WELCOME

The IEEE Magnetics Society Conference, “Intermag Europe 2008”, will be held from Sunday, May 4th, until Thursday, May 8th, at the Palacio Municipal de Congresos in Madrid, Spain. Intermag is the premier conference on applied magnetism and related technologies. Members of the international scientific and engineering communities interested in recent developments in these topics are invited to attend the conference.

We have planned an exciting and informative set of symposia, tutorial sessions and invited talks, regular oral and poster presentations and technical exhibitions reviewing the latest developments in this field.

Intermag Europe 2008 is a unique event. We are delighted to announce that this year’s Nobel Laureates in Physics, Prof. Albert Fert and Prof. Peter Grünberg have confirmed their attendance at the 2008 Intermag Conference. A GMR Nobel Celebration has been arranged for the evening on Monday May 5th, where Prof. Grünberg will deliver a lecture on “From Spin Waves to Giant Magnetoresistance and Beyond” and Prof. Fert will lecture on “Emerging Directions in Spintronics”. Other technical events and celebrations in recognition of the Nobel Prize for the discovery of GMR are also planned. We hope that members of the IEEE Magnetics Society and researchers with interests in the field will join us for this special occasion.

Finally we also hope you will enjoy visiting Madrid and experiencing Spanish culture. On behalf of the Management Committee of Intermag Europe 2008, we look forward to seeing you in Madrid.

Manuel Vázquez

Ron Indeck

General Chairmen

LOCATION

Madrid is the cosmopolitan capital city of Spain. It is the home of the administration of the Spanish government and Parliament as well as the residence of the monarch. It is one of the most important cities in Spain in the financial and industrial sectors. Madrid is a cosmopolitan and multi-ethnic city with more than 4 million inhabitants and is characterised by intense cultural and artistic activities as well as a vibrant nightlife.

Madrid is also a centre for science and technology. In Madrid there are 6 public and 9 private universities and about 30,000 students study science and technology. More than 50 research centers in different branches and institutes provide a dynamic scientific community. For more information about science and technology in Madrid, go to www.madrimasde.org/English/default.asp

Intermag Europe 2008 will be held at the Palacio Municipal de Congresos, located in the “Campo de las Naciones”, the new financial hub of the city, which is well connected with the centre and only five minutes from Barajas Airport.

Further information about Madrid can be found on the web at: www.esmadrid.es or www.turismomadrid.es.

WEATHER

Springtime is the nicest season of the year in Madrid. The days are long and the temperatures pleasant, though it can cool down at night. The average temperature in May is around 16º C with a maximum of 22º C and minimum of 9º C. Rain is not uncommon in spring.

TRANSPORTATION IN MADRID

Underground/Subway: The lines are differentiated by colour and are numbered from 1 to 13. Tickets can be purchased in every station from ticket offices or automated machines. Single tickets cost 1 €. Metrobus, which is a 10 journey travel card valid for underground and buses, costs 6.70 €. The underground/subway runs from 6:00 am to 1:30 am.

Line 8 (pink line) goes to the station “Campo de las Naciones” where the conference venue is located.

City Buses: The city buses are a good alternative to the subway. Bus single tickets can be paid directly to bus driver. The buses run from 6:00 am to 11:00 pm. Night buses (called “buhos”) run less frequently. The price is the same, 1 €. Traffic jams in Madrid are frequent

For more information please visit the following website: http://www.emtmadrid.es/

Tourist Travel Pass: A Tourist Travel Pass can be used on all public transport in the city as many times as required within its period of validity. There are five types of pass valid for 1 to 7 days. The card can be purchased at all stations in the subway network, at the Centro de Atención al Viajero (Passenger Assistance Centre), at both airport stations (line 8) and at Tourist Offices.

Area A, comprising the services of the Metro and EMT de Madrid (buses).

TOURIST TRANSPORT CARD (PRICE IN EURO)					
	A Area				
	1 day	**2 days**	**3 days**	**5 days**	**7 days**
Adult	4.00	7.20	9.60	15.00	20.80

Madrid Public Transport Information:
Please visit www.ctm-madrid.es

You can also find an underground map at:
www.metromadrid.es/acc_resources/pdfs/Plano_Metro_2007.pdf

Taxis: Taxis in Madrid are white and are distinguished with a diagonal red band on the front doors. A green light on top of the taxi indicates if it is available. The taxi should always charge by the taxi-meter that runs according to distance covered, the urban area, the day of the week (higher fares on holidays), and the pickup point (higher fares for pickups in bus stations, train stations and airport). Passengers are never required to pay additional fares for luggage if there is enough space in the boot. Additional fares are shown on information signs on the back windows of the taxi.

Car Rental: Car rental is not recommended to get around Madrid due the traffic. Parking in Madrid is expensive and always difficult. A large part of the tourist area is not accessible by car.

ACCESS TO MADRID CENTRE FROM MADRID AIRPORT

By Underground/Subway

- From Terminals 1, 2 and 3 (T1, T2 and T3): Connection to underground (metro) line 8, the underground station is called “Aeropuerto T1-T2-T3”.
- From Terminal 4 (T4): Connection to underground line 8, the underground station is called “Aeropuerto T4”.

The metro fare to downtown Madrid is 2 Euros but involves a change of train.

By Bus: Number 200 to “Avenida de America” bus station. There you can find connection to underground lines: 4, 6, 7 and 9.

By Taxi: The approximate cost from the airport to the city centre is around 30 €.

ACCESS TO INTERMAG 2008 VENUE

Venue: Palacio Municipal de Congresos,
Avenida de la Capital de España Madrid, 7, 28042 Madrid.

Underground/Subway: Line 8, Station “Campo de las Naciones”

Access Map: Please visit
http://www.madridespaciosycongresos.es/palacio/situacion_i.cfm

HOTEL ACCOMMODATION

Participants interested in making a hotel reservation, should check the accommodation offer on the website and follow the procedure. A hotel confirmation showing the amount received will be issued and sent as soon as the payment is received. For further information about hotel reservations please contact sureta@siasa.es.

ACCOMMODATION FOR STUDENTS

http://www.student-accommodation-madrid.com/
http://www.madridflatmate.com/

LUNCH, TAPAS AND DINNER

Spain has a different dining schedule than some other countries. Lunchtime typically starts at 1:30 pm and can finish as late as 4:00 pm. Dinner starts after 9:00 pm and many restaurants are not open until this time.

One of Madrid's main attractions is its great number of bars and taverns where you are able to relax after a busy day, enjoy a glass of wine or a beer accompanied by a tasty 'tapa'. "Tapeo" has existed as a pleasant and healthy custom in Spain since the 13th century, when the Castillian King Alphonse X ("the Wise") forced bartenders to serve something to eat when customers ordered wine. Today tapas are small snacks between meals, though on many occasions tapas can substitute for meals.

CONFERENCE REGISTRATION

Advance registration fees can be paid in € or US$. The advanced registration deadline is March 31st 2008. Advanced registration and full payment must be received before March 31st. Registration payments received after this date or on-site will be at the higher rates.

Please note that the IEEE Magnetics Society has provided a special discount to the registration fee for Society members wishing to attend Intermag 2008. This $100 discount is in addition to the usual IEEE member discount. Participants are advised to join the Society on-line at www.Intermagconference.com/intermag2008. Those registering on-site can join the Society at registration to take advantage of the discount.

REGISTRATION FEES	Advanced Registration Before 31 March '08	On-Site Registration
IEEE Magn. Soc. Members	390 €/ 570 $	470 €
IEEE Members	460 €/ 670 $	540 €
Non-IEEE Members	550 €/ 800 $	650 €
Students IEEE Magn. Soc. Members Unemployed Retiree	175 €/ 255 $	195 €
Students IEEE Members Unemployed Retiree	230 €/ 335 $	250 €
Students non-IEEE Members Unemployed Retiree	275 €/ 400 $	300 €

Advanced registration via the web is the most convenient way to register and is highly recommended. On the conference website you will find links to register on-line or to download a PDF file. www.Intermagconference.com/intermag2008

The registration fee includes:
- Access to all Scientific Sessions
- Digest CD
- Morning coffee
- Evening Bierstube
- GMR Nobel Celebration
- Awards Ceremony
- Plenary Lecture
- Magnetics Society Reception

All conference attendees including invited speakers must pay the appropriate registration fee.

All attendees will be required to wear Intermag 2008 name badges at all times.

The use of cameras, videotaping and/or recording devices in the technical sessions is prohibited.

On-site Registration:

Registration on-site can be paid only in Euros. Payment in Euros can be made in cash or by MasterCard, Visa or American Express credit cards only.

The Conference Registration Desk, located in the main lobby of the Palacio Municipal de Congresos, will be open during the following hours:

- Sunday May 4th. 4:00 pm - 7:00 pm
- Monday May 5th 8:00 am - 6:00 pm
- Tuesday May 6th 8:30 am - 6:00 pm
- Wednesday May 7th 8:30 am - 6:00 pm

Cancellation Policy:

Cancellations of registrations paid in Euros must be received by e-mail at sureta@siasa.es or fax (34 91458 10 88). Payments will be refunded less a 50 € service charge before March 31st. After March 31st, cancellations will be accepted but not refunded. Substitutions may be made prior to April 20th.

Cancellation of registrations paid in US$ must be received in writing at YesEvents:

Intermag 2008 Conference c/o YesEvents
P.O. Box 32862
Baltimore, MD 21282 USA

Payments will be refunded less a $75.00 service charge before March 31st. After 31st, cancellations will be accepted but not refunded. Substitutions may be made prior to April 20th.

VISA REQUIREMENTS

EU citizens need only their national identity card or passport to enter Spain. Citizens of the United States, Australia, Canada, Japan, South Korea and Singapore do not need a visa to visit Spain for up to 90 days.

Citizens from other countries should contact their local Spanish Embassy or Consulate for details regarding visa applications. Please contact the embassy or consulate as soon as possible in order to determine your particular visa requirements.

For additional information please visit:
www.mae.es/en/webembajadasconsulados/

If you need a personal letter of invitation to obtain a visa, please contact visaintermag2008@icmm.csic.es, providing your full name, complete mailing address and reference number of the submitted digest. An original letter will be sent to you by post.

Please note that a letter of invitation will be provided to assist delegates obtaining visa or permission to attend the conference and should not be considered as an official invitation covering the registration fee or other expenses. Applications for invitation letters must be received by April 1st 2008.

Citizens from all countries must carry a valid identity card or passport at all times.

ORAL PRESENTATION

Invited talks are a 25 minutes presentation with 5 minutes discussion. Contributed talks are 12 minutes plus 3 minutes discussion. Session Chairs will keep all sessions strictly to time to allow delegates to move between sessions.

All accepted oral presentations are to be made using LCD projectors connected to the author's personal computer. Authors are advised to bring as USB flash memory as a back-up. No alternative presentation facilities will be provided.

Only standard PC-style VGA connections to the LCD projector will be supplied. You must supply any adaptor required for your computer. Macintosh users must make sure that "mirroring" is activated.

SPEAKER PRACTICE ROOM

Speakers may use the Luxemburgo Room on the first floor to practice their presentations. Audiovisual equipment will be available for authors to use. This room will be open as follows:

Monday	8:00 am – 6:30 pm
Tuesday	8:30 am – 6:30 pm
Wednesday	8:30 am – 6:30 pm
Thursday	8:30 am – 1:00 pm

A booking sheet is available on the practice room door allowing users to book the room. Bookings are allowed for 20 minute periods only.

POSTER SESSIONS

Poster presentations will consist of visual materials about the work presented on a designated board. An author must be available to answer questions during a significant part of the session. An author should be present for the first and last 30 minutes of morning sessions and the last 60 minutes of afternoon sessions. The conference provides a small sign designating the paper number to be posted on each board. Mounting materials will be provided.

For the first time Intermag 2008 will include invited poster presentations. There will be one invited poster in each half day session. Invited posters will be allocated 2 poster boards.

Papers related to posters where the authors did not attend the conference or were not available to discuss their work will not be published.

Poster Area: Polivalente Room on the 3rd floor of the conference venue.

Posters should be displayed from 9:00 am – 1:00 pm or from 2:30 pm – 6:30 pm

Poster board size is 95cm high by 130cm wide. Note this is landscape style.

Authors should set up their posters at least 15 minutes before the session starts. Presenters must be by their posters from 9:00 am to 9:30 am and from 12:30 pm to 1:00 pm for the morning session and from 5:30 pm to 6:30 pm for the afternoon session.

Authors are reminded to remove their posters promptly at the end of their session. Posters not removed will be discarded.

PUBLICATIONS ROOM

The Publication Room will be located in the Dublin Room on the second floor. The status of all papers will be displayed and authors should check periodically on their papers. Authors may leave messages for the editor for their paper. Each editor will post a notice of times at which he/she can be found in the publication room. Editors will respond to messages and questions as promptly as possible. This room will be open as follows:

Monday to Wednesday:	9:00 am – 6:00 pm
Thursday:	9:00 am – 4:00 pm

Session Chairs are requested to visit the editor for their session to support the completion of the reviewing process for all papers in their session.

TUTORIAL

The IEEE Magnetics Society Education Committee has organized a tutorial on "Multiferroics". The tutorial will be at a level for a novice in the subject but should be of interest to specialists and non-specialists.

The tutorial program is:

Session Chair:	J.W. Harrell
Date:	Sunday, May 4th, 2008
Time:	5:00 pm – 7:00 pm
Room:	Auditorio A

Speakers:

James Scott, Cambridge (UK)
Wilfrid Prellier, CRISMAT (France)
Gopalan Srinivasa, Oakland University (USA)

GMR NOBEL CELEBRATION

We are delighted to announce that this year's Nobel Laureates in Physics, Professor Albert Fert and Professor Peter Grünberg have confirmed their attendance at the 2008 Intermag Conference in Madrid. A GMR Nobel Celebration (session YA) has been arranged for the evening on Monday, May 5th. This special session will be preceded by a symposium on The Importance of GMR (session BA).

Session YA
GMR Nobel Celebration
5:10 pm Monday May 5th: Auditorio A

Session chair: Manuel Vazquez,
General Chair Intermag Europe 2008

5:10 pm Opening Remarks
Prof. Carl Patton
IEEE Magnetics Society President

5:20 pm "From Spin Waves to Giant Magneto-resistance and Beyond"
Prof Peter Grünberg, NL
Forschungszentrum Jülich

6:00 pm "Emerging Directions in Spintronics"
Prof Albert Fert, NL
CNRS, Université Paris-Sud

6:40 pm Recognition from the IEEE
Lew Terman
President IEEE

6:50 pm Closing Remarks
Prof. Manuel Vázquez
Conference Chair Intermag 2008

7:15 pm Celebratory Reception, Polivalente Room
Toast to Nobel Laureates
Prof. F. Marcellán (Secretary of State of Science and Technology, MEC)
Prof. C. Martínez (President of the Spanish National Research Council, CSIC)

7:45 pm Close

IEEE MAGNETICS SOCIETY ANNUAL GENERAL MEETING

This meeting is open to all Intermag participants. Please come to learn what the IEEE Magnetics Society is doing and the benefits of joining the Society. The meeting will be held on Tuesday, May 6th, at 6:30 pm - 7:30 pm in Auditorio A. Please sit towards the front of the Auditorium.

AWARDS AND PLENARY SESSION

4:40 pm Wednesday May 7th: Auditorio A
Session Chair: Bruce Gurney

IEEE Magnetics Society Awards

IEEE Reynold B. Johnson Information Storage Device Award

Prof. Stanley Charap
Professor of Electrical and Computer Engineering, Carnegie-Melon University, Emeritus

The IEEE Daniel E. Noble Award

Dr. James M. Daughton (NVE Corporation)
Dr. Stuart Parkin (IBM, San Jose)
Dr. Saied Tehrani (Freescale Semiconductor)

The Magnetics Society Achievement Award

Prof. Jack H. Judy
Professor of Electrical Engineering, University of Minnesota, Emeritus

Newly Elected Fellows of the IEEE

Roy W. Chantrell, University of York
Vincent G. Harris, Northeastern University
Jinliang He, Tsinghua University
Thomas D. Howell, San Jose State University
Hiroaki Muraoka, Tohoku University
Lalita Udpa, Michigan State University
John Wikswo, Vanderbilt University
Jian-Gang Zhu, Carnegie Mellon University

2007 Magnetics Society Distinguished Lecturers

Matthias Bode, Argonne National Lab
Vincent Harris, Northeastern University
Sara Majetich, Carnegie Mellon University
Takao Suzuki, Toyota Technical Institute

IEEE Magnetics Society Best Student Paper Award

Following the establishment of this prestigious prize by the IEEE Magnetics Society in 2008, the selection of the five finalists has been made after a full review of all students entering the competition by the Programme Committee Co-Chairs for Intermag 2008. This selection has been based solely on the likely quality/impact of the work. The five finalists will receive a cash award from the Magnetics Society as well as recognition for their achievement.

The eventual winner of the award will be selected by a transnational panel of four young scientists who have recently completed their PhDs and who will visit each presentation, whether poster or oral, to assess the papers according to the following criteria:

1. The quality/impact of the work
2. The student contribution and involvement in the work
3. The quality of the presentation by the student.

Each criteria will make an equal contribution to the assessment. The assessment of the panel will be overseen by Prof. J W Harrell, the Chairman of the IEEE Magnetics Society Education Committee and Dr Bruce Gurney, the Chairman of the Awards Committee. The award will be made to the student achieving the highest overall ranking in the three criteria.

Please note that students associated in any way with any persons involved in the selection of the finalists or the eventual winner have been declared ineligible in the competition.

Finalist: Pedram Khalili Amiri   Paper: CV – 01
Title: Integrated on-chip microstrip lines
with Co-Ta-Zr magnetic films
P. K. Amiri, B. Rejaei, Y. Zhuang, M. Vroubel,
D. Lee, S. Wang & J. Burghartz (Netherlands)

Finalist: Karen Livesey   Paper: HC – 02
Title: Nonlinear processes during switching
of a thin Permalloy film in different geometries
K. Livesey, H. Nembach, M. Kostylev, P. Martin-Pimentel, S. Hermsdoerfer, B. Leven, R. Stamps, B. Hillebrands (Australia)

Finalist: Hiroyuki Tomita   Paper: AA – 04
Title: Real Time Measurements of Spin-Transfer Switching
in CoFeB/MgO/CoFeB Magnetic Tunnel Junctions
H. Tomita, K. Konishi, T. Nozaki, M. Shiraishi, H. Kubota,
A. Fukushima, S. Yuasa, Y. Suzuki (Japan)

Finalist: Takayuki Ishikawa   Paper: AC – 07
Title: Spin-dependent tunneling conductance in fully epitaxial Co2MnSi/MgO/Co2MnSi tunnel junctions
T. Ishikawa, N. Itabashi, K. Matsuda, T. Uemura,
M. Yamamoto (Japan)

Finalist: Benoit Georges   Paper: CB – 06
Title: Phase locking of a Spin Transfer Oscillator
to an external microwave current : a milestone
for the synchronization of a large assembly of STOs
B. Georges, J. Grollier, M. Darques, V. Cros,
C. Deranlot, G. Faini, A. Fert (France)

In addition, the 2008 Student Travel Grants will be presented.

Plenary Lecture
Session Chair: Josef Fidler

Following the awards ceremony at approximately 5.40 pm on Wednesday, May 7th the Intermag Plenary lecture will be presented. The speaker is Prof. Ludwig Schultz of IFW Dresden whose title will be:

"Riding on Magnetic Fields - Macroscopic Interaction
of Ferromagnetic and Superconducting Permanent Magnets"

Abstract:
Different concepts for magnetic levitation are discussed. The conventional system is the Trans¬rapid now running between Shanghai Airport and the city centre. Our approach is a passive super¬conducting magnetically levitated system using bulk superconductors cooled to 77 K. At low temperatures, superconductors can freeze in a magnetic field of any configuration. Hence they act as permanent magnets but with a magnetic remanence, which is, for YBaCuO material, far larger than that of ferromagnetic permanent magnets. The ability to freeze in a magnetic field can be used for completely new applications. This will be experimentally demonstrated for different types of superconducting magnetically levitated trains, which can either be in an upright or a hanging position or, moving along a wall without any mechanical contact. With regard to scaling-up, the SupraTrans project will be presented.

Biography:
Ludwig Schultz studied physics at the University of Goettingen and received his Ph.D. in 1976 with a thesis on flux pinning in superconductors. He continued as a research assistant at the Institute of Metal Physics of the University of Goettingen and as a postdoc at IBM Thomas J. Watson Research Center in Yorktown Heights. In 1980 he joined Siemens Research Labs at Erlangen. In 1993 he accepted a call to become a full professor at TU Dresden and Director of the Institute of Metallic Materials at the Leibniz Institute of Solid State and Materials Research (IFW) Dresden. On April 1, 2008 he will be promoted to be the Scientific Director of this Institute. His main activities concern permanent magnets, CMR materials, magnetic thin films, magnetic shape memory alloys, superconducting materials and superconducting levitation systems. He authored or co-authored more than 650 publications with more than 13,000 citations, filed 65 patents and founded 2 companies: Evico and Evico Magnetics.

Magnetics Society Reception
Invitation: Prof. Manuel Vázquez
General Chair Intermag Europe 2008

Following the Plenary lecture a Magnetics Society reception will be held in the Polivalente Room for all participants at Intermag Europe 2008. This reception has been provided by special funding from the IEEE Magnetics Society.

BIERSTUBE AND COFFEE

A coffee service will be available Monday through Thursday mornings in the poster and exhibition area in Polivalente Room located on the third floor, from 9:00 am – 10:00 am.

On Tuesday evening, the Bierstube will be held in the Polivalente Room, from 6:00 pm - 7:00 pm. During registration on Sunday May 4th the Bierstube will be held in the foyer of the conference centre.

EXHIBITION

The Exhibition will be located in the Polivalente Room. This large space will allow us to accommodate the exhibition, poster area and catering service for morning coffee and afternoon bierstube.

Exhibition hours:

• Monday May 5th	9:00 am - 7:00 pm
• Tuesday May 6th	9:00 am - 7:00 pm
• Wednesday May 7th	9:00 am - 7:00 pm
• Thursday May 8th	9:00 am - Noon

Intermag 2008 Exhibitors (as of February 20)

Company / Institution	Country	Booth
ATOMISTIX	Denmark	28
BARTINGTON INSTRUMENTS LIMITED	UK	14
DCA Instruments Oy	Finland	22
HERAUS. FNC	USA	16
HITACHI METALS, Ltd.	Japan	10
INTA Instituto Nacional de Técnica Aeroespacial	Spain	13
KLA-Tencor Corp.	USA	2
MAGNET-PHYSIK Dr. Steingroeven GmbH,	Germany	15
METROLAB INSTRUMENTS, S.A.	Switzerland	12
NANOMAGNETICS INSTRUMENTS Ltd.	UK - Turkey	7 & 8
NANOSCAN Ltd.	Switzerland	1
NEOARK Corporation	Japan	6
PRINCETON MEASUREMENTS CORP.	USA	5
QUANTUM DESING	USA	3
SERVICIENCIA, S.L.	Spain	9
SINGULUS NANO DEPOSITION TECHNOLOGIES GmbH	Germany	4
TECO, Rene Koch	Switzerland	11

IEEE MAGNETICS SOCIETY MEMBERSHIP

If you are not already a member of the IEEE Magnetics Society we advise you to join and take advantage of the special discount for this conference. The difference between the Magnetic Society member rate and the non-member rate is significantly more than the membership fee. Join now by going on-line at www.ieeemagnetics.org and follow the links. A membership desk will be available at registration but significant delays may occur.

Through the IEEE Magnetics Society you get unlimited access to all issues of the IEEE Transactions on Magnetics since the journal's inception in 1969 with unlimited downloads. This includes all Intermag Proceedings as well as other topical conferences published in the Transactions. Membership also includes a CD-ROM copy of the Transactions each year. By joining, you become a part of the world's largest and best known organization in magnetics. You also gain access to local chapter events, technical activities and student sponsorship for conference travel.

STUDENT TRAVEL GRANTS

The IEEE Magnetic Society will award travel grants of up to $1000 each to a limited number of students who wish to attend Intermag Europe 2008. These grants are intended to partially offset travel costs. Support is for current graduate students only. Post-doctoral workers and undergraduate students are ineligible. Students who have previously received travel support from the Magnetics Society are also ineligible

Preference will be given to Student Members of the Magnetics Society. Preference will also be given to students nearing completion of their studies and presenting conference papers. The student´s supervisor must also be a member of the Magnetics Society. The student's supervisor must write a brief letter of endorsement for the applicant. A second endorsement from a full member of the IEEE Magnetic Society is also required.

Shortly after the conference, grant recipients must submit a short account of their experience for possible inclusion in the IEEE Magnetic Society Newsletter. Forms and instructions for applicants are available at:

www.intermagconference.com/intermag2008.

Applications and all letters of endorsement must be submitted before March 7th 2008. Inquiries should be sent to the Student Travel Grants Co-Coordinator:

M. J. Carey, Hitachi GST, San Jose, CA (matthew.carey@hitachigst.com).

Students wishing to apply should also visit the IEEE Magnetics Society website at: www.ieee.magnetics.org.

IEEE MAGNETICS SOCIETY

President . . . . .Carl Patton

Vice President . . . . .Randall Victora

Secretary/Treasurer . . . . .Takao Suzuki

Past President . . . . .Kevin O'Grady

Executive Director . . . . .Diane Melton

ELECTED IEEE MAGNETICS SOCIETY ADMINISTRATIVE COMMITTEE MEMBERS

Terms expiring December 31, 2008

G. Bertotti; M. Coey; J. Fidler; S. Majetich; M. Pasquale; C. Ross; D. Weller; R. Wood

Terms expiring December 31, 2009

C-R Chang; R. W. Chantrell; B. Dieny; R. Fontana; P. Freitas; D. Jiles; J-U Thiele; S. Ueno

Terms expiring December 31, 2010

J. Chapman; O. Heinonen; B. Hillebrands; D. Litvinov; H. Muraoka; M. Pardavi-Horvath; B. Terris; U. Varshney

Appointed Committee Chairs: L. Folks; R. Goldfarb; B. Gurney; J.W. Harrell; R. Hasegawa; A. Hoffmann; R. Indeck; C. Korman; D. Lavers; R. D. McMichael

Council Representatives: A. Edelstein (Sensors); D. Litvinov and R. Rannow (Nanotechnology); R. Goldfarb and A. Zeller (Superconductivity)

Newsletter Editors: P. Dhagat; A. Jander

FUTURE CONFERENCES

2008 MMM Conference - Austin (Texas), November 10-14

2009 Intermag Conference - Sacramento (California), May 4-8

2010 Joint MMM/Intermag Conference - San Francisco (California), January 17-21

2010 MMM - Scottsdale, Arizona, October 31-November 4

2011 Intermag Asia Conference – Taipei, May
(No specific dates have been confirmed)

INTERMAG EUROPE 2008 CONFERENCE MANAGEMENT COMMITTEE

Chairmen . . . . .Manuel Vázquez
Ronald S. Indeck

Program Co-Chairs . . . . .Josef Fidler
Bruce Terris
Kevin O'Grady

Local Chair . . . . .María del Puerto Morales

Publication Co-Chairs . . . . .Jacques Miltat
Sara Majetich

Treasurers . . . . .Oksana Chubykalo-Fesenko
Jan-Ulrich Thiele

Exhibits and Industrial Support . . . . .Marta San Román
Marina Díaz Michelena

Website, Printing and Publicity . . . . .Luis López Díaz
Petru Andrei

Conference Coordinator . . . . .Mercedes del Portillo
Siasa Congresos, S.A.

Conference Administration . . . . .Diane S. Melton
Courtesy Associates

PROGRAM COMMITTEE MEMBERS

Josef Fidler (Co-Chair), Kevin O'Grady (Co-Chair), Bruce Terris (Co-Chair), Fatih Anaya, Antero Arkkio, Jose Manuel Barandiaran, Xiaoping Bian, Alfonso Cebollada, Roy Chantrell, John Chapman, Bernard Dieny, Fatih Erden, Jürgen Fassbender, Dino Fiorani, Josep Fontcuberta, Paulo Freitas, Jesus M. Gonzalez, Simon Greaves, Oliver Gutfleisch, George Hadjipanayis, Ryusuke Hasagawa, Olle Heinonen, Laura Heyderman, Burkard Hillebrands, Ronnie Jansen, David Jiles, Alan B. Johnston, Ganping Ju, Des Mapps, Wolfram Maass, María del Puerto Morales, Bruno Marchon, Philip Marketos, Josep Nogues, Fernando C. Palacio, Larissa Panina, Amanda Petford-Long, Johannes Paulides, Theo Rasing, Dafiné Ravelosona, Manfred Ruehrig, Manfred Schabes, Rudolf Schaefer, Thomas Schrefl, John Snyder, Alexandru Stancu, Jonathan Z Sun, Tom Thomson, Raul Valenzuela, Masahiro Yamaguchi, Manuel Vazquez, Marylin Wun Fogle.

PUBLICATION COMMITTEE

Jacques Miltat (Co-Chair), Sara Majetich (Co-Chair), Claudio Aroca, Juan Bartolomé, Xavier Battle, Giorgio Bertotti, Matthias Bode, Ekkes Bruck, Mairbek Chshiev, Pietro Gambardella, Julie Grollier, Robert Hicken, Bert Koopmans, Chih-Huang Lai, Roland Mattheis, Jeffrey McCord, Jim Miles, Uli Nowak.

LOCAL COMMITTEE

María del Puerto Morales (Chair), Agustina Asenjo, Giovanni Badini-Confalonieri, Julio Camarero, Federico Cebollada, Patricia Crespo, Jose Miguel García, Mar García, Miguel Angel García, Elvira González, Marian González, Yves Huttel, Marco Maicas, Pilar Marín, Benjamin Martínez, Javier Palomares, Jose Luis Prieto.

ADDITIONAL INFORMATION

If you would like to receive more information about Intermag 2008 or to be placed on the Intermag Conference mailing list, please contact Siasa Congresos, S.A. at:

INTERMAG 2008
Siasa Congresos, S.A.
Paseo de la Habana, 134
28036 Madrid, Spain
E-mail:sureta@siasa.es

You may also access complete conference information through the web at the Intermag home page at:

www.intemagconference.com/intermag2008

PROGRAM AT A GLANCE

	Session	Session Title	Location
Sunday Registration 4:00 pm – 7:00 pm			Main Entrance Hall
Sunday Tutorial 5:00 pm – 7:00 pm	ZA	IEEE Magnetics Society Education Committee Tutorial: Multiferroics	Auditorio A
Monday Oral Sessions 9:30 am – 12:30 pm	AA	Spin-Torque Switching	Auditorio A
	AB	Domain Walls in Nanowires	Madrid
	AC	Magnetic Tunnel Junctions - I	Roma
	AD	Thin Films: Interface and Transport Properties	Paris
	AE	Heat and Microwave Assisted Recording	Londres
	AF	Characterization and Measurement Techniques - I	Berlin
	AG	Transformers and Inductors - I	Amsterdam
	AH	Magnetoimpedance	Caracas
Monday Poster Sessions 9:00 am – 1:00 pm	AL	Motors and Actuators - I	Polivalente Room
	AM	Magnetic Sensors - I	Polivalente Room
	AN	Magnetic Oxides & Heusler Alloys - I	Polivalente Room
	AO	Transport Theory and Semiconductors Spintronics	Polivalente Room
	AP	Longitudinal and Particulate Media	Polivalente Room
	AQ	Magnetic Nanoclusters and Nanoparticles - I	Polivalente Room
	AR	Soft Magnetic Materials & EMC	Polivalente Room
	AS	GMR for Multilayers and Nanostructures	Polivalente Room
	AT	Fundamental Properties for Applications	Polivalente Room
	AU	Permanent Magnet Materials – Applications - I	Polivalente Room
	AV	Intermetallics and Other Hard Magnets	Polivalente Room
Monday Oral Sessions 2:30 pm – 5:00 pm	BA	Symposium on the Importance of GMR	Auditorio A
	BB	Head-Media Interface and Tribology - I	Madrid
	BC	MEMS and Miniature Magnetic Sensors	Roma
	BD	Magnetic Sensors - II	Paris
	BE	Molecular and Novel Materials - I	Londres
	BF	Magnetic Semiconductors - I	Berlin
	BG	Microwave Materials and Devices - I	Amsterdam
	BH	Multilayer Films and Superlattices - I	Caracas
Monday GMR Nobel Celebration 5:10 pm	YA	GMR Nobel Celebration	Auditorio A
Tuesday Oral Sessions 9:30 am – 12:30 pm	CA	Symposium on Biomedical Applications	Auditorio A
	CB	Spin Torque Oscillators - I	Madrid
	CC	MgO Magnetic Tunnel Junctions - I	Roma
	CD	Magnetic Microscopy - I	Paris
	CE	Exchange Bias - I	Londres
	CF	Electrical Steels and Inductor Cores	Berlin
	CG	Thin films: Surface and Anisotropy Properties	Amsterdam
	CH	Magnetic Shape Memory Alloys	Caracas
Tuesday Poster Sessions 9:00 am – 1:00 pm	CL	Permanent Magnet Machines - I	Polivalente Room
	CM	Magnetic Micro and Nanostructures	Polivalente Room
	CN	Micromagnetics – I	Polivalente Room
	CO	Nanostructured Hard Magnetic Materials - I	Polivalente Room
	CP	Hysteresis Modelling - I	Polivalente Room
	CQ	Soft Magnetic Materials and Applications - I	Polivalente Room
	CR	Magnetic Nanoclusters and Nanoparticles - II	Polivalente Room
	CS	Perpendicular Granular Media	Polivalente Room
	CT	Perpendicular High Ku Media	Polivalente Room
	CU	Bit Patterned Media - I	Polivalente Room
	CV	Microwave Materials and Devices – II	Polivalente Room
	CW	Characterization and Measurement Techniques - II	Polivalente Room
Tuesday Oral Sessions 2:30 pm – 5:30 pm	DA	Bit Patterned Media - II	Auditorio A
	DB	Symposium on Magnetic Modeling	Madrid
	DC	GMR in Nanocontacts and Constrictions	Roma
	DD	Permanent Magnet Machines - II	Paris
	DE	Soft Magnetic Wires	Londres
	DF	Recording Systems and Servo - I	Berlin
	DG	Life Sciences: Techniques and Instrumentation - I	Amsterdam
Tuesday Poster Sessions 2:30 pm – 6:30 pm	DL	Ultrathin Films and Surface Effects - I	Polivalente Room
	DM	Ultrathin Films and Surface Effects - II	Polivalente Room
	DN	Magnetic Microscopy - II	Polivalente Room
	DO	Magneto-Optic Materials and Devices	Polivalente Room
	DP	Spin Torque Oscillators – II	Polivalente Room
	DQ	Life Science and Applications - I	Polivalente Room
	DR	Magnetic Elements and Antidot Arrays	Polivalente Room
	DS	Microwave Systems	Polivalente Room
	DT	RE-TM Borides and Magnet Processing	Polivalente Room
	DU	Permanent Magnet Materials - Applications - II	Polivalente Room
	DV	Manganites	Polivalente Room
	DW	Transformers and Inductors - II	Polivalente Room
Tuesday Annual General Meeting 6:40 pm – 7:40 pm	XA	IEEE Magnetics Society Annual General Meeting (All Intermag attendees welcome)	Auditorio A

Wednesday
Oral Sessions

9:30 am – 12:30 pm	EA	Symposium on Spin Transfer and Dynamics	Auditorio A
	EB	Motor and Actuators - II	Madrid
	EC	Magnetic Nanostructures - I	Roma
	ED	Perpendicular Media	Paris
	EE	Magnetic Nanoparticles - I	Londres
	EF	Recording Physics, Models and Theory - I	Berlin
	EG	Soft Magnetic Materials and Applications - II	Amsterdam
	EH	Magneto-Dielectric Materials	Caracas

Wednesday
Poster Sessions

9:00 am – 1:00 pm	EL	Permanent Magnet Machines - III	Polivalente Room
	EM	Exchange Bias - II	Polivalente Room
	EN	Shielding, Levitation and Transport	Polivalente Room
	EO	Molecular and Novel Materials - I	Polivalente Room
	EP	Magnetodynamics and Millimetre Wave Devices	Polivalente Room
	EQ	Magnetic Semiconductors - II	Polivalente Room
	ER	Magnetic Semiconductors - III	Polivalente Room
	ES	Recording Heads	Polivalente Room
	ET	Magnetoelastic and Magnetoelectric Materials	Polivalente Room
	EU	Ferrite Dynamics and Applications	Polivalente Room
	EV	Magnetostrictive Shape Memory Alloys/Devices	Polivalente Room
	EW	Multiferroics, Ferrites and Other Materials	Polivalente Room
	EX	Magnetic Tunnel Junctions - II	Polivalente Room

Wednesday
Oral Sessions

2:30 pm – 4:30 pm	FA	Symposium on Spin Torque Transfer for MRAM	Auditorio A
	FB	Spin Injection and Spin Hall Effect	Madrid
	FC	Magneto-Electronic Devices	Roma
	FD	Magnetic Oxides & Heusler Alloys - II	Paris
	FE	Life Science and Applications - II	Londres
	FF	Microwave Devices and FMR	Berlin
	FG	Nanostructured Hard Magnetic Materials - II	Amsterdam
	FH	Oxide Multiferroics and Ferrites	Caracas

Wednesday
Awards and Plenary Session

4:40 pm – 6:40 pm	WA	IEEE Magnetics Society Awards Ceremony Intermag Plenary Session	Auditorio A

Plenary Reception

6:45 pm – 8:00 pm		Magnetics Society Plenary Reception	Polivalente Room

Thursday
Oral Sessions

9:30 am – 12:30 pm	GA	Symposium on Bit Patterned Media	Auditorio A
	GB	MR Based Heads (GMR, MTJ, CPP)	Madrid
	GC	Ultrafast Dynamics	Roma
	GD	MRAM	Paris
	GE	Magnetic Nanoparticles - II	Londres
	GF	Head-Media Interface and Tribology - II	Berlin
	GG	Hysteresis Modelling - II	Amsterdam
	GH	Permanent Magnet Materials - Applications - III	Caracas

Thursday
Poster Sessions

9:00 am – 1:00 pm	GL	Multilayer Films and Superlattices - II	Polivalente Room
	GM	Permanent Magnet Machines - IV	Polivalente Room
	GN	Motors and Actuators - III	Polivalente Room
	GO	Life Sciences: Techniques and Instrumentation - II	Polivalente Room
	GP	Switched Reluctance Machines	Polivalente Room
	GR	Soft Nanocrystalline Alloys	Polivalente Room
	GS	Power and Control Magnetics	Polivalente Room
	GT	Spin Torque Excitations in Nanomagnets	Polivalente Room
	GU	Magnetocaloric Effect and Materials	Polivalente Room
	GV	Fast Switching of Films and Nanostructures	Polivalente Room
	GW	Computational Magnetics	Polivalente Room
	GX	Miscellaneous – I	Polivalente Room
	GY	Miscellaneous – II	Polivalente Room

Thursday
Oral Sessions

2:30 pm – 5:30 pm	HA	Symposium on the Roadmap for Spintronics	Auditorio A
	HB	Inductive Recording Heads and Materials	Madrid
	HC	Magnetization Dynamics	Roma
	HD	Micromagnetics – II	Paris
	HE	Permanent Magnet Materials	Londres
	HF	Life Science and Applications - III	Berlin
	HG	Magnetoelastic Materials and Devices	Amsterdam
	HH	Current Induced DW Motion	Caracas

Thursday
Poster Sessions

2:30 pm – 6:30 pm	HL	Recording Systems and Servo - II	Polivalente Room
	HM	Recording Systems, Coding and Channel - I	Polivalente Room
	HN	Magnetic Nanoclusters and Nanoparticles - III	Polivalente Room
	HO	Head-Media Interface and Tribology – III	Polivalente Room
	HP	Soft Films	Polivalente Room
	HQ	Domain Walls in Nanowires and Thin Films	Polivalente Room
	HR	MgO Magnetic Tunnel Junctions - II	Polivalente Room
	HS	Ab Initio Calculations	Polivalente Room
	HT	Recording Systems, Coding and Channel - II	Polivalente Room
	HU	Multilayer Films and Superlattices - III	Polivalente Room
	HV	Magneto-Optic, HAMR and Novel Recording	Polivalente Room
	HW	Recording Physics, Models and Theory - II	Polivalente Room

Thursday
Closing Reception

8:30 pm – 10:00 pm		Government of the Autonomous Community of Madrid (by invitation)	Real Casa de Correos, Plaza de la Puerta del Sol

SUNDAY
AFTERNOON
5:00

AUDITORIO A

Session ZA
TUTORIAL ON MULIFERROICS
J. W. Harrell, Chair

5:00

ZA-01. Multiferroic and Magnetoelectric Materials. ***(Invited)*** *J.F. Scott*[1] *1. Earth Sciences, Cambridge University, Cambridge, United Kingdom*

5:40

ZA-02. Multiferroic materials: from bulk to thin films. ***(Invited)*** *W. Prellier*[1] *1. ENSICAEN, CNRS, Caen, France*

6:20

ZA-03. Multiferroic Composites: Magnetoelectric Effects, Sensors and High Frequency Devices. ***(Invited)*** *G. Srinivasan*[1] *1. Physics, Oakland University, Rochester, MI*

MONDAY
MORNING
9:30

AUDITORIO A

Session AA
SPIN-TORQUE SWITCHING
Xian Jiang, Chair

9:30

AA-01. Magneto-optical and spin transfer switching properties of current-perpendicular-to plane spin valves with perpendicular magnetic anisotropy. ***(Invited)*** *K. Aoshima*[1], N. Funabashi[1], K. Machida[1], Y. Miyamoto[1], N. Kawamura[1], K. Kuga[1], N. Shimidzu[1], T. Kimura[2] and Y. Otani[2] *1. Science & Technical Research Laboratories, Japan Broadcasting Corp., Setagaya, Tokyo, Japan; 2. The Institute for Solid State Pysics, The Tokyo University, Kashiwa, Chiba, Japan*

10:00

AA-02. Time-resolved magnetization switching induced by spin-transfer in Magnetic MgO tunnel junctions. *T. Devolder*[1], J. Hayakawa[2,3], K. Ito[2], H. Takahashi[2], S. Ikeda[3], P. Crozat[1], J.V. Kim[1], C. Chappert[1] and H. Ohno[3] *1. Institut d'Electronique Fondamentale, ORSAY Cedex, France; 2. Advanced Research Laboratory, Hitachi, Ltd, Tokyo, Japan; 3. Laboratory for Nanoelectronics and Spintronics,, Research Institute of Electrical Communication, Tohoku University, Sendai, Japan*

10:15

AA-03. Coherent control of spin transfer torque magnetization dynamics. S. Serrano-Guisan[1], K. Rott[2], G. Reiss[2], B. Ocker[3], J. Langer[3] and *H.W. Schumacher*[1] *1. Physikalisch-Technische Bundesanstalt, Braunschweig, Germany; 2. Department of Physics, University of Bielefeld, Bielefeld, Germany; 3. Singulus Nano Deposition Technologies GmbH, Kahl am Main, Germany*

10:30

AA-04. Real Time Measurements of Spin-Transfer Switching in CoFeB/MgO/CoFeB Magnetic Tunnel Junctions. *H. Tomita*[1], K. Konishi[1], T. Nozaki[1], M. Shiraishi[1], H. Kubota[2], A. Fukushima[2], S. Yuasa[2] and Y. Suzuki[1] *1. Osaka university, Toyonaka, Osaka, Japan; 2. National Institute of Advanced Industrial Science and Technology (AIST), Tsukuba, Japan*

10:45

AA-05. Observation of intermediate states in large magnetic tunnel junctions with composite free layer. X. Yao[1], R. Malmhall[2], R. Ranjan[2] and *J. Wang*[1] *1. MINT Center & Electrical and Computer Engineering Department, Univ. Of Minnesota, Minneapolis,, MN; 2. Yadav Technology, Fremont, CA*

11:00

AA-06. Spin transfer switching in magnetic tunnel junctions with several compositions of the free layer. *D. Watanabe*[1], M. Oogane[1], Y. Ando[1] and T. Miyazaki[2] *1. Applied Physics, Tohoku University, Sendai, Japan; 2. WPI-AIMR, Tohoku University, Sendai, Japan*

11:15

AA-07. Spin Torque Induced Magnetization Switching Variations. *X. Wang*[1], W. Zhu[1], M. Siegert[1] and D. Dimitrov[1] *1. Seagate Technology, Bloomington, MN*

11:30

AA-08. Spin-torque driven ferromagnetic resonance of Co/Ni synthetic layers in spin valves. W. Chen[1], G. de Loubens[1], J.L. Beaujour[1], *A.D. Kent*[1] and J.Z. Sun[2] *1. Physics, New York University, New York, NY; 2. IBM T. J. Watson Research Center, IBM, Yorktown Heights, NY*

11:45

AA-09. Spin torque transfer in deep submicron annular cpp-gmr devices. *M.T. Moneck*[1], X. Zhu[1] and J. Zhu[1] *1. Electrical & Computer Engineering, Carnegie Mellon University, Pittsburgh, PA*

12:00

AA-10. Effective description of planar spin-transfer devices. *Y. Bazaliy*[1,2] *1. Department of Physics and Astronomy, University of South Carolina, Columbia, SC; 2. Institute of Magnetism, National Academy of Science, Kyiv, Ukraine*

12:15

AA-11. Magnetization reversal driven by spin-injection : a mesoscopic spin transfer effect. *J. Wegrowe*[1] *1. LSI, Ecole Polytechnique, Palaiseau, France*

MONDAY MORNING 9:30 — MADRID

Session AB
DOMAIN WALLS IN NANOWIRES
Del Atkinson, Chair

9:30

AB-01. **Current-Induced Magnetic Domain Wall Motion at Low Current Density via Perpendicular Anisotropy.** *S. Jung*[1], W. Kim[2], T. Lee[2], K. Lee[3] and H. Lee[1] *1. Physics, POSTECH, Pohang, South Korea; 2. Materials Science, KAIST, Daejeon, South Korea; 3. Materials Science and Engineering, Korea University, Seoul, South Korea*

9:45

AB-02. **Current-induced Domain Wall Transformations and Vortex Core Displacement.** *L. Heyne*[1], D. Backes[1,2], T.A. Moore[1], S. Krzyk[1], M. Kläui[1], U. Rüdiger[1], L.J. Heyderman[2], A. Fraile Rodriguez[2], F. Nolting[2], O. Mentes[3], M. Nino[3], A. Locatelli[3], K. Kirsch[4] and R. Mattheis[4] *1. Universität Konstanz, Konstanz, Germany; 2. Paul Scherrer Institut, Villigen, Switzerland; 3. Sincrotrone Trieste, Trieste, Italy; 4. Institute of Photonic Technology, Jena, Germany*

10:00

AB-03. **Dynamics of domain walls in soft magnetic nanostripes: soliton approach.** *K. Gusliyenko*[1], J. Lee[1] and S. Kim[1] *1. Research Center for Spin Dynamics & Spin-Wave Devices and Nanospintronics Laboratory, Materials Science & Eng. Dept., Seoul National University, Seoul, South Korea*

10:15

AB-04. **Pinning and propagation of vortex domain walls in triangular anti-notches.** *K.J. O'Shea*[1], J.N. Chapman[1], S. McVitie[1] and Y.H. Wu[2] *1. Physics and Astronomy, University of Glasgow, Glasgow, United Kingdom; 2. Electrical and Computer Engineering, National University Singapore, Singapore, Singapore*

10:30

AB-05. **Domain wall pinning mechanism in ferromagnetic nanowires.** *D. Petit*[1], A. Jausovec[1], E. Lewis[1], H.T. Zeng[1], L. O'Brien[1], D. Read[1] and R.P. Cowburn[1] *1. Physics, Imperial College London, London, United Kingdom*

10:45

AB-06. **The dependence of wire width and trap geometry on domain wall pinning behaviour in nanowires.** *L.K. Bogart*[1], D. Eastwood[1], D. Atkinson[1], D. McGrouther[2], K. O'Shea[2], S. McVitie[2] and J. Chapman[2] *1. Physics, Durham University, Durham, United Kingdom; 2. Physics and Astronomy, University of Glasgow, Glasgow, United Kingdom*

11:00

AB-07. **Propagation field of notched permalloy nanowires.** *P. Warnicke*[1], A. Himeno[2], S. Kasai[2] and T. Ono[2] *1. Department of Engineering sciences, Division for solid state physics, Uppsala, Sweden; 2. Institute for Chemical Research, Division of materials research, Kyoto, Japan*

11:15

AB-08. **Measuring domain wall coherence lengths using a chirality filter.** *E. Lewis*[1], D. Petit[1], A. Jausovec[1], L. O'Brien[1], H. Zeng[1], D. Read[1] and R. Cowburn[1] *1. Imperial College London, London, United Kingdom*

11:30

AB-09. **Dynamic of depinning of a magnetic domain wall from a single defect.** *F. Montaigne*[1], J. Briones[1], D. Lacour[1], M. Hehn[1], M.J. Carey[2] and J. Childress[2] *1. Laboratoire de Physique des Matériaux, Nancy-University, CNRS, Vandoeuvre lès Nancy, France; 2. Hitachi San Jose Research Center, San Jose, CA*

11:45

AB-10. **Direct observation of the Walker breakdown during field driven domain wall (DW) motion in Permalloy nanowires.** *R. Mattheis*[1] and S. Glathe[1] *1. Photonic Intrumentation, IPHT, Jena, Germany*

12:00

AB-11. **Control of field driven domain wall (DW) motion by transversal fields: suppression of Walker breakdown and giant velocities.** *S. Glathe*[1], R. Mattheis[1] and T. Mikolajick[2] *1. Photonic Intrumentation, IPHT, Jena, Germany; 2. Institute of Electronic and Sensor Materials, TU Bergakademie Freiberg, Freiberg, Germany*

12:15

AB-12. **Domain-Wall Trapping by Localized Field on Submicron Permalloy Wire.** *L. Ji*[1], A. Orlov[1], G.H. Bernstein[1] and W. Porod[1] *1. Electrical Engineering, University of Notre Dame, Notre Dame, IN*

MONDAY MORNING 9:30 — ROMA

Session AC
MAGNETIC TUNNEL JUNCTIONS - I
Wolfram Maass, Chair

9:30

AC-01. **Tunnel magnetoresistance over 100 % in MgO based magnetic tunnel junction films with perpendicular magnetic $L1_0$-FePt electrodes.** *M. Yoshikawa*[1], E. Kitagawa[1], T. Nagase[1], T. Daibou[1], M. Nagamine[1], K. Nishiyama[1], T. Kai[1], N. Shimomura[1], M. Amano[1], S. Takahashi[1], T. Kishi[1] and H. Yoda[1] *1. Corporate Research & Development Center, TOSHIBA Corporation, Kawasaki, Japan*

9:45

AC-02. Interfacial Oxidation Enhanced Perpendicular Magnetic Anisotropy in Low Resistance Magnetic Tunnel Junctions Composed of Co/Pt Multilayer Electrodes. *J. Park*[1], C. Park[2] and J. Zhu[1] *1. Carnegie Mellon University, Pittsburgh, PA; 2. Western Digital Corporation, Fremont, CA*

10:00

AC-03. Large Tunneling Anisotropic Magnetoresistance in a Magnetic Tunnel Junction with a Single Ferromagnet CoPt. *B. Park*[1], J. Wunderlich[1], S. Joo[2], K. Jung[2], K. Shin[2], A. Shick[3] and T. Jungwirth[3,4] *1. Hitachi Cambridge Laboratory, Cambridge, United Kingdom; 2. Nano Device Research Center, KIST, Seoul, South Korea; 3. Institute of Physics ASCR, Pargue, Czech Republic; 4. School of Physics and Astronomy, University of Nottingham, Nottingham, United Kingdom*

10:15

AC-04. Crossover from Kondo assisted suppression to cotunneling enhancement of tunneling magnetoresistance via ferromagnetic nanodots in MgO tunnel barriers. *H. Yang*[1,2], S. Yang[1] and S. Parkin[1] *1. IBM Almaden Research Center, San Jose, CA; 2. ECE, National University of Singapore, Singapore, Singapore*

10:30

AC-05. Magneto-Coulomb effects through isolated nanoparticles connected to ferromagnetic electrodes. *A. Bernand-Mantel*[1], P. Seneor[2], B. Dlubak[2], V. Cros[2], S. Fusil[2], K. Bouzehouane[2], C. Deranlot[2], A. Vaures[2], R. Guillemet[2], F. Petroff[2] and A. Fert[2] *1. Kavli Institute of Nanoscience, Delft University of Technology, Delft, Netherlands; 2. Unite Mixte de Physique CNRS/Thales associated with University Paris-sud, Palaiseau, France*

10:45

AC-06. Fabrication and characterization of magnetic tunnel junctions using Co_2MnSi electrode and MgO tunneling barrier. *S. Tsunegi*[1], Y. Sakuraba[2], M. Oogane[1], K. Takanashi[2] and Y. Ando[1] *1. Applied physics, Tohoku University, Sendai, Japan; 2. Institute for Materials Research, Tohoku University, Sendai, Japan*

11:00

AC-07. Spin-dependent tunneling conductance in fully epitaxial $Co_2MnSi/MgO/Co_2MnSi$ tunnel junctions. *T. Ishikawa*[1], N. Itabashi[1], K. Matsuda[1], T. Uemura[1] and M. Yamamoto[1] *1. Division of Electronics for Informatics, Hokkaido University, Sapporo, Japan*

11:15

AC-08. Spin-polarized tunneling characteristics of the room temperature spin filter CoFe2O4. *A.V. Ramos*[1], R. Mattana[2], F. Petroff[2], T.S. Santos[3,4], G. Miao[3] and J.S. Moodera[3] *1. DSM/DRECAM/SPCSI, CEA Saclay, Gif-sur-Yvette, France; 2. Unite Mixte de Physique, CNRS/Thales, Palaiseau, France; 3. Francis Bitter Magnet Laboratory, MIT, Cambridge, MA; 4. Argonne National Laboratory, Argonne, IL*

11:30

AC-09. *In Situ* Lorentz Study of Disorder, Fluctuations, and Breakdown in Magnetic Tunnel Junctions. *S.E. Russek*[1], J.M. Shaw[1] and R. Geiss[1] *1. National Institute of Standards and Technology, Boulder, CO*

11:45

AC-10. Pulse Width Dependence of Barrier Breakdown in MgO Magnetic Tunnel Junctions. *J. Hérault*[1], R. Sousa[1], C. Papusoi[1], Y. Conraux[2], I. Prejbeanu[2], K. Mackay[2], J. Nozières[2] and B. Dieny[1] *1. Spintec (URA 2512 CEA/CNRS), Grenoble, France; 2. Crocus Technology, Grenoble, France*

12:00

AC-11. Spin dependent transport through an organic semiconductor tunnel barrier. *C. Barraud*[1,2], P. Seneor[1,2], R. Mattana[1,2], R. Guillemet[1,2], S. Fusil[1,2], K. Bouzeehouane[1,2], C. Deranlot[1,2], A. Vaures[1,2], F. Petroff[1,2], A. Fert[1,2], P. Graziosi[3], L. Hueso[3], I. Bergenti[3] and V. Dediu[3] *1. Unité Mixte de Physique CNRS/Thales, Palaiseau, France; 2. Department of Physics, University of Paris-Sud 11, Orsay, France; 3. Istituto per lo Studio dei Materiali Nanostrutturati, ISMN-CNR, Bologna, Italy*

12:15

AC-12. Theoretical studies on spin-dependent conductance in FePt/MgO/FePt(001) magnetic tunnel junctions. Y. Taniguchi[1], Y. Miura[1], K. Abe[1] and *M. Shirai*[1] *1. Research Institute of Electrical Communication, Tohoku University, Sendai, Japan*

MONDAY MORNING 9:30 — PARIS

Session AD
THIN FILMS: INTERFACE AND TRANSPORT PROPERTIES
Sergej Demokritov, Chair

9:30

AD-01. Fe-induced spin-polarized electronic states in a realistic semiconductor tunnel barrier. *M. Marangolo*[1] and F. Finocchi[1] *1. INSP, Université Pierre et Marie Curie, Paris, France*

9:45

AD-02. Spin polarised electrodes and interfaces in organic spintronic devices. *I. Bergenti*[1], A. Dediu[1], F. Borgatti[1], A. Riminucci[1], L.H. Hueso[5], F. Casoli[2], Y. Zhan[3], C. Pernechele[4] and M. Solzi[4] *1. ISMN CNR, Bologna, Italy; 2. CNR-IMEM, Parma, Italy; 3. Department of Physics,IFM, Linköping University, Linköping, Sweden; 4. Dipartimento di Fisica, Università di Parma, Parma, Italy; 5. Department of Physics and Astronomy, University of Leeds, Leeds, United Kingdom*

10:00

AD-03. Voltage control of the in-plane magnetic hysteresis in Fe/Au/Fe(001) and Fe (001) ultrathin films grown on GaAs (001) surface. K. Ohta[1], *Y. Suzuki*[1], T. Maruyama[1], T. Nozaki[1], T. Shinjo[1], M. Shiraishi[1], S. Ha[2], C. You[2] and W. Van Roy[3] *1. Engineering Science, Osaka University, Toyonaka, Japan; 2. Department of Physics, Inha University, Incheon 402-751, South Korea; 3. IMEC, B-3001 Leuven, Belgium*

10:15

AD-04. Extraordinary increase of the resistivity and decrease of the Curie temperature in ultrathin LSMO films capped with Au. *M. Cantoni*[1], S. Brivio[1], D. Petti[1], A. Cattoni[1], R. Bertacco[1], A.A. Sidorenko[2], G. Allodi[2], M. Ghidini[2] and R. De Renzi[2] *1. Physics, Politecnico di Milano, Como, Italy; 2. Physics, Università di Parma, Parma, Italy*

10:30

AD-05. Influence of interfacial oxygen on spin filtering and antiferromagnetic coupling in single-crystalline Fe/MgO/Fe(001) magnetic tunnel junctions. *F. Bonell*[1], S. Andrieu[1], C. Tiusan[1], A.M. Bataille[1], B. Kierren[1], F. Montaigne[1] and G. Lengaigne[1] *1. Nanomagnetism and Spintronics Team, Laboratoire de Physique des Matériaux - Université Henry Poincarré - UMR 7556, Vandoeuvre-lès-Nancy, France*

10:45

AD-06. Interface magnetism in ultra-thin Mo/Co multilayers. *L. Baczewski*[1], K. Mergia[2], J. Kisielewski[3], A. Maziewski[3] and F. Ott[4] *1. Institute of Physics Polish Academy of Sciences, Warsaw, Poland; 2. Institute of Nuclear Technology and Radiation Protection, Athens, Greece; 3. Institute of Experimental Physics, University of Bialystok, Bialystok, Poland; 4. Laboratoire Leon Brillouin, CEA, Saclay, France*

11:00

AD-07. Noncollinear Surface Spin Density of equiatomic NiMn alloy on Cu(001). *C. Gao*[1], A. Ernst[1], A. Winkelmann[1], J. Henk[1], W. Wulfhekel[1,2], P. Bruno[1] and J. Kirschner[1] *1. Max Planck Institute of MicrostrcutrurePhysics, Halle (Saale), Germany; 2. Physikalisches Institut, Universität Karlsruhe (TH), Karlsruhe, Germany*

11:15

AD-08. Room temperature ferromagnetism in pristine and Mn-doped ZnO thin films. *H. Nguyen*[1], E. Chikoidze[2] and Y. Dumont[2] *1. Faculté des Sciences et Techniques, Université F. Rabelais, Laboratoire LEMA, UMR 6157 CNRS/CEA, Tours, France; 2. GeMAC, UMR 8635, CNRS-University of Versailles, Meudon, France*

11:30

AD-09. Tailoring the magnetic properties of all-ferromagnetic artificial FeCu(111) alloy thin films. *M. Niño*[1,2], J. Camarero[1], W. Kuch[3], R. Abrudan[3,4], N. Mikuszeit[1,5], C. Tieg[4,6], M.P. Jigato[1], J. Kirschner[4], J. de Miguel[1] and R. Miranda[1,7] *1. Departamento de Física de la Materia Condensada, Instituto de Materiales "Nicolás Cabrera" and Universidad Autonoma de Madrid, Madrid, Spain; 2. ELETTRA-Sincrotrone Trieste, Basovizza, Italy; 3. Institut für Experimentalphysik, Freie Universität Berlin, Berlin, Germany; 4. Max-Planck Institut für Mikrostrukturphysik, Halle, Germany; 5. Institut für Angewandte Physik, Universität Hamburg, Hamburg, Germany; 6. European Synchrotron Radiation Facility-ESRF, Grenoble, France; 7. Instituto Madrileño de Estudios Avanzados en Nanociencia IMDEA-Nanociencia, Madrid, Spain*

11:45

AD-10. Magnetic properties of ultra thin magnetite film grown by molecular beam epitaxy. *S.K. Arora*[1], W. HanChun[1], I.V. Shvets[1], O.N. Mryasov[2], H. Yao[3] and W.Y. Ching[3] *1. Centre for Adaptive Nanostructures and Nanodevices (CRANN), School of Physics, Trinity College Dublin, Dublin, Dublin, Ireland; 2. Seagate Research Center, Seagate Technology, Pittsburgh, PA, 15222, PA; 3. Department of Physics, University of Missouri-Kansas City, Kansas City, MO, 64110, KS*

12:00

AD-11. Structure and magnetism of ultra-thin chromium layers on W(110). *B. Santos*[1,2], J.M. Puerta[3], J.I. Cerda[3], R. Stumpf[4], K. von Bergmann[5], R. Wiesendanger[5], M. Bode[5,6], K.F. McCarty[4] and J. de la Figuera[1,2] *1. Instituto de Quimica-Fisica Rocasolano, CSIC, Madrid, Madrid, Spain; 2. Centro de Microanalisis de Materiales, Universidad Autonoma de Madrid, Madrid, Madrid, Spain; 3. Instituto de Ciencia de Materiales de Madrid, CSIC, Madrid, Madrid, Spain; 4. Sandia National Laboratories, Livermore, CA; 5. Institute of Applied Physics and Microstructure Research Center, University of Hamburg, Hamburg, Germany; 6. Center for Nanoscale Materials, Argonne National Laboratory, Argonne, IL*

12:15

AD-12. Quantum-size induced oscillations of the electron-spin motion in Au films on Co(001). *L. Tati Bismaths*[1], L. Joly[2], F. Scheurer[1] and W. Weber[1] *1. Institut de Physique et Chimie des Matériaux de Strasbourg,, Strasbourg, France; 2. Swiss Light Source, Villigen, Switzerland*

MONDAY MORNING 9:30 LONDRES

Session AE
HEAT AND MICROWAVE ASSISTED RECORDING
Duane Karns, Chair

9:30

AE-01. Monolithically-fabricated hybrid head for near field assisted magnetic recording. *(Invited)* *S. Miyanishi*[1], K. Innami[1], T. Naka[1], T. Kitazawa[1], M. Yagura[1], N. Teraguchi[1], Y. Murakami[1] and A. Takahashi[1] *1. Advanced Technology Research Laboratories, SHARP CORPORATION, Tenri, Nara, Japan*

10:00

AE-02. Exploiting far- and nar-fiel optics to develop energy efficient transducer for heat-assisted magnetic recording. *R. Ikkawi*[1], N. Amos[1], A. Krichevsky[1], A. Lavrenov[1], D. Litvinov[2] and S. Khizroev[1] *1. Electrical Engineering, University of California, Riverside, Riverside, CA; 2. Center for Nanomagnetic Systems, University of Houston, Houston, TX*

10:15

AE-03. Design and characterization of a media thermal stack for confining lateral thermal heat flow. *D. Karns*[1], G. Ju[1], A. Itagi[1] and B. Lu[1] *1. Seagate Technologies, Pittsburgh, PA*

10:30

AE-04. Domain structure in TbFeCo/FePt-grains composite film and Cu doping effect on Curie temperature of FePt grains. *A. Itoh*[1], A. Tsukamoto[1], F. Chino[2], S. Iwase[2], Y. Sano[2] and K. Okayama[2] *1. Dep. of Electronics and Computer Science, College of Science and Technology, Nihon University, Funabashi, Chiba, Japan; 2. Dep. of Electronics, Graduate School of Nihon University, Funabashi, Chiba, Japan*

10:45

AE-05. Magnetic properties of amorphous magnetic film on self-assembled convex pattern. *N. Iwata*[1], D. Honda[1], Y. Murakami[1] and A. Takahashi[1] *1. Advanced Technology Research Laboratories, SHARP CORPORATION, Tenri, NARA, Japan*

11:00

AE-06. Comparison of Dual and Thermal Gradient Recording Methods for Thermally Assisted Magnetic Recording. *F. Akagi*[1], T. Matsumoto[1] and M. Igarashi[1] *1. Hitachi, Ltd., Tokyo, Japan*

11:15

AE-07. Investigation of magnetic reversal modes for Heat Assisted Magnetic Recording. *R.F. Evans*[1], P. Asselin[2], D. Hinzke[1], U. Nowak[1] and R.W. Chantrell[1] *1. Physics, University Of York, York, England, United Kingdom; 2. Seagate Research, Pittsburgh, PA*

11:30

AE-08. Modeling of thermally-activated switching of single phase, exchange-coupled and graded media. *O. Chubykalo-Fesenko*[1], U. Atxitia[1] and D. Suess[2] *1. POMT, Instituto de Ciencia de Materiales de Madrid, CSIC, Madrid, Spain; 2. Vienna University of Technology, Vienna, Austria*

11:45

AE-09. Application of plasmon resonances to all-optical magnetic recording. *I. Mayergoyz*[1], Z. Zhang[1], P. McAvoy[1] and C. Krafft[2] *1. ECE Department and UMIACS, University of Maryland, College Park, MD; 2. Laboratory for Physical Sciences, College Park, MD*

12:00

AE-10. Narrow Track Confinement by AC Field Generation Layer in Microwave Assisted Magnetic Recording. *Y. Tang*[1] and J. Zhu[1] *1. Electrical and Computer Engineering, Carnegie Mellon University, Pittsburgh, PA*

12:15

AE-11. LLG Simulation of Microwave Assisted Switching in Isolate Particle. *M. Igarashi*[1], Y. Suzuki[1], H. Miyamoto[1], Y. Maruyama[2], H. Fukui[2] and Y. Shiroishi[2] *1. Hitachi, Ltd., Kokubunji, Tokyo, Japan; 2. Hitachi Global Storage Technology, Odawara, Kanagawa, Japan*

MONDAY MORNING 9:30 BERLIN

Session AF
CHARACTERIZATION AND MEASUREMENT TECHNIQUES I
Ernie Hill, Chair

9:30

AF-01. Hyperfine field distribution in the Heusler compound Co_2FeAl probed by ^{59}Co NMR. *S. Wurmehl*[1], J.T. Kohlhepp[1], H. Swagten[1], B. Koopmans[1], C. Blum[2], B. Balke[2], G.H. Fecher[2] and C. Felser[2] *1. Applied Physics, Eindhoven University of Technology, Eindhoven, Netherlands; 2. Institut für Anorganische und Analytische Chemie, Johannes Gutenberg-University, Mainz, Germany*

9:45

AF-02. Shedding light on magnetoelastic coupling and magnetostriction at an atomic level. *S. Pascarelli*[1], M. Ruffoni[1], A. Trapananti[1], O. Mathon[1], Y. Joly[2], R. Pettifer[3], M. Pasquale[4], A. Magni[4], C.P. Sasso[4], F. Celegato[4] and E. Olivetti[4] *1. European Synchrotron Radiation Facility, Grenoble, France; 2. Institut NEEL, CNRS/UJF, Grenoble, France; 3. Dept. of Physics, Univ. of Warwick, Coventry, United Kingdom; 4. INRIM, IENGF, Torino, Italy*

10:00

AF-03. Detection of magnetic reversal at a DW pinning site in Ni80Fe20 nanowires using concurrent Magneto-Optical Kerr Effect (MOKE) and electrical measurements. *H.T. Zeng*[1], D. Read[1], D. Petit[1], L. O'Brien[1], E. Lewis[1], A. Jausovec[1] and R. Cowburn[1] *1. Physics, Imperial College London, London, United Kingdom*

10:15

AF-04. Material selective sensitivity of magneto-optical Kerr effect in NiFe/Au/Co/Au periodic multilayers. *K. Postava*[1,2], M. Tekielak[1], P. Mazalski[1], A. Maziewski[1], A. Stupakiewicz[1], M. Urbaniak[3], B. Szymanski[3] and F. Stobiecki[3] *1. Laboratory of Magnetism, University of Bialystok, Bialystok, Poland; 2. Department of Physics, Technical University of Ostrava, Ostrava - Poruba, Czech Republic; 3. Institute of Molecular Physics, Polish Academy of Sciences, Poznan, Poland*

10:30

AF-05. Magnetic images of a surface crack on a heated specimen with the use of an area type magnetic camera with high spatial resolution. J. Lee[1] and *J. Hwang*[2] *1. Department of Information and Communication Engineering, Chosun University, Gwangju, South Korea; 2. Department of Information and Communication Engineering, Graduate School of Chosun University, Gwangju, South Korea*

10:45

AF-06. Magnetostriction of Iron at Low Temperatures Observed with X-Ray Diffraction. *E. Arakawa*[1] and N. Aizawa[1] *1. Physics Dept., Tokyo Gakugei University, Koganei,, Tokyo, Japan*

11:00

AF-07. Enhancement of magneto-optical Kerr signal from the nano-structure by employing anti-reflection coated substrate. *C. You*[1] and D. Kim[1] *1. Department of Physics, Inha University, Incheon, South Korea*

11:15

AF-08. Selective Magnetometry using a single x-ray absorption edge. *J. Chaboy*[1], M. Laguna-Marco[1], C. Piquer[1], R. Boada[1], H. Maruyama[2] and N. Kawamura[3] *1. ICMA, Zaragoza, Zaragoza, Spain; 2. Graduate School of Science, Hiroshima University, Higashi-Hiroshima, Japan; 3. SPring-8/JASRI, Sayo, Hyogo, Japan*

11:30

AF-09. Open-circuit one-port network analyzer ferromagnetic resonance. C. Bilzer[1], *T. Devolder*[1], P. Crozat[1] and C. Chappert[1] *1. Institut d'Electronique Fondamentale, ORSAY Cedex, France*

11:45

AF-10. Discrimination of metallic coins using the scan type magnetic camera. J. Lee[1] and *J. Jun*[2] *1. Department of Information and Communication Engineering, Chosun University, Gwangju, South Korea; 2. Department of Information and Communication Engineering, Graduate School of Chosun University, Gwangju, South Korea*

12:00

AF-11. Apparent Image Effect in Closed-Circuit Magnetic Measurements. A.K. Higgins[1], *C.H. Chen*[1], C.D. Graham[2] and R.M. Strnat[3] *1. University of Dayton Magnetics Lab, Dayton, OH; 2. University of Pennsylvania, Philadelphia, PA; 3. Magnetic Instrumentation, Inc, Indianapolis, IN*

12:15

AF-12. A GMR Based System for Pulsed Eddy Current NDE of Aircraft Structures. G. Yang[1], *L. Udpa*[1] and S. Udpa[1] *1. msu, East Lansing, MI*

MONDAY
MORNING
9:30

AMSTERDAM

Session AG
TRANSFORMERS AND INDUCTORS I
Saibal Roy, Chair

9:30

AG-01. Fabrication and analysis of high-performance integrated solenoid inductor with magnetic core. *(Invited)* *D. Lee*[1], K. Hwang[2] and S.X. Wang[1] *1. Materials Science and Engineering, Stanford University, Stanford, CA; 2. Intel Corporation, Folsom, CA*

10:00

AG-02. Thin Film Integrated Power Inductor on Si and Its Performance in a 8MHz Buck Converter. *N. Wang*[1], T. O'Donnell[1], R. Meere[1], F. Rhen[1], S. Roy[1] and C. O'Mathuna[1] *1. Microsystems Centre, Tyndall National Institute, Cork, Ireland*

10:15

AG-03. CoNiFe applied in Microinductors for integrated dc-dc converters. *T. El mastouli*[1], J. Laur[1], J. Sanchez[1], M. Brunet[1], D. Bourrier[1] and M. Dilhan[1] *1. ISGE, Laboratory for Analysis and Architectures of Systems (LAAS - CNRS), Toulouse Cedex 4, France*

10:30

AG-04. High Q and High Current NiZnCu ferrite inductor for On-chip power module. *S. Bae*[1,2], Y. Hong[1,2], J. Lee[1,2], G.S. Abo[1,2], J. Jalli[1,2], A. Lyle[1,2], H. Han[1,2] and G.W. Donohoe[3] *1. Department of Electrical and Computer Engineering, University of Alabama, Tuscaloosa, AL; 2. MINT Center, University of Alabama, Tuscaloosa, AL; 3. Department of Electrical and Computer Engineering, University of Idaho, Moscow, ID*

10:45

AG-05. Synthesis of Bi-Zn-Al-B-Si-O nano-glass by sol-gel method for multilayer chip inductors. *S. An*[1] and S. Wi[1] *1. EMC R&D Group, Samsung Electro-Mechanics, Gyunggi-Do, South Korea*

11:00

AG-06. Electrically Tunable Thin Film Magnetic Core using Synthetic Antiferromagnet Structure. *N. An*[1], A. Jander[1] and P. Dhagat[1] *1. Electrical Engineering&Computer Science, Oregon State University, Corvallis, OR*

11:15

AG-07. The effect of magnetic coating layer thickness on the performance of tunable magnetic inductors. N. Ning[1], *X. Li*[1], H. Seet[1], W. Ng[1] and Y. Xu[2] *1. Mechanical Engineering, National University of Singapore, Singapore, Singapore; 2. Electrical and Computer Engineering, National University of Singapore, Singapore, Singapore*

11:30

AG-08. Audible noise from amorphous metal and silicon steel based transformer core. *D. Azuma*[1] and R. Hasegawa[1] *1. Metglas, Inc., Conway, SC*

11:45

AG-09. Development of a Novel Three-Phase Laminated Core Variable Inductor. *K. Nakamura*[1], S. Hisada[1], K. Arimatsu[2], T. Ohinata[2], K. Sakamoto[2] and O. Ichinokura[1] *1. Graduate School of Engineering, Tohoku University, Sendai, Japan; 2. Tohoku Electric Power Co., Inc., Sendai, Japan*

12:00

AG-10. Magneto-mechanical resonance in a 3-phase transformer core under PWM voltage excitation. X. Yao[1], *P.P. Thant*[2], A.J. Moses[1] and F. Anayi[1] *1. School of Engineering, Cardiff University, Wolfson Centre for Magnetics, Cardiff, Wales, United Kingdom; 2. Drilling & Measurements, Schlumberger, Aberdeen, Scotland, United Kingdom*

12:15

AG-11. Modeling the mutual impedances of non-coaxial inductors for induction heating applications. *C. Carretero*[1,3], J. Acero[1], R. Alonso[2], J. Burdío[1] and F. Monterde[3] *1. Dept. of Electronics Engineering and Communications, University of Zaragoza, Zaragoza, Spain; 2. Dept. of Applied Physics, University of Zaragoza, Zaragoza, Spain; 3. Bosch-Siemens Home Appliances Group, Montañana (Zaragoza), Spain*

MONDAY
MORNING
9:30

CARACAS

Session AH
MAGNETOIMPEDANCE
Larissa Panina, Chair

9:30

AH-01. High-frequency transverse incremental permeability and magnetoimpedance effect in CoFeHfO magnetic oxide nanofilms. A. Le[1], M. Phan[2], V. Manuel[3], *H. Lee*[4], Q. Nguyen[1] and S. Yu[1] *1. BK 21 Physics Program and Department of Physics, Chungbuk National University, Cheongju 361-763, South Korea; 2. Advanced Composites Centre for Innovation and Science, University of Bristol, Queen's Building, Bristol, United Kingdom; 3. De Instituto de Ciencia de Materiales de Madrid, CSIC, Campus de Cantoblanco, 28049 Madrid, Spain; 4. Department of Physics Education, Kongju National University, Kongju 314-701,, South Korea*

9:45

AH-02. Width dependence of magneto-impedance in sandwiched films. D. de Cos[1], *A. Garcia-Arribas*[1] and J. Barandiaran[1] *1. Electricidad y Electronica, Universidad del Pais Vasco, Bilbao, Spain*

10:00

AH-03. Annealing effects on the microwave absorption properties of nanocrystalline $Fe_{79}Si_{16}B_5$ microwires. *M. Han*[1], L. Deng[1] and D. Liang[1] *1. State Key Laboratory of Electronic Thin Films and Integrated Devices, University of Electronic Science and Technology of China, Chengdu, Sichuan, China*

10:15

AH-04. Microwave absorption of amorphous microwires carrying a low frequency ac current. *A.G. Gorriti*[1], I. Carabias[1], P. Marin[1] and A. Hernando[1] *1. Instituto de Magnetismo Aplicado, Las Rozas, Madrid, Spain*

10:30

AH-05. Magneto Impedance Behavior in Co/Cu/Co/NiFe Pseudo Spin Valve with a nano-oxide layer after Annealing Treatment. *W. Chien*[1,4], R. Hung[2], C. Lo[2,4], Y. Yao[1,3], K. Chang[4], E. Lai[4], Y. Chen[4], K. Hsieh[4], C. Lu[4] and P. Lin[1,4] *1. Department of Materials Science and Engineering, National Chiao Tung University, Hsinchu, Taiwan; 2. Electronics and Optoelectronics Research Laboratories, Industrial Technology Research Institute, Hsinchu, Taiwan; 3. Department of Materials Engineering, Tatung University, Taipei, Taiwan; 4. Emerging Central Lab, Macronix International Co. Ltd, Hsinchu, Taiwan*

10:45

AH-06. Analysis of the intrinsic field sensitivity and noise of magnetoimpedance sensors. *L. Melo*[1], D. Menard[2], A. Yelon[2], B. Dufay[3], O. Mareschal[3], S. Saez[3] and C. Dolabdjian[3] *1. Electrical Engineering, Ecole Polytechnique de Montreal, Montreal, QC, Canada; 2. Engineering Physics, Ecole Polytechnique de Montreal, Montreal, QC, Canada; 3. GREYC, ENSICAEN and University of Caen, Caen, France*

11:00

AH-07. Magneto impedance study in magneto tunneling junctions with different thickness of its barrier layer. W. Chien[1], *Y. Yao*[2], J. Wu[2], C. Lo[3], P. Lin[1] and X. Han[4] *1. The Department of Materials Science and Engineering, National Chiao Tung University, Hsinchu, Taiwan; 2. Department of Materials Engineering, Tatung University, Taipei, Taiwan; 3. Electronics and Optoelectronics Research Laboratories, Industrial Technology Research Institute, Hsinchu, Taiwan; 4. Institute of Physics, Chinese Academy of Sciences, Beijing, China*

11:15

AH-08. Development of thin microwires with enhanced magnetic softness and GMI. V. Zhukova[2], M. Ipatov[1], J. Gonzalez[1], J. Blanco[2] and *A. Zhukov*[1,3] *1. Dept. of Phys. Materials, Basque Country University, San Sebastian, Spain; 2. Dpto. de Física Aplicada, EUPDS, Basque Country University, San Sebastian, Spain; 3. TAMAG Ibérica S.L., Parque Tecnológico de Miramón, Paseo Mikeletegi 56, 1 Planta,, San Sebastian, Spain*

11:30

AH-09. Dependence of magneto-impedance on magnetic states in manganeses. *J. Li*[1], H. Chou[1] and C. Lin[1] *1. Department of Physics and Center of Nanoscience, National Sun Yat-sen University, Kaohiung, Taiwan*

11:45

AH-10. Temperature Dependence of Magnetoimpedance and Anisotropy in Nanocrystalline Finemet Wire. *B. Hernando*[1], J. Olivera[1], M. Sánchez[1], V.M. Prida[1] and R. Varga[2] *1. Fisica, Universidad de Oviedo, Oviedo, Asturias, Spain; 2. Inst. Physics, Fac.Sci.,UPJS, Park Angelinum, Kosice, Slovakia*

12:00

AH-11. Asymmetrical magnetoimpedance in CoFeSiB/CoNi layered microwires. J. Torrejon[1], G. Badini[1] and *L.V. Panina*[2] *1. Magnetism, ICMM (CSIC), Madrid, Spain; 2. School of Computing, Communication and Electronics, University of Plymouth, Plymouth, United Kingdom*

12:15

AH-12. Role of the interdomain wall in the giant magneto-impedance effect of thin microwires. *H. Chiriac*[1], T. Óvári[1] and S. Corodeanu[1] *1. National Institute of Research and Development for Technical Physics, Iasi, Romania*

MONDAY
MORNING
9:00

POLIVALENTE

Session AL
MOTORS AND ACTUATORS I
(POSTER SESSION)
Elena Lomonova, Chair

AL-01. Development of an Axial-flux Spindle Motor for the Slim Optical Disc Drive. *G. Yan*[1], G. Huang[1], H. Wang[1] and L. Hsu[2] *1. Micro/Meso Mechanical Manufacturing Section, Metal Industries Research & Development Center, Kaohsiung, Taiwan; 2. Electric Motor Technology Research Center, National Cheng Kung University, Tainan, Taiwan*

AL-02. Developments of a direct driven linear tubular generator for wave energy extraction. *C. Liu*[1], S. Yan[1], C. Lin[1], H. Lin[1], M. Lai[1] and C. Hwang[2] *1. Electrical Engineering, National Sun Yat-Sen University, Kaohsiung, Taiwan; 2. Electrical Engineering, Feng Chia University, Taichung, Taiwan*

AL-03. Mechanical resonance in non-oriented electrical steels induced by magnetostriction under pwm excitations. *S. Somkun*[1], A. Moses[1] and P. Anderson[1] *1. Wolfson Centre for Magnetics, Cardiff University, Cardiff, United Kingdom*

AL-04. Analysis of concentric magnetic gears using three dimensional scalar magnetic potential finite element method. L. Xinhua[1,2], C. K.t[1], J. J.z[2] and *J. Linni*[1] *1. Department of Electrical and Electronic Engineering, The University of Hong Kong, Hong Kong, China; 2. School of Automation, Shanghai University, Shanghai, China*

AL-05. Reduction of the Toque Ripple and Unbalanced Magnetic Force of a Rotatory Two-Phase Transverse Flux Machine by Using Herringbone Teeth. G. Jang[1], *H. Ahn*[1], J. Chang[2], S. Chung[2] and D. Kang[2] *1. Dept. of Mechanical Engineering, PREM Lab., Hanyang University, Seoul, South Korea; 2. Korea Electrotechnology Research Institute, Changwon, South Korea*

AL-06. EVALUATION OF INDUCTION HEATING APPLICATION OF LINEAR INDUCTION MOTOR BY USING FEM CALCULATION. *T. Yamada*[1] and K. Fujisaki[2,3] *1. Nittetsu Plant Designing Corpolation, Futtsu, Japan; 2. Nippon Steel Corpolation, Futtsu, Japan; 3. Graduated School of Environmental Studies, Tohoku University, Sendai, Japan*

AL-07. Calculation of Stator End-winding Reactance of an Induction Machine Based on Magnetic Energy by 3-D Finite Element Analysis. *R. Lin*[1] and A. Arkkio[1] *1. Helsinki University of Technology, Espoo, Finland*

AL-08. Investigation of carrier loss of induction motors considering skin effect in electrical steel sheets. *K. Yamazaki*[1] and N. Fukushima[1] *1. Dept. of Electrical, Electronics and Computer Engineering, Chiba Institute of Technology, Narashino, Chiba, Japan*

AL-09. Characteristics Analysis of 3DOF Spherical Motor for robotic wrist motor. *S. Won*[1] and J. Lee[1] *1. Electrical Eng., Hanyang University, Seoul, South Korea*

AL-10. Electro-Magnetically Excited Vibration Testing for a Vibro-Acoustic Investigation on PMSMs in Hard Disk Drives. S. Suwankawin[1] and *T. Jintanawan*[2] *1. Electrical Engineering, Chulalongkorn University, Bangkok, Thailand; 2. Mechanical Engineering, Chulalongkorn University, Bangkok, Thailand*

AL-11. A Study on the Multi-Objective Optimal Design of Interior Permanent Magnet Synchronous Motor. *K. Kim*[1] and J. Lee[1] *1. Dept. of electrical engineering, hanyang university, seoul, South Korea*

AL-12. Analysis on Operating Characteristics of Auto Focusing VCM Actuator. Y. Choi[1], Y. Kim[1], G. Cho[1], *Z. Piao*[1], B. Min[1], H. Baek[1] and B. Chae[2] *1. Department of Electrical Engineering, Chosun University, Gwangju, South Korea; 2. Department of Electrical and Control Engineering, Korea Polytechic V College, Gwangju, South Korea*

AL-13. Development of Laser Beam Steering System Using Three Magnetostrictive Actuators. *J. Jung*[1], Y. Park[1] and K. Im[1] *1. Mechatronics Engineering, Chungnam National University, Daejeon, South Korea*

MONDAY
MORNING
9:00

POLIVALENTE

Session AM
MAGNETIC SENSORS I
(POSTER SESSION)
Giovanni Badini-Confalonieri, Chair

AM-01. Magnetization process and induced pulse voltage of FeCoV wire implemented in tiny sensor chip. H. Tanaka[1], T. Kusunoki[1], T. Yamada[1], *Y. Takemura*[1], S. Abe[2], S. Kohno[3] and H. Kondo[3] *1. Department of Electrical & Computer Engineering, Yokohama National University, Yokohama, Japan; 2. Kanagawa University, Yokohama, Japan; 3. Nikkoshi Co., Ltd., Tokyo, Japan*

AM-02. The effect of ultrasonic resonance on impedance in magnetic rods. *H. Osada*[1], S. Nakamura[1], H. Hatafuku[1], S. Chiba[1] and H. Oka[1] *1. Iwate University, Morioka, Japan*

AM-03. Electrical Isolators based on Tunneling Magnetoresistance Technology. *C. Reig*[1], M.D. Cubells-Beltrán[1], D. Ramírez[1], S. Cardoso[2] and P.P. Freitas[2] *1. Electronic Engineering, Universitat de València, Burjassot, Spain; 2. Microsistemas e Nanotecnologias, INESC, Lisboa, Portugal*

AM-04. Introduction of a Base-Model for Eddy Current Testing of Printed Circuit Boards. H. Bayani[1], M. Nishino[1], *S. Yamada*[1] and M. Iwahara[1] *1. Division of Biological Measurement and Applications, Kanazawa University, Kanazawa, Japan*

AM-05. Orthogonal Fluxgate with Tube Core Operated in Fundamental Mode. *E. Paperno*[1], E. Wiess[1] and A. Plotkin[1] *1. Electrical and Computer Engineering, Ben-Gurion University of the Negev, Beer-Sheva, Israel*

AM-06. Test of multiturn sensors by a system generating rotating electromagnetic fields with high rotational frequencies. *H. Koebe*[1], D. Schmidt[1], M. Scherzinger[2], K. Bauer[2] and R.M. Mattheis[1] *1. Photonic Intrumentation, IPHT, Jena, Germany; 2. Novotechnik, Ostfildern, Germany*

AM-07. External and internal bias field effect on giant magneto impedance profile. *H. Kim*[1], S. Park[1], D. Kim[1] and W. Jeung[1] *1. Division of Materials Science & Engineering, Korea Institute of Science and Technology, Seoul, South Korea*

AM-08. Magnetic Gradiometer for Magnetic Moment Measurement using Two Cesium Magnetometer in Earth's Magnetic Field Background. *P. Park*[1], Y. Kim[1], W. Kim[1] and V.Y. Shifrin[2] *1. Electromagnetic Metrology Group, Korea Research Institute of Standards and Science(KRISS), Daejeon, South Korea; 2. D. I. Mendeleyev Institute for Metrology (VNIIM), St. Petersburg, Russian Federation*

AM-09. Surface flaws detection using AC magnetic field sensing by a thin film inductive micro sensor. *K. Kim*[1], Y. Cha[1], J. Kim[2], J. Sohn[2] and Y. Yoo[2] *1. Physics, Yeungnam University, Gyeongsan, South Korea; 2. Institute of Nova Magnetics, Nova Magnetics, Incheon, South Korea*

AM-10. Linear magnetoresistance of NiO-spin valve device. *S. Lee*[1], Y. Park[2], D. Hwang[3] and J. Rhee[4] *1. Oriental Biomedical Engineering, Sangji University, Wonju, Gangwondo, South Korea; 2. Oriental Western Biomedical Engineering, Sangji University, Wonju, Gangwondo, South Korea; 3. Applied Physics and Electronics, Sangji University, Wonju, Gangwondo, South Korea; 4. Physics, Sookmyung Women's University, Seoul, Seoul, South Korea*

AM-11. Temperature Characteristics of Magnetic Rotation Angle Sensors With Spin-Valve GMR Films. *Y. Abe*[2], T. Ono[2] and T. Kawai[1] *1. New Business Development Center, Hitachi Metals, Tokyo, Japan; 2. OE Device Center, Hitachi Metals, Mooka, Japan*

AM-12. A simple design of an orthogonal fluxgate magnetometer of fundamental mode. *I. Sasada*[1] and H. Kashima[1] *1. Applied Science for Electronics and Materials, Kyushu University, Kasuga, Japan*

AM-13. Nitride based (AlGaN/GaN) micro-Hall sensor. A. Bengoechea[1], *C. Aroca*[1], M.A. Sanchez-Garcia[1], E. Lopez[2] and P. Sanchez[1] *1. ISOM, Universidad Politecnica de Madrid, Madrid, Madrid, Spain; 2. Fisica de Materiales, Universidad Complutense de Madrid, Madrid, Madrid, Spain*

AM-14. Enhancement of sensitivity in a magnetic sensor by combining planar Hall resistance and giant Magnetoresistance. *H. Tran Quang*[1], S. Oh[1], D. Nguyen Huu[2] and C. Kim[1] *1. Department of Materials Science and Engineering, Chungnam National University, Daejeon, South Korea; 2. College of Technology, Vietnam National University, Hanoi, Viet Nam*

AM-15. Detection of magnetic particles for biological applications using a local-Hall device. *S. Joo*[1,2], Y. Kim[1], W. Lee[1], J. Lee[1], J. Hong[1,2], K. Rhie[1,2] and K. Shin[2] *1. Applied Physics, Korea university, Seoul, South Korea; 2. Center for Spintronics Research, KIST, Seoul, South Korea*

AM-16. Fabrication and Characterization of Silicon Micro Hall Sensors for Scanning Hall Probe Microscopy (SHPM) Using Multiple Feedback Techniques. *R. Akram*[1], M. Dede[1] and A. Oral[1] *1. Department of Physics, Bilkent University, 06800, Ankara, Turkey*

AM-17. Magneto-impedance property in a micromachined magnetic LC-sensor device. *A. Le*[1], S. Yu[1], H. Lee[2] and V. Manuel[3] *1. BK 21 Physics Program and Department of Physics, Chungbuk National University, Cheongju 361-763, South Korea; 2. Department of Physics Education, Kongju National University, Kongju 314-701,, South Korea; 3. De Instituto de Ciencia de Materiales de Madrid, CSIC, Campus de Cantoblanco, 28049 Madrid, Spain*

MONDAY
MORNING
9:00

POLIVALENTE

Session AN
MAGNETIC OXIDES & HEUSLER ALLOYS I (POSTER SESSION)

Atsufumi Hirohata, Chair

AN-01. Half-metallic magnetic materials and hybrid spintronic Structures. ***(Invited)*** *Y. Xu*[1] *1. Department of Electronics, The University of York, York, United Kingdom*

AN-02. Searching for quaternary Heusler alloys with half-metallicity. *X. Dai*[1], G. Liu[1], G. Fecher[1] and C. Felser[1] *1. Institut für Anorganische und Analytische Chemie, Johannes Gutenberg-Universität Mainz, Mainz, Germany*

AN-03. Universal scaling of the anomalous Hall effect in Fe3O4. *A. Fernández-Pacheco*[1,2], J.M. De Teresa[2], J. Orna[1,2], L. Morellón[1,2], P.A. Algarabel[2], J.A. Pardo[1,3] and M.R. Ibarra[1,2] *1. Instituto de Nanociencia de Aragón, Zaragoza, Spain; 2. Instituto de Ciencias de los Materiales de Aragón, Zaragoza, Spain; 3. Departamento de Ciencia y Tecnología de Materiales y Fluidos, Universidad de Zaragoza, Zaragoza, Spain*

AN-04. Optimization of the Postgrowth Oxidation Preparation Process of Fe3O4/GaAs(100) Hybrid Structure. *S. Hassan*[1], Y. Xu[1], K. Wilson[3], S. Thompson[2] and G. Van der Laan[4] *1. Electronics, University of York, York, United Kingdom; 2. Physics, University of York, York, United Kingdom; 3. Chemistry, University of York, York, United Kingdom; 4. Daresbury Laboratory, Warrington, United Kingdom*

AN-05. Magnetic and transport properties of polycrystalline CaRu1-xMoxO3. *Y. Ying*[1], Y. Lee[1], K. Kim[2], H. Pan[3] and Y. Zhang[3] *1. Quantum Photonic Science Research Center and BK21 Program Division of Advanced Research and Education in Physics, Hanyang University, Seoul, South Korea; 2. Sunmoon University, Asan, South Korea; 3. National High Magnetic Field Laboratory, University of Science and Technology of China, Hefei, China*

AN-06. Atomic and electronic structure in ferromagnetic/superconducting oxide interfaces. *M. Varela*[1], J. Garcia-Barriocanal[2], A.R. Lupini[1], W. Luo[3,1], Z. Sefrioui[2], S.T. Pantelides[3,1], C. Leon[2], J. Santamaria[2] and S.J. Pennycook[1,3] *1. Materials Science and Technology Division, Oak Ridge National Laboratory, Oak Ridge, TN; 2. Departmento de Física Aplicada III, Universidad Complutense de Madrid, Madrid, Spain; 3. Department of Physics and Astronomy, Vanderbilt University, Nashville, TN*

AN-07. Magnetic phase coupled to an electric memory state in d^0 oxide ZrO_2 films. *Y. Jo*[1], M. Jung[1], I. Hwang[2], B. Park[2] and S. Lee[3] *1. Korea Basic Science Institute, DAEJEON, South Korea; 2. Konkuk University, SEOUL, South Korea; 3. Pohang University of Science and Technology, POHANG, South Korea*

AN-08. Perovskite-oxide pseudo spin valve structure. *Y. Chan*[1], W. Cheng[1], H. Lau[1] and C. Leung[1] *1. Department of Applied Physics, The Hong Kong Polytechnic University, Hong Kong, China*

AN-09. Grain-size effects on magnetic properties of sputtered Co_2MnSi films. S. Ladak[2] and *A. Hirohata*[1] *1. Department of Electronics, University of York, York, United Kingdom; 2. Department of Physics, University of York, York, United Kingdom*

AN-10. Effect of Nd doping on the spin polarization of Co_2MnSi Heusler alloy. *A. Rajanikanth*[1,2], Y.K. Takahashi[2] and K. Hono[2,1] *1. International Center for Young Scientists, NIMS, Tsukuba, Ibaraki, Japan; 2. Magentic Materials Center, NIMS, Tsukuba, Ibaraki, Japan*

AN-11. Anisotropy and magnetic dynamic properties of Co_2MnGe Heusler compound. *M. Belmeguenai*[2,1], F. Zighem[1], G. Woltersdorf[2], Y. Roussigné[1], S. Chérif[1], K. Westerholt[3] and G. Bayreuther[2] *1. LPMTM Université Paris13, Villetaneuse, France; 2. Institut für Experimentelle Physik, Universität Regensburg, Regensburg, Germany; 3. Ruhr-Universität Bochum, Bochum, Germany*

AN-12. The effects of annealing temperature on structural and chemical properties of the $Co_2Cr_{0.6}Fe_{0.4}Al$ surface and its relevance for the electron spin polarization at the surface. *J. Wüstenberg*[1], J. Fischer[1], A. Conca[2], M. Jourdan[2], M. Aeschlimann[1] and M. Cinchetti[1] *1. Institute of Physics, University of Kaiserslautern, Kaiserslautern, Germany; 2. Institute of Physics, Johannes Gutenberg University Mainz, Mainz, Germany*

AN-13. The Different Capping Layer Influence on the Magnetic, Electronic and Structural Properties of the Co2MnGa/GaAs(100) Hybrid Structure. *S. Hassan*[1], J.S. Claydon[1], W. Zhang[1], Y. Xu[1], C.D. Damsgaard[2], J.B. Hansen[2], C.S. Jacobsen[2] and G. Van der Laan[3] *1. Electronics, University of York, York, United Kingdom; 2. Physics, Technical University of Denmark, Lyngby, Denmark; 3. Daresbury Laboratory, Warrington, United Kingdom*

MONDAY
MORNING
9:00

POLIVALENTE

Session AO
TRANSPORT THEORY AND SEMICONDUCTORS SPINTRONICS (POSTER SESSION)

Dafine Ravelosona, Chair
Joerg Wunderlich, Chair

AO-01. Penetration depth of transverse spin current in ferromagnetic metals. *T. Tomohiro*[1,2], Y. Satoshi[3], I. Hiroshi[1] and A. Yasuo[3] *1. Nanotechnology Research Institute, National Institute for Advanced Industrial Science and Technology, Tsukuba, Japan; 2. Institute of Applied Physics, University of Tsukuba, Tsukuba, Japan; 3. Department of Applied Physics, Graduate School of Engineering, Tohoku University, Sendai, Japan*

AO-02. Effect of Spin Memory Loss at Interfaces of Ferromagnet/Normal Metal on Spin-Transfer Torque. *S. Lee*[1] and K. Lee[1] *1. Korea University, Seoul, South Korea*

AO-03. Magnetic and structural properties of fully epitaxial Fe_3O_4/MgO/GaAs(100) for spin injection. *P. Wong*[1], W. Zhang[1], Y. Xu[1] and S.M. Thompson[2] *1. Spintronics and Nanodevice Laboratory, Department of Electronics, University of York, York, United Kingdom; 2. Department of Physics, University of York, York, United Kingdom*

AO-04. The effect of screening on extracted tunneling barrier parameters. *S. Bonetti*[1], J. Persson[1] and J. Åkerman[1] *1. Microelectronics and Applied Physics, Royal Institute of Technology (KTH), Kista-Stockholm, Sweden*

AO-05. Rectification effect in the medium with noncoplanar magnetic structure. *O.G. Udalov*[1] and A.A. Fraerman[1] *1. Institute for physics of microstructures RAS, Nizhny Novgorod, Nizhegorodskaya oblast', Russian Federation*

AO-06. Physical and electrical study of Permalloy/Al2O3/Si diodes for spin injection into silicon. *N. Bruyant*[1], R. Benabderrahmane[1], M. Kanoun[1], C. Baraduc[1], H. Achard[2] and A. Bsiesy[3] *1. SPINTEC, CEA CNRS, Grenoble, France; 2. LETI-Minatec, CEA, Grenoble, France; 3. SPINTEC, Université Joseph Fourier, Grenoble, France*

AO-07. Efficient spin injection and spin filtering in semiconductors by utilizing the k^3-Dresselhaus spin-orbit effect. *T. Fujita*[1,2], M. Jalil[1] and S. Tan[2] *1. Electrical and Computer Engineering Department, National University of Singapore, Singapore, Singapore; 2. Data Storage Institute, Singapore, Singapore*

AO-08. Electric field effect on spin diffusion in a semiconductor channel. *J. Kwon*[1], H. Koo[1], J. Eom[2,1], J. Chang[1] and S. Han[1] *1. Center for Spintronics Research, Korea Institute of Science and Technology, Seoul, South Korea; 2. Department of Physics, Sejong University, Seoul, South Korea*

AO-09. Effect of dynamical nuclear polarization on the transport through double quantum dots. *J. Inarrea*[1,2] and G. Platero[2] *1. Fisica, Universidad Carlos III, Leganes, Spain; 2. CSIC, Madrid, Madrid, Spain*

AO-10. Spin Current Characteristics in a Quantum Dot- Ferromagnetic Contacts Sandwich Structure. *W. Chen*[1], M. Jalil[1] and S. Tan[2] *1. Electrical & Computer Engineering, National University of Singapore, Singapore, Singapore; 2. Data Storage Institute, Singapore, Singapore*

AO-11. Transport of carbon nanotubes coupled to ferromagnetic electrodes. *S. Sun*[1] *1. Department of Applied Physics, National university of Kaohsiung, Taiwan, Kaohsiung, Taiwan*

AO-12. The Effects of Cotunneling and Spin Flip on The Spin Polarized Transport in A Ferromagnetic Single Electron Tunneling Transistor. *M. Ma*[1] and M. Jalil[1] *1. Department of Electrical and Computer Engineering, Information Storage Materials Laboratory, Singapore, Singapore*

AO-13. Self-sustained spin-polarized current oscillations in diluted magnetic semiconductor superlattices. *R. Escobedo*[1], M. Carretero[2,3], L.L. Bonilla[2,3] and G. Platero[4] *1. Matemática Aplicada, Universidad de Cantabria, Santander, Cantabria, Spain; 2. G. Milan Institute of Modeling, Simulation and Industrial Mathematics, Universidad Carlos III de Madrid, Leganés, Madrid, Spain; 3. Unidad Asociada al Instituto de Ciencia de Materiales de Madrid, CSIC, Madrid, Madrid, Spain; 4. Instituto de Ciencia de Materiales, CSIC, Madrid, Madrid, Spain*

AO-14. Modeling of Spin-Transfer Torque in Magnetic Multilayers with Noncollinear Magnetizations. *H. Morise*[1] and S. Nakamura[1] *1. Corp. R&D Ctr., Toshiba Corp., Kawasaki, Kanagawa, Japan*

AO-15. FMR studies of single permalloy layers sandwiched by Al. *H.J. Hurdequint*[1], N. Sergeeva[1] and J. Ben Youssef[2] *1. Laboratoire de Physique des Solides, CNRS-Universite Paris-Sud, Orsay, France; 2. Laboratoire de Magnetisme de Bretagne, CNRS-Universite de Bretagne-Ouest, Brest, France*

AO-16. Verifying a sole effect of tunnel barrier on spin transport by spin-polarised photoexcitation. *K. Lee*[1], T. Trypiniotis[1], H. Kurebayashi[1], S.N. Holmes[1,2], W.S. Cho[1], J.A. Bland[1], K.I. Lee[3] and K.H. Shin[3] *1. Physics, Cavendish Laboratory, Cambridge, United Kingdom; 2. Toshiba Research Europe Limited, Toshiba Cambridge Research Laboratory, Cambridge, United Kingdom; 3. Center for Spintronics Research, Korea Institute of Science and Technology, Seoul, South Korea*

AO-17. Polarization dependence of phonon replica peaks in spin-LEDs. *R. Mansell*[1], J. Laloë[1], S.N. Holmes[2], A. Petrou[3], I. Farrer[1], G. Jones[1] and T. Bland[1] *1. Department of Physics, University of Cambridge, Cambridge, United Kingdom; 2. Toshiba Cambridge Research Laboratory, Cambridge, United Kingdom; 3. Department of Physics, SUNY, Buffalo, NY*

AO-18. Comparison of room temperature polymeric spin-valves with different organic components. *D. Dhandapani*[1], N.A. Morley[1], A. Rao[1], A. Das[2], M. Grell[2] and M.R. Gibbs[1] *1. Engineering Materials, University of Sheffield, Sheffield, United Kingdom; 2. The Department of Physics and Astronomy, University of Sheffield, Sheffield, United Kingdom*

AO-19. Measurement of the spin polarization of rare earth – transition metal Laves phase compounds by point contact Andreev reflection. *C.G. Morrison*[1], K.N. Martin[1], G.J. Bowden[1], P.A. de Groot[1] and R.C. Ward[2] *1. School of Physics and Astronomy, University of Southampton, Southampton, Hampshire, United Kingdom; 2. Clarendon Laboratory, University of Oxford, Oxford, Oxfordshire, United Kingdom*

MONDAY
MORNING
9:00

POLIVALENTE

Session AP
LONGITUDINAL AND PARTICULATE MEDIA (POSTER SESSION)
Dimitris Niarchos, Chair

AP-01. Vapor phase synthesis of $L1_0$ FePt nanopowders and their magnetic properties. *J. Yu*[1], D. Lee[1], B. Kim[1] and T. Jang[2] *1. Department of Powder Materials Research, Korea Institute of Materials Science, Changwon, Gyeongnam, South Korea; 2. Dept. of Electronic Materials Engineering, Sunmoon University, Asan, Choongnam, South Korea*

AP-02. Two easy axes effect on nanosized spherical particles for advanced tape storage. *Y. Wang*[1] and J. Zhu[1] *1. Electrical and Computer Engineering, Carnegie Mellon University, Pittsburgh, PA*

AP-03. Synthesis and self-assembly of phase-, size- and shape-controlled $L1_0$-FePt nanorods by a modified polyol process. *L.C. Varanda*[1] and M. Jafelicci Jr.[2] *1. Físico-Química, Instituto de Química de São Carlos - USP, São Carlos, São Paulo, Brazil; 2. Físico-Química, Instituto de Química de Araraquara - UNESP, Araraquara, São Paulo, Brazil*

AP-04. Playback performance of facing targets sputtered tape media on moving tape substrate with a high speed. *S. Matsunuma*[1], T. Inoue[2], T. Doi[2], T. Matsuu[3], A. Hashimoto[3], H. Fujiura[3], K. Hirata[3] and S. Nakagawa[3] *1. R&D Division, Hitachi Maxell, Tsukubamirai, Ibaraki, Japan; 2. Advanced Tape Division, Hitachi Maxell, Oyamazaki, Kyoto, Japan; 3. Department of Physical Electronics, Tokyo Institute of Technology, Meguro, Tokyo, Japan*

AP-05. A possibility of >15Gbit/in2 recording density system with fine MP tape and GMR head. *N. Sekiguchi*[1], M. Terakawa[1], T. Akasaka[1], T. Fukuda[1], Y. Kamoshita[1], H. Ohnuma[1], K. Maeshima[1] and M. Yamaga[1] *1. CDG, SONY, Tagajo, Japan*

AP-06. Investigation of thermal de-magnetization effects in data recorded on barium ferrite recording media. *M.L. Watson*[1], T.W. Feebeck[1], R.A. Beard[1] and S.M. Kientz[1] *1. Storage Group, Sun Microsystems, Louisville, CO*

MONDAY
MORNING
9:00

POLIVALENTE

Session AQ
MAGNETIC NANOCLUSTERS AND NANOPARTICLES I (POSTER SESSION)
Marcelo Knobel, Chair

AQ-01. Influence of the capping molecule on the magnetic behavior of thiol capped gold nanoparticles. *P. Crespo*[1], E. Guerrero[2], M. Muñoz-Márquez[2], A. Hernando[1] and A. Fernández[2] *1. Instituto de Magnetismo Aplicado, Universidad Complutense de Madrid, P.O. Box 28230 Las Rozas,Madrid, Madrid, Spain; 2. Instituto de Ciencia de Materiales de Sevilla, CSIC-US, Av. Américo Vespucio 49, 41092-Sevilla, Sevilla, Spain*

AQ-02. XMCD study of thiol capped Au nanoparticles. V. Bouzas[1], *M. Garcia*[1], P. Andrea[4], D. Haskel[2], G. Ruggeri[4] and C. de Julian Fernandez[3] *1. Dpt. Materials Science, University Complutense, MAdrid, Madrid, Spain; 2. Advanced Photon source, Argonne National Laboratory, Argonne, IL; 3. Molecular Magnetism Laboratory, University of Florence, Florence, Florence, Italy; 4. Dpt. of Chemistry and Industrial Chemistry, University of Pisa, Pisa, Pisa, Italy*

AQ-03. Local structure, optical and magnetic studies of Ni nanostructures embedded in SiO_2 matrix by ion implantation. *S.K. Sharma*[1], R. Kumar[2], M. Knobel[3], P. Kumar[4], P. Thakur[5], K.H. Chae[6], W.K. Choi[7], D. Kanjilal[8] and R. Kumar[9] *1. DFMC, Unicamp, Campinas, SP, Brazil; 2. Materials Science Division, IUAC, New Delhi, Delhi, India; 3. DFMC, Unicamp, SP, Campinas, Brazil; 4. Materials Science Division, IUAC, New Delhi, Delhi, India; 5. Materials Science and Technology Research Division, KIST, Cheongrang, Seoul, Korea, South Korea; 6. Materials Science and Technology Research Division, KIST, Cheongrang, Seoul, Korea, South Korea; 7. Thin Film Materials Research Center, KIST, Cheongrang, Seoul, Korea, South Korea; 8. Materials Science Division, IUAC, New Delhi, Delhi, India; 9. Physics, Ch. Charan Singh University, Meerut, Meerut, India*

AQ-04. Surface contribution to magnetic anisotropy energy in Fe_3O_4 nanoparticles. *N. Pérez*[1,2], P. Guardia[1,2], A.G. Roca[3], M.P. Morales[3], C.J. Serna[3], F. Bartolomé[4], L.M. García[4,5], A. Labarta[1,2] and X. Batlle[1,2] *1. Física Fonamental, Universitat de Barcelona, Barcelona, Catalunya, Spain; 2. Institut de Nanociència i Nanotecnologia IN2UB, Universitat de Barcelona, Barcelona, Catalunya, Spain; 3. Instituto de Ciencia de Materiales de Madrid, CSIC, Madrid, Madrid, Spain; 4. Instituto de Ciencia de Materiales de Aragón, CSIC, Zaragoza, Aragón, Spain; 5. Física de la Materia Condensada, Universidad de Zaragoza, Zaragoza, Aragón, Spain*

AQ-05. Microscopic, structural and magnetic investigation of polymer-encapsulated iron oxide nanoparticles. *A.R. Rodriguez*[1], J.H. Coaquira[2], J.G. Santos[1], L.B. Silveira[1], E.M. Marmolejo[1], W. Tennpohl[1], J.P. Sinnecker[3], M.A. Novak[3], D. Rabelo[4] and P.C. Morais[2] *1. Physics, Fundação Universidade Federal de Rondônia, Ji-Paraná, RO, Brazil; 2. Physics, Universidade de Brasília, Brasília, DF, Brazil; 3. Physics, Universidade Federal de Rio de Janeiro, Rio de Janeiro, RJ, Brazil; 4. Chemistry, Universidade Federal de Goiás, Goiânia, GO, Brazil*

AQ-06. Magnetite Nanoparticles With No Surface Spin Canting. *A. Roca*[1], D. Niznansky[2], M. González-Fernández[1], M. Morales[1] and C. Serna[1] *1. Instituto de Ciencia de Materiales de Madrid (CSIC), Madrid, Spain; 2. Department of Inorganic Chemistry, Charles University, Prague, Czech Republic*

AQ-07. Synthesis and characterization of anisotropic magnetic nanoparticles for lab-on-a-bead applications. *N. Kataeva*[1], J. Schotter[1] and H. Brueckl[1] *1. Nano-System-Technologies, Austrian Research Centers GmbH, Vienna, Austria*

AQ-08. Magnetic Properties of γ-Fe_2O_3 Nanoparticles Precipitated in Alginate Hydrogels. *L.E. Wenger*[1], G.M. Tsoi[1], P.P. Vaishnava[2], R. Naik[3], U. Senaratne[3], E.C. Buc[3] and V.M. Naik[4] *1. Physics, University of Alabama at Birmingham, Birmingham, AL; 2. Physics, Kettering University, Flint, MI; 3. Physics & Astronomy, Wayne State University, Detroit, MI; 4. Natural Sciences, University of Michigan-Dearborn, Dearborn, MI*

AQ-09. Intermatrix synthesis of magnetic nanocrystals by frontal polymerization and subsequent pyrolysis on iron containing monomer. *E.D. Maciejewska*[1], M. Leonowicz[1], A. Pomogailo[2] and G. Dzhardimalieva[2] *1. Faculty of Material Science and Engineering, Warsaw University of Technology, Warsaw, Poland; 2. Institute of Chemical Physics RAS, Chernogolovka, Russian Federation*

AQ-10. Synthesis of L10 (FePt)1-xAux Nanoparticle Monolayer on Polyimide Substrate. *J. Kim*[1], R. Kim[1], N. Oh[1], H. An[1], C. Yoon[1], Y. Kim[1] and C. Kim[1] *1. Materials Science and Engineering, Hanyang University, Seoul, South Korea*

AQ-11. Co-CoO Nanoparticles Prepared by Reactive Gas Phase Aggregation. *J.A. De Toro*[1], J.P. Andrés[1], J.A. González[1], P.S. Normile[1], T. Muñoz[1], P. Muñiz[1], A.J. Barbero[1] and J.M. Riveiro[1] *1. Departamento de Fisica Aplicada, Universidad de Castilla-La Mancha, Ciudad Real, Spain*

AQ-12. Magnetism of ε-Fe_2O_3 nanoparticles modified by Al and Ga substitution. *J. Poltierova Vejpravova*[1], P. Brazda[2], D. Niznansky[2], S. Danis[1], S. Burianova[1] and V. Sechovsky[1] *1. Faculty of Mathematics and Physics, DCMP, Charles University Prague, Prague 2, Czech Republic; 2. Faculty of Science, DIC, Charles University Prague, Prague 2, Czech Republic*

AQ-13. The first ternary intermetallic Heusler nanoparticles: Co2FeGa. *L. Basit*[1], A. Yella[1], S.A. Nepijko[2], V. Ksenofontov[1], G.H. Fecher[1], W. Tremel[1] and C. Felser[1] *1. Chemistry, Inst. for Inorganic & Analytical Chemistry, Mainz, Germany; 2. Physics, Institute of Physics, Johannes Gutenberg - University, Mainz, Germany*

AQ-14. Giant diamagnetism in AuFe nanoparticles. *J. Wu*[1], M. Jung[2], J. Min[3], H. Liu[1,4], J. Cho[3] and Y. Kim[3] *1. Institute for Nano Science, Korea University, Seoul 136-713, South Korea; 2. Quantum Materials Research Team, Korea Basic Science Institute, Daejeon 305-333, South Korea; 3. Department of Materials Science and Engineering, Korea University, Seoul 136-713, South Korea; 4. College of Chemistry and Chemical Engineering, Henan University, Kaifeng 475001, China*

AQ-15. XMCD studies of core-shell FeRh nanoparticles. *A. Smekhova*[1], D. Ciuculescu[2], F. Wilhelm[1], C. Amiens[2], A. Rogalev[1] and B. Chaudret[2] *1. European Synchrotron Radiation Facility, Grenoble, France; 2. Laboratoire de Chimie de Coordination du CNRS, Toulouse, France*

AQ-16. Surface-induced magnetic anisotropy of impurities. *A. Szilva*[1], L. Szunyogh[1], G. Zarand[1] and C. Muñoz[2] *1. Department of Theoretical Physics, Budapest University of Technology and Economics, Budapest, Hungary; 2. Instituto de Ciencia de Materiales de Madrid, Consejo Superior de Investigaciones Científicas, Madrid, Spain*

AQ-17. Exchange bias in inverted AFM-core|FiM-shell nanoparticles. *G. Salazar-Alvarez*[1], A. López-Ortega[2], J. Sort[3], S. Suriñach[2], M.D. Baró[2] and J. Nogués[4] *1. Institut Catala de Nanotecnologia, Bellaterra, Barcelona, Spain; 2. Departament de Física, Universitat Autònoma de Barcelona, Bellaterra, Barcelona, Spain; 3. Institució Catalana de Recerca i Estudis Avançats (ICREA) and Departament de Física, Universitat Autònoma de Barcelona, Bellaterra, Barcelona, Spain; 4. Institució Catalana de Recerca i Estudis Avançats (ICREA) and Institut Català de Nanotecnologia, Universitat Autònoma de Barcelona, Bellaterra, Barcelona, Spain*

MONDAY
MORNING
9:00

POLIVALENTE

Session AR
SOFT MAGNETIC MATERIALS AND EMC (POSTER SESSION)
Aready Zhukov, Chair

AR-01. Analysis of Conduction Noise Attenuation by Magnetic Composite Sheets on Microstrip Line by Finite Element Method. *S. Kim*[1], S. Kim[1] and G. Ryu[1] *1. Materials Engineering, Chungbuk National University, Cheongju, South Korea*

AR-02. Microwave Absorbers of Two-layer (Dielectric/Magnetic) Composite Laminates for Wide Oblique Incidence Angles. *S. Kim*[1] and J. Kim[1] *1. Materials Engineering, Chungbuk National University, Cheongju, South Korea*

AR-03. Left-handed properties in the combined structures of cut-wire pair and continuous wire. *V. Dinh Lam*[1], J. Kim[1], N. Thanh Tung[1], S. Lee[1] and Y. Lee[1] *1. Hanyang University, Seoul, South Korea*

AR-04. Electromagnetic interference and shielding of valve hall in HVDC converter station. *C. Gao*[1], Z. Zhao[1] and S. Wang[2] *1. North China Electric Power University, Baoding, China; 2. Northeast Electric Power Design Institute, Changchun, China*

AR-05. Study of coupling on parallel microstrip lines due to magnetic absorber sheet. *V.B. Bregar*[1], J. Koselj[1] and B. Drnovsek[1] *1. Nanotesla Institute, Ljubljana, Slovenia*

AR-06. The influence of the construction of secondary reaction plate on the transverse edge effect in Single-sided linear induction motor. *S. Lee*[1], H. Lee[2], S. Go[1], K. Kim[1], D. Jung[1] and J. Lee[1] *1. Hanyang university, Seoul, South Korea; 2. Korea Railroad Research Institute, Uiwang, South Korea*

AR-07. RF conduction in-line noise suppression effects for the NiFe and Fe magnetic composite. *K. Kim*[1], J. Ryu[2], S. Lee[2], S. Lee[2], Y. Choa[3] and S. Oh[4] *1. Physics, Yeungnam University, Gyeongsan, South Korea; 2. Composite Materials, Korea Institute of Materials Science, Changwon, South Korea; 3. Dept.of Chemical Engineering, Hanyang University, Ansan, South Korea; 4. Dept. of Materials Science and Engeering, Seoul National University of Technology, Seoul, South Korea*

AR-08. Optimal bulk content of sulfur for high magnetic induction in inhibitor-free 3% Si-Fe strips. *S. Kim*[1], J. Soh[1], J. Oh[1], S. Cho[1], S. Han[2] and N.H. Heo[1] *1. Advanced Materials Group, Korea Electric Power Research Institute, Daejon, CN, South Korea; 2. Chungnam National University, Daejeon, CN, South Korea*

AR-09. Performance Improvement of PM Synchronous Motor by Using Soft Magnetic Composite Material. *G.V. Cvetkovski*[1] and L.B. Petkovska[1] *1. Faculty of Electrical Engineering and Information Technologies, Ss. Cyril & Methodius University, Skopje, Macedonia*

AR-10. Magnetic entropy change of V substituted Ni-Mn-Ga Heusler alloy. *S. Min*[1], Y. Zhang[1], K. Kim[2,3], Y. Kim[2,3], S. Yu[1], K. Lee[4] and Y. Kim[5] *1. BK21 Physics Program and Department of Physics, Chungbuk National University, Cheongju, South Korea; 2. School of Electrical & Computer Engineering, Chungbuk National University, Cheongju, South Korea; 3. CBNU BK21 Chungbuk Information Technology Center, Chungbuk National University, Cheongju, South Korea; 4. Superconductivity Lab., Korea Research Institute of Standard and Science, Taejon, South Korea; 5. Engineering, Korea Institute of Science and Technology, Seoul, South Korea*

AR-11. Ferroresonance phenomena in electric circuits including amorphous cores. N. Banu[1], E. Barbisio[1], O. Bottauscio[2], *M. Chiampi*[1], G. Crotti[2] and D. Giordano[2] *1. Ingegneria Elettrica, Politecnico di Torino, Torino, Italy; 2. Electromagnetics, Istituto Nazionale di Ricerca Metrologica, Torino, Italy*

AR-12. Harmonic Distortion of Magnetizing Current in Combined Wound Toroidal Cores. J. Chojnacki[1], P. Liszewski[1], *M. Soinski*[2], W. Pluta[2], R. Rygal[2], S. Zurek[3] and P. Pinkosz[4] *1. ABB Sp. z o.o., 04-713 Warsaw, Pszasnysz Branch, Poland; 2. Czestochowa University of Technology, Faculty of Electrical Engineering, 42-200 Czestochowa, Poland; 3. Wolfson Centre for Magnetics, School of Engineering, Cardiff University, Cardiff, CF24 2AA, United Kingdom; 4. Magneto Ltd, 42-224 Czestochowa, Poland*

AR-13. The Characterisation of NiFe Cores for High Current Micro-inductors. *B. Jamieson*[1], T. O'Donnell[1], N. Wang[1], J. Godsell[1] and S. Roy[1] *1. Microsystems Centre, Tyndall National Institute, Cork, Ireland*

MONDAY
MORNING
9:00

POLIVALENTE

Session AS
GMR FOR MULTILAYERS AND NANOSTRUCTURES (POSTER SESSION)
Thomas McLaughlin, Chair

AS-01. FABRICATION OF 8X8 ARRAY OF SPIN VALVE PILLARS AND MR CHARACTERIZATION. *A. Lyle*[1,2], Y. Hong[1,2], B.C. Choi[3], J. Rudge[3], G.S. Abo[1,2], S. Gee[1,4], H. Han[1,2], J. Jalli[1,2] and G.W. Donohoe[5] *1. Electrical and Computer Engineering, University of Alabama, Tuscaloosa, AL; 2. MINT Center, University of Alabama, Tuscaloosa, AL; 3. Physics and Astronomy, University of Victoria, Victoria, BC, Canada; 4. Seagate Technology, Bloomington, MN; 5. Electrical and Computer Engineering, University of Idaho, Moscow, ID*

AS-02. Two-dimensional imaging of giant magnetoresistance with improved sensitivity. *R.A. Armstrong*[1], S.M. Stirk[1], R.T. Mennicke[1], A.F. Lee[2], J.A. Matthew[1] and S.M. Thompson[1] *1. Physics, University of York, York, United Kingdom; 2. Chemistry, University of York, York, North Yorkshire, United Kingdom*

AS-03. Magnetic degradation of GMR spin-valve multi-layers due to electromigration induced failures. *J. Jiang*[1], S. Bae[1] and H. Ryu[2] *1. Electrical and Computer Engineering, National University of Singapore, Singapore, Singapore; 2. IT Convergence & Components Laboratory, ETRI, Daejon, Yuseong-Gu, South Korea*

AS-04. High spin polarization of epitaxial films with artificial alternate monatomic $[Fe/Co]_n$ superlattice. I. Chu[1], A. Rajanikanth[2], Y. Takahashi[2], K. Hono[2], *M. Doi*[1] and M. Sahashi[1] *1. Department of Electronic Engineering, Tohoku University, Sendai, Japan; 2. National institute for materials Science, Tsukuba, Japan*

AS-05. Microstructure, magnetoresistance and interlayer coupling studies in FePt/Os/FePt thin films. *C. Shih-Yuan*[1], Y. Yeong-Der[2], W. Jenn-Ming[1] and Y. Chin-Chung[3] *1. Materials Science and Engineering, National Tsing Hua University, Taipei, Taiwan; 2. Materials Engineering, Tatung University, Taipei, Taiwan; 3. Applied Physics, National University of Kaohsiung, Kaohsiung, Taiwan*

AS-06. **Novel Granular Thin Film Device Structure.** *S. Regunathan*[1] and V. Ng[1] *1. Information Storage Materials Laboratory, Dept of Electrical and Computer Engg, National University of Singapore, Singapore, Singapore*

MONDAY
MORNING
9:00

POLIVALENTE

Session AT
FUNDAMENTAL PROPERTIES FOR APPLICATIONS (POSTER SESSION)
Roy Chantrell, Chair
Oksana Fesenko Chubykalo, Chair

AT-01. **Nature and entropy content of the magnetic transitions in pure and pseudo-binary Laves phases RCo_2** *M. Parra-Borderías*[1], F. Bartolomé[1], J. Herrero-Albillos[2] and L.M. García[1] *1. Instituto de Ciencia de Materiales de Aragón, CSIC-Universidad de Zaragoza, Zaragoza, Spain; 2. Department of Materials Science, University of Cambridge, Cambridge, United Kingdom*

AT-02. **Estimating magnetic entropy change by a mean-field scaling method and the effect of magnetic irreversibility in first-order transitions.** *J.S. Amaral*[1], N.O. Silva[1,2] and V.S. Amaral[1] *1. Physics and CICECO, Universidade de Aveiro, Aveiro, Portugal; 2. Materia Condensada, Facultad de Ciencias, Zaragoza, Spain*

AT-03. **Magnetic and structural phase transitions in magnets with a NaCl structure.** *F.A. Kassan-Ogly*[1] and B.N. Filippov[2] *1. Department of Theoretical and Mathematical Physics, Institute of Metal Physics, Ekaterinburg, Sverdlovskaya oblast, Russian Federation; 2. Lab. of Micromagnetics, Institute of Metal Physics, Ekaterinburg, Sverdlovsk region, Russian Federation*

AT-04. **The magnetic phase transition and electronic properties of CoS2-xSex.** *M. Otero-Leal*[2], F. Rivadulla[1] and J. Rivas[2] *1. Depto. Química-Física, Universidad de Santiago de Compostela, Santiago de Compostela, La Coruña, Spain; 2. Fisica Aplicada, Universidad de Santiago de Compostela, Santiago de Compostela, La Coruña, Spain*

AT-05. **Symmetry breaking effects in epitaxial magnetic thin films.** *E. Jiménez*[1], N. Mikuszeit[1,2], D. Ecija[1], J. Gallego[3], N. Sacristán[1,4], J. Vogel[5], J. Camarero[1] and R. Miranda[1,6] *1. Departamento de Física de la Materia Condensada and Instituto de Materiales "Nicolás Cabrera", Universidad Autonoma de Madrid, Madrid, Spain; 2. Institut für Angewandte Physik, Universität Hamburg, Hamburg, Germany; 3. Instituto de Ciencia de Materiales de Madrid ICMM, CSIC, Madrid, Spain; 4. Escuela Universitaria de Informática, Universidad de Valladolid, Segovia, Spain; 5. Institut Néel, CNRS, Grenoble, France; 6. Instituto Madrileño de Estudios Avanzados en Nanociencia, IMDEA-Nanociencia, Madrid, Spain*

AT-06. **Cobalt doped β-peptide nanotubes: a new class of spintronic materials.** *B. Sanyal*[1], P.I. Arvidsson[2,3] and O. Eriksson[1] *1. Department of Physics, Uppsala University, Uppsala, Sweden; 2. Department of Biochemistry and Organic Chemistry, Uppsala University, Uppsala, Sweden; 3. Discovery CNS \& Pain Control, AstraZeneca R\&D, S\"{o}dert\"{a}lje, Sweden*

AT-07. **Magnetotransport Properties of $Y_2Fe_{17-x}Co_x$ Single Crystals.** *J. Stankiewicz*[1], K.P. Skokov[2], A.G. Khokholkov,[2], J. Bartolomé[1] and Y.G. Pastushenkov[2] *1. Instituto de Ciencia de Materiales, CSIC - Universidad de Zaragoza, Zaragoza, Spain; 2. Faculty of Physics, Tver State University, Tver, Russian Federation*

AT-08. **Weiss oscillations modulated by microwave radiation.** *J. Inarrea*[1,2] and G. Platero[2] *1. Physics, Universidad Carlos III, Leganes, Spain; 2. CSIC, Leganes. Madrid, Spain*

AT-09. **Nonlinear modulation of spin-orbit interaction in a semiconductor channel.** *H. Koo*[1], J. Kwon[1], J. Eom[2,1], J. Chang[1] and S. Han[1] *1. Center for Spintronics Research, Korea Institute of Science and Technology, Seoul, South Korea; 2. Department of Physics, Sejong University, Seoul, South Korea*

AT-10. **Ordinary Magnetoresistance of Individual Single-Crystalline Bi Nanowires.** *J. Ham*[1], D. Kim[2], W. Shim[1], J. Kim[1], K. Lee[1], W. Jeung[2] and W. Lee[1] *1. Department of Materials Science and Engineering, Yonsei University, Seoul, South Korea; 2. Division of Material Research, KIST, Seoul, South Korea*

AT-11. **The effects of spin relaxation on spin transfer switching of a non-collinear giant magnetoresistance device.** *N. Chung*[1,2], M.B. Abdul Jalil[1], S. Tan[2], J. Guo[1] and B. AL Sundaram[2] *1. Information Storage Materials Laboratory, Electrical and Computer Engineering Department, National University of Singapore, Singapore, Singapore; 2. Spintronics, Media and Interfaces Division, Data Storage Institute, Singapore, Singapore*

AT-12. **Patterning of magnetic structures on austenitic stainless steel by ion beam nitriding.** *E. Menéndez*[1], A. Martinavicius[2], M.O. Liedke[2], G. Abrasonis[2], J. Fassbender[2], J. Sort[3], S. Suriñach[1], M.D. Baró[1] and J. Nogués[4] *1. Physics, Universitat Autònoma de Barcelona, Bellaterra, Spain; 2. Institute of Ion Beam Physics and Materials Research, Forschungszentrum Dresden-Rossendorf, Dresden, Germany; 3. Physics, Institució Catalana de Recerca i Estudis Avançats (ICREA) and Universitat Autònoma de Barcelona, Bellaterra, Spain; 4. Institució Catalana de Recerca i Estudis Avançats (ICREA) and Institut Català de Nanotecnologia, Bellaterra, Spain*

AT-13. **Synthesis and characterization of particulate magneto polymer composite at microwave frequencies.** *S. Borah*[1] and N.S. Bhattachyaryya[1] *1. Physics, Tezpur University, Tezpur, Assam, India*

AT-14. **Nanocrystals formation in $Ce_{100-x}Al_x$ (x=45, 50) ribbons by rapid solidification from the liquid state.** *B. Idzikowski*[1], Z. Sniadecki[1] and D. Kaczorowski[2] *1. Institute of Molecular Physics, Polish Academy of Sciences, Poznan, Poland; 2. Institute of Low Temperature and Structure Research, Polish Academy of Sciences, Wroclaw, Poland*

AT-15. **Noise enhanced stability of magnetic systems.** *M. Trapanese*[1] *1. Dipartimento di Ingegneria Elettrica, Elettronica e delle Telecomunicazioni, University of Palermo, Palermo, Italy*

MONDAY
MORNING
9:00

POLIVALENTE

Session AU
PERMANENT MAGNET MATERIALS — APPLICATIONS I (POSTER SESSION)
Roland Groessinger, Chair

AU-01. **Implementing mixture design to predict magnetic properties of hybrid bonded magnets.** *J. Hsu*[1], P. Sharma[1] and A. Verma[2] *1. Physics, National Taiwan University, Taipei, Taiwan; 2. Moserbaer India Ltd, Greater Noida, India*

AU-02. Establishment of multipole magnetizing method and apparatus using a heating system for Nd-Fe-B isotropic bonded magnets. *H. Komura*[1], M. Kitaoka[1], T. Kiyomiya[1] and Y. Matsuo[1] *1. R & D, FDK Corporation, Kosai, Japan*

AU-03. Investigation of eddy current loss in divided Nd-Fe-B sintered magnets for synchronous motors due to insulation resistance and frequency. *K. Yamazaki*[1], M. Shina[1], M. Miwa[2] and J. Hagiwara[2] *1. Dept. of Electrical, Electronics and Computer Engineering, Chiba Institute of Technology, Narashino, Chiba, Japan; 2. TDK Corporation, Ichikawa, Chiba, Japan*

AU-04. Outer Rotor Consequent-pole Bearingless Motor Improved Start-up Characterinstics. T. Yamada[1], *Y. Nakano*[1], J. Asama[1], A. Chiba[1], T. Fukao[1], T. Hoshino[2] and A. Nakajima[2] *1. Electrical Engineering, Tokyo University of Science, Chiba, Japan; 2. Japan Aerospace Exploration Agency(JAXA), Tokyo, Japan*

AU-05. Study of the Static Force by the Difference in the Winding Structure of Permanent Magnet Type Linear Synchronous Motor. *K. Suzuki*[1], Y. Kim[2] and H. Dohmeki[1] *1. Department of Electrical and Electronic Engineering, Musashi Institute of Technology, Tokyo, Japan; 2. Department of Electrical Engineering, Colleage of Engineering Chosun University, Gwangju, South Korea*

AU-06. Proposal of the Air-core Type Linear Synchronous Motor Using the Air Levitation System. *K. Suzuki*[1], Y. Kim[2] and H. Dohmeki[1] *1. Department of Electrical and Electronic Engineering, Musashi Institute of Technology, Tokyo, Japan; 2. Department of Electrical Engineering, College of Engineering Chosun University, Gwanju, South Korea*

AU-07. Thrust Optimization of Linear Oscillatory Actuator Using Permeance Analysis Method. *M. Norhisam*[1], F. Azhar[1], H. Hashim[1], M. Nirei[2], H. Wakiwaka[3] and A. Razak J.[4] *1. Electrical & Electronic Engineering Department, Universiti Putra Malaysia, Serdang, Selangor, Malaysia; 2. Faculty of Engineering, Nagano National College of Technology, Tokuma, Nagano, Japan; 3. Faculty of Engineering, Shinshu University, Wakasato Nagano, Japan; 4. Research and Development, Malaysian Palm Oil Board, Kajang, Malaysia*

AU-08. Optimal design of barrier shape improve torque of interior permanent magnet synchronous motor. *C. Jin*[1] and J. Lee[1] *1. Hanyang University, Seoul, South Korea*

AU-09. Feasibility Study of a Passive Magnetic Bearing Using the Ring Sahped Permanent Magnets. *T. Azukizawa*[1], S. Yamamoto[1] and N. Matsuo[1] *1. Kobe University, Kobe, Japan*

AU-10. Design Considerations of Axial Ring magnet. *C. Li*[1], M. Devine[1] and G. Hatch[1] *1. Dexter Magnetic Technologies, Hicksville, NY*

MONDAY
MORNING
9:00

POLIVALENTE

Session AV
INTERMETALLICS AND OTHER HARD MAGNETS (POSTER SESSION)
Reiko Sato, Chair

AV-01. Effect of microstructure refinment on magnetic properties of Fe-Pt thin films. *F.T. Yuan*[1], H.W. Huang[2], W.M. Liao[4], H.W. Chang[1], D.H. Wei[1], S.K. Chen[2], Y.D. Yao[3] and H.Y. Lee[4] *1. Institute of Physics, Academia Sinica, Taipei, Taiwan; 2. Materials Science and Engineering, Feng Chia University, Taichung, Taiwan; 3. Material Engineering, Tatung University, Taipei, Taiwan; 4. National Synchrotron Radiation Research Center, Hsinchu, Taiwan*

AV-02. Magnetization reversal mechanism and intrinsic properties of FePt (110) epitaxial thin films. S. Fong[1,2], K. Cheng[1,2], D. Wei[1,4], C. Yu[3], C. Lin[2], F. Yuan[1], H. Chang[1], Y. Liou[1], T. Chin[2] and *Y. Yao*[4] *1. Institute of Physics, Academia Sinica, Taipei, Taiwan; 2. Department of Materials Science and Engineering, National Tsing Hua University, HsinChu, Taiwan; 3. Department of Applied Physics, National University of Kaohsiung, Kaohsiung, Taiwan; 4. Department of Materials Engineering, Tatung University, Taipei, Taiwan*

AV-03. Effect of Au underlayer on magnetic properties and ordering of CoPt thin films. *F.T. Yuan*[1], H.W. Huang[2], A.C. Sun[3], D.H. Wei[1], H.W. Chang[1], S.K. Chen[2] and Y.D. Yao[4] *1. Academia Sinica, Physics, Taipei, Taiwan; 2. Materials Science and Engineering, Feng Chia University, Taichung, Taiwan; 3. Physics, National Taiwan University, Taipei, Taiwan; 4. Materials Engineering, TaTung University, Taipei, Taiwan*

AV-04. Strain effect on the spin reorientation of epitaxial Nd-Fe-B films. *A. Kwon*[1], V. Neu[1], V. Matias[2], J. Hänisch[2], R. Hühne[1], B. Holzapfel[1], L. Schultz[1] and S. Fähler[1] *1. Institute for Metallic Materials, IFW Dresden, Dresden, P.O. Box 270116, D-01171, Germany; 2. Los Alamos national laboratory, NM 87545, NM*

AV-05. Magnetic properties and structure of Nd-Fe-B thin films with Ta buffer layer prepared on MgO(100) substrate. *H. Ishioka*[1], T. Sato[2], H. Kato[1], H. Fujino[1] and T. Shima[1] *1. Faculty of Engineering, Tohoku Gakuin University, Tagajo, Japan; 2. Toyota Central R&D Lab, Nagakute, Japan*

AV-06. In field magnetic domain observation of Nd-Fe-B thin film by magnetic force microscopy. *T. Iwasa*[1], H. Ishioka[1], H. Kato[1], T. Sato[2] and T. Shima[1] *1. Faculty of Engineering, Tohoku Gakuin University, Tagajo, Japan; 2. Toyota Central R&D Labs., Nagakute, Japan*

AV-07. Improvement in magnetic properties of PLD-made Nd-Fe-B thick film magnets. *M. Nakano*[1], H. Takeda[1], F. Yamashita[2], T. Yanai[1] and H. Fukunaga[1] *1. Electronics and Electrical Engineering, Nagasaki University, Nagasaki, Japan; 2. Matsushita Electric Industrial Co., Ltd., Osaka, Japan*

AV-08. Electrodeposited Co-Pt-(P) thick films prepared by low temaperature process. T. Tomimatsu[1], *M. Nakano*[1], T. Yanai[1], N. Fujita[2] and H. Fukunaga[1] *1. Electronics and Electrical Engineering, Nagasaki University, Nagasaki, Japan; 2. Nara National College of Technology, Yamatokouriyama, Japan*

AV-09. Some magnetic properties of YTiFe11-xSixC carbides. *B.C. Cizmas*[1], L. Bessais[2] and C. Djega-Mariadassou[2] *1. Department of Physics, Transilvania University of Brasov, Brasov, Romania; 2. ICMPE, UMR7182 CNRS, Université de Paris XII, Thiais, France*

AV-10. A magnetic and Mössbauer spectral study of the $Lu(Fe_{1-x}Al_x)_2$ compounds. *C.L. Piquer*[1], M. Laguna-Marco[1,2], J. Chaboy[1], R. Boada[1] and F. Plazaola[3] *1. Instituto de Ciencia de Materiales de Aragón, 50009 Zaragoza, Zaragoza, Spain; 2. Advanced Photon Source, Argonne National Laboratory, 9700 S, Cass Avenue, Argonne 60439, IL; 3. Departamento de Electricidad y Electrónica, Universidad del País Vasco (UPV/EHU), Apartado 644, 48080 Bilbao, Vizcaya, Spain*

AV-11. Magnetic properties of YCo_XNi_{3-X} compounds. *E. Burzo*[1], R. Tetean[1] and I.G. Deac[1] *1. Faculty of Physics, Babes-Bolyai University, Cluj Napoca, Romania*

AV-12. Magnetostriction in Sm_2Fe_{17} before and after nitrogenation. *H. Chen*[1], J. Xu[1], Y. Zhang[1], H. Du[1], C. Wang[1] and Y. Yang[1] *1. Physics School, Peking University, Beijing, China*

AV-13. Magnetic properties of Zr-doped Lu_2Fe_{17} single crystal and its hydride. *E. Tereshina*[1,2], A. Andreev[1] and H. Drulis[3] *1. Institute of Physics of the Academy of Sciences of the Czech Republic, Prague, Czech Republic; 2. Department of Condensed Matter Physics, Faculty of Mathematics and Physics, Charles University, Prague, Czech Republic; 3. Institute of Low Temperature and Structure Research, Wroclaw, Poland*

AV-14. Crystalline and local structure of $SmCo_5$ based alloys. *V.P. Menushenkov*[1], A.P. Menushenkov[2], R.V. Chernikov[2], V.V. Sidorov[2] and T.A. Sviridova[1] *1. State Technological University "Moscow Institute of Steel and Alloys", Moscow, Russian Federation; 2. Moscow Engineering Physics Institute (State University), Moscow, Russian Federation*

AV-15. Impact of Aluminium on the magnetic properties of RT2 compounds (R = rare-earth, T = transition metal) through the modification of the electronic structure. *R. Boada*[1], J. Chaboy[1], M.A. Laguna-Marco[1,2], C. Piquer[1] and F. Jiménez-Villacorta[3] *1. Física de la Materia Condensada, Instituto de Ciencia de Materiales de Aragón, Zaragoza, Zaragoza, Spain; 2. Advanced Photon Source, Argonne National Laboratory, Chicago, IL; 3. SpLine / Spanish CRG (BM25), European Synchrotron Radiation Facility, Grenoble, France*

MONDAY AFTERNOON 2:30 — AUDITORIO A

Session BA
SYMPOSIUM ON THE IMPORTANCE OF GMR
Sarah Thompson, Chair

2:30

BA-01. A History of Magnetic Recording Areal Density Improvements — A Transducer Perspective. ***(Invited)*** *R. Fontana*[1] *1. IBM Almaden Research Center (retired), San Jose, CA*

3:00

BA-02. The Spin Valve GMR Sensor. ***(Invited)*** *B. Gurney*[1] *1. San Jose Research Center, Hitachi Global Storage Technologies, San Jose, CA*

3:30

BA-03. GMR spin valves, tunneling magnetoresistive devices, and beyond: transport, magnetism, and materials science. ***(Invited)*** *O. Heinonen*[1], E.W. Singleton[1], B.W. Karr[1], Z. Gao[1], H. Cho[1] and Y. Chen[1] *1. Seagate Technology, Bloomington, MN*

4:00

BA-04. GMR and TMR Sensors for non-storage applications. ***(Invited)*** *M. Ruehrig*[1], G. Rieger[1] and J. Wecker[1] *1. Corporate Technology MM1, Siemens AG, Erlangen, Germany*

4:30

BA-05. Spintronic devices for memory and logic applications. ***(Invited)*** *B. Dieny*[1], R. Sousa[1] and G. Prenat[1] *1. SPINTEC, CEA/CNRS/UJF/INPG, Grenoble, France*

MONDAY AFTERNOON 2:30 — MADRID

Session BB
HEAD-MEDIA INTERFACE AND TRIBOLOGY -I
Bo Liu, Chair

2:30

BB-01. A dynamic scratch test to study read/write head degradation due to head disk interactions. *A. Wallash*[1], H. Zhu[1] and D. Chen[2] *1. Advanced Technology, Hitachi GST, San Jose, CA; 2. Mechanical Engineering Department, UC Berkeley, Berkeley, CA*

2:45

BB-02. Effect of Segregant Surface Energy on PMR Media Roughness. *Q. Dai*[1], H. Do[1], K. Takano[1] and B. Marchon[1] *1. Hitachi GST, San Jose, CA*

3:00

BB-03. Stress Induced Permanent Magnetic Signal Degradation of PMR System. *S. Lee*[1], S. Hong[1], N. Kim[1], J. Ferber[1], X. Che[1] and B.D. Strom[2] *1. Samsung Information Systems America, San Jose, CA; 2. Apple Inc., Cupertino, CA*

3:15

BB-04. Scratch Induced Demagnetization of Perpendicular Magnetic Disk. *M. Furukawa*[1], J. Xu[1], Y. Shimizu[1] and Y. Kato[1] *1. Central Research Laboratory, Hitachi, Ltd., Fujisawa-shi, Kanagawa-ken, Japan*

3:30

BB-05. Lubricant dynamics on a slider: "the waterfall effect" *B. Marchon*[1], X. Guo[1], A. Moser[1], R. Kroeker[2] and F. Crimi[2] *1. San Jose Research Center, Hitachi GST, San Jose, CA; 2. Server Business Unit, Hitachi GST, San Jose, CA*

3:45

BB-06. Effect of Thermal Bonding on Frictional Properties of Monolayer Lubricant Films Coated on Magnetic Disk Surfaces. *H. Zhang*[1], Y. Mitsuya[2], A. Fuwa[1], Y. Fujikawa[1] and K. Fukuzawa[1] *1. Nagoya University, Nagoya, Japan; 2. Nagoya Industrial Science Research Institute, Nagoya, Japan*

4:00

BB-07. Experimental Comparisons of Spreading and Replenishment Flows of Molecularly Thin Lubricant Films Coated on Magnetic Disks. *Y. Mitsuya*[1], H. Zhang[2], J. Ohgi[2] and K. Fukuzawa[2] *1. Nagoya Industrial Science Research Institute, Nagoya, Japan; 2. Micro-Nano Systems Engineering, Nagoya University, Nagoya, Japan*

4:15

BB-08. Coverage Analysis of Molecularly Thin Lubricant Films using Molecular Dynamics Simulations and CAICISS Measurements. *Y. Ikai*[1], N. Nakamura[1], H. Chiba[1] and T. Imamura[1] *1. Fujitsu Laboratories Ltd., Atsugi 243-0197, Japan*

4:30

BB-09. Time Dependence of Head-Media Interference at Low Fly Heights. *J. He*[1], J. Hopkins[1], S. Duan[1] and K. Johnson[1] *1. HGST, San Jose, CA*

4:45

BB-10. Air bearing surface designs for less humidity sensitivity. *S. Zhang*[1], G. Tyndall[1] and M. Suk[1] *1. Advanced Technology, Samsung Infromation Systems America, San Jose, CA*

MONDAY AFTERNOON 2:30 — ROMA

Session BC
MEMS AND MINIATURE MAGNETIC SENSORS
Eckhard Quandt, Chair

2:30

BC-01. Electroplated Co-rich CoPt thick films and patterned arrays for magnetic MEMS. *N. Wang*[1,2] and D.P. Arnold[1] *1. Interdisciplinary Microsystems Group, Dept. of Electrical and Computer Engineering, University of Florida, Gainesville, FL; 2. Materials Science and Engineering, University of Florida, Gainesville, FL*

2:45

BC-02. Optical technique for measuring magnetic MEMS vibrations. *V. de Manuel*[1], R. del Real[2], M. Díaz-Michelena[3], I. Arruego[4], I. Lucas[5] and H. Guerrero[6] *1. Space Programs and Space Sciences, INTA, Torrejón de Ardoz, Madrid, Spain; 2. Space Programs and Space Sciences, INTA, Torrejón de Ardoz, Madrid, Spain; 3. Space Programs and Space Sciences, INTA, Torrejón de Ardoz, Madrid, Spain; 4. Space Programs and Space Sciences, INTA, Torrejón de Ardoz, Madrid, Spain; 5. Space Programs and Space Sciences, INTA, Torrejón de Ardoz, Madrid, Spain; 6. Space Programs and Space Sciences, INTA, Torrejón de Ardoz, Madrid, Spain*

3:00

BC-03. Design of Axial Flux Machine for Micro Flywheel Energy Storage System. J. Yi[1], K.W. Lee[2], S. Jeong[2], *M. Noh*[1] and S.S. Lee[2] *1. Mechatronics Engineering, Chungnam National University, Daejeon, South Korea; 2. Mechanical Engineering, KAIST, Deajeon, South Korea*

3:15

BC-04. Magnetic hysteresis loop micro sensor for wafer level testing of magnetic films. *E. Flick*[1], K. Feindt[2] and H.H. Gatzen[1] *1. Leibniz Universitaet Hannover, Institute for Microtechnology, Garbsen, Germany; 2. innomas GmbH, Ilmenau, Germany*

3:30

BC-05. Thin Film Magneto-Impedance Sensor Integrated with L-10 FePt Thin Film Bias Magnet. *K. Ohmori*[1], K. Tan[2], K. Itoi[1], K. Nagasu[1], Y. Uemichi[1], T. Aizawa[1] and R. Yamauchi[1] *1. Microdevice department,Electron Device laboratory, Fujikura Ltd., Sakura, Chiba, Japan; 2. Akita research institute of advanced technology(AIT), Akita, Japan*

3:45

BC-06. PWM Type Amorphous Wire CMOS IC Magneto-Impedance Sensor Having High Temperature Stability. *Y. Nakamura*[1], T. Uchiyama[1], C.M. Cai[2] and K. Mohri[3] *1. Nagoya University, Nagoya, Japan; 2. Aichi Steel Co., Tokai, Japan; 3. Aichi Micro Intelligent Co., Tokai, Japan*

4:00

BC-07. Microfabrication process and characteristics of thin-film noise suppressor integrated onto the re-wiring layer of a LSI chip. *M. Yamaguchi*[1], T. Fukushima[1], T. Akiba[2] and A. Nakamura[2] *1. Dept. of Electrical and Communication Engineering, Tohoku University, Sendai, Miyagi, Japan; 2. Division of Process & Device Analysis Engineering Development, Renesas Technology Corp., Kodaira, Tokyo, Japan*

4:15

BC-08. Investigation of Magneto Impedance Sensors in Micro Scale for an Application to Chip-cytometer. *D. Kim*[1,2], H. Kim[1], D. Chun[1], W. Lee[2] and W. Jeung[1] *1. Functional Materials Research Center, Korea Institute of Science and Technology, Seoul, South Korea; 2. Material Science & Engineering, Yonsei University, Seoul, South Korea*

4:30

BC-09. Development of Low Noise GMI Sensor and Its Applications. *H. Aoyama*[1], M. Yamamoto[1], Y. Honkura[1] and K. Sumi[2] *1. Electronic & magnetic product division, Aichi Steel Corporation, Tokai, Aichi, Japan; 2. Toyota Central Research Laboratory, Nagakute, Aichi, Japan*

4:45

BC-10. 3-Axis Compact Electric Compass Using Maneto-Impedance Sensor. *M. Yamamoto*[1] and Y. Honkura[1] *1. Aichi Steel Corporation, Aichi-ken, Japan*

MONDAY
AFTERNOON
2:30

PARIS

Session BD
MAGNETIC SENSORS II
Joachim Wecker, Chair

2:30

BD-01. Giant magnetoresistive sensors for DNA microarray. *L. Xu*[1], H. Yu[2], S. Han[1], S. Osterfeld[1], R.L. White[1], N. Pourmand[2] and S.X. Wang[1] *1. Materials Science and Engineering, Stanford University, Stanford, CA; 2. Stanford Genome Technology Center, Stanford University, Palo Alto, CA*

2:45

BD-02. Device for individualized detection of articles containing magnetic microwires based on ferromagnetic resonance. P. Marín[1,2], D. Cortina[3], J. Calvo[3] and *A. Hernando*[1,2] *1. Instituto de Magnetismo Aplicado, Universidad Complutense de Madrid, Las Rozas, Madrid, Spain; 2. Departamento de Física de Materiales, Universidad Complutense de Madrid, Madrid, Spain; 3. Micromag 2000, S.L., Las Rozas, Spain*

3:00

BD-03. Two-domain model for orthogonal fluxgate. *M. Butta*[1] and P. Ripka[1] *1. CVUT v Praze - FEL - MagLab, Praha, Czech Republic*

3:15

BD-04. Fabrication and characterization of magnetic tunnel junction field sensors with a Co_2MnSi thin film. *M. Masuda*[1], T. Uemura[1], K. Matsuda[1] and M. Yamamoto[1] *1. Division of Electronics for Informatics, Graduate School of Information Science and Technology, Hokkaido University, Sapporo, Japan*

3:30

BD-05. High sensitive thin film wattmeter using magnetic thin film. *H. Tsujimoto*[1], H. Toratani[1] and Y. Deguti[1] *1. Faculty of Engineering, Osaka City University, Osaka, Japan*

3:45

BD-06. Acoustic Interferometer Based on Magnetostrictive Delay Lines. C. Petridis[1], V. Vassiliou[1], M. Kollár[2] and *E. Hristoforou*[1] *1. Mining and Metallurgy Engineering, National Technical University of Athens, Athens, Greece; 2. Electrical Engineering and Information Technology, Slovak University of Technology in Bratislava, Bratislava, Slovakia*

4:00

BD-07. 2D magnetic sensor based on planar Hall effect and surface nano-structuration. J. Briones[1], *F. Montaigne*[1], M. Hehn[1], G. Lengaigne[1] and D. Lacour[1] *1. Laboratoire de Physique des Matériaux, Nancy-University, CNRS, Vandoeuvre lès Nancy, France*

4:15

BD-08. Advanced Techniques for Modelling and Detection of Cracks in Hot Wire Steel. R. Marklein[1] and *M. Rahman*[1] *1. Department of Electrical Engineering and Computer Science, University of Kassel, Kassel, Germany*

4:30

BD-09. Thermally modulated flux concentrator for minimizing 1/f noise in magnetic sensors. *W. Wang*[1] and Z. Jiang[1] *1. Electrical Engineering, University of Wisconsin - Milwaukee, Milwaukee, WI*

4:45

BD-10. Nanoscale InAs Hall Crosses Excited with Localized Magnetic and Electric Fields. *L. Folks*[1], A.S. Troup[2], T.D. Boone[1], J.A. Katine[1], G.J. Sullivan[3], M. Field[3], E. Marinero[1] and B.A. Gurney[1] *1. San Jose Research Center, Hitachi Global Storage Technologies, San Jose, CA; 2. Hitachi Cambridge Laboratory, Cambridge, United Kingdom; 3. Teledyne Scientific Company, Thousand Oaks, CA*

MONDAY AFTERNOON 2:30 — LONDRES

Session BE
MOLECULAR AND NOVEL MATERIALS-I
Fernando Palacio, Chair

2:30

BE-01. Field dependence of the magnetocaloric effect beyond the mean field approach: a universal curve for the magnetic entropy change. ***(Invited)*** *V. Franco*[1] and A. Conde[1] *1. Department of Condensed Matter Physics, Sevilla University, Sevilla, Spain*

3:00

BE-02. Isothermal and adiabatic measurements and modeling of sign switching magnetocaloric effect in NiMnSn. *L. Giudici*[1,2], C.P. Sasso[1], M. Kuepferling[1], M. Pasquale[1] and V. Basso[1] *1. Electromagnetism Department, INRIM, Torino, Italy; 2. Physics Department, Politecnico di Torino, Torino, Italy*

3:15

BE-03. Magnetocaloric properties of $La(Fe,Co,Si)_{13}$ bulk material prepared by powder metallurgy. *M. Katter*[1], V. Zellmann[1], G. Reppel[1] and K. Uestuener[1] *1. Vacuumschmelze GmbH & Co. KG, Hanau, Germany*

3:30

BE-04. Magnetocaloric Properties and Structure of the $Gd_5Ge_{1.8}Si_{1.8}Sn_{0.4}$ Compound. *V. Provenzano*[1], T. Zhang[1,2], A.J. Shapiro[1], Y.G. Chen[2] and R.D. Shull[1] *1. Magnetic Materials Group, NIST, Gaithersburg, MD; 2. School of Materials Science and Engineering, Sichuan University, Chengdu, China*

3:45

BE-05. Ferromagnetism in graphite induced by ion irradiation. *M.A. Ramos*[1], A. Climent-Font[2], A. Muñoz-Martin[2], M. Garcia-Hernandez[3], A. Asenjo[3] and P.D. Esquinazi[2,4] *1. Fisica de la Materia Condensada, Universidad Autonoma Madrid, Madrid, Spain; 2. Centro de Microanalisis de Madrid (CMAM), Universidad Autonoma Madrid, Madrid, Spain; 3. Instituto de Ciencia de Materiales de Madrid (ICMM), Consejo Superior de Investigaciones Cientificas (CSIC), Madrid, Spain; 4. Superconductivity and Magnetism Division, Institut für Experimentelle Physik II, Fakultät für Physik und Geowissenschaften, University of Leipzig, Leipzig, Germany*

4:00

BE-06. Magnetic properties of TiO_2/γ-Fe_2O_3 nanocomposites designed for photocatalytic applications. *V. Sechovsky*[1], V. Tyrpekl[2], J. Poltierova Vejpravova[1], S. Danis[1], B. Bittova[1] and D. Niznansky[2] *1. Department of Condensed Matter Physics, Charles University in Prague, Prague 2, Czech Republic; 2. DIC, Charles University Prague, Prague, Czech Republic*

4:15

BE-07. Elastic model for complex hysteresis in molecular magnets. *C. Enachescu*[1], L. Stoleriu[1], A. Stancu[1] and A. Hauser[2] *1. Department of Physics, Alexandru Ioan Cuza University, Iasi, Romania; 2. Department of Physical Chemistry, Universite de Geneve, Geneva, Switzerland*

4:30

BE-08. Various relaxation behaviors in one dimensional chain-like molecular magnet $[Fe^{II}(\Delta)Fe^{II}(\Lambda)(ox)_2(phen)_2]_n$ at low temperature. *J. Her*[1,3], C. Sun[1,3], C. Chou[1,3], C. Chan[1,3], C. Lin[1,3], H. Yang[1,3], L. Li[2,4], K. Lin[2,4] and S. Taran[1,3] *1. Department of Physics, National Sun Yat-sen University, Kaohsiung, Taiwan; 2. Department of Chemistry, National Chung-Hsing University, Taichung, Taiwan; 3. Center for Nanoscience and Nanotechnology, National Sun Yat-sen University, Kaohsiung, Taiwan; 4. Center of Nanoscience and Nanotechnology, National Chung-Hsing University, Taichung, Taiwan*

MONDAY AFTERNOON 2:30 — BERLIN

Session BF
MAGNETIC SEMICONDUCTORS -I
Jodseph Fontcuberta, Chair

2:30

BF-01. Study of the origin of the spin polarization in the Co-doped $(La,Sr)TiO_3$ diluted magnetic oxide. *O. Copie*[1], G. Herranz[1], M. Bibes[1], R. Mattana[1], F. Petroff[1], K. Bouzehouane[1], H. Jaffres[1], E. Jacquet[1], J. Maurice[1], V. Cros[1], M. Basletic[2], E. Tafra[2], A. Hamzic[2], A. Barthelemy[1] and P. Bencok[3] *1. Unité Mixte de Physique CNRS THALES, Palaiseau, France; 2. Department of Physics, Faculty of Science, University of Zagreb, Zagreb, Croatia; 3. European Synchrotron Radiation Facility, Grenoble, France*

2:45

BF-02. Ultrafast laser spectroscopy of GaMnAs. *E. Rozkotová*[1], P. Horodyská[1], P. N ěmec[1], D. Sprinzl[1], F. Trojánek[1], P. Mal ý[1], V. Novák[2], K. Olejník[2], M. Cukr[2] and T. Jungwirth[2] *1. Faculty of Mathematics and Physics, Charles University in Prague, Prague, Czech Republic; 2. Institute of Physics, AS CR, Prague, Czech Republic*

3:00

BF-03. Preparation and properties of cobalt doped ZnO nanowires. *I. Enculescu*[1], E. Matei[1], M. Sima[1], S. Granville[2], J. Ansermet[2] and R. Neumann[3] *1. National Institute for Materials Physics, Magurele, Ilfov, Romania; 2. Institut de Physique des Nanostructures, EPFL, Lausanne, Switzerland; 3. Materials Research, GSI, Darmstadt, Germany*

3:15

BF-04. Room temperature ferromagnetism of FeCo-codoped ZnO nanorods prepared by chemical vapor deposition. J. Chen[1], Y. Yan[2], J. Liu[1], M. Yu[1], A. West[1] and *W. Zhou*[1] *1. Advanced Materials Research Institute, University of New Orleans, New Orleans, LA; 2. National Renewable Energy Laboratory, Golden, CO*

3:30

BF-05. Magnetic interactions in (Zn,Co)O - effects of heat treatment and co-doping. *M. Wikberg*[1], P. Svedlindh[1], V. Coleman[2,3], R. Knut[2], O. Karis[2], D. Iusan[2], B. Sanyal[2] and G. Westin[3] *1. Engineering Sciences, Uppsala University, Uppsala, Sweden; 2. Physics, Uppsala University, Uppsala, Sweden; 3. Materials Chemistry, Uppsala University, Uppsala, Sweden*

3:45

BF-06. Growth of $Zn_{1-x}Mn_xO$ nanorod arrays in aqueouse solution. *Y. Fang*[1], J. Persson[1], M. Göthelid[1] and J. Åkerman[1] *1. Department of Microelectronics and Applied Physics, Royal Institute of Technology, Stockholm-Kista, Sweden*

4:00

BF-07. Investigation of ferromagnetism in N and Mn co-sputtered ZnO. *J. Persson*[1], S. Bonetti[1], M. Göthelid[1], O. Tjernberg[1], J. Åkerman[1], M. Wikberg[2] and O. Karis[2] *1. Material Physics, KTH, Kista, Sweden; 2. Departement of physics, Uppsala University, Uppsala, Sweden*

4:15

BF-08. Andreev and Optical Measurement of Spin polarisation in ZnO Based Dilute Magnetic Semiconductors. *J.R. Neal*[1], K. Yates[2], A.J. Behan[1], D.S. Score[1], H.J. Blythe[1], A.M. Fox[1], L.F. Cohen[2] and G.A. Gehring[1] *1. Physics and Astronomy, The University of Sheffield, Sheffield, United Kingdom; 2. Blackett Laboratory, Imperial College, London, United Kingdom*

4:30

BF-09. Magnetic behaviour of Fe implanted TiO_2 thin films. *R. Sanz*[1], M. Hernandez-Vélez[1,2], T. Kubart[3], D. Martin[3] and J. Jensen[3] *1. Department of optical, magnetic and transport properties, Instituto de Ciencia de Materiales, CSIC, Madrid, Spain; 2. Fisica Aplicada, Universidad Autónoma, Madrid, Spain; 3. Department of Engineering Sciences, Ångström Laboratory, Uppsala University, Uppsala, Sweden*

4:45

BF-10. (Ga,Mn)As ultrathin films with high Mn concentration. *J. Deng*[1,2], W. Wang[1], L. Chen[1], J. Lu[1], Y. Ji[1] and J. Zhao[1] *1. Institute of Semiconductors, Chinese Academy of Sciences, Beijing, China; 2. Department of Physics, University of Science and Technology of China, Hefei, China*

MONDAY AFTERNOON 2:30 — AMSTERDAM

Session BG
MICROWAVE MATERIALS AND DEVICES I
Nian-Xiang Sun, Chair

2:30

BG-01. Non-resonant parametric recovery of spin-wave signals. *S. Schäfer*[1], A.V. Chumak[1], A.A. Serga[1] and B. Hillebrands[1] *1. Fachbereich Physik and Forschungsschwerpunkt MINAS, Technische Universität Kaiserslautern, Kaiserslautern, Germany*

2:45

BG-02. Reflectivity of microwave signal in ferromagnetic wires. *A. Yamaguchi*[1,2], N. Higashio[1], K. Motoi[1], T. Kishimoto[1] and H. Miyajima[1] *1. Department of Physics, Keio University, Yokohama, Kanagawa, Japan; 2. PRESTO, Tokyo, Japan*

3:00

BG-03. Ferromagnetic resonance on FeSiB thin films displaying spin reorientation transition. *M. Coisson*[1], F. Celegato[1], P. Tiberto[1] and F. Vinai[1] *1. Electromagnetics, INRIM, Torino, TO, Italy*

3:15

BG-04. Correlation receiver of below-noise pulsed signals based on the parametric interactions of spin waves in magnetic films. G.A. Melkov[1], V.I. Vasyuchka[1], V.A. Moiseienko[1] and *A.N. Slavin*[2] *1. Faculty of Radiophysics, Kiev National Taras Shevchenko University, Kiev, Ukraine; 2. Department of Physics, Oakland University, Rochester, MI*

3:30

BG-05. Electronically Tunable Miniaturized Antennas on Magnetoelectric Substrates with Enhanced Performance. *N. Sun*[1], G. Yang[1], A. Daigle[1], J. Lou[1], M. Liu[1], O. Obi[1], S. Stoute[1], C. Pettiford[1], J. Wang[1] and K. Naishadham[2] *1. Electrical and Computer Eng., Northeastern University, Boston, MA; 2. RF communications Groups, Draper Laboratory, Cmabridge, MA*

3:45

BG-06. On the study of left handed coplanar waveguide zeroth order resonator on ferrite substrate. *M.A. Abdalla*[1] and Z. Hu[1] *1. School of Electrical and Electronic Engineering, University of Manchester, Manchester, United Kingdom*

4:00

BG-07. Observation of bright and dark spin wave envelope solitons in periodic magnetic film structures. A. Ustinov[1], N. Grigorieva[1] and *B. Kalinikos*[1] *1. Physical Electronics and Technology, St.Petersburg Electrotechnical University, St.Petersburg, Russian Federation*

4:15

BG-08. Measurement System of FMR Linewidth ΔH_ω of Ferrite using a Shorted Stripline. *S. Takeda*[1] and H. Suzuki[2] *1. Magnontech, Ltd., Kumagaya, Japan; 2. KEYCOM Corp., Tokyo, Japan*

4:30

BG-09. On the study of ferrite coupled coplanar waveguide. *M.A. Abdalla*[1] and Z. Hu[1] *1. School of Electrical and Electronic Engineering, University of Manchester, Manchester, United Kingdom*

MONDAY
AFTERNOON
2:30

CARACAS

Session BH
MULTILAYER FILMS AND SUPERLATTICES I
A. Cebollada, Chair

2:30

BH-01. (110)-textured La2/3Ca1/3MnO3 thin films. Optimal electrodes in manganite tunnel junctions. *I.C. Infante*[1], F. Sánchez[1], J. Fontcuberta[1], M. Wojcik[2], E. Jedryka[2], S. Estradé[3], F. Peiró[3], J. Arbiol[3,4], V. Laukhin[5] and J.P. Espinós[6] *1. Magnetic Materials and their Applications, Institut de Ciència de Materials de Barcelona, Bellaterra, Barcelona, Spain; 2. Institute of Physics, Polish Academy of Sciences, Warszawa, Warszawa, Poland; 3. Dept. d'Electrònica, EME/CeRMAE/IN2UB, Universitat de Barcelona, Barcelona, Barcelona, Spain; 4. TEM-MAT, Serveis Cientificotècnics, Universitat de Barcelona, Barcelona, Barcelona, Spain; 5. Institució Catalana de Recerca i Estudis Avançats (ICREA), Barcelona, Barcelona, Spain; 6. Instituto de Ciencia de Materiales de Sevilla ICMSE (CSIC-USE), Sevilla, Sevilla, Spain*

2:45

BH-02. Observation of large tunneling magnetoresistance in Fe-MgO-Fe epitaxial multilayers using STM double tunneling experiments. *J. Lee*[1,2], C. Krafft[2] and R.D. Gomez[1,2] *1. Electrical and Computer Engineering, University of Maryland, College Park, MD; 2. Laboratory for Physical Sciences, Collegs Park, MD*

3:00

BH-03. Multifunctional Ni/Au Multilayered Nanowires. *M. Cho*[1], J. Cho[2,3], J. Wu[4], J. Min[2], J. Lee[2], B. An[2] and Y. Kim[2] *1. Program in Micro/Nano System, Korea University, Seoul, South Korea; 2. Department of Materials Science and Engineering, Korea University, Seoul, South Korea; 3. Korea Electronic Technology Institute, Korea University, Gyeonggi, South Korea; 4. Institute for Nano Science, Korea University, Seoul, South Korea*

3:15

BH-04. Novel phenomena in multi-layer composite structure observed by anomalous Hall effect measurement. *S. Das*[1], T. Ichihara[1], H. Suzuki[1] and Y. Matsuda[2] *1. Central Research Laboratory, Hitachi Ltd., Odawara, Kanagawa, Japan; 2. Head Development, Hitachi Global Storage Technologies, Odawara, Kanagawa, Japan*

3:30

BH-05. Band and bubble domains in AF coupled [Co/Pt]/Ru multilayers. *C. Bran*[1,2], O. Hellwig[3], U. Wolff[1], L. Schultz[1] and V. Neu[1] *1. IFW Dresden, Dresden, Germany; 2. IMPRS "Dynamical Processes in Atoms, Molecules and Solids", Dresden, Germany; 3. Hitachi Global Storage Technologies, San Jose, CA*

3:45

BH-06. Exchange-spring behavior in Fe-FePt thin films studied via synchrotron radiation. *B. Laenens*[1], N. Planckaert[1], J. Demeter[1], K. Temst[1], A. Vantomme[1], C. Strohm[2], R. Rüffer[2] and J. Meersschaut[1] *1. Instituut voor Kern- en Stralingsfysica and INPAC, Katholieke Universiteit Leuven, Celestijnanlaan 200D, B-3001 Leuven, Belgium; 2. ESRF, Rue Jules Horowitz 6, Boîte Postale 220 38043 Grenoble, France*

4:00

BH-07. How to retrieve more information on magnetic films from microwave permeability measurements. *O. Acher*[1], V. Dubuget[1,2] and S. Dubourg[1] *1. Departement Matériaux, CEA, Monts, France; 2. UMR 6157 LEMA, Tours, France*

4:15

BH-08. The effect of FePt layer on the transition temperature of FeRh layer. *N.T. Nguyen*[1], Y.Y. Hnin[1] and T. Suzuki[1] *1. Information Storage Materials Laboratory, Toyota Technological Institute, Nagoya, Japan*

4:30

BH-09. Effects of perpendicular interlayer coupling on canting angles of TbCo sublattice magnetization by x-ray magnetic circular dichroism. *M. Lin*[1], P. Huang[1], Y. Wu[1], H. Hou[1], C. Lai[1], H. Lin[2] and F. Chang[2] *1. Department of Materials Science and Engineering, National Tsing Hua University, Hsinchu, Taiwan; 2. National Synchrotron Radiation Research Center, Hsinchu, Taiwan*

4:45

BH-10. Magnetization reversal in thermally processed Fe/SmCo spring magnets. *J.E. Davies*[1], Y. Choi[2], J.P. Liu[3], J.S. Jiang[2], S.D. Bader[2], R.D. Shull[1] and K. Liu[4] *1. Metallurgy/Magnetic Materials, NIST, Gaithersburg, MD; 2. Materials Science Division, Argonne National Laboratory, Argonne, IL; 3. Physics Department, University of Texas, Arlington, TX; 4. Physics Department, University of California, Davis, CA*

MONDAY
AFTERNOON
5:10

AUDITORIO A

Session YA
NOBEL PRIZE CELEBRATION
Manuel Vazquez, Chair

TUESDAY
MORNING
9:30

AUDITORIO A

Session CA
SYMPOSIUM ON BIOMEDICAL APPLICATIONS
Axel Hoffman, Chair

9:30

CA-01. Non-invasive Measurement of Tissue Iron Concentrations with Magnetic Resonance Imaging. ***(Invited)*** *T.G. St Pierre*[1] *1. School of Physics, University of Western Australia, Perth, WA, Australia*

10:00

CA-02. Exploring the frontiers of magnetic nanoparticles prepared in microemulsions: from ferrofluids to biomedical applications. ***(Invited)*** *J. Rivas*[1,2] and M. Lopez Quintela[2,1] *1. Laboratory of Magnetism and Nanotechnology(NANOMAG), University of Santiago de Compostela, Santiago de Compostela, A Coruña, Spain; 2. Laboratory of Magnetism and Nanotechnology(NANOMAG), University of Santiago de Compostela, Santiago de Compostela, A Coruña, Spain*

10:30

CA-03. Spintronic biochips for biomolecular recognition detection. ***(Invited)*** *P. Freitas*[1,2], V. Martins[1,3], F. Cardoso[1,2], S. Cardoso[1], V. Chu[1], J. Conde[1,3], J. Loureiro[1,2], J. Germano[5,4], L. Sousa[5,4] and M. Piedade[5,4] *1. INESC MN, Lisbon, Portugal; 2. Physics Department, Instituto Superior Tecnico, Lisbon, Portugal; 3. Chemical and Bioengineering Department, Instituto Superior Tecnico, Lisbon, Portugal; 4. Electrical Engineering Department, Instituto Superior Tecnico, Lisbon, Portugal; 5. INESC ID, LISBON, Portugal*

11:00

CA-04. In vivo sensing, moving and heating of magnetic nanoparticles in the human body. ***(Invited)*** *Q. Pankhurst*[1] *1. London Centre for Nanotechnology, London, United Kingdom*

11:30

CA-05. Room-temperature detection of single magnetic biomolecular labels with Hall devices*. ***(Invited)*** *G. Mihajlovic*[1], K. Aledealat[2], P. Xiong[2], S. von Molnár[2], M. Field[3], G.J. Sullivan[3], K. Ohtani[4] and H. Ohno[4] *1. Materials Science Division, Argonne National Laboratory, Argonne, IL; 2. Center for Materials Research and Technology (MARTECH) and Department of Physics, Florida State University, Tallahassee, FL; 3. Teledyne Scientific Company LLC, Thousand Oaks, CA; 4. Laboratory for Electronics Intelligent Systems, Research Institute of Electrical Communication, Tohoku University, Sendai, Japan*

TUESDAY
MORNING
9:30

MADRID

Session CB
SPIN TORQUE OSCILLATORS - I
Andrew Kent, Chair

9:30

CB-01. Spin transfer induced microwave emission and spin diode effects in MgO based magnetic tunnel junctions. B. Georges[1], V. Cros[1], *J. Grollier*[1], A. Fert[1], A. Fukushima[2], H. Kubota[2], K. Yakushiji[2], S. Yuasa[2] and K. Ando[2] *1. UMR CNRS-Thales, Palaiseau, France; 2. National Institute of Advanced Industrial Science and Technology (AIST), Tsukuba, Japan*

9:45

CB-02. Quantized spin wave modes in magnetic tunnel junctions. *A. Helmer*[1], T. Devolder[1], J. Hayakawa[2,3], K. Ito[2], H. Takahashi[2], S. Ikeda[3], P. Crozat[1], J.V. Kim[1], C. Chappert[1] and H. Ohno[3] *1. Institut d'Electronique Fondamentale, Université Paris-Sud, Orsay, France; 2. Advanced Research Laboratory, Hitachi, Ltd, Tokyo, Japan; 3. Laboratory for Nanoelectronics and Spintronics, Research Institute of Electrical Communication, Tohoku University, Sendai, Japan*

10:00

CB-03. Low field spin-transfer induced precession in a pinned SAF layer for high frequency devices. *A.M. Deac*[1,3], W.H. Rippard[1] and J.A. Katine[2] *1. NIST, Boulder, CO; 2. Hitachi San Jose Research Center, San Jose, CA; 3. Institut fuer Festkoerperforschung, Forschungszentrum Juelich GmbH, Juelich, Germany*

10:15

CB-04. Spin-polarized current induced excitations in a synthetic antiferromagnet. *D. Gusakova*[1,2], D. Houssameddine[1], U. Ebels[1], M. Cyril[2], B. Dieny[1] and L. Buda-Prejbeanu[1] *1. SPINTEC URA 2512, Grenoble, France; 2. 2LIMN/DIHS/LETI CEA-Grenoble, Grenoble, France*

10:30

CB-05. Tuning the Coherence of Spin-Torque-Driven Dynamics in Nanomagnetic Oscillators. *(Invited)* *K. Thadani*[1], G. Finocchio[3], Z.P. Li[2], O. Ozatay[2], J.C. Sankey[1], I.N. Krivorotov[4], Y.T. Cui[2], R.A. Buhrman[2] and D.C. Ralph[1] *1. Physics, Cornell University, Ithaca, NY; 2. Applied & Engineering Physics, Cornell University, Ithaca, NY; 3. University of Messina, Messina, Italy; 4. University of California-Irvine, Irvine, CA*

11:00

CB-06. Phase locking of a Spin Transfer Oscillator to an external microwave current : a milestone for the synchronization of a large assembly of STOs. *B. GEORGES*[1], J. Grollier[1], M. Darques[1], V. Cros[1], C. Deranlot[1], G. Faini[2] and A. Fert[1] *1. Unité Mixte de Physique CNRS/Thales (CNRS-UMR137), Palaiseau, France; 2. Phynano team, Laboratoire de Photonique et Nanostructures, LPN - CNRS, Marcousis, France*

11:15

CB-07. Magnetic point-contact precession frequency vs. magnetic field angle – The prospect for spin torque oscillator operation at 65 GHz. S. Bonetti[1], J. Persson[1], F.B. Mancoff[2] and *J. Åkerman*[1] *1. Microelectronics and Applied Physics, Royal Institute of Technology (KTH), Kista-Stockholm, Sweden; 2. Technology Solutions Organization, Freescale Semiconductor Inc., Chandler, AZ*

11:30

CB-08. Asymmetric lineshapes in spin-torque nano-oscillators near threshold. *J. Kim*[1], Q. Mistral[1], C. Chappert[1], V.S. Tiberkevich[2] and A.N. Slavin[2] *1. Institut d'Electronique Fondamentale, CNRS / Univ. Paris Sud, Orsay, France; 2. Department of Physics, Oakland University, Rochester, MI*

11:45

CB-09. Experimental and theoretical study of spin-torque microwave excitation linewidths in nanocontacts subject to out-of-plane external fields. *M. Pasquale*[1], C. Serpico[2], P. Anzalone[3], G. Bertotti[1], M. Pufall[4] and W. Rippard[4] *1. Divisione Elettromagnetismo, INRIM, Torino, Italy; 2. Dipartimento di Ingegneria Elettrica, Università di Napoli "Federico II", Napoli, Italy; 3. Dipartrimento di Ingegneria Elettrica Industriale, Politecnico di Torino, Torino, Italy; 4. Electromagnetics Division, NIST, Boulder, CO*

12:00

CB-10. The frequency of microwave oscillation on domain wall magnetoresistance elements. *H. Endo*[1], K. Shirafuji[1], H. Suzuki[1], M. Doi[1], M. Takagishi[2], H.N. Fuke[2], H. Iwasaki[2] and M. Sahashi[1] *1. Department of Electronic Engineering, Tohoku University, Sendai, Japan; 2. Corporate Research & Development Center, Toshiba Corporation, Kawasaki, Japan*

12:15

CB-11. Spin wave Doppler shift. *V. Vlaminck*[1] and M. Bailleul[1] *1. GEMME, IPCMS, Strasbourg, France*

TUESDAY
MORNING
9:30

ROMA

Session CC
MgO MAGNETIC TUNNEL JUNCTIONS I
Bernard Dieny, Chair

9:30

CC-01. Equilibrium and out-of-equilibrium spintronic phenomena in single crystal MgO based magnetic tunnel junctions. *(Invited)* *C. Tiusan*[1], F. Greullet[1], F. Bonell[1], M. Hehn[1], S. Andrieu[1], C. Bellouard[1], F. Montaigne[1], D. Halley[2], M. Bowen[2], W. Weber[2], E. Snoeck[3], F. Aliev[4], E. Popova[5] and A. Schuhl[6,1] *1. Nancy Université- CNRS, Laboratoire de Physique des Materiaux - UMR7556, Vandoeuvre les Nancy, Lorraine, France; 2. Institut de Physique et Chimie des Matériaux, Strasbourg, Alsace, France; 3. CEMES, Toulouse, France; 4. University of Madrid, Madrid, Spain; 5. Université de Versailles, Laboratoire de Magnétisme et d'Optique de Versailles, Versailles, France; 6. SPINTEC, Grenoble, France*

10:00

CC-02. Nature of Voltage Dependence of Spin Transfer Torque in Magnetic Tunnel Junctions. *(Invited)* *M. Chshiev*[1], I. Theodonis[2,3], N. Kioussis[2], A. Kalitsov[2] and W. Butler[1] *1. Center for Materials for Information Technology, University of Alabama, Tuscaloosa, AL; 2. Department of Physics and Astronomy, California State University, Northridge, CA; 3. Department of Physics, National Technical University, Zografou, Athens, Greece*

10:30

CC-03. Magnetic tunnelling junctions based on MgO(001) epitaxial barriers: from the interfacial spin dependent electronic structure to the ultimate TMR. *A. Cattoni*[1], D. Petti[1], M. Cantoni[1], S. Brivio[1] and R. Bertacco[1] *1. Center LNESS - Department of Physics, Politecnico di Milano, Como, Italy*

10:45

CC-04. Magnetic Tunnel Junctions with MgO Tunnel Barriers and NiFeSiB/CoFeB Hybrid Free Layers. *J. Cho*[1], D. Kim[1], T. Wang[1], S. Isogami[2], M. Tsunoda[2], M. Takahashi[2] and Y. Kim[1] *1. Department of Materials Science and Engineering, Korea University, Seoul, South Korea; 2. Department of Electronic Engineering, Tohoku University, Sendai, Japan*

11:00

CC-05. The Surface Electronic Structure: a Key Parameter in Low Resistance Area Single Crystal Magnetic Tunnel Junctions. *P. Zermatten*[1], M. Miron[1], G. Gaudin[1], A. Schuhl[1], F. Greullet[2], M. Hehn[2] and C. Tiusan[2] *1. SPINTEC, CEA/CNRS, Grenoble, France; 2. LPM, CNRS/UHP, Nancy, France*

11:15

CC-06. Transport characterization of the single and double magnetic tunnel junctions using point contact spectroscopy. *A. Iovan*[1], S. Cherepov[1], A. von Bieren[1], S. Andersson[1] and V. Korenivski[1] *1. Nanostructure Physics, KTH, Stockholm, Sweden*

11:30

CC-07. Magnetotransport properties of MgO-based epitaxial magnetic tunnel junctions with a nonmagnetic electrode. *R. Matsumoto*[1,2], A. Fukushima[1], T. Nagahama[1], Y. Suzuki[1,2], K. Ando[1] and S. Yuasa[1] *1. Nanoelectronics Research Institute, National Institute of Advanced Industrial Science and Technology (AIST), Tsukuba, Japan; 2. Graduate School of Engineering Science, Osaka University, Toyonaka, Japan*

11:45

CC-08. High bias tunneling magnetoresistance and low frequency noise in fully epitaxial Fe/C/MgO/Fe(001) magnetic tunnel junctions. D. Herranz[1], R. Guerrero[1], R. Villar[1], *F.G. Aliev*[1], F. Greullet[2], C. Tiusan[2] and M. Hehn[2] *1. Fisica Materia Condensada, CIII, Universidad Autonoma de Madrid, Madrid, Madrid, Spain; 2. Laboratoire de Physique des Matériaux, Nancy Université, Nancy, France*

12:00

CC-09. 1/f magnetic noise dependence on free layer thickness in linear MgO magnetic tunnel junctions. *P. Wisniowski*[1], J.M. Almeida[1] and P.P. Freitas[1] *1. INESC-MN, Lisbon, Portugal*

12:15

CC-10. Hybrid Magnetic Tunnel Junction-MEMS device for 1/f noise supression. *A.A. Guedes*[1,2], S.B. Patil[1], P. Wisniowski[1], V. Chu[1], J.P. Conde[1,2] and P.P. Freitas[1,2] *1. INESC-MN, Lisbon, Portugal; 2. Instituto Superior Tecnico, Lisbon, Portugal*

TUESDAY
MORNING
9:30

PARIS

Session CD
MAGNETIC MICROSCOPY I
Amanda Petford-Long, Chair

9:30

CD-01. Field driven ferromagnetic phase evolution originating from the domain boundaries in antiferromagnetically coupled perpendicular anisotropy films. *T. Hauet*[1], C.M. Günther[2], O. Hovorka[3], A. Berger[3], M. Im[4], P. Fischer[4] and O. Hellwig[1] *1. Hitachi Gst, San Jose, CA; 2. BESSY mbH, Berlin, Germany; 3. CIC NanoGUNE Consolider, Donostia, Spain; 4. Center for X-Ray Optics, Lawrence Berkeley National Laboratory, Berkeley, CA*

9:45

CD-02. Magnetization indicator film for Lorentz transmission electron microscopy measurements of perpendicularly magnetized nanostructures. *J.W. Lau*[1] *1. Metallurgy Division, National Institute of Standards and Technology, Gaithersburg, MD*

10:00

CD-03. Effect of in-situ FIB trimming on the spin configurations of hexagonal shaped ferromagnetic elements. *S.Y. Lua*[1,3], S.S. Kushvaha[2], Y. Wu[2], K. Teo[2] and T. Chong[3] *1. NUS Graduate School for Integrative Sciences and Engineering, National University of Singapore, Singapore, Singapore; 2. Department of Electrical and Computer Engineering, National University of Singapore, Singapore, Singapore; 3. Data Storage Institute, Singapore, Singapore*

10:15

CD-04. Ballistic electron magnetic microscopy on Co/Cu/NiFe spin valves. *A. Kaidatzis*[1], S. Rohart[1], A. Thiaville[1] and J. Miltat[1] *1. Laboratoire de Physique des Solides, Orsay, France*

10:30

CD-05. Mapping Atomic-Scale Spin Structures on Insulators by Magnetic Exchange Force Microscopy. *(Invited)* *R.M. Wiesendanger*[1] *1. Institute of Applied Physics, University of Hamburg, Hamburg, Germany*

11:00

CD-06. 120° antiferromagnetic Néel structure of Mn monolayer on Ag(111). *C. Gao*[1], W. Wulfhekel[1,2] and J. Kirschner[1] *1. Max Planck Institute of MicrostrcutrurePhysics, Halle (Saale), Germany; 2. Physikalisches Institut, Universität Karlsruhe (TH), Karlsruhe, Germany*

11:15

CD-07. The role of the spin-orientation of the tip in spin-polarized scanning tunneling microscopy in external magnetic fields. *D. Sander*[1], G. Rodary[1], S. Wedekind[1] and J. Kirschner[1] *1. Max Planck Institute, Halle, Germany*

11:30

CD-08. Theoretical description of the high-frequency magnetic force microscopy (HF-MFM) technique. *M.R. Koblischka*[1] and U. Hartmann[1] *1. Institute of Experimental Physics, University of the Saarland, Saarbruecken, Germany*

11:45

CD-09. Imaging a single domain wall position by Extraordinary Hall Effect in nanostructured thin films with perpendicular anisotropy. *M. Miron*[1], P. Zermatten[1], G. Gaudin[1] and S. Alain[1] *1. SPINTEC (CNRS/CEA), Grenoble, France*

12:00

CD-10. Hall imaging of the history dependence of the magneto-caloric effect in Gd5Si2.09Ge1.91. *M. Kuepferling*[1], J. Moore[2], V. Basso[1], C.P. Sasso[1], L. Giudici[1] and L. Cohen[2] *1. Department for Electromagnetism, National Institute of Metrological Research, Torino, Italy; 2. The Blackett Laboratory, Imperial College of Science, London, United Kingdom*

12:15

CD-11. Imaging perpendicularly recorded data with servo feedback control. C. Tseng[1], P. McAvoy[1], *I.D. Mayergoyz*[1] and C. Krafft[2] *1. Department of Electrical and Computer Engineering, University of Maryland, College Park, MD; 2. Laboratory for Physical Sciences, College Park, MD*

TUESDAY MORNING 9:30 — **LONDRES**

Session CE
EXCHANGE BIAS I
Josep Nogues, Chair

9:30

CE-01. Reversible exchange bias in ideal antiferromagnetic alloys. *D. Lederman*[1] and M. Cheon[1] *1. Department of Physics, West Virginia University, Morgantown, WV*

9:45

CE-02. Role of anisotropies on the asymmetric magnetization reversal behavior in exchange-biased systems. E. Jiménez[1], *J. Camarero*[1], J. Sort[2], J. Nogués[3], N. Mikuszeit[1,4], J. García-Martín[5], A. Hoffmann[6], B. Dieny[7] and R. Miranda[1,8] *1. Departamento de Física de la Materia Condensada and Instituto de Materiales "Nicolás Cabrera", Universidad Autonoma de Madrid, Madrid, Spain; 2. Departament de Física, Institució Catalana de Recerca i Estudis Avançats (ICREA) and Universitat Autònoma de Barcelona, Bellaterra, Spain; 3. Institució Catalana de Recerca i Estudis Avançats (ICREA) and Institut Català de Nanotecnologia, Bellaterra, Spain; 4. Institut für Angewandte Physik, Universität Hamburg, Hamburg, Germany; 5. Instituto de Microelectrónica de Madrid CNM-CSIC, Tres Cantos, Spain; 6. Materials Science Division and Center for Nanoscale Materials, Argonne National Laboratory, Argonne, IL; 7. SPINTEC, URA2512, CNRS/CEA, Grenoble, France; 8. Instituto Madrileño de Estudios Avanzados en Nanociencia IMDEA-Nanociencia, Madrid, Spain*

10:00

CE-03. Asymmetric magnetization reversal behavior in exchange-biased multilayers in different antiferromagnetic thickness ranges. *D. Spenato*[1], V. Castel[1], S.P. Pogossian[1], C. Le Graët[1], D.T. Dekadjevi[1] and J. Ben Youssef[1] *1. Laboratoire de Magnétisme de Bretagne, CNRS/FRE 2997, Université de Bretagne Occidentale, Brest, France*

10:15

CE-04. Tailoring of dynamic magnetic properties of ferromagnetic thin films by ultra-thin IrMn layers. *J. McCord*[1], R. Kaltofen[2] and L. Schultz[1] *1. Institute for Metallic Materials, IFW Dresden, Dresden, Germany; 2. Institute for Integrative Nanosciences, IFW Dresden, Dresden, Germany*

10:30

CE-05. Local magnetization studies by Magnetic Force and Kerr microscopy of exchange bias in Co/CoO patterned dots. *U. Wolff*[1], S. Suck[2], D. Givord[2], J. Mc Cord[1], L. Schultz[1] and V. Neu[1] *1. IFW Dresden, Dresden, Germany; 2. Institut Neel, Grenoble, France*

10:45

CE-06. Control of crystallographic orientation in IrMn/CoFe exchange bias systems. *N. Aley*[1], G. Vallejo-Fernandez[1], K. O'Grady[1], B. Lafferty[2], J. Agnew[2] and Y. Lu[2] *1. Physics, University of York, York, United Kingdom; 2. Seagate Technology Ltd., Derry, United Kingdom*

11:00

CE-07. Magnetoresistance in positive and negative exchange bias Ni/FeF_2 bilayered 200 nm antidots. *M. Kovylina*[1,2], R. Morales[3,4], J. Villegas[4], M. Erekhinsky[4], I.V. Roshchin[4], A. Labarta[1,2], I.K. Schuller[4] and X. Batlle[1,2] *1. Fisica Fundamental, Universidad de Barcelona, Barcelona, Barcelona, Spain; 2. Institut de Nanociència i Nanotecnologia (IN2UB), Barcelona, Barcelona, Spain; 3. Departamento de Física, Universidad de Oviedo, Oviedo, Oviedo, Spain; 4. Physics Department, University of California-San Diego, San Diego, CA*

11:15

CE-08. Exchange coupled IrMn/CoFe networks on mesoporous alumina. *N.N. Shams*[1], M. Rahman[1] and C. Lai[1] *1. Materials Science and Engineering, National Tsing-Hua University, Hsinchu, Taiwan*

11:30

CE-09. Effects of nonmagnetic additives in metallic antiferromagnets on exchange bias. *M. Fecioru-Morariu*[1], S. Ali[1], C. Papusoi[2], M. Sperlich[1] and G. Güntherodt[1] *1. Physikalisches Institut (IIA), RWTH Aachen University, Aachen, Germany; 2. SPINTEC, CEA/CNRS, Grenoble, France*

11:45

CE-10. Negative and positive exchange bias in polycrystalline Ni/FeF_2 thin films. *R. Morales*[1,2], J. Alameda[1] and I. Schuller[2] *1. Dpto. de Fisica, Universidad de Oviedo, Oviedo, Spain; 2. Physics Department, University of California San Diego, La Jolla, CA*

12:00

CE-11. Large exchange bias IrMn/CoFe for magnetic tunnel junctions. *L.E. Fernandez-Outon*[1], K. O'Grady[1], M. Zhou[2] and M. Pakala[2] *1. Physics, The University of York, York, United Kingdom; 2. Western Digital Fremont Inc., Fremont, CA*

12:15

CE-12. Observation of Metastable Remanence States in Pinned Antiferromagnetically Coupled Ferromagnetic Layers. *K. Srinivasan*[1], S. Wong[1], S.N. Piramanayagam[1] and R. Sbiaa[1] *1. Spintronics, Media and Interface Division, Data Storage Institute, A*STAR, Singapore, Singapore*

TUESDAY MORNING 9:30 — BERLIN

Session CF
ELECTRICAL STEELS AND INDUCTOR CORES
Anthony Moses, Chair

9:30

CF-01. Effect of hot and cold rolling on grain size and texture in FeSi strips with a Si-content larger than 2 wt%. P.R. Calvillo[1], H. Hermann[2], J. Verstraete[1], *J. Schneider*[1,2] and Y. Houbaert[1] *1. Metallurgy and Materials Science, Universiteit Gent, Gent-Zwijnaarde, Belgium; 2. Institut für Metallformung, Technische Universität Bergakademie Freiberg, Freiberg, Germany*

9:45

CF-02. Magnetization processes of Fe(Si,Al)-steels with homogeneous and inhomogeneous distribution of (Si,Al). J. Schneider[1], J. Verstraete[1], K. Verbeken[1] and *Y. Houbaert*[1] *1. Metallurgy and Materials Science, Universiteit Gent, Gent-Zwijnaarde, Belgium*

10:00

CF-03. Effects of Si content on the magnetic properties of Fe-Si alloy powder cores. *P. Jang*[1], B. Lee[1] and I. Jeong[2] *1. Div. of Applied Science, Cheongju University, Cheongju, Chungcheongbuk-do, South Korea; 2. R&D Center, Changsung Corp., Incheon, South Korea*

10:15

CF-04. An In-depth Study of the Barkhausen Emission Signal Properties of the Plastically Deformed Fe-2%Si Alloy. *L. Piotrowski*[1], B. Augustyniak[1], M. Chmielewski[1] and F.J. Landgraf[2] *1. Dept. of Appl. Phys. and Math., Gdansk University of Technology, Gdansk, Poland; 2. Dept. of Met. Eng., University of Sao Paulo, Sao Paulo, Brazil*

10:30

CF-05. Correlation between core loss and microstructure for Fe-Si powder cores. *S. Takemoto*[1] and T. Saito[1] *1. R&D Center, Daido Steel, Nagoya, Japan*

10:45

CF-06. Effect of surface magnetic domain structure on iron loss of thin-gauged 3% si-fe sheets. *H. Jung*[1], J. Kim[1] and S. Kim[2] *1. Metallurgy and Material Science, Hanyang University, Ansan, South Korea; 2. Machinery and Materials Group, Korea Electric Power Research Institute, Taejeon, South Korea*

11:00

CF-07. Specific total loss components under axial magnetization in electrical steel sheets with different degree of Goss texture. *W. Pluta*[1] *1. Electrical Engineering Faculty, Czestochowa University of Technology, Czestochowa, Poland*

11:15

CF-08. Three Dimensional Polycrystal Magnetic Field Analysis of Electrical Steel. *K. Fujisaki*[1,2] *1. Technical Development Bureau, Nippon Steel Corporation, Futtsu-city, Chiba-prefecture, Japan; 2. Graduate School of Environmetal Studies, Tohoku University, Sendai, Japan*

11:30

CF-09. Improvement of the Bertotti's formula for energy loss in soft magnetic materials. *K. Sokalski*[1] and J. Szczyglowski[1] *1. TU Czestochowa, Czestochowa, Poland*

11:45

CF-10. Influence of improving efficiency using Fe-P-B-Nb type ultra low loss glassy metal dust core on inductor for large-current. *H. Matsumoto*[1], Y. Yamada[1] and A. Urata[1] *1. RESEARCH AND DEVELOPMENT UNIT, NEC TOKIN, Sendai, Japan*

12:00

CF-11. Soft-magnetic Fe-based nanocrystalline thick ribbons. M. Lee[1], C. Lin[1], *S. Wang*[1] and T. Chin[2] *1. Department of Materials Science and Engineering, National Tsing Hua University, Hsinchu, Taiwan; 2. Department of Materials Science and Engineering, Feng Chia University, Taichung, Taiwan*

12:15

CF-12. Gas flow effects to the magnetic properties of current annealed Vitroperm samples. *V. de Manuel*[1] and R. Pérez del Real[2] *1. Space Programs and Space Sciences, INTA, Torrejón de Ardoz, Madrid, Spain; 2. Space Programs and Space Sciences, INTA, Torrejón de Ardoz, Madrid, Spain*

TUESDAY MORNING 9:30 — AMSTERDAM

Session CG
THIN FILMS: SURFACE AND ANISOTROPY PROPERTIES
Fernando Briones, Chair

9:30

CG-01. Routes to Create Ultrathin Co Films with Perpendicular Magnetic Easy Axis. *S. Gallego*[1] and C. Muñoz[1] *1. Inst. Ciencia Materiales Madrid, Madrid, Spain*

9:45

CG-02. Perpendicular magnetic anisotropy at Co/Oxide interfaces. *Y. Dahmane*[1], S. Auffret[1], U. Ebels[1], B. Rodmacq[1] and B. Dieny[1] *1. CEA Grenoble, Grenoble, France*

10:00

CG-03. Giant magnetic anisotropy of Fe_3Pt alloy thin films with various crystallographycal orientations. H. Yamamoto[1] and *T. Suzuki*[1] *1. Information Storage Materials Laboratory, Toyota Technological Institute, Nagoya, Japan*

10:15

CG-04. Uniaxial anisotropy and temperature driven magnetization reversal of Fe deposited on a MnAs/GaAs(001) magnetic template. R. Breitwieser[2], *M. Marangolo*[1], M. Sacchi[2,3], C. Spezzani[4], L. Coelho[5], J. Milano[6], V. Etgens[1], J. Lüning[2] and N. Jaouen[3] *1. INSP, Université Pierre et Marie Curie, Paris, France; 2. Laboratoire de Chimie Physique - Matière et Rayonnement, UPMC - Univ.Paris 6, Paris, France; 3. Synchrotron SOLEIL, Paris, France; 4. Sincrotrone Trieste S.C.p.A, Trieste, Italy; 5. Universidade Federal de Minas Gerais, Minas Gerais, Brazil; 6. Centro Atómico Bariloche and Instituto Balseiro-UNCuyo, CNEA, Bariloche, Argentina*

10:30

CG-05. Magnetic anisotropy control by ion irradiation. *A. Mougin*[1], H. Cruguel[2], C. Beigné[3], A. Marty[3], J. Ferré[1], Y. Samson[3], O. Plantevin[2], F. Fortuna[2] and H. Bernas[2] *1. LPS, Univ. Paris Sud, UMR CNRS 8502, Orsay, France; 2. CSNSM, Univ. Paris-Sud, UMR CNRS 8609, Orsay, France; 3. DRFMC/SP2M, CEA, Grenoble, France*

10:45

CG-06. Study of magnetic structures on the nanoscale: a multiscale approach based on first principles calculations. *L. Szunyogh*[1], L. Udvardi[1], A. Antal[1], B. Lazarovits[2,1] and B. Újfalussy[2] *1. Department of Theoretical Physics, Budapest University of Technology and Economics, Budapest, Hungary; 2. Research Institute of Solid State Physics and Optics, Hungarian Academy of Sciences, Budapest, Hungary*

11:00

CG-07. Magnetooptic sensing using ultrathin ferromagnetic films. *E. Liskova*[1] and S. Visnovsky[1] *1. Institute of Physics, Charles University, Prague, Czech Republic*

11:15

CG-08. Nonuniform RKKY magnetism in nanosized films, wires and spheres. *E. Meilikhov*[1] and R. Farzetdinova[1] *1. Kurchatov Institute, Moscow, Russian Federation*

11:30

CG-09. Spin Dynamics of Ge:Mn Thin Films. *O. Kazakova*[1], R. Morgunov[2], M. Farle[3] and L. Ottaviano[4] *1. NPL, Teddington, United Kingdom; 2. IPCP, Chernogolovka, Russian Federation; 3. Universitat Duisburg-Essen, Duisburg, Germany; 4. Università dell'Aquila, Coppito L'Aquila, Italy*

11:45

CG-10. Magnetoelastic coupling in epitaxial monolayers: The role of lattice strain. *D. Sander*[1], Z. Tian[1] and J. Kirschner[1] *1. Max Planck Institute, Halle, Germany*

12:00

CG-11. Spin-reorientation transitions induced by coinage-metal capping of Co/Ru(0001) studied by spin-polarized low energy electron microscopy. F. El Gabaly[1,2], A.K. Schmid[2], K.F. McCarty[3] and *J. de la Figuera*[4,1] *1. Centro de Microanalisis de Materiales, Universidad Autonoma de Madrid, Madrid, Madrid, Spain; 2. Berkeley National Laboratory, Berkeley, CA; 3. Sandia National Laboratories, Livermore, CA; 4. Instituto de Quimica-Fisica Rocasolano, CSIC, Madrid, Madrid, Spain*

12:15

CG-12. Magnetic Properties of Single-Crystalline FeRh Alloy Thin Films. S. Inoue[1], Y.Y. Hnin[1], *N.T. Nguyen*[1] and T. Suzuki[1] *1. Information Storage Materials Laboratory, Toyota Technological Institute, Nagoya, Japan*

TUESDAY MORNING 9:30 — CARACAS

Session CH
MAGNETIC SHAPE MEMORY ALLOYS
Thomas Lograsso, Chair

9:30

CH-01. Controlling the microstructure in Ni-Mn-Ga alloys. *M. Pötschke*[1], F. Thoss[1], U. Gaitzsch[1], C. Hürrich[1], S. Roth[1], B. Rellinghaus[1] and L. Schultz[1] *1. Institute for Metallic Materials, IFW Dresden, Dresden, Germany*

9:45

CH-02. Field, stress and temperature controlof the phase transitions in $Ni_{55}Mn_{20}Ga_{25}$ single crystal. *C.P. Sasso*[1], M. Pasquale[1] and L. Giudici[1,2] *1. Electromagnetics, INRiM, Torino, Italy; 2. Physics, Politecnico di Torino, Turin, Italy*

10:00

CH-03. Effect of annealing conditions on the structure formation in NiMnGa shape memory alloys. *R. Wroblewski*[1] and M. Leonowicz[1] *1. Faculty of Materials Science and Engineering, Warsaw University of Technology, Warsaw, Poland*

10:15

CH-04. Magnetic-field induced strain in 5M polycrystalline alloy. *U. Gaitzsch*[1], C. Huerrich[1], M. Pötschke[1], S. Roth[1] and L. Schultz[1] *1. Inst metal mater, IFW Dresden, Dresden, Germany*

10:30

CH-05. Angular dependence of magnetic shape memory effect – model and experiment. *O. Heczko*[1,2] *1. Institute for Metallic Materials, IFW Dresden, Dresden, Germany; 2. Laboratory of Materials Science, Helsinki University of Technology, Helsinki, Finland*

10:45

CH-06. Magnetic properties of rapidly quenched Ni-Mn-Ga wires. *C. Gomez-Polo*[1], J. Pérez-Landazábal[1], V. Recarte[1], V. Sánchez-Alarcos[1] and G. Badini[2] *1. Dept. Fisica, Universidad Publica de Navarra, Pamplona, Spain; 2. Instituto de Ciencia de Materiales, CSIC, Madrid, Spain*

11:00

CH-07. Comparative study of structural and magnetic properties of bulk and powder Ni52Fe17Ga27Co4 magnetic shape memory alloy. *J. Liu*[1], N. Scheerbaum[1], D. Hinz[1] and O. Gutfleisch[1] *1. Institute for Metallic Materials, IFW Dresden, Dresden, Germany*

11:15

CH-08. Magnetocaloric effect and martensitic transition in Ni-Mn-In alloys under hydrostatic pressure. *J. Lyubina*[1], O. Gutfleisch[1], K. Nenkov[1], L. Mañosa[2], X. Moya[2], A. Planes[2], M. Barrio[3], J. Tamarit[3], S. Aksoy[4], T. Krenke[4] and M. Acet[4] *1. Institute for Metallic Materials, IFW Dresden, P.O. Box 270116, D-01171 Dresden, Germany; 2. Facultat de Fisica, Dept. d'Estructura i Constituents de la Materia, Universitat de Barcelona, Diagonal 647, E-08028 Barcelona, Spain; 3. Dept. de Fisica i Enginyeria Nuclear, Universitat Politecnica de Catalunya, Diagonal 647, 08028-Barcelona, Spain; 4. Experimentalphysik, Universität Duisburg-Essen, D-47048 Duisburg, Germany*

11:30

CH-09. Magnetic domain reorganization and twin boundary dynamics in magnetic shape memory alloys. *(Invited)* *J. McCord*[1] *1. Institute for Metallic Materials, IFW Dresden, Dresden, Germany*

12:00

CH-10. Exchange bias in Ni-rich ferromagnetic shape memory alloys Ni-Mn-Sn. *V. Khovaylo*[1], V. Koledov[1], V. Shavrov[1], A. Korolyov[2], M. Ohtsuka[3], H. Miki[4] and T. Takagi[4] *1. Institute of Radioengineering and Electronics, Moscow, Russian Federation; 2. Institute of Metal Physics, Ekaterinburg, Russian Federation; 3. Institute of Multidisciplinary Research for Advanced Materials, Tohoku University, Sendai, Japan; 4. Institute of Fluid Science, Tohoku University, Sendai, Japan*

12:15

CH-11. Magnetic and shape memory properties of FeMnSi-based glass-coated microwires. H. Chiriac[1], *N. Lupu*[1], C.M. Craciunescu[2], S. Corodeanu[1] and M. Grigoras[1] *1. Magnetic Materials and Devices, National Institute of Research and Development for Technical Physics, Iasi, Romania; 2. "Politehnica" University, Timisoara, Romania*

TUESDAY
MORNING
9:00

POLIVALENTE

Session CL
PERMANENT MAGNET MACHINES I (POSTER SESSION)
Phil Anderson, Chair

CL-01. Analytical computation and experimental verification of magnetic core loss of permanent magnet generator considering the wind turbine speed. S. Jang[1], *K. Ko*[1], J. Choi[1] and H. Cho[2] *1. Chungnam Nat'l Univ, Daejeon, South Korea; 2. Korea Institute of Machinary & Materials, Daejeon, South Korea*

CL-02. Stator core loss prediction in large synchronous machines. *A. Knight*[1], S. Troitskaia[1] and Y. Zhan[1] *1. Electrical and Computer Eng, University of Alberta, Edmonton, AB, Canada*

CL-03. Design and analysis of ultra high-speed permanent magnet generator driven by gas turbine for micro scale power generation. S. Jang[1], *K. Ko*[1], J. Choi[1] and Y. Lee[2] *1. Chungnam Nat'l Univ, Daejeon, South Korea; 2. Korea Institute of Science of Technology, Seoul, South Korea*

CL-04. Electromagnetic Performance Analysis and Vector Control of a Flux-Controllable Stator-PM Brushless Motor with Skewed Rotor. *M. Cheng*[1], X. Zhu[1,2], W. Hua[1] and H. Jia[1] *1. School of Electrical Engineering, Southeast University, Nanjing, China; 2. School of Electrical Information Engineering, Jiangsu University, Zhenjiang, China*

CL-05. Permanent magnet optimization for reduction of cogging torque of BLDC motor using response surface methodology. J. Lee[1], *H. Shim*[1] and S. Wang[1] *1. Mechatronics, Gwangju Institute of Science and Technology, Gwangju, South Korea*

CL-06. Design of Direct-Coupled, Small Scaled Permanent Magnet Generators for Wind Turbines. S. Jang[1], H. Kim[1], *J. Choi*[1], D. You[1], S. Lee[2] and B. Kim[3] *1. Chungnam National University, Dae-jeon, South Korea; 2. Korea Institute of Industrial Technaology, Kwangju, South Korea; 3. Korea Electric Power Research Institute, Daejeon, South Korea*

CL-07. Design and experimental evaluation of synchronous machine without iron loss using double-sided halbach magnetized permanent magnet rotor in high power fess. *D. You*[1], S. Jang[1], K. Ko[1] and S. Choi[2] *1. chungnam national univ., daejeon, South Korea; 2. Korea Institute of Machinery and Materials, Daejeon, South Korea*

CL-08. Experimental method for determining magnetically nonlinear characteristics of electric machines with magnetically nonlinear and anisotropic iron core, damping windings and permanent magnets. *G. Stumberger*[1,2], T. Marcic[2], B. Stumberger[1,2] and D. Dolinar[1] *1. Faculty of electrical engineering and computer science, University of Maribor, Maribor, Slovenia; 2. TECES, Maribor, Slovenia*

CL-09. Detent force minimization of permanent magnet linear synchronous motor by means of two different methods. *Y. Zhu*[1] and Y. Cho[1] *1. Electrical Engineering, Dong-A University, Busan, South Korea*

CL-10. A STUDY ON THE IRREVERSIBLE MAGNET DEMAGNETIZATION IN SINGLE-PHASE LINE-START PERMANENT MAGNET RELUCTANCE MOTOR. J. Hong[2], H. Nam[3] and *T. Kim*[1] *1. Electrical Engineering, Gyeongsang National University, Jinju, South Korea; 2. Hanyang University, Seoul, South Korea; 3. LG Electronics, Changwon, South Korea*

CL-11. Design of IPM type BLDC motor considering demagnetization characteristics. *B. Yang*[1], S. Hong[1] and B. Kwon[1] *1. Hanyang Unv., Ansan, South Korea*

CL-12. Characteristic analysis of Permanent Magnet Motor Considering Anisotropic Characteristics of Electrical Steel Sheets. *S. Kwon*[1], J. Lee[1], K. Ha[2] and J. Hong[1] *1. Department of Mechanical Engineering, Hanyang Univeristy, Seoul, South Korea; 2. POSCO Technical Research Laboratories, Pohang, South Korea*

TUESDAY MORNING 9:00 — POLIVALENTE

Session CM
MAGNETIC MICRO- AND NANOSTRUCTURES (POSTER SESSION)
Tom Thomson, Chair

CM-01. Nonlinear eigenmodes of monodomain magnetic squares. ***(Invited)*** *V.E. Demidov*[1], U. Hansen[1], S.O. Demokritov[1] and M. Kostylev[2] *1. Institute for Applied Physics, University of Muenster, Muenster, Germany; 2. School of Physics, University of Western Australia, Crawley, WA, Australia*

CM-02. Synthesis and Magnetic Properties of Au Doped CoPt Nanowires. *J. Min*[1], J. Wu[2], J. Lee[1], J. Ju[3] and Y. Kim[1] *1. Department of Materials Science and Engineering, Korea University, Seoul, South Korea; 2. Institute for Nano Science, Korea University, Seoul, South Korea; 3. Cooperative Center for Research Facilities, Sungkyunkwan University, Suwon, South Korea*

CM-03. FMR studies of interactions effects in magnetic nanowires arrays. O.C. Trusca[1,2], D. Cimpoesu[1], A. Diaconu[4], I. Dumitru[4], J. Lim[1,3], X. Zhang[1,3], J.B. Wiley[1,3], A. Stancu[4] and *L. Spinu*[1,2] *1. Advanced Materials Research Institute, University of New Orleans, New Orleans, LA; 2. Department of Physics, University of New Orleans, New Orleans, LA; 3. Department of Chemistry, University of New Orleans, New Orleans, LA; 4. Faculty of Physics, "Alexandru Ioan Cuza" University, Iasi, Romania*

CM-04. Thermal coercivity mechanism in Fe nanoribbons and stripes. *F. Garcia-Sanchez*[1] and O. Chubykalo-Fesenko[1] *1. POMT, Instituto de Ciencia de Materiales de Madrid, CSIC, Madrid, Spain*

CM-05. Patterning of magnetic films by focused ion beam irradiation. *S. Tibus*[1], D. Makarov[2], C.T. Rettner[3], T. Thomson[4], B.D. Terris[4], T. Schrefl[5] and M. Albrecht[1] *1. Institute of Physics, Chemnitz University of Technology, Chemnitz, Germany; 2. Department of Physics, University of Konstanz, Konstanz, Germany; 3. IBM Almaden Research Center, San Jose, CA; 4. San Jose Research Center, Hitachi Global Storage Technologies, San Jose, CA; 5. Department of Engineering Materials, University of Sheffield, Sheffield, United Kingdom*

CM-06. A novel bottom-up fabrication process for controllable sub-100nm magnetic multilayer devices. *M. Kao*[1], J. Ou[1] and J. Wu[1] *1. Physics, National Changhua University of Education, Changhua, Taiwan*

CM-07. Self-organised hexagonal patterns of independent magnetic nanodots. T. Bobek[1], N. Mikuszeit[2], J. Camarero[2], S. Kyrsta[3], L. Yang[1], M. Niño[2], C. Hofer[4], L. Gridneva[5], A. Persson[5], D. Arvanitis[5], R. Miranda[2,6], *J.J. de Miguel*[2], C. Teichert[4] and H. Kurz[1] *1. Institute of Semiconductor Electronics, RWTH-Aachen, Aachen, Germany; 2. Dept. Fisica de la Materia Condensada, C-3, Univ. Autonoma de Madrid, Madrid, Spain; 3. Materials Chemistry, RWTH-Aachen, Aachen, Germany; 4. Institut für Physik, Montanuniversität Leoben, Leoben, Austria; 5. Department of Physics, Uppsala University, Uppsala, Sweden; 6. IMDEA-Nano, Madrid Institute of Advanced Studies in Nanotechnology, Madrid, Spain*

CM-08. Transverse Rectifier Based on Hybrid Magnetic/Superconducting Nanodevices. *D. Perez de Lara*[1], E.M. Gonzalez[1], J.V. Anguita[2] and J.L. Vicent[1] *1. Fisica de Materiales, Universidad Complutense de Madrid, Madrid, Spain; 2. Instituto Microelectronica, Madrid, CSIC, Tres Cantos, Madrid, Spain*

CM-09. Electrical transport study of patterned lateral Niobium-Permalloy junctions. *S.R. Bakaul*[1,2], K. Li[3], G. Han[2] and Y. Wu[1] *1. Electrical and Computer Engineering, National University of Singapore, Singapore, Singapore; 2. Spintronic, Media and Interface, Data Storage Institute, Singapore, Singapore; 3. Industrial Materials Institute, Boucherville, QC, Canada*

CM-10. Finite size effects in [Co(1nm)/Bi(2.5nm)]n line-structures. *C. Christides*[1] and T. Speliotis[2] *1. Department of Engineering Sciences, University of Patras, Patras, 26504, Greece; 2. Institute of Materials Science, NCSR Demokritos, Athens, 153 10, Greece*

TUESDAY MORNING 9:00 — POLIVALENTE

Session CN
MICROMAGNETICS I (POSTER SESSION)
Gino Hrkac, Chair

CN-01. Dynamic and temperature effects in spin-transfer switching. H. Pham[1,2], D. Cimpoesu[1,3], A. Stancu[3] and *L. Spinu*[1,2] *1. Advanced Materials Research Institute, University of New Orleans, New Orleans, LA; 2. Department of Physics, University of New Orleans, New Orleans, LA; 3. Department of Physics, "Al. I. Cuza" University, Iasi, Romania*

CN-02. Analysis of spin transfer switching speed in magnetic nano-structures. J. Guo[1], T. Seng Ghee[2], *J. Mansoor Bin Abdul*[1] and L. Lin[1] *1. National University of Singapore, Singapore, Singapore; 2. Data Storage Institute, Singapore, Singapore*

CN-03. **Current induced domain wall motion in ferromagnetic wires with out-of-plane magnetization.** *H. Szambolics*[1,3], J. Toussaint[1,3], A. Marty[4], I. Miron[2] and L. Buda-Prejbeanu[2,3] *1. Department of Nanosciences, Institut Neel, CNRS, Grenoble, France; 2. Laboratoire SPINTEC, CEA-CNRS, Grenoble, France; 3. Institut National Polytechnique de Grenoble, Grenoble, France; 4. Laboratoire SP2M, CEA-CNRS, Grenoble, France*

CN-04. **Fast magnetization switching with short pulses.** *W. Scholz*[1], T.M. Crawford[2], T.W. Clinton[1], T. Ambrose[1], S. Kaka[1] and S. Batra[1] *1. Research, Seagate, Pittsburgh, PA; 2. USC NanoCenter, Univ. of South Carolina, Columbia, SC*

CN-05. **Micromagnetic Simulations of Domain Wall Depinning Forced by Oscillating Fields.** *O. Alejos Ducal*[1], E. Martínez Vecino[2], L. López Díaz[3] and L. Torres Rincón[3] *1. Electricidad y Electrónica, Universidad de Valladolid, Valladolid, Valladolid, Spain; 2. Ingeniería Electromecánica, Universidad de Burgos, Burgos, Burgos, Spain; 3. Física Aplicada, Universidad de Salamanca, Salamanca, Salamanca, Spain*

CN-06. **Effects of Shape Anisotropy on the Walker Breakdown Field in Field-Driven Domain Wall Motion.** *W. Kim*[1], S. Jung[2], H. Lee[2] and K. Lee[1] *1. Korea University, Seoul, South Korea; 2. POSTECH, Pohang, South Korea*

CN-07. **Testing the theory of nucleation in infinite square prism—micromagnetic simulations.** *K.M. Lebecki*[1] *1. Institute of Physics, PAS, Warsaw, Poland*

CN-08. **Finite difference and edge finite element approaches for dynamic micromagnetic modeling.** *A. Manzin*[1], B. Van de Wiele[2], O. Bottauscio[1], M. Chiampi[3], L. Dupré[2] and F. Olyslager[4] *1. Istituto Nazionale di Ricerca Metrologica, Torino, Italy; 2. Department of Electrical Energy, Systems and Automation, Ghent University, Ghent, Belgium; 3. Department of Electrical Engineering, Politecnico di Torino, Torino, Italy; 4. Department of Information Technology, Ghent University, Ghent, Belgium*

CN-09. **Computation of magnetization normal oscillations and resonant frequencies for ferromagnetic nanoparticles.** *M. d'Aquino*[1], C. Serpico[2], G. Miano[2] and G. Bertotti[3] *1. Dipartimento per le Tecnologie, Università di Napoli "Parthenope", Napoli, Italy; 2. Dipartimento di Ingegneria Elettrica, Università di Napoli "Federico II", Napoli, Italy; 3. Istituto Nazionale di Ricerca Metrologica (INRiM), Torino, Italy*

CN-10. **Micromagnetic modeling of magnetization switching mechanisms in high magnetoresistance tunnel junctions.** *L. Torres*[1], G. Finocchio[2], M. Carpentieri[2], E. Martinez[3], E. Jaromirska[1], O. Alejos[4] and L. Lopez-Diaz[1] *1. Dept. Fisica Aplicada, Universidad de Salamanca, Salamanca, Spain; 2. University of Messina, Messina, Messina, Italy; 3. Universidad de Burgos, Burgos, Burgos, Spain; 4. Universidad de Valladolid, Valladolid, Valladolid, Spain*

CN-11. **Effect of Sawtooth Shape on Switching Process of Write Head.** *S. Wang*[1], D. Wei[1] and K. Gao[2] *1. Dept. of Materials Science and Engineering, Tsinghua University, Beijing, China; 2. Seagate Technology Seagate Technology, Bloomington, MN*

CN-12. **Micromagnetic study of read sensitivity: Influence of curved hard bias and granular media.** *L. Wang*[1], G.C. Han[1], S.G. Wu[1] and B. Liu[1] *1. Spintronics, Media and Interface, Data Storage Institute, Singapore, Singapore*

TUESDAY
MORNING
9:00

POLIVALENTE

Session CO
NANOSTRUCTURED HARD MAGNETIC MATERIALS - I (POSTER SESSION)
Thomas Schrefl, Chair

CO-01. **Remanence analysis of nanocrystalline, epitaxial $SmCo_5$ films in high pulsed fields up to 35 T.** *V. Neu*[1], J. Freudenberger[1], A. Singh[1] and L. Schultz[1] *1. Institute for Metallic Materials, IFW Dresden, Dresden, Germany*

CO-02. **Effect of Ga addition on the magnetic properties of $Nd_{60}Fe_{30}Al_{10-x}Ga_x$ alloy.** *W. Kaszuwara*[1], B. Michalski[1], M. Leonowicz[1] and J. Latuch[1] *1. Faculty of Materials Science and Engineering, Warsaw University of Technology, Warsaw, Poland*

CO-03. **Ab initio calculation of the magnetic structures in $Nd_2Fe_{14}B/\alpha$-Fe nanocomposite materials.** *Y. Toga*[1], H. Tsuchiura[1] and A. Sakuma[1] *1. Applied Physics, Tohoku University, Sendai, Japan*

CO-04. **Nanostructure and Magnetic Properties of Nd-Fe-B Thin Film Fabricated by UHV Sputtering.** *D. Ogawa*[1], T. Akiya[2], M. Oogane[1], H. Kato[2,3] and Y. Ando[1] *1. Department of Applied Physics, Tohoku University, Sendai, Japan; 2. New Industry Creation Hatchery Center (NICHe), Tohoku University, Sendai, Japan; 3. Department of Applied Mathematics and Physics, Yamagata University, Yonezawa, Japan*

CO-05. **Effect of Nd and Nd_2O_3 layers on the magnetic properties for Nd-Fe-B thin films.** *N. Oka*[1], T. Sato[2], H. Kato[1] and T. Shima[1] *1. Faculty of Engineering, Tohoku Gakuin University, Tagajo, Japan; 2. Toyota Central R&D Labs., Nagakute, Japan*

CO-06. **Refinement of surface morphology of Nd-Fe-B thin film by low temperature deposition.** *H. Kato*[1], I. Honda[1], T. Sato[2] and T. Shima[1] *1. Faculty of Engineering, Tohoku Gakuin University, Tagajo, Japan; 2. Toyota Central R&D Labs., Nagakute, Japan*

CO-07. **Enhancement of coercivity for Nd-Fe-B thin films with Tb and Dy layer.** *T. Sato*[1], N. Oka[2], H. Kato[2] and T. Shima[2] *1. Toyota Central R&D Labs., Inc., Aichi, Japan; 2. Faculty of Engineering, Tohoku Gakuin University, Tagajyo, Japan*

CO-08. **FePt-based nanocomposite ribbons as exchange coupled magnets.** *A. Crisan*[1,2], O. Crisan[1], N. Randrianantoandro[2] and I. Skorvanek[3] *1. National Institute for Materials Physics, Bucharest-Magurele, Romania; 2. Laboratoire de Physique de l'Etat Condense, Universite du Maine, Le Mans, France; 3. Institute of Experimental Physics, Slovak Academy of Sciences, Kosice, Slovakia*

Session CP
HYSTERESIS MODELLING I
(POSTER SESSION)
A. Petru, Chair

CP-01. Genetic algorithm for Jiles-Atherton parameters optimization. *F.A. Cuéllar*[1] and A. Mendoza[2] *1. Physics Department, Universidad Nacional de Colombia, Bogotá, Colombia; 2. Grupo de Materiales Magnéticos y Nanoestructuras, Universidad del Quindío, Armenia, Colombia*

CP-02. Angle Difference between B vector and H vector in Anisotropic Electrical Steel. *K. Fujisaki*[1,2] and S. Satou[3] *1. Technical Development Bureau, Nippon Steel Corporation, Futtsu-city, Chiba-prefecture, Japan; 2. Graduate School of Environmetal Studies, Tohoku University, Sendai-city, Miyagi-prefecture, Japan; 3. N-Teck Ohita Corporation, Ohita-city, Japan*

CP-03. Data collapse and viscosity in three-dimensional magnetic systems. A. Adedoyin[1] and *A. Petru*[1] *1. Electrical and Computer Engineering, Florida State University, Tallahassee, FL*

CP-04. A Simplified Iron Loss Model for Laminated Magnetic Cores. *E. Dlala*[1] *1. Department of Electrical Engineering, Helsinki University of Technology, Espoo, Finland*

CP-05. Modeling of Vector Hysteresis of Soft Magnetic Composite Material. *Y. Guo*[1], H. Lu[2], J. Zhu[1], Z. Lin[1], J. Zhong[1] and S. Wang[3] *1. Faculty of Engineering, University of Technology Sydney, Sydney, NSW, Australia; 2. Faculty of Information Technology, University of Technology Sydney, Sydney, NSW, Australia; 3. Faculty of Electrical Engineering, Xi'an Jiaotong University, Xi'an, Shaanxi, China*

CP-06. Analysis of the local material degradation near cutting edges of electrical steel sheets. *G. Crevecoeur*[1], P. Sergeant[1], L. Dupre[1], L. Vandenbossche[1] and R. Van de Walle[2] *1. Departement of Electrical Energy, Systems and Automation, Ghent University, Ghent, Belgium; 2. Department of Electronics and Information systems, Ghent University, Ghent, Belgium*

CP-07. Modelling of magnetostrictive material and linear controling of nonlinear magnetostrictive drive system based on SVM. J. An[1], *Q. Yang*[1], Z. Ma[1], H. Chen[1], L. Hou[1], W. Yang[1] and F. Liu[1] *1. hebei university of technology, Tianjin, China*

CP-08. Modelling hysteresis of a first order magneto-structural phase transformation. *V. Basso*[1], M. Lo Bue[2], C.P. Sasso[1] and M. Küpferling[1] *1. INRIM, Torino, Italy; 2. SATIE, ENS Cachan, CNRS, UniverSud, Cachan, France*

CP-09. The Preisach distribution and the symmetry of the local hysterons in strongly interacting nanoparticulate systems. *R. Tanasa*[1] and A. Stancu[1] *1. Department of Physics, "Alexandru Ioan Cuza" University, Iasi, Romania*

TUESDAY
MORNING
9:00

POLIVALENTE

Session CQ
SOFT MAGNETIC MATERIALS AND APPLICATIONS I
(POSTER SESSION)
Andy Knight, Chair

CQ-01. Magnetic and magneto-thermal properties of RFe4Ge2(R=Er,Dy) compounds. *P. Kumar*[1], N.K. Singh[1], K.G. Suresh[1] and A.K. Nigam[2] *1. Physics, IIT Bombay, Mumbai, Maharastra, India; 2. Tata Institute of Fundamental Research, Tata Institute of Fundamental Research, Mumbai, Maharastra, India*

CQ-02. Capacity of magnetic inductive parameters on annealing characterization of cold rolled low carbon steel. *K. Gurruchaga*[1,2], A. Martínez-de-Guerenu[1], M. Soto[1,2] and F. Arizti[1,2] *1. CEIT, San Sebastian, Spain; 2. Tecnun, San Sebastian, Spain*

CQ-03. A fully digital magnetic property measurement system. *M. Soto*[1,2], A. Martínez-de-Guerenu[1], K. Gurruchaga[1,2] and F. Arizti[1,2] *1. CEIT, San Sebastian, Spain; 2. Tecnun (University of Navarra), San Sebastian, Spain*

CQ-04. Preparation and magnetorheology of solvent-cast magnetite nanoparticle and poly(vinyl butyral) composite. *B. Park*[1], J. You[1], F. Fang[1] and H. Choi[1] *1. Department of Polymer Science and Engineering, Inha University, Incheon, South Korea*

CQ-05. 3D Magnetic Field Analysis by Homogenization Method for Thin Steel Plate of Magnetic Field. *K. Fujisaki*[1,2], M. Fujikura[1], J. Mino[3] and S. Satou[4] *1. Technical Development Bureau, Nippon Steel Corporation, Futtsu-city, Chiba-prefecture, Japan; 2. Graduate School of Environmetal Studies, Tohoku University, Sendai-city, Japan; 3. Nippon Steel Engineering Corporation, Tokyo, Japan; 4. N-Teck Ohita Corporation, Ohita, Japan*

CQ-06. Field Coil for Magneto-Optic Switching : Capacitance Considerations. *J. Tioh*[1], M. Mina[1] and R. Weber[1] *1. Electrical and Computer Engineering, Iowa State University, Ames, IA*

CQ-07. Power loss measurement and prediction of soft magnetic powder composites magnetised under non-sinusoidal excitation. P. Marketos[1], *J.P. Hall*[1] and S.E. Zirka[2] *1. School of Engineering, Cardiff University, Cardiff, Wales, UK, United Kingdom; 2. Department of Applied Physics and Technology, Dnepropetrovsk National University, Dnepropetrovsk, Ukraine*

CQ-08. Electromagnetic Wave Absorption Characteristics of Powder-Type Magnetic Wood Considering the Mixing Ratios of Two Types of Magnetic Powder. *H. Oka*[1], Y. Yanagidate[1], H. Osada[1], K. Kubota[1], Y. Namizaki[2] and F.P. Dawson[3] *1. Iwate University, Morioka, Japan; 2. Iwate Industrial Research Institute, Morioka, Japan; 3. University of Toronto, Toronto, ON, Canada*

CQ-09. Influence of asymmetry in stator geometry and magnetic circuit on cogging torque in PM brushless machines. *Z. Zhu*[1], J. Chen[1], L. Wu[1] and D. Howe[1] *1. University of Sheffield, Sheffield, United Kingdom*

CQ-10. Electromagnetic modeling of a novel linear oscillating actuator. *Z. Zhu*[1], X. Chen[1], D. Howe[1] and S. Iwasaki[2] *1. University of Sheffield, Sheffield, United Kingdom; 2. IMRA UK Research Center, Brighton, United Kingdom*

CQ-11. Non-oriented electrical steel and magnetostriction: a review. *A.M. Severino*[1] *1. Departamento de Física - CCNE, Universidade Federal de Santa Maria, Santa Maria, Rio Grande do Sul, Brazil*

CQ-12. Optimization of Design Parameters for Ferrite Inductor for 10 MHz On-chip Power Module. *S. Bae*[1,2], Y. Hong[1,2], J. Lee[1,2], J. Jalli[1,2], G.S. Abo[1,2], A. Lyle[1,2], H. Han[1,2] and G.W. Donohoe[3] *1. Department of Electrical and Computer Engineering, University of Alabama, Tuscaloosa, AL; 2. MINT Center, University of Alabama, Tuscaloosa, AL; 3. Department of Electrical and Computer Engineering, University of Idaho, Moscow, ID*

TUESDAY
MORNING
9:00

POLIVALENTE

Session CR
MAGNETIC NANOCLUSTERS AND NANOPARTICLES II (POSTER SESSION)
Patricia de la Presa, Chair

CR-01. Magnetic properties of cobalt ferrite nanoparticles obtained by non-aqueous synthesis. *C. Vázquez-Vázquez*[1], C. Mateo-Mateo[1], M. Buján-Núñez[1], M. López-Quintela[1], D. Serantes[2], D. Baldomir[2] and J. Rivas[2] *1. Facultad de Química. Departamento de Química Física, Universidad de Santiago de Compostela, Santiago de Compostela, A Coruña, Spain; 2. Facultad de Física. Departamento de Física Aplicada, Universidad de Santiago de Compostela, Santiago de Compostela, A Coruña, Spain*

CR-02. Magnetic Properties of Nano-composite Particles of FePt/FeRh. *Y. Hnin*[1], S. Inoue[1], N.T. Nam[1], T. Suzuki[1] and Y. Hirotsu[2] *1. Information Storage Materials Laboratory, Toyota Technological Institute, Nagoya, Japan; 2. The Institute of Scientific and Industrial Research, Osaka University, Osaka, Japan*

CR-03. Synergic application of albumin nanoparticles: combination of Photodynamic Therapy with Cellular Hyperthermia. M.M. Andrade Rodrigues[1], A.R. Simioni[1], F.L. Primo[2,1], M.P. Siqueira-Moura[2], Z.G. Lacava[3], P.C. Morais[4] and *A.C. Tedesco*[1] *1. Departamento de Química, Grupo de Fotobiologia e Fotomedicina, Faculdade de Filosofia, Ciências e Letras de Ribeirão Preto, Universidade de São Paulo, 14040-901, Brazil, Ribeirão Preto, SP, Brazil; 2. Faculdade de Ciências Farmacêuticas de Ribeirão Preto, Universidade de São Paulo, Ribeirão Preto-SP, 14040-903, Brazil, Ribeirão Preto, SP, Brazil; 3. Universidade de Brasília, Instituto de Ciências Biológicas, Brasília DF 70910-900, Brazil, Ribeirão Preto, DF, Brazil; 4. Universidade de Brasília, Instituto de Física, Núcleo de Física Aplicada, Brasília DF 70910-900, Brazil, Ribeirão Preto, DF, Brazil*

CR-04. Synthesis of Ni nanoparticles by dc magnetron sputtering. H. Cui[1], *M. Sanz*[1], M. Maicas[1] and C. Aroca[1] *1. ISOM, Universidad Politécnica de Madrid, Madrid, Madrid, Spain*

CR-05. Influence of the Si substrate on the transport and magnetotransport properties of nanostructured FeAg thin films. *J. Alonso*[1], M. Fdez-Gubieda[1], J. Barandiarán[1], J. Chaboy[3], L. Fernández Barquín[4], I. Orue[2], A. Svalov[1] and N. Kawamura[5] *1. Electricidad y Electrónica, Universidad del País Vasco, Bilbao, Spain; 2. SGIKER, Servicios Generales de medidas magnéticas, Universidad del País Vasco, Bilbao, Spain; 3. Instituto de Ciencia de Materiales de Aragón, CSIC-Universidad de Zaragoza, Zaragoza, Spain; 4. CITIMAC, Universidad de Cantabria, Santander, Spain; 5. Japan Synchrotron Radiation Research Institute, Kouto, Japan*

CR-06. WITHDRAWN

CR-07. Characterization of nanocrystalline iron oxide powder modified by electroless nickel plating. C. Lin[1], *C. Tsay*[1], T. Yang[1], R. Yang[2], D. Hung[3] and Y. Yao[3] *1. Materials Science and Engineering, Feng Chia University, Taichung, Taiwan; 2. Dept. of Aerospace and Systems Engineering, Feng Chia Univ, Taichung, Taiwan; 3. Institute of Physics, Academia Sinica, Taipei, Taiwan*

CR-08. Functionalized silica coated maghemite nanoparticles prepared by the microemulsion method for biomedical applications. *A. Drmota*[1], A. Ko šak[2] and A. Znidar ši č[1,2] *1. Kolektor Nanotesla Institute, Ljubljana, Slovenia; 2. Kolektor Magma d.o.o., Ljubljana, Slovenia*

CR-09. Magnetic nanoparticles obtained by ultrahigh vacuum glancing angle deposition technique at high temperature. *X. Bendaña*[1], E. Ferreiro[1], G. Armelles[1], A. Cebollada[1] and J. Garcia Martin[1] *1. Instituto de Microelectrónica de Madrid IMM-CNM-CSIC, Tres Cantos, Madrid, Spain*

CR-10. Magnetic properties of nanocrystalline Co thin films grown on glass. *B. Presa*[1], R. Matarranz[1], M.C. Contreras[1], J.F. Calleja[1], L.E. Fernandez-Outon[2] and K. O'Grady[2] *1. Departamento de Física, Universidad de Oviedo, Oviedo, Principado de Asturias, Spain; 2. Department of Physics, The University of York, York, United Kingdom*

CR-11. Core-shell magnetic behaviour of iron ultrathin films prepared by sputtering at very low temperatures. F. Jiménez-Villacorta[1], *R.M. Morillas*[1], E. Salas[1], E. Céspedes[1] and C. Prieto[1] *1. Instituto de Ciencia de Materiales de Madrid - CSIC, Madrid, Spain*

CR-12. Preparation and magnetic properties of disordered CdFe2O4 thin films. *H. Akamatsu*[1], Y. Zong[1], Y. Fujiki[1], K. Kamiya[1], K. Fujita[1], S. Murai[1] and K. Tanaka[1] *1. Material Chemistry, Kyoto University, Kyoto, Japan*

CR-13. Controlled synthetic conditions of FePt nanoparticles with high magnetization for biomedical applications. *D. Wei*[1,4], D. Hung[2], C. Ho[3], P. Chen[3] and Y. Yao[4] *1. Institute of Physics, Academia Sinica, Taipei, Taiwan; 2. Department of Information and Telecommunications Engineering, Ming Chuan University, Taipei, Taiwan; 3. Department of Chemical Engineering, Tunghai University, Taichung, Taiwan; 4. Department of Materials Engineering, Tatung University, Taipei, Taiwan*

CR-14. Properties of Co-HfO2 nanogranular magnetic thin films. *M. Chadha*[1] and V. Ng[1] *1. ECE, National University of Singapore, Singapore, Singapore*

CR-15. Fe_3O_4 incorporated AOT-Alginate - composite nanoparticles for drug delivery. C. Sudakar[1], A. Dixit[1], R. Regmi[1], *R. Naik*[1], G. Lawes[1], V.M. Naik[2], P.P. Vaishnava[3], U. Toti[4] and J. Panyam[4] *1. Department of Physics and Astronomy, Wayne State University, Detroit, MI; 2. Department of Natural Sciences, University of Michigan-Dearborn, Dearborn, MI; 3. Department of Physics, Kettering University, Flint, MI; 4. College of Pharmacy, University of Minnesota, Minneapolis, MN*

CR-16. Iron Oxide Nanoparticles Embedded in Thermoplastic Polymers for Magneto-optical Devices. G. Carotenuto[2], *D. Davino*[1], A. Longo[2], V. Pagliarulo[1], G. Pepe[3] and C. Visone[1] *1. Engineering Department, University of Sannio, Benevento, Italy; 2. Istituto per i materiali compositi, CNR, Napoli, Italy; 3. Coherentia INFM - Physics Department, Università di Napoli Federico II, Napoli, Italy*

CR-17. Novel single-step synthesis of Fe1-xCox and MgO based core-shell structured nanospheres: High magnetization particles for biomedicine, catalysis and spintronics applications. *C. Martinez-Boubeta*[1], L. Balcells[1], F. Sandiumenge[1], L. Casas[3], A. Calleja[1], V. Laukhin[1,2], C. Monty[4] and B. Martínez[1] *1. ICMAB, Bellaterra, Barcelona, Spain; 2. Institut Catalá de Recerca i Estudis Avançats (ICREA), Passeig Lluís Companys 23, Barcelona, Spain; 3. Unitat de Cristallografía i Mineralogia, Dept. Geologia-UAB, Bellaterra, Barcelona, Spain; 4. CNRS/Procédés, Matériaux et Energie Solaire (PROMES), Font Romeu, France*

TUESDAY
MORNING
9:00

POLIVALENTE

Session CS
PERPENDICULAR GRANULAR MEDIA (POSTER SESSION)
Simon Greaves, Chair

CS-01. High Perpendicular Anisotropy Layers stacked Exchange Coupled Composite Media. *S. Oikawa*[1], T. Maeda[1] and A. Takeo[1] *1. Hard Disk Drive Development Dept., TOSHIBA Corporation, Kawasaki, Japan*

CS-02. Segregation Mechanisms in Co-based Oxide Recording Media. *E.E. Marinero*[1], D.T. Margulies[1], B.R. York[1] and P. Rice[2] *1. Hitachi San Jose Research Center, San Jose, CA; 2. IBM Almaden Research Center, San Jose, CA*

CS-03. Pseudo-hcp material and its evaluation for perpendicular recording media. *S. Saito*[1] and M. Takahashi[2,1] *1. Electronic engineering, Tohoku university, Sendai, Miyagi, Japan; 2. New industry creation hatchery center, Tohoku univ., Sendai, Miyagi, Japan*

CS-04. Magnetic interaction between recording layer and soft underlayer in granular-type perpendicular magnetic recording media with thin intermediate layer. *K. Shintaku*[1] *1. Akita Research Institute of Advanced Technology, Akita Prefectural R&D Center, Akita, Japan*

CS-05. A new method for controlling an exchange coupling of perpendicular recording media. *J. Ariake*[1] and N. Honda[1] *1. AIT, Akita Prefectural R&D Center, Akita, Japan*

CS-06. A study of perpendicular magnetic recording media with an exchange control layer. *K. Tang*[1], K. Takano[1], G. Choe[1], G. Wang[1], J. Zhang[1], X. Bian[1] and M. Mirzamaani[1] *1. Hitachi Global Storage Technologies, San Jose, CA*

CS-07. Al-N; a hexagonal-nitride seed layer underlayered Ru in granular-type perpendicular media. *S. Ishibashi*[1], S. Saito[1], A. Hashimoto[1] and M. Takahashi[2,1] *1. Dept. of Electronics Engineering, Tohoku University, Sendai, Japan; 2. New Industry Creation Hatchery Center, Tohoku University, Sendai, Japan*

CS-08. Granular perpendicular soft layer with tunable anisotropy energy in exchange coupled composite media. *H. Hou*[1], M. Lin[1], R. Liao[1], C. Lai[1], R. Chen[2] and C. Lee[2] *1. Department of Materials Science and Engineering, National Tsing Hua University, Hsinchu, Taiwan; 2. China Steel Corporation, Kaohsiung, Taiwan*

CS-09. Effect of deposition condition of Ru-oxide/Ru bilayers on magnetic properties and orientation of CoPtCr-SiO_2 perpendicular recording media. *T. Matsuu*[1], A. Hashimoto[1], K. Hirata[1], H. Fujiura[1], S. Matsunuma[2], T. Inoue[2], T. Doi[2] and S. Nakagawa[1] *1. Dept. of Physical Electronics, Tokyo Institute of Technology, Tokyo, Japan; 2. Hitachi Maxell, Ibaraki, Japan*

CS-10. Remanence measurements of perpendicular recording media. *T. Deakin*[1], C. Bunce[1], K. O'Grady[1] and S.Z. Wu[2] *1. Department of Physics, The University of York, York, United Kingdom; 2. Seagate Media Research, Fremont, CA*

CS-11. Microwave-assisted magnetization reversal in exchange spring media. *M.A. Bashir*[1], J. Dean[1], T. Schrefl[1], A. Goncharov[1], G. Hrkac[1], S. Bance[1], D.A. Allwood[1] and D. Suess[2] *1. Engineering Materials, University Of Sheffield, Sheffield, United Kingdom; 2. Solid State Physics, Vienna University of Technology, Vienna, Austria*

CS-12. Micromagnetic Simulations of Cluster-pinned Recording Media. *C. Loke*[1], S. Greaves[1] and H. Muraoka[1] *1. RIEC, Tohoku University, Sendai, Miyagi, Japan*

CS-13. Effects of exchange and dipolar interactions on the determination of intrinsic switching field distributions in perpendicular recording media. *Y. Liu*[1], K.A. Dahmen[1], O. Hovorka[2] and A. Berger[2] *1. Department of Physics, University of Illinois at Urbana-Champaign, Urbana, IL; 2. CIC nanoGUNE Consolider, Donostia - San Sebastián, Spain*

CS-14. Hybrid Soft Underlayer for Perpendicular Recording Media. *Y. Dong*[1] and R. Victora[1] *1. Department of Electrical and Computer Engineering, The Center for Micromagnetics and Information Technologies (MINT), University of Minnesota, Minneapolis, MN*

CS-15. Fast precessional switching in exchange spring media. *D. Suess*[1], J. Fidler[1], J. Dean[2] and T. Schrefl[2] *1. Institut of Solid State Physics, Technical University of Vienna, Vienna, Austria; 2. Department of Engineering Materials, The University of Sheffield, Sheffield, UK., Sheffield, United Kingdom*

TUESDAY MORNING 9:00 — POLIVALENTE

Session CT
PERPENDICULAR HIGH KU MEDIA (POSTER SESSION)
Mohammad Mirzamaani, Chair

CT-01. Co-rich Co-Pt films with low ordering temperature and high perpendicular hard magnetic properties for high-density magnetic recording media. *S. Chen*[1,2], P. Kuo[3], C. Shen[3], Y. Fang[3] and S. Hsu[3] *1. Department of Materials Engineering, MingChi University of Technology, Taipei, Taiwan; 2. Center for Nanostorage Research, National Taiwan University, Taipei, Taiwan; 3. Institute of Materials Science and Engineering, National Taiwan University, Taipei, Taiwan*

CT-02. Microstructure and magnetic properties of FePt films on anodized aluminum oxide membranes. *C. Yu*[1], S. Chen[2], Y. Yao[3] and J. Wu[2] *1. Department of Applied Physics, National University of Kaohsiung, Kaohsiung, Taiwan; 2. Department of Materials Science and Engineering, National Tsing Hua University, Hsinchu, Taiwan; 3. Department of Materials Engineering, Tatung Universit, Taipei, Taiwan*

CT-03. Effect of MgO addition on structural and magnetic properties of (001) textured FePt thin films. A. Sun[1,2], Y. Tsai[3], F. Yuan[4], *J. Hsu*[1,2] and P. Kuo[3] *1. Physics, National Taiwan University, Taipei, Taiwan; 2. Center for Nanostorage Research, National Taiwan University, Taipei, Taiwan; 3. Materials Science and Engineering, National Taiwan University, Taipei, Taiwan; 4. Physics, Academia Sinica, Taipei, Taiwan*

CT-04. Thickness Dependence on (001) Texture Evolution and Magnetic Properties of Sputter-Deposited FePt:MgO Nanocomposite Films. H. Kim[1], *K. Kim*[1], S. Lee[1] and W. Jeung[2] *1. Materials Science and Engineering, Korea University, Seoul, South Korea; 2. Korea Institute of Science and Technology, P.O.Box 131, Seoul, South Korea*

CT-05. Dependence of ordering kinetics of FePt thin films on substrates. *C. Zha*[1,2], S. He[1], B. Ma[1], Z. Zhang[1], F. Gan[1] and Q. Jin[1] *1. Department of Optical Science and Engineering, Fudan University, Shanghai, China; 2. Department of Microelectronics and Applied Physics, Royal Institute of Technology, Stockholm, Sweden*

CT-06. Domain reversal behavior of ultrathin FePt:C films. *H. Ko*[1], P. Alagarsamy[1], S. Shin[1], W. Byun[2] and S. Kim[2] *1. Physics, KAIST, Daejoen, South Korea; 2. Material Science, KAIST, Daejeon, South Korea*

CT-07. Fabrication of easy-axis-aligned ultrahigh-density FePt nanoparticles. *Y. Wu*[1], L. Wang[1] and C. Lai[1] *1. Materials Science and Engineering, National Tsing Hua University, Hsinchu, Taiwan*

CT-08. Structural and magnetic properties of textured Fe/FePt bilayer. S.H. He[1], B. Ma[1], *C.L. Zha*[1], Z.Z. Zhang[1] and Q.Y. Jin[1] *1. Department of Optical Science and Engineering, Fudan University, Shanghai, Shanghai, China*

CT-09. Control of Curie temperature of FePt(Cu) films prepared from Pt(Cu)/Fe bilayers. J. Ikemoto[1], *Y. Imai*[1] and S. Nakagawa[1] *1. Dept. of Physical Electronics, Tokyo Institute of Technology, Tokyo, Japan*

CT-10. Exchange Coupling Assisted FePtC Perpendicular Recording Media. *J. Hu*[1], J. Chen[2], Y. Ding[1], B. Lim[1], W. Phyoe[1] and B. Liu[1] *1. Data Storage Institute, Singapore, Singapore; 2. Department of Materials Science and Engineering, National University of Singapore, Singapore, Singapore*

CT-11. Epitaxial thin $SmCo_5$ films with perpendicular anisotropy. *M. Seifert*[1], V. Neu[1] and L. Schultz[1] *1. Institute for Metallic Materials, IFW Dresden, Dresden, Germany*

CT-12. Studies on $Sm(Co,Cu)_5$ thin films with perpendicular anisotropy for extremely high areal density recording. *X. Liu*[1], H. Zhao[1], Y. Kubota[2] and J. Wang[1] *1. The Center for Micromagnetics and Information Technologies, Department of Electrical and Computer Engineering, University of Minnesota, Minneapolis, MN; 2. Seagate Research, Pittsburgh, PA*

CT-13. Second order anisotropy in exchange spring systems. *B.F. Valcu*[1], A. Dobin[1] and E. Girt[1] *1. Seagate Technology, Fremont, CA*

TUESDAY MORNING 9:00 — POLIVALENTE

Session CU
BIT PATTERNED MEDIA I (POSTER SESSION)
Branson Belle, Chair

CU-01. Magnetic recording in patterned media at 5 - 10 Tbit/in^2 *S. Greaves*[1], Y. Kanai[2] and H. Muraoka[1] *1. RIEC, Tohoku University, Sendai, Japan; 2. IEE, Niigata Instiute of Technology, Kashiwazaki, Japan*

CU-02. Characterisation of a 2 Tbit/in^2 patterned media recording system. *N. Degawa*[1], S.J. Greaves[1], H. Muraoka[1] and Y. Kanai[2] *1. RIEC, Tohoku University, Sendai, Miyagi, Japan; 2. IEE, Niigata Institute of Technology, Niigata, Niigata, Japan*

CU-03. Simulation Study of High Density Bit Patterned Media with Inclined Anisotropy. *N. Honda*[1], K. Yamakawa[1] and K. Ouchi[1] *1. Research Institue of Advanced Technology, Akita Prefectural R & D Center, Akita-shi, Japan*

CU-04. Writability in Discrete Track Media. *K. Moon*[1], C. Che[1], Y. Tang[2], M.T. Moneck[2], J. Zhu[2] and N. Takahashi[3] *1. Samsung Information Systems America, San Jose, CA; 2. ECE Department, Carnegie Mellon University, Pittsburgh, PA; 3. Fuji Electric Advanced Technology, Nagano, Japan*

CU-05. Magnetization switching experiments on sub-micron Co/Pt multilayer dot with pulse field generator with nanoseconds duration. *N. Kikuchi*[1], I. Atsuo[1], S. Okamoto[1] and O. Kitakami[1] *1. IMRAM Tohoku University, Sendai, Japan*

CU-06. Dot size dependence of magnetic properties in CoPt dot arrays fabricated using diblock copolymer. *K. Kimura*[1], Y. Kamata[1], T. Maeda[1], Y. Isowaki[1] and A. Kikitsu[1] *1. Storage Materials & Devices Laboratory, Corporate Research & Development Center, Toshiba Corporation, Kawasaki, Kanagawa, Japan*

CU-07. Study on ferro-antiferromagnetic transition in $L1_0$ FePtRh film for bit patterning. *T. Hasegawa*[1], J. Miyahara[1], Y. Fu[2], T. Wang[2], H. Saito[1] and S. Ishio[1] *1. Materials Science and Engineering, Akita University, Akita, Japan; 2. Venture Business Laboratory, Akita University, Akita, Japan*

CU-08. CoCrPt-SiO_2 films on spherical SiO_2 particle arrays. *C. Brombacher*[1], F. Springer[2], H. Rohrmann[4], M. Kratzer[4], M. Parlinska[3], S. Meier[3], P. Kappenberger[3] and M. Albrecht[1] *1. Institute of Physics, Chemnitz University of Technology, D-09107 Chemnitz, Germany; 2. Department of Physics, University of Konstanz, D-78457 Konstanz, Germany; 3. Nanoscale Materials Science, Empa, CH-8600 Dübendorf, Switzerland; 4. Data Storage, OC Oerlikon Balzers AG, FL-9496 Balzers, Liechtenstein*

CU-09. Fabrication of nanomagnet arrays by exfoliating thin films sputter-deposited onto molds. *H. Oshima*[1,2], H. Kikuchi[1,2], H. Nakao[1,2], K. Itoh[1,2], T. Morikawa[3], H. Tamura[4], K. Nishio[5,6] and H. Masuda[5,6] *1. Fujitsu Laboratories Ltd., Atsugi 243-0197, Japan; 2. Yamagata Fujitsu Ltd., Higashine 999-3701, Japan; 3. Fujitsu Laboratories Ltd., Akashi 674-8555, Japan; 4. Fujitsu Ltd., Kawasaki 211-8588, Japan; 5. Kanagawa Academy of Science and Technology, Sagamihara 229-1131, Japan; 6. Tokyo Metropolitan University, Hachioji 192-0397, Japan*

CU-10. Design of Ni-Mold for Discrete Track Media. *K. Ichikawa*[1], T. Usa[2], K. Nishimaki[2] and K. Usuki[1] *1. Recording Media Research Laboratories, FUJIFILM Corp., Odawara Kanagawa, Japan; 2. Production Engineering & Development Center, FUJIFILM Corp., Odawara Kanagawa, Japan*

TUESDAY
MORNING
9:00

POLIVALENTE

Session CV
MICROWAVE MATERIALS AND DEVICES -II (POSTER SESSION)
Masahiro Yamaguchi, Chair

CV-01. Integrated on-chip microstrip lines with Co-Ta-Zr magnetic films. *P. Khalili Amiri*[1], B. Rejaei[1], Y. Zhuang[1], M. Vroubel[1], D. Lee[2], S. Wang[2] and J. Burghartz[3,1] *1. Delft Institute of Microsystems and Nanoelectronics (DIMES), Delft University of Technology, Delft, Netherlands; 2. Department of Materials Science and Engineering, Stanford University, Stanford, CA; 3. Institute for Microelectronics Stuttgart (IMS CHIPS), Stuttgart, Germany*

CV-02. Optimal Design of Microwave Absorbers Using Ferrite-epoxy and Iron-epoxy Composites. *R. Yang*[1], S. Hsu[1], C. Lin[2] and C. Tsay[2] *1. Aerospace and Systems Engineering, Feng Chia University, Taichung, Taiwan; 2. Materials Science and Engineering, Feng Chia University, Taichung, Taiwan*

CV-03. Strong Magnetoelectric Coupling at Microwave Frequencies in Metallic Magnetic Film / PZT Composites. *C.I. Pettiford*[1], J. Lou[1], L. Russell[1] and N.X. Sun[1] *1. Northeastern University, Boston, MA*

CV-04. Nonlinear electrical tuning of ferromagnetic resonance in YIG film - PZT layered structures. *Y. Fetisov*[1] and G. Srinivasan[2] *1. Moscow State Institute of Radio Engineering, Electronics and Automation, Moscow, Russian Federation; 2. Physics Department, Oakland University, Rochester, MI*

CV-05. Generation of chaotic spin waves in magnetic film active feedback rings through four-wave parametric processes. A. Kondrashov[1], A. Ustinov[1], T. Stemler[2], *B. Kalinikos*[1,3], M. Wu[3] and H. Benner[2] *1. Physical Electronics and Technology, St.Petersburg Electrotechnical University, St.Petersburg, Russian Federation; 2. Institute for Solid State Physics, Darmstadt University of Technology, Darmstadt, Germany; 3. Department of Physics, Colorado State University, Fort Collins, CO*

CV-06. Particle Effect of Electromagnetic Penetration in High Frequency in H Field and B Field application. *K. Fujisaki*[1,2] *1. Technical Development Bureau, Nippon Steel Corporation, Futtsu-city, Chiba-prefecture, Japan; 2. Graduate School of Environmetal Studies, Tohoku University, Sendai, Japan*

CV-07. The X-band permittivity of iron-epoxy composites under the magnetic field. *H. Dung Shing*[1], S. Hsu[3], W. Liang[3], C. Lin[2], C. Tsay[2], Y. Yao[4] and R. Yang[3] *1. Department of Information and Tele. Engineering, Ming Chuan University, Taipei, Taiwan; 2. Department of Material Science and Engineering, Feng Chia University, Taichung, Taiwan; 3. Department of Aerospace and Systems Engineering, Feng Chia University, Taichung, Taiwan; 4. Department of Materials Engineering, Tatung University, Taipei, Taiwan*

CV-08. High-frequency Magnetic Properties and Attenuation Characteristics for Barium Ferrite Composites. *Z. Li*[1], G. Lin[1], Y. Wu[1] and L. Kong[1] *1. Temasek Laboratories, National University of Singapore, Singapore, Singapore*

CV-09. High frequency property of polyol-derived FeCo nanoparticles for EWA application. *D. Kodama*[1], K. Shinoda[2], R.J. Joseyphus[3], Y. Shimada[4], K. Tohji[1] and B. Jeyadevan[1] *1. Graduate School of Environmental Studies, Tohoku University, Sendai, Japan; 2. Institute of Multidisciplinary Research for Advanced Materials, Tohoku University, Sendai, Japan; 3. Department of Physics, National Institute of Technology, Tiruchirappalli, India; 4. Department of Electrical and Communication Engineering, Tohoku University, Sendai, Japan*

CV-10. Noise Suppression Effectiveness of Fe-Si-Al Magnetic Composite Thick Film on the Signal Transmission Cable. *K. Lee*[1], D. Kang[1], I. Byun[1], I. Jeong[1] and S. Kim[2] *1. R & D Center, Chang Sung Corporation, Incheon, South Korea; 2. Nano-Materials Research Center, Korea Institute of Science and Technology, KIST, Seoul, South Korea*

CV-11. Microwave absorption properties in Bi-substitute Yttrium Iron Garnet. *D. Hung*[1], Y. Fu[2] and Y. Yao[3] *1. Information & Telecommunications Engineering, Ming Chuang University, Taipei, Taiwan; 2. Department of Materials Science and Engineering,, National Dong Hwa University, Hualien, Taiwan; 3. Department of Materials Engineering, Tatung University, Taipei, Taiwan*

CV-12. Preparation and characterization of nano-fiber nonwoven textile for electromagnetic wave shielding. *M. Sonehara*[1,2], T. Sato[2], M. Takasaki[1], H. Konishi[3], K. Yamasawa[2] and Y. Miura[2] *1. Satellite Venture Business Laboratory, Shinshu University, Ueda, Japan; 2. Spin Device Technology Center, Shinshu University, Nagano, Japan; 3. Faculty of Textile Science and Technology, Shinshu University, Ueda, Japan*

TUESDAY MORNING 9:00 — POLIVALENTE

Session CW
CHARACTERIZATION AND MEASUREMENT TECHNIQUES II (POSTER SESSION)

Philip Marketos, Chair
Stan Zurek, Chair

CW-01. Characterization of iron magnetic nanoparticles by termomagnetogravimetry. J.C. Aphesteguy[1], *S.E. Jacobo*[1], C.E. Rodriguez Torres[2], M.B. Fernández van Raap[2] and F.H. Sanchez[2] *1. Chemistry, Universidad de Buenos Aires, Buenos Aires, Argentina; 2. Physics IFLP (CONICET), FCE, Universidad Nacional de La Plata, La Plata, Argentina*

CW-02. Magnetization reversal study in a permalloy wire with 3 dissimilar trenches by using real-time magnetic force microscopy. *K. Cheng*[1,2], C. Yu[1], S. Lee[1], Y. Liou[1], Y. Yao[3], J. Wu[3] and J. Huang[2] *1. Institute of Physics., Academia Sinica., Taipei, Taiwan; 2. Department of Materials Science and Engineering, National Tsing-Hua University, Hsinchu, Taiwan; 3. Department of Materials Engineering, Tatung University, Taipei, Taiwan*

CW-03. Diffracted magneto-optical Kerr effects of one-dimensional magnetic gratings. *J. Kim*[1], G. Lee[1], Y. Lee[1], J. Rhee[2] and C. Yoon[3] *1. Quantum Photonic Science Research Center and BK21 Program Division of Advanced Research and Education in Physics, Hanyang University, Seoul, South Korea; 2. BK21 Physics Research Division and Department of Physics, Sungkyunkwan University, Suwon, South Korea; 3. Division of Advanced Materials Science, Hanyang University, Seoul, South Korea*

CW-04. Strain induced ferrimagnetism in Mn2As and Fe2As thin films. *J. Kim*[1], Y. Hwang[1], J. Choi[1] and S. Cho[1] *1. Univ.of Ulsan, Ulsan, South Korea*

CW-05. Electron paramagnetic resonance studies of diluted magnetic semiconductors Si<_1-x>Mn<_x>Te<_1.5> crystals. *Y. Hwang*[1], Y. Um[1], J. Choi[1], S. Cho[1], S. Na[2] and J. Kim[2] *1. Physics, University of Ulsan, Ulsan, South Korea; 2. Physics, Pusan National University, Pusan, South Korea*

CW-06. Metallographic Investigations of $Co_2FeAl_{1-x}Si_x$ Heusler-Compounds. *C.G. Blum*[1], G.H. Fecher[1], B. Balke[1] and C. Felser[1] *1. Institut für Anorganische und Analytische Chemie, Johannes Gutenberg-University, Mainz, Germany*

CW-07. Magnetic entropy change in $La_{0.5}Nd_{0.2}Sr_{0.3}MnO_3$ peroveskite. *J. Cho*[1], S. Ko[1], Y. Ahn[1] and E. Choi[2] *1. Chemistry, Konyang University, Nonsan Chungnam, South Korea; 2. Opthalmic Optics, Konyang University, Daejeon, South Korea*

CW-08. Magnetic behavior and magnetoimpedance effect in Cobalt-based ribbons. *A. Rosales-Rivera*[1], M. Gomez-Hermida[1], A. Velasquez[1], D. Muraca[2] and H. Sirkin[2] *1. Laboratorio de Magnetismo y Materiales Avanzados, Universidad Nacional de Colombia, Manizales, Caldas, Colombia; 2. Física, Universidad de Buenos Aires, Buenos Aires, Argentina*

CW-09. Correlation between surface magnetic field and Barkhausen noise in grain-oriented electrical steel. *S. Zurek*[1], P. Marketos[1], S. Tumanski[2], H.V. Patel[3] and A.J. Moses[1] *1. School of Engineering, Cardiff University, Cardiff, Wales, UK, United Kingdom; 2. Institute of Electrical Theory and Measurements, Warsaw University of Technology, Warsaw, Poland; 3. Industry and Innovation Division, National Physical Laboratory, Middlesex, England, United Kingdom*

CW-10. Comparison of properties of magnetoacoustic emission and mechanical Barkhausen effects for P91 steel after plastic flow and creep. *B. Augustyniak*[1], M. Chmielewski[1], L. Piotrowski[1] and Z. Kowalewski[2] *1. Gdansk University of Technology, Gdansk, Poland; 2. Polish Academy of Science, IPPT, Warsaw, Poland*

CW-11. Magnetic and microstructural investigation of pipeline steels. *G. Roland*[1], E. Jose[2], A. Jose[3], K. Franz[4], M. Nasir[1], E. Chistian[1], P. Karin[1] and H. Jose[3] *1. Inst. of Solid State Physics, Techn. Univ. Vienna, Vienna, Austria; 2. ESIME-Zacatenco, Instituto Politécnico Nacional, Mexico City, Mexico; 3. ESIQIE, Instituto Politécnico Nacional, Mexico City, Mexico; 4. Techn Univ Vienna, Inst. f. Sensor u. Atuatorsysteme, Vienna, Austria*

CW-12. A Pulsed Field Magneto-optic Kerr Effect Magnetometer for Studying Magnetic Thin-Films and Nanostructures. *D. Atkinson*[1] and J.A. King[1] *1. Physics, Durham University, Durham, United Kingdom*

CW-13. A novel application of high resolution scanning electron microscopy for perpendicular recording media characterization. *E.T. Yen*[1], L. Lee[1], B. Lu[1] and O. Mryasov[2] *1. Seagate Technology, Fremont, CA; 2. Seagate Technology, Pittsburg, PA*

CW-14. Magnetic image detection of the stainless-steel welding part inside the multi-layered tube structure. *T. Hayashi*[1,2], H. Yamada[1], T. Kiwa[1], K. Tsukada[1] and M. Tamazumi[3] *1. Graduate School of Natural Science & Technology, Okayama University, Okayama, Japan; 2. Pulstec Industrial Co., Ltd, Hamamatsu, Japan; 3. Uno Kogyo Co.,Ltd, Okayama, Japan*

CW-15. Transient Eddy Current Measurement for the Characterization of Depth and Conductivity of a Conductive Plate. *W. Cheng*[1] *1. NDE Center, Japan Power Engineering and Inspection Corporation, Yokohama, Japan*

CW-16. Multidirectional Remanent Flux Leakage Transducers for Evaluation of Stress and Fatigue Loaded Steel Samples. T. Chady[1] and *G. Psuj*[1] *1. Department of Electrical and Computer Engineering, Szczecin University of Technology, Szczecin, Poland*

TUESDAY AFTERNOON 2:30 — AUDITORIO A

Session DA
BIT PATTERNED MEDIA II
Kaizhong Gao, Chair

2:30

DA-01. Understanding Adjacent Track Erasure in Discrete Track Media. *Y. Tang*[1], X. Che[2] and J. Zhu[1] *1. Electrical and Computer Engineering, Carnegie Mellon University, Pittsburgh, PA; 2. Samsung Information Systems America, San Jose, CA*

2:45

DA-02. 10 Tb/in^2 recording simulations on patterned domain wall assisted media. *A.Y. Dobin*[1], H.J. Richter[1], J. Xue[1] and D. Weller[1] *1. Seagate Technology LLC, Fremont, CA*

3:00

DA-03. Patterned media for 10 Tbit/in2 utilizing dual-section "ledge" elements. ***(Invited)*** *V. Lomakin*[1,2], B. Livshitz[1,2], S. Li[1,2], A. Inomata[4], R. Choi[1] and N. Bertram[2,3] *1. ECE, University of California, San Diego, La Jolla, CA; 2. Center for Magnetic Recording Research,, University of California, San Diego, La Jolla, CA; 3. Hitachi San Jose Research Center, San Jose, CA; 4. Storage Systems Laboratories, Fujitsu Laboratories Ltd., Kanagawa, Japan*

3:30

DA-04. Characterization of timing jitter in synchronous writing of bit patterned media. *Y. Tang*[1] and X. Che[1] *1. Samsung, San Jose, CA*

3:45

DA-05. Formation of multilayered Co/Pd nano-dot array with an areal density of 1 Tb/in^2 *J. Wi*[1], H. Lee[1], K. Lim[1], T. Kim[2], K. Shin[3] and K. Kim[1] *1. Department of Materials Science and Engineering, Seoul National University, Seoul, South Korea; 2. Department of Advanced Materials Engineering, Sejong University, Seoul, South Korea; 3. Future Technology Research Division, Korea Institute of Science and Technology, Seoul, South Korea*

4:00

DA-06. SUB 100 nm FePt NANODOT ARRAYS FOR ULTRAHIGH-DENSITY MAGNETIC RECORDING. *H. Ko*[1], P. Alagarsamy[1], K. Lee[1], S. Shin[1], J. Jung[2] and H. Jung[2] *1. Physics, KAIST, Daejeon, South Korea; 2. Chemical and Biomolecular Engineering, KAIST, Daejeon, South Korea*

4:15

DA-07. Dot size dependence of magnetization reversal process in $L1_0$ FePt dot arrays. D. Wang[1], T. Seki[1], *K. Takanashi*[1] and T. Shima[2] *1. Institute for Materials Research, Tohoku University, Sendai, Miyagi, Japan; 2. Faculty of Engineering, Tohoku-gakuin University, Tagajyo, Miyagi, Japan*

4:30

DA-08. Separating dipolar broadening from the intrinsic switching field distribution in perpendicular bit patterned media. *O. Hellwig*[1], A. Moser[1], A. Berger[1,2], T. Thomson[1,3], E. Dobisz[1], Z.Z. Bandic[1], H. Yang[1], D. Kercher[1] and E.E. Fullerton[1,4] *1. San Jose Research Center, Hitachi Global Storage Technologies, San Jose, CA; 2. CIC Nanogune, Donastia, Spain; 3. University of Manchester, Manchester, United Kingdom; 4. Center for Magnetic Recording Research, University of California at San Diego, La Jolla, CA*

4:45

DA-09. Low Temperature Remanence Loop Measurements of Ion-Milled Patterned Media. *B.D. Belle*[1], F. Schedin[1], T.V. Ashworth[2], E.W. Hill[1], P.W. Nutter[1], H.J. Hug[3] and J.J. Miles[1] *1. School of Computer Science, The University of Manchester, Manchester, United Kingdom; 2. Institute fuer Physik, Universitaet Basel, Basel, Switzerland; 3. EMPA, Dübendorf, Switzerland*

5:00

DA-10. Magnetic properties of exchange-coupled composite nanoparticles and nanopatterns. *D. Goll*[1], A. Breitling[1] and S. Macke[1] *1. Max-Planck-Institute for Metals Research, Stuttgart, Germany*

5:15

DA-11. Study of gas cluster ion beam planarization for discrete track magnetic disks. *K. Nagato*[1,2], H. Tani[3], Y. Sakane[4], N. Toyoda[5], I. Yamada[5], M. Nakao[1] and T. Hamaguchi[1] *1. The University of Tokyo, Bunkyo-ku, Tokyo, Japan; 2. Japan Society for the Promotion of Science, Chiyoda-ku, Tokyo, Japan; 3. Hitachi Global Storage Technologies Japan Ltd., Odawara-shi, Kanagawa-ken, Japan; 4. Western Digital Media Operations, San Jose, CA; 5. University of Hyogo, Himeji-shi, Hyogo-ken, Japan*

TUESDAY AFTERNOON 2:30 — MADRID

Session DB
SYMPOSIUM ON MAGNETIC MODELING
Oksana Fesenko Chubykalo, Chair

2:30

DB-01. Dynamic edge mode modeling and edge property measurements in magnetic nanostructures. ***(Invited)*** *R.D. McMichael*[1,3], B.B. Maranville[2,3], D.W. Abraham[4], C.A. Ross[5] and V.P. Chuang[5] *1. Center for Nanoscale Science and Technology, NIST, Gaithersburg, MD; 2. Center for Neutron Research, NIST, Gaithersburg, MD; 3. Metallurgy Divison, NIST, Gaithersburg, MD; 4. IBM Thomas J. Watson Research Center, Yorktown Heights, NY; 5. Department of Materials Science and Engineering, Massachusetts Institute of Technology, Cambridge, MA*

3:00

DB-02. Spin injection driven magnetization dynamics: physical insights gained from numerical micromagnetics. ***(Invited)*** *D.V. Berkov*[1] and J. Miltat[2] *1. Magnetic and Optical Systems, Innovent Technology Development, Jena, Germany; 2. Laboratoire de Physique des Solides, University Paris-Sud & CNRS, Orsay, France*

3:30

DB-03. Hierarchical multi-scale model: application to FePt. ***(Invited)*** *U. Nowak*[1] *1. Physics, University of York, York, United Kingdom*

4:00

DB-04. Micromagnetics of Patterned Media Recording. ***(Invited)*** *T. Schrefl*[1], A. Goncharov[1], J. Dean[1], G. Hrkac[1] and S. Bance[1] *1. University of Sheffield, Sheffield, United Kingdom*

4:30

DB-05. MODELING THE MAGNETIC PROPERTIES OF NANOPARTICLES: FINITE-SIZE, SURFACE AND EXCHANGE BIAS EFFECTS. ***(Invited)*** *O. Iglesias*[1,2], X. Batlle[1,2] and A. Labarta[1,2] *1. Dpt. Física Fonamental, Universitat de Barcelona, Barcelona, Spain; 2. Institut de Nanociència i Nanotecnologia de la UB (IN2UB), Barcelona, Spain*

5:00

DB-06. Modeling the temperature dependent free energy barrier for magnetization reversal in nanomagnets. ***(Invited)*** *T.C. Schulthess*[1], C. Zhou[1], O.N. Mryasov[2], D.M. Nicholson[1], M. Eisenbach[1] and P.R. Kent[1] *1. Oak Ridge National Laboratory, Oak Ridge, TN; 2. Seagate Research, Pittsburgh, PA*

TUESDAY AFTERNOON 2:30 — ROMA

Session DC
GMR IN NANOCONTACTS AND CONSTRICTIONS
Jeff Childress, Chair

2:30

DC-01. Effective resistance mismatch and magnetoresistance of a CPP-GMR system with current-confined-paths. *J. Sato*[1], K. Matsushita[1] and H. Imamura[1] *1. Advanced Industrial Science and Technology, Tsukuba, Japan*

2:45

DC-02. Current-perpendicular-to-plane magnetoresistances of CoFeB-based exchange-biased spin valves and CoFeB/Ru multilayers. *C. Ahn*[1], K. Shin[1] and W. Pratt Jr.[2] *1. Center for Spintronics Research, Korea Institute of Science and Technology, Seoul, South Korea; 2. Department of Physics and Astronomy, Michigan State University, East Lansing, MI*

3:00

DC-03. Magnetoresistance and switching properties of Co_xFe_{100-x}/Pd-based perpendicular anisotropy single and dual spin valves without exchange bias. *R. Law*[1,2], R. Sbiaa[1], T. Liew[1] and T. Chong[1] *1. Data Storage Institute, A*STAR (Agency for Science, Technology and Research), Singapore, Singapore; 2. NUS Graduate School for Integrative Sciences & Engineering, National University of Singapore, Singapore, Singapore*

3:15

DC-04. Magnetic structure of domain walls confined in a nano-oxide layer. *K. Matsushita*[1], J. Sato[1] and H. Imamura[1] *1. Nanotechnology Research Institute, AIST, Tsukuba, Ibaraki, Japan*

3:30

DC-05. MICROMAGNETIC STUDY ON DOMAIN WALL SIZE FOR NANOCONTACT MAGNETORESISTANCE IN SPIN VALVE STRUCTURE. *M. Takagishi*[1], H.N. Fuke[1], S. Hashimoto[1] and H. Iwasaki[1] *1. Corporate R&D Center, TOSHIBA Corporation, Kawasaki, Japan*

3:45

DC-06. Effect of surface scattering on magnetoresistance. X. Chen[1] and *R.H. Victora*[2] *1. Department of Physics, University of Minnesota, Minneapolis, MN; 2. Department of Electrical & Computer Engineering, University of Minnesota, Minneapolis, MN*

4:00

DC-07. CPP-GMR characteristics of full epitaxial spin valves film with alternate monatomic $[Fe/Co]_n$ superlattice. I. Chu[1], *T. Mano*[1], M. Doi[1] and M. Sahashi[1] *1. Department of Electronic Engineering, Tohoku University, Sendai, Japan*

4:15

DC-08. Spin transfer magnetization dynamics in ultra small nanocontacts elaborated by CT-AFM nanolithography. M. Darques[1], B. Georges[1], A. Ruotolo[1], *V. Cros*[1], S. Fusil[1], J. Grollier[1], R. Guillemet[1], K. Bouzehouane[1], C. Deranlot[1] and A. Fert[1] *1. Unite Mixte de Physique CNRS/Thales, Palaiseau, France*

4:30

DC-09. Layered annular magnetic bridges for storage and logic applications. *F.J. Castano*[1], B.G. Ng[1], C.H. Nam[1] and C.A. Ross[1] *1. Depart. of Material Science and Engineering, MIT, Cambridge, MA*

4:45

DC-10. Investigation of strong biquadratic coupling in Co_2MnSi based trilayer structures. *Y. Sakuraba*[1], S. Bosu[1], K. Saito[1], H. Wang[1], S. Mitani[1] and K. Takanashi[1] *1. Institute for materials research, Tohoku univ., Sendai, Miyagi, Japan*

5:00

DC-11. CPP magnetoresistance effect through Graphene sheets. *E.W. Hill*[1], T.G. Mohiuddin[1], D. Elias[1], A.K. Geim[1], F. Schedin[1], K. Novoselov[1], P. Blake[1] and A. Zhukov[1] *1. Centre for Mesoscience and Nanotechnology, The University of Manchester, Manchester, United Kingdom*

5:15

DC-12. Magnetoresistance and energy model of Alq3-based spintronic devices. *L.E. Hueso*[1,2], V. Dediu[2], I. Bergenti[2], A. Riminucci[2], P. Graziosi[2], F. Borgatti[2], F. Cassoli[3], Y. Zhan[2], C. Taliani[2] and M.P. de Jong[4] *1. Department of Physics, University of Leeds, Leeds, United Kingdom; 2. ISMN, CNR, Bologna, Italy; 3. IMEM, CNR, Parma, Italy; 4. Nanoelectronics Group, University of Twente, Enschede, Netherlands*

TUESDAY
AFTERNOON
2:30

PARIS

Session DD
PERMANENT MAGNET MACHINES II
Antero Arkkio, Chair

2:30

DD-01. A novel 'pseudo' direct-drive brushless permanent magnet machine. *K. Atallah*[1], J. Rens[1], S. Mezani[1] and D. Howe[1] *1. Electronic & Electrical Engineering, The University of Sheffield, Sheffield, United Kingdom*

2:45

DD-02. Design optimization of a single-phase permanent magnet synchronous generator. *J. El Hayek*[1], J. Brünisholz[2] and P. Pittet[3] *1. Industrial Technologies, University of Applied Sciences Western Switzerland, Fribourg, Switzerland; 2. ATPS, ABB, Turgi, Switzerland; 3. Power Service, ALSTOM Ltd, Baden, Switzerland*

3:00

DD-03. An Ultra-High Speed PM Motor for Small Milling Machine Applications. J. Asama[1], *K. Maruyama*[1], Y. Yanagihara[1] and A. Chiba[1] *1. Electrical Engineering, Tokyo University of Science, Noda, Chiba, Japan*

3:15

DD-04. Design and analysis of a novel hybrid excitation synchronous machine with asymmetrically stagger permanent magnet. Y. Chengfeng[1], *L. Heyun*[1], G. Jian[1] and Z. Ziqiang[2] *1. School of Electrical Engineering, Southeast University, Nanjing, China; 2. Department of Electronic and Electrical Engineering, University of Sheffield, Sheffield, United Kingdom*

3:30

DD-05. Novel axial flux permanent magnet synchronous machines with segmented and laminated stator configuration. *W. Fei*[1] and P. Luk[1] *1. Department of Aerospace Power and Sensors, DCMT Cranfield University, Shrivenham, Wiltshire SN6 8LA, United Kingdom*

3:45

DD-06. Modeling of a linear and rotative permanent magnet actuator. *G. Krebs*[1], A. Tounzi[1], B. Pauwels[2], D. Willemot[2] and F. Piriou[1] *1. L2EP-USTL, Villeneuve d'Ascq, France; 2. Psicontrol Mechatronics, Ieper, Belgium*

4:00

DD-07. Analysis and experimental verification of a single phase, quasi-Halbach magnetised tubular permanent magnet motor with non-ferromagnetic supporting tube. *J. Wang*[1], T. Ibrahim[1] and D. Howe[1] *1. Electronic and Electrical Engineering, University of Sheffield, Sheffield, United Kingdom*

4:15

DD-08. Optimization of a sea wave energy harvesting electromagnetic device. *M. Trapanese*[1] *1. Dipartimento di Ingegneria Elettrica, Elettronica e delle Telecomunicazioni, University of Palermo, Palermo, Italy*

4:30

DD-09. Design and characteristic analysis on the short-stator linear synchronous motor for high-speed Maglev propulsion. *H. Cho*[1], H. Sung[1], S. Sung[1], D. You[2] and S. Jang[2] *1. Maglev Research Team, Korea Institute of Machinery and Materials, Daejeon, South Korea; 2. Electrical Engineering, Chungnam National University, Daejeon, South Korea*

4:45

DD-10. Eddy-current stator solid steel back-iron losses in small rotary brushless permanent magnet machines. *J.J. Paulides*[1], K.J. Meessen[1] and E.A. Lomonova[1] *1. Technical university Eindhoven, Eindhoven, Netherlands*

5:00

DD-11. Experimental Method and Verification to Characterize the Unbalanced Magnetic Force in Electric Motors. *C. Lee*[1] and G. Jang[1] *1. Dept. of Mechanical Engineering, PREM Lab., Hanyang University, Seoul, South Korea*

5:15

DD-12. Study of an electromagnetic gearbox involving two PM synchronous machines using 3D-FEM. *M. Aubertin*[1], A. Tounzi[1] and Y. Le Ménach[1] *1. L2EP - USTL, Villeneuve d'Ascq, France*

TUESDAY
AFTERNOON
2:30

LONDRES

Session DE
SOFT MAGNETIC WIRES
Kleber Pirota, Chair

2:30

DE-01. Domain wall propagation in thin magnetic wires. ***(Invited)*** *R. Varga*[1], K. Richter[1], A. Zhukov[2] and V. Larin[3] *1. Institute of Physics, Faculty of Sciences, UPJS, Kosice, Slovakia; 2. Dept. Fisica de Materiales, Fac. Quimica, UPV/EHU, San Sebastian, Spain; 3. MFTI, Kishinev, Moldova*

3:00

DE-02. Domain wall propagation in nearly zero magnetostrictive amorphous microwires. *H. Chiriac*[1], T. Óvári[1] and M. Tibu[1] *1. National Institute of Research and Development for Technical Physics, Iasi, Romania*

3:15

DE-03. Electromagnetic wave absorbing material based on magnetic microwires. *P. Marín*[1,2], D. Cortina[3] and A. Hernando[1,2] *1. Instituto de Magnetismo Aplicado, Universidad Complutense de Madrid, Las Rozas, Madrid, Spain; 2. Física de Materiales, Universidad Complutense de Madrid, Madrid, Spain; 3. Micromag 2000, S.L., Las Rozas, Spain*

3:30

DE-04. Experimental determination of relation between helical anisotropy and torsion stress in amorphous magnetic microwires. *A. Chizhik*[1], A. Zhukov[1], J. Blanco[2], J. Gonzalez[1], P. Gawronski[3] and K. Kulakowski[3] *1. Dpto. Fisica de Materiales, Universidad del Pais Vasco, San Sebastian, Giupuzcoa, Spain; 2. Departamento Física Aplicada I, EUPDS, Universidad del Pais Vasco, San Sebastian, Guipuzcoa, Spain; 3. Faculty of Physics & Applied Computer Science, AGH University of Science & Technology, Cracow, Poland*

3:45

DE-05. Circular magnetoelastic anisotropy induced in the nucleus of FeSiB/CoNi soft-hard biphase microwire. *J. Torrejón*[1], M. García-Hernández[1], G. Infante[1], K.J. Merazzo[1] and G. Badini[1] *1. Magnetism, ICMM (CSIC), Madrid, Madrid, Spain*

4:00

DE-06. Temperature behaviour of magnetic anisotropy of nanocrystallized Finemet-based glass-coated microwires. *V. Dubuget*[1,2], A. Adenot-Engelvin[1] and F. Bertin[1] *1. CEA, Monts, France; 2. LEMA, UMR CNRS 6157, TOURS, France*

4:15

DE-07. Temperature Dependence of the Magnetization Reversal Process and Domain Structure in Fe77.5-xNixSi7.5B15 Magnetic Microwires. J. Olivera[1,2], *M. Sánchez*[1], V.M. Prida[1], R. Varga[2], V. Zhukova[3], A.P. Zhukov[3] and B. Hernando[1] *1. Fisica, Universidad de Oviedo, Oviedo, Asturias, Spain; 2. Inst. Physics, Fac. Sci., UPJS, Park Angelinum, Kosice, Slovakia; 3. Dpto. de Física de Materiales, Fac. Químicas, Universidad del Pais Vasco, San Sebastián, Guipúzcoa, Spain*

4:30

DE-08. Synthesis and Characterization of Fe/FeOx Core/Shell Nanowires. *J. Lee*[1], J. Lee[1], K. Jeon[2], J. Wu[1], H. Kim[1], J. Lee[1], Y. Suh[2] and Y. Kim[1] *1. Department of Materials Science and Engineering, Korea University, Seoul, Seoul, South Korea; 2. Fusion Biotechnology Research Center, Korea Research Institute of Chemical Technology, Daejeon, South Korea*

4:45

DE-09. Structure and Magnetic properties of electrodeposited cobalt nanowires in polycarbonate membrane. *S.r. Vishnubhotla*[1], C. Kim[1] and S. Yoon[2] *1. Chungnam National University, Daejeon, South Korea; 2. Andong National University, Daejeon, South Korea*

5:00

DE-10. Structural and thermal behaviour of nanocrystalline nanowires. M.J. Vieyra[1], *T. Meydan*[1] and F. Borza[1] *1. Cardiff School of Engineering, Wolfson Centre for Magnetics, Cardiff, South Glamorgan, United Kingdom*

5:15

DE-11. Silicon steel wire with low magnetic losses. *T. Yonamine*[1], M. Fukuhara[1], N.A. Castro[2], F.G. Landgraf[3] and F.P. Missell[1,4] *1. Divisão de Metrologia de Materiais, Instituto Nacional de Metrologia, Normalização e Qualidade Industrial-INMETRO, Duque de Caxias, Rio de Janeiro, Brazil; 2. Instituto de Pesquisas Tecnológicas-IPT, São Paulo, São Paulo, Brazil; 3. Departamento de Metalurgia e Materiais, Escola Politécnica da Universidade de São Paulo - EPUSP, São Paulo, São Paulo, Brazil; 4. Centro de Ciências Exatas e Tecnológicas, Universidade de Caxias do Sul, Caxias do Sul, Rio Grande do Sul, Brazil*

TUESDAY AFTERNOON 2:30 — BERLIN

Session DF
RECORDING SYSTEMS AND SERVO I
Aleksandar Kavcic, Chair

2:30

DF-01. A proposed "747" test to establish the areal-density capability of a magnetic recording system based only on data-block failure rate. Z. Jin[1], M. Salo[1] and *R. Wood*[1] *1. HDD AdTech, Hitachi GST, San Jose, CA*

2:45

DF-02. Probabilistic Analysis of Off-track Capability for Higher Track Density Disk Drives. *K. Aruga*[1], H. Ueno[1], T. Iwase[1] and Y. Ogawa[1] *1. HDD division (E3-333), Fujitsu Limited, Kawasaki, 211-8588, Japan*

3:00

DF-03. Analysis of cross track response using a three dimensional model for Perpendicular Read Heads. *Z. Liu*[1], B. Chen[1] and S. Zhang[1] *1. Data Storage Institute, Singapore, Singapore*

3:15

DF-04. The reliability evaluation of piezoelectric micro actuators with application in hard disk drives. *Z. He*[1], H. Loh[2] and E. Ong[1] *1. A*Star, Data Storagae Institute, Singapore, Singapore; 2. Mechanical Engineering Department, National University of Singapore, Singapore, Singapore*

3:30

DF-05. A slider with an integrated microactuator (SLIM) for second stage actuation in hard disc drives. *H.H. Gatzen*[1], P.J. Freitas[2], E. Obermeier[3] and J. Robertson[4] *1. Institute for Microtechnology, Leibniz Universitaet Hannover, Garbsen, Germany; 2. INESC-MN, Lisboa, Portugal; 3. Microsensor & Actuator Technology, Berlin University of Technology, Berlin, Germany; 4. Department of Engineering, University of Cambridge, Cambridge, United Kingdom*

3:45

DF-06. Integrated electromagnetic second stage micro actuator for a hard disk recording head. *D. Dinulovic*[1], H. Saalfeld[1] and H.H. Gatzen[1] *1. Institute for Microtechnology, Leibniz Universitaet Hannover, Garbsen, Germany*

4:00

DF-07. Characterization of timing based servo signals. G. Cherubini[1], *R.D. Cideciyan*[1], E. Eleftheriou[1] and P.V. Koeppe[2] *1. IBM Research, Zurich Research Laboratory, Rueschlikon, Switzerland; 2. IBM Systems and Technology Group, San Jose, CA*

4:15

DF-08. Evaluation of printed servo patterns. *B. Baker*[1] *1. Redwood Technology, Redwood City, CA*

4:30

DF-09. Overwrite performance change due to air-flow induced vibration of head stack assembly. *E. Jang*[1] and J. Chang[1] *1. HDD R&D, Samsung Information Systems America, San Jose, CA*

4:45

DF-10. Reduced Order Models for Efficient Simulation of Hard Disk Drive Operational Shock Responses. *W. Lin*[1], E. Ong[1], J. Mou[1], E. Ong[1] and S. Hu[2] *1. Data Storage Institute, Singapore, Singapore; 2. Nitto Denko Corporation, Kameyama, Japan*

5:00

DF-11. A Case for Redundant Arrays of Hybrid Disks (RAHD). *F. Wang*[1], N. Helian[1], D. Deng[1], S. Wu[1], C. Liao[1], M. Rashidi[1] and A. Parker[2] *1. Centre for Grid Computing, Cambridge-Cranfield HPCF, Cranfield, United Kingdom; 2. Cavendish Laboratory, Cambridge University, Cambridge, United Kingdom*

5:15

DF-12. What is the future of hard disk drive, death or rebirth? *Y. Deng*[1], F. Wang[1] and N. Helian[2] *1. School of Engineering, Cranfield University, Bedforshire, United Kingdom; 2. London Metropolitan University, London, United Kingdom*

TUESDAY AFTERNOON 2:30 — AMSTERDAM

Session DG
LIFE SCIENCES: TECHNIQUES AND INSTRUMENTATION I
Quentin Pankhurst, Chair

2:30

DG-01. Signal and Power Transmission in Real-time Internal Irradiation Dose Measurement System. *K. Shinohe*[1], T. Takura[1], F. Sato[1], H. Matsuki[1], S. Yamada[2] and T. Sato[3] *1. Graduate School of Engineering, Tohoku University, Sendai, Miyagi, Japan; 2. Graduate School of Medicine, Tohoku University, Sendai, Miyagi, Japan; 3. NEC Torkin Corp., Sendai, Miyagi, Japan*

2:45

DG-02. Imaging of electric permittivity and conductivity using MRI. *M. Sekino*[1], S. Tatara[1] and H. Ohsaki[1] *1. Department of Advanced Energy, Graduate School of Frontier Sciences, The University of Tokyo, Kashiwa, Chiba, Japan*

3:00

DG-03. Optimization of coil structure in resonant circuit implant for hyperthermia using MRI. J. Kunisaki[1], M. Shimizu[1], K. Kamio[1], S. Hiroe[1], T. Yamada[1] and *Y. Takemura*[1] *1. Division of Electrical and Computer Engineering, Yokohama National University, Yokohama, Japan*

3:15

DG-04. Calculation of minimum parameters required for low-field low-size nano nuclear magnetic resonance (nanoNMR). *P. Gomez*[1,2], S. Khizroev[2] and D. Litvinov[3] *1. Electrical Engineering, Florida International University, Miami, FL; 2. Electrical Engineering, University of California Riverside, Riverside, CA; 3. Electrical Engineering, University of Texas, Houston, TX*

3:30

DG-05. Microwave radiometry for early breast cancer detection. *M.P. Costin*[1,2] and O. Baltag[2] *1. Computer Science Institute, Romanian Academy, Iasi, Romania; 2. Faculty of Biomedical Engineering, University of Medicine and Pharmacy, IASI, IASI, Romania*

3:45

DG-06. Microwave resonator devices for ferromagnetic resonance detection of magnetic beads. *S. Ghionea*[1], P. Dhagat[1] and A. Jander[1] *1. Department of Electrical Engineering and Computer Science, Oregon State University, Corvallis, OR*

4:00

DG-07. Magnetic Immunoassays – New Methods of Biochemical Diagnostics Based on Detection of Magnetic Nanoparticles by Non-Linear Magnetization. *P. Nikitin*[1], P. Vetoshko[2], M. Nikitin[3] and T. Ksenivich[1] *1. Natural Science Center, General Physics Institute, Russian Academy of Sciences, Moscow, Russian Federation; 2. Institute of Radioengineering and Electronics, Russian Academy of Sciences, Moscow, Russian Federation; 3. Department of Molecular & Biological Physics, Moscow Institute of Physics & Technology, Dolgoprudny, Moscow Region, Russian Federation*

4:15

DG-08. Giant magnetoresistance sensors for lateral flow tests. *C. Marquina*[1], J.M. De Teresa[1], J. Sesé[2], V. Grazú[2], B. Velasco[3], P. Freitas[4] and R. Ibarra[1,2] *1. Instituto de Ciencia de Materiales de Aragon, CSIC-Universidad de Zaragoza, Zaragoza, Spain; 2. Instituto de Nanociencia de Aragon, Universidad de Zaragoza, Zaragoza, Spain; 3. CerTest Biotec, Zaragoza, Spain; 4. INESC, MN, Inst Engn Sistemas Computadores Microsyst & Nanot, Lisbon, Portugal*

4:30

DG-09. Magnetic-Entasis Biorecognition Platform: Self Assembly of Magnetic Nanoparticles for Detection of Magnetically Labeled Biomolecules. Y. Yamamoto[1], T. Yamanaka[1], *Y. Morimoto*[1], S. Sakamoto[3], Y. Mochiduki[3], M. Abe[4], H. Handa[3] and A. Sandhu[1,2] *1. Quantum Nanoelectronics Research Center, Tokyo Institute of Technology, Tokyo, Japan; 2. Department of Electrical and Electronic Engineering, Tokyo Institute of Technology, Tokyo, Japan; 3. Graduate School of Bioscience and Biotechnology, Tokyo Institute of Technology, Tokyo, Japan; 4. Department of Physical Electronics, Tokyo Institute of Technology, Tokyo, Japan*

4:45

DG-10. Magnetic bar array with linker technology for detection and investigation of non-magnetic molecules. *D. Lee*[1], L.A. Roberts[2], E. Peroziello[3], R. Fontana[4], S. Maat[4], M. Nemat-Gorgani[2], S. Hoon[2] and R.L. White[1] *1. Dept. of Materials Science and Engineering, Stanford University, Stanford, CA; 2. Stanford Genome Technology Center, Stanford University, Stanford, CA; 3. Center for Integrated Systems, Stanford University, Stanford, CA; 4. Hitachi Global Storage Technologies, San Jose, CA*

TUESDAY AFTERNOON 2:30

POLIVALENTE

Session DL
ULTRATHIN FILMS AND SURFACE EFFECTS I (POSTER SESSION)
Alexandra Mougin, Chair

DL-01. Voltage control of magnetic anisotropy in an ultrathin Fe film. *T. Maruyama*[1], K. Ohta[1], N. Toda[1], T. Nozaki[1], T. Shinjo[1], M. Shiraishi[1] and Y. Suzuki[1] *1. Engineering science, Osaka university, Toyonaka, Japan*

DL-02. Angular dependence of two magnon scattering in ultrathin ferromagnets. *P. Landeros*[1], R.E. Arias[2] and D.L. Mills[3] *1. Departamento de Física, Universidad Técnica Federico Santa María, Valparaíso, Valparaíso, Chile; 2. Departamento de Física, Universidad de Chile, Santiago, Chile; 3. Department of Physics and Astronomy, University of California, Irvine, CA*

DL-03. CEMS study of epitaxial $Co_2Cr_{0.6}Fe_{0.4}Al$ thin films. *V. Ksenofontov*[1], C. Herbort[2], M. Jourdan[2] and C. Felser[1] *1. Institute of Inorganic and Analytical Chemistry, Johannes Gutenberg-University Mainz, 55099 Mainz, Germany; 2. Institute of Physics, Johannes Gutenberg - University, 55099 Mainz, Germany*

DL-04. Morphology-induced oscillations of the electron-spin motion in Fe films on Ag(001). *L. Tati Bismaths*[1], L. Joly[2], F. . Scheurer[1] and W. Weber[1] *1. Institut de Physique et Chimie des Matériaux de Strasbourg,, Strasbourg, France; 2. Swiss Light Source, Villigen, Switzerland*

DL-05. Ferromagnetic Resonance of Disordered FePt Thin Films. J. Gómez[1], M. Vásquez Mansilla[1] and *A. Butera*[1] *1. Centro Atomico Bariloche and Instituto Balseiro, Bariloche, Rio Negro, Argentina*

DL-06. Magnetization processes in ultrathin Co film grown on stepped Si(111) substrate. *A. Stupakiewicz*[1,2], A. Fleurence[2], A. Maziewski[1], T. Maroutian[2], P. Gogol[2], B. Bartenlian[2], R. Mégy[2] and P. Beauvillain[2] *1. University of Bialystok, Bialystok, Poland; 2. Institut d'Electronique Fondamentale, Universite Paris XI, CNRS, UMR 8622, Orsay, France*

DL-07. Effects of Co/Sm composition on the ordered phase formation in Sm-Co thin films grown on Cu(111) single-crystal underlayers. *Y. Nukaga*[1], M. Ohtake[1], F. Kirino[2] and M. Futamoto[1] *1. Faculty of Science and Engineering, Chuo University, Tokyo, Japan; 2. Graduate School of Fine Arts, Tokyo National University of Fine Arts and Music, Tokyo, Japan*

DL-08. Analysis of the multiferroic properties in $BiMnO_3$ epitaxial thin films. *M. Grizalez*[1,2], J.C. Caicedo[2] and P. Prieto[3] *1. Universidad de la Amazonia, Florencia, Caquetá, Colombia; 2. Universidad del Valle, Cali, Valle del Cauca, Colombia; 3. Centro de Excelencia en Nuevos Materiales, Cali, Valle del Cauca, Colombia*

DL-09. Electric and magnetic properties of multiferroic $BiFeO_3$ and $YMnO_3$ thin films. J.A. Zapata[1], J. Narvaez[1], W. Lopera[1], *M.H. Gómez*[1] and P. Prieto[2] *1. Physics, Universidad del Valle, Cali, Valle del Cauca, Colombia; 2. Centro de Exelencia en Nuevos Materiales, Cali, Valle del Cauca, Colombia*

DL-10. Graphene/Ni(111) system: Spin- and angle-resolved photoemission studies. Y.S. Dedkov[1], *M. Fonin*[2], U. Rüdiger[2] and C. Laubschat[1] *1. TU Dresden, Dresden, Germany; 2. University of Konstanz, Konstanz, Germany*

DL-11. Epitaxial growth of SrM(00*l*) film on Au(111). *A. Kaewrawang*[1], G. Ishida[1], X. Liu[1] and A. Morisako[1] *1. Information Engineering, Shinshu University, Nagano, Japan*

DL-12. Surface characteristics of atomic-level Co-Cu thin film system : Molecular dynamics simulation. *B. Kim*[1], K. Chae[1] and Y. Chung[1] *1. Department of Materials Science and Engineering, Hanyang University, Seoul, South Korea*

DL-13. Measurement of interface pinning at a metallic ferromagnetic thin film interface using inductive magnetometry. *K.J. Kennewell*[1], M. Ali[2], M. Kostylev[1], D. Greig[2], B.J. Hickey[2] and R.L. Stamps[1] *1. School of Physics, University of Western Australia, Crawley, WA, Australia; 2. Department of Physics & Astronomy, University of Leeds, Leeds, United Kingdom*

DL-14. Study of the magnetic properties of MnAs thin films as a function of the film thickness. *J. Milano*[1,2], L.B. Steren[1,2], A. Repetto Llamazares[2], V. Garcia[3], M. Marangolo[3], M. Eddrief[3] and V.H. Etgens[3] *1. CNEA-CONICET, San Carlos de Bariloche, Río Negro, Argentina; 2. Instituto Balseiro, UNCuyo, San Carlos de Bariloche, Río Negro, Argentina; 3. Institut des NanoSciences de Paris, INSP, Université Pierre et Marie Curie-Paris 6, Université Denis Diderot-Paris 7, CNRS UMR 7588, París, France*

DL-15. Fe-doping Effect on Morphologic and Magnetotransport Properties of La2/3Ca1/3Fe1-yMnyO3 thin films. *O.L. Arnache Olmos*[1], A. Hoffmann[2], D.A. Giratá[1] and M.E. Gomez[3] *1. Instituto de Física, Universidad de Antioquia, Medellín, Antioquia, Colombia; 2. Materials Science Division, Argonne National Laboratory, Argonne, IL; 3. Department of Phisics, Universidad del Valle, Cali, Valle, Colombia*

TUESDAY AFTERNOON 2:30

POLIVALENTE

Session DM
ULTRATHIN FILMS AND SURFACE EFFECTS II (POSTER SESSION)
Juergen Fassbender, Chair

DM-01. A study on surface magneto-optical Kerr effect of ultra thin Fe films on various GaAs substrates. *W. Guan*[1], T. Shen[1] and G. Jones[1] *1. Joule Physics Laboratory, University of Salford, Salford, United Kingdom*

DM-02. Composite oxide buffer layers for (002) Fe/MgO/Fe magnetic tunneling junctions. *H. Huang*[1], P. Huang[1] and C. Lai[1] *1. Department of Materials Science and Engineering, National Tsing Hua University, Hsinchu, Taiwan*

DM-03. Stripe magnetic domains in sputtered permalloy films. *D. Hrabovský*[1], M. Rubio-Roy[2], J. Caicedo-Roque[1], E. Bertan[2] and J. Fontcuberta[1] *1. ICMAB - CSIC, Bellaterra, Spain; 2. FAO, University of Barcelona, Barcelona, Spain*

DM-04. Influence of capping layers on magnetic anisotropy in Fe/MgO/GaAs(100) ultrathin films. *P. Wong*[1], W. Zhang[1], Y. Xu[1], Y. Fu[2], Z. Huang[2], Y. Zhai[2], Y. Xu[3], H. Zhai[3] and S.M. Thompson[4] *1. Spintronics and Nanodevice Laboratory, Department of Electronics, University of York, York, United Kingdom; 2. Department of Physics, Southeast University, Nanjing, China; 3. Center for Materials Analysis, Nanjing University, Nanjing, China; 4. Department of Physics, University of York, York, United Kingdom*

DM-05. Calculation of resonant standing spin wave mode response induced by a coplanar stripline. *K.J. Kennewell*[1], M. Kostylev[1] and R.L. Stamps[1] *1. School of Physics, University of Western Australia, Crawley, WA, Australia*

DM-06. Ga^+ ion irradiation-induced out-of-plane magnetization in Pt/Co(3nm)/Pt films. *J. Jaworowicz*[1,2], M. Kisielewski[1,2], A. Maziewski[1,2], I. Sveklo[1], J. Jamet[1], J. Ferré[1], . Mougin[1], N. Vernier[1] and J. Fassbender[3] *1. Laboratoire de Physique des Solides, Orsay, France; 2. Laboratory of Magnetism, University of Bialystok, Bialystok, Poland; 3. Institute of Ion Beam Physics and Materials Research, Forschungszentrum Dresden-Rossendorf, Dresden, Germany*

DM-07. Intermixing and spin-pumping effects on Gilbert damping of CoFeB. *S. Huang*[1], C. Wang[1], J. Song[1], C. Lai[1], W. Chen[2], S. Yang[2], K. Shen[2] and H. Bor[3] *1. Department of Materials Science and Engineering, National Tsing Hua University, Hsinchu, Taiwan; 2. Electronics Research and Service Organization, Industrial Technology Research Institute, Hsinchu, Taiwan; 3. Materials and Electro-Optics Research Division, Chuang-Shan institute of Science and Technology, Taoyoun, Taiwan*

DM-08. FMR Studies of $Ga_{1-x}Mn_xAs$ thin layers with x>0.1. *K. Khazen*[1], M. Cubukcu[1], H. von Bardeleben[1], J. Cantin[1], S. Ohya[2,3], K. Ohno[2] and M. Tanaka[2] *1. Institut des NanoSciences de Paris(INSP)Université- Paris 6, UMR 7588 au CNRS, Paris, Ile de France, France; 2. Electronic Engineering, The University of Tokyo, Tokyo, Japan; 3. Japan Science and Technology Agency, Kawaguchi-shi, Saitama, Japan*

DM-09. Large scale surface magnetic domains in magnetite thin films studied by spin-polarized scanning electron microscopy. *E. Kaji*[1], A. Subagyo[1] and K. Sueoka[1] *1. Graduate School of Information Science and Technology, Hokkaido University, Sapporo, Japan*

DM-10. Determination of the Gilbert damping factor in $Ga_{0.93}Mn_{0.07}As$/GaAs Thin Layers. *K. Khazen*[1], M. Cubukcu[1], H. von Bardeleben[1], J. Cantin[1], V. Novak[2], K. Olejnik[2] and M. Cukr[2] *1. Institut des NanoSciences de Paris(INSP)Université- Paris 6, UMR 7588 au CNRS, Paris, Ile de France, France; 2. Institute of Physics AS CR, Praha, Czech Republic*

DM-11. Experimental evidence for bulk and interfacial contributions to static and dynamic properties of Py/Al$_2$O$_3$. C. Le Graet[1], D.T. Dekadjevi[1], S. Pogossian[1], D. Spenato[1] and *J. Ben Youssef*[1] *1. Physics, LMB/UBO/CNRS, Brest, Bretagne, France*

DM-12. Asymmetry of polycrystalline Fe thin films showing bcc (110) growth orientation on glass substrates using second-harmonic generation. *F. Lee*[1], J. Jeong[1], H. Lee[1], K. Lee[1], J. Kim[1] and S. Shin[1] *1. department of Physics, Korea Advanced Institute of Science, Daejeon, South Korea*

DM-13. Transition to antiferromagnetic interlayer coupling at the Cu spacer thickness of 2 nm in bottom spin valve films with $Co_{1-x}Fe_x$/Cr-NOL. *K. Sawada*[1], K. Futatsukawa[1], M. Doi[1], N. Hasegawa[2] and M. Sahashi[1] *1. Tohoku university, Sendai, Japan; 2. ALPS electric corporation, Niigata, Japan*

DM-14. The Effect of CoFe Surface Pre-Oxidation on Magnetic Tunnel Junctions. *P. Pong*[1] and W.F. Egelhoff[1] *1. Magnetic Materials Group, National Institute of Standards and Technology, Gaithersburg, MD*

TUESDAY AFTERNOON 2:30 **POLIVALENTE**

Session DN
MAGNETIC MICROSCOPY II (POSTER SESSION)
Manfred Rührig, Chair

DN-01. Time-resolved magnetization dynamics in magnetic microstructures. *D. Bayer*[1], J. Miguel[2], J. Sanchez-Barriga[3], J. Kurde[2], M. Piantek[2], F. Kronast[3], M. Cinchetti[1], B. Heitkamp[3], H. Dürr[3], W. Kuch[2] and M. Aeschlimann[1] *1. University of Kaiserslautern, Kaiserslautern, Germany; 2. Freie Universität Berlin, Berlin, Germany; 3. BESSY GmbH, Berlin, Germany*

DN-02. Anisotropic x-ray magnetic linear dichroism at Fe, Co and Ni L edges: Interfacial coupling revisited. *G. van der Laan*[1] and E. Arenholz[2] *1. Diamond Light Source, Didcot, Oxfordshire, United Kingdom; 2. ALS, Berkeley, CA*

DN-03. Topological hysteresis in superconductors and ferromagnets. *R. Prozorov*[2,1] and P.C. Canfield[2,1] *1. Physics and Astronomy, Iowa State University, Ames, IA; 2. Ames Laboratory, Ames, IA*

DN-04. Avalanches through windows: multiscale visualization in magnetic thin films. *G. Durin*[1], A. Magni[1], S. Zapperi[2,3] and J.P. Sethna[4] *1. Istituto Nazionale di Ricerca Metrologica, Torino, Italy; 2. Dep.of Physics, University of Modena and Reggio Emilia, CNR-INFM National Center on nanoStructures and bioSystems at Surfaces (S3), Modena, Italy; 3. ISI foundation, Torino, Italy; 4. Physics Department, LASSP, Cornell University, Ithaca, NY*

DN-05. Direct observation on a systematic change of the magnetic domain structure with temperature in 50 nm-MnAs/GaAs(001). *J. Kim*[1], Y. Lee[1], K. Ryu[2], S. Shin[2] and H. Akinaga[3] *1. Quantum Photonic Science Research Center and BK21 Program Division of Advanced Research and Education in Physics, Hanyang University, Seoul, South Korea; 2. Department of Physics and Center for Nanospinics of Spintronic Materials, Korea Advanced Institute of Science and Technology, Daejeon, South Korea; 3. Nanotechnology Research Institute, National Institute of Advanced Industrial Science and Technology, Tsukuba, Japan*

DN-06. Magnetic domain structure coupled with temperature and applied voltage in multiferroic $Bi_{0.7}Dy_{0.3}FeO_3$ thin films. *V.R. Palkar*[1], P. Kovur[1], S.P. Dattagupta[1] and S. Bhattacharya[2] *1. Electrical Engineering, Indian Institute of Technology Bombay, Mumbai, Maharashtra, India; 2. Condensed Matter Physics, Tata Institute of Fundamental Research, Mumbai, Maharashtra, India*

DN-07. A detailed magnetization reversal in a single Ni-Fe elliptical dot with several dot sizes. *Y. Endo*[1], H. Fujimoto[2], R. Nakatani[2,3] and M. Yamamoto[2] *1. Dept. of Electrical and Communication Engineering, Tohoku University, Sendai, Japan; 2. Dept. of Materials Science and Engineering, Osaka University, Suita, Japan; 3. Center for Atomic and Molecular Technologies, Osaka University, Suita, Japan*

DN-08. High-resolution MFM imaging of in-plane magnetic field using transient oscillation. *H. Saito*[1], G. Egawa[1], S. Ishio[1] and G. Li[2] *1. Faculty of Engineering and Resource Science, Akita University, Akita, Japan; 2. School of Physics Science & Technology, Southwest University, Chongqing, China*

DN-09. Characterization of coercivity of magnetic force microscopy probes. *M. Jaafar*[1], A. Jacas[1], W. Rosa[1] and A. Asenjo[1] *1. Instituto de Ciencia de Materiales de Madrid, ICMM-CSIC, Madrid, Spain*

DN-10. Calibration of MFM probe tips for measurements in external in-plane magnetic fields. *A. Ehresmann*[1], T. Weis[1], D. Engel[1], V. Höink[2], J. Schmalhorst[2] and G. Reiss[2] *1. Institute of Physics and Centre for Interdisciplinary Nanostructure Science and Technology (CINSaT), University of Kassel, Kassel, Germany; 2. Thin Films and Nanostructures, Department of Physics, University of Bielefeld, Bielefeld, Germany*

DN-11. An experimental investigation of the magnetically active volume in a magnetic force microscopy tip. N.E. Mateen[1], *M. Gibbs*[1] and M. Rainforth[1] *1. Department of Engineering Materials, University of Sheffield, Sheffield, United Kingdom*

DN-12. Plateau probes to enhance the capabilities of magnetic force microscopy. *N. Amos*[1], R. Ikkawi[1], R. Fernandez[1], A. Lavrenov[1], A. Krichevsky[1], D. Litvinov[2] and S. Khizroev[1] *1. Electrical Engineering, University of California, Riverside, Riverside, CA; 2. Center for Nanomagnetic Systems, University of Houston, Houston, TX*

DN-13. Fabrication of Magnetic Force Microscopy Tips via Electrodeposition and Focused Ion Beam Milling. *O. Cespedes*[1], A. Luu[1], F.F. Rhen[1] and J.D. Coey[1] *1. Physics Department, Trinity College Dublin, Dublin, Ireland*

DN-14. Contact Mode Scanning Hall Probe Microscopy. *T. Ohashi*[1], H. Osawa[1] and A. Sandhu[1,2] *1. Quantum Nanoelectronics Research Center, Tokyo Institute of Technology, Tokyo, Japan; 2. Electrical and Electronic Engineering, Tokyo Institute of Technology, Tokyo, Japan*

DN-15. Variable Temperature-Scanning Hall Probe Microscopy (VT-SHPM) with GaN/AlGaN Two-Dimensional Electron Gas (2DEG) Micro Hall Sensors in 4-400K range, Using Novel Quartz Tuning Fork AFM Feedback. *R. Akram*[1], M. Dede[1] and A. Oral[1] *1. Department of Physics, Bilkent University, 06800, Ankara, Turkey*

TUESDAY
AFTERNOON
2:30

POLIVALENTE

Session DO
MAGNETO-OPTIC MATERIALS AND DEVICES (POSTER SESSION)
Jaroslav Hamrle, Chair

DO-01. Optical reading from videotapes using magnetic garnet film. *M. Kishida*[1], N. Hayashi[1], K. Iwasaki[2], H. Umezawa[2] and T. Nomura[3] *1. Science and Technical Research Laboratories, NHK (Japan Broadcasting corporation), Tokyo, Japan; 2. Research & Development Division, FDK Corporation, Sizuoka, Japan; 3. Department of Electrical, Electronics and Information Engineering, Shizuoka Institute of Science and Technology, Sizuoka, Japan*

DO-02. The influence of the implantation on the magneto-optical properties of $(YBiCaSmLu)_3(FeGeSi)_5O_{12}$ surface. *L. Kalandadze*[1] *1. Batumi State University, Batumi, Georgia*

DO-03. On System Optimization for Magneto-Optic Switching: Material Considerations. *S. Kemmet*[1], M. Mina[1] and R.J. Weber[1] *1. Electrical and Computer Engineering, Iowa State University, Ames, IA*

DO-04. Practical magneto-optic spatial light modulator with single magnetic domain pixels. *K. Iwasaki*[1], H. Mochizuki[1], H. Umezawa[1] and M. Inoue[2] *1. Research and Development Division, FDK CORPORATION, 2281 Washizu, Kosai-Shi, Shizuoka, Japan; 2. Toyohashi University of Technology, 1-1 Hibarigaoka, Tennpakucho, Toyohashi-shi, Aichi, Japan*

DO-05. Enhanced magneto-optics in magnetic nanostructures, magnetophotonic crystals and semiconductors. *A. Granovsky*[1], E. Ganshina[1], N. Perov[1], A. Vinogradov[2], A. Orlov[3], Y. Kalinin[4], A. Khanikaev[5] and M. Inoue[5] *1. Faculty of Physics, Moscow State University, Moscow, Russian Federation; 2. Institute for Theoretical and Applied Electromagnetics, Moscow, Russian Federation; 3. State Research Institute for the Rare-Metal Industry, Moscow, Russian Federation; 4. Department od Solid State Physics, Voronezh State Technical University, Voronezh, Russian Federation; 5. Department of Electrical and Electronic Engineering, Toyohashi University of Technology, Toyohashi, Japan*

DO-06. Temperature properties of magneto-optic film and the non-destructive testing of a paramagnetic specimen. J. Lee[1] and *R. Wang*[2] *1. Department of Information and Communication Engineering, Chosun University, Gwangju, South Korea; 2. Department of Information and Communication Engineering, Graduate School of Chosun University, Gwangju, South Korea*

DO-07. Enhanced magneto-optical diffraction by gyrotropic gratings. *Y. Lu*[1], M. Cho[1], J. Kim[1], G. Lee[1], Y. Lee[1] and J. Rhee[2] *1. Quantum Photonic Science Research Center and BK21 Program Division of Advanced Research and Education in Physics, Hanyang University, Seoul, South Korea; 2. BK21 Physics Research Division and Department of Physics, Sungkyunkwan University, Suwon, South Korea*

DO-08. Surface plasmon resonance effects in the magneto-optical activity of Ag/Co/Ag trilayers. *E. Ferreiro*[1], X. Bendaña[1], J. González-Díaz[1], A. García-Martín[1], J. García-Martín[1], G. Armelles[1], A. Cebollada[1], D. Meneses[2] and E. Muñoz-Sandoval[2] *1. Instituto de Microelectrónica de Madrid, IMM (CNM-CSIC), Tres Cantos, Spain; 2. Advanced Materials Department, IPICYT, San Luis Potosí, Mexico*

DO-09. Magneto-optical properties of wider gap magnetic semiconductor ZnMnTe and ZnMnSe films. *M. Imamura*[1], A. Okada[2] and H. Higuchi[1] *1. Fukuoka Inst. of Tech., Fukuoka, Japan; 2. Mitsubishi Electric Corp., Amagasaki, Japan*

DO-10. Magnonic crystals-theory, experiment, parametric processes. *S.A. Nikitov*[1], S. Bankov[1], Y. Filimonov[1], A. Kozhevnikov[1] and S. Vysotsky[1] *1. IRE, RAS, Moscow, Russian Federation*

DO-11. Enhanced magneto-optical activity in au/co/au nanodisks with localized surface plasmon resonances. *J.B. Gonzalez-Diaz*[1], G. Armelles[1], A. García-Martín[1], A. Cebollada[1], J.M. García-Martín[1], B. Sepúlveda[2,1], M. Käll[2] and L. Balcells[3] *1. Instituto de Microelectrónica de Madrid, IMM (CNM-CSIC), Tres Cantos, Spain; 2. Chalmers University of Technology, Göteborg, Sweden; 3. Institut de Ciència de Materials de Barcelona, Bellaterra, Spain*

DO-12. Magnetic inverse opals. *D. Hrabovsky*[1], E. Taboada[1], M. Lopez[2], J. Fontcuberta[1], C. Lopez[2] and A. Roig[1] *1. Institut de Ciència de Materials de Barcelona (CMAB-CSIC), Bellaterra, Spain; 2. Instituto de Ciencia de Materiales de Madrid (ICMM-CSIC), Madrid, Spain*

DO-13. Controllability of growth-induced anisotropy of thin garnet films grown on (210)-oriented substrates. *S. Tkachuk*[1], D. Bowen[1], C. Krafft[2] and I.D. Mayergoyz[1,3] *1. Electrical and Computer Engineering, University of Maryland, College Park, MD; 2. Laboratory for Physical Sciences, College Park, MD; 3. UMIACS, University of Maryland, College Park, MD*

DO-14. Adjustable Faraday rotation by using one dimensional magnetophotonic crystals. *M. Hamidi*[1], A. Bananej[3], M. Tehranchi[1,2] and M. Ghanaat Shoar[1] *1. laser and plasma resurch institute, Shahid Beheshti University, Tehran, Iran; 2. physics department, Shahid Beheshti University, Tehran, Iran; 3. Laser and Optics Research School, Tehran, Iran*

DO-15. Optical Tamm states in 1D magnetophotonic crystals. T. Goto[1], *A. Baryshev*[1,4], M. Inoue[1], A. Merzlikin[2], A. Vinogradov[2] and A. Granovsky[3] *1. Toyohashi University of Technology, Toyohashi, Japan; 2. Institute for Theoretical and Applied Electromagnetics, Moscow, Russian Federation; 3. Moscow State University, Moscow, Russian Federation; 4. Ioffe Physico-Technical Institute, St. Petersburg, Russian Federation*

DO-16. Magneto-plasmonic nanostructures: a way to control surface plasmon excitation for Biosensor application. *D. Regatos*[1], A. Calle[2], A. Cebollada[2], L. Lechuga[1] and A. Armelles[2] *1. Nanobiosensor and Molecular nanobiophysics Group, Research Center on Nanoscience and Nanotechnology (CIN2: CSIC-ICN), Bellaterra, Barcelona, Spain; 2. Microelectronics Institute of Madrid (IMM-CNM), Tres Cantos, Madrid, Spain*

DO-17. Layered bismuth iron garnet films for magneto-optical applications. *M. Kucera*[1] and R. Gerber[2] *1. Faculty Math. & Physics, Charles University, Prague, Czech Republic; 2. School of Sciences, Salford University, Salford, United Kingdom*

TUESDAY AFTERNOON 2:30

POLIVALENTE

Session DP
SPIN TORQUE OSCILLATORS - II (POSTER SESSION)
Jean-Eric Wegrowe, Chair

DP-01. Thermal properties of Spin Torque Oscillators: Singularity in Effective Energy. *P.B. Visscher*[1] and S. Wang[1] *1. Department of Physics and MINT Center, University of Alabama, Tuscaloosa, AL*

DP-02. Spin torque induced RF-oscillations of the magnetic end domains in CoFeB/MgO/CoFeB nanopillars under subtreshold currents. *S. Cornelissen*[1,3], M. van Kampen[1], G. Hrkac[2], T. Schreffl[2] and L. Lagae[1] *1. NEXTNS, IMEC, Heverlee(Leuven), Belgium; 2. Department of Engineering Materials, University of Sheffield, Sheffield, United Kingdom; 3. EHSAT, K.U.Leuven, Leuven, Belgium*

DP-03. Experimental Study of Current-Driven Spin-Wave Excitations in GMR Nanopillars. *Q. Mistral*[1], J. Kim[1], T. Devolder[1], P. Crozat[1], C. Chappert[1], J. Katine[2], M. Carey[2] and K. Ito[3] *1. Institut d'Electronique Fondamentale, CNRS / Univ. Paris Sud, Orsay, France; 2. Hitachi Global Storage Technologies, San Jose, CA; 3. Advanced Research Laboratory, Hitachi, Tokyo, Japan*

DP-04. Influence Of The Spin Current Polarization And Direction On The Current-Excited Spin Waves In A Nanopillar Spin Valve: A Micromagnetic Study. *A.V. Khvalkovskiy*[1,2], B. Georges[1], J. Grollier[1], Y.V. Gorbunov[3], K.A. Zvezdin[2], V. Cros[1], H. Jaffres[1] and A. Fert[1] *1. Unité Mixte de Physique CNRS/Thales, Palaiseau, France; 2. A.M. Prokhorov General Physics Institute of RAS, Moscow, Russian Federation; 3. Institute of Microtechnology – Spin MT ltd., Moscow, Russian Federation*

DP-05. Angular dependence of generation linewidth of in-plane-magnetized anisotropic spin-torque oscillator. *V. Tyberkevych*[1] and A. Slavin[1] *1. Department of Physics, Oakland University, Rochester, MI*

DP-06. Mutual phase-locking of two spin-torque oscillators: Influence of time delay of a coupling signal. O. Prokopenko[1], *V. Tyberkevych*[2] and A. Slavin[2] *1. Faculty of Radiophysics, Kiev National Taras Shevchenko University, Kiev, Ukraine; 2. Department of Physics, Oakland University, Rochester, MI*

DP-07. Influence of the Demagnetizing Field in Spin Dynamics with A Perpendicular-to-Plane Polarizer. *C. Jui-Hang*[1] and C. Ching-Ray[1] *1. Department of Physics, National Taiwan University, Taipei, Taiwan*

DP-08. Investigation of spin-wave radiation and current controlled three-magnon-scattering in spin-torque nanocontact devices. *H. Schultheiss*[1], X. Janssens[2], M. van Kampen[2], S. Cornelissen[2], F. Ciubotaru[1], A. Laraoui[1], B. Leven[1], A.N. Slavin[3], L. Lagae[2] and B. Hillebrands[1] *1. Fachbereich Physik and Forschungsschwerpunkt MINAS, TU Kaiserslautern, Kaiserslautern, Germany; 2. IMEC, Leuven, Belgium; 3. Oakland University, Rochester, MI*

DP-09. Mutual phase-locking in high frequency microwave nanooscillators as function of field angle. *G. Hrkac*[1], T. Schrefl[1], S. Bance[1], A. Goncharov[1], J. Dean[1], D. Allwood[1], D. Suess[2] and J. Fidler[2] *1. University of Sheffield, Sheffield, United Kingdom; 2. Vienna University of Technology, Vienna, Austria*

DP-10. Non-stationary analysis of large magnetization dynamics in nanoscale spin-valves. *G. Finocchio*[1], L. Torres[2], M. Carpentieri[1], G. Consolo[1] and B. Azzerboni[1] *1. University of Messina, Messina, Italy; 2. Universidad de Salamanca, Salamanca, Spain*

DP-11. Magnetic Vortex Oscillators driven by Spin-Polarized Current and Perpendicular Anisotropy at Zero-Field. *V. Puliafito*[1], B. Azzerboni[1], G. Consolo[1], G. Finocchio[1], L. Torres[2] and L. Lopez-Diaz[2] *1. Dipartimento di Fisica della Materia e Tecnologie Fisiche Avanzate, University of Messina, Messina, Italy; 2. Departamento de Fisica Aplicada, University of Salamanca, Salamanca, Spain*

DP-12. Linear and Nonlinear Frequency Modulation of Nanocontact Spin-Transfer Oscillators: A Micromagnetic Study. *G. Consolo*[1], V. Puliafito[1], L. Lopez-Diaz[2] and B. Azzerboni[1] *1. Dipartimento di Fisica della Materia e Tecnologie Fisiche Avanzate, University of Messina, Messina, Italy; 2. Departamento de Fisica Aplicada, University of Salamanca, Salamanca, Spain*

DP-13. Intrinsic Capacitance Effect on Microwave Power Spectra of Spin-Torque Oscillator with Thermal Noise. *B. Guan*[1], Y. Zhou[2], F. Shin[1] and J. Åkerman[2] *1. Applied Physics, The Hong Kong Polytechnic University, Hong Kong, China; 2. Institute of Microelectronics and Information Technology, Royal Institute of Technology, Stockholm-Kista, Sweden*

DP-14. Spin torque oscillator phase locking to a noisy alternating current. *E. Iacocca*[1], Y. Zhou[1], J. Persson[1] and . Johan[1] *1. Institute of Microelectronics and Information Technology, Royal Institute of Technology, Stockholm-Kista, Sweden*

DP-15. Point contact Spin Torque Oscillators at high magnetic fields: Non-monotonic field dependence of oscillation threshold current. S. Bonetti[1], *J. Garcia*[1], J. Persson[1], F.B. Mancoff[2] and J. Åkerman[1] *1. Microelectronics and Applied Physics, Royal Institute of Technology (KTH), Kista-Stockholm, Sweden; 2. Technology Solutions Organization, Freescale Semiconductor Inc., Chandler, AZ*

DP-16. Time-dependent locking between a spin torque oscillator and an ac current. *Y. Zhou*[1], J. Persson[1] and J. Åkerman[1] *1. Institute of Microelectronics and Information Technology, Royal Institute of Technology, Stockholm, Sweden*

TUESDAY AFTERNOON 2:30 — POLIVALENTE

Session DQ
LIFE SCIENCE AND APPLICATIONS-I (POSTER SESSION)
Weilie Zhou, Chair

DQ-01. Estimation method on multiple sources of MEG based on columnar structure of the cerebral cortex. ***(Invited)*** *H. Fukuda*[1], M. Odagaki[1], O. Hiwaki[1], A. Kodabashi[2] and T. Fujimoto[2] *1. Graduate School of Information Sciences, Hiroshima City University, Hiroshima, Japan; 2. Fujimoto Hayasuzu Hospital, Miyakonojo, Japan*

DQ-02. Stochastic resonance in phase synchronization of auditory steady state responses in MEG. *K. Tanaka*[1], M. Kawakatsu[2] and I. Nemoto[1,2] *1. Research Center for Advanced Technologies, Tokyo Denki Universtiy, Inzai, Chiba, Japan; 2. School of Information Environment, Tokyo Denki University, Inzai, Chiba, Japan*

DQ-03. Preparation, Characterization and Testing of Magnetic Carriers for Arsenic Removal from Water. *A.M. Estevez*[1], J.M. Rodriguez[1], A. Alvaro[1] and P.A. Augusto[2,1] *1. Department of Chemical Engineering, University of Salamanca, Salamanca, Castilla y Leon, Spain; 2. DEQ, Faculdade de Engenharia da Universidade do Porto, Porto, Portugal*

DQ-04. Synthesis of superparamagnetic nanoparticles by non conventional routes and their feasible application as contrast agents. *R. Costo*[1], A.G. Roca[1], M. Morales[1] and S. Veintemillas-Verdaguer[1] *1. Materiales Particulados, Instituto de Ciencia de Materiales de Madrid, Madrid, Madrid, Spain*

DQ-05. Magnetic properties of iron oxyhydroxynitrate nanoparticles. *N.J. Silva*[1], V.S. Amaral[2], L.D. Carlos[2], A. Millán[1], F. Palacio[1], B. Rodríguez-González[3], L.M. Liz-Marzán[3], T. Berquó[4], F. Fauth[5] and V. de Zea Bermudez[6] *1. Fisica de la Materia Condensada, Instituto de Ciencia de Materiales de Aragón, CSIC/Universidad de Zaragoza, Zaragoza, Spain; 2. Departamento de Física and CICECO, Universidade de Aveiro, Aveiro, Portugal; 3. Departmento de Quimica Fisica, Universidad de Vigo, Vigo, Spain; 4. Institute for Rock Magnetism, University of Minnesota, Minneapolis, MN; 5. LLS, BM16-ESRF, Grenoble, France; 6. Departmento de Química, Universidade de Trás-os-Montes e Alto Douro and CQ-VR, Vila Real, Portugal*

DQ-06. Biosorption of Cu(II) ions by magnetically labeled yeast. *S.V. Gorobets*[1], V.V. Lizunov[1] and I.V. Dem'yanenko[1] *1. National Technical University of Ukraine "Kyiv Polytechnic Institute", Kyiv, Ukraine*

DQ-07. COATING of cobalt ferrite nanoparticles with silica for an in-vitro gmr biosensor agent. *S. Tang*[1], S. Bae[1] and W. Lee[2] *1. Electrical and Computer Engineering, Biomagnetics Laboratory (BML), National University of Singapore, Singapore 117576, Singapore, Singapore; 2. Dept of Physics, Sookmyung Women's University, Seoul 140-742, Seoul, Seoul, South Korea*

DQ-08. Effect of Metallic-coating Thickness of Thermosensitive Magnetic Powder for Cancer Therapy. *T. Takura*[1], F. Sato[1], H. Matsuki[1] and T. Sato[2] *1. Dept. of Electrical and Communication Engineering, Graduate School of Engineering, Tohoku University, Sendai, Miyagi, Japan; 2. NEC Tokin Corp., Sendai, Japan*

DQ-09. Fe Oxide Nanoparticles produced by laser pyrolysis for biomedical applications. *V. Bouzas*[1], R. Costo[2], M. García[1], M. Morales[2] and S. Veintemillas-Verdaguer[2] *1. Dpt. Material Science, Universidad Complutense de Madrid, Madrid, Madrid, Spain; 2. Institute of Materials Science, CSIC, Madrid, Madrid, Spain*

DQ-10. Magnetic properties and potential biomedical applications of CM-CL-SPIONs. *M. Lin*[1], J. Gu[1], T. Veres[3], J. Dobson[1], H. Lee[2], M. Muhammed[4] and D. Kim[1] *1. Institute of Science and Technology in Medidicine, Keele University, Stoke-on-Trent, United Kingdom; 2. Department of Materials Science and Engineering, Myongji University, Kyunggi-do, South Korea; 3. Industrial Materials Institute, National Research Council Canada, Boucherville, QC, Canada; 4. Materials Chemistry Division, Royal Institute of Technology, Stockholm, Sweden*

Session DR
MAGNETIC ELEMENTS AND ANTIDOT ARRAYS (POSTER SESSION)
Feng Luo, Chair

DR-01. Controlling vortex chirality in magnetic submicron dots by modulating the magnetic properties in lateral direction. *Z. Zhong*[1], H. Zhang[1], X. Tang[1], Y. Jing[1], L. Jia[1] and L. Zhang[1] *1. State Key Laboratory of Electronic Thin Films and Integrated Devices, University of Electronic Science and Technology of China, Chengdu, Sichuan, China*

DR-02. Helical states in multilayer nanomagnets. *V. Mironov*[1], A. Fraerman[1], B. Gribkov[1], S. Gusev[1], S. Vdovichev[1], B. Hjorvarsson[2] and H. Zabel[3] *1. Institute for physics of microstructures RAS, Nizhniy Novgorod, Russian Federation; 2. Uppsala University, Uppsala, Sweden; 3. Ruhr-University, Bochum, Germany*

DR-03. Double vortex interaction of micron-sized elliptical Py element studied by real-time Kerr microscopy. *B. Hong*[1], J. Bland[1] and J. Jeong[1,2] *1. Cavendish Laboratory, Cambridge University, Cambridge, United Kingdom; 2. Department of Materials Science and Engineering, Chungnam National University, Daejeon, South Korea*

DR-04. Evolution of mixed states composed of vortex cores and anti-vortex cores in different helicities under external field. *Z. Wei*[1], M. Lai[1], C. Lee[1], Z. San[1], Y. Hsieh[1] and T. Ho[1] *1. National Tsing Hua University, Hsinchu, Taiwan*

DR-05. Effect on the dipole-dipole interaction between adjacent dots in Ni-Fe elliptical dot arrays. *Y. Endo*[1], H. Fujimoto[2], Y. Kawamura[2], R. Nakatani[2,3] and M. Yamamoto[2] *1. Dept. of Electrical and Communication Engineering, Tohoku University, Sendai, Japan; 2. Dept. of Materials Science and Engineering, Osaka University, Suita, Japan; 3. Center for Atomic and Molecular Technologies, Osaka University, Suita, Japan*

DR-06. The effect of dipolar interaction on the magnetization reversal of nano-patterned permalloy dots array. *Y. Tsai*[1], C. Chang[1], J. Wang[1], J. Wu[1] and L. Horng[1] *1. Taiwan SPIN Research Center, National Changhua University of Education, Changhua, Taiwan*

DR-07. Interaction in soft magnetic bilayers nanoscale arrays. *J.E. Davies*[2], L.H. Bennett[1,2], E. Della Torre[1,2], B.C. Choi[3], S.N. Piramanayagam[4] and E. Girgis[5] *1. George Washington University, Washington, DC; 2. National Institute of Standards and Technology, Gaithersbug, MD; 3. University of Victoria, Victoria, BC, Canada; 4. Data Storage Institute, Singapore, 117 608, Singapore; 5. National Research Center, Dokki, Giza, Egypt*

DR-08. Magnetic imaging and angle-resolved magnetoresistance behaviour of micropatterned films containing Co antidots. *E. Celasco*[1,2], P. Martino[1], A. Chiolerio[1], F. Celegato[3] and P. Allia[1] *1. Physics, Polytechnic of Turin, Turin, Italy; 2. Physics, Materials and Microsystems Laboratory (χ-lab)- LATEMAR Unit, Chivasso (TO), Italy; 3. INRIM, Torino, Italy*

DR-09. Analysis of the nucleation-propagation sequence in the magnetization reversal of antidot arrays. *F. García-Sánchez*[1], E. Paz[1], O. Fesenko-Chubykalo[1], F. Palomares[1], J. González[1], F. Cebollada[2], J. Haba[2], R. Yanes[1] and U. Atxitia[1] *1. Instituto de Ciencia de Materiales de Madrid, CSIC, 28049 Cantoblanco, Madrid, Spain; 2. Física Aplicada a las Tec.de la Inf., Univ. Politécnica de Madrid, 28031 Madrid, Spain*

DR-10. Magnetic behaviour of Ni antidot arrays on alumina nanoporous membranes. *P. Prieto*[1], A.J. Chaves-Neto[3], K.R. Pirota[2], M. Knobel[3] and J.M. Sanz[1] *1. Física Aplicada, Universidad Autónoma de Madrid, Madrid, Spain; 2. Instituto de Ciencia de Materiales de Madrid, CSIC, Madrid, Spain; 3. Instituto de Física" Gleb Wataghin", Universidad Estadual de Campinas, Campinas, Brazil*

DR-11. TAILORING magnetization reversal mode and switching field of magnetic nanostructure with perpendicular anisotropy. *M. Rahman*[1], N.N. Shams[1], Y. Wu[1] and C. Lai[1] *1. Materials Science and Engineering, National Tsing Hua University, Hsinchu, Taiwan*

DR-12. Property variation in coupled permalloy nanostructures. *A.O. Adeyeye*[1], S. Jain[1] and N. Singh[2] *1. Electrical and Computer Engineering, National University of Singapore, Singapore, Singapore; 2. Institute of Microelectronics, Singapore, Singapore*

TUESDAY
AFTERNOON
2:30

POLIVALENTE

Session DS
MICROWAVE SYSTEMS (POSTER SESSION)
Vasil Tyberkevych, Chair

DS-01. Double Ferromagnetic Resonance Absorption Of Non-Saturated States In Arrays of Bi-Stable Magnetic Nanowires. *J. De La Torre Medina*[1], J. Olais-Govea[2], A. Encinas[2] and L. Piraux[1] *1. Université Catholique de Louvain, Louvain-la-Neuve, Belgium; 2. Instituto de Física, San Luis Potosí, Mexico*

DS-02. Soft magnetic properties and high frequency characteristics in FeCoSi/native-oxide multilayer films. H. Zuo[1], *S. Ge*[1], Z. Wang[1], Y. Xiao[1] and D. Yao[1] *1. Key Laboratory for Magnetism and Magnetic Materials of Ministry of Education, Lanzhou University, Lanzhou, China*

DS-03. Excellent low loss performance of microwave permeability in high resistive CoFeHfO films by thermal annealing. *K. Dong Young*[1], Y. Seok Soo[1], R. B. Parvatheeswara[2], K. CheolGi[2] and T. Migaku[3] *1. Department of Physics, Andong National University, Andong, South Korea; 2. School of Nano-Science and Engineering, Chungnam National University, Daejon, South Korea; 3. Electronic Engineering, Tohoku University, Sendai, Japan*

DS-04. MAGNETOIMPEDANCE EFFECT IN SANDWICHED AND MULTILAYERED AMORPHOUS FILMS: SIMULATION AND EXPERIMENTS. *M.A. Corrêa*[1], F. Bohn[2], A. Viegas[3], A. de Andrade[5] and R. Sommer[4] *1. Centro de Ciências Exatas e Tecnológicas, Universidade Federal do Pamapa, Caçapava do Sul, Rio Grande do Sul, Brazil; 2. Departamento de Física, Universidade Federal de Santa Maria, Santa Maria, Rio Grande do Sul, Brazil; 3. Departamento de Física, Universidade Federal de Santa Catarina, Santa Maria, Santa Catarina, Brazil; 4. Centro Brasileiro de Pesquisas Fisicas, Rio de Janeiro, Rio de Janeiro, Brazil; 5. Universidade Federal de Santa Maria, Frederico Westphalen, Rio Grande do Sul, Brazil*

DS-05. Complex impedance and capacitance spectra characterizations of MgO-based MTJs with/without Mg doping. J. Huang[1,2], *C. Hsu*[1,2], W. Chen[1], S. Chen[3] and C. Liu[3] *1. Physics, National Cheng-Kung University, Tainan, Taiwan; 2. Institute of Innovations and Advanced Studies, National Cheng-Kung University, Tainan, Taiwan; 3. Materials Science and Engineering, National Cheng-Kung University, Tainan, Taiwan*

DS-06. A modulated microwave absorption study of $FeNbO_4$ G. Alvarez[1], R. Font[2], J. Portelles[2], R. Zamorano[3] and *R. Valenzuela*[1] *1. Instituto de Investigaciones en Materiales, Universidad Nacional Autonoma de Mexico, Mexico City, D.F., Mexico; 2. Fisica Aplicada, Universidad de la Habana, Havana, Havana, Cuba; 3. Ciencia de los Materiales, Instituto Politecnico Nacional, Mexico City, D.F., Mexico*

DS-07. IrMn/CoFe-SiO_2/IrMn exchange coupled nanostrucutre for high frequency applications. *N.N. Shams*[1], M. Rahman[1], Y. Wu[1] and C. Lai[1] *1. Materials Science and Engineering, National Tsing-Hua University, Hsinchu, Taiwan*

DS-08. Permeability of ferromagnetic microwires composites/metamaterials and potential applications. *L. Liu*[1], L. Kong[1], G. Lin[1] and S. Matitsine[1] *1. Temasek Lab, National University of Singapore, Singapore, Singapore*

DS-09. Microwave permeability of amorphous FeCoSiB thin films on flexible substrates. *M. Han*[1], Y. Ou[1], L. Deng[1], J. Xie[1] and H. Lu[1] *1. State Key Laboratory of Electronic Thin Films and Integrated Devices, University of Electronic Science and Technology of China, Chengdu, Sichuan, China*

DS-10. Magnetic damping in exchange-coupled IrMn/ CoFe multilayers for microwave applications. *R. Jiang*[1], C. Lai[1] and J. Lin[2] *1. Department of Materials Science and Engineering, National Tsing Hua University, Hsinchu, Taiwan; 2. Centre for Condensed Matter Sciences, National Taiwan University, Taipei, Taiwan*

TUESDAY
AFTERNOON
2:30

POLIVALENTE

Session DT
RE-TM BORIDES AND MAGNET PROCESSING (POSTER SESSION)
Javier Palomares, Chair

DT-01. Synthesis of nano-crystalline barium hexaferrite using a reactive co-precipitated precursor. *M. Montazeri-Pour*[1] and A. Ataie[1] *1. School of Metallurgy and Materials Engineering, University of Tehran, Tehran, Tehran, Iran*

DT-02. Development of anisotropic NdFeB bonded magnet MAGFINE with high heat resistance for automobile use. *K. Noguchi*[1], C. Mishima[1], H. Matsuoka[1] and Y. Honkura[1] *1. Aichi Steel Corporation, Tokai-shi, Aichi-ken, Japan*

DT-03. Effects of conventional HDDR process and the additions of Co and Zr on anisotropy of HDDR PrFeB-type magnetic materials. *J. Han*[1], C. Wang[1], H. Du[1], H. Chen[1] and Y. Yang[1] *1. School of Physics, Peking University, Beijing, China*

DT-04. Magnetic properties and structure for bonded magnet using Dy-F coated NdFeB powder. *M. Komuro*[1] and S. Yuichi[1] *1. Energy and Enviroment Laboratory, Advanced Research Laboratory, Hitachi, Ibaraki, Japan*

DT-05. Effect of grain size and hot-deformation temperature on texture in die-upset Nd-Fe-B magnet. *H. Kwon*[1] and J. Lee[1] *1. Materials Science and Engineering, Pukyong National University, Busan, South Korea*

DT-06. Boron enriched stoichiometric melt spun $RE_2(Fe,Co)_{14}B$-based alloys with enhanced coercivity. *I. Betancourt*[1,2], T. Schrefl[1] and H. Davies[1] *1. Department of Engineering Materials, University of Sheffield, Sheffield, South Yorkshire, United Kingdom; 2. Departamento de Materiales Metalicos y Ceramicos, Instituto de Investigaciones en Materiales, Universidad Nacional Autonoma de Mexico, Mexico, D.F. 04510, Mexico*

DT-07. The copper, titanium and carbon influence on properties of permanent magnets based on FeNdB alloy. *G.P. Brekharya*[1], V. Vystavkina[2] and K. Elena[1] *1. Solid State Physics, Dneprodzerzhinsk Technical StateUniversity, Dneprodzerzhinsk, Ukraine; 2. Materials Science, Zaporozhye State University, Zaporozhye, Ukraine*

DT-08. Effect of heat treatment on the magnetic property and microstructure of sintered Nd-Fe-B magnets. *W. Li*[1], T. Ohkubo[1,2] and K. Hono[1,2] *1. National Institute for Materials Science, Tsukuba, Japan; 2. CREST, JST, Japan*

DT-09. Field-induced coercivity enhancement phenomena in sintered Nd-Fe-B magnets. *H. Kato*[1,2], T. Akiya[2] and K. Koyama[3] *1. Department of Applied Mathematics and Physics, Yamagata University, Yonezawa, Japan; 2. New Industry Creation Hatchery Center, Tohoku University, Sendai, Japan; 3. Institute for Materials Research, Tohoku University, Sendai, Japan*

DT-10. Small angle neutron scattering study of interface nanostructure in sintered Nd-Fe-B magnets. *T. Akiya*[1], H. Kato[1,2], M. Takeda[3], J. Suzuki[3], D. Yamaguchi[4], S. Koizumi[4], M. Sagawa[5] and K. Koyama[6] *1. New Industry Creation Hatchery Center, Tohoku Univ., Sendai, Miyagi, Japan; 2. Department of Applied Mathematics and Physics, Yamagata Univ., Yonezawa, Yamagata, Japan; 3. Quantum Beam Science Directorate, Japan Atomic Energy Agency (JAEA), Tokai-mura, Naka-gun, Ibaraki, Japan; 4. Advances Science Research Center, Japan Atomic Energy Agency (JAEA), Tokai-mura, Naka-gun, Ibaraki, Japan; 5. Intermetallics Co., Ltd,, Kyoto, Japan; 6. Institute for Materials Research, Tohoku University, Sendai, Miyagi, Japan*

DT-11. Reduction of sensitivity to sintering temperature for Nd-Fe-B magnets through co-doping Zr and Nb. *M. Yan*[1], X. Cui[1], L. Yu[1] and T. Ma[1] *1. Department of Materials Science and Engineering, Zhejiang University, Hangzhou, China*

DT-12. Structure and magnetic properties of low neodymium magnets containing minor addition of molybdenum. *M. Spyra*[1] and M. Leonowicz[1] *1. Faculty of Materials Science and Engineering, Warsaw University of Technology, Warsaw, Poland*

TUESDAY
AFTERNOON
2:30

POLIVALENTE

Session DU
PERMANENT MAGNET MATERIALS - APPLICATIONS II (POSTER SESSION)
Tom Woodcock, Chair

DU-01. Multi-tooth Flux Switching PM Brushless ac Machines for High Torque Direct-Drive Applications. *Z. Zhu*[1], J. Chen[1], D. Howe[1], S. Iwasaki[2] and R. Deodhar[2] *1. University of Sheffield, Sheffield, United Kingdom; 2. IMRA UK Research Center,University of Sussex, Brighton, United Kingdom*

DU-02. Optimum Design of Transverse Flux Linear Motor for Weight Reduction and Improvement Thrust Force Using Response Surface Methodology. *D. Hong*[1], B. Woo[1] and D. Kang[1] *1. Korea Electrotechnology Research Institute, Changwon, South Korea*

DU-03. 2D analytical calculation of the no-load induced EMF in an axial flux slotted permanent magnet machine. *J. Pérez*[1] and F. Frechoso[1,2] *1. Electrical Engineering, Universidad de Valladolid, Valladolid, Spain; 2. Member, IEEE, Valladolid, Spain*

DU-04. Modeling permanent magnet axial flux machine with Lie's symmetries. L.T. Loureiro[1], J.R. Zabadal[2], *A.F. Flores*[1] and R.P. Homrich[1] *1. Electrical Engineering, Universidade Federal do Rio Grande do Sul, Porto Alegre, Rio Grande do Sul, Brazil; 2. Nuclear Engineering, Universidade Federal do Rio Grande do Sul, Porto Alegre, Rio Grande do Sul, Brazil*

DU-05. Optimal Design of an SPM Motor Using Taguchi Method and Genetic Algorithms. *C. Hwang*[1], L. Lyu[1], P. Li[1] and C. Liu[2] *1. EE, Feng Chia University, Seatwen, Taichung, Taiwan; 2. EE, National Sun Yat-sen University, Kaohsiung, Taiwan*

DU-06. On the Material and Temperature Impacts of Interior Permanent Magnet Machine for Electric Vehicle Applications. *A. Wang*[1], H. Li[1] and C. Liu[2] *1. Electrical Engineering, North China Electric power university, Baoding, Hebei, China; 2. Electrical Engineering, National Sun Yat-Sen University, Kaohsiung, Taiwan*

DU-07. Fabrication and properties of FePt thick films for micro-machine application. *P. Jang*[1], B. Lee[1], K. Rhie[2] and S. Choi[2] *1. Div. of Applied Science, Cheongju University, Cheongju, Chungcheongbuk-do, South Korea; 2. Department of display, semiconductor and physics, Korea University, Chochiwon, Chungcheongnam-do, South Korea*

DU-08. Optimum Design of 60 W Longitudinal Flux Linear Motor for Weight Reduction and Improvement Performance Using DOE. *D. Hong*[1], B. Woo[1] and D. Kang[1] *1. Korea Electrotechnology Research Institute, Changwon, South Korea*

DU-09. Optimal Design of a Small PM Wind Synchronous Generator for Wide Range of Winds Speed. *B. Ebrahimi*[1], J. Faiz[1], M. Rajabi Sebdani[1] and M.A. Khan[2] *1. Department of Electrical and Computer Engineering, University of Tehran, University of Tehran, Tehran, Iran; 2. Department of Electrical Engineering, University of Cape Town, Cape Town, South Africa*

DU-10. Analytical analysis of magnetic field and back electromotive force calculation of an axial-flux permanent magnet synchronous generator with coreless stator. *P. Virti č*[1], P. Pi šek[1], T. Mar či č[1], M. Hadziselimovi č[1,2] and B. Štumberger[1,2] *1. TECES, Development centre for electrical machines, Maribor, Slovenia; 2. Faculty of Electrical Engineering and Computer Science, University of Maribor, Maribor, Slovenia*

TUESDAY
AFTERNOON
2:30

POLIVALENTE

Session DV
MANGANITES (POSTER SESSION)
Gervasi Herranz, Chair

DV-01. Theoretical and experimental studies of structural characteristics, magnetic response and electronic properties of Sr_2FeMnO_6 double cubic Perovskite. *J.A. Rodriguez*[1], D.A. Landinez-Tellez[1], R. Cardona[1], F.E. Fajardo[1] and J. Roa-Rojas[1] *1. Physics Dept., Universidad Nacional de Colombia, Bogotá, D. C., Colombia*

DV-02. Local probe studies on $Pr_{1-x}Ca_xMnO_3$ system. *A.M. Lopes*[1,2], T.M. Mendonça[1,2], J.S. Amaral[3], A.M. Pereira[1], P.B. Tavares[4], Y. Tomioka[5], Y. Tokura[6], J.G. Correia[7,2], V.S. Amaral[3] and J.P. Araújo[1] *1. Department of Physics and IFIMUP, Univ. of Porto, Porto, Portugal; 2. EP, CERN, Geneva, Switzerland; 3. Department of Physics and CICECO, Univ. of Aveiro, Aveiro, Portugal; 4. Department of chemistry and CQ-VR, Univ. of Tras-os-Montes e Alto Douro, Vila Real, Portugal; 5. CERC, National Institute of Advanced Industrial Science and Technology, Tsukuba, Japan; 6. Department of Applied Physics, Univ. of Tokyo, Tokyo, Japan; 7. Instituto Tecnólogico Nuclear, Sacavém, Portugal*

DV-03. Complex magnetic behaviour in anion deficient manganite superstructures R. Cortés-Gil1,2, J. M. Alonso2,3, A. Hernando2,4, M. L. Ruiz-González1, M. García-Hernández3, M. Vallet-Regí2,5, J. M. González-Calbet1,2,* 1Departamento de Química Inorgánica, Facultad de Químicas, Universidad Complutense, 28040-Madrid, Spain 2Instituto de Magnetismo Aplicado, UCM-CSIC-RENFE, Las Rozas, P.O. Box 155, 28230-Madrid, Spain 3Instituto de Ciencia de Materiales, CSIC, Sor Juana Inés de la Cruz s/n, 28049-Madrid, Spain 4Departamento de Física de Materiales, Facultad de Físicas, Universidad Complutense, 28040-Madrid, Spain 5Departamento de Química Inorgánica y Bioinorgánica, Facultad de Farmacia, Universidad Complutense, 28040- Madrid, Spain. *J.M. González-Calbet*[1] *1. Quimica Inorgánica, UCM, Madrid, Spain*

DV-04. Anisotropic magnetoresistance in ferromagnetic manganites. *M. Granada*[1], J. Rojas Sánchez[1], L.B. Steren[1], J.D. Fuhr[1] and B. Alascio[1] *1. Centro Atómico Bariloche (Comisión Nacional de Energía Atómica) and CONICET, San Carlos de Bariloche, Río Negro, Argentina*

DV-05. Comparative study of magnetic ordering in bulk and nanometer-sized $La_{0.4}Ca_{0.6}MnO_3$ manganite. *E. Rozenberg*[1], M. Auslender[1], A.I. Shames[1], I. Felner[2], E. Sominski[3], A. Gedanken[3], A. Pestun[4] and Y. Mukovskii[4] *1. Physics, BGU of the Negev, Beer-Sheva, Israel; 2. Physics, The Hebrew University, Jerusalem, Israel; 3. Chemistry, Bar-Ilan University, Ramat-Gan, Israel; 4. Moscow Steel and Alloys Institute, Moscow, Russian Federation*

DV-06. EMR probing of magnetic ordering in $Pr_{1-x}Sr_xMnO_3$ (x = 0.22, 0.24, 0.26) manganite single crystals. *A.I. Shames*[1], E. Rozenberg[1], Y.M. Mukovskii[2] and G. Gorodetsky[1] *1. Physics, Ben Gurion University of the Negev, Be'er-Sheva, Israel; 2. Moscow Steel and Alloys Institute, Moscow, Russian Federation*

DV-07. Magnetic and magnetoresistive properties of $Pr_{1-x}Ca_xCoO_3$ (x =0.3, 0.5) cobaltites. *I.G. Deac*[1], R. Tetean[1], D. Andreica[1,2] and E. Burzo[1] *1. Physics, Universitatea Babes-Bolyai, Cluj-Napoca, Romania; 2. Laboratory for Muon-Spin Spectroscopy, Paul Scherrer Institut, Villigen, Switzerland*

DV-08. Magnetism of LCMO/YBCO thinfilm epitaxial heterostructures. *N.M. Nemes*[1,3], M. García-Hernández[1], Z. Szatmári[2], T. Fehér[2], F. Simon[2], J. García-Barriocanal[3], F.Y. Bruno[3], C. Leon[3], C. Miller[3], Z. Sefrioui[3], C. Visani[3] and J. Santamaría[3] *1. Instituto de Ciencia de Materiales de Madrid, Consejo Superior de Investigaciones Cientificas, Madrid, Spain; 2. Institute of Physics, Budapest University of Technology and Economics, Budapest, Hungary; 3. GFMC, Dpto. Fisica Aplicada III, Universidad Complutense de Madrid, Madrid, Spain*

DV-09. In-situ strain effect on extrinsic electrical transport and magnetotransport in $La_{0.7}Sr_{0.3}MnO_3$ films. *R. Gangineni*[1], L. Schultz[1], I. Mönch[1] and K. Dörr[1] *1. Institute for Metallic Materials, Leibniz Institute for Solid State and Materials Research Dresden, Dresden, Saxony, Germany*

DV-10. Effect of Cr Doping on the Magnetic Properties of $La_{0.3}Ca_{0.7}MnO_3$ *L.E. Wenger*[1], G.M. Tsoi[1], R. Suryanarayanan[2] and T. Sudyoadsuk[3] *1. Department of Physics, University of Alabama at Birmingham, Birmingham, AL; 2. Laboratoire de Physico-Chimie de l'Etat Solide, CNRS, Université Paris-Sud, Orsay, France; 3. Department of Chemistry, Ubon Ratchathani University, Ubon Ratchathani, Thailand*

DV-11. 1/f noise study of electron transport in $La_{0.82}Ca_{0.18}MnO_3$ single crystals. *X. Wu*[1,2], G. Jung[2], B. Dolgin[2], V. Markovich[2], Y. Yuzhelevski[2], M. Belogolovskii[3,4], Y.M. Mukovskii[5], K. Suzuki[1] and G. Gorodetsky[2] *1. Materials Engineering, Monash University, Clayton, VIC, Australia; 2. Physics, Ben Gurion University, Beer Sheva, Israel; 3. Donetsk Physical and Technical Institute, National Academy of Sciences of Ukraine, Donetsk, Ukraine; 4. Scientific and Industrial Concern 'Nauka', Kyiv, Ukraine; 5. Moscow State Steel and Alloys Institute, Moscok, Russian Federation*

DV-12. Effect of substrate orientation on magnetic anisotropy and 1/f noise in La0.7Sr0.3MnO3 thin films. *L. Mechin*[1], P. Perna[1,2], M. Saib[1], S. Flament[1], C. Barone[1,3], D. Fadil[1] and J. Routoure[1] *1. GREYC-ENSICAEN, CNRS, Caen, France; 2. DiMSAT, University of Cassino, Cassino, Italy; 3. Dipartimento di Fisica "E.R. Caianiello", University of Salerno, Salerno, Italy*

DV-13. Room temperature giant magnetoimpedance in La0.67Sr0.33MnO3. *M. Ramanathan*[1] *1. Department of Physics, National Univeristy of Singapore, Singapore, Singapore*

DV-14. Electroresistance in mixed valence manganites. *N. Biskup*[1], A. de Andrés[1] and M. Garcia Hernandez[1] *1. ICMM, Madrid, Spain*

DV-15. Impedance spectroscopy of magnetoresistive manganite films exhibiting electric-pulse-induced resistance switching. *T. Nakamura*[1], K. Homma[1], T. Yakushiji[1] and K. Tachibana[1] *1. Department of Electronic Science and Engineering, Kyoto University, Kyoto, Japan*

DV-16. Strain effect on MnO_6 octahedrons in the colossal magnetoresistance (CMR) films. C. Wu[1], *H. Chou*[1] and F. Yuan[1] *1. National Sun Yat-sen University, Kaohsiung, Taiwan*

DV-17. Pulsed current induced multi level resistivity switching in two magnetodielectrics: antiferromagnetic Nd0.5Ca 0.5MnO3 and ferromagnetic La2NiMnO6. *M. Ramanathan*[1] *1. Physics, National university of Singapore, Singapore, Singapore*

TUESDAY AFTERNOON 2:30 — POLIVALENTE

Session DW
TRANSFORMERS AND INDUCTORS II (POSTER SESSION)
Oriano Bottauscio, Chair

DW-01. Design optimization of a non-contact rapid charging inductive power supply system for electric-driven vehicles based on finite-element electromagnetic field analyses. *Y. Kamiya*[1], Y. Daisho[1], R. Yokoyama[1] and S. Takahashi[2] *1. Graduate School of Environment and Energy Engineering, Waseda Univ., Tokyo, Japan; 2. Showa Aircraft, Tokyo, Japan*

DW-02. An Analytical Model of the Electromagnetic Efficiency of Litz-Wire Windings for Domestic Induction Heating Systems. *J. Acero*[1], R. Alonso[2], J.M. Burdio[1], L.A. Barragan[1] and J.I. Artigas[1] *1. Electronic Engineering and Communications, University of Zaragoza, Zaragoza, Zaragoza, Spain; 2. Applied Physics, University of Zaragoza, Zaragoza, Zaragoza, Spain*

DW-03. High Frequency Coaxial Transformer for DC/DC Converter Used in Solar PV Systems. *J. Lu*[1], X. Yang[2] and F. Dawson[3] *1. School of Eng., Griffith University, Brisbane, QLD, Australia; 2. Province-Ministry Joint Key Laboratory of Electromagnetic Field and Electrical Apparatus Reliability, Hebei University of Technology, Tianjin,, Hebei, China; 3. Department of Electrical and Computer Engineering, University of Toronto, Toronto, ON, Canada*

DW-04. Novel EU core variable inductor. *M. Xianmin*[1], L. Fengchun[1], W. Jianze[2] and J. Yanchao[2] *1. Department of Electrical and Electronics Engineering, DaLian University of Technonlogy, DaLian, LiaoNing, China; 2. School of Electrical Engineering and Automation, Harbin Instituted of Technology, Harbin, HeiLongJiang, China*

DW-05. Stability analysis of contact-less electrical energy detachable transformer. H. Chen[1], *Q. Yang*[1], J. Li[1], S. Yang[1] and S. Hou[1] *1. Hebei University of Technology, Tianjin, China*

DW-06. A Forced Vibration Analysis of Cable-type Power Transformer Winding by the Pseudospectral Method. J. Ha[1], *H. Chung*[1], S. Woo[1], P. Shin[1] and J. Lee[1] *1. Hongik University, Jochiwon, Chungnam 339-701, South Korea*

DW-07. Coupled three phase inductors for interleaved inverter switching. *A. Knight*[1], J. Ewanchuk[1] and J.C. Salmon[1] *1. Electrical and Computer Eng, University of Alberta, Edmonton, AB, Canada*

DW-08. A novel approach to extending the linearity range of displacement inductive sensor. *M.S. Damnjanovic*[1], L. Zivanov[1], L. Nagy[1], S. Djuric[1] and B. Biberdzic[1] *1. Department of Electronics, Faculty of Technical Sciences, Novi Sad, Serbia*

DW-09. A New Technique for Measuring Ferrite Core Loss under DC Bias Conditions. *C. Baguley*[1], U.K. Madawala[1] and B. Carsten[2] *1. ECE, University of Auckland, Auckland, New Zealand; 2. Power Conversion Consulting and Research, Corvallis, OR*

TUESDAY AFTERNOON 6:30 — AUDITORIO A

Session XA
IEEE MAGNETICS SOCIETY ANNUAL GENERAL MEETING

WEDNESDAY MORNING 9:30 — AUDITORIO A

Session EA
SYMPOSIUM ON SPIN TRANSFER AND DYNAMICS
Thibaud Devolder, Chair

9:30

EA-01. Spin-torque oscillator in the presence of thermal noise. ***(Invited)*** *A.N. Slavin*[1], J. Kim[2] and V. Tiberkevich[1] *1. Department of Physics, Oakland University, Rochester, MI; 2. Institut d'Electronique Fondamentale, Universite Paris-Sud, Orsay, France*

10:00

EA-02. Frequency Pulling and Locking in RF Assisted Spin-Torque Switching. ***(Invited)*** *S.H. Florez*[1], J.A. Katine[1], M. Carey[1], O. Ozatay[1] and L. Folks[1] *1. Hitachi Global Storage Technologies, San Jose, CA*

10:30

EA-03. Time-Domain Studies of Nonlinear Magnetization Dynamics Excited by Spin Transfer Torque. ***(Invited)*** *I. Krivorotov*[1], N. Emley[2], J. Sankey[2], G. Finocchio[3], L. Torres[4], B. Azzerboni[3], R. Buhrman[2] and D. Ralph[2] *1. Department of Physics and Astronomy, University of California, Irvine, Irvine, CA; 2. Cornell University, Ithaca, NY; 3. Dipartimento di Fisica della Materia e Tecnologie Fisiche Avanzate, University of Messina, Messina, Italy; 4. Departamento de Fisica Aplicada, Universidad de Salamanca, Salamanca, Spain*

11:00

EA-04. Current-driven vortex oscillations in metallic nanocontacts. ***(Invited)*** Q. Mistral[1], M. van Kampen[2], G. Hrkac[3], *J. Kim*[1], T. Devolder[1], P. Crozat[1], C. Chappert[1] and L. Lagae[2] *1. Institut d'Electronique Fondamentale, CNRS / Univ. Paris Sud, Orsay, France; 2. IMEC, Leuven, Belgium; 3. Department of Engineering Materials, University of Sheffield, Sheffield, United Kingdom*

11:30

EA-05. Self-Torque Induced by Local Spin-Transfer Effect and Lateral Spin Diffusion in Magnetic Layers with Inhomogeneous Magnetization. ***(Invited)*** *K. Lee*[1] *1. Korea University, Seoul, South Korea*

12:00

EA-06. Spin Torque Influence on the High Frequency Magnetization Fluctuations in Magnetic Tunnel Junctions. ***(Invited)*** S. Petit[1], N. de Mestier[1], C. Thirion[1], U. Ebels[1], Y. Liu[2], M. Li[2], P. Wang[2] and *C. Baraduc*[1] *1. SPINTEC, CEA/CNRS, Grenoble, France; 2. Headway Technologies, Milpitas, CA*

WEDNESDAY MORNING 9:30 — MADRID

Session EB
MOTOR AND ACTUATORS II
Johannes Paulides, Chair

9:30

EB-01. Design considerations of tubular flux-switching permanent magnet machines. ***(Invited)*** *J. Wang*[1], W. Wang[1], K. Atallah[1] and D. Howe[1] *1. Electronic and Electrical Engineering, University of Sheffield, Sheffield, United Kingdom*

10:00

EB-02. Linear induction motors with modular winding primaries and wound rotor secondaries. *J. Eastham*[1], T. Cox[1,2] and J. Proverbs[2] *1. The University of Bath, Bath, United Kingdom; 2. Force Engineering, Shepshed, United Kingdom*

10:15

EB-03. Magnetic Actuator Design using Level Set based Topology Optimization. S. Park[1], *S. Min*[1], S. Yamasaki[2], S. Nishiwaki[2] and J. Yoo[3] *1. Mechanical Engineering, Hanyang University, Seoul, South Korea; 2. Aeronautics and Astronautics, Kyoto University, Kyoto, Japan; 3. Mechanical Engineering, Yonsei University, Seoul, South Korea*

10:30

EB-04. Comparsion of numerical and analytical simulation of saturated zig-zag flux in induction machines. A. Binder[1], *T. Knopik*[1] and R. Hagen[1] *1. Institute for Electrical Energy Conversion, Technische Universität Darmstadt, Darmstadt, Germany*

10:45

EB-05. Newly structured double excited 2-DOF motor for security camera. *J. Lee*[1], D. Kim[2], S. Baek[1] and B. Kwon[1] *1. Hanyang University, Ansan, South Korea; 2. Korea Electronics Technology Institute, Gwang-ju, South Korea*

11:00

EB-06. 3-D Finite Element Analysis of Magnetic Forces Exerted on Stator End-windings of an Induction Motor. *R. Lin*[1] and A. Arkkio[1] *1. Helsinki University of Technology, Espoo, Finland*

11:15

EB-07. Magnetoelastic Characteristics of the Multilayered Magnetostrictive Thin Film with Polyimide Substrate for Micro Actuator. *H. Lee*[1] and C. Cho[1] *1. Mechanical Engineering, Inha University, Incheon, South Korea*

11:30

EB-08. Analysis of the force produced by speed-induced eddy currents in an xy-actuator. *A.F. Flores Filho*[1], N.F. Baggio Filho[1] and M.A. da Silveira[2] *1. Post-graduate Programme in Electrical Engineering, Federal University of Rio Grande do Sul, Porto Alegre, RS, Brazil; 2. Post-graduate Programme in Engineering – Environment, Energy and Materials, Lutheran University of Brazil, Canoas, RS, Brazil*

11:45

EB-09. An Extension to Multiple Coupled Circuits Modeling of Induction Machines to Include Variable Degrees of Saturation Effects. M. Ojaghi[1] and *J. Faiz*[1] *1. Department of Electrical and Computer Engineering, University of Tehran, Tehran, Iran*

12:00

EB-10. Switched Reluctance Motor with External Rotor for Fan in Air-condition. *H. Chen*[1] *1. College of Information and Electrical Engineering, China University of Mining & Technology, Xuzhou, Jiangsu, China*

12:15

EB-11. End turn leakage reactance of concentrated modular winding stators. *T. Cox*[1,2], J. Eastham[1] and J. Proverbs[2] *1. The University of Bath, Bath, United Kingdom; 2. Force Engineering, Shepshed, United Kingdom*

WEDNESDAY MORNING 9:30 — ROMA

Session EC
MAGNETIC NANOSTRUCTURES I
Olav Hellwig, Chair

9:30

EC-01. X-ray and valence band photoemission microscopy of ultra-thin magnetic cobalt films on ruthenium. *A. Mascaraque*[1], L. Perez[1], L. Aballe[2], T. Onur Mentes[2], J.F. Marco[3], F. El Gabaly[4,5], C. Klein[5], A.K. Schmid[5], K.F. McCarty[6], A. Locatelli[2] and J. de la Figuera[3,4] *1. Dpto. de Fisica de Materiales, Universidad Complutense de Madrid, Madrid, Madrid, Spain; 2. Elettra - Sincrotrone Trieste, Trieste, Italy; 3. Instituto de Quimica-Fisica Rocasolano, CSIC, Madrid, Madrid, Spain; 4. Centro de Microanalisis de Materiales, Universidad Autonoma de Madrid, Madrid, Madrid, Spain; 5. Berkeley National Laboratory, Berkeley, CA; 6. Livermore National Laboratories, Livermore, CA*

9:45

EC-02. Magnetostatic interactions in an artificial two-phase magnet. *S. Sievers*[1], S. Schnittger[2], K. Braun[1], U. Siegner[1] and C. Jooss[2] *1. Physikalisch-Technische Bundesanstalt, Braunschweig, Germany; 2. Institut für Materialphysik, Universität Göttingen, Göttingen, Germany*

10:00

EC-03. 360° domain wall generation in the soft layer of magnetic tunnel junctions. *F. Montaigne*[1], M. Hehn[1], D. Lacour[1], J. Briones[1], R. Belkhou[2,3], S. El Moussaoui[2,3], F. Maccherozzi[2,3] and N. Rougemaille[4] *1. Laboratoire de Physique des Matériaux, Nancy-University, CNRS, Vandoeuvre lès Nancy, France; 2. Synchrotron SOLEIL, Gif-sur-Yvette, France; 3. Synchrotron ELETTRA, Basovizza, Italy; 4. Institut Néel, CNRS & Université Joseph Fourier, Grenoble, France*

10:15

EC-04. Magnetic reversal in patterned nanostructures with circular exchange-bias. *M. Tanase*[1], A.K. Petford-Long[1], O.G. Heinonen[2], K.S. Buchanan[3], J. Sort[4] and J. Nogues[4] *1. Materials Science Division, Argonne National Laboratory, Lemont, IL; 2. Seagate Technology, Bloomington, MN; 3. Center for Nanoscale Materials, Argonne National Laboratory, Lemont, IL; 4. Universitat Autonoma de Barcelona, Bellaterra, Spain*

10:30

EC-05. Static and dynamic properties of exchange bias modulated thin films. *C. Hamann*[1], J. McCord[1], R. Kaltofen[2], I. Mönch[2], R. Schäfer[1] and L. Schultz[1] *1. Institute for Metallic Materials, IFW Dresden, Dresden, Germany; 2. Institute for Integrative Nanosciences, IFW Dresden, Dresden, Germany*

10:45

EC-06. Dynamic splitting of azimuthal spin wave modes in circular magnetic dot in vortex ground state. *K.Y. Guslienko*[1], A.N. Slavin[2], V. Tyberkevych[2] and S.K. Kim[1] *1. Research Center for Spin Dynamics and Spin-Wave Devices and Nanospintronics Laboratory, Seoul National University, Seoul, South Korea; 2. Department of Physics, Oakland University, Rochester, MI*

11:00

EC-07. Enhancment of superconductive vortex pinning through formation of magnetic vortices. *A. Hoffmann*[1,2], L. Fumagalli[3], N. Jahedi[3], J.C. Sautner[3], J.E. Pearson[1], G. Mihajlovi ć[1] and V. Metlushko[3] *1. Materials Science Division, Argonne National Laboratory, Argonne, IL; 2. Center for Nanoscale Materials, Argonne National Laboratory, Argonne, IL; 3. Electrical and Computer Engineering, University of Illinois at Chicago, Chiacgo, IL*

11:15

EC-08. Beams of spin waves guided by permalloy micro-stripes. *V.E. Demidov*[1], S.O. Demokritov[1], K. Rott[2], P. Krzysteczko[2] and G. Reiss[2] *1. Institute for Applied Physics, University of Muenster, Muenster, Germany; 2. Department of Physics, Bielefeld University, Bielefeld, Germany*

11:30

EC-09. Direct magnetic patterning on paramagnetic FeAl sheets by ion irradiation through poly(methyl methacrylate) and porous alumina shadow masks. *E. Menéndez*[1], j. sort[2], E. Jiménez[3], J. Camarero[3], O. Liedke[4], J. Fassbender[4], D. Baró[1], S. Suriñach[1], S. Deevi[5], K. Rao[6], A. Weber[7], L. Heyderman[7], J. Sommerlatte[8], K. Nielsch[8] and J. Nogues[9] *1. Departament de Física, Universitat Autònoma de Barcelona, 08193 Bellaterra, Barcelona, Spain; 2. ICREA and Departament de Física, Universitat Autònoma de Barcelona, 08193 Bellaterra, Spain; 3. Surface Science Lab (LASUAM, Lab. de Física de Superficies), Dpto. Física de la Materia Condensada, Universidad Autónoma de Madrid, 28049 Madrid, Barcelona, Spain; 4. Institute of Ion Beam Physics and Materials Research, Forschungszentrum Dresden, 01314 Rossendorf, Germany; 5. Research Center, Chrysalis Technologies Incorporated, 23234 Richmond, WA; 6. Department of Materials Science and Engineering, Royal Institute of Technology, 10044 Stockholm, Sweden; 7. Paul Scherrer Institut, 5232 Villigen, Switzerland; 8. Max Planck Institute of Microstructure Physics, 06120 Halle, Germany; 9. ICREA and Institut Català de Nanotecnologia, Campus UAB, 08193 Bellaterra, Spain*

11:45

EC-10. Transverse magnetization in Nickel nanowire arrays patterned from Cu/Ni/Cu epitaxial films. *M. Ciria*[1], J.L. Diez-Ferrer[2], J.I. Arnaudas[2,1], B.G. Ng[3], F.J. Castaño[3], R.C. O'Handley[3], E.S. Friend[3] and C.A. Ross[3] *1. ICMA, CSIC-Universidad de Zaragoza, Zaragoza, Spain; 2. Instituto de Nanociencia de Aragón, Universidad de Zaragoza, Zaragoza, Spain; 3. Department of Materials Science and Engineering, Massachusetts Institute of Technology, Cambridge, MA*

12:00

EC-11. Magnetostatic dipolar domain wall pinning in chains of Permalloy triangular rings micromagnets. *P. Vavassori*[1,2], D. Bisero[2], V. Bonanni[2], A. Busato[2], M. Grimsditch[3], K. Lebecki[4], V. Metlushko[5] and B. Ilic[6] *1. CIC nanoGUNE, San Sebastian, Spain; 2. CNISM, CNR-INFM S3, and Dipartimento di Fisica, Universita` di Ferrara, Ferrara, Italy; 3. Materials Science Division, Argonne National Laboratory, Argonne, IL; 4. Institute of Physics, Polish Academy of Sciences, Warsaw, Poland; 5. Department of Electrical and Computer Engineering, University of Illinois at Chicago, Chicago, IL; 6. Cornell Nanofabrication Facility, Cornell University, Ithaca, NY*

12:15

EC-12. Partial frequency band gap in 1D magnonic crystals. *M. Kostylev*[1], G. Gubbiotti[2], P. Schrader[1], G. Carlotti[2], A.O. Adeyeye[3], S. Goolaup[3], N. Singh[3] and R.L. Stamps[1] *1. School of Physics, University of Western Australia, Crawley, WA, Australia; 2. CNISM, Dipartimento di Fisica, Universita di Perugia, Perugia, Italy; 3. Department of Electrical and Computer Engineering, National University of Singapore, Singapore, Singapore*

Session ED
PERPENDICULAR MEDIA
S. Piramanayagam, Chair

9:30

ED-01. Head-to-SUL spacing reduction with a magnetic seed and the effect on perpendicular recording characteristics. *G. Choe*[1], M. Minardi[1], K. Zhang[1] and M. Mirzamaani[1] *1. Hitachi GST, 5600 Cottle Road, San Jose, CA*

9:45

ED-02. Reduction of transition layer thickness showing incoherent switching behavior in single CoCrPt-SiO_2 perpendicular media. *H. Jung*[1], M. Kuo[1], S. Malhotra[1] and G. Bertero[1] *1. Western Digital Media Inc., San Jose, CA*

10:00

ED-03. Compositional structure and magnetic properties of CoCrPt-SiO_X Perpendicular Recording Medium. *M. Futamoto*[1], T. Handa[1] and Y. Takahashi[2] *1. Faculty of Science and Engineering, Chuo University, Tokyo, Japan; 2. Central Research Laboratory, Hitachi, Ltd., Tokyo, Japan*

10:15

ED-04. Exactly Lattice Matched Novel Under Layers (LML) in Perpendicular Media. *A. Ajan*[1], T. Sugimoto[1] and T. Uzumaki[1] *1. Magnetic Media Laboratory, Fujitsu Laboratories Ltd., 10-1 Morinosato-Wakamiya, Atsugi, Japan*

10:30

ED-05. Magnetic and Recording Characteristics of CoCrPt-Oxide Media with a Mixture of SiO2 and TiO2. *I. Tamai*[1], R. Araki[1] and K. Tanahashi[1] *1. Central Research Laboratory, Hitachi,Ltd., Odawara-shi, Kanagawa-ken, Japan*

10:45

ED-06. Investigation of high and low Mobility sputter conditions to enhance decoupling in oxide composite media. *H. Lee*[1], S. Kong[2], H. Lee[2], H. Oh[2], V.W. Guo[1], J. Zhu[1] and D.E. Laughlin[1] *1. Electrical and Computer Engineering, Carnegie Mellon University, Pittsburgh, PA; 2. Samsung Advanced Institute of Technology, Yongin-Si, Gyeonggi-Do, South Korea*

11:00

ED-07. High-Resolution TEM Analysis Of Perpendicular CoCrPt-SiO_2 Media. *R. Araki*[1], Y. Takahashi[1], I. Takekuma[2] and S. Narishige[2] *1. Central Research Laboratory, Hitachi Ltd., 1-280 Higashi-koigakubo Kokubunji-shi, Tokyo, Japan; 2. Central Research Laboratory, Hitachi Ltd., 2880 Kozu, Odawara, Kanagawa, Japan*

11:15

ED-08. Epitaxially grown FCC/BCC/HCP multi-underlayers for high performance perpendicular recording media. *G. Choe*[1], X. Xu[1], K. Tang[1] and X. Bian[1] *1. Hitachi GST, San Jose, CA*

11:30

ED-09. A General Method to Fabricate Exchange Coupled Composite Media with Graded Structure for Energy Assisted Magnetic Recording. *H. Zhao*[1], H. Wang[1] and J. Wang[1] *1. ECE, University of Minnesota, Minneapolis, MN*

11:45

ED-10. Tuning pinning-site size of percolated perpendicular media (PPM) fabricated on pre-patterned substrates. *M. Rahman*[1], C. Lai[1] and D. Suess[2] *1. Materials Science and Engineering, National Tsing Hua University, Hsinchu, Taiwan; 2. Solid state physics, Vienna University of Technology, Vienna, Austria*

12:00

ED-11. Effect of carbon cosputtering in the growth of ultra-thin FePt particulate films on oxidized Si substrates. *P. Alagarsamy*[1], S. Tomoko[2], T. Yukiko K[1] and K. Hono[1,2] *1. Magnetic Materials Center, National Institute for Materials Science, Tsukuba, Ibaraki, Japan; 2. Graduate School of Pure and Applied Sciences, University of Tsukuba, Tsukuba, Ibaraki, Japan*

12:15

ED-12. Effect of carbon mixing on the perpendicular anisotropy of FePt thin film. *S. Lee*[1], M. Kim[1] and J. Park[1] *1. Materials Science and Engineering, Korea Advanced Institute of Science and Technology, Daejeon, South Korea*

WEDNESDAY
MORNING
9:30

LONDRES

Session EE
MAGNETIC NANOPARTICLES I
Gangping Ju, Chair

9:30

EE-01. Radio-frequency transverse susceptibility studies of effective magnetic anisotropy in nanoparticle assemblies. *H. Srikanth*[1], P. Poddar[2,1], M. Morales[1] and N. Frey[1] *1. Department of Physics, University of South Florida, Tampa, FL; 2. National Chemical Laboratory, Pune, India*

9:45

EE-02. Magnetic properties characterization of single IBICVD fabricated magnetic particles. *T. Suzuki*[1], Y. Pogoryelov[1] and A. Htoo[1] *1. Information Storage Materials Laboratory, Toyota Technological Institute, Nagoya, Aichi, Japan*

10:00

EE-03. Ground states in ferromagnetic nanotubes. P. Landeros[1], O. Suarez[1], A. Cuchillo[1] and *P. Vargas*[1] *1. Departamento de Física, Universidad Técnica Federico Santa María, Valparaiso, Valparaiso, Chile*

10:15

EE-04. A study of the magnetic behavior of Ni/Cu multilayer nanowire arrays, using FORC diagrams. *F. Beron*[1], L. Carignan[1], D. Menard[1] and A. Yelon[1] *1. Génie physique, École Polytechnique de Montréal, Montréal, QC, Canada*

10:30

EE-05. Magnetic properties of metal/silicon nanocomposites tailored by specific metal precipitation. *P. Granitzer*[1], K. Rumpf[1] and H. Krenn[1] *1. Institute of Physics, Karl Franzens University Graz, Graz, Austria*

10:45

EE-06. Polymer nanocomposites with embedded Cobalt nanoparticles. *S.N. Kale*[1], S.H. Hatamie[1] and S.D. Kulkarni[2] *1. Department of Electronics-Science, Fergusson College, Pune, Maharashtra, India; 2. Centre for Materials Characterization, National Chemical Laboratory, Pune, Maharashtra, India*

11:00

EE-07. Temperature Dependence of Magnetic Correlations within a Magnetite Nanoparticle Assembly. *K. Krycka*[1], C. Hogg[2], Y. Ijiri[3], R. Booth[2], J. Borchers[1], W. Chen[1], M. Laver[1], T. Gentile[1], B. Maranville[1], B. Breslauer[3] and S. Majetich[2] *1. NIST Center for Neutron Research, Gaithersburg, MD; 2. Carnegie Mellon University, Pittsburgh, PA; 3. Oberlin College, Oberlin, OH*

11:15

EE-08. First-order Magnetic Phase Transition in Manganese Phosphide Nanorods. R. Booth[1] and *S. Majetich*[1] *1. Physics Department, Carnegie Mellon University, Pittsburgh, PA*

11:30

EE-09. Self-assembly Nanoscale Triangular Shaped Fe64Ni36 Dot Arrays. *D. Niu*[1], X. Zou[2], J. Wu[2] and Y. Xu[1] *1. Spintronics and Nanodevice Laboratory, Department of Electronics, The University of York, York, United Kingdom; 2. Department of Physics, University of York, York, United Kingdom*

11:45

EE-10. Monodispersive doped iron core-shell nanoclusters: synthesis, transport and magnetic properties. *Y. Qiang*[1], A. Sharma[1] and D. Meyer[1] *1. Physics, University of Idaho, Moscow, ID*

12:00

EE-11. Porous Silicon/Metal Hybrid System with Ferro and Paramagnetic Behaviour. *K. Rumpf*[1], P. Granitzer[1] and H. Krenn[1] *1. Institute of Physics, Karl Franzens University Graz, Graz, Austria*

12:15

EE-12. Electrical Resistance and Magnetoresistance of Glass Ceramics Containing Magnetite Nanoparticles. *P. Allia*[1], F. Celegato[2], M. Coisson[2], P. Tiberto[2], F. Vinai[2] and O. Bretcanu[3] *1. Politecnico di Torino, Torino, Italy; 2. INRIM, Torino, Italy; 3. Imperial College, London, United Kingdom*

WEDNESDAY
MORNING
9:30

BERLIN

Session EF
RECORDING PHYSICS, MODELS AND THEORY - I
Masukazu Igarashi, Chair

9:30

EF-01. Switching field distribution reduction and effective write gradient enhancement in domain wall assisted media. *A.Y. Dobin*[1] *1. Seagate Technology LLC, Fremont, CA*

9:45

EF-02. A Simple Model for Optimal Read Width due to Finite Write Width and Off-track Interference. *Z. Jin*[1] and H.N. Bertram[1,2] *1. Hitachi GST, San Jose, CA; 2. CMRR, UCSD, La Jolla, CA*

10:00

EF-03. Micromagnetic Study of Short and Long Yoke PMR Head Trailing Shield. *A.F. Torabi*[1], D. Bai[2], T. Pan[2], S. Li[2], S. Song[2], L. Zhong[2], L. Wang[2], K. Stoev[2] and S. Mao[2] *1. Western Digital Corporation, San Jose, CA; 2. Western Digital Corporation, Fremont, CA*

10:15

EF-04. Reduction in Switching Field for a Granular Perpendicular Medium Using Microwave Assisted Magnetic Recording. *S. Batra*[1] and W. Scholz[1] *1. Seagate technology, Pittsburgh, PA*

10:30

EF-05. A Trailing Shield Perpendicular Writer Design with Tapered Write Gap for High Density Recording. *L. Guan*[1], J. Smyth[1], M. Dovek[1], S. Chan[2] and T. Shimizu[2] *1. Headway Technologies, Milpitas, CA; 2. SAE Magnetics (H.K.) Ltd, Hong Kong, China*

10:45

EF-06. Time-dependent fields and anisotropy dominated magnetic media. *K. Rivkin*[1], N. Tabat[1] and S. Foss-Schroeder[1] *1. Seagate Technology, Edina, MN*

11:00

EF-07. Effect Of Interlayer on Read Write Process in Perpendicular Recording. *K. Gao*[1], V. Sapozhnikov[1], A. Zheng[2] and O. Heinonen[1] *1. Seagate Technology, Bloomington, MN; 2. Seagate Technology, Fremont, CA*

11:15

EF-08. Infulence of negative field on media noise in combination of capped medium and shielded pole head. *T. Ichihara*[1], H. Kashiwase[1], H. Nakagawa[1], H. Nemoto[1] and M. Mochizuki[2] *1. Central Research Laboratory, Hitachi Ltd., Odawara, Kanagawa, Japan; 2. Hitachi Grobal Storage Technologies, Fujisawa, Kanagawa, Japan*

11:30

EF-09. Investigation on magnetic fields from field genarating layer in MAMR. *K. Yoshida*[1], E. Uda[1], N. Udagawa[1] and Y. Kanai[2] *1. Information and Communications Engineering, Kogakuin University, Tokyo, Japan; 2. Niigata Institute of Technology, Kashiwazaki, Niigata, Japan*

11:45

EF-10. Effect of media reversal mode on head footprint. *B.F. Valcu*[1], B. Allimi[2], A. Dobin[1], R. Lynch[1] and R. Brockie[1] *1. Seagate Technology, Fremont, CA; 2. Department of Materials Science and Engineering, University of Connecticut, Storrs, CT*

12:00

EF-11. Magnetic recording readback responses in three-dimensions for multi-layered recording media configurations. ***(Invited)*** *R. Wood*[1] and D.T. Wilton[2] *1. HDD AdTech, Hitachi GST, San Jose, CA; 2. School of Mathematics and Statistics, University of Plymouth, Plymouth, United Kingdom*

WEDNESDAY AMSTERDAM
MORNING
9:30

Session EG
SOFT MAGNETIC MATERIALS AND APPLICATIONS II
Francis Johnson, Chair
Jorge Guerra, Chair

9:30

EG-01. Direct observation of magnetocaloric effect with pulsed-field magnet. *T.T. Nguyen*[1], E. Brück[1], C. D. T[1], O. Tegus[2], J. Klaasse[1] and J. Buschow[1] *1. Faculty of Science, Universiteit van Amsterdam, Van der Waals-Zeeman Institute for Experimental Physics, Amsterdam, Netherlands; 2. Inner Mongolia Normal University, Key Laboratory for Physics and Chemistry of Functional Materials, Hohhot, China*

9:45

EG-02. The dc & ac properties of soft magnetic materials for the operational conditions found in novel electrical devices. *H.V. Patel*[1], M.J. Hall[1], O. Thomas[1] and S.C. Harmon[1] *1. Industry & Innovation Division, National Physical Laboratory, Hampton Road, Teddington, Middlesex, TW11 0LW, United Kingdom*

10:00

EG-03. Eddy current effects and pinning effects in Fe and Ni single crystals with low defect densities. *S. Takahashi*[1] and S. Kobayashi[1] *1. Faculty of Engineering, Iwate University, Morioka, Japan*

10:15

EG-04. Experimental Prediction of Iron Losses in Electromagnetic Devices. *G. Almandoz*[1], E. Ritchie[2], J. Poza[1] and A. Gonzalez[3] *1. University of Mondragon. Faculty of Engineering, Arrasate, Spain; 2. Aalborg University. Institute of Energy Technology, Aalborg, Denmark; 3. ORONA Elevator Innovation Center, Hernani, Spain*

10:30

EG-05. Miniature iron-gallium actuator with displacement magnifying mechanism. *M. Ghodsi*[1], T. Ueno[1], C. Sze Keat[2], T. Yano[2] and T. Higuchi[1] *1. Precision Eng. Department, The University of Tokyo, Tokyo, Japan; 2. Mechano Transformer Corporation, Kawasaki, Japan*

10:45

EG-06. Application of magnetoelastic sensors for monitoring of the combustion process in diesel engines for locomotives. *A. Bienkowski*[1], R. Szewczyk[1,2] and J. Salach[1] *1. Institute of Metrology and Measuring Systems, Warsaw University of Technology, Warsaw, Poland; 2. Industrial Research Institute for Automation and Measurements PIAP, Warsaw, Poland*

11:00

EG-07. Longitudinal and transverse magnetoimpedance in FeNi/Cu/FeNi multilayers with longitudinal and transverse anisotropy. *D. de Cos*[1], J.M. Barandiaran[1], A. Garcia-Arribas[1], V.O. Vas′kovskiy[2] and G.V. Kurlyandskaya[1,2] *1. Electricity and Electronics, Basque Country University UPV-EHU, Leioa, Bizkaia, Spain; 2. Physics of Magnetic Phenomenon, Ural State University named under A.M.Gorky, Ekaterinburg, Russian Federation*

11:15

EG-08. Magnetorheological characteristics of carbonyl iron embedded suspension polymerized poly(methyl methacrylate) microbead. J. You[1], B. Park[1] and *H. Choi*[1] *1. Department of Polymer Science and Engineering, Inha University, Incheon, South Korea*

11:30

EG-09. Effect of Slit Patterning Perpendicular to Magnetic Easy Axis In Thin Film Inductors. *T. Masai*[1,2] and Y. Kitamoto[2] *1. TDK, Minami-alps city, Yamanashi pref., Japan; 2. Innovative and Engineerd Materials, Tokyo Institute of Technolgy, 4259 Nagatsuta, MIdori-ku, Yokohama, Japan*

11:45

EG-10. Miniaturization of antenna using Y-type hexagonal ferrite. *K. Kawano*[1] and Y. Okamoto[1] *1. Product Development HQ, TAIYO YUDEN CO.,LTD., Takasaki-shi, Japan*

12:00

EG-11. Development of Axial Flux Permanent Syncrnous Motor by using High-Density Magnetic Composites. *H. Nakai*[1], T. Arakawa[1], K. Hiramoto[1], S. Tajima[1] and Y. Inaguma[2] *1. Toyota Central R&D labs., INC., Aichi, Japan; 2. Daido Institute of Technology, Nagoya, Japan*

12:15

EG-12. Validation of Voltage and Current Waveforms of Nonlinear Inductors Computed with a Novel Finite Element Methodology. *R. Salas*[1] and J. Pleite[1] *1. Tecnologia Electronica, Universidad Carlos III de Madrid, Leganés, Spain*

WEDNESDAY MORNING 9:30 — CARACAS

Session EH
MAGNETO-DIELECTRIC MATERIALS
J. Mira, Chair

9:30

EH-01. Spin control by doping non-magnetic ions in magnetic ordering type of multiferroic materials. *K. Choi*[1], S. Kim[1], B. Lee[2] and C. Kim[1] *1. Physics, Kookmin Univ., Seoul, South Korea; 2. Hankuk University of Foreign Studies, Yongin, South Korea*

9:45

EH-02. Dielectric and magnetic properties of low-temperature sintered Ni0.24Cu0.21Zn0.55Fe1.96O4+xPb0.95Sr0.05(Zr0.52Ti0.48)O3 composites. *L. Jia*[1], H. Zhang[1], S. Bao[1] and Z. Zhong[1] *1. university of electronic science and technology of China, chengdu, Sichuan, China*

10:00

EH-03. Processing related magneto-dielectric properties of Ni-Zn-Co ferrite ceramics. *L. Kong*[1], Z. Li[1] and G. Lin[1] *1. Temasek Laboratories, National University of Singapore, Singapore, Singapore*

10:15

EH-04. Dielectric properties of the charge-ordered oxyborate Fe_2OBO_3 M. Sanchez-Andujar[2], *J. Mira*[1], B. Rivas-Murias[2], S. Yanez-Vilar[2], N. Biskup[3], J. Rivas[1] and M. Senaris-Rodriguez[2] *1. Fisica Aplicada, Universidade de Santiago de Compostela, Santiago de Compostela, Spain; 2. Quimica Fundamental, Universidade da Coruna, A Coruna, Spain; 3. ICMM, Consejo Superior de Investigaciones Científicas, Madrid, Spain*

10:30

EH-05. Magneto-electric Effects in Single Crystal Hexaferrite-Piezoelectric Bilayers. V. Mathe[1] and *G. Srinivasan*[1] *1. Physics, Oakland University, Rochester, MI*

10:45

EH-06. Anisotropic Susceptibility and Weak Magnetic Moment of $YbMnO_3$ Single Crystal. *J. Fontcuberta*[1], M. Gospodinov[2] and V. Skumryev[3] *1. Institut de Ciència de Materials de Barcelona, CSIC, Campus UAB, 08193 Bellaterra, Spain; 2. Institute of Solid State Physics, Bulgarian Academy of Sciences, 1784 Sofia, Bulgaria; 3. Institut Català de Recerca i Estudis Avançats (ICREA), and Departament de Física, Universitat Autònoma de Barcelona, 08193 Bellaterra, Spain*

11:00

EH-07. Pressure effect on the magnetic ordering in $BiMnO_3$ *C. Chou*[1,2], C. Lin[1,2], S. Taran[1,2], C. Huang[1,2], J. Her[1,2], C. Sun[1,2], C. Chan[1,2], H. Sakurai[3], E. Takayama-Muromachi[3] and H. Yang[1,2] *1. Department of Physics, National Sun Yat-Sen University, Kaohsiung, Taiwan; 2. Center for Nanoscience and Nanotechnology, National Sun Yat-Sen University, Kaohsiung, Taiwan; 3. National Institute for Materials Science, Tsukuba, Japan*

11:15

EH-08. Magnetic properties of Ga substituted $NiCr_{1.9-x}Ga_xFe_{0.1}O_4$ *G. Ahn*[1], S. Park[1], S. Park[2] and C. Kim[2] *1. HANARO Utilization Technology Development Center, Korea Atomic Energy Research Institute(KAERI), Daejeon, South Korea; 2. Dept. of Physics, Kookmin University, Seoul, South Korea*

11:30

EH-09. Synthesis and magneocaloric effect of functional perovskites by sol-gel reaction. K. Jeongju[1], A. Yangkyu[1] and *C. Eun Jung*[2] *1. Chemistry, Konyang University, Nonsan, Chungnam, South Korea; 2. Opthalmic Optic, Konyang University, Nonsan, Chungnam, South Korea*

11:45

EH-10. Ferrimagnetic $Ba_{0.5}Sr_{1.5}Zn_2Fe_{12}O_{22}$ (Zn-Y) single crystal barium ferrites. *J. Jalli*[1,2], Y. Hong[1,2], S. Gee[1,3], J. Lee[1,2], S. Bae[1,2], G.S. Abo[1,2], A. Lyle[1,2], H. Han[1,2], J. Kim[4], H. Lee[4] and S. Lee[4] *1. Electrical and Computer Engineering, University of Alabama, Tuscaloosa, AL; 2. MINT Center, University of Alabama, Tuscaloosa, AL; 3. Seagate Technology, Bloomington, MN; 4. Pohang Superconductivity Center, Pohang University of Science and Technology, Pohang, South Korea*

12:00

EH-11. Increment of saturation magnetization and reduction of electric coercive field in multiferroic Bi ferrite films by adding cobalt. *H. Naganuma*[1], J. Miura[1] and S. Okamura[1] *1. Department of Applied Physics, Tokyo University of Science, Tokyo, Japan*

12:15

EH-12. Influence of oxygen and nitrogen on magnetic properties of soft magnetic CoFeZr nanoparticles embedded in alumina dielectric matrix. *A. Fedotov*[1], J. Fedotova[1], Y. Kalinin[2], A. Sitnikov[2], V. Fedotova[3] and Y. Ilyashuk[1] *1. Belarusian State University, Minsk, Belarus; 2. Voronezh State Technical University, Voronezh, Russian Federation; 3. Joint Institute of Solids and Semiconductors Physiscs, Minsk, Belarus*

WEDNESDAY MORNING 9:00 — POLIVALENTE

Session EL
PERMANENT MAGNET MACHINES III (POSTER SESSION)
Jiabin Wang, Chair

EL-01. Determining parameters of a line-start interior permanent magnet synchronous motor model by the differential evolution. *T. Mar či č*[1], G. Štumberger[2,1], B. Štumberger[2,1], M. Hadziselimovi č[2,1] and P. Virti č[1] *1. TECES, Research and Development Centre for Electrical Machines, Maribor, Slovenia; 2. University of Maribor, Faculty of Electrical Engineering and Computer Science, Maribor, Slovenia*

EL-02. Design and performance measurement of high speed permanent magnet synchronous motor with full-ring magnet for axial-flow turbo fan. S. Jang[1], *J. Park*[1], K. Ko[1] and J. Hwang[2] *1. Electrical Engineering, Chungnam National University, Daejeon, South Korea; 2. MAGPLUS, Daejeon, South Korea*

EL-03. Finite element analysis of stator winding faults in permanent magnet brushless AC motors. *J.A. Farooq*[1], T. Raminosoa[1], A. Djerdir[1] and A. Miraoui[1] *1. Electrical Engineering and Control Systems, University of Technology Belfort Montbeliard, Belfort, France*

EL-04. Analysis method for considering the effect of magnetic cross saturation of IPMSM. *Y. Kim*[1], I. Jung[1], J. Hur[1] and J. Hong[2] *1. KETI, Bucheon, South Korea; 2. Hanyang University, Seoul, South Korea*

EL-05. Design and finite-element analysis of interior permanent magnet synchronous motor with flux barriers. *B. Stumberger*[1], G. Stumberger[1], M. Hadziselimovic[1], T. Marcic[2], P. Virtic[2], V. Gorican[1] and M. Trlep[1] *1. University of Maribor, Faculty of EE&CS, Maribor, Slovenia; 2. TECES, Development centre for Electrical Machines, Maribor, Slovenia*

EL-06. Performance of IPMSM for Electro-Hydraulic Power Steering with Electric Driven Pump Unit. *Y. Kim*[1], S. Rhyu[1], J. Hur[1] and J. Hong[2] *1. KETI, Bucheon, South Korea; 2. Hanyang University, Seoul, South Korea*

EL-07. Influence of driving methods on dynamic torque characteristic of high-speed permanent magnet synchronous motor with hall sensor. S. Jang[1], *U. Lee*[1], D. You[1], J. Park[1] and T. Sung[2] *1. Chungnam National University, Daejeon, South Korea; 2. Korea Electric Power Research Institute, Daejeon, South Korea*

EL-08. Thrust Ripple Minimization of Permanent Magnet Linear Synchronous Motor by the Notch and the Auxiliary-teeth. *D. Lee*[1], K. Jang[1] and G. Kim[1] *1. Electrical Engineering, Changwon National University, Changwon, Gyeongsangnam-do, South Korea*

EL-09. A Study on the Vibration Characteristic According to PM Arrangement in PMLSM. *D. Lee*[1], S. Lee[1], K. Jang[1] and G. Kim[1] *1. Electrical Engineering, Changwon National University, Changwon, Gyeongsangnam-do, South Korea*

EL-10. Flux Barrier Design to Improve Torque Characteristics of Double-layer Interior Permanent Magnet Synchronous Motor. *S. Kim*[1], J. Jung[1], J. Hong[1] and S. Lee[2] *1. Department of Mechanical Engineering, Hanyang University, Seoul, South Korea; 2. Research Center, Korea Institute of Industrial Technology, Gwangju, South Korea*

EL-11. Study on High Efficiency Performance in Interior Permanent Magnet Synchronous Motor with Double-layer PM Design. *L. Fang*[1], J. Jung[1], B. Lee[1] and J. Hong[1] *1. Department of Mechanical Engineering, Hanyang University, Seoul, South Korea*

EL-12. A new PMLSM having 9 pole 10 slot structure and its shape optimal design for detent force reduction. *C. Koh*[1], I. Hwang[1] and H. Yoon[1] *1. School of Electrical & Computer Engineering, Chungbuk National University, Cheongju, Chungbuk, South Korea*

WEDNESDAY
MORNING
9:00

POLIVALENTE

Session EM
EXCHANGE BIAS II (POSTER SESSION)
Jordi Sort, Chair

EM-01. The role of uncompensated spins in exchange biasing. *(Invited)* *H.J. Hug*[1,2], I. Schmid[1] and P. Kappenberger[1] *1. Nanoscale Materials Science, Empa, Duebendorf, Switzerland; 2. Institute of Physics, University of Basel, Basel, Switzerland*

EM-02. Measuring exchange anisotropy in Fe/MnPd using inductive magnetometry. *K.J. Kennewell*[1], X. Ji[2], J. Hu[1], K.M. Krishnan[2] and R.L. Stamps[1] *1. School of Physics, University of Western Australia, Crawley, WA, Australia; 2. Materials Science and Engineering, University of Washington, Seattle, WA*

EM-03. Dependence of the training effect on the antiferromagnet structure in the domain state model for exchange bias. *A.G. Biternas*[1], U. Nowak[1] and R.W. Chantrell[1] *1. Department of Physics, University of York, York, United Kingdom*

EM-04. Temperature Dependence of IrMn Pinning: Single Crystal versus Polycrystalline Effects. *P. Pong*[1], C.L. Dennis[1] and W.F. Egelhoff[1] *1. Magnetic Materials Group, National Institute of Standards and Technology, Gaithersburg, MD*

EM-05. Exchange coupling between an amorphous ferromagnet and a crystalline antiferromagnet. *M. Fecioru-Morariu*[1], G. Güntherodt[1], M. Rührig[2], A. Lamperti[3] and B. Tanner[3] *1. Physikalisches Institut (IIA), RWTH Aachen University, Aachen, Germany; 2. Corporate Technology, CT MM 1, Innovative Electronics, SIEMENS AG, Erlangen, Germany; 3. Department of Physics, Durham University, Durham, United Kingdom*

EM-06. Local exchange anisotropy of epitaxial and polycrystalline MnIr/CoFe bilayers. H. Kato[2], *T. Kato*[1], S. Tsunashima[2] and S. Iwata[1] *1. Department of Quantum Engineering, Nagoya University, Nagoya, Aichi, Japan; 2. Department of Electrical Engineering and Computer Science, Nagoya University, Nagoya, Aichi, Japan*

EM-07. The significant enhancement of the thermal stability in Co/Cu/Co/IrMn spin valve through insert 1nm FeMn layer. L. Wang[1], Q.Q. Qin[1], *H.X. Wei*[1] and X.F. Han[1] *1. Institute of Physics, Beijing, China*

EM-08. Exchange bias in Cu/Ni/FeMn trilayer with perpendicular magnetic anisotropy. *L.T. Tu*[1] and C. Kim[1] *1. Department of Materials Science and Engineering, Chungnam National University, Deajeon, South Korea*

EM-09. Parallel and perpendicular exchange biases in epitaxial FePt-FeMn multilayers with different crystalline orientations. N.N. Phuoc[1] and *T. Suzuki*[1] *1. Information Storage Materials Laboratory, Toyota Technological Institute, Nagoya, Aichi, Japan*

EM-10. Enhanced Exchange Anisotropy by ultra-thin Co_xFe_{100-x} (x > 80) Layer Insertion at the Interface of $L1_2$-ordered $Mn_3Ir/Co_{65}Fe_{35}$ Bilayers. *K. Komagaki*[1], M. Tsunoda[2], K. Noma[1], H. Kanai[1], K. Kobayashi[1], Y. Uehara[1] and M. Takahashi[2] *1. Advanced Head Technology Department, Head Division, FUJITSU LIMITED, Nagano, Japan; 2. Department of Electronic Engineering, Tohoku University, Sendai, Japan*

EM-11. Lateral grain size effect on exchange bias in polycrystalline FeNi/FeMn bi-layer films. P. Sharma[1], T. Huang[1], A. Sun[1] and *J. Hsu*[1] *1. Physics, National Taiwan University, Taipei, Taiwan*

EM-12. The influence of different Mn-oxide structures on the exchange bias field in NiFe/Mn-oxide bilayers. J. Guo[1], T. Chen[1], Y. Chiu[1], H. Ouyang[1], *K. Lin*[1], E. Vass[2] and J. van Lierop[3] *1. Department of Materials Engineering, National Chung Hsing University, Taichung, Taiwan; 2. Institut for Experimentalphysik, University of Innsbruck, Innsbruck, Austria; 3. Department of Physics and Astronomy, University of Manitoba, Winnipeg, MB, Canada*

EM-13. Effect of the ferromagnetic layer thickness on the blocking temperature in IrMn/CoFe exchange couples. *G. Vallejo-Fernandez*[1], L.E. Fernandez-Outon[1], B. Kaeswurm[1] and K. O'Grady[1] *1. Physics, The University of York, York, North Yorkshire, United Kingdom*

EM-14. Probing the influence of in-plane roughness on magneto-resistance in spin-valves using off-specular reflectivity techniquestechniques. *J. Park*[1], C. Furjanic[1], D. Draganova[1], C. Chen[1], S.M. Watson[2], J.A. Borchers[2], M. Carey[3], P. Sparks[1] and J.C. Eckert[1] *1. Physics, Harvey Mudd College, Claremont, CA; 2. NIST Center for Neutron Research, Gaithersburg, MD; 3. Hitachi Global Storage Technologies, San Jose, CA*

Session EN
SHIELDING, LEVITATION AND TRANSPORT (POSTER SESSION)
Claudio Aroca, Chair

EN-01. Intuitive operation of magnetically driven fish-type microrobot using smart interface. *T. Honda*[1], K. Ono[1] and J. Yamasaki[1] *1. Department of Applied Science for Integrated System Engineering, Kyushu Institute of Technology, Kitakyushu, Fukuoka, Japan*

EN-02. Three-dimensional motion of a small object by using a new magnetic levitation system having four I-shaped electromagnets. *T. Ohji*[1], H. Hara[1], K. Amei[1] and M. Sakui[1] *1. University of Toyama, Toyama, Japan*

EN-03. A Novel Design of a Disk-Shaped Bearingless PM Motor for Artificial Hearts. J. Asama[1], *Y. Kishi*[1] and A. Chiba[1] *1. Electrical Engineering, Tokyo University of Science, Noda, Chiba, Japan*

EN-04. Effect of the active damper coils of the superconducting magnetically levitated bogie in case of acceleration. *S. Ohashi*[1] *1. Electrical and Electric Engineering, Kansai University, Osaka, Japan*

EN-05. Assessing the Maglev Force Capabilities of Two Passive Flat Guideway Topologies when using Electrodynamic Wheels. *J. Bird*[1,2] *1. Advanced Technology Center, General Motors Corporation, Torrance, CA; 2. Electrical and Computer Engineering, University of Wisconsin-Madison, Madison, WI*

EN-06. Magnetic levitation with minimum power consumption using disturbance compensation. *J. Ahn*[1], S. Kim[2], J. Lee[1] and J. Choi[3] *1. Electrical Engineering, Hanyang University, Seoul, South Korea; 2. Electrical Engineering, Yuhan College, Buchon, Gyeonggi, South Korea; 3. Industry Application Researh Division, Korea Electrotechnology Research Institute, Changwon, Gyeongnam, South Korea*

EN-07. Design and Dynamic Analysis of Rectangular-Surface Electromagnets for Levitation Applications. S. Jang[1], *J. Choi*[1], J. Park[1], H. Sung[2] and S. Sung[2] *1. Chungnam National University, Dae-jeon, South Korea; 2. Korea Institute of Machinery&Materials, Daejeon, South Korea*

EN-08. Basic Characteristics of an Active Thrust Magnetic Bearing with a Cylindrical Rotor Core. *K. Hijikata*[1], S. Kobayashi[1], M. Takemoto[1], Y. Tanaka[1], A. Chiba[2] and T. Fukao[1] *1. Mechanical Systems Engineering, Musashi Institute of Technology, Setagaya-ku, Tokyo, Japan; 2. Electrical Engineering, Tokyo University of Science, Noda-shi, Chiba, Japan*

EN-09. Magnetically-Levitated Steel Plate Conveyance System Using Electromagnets and a Transverse-Flux Linear Induction Motor. *J. Choi*[1] and Y. Baek[1] *1. Mechanical Engineering, Yonsei University, Seoul, South Korea*

EN-10. Combination resonance of a rigid body levitated above a diamagnetic slab. *T. Sugiura*[1] and T. Hosono[1] *1. Mechanical Engineering, Keio University, Yokohama, Japan*

EN-11. Dynamic shielded room for biomagnetism. D. Costandache[1] and *O. Baltag*[1] *1. University of Medicine and Pharmacy "Gr.T.Popa", Iasi, Romania*

EN-12. Magnetic shielding design for magneto-electronic devices protection. *W. Wang*[1] and Z. Jiang[1] *1. Electrical Engineering, University of Wisconsin - Milwaukee, Milwaukee, WI*

EN-13. Measurement and calculation of shielding performance of reinforced concrete structures. *M. Zhang*[1], Z. Zhao[1] and X. Cui[1] *1. North China Electric Power University, Baoding, Hebei, China*

EN-14. Reduction of magnetic shaking flux leakage from loosely coupled cylindrical magnetic shield shells having active compensation. *I. Sasada*[1] and R. Takahashi[1] *1. Applied Science for Electronics and Materials, Kyushu University, Kasuga, Japan*

EN-15. Analysis of perforated magnetic shields. *P. Sergeant*[1], R. Sabariego[2], G. Crevecoeur[1], C. Geuzaine[2] and L. Dupre[1] *1. Department of Electrical Energy, Systems and Automation, Ghent university, Gent, Belgium; 2. Department of Electrical Engineering and Computer Science, University of Liege, Liege, Belgium*

EN-16. Optimal Design and Analysis of Faraday Shield Used in High Frequency Coaxial Transformer. X. Yang[1] and *J. Lu*[2] *1. Province-Ministry Joint Key Laboratory of Electromagnetic Field and Electrical Apparatus Reliability, Hebei University of Technology, Tianjin, China; 2. School of Eng., Griffith University, Brisbane, QLD, Australia*

EN-17. Electromagnetic wave absorption properties of double layers absorbers made of hollow glass microspheres electroless plated with FeCoNiB and NiCoZn ferrites. *M. Han*[1], F. Xiao[1] and Y. Ou[1] *1. State Key Laboratory of Electronic Thin Films and Integrated Devices, University of Electronic Science and Technology of China, Chengdu, Sichuan, China*

EN-18. Open-type Magnetic Shield Structure and its Performance. *M. Fujikura*[1], K. Segawa[1], K. Chikuma[1], K. Fujisaki[1], J. Mino[2], T. Morita[2], T. Saito[3], H. Hirano[3] and T. Shinnoh[3] *1. Nippon Steel corporation, Chiba, Japan; 2. Nippon Steel Engineering Co., LTD., Tokyo, Japan; 3. Kajima Corporation, Tokyo, Japan*

EN-19. The Estimation on the shield capability of the Magnetic Shielding Room depending on the setting direction of GO based on the analysis with Homogenization Method for Thin Steel Plate. Y. Tomizawa[1], *K. Fujisaki*[2,3], M. Fujikura[2], J. Mino[4], S. Tamaki[5] and T. Morita[6] *1. Industrial Plant Engineering, Taiheikogyo Co.,Ltd, Toukai, Japan; 2. Technical Development Bureau, Nippon Steel Corp., Futtsu, Japan; 3. Graduate School of Environmental Studies, Tohoku University, Sendai, Japan; 4. Building Construction & Steel Structures, Nippon Steel Engineering Co.,Ltd, Chiyoda, Japan; 5. Nagoya Works, Nippon Steel Corp., Toukai, Japan; 6. NS Construction, Chiyoda, Japan*

EN-20. Open-Type Magnetically Shielded Room Combined with Square Cylinders made of Magnetic and Conductive Materials for MRI. *K. Yamazaki*[1], S. Hirosato[1], K. Kamata[2], K. Muramatsu[3], K. Kobayashi[4] and A. Haga[5] *1. Takenaka Corp., Chiba, Japan; 2. Kagoshima National College of Technology, Kagoshima, Japan; 3. Saga University, Saga, Japan; 4. Iwate University, Iwate, Japan; 5. Tohoku-Gakuin University, Miyagi, Japan*

EN-21. Shield Duct to Prevent Magnetic Field Leakage through Openings in Double-layered Magnetically Shielded Rooms. *K. Yamazaki*[1], Y. Hatsukade[2], S. Tanaka[2] and A. Haga[3] *1. Takenaka Corp., Chiba, Japan; 2. Toyohashi University of Technology, Toyohashi, Japan; 3. Tohoku-Gakuin University, Miyagi, Japan*

EN-22. Features of a Wall with Open-type Magnetic Shield. *T. Saito*[1] *1. Kajima Corporation, Tokyo, Japan*

EN-23. Analysis of the shielding effectiveness of rectangular enclosure of metal structures with apertures. *M. Zhang*[1], Z. Zhao[1], C. Gao[1] and S. Wang[2] *1. North China Electric Power University, Baoding, Hebei, China; 2. Northeast Electric Power Design Institute, Changchun, Jilin, China*

WEDNESDAY MORNING 9:00 — POLIVALENTE

Session EO
MOLECULAR AND NOVEL MATERIALS-II (POSTER SESSION)
Clara Marquina, Chair

EO-01. Effect of La-substitution on magnetic and ferroelectric properties of $Bi_{(1-x)}La_xDy_{0.3}FeO_3$ system. *P. Kovur*[1], S.P. Duttagupta[1] and V.R. Palkar[1] *1. Electrical Engineering, Indian Institute of Technology Bombay, Mumbai, Maharashtra, India*

EO-02. Thermomagnetic characterization of the $CeNi_4Cr$ compound. *T. Tolinski*[1], A. Kowalczyk[1], M. Reiffers[2], E. Gazo[2], M. Zapotokova[2] and G. Chelkowska[3] *1. Institute of Molecular Physics, Polish Academy of Sciences, Poznan, Poland; 2. Institute of Experimental Physics, SAS, Kosice, Slovakia; 3. Institute of Physics, Silesian University, Katowice, Poland*

EO-03. Two dimensional ferromagnetic clusters in Ho0.8La0.2Mn2O5. *H. Chou*[1], C. Yu[1], C. Wang[2], C. Wu[2] and W. Li[2] *1. Physics, National Sun Yat-sen Unversity, Kaohsiung, Taiwan; 2. Physics and Center for Neutron Beam Application, National Central University, Jhongli, Taiwan*

EO-04. The switching behavior of spin transition [Fe(PM-BiA)2(NSC)2] compound derived from pressure pulse type experiments. *R. Tanasa*[1], A. Stancu[1], J. Linares[2], E. Codjovi[2], F. Varret[2] and J. Letard[3] *1. Department of Physics, "Alexandru Ioan Cuza" University, Iasi, Romania; 2. Groupe d'Etude de la Matière Condensée (GEMaC) CNRS-UMR 8635, Université de Versailles, Versailles, France; 3. Groupe des Sciences Moléculaires, Institut de Chimie de la Matière Condensée de Bordeaux, UPR No. 9048 CNRS-Université Bordeaux I, Pessac, France*

EO-05. Magnetic Properties of Zr_9Ni_{11} Intermetallic Compound. *V. Provenzano*[1], R.D. Shull[1], R.M. Waterstrat[1], L.H. Bennett[1,2], E. Della Torre[1,2] and H. Seyoum[3] *1. Magnetic Materials Group, NIST, Gaithersburg, MD; 2. Physics Department, George Washington University, Washington, DC; 3. Physics Department, University of the District of Columbia, Washington, DC*

EO-06. First-Order Reversal Curve Analysis of Spin-Transition Thermal Hysteresis Under Pressure in Terms of Physical-Parameter Distributions and Their Correlations. *A. Rotaru*[1,2], J. Linares[1], E. Codjovi[1], F. Varret[1] and A. Stancu[2] *1. Physique, GEMAC-Versailles University, Versailles, Yvelines, France; 2. Physique, Alexandru Ioan Cuza University, Iasi, Iasi, Romania*

EO-07. Thermodynamic and electronic properties of DyNi4Si compound. *M. Falkowski*[1], A. Kowalczyk[1], M. Reiffers[2], T. Tolinski[1], E. Gazo[2], M. Zapotokova[2] and G. Chelkowska[3] *1. Institute of Molecular Physics, Polish Academy of Sciences, Smoluchowskiego 17, Poznan, Poland; 2. Institute of Experimental Physics, Slovak Academy of Sciences, Watsonova 47, Kosice, Slovakia; 3. Institute of Physics, Silesian University, Uniwersytecka 4, Katowice, Poland*

EO-08. Multiferroic, electronic and structural properties of Sr_2TiMnO_6 perovskite: experimental and ab-initio studies. *J.A. Rodriguez*[1], D.A. Landinez-Tellez[1], C. Salazar-M[1], P. Pureur[2], F.E. Fajardo[1] and J. Roa-Rojas[1] *1. Dept. of Physics, Universidad Nacional de Colombia, Bogotá, D. C., Colombia; 2. Institute of Physics, Universidade Federal do Rio Grande do Sul, Proto Alegre RS, Brazil*

EO-09. Physical Properties in Powder, Bulk and Thin Films of La2/3Ca1/3CrxMn(1-x)O3 with Low Doping. *D.L. Quintero*[1] and D. Girata[1] *1. Physics Institute, Universidad de Antioquia, Medellin, Antioquia, Colombia*

EO-10. Magnetic relaxation behavior in $Nd_{0.5}Sr_{0.5}MnO_3$: observation of negative imaginary component of ac magnetic susceptibility. *A.N. Ulyanov*[1], H.D. Quang[2], K.W. Lee[3], S.C. Yu[4], N.H. Sinh[5], Y.M. Kang[1] and S.I. Yoo[1] *1. Department of Materials Science and Engineering, Seoul National University, Seoul 151-744, South Korea; 2. Solid State Physics Group, Department of Physics & Astronomy and SUPA Graduate School, University of Glasgow, G12 8QQ, United Kingdom; 3. Korea Research Institute of Standards and Science, Yusong, Taejon 305-340, South Korea; 4. Department of Physics, Chungbuk National University, Cheongju 361-763, South Korea; 5. Cryogenics Laboratory, Department of Physics, College of Natural Science, Hanoi National University, 334 Nguyen Trai Road, Thanh Xuan, Hanoi, Viet Nam*

EO-11. Synthesis and characterization of multiferroic polycrystalline transition metal doped $BiFeO_3$ thin films. P. Kharel[1], S. Talebi[2,1], C. Sudakar[1], M.B. Sahana[1], *V.M. Naik*[2], R. Naik[1] and G. Lawes[1] *1. Department of Physics and Astronomy, Wayne State University, Detroit, MI; 2. Department of Natural Sciences, University of Michigan-Dearborn, Dearborn, MI*

WEDNESDAY MORNING 9:00 — POLIVALENTE

Session EP
MAGNETODYNAMICS AND MILLIMETRE WAVE DEVICES (POSTER SESSION)
Andrei Slavin, Chair

EP-01. Influence of current induced magnetic inhomogeneities on spin wave propagation. *T. Neumann*[1], A.A. Serga[1], M.P. Kostylev[2] and B. Hillebrands[1] *1. Fachbereich Physik und Forschungsschwerpunkt MINAS, TU Kaiserslautern, Kaiserslautern, Germany; 2. School of Physics, University of Western Australia, Crawley, WA, Australia*

EP-02. A YIG/GGG/GaAs-Based Magnetically Tunable Wideband Microwave Band-Pass Filter Using Cascaded Band-Stop Filters*. G. Qiu[1], B.T. Wang[2] and *C.S. Tsai*[1,3] *1. Dept of Electrical Engineering and Computer Science, and Institute of Surface and Interface Science, University of California, Irvine, CA; 2. Wang, NMR Inc., Livermore, CA; 3. Institute of Electrooptics Engineering, National Taiwan University, Taipei, Taiwan*

EP-03. Bistable control of ferromagnetic resonance frequencies in ferromagnetic trilayered dots. *Y. Nozaki*[1], K. Tateishi[1], S. Taharazako[1], S. Yoshimura[1] and K. Matsuyama[1] *1. Dept. of Electronics, Kyushu University, Fukuoka, Japan*

EP-04. An Electric Field Tunable Millimeter-Wave Ferrite-Piezoelectric Phase Shifter. A.S. Tatarenko[1] and *G. Srinivasan*[1] *1. Physics, Oakland University, Rochester, MI*

EP-05. Design of Scandium and Indium doped hexaferrite microstripline phase shifters for X-band applications. T. Sakai[1], *C. Chinnasamy*[1], V. Ilancheliyan[1], S. Yoon[1], C. Vittoria[1] and V.G. Harris[1] *1. Electrical&Computer Engineering, Northeastern university, Boston, MA*

EP-06. Propagation characteristics of magnetostatic surface waves in a YIG-based one-dimensional magnonic crystal composed of rubber magnets. *K. Togo*[1], K. Hatafuku[1], M.E. Dokukin[1], J. Kim[1], K. Shin[2] and M. Inoue[1] *1. Toyohashi University of Technology, Toyohashi, Japan; 2. Kyungsung University, Pusan, South Korea*

EP-07. A magnetosensitive microwave absorption characterization of terbium. *G. Alvarez*[1], H. Montiel[2], R. Zamorano[3] and R. Valenzuela[1] *1. Departamento de Materiales Metálicos y Cerámicos, Instituto de Investigaciones en Materiales de la Universidad Nacional Autónoma de México, Ciudad de México, México DF, Mexico; 2. Centro de Ciencias Aplicadas y Desarrollo Tecnológico de la Universidad Nacional Autónoma de México, Ciudad de México, México DF, Mexico; 3. Departamento de Ciencias de los Materiales, Instituto Politécnico Nacional, Ciudad de México, México DF, Mexico*

EP-08. Magnetic tuning of surface acoustic wave devices within high frequency range. *C. Cavaco*[1], L.A. Francis[2,1], L. Lagae[1] and G. Borghs[1] *1. IMEC, Leuven, Belgium; 2. Université catholique de Louvain, Louvain-la-Neuve, Belgium*

EP-09. Microwave Absorption Properties of The Hierarchically Branched Ni Nanowires Composites. *L. Qiao*[1], J. Wang[1], X. Han[1], B. Gao[1], F. Wen[1] and F. Li[1] *1. Lanzhou University, Institute of Applied Magnetism, Key Laboratory for Magnetism and Magnetic Materials of Ministry of Education, LanZhou, Gansu, China*

WEDNESDAY
MORNING
9:00

POLIVALENTE

Session EQ
MAGNETIC SEMICONDUCTORS-II (POSTER SESSION)
Benjamin Martinez, Chair

EQ-01. Magnetoresistance in Co/ZnO films. X. Li[1,2], Z. Quan[2], *X. Xu*[2] and H. Wu[2,1] *1. College of Chemistry and Chemical Engineering, Taiyuan University of Technology, Taiyuan, Shanxi, China; 2. School of Chemistry and Materials Science, Shanxi Normal University, Linfen, Shanxi, China*

EQ-02. Temperature dependent magneto-transport studies in ferromagnetic $Ge_{1-x}Mn_xTe$. *C. Sim*[1,2], W. Chen[2], S. Lim[2], J. Bi[1], K. Teo[1], T. Liew[2] and T. Chong[2] *1. Electrical & Computer Engineering, National University of Singapore, Singapore, Singapore; 2. Data Storage Institute, Singapore, Singapore*

EQ-03. Exponential decrease of neutral dangling bonds density in rare-earth doped amorphous Si films. W. Iwamoto[1], *P.G. Pagliuso*[1], C. Rettori[1] and A.R. Zanatta[2] *1. DEQ, IFGW - Unicamp, Campinas, São Paulo, Brazil; 2. Instituto de Física de São Carlos, USP, São Carlos, São Paulo, Brazil*

EQ-04. Study on absence of room-temperature ferromagnetism in the Mn-AlN films with various Mn concentrations. *T. Sato*[1], Y. Endo[2], Y. Kawamura[1], F. Kirino[3], R. Nakatani[1] and M. Yamamoto[1] *1. Department of Materials Science and Engineering, Osaka University, Osaka, Japan; 2. Department of Electrical and Communication Engineering, Tohoku University, Sendai, Japan; 3. Conservation of Cultural Property, Tokyo National University of Fine Arts and Music, Tokyo, Japan*

EQ-05. Growth parameter dependence of structural characterization of diluted magnetic semiconductor (Ga,Cr)As. *J. Lu*[1], J. Bi[1], W. Wang[1], G. Gan[1], H. Meng[1], H. Zheng[1] and J. Zhao[1] *1. State Key Laboratory for Superlattices and Microstructures, Institute of Semiconductors, Chinese Academy of Sciences, Beijing, China*

EQ-06. Coexistence of ferromagnetism and paramagnetism in highly dilute $Ga_{1-x}Mn_xN$. *D. Sedmidubsk ý*[1], Z. Sofer[1], J. Hejtmánek[2], M. Mary ško[2] and K. Jurek[2] *1. Institute of Chemical Technology, Prague, Czech Republic; 2. Institute of Physics ASCR, v.v.i., Prague, Czech Republic*

EQ-07. Effect of strain relaxation on the anisotropic magnetoresistance of GaMnAs microbars. *E. De Ranieri*[1], K. Olejník[2], K. Vyborn ý[2], A.C. Irvine[1], R.P. Campion[3], B.L. Gallagher[3], T. Jungwirth[2,3], H. Sirringhaus[1] and J. Wunderlich[4,2] *1. Microelectronics Research Centre, University of Cambridge, Cambridge, United Kingdom; 2. Institute of Physics ASCR, Prague, Czech Republic; 3. School of Physics and Astronomy, University of Nottingham, Nottingham, United Kingdom; 4. Hitachi Cambridge Laboratory, Cambridge, United Kingdom*

EQ-08. Preparation of $(Ge_{1-y}Pb_y)_{1-x}Mn_xTe$ thin films and their magnetic properties. *H. Asada*[1], Y. Fukuma[2], D. Kitabori[1], A. Ohji[1], Y. Kamimoto[1] and T. Koyanagi[1] *1. Department of Materials Science and Engineering, Yamaguchi University, Ube, Japan; 2. Yamaguchi Prefectural Industrial Technology Institute, Ube, Japan*

EQ-09. Properties of ternary rare earth REXY compounds with 18 valence electrons. *F. Casper*[1] and C. Felser[1] *1. Institute for inorganic and analytical chemistry, Mainz, Germany*

EQ-10. Effect of local magnetic field on the transport properties of GaMnAs. *J. Suh*[1,2], J. Chang[1], E. Kim[2], M. Sapozhnikov[3] and A. Fraerman[3] *1. Center for Spintronics Research, KIST, Seoul, South Korea; 2. Quantum-Function Spinics Lab. and Department of Physics, Hanyang University, Seoul, South Korea; 3. Institute for Physics of Microstructures RAS, Nizhny Novgorod, Russian Federation*

WEDNESDAY
MORNING
9:00

POLIVALENTE

Session ER
MAGNETIC SEMICONDUCTORS - III
(POSTER SESSION)
Alicia Andres, Chair

ER-01. Structural and magnetic properties of Co-doped ZnO thin films. *M. Fonin*[1], G. Mayer[1], S. Voss[1], E. Goering[2], U. Rüdiger[1], R. Schneider[3] and D. Gerthsen[3] *1. Fachbereich Physik, Universität Konstanz, Konstanz, Germany; 2. Max Planck-Institut für Metallforschung, Stuttgart, Germany; 3. Laboratorium für Elektronenmikroskopie, Universität Karlsruhe, Karlsruhe, Germany*

ER-02. Ferromagnetism observed in transition metal doped high K oxides. *Q. Wen*[1], H. Zhang[1], Y. Song[1], Q. Yang[1] and Y. Liu[1] *1. State Key Laboratory of Electronic Films and Integrated Devices,, University of Electronic Science and Technology of China, Chengdu, Sichuan, China*

ER-03. Evidence of oxygen vacancies enhancing the room temperature ferromagnetism in CeO_2 nanopowders. M. Li[1], *S. Ge*[1], Y. Zuo[1], X. Zhou[1], L. Zhang[1] and S. Yan[1] *1. Lanzhou University, Lanzhou, China*

ER-04. Zeeman splitting induced positive magnetoresistance in Co-doped ZnO and Co-doped Cu_2O ferromagnetic nanoparticles. Y. Tian[1,2], J. Antony[1], R. Souza[1], D. Meyer[1], A. Sharma[1] and *Y. Qiang*[1] *1. Department of Physics, University of Idaho, Moscow, ID; 2. School of Physics and Microelectronics, Shandong University, Jinan, Shandong, China*

ER-05. ZnO:Co films obtained by oxidation of ZnTe and Co diffusion. *I. Mínguez Bacho*[1], O. de Melo[2,3], R. Sanz[1], A. Climent-Font[3,4], A. Jacas Rodriguez[1] and M. Hernández-Vélez[1,3] *1. ICMM-CSIC, Madrid, Spain; 2. Facultad de Física, Universidad de La Habana, La Habana, Cuba; 3. Departamento de Física Aplicada, Universidad Autónoma de Madrid, Madrid, Spain; 4. Centro de Micro-Análisis de Materiales, Universidad Autónoma de Madrid, Madrid, Spain*

ER-06. Magnetic properties of TiO_2 /Co_3O_4 system. *A. Serrano*[1], A. Quesada[1,4], I. Lorite[2], L. Pérez[1], J. Fernandez[2], J. Costa-Kramer[3], M. Martin-Gonzalez[3], S. Steplecaru[3], J. Llopis[1] and M. Garcia[1] *1. Dpt Material Science, Universidad Complutense de Madrid, Madrid, Spain; 2. Dpt Electroceramics, Institute for Ceramic and glasses - CSIC, Madrid, Madrid, Spain; 3. Institute of Microelectronics, CSIC, Madrid, Madrid, Spain; 4. Institut for applied magnetism, Universidad Complutense de Madrid, Las Rozas, Madrid, Spain*

ER-07. EXPERIMENTAL EVIDENCE OF DOUBLE-EXCHANGE CONTRIBUTION TO FERROMAGNETISM IN Mn-Zn-O: A XANES ANALYSIS. *A. Quesada*[1,2], F. Rubio Marcos[4], M. García[2], J. Fernández[4], F. Wilhelm[3], A. Rogalev[3], J. Llopis[2] and A. Hernando[1,2] *1. Institute of Applied Magnetism, Las Rozas, Madrid., Madrid, Spain; 2. Departamento Física de Materiales, Facultad de Ciencias Físicas. Universidad Complutense de Madrid., Madrid, Madrid, Spain; 3. ID12, European Synchrotron Radiation Facility., Grenoble, Isère, France; 4. Departamento de Cerámica, Instituto de Cerámica y Vidrio.CSIC., Cantoblanco, Madrid, Spain*

ER-08. Ferromagnetism in bulk Co-Zn-O. *E. Enríquez*[1], A. Quesada[1,2], F. Rubio-Marcos[3], L. Pérez[1], I. Lorite[3], M. García[1], M. Martín-González[4], J. Costa-Kramer[4], S.C. Steplecaru[4], J. Fernández[3] and J. LLopis[1] *1. Dpt. Materials Science, Universidad Complutense de Madrid, Madrid, Madrid, Spain; 2. Institute for applied Magnetism, Universidad Complutense de Madrid, Las Rozas, Madrid, Spain; 3. Institute for Glass and Ceramics, CSIC, Madrid, Madrid, Spain; 4. Institute for Microelectronic, CSIC, Madrid, Madrid, Spain*

ER-09. Magnetism and Transport Properties of ZnO films doped with Co or Mn and Al. *G. Gehring*[1], A.J. Behan[1], A. Mokhtari[1], H.J. Blythe[1], D. Score[1], J.R. Neal[1] and M. Fox[1] *1. Physics and Astronomy, University of Sheffield, Sheffield, United Kingdom*

ER-10. Ferromagnetism of manganese-doped indium tin oxide films deposited on flexible polymer substrates. *T. Nakamura*[1], K. Tanabe[1], S. Isozaki[1] and K. Tachibana[1] *1. Department of Electronic Science and Engineering, Kyoto University, Kyoto, Japan*

WEDNESDAY
MORNING
9:00

POLIVALENTE

Session ES
RECORDING HEADS
(POSTER SESSION)
Robert Lamberton, Chair

ES-01. Fabrication of shielded planar type single-pole head. *K. Ise*[1], T. Kiya[1], K. Taguchi[1] and K. Yamakawa[1] *1. AIT, Akita Prefectural R&D Center, Akita, Japan*

ES-02. New Type Side Shield Head for Ultra High Density Recording. *Y. Kim*[1], S. Kukhyun[1] and K. Na[1] *1. HDD Core Tech TF, SAIT(Samsung Advanced Institute of Technology), Yongin-Si, Gyeonggi-Do, South Korea*

ES-03. Optimal Side Shield Write Head Design for Ultra High Recording Density. *Y. Kim*[1], S. Kukhyun[1] and K. Shin[1] *1. HDD Core Tech TF, SAIT(Samsung Advanced Institute of Technology), Yongin-Si, Gyeonggi-Do, South Korea*

ES-04. Magnetic 1/f noise in MgO tunneling magnetoresistive sensors. *N. Smith*[1], D. Mauri[1], J.A. Katine[1] and Y. Hong[1] *1. Hitachi Global Storage Technologies, San Jose, CA*

ES-05. Proposal of new method to fabricate nano-contacts in CoFe-NOL. *Y. Shiokawa*[1], Y. Saki[1], S. Kawasaki[1], M. Doi[1] and M. Sahashi[1] *1. Electronic Engineering, Tohoku univ., Sendai, Japan*

ES-06. Effect of Spin Transfer Torque on 1/f Noise in TMR Heads. *J. Masuko*[1], H. Akimoto[1], H. Kanai[1] and Y. Uehara[1] *1. Fujitsu Limited, Nagano, Japan*

ES-07. The role of pre-oxidation on the interface structure of Co/MgO multilayers. *D.S. Eastwood*[1], W.F. Egelhoff, Jr.[2] and B.K. Tanner[1] *1. Physics, Durham University, Durham, United Kingdom; 2. National Institute of Standards and Technology, Gaithersburg, MD*

ES-08. Hard bias effect on magnetic noise in different types of tunnel magnetoresistive heads. *G. Han*[1], B. Zong[1], P. Luo[1] and Z. Guo[1] *1. Data Storage Institute, A*STAR, Singapore, Singapore*

ES-09. Effect of annealing and barrier thickness on MgO-based Co/Pt and Co/Pd multilayered perpendicular magnetic tunnel junctions. *L. Ye*[1], C. Lee[1,2], J. Syu[1,3], Y. Wang[1], K. Lin[4], Y. Chang[4] and T. Wu[1,2] *1. Taiwan SPIN Research Center, National Yunlin University of Science and Technology, Douliou, Taiwan; 2. Graduate School of materials science, National Yunlin University of Science and Technology, Douliou, Taiwan; 3. Graduate School of Optoelectronics, National Yunlin University of Science and Technology, Douliou, Taiwan; 4. Laser Application Technology Center, Industrial Technology Research Institute, Tainan, Taiwan*

ES-10. Effects of Current-Confined-Path on the Spin-Torque Noise in CPP-GMR Heads with a Current-Screen Layer. *M. Shiimoto*[1], H. Katada[1], K. Nakamoto[1] and H. Hoshiya[1] *1. Central research laboratory, Hitachi, Ltd., Odawara-shi, Kanagawa-ken, Japan*

ES-11. Electrical 1/f noise in CPP-GMR with current-confined-pass nano-oxide layer. *M. Shimizu*[1], M. Takagishi[1], M. Takashita[1] and H. Iwasaki[1] *1. Corporate Research & Development Center, Toshiba corporation, Kawasaki, Japan*

ES-12. Dependence of Thermal Stability on Cap Layer and Top Lead for Current Screen CPP-GMR Sensor. *K. Hoshino*[1], H. Hoshiya[1] and Y. Sato[1] *1. Storage Technology Research Center, Central Research Laboratory, Hitachi, Ltd., Odawara-shi, Japan*

WEDNESDAY
MORNING
9:00

POLIVALENTE

Session ET
MAGNETOELASTIC AND MAGNETOELECTRIC MATERIALS (POSTER SESSION)
Nicoleta Lupu, Chair

ET-01. Stoichiometry and sintering temperature influence on magnetostrictive properties of cobalt ferrites. *L. Boutiuc*[1], O. Caltun[1], I. Dumitru[1], M. Feder[2], N. Lupu[3] and H. Chiriac[3] *1. 'Alexandru Ioan Cuza" University, Iasi, Romania; 2. National Institute of Material Physics, Bucharest, Romania; 3. National Institute of R&D for Technical Physics, Iasi, Romania*

ET-02. Spontaneous magnetostriction of $R_2Fe_{13.6}Si_{3.4}$ (R = U, Lu). *A.V. Andreev*[1] and S. Dani š[2] *1. Institute of Physics, Prague, Czech Republic; 2. Charles University, Prague, Czech Republic*

ET-03. Tuning the magneto-electric effect of multiferroic composites via crystallographic texture. *M. Vopsaroiu*[1], M. Stewart[1], M. Cain[1] and G. Srinivasan[2] *1. Functional Materials, National Physical Laboratory, Teddington, United Kingdom; 2. Physics Department, Oakland University, Rochester, MI*

ET-04. Multiferroic properties of spin-spray deposited Ni0.23Co0.13Fe2.64O4 ferrite film on PZT substrate. *M. Liu*[1], O. Obi[1], J. Lou[1], S. Stoute[1], Y. Chen[1], V.G. Harris[1] and N.X. Sun[1] *1. Electrical and Computer engineering, Northeastern University, Bosotn, MA*

ET-05. Stress and magneto-elastic properties control of amorphous Fe80B20 thin films during triode sputtering deposition. *I. Fernández-Martínez*[1], J.L. Costa-Krämer[1] and F. Briones[1] *1. Inst. Microlectronica Madrid, CNM-CSIC, Tres CAntos, Spain*

ET-06. Poisson ratio of amorphous nanoporous alumina as determined from thermal expansion of Ni nanowires at low temperatures. *C.A. Ramos*[1], E. Vassallo Brigneti[1], S. García[2] and M. Vázquez[2] *1. Centro Atómico Bariloche and Insituto Balseiro, Comisión Nacional de Energía Atómica and Universidad Nacional de Cuyo, S. C. de Bariloche, Rio Negro, Argentina; 2. Instituto de Ciencias de Materiales, CSIC, Madrid, Spain*

ET-07. Customizing the magnetic properties of magnetostrictive amorphous $(Fe_{80}Co_{20})_{80}B_{20}$ multilayers with orthogonal anisotropies by using different buffer layers to control the induced-deposition stress. *M. González-Guerrero*[1], J. Prieto[2], P. Sánchez[1] and C. Aroca[1] *1. Física Aplicada, ETSI Telecomunicación UPM, Madrid, Madrid, Spain; 2. ISOM, Universidad Politécnica de Madrid, Madrid, Madrid, Spain*

ET-08. Low Temperature Magnetoelastic Effects In Template Grown Ferromagnetic Nanowires. *J. De La Torre Medina*[1], M. Darques[1] and L. Piraux[1] *1. Université Catholique de Louvain, Louvain-la-Neuve, Bravant Wallon, Belgium*

ET-09. Magnetostriction of Fe-Ti alloys. *C. Bormio-Nunes*[1], A.B. Belarmino[1], C.T. Santos[1], V.C. Ugeda[1], L. Ghivelder[2] and C.A. Baldan[1] *1. Escola de Engenharia de Materiais, Universidade de Sao Paulo, Lorena, Sao Paulo, Brazil; 2. Instituto de Física, UFRJ, Rio de Janeiro, RJ, Brazil*

WEDNESDAY
MORNING
9:00

POLIVALENTE

Session EU
FERRITE DYNAMICS AND APPLICATIONS (POSTER SESSION)
Patrick Queffelec, Chair

EU-01. Picosecond magnetization dynamics of single-crystal Fe_3O_4 thin films. *C. Bunce*[1], J. Wu[1], R. Chantrell[1], Y. Lu[2] and Y. Xu[2] *1. Department of Physics, University of York, York, United Kingdom; 2. Electronics, University of York, York, United Kingdom*

EU-03. Deconvolution of the ferromagnetic resonance absorption through the Verwey transition of magnetite. *H. Montiel*[1], G. Alvarez[2], R. Valenzuela[2] and R. Zamorano[3] *1. Tecnociencia, CCADET-UNAM, Mexico DF., Mexico DF., Mexico; 2. Metalicos y Ceramicos, IIM-UNAM, Mexico D.F., Mexico, D.F., Mexico; 3. Fisica, ESFM-IPN, Mexico D.F., Mexico, D.F., Mexico*

EU-04. Dynamic Magnetic Properties of $NiFe_2O_4$ Nanoparticles Embedded in SiO_2 Matrix. S. Mitra[1], *K. Mandal*[1] and E. Choi[2] *1. Materials Science, S. N. Bose National Centre for Basic Sciences, Kolkata, West Bengal, India; 2. National High Magnetic Field Laboratory, Tallahassee, FL*

EU-05. Analyzing the permeability and permittivity dispersion spectra of $(Ni_{0.4}Zn_{0.59}Co_{0.01})$ $Fe_{1.98}O_4$ spinel ferrites with Fe deficiency. *M. Han*[1] and L. Deng[1] *1. State Key Laboratory of Electronic Thin Films and Integrated Devices, University of Electronic Science and Technology of China, Chengdu, Sichuan, China*

EU-06. Magnetic and Microwave properties Sm-doped $SrFe_{12}O_{19}$ single crystals. *J. Jalli*[1,2], Y. Hong[1,2], S. Gee[1,3], J. Lee[1,2], S. Bae[1,2], G.S. Abo[1,2], A. Lyle[1,2], H. Han[1,2], J. Kim[4], H. Lee[4] and S. Lee[4] *1. Electrical and Computer Engineering, University of Alabama, Tuscaloosa, AL; 2. MINT Center, University of Alabama, Tuscaloosa, AL; 3. Seagate Technology, Bloomington, MN; 4. Pohang Superconductivity Center, Pohang University of Science and Technology, Pohang, South Korea*

EU-07. Relaxation Effect of $NiCr_{1.8}In_{0.1}Fe_{0.1}O_4$ with Magnetic Anisotropy. *S. Park*[1], D. Choi[1] and C. Kim[1] *1. Department of Physics, Kookmin University, Seoul, South Korea*

EU-08. Temperature dependence of magnetic losses in soft ferrites. *F. Fiorillo*[1], C. Beatrice[1] and L. Zhemchuzhna[1] *1. Istituto Nazionale di Ricerca Metrologica INRIM, Torino, Italy*

EU-09. Suppression of GHz noise emitted from a four-layered PWB with a ferrite-plated inner ground layer. S. Yoshida[1], *K. Kondo*[1] and T. Kubodera[2] *1. NEC TOKIN Corporation, Sendai Miyagi, Japan; 2. System Design Laboratory Co., Ltd., Ebina Kanagawa, Japan*

EU-10. Fabrication of novel chip temperature sensing device using Mn substituted Li-Zn-Cu ferrite. *M. Naoe*[1], M. Oishi[1], S. Okazaki[1], T. Sato[1], K. Yamasawa[1] and Y. Miura[1] *1. Spin Device Technology Center, Shinshu University, Nagano, Japan*

EU-11. Effect of Co-Z type ferrite on broadband antenna miniaturization. *J. Choi*[1], K. Moon[1], J. Kim[1] and I. Kim[2] *1. Metallurgy and materials engineering, Hanyang university, Ansan, South Korea; 2. Central R&D institute, Samsung eletro-mechanics Co. LTD., Suwon, South Korea*

WEDNESDAY
MORNING
9:00

POLIVALENTE

Session EV
MAGNETORESTRIVTIVE SHAPE MEMORY ALLOYS/DEVICES (POSTER SESSION)
Simon Busbridge, Chair

EV-01. Enhancement of magnetostriction in internally-biased Terfenol-D 2-2 composites. L. Garcia-Gancedo[1], *S.C. Busbridge*[2] and T.W. Button[1] *1. IRC in Materials Processing, School of Engineering, University of Birmingham, Birmingham, United Kingdom; 2. School of Environment and Technology, University of Brighton, Brighton, United Kingdom*

EV-02. Magnetoelastic properties of Tb-Dy-Ho-Fe-Co alloys. *I. Tereshina*[1], G. Burkhanov[1], O. Chistyakov[1], S. Nikitin[2] and G. Politova[2] *1. Baikov Institute of Metallurgy and Material Science RAS, Moscow, Russian Federation; 2. Faculty of Physics, M.V. Lomonosov Moscow State University, Moscow, Russian Federation*

EV-03. Modeling of bimorph type cantilever for actuators. *G. Yun*[1,2] and B. Narsu[1] *1. department of physics, inner mongolia university, Hohhot, inner mongolia, China; 2. department of physics, inner mongolia normal university, Hohhot, inner mongolia, China*

EV-04. Microstructure and magnetic properties of Fe-Ga composite. *K. Perduta*[1], S. Busbridge[1] and M. Nabialek[2] *1. School of Engineering, University of Brighton, Brighton, United Kingdom; 2. Institute of Physics, Czestochowa University of Technology, Czestochowa, Poland*

EV-05. Giant Magnetostriction on the Metamagnetic Transition of the Ho_5Ge_4 *A.M. Pereira*[1], P. Algarabel[2], C. Sacristan[3], L. Morellon[2,3], C. Magen[4], M.R. Ibarra[2,3], J.B. Sousa[1] and J.P. Araujo[1] *1. IFIMUP Faculdade de Ciências da Universidade do Porto, Porto, Portugal; 2. ICMA - Universidad de Zaragoza and Consejo Superior de Investigaciones Científicas, Zaragoza, Spain; 3. Instituto de Nanociencia de Aragón, Universidad de Zaragoza, Zaragoza, Spain; 4. Oak Ridge Natl Lab, High Temp Mat Lab, Oak Ridge, TN*

EV-06. Voltage controlled magnetic properties of polycrystalline Terfenol-D film on PMN-PT single crystal substrate. *J. Kim*[1], V. Ravindranath[1] and S. Shin[1] *1. Physics, KAIST, Daejeon, South Korea*

EV-07. Study of giant magnetostrictive acceleration sensors. R. Yan[1], *Q. Yang*[1], W. Yang[1], S. Hou[1,2], F. Liu[1] and W. Yan[1] *1. Hebei University of Technology, Tianjin, China; 2. Tianjin University of Commerce, Tianjin, China*

EV-08. Influence of the magnetic anisotropy on the magnetic entropy change of Ni2MnGa memory shape alloy. *J.C. Leitão*[1], D. Rocco[1], J. Amaral[1], M. Reis[1], V. Amaral[1], N. Martins[2] and P. Tavares[2] *1. Physics, Universidade de Aveiro, Aveiro, Aveiro, Portugal; 2. Chemistry, Universidade de Trás-os-Montes e Alto Douro, Vila Real, Vila Real, Portugal*

EV-09. Coincidence of magnetic and martensitic transition in NiMnGa thin films obtained by changing growth parameters. *F. Albertini*[1], F. Casoli[1], S. Fabbrici[1], L. Righi[2], V.A. Chernenko[3], S. Besseghini[3] and A. Gambardella[3] *1. IMEM-CNR, Parma, Italy; 2. Dipartimento Chimica GIAF, Università di Parma, Parma, Italy; 3. IENI – CNR, Lecco, Italy*

EV-10. MFM domain imaging of textured Ni-Mn-Ga/substrate thin film composites. *R. Lopez Anton*[1,2], V. Chernenko[3], J. Barandiaran[4], I. Orue[4], S. Besseghini[3], M. Ohtsuka[5] and A. Gambardella[3] *1. ISIS, STFC Rutherford Appleton Laboratory, Didcot, United Kingdom; 2. ICMA, CSIC-Universidad de Zaragoza, Zaragoza, Spain; 3. CNR-IENI, Lecco, Italy; 4. Universidad del Pais Vasco, Bilbao, Spain; 5. IMRAM, Tohoku University, Sendai, Japan*

WEDNESDAY
MORNING
9:00

POLIVALENTE

Session EW
MULTIFERROICS, FERRITES AND OTHER MATERIALS (POSTER SESSION)
Aria Yang, Chair

EW-01. Substrate dependent structure and magnetic properties in HoMnO3 films. *T. Han*[1] and J. Lin[2] *1. Department of Applied Physics, National University of Kaohsiung, Kaohsiung, Taiwan; 2. Center for Condensed Matter Sciences, National Taiwan University, Taipei, Taiwan*

EW-02. Effect of iron-doping on the structural and magnetic properties of LuMnO3. J. Lin[1] and *T. Han*[2] *1. Center for Condensed Matter Sciences, National Taiwan University, Taipei, Taiwan; 2. Department of Applied Physics, National University of Kaohsiung, Kaohsiung, Taiwan*

EW-03. Magnetic hysteresis in $ErFeO_3$ near the 4.1 K ordering transition. *L.T. Tsymbal*[1], Y.B. Bazaliy[2,3], G.N. Kakazei[3,4], F.J. Palomares[4] and P.E. Wigen[5] *1. O. Galkin Donetsk Physics and Technology Institute, Donetsk, Ukraine; 2. University of South Carolina, Columbia, SC; 3. Institute of Magnetism, National Academy of Science, Kyiv, Ukraine; 4. Instituto de Ciencia de Materiales de Madrid, Madrid, Spain; 5. Ohio State University, Columbus, OH*

EW-04. Mössbauer studies of ^{57}Fe-doped in $LiCoPO_4$ at low temperatures. *S. Moon*[1] and C. Kim[1] *1. Department of Physics, Kookmin University, Seoul, South Korea*

EW-05. Effects of gallium distribution on terbium bismuth gallium iron garnet. *I. Park*[1] and C. Kim[1] *1. Physics, Kookmin University, Seoul, South Korea*

EW-06. Physical properties of $Fe_{3-x}Mg_xO_4$ ferrite films on MgO(001) and $SrTiO_3$(001) grown by molecular beam epitaxy. *D. Lee*[1] and G. Chern[2] *1. Electrical Engineering Department, Da-Yeh University, Chang-Hua, Taiwan; 2. Physics, National Chung Cheng University, Chia-Yi, Taiwan*

EW-07. Enhancement of magnetoelastic properties of highly magnetostrictive cobalt ferrite through control of sintering conditions. *I. Nlebedim*[1], N. Ranvah[1], A.J. Moses[1], D.C. Jiles[1], P.I. Williams[1], Y. Melikhov[1], J.E. Snyder[1] and F. Anayi[1] *1. Wolfson Centre for Magnetics, Cardiff School of Engineering, Cardiff, United Kingdom*

EW-08. Comparative study of the microstructural and magnetic properties of cobalt ferrites synthesized by ceramic and oxidation wet methods. M. Feder[2], L. Diamandescu[2], I. Bibicu[2], *O.F. Caltun*[1], I. Dumitru[1], L. Boutiuc Hrib[1], H. Chiriac[3], N. Lupu[3], M. Vilceanu[4] and V. Vilceanu[4] *1. Physics, Al, I. Cuza University, Iasi, Romania; 2. National Institute of Materials Physics, Bucharest-Magurele, Romania; 3. National Institute of R&D for Technical Physics, Iasi, Romania; 4. AferoExim ltd., Buharest, Romania*

EW-09. Nonequilibrium cation influence on the Néel temperature in ZnFe2O4. *I. Al-Omari*[1], H.M. Widatallah[1], F.R. Sives[2] and S.J. Stewart[1,2] *1. Physics, Sultan Qaboos University, Muscat, Oman; 2. IFLP-CONICET and Departamento de Física, Universidad Nacional de La Plata, La Plata, Argentina*

EW-10. Synthesis and magnetic properties of surface coated magnetite superparamagnetic nanoparticles. *K. Kim*[1], M. Kim[2], Y. Choa[2], Y. Cha[1], T. Hwang[1] and D. Kim[1] *1. Dept. of Physics, Yeungnam University, Gyeongsan, South Korea; 2. Dept. of Chemical Engineering, Hanyang University, Ansan, South Korea*

EW-11. Magnetic properties of $Hf_{1-x}R_xFe_6Ge_6$ compounds. *J. Rubín*[1], C. Piquer[1], N. Plugaru[1], J. Bartolomé[1] and F. Grandjean[2] *1. Instituto de Ciencia de Materiales de Aragón, 50009 Zaragoza, Spain; 2. Dept. of Physics, Université de Liège, B-4000 Sart-Tilman, Belgium*

EW-12. Mössbauer study of iron sulfide nano-compound. *S. Hyun*[1], I. Shim[1] and C. Kim[1] *1. Physics, Kookmin University, SEOUL, South Korea*

EW-13. Preparation of Metal-Polymer composite films by metal- polymer co-electrodeposition method. *N. Fujita*[1], M. Matsuba[1], Y. Toujou[1], T. Kazuya[1], N. Satoru[1], I. Masanobu[2] and I. Mitsuteru[2] *1. Nara National College of Technology, Yamatokoriyama, Japan; 2. Toyohashi University of Technology, Toyohashi, Japan*

EW-14. Nonlinear homogenisation technique for saturable soft magnetic composites. *O. Bottauscio*[1], M. Codegone[3], V. Chiado' Piat[3], M. Chiampi[2] and A. Manzin[1] *1. Electromagnetics, Istituto Nazionale di Ricerca Metrologica, Torino, Italy; 2. Dip. Ingegneria Elettrica, Politecnico di Torino, Torino, Italy; 3. Dip. Matematica, Politecnico di Torino, Torino, Italy*

EW-15. Structural and magnetic properties of nanocrystalline strontium hexaferrite prepared by an ionic reaction technique. J. Araujo[1], F. Cabral[1,4], *J. Soares*[2], M. Ginani[3], F. Machado[4] and J. Cunha[5] *1. Departamento de Física Teórica e Experimental, Universidade Federal do Rio Grande do Norte, Natal, Rio Grande do Norte, Brazil; 2. Departamento de Física, Universidade do Estado do Rio Grande do Norte, Mossoró, Rio Grande do Norte, Brazil; 3. Departamento de Química, Universidade Federal do Rio Grande do Norte, Natal, Rio Grande do Norte, Brazil; 4. Departamento de Física, Universidade Federal de Pernambuco, Recife, Pernambuco, Brazil; 5. Instituto de Física, Universidade Federal do Rio Grande do Sul, Porto Alegre, Rio Grande do Sul, Brazil*

WEDNESDAY
MORNING
9:00

POLIVALENTE

Session EX
MAGNETIC TUNNEL JUNCTIONS -II (POSTER SESSION)
Berthold Ocker, Chair

EX-01. Tunnel spin-polarization of low-work-function ferromagnets. *R. Patel*[1], B. Min[1], S. Dash[1], M. de Jong[1] and R. Jansen[1] *1. MESA+ Institute for Nanotechnology, University of Twente, Enschede, Netherlands*

EX-02. Strain dependence of magnetoresistance in magnetostrictive magnetic tunnel junctions. *J.G. Deak*[1] *1. Advanced Technology, NVE Corporation, Eden Prairie, MN*

EX-03. Broadband Ferromagnetic Resonance Linewidth Measurements of Magnetic Tunnel Junction Multilayers. *J. Sierra*[1], F. Aliev[1], R. Heindl[2], S. Russek[2] and W. Rippard[2] *1. Condensed Matter Physics, UAM, Madrid, Spain; 2. NIST, Boulder, CO*

EX-04. Effect of interface roughness on magnetoresistance and magnetization switching in magnetic tunnel junction. *B. Chun*[1], M. Coey[1], S. Lee[2], J. Hwang[2], J. Rhee[2], H. Yim[2], T. Kim[3], Y. Kim[4] and Y. Kim[4] *1. School of Physics, Trinity College, Dublin, Ireland; 2. Department of Physics, Sookmyung Women's University, Seoul, South Korea; 3. Nanotechnology and Advanced Materials Engineering, Sejong University, Seoul, South Korea; 4. Department of Materials Science and Engineering, Korea University, Seoul, South Korea*

EX-05. Appearance of a tunneling spectrum peak by electrical breakdown of tunneling junction. *K. Horikiri*[1] and K. Shiiki[1] *1. Applied Physics and Physico-Informatics, Keio University, Yokohama, Kanagawa, Japan*

EX-06. Magnetostriction and tunneling magnetoresistance of Co/AlOx/Co/IrMn junctions. *Y. Chen*[1,2], S. Jen[1,2] and Y. Yao[2,1] *1. Institute of Physics, Academia Sinica, Institute of Physics, Taipei, Taiwan; 2. Department of Materials Engineering, Department of Materials Engineering, Tatung University, Taipei, Taiwan*

EX-07. Magneto-transport in a single nano-object with a conductive AFM. P. Zermatten[1], *G. Gaudin*[1] and A. Schuhl[1] *1. SPINTEC, CEA/CNRS, Grenoble, France*

EX-08. Huge electron mean free path in MgO - Detection of the valence band in buried Co2MnSi-MgO half-metallic ferromagnetic tunnel junctions by means of photo emission spectroscopy. *B. Balke*[1], G.H. Fecher[1], A. Gloskowskii[1], S. Ouardi[1], C. Felser[1] and M. Yamamoto[2] *1. University Mainz, Mainz, Germany; 2. Graduate School of Informatic Science and Technology, Hokkaido University, Sapporo, Japan*

EX-09. X-ray magnetic dichroism studies of half-metallic Heusler alloys and magnetic tunnel junctions. *N.D. Telling*[1], P.S. Keatley[2], G. van der Laan[1,5], R.J. Hicken[2], E. Arenholz[3], Y. Sakuraba[4], M. Oogane[4], Y. Ando[4] and T. Miyazaki[4] *1. Magnetic Spectroscopy Group, STFC Daresbury Laboratory, Warrington, United Kingdom; 2. School of Physics, University of Exeter, Exeter, United Kingdom; 3. Advanced Light Source, Lawrence Berkeley National Laboratory, Berkeley, CA; 4. Department of Applied Physics, Tohoku University, Aoba-yama 6-6-05, Japan; 5. Diamond Light Source Ltd, Harwell Science and Innovation Campus, Didcot, Oxfordshire, United Kingdom*

EX-10. Fabrication of magnetic tunnel junctions with Co_2FeSi Heusler alloy and MgO crystalline barrier. *W. Lim*[1], G. Choi[1] and T. Lee[1] *1. Department of Materials Science and Engineering, KAIST, Daejeon, South Korea*

EX-11. (110) manganite electrodes for magnetic tunnel junctions. *I.C. Infante*[1], F. Sánchez[1], J. Fontcuberta[1], S. Fusil[2], K. Bouzehouane[2], G. Herranz[2] and A. Barthélémy[2] *1. Magnetic Materials and their Applications, Institut de Ciència de Materials de Barcelona, Bellaterra, Barcelona, Spain; 2. Unité Mixte de Physique CNRS/Thales, Orsay, France*

EX-12. Magneto-transport characteristics of magnetic tunnel junction with a synthetic antiferromagnetic amorphous CoFeSiB free-layer. *B. Chun*[1], M. Coey[1], S. Lee[2], J. Hwang[2], J. Rhee[2], H. Yim[2], T. Kim[3] and Y. Kim[4] *1. School of Physics, Trinity College, Dublin, Ireland; 2. Department of Physics, Sookmyung Women's University, Seoul, South Korea; 3. Nanotechnology and Advanced Materials Engineering, Sejong University, Seoul, South Korea; 4. Department of Materials Science and Engineering, Korea University, Seoul, South Korea*

EX-13. Structure and magnetic properties of epitaxial full-Heusler alloy $Co_2FeAl_{0.5}Si_{0.5}$ films on MgO-buffered MgO (001) substrates and TMR using their electrodes. *H. Sukegawa*[1,2], W. Wang[2], R. Shan[2] and K. Inomata[2] *1. International Center for Young Scientists (ICYS), National Institute for Materials Science (NIMS), Tsukuba, Japan; 2. Magnetic Material Center, National Institute for Materials Science (NIMS), Tsukuba, Japan*

EX-14. Coherent effects for electronic equilibrium and transport in perfect magnetic junctions. *Y.G. Pogorelov*[1] and H.G. Silva[2,1] *1. IFIMUP/IN, Universidade do Porto, Porto, Porto, Portugal; 2. CEOT, Universidade do Algarve, Faro, Algarve, Portugal*

EX-15. Spin Transport in a Double Magnetic Tunnel Junction Quantum Dot System with Noncollinear Magnetization. *M. Ma*[1] and M. Jalil[1] *1. Department of Electrical and Computer Engineering, Information Storage Materials Laboratory, Singapore, Singapore*

WEDNESDAY AFTERNOON 2:30 — AUDITORIO A

Session FA
SYMPOSIUM ON SPIN TORQUE TRANSFER FOR MRAM
J. Wang, Chair

2:30

FA-01. Spin torque effects in magnetic nanostructures. ***(Invited)*** *R. Buhrman*[1] *1. Cornell University, Ithaca, NY*

3:00

FA-02. The development of magnetic tunnel junction memory: from first devices to Mbit MRAMs to emerging spin-torque transfer MRAMs. ***(Invited)*** *W.J. Gallagher*[1] *1. IBM Watson Research Center, Yorktown Heights, NY*

3:30

FA-03. Spin torque devices for high density MRAM and nano-oscillators. ***(Invited)*** *N.D. Rizzo*[1], R.W. Dave[1], F.B. Mancoff[1], P.G. Mather[1], B. Butcher[1] and S. Tehrani[1] *1. Technology Solutions Organization, Freescale Semiconductor, Chandler, AZ*

4:00

FA-04. Spin Torque Transfer Switching of Perpendicular Magnetoresistive elements for High Density MRAMs. ***(Invited)*** *H. Yoda*[1], T. Kishi[1], T. Kai[1], T. Nagase[1], M. Yoshikawa[1], M. Nakayama[1], E. Kitagawa[1], M. Amano[1], H. Aikawa[1], N. Shimomura[1], K. Nishiyama[1], T. Daibou[1], S. Takahashi[1], S. Ikegawa[1], K. Yakushiji[2], T. Nagahama[2], H. Kubota[2], A. Fukushima[2], S. Yuasa[2], Y. Nakatani[3], M. Oogane[4], Y. Ando[4], Y. Suzuki[5,2], K. Ando[2] and T. Miyazaki[6] *1. Corporate R & D center, Toshiba, Kawasaki, Japan; 2. Nanoelectronics Research Institute, AIST, Tsukuba, Japan; 3. Computer Science, The University of Electro-Communications, Tokyo, Japan; 4. Applied Physics, Tohoku University, Sendai, Japan; 5. Materials Engineering Science, Osaka University, Osaka, Japan; 6. WPI Advanced Institute for Materials Research, Tohoku University, Sendai, Japan*

WEDNESDAY AFTERNOON 2:30 — MADRID

Session FB
SPIN INJECTION AND SPIN HALL EFFECT
M Jong, Chair

2:30

FB-01. Giant Spin Hall Effect in Perpendicularly Spin-Polarized FePt/Au Devices. ***(Invited)*** *T. Seki*[1], Y. Hasegawa[1], S. Mitani[1], K. Takanashi[1], S. Takahashi[1,2], S. Maekawa[1,2], H. Imamura[3,2] and J. Nitta[4] *1. Institute for materials research, Tohoku Univ., Sendai, Japan; 2. CREST, Japan Science and Technology Agency, Tokyo, Japan; 3. National Institute of Advanced Industrial Science and Technology, Tsukuba, Japan; 4. Graduate School of Engineering, Tohoku University, Sendai, Japan*

3:00

FB-02. Electrical Generation, Modulation and Detection of Spin Currents in Silicon in a Lateral Transport Geometry. *B. Jonker*[1], O. van 't Erve[1], G. Kioseoglou[1], A. Hanbicki[1], C. Awo-Affouda[1], M. Holub[1], C. Li[1] and P. Thompson[1] *1. Naval Research Laboratory, Washington, DC*

3:15

FB-03. Electrical transport properties of MgO/ferromagnet contacts to p-Si for spin injection and detection. *T. Dimopoulos*[1], T. Uhrmann[1], D. Schwarz[1], V. Lazarov[2], D. Kirk[2], A. Kohn[2], S. Weyers[3], U. Paschen[3] and H. Brückl[1] *1. Nano-System-Technologies, Austrian Research Centers GmbH - ARC, Vienna, Austria; 2. Department of Materials, University of Oxford, Oxford, United Kingdom; 3. Microelectronic Circuits and Systems, Fraunhofer Institute, Duisburg, Germany*

3:30

FB-04. Spin Coulomb Drag: a Limitation for Spintronics? ***(Invited)*** *I. D'Amico*[1] and C.A. Ullrich[2] *1. Physics, University of York, York, United Kingdom; 2. Physics and Astronomy, University of Missouri-Columbia, Columbia, MO*

4:00

FB-05. Organic spintronics: on the spin injection at the CuPc/GaAs interface. *M. Cinchetti*[1], H. Ding[2], Y. Gao[2], J. Wüstenberg[1], M. Sánchez Albaneda[1], O. Andreyev[1], M. Bauer[1] and M. Aeschlimann[1] *1. Department of Physics, University of Kaiserslautern, Kaiserslautern, Germany; 2. Department of Physics and Astronomy, University of Rochester, Rochester, NY*

4:15

FB-06. Spin injection through MgO tunnel barrier in an InAs quantum well semiconductor. *S.H. Shim*[1,2], Y.J. Park[1,3], J. Chang[1], Y. Lee[2], J. Moodera[3] and S. Han[1] *1. Center for Spintronics Research, Korea Institute of Science and Technology, Seoul, South Korea; 2. National Research Laboratory for Nano Device Physics, Department of Physics, Korea University, Seoul, South Korea; 3. Francis Bitter Magnet Laboratory, Massachusetts Institute of Technology, Cambridge, MA*

WEDNESDAY AFTERNOON 2:30 — ROMA

Session FC
MAGNETO-ELECTRONICS DEVICES
Claude Chappert, Chair

2:30

FC-01. High sensitivity spin valve sensors with antiferromagnetically coupled flux guides. *I.G. Trindade*[1,2], J. Oliveira[2], J. Teixeira[2], J.B. Sousa[1,2], P.P. Freitas[3], S. Cardoso[3] and R.C. Chaves[3] *1. Physics, Faculdade de Ciências da Universidade do Porto, Porto, Portugal; 2. IFIMUP-IN, Porto, Portugal; 3. INESC-MN-IN, Lisboa, Portugal*

2:45

FC-02. Gate Controlled Magnetoresistance in a Balistic Nanodevice. S. Kumar[1,2], S. Tan[1] and *M. Jalil*[2] *1. SMI, Data Storage Institute, Singapore, Singapore; 2. ISML, ECE, National University of Singapore, Singapore, Singapore*

3:00

FC-03. **Magnetic-tunnel-junction-based programmable logic devices by spin transfer torque switching.** X. Yao[1], Y. Zhang[1], H. Meng[1] and *J. Wang*[1] *1. MINT Center & Electrical and Computer Engineering Department, Univ. Of Minnesota, Minneapolis,, MN*

3:15

FC-04. **Transport properties of fully epitaxial magnetic tunnel transistor with a MgO barrier.** *T. Nagahama*[1], H. Saito[1,2] and S. Yuasa[1] *1. AIST, Tsukuba, Ibaraki, Japan; 2. PRESTO, Japan Science and Technology Agency, Kawaguchi, Saitama, Japan*

3:30

FC-05. **A Planar Magnetic Content Addressable Memory Cell.** *W. Wang*[1] and Z. Jiang[1] *1. Electrical Engineering, University of Wisconsin - Milwaukee, Milwaukee, WI*

3:45

FC-06. **Investigation on Magneto-Optoelectronic properties in Metal/Organic Heterostructure Films.** *N. Lee*[1], T. Kim[1], J. Lee[2], H. Cho[3] and C. Lee[3] *1. Department of Physics, Ewha Womans University, Seoul, South Korea; 2. Microgate, Inc., Anyang, South Korea; 3. School of Electrical Engineering & Computer Science, Seoul National University, Seoul, South Korea*

4:00

FC-07. **Electrical switching controlled by magnetic field.** J. Lee[1], S. Joo[1,4], T. Kim[1], *J. Hong*[1,4], K. Rhie[1,4], B. Lee[2], T. Kim[3] and K. Shin[4] *1. Applied Physics, Korea University, Chochiwon, South Korea; 2. Physics, Inha University, Incheon, South Korea; 3. Physics, Pohang University of Science and Technology, Pohang, South Korea; 4. Korea Institute of Science and Technology, Seoul, South Korea*

4:15

FC-08. **Micromagnetic Investigation of Interaction between Spin-Polarized Current and Spin-wave.** *S. Seo*[1] and K. Lee[1] *1. Korea University, Seoul, South Korea*

Session FD
MAGNETIC OXIDES & HEUSLER ALLOYS II
Jacobo Santamaria, Chair

2:30

FD-01. **Ferromagnetic oxides for spin filtering.** ***(Invited)*** *J. Fontcuberta*[1], A. Barthelemy[2], M. Bibes[2], U. Lüders[1], M. Gajeck[2], K. Bouzehouane[2], J.F. Bobo[3], S. Fusil[2], E. Jacquet[2], J.P. Contour[2], A. Fert[2], F. Sánchez[1], X. Martí[1], F. Rigato[1], V. Laukhin[1], V. Skumryev[1] and M. Varela[4] *1. ICMAB-CSIC, Bellaterra, Spain; 2. Unité Mixte de Physique CNRS-Thales,, Palaiseau, France; 3. Lab. de Nanomagnétisme pour l'Hyperfréquence CNRS-ONERA, Toulouse, France; 4. Dept. Física Aplicada i Òptica. U. Barcelona, Barcelona, Spain*

3:00

FD-02. **Giant planar Hall effect in epitaxial Fe_3O_4 thin films and its temperature dependence.** *J.M. De Teresa*[1], A. Fernandez-Pacheco[1,2], J. Orna[2], L. Morellon[1,2], P. Algarabel[1], J.A. Pardo[2,3] and R. Ibarra[1,2] *1. Instituto de Ciencia de materiales de Aragon, CSIC-University of Zaragoza, Zaragoza, Spain; 2. Instituto de Nanociencia de Aragon, University of Zaragoza, Zaragoza, Spain; 3. Departamento de Ciencia y Tecnologia de Materiales y Fluidos, University of Zaragoza, Zaragoza, Spain*

3:15

FD-03. **Time resolved precessional magnetization dynamics in Fe_3O_4 thin films measured by pulsed inductive microwave magnetometry.** *S. Serrano-Guisan*[1], C. Boothman[2], M. Abid[2], J.D. Coey[2] and H.W. Schumacher[1] *1. Physikalisch-Technische Bundesanstalt, Braunschweig, Germany; 2. CRANN and School of Physics, Trinity College, Dublin, Ireland*

3:30

FD-04. **Angular dependence of the magnetoresistance measured across a single-grain boundary.** *L.B. Steren*[1], G. Alejandro[1], J.C. Rojas Sanchez[1], E.N. Monteblanco Vinces[1] and H. Pastoriza[1] *1. Physics, Centro Atomico Bariloche, S.C. Bariloche, Rio Negro, Argentina*

3:45

FD-05. **Antiferromagnetic Heusler compounds with high spin-polarization.** G. Liu[1], X. Dai[1], G. Fecher[1] and *C. Felser*[1] *1. Institution for Inorganic and Analytical Chemistry,Johannes Gutenberg University of Mainz, Mainz, Germany*

4:00

FD-06. Exchange constant and magnetic anisotropy in Co_2-based Heusler compounds. *J. Hamrle*[1], O. Gaier[1], B. Hillebrands[1], M. Jourdan[2], H. Schneider[2], G. Jakob[2], T. Kubota[3], Y. Sakuraba[3], M. Oogane[3], Y. Ando[3] and C. Felser[4] *1. Fachbereich Physik, Technische Universität Kaiserslautern, Kaiserslautern, Germany; 2. Institut für Physik, Johannes-Gutenberg-Universität, Mainz, Germany; 3. Department of Applied Physics, Graduate School of Engineering, Tohoku University, Sendai, Japan; 4. Institute of Inorganic and Analytical Chemistry, Johannes-Gutenberberg-Universität, Mainz, Germany*

4:15

FD-07. Spin transitions in $DyCoO_3$ investigated by measuring the electric quadrupole interactions. F.H. Cavalcante[1], *A.W. Carbonari*[1], G.A. Cabrera-Pasca[1], J. Mestnik-Filho[1] and R.N. Saxena[1] *1. CRPq, IPEN, Sao Paulo, Sao Paulo, Brazil*

WEDNESDAY AFTERNOON 2:30 — LONDRES

Session FE
LIFE SCIENCE AND APPLICATIONS II
Angel Millan, Chair

2:30

FE-01. Prototyping and Evaluation of Magnetic Communication Coils between Inside and Outside of Body for Controlling FES. *K. Kato*[1], M. Goto[1], K. Sugano[1], M. Miyashita[1], F. Sato[1], H. Matsuki[1], Y. Handa[2] and T. Sato[3] *1. Department of Electrical and Communication Engineering, Graduate School of Engineering, Tohoku University, Sendai, Miyagi, Japan; 2. Graduate School of Medicine, Tohoku University, Sendai, Japan; 3. NEC TOKIN Corp., Sendai, Japan*

2:45

FE-02. Bone Tissue Engineering using Magnetically Oriented Collagen. *T. Shinohara*[1], T. Saito[2], D. Saito[1], A. Nakahira[3], M. Aoki[4] and M. Kotani[2] *1. Research Institute for Advanced Technologies, Tokyo Denki University, Inzai-shi, Chiba Pref., Japan; 2. Graduate School of Engineering, Tokyo Deki University, Kanda, Tokyo, Japan; 3. Graduate School of Engineering, Osaka Prefecture University, Sakai, Japan; 4. Neomax, Hitachi Metals, Ltd, Oomachichou, Saga Pref., Japan*

3:00

FE-03. Modification of motor evoked potentials caused by electrical peripheral nerve stimulation in transcranial magnetic stimulation. *O. Hiwaki*[1], M. Odagaki[1], F. Hiroshi[1], A. Kodabashi[2] and T. Fujimoto[2] *1. Graduate School of Information Sciences, Hiroshima City University, Hiroshima, Japan; 2. Fujimoto Hayasuzu Hospital, Miyakonojyo, Japan*

3:15

FE-04. Detection of the terrestrial magnetism in migrating birds: Is it a question of vision? *S. Migalski*[1,2], T. Meydan[2], J.T. Erichsen[1] and V.P. Bingman[3] *1. Optometry and Vision Sciences, Cardiff University, Cardiff, United Kingdom; 2. Engineering, Cardiff University, Cardiff, United Kingdom; 3. Psychology, Bowling Green State University, Bowling Green, OH*

3:30

FE-05. Computation of Current Distribution in Rat Head by Transcranial Magnetic Stimulation and Electroconvulsive Therapy. *M. Lu*[1], S. Ueno[2], T. Thorlin[3], P. Miranda[1] and M. Persson[4] *1. Institute of Biophysics and Biomedical Engineering, Faculty of Sciences, University of Lisbon, Lisbon, Portugal; 2. Department of Applied Quantum Physics, Graduate School of Engineering, Kyushu University, Fukuoka, Japan; 3. Institute for Clinical Neuroscience, Sahlgrens University Hospital, Gothenburg, Sweden; 4. Department of Signals and Systems, Chalmers University of Technology, Gothenburg, Sweden*

3:45

FE-06. Spintronic biosensors based on Fe/MgO/Fe(001) tunnelling junctions. *R. Bertacco*[1], S. Brivio[1], M. Cantoni[1], A. Cattoni[1] and D. Petti[1] *1. Center LNESS, Politecnico di Milano, Como, Italy*

4:00

FE-07. MTJ based biosensor with top Au electrodes and functionalization layers. *F.A. Cardoso*[1,2], S. Cardoso[1,2], V.C. Martins[1,3] and P.P. Freitas[1,2] *1. INESC-MN, Lisboa, Portugal; 2. Instituto Superior Tecnico, Lisboa, Portugal; 3. Center for Biological and Chemical Engineering (CEBQ), Lisboa, Portugal*

4:15

FE-08. Stem Cell Separator and Counter. *J. Loureiro*[1,2], S. Cardoso[1,2], C.L. Silva[2,3], J.M. Cabral[2,3] and P.P. Freitas[1,2] *1. INESC-Microsystems and Nanotechnologies, Lisbon, Portugal; 2. Instituto Superior Técnico (IST), Lisbon, Portugal; 3. CEBQ - IST, Lisbon, Portugal*

WEDNESDAY AFTERNOON 2:30 — BERLIN

Session FF
MICROWAVE DEVICES AND FMR
Raul Valenzuela, Chair

2:30

FF-01. Experimental realization of spin-wave logic gates. *A.A. Serga*[1], T. Schneider[1], B. Leven[1], B. Hillebrands[1], M.P. Kostylev[2] and R.L. Stamps[2] *1. Fachbereich Physik und Forschungsschwerpunkt MINAS, Technische Universität Kaiserslautern, Kaiserslautern, Germany; 2. School of Physics, University of Western Australia, Crawley, WA, Australia*

2:45

FF-02. Microwave signal processor based on spin waves in permalloy (Py) films. G.A. Melkov[1], Y.V. Koblyanskiy[1], R.A. Slipec[1], A.V. Talalaevskij[1] and *A.N. Slavin*[2] *1. Faculty of Radiophysics, Kiev National Taras Shevchenko University, Kiev, Ukraine; 2. Department of Physics, Oakland University, Rochester, MI*

3:00

FF-03. Design and optimization of one-dimensional YIG film based magnonic crystal. *A. Chumak*[1,2], A.A. Serga[1] and B. Hillebrands[1] *1. Fachbereich Physik und Forschungsschwerpunkt MINAS, Technische Universität Kaiserslautern, Kaiserslautern, Germany; 2. Department of Radiophysics, Taras Shevchenko National University of Kiev, Kiev, Ukraine*

3:15

FF-04. Experimental Verification of Skin Effect Suppression in Multilayer Thin-Film Conductor Taking Advantage of Negative Permeability of Magnetic Film beyond FMR frequency. S. Shiozawa[1], Y. Shimada[1], *M. Yamaguchi*[1], K. Kim[2], Y. Zhuang[3], M. Vroubel[3] and B. Rejaei[3] *1. Electrical and Communication Engineering, Tohoku University, Sendai, Japan; 2. Physics, Yeungnam University, Gyeongsan, South Korea; 3. Electronic Components, Technology, and Materials, Delft University of Technology, Delft, Netherlands*

3:30

FF-05. Selective excitation and imaging of precessional modes in soft-magnetic squares. *A. Neudert*[1], P.S. Keatley[1], V.V. Kruglyak[1], J. McCord[2] and R.J. Hicken[1] *1. School of Physics, University of Exeter, Exeter, United Kingdom; 2. Institute for Metallic Materials, IFW Dresden, Dresden, Germany*

3:45

FF-06. Electrically detected ferromagnetic resonance in electrodeposited spin valves under AC excitation. *N. Biziere*[1], E. Murè[1] and J. Ansermet[1] *1. Institut de Physique des nanostructures, Ecole Polytechnique Federale de Lausanne, Lausanne, Switzerland*

4:00

FF-07. Ferromagnetic resonance modes below the critical thickness of stripe domain formation. *J. McCord*[1], A. Gerber[2] and E. Quandt[2] *1. Institute for Metallic Materials, IFW Dresden, Dresden, Germany; 2. Institute for Inorganic Functional Materials, CAU Kiel, Kiel, Germany*

4:15

FF-08. Ferromagnetic resonance study of Fe/FePt coupled films with perpendicular anisotropy. *D. Schmool*[1], A. Apolinário[1], F. Casoli[2] and F. Albertini[2] *1. Physics, Universidade do Porto, Porto, Portugal; 2. IMEM, CNR, Parma, Italy*

Session FG

NANOSTRUCTURED HARD MAGNETIC MATERIALS - II

Oliver Gutfleisch, Chair

2:30

FG-01. Inter-phase exchange coupling in $Sm(Co,Cu)_5$/α-Fe nanocomposite obtained by mechanical milling and annealing. *V. Pop*[1,2], O. Isnard[2], D. Givord[2] and I. Chicinas[3] *1. Faculty of Physics, Babes-Bolyai University, 400084 Cluj-Napoca, Romania, Cluj-Napoca, Romania; 2. Institut Néel, CNRS, associé à l'Université Joseph Fourier de Grenoble, BP166, 38042 Grenoble, Cedex 9, France, Grenoble, France; 3. Materials Sciences and Technology Dept., Technical University of Cluj-Napoca, 103-105 Muncii ave., 400641 Cluj-Napoca, Romania, Cluj-Napoca, Romania*

2:45

FG-02. Isotropic $Sm_x(Co,Fe,Mn)_{100-x}$ Magnets Via High-Energy Ball Milling. *A. Gabay*[1], J. Liu[2] and G.C. Hadjipanayis[1] *1. University of Delaware, Newark, DE; 2. Electron Energy Corporation, Landisville, PA*

3:00

FG-03. Effect of TiC and Cr additions on magnetic properties of nanocrystalline (Pr,Nd)FeB alloys. V.C. de Franco[2], R.K. Murakami[3], H.R. Rechenberg[4], T. Yonamine[1], *F.P. Missell*[1,2] and V. Villas-Boas[2] *1. Divisão de Metrologia de Materiais, INMETRO, Duque de Caxias, Rio de Janeiro, Brazil; 2. Centro de Ciências Exatas e Tecnologia, Universidade de Caxias do Sul, Caxias do Sul, Rio Grande do Sul, Brazil; 3. Universidade do ABC, Santo André, São Paulo, Brazil; 4. Instituto de Física, Universidade de São Paulo, São Paulo, São Paulo, Brazil*

3:15

FG-04. Two Major Effects of Process Temperature on the Characteristic of Bulk Nanostructured Nd-Fe-B / Fe-Co Composite Magnets. *C.H. Chen*[1], Y. Shen[2], M. Huang[3] and A.K. Higgins[1] *1. University of Dayton Research Institute, Dayton, OH; 2. FutureTek Corp, Dayton, OH; 3. UES / Wright Patterson Air Force Base, Dayton, OH*

3:30

FG-05. $Nd_2Fe_{14}B$ based Magnetic Nanocomposites Synthesized by Electrodeposition, Microemulsion and Melt Spinning Techniques. *R. Ramanujan*[1], Z. Liu[1], S. Viswanathan[1], P.K. Deheri[1] and S. Shukla[1] *1. School of Mater. Sci. Eng., Nanyang Tech. Univ., Singapore, Singapore*

3:45

FG-06. Improvement in Morphology and Magnetic Properties of Thick Nanocomposite Film-Magnets with Multi-Layered Structure. *H. Fukunaga*[1], H. Nakayama[1], M. Nakano[1], M. Ishimaru[2], M. Itakura[2] and F. Yamashita[3] *1. Department of Electrical Engineering and Electronics, Nagasaki University, Nagasaki, Nagasaki, Japan; 2. Department of Applied Science for Electronics and Materials, Kyushu University, Kasuga, Fukuoka, Japan; 3. Matsushita Electric Industrial Co., Ltd., Daito, Osaka, Japan*

4:00

FG-07. Magnetic properties of Nd-Fe-B thin films with island structure prepared on Mo buffer layer. *T. Shima*[1], H. Kato[1] and T. Sato[2] *1. Faculty of Engineering, Tohoku Gakuin University, Tagajo, Japan; 2. Toyota Central R&D Labs., Nagakute, Japan*

4:15

FG-08. Highly Coercive Nanocrystalline Electro-Deposited CoPt Thin Films. *K. Zuzek Rozman*[1], J. Kovac[2], P.J. McGuiness[1] and S. Kobe[1] *1. Department for Nanostructured Materials, Jozef Stefan Institute, Ljubljana, Slovenia; 2. Department of Surface Engineering and Optoelectronics, Jozef Stefan Institute, Ljubljana, Slovenia*

WEDNESDAY AFTERNOON 2:30 — CARACAS

Session FH
OXIDE MULTIFERROICS AND FERRITES
Yevgen Melikhov, Chair

2:30

FH-01. Magnetism and magnetocaloric effect in multiferroic $LuFe_2O_4$ J. Gass[1], N. Frey[1], M. Phan[1], *H. Srikanth*[1], M. Angst[2], B. Sales[2] and D. Mandrus[2] *1. Department of Physics, University of South Florida, Tampa, FL; 2. Materials Science and Technology Division, Oak Ridge National Laboratory, Oak Ridge, TN*

2:45

FH-02. Design and processing of new ferrite materials from an atomistic perspective. *A. Yang*[1], A. Geiler[1], X. Zuo[2], C. Vittoria[1] and V.G. Harris[1] *1. Center for Microwave Magnetic Materials and Integrated Circuits, Electrical and Computer Engineering, Northeastern University, Boston, MA; 2. College of Information Technical Science, Nankai University, Tianjin, China*

3:00

FH-03. Texture analysis of ferrite materials by means of electron backscatter diffraction (EBSD). *A.D. Koblischka-Veneva*[1], M.R. Koblischka[2] and F. Muecklich[1] *1. Institute for Functional Materials, University of the Saarland, Saarbruecken, Saarland, Germany; 2. Institute of Experimental Physics, Saarland University, Saarbrucken, Saarland, Germany*

3:15

FH-04. Oxide electrode on LAO (110) substrate for studying low-symmetry perovskite oxides. *J. Kim*[1], J. Kim[1], H. Na[1], B. Lee[1], I. Choi[1], C. Jung[1] and S. Chae[2] *1. Dept. of Physics, Hankuk University of Foreign Studies, Yongin, Kyunggi-do, South Korea; 2. School of Physics and Astronomy, Seoul National University, Seoul, South Korea*

3:30

FH-05. Mössbauer studies of the $Co_{1-x}Zn_xFe_2O_4$ Ferrite. Y. Zhang[1], X. Yuan[1], Z. Ren[1], Z. Kou[1], X. Bai[2], *Y. Zhai*[1,2], Y. Xu[3], J. Du[2] and H. Zhai[2] *1. Department of Physics, Southeast University, Nanjing, Jiangsu, China; 2. National Laboratory of Solid Microstructures, Nanjing University, Nanjing, Jiangsu, China; 3. Department of Electronics, University of York, York, United Kingdom*

3:45

FH-06. Synthesis of iron oxide nanoparticles of controlled size, shape and magnetic properties. *P. Guardia*[1], A. Labarta[1] and X. Batlle[1] *1. Fundamental Physics, UB, Barcelona, Catalunya, Spain*

4:00

FH-07. The dispersion of $BaFe_{12}O_{19}$ particles in a liquid. *D. Lisjak*[1] and M. Drofenik[1,2] *1. Jozef Stefan Institute, Ljubljana, Slovenia; 2. Faculty of Chemistry and Chemical Engineering, University of Maribor, Maribor, Slovenia*

4:15

FH-08. FREEZE Granulation:A novel technique for low-loss MnZn ferrites. *V. Tsakaloudi*[1], G. Kogias[1] and V.T. Zaspalis[1] *1. Laboratory of Inorganic Materials, Centre for Research and Technology Hellas, Thermi-Thessaloniki, Greece*

WEDNESDAY AFTERNOON 4:40 — AUDITORIO A

Session WA
INTERMAG PLENARY SESSION
Josef Fidler, Chair

THURSDAY MORNING 9:30 — AUDITORIO A

Session GA
SYMPOSIUM ON BIT PATTERNED MEDIA
Manfred Schabes, Chair

9:30

GA-01. Achieving tight physical and magnetic sigmas in bit patterned media recording disks. *(Invited)* *D. Weller*[1], A.Y. Dobin[1], D. Kuo[1], K.Y. Lee[1], J. Hwu[1], X. Yang[3], S. Xiao[3], G. Gauzner[1], M. Feldbaum[1], M. Ostrowski[2], G. Ju[3], H.J. Richter[1], B. Lu[1], B. Valcu[1], X. Zhu[3] and R. van de Veerdonk[3] *1. Media R&D, Seagate Technology, Fremont, CA; 2. Recording Heads Operations, Seagate Technology LLC, Normandale, MN; 3. Research, Seagate Technology LLC, Pittsburgh, PA*

10:00

GA-02. Modeling and Simulation of the Writing Process on Bit-Patterned Perpendicular Media. *(Invited)* *H. Muraoka*[1], S.J. Greaves[1] and Y. Kanai[2] *1. RIEC, Tohoku University, Sendai, Japan; 2. Niigata Institute of Technology, Kashiwazaki, Japan*

10:30

GA-03. Nanoscale perpendicular magnetic island arrays fabricated by extreme ultraviolet interference lithography. *(Invited)* *F. Luo*[1], L.J. Heyderman[1] and H.H. Solak[1] *1. Laboratory for Micro- and Nanotechnology, Paul Scherrer Institut, Villigen, Switzerland*

11:00

GA-04. Magnetic films on self-assembled nanoparticles: An approach for bit-patterned media. *(Invited)* *M. Albrecht*[1], C. Brombacher[1], H. Rohrmann[2], P. Kappenberger[4], O. Hellwig[3], A. Goncharov[5] and T. Schrefl[5] *1. Institute of Physics, Chemnitz University of Technology, Chemnitz, Germany; 2. Data Storage, OC Oerlikon Balzers AG, Balzers, Liechtenstein; 3. San Jose Research Center, Hitachi Global Storage Technologies, San Jose, CA; 4. Nanoscale Materials Science, Empa, Duebendorf, Switzerland; 5. Department of Engineering Materials, University of Sheffield, Sheffield, United Kingdom*

11:30

GA-05. Self-Assembly Pattern Multiplication for 1Tb/in^2 Patterned Media Templates. *(Invited)* *R. Ruiz*[1], E. Dobisz[1], D.S. Kercher[1], T. Wu[1], T.R. Albrecht[1], H. Kang[2] and P.F. Nealey[2] *1. San Jose Research Center, Hitachi Global Storage Technologies, San Jose, CA; 2. Department of Chemical and Biological Engineering, University of Wisconsin, Madison, WI*

12:00

GA-06. Fabrication and Characterization of High-density Patterned Media. *(Invited)* *N. Yasui*[1,2], S. Ichihara[1], T. Nakamura[1], A. Imada[1], T. Saito[1], R. Horie[1], Y. Ohashi[1], T. Den[1], K. Miura[2] and H. Muraoka[2] *1. Canon Research Center, Tokyo, Japan; 2. RIEC, Tohoku Univ., Sendai, Japan*

THURSDAY MORNING 9:30 — MADRID

Session GB
MR BASED HEADS (GMR, MTJ, CPP)
Brendan Lafferty, Chair

9:30

GB-01. An investigation of noise increased in TMR readers during drive operation. *P. Wong*[1] *1. SAE Magnetics (HK) Ltd, Hong Kong, China*

9:45

GB-02. Improvement of TMR effect of magnetic tunneling junctions with very thin MgO barrier sputtered by noble gas mixture at low RA product below 1.0 Ωμm^2 *K. Noma*[1], K. Komagaki[2], K. Sunaga[2], H. Kanai[2], Y. Uehara[2] and T. Umehara[1] *1. Head Manufacturing, Fujitsu Ltd., Nagano, Japan; 2. Advanced Head Technology, Fujitsu Ltd., Nagano, Japan*

10:00

GB-03. Atomic layer deposition Al2O3 films for permanent magnet isolation in TMR read heads. *M. Kautzky*[1], A. Demtchouk[1], Y. Chen[1], S. McKinlay[1], K. Brown[1] and J. Xue[1] *1. Advanced Transducer Development, Seagate Technology, Bloomington, MN*

10:15

GB-04. Analysis of the current-confined-paths in the film plane for CPP-GMR films. *H. Fukuzawa*[1], M. Hara[1], H. Yuasa[1] and Y. Fuji[1] *1. Corporate R&D Center, Toshiba Corporation, Kawasaki, Japan*

10:30

GB-05. **Development of CPP-GMR Heads for High-Density Magnetic Recording. *(Invited)*** *J.R. Childress*[1], M.J. Carey[1], S. Maat[1], N. Smith[1], X. Liu[1], H. Balamane[1], S. Chandrashekariaih[1], T.D. Boone[1], R.E. Fontana[1], P. Vanderheijden[1], Y. Hong[1], K. Carey[1], J. Tabib[1], J. Li[1], B. York[1], T. Lin[1], J.A. Katine[1], W. Jayasekara[1], N. Robertson[1], M. Alex[1], J. Moore[1] and C. Tsang[1] *1. Hitachi Global Storage Technologies, San Jose, CA*

11:00

GB-06. **Current Confined Path (CCP) Giant Magneto Resistive (GMR) Sensors.** *X. Peng*[1], P. Kolbo[1], K. Nikolaev[1], S. Chen[1], Z. Wang[1], T. Boonstra[1], P. Anderson[1], S. Kalderon[1], P. Czoschke[1], A. Morrone[1], D. Dimtrov[1], S. Xue[1] and Y. Chen[1] *1. RHO, Seagate Technology, Bloomington, MN*

11:15

GB-07. **Current Density Limitation by Spin Transfer Torque for CPP-GMR Heads.** *K. Yamada*[1], M. Takagishi[1], M. Takashita[1] and H. Iwasaki[1] *1. Corporate R&D Center, Toshiba Corporation, Kawasaki, Japan*

11:30

GB-08. **Suppression of spin-torque in current perpendicular to the plane spin-valves by addition of Dy caps.** *S. Maat*[1], M.J. Carey[1], N. Smith[1] and J.R. Childress[1] *1. Hitachi Global Storage Technologies, San Jose, CA*

11:45

GB-09. **Transport and magnetic properties of CPP-GMR sensor with CoMnSi Heusler alloy.** *T. Mizuno*[1], Y. Tsuchiya[1], T. Machita[1], S. Hara[1], D. Miyauchi[1], K. Shimazawa[1], K. Noguchi[1] and K. Tagami[1] *1. SQ Research Center, TDK CORPORATION, 543 Otai, Saku-shi, Nagano, Japan*

12:00

GB-10. **Mesoscopic Extraordinary Magnetoresistance and the Effects of Impact Ionization and Velocity Saturation. *(Invited)*** *T.D. Boone*[1], L. Folks[1], J.A. Katine[1], E.E. Marinero[1], N. Smith[1] and B.A. Gurney[1] *1. San Jose Research Center, Hitachi Global Storage Technologies, San Jose, CA*

THURSDAY
MORNING
9:30

ROMA

Session GC
ULTRAFAST DYNAMICS
Juergen Fassbender, Chair

9:30

GC-01. **Ultrafast Magnetic Switching with Terahertz Fields. *(Invited)*** *H. Siegmann*[1], S.J. Gamble[2,6], M.H. Burkhardt[2,6], A. Kashuba[3], R. Allenspach[4], S.S. Parkin[5] and J. Stöhr[6] *1. PULSE Center Stanford University, Stanford, CA; 2. Dept. of Applied Physics, Stanford University, Stanford, CA; 3. Bogolyubov Institute for Theoretical Physics, Kiev, Ukraine; 4. IBM Research, Zurich Research Laboratory, 8803 Rueschlikon, Switzerland; 5. IBM Almaden Research, San Jose, CA; 6. Stanford Synchrotron Radiation Laboratory, Stanford, CA*

10:00

GC-02. **Terahertz Emission Spectroscopy as a Probe of Laser-Induced Ultrafast Demagnetization Dynamics. *(Invited)*** *E. Beaurepaire*[1], J. Arabski[1], M. Vomir[1], J. Bigot[1], S.M. Harrel[2], J.M. Schleicher[2] and C.A. Schmuttenmaer[2] *1. IPCMS-GEMME, CNRS, Strasbourg, France; 2. Dept. of Chemistry, Yale University, New Haven, CT*

10:30

GC-03. **Atomistic and Multiscale calculations of picosecond magnetisation dynamics. *(Invited)*** *R.W. Chantrell*[1], U. Nowak[1], O. Chubykalo-Fesenko[2] and A. Rebei[3] *1. Physics, The University of York, York, United Kingdom; 2. ICMM, Madrid, Spain; 3. Seagate Research, Pittsburgh, PA*

11:00

GC-04. **Femtosecond transfer of angular momentum in ferromagnets probed by X-ray spectroscopy. *(Invited)*** *H.A. Dürr*[1] *1. BESSY, Berlin, Germany*

11:30

GC-05. **Laser-induced reorientation of spins in Co/SmFeO3 heterostructures.** *J. Loïc*[1], F. Nolting[1], A. Kirilyuk[2], R. Pisarev[3], T. Rasing[2] and A. Kimel[2] *1. SLS, Paul Scherrer Institut, Villigen-PSI, Switzerland; 2. IMM, Radboud University Nijmegen, Radboud, Netherlands; 3. Ioffe Physical Technical Institute, St. Petersburg, Russian Federation*

11:45

GC-06. **Heusler alloys: The role of band structure on the ultrafast demagnetization.** *T. Roth*[1], D. Steil[1], A. Conca[2], M. Jourdan[2], M. Aeschlimann[1] and M. Cinchetti[1] *1. Physics, TU Kaiserslautern, Kaiserslautern, Germany; 2. Institute of Physics, University of Mainz, Mainz, Germany*

12:00

GC-07. Dynamics of the coercivity in (ultrafast) pump-probe experiments. *D. Steil*[1], T. Roth[1], M. Cinchetti[1] and M. Aeschlimann[1] *1. FB Physik, AG Aeschlimann, TU Kaiserslautern, Kaiserslautern, Germany*

12:15

GC-08. LLB-Micromagnetic modelling of ultra-fast optical magnetisation dynamics. *U. Atxitia*[1], O. Chubykalo-Fesenko[1], N. Kazantseva[2], D. Hinzke[2], U. Nowak[2] and R.W. Chantrell[2] *1. POMT, ICMM-CSIC, Madrid, Spain; 2. Department of Physics, University of York, York, United Kingdom*

THURSDAY MORNING 9:30 — PARIS

Session GD
MRAM
Freitas Paulo, Chair

9:30

GD-01. Switching Characteristics and Bias Voltage Dependence of Spin Torque Switching in MgO based Magnetic Tunnel Junctions. *S. Oh*[1], K.T. Nam[1], J.E. Lee[1], W.J. Kim[1], J.H. Jeoung[1], D.K. Kim[1], S.Y. Lee[1], K. Kim[2], U. Chung[1] and J.T. Moon[1] *1. Memory Division, Semiconductor Business, Samsung Electronics Co., LTD., Yongin-City, Gyeonggi-Do, South Korea; 2. Semiconductor Device Lab, Samsung Advanced Institute of Technology, Yongin-City, Gyeonggi-Do, South Korea*

9:45

GD-02. Impact of antiferromagnet-induced magnetization fluctuation control on switching current distribution reduction in MRAM. *Y. Katoh*[1], H. Hada[1] and N. Kasai[1] *1. Device Platforms Research Laboratories, NEC Corporation, Kanagawa, Japan*

10:00

GD-03. Spin Torque Random Access Memory down to 22nm Technology. *X. Wang*[1], Y. Chen[1], H. Li[1], D. Dimitrov[1] and H. Liu[1] *1. Seagate Technology, Bloomington, MN, MN*

10:15

GD-04. Multilevel Magnetic Random Access Memory Based on Spin Transfer Torque Switching. *Y. Zhang*[1], X. Yao[1] and J. Wang[1] *1. MINT Center & Electrical and Computer Engineering Department, University of Minnesota, Minneapolis, MN*

10:30

GD-05. Heat-assisted magnetization reversal using pulsed laser irradiation in patterned magnetic thin film with perpendicular anisotropy. *K. Waseda*[1], R. Doi[1], B. Purnama[1], S. Yoshimura[1], Y. Nozaki[1] and K. Matsuyama[1] *1. Dept. of Electronics, Kyushu University, Fukuoka, Japan*

10:45

GD-06. Estimation of Thermal Stability Factor in Current-Induced Magnetization Switching. *H. Suh*[1] and K. Lee[1] *1. Korea University, Seoul, South Korea*

11:00

GD-07. Nano-ring MTJ and nano-ring MRAM. *X. Han*[1], Z. Wen[1] and H. Wei[1] *1. State Key Lab of Magnetism, Institute of Physics, CAS, Beijing, China*

11:15

GD-08. Magnetic characterization of embedded MgO ferromagnetic contacts for spin injection in silicon. *T. Uhrmann*[1], T. Dimopoulos[1], D. Schwarz[1], V. Lazarov[2], D. Kirk[2], A. Kohn[2], S. Weyers[3], U. Paschen[3] and H. Brückl[1] *1. Nano-Systemtechnologies, Austrian Research Centers GmbH - ARC, Vienna, Austria; 2. Department of Materials, University of Oxford, Oxford, United Kingdom; 3. Fraunhofer Institute of Microelectronic Circuits and Systems, Duisburg, Germany*

11:30

GD-09. High thermal stability and low switching current in a perpendicular-CPP-GMR with an ultrathin epitaxial FePt free layer. *K. Yakushiji*[1], S. Yuasa[1], A. Fukushima[1], H. Kubota[1], T. Nagahama[1], T. Katayama[1] and K. Ando[1] *1. National Institute of Advanced Industrial Science and Technology (AIST), Tsukuba, Japan*

11:45

GD-10. Stress assisted reversal of perpendicular magnetization of thin films with giant magnetostriction constant. *N. Saito*[1] and S. Nakagawa[1] *1. Dept. of Physical Electronics, Tokyo Institute of Technology, Tokyo, Japan*

12:00

GD-11. A Novel Macro-Model for Spin-Transfer-Torque based Magnetic-Tunnel-Junction Elements. *S. Lee*[1], H. Lee[1], S. Lee[1] and H. Shin[1] *1. Information Electronics Engineering, Ewha W. Univ., Seoul, South Korea*

12:15

GD-12. Random number generation by current induced magnetization switching in a MgO magnetic tunnel junction. *A. Fukushima*[1], K. Yakushiji[1], H. Kubota[1], S. Yuasa[1] and K. Ando[1] *1. NeRI, AIST, Tsukuba, Ibaraki, Japan*

THURSDAY MORNING 9:30 — LONDRES

Session GE
MAGNETIC NANOPARTICLES II
Dino Fiorani, Chair

9:30

GE-01. Towards dense regular arrays of FePt nanomagnets by gas phase deposition onto bacterial S-layers within a horizontal magnetic field. *U. Queitsch*[1], D. Pohl[1], A. Blüher[2], M. Mertig[2], L. Schultz[1] and B. Rellinghaus[1] *1. Metastable and Nanostructured Materials, Leibniz Institute for Solid State and Materials Research Dresden, Dresden, Saxony, Germany; 2. Max Bergmann Center of Biomaterials, Dresden University of Technology, Dresden, Saxony, Germany*

9:45

GE-02. Magnetic anisotropy of a single Fe atom on Pt(111). *T. Schuh*[1], T. Balashov[1], A.F. Takacs[1], W. Wulfhekel[1], A. Ernst[2], S. Ostanin[2], J. Henk[2], P. Bruno[2], T. Miyamachi[3] and S. Suga[3] *1. Physikalisches Institut, Universität Karlsruhe, Karlsruhe, Germany; 2. Max-Planck Institut für Mikrostrukturphysik, Halle, Germany; 3. Graduate School of Engineering Science, Osaka University, Osaka, Japan*

10:00

GE-03. High-moment synthetic magnetic nanoparticles for biomedical applications. *W. Hu*[1], R.J. Wilson[1], C.M. Earhart[1], A. Koh[1,2], A.Z. Faranesh[3], R. Sinclair[1], S. Guccione[3] and S.X. Wang[1,4] *1. Materials Science & Engineering, Stanford University, Stanford, CA; 2. Mechanical Engineering, Stanford University, Stanford, CA; 3. Radiology, Stanford University, Stanford, CA; 4. Electrical Engineering, Stanford University, Stanford, CA*

10:15

GE-04. Highly anisotropic FePt nanomagnets obtained via Fe ion implantation on Pt films. *R.A. Lukaszew*[1,2], C. Clavero[1] and J.R. Skuza[2] *1. Applied Science Dept., College of William and Mary, Williamsburg, VA; 2. Physics Department, College of William and Mary, Williamsburg, VA*

10:30

GE-05. Surface relaxation and magnetism in mondisperse binary metal nanoparticles. *(Invited)* *M. Farle*[1] *1. Physik, Universitaet Duisburg-Essen, Duisburg, Germany*

11:00

GE-06. Synthesis and characterisation of polymer-coated Fe nanoparticles with high magnetisation. J. Marin[2], *A. Garcia Prieto*[1], I. Orue[3], J. Vilas[2], M. Fdez-Gubieda[1] and L.M. Leon[2] *1. Dpto Electricidad y Electronica, Universidad del Pais Vasco - UPV/EHU, Bilbao, Spain; 2. Dpto Química Macromolecular, Universidad del Pais Vasco - UPV/EHU, Bilbao, Spain; 3. SGIKER Medidas Magnéticas, Vicerrectorado de Investigación, Universidad del Pais Vasco - UPV/EHU, Bilbao, Spain*

11:15

GE-07. Bulk-like magnetic properties in Fe_3O_4 nanoparticles: surface anisotropy, orbital moment and crystal quality. N. Pérez[1,2], P. Guardia[1,2], A.G. Roca[3], M.P. Morales[3], C.J. Serna[3], F. Bartolomé[4,5], L.M. García[4,5], J. Bartolomé[4,5], J.C. Cezar[6], A. Labarta[1,2] and *X. Batlle*[1,2] *1. Física Fonamental, Universitat de Barcelona, Barcelona, Catalonia, Spain; 2. Institut de Nanociencia i Nanotecnologia IN2UB, Universitat de Barcelona, Barcelona, Catalonia, Spain; 3. ICMM, CSIC, Madrid, Madrid, Spain; 4. ICMA, CSIC, Zaragoza, Aragón, Spain; 5. Física de la Materia Condensada, Universidad de Zaragoza, Zaragoza, Aragón, Spain; 6. ESRF, Grenoble, France*

11:30

GE-08. On the spin reorientation of magnetic nano-dot arrays: Co/Au versus Co/Pt on SiGe. *A. Persson*[1], L. Gridneva[1], M.A. Niño[2], J. Camarero[2], J.J. de Miguel[2], R. Miranda[2], C. Hofer[3], C. Teichert[3], T. Bobek[4] and D. Arvanitis[1] *1. Physics Department, Uppsala University, Uppsala, Sweden; 2. Departamento de Física de la Materia Condensada, Universidad Autonoma de Madrid, Madrid, Spain; 3. Institut für Physik, Montanuniversität Leoben, Leoben, Austria; 4. Institute of Semiconductor Electronics, Aachen University, Aachen, Germany*

11:45

GE-09. Perpendicular anisotropy in Co/Pt granular multilayers. *J. Bartolome*[1], L. García Vinuesa[1], F. Bartolomé[1], J. Stankiewicz[1], F. Luis[1], F. Petroff[2], C. Deranlot[2], F. Wilhelm[3], A. Rogalev[3], P. Bencok[3] and N.B. Brookes[3] *1. Instituto de Ciencia de Materiales de Aragón, CSIC/U. de Zaragoza, Zaragoza, Spain; 2. Unité Mixte de Physique, CNRS/Thales, Orsay (Paris), France; 3. ESRF, Grenoble, France*

12:00

GE-10. Evidence of L10 chemical order in CoPt nanoclusters: direct observation and magnetic signature. *F. Tournus*[1], A. Tamion[1], N. Blanc[1], A. Hannour[1], L. Bardotti[1], B. Prével[1], P. Ohresser[2], E. Bonet[3], T. Epicier[4] and V. Dupuis[1] *1. LPMCN, Université de Lyon; Univ. Lyon 1; CNRS, Villeurbanne, France; 2. Synchrotron SOLEIL, Gif sur Yvette, France; 3. Institut Néel, CNRS/UJF, Grenoble, France; 4. MATEIS, CNRS; INSA Lyon; Université de Lyon, Villeurbanne, France*

12:15

GE-11. Magnetic Hardening of FePt Nanomagnets by Ultra Short Time In-Flight Annealing. E. Mohn[1], *B. Rellinghaus*[1] and L. Schultz[1] *1. Institute for Metallic Materials, IFW Dresden, Dresden, Germany*

THURSDAY MORNING 9:30 — BERLIN

Session GF
HEAD-MEDIA INTERFACE AND TRIBOLOGY II
Singh Bhatia, Chair

9:30

GF-01. Flying Characteristics on Discrete Track and Patterned Media With Thermal Protrusion Slider. *(Invited)* *B.E. Knigge*[1], Z.Z. Bandic[1] and D. Kercher[1] *1. San Jose Research Center, Hitachi Global Storage Technologies, San Jose, CA*

10:00

GF-02. Nonuniform distribution of molecularly thin lubricant caused by inhomogeneous buried layers of discrete track media. *K. Fukuzawa*[1,2], T. Muramatsu[1], H. Amakawa[1], S. Itoh[1] and H. Zhang[1] *1. Micro/Nano Systems Engineering, Nagoya University, Nagoya, Japan; 2. PRESTO, JST, Kawaguchi, Japan*

10:15

GF-03. Parametric Study of Contact Performance for Discrete Track Recording Media Using Finite Element Analysis. C. Yeo[1] and *A.A. Polycarpou*[1] *1. Mechanical Science and Engineering, Univ. of Illinois at Urbana-Champaign, Urbana, IL*

10:30

GF-04. Numerical and Experimental Investigation of "Flyability" of Sliders on Discrete Track Recording Media. *Y. Yoon*[1], M. Duwensee[2], J. Lin[3], S. Suzuki[3] and F.E. Talke[1] *1. Mechanical Engineering, University of California, San Diego, La Jolla, CA; 2. Hitachi Global Storage Technologies, San Jose, CA; 3. Western Digital Corporation, San Jose, CA*

10:45

GF-05. Dynamic analysis schemes for flying head sliders over discrete track media. *S. Fukui*[1], T. Kanamaru[1] and H. Matsuoka[1] *1. Dept. of Applied Mathematics and Physics, Tottori University, Tottori City, Japan*

11:00

GF-06. Effect of van der Waals Force on Ultimate Head-to-Disk Interface. *K. Ono*[1] *1. Storage Technology Research Center, Hitachi Central Research Laboratory, Fijisawa-shi, Japan*

11:15

GF-07. STUDY ON CONTACT OF THERMAL ACTUATED SLIDER AND DISK. *M. Zhang*[1], B. Liu[1,2] and S. Hu[1] *1. Spintronics, Media and Interface Division, Data Storage Institute, Singapore, Singapore; 2. Nanyang Technological University, Singapore, Singapore*

11:30

GF-08. Numerical and Experimental Analyses of Nanometer-scale Flying Height Control of Magnetic Head with Heating Element. *J. Juang*[1], T. Nakamura[3], B. Knigge[1], Y. Luo[2], W. Hsiao[2], K. Kuroki[3], F. Huang[1] and P. Baumgart[1] *1. San Jose Research Center, Hitachi GST, San Jose, CA; 2. Hitachi GST, San Jose, CA; 3. Hitachi GST, Fujisawa-shi, Kanagawa-ken, Japan*

11:45

GF-09. Dynamics of Fly-Contact Head-Disk Interface. *S. Yu*[1], B. Liu[1], W. Hua[1], W. Zhou[1] and C. Wong[1] *1. Data Storage Institute, Singapore, Singapore*

12:00

GF-10. Slider Optical Constant Distribution, n and k Correlation, and FH Measurement Accuracy. *Z. Yuan*[1], C. Ong[1], B. Liu[1], J. Liu[2] and S. Yoshida[2] *1. DSI, Singapore, Singapore; 2. Hitachi Asia, SG, Singapore*

12:15

GF-11. A Method for Identification of Pitch and Roll Stiffness of Head-Gimbal Assembly at Flying State. *Q. Zeng*[1], Y. Fu[1], C. Yang[1], B. Aujla[1] and E. Cha[1] *1. SAE Magnetics, Milpitas, CA*

THURSDAY
MORNING
9:30

AMSTERDAM

Session GG
HYSTERESIS MODELLING II
Alexandru Stancu, Chair

9:30

GG-01. 2D finite element simulations for bulk steel hysteresis curve derivations. *P. Meilland*[1], S. He[2], S. Depeyre[2], M. Bernadou[2] and J. Cagnol[2] *1. ArcelorMittal Maizières Research, Maizières-lès-Metz, France; 2. Pôle Universitaire Léonard de Vinci, Paris-La Défense, France*

9:45

GG-02. Rotational saturation properties of isotropic vector hysteresis models using vectorized stop and play hysterons. *T. Matsuo*[1] *1. Electrical Engineering, Kyoto University, Kyoto, Japan*

10:00

GG-03. Viscous behavior of ferromagnets in the voltage and current driven regimes. S.E. Zirka[1], Y.I. Moroz[1], P. Marketos[2], *A.J. Moses*[2] and D.C. Jiles[2] *1. Department of Applied Physics and Technology, Dnepropetrovsk National University, Dnepropetrovsk, Ukraine; 2. School of Engineering, Cardiff University, Cardiff, Wales, UK, United Kingdom*

10:15

GG-04. Size effects influence on hysteresis and relaxation for a Random Anizotropy Ising System. *C. Enachescu*[1] and A. Stancu[1] *1. Department of Physics, Alexandru Ioan Cuza University, Iasi, Romania*

10:30

GG-05. Correction of permeability of a soft ferromagnet measured by using vibrating sample magnetometer. *M. Chan*[1], C. Ong[1] and Y. Wong[1] *1. Department of Applied Physics and Materials Research Center, The Hong Kong Polytechinc University, Hong Kong, China*

10:45

GG-06. The temperature dependence of magnetostatic interactions in nanowires systems. *A. Diaconu*[1], I. Dumitru[1] and A. Stancu[1] *1. Department of Solid State and Theoretical Physics, "Alexandru Ioan Cuza" University, Iasi, Iasi, Romania*

11:00

GG-07. A magnetostriction model with stress dependence for real-time control applications. *D. Davino*[1], A. Giustiniani[2] and C. Visone[1] *1. Engineering Department, University of Sannio, Benevento, Italy; 2. DIIIE, University of Salerno, Salerno, Italy*

11:15

GG-08. An Improved Engineering Model of Vector Magnetic Properties of Grain-oriented Electrical Steels. Y. Zhang[1], Y. Eum[2], *C. Koh*[2] and D. Xie[1] *1. School of Electrical Engineering, Shenyang University of Technology, Shenyang, Liaoning 110023, China; 2. School of Electrical & Computer Engineering, Chungbuk National University, Cheongju,Chungbuk 361- 763, South Korea*

11:30

GG-09. Magnetic behaviour of assemblies of nanoparticles with core/shell morphology:Interparticle interaction effects. *M. Vasilakaki*[1], K.N. Trohidou[1] and J.A. Blackman[2] *1. Institute of Materials Science,NCSR "Demokritos", Athens, Greece; 2. Departmen of Physics, Reading University, Reading, United Kingdom*

11:45

GG-10. Compensation of Hysteresis and Time- dependent Error for Magnetostrictive Actuators. *H. Choi*[1] and Y. Park[1] *1. Mechatronics Engineering, Chungnam National University, Daejeon, South Korea*

12:00

GG-11. Rotational hysteresis first-order reversal curves diagrams as test problem for vectorial hysteresis models. *L. Stoleriu*[1], P. Postolache[1], P. Andrei[2] and A. Stancu[1] *1. Department of Physics, Alexandru Ioan Cuza University, Iasi, Romania; 2. Department of Electrical and Computer Engineering, Florida State University and Florida A&M University, Tallahassee, FL*

12:15

GG-12. Identification of the parameters of reduced vector Preisach model by neural networks. *M. Trapanese*[1] *1. Dipartimento di Ingegneria Elettrica, Elettronica e delle Telecomunicazioni, University of Palermo, Palermo, Italy*

THURSDAY
MORNING
9:30

CARACAS

Session GH
PERMANENT MAGNET MATERIALS - APPLICATIONS III
Jesus Gonzalez, Chair

9:30

GH-01. Analysis of Permanent Magnet Demagnetization Accounting for Minor BH-curves. *Y. Zhilichev*[1] *1. Magnequench International, Inc, Durham, NC*

9:45

GH-02. A Hybrid Dual-Memory Motor. *C. K.t.*[1], G. Yu[1,2] and J. Jianzhong[2] *1. Electrical and Electronic Engineering, the University of Hong Kong, Hongkong, China; 2. Automation, Shanghai University, Shanghai, China*

10:00

GH-03. Study on Detachment of a Permanent Magnet-Wheel for a Wall-Climbing Mobile Robot using Magnetic Inducement. *H. Yi*[1], J. Kim[1] and S. Han[2] *1. Mechanical Engineering, Yeungnam University, Gyeongsan, Gyeongsangbuk-do, South Korea; 2. Automobile engineering, Yeungnam College of Science & Technology, Daegu, South Korea*

10:15

GH-04. Ironless and leakage free voice-coil motor made of bounded magnets. G. Lemarquand[1], *M. Remy*[2], B. Castagnede[1] and G. Guyader[2] *1. LAUM, Universite du Maine, Le Mans, France; 2. Renault, Guyancourt, France*

10:30

GH-05. Generic Algorithm-Based Optimal Design of New Electromagnetic Engine Valve Actuator for Reduction of Transition Time. *J. Kim*[1], K. Han[2] and J. Chang[3] *1. Mechanical Engineering, Yeungnam University, Gyeongsan, Gyeongsangbuk-do, South Korea; 2. Electrical Engineering, Florida Institute of Technology, Melbourne, FL; 3. Transverse Flux Machines Research Group, Korea Electrotechnology Research Institute, Changwon, Kyungsangnam-Do, South Korea*

10:45

GH-06. Self-Assembly of Millimeter-Scale Components using Integrated Micromagnets. *S.B. Shetye*[1] and D.P. Arnold[1] *1. Interdisciplinary Microsystems Group, University of Florida, Gainesville, FL*

11:00

GH-07. Minimization of Cogging Torque in an IPM Machine. *C. Hwang*[1], P. Li[1] and C. Liu[2] *1. EE, Feng Chia University, Seatwen, Taichung, Taiwan; 2. EE, National Sun Yat-sen University, Kaohsiung, Taiwan*

11:15

GH-08. Static Eccentricity Fault Diagnosis in Permanent Magnet Synchronous Motor using Time Stepping Finite Element Method. *B. Ebrahimi*[1], J. Faiz[1] and A. Zargham Nejhad[1] *1. Department of Electrical and Computer Engineering, University of Tehran, University of Tehran, Tehran, Iran*

11:30

GH-09. Six-degree-of-freedom motion analysis of a planar actuator with a magnetically levitated mover by six-phase current controls. *Y. Ueda*[1] and H. Ohsaki[1] *1. Department of Advanced Energy, The University of Tokyo, Kashiwa, Japan*

11:45

GH-10. Optimal Halbach Permanent Magnet Shapes for Slotless Tubular Actuators. *J.J. Paulides*[1], K.J. Meessen[1], B.L. Gysen[1] and E.A. Lomonova[1] *1. Technical university Eindhoven, Eindhoven, Netherlands*

12:00

GH-11. Development of Inverse Magnetostrictive Actuator. *H. Park*[1], Y. Park[1] and H. Choi[1] *1. Mechatronics Engineering, Chungnam National University, Daejeon, South Korea*

GH-12. WITHDRAWN

THURSDAY
MORNING
9:00

POLIVALENTE

Session GL
MULTILAYER FILMS AND SUPERLATTICES II (POSTER SESSION)
Alex Dobin, Chair

GL-01. Interface effects in the magnetic properties of $La_{0.7}Sr_{0.3}MnO_3/SrTiO_3$ heterostructures. ***(Invited)*** *F.Y. Bruno*[1], J. Garcia-Barriocanal[1], A. Rivera[1], Z. Sefrioui[1], C. Leon[1], J. Santamaria[1], N.M. Nemes[2], M. Garcia-Hernandez[2], M. Varela[3] and S.J. Pennycook[3] *1. GFMC. Dpto. Fisica Aplicada III., Universidad Complutense de Madrid, Madrid, Madrid, Spain; 2. Instituto de Ciencia de Materiales de Madrid, Consejo Superior de Investigaciones Cientificas, Cantoblanco, Madrid, Spain; 3. Condensed Matter Science Division, Oak Ridge National Laboratory, Oak Ridge, TN*

GL-02. Control of the degree of out-of-plane anisotropy of CoFe/Tb multilayer by applying an external in-plane field during film deposition. *K. Lee*[1], Y. Jang[1], J. Kim[1], S. Lee[1] and B. Cho[1] *1. School of Photonics, MSE, GIST, Gwangju, South Korea*

GL-03. Effect of the Cr insertion layer on synthetic antiferromagnetic coupling in magnetic tunnel junctions. *K. Kim*[1], W. Kim[2], S. Oh[2], D. Kim[2], I. Hwang[1], K. Kim[1], S. Seo[1], J. Jeong[2], K. Nam[2] and J. Lee[2] *1. Semiconductor Devices Lab, Samsung Advanced Institute of Technology (SAIT), Yongin-Si, Gyeonggi-Do, South Korea; 2. Process Development Team, Samsung Electronics Co., Ltd, Yongin-Si, Gyeonggi-Do, South Korea*

GL-04. Preparation and magnetic characterization of Fe/MgO layered granular thin films. A. García-García[1], J.A. Pardo[2,3], *P.A. Algarabel*[1], C. Magén[4], P. Štrichovanec[2], L. Morellón[1,2], J.M. De Teresa[1], A. Vovk[2] and M.R. Ibarra[1,2] *1. Instituto de Ciencia de Materiales de Aragón, Universidad de Zaragoza-CSIC, Zaragoza, Spain; 2. Instituto de Nanociencia de Aragón, Universidad de Zaragoza, Zaragoza, Spain; 3. Departamento de Ciencia y Tecnología de Materiales y Fluidos, Universidad de Zaragoza, Zaragoza, Spain; 4. Centre d'Elaboration de Matériaux et d'Etudes Structurales, CNRS, Toulouse, France*

GL-05. FMR Investigation of (Ga_{1-x},Mn_x)As Tri-layers. *M. Cubukcu*[1], K. Khazen[1], H. von Bardeleben[1], J. Cantin[1], M. Elsen[2], H. Jaffrès[2], J. George[2], L. Thevenard[3] and A. Lemaître[3] *1. Institut des Nanosciences de Paris (INSP), Université Paris 6, UMR 75-88 au CNRS, Paris, Ile de France, France; 2. Unité Mixte de Physique CNRS-Thales, associée à l'Université Paris XI, Palaiseau, Ile de France, France; 3. Laboratoire de Photonique et Nanostructures, Marcoussis, Ile de France, France*

GL-06. Interplay between magnetic anisotropy and interlayer exchange coupling in amorphous CoSi / Si multilayers. *L.M. Álvarez-Prado*[1], C. Quirós[1], L. Zárate[1], J.I. Martín[1] and J.M. Alameda[1] *1. Departamento de Física, Universidad de Oviedo, Oviedo, Asturias, Spain*

GL-07. Creation of out–of–plane magnetization ordering by increasing multilayer number N in $[Co/Au]_N$ multilayers. *M. Tekielak*[1,2], P. Mazalski[1], A. Maziewski[1,3], R. Schäfer[2], J. McCord[2], B. Szymanski[4], M. Urbaniak[4] and F. Stobiecki[4] *1. Department of Physics, Univeristy of Bialystok, Bialystok, Poland; 2. Leibniz-Institut für Festkörper- und Werkstofffforschung Dresden e.V, Dresden, Germany; 3. Laboratoire de Physique des Solides, Université Paris-Sud, Orsay, France; 4. Institute of Molecular Physics, Polish Academy of Sciences, Poznan, Poland*

GL-08. Magnetostatic waves in the magnetic/nonmagnetic periodic structures. *M. Krawczyk*[1] *1. Faculty of Physics, Adam Mickiewicz University, Poznan, Poland*

GL-09. Investigations on magnetic properties of NiFe film doped with Gd by ferromagnetic resonance. Y. Fu[1], L. Sun[1,3], J. Wang[1], Z. Kou[1], *Y. Zhai*[1,2], X. Bai[2], J. Wu[3], Y. Xu[4], J. Du[2], H. Lu[2] and H. Zhai[2] *1. Department of Physics, Southeast University, Nanjing, Jiangsu, China; 2. National Laboratory of Solid Microstructures, Nanjing University, Nanjing, Jiangsu, China; 3. Department of Physics, University of York, York, United Kingdom; 4. Department of Electronics, University of York, York, United Kingdom*

GL-10. Hard Magnetic Nanocomposite [NdFeBNbCu/FeBSi]xn Multilayer Films with Low Crystallization Temperature. *H. Chiriac*[1], M. Grigoras[1], N. Lupu[1] and M. Urse[1] *1. National Institute of Research & Development for Technical Physics, Iasi, Romania*

GL-11. Magneto-optical circular dichroism properties of fept layers with perpendicular anisotropy. *C. de Julian Fernandez*[1], R. Novak[2], F. Albertini[3], F. Casoli[3], S. Fabbrici[3] and A. Caneschi[1] *1. Chemistry, INSTM- University of Florence, Sesto Fiorentino (FI), Italy; 2. Physics, INSTM-University of Florence, Sesto Fiorentino (FI), Italy; 3. Magnetic Materials, IMEM - CNR, Parma, Italy*

GL-12. Structural and Magnetic Properties of Fe/Polyimide Multilayer Thin Film. *J. Kim*[1], S. Kim[1], N. Oh[1], H. An[1], J. Kim[1], D. Jeong[1], C. Kim[1] and C. Yoon[1] *1. Materials Science and Engineering, Hanyang University, Seoul, South Korea*

GL-13. The magnetic anisotropies of FeCo and FeCoGd films. L. Sun[1,2], J. Wang[1], Y. Fu[1], Z. Kou[1], *Y. Zhai*[1,4], X. Bai[4], J. Wu[3], Y. Xu[2], J. Du[4], H. Lu[4] and H. Zhai[4] *1. Department of Physics, Southeast University, Nanjing, Jiangsu, China; 2. Department of Physics, University of York, York, United Kingdom; 3. Department of Electronics, University of York, York, United Kingdom; 4. National Laboratory of Solid Microstructures, Nanjing University, Nanjing, Jiangsu, China*

THURSDAY
MORNING
9:00

POLIVALENTE

Session GM
PERMANENT MAGNET MACHINES IV (POSTER SESSION)
Aly Flores Filho, Chair

GM-01. The energy loss by drag force of superconductor flywheel energy storage system with permanent magnet rotor. *J. Lee*[1], Y. Han[1], S. Jung[1], T. Sung[1] and B. Park[1] *1. Korea Electric Power Research Institute, Daejeon, South Korea*

GM-02. Analysis of eddy-current loss in a double-stator cup-rotor PM machine. *S. Niu*[1], K. Chau[1] and J. Jiang[2] *1. Depart. of Electrical and Electronic Engineering, The University of Hong Kong, Hong Kong, China; 2. School of Electromechanical Engineering and Automation, Shanghai University, Shanghai, China*

GM-03. Comparison of stator-permanent-magnet brushless machines. *C. Liu*[1] and K. Chau[1] *1. Dept. of Electrical and Electronic Engineering, The University of Hong Kong, Hong Kong, China*

GM-04. Segmentation of magnets to reduce losses in permanent magnet synchronous machines. *P. Sergeant*[1] and A. Van den Bossche[1] *1. Department of Electrical Energy, Systems and Automation, Ghent university, Gent, Belgium*

GM-05. Cogging Torque Reduction in Brushless DC Motors Due to the Magnetization Distribution in Permanent Magnets. *T. Ishikawa*[1], K. Yonetake[1], M. Matsunami[1] and M. Tsuchiya[2] *1. Electronic Engineering, Gunma University, Kiryu, Japan; 2. Tokyo Parts Industrial Co.,LTD., Isesaki, Japan*

GM-06. Negative Stiffness of Toroidally-Wound BLDC Machine. *M. Noh*[1] and H. Lee[1] *1. Mechatronics Engineering, Chungnam National University, Daejeon, South Korea*

GM-07. A STUDY ON THE DESIGN OF AN INSET PERMANENT MAGNET TYPE FLUX-REVERSAL MACHINE. *T. Kim*[1] *1. Electrical Engineering, Gyeongsang National University, Jinju, South Korea*

GM-08. A Comprehensive Comparsion of Flux-Switching and Flux-Reversal Brushless PM Machines. *H. Wei*[1], C. Ming[1], Z. Wenxiang[1], Z. Jianzhong[1] and J. Hongyun[1] *1. School of Electrical Engineering, Southeast University, Nanjing, 210096, China*

GM-09. Optimization and electromagnetic analysis of stator interior permanent magnet machine with minimum cogging torque. J. Zhang[1], *M. Cheng*[1] and W. Zhao[1] *1. school of electrical engineering, Southeast University, Nanjing, Jiangsu, China*

GM-10. Design and analysis of line-starting three- and single-phase interior permanent magnet synchronous motors; direct comparison to induction motor characteristics. *T. Marčič*[1], B. Štumberger[2,1], G. Štumberger[2,1], M. Hadziselimović[2,1], P. Virtič[1] and D. Dolinar[2,1] *1. TECES, Research and Development Centre for Electrical Machines, Maribor, Slovenia; 2. University of Maribor, Faculty of Electrical Engineering and Computer Science, Maribor, Slovenia*

GM-11. Design and analysis of large capacity line-start permanent magnet synchronous motors. *Q. Lu*[1] and Y. Ye[1] *1. college of electrical engineering, Hangzhou, Zhejiang, China*

GM-12. An Application of the Latin Hypercube Sampling Strategy for Optimal Design of Large Scale Permanent magnet pole using Adaptive Response Surface Method. P. Shin[1], *S. Woo*[1], Y. Zhang[2] and C. Koh[2] *1. Electrical Engineeirng, Hongik University, Chungnam, South Korea; 2. Electrical and Computer Engineering, Chungbuk National University, Chungbuk, South Korea*

THURSDAY
MORNING
9:00

POLIVALENTE

Session GN
MOTORS AND ACTUATORS III
(POSTER SESSION)
Ranran Lin, Chair

GN-01. Development of an axial-flux brushless motor for low-profile fan applications. *L. Hsu*[1], C. Huang[1], M. Tsai[1] and G. Yan[2] *1. Electric Motor Technology Research Center,National Cheng Kung University, Tainan, Taiwan; 2. Metal Industries Research & Development Centre, Kaohsiung, Taiwan*

GN-02. Sliding Mode Control for Optical Image Stabilization Actuators. *H. Yu*[1,2], T. Liu[1] and C. Chiang[1] *1. Department of Mechanical Engineering, National Chiao Tung University, Hsinchu, Taiwan; 2. Electronics and Opto-electronics Research Laboratories, Industrial Technology Research Institute, Hsinchu, Taiwan*

GN-03. Characteristic Comparison between the Spiral and Lamination Stator in Axail Field Slotless Machines. *S. Lee*[1], J. Hong[1], T. Lee[2] and J. Park[2] *1. Automotive Engineering, Hanyang university, Seoul, South Korea; 2. Mechanical Engineering, Hanyang university, Seoul, South Korea*

GN-04. Investigation and comparison of inductance calculation methods in interior permanent magnet synchronous motors. *T. Sun*[1], S. Kwon[1], J. Lee[1] and J. Hong[1] *1. Department of Mechanical Engineering, Hanyang University, Seoul, South Korea*

GN-05. Two-DOF micro magnetostrictive bending actuator for wobbling motion. *T. Ueno*[1], C. Saito[2], N. Imaizumi[2] and T. Higuchi[1] *1. University of Tokyo, Tokyo, Japan; 2. Namiki Precision Jewel Co., LTD, Tokyo, Japan*

GN-06. Thrust calculations and measurements of cylindrical linear oscillatory actuator with halbach array moving magnet using transfer relations theorem. S. Jang[1], *H. Kim*[1], J. Choi[1] and S. Lee[2] *1. Chungnam National University, Daejeon, South Korea; 2. Korea Institute of Industrial Technology, Kwangju, South Korea*

GN-07. CHARACTERISTIC ANALYSIS OF A FLUX-REVERSAL MOTOR WITH FOUR-SWITCH CONVERTER. H. Kang[2], *T. Kim*[1] and B. Lee[2] *1. Electrical Engineering, Gyeongsang National University, Jinju, South Korea; 2. Sungkyunkwan University, Suwon, South Korea*

GN-08. Iron Loss Calculation in an Amorphous Transformer Using Coupled Preisach Modeling & Finite Element Method. *Y. Cho*[1] and S. Mun[1] *1. Electrical Engineering, Hanbat National University, Daejeon, South Korea*

GN-09. Reduction of Lateral Force using V-skew in Permanent Magnet Linear Synchronous Motor. *D. Lee*[1], K. Jang[1] and G. Kim[1] *1. Electrical Engineering, Changwon National University, Changwon, Gyeongsangnam-do, South Korea*

GN-10. Axial-gap type permanent magnet motor modeling for transient analysis. *S. Won*[1], J. Choi[1] and J. Lee[1] *1. Electrical Eng., Hanyang University, Seoul, South Korea*

GN-11. Analysis of Total Harmonic Distortion in microspeaker considering electromagnetic mechanical acoustic coupling effect. *J. Kwon*[1], S. Hwang[1] and G. Hwang[2] *1. Mechanical Engineering, Pusan National University, Busan, Busan, South Korea; 2. Computer Engineering, Youngsan University, Yangsan-city, Kyungnam-do, South Korea*

THURSDAY
MORNING
9:00

POLIVALENTE

Session GO
LIFE SCIENCES: TECHNIQUES AND INSTRUMENTATION II
(POSTER SESSION)
Jose Rivas, Chair

GO-01. Wide dynamic range digital FLL system using high-T_c SQUID for biomagnetic measurements. *D. Oyama*[1,2], K. Kobayashi[1], M. Yoshizawa[1] and Y. Uchikawa[3] *1. Graduate School of Engineering, Iwate University, Morioka, Iwate, Japan; 2. Japan Society for the Promotion of Science Research Fellow, Tokyo, Japan; 3. Department of Electronics and Computer Engineering, School of Science and Engineering, Tokyo Denki University, Hatoyama, Saitama, Japan*

GO-02. Double relaxation oscillation SQUID mounted on Pulse Tube cryocooler. *M.J. Eshraghi*[1] and I. Sasada[1] *1. Applied science for electronics and materials, Kyushu University, Kasuga, Fukuoka, Japan*

GO-03. Quantitative magnetic immunoassays with a SQUID by means of mutual inductance calculations. *A. Bruno*[1], H.R. Carvalho[1], S.R. Louro[1] and C. Paulo[1] *1. Physics, Pontifical Catholic University of Rio de Janeiro, Rio de Janeiro, Brazil*

GO-04. Detection of MCG signal by using MgB_2 SQUID on pulse-tube cooler. *D. Oyama*[1,2], Y. Harada[3], Y. Fujine[1], K. Kobayashi[1], Y. Uchikawa[4] and M. Yoshizawa[1] *1. Graduate School of Engineering, Iwate University, Morioka, Iwate, Japan; 2. Japan Society for the Promotion of Science Research Fellow, Tokyo, Japan; 3. Japan Science and Technology Agency Innovation Satellite Iwate, Morioka, Iwate, Japan; 4. Department of Electronics and Computer Engineering, School of Science and Engineering, Tokyo Denki University, Hatoyama, Saitama, Japan*

GO-05. Biomagnetic Signal Detection Using Very High Sensitive MI Sensor for Medical Applications. *T. Uchiyama*[1], S. Tajima[1], S. Shibata[1], L. Ji[1] and K. Bushida[2] *1. Electrical Engineering, Nagoya University, Nagoya, Japan; 2. UNITIKA LTD, Tokyo, Japan*

GO-06. Giant magnetoimpedance of electrochemically surface modified Co-based amorphous ribbons. *V. Fal Miyar*[1], M. Cerdeira[1], J.A. García[1], A.P. Potatov[2], .R. Pierna[3], F.F. Marzo[3], J.M. Barandiarán[4] and G.V. Kurlyandskaya[4] *1. Department of Physics, University of Oviedo, Oviedo, Asturias, Spain; 2. Institute of Metal Physics, Ekaterinburg, Russian Federation; 3. Dpto. de Ingeniería Química y Medio Ambiente, Universidad del País Vasco, San Sebastián, Basque Country, Spain; 4. Department of Electricity and Electronics, Basque Country University, Bilbao, Basque Country, Spain*

GO-07. Spatially arterial pulse diagnostic apparatus using array Hall devices. *S. Lee*[1], G. Kim[2], M. Ahn[3], Y. Park[3], D. Hwang[1], J. Rhee[4] and H. Yoon[5] *1. Oriental Biomedical Engineering, Sangji University, Wonju, Gangwondo, South Korea; 2. Oriental Medicine Science, Sangji University, Wonju, Gangwondo, South Korea; 3. Oriental-western Biomedical Engineering, Sangji University, Wonju, Gangwondo, South Korea; 4. Physics, Sookmyung Women's University, Seoul, Seoul, South Korea; 5. Biomedical Engineering, Yonsei University, Wonju, Gangwondo, South Korea*

GO-08. Various Types of Hall Sensors for Single Particle Detection. *O. Kazakova*[1], J. Gallop[1], D. Cox[1,2], A. Cuenat[1], L. Brown[1], K. Suzuki[3], L. Bernau[4] and I. Utke[4] *1. NPL, Teddington, United Kingdom; 2. Surrey University, Guilford, United Kingdom; 3. NTT Basic Research Laboratories, Kanagawa, Japan; 4. EMPA, Thun, Switzerland*

GO-09. Microwaves Doppler transducer for noninvasive monitorisation of the cardiorespiratory activity. *O.I. Baltag*[2] and M.P. Costin[1,2] *1. Computer Science Institute, Romanian Academy, Iasi, Romania; 2. Faculty of Biomedical Engineering, "Gr.T.Popa"University of Medicine and Pharmacy, IASI, Romania*

GO-10. Investigating the cortical connectivity in the brain by combined TMS and EEG. *K. Iramina*[1,2], T. Arimatsu[1], H. Sato[1], A. Hyodo[2], T. Hayami[3] and S. Ueno[4] *1. Department of Intelligent Systems, Kyushu University, Fukuoka, Japan; 2. Graduate School of Systems Life Sciences, Kyushu University, Fukuoka, Japan; 3. Digital Medicine Initiative, Kyushu University, Fukuoka, Japan; 4. Department of Applied Quantum Physics, Kyushu University, Fukuoka, Japan*

GO-11. Fabrication of new magnetic micro-machines for low-invasive surgery. C. Troisi[1], M. Knaflitz[1], E. Olivetti[2], L. Martino[2] and *G. Durin*[2] *1. Dep. of Electronics, Politecnico di Torino, Torino, Italy; 2. Istituto Nazionale di Ricerca Metrologica, Torino, Italy*

GO-12. Magnetic Tracking of Eye Motion in Small, Fast-Moving Animals. *A. Plotkin*[1], E. Paperno[1], G. Vasserman[2] and R. Segev[2] *1. Electrical and Computer Engineering, Ben-Gurion University of the Negev, Beer-Sheva, Israel; 2. Life Sciences, Ben-Gurion University of the Negev, Beer-Sheva, Israel*

GO-13. Minimization of Computational Errors in Diffusion Simulation of Nuclear Magnetization. *T. Imae*[1,2], H. Shinohara[2], M. Sekino[3], H. Ohsaki[3], S. Ueno[4], K. Mima[1] and K. Ootomo[1] *1. Department of Radiology, University of Tokyo Hospital, Tokyo, Japan; 2. Graduate School of Human Health Science, Tokyo Metropolitan University, Tokyo, Japan; 3. Graduate School of Frontier Sciences, University of Tokyo, Chiba, Japan; 4. Graduate School of Engineering, Kyushu University, Fukuoka, Japan*

GO-14. Discriminative detection of extracellular and intracellular sodiums in nerve fibers by magnetic resonance spectroscopy. *S. Yamaguchi-Sekino*[1], H. Tatsuoka[2], M. Sekino[3], H. Ohsaki[3], Y. Abe[1] and S. Ueno[4] *1. Department of Biomedical Engineering, Graduate School of Medicine, The University of Tokyo, Tokyo, Japan; 2. Research Center for Frontier Medical Engineering, Chiba University, Chiba, Japan; 3. Department of Advanced Energy, Graduate School of Frontier Sciences, The University of Tokyo, Chiba, Japan; 4. 4Department of Applied Quantum Physics, Graduate School of Engineering, The Kyusyu University, Fukuoka, Japan*

GO-15. Detection of single Magnetic bead using Spin Valve Structure for an Array of PHR Sensor. *S. Oh*[1], H. Tran Quang[1], K. Kim[1] and C. Kim[1] *1. Chung nam univ., Daejeon, South Korea*

THURSDAY
MORNING
9:00

POLIVALENTE

Session GP
SWITCHED RELUCTANCE MACHINES (POSTER SESSION)
Jeremy Hall, Chair

GP-01. Extraction of design parameters of linear switched reluctance motor based on force calculation. S. Jang[1], *J. Park*[1], J. Choi[1] and H. Sung[2] *1. Electrical Engineering, Chungnam National University, Daejeon, South Korea; 2. Korea Institute of Machinery & Materials, Daejeon, South Korea*

GP-02. Dynamic Analysis of Rotor Eccentricity in Switched Reluctance Motor with Parallel Winding. *L. Jian*[1] *1. Electrical Engineering, Dong-A University, Busan, South Korea*

GP-03. Comparison of 12/8 and 6/4 Switched Reluctance Motor: Noise and Vibration Aspects. *L. Jian*[1] *1. Electrical Engineering, Dong-A University, Busan, South Korea*

GP-04. Comparison of iron losses in switched reluctance motor with different winding arrangements and switching sequences. *T. Sun*[1] and J. Hong[1] *1. Department of Mechanical Engineering, Hanyang University, Seoul, South Korea*

GP-05. Optimum Design Criteria for Maximum Torque Density and Minimum Torque Ripple of Synchronous Reluctance Motor according to the Rated Wattage using Response Surface Methodology. *Y. Choi*[1] and S. Mun[1] *1. Electrical Eng., Hanbat National University, Deajeon, South Korea*

GP-06. The Evaluation of On-line Observer System of Synchronous Reluctance Motor Using a Coupled FEM & Preisach Model. *H. Lim*[1], J. Lee[1], M. Lee[1] and D. Lee[2] *1. Electrical Engineering, Hanbat National University, Daejeon, South Korea; 2. Electrical Engineering, Hanyang University, Seoul, South Korea*

GP-07. Design and Characteristic Analysis of Synchronous Reluctance Motors with Axial Lamination Rotor. *S. Hahn*[1], J. Hong[1], J. Kim[1] and D. Koo[2] *1. Department of Electrical Engineering, Dong-A University, Busan, South Korea; 2. Mechatronics Research Group, Korea Electrotechnology Research Institute, Changwon, South Korea*

GP-08. Design Solutions To Minimize Iron Core Loss In Synchronous Reluctance Motors Using Preisach Model & Finite Elements Method(FEM). *H. Lim*[1], J. Lee[1], M. Lee[1] and D. Lee[2] *1. Hanbat National University, Daejeon, South Korea; 2. Electrical Engineering, Hanyang University, Seoul, South Korea*

GP-09. Optimum Design of Synchronous Reluctance Motors Based on Torque/Volume Using Finite Element Method & Sequential Unconstrained Minimization Technique. *S. Mun*[1] and Y. Cho[1] *1. Electrical Engineering, Hanbat National University, Daejeon, South Korea*

GP-10. Reduced windage loss rotor of SRM using magnetic saturation for high speed application. *S. Won*[1] and J. Lee[1] *1. Electrical Eng., Hanyang University, Seoul, South Korea*

GP-11. Calculation of force characteristics of an electromechanical system using co-energy. *M. Hadziselimovic*[1,2], P. Virtic[1], G. Stumberger[1,2], T. Marcic[1] and B. Stumberger[1,2] *1. University of Maribor, FE&CS, Maribor, Slovenia; 2. TECES, Maribor, Slovenia*

THURSDAY
MORNING
9:00

POLIVALENTE

Session GR
SOFT NANOCRYSTALLINE ALLOYS (POSTER SESSION)

Daichi Azuma, Chair
Patricia Crespo, Chair

GR-01. Exchange bias in surface-crystalline FeNbB ribbons. *L. Kraus*[1], O. Zivotsk ý[2], K. Postava[2], P. Švec[3] and D. Jani čkovi č[3] *1. Institute of Physics v.v.i., Academy of Sciences of the Czech Republic, Prague, Czech Republic; 2. Department of Physics, Technical University of Ostrava, Ostrava, Czech Republic; 3. Institute of Physics, Slovak Academy of Sciences, Bratislava, Slovakia*

GR-02. Surface magnetic properties and depth sensitivity of as-quenched FeNbB ribbons. *O. Zivotsky*[1], K. Postava[1], L. Kraus[2], K. Hrabovska[1] and J. Pistora[1] *1. Department of Physics, VSB-Technical University of Ostrava, Ostrava, Czech Republic; 2. Institute of Physics, Academy of Sciences of the Czech. Rep., Prague, Czech Republic*

GR-03. Some Magnetic Properties of Bulk Amorphous Fe-Co-Zr-Hf-Ti-W-B-(Y) Alloys. *M. Hasiak*[1], K. Sobczyk[2], J. Zbroszczyk[2], W. Ciurzynska[2], J. Olszewski[2], M. Nabialek[2], J. Kaleta[1], J. Swierczek[2] and A. Lukiewska[2] *1. Institute of Materials Science and Applied Mechanics, Wroclaw University of Technology, Wroclaw, 50-370, Poland; 2. Institute of Physics, Czestochowa University of Technology, Czestochowa, 42-200, Poland*

GR-04. Magnetic properties of as - quenched Fe87-xZr3.5Nb3.5B6Cux nanocrystalline ribbons. *J. Hu*[1], B. Li[2], H. Qin[1], R. Zhang[1] and M. Jiang[1] *1. Department of Physics, Shandong University, Jinan, China; 2. Central Iron & Steel Research Institute, Beijing, China*

GR-05. Dynamics of the magnetic susceptibility of milled FexAl100-x (x = 70,71) alloys. D. Alba Venero[2], R. Rodríguez García[2], *L. Fernández Barquín*[2], E. Apiñaniz[1], J.J. Garitaonandia[1] and F. Plazaola[1] *1. University of the Basque Country, Bilbao, Spain; 2. Universidad de Cantabria, CITIMAC, Santander, Spain*

GR-06. EXAFS studies and magnetic behavior of FeCuZr Ball-milled alloys. *A. Martinez*[1], J.J. Romero[1], G. Castro[2], A. Yang[3], V.G. Harris[3], J.C. Woicik[4], A. Hernando[1] and P. Crespo[1] *1. Intituto de Magnetismo Aplicado, Las Rozas, Madrid, Spain; 2. Sp-line European Synchrotron Radiation Facility, ESRF, Grenoble, France; 3. Northeastern University, Boston, MA; 4. National Institute of Science and Technology, Gaithersburg, MD*

GR-07. Mossbauer and structural studies of the system FeAlNb prepared by mechanical alloying. *L.E. Zamora*[1,3], G.A. Perez Alcazar[1,3], J.M. Greneche[2] and J.M. Gonzalez[3] *1. Fïsica, Universidad del Valle, Cali, Valle, Colombia; 2. Laboratoire de Etat Condense, Université du Maine, 72085, Cedex 9, Le Mans, France; 3. Unidad Asociada, ICMM-IMA, Apdo. 155, 28230 Las Rozas, Madrid, Madrid, Spain*

GR-08. Magnetic and structural characterization of mechanically alloyed Fe50Co50 samples. *G.A. Pérez Alcázar*[1], L.E. Zamora Alfonso[1], J.F. Marco[2], J.J. Romero[3], J.M. Gonzalez[4] and F.J. Palomares[5] *1. Physics, Universidad del Valle, Cali, Valle, Colombia; 2. Instituto de Física-Química Rocasolano, CSIC, C/Serano, 119. 28006, Madrid, Madrid, Spain; 3. Instituto de Magnetismo Aplicado, UC, P.O. Box 155, 28360, Las Rozas, Madrid, Madrid, Spain; 4. Unidad Asociada, ICMM-IMA, P.Box 155, 28360, Las Rozas, Madrid, Madrid, Spain; 5. Instituto de Ciencia de Materiales de Madrid, CSIC, C/Sor Juana Inés de la Cruz, 28049, Cantoblanco, Madrid, Madrid, Spain*

GR-09. Residual strain induced in a crystal lattice upon annealing under stretching load in soft-magnetic Fe-based nanocrystalline alloys. *N.V. Ershov*[1], Y.P. Chernenkov[2], V.I. Fedorov[2], V.A. Lukshina[1] and A.P. Potapov[1] *1. Institute of Metal Physics, Ural Division, Russian Academy of Sciences, Yekaterinburg, Russian Federation; 2. St.-Petersburg Institute of Nuclear Physics, Russian Academy of Sciences, Gatchina, Russian Federation*

GR-10. Magnetic properties and reaction kinetics of synthesized Fe-Ni-Co alloy during H2 reduction of Ni0.5Co0.5Fe2O4. M. Bahgat[1], *M. Paek*[1] and J. Pak[1] *1. Metallurgical and material engineering, Hanyang university, Ansan, South Korea*

GR-11. Magnetocaloric effect in the FeCrCuNbSiB amorphous materials. *A. Kolano-Burian*[1], M. Kowalczyk[2], R. Kolano[1], R. Szymczak[3], H. Szymczak[3], T. Kulik[2] and J. Szynowski[1] *1. Institute of Non-Ferrous Metals, Gliwice, Poland; 2. Faculty of Materials Science and Engineering, Warsaw University of Technology, Warsaw, Poland; 3. Institute of Physics, Polish Academy of Sciences, Warsaw, Poland*

GR-12. Thermal and magnetic field-induced martensite-austenite transformation in melt spun Mn50Ni40In10 ribbons. *J.L. Sanchez Llamazares*[1], B. Hernando[1], J.D. Santos[1], M.J. Pérez[1], C. García[2], J. González[2] and R. Varga[3] *1. Departamento de Fisica, Universidad de Oviedo, Oviedo, Asturias, Spain; 2. Departamento de Física de Materiales, Universidad del País Vasco, San Sebastián, Spain; 3. Institute of Physics, UPJS, Kosice, Slovakia*

GR-13. Influence of the Fe/B ratio on the magnetocaloric response of $Fe_{92-x}Cr_8B_x$ (x=12, 15) amorphous alloys. *V. Franco*[1], A. Conde[1] and L.F. Kiss[2] *1. Department of Condensed Matter Physics, Sevilla University, Sevilla, Spain; 2. Research Institute for Solid State Physics and Optics, Hungarian Academy of Sciences, Budapest, Hungary*

GR-14. XMCD-PEEM imaging of the micromagnetic structure of Co_2FeSi Heusler compound. *A. Gloskovskii*[1], C. Blum[1], J. Barth[1], G. Fecher[1], P. Nagel[2], S. Schuppler[2], G. Schönhense[3] and C. Felser[1] *1. Institut für Anorganische Chemie und Analytische Chemie, Johannes Gutenberg - Universität, Mainz, Germany; 2. Forschungszentrum Karlsruhe, Institut für Festkörperphysik, Karlsruhe, Germany; 3. Institut für Physik, Johannes Gutenberg - Universität, Mainz, Germany*

GR-15. Transport and Magnetism in $Nd_5Si_{1.45}Ge_{2.55}$ *A.M. Pereira*[1], C. Magen[4], P. Algarabel[2], L. Morellon[2,3], M.E. Braga[1], F. Carpinteiro[1], M.R. Ibarra[2,3], J. Ventura[1], J.B. Sousa[1] and J.P. Araujo[1] *1. IFIMUP Faculdade de Ciências da Universidade do Porto, Porto, Portugal; 2. ICMA - Universidad de Zaragoza and Consejo Superior de Investigaciones Científicas, Zaragoza, Spain; 3. Instituto de Nanociencia de Aragón, Universidad de Zaragoza, Zaragoza, Spain; 4. Oak Ridge Natl Lab, High Temp Mat Lab, Oak Ridge, TN*

GR-16. Magnetism and phase transformation in Fe / Fe oxide milled nanopowders. *O. Crisan*[1], R. Nicula[2] and I. Skorvanek[3] *1. National Institute for Materials Physics, Bucharest-Magurele, Romania; 2. Institute of Physics, Rostock University, Rostock, Germany; 3. Institute of Experimental Physics, Slovak Academy of Sciences, Kosice, Slovakia*

GR-17. Magnetic properties of high Bs Fe-based amorphous powders produced by Spinning Water Atomization Process (SWAP). *I. Otsuka*[1], K. Wada[1], Y. Maeta[1], T. Kadomura[1] and M. Yagi[2] *1. EPSON ATMIX CORPORATION, Hachinohe-shi, Aomori-ken, Japan; 2. Sojo University, Kumamoto, Japan*

GR-18. Study on the microstructure and soft magnetic properties of Ni-Fe particles synthesized by a conventional and a microwave-assisted polyol method. *Y. Shimada*[1], Y. Endo[1], S. Okamoto[2], M. Yamaguchi[1] and O. Kitakami[2] *1. Dept. of Electrical and Communication Engineering, Tohoku University, Sendai, Japan; 2. IMRAM, Tohoku Univ., Sendai, Japan*

GR-19. Synthesis, Phase Transfer and Magnetic Properties of Monodisperse Magnetite Nanocubes. *H. Yang*[1], D. Hasegawa[2], M. Takahashi[1] and T. Ogawa[2,3] *1. Niche, Tohoku University, Sendai, MIyagi, Japan; 2. Dep. of Electronics Engineering, Tohoku University, Sendai, MIyagi, Japan; 3. Cress, Tohoku University, Sendai, MIyagi, Japan*

GR-20. Size controlled Fe nanoparticles through polyol process and their magnetic properties. *R.J. Joseyphus*[1,2], K. Shinoda[2], D. Kodama[2] and B. Jeyadevan[2] *1. Department of Physics, National Institute of Technology, Tiruchirappalli, Tamilnadu, India; 2. Graduate School of Environmental Studies, Tohoku University, Sendai, Miyagi, Japan*

GR-21. Magnetic behaviour of $Gd_4(Co_{1-x}Cu_x)_3$ compounds. *T.M. Seixas*[1,2], M.A. Salgueiro da Silva[2], J.M. Machado da Silva[1,2], H.F. Braun[3] and G. Eska[3] *1. Instituto de Física dos Materiais da Universidade do Porto (IFIMUP), Porto, Portugal; 2. Departamento de Física da Universidade do Porto, Rua do Campo Alegre, 687, 4169-007, Porto, Portugal; 3. Physikalisches Institut, Universitaet Bayreuth, D – 95440, Bayreuth, Germany*

GR-22. Exact Calculation of The Magnetostatic Interaction in Arrays of Nanowires. *J. Velázquez*[1] *1. CAI Difracción Rayos X, Universidad Complutense de Madrid, Madrid, Spain*

THURSDAY
MORNING
9:00

POLIVALENTE

Session GS
POWER AND CONTROL MAGNETICS (POSTER SESSION)
David Howe, Chair

GS-01. Performance Analysis of Flyback Converter Based on Time-stepping FEA Incorporating Magnetic Hysteresis Effect. J. Chen[1], *Y. Guo*[2], J. Zhu[2] and Z. Lin[2] *1. College of Electromechanical Engineering, Donghua University, Shanghai, Shanghai, China; 2. Faculty of Engineering, University of Technology Sydney, Sydney, NSW, Australia*

GS-02. Chaoization of Permanent Magnet Synchronous Motors Using Stator Flux Regulation. *Z. Wang*[1] and K. Chau[1] *1. Department of Electrical and Electronic Engineering, The University of Hong Kong, Hong Kong, China*

GS-03. Fundamental Resarch about Parameter Design of Contactless Power Station for Moving Electric Loads. *N. Nakajima*[1], Y. Kakubari[1], F. Sato[1] and H. Matsuki[1] *1. Tohoku University, Sendai, Miyagi, Japan*

GS-04. Experimental Verification and Performance Analysis of Permanent Magnet Wind Turbine Generators considering Magnetic Losses using D-Q Axis Model. S. Jang[1], *J. Choi*[1], K. Ko[1] and B. Kim[2] *1. Chungnam National University, Dae-jeon, South Korea; 2. Korea Electric Power Research Institute, Daejeon, South Korea*

GS-05. Design, Fabrication and Experimental Validation of a Miniaturized Generator with Planar Coils via Genetic Algorithm. *P. Chao*[1], J. Shen[2], E. Chiu[1] and J. Huang[2] *1. Electrical and Control Engineering, National Chiao Tung University, Hsinchu, Taiwan; 2. Mechanical Engineering, Chung Yuan Christian Univ., Chung Li, Taiwan*

GS-06. Electromagnetic Analysis and Parameter Estimation of Permanent Magnet Wind Turbine Generators Considering Skew Effects. S. Jang[1], *J. Choi*[1] and K. Ko[1] *1. Chungnam National University, Dae-jeon, South Korea*

GS-07. Operating time estimation in acceleration and deceleration mode of high power FESS using electromagnetic field analysis of PM synchronous motor/generator. *D. You*[1], S. Jang[1], J. Lee[2] and T. Sung[2] *1. chungnam national univ., daejeon, South Korea; 2. Korea Electric Power Research Institute, Daejeon, South Korea*

GS-08. Magnetic Switch Topologies. *W. Johnson*[1] *1. Electrical and Computer Engineering, University of Kentucky, Lexington, Ky, KY*

THURSDAY
MORNING
9:00

POLIVALENTE

Session GT
SPIN TORQUE EXCITATIONS IN NANOMAGNETS (POSTER SESSION)
Dafine Ravelosona, Chair

GT-01. Influence of Notch Shape and Size on Current-Driven Domain Wall Motions in a Magnetic Nanowire. H. Murakami[1], *T. Komine*[1], T. Nagayama[1], R. Sugita[1] and Y. Hasegawa[2] *1. Department of Media and Telecommunications Engineering, Ibaraki University, Hitachi, Ibaraki, Japan; 2. Saitama University, Saitama, Saitama, Japan*

GT-02. Multi-level transitions of closely-arranged spin valve pillars by spin transfer switching. *N. Funabashi*[1], K. Machida[1], K. Aoshima[1], Y. Miyamoto[1], N. Kawamura[1], K. Kuga[1] and N. Shimidzu[1] *1. NHK Science & Technical Research Laboratories, Tokyo, Japan*

GT-03. Dependence of current induced switching properties on MgO formation method. *J. Langer*[1], J. Wrona[1], B. Ocker[1], W. Maass[1], A. Thomas[2], K. Rott[2], M. Schaefers[2] and G. Reiss[2] *1. Singulus Nano Deposition Technologies GmbH, Kahl am Main, Germany; 2. Department of Physics, Bielefeld University, Bielefeld, Germany*

GT-04. Dynamics of current-induced magnetic switching of a single-molecule magnet. *M. Misiorny*[1] and J. Barnas[1,2] *1. Department of Physics, Adam Mickiewicz University, Poznan, Poland; 2. Institute of Molecular Physics, Polish Academy of Science, Poznan, Poland*

GT-05. Spin mechatronics to facilitate spin transfer switching in magnetic tunnel junction. S. Kumar[1,2], *N. Chen*[1], S. Tan[1] and M. Jalil[2] *1. SMI, Data Storage Institute, Singapore, Singapore; 2. ISML, ECE, National University of Singapore, singapore, Singapore*

GT-06. Spin transfer in Co/Cu/Co nanocontacts. *M.N. Baibich*[1], M.P. de Lucena[1], D.L. Baptista[1], R.B. da Silva[1], J.E. Schmidt[1] and L.G. Pereira[1] *1. Instituto de Fisica UFRGS, Porto Alegre, RS, Brazil*

GT-07. On the relation of the inelastic spin torque and the spin polarization. *W. Wulfhekel*[1], A.F. Takacs[1], T. Balashov[1], M. Däne[2], A. Ernst[2] and P. Bruno[2] *1. Physikalisches Institut, Universität Karlsruhe, Karlsruhe, Germany; 2. Max-Planck Institut für Mikrostrukturphysik, Halle, Germany*

GT-08. Microscopic theory of spin transfer torque based on the spin spiral texture. *Y. Le Maho*[1] and F. Piechon[2] *1. Institut d'Electronique Fondamentale, CNRS / Univ. Paris Sud, Orsay, Paris, France; 2. Laboratoire de Physique des Solides, CNRS / Univ. Paris Sud, Orsay, Paris, France*

GT-09. Current-induced domain wall motion in permalloy nanowires. *W. Zhang*[1], P. Wong[1], Y. Xu[1], X. Zou[2] and J. Wu[2] *1. Spintronics and Nanodevice Laboratory, Department of Electronics, University of York, York, United Kingdom; 2. Department of Physics, University of York, York, United Kingdom*

GT-10. Spin transfer switching in magnetic tunnel junction using a composite free layer. *W. Chen*[1], D. Wang[1], C. Yen[1], Y. Lee[1], S. Yang[1], C. Shen[1], C. Tsai[1], C. Hung[1], K. Shen[1] and M. Kao[1] *1. Electronics and Optoelectronics Research Lab. (EOL), Industrial Technology Research Institute (ITRI), Hsinchu, Taiwan*

GT-11. Current-induced Domain Wall Motion in L- and C-shaped Permalloy Nanowires. *J. Yoon*[1,4], J. Lee[2,3], C. You[4], S. Choe[3], K. Shin[2] and M. Jung[1] *1. Quantum Material Research Team, Korea Basic Science Institute, Daejeon, South Korea; 2. Center for Spintronics Research, Korea Institute of Science and Technology, Seoul, South Korea; 3. physics, Seoul National University, Seoul, South Korea; 4. physics, Inha University, Incheon, South Korea*

GT-12. Experimental study of thermally activated magnetization reversal with a spin-transfer torque in a nanowire. *K. Seon Ock*[1], W. Kim[1], T. Lee[1], K. Kim[2], S. Choe[2], Y. Jang[3], S. Yoon[3] and B. Cho[3] *1. Department of Materials Science and Engineering, Korea Advanced Institute of Science and Technology, Daejeon, South Korea; 2. Department of Physics and Astonomy, Seoul National Univesity, Seoul, South Korea; 3. Department of Materials Science and Engineering, Gwangju Institute of Science and Technology, Gwangju, South Korea*

GT-13. Spin-Transfer Switching in Elliptical Spin Valves in Subnanosecond Regime. *R. Heindl*[1], T. Silva[1], W. Rippard[1], S. Russek[1] and J. Katine[2] *1. Electromagnetics Division - Magnetics Group, National Institute of Standards and Technology (NIST), Boulder, CO; 2. Hitachi San Jose Research Center, San Jose, CA*

GT-14. Shape dependence of current-induced magnetization switching. *C. Tsai*[1], Y. Lee[1], D. Wang[1], W. Chen[1], C. Yen[1], C. Shen[1], S. Yang[1], C. Hung[1], K. Shen[1] and M. Kao[1] *1. Electronics and Optoelectronics Research Laboratories, Industrial Technology Research Institute, Hsinchu, Taiwan*

GT-15. Static and Dynamic Depinning Current Density in Current-Induced Domain Wall Motion. *S. Seo*[1], H. Lee[2], W. Kim[3], T. Lee[3], S. Choe[4], D. Kim[5] and K. Lee[1] *1. Korea University, Seoul, South Korea; 2. POSTECH, Pohang, South Korea; 3. KAIST, Daejon, South Korea; 4. Seoul National University, Seoul, South Korea; 5. Chungbuk National University, Cheongju, South Korea*

GT-16. Current-assisted variation of magnetization reversal process in tri-layer-ring spin valve. *D. Chen*[1], C. Yu[2] and Y. Yao[1,3] *1. Department of Material Science and Engineering, National Chiao Tung University, Hsinchu, Taiwan; 2. Institute of Physics, Academia Sinica, Taipei, Taiwan; 3. The Department of Materials Engineering, Tatung University, Taipei, Taiwan*

GT-17. Domain wall dynamics in the microwave frequency range probed by Spin diode effect. S. Laribi[1,2], *A. Anane*[1], J. Grollier[1], V. Cros[1], K. Bouzehouane[1], G. Faini[3] and A. Fert[1] *1. Unité Mixte de Physique CNRS/Thales and Université Paris Sud 11, Route départementale 128, 91767, Palaiseau, France; 2. ST Microelectronics, 850 Rue Jean Monnet, 38926, Crolles, France; 3. Phynano team, Laboratoire de Photonique et Nanostructures, LPN-CNRS, Route de Nozay, 91460, Marcoussis, France*

GT-18. Current induced domain wall motion with step structure. *H. Ashida*[1], T. Ochiai[1], Y. Shimizu[1] and A. Tanaka[1] *1. Fujitsu Limited., Atsugi, 243-0197, Japan*

THURSDAY MORNING 9:00 — POLIVALENTE

Session GU
MAGNETOCALORIC EFFECT AND MATERIALS (POSTER SESSION)
Julia Lyubina, Chair

GU-01. Magnetocaloric Effect in Ni-Mn-Ga Alloys. *K. Mandal*[1], D. Pal[1], O. Gutfleisch[2], J. Lyubina[2] and N. Scheerbaum[2] *1. Materials Science, S. N. Bose National Centre for Basic Sciences, Kolkata, West Bengal, India; 2. Institut für Metallische Werkstoffe, Leibniz Institute für Festkörper- und Werkstoffforschung Dresden (IFW Dresden), Dresden, saxony, Germany*

GU-02. Magnetic properties and magnetocaloric effect in $Tb_8Co_{16-X}A_X$ compounds where A=Al or Cu and x ≤ 4. *R. Tetean*[1], E. Burzo[1] and I.G. Deac[1] *1. Physics, Babes-Bolyai University, Cluj Napoca, Romania*

GU-03. Synthesis and evaluation of magnetocaloric effect of rare earth nitrides. *Y. Hirayama*[1], S. Nishio[1], T. Kusunose[2], T. Nakagawa[3] and T.A. Yamamoto[1] *1. Graduate School of Engineering, Osaka University, Osaka, Japan; 2. Institute of Scientific and Industrial Research, Osaka University, Osaka, Japan; 3. Graduate School of Science and Engineering, Tokyo Institute of Technology, Tokyo, Japan*

GU-04. Anisotropy of magnetocaloric effect in R2Fe17 single crystals with heavy RE metals and Y. *K.P. Skokov*[1], Y.G. Pastushenkov[1], Y.S. Koshkid'ko[1], T.I. Ivanova[2] and S.A. Nikitin[2] *1. Department of Physics, Tver State University, Tver, Russian Federation; 2. Department of Physics, Moscow State University, Moscow, Russian Federation*

GU-05. Magnetocaloric effect in $Gd4(Bi_xSb_{1-x})_3$ alloys. *N.A. de Oliveira*[1] and M.B. Gomes[1] *1. Instituto de Física, Universidade do Estado do Rio de Janeiro, Rio de Janeiro, Brazil*

GU-06. Magnetocaloric effect in $La(Fe_xSi_{1-x})_{13}$ under applied pressure. *N.A. de Oliveira*[1], L.G. de Medeiros Jr[1] and A. Troper[1,2] *1. Instituto de Física, Universidade do Estado do Rio de Janeiro, Rio de Janeiro, Brazil; 2. Centro Brasileiro de Pesquisas Físicas, Rio de Janeiro, Brazil*

GU-07. Magnetocaloric Effect of the PrNi5-xCox Hard Magnets. *D.L. Rocco*[1], R.P. Fernandes[2], M.S. Reis[1], J.S. Amaral[1], V.S. Amaral[1], J.P. Araújo[3], P.B. Tavares[4] and A.A. Coelho[5] *1. Departamento de Física e CICECO, Universidade de Aveiro, Aveiro, Portugal; 2. Technische Universität Hamburg-Harburg, Institut für Keramische Hochleistungswerkstoffe, Hamburg, Germany; 3. IFIMUP, Departamento de Física, Universidade do Porto, Porto, Portugal; 4. Departamento de Química and CQ-VR, Universidade de Trás-os-Montes e Alto Douro, Vila Real, Portugal; 5. Departamento de Física Gleb Wataguin, Universidade Estadual de Campinas – UNICAMP, Campinas, Brazil*

THURSDAY MORNING 9:00 — POLIVALENTE

Session GV
FAST SWITCHING OF FILMS AND NANOSTRUCTURES (POSTER SESSION)
Karsten Kuepper, Chair

GV-01. Laser induced magnetisation switching in films with perpendicular anisotropy: a comparison between measurements and an LLB macro-spin model. C. Bunce[1], *J. Wu*[1], G. Ju[2], B. Lu[2], D. Hinzke[1], N. Kazantseva[1], R. Chantrell[1] and U. Nowak[1] *1. Department of Physics, University of York, York, United Kingdom; 2. Seagate Research, 1251 Waterfront Place, Pittsburgh, PA*

GV-02. Spin dynamics in patterned nanoscale Fe dot arrays. *J. Wu*[1], S. Lepadatu[1], C. Bunce[1], X. Zou[1], D. Niu[2], Y.B. Xu[2], R. Chantrell[1] and G.P. Ju[3] *1. Physics, University of York, York, United Kingdom; 2. Electronics, University of York, York, United Kingdom; 3. Seagate Research, Pittsburgh, PA*

GV-03. FMR study of self-organized plane arrays of metallic magnetic elements. *M. Kostylev*[1], R. Magaraggia[1], F.Y. Ogrin[2], V. Mescheryakov[3,4], N. Ross[1] and R.L. Stamps[1] *1. School of Physics, University of Western Australia, Crawley, WA, Australia; 2. School of Physics, University of Exeter, Exeter, United Kingdom; 3. Moscow Institute of Radioelectronics and Automation, Moscow, Russian Federation; 4. Instutute of Crystallography of Russian Academy of Science, Moscow, Russian Federation*

GV-04. Complex broadband magnetic response of periodic arrays of FeNi dots and of Fe/Cr multilayers studied by using FMR-VNA technique. J. Sierra[1], *A. Awad*[1], V. Pryadun[1], F. Aliev[1] and G. Kakazei[2] *1. Departamento de Fisica de la Materia Condensada, Universidad Autonoma de Madrid, Spain, Madrid, Spain; 2. Institute of Magnetism NASU, Kiev, Ukraine*

GV-05. Linear and Nonlinear Dynamics of the Gyrotropic Motion of a Magnetic Vortex in Ferromagnetic Nanodots. *K. Lee*[1] and S. Kim[1] *1. Research Center for Spin Dynamics and Spin-Wave Devices & Nanospintronics Laboratory, Seoul National University, Seoul, South Korea*

GV-06. Nonlinear phenomena in magnetic nanoparticle systems at microwave frequencies. *M. Pardavi-Horvath*[1], G.S. Makeeva[2] and O.A. Golovanov[3] *1. SEAS, The George Washington University, Washington, DC; 2. Penza State University, Penza, Russian Federation; 3. Penza Military Institute of Artillery, Penza-5, Russian Federation*

GV-07. Parametric spin wave excitation and cascaded processes in thin films. *K. Livesey*[1], M. Kostylev[1] and R. Stamps[1] *1. School of Physics, University of Western Australia, Crawley, WA, Australia*

GV-08. Micromagnetic modeling of the magnetization dynamics in a circularly exchange biased tunnel junction. *O.G. Heinonen*[1], D.K. Schreiber[2] and A.K. Petford-Long[3] *1. Seagate Technology, Bloomington, MN; 2. Materials Science and Engineering, Northwestern University, Evanston, IL; 3. Materials Science Division, Argonne National Laboratory, Argonne, IL*

GV-09. WITHDRAWN

GV-10. Size dependence of the magnetic switching of Co-nanoislands studied by spin-polarized scanning tunneling spectroscopy. *D. Sander*[1], S. Wedekind[1], G. Rodary[1] and K. Jürgen[1] *1. Max Planck Institute, Halle, Germany*

THURSDAY MORNING 9:00 — POLIVALENTE

Session GW
COMPUTATIONAL MAGNETICS (POSTER SESSION)
Claudio Serpico, Chair

GW-01. Chemical order and size effects on the magnetic anisotropy of FePt and CoPt nanoparticles. *F. Tournus*[1], S. Rohart[1,2] and V. Dupuis[1] *1. LPMCN, Université de Lyon; Univ. Lyon 1; CNRS, Villeurbanne, France; 2. LPS, Université Paris Sud; CNRS, Orsay, France*

GW-02. A study of the optimum dose of ferromagnetic nanoparticles suitable for cancer therapy using magnetic fluid hyperthermia. *M. Pavel*[1,2], G. Gradinariu[1,2] and A. Stancu[1] *1. Department of Solid State and Theoretical Physics, "Alexandru Ioan Cuza" University, Faculty of Physics, Iasi, Romania; 2. Department of Oncology, University of Medicine and Pharmacy "Gr. T. Popa", Iasi, Romania*

GW-03. Influence of dipole interaction and thermal effect on static magnetization process of magnetic nanoparticle assembly. *D. Hasegawa*[1], T. Ogawa[2] and M. Takahashi[3] *1. Electronic Engineering, Tohoku University, Sendai, Japan; 2. CRESS, Tohoku University, Sendai, Japan; 3. NICHe, Tohoku University, Sendai, Japan*

GW-04. Numerical Modeling and Characterization of Micromachined Flexible Magnetostrictive Thin Film Actuator. *H. Lee*[1] and C. Cho[1] *1. Mechanical Engineering, Inha University, Incheon, South Korea*

GW-05. Semi-analytical calculation of the armature reaction in a slotted tubular permanent magnet actuator with distributed windings. *B. Gysen*[1], J. Paulides[1], E. Lomonova[1] and A. Vandenput[1] *1. Electrical Engineering, Eindhoven University of Technology, Eindhoven, Netherlands*

GW-06. Sequential optimization method for the design of electromagnetic devices. G. Lei[1], *Y. Guo*[2] and J. Lavers[3] *1. College of Electrical and Electronic Engineering, Huazhong University of Science and Technology, Wuhan, HuBei, China; 2. Faculty of Engineering, University of Technology, Sydney, NSW, Australia; 3. Department of Electrical and Computer Engineering, University of Toronto, Toronto, ON, Canada*

GW-07. A new field-circuit coupled method for the computation of additional losses in transformer. G. Jian[1], *L. Heyun*[1] and H. Siulau[2] *1. School of Electrical Engineering, Southeast University, Nanjing, Jiangsu, China; 2. Department of Electrical Engineering, Hong Kong Polytechnic University, Hong Kong, Hong Kong, China*

GW-08. Accurate eddy current losses computation for ferromagnetic cores working in strongly distorted regimes. *L. Mandache*[1], D. Topan[1] and K. Al-Haddad[2] *1. Electrical Engineering, University of Craiova, Craiova, Romania; 2. Genie Electrique, Ecole de Technologie Superieure, Montreal, QC, Canada*

GW-09. Modeling of effect of plastic deformation on Barkhausen noise and magnetoacoustic emission in iron with 2% silicon. *M.J. Sablik*[1], B. Augustyniak[2] and F.J. Landgraf[3] *1. Mechanical and Materials Engineering Div., Bldg. 139,, Southwest Res. Inst., San Antonio, TX; 2. Physics, Gdansk Institute of Technology, Gdansk, Poland; 3. Metallurgical Engineering, University of Sao Paulo, Sao Paulo, Brazil*

GW-10. Fluxmetric and Magnetometric Demagnetizing Factors in Cylindrical and Rectangular Geometries. *A. Vashghani Farahani*[1] and A. Konrad[1] *1. Electrical and computer engineering, University of Toronto, Toronto, ON, Canada*

GW-11. Transmutation of momentum into position in magnetic vortices. *S. Komineas*[1] and N. Papanicolaou[2] *1. Max-Planck Institute, Dresden, Germany; 2. Department of Physics, University of Crete, Heraklion, Greece*

GW-12. Reduction Design of Eddy Current Loss in Permanent Magnet. *J. Jung*[1], S. Lee[1] and J. Hong[1] *1. Department of Mechanical Engineering, Hanyang University, Seoul, South Korea*

THURSDAY MORNING 9:00 — POLIVALENTE

Session GX
MISCELLANEOUS I (POSTER SESSION)
Federico Cebollada, Chair

GX-01. Magnon thermalization and formation of coherent Bose-Einstein condensate. *S.O. Demokritov*[1], V.E. Demidov[1], O. Dzyapko[1], G.A. Melkov[2] and A.N. Slavin[3] *1. Institute for Applied Physics, University of Muenster, Muenster, Germany; 2. Department of Radiophysics, National Taras Schevchenko University of Kiev, Kiev, Ukraine; 3. Department of Physics, Oakland University, Rochester, MI*

GX-02. Critical Temperature for Thermal Runaway in a Magnetic Material. F. Farahmand[1], *F.P. Dawson*[1] and J. Lavers[1] *1. ECE, The University of Toronto, Toronto, ON, Canada*

GX-03. Effects of double-axis electromagnetic stirring in continuous casting. *R. Otake*[1], T. Yamada[2], R. Hirayama[3], K. Fujisaki[1,3], S. Shimasaki[1] and S. Taniguchi[1] *1. Graduate school of TOHOKU university, Sendai, Japan; 2. Nittetsu Plant Designing Corp., Futtsu, Japan; 3. Nippon Steel Corp., Futtsu, Japan*

GX-04. Diamagnetic levitation of solids at micro scale. *C. Pigot*[1], G. Poulin[1] and R. Gilbert[1] *1. Magnetic Microsystems, G2ELab, Grenoble, France*

GX-05. Construction of Quasi-Cyclic LDPC Codes and the Performance over Magnetic Recording Channels. *X. Liu*[1], H. Cheng[1] and Z. Wang[2] *1. Dept. of Electronics & Comm. Engr., Sun Yat-Sen University, Guangzhou, Guangdong, China; 2. School of Electrical Engineering and Computer Science, Oregon State University, Corvallis, OR*

GX-06. A Novel Electromagnetic Device for Latching Valve in Automotive Engine. *J. Kim*[1] and J. Chang[2] *1. Mechanical Engineering, Yeungnam University, Gyeongsan, Gyeongsangbuk-do, South Korea; 2. Transverse Flux Machines Research Group, Korea Electrotechnology Research Institute, Changwon, Kyungsangnam-Do, South Korea*

GX-07. Air gag's influence on the performance of the transformer of an electromagnetic pump. *D. Morinigo*[2,1], M.A. Rodríguez[1,2], A. Rivas[1] and J. Martin[1] *1. Light Alloys, CIDAUT Foundation, Valladolid, Spain; 2. Electrical Engineering, University of Valladolid, Valladolid, Spain*

GX-08. A New Calibration Procedure for Magnetic Tracking Systems. *A. Plotkin*[1], V. Kucher[1], Y. Horen[2] and E. Paperno[1] *1. Electrical and Computer Engineering, Ben-Gurion University of the Negev, Beer-Sheva, Israel; 2. Electrical and Electronic Engineering, Shamoon College of Engineering, Beer-Sheva, Israel*

GX-09. Microstructural changes in Fe-doped $Gd_5Si_2Ge_2$ *B. Podmiljsak*[1], I. Skulj[2], B. Markoli[3], P. McGuiness[1] and S. Kobe[1] *1. Jozef Stefan Institute, Ljubljana, Slovenia; 2. Institute of Metals and Technology, Ljubljana, Slovenia; 3. University of Ljubljana, Ljubljana, Slovenia*

GX-10. Stress-strain relationship of magnetorheological fluids under tension mode. *S.A. Mazlan*[1], N.B. Ekreem[1] and A.G. Olabi[1] *1. School of Mechanical and Manufacturing Engineering, Dublin City University, Dublin, Ireland*

GX-11. Novel magnetic composite particles of carbonyl iron embedded in polystyrene and their magnetorheological characteristics. F. Fang[1] and *H. Choi*[1] *1. Department of Polymer Science and Engineering, Inha University, Incheon, South Korea*

GX-12. Barkhausen noise statistical properties in ferromagnetic thin films: dimensionality and range of the relevant interactions. *F. Bohn*[1], M.A. Corrêa[2,1], A. Viegas[3], L.F. Schelp[1] and R.L. Sommer[4] *1. Departamento de Física, Universidade Federal de Santa Maria, Santa Maria, RS, Brazil; 2. Campus Caçapava do Sul, Universidade Federal do Pampa, Caçapava do Sul, RS, Brazil; 3. Departamento de Física, Universidade Federal de Santa Catarina, Florianópolis, SC, Brazil; 4. Centro Brasileiro de Pesquisas Físicas, Rio de Janeiro, RJ, Brazil*

THURSDAY
MORNING
9:00

POLIVALENTE

Session GY
MISCELLANEOUS II
(POSTER SESSION)
Puerto Morales, Chair

GY-01. Coloring media by using nanopipette to store more data. *M. Rashidi*[1] and F. Wang[1] *1. Centre for Grid Computing, Cambridge-Cranfield HPCF, Cranfield, United Kingdom*

GY-02. AFM friction investigation with temperature. *D. Kim*[1] *1. Samsung Information Systems America, Inc, San Jose, CA*

GY-03. Arsenic Removal from Water by Magnetic Separation: A Review and a Case Study Using Magnetic Aggregates and Magnetic Stabilized Bed. A.M. Estevez[1], *P.A. Augusto*[2,1], J.M. Rodriguez[1] and A. Alvaro[1] *1. Department of Chemical Engineering, University of Salamanca, Salamanca, Castilla y Leon, Spain; 2. DEQ, Faculdade de Engenharia da Universidade do Porto, Porto, Portugal*

GY-04. Investigation of Nanoparticle Clusterization in Magnetic Fluids Driven by Surface-Coating Desorption. *F.M. Oliveira*[1], P.C. Morais[1], K.S. Neto[1], A.P. Canizares[1] and L.C. Figueiredo[1] *1. Instituto de Física, Universidade de Brasília, Brasília, Brasília/DF, Brazil*

GY-05. Detection of Low-Concentration Magnetic Fluid inside Body by Needle-Type GMR Sensor. *S. Yamada*[1], C.P. Gooneratne[1], M. Iwahara[1] and M. Kakikawa[1] *1. Institute of Nature and Environmental Technology, Faculty of Engineering, Kanazawa University, Kanazawa, Ishikawa, Japan*

GY-06. Suppression of electromyogram of hand muscle elicited by transcranial magnetic stimulation over the primary motor cortex. *M. Odagaki*[1], S. Ohishi[1], H. Fukuda[1] and O. Hiwaki[1] *1. Graduate School of Information Sciences, Hiroshima City University, Hiroshima, Japan*

GY-07. Formation of beta-Sheet Rich Fibrils in Cortex Cells from Mice Fetuses Cultured with Ferritin and Exposed to Radio Frequency Magnetic Fields. *O. Cespedes*[1], O. Inomoto[1], S. Kai[1] and S. Ueno[1] *1. Applied Quantum Physics Department, Kyushu University, Fukuoka, Japan*

GY-08. Effects of Radio Frequency Magnetic Fields on the Iron Release from Cage Proteins via 6-Hydroxydopamine. *O. Cespedes*[1] and S. Ueno[1] *1. Applied Quantum Physics Department, Kyushu University, Fukuoka, Japan*

GY-09. Short and long duration of rTMS effects on perceptual reversals. S. Ge[1], T. Hayami[2], A. Hyodo[3], S. Ueno[4] and *K. Iramina*[1,3] *1. Department of Intelligent Systems, Kyushu University, Fukuoka, Japan; 2. Digital Medicine Initiative, Kyushu University, Fukuoka, Japan; 3. Graduate School of Systems Life Sciences, Kyushu University, Fukuoka, Japan; 4. Department of Applied Quantum Physics, Kyushu University, Fukuoka, Japan*

Session HA
SYMPOSIUM ON THE ROADMAP FOR SPINTRONICS
Yongbing Xu, Chair
Atsufumi Hirohata, Chair

2:30

HA-01. Prospects for Spin Memory Devices and Their Element Technologies in the Next 10 Years. ***(Invited)*** *S. Nakamura*[1] *1. Corporate R&D Center, Toshiba Corporation, Kawasaki, Japan*

3:00

HA-02. Spintronics devices based on the Tunneling Anisotropic Magnetoresistance and the Coulomb Blockade Anisotropic Magnetoresistance effect. ***(Invited)*** *J. Wunderlich*[1,2], B. Park[1], A.C. Irvine[3], A. Shick[2], R.P. Campion[4], V. Novak[2], D.A. Williams[1], B.L. Gallagher[4] and T. Jungwirth[2,4] *1. Hitachi Europe Ltd., Hitachi Cambridge Laboratory, Cambridge, United Kingdom; 2. Institute of Physics ASCR, Prague, Czech Republic; 3. Microelectronics Research Centre, University of Cambridge, Cambridge, United Kingdom; 4. School of Physics and Astronomy, University of Nottingham, Nottingham, United Kingdom*

3:30

HA-03. Engineering magnetic nanostructures into complex devices for spin electronics. ***(Invited)*** *C. Chappert*[1,2] *1. IEF, CNRS - UMR 8622, Orsay, France; 2. IEF, Université Paris Sud, Orsay, France*

4:00

HA-04. Manipulating single spins and coherence for semiconductor spintronics. ***(Invited)*** *D.D. Awschalom*[1] *1. Center for Spintronics and Quantum Computation, University of California, Santa Barbara, CA*

4:30

HA-05. The road to silicon spintronics. ***(Invited)*** *R. Jansen*[1] *1. MESA+ Institute for Nanotechnology, University of Twente, Enschede, Netherlands*

5:00

HA-06. Spin Manipulation in Semiconductors and Metals. ***(Invited)*** *H. Ohno*[1,2] *1. Laboratory for Nanoelectronics and Spintronics, Research Institute of Electrical Communication, Tohoku University, Sendai, Japan; 2. ERATO, JST, Sendai, Japan*

Session HB
INDUCTIVE RECORDING HEADS AND MATERIALS
Alan Johnston, Chair

2:30

HB-01. Micromagnetic Model Analysis of a Single-Pole-Type Head for 1 – 2 Tbit/in^2 *Y. Kanai*[1], K. Hirasawa[1], T. Tsukamoto[1], K. Yoshida[2], S. Greaves[3] and H. Muraoka[3] *1. Niigata Institute of Technology, Kashiwazaki, Japan; 2. Kogakuin University, Tokyo, Japan; 3. Tohoku University, Sendai, Japan*

2:45

HB-02. 1 Turn Solenoid PMR Writer Design for High Frequency Writing. *E. Kim*[1] and K. Sunwoo[1] *1. HDD Core Tech TF, Samsung Advanced Institute of Technology, Yongin, Kyoungki-Do, South Korea*

3:00

HB-03. Advanced heads for areal desnity at 500Gb/in2 and towards 1Tb/in2. ***(Invited)*** *M. Ho*[1], S. Mao[1], S. Li[1], L. Zhong[1], E. Champion[1], S. Song[1], J. Wang[1], T. Pan[1], K. Stoev[1], C. Macchioni[1], Y. Chen[1], L. Wang[1], Q. Leng[1], M. Pakala[1], Y. Li[1], U. Tran[1], M. Chapline[1], W. Yu[1], L. Hong[1], D. Li[1] and Y. Shen[1] *1. Western Digital Corp, Fremont, CA*

3:30

HB-04. Writing performance of a planar single-pole head with a main pole fabricated by ion beam milling. *Y. Ohsawa*[1,2], K. Yamakawa[2] and H. Muraoka[2] *1. CR&D center, Toshiba Corp., Kawasaki, Japan; 2. RIEC, Tohoku Univ., Sendai, Japan*

3:45

HB-05. Thin film processing realities for Tbit/in^2 recording. *R. Fontana*[1], N. Robertson[1] and S. Hetzler[2] *1. Hitachi GST, San Jose, CA; 2., IBM Research Division, San Jose, CA*

4:00

HB-06. Exchange Coupling in Synthetic Antiferromagnetic Multilayers for Write Head. *Y. Xu*[1], H. Jiang[2], K. Sin[2], Y. Chen[2] and J. Wang[1] *1. Dept. of Electrical and Computer Engineering, University of Minnesota, Minneapolis, MN; 2. Western Digital Corporation, Fremont, CA*

4:15

HB-07. Laminated high moment FeCo films for perpendicular magnetic recording. *B. Ocker*[1], K. Schuller[1], J. Wrona[1], J. Langer[1] and W. Maass[1] *1. Singulus Nano Deposition Technologies GmbH, Kahl am Main, Germany*

4:30

HB-08. Comparison of Electrical and Magnetic Flux Rise Times in Tape Heads Using Impedance Measurements and High Speed Kerr Magnetometry. A. Kaya[1,3], *J.A. Bain*[1], J.P. Nibarger[2] and K.D. McKinstry[2] *1. Carnegie Mellon University, Pittsburgh, PA; 2. Sun Microsystems, Louisville, CO; 3. Hitachi Global Storage, San Jose, CA*

4:45

HB-09. Crosstalk between write transducers. P. Herget[1] and *R.G. Biskeborn*[1] *1. IBM Corporation, San Jose, CA*

THURSDAY AFTERNOON 2:30 — ROMA

Session HC
MAGNETIZATION DYNAMICS
Bob Stamps, Chair

2:30

HC-01. Dynamic interaction between vortices, antivortices and holes in domain walls investigated by means of time resolved Photoemission Electron Microscopy (PEEM). ***(Invited)*** *K. Kuepper*[1], S. Wintz[1], M. Buess[2], J. Raabe[2], C. Quitmann[2] and J. Fassbender[1] *1. Ion Beam Physics and Materials Research, FZ Dresden-Rossendorf e. V., Dresden, Germany; 2. Swiss Light Source, Paul Scherrer Institut, Villigen, Switzerland*

3:00

HC-02. Current-induced resonant motion of the magnetic vortex core in a ferromagnetic circular disk. ***(Invited)*** *S. Kasai*[1], F. Peter[2], M. Im[2], K. Yamada[1], Y. Nakatani[3], K. Kobayashi[1], H. Kohno[4] and T. Ono[1] *1. Institute for Chemical Research, Kyoto University, Uji, Kyoto, Japan; 2. Center for X-Ray Optics, Lauence Berkeley National Lab, Berkeley, CA; 3. Department of Computer Science, University of Electro-communications, Chofu, Tokyo, Japan; 4. Graduate School of Engineering Science, Osaka University, Toyonaka, Osaka, Japan*

3:30

HC-03. Elementary Eigenmodes of Magnetic Vortex Gyrotropic Motions in Magnetic Nanoelements. *K. Lee*[1], S. Kim[1], D. Jung[1], Y. Yu[1] and Y. Choi[1] *1. Research Center for Spin Dynamics and Spin-Wave Devices & Nanospintronics Laboratory, Seoul National University, Seoul, South Korea*

3:45

HC-04. Unidirectional switching of the vortex core polarization by excitation with rotating magnetic fields. *H. Stoll*[1], B. Van Waeyenberge[1,2], K. Chou[1], M. Curcic[1], M. Weigand[1], V. Sackmann[1], A. Puzic[1], A. Vansteenkiste[2], T. Tyliszczak[3], G. Woltersdorf[4], C.H. Back[4] and G. Schuetz[1] *1. Max Planck Institute for Metals Research, Stuttgart, Germany; 2. Department of Subatomic and Radiation Physics, Ghent University, Gent, Belgium; 3. Advanced Light Source, LBNL, Berkeley, CA; 4. Department of Physics, University of Regensburg, Regensburg, Germany*

4:00

HC-05. Spin-dynamics and mode structure in lithographically patterned Permalloy nanostructures. *J.M. Shaw*[1], M. Schneider[1,2], T. Silva[1], R. McMichael[3], S. Kim[1], W. Johnson[1] and P. Kabos[1] *1. National Institute of Standards and Technology, Boulder, CO; 2. University of Montana, Missoula, MT; 3. National Institute of Standards and Technology, Gaithersburg, MD*

4:15

HC-06. Microwave-assisted switching and demagnetizing of NiFe thin films patterned in micro-elements : a domain structure study by Kerr effect. *M. Laval*[1], J. Bonnefois[1], J. Bobo[1], F. Issac[2] and F. Boust[2] *1. LNMH, CNRS ONERA, Toulouse, France; 2. DEMR, ONERA, Toulouse, France*

4:30

HC-07. Modeling of microwave-assisted switching in micron-size magnetic ellipsoids. R. Yanes[1], *O. Chubykalo-Fesenko*[1], P. Martin Pimentel[2], B. Leven[2], B. Hillebrands[2], V. Tyberkevich[3] and A. Slavin[3] *1. POMT, Instituto de Ciencia de Materiales de Madrid, CSIC, Madrid, Spain; 2. Technische Universitaet Kaiserslautern, Kaiserslautern, Germany; 3. Department of Physics, Oakland University, Rochester, MI*

4:45

HC-08. Nonlinear processes during switching of a thin Permalloy film in different geometries. *K. Livesey*[1], H. Nembach[2], M. Kostylev[1], P. Martin-Pimentel[2], S. Hermsdoerfer[2], B. Leven[2], R. Stamps[1] and B. Hillebrands[2] *1. School of Physics, University of Western Australia, Crawley, WA, Australia; 2. Fachbereich Physik und Forschungsschwerpunkt MINAS, Technische Universitaet Kaiserslautern, Kaiserslautern, Germany*

5:00

HC-09. Precessional magnetization reversal in composite patterned media: Dependence on applied field parameters. *B. Livshitz*[1], H.N. Bertram[2,3], A. Inomata[4] and V. Lomakin[1] *1. Department of Electrical and Computer Engineering, UCSD, San Diego, CA; 2. Center for Magnetic Recording Research, UCSD, San Diego, CA; 3. Research Center, Hitachi Global Storage, San Jose, CA; 4. Storage and Intelligent Systems Laboratories, Fujitsu Laboratories Ltd, Atsugi, Japan*

5:15

HC-10. Dynamics of bubble domains in nanodots with high anisotropy. *C. Moutafis*[1], S. Komineas[2], C.F. Vaz[3], J.C. Bland[1], T. Shima[4], T. Seki[5] and K. Takanashi[5] *1. Cavendish Laboratory, Cambridge University, Cambridge, United Kingdom; 2. Max-Planck Institute for the Physics of Complex Systems, Dresden, Germany; 3. Applied Physics, Yale University, New Haven, CT; 4. Faculty of Engineering, Tohoku-Gakuin University, Tagajyo, Japan; 5. Institute for Materials Research, Tohoku University, Sendai, Japan*

THURSDAY
AFTERNOON
2:30

PARIS

Session HD
MICROMAGNETICS II
Massimiliano d'Aquino, Chair

2:30

HD-01. Control of domain wall motion in Permalloy nanowires using magnetostatic interactions. *S. Basu*[1], D. Allwood[1] and T. Schrefl[1] *1. Department of Engineering Materials, University of Sheffield, Sheffield, United Kingdom*

2:45

HD-02. Domain wall depinning from a notch under oscillating currents: the role of non-adiabaticity. *E. Martinez*[1], L. Lopez-Diaz[2], O. Alejos[3] and L. Torres[2] *1. Ingenieria Electromecanica, University of Burgos, Burgos, Burgos, Spain; 2. Fisica Aplicada, University of Salamanca, Salamanca, Spain; 3. Electricidad y Electronica, University of Valladolid, Valladolid, Spain*

3:00

HD-03. Spin-Polarized Current Induced Switching of Composite Free Layers. *C. Yen*[1], W. Chen[1], Y. Chen[1], D. Wang[1], C. Shen[1], S. Yang[1], C. Tsai[1], Y. Lee[1], C. Hung[1], K. Shen[1] and M. Kao[1] *1. Electronics and Optoelectronics Research Laboratories (EOL), Industrial Technology Research Institute (ITRI), Hsinchu, Taiwan*

3:15

HD-04. Switching of vortex chirality in $Ni_{80}Fe_{20}$/Cu/Co nanopillars by a spin-polarized current pulse. *B.C. Choi*[1], Y.K. Hong[2], J. Rudge[1], E. Girgis[1], J. Kolthammer[1], A. Lyle[2] and G.W. Donohoe[3] *1. Department of Physics & Astronomy, University of Victoria, Victoria, BC, Canada; 2. Department of Electrical and Computer Engineering, University of Alabama, Tuscaloosa, AL; 3. 2Department of Electrical and Computer Engineering, University of Idaho, Moscow, ID*

HD-05. WITHDRAWN

3:30

HD-06. Temperature dependent exchange stiffness in FePt. *D. Hinzke*[1], R.F. Evans[1], U. Nowak[1], R.W. Chantrell[1], U. Atxitia[2], O. Chubykalo-Fesenko[2], P. Asselin[3] and O.N. Mryasov[3] *1. Physics, University of York, York, United Kingdom; 2. Instituto de Ciencia de Materiales de Madrid, Madrid, Spain; 3. Seagate Research, 1251 Waterfront Place, Pittsburgh, PA*

3:45

HD-07. An alternative finite element scheme for dynamic micromagnetic computations. *A. Manzin*[1], O. Bottauscio[1] and M. Chiampi[2] *1. Istituto Nazionale di Ricerca Metrologica, Torino, Italy; 2. Ingegneria Elettrica, Politecnico di Torino, Torino, Italy*

4:00

HD-08. Innovative weak formulation for the Landau-Lifschitz-Gilbert equation. *H. Szambolics*[1,2], J. Toussaint[1,2], L.D. Buda-Prejbeanu[2,3], F. Alouges[4], E. Kritsikis[2,3] and O. Fruchart[1] *1. Department of Nanosciences, Institut Neel, CNRS, Grenoble cedex 9, France; 2. Institut National Polytechnique de Grenoble, Grenoble, France; 3. Laboratoire SPINTEC, CEA, Grenoble, France; 4. Laboratoire de Mathématique, Université Paris XI, Orsay, France*

4:15

HD-09. Stochastic dynamics and optimal switching paths in thermally activated magnetization processes of ferromagnetic nanoparticles. *C. Serpico*[1], G. Bertotti[2], C.S. Ragusa[3], M. d'Aquino[4], I.D. Mayergoyz[5] and P. Ansalone[3] *1. Dipartimento di Ingegneria Elettrica, Università di Napoli "Federico II", Napoli, Italy; 2. Istituto Nazionale di Ricerca Metrologica (INRiM), Torino, Italy; 3. Dipartimento di Ingegneria Elettrica, Politecnico di Torino, Torino, Italy; 4. Dipartimento per le Tecnologie, Università di Napoli "Parthenope", Napoli, Italy; 5. ECE Department and UMIACS, University of Maryland, College Park, MD*

4:30

HD-10. A Study of Pseudoelastic Phenomenon in Ferromagnetic Shape Memory Alloy NiMnGa by Phase-field Simulation. *X. Ma*[1], P. Wu[1], J. Zhang[2] and L. Chen[2] *1. Department of Physics, University of Science and Technology Beijing, Beijing, China; 2. Department of Materials Science and Engineering, The Pennsylvania State University, University Park, PA*

4:45

HD-11. Effects of nanowire roughness on spin wave propagation. *S. Bance*[1], T. Schrefl[1], D. Allwood[1], G. Hrkac[1] and A. Goncharov[1] *1. University of Sheffield, Sheffield, United Kingdom*

5:00

HD-12. Effect of interface exchange coupling on the reversal of single antiferromagnetic grains in exchange bias systems. *J. Jackson*[1], U. Nowak[1] and R. Chantrell[1] *1. Physics, University of York, York, United Kingdom*

THURSDAY AFTERNOON 2:30

LONDRES

Session HE
PERMANENT MAGNET MATERIALS
George Hadjipanayis, Chair

2:30

HE-01. Microtexture and Magnetic Microstructure of Sputtered NdFeB Thick Films Destined for Application in Micro-Electro-Mechanical Systems (MEMS). *T.G. Woodcock*[1], K. Khlopkov[1], A. Walther[2], N.M. Dempsey[2], D. Givord[2] and O. Gutfleisch[1] *1. Institute for Metallic Materials, IFW Dresden, Dresden, Germany; 2. Insitut Néel, CNRS, Grenoble, France*

2:45

HE-02. Temperature dependent anisotropy in epitaxial Pr-Co films. *A.K. Patra*[1], M. Eisterer[2], R. Biele[1,3], S. Fähler[1], L. Schultz[1] and V. Neu[1] *1. IFW Dresden, Dresden, Germany; 2. Atomic Institute of the Austrian Universities, Vienna, Austria; 3. University of Technology Dresden, Dresden, Germany*

3:00

HE-03. Sintered Sm_2Co_{17}-based Magnets with Small Additions of Indium. *A. Gabay*[1], M. Marinescu[2], J. Liu[2] and G.C. Hadjipanayis[1] *1. University of Delaware, Newark, DE; 2. Electron Energy Corporation, Landisville, PA*

3:15

HE-04. Prediction of temperature demagnetization of bonded rare earth magnets by finite element analysis. *T. Schliesch*[1] and T. Lindner[1] *1. Max Baermann GmbH, Bergisch Gladbach, Germany*

3:30

HE-05. New Dy-substituted Ba hexaferrites with high coercivity. *G. Litsardakis*[1], I. Manolakis[1], A. Stergiou[2], C. Serletis[2] and K.G. Efthimiadis[2] *1. Dept. of Electrical & Computer Engineering, Aristotle University, Thessaloniki, Greece; 2. Dept. of Physics, Aristotle University, Thessaloniki, Greece*

3:45

HE-06. Strain-induced exchange bias effects in chemically ordered Pt_3Fe single crystal. *S. Kobayashi*[1], S. Takahashi[1], Y. Kamada[1] and H. Kikuchi[1] *1. Faculty of Engineering, Iwate University, Morioka, Japan*

4:00

HE-07. Fe-Pt thick film magnets prepared by high-speed PLD method. S. Shibata[1], *M. Nakano*[1], T. Yanai[1] and H. Fukunaga[1] *1. Electronics and Electrical Engineering, Nagasaki University, Nagasaki, Japan*

4:15

HE-08. Coercivity generation of surface Nd2Fe14B grains and mechanism of fcc-phase formation at Nd/Nd2Fe14B interface in Nd-sputtered Nd-Fe-B sintered magnets. *T. Fukagawa*[1] and S. Hirosawa[1] *1. Magnetic Materials Research Laboratory NEOMAX Company, Hitachi Metals, Ltd., 2-15-17, Egawa, Shimamoto-cho, Mishima-gun, Osaka, Japan*

4:30

HE-09. Wettability and interfacial microstructure between $Nd_2Fe_{14}B$ and Nd-rich phases in Nd-Fe-B alloys. *R. Goto*[1], S. Nishio[1], M. Matsuura[1], N. Tezuka[1] and S. Sugimoto[1] *1. Department of Materials Science, Tohoku University, Sendai, Japan*

4:45

HE-10. The role of Cu addition in the coercivity enhancement of sintered Nd-Fe-B magnets. *T. Ohkubo*[1,2], W. Li[1], K. Hono[1,2], T. Akiya[3] and H. Kato[3] *1. National Institute for Materials Science, Tsukuba, Japan; 2. CREST, JST, Japan; 3. Tohoku University, Sendai, Japan*

5:00

HE-11. Magnetic Properties of Sm2Co17 & Sm2Co7 Sputtered and Post-annealed Thin Films. Effect of Mo Underlayer. *I. Lucas*[1], M. Maicas[2], L. Pérez[3] and M. Díaz - Michelena[1] *1. Dto: Space Programs and Space Sciences, I.N.T.A., 28850 Torrejón de Ardoz, Madrid, Spain; 2. (ISOM) ETSI Telecomunicación, Universidad Politécnica de Madrid (UPM), Madrid, Madrid, Spain; 3. Dto:Física de Materiales, Universidad Complutense de Madrid (UCM), Madrid, Madrid, Spain*

5:15

HE-12. Preparation and magnetic study of the $CoFe_2O_4$-$CoFe_2$ nanocomposite powders. F. Cabral[1,2], *F. Machado*[1], J. Araújo[2], J. Soares[3], A. Rodrigues[1] and A. Araújo[2] *1. Departamento de Física, Universidade Federal de Pernambuco, Recife, Pernambuco, Brazil; 2. Departamento de Física Teórica e Experimental, Univesidade Federal do Rio Grande do Norte, Natal, Rio Grande do Norte, Brazil; 3. Departamento de Física, Univesidade do Estado do Rio Grande do Norte, Mossoró, Rio Grande do Norte, Brazil*

THURSDAY
AFTERNOON
2:30

BERLIN

Session HF
LIFE SCIENCE AND APPLICATIONS-III
Ricardo Ibarra, Chair

2:30

HF-01. Bimodal use of maghemite nanoparticles as contrast agents for magnetic resonance imaging (T1 and T2 CA's) through modulation of their stabilizing coating. ***(Invited)*** E. Taboada[1], *A. Roig*[1], E. Rodriguez[2] and M. Delville[3] *1. Institut de Ciència de Materials de Barcelona, ICMAB-CSIC, Bellaterra, Spain; 2. Center for Molecular Imaging Research, MGH-Harvard Medical Hospital, Boston, MA; 3. Institut de Chimie de la Matière Condensée de Bordeaux, ICMCB-CNRS, Bordeaux, France*

3:00

HF-02. Magnetic Hyperthermia with Fe_3O_4 nanoparticles: the Influence of Particle Size and Domain Structure on Energy Absorption. *G.F. Goya*[1], E. Lima Jr.[2], A.D. Arelaro[2], T. Torres[1], H.R. Rechenberg[2], L. Rossi[3], C. Marquina[4,1] and M.R. Ibarra[1,4] *1. Nanoscience Institute of Aragon, University of Zaragoza, Zaragoza, Zaragoza, Spain; 2. Physics Institute, University of Sao Paulo, Sao Paulo, Sao Paulo, Brazil; 3. Chemistry Institute, University of Sao Paulo, Sao Paulo, Sao Paulo, Brazil; 4. Instituto de Ciencia de Materiales de Aragón-CSIC, University of Zaragoza, Zaragoza, Zaragoza, Spain*

3:15

HF-03. Synthesis and Cellular Uptake of Foliate-Conjugated Hydrophobic Superparamagnetic Iron Oxide Nanoparticles. *K. Woo*[1], J. Moon[1,2], K. Choi[3], K. Yoon[3] and T. Seong[2] *1. Nano-Materials Research Center, KIST, Seoul, South Korea; 2. Department of Materials Science and Engineering, Korea University, Seoul, South Korea; 3. Institute for Radiological Imaging Science, Wonkwang University School of Medicine, Iksan, South Korea*

3:30

HF-04. Water based colloids of Fe_3O_4/SiO_2 magnetic nanoparticles with core/shell structure for magnetic hyperthermia. *M.A. Gonzalez-Fernandez*[1], T. Torres[2], M.A. Verges[3], G.F. Goya[2], C.J. Serna[1] and M.P. Morales[1] *1. Instituto de Ciencia de Materiales de Madrid, CSIC, Madrid, Spain; 2. Institute of Nanoscience of Aragon (INA), University of Zaragoza, Zaragoza, Spain; 3. Department of Organic and Inorganic Chemistry, Universidad de Extremadura, Badajoz, Spain*

3:45

HF-05. Antiferromagnetic susceptibility in ferritin. *N.J. Silva*[1], A. Urtizberea[1], A. Millán[1], F. Palacio[1], E. Kampert[2], U. Zeitler[2], H. Rakoto[3] and V.S. Amaral[4] *1. Fisica de la Materia Condensada, Instituto de Ciencia de Materiales de Aragón CSIC/Universidad de Zaragoza, Zaragoza, Spain; 2. Radboud Univ. Nijmegen, High Field Magnet Lab, Nijmegen, Netherlands; 3. LNCMP, Toulouse, France; 4. Departamento de Física and CICECO, Universidade de Aveiro, Aveiro, Portugal*

4:00

HF-06. Iron oxide *versus* $Fe_{55}Pt_{45}$@Fe_2O_3 ferromagnetic nanoparticles: improved magnetic properties of core/shell nanostructure for biomedical applications. *L.C. Varanda*[1], F.J. Santos[2], I. Momotaro[3] and M. Jafelicci Jr.[2] *1. Físico-Química, Instituto de Química de São Carlos - USP, São Carlos, São Paulo, Brazil; 2. Físico-Química, Instituto de Química de Araraquara - UNESP, Araraquara, São Paulo, Brazil; 3. Física, Faculdade de Ciências - UNESP, Bauru, São Paulo, Brazil*

4:15

HF-07. Surface modified superparamagnetic nanoparticles as a novel magnetic carrier. *M. Lin*[1], S. Li[2], J. Gu[1], H. Lee[3], M. Mamoun[2] and D. Kim[1] *1. Institute of Science and Technology in Medidicine, Keele University, Stoke-on-Trent, United Kingdom; 2. Materials Chemsitry Divisions, Royal Institute of Technology, Stockholm, Sweden; 3. Department of Materials Science and Engineering, Myongji University, Kyunggi-do, South Korea*

4:30

HF-08. Magnetic porous hollow silica nanospheres for biomedicine application. H. Ma[1], J. Zhou[1], D. Caruntu[1], M. Yu[1], J. Chen[2], C. O'Connor[1] and *W. Zhou*[1] *1. Advanced Materials Research Institute, University of New Orleans, New Orleans, LA; 2. Key Lab for Nanomaterials, Ministry of Education, Beijing University of Chemical Technology, Beijing, Beijing, China*

4:45

HF-09. Hysteresis power loss heating of ferromagnetic nano-particles designed for magnetic thermoablation. *E. Kita*[1], H. Yanagihara[1], S. Hashimoto[2], K. Yamada[2], T. Oda[2], M. Kishimoto[3] and A. Tasaki[1] *1. Institute of Appield Physics, University of Tsukuba, Tsukuba, Ibaraki, Japan; 2. Institute of Clinical Medicine, University of Tsukuba, Tsukuba, Ibaraki, Japan; 3. Hitachi Maxell, Ltd.,, Oyamazaki, Kyoto, Japan*

Session HG
MAGNETOELASTIC MATERIALS AND DEVICES
Mike Gibbs, Chair

2:30

HG-01. The local atomic Joule magnetostriction of $Fe_{81}Ga_{19}$ *M.P. Ruffoni*[1], S. Pascarelli[1], R. Grössinger[2], R. Sato-Turtelli[2] and R.F. Pettifer[3] *1. European Synchrotron Radiation Facility, Grenoble, France; 2. Technical University of Vienna, Vienna, Austria; 3. Department of Physics, University of Warwick, Coventry, United Kingdom*

2:45

HG-02. The Effect of Tempering on the Magnetostriction of Fe-Ga Alloys. *T.A. Lograsso*[1,2] and M. Huang[1] *1. Institute for Physical Research and Technology, Iowa State University, Ames, IA; 2. Materials and Engineering Physics, Ames Laboratory, Ames, IA*

3:00

HG-03. Magnetic field and stress dependence of FeGa 3-D shaped polycrystalline magnetostrictive materials properties. *N. Lupu*[1] and H. Chiriac[1] *1. Magnetic Materials and Devices, National Institute of Research and Development for Technical Physics, Iasi, Romania*

3:15

HG-04. Magnetostriction of Fe-X (X = B, Al, Ga,Si, Ge) intermetallic alloys. *G. Roland*[1], S. Reiko[1] and M. Nasir[1] *1. Inst. of Solid State Physics, Techn. Univ. Vienna, Vienna, Austria*

3:30

HG-05. Magnetic and magnetoelastic properties of electrodeposited FeGa/CoFeB multilayered films and nanowires arrays. *N. Lupu*[1], P. Pascariu[1], C. Gherasim[1] and H. Chiriac[1] *1. Magnetic Materials and Devices, National Institute of Research and Development for Technical Physics, Iasi, Romania*

3:45

HG-06. Modelling and experimental analysis of magnetostrictive devices: from the material characterisation to their dynamic behaviour. *O. Bottauscio*[1], R. Bonin[1], A. Lovisolo[1], P. Roccato[2], C. Sasso[1] and M. Zucca[1] *1. Electromagnetics, Istituto Nazionale di Ricerca Metrologica, Torino, Italy; 2. Dip. Ingegneria Elettrica, Politecnico di Torino, Torino, Italy*

4:00

HG-07. Design of a multipurpose magnetostrictive device. O. Bottauscio[1], A. Lovisolo[1], P. Roccato[2] and *M. Zucca*[1] *1. Electromagnetics, INRIM, Torino, Italy; 2. Dip. Ing. Elettrica, Politecnico di Torino, Torino, Italy*

4:15

HG-08. Temperature dependence of magnetostriction of $Co_{1+x}Ge_xFe_{2-2x}O_4$ for magnetostrictive sensor and actuator applications. *N. Ranvah*[1], I.C. Nlebedim[1], S.H. Song[2], Y. Melikhov[1], J.E. Snyder[1], D.C. Jiles[1], A.J. Moses[1] and P.I. Williams[1] *1. Wolfson Centre for Magnetics, Cardiff University, Cardiff, Wales, United Kingdom; 2. Materials Science and Engineering Department, Iowa State University, Ames, IA*

4:30

HG-09. Magnetostriction studies on antiferromagnetic MnxFe100-x (30≤x≤55) alloys. *M. Yan*[1], T. Ma[1], J. Zhang[1] and Y. Xu[1] *1. Department of Materials Science and Engineering, Zhejiang University, Hangzhou, China*

4:45

HG-10. Magnetic softening of magnetostrictive $(Fe_{80}Co_{20})_{80}B_{20}$ amorphous thin films with a thickness modulation of the magnetic anisotropy. *J. Prieto*[2], M. González-Guerrero[1], D. Ciudad[1], P. Sánchez[1] and C. Aroca[1] *1. Física Aplicada, ETSI Telecomunicación UPM, Madrid, Madrid, Spain; 2. ISOM, Universidad Politécnica de Madrid, Madrid, Madrid, Spain*

5:00

HG-11. Fine structure observation near critical temperature in $Gd_5Si_{1.95}Ge_{2.05}$ *R.L. Hadimani*[1], Y. Melikhov[1], J.E. Snyder[1] and D.C. Jiles[1] *1. Wolfson Centre for Magnetics, Cardiff University, Cardiff, Wales, United Kingdom*

5:15

HG-12. On the nature of the Griffiths-like phase behaviour in Gd_5Ge_4 giant magnetocaloric alloy. *N. Pérez*[1,2], F. Casanova[2,3], F. Bartolomé[4,5], L.M. García[4,5], S. DeBrion[6], A. Labarta[1,2] and X. Batlle[1,2] *1. Fisica Fonamental, Universitat de Barcelona, Barcelona, Catalonia, Spain; 2. Institut de Nanociencia i Nanotecnologia IN2UB, Universitat de Barcelona, Barcelona, Catalonia, Spain; 3. Physics Department, University of California (UCSD), San Diego, CA; 4. Instituto de Ciencia de Materiales de Aragón, CSIC, Zaragoza, Aragón, Spain; 5. Física de la Materia Condensada, Universidad de Zaragoza, Zaragoza, Aragón, Spain; 6. Institut Néel, CNRS-UJF, Grenoble, France*

Session HH
CURRENT INDUCED DW MOTION
Joo-Von Kim, Chair

2:30

HH-01. Spin Dynamics and Gilbert damping of a nanomagnet connected to leads. *A. Núñez*[1] and R. Duine[2] *1. Departamento de Física, Facultad de Ciencias Físicas y Matemáticas, Universidad de Chile, Santiago, Chile; 2. Institute for Theoretical Physics, Utrecht University, Utrecht, Netherlands*

2:45

HH-02. Race track memories seen from an ab-initio point of view. *P. Weinberger*[1,2] *1. Center for Computational Nanoscience, Vienna, Austria; 2. Department of Physics, New York University, New York, NY*

3:00

HH-03. DETECTION OF CURRENT-INDUCED OSCILLATIONS OF PINNED DOMAIN WALLS. *M. Kläui*[1], D. Bedau[1], S. Krzyk[1], G. Faini[2], L. Vila[2] and U. Rüdiger[1] *1. Physics, University of Konstanz, Konstanz, Germany; 2. LPN-CNRS, Marcoussis, France*

3:15

HH-04. Current-induced switching of the magnetic vortex core in a ferromagnetic circular dot. *K. Yamada*[1], S. Kasai[1], Y. Nakatani[2], K. Kobayashi[1], H. Kohno[3], A. Thiaville[4] and T. Ono[1] *1. Institute for Chemical Research, Kyoto University, Uji, Kyoto, Japan; 2. Department of Computer Science, University of Electro-Communications, Chofu, Tokyo, Japan; 3. Graduate School of Engineering Science, Osaka University, Toyonaka, Osaka, Japan; 4. Laboratoire de Physique des Solides, CNRS and Univ. Paris-Sud, Orsay, France*

3:30

HH-05. Magnetization reversal control using a current pulse in Permalloy nanowires. *Y. Togawa*[1], T. Kimura[1,2], K. Harada[1,3], T. Akashi[4], T. Matsuda[1,3], A. Tonomura[1,3] and Y. Otani[1,2] *1. Frontier Research System, Institute of Physical and Chemical Research (RIKEN), Wako, Saitama, Japan; 2. Institute for Solid State Physics, University of Tokyo, Kashiwa, Chiba, Japan; 3. Advanced Research Laboratory, Hitachi, Ltd., Hatoyama, Saitama, Japan; 4. Hitachi High-Technologies Co., Hitachinaka, Ibaraki, Japan*

3:45

HH-06. Stochastic magnetic field driven domain wall motion in a spin-valve nanowire. *X. Jiang*[1], L. Thomas[1], R. Moriya[1], M. Hayashi[1], B. Bergman[1], C. Rettner[1] and S. Parkin[1] *1. IBM Almaden Research Center, San Jose, CA*

4:00

HH-07. Stochastic domain wall motion under a polarized current in wires with perpendicularly magnetized layers. *C. Burrowes*[1], D. Ravelosona[1], D. Stanescu[1], N. Vernier[1], C. Chappert[1], B. Terris[2], J. Katine[2] and E. Fullerton[3] *1. Institut d'Electronique Fondamentale, Orsay, France; 2. HitachiGST, San Jose, CA; 3. UC San Diego, San Diego, CA*

4:15

HH-08. Effect of anisotropy distribution on domain wall motion in nanowires with perpendicular anisotropy. *Y. Nakatani*[1] and T. Ono[2] *1. Department of Computer Science, University of Electro-Communications, Tokyo, Japan; 2. Kyoto University, Uji, Japan*

4:30

HH-09. Current-driven domain wall motion, nucleation, and propagation in a Co/Pt multi-layer strip with a stepped structure. *T. Suzuki*[1], S. Fukami[1], K. Nagahara[1], N. Oshima[1] and N. Ishiwata[1] *1. Device Platforms Res. Labs., NEC, Sagamihara, Kanagawa, Japan*

4:45

HH-10. Current-Driven Domain Wall Motion in CoCrPt Wires with Perpendicular Magnetic Anisotropy. H. Tanigawa[1], K. Kondou[1], T. Koyama[1], K. Nakano[1], S. Kasai[1], N. Ohshima[2], S. Fukami[2], N. Ishiwata[2] and *T. Ono*[1] *1. Institute for Chemical Research, Kyoto University, Uji, Japan; 2. Device Platforms Research Laboratories, NEC Corporation, Sagamihara, Japan*

5:00

HH-11. Intrinsic threshold current density of domain wall motion in nano-strips with perpendicular magnetic anisotropy for use in low-write-current MRAMs. *S. Fukami*[1], T. Suzuki[1], N. Ohshima[1], K. Nagahara[1] and N. Ishiwata[1] *1. Device Platforms Research Laboratories, NEC Corporation, Sagamihara, Japan*

5:15

HH-12. Current domain wall dragging in GaMnAs. *N. VERNIER*[1,3], L. Thevenard[2], A. Lemaitre[2], A. Miard[2], G. Faini[2], L. Vila[2], J. Ferré[3] and J. Adam[3] *1. IEF, Université Paris-Sud, Orsay, France; 2. LPN, CNRS, Marcoussis, France; 3. LPS, Université Paris-sud, Orsay, France*

THURSDAY AFTERNOON 2:30 | POLIVALENTE

Session HL
RECORDING SYSTEMS AND SERVO II (POSTER SESSION)
Mark Bedillion, Chair

HL-01. Aerodynamic damping on vibration of rotating disks and effects of shroud and top cover. *T. Eguchi*[1] *1. Central Research Laboratory, Hitachi, Ltd., Fujisawa, Ibaraki, Japan*

HL-02. Adaptive frequency identification method for multiple unknown disturbances in HDDs. *Q. Jia*[1] and Z. Wang[2] *1. Storage Mechanics Lab, Hitachi Asia Ltd, Singapore, Singapore; 2. School of Electrical Engineering and Computer Science, Oregon State University, Corvallis, OR*

HL-03. A disturbance observer design for SPM-based data storage system. *J. Moon*[1], C. Chung[1], C. Lee[1] and Y. Kim[2] *1. Electrical Engineering, Hanyang University, Seoul, South Korea; 2. Devices & Materials Lab., LG Elite, Seoul, South Korea*

HL-04. A discrete-time modified sliding mode proximate time optimal servomechanism for SPM-based data storage systems. *J. Jeong*[1], C. Lee[1], C. Chung[1] and Y. Kim[2] *1. Electrical Engineering, Hanyang University, Seoul, South Korea; 2. Devices & Materials Lab., LG Elite, Seoul, South Korea*

HL-05. Magnetic recording performance of 'Bit Printing method' on PMR media and its extendability to the higher areal density. *A. Morooka*[1], M. Nagao[1], T. Yasunaga[1] and K. Nishimaki[2] *1. Recording Media Research Laboratories, FUJI FILM co.,LTD., Odawara, Japan; 2. Production Engineering & Development Center, FUJI FILM co.,LTD., Odawara, Japan*

HL-06. Using steady solutions of Reynolds-Averaged Navier Stokes (RANS) equations to estimate flow induced vibrations (FIV) of hard disk drive carriage arms. *T. Yip*[1], E. Ong[1], A. Yudhanto[1], Z. He[1] and Q. Zhang[1] *1. Data Storage Institute, Singapore, Singapore*

HL-07. A Novel Settling Controller for Dual-stage Servo Systems. *J. Zhang*[1], C. Du[1] and S. Ge[2] *1. Data Storage Institute, Singapore, Singapore; 2. Department of Electrical & Computer Engineering, National University of Singapore, Singapore, Singapore*

HL-08. PES Generation and Evaluation for Bit Patterned Servo. *S. Zhang*[1] and W. Wong[1] *1. Data Storage Institute, Singapore, Singapore*

THURSDAY AFTERNOON 2:30 | POLIVALENTE

Session HM
RECORDING SYSTEMS, CODING AND CHANNELS - I (POSTER SESSION)
Roger Wood, Chair

HM-01. Mean-Adjusted PDNP Detector for Perpendicular Recording Channels With NLTS. *Z. Wu*[1], P.H. Siegel[1], J.K. Wolf[1] and N. Bertram[1,2] *1. Center for Magnetic Recording Research, University of California, San Diego, La Jolla, CA; 2. Hitachi Global Storage Technologies, San Jose, CA*

HM-02. Ordered statistics soft decoding of Reed-Solomon codes over intersymbol interference channels. F.Y. Lim[1], *A. Kav či ć*[1] and M. Fossorier[1] *1. University of Hawaii, Manoa, Honolulu, HI*

HM-03. Enhanced Message Passing in Turbo Product Code. *N. Yeh*[1], P. Steiner[1] and Y. Li[1,2] *1. Seagate Technology, Fremont, CA; 2. Presently with AMD, Yardley, PA*

HM-04. A New Burst Detection Method Using Parity Check Matrix of LDPC Code for Bit Flipping Burst-like Signal Degradation. *Y. Nakamura*[1], M. Nishimura[1], Y. Okamoto[1], H. Osawa[1] and H. Muraoka[2] *1. Graduate School of Science and Engineering, Ehime University, Matsuyama, Japan; 2. RIEC, Tohoku University, Sendai, Japan*

HM-05. Low-Complexity LDPC Decoder Architecture for High-Speed Magnetic Recording. *C. Zhang*[1,2], Z. Wang[3], L. Li[1,2], J. Lin[1,2] and M. Gao[1,2] *1. Institute of VLSI Design, Physics Department, Nanjing University, Nanjing, Jiangsu, China; 2. Key Laboratory of Advanced Photonic and Electronic Materials, Nanjing University, Nanjing, Jiangsu, China; 3. School of Electrical Engineering and Computer Science, Oregon State University, Corvallis, OR*

HM-06. Message-Passing Detector with Serial Concatenated Codes for PMR Channel. *D. Park*[1], J. Lee[1] and J. Lee[2] *1. School of Electronic Engineering, Soongsil University, Seoul, South Korea; 2. Storage System Division, Samsung Electronics, Suwon, South Korea*

HM-07. Hardware-Efficient LDPC Decoding for Magnetic Recording. Z. Cui[1], Z. Wang[1], *X. Zhang*[2] and Q. Jia[3] *1. Oregon State University, Corvallis, OR; 2. Case Western Reserve University, Cleveland, OH; 3. Hitachi Asia Ltd, Singapore, Singapore*

HM-08. Perpendicular Magnetic Recording Channel Equalization Based on Gaussian Sum Approximation. *S. Choi*[1], G. Kong[1], H. Cho[1], D. Lee[1], J. Lee[3] and J. Lee[2] *1. School of Electrical and Electronic Engineering, Yonsei University, Seoul, South Korea; 2. School of Electronic Engineering, Soongsil University, Seoul, South Korea; 3. Storage System Division, Samsung Electronics, Suwon, South Korea*

HM-09. Simplified Neural Network Equalizer with Noise Whitening Function for GPRML System. H. Osawa[1], *M. Hino*[1], N. Shinohara[1], Y. Okamoto[1], Y. Nakamura[1] and H. Muraoka[2] *1. Graduate School of Science and Engineering, Ehime University, Matsuyama, Japan; 2. RIEC, Tohoku University, Sendai, Japan*

HM-10. Digital Storage Channel Equalization Using A Bilinear Recursive Polynomial System. *S. Choi*[1], H. Cho[1], G. Kong[1], J. Lee[3] and J. Lee[2] *1. School of Electrical and Electronic Engineering, Yonsei University, Seoul, South Korea; 2. School of Electronic Engineering, Soognsil University, Seoul, South Korea; 3. Storage System Division, Samsung Electronics, Suwon, South Korea*

HM-11. Interleaved Modified Array Codes (IMAC) Hardware Design and Performance for High-Rate Perpendicular Magnetic Recording Systems. *P. Leekul*[1,3], W. Singhaudom[1] and P. Supnithi[1,2] *1. Faculty of Engineering, King Mongkut's Institute of Technology Ladkrabang, Bangkok, Thailand; 2. Data Storage Technology and Applications Research Center (D*STAR), King Mongkut's Institute of Technology Ladkrabang, Bangkok, Thailand; 3. Research Center for Communications and Information Technology (ReCCIT), King Mongkut's Institute of Technology Ladkrabang, Bangkok, Thailand*

HM-12. **Nonbinary LDPC codes for 4K-byte sectors.** W. Chang[1] and *J. CRUZ*[1] *1. The University of Oklahoma, Norman, OK*

THURSDAY
AFTERNOON
2:30

POLIVALENTE

Session HN
MAGNETIC NANOCLUSTERS AND NANOPARTICLES III (POSTER SESSION)
Leonard Spinu, Chair

HN-01. **Magnetic properties of self-assembled cobalt nanoparticles crystal superlattices.** M. Varon[1], L. Peña[2], L. Balcells[2], V.F. Puntes[1] and *B. Martinez*[2] *1. Institut Català de Nanotecnologia, Bellaterra, Barcelona, Spain; 2. Magnetic Materials, ICMAB-CSIC, Bellaterra, Barcelona, Spain*

HN-02. **One-Dimensional Hierarchical Nanostructure Generated by Coating SiOX Nanowires with L10 CoPt Nanoparticles.** *J. Kim*[1], J. Kim[1], J. Park[1], K. Baek[1], H. Woo[1], S. Kim[1], C. Kim[1] and C. Yoon[1] *1. Materials Science and Engineering, Hanyang University, Seoul, South Korea*

HN-03. **Effects of oxidation and particle size on saturation magnetization of iron nanoparticles.** *H. Matsuura*[1], K. Seto[2], K. Kawano[1], M. Takahashi[3] and T. Ogawa[4] *1. TAIYO YUDEN Co.,Ltd., Takasaki-shi, Japan; 2. Dept. of Elec. Eng., Tohoku Univ., Sendai, Japan; 3. NICHe, Tohoku Univ., Sendai, Japan; 4. CRESS, Tohoku Univ., Sendai, Japan*

HN-04. **Phase transition of the escape rate for ferromagnetic nanoparticles: A magnetic quantum tunneling study.** *J. Florez*[1] and P. Vargas[1] *1. Phys. Dept. USM, Valparaiso, Chile*

HN-05. **Magnetic characterization of nanowire arrays using first order reversal curves.** R. Lavín[1], *J.C. Denardin*[1], J. Escrig[1], D. Altbir[1], A. Cortés[2] and H. Gómez[2] *1. Física, USACH, Santiago, Chile; 2. Química, UCV, Valparaíso, Chile*

HN-06. **AC susceptibility study of spin dynamics in Fe-doped $La_{0.7}Pb_{0.3}Mn_{0.8}Fe_{0.2}O_3$** *L. Fernandez Barquin*[1], J. Gutiérrez[2], J. Barandiaran[2], J. Bermejo[2] and S. Kaul[3] *1. CITIMAC, Facultad de Ciencias, Universidad de Cantabria, Santander, Cantabria, Spain; 2. Electricidad y Electrónica, UPV / EHU, Fac. Ciencia y Tecnología, Bilbao, Bizkaia, Spain; 3. School of Physics, University of Hyderabad, Hyderabad, India*

HN-07. **Exchange coupling in core(ferromagnet)-shell(antiferromagnet) structured nano-particles.** N.N. Phuoc[1], *T. Suzuki*[1], R.W. Chantrell[2] and U. Nowak[2] *1. Information Storage Materials Laboratory, Toyota Technological Institute, Nagoya, Aichi, Japan; 2. Department of Physics, University of York, York, United Kingdom*

HN-08. **Single cobalt clusters embedded in isolating matrix.** C. Raufast[1], *A. Tamion*[1], V. Dupuis[1], T. Fournier[2], T. Crozes[2], E. Bernstein[1], E. Bonet[2] and W. Wernsdorfer[2] *1. Laboratoire de Physique de la Matière Condensée et Nanostructures, Lyon, France; 2. Institut Néel, CNRS, Grenoble, France*

HN-09. **Thermal relaxation phenomena probed by transverse susceptibility measurements performed at different frequecies.** *J. Calleja*[1], C. Radu[2], L. Spinu[2], R. Matarranz[1], B. Presa[1] and M. Contreras[1] *1. Física, Universidad de Oviedo, Oviedo, Spain; 2. AMRI, University of new Orleans, New Orleans, LA*

HN-10. **Self-ordered growth of ferrite nanopyramids.** *F. Rigato*[1], B.B. Nelson-Cheeseman[2], J. Caicedo Roque[1], D. Hrabovsk ý[1], F. Sánchez[1] and J. Fontcuberta[1] *1. Magnetic Materials, ICMAB, Bellaterra, Barcelona, Spain; 2. Materials Science and Engineering, University of California, Berkeley, CA*

HN-11. **On the low-temperature dependence of the nanoparticle interactions in the $Mn_xZn_{1-x}Fe_2O_4$ system.** *A. Mendoza*[1], O. Marín[2], D. Reyes[3], A. Ovidio[1] and P. Prieto[3] *1. Physics Department, Universidad Nacional de Colombia, Bogotá, Colombia; 2. Magnetic Materials and Nanoestructures, Universidad del Quindío, Armenia, Colombia; 3. Thin Films Group, Universidad del Valle, Cali, Colombia*

HN-12. **Magnetostatic interactions between magnetic nanotubes.** *J. Escrig*[1], S. Allende[1], D. Altbir[1], P. Landeros[2] and M. Bahiana[3] *1. Departamento de Fisica, Universidad de Santiago de Chile, Santiago, Chile; 2. Departamento de Fisica, Universidad Tecnica Federico Santa Maria, Valparaiso, Chile; 3. Instituto de Fisica, Universidade Federal do Rio de Janeiro, Rio de Janeiro, Brazil*

HN-13. **Magnetic nanowires: from synthesis to permanent magnet applications.** *G. Viau*[1], Y. Soumare[2], T. Maurer[3], J. Piquemal[2], F. Ott[3] and G. Chaboussant[3] *1. LPCNO, INSA Toulouse, TOULOUSE, France; 2. ITODYS, Université Paris7, PARIS, France; 3. LLB, CEA Saclay, ORSAY, France*

HN-14. **Numerical simulation of magnetic cluster in transition region.** *H. Endo*[1], Y. Uesaka[1], Y. Nakatani[2], N. Hayashi[3] and H. Fukushima[4] *1. Nihon University, Koriyama, Fukushima, Japan; 2. University of Electro-Communications, Chofu, Japan; 3. Individual capacity, Tokyo, Japan; 4. Individual capacity, Chiba, Japan*

HN-15. **Ligand exchange in gold-coated FePt nanoparticles.** *P. de la Presa*[1], T. Rueda[1], M. Morales[2] and A. Hernando[1] *1. Instituto de Magnetismo Aplicado, UCM, Las Rozas, Madrid, Spain; 2. ICMM-CSIC, Madrid, Madrid, Spain*

HN-16. **Magnetic behavior of oleate-capped monodisperse iron oxide nanoparticles prepared in polyol solutions.** *G. Caruntu*[1,2], D. Caruntu[1,2] and C.J. O'Connor[1,2] *1. Advanced Materials Research Institute, New Orleans, LA; 2. Chemistry Department, University of New Orleans, New Orleans, LA*

HN-17. **Interplay Between Magnetic Coupling of Magnetic Nanoparticles and Magnetic/Superconducting Proximity Effect.** *E. Navarro*[1], Y. Huttel[2], A. Cebollada[3], A. Perez-Junquera[4], M. Velez[4], J.I. Martin[4], J.M. Alameda[4] and J.L. Vicent[1] *1. Fisica Materiales, Univ. Complutense, Madrid, Spain; 2. Instituto Ciencia de Materiales, CSIC, Madrid, Spain; 3. Instituto Microelectronica de Madrid, CSIC, Madrid, Spain; 4. Fisica, Universidad de Oviedo, Oviedo, Spain*

THURSDAY AFTERNOON 2:30 POLIVALENTE

Session HO
HEAD-MEDIA INTERFACE AND TRIBOLOGY - III (POSTER SESSION)
Bernhard Knigge, Chair

HO-01. Lube depletion caused by thermal-desorption in heat assisted magnetic recording. *Y. Ma*[1] and B. Liu[1] *1. Data Storage Insitute, Singapore, Singapore*

HO-02. Study of slider's flying behavior under by various temperature and humidity conditions. *T. Watanabe*[1] and K. Kusakawa[1] *1. Fuji Electric Device Technology Co.,Ltd, Matsumoto, Japan*

HO-03. A novel simulation of air/liquid bearing based on lattice Boltzmann method. *D. Kim*[1], M.S. Jhon[1] and H. Kim[1] *1. Depart of Chemical Engineering and Data Storage Systems Center, Carnegie Mellon University, Pittsburgh, PA*

HO-04. Numerical Simulation of Touchdown/Takeoff of Sphere-Pad Slider. *H. Li*[1], J. Li[2], J. Xu[2], Y. Shimizu[2], K. Ono[2] and S. Yoshida[1] *1. Storage Mechanics Laboratory, Hitachi Asia Ltd., Singapore, Singapore; 2. Central Research Laboratory, Hitachi Ltd., Kanagawa, Japan*

HO-05. Dynamically controlled thermal flying-height control slider. *T. Shiramatsu*[1], T. Atsumi[1], M. Kurita[1], Y. Shimizu[1] and H. Tanaka[2] *1. Central Research Laboratory, HITACHI, Ltd, Fujisawa-shi, Kanagawa-ken, Japan; 2. Hitachi Global Storage Technologies Japan, Ltd., Odawara-shi, Kanagawa-ken, Japan*

HO-06. Transient analysis of micro thermal actuator for flying height control. *J. Liu*[1], J. Li[2], H. Li[1], J. Xu[2] and S. Yoshida[1] *1. Storage Mechanics Laboratory, R&D Center, Hitachi Asia Ltd, Singapore, Singapore; 2. Storage Technology Research Center, Hitachi Ltd, Fujisawa, Japan*

HO-07. Origin of Heater Induced Voltage in Magnetic Recording Heads. *D. Song*[1] and M.T. Johnson[1] *1. Seagate Technologies, Bloomington, MN*

HO-08. Signal modulation study of TuMR reader near head/disk contact. *N. Kim*[1], Y. Tang[1] and X. Che[1] *1. Samsung Information Systems America, San jose, CA*

HO-09. Nano-mechanics of Perfluoropolyether Films: Compression vs. Tension. Q. Guo[1,2], P. Chung[1] and *M.S. Jhon*[1] *1. Depart of Chemical Engineering and Data Storage Systems Center, Carnegie Mellon University, Pittsburgh, PA; 2. Seagate Technology, Fremont, CA*

HO-10. Ultraviolet Bonding of PFPE with Carbon Overcoat: Surface Energy and Spreading. H. Chen[2], *P. Chung*[1] and M.S. Jhon[1] *1. Depart of Chemical Engineering and Data Storage Systems Center, Carnegie Mellon University, Pittsburgh, PA; 2. Hewlett-Packard Company, San Diego, CA*

HO-11. Binary Mixture Lubricant Film of PFPE Lubricants. *P. Chung*[1], H. Chen[2] and M.S. Jhon[1] *1. Depart of Chemical Engineering and Data Storage Systems Center, Carnegie Mellon University, Pittsburgh, PA; 2. Hewlett-Packard Company, San Diego, CA*

HO-12. A Study on Design and Analysis of New Lubricant for Near Contact Recording. *D. Shirakawa*[1] and K. Ohnishi[1] *1. Asahi Glass Co., Ichihara-shi, Chiba, Japan*

HO-13. A new contact model for head disk interface (HDI) with ultrathin liquid film and ultrasmall spacing. *H. Matsuoka*[1], H. Kokumai[1] and S. Fukui[1] *1. Department of Applied Mathematics and Physics, Faculty of Engineering, Tottori University, Tottori, Japan*

HO-14. Density Dependence of Carbon/Magnetic layer for Corrosion/Scratch Resistance on Head-Disk-Interface. *H. Tani*[1] and M. Shoda[1] *1. Head media interface technology, Hitachi Global Storage Technologies Japan, Fujisawa-shi, Kanagawa-ken, Japan*

THURSDAY AFTERNOON 2:30 POLIVALENTE

Session HP
SOFT FILMS (POSTER SESSION)
Alfredo Garcia-Arribas, Chair

HP-01. Crystal structure as an origin of high anisotropy field of FeCoB films with Ru underlayer. A. Hashimoto[1], K. Hirata[1], T. Matsuu[1], S. Saito[2] and *S. Nakagawa*[1] *1. Dept. of Physical Electronics, Tokyo Institute of Technology, Tokyo, Japan; 2. Electronic Engineering, Tohoku University, Sendai, Japan*

HP-02. Magnetic properties and crystallographic structure of Fe3Pt thin films on glass substrate. *S. Hsiao*[1], S. Chen[1], Y. Hsu[1], H. Lee[2], W. Chang[3] and F. Yuan[4] *1. Materials science and engineering, Feng Chia University, Taichung, Taiwan; 2. National Synchrotron Radiation Research Center, Hsinchu, Taiwan; 3. Phyics, National Chung Cheng University, Chiayi, Taiwan; 4. Physics, Academia sinica, Taipei, Taiwan*

HP-03. Suppression Of Sm Segregation And Improvement In Thermal Stability By Introducing Ru Underlayer In Co-Sm Amorphous Films. *K. Ikeda*[1,2], T. Suzuki[1] and T. Sato[2] *1. R&D center, Taiyo Yuden Co., Ltd., Gunma, Japan; 2. Spin device technology center, Shinshu University, Nagano, Japan*

HP-04. Magnetic properties of FeCo films prepared by hydrogenous gas reactive sputtering. *X. Liu*[1] and A. Morisako[2] *1. Department of Information Engineering, Shinshu University, Nagano, Naganoken, Japan; 2. Spin device technology center, Shinshu University, Nagano, Nagano, Japan*

HP-05. Nanocrystallyne permalloy thin films obtained by nitrogen IBAD. *P. Prieto*[1], J. Camarero[2], J.F. Marco[3], E. Jimenez[2], J.M. Benayas[1] and J.M. Sanz[1] *1. Física Aplicada, Universidad Autónoma de Madrid, Madrid, Spain; 2. Física de la Materia Condensada, Universidad Autónoma de Madrid, Madrid, Spain; 3. Instituto de Química Física Rocasolano, CSIC, Madrid, Spain*

HP-06. Ultra-Soft and High Magnetic Moment CoFe Films Directly Electrodeposited from a B-Reducer Contained Solution. *B. Zong*[1], G. Han[1], L. Wang[1], G. Leonard[1], J. Sze[1], L. Shen[2], H. Tan[2], Y. Loh[1], B. Lim[1] and B. Liu[1] *1. SMI, Data Storage Institute, A-Star, Singapore, Singapore; 2. Institute of Materials Research & Engineering, A-Star, Singapore, Singapore*

HP-07. Soft-magnetic CoNiFeP alloy films for high frequency applications. F.M. Rhen[1] and *S. Roy*[1] *1. Microsystems Center, Tyndall National Institute, Cork, Ireland*

HP-08. Spin re-orientation transition in amorphous FeBSi thin-films submitted to thermal treatments. *P. Tiberto*[1], F. Celegato[1], M. Coisson[1] and F. Vinai[1] *1. INRIM, Torino, Italy*

HP-09. Electroplated Ni_xFe_{100-x}/FeCo Multi-layer Films for Perpendicular Write Heads. *Y. Miyake*[1], M. Matsuoka[1], M. Kato[1], H. Kanai[1] and Y. Uehara[1] *1. fujitsu ltd, Nagano, Japan*

HP-10. High temperature electrodeposited multilayer amorphous alloy suitable for integrated inductors. *P. McCloskey*[1], B. Jamieson[1], T. O'Donnell[1], D. Gardner[2], M. Morris[3] and S. Roy[1] *1. Microsystems Center, Tyndall National Institute, Cork, Ireland; 2. Circuit Research lab, INTEL Corporation, Santa Clara, CA; 3. Chemistry department, University College Cork, Cork, Ireland*

HP-11. Magnetic properties of sputtered permalloy/molibdenum multilayers. *M. Romera*[1], M. Maicas[1], R. Ranchal[2], D. Ciudad[1], E. López[2] and P. Sánchez[1] *1. ISOM, Universidad Politécnica de Madrid, Madrid, Madrid, Spain; 2. Física de Materiales, Universidad Complutense de Madrid, Madrid, Madrid, Spain*

HP-12. Effects of capping layers on damping constants and magnetic properties of CoFeB. *J. Song*[1], C. Wang[1], S. Huang[1], C. Lai[1], W. Chen[2], S. Yang[2] and K. Shen[2] *1. Department of Materials Science and Engineering, National Tsing Hua University, Hsinchu, Taiwan; 2. ERSO, Industrial Technology Research Institute, Hsinchu, Taiwan*

HP-13. Direct Observation of Barkhausen Avalanches during Nucleation-Mediated Magnetization Reversal on a nanoscale. *M. Im*[1], P. Fischer[1], D. Kim[2] and S. Shin[3] *1. CXRO, LBNL, Berkeley, CA; 2. Department of Physics, Chungbuk National University, Cheongju 361-763, South Korea; 3. Department of Physics and Center for Nanospinics of Spintronic Materials, Korea Advanced Institute of Science and Technology, Daejeon 305-701, South Korea*

HP-14. Magnetotransport and exchange-bias in CoCu electrodeposited granular alloys. *M. Plaza*[1], L. Perez[1], M. Sánchez[1], A. Fernández-Pacheco[2,3] and J. de Teresa[2] *1. Dpt. Fisica de Materiales, Universidad Complutense de Madrid, Madrid, Spain; 2. Instituto de Ciencia de Materiales de Aragón, CSIC-Universidad de Zaragoza, Zaragoza, Spain; 3. Instituto de Nanociencia de Aragón, Universidad de Zaragoza, Zaragoza, Spain*

HP-15. High magnetic moment soft thin films for flux concentrators. *I.G. Trindade*[1,2], J. Oliveira[1,3], J. Teixeira[1], R. Fermento[1], J.B. Sousa[1,2], S. Cardoso[4], P.P. Freitas[4], J.E. Snyder[5] and A. Raghunathan[5] *1. IFIMUP-IN, Porto, Portugal; 2. Physics, Faculdade de Ciências da Universidade do Porto, Porto, Portugal; 3. Faculdade de Ciências da Universidade do Minho, Braga, Portugal; 4. INESC-MN-IN, Lisboa, Portugal; 5. Wolfson Centre for Magnetics, School of Engineering, Cardiff University, Cardiff, United Kingdom*

THURSDAY
AFTERNOON
2:30

POLIVALENTE

Session HQ
DOMAIN WALLS IN NANOWIRES AND THIN FILMS (POSTER SESSION)
Dorothee Petit, Chair

HQ-01. Controlling Domain Wall Pinning in Planar Nanowires with Transverse Field and its Application in a Magnetic Memory Cell. *D. Atkinson*[1], D.S. Eastwood[1] and L.K. Bogart[1] *1. Physics, Durham University, Durham, United Kingdom*

HQ-02. Bi-stable memory element based on pinned domain walls in pairs of notches. *E. Martinez*[1], L. Lopez-Diaz[2], O. Alejos[3] and L. Torres[2] *1. Ingenieria Electromecanica, University of Burgos, Burgos, Burgos, Spain; 2. Fisica Aplicada, University of Salamanca, Salamanca, Spain; 3. Electricidad y Electronica, University of Valladolid, Valladolid, Spain*

HQ-03. Shingle shot detection of the magnetic domain wall motion by using the TMR effect. *K. Kondou*[1], N. Ohshima[2], S. Kasai[1], Y. Nakatani[3] and T. Ono[1] *1. Institute for Chemical Research, Kyoto University, Uji, Kyoto, Japan; 2. Device Platforms Reseach Laboratories, NEC Corp., Sagamihara, Kanagawa, Japan; 3. Department of Computer Science, University of Electro-communications, Chofu, Tokyo, Japan*

HQ-04. Domain wall injection study in spin valve system with different geometry reservoirs. *K. Cheng*[1,2], C. Yu[1], S. Lee[1], Y. Liou[1], Y. Yao[3], J. Wu[3] and J. Huang[2] *1. Institute of Physics., Academia Sinica., Taipei, Taiwan; 2. Department of Materials Science and Engineering, National Tsing-Hua University, Hsinchu, Taiwan; 3. Department of Materials Engineering, Tatung University, Taipei, Taiwan*

HQ-05. Magnetization reversal with domain wall motion in NiFe nanodevices with different pinning sites. *Y. Zhou*[1], D. Stickler[2], Y. Du[1], E. Ahmad[1], Z. Lu[1], H.P. Oepen[2], D. Wilton[1] and G. Pan[1] *1. Faculty of Technology, University of Plymouth, Plymouth, Devon, United Kingdom; 2. Institut für Angewandte Physik, Universität Hamburg, Jungiusstr, Hamburg, Germany*

HQ-06. Magnetoresistance of transverse and vortex domain walls in permalloy submicron wires. *C. Yu*[1], S. Lee[1], K. Cheng[1], D. Chen[2], E. Haung[3] and Y. Liou[1] *1. physics, academica sinica, Taipei, Taiwan; 2. Materials Science & Engineering, Chiao Tung University, Hsinchu, Taiwan; 3. Materials Science & Engineering, University of Tennessee, Knoxville, TN*

HQ-07. Domain wall magnetoresistance effect in nanobridges. Y. Chen[1], *J. Hsu*[1], C. Yu[2], K. Cheng[2], S. Lee[2], Y. Liou[2] and Y. Yao[2] *1. Physics, National Taiwan University, Taipei, Taiwan; 2. Physics, Academia Sinica, Taipei, Taiwan*

HQ-08. Effect of period and linewidth on the magnetization reversal of thin film wire arrays. *S. Moralejo*[1], C. Redondo[1], F.J. Castano[2], C.A. Ross[2] and F. Castano[1] *1. Depart. Química Física, Univ. País Vasco, Lejona, Vizcaya, Spain; 2. Depart. of Material Science and Engineering, MIT, Cambridge, MA*

HQ-09. Edge Roughness effect on the magnetization reversal process of spin valve submicron wires. *T. Chiang*[1,2], C. Yu[1], Y. Chen[1], S. Lee[1] and G. Guo[2] *1. Institute of physics, Academia sinica, Taipei, Taiwan; 2. Physics, National Taiwan University, Taipei, Taiwan*

HQ-10. Study on domain wall moving in a permalloy ring structure. *D. Chen*[1], C. Yu[2] and Y. Yao[3,1] *1. Department of Material Science and Engineering, National Chiao Tung University, Hsinchu, Taiwan; 2. Institute of Physics, Academia Sinica, Taipei, Taiwan; 3. The Department of Materials Engineering, Tatung University, Taipei, Taiwan*

HQ-11. Magnetic domain wall pinning by the stray field of a ferromagnetic dot array. *P.J. Metaxas*[1,3], J. Jamet[1], J. Ferré[1], P. Zermatten[2], G. Gaudin[2], B. Rodmacq[2], A. Schuhl[2] and R.L. Stamps[3] *1. Laboratoire de Physique des Solides (UMR CNRS 8502), Université Paris-Sud, Orsay, France; 2. SPINTEC (URA 2512 CNRS/CEA), CEA, Grenoble, France; 3. School of Physics, University of Western Australia, Perth, WA, Australia*

HQ-12. Ratchet effects on domain wall motion in 2D magnetic amorphous thin film with arrays of asymmetric holes. *J.I. Martín*[1], A. Pérez-Junquera[1], V.I. Marconi[2], A.B. Kolton[2], L.M. Álvarez-Prado[1], Y. Souche[3], A. Alija[1], M. Vélez[1], J.V. Anguita[4], J.M. Alameda[1] and J.R. Parrondo[2] *1. Departamento de Física, Universidad de Oviedo - CINN, Oviedo, Asturias, Spain; 2. Física Atómica, Molecular y Nuclear, and GISC, Universidad Complutense de Madrid, Madrid, Comunidad de Madrid, Spain; 3. NANO, Institut Néel, CNRS and Universite Joseph Fourier, Grenoble, Grenoble, France; 4. Dispositivos, Sensores y Biosensores, Instituto de Microlectrónica de Madrid (CNM-CSIC), Madrid, Comunidad de Madrid, Spain*

THURSDAY
AFTERNOON
2:30

POLIVALENTE

Session HR
MgO MAGNETIC TUNNEL JUNCTIONS II (POSTER SESSION)
Coriolan Tiusan, Chair

HR-01. Annealing temperature dependence of tunnel magnetoresistance in MgO-barrier magnetic tunnel junctions with CoFeB electrodes. ***(Invited)*** *S. Ikeda*[1], J. Hayakawa[2], Y. Lee[1], K. Miura[2,1], H. Hasegawa[1,2], F. Matsukura[1] and H. Ohno[1] *1. Laboratory for Nanoelectronics and Spintronics, RIEC, Tohoku Univ., Sendai, Japan; 2. Advanced Research Laboratory, Hitachi, Ltd., Tokyo, Japan*

HR-02. Effects of MgO barrier thickness on magnetic anisotropy energy constant in perpendicularly magnetic tunnel junctions of $(Co/Pd)_n/MgO/(Co/Pt)_n$ *J. Lee*[1,3], C. Lee[1,2], L. Ye[1], S. Wang[1,2], Y. Wang[1], K. Lin[4], Y. Chang[4] and T. Wu[1,2] *1. Taiwan SPIN Research Center and Graduate School of Engineering Science and Technology, National Yunlin University of Science and Technology, Douliou, Taiwan; 2. Graduate school of materials science, National Yunlin University of Science and Technology, Douliou, Taiwan; 3. Graduate school of Engineering Science and Technology, National Yunlin University of Science and Technology, Douliou, Taiwan; 4. Laser Application Technology Center, Industrial Technology Research Institute, Tainan, Taiwan*

HR-03. Magnetoresistance Behavior of Bottom Exchange Biased Perpendicular Magnetic Tunnel Junction Based on Pd/Co Multilayers. D. Lim[1], *K. Kim*[1], S. Lee[1], S. Kim[2] and W. Jeung[3] *1. Materials Science and Engineering, Korea University, Seoul, South Korea; 2. Mechanical Design and Automation Engineering, Seoul National University of Technology, Seoul, South Korea; 3. Korea Institute of Science and Technology, P.O.Box 131, Seoul, South Korea*

HR-04. Improvement of (100) orientation of MgO films deposited at room temperature for perpendicular MTJ. *H. Ohmori*[1] and S. Nakagawa[1] *1. Dept. of Physical Electronics, Tokyo Institute of Technology, Tokyo, Japan*

HR-05. Magnetic tunnel junctions formed by oxidation of Mg. *W. Raberg*[1], T. Bever[1], M. Hawraneck[1,2], S. Koss[1,3], S. Schmitt[1] and J. Zimmer[1] *1. Technology development Sense & Control, Infineon Technologies AG, Neubiberg, Germany; 2. Institut für Materialwissenschaften, Technische Universität Darmstadt, Darmstadt, Germany; 3. Institut für Festkörperphysik, Universität Hannover, Hannover, Germany*

HR-06. Influence of boron concentration on tunnel magnetoresistance in CoFeB/MgO/CoFeB magnetic tunnel junctions. *K. Tsunekawa*[1], Y. Nagamine[1], Y. Choi[1], F. Ernult[1], D.D. Djayaprawira[1] and Y. Kitamoto[2] *1. Electronic Devices Engineering Headquarters, Canon ANELVA Corp., Kawasaki-shi, Kanagawa, Japan; 2. Tokyo Institute of Technology, Yokohama-shi, Kanagawa, Japan*

HR-07. Temperature dependence of magnetoresistance in epitaxial Fe/MgO/Fe/IrMn magnetic tunnel junctions. S. Wang[1,2], *R. Ward*[1], G. Du[2], X. Han[2], C. Wang[3] and A. Kohn[3] *1. Department of Physics, University of Oxford, Oxford, United Kingdom; 2. Institute of Physics, Chinese Academy of Sciences, Beijing, China; 3. Department of Materials, University of Oxford, Oxford, United Kingdom*

HR-08. The XRD analysis of pseudo and exchange bias spin valve of MgO based magnetic tunnel junctions. *J. Kanak*[1], P. Wisniowski[2], A. Zaleski[1], S. Cardoso[2], P.P. Freitas[2] and T. Stobiecki[1] *1. AGH University of Science and Technology, Krakow, Poland; 2. INESC Microsystems and Nanotechnologies, Lisbon, Portugal*

HR-09. The electrical properties of the radically oxidized MgO prepared in different oxidation condition. *C. Shen*[1], S. Yang[1], C. Yen[1], W. Chen[1], Y. Lee[1], D. Wang[1], C. Tsai[1], C. Hung[1], K. Shen[1] and M. Kao[1] *1. Electronics and Optoelectronics Research Lab (EOL), Industrial Technology Research Institute (ITRI), Hsinchu, Taiwan*

HR-10. Effect of Thermal Treatment on Chemical States of CoFeB/MgO/CoFeB Tunnel Junctions. *Y. Han*[1], S. Lee[1], J. Hong[1], M. Jung[2] and H. Shin[2] *1. Materials Science and Engineering, Yonsei University, Seoul, South Korea; 2. Pohang Accelerator Laboratory, POSTECH, Pohang, Kyungbuk, South Korea*

HR-11. Ab intio calculations of the TMR in magnetic tunnel junctions (MTJ): application to Fe/MgO/Fe. *I. Arias*[1], J.I. Cerdá[1] and M. Muñoz[1] *1. Intercaras y crecimiento, Instituto de Ciencia de Materiales de Madrid, Madrid, Madrid, Spain*

HR-12. Substrate biasing effect on the MgO (001) growth in CoFeB/MgO/CoFeB TMR junctions. *G. Choi*[1], W. Lim[1] and T. Lee[1] *1. Department of Materials Science and Engineering, KAIST, Daejeon, South Korea*

HR-13. The bias voltage dependence of inverted magnetoresistance on the annealing temperature in MgO-based magnetic tunnel junctions. *J. Feng*[1], G. Feng[1] and J. Coey[1] *1. CRANN and school of physics, Trinity College, Dublin, Ireland*

HR-14. Detection of an infra red magnetorefractive effect from a layered Fe/MgO/Fe magnetic tunnel junction. R.T. Mennicke[1], R. Berryman[1], F. Ernult[2], H. Wang[2], Y. Nogi[2], J.A. Matthew[1], *S.M. Thompson*[1], S. Mitani[2] and K. Takanashi[2] *1. Physics, University of York, York, North Yorkshire, United Kingdom; 2. Institute for Materials Research, Tohoku University, Sendai, Miyagi, Japan*

HR-15. Low Frequency Noise in MgO Magnetic Tunnel Junctions: Hooge's Parameter Dependence on Bias Current Density. *J.M. Almeida*[1,2] and P.P. Freitas[1,2] *1. INESC - MN, Lisbon, Portugal; 2. Physics, IST, Lisbon, Portugal*

HR-16. Magnetization reversal processes of nanostructured magnetic tunnel junction rings. *C. Chen*[1], C. Chao[1], C. Kuo[1], J. Ou[1], L. Horng[1], J. Wu[1], T. Wu[2], J. Yang[3], S. Isogami[4], M. Tsunoda[4] and M. Takahashi[4] *1. Taiwan SPIN Research Center,National Changhua University of Education, Changhua, Taiwan; 2. Taiwan SPIN Research Center, National Yunlin University of Science & Technology, Yunlin, Taiwan; 3. Institute of Optoelectronic Sciences, National Taiwan Ocean University, Keelung, Taiwan; 4. Graduate school of Electronic Engineering, Tohoku University, Sendai, Japan*

THURSDAY AFTERNOON 2:30 — POLIVALENTE

Session HS
AB INITIO CALCULATIONS (POSTER SESSION)
Oleg Mryasov, Chair
Laszlo Szunyogh, Chair

HS-01. First-principles calculations of structural and magnetic properties of Fe/MgO/Fe with interfacial Mg vacancy. *C. Kim*[1], G. Yoon[1] and Y. Chung[1] *1. Materials Science and Engineering, Hanyang University, Seoul, South Korea*

HS-02. Ab-initio spin-dependent electronic transport calculations of MTJ with low band-gap insulating oxides with rock salt structure. *A. Furuya*[1], A. Fujisaki[1], H. Kanai[2], K. Noma[2], K. Kobayashi[2] and Y. Uehara[2] *1. Simulation Technology Development Division, FUJITSU Advanced Technologies Ltd, Kawasaki, kanagawa, Japan; 2. Head Division, Storage Products Group, Fujitsu Ltd, Nagano, Nagano, Japan*

HS-03. Inhomogeneity and magnetism in diluted magnetic semiconductors. *B. Sanyal*[1], R. Knut[1], O. Granas[1], D.M. Iusan[1], O. Karis[1] and O. Eriksson[1] *1. Department of Physics, Uppsala University, Uppsala, Sweden*

HS-04. Interface magnetism in Fe_2O_3-$FeTiO_3$ heterostructures. *S. Sadat Nabi*[1] and R. Pentcheva[1] *1. department of earth and environmental sciences, section crystallography, Ludiwig Maximilain University of Munich, Munich, Germany*

HS-05. Charge, magnetic and orbital order at perovskite interfaces. *R. Pentcheva*[1] and W.E. Pickett[2] *1. Department of Earth and Environmental Sciences,Section Crystallography, University of Munich, Munich, Germany; 2. Department of Physics, University of California, Davis, CA*

HS-06. Magnetism of conduction band, exchange interactions and magneto-caloric effects in pure hcp Gd: a first-principles calculations. *S. Khmelevskyi*[1], A.V. Ruban[2], I. Turek[3] and P. Mohn[1] *1. Center for Computational Materials Science, Vienna Technical University, Vienna, Austria; 2. Royal Unicersity of Technology, Stockholm, Sweden; 3. Charles University, Prague, Czech Republic*

HS-07. Ab-initio magneto-optical properties of bcc Ni/Ni(100). *C. Etz*[1], A. Vernes[1], L. Szunyogh[1,2] and P. Weinberger[1] *1. Center for Computational Materials Science, Vienna University of Technology, Vienna, Austria; 2. Department of Theoretical Physics, Budapest University of Technology and Economics, Budapest, Hungary*

HS-08. Influence of external magnetic field on the resistivity of a one-dimensional Neel type magnetic domain wall in presence of Rashba spin-orbit coupling. *M. Ghanaatshoar*[1], V. Fallahi[1], M.M. Tehranchi[1] and A. Phirouznia[2] *1. Laser and Plasma research institute, Shahid Beheshti University, Tehran, Tehran, Iran; 2. Department of physics, Azarbaijan University of Tarbiat Moallem, Tabriz, Eastern Azarbaijan, Iran*

HS-09. *Ab-initio* study on the magnetic structures in the ordered Mn_3Pt alloy. *Y. Kota*[1], H. Tsuchiura[1] and A. Sakuma[1] *1. Applied Physics, Tohoku University, Sendai, Japan*

HS-10. Half-metallicity of the bulk and the (001) surface for full Heusler alloy Co_2HfSi: a first-principles study. Y. Jin[1] and *J. Lee*[1] *1. Physics, Inha University, Incheon, South Korea*

HS-11. Magnetic properties of the antiperovskite Co_4N(001) surfaces: a first-principles study. *I. Kim*[1], B. Bialek[2] and J. Lee[2] *1. Grad. Inst. Ferrous Tech. (GIFT), POSTECH, Pohang, South Korea; 2. Physics, Inha University, Incheon, South Korea*

HS-12. A first principles study of Thiol-Capped Au Nanoparticles. *R. Cuadrado*[1] and J. Cerdá[1] *1. Intercaras y Crecimiento, Instituto de Ciencia de Materiales de Madrid, Madrid, Madrid, Spain*

HS-13. The Study of Magnetic Properties of Fe2Sm Using Ab- Initio Calculation. M. Imaizumi[1], *L.C. Varanda*[2] and M. Jafelicci Jr[3] *1. Fisica, Universidade Estadual Julio de Mesquita Filho, Bauru, S.Paulo, Brazil; 2. Química, Universidade de São Paulo, São Carlos, Sâo Paulo, Brazil; 3. Qúimica, Universidade Estadual Paulista Júlio de Mesquita Filho, Araraquara, Sâo Paulo, Brazil*

HS-14. Energy spectrum of S=1/2 Heisenberg systems via a recursive diagonalization method. *F.C. Souza*[1] and V.L. Líbero[1] *1. Departamento de Física e Informática, Instituto de Física de São Carlos, Universidade de São Paulo, São Carlos, São Paulo, Brazil*

HS-15. Density Functional Theory for Heisenberg Spin-1/2 Chains With Bond Defects. *V.L. Líbero*[1] and P.H. Penteado[1] *1. Departamento de Física e Informática, Instituto de Física de São Carlos, Universidade de São Paulo, São Carlos, São Paulo, Brazil*

HS-16. Ab initio DFT study of half-metallic character in Sr_2CoReO_6 complex perovskite. *J. Roa-Rojas*[1], M. Bonilla[1], J.A. Rodriguez[1], F. Fajardo[1] and D.A. Landinez-Tellez[1] *1. Dept. of Physics, Universidad Nacional de Colombia, Bogotá, D. C., Colombia*

THURSDAY AFTERNOON 2:30 — POLIVALENTE

Session HT
RECORDING SYSTEMS, CODING AND CHANNELS-II (POSTER SESSION)
Jae Moon, Chair

HT-01. Combinations of decoding algorithm for LDPC codes by tensor product decoding. *H. Kamabe*[1] *1. Information Science, Gifu University, Gifu, Gifu, Japan*

HT-02. Performance Evaluation of Combined Post-processor Based on Likely Error Pattern and Parity Check Targeting under Write Pre-compensation in PMR Channel with NLTS. Y. Okamoto[1], *T. Bushisue*[1], Y. Nakanura[1], H. Osawa[1] and H. Muraoka[2] *1. Graduate School of Science and Engineering, Ehime University, Matsuyama, Ehime, Japan; 2. RIEC, Tohoku University, Sendai, Japan*

HT-03. Performance comparison of various error correcting strategies using perpendicular magnetic recording data series. *S. Mita*[1] and H. Matsui[1] *1. Toyota Technological Institute, Nagoya, Japan*

HT-04. EPCC-based Channel-Optimized LDPC coding. H.S. Alhussien[1] and *J. Moon*[1] *1. CDSLAB, Electrical and Computer Engineering, University of Minnesota Twin Cities, Minneapolis, MN*

HT-05. On Imposing an RLL Constraint without Explicit RLL Coding. *J. Park*[1] and J. Moon[1] *1. Electrical and Computer Engineering, University of Minnesota, Minneapolis, MN*

HT-06. On the use of averaging to estimate the dibit response. *M. Ting*[1] *1. Seagate Technology, Pittsburgh, PA*

HT-07. Two-Dimensional Pulse Response and Media Noise Modeling for Bit-Patterned Media Channels. S. Nabavi[1,2], *V. Bhagavatula*[1,2] and J.A. Bain[1,2] *1. Data Storage Systems Center (DSSC),, Pittsburgh, PA; 2. ECE, Carnegie Mellon University, Pittsburgh, PA*

HT-08. Soft Feedback Equalization for Patterned Media Storage. *M. Keskinoz*[1] *1. Electronics Engineering, Sabanci University, Istanbul, Turkey*

HT-09. Signal Modeling for Ultra-high Density Bit Patterned Media and Performance Evaluation. *S. Zhang*[1], Z. Qin[1] and X. Zou[1] *1. Data Storage Institute, Singapore, Singapore*

HT-10. Equalization and detection for patterned media recording. *S. Karakulak*[1], P.H. Siegel[1], J.K. Wolf[1] and H. Bertram[1,2] *1. Electrical and Computer Engineering Dept., Center for Magnetic Recording Research, UCSD, La Jolla, CA; 2. Hitachi Global Storage Technologies, San Jose, CA*

HT-11. Understanding sources of errors in bit patterned media to improve read channel performance. *Y. Shi*[1], P.W. Nutter[1] and J.J. Miles[1] *1. School of Computer Science, The University of Manchester, Manchester, United Kingdom*

HT-12. Global timing control for tape storage channels. *S. Ölçer*[1], J. Jelitto[1] and R.A. Hutchins[2] *1. IBM Zurich Research Laboratory, Rüschlikon, Zürich, Switzerland; 2. IBM STG, Tucson, AZ*

THURSDAY AFTERNOON 2:30 — POLIVALENTE

Session HU
MULTILAYER FILMS AND SUPERLATTICES III (POSTER SESSION)
Hong-Sik Jung, Chair

HU-01. Multilayered thin film structure for negative permeability. *S. Cho*[1], J. Kim[1] and K. Kim[2] *1. Metallurgy and materials engineering, Hanyang University, Ansan, South Korea; 2. Physics, Yeungnam University, Gyeongsan, South Korea*

HU-02. Interlayer exchange coupling in $Co_2FeAl_{0.5}Si_{0.5}$/Cr/$Co_2FeAl_{0.5}Si_{0.5}$ trilayers. *T. Furubayashi*[1], K. Kodama[2], K. Inomata[1] and K. Hono[1] *1. Magnetic Materials Center, National Institute for Materials Science, Tsukuba, Japan; 2. Graduate School of Pure and Applied Sciences, University of Tsukuba, Tsukuba, Japan*

HU-03. Thickness and Temperature Dependence of Extraordinary Hall Effect in Interlayer Coupled [Pt/Co]$_5$/Ru/[Co/Pt]$_5$ Multilayers with Perpendicular Anisotropy. *J. Zhao*[1], Y. Wang[1], S. Zhang[2] and X. Han[1] *1. State Key Laboratory of Magnetism, Institute of Physics, Chinese Academy of Science, Beijing, Beijing, China; 2. Department of Physics and Astronomy, University of Missouri–Columbia, Columbia, MO*

HU-04. Effect of antiferromagnetic interlayer coupling on domain wall creep in a system with perpendicular anisotropy. *P.J. Metaxas*[1,2], J. Jamet[1], J. Ferré[1], B. Rodmacq[3], B. Dieny[3] and R.L. Stamps[2] *1. Laboratoire de Physique des Solides (UMR CNRS 8502), Université Paris-Sud, Orsay, France; 2. School of Physics, University of Western Australia, Crawley, WA, Australia; 3. SPINTEC (URA 2512 CNRS/CEA), CEA, Grenoble, France*

HU-05. Spin-glass-like magnetic behaviour of Tb/Si and Tb/Ti nanoscale multilayers. *A.V. Svalov*[1,2], V.O. Vas'kovskiy[1], J.M. Barandiarán[2], I. Orue[3], R. Lopez Anton[4,5] and G.V. Kurlyandskaya[2] *1. Ural State University, Ekaterinburg, Russian Federation; 2. Electricidad y Electrónica, Universidad del País Vasco (UPV/EHU), Bilbao, Spain; 3. SGiker, Universidad del País Vasco (UPV/EHU), Bilbao, Spain; 4. Instituto de Ciencia de Materiales de Aragón, CSIC-Universidad de Zaragoza, Zaragoza, Spain; 5. ISIS Facility, Science and Technology Facilities Council, Rutherford Appleton Laboratory, Harwell Science and Innovation Campus, Didcot, United Kingdom*

HU-06. Magnetoimpedance in permalloy-based multilayers: effect of Ag and Cu spacers. *A. de Andrade*[1], A. Viegas[2], R. da Silva[3], M. Corrêa[4] and R. Sommer[5] *1. Universidade Federal de Santa Maria, Frederico Westphalen, Rio Grande do Sul, Brazil; 2. Universidade Federal de Santa Catarina, Florianópolis, Santa Catarina, Brazil; 3. Universidade Federal do Rio Grande do Sul, Porto Alegre, Rio Grande do Sul, Brazil; 4. Universidade Federal do Pampa, Caçapava do Sul, Rio Grande do Sul, Brazil; 5. Centro Brasileiro de Pesquisas Fisicas, Rio de Janeiro, Rio de Janeiro, Brazil*

HU-07. Structural Characterization of Ferromagnetic Mn/ZnO Multilayers. *E. Céspedes*[1], A. Espinosa[1], M. García-Hernández[1], A. de Andrés[1] and C. Prieto[1] *1. Instituto de Ciencia de Materiales de Madrid, Consejo Superior de Investigaciones Científicas (CSIC), Madrid, Spain*

HU-08. Structural control of magnetic properties in Co/Pd multilayer for heat assisted perpendicular MRAM application. B. Purnama[1], K. Waseda[1], S. Yoshimura[1], Y. Nozaki[1] and *K. Matsuyama*[1] *1. Electronics, Kyushu University, Fukuoka, Japan*

HU-09. Antiferromagnetic Exchange Coupling at Interface between Fe_3O_4(001) and Fe(001) Epitaxial Films. *H. Yanagihara*[1], A. Ohnishi[1], J. Hagiwara[1], Y. Toyada[1] and E. Kita[1] *1. Applied Physics, Univ. Tsukuba, Tsukuba, Japan*

HU-10. Preparation of Longitudinally Oriented CoCrPt Thin Film in GMR Head at Room Temperature. X. Liu[1], Z. Li[1], S. Li[1], W. Shi[1], *F. Wei*[1], D. Wei[2] and J. Cao[3] *1. Lanzhou University, Research Institute of Magnetic Materials, Lanzhou, Gansu, China; 2. Tsinghua University, Key Laboratory of Advanced Materials Department and Engineering, Beijing, China; 3. Lanzhou University, Research Institute of Magnetic Materials(Now woking in INESC-Microsystems and Nanotechnologies (INESC-MN), R.Alves Redol 9-1, 1000-29 Lisbon, Portugal), Lanzhou, Gansu, China*

HU-11. Molecular dynamics investigation on interfacial mixing behavior in transition metals (Fe, Co, Ni)- Al multilayer system. *S. Lee*[1], H. Park[1] and Y. Chung[1] *1. Department of Materials Science & Engineering, Hanyang University, Seoul, South Korea*

HU-12. Intermedium zero-magnetization state in Co/TiO2/Co trilayer. Y. Wu[1,2], *J.G. Lin*[1,3] and C. Chang[2,3] *1. Center for Condensed Matter Sciences, National Taiwan University, Taipei, Taiwan; 2. Department of Physics, National Taiwan University, Taipei, Taiwan; 3. Center for Nanostorage research, National Taiwan University, Taipei, Taiwan*

HU-13. Fe_3O_4/MgO/Fe heteroepitaxial structures for magnetic tunnel junctions. *J. Orna*[1,2], L. Morellon[1,2], P.A. Algarabel[2], J.A. Pardo[1,3], S. Sangiao[1], C. Magen[4], J.M. De Teresa[2] and M.R. Ibarra[1,2] *1. Instituto de Nanociencia de Aragón (INA), Universidad de Zaragoza, Zaragoza, Spain; 2. Instituto de Ciencia de Materiales de Aragon (ICMA), Universidad de Zaragoza-CSIC, Zaragoza, Spain; 3. Departamento de Ciencia y Tecnología de Materiales y Fluidos, Universidad de Zaragoza, Zaragoza, Spain; 4. Materials Science and Technology Division, Oak Ridge National Laboratory, Oak Ridge, TN*

HU-14. Thermal stability of top-type synthetic antiferromangetic spin-valve structure in (001) orientated MgO-based MTJs. *C. Chen*[1], C. Lai[1], W. Chen[2], K. Shen[2] and H. Bor[3] *1. Department of Materials Science and Engineering, National Tsing Hua University, Hsinchu, Taiwan; 2. Electronics Research and Service Organization, Industrial Technology Research Institute, Hsinchu, Taiwan; 3. Materials and Electro-Optics Research Division, Chuang-Shan institute of Science and Technology, Tauyoun, Taiwan*

THURSDAY AFTERNOON 2:30 — POLIVALENTE

Session HV
MAGNETO-OPTIC, HAMR AND NOVEL RECORDING (POSTER SESSION)
Takao Suzuki, Chair

HV-01. Numerical Analysis of Heat Transfer Mechanisms Induced by Laser Heating in Far- and Near-Field HAMR Systems. *R. Ikkawi*[1], N. Amos[1], A. Balandin[1], D. Litvinov[2] and S. Khizroev[1] *1. Electrical Engineering, University of California, Riverside, Riverside, CA; 2. Center for Nanomagnetic Systems, University of Houston, Houston, TX*

HV-02. Micromagnetic studies of probe recording on magnetic nanocaps. *A. Goncharov*[1], T. Schrefl[1], P. Kappenberger[2], G. Hrkac[1], J. Dean[1], S. Bance[1] and M. Albrecht[3] *1. Engineering Materials, The University of Sheffield, Sheffield, United Kingdom; 2. Nano-scale Materials Science, Empa-Materials Science & Technology, Dübendorf, Switzerland; 3. Surface and Interface Physics, Chemnitz University of Technology, Chemnitz, Germany*

HV-03. Compositional dependence of g-factor and damping constant of GdFeCo amorphous alloy films. *T. Kato*[1], K. Nakazawa[2], R. Komiya[2], N. Nishizawa[3], S. Tsunashima[2] and S. Iwata[1] *1. Department of Quantum Engineering, Nagoya University, Nagoya, Aichi, Japan; 2. Department of Electrical Engineering and Computer Science, Nagoya University, Nagoya, Aichi, Japan; 3. Osaka University, Suita, Osaka, Japan*

HV-04. Magneto-optical properties of nanometer crystal giant magneto-optical BiAlDyIG thin film materials post-treated by rapid recurrent thermal annealing (RRTA) method. *Q. Yang*[1], H. Zhang[1], Q. Wen[1] and Y. Liu[1] *1. University of Electronic Science and Technology of China, Chengdu, Sichuan, China*

HV-05. Prospect for Optically Assisted Magnetic Recording using Amorphous Film of Rare Earth-Transition Metal Alloy. *M. Murakami*[1] *1. Electro-mechanical Components Business Unit, Panasonic Electronic Devices Co., Ltd., Kadoma, Osaka, Japan*

THURSDAY AFTERNOON 2:30 — POLIVALENTE

Session HW
RECORDING PHYSICS, MODELS AND THEORY - II (POSTER SESSION)
Werner Scholz, Chair

HW-01. Feasibility of Perpendicular Magnetic Printing at 1 Tbit/inch^2 *T. Komine*[1], T. Murata[1], Y. Sakaguchi[1], Y. Hosoya[1], N. Suhaimi[1] and R. Sugita[1] *1. Department of Media and Telecommunications Engineering, Ibaraki University, Hitachi, Ibaraki, Japan*

HW-02. Off-Track Performance and Track-Edge Structure in Narrow Track Perpendicular Magnetic Recording. *K. Miura*[1], T. Ogawa[1], H. Muraoka[1], H. Aoi[1] and Y. Nakamura[1] *1. RIEC, Tohoku University, Sendai, Miyagi, Japan*

HW-03. Microwave assisted magnetization reversal and its thermal activation. *S. Okamoto*[1], N. Kikuchi[1] and O. Kitakami[1] *1. IMRAM, Tohoku University, Sendai, Japan*

HW-04. Prediction on the recording performance of exchange coupled composite media and discrete track media. *Y. Tahk*[1], J. Lee[1] and S. Lee[1] *1. Storage System Division, Samsung Electronics, Suwon, South Korea*

HW-05. Attempt Frequency with Respect to Field Dependence and Modified Sharrck'S Formula for Perpendicular Recording Media. *M. Igarashi*[1] and Y. Sugita[2] *1. Hitachi, Ltd., Kokubunji, Tokyo, Japan; 2. Tohoku Institute of Technology, Sendai, Miygi, Japan*

HW-06. Effect of demagnetizing field distribution in discrete track media recording. *Y. Kawato*[1], A. Nakamura[1], A. Yatagai[2], Y. Nishida[2], K. Ito[1], S. Nosaki[1], Y. Hirayama[1] and Y. Hosoe[1] *1. Central Research Laboratory, Hitachi, Ltd., Kokubunji, Tokyo, Japan; 2. Advanced HDD Technology Laboratory, Hitachi Global Storage Technologies, Fujisawa, Kanagawa, Japan*

HW-07. The effect of write head current on adjacent track erasure. *J.S. Dean*[1], M.A. Bashir[1], A. Goncharov[1], G. Hrkac[1], S. Bance[1], T. Schrefl[1], A. Cazacu[2], M. Gubbins[2], R.R. Lamberton[2] and D. Suess[3] *1. Engineering materials, Univerisity of Sheffield, Sheffield, United Kingdom; 2. Seagate Technology, Derry, United Kingdom; 3. Solid State Physics, Vienna University of Technology, Vienna, Austria*

HW-08. Study of Overwrite Generated Twisted Transition Written by Trapezoid Shape Single Pole. *S. Hu*[1], Z. Yuan[1] and B. Liu[1] *1. Data Storage Institute, Singapore, Singapore*

HW-09. Reverse DC erase noise analysis on exchange coupled composite PMR media. *S. Hong*[1], Y. Tang[1] and X. Che[1] *1. SISA, San Jose, CA*

HW-10. Influence of the media magnetization patterns on the domain structure in the reader stack with the asymmetric stabilization. E. Haftek[1], *V. Nandakumar*[2] and M. Benakli[3] *1. Electrical Integration, Seagate Technology, Bloomington, MN; 2. Servo Format Engineering, Seagate Technology, Shakopee, MN; 3. Recording Sub-systems Organization, Seagate Technology, Bloomington, MN*

HW-11. A Novel Algorithm for Unknown Periodic Disturbance Cancellation in HDD. *L. Hui*[2,1], D. Chunling[1] and W. Youyi[2] *1. MRC, DSI, Singapore, Singapore; 2. NTU, Singapore, Singapore*

ZA-01

Multiferroic and Magnetoelectric Materials.

J. F. Scott
Earth Sciences, Cambridge University, Cambridge, United Kingdom

J. F. Scott
Cambridge University

In this tutorial I will do five things: First a discussion is given of the general symmetry ideas and notation used to describe materials that are simultaneously ferromagnetic (or antiferromagnetic) and ferroelectric (or antiferroelectric). A comparison is given with electrets and with pyroelectrics, some of which can be ferroelectric (e.g., GeTe), depending upon their electrical conductivity, and some of which (e.g., ZnO or CdS wurtzite structures) can be pyroelectric but not ferroelectric. This point is used to discuss ZnO:Li, which many authors claim to be ferroelectric.
In the second part of the talk I will give a brief status report on random access memories (RAMs) and describe the present state of ferroelectric RAMs (FRAMs), magnetic MRAMs, and explain why multiferroelectric magnetoelectric RAMs are potentially attractive: Fast, low-power, voltage-driven WRITE operations, followed by nondestructive magnetic READ operations (which require no re-set).
In the third part of the tutorial I will describe the basic physics of switching, and how this controls the speed of ferroelectric and magnetic domain walls in devices [Catalan et al.], as well as the basic phenomenon of magnetocapacitance [Scott; Glass et al.]. I show that magnetodielectric effects in which the dielectric constant changes near T(Neel) are normally small (<1%), negative, and scale with temperature T as the magnetism M(T) does or as the magnetic energy <Sj . Sj+1> does. By comparison, external artifacts due to Maxwell-Wagner space charge can be very large (>1000%), positive, and have T-dependences which do not vary as M(T) [Catalan; Catalan and Scott].
In the fourth part of the talk I will discuss the extension of present searches for room-temperature multiferroics from oxides to fluorides [Blinc], with illustrations from K3Fe5F15 (Tc = 125K) and Sr3(FeF6)2.
Finally, in the last part of the tutorial I will provide an up-date on BiFeO3, the most popular multiferroic material at present; I will emphasize the new, unpublished, discoveries [Palai et al.] of a metal-insulator transition in this material at 931C (atmospheric pressure) and 47 GPa (room temperature). This is shown schematically in Figure 1. This is the only know metal-insulator in a ferroelectric magnet. And I will discuss the new [Singh et al., arXiv 2007; Cazayous et al., arXiv 2007] and unexpected magnetic spin-reorientation transition at 200K (one sample) or 140K (another sample), and the spin-glass transition at 29.4K.

R. Palai et al., Physical Review B (January 2008).

G. Catalan et al., Phys. Rev. Letters (January 2008).

M. Singh et al., condmat arXiv December 2007.

R. Blinc et al., J. Appl. Phys. (2008).

M. Cazayous et al., condmat arXiv December 2007.

J. F. Scott, Phys. Rev. B16, 2329 (1977)

A. Glass et al., Commun. Sol. St. Phys. (1977).

G. Catalan, Appl. Phys. Lett. (2005).

G. Catalan and J. F. Scott, Nature 448, E4 (2007).

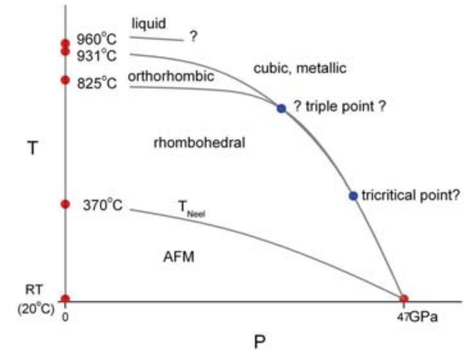

Schematic phase diagram of bismuth ferrite, showing metal-insulator transition to cubic phase and orthorhombic beta phase.

ZA-02

Multiferroic materials: from bulk to thin films.

W. Prellier
ENSICAEN, CNRS, Caen, France

Transition metal oxides with perovskite-type structure exhibit a rich spectrum of interesting properties, including magnetism, ferroelectricity, strongly correlated electron behaviour, superconductivity, magnetoresistance, half metals etc., which have become the research area of great interest among the scientific community for decades. Previously, perovskite oxides were considered as pure academic materials, but the discovery of superconductivity at high temperatures in cuprates and soon after of colossal magnetoresistance in manganites, makes that they are now regarded as potential candidates for various applications in electronics, such as memory elements, actuators and sensors.

There exist very few materials which exhibit multiple functional properties -one such class of material is called multiferroics. Multiferroics are interesting because they possess simultaneously ferromagnetic and ferroelectric polarization and there might be a coupling between them. Thus, the magnetic polarization could be switched by applying an electric field likewise the ferroelectric polarization can be switched by applying a magnetic field. As a consequence, they offer rich physics and novel devices concepts, which recently nested a great interest among the researchers.

During this tutorial, the recent experimental status, both in bulk single-phase and in thin film form, will be presented. Current study on the ceramic compounds in bulk form including Bi(Fe,Mn)O3, REMnO3 and the series of REMn2O5 single crystals (RE=rare earth) will be discussed in the first part. A detailed overview on multiferroic thin films and artificially grown structures (multilayers and nanocomposites) will be presented in a second part. A peculiar attention will be given to the BiFeO3 compound, which has been among the one of the few naturally existing multiferroic materials, that has been studied extensively in the past few decades, both in the form of bulk and thin films. Finally, some possible applications in spintronics will be discussed.

This work was carried out in the frame of the Network Of Excellence FAME (FP6-5001159-1), the STREP project MAnipulating the COpling in Multiferroic FIlms (NMP3-CT-2006-033221) supported by the European Commission and by the CNRS, France. Partial support from the ANR (NT05-1-45177, NT05-3-41793) is also acknowledged.

ZA-03

Multiferroic Composites: Magnetoelectric Effects, Sensors and High Frequency Devices.

G. Srinivasan
Physics, Oakland University, Rochester, MI

Multiferroics with two or more ferroic (ferroelectric, ferro/ferri/anti-ferromagnetic, ferroelastic) orderings have attracted considerable interests in recent years. Single-phase multiferroics are rare and their magnetoelectric (ME) responses are either weak or occur at temperatures too low for practical applications. Ferromagnetic-piezoelectric composites, however, show strong ME coupling at ambient temperatures. The ME effect here is a product-property mediated by elastic deformation, i.e., an electric polarization is induced by an ac magnetic field in the presence of a dc bias field. So far, three kinds of ME composites have been investigated: (a) ferrite and piezoelectric ceramics (e.g., lead-zirconate-titanate), (b) magnetic metals/alloys and piezoelectric ceramics, and (c) magnetic alloys and piezoelectric polymers. The composites show a rich variety of phenomena including giant low-frequency ME interactions and enhanced coupling when magnetic and/or electric sub-systems are at resonance.

This tutorial presentation will focus on recent developments in the physics, materials science and applications of composite multiferroics.

We will discuss single crystal and polycrystalline bulk and layered composites; epitaxial heterostructures; ferrites, shape memory alloys, or transition metal/alloy based multiferroics; polymer ferroelectric-ferromagnetic composites; ME characterization techniques and the theory of ME phenomena. The potential use of composites for magnetic field sensors and transduceres, memory devices, and dual electric and magnetic field tunable microwave and mm-wave devices will also be discussed.

The review will conclude with an outlook on future possibilities and challenges in the field of multiferroic magnetoelectric compsoites.

1. "Multiferroic magnetoelectric composites: Historical perspective, status, and future direction," Ce-Wen Nan, M. I. Bichurin, S. Dong, D. Viehland, and G. Srinivasan, in press, J. Appl. Phys., 2008.

AA-01

Magneto-optical and spin transfer switching properties of current-perpendicular-to plane spin valves with perpendicular magnetic anisotropy.

K. Aoshima[1], N. Funabashi[1], K. Machida[1], Y. Miyamoto[1], N. Kawamura[1], K. Kuga[1], N. Shimidzu[1], T. Kimura[2], Y. Otani[2]
1. Science & Technical Research Laboratories, Japan Broadcasting Corp., Setagaya, Japan; 2. The Institute for Solid State Pysics, The Tokyo University, Kashiwa, Japan

1. Introduction

Magneto-optical (MO) observation of spin transfer switching (STS) by visible light has been demonstrated using the current-perpendicular-to-plane spin-valve (CPP-SV) device with a transparent top electrode [1]. However, because of its in-plane magnetic anisotropy, the detected MO signal was not sufficient for useful applications, such as a MO light modulation device driven by STS or a time resolved STS observation [1]. To accomplish those MO devices driven by STS, large MO effect and an efficient spin transfer are both required at a same time. It is well-known that magnetic materials with perpendicular anisotropy have larger MO effect compare to that with in-plane anisotropy. Although the STS with the perpendicular anisotropy have been succeeded for MRAM application to reduce switching field [2], MO properties of the sandwich structure such as the CPP-SV structure have not been investigated. In this paper we show MO properties of CPP-SV stacks with perpendicular anisotropy using GdFe free layer, as well as their STS properties.

2. Experiment

The film stacks of the CPP-SV is substrate/bottom electrode/Tb-Fe-Co(20)/ $Co_{75}Fe_{25}$ (1)/Cu(6)/Gd-Fe(t)/Cu(3)/Ru(3) (in nm). The films were deposited by DC magnetron sputtering system and annealed at 190 °C in vacuum without magnetic field. Tb_{32}-Fe-Co (at%) and $Gd_{30}Fe_{70}$ (at%) layers serve as the pinned and the free layer, respectively. In these compositions, magnetic moment direction of Tb and Gd are aligned parallel with the applied magnetic field at room temperature [3]. MO measurements were carried out in the wave length of 780 nm. CPP-SV devices were fabricated by electron beam lithography and lift-off method. Transport properties were measured by 4-point probe method. STS properties were evaluated by pulsed current of which duration is 1 µs at a magnetic field of -70 Oe. Positive current corresponds to current flowing from the bottom to the top electrode.

3. Results and Discussion

The inset of fig. 1 shows Kerr rotation (θ_k) for Gd-Fe 10 nm sample versus applied field. It has steps which correspond to the switching of the Gd-Fe (smaller coercivity, $H_c \approx 300$ Oe) and Tb-Fe-Co (lager Hc≈ 6.5 kOe) layer. This indicates that Gd-Fe and Tb-Fe-Co layer exhibit sufficient property for the free and the pinned layer respectively. Figure 1 shows the θ_k of Gd-Fe for various thickness. θ_k is about 0.18 ° for samples which thickness is more than 20 nm, and decreased with a decrease of the Gd-Fe thickness for thinner than 20 nm. This reduction was explained that the Gd-Fe thickness became thinner (<20nm) than a penetration depth of the light. And a sign of θ_k was changed from positive to negative for the samples thickness of 6 nm or less. Cause of the sign change is not clear here. But we speculate that slight composition change may occur near the interface of GdFe due to an intermixing. Figure 2 (a) shows schematic figure of the fabricated CPP-SV and direction of current flow and magnetic field. Figure 2 (b) and (c) show Magneto Resistance (MR) response curve and STS property of CPP-SV with Gd-Fe 10 nm, respectively. The MR ratio was about 0.06%. Small MR is attributed to large resistivity of TbFeCo and GdFe (about 200 µΩcm). Switching current from high to low resistance and low to high resistance were -3.1×10^7 A/cm^2 and 1.6×10^7 A/cm^2, respectively. Resistance change was about 0.3 mΩ which is consistent with the resistance change obtained from the MR curve. These results demonstrate that STS was succeeded with GdFe free layer which shows large Kerr rotation. CPP-SV using GdFe free layer with perpendicular anisotropy would have great potential to improve light modulation property of those MO devices.

[1] K. Aoshima, N. Funabashi, K. Machida, Y. Miyamoto, N. Kawamura, K. Kuga, N. Shimidzu, F. Sato, T. Kimura, and Y. Otani, Appl. Phys. Lett. **91** pp. 052507-1-3 (2007)

[2] S. Mangin, D. Ravelosona, J. Katine, M. Carey, B. Terris, and E. Fullerton, Nature Mater., **5** , pp. 210-215 (2006)

[3] X. Jiang, L, Gao, J. Sun, and S. S. Parkin, Phys. Rev. Lett. **97** pp. 217202-1-4 (2006)

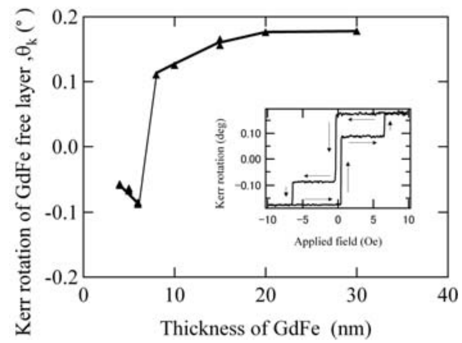

Fig. 1 Kerr rotation of GdFe free layer versus thickness of GdFe for spin-valve stacks of substrate/Ru/Cu/TbFeCo/CoFe/Cu/GdFe [4-30 nm]/Cu/Ru. The solid line is guide to the eye. Inset shows Kerr hysteresis loop of the spin-valve stack of GdFe [10 nm].

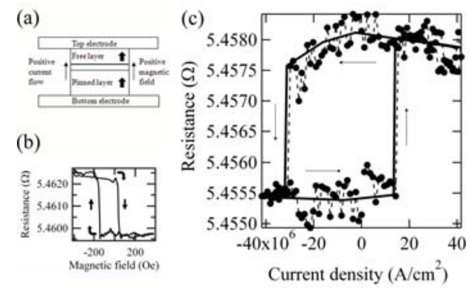

Fig. 2 (a) Schematic figure of the device with the direction of current flow and the magnetic field. A MR response curve (b) and a spin transfer switching curve (c) for the spin valve with 10 nm GdFe free layer (Resistance indicates dV/dI). The solid line is guide to the eye.

AA-02

Time-resolved magnetization switching induced by spin-transfer in Magnetic MgO tunnel junctions.

T. Devolder[1], J. Hayakawa[2,3], K. Ito[2], H. Takahashi[2], S. Ikeda[3], P. Crozat[1], J. V. Kim[1], C. Chappert[1], H. Ohno[3]

1. Institut d'Electronique Fondamentale, ORSAY Cedex, France; 2. Advanced Research Laboratory, Hitachi, Ltd, Tokyo, Japan; 3. Laboratory for Nanoelectronics and Spintronics,, Research Institute of Electrical Communication, Tohoku University, Sendai, Japan

The spin-transfer torque can switch the magnetization of a nanomagnet [1], which is considered as a promising route to ensure the scalability of programming in high density Magnetic Random Access Memories. One important issue is whether fast writing can be achieved in a routine manner in the magnetic tunnel junctions (MTJ) with high magneto-resistance ratios that are needed for efficient memory reading. In this paper, we study spin-transfer switching induced by fast voltage pulses in MgO-based magnetic tunnel junctions.

Our devices are patterned from a MTJ of composition CoFeB (2.5 nm, free layer)/MgO (0.9) /CoFeB (6)/Ru(0.8)/CoFe(5)/MnIr(8). The MTJ is patterned in a pillar-shaped rectangle of size 100x300 nm. The long axis is parallel to the pinning direction.

The quasi-static properties of the MTJ are consistent with the uniaxial anisotropy expected from the sample elongated shape. The two remanent states have resistances of 286 and 364 W. Spin transfer loops (i.e. I-V curves) indicate quasi-static switching voltages to are 0.6 V±0.1 V for the AP to P transition and 0.6 V±0.1 V for the P to AP transition.

For time-resolved switching experiments, we first prepare the sample in the remanent P state using a proper field history. A (negative) voltage step Vstep=-0.5 V with a rise time of 55 ps is then sent to a 50 W line feeding the sample. Due to the reflection at the high impedance device, the voltage across the device is almost twice this incident voltage, hence it is near -1V. After amplification, the transmitted voltage is recorded with either a sampling (i.e. stroboscopic) oscilloscope with a bandwidth of 26 GHz (Fig.1A) or a single-shot oscilloscope with a bandwidth of 13 GHz (Fig.1B). With these set-up, the transmitted voltage abruptly decreases when the device transits in the high resistance state (Fig. 1A inset).

From single shot switching records (Fig. 1B), we could determine individual switching instants, and the distribution thereof. They are randomly distributed with a mean value of 5.3 ns. Note that the widely used stroboscopic techniques, such as pump-probe optical techniques [2] or electrical sampling (Fig.1A or [3]) can fail to describe accurately the switching main characters. Indeed in these techniques, any time-resolved curve must be reconstructed from a large number of switching tests, and the present stochasticity renders this reconstruction inoperative.

Knowing the shape of the current pulse, we translate the voltage traces into magneto-resistance traces (Fig. 2). Three main interesting features are worth noticing. First, there is an incubation delay before anything happens after the onset of the voltage step. The resistance stays quiet during that delay. Secondly, there is a fast transition from P to AP resistance that takes circa 0.4 ns. Finally, there is a large ringing after switching. To study this ringing, we have averaged 20 traces, those traces having been selected to have the same switching instant 1.650 ns. This averaging procedure (Fig. 2A) confirms that the ringing is reproducible.

We have repeated this procedure with other selected switching instants (Fig. 2B). It is striking to notice once the stochastically varying incubation delay is passed, the resulting time evolutions of the electrical resistance seem identical within the measurement accuracy. This is our central conclusion: the switching instant fluctuates but the resistive signature of the switching trajectory after the incubation delay is deterministic.

Figures

Figure 1: (color online): Inset: sketch of the incident and transmitted voltage pulses when a device switches from P to AP. The dotted line rectangle zooms on the pulse plateau. Main panel: zoom on the plateau of the transmitted voltage. Each switching trials is displayed with a different color. Panel A is measured with a sampling 26 GHz oscilloscope. Panel B: is measured with a single shot 13 GHz oscilloscope.

Figure 2: (color online): Panel A: top curve: single shot switching event measured with 13 GHz bandwidth. Bottom curve; average of 20 single shot switching events having the same switching instant. Panel B: average of single shot switching events with switching instants of 0.7 (black), 2.8 (red), and 4.9 ns (blue). Data are plotted versus time elapsed after switching, and are vertically offset.

[1] J. A. Katine et al., Phys. Rev. Lett. 84, 3149 (2000).

[2] Y. Acremann et al., Phys. Rev. Lett. 96, 217202 (2006).

[3] N. C. Emley et al. Phys. Rev. Lett. 96, 247204 (2006).

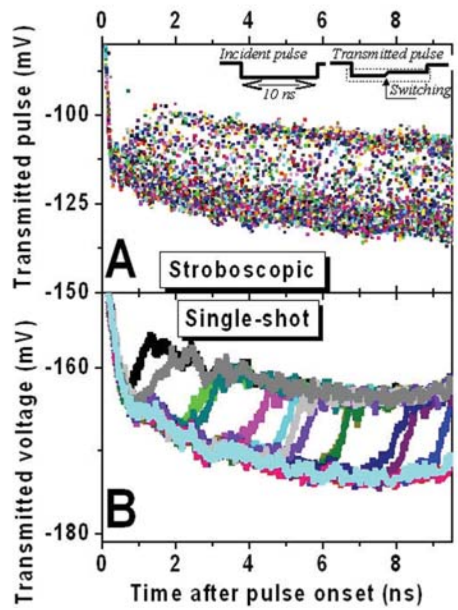

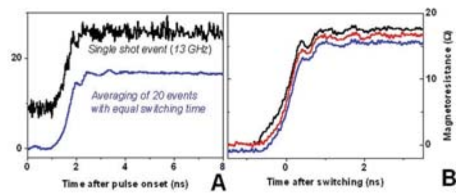

AA-03

Coherent control of spin transfer torque magnetization dynamics.

S. Serrano-Guisan[1], K. Rott[2], G. Reiss[2], B. Ocker[3], J. Langer[3], *H. W. Schumacher*[1]
1. Physikalisch-Technische Bundesanstalt, Braunschweig, Germany; 2. Department of Physics, University of Bielefeld, Bielefeld, Germany; 3. Singulus Nano Deposition Technologies GmbH, Kahl am Main, Germany

We study time resolved precessional magnetization dynamics induced by spin momemtum transfer in CoFeB/MgO/CoFeB based magnetic tunnelling junctions (MTJ). Our experiments are performed at room temperature on elliptical MTJ nanopillars having lateral dimensions down to 120 nm [1]. The MTJ stacks were sputter deposited in a Singulus TIMARIS 10 Target PVD module. In static magnetic fields the CoFeB free layers of the nanopillars show a well defined mainly single domain switching behaviour. Spin transfer torque precession of the CoFeB free layer is excited by application of ultra short current pulses with pulse duration from 0.16 to 5 ns duration and with current densities around 10^6 A/cm^2. The time resolved precession of the free layer is studied by measuring the time resolved tunnelling magneto resistance (TMR) change of the MTJ using a fast sampling oscilloscope. Superposition of a weak dc bias current on the excitation pulse allows detecting both the spin torque precession during the current pulse and the magnetization ringing after pulse termination (Fig. 1).
From the decay of the ringing the effective Gilbert damping parameter α of the MTJ free layer is derived (Fig 1a). Additionally, the modification of α under the influence of STT is accessible from the decay of the STT precession during a long current pulse (Fig.1b). Depending on the relative orientation the free and pinned layer magnetization the STT leads to an enhaced or reduced effective damping in agreement with theoretical predictions.
The magnetization ringing further provides information on the non-equilibrium orientation of the free layer magnetization upon pulse termination. This is of major importance e.g. to evaluate the reliability of spin torque magnetization switching employing ultra short current pulses. We show that by adapting the duration of the excitation pulse to integer multiples of the period of the spin torque precession the magnetization ringing can be coherently suppressed (Fig. 2). Such coherent control of spin torque dynamics is a prerequisite for ultra fast ballistic spin transfer torque magnetization reversal.
STT magnetization reversal under application of a 10 mT hard axis bias field is shown in Fig. 3. Fig. 3(a) shows switching by a 5 ns current pulse of 4×10^6 A/cm^2 current density. At the pulse inset the magnetization performs a precessional overshoot followed by damped precession. Upon pulse termination the magnetization relaxes to the reversed equilibrium state.
Figure 3(b) shows biased STT switching by 100 and 500 ps pulses. Again, the initial overshoot is observed. It is now followed by a pronounced magnetization ringing indicating non equilibrium magnetization alignment upon pulse termination. Furthermore the reduced voltage signal measured in the reversed state speaks for a reduced switching reliability.
Finally Fig. 3(c) shows switching for a 1 ns pulse. Here the pulse duration is coherently matched to the duration of the precessional overshoot observed for the 5 ns pulse. Upon pulse decay the magnetization is near the reversed equilibrium state and the magnetization ringing is suppressed. Furthermore, for the coherently optimized pulse a high switching reliability is found.
Such biased quasi ballistic STT magnetization reversal could allow ultra fast and yet reliable STT memory operation.

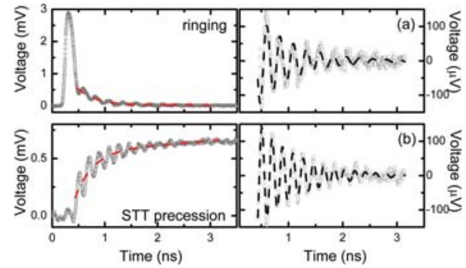

Fig. 1: Time resolved TMR signal for 160 ps pulse (a) and pulse step (b). Current density (a) 9×10^6 and (b) 3×10^6 A/cm^2. 24 mT hard axis field . Left: raw data. Right: precession data obtained by subtracting RC low pass response (red line) from raw data. Precession parameters are derived from fitting (black line).

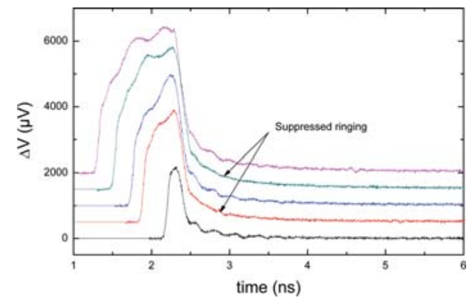

Fig. 2: Coherent control of STT precession by tailoring pulse duration. When the pulse terminates after an integer number of full precessional turns the magnetization ringing is suppressed.

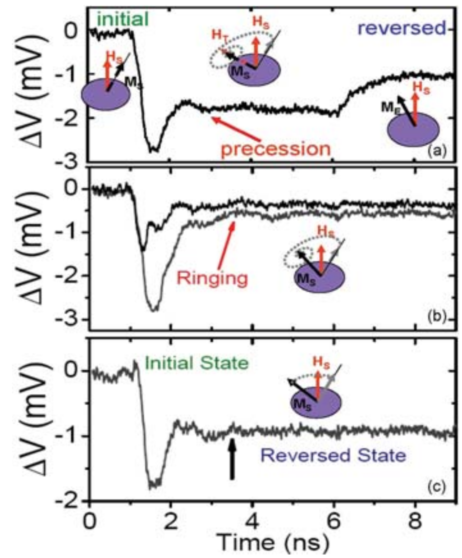

Fig. 3: Biased STT magnetization switching: (a) 5 ns pulse (b) 100 ps (black) and 500 ps pulse (grey), (c) 1 ns pulse.

AA-04

Real Time Measurements of Spin-Transfer Switching in CoFeB/MgO/CoFeB Magnetic Tunnel Junctions.

H. Tomita[1], K. Konishi[1], T. Nozaki[1], M. Shiraishi[1], H. Kubota[2], A. Fukushima[2], S. Yuasa[2], Y. Suzuki[1]

1. Osaka university, Toyonaka, Japan; 2. National Institute of Advanced Industrial Science and Technology (AIST), Tsukuba, Japan

Introduction

Spin-transfer magnetization switching has received increasing attention as a novel magnetization switching technique without external magnetic field. This technique has a potential to lower the writing current in the magnetoresistive random access memory (MRAM) compared with the classical magnetic field writing. Coherent amplification of the precession and successive switching of the free-layer magnetization in a CPP-GMR device was demonstrated by I. N. Krivorotov et al. [1] at low temperature (40 K). For real application, however, the mechanism of the room temperature switching of the magnetic tunnel junctions (MTJs) where the thermal fluctuation may play important role [2,3] must be clarified. In this study, we performed time-resolved measurements of current-induced magnetization switching in MgO-based MTJs using a high speed single-shot oscilloscope to understand the switching process.

Experimental method

The layer structure of the measured MTJs is MgO substrate/buffer/PtMn/CoFe /Ru/CoFeB(3.0)/Mg(0.6)/MgO(0.6)/CoFeB(2.0)/cap (numbers are thickness in nm). Pillars of 70×160 nm^2 in size were fabricated from the film using an electron-beam lithography and an Ar-ion milling. Applied magnetic field direction and MTJ's easy axis inclined by 30 degrees. Schematic illustration of the measurement system is shown in figure 1. After initializing the magnetization to the parallel state, a DC pulse with duration time of 10 ns was applied from a pulse generator to the MTJ through a power divider. A reflected pulse from the MTJ was recorded by the high-speed storage oscilloscope (Band width: 18 GHz, Sampling rate: 50 GS/s).

Results

In figure 2, the typical reflected pulse signals are shown. Amplitude of the applied current pulse was 2.0 mA(J = 1.8 × 10^7 A/cm^2). In the case of light color line, we can see no voltage transition in the reflected pulse signal. In contrast, in the case of dark color line, clear voltage step appears after a waiting time of about 5 ns. Here, we define the waiting time as the time delay between the initial rise of the reflected pulse signal and the onset of the voltage step. The transition indicates a magnetization switching from the parallel to the anti-parallel state. Although considerably long waiting time was observed, the transition time from parallel state to the anti-parallel state was found to be very short (300 ps for example). This result agrees well with micromagnetic calculations [3]. Repetitive several hundreds measurements were performed under the same condition with different current amplitudes. The distribution of the waiting time in the switching process appears in the figure 3. The amplitudes of the applied currents were 2.0 mA(J = 1.8 × 10^7 A/cm^2) and 1.7 mA(J = 1.5 × 10^7 A/cm^2). We can clearly see that the distribution of the waiting time shift to the longer time range with decreasing the current amplitude. Further analyses of the data revealed a correlation between the waiting time and the transition time. We will try to discuss the detailed switching mechanism in the talk.

This study was partly supported by New Energy and Industrial Technology Development Organization (NEDO) and a Grant-in-Aid for Scientific Research (A)-19206002 of JSPS.

[1] I. N. Krivorotov et al, Science 307. 228 (2005)

[2] R. H. Koch, J. A. Katine, and J. Z. Sun, Phys. Rev. Lett. 92. 088302 (2004)

[3] M. D. Stiles and J. Miltat, Top. Appl. Phys. 101, 225 (2006)

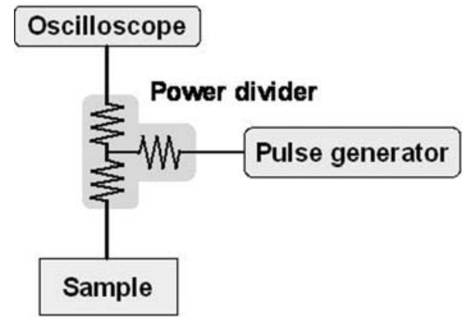

Fig.1 Measurement system

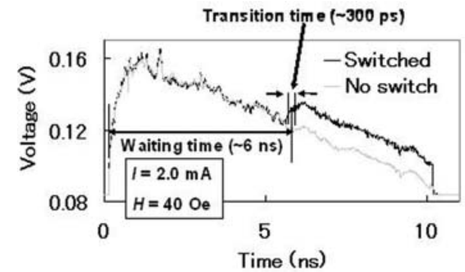

Fig.2 Time-resolved voltage signal of switching

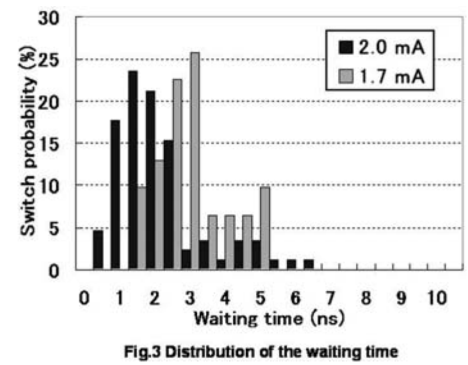

Fig.3 Distribution of the waiting time

AA-05

Observation of intermediate states in large magnetic tunnel junctions with composite free layer.

X. Yao[1], R. Malmhall[2], R. Ranjan[2], *J. Wang*[1]
1. MINT Center & Electrical and Computer Engineering Department, Univ. Of Minnesota, Minneapolis,, MN; 2. Yadav Technology, Fremont, CA

Current-induced magnetization switching (CIMS) has advantages of device scaling compared to the traditional field-induced switching. Several groups reported the existence of an intermediate state in GMR devices due to the multidomain formation [1-3] by the spin-polarized current. In this paper, we discuss the current-driven switching behaviour of large MTJ devices with a composite free layer, with the emphasis on the intermediate state observation. To generate and control reversible intermediate states is one of ways to realize the multilevel spintronic devices such as MRAM.

The composite free layer structure is CoFeB/CoFeB-oxide/CoFeB. CoFeB-oxide layer acts as a nano-current-confined (NCC) structure, which can reduce the critical switching current density (Jc) of the devices [4,5]. Same as FeSiO NCC layer, CoFe prefers to form the cores and the oxide material together with small element boron prefer at the grain boundary. Fig1a shows the hysteresis loops of the CoFeB-oxide samples with different oxide fraction. Film thickness fixed at 12 nm. With the increase of the oxide fraction, both the squareness and the coercivity were decreased. The decrease of the squareness indicates that part of CoFe grains are decoupled by the oxide grain boundary, and switch gradually. And the decrease of the film coercivity shows that the grain size of the CoFe decreases. Film became superparamagnetic when oxide fraction is higher than 40% (insert of fig.1 a). The hybrid free layer with different NCC layer thickness was studied (fig.1b)(oxide fraction fixed at 30 at%). With increase of the NCC layer thickness from 1nm to 3 nm, the saturation magnetization keeps constant, and its coercivity increases slowly. The insert of fig.1b shows the superparamagnetic behaviour of a single NCC layer with 3 nm thickness.

The sample with full MTJ structure was deposited by sputtering method. The film structure is: SiO2/Bottom electrode/IrMn/CoFe/Ru/CoFeB/MgO/ composite free layer/top electrode. The composite free layer is: CoFeB 2nm /CoFeB-oxide30at% (NCC layer)3nm/CoFeB 1nm. The sample was patterned by e-beam lithography into 200 nm*600 nm with different shape (bar and ellipse) in order to observe the intermediate states. For ellipse shape sample, the hysteresis loop and the current-induced switching are shown in fig2 a-c. When the bias field changed from the switching field (Hsw) to the offset field, Jc increases and reaches to 5*10^6 A/cm2 when the bias field equals to the offset field. From AP to P state switch, an intermediate state (IM) is observed in both field-driven and current-driven switching. Fig2c shows the CIMS switching from P to AP state. Different from the AP to P switch, the switching is sharp and there is no intermediate state. The final AP state is confirmed by measuring the resistance using a small current (2*10^-5 A) at zero field after each scan. The bar shape sample also has an intermediate state (fig.2d~f). Fig.2e and 2f show the minor loops of current-driven switching. IM state also exists when applying a negative current, which is different from the ellipse shape sample. As expected for MTJ with large size, there may be multidomain structure in its free layer. However, this cannot explain the distinct and reversible intermediate states observed in this work. The repeatable and distinct intermediate states may come from the pinning sites induced by the granular type nano-current-channel layer. Detailed discussion will be addressed in the full paper.

[1] T. Yang, et al, J. Appl. Phys., 97 (2005) 064304

[2] Y. Jiang, et al, Appl. Phys. Lett., 89 (2006) 122514

[3] D. Ravelosona, et al, Phys. Rev. Lett., 96 (2006) 186604

[4] H. Meng, J. P. Wang, IEEE Trans. Magn. 41 (2005) 2612

[5] H. Meng, J. P. Wang, Appl. Phys. Lett., 89 (2006) 152509

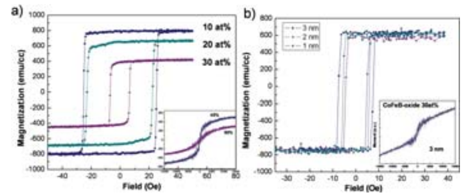

Fig.1 (a) Hysteresis loops of CoFeB- oxide films (12 nm) with different oxide fraction. Insert shows superparamagnetic behavior above 40 at%. (b) Hysteresis loops of hybrid free layer with different NCC layer thickness. Insert shows superparamagnetic behavior of a single CoFeB-oxide layer with 3nm.

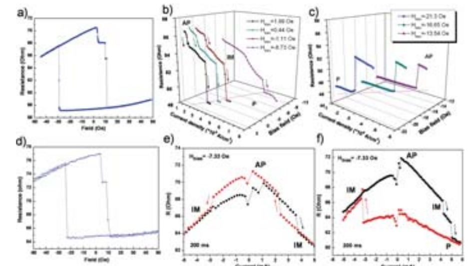

Fig.2 Ellipse shape sample: hysteresis loop (a); current-induced magnetization switching (CIMS) curves: from AP to P (b); from P to AP (c) under different bias field. Bar shape sample: hysteresis loop (d); minor loops of current-induced switching (e and f).

AA-06

Spin transfer switching in magnetic tunnel junctions with several compositions of the free layer.

D. Watanabe[1], M. Oogane[1], Y. Ando[1], T. Miyazaki[2]
1. Applied Physics, Tohoku University, Sendai, Japan; 2. WPI-AIMR, Tohoku University, Sendai, Japan

Current induced magnetization switching has a potential as a key technology for a writing scheme in high-density MRAM. To achieve it, the critical current for the switching should be reduced from the value reported recently [1] because applying current is restricted by a peripheral circuit in MRAM. Theoretical predictions [2] have suggested that critical current was proportional to the magnetic parameter $\alpha M_s^2/g$, where α, M_s^2, g were respectively damping constant, saturation magnetization, and spin-transfer efficiency which was described as $g = P/(1+P^2\cos\theta)$ (P: spin polarization) in MTJ [3]. To utilize it as a lead for reducing critical current, it is important that the relation between the magnetic parameters of small ferromagnet and critical current is confirmed experimentally.

Magnetic tunnel junctions (MTJs) were prepared using UHV sputtering system with the structure of buffer/IrMn/CoFe/Ru/CoFeB/MgO/CoFeB/Ta/capping on an oxidized Si wafer. The first and second CoFeB correspond to pinned and free layer, respectively. The free layer has a thickness of 2 nm and compositions altered as $(Co_{50}Fe_{50})_{100-x}B_x$ (x = 20,25,30). The films were fabricated into a size of about 100×200 nm^2 by electron beam lithography and ion milling. Tunnel magnetoreistance (TMR) loops with sweeping magnetic field and current were obtained using 4-probe lock-in amplifier method. Applied current was pulsed with a duration ranging from 10 μs to 100 ms and defined flowing from bottom to top electrode as a positive. The α value of each free layer in the TMR multilayer was evaluated using FMR method by which the intrinsic value without the effect from magnetic inhomogeneity can be obtained [4]. The M_s was measured by VSM.

Fig. 1 shows the TMR ratios as a function of resistance area product (RA) in each MTJ with x = 20,25,30 after annealing at 325°C under a magnetic field of 1 T. The TMR ratios with x = 20 were 100-120% at around RA = 10 Ωμm^2. However, the TMR ratios were reduced rapidly with increasing boron density of the free layer because the annealing temperature was not enough to crystallize the CoFeB, which was necessity for high TMR ratio in MgO-based MTJs. The inset in Fig. 1 shows typical TMR loops with magnetic field and current scan, respectively, in the MTJ with x = 20. Good agreement in the resistances between two magnetization states is confirmed. The inset in Fig. 2 shows the dependence of the critical current on the current pulse width. Solid lines are the fitting result using thermal activation model which defined critical current as $I_c^{\pm} = I_{c0}^{\pm}[1-k_BT/E\ln(\tau_p/\tau_0)]$ [5], where k_B, E, τ_p, τ_0 are Boltzmann constant, activation energy, pulse width, and inverse of attempted frequency (~10^9 GHz), respectively. The symbol + (–) means a magnetization switching from anti-parallel(AP) to parallel(P) (P to AP) state. The critical current density $J_{c0} = (I_{c0}^{+}-I_{c0}^{-})/2A$ (A: junction area) and thermal stability E/k_BT could be obtained from the fitting. These parameters are comparable for different MTJs and considered as an indicator for devices. From the fitting to the inset in Fig.2, both $J_{c0} = 6.7\times10^6$ A/cm^2 and $E/k_BT = 33.2$ were estimated. The J_{c0} observed in each MTJs and the parameter $\alpha M_s^2/g$ are plotted in the vertical and horizontal axis of Fig. 2, respectively. In the calculation of $\alpha M_s^2/g$, experimentally obtained values, α = 0.014, 0.014, 0.017 and M_s = 1370, 1150, 950 emu/cc, in the free layer with x = 20, 25, 30 were used, respectively. The line in Fig. 2 has the slope of $4\pi ed/h$ which is the proportionality coefficient in the theory, where d is set to 2 nm as the free-layer thickness. Because the measured values were in nearly agreement with theoretical line in Fig. 2, the theoretical relation between the J_{c0} and the magnetic parameter $\alpha M_s^2/g$ was confirmed experimentally.

This work was partially supported by R & D for Next-Generation Information Technology of MEXT and SCOPE of MIC.

[1] Z. Diao *et al*., Appl. Phys. Lett. 87, 232502 (2005).

[2] J. C. Slonczewski, J. Magn. Magn. Mater. 159, L1 (1996).

[3] J. C. Slonczewski, Phys. Rev. B 71, 024411 (2005).

[4] S. Mizukami *et al*., Phys. Rev. B 66, 104413 (2002).

[5] R. H. Koch *et al*., Phys. Rev. Lett. 92, 088302 (2004).

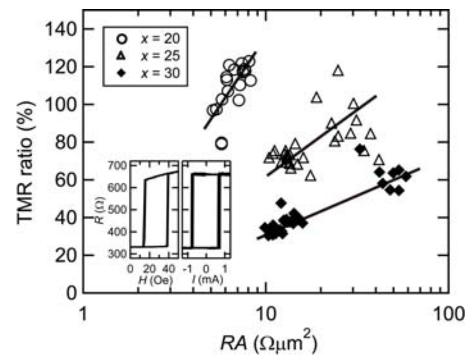

Fig.1 TMR ratios versus *RA*. Inset: Typical TMR loops for field and current scan.

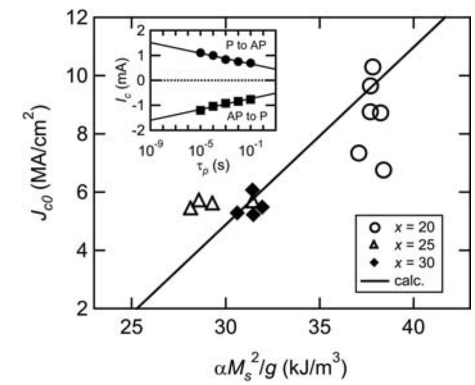

Fig.2 Relation between J_{c0} and predicted parameter. Inset: Fitting results of I_c versus τ_p.

AA-07

Spin Torque Induced Magnetization Switching Variations.

X. Wang, W. Zhu, M. Siegert, D. Dimitrov
Seagate Technology, Bloomington, MN

Fast magnetization switching under spin torque current excitation and sufficient thermal stability at room temperature are two main design criterions for spin torque magnetic random access memory (MRAM). When characterizing spin torque induced magnetization switching, both the averaged switching behavior and the switching variations are critical. Here spin torque induced magnetization switching variations are studied based upon experimental measurement and theoretical modeling. The study covers a wide time range, from the short time dynamic switching (10 nanosecond) to the long time thermal switching (0.1 sec). The modeling and the experimental measurements provide valuable information and tools for design tradeoffs between current switching magnitude, switching variations, switching speed and thermal stability.

Square wave polarized current pulses with different pulse durations and amplitudes are used to switch free layers of the magnetic tunneling junctions. Figure 1a shows the measured switching current variations as a function of the pulse width. As the pulse width decreases, mean switching current increases. The switching current standard deviation remains almost constant for long pulse width and starts to increase when the switching time decreases to certain threshold. Figure 1b shows the measured switching time standard deviation versus the measured mean switching time for constant current amplitude. It is found that the switching time variation is almost the same as the mean switching time for long time switching process and the ratio of the switching time variation to the mean switching time decreases for short time switching process. When standard deviations of the switching current or time are normalized to their means, the coefficients of variation of the switching current or time are obtained. Interesting enough, experimental data shows the coefficient of variation of the switching time decreases while the coefficient of variation of the switching current could increases as the current pulse width scales down from the long time thermal reversal region to the short time dynamic reversal region.

We have solved stochastic Landau-Lifshitz-Gilbert (LLG) equation with spin torque term at room to describe the switching time mean/variations and switching current mean/variations [1]. Figure 2 shows an example of the modeled coefficient of variation and standard deviation of variation of the switching current and the switching time. The model results show the same trend as that of the experimental measurements in Figure 1. In this comparison, only trend matters because the model parameters have not been calibrated to experimental measurement condition. Figure 3 shows an example of model data calibration on the switching current standard deviation versus the pulse width. In this presentation, we will show detailed model data calibrations on spin torque induced switching variations for the whole time range. We will explain the physics for the this different scaling behavior of switching current variation and switching time variation as time scales down from second to nanosecond region.

[1]: X.Wang, Y.Zheng, H. Xi and D. Dimitar, “Thermal Fluctuation Effects on Spin Torque Induced Switching: Mean and Variations”, to be published on J.Appl. Phys.

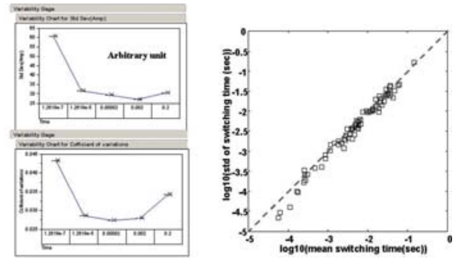

Measured switching current variations versus pulse width and switching time variations versus mean switching time.

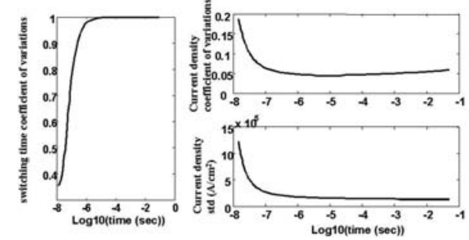

Modeled switching current and switching time variations (standard deviation/mean and standard deviation) versus pulse width.

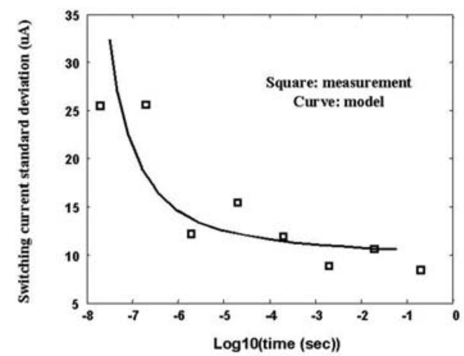

Experimental measurement and model calibration on switching current standard deviation.

AA-08

Spin-torque driven ferromagnetic resonance of Co/Ni synthetic layers in spin valves.

W. Chen[1], G. de Loubens[1], J. L. Beaujour[1], *A. D. Kent*[1], J. Z. Sun[2]
1. Physics, New York University, New York, NY; 2. IBM T. J. Watson Research Center, IBM, Yorktown Heights, NY

Spin-torque-driven ferromagnetic resonance (ST-FMR) in nanostructured magnetic junctions has recently been observed both in magnetic tunnel junctions and in spin-valves [1, 2]. It is a quantitative tool for measuring the magnetic anisotropy and damping of magnetic layers in confined nanojunctions [3]. It also enables measurement of spin transfer torques [4]. Using this method, we have measured the anisotropy and damping of Co/Ni synthetic layers in spin-valves [5]. We also measured the torque acting on this layer. Experiments were conducted on ||[t nm Co 2t nm Ni]×1.2/t| 10 nm Cu| 12 nm Co|| layer structures patterned to ~50 nm lateral dimensions using a nanostencil process. We varied the Co thickness t from 0.1 to 0.4, tuning the magnitude of the Co/Ni synthetic layer's net anisotropy, while the total magnetic moment and thickness of the free layer were kept nearly constant. Field swept ST-FMR measurements were conducted with a magnetic field applied perpendicular to the layer surface. A microwave current was fed into the spin valve junctions at a fixed frequency between 1 and 20 GHz. The field-swept resonance lines were measured as a function of microwave frequency, power and dc current bias. In a low rf power, linear response regime, magnetic anisotropy constants and damping parameters were determined. These results were compared with those obtained from same-stack extended films measured using conventional rf field driven FMR. The layers confined in spin valves have a lower resonance field as shown in Fig. 1(a), which is associated with the effect of both dipolar fields acting on the Co/Ni layer emanating from other magnetic layers in the device, and finite size effects on the spin wave spectrum. The layers confined in spin valves also have a narrower resonance linewidth, and approximately the same linewidth vs frequency slope, as shown in Fig. 1 (b), implying the same damping parameter and a lower magnetic inhomogeneity in the confined structure.

The high-field spin-torque instability threshold currents were determined from measurements of the resonance linewidth vs dc bias (Fig. 2), and the results are in accord with the ones obtained from I-V measurements. The magnitude of spin transfer torque was estimated from both the zero dc bias resonance line and from the change of the resonance linewidth with dc current. These two sets of results are in agreement with each other, and consistent with a sinusoidal dependence of the torque on the angle between the Co and Co/Ni synthetic layer magnetization for 60°~80°. At higher rf power, asymmetric lineshapes were observed, which we associate with large angle precessional dynamics of the free layer.

[1] A. A. Tulapurkar et al., Nature 438, 339 (2005)

[2] J. C. Sankey et al., Phys. Rev. Lett. 96, 227601 (2006)

[3] G. D. Fuchs et al., Appl. Phys. Lett. 91, 062507 (2007)

[4] J. C. Sankey et al., Nat. Phys. 4, 67 (2008)

[5] W. Chen et al., Appl. Phys. Lett. 92, 012507 (2008)

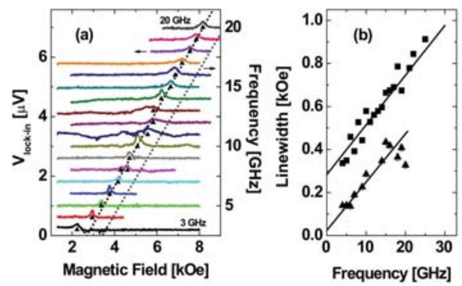

Fig. 1: (a) ST-FMR signal as a function of applied perpendicular magnetic field at different frequencies, from 3 up to 20 GHz. Resonance fields of a 50 x 150 nm2, t=0.4 Co/Ni synthetic free layer in a spin valve; black dashed line: corresponding linear fit; gray dashed line: a linear fit of resonance field vs rf frequency of an extended film with the same Co/Ni layer stack. (b) Linewidth vs rf frequency for the spin valve junction and the extended film, together with their corresponding linear fits.

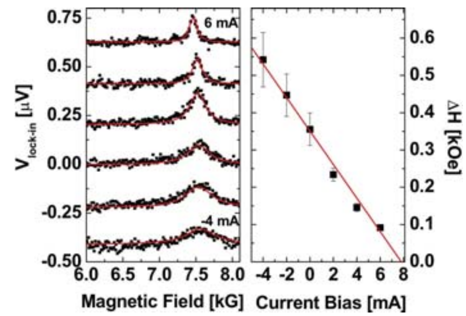

Fig. 2: (a) ST-FMR signal as a function of applied field at different dc currents. The rf frequency was set as 18 GHz, and the rf amplitudes were varied to keep the resonance in a linear response regime for each dc current from -4 to 6 mA in 2 mA steps. Solid lines are Lorentzian fits of each data set. (b) Linewidth vs dc current.

AA-09

Spin torque transfer in deep submicron annular cpp-gmr devices.

M. T. Moneck, X. Zhu, J. Zhu
Electrical & Computer Engineering, Carnegie Mellon University, Pittsburgh, PA

The ability of a spin polarized current to impart a torque on a magnetic film through spin momentum transfer has been the subject of much interest in recent years. The majority of experimental spin transfer research has focused on magnetic point contacts or nanopillars with a linear in-plane magnetization mode [1],[2]. Annular current-perpendicular-to-plane (CPP) multilayer giant-magnetoresistive (GMR) devices offer many advantages such as the absence of magnetic stray field and robust magnetic switching [3],[4]. In this paper, we present an experimental demonstration of the spin torque transfer effect in annular CPP-GMR devices at deep submicron dimensions when switched by a vertically injected current.

Each CPP-GMR annular element, shown schematically in Fig. 1(a) and experimentally in Fig. 1(b), is patterned to a 600 nm outer diameter and 200 nm inner diameter from a sputter deposited film stack with the following structure: Ta (50 Å)/ Cu (500 Å)/ Ta (30 Å)/ NiFe (20 Å)/ CoFe (10 Å)/ Cu (35 Å)/ [CoFe (10 Å)/ Cu (3-5 Å)]x4/ CoFe (110 Å)/ Cu (1500 Å). In this pseudo spin-valve design, the element free layer consists of a Ni81Fe19/Co90Fe10 composite stack, and the reference layer consists of a Co90Fe10 film containing nano-Cu insertions for an increase in the CPP-GMR effect [5]. Both readback and switching of the reference and free layer circular orientation is performed by vertically injecting current through the stack, using the four-point probe test structure shown in the inset of Fig. 1(b), where each test structure is fabricated by a combination of electron beam lithography, optical lithography, and ion milling [5].

The switching of the annular CPP-GMR devices occurs through two mechanisms, one being the Amperean field generated from the injected current and the other being spin momentum transfer. Fig. 2 represents two magnetoresistance curves taken for the annular CPP-GMR elements. Each curve was produced by sweeping a DC current to switch the circular magnetization of the free layer between parallel and anti-parallel states while maintaining the state of the reference layer. For the black curve, the reference layer was clockwise, while the counterclockwise orientation was used for the gray curve. The large disparity between the switching currents of the two curves is a direct result of spin transfer. The major contribution to the switching is the Amperean field, which is independent of the magnetization chirality of the reference layer. If acting under this field alone, the device would switch symmetrically at approximately 13 mA, corresponding to a current density of 5.2x10^6 A/cm^2. Conversely, spin transfer does depend on the magnetization chirality of the reference layer and acts to either assist the Amperean field or work against it. In the case where the reference layer is magnetized counterclockwise, the spin transfer torque acts to assist the Amperean field, thus lowering the switching current by 1.3-3.2 mA, depending on the direction of the injected current. For a reference layer magnetized clockwise, the spin transfer torque acts against the Amperean field by the same amount. In both cases, the spin transfer effect clearly has a measurable impact on the switching properties.

[1] M. Tsoi, A. G. M. Jansen, J. Bass, W.-C. Chiang, M. Seck, V. Tsoi, and P. Wyder, Phys. Rev. Lett., 80, 4281 (1998)

[2] J. A. Katine, F. J. Albert, and R. A. Buhrman, Appl. Phys. Lett., 77, 3809 (2000)

[3] J. G. Zhu, Y. Zheng, G. A. Prinz, J. App. Phys., 87, 6668 (2000)

[4] X. Zhu, J. G. Zhu, U.S. Patent 6,956,297 B2 (18 Oct. 2005)

[5] M. T. Moneck and J.-G. Zhu, J. Appl. Phys., 99, 08H709-1 (2006)

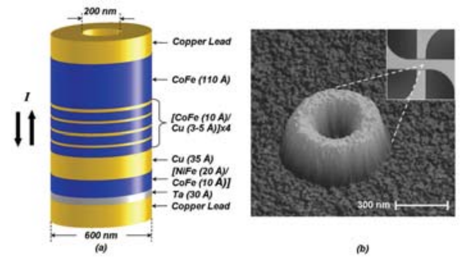

Fig. 1. (a) A schematic diagram of an annular CPP-GMR element and (b) an atomic force microscope image of a fabricated ring where the inset represents the four-point probe test structure used for probing the individual elements.

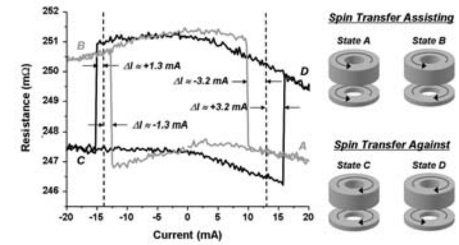

Fig. 2. Magnetoresistance curves demonstrating evidence of spin transfer torque both asssiting and acting against the switching of the CPP-GMR element free layer. The states of the thin free layer and thick reference layer at points A, B, C, and D are represented by the schematic diagrams on the right hand side of the image.

AA-10

Effective description of planar spin-transfer devices.

Y. Bazaliy
1. Department of Physics and Astronomy, University of South Carolina, Columbia, SC; 2. Institute of Magnetism, National Academy of Science, Kyiv, Ukraine

Spin-polarized currents are able to change the magnetic configuration of nanostructures through the spin-transfer effect proposed more than a decade ago [1,2]. Intensive research is currently directed at understanding the basic physics of this non-equilibrium interaction and designing magnetic nanodevices with all-electric control. In those devices spin transfer torques play a key role creating dynamic regimes that are not present in conventional magnetic systems. Unfortunately full dynamic study is not straightforward even for simple spin transfer devices due to the nonlinearity of the Landau-Lifshitz-Gilbert (LLG) equation governing the magnetization motion. A simple device consists of a dynamic magnet (free layer) influenced by the current coming from a stationary spin polarizer (fixed layer) [2,3]. When magnetic anisotropy of the free layer is an easy axis parallel to the spin polarizer direction, the problem can be solved exactly [2,4] But if in addition the easy plane anisotropy of actual devices [5] is accounted for, and/or the polarizer direction is different, the calculations become much more involved. As the anisotropy gets more complicated, additional dynamic features appear: "canted states" [4,6], multiple precession states [6], "magnetic fan" regimes [6], etc. Experimentally, the easy plane anisotropy energy is usually much larger than the easy axis energy, i.e., the system is in the regime of a planar spintronic device [7] (Fig. 1). Fortunately, the limit of dominating easy plane energy is characterized by a simplification of the dynamic equations [8], which mathematically arises from the existence of a small parameter: the ratio of the energy modulation within the plane to the easy plane energy. Physically, the magnetization moves with little deviations from the easy plane and thus can be well described by the in-plane angle governed by an effective planar equation.

In Ref [8] effective equation was derived in the absence of spin-transfer torques. In this work we derive the effective planar equation that takes into account spin transfer torques in general form [9]. Importantly, effective equation has the form of Newton's equation of motion for an effective particle in external potential with a variable viscous friction coefficient. The advantage of such a description is that the motion of the effective particle can be qualitatively understood by applying the usual energy conservation and dissipation arguments. In the absence of current, the effective friction turns out to be a positive constant, so after an initial transient motion the system always ends up in one of the minima of the magnetic energy. However, when current is present, effective friction and energy are modified. Such a modification reflects the physical possibility of extracting energy from the current source, and leads to the emergence of the qualitatively new dynamic regimes: jumps between the minima which correspond to current induced switching events, and persistent oscillations which correspond to the precession states induced by spin-transfer torques.

The power of the planar approach is demonstrated in two cases. First, we analytically calculate the boundaries between different precession cycles [11,6] in the nanopillar device. So far, those boundaries were studied only numerically [6]. Our analytical calculation based on the effective particle analogy is surprisingly simple [10] Second, we the study current-induced switching in a spin-flip transistor [12] and find a new equilibrium stabilized by the current [9]. This stabilization is highly counterintuitive in the following sense: the direction found in Ref. [9] is not stabilized by the anisotropy torques (it is a saddle point) and the added spin transfer torque repels the system from this direction as well. The phenomenon is dubbed as stabilization by repulsion. Even though the conclusion is counterintuitive, it is completely confirmed by the no-approximation calculations and numeric modeling. We show that stabilization by repulsion is closely connected to the dissipation in the system and happens in the overdamped regime already noticed in the conventional case without the spin-transfer torques [8].

[1] L. Berger, J. Appl. Phys., **49**, 2156 (1978); Phys. Rev. B **33**, 1572 (1986); J. Appl. Phys. **63**, 1663 (1988).

[2] J. Slonczewski, J. Magn. Magn. Mater. **159**, L1 (1996).

[3] J. Z. Sun, Phys. Rev. B **62**, 570 (2000).

[4] Ya. B. Bazaliy, B. A. Jones, and S. C. Zhang, cond-mat/0009034; J. Appl. Phys., **89**, 6793 (2001); Physica B, **329-333**, 1290 (2003); Phys. Rev. B, **69**, 094421 (2004).

[5] J. A. Katine *et al.*, Phys. Rev. Lett., **84**, 3149 (2000).

[6] see detailed references in papers [9] and [10].

[7] A. Brataas, G. E. W. Bauer, and P. J. Kelly, Phys. Rep., **427**, 157 (2006).

[8] C. J. G.-Cervera, Weinan E, J. Appl. Phys., **90**, 370 (2001).

[9] Ya. B. Bazaliy, Appl. Phys. Lett. **91**, 262510 (2007).

[10] Ya. B. Bazaliy, Phys. Rev. B **76**, 140402(R) (2007).

[11] S. I. Kiselev *et al.*, Nature, **425**, 380 (2003).

[12] X. Wang, G. E. W. Bauer, and T. Ono, Jap. J. Appl. Phys., **45**, 3863 (2006).

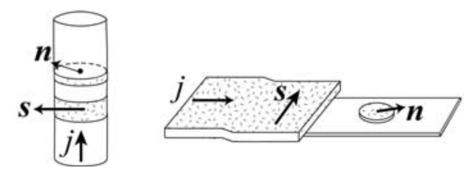

Planar spin-transfer devices driven by current *j*. Hashed parts are ferromagnetic, white parts are made of non-magnetic metal.

AA-11

Magnetization reversal driven by spin-injection : a mesoscopic spin transfer effect.

J. Wegrowe
LSI, Ecole Polytechnique, Palaiseau, France

A mesoscopic description of spin-transfer effect is proposed, based uniquely on the spin-injection mechanism occurring at the junction with a ferromagnet. The effect of spin-injection is to modify locally, in the ferromagnetic configuration space, the density of magnetic moments. The corresponding gradient leads to a current-dependent diffusion process of the magnetization. In order to describe this effect, the dynamics of the magnetization of a ferromagnetic single domain is reconsidered in the framework of the thermokinetic theory of mesoscopic systems.
Assuming an Onsager cross-coefficient that couples the currents, it is shown that spin-dependent electric transport leads to a correction of the Landau-Lifshitz-Gilbert equation of the ferromagnetic order parameter with supplementary diffusion terms. The consequence of spin-injection in terms of activation process of the ferromagnet is deduced, and the expressions of the effective energy barrier and of the critical current are derived. Magnetic fluctuations are also calculated: the correction to the fluctuations due to spin-injection is similar to that obtained for the correction of the activation process. These predictions are consistent with the measurements of spin-transfer obtained in the activation regime and for ferromagnetic resonance under spin-injection.
The motivation for a classical mesoscopic analysis was the need to account for the following highly specific properties observed in spin-transfer
experiments that can hardly be accounted for in direct microscopic approaches [1]. First, in single domain
ferromagnets, the reversible part of the hysteresis loop is not significantly modified under current injection, while the irreversible jump is drastically modified [1]. Second, the amplitude of spin-transfer is proportional to the giant magnetoresistance and to the amplitude of the current. Third, the
N\'eel-Brown activation law is still valid under current injection, with a correction of the barrier height that is quasi-symmetric under both the permutation of the magnetic configuration (parallel to anti-parallel and inversely) and the change of the direction of the current. "Quasi"-symmetric means here
that a quantitative shift (a factor 2 to 4 in general) is systematically observed in the amplitude of spin transfer for both transitions in spin-valve structures. Fourth, this last
quasi-symmetry is also observed in the context of ferromagnetic resonance under current injection close to the equilibrium states (i.e. with an weak spin-injection).

[1] J.-E. Wegrowe, M. C. Ciornei, H.-J. Drouhin, J. Phys.: Condens. Matter {\bf 19}, 165213 (2007).

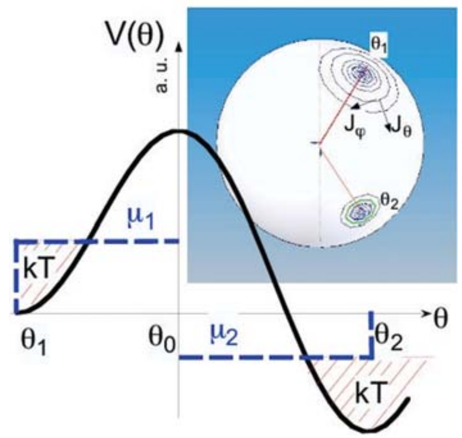

The configuration space of the ferromagnetic order parameter is represented by a sphere of radius unity. The double well shown is a projection over the plane that contains the two equilibrium states at θ1 and θ2, and the top of the barrier at θ0. The step approximation for the chemical potential is plotted with the thermal fluctuations sketched by the dashed area around the two minima.

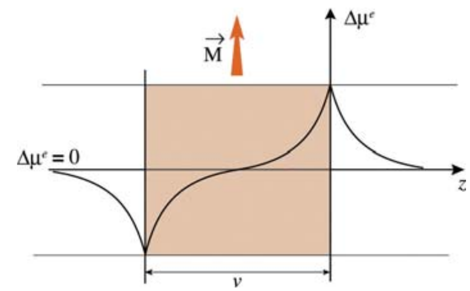

Illustration of the spin-accumulation occurring in a nanoscopic ferromagnetic layer with its two non-ferromagnetic contacts: the profile of the electrochemical potential difference $\Delta\mu$ is plotted as a function the spatial coordinate z.

AB-01

Current-Induced Magnetic Domain Wall Motion at Low Current Density via Perpendicular Anisotropy.

S. Jung[1], W. Kim[2], T. Lee[2], K. Lee[3], H. Lee[1]
1. Physics, POSTECH, Pohang, South Korea; 2. Materials Science, KAIST, Daejeon, South Korea; 3. Materials Science and Engineering, Korea University, Seoul, South Korea

The current-induced motion of magnetic domain wall (DW) carries great potentials for applications such as nano-scaled logic and memory devices. To achieve this goal, a large reduction in the threshold current density Jc for the domain wall motion is highly desired. Here we show that by introducing and properly exploiting the perpendicular magnetic anisotropy (PMA), Jc can be reduced by one or even two orders of magnitude in experimentally accessible parameter regimes. The PMA changes the easy axis of the magnetization from the wire direction to the direction perpendicular to the wire plane. For a defect-free magnetic nanowire, the theory predicts [1] that Jc is related to adverse effects suppressing the DW motion such as anisotropy Kd associated with the tilting of the DW. Analyzing the DW motion following the Thiele's approaches [2], we found that the change of the easy axis significantly influences Kd so that the Kd of the PMA wire is considerably different from that of the in-plane anisotropy (IMA) wire, which leads to the reduction of Jc. We calculated analytically Kd as a function of the wire width w for a given wire thickness t. By tuning w properly, Kd can be suppressed to arbitrarily small values, which in turn reduces Jc considerably. This tuning of w for the PMA wire is much easier than the IMA wire since Kd for the PMA wire depends on the ratio w/l while Kd for the IMA wire depends on the ratio w/t where l is the DW width. The analytic result is in good agreement with the prediction of our micromagnetic simulations of the LLG equation with spin transfer torque terms. We also performed the micromagnetic simulation to see the DW motion in realistic nanowire with a single notch, edge roughness, and/or PMA fluctuations. Despite of these imperfections, we found that the Jc of the PMA wire with experimentally reasonable parameters is also much smaller than the IMA wire because of the difference in the anisotropy Kd. Especially, the resulting Jc is insensitive to domain wall pinning forces related to the imperfections and also to the non-adiabaticity, both of which are hard to control in experiments. These results suggest that the PMA wire is useful for DW-based nano-scale magnetoelectric devices and also allows probing fundamental aspects of spin and magnetization dynamics.

[1] G. Tatara, H. Kohno, Phys. Rev. Lett. 92, 086601 (2004)

[2] A. A. Thiele, Phys. Rev. Lett. 30, 230 (1973)

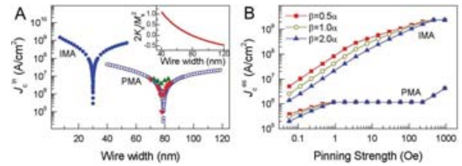

Fig. 1. (A) For a defect-free wire, Jc of a PMA wire and an IMA wire. Jc of a PMA wire is in good agreement with 1D (downward triangle) and 2D (upward triangle) LLG simulations. Inset: Demagnetization factor for a PMA wire. (B) In the presence of the pinning potential, Jc of a PMA wire and an IMA wire for various non-adiabaticities.

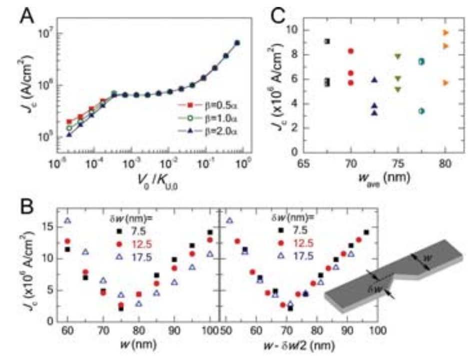

Fig. 2. LLG simulations results for Jc of a PMA wire in the presence of the magnitude fluctuation of the PMA for various non-adiabaticities (A), in the presence of a single notch (B), and in the presence of both wire edge roughness and fluctuations of the PMA as a function of averaged wire width (C). Lower inset: Schematic of a notch.

AB-02

Current-induced Domain Wall Transformations and Vortex Core Displacement.

L. Heyne[1], D. Backes[1,2], T. A. Moore[1], S. Krzyk[1], M. Kläui[1], U. Rüdiger[1], L. J. Heyderman[2], A. Fraile Rodriguez[2], F. Nolting[2], O. Mentes[3], M. Nino[3], A. Locatelli[3], K. Kirsch[4], R. Mattheis[4]
1. Universität Konstanz, Konstanz, Germany; 2. Paul Scherrer Institut, Villigen, Switzerland; 3. Sincrotrone Trieste, Trieste, Italy; 4. Institute of Photonic Technology, Jena, Germany

The feasibility of the manipulation of magnetic domains and domain walls by spin-polarized current injection is of great scientific interest and has large potential for applications. Controlled manipulation of current-induced domain wall motion is crucial for any devise based on this effect. This requires an in-depth understanding of the underlying theory.
The influence of spin-polarized current on the magnetization can be described theoretically by an adiabatic and a non-adiabatic term added to the Landau-Lifshitz-Gilbert equation of motion [1,2]. Here especially the magnitude of the non-adiabatic term, the so called non-adiabaticity constant β is currently much under debate and for controlled domain wall motion a detailed knowledge of this term is necessary. In particular the relation between β and the damping constant α is debated. While some predict that $\beta=\alpha$ [3,4] other found that in general $\beta\neq\alpha$ [5,6].
Thus experiments addressing this topic are of utmost importance. Current-induced domain wall motion has been observed by a number of groups using different techniques [7-11], but so far detailed statements concerning β could not be deduced.
We present new results on the interaction of spin-polarized currents with the spin configuration studied by direct imaging using X-ray photoemission electron microscopy.
In a magnetic wire, two domain wall configurations prevail: the vortex wall (VW) and the transverse wall (TW). VWs are characterized by the magnetization curling in-plane around the vortex core and the polarity of the vortex core. The sense of rotation can be either clockwise or counterclockwise. In a TW the magnetization rotates in-plane by 180° similar to a Néel wall.
In 1000 nm wide and 28 nm thick Permalloy wires, VWs are energetically more favorable, due to their lower stray field. In these wires we observed not only current-induced domain wall motion but also current-induced DW transformations [12]. Due to the spin torque effect additional vortices are created, so that a single VW is transformed to a double VW. But not only DW nucleations, but also DW annihilations were observed.
This indicates that the spin-polarized current not only displaces DWs but also has a profound influence on the internal structure of the DW. To further study this effect magnetic wires where VWs as well as TW can coexist were examined [13]. In these wires periodic transformations between the two DW types are predicted to occur under current injection.
We studied current-induced domain wall motion in 1500 nm wide and 8 nm thick Permalloy wires and observed propagation and transformation of the DWs after current pulse injection.
In Fig. 1 an XMCD image sequence of such transformations is shown. The bottom row shows results from a corresponding simulation [14]. The initial TW (a) is transformed to a clockwise VW (b) by a 25 µs long 10^{12} A/m^2 strong current pulse. (c) A further injection results in a TW but with opposite transverse component compared to the initial TW. (d) The next injection yields an off-center VW. (e) Subsequent injection results again in a VW with same sense of rotation as in (b) and (d). To exclude thermal effects as a possible cause for these transformations we can make use of the fact that for a given initial spin structure the spin torque predicts transformations to VWs with always the same sense of rotation, whereas for thermally induced transformations both kind of VWs should occur equally often. Since we only observe transformations to clockwise VWs, this clearly rules out thermal effects and fits to theoretical predictions under the assumption that the non-adiabaticity parameter β does not equal the damping constant α [15].
Furthermore we observe current-induced vortex core displacements in magnetic disks. It is shown that the direction of the vortex core displacement depends on the vortex core polarity, but not on the sense of rotation in agreement with theory [16].
This also shows the fundamental difference of current- and field-induced displacements, where the direction depends solely on the sense of rotation.

[1] A. Thiaville et al., Europhys. Lett. 69, 990 (2005)
[2] S. Zhang, and Z. Li, Phys. Rev. Lett. 93, 127204 (2004)
[3] Y. Tserkovnyak et al., Phys. Rev. B 74, 144405 (2006)
[4] S. E. Barnes et al., Phys. Rev. Lett. 95, 107204 (2005)
[5] J. Xiao et al., Phys. Rev. B 73, 054428 (2006)
[6] H. Kohno et al., J. Phys. Soc. Jap. 75, 113706 (2006)
[7] N. Vernier et al., Europhys. Lett. 65, 526 (2004)
[8] J. Grollier et al., Appl. Phys. Lett. 83, 509 (2003)
[9] A. Yamaguchi et al., Phys. Rev. Lett. 92, 077205 (2004)
[10] L. Thomas et al., Nature 443, 197 (2006)
[11] M. Kläui et al., Appl. Phys. Lett. 83, 105 (2003), Phys. Rev. Lett. 94, 106601 (2005)
[12] M. Kläui et al., Appl. Phys. Lett. 88, 232507 (2006)
[13] M. Laufenberg et al., Appl. Phys. Lett. 88, 52507 (2006)
[14] LLG Micromagnetics Simulator
[15] L. Heyne et al., Phys. Rev. Lett., in press
[16] J. Shibata et al., Phys. Rev. B 73, 020403(R) (2006)

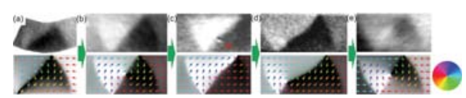

Fig.1

AB-03

Dynamics of domain walls in soft magnetic nanostripes: soliton approach.

K. Gusliyenko, J. Lee, S. Kim
Research Center for Spin Dynamics & Spin-Wave Devices and Nanospintronics Laboratory, Materials Science & Eng. Dept., Seoul National University, Seoul, South Korea

Recently the motion of domain walls (DWs) driven by magnetic field or spin polarized current in magnetic nanostripes became of considerable interest. One of the central issues is to understand DW motions under an applied magnetic field (H) stronger than a critical field (the Walker field), H_w. When H is applied to "head-to head" ("tail-to tail") DW in nanostripes, the DW propagates along (against) **H** direction increasing its velocity with increasing H below H_w. But for $H> H_w$, the average velocity v decreases considerably [1] and DW oscillations occur [2].

In this talk, we report a soliton approach to the description of moving DWs in nanostripes that reveal oscillations in high-H regime or a steady movement in low-H regime. Our model explains DW dynamics by the motions of a limited number of magnetic topological solitons [vortices (V) and antivortices (AV)], via their emission, gyrotropic motion and absorption. The vortex or antivortex walls (VW or AVW) contain a single V(AV) and some solitons at the stripe edges [3]. V and AV bear topological charges q related to their cores and have non-zero gyrovectors [4]. The gyrovectors result in V(AV) gyrotropic motion determined by the magnetic energy W. The transverse walls (TW) correspond to half-integer ($q=\pm1/2$) topological solitons located on the edges [3]. The VW(AVW) have also half-integer q similar to ones in the TW. The emission of V(AV) changes the edge soliton charges from +1/2(-1/2) to -1/2(+1/2). The relatively slow gyromotions lead to essential decrease of v due to V(AV) motions against the **H** direction.

To find the soliton trajectories and traveling times, we use the Landau-Lifshitz equation of motion (LLG) in the form of Thiele's equation of motion of the soliton core position $\mathbf{X}=(X,Y)$ in the stripe x-y plane [4]. We use the energy decomposition $W(\mathbf{X})=\kappa Y^2/2-\lambda \mathbf{XH}+\mu \mathbf{z}[\mathbf{X}\times\mathbf{H}]$, where the first term describes W variation in the transverse direction of nanostripe (κ is the stiffness coefficient), the 2nd and 3rd terms describe the motion of DW as a whole and interaction of V(AV) with **H** [4]. $\lambda=2M_s wL$, $\mu\approx 2M_s wL$ ($\mu\approx 0$) for V(AV), L and w are the nanostripe thickness and width.

By solving the equations of motion for X and Y, the trajectories of V(AV) are found. For a steady motion perpendicularly to the nanostripe length, a quasi-1D solution $dX/dt=D_{xx}^{-1}\partial W/\partial X$ exists, which corresponds to the viscous DW motion [5]. This motion is stable in low fields and occurs only for TW or VW in infinitely long stripes. The components $D_{\alpha\beta}$ of the damping tensor are calculated for TW(VW) and the TW(V) velocity can be written as $dX/dt=\lambda H/|D_{xx}|$. The moving V experiences a force due to the field H, which pushes the vortex perpendicularly to the stripe length. The equation of motion for Y (VW) has a stationary point Y_0. The field when Y_0 reaches the stripe edge is the critical field H_w and means beginning of oscillations of the DW internal structure. Estimation yields $H_w=\alpha 2\pi M_s L/w$. I.e., the critical field in nanostripes ($L/w<<1$) is essentially reduced comparing to bulk 1D case [5]. The DW velocity reaches the maximum value $v_m=2\gamma M_s L$ for nanostripe that is essentially smaller than the Walker result [5]. The explicit trajectories of the V(AV) gyrotropic motions within the VW(AVW) for $H>H_w$ between their emission and absorption at the nanostripe edges are calculated. They are quite complicated, but for the LLG damping $\alpha<<1$ we get the simple parabolas. The values of κ determining their slope are different for V(AV) and were calculated numerically. The traveling time t_S of V(AV) between the stripe edges is $t_S=\pi\gamma/H$ within the limit $\alpha<<1$ (or $H>>H_w$). It does not depend on the nanostripe sizes L, w and intrinsic material parameters M_s, α. The traveling time t_{TW} of the edge solitons between the absorption and emission of V(AV) can be neglected comparing to t_S. The period of the DW oscillations is $\approx 2t_S$ and the eigenfrequency is the Larmor frequency, $\omega=\gamma H$. To calculate v at $H>H_w$, we average the DW velocity over the oscillation period and get $v\approx v_{TW}t_{TW}/t_s$. This equation describes a considerable v drop just above H_w, $v\approx(0.1\surd 0.2)v_m$, which was observed experimentally in nanostripes [1].

We also conducted micromagnetic simulations [6] assuming rectangular permalloy nanostripes with L=10 nm, $w=60\surd 240$ nm. The simulated DW velocity v increases linearly with increasing H ($H<H_w$). Just above H_w, v decreases remarkably [1,3]. Above H_w, $v(H)$ is constant, and the oscillatory motions of DWs appear [3]. The dependence of $t_S=\pi\gamma/H$ for VW and AVW is in good agreement with simulations. We confirmed that t_{TW} is small (<1 ns) and in high fields only VW and AVW represent the DW oscillations until a chaotic regime revealing multi-soliton states. The simulated V(AV) core trajectories were well fitted to the parabolic equations $X(Y)$ and $\kappa>0$ ($\kappa<0$) for the VW(AVW) were calculated. Recent experimental observations of DW motion in the nanostripes [1,2] can be explained by our model.

This work was supported by Creative Research Initiatives (Research Center for Spin Dynamics & Spin-Wave Devices) of MOST/KOSEF.

[1] G. Beach et al., Nature Mater. 4, 741 (2005); Phys. Rev. Lett. 97, 057203 (2006).

[2] M. Hayashi et al., Nature Phys. 3, 21 (2007).

[3] J. Lee et al., Phys. Rev. B 76, 184408 (2007);

[4] K.Y. Guslienko et al., Phys. Rev. Lett., submitted.

[5] N.L. Schryer, and L.R. Walker, J. Appl. Phys. 45, 5406 (1974).

[6] We used the OOMMF code, http://math/nist.gov/oommf. The parameters were as follows: the saturation magnetization M_s=0.86 MA/m, the exchange stiffness A=13 pJ/m, and α=0.01.

AB-04

Pinning and propagation of vortex domain walls in triangular anti-notches.

K. J. O'Shea[1], J. N. Chapman[1], S. McVitie[1], Y. H. Wu[2]
1. Physics and Astronomy, University of Glasgow, Glasgow, United Kingdom; 2. Electrical and Computer Engineering, National University Singapore, Singapore, Singapore

Domain walls (DWs) in ferromagnetic nanowires are currently the focus of intense research activity due to their potential applications in spintronic devices [1]. A greater understanding of the fundamental properties and behaviour of DWs is required, however, before such devices can be realised. The nanostructures investigated here are shown schematically in fig. 1a. They were fabricated by electron beam lithography in thermally evaporated Ni_{80} Fe_{20}. For wires of 350 nm width and 20 nm thickness, the favoured head-to-head wall structure is a vortex DW (VDW) according to the DW structure phase diagram [2]. Application of a field approximately perpendicular to the wire resulted in the nucleation of a DW between the anti-notch and the diamond end-shape. Thereafter DWs were driven along the wire with a parallel field, the direction of the field being chosen to drive the wall towards the anti-notch. Here we explore the effect of triangular anti-notches of constant width, 400 nm, and heights varying between 100-675 nm.

Characterisation of the magnetic behaviour was carried out using the Fresnel mode of Lorentz microscopy [3]. Magnetic contrast arises at the positions of DWs and also at the edges of the structure where M lies parallel to the edges. Regions of increased or decreased intensity appear superimposed on the defocused image of the nanowire. The thick dark fringe along the upper edge of the wire, indicated by A in fig. 1b, indicates that this section of the wire is oppositely magnetised to the wider end region at B where the dark fringe is along the lower edge. The magnetisation configuration is illustrated in fig. 1a. The appearance of the vortex core, white or black, depends directly on the sense of rotation of the magnetisation around it; here a clockwise (cw) VDW is shown. The anti-notch gradient α, for an anti-notch 100 nm high is 27°, which means that the magnetisation only has to deviate modestly from the direction in the main body of the wire to align with the gentle slope of the anti-notch. Figure 2a shows that under only a small applied field the VDW enters the anti-notch to form the configuration shown in fig. 2b, suggesting that the anti-notch acts as a potential well.

For an anti-notch of height 675 nm, however, the anti-notch acts as a potential barrier and the clockwise VDW is pinned just in front of it, fig. 2c. In this case, α is 59° and the magnetisation in the notch lies approximately perpendicular to the wire, as seen from the thick dark fringe at positions C and D in fig. 2c. Thus this anti-notch acts as a potential barrier for a cw VDW, the magnetisation distribution being as shown schematically in fig. 2d. Not surprisingly different behaviour is observed in the two cases as the field is increased. For the shallower anti-notch, the VDW distorts and it extends into the far side of the wire, fig. 2e. Simultaneously, the vortex core is forced further into the apex of the anti-notch prior to depinning. Reversal occurs at 67 Oe. In the second case, the VDW is never stable in the anti-notch, reversal occurring abruptly at a field ≈75 Oe.

Somewhat different behaviour is observed if the chirality of the VDW is changed. Fig. 3a shows that the ccw VDW is pinned in the 100 nm anti-notch in a similar manner to the cw VDW. However, the ccw VDW interacts with the 675 nm anti-notch in an entirely different manner, figs. 3b and c. The magnetisation of the leading domain has a component pointing perpendicularly upwards and hence in a similar sense to the magnetisation in the anti-notch. Thus the DW enters the anti-notch suggesting that for a ccw VDW the anti-notch acts as a potential well for for both low and high values of α. Under increasing applied fields both DW structures distort and extend into the wire, figs. 3d and e, before depinning at fields of 72 and 76 Oe respectively. In summary a 100 nm high anti-notch attracts VDWs of both chiralities whilst the behaviour of a 675 nm high anti-notch depends on the chirality of the incoming VDW.

[1] D. A. Allwood, G. Xiong, C. C. Falkner, D. Atkinson, D. Petit, R. P. Cowburn, Science 309, 1688 (2005).

[2] Y. Nakatani, A. Thiaville, J. Militat, J. Magn. Magn. Mater. 290, 750 (2005).

[3] J. N. Chapman, M.R. Scheinfein, J. Magn. Magn. Mater. 200, 729 (1999).

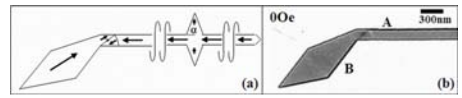

Figure 1: (a) schematic of the nanostructure and the magnetisation distribution supported. (b) Fresnel image of the cw VDW.

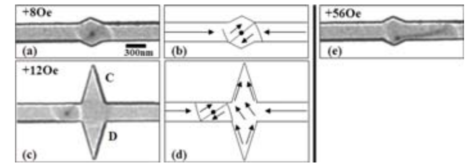

Figure 2: (a) Fresnel image of the VDW inside the 100 nm anti-notch; (b) corresponding schematic. (c) Fresnel image of the VDW pinned outside the 675 nm anti-notch; (d) corresponding schematic. (e) Fresnel image of the VDW being pulled away from the 100 nm anti-notch.

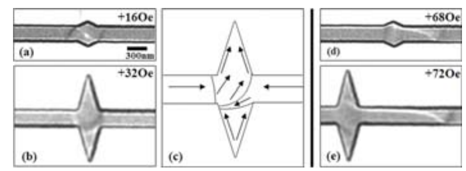

Figure 3: Fresnel images of the ccw VDW at (a) the 100 nm and (b) the 675 nm anti-notches. (c) schematic of the magnetisation distribution in (b). Fresnel images of the DWs as they are pulled away from (d) the 100 nm and (e) the 675 nm anti-notches.

AB-05

Domain wall pinning mechanism in ferromagnetic nanowires.

D. Petit, A. Jausovec, E. Lewis, H. T. Zeng, L. O'Brien, D. Read, R. P. Cowburn
Physics, Imperial College London, London, United Kingdom

The chirality dependent [1] interaction mechanism between transverse domain walls (TDWs) in Permalloy nanowires and artificially patterned traps is studied using high sensitivity spatially resolved Magneto Optical Kerr Effect measurements. The DWs are created at the C-shaped end of the structures using external magnetic fields. The pinning from T shaped traps is investigated, where a DW travelling in the horizontal arm is pinned by the vertical arm (see Fig. 1). The chirality of the incoming DW and the micromagnetic configuration in the trap are independently controlled using external magnetic fields and by placing the transverse arm either inside the curvature of the C ("In"), or outside ("Out"), allowing all four different DW/trap configurations to be studied. The pinning strength (Fig. 2) as well as the potential energy profile created by the traps are measured for all cases, and the roles of the different DW characteristic parameters, such as the sign of the DW charge, the DW core orientation and the magnetic charge distribution within the DW, are separately assessed. It is found that whether or not the core of the DW is aligned with the transverse arm of the T affects the shape of the main potential experienced by the DW, whereas the pinning strength strongly depends on which side of the V-shaped TDW interacts with the trap. These effects are discussed in terms of the magnetostatic interaction between the DW and the junction. We also present results of numerical simulations which are in excellent qualitative agreement with the experiments. Finally, a chirality analysing and filtering mechanism is experimentally demonstrated.

[1] D. Petit, A.-V. Jausovec, D. Read and R. P. Cowburn, Cond-Mat arXiv:0711.5026v2

FIB image of a 200 nm wide, 7 nm thick C-shaped nanowire containing a T-shaped trap. The transverse arm is placed outside the curvature of the C.

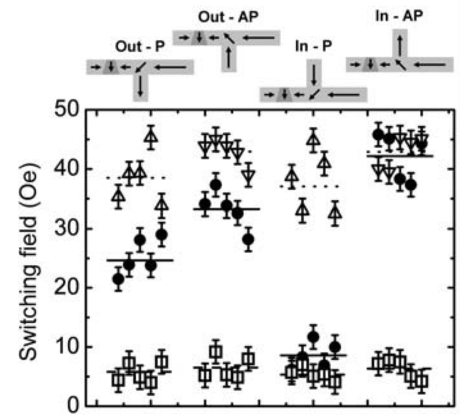

Propagation (open squares), transmission (full circles), and nucleation (open triangles) fields for five structures of each of the four TDW/trap arrangements. The strong dependency of the transmission field with the configuration is clearly seen.

AB-06

The dependence of wire width and trap geometry on domain wall pinning behaviour in nanowires.

L. K. Bogart[1], D. Eastwood[1], D. Atkinson[1], D. McGrouther[2], K. O'Shea[2], S. McVitie[2], J. Chapman[2]
1. Physics, Durham University, Durham, United Kingdom; 2. Physics and Astronomy, University of Glasgow, Glasgow, United Kingdom

The behaviour of magnetic domain walls (DWs) in nanowires has attracted much attention with potential applications including spintronic logic [1] and memory devices [2]. In these devices information is encoded in the magnetic states of domains in lithographically patterned nanowires. Quantitative correlation between the depinning field and pinning site geometry is highly relevant to both field and spin-polarised current induced domain wall behaviour and may ultimately lead to optimising the control and efficiency of these devices.
Experiment
Two samples of permalloy nanowires of the same nominal dimensions were fabricated using different lithographic techniques. Each nanowire was ten nanometres thick and contained a micron-scale nucleation pad on one end [3] and was sharply tapered at the other [4]. Wire widths ranged from 600 nm to 200 nm, with each structure containing a single pinning site along one side of the wire. The pinning potential of two different pinning site geometries was investigated, including triangular and rectangular shaped sites in the notch and prominence configuration. The first set of samples was prepared using electron beam lithography, thermal evaporation and 'lift-off' techniques. Spatially resolved magnetisation analysis was performed using a high sensitivity focused magneto-optic Kerr effect (MOKE) magnetometer. Placing the laser spot over pad/wire junctions and after the pinning sites allowed for the study of DW injection and also to quantify the pinning potential as a function of site geometry. The second set of nanowires was prepared by thermally evaporating films onto a silicon nitride membrane which was then directly patterned using focussed ion beam (FIB) milling. DW pinning behaviour was imaged using Lorentz transmission electron microscopy (TEM). The spin structure of pinned DWs was also investigated using the OOMMF micromagnetic code [5].
Results
Fig. 1 shows the average DW injection fields for different wires of the same nominal dimensions as a function of wire width. As the wire width decreases the field required to inject a DW increases significantly as is consistent with the pad/wire junction forming a symmetrical potential well. For narrow wire widths there is a large spread in measured injection fields; this suggests such widths can support metastable DW flavours since these dimensions are close to the transverse wall (TW)-vortex wall (VW) phase transition line [6]. OOMMF micromagnetic simulations support this and suggest that an extreme asymmetric TW state is stable beyond the regime obtained by Nakatani et al.[6]. MOKE hysteresis loops reveal how the DW depinning behaviour depends strongly on the chirality of the DW, although for a fixed wire width the depinning fields are relatively insensitive to the geometry of the pinning site. Asymmetric pinning sites lift the energy degeneracy of metastable wall types, as is shown by the two distinct switching steps in Fig.2. Both TEM images and OOMMF simulations show clearly how the location at which a DW pins and the depinning field depend on the wall flavour and chirality (Figs.3 and 4), which is in good agreement with Hayashi et al [7]. A systematic investigation into the relationship between pinning site geometry and DW pinning behaviour will be presented.

[1] D. A. Allwood, et al., Science 309, 1688 (2005)

[2] S. S. P. Parkin, U.S. Patent No. US 683 400 5 (2004)

[3] R. P. Cowburn, et al., J. Appl. Phys., 91 (10) 6949 (2002)

[4] K. J. Kirk, et al., Appl. Phys. Lett. 75, 6461 (2001)

[5] R. D. McMichael and M. J. Donahue, IEEE Trans. Mag. 33, 4167 (1997).

[6] Y. Nakatani, et al., J. Magn. Magn. Mater., 290, 750 (2005)

[7] M. Hayashi, et al., Phys. Rev. Lett., 97, 207205 (2006)

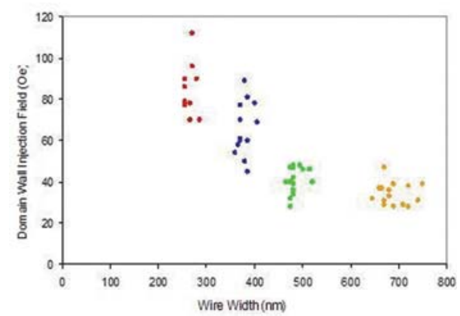

Average DW injection fields as a function of wire width.

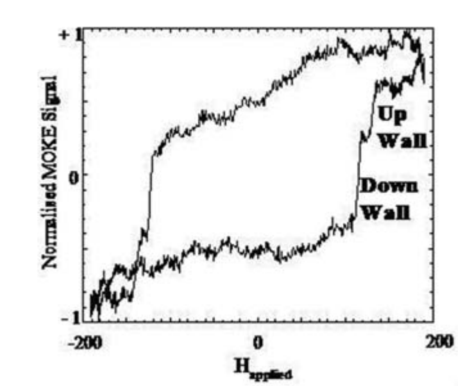

MOKE hysteresis loop showing two DW depinning fields from a 200 nm deep rectangular notch in a 300nm wire

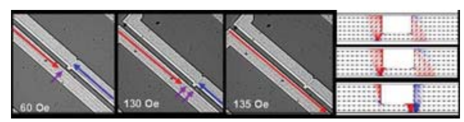

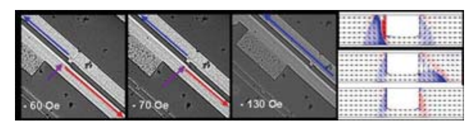

Fig. 3 (up) & Fig. 4 (down) TEM images and complimentary OOMMF simulations showing DW pinning behaviour at a rectangular notch in a 300 nm wide wire. (Purple arrows indicate DW; red and blue arrows indicate domain magnetisation respectively.)

AB-07

Propagation field of notched permalloy nanowires.

P. Warnicke[1], A. Himeno[2], S. Kasai[2], T. Ono[2]
1. Department of Engineering sciences, Division for solid state physics, Uppsala, Sweden; 2. Institute for Chemical Research, Division of materials research, Kyoto, Japan

The propagation field for magnetic vortex domain walls was experimentally investigated in notched nanowires of permalloy. Wires with sub-micrometer width and variable notch depth were fabricated using a lithography process. Vortex walls were nucleated and depinned by applied magnetic fields and observed with magnetic force microscopy. Numerical results were obtained by micromagnetic simulations.
Patterned ferromagnetic films have attracted increasing attention due to their promising applicability in data transfer and storage technology [1, 2]. By decreasing the thickness of a ferromagnetic structure, the magnetization is forced to align in-plane due to the shape anisotropy. In addition, by decreasing the width we obtain a wire and the magnetization is forced to align parallel with the wire axis. As a result, regions between opposite magnetizations in this wire form domain walls (DW). Typically, there are two types of domain walls; transverse and vortex domain walls. The type is determined by the geometry of the wire [3]. Vortex walls have a curling spin distribution and a small stray field that enable high density packing without interference with neighboring magnetic domains. A domain wall, trapped in the wire, can be manipulated by applied electric currents [4-8] or magnetic fields [9, 10]. In order to control the position of a magnetic wall, artificial constrictions can be introduced that reduce the number of equilibrium positions along the wire [11]. Understanding how domain walls couple with the notches under an externally applied magnetic field is important for successful manipulation of the information bits.
In this report we investigate the vortex depinning properties in nano wires with symmetrical notches on one side. The depth of the notches was varied between 20 nm and 80 nm.
The nanowires were fabricated on native silicon wafers capped with a 200 nm SiO_2 oxide and spin-coated with a negative resist. The geometry is defined by the wire width w = 240 nm, thickness h = 20 nm, notch period l = 480 nm and notch depth d. The patterning was done by electron-beam (EB) lithography, the deposition by EB evaporation and the lift-off process using chemical solvents. The numerical calculations were performed using the public micromagnetic OOMMF code [12] and standard parameters for permalloy; a saturation magnetization of 860 kA/m, an exchange constant of 13 pJ/m and zero magneto-crystalline anisotropy. A damping coefficient of 0.02 and a cell size 5 nm $\times$ 5 nm $\times$ h nm were used. Simulations were performed on a wire segment including five notches with the trapped vortex at the central pinning site. This segment size is sufficient in the sense that the magnetostatic interference of the wire ends has a negligible effect on the propagation field.
In Figure 1, the propagation field H_p is shown for wires with a notch depth between 0 nm and 80 nm. Experimental values are taken as the average H_p from 10 different symmetrical wires. Lateral discrepancies, originating from the finite resolution in the lithography process, are indicated by the standard deviation of the data. This effect is significantly enhanced for the deeper notches. Natural defects heavily influence the pinning strength of a notch-free wire. The simulated H_p of 0.05 mT $\pm$ 0.05 mT can be compared with the experimental value of 1 mT and results from an absence of edge roughness. The magnetization profile of the wires with $20 \leq d \leq 80$ is shown in the inset.
In conclusion, the notch geometry influences the pinning potential of a trapped vortex in the studied nano wires. Experimental and numerical results are well correlated for deeper notches, i.e. $d \geq$ 40 nm, but diverge at small d due to unavoidable edge roughness in the fabricated samples.

[1] D. A. Allwood et al., Science 309, 1688 (2005).
[2] S. S. P. Parkin, U.S. Patent No. 683 400 5 (2004).
[3] Y. Nakatani, A. Thiaville, and J. Miltat, Journal of Magnetism and Magnetic Materials 290-291, 750 (2005).
[4] J. Grollier et al., Applied Physics Letters 83, 509 (2003).
[5] M. Klaui et al., Applied Physics Letters 83, 105 (2003).
[6] E. Saitoh et al., Nature 432, 203 (2004).
[7] N. Vernier et al., Europhysics Letters 65, 526 (2004).
[8] A. Yamaguchi et al., Physical Review Letters 92, 077205 (2004).
[9] G. S. D. Beach et al., Nature Materials 4, 741 (2005).
[10] T. Ono et al., Science 284, 468 (1999).
[11] A. Himeno, S. Kasai, and T. Ono, Applied Physics Letters 87, 243108 (2005).
[12] The OOMMF package is available at http://math.nist.gov/oommf/

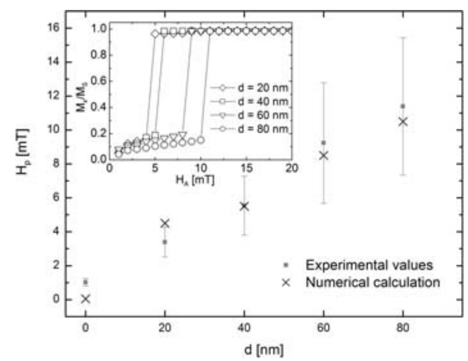

Figure 1 The propagation field for wires with 0 ≤ *d* ≤ 80 nm. The inset shows the simulated magnetization profile for some of the nano wires.

AB-08

Measuring domain wall coherence lengths using a chirality filter.

E. Lewis, D. Petit, A. Jausovec, L. O'Brien, H. Zeng, D. Read, R. Cowburn
Imperial College London, London, United Kingdom

The interaction of a magnetic domain wall (DW) with artificially-created defects in a nanostrip is important for DW-based data storage devices [1,2], in which it is required to controllably propagate DWs. Because the interaction will in general depend on the DW chirality [3] (that is, the sense of rotation of the spins across the DW), it is necessary to consider the phenomenon of Walker breakdown [4], in which the DW structure oscillates as it propagates along the strip under a field greater than the 'Walker field' H_W. In the case of a transverse DW, which is the stable structure for our nanostrips (cross-section 90 x 7 nm^2), the DW core continually switches between the two transverse orientations.

We can detect these structural changes using a 'chirality filter': we fabricate l-shaped $Ni_{80}Fe_{20}$ nanostrips with a transverse arm crossing the main wire (Fig. 1 (i), (ii)) so that approaching DWs either transmit through the cross, or are blocked, depending on whether the DW core magnetisation is parallel or antiparallel to the magnetisation in the transverse arm. We create DWs of known chirality at varying distances d from the filter and use spatially-resolved MOKE (laser spot diameter ~5 μm)to measure the switching field of the latter part of the strip. From this, we can infer the orientation of the DW as it reaches the transverse arm: the switching field corresponding to transmission (~110 Oe) is roughly half that corresponding to blocking of the DW and subsequent re-nucleation of a new domain (~200 Oe); the propagation field is ~10 Oe. We find that chirality reversal never occurs below a certain distance, but that at long distances, the chirality is not a well-defined function of the distance travelled (Fig. 2). We therefore characterise the motion by a 'DW coherence length', L, over which the DW chirality is effectively preserved; L = (1.1±0.1) μm for our nanostrips.

We have also measured the field-dependence of L: we fabricate structures with varying corner radii of curvature, so that the DW de-pins and moves towards the cross at different fields. L was measured for four different fields. Analytical and numerical calculations [5] and related experiments [6] predict DW motion with a characteristic dependence of velocity and temporal oscillation frequency on the applied field. From these, a spatial 1/2 period can be extracted, which we associate with our measured L: it is expected to decrease sharply just above H_W, and tend to a constant in large applied fields. Our measurements of L are indeed consistent with this picture, with L tending to around 0.35 μm at high fields.

In addition, we have experimentally demonstrated extension of L to metre length scales by passing the DW through a series of closely-spaced filters. We fabricate U-shaped nanostrips with many transverse arms of spacing d = 0.25 μm (Fig. 1 (iii), (iv)). A DW is created in one corner by application of a large field pulse, followed by an oscillating horizontal field with maximum magnitude in between the transmission and nucleation fields, so that no new domains can be nucleated. In the absence of chirality reversal, the DW should continually move back and forth between the two corners of the U-shape; if the DW chirality reverses at any point, it will not be able to transmit through the crosses and the magnetisation switching of the structure will stop. We find that even after $4x10^4$ cycles of the horizontal field, we still measure switching at the centre of the structure, corresponding to chirality-conserving motion of the DW over a total distance of 3.2 m.

1. S. S. Parkin, US Patent 6,834,005 (2004)

2. Allwood, Cowburn et al.,Science 309, 1688 (2005)

3. D. Petit et al., arXiv:0711.5026v2 (2007)

4. N. L. Schryer and L. R. Walker, J. Appl. Phys. 45, 5406 (1974)

5. A. Thiaville and Y. Nakatani, Spin Dynamics in Confined Magnetic Structures III, p. 161 (2006)

6. M. Hayashi et al., Nature Physics 3(1), 21 (2007)

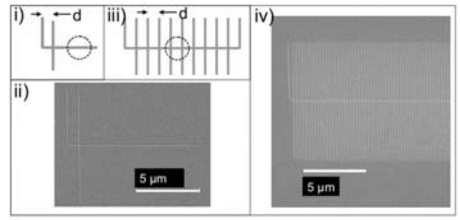

Figure 1: (i, ii) Schematic and SEM image of L-shaped nanostrip with single transverse arm. (iii, iv) Schematic and SEM image of a U-shaped nanostrip with many transverse arms of spacing d = 250 nm. The whole structure is 80 μm long. The dashed circles in (i) and (iii) indicate the position of the MOKE measurements.

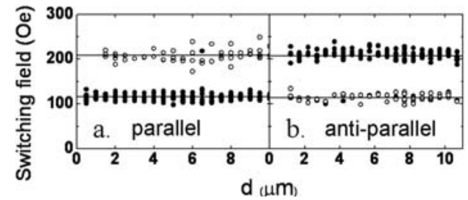

Figure 2: Switching fields as a function of distance d travelled to the filter. Each filled circle corresponds to a measurement on a separate structure; open circles correspond to secondary transitions. The lower-field transition corresponds to transmission, the higher to re-nucleation. (a) Domain walls created with core magnetisation parallel to the filter always transmit for d≤1 μm, consistent with a coherence length L > 1 μm. (b) Domain walls created with core magnetisation anti-parallel to the filter: the smallest value of d measured is 1.2 μm, at which chirality reversal is aleady observed, consistent with L<1.2 μm.

Dynamic of depinning of a magnetic domain wall from a single defect.

F. Montaigne[1], J. Briones[1], D. Lacour[1], M. Hehn[1], M. J. Carey[2], J. Childress[2]
1. Laboratoire de Physique des Matériaux, Nancy-University, CNRS, Vandoeuvre lès Nancy, France; 2. Hitachi San Jose Research Center, San Jose, CA

The propagation and the pinning have always been key issues in magnetism. Recently, these aspects have been revisited in nanostructures. We present here results on dynamics of depinning from a single defect in a submicronic stripe.
A spin valve multilayer is patterned by electron beam lithography and Ar ion beam etching in order to create and manipulate a magnetic DW in a submicron wire 500 nm wide and 20 µm long. A nucleation pad is present on one side of the wire and a notch is positioned along the wire. Figure 1(a) shows a scanning electron microscopy (SEM) picture of a completed device. GMR measurements allow us to locate precisely the DW between the electrical contacts.
Figure 2 represents different cycles obtained by sweeping the field from 300 to -300 Oe (and back). Starting from an antiparallel configuration of magnetizations, the AP->P propagation of a domain wall from the injection pad to the notch is associated with a drop in resistance. The magnetization in the pad reverses at fields below 30 Oe but the propagation of this reversed domain is limited by the nucleation pad neck as shown by the MFM image on figure 1(b). Then, this domain is further injected in the wire at the so-called injection field and propagates to the notch. The notch acting as a pinning site stops its propagation (see MFM picture on figure 1(c)). Further increase of the field is necessary to depin the DW. At the so-called depinning field, the normalized resistance of the device drops to 0% corresponding to the parallel state. Sweeping the field backwards results in similar phenomena for P->AP propagation.
Figure 2 clearly shows that this cycle is not fully reproducible. While the domain wall is trapped at the same position (same intermediate resistance), the exact value of the injection and depinning fields varies from experiment to experiment. Histogram of the depinning fields values are represented in figure 3 for the two propagations. Significant differences in the statistics are observed. These differences are mainly due to the effect of the dipolar field originating from the hard layer (cf. ref 1). The statistic is rather simple for the AP->P propagation with two peak centred around 124 and 225 Oe. For the P->AP propagation, the distribution is much more complex. In order to get more insight in the depinning process, time resolved relaxation measurements have been performed. After injection of the domain wall in the notch, the field is kept at constant value. The time of depinning is represented in figure 3 for different field values for the AP->P propagation. It appears clearly that for field around 124 Oe, the probability of transmission saturates at 58% whereas for higher fields, there is a 58% probability of immediate depinning. The results can be explained considering that two different types of domain wall are pinned in the notch.

(1) J. Briones et al., Appl. Phys. Lett. 92(3) (2008)

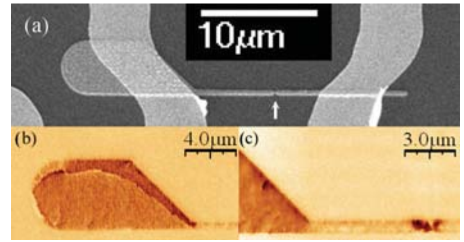

(a) SEM image of a device. The white arrow indicates the position of the notch. (b) and (c) MFM images of the domain wall trapped respectively in the pad before injection and at the notch vicinity before depinning.

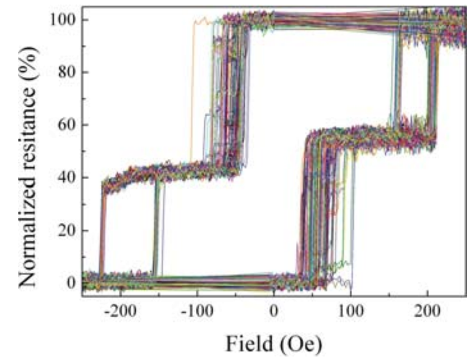

Normalized resistance recorded during 440 different hysteresis loops. 0% corresponds to the parallel state (P) and 100% to the anti parallel state (AP).

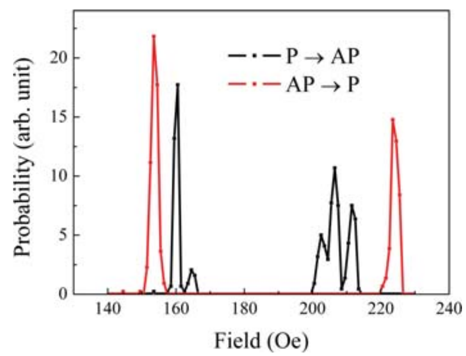

Statistical distribution of the depinning field for parallel to antiparallel propagation (full symbols) and antiparallel to parallel propagation (full symbols). For the late case, absolute value of the field is considered.

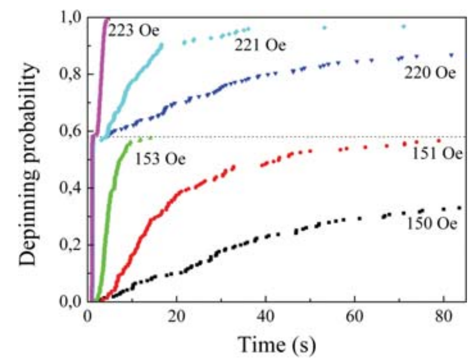

Integrated probability of depinning as a function of time for several value of magnetic field. Dotted line represent s the 0.58 value (see text).

AB-10

Direct observation of the Walker breakdown during field driven domain wall (DW) motion in Permalloy nanowires.

R. Mattheis, S. Glathe
Photonic Intrumentation, IPHT, Jena, Germany

The investigation of DW motion in soft magnetic materials started in the 1930`s with the experiments of Sixtus and Tonks [1]. Forty years later Walker analysed the DW motion theoretically and found a periodic component in the forward motion of field driven DWs above a critical driving field Hw. Below this so called Walker breakdown field one finds steady state motion of the DW. Increasing the external driving field above Hw the DW movement became turbulent because of a periodic change of the DW chirality due to a nucleation and motion of an antivortex and vortex, respectively. This behaviour was found and confirmed in several simulations e.g. [2,3,4]. Up to date only one experimental study addressing the frequencies connected to the change of the DW chirality was published [5].
We investigated the DW motion in Permalloy (Py) nanostrips in terms of time resolved resistance measurements to visualise the whole process in more detail. We use additionally to the longitudinal driving field Hl a transversal field Ht to change the nucleation conditions of the DW. This gives us an additional parameter to influence the dynamics of DW motion. The 20 nm thick and 45 µm long Py nanostrip is part of a GMR stack whose resistance depends on the magnetisation direction of the Py layer with respect to the wire axis. The GMR stack was deposited by means of physical vapour deposition and patterned via photolithography and Ar ion etching under tilt.
Fig. 1 shows the DW propagation in a 150 nm wide nanostrips under different applied transversal and longitudinal driving fields Ht and Hl. The bold (thin) graph represents the temporal evolution of the voltage (velocity). In the first picture (Ht = 19.5 kA/m and Hl = 5.7 kA/m) one can clearly separate intervals of DW forward motion and intervals where the DW stops or even move backwards. This behaviour fits very well to the DW motion during the Walker breakdown process as shown by micromagnetic simulations [3,4]. Here the DW is accelerated by the external magnetic field and propagates uniformly along the nanostrips. After a certain time an antivortex and vortex respectively is nucleated at one edge of the nanostrips and moves across the nanostrips, while the chirality of the initial DW is reversed. During this antivortex (vortex) movement the initial DW stops basically with respect to the wire axis. Thus the mean velocity drops drastically if the Walker breakdown occurs. In our experiment the maximum velocity is in the range of (980 ± 200) m/s and the mean velocity is 540 m/s.
Simulations of a 20nm*200nm*4000nm Py layer with an edge roughness of dr = 20 nm have shown that the Walker breakdown is not highly periodically like in perfect wires [2,3,4]. Due to the existing edge roughness in our nanostrips the DW motion is different in every single experiment. For that reason we are not able to average over many measurements to get low-noise charts.
If the transversal field is increased the longitudinal field necessary for the nucleation of a reversed domain is decreased. For these field parameters we get only 3 clear Walker breakdown processes meanwhile the DW basically don't move with respect to the wire axis. Due to the increased transversal field the nucleation of an antivortex or vortex is partially suppressed, increasing the intervals where the DW moves. Thus the mean velocity is increased by 33 % while the maximum velocity is still (1000 ± 50) m/s. Increasing the transversal field to 21.5 kA/m the Walker breakdown is suppressed completely an we get an almost steady state motion. Now the maximum velocity is nearly equivalent to the mean velocity, which is now 990 m/s. For these 3 charts the mean velocity is increased due to the stepwise suppression of the Walker breakdown, while the maximum velocity is nearly constant. For Ht = 24 kA/m and Hl = 4.8 kA/m the maximum velocity is increased slightly, thus we get a larger mean velocity due to the increased maximum velocity. This rise of DW velocity below the Walker breakdown although the longitudinal driving field is decreased can be explained by the broadening of the DW and the reduction of the DW angle [6].
In conclusion we are able to verify the Walker breakdown process in single measurements. Additionally we can tune the DW movement around the initiation of the Walker breakdown due to an applied transversal field.

[1] A. Kunz, J. Appl. Phys.99, 08G107 (2006)

[2] A. Thiaville et al., in "Spin Dynamics in Confined Magnetic Structures I", Springer Series: Topics in Applied Physics, Vol. 83, Hillebrands, B. and Ounadjela, K. (Eds.) (2002)

[3] J.-Y. Lee et al., Phys. Rev. B, 76, 184408 (2007)

[4] M. Hayashi et al., Nat. Phys., 3, 21 - 25 (2007)

[6] D. Allwood, M. Bryan and D. Atkinson, private communication

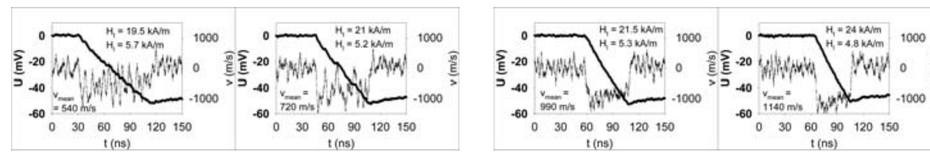

Fig. 1: DW propagation in a 20nm * 150nm * 45000nm nanostrip under given applied fields Ht and Hl in kA/m. Shown is the temporal evolution of the voltage (bold) and the velocity (thin).

AB-11

Control of field driven domain wall (DW) motion by transversal fields: suppression of Walker breakdown and giant velocities.

S. Glathe[1], R. Mattheis[1], T. Mikolajick[2]
1. Photonic Intrumentation, IPHT, Jena, Germany; 2. Institute of Electronic and Sensor Materials, TU Bergakademie Freiberg, Freiberg, Germany

In the past few years field and current driven dw motion became a field of strong experimental and theoretical activity e.g. [1 - 3]. These efforts are driven by potential application in data storage (Race Track Memory [4]) and sensor device applications (Multiturn sensor [5]). Within the development of the Multiturn sensor the question occurred in which way large transversal fields can influence the propagation of DWs. Up to now there are only micromagentic simulations at low transversal fields dealing with this topic [6, 7].
We investigated the DW motion under the influence of strong transversal fields in Permalloy (Py) nanostrips. The 20 nm thick Py layer is part of a GMR stack deposited using physical vapour deposition and patterned via photolithography and Ar ion etching under tilt. Due to a magnetisation reversal of the Py sense layer we get a change in the GMR resistance in the order of 5 %. This variation of the GMR resistance is measured in terms of a change in voltage. Thus we investigated the DW propagation by means of time resolved voltage measurements. Using the slope of the voltage jump one can calculate the DW velocity. The required longitudinal and transversal fields are generated by two coils adjusted orthogonally to each other.
To perform a measurement we first applied a constant transversal field and then an alternating longitudinal field by means of a triangular signal. If the nucleation field of a DW is reached a DW is injected into the nanostrips and driven through the whole Py wire within some µs at constant transversal and longitudinal driving field without pinning events.
Fig. 1 shows the longitudinal component of the nucleation field (bold), which is the driving field Hdr of the DW, and the DW velocity (thin) as a function of the transversal field. The longitudinal component of the driving field is reduced with increasing transversal field. This can be explained by the reduction of the DW angle by increasing the transversal field and thus a reduction of exchange energy stored in the DW. Micromagnetic simulations show two effects of the transversal field on a static DW. Firstly, the DW width is increased by the factor of two (Ht = 32 kA/m) and secondly, the magnetisation direction of the domains is tilted in the direction of the transversal field, resulting in a reduced DW angle. At highest applied transversal fields of Ht = 50 kA/m one get a DW angle in the order of 60° and a longitudinal field component in the order of 0,8 kA/m is necessary for the nucleation of the reversed domain.
For small transversal fields (|Ht| < 10 kA/m) the velocity decreases slightly with decreasing Hdr. Hence we get a positive DW mobility (dv/dHdr). Increasing the transversal field to higher values a jump of the DW velocity occurs at |Ht| = 20 kA/m by the factor of about 2. This rise is due to the suppression of the Walker breakdown process [1, 7], as shown in detail elsewhere. The transversal field stabilizes the DW core magnetisation parallel to Ht and suppresses the nucleation and propagation of an antivortex and vortex respectively. Thus we get DW motion below Walker breakdown at relatively high driving fields compared to DW motion without transversal fields [3].
Increasing the transversal fields to values above 20 kA/m we get a further rise of DW velocity while the driving field Hdr is decreased, resulting in a negative DW mobility. For pure longitudinal fields (Ht=0) one gets a negative DW mobility only in the transition region between DW motion above and below Walker breakdown [3]. This transition is observed at |Htrans| = 20 kA/m as explained above. Thus the rise in DW velocity for |Htrans| > 20 kA/m must have different origin. We explain this behaviour with the broadening of the DW and the reduction of the DW angle. A 1-D-model developed by Allwood et al. [8] predicts a dramatic increase of DW velocity with decreasing DW angle and a moderate rise with increasing DW width. Due to these effects we get maximum velocities of v = 8000 m/s, which is 5 times higher than the maximum published velocity of field driven DWs in Py [9].

[1] J.-Y. Lee, K.-S. Lee, S. Choi, K. Y. Guslienko and S.-K. Kim, Phys. Rev. B, 76, 184408 (2007)

[2] M. Hayashi, L. Thomas, C. Rettner, R. Moriya and S.S.P. Parkin, Nat. Phys., 3, 21-25 (2007)

[3] G. Beach, C. Nistor, C. Knutson, M. Tsoi and J. Erskine, Nat. Mat., 4, 741-744 (2005)

[4] S.S.P. Parkin, The Magnetic Race Track - Current Driven Motion of Domain Walls, http://online.kitp.ucsb.edu/online/spintr_c06/parkin/ (12/2007)

[5] M. Diegel, R. Mattheis, E. Halder, IEEE Transac. on Magn. 404, 2655

[6] A. Kunz, private communication

[7] A. Thiaville et al., in “Spin Dynamics in Confined Magnetic Structures I”, Springer Series: Topics in Applied Physics, Vol. 83, Hillebrands, B. and Ounadjela, K. (Eds.) 002

[8] D. Allwood, M. Bryan and D. Atkinson, private communication

[9] D. Atkinson Cowburn et al., Nat. Mater. 2, 85 (2003)

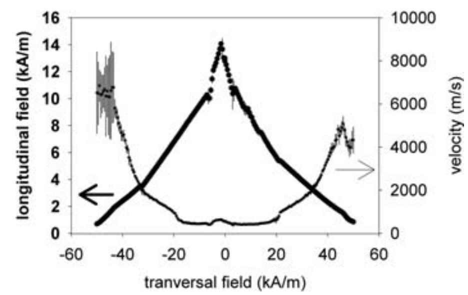

Figure 1: Longitudinal component of the nucleation field and DW velocity in dependence on the transversal field

AB-12

Domain-Wall Trapping by Localized Field on Submicron Permalloy Wire.

L. Ji, A. Orlov, G. H. Bernstein, W. Porod
Electrical Engineering, University of Notre Dame, Notre Dame, IN

We present a novel method to trap a domain wall on a submicron permalloy wire. The trapping is accomplished by the stray field generated by a rectangular permalloy bar placed at a right angle next to the wire.

Simulations of this structure have been performed by the standard OOMMF simulator. The wire dimension is 7um in length, including a large circular pad to initiate the magnetic switching, and a sharpened end for domain wall annihilation. For this study, the wire width is 200nm. A 300*1500nm rectangular bar is placed 30nm away from the wire, as shown in Figure 1a). The thickness of the wire and the bar is 10nm.Initially, the structure is saturated in the +y direction perpendicular to the wire. When the external field is relaxed, the bar will maintain the magnetization in the +y direction, while on the wire, a head-to-head domain wall is naturally trapped in the vicinity of the bar, as shown in Figure 1b). Then, an external field is gradually increased in the +x direction along the wire. The domain wall will remain at that position until the external field is sufficiently large to drive it out. For our geometry, this critical field is +75 Oe. After +75 Oe, the wire is magnetized to the right. When the external field is decreased to zero and then is increased in the –x direction, switching starts from the circular pad. At about -70 Oe, the domain wall moves out of the pad and starts to propagate along the wire. When it travels to the left of the rectangular bar, the stray field from the bar is pointing to the right, which opposes the external field, and a domain wall is trapped until the external field is large enough to drive it out, as shown in Figure 1c) and 1d). However, if the field is increased to +x direction again, when a domain wall travels to the left of the bar, the stray field would facilitate the propagation of domain wall, so no domain wall will be trapped.

Sample with the same dimension as in the above simulation was fabricated by electron beam lithography. A SEM image is shown in Figure 2 a). Copper contacts are made upon the wire as shown in Figure 2b) for four-probe measurement. Sample is first magnetized in the +y direction, when the external field is removed, the rectangular bar is magnetized upwards. And a domain wall is trapped on the wire as shown in MFM image, as shown in Figure 3. The wire is then magnetized in the +x direction by a field of 200 Oe.

A full magneto-resistance resistance measurement loop is then performed. External field is increased from 0 to +80 Oe in the +x direction first. No domain wall is trapped. When the field starts to decrease in the –x direction, a domain wall is trapped between -40~ -60 Oe, indicated by a resistance change of about 0.2Ω due to AMR effect. The magneto-resistance measurement result can be observed in Figure 4.

Due to the fact that domain wall is only trapped on one side of the loop and it is purely decided by the magnetization of the rectangular bar, it can be used as an electronic read-out for the magnetic QCA(Magnetic Quantum Cellular Automata)[1] to determine the output dot's magnetization. This method of domain wall trapping may also be useful for the study of current-induced domain-wall motion, since it does not require a physical constriction on the wire [2].

Figure 1. OOMMF simulation results.

Figure 2. SEM images of the sample.

Figure 3. MFM images of the pattern after initialization.

Figure 4. Magnetoresistance measurement result.

[1] A. Imre, G. Csaba, L. Ji, A. Orlov, G. H. Bernstein, W. Porod, Science 311, 205 – 208 (2006)

[3] M. Tsoi, R. E. Fontana, and S. S. P. Parkin, Applied Physics Letter 83, 2617 (2003)

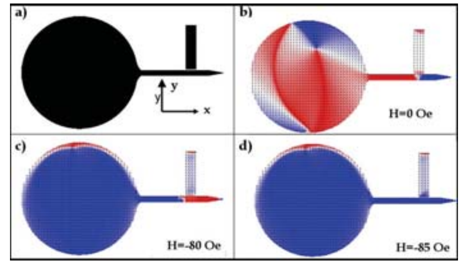

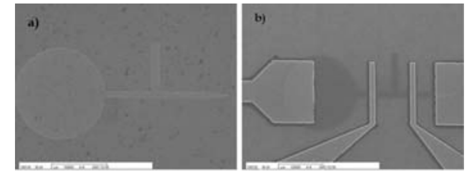

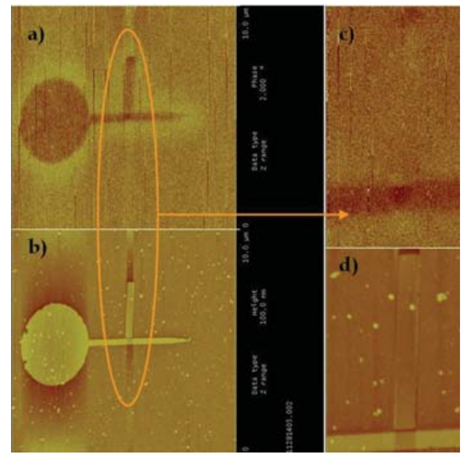

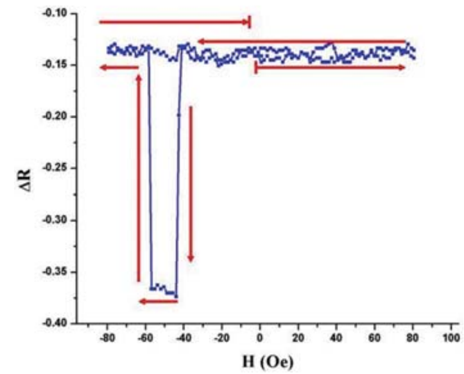

AC-01

Tunnel magnetoresistance over 100 % in MgO based magnetic tunnel junction films with perpendicular magnetic $L1_0$-FePt electrodes.

M. Yoshikawa, E. Kitagawa, T. Nagase, T. Daibou, M. Nagamine, K. Nishiyama, T. Kai, N. Shimomura, M. Amano, S. Takahashi, T. Kishi, H. Yoda
Corporate Research & Development Center, TOSHIBA Corporation, Kawasaki, Japan

Spin transfer torque switched elements with a perpendicular magnetic anisotropy were thought to be suitable for high density magnetoresistive random access memory (MRAM) application because they have potentials to reduce the critical switching current density while maintaining the thermal stability at small element size [1]. Some experimental results for the spin transfer torque switching in MgO based MTJs with perpendicular magnetic anisotropy were reported [2,3]. However, reliability of the materials is not adequate. In this paper, the MgO based MTJ film with $L1_0$-FePt electrodes, which was a promising material for high density MRAM, was studied and successfully developed to have high TMR ratio over 100 % at room temperature.
The MTJ stacks of a capping-layer/top $L1_0$-FePt(3)/MgO(1.5)/interface-layer(2)/bottom $L1_0$-FePt(10)/underlayer/substrate (thicknesses in nanometers) were deposited on thermal oxidized Si substrates by a DC/RF magnetron sputtering method, where the interface layers consisted of polycrystalline Fe and FeCo. The bottom $L1_0$-FePt electrode was formed on a heated substrate. The top $L1_0$-FePt electrode was annealed in-situ after deposition. The substrate temperature and the post-annealing temperature were optimized in the range from 673 K to 773 K. Magnetic properties were measured using a vibrating sample magnetometer. The TMR ratio was measured at room temperature by the current-in-plain tunneling method [4].
Figure 1 shows a typical magnetization versus applied magnetic field (M-H) curve of the FePt/MgO/Fe/FePt-MTJ film. The enough coersive force difference between the top and bottom electrodes, whose coersive forces were 0.6 kOe and 2.5 kOe, respectively, was obtained. A typical TMR ratio was around 100 % and a maximum value was 120 %. Then, Figure 2 shows the plots of the TMR ratio as a function of the top FePt electrode thickness for the FePt/MgO/FeCo/FePt-MTJ films. The TMR ratio was not dependent on the top FePt electrode thickness and approximately constant around 100 %. A transmission electron microscopy analysis for the FePt/MgO/Fe/FePt-MTJ film shows that the smooth MgO barrier with good (001) orientation was formed and the FePt electrodes had high (001) orientation (not shown here). On the other hands, the TMR ratio was decreased as the interface Fe layer thickness became thin. No TMR was observed in the case that the interface Fe layer was not inserted (not shown here). This is because the lattice mismatch at the MgO(001)/FePt(001) interface is too large for the MgO film to grow epitaxially and the morphology and the (001) orientation of the MgO barrier become degraded. The insertion of the interface layer is required for the relaxation of the lattice mismatch between MgO(001) and FePt(001).
Consequently, the high TMR ratio over 100 % in the $L1_0$-FePt/MgO/Fe(FeCo)/$L1_0$-FePt MTJ films was obtained at room temperature. The recent theoretical calculation predicted the TMR over 300 % in an epitaxial $L1_0$-FePt/MgO/$L1_0$-FePt(001) MTJ [5] as well as the large one in an epitaxial Fe/MgO/Fe(001) MTJ [6]. The much higher TMR ratio can be obtained by optimization of the interface layer inserted between MgO and FePt.
A portion of this work was supported by NEDO.

[1]S. Mangin *et al.*, Nature Materials, 5, 210 (2006)

[2]M. Nakayama *et al.*, Abstract of 52nd Annual Conference on Magnetism and Magnetic Materials, BB-09, p.81 (2007)

[3]T. Nagase *et al.*, American Physical Society March meeting 2008, New Orleans, LA, to be submitted

[4]D. C. Worledge *et al.*, Appl. Phys. Lett., 83, 84 (2003)

[5]Y. Taniguchi *et al.*, Abstract of 6th International Symposium on Metallic Multilayers, TUE-06, p.71 (2007)

[6]W. H. Butler *et al.*, Phys. Rev. B, 63, 054416 (2001)

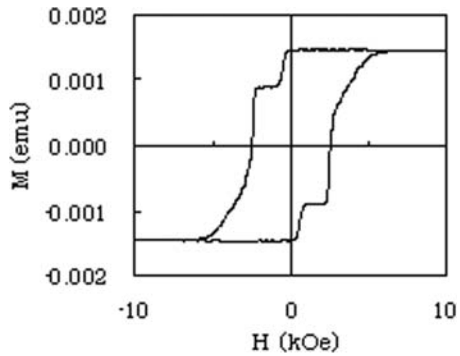

Fig. 1. Typical M-H curve of the FePt/MgO/Fe/FePt-MTJ film.

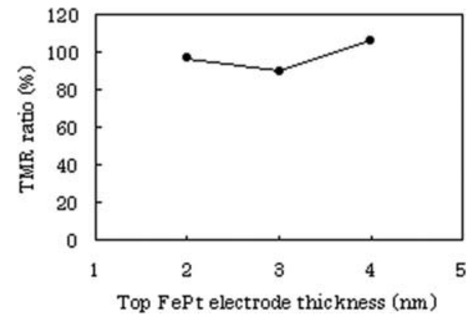

Fig. 2. TMR ratio as a function of the top FePt electrode thickness for the FePt/MgO/FeCo/FePt-MTJ films.

Interfacial Oxidation Enhanced Perpendicular Magnetic Anisotropy in Low Resistance Magnetic Tunnel Junctions Composed of Co/Pt Multilayer Electrodes.

J. Park[1], C. Park[2], J. Zhu[1]
1. Carnegie Mellon University, Pittsburgh, PA; 2. Western Digital Corporation, Fremont, CA

Introduction

Magnetic tunnel junctions (MTJs) using perpendicular magnetic anisotropy (PMA) have been suggested as the promising candidate to overcome the density limits of the present in-plane-magnetized junctions for scalable magnetic memory application [1]. In the previous study, authors experimentally demonstrated pMTJs composed of Co/Pt multilayers with PMA, which yielded robust tunneling magnetoresistance (TMR) of ~15% TMR ratio [2]. In this study, low resistive pMTJs with thin AlOx tunnel barrier by natural oxidation have been investigated. On optimizing the tunnel barrier, the authors focus on verifying the effect of oxidizing Co monolayer adjacent to AlOx barrier. This has been designed in order to enhance the PMA of Co/Pt multilayer by producing rich Co-O bonding at the interface [3]. As results, magnetization switching behavior has been improved and well-defined transition between parallel and anti-parallel states is obtained at the pMTJ device of ~100 Ω●μm2 resistance-area (RA) product.

Experimental

All film stacks including magnetic layers, leads and tunnel barrier were prepared by rf/dc sputtering below 3×10-7 Torr base pressure. The typical oxidation procedure of AlOx barrier and Co adjacent layers is depicted in Fig. 1. In this figure, each natural oxidation process has been optimized for the full oxidation of ~5 Å Al layer. For enriching Co-O bonding at the bottom interface, 3 Å thick Al is deposited on top of the bottom Co adjacent layer prior to the 1st oxidation. For the top interface oxidation, monolayer thick Co is deposited on top of 3 Å Al layer followed by the 3rd oxidation step. After film deposition, magnetization switching has been investigated by film level perpendicular hysteresis and TMR transfer curves of micro-fabricated MTJ test patterns.

Results and discussion

The oxidation effect of adjacent Co monolayer on perpendicular hysteresis loop is shown in Fig. 2. MTJ film without Co oxidation has dispersed switching field both in soft and hard layers, which can be attributed to the lack of Co/Pt interface anisotropy in the vicinity of Co-AlOx interface and orientational incoherence especially on the soft Co adjacent layer on top of amorphous AlOx layer. On the contrary, MTJ film with treated Co adjacent layers shows sharp magnetization switching in the both layers. This improvement is also confirmed in the TMR measurement result. Fig. 3 shows MR behavior of two MTJ devices with (a) non-oxidized and (b) oxidized Co interfacial layers. In the non-treated MTJ device, the magnetization of the soft layer appears to be completely tilted with the hard layer being partially tilted. However, the treated device shows well-defined parallel and anti-parallel states and reproducible magnetization switching at the junction of ~100 Ω●μm2 RA product. Thus abundant Co-O bonding at the barrier interface is believed to enhance the PMA of Co/Pt multilayer and magnetization switching property. This consideration should be very important for possible perpendicular spin-torque-transfer application, in which thick adjacent layers are expected to be advantageous for high spin polarization. Therefore, the effect of adjacent layer thickness on the PMA will be also discussed.

[1] N. Nishimura, T. Hirai, A. Koganei, T. Ikeda, K. Okano, Y. Sekiguchi, and Y. Osada, J. Appl. Phys., 97, 10C919 (2002)

[2] J. Park, C. Park, T. Jeong, M. T. Moneck and J. Zhu, 52nd MMM conference, AB-02 (2007)

[3] A. Manchon, S. Pizzini, J. Vogel, V. Uhlir, L. Lombard, C. Ducruet, S. Auffret, B. Rodmacq, B. Dieny, M. Hochstrasser and G. Panaccione, 52nd MMM conference, AB-05 (2007)

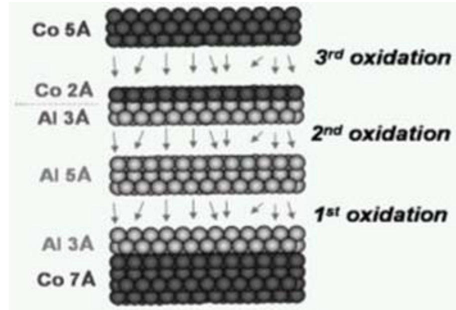

Fig. 1 A schematic description on the oxidation of tunnel barrier and Co adjacent layers by repeated natural oxidation methods.

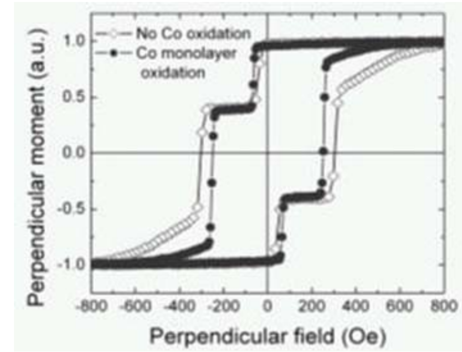

Fig. 2 Perpendicular hysteresis loops of two pMTJ samples with same deposition stacks but different Co adjacent layer oxidation during tunnel barrier formation.

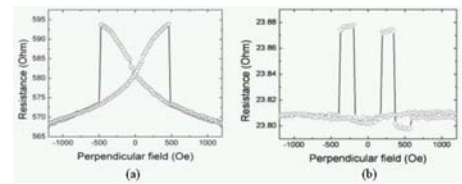

Fig. 3 Perpendicular tunneling magnetoresistance curves of pMTJ samples with the structure Pt 50Å/[Co 6Å/Pt 18Å]×4/Co 7Å/AlOx (naturally oxidized)/Co 7Å/Pt 18Å/Co 7Å/Pt 50Å where the Co layers adjacent to the AlOx barrier are (a) not oxidized and (b) naturally oxidized. The different resistance levels in (a) and (b) result from using different leads and pattern sizes between the two samples.

AC-03

Large Tunneling Anisotropic Magnetoresistance in a Magnetic Tunnel Junction with a Single Ferromagnet CoPt.

B. Park[1], J. Wunderlich[1], S. Joo[2], K. Jung[2], K. Shin[2], A. Shick[3], T. Jungwirth[3,4]
1. Hitachi Cambridge Laboratory, Cambridge, United Kingdom; 2. Nano Device Research Center, KIST, Seoul, South Korea; 3. Institute of Physics ASCR, Pargue, Czech Republic; 4. School of Physics and Astronomy, University of Nottingham, Nottingham, United Kingdom

A magnetic tunnel junction consisting of two ferromagnetic (FM) layers separated by a tunnel barrier exhibits a large tunnel magnetoresistance (TMR), depending on the relative magnetization direction of the two FM layers. This originates from the spin-polarized tunneling from the FM/Insulator interface. Recently, a similar magnetoresistnace effect (so-called tunneling anisotropic magnetoresistance, TAMR) is observed in the tunnel junctions with only one FM layer where the TMR is not present. Studies in ferromagnetic semiconductor devices showed that TAMR response can in principle be huge and richer than TMR, with the magnitude and sign dependent on the magnetic field orientation and electric fields. Theoretical work predicted [1] that the TAMR effect is generic in FMs with spin orbit(SO)-coupling, including the transition metal systems. Experimental demonstration of the TAMR in a metallic tunnel junction has recently been reported in an epitaxial Fe/GaAs/Au [2] and CoFe/tunnel barrier (MgO, Al2O3)/CoFe structures [3]. The observed TAMR in those structures is relatively small, bellow 0.5%, consistent with the weak SO-coupling. In this work we present a study of tunnel devices with a single FM electrode of Co/Pt multilayer in which large and tunable magnetic anisotropies are generated at the interfaces by combined effects of induced moments and strong SO-coupling. We show that engineering the interfaces adjacent to the tunnel barrier enhances the TAMR effect by an order(s) of magnitude.
Our tunneling devices, schematically illustrated in Fig. 1(a), were grown by magnetron sputtering on a thermally oxidized Si wafer. The Ta/Pt seed layer was chosen to initiate growth of a textured Pt(111)/Co ferromagnetic film with a strong out-of-plane magnetocrystalline anisotropy. The tunnel barrier was fabricated by plasma oxidation of 1.6 nm Al layer. Two types of multilayers are investigated: samples A have the alternating sequence of Pt and Co layers beneath the AlOx barrier terminated by 0.5 nm (two monolayers) Pt film while samples B have this top Pt film in the FM electrode omitted. Devices were mounted on a rotating sample holder allowing the application of magnetic fields up to 10 T at an arbitrary in-plane and out-of-plane angle.
Fig. 1(b) compares magnetization and magnetotransport anisotropy data measured in samples A and B. Wide and square hysteresis loops in perpendicular magnetic fields, shown in the insets, confirm the strong magnetic anisotropy with out-of-plane easy axis in both devices. The anisotropic magnetotransport in the two tunneling devices is, however, fundamentally different. The resistances of the device are taken at a magnetic field of 10T rotating from the perpendicular (θ=0) to the in-plane (θ=90) direction. In both samples the TAMR has the expected uniaxial symmetry but the magnitude of the effect is enhanced by 2 orders of magnitude in sample A. As the transport characteristics of TMR or TAMR tunneling devices are expected to be strongly influenced by the nature of the surface layers of the FM electrode we attribute the large TAMR signal in sample A to the induced moment and strong SO-coupling in the two-monolayer Pt film inserted between Co and the tunnel barrier. In sample B, the topmost layer in contact to the barrier is 1 nm Co film and therefore this tunneling device behaves effectively as a Co/barrier/normal metal for which the magnetotransport anisotropy is expected to be comparably weak.
The analysis is based on calculating density of states (DOS) anisotropies in the FM electrode with respect to the orientation of the magnetization (Fig1. (c)). For the Co/Pt model system we find a complex structure of the DOS near the Fermi energy with the main features shifted by 10's of meV when comparing the two magnetization orientation curves. The Co-film, on the other hand, has a nearly featureless DOS near the Fermi level which depends very weakly on the magnetization direction. The relative difference between DOSs for the in-plane and out-of-plane magnetizations, which we relate to the tunneling conductance anisotropy, shows an oscillatory behavior as a function of energy for the Co/Pt with a magnitude of up to 20% (Fig 1. (d)). For the Co film the magnitude and the energy dependence of the anisotropy is substantially weaker. These theoretical results are qualitatively consistent with measurements in samples A and B presented above. We will discuss further on the dependence of the TAMR on magnetic field, temperature, and bias voltage for both samples.

[1] A. B. Shick, F. Maca, J. Masek, and T. Jungwirth, Phys. Rev. B 73, 024418 (2006).

[2] J. Moser et al., Phys. Rev. Lett. 99, 056601 (2007). [3] Li Gao et al, Phys. Rev. Lett. 99, 226602 (2007).

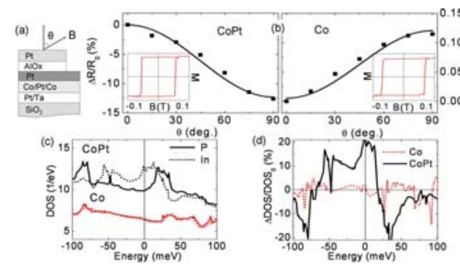

Figure 1. (a) schematic layer structures of device. (b) TAMR [(R(θ) − R(θ=0))/R(θ=0)] at -5 mV bias and 4 K. Insets: SQUID magnetization measurements in out of plane magnetic fields (c) Theoretical DOSs for perpendicular (P) and in plane (In) magnetization. (d) relative DOS anisotropy [(DOS_In − DOS_P)/DOS_P] as a function of energy for the Pt/Co and Co model systems

AC-04

Crossover from Kondo assisted suppression to cotunneling enhancement of tunneling magnetoresistance via ferromagnetic nanodots in MgO tunnel barriers.

H. Yang[1,2], S. Yang[1], S. Parkin[1]
1. IBM Almaden Research Center, San Jose, CA; 2. ECE, National University of Singapore, Singapore, Singapore

The magneto-transport properties of magnetic granular alloys and magnetic tunnel junction devices with magnetic nanodots embedded in amorphous dielectric matrices [1,2] and tunnel barriers [3,4] respectively, have been studied by several groups but no systematic studies of the dependence on these properties on the nanodot size have been made.
Here we show that a wide range of magneto-transport properties in magnetic tunnel junctions with barriers containing magnetic nanodots can be accounted for by Kondo-like physics and that as the size of these nanodots is systematically increased the tunnelling properties change from those characteristic of Kondo tunnelling which suppresses the TMR near zero bias, to those of correlated tunneling which increases the TMR at low bias.
The MTJ device is composed of CoFe ferromagnetic (F) electrodes, and an MgO tunnel barrier. Both F electrodes are exchange biased but the exchange bias field is designed to be significantly stronger for the lower electrode so that the moment of each electrode can be switched independently. A thin CoFe layer of nominal thickness t_{ND} is inserted in the middle of the MgO layer. When this layer is thinner than ~2 nm it forms a discontinuous layer of nanodots, as revealed by plan-view transmission electron microscopy (TEM). This means that the diameter of the nanodots is considerably larger than the nominal layer thickness.
The magneto-transport properties of the MTJs are considerably affected by the presence of the nanodots in the MgO tunnel barrier, as shown in Figure 1. In particular, as the temperature is reduced, the resistance of the MTJ increases, but at a greater rate, the smaller the nanodot size. This is due to a Coulomb blockade (CB) effect, which has previously been seen in MTJs formed with discontinuous Co and Fe layers within alumina [4-7] and MgO [8] tunnel barriers. At high temperatures and bias voltages the tunneling is dominated by sequential tunneling through the nanodots since the barrier is very thick (thus direct tunneling across the MgO barrier is small). The nanodots are so small that there is a significant increase in energy when an electron tunnels onto a dot which, at low temperature and bias compared to this energy, thereby depresses the tunneling conductance across the MTJ device. From the fits of the temperature dependence of the tunneling resistance a characteristic temperature T_{CB}, below which CB effects are important, can be derived. T_{CB} is proportional to the charging energy needed to add a single electron to the dot. CB effects are observed when t_{ND} <1.8nm with T_{CB} increasing to ~330 K when t_{ND} = 0.05 nm. The calculated CB energy is consistent with the average size of the nanodots inferred from plan-view TEM micrographs. For example, when t_{ND}= 0.45nm, the CB energy is ~53 meV which gives a nanodot diameter of ~2.6 nm.
There are several other characteristic features of Kondo assisted tunneling, which we observe in MTJs with nanodots. One of these is a peak in the tunneling conductance versus bias voltage curve centered at zero voltage which has a characteristic width proportional to the strength of the Kondo interaction i.e. the Kondo temperature T_K. The crossover from Kondo to cotunneling behaviour is likely correlated with suppression of the fluctuations of the nanodot magnetic moments. Although the tunneling characteristics for the smallest nanodots can be described by Kondo physics, the possibility of observing Kondo phenomenon involving quantum dots with large magnetic moments requires a stronger theoretical foundation and remains an open question.

[1] Mitani, S. et al. Enhanced magnetoresistance in insulating granular systems: evidence for higher-order tunneling. Phys. Rev. Lett. 81, 2799 (1998).

[2] Milner, A., Gerber, A., Groisman, B., Karpovsky, M. & Gladkikh, A. Spin-dependent electronic transport in granular ferromagnets. Phys. Rev. Lett. 76, 475 (1996).

[3] Takahashi, S. & Maekawa, S. Effect of Coulomb blockade on magnetoresistance in ferromagnetic tunnel junctions. Phys. Rev. Lett. 80, 1758-1761 (1998).

[4] Sukegawa, H., Nakamura, S., Hirohata, A., Tezuka, N. & Inomata, K. Significant Magnetoresistance Enhancement due to a Cotunneling Process in a Double Tunnel Junction with Single Discontinuous Ferromagnetic Layer Insertion. Phys. Rev. Lett. 94, 068304 (2005).

[5] Schelp, L.F. et al. Spin-dependent tunneling with Coulomb blockade. Phys. Rev. B 56, R5747-R5750 (1997).

[6] Yakushiji, K. et al. Enhanced spin accumulation and novel magnetotransport in nanoparticles. Nature Mater. 4, 57-61 (2005).

[7] Fettar, F. et al. Temperature and voltage dependence of the resistance and magnetoresistance in discontinuous double tunnel junctions. Phys. Rev. B 65, 174415 (2002).

[8] Ernult, F. et al. Spin-dependent single-electron-tunneling effects in epitaxial Fe nanoparticles. Appl. Phys. Lett. 84, 3106-3108 (2004).

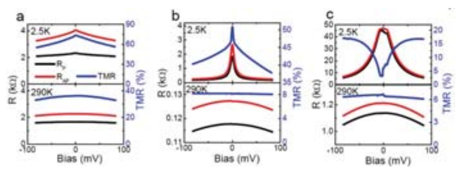

Fig. 1 The temperature and bias voltage dependence of the dc resistance and tunneling magnetoresistance (TMR) of a MTJ without the nanodot layer (a) and with a nanodot layer in (b & c). The nanodot layer thickness is 0.45 nm in (b) and 1.2 nm in (c).

AC-05

Magneto-Coulomb effects through isolated nanoparticles connected to ferromagnetic electrodes.

A. Bernand-Mantel[1], P. Seneor[2], B. Dlubak[2], V. Cros[2], S. Fusil[2], K. Bouzehouane[2], C. Deranlot[2], A. Vaures[2], R. Guillemet[2], F. Petroff[2], A. Fert[2]
1. Kavli Institute of Nanoscience, Delft University of Technology, Delft, Netherlands; 2. Unite Mixte de Physique CNRS/Thales associated with University Paris-sud, Palaiseau, France

What is now emerging in the field of spintronics is the investigation of the spin transport properties of structures in which the central element is a nano-object connected to ferromagnetic electrodes. The capacitance of this nano-object can be small enough that the energy needed to add an electron on it becomes larger than the thermal energy at low temperature, leading to discrete voltage jumps of e/C in the I-V characteristics called Coulomb blockade ”staircases”. The interesting aspects of this new field of nano-spintronics come from the interplay between this Coulomb blockade effects and magnetic properties [1]. This subject has motivated a lot of theoretical works in the past decade.
They predict the observation of a magnetoresistance effect related to spin dependant transport and spin accumulation in systems with at least two ferromagnetic elements [2,3].
We investigate Coulomb blockade and magnetic properties in a single nonmagnetic metallic nanoparticle connected to ferromagnetic leads. A layer containing metallic clusters of a few nanometers in diameter embedded in an oxide layer of alumina is grown by sputtering. After an optical lithography process, the fabrication is carried out using a conductive tip AFM where the nanoindentation process is electrically monitored in real time. With this simple technique, we contact single particles of a few nanometers in size [4]. A schematic representation of the sample is shown in figure 1.
The I-V characteristics of this system measured at 1.5K show typical Coulomb blockade effects and are in excellent agreement with numerical simulations of transport through a unique nanoparticle (see figure 2). We observe magnetoresistance effects in samples containing single Au, Cu and Al nanoparticles connected with ferromagnetic electrodes. Besides spin accumulation effects, we are able to distinguish another type of magneto-Coulomb effect. This effect is linked to the magnetic anisotropy of the ferromagnetic electrodes and can occur even when a single ferromagnetic element is present in the system.
A measurement of this effect is shown in figure 2. We present I-V curves obtained at low temperature on a sample containing an Au nanoparticle of around 5nm in diameter with a magnetic field of 500 Oe applied in different directions. We see a clear difference in the I-V curves measured with a magnetic field applied at 0 and 90 degrees. We find out by realizing simulations that the magnetic electrode acts as a gate on the single electron device. The magnetoresistance presents an oscillation as function of bias voltage and can be as strong as -70% showing evidence for Coulomb blockade driven anisotropic magnetoresistance in metallic single electron devices.

[1] P. Seneor et al., J. Phys. Cond. Mat., 19, 165222 (2007)

[2] J.Barnas and A. Fert, Phys. Rev. Lett., vol. 80, 1158, (1998)

[3] S. Takahashi and S.Maekawa,Phys. Rev. Lett., vol.80, 1758, (1998)

[4] A. Bernand-Mantel et al., Appl. Phys. Lett.,, 062502 (2006)

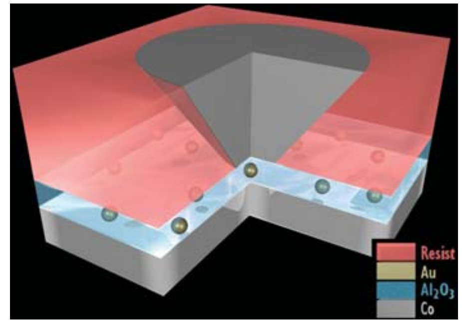

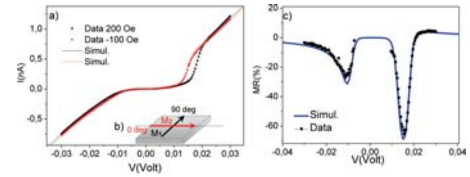

AC-06

Fabrication and characterization of magnetic tunnel junctions using Co_2MnSi electrode and MgO tunneling barrier.

S. Tsunegi[1], Y. Sakuraba[2], M. Oogane[1], K. Takanashi[2], Y. Ando[1]

1. Applied physics, Tohoku University, Sendai, Japan; 2. Institute for Materials Research, Tohoku University, Sendai, Japan

Introduction

Some of full-Heusler alloys (Co_2MnSi, Co_2MnGe, etc.) attract much interest in recent spintronics field because they have been predicted to possess half-metallic electronic structure. We have demonstrated giant TMR ratio of 159% at 2 K in magnetic tunnel junctions (MTJs) with Co_2MnSi/Al-O/CoFe structure; this result indicates the half-metallic property of Co_2MnSi (CMS). [1] However, the TMR ratio decreased drastically with increasing of temperature. We considered that the large temperature dependence was originated from the destruction of half-metallic gap due to thermal fluctuation of DOS at the Fermi level.

Although this TMR ratio is outstanding in the MTJs with conventional Al-O barrier, recent works on the MTJs with MgO barrier showed more excellent performance due to coherent tunneling mechanism through (001)-oriented crystalline MgO barrier. [2] Miura et al. showed coherent tunneling through the Δ_1 band could also occur in a CMS/MgO/CMS-MTJ, theoretically. [3] As the edge of Δ_1 band of CMS exists apart from the Fermi level, a large TMR ratio at RT can be realized in MTJs using both CMS electrode and MgO tunneling barrier.

In this study, we fabricated the high-quality Co_2MnSi/MgO/CoFe-MTJs and investigated their spin-dependent tunneling properties.

Experiments

We fabricated fully-epitaxial MTJs with Co_2MnSi/MgO/CoFe-structure on the single crystalline MgO substrates. The CMS bottom electrode was deposited by magnetron sputtering system at RT and annealed at 500°C to obtain good chemical ordering. The MgO tunneling barrier was formed by EB-evaporation system under 10^{-7} Pa. All the MTJs were patterned into 4-terminal structure by photo-lithography and Ar ion milling. The differential conductance G ($=dI/dV$) was measured using standard ac lock-in technique. A positive bias voltage is defined as electrons tunneling from the bottom CMS to the top CoFe electrode.

Results and discussions

Figure 1 shows temperature dependence of TMR ratio and the typical MR curves for the Co_2MnSi/MgO/CoFe-MTJ and the Co_2MnSi/Al-O/CoFe-MTJ. The Co_2MnSi/MgO/CoFe-MTJ shows TMR ratios of 217% at 300 K and 753% at 2 K. The TMR ratio of 753% at LT is the highest in MTJs using Heusler alloy electrodes and larger than that for CoFe/MgO/CoFe-MTJ, 300%, reported in ref [4]. This result reveals that half-metallicity of CMS can be realized in the MTJ with MgO tunneling barrier. In addition, the TMR ratio at RT is drastically improved, compared with that for the MTJ with Al-O barrier. However, the temperature dependence of TMR ratio is still large.

Figure 2-(a) shows the bias voltage dependence of conductance for parallel magnetization configuration (G_P). For reference, G_P for the CMS/Al-O/CoFe-MTJ is shown together. In the CMS/Al-O/CoFe-MTJ, the crucial rise of G_P is observed at the negative bias voltage. This behavior of G_P reflects very small energy separation (ca. 10 meV) between the conduction band and the Fermi level of the CMS. [5] On the other hand, in the CMS/MgO/CoFe-MTJ, the crucial rise of G_P at the negative bias voltage is suppressed at both RT and LT. In addition, dip structures, being similar to that for the CoFeB/MgO/CoFeB-MTJ reported previously, are observed at ±400 mV. [6] We infer that these dip structures are related to the coherent tunneling process through the MgO barrier.

Figure 2-(b) shows the bias voltage dependence of conductance for anti-parallel magnetization configuration (G_{AP}). G_{AP} at LT increases sharply at low bias voltage compared with G_P or G_{AP} at RT. This large voltage dependence of G_{AP} at low bias can be originated from inelastic tunneling processes at the CMS/MgO interface. There are two possible explanations for the large inelastic tunneling probability in the MTJs with CMS electrodes; magnon excitations due to the low Curie temperature at the CMS surface and magnetic impurity scatterings caused by Mn and Si oxide.

In summary, we have succeeded to fabricate the high-quality Co_2MnSi/MgO/CoFe-MTJs and obtained the highest TMR ratio in MTJs using Heusler alloy electrodes.

This work was supported in part by Research and Development for Next-Generation Information Technology of MEXT.

[1] Sakuraba, *et al. Jpn. J. Appl. Phys.* 44 L1100-1102 (2005)

[2] Hayakawa, *et al. Appl.Phys. Lett.* 89, 232510 (2006)

[3] Miura *et al. J. Phys. Con. Matt.* 19 36 (2007)

[4] Parkin *et al. Nat. Mater.* 3, 862 (2006)

[5] Sakuraba, *et al. Appl. Phys. Lett.* 89, 052508 (2006)

[6] K. Ono *et al. J. Appl. Phys.* 99 08A905 (2006)

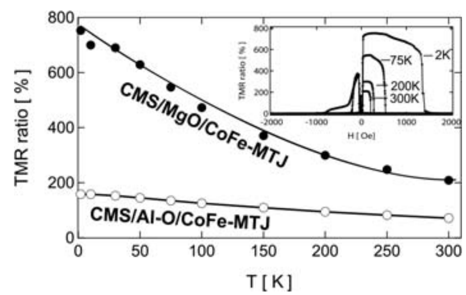

Fig.1 Temperature dependence of TMR ratio and inset shows MR curves in CMS/MgO/CoFe-MTJ

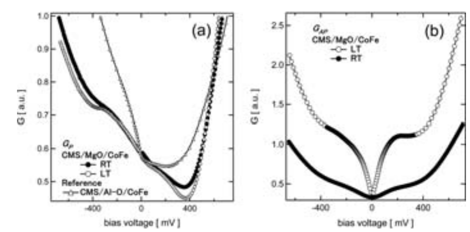

Fig.2 (a) Bias voltage dependence of G_P Fig.2 (b) Bias voltage dependence of G_{AP}

AC-07

Spin-dependent tunneling conductance in fully epitaxial $Co_2MnSi/MgO/Co_2MnSi$ tunnel junctions.

T. Ishikawa, N. Itabashi, K. Matsuda, T. Uemura, M. Yamamoto
Division of Electronics for Informatics, Hokkaido University, Sapporo, Japan

Co-based full-Heusler alloy (Co_2YZ) thin films have attracted much interest as a promising ferromagnetic electrode material for spintronic devices [1,2]. This is because of the half-metallic ferromagnetic (HMF) nature theoretically predicted for many of these alloys, and because of their high Curie temperatures, which are well above room temperature (RT). We recently demonstrated high tunnel magnetoresistance (TMR) ratios of up to 182% at RT and 705% at 4.2 K for fully epitaxial magnetic tunnel junctions (MTJs) with Co_2MnSi (CMS) thin films as both the lower and upper electrodes and a MgO (001) tunnel barrier [3]. Our purpose in the present study is to investigate the bias voltage (V) dependence of the spin-dependent tunneling conductance and clarify its origin for the CMS/MgO/CMS MTJs (CMS-MTJs) that feature high TMR ratios. We investigated V dependences of R_P and R_{AP}, where R_P and R_{AP} are the respective tunneling resistances for the parallel (P) and antiparallel (AP) magnetization alignments, along with the differential conductance (G = dI/dV) vs V characteristics for P and AP (G_P and G_{AP}, respectively). The latter characteristics were measured using a standard lock-in method. The second derivative d^2I/dV^2 was obtained mathematically from the dI/dV vs V characteristics.
Figure 1(a) shows R_P and R_{AP} as a function of V at 4.2 K for a CMS-MTJ that showed a TMR ratio of 679% at 4.2 K (176% at RT). The bias voltage was defined with respect to the lower CMS electrode. R_{AP} of the CMS-MTJ showed a strong V dependence, especially in the V range of $|V| \leqq 100$ mV, while R_P exhibited a very weak dependence on V. This highly cusp-like dependence of R_{AP} in the range of $|V| \leqq 100$ mV faded away at RT.
Figure 1(b) shows G vs V for P and AP at 4.2 K. A marked increase of G_{AP} with increasing V was clearly visible in the V range of $|V| \leqq 70$ mV, which corresponds to the cusp-like structure in the R_{AP} vs V. Figure 2 shows typical d^2I/dV^2 spectra at 4.2 K. Clear structures in the range of $|V| \leqq 100$ mV characterized by peaks at around $\pm$ 4 mV are observed in the d^2I/dV^2 spectra for AP, indicating magnon excitations due to hot electrons in the collector.
The G_P spectra exhibited a broad, nearly flat region for $|V| \leqq 0.36$ V, and G_P increased sharply at V ~ 0.36 V. The G_{AP} spectra showed a similar region for $|V| \leqq 0.21$ V except the range of $|V| \leqq 0.07$ V. These sharp increases can be ascribed to direct tunneling from the minority-spin band below the Fermi level (E_F) or to the minority-spin band above E_F. From the characteristic structures in both spectra of G and d^2I/dV^2 indicated by the arrows in Figs. 1(b) and 2, we estimated an energy gap for the minority-spin band of about 0.36 eV with the E_F position being near the middle of the half-metallic gap.
These spin-dependent tunneling characteristics for the CMS-MTJs along with the large TMR ratios can be explained as follows: 1) Due to the half-metallic gap, the tunneling conductance for AP should be significantly decreased. 2) At low temperatures, where kT energy is much lower than the magnon excitation energy, we should consider only the tunneling from the majority-spin band in the emitter to the interface states of the minority-spin band in the collector for AP [4]. Hot electrons associated with the bias voltage excite magnons in the collector. Electrons are then scattered from the interface states in the minority-spin band to the majority-spin band in the collector. This results in the considerable increase of the tunnel conductance for AP by increasing V in the range of $|V| \leqq$ 100 mV.

In summary, we showed a HMF nature of CMS thin films incorporated into MTJs as ferromagnetic electrodes through the spin-dependent tunneling conductance characteristics. It was experimentally shown that spin-flip scattering from the interface states of the minority-spin band to the majority-spin band in the collector electrode by the hot-electron effect is a dominant factor for the tunneling characteristics of half-metallic Heusler alloy-based MTJs.

[1] T. Marukame et al., Appl. Phys, Lett., vol. 90, p. 012508, 2007.

[2] T. Ishikawa et al., Appl. Phys. Lett., vol. 89, p. 192505, 2006.

[3] T. Ishikawa et al., unpublished.

[4] Ph. Mavropoulos et al., Phys. Rev. B, vol. 72, p. 174428, 2005.

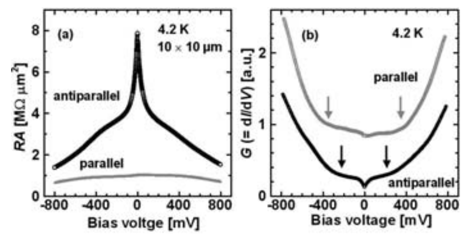

Fig. 1. (a) RA_P and RA_{AP} at 4.2 K for a fully epitaxial CMS/MgO/CMS MTJ (t_{MgO} = 2.2 nm) as a function of bias voltage. (b) G (= dI/dV) spectra at 4.2 K for the P and AP alignments.

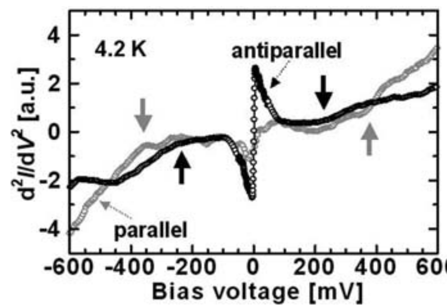

Fig. 2. d^2I/dV^2 spectra for the P and AP alignments at 4.2 K for a CMS/MgO/CMS MTJ which is the same as that shown in Fig. 1. Solid arrows are explained in the main text.

AC-08

Spin-polarized tunneling characteristics of the room temperature spin filter CoFe2O4.

A. V. Ramos[1], R. Mattana[2], F. Petroff[2], T. S. Santos[3,4], G. Miao[3], J. S. Moodera[3]
1. DSM/DRECAM/SPCSI, CEA Saclay, Gif-sur-Yvette, France; 2. Unite Mixte de Physique, CNRS/Thales, Palaiseau, France; 3. Francis Bitter Magnet Laboratory, MIT, Cambridge, MA; 4. Argonne National Laboratory, Argonne, IL

The generation of highly spin-polarized electron currents at room temperature is the basis of most spin-based device technologies. One approach known as spin filtering, has the potential of generating 100%-polarized currents by the spin selective transport of electrons across a ferromagnetic tunnel barrier [1]. While efficient spin filtering at room temperature is highly attractive for applications such as ultra sensitive detectors and spin injection into semiconductors, the selection of materials having the necessary magnetic and electronic properties is quite limited. Cobalt ferrite (CoFe2O4) is one very good candidate because it is a ferrimagnetic insulator with a remarkably high Curie temperature (793 K). In this work, we demonstrate that room temperature spin filtering may indeed be obtained in magnetic tunnel junctions (MTJs) containing CoFe2O4 tunnel barriers.

Fully epitaxial MTJs containing CoFe2O4(111) tunnel barriers have been grown by oxygen plasma-assisted molecular beam epitaxy. Their structural, chemical and magnetic properties are studied by a number of in situ and ex situ characterization techniques [2], as these are known to significantly impact the spin filter capability of complex magnetic oxides. We also pay special attention to the magnetization reversal behavior of the magnetic barrier and its magnetic counter electrode, which is yet another crucial step towards the successful measurement of TMR. Following the optimization of the CoFe2O4-based systems, we focus on the spin-polarized tunneling characteristics using two different measurement techniques: Tunneling magnetoresistance (TMR) measurements and the Meservey Tedrow technique. These spin polarized transport measurements first reveal significant TMR values both at low temperature and at room temperature [3]. In addition, the TMR ratio follows a unique bias dependence that has been theoretically predicted to be the signature of spin filtering in magnetic tunnel barriers. In the case of the Meservey Tedrow measurements, we once again demonstrate spin polarization in CoFe2O4-based tunnel barriers using Al superconducting electrodes as the spin analyzer. The results from the spin polarized transport measurements allow us to address the influence of defects such as oxygen vacancies on the spin polarization, as well as the role played by different spin-detecting electrodes. We therefore show that CoFe2O4 tunnel barriers provide a model system to investigate spin filtering in a wide range of temperatures.

[1] J. S. Moodera, T. S. Santos and T. Nagahama, J. Phys. Cond. Mat. 19, 165202 (2007).

[2] A. V. Ramos, et al., Phys. Rev. B 75, 224421 (2007).

[3] A. V. Ramos, et al., Appl. Phys. Lett. 91, 122107 (2007).

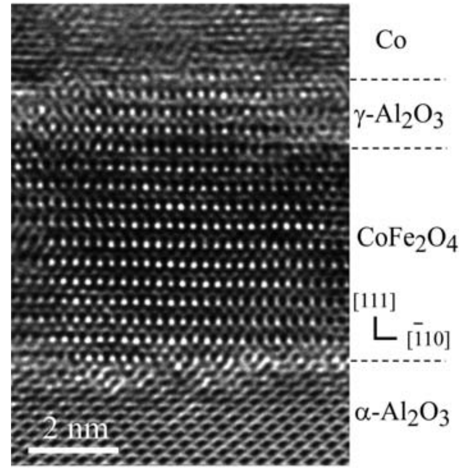

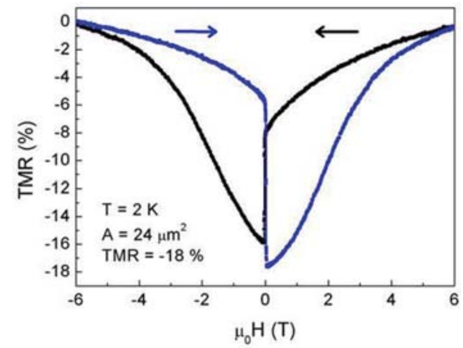

In Situ Lorentz Study of Disorder, Fluctuations, and Breakdown in Magnetic Tunnel Junctions.

S. E. Russek, J. M. Shaw, R. Geiss
National Institute of Standards and Technology, Boulder, CO

Nanoscale disorder and fluctuations in magnetic tunnel junctions (MTJs) have been imaged using TEM and Lorentz microscopy. The observed disorder and fluctuations give rise to Barkhausen and 1/f noise in MTJ sensors, which limit the ability of MTJs to be used in pT sensor applications. To study how nanoscale magnetic and microstructural variations affect device performance an active probe was fabricated that allows imaging, in both TEM and Lorentz modes, of devices while magnetic fields and currents are applied. The probe has xy field coils, integrated device current supply and low noise amplifiers. MTJ devices were fabricated on silicon nitride membranes with elliptical shapes and dimensions down to 3 μm as seen in Fig. 1. Both device orientations, with the fixed layer parallel and perpendicular to the easy axis, are included on each sample. The layer thicknesses of the MTJ stack, dielectrics, and electrodes were reduced to allow high resolution imaging of active devices in the TEM. The stack structure was Si_3N_4/5nm Ta/5nm Cu/ 10nm $Ir_{20}Mn_{80}$/ 3nm $Co_{90}Fe_{10}$/ 1.8 nm Al_2O_3/ 2 nm $Co_{90}Fe_{10}$/ 20 nm $Ni_{80}Fe_{20}$/ 5nm Ta and several process conditions using different preoxidation treatments before barrier formation were used to change the interfacial morphology.

The magnetic structure in both the 3 nm thick $Co_{90}Fe_{10}$ fixed layer as well as in the 22 nm thick $Co_{90}Fe_{10}$/$Ni_{80}Fe_{20}$ free layer were resolved as seen in Fig. 2. The patterned elliptical structures consist of both free and fixed layer while the surrounding area consists of only the lower fixed layer. In unannealed samples there was considerable disorder in the fixed layer, which is seen as a ripple structure outside the ellipse. The structure in the fixed layer disappeared after annealing in a magnetic field as seen in Fig. 3. The unannealed MTJs, as shown in Figs. 2 and 3, show a complex multidomain state at zero field. The annealed MTJs show less disorder although they still show the presence of vortices.

Fig. 4 shows a 20 μm MTJ which has a trapped vortex. As seen in the figure, the vortex can be moved *in situ* with an applied magnetic field. The *in-situ* magnetoresistance is shown along with the *ex-situ* magnetoresistance data taken on a probe station before mounting on the Lorentz probe. The left inset shows voltage versus current (IV) data taken while imaging in the TEM.

In addition to monitoring the resistance and IV curves during imaging, thermal fluctuations of the magnetization and breakdown phenomena can be observed while the current and field remain fixed. The Lorentz images can be obtained at 30 frames/s which is well suited to observing sources of 1/f noise and barrier breakdown. At high voltages across the device breakdown events occur and localized damaged regions are formed which can be seen in both TEM and Lorentz mode.

MTJ stacks with preoxidation steps before formation of the tunnel barrier showed less ripple structure [1], which correlates well with cross sectional TEM images showing that pre-oxidation improves interface flatness.

[1]Justin M. Shaw, Roy Geiss, and Stephen Russek, Dynamic Lorentz microscopy of micromagnetic structure in magnetic tunnel junctions, Appl. Phys. Lett. 89, 212503 (2006)

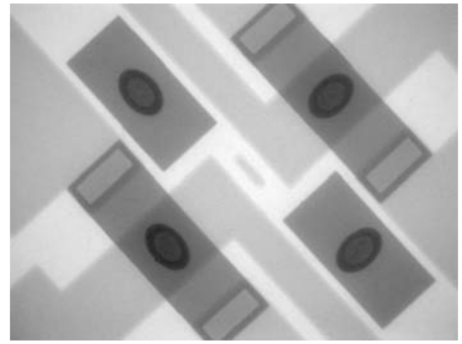

TEM image of 5 x 10 μm MTJs. The junctions on the lower left and upper right are fully contacted functional devices.

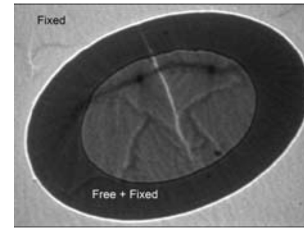

Lorentz micrograph of MTJ in zero field showing magnetic structure in both the free layer and the fixed layer.

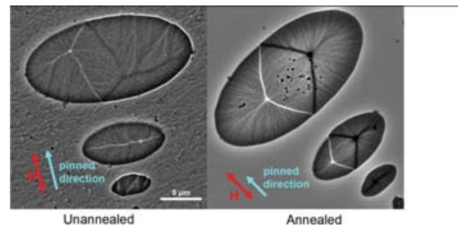

Lorentz images of MTJs before anneal (left image) and after anneal (right image). The MTJs show considerably more disorder before annealing. The regions surrounding the patterned elements show disordered structure in the fixed layer which disappears after annealing.

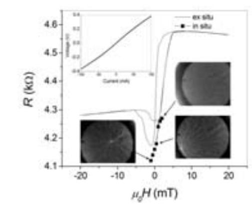

Plot of the magnetoresistance measured *in situ* and *ex situ*. The images show the magnetic state which consists of a vortex moving from the lower left to the upper right. Ripple can be seen around the vortex indicating the presence of disorder. An *in situ* IV plot is shown in the upper left inset.

AC-10

Pulse Width Dependence of Barrier Breakdown in MgO Magnetic Tunnel Junctions.

J. Hérault[1], R. Sousa[1], C. Papusoi[1], Y. Conraux[2], I. Prejbeanu[2], K. Mackay[2], J. Nozières[2], B. Dieny[1]
1. Spintec (URA 2512 CEA/CNRS), Grenoble, France; 2. Crocus Technology, Grenoble, France

Studies of time-dependent dielectric breakdown (TDDB) in magnetic tunnel junctions (MTJ) are usually carried out by applying a DC voltage while recording the time to breakdown [1]. The normal operation conditions of an MTJ in a memory device require applying a large number of read/write voltage pulses. This work reports on the breakdown behavior of MgO tunnel barrier when submitted to consecutive voltage pulses. The studied junction structure was Ta 50/ PtMn 20/ CoFe 2/ Ru 0.8/ CoFeB 2/ MgO 1.1/ CoFeB 2.5/ NiFe 2.5/ IrMn 6.5/ Ta 5 (thickness in nm). The measured devices were ellipses of 0.25µm x 0.3µm nominal diameter showing 35% TMR and an R×A value of 150-200 $\Omega\mu m^2$.
The experimental procedure consisted in applying a sequence of pulses of constant width and amplitude up to observation of barrier breakdown. This has been repeated for 10ns, 100ns and 1µs pulse widths and 1.7V pulse amplitude, corresponding to an electric field of 15×10^9 V/m. The results are shown in Fig.1 where the fraction of barrier failures is plotted as a function of the total cumulated pulse time. The data are well described by a Weibull distribution, clearly establishing an equivalence between the present reliability test procedure and previous studies of the time to breakdown distribution on junctions under DC bias [1,2]. The Weibull distribution is defined by the scale parameter η, representing the total cumulated time for which 63.2% of MTJ have failed, and shape parameter β, the slope of a straight line fit to the data, reflecting the distribution of time dependent breakdown failures. The β parameter generally depends on the quality of MTJ fabrication (deposition and patterning), whereas η is mostly dependent on the test conditions [2], in particular the applied voltage.
The results also show that η has two different regimes. In the short pulse width regime (below 100ns), there is a significant increase in η, while for pulses of 100ns and longer, η remains essentially unchanged. This phenomenon has already been observed in thicker SiO_2 barriers where it is attributed to a combination of charge trap creation and trapped charge relaxation [3]. However the observed increase by three orders of magnitude of the total cumulated time to barrier breakdown failure is much larger than initially expected. This might be related to a temperature effect, since the applied 1.2mW pulse power should result in a quasi-static temperature increase of 130°C. For longer pulse widths, the device has time to reach quasi-static thermal equilibrium. In contrast, for 10ns pulse widths, this is not the case since the characteristic temperature rise time has been measured to be 8-10ns. To verify this assumption, measurements were performed at 100°C and 150°C using a hot chuck while applying 10ns pulses. The effect of temperature increase is an acceleration of the barrier breakdown. Both η and β, the parameters describing the Weibull lifetime distribution, are clearly affected by the temperature. At 150°C, the β parameter increases to the value found for 100ns pulses and longer while η, although reduced from its room temperature value, still remains greater than η for the long pulse widths. Therefore when choosing the operation conditions to optimize junction reliability, i.e maximize both η and β, the junction temperature has to be taken into account as well as pulse voltage and duration.

[1] J. Åckerman, P. Brown, M. DeHerrera, M. Durlam, E. Fuchs, D. Gajewski, M. Griswold, J. Janesky, J. J. Nahas, and S. Tehrani, IEEE Transactions on Device and Materials Reliability, Vol.4, No.3, September 2004

[2] J. Das, R. Degraeve, P. Roussel, G. Groeseneken, G. Borghs, and J. De Boeck, J. Appl. Phys., Vol.91, No.10, 7712, May 2002

[3] E. Rosenbaum and C. Hu, IEEE Electron Device Letters, Vol.12, No.6, June 1991

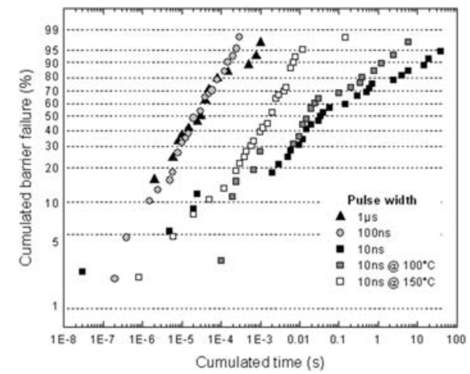

Fig.1: Time dependent barrier breakdown failure in 1.1nm MgO barriers. The stress voltage was applied in pulses of varying width maintaining a constant amplitude of 1.7V.

AC-11

Spin dependent transport through an organic semiconductor tunnel barrier.

C. Barraud[1,2], P. Seneor[1,2], R. Mattana[1,2], R. Guillemet[1,2], S. Fusil[1,2], K. Bouzeehouane[1,2], C. Deranlot[1,2], A. Vaures[1,2], F. Petroff[1,2], A. Fert[1,2], P. Graziosi[3], L. Hueso[3], I. Bergenti[3], V. Dediu[3]
1. Unité Mixte de Physique CNRS/Thales, Palaiseau, France; 2. Department of Physics, University of Paris-Sud 11, Orsay, France; 3. Istituto per lo Studio dei Materiali Nanostrutturati, ISMN-CNR, Bologna, Italy

At the interface between « classic » spintronics and organic electronics, organic spintronics has been the focus of a growing interest since 2002 and the first observation of magnetoresistance effects through sexithiophene (T6) films [1]. Since then, most of the successful studies have dealt with aluminium tris(8-hydroxyquinoline) (Alq3). Usually a thick Alq3 layer (about 100nm) is inserted between (La,Sr)MnO3 and cobalt or between two transition metals [2,3]. In this thickness range, associated to a diffusive transport, both positive and negative magnetoresistance have been observed. To understand this disparity between these results, it is necessary to probe the spin polarization at the ferromagnet/organic semiconductor interfaces. One approach is to study magnetic tunnel junctions composed of organic semiconductors. However very few reported on spin polarized tunnel transport [4]. This is partly due to the difficulties encountered when trying to elaborate a homogeneous nanometer thick organic layer over a micron size surface avoiding pinholes. Our solution is to reduce dramatically the size of the tunnel junction and use (La,Sr)MnO3 as a spin analyser [5]. We report on the fabrication and magneto-transport properties of (La,Sr)MnO3/Alq3/Co nanometer scale area magnetic tunnel junctions in which the few nanometer thick organic semiconductor Alq3 acts as a tunnel barrier.

(La,Sr)MnO3/Alq3 bilayers are first grown by a pulsed plasma deposition method developed at the ISMN [6]. Roughness is then characterized by atomic force microscopy. As expected the observed 20 nm peak to peak roughness (see figure 2) prohibits the elaboration of reliable micron size area nanometer thick tunnel junctions. To avoid short-circuits, as a prerequisite, we realize junctions over areas in the nanometer range for which the Alq3 thickness is kept homogeneous.

In order to create such nanometer size tunnel junctions, the fabrication is carried out using a combination of UV lithography and conductive tip AFM nanoindentation process where the tip-sample resistance is monitored in real time [7]. With this technique, we are able to control the section (about few tenth nm2) of the nanocontact. Moreover, by indenting further, we can also vary the organic tunnel barrier thickness. As a final step, cobalt is deposited into the nanocontact forming a magnetic tunnel junction enabling the study spin dependent tunnelling through the Alq3 layer.

We will present magneto-transport measurements performed on (La,Sr)MnO3/Alq3/Co nanojunctions. The thicknesses of the organic tunnel barriers are in the nm range and the junction areas are less than few tenth nm2. The non-linear I(V) curves measured indicate the occurrence a tunnel transport through the organic barrier. On figure 2, we show a magnetoresistance curve obtained at low temperature. The high positive magnetoresistance (more than 200%) observed indicates that the magnetic and electronic properties are preserved at the (La,Sr)MnO3/Alq3 and Alq3/Co interfaces. We will discuss on the sign and amplitude of the magnetoresistance.

This work is funded by the EU under the NMP/STREP project OFSPIN (STRP 033370)

[1] V. Dediu et al., Solid State Communication, 122, 181 (2002)

[2] Z.H. Xiong et al., Nature, 427, 821 (2004)

[3] S. Pramanik et al., Phys. Rev. B 74, 235329 (2006)

[4] T. S. Santos, Phys. Rev. Lett. 98, 016601 (2007)

[5] J.M. De Teresa et al., Science 286, 507 (1999)

[6] V. Dediu et al., Supercond. Sci. Technol. 8, 160 (1995)

[7] K. Bouzehouane et al. Nanolett. 3 1599 (2003)

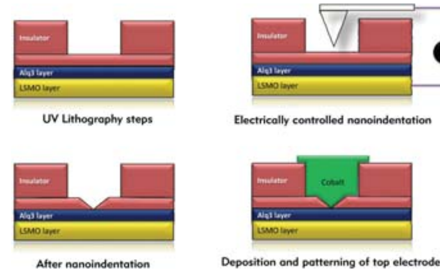

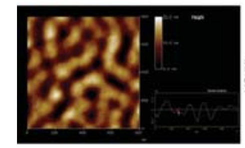

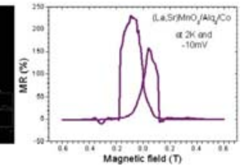

AC-12

Theoretical studies on spin-dependent conductance in FePt/MgO/FePt(001) magnetic tunnel junctions.

Y. Taniguchi, Y. Miura, K. Abe, *M. Shirai*
Research Institute of Electrical Communication, Tohoku University, Sendai, Japan

Recently, extensive research activities have been devoted to non-volatile magnetoresistive random access memories (MRAMs) which exploit magnetic tunnel junctions (MTJs) as memory cells. When each cell-size is reduced in order to fabricate ultra-high density MRAMs, it is inevitable to improve the stability of the magnetization direction at each MTJ against thermal fluctuations at finite temperatures. A possible way to overcome this problem is adopting ferromagnetic materials with large magneto-crystalline anisotropy, such as L10-ordered FePt, as electrodes of MTJs. So far, a tunneling magnetoresistance (TMR) ratio of 18% has been observed at room temperature in the MTJ with an ordered FePt electrode and an amorphous Al-O barrier [1]. On the other hand, huge TMR ratios over 400% at room temperature have been reported for MTJs with use of single-crystalline MgO as a barrier material [2, 3]. Thus, it is worth while investigating the possibility to improve the TMR ratio by using the MgO barrier in the MTJs with FePt electrodes. In the present work we investigate electronic structures and spin-dependent transport properties of FePt/MgO/FePt(001) MTJs theoretically by using a first-principles ultra-soft pseudopotential method implemented in the quantum ESPRESSO code [4, 5]. The in-plane lattice constant is assumed to be identical with that of bulk FePt, 0.386 nm, and the interlayer separations in the MTJs are fully relaxed so as to minimize the total energy of the system.

First, we have calculated the electronic band-structure along the [001] direction of bulk FePt. As a result, we have found that the totally symmetric Δ1 band crosses the Fermi level both in the majority and minority spin states. The minority-spin Δ1 band is predominantly composed of Fe and Pt dz2 orbitals at the Fermi level, while the majority-spin Δ1 band is constructed from Fe and Pt pz and s orbitals. Since the Δ1 band electrons predominantly transmit the MgO barier [6, 7], huge TMR ratios can not be expected in the FePt/MgO/FePt(001) MTJs from the symmetry consideration of electronic band-structures in the bulk FePt and MgO. Next, we have investigated the energetically favorable atomic structure of the FePt/MgO(001) interface. By calculating the adhesion energy of the interface, we have found that the Fe-terminated interface, in which the Fe atom is located on top of the O atom, has strong bonding with MgO layer as compared with the other structures including the Pt-terminated interfaces. Moreover, the formation energy is lower for the Fe-terminated interface than that for the Pt-terminated interface. These results make a remarkable contrast to the FePt(001) surface; i.e. the Pt-terminated surface is more stable than the Fe-terminated surface. The formation of Fe-O bonding significantly contribute to the stability of the Fe-terminated FePt/MgO(001) interface. In fact, the Fe-O distance at the Fe-terminated interface is 0.22 nm, which is much shorter than the Pt-O distance, 0.26 nm, in the Pt-terminated interface.

Finally, we have investigated the tunneling conductance of FePt/MgO/FePt(001) MTJs. It is confirmed that theΔ1 band predominantly contributes to the tunneling conductance for both majority-spin and minority-spin channels. The tunneling conductance as a function of in-plane components of electron wave-vector shows a sharp peak around the center of the two-dimensional Brillouin zone as usual. In the parallel magnetization configuration, the tunneling conductance via the majority-spin channel shows almost the same values for the MTJs with the Fe- and Pt-terminated interface. On the other hand, the tunneling conductance via the minority-spin channel depends significantly on the interface structure of the MTJ; i.e. the conductance for the Fe-terminated interface is two orders of magnitude smaller than that through the Pt-terminated interface. The remarkable reduction of the tunneling conductance can be attributed to the scattering of dz2 electrons in the interfacial Fe layer, where the atomic potential acting on Fe dz2 electrons is altered from that in the bulk FePt due to the Fe-O bond formation. As the consequence, the TMR ratio evaluated for the MTJ with the Fe-terminated interface and five MgO layers exceeds 400%, which is in contrast to that of about 70% for the MTJ with the Pt-terminated interface. In conclusion, the Fe-terminated interface is more desirable for obtaining larger TMR ratio in the FePt/MgO/FePt(001) MTJs.

This work is partly supported by a Grant-in-Aid for Scientific Research in Priority Areas, “Creation and Control of Spin Current” (Grant No. 19048002) and “Development of New Quantum Simulators and Design” (Grant No. 17064001), from MEXT.

[1] S. Mitani, K. Tsukamoto, T. Seki, T. Shima, and K. Takanashi, IEEE Trans. Magn., vol.41, no.10, pp.2606-2608, 2005.

[2] S. Yuasa, A. Fukushima, H. Kubota, Y. Suzuki, and K. Ando, Appl. Phys. Lett., vol.89, art.no.042505, 2006.

[3] S. Ikeda, J. Hayakawa, Y. M. Lee, F. Matsukura, Y. Ohno, T. Hanyu, and H. Ohno, IEEE Trans. Electron Dev., vol.54, no.5, pp.991-1002, 2007.

[4] S. Baroni, A. Dal Corso, S. de Gironcoli, and P. Giannozzi, http://www.pwscf.org

[5] A. Smogunov, A. Dal Corso, and E. Tosatti, Phys. Rev. B, vol.70, art.no.045417, 2004.

[6] W. H. Butler, X.-G. Zhang, and T. C. Schulthess, Phys. Rev. B, vol.63, art.no.054416, 2001.

[7] W. H. Butler, X.-G. Zhang, S. Vutukuri, M. Chshiev, and T. C. Schulthess, IEEE Trans. Magn., vol.41, no.10, pp.2645-2648, 2005.

AD-01

Fe-induced spin-polarized electronic states in a realistic semiconductor tunnel barrier.

M. Marangolo, F. Finocchi
INSP, Université Pierre et Marie Curie, Paris, France

Since a ferromagnetic metal (FM) provides a natural spin-polarized source, FM/semiconductor (SC) junctions have been extensively studied as integrated devices for spintronics applications. Whenever a Fm/SC interface is created, the electronic states on the metal side with energies comprised between the SC valence band top and the Fermi energy EF decay exponentially in the SC. Called metal-induced gap states (MIGS), they are spin-polarized in the case of FM/SC junction. Their spatial behavior is crucial in spintronics, since it drives the tunnelling current. In this respect, it was shown that spin accumulation on the SC side can be obtained by means of a high enough FM/SC Schottky barrier or a tunnel barrier with resistance comparable to that of the semiconductor1, thus remedying the resistance mismatch problem2.
We consider the Fe/ZnSe(001) hetero-junction, which has been studied experimentally by our group to such a degree that it can be considered as a prototype of low reactive FM/SC interfaces. The mismatch between bcc Fe and ZnSe is quite small (1.1%). The interface is sharp without any loss of magnetic moment 3. Chemical reactivity was not observed by spectroscopic measurements even if Zn atoms are released in the Fe film and Se atoms are detected on the growth front4. By first-principles calculations, we show that the formation of an intermixed Fe-Zn monolayer with interface Se-Fe bonding is favored with respect to ideal hetero-junctions. Since the averaged transmission polarization in the generalized Jullière model is indirectly linked to the interface polarization at the Fermi level and to the decay profile of polarized MIGS, we analyze by DFT calculations the influence of the structure of realistic interfacial phases on the spin polarization and on the electronic structure of the SC tunnel barrier.
The electronic DOS of ideal and intermixed hetero-junctions are shown in figure 2. Two main features are worth to be noticed:
(i) close to the Fermi level, minority spin states dominate at the interface of ideal hetero-junctions, leading to a stronger spin polarization than in the intermixed interfaces (see Fig.2);
(ii) the amplitude of the MIGS polarization within the semiconductor strongly depends on the interface geometry (see Fig.3).
In conclusion, a Fe-Zn intermixed buffer monolayer at the Fe/ZnSe(001) interface, which is here predicted to be energetically favored, dramatically affects the interface electronic structure. Intermixed junctions have little negative polarization at EF, with respect to ideal Fe/ZnSe(001) interfaces. As far as spintronics is concerned, one important consequence is the strong reduction of the MIGS spin polarization inside the SC barrier, since spin injection depends on the competition between the majority and minority channels. The most favoured architecture for spintronics applications is the ideal Zn/Fe junctions; we are currently exploring the possibility that similar interfaces could be stabilized by low-temperature growth in Zn-rich environments.

REFERNCES:

1 A. Fert and H. Jaffrès, Phys. Rev. B 64, 184420 (2001)
2 G. Schmidt et al., Phys. Rev. B 62, R4790 (2000).
3 M. Marangolo et al., Phys. Rev. Lett. 88, 217202 (2002).
4 M. Eddrief, M.Marangolo et al., Phys. Rev. B 73, 115315 (2006); Appl. Phys. Lett. 81, 4553 (2002).

CAPTIONS:
FIG. 1: (Color online) Sketch of the superlattice adopted for DFT calculations.
FIG. 2: (Color online) Computed Local Density of States (DOS) of ideal interfaces (left) and intermixed interfaces (right). Black and red curves refer to majority and minority spin components, respectively. In top (a) and (b) panels, the LDOS on the interface (I) and inner (I+3) Fe layers is drawn.
FIG.3 LDOS at the Fermi energy within the ZnSe substrate as a function of the distance from the interface. Ideal (left) and intermixed (right) interfaces. The semi-logarithmic scale evidences the exponential decay of the spin-up (full symbols) and spin-down (open symbols) MIGS within the semiconductor.

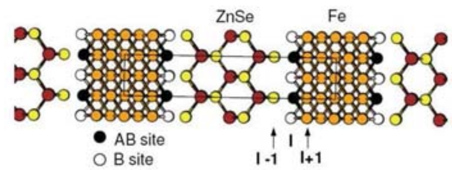

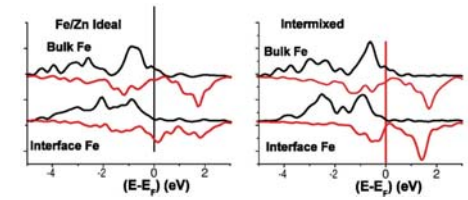

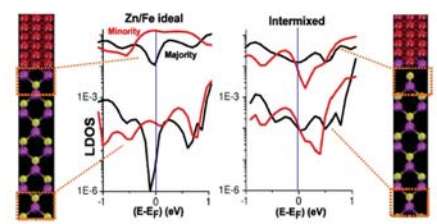

AD-02

Spin polarised electrodes and interfaces in organic spintronic devices.

I. Bergenti[1], A. Dediu[1], F. Borgatti[1], A. Riminucci[1], L. H. Hueso[5], F. Casoli[2], Y. Zhan[3], C. Pernechele[4], M. Solzi[4]
1. ISMN CNR, Bologna, Italy; 2. CNR-IMEM, Parma, Italy; 3. Department of Physics,IFM, Linköping University, Linköping, Sweden; 4. Dipartimento di Fisica, Università di Parma, Parma, Italy; 5. Department of Physics and Astronomy, University of Leeds, Leeds, United Kingdom

Applications of organic semiconductors into spintronic domain, motivated by unquestionable advantage of weak spin-orbit coupling and hyperfine interaction, have been recently successfully demonstrated[1]. Magnetoresistive spin valves and magnetic tunnel junction based on archetypal organic materials Alq3 have been experimentally obtained [2,3]. In spite of the different mechanism, injection/transport for Spin Valves and tunnelling for magnetic tunnel junction, their performances are affected not just by the properties of their constituents but also by their metal/organic interfaces. Investigations on ferromagnet/organic interfaces are crucial in vertical devices, which typically include the deposition of a ferromagnetic contact on top of organic materials. Such deposition is by its nature critical: penetration of atoms, formations of complexes and cluster can be expected.
Morphology and disorder of ferromagnetic thin films, possible intermixing or interdiffusion at the interface may change the magnetic properties of the FM films and affect the intensity of spin valve effect. For this reason a detailed characterization of ferromagnetic metal/organic semiconductor heterostructures is necessary in order to understand and predict the device behaviour.
Hybrid spin valves with highly spin polarized manganite La2/3Sr1/3MnO3 and Cobalt as ferromagnetic electrodes and Alq3 as organic transport layer have been investigated (for experimental details see [4]). Room temperature operation have been obtained trough the control of interfacial properties and interface engineering.
We present a full magnetic and morphological characterization of ferromagnetic films used as electrodes in spin valves devices and we correlate the results with the Spin valve device performance. 20 nm thick LSMO epitaxial films present a XMCD signal at room temperature indicating a good surface magnetisation. AFM investigations on 100 nm thick Alq3 films grown on epitaxial LSMO indicate a very smooth surface (rms 1 nm). A template growth of Co layers on top of organic semiconductor is observed. Magnetic characterization by MOKE and SQUID indicates the presence of a uniaxial anisotropy.
X ray magnetic reflectivity indicates that sharp Co/Alq3 interfaces are obtained in presence of a thin AlOx tunnel barrier(fig.1). An intermixing region of 2 nm has been measured. The tunnel barrier prevents the degradation of the interface and improves the quality of the SV effect reaching the room temperature operation.

[1]Sanvito S. J. Mat. Chem. 17, 4455 (2007) and references therein

[2]Xiong, Z.H., Wu, D., Vardeny, Z.V. & Shi, J. Nature 427, 821-824 (2004)

[3]Santos, T.S., Lee, J.S., Migdal, P., Lekshmi, I.C., Satpati, B. & Moodera, J.S. Phys. Rev. Lett. 98, 016601 (2007)

[4]Hueso, L.E., Riminucci, A., Bergenti, I., Zhan, Y. & Dediu, V. Adv. Mater. 19, 2639-2642 (2007).

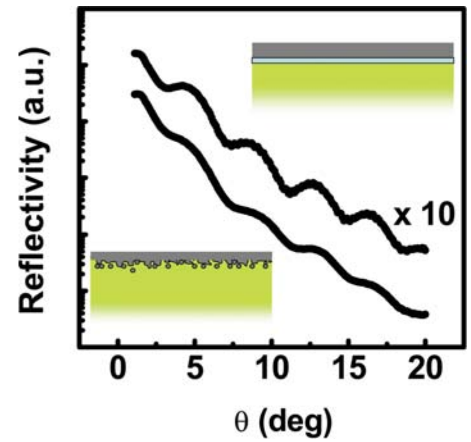

X-ray reflectivity data at a grazing angle of a Cobalt film grown on top of Alq3 (lower curve) and Alq3/AlOx (upper curve). Reflectivity data indicate a sharp Co interface in presence of a tunnel barrier as shown in the pictures

AD-03

Voltage control of the in-plane magnetic hysteresis in Fe/Au/Fe(001) and Fe (001) ultrathin films grown on GaAs (001) surface.

K. Ohta[1], *Y. Suzuki*[1], T. Maruyama[1], T. Nozaki[1], T. Shinjo[1], M. Shiraishi[1], S. Ha[2], C. You[2], W. Van Roy[3]
1. Engineering Science, Osaka University, Toyonaka, Japan; 2. Department of Physics, Inha University, Incheon 402-751, South Korea; 3. IMEC, B-3001 Leuven, Belgium

The voltage controlled magnetization reversal has been proposed as a most energy saving writing method [1-4]. However, only few experimental results have been reported up-to-now [4, 5]. Here, we report voltage control of an in-plane magnetization at room temperature using a Schottky junction with a magnetic multilayer [2, 3].

In Fig. 1, schematic cross section of the sample is shown. N-type GaAs (001) layer (n=5x10^{17} cm^{-3}) was grown epitaxially on a GaAs substrate. Then Fe/Au/Fe/Au(001) magnetically coupled layers or Fe/Au (001) layers were grown on Ga-rich GaAs surface at room temperature. After the depositions, the metallic layers were cut into an oval shape (600 μm x 300 μm) to form a Schottky diode.

The samples show typical diode characteristics with break down voltage of about 2 volts. The bottom Fe layer shows a large uniaxial and a small 4-fold in-plane anisotropy. The hard axis ([1-10]) saturation field is about 950 Oe for the 1 nm thick Fe layer whereas the easy axis coercive force is less than 20 Oe. The sample with n-GaAs/Fe(0 nm≦d≦3.6 nm)/Au(3.4 nm)/Fe(1.5 nm)/Au(5 nm) structure shows clear oscillation of the interlayer exchange coupling strength as a function of the bottom Fe layer thickness, d [6]. Long lasting oscillation with 6 maxima reveals high electron coherency in the Fe layer. A Kerr ellipticity, η_K, hysteresis curve obtained for the n-GaAs/Fe(0.85 nm)/ Au(2.8 nm)/ Fe(1.5 nm)/Au(5.0 nm) coupled layer is shown in Fig. 2 (a). Here, the external magnetic field was applied along to [010] direction (45 degree from the easy axis.). A hysteresis with three successive magnetic switchings is observed. Between the first and 2nd jumps, η_K continuously increases with increase of the external field because of a continuous rotation of the magnetization.

To observe a bias voltage effect, we modulated the bias voltage and detected the same frequency component in the η_K signal using a lock-in amplifier. Fig. 2 (b) shows a response to the bias voltage modulation, i.e. $d\eta_K/dV$ signal. Considerable $d\eta_K/dV$ signal was observed where η_K hysteresis shows the finite slope. For 1 Vp-p modulation the signal amplitude is about 0.3 % of the η_K. The origin of the effect can be either a change in the coupling strength [3] or the magnetic anisotropy [2]. To make this clear, we have examined the sample with a single Fe layer and obtained same kind of responses. Therefore, we tentatively conclude that the main contribution to the hysteresis modulation is a change in the in-plane magnetic anisotropy by the voltage across the Schottky junction. From symmetry, the electric field perpendicular to the film should affect to the perpendicular anisotropy. Here, we could control, however, the in-plane anisotropy by the perpendicular electric field. This may be attributed to the special symmetry of the GaAs (001) surface where an in-plane electric polarization may appear.

This result reveals a control of in-plane magnetization process by a voltage application and will be useful as a low energy consumption writing technique for the solid state magnetic memories.

Acknowledgements This research was partly supported by a SCOPE program of MIC and a Grant-in-Aid for Scientific Research (A)-19206002 of JSPS.

[1] C.-Y. You and S. D. Bader, J. Magn. Magn. Mater. 195 (1999) 488.

[2] X. Nie, S. Blügel, German patent:PCT/DE99/02840.

[3] C.-Y. You and Y. Suzuki, J. Magn. Magn. Mater. 293 (2005) 774.

[4] P. Borisov, A. Hochstrat, Xi Chen, W. Kleemann, and C. Binek, Phys. Rev. Lett., 94 (2005)117203-1-4.

[5] M. Weisheit, S. Fähler, A. Marty, Y. Souche, C. Poinsignon, D. Givord, Science 315 (2007) 349.

[6] S.N.Okuno and K. Inomata Phys. Rev. B, 51(1995)6139.

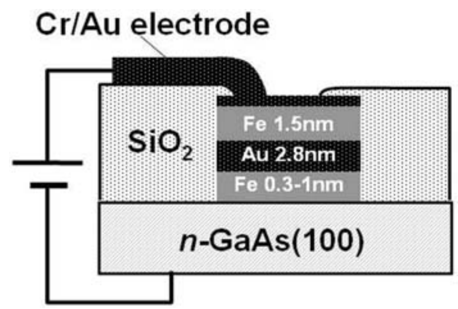

Fig. 1 Sample structure. An Fe/Au multilayer and an *n*-GaAs compose a Schottky diode.

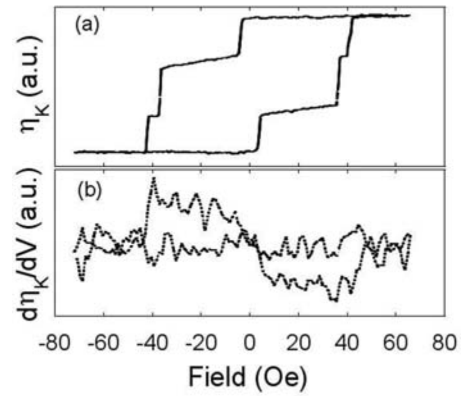

Fig. 2 (a) Magneto-optical Kerr ellipticity, η_K, hysteresis loop. (b) $d\eta_K/dV$ signal. $d\eta_K/dV$ signal reveals a change in the magnetc hysteresis by a voltage application.

AD-04

Extraordinary increase of the resistivity and decrease of the Curie temperature in ultrathin LSMO films capped with Au.

M. Cantoni[1], S. Brivio[1], D. Petti[1], A. Cattoni[1], R. Bertacco[1], A. A. Sidorenko[2], G. Allodi[2], M. Ghidini[2], R. De Renzi[2]
1. Physics, Politecnico di Milano, Como, Italy; 2. Physics, Università di Parma, Parma, Italy

The electric and magnetic properties of manganites are extremely sensitive to the concentration of free carriers. These properties can be varied not only by hole-doping the material, but also by designing a heterostructure where light or an externally applied electric field might effectively modulate the carrier concentration.[i] The presence of an interface represents, by itself, a significant perturbation of the electronic properties of perovskite manganites. The interface with a metal is known to affect the chemical and electronic environment of strongly correlated oxides, and can change basic electronic parameters, such as the Hubbard energy U, the electronic bandwidths, or the exchange energies.[ii]
We have widely investigated the effect of depositing a metal layer on ultrathin films of $La_{2/3}Sr_{1/3}MnO_3$(LSMO) grown on $SrTiO_3$(001)substrates (STO).[iii] Magnetization curves taken with a SQUID apparatus on 4 nm thick epitaxial LSMO layers (Fig. 1) show a dramatic reduction of the Curie temperature upon deposition of 2 nm of Au (185 K); upon insertion of a 2 nm thick STO buffer layer the effect is only reduced but the decrease of T_C is still relevant (60K). The latter finding, coupled to a detailed XPS investigation of the Au/LSMO interface showing negligible chemical reactions and interdiffusion, suggests that the effect might have an electrostatic origin. SQUID data on 8 nm thick LSMO films only show a small reduction of T_C: the effect is limited to layers with thickness slightly exceeding the "dead layer" typically developing at the LSMO/STO(substrate) interface (~3 nm). In thicker films, where the non-dead layer is thicker than the screening length (a few units cells in LSMO), the reduction of T_C is averaged out and tends to disappear.
Due to the strong connection between magnetism and transport in manganites, we have also investigated the effect of Au capping on the resistivity of ultrathin LSMO films. The resistivity vs. temperature is shown in Fig. 2: upon deposition of 2 nm of Au onto 4 nm of LSMO, we can see a strong decrease of the temperature T_p where the metal to insulator transition takes place (ΔT_p>250 K), in agreement with the observed decrease of T_C. Furthermore, the shift of T_p is accompanied by an extraordinary increase of the film resistivity at T_p, by four orders of magnitude. This is an unexpected result, that can be measured only due to the granularity of the thin Au film, avoiding a short circuit in the four probe measurements. In addition the I(V) characteristics measured in the four probe configuration display high non linearity and negative differential resistivity, that indicate a non uniform resistivity in the film due to the phase separation of the LSMO induced by the granularity of the Au overlayer. As a matter of fact NMR measurements show a strong reduction of the double exchange signal from LSMO upon Au deposition, and SQUID detects a corresponding reduction of the macroscopic moment. The missing NMR and SQUID signals may be attributed to antiferromagnetic-insulating phases. In these separated films, then, conduction takes place via filamentary paths of conductive (ferromagnetic) manganite well separated by large regions of insulating (antiferromagnetic) LSMO.
These results indicates that the magnetic and electric properties of ultrathin LSMO films can be largely modified simply upon creation of a contact with a noble metal like Au. Detailed field effect experiments are currently performed in our laboratory to clarify if it is possible to produce sizable effects on magnetism in these films, in analogy to multiferroicity, or use these films as active channels in MOS-like devices.

[i] For a review, see C. H. Ahn et al., Rev. Mod. Phys. 78, 1185 (2006);
[ii] S. Altieri, H. L. Tjeng, F. C. Voogt, T. Hibma, O. Rogojanu, and G. Sawatzky, Phys. Rev. B 66, 155432 (2002);
[iii] R. Bertacco, S. Brivio, M. Cantoni, A. Cattoni, D. Petti, M. Finazzi, F. Ciccacci, A. A. Sidorenko, M. Ghidini, G. Allodi, and R. De Renzi, Appl. Phys. Lett. 91, 102506 (2007).

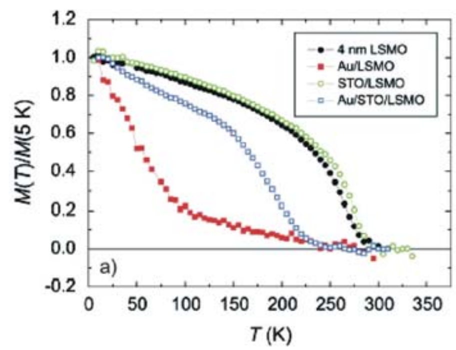

Figure 1: Normalized magnetization vs. temperature curves measured by SQUID on different heterostructures; the LSMO, STO and Au thicknesses are, respectively, 4, 2 and 2 nm.

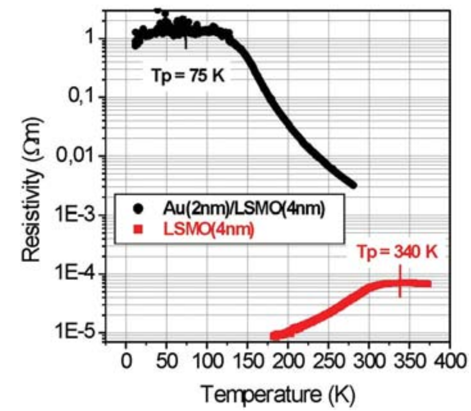

Figure 2: Resistivity vs. temperature for 4 nm of LSMO with (black) and whitout (red) 2 nm of Au

AD-05

Influence of interfacial oxygen on spin filtering and antiferromagnetic coupling in single-crystalline Fe/MgO/Fe(001) magnetic tunnel junctions.

F. Bonell, S. Andrieu, C. Tiusan, A. M. Bataille, B. Kierren, F. Montaigne, G. Lengaigne
Nanomagnetism and Spintronics Team, Laboratoire de Physique des Matériaux - Université Henry Poincarré - UMR 7556, Vandoeuvre-lès-Nancy, France

The large tunnel magneto-resistance (TMR) measured in single-crystal Fe/MgO/Fe magnetic tunnel junctions (MTJs) [1] makes them serious candidates for applications. However, tailoring the electronic transport in these MTJs remains a challenge of great interest to improve their performances and our understanding on the tunneling mechanisms.
Several studies aimed at tuning the conductivities of the different tunneling channels responsible for the TMR, by inserting symmetry-dependant metallic barriers (Co or Cr films) [2,3]. Another possibility is to deal with interfacial chemistry between Fe and MgO. The interest of this approach was demonstrated in C doped MTJs.
We present here the first results on epitaxial MTJs with an oxygen doped Fe/MgO interface. Using X-ray photoelectrons spectroscopy (XPS), the amount of deposited O can be precisely controlled in the sub-monolayer regime (fig. 1). Moreover, scanning tunneling microscopy (STM) observations performed *in vacuo* provide atomically resolved maps of the Fe electrons tunneling efficiency (fig. 2). The adsorption kinetics monitored by XPS show the presence of two regimes, explained by the appearance of different O-related species in STM images (fig. 2 b). STM also evidences the O location on the hollow site of the Fe surface unit cell (fig. 2 c), a precious information for band structure *ab initio* calculations.
The precise control of both the O amount and the MgO thickness (growth assisted with RHEED intensity oscillations) allows us to investigate the properties of Fe/O/MgO/Fe MTJs at equilibrium (coupling between electrodes), and out of equilibrium (by biasing MTJs).
Biased O doped junctions preserve a large TMR (>90%) and exhibit interesting conductance features. In particular, the curves shown in fig. 3 seem to indicate that the interfacial O totally filters the low-bias Δ_5 tunneling channel (disappearance of the local maximum at zero bias).
Concerning the antiferromagnetic coupling between the Fe films observed at equilibrium in simple Fe/MgO/Fe multilayers (black curve in fig. 4), we find that the magnetization reversal of the *top* Fe film is strongly modified by the presence of O at the *bottom* Fe/MgO interface. The dependence of the coupling on the O coverage (brown curve in fig. 4) will be discussed by the light of the XPS/STM results.

[1] S. Yuasa et al., Nat. Mater. 3 (2004) 868.

[2] S. Yuasa et al., Appl. Phys. Letters 89, 042505.

[3] F. Greullet, Phys. Rev. Lett. 99, 187202.

[4] R. Guerrero et al., Appl. Phys. Letters 91 (13), 132504, (2007).

[5] C. Tiusan et al., Appl. Phys. Letters 88, 62512, (2006).

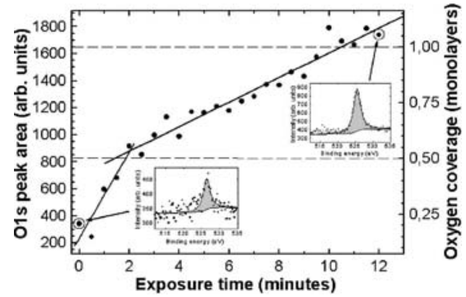

Area of the O1s XPS peak versus exposure time (left axis), and corresponding oxygen coverage (right axis). Insets : experimental spectra.

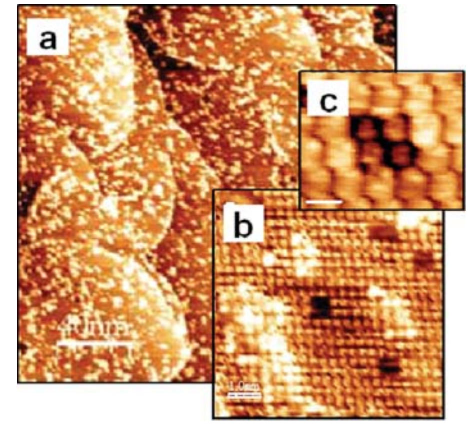

STM images of an oxygen covered Fe(001) surface (tip-sample voltage : -500 mV ; current : 1 nA ; oxygen coverage : 0.6 ML). Scale bars : (a) 40 nm. (b) 1 nm. (c) 0.3 nm.

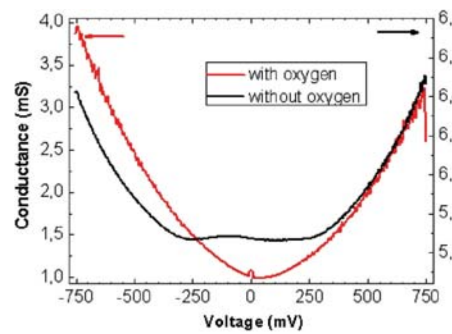

Conductances of Fe/MgO(2.5nm)/Fe MTJs versus bias voltage in the parallel configuration of magnetizations, without interfacial oxygen (black) and with 1 ML of interfacial oxygen (red). Positive bias corresponds to electrons flowing from the bottom electrode to the top one.

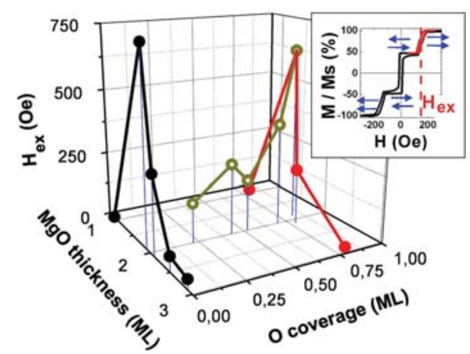

Reversal magnetic field of the soft Fe(001) layer versus the MgO barrier thickness and the interfacial oxygen coverage of Fe/O/MgO/Fe(001) multilayers. Inset : magnetization curve measured with VSM. The arrows represent the magnetization directions of the two Fe layers.

AD-06

Interface magnetism in ultra-thin Mo/Co multilayers.

L. Baczewski[1], K. Mergia[2], J. Kisielewski[3], A. Maziewski[3], F. Ott[4]
1. Institute of Physics Polish Academy of Sciences, Warsaw, Poland; 2. Institute of Nuclear Technology and Radiation Protection, Athens, Greece; 3. Institute of Experimental Physics, University of Bialystok, Bialystok, Poland; 4. Laboratoire Leon Brillouin, CEA, Saclay, France

An exciting area of materials engineering and related physics is the increased complexity and emerging new phenomena when building materials on the nanoscale level. Local interactions at the interfaces between two different materials with different properties play an important role due to spin, charge and lattice degrees of freedom interplay. Thin film deposition techniques allow to create model magnetic multilayers where important magnetic properties such as the magnetization, anisotropy and exchange parameters can be tuned. Important influence of Mo/Co interface on magnetic and magnetooptical properties of ultra-thin Co films was recently reported [1,2].
The purpose of this study has been to investigate the Mo/Co interface magnetic structure i.e. to determine: (i) if the Mo acquires the magnetic moment in the vicinity of Co and (ii) its magnetic coupling direction with the Co. In order to ascertain whether there is a surface magnetization state of Mo, samples with different Mo thickness were fabricated by MBE deposition technique. The crystallographic structure of the layers was monitored in-situ by RHEED, which showed that the in-plane directions relation Mo(110)/Co(0001) was satisfied for every sample. Samples were grown by a molecular beam epitaxy (MBE) system with the vacuum level in the range of 10-10 Torr. Sapphire Al2O3 wafers with the orientation (11-20) were used as substrates, on which a Mo buffer layer was deposited at 1000 deg C. Next Au buffer layer was deposited and annealed at 200 deg C for 15 min. All subsequent layers were deposited at room temperature. Co and Mo were evaporated from electron guns and Au from effusion cell at the rates lower than 0.5 Å/s. The multilayer samples were deposited with varying Mo layer thickness and constant Co layer thickness:
Al203/Mo/Au/(Co 25/ Mo d)x 20 /Pt
where d = 0.5, 1.0, 1.5 and 2.0 nm.
Standard thicknesses of Mo and Au buffer (b) and overlayer (o) were chosen as: dbMo=20 nm, dbAu=20 nm, doPt=8 nm. Cobalt film thickness d = 2.5 nm was chosen in the range where the in-plane anisotropy is present in such Mo/Co structures. The growth mode, crystalline structure and purity of the constituent layers were monitored in-situ by RHEED and Auger spectroscopy, respectively. Detailed structural analysis regarding constituent layers thickness, density and interface roughness was performed ex-situ by X-ray reflectivity. Multilayers magnetic structure was studied by polarized neutron reflectivity (PNR) and magnetisation measurements. Hysteresis loops and magnetization temperature dependence M(T) were measured using SQUID magnetometer. The PNR measurements were carried out on the PRISM instrument at Laboratoire Léon-Brillouin, CEA-Saclay, at 10 K and with an in-plane external magnetic field of 1.0 T in order to magnetically saturate the samples. The wavelength used was 0.43 nm and the Q-range was from 0.05 to 2.2 nm-1. The spin-up and spin-down reflectivities (R+, R-) of the all samples were measured. The data have been corrected for the polarization efficiency. The least squares fitting of all the reflectivity data (X-rays and neutrons) was made using the SimulReflec software [3]. For the scattering lengths of X-rays and neutrons and absorption cross sections the tabulated values were employed.
From the PNR data of four Mo/Co samples the Mo and Co magnetic moments have been determined. In all the Mo/Co multilayers it was found that a magnetic moment has been induced in the Mo and that the Mo layer is antiferromagnetically coupled to the Co layer. The product of the molybdenum layer thickness by its moment is almost constant for all studied Mo/Co samples, which demonstrates that only a top slab of molybdenum layer close to the interface with Co is magnetically active. The thickness of this slab is less or equal to 4 ML and the induced molybdenum magnetic moment higher or equal to 0.8 mB/at (thinner magnetically active slabs imply larger Mo moments). It seems that the inetrface roughness is further reducing the number of Mo next neighbours, distorts the bond lengths and angles and between 3 to 4 monolayers of Mo acquire a magnetic moment. Also, the lattice strain occurring at the interfaces during epitaxial growth of hcp Co on Mo bcc metal can influence the ordering at the interface. Large magnetic moments for V have been already reported for the systems of Fe/V [4] and Co/V [5] but this is the first experimental evidence of an induced magnetic moment in Mo.

[1] R.Gieniusz, L.T.Baczewski, Z.Kurant, A.Maziewski, A.Wawro, Journal of Magnetism and Magnetic Materials, 310, Issue 2, Part 3, (2007), 2198

[2]K.Postava, Z.Kurant, A.Maziewski, A.Stupakiewicz, L.T.Baczewski, A.Wawro, M.Aoyama, T.Yamaguchi, Applied Surface Science, 254 (2007) 360

[3]www.llb.cea.fr/prism/programs/simulreflec/, version 1.9

[4] Y. Huttel, G. van der Laan, T.K. Johal, N.D. Telling, P. Bencok, Phys Rev B 68 (2003) 174405

[5] A. Scherz, H. Wende, P. Poulopoulos, J. Lindner, K. Baberschke, F. Wilhelm, N. B. Brookes, P. Blomquist, R. Wäppling Phys. Rev. B vol.64 (2001) 180407 (R)

AD-07

Noncollinear Surface Spin Density of equiatomic NiMn alloy on Cu(001).

C. Gao[1], A. Ernst[1], A. Winkelmann[1], J. Henk[1], W. Wulfhekel[1,2], P. Bruno[1], J. Kirschner[1]
1. Max Planck Institute of MicrostrcutrurePhysics, Halle (Saale), Germany; 2. Physikalisches Institut, Universität Karlsruhe (TH), Karlsruhe, Germany

The surface spin density of the antiferromagnet is important in determining the exchange interaction across the antiferromagnet/ferromagnet interface. The atomic scale understanding of the antiferromagnetic surfaces is, however, very limited due to the limited resolution of the traditional techniques. In this joint experimental and theoretical investigation we show by spin-polarized scanning tunneling microscopy (Sp-STM) that the surface spin density of NiMn films is non-collinear in space (a variation of the direction of the spin polarization with the coordinates) and energy (a variation of the direction of the spin polarization with the energy of the electrons). The very reason for this effect is the broken surface symmetry, as is supported by first-principles electronic-structure calculations.

Chemically ordered Ni50Mn50 grown on Cu(001) has a structure similar to that of the respective bulk (L10), with Ni and Mn atomic sheets oriented perpendicular to the Cu(001) surface [1]. A careful analysis of the atomically resolved STM image shows that in addition to the c(2x2) chemical ordered arrangement of the Ni and Mn atoms, a p(2x2) reconstruction was present due to the slightly different coordinates of every second Mn (Ni) atom of the surface layer. The layer thickness and the coordinates of the surface atoms were determined quantitatively with the LEED-IV measurements and simulations.

The Sp-STM measurements were performed in the differential magnetic mode at 300 K [2]. A ferromagnetic CoFe-SiB ring whose magnetization can be switched periodically was used as STM electrode. A major advantage of this method is that the ring has a well-defined direction of in-plane spin sensitivity, determined by its shape. Further, the signal is of purely magnetic origin. This technique is therefore well suited for investigating alloy films.

Two different spin patterns were observed at positive bias voltages (from 0.1 V to 0.5 V) as shown in Fig. 1. One displays a checkerboard structure (domain 1) whose unit cell coincides with the c(2x2) chemical unit cell (3.6 Å x 3.6 Å) while the other exhibits parallel lines (domain 2), the separation of which equals that of adjacent Mn sheets (3.6 Å). The two spin patterns reflect two magnetically equivalent, orthogonal structural domains distinguished by the orientations of the Mn sheets either along [100] or along [010]. The two patterns appear differently in the spin-resolved STM image because the projections of their spin polarizations onto the spin-sensitive direction of the STM differ reflecting the non-collinearity of the spin polarization in real space. As the bias voltages change from positive to negative (-0.1 V), the pattern in domain 1 changes from high contrast c(2x2) to weak contrast p(2 x 2) cells. In domain 2, the ordered feature disappears at negative voltages. The change of the spin unit cell in domain 1 from c(2x2) to p(2x2) indicates a change of the direction of the spin polarization of individual atoms as a function of the energy of the electrons which can be defined as a non-collinearity of the spin polarization in the energy domain.

The observed non-collinear surface spin density in both space and energy domain was attributed to the symmetry breaking at the surface due to the surface reconstruction. This mechanism requires spin-orbit interaction as a means to couple the orbital degrees of freedom (which are sensitive to the atomic displacements) to the spin degrees of freedom (which determine the spin polarization of the tunnel current). To support the above explanation of non-collinearity, scalar-relativistic and fully relativistic first-principles electronic structure calculations were carried out for 6ML-NiMn films on Cu(001) within the local spin-density approximation to density-functional theory, using Korringa-Kohn-Rostoker methods for layered systems. Both the unreconstructed and the experimental geometry were considered in the self-consistent calculations. For NiMn bulk, the collinear antiferromagnetic phases are energetically preferred to the ferromagnetic phase. The magnetic moments of nearest-neighbor Mn atoms in the film couple antiferromagnetically whereas those of second-nearest Mn atoms couple ferromagnetically. The total energy of the reconstructed p(2 x2) cell (with atomic positions taken from the LEED-IV analysis) is lower than that of the ideal c(2 x 2) cell, thus supporting the LEED-IV analysis. The spin resolved density of states of the surface atoms shows that close to the Fermi level, Mn shows high (low) spin polarization above (below) the Fermi level in agreement with the experimental observations.

[1] C. Tieg, W. Kuch, S. G. Wang, and J. Kirschner, Phys. Rev. B 74, 094420 (2006).

[2] C. L. Gao, U. Schlickum, W.Wulfhekel, and J. Kirschner, Phys. Rev. Lett. 98, 107203 (2007).

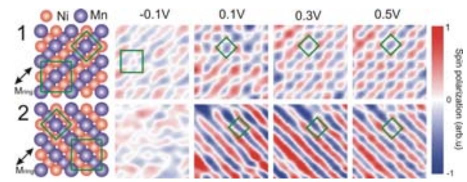

Fig.1 Spin-resolved STM images of NiMn for selected bias voltages on the sample (-0.1V to 0.5V, as indicated on the top) at domain 1 (top row) and domain 2 (bottom row). The structures of the domains are sketched on the left. The images of dimension 3nm_3nm were taken successively at a fixed tunnel current (3 nA). Mring represents the spin sensitive direction of the STM tip. The p(2 x2) (large green square) and c(2x2) (small green square) cells are marked.

AD-08

Room temperature ferromagnetism in pristine and Mn-doped ZnO thin films.

H. Nguyen[1], E. Chikoidze[2], Y. Dumont[2]
1. Faculté des Sciences et Techniques, Université F. Rabelais, Laboratoire LEMA, UMR 6157 CNRS/CEA, Tours, France; 2. GeMAC, UMR 8635, CNRS-University of Versailles, Meudon, France

Theorists have predicted that ferromagnetism (FM) at high temperature could be obtained in various semiconductors if we substitute metal ion by Mn and having a high concentration of holes in those systems. Actually room temperature FM was experimentally observed in many transition-metal (TM)-doped semiconducting oxides under the thin film form. However, the phenomenon is not exactly as what theory supposed, because the compounds are found to be n-type.
Room temperature FM was observed in pristine ZnO thin films grown on Al2O3 substrates. The FM in this compound unlikely originates from oxygen vacancies but from other kind of defects. Magnetization of very thin films is much larger than that of the thick films indicating that defects must be located mostly at the surface and/or the interface between the film and the substrate.
Data on Fe:ZnO and Mn:ZnO films show that a TM doping does not play any essential role in introducing the magnetism into ZnO. However, in the case of Mn doping, the magnetic moment could be enhanced only slightly. Hall effect measurements reveal that the incorporation of Mn does not change the carriers type (both ZnO and Mn:ZnO films are n-type), but decreases the carrier concentration and increases Hall mobility, resulting in more resistive Mn:ZnO films. Since no anomalous Hall effect was observed, one must conclude that the observed FM is not due to the interaction between the free-carrier and the Mn impurity, but other effects. Studying on very thin films of ZnO would elucidate the issue if there were any modification of the ordering at the surface/interface.

AD-09

Tailoring the magnetic properties of all-ferromagnetic artificial FeCu(111) alloy thin films.

M. Niño[1,2], J. Camarero[1], W. Kuch[3], R. Abrudan[3,4], N. Mikuszeit[1,5], C. Tieg[4,6], M. P. Jigato[1], J. Kirschner[4], J. de Miguel[1], R. Miranda[1,7]
1. Departamento de Física de la Materia Condensada, Instituto de Materiales "Nicolás Cabrera" and Universidad Autonoma de Madrid, Madrid, Spain; 2. ELETTRA-Sincrotrone Trieste, Basovizza, Italy; 3. Institut für Experimentalphysik, Freie Universität Berlin, Berlin, Germany; 4. Max-Planck Institut für Mikrostrukturphysik, Halle, Germany; 5. Institut für Angewandte Physik, Universität Hamburg, Hamburg, Germany; 6. European Synchrotron Radiation Facility-ESRF, Grenoble, France; 7. Instituto Madrileño de Estudios Avanzados en Nanociencia IMDEA-Nanociencia, Madrid, Spain

The magnetic properties of a given material are strongly related to its crystalline structure. Among others, aspects as important as the magnetic moment per atom, the type of magnetic long-range order (ferro- or antiferromagnetic), or the coercive field are extremely sensitive to any modification of the interatomic distances or the chemical environment. Iron-based structures are an example of this subtle interplay between structural and magnetic properties, and have consequently attracted extensive attention. A great variety of properties has been predicted if the structure and lattice parameter of Fe could be changed from their bulk properties [1]. In this presentation we will show the growth of artificial Fe_xCu_{1-x}[111] thin films and the influence of thickness, concentration, and temperature on the electronic and element-resolved magnetic properties.
Iron-copper alloys of these otherwise immiscible elements have to be synthesized artificially by using far-from-equilibrium producing techniques. FeCu alloy thin films were grown at room temperature codepositing simultaneously Fe and Cu onto a Cu(111) substrate precovered with a surfactant Pb layer. The latter reduces the film roughness and, at the same time, prevents the segregation of the two components by reducing the atom mobility on the surface layer [2]. Element-resolved magnetic measurements were performed in remanence by x-ray magnetic circular dichroism (XMCD) at the Fe and Cu $L_{2,3}$ absorption edges at the UE56/2-PGM2 beamline at BESSY.
Figure 1 shows total electron yield absorption spectra XAS (top) for positive and negative helicity (black and red curves, respectively) and the difference, the magnetic dichroism XMCD(bottom), at the Fe and Cu $L_{2,3}$ absorption edges of a 37 monolayers (ML) $Fe_{55}Cu_{45}$ film on Cu(111). The induced magnetic moment of the Cu atoms is also clearly visible in the XMCD spectra. Fe and Cu moments are aligned parallel, as can be seen from the identical sign of the Fe and Cu dichroism. The evaluation of the magnetic moments by sum rule analysis reveals an Fe spin moment smaller than that of bulk Fe. The induced moment at the Cu atoms is slightly larger than that found in artificial FeCu(100) alloys [3].
A non-ferromagnetic behavior is found up to ~15 ML of alloy, and above 120 K. For thicker films, a low spin phase ferromagnetic behavior is found at room temperature. The evaluation of the magnetic moments by sum rule analysis reveals the magnetic moment of both the Fe and Cu atoms increases as the thickness of the alloy increases (see Fig.2 (a)). These changes are related to the structural fcc-bcc transformation that takes place with increasing thickness (see Fig.2 (b)). The structural change in the alloy is reflected in the change of the XAS line shape just above the Cu-L_3 edge, where a two-peaked feature converts to a single peak when the thickness of the alloy increases. Additionally, an enhancement in intensity for the alloy film is observed at the Cu-L_3 edge, ~934 eV photon energy. Since the XAS spectra reflects the Cu unoccupied density of states above the Fermi edge, this can be judged as manifestation of an enhanced number of unoccupied Cu d-like states in FeCu with respect to pure Cu metal.
Low temperature measurements show that the fcc–bcc structural transition can also occur by decreasing the
temperature. Additionally, this structural transition is delayed when the concentration of the Fe in the alloy is smaller. Our findings demonstrate that it is possible to tune at will the magnetic moments of the iron, and therefore the Cu, atoms by combining the appropriate thickness and chemical composition of the alloy.

[1] V. M. García-Suárez *et al.*, J. Phys.: Condens. Matter **16**, 5453 (2004).

[2] J. Camarero *et al.*, Phys. Rev. Lett. **81**, 850 (1998).

[3] W. Kuch *et al.*, Phys. Rev. B **58**, 8556 (1998).

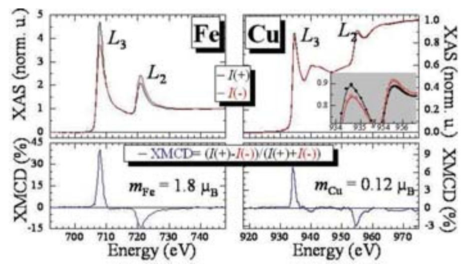

XAS (top) and XMCD (bottom) spectra of 37 ML $Fe_{55}Cu_{45}$ at the Fe-$L_{2,3}$ (left) and Cu-$L_{2,3}$ (right) edges.

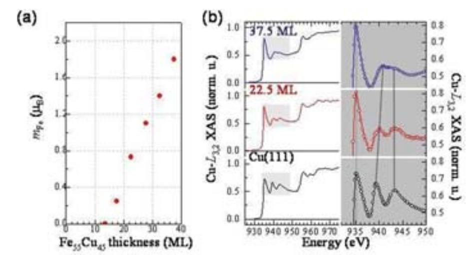

(a) Thickness-dependent Fe magnetic moment of a $Fe_{55}Cu_{45}$ alloy. (b) Cu $L_{3,2}$-XAS spectra for different thicknesses. The insets are magnifications of the marked areas. Two peaks around 942 eV photon energy (gray dotted lines) indicate an fcc-Cu like structure, whereas one peak indicates a bcc-like structure.

AD-10

Magnetic properties of ultra thin magnetite film grown by molecular beam epitaxy.

S. K. Arora[1], W. HanChun[1], I. V. Shvets[1], O. N. Mryasov[2], H. Yao[3], W. Y. Ching[3]
1. Centre for Adaptive Nanostructures and Nanodevices (CRANN), School of Physics, Trinity College Dublin, Dublin, Ireland; 2. Seagate Research Center, Seagate Technology, Pittsburgh, PA, 15222, PA; 3. Department of Physics, University of Missouri-Kansas City, Kansas City, MO, 64110, KS

Epitaxial hetero-structures based on Magnetite, Fe_3O_4, have attracted considerable interest due to its half metallic ferromagnetic nature, high Curie temperature (838 K) and presence of a metal-insulator transition at 120 K, (Verwey transition). Magnetic properties of epitaxial Fe_3O_4/MgO (100) hetero-structure are found to be strongly influenced by their method of preparation, presence of intrinsic defects (antiphase boundaries, APB). Presence of APBs led to non saturation of magnetization in high magnetic fields and superparamagnetic behavior for ultrathin (<5 nm) films. Here, we report a detailed magnetization studies on well characterized epitaxial Fe_3O_4 thin films (2-20 nm thickness) grown on MgO (100) using oxygen plasma molecular beam epitaxy (MBE) technique. We find that the films exhibit a ferromagnetic behavior down to 2 nm thickness and possess magnetic moments greater than that of bulk magnetite. Our results are in direct contrast to previously accepted dead layer interface model or a super-paramagnetic behavior for ultra thin films of magnetite [1,2]. In order to find the origin of enhanced magnetic moment, we considered various possibilities such as contribution from Fe_3O_4-MgO interface, surface terminations and defects (cationic and anionic). From detailed spin-polarized density functional theory based calculations of Fe_3O_4-MgO interface, we estimate that the spin moments of the Fe ions in the vicinity of the Fe_3O_4-MgO interface are marginally enhanced but these changes are insufficient to explain the observed results. Orbital moment contribution for the surface Fe atoms also turn out to be quite small. The non-compensation of spin-moments between the tetrahedral (A) and octahedral (B)- sublattices inferred to be the main factor contributing to the observed enhanced magnetic moment.

[1] F.C. Voogt, T.T.M. Palstra, L. Niesen, O.C. Rogojanu, M.A. James and T. Hibma, Phys. Rev. B 57, R8107 (1998)

[2] Y. Zhou, Ciaran McEvoy, R. Ramos and I.V. Shvets, J. Appl. Phys. 99, 08J111(2006)

AD-11

Structure and magnetism of ultra-thin chromium layers on W(110).

B. Santos[1,2], J. M. Puerta[3], J. I. Cerda[3], R. Stumpf[4], K. von Bergmann[5], R. Wiesendanger[5], M. Bode[5,6], K. F. McCarty[4], J. de la Figuera[1,2]
1. Instituto de Quimica-Fisica Rocasolano, CSIC, Madrid, Spain; 2. Centro de Microanalisis de Materiales, Universidad Autonoma de Madrid, Madrid, Spain; 3. Instituto de Ciencia de Materiales de Madrid, CSIC, Madrid, Spain; 4. Sandia National Laboratories, Livermore, CA; 5. Institute of Applied Physics and Microstructure Research Center, University of Hamburg, Hamburg, Germany; 6. Center for Nanoscale Materials, Argonne National Laboratory, Argonne, IL

Chromium is a transition metal with a rich variety of magnetic properties that has been the focus of many studies. It is an itinerant antiferromagnet (AFM) in the bulk and presents an incommensurate spin density wave. In thin films the coupling with the substrate transforms this AFM spin-density wave (SDW) from an incommensurate to a commensurate one. Furthermore, the current interest in spintronics has been partially initiated by the discovery of the giant magnetoresistance effect in Fe/Cr multilayers. Further progress in this area depends on atomic level control in the manufacturing of spintronic devices.
Surprisingly, structural and magnetic characterizations of ultra-thin Cr films on W(110), a common substrate for thin metal films because of its resistance to alloying, are scarce. Most studies actually focus on the thick-Cr regime, where the surface is assumed to be a proxy of bulk Cr. One basic question is whether ultra-thin films of Cr on W(110) present magnetic ordering, and if so, what kind. The problem is challenging because few methods are capable of detecting antiferromagnetism in such thin layers. Recent ab-initio calculations indicate that a monolayer might be magnetic. Here we present a combined low-energy electron diffraction intensity-versus-voltage (LEED IV), spin-polarized (SP)-STM, and ab-initio theory study with the aim of obtaining a thorough understanding of the atomic and magnetic structure of Cr films a few atomic layers thick on W(110). LEED IV is the classic tool for determining the interlayer separation of the first few atomic surface layers with errors in the 0.01-0.02 Angstrom range. A satisfactory comparison of LEED with ab-initio density functional theory (DFT) is also a mature approach and, in general, is considered the gold standard for surface structure determinations. Well-converged spin-polarized DFT calculations usually predict surface relaxations in good agreement with experiment even for magnetic materials. Finally, SP-STM is one of the few techniques able to measure local antiferromagnetic order on surfaces. By depositing a ferromagnetic film on the tunneling tip, images with atomic contrast related to the magnetic structure of the surface can be acquired. The sensitivity of the tip to either in-plane or out-of-plane surface magnetic moments can be tuned by applying magnetic fields.
The first-principles calculations predict a very different surface relaxation for antiferromagnetic and non-magnetic Cr films. Only in the antiferromagnetic case is the calculated relaxation compatible with that determined by LEED IV. This strongly suggests that films of one, two and three atomic layers of Cr on W(110) have antiferromagnetic short-range order. As seen in the figure, SP-STM data confirm this finding: The Cr monolayer on W(110) shows characteristic stripes along the [001] direction due to the antiferromagnetic order of nearest-neighbor Cr atoms. Additionally, the SP-STM data of the Cr monolayer reveal a periodically varying magnetic amplitude that peaks every ~7.7 nm. On thick Cr(110) films the signature of an incommensurate spin density wave, existing in two different orientations, is found. We also compare the LEED IV and ab-initio relaxations of bare W(110) and bulk-like Cr(110) surfaces.

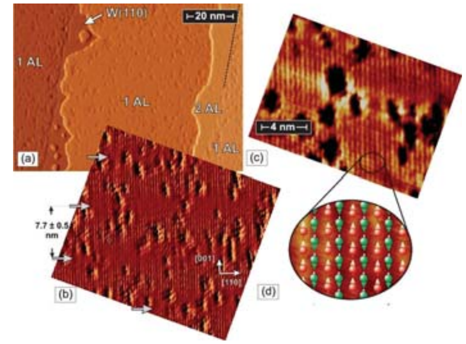

Spin-polarized STM images of a mostly monolayer thick film of Cr on W(110).

AD-12

Quantum-size induced oscillations of the electron-spin motion in Au films on Co(001).

L. Tati Bismaths[1], L. Joly[2], F. Scheurer[1], W. Weber[1]
1. Institut de Physique et Chimie des Matériaux de Strasbourg,, Strasbourg, France; 2. Swiss Light Source, Villigen, Switzerland

In many of the most intriguing new concepts of contemporary magnetism such as the reversal of the magnetization by spin-polarized electron currents, it is of crucial importance to understand the interaction of spin-polarized electrons with a ferromagnetic material. Due to spin-dependent scattering the spin polarization vector of the interacting electrons is expected to change. We measured this spin motion, comprising an azimutal precession and a polar rotation around the magnetization direction of the ferromagnet, in the past both in transmission and in reflection geometry on simple ferromagnetic systems [1-3]. Of even more interest both from the fundamental and from the practical point of view are quantum-well structures in which standing electron waves are formed. The existence of such quantum-well states is at the origin of a number of different oscillatory phenomena in thin films, such as the oscillatory exchange coupling between two ferromagnetic layers separated by a non-magnetic spacer layer.

Here we report on spin-polarized electron reflection experiments in which the electron-spin motion is studied in spin-dependent quantum-well structures. Oscillations of the electron-spin motion due to quantum interference are observed in the system Au/Co(001) as a function of the Au-overlayer thickness. The reflectivity as well as the spin-motion data can be well interpreted in terms of a simple Fabry-Pérot interferometer model. We discuss the influence of the spin-dependent reflectivity, the inelastic mean free path, the scattered electron intensity contribution, and the growth mode on the behaviour of the electron-spin motion within the interferometer model.

[1] W. Weber et al., Science 291, 1015 (2001)

[2] W. Weber et al., Phys. Rev. B 66, R100405 (2002)

[3] L. Joly et al., Phys. Rev. Lett. 96, 137206 (2006)

AE-01

Monolithically-fabricated hybrid head for near field assisted magnetic recording.

S. Miyanishi, K. Innami, T. Naka, T. Kitazawa, M. Yagura, N. Teraguchi, Y. Murakami, A. Takahashi
Advanced Technology Research Laboratories, SHARP CORPORATION, Tenri, Japan

Introduction

Thermally assisted magnetic recording is one of key concepts to achieve high density magnetic recording beyond 1 Tb/inch^2. There have been several experimental reports concerning the thermal assisted recording [1-6]. Especially in the field of the hybrid magnetic recording, near field optics has been adopted as a nanoscale thermal source [4-6]. In particular, we have proposed a surface plasmon and magnetic field applicable synchronously hybridized (SMASH) head that generates magnetic field and surface plasmon at nanosized region. We have demonstrated the capability of the SMASH head for the near-field assisted magnetic recording [4]. Several groups have proposed hybrid magnetic heads combined with an optical waveguide or an optical fiber unit [5-6]. However, precise optical alignment with the near field generator and a light source remains difficult. There is no tangible proposal how to hybridize the head with a laser device.

In this paper, we show a monolithically-fabricated hybrid head with a GaAs-based laser diode for the near field assisted magnetic recording. The hybrid head is composed of a laser diode and a generator of the near field and the magnetic field. We confirm localization of the near field on the generator on the hybrid head using near field scanning optical microscope (NSOM).

Experimental

Figure 1 shows a mock-up assembly image of the monolithically-fabricated hybrid head. The size of hybrid head is less than that of a femto-slider. The components of the laser diode and the generator are located in the center of trailing edge of the slider. The near-field and magnetic field generator consists of double layered metals and the upper layer has a 200 nm width slit. The lower layer is deposited on the SiN insulator layer on the GaAs substrate. The slit produces a bottleneck structure. The magnetic field is mainly generated around the bottleneck structure by feeding current through the metal double layers. The laser diode is monolithically fabricated on the substrate, where the position of laser diode's active layer is adjusted to that of the generator as the emitted laser beam effectively enters into the bottleneck structured portion.

Results and discussion

Figure 2 shows a scanning electron microscopic image observed from the air bearing surface side around the generator on the slider. The generator with the bottleneck structure is located in front of the high mesa laser ledge. The precise optical alignment between the generator and the laser beam has been accomplished using monolithically fabrication process. Figure 3 shows the NSOM image around the bottleneck region of generator. Near field is locally generated on the top and bottom edge of the bottleneck structure, where the near field intensity is designated as bright part. We confirmed that the near field intensity exponentially decreases with the scanning z-height of the SNOM probe.

[1] K. Kojima et al., IEEE Trans. Magn., **37**, 1406 (2001).

[2] S. Miyanishi et al., J. Appl. Phys., **93**, 7801 (2003).

[3] T. E. Schlesinger et al., Jpn. J. Appl. Phys., **41**, 1821 (2002).

[4] S. Miyanishi et al., IEEE Trans. Magn., **41**, 2817 (2005).

[5] F. Tawa et al., J. Appl. Phys., **101**, 09H503 (2007).

[6] H. Masakazu et al., IEICE Trans. Electron., **E90-C**, 105 (2007).

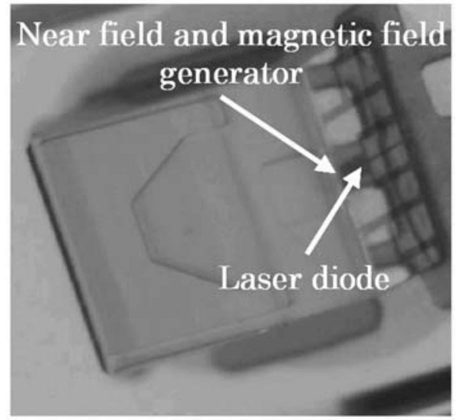

Fig.1 Mock-up assembly image of monolithically-fabricated hybrid head.

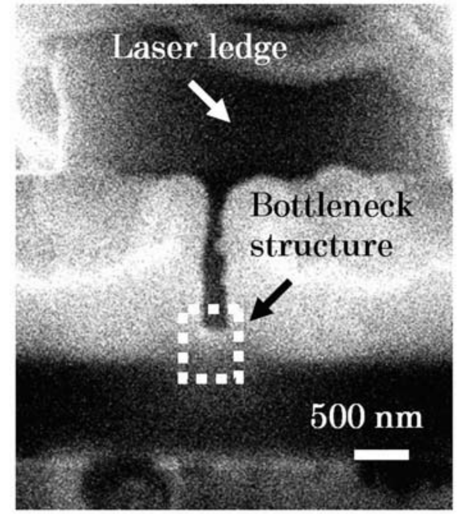

Fig.2 Scanning electron microscopic image around the generator on the hybrid head.

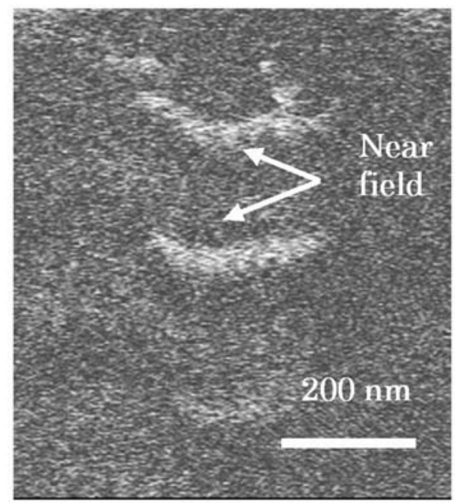

Fig.3 Near field scanning optical microscopic image around the generator on the hybrid head in the enclosed area in Fig.2.

AE-02

Exploiting far- and nar-fiel optics to develop energy efficient transducer for heat-assisted magnetic recording.

R. Ikkawi[1], N. Amos[1], A. Krichevsky[1], A. Lavrenov[1], D. Litvinov[2], S. Khizroev[1]
1. Electrical Engineering, University of California, Riverside, Riverside, CA; 2. Center for Nanomagnetic Systems, University of Houston, Houston, TX

Recently, it became clear that the conventional magnetic recording schemes are coming to end because of the superparamagnetic limit. Heat-assisted magnetic recording (HAMR) may have potential to extend the data densities to 10 Terabit/in2. In order to record information, HAMR will use not only magnetic but also thermal energy. Therefore, a recording media with substantially higher anisotropy could be utilized. In one of the proposed implementations, a laser beam in the near field, co-aligned with the recording field, heats up a local region to the temperature close to the Curie point. The key challenge in this implementation is to develop a near-field transducer capable of delivering over 50 µW into a spot diameter of 30 nm. The traditional fiber schemes are barely capable of producing 10 nW. To resolve this issue, a laser diode could be placed with the emitting edge only a few nanometers away from the recording media [1]. The light can propagate through a nano-aperture on the surface of an aluminum-coated emitting edge.
The transducer is required to focus light into a spot with a diameter less than 50nm. Knowing that classical optics is diffraction limited to approximately half the wavelength, an approach to combine both: far-field and near-field optics will be employed to focus light not only to a nanoscale spot, but also to superiorly enhance its power efficiency to deliver sufficient power to elevate the disk temperature. The foundation for employing far- and near-field optics arise from current limitations in collimating laser diode beams caused by exceedingly high beam divergence at the faucet of commercial semiconductor lasers. This novel device will firstly focus light into a diffraction limited spot on a metallic thin film where nanoscale apertures acting as focusing antennas will focus the light further to spots of less than 50nm diameter and more than 500nW of power. Figure 1top exemplifies how the first plano-covex lens will collimate the beam, then get focused to a diffraction limited spot in the order of a few microns on the air-bearing surface of the contact forming lens by the second plano-convex lens. It has been numerically modeled that such focusing method improves the power transmission efficiency by at least two orders of magnitude relative to defining the nanoapertures directly on a metalized laser faucet. The design of so called "aperturless" probes to conceive an adequately high energy throughput near-field system remains to be a decisive element. Numerical simulations have indicated evident dependence between the aperture geometry and its transmission efficiency and focusing capabilities (figure 1bottom).

[1] R. Ikkawi, N. Amos, A. Krichevsky, R. Chomko, D. Litvinov, S. Khizroev, "Nanolasers to enable data storage beyond 10 terabit/in2, "Appl. Phys. Lett. 91 (15), 3115-6 (2007)

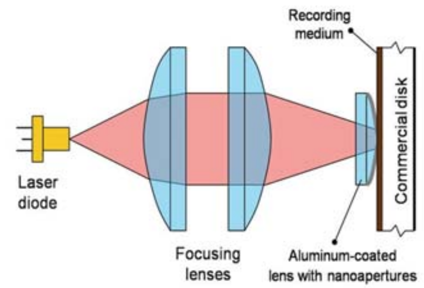

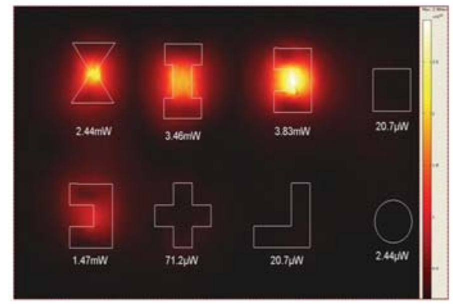

AE-03

Design and characterization of a media thermal stack for confining lateral thermal heat flow.

D. Karns, G. Ju, A. Itagi, B. Lu
Seagate Technologies, Pittsburgh, PA

Abstract
We report on a pump-probe tool, referred to as the scanning pump-probe spin stand, which enables the measurement of the lateral thermal profile created in a medium of interest by a static or scanning incident focused laser beam. This tool enables the relative quantization of lateral diffusivity for experimental samples. The tool utilizes a 405 nm diode laser focused through an objective lens with a numerical aperture of 0.85 for probing the thermal profile in the medium. This is a similar configuration to the Blu-Ray and HD-DVD configurations. Using experimentally measured material properties, good agreement between experiment and modeling was achieved for the complete structure of an exemplary high density optical storage media. The media stack consists of a substrate, heat sink layer, seed layer, recording layer and a protective overcoat. Effects of layer thickness and materials on the lateral thermal flow have been studied. Non-static cases have been examined and the thermal stack optimized to assure thermal confinement and minimal thermal spread in the sample during motion. With an optimized stack design the thermal profile measured by the scanning pump probe spin stand is close to the minimum expected for both the static and non-static cases, indicating strong lateral thermal confinement and good heat sinking into the substrate material.

Experimental results
The heat sink thickness series of disks has the following structure, CuX with a vertical thermal conductivity of 250 W/(mK)on glass with a thermal conductivity of roughly 1 W/(mK)and a high Curie temperature recording layer. The disk without a heat sink produces a narrow thermal profile with a FWHM of only ~450 nm, and very small thermal tails roughly 3% of the peak signal at 1 µm from the peak signal as shown in figure 1. The narrow profile is a result of the low thermal conductivity and thus strong lateral thermal confinement in the recording medium. When a thin, 50 nm, heat sink is added the heat is allowed to spread laterally. The disk with a heat sink thickness of 50 nm produces a considerable amount of thermal spread in the medium. As the heat sink becomes thicker, it allows the heat to be conducted away from the recording medium and reduces thermal spreading in the recording medium. The data did show the general form expected from modeling.
The heat sink is needed to allow thermal diffusion away from the magnetic recording layer when the disk is spinning. Otherwise, a teardrop thermal profile will form and the trailing edge will be extended and yield a poor thermal gradient. This effect can be observed in figure 2.
To reduce the thermal spreading induced by the heat sink material with a high thermal conductivity a seed layer is utilized. The seed layer is designed to allow heat flow from the recording medium to the heat sink but not back into the recording medium from the heat sink. This should produce a narrow FWHM and minimize re-heating effects far away from the thermal source known as tails or shoulders. The data shown in figure 3 represents the FWHM of the measured thermal profile versus the seed layer thickness. It is clear that the thicker seed layer is effectively reducing the measured FWHM. The minimum measured FWHM is 540 nm, which is smaller than the measured value of 720 nm from the reference disk without a heat sink or a seed layer.
The last step is to utilize all of the knowledge gained and fabricate a disk that maintains thermal confinement when spinning. The heat sink should be sufficiently thick with a high thermal conductivity. Also, the seed layer must be properly designed to alleviate lateral heat flow. The measured thermal profile for the disk spinning at ~11 m/s remains symmetric and the FWHM remains approximately 486 nm.
Conclusions
A XY scanning pump probe spin stand was constructed. This system can be used to measure the later thermal profile created in a medium by an incident pump laser by utilizing a probe laser. The probe laser is modulated and fed into a lock-in amplifier to increase the system sensitivity. The medium can also be measured as a static or spinning disk. This allows the thermal bloom due to medium motion to be measured. A recording layer can show good thermal confinement without a heat sink. However, if the medium is spinning a heat sink is required to conduct heat away from the recording layer and minimize the tear drop effect. However, lateral thermal bloom can occur for a heat sink that is not thick enough. A design of seed layer can be optimized to reduce the effects of lateral thermal bloom when media is static and spinning.

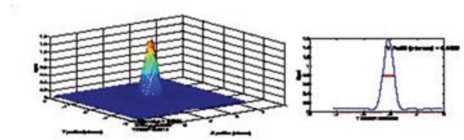

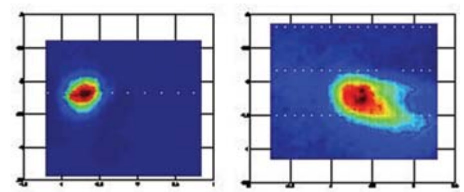

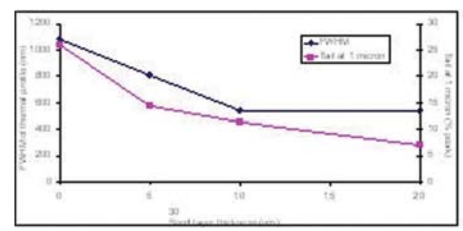

AE-04

Domain structure in TbFeCo/FePt-grains composite film and Cu doping effect on Curie temperature of FePt grains.

A. Itoh[1], A. Tsukamoto[1], F. Chino[2], S. Iwase[2], Y. Sano[2], K. Okayama[2]
1. Dep. of Electronics and Computer Science, College of Science and Technology, Nihon University, Funabashi, Japan; 2. Dep. of Electronics, Graduate School of Nihon University, Funabashi, Japan

Thermally assisted magnetic recording (TAMR) can solve fundamental problems concerning thermal fluctuation and write capability in magnetic recording. Although the advantages of TAMR in increasing areal density, it has implementation issues such as optimization of thermal profile and the magnetic head. Rausch et al. reported[1)] that there exists an optimal alignment between them, which minimizes the transition length, and parameter effects by using a systematic thermal Williams-Comstock recording model (explicitly included thermal term : $dHc/dT \times dT/dx$). Moreover, grain size dominates transition noise in present granular perpendicular media.
In this study, we report a micromagnetic modeling analysis of the composite magnetic recording media, consisting of FePt granular under layer that act as a domain pinning of TbFeCo continuous layer and yield smooth transition boundaries. TbFeCo is well known as magneto-optical recording media and thermal property such as Tc and dHc/dT is rather controllable by adequate tuning of composition ratio. Therefore, we also performed thermal characterizations of FePt nano-particles by Cu doping.

1. Micromagnetic simulation of composite magnetic recording media

We performed 3-dimensional LLG simulations for estimating domain shapes in TbFeCo/FePt-grains composit film. Two models containing different grain diameter d and spacing s were employed. For overcome the recording density of 1 Tbit/inch^2, d and s have to be decreased until comparable scale with the domain wall width W_d, and it causes difficulty to predict the domain structure. At the Model 1(d = 5 nm, s = 3 nm) period of each grains p is nearly equal to W_d and Model 2 (d = 4 nm, s = 2 nm) is higher density model. Fig. 1 shows initial state of magnetization of the film (Model 2).
Fig. 2 shows the temperature dependence of domain diameter $D_d$at the boundary of TbFeCo/FePt, at the surface of TbFeCo, respectively. The material parameters are estimated from experimental reports and calculation with mean field approximation. Simulated result shows magnetic domain could be formed on all the cases. Well isolated and exchange decoupled FePt grains, pined and defined the domain shape of the continuous layer. Moreover, we found that D_d < 23 nm (it is suitable at 1.3 Tbit/inch^2) could be formed even under the condition of $p < W_d$. In addition, for the simulation, with an exchange break between the granular and continuous layers, the initial domain shrunk and disappeared. The introduction of a granular layer pins the magnetization of the exchange-coupled layer. Furthermore, it is confirmed that domain shape is smoother at the surface of TbFeCo layer. This smoothening of domain shape contributes to a reduction of the medium noise caused by magnetization transition due to magnetic irregularities or magnetic clusters.

2. Cu doping effect on Curie temperature *Tc* of FePt grains

We investigated the effect of Cu doping to Tc within FePt particles (FePt, Tc = 770 K) prepared by Rapid Thermal Annealing (RTA) method[2)]. Cu doped Pt/Fe film was fabricated by RF magnetron sputtering onto thermally oxidized Si substrates. First the FeCu and then the Pt layers were deposited, and then RTA was done by using a 2 kW lamp in a vacuum chamber at a pressure of 9 x 10^{-4} Pa. The heating rate was 100 K/sec.
As-deposited double-layer Pt/FeCu (total film thickness is 3.8 nm) was continuous films, and after 773 K at 1 sec. RTA, well isolated particles formed. Fig. 3 shows the typical results of temperature dependence of Coercivity determined from magneto-optically (Kerr ellipticity) measured perpendicular hysteresis loops. It is clear that Tc successively and sensitively reduced by increasing the amount of Cu doping. Moreover, advantageously large value of dHc/dT (around 160 Oe/K) was appeared in each case.

3. Acknowledgements

This work is partially supported by a Grant-in-Aid for Scientific Research from the Ministry of Education, Culture, Sports, Science and Technology in Japan, No. 18560347, and Storage Research Consortium, No. 50739.

1) T. Rausch et al., *IEEE. Trans. Magn.*, vol. 40,No. 1, pp. 137–147 (2004).

2) A. Itoh et al., *J. Appl. Phys.*, 99, 08Q906 (2006).

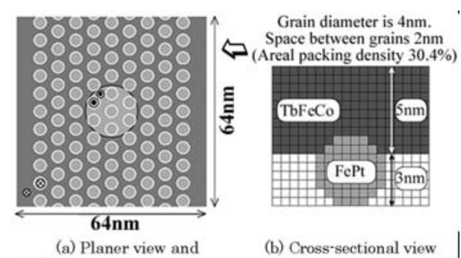

Fig. 1 Initial state of magnetization of the film(Model2)

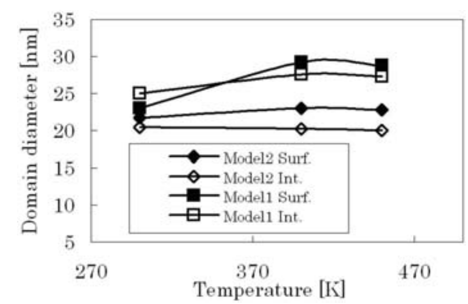

Fig. 2 Temperature dependence of domain diameter

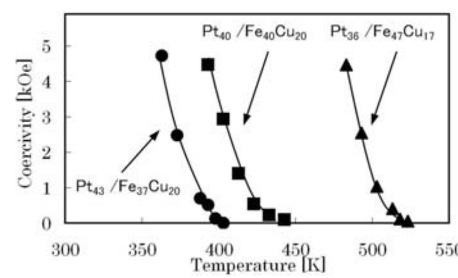

Fig. 3 Temperature dependence of Coercivity

AE-05

Magnetic properties of amorphous magnetic film on self-assembled convex pattern.

N. Iwata, D. Honda, Y. Murakami, A. Takahashi
Advanced Technology Research Laboratories, SHARP CORPORATION, Tenri, NARA, Japan

Introduction

Several fabrication methods for bit patterned media are proposed, for example, combination of self-assembled molecules and dry etching [1], nanoholes and electrodeposition [2]. However, these methods require drastic change of the conventional media manufacturing process. We introduced a newly developed self-assembled convex pattern method as an underlayer of amorphous TbFeCo thin film media. The convex pattern can be easily fabricated using conventional sputtering and reactive ion etching (RIE) equipments. TbFeCo is one of the hopeful candidates for near field assisted magnetic recording [3] because of its high perpendicular anisotropy and low Curie temperature, but it is necessary to reduce the exchange coupling force at the magnetic domain boundaries to achieve the area densities of over 1 Tbits/inch^2. In this paper, we report magnetic properties and magnetic domain size to confirm the effect of convex pattern.

Experiment

Firstly, we deposited Ta on a Si substrate using a sputtering machine with RF bias applied. Fabricated dots had the periodicity around 25 nm on the Si substrate. After Ta deposition, Si substrate was reactive-ion-etched in fluoride gas atmosphere using the Ta dots as an etching mask. Atomic force microscope (AFM) images after the RIE is shown in Fig.1. The convex pattern after RIE had the periodicity of around 28 nm, the height of around 15 nm and the maximum angle to the substrate plane at the steep region of the convex curve was 75 degrees. A TbFeCo film and a Ta capping film were deposited onto the convex pattern and magnetic properties were evaluated using a vibration sample magnetometer and a magnetic force microscope (MFM).

Results and discussions

Fig.2 shows the normalized remanence coercivity (H_r) of the fabricated samples on a flat Si substrate (a) and on the convex pattern (b) both with a 50 nm-thick TbFeCo film as a function of applied field angle (θ) from the direction normal to the substrate plane. The TbFeCo on the flat substrate (a) indicated monotonous increase showing almost the same tendency of the theoretical domain wall (DW) type curve. On the other hand, normalized remanence coercive force on the convex pattern (b) decreased with similar tendency of the Stoner-Wohlfarth model (S-W) from 0 degree to 45 degrees, and it showed further decrease in larger angles. These results indicate the magnetization reversal modes are different between sample (a) and sample (b), and the TbFeCo on the pattern has regions whose easy axes are rather close to parallel than to normal to the substrate plane.

Fig.3 shows MFM images of the 50 nm-thick TbFeCo film on the convex pattern. The small magnetic domains are observed whose diameters are around 50 nm.

Summary

Reduction of magnetic domain size was confirmed in the amorphous TbFeCo film deposited on the self-assembled convex pattern. The reduction is attributed to the change of the anisotropy direction and the decrease of exchange coupling force at the steep region of the convex curve. This result indicates the possibility of realizing amorphous film patterned media which can be preferable for near field assisted magnetic recording.

[1] K. Naito et al, IEEE Trans. Magn., **38**, 1949-1951 (2002).

[2] H. Kikuchi et al, IEEE Trans. Magn., **41**, 3226-3228 (2005)

[3] S. Miyanishi et al, IEEE Trans. Magn., **41**, 2817-2821 (2005)

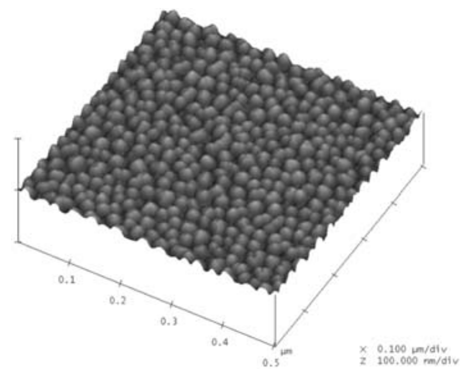

Fig.1 AFM image of self-assembled convex pattern after RIE with a periodicity of around 28 nm.

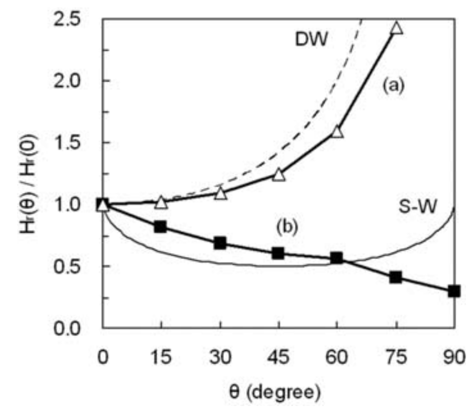

Fig.2 Normalized H_r for TbFeCo (50 nm) films on the flat substrate (a) and that on the convex curve pattern (b) as a function of applied field angle from the substrate normal, θ.

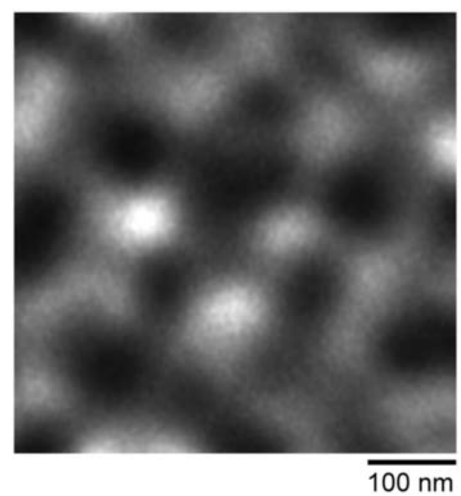

Fig.3 MFM image of TbFeCo (50 nm) films on the convex pattern.

Comparison of Dual and Thermal Gradient Recording Methods for Thermally Assisted Magnetic Recording.

F. Akagi, T. Matsumoto, M. Igarashi
Hitachi, Ltd., Tokyo, Japan

Introduction

Thermally assisted magnetic recording (TAR), which combines thermo-magnetic writing with magnetic reading, is a promising system for achieving a high areal recording density [1,2,3]. TAR is classified into some recording methods depending on the dimensions of the light spot and head-field. In this study, we compared the write performance of the dual gradient recording method (DGRM) and the thermal gradient recording method (TGRM). The DGRM combines a small light spot with a head-field with a sharper field gradient. The TGRM combines a small light spot with a large head-field.

Calculation Method

The recording process was calculated using the Landau-Lifshitz-Gilbert equation, which adds a stochastic thermal field to an effective field [4]. The output signal and the noise were calculated using a Fourier transform of the averaged magnetization in the track-width direction. The magnetic characteristics of the medium at 300 K are shown in Table 1. The temperature dependence of the anisotropy field (H_k) was calculated using a Brillouin function [5] and the Curie temperature was 550 K. The thermal profile was assumed to be a Gaussian distribution, the half width of which was 80 nm and the temperature increased by 250 degrees. The head-field (H_h) for DGRM was calculated with single-pole-type head and that for TGRM was a uniform field.

Results and Discussion

Figure 1 shows the MH major loops for H_k of 17 kOe and 25 kOe. The sweep rate was 625 Oe/ns, which was equal to the recording speed. The nucleation field (H_n) intensity for H_k of 17 kOe was 7 kOe and that for H_k of 25 kOe was 12 kOe. If the magnetic field that is stronger than H_n is applied to the medium, magnetizations will begin to reverse without thermal. Figure 2 shows the comparison of recorded magnetization patterns at 1000 kfci between DGRM and TGRM. The head-field intensity was 12 kOe. The magnetization patterns of DGRM for both H_k were clearly observed. The magnetization pattern of TGRM for H_k of 17 kOe was not observed, but that for H_k of 25 kOe was clearly observed because the uniform head-field, which was stronger than H_n for H_k of 17 kOe, erased the recorded magnetization pattern. Figure 3 shows the comparison of the magnetization patterns at 122 kfci between DGRM and TGRM. It was found that the magnetization pattern for DGRM was clearly observed, but there were reversal magnetizations in the bit for TGRM because a uniform head-field was applied to the recorded bit, which caused the reversal magnetizations.

Conclusion

It is cleared that a head-field of TGRM strictly affects recorded magnetization patterns in comparison with DGRM.

[1] H. Saga, H. Nemoto, H. Sukeda, and M. Takahashi, Jpn. J. Appl. Phys. Vol.38, 1839 (1999).

[2] T. W. Mcdaniel, J. Phys.: Condens. Matter vol.17 (2005) R315

[3] F. Akagi, M. Igarashi, A. Nakamura, M. Mochizuki, H. Saga, T. Matsumoto, and K. Ishikawa, Jpn. J. Appl. Phys. Vol.43, 7483 (2004).

[4] F. Akagi, M. Igarashi, K. Yoshida, Y. Nakatani, and N. Hayashi, IEEE Trans. Magn. vol.37, 1534 (2001).

[5] J.-U. Thiele, K. R. Coffey, M. F. Toney, J. A. Hedstrom, and A. J. Kellock, J. Appl. Phys. vol.91, 15 (2002).

Grain Diameter <D>(nm)	σD/<D>(%)	Thickness (nm)	M_s (emu/cm^3)	$\langle H_k \rangle$(kOe)	$\sigma H_k/\langle H_k \rangle$(%)
6.5	15	20	350	17,25	5

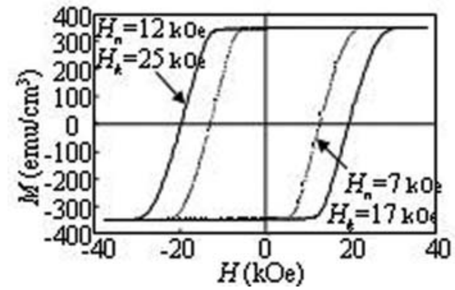

Fig. 1 MH major loops

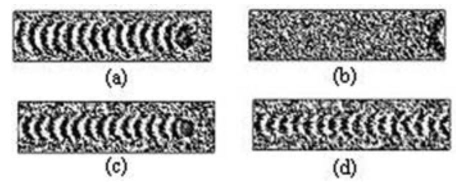

Fig. 2 Magnetization patterns at 1000 kfci for H_h of 12 kOe (a) DGRM, H_k = 17 kOe (b) TGRM, H_k = 17 kOe (c) DGRM, H_k = 25 kOe (d) TGRM, H_k = 25 kOe

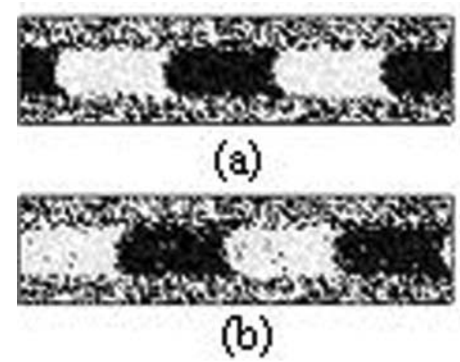

Fig. 3 Magnetization patterns at 122 kfci for H_k of 25 kOe and H_h of 12 kOe (a) DGRM (b) TGRM

AE-07

Investigation of magnetic reversal modes for Heat Assisted Magnetic Recording.

R. F. Evans[1], P. Asselin[2], D. Hinzke[1], U. Nowak[1], R. W. Chantrell[1]
1. Physics, University Of York, York, United Kingdom; 2. Seagate Research, Pittsburgh, PA

Heat assisted magnetic recording (HAMR) is a promising technological innovation which utilises a laser heat source to reduce the coercivity of recording media so that magnetic information can be written in a reliable way. To achieve a sufficiently low coercivity requires substantial heating of the recording media, often in the vicinity of the Curie temperature. At such high temperatures conventional micromagnetic models cease to accurately represent the physical situation and new approaches are required to understand magnetic effects near the phase transition. However, the intention with HAMR is also to increase the magnetic data density through the use of high anisotropy materials, such as FePt and CoPt. Such an increase in data storage density presents a problem in itself, arising from very significant finite size effects as data densities approach 1 Terabit per square inch. Thus HAMR provides a significant challenge to our understanding and knowledge of magnetic phenomena at nanoscopic sizes and near the Curie temperature.

In this digest we use an atomistic Heisenberg approach to investigate the reversal process for 10 nm FePt grains with heat assisted writing. The room temperature coercivity of the grains was assumed to be 5 Tesla, correlating with approximately 50% L_10 ordering. Due to the small size of the grains, they also have a reduced Curie temperature of 680 K compared to around 750 K in Bulk. The atomistic simulations properly take into account the thermal fluctuations of the magnetisation length and direction which are not included in conventional micromagnetic models. The reversal mechanism is a statistical process and has been investigated by repeatedly writing a single grain with varying laser power. The effects of laser heating are modelled with a pseudo three-dimensional discretised heat transfer model. The cooling process is simulated by moving the laser away from the target grain as would occur in an actual device with revolving media. This results in a cooling time of around 350 picoseconds from Tc to room temperature. In order to accurately reflect the present situation at the device level, a maximum external applied write field of 0.8 Tesla has been used. Due to the high anisotropy, simulations of the temperature dependence of the anisotropy field show that the write field is ineffectual below a temperature of 640 K. This leads to the concept of a critical cooling time, which defines the length of time where the external field is greater than the anisotropy field.

We find that in order to reliably reverse the grain, the maximum temperature of the grain must exceed the Curie temperature, which coincides with a change in the reversal mechanism. Specifically, instead of precessional reversal, where the magnetisation vector rotates around the anisotropy axis, the length of magnetisation passes through zero and reforms in the opposite direction, a process known as linear reversal. This arises from the fact that the mean reversal time of the precessional mode is longer than the critical cooling time, so precessional reversal is thus unlikely to occur. Cooling through the Curie temperature, however, has no such limitation since the magnetisation can reform in the correct direction due to the large susceptibility at T_c. A plot of the time dependence of the magnetisation for a single reversal is shown in Fig. 1. The data shows the rapid decrease in magnetisation when the laser is turned on, and the linear change in the z-component of M as the system is cooled through the Curie temperature.

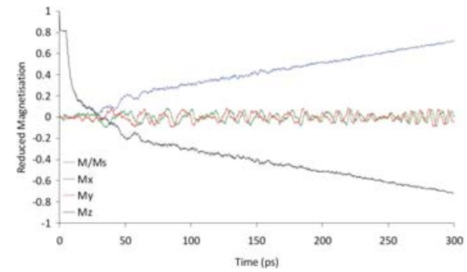

Plot of time dependence of the magnetisation of a single 10 nm FePt grain. The external applied field of 0.8 Tesla is in the negative z-direction. The data show a rapid decrease in the length of the magnetisation, as well as a linear change in the z-component.

AE-08

Modeling of thermally-activated switching of single phase, exchange-coupled and graded media.

O. Chubykalo-Fesenko[1], U. Atxitia[1], D. Suess[2]
1. POMT, Instituto de Ciencia de Materiales de Madrid, CSIC, Madrid, Spain; 2. Vienna University of Technology, Vienna, Austria

The superparamagnetic limitation of the current magnetic recording media has stimulated an extensive search for alternative ideas. Among those, the exchange-coupled composite (ECC) media has been suggested [1,2] as a possibility to decrease the necessary recording field without deterioration of the thermal stability. The graded media [3] has a further advantage in decreasing the nucleation field while maintaining the same energy barrier as the ECC one. Most of the extensive work on the media optimisation has been performed using the zero-temperature micromagnetic framework. In this case, the energy barrier is normally evaluated through the minimum energy path separated the two minima in the static many-body magnetisation landscape. The questions related to the change of energy landscape with temperature, related to thermodynamics such as the free energy and entropy are normally ignored, therefore, limiting the problem to relatively law temperatures.
In the present work, we use the Langevin dynamics approach, integrating the stochastic Landau-Lifshitz-Gilbert equation to simulate the switching properties of the single-phase, ECC and graded media. The atomistic approach with simple cubic lattice with a=0.33 nm, for simplicity has been used. To simulate the most favorable situation we assume an elongated grain with 24nm length and 1.5 x 1.5 nm base dimension. The hard media phase had an anisotropy constant Khard(T=0)= 3.6 10^7 erg/cc. The soft media phase was considered to have an anisotropy constant Ksoft(T=0) =Khard/6 and the graded media - the variation of the anisotropy constant following the quadratic dependence [4]. Fig. 1 presents results on the switching times of three ferromagnetic grains : single hard phase, ECC and graded media, as a function of the inverse temperature. The switching process of the graded media occurs clearly much faster than other alternatives. Assuming the Arrhenius-Neel law with static magnetisation landscape approach, this gives a reversal constant for the single grain 8 10^{-14} s, and much larger value for the graded media 4 10^{-12} s. The thermodynamic averaging of magnetic properties of different grain types also suggests that the energy barriers depend differently on temperature for different media.
Furthermore, we have also investigated the switching process for ECC grains with different exchange values. This introduces different dependences of magnetisation on temperature in both soft and hard grains. Different situations: high Tc soft/low Tc hard and lowTc hard /high Tc soft have been considered.

[1] D.Suess et al Appl. Phys. Lett. 87 (2005) 012504

[2] R.H.Victora and X-Shen, IEEE Trans Magn 41 (2005) 537.

[3] D.Suess, Appl. Phys. Lett. 89 (2006) 113105.

[4] Z.Lu, P.B.Vissher and W.H.Butler, IEEE Trans Magn 43 (2007) 2941.

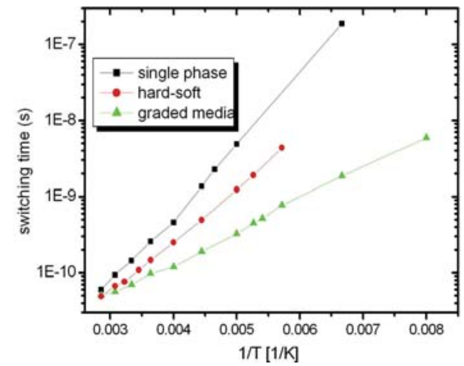

Fig.1 The switching time of single phase, ECC and graded grain as a function of the inverse temperature. The exchange parameters J=6.53 10^{-14} erg and the magnetisation value Ms(T=0) =600 emu/cc was considered to be the same in all cases.

AE-09

Application of plasmon resonances to all-optical magnetic recording.

I. Mayergoyz[1], Z. Zhang[1], P. McAvoy[1], C. Krafft[2]
1. ECE Department and UMIACS, University of Maryland, College Park, MD; 2. Laboratory for Physical Sciences, College Park, MD

It has been recently demonstrated [1] that magnetization reversals can be achieved in a reproducible way by using only circularly polarized laser pulses, that is without applying any external magnetic fields. The direction of magnetization reversals is controlled by the helicity of light. It is believed that these magnetization reversals occur due to the combination of the local laser heating of magnetic media close to the Curie temperature and the simultaneous action of circularly polarized light as a magnetic field with the direction parallel to the light wave vector. Furthermore, right- and left-handed circularly polarized waves act as magnetic fields of opposite directions. The performed experiments [1] have demonstrated femtosecond magnetization reversals of 100um spots on magnetic media.
The purpose of this paper is to theoretically and numerically demonstrate that plasmon resonances in metallic nanoparticles can be efficiently used for all-optical magnetization reversals of nanoscale spots of magnetic media. These magnetization reversals can be achieved by focusing of light at nanoscale and, at the same time, preserving its circular polarization. The above two conditions can be simultaneously achieved by exciting specific plasmon modes in metallic nanoparticles with uniaxial symmetry. Our analysis has been based on the treatment of plasmon resonances as an eigenvalue problem for specific boundary integral equations [2-5]. By using this mathematical machinery, we have been able to identify two identical and ninety degree-shifted in space plasmon modes for several promising nanoparticle designs. Such two plasmon modes have the same resonance frequency and can be simultaneously excited by the incident circularly polarized light resulting in dramatic nanoscale enhancement (focusing) of this light. The two particular designs that have been extensively studied are spherical and cylindrical silver nanoshells on dielectric substrates. Nanoshells are very attractive because, by controlling their thickness, plasmon resonances can be shifted into the 800 nm – 1000 nm wavelength region. In this region, the ratio of the real part to imaginary part of silver dielectric permittivity achieves its maximum values. This results in very strong local enhancement of the incident light intensity. It is worthwhile to note [2-5] that resonance frequencies and plasmon resonance fields depend on nanoparticle shape, but they are scale invariant with respect to particle dimensions, provided that these dimensions are appreciably smaller than the free-space wavelength. This scaling property can be utilized for scaling plasmon modes to various storage densities. The numerically identified plasmon modes for spherical and cylindrical shells with silicon cores are illustrated in Figures 1 and 2, respectively. In the paper, the detail exposition of the theoretical and numerical aspects of our analysis of circularly polarized plasmon modes will be presented. The coupling of these plasmon modes to incident laser radiation as well as their time-dynamics of excitation and dephasing will be discussed as well.

[1] C. D. Stanciu, F. Hansteen, A. V. Kimel, A. Kirilyuk, A. Tsukamoto, A. Itoh, and Th. Rasing, Physical Review Letters 99, 047601 (2007).

[2] D. R. Fredkin and I. D. Mayergoyz, Physical Review Letter 91, 253902 (2003).

[3] I. D. Mayergoyz, D. R. Fredkin and Z. Zhang, Physical Review B 72, 155412 (2005).

[4] I. D. Mayergoyz, Z. Zhang and G. Miano, Physical Review Letters 98, 147401 (2007).

[5] I. D. Mayergoyz and Z. Zhang, IEEE Transactions on Magnetics 43, pp.1689-1692 (2007).

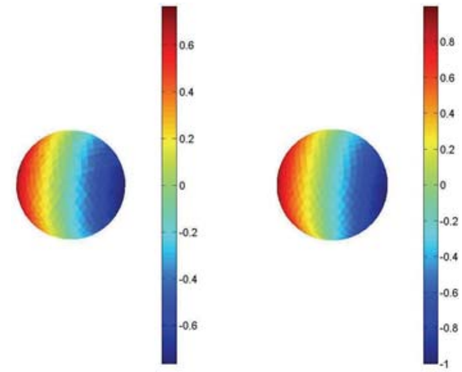

Figure 1: Plasmon mode of spherical silver nanoshell with silicon core on glass substrate. The left and right hand side spheres are the interior and exterior surfaces of the shell, respectively; the red and blue colors represent positive and negative surface charges, respectively; color bars indicate the normalized surface charge density. The resonance permittivity is –36.76 and the corresponding wavelength is 861 nm.

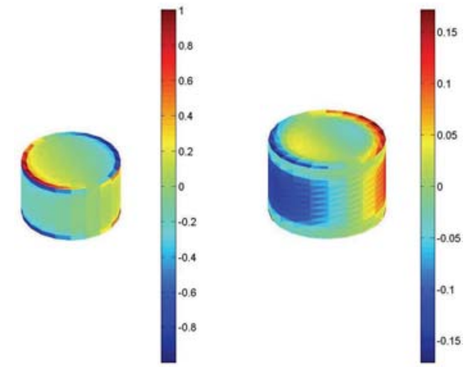

Figure 2: Plasmon modes of cylindrical silver nanoshell with silicon core on glass substrate. The left and right hand side cylinders are the interior and exterior surface of the shell, respectively; the red and blue colors represent positive and negative surface charges, respectively; color bars indicate the normalized surface charge density. The resonance permittivity is -48.94 and the corresponding wavelength is 985 nm.

AE-10

Narrow Track Confinement by AC Field Generation Layer in Microwave Assisted Magnetic Recording.

Y. Tang, J. Zhu
Electrical and Computer Engineering, Carnegie Mellon University, Pittsburgh, PA

In present perpendicular magnetic recording system, the track width is mainly decided by the width of main pole in the writer. Consequently, keep scaling down the writer dimension is necessary for achieving high track density. However, when the width of main pole is less than 60 nm, the strength of magnetic field beneath the pole tip is significantly degraded, which will cause writability issues in recording. Meanwhile, single domain is preferred in the ultra narrow pole when the current is turned off, which will induce sever remanent field erasure. Considering the two reasons above, it is a challenge to writer designs for track density beyond 400 TPI.
We have proposed microwave assisted magnetic recording (MAMR) based on the ferromagnetic resonance phenomena1. Based on present trailing shielded pole head, a perpendicular spin torque driven oscillator2 is inserted between the trailing shield and main pole, which will generate localized ac field at microwave frequency regime. Our simulation indicated, with the presence of a high frequency AC field, media can be switched by a write field well below the media coercivity. A major benefit in this novel recording scheme is high Ku magnetic material can be used as recording media. Hence, we can keep squeezing the grain size and increasing the recording areal density. On the hand, since both ac field and head field are needed for media switching, the recording track width depends on the overlap area of the ac field and head field. A narrow track can be obtained by only shrinking the dimension of ac field generation layer (FGL).
In our simulation, the recording fields from a trailing shielded pole head is calculated by FEM. The width of main pole is 120 nm and spacing between shield and pole is 50 nm. The maximum head field on the media is assumed 12 kOe. The thickness of ac FGL is 15 nm. The maximum ac field on the media is assumed 3 kOe. And the ac field frequency is 42 GHz in recording. The height and width of ac FGL are identical. The recording performances on a single hard magnetic layer are studied. The size of media grains is 5 nm and thickness is 10 nm. The crystalline anisotropy field of media is 10 kOe and 30 kOe for conventional recording and MAMR, respectively. In MAMR, the offset between the ac FGL and main pole is optimized to maximize on-track signals. Figure 1 shows the recording patterns at 1000 KFCI for the conventional perpendicular recording and MAMR. In the conventional recording, the curvature of transitions at the track edges is significant, which leads to large ATE and low track density. For MAMR with 100 nm width ac FGL, narrow and straight transitions are obtained due to the well confined overlap region of ac field and head field. And track width is obvious decreased by shrinking the FGL width from 100 nm to 50 nm. The quantitive magnetic write width (MWW) is calculated from the cross track profiles of on-track signals in frequency domain, which is shown in figure 2. For a 120 nm writer with 50 nm FGL, the track density reaches 451 TPI. Since the curvature of transitions is almost eliminated in MAMR, the SNR will also be improved due to the missed side signals in the read back process.

[1] J. Zhu, X. Zhu and Y. Tang, IEEE Trans. Magn., vol. 44, pp. 125, 2008.

[2] X. Zhu and J. Zhu, IEEE Trans. Magn., vol. 42, pp. 2670-2672, 2006

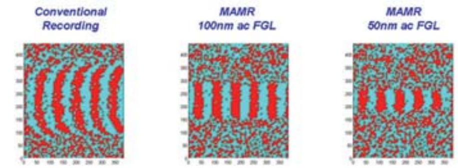

Figure 1. Recording at 1000 KFCI with a 120 nm wide writer in conventional recording and MAMR.

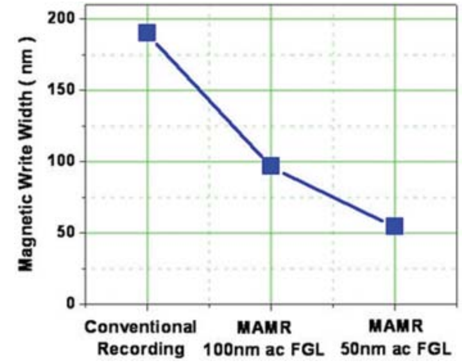

Figure 2. Comparisons of magnetic write width (MWW) in conventional recording and MAMR.

AE-11

LLG Simulation of Microwave Assisted Switching in Isolate Particle.

M. Igarashi[1], Y. Suzuki[1], H. Miyamoto[1], Y. Maruyama[2], H. Fukui[2], Y. Shiroishi[2]
1. Hitachi, Ltd., Kokubunji, Japan; 2. Hitachi Global Storage Technology, Odawara, Japan

As recording bit density of hard-disk drives (HDD) becomes higher, volume for a bit becomes smaller, requiring larger media anisotropy energy to keep thermal stability and exceeding the physical limit of conventional magnetic head writability. Microwave assisted recording with a microwave generator of spin torque has recently been proposed as one of the promising candidates of next generation recording technology [1].
However, our preliminary study revealed that required field for switching in a single domain particle with microwave [2] is not so small as the case reported. This suggests that a certain important factor in the recording media is missed at the single domain particle.
In this work, intra-grain exchange coupling effect was investigated to be the factor. A sub-grain is with the large exchange field when the direction of the sub-grain magnetization is different from the exchange coupled neighbors. If a certain sub-grain meets a resonance condition and its magnetization starts rotate on, a large high frequency exchange field will affect resonance of the adjacent sub-grains and finally entire magnetic particle. We have investigated the switching characteristic assisted by microwave for an isolated particle composed of sub-grains using the LLG (Landau Lifshitz Gilbert) simulation.
A hexagonal prism grain with a diameter D of 8.5 nm and a height t_{mag} of 12.0 nm was used to simulate an isolated single grain. The grain was divided into two sub-grains in the direction of the height (z-axis). In each sub-grain, the magnetization rotates coherently and interacts with the neighbor by the exchange coupling. The easy axis of each grain was in the direction of the height. The value of the uniaxial perpendicular anisotropy energy K_u was assumed to be 13.5 Merg/cc (H_k=30 kOe). The time evolutions of the magnetizations in the sub-grains were calculated by solving the LLG equation. The switching time was investigated up to 3ns with changing strength of the microwave, its frequency, and the external field.
Figure 1 shows the time dependences of the z-components of the sub-grains at AC-field of 5 kOe, AC-frequency of 50 GHz, and the external field of 6 kOe. Both sub-grain magnetizations show almost similar behavior with small vibration and do not switch up to 0.1ns. When the time exceeds 0.1ns, the difference of the both becomes remarkable and each sub-grain switched around 0.2ns. It should be noted that large exchange fields have effected to the other sub-grains from 0.1ns to 0.2ns.
Figure 2 shows the switching field at AC-field of 6 kOe as a function of the frequency for a magnetic particle separated into two parts (Twin) along with a single domain particle. The switching field is defined as a minimum field where the switching can be completed within 3ns after the fields application. The switching field decreases with increasing the AC-frequency below an optimum AC-frequency f_{opt}, above which the switching field increases with increasing the AC-frequency. The f_{opt} increases with increasing the angle between the external field and the magnetization easy axis θ_h. On the other hand, the switching field slightly depends on the AC-frequency and its value is almost equal to the Stoner-Wohlfarth field.
Thus a large effect of microwave assistance is achieved through exchange coupling between the sub-grains in an isolate particle.

[1] J. G. Zhu and X. Zhu, 'Microwave Assisted Magnetic Recording'TMRC2007 B6.

[2] W. Scholz, S. Batra, 'Micromagnetic Modeling of Ferromagnetic Resonance Assisted Switching', MMM2007 CC-10.

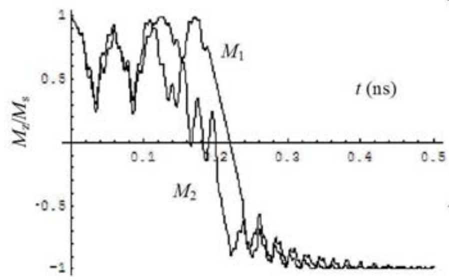

Fig. 1. Time dependences of sub-grain's magnetizations.

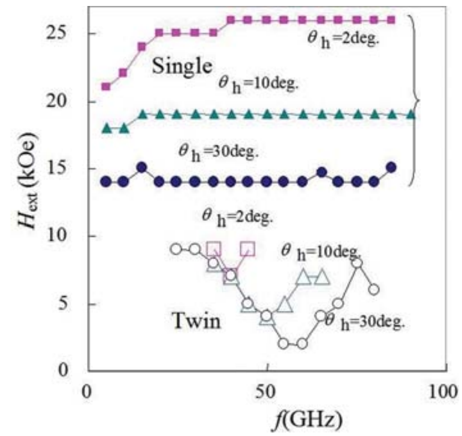

Fig. 2. Switching field as a function of frequency for a magnetic particle with two parts (Twin) and a single part (H_k =30 kOe).

AF-01

Hyperfine field distribution in the Heusler compound Co_2FeAl probed by ^{59}Co NMR.

S. Wurmehl[1], J. T. Kohlhepp[1], H. Swagten[1], B. Koopmans[1], C. Blum[2], B. Balke[2], G. H. Fecher[2], C. Felser[2]

1. Applied Physics, Eindhoven University of Technology, Eindhoven, Netherlands; 2. Institut für Anorganische und Analytische Chemie, Johannes Gutenberg-University, Mainz, Germany

The Heusler compound Co_2FeAl is reported to occur in various structures ranging from the completely ordered *L2₁* to the completely disordered *A2* structure type. The difference in *B2* and *A2* structured Co_2FeAl thin films was already reported by Inomata *et al.* [1] using the spin echo nuclear magnetic resonance (NMR). NMR provides a tool to obtain the local environment by measuring the resonance frequencies and consequently probing the local hyperfine magnetic fields, revealing next neighboring shells of the NMR active atoms. This method is thus suitable to study the local structure of Heusler compounds [2]. Inomata *et al.* [1] observed a line splitting due to Co atoms experiencing a random distributions of Fe and Al in thin films of Co_2FeAl.
In this work, NMR is used to probe the structure of Co_2FeAl bulk samples. It will be shown that NMR is a very suitable tool to uniquely study the local structure of magnetic materials by probing the direct local environments of the active atoms and resolving next neighboring shells. A study of bulk samples provides the unique possibility to verify the intrinsic generic structural properties of a certain material.
As shown in figure 1 (a,b), the ^{59}Co NMR spectrum of the bulk Co_2FeAl samples (as-melted) revealed a splitting into main and sub-lines. These main lines originate from the distribution of Fe and Al in the neighbouring shells of the ^{59}Co nuclei. Each main resonance line can be attributed to a certain distribution of Fe and Al in the first shell of the ^{59}Co nuclei in agreement with the results of Inomata *et al.* [1]. A complete intermixing of the Fe and Al atoms leads to a structure type different from $L2_1$, the *B2* structure. From a crystallographic point of view, a basic requirement of the *B2* structure is an entire random distribution of Fe and Al of the Wyckhoff 1*a* position. The random distribution of Fe and Al (*B2* type) is described by a binomial distribution, revealing the probability $P(n,x)$ for a particular environment of the form n Fe atoms + (8-n)Al atoms in the first shell of the Co central atom. A comparison between the fitted relative areas of the resonance lines (grey line in fig. 1) with the probabilities given by a random distribution of Fe and Al demonstrates that as-melted Co_2FeAl bulk samples mainly exhibit a *B2* type structure with contributions of a $L2_1$ type structure of about 10%. This $L2_1$ contributions were not apparent in the NMR spectrum of Co_2FeAl thin films [1].
The structure of the bulk samples can be changed by annealing (figure 1 (c,d)). The NMR spectrum of a bulk sample annealed at 1300 K consists of several main lines with an underlying sub-structure similar to the NMR spectrum of an as-melted sample. However, the main lines are less resolved after annealing and seem to merge. It was not possible to sufficiently fit the main lines of the spectrum of the annealed sample using only the Gaussian lines expected for a pure *B2* type ordering or a mixture of *B2* and $L2_1$. These observations point to a loss of the high degree of order as shown for the as-melted sample. A satisfactory fit was obtained by implementation of an additional broad resonance line. Interestingly, the additional very broad line exhibits the characteristic resonance frequency and width of a completely *A2* ordered Co_2FeAl sample as shown by Inomata *et al.* [1]. It seems that annealing at 1300 K leads to a mixture of *B2* and *A2* contributions. According to Balke *et al.*, annealing at 1300 K leads to Co_2FeAl samples with a mixture of *A2* and *B2* contributions [2], thus supporting our NMR results.
Summarising our results, additional contributions of structural phases as $L2_1$ and *A2* can be excluded to cause the sub-lines. However, a random distribution of Fe and Al may not only affect the composition of the first coordination shell of the ^{59}Co nuclei but may also affect the composition of higher shells. Thus, the sub-structure is related to different higher shell environments of the ^{59}Co nuclei. This sub-structure of the resonance lines was not resolved in ^{59}Co NMR spectrum of thin Co_2FeAl films [1], pointing to a more pronounced long range order in the bulk samples than in thin film samples.
This NMR study demonstrates the possibility to further improve the degree of order in Co_2FeAl, which may lead to high TMR ratios when implemented in magnetic tunnel junctions.

[1] K. Inomata, S. Okamura, A. Miyazaki, M. Kikuchi, N. Tezuka, M. Wojcik, E. Jedryka, J. Phys. D: Appl. Phys. 39 (2006) 816.

[2] S. Wurmehl, J. T. Kohlhepp, H. J. Swagten, M. Wojcik, B. Balke, C. G. F. Blum, V. Ksenofontov, G. H. Fecher, C. Felser, Appl. Phys. Lett. 91 (2007) 052506

[3] B. Balke, G. H. Fecher, C. Felser, Appl. Phys. Lett 90 (2007) 242503.

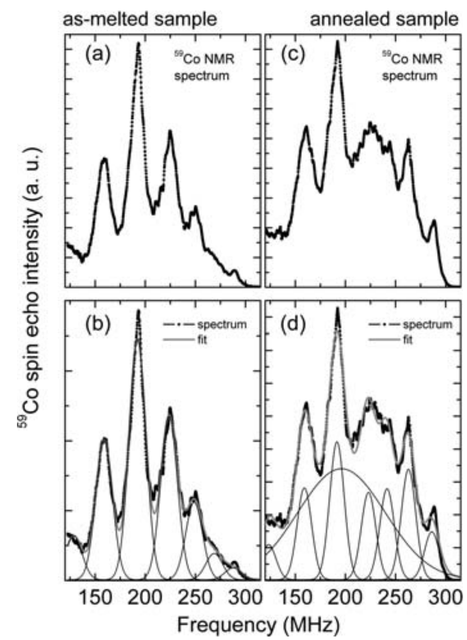

The ^{59}Co spin echo intensity in Co_2FeAl bulk samples (a,c) as a function of frequency in comparison with a fit (grey line) (b,d) for the as-melted (a,b) and annealed sample (c,d).

AF-02

Shedding light on magnetoelastic coupling and magnetostriction at an atomic level.

S. Pascarelli[1], M. Ruffoni[1], A. Trapananti[1], O. Mathon[1], Y. Joly[2], R. Pettifer[3], M. Pasquale[4], A. Magni[4], C. P. Sasso[4], F. Celegato[4], E. Olivetti[4]

1. European Synchrotron Radiation Facility, Grenoble, France; 2. Institut NEEL, CNRS/UJF, Grenoble, France; 3. Dept. of Physics, Univ. of Warwick, Coventry, United Kingdom; 4. INRIM, IENGF, Torino, Italy

The local character and chemical selectivity of X-ray Absorption Spectroscopy (XAS) has been used to address the complex problems of magnetoelastic coupling and magnetostriction at the atomic level. This has been made possible thanks to recent developments in the field of synchrotron radiation based methods, which have enabled the measurement of femtometer atomic displacements [1]. In principle any reproducible subtle distortion of the local structure induced by an external perturbation can now be investigated and quantified. Phenomena such as magnetostriction, electrostriction, piezoelectric or magnetic effects, elastic compliance or thermal expansion may be investigated from an atomic point of view, so that we can understand which atomic movements are responsible for the macroscopic effect that we observe.

Up to now, experimental input relied essentially on macroscopic quantities where the important atomic information is averaged out over different chemical bonds, defects, etc. Being able to be not only “local” but also “chemical selective” opens an enormous potential for the study of complex and disordered systems.

Here we will focus on ferromagnetic materials, and investigate magnetoelastic coupling and magnetostriction at the atomic level. Since the spin system in a ferromagnetic system is coupled to atomic displacements, due to the spin-orbit interaction, and since the static portion of this interaction results in a shift in the equilibrium atomic positions, we can now detect the effects of magnetization on the local structure [1]. Magnetoelastic coupling, i.e. the dependence of Magneto-Crystalline Anisotropy (MCA) energy on lattice strain, is the subject of intensive theoretical and experimental work nowadays because it governs the behaviour of technologically interesting ferromagnetic systems for high-density magneto-optical storage and magnetostrictive applications. The understanding of magnetostriction, and its theoretical description, still remains a great challenge because it is difficult to determine the dependence of MCA energy on lattice strain. In this respect, direct measurements of local strain values, as well as their evolution with pressure, can give a fundamental input to gain physical insight into this complex problem.

One of the first problems we addressed is the investigation of local atomic displacements induced by anisotropic magnetostriction in FeCo and how these are affected by a modification of the volume of the unit cell. Here magnetoelastic coupling is found to favor enhancement of atomic displacements with decreasing volume, contrary to expectations based only on the commonly accepted “stiffening” of bonds with compression [2]. State-of-the-art ab-initio electronic structure calculations of the evolution of magnetocrystalline anisotropy energy with tetragonal strain in FeCo are found capable of predicting correctly even such tiny effects, where the energies in play are of the order of the μeV. This kind of information, obtained through the combination of experiment and theory, is fundamental to be able to guide the search for materials with improved properties.

The second problem that we are now looking at is trying to apply these methods to elucidate the atomic origin of the giant magnetostriction observed in rare-earth transition metal compounds. It is well known for example that in rare-earth-Fe_2 (RE-Fe_2) compounds, the huge anisotropy of the 4f electron cloud, the high moment, and the high Curie temperature, lead to large magnetostriction. In these systems, when the orientation of the magnetic moment of the 4f shell is rotated with respect to the crystallographic axes by an external magnetic field, it is assumed that the anisotropic 4f charge density is rigidly co-rotated and displacements of RE atoms from their equilibrium position could occur. Internal distortions in $TbFe_2$ were predicted 40 years ago [3] but to date have not yet been detected. In the attempt to identify and eventually quantify RE atomic displacements in RE-Fe_2 compounds, we have initiated a XAS study on amorphous films of $TbFe_2$, $DyFe_2$ and $TbDyFe_2$ at the Fe K and RE L_3 absorption edges. To detect bond strain induced by magnetostriction the sample is magnetically saturated under a magnetic field applied on the plane of the film. We then measure changes in photoelectron scattering path length induced by local atomic distortions arising only from the rotation of the magnetic field, using XAS in a differential mode [4].

Preliminary results show that the large differential XAS signal observed at the RE L_3 edge can be qualitatively and quantitatively described using ab-initio fully relativistic multiple scattering theory, and can be directly associated to the polarization of the RE 4f and 5d orbitals due to the very strong spin-orbit interaction. This effect is therefore not directly related to the displacement of the RE, but only to a distortion of the charge density around the RE. These calculations also show that we may have the sensitivity to the displacement of the RE in the [111] direction, and a first estimate gives a value of ~ 0.013 Å, in agreement with ab – initio electron theory that predicted that the aspherical 4f charge density may produce large magnetostrictive strains [5].

[1] R.F. Pettifer et al., Nature 435, 78 (2005)

[2] S. Pascarelli et al., Phys. Rev. Lett. 99, 237204 (2007)

[3] E.R. Callen and H.B. Callen, Phys. Rev. 129, (1963)

[4] M. P. Ruffoni et al., AIP Conf. Proc. 882, 838 (2007)

[5] S. Buck and M. Fahnle, J. Magn. and Magn. Mat. 204 L1-L4 (1999)

AF-03

Detection of magnetic reversal at a DW pinning site in Ni80Fe20 nanowires using concurrent Magneto-Optical Kerr Effect (MOKE) and electrical measurements.

H. T. Zeng, D. Read, D. Petit, L. O'Brien, E. Lewis, A. Jausovec, R. Cowburn
Physics, Imperial College London, London, United Kingdom

The ability to measure both the magnetic and electrical transport properties of ferromagnetic nanostructures in-situ with the same instrument is highly desirable in current nanomagnetism research, enabling resistance changes to be easily correlated with an associated change in magnetization. This change in resistance can then be used to infer the presence of different magnetic configurations, such as the type of domain wall present in the nanowire (1). We have modified a commercial MOKE magnetometer to be able to position 16 electrical contacts with a pitch of 125µm (Fig. 1) for concurrent transport measurements of our samples.

Using this setup, we have measured the anisotropic magnetoresistance (AMR) due to transverse domain walls (TDWs) in 10nm thick, 180nm wide Ni80Fe20 nanowires. These were fabricated into an L shape using electron beam lithography and thermal deposition, with a symmetric double outward notch located along the horizontal arm acting as a pinning centre for the TDWs (Fig.2). The geometry of the L-wire allows an external field to create TDWs in the corner, and the magnetization of the horizontal arm can be reversed by propagating this wall along the length of the wire. With a double outward notch, a potential well for the TDW is introduced (2), so a field higher than the propagation field must be applied to move the TDW past the notch and to switch the rest of the wire. We call this the transmission field, and it has been measured by MOKE to be ±78 Oe for the sample presented here. This is appreciably lower than the saturating field required resetting the wire magnetization into the single domain state (±162 Oe). Four-terminal magnetoresistance measurements taken across the pinning site on the same sample enable us to detect the presence or absence of a TDW at the trap, since the magnetization of the DW core lies orthogonal to the current flow direction, and contributes to a lowering of the resistance. The field values corresponding to transitions in the AMR signal are shown to match the switching fields obtained from the MOKE measurements (Fig. 3).

We also found that the amplitude of the DW AMR signal decreases as the external field pushing the DW at the notch approaches the transmission field value. This is believed to be a consequence of thermally activated magnetization reversal (3), numerical simulations of the DW depinning process were carried out using the OOMMF code.

1) M. Hayashi et al. Phys. Rev. Lett. 97, 20 (2006)

2) D. Petit et al. Cond-Mat arXiv:0711.5026v2

3) A. Himeno et al. J. Magn. Magn. Mat. 286, 167 (2005)

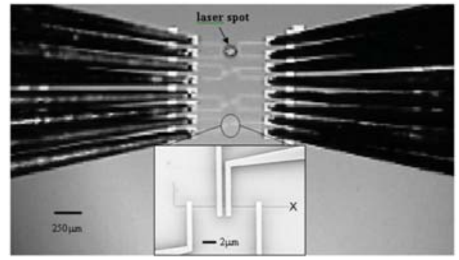

Fig. 1: CCD camera image of 16-way probes on Au contacts, with the MOKE laser spot focused on one of the nanostructures. Inset: SEM image of an L-wire with four terminal contacts. The laser spot is placed at X.

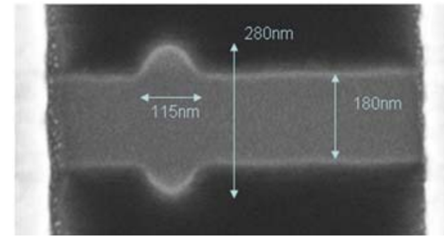

Fig. 2: SEM image of the double outward notch between two Au contacts, for an inter-contact spacing of 800nm.

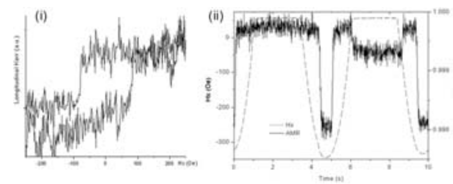

Fig. 3: (i) MOKE data showing switching at ±78 Oe through the notch, corresponding to transmission. (ii) Plot of AMR signal and x field component as a function of time for the L-wire. In the first half of the field cycle (field at 0.1Hz), the wire is reset and no DW is trapped at the notch. A field pulse at 5s creates a DW in the corner, and this is propagated into the notch at 6s, where it remains until 8.7s under a constant x field. The x field values at these transitions are 36 Oe and -77 Oe, indicating pinning and subsequent withdrawal of a TDW at the notch. The prominent dips in AMR are a result of pulses along the y-axis used to reset and inject the DWs, which gives rise to a global AMR effect.

AF-04

Material selective sensitivity of magneto-optical Kerr effect in NiFe/Au/Co/Au periodic multilayers.

K. Postava[1,2], M. Tekielak[1], P. Mazalski[1], A. Maziewski[1], A. Stupakiewicz[1], M. Urbaniak[3], B. Szymanski[3], F. Stobiecki[3]
1. Laboratory of Magnetism, University of Bialystok, Bialystok, Poland; 2. Department of Physics, Technical University of Ostrava, Ostrava - Poruba, Czech Republic; 3. Institute of Molecular Physics, Polish Academy of Sciences, Poznan, Poland

Magneto-optical (MO) effects have been recently extensively applied to study thin-film magnetic phenomena as magnetic anisotropy, magnetization reversal, interlayer coupling, and magnetization dynamics [1]. Main advantages of the MO effects are their high near-surface sensitivity, nondestructive character, and possibility to measure all components of the magnetization vector in the frame of the magneto-optic vector magnetometry [2]. Depth sensitivity of MO effects was systematically studied by Traeger [3] and Hubert [4] using modeling of the MO effect from a buried thin MO film in a non-magnetic surrounding. Separation of polar MO signal from films in different depth was presented by Ferre [5] and Hamrle [6] in the case of Co films separated by Au spacer. Depth sensitivity of longitudinal Kerr effect in Fe/Cr/Fe structure was demonstrated by Nyvlt [7].
In this paper, we propose to use a selective sensitivity of magneto-optical Kerr effect for separation of signals from different materials in a periodic multilayer. The method of material selectivity is demonstrated on the magnetostaticaly coupled periodic multilayers [Ni80Fe20(2 nm)/Au(2 nm)/Co(0.8 nm)/Au(2 nm)]10 prepared by sputter deposition on a silicon substrate [8].
A.Theoretical background
Magneto-optical selective sensitivity described in this paper is based on differences between magneto-optical and optical parameters of different MO materials, which results in different phases of MO complex response. Figure 1 shows modelled magneto-optic contributions from particular layers of the structure in the MO complex plane. The coordinates correspond to the polar MO Kerr rotation and ellipticity. Normal incidence and the light wavelength of 640 nm is used in the model based on Yeh's matrix formalism. Deeper layers contribute less to the overall signal due to the light absorption. This corresponds to points close to the origin. Total MO response of Co and NiFe can be obtain in reasonable approximation by summing contributions of all Co and NiFe layers, respectively. Different azimuths of Co and NiFe in the complex plane gives possibility for separation of their MO signals.
B.Experimental demonstration
Similarly as for depth sensitivity, different methods for MO signal separation can be proposed: (i) adjustment of wavelength of inspected optical beam, (ii) phase adjustment of magnet-optic ellipsometer using Babinet-Soleil compensator, and (iii) numerical linear combination of measured Kerr rotation and ellipticity. In this study, we demonstrate separation of Co and NiFe contribution by linear combination of measured Kerr rotation and Kerr ellipticity. In the separation we use a matrix relation between the vector consisting of Kerr rotation and ellipticity and the vector of magnetic signals from Co and NiFe. Matrix inversion enables to evaluate the weight coefficients for the linear combinations. We expect that the Co film has its polar component close to saturated value everywhere except for low magnetic fields. Figure 2 shows separated MO hysteresis loops of Co and NiFe. From the obtained hysteresis loops we deduce that magnetization of Co reverses from up to down direction via a domain structure changes. However, in the case of NiFe the perpendicular field forces the magnetic moments to rotate toward the field direction. Without field, due to magnetostatic coupling between Co and NiFe layers [8], the magnetization of NiFe is inclined by the angle of approximately 20 degree from the in-plane direction.

[1] Z. Q. Qiu and S. D. Bader, J. Magn. Magn. Mater. 200 (1999) 664-678.

[2] S. Visnovsky, R. Lopusnik, M. Bauer, J. Bok, J. Rassbender, and B. Hillebrands, Opt. Express 9 (2001) 121-135.

[3] G. Traeger, L. Wenzel, and A. Hubert, Phys. Stat. Sol. (a) 131 (1992) 201-227.

[4] A. Hubert and G. Traeger, J. Magn. Magn. Mater. 124 (1993) 185-202.

[5] J. Ferre, P. Meyer, M. Nyvlt, S. Visnovsky, and D. Renard, J. Magn. Magn. Mater. 165 (1997) 92-95

[6] J. Hamrle, J. Ferre, M. Nyvlt, S. Visnovsky, Prys. Rev. B 66 (2002) 224423.

[7] M. Nyvlt, M. Przybylski, J. Grabowski, and J. Kirschner, J. Appl. Phys. 98 (2005) 033516.

[8] M. Urbaniak, F. Stobiecki, and B. Szymanski, J. Appl. Phys. 101 (2007) 013905

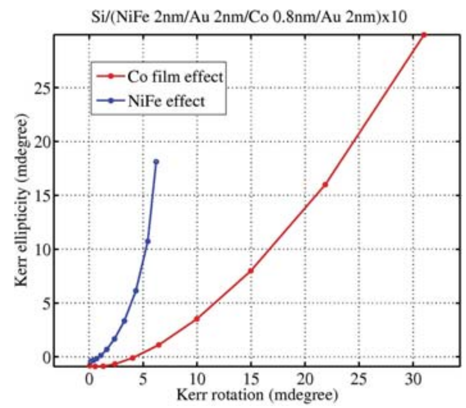

Magneto-optical contributions of particular Co and NiFe layers in the multilayer periodic system are shown in the complex MO plane. Points on the lines close to the origin correspond to layers from the top of the structure. Different directions of the Co and NiFe contributions gives possibility for material selective sensitivity.

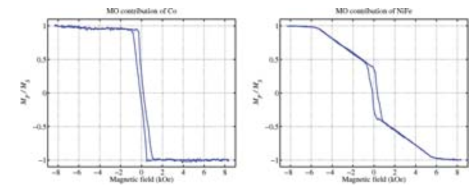

Magneto-optic contributions of Co and NiFe layers are shown.

AF-05

Magnetic images of a surface crack on a heated specimen with the use of an area type magnetic camera with high spatial resolution.

J. Lee[1], *J. Hwang*[2]
1. Department of Information and Communication Engineering, Chosun University, Gwangju, South Korea; 2. Department of Information and Communication Engineering, Graduate School of Chosun University, Gwangju, South Korea

When a metal or electric conductor is placed in an electromagnetic field, the distribution of the magnetic field becomes distorted around the object as a result of the direct current input, magnetizer, alternative current, eddy current, pulsed current, or residual magnetization. Cracks in the structure can be detected and evaluated by analyzing the distorted electromagnetic field. Hence, measuring and displaying the quantitative electromagnetic field in real time is an important methodology for a quantitative non-destructive evaluation (QNDE). The novel micro-array method of Hall sensors, as shown in Fig. 1, was proposed in previous research [1]. That array method enabled 2-dimensional magnetic field measurement with high spatial resolution with the use of the simplified connections. A wide range of magnetic fields could be measured quantitatively with high spatial resolution.

This paper proposes a non-destructive testing (NDT) method with the use of an area type magnetic camera and the above-mentioned micro-array method, in order to detect cracks on a specimen at high temperatures. Fig. 1 (b) shows the principle used to obtain the magnetic images of a surface crack on the heated specimen, with the use of an area type magnetic camera with high spatial resolution. Distilled water has a boiling point of 100 °C at atmospheric pressure. Therefore, the Hall sensor array, which is submerged in the distilled water, can be protected from an external high temperature of several hundred degrees centigrade until the container, which is filled with distilled water, is broken. If the Hall voltage of each Hall sensor changes with respect to the external magnetic field at the boiling point of the liquid, the crack can be detected in a high temperature environment with the use of the magnetic camera submerged in the liquid, as proposed in this paper.

The ferromagnetic specimens, which are 100×200×5 mm in size and each have slits as shown in Fig. 2, were used to verify the proposed NDT method with the use of the high spatial magnetic camera in a high temperature environment. Fig. 3 shows the magnetic images of each specimen at 170 °C. Magnetic intensity increases with respect to the width and depth of each crack. Also, the integrated values of maximum and minimum $\partial V_{RMS}/\partial x$ have a strong relationship to the width and depth of the crack, as shown in Fig. 4.

[1] J. Lee, J. Jun and J. Hwang, "Magnetic Sensor Array and Apparatus for Detecting Defect Using the Magnetic Sensor Array", Patent Cooperation Treaty, PCT/KR2007/003801., 2007.

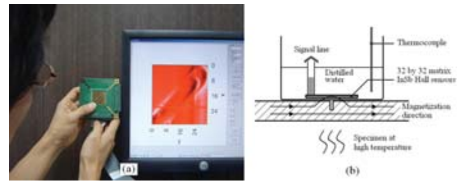

Fig. 1. (a) The visualization of the residual magnetic field around a clip by using 1,024 Hall sensors array with 0.78 mm spatial resolution, (b) principle of the high temperature magnetic camera.

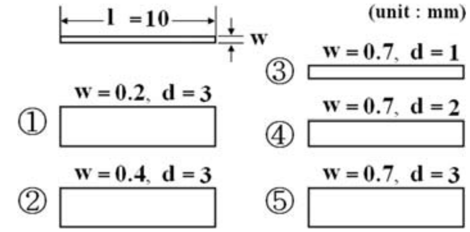

Fig . 2. Specimen.

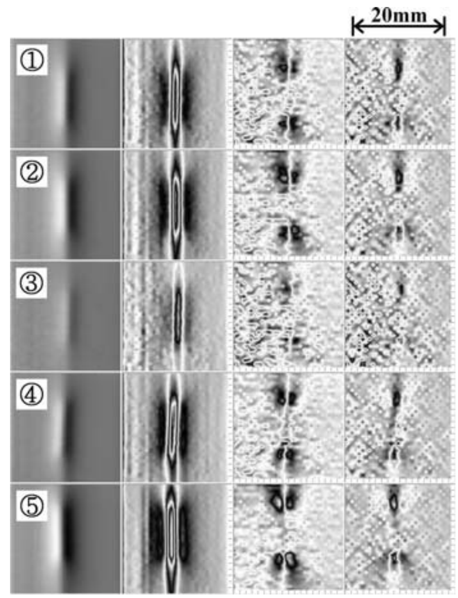

Fig. 3. Magnetic images on each crack and its processed images.

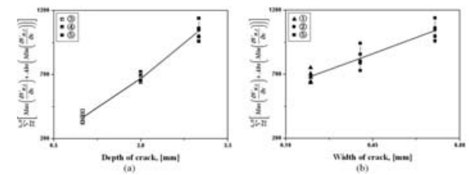

Fig. 4. The relationship between the integrated processed output and the width, depth of crack.

AF-06

Magnetostriction of Iron at Low Temperatures Observed with X-Ray Diffraction.

E. Arakawa, N. Aizawa
Physics Dept., Tokyo Gakugei University, Koganei,, Japan

Variations of iron magnetostrictive coefficient $\lambda^{\gamma,2}$ in the direction of easy-axis magnetization at low temperature region have been reported [1]. A minor maximum at 200 K was observed with a strain gauge extensometer [1]. No minor maximum was, however, found at that temperature region with the strain gauge extensometer and a capacitance dilatometry [1]. Theoretically, $\lambda^{\gamma,2}$ of ferromagnets should fall monotonically to zero with increasing temperature [2]. For measurements at the low temperature region, the coefficients obtained by the strain gauges were said to be less reliable because of magnetoresistance [3]. Correction of low-temperature contraction to values observed with a strain gauge was in the order of tens of micron. Recently, a technique with X-ray diffraction to observe magnetostriction was improved [4]-[6]. As it observed a *d*-space displacement of crystalline specimen, a correction of specimen position due to the low-temperature contraction was relatively easy. As it was a non-electric technique, a correction of the magnetoresistance for a probe was not concerned. Therefore, reliability of the X-ray technique was not changed principally even if at such low temperature region. The purpose of this study was to determine the values of iron $\lambda^{\gamma,2}$ with the X-ray diffraction technique at the low temperature region.

The experiment was performed on beamline BL15B1 of the Photon Factory at KEK, Japan. Photon energy of incident π-polarized X-rays to a specimen in a transverse configuration of magnetization was set to a resonant energy at Fe *K* absorption edge, 7.111 keV, 1.744 Å [4]. The specimen was a single crystal of iron, 99.94+%, Monocrystals Co. It was a disk of 6.0 mm diameter and 2.0 mm thick. Flat plane of the specimen was (110) and polished sub-micron. The [001] axis of the specimen was vertical, parallel to the magnetic field of an electromagnet and perpendicular to the scattering plane. In the transverse configuration, a quantitative magnetostriction of perpendicular component to the saturation magnetization could be determined and a saturation of magnetization could be confirmed during cyclic magnetization [4], [5]. We set the specimen cool down from room temperature to 100 K and warm up to 300 K with a cryostat. To determine $\lambda^{\gamma,2}$, we measured rocking curves of 220 diffraction intensity at zero magnetic fields and observed magnetic field dependence of the diffraction precisely.

Temperature dependence of $\lambda^{\gamma,2}$ observed was shown in Fig. 1. In the analysis, a magnetostrictive volume change was neglected [4]. The minor maximum at 200 K was not obvious in this experiment. All measurement time in this experiment was approximately four days, which included time to wait thermal equilibrium and time to adjust specimen position and angle. Reported experimental and theoretical results were also plotted in Fig. 1 [1], [3], [4], [7]. Curves of the magnetoelastic coupling coefficient $B^{\gamma,2}$ were converted from $-\lambda^{\gamma,2}c^{\gamma}$, where c^{γ} was an elastic constant, for cubic symmetry [1], and plotted in Fig. 2. In the conversion, c^{γ} was taken from Rayne and Dever [8], [9].

[1] Etienne du Trémolet de Lacheisserie, Magnetostriction: Theory and Applications of Magnetoelasticity, CRC Press, Boca Raton, 1993, chap. 1, pp. 24-29, chap. 2 pp. 89-94, chap. 3, pp. 131-142, and chap. 3, pp. 165-179.

[2] Earl R. Callen and Herbert B. Callen, *Phys. Rev.,* vol. 129, pp. 578-593, 1963.

[3] Herbert B. Callen and Earl R. Callen, *Phys. Rev.,* vol. 132, pp. 991-996, 1963.

[4] Etsuo Arakawa, Koh-ichi Maruyama, Koichi Mori, Hidetaka Nishigaitsu, and Noriyuki Aizawa, *IEEE Transactions on Magnetics,* vol. 41, pp. 3718-3720, 2005.

[5] Etsuo Arakawa, Koichi Mori, and Hidetaka Nishigaitsu, *IEEE Transactions on Magnetics,* vol. 42, pp. 81-83, 2006.

[6] Etsuo Arakawa, Noriyuki Aizawa, Yongjun Park, and Jae-Young Choi, *J. Phys. Chem. Sol,* vol. 68, pp 2138-2142, 2007.

[7] L. Dominguez and K. Kulakowski, *J. Magn. Magn. Mat.,* vol. 185, pp. 121-126, 1998.

[8] J. A. Rayne and Chandrasekhar, *Phys. Rev.,* vol. 122, pp. 1714-1716, 1961.

[9] D. J. Dever, *J. Appl. Phys.,* vol. 43, pp. 3293-3301, 1972.

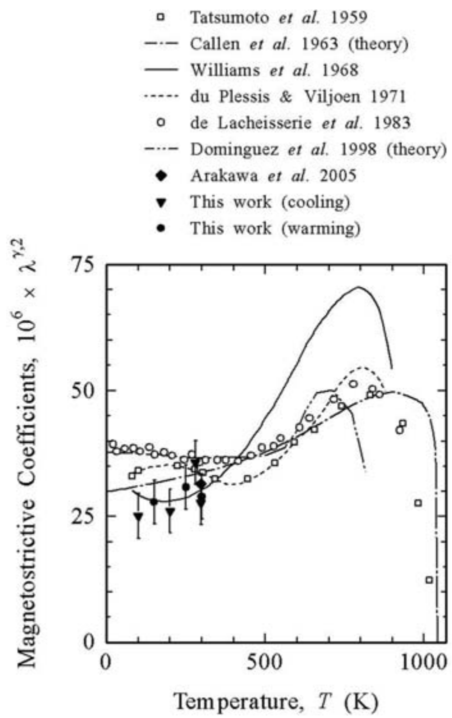

Fig. 1. Temperature dependence of $\lambda^{\gamma,2}$ in iron.

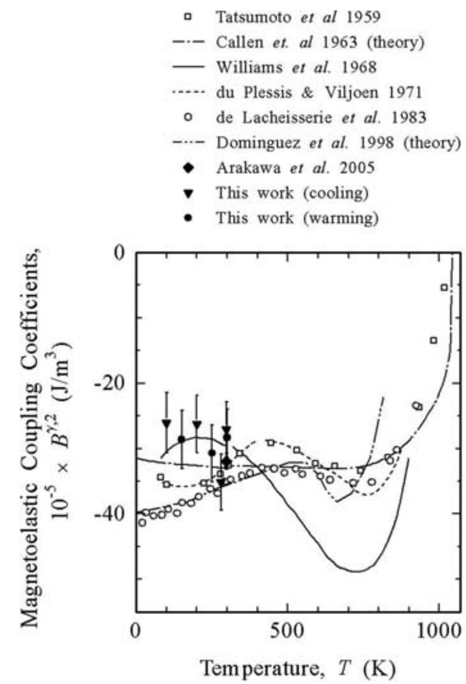

Fig. 2. Temperature dependence of $B^{\gamma,2}$ in iron.

AF-07

Enhancement of magneto-optical Kerr signal from the nano-structure by employing anti-reflection coated substrate.

C. You, D. Kim
Department of Physics, Inha University, Incheon, South Korea

Detection of the magnetic dynamics of the ferromagnetic nanowire and nanodot is an important research subject, because of its rich physics [1] and technical importance [2]. Magneto-optical Kerr effect (MOKE) is one of the promising technologies for detecting magnetic signal from a ferromagnetic body due to its sub-monolayer sensitivity and relatively simple experimental setup. With combining a pump probing technique, MOKE has an ultra-fast time resolving power [3]. However, the beam spot size is limited about sub-micron due to the diffraction limit of the light, it cause the limitation of the spatial resolution. Since the interesting nanowire/nanodot size is smaller than the beam spot, it causes unwanted degradation of the MOKE signal for the nanostructure. Cowburn <it>et al.~~<\>> [4] and Beach <it>et al.~~<\>> [5] overcame the poor signal qualities by taking numerous numbers of averages. Furthermore when we reduce the beam spot size too small, the nanostructure will be heated, and the uncertainty of the system temperature will prevent from correct interpretation of observed data.

In this study, we propose new measurement technique which can enhance the MOKE signal form the nanowire and nanodot. The main idea is illustrated in Fig. 1. The focused laser beam consists of two parts: one is on the nanostructure and the other is on the substrate. The MOKE signal is proportional to $\Delta R/(R_{sub} + R_{nano})$, where ΔR is the difference of the reflectivity for two magnetic states and the R_{sub} (R_{nano}) is reflectivity of substrate (nanostructure) part. While there is no contribution to the ΔR from the substrate, the contribution from R_{sub} is significant in sub-micron sized nanostructure due to the large area of substrate part when the beam size of order of micron. If we reduce the reflected light from the substrate, then the MOKE signal can be enhanced. This is the key part of this study. As shown in Fig. 1, we employ an anti-reflection coated substrate instead of usual substrate. The anti-reflection condition for the single wavelength and a constant incident angle is easily found with a dielectric multilayer stack.

The calculated results are shown in Fig. 2. The MOKE signals in Fig. 2 (a) are calculated [6] for 20-nm thick Fe nanowire with various wire width for the Gaussian beam of radius of 1500 nm. Without anti-reflection coating (R_{sub} = 30 %), the MOKE signal is significantly dropped with wire width. However, when anti-reflection coating layer exist (R_{sub} = 0.7 %), the MOKE signal is slightly reduced from its bulk value. Even for the 100-nm wide nanowire, the MOKE signal is 78 % of the bulk value. Fig. 2 (b) shows the MOKE signals for various beam sizes with a 100-nm wide Fe nanowire. When the beam diameter is comparable to the wire width, the MOKE signal is almost its bulk value. Without anti-reflection coating (R_{sub} = 30 %), the signal decreases rapidly as the bean radius increases. However, with anti-reflection coating, (R_{sub} = 0.7 %) the MOKE signal is maintains 78 % of its bulk value for 1500-nm beam radius.

We found that the MOKE signal from the nanostructure can be enhanced to 78 % of its bulk values for 1500-nm radius beam with anti-reflection coating layer. This proposed method can improve the signal to noise ratio and reduce the number of averaging in the nanostructures MOKE experiments.

[1] Luc Thomas, M. Hyayashi, X. Jiang, R. Moriya, C. Rettner, S. Parkin, Science 315, (2007) 1553.

[2] S. S. P. Parkin, US. Patent No. 6834005 (2004).

[3] J.-Y. Bigot, L. Guidoni, E. Beaurepaire, and P. N. Saeta, Phys. Rev. Lett. 93, (2004) 077401.

[4] D. A. Allwood, G. Xiong, M. D. Cooke, C. C. Faulkner, D. Atkinson, N. Vernier, and R. P. Cowburn, Science 296 (2002) 2003.

[5] G. S. D. Beach, C. Nistor, C. Knutson, M. Tsoi, and J. L. Erskine, Nat. Mat. 4 (2005). 741.

[6] C.-Y. You and S.-C. Shin, J. Appl. Phys. 84 (1998) 541.

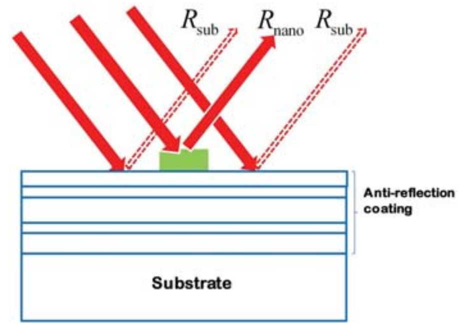

Fig. 1 Schematics of anti-reflection coated substrate MOKE measurement.

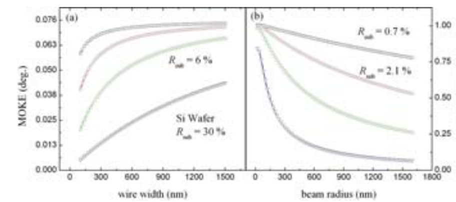

Fig. 2 MOKE signal and normalized by its bulk MOKE signal are plotted for (a) various wire width for a 1500-nm radius Gaussian beam, (b) various beam radius for a 100-nm wide Fe nanowire.

AF-08

Selective Magnetometry using a single x-ray absorption edge.

J. Chaboy[1], M. Laguna-Marco[1], C. Piquer[1], R. Boada[1], H. Maruyama[2], N. Kawamura[3]
1. ICMA, Zaragoza, Spain; 2. Graduate School of Science, Hiroshima University, Higashi-Hiroshima, Japan; 3. SPring-8/JASRI, Sayo, Japan

The possibility of disentangling the magnetic contribution of different atomic species within the same material has been a challenge from long time. Most of experimental techniques aimed to study the magnetic properties of materials are sensitive to the total magnetisation of the measured system and, consequently, they can not discern between the contributions of different atoms in the material.
Within this scenario X-ray Magnetic Circular Dichroism (XMCD), the difference in absorption of left- and right-circularly polarized x-rays by a magnetized sample, emerges as an outstanding tool to study magnetism by incorporating the element specificity of core level spectroscopies [1], combined with the application of magneto–optical sum rules [2,3] allowing quantitative magnetic measurements at the atomic level.
These capabilities are now incorporated as a standard tool to study the localised magnetism in many systems. However, the application of XMCD to the study of the conduction band magnetism is not so straightforward. Here, we show
that the atomic selectivity is not lost when XMCD probes the delocalised states. On the contrary, it provides a direct way of disentangling the magnetic contributions to the conduction band coming from the different elements in the material.
In this work we report on an XMCD study performed as a
function of the temperature at the rare-earth L_2-edge in the case of RT_2 (R = rare-earth, T = 3d transition metal) materials. According to previous works the analysis of the R L_2-edge XMCD spectra shows the presence of a magnetic contribution coming from the transition metal even when the rare-earth is probed. Indeed, the RT_2 compounds show a
different XMCD shape for different transition metal (Al, Fe and Co). This behaviour cannot be explained
in terms of the current knowledge of the rare-earth XMCD signals at the L-absorption edges. On the contrary, the fact that the magnetic properties of the R counterpart (Al, Fe and Co) are clearly different suggests that the origin of such a behavior stems from an *unexpected* contribution arising from the T sublattice [4-6]. To account for such anomalous behaviour we have considered that the XMCD at the L_2 absorption edges is not exclusively due to the rare-earth being probed itself, but there is also a contribution from the neighbouring magnetic transition-metal atoms. In this way, the XMCD signal can be decomposed as the addition of two contributions one exclusively due to the rare-earth, $XMCD_R$, and the second due to the transition metal, $XMCD_T$. Within an atomic picture the rare-earth contribution is mainly determined by the 4f electrons and, because they are close to the free-ion values, we can assume that $XMCD_R$ contribution to the XMCD spectrum corresponds to the whole XMCD spectrum of the RAl_2 compound, as Al atoms do not carry magnetic moment, and thus $XMCD_T$ should be zero. Under these assumptions it is possible to isolate the contribution of the transition metal to the R L_2-XMCD by subtracting from each recorded dichroic spectrum that RAl_2 with the same R. In this way, the same absorption edge yields the temperature dependence of the magnetisation of both sublattices $M_R(T)$ and $M_T(T)$. The total magnetisation built up from the values determined from the XMCD spectra shows a remarkable good agreement with the experimental values of the magnetisation measured in a commercial SQUID magnetometer at the same experimental conditions .

The reported results show the success into disentangling the magnetic contribution of different atomic species by using a single x-ray absorption edge. The addition of both individual sublattice magnetisations according to their ferrimagnetic coupling reproduces fair well the temperature dependence of the macroscopic magnetisation. Moreover, these results show that the atomic selectivity is not lost when XMCD probes the delocalised states. On the contrary, XMCD is a simultaneous fingerprint of the magnetic contributions to the conduction band coming from the different elements in the material. Taking advantage of this peculiarity we have proposed a direct method of disentangling these contributions. A consequence we have
demonstrated that it is possible to perform element-specific magnetometry by using a single x-ray absorption edge.

[1] T. Funk, A. Deb, S. J. George, H. Wang and S. P. Cramer, Coordination Chemistry Reviews 249}, 3 (2005).

[2] B. T. Thole, P. Carra, F. Sette and G. van der Laan, Phys. Rev. Lett. 68, 1943 (1992).

[3] P. Carra, B. T. Thole, M. Altarelli and X. Wang, Phys. Rev. Lett. 70, 694 (1993).

[4] M. A. Laguna-Marco, “A new insight into the interpretation of the T K-edge and R $L_{2,3}$-edges XMCD spectra in R-T intermetallics. (Prensas Universitarias de Zaragoza, Zaragoza, 2007).

[5] M. A. Laguna-Marco, J. Chaboy, C. Piquer, H. Maruyama, N. Ishimatsu, N. Kawamura, M. Takagaki, M. Suzuki, Phys. Rev. B 72, 052412 (2005).

[6] M. A. Laguna-Marco, J. Chaboy and H. Maruyama,

Phys. Rev. B 72, 094408 (2005).

AF-09

Open-circuit one-port network analyzer ferromagnetic resonance.

C. Bilzer, *T. Devolder*, P. Crozat, C. Chappert
Institut d'Electronique Fondamentale, ORSAY Cedex, France

Broadband spectrometers based on transmission coplanar waveguides have recently found much success for extracting the magnetic permeability and the ferromagnetic resonance (FMR). Here, we describe an simpler instrument based on a coplanar waveguide (CPW) terminated by an open-circuit. We demonstrate a scheme to transform reflexion parameters into permeability spectra, and compare our evaluation method to measurements performed using the standardized transmission geometry.

The Network Analyser (NA) FMR technique is usually implemented using a transmission geometry, where a thin film is flipped onto the CPW [1] whose reflexion/transmission properties are monitored. The scattering matrix of the so-loaded CPW are used to extract the permeability spectra and the field dependence thereof. NAFMR set-up free of electrical artefacts are not easy to fabricate, and the measurement method is prone to errors, due to some non-repeatability of the electrical contacts during the microwave calibration of the circuitry.

In the present paper, we demonstrate a simple modification of the set-up that avoids a large part of the time-consuming and error-prone calibration procedure. Our instrument is based on a CPW terminated by an open-circuit. This geometry ensure the formation of a standing wave with no RF field near the open-circuit side of the CPW, where the sample is placed. The permeability is thus measured closer to the linear excitation regime that in transmission geometry set-ups. We analyze our configuration, and establish a scheme to deduce permeability spectra. We finally compare our method to measurements performed using the standardized transmission geometry.

The core of our set-up is a CPW, on which we load a thin film. We start by measuring the reflexion parameters S11,refR of the loaded CPW with a saturating field along (y). In doing so, the RF excitation field is parallel to the magnetization, such that the magnetic susceptibility c vanishes, providing a reference measurement. We then rotate the field to align the magnetization parallel to the CPW, in order to get RF field perpendicular to magnetization, and thus to get a finite c. We record the new reflexion parameter S11R (Fig.1).

We write g0 and g the propagation constants (wave vectors) of the CPW when respectively unloaded and loaded. We write mr the relative effective permeability of the medium surrounding the CPW when loaded with the sample. We have mr = 1 + xc, where x<<1 is a filling factor and c is the sample's magnetic susceptibility.

Some algebra and simplifications are needed to derive the relationship between the magnetic permeability and the reflexion parameter. The reflexion parameter of a loaded CPW terminated by an open-circuit at port 2 is found to be approximately S11R=exp(-2gl), such that we can calcule X an estimator of the magnetic susceptibility using:

X=ln(S11R)/ln(S11Rref)-1

We have measured susceptibility spectra in both geometries: open-circuit CPW and conventional transmission CPW. The two Kittel plots obtained from the two techniques coincide almost perfectly. The relative error (Fig. 2C)is less that a percent, except at low FMR frequencies. Similarly, the linewidth determined from open-circuit measurement is very similar to the exact one.

In conclusion, we have introduced a new method to perform Network Analyser Ferromagnetic Resonance measurements. The method relies on the measurement of the microwave reflexion parameter of a coplanar waveguide terminated by an open-circuit, and loaded with a magnetic thin film. This method drastically simplifies the implementation of NAFMR, since it allows for a more compact set-up with only one probe. It requires a calibration procedure that is considerably faster than the one needed in the usual transmission 2-port geometry. By comparing with a standardized technique [1], we have shown that the open-circuit method provides reliable measurements of the ferromagnetic resonance frequencies and linewidth.

Figure 1: Complex reflexion coefficient S11R versus frequency from 50 MHz to 15 GHz for a CPW loaded with a CoFe 40nm film, submitted to a field of 40 mT along the CPW direction (black curve), or perpendicular to the CPW (red dotted curve). Inset: sketch of the set-up.

Figure 2: Comparison of the FMR resonance frequencies and linewidth obtained from the exact susceptibility determined from a 2-port analysis and the values obtained from the approximate magnetic susceptibility X.

[1] C. Bilzer, T. Devolder, P. Crozat, C. Chappert, S. Cardoso and P. P. Freitas, J. Appl. Phys. 101, 074505 (2007).

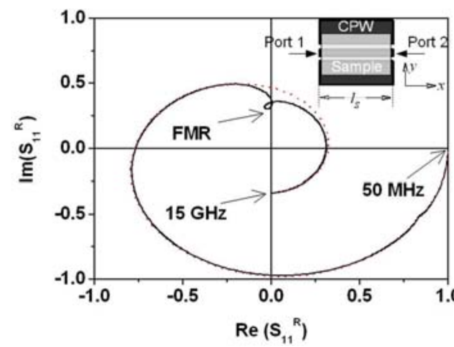

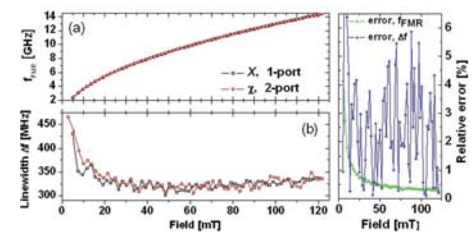

AF-10

Discrimination of metallic coins using the scan type magnetic camera.

J. Lee[1], *J. Jun*[2]
1. Department of Information and Communication Engineering, Chosun University, Gwangju, South Korea; 2. Department of Information and Communication Engineering, Graduate School of Chosun University, Gwangju, South Korea

Fig. 1 shows the diameters and weights of coins from different countries. Coins, which have similar sizes and weights, could be used for criminal purposes because of the large differences in economic values (the exchange rates). The coins consist of paramagnetic metals or magnetically combined metals, such as gold, silver, copper, bronze, brass, aluminum, zinc, tin, nickel, platinum, iron and rhodium. Thus, skilled workers have been necessary to discriminate the coins.
In this paper, an algorithm for discriminating the coins by using a scan type magnetic camera is proposed. The device uses the linearly integrated Hall sensors array (LIHaS) [1] and the complex induced current - magnetic flux leakage method (CIC-MFL) [2]. The 64 InSb Hall sensors are linearly integrated on the Ni-Zn ferrite wafer to a spatial resolution of 0.52mm, as shown in Fig. 2 (a). Current is induced in a coin by using a small yoke type magnetizer (hereafter referred to as simply a magnetizer), which is positioned on the LIHaS, as shown in Fig. 2 (b). The pole interval of the magnetizer is 12 mm. The 255 mA alternative current with 1 kHz is run through the 1,110 turns of coil on the magnetizer.
The distribution of the magnetic field intensity [3] around each coin was measured in the 1 mm of lift-off, and processed by $\partial V_{RMS}/\partial x$, as shown in Fig. 3. The peak-distances and the integrated maximum values of $\partial V_{RMS}/\partial x$ could be used to discriminate the coins, as shown in Fig.4. 44 cases, using 22 coins of 12 kinds from 10 countries, were examined to verify the proposed algorithm.

[1] J. Hwang, J. Lee, et., al. : Scan type magnetic camera images with a high spatial resolution for NDT obtained by using a LIHaS, Proc. of IEEE IST, (2007), 1-6

[2] J. Jun, J. Lee and D. Park : NDT of a nickel coated inconel specimen using by the CIC-MFL method and LIHaS, Journal of the KSNT, 27, (2007), 383-390

[3] J. Jun, J. Hwang, K. Kim, K. Ogawa and J. Lee : Development of signal processing circuit of a magnetic camera for the NDT of a paramagnetic material, Key Engineering Materials, 353-358, (2007), 2379-2382

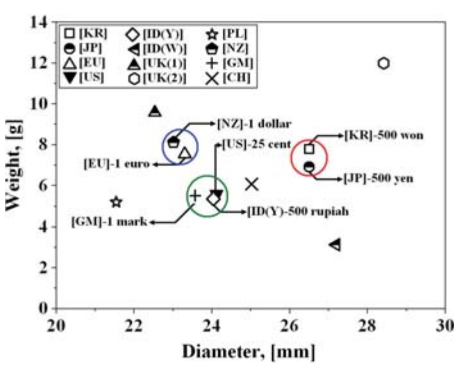

Fig. 1. Diameters and weights of metallic coins.

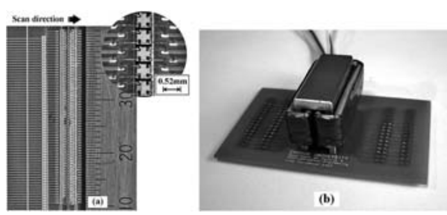

Fig. 2. Linearly integrated Hall sensor array ((a), LIHaS) and the yoke type magnetizer (b).

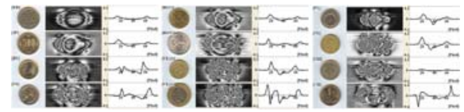

Fig. 3. Coins, $\partial V_{RMS}/\partial x$ images and section view.

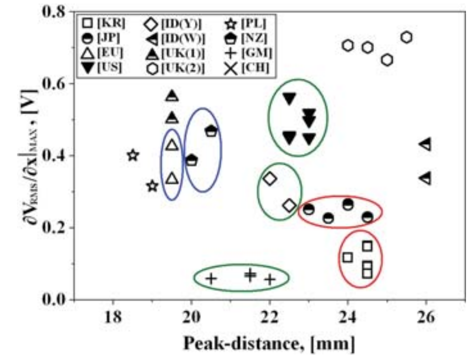

Fig. 4. Experimental results to discriminate coins.

AF-11

Apparent Image Effect in Closed-Circuit Magnetic Measurements.

A. K. Higgins[1], *C. H. Chen*[1], C. D. Graham[2], R. M. Strnat[3]
1. University of Dayton Magnetics Lab, Dayton, OH; 2. University of Pennsylvania, Philadelphia, PA; 3. Magnetic Instrumentation, Inc, Indianapolis, IN

Magnetic measurements made "open circuit," typically using a VSM with the sample in the gap of an electromagnet, are subject to error from the image effect, so called because in the ideal case a magnetic image of the sample appears in the electromagnet pole pieces. The usual result is an apparent drop in the measured magnetization as the pole pieces approach saturation.
Closed-circuit measurements are not considered subject to the image effect. However, when measuring permanent magnet samples clamped between the pole pieces of an electromagnet, we observe a phenomenon like the image effect, as shown in Fig. 1. The drop in apparent magnetization can appear in quite low fields and can be large, approaching 50%. The effect depends on the length-to-diameter ratio of the sample, and is minimal for L/D greater than about 1.8. A series of experiments leads us to believe it originates in a non-uniform saturation of the electromagnet pole tips.
Samples were cylinders about 1.2 cm in diameter, with a range of L/D values from 1.8 to 0.23. They were clamped between moveable electromagnet Fe-Co pole pieces as shown in Fig. 2. Flux density B is measured with a centrally-located coil, and the field intensity H just outside the sample is measured with a pair of concentric coils of slightly different diameters, connected in series opposition. The magnetization is given by $B–H=4\pi M$ gauss. With no sample present, B is linear with H and $4\pi M$ is zero over the range of magnet gaps.
We find that:
1. The effect occurs for both hard and soft magnetic materials, with Hc from about 10 to more than 20,000 Oe and $4\pi M_s$ from about 6000 to more than 20,000 gauss.
2. The drop in apparent magnetization occurs at lower fields for materials with higher magnetic saturation.
3. Both the B and the H signals are affected.
4. The presence of a sample lowers the measured maximum field at a given magnet air gap.
5. The magnitude of the effect decreases as the value of L/D increases, and is negligible for L/D greater than 1.8.
6. The effect appears only in the first and third quadrants of the hysteresis loop.
We believe that the pole tips of the electromagnet approach saturation first in the regions immediately adjacent to the ends of the sample, as suggested by Fig. 2, because the sample magnetization increases the local flux density in the pole pieces. This happens at lower applied fields when the sample magnetization is higher. The diameter of the pole tips is much larger than that of the sample, so the magnetization of the pole tips becomes non-uniform. As the magnet current increases, the additional magnetic flux is forced to leave and enter the pole pieces primarily in an annular ring surrounding the sample cylinder. Thus the flux density outside the sample increases more than inside the sample, and the measuring coils record lower values of both B and H than they would if the flux density remained uniform. As the distance between the pole faces increases, the natural tendency of the flux density to become uniform causes the non-uniformity at the mid-plane of the sample to decrease.
Since no part of the pole pieces approaches saturation in the second quadrant (where the sample magnetization lowers the flux density in the pole pieces), second-quadrant measurements are not affected and short samples can be used. To measure high-field magnetization accurately, it is necessary to use samples with L/D > 1.8; even then there will be some uncertainty in the field. In addition, the radial variation of flux at the ends of the sample will be different from that at the center. It is possible that the error might be diminished by reducing the area of the pole tips relative to the cross-sectional area of the sample, or by changes in the geometry of the measuring coils.

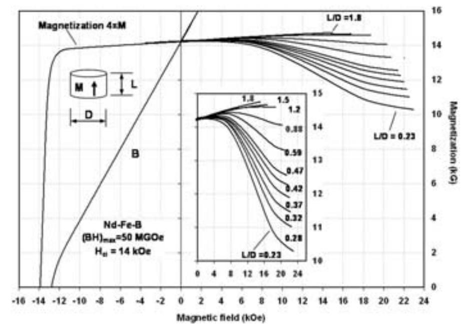

Fig.1. Magnetization distortions for testing in closed circuit: Nd-Fe-B magnet with different values of L/D

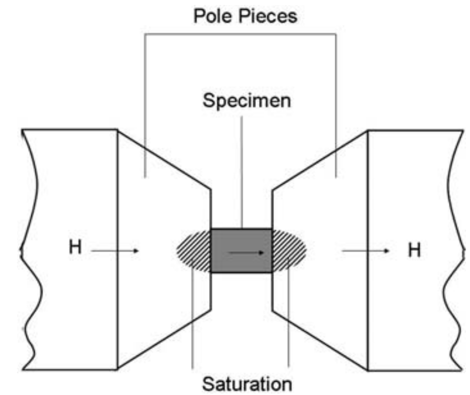

Fig.2. Sample/pole-piece configuration for closed-circuit magnetic measurement in a hysteresigraph

AF-12

A GMR Based System for Pulsed Eddy Current NDE of Aircraft Structures.

G. Yang, *L. Udpa*, S. Udpa
msu, East Lansing, MI

Abstract— Research in nondestructive evaluation of aircraft is constantly pushing the envelope in regard to the detection of increasingly smaller cracks that are embedded deep in layered aircraft structures. This paper, presents the design and development of a nondestructive inspection system that uses a pulse excitation signal to generate a field that is detected via GMR field sensors. Experimental signals are analyzed to detect the presence of cracks under fasteners.

Index Terms—Giant Magneto Resistive (GMR) sensors, eddy current, nondestructive evaluation

I. Introduction

A major challenge in the inspection of aging aircraft is the detection and characterization of cracks that occur around fastener holes in multi-layered wing structures. The large number of potential flaw sites has contributed to interest in the development of fast and reliable NDE techniques for detecting such cracks. Eddy current testing methods have served as the primary NDE modality in the aircraft industry for more than 50 years [1]. Though the technique is powerful in principle, the inspection process is often time consuming since the impedance plane signal returned by the probe is difficult to interpret and often requires special operator training. Furthermore, conventional eddy current systems are limited by the depth of penetration of fields or skin depth. This has led to the development of the pulsed eddy current testing method [2]. More recently, alternate sensors such as magneto-optic imaging (MOI) [3] sensors and giant magneto-resistive (GMR) [4] sensors have been used in conjunction with eddy current excitation to detect fields associated with the induced currents, particularly when the field levels are low and finer spatial resolution of flaws are desired.

This paper describes a system that combines the advantages of pulsed eddy current excitation with the enhanced bandwidth and sensitivity of Giant Magneto Resistive (GMR) based field sensors to maximize the probability of detecting small cracks under fasteners in airframe structures.

II. Field Measurement Approach

A schematic of the experimental system is shown in Figure 1. A current foil with a GMR sensor placed symmetrically is excited by a 50 Hz square wave. When the probe is at a defect free location, the field at the GMR sensor is largely tangential to the test object and the signal measured is close to zero. When the symmetry of the induced current is disturbed by rivets and cracks, a transient signal can be measured by the GMR sensor. The GMR signal contains information relating to discontinuities in the sample. As the rivet and subsurface defect are located in different layers of the sample, the temporal evolution of the measured signal is indicative of the state of the different layers of the specimen. Consequently, the rivet and subsurface defect can be efficiently detected and separated by analyzing the temporal evolution the GMR sensor signal.

III. Results

The test sample consists of two layers of aluminum with a rivet and a subsurface radial crack as shown in Figure 2. When the probe scans the surface of the sample, the transient time signal from the GMR sensor is sampled and stored for each sensor position.

The response from the GMR sensor is shown in Figure 3. The curve labeled 1 is the low amplitude signal due to a symmetric geometry, the curve labeled 2 is caused by the asymmetry due to the rivet alone, whereas the curve labeled 3 is due to the asymmetry caused by the rivet and crack under the fastener head.

IV. Conclusions

A new inspection system that uses pulsed eddy current excitation applied to a planar coil and employing a GMR sensor for measuring fields associated with induced currents has been proposed. Initial results obtained show the system is capable of detecting small cracks buried under the fastener head in a multilayer geometry.

1. K. Nguyen, D. J. Hagemaier, “ Automated Eddy Current Scanning of Aircraft for Corrosion Detection”, Material. Evaluation,

Vol. 52, no.1, pp.91-95, 1994.

2. A. Sophiana, G. Yun. Tian, D. Taylora, and J. Rudlin, “Design of a pulsed eddy current sensor for detection of defects in

aircraft lap-joints”, Sensors and Actuators A, Vol.101, pp.92–98, 2002.

3. G. L. Fitzpatrick, “Imaging Near Surface Flaws in Ferromagnetic Materials Using Magneto-Optic Detectors,” Review of

Progress in Quantitative Nondestructive Evaluation, Vol. 4A, pp.807-818, 1985.

4. N. Nair., V. Melapudi., J. Hector, X. Liu, Y. Deng, Z. Zeng, L. Udpa, J. M. Thomas, and S. Udpa, “A GMR-Based Eddy

Current System for NDE of Aircraft Structures”, IEEE Transactions on Magnetics, Vol. 42, no. 10, pp.3312-3314, 2006.

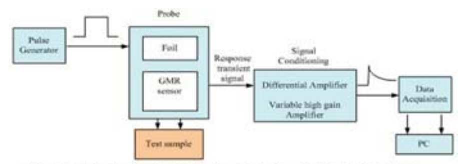

Figure 1. Schematic diagram of the Pulsed GMR system

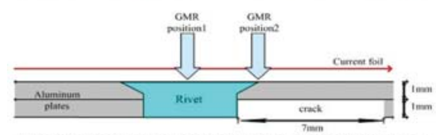

Figure 2. Cross-section of the multilayer sample geometry

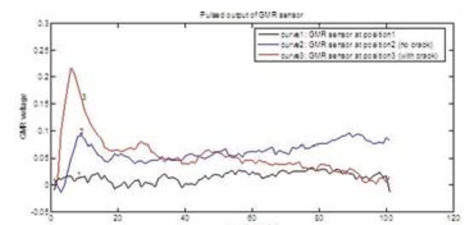

Figure 3. Pulsed response of GMR sensor detection at different positions

AG-01

Fabrication and analysis of high-performance integrated solenoid inductor with magnetic core.

D. Lee[1], K. Hwang[2], S. X. Wang[1]

1. Materials Science and Engineering, Stanford University, Stanford, CA; 2. Intel Corporation, Folsom, CA

Introduction:

Use of magnetic core with high permeability in the integrated inductor was proposed decades ago to significantly increase the inductance by the relative permeability of the magnetic material used [1]. However, the reported inductance enhancements over air core so far have been very limited. Here we present the high performance integrated inductors with a single layer of magnetic core, low coil resistance and small area consumption. The inductor devices show inductance enhancements as high as 34 times over the air core and large inductance densities, and their properties can be accurately described by the analytical models we used in the design process.

Experiments:

Based on the established analytical models for discrete inductors, the careful analyses of our previous experimental results [2], and the comparison with the results of finite element electromagnetic field simulation tools, we were able to put forward a set of analytical models to describe the device properties of integrated solenoid inductors. Design parameters were optimized using these models to achieve a high inductance while maintaining the lateral device area < 1 mm^2 and the coil resistance < 1 Ω.

The integrated inductors were fabricated on Si wafers. 5 μm thick copper was used as the conductor layer, and 2 μm thick CoTaZr alloy with the relative permeability of ~600 [3] was chosen as the magnetic core layer. Polyimide was used as the interlayer insulating material. Fig. 1 shows an integrated magnetic inductor having the number of coil turns N = 17.5 with the probe pads and ground ring.

The frequency-dependent device properties of the inductors were measured using a network analyzer.

Results and Discussion:

The inductance increased with the number of turns and reached a value of 70.2 nH at 10 MHz with N = 17.5 (Fig. 2(a)). This is an enhancement by a factor of 34 from 2.0 nH of the air core inductor with the identical geometry, which is higher than the recently reported record-high inductance enhancement by 19 [4]. The device area for N = 17.5 is 0.88 mm^2, corresponding to an inductance density of 80 nH/mm^2, with DC resistance of 0.67 Ω. This is significantly more than the reported 20~40 nH/mm^2 for coil resistances less than 1 Ω [5]. By shrinking the lateral dimensions while maintaining the vertical dimensions unchanged, the inductance density further increased to 219 nH/mm^2 without affecting the coil resistance significantly.

The measured inductance values and the calculations using the analytical models were compared in Fig. 2(a). The demagnetization effect in the finite-sized magnetic core was mainly considered in estimating the magnetic contribution to the inductance. The good agreements confirm that the analytic models can accurately describe the inductances of air core and magnetic inductors. The expected inductance enhancement was about 37× for N = 17.5, which is very close to the observed enhancement of 34×.

The use of magnetic core comes with the cost of introducing magnetic power losses at high frequencies. The resistance for the magnetic inductor increases significantly with the frequency, and this is greater for higher number of turns N. A higher N generates a larger inductance gain, and this in turn results in a higher magnetic core contribution to the resistance at high frequencies according to the fundamental trade-off described by the analytical models. Resistance and quality factor were calculated and compared with the measurement data for N = 17.5 as shown in Fig. 2(b). The excellent agreements between the calculation and measurement results confirm the validity of the proposed analytical models. The quality factor was above 6 at 20-30 MHz for N = 17.5.

In summary, we have designed and fabricated high performance magnetic inductor devices suitable for integration to a semiconductor chip. The device properties of the integrated magnetic inductors are well understood with improved analytical models and can be further optimized for various applications and frequency ranges of interest.

[1] R.F. Sohoo, IEEE Trans. Magn., v.15, p.1803, 1979.

[2] L. Li et al., IEEE Trans. Magn., v.43, p.3168, 2007.

[3] D.W. Lee and S.X. Wang, J. Appl. Phys., v.99, p.08F109, 2006.

[4] D.S. Gardner et al., IEEE Trans. Magn., v.43, p.2615, 2007.

[5] S.C.O. Mathuna et al., IEEE Trans. Power Electron., v.20, p.585, 2005.

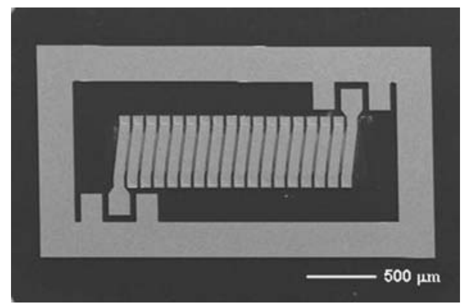

Fig. 1 SEM image of the fabricated magnetic inductor with N = 17.5

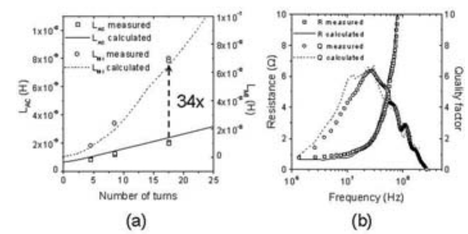

Fig. 2 Comparison of the measured and calculated data: (a) inductance values for the air core, L_{AC}, and magnetic inductors, L_{MI}, and (b) resistance and quality factor for the magnetic inductor with N = 17.5

AG-02

Thin Film Integrated Power Inductor on Si and Its Performance in a 8MHz Buck Converter.

N. Wang, T. O'Donnell, R. Meere, F. Rhen, S. Roy, C. O'Mathuna
Microsystems Centre, Tyndall National Institute, Cork, Ireland

It is an ever increasing demand to miniaturize the voltage regulators in the portable electronic devices. Although there has been considerable recent progress in the integration of the active parts of such converters, significant miniaturization of the overall converter is retarded by the need to miniaturize and integrate the passive components[1-11]. Recently, some DC/DC converters with inductors integrated into the converter package have been introduced[12-13]. The technology developed by authors is to seek a different approach by integrating inductors on to silicon using cost-effective and standard IC fabrication compatible techniques. This provides monolithic power-supply-on-chip (PSOC) solutions with an adequate performance for low power consumption applications in the portable electronic devices, such as PDAs, mobile phones[14].
The fabricated inductor consists of a single layer of race track shaped copper winding (7 turns) sandwiched between two layers of magnetic material (NiFe alloy) deposited by electroplating. Its inductance is approximately 0.45 uH. The frequency response test shows that the inductance can hold up to at least 20 MHz. The maximum Q factor is about 12 at 5 MHz, which is the highest reported Q factor of a micro-fabricated inductor realized using standard electrochemical deposition technique. The bias current characteristic test shows the inductance only drops by approximately 10% with a 500mA DC current, which implies that it is capable of handling at least 500mA current without saturation.
MIC2285YML is a commercially available buck converter with a fixed switching frequency of 8MHz from Micrel[15]. It requires a 0.5 uH external inductor. An inductor from Murata with an inductance of 0.47 uH was originally mounted on the test board. The micro-fabricaetd thin film inductor was used to replace the chip inductor. A picture of the converter evaluation board with micro-inductor wire bonded on top is shown in fig. 1. The measured efficiencies of the buck converter using the on silicon integrated thin film inductor with various load currents are shown in Figure 2. The efficiencies of the converter using the original chip inductor are also shown in the graph for comparison. The full specifications of the tested inductors and the break down of the losses in both tested inductors will be detailed in the full paper.
When using the thin film inductor, the converter efficiency is still over 80% for the load current between 0.1 A and 0.25A. The difference in converter maximum efficiency between using the commercially available thinnest chip inductor and Tyndall integrated inductor is approximately 3%. The work demonstrated the feasibility of implementing thin film integrated inductors in a DC/DC converter. Although the thin film inductor has a relatively larger footprint area (2 * 5.75 mm2) compared to that of the tested Murata chip inductor (2*1.25 mm2), the thickness of the effective part of the device is less than 0.15mm whereas the chip inductor is 0.55mm thick. This can be a great advantage when a very small thickness is required in particular applications. Moreover, the IC fabrication compatible process developed by authors enables to fabricate inductors onto the same substrate of the power management IC to realize a truly monolithic DC/DC converter without requirement of using external inductors.

[1]Y. Fukuda et. al., IEEE Trans on Magn, Vol. 39, July 2003, pp 2057.

[2]T. Sato et. al., Proc. of Int. Power Elec Conf., Tokyo, 2000, pp. 303.

[3]E. J. Brandon et. al., IEEE Trans on Magn, Vol. 39, 2003, pp 2049.

[4]C.H. Ahn et al., IEEE Trans. Ind. Electronics, 45 (1998) pp. 866.

[5] J. W. Park et. al, IEEE Trans on Magn, Vol. 39, No. 5, 2003, pp 3184.

[6]J. Y. Park et. al, IEEE Trans on Magn, vol. 35, no. 5, 1999, pp 4291.

[7]K. Kawabe, et. al, IEEE Trans. On Magn, Vol. 20, No. 5, 1984, pp.1804.

[8]O. Oshiro, et. al, IEEE Trans. On Magn,Vol. 23, No. 5, 1987, pp. 3759.

[9]N. Wang, et. al, Journal of MMM, 316, 2007, pp. e233.

[10]M. Yamaguchi, et. al, IEEE Trans. On Magn, 31(6), 1995, pp.4229.

[11]N. Wang et. al, J. Mag. and Magn. Mat., Vol 290-291, 2005, pp. 1347.

[12]EN5312Q product datasheet, Enpirion, http://www.enpirion.com/pdfdocuments/EN5312Q%20Rev%2011.pdf

[13] MIC3385 product datasheet, Micrel, http://www.micrel.com/_PDF/mic3385.pdf

[14]S.C. O'Mathuna, et. al, IEEE Trans on Power Electronics, vol. 20, no. 3, 2005, pp585.

[15]MIC2285YML product datasheet, Micrel, http://www.micrel.com/_PDF/mic2285.pdf

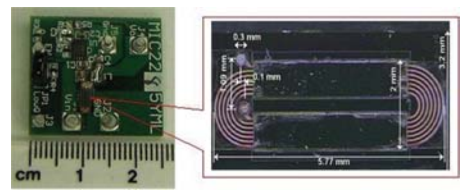

Tyndall micro-inductor mounted on an 8 MHz commercially available buck converter evaluation board

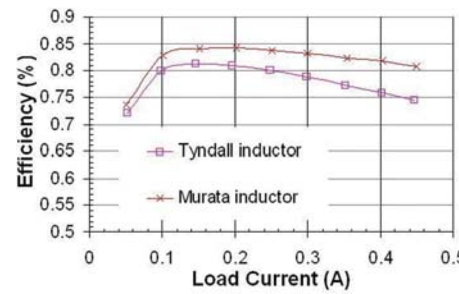

Measured buck converter efficiency operating at 8MHz using chip inductor and thin film integrated inductor with Vin=3.6 V, Vout=1.8V.

AG-03

CoNiFe applied in Microinductors for integrated dc-dc converters.

T. El mastouli, J. Laur, J. Sanchez, M. Brunet, D. Bourrier, M. Dilhan
ISGE, Laboratory for Analysis and Architectures of Systems (LAAS - CNRS), Toulouse Cedex 4, France

1. Introduction:
As it is necessary to reduce size and weight of electronic devices for portable micro-systems, manufacturing of magnetic components dedicated to power conversion becomes essential. This miniaturization requires developing new techniques and materials that increase the efficiency of micro-inductors associated in integrated DC-DC converters. This paper deals firstly with the optimisation of the electrodeposition of CoNiFe and with the integration on silicon of “spiral-type” inductor topology. Electroplating techniques are used to achieve the copper conductor and the CoNiFe laminated magnetic core and several investigations on the electroplating bath’s parameters have been realized in order to obtain the adequate magnetic properties. Finally, a 1µH micro-inductor prototype has been fabricated and characterized.
The proposed structure consists in a copper spiral sandwiched between two laminated magnetic layers. The laminated magnetic core would reduce the effects induced by the influence of eddy currents and skin effect due to the high frequency switching operation. As the energy density in micro-inductors is limited by the saturation flux density Bsat of magnetic core, Bsat has to be high. In our case, the material for the magnetic core selected is CoNiFe which presents a very high Bsat (>2T), low coercive field Hc (<8Oe) [1] and a thin film magnetic permeability µ of about 1000. This magnetic material has been selected to replace the NiFe (80%-20%) classically used for this kind of the integrated devices. The NiFe have a low Bsat = 1T [1]. The main feature of CoNiFe is the resisitivity of about 30µΩ.cm which is considerably better than the NiFe which has a resistivity about 20 µΩ.cm.
2. Optimization and characterization of electrodeposited CoNiFe:
Studies made on CoNiFe have shown that the best ratio of CoNiFe is about 60%-15%-25% [1], and to achieve this ratio several bath formulations have been investigated. We have chosed to work on the bath presented in [2], our work aimed to optimize an electroplating process enables the electrodeposition of thick Co60%Ni15%Fe25% with good adhesion to substrate and with optimal magnetic properties. To achieve our goal, several parameters have been investigated by changing temperature, pH, current density of plating process and concentrations of additives (saccharin and Sodium Lauryl sulphate or thiourea). The details of the optimisation process will be given in the final paper. The optimal deposit conditions selected are: Bath temperature of 40°C, current density of 3A/dm2 and pH of 1.5. These conditions were used for the realized inductor’s magnetic core. The composition of the magnetic layer determined by quantitative energy dispersive X-ray analysis. The measurement shows a CoNiFe layer of the following stoechiometry (60%-15%-25%).
The magnetic characteristics of CoNiFe electrodeposited layers extracted from the Hysterisis loop are: Bsat of 2.2T, Hc of 10Oe and relative permeability (µr) of 250. These characteristics are measured by SQUID and Vibrating Sample Magnetometer. The coercive field (Hc) can be reduced by applying a magnetic field during plating to induce a hard axis (and easy axis) in the direction of the magnetic flux in the structure. The resistivity is measured by the four point probes method. The measured resistivity value is 30 µΩ.cm.
3. Microfabrication and electrical characterization of microinductors prototype:
With development of the CoNiFe electrodeposition and using the process sequence of the micro-inductor fabrication, we have been successfully realized devices of the “spiral type” structure. Figure 1 represents the cross section of a “spiral type” prototype showing the copper spiral located between CoNiFe laminated magnetic core.
The measurements of the inductance and the series resistance of the realized prototype as a function of frequency were done using impedance analyzer (Agilent 4294A 0-110MHz). For frequency less than 1MHz, the fabricated prototype shows nearly constant inductance value and dc series resistance of about respectively 1µH and 1.2Ω. However, for the frequencies superior to 1MHz, on one hand, the inductance value slightly decreases with increasing frequency. On the other hand, the resistance increases due to losses that are mainly in the magnetic core, since the lamination is beneficial for frequencies up to 500 kHz. For greater frequency, eddy currents are generated in the magnetic core.
These micro-inductors are used in dc-dc converters. These measurements have been carried out at 2 and 3MHz. That confirmed the presence of previously mentioned resistive effect.

[1] E. I. Cooper, C. Bonhote, J; Heidmann, Y. Hsu, P. Kern, J. W. Lam, M. Ramasubramanian, N. Robertson, L. T. Romankiw, H. Xu, “Recent development in high-moment electroplated materials for recording heads”, IBM J. RES & DEV. VOL. 49 NO.1 January 2005.

[2] Peter T.Tang, “Pulse reversal plating of nickel and nickel alloys for microgalvanics,” Electrochimica Acta 47 (2001) 61-66.

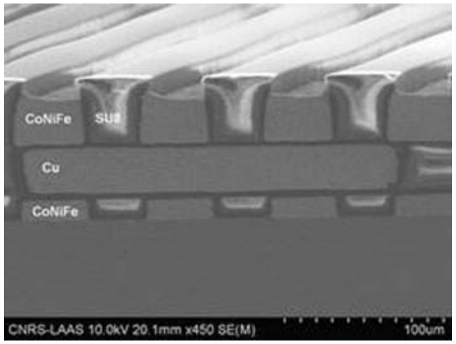

Fig.1. Cross section of a spiral-type prototype

AG-04

High Q and High Current NiZnCu ferrite inductor for On-chip power module.

S. Bae[1,2], Y. Hong[1,2], J. Lee[1,2], G. S. Abo[1,2], J. Jalli[1,2], A. Lyle[1,2], H. Han[1,2], G. W. Donohoe[3]
1. Department of Electrical and Computer Engineering, University of Alabama, Tuscaloosa, AL; 2. MINT Center, University of Alabama, Tuscaloosa, AL; 3. Department of Electrical and Computer Engineering, University of Idaho, Moscow, ID

Electric power consumption by CPU in desktop, laptop and smart phone are 70 ~ 100 W, 10 ~ 30 W and 1 ~ 2 W, respectively. At present, about 1 V is supplied to CPUs; therefore, current is increased up to 100 A in desktops. However, a high current acceptable on-chip dc-dc converter has not yet been developed.

In this paper, we present a ferrite planar inductor with Q over 50 for 10 ~ 100 MHz for a 1 ~ 2 W buck type dc-dc converter module with 0.25 V and 5 A output. HFSS simulations were performed on three different inductor structures to evaluate inductance. These structures are shown in Fig. 2(a); namely UA-SS, UA-DS, and UA-C. We have also compared performance of NiZnCu ferrite inductor (UA-C) to CoNbZr magnetic inductor (UA-C).

A spiral structure is used because of its high L/mm2 property. Copper coil with area of 5 mm x 5 mm was designed on 600 μm thick Si. Cu coil thicknesses are 50 μm and 15 μm at 10 MHz and 100 MHz, respectively. These thicknesses are greater than the skin depth at a given frequency. Accordingly, cross sectional coil area was designed over 25,000 μm2 to withstand joule heating by maximum 5 A rated current [2,3]. Therefore, coil width is fixed at 500 μm. We used two different magnetic materials for UA-C inductor, which are CoNbZr with μ (permeability) = 1000 up to fr = 0.7 GHz and NiZnCu ferrite with μ = 40 at 50 MHz and 20 at 100 MHz, for comparison of inductor performance. In principal, inductor needs inductance of 125 ~ 30 nH at 10 ~ 100 MHz [4]. Values of L, Q, R and C are calculated from simulated S parameters [5], which are generated by Ansoft HFSS simulation.

Figure 2(b) shows frequency dependence of inductance for three types of inductor. It is found that the highest inductance of 1.372 μH at 10 MHz was obtained from the type UA-C inductor. This inductance is 790% higher than air-core inductor. It is attributed to reduction of leakage magnetic flux due to closed magnetic edges. Therefore, we choose the UA-C structure to compare quality factor for two different magnetic materials; CoNbZr and NiZnCu ferrite.

From our simulation results, inductor performance is given in Table I. The NiZnCu ferrite film UA-C inductor has smaller parasitic C, large insulation property represented by R1 (resistance between copper coil and substrate) and R2 (resistance between coils), and a high Q value as compared to both air-core and CoNbZr UA-C inductors. Quality factor Q for NiZnCu UA-C and CoNbZr UA-C inductors are 97.5 and 1.3 at 100 MHz, respectively.

In addition, the effects of top ferrite film thickness and tan δ on the Q factor were investigated for UA-C inductor which has 2.5 turns and 3 μm thick bottom ferrite. The results are presented in Fig.3 The quality factor Q increases with increasing the top ferrite thickness and also with permeability. On the other hand, the quality factor Q decreases with increasing loss tan δ and is higher for smaller permeability.

In conclusion, the following design and material properties are required to achive Q of 50 of inductor at 10 MHz for 0.25 V and 5 A dc-dc converter module: inductor structure – UA-C, thickness of top NiCuZn ferrite > 100 μm, permeability of ferrite > 20, copper thickness > 2 x Skin depth, and loss tan δ < 0.02.

[1] [1] S.C.O. Matuna, et al., IEEE Trans. On Power Elec., Vol.20, No.3, p585, May 2005

[2] I. Kowase, et al., IEEE Trans. On Mag., Vol. 41, pp. 3991-3993, Oct. 2005

[3] S. Prabhakaran, et al., 35th IEEE Power Electronics Specialists Conf., Vol. 6, pp. 4467-4472, 2004

[4] P-L. Wong, et al., IEEE Trans. On Power Elec., Vol. 17, pp. 485-492, Jul. 2002

[5] T. Kuribara, et al.,IEEE Trans. On Mag., Vol. 38, pp. 3159-3161, Sep. 2002.

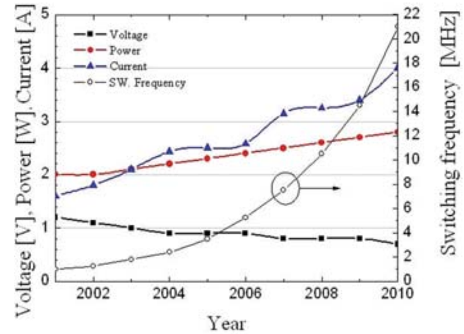

Fig. 1. Trand in voltage, current, power, and switching frequency for single dc-dc converter [1]

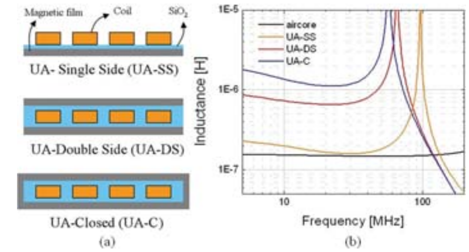

Fig. 2. (a) Inductor structures and (b) Frequency dependencies of inductance with various inductor structures

		Air-core inductor	CoNbZr inductor	NiCuZn ferrite inductor	Comparison
Structure		Spiral 1.5 T	Spiral 1.5 T	Spiral 1.5 T	-
Coil area [mm2]		10 ×10	10 × 10	10 × 10	-
Thickness [μm]	mag. film	N/A	5 (μ = 1000)	5 (μ = 20)	-
	insulator	N/A	5	N/A	-
Inductance [nH]		32	37	35	- 5.4 %
Q		62.5	1.28	97.5	+ 7517 %
C21 [pF]		0.8308	1.6408	1.1002	- 32.9 %
C22 [pF]		0.9588	1.6087	1.1785	- 26.7 %
R1 [Ω]		119066	84835	475757	+ 461 %
R2 [Ω]		28653	111233	279093	+ 151 %

Table 1. Comparisons of electrical and physical properties at 100 MHz between magnetic metal alloy inductor and ferrite inductor.

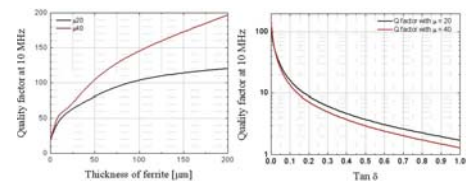

Fig. 3. The effects of ferrite thickness and loss tan δ on Q factor of inductor.

AG-05

Synthesis of Bi-Zn-Al-B-Si-O nano-glass by sol-gel method for multilayer chip inductors.

S. An, S. Wi
EMC R&D Group, Samsung Electro-Mechanics, Gyunggi-Do, South Korea

Introduction

Recently, with the rapid development of mobile communication and miniaturization of electronic devices, low-cost are greatly demanded. NiZnCu ferrites are extensively used in the fabrication of multilayer chip inductors (MLCI) because of their relatively low sintering temperatures, high permeability in the high frequency region, high electrical resistivity, mechanical hardness, and chemical stability [1-2]. To fabricate MLCIs, ferrite layers and internal conductors are alternately laminated and then co-fired to form the monolithic structure. In MLCIs, Ag (melting point=961 ^{o}C) is used as the internal electrode material due to its low resisivity and lower cost. For successful fabrication of MLCI, the sintering temperature of NiZnCu ferrite should be reduced to 900 ^{o}C to realize the co-firing of the ferrite and Ag electrode materials. For this purpose, suitable amount of low melting-point sintering aids such as Bi_2O_3, MoO_3, V_2O_5 and glass are usually introduced into NiZnCu ferrites [3]. In this work, Bi-Zn-Al-B-Si-O nano-glass was used as a sintering aid for the densification of the NiZnCu ferrites and the initial permeability, quality factor, density and saturation magnetization were also measured.

Experiments

$Bi(NO_3)_35H_2O$, $Al(NO_3)_39H_2O$, $Zn(NO_3)_26H_2O$, $C_3H_9BO_3$ and $Si(OC_2H_5)_4$ were dissolved in 2-methoxyethanol and acetic acid. The solution was refluxed at 60 ^{o}C for 24 h and dried at 120 ^{o}C for 48 h in oven. The obtained powder was annealed at 300 ^{o}C for 2 h in air and finely nano-glass powdered. NiZnCu ferrites powders were mixed with an appropriate amount of 0.1-2.0 wt% Bi-Zn-Al-B-Si-O nano-glass powders. The granulated powder with an amount of 0.5 wt% polyvinyl alcohol as a binder was pressed at a pressure of 2000 kgcm^{-1} to form green toroidal specimens. The specimens were kept at 600 ^{o}C for 1 h in order to decompose and vaporize the organic components and then sintered at 840-900 ^{o}C for 2 h in air. Initial permeability and quality factor of sintered toroidal specimens were measured using a HP4286 impedance analyzer. The saturation magnetization and coercivities of the powders were measured with a vibrating sample magnetometer at a maximum applied field of 5 kOe at room temperature.

Results and discussion

Bi-Zn-Al-B-Si-O nano-glass was prepared by sol-gel method. The x-ray diffraction patterns of the compounds showed a non-crystalline phase in the nano-glass materials. Figure 1 shows the SEM images of nano-glass annealed at 300 ^{o}C. According to SEM images, the particle size was estimated to 60.3 nm with narrow size distribution. Using sol-gel method, nano-sized glass materials can be obtained, which have larger surface area and larger surface free energy than micron-sized glass materials prepared by the conventional melt-quenching method. As shown in Fig. 2, permeability increases with the increase in the nano-glass content in NiZnCu ferrite. The increase in initial permeability with nano-glass content may be primarily attributed to the increase in bulk density. It is known that ferrites with higher density and larger average grain size possess a higher initial permeability [4]. The initial permeability of 0.1 wt% nano-glass added sample was about 62.6. It should a sharp increase from 0.4 wt% to 0.5 wt% nano-glass addition, and then reached the maximum value (211.2) at 1.0 wt% addition level. Beyond 1.0 wt% addition level the initial permeability decrease again with further increase in the nano-glass content. The quality factor and saturation magnetization of 0.5 wt% nano-glass added sample for NiZnCu ferrites sintered at 880 ^{o}C was about 143 and 386 emu/cc, respectively. As a result, Bi-Zn-Al-B-Si-O nano-glass systems were found to be useful as sintering aids for MLCIs.

[1] J. Murbe and J. Topfer, J. Electroceramics, 15, 215 (2005).

[2] H. Su, H. Zhang, X. Tang, L. Jia, and Q. Wen, Mater. Sci. Eng. B, 129, 172 (2006).

[3] H. Su, H. Zhang, and X. Tang, Mater. Sci. Eng. B, 117, 231 (2005).

[4] E. C. Snelling, Soft Ferrites, 2nd ed, Butterworths, London, (1998)

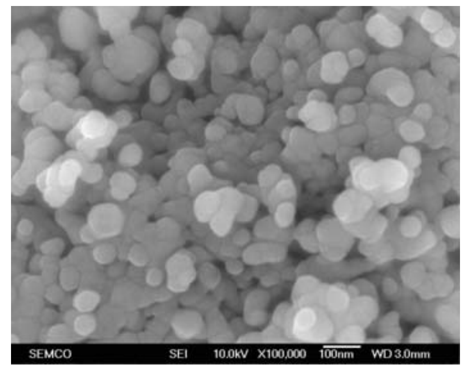

Fig. 1. Scanning electron micrograph of the microstructure of a representative Bi-Zn-Al-B-Si-O nano-glass annealed at 300 ^{o}C, for 2 h in air.

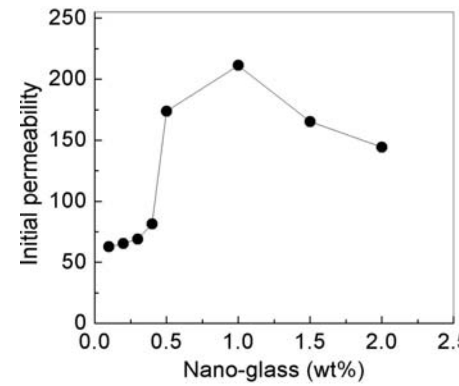

Fig. 2. Initial permeability (at 1 MHz) as a function of the concentration of a sintering additive for NiZnCu ferrites sintered at 880 ^{o}C.

AG-06

Electrically Tunable Thin Film Magnetic Core using Synthetic Antiferromagnet Structure.

N. An, A. Jander, P. Dhagat
Electrical Engineering&Computer Science, Oregon State University, Corvallis, OR

We demonstrate an electrically tunable thin film magnetic core using a synthetic antiferromagnet (SAF) structure. It consists of two ferromagnetic layers antiferromagnetically coupled together through an exchange coupling layer. Variation of susceptibility is achieved by leading a current through the SAF structure. The experimental data show that with 2mA internal current, a tuning range (relative change in susceptibility) of 10% can be achieved at 800Hz. Substantial further improvements in tuning range is expected by optimizing the structural designs and exchange coupling strength.

Fig. 1 shows the SAF test structure. It contains three parts: Part (1) and (3) are two Al strips, they serve as electrical contacts for the internal current; Part (2) are 600 parallel SAF lines, each of which is comprised of two 12-nm-thick NiFe layers coupled through a 0.7-nm-thick Ru layer (Fig. 2). This structure, covering an area of approximately 1cm2, provides enough magnetic material for "bulk" susceptibility measurements. The width and the spacing of the SAF lines are 10 µm and 5 µm respectively.

Fig.3 illustrates the experiment setup. The Helmholtz coils are used to produce a uniform ac field. About 6 Oe, 800 Hz magnetic field is applied parallel to the SAF lines. The current source is used to apply current pulses to the SAF test structure. The purpose of using current pulse instead of dc current is to eliminate thermal effects. The signal induced in the pick-up coils by the SAF test structure is detected using a lock-in amplifier. The change in induced voltage as a function of current pulse amplitude is measured with the oscilloscope.

Fig. 4 shows the susceptibility change as a function of internal current. $\Delta\chi/\chi$ represents the relative change in susceptibility, which is proportional to the induced voltage. As predicted in our previous analysis (1), the susceptibility increases with current. This is because the magnetic field generated by the internal current rotates the magnetizations of the two NiFe layers, which results in a net magnetization change along the applied field.

In conclusion, the susceptibility of thin film magnetic core can be adjusted by an internal current. The experiment results are consistent with the model developed in our previous work. By incorporating the SAF structures into the cores, electrically tunable, on-chip inductors can be realized.

(1) An, N. and Jander, A., Electrically Tunable Susceptibility of Synthetic Antiferromagnet Lines, IEEE Transactions on Magnetics, VOL.42, NO.10, 3383 (2006).

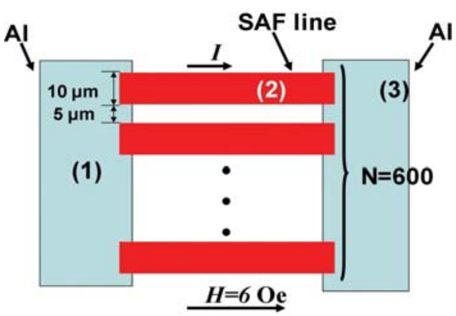

Fig.1. Top view of the SAF test structure

Fig.2. Cross sectional view of the SAF line

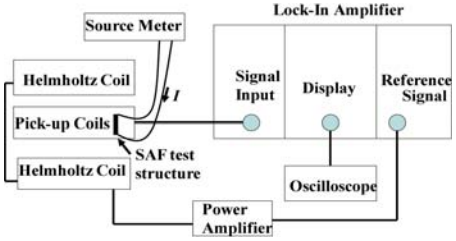

Fig.3. Experiment setup

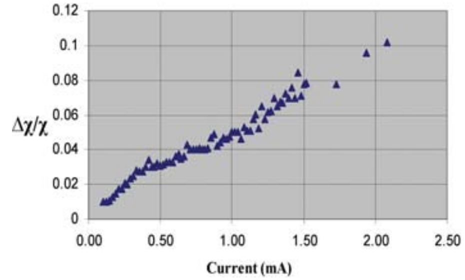

Fig.4. Magnetic susceptibility change versus internal current

AG-07

The effect of magnetic coating layer thickness on the performance of tunable magnetic inductors.

N. Ning[1], *X. Li*[1], H. Seet[1], W. Ng[1], Y. Xu[2]
1. Mechanical Engineering, National University of Singapore, Singapore, Singapore; 2. Electrical and Computer Engineering, National University of Singapore, Singapore, Singapore

A tunable magnetic inductor has been reported recently [1]. The tuning effect of such tunable magnetic inductor is achieved by modulating the permeability of the soft magnetic layer in a magnetic inductor body of either sandwiched thin film structure or composite wire structure, via applying a bias magnetic field generated by the insulated coil wound on the magnetic inductor body. In a further understanding of the performance of the tunable magnetic inductor of composite wire structure, the tunability of inductance in relation to one of the key parameters in such tunable inductor - the magnetic coating layer thickness, is presented in this paper.
Samples of the magnetic inductor body of composite wire structure were produced by electroplating a layer of $Ni_{80}Fe_{20}$ with varying thickness t_m of 2.3 - 6.2 µm, onto a Cu wire of 20 µm in diameter and 2 cm in length. The resultant inductance L, resistance R, and quality factor Q of the inductor samples, under the application of a DC bias magnetic field H_{ex} varying from 0 to 43 Oe along the length of the wires, were measured at room temperature using a precision impedance analyzer (HP4294A). The rms value of the AC current through the inductor was kept constant at 10 mA, and the frequency *f* of the current was varied from 100 kHz to 110 MHz. To represent the tunablity of the inductance, the relative variation of inductance was defined as $\Delta L/L_0=(L-L_0)/L_0$, where L_0 is the inductance of the tunable magnetic inductor without a bias magnetic field.
Fig. 1 (a) and (b) show relative variation of inductance $\Delta L/L_0$ versus the bias magnetic field H_{ex} for the studied inductors of different t_m ranging from 2.3 µm to 6.2 µm, at a low frequency of 100 kHz and at a high frequency of 100 MHz, respectively. As can be seen in Fig. 1 (a), the curves for t_m = 2.3 µm and t_m=3.6 µm are similar, which can be described as a pattern that the larger the values of t_m, the larger the values of $\Delta L/L_0$, whereas the curves for t_m=4.4 µm and t_m= 6.2 µm are similar in a different pattern, in which the larger the values of t_m, the smaller the values of $\Delta L/L_0$. Interestingly, as can be observed in Fig. 1 (b), all the curves appear to follow a same pattern, in which the larger the values of t_m, the smaller the values of $\Delta L/L_0$.
These pattern differences as observed in Fig. 1 (a) and (b), are possibly because the increase of the coating thickness tilts the direction of the easy axis towards the wire axis, as the samples were electroplated with constant plating current. Given that the easy axis makes an angle θ_k with the circumferential direction, the field dependence of the transverse susceptibility can be calculated [2], provided that the simple model of a uniaxial single domain is used, as shown in Fig. 1 (c).
As t_m increases, θ_k increases. When θ_k increases to certain level, e.g. 60°, the dominating magnetization process in the coating layer is changed from domain displacement to moment rotation.
At the frequency of 100 kHz, for the magnetic inductor of t_m=2.3 and 3.6 µm, the domain wall movements in the coating layer were nearly damped, and the moment rotations thus dominated the magnetization process. Therefore, the circumferential permeability μ_t, and thus $\Delta L/L_0$, increased with increasing bias field until reaching the anisotropy field (about 1.7 Oe in this case). After the maximum value of μ_t was reached, μ_t, so did $\Delta L/L_0$, decreased with increasing H_{ex}, until the magnetization was saturated. When the coating thickness t_m increased to a certain level, e.g. 4.4 µm, the domain displacement dominated the magnetization process. The total circumferential permeability monotonically decreased with respect to the bias field.
At the frequency of 100 MHz, for the inductor of all thicknesses discussed, the moment rotations dominate the magnetization process. μ_t and $\Delta L/L_0$ decreased with increasing t_m and θ_k.
The results indicate that there is a critical thickness for the coating layer, below which the tunability of L under a weak bias magnetic field is high (up to 50.6% at 100 kHz and 5.3% at 100 MHz, when H_{ex} is 1.7 Oe) and is proportional to the coating layer thickness t_m, and above which the tunability of L under a weak bias field is low (up to 6.6% at 100 kHz and 2.5% at 100 MHz, when H_{ex} is 1.7 Oe) and is inversely proportional to t_m. To the tunability of L of such tunable magnetic inductors, the increase of t_m has an equivalent effect as decreasing the operating frequency *f*. The thickness and the operating frequency *f* together determine that the dominating magnetization process in the coating layer is the domain displacement or moment rotation, which consequently determines the response of inductance, resistance, and quality factor of the tunable magnetic inductor.

[1] N. Ning, X. P. Li, J. Fan, W. C. Ng, Y. P. Xu, X. Qian, and H. L. Seet, IEEE Trans. Magn. 42, 1585 (2006).

[2] X. P. Li, Z. J. Zhao, H. L. Seet, W. M. Heng, T. B. Oh, and J. Y. Lee, J. Appl. Phys. 94, 6655 (2003).

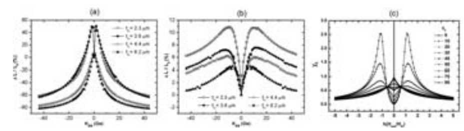

Fig.1 (a) $\Delta L/L_0$ versus H_{ex} for inductors of different tm at 100 kHz; (b) $\Delta L/L_0$ versus H_{ex} for inductors of different tm at 100 MHz; (c) Simulation results of the bias field dependence of the normalized transverse susceptibility at different θ_k.

AG-08

Audible noise from amorphous metal and silicon steel based transformer core.

D. Azuma, R. Hasegawa
Metglas, Inc., Conway, SC

1. Introduction
The most important property of a transformer core is core loss or no-load loss in light of its energy efficiency. At this point Fe-based amorphous metals are superior to the conventional silicon steel as a core material. As another aspect, audible noise from transformer becomes an additional important factor, since electric power distribution systems are close to the residential area with increasing population density due to the recent industrial growth. It has been recognized that a transformer based on Fe-based amorphous metals is noisier than that based on silicon steels. The noise of a transformer consists of the following two parts: (1) No-load noise caused by magnetization of a core. It is generally assumed that no-load noise arises from magnetostriction; (2) load noise caused by electromagnetic force in conducting windings. Though there are several standards for measurement methods of transformer noise, these methods are not for transformer cores [1]-[3]. It, however, is important to measure audible noise of a core, because the source of no-load noise is from a magnetized core and when a direct comparison among noises from cores with different materials is needed. In this article we report on the measurement results of audible noise generated from magnetized model cores based on Metglas® 2605SA1 and newly developed 2605HB1 alloys [4], and M3 silicon steel for distribution transformers in hemi-anechoic chamber accordance with ISO 3744 Standard [5].
2. Experimental
Configurationally same model cores based on SA1, HB1 alloys and M3 silicon steel were prepared weighing about 73 kg for SA1 core, 75 kg for HB1 and 89 kg for M3 material. The annealing temperatures for amorphous cores were 320°C - 350°C for and 300°C - 330°C for SA1 and HB1 alloy, respectively. A DC magnetic field of 2000A/m was applied along cores' circumference direction during heat treatment to induce magnetic anisotropy in the amorphous metal-based cores. Audible noise measurement on excited cores was conducted in a hemi-anechoic chamber (4.0 m x 3.7 m x 3.0 m) qualified in accordance with ISO 3744 Standard. Sound power levels were determined by sound pressure levels from 100 Hz to 25 kHz measured by ten fixed microphones located on a 1.4 m radius hemispherical measurement surface.
3. Results and Discussion
Fig.1 depicts exciting power as a function of induction for amorphous metal-based cores and for an M3-based core. Exciting power is lower than that of M3 for induction level below 1.4 T and 1.5 T for amorphous SA1 and HB1 core, respectively. Fig. 2 illustrates A-weighted sound power level [5] for cores shown in Fig. 1 as a function of operating induction. M3 core shows the lowest sound power level above induction level of 1.3 T. It is noted that in the core based on HB1 material the operating flux density can be increased by about 0.05 T with the same noise level as that of SA1. Since operating flux density of M3-based transformer is usually 1.6 T at 60 Hz, its sound power level is 56 dB according to Fig.2. The same level of noise is generated from SA1 and HB1 cores at the typical operating induction of each material (SA1: 1.35 T, HB1: 1.4 T). Above results do not necessarily reflect the audible noise of a finished transformer, since the measurement was conducted on the same core configuration and the actual core design for the same rating transformer depends on material grade, transformer specification etc. However it has been reported that optimally designed 25 kVA transformers had noise levels at 33 dB and 40 dB for amorphous metal and silicon steel based units, respectively [6]. The amorphous metal use in these units was an Fe based SA1-like alloy. When we use HB1 alloy, a noise level lower than 33 dB would be expected.

[1] IEC60076-10 Standard (2001)

[2] IEEE Std C57. 12. 90 (1999)

[3] JIS C 4304 Standard (2005)

[4] Y. Ogawa, M Naoe, Y. Yoshizawa and R. Hasegawa, J. Magn. Magn. Matrls. 304 (2006) e675

[5] ISO 3744 Standard (1994)

[6] H. W. Ng, R. Hasegawa, A.C. Lee and L.A. Lowdermilk, Proceedings of IEE, 79 (1991) 1608

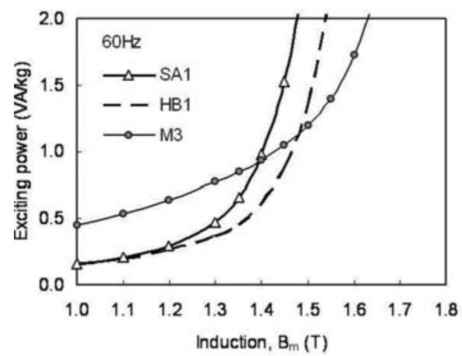

Fig. 1 Exciting power at 60 Hz as a function of operating induction.

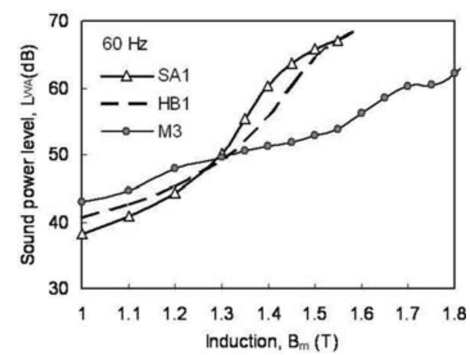

Fig. 2 A-weighted sound power level taken at 60 Hz as a function of operating induction.

AG-09

Development of a Novel Three-Phase Laminated Core Variable Inductor.

K. Nakamura[1], S. Hisada[1], K. Arimatsu[2], T. Ohinata[2], K. Sakamoto[2], O. Ichinokura[1]
1. Graduate School of Engineering, Tohoku University, Sendai, Japan; 2. Tohoku Electric Power Co., Inc., Sendai, Japan

Introduction

Importance of stabilizing line voltage in electric power systems is increasing every year, as a result of increasing nonlinear loads and introducing renewable and distributed energy resources such as fuel cells, wind-turbine, and photovoltaic power. One effective solution of this problem is reactive power compensation.

A variable inductor, which can be used as a reactive power compensator [1], consists of only magnetic core and coils, but can control its winding inductance by using magnetic saturation. Hence, it can generate from leading to lagging reactive power continuously by combining with a fixed capacitor. The variable inductor has a simple and robust structure, high reliability, and low cost. These features are suited for applications in electric power systems.

This paper presents a novel three-phase laminated core variable inductor to reduce size and weight as compared with a conventional single-phase variable inductor. First, characteristics of the proposed variable inductor are calculated by reluctance network analysis (RNA) and finite element analysis (FEA). Next, a trial 4 kVA variable inductor is demonstrated.

Characteristics of a three-phase laminated core variable inductor

Fig. 1 illustrates a schematic diagram of the proposed three-phase laminated core variable inductor. Primary windings N_1 turn around the six yokes and connected to dc control voltage V_{DC}. Contrary to this, secondary windings N_u, N_v, N_w turn around the six legs respectively and connected to a three-phase ac power source. In the figure, the arrows indicate primary and secondary flux flows. Effective inductance of the secondary winding can be controlled by primary dc excitation since the both fluxes share magnetic paths in the yokes. Fig. 2 shows the specifications of the proposed variable inductor.

RNA is employed to estimate performance of the proposed variable inductor [2]. At the beginning, the core is divided into multiple elements as shown in Fig. 3(a). Surrounding space is also divided to consider flux leakage. Every divided element is expressed in a three-dimensional magnetic circuit as shown in Fig. 3(b). In the core region, these reluctances are determined by a *B-H* curve of core material and dimensions of the element. On the other hand, in the space region, reluctances are given by a vacuum permeability and the dimensions.

Fig. 4(a) shows the reactive power characteristics of the variable inductor calculated by RNA and FEA, and (b) indicates the calculated total distortion factor of the secondary currents i_u, i_v, i_w. From the figures, it is understood that the proposed variable inductor can control the reactive power linearly and continuously, and that the secondary current is almost sinusoidal.

Demonstration of a trial 4 kVA variable inductor

Based on the above results, we tried to make a 4 kVA three-phase laminated core variable inductor. The specifications of the trial variable inductor are the same as Fig. 2. Fig. 5 shows a photo of the trial variable inductor. Fig. 6(a) shows the measured reactive power characteristics, and (b) indicates the total distortion factor of the secondary current. These figures indicate that the proposed variable inductor has good controllability and sinusoidal output current as in the case of the calculation.

Conclusion

The novel three-phase laminated core variable inductor has been proposed. This paper has indicated that the proposed variable inductor can control the reactive power linearly and the harmonics are remarkably low.

[1] K. Nakamura et. al., *IEEE Trans. Magn.*, **36**, 3565 (2000).

[2] K. Tajima, A. Kaga, Y. Anazawa, O. Ichinokura, *IEEE Trans. Magn.*, **29**, 3225 (1993).

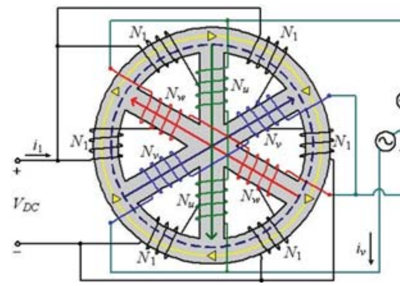

Fig. 1 Schematic diagram of the proposed three-phase laminated core variable inductor.

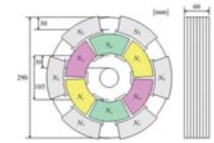

N_1	114 turns×6 0.762 Ω
N_u, N_v, N_w	208 turns×2 0.906 Ω
Voltage	200 V
Rated capacity	4 kVA
Control current	DC 0 to 30 A
Core material	Non-oriented silicon steel

Fig. 2 Specifications of the proposed variable inductor.

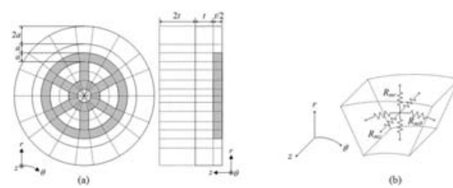

Fig. 3 Division of the core based on RNA and 3-D magnetic circuit.

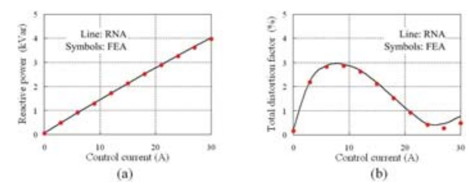

Fig. 4 Calculated reactive power characteristics (left) and total distortion factor (right).

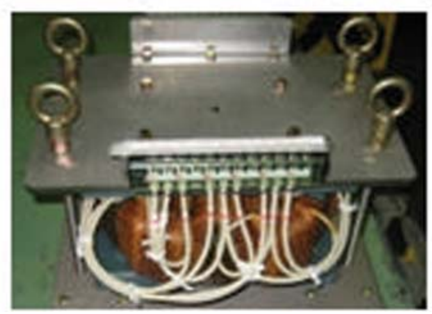

Fig. 5 Photo of the trial variable inductor.

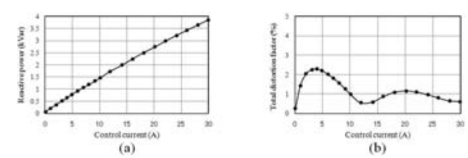

Fig. 6 Measured reactive power characteristics (left) and total distortion factor (right).

AG-10

Magneto-mechanical resonance in a 3-phase transformer core under PWM voltage excitation.

X. Yao[1], *P. P. Thant*[2], A. J. Moses[1], F. Anayi[1]
1. School of Engineering, Cardiff University, Wolfson Centre for Magnetics, Cardiff, United Kingdom; 2. Drilling & Measurements, Schlumberger, Aberdeen, United Kingdom

The causes and reduction of transformer noise has been the subject for many articles even before discovering that magnetostriction was the main source of noise in transformer cores. However, only sinusoidal excitation was considered in most of these studies.
Transformers subjected to PWM excitation are becoming more common in industrial applications such as active power line conditioner and renewable energy supply systems[1].
Therefore,improvement in the performance of cores under PWM excitation has become prominent. Very limited research has been reported on acoustic noise for transformer core under PWM excitation[2]with almost no study has been reported on magneto-mechanical resonance in cores. If a transformer core is subjected to resonance under magnetisation, the vibration of the core can enhance the output acoustic noise of the core as well as flapping of laminations which could lead to damage of the surface insulation coating.
In this investigation, acoustic noise and vibration behavior of a model 3-phase transformer core under PWM excitation at no-load condition with increasing switching frequency were analysed.
The core was assembled using laminations each of 0.27 mm thick grain-oriented 3%-Si electrical steel which Thant and Moses suggested that it would resonate when magnetised at approximately 1.5 kHz in the form of Epstein strips[3]. The core dimensions and positions at which acoustic noise and vibration were measured are shown in fig.1.
A 3-phase PWM inverter was used to supply the three primary windings with delta-connection and enabled the core to be magnetised up to 1.5 T. Sound pressure was recorded using a microphone[2], which was placed 0.5 m vertically above the core and moved among point 1, 2, 3 and point 5 in turn; vertical vibration of the core surface at points 1,2,3 and horizontal displacement on the side of the core at point 4 were measured using single-point laser vibrometer(SPLV)[3], vibration signal from SPLV were recorded by a digital oscilloscope.
Throughout the experimental work, modulation index m_a was in the range of 0.5 to 1.2. Switching frequency f_s was varied from 1 to 3 kHz while the magnetisation frequency f was set at 50 and 100 Hz.
Results of resultant acoustic noise and average peak-to-peak horizontal displacement at point 4 are shown in Table 1.
Fig.2(a-c) show the harmonic components of horizontal displacement at point 4 under PWM excitation at modulation index m_a=0.6,f=50 Hz,B_{peak}=1.5 T,f_s=1, 2 and 3 kHz respectively. The results obtained under PWM excitation were compared with measurements made under sinusoidal excitation at corresponding condition.
The displacement at fundamental frequency decreased with f_s increasing and increased harmonic components of 3-4 kHz was observed. However,at f_s=3 kHz(fig.2 c),the amplitude of harmonic component at 3 kHz is higher than at f_s=1 kHz and 2 kHz, indicating a magneto-mechanical resonance behavior.
The resultant acoustic noise measured under PWM excitation is around 11-13 dB greater than under corresponding sinusoidal excitation due to higher harmonics in the core vibration. The average result of horizontal displacement is decreased around 0.05 µm with increasing f_s from 1 kHz to 3 kHz is due to the lower amplitude of harmonic content of the displacement. Similar trends in vertical vibration were found above other points on the core surface with increasing f_s.
Results shows that acoustic noise and displacement decrease with increasing f_s for the 3-phase core under PWM excitation. However,near the resonance frequency(when f_s=3 kHz), amplitude of harmonic component at 3 kHz increases. The observed magneto-mechanical resonance phenomenon could be regarded as a possible cause of deterioration of transformer cores performance by increasing vibration and acoustic noise.

[1]Z.Chen, F. Blaabjerg, IEEE Power Electronics Society Newsletter,vol.18,no.3,pp.15-18,2006.

[2]Y.X.Guang, T.P.P.Phway, A.J.Moses, F.Anayi, 17th Int.Conf.on Electrical Machines (ICEM) 514 OTM4-4, 2006.

[3]T.P.P.Phway, A.J. Moses, JMMM, 316, 468-471, 2006.

Magnetisation frequency	Modulation index	Switching frequency[kHz]	Resultant acoustic noise(dB)	Displacement (µm)
sine 50 Hz	--	--	39.5	0.48
PWM 50 Hz	0.6	1	52.8	0.59
		2	51.6	0.56
		3	50.8	0.54

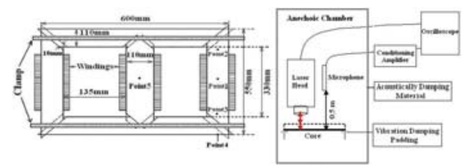

Fig.1 Layout of 3-phase model transformer core showing local measurement points, acoustic noise and vibration measurement setup in anechoic chamber

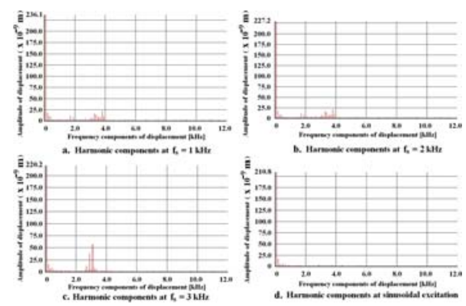

Fig.2 Harmonic components of displacement under PWM and sinusoidal voltage excitation

AG-11

Modeling the mutual impedances of non-coaxial inductors for induction heating applications.

C. Carretero[1,3], J. Acero[1], R. Alonso[2], J. Burdío[1], F. Monterde[3]
1. Dept. of Electronics Engineering and Communications, University of Zaragoza, Zaragoza, Spain; 2. Dept. of Applied Physics, University of Zaragoza, Zaragoza, Spain; 3. Bosch-Siemens Home Appliances Group, Montañana (Zaragoza), Spain

Abstract
A model of the coupling impedance between two non-coaxial single turn circular placed into two parallel planes that are located inside a multilayer media is derived. The model has been tested and validated by means of measurements.

Introduction
Domestic induction cookers consists of an electronic power stage [1], that supplies medium-frequency current, between 20 to 100 kHz, to a resonant tank that consists of an inductor and a series connected resonant capacitor. The inductor system, that is composed by a coil and the multilayer media, can be electrically modelled by its frequency dependent impedance Z(ω) that consists of a serial RL circuit [2] [3] that can be evaluated from analytical expressions, as shown in Fig. 1, where the expressions of $A_{k\omega}(\beta)$ and $B_{k\omega}(\beta)$ are functions of the positions and the physical properties of the layers. Usually, a domestic induction cooker has got more than one cooking zone, but each of them is made up one inductor and it works independent to another. However, recent developments include cooking areas composed by several coupled inductors, thus, it is necessary to model the coupling among them. We define the impedance matrix $\mathbf{Z}(\omega)$ for a n-coil system, where each element Z_{ij} is the ratio of the voltage induced in the coil i by the electric field of the inductor j, divided by the current that inductor j drives.

Analytical Model
The coupling impedance expressions between two filiform single turn inductor placed inside a multilayer media is carried out by integrating the electric field along the turn i. This expression is performed in the same way as shown [4] in a single parameter integral and its final expression appears in Fig. 2. The multilayer contribution is included in the expressions of coefficients $A_{k\omega}(\beta)$ and $B_{k\omega}(\beta)$. As a consequence of the reciprocity theorem, we have $Z_{ij} = Z_{ji}$ and the impedance matrix is symmetric.

Experimental Arrangement
An experimental set-up has been built to test the analytical expressions. It consists of two equal PCB loops of a radius equal to 30 mm. and a negligible thickness and width. These are located in the same plane, at different distances l (Fig. 2) between their centres (from 61 mm. to 90 mm.). Besides, the layer under inductors can be ferrite (insulator with μ_r=2000) or the vacuum at a distance of 1.7 mm, and the layer above inductors may be F114 steel, copper, aluminum or the vacuum at a distance of 4 mm.

The coupling impedance has been carried out by means of a one channel precision LCR-meter E4980A at a frequency range from 1 kHz to 1 MHz. The procedure is to measure the direct series impedance and the opposite series impedance of the two inductor, then, we obtain the values $Z_{direct} = Z_{11}+Z_{22}+Z_{12}+Z_{21}$ and $Z_{opposite}=Z_{11}+Z_{22}-Z_{12}-Z_{21}$, therefore, $Z_{direct}-Z_{opposite}=2*(Z_{12}+Z_{21})=4*Z_{12}$.

Main Results
A comparison between experimental and analytical results can be shown in Fig 3.

Conclusions
A new analitical model of the coupling impedance between inductors placed inside a multilayer media has been developed and experimentally verified for a single turn configuration. This model can be easily extended to n-turns inductors.

[1] S. Llorente, F. Monterde, J.M. Burdío, J. Acero, "A comparative study of resonant inverter topologies used in induction cooking." IEEE Applied Power Electronics Conference and Exposition (APEC'02). Rec., 2002, pp. 1168-1174.
[2] J. Acero, R. Alonso, J.M. Burdío, L.A. Barragán, and D. Puyal, "Analytical equivalent impedance for a planar circular induction heating system." IEEE Trans. on Magnetics, vol. 42, pp. 84-86, Jan. 2006.
[3] J. Acero, R. Alonso, L.A. Barragán, J.M. Burdío, "Modeling of planar spiral inductors between two multilayer media for induction heating aplications." IEEE Trans. on Magnetics, vol. 42, no. 11, pp. 3719 - 3729, November 2006.
[4] J. T. Conway, "Inductance calculations for noncoaxial coils using bessel functions". IEEE Transactions on Magnetics, vol. 43, no. 3, pp. 1023 - 1034, March 2007.

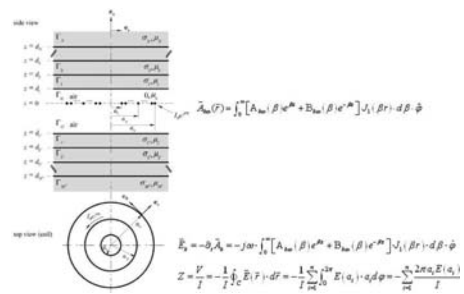

Fig. 1. Model of a planar inductor between two multilayer media.

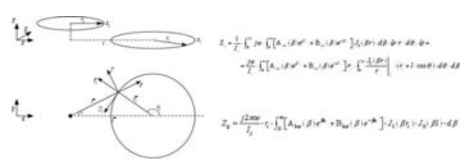

Fig. 2. Model of coupling between one turn inductors.

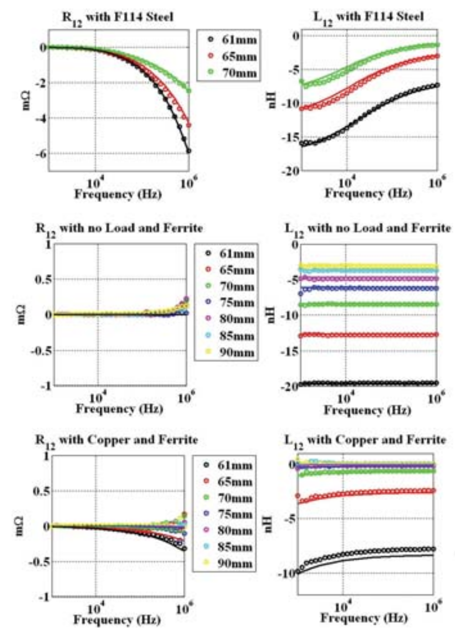

Fig. 3. Simulated data is represented using a solid line and measured data is plotted with circle symbols.

AH-01

High-frequency transverse incremental permeability and magnetoimpedance effect in CoFeHfO magnetic oxide nanofilms.

A. Le[1], M. Phan[2], V. Manuel[3], *H. Lee*[4], Q. Nguyen[1], S. Yu[1]
1. BK 21 Physics Program and Department of Physics, Chungbuk National University, Cheongju 361-763, South Korea; 2. Advanced Composites Centre for Innovation and Science, University of Bristol, Queen's Building, Bristol, United Kingdom; 3. De Instituto de Ciencia de Materiales de Madrid, CSIC, Campus de Cantoblanco, 28049 Madrid, Spain; 4. Department of Physics Education, Kongju National University, Kongju 314-701,, South Korea

In this letter, high-frequency magneto-transport properties in CoFeHfO magnetic oxide nanofilms have been thoroughly investigated by means of transverse incremental permeability (TPR) and magnetoimpedance (MI) measurements. CoFeHfO films with varying thicknesses (t = 1, 1.5, 1.8 and 2.4 μm) were fabricated by oxygen reactive rf-sputtering method. The circle-type film samples were put into a solenoid coil with 10 turns and 10 mm in length. The changes of transverse incremental permeability along the easy and hard axes of the film sample and of MI effect were measured using an rf impedance analyzer HP 4191A in the high-frequency range of 100 – 1000 MHz and a varying external dc magnetic field within 300 Oe. The solenoid coil was located in the perpendicular direction to the external field for measuring transverse incremental permeability. The single-layered film samples with different thicknesses were cut into 15 mm long and 2 mm wide for all MI measurements. The shape of each sample was determined by a mask on the substrate. The experimental analyses revealed that the nanostructure of Co-Fe-Hf-O films prepared consists of α-Fe(Co)-rich bcc nanograins embedded in an HfO_2-rich amorphous matrix. It is the formation of a granular-type nanostructure that results in the excellent soft magnetic properties of this film. In addition, the insulating HfO_2-rich amorphous matrix contributes to the high electrical resistivity that significantly suppresses eddy current loss, and, consequently, gives rise to a good high-frequency performance. It is noteworthy that the study of TPR and MI spectra provides deeper physical insights of the complex nature of high-frequency magneto-transport behaviors in the CoFeHfO film material. The results obtained show that the magnitude of TPR values increases with increasing frequency, reaching a maximum value at 710 MHz, and then decreases at higher frequencies. TPR curves measured at the same frequency of 710 MHz along the easy and hard axes of sample are displayed in Fig 1. It can be seen also that the magnitude of TPR increases with increasing film thickness, indicating the increase of magnetic softness. Furthermore, the TPR curves measured along the easy-axis direction shows a single-peak feature at zero magnetic field (Fig. 1a), whereas those measured along the hard-axis direction have a double-peak feature (Fig. 1b). This evidently indicates an existence of magnetic anisotropy and its dispersion in the film. It is worth noting that the width of measured TPR peaks can reflect the distribution of anisotropy field. As can be seen clearly from Fig. 1b, the anisotropy field, corresponding to the peak field (H_k), significantly decreases from 42.6 Oe to 37.8 Oe as the film thickness increases from 1 to 2.4 μm. This result coincides with that obtained from the magnetization measurements. It has been shown that the decrease of anisotropy field is related to the increase of magnetic softness. Therefore, it is reasonable to conclude that the magnitude of anisotropy field and TPR depends on the degree of the magnetic softness. Apart from this, an asymmetry in the measured TPR curves appears to occur, which is likely to be due to the anisotropy dispersions in relation to the magnetization process. To further clarify the high-frequency magnetic behavior in CoFeHfO material, the high-frequency MI effect in Co-Fe-Hf-O magnetic nanofilms with different thicknesses has been also performed. It is worth noting that, in the investigated frequency range of 100 – 1000 MHz, the MI ratio first increases with increasing frequency, reaches a maximum at 696 MHz, and then decreases at higher frequencies (see Fig. 2 and its inset, for the t = 1.8 μm film). In addition, the maximum MI ratio significantly increases as the film thickness increases from 1 to 2.4 μm. It has been demonstrated that the large increase of MI effect at high frequencies is related to the ferromagnetic resonance (FMR) effect as clearly evidenced from the frequency-dependent measurement (both real and imaginary parts) of ac complex permeability. These obtained results indicate that the ferromagnetic resonance plays an important factor for large increase of transverse incremental permeability at high frequencies and, hence the MI effect in CoFeHfO nanofilms.

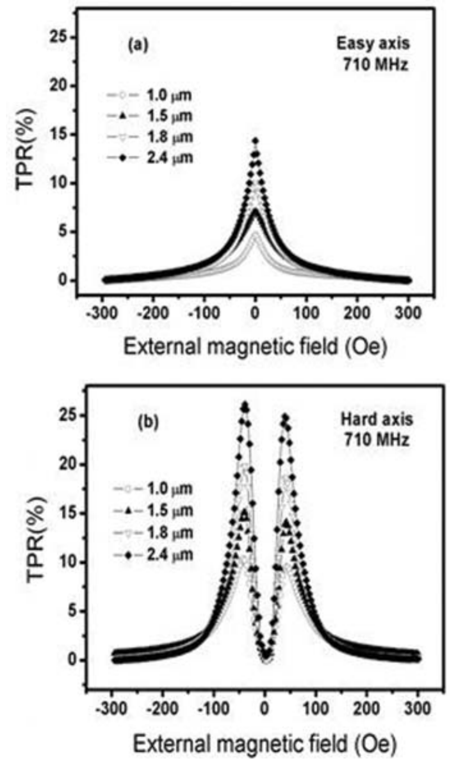

Figure 1

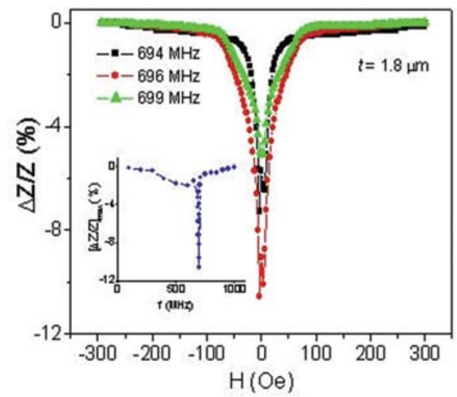

Figure 2

AH-02

Width dependence of magneto-impedance in sandwiched films.

D. de Cos, *A. Garcia-Arribas*, J. Barandiaran
Electricidad y Electronica, Universidad del Pais Vasco, Bilbao, Spain

The magneto-impedance (MI) has been measured for a series of sandwiched Ni-Fe/Au/Ni-Fe samples with different widths. The magnitude and sensibility of the MI are analyzed as a function of both the applied magnetic field and the frequency. Our results clearly show that the width dependence of these figures of merit is mainly a consequence of the external inductance determined by the geometry of the sample.
Sandwiched samples (each layer 500 nm thick) were sputtered onto a glass substrate placed in a magnetic field to induce a transverse anisotropy during the deposition. The wafer was patterned out by conventional photolithography methods and dry-etched to obtain samples 5 mm long and 20, 50, 100, and 200 μm wide. The preparation was completed with a thermal treatment to relax internal stresses.
The MI measurements have been performed using RF techniques: the sample is placed in a 50 Ω microstrip line situated in the central region of a pair of Helmholtz coils. The impedance is obtained from S_{11} parameter measurements made by a network analyzer, after proper calibration and mathematical subtraction of the non desired high frequency contributions of the test fixture [1]. We present measurements results up to 500 MHz were quasi-static processes dominates the MI behavior [2].
The MI curves show the typical two-peak shape that corresponds to well-defined perpendicular anisotropy of H^k = 7.4 Oe.
The real and imaginary parts of the impedance are analyzed independently to understand their relevance in the behavior of the magnitude and sensibility of MI. Figure 1 shows the frequency dependence of both real and imaginary parts for the samples with different widths. The impedance shown has been measured for maximum (applied magnetic field equals to the anisotropy field) and minimum (without magnetic field) impedance.
The curves for the real part are very similar for the widest samples (200, 100 and 50 μm). The magneto-impedance corresponding to the real part is, for these samples, ranging between 160 and 180% at 500 MHz. The narrowest sample (20 μm) only reach 38%.
In the imaginary part, the slope that is measured at zero field is caused by the external self-inductance. At the anisotropy field, the impedance grows rapidly at low frequencies, but its slope gradually equals that of zero field at higher frequencies. Consequently, the relative MI is huge at low frequencies but decreases significantly when the frequency increases.
The relevant parameter to determine the performance of the samples is the MI of the absolute value of the impedance. Therefore, the combined behavior of real and imaginary parts must be examined. At low frequency, the imaginary part is small and the impedance is dominated by the real part so, although the MI of the imaginary part is really large, it has no consequences in the MI of the absolute vale. On the contrary, at high frequencies, the impedance is dominated by the imaginary part and, although the MI of the real part is really high, the overall MI of the absolute value is not. Using these simple argument, we can explain the behavior of the MI for the absolute value of the impedance as a function of the frequency shown in figure 2: increase while the real part is greater than the imaginary part and decrease after that. The important parameter is then the frequency at which the value of the real parts equals the imaginary parts. This happens at 196, 260, and 295 MHz for the samples 200, 100, and 50 μm wide respectively. In consequence, 50 μm wide sample takes larger MI values since MI is growing longer (up to higher frequencies). And the ultimate reason for this is that the self-inductance of the 50 μm wide sample is smaller, for geometrical reasons, than the ones of 200 and 100 μm samples.
Sample 20 μm wide behaves considerably different and other factors must be taken into account, as flux loss [3]. All those aspects will be discussed in the full length paper.

[1] D. de Cos, A. Garcia-Arribas, and J. M. Barandiaran, Sens. Actuators, A **115**, 368 (2004).

[2] J. M. Barandiaran, A. Garcia-Arribas, and D. de Cos, J. Appl. Phys. **99**, 103904 (2006).

[3] D. de Cos, L. V. Panina, N. Fry, I. Orue, A. Garcia-Arribas, and J. M. Barandiaran, IEEE Trans. Magn. **41** 2367 (2005).

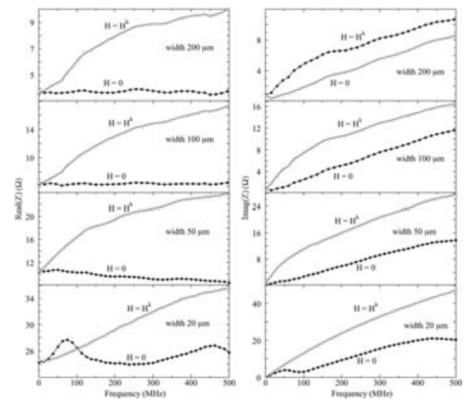

Real and imaginary parts of the impedance for samples with different widths.

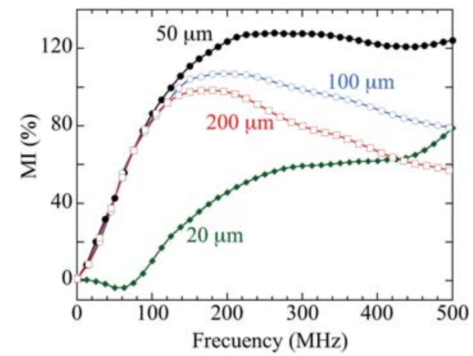

Magneto-impedance for samples with different widths.

AH-03

Annealing effects on the microwave absorption properties of nanocrystalline $Fe_{79}Si_{16}B_5$ microwires.

M. Han, L. Deng, D. Liang
State Key Laboratory of Electronic Thin Films and Integrated Devices, University of Electronic Science and Technology of China, Chengdu, China

Fe-based amorphous and nanocrystalline wires have been widely reported for their giant magnetoimpedance (GMI) effect, and have been mainly exploited for sensor developments, such as magnetic field sensors, position sensors etc. [1] Recently, there was an ever increasing interest in studying the electromagnetic (EM) wave absorbers due to their applications in anti-EM interference coatings, microwave darkrooms [2]. It is well known that Fe-based nanocrystalline materials can be fabricated by properly annealing amorphous Fe-Si-B alloy: nano scale α-Fe grains are embedded in an amorphous matrix [3]. However, to our best of knowledge, the possible application of Fe-Si-B nanocomposite in EM wave absorber has not been well exploited yet, especially in forms of microwires.

$Fe_{79}Si_{16}B_5$ microwires were fabricated by the melt extract method. Annealing treatments on magnetic wires under argon atmosphere for 1 hour were carried out at 600 ^{0}C and 750 ^{0}C respectively. The M-H loops were measured for the heat treated microwires on a vibrating sample magnetometer (VSM). The heat treated microwires were cut into 1 mm, and homogenously mixed with wax (the microwires / wax weight ratio is about 1:2), then the complex relative permittivity ($\varepsilon_r = \varepsilon' - j\varepsilon''$) and the complex relative permeability ($\mu_r = \mu' - j\mu''$) were measured on an Agilent 8720ET Network Analyzer within the frequency range of 1 GHz – 18 GHz.

The morphology of as-prepared microwires with the average diameter of 33 μm is shown in Fig. 1(a). The DSC curve is shown in Fig. 1(b), and two exothermic peaks are found at 532 ^{0}C and 665 ^{0}C. The first peak is believed due to the formation of α-Fe nanocrystalline grains. The second peak is due to the formation of non-magnetic borides (Fe_2B), as shown in Fig. 1(c). Magnetic hysteresis (M-H) loops are shown in Fig. 1(d). Both the as-prepared microwires and the microwires annealed at 600 ^{0}C show good soft magnetic properties. Their coercivity values are about 5 Oe. However, the coercivity of microwires annealed at 750 ^{0}C is about 110 Oe, its larger coercivity is believed due to the formation of non-magnetic phase Fe_2B, which hinders the movement of domain walls. The large permittivity values (for instance, for microwires annealed at 750 ^{0}C, ε' = 45 at 1 GHz) are believed due to the good conductivity characteristics of microwires. The permeability spectra for the annealed microwires are shown in Fig. 1(e). Interestingly, there are two dispersion peaks for each spectrum. The peak at lower frequency is believed due to the domain wall movement, the other one is believed due to the spin rotation. The EM wave absorbing performances are generally evaluated using the reflection loss (RL) in dB unit. With the measured permittivity and permeability values, we can evaluate their EM wave absorption performances based on the following equations [4]:

$Z_{in} = Z_0(\mu_r/\varepsilon_r)^{1/2}\tanh\{j(2\pi ft/c)(\mu_r\varepsilon_r)^{1/2}\}$ —-(1)

$RL = 20\log|(Z_{in}-Z_0)/(Z_{in}+Z_0)|$——(2), where Z_0 is the impedance of free space; t is the thickness of an absorber; *c* is the speed of light. As shown in Fig. 1(f), if *t* is 1.25 mm, the microwires annealed at 600 ^{0}C show better absorption performances: for microwires annealed at 600 ^{0}C, the minimum RL is -15.8 dB at 15 GHz; while for microwires anneal at 750 ^{0}C, the minimum RL is -9.4 dB at 14. 33 GHz.

[1] M. Han, D. F. Liang, L. J. Deng, J. Mater. Sci. Vol. 40, (2005) 5573.

[2] M.R. Meshram, N.K. Agrawal, B. Sinha, P. S. Misra, J. Magn. Magn. Mater. 271 (2004) 207.

[3] M. McHenry, M. Willard, D. Laughlin, Prog. Mater. Sci. 44, (1999) 291.

[4] Y. Naito, K. Suetake, IEEE Trans. Microwave Theory Tech. 19 (1971) 65.

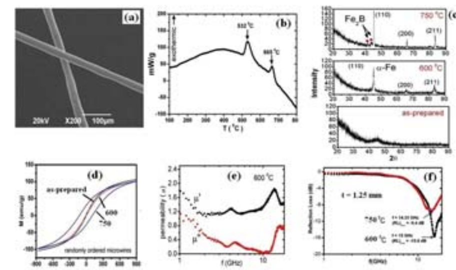

Fig. 1. (a) SEM images of as-prepare microwires; (b) DSC curve; (c) XRD patterns; (d) M-H loops; (e) microwave permeability spectra; (f) reflection loss of microwire/wax composites.

Microwave absorption of amorphous microwires carrying a low frequency ac current.

A. G. Gorriti, I. Carabias, P. Marin, A. Hernando
Instituto de Magnetismo Aplicado, Las Rozas, Spain

There is a growing interest in the study of glass coated amorphous microwires, Fe or Co rich, because they show very interesting magnetic properties with a broadband range of applications. Among others, they present ferromagnetic resonance and therefore absorb electromagnetic energy on the microwave region of the spectrum [1].

These microwires consist of an inner core of an amorphous metallic composition of typically tens of µm coated with glass. They are obtained by an extracting melt-spinning technique, based on Taylor's classical method [2]. A SEM image of a microwire is shown in Figure 1.

Their magnetic properties are strongly dependent on the composition of the metallic core, and the magnetization process on the magnetostriction constant ant the magnetoelastic anisotropy induced by internal stresses [3]. These affect the ferromagnetic resonance (FMR) which is responsible for the absorption of microwave energy.

These absorption properties are unique and depend on several factors, such as, composition, diameter relation between the inner metallic core and the glass coat, temperature, applied tension along the wire, applied external low frequency magnetic field, etc. Which enable the use of these microwires in applications ranging from microwave absorbers to magnetic tags. But, to fully develop these applications a deep understanding of the relation between the physical processes and the parameters that affect them is needed.

It is well known that the absorption mechanisms are altered by an applied low frequency magnetic field parallel to the microwire [3]. However, in this communication we want to show that this is also the case when the wire transports an alternating low frequency current.

The microwave absorption was measured inside a microwave anechoic chamber with helical antennas at a frequency of 1.29 GHz. An antenna emitted a circular polarized electromagnetic wave, generated by an ESG Analog Signal Generator, while the other received the signal via an EMC Spectrum Analyzer. At the same time, the microwire transported a low frequency (f = 10 Hz) alternating current (I). Data was recorded in the time domain and it showed that the microwire modulated the emitted signal with a period equal to 1/ f (see Figure 3).

The amplitude of the modulation depends on the amplitude of the applied field, it increases with increasing field amplitude up to a value where it stabilizes (the microwire is saturated). Figure 2 shows different modulations for different current intensities, and Figure 3 the amplitude of the modulation versus the intensity of the applied current. In this case, the microwire had a composition of Mn7Co69Si11B13, and the current was sinusoidal. We will also show how the modulation follows other types of current, such as square.

These experiments show a promising future for the absorption of microwaves with microwires.

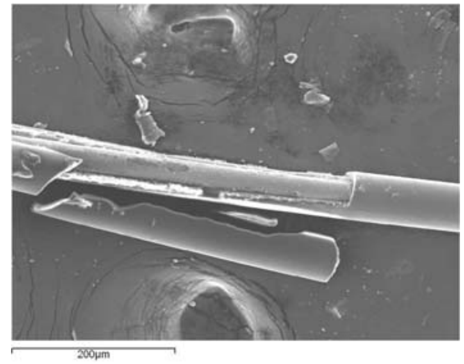

Figure 1. SEM image of an amorphous microwire. Metallic diameter of 18 µm and glass diameter of 45 µm.

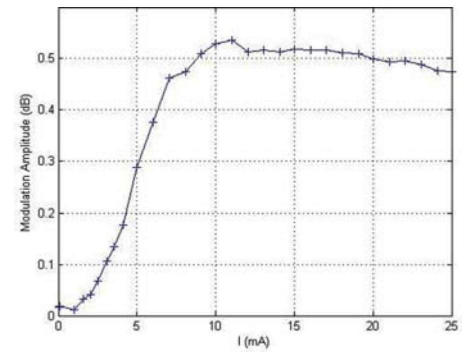

Figure 2. Change of the amplitude of the modulation with the intensity of the current.

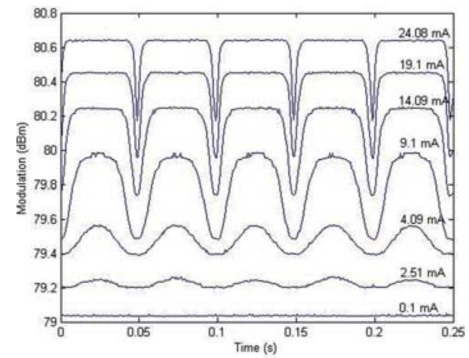

Figure 3. Modulations for different current intensities. Note that the curves have been shifted for clarity purposes.

[1]. Acher O., Jacquart P. and Boscher C. Investigation of high frequency permeability of thin amorphous wires. IEEE Trans. Magnetics 30, 6, 4542-4544, 1994.

[2]. Taylor G.F. A method for drawing metallic filaments and discusión of their properties and uses. Phys. Rev 24, 6555-60, 1924.

[3]. Marin P. and Hernando A. Magnetic Microwires: Manufacture, Properties and Applications. Encyclopedia of Materials: Science and Technology. Elsevier Science, The Netherlands, 1-9, 2004

AH-05

Magneto Impedance Behavior in Co/Cu/Co/NiFe Pseudo Spin Valve with a nano-oxide layer after Annealing Treatment.

W. Chien[1,4], R. Hung[2], C. Lo[2,4], Y. Yao[1,3], K. Chang[4], E. Lai[4], Y. Chen[4], K. Hsieh[4], C. Lu[4], P. Lin[1,4]
1. Department of Materials Science and Engineering, National Chiao Tung University, Hsinchu, Taiwan; 2. Electronics and Optoelectronics Research Laboratories, Industrial Technology Research Institute, Hsinchu, Taiwan; 3. Department of Materials Engineering, Tatung University, Taipei, Taiwan; 4. Emerging Central Lab, Macronix International Co. Ltd, Hsinchu, Taiwan

Magnetic tunneling junctions (MTJs) and pseudo spin valves (PSVs) show great promise for applications in Magnetoresistive Random Access Memory (MRAM), pick-up heads, and magnetic sensors. It is well known that due to the oxidation and diffusion effects, the DC MR ratio of the PSV decreases as the annealing temperature increases. [1]. However, the characteristics of annealing treatment (AT) in PSV are hard to differentiate by non-destructive analysis. Recently, it is shown that the impedance spectroscopy can provide evidences to identify interface or metal layers characteristics by using equivalent circuit analysis [2, 3]. In this study we extend our previous work [4,5] to report on the frequency response features of the magneto impedance (MI) behavior of PSVs with a nano-oxide layer (NOL) after AT.
The PSV ($1cm^2$) with Ta (0.6 nm)/Co-NOL/Co (3 nm)/Cu (5 nm)/Co (1 nm)/NiFe (3 nm)/substrate has been fabricated by e-gun evaporation at room temperature (R_T). The nano-oxide layer was obtained by oxidizing the thin magnetic layers of Co for ten minutes naturally. The sample was subsequently annealed from R_T to 200°C for 30 minutes. The MI behavior was determined by using the HP4194 impedance analyzer with the HP16047D fixture ranging from 100 Hz to 40 MHz.
As the AT temperature increases from R_T to 200°C, the resistance of the PSV with NOL increases from 5.00 to 6.32 ohm and DC MR ratio of the PSV decreases from 5.41 to 0.48 %. The effective capacitance was studied by imaginary part of impedance (Im (Z)) curves, as shown in Fig. 1. Im (Z) reaches a minimum at roll-off frequency (f_{roll}). This f_{roll} is a function of AT temperature, and we find that it increases linearly from 345 to 465 kHz as the AT temperature increases from R_T to 200°C. According to the effective capacitance calculation $f_{roll} = 1 / (2\pi R_{eff} C_{eff})$, the effective capacitance should reversely proportional to the f_{roll} and the estimative values of C_{eff} decrease from 21.8 to11.8 nF as AT temperatures increase from R_T to 200°C. As plotted in Fig. 2, the coercivity (H_C) of the Co layer is 20 Oe, and H_C of the Co-NiFe layers is 12 Oe in the PSV that deposited at R_T. When the AT temperature increases to 140°C, the H_C of Co shows incoherent in the PSV apparently due to the oxidation in Co layer. The experimental data of f_{roll}, which increases as AT temperature increased from room temperature to 140°C, suggest the increase of the oxidative thickness of Co layer. For the AT temperatures higher than 140°C, it is difficult to distinguish the H_C between Co and Co-NiFe, and this implies that the oxidation reaction extends from Co to Cu layers. This effect could be regarded as two capacitors in serial and as results the effective capacitance decreases as shown in the inset panels in Fig. 2.
In summary, the magneto impedance behavior in the Co/Cu/Co/NiFe pseudo spin valve with a nano-oxide layer after AT has been studied. Its roll-off frequency increases from 345 to 465 kHz, and the effective capacitance decreases from 21.8 to11.8 nF as the AT temperature increases from R_T to 200°C. We can utilize the equivalent capacitor circuit to explain the NOL behavior with AT. This study shows that the impedance analysis is a useful technique, and its nondestructive measurement is more widely appreciated.

[1] Chih-Huang Lai, C. J. Chen and T. S. Chin, J. Appl. Phys. 89, 6928 (2001)

[2] M. F. Gillies, A. E. T. Kuiper, R. Coehoorn and J. J. T. M. Donkers, J. Appl. Phys. 88, 429 (2000)

[3] J. C. A. Huang and H. S. Hsu, Appl. Phys. Lett. 87, 132503 (2005)

[4] W.C. Chien, C. K. Lo, L. C. Hsieh, Y. D. Yao, X. F. Han, Z. M. Zeng, T. Y. Peng, and P. Lin, Appl. Phys.Lett., 89, 202515 (2006)

[5] W. C. Chien, T. Y. Peng, L. C. Hsieh, C. K. Lo, and Y. D. Yao, IEEE Trans. Magn., 42, 10 (2006)

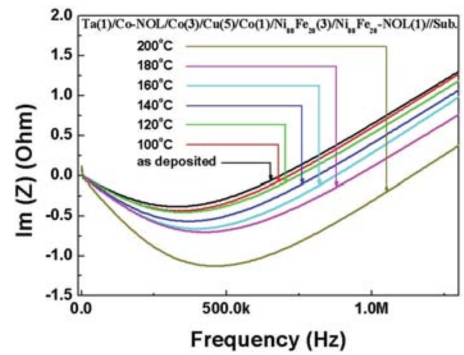

Fig1. Imaginary part of impedance curves for PSV with different AT temperature ranging from R_T to 200°C.

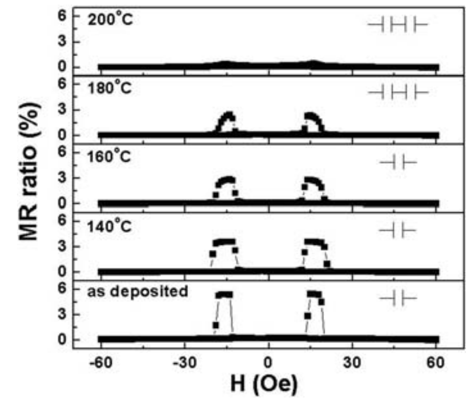

Fig2. The hysteresis loops of the PSV with AT temperatures R_T, 140°C, 160°C, 180°C, 200°C, respectively. The inset panels show the equivalent capacitor modes.

AH-06

Analysis of the intrinsic field sensitivity and noise of magnetoimpedance sensors.

L. Melo[1], D. Menard[2], A. Yelon[2], B. Dufay[3], O. Mareschal[3], S. Saez[3], C. Dolabdjian[3]
1. Electrical Engineering, Ecole Polytechnique de Montreal, Montreal, QC, Canada; 2. Engineering Physics, Ecole Polytechnique de Montreal, Montreal, QC, Canada; 3. GREYC, ENSICAEN and University of Caen, Caen, France

The giant magnetoimpedance (GMI) effect is observed when the impedance of a magnetically soft conductor is measured as a function of frequency of the drive current and the applied external dc field.[1] Technological applications of the GMI effect such as magnetic, current and stress sensors[1] primarily require high impedance variation, high intrinsic sensitivity to dc and ac fields and low intrinsic magnetic noise. The magnitude of the effect, ΔZ, is commonly given by the change of impedance relative to the impedance at saturation. The sensitivity, *S* (in units of %/Oe or %/T), is proportional to the derivative of ΔZ with respect to the applied dc field. The magnetic noise, *MN* (in units of T/√Hz), which is a quantity proportional to the voltage-noise-to-sensitivity ratio, defines the minimum measurable field in 1Hz bandwidth and dictates sensor performance. In this work, the experimental and theoretical behaviour of *S* and *MN* are analyzed as a function of frequency and applied fields, including the effect of a dc bias current, for a Co-based magnetic conductor. A procedure to obtain the external parameters yielding the highest *S* and minimum *MN* is outlined.

We have recently proposed a simple model to evaluate the GMI *MN* and *S* in the MHz regime of anisotropic magnetic wires.[2] The model accounts for a biasing dc circumferential field, H_{bias}, which is included in the internal field of a single domain cylindrical magnetic conductor. For given frequency, H_{bias} and easy axis direction, *S* is evaluated as a function of the external axial dc field, $H_{\rm ext}$. The field yielding the maximum sensitivity (S^{max}), $H_{\rm ext}^{max}$, is determined, defining the sensor working point. The *MN* is then evaluated at $H_{\rm ext}^{max}$. For helical magnetic structures having the easy magnetization axis close to circumferential, calculations show that both S^{max} and *MN* (at $H_{\rm ext}^{max}$) decrease for increasing H_{bias}.[2] The field H_{bias} essentially increases the internal field, which effectively makes the wire magnetically harder and hence, less sensitive to the driving signal when $H_{\rm ext}$ is applied.

Calculated normalized sensitivity, Λ, as a function of $H_{\rm ext}$ and H_{bias} at 10MHz for a 35μm diameter is presented in Fig. 1. The quantity Λ is given by $\Lambda=H_kS$, where H_k is the anisotropy field of the wire and $S=d\eta/dH_{\rm ext}$. $\eta=(\xi\mu_{\rm t}^{1/2}-1)\cos^2\theta$, ξ is a function of the wave vectors and material parameters,[2] $\mu_{\rm t}$ is the transverse permeability and θ is the angle between the static magnetization direction and the direction of $H_{\rm ext}$. The permeability depends on frequency, internal field and magnetic damping. The parameter values used in the calculations are typical for Co-rich amorphous wires. Also, we have used H_k=1.4Oe and an easy axis angle of 72° (relative to the axial direction) in the calculations. We observe in Fig. 1 that for this frequency and easy axis angle, *S* broadens with S^{max} (black points) decreasing when H_{bias} is applied (see also broken lines A and B), as a consequence of the increase of the internal field.

This may not be the case for a wire with an axial easy axis. Figure 2 shows experimental results of $\Delta Z/R_{dc}$ and *S* from the measurement of the impedance of an as-cast Co-based wire as a function of $H_{\rm ext}$, when the wire was submitted to a dc bias current, i_{bias}. The impedance was measured in a HP 8753B Network Analyzer (NA). For the i_{bias}, injected into the device, we used the bias input of the NA. The experimental sensitivity shown in Fig. 2 was then obtained from the numerical derivative of the impedance versus field curve. In Fig. 2*a*, $\Delta Z/R_{dc}$ and *S* vs. $H_{\rm ext}$ at *f*=10MHz and 100MHz for i_{bias}=20mA are shown. This value of i_{bias} is equivalent to a H_{bias}~2Oe at the surface of the wire, which is close to the H_k of this sample. Figure 2*b* shows *S* vs. $H_{\rm ext}$ at *f*=100MHz for i_{bias}=40mA, 20mA and 4mA. These results show that there are optimal frequency and dc bias conditions to maximize the sensitivity. The high S^{max} for a non-zero H_{bias} opens the possibility for the observation of very low values of *MN* predicted by the theory.[2]

In this work, the behavior of *S* and *MN* are analysed and compared with experiment at frequencies up to 500MHz on Co-based amorphous wires.

[1] M. Knobel, M. Vazquez and L. Kraus, in Handbook of Magnetic Materials 15, K.H.J. Buschow, ed., Elsevier (2003).

[2] L.G.C. Melo et al., IEEE Trans. Magn., 43, 2992 (2007), and L.G.C. Melo et al., J. Appl. Phys., accepted, Nov. 2007.

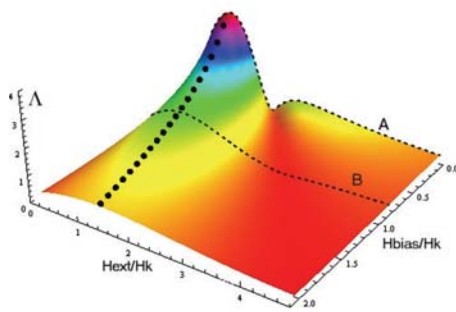

Figure 1. Normalized sensitivity as a function of applied fields at 10MHz for a wire with (almost) circumferential easy axis angle.

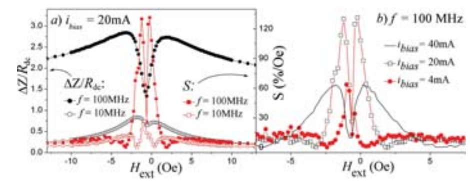

Figure 2. Experimental results for an as-cast amorphous microwire (R_{dc}=20Ω). *a*) $\Delta Z/R_{dc}$ and *S* for i_{bias}=20mA and *f*=10MHz and 100MHz. *b*) *S* for *f*=100MHz and i_{bias}=40mA, 20mA and 4mA.

AH-07

Magneto impedance study in magneto tunneling junctions with different thickness of its barrier layer.

W. Chien[1], *Y. Yao*[2], J. Wu[2], C. Lo[3], P. Lin[1], X. Han[4]
1. The Department of Materials Science and Engineering, National Chiao Tung University, Hsinchu, Taiwan; 2. Department of Materials Engineering, Tatung University, Taipei, Taiwan; 3. Electronics and Optoelectronics Research Laboratories, Industrial Technology Research Institute, Hsinchu, Taiwan; 4. Institute of Physics, Chinese Academy of Sciences, Beijing, China

Magneto impedance (MI) in magneto tunneling junctions (MTJ) has been extensively studied in recent years [1, 2]. The equivalent circuit model composed of a resistance component and two sets of parallel resistance (R) and capacitance (C) components in series, has been utilized to describe the individual impedance contribution from lead of cross pattern, barrier and interface [3]. Therefore, in this study we extend our recent work to investigate a MTJ with different thicknesses of AlOX by means of a non-destructive method - impedance spectroscopy and use mathematic method to predict high frequency behavior of MTJ by equivalent circuit.
The MTJ with structure of Ru (5nm)/Cu (10nm)/Ru (5nm)/IrMn (10nm)/CoFeB (4nm)/Al (x = 0.8, 1.1, or 1.2 nm)-oxide/CoFeB (4nm)/Ru (5nm), which was deposited on Si/SiO wafer by using Magnetron Sputtering System with its junction area of 6um x 6um. As an example, its structure and equivalent circuit are shown in Fig. 1 for sample with x = 1.2 nm. The frequency was raised to 40 MHz, and the magneto impedance, MZ = |Z|eiθ = R+iX in which X = XL-XC, of an MTJ device was studied. The MZ ratio is defined as 100 % × (|MZ|AP-|MZ|P) / |MZ|P, where the subscript P (AP) stands for the parallel (anti-parallel) magnetization orientation state of the MTJ. The magneto resistance ratio (MR) and magneto reactance ratio (MX) are all defined similarly. In fact the whole system contains non-ignorable parasitic inductance and capacitance from wires, and these terms have effect on the shift of resonant frequency. However, these sensing wires do not have any contribution to the MI, and can not prevent us from analyzing general MI phenomena. The AC behavior was determined by using the HP4194 impedance analyzer with the 16047D fixture. A two-point contact was used in a frequency range from 100 Hz to 40 MHz with an electromagnet which supplied a dc field up to 500 Oe.
From our experimental data, the real part of the impedance value at the crossover frequency (fc) at which the real part of the impedance in the parallel state is equal to that in the anti-parallel state, is a single value for samples with x = 1.2 and 1.1 nm. However, as shown in Fig. 2, the resistance difference between the anti-parallel state and the parallel state (RAP-RP) as a function of the frequency between 100Hz to 40MHz for sample with x = 0.8 nm behaviors like a damping oscillating, and its amplitude decreases as frequency increases, which is quite consistent with the calculated value based on the Maxwell-Wagner model due to the reduction of the barrier thickness. From the frequency dependence of the imaginary part of impedance (XAP, XP) for the MTJ in the parallel and anti-parallel states, the effective capacitance increases from 64.10 to168.81 and 184.90 pF as the barrier thickness decreases from 1.2 to 1.1 and 0.8 nm, respectively. This means that the effective thickness of barrier decreases which cause the effective capacitance increases.
In summary, from the frequency dependence of the magneto impedance for the MTJ in the parallel and anti-parallel states. The RAP and RP curves decrease with increasing frequency, which indicates that the MTJ includes a significant capacitance effect. A Maxwell-Wagner model capacitor consisting of dielectric material with the equivalent circuit theory has been used to analyze our experimental data. We have shown that with an AC current in MTJ, the magnetic behavior can be switched by both the barrier thickness and the driving frequency.

Finally, This work was supported by the Sapintia Education Foundation.

[1] M. F. Gillies, A. E. T. Kuiper, R. Coehoorn and J. J. T. M. Donkers, J. Appl. Phys. 88, 429 (2000)

[2] W.C. Chien, C. K. Lo, L. C. Hsieh, Y. D. Yao, X. F. Han, Z. M. Zeng, T. Y. Peng, and P. Lin, Appl. Phys.Lett., 89, 202515 (2006)

[3] W. C. Chien, L. C. Hsieh, T. Y. Peng, C. K. Lo, Y. D. Yao, X. F. Han and P. Lin IEEE Trans. Magn., 43, 2812 (2007).

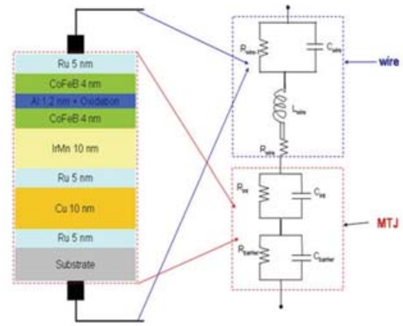

The structure of the magneto tunneling junctions is Ru (5nm) /Cu (10nm) /Ru(5nm) /IrMn(10nm) /CoFeB(4nm) /Al(1.2nm)-oxide /CoFeB (4nm) /Ru (5nm) and equivalent circuit with contributions from magneto tunneling junctions.

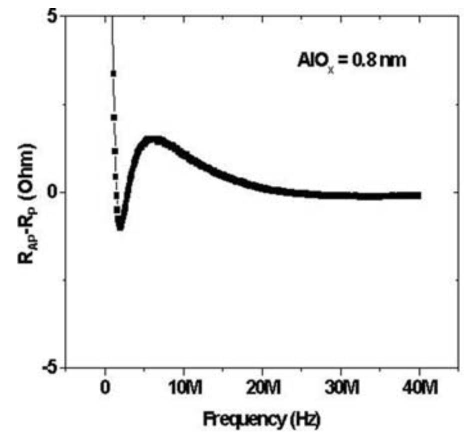

The resistance difference between the anti-parallel state and the parallel state (RAP-RP) as a function of the frequency between 100Hz to 40MHz for sample with x = 0.8 nm.

AH-08

Development of thin microwires with enhanced magnetic softness and GMI.

V. Zhukova[2], M. Ipatov[1], J. Gonzalez[1], J. Blanco[2], *A. Zhukov*[1,3]
1. Dept. of Phys. Materials, Basque Country University, San Sebastian, Spain; 2. Dpto. de Física Aplicada, EUPDS, Basque Country University, San Sebastian, Spain; 3. TAMAG Ibérica S.L., Parque Tecnológico de Miramón, Paseo Mikeletegi 56, 1 Planta,, San Sebastian, Spain

Ferromagnetic metallic glass coated microwires (usually of 15-30 μm in diameter) exhibit a number of outstanding magnetic properties such as magnetic bistabilty and GMI effect [1-3]. Recent studies allow improving of magnetically soft properties and GMI effect of glass coated microwires but keeping the microwires diameter generally above 10 μm [1,2]. The demagnetizing factor affects the domain structure and magnetic properties when the geometric ratio of microwire diameter to its longitude becomes low enough [3]. Therefore the development of magnetically soft microwires with reduced diameter (below 10 μm) is quite important for micro-miniaturized sensor application [4].

In this paper we studied the GMI effect (GMI ratio, ΔZ/Z, and the off-diagonal impedance tensor component $\xi_{\phi z}$) and hysteretic magnetic properties in ultra-thin amorphous glass-coated microwires with nearly-zero and negative magnetostriction constant and metallic nucleus diameter ranging within 6 and 16 μm have been systematically studied.

Both ΔZ/Z, and hysteresis loops of nearly-zero $Co_{67.1}Fe_{3.8}Ni_{1.4}Si1_{4.5}B_{11.5}Mo_{1.7}$ microwires magnetostrictive exhibit strong sensitivity to the ratio, ρ, the metallic nucleus diameter to the total microwire diameter. The hysteresis loops exhibit low coercivity (generally below 15 A/m) with well defined magnetic anisotropy field, H_k (see Fig.1a). H_k increases when ρ decreases (see Fig.1b).

Field dependence of the off-diagonal voltage response of nearly zero magnetostriction ($\lambda_s \approx -3x10^{-7}$) $Co_{67.1}Fe_{3.8}Ni_{1.4}Si1_{4.5}B_{11.5}Mo_{1.7}$ with metallic nucleus diameter of 6.0, 7.0 and 8.2 μm exhibits anti-symmetrical shape with almost linear growth within the field range from $-H_m$ to H_m associated with the anisotropy field (Fig.2a).

DC and even pulsed current significantly affects the off- diagonal MI curves of $Co_{67.1}Fe_{3.8}Ni_{1.4}Si1_{4.5}B_{11.5}Mo_{1.7}$ microwires with vanishing magnetostriction constant: voltage pulse with the peak value above some critical value reduces the linear region (Fig.2b). Under DC current annealing the Hm decreases from 480 A/m in as-cast state to 230 A/m after 5 min annealing with 50 mA current.

High negative magnetostriction microwire $Co_{74}B_{13}Si_{11}C_2$ ($\lambda_s \approx -10^{-6}$) with metallic diameter of 10 μm possesses hysteretic off-diagonal MI curve in as-prepared state. DC joule heating affects the character of the magnetic field dependence of ξϕz for $Co_{74}B_{13}Si_{11}C_2$ microwire: the hysteretic MI curve transforms into the unhysteretic one with large enough nearly-linear region.

The obtained results allow us to tailor the microwire magnetic properties for its application in magnetic sensors through the selection of their composition and/or thermal treatment conditions.

1. D.C. Jiles, Acta Materialia 51 (2003) 5907.

2. K.R. Pirota, L. Kraus, H. Chiriac, and M. Knobel, J. Magn. Magn. Mater. 221 (2000) L243.

3. A. P. Zhukov, M. Vázquez, J. Velázquez, H. Chiriac and V. Larin, J. Magn. Magn. Mater. 151 (1995) 132.

4. K. Mohri and Y. Honkura, Sensors letters, 5 (2007) 267.

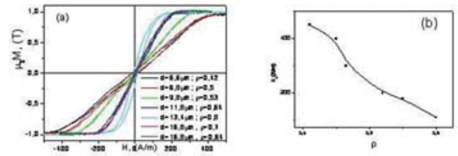

Fig.1 Hysteresis loops (a) and Hk(ρ) dependence of $Co_{67.1}Fe_{3.8}Ni_{1.4}$ $Si_{14.5}B_{11.5}Mo_{1.7}$ microwires

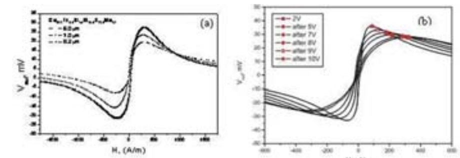

Fig.2. Field dependence of the off-diagonal voltage response for different microwires diameters (a) and effect of pulse annealing with different pulse amplitude on off diagonal GMI (b) of nearly zero magnetostriction $Co_{67.1}Fe_{3.8}Ni_{1.4}Si_{14.5}B_{11.5}Mo_{1.7}$ microwires.

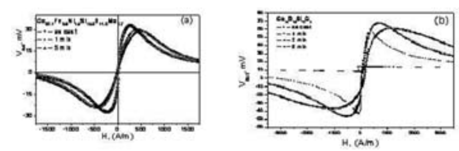

Fig. 3. Field dependence of the off-diagonal voltage response of $Co_{67}Fe_{3.85}Ni_{1.45}B_{11.5}Si_{14.5}Mo_{1.7}$ Joule-heated microwire annealed with 50 mA currents for different time (a) and $Co_{74}B_{13}Si_{11}C_2$ microwire in as-prepared state and annealed with 50 mA currents for different time.

Dependence of magneto-impedance on magnetic states in manganeses.

J. Li, H. Chou, C. Lin
Department of Physics and Center of Nanoscience, National Sun Yat-sen University, Kaohiung, Taiwan

There has been much interest in the magneto-resistive behavior of the manganese oxides, due to the remarkable reduction in the resistivity by the application of a magnetic field. To our acknowledgement, few works of higher frequency transport properties of manganese oxides have been systematically reported [1,2]. Experimental results have demonstrated that the magneto-impedance at higher frequency can be sensitively affected by magnetic states on the sintered manganese oxides, called giant magneto-impedance (GMI) effects. In this work, the impedance spectroscopy of $La_{0.67}Sr_{1.33}MnO_4$ and $La_{0.67}Sr_{0.33}MnO_3$ were applied to characterize the ac properties behind and after Curie temperature (T_c). Our work provides further understanding of the dielectrics variation during the phase transition from an antiferromagnetic (AFM) insulating phase or a ferromagnetic (FM) metallic phase to a paramagnetic (PM) insulating phase.

In this study, thin films of $La_{0.67}Sr_{1.33}MnO_4$ and $La_{0.67}Sr_{0.33}MnO_3$ were deposited on $SrTiO_3$ (001) substrate by an off-axis RF sputtering method [3]. The impedance spectra were measured from 125K to 291K by using HP4284A network analyzer, in the frequency range of 20Hz to 1MHz.

Fig.1 shows the frequency dependence of the imaginary component of the complex impedance, $Z(f) = R(f)+ iX(f)$, for the $La_{0.67}Sr_{1.33}MnO_4$ thin film in T~125K - 291K. For T < 156 K, the resistive component (R) and the absolute value of the reactive component (-X) decrease monotonically with frequency and exhibits negative curvatures for the entire frequency range. When T > 156 K, the curvature of R(f) for exhibits a plateau at low frequency and decreasing monotonically at higher frequency while the curvature of -X (f) shows an up-down bump with maximums at certain frequencies. These bumps intensities decrease and the frequency of the peak intensity increase with the frequency, as shown in the inset. The evolution of the impedance spectra is coincident with the AFM phase transition of $La_{0.67}Sr_{1.33}MnO_4$ thin film, in which the antiferromagnetic (AFM) to paramagnetic (PM) insulating phase transition appears within T~156~185K. [4]

The high frequency impedances of $La_{0.67}Sr_{0.33}MnO_3$ thin film are plotted in Fig. 2. The reactive component (X) appears an increasing curve as a function of frequency for T < 329K. When at T > 329K, the X decreases with raising frequency (as shown in the inset). The evolution of the impedance spectra is in correspondence to the FM-PM transition at T~329 K. The observed diverse feature of spectra on $La_{0.67}Sr_{1.33}MnO_4$ and $La_{0.67}Sr_{0.33}MnO_3$ may be correlated with different nature of FM/PM and AFM/PM states.

These magneto-impedance spectra are further analyzed based on an equivalent circuit that composes of resistances (R) and capacitances (C) to the grains and grain-boundaries. The results of our work may provide a fundamental understand of the higher frequency conduction in manganese oxides. Details of the analysis will be presented in the conference.

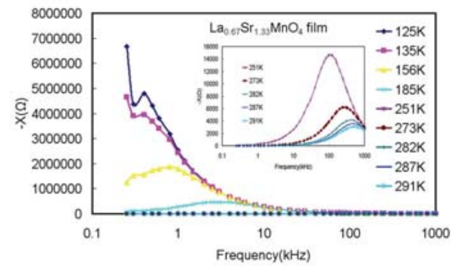

Fig. 1 The frequency dependence of the imaginary component of the complex impedance for the $La_{0.67}Sr_{1.33}MnO_4$ thin film in T~125-291K. The inset shows the detail of the curves for T>251K.

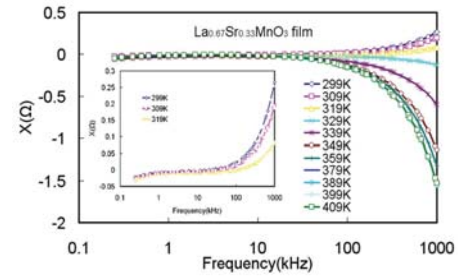

Fig. 2 The frequency dependence of the imaginary component of the complex impedance for the $La_{0.67}Sr_{0.33}MnO_3$ thin film in T~299-409K. The inset shows the detail of the curves for T<319K.

[1]C.M.Fu,C.J.Lai,H.S.Hsu,and Y.C.Chao, J. Appl. Phys. 91 (2002) 10

[2] C. Y. Hsu, H. Chou, B. Y. Liao and J. C. Andruw Huang, Appl. Phys. Lett. 89, 262510 (2006)

[3] Z. J. Huang, Ms thesis, Nat'l San-Yat-Sen Univ. (2003)

[4] W Prellier,Ph Lecoeure and B Mercey, J. Phys. 13 (2001) R915-R944

AH-10

Temperature Dependence of Magnetoimpedance and Anisotropy in Nanocrystalline Finemet Wire.

B. Hernando[1], J. Olivera[1], M. Sánchez[1], V. M. Prida[1], R. Varga[2]
1. Fisica, Universidad de Oviedo, Oviedo, Spain; 2. Inst. Physics, Fac.Sci.,UPJS, Park Angelinum, Kosice, Slovakia

The study of the temperature dependence on magnetoimpedance (MI) effect is important for controlling the thermal stability of MI-based sensor devices in amorphous magnetic materials [1]. The MI effect in ferromagnetic materials describes the change of the material's impedance due to the variations on the penetration depth of an ac current flowing across the sample under the influence of the static applied magnetic field [2]. An $Fe_{73.5}Cu_3Nb_1Si_{13.5}B_9$ (Finemet) wire fully nanocristallized after one hour annealing at 565°C [3], with 133 µm in diameter and 1.5 cm in length, was chosen for the temperature measurements of MI effect by employing a cryogenic chamber, where the temperature of the sample can be varied from 80 to 340 K. The MI effect has been collected as a function of a dc magnetic field $-5000 < H_{dc} < 5000$ A/m, with a driving current amplitude of I_{rms} = 5 mA and a frequency of 1kHz, for all measured temperatures. It has been found that MI effect exhibits a characteristic temperature dependent behaviour in these samples, where a double peak is obtained at low temperature (Fig. 1 a), while it changes into a single peak shape near room temperature (Fig. 1 b). A peculiar asymmetry in the double peak behaviour as a function of the applied magnetic field is clearly observed in the low temperature regime, in comparison with other previously studied wires [1], since the highest peak of the MI maximum is found in the direction of the static field at which the sample was saturated, meanwhile the smaller maximum is found in the opposite magnetic field direction. These measurements can be explained in terms of competition between different existing anisotropies in the sample, taking into account the revised core-shell model [4]. This investigation brings information about the thermal evolution of magnetization dynamics, anisotropy, and the magnitude of the MI effect in this kind of nanocrystalline ferromagnetic samples.

[1] K. Mohri, T. Uchiyama, L.P. Shen, C.M. Cai, L.V. Panina, Y. Honkura, M. Yamamoto, IEEE Trans. Magnetics 38, 3063 (2002).

[2] L. V. Panina, K. Mohri, K. Bushida, M. Noda, J. Appl. Phys. 76, 6198 (1994).

[3] B. Hernando, J. Olivera, M. L. Sánchez, V. M. Prida, M. J. Pérez, J. D. Santos, P. Gorria, F. J. Belzunce, Physics of Metals and Metallography 102, (Suppl. 1), S13 (2006).

[4] D.-X. Chen, L. Pascual, F.J. Castaño, M. Vazquez, A. Hernando, IEEE Trans. Magnetics 37, 994 (2001).

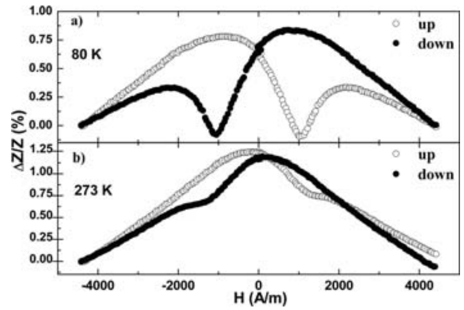

Fig.1. MI effect dependence on the applied magnetic field measured at two different temperatures: a) T = 80K, b) T= 273 K.

AH-11

Asymmetrical magnetoimpedance in CoFeSiB/CoNi layered microwires.

J. Torrejon[1], G. Badini[1], *L. V. Panina*[2]
1. Magnetism, ICMM (CSIC), Madrid, Spain; 2. School of Computing, Communication and Electronics, University of Plymouth, Plymouth, United Kingdom

Magnetoimpedance (MI) is an expanding area of current research finding applications in magnetic sensor technology and smart sensory composites. Various soft magnetic materials such as amorphous or nanocrystalline wires and ribbons show large change in high frequency impedance for a characteristic fields of few Oe, having a sensitivity in the range of 50-100%/Oe. This high sensitivity makes MI elements very attractive for low field detection. However, typically, MI characteristics are essentially non linear near the zero field point with strongly reduced sensitivity. Therefore, the sensor operational region should be shifted by applying a dc bias field or current. This could be disadvantageous for many practical applications, for example, where low energy consumption is required or in smart sensory composite with remote interrogation. Establishing asymmetrical magnetic configuration helps to improve linearity and reduce the needed dc bias [1]. Here we report asymmetrical MI in CoFeSiB glass coated amorphous microwires with electroplated semi hard CoNi outer shell. This additional magnetic layer creates a magnetostatic bias and also modifies the wire magnetic anisotropy. The MI characteristics have essentially linear portion near zero field with sensitivity up to 20%/Oe.

Multilayer microwire samples were prepared by combining Taylor-Ulitovsky method to produce $(Co_{0.94}Fe_{0.06})_{72.5}Si_{12.5}B_{15}$ amorphous core (17.4 µm in diameter) coated with glass (12.1 µm), with further sputtering Au nanolayer (30 nm) and electroplating $Co_{90}Ni_{10}$ magnetic layer. The inner core with small negative magnetostriction and soft magnetic properties showed large MI. The Au nanolayer played a role of electrode/substrate for subsequent electroplating a semi hard magnetic shell the thickness of which was varied in the range of 0-12 µm by changing the electroplating parameters [2]. Changing the thickness of CoNi layer allows controlling the magnetostatic bias and induced helical anisotropy [3]. The samples were investigated at low-field with the outer shell in a demagnetised state and magnetised in positive and negative sense with the field of 0.5-1 kOe. The dc magnetization behavior of the samples was investigated by measuring B-H loops by VSM method and hysteresis modeling to obtain anisotropy and magnetostatic field characteristics (no shown here). The loops are shifted in a positive or negative direction depending on the CoNi layer magnetization and reveal a slightly helical anisotropy with the angle of about 15° with respect to the circumference.

The MI characteristics of multilayer wires were found from measurements of S_{11} parameter with the help of vector network analyzer HP8753E sweeping in frequency from 1 MHz to 500 MHz. The sample is housed as a central conductor in microstrip line of 50 Ω characteristic impedance with SMA connectors at both ends, one of which is loaded with a precision 50 Ω termination and the other is connected to the VNA. The outer shells of the samples are shorter than the inner soft magnetic core to exclude them from electrical connections. The test fixture was placed inside a long solenoidal coil producing a magnetic field of increasing values up to 50 Oe.

Figure 1a shows the MI plots at 50 MHz for a multilayer micowire with t_{CoNi}= 3 µm when the hard magnetic layer is in a demagnetised and magnetized state. The insert shows the same plots at a larger field scale. For demagnetized CoNi layer, the MI characteristics show two symmetrical peaks typical of a transverse anisotropy. When this layer is magnetized in a high field (± 1 kOe), the MI plots reveal asymmetry and a shift due to induced magnetostatic bias field. It also appears that the anisotropy in the inner soft magnetic layer depends on the magnetization state of the outer hard magnetic layer. Increasing the thickness of the hard magnetic layer increases the biasing effect as shown in Fig.1b, however, the induced anisotropy also increases which reduces the sensitivity. At optimal conditions of t_{CoNi}= 3 µm, the MI characteristics are almost linear near the zero sensed field with the nominal change in impedance of about 50% in the field range of -1 Oe -2.5 Oe. The obtained linear highly sensitive MI characteristics in layered microwires without using any external dc bias demonstrate that this new family of MI materials can be very promising in magnetic sensor applications

[1] L.V. Panina. Journal of Magnetism and Magnetic Materials 249 (2002) 278–287.

[2] K. Pirota, M. Provencio, K. García, P. Mendoza, M. Hernandez-Velez and M. Vázquez, J. Magn. Magn. Mater. 290 (2005) 68-73.

[3] J. Torrejón, L. Kraus, K. R. Pirota, G. Badini and M. Vázquez. J. Appl. Phys. 101 (2007) 09N105.

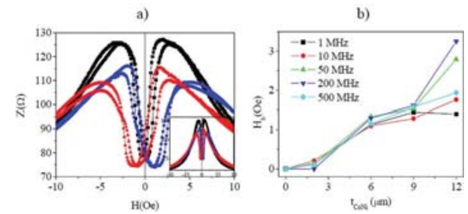

Fig. 1.- (a) MI characteristics of multilayered wire with t_{CoNi}= 3 µm when it is demagnetised (black squares), and magnetized positively (blue circles) or negatively (red triangles). Frequency is 50 MHz. (b) Bias field dependence on the CoNi thickness for selected frequencies deduced from MI plots.

AH-12

Role of the interdomain wall in the giant magneto-impedance effect of thin microwires.

H. Chiriac, T. Óvári, S. Corodeanu
National Institute of Research and Development for Technical Physics, Iasi, Romania

Nearly zero magnetostrictive glass-coated amorphous microwires with metallic nucleus diameters ranging between 1 and 40 µm and the glass coating thickness between 1 and 30 µm, display excellent soft magnetic properties and an appropriate domain structure for a sensitive giant magneto-impedance (GMI) response, suitable for sensor applications [1].
The interdomain wall that separates the main regions of the magnetic structure in these microwires has been recently investigated [2]. It has been shown that the interdomain wall between the inner core (IC) and the outer shell (OS) has a large width in case of nearly zero magnetostriction, such as in $Co_{68.15}Fe_{4.35}Si_{12.5}B_{15}$ microwires. In this case, the interdomain wall reaches within the region that responds in the high frequency GMI effect, region determined by the skin effect through the magnetic penetration depth. The GMI effect has been recently employed as an experimental method in the investigation of the interdomain wall in thicker microwires, i.e. with the metallic nucleus diameter around 20 µm [2], microwires that have been also analyzed for the optimization of the GMI effect [3].
The aim of this paper is to investigate the role of the interdomain wall in the GMI effect of thin microwires, i.e. with the metallic nucleus diameter close to 1 µm. The importance of such thin microwires emerges from their potential applications as sensors in spintronic devices.
With this aim, we prepared glass-coated amorphous microwires with the nominal composition $Co_{68.15}Fe_{4.35}Si_{12.5}B_{15}$, with the metallic nucleus diameter of 1.5 µm and the glass coating thickness of 7.5 µm. GMI measurements have been performed at frequencies of the ac driving current between 10 and 500 MHz on both as-cast samples and on samples with the glass coating completely removed by chemical etching.
The GMI ratio, defined as the difference between the impedance at the measuring field and the impedance at the maximum field divided by the latter, displays a maximum at each frequency in the case of as-cast samples, its position being symmetric with respect to the applied dc field. The most sensitive response is obtained at 100 MHz. Such maxima are linked to the transverse anisotropy field, i.e. once the applied field overcomes it, the GMI response is the largest since the magnetic moments are free to follow the circumferential field created by the ac driving current.
Glass removal leads to a significant change in the shape of the GMI curve. The most sensitive response is again obtained at 100 MHz. Fig. 1 shows the GMI response at 100 MHz for an as-cast sample and for the same sample after glass removal. The GMI ratio decreases monotonically with the applied field, without going through a maximum. This change in the GMI behavior is associated with the important stress relief caused by glass removal. Consequently, the transverse anisotropy field decreases abruptly, becoming almost negligible.
In order to fully understand this behavior, one has to consider the presence and the parameters of the interdomain wall, and the changes these parameters suffer as a result of glass removal, due to the large width of the wall in these microwires. Therefore, we have calculated the position and the width of the interdomain wall in the as-cast state, as well as their changes with glass removal.
The as-cast microwire has a calculated interdomain wall width of 175 nm located between the radial coordinates 0.686 µm and 0.861 µm. This leaves space just for an extremely thin OS (less than 40 nm), but nevertheless with a quite large circumferential anisotropy. Glass removal leads to a drastic decrease of the axial tensile stress, which practically results in the expansion of the interdomain wall with almost 30% of its initial width and in the vanishing of the thin OS. The observed GMI behavior of the microwire with the glass coating removed is perfectly plausible under these circumstances.
Summarizing, the characteristics of the GMI response of thin microwires are a consequence of the interplay between the magnetic penetration depth, the location and width of the interdomain wall, their changes with glass removal, as well as of the general characteristics of the microwire's domain structure (e.g., presence or absence of the OS and OS thickness).

[1] A. Zhukov, J. Magn. Magn. Mater. 242-245 (2002) 216.

[2] H. Chiriac, T.-A. Óvári, S. Corodeanu, G. Ababei, Phys. Rev. B 76 (2007) 214433.

[3] H. Chiriac, S. Corodeanu, M. Tibu, T.-A. Óvári, IEEE Trans. Magn. 43 (2007) 2977.

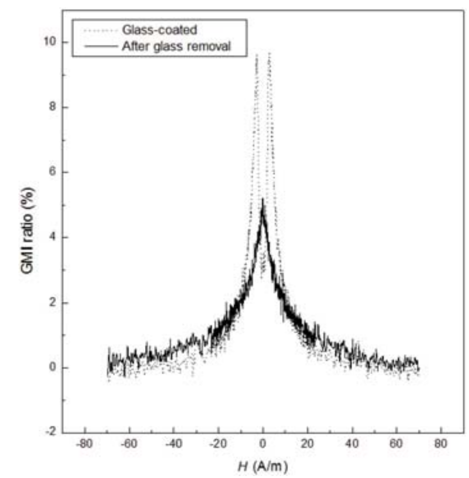

Fig. 1. GMI response at 100 MHz of an as-cast glass-coated microwire with the metallic nucleus diameter of 1.5 µm and the glass coating thickness of 7.5 µm, and of the same microwire after glass removal.

AL-01

Development of an Axial-flux Spindle Motor for the Slim Optical Disc Drive.

G. Yan[1], G. Huang[1], H. Wang[1], L. Hsu[2]
1. Micro/Meso Mechanical Manufacturing Section, Metal Industries Research & Development Center, Kaohsiung, Taiwan; 2. Electric Motor Technology Research Center, National Cheng Kung University, Tainan, Taiwan

I. INTRODUCTION AND MOTIVATION

Slim optical disc drives are popular and manufactured to be very thin for use in portable terminals such as notebook computer. However, there is still a strong demand for the optical disc drive with thinner thickness. To accommodate this demand, the spindle motor is one of important elements that require high efficiency and compact size. As the height of the optical disk drive is reduced, it is more difficult to design a spindle motor to satisfy the above requirements with radial-flux type. Therefore, an axial-flux motor has been proposed to achieve smaller size due to its low profile.

As shown in Fig.1, the proposed motor is composed of a rotor with high-energy magnet, NdFeB, and a stator with windings piled up on PCB board. Besides, there is no cogging torque due to the slotless base plate. In this study, the axial-flux motor is chosen as 3 phases, 6 winding coils and 8 poles. Under the design procedure, the parameters of the motor structure are determined by the equivalent magnetic circuit. FEA, using ANSOFT Maxwell software, is then applied to verify the design calculations and result.

II. MOTOR DESIGN

The main issue of the structure design is to minimize the height in the axial direction. Fig. 2 shows the mechanical structure of the proposed motor. The height from the bottom plate to the upper cover is reduced to 4.2mm, where the conventional one has the height about 6.8mm.

In the electromagnetic design, the torque constant is the major design consideration. For the application of the slim optical disc drive, the expectant value is about 3.5 mNm/A. A three-dimensional finite-element analysis is employed to calculate the flux density distribution in the steady-state as illustrated in Fig. 3. Local hot-spots in the flux density appear in the rotor yoke above the inter-pole regions. The average flux density in the air gap is about 0.4~0.5 Telsa. This leads the number of the turns per coil should be greater than 30.

III. POTOTYPING AND BERIEF CONCLUDSION

From the design outlined in the previous section, a prototype is constructed as shown in Fig. 4. The comparison between the prototyped motor and the conventional one is also shown in this figure. In this paper, the decrease in size of this motor, as compared with the conventional one, is up to 55%. An experimental device to measure the characteristics of the developed motor by using the forcemeter is setup. After the spindle motor reaches the highest speed under no load condition, the load weight is applied. Then, current and speed are measured with the supply voltage of 5 V. According to the experimental measurement of the torque-current curve, the torque constant is about 3.2mNm/A. This is 8.5% less than the expectant value but acceptable, while the rated speed is about 6000rpm. With the improvement of the tilt and axial repeatable run-out (RRO) characteristics, the developed motor has great potential for the novel optical disc player applications in the near future.

[1]G. H. Jang and J. H. Chang, “Development of dual air gap printed coil BLDC motor,” IEEE Trans. Magn., vol. 35, no. 3, pp. 1789-1792, May, 1999.

[2]G. H. Jang and J. H. Chang, “Development of an axial-gap spindle motor for computer hard disk drivers using PCB and dual air gaps,” IEEE Trans. Magn., vol. 38, no. 5, pp. 3297-3299, Sep. 2002.

[3]Ansoft Corporaton, Maxwell 3D Field Simulation, Release Notes, 2001.

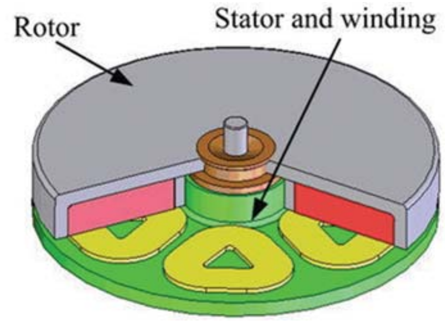

Fig. 1 Axial-flux type motor

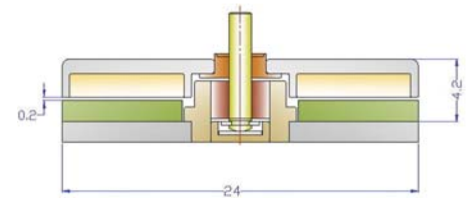

Fig. 2 Structure of the proposed motor

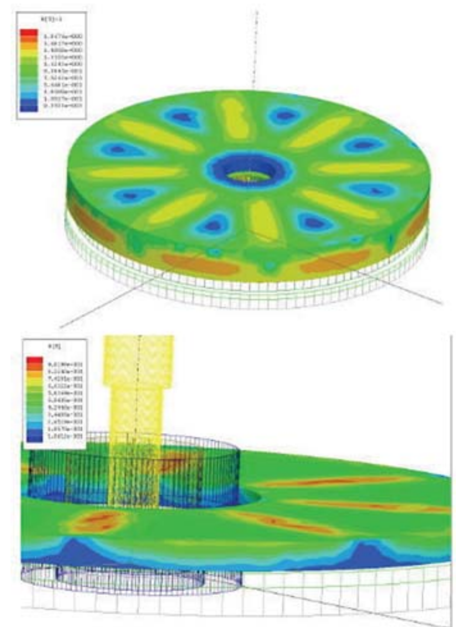

Fig. 3 Distribution of flux density determined by FEA.

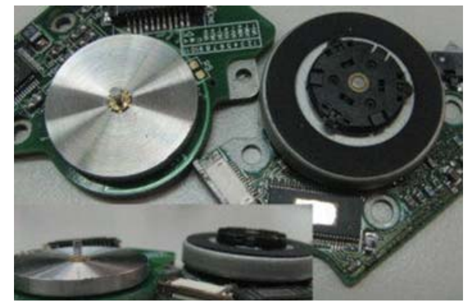

Fig. 4 Prototyped result and comparison with conventional motor

AL-02

Developments of a direct driven linear tubular generator for wave energy extraction.

C. Liu[1], S. Yan[1], C. Lin[1], H. Lin[1], M. Lai[1], C. Hwang[2]
1. Electrical Engineering, National Sun Yat-Sen University, Kaohsiung, Taiwan; 2. Electrical Engineering, Feng Chia University, Taichung, Taiwan

Introduction:
The ever increasing demands for generating electricity from various carbon-free renewable energy sources have drawn the attentions of developing appropriate mechanical/electrical conversion systems that can fulfill these special requirements. A linear tubular generator (LTG), with slotless stator windings and quasi-Halbach mover permanent magnet (PM) arrangement that can operate in reciprocating manner to incorporate with the available wave energy extraction mechanisms, will be reported in this paper.
Though the design concepts of linear tubular electric machines are quite common [1], detailed electromagnetic characteristic investigations will be required at the objective operational modes and mechanical inputs. The stator winding flux linkages contributed from those ring-shape mover PMs with radial, axial, and quasi-Halbach flux directions will be respectively calculated from three-dimensional (3-D) finite element method (FEM), and the induced voltages at the specific wave energy input patterns will then be devised. Based on these system electromagtic characteristics and the offshore site measurement data, applicability of the proposed LTG for wave energy extraction can then be assessed.
The Linear Tubular Generator:
Figure 1 shows the conceptual structure of a LTG, and the three possible mover PM arrangements are illustrated in Fig. 2. As the main flux direction in the mover is determined by the magnetization of PMs, the interaction rates and directions between stator windings and mover fluxes will dominant the generator voltage supplies. With a guided flux path through the mover PMs, investigations showed that the LTG with quasi-Halbach mover PM array will provide better overall performance. The 3-D meshes, flux density distribution, and stator induced flux linkages of this arrangement are illustrated in Fig. 3.
Operation and Applicability Evaluations:
Based on the long-term site measurements and the wave energy conversion mechanisms [2], the offshore wave energy distribution surrounding Taiwan and the buoy velocity pattern at the corresponding northeast area are illustrated in Fig. 4. By combining the flux linkages and the damped velocity patterns, with $|V(t)|=|d/dt(\lambda(x,t))|=|\upsilon(t)*d/dx(\lambda(x,t))|$, the voltages that are induced from the proposed LTG with quasi-Halbach rotor PM array can be devised and shown in Fig. 5. Evidently after a power conditioning device, the generated electricity can be stored and supplied to the utility system through sub sea cables. From such preliminary assessments, applicability of the proposed LTG for wave energy extraction can be validated.

[1] J. Wang, G. W. Jewell, and D. Howe, IEEE Trans. Magn., 35, 1986 (1999).

[2] U. A. Korde, Ocean Eng., 29, 1343 (2002).

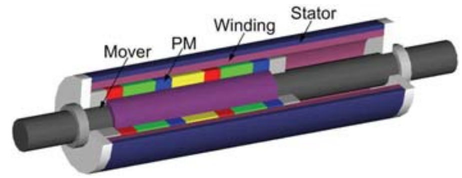

Fig. 1. Structure of a linear tubular generator.

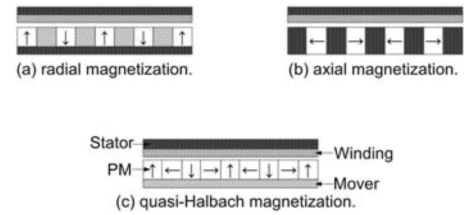

Fig. 2. Three different LTG mover PM arrangements.

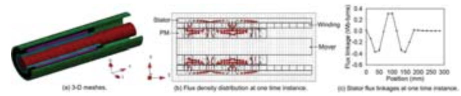

Fig. 3. Investigations of the LTG with quasi-Halbach rotor PM array by 3-D FEM.

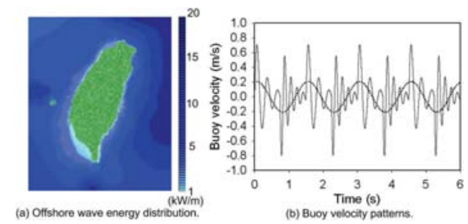

Fig. 4. Offshore wave energy distribution surrounding Taiwan and velocity patterns of the buoy at the northeast offshore area.

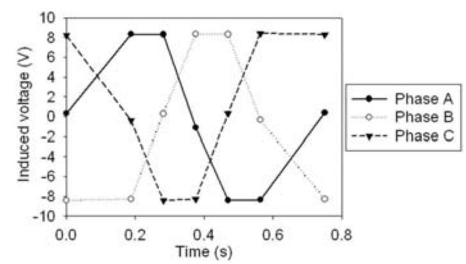

Fig. 5. Induced voltages of the proposed LTG.

AL-03

Mechanical resonance in non-oriented electrical steels induced by magnetostriction under pwm excitations.

S. Somkun, A. Moses, P. Anderson
Wolfson Centre for Magnetics, Cardiff University, Cardiff, United Kingdom

Magnetostriction (MS) is a source of acoustic noise and vibrations in induction motors [1]. The acoustic noise can reach its peak if the resonance occurs [2]. Magnetostriction-induced mechanical resonance in electrical steels commonly used in motor cores has been recently studied [3]. In the case of a PWM inverter-fed induction motor, there are high frequency components in the flux density (B) waveform, which may resonate [4]. In this work, non-oriented (NO) electrical steels under PWM excitation are studied and the effect of mechanical resonance is also taken into consideration, which could be useful for noise prediction during the motor design process.

Firstly, a strip of M400-50A NO steel 30 cm long and 3 cm wide was magnetised under sinusoidal waveform at 1.0 T peak flux density (B_p) from 500 to 4000 Hz. One end of the strip was clamped, while the displacement was measured at the other end with the aid of a single point laser vibrometer [3]. MS was calculated as the ratio of the displacement to the magnetic path length. At the magnetised frequency of 2250 Hz, the mechanical resonance occurs at 4500 Hz, which is twice of the magnetised frequency. The averaged value of peak to peak magnetostriction (MS_{pp}) was around 21.54 microstrain (με), 14 times higher than that at 500 Hz.

Secondly, PWM waveforms were applied to the strip at B_p=1.0 T. The relation between modulation index (m_i) and fundamental frequency (f_o) was set similar to that in a commercial inverter, which m_i=0.5 at f_o=25 Hz and m_i=1.0 at f_o=50 Hz. The switching frequency (f_{sw}) was selected as either 1687 Hz or 2250 Hz. MS_{pp} under PWM excitations are higher than that under sinusoidal excitation both at f_o=25 and f_o=50 Hz as shown in table 1. MS_{pp} at f_{sw}=2250 Hz is higher that that at f_{sw}=1687 Hz due to the effect of the resonance on the sample. There is significant fluctuation in the butterfly loops of MS when the switching frequency is equal to the resonance frequency even though the amplitude of B is lower than that at 1687 Hz as shown in figure 1. Figure 2 shows closer views of spectrum analysis of B and MS. High frequency components of MS are the same as those of B because the ripples in B do not change the sign of MS. At f_{sw}=2250 Hz, the highest frequency cluster happens at 4500 Hz, which is equal to the resonant frequency, with the peak value around 0.06 με.

MS_{pp} under PWM excitation can be up to 28% higher than that under sinusoidal excitation if the switching frequency matches the resonant frequency of the material. A small value of B can amplify very high value of MS if resonance occurs. Although this experiment was conducted on a single strip, similar effects would be expected in a motor core with different resonant frequencies. Large acoustic noise could be created if the switching frequency of the inverter coincides with the resonant frequency of the motor core.

[1] P. Cester, "Magnetostriction as a Source of Noise and Vibrations, Design and Measurement Set-up on an Experimental Induction Motor," in Summer Seminar of the Nordic Network for Multi Disciplinary Optimised Electric Drives. Taipalsaari, Finland, 2002, pp. 3.

[2] F. Kako, T. Tsuruta, K. Nagaishi, and H. Kohmo, "Experimental Study on Magnetic Noise of Large Induction Motors," IEEE Transactions on Power Apparatus and Systems, vol. PAS-102, pp. 2805-2810, 1983.

[3] T. P. P. Phway and A. J. Moses, "Magnetisation-induced mechanical resonance in electrical steels," Journal of Magnetism and Magnetic Materials, vol. 316, pp. 468-471, 2007.

[4] R. J. M. Belmans, D. Verdyck, W. Geysen, and R. D. Findlay, "Electro-mechanical analysis of the audible noise of an inverter-fed squirrel-cage induction motor," Industry Applications, IEEE Transactions on, vol. 27, pp. 539-544, 1991.

f_o (Hz)	Sine (με)	PWM f_{sw}=1687Hz (με)	PWM f_{sw}=2250Hz (με)
25	1	1.10	1.28
50	1.05	1.18	1.21

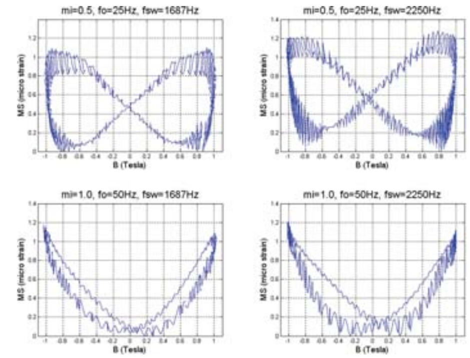

Butterfly loops of magnetostriction under PWM excitation

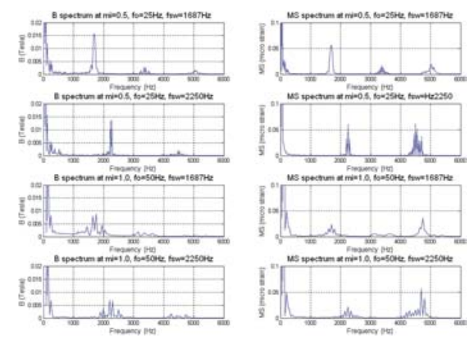

Harmonic analysis of flux density and magnetostriction at B_p=1.0 T

AL-04

Analysis of concentric magnetic gears using three dimensional scalar magnetic potential finite element method.

L. Xinhua[1,2], C. K.t[1], J. J.z[2], *J. Linni*[1]
1. Department of Electrical and Electronic Engineering, The University of Hong Kong, Hong Kong, China; 2. School of Automation, Shanghai University, Shanghai, China

I.INTRODUCTION
Compared with mechanical gears, magnetic gears have many advantages such as free from lubrication, inherent overload protection, no mechanical fatigue, low noise and high efficiency. However, due to its poor torque density, the traditional magnetic gear has not received much attention. Recently, a concentric magnetic gear topology has been proposed, which can produce high torque density [1]. However, the 2D-FEM analysis results exhibited serious errors with respect to the actual results. Namely, the measured static torque was about 30% lower than the calculated value in [2]. Although [2] has ever pointed out that such errors might be due to the large end effect, the use of 3D-FEM for such purpose is absent in literature.
In this paper, a 3D-FEM will be newly developed to analyze concentric magnetic gears. The key is to adopt the scalar magnetic potential so that the required data manipulation and computation can be significantly reduced.
II.APPROACH
For the 2D-FEM, vector magnetic potential is commonly used. However, for the 3D-FEM, if vector magnetic potential is adopted, the unknown variables will be three times the number of nodes since each vector potential has three directional variables. Based on scalar magnetic potential, the number of unknown variables is only the number of nodes of volume meshing [3]. Hence, the required memory and time for data manipulation and computation can be significantly reduced.
The magnetic gear shown in Fig. 1 can be represented by a boundary-value problem as given by: $\nabla(\mu\nabla\phi)=0$ in Ω; $\phi=\phi_0$ on S_1; $\mu(\partial\phi/\partial n)=-B_n$ on S_2 and the interface boundary condition of the PM is given by: $(\mu(\partial\phi^i/\partial n))-(\mu(\partial\phi^o/\partial n))=\sigma$, where the models of the PM and the calculated region are shown in Fig. 2. Consequently, it can be derived as a set of algebraic equations $[K][\phi]=[P]$ where $[\phi]$ is the vector of unknown scalar magnetic potentials and the contributions of each element to $[K]$ and $[\phi]$ are calculated by: $k_{ij}=\int_\Omega \mu\nabla N_i\nabla N_i d\Omega$, $p_i=\int_S N_i\sigma ds$. By using the Newton-Raphson iteration method and incomplete Cholesky conjugate gradient method, the above matrix equation can be solved with good convergence.
III.RESULTS
The parameters of the concentric magnetic gear used for exemplification are listed in Table I. Firstly, the magnetic gear is analyzed by the 2D-FEM, and Fig. 3(a) shows the static torque characteristics. Secondly, the developed 3D-FEM is used to analyze the magnetic gear and the static torque characteristics without and with the end effect are shown in Fig. 3(b) and Fig. 3(c), respectively. It can be found that their maximum static torques are very different, which is due to significant leakage flux at both ends of the magnetic gear. For verification, Fig. 3(d) shows the measured static torque characteristic in the outer rotor, which closely matches with Fig. 3(c).
Table II gives a comparison of their maximum static torques and computation times. Although the 2D-FEM can quickly get the result, typically 9 s per computation, the result exhibits a serious error, about 32%. Taking into account the end effect, the newly developed 3D-FEM can provide the result which closely agrees with the measured result, less than 7% error. Due to the use of scalar magnetic potential, the developed 3D-FEM computation time is typically 405 s per computation, which is very acceptable. Also, it can be found that the 3D-FEM (without considering the end effect) is slightly less accurate than the 2D-FEM, which is actually due to different segmentations of the airgaps along the circumferential direction. For the 2D-FEM, the inner and outer airgaps are divided into 450 and 550 segments, respectively; whereas, for the 3D-FEM, the two airgaps are both divided into 264 segments.

[1]K. Atallah and D. Howe, “A novel high-performance magnetic gear,” IEEE Trans. Mag., Vol. 37, No. 4, 2001, pp. 2844-2846.

[2]K. Atallah, S. D. Calverley and D. Howe, “Design, analysis and realization of a high-performance magnetic gear,” IEE Proc.-Elect. Power Appl., Vol. 151, No. 2, 2004, pp. 135-143.

[3]I.D. Mayergoyz, M.V.K. Chari and J. D’Angelo, “A new scalar potential formulation for three-dimensional magnetostatic problems,” IEEE Trans. Mag., Vol. 23, No. 6, 1987, pp. 3889-3894.

TABLE I PARAMETERS OF MAGNETIC GEAR

No. of pole pairs in inner rotor	3
No. of pole pairs in outer rotor	22
No. of ferromagnetic segments in stator	25
Outside radius of outer rotor yoke (mm)	97
Inside radius of outer rotor yoke (mm)	92
Outside radius of stator segment (mm)	85
Inside radius of stator segment (mm)	72
Outside radius of inner rotor yoke (mm)	67.4
Inside radius of inner rotor yoke (mm)	30
Stack length (mm)	40
Height of PMs in outer rotor (mm)	6
Height of PMs in inner rotor (mm)	4
Remanence of PMs (T)	1.1
Coercivity of PMs (kA/m)	894

TABLE II COMPARISON BETWEEN ANALYSIS RESULTS

	Max. static torque (Nm)	Computation time (s)	Error (%)
2D-FEM	84.5	9	32.0
3D-FEM without end effect	88.1	408	37.7
3D-FEM with end effect	68.4	405	6.9

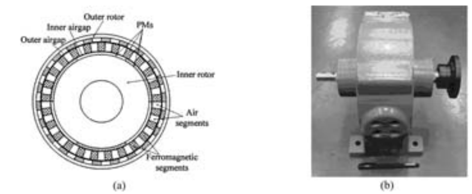

Fig. 1. Concentric magnetic gear. (a) Schematic diagram. (b) Prototype.

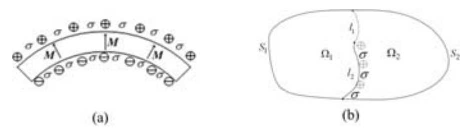

Fig. 2. Models. (a) PMs. (b) Calculated region.

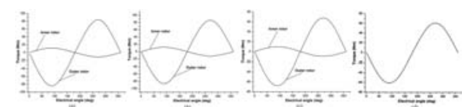

Fig. 3. Static torque characteristics. (a) 2D-FEM. (b) 3D-FEM without end effect. (c) 3D-FEM with end effect. (d) Measured.

AL-05

Reduction of the Toque Ripple and Unbalanced Magnetic Force of a Rotatory Two-Phase Transverse Flux Machine by Using Herringbone Teeth.

G. Jang[1], *H. Ahn*[1], J. Chang[2], S. Chung[2], D. Kang[2]
1. Dept. of Mechanical Engineering, PREM Lab., Hanyang University, Seoul, South Korea; 2. Korea Electrotechnology Research Institute, Changwon, South Korea

Transverse flux machine (TFM) has been considered as one of the promising driving machines especially at the low-speed applications because it has higher power density and torque than conventional electrical motors. However, it tends to generate big torque ripple and unbalanced magnetic force due to its inherent complicated structure, and they may result in the magnetically induced vibration and noise. Prior researchers have investigated to reduce the torque ripple and unbalanced magnetic force. Masmoudi et al. analyzed the magnet-skewing of a TFM rotor to reduce cogging torque [1]. But their design generates the unbalanced magnetic force due to the asymmetry of magnet. Jang et al. proposed a TFM without generating the unbalanced magnetic force by using symmetric multi-pair cores [2]. But their design still has big torque ripple. This paper investigates the characteristics of torque ripple and unbalanced magnetic force of a rotatory two-phase TFM due to the teeth geometry by using the 3-dimensional finite element method, and it develops a rotatory two-phase TFM with herringbone teeth to reduce the torque ripple and to eliminate the unbalanced magnetic force.

Fig. 1 shows a rotatory two-phase TFM with the rated speed of 300 rpm. Stator is composed of soft magnetic composite(SMC) to reduce iron loss, and it has upper and lower cores corresponding to phase A and B. Each core has circumferentially 32 teeth up and down, shifted by 1/2 tooth pitch (180 electrical degree, 5.625 mechanical degree). Rotor has 32 pairs of north pole, SMC and south pole, and they are alternatively arranged along the circumferential direction. Rectangular shape of current with the 1,250 Amphere-turns is applied to the coils of each phase.

Full finite element model is developed to analyze the whole motor. The number of 8-node hexahedral element of full model is 647,681. This model is divided every 0.28125 degree in the circumferential direction. ANSYS, a commercial finite element program, is used to solve the magnetic field. Torque and magnetic force are calculated by using the virtual work method every 0.28125 degree while the rotor passes a period of pole pair.

Magnetic field of the electric motors generates the torque ripple which is the major source of noise and vibration. Skew teeth may be one of the possible solutions to reduce the torque ripple. But they may generate the unbalanced magnetic force in the axial direction. This research investigates the magnetic field, torque ripple and unbalanced magnetic force for the five cases, i.e. (1) conventional straight teeth as shown in Fig. 1, (2) skew teeth for phase A and B in same direction, (3) skew teeth for phase A and B in opposite direction, (4) herringbone teeth for phase A and B in same direction, and (5) herringbone teeth for phase A and B in opposite direction. Fig. 2 shows the teeth geometry from the cases 2 to 5.

Fig. 3 shows the torque ripple and the axial unbalanced magnetic force for 5 cases. The skew angle of teeth is 10.43 degrees. Skew or herringbone teeth from the cases 2 to 5 reduce the torque ripple by approximately 43 %, compared with the conventional straight teeth of the case 1. Torque characteristics of case 2 and 3 are identical, and torque ripple of case 4 is the smallest of all. However, case 2 and 3 with skew teeth generate the unbalanced magnetic force in axial direction, because they have asymmetric magnetic field in axial direction. Fig. 4 shows the magnetic field of skew teeth and herringbone teeth. In Fig. 4 (b), herringbone teeth generates the symmetric magnetic field with respect to the mid plane of each core even though upper and lower teeth are shifted by 1/2 tooth pitch. It explains that TFMs with herringbone teeth do not generate the unbalanced magnetic force. This research may contribute to the sound operation of TFMs by reducing the magnetically induced vibration and noise originated from torque ripple and unbalanced magnetic force.

[1] A. Masmoudi, A. Njeh, and A. Elantably, "On the analysis and reduction of the cogging torque of a claw pole transverse flux permanent magnet machine," European Transactions on Electrical Power, vol. 15, pp. 513-526, 2005

[2] G.H. Jang, N.K. Park, C.I. Lee, J.H. Chang, S.W. Jeong, and D.H. Kang, "Reduction of the unbalanced magnetic force of a transverse flux machine by using symmetric multi-pair cores," Journal of Applied Physics, accepted for publication, vol. 103, May 2008

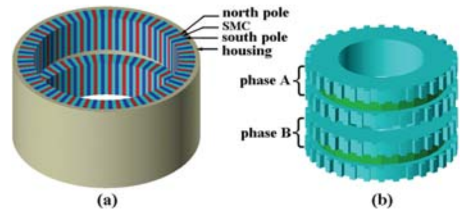

Fig. 1 A rotatory two-phase TFM (a) Rotor (b) Stator with conventional straight teeth (Case 1)

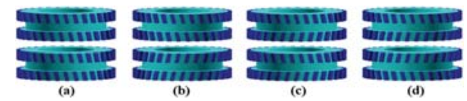

Fig. 2 A TFM with different teeth geometry (a) Case 2 (b) Case 3 (c) Case 4 (d) Case 5

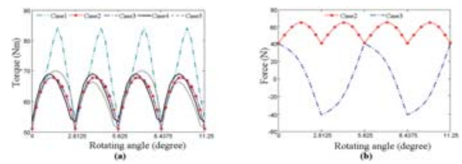

Fig. 3 Torque ripple and axial unbalanced magnetic force due to teeth geometry (a) Torque ripple (b) Axial unbalanced magnetic force

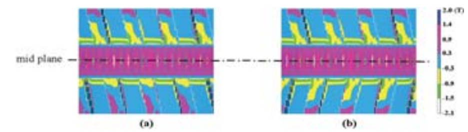

Fig. 4 Magnetic flux density (a) Skew teeth (b) Herringbone teeth

AL-06

EVALUATION OF INDUCTION HEATING APPLICATION OF LINEAR INDUCTION MOTOR BY USING FEM CALCULATION.

T. Yamada[1], K. Fujisaki[2,3]

1. Nittetsu Plant Designing Corpolation, Futtsu, Japan; 2. Nippon Steel Corpolation, Futtsu, Japan; 3. Graduated School of Environmental Studies, Tohoku University, Sendai, Japan

Introduction

Induction heating application of linear induction motor which uses electromagnetic AC field is investigated. Although linear induction motor application to thin steel sheet is usually used for conveyance, it is also considered to be used as induction heating application, because eddy current is generated in steel sheet. However, in this case, since the thin steel sheet is ferromagnetic material, it is expected that the meandering of the thin steel sheet caused by the electromagnetic force in the normal direction is influence on the product quality. Because the normal force is too difficult to handle the linear induction motor and thin steel sheet, the reduction of the normal force is an important problem to apply it to such a process. As shown in Fig.1, the normal force of the linear induction motor consists of a repulsive force caused by Lorentz force and an attractive force caused by magnetization. To evaluate the basic characteristic of linear induction motor, 2D electromagnetic field calculation by means of finite element method (FEM) is typically used as simplified method. However, because the real equipment is 3D model and especially eddy current shows complex behavior, it is necessary for the detailed investigation to evaluate by 3D electromagnetic field calculation. The aim of this study is to evaluate the characteristic of the electromagnetic force in a single side linear induction motor from the point of view of the comparison with 2D FEM calculation and 3D one.

Comparison result

Frequency characteristic of the electromagnetic force in the normal direction calculated by Maxwell stress method is shown in Fig.2. Here, the electromagnetic force calculated from 2D model is converted value by the steel sheet width of the 3D model. The normal force of the both models decreases as the frequency increases and changes from the attractive force to the repulsive force at 2kHz in 2D model and 5kHz in 3D model respectively. As shown in Fig.3, though the repulsive force caused by Lorentz force increases as frequency increases, on the other hand, the attractive force caused by magnetization is considered to be constant at any frequency. Therefore, a crossover frequency which the attractive force and the repulsive force become equal exists in the frequency characteristic [1]. Therefore, the effect of the normal direction is considered to be removed by operating at the crossover frequency. Also, the crossover frequency of the 3D model is large in comparison with 2D one. This reason is considered that the flow pattern of the eddy current in the steel sheet differs between 2D model and 3D model. The eddy current density vector of the 3D model at frequency 20kHz is shown in Fig.4. 2D calculation model of the linear motor assumes only center section in the width direction like enclosed area by dotted line in Fig.4. On the other hand, because the 3D model has edge part of the steel sheet, the eddy current returns at the edge part of the steel sheet. Usually, Lorentz force in the steel sheet operates as repulsive force mode in the normal direction. However, the eddy current which returns around the edge part of the steel sheet makes the steel sheet an electromagnetic force as attractive force mode in the normal direction and the total quantity of the Lorentz force operates as repulsive force is reduced due to the attractive force at the edge part. As a result, it is considered that the crossover frequency of the 3D model becomes large in comparison with 2D model.

[1] T.Yamada, K.Fujisaki, “Application of Linear Induction Motor for Tension Supply and Heating to Thin Steel Sheet” IEEJ Trans, IA, Vol.127, No.7, 2007, pp707-714 (in Japanase).

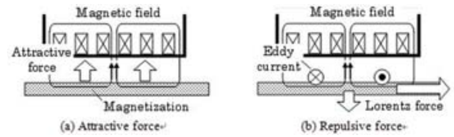

Fig.1 Electromagnetic force in thin steel sheet.

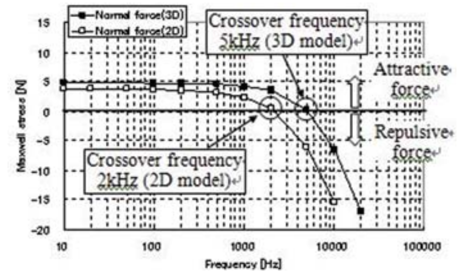

Fig.2 Frequency characteristic of normal force.

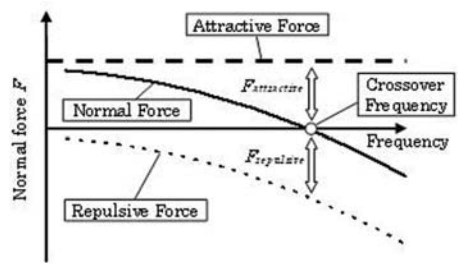

Fig.3 Mechanism of crossover frequency.

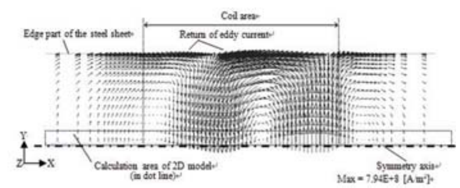

Fig.4 Eddy current density vector of the 3D model at frequency 20kHz (ωt=0°).

AL-07

Calculation of Stator End-winding Reactance of an Induction Machine Based on Magnetic Energy by 3-D Finite Element Analysis.

R. Lin, A. Arkkio
Helsinki University of Technology, Espoo, Finland

I. INTRODUCTION

This paper illustrates a procedure for calculating the end-winding reactance of an induction machine by 3-D finite element analysis.

II. MODEL AND METHODS

A. Model

According to IEC, the end-winding reactance should be measured when all the rotary parts are removed, so no rotary parts in this model. To analyze the energy, the core region is divided into 4 same parts with equal 10 cm in axial length. The model is shown in Fig. 1.

B. Methods

The simulations use current sources and a time-harmonic analysis. The following equation is solved:

$\nabla\times[\boldsymbol{\upsilon}(\nabla\times\underline{\boldsymbol{A}})]+j\omega\boldsymbol{\sigma}\underline{\boldsymbol{A}}=\underline{\boldsymbol{J}}$, (1)

where $\underline{\boldsymbol{A}}$ and $\underline{\boldsymbol{J}}$ are the complex vectors of vector potential and current density. The number of DOFs to solve is 272944.

Since no rotary parts, the flux is just stator leakage Φ_l, which contains slot leakage Φ_{sl}, tooth-top leakage Φ_{tl} and end-winding leakage Φ_{el}. Correspondingly, the total magnetic energy in the model W_l consists of slot leakage energy W_{sl}, tooth-top leakage energy W_{tl} and end-winding leakage energy W_{el}. Also, the sum of W_{sl} and W_{tl} is proportional to the axial length l of stator iron core.

Without the end-windings, the energy in parts 1-4 originates only from slot leakage and tooth-top leakage. Then, the energy in each part should be equal since every part is the same.

The end-windings can affect the energy in the iron cores, especially in the core ends. Part 1 is far from the end-windings, so it is assumed that the energy W_1 in part 1 is not affected by the end-windings, which originates only from slot leakage and tooth-top leakage. Hence, the produced energy by the end-windings can be calculated by

$W_{el}=W_l-4W_1$. (2)

C. End-winding Reactance

The time-average value of magnetic energy W_V in volume V is calculated by

$W_V=0.25\int\mathrm{Re}\{\underline{\boldsymbol{H}}^*\underline{\boldsymbol{B}}\}\mathrm{d}V$, (3)

where $\underline{\boldsymbol{H}}$ and $\underline{\boldsymbol{B}}$ are the complex vectors of field strength and flux density.

The end-winding reactance per phase X_{ew} is calculated by

$X_{ew}=8\omega pW_{el}/(mI^2)$, (4)

where I is the rms value of current, p and m are the number of pole pairs and phases.

III. RESULTS

A. Flux Density in Core Region

To analyze the end-winding effects, 4 lines parallel to the axial direction are chosen: line 1 in the air, lines 2 and 4 in the stator yoke and line 3 in the stator tooth. Figs. 2 and 3 plot the variation of flux density along these lines.

B. Magnetic Energy

Based on (3), Table I lists the time-average values of energy in different parts of the model.

C. End-winding Reactance

X_{ew} is calculated by (2) and (4). In this model, p = 3, m = 3 and I = 270 A. The calculation result of X_{ew} is 0.0326 Ω, and the given experiential value is 0.0248 Ω, so the relative error is 31.5%.

IV. CONCLUSIONS

In Figs. 2 and 3, the magnetic field in the ends of iron core is affected by the end-windings. The flux density in part 4 is stronger than in parts 1-3. Besides, Table I shows that the magnetic energy in part 4 is 2.1% larger than in parts 1, 2 and 3, due to the end-windings. Although the relative error between the calculation result and given value is not small, it is acceptable since the given value is based on the rough semi-experiential analytical formula.

The results verify that the end-windings affect the magnetic field in the core ends. And the effects on the flux density are stronger than that on the magnetic energy in the core ends.

Geometric Part	Magnetic Energy [J]
Whole model	6.813665
Part 1	1.466751
Part 2	1.466755
Part 3	1.466971
Part 4	1.497927

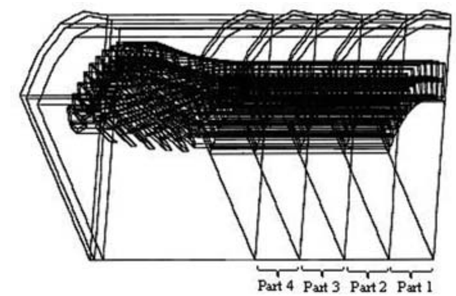

Fig. 1. The model of the machine without rotary parts.

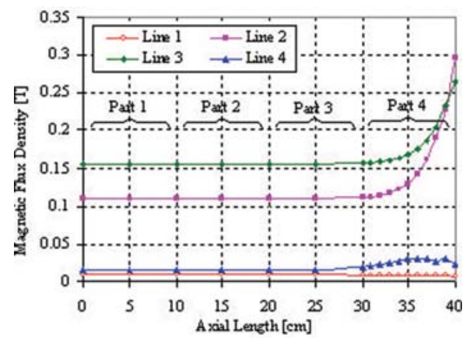

Fig. 2. The variation of magnetic flux density (magnitude of real parts) as the axial length of stator iron core.

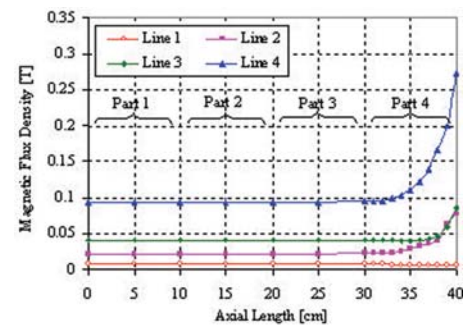

Fig. 3. The variation of magnetic flux density (magnitude of imaginary parts) as the axial length of stator iron core.

AL-08

Investigation of carrier loss of induction motors considering skin effect in electrical steel sheets.

K. Yamazaki, N. Fukushima
Dept. of Electrical, Electronics and Computer Engineering, Chiba Institute of Technology, Narashino, Japan

Induction motors driven by PWM inverters are widely applied to the industry as variable speed motors. However, it is well known that the efficiency of the motor often decrease due to the carrier harmonics that cause the harmonic copper and core losses in the motor. The estimation of the carrier harmonic losses at each part of the motor is desired.

Owing to the progress of computers, the electromagnetic field analysis using the finite element method became a powerful tool to estimate the losses of the motors. In most of the analyses, the stator and the rotor cores are modeled as the solid magnetic material without the conductivity and the core loss is calculated in the post process from the time-variation of the flux density obtained by the finite element analysis [1]. In these cases, the axial variation of the flux density within the electrical steel sheet is neglected.

However, when the frequency of the magnetic field is high, it can be considered that the flux concentrates at the surface of the electrical steel sheets due to the skin effect. The frequency of the carrier harmonics of the PWM inverter is kHz order. Therefore, the eddy current analysis considering the axial flux distribution within the sheet will be required for the correct estimation of the core loss caused by the carrier harmonics.

In this paper, we investigate the carrier harmonic losses in the induction motors from both sides of measurement and calculation. In the measurement, the motor is driven by both the PWM inverter and sinusoidal power supply at the same fundamental voltage condition. Then the total carrier harmonic loss is obtained by the subtraction. On the other hand, the carrier losses generated at the primary windings, secondary conductor, stator and rotor cores cannot be separated by the measurement. Therefore, we also introduce the 3-D finite element analysis considering the skin effect of the electrical steel sheets, which can calculated the losses separately. The measured and calculated total carrier harmonic loss is compared to verify the validity.

Fig.1 shows the voltage waveform and included harmonics of the PWM inverter. The fundamental and carrier frequency is 50 and 3.3kHz, respectively. In this case, around the 66i-th (i=1, 2…) harmonics are remarkable.

Fig.2 shows the 3-D finite element mesh. The analyzed motor is a 750W cage induction motor. The analyzed region is reduced as half of the electrical steel sheet of the motor. The number of the time-step per one time period is set as 1,024 to consider the carrier harmonics of the PWM inverter correctly. The rotor region is shifted at each time step due to the rotational speed of the rotor.

Fig. 3 shows the calculated eddy current distribution of the electrical steel sheet. It can be seen that the currents increase when the motor is driven by the inverter. Fig. 4 shows the calculated flux density waveform at the teeth. It indicates that the harmonic ripples are concentrated at the surface of the electrical steel sheet due to the skin effect. The waveform at the inside of the sheet is almost sinusoidal.

Fig. 5 shows the calculated and measured carrier harmonic losses. The loss calculated by the 2-D finite element method assuming the uniform flux density within sheet is also shown for the comparison. The result of the 2-D method clearly overestimates the carrier harmonic core losses because it neglects the skin effect. On the other hand, the result of the 3-D analysis agrees well with the measured results. In addition, it is clarified that the main components of the carrier harmonic losses in the induction motor are the stator and rotor core losses.

[1] K. Yamazaki and Y. Abe, "Loss analysis of induction motors considering carrier harmonics" IEEJ Trans. on IA, vol.126, no.4 pp.379-384 (2006)

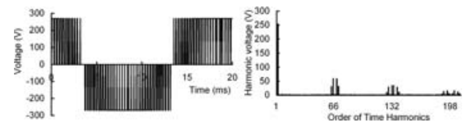

Fig.1. Voltage waveform of inverter and included harmonics.

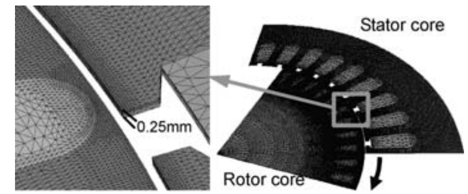

Fig.2. 3-D finite element mesh (Half of a steel sheet).

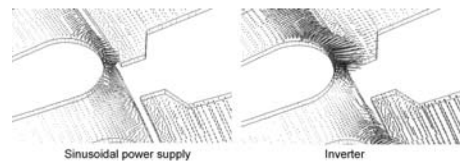

Fig.3 Calculated eddy current distribution of core.

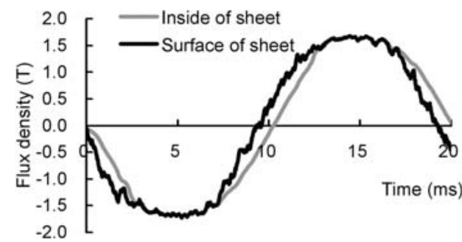

Fig.4. Calculated flux density waveform at teeth.

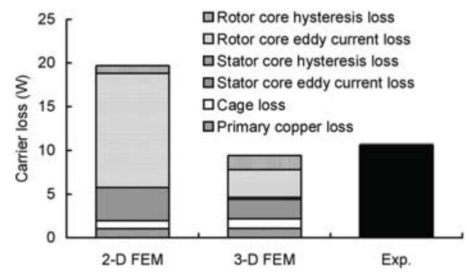

Fig.5. Calculated and experimental carrier losses.

AL-09

Characteristics Analysis of 3DOF Spherical Motor for robotic wrist motor.

S. Won, J. Lee
Electrical Eng., Hanyang University, Seoul, South Korea

The spherical motor for robotic wrist is growingly attracting interest from researchers and engineers who study the automatic control and robotics because it can change its rotating axis orientation arbitrary. Among the spherical motors, the permanent magnet spherical motor has potential to be adopted in a number of areas of robotic applications because it is very simple to implement 3DOF operations [1].
However, the spherical motor has some problems in predicting its characteristics because we have to perform 3-dimensional analysis to calculate the spherical motor torque which has three directional components of basis coordinate axis. 3-dimentional analysis itself is not so difficult but, in this case, the structure of spherical motor is somewhat complicated like Fig. 1, it takes several hours to finish a 3-dimensional simulation. Considering the rotating axis orientation is not fixed, the analysis of spherical motor characteristics takes such a long time compared with ordinary single axis rotating motor.
To solve this problem, we use a novel calculation method of the spherical motor torques and back-emfs at any arbitrary axis with a given magnetic flux density field data by 3D finite element analysis and current values of each coil elements [2]. Using this method, we can calculate the spherical robotic wrist motor torques at any rotating axis and this method saves calculation time dramatically because it needs just one static 3D finite element analysis for getting flux density field data. It is very important to save calculation time because we have to calculate torque vectors and back-emfs at every time step from start to end while the rotor is moving to designated position to predict the behavior of a spherical motor.
To verify this method, we manufactured a spherical motor and compared the simulated values with the measured data. It is found that the simulation values are in good agreement with the measured values, so it is confirmed that the presented method is very useful in analysis of a spherical motor.

1. Liang Yan, I-Ming Chen, Chee Kian Lim, Guilin Yang, Wei Lin, Kok-Meng Lee, "Design and analysis of a permanent magnet spherical actuator", Intelligent Robots and Systems, 2005. (IROS 2005). 2005 IEEE/RSJ International Conference on, 2-6 Aug. 2005 Page(s):691 - 696v.

2. S.H.Won, J.S.Ahn, J.Lee, "Dynamic Characteristics Analysis of LDM for the Electric Screen Door System", J. Appl. Phys.,Vol.99, No.8, Part 2&3, 15 Apr. 2006, Page(s):08R311

The spherical motor structure and the current driver

AL-10

Electro-Magnetically Excited Vibration Testing for a Vibro-Acoustic Investigation on PMSMs in Hard Disk Drives.

S. Suwankawin[1], *T. Jintanawan*[2]

1. Electrical Engineering, Chulalongkorn University, Bangkok, Thailand; 2. Mechanical Engineering, Chulalongkorn University, Bangkok, Thailand

Acoustic noise recently becomes new criteria for hard disk drive (HDD) design. Noise that generated from the spindle motor partly contributes to the overall noise of HDD. For the fluid dynamic bearing (FDB) motors in HDDs, electromagnetic (EM) forces are the major source of vibro-acoustic noise [1, 2]. The Permanent Magnet Synchronous Motors (PMSMs) for HDD consist of many tiny components, including the motor base and spindle hub. Both structural components are the major paths of noise, because they play an important role for vibro-acoustic transmission.

The modal vibration testing on the motor structure is usually performed to explore its inherent vibro-acoustic behavior [1, 3]. For the small-sized PMSMs in HDD and expanded range of the interested audible frequency up to 20 kHz, the vibration testing on the motor with the mechanical excitation [1, 3] might not be appropriate, because the mechanical impulsive forces contain an insufficient energy for exciting the high-frequency modes. The present work therefore proposes a technique of vibration testing on the miniature PMSMs for HDD through the use of sine-swept, EM-excitation. Compared with the conventional mechanical excitation, the EM excitation is more natural to the actual EM forces that are the major noise source in the motor operation.

EM-EXCITED VIBRATION TESTING

With the motor rating of 10 Vp-p and 1.5-A maximum current and the designed bandwidth of 0.1-20 kHz for the EM-excited vibration testing, it is applicable to design the amplifier that functions within these criteria. In this case, the linear power amplifier (200-W-STK4028II model) is used as the V-to-I amplifier. With a low total harmonic distortion (0.4% THD) of STK4028II, a perfectly sinusoidal current is satisfactorily obtained. The use of V-to-I amplifier helps avoid the high-frequency contents due to switching of the inverter.

In the implementation, the sine-swept source signal was supplied by the function generator from Agilent-35670 dynamic signal analyzer (DSA). This signal was amplified with the V-to-I amplifier and then fed to the motor. During the operation, as the frequency swept, the V-to-I amplifier varies the phase voltage accordingly in order to regulate the phase current at the constant value. To validate the effectiveness of the V-to-I amplifier, the spectrum of the phase current for the whole range of audible frequencies (0.1-20 kHz) is illustrated in Figure 1.

For the test setup, the PMSM for HDD is excited by featuring a sine-swept and controlled current with a constant amplitude that supplied by the V-to-I amplifier to only one phase of the motor, ensuring a constant level of EM force at all various frequencies from 0.1 to 20 kHz. The flexural vibrations from both the motor base and the spindle hub are measured at various positions, using the Laser Doppler Vibrometer (LDV). Signals of the measured vibration and the phase current are fed to the DSA to determine the frequency response functions (FRFs).

VIBRO-ACOUSTIC PHENOMENA OF THE PMSMS FOR HDD

The FRFs were compared with the measured sound power spectrum (SPW) of the spin motor in Figure 2. The vibro-acoustic modes and their corresponding natural frequencies can be identified at peaks of the FRFs. With the proposed sine-swept EM-excitation, all the vibro-acoustic modes, especially at high frequencies, can be completely seen. For all measured FRFs, there exist a single mode at ~2.4 kHz and another two groups of the high-density and undistinguished modes at frequency ranges of 7-12 kHz and 14-20 kHz, respectively. Each vibro-acoustic mode can be identified in the FRFs that measured either at the motor base or at the spindle hub, indicating that the motor exhibits coupled vibrations of the base and hub.

A comparison of both the vibration and sound spectra in Fig. 2 shows that the natural frequencies of all vibro-acoustic modes found in the FRFs closely match with the sound resonance frequencies, i.e. the frequencies where the mountain peaks exist in the sound spectrum.

[1]N. Ajavakom, et. al., Microsystem Technologies, DOI 10.1007/s00542-006-0372-z, 2007.

[2]C. Bi, et. al., IEEE Trans. Magnetics, vol. 39, pp. 800–805, 2003.

[3]C. Wang, et. al., IEE Proc. Elect. Power Appl, vol. 12, pp. 29-36, 2004.

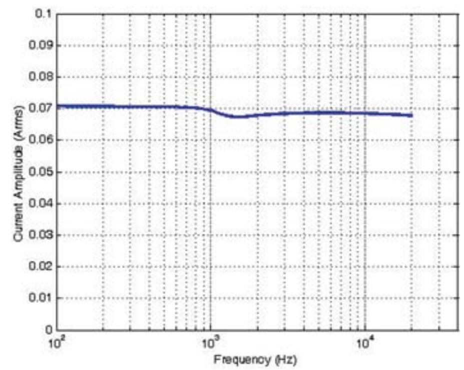

Fig. 1. Spectrum of the phase current with the setting value of 100 mA peak.

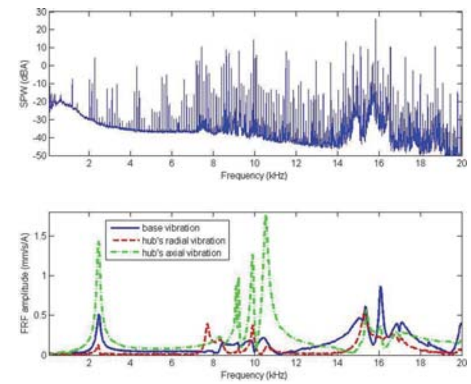

Fig. 2. Sound power spectrum (top) vs. the FRFs (bottom) obtained from the EM-excited vibration testing.

AL-11

A Study on the Multi-Objective Optimal Design of Interior Permanent Magnet Synchronous Motor.

K. Kim, J. Lee
Dept. of electrical engineering, hanyang university, seoul, South Korea

1.INTRODUCTION
Traction motors for vehicles such as fuel cell and hybrid electric vehicle are main application area of an interior permanent magnet synchronous motor (IPMSM). The reason for these applications is driving characteristics of high torque performance when starting mode and wide constant power range by field weakening control [1],[2].
In the paper, the multi-objective optimal design of IPMSM is proposed in order to increase high reluctance torque, low cogging torque, low torque ripple and low THD of back EMF. Because there are many design variables related to shape and arrangement of permanent magnet, representative design variables are suggested and optimized by experimental design method with finite element method (FEM) [3]. For the comparison of reluctance torque, the d-axis and q-axis inductances by FEM are calculated. Finally, the prototypes of IPMSM are experimented for the verification of multi-objective design results.
2.OPTIMAL ROTOR DESIGN OF IPMSM
The rotor model with flat type magnet can not have high inductance difference and saliency which means the ratio of q-axis inductance to d-axis inductance just because of difficulty in security of q-axis flux path in the rotor core. Therefore there is limit to increase the reluctance torque. In the paper, in order to improve the performance of reluctance torque of IPMSM, the multi-objective design of V shape magnet model by using Taguchi method is proposed. Fig. 1 shows the representative design variables of V shape magnet model. The variable RL means the ratio of magnet length to barrier length. Each design variable has three levels and noise factor is set as tolerance levels of slot open width. Each rotor model for Taguchi analysis has the same volume of permanent magnet from an economical point of view.
Orthogonal array L9 is used with multi-objective function. The multi-objective optimal design can be performed by using normalized SN ratio and weighting function of each object function. The values of SN ratio according to object functions are normalized by using mean and standard deviation of SN ratio. After that, the optimal values of multi-object function using weighting function are calculated. For the high reluctance torque, the weighting function for maximum torque is decided as 0.5. The weighting functions of emf and torque ripple are set as 0.3 and 0.2, separately. The main effect plot of SN ratio of multi-objective function is shown in Fig. 2. Therefore, optimized design values of V shape rotor can be selected as A3, B1 and C1.
In order to verify reluctance torque, the d and q-axis inductances according to load angle are analyzed by FEM and total torque is separated with reluctance torque and magnetic torque as shown in Fig. 3. Because of high reluctance torque of V shape magnet model over load angle of 110 degree, the total torque of V shape magnet model is superior to that of flat type magnet model. Fig. 4 shows the experimental set for the verification of optimal design results.
3.CONCLUSION
This paper proposed the multi-objective optimal design of IPMSM for the purpose of high torque density and wide constant power region owing to high reluctance torque by experimental design method with FEM.

[1] K.C. Kim, D.H. Koo, J.P. Hong and J. Lee, “A study on the characteristics due to pole-arc to pole-pitch ratio and saliency to improve torque performance of IPMSM”, IEEE Transactions on Magnetics, vol. 43, no. 6, pp. 2516-2518, June 2007

[2] Ching-Tsai Pan, S-M, Sue, “A linear maximum torque per ampere control for IPMSM drives over full-speed range”, IEEE Transactions on Magnetics, vol. 20, no. 2, pp.359-366, June 2005

[3] Jiju Antony, Design of Experiments for Engineers and Scientists, Butterworth Heinemann, 2003

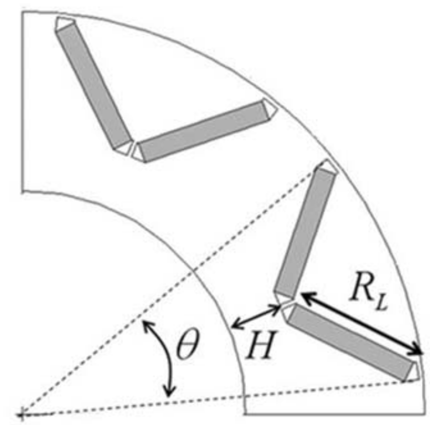

Fig. 1. Representative design variables

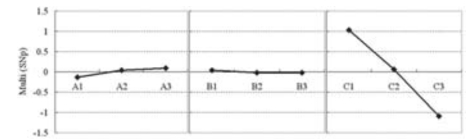

Fig. 2. Main effect results

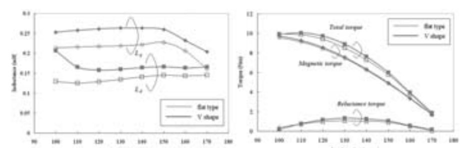

Fig. 3. Comparison results

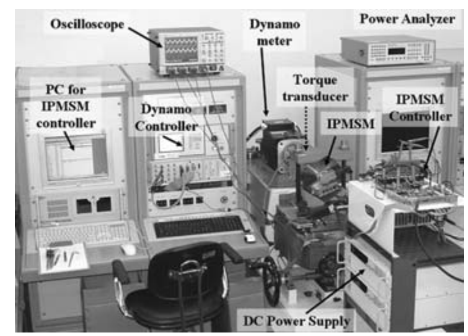

Fig. 4. Experimental set for IPMSM

AL-12

Analysis on Operating Characteristics of Auto Focusing VCM Actuator.

Y. Choi[1], Y. Kim[1], G. Cho[1], *Z. Piao*[1], B. Min[1], H. Baek[1], B. Chae[2]
1. Department of Electrical Engineering, Chosun University, Gwangju, South Korea; 2. Department of Electrical and Control Engineering, Korea Polytechic V College, Gwangju, South Korea

1. Introduction
Auto focusing actuator for mobile camera module can be classified into stepping motor type, ultrasonic wave type and VCM type. Stepping motor type has strengths of being powerful and highly reliable, but has weakness of big in size and high prime cost. Ultrasonic wave motor type is a type operated by micro precision ultrasonic motor made with piezoelectric ceramic, and due to its advantage of making into compact and slim size, it has been developed and researched for auto focusing camera module. However, due to material's hysteresis and problem in reliability with quick abrasion on friction part and problem with impact due to easily breakable material make ultrasonic wave motor type difficult for application[1]. VCM type is fast in response, high in precision, and excellent in size and prime cost aspects, but as it needs continuous power to be fixed on focal point of lenses, it requires relatively larger power consumption, and has weakness of being fragile on impact[2]. Therefore, by making the most of strengths existing type has at the same time, research on actuator that is improved in reliability and advantageous for making into compact size is needed.
In this paper, VCM actuator designed a similar structure with operating theory of hard drive's rotary type actuator. When rotary type VCM actuator rotates with the center of lens as its basis, it makes up-and-down motion by lens guide with cam shape. Therefore, this kind of structure allows advantages of lower power consumption, rugged structure to impact and vibration, and easy to be made in slim type. Also, in this paper, validity of the designed VCM actuator was verified through inquires on the maximum motion displacement characteristic, displacement response characteristics, hysteresis response characteristics with self made laser displacement sensor-applied characteristics evaluation system in order to evaluate characteristics of the designed VCM actuator.
2. Experiment results of VCM acuator
Specifications of produced VCM actuator is on Table 1. Material of Leaf spring is SUS 301, and yoke is made of Gray cast iron with high permeability. As the result of supplies normal operating voltage 2.75 [V] to the designed VCM actuator and measuring moving part with laser displacement meter, when the maximum rating voltage was supply, the maximum motion displacement value was measured as 509[μm] and it is as in Figure 1. Resistance of VCM actuator is ratio of current consumption to input voltage in the maximum motion displacement, which is 33.1[Ω], the maximum current consumption was 83.2 [μm], and the power consumption at this point was 229 [mW]. In addition, in order to confirm charactercs of durability, VCM actuator was measured of changes after repeating 100,000 times from the minimum motion displacement to the maximum displacement, and to check reliability, hysteresis changes were measured every 5,000 times after the 100,000 times of operation, and as the result, it was confirmed that hysteresis change was insignificant by the maximum value of 15 [μm]. Figure 2 predicts increase of Hysteresis change for 100,000 times of operation using Weibull 6, and it draws a result of changing up to 20 [μm] after 150,000 times.
3. Conclusions
In this paper, mobile device mountable VCM actuator for auto focus control was made, and in order to analyze operating characteristic of produced VCM actuator, tests of the maximum motion displacement characteristics and hysteresis response characteristics were selected to perform experiment. As the result of the experiment, operating displacement above 509 [μm] under normal voltage used in mobile device was confirmed. Also, as the maximum motion displacement and hysteresis displacement value are small after repeated test of 100,000 times from the minimum motion displacement to the maximum motion displacement, it was verified by the test that durability and reliability have been secured.

[1] M.J. Jung,"Zoom and autofocusing actuator used in camera phone",EP&C/Technical Report/actuator., Korea, pp 92~97.

[2] F.Jogensen., "The complete handbook og magnetic recoding",McGraw-Hill international editions.

Physical specfication			Electrical specification		
Hight	Length	Width	Resistance	Turns	Daimeter
4.5[mm]	7.9 [Φ]	7.9 [Φ]	33[Ω]	140[T]	0.06 [Φ]

Figure 1. The results of maximum displacement

Figure. 2 Degradation of hysteresis in the weibull 6

AL-13

Development of Laser Beam Steering System Using Three Magnetostrictive Actuators.

J. Jung, Y. Park, K. Im
Mechatronics Engineering, Chungnam National University, Daejeon, South Korea

Over the past 20 years, laser processing systems have found their way in countless industrial applications such as welding, cutting, scribing, engraving, drilling and marking. Laser beam steering system is used to position the laser focus onto the workpiece. Galvanometer is widely used for laser beam steering, but it needs two separate mirrors for two- axis control. Thus, this paper proposes one-mirror laser beam steering system using three magnetostrictive actuators.

Fig. 1 shows a schematic view in two- and three-dimension of the proposed laser beam steering system. The system consists of three magnetostrictive actuators, notch flexure hinge and a mirror. The dimensions of the system are 91 mm in diameter and 112 mm in height. The sizes of mirror are 25.4 mm in diameter and 8 mm in thickness.

The components of the magnetostrictive actuator are magnetostrictive material rod (Terfenol-D) with Ø10 mm x L50 mm surrounded by 880 turns of coil, cylinder-type permanent magnet, 7.5 MPa of preloading spring, push rod, flux paths, and housing. The magnetostrictive actuator generated 30 μm of displacement and about 200 N of force with 2 amperes of current.

A notch flexure hinge is designed to convert linear motion from magnetostrictve actuator into an angular motion. The parameters to be determined are notch radius R, notch thickness t, notch length b, flexure length l. The optimized values for the parameters are R=2 mm, t=1 mm, b=10 mm and l=24.5 mm. The notch flexure hinge is made of aluminum. The maximum displacement and angle can be calculated.

$\theta_{max}=(4KR/K_tEt)\sigma_{max}=2.4$ *mrad (1)*

$x_{max}=2l\theta_{max}=117.6\mu m$ *(2)*

,where stress concentration factor $K_t=1.119$*, maximum stress* $\sigma_{max}=54\times10^3 mN/mm^2$*, correction factor* $K=0.4485$*, Young's modulus of aluminum* $E=72\times10^6 mN/mm^2$ *and yield stress of aluminum* $\sigma_y=270\times10^3 mN/mm^2$ *[1].*

Fig. 2 shows the experimental setup for the measurements of displacement of flexure hinge, marked as X_1 and X_2. Experimental setup consists of the three magnetostrictive actuators, platform, a current driver for current amplification, power supply and two ADE 4810 Microsense II capacitive sensors with the resolution of 1 nm for the displacement measurement. Magnetostrictive actuator exhibits significant hysteresis over the operating range. The Preisach model is modified and used to compensate hysteresis[2]. Hysteresis-compensated chopping waves are introduced to hinges A and B simultaneous. After 10-seconds, another hysteresis-compensated chopping wave is introduced to hinge C. Using the measured displacements at X_1 and X_2, an angle can be calculated by using the relationship $\theta=(X_1-X_2)/L$.

Fig. 3 (a) shows the measured displacements and Fig. 3 (b) the calculated angle. The mirror can be rotated up to angle of 1.45 mrad, which is smaller than calculated maximum angle of 2.4 mrad.

[1] Stuart T. Smith, "Flexures: elements of elastic mechanisms", CRC Press; 2000.

[2] Kyoung-Bin Im, "Hysteresis Compensation and Control of Magnetostrictive Actuator Using Modified Preisach Model", Master's thesis at Chungnam National University in Korea, 2007.

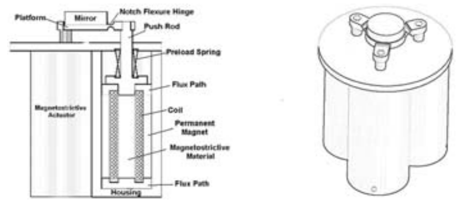

Fig. 1 Schematic of the laser beam steering system

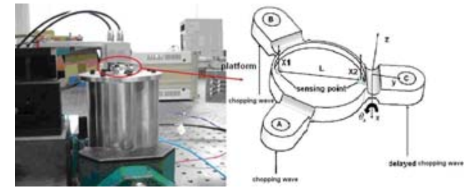

Fig. 2 Photograph for the displacement and angle test.

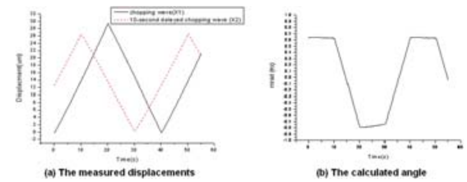

Fig. 3 Experiment result of laser beam steering system

AM-01

Magnetization process and induced pulse voltage of FeCoV wire implemented in tiny sensor chip.

H. Tanaka[1], T. Kusunoki[1], T. Yamada[1], *Y. Takemura*[1], S. Abe[2], S. Kohno[3], H. Kondo[3]
1. Department of Electrical & Computer Engineering, Yokohama National University, Yokohama, Japan; 2. Kanagawa University, Yokohama, Japan; 3. Nikkoshi Co., Ltd., Tokyo, Japan

A fast magnetization reversal accompanied with a large Barkhausen jump in a magnetic wire is utilized in speed sensor, rotation sensor, and other applications [1,2]. A twisted Vicalloy wire has been the optimum material yielding this phenomenon, which reveals longitudinal anisotropy with coercive force of about 20 Oe in the outer shell (soft layer) and 80 Oe in the inner core (hard layer) [3]. When the magnetization of soft layer is switched parallel/antiparallel to that of hard layer by an external field, positive/negative output voltages are induced in the pickup coil respectively. Previously, the magnetization of the hard layer was not reversed in order to obtain high output voltage owing to switching of the soft layer. The positive/negative outputs were asymmetric in amplitude, which arose from the asymmetric magnetization reversal of parallel /antiparallel switching due to the magnetostatic coupling between the soft/hard layers under the antiparallel alignment and the demagnetizing field under the parallel alignment. These demagnetizing field and magnetostatic coupling increase with shortening the wire length. The output voltage due to the switching of the soft layer was significantly reduced according with the increased magnetostatic coupling between the soft/hard layers in short wires. This characteristic prevents miniaturization of the sensor size. In this paper, magnetization process under an applied magnetic field larger than that in the previous method was studied. In this case, the hard layer was also switched. It was found that the pulse voltage owing to the large Barkhausen jump during magnetization reversal of the soft layer was successfully obtained in short wires (~3 mm).
A twisted Vicalloy (Fe40-Co50-V10) wire of 0.25 mm diameter was used. A pickup coil of 50 turns was located at the center of the wire. The wire length was changed from 1.5 to 9 mm. An alternating magnetic field at 1 Hz was applied to the wire by a solenoid coil. As the hard layer was reversed, the switching of the soft layer was always antiparallel reversal to the hard layer as shown by insersions in Fig. 2. The amplitude of the output voltage during the magnetization reversal of the soft layer was measured as a function of the applied field strength as shown in Fig.1. The range of the applied field where the output voltage was obtained shifted to higher field strength with shortening the wire length. It was because that the higher field was required in order to switch the hard layer against the larger magnetostatic coupling between the hard and soft layers. Magnetization curves were also measured. The maximum applied field strength for each length of the wires was determined by that for obtaining the maximum output voltage in Fig. 1. All wires exhibited the large Barkhausen jump during the magnetization reversal of the soft layer. It was switched in decreasing the magnetic field for the wires shorter than 4.5 mm, whereas it was reversed in increasing the magnetic field for 6 - 9 mm wires as indicated in Fig. 2. The magnetization of the soft layer in the wires shorter than 4.5 mm was autonomously switched by the large demagnetizing field under the parallel alignment. This successful observation of the induced pulse voltage accompanied with the large Barkhausen jump in the Vicalloy wires as short as 3 mm is significant for sensor applications, especially for implementing as tiny sensor chips.

[1] M. Vázquez et al., IEEE MAG. 30, 907, 1994.

[2] A. Chizhik et al., JMMM 294, e167, 2005.

[3] S. Abe and A. Matsushita, IEEE MAG 31, 3152, 1995.

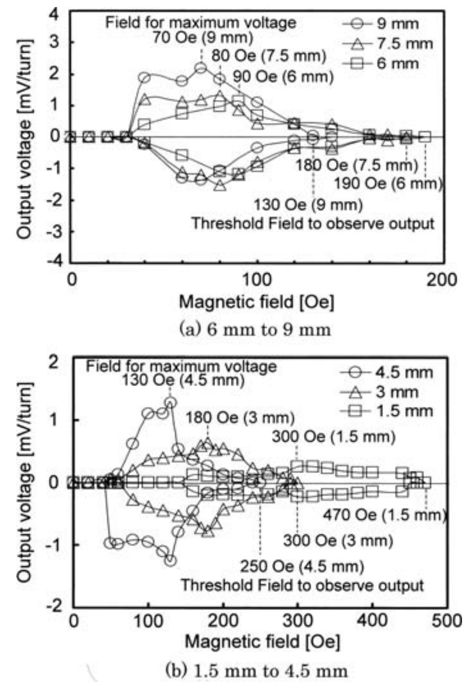

Fig.1 Output voltage induced in Vicalloy wires of 1.5-9 mm length as a function of magnetic field strength

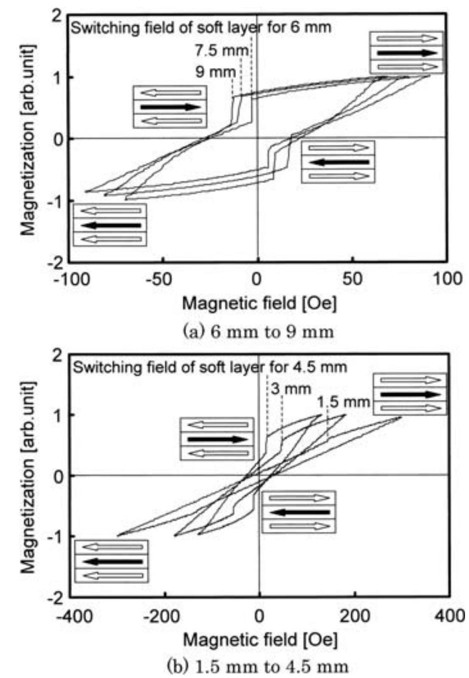

Fig.2 Magnetization curves of Vicalloy wires of 1.5-9 mm length.

AM-02

The effect of ultrasonic resonance on impedance in magnetic rods.

H. Osada, S. Nakamura, H. Hatafuku, S. Chiba, H. Oka
Iwate University, Morioka, Japan

__Introduction__

When an ultrasonic wave is applied to the end of a magnetic rod, elastic standing waves are generated inside the rod [1]. In this experiment, both ends of the sample are the anti-nodes of the standing wave, and the anti-nodes and nodes are located along a line of the rod. The positions of the anti-nodes and nodes of the standing wave can be observed from the amplitude of the induced electromotive force in the detector coil wound around the rod by means of the inverse effect of magnetostriction [2].

This phenomenon is reversible. That is, the standing wave also can be generated by applying a high frequency voltage using the detector coil as a magnetization coil.

This report describes the change in impedance with the positions of the anti-nodes and nodes of the standing wave in magnetic rods.

__Experimental results and Discussion__

Figure 1 shows the scheme of the experimental device. The sample (magnetic rod) is supported at both ends by the ultrasonic transducer and a needle is installed in the magnetization coil. A bias magnetostriction is given to the sample by applying a DC magnetic field. The AC signal is inputted to the magnetization coil from the LCR meter, and an elastic standing wave is generated in the sample. Simultaneously, the impedance of the magnetization coil is measured by the LCR meter. In addition, generation of the elastic standing wave is checked by observing the induced electromotive force (EMF) from the ultrasonic transducer bonded to the sample end.

Figure 2 and 3 shows the measurement result for the impedance and the induced electromotive force in he sensing coil on a ferrite rod sample (ϕ5 x 100 mm). The impedance was measured at intervals of 1 mm by setting the ultrasonic transducer side to 0 mm. When the frequency of the magnetization coil is 381.2 kHz, the cycle of the ferrite rod is $n = 7$, and the speed of the ultrasonic wave is $v = 5.5 \times 10^3$ m/s. This figure shows that resistance reaches a local maximum at a position where induced EMF is either at a local maximum or local minimum. Moreover, resistance reaches a local minimum in the position where induced EMF is zero. On the other hand, inductance reaches a local minimum in the position where induced EMF is either at a local maximum or local minimum, and reaches a local maximum in the position where the induced EMF is zero.

When generating an elastic standing wave by means of ultrasonic resonance phenomenon in a magnetic rod, it is thought generally accepted that the magnetic flux inside the magnetic rod is concentrated at the node of the standing wave, and in the part of the anti-node that comes out of or enters the magnetic rod (see Fig. 4). Therefore, when a magnetization coil is in the position of a node, the magnetic flux generated from the coil goes outside in, and out from the position of the adjoining anti-node. On the other hand, when a magnetization coil is in the position of an anti-node, a standing wave is not generated and the magnetic flux runs through the magnetic rod. This difference in the magnetic flux state inside a sample may be the reason for changes in the impedance of the coil because of the position of an anti-node and a node.

Since it is generally accepted that change of such impedance changes also with the stress inside the magnetic rods, it is thought that the state of the inside can be observed in a non-destructive way by measuring the impedance change.

[1] H. Hatafuku, C. Sarudate, A. Konno, IEEE Trans. Magn., vol. 38, No. 5, 2002, pp. 3309-3311.

[2] Chikazumi, Physics of Ferromagnetizm, 2nd edition, 1997, p. 377 Oxford.

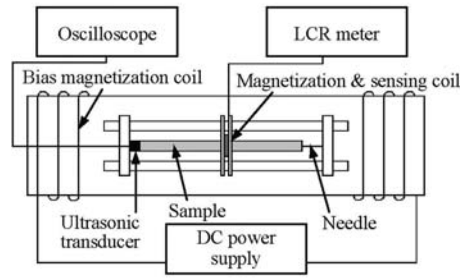

Fig. 1 Scheme of an experimental device.

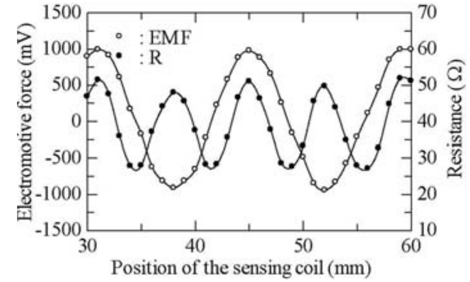

Fig. 2 Resistance and EMF of the sensing coil on the ferrite rod.

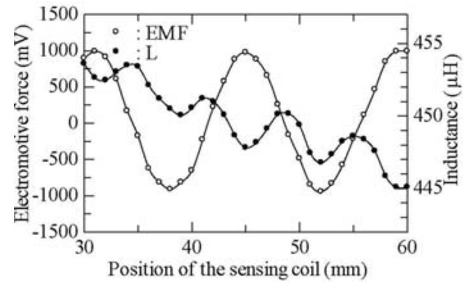

Fig. 3 Inductance and EMF of the sensing coil on the ferrite rod.

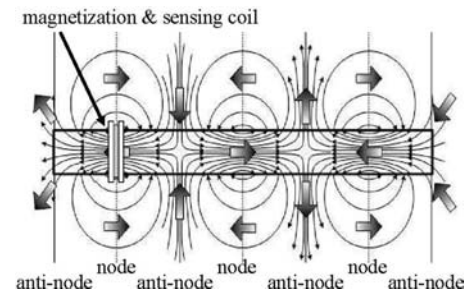

Fig. 4 State of the magnetic flux when generating the elastic standing wave.

AM-03

Electrical Isolators based on Tunneling Magnetoresistance Technology.

C. Reig[1], M. D. Cubells-Beltrán[1], D. Ramírez[1], S. Cardoso[2], P. P. Freitas[2]
1. Electronic Engineering, Universitat de València, Burjassot, Spain; 2. Microsistemas e Nanotecnologias, INESC, Lisboa, Portugal

1. Introduction

Signal isolator devices are widely used in many electronics systems. Optical isolators and capacitive or inductive couplers are often limited in linearity and frequency performance; they need a notable power consumption and they display a considerable size and usually require hybrid packaging. From the early work of T.M. Herman et al. [1], some approaches have been carried out in the sense of using MR tecnologies in the basis of novel electrical isolators. TMR structures have been used for digital isolators [2], [3] and spin-valve structures for analog isolators [4]. In this work we study the possibility of using magnetic tunnel junctions (MTJ) based full bridges in order to design analog magnetically coupled isolators. MTJ display some advantages when compared to spin-valve, namely smaller devices and higher magnetoresistance levels (and then higher sensitivity devices).

2. Experiment

The sensing structure was deposited by ion beam sputtering (IBD) onto 3” Si/SiO2 1000 Å substrates. The final magnetic tunnel junction configuration was: Al(600Å)/Ta(90Å)/NiFe(70Å)/MnIr(250Å)/CoFe(50Å)/Al2O3(12Å)/CoFe (50Å)/NiFe(25Å)/Ta(60Å)/TiW(300Å). The wafer was 90° rotated after the oxidation step in order to ensure a crossed-axis linear configuration. The fabrication of the sensors required six lithographic steps. In the first one, the TMR stacks were patterned by direct laser writing on photoresist followed by soft sputter etching. In the second step, 2×15 µm2 junction areas were defined by selective sputter etching. The contact leads [0.150µm Al98.6Si1.0Cu0.4/150Å TiW(N)] were then defined by lift off, for a full Wheatstone bridge configuration. A Al2O3 layer was used as isolation barrier. The driven current strips were then deposited and patterned. Pads were opened for external contacts by wet etching in the last lithographic step. Some fabricated sensors were cut into 8.2mm×8.2mm dies and then encapsulated into chip-carriers for testing purposes. The micrograph of the die, as well as the function explanation, is shown in Fig. 1.

3. Results and Discuss

Single resistance test structures were also included on the wafers to perform basic characterizations. A direct current was driven through the integrated current strips, running just above the single MTJ structures. A typical response is displayed in Fig. 1. As observed, the linearity of single MTJ structures is notable even when working alone. In order to characterize the linearity and the sensitivity of the devices, they were fed at a constant direct current of 10mA (through terminals A and B) and the output voltage taken from terminals C and D. A direct current was injected through terminals Iin-Iout with a hysteresis-detecting loop scheme. Results are shown in Fig. 2. To demonstrate the capability of these devices for acting as analog isolators, different electrical signals were applied through the input terminals, with the help of a signal generator. An illustrative result is shown in Fig. 3, for a triangular example.

<p>[1] T.M. Hermann, W.C. Black and S. Hui, “Magnetically Coupled Linear Isolator”, IEEE Trans. on Magnetics, vol. 33, pp. 4029-4031, 1997

[2] D. Wang, M. Tondra, C. Nordman, Z. Qian, J.M. Daughton, E. Lange, D. Brownell, L. Tran and J. Schuetz, “Prototype spin-dependent tunneling isolators integrated with circuit electronics”, J. of Appl. Phys., vol. 91, pp. 8405-8407, 2002

[3] Z. Qian, D. Wang, J. Daughton, M. Tondra, E. Lange, C. Nordman, A. Popple, J. Myers and J. Schuetz, “Magnetoresistive signal isolators employing linear spin-valve sensing resistors”, J. of Appl. Phys., vol. 93, pp. 6870-6872, 2003

[4] Z. Qian, D. Wang, J.M. Daughton, M. Tondra, C. Nordman and A. Popple, “Linear Spin-Valve Bridge Sensing Devices”, IEEE Trans. on Magnetics, vol. 40, pp. 2643-2645, 2004

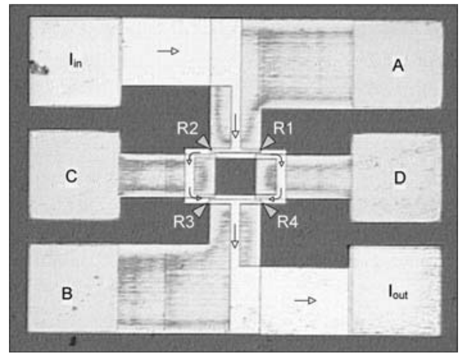

Micrograph of the prototypes

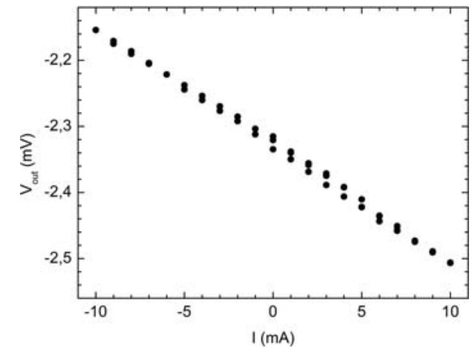

Estatic response of the device

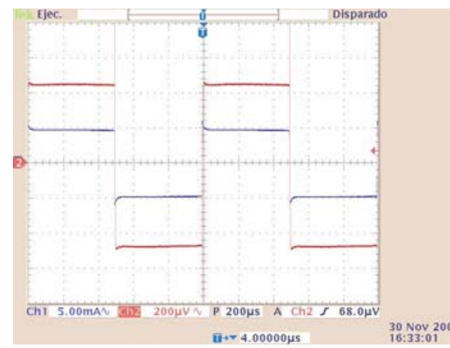

A typical oscillogram

AM-04

Introduction of a Base-Model for Eddy Current Testing of Printed Circuit Boards.

H. Bayani, M. Nishino, *S. Yamada*, M. Iwahara
Division of Biological Measurement and Applications, Kanazawa University, Kanazawa, Japan

Introduction

Eddy current testing (ECT) is an effective non-destructive method for defect inspection of printed circuit boards[1,2], although two difficulties need to be solved.First,eddy-currents should be induced efficiently in thin and narrow printed circuits.For this purpose a Meander-type excitation coil is used as shown in Fig.1.Second, the pattern of the conductor on PCB is not uniform and is different from conventional ECT,so the output of the ECT probe includes many kind of signals originated from not only defects but also PCB pattern.Consequently,introducing a technique which selects only the defect signal is indispensable for this application.Base-Model method provides the required tools for getting the signals produced by a non-defected PCB directly from its pattern sheet.

Method

1.Disassembling the PCB pattern:It is possible to consider a PCB pattern geometry as an assembling of some basic parts as seen in Fig.2.In this way a complicated pattern could be separated into basic parts.

2.Probe details and physical quantity measurement:A long Meander-type coil is utilized as an excitation coil.To simulate the coil, we use four straight long conductive strips located parallel to each other and carrying equal currents which are in opposite direction in the adjacent strips as seen in Fig.3.The physical quantity which we calculate here is the magnetic flux density due to interaction between the Meander coil and a PCB basic part.Unfortunately there is no analytical solution to such a problem;hence,we use numerical method to solve the problem.Using FEMLAB package,we simulated a Meander coil above a basic part in a 3D mode while quadratic element was considered to obtain an acceptable smoothed result.Since the legs of the coil was supposed to be very long in y-direction and they had periodicity in x-direction,the magnetic field has only tangential component at infinity.Hence,the Dirichlet boundary condition was applied to the problem.

3.Simulation of scanning process and image processing: we put the part in a reference position and ran the package to obtain the magnetic flux density.Then we moved the position of the PCB part one step on the x-direction.Here we considered each step to be 25 um as in the experiment.After running the program and getting result,the same procedure was repeated for a new position of the PCB part.We repeated the procedure 10 times.For simulating the y-direction scanning process we measure the magnetic flux density on each central line between the strips of the Meander coil which are shown by dashed lines in Fig.3.As the PCB part was moved 10 steps and we also had 3 central lines, we got 30 columns of data.These data were gathered in a matrix to be used for image processing step.To obtain an image of the PCB part,numerical gradient of the aforementioned matrix was taken as an edge detection process.A median filter was also applied to get a clearer image as in Fig.4.One of the most important points in the calculation is related to the width of the sensing area of magnetic sensor which we should take into account.The GMR sensor used in the experiment has a sensing area about 100 um by 100 um; hence,we should consider the effective sensing area as a surface, not as a point, to obtain a more realistic result as close as possible to the experimental result.The wide-area sensing effect causes the final image to be a little blurred in comparison with the result of a point-sensor.On the other hand, calculated results obtained by the Base-Model shows that the resolution of the final image of the basic part is inversely proportional to the scanning step size.

Experimental Results and conclusion

The probe used in the experiment consists of a long Meander coil as an exciter and a SV-GMR sensor to measure the magnetic flux density. The sensor was mounted on the long Meander coil and its sensing axis was set to detect the magnetic flux density, only in the scanning direction. In this research, sinusoidal current of 200 mA at a frequency of 5 MHz was fed to the Meander coil. A lock-in amplifier was used as a data acquisition system for measuring the ECT signal from the sensor. By scanning a small part of a PCB in an experimental situation and applying image processing technique; we get the patterns which can be seen in Fig.3.Subtracting the signal obtained by the method from the signal by the experiment gives the defect signal on a clear background without the complicated PCB conductor pattern.The Base-Model method shows a considerable development in PCB inspection and could be extended to other areas of ECT inspection where the test piece is made of a complicated pattern as well.

[1]S. Yamada, H. Fujiki, M. Iwahara, S.C. Mukhopadhyay and F.p. Dawson, IEEE Trans. Mag. VOL. 33, 5, Sep. 1997.

[2]K. Chomsuwan, S. Yamada, M. Iwahara, IEEE Trans. Mag. VOL. 41, 10, Oct. 2005.

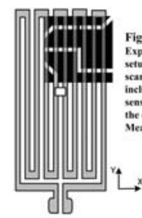

Fig. 1. Experimental setup of a 2D scanning system including a GMR sensor placed at the center of a Meander coil

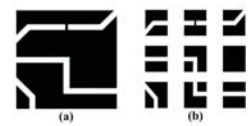

Fig. 2. (a) A typical simple PCB pattern sheet, (b) disassembled to nine basic parts.

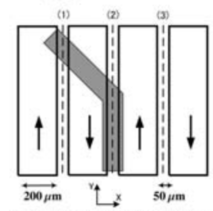

Fig. 3. Top view of 3D FEM simulation of the problem. An open-elbow PCB basic part, 100 um width, shown in gray is set 50 um under four legs of Meander coil.

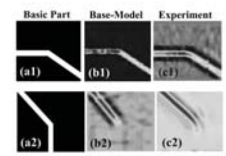

Fig. 4. (a1), (a2) Basic parts obtained after disassembling,
(b1), (b2) Base-Model results of scanning simulation based on 3D FEM analysis,
(c1), (c2) Experimental results of the same pattern PCB,
Scanning direction is the same as Y direction in Fig. 2.

Orthogonal Fluxgate with Tube Core Operated in Fundamental Mode.

E. Paperno, E. Wiess, A. Plotkin
Electrical and Computer Engineering, Ben-Gurion University of the Negev, Beer-Sheva, Israel

A new operating mode has been recently suggested for orthogonal fluxgates with amorphous wire core [1]-[4]. In this mode, a dc component is added to the fluxgate ac excitation and their output is detected at the fundamental rather than at the second harmonic. The fundamental-mode operation increases the sensitivity of the orthogonal fluxgates [1], reduces their offset [2], noise [3], and thermal drift [4], thus, making them competitive with state of the art parallel fluxgates [5].

In this work, we suggest applying the fundamental-mode operation to a different type of fluxgates; namely, to orthogonal fluxgates with tube core (see Fig. 1). Excitation current in these fluxgates flows through the toroidal coil wound around the tube core, whereas in the orthogonal fluxgates with amorphous wires, it flows directly through the wire core. Having no excitation current inside the core reduces its heating and, hence, decreases its thermal drift. Employing the toroidal coil also allows decreasing the excitation current, by simply increasing the number of coil turns, while keeping the same intensity of the excitation field.

Our experiments with a tube-core fluxgate (see Fig. 1) have shown a much higher efficiency of the new operating mode as compared with the second-harmonic mode.

To assemble the fluxgate core, we cut a 50x50-mm square from a 22-µm thick Metglas 2705M amorphous ribbon and coiled it inside a nonconductive pipe, aligning the Metglas magnetic anisotropy circumferentially.

We have found that the excitation with a 6-mA rms ac and 40-mA dc currents provides the maximum signal to noise ratio (SNR) in the fundamental mode. The maximum SNR in the second-harmonic mode was obtained for the same 6-mA ac excitation.

Adding the dc component to the ac excitation has caused a dramatic noise reduction. This effect is especially pronounced at relatively low frequencies (see Fig. 2). One can see from Fig. 2 that the large enough dc bias suppresses the fluxgate noise down to the spectrum analyzer noise floor.

The fluxgate sensitivity increases with frequency in both modes. At a 32-kHz fundamental, it exceeds by a factor of 12.5 the sensitivity at the second-harmonic.

In the fundamental mode, the fluxgate resolution reaches 10 pT/sqrtHz at 1 Hz, which is by an order of magnitude better than in the second-harmonic mode.

The resolution obtained in the fundamental mode exceeds that of a fluxgate with amorphous wire core [3]. We have also observed an about two times lower thermal drift of the fluxgate output compared to [4]. This allows us to conclude that the orthogonal fluxgate with tube core, operated in the fundamental mode, outperforms its counterpart with amorphous wire core.

[1] I. Sasada, “Orthogonal fluxgate mechanism operated with dc biased excitation,” J. Appl. Phys., vol. 91, pp. 7789–7791, May 2002.

[2] I. Sasada, “Symmetric response obtained with an orthogonal fluxgate operated in fundamental mode, IEEE Trans. Magn., vol. 38, pp. 3377–3379, Sep. 2002.

[3] E. Paperno, “Suppression of magnetic noise in the fundamental-mode orthogonal fluxgate,” Sensors and Actuators A: Physical, vol. 116, pp 405-409, Oct. 2004.

[4] A. Plotkin, E. Paperno, A. Samohin, and I. Sasada, “Compensation of the thermal drift in the sensitivity of fundamental-mode orthogonal fluxgates,” accepted for publication in J. Appl. Phys., vol. 99, 08B305, pp. 1-3, Apr. 2006.

[5] P. Ripka, “Advances in fluxgate sensors,” Sensors and Actuators A: Physical, vol. 106, pp 8-14, Sep. 2003.

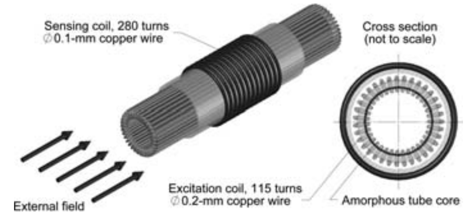

Fig. 1. Orthogonal fluxgate with tube core.

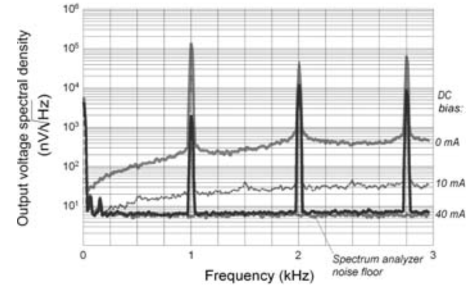

Fig. 2. Comparison between the output signal voltage spectra obtained for different dc bias currents at the same excitation frequency of 1 kHz. A 40 mA dc bias corresponds to a purely unipolar excitation of the fluxgate core (fundamental mode), and a zero dc bias corresponds to a purely bipolar excitation (second-harmonic mode).

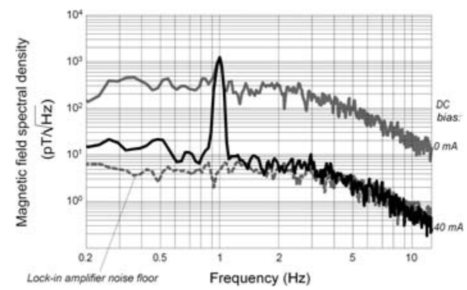

Fig. 3. The fluxgate noise spectra. A 7 nT rms external magnetic field is applied to the fluxgate at a 1 Hz frequency. Note that the noise in the fundamental mode is by an order of magnitude lower than in the second-harmonic mode. (The spectrum line width is 12.5/400 Hz.)

AM-06

Test of multiturn sensors by a system generating rotating electromagnetic fields with high rotational frequencies.

H. Koebe[1], D. Schmidt[1], M. Scherzinger[2], K. Bauer[2], R. M. Mattheis[1]
1. Photonic Intrumentation, IPHT, Jena, Germany; 2. Novotechnik, Ostfildern, Germany

Magnetic domain wall based devices have high potential for magnetic storage like high-density memory as proposed by Parkin [1] and Cowburn [2]. For automotive application there is another prospective sensor system, a multiturn sensor [3], which is able to detect and storage the number of turns of a wheel or of other rotating parts of an automobile. Multiturn sensors are necessary for the realization of 'steer-by-wire' or 'drive-by-wire'-concepts. We developed such sensors at the IPHT in cooperation with the Novotechnik factory [4]. A multiturn sensor consists of a GMR-stack which is patterned in a long, narrow helical lane (thickness of 40 nm, width of 150 nm and length of 4 mm). At one end of the helix an enlarged area acting as a domain wall generator is placed, which is responsible for the injection of a domain wall every 180° of rotation whereas the other end of the helix ends in a tapered geometry to avoid domain wall injection from that side of the helix. There is a magnetic window for the functionality of the sensor: the rotating field must be large enough for the reliable injection and transportation of the domain wall and must not exceed the field which could be able to generate a domain wall outside the domain wall generator. The detailed functionality of this sensor was described in [5], see Fig. 1.

For the qualification of such a sensor type with respect to any possible failure, the sensor has to be tested to work correctly for at least 10 millions of revolutions. Every rotation has to be qualified with respect to the correct domain wall motion within the magnetic field window between 10 and 50 mT. We developed a measurement system to realize the qualification process in a short time. The core of this measurement device consists of two serial oscillating circuits containing a stator of an electric motor, a capacitor and a resistor (Fig. 2). There the rotating magnetic field is generated inside the stator of the motor. The capacitors compensate the inductance of the stator and the resistor limits the current and accommodates the impedance of the circuit to the amplifier. The operating and rotational frequency is determined by the resonance frequency of the oscillating circuit. We achieve rotational frequencies of 2 kHz. In addition to that, our system allows changing the rotation direction immediately, because one pair of coils of the motor is placed in an H-bridge consisting of 8 IGBTs (Fig. 2). This enables us to change the direction of the current flow within some microseconds. A microcontroller controls the whole system and is connected to a PC via USB, which collects the data provided by the uC. The voltage of the sensor is read by a high speed ADC. This allows us at least 10 voltage measurements within every half rotation.

In this way we can apply three different test regimes:

a) Test of the domain transportation process through the spiral by rotating the magnetic field in the direction of the sense of the spiral and measuring the correct transport to the innermost point of the spiral (determination of the minimum magnetic field).

b) Test of the stability of the sensor against high magnetic fields by rotating the field in the reverses sense with respect to the sense of the helix by checking the generation of any domain wall by testing the outer part of the spiral against domain wall movement.

c) Full test of the sensor by complete filling and emptying the sensor at least 10 Mio times repeatedly.

The system will be presented and first results of the tests will be discussed with respect to the qualification of the new multiturn sensor for automotive application.

[1] S. S. P. Parkin, US Patents 6834005, 6898132, 6920062, 7031178 (2004-5).

[2] D.A. Allwood, G. Xiong, R.P. Cowburn, Appl. Phys. Lett. 89 (2006) 102504, WO 0241492, WO 03/0838874

[3] R. Mattheis, M. Diegel, U. Huebner and E. Halder, IEEE Trans. Magn. 42, 3297, (2006)

[4] http://www.novotechnik.de/

[5] M. Diegel, R. Mattheis and E. Halder, Sensor Letters 5 (2007) 118

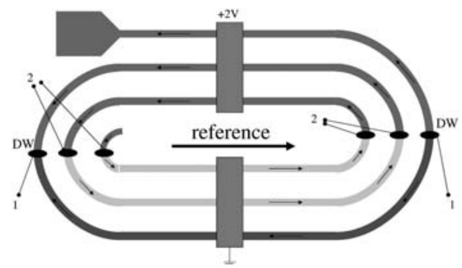

Figure 1: Layout of the multiturn sensor. The supply voltage is applied at the grey, squared contact pads and the magnetization states of the lanes can be measured at the black taps. The arrows show the direction of the magnetization. The colour-code is: dark grey - high resistance, light grey - low resistance. Possible potential states are shown: Number 1 => medium state (potential divider of two similar resistors). Number 2 => low state (potential divider of a high and a low resistor).

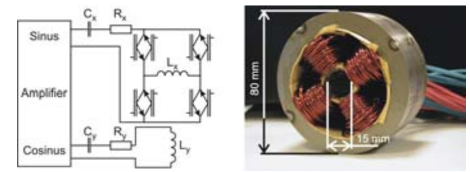

Figure 2: Left: a draft of the serial oscillation circuit and the H-bridge that is used to turn the direction of the rotation. The photo on the right hand side shows the stator of the electric motor in which the magnetic field is generated.

AM-07

External and internal bias field effect on giant magneto impedance profile.

H. Kim, S. Park, D. Kim, W. Jeung
Division of Materials Science & Engineering, Korea Institute of Science and Technology, Seoul, South Korea

Conventionally, giant magneto impedance (GMI) effect shows symmetric behavior with respect to external magnetic field since its mechanism is based on alternating transverse permeability, whose magnitude is irrelevant to the sign of the external field. For the practical application of GMI devices, many efforts were devoted to induce asymmetric giant magneto impedance (AGMI) effect [1~3]. Representatively, J. G. S. Duque et al. [2] showed that exchange coupling between soft magnetic core and hard magnetic surface, which is formed during field annealing process, can break the symmetry and induce AGMI effect. In addition, N A Buznikov et al, based on the Mawell and Landau-Lifschitz-Gilbert equation, proposed a theoretical model that can explain the mechanism of exchange biased AGMI effect [3].

However, all these works were based on amorphous soft magnetic wires and, to our best knowledge, no efforts were made to investigate AGMI in crystalline soft magnetic materials. In this work, we examined AGMI profile in electroplated CoFeNi crystalline wires, of which the asymmetry was induced by internal magneto static coupling between soft magnetic CoFeNi wire and mechanically attached AlNico hard magnet.

Experimentally, using photolithography process, device patterns having dimensions 150 μm × 7500 μm (width × length) were formed on SUS wafer. CoFeNi micro-wire was electroplated on the patterns with thickness 1 μm. For the investigation of internal bias field effect, AlNiCo (1mm^2 × 20 μm (diameter × thickness) hard magnet mechanically attached on the CoFeNi micro-wire using epoxy. Distance of the two devices was 200 μm in this experiment. VSM was used for the measurement of magnetic properties of the devices. For the impedance measurement we used a function generator as a ac signal source while rms value of device ac voltage was converted to dc value using AD8361 rf detector chip and then amplified in order to increase signal to noise ratio.

Figure 1. shows the GMI profile of original CoFeNi device which clearly illustrates typical symmetric behavior. Total GMI ratio was measured to be 60 % and impedance maximum field was consistent with anisotropy field, which was confirmed with VSM measurement. When the hard magnet was attached, AlNiCo greatly influenced the GMI profile and induced AGMI effect. (Figure 2) We ascribe this effect to the magneto static coupling between soft magnetic CoFeNi wire and AlCoNi hard magnet. Since the coercive field of AlNiCo is larger than the operating external field range (-80 ~ +80 Oe), internal stray field from hard magnetic layer, which is antiferromagnetically coupled to the soft layer acts as a bias field. Accordingly, it helps the longitudinal magnetization of the device when the external magnetic field is parallel to the magnetization direction of the hard magnet while pins the magnetization of the soft magnetic device on the other. Therefore, the total effective anisotropy of the device becomes asymmetric with respect to the external magnetic field and it is represented as a different maximum value in Figure 2. Furthermore, not only the maximum impedance value but also external field point at maximum impedance is shifted due to asymmetric effective anisotropy. This characteristic of AGMI can be advantageous for the practical application of GMI devices.

Figure 1. GMI profile of original CoFeNi device
Figure 2. GMI profile of CoFeNi device with AlNiCo hard magnet

1. Stress-induced asymmetric magneto-impedance in melt-extracted Co-rich amorphous wires.

P. Ciureanu, I. Khalil, L. G. C. Melo, P. Rudkowski, A. Yelon, Journal of Magnetism and Magnetic Materials 249 (2002) 305-309.

2. Asymmetric impedance in field-annealed Co-based amorphous wires and its bias field dependence.

J. G. S. Duque, A. E. P. De Araujo, M. Knobel, Journal of Magnetism and Magnetic Materials 299 (2006) 419-424

3. A model for exchange-biased asymmetric giant magneto-impedance in amorphous wires.

N. A. Buznikov, S. S. Yoon, C. G. Kim, C. O. Kim, Journal of Physics D: Applied Physics 39 (2006) 3525-3530

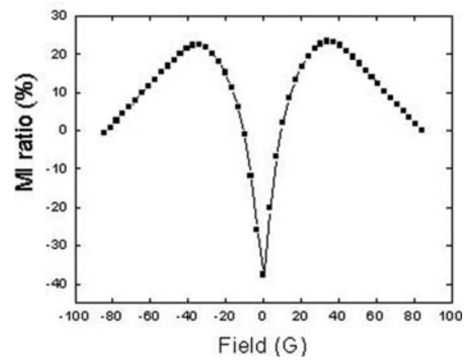

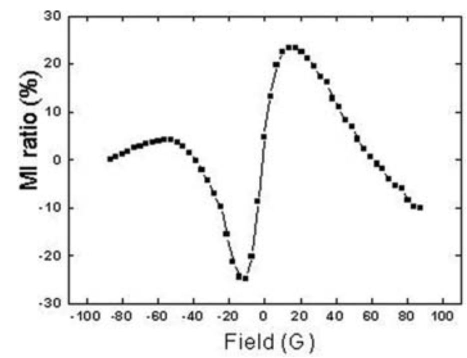

AM-08

Magnetic Gradiometer for Magnetic Moment Measurement using Two Cesium Magnetometer in Earth's Magnetic Field Background.

P. Park[1], Y. Kim[1], W. Kim[1], V. Y. Shifrin[2]
1. Electromagnetic Metrology Group, Korea Research Institute of Standards and Science(KRISS), Daejeon, South Korea; 2. D. I. Mendeleyev Institute for Metrology (VNIIM), St. Petersburg, Russian Federation

1.Introduction
The atom magnetic resonance (AMR) technique based on the optical pumping polarization of gaseous samples provides very high sensitivity which difficult to realize at pplication in a variable Earth magnetic field. Usually arth magnetic field variation is thousand times bigger than cesium magnetometer sensitivity.
Used in geophysics optical pumping method employing two or more sensors is a effective way of measuring local magnetic field sources parameters at Earth's magnetic field (EMF) background.
It allows fully use the magnetometers sensitivity reducing the least measured field increment to (1 – 2) pT.
With optically pumped gradiometer (OPG), we can precisely measure also effect of the magnetized technical objects in motion that is important for some practical application.
EMF variations are quite uniform at the Earth surface and have the gradient level about 0.01-0.05 nT/km depending on the points of observation. It means the EMF magnetic field variations are the same at distance about 100 m within (1-5) pT difference. For instance, when measuring the magnetic field difference at two points using two ideal (free from the instrumentation noise) identical magnetometers having the base (distance) of 100 m between the sensors, we can get the stable output signal without any variations within 1-5 pT. This instrument is the magnetic gradiometer. When a magnetized object is within the range of the sensor, the balance of two sensors change and the difference is detected.
2. Experimental Apparatus
Fig.1 represents the block-diagram example of Cesium gradiometer application.
In this case Cesium gradiometer measured projection increments of a total magnetic flux density on the basis of 7 m is effected by two cars of different sizes.
Frequencies of the AMR signals from the magnetometers, which are proportional to the magnetic field, were compared at the phase detector. The frequency difference was converted to current and compensated the magnetic field difference inside the Cesium sensor 1 to maintain the equal phases (or frequencies) on the inputs of the phase detector. So the voltage across the standard resistor, which is located in the feedback coil circuit, represents the magnetic field difference between the two sensors.
The car, as an example of the magnetized object, was used for the determination of its space distribution of magnetic field projection on the EMF direction, effective magnetic moment, and the maximum distance for detection.
3.Calculation and Results
The magnetic field distribution of the dipole magnetization of an object is determined by formula 1:

where H-magnetic field strength(A/m), M-magnetic moment(A.m2), R- distance from the object to the point of the measurement(m), x, y - axial and perpendicular coordinates of the measuring point.

Fig.1 shows the result of these measurements. The distance of reliable detection the mini-car Tico and the ordinary size car Excel was 50 m and 68 m respectively.
In order to demonstrate the effectiveness of the scanning of an object, the Cesium AMR gradiometer was designed using the ordinary commercial AMR magnetometers.

[1] P. G. Park, Y. G. Kim, V. Ya. Shifrin, and V. N. Khorev, "Precise standard system for low dc magnetic field reproduction", Rev. Sci. Instrum., vol.73, no 8, pp.3107-3111, Aug. 2002.

[2] V. Ya. Shifrin, V. N. Khorev, and P. G. Park, "A Standard Quantum Measuring System for Reproduction and Measurement of Low Direct Magnetic Field in the Range 0.1 uT -1.5 mT", IEEE Trans. Instrum. Meas., vol. 54, no.2, pp.727-729, Apr. 2005.

[3] V. Ya. Shifrin, V. N. Khorev and P. G. Park, "A high-precision system for direct current reproduction based on atomic magnetic resonance in helium-4", Metrologia, vol.36, pp. 171-177, 1999.

$$H = \frac{M}{4\pi} \cdot \frac{2x^2 - y^2}{R^5}$$

formula 1

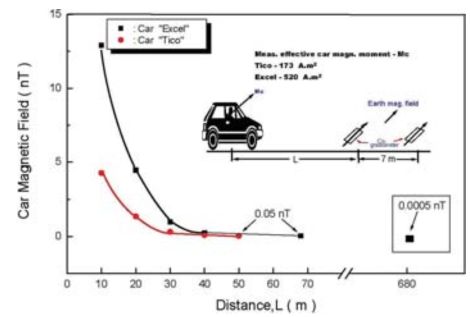

Fig. 1. Block diagram and measurement result of Cesium magnetic gradiometer.

AM-09

Surface flaws detection using AC magnetic field sensing by a thin film inductive micro sensor.

K. Kim[1], Y. Cha[1], J. Kim[2], J. Sohn[2], Y. Yoo[2]
1. Physics, Yeungnam University, Gyeongsan, South Korea; 2. Institute of Nova Magnetics, Nova Magnetics, Incheon, South Korea

The role of electromagnetic-based non-contact and non-destructive evaluation (NDE) of metallic components in engineering industry is increasing [1, 2]. It has been mainly applied for inspection of metal constructions, pipes, parts of plains, and nuclear power plants, etc.. Especially, in order to detect the surface flaws on metallic nonmagnetic and magnetic specimens, the changes of alternative current (AC) magnetic fields detection using the inductive coil sensor with AC source driving to specimens is one of good technique [3]. Induction coil sensors are one of the oldest and most well-known types of magnetic sensors, which transfer function results from fundamental Faraday's law. Today, induction coils are still in common use for their important advantages: simplicity of operation and design, wide frequency bandwidth, shielding from external electromagnetic noise sources and large dynamics. Therefore, we have performed the nondestructive testing (NDT) to detect the metallic surface flaws using the inductive planar micro sensor with a single straight AC driving coil.

The thin film inductive micro sensor was fabricated on AlTiC substrate using photolithography process. The thin film micro sensor has a dimension of 288 μm ×360 μm with the thickness of 23 μm. The Cu pick-up coil (2.5 μm × 3.5 μm) with 40 turns and CoFeNi magnetic film as a magnetic core were deposited by electrolyte process. The size of a magnetic core is 120 μm × 145 μm × 5 μm with the 0.6 μm-spaced gap between top and bottom layer. Figure 1 shows a schematic draw and real photo images of the thin film sensor. To apply the AC magnetic fields to specimens, a single straight coil with the diameter of 120 μm was used, which was placed in the edge side of the magnetic gap on thin film sensor. The driving Cu coil generates the AC magnetic fields with the frequency range of about 1.6 MHz, which magnetic fields were applied to the artificial cracks on specimen. In order to detect the flaws on surface of the specimens, the thin film sensor probe was moved on surface of specimens with 0.5 mm ~ 1 mm of flying height and 4 mm/s of scan speed, which was controlled by x, y-axis scanner. The 5 mm-thick nonmagnetic Al and magnetic FeC specimens were prepared with the artificial slit typed flaws. The induced output signals were amplified and filtered by the amplifier. Fig. 2 shows the measuring results with the change of depth and width of slit typed flaws on Al and carbon steel. For an Al specimen, the intensity of the induced voltage was increased with the increment of slit width; on the contrary, the induced voltage was slightly decreased with the increment of slit depth. For a carbon steel specimen, the output signal was slightly decreased with the increase of slit width and depth, respectively. The obtained output signals were good coincidence with the positions of slit flaws. As results, the induced output signal is dominant on nonmagnetic specimen in comparison that on magnetic specimen. It could be related with the relatively different skin depth effects by means of the high permeable magnetic specimens. Fig. 3 shows the real photo images of the coins (Euro, cent) and the obtained image with the 0.1 mm on one-axis of pixel resolution, which results from the scanning by thin film sensor. Unlike the optical method, the eddy current measurement gives information not only on the actual profile but also on the material. As results, the positions and shapes of surface crack on various metallic specimens were easily detected with high sensitivity. Also, the inductive thin film micro sensor makes it possible to apply in imaging metallic profiles.

[1] Cavoit C, Rev. Sci. Instrum 77, 064703 (2006).

[2] Slawomir Tumanski, Meas. Sci. Technol 18, R31 (2007).

[3] Ki Hyeon Kim, et. al., Phys. Stat. Sol. (a), 204(12), 4083 (2007)

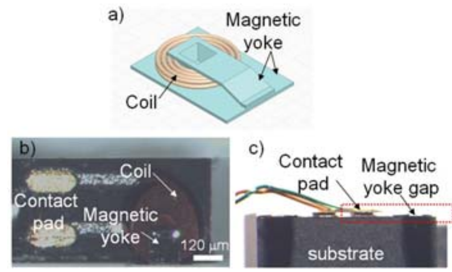

Fig. 1 A schematic of thin film inductive senor a), top view b) and side view of real image

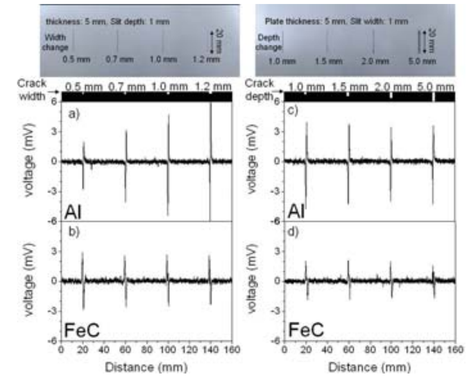

Fig. 2 The measured output signal with the change of depth and width of slit typed flaws on Al and carbon steel.

Fig. 3 Optical photo images a), c) and scanned images b), d) by inductive thin film sensor, respectively.

AM-10

Linear magnetoresistance of NiO-spin valve device.

S. Lee[1], Y. Park[2], D. Hwang[3], J. Rhee[4]
1. Oriental Biomedical Engineering, Sangji University, Wonju, South Korea; 2. Oriental Western Biomedical Engineering, Sangji University, Wonju, South Korea; 3. Applied Physics and Electronics, Sangji University, Wonju, South Korea; 4. Physics, Sookmyung Women's University, Seoul, South Korea

The selective magnetic giant magnetoresistance-spin valve (GMR-SV) device includes bio-magnetic materials, such as magnetic beads coated with Streptavidin particles and bio-tin particles whose superious properties can be harnessed to make a sufficiently effective nano-bio device in the future [1]. Presently, the study of the detailed response and behavior of bio-molecules and cells attached to magnetic beads or nano-particles is a very important factor in the biological and medical sciences[2,3].

In this research, with a focus on the nano-magnetic sensitive GMR-SV device for biosensor, we investigated the Property of the linear MR of the fabricated device through experiments.

The sample structure of the GMR-SV device prepared on the substrate of Corning glass (#7059) was made of NiO (300 Å)/NiFe (20 Å)/CoFe (10 Å)/Cu (26 Å)/(CoFe (10 Å)/NiFe (40 Å) multilayers. The direction of the uniaxial anisotropy applied on the deposition of the GMR-SV multilayer was parallel or counter-parallel to the plane of the device with a length of 15 μm. The micro-patterning device with the real region of 2×5 μm^2 formed the two-probe Al (500 Å)/Cu (200 Å) electrode

The coercivity (H_c), exchange coupling field (H_{ex}), magnetoresistance ratio (MR(%)), and magnetic sensitivity (MS) of the above-mentioned sample and device were measured.

Fig. 1 shows the magnetoresistive (MR) curves for the NiO-SV device, which were measured by the two-probe method. As shown in Fig. 1(a) and 1(b), from the major loop of the MR curve measured in the easy axis. The values of H_{ex}, H_c, MR, and MS values were 120 Oe, 90 Oe, 4.2 %, and 0.3 %/Oe, respectively. Especially, Fig. 1(b) showed that the intensity of interlayer coupling of between the bottom-pinned NiFe/CoFe layer and the top free CoFe/NiFe layer was about 8.0 Oe. It seems like the effect by the difference between the initial direction of magnetization configuration and the direction of the measuring current was larger than that of the demagnetization (shape anisotropy) effect.

To change to the transversal direction corresponding to the width of the biosensor with the longitudinal direction property of the easy axis for the NiO-SV device, we performed vacuum thermal annealing at 200 ^oC for 1 hr under the permanent magnet of 300 Oe.

Fig. 2 shows the values of H_{ex}, H_c, and MR measured MR curves before and after the annealing process with about 120 Oe and 90 Oe, and 4%. The easy axis minor loop with the H_c of 20 Oe before annealing was changed to the minor loop with the H_c of 2 Oe without the intensity of interlayer coupling and hysteresis property after annealing. From these results, if the final MR curve is in linear proportion to a slightly external magnetic field on the neighboring region of 0 Oe after the annealing process, the enhanced minor MR loop will be used in the detection of magnetic nanoparticles by the biosensor.

Although the magnetic sensitivity was decreased, the reason to perform the linear magnetic property through the thermal annealing process was to obtain the optimum condition to minimize and respond to the coercivity of the GMR-SV device in the surrounding region of 0 Oe by a subtle external magnetic field with increase and decrease. When the GMR-SV device is used as a biosensor with the ultra-micro-magnetic field, the prepared important characteristics include sufficient magnetic sensitivity and large output amplitudes. Therefore, the direction between the magnetization of pinned layer and the magnetization of free layer should be occurred to be orthogonal to each other. The MR property of the micro-patterned device should be had the linear sensitivity and GMR effect caused by the AMR effect and included the large amplitude.

This work was supported by the Korea Foundation for International Cooperation of Science & Technology(KICOS)in 2007.

[1] G. Li, S. Sun, R. J. Wilson, R. L. White, N. Pourmand, S. X. Wang, Sens. Acut. A 126, 98 (2006).

[2] S. H. Park, K. S. Soh, M. C. Ahn, D. G. Hwang, S. S. Lee, J. Kor. Mag. Soc. 16, 157S (2006).

[3] B. M. de Boer, J. A. H. M. Kahlman, T. P. G. H. Jansen, H. Duric, J. Veen, Biosens. Bioelectron. 22, 2366 (2006).

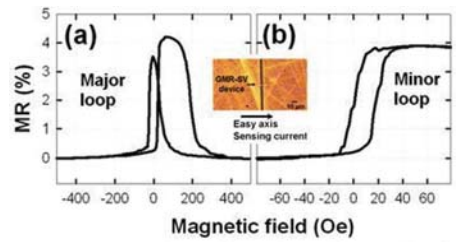

Fig. 1. Magnetoresistive curves measured by the two-probe method for the micro-post-patterned NiO-SV device: (a) The major loop of the MR curve according to the easy axis and (b) the minor loop of the MR curve according to the easy axis. Inset is the feature of micro-patterning size of 2×5 μm^2 and the direction of the easy axis.

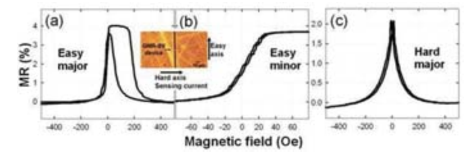

Fig. 2. Magnetoresistive curves measured by the two-probe method for the micro-post-patterned and post-annealed NiO-SV device: (a) The major loop of the MR curve according to the easy axis, (b) the minor loop of the MR curve according to the easy axis, and (c) the major loop of the MR curve according to the hard axis. Inset is the feature of micro-patterning size of 2×5 μm^2 and the direction of the easy axis and hard axis.

AM-11

Temperature Characteristics of Magnetic Rotation Angle Sensors With Spin-Valve GMR Films.

Y. Abe[2], T. Ono[2], T. Kawai[1]
1. New Business Development Center, Hitachi Metals, Tokyo, Japan; 2. OE Device Center, Hitachi Metals, Mooka, Japan

Introduction

Magnetic rotation angle sensors have high reliability as a non-contact type, and magnetic sensors with AMR films are widely used. But, more sensitive and temperature stable sensors are required for precise angle detections even at elevated temperatures.

Spin-Valve GMR(SV-GMR) films have generally larger MR ratio and smaller temperature coefficient than those of AMR films, then magnetic sensors with SV-GMR films are one of the candidates replacing current magnetic sensors with AMR films.

D.Hammerschmidt et al. has already reported the SV-GMR sensors for automobile applications[1]. But their sensors uses an anti-ferromagnetic(AF) film for the pinned layer, then the temperature characteristics are restricted by the blocking temperature of the AF film. To achieve better temperature characteristics, SV-GMR films without any AF films are required.

The present paper investigated temperature characteristics of magnetic rotation angle sensors with SV-GMR films prepared using synthetic anti-ferromagnetic layer(SyAF) as the pinned layer without any AF films.

Experiment

SV-GMR films were deposited on Si wafer substrates by DC magnetron sputtering technique. The pinned layer structure is only CoFe/Ru/CoFe without any AF films. The typical composition of the SV-GMR films is Substrate/CoFe(2.1nm)/Ru(0.4nm)/CoFe(2.0nm)/Cu(2.2nm)/CoFe(1.0nm)/NiFe(2.0nm)/Capping layer. The pinned direction of these films is parallel to the direction of the magnetic field applied during sputtering the first CoFe layer. The rotation angle sensors with a pair of full-bridge were prepared by a conventional photolithograph process to detect angles from 0 to 360 degree. The directions of the pinned layers were set rectangular between full-bridges and set anti-parallel in the half bridges. This setting promises better temperature characteristics. The rotation angle measurements were carried out in the 2-axis Helmholtz coil with 24kA/m magnetic field, applying 5V DC in the bridges.

Results

The typical MR ratio of the SV-GMR films was 10% and the temperature dependence of MR ratio was flat up to 573K, much better than that of SV-GMR using PtMn AF film as the pinned layer.

The output voltage(peak to peak) of the sensors was around 450mV and the temperature coefficient of the output was –0.25%/K up to 453K. The temperature drift of the offset voltage of the full bridges was 0.01mV/K. Measured angle errors at room temperature were less than ±0.5 degree after compensating both offset voltages and output amplitudes. Up to453K, the measured angle errors were kept within ±0.5 degree after the compensation at each temperature. The results are plotted in Figures 1 and 2 including hysteresis angle errors.

Magnetic field intensity dependence upon the measured angle errors was also evaluated. The angle error at 4.8kA/m was ±1.5 degree, but the error was reduced as the magnetic field intensities increase. The error was less than ±0.5degree at 16kA/m and more. The results are plotted in Fig.3.

Then we conclude that magnetic rotation angle sensors using SV-GMR film of SyAF pinned layer without any AF films possess both excellent temperature characteristics and high sensitivities.

References

[1]D.Hammerschmidt et al. SAE 2005 World Congress & Exhibition(2005-01-0462)

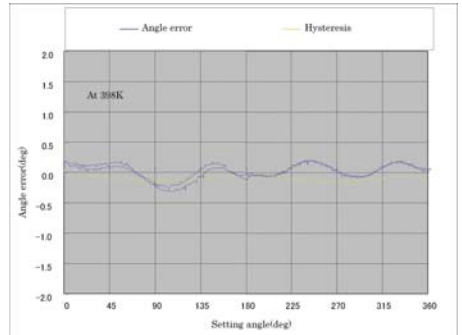

Fig.1 Angle errors at 398K

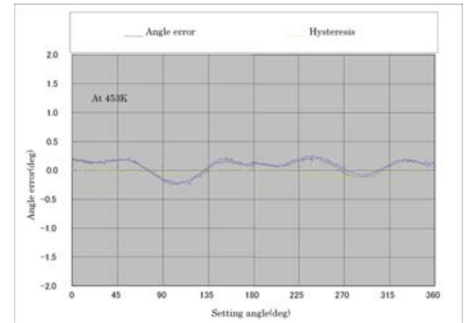

Fig.2 Angle errors at 453K

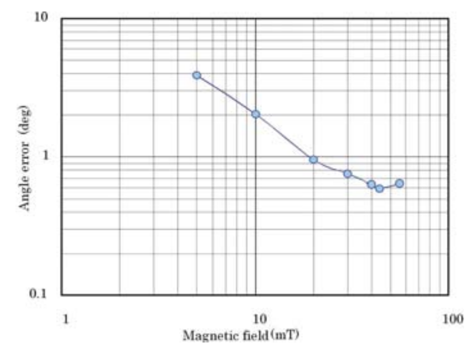

Fig.3 Magnetic field dependence of angle errors

AM-12

A simple design of an orthogonal fluxgate magnetometer of fundamental mode.

I. Sasada, H. Kashima
Applied Science for Electronics and Materials, Kyushu University, Kasuga, Japan

In this paper, we will provide a simple realization of an orthogonal fluxgate magnetometer of fundamental mode [1-2], in which the ac excitation current, supplied directly to the thin magnetic wire core typically, is biased by a dc current having magnitude larger or equal to the that of the ac current. In this simple design, we avoided to incorporate bias flipping that can null offset in principle [3] to make an electronic circuit simple. The circuit presented in this paper in detail (including element values) can be fabricated by those who want to use for their own researches.
Fig. 1 shows the structure of the sensor head that using a magnetic wire [4], in which the wire core is bent in a U-shape so that offset caused by the small swing of the magnetization synchronized with the driving current under no applied magnetic field may be cancelled between two straight sections of the U-shape. Also by increasing dc bias current one can reduce the offset substantially although this incurs additional power consumption. Fg. 2 show a detail of the electronics, where 118 kHz sinusoidal voltage can be generated with a single logic NAND gate followed by a tuned filter in the feedback path. dc bias current is simply superposed at the terminal of the high-side of the U-shaped core. A 10 Ω resistor is for monitoring the driving current. A phase-sensitive detector is made by using a modulation function of AD630 (Analog Devices) which is followed by a first-order low-pass filter having cutoff frequency≈130 Hz. An input-output characteristic of the designed magnetometer is almost straight within the range ±16 uT and the sensitivity is 0.5V/uT. The system noise measured while keeping the sensor head in a five-shell magnetic shield revealed to be 0.18 nT in the root-mean-square scale for the 130 Hz bandwidth. Because of a limited supply of the amorphous magnetic wire, one can use etched amorphous ribbon core of Metglas 2714A. Our first design is shown in Fig. 3 where the length of the sample is 40 mm and the width of leg is 0.2 mm. The edges of the core can be stably soldered to the lead wire by using a narrow and long printed circuit board or machin cut circuit board. The sensor core can then be inserted into a thin solenoid coil used as a pickup coil. In our first experiments, the sensitivity obtained with a 350 turn pickup coil was 0.57 V/100 µT normalized to the amplitude gain equal to unity. This etched core head exhibited very small hysteresis when the polarity of the applied magnetic field was reversed. This may be overcome by redesigning the connecting part more round.

[1]I. Sasada, Journal of Appl. Phy., Vol. 91, No. 10 pp. 7789 (2002)

[2]I. Sasada, IEEE. Trans. Magn., Vol. 38, No. 5, pp. 3377-3379 (2002)

[3]I. Sasada, and T. Usui, Proc. of IEEE Sensors 2003, Conference 2, Vol. I, pp. 468-471 (2003)

[4]K. Goleman, and I. Sasada, Trans. Magn. Soc. Japan, 5, pp. 101-104 (2005)

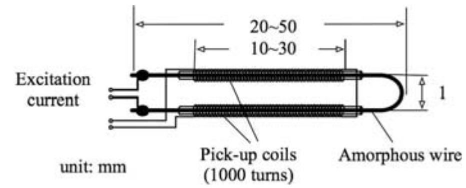

Fig. 1 Sensor head

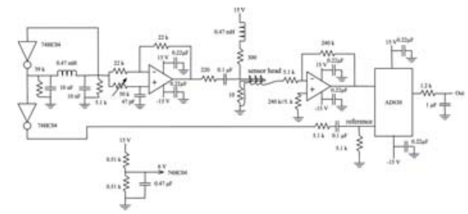

Fig. 2 Circuit for the orthogonal fluxgate of fundamental mode.

Fig. 3 Pattern for the etched ribbon core.

AM-13

Nitride based (AlGaN/GaN) micro-Hall sensor.

A. Bengoechea[1], *C. Aroca*[1], M. A. Sanchez-Garcia[1], E. Lopez[2], P. Sanchez[1]
1. ISOM, Universidad Politecnica de Madrid, Madrid, Spain; 2. Fisica de Materiales, Universidad Complutense de Madrid, Madrid, Spain

Magnetization measurements in micro and nano sized materials can been performed using micro Hall sensors. A real improvement is to place a magnetic material on top of a semiconductor heterostructure where a two dimensional electron gas (2DEG) is generated at few nanometers from surface. GaAs-based systems have been extensively used in the past because of their long electron mean free path[1,2] and high RH constant. However, GaAs heterostructures are very sensitive to temperature and that produces stability problems during measurements, reducing their application range. Additionally there are concerns about its toxicity when used for biological applications.

In this work we present magnetization measurements in a micrometric size ferromagnetic thin film (Fig. 1) using a triple Hall sensor based on a 2DEG (Al,Ga)N/GaN heterostructure grown by plasma-assisted MBE. Figure 2 shows the charge distribution versus depth, in the AlGaN/GaN heterostructure, calculated from capacity-voltage measurement, while the inset shows the temperature dependence of the charge density and carrier mobility obtained from Hall effect measurements. These results confirm the presence of a high mobility channel (2DEG) at the AlN/GaN interface. The main advantages of this nitride-based Hall sensor are its high temperature stability [3,4] and its truly compatibility with any biological application.

Using lift off procedures a 100 nm thick Permalloy (Ni80Fe20) bar was grown by Ar sputtering. The bar size was the adequate to produce a strong dispersion magnetic field in two of the sensors, in such a way that these sensors are sensitive to a magnetic field applied perpendicular to the sample and to the dispersion field produced by the magnetic material (positive in one sensor and negative in the other). The central Hall sensor is only sensitive to the magnetic field applied perpendicular to the sample. When a magnetic field is applied parallel to the sample plane, the Hall sensor signal is mainly due to the dispersion field that is directly related with the sample magnetization.

Figure 4 shows an hysteresis loop measured with an in-plane magnetic field applied along the magnetic bar. This hysteresis loop shows an unexpected high coercive value and a shape similar to the one observed in thicker samples [5]. This effect is possibly due to an interaction between the heterostructure semiconductor surface and the magnetic material and it should be avoided to improve the sensor performance.

[1] "Local Hall effect in hybrid ferromagnetic/semiconductor devices" Hong et al. Appl. Phys. Lett. 90, 023510 (2007).

[2] "Magnetoresistance of a two-dimensional electrón gas due to a single magnetic barrier and its use for nanomagnetometry". V. Kubrak et al. Appl. Phys. Lett. 74, 17, 2507 (1999).

[3] "High temperature electrical investigations of (Al,Ga)N/GaN heterostructures – Hall sensor applications". Consejo et al, phys. stat. sol. c (2), No 4, 1438-1443 (2005).

[4] "High temperature Hall effect sensors based on AlGaN/GaN heterojunctions" Lu et al. J. Appl. Phys. 99, 114510 (2006).

[5] "Effects of spacer layer on growth,stress and magnetic properties of sputtered permalloy film" S.F. Cheng. et al J. Mag: Mag. Mat 282 (2004) 109–114

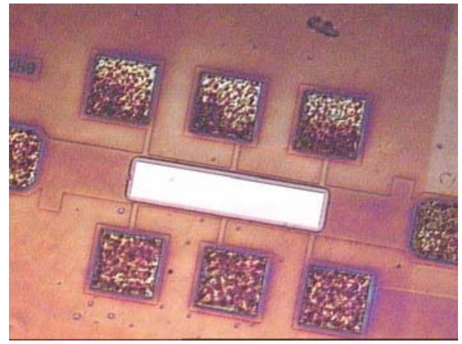

Figure 1.-Device micrography

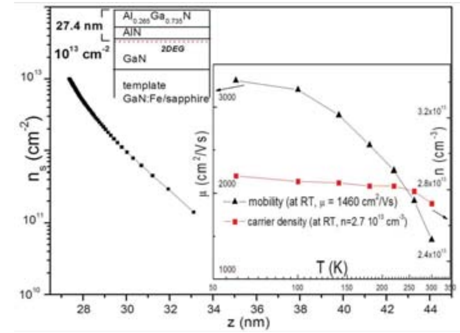

figure 2.-Bidimensional charge distribution. insets: heterostructure scheme, mobility and charge density vs temperature

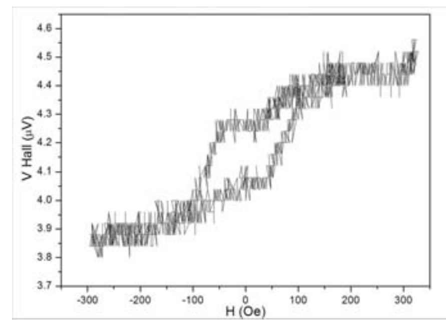

Figure 3.- Py hysteresys loop (V Hall vs applied magnetic field)

AM-14

Enhancement of sensitivity in a magnetic sensor by combining planar Hall resistance and giant Magnetoresistance.

H. Tran Quang[1], S. Oh[1], D. Nguyen Huu[2], C. Kim[1]

1. Department of Materials Science and Engineering, Chungnam National University, Daejeon, South Korea; 2. College of Technology, Vietnam National University, Hanoi, Viet Nam

Introduction:

Sensor designs to combine magnetoresistance and planar Hall resistance (PHR) by using bridge type and different contact arrangements were reported. However, the review of the literature reveals that there is no available report so far on the role of sensitivity of the magnetic sensor with a tilt angle of the cross junction bars. We report here a new kind of magnetic sensor by combining giant magnetoresistance (GMR) and PHR in order to enhance the sensitivity of magnetic sensor while taking into account the contribution of a tilt angle of cross junction using spin-valve structure. In order to understand the experimental data, a simple calculation based on Stoner-Wohlfarth model is introduced.

The first order approximation of Stoner-Wohlfarth energy of rotation process of magnetization in spin-valve structure was reported [1]. The energy term of the Stoner-Wohlfarth model can be rewritten as follow:

$E=K_u t\sin^2\theta - M_s tH\cos(\alpha - \theta) - J\cos(\beta - \theta)$ (1)

here, the t, θ, K_u, M_s are the thickness, the angle between magnetization and easy axis direction, the effective anisotropy constant, and the saturation magnetization of the free layer, respectively. J is the interlayer coupling, α is the measurement angle between external magnetic field and easy axis, and the β is the angle between the exchange bias field direction and the easy axis of free layer.

The four terminal Hall bars with a tilt angle ζ is shown in Fig. 1, When M makes an angle θ with J, under transverse magnetic field, the total resistance of junction with the tilt angle ζ can be approximately described as:

$R = R_{PHR} + R_d + \Delta R_{GMR}$ (2)

where $R_{PHR} = (R_{\parallel} - R_{\perp})\sin\theta\cos\theta$ is the planar Hall resistance component, $R_d = R_{\perp}\sin\zeta$ is the drift resistance [2], $\Delta R_{GMR} = R_0(1 - \cos\theta)$ is the GMR component.

The output voltage profiles with different values of tilt angles can be calculated theoretically by combining Eq. (1) and Eq. (2) under the condition that the energy E is minimal.

Experiments and results:

Spin-valve structures of Ta(5)/NiFe(6)/Cu(3)/NiFe(3)/IrMn(15)/Ta(5) (nm) were fabricated using a four-gun dc magnetron sputtering system and were patterned into four terminal Hall bars (Fig. 1). The variation of angle ζ is set to 0, 4, 8, 10, 30, 45 degrees. The exchange bias field direction and the current direction were aligned parallel to the long terminals *a* and *b*. Output voltages were measured from the short terminals *c* and *d* at room temperature under the application of external magnetic fields ranging from -45 Oe to 45 Oe along the direction of the film plane.

The voltage profiles of cross junctions with various tilt angles showing in Fig. 2 were measured by a Keithley 2182A Nanovoltmeter, whose sensitivity is 10 nV.

Discussion:

The result of separation PHR and GMR components of junction with $\zeta = 10^o$ is showed in Fig. 3. The increase of resistance in the positive magnetic direction is larger when compare with the decrease in negative magnetic field range. The increase and decrease in resistance are due to the contribution from GMR component and PHR component. This results in increase the sensitivity of magnetic sensor.

The sensitivity of various tilt angles of sensor elements is estimated and is given in table 1.

In conclusion, the magnetic sensors with various tilt angles utilize better sensitivity in compared with PHR or GMR sensor. A simple model is introduced to understand the role of contribution of GMR and PHR to the total output voltage.

[1] Tran Quang Hung et al, Phys. Stat. Sol. b, 244, 4431 (2007).

[2] D. Y. Kim et al, J. Appl. Phys., 88, 3490 (2002).

Angle (°)	0	4	8	10	30	45
Sensitivity (μV/Oe)	7.48	7.55	7.60	7.72	9.10	9.53

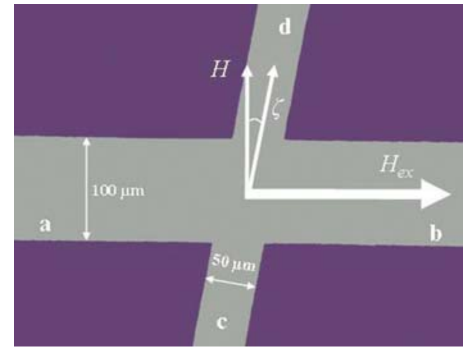

Fig. 1 Junction geometry with a tilt angle ζ

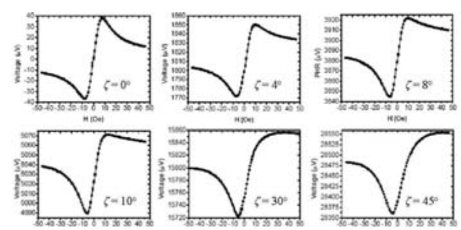

Fig. 2 Voltage profiles of cross junctions with different tilt angles

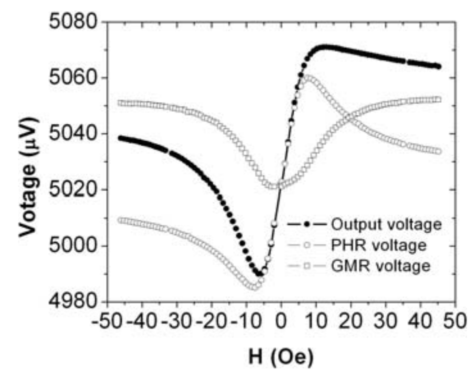

Fig. 3 PHR and GMR components separated from output voltage of junction with $\zeta = 10^o$

AM-15

Detection of magnetic particles for biological applications using a local-Hall device.

S. Joo[1,2], Y. Kim[1], W. Lee[1], J. Lee[1], J. Hong[1,2], K. Rhie[1,2], K. Shin[2]
1. Applied Physics, Korea university, Seoul, South Korea; 2. Center for Spintronics Research, KIST, Seoul, South Korea

The sensor for nano-scale magnetics has potential applications in fundamental study of biological interactions as well as utilities in bio-analysis and biomedical applications. Micro-magnetic sensors proposed thus far are based on magnetoresistive technologies such as GMR and TMR which suffer from nonlinear responses and saturation at low field. Another kind of sensor is Hall device which has difficulty in the integration of sensor array and requires a bulky system caused by using AC magnetic field. To overcome the drawbacks of these conventional devices, we have fabricated a magnetic sensor made of InAs 2DEG and its signal is detected by measuring longitudinal resistance.

The structure of our device is displayed in a scanning electron microscope image as shown in Fig. 1(a). An InAs 2DEG mesa, with a current channel from I+ to I– and two voltage probes denoted as B and C was patterned by electron beam lithography. The current channel is 2.8 μm wide and the voltage probes are separated about 2.8 μm from center to center. A single magnetic particle was manipulated on top of the InAs 2DEG mesa. The InAs 2DEG resides 35.5 nm below the surface. The mobility and the carrier density of InAs 2DEG (2-demensional electron gas) is 7.86 m2/Vsec and 2.0 × 1016 m–2 respectively, at T= 2 K and 2.0 m2/Vsec and 2.1 × 1016 m–2 at room temperature (RT). Since the mean free path at 2 K is 1.85 μm, the transport mechanism at 2 K can be treated as ballistic motion. Fig, 1(a) show in which the widths of the current channel and the voltage probe are 2.8 μm, and the size of magnetic particle is 2.8 μm.

In a conventional Hall sensor magnetic particles are located on the center of a cross-shaped Hall sensor. But our device can obtain a signal when the magnetic particle place in the middle of two neighboring voltage probes. Resistance was measured using a DC measurement and a standard lock-in technique with low-frequency (98 Hz) ac of 10μA. The signals were measured by passing a current through terminal [I+] and [I–] while the voltage was measured between a pair of probes [B] and [C]. When an external magnetic field (Bext) is applied, a magnetic particle is located between voltage probes and the stray field generated by the magnetic particle leads to the variation of resistance (see RBC in Fig1.(b)).

Further miniaturization of our device to submicron dimensions will lead to a high performance biological sensor for detection of nanometer-size particles.

[1] Sungjung Joo et al.Korean phys.Soc 48,642(2006)

[2] Daniel L. Graham et al. TRENS in Biotechnology vol.22 No.9(2004)

[3] G. Landry, M. M. Miller, B. R. Bennett, and M. Johnson Applied physics letters Vol 85, #20(2004)

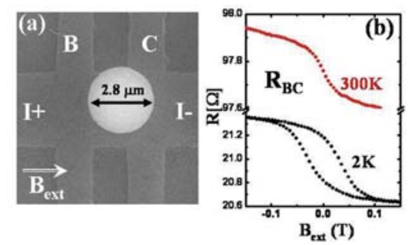

Fig.1 (a) Scanning electron micrograph of the device. (b) Longitudinal resistance (RBC) at 2K and 300K.

AM-16

Fabrication and Characterization of Silicon Micro Hall Sensors for Scanning Hall Probe Microscopy (SHPM) Using Multiple Feedback Techniques.

R. Akram, M. Dede, A. Oral
Department of Physics, Bilkent University, 06800, Ankara, Turkey

In this report we present the fabrication and characterization of Silicon on Insulator (SOI) micro hall sensors for scanning hall probe microscopy (SHPM) using different feedback configurations. Compatibility of fabrication process with standard CMOS fabrication process and controllability on the characteristics parameters of Silicon makes them a more advantageous, for hall probe applications, over other compound semiconductors (AlGaAs/GaAs, InSb and AlGaN/GaN) which are mainly based on 2DEG heterostructures or thin films.
Silicon micro hall probes were produced using optical lithography and reactive ion etching of SOI wafers. The active area of the hall probes were ~1x1μm^2 with the thickness ranging from 250nm to 500nm, the picture of the Hall probe is shown in Figure 1. These probes have been characterized based on their electric (V_H vs. I_H), magnetic (R_H vs. I_H), noise and temperature characteristics. Figure 2 shows a dependency of Hall voltage, V_H, and Hall coefficient, R_H, on the Hall current. A typical value of Hall coefficient, carrier concentration and series resistance of the Hall sensors were 0.95mΩ/G, 2.2x10^{19}cm^{-2} and 22kΩ at room temperature with Hall current of 500μA.
Application of Silicon Hall sensors in SHPM have been investigated using conventional scanning tunneling microscopy (STM) feedback and a novel Quartz Tuning Fork (QTF) in atomic force-guided scanning (AFM) Hall probe microscopy (SHPM). Simultaneous scans of magnetic and topographic data at various pressures (from atmospheric pressure to high vacuum) at temperatures ranging from 77K to 300K will also be presented for different samples to illustrate the capability of Silicon Hall sensors in variable temperature-SHPM.

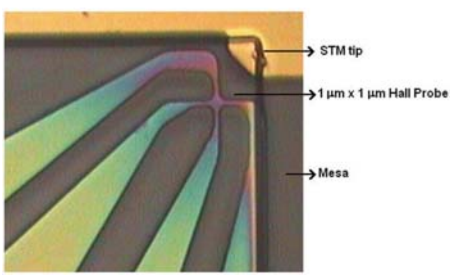

Si 1μmx1μm Hall probe with STM Tip.

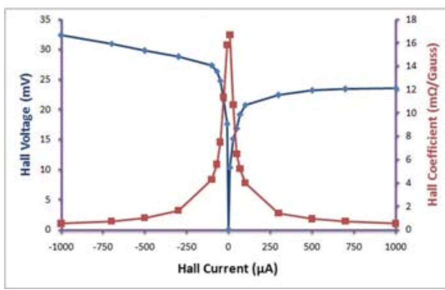

Electrical (V_H vs. I_H) and Magnetic (R_H vs. I_H) Characteristics of Si 1μmx1μm Hall probe.

AM-17

Magneto-impedance property in a micromachined magnetic LC-sensor device.

A. Le[1], S. Yu[1], H. Lee[2], V. Manuel[3]
1. BK 21 Physics Program and Department of Physics, Chungbuk National University, Cheongju 361-763, South Korea; 2. Department of Physics Education, Kongju National University, Kongju 314-701,, South Korea; 3. De Instituto de Ciencia de Materiales de Madrid, CSIC, Campus de Cantoblanco, 28049 Madrid, Spain

In recent years, an increasing interest in the development of miniaturized smart structures and systems, particularly on micro and nano electromechanical systems (MEMS and NEMS) and integrated sensor systems have evolved a new page in the science and engineering field. In order to approach this, we have proposed and developed a novel micromagnetic LC-sensor device with soft ferromagnetic microwires as sensing element, giving an emphasis on the use of resonance effect from LC-components to improve the sensitivity of sensor. A micro LC-sensor device consists of a solenoidal microinductor with a bundle of soft magnetic microwires as a core and a capacitor connected in parallel to the microinductor. The solenoidal microinductors were fabricated with varying dimensions of 500 – 1000 μm in length, 200 μm in width, 75 μm in height, and with 10 – 20 turns by adapting the MEMS techniques including the spin coating of photoresist, ultraviolet lithography (UV-LIGA) process, and metal electroplating. To form a LC-electric circuit, the varying external capacitors from 1 - 100 pF were connected in parallel to the microinductors. Magneto-impedance (MI) measurements were conducted using an rf impedance analyzer (HP4191A) in a wide range of frequencies from 1 MHz – 1000 MHz and a varying dc magnetic field within 300 Oe. Because the permeability of soft magnetic microwires core varies rapidly as the external magnetic field changes causing a large variation in the inductance of microinductors and, therefore the impedance of the micro LC-sensor device. It is important to note that the impedance variation of a micro LC-sensor device can be significantly improved by working at resonant conditions in a LC-electric circuit. In our present case, the magnitude of impedance changes was extremely enhanced by adjusting the measuring frequencies at near the resonance point. This originates from both the strong change in permeability of the microwires caused by external magnetic field and the LC resonance effect of the sensing elements. In the present work, the largest MI ratio up to 500% with very sharp peak was obtained at a frequency of 263.4 MHz for a micro LC-device with an external capacitor value of 10 pF as shown in Fig. 1. The calculated maximum field sensitivity of the micro LC-device reached an extremely high value of 420 %/Oe. This value is of practical importance in the development of highly sensitive micromagnetic sensors that can operate at high-frequency region. It is also noteworthy that the resonant frequency and the field sensitivity of LC-sensor devices were considerably altered with change in external capacitor values. Our experimental results have been demonstrated that the resonance frequency of micro LC-sensor devices decreases from 569 MHz to 72 MHz when the external capacitor value increases from 1 pF to 100 pF as shown in Fig. 2. This indicates that by changing values of external capacitor, the operating frequency of the sensor device can be precisely tuned for desirable purposes. It is worth to noting that the field sensitivity of micro LC-sensor devices also alters as the external capacitors changes (see Fig. 2). Consequently, an appropriate selection of the external capacitor for making a LC-resonant circuit is necessary for the design and fabrication of practical micromagnetic sensors with desired sensitivity and operating frequency.

To clarify the influence of core material, we examined the effect of number of microwire cores on the sensing characteristics of device. Here, the dimensions of microinductor and the external capacitor were fixed, whereas the number of microwires (n) was varied from 1 - 5. The experimental results showed that the sensitivity of device increased with increasing the number of microwire cores in the sensing element. As one can see clearly from inset of Fig. 1 the calculated field sensitivity increases from 40 %/Oe to 92 %/Oe as the number of sensing microwire cores increases from 1 to 5. In our present case, the increase in sensitivity is likely due to the dynamic magnetic interaction between the ferromagnetic microwire cores in the sensing element under the influence of high-frequency excitation current. Finally, it is interesting to mention that the feature of a LC-sensor circuit can be ideally used for developing highly sensitive microsensor devices or for improving the sensitivities of magnetic sensors. This also opens up a new opportunity to design smart microsensor structures containing short magnetic microwires for a variety of engineering and technological applications.

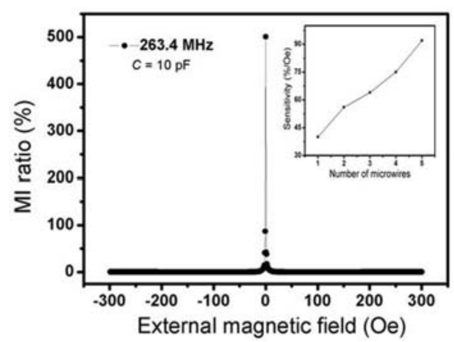

Figure 1

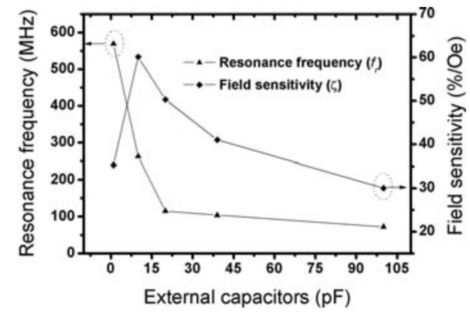

Figure 2

AN-01

Half-metallic magnetic materials and hybrid spintronic Structures.

Y. Xu
Department of Electronics, The University of York, York, United Kingdom

The second generation spintronic devices, integrating magnetic materials with semiconductor devices, will not just improve the existing capabilities of electronic devices, but will have new functionalities enabling future computers to run faster, but consume less power, which is expected to have a impact comparable to the development of transistors 50 years ago. There are currently two classes of material systems exploited for use in the second generation spintronics a) Dilute magnetic semiconductors, b) Hybrid magnetic/semiconductor spintronic structures. The dilute magnetic semiconductors might offer opportunities of easy integration with conventional semiconductor devices, but the challenges are to increase their Curie temperatures and their magnetization apart from understanding the origin of the ferromagnetism in this system. The hybrid spintronic structures have the advantages of high Curie temperatures, well controlled magnetic properties, and easy integration with current magnetic technologies; in particular, by integrating half-metallic magnetic materials as high efficient spin sources [1]. In this invited presentation, we will report our studies of three types of promising hybrid spintronics materials and devices based ferromagnetic metals and half-metallic oxides and Heusler alloys.

The hybrid spintronic structures integrating half-metallic magnetic oxides and Heusler alloys are exciting for the second generation spintronics as a 100% spin polarisation is expected for high efficient spin injection. By using post-growth annealing, we have synthesized epitaxial magnetic oxide Fe3O4 on GaAs(100) and the unit cell of the Fe3O4 was found to be rotated by 45 degree to match of GaAs [2]. The formation of the ferrimagnetic Fe3O4 rather than Fe2O3 or other ion oxides has been further confirmed by XPS and XMCD measurements. The ultrathin films have a uniaxial anisotropy possibly related to the strain due to the lattice mismatch. The system has a moderate Schottky barrier of around 0.3-0.4eV, which is favorable for spin-injection [3]. Furthermore, the films were found to have a bulk like moment down to 3-4 nm indicating a sharp interface. We are currently developing high efficient spin-LED with this half metallic Fe3O4.

In the Heusler alloy systems, such as Co2MnGa on GaAs, we found that the magnetic moment was reduced by more than 50% for the thickness down to 5nm. Using the elementary specific XMCD technique, we have further found that the reduced spin moments come from the Mn rather than the Co, but the orbital moments are not reduced [4]. Our studies suggested that more work is needed to improve the growth of Heusler alloy/semiconductor hybrid spintronics structures to have a clean interface in order to make use of this encouraging material system.

In the ferromagnetic metal based system, while our previous XMCD study demonstrated that the Fe atoms on GaAs (100) are ferromagnetic down to submonolayer at room temperatures [5], our studies of Co and Ni show that the Co atoms are similar to that of Fe with bulk-like spin moments down to submonolayer, but the Ni atoms lost their magnetic moments on the GaAs surface [6]. This demonstrated clearly that the magnetism of ferromagnetic metal/semiconductor interface depends strongly on the materials used.

We have fabricated a vertical hybrid ferromagnetic/III-V semiconductor/ferromagnetic spintronic devices namely, Co/GaAs (50nm, n-type)/Al0.3Ga0.3As (200nm, n-type)/ FeNi and studied their magneto transport properties [7]. The I-V characteristics revealed Schottky/tunneling type behavior and are dependent on external fields beyond a bias voltage of 5 V indicating that a high barrier related to interface oxide layer has been introduced in the device. The MR shows a strong dependence both on bias current and applied field. A 12% change in MR has been observed at room temperature, which is far larger than that of conventional AMR effect indicating strong spin injection and detection occurred in this device. The device also exhibited interesting field dependent MR behaviour which could be compared to field effect transistor characteristics. We are currently working on full epitaxial Fe/GaAs/Fe vertical devices with magnetic interfaces, and this structure might offer an opportunity to have a large room temperature electric spin injection and detection essential for the operation of the second generation spintronic devices.

Acknowledgement: The author acknowledges the contributions from Yongxiong Lu, Ehsan Ahmad, Jill Claydon, Sameh Hassan, and Iain Will in York Spintronics Laboratory; Gerrit van der Laan in UK Diamond Light Sources; Christian Damsgaard, Jørn Bindslev Hansen, Claus Jacobsen in Technical University of Denmark; and Stuart Holmes in Toshiba.

[1] Y.B. Xu, E. Ahmad, J. S. Claydon, Y.X. Lu, S. S. A. Hassan, I. G. Will and B. Cantor, J. Magn. Magn. Mater. 304, 69 (2006).

[2] Y. X. Lu, J. S. Claydon, Y. B. Xu, D. M. Schofield, S. M. Thompson, G. van der Laan, Phys. Rev. B, 70, 233304 (2004)

[3] Hassan SSA, Xu YB, Ahmad E, Lu YX, IEEE Trans on Magn. 43, 2875 (2007)

[4] S.S.A. Hassan, Y.B. Xu, Christian Damsgaard, Jørn Bindslev Hansen, Claus Jacobsen, Gerrit van der Laan, to be submitted, 2008

[5] J. S. Claydon, Y.B. Xu, M. Tselepi, J.A.C. Bland, G. van der Laan, Phys. Rev. Lett., 93 16 (2004).

[6] Y.B. Xu et al, to be submitted, 2008

[7] E. Ahmad, A. Valavanis J. S. Claydon, Y. X. Lu and Y. B. Xu, IEEE Trans on Magn. 41, 2592, (2005)

AN-02

Searching for quaternary Heusler alloys with half-metallicity.

X. Dai, G. Liu, G. Fecher, C. Felser
Institut für Anorganische und Analytische Chemie, Johannes Gutenberg-Universität Mainz, Mainz, Germany

In this work, we will focus on the searching for the quaternary half-metallic Heusler alloys by the first-principle calculations. As an example, the Heusler-type CoFeMnSi with different superstructures have been investigated. A semi-experiential rule to develop quaternary half-metallic Heusler alloys will be also presented. As a Heusler-type compound with four different elements, there exist three non-equivalent highly-ordered alignments of atoms as shown in Fig 1.

We optimize the lattice constants for CoFeMnSi compounds with different superstructures and calculated their electronic structures with the optimized lattice constants. The calculated results were shown in Fig. 2. For the type I structure, the Fermi level verily lies in an energy gap of the spin-down states. For the type II structure, the electronic structure is similar to that of type I. However, the Fermi level lies in a deep valley in the spin-down states but not a real gap. As to type III arrangement, a spin-polarization behavior of the general ferromagnets was observed at the Fermi level. These results indicate that the CoFeMnSi compound with type I or type II structure is half-metallic ferromagnet while the type III anti-sites will destroy the half-metallicity. Fortunately, based on an experiential rule discussed in ref.1, we can predict that the CoFeMnSi composition will firstly favor the type I superstructure, secondly type II, which is also confirmed by our calculations of total energy.

As discussed in our previous works, the half-metallic band gap in Heusler alloys results from two mechanisms: covalent band gap and d-d band gap. The former roots in the covalent hybridization between the nearest atoms. The hybridization leads to the formation of bonding and antibonding bands, which further generates a band gap between the bonding and antibonding bands. The origin of d-d band gap has been elucidated in Ref.2. It was shown that the gap arises between the occupied tIu and the unoccupied eu states which are exclusively localized in space at the A and C sites since the d orbitals of the atoms at B sites do not transform with the u representations [2]. The final width of energy gap for a compound will be determined by the smaller one of the covalent band gap and the d-d band gap.

Based on the analysis of the electronic structures of the CoFeMnSi with different superstructures, one can see the high valence transition metal atom (like Co, Ni elements) is not proper one to occupy the B sites as the contributor of the covalent band gap. As in CoFeMnSi compound, when the Co atom is at the B site, its spin-down states have to strongly hybridize with that of Fe since they have many spin-down states distribute in the similar energy area, which makes the d electrons delocalize, so the bonding and antibonding states difficult to form. At the same time, the d-d band gap was also difficult to form due to the absence of the spin-down states with similar energies in Mn and Fe atoms. However, when the Mn atom is at B site, the Co and Fe atoms have quite many spin-down states at the similar energy area, which is easy to generate a tIu-eu band gap. As shown in Ref. [3], the covalent hybridization is easy to occur between the lower-energy d states of the high-valent transition metal Co atom and the higher-energy d states of the lower-valent transition metal Mn atoms, which lead to the formation of band gap between the bonding and antibonding bands. The bonding hybrids are localized mainly at the high-valent transition metal atom site, while the unoccupied antibonding states are localized mainly at the lower valent transition metal site.

In summary, a good field to develop new half-metallic materials is the quaternary Heusler alloys. The preferred route is to combine the compounds that have been already grown in the Heusler L21 lattice, which is advantageous to the realistic synthesis. In the quaternary compounds, the atomic positions must be considered as an important aspect.

[1] C. M. Fang, G. A. de Wijs, and R. A. de Groot, J. Appl. Phys. 91, 8340 (2002).

[2] I. Galanakis, P. H. Dederichs, and N. Papanikolaou, Phys. Rev. B 66, 174429 (2002).

[3] H. van Leuken and R. A. de Groot, Phys. Rev. Lett. 74, 1171 (1995).

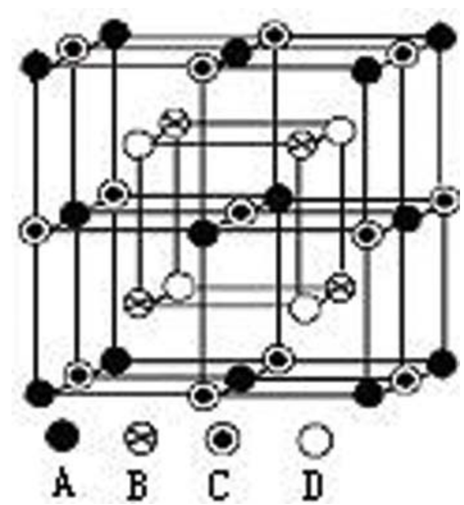

Three non-equivalent CoFeMnSi atomic arrangements: Type I: Co is at C site, Fe at A site and Mn at B site. Type II: Co is at C site, Fe at B site, and Mn at A site. Type III: Co is at B site, Fe at C site, and Mn at A site.

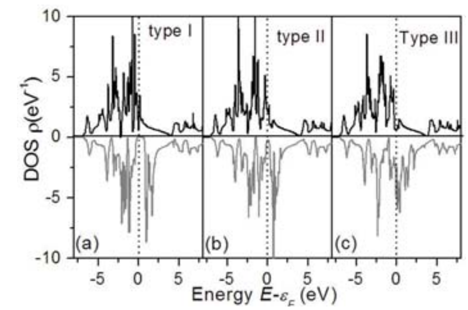

Figure 2 The DOSs of CoFeMnSi composition

AN-03

Universal scaling of the anomalous Hall effect in Fe3O4.

A. Fernández-Pacheco[1,2], J. M. De Teresa[2], J. Orna[1,2], L. Morellón[1,2], P. A. Algarabel[2], J. A. Pardo[1,3], M. R. Ibarra[1,2]

1. Instituto de Nanociencia de Aragón, Zaragoza, Spain; 2. Instituto de Ciencias de los Materiales de Aragón, Zaragoza, Spain; 3. Departamento de Ciencia y Tecnología de Materiales y Fluidos, Universidad de Zaragoza, Zaragoza, Spain

The origin of the Anomalous Hall effect (AHE), present in magnetic materials, has been a controversial issue for decades, where theories based on intrinsic [1] or extrinsic contributions [2,3] tried to explain this effect. A recent theory [4] based on multi-band ferromagnetic metals with dilute impurities seems to have solved this complex scenario where three regimes can be distinguished as a function of the longitudinal conductivity. In the dirty regime (σxx<104Ω-1cm-1), as it is the case of magnetite, a relationship σH∝σxx1.6 is predicted, caused by the damping of the intrinsic contribution.

We report a systematic study of the AHE in epitaxial Fe3O4 thin films grown on MgO (001) within a wide range of thicknesses (5-150nm) and in the temperature range from 300K down to 60K. Fe3O4 thin films were grown on MgO (001) substrates by pulsed laser deposition. Structural and magnetic characterization indicate a 001-oriented epitaxial growth as well as a high cristallinity of the films. For electrical transport measurements a two-step lithography process was carried out. The typical electrode for the flow of the current was 300 μm wide and additional pads were patterned for the measurements of the voltage drop [5]. The values for the resistivity at room temperature increase monotonically for decreasing film thickness (from 5.46 mΩcm for the 150 nm film to 121.4 mΩcm for the 5 nm film)This result is mainly associated with the increase of anti-phase boundaries (APB) density [6].

We have measured the AHE for the different thickness in the temperature range from 300K down to 60K and with fields up to 11kOe (see Fig 1 and 2). In this range of magnetic fields, the contribution of the AHE dominates completely the Hall effect. The values for ρH increase in modulus monotonously when the temperature diminishes, presenting a huge enhancement as the temperature the Verwey transition is approached. This effect is related with changes in the electronic structure and the spin-orbit coupling that occurs at the transition [7]. In figure 3 we show the absolute value of the Hall conductivity at maximum field as a function of the longitudinal conductivity for all the samples measured. In spite of the different thicknesses and measurement temperature, the relationship σH ∝ σxx1.6 (dashed line) is followed in all cases, as it is expected in the dirty range of conductivities. Together with our results, other measurements found in the literature for the AHE in magnetite have also been plotted. These data approximately match with ours, revealing the same physical origin in all cases. All these facts support the belief that the relationship σH ∝ σxx1.6 is universal for this low-conductivity regime.

[1] R. Karplus and J.M. Luttinger, Phys. Rev. 95, 1154 (1954)

[2] J. Smit, Physica (Utretch) 21, 877 (1955), 24, 39 (1958)

[3] L. Berger, Phys. Rev. B 2, 4559 (1970)

[4] S. Onoda, N. Sugimoto, and N. Nagaosa, Phys. Rev. Lett. 97, 126602 (2006)

[5] J.M. De Teresa et al, Microelectr. Eng. 84, 1660 (2007)

[6] W. Eerenstein et al, Phys. Rev. B 66, 201101(R) (2002)

[7] F. Walz, J. Phys.: Condens. Matter 14 R285(2002)

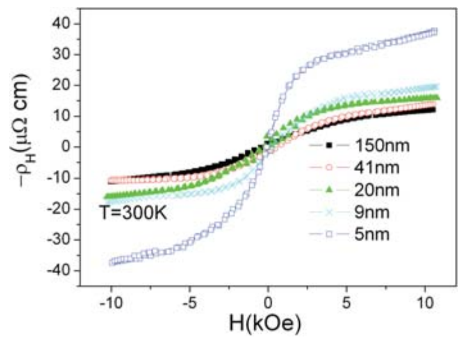

FIGURE 1. Hall resistivity at room temperature as a function of thickness

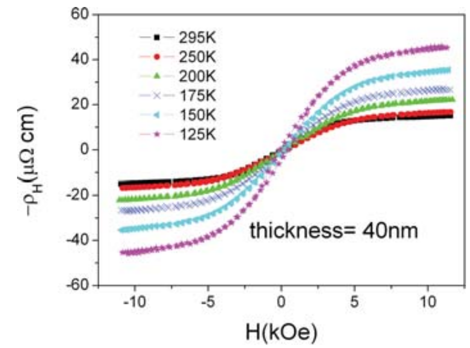

FIGURE 2. Hall resistivity isotherms in a film of 40 nm for temperatures above the transition

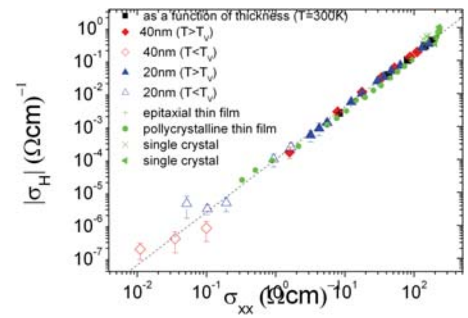

FIGURE 3. Relationship between the magnitude of the Hall conductivity at 11kOe and the longitudinal conductivity for our films and data taken from literature

AN-04

Optimization of the Postgrowth Oxidation Preparation Process of Fe3O4/GaAs(100) Hybrid Structure.

S. Hassan[1], Y. Xu[1], K. Wilson[3], S. Thompson[2], G. Van der Laan[4]
1. Electronics, University of York, York, United Kingdom; 2. Physics, University of York, York, United Kingdom; 3. Chemistry, University of York, York, United Kingdom; 4. Daresbury Laboratory, Warrington, United Kingdom

One of the most promising spintronic materials is the half-metallic oxides as they have high spin polarisation at the Fermi level making them useful in the application of magnetoresistive devices. Magnetite (Fe3O4) is a robust ferrimagnetic material with a Curie temperature of 858 K [1]. Theoretical band calculations predict a half-metallic character with only minority spin (spin down) electrons present at the Fermi level [2,3]. In order to introduce the half-metallic materials in the spintronic technologies, one needs to integrate them with the semiconductors of conventional electronics.
Recently, we succeeded in growing monocrystalline ultrathin films of Fe3O4 on GaAs substrate by molecular beam epitaxy (MBE) using post-growth annealing of the Fe film in a partial pressure of oxygen [4]. The results suggested that the film structures and properties might depend on the grow conditions. In the present work, we have carried out a detailed RHEED, XAS, XMCD, XPS and AGFM study of the effect of the O2 pressure on the sample's structures and magnetic properties, and the optimised pressure was found to be around 4-8x10-4mbar.
Seven samples have been prepared using MBE growth facilities at the University of York. They consisted of a 6nm thin Fe films on GaAs substrates transformed to magnetite by in-situ exposure to a variety of O2 pressure ranging from 1.25 x 10-5 mbar to 8 x 10-4 mbar at a fixed controlled temperature of 180oC for 10 minutes. The temperature used in this study is lower than that of 230 oC reported previously [4]. This is to reduce possible intermixing at the interface.
The in-situ RHEED patterns confirmed the growth of Fe3O4 of all seven samples. However, as RHEED is surface sensitive and cannot differentiate between Fe3O4 and maghemite γ-Fe2O3, we have further studied these samples using XPS technique. The XPS measurements showed widened and shake-up satellite free spectra confirming the growth of Fe3O4 rather than γ-Fe2O3. Interestingly, the samples oxidised at low Oxygen pressures have shown a small shoulder on the Fe 2p3/2 spectra at a binding energy of about 707 eV, which could be attributed to a certain percentage of unoxidised metallic Fe beneath the surface magnetite layer [5].
The XAS and XMCD measurement have been carried out at the station 1.1 on the SRS in Daresbury Labs. Figure 1 shows the XMCD spectra of the 6nm Fe3O4 prepared at different oxygen pressures and normalized to the FeOH3+ Peak. The XAS and XMCD results have further confirmed that, with increasing the oxygen pressure up to 8x10-4 mbar, better quality magnetite samples with a reduced contribution from any other phases can be obtained. The contribution of metallic Fe has been subtracted and the spin and orbital magnetic moment have been calculated from the Sum rules. The detailed results will be presented at the conference.
The AGFM measurements showed a change on the coercive fields from couple of Oersted up to 75 Oersted for the different samples which could be used to tailor the magnetic properties of the prepared samples by using different oxygen pressure. Moreover the samples prepared at the lower O2 pressure showed a double switching, which could be attributed to unoxidised metallic Fe saturate independently from the rest of the magnetite thin film.

1. M.L. Glasser, F.J. Milford, Phys. Rev. 130, 1783 (1963).

2. Yanase, K. Siratori, J. Phys. Soc. Jap. 53, 312 (1984).

3. Yanase, N. Hamada, J. Phys. Soc. Jap 68, 1607 (1999).

4. Y.X. Lu, J.S. Claydon, Y.B. Xu, D.M. Schofield, S.M. Thompson, J. Appl. Phys. 95, 7228 (2004).

5. S Jain, A O Adeyeye, S Y Chan and C B Boothroyd, J. Phys. D: Appl. Phys. 37, 2720 (2004).

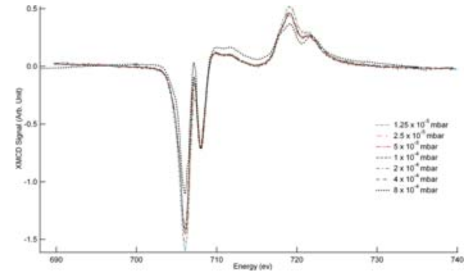

Figure 1: XMCD of 6nm Fe3O4 prepared at different oxygen pressures and normalized to the FeOH3+ Peak.

AN-05

Magnetic and transport properties of polycrystalline CaRu1-xMoxO3.

Y. Ying[1], Y. Lee[1], K. Kim[2], H. Pan[3], Y. Zhang[3]
1. Quantum Photonic Science Research Center and BK21 Program Division of Advanced Research and Education in Physics, Hanyang University, Seoul, South Korea; 2. Sunmoon University, Asan, South Korea; 3. National High Magnetic Field Laboratory, University of Science and Technology of China, Hefei, China

Recently, ruthenates have been widely investigated for their peculiar properties, such as the unconventional superconductivity in Sr2RuO4 and the ferromagnetic (FM) metallic behavior in SrRuO3 [1,2]. CaRuO3, similar to SrRuO3, has an orthorhombically distorted GdFeO3-type structure and shows a metallic conductivity. On the other hand, the magnetic properties are significantly different from those of SrRuO3 [2]. The detailed magnetic structure of CaRuO3 is still unclear. The main debate focuses on whether there exists antiferromagnetic and/or FM spin interaction in CaRuO3. The ground state of CaRuO3 is sensitive to the impurity doping. The recent works exhibit that a disorder is doped into CaRuO3 by the partial substitution with foreign elemental ions such as Cr3+, Sn4+, Mn4+, Ti4+ and Fe3+ [2]. Thus, CaRuO3 is believed to be a compound that is on the verge of magnetic ordering. Even though many transition-metal ions were introduced into CaRuO3 up to now, few works have been devoted to the doping effect of Mo ions in CaRuO3. In this work, the magnetic and the transport properties of polycrystalline CaRu1-xMoxO3 have been studied.
Polycrystalline CaRu1-xMoxO3 (x = 0 and 0.02) perovskite samples were synthesized by the conventional solid-state reaction. The XRD spectra show that both kinds of samples are in a single phase of the Pbnm orthorhombic structure (not shown here). The resistivity measurements were performed by the conventional four-probe method in a temperature regime between 10 and 300 K. The magnetic properties were measured by using a superconducting quantum interference device magnetometer.
Figure 1 presents the temperature dependence of magnetization M(T) investigated in zero field cooling (ZFC) and field cooling (FC) modes with an applied field of 1000 Oe. As shown in Fig. 1, in the low temperature region, the magnetization of CaRuO3 shows a remarkable increase with decreasing temperature, which indicates the formation of the FM order. The ZFC curve and the FC curves are divided below 12.7 K, which is a character of the spin-glass state. This implies the existence of the short-range antiferromagnetic spin interaction, which makes the spin order frozen at low temperatures. For the CaRu0.98Mo0.02O3 sample, both ZFC and FC curves are nearly superposed on those of CaRuO3, respectively. It seems that the Mo ionic doping hardly changes the magnetic properties of this system. According to the M(H) curves (Fig. 2), the FM interaction begins to take place above 15 K while the AFM one exists only below 12.7 K (seen in Fig. 1). The doping of Mo ions hardly affects the AFM interaction but enhances the FM one. The temperature-dependent resistivity, ρ(T), curves of CaRuO3 show a metallic conductivity in the high temperature region and an insulating state at low temperatures, but the value of resistivity is small in the whole temperature region (Fig. 3). CaRu0.98Mo0.02O3 reveals an insulating behavior in the investigated temperature range. The doping of Mo ions enhances the insulating properties. According to variable-range hopping model, the electrons become more localized with the doping of Mo ions, which results in the lager resistivity of CaRu0.98Mo0.02O3 with respect to CaRuO3.

[1] Y. Maeno, H. Hashimoto, K. Yoshida, S. Nishizaki, T. Fujita, J. G. Bednorz, and F. Lichtenberg,

Nature 372, 532 (1994).

[2] G. Cao, S. McCall, M. Shepard, J. E. Crow, and R. P. Guertin, Phys. Rev. B 56, 321 (1997).

[3] T. He and R. J. Cava, J. Phys.: Condens. Matter 13, 8347 (2001).

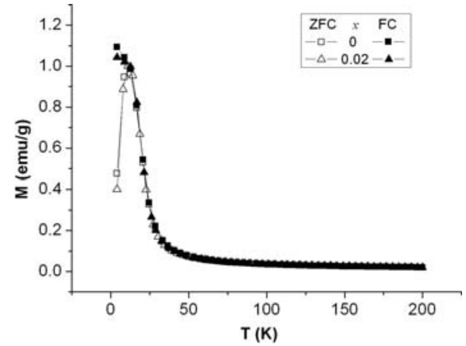

Fig. 1. Temperature dependence of the magnetization for CaRu1-xMoxO3.

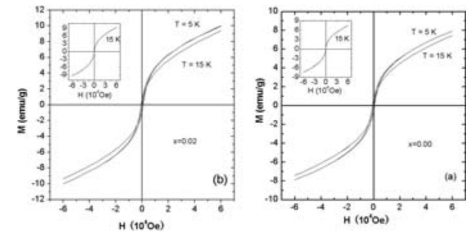

Fig. 2. Magnetization as a function of applied magnetic field for CaRu1-xMoxO3. x = (a) 0 and (b) 0.02.

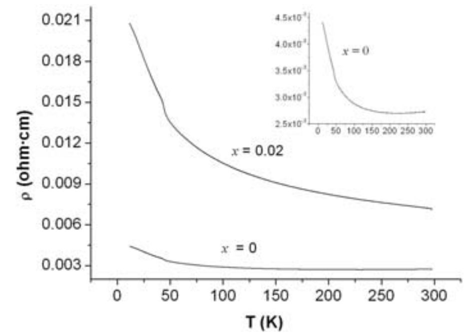

Fig. 3. Temperature dependence of the resistivity for CaRu1-xMoxO3.

AN-06

Atomic and electronic structure in ferromagnetic/superconducting oxide interfaces.

M. Varela[1], J. Garcia-Barriocanal[2], A. R. Lupini[1], W. Luo[3,1], Z. Sefrioui[2], S. T. Pantelides[3,1], C. Leon[2], J. Santamaria[2], S. J. Pennycook[1,3]
1. Materials Science and Technology Division, Oak Ridge National Laboratory, Oak Ridge, TN; 2. Departmento de Física Aplicada III, Universidad Complutense de Madrid, Madrid, Spain; 3. Department of Physics and Astronomy, Vanderbilt University, Nashville, TN

Ferromagnetic/superconducting oxide interfaces have received a great deal of attention due to their intriguing physical properties [1-11], such as the giant magnetoresistance (GMR) found in $YBa_2Cu_3O_{7-x}/La_{0.7}Ca_{0.3}MnO_3$ (YBCO/LCMO) superlattices [7,10] and a strong interplay between ferromagnetism and superconductivity [3] which suggests of a long range proximity effect [4]. Since these systems have significant potential towards applications of spin injection from a ferromagnet into a superconducting electrode, such heterostructures where a high Tc superconductor (a cuprate) and a manganite exhibiting colossal magnetoresistance are combined have attracted significant attention in the past few years [1-11]. Reduced dimensionality, novel interactions and/or the aforementioned proximity effects across the interfaces can give rise to unexpected physical behaviors. The possibility of interface charge transfer drastically affecting the interface properties has been recently examined [9,11,12]. But harnessing these phenomena relies on a detailed understanding of the structure, chemistry and physical properties of these interfaces with atomic resolution, in real space.

For this aim, aberration corrected scanning transmission electron microscopy (STEM) and electron energy loss spectroscopy (EELS) combined with first principles calculations have proven to be very effective to improve our understanding of such systems [13]. STEM-EELS is a most powerful tool to study the structure, chemistry and electronic properties of these oxides, with atomic resolution and in real space and sensitivity to single atoms [14]. EELS chemical imaging with atomic resolution has been achieved [15-17]. Furthermore, in perovskites the O 2p bands and the transition metal 3d bands are very close to the Fermi level so the electronic properties can be probed by studying the fine structure on the O K edge and the transition metal L edge.

Here, we study the interaction between a high Tc superconductor and a manganite with colossal magnetoresistance by these techniques. High quality superconducting/ferromagnetic YBCO/LCMO and superconducting/antiferromagnetic $YBa_2Cu_3O_{7-x}/LaMnO_3$ (YBCO/LMO) superlattices grown by high pressure oxygen sputtering [2-4] were studied in a scanning transmission electron microscope (STEM) equipped with a Nion aberration corrector and a Gatan Enfina Electron Energy Loss Spectrometer. Both superconductivity and ferromagnetism are strongly suppressd in each other's presence [2,3]. Atomic resolution Z-contrast images show that the interfaces are coherent and free of defects [18, 19]. Elemental profiles show the interface stacking sequence to be CuO_2-BaO-MnO_2-La/CaO- MnO_2-… [18, 19]. The absence of interfacial CuO chains explains the lack of superconductivity in ultrathin YBCO layers (1 or 2 unit cells thick) sandwiched in between manganite layers.

EELS measurements in ferromagnetic/superconducting LCMO/YBCO superlattices suggest significant hole enrichment in the manganite together with electron localization in the superconding side of the interface, while density-functional theory shows how the first manganite layer at the interface has a lower magnetic moment than expected according to the nominal doping. Interpretation of the energy loss fine structure in terms of charge transfer from the ferromagnet will be discussed. As a result, superconductivity is suppressed in the superconductor, and the magnetization in the ferromagnet interface layer is depressed [6]. Interestingly, in antiferromagnetic/ superconducting LMO/YBCO superlattices ferromagnetism is induced in the LMO when its thickness is above five unit cells. The onset of ferromagnetism is accompanied by a strong depression of the superconductivity, similar to that found in LCMO/YBCO superlattices. The possibility of charge transfer at the interfaces being involved in this phenomenon will also be examined. Since interface vacancies may also be present and condition the system properties their role will also be discussed.

Acknowledgements: This work was supported by the Office of Basic Energy Sciences, Divisions of Materials Sciences and Engineering (MV, ARL, WL, SJP) and the McMinn Endowment at Vanderbilt University (STP). Work at UCM (JGB, CL, JS) supported by CICYT MAT 2005-06024-C01-02.

[1] V. A. Vas'ko et al., Phys. Rev. Lett. **78**, 1134 (1997)

[2] P. Prieto et al., J. Appl. Phys. **89**, 8026 (2001)

[3] Z. Sefrioui et al., Appl. Phys. Lett. **81**, 4568 (2002)

[4] Z. Sefrioui et al., Phys. Rev. B **67**, 214511(2003)

[5] V. Peña et al., Phys. Rev. B **69**, 224502 (2004)

[6] A. Hoffmann et al, Phys. Rev. B **72**, 140407 (2005)

[7] V. Peña et al., Phys. Rev. Lett. **94**, 057002 (2005)

[8] V. Peña et al., Phys. Rev. B **73**, 104513 (2006)

[9] S. Yunoki et al., Phys. Rev. B **76**, 064532 (2007)

[10] C. Visani et al., Phys. Rev. B **75**, 054501 (2007)

[11] J. Chakhalian et al., Science **318**,1114-1117 (2007)

[12] M. Varela et al., arXiv:cond-mat/0508564 (2005)

[13] M. Varela et al., Annu. Rev. Mater. Res. **35**, 539 (2005)

[14] M. Varela et al., Phys. Rev. Lett. **92**, 095502 (2004)

[15] M. P. Oxley et al., Phys. Rev. B **76**, 64303 (2007)

[16] M. Bosman et al., Phys. Rev. Lett. **99**, 086102 (2007)

[17] Koji Kimoto et al., Nature **450**, 702 (2007)

[18] M. Varela et al., Solid. State Elect. **47**, 2245 (2003)

[19] M. Varela et al., J. Mat. Sci., **41**, 4389 (2006)

AN-07

Magnetic phase coupled to an electric memory state in d^0 oxide ZrO_2 films.

Y. Jo[1], M. Jung[1], I. Hwang[2], B. Park[2], S. Lee[3]
1. Korea Basic Science Institute, DAEJEON, South Korea; 2. Konkuk University, SEOUL, South Korea; 3. Pohang University of Science and Technology, POHANG, South Korea

Introduction

To understand the unexpected ferromagnetism shown in the d^0 oxide film of HfO_2 [1], we have studied the d^0 oxide film of ZrO_2 with oxygen-vacant, which shows bistable resistive switching between high-resistance (HR) and low-resistance (LR) states by applying external voltage at room temperature. We find that the HR state is ferromagnetic and insulating and the LR state is non-magnetic and metallic. This suggests that the magnetic phase in our d^0 thin films is strongly coupled with the electric memory state induced by an external electric field. HR ferromagnetism of our ZrO_2 thin film achieved at room temperature can generate new functional spin devices, such as electric-field-controlled magnetic data storage and magnetically recorded ferroelectric memory devices, in which the electric field is used as an alternative means for controlling the magnetic configuration.

Experimental details

Our experiments were carried out with ZrO_2 thin films made by dc reactive sputtering. During deposition, the substrate temperature and the working pressure of

the ($Ar+O_2$) gas were kept at 300 °C and 5 mTorr, respectively. The ratio of the O_2 partial pressure to the working pressure was lowered to 5% to make oxygen-vacant samples. For transport measurements, 100-μm-diameter Pt top electrodes were deposited at room temperature by dc sputtering with a shadow mask. Micro manipulated probe station was used for transport measurements. The magnetic properties were characterized with a superconducting quantum interference device magnetometer.

Results and discussion

Fig. 1 shows the typical current-voltage (I-V) characteristics of our ZrO_2 thin films. The application of a voltage induces reversible switching between the HR and the LR states with slightly capricious switching voltages. This bistable resistance switching is applicable to nonvolatile resistance random

access memory (RRAM) device. As seen in Fig. 2, the temperature dependence of the resistance of HR state plotted with lnR versus $1/T^{1/4}$, which is typical form of variable-range hopping model, is linear in the temperature regions of 150 K < T < 300 K and 50 K < T < 150 K. The best fit gives the values of T_0 = 6.8 eV and 28.4 meV in the high- and the low-temperature regions, respectively. On the other hand, the resistance decrease of the LR state on cooling is suggestive of a metallic nature. Fig. 3 shows the hysteresis loop of HR state at room temperature. The coercive field is about 50 Oe, and it saturates above 1.5 kOe. One of the simplest models to explain the high-resistance state

for slow-moving electrons in a dielectric crystal is a lattice polaron model, leading to a high-resistance state. In an analogous manner to the lattice polaron, if an electron tends to distort the magnetic polarization in a magnetic material, then it would induce a local ferromagnetic ordering, this is called a bound magnetic polaron model [2].

Conclusion

From the results in our d^0 ZrO_2 films, we can elucidate the fact that the magnetic phase can be controlled by an electric field. These ferromagnetic and insulating phases at HR state are intrinsic and can be understood in terms of bound magnetic polaron model.

[1] M. Venkatesan, C. B. Fitzgerald, and J. M. D. Coey, Nature, **430**, 630 (2004).

[2] J. B. Torrance, M. W. Shafer, and T. R. McGuire, Phys. Rev. Lett. **29**, 1168 (1972); J. M. D. Coey, M. Venkatesan and C. B. Fitzgerald, Nature Matet. **4**, 173 (2005).

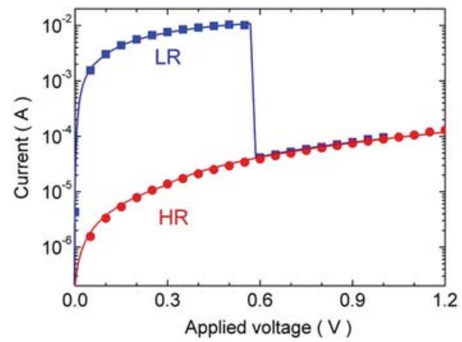

Typical current-voltage (I-V) characteristics measured at room temperature for a ZrO_2 thin film.

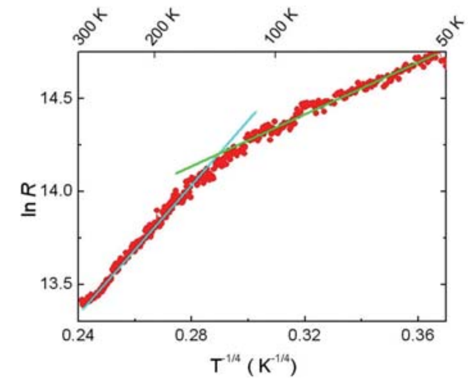

Temperature dependences of the electrical resistances. HR data plotted as ln R versus $T^{-1/4}$. The solid lines are linear fits.

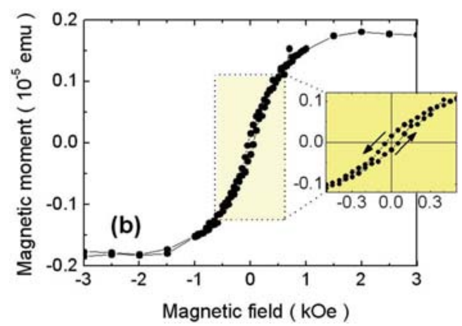

Magnetization data for the HR state, which is obtained after subtracting the diamagnetic contribution of the LR magnetization from the magnetization measured at the HR state. The inset represents the low-field data, which shows a clear hysteresis loop.

AN-08

Perovskite-oxide pseudo spin valve structure.

Y. Chan, W. Cheng, H. Lau, C. Leung
Department of Applied Physics, The Hong Kong Polytechnic University, Hong Kong, China

Giant magnetoresistive (GMR) effect has been extensively studied in both theoretical and practical aspects. While most of the investigations were focused on metallic multilayers, only a few studies have demonstrated GMR in all-oxide structures.

In this work, we fabricated all-perovskite oxide pseudo spin valve (PSV) structures. $LaNiO_3$ (LNO), a Pauli paramagnet with high electrical conductivity [1], was used as the spacer material. For ferromagnetic electrodes, $La_{0.67}Sr_{0.33}MnO_3$ (LSMO) and $La_{0.67}Sr_{0.33}Mn_{0.95}Ru_{0.05}O3$ (LSMRO) were chosen. Bulk LSMO is ferromagnetic at room temperature, has been predicted to be half metallic, and has a fairly good conductivity [2]. On the other hand, substitution of Mn by Ru in LSMO could lead to an enhanced coercivity compared with LSMO, while retaining the high Curie temperature and conductivity [3]. Since a sharp steplike magnetoresistance can be achieved in PSV only when there is a high contrast in coercivities between two ferromagnetic layers, LSMRO was a suitable candidate material for the ferromagnetic electrode layer. Crucially, the perovskite structures of all the three materials, with similar lattice parameters (a_{LNO} = 3.84 Å, a_{LSMO} = 3.87 Å, a_{LSMRO} = 3.86 Å), permitted epitaxial growth of the structure under suitable conditions.

LSMRO(100nm)\LNO(15nm)\LSMO(50nm) PSV structure was deposited on $LaAlO_3$ (LAO) (001) substrates by pulsed laser deposition. All the layers were deposited under an oxygen pressure of 150mTorr. The substrate temperature required for the deposition of LSMRO film (830°C [3]) was higher than that of LNO and LSMO (650°C); the combination of such a high substrate temperature and oxygen pressure avoided Ru deficiency in the final films due to its high volatility [3]. Therefore, LSMRO was deposited as the bottom layer to minimize interdiffusion effect among different materials.

Fig.1 depicts the X-ray diffraction profile of a trilayer film sample. The lattice parameters of LNO and LSMO were so close that they could not be separated from the scan. For the LSMRO, the 5%-Ru doping has caused an enlargement of the lattice parameter in the film, which was similar to the observation by Yamada et al [3]. Temperature-dependent resistance measurements of single-layer LSMO and LSMRO films on LAO (001), 50 and 100 nm in thickness, indicated Curie temperatures of 330°C for both layers.

Fig. 2 shows the hysteresis measurements of the PSV at various temperatures, down to 77 K. As the temperature was reduced below 200 K, a double-coercivity behaviour was observed in the sample. At 77 K, the coercivity of LSMRO was about 300 Oe, approximately five times the coercivity of the LSMO layer. This clearly indicated the coercivity enhancement effect by Ru doping in LSMO.

Fig.3(a) shows the current-in-plane MR measurements of a PSV sample at 10 K, with current applied parallel and perpendicular to the external field. The corresponding measurements of LSMRO is illustrated in Fig. 3(b), which showed clear signs of anisotropic magnetoresistance (AMR) effect. On the other hand, no AMR effect was observed in LSMO single layer samples (data not shown). A direct comparison of Fig. 3(a) and (b) clearly indicated AMR contributions of the LSMRO layer to the transport behaviour of the PSV at high magnetic fields (~ 500 – 700 Oe). Yet at low fields values (~ 150 – 200 Oe), a pair of resistance peaks were observed for the measurements of PSV in orthogonal directions. These are signs for the occurrence of GMR in the PSV sample.

1. X. Q. Xu, J. L. Peng, Z. Y. Li, H. L. Ju, and R. L. Greene, Phys. Rev. B 48, 1112 (1993).

2. R. J. Soulen, Jr., J. M. Byers, M. S. Osofsky, B. Nadgorny, T.Ambrose, S. F. Cheong, P. R. Broussard, C. T. Tanaka, J.Nowak, J. S. Moodera, A. Barry, and J. M. D. Coey, Science 282, 85 (1998).

3. H. Yamada, M. Kawasaki, and Y. Tokura, Appl. Phys. Lett. 86, 192505 (2005).

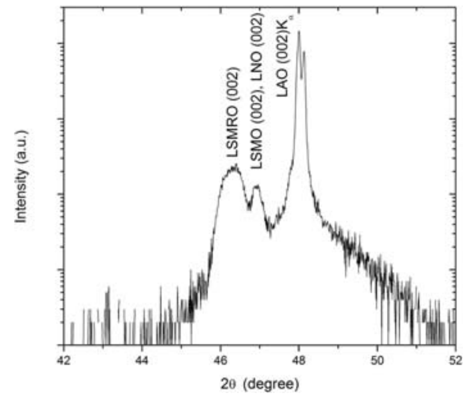

Fig. 1 X-ray diffraction profile of the trilayer structure

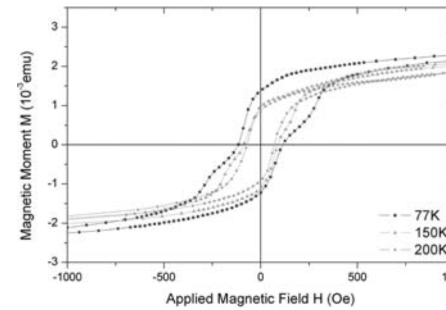

Fig. 2 Hysteresis loops of the trilayer at different temperatures

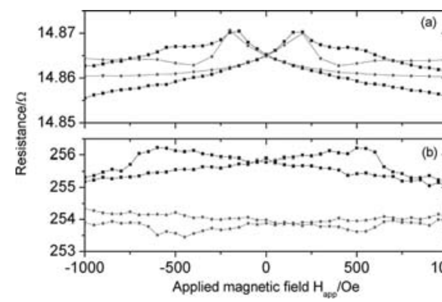

Fig. 3 Magnetoresistance measurements of (a) the trilayer and (b) the single layer LSMRO thin film at 10K

AN-09

Grain-size effects on magnetic properties of sputtered Co_2MnSi films.

S. Ladak[2], *A. Hirohata*[1]

1. Department of Electronics, University of York, York, United Kingdom; 2. Department of Physics, University of York, York, United Kingdom

In order to exploit 100% spin polarisation induced by spontaneous magnetisation, a half-metallic ferromagnet (HMF) has been intensively investigated [1]. The HMF possesses a bandgap δ at the Fermi level E_F only for its minority spins, achieving 100% spin polarisation at E_F, however, to date there has been no experimental report on the half-metallicity at room temperature (RT), which is crucial for future device applications. Among theoretically proposed HMFs, the Heusler alloys hold the greatest potential to realise the half-metallicity at RT due to their high Curie temperature (above RT), lattice constant matching with major substrates (such as III-V semiconductors and MgO), and large δ at E_F in general. Recently, a magnetic tunnel junction (MTJ) with an epitaxial $L2_1$ Co_2MnSi film has been reported to show very large tunneling magnetoresistance (TMR) ratios of 70% at RT and 159% at 2 K [2]. These are the largest TMR ratio obtained in a MTJ with a Heusler alloy film and AlO*x* barrier. Even so, such rapid decrease in the TMR ratio with increasing temperature does not follow the temperature dependence of the magnetisation, suggesting that a small fraction of atomically disordered phases cannot be ignored in the spin-polarized electron transport at a finite temperature. The elimination of such disordered phases, especially near the barrier interface, improves the TMR ratios further and realizes the half-metallicity at RT. In this study, we fabricate polycrystalline Co_2MnSi films with controlled grain sizes by sputtering in order to investigate both magnetic and structural properties of both grain-boundary and bulk regions.

Samples were prepared using a controlled plasma HiTUS sputtering system [3], where the target bias was adjusted to deposit Co_2MnSi films with a series of grain sizes. MgO(001) substrates were cleaned with acetone and annealed at 573 K for 20 min. at a base pressure of 3×10^{-5} Pa. The plasma was generated by an RF field at 3×10^{-1} Pa Ar pressure and steered onto a target with a DC bias from –250 to –990 V), giving control of the deposition rate. This results in the change of grain size. The Co_2MnSi film thickness was maintained at 23 nm with a 2nm thick Ru capping layer. These films were annealed at 760 K for 3 hours. Magnetisation curves were measured with using a PMC AGFM. The grain size analysis was carried out by TEM, and the crystalline structures were characterised by X-ray diffraction (XRD).

Figure 1 shows the magnetisation curves of the films after annealing. The films provide almost no magnetic moment before annealing. It is well established that the grain size becomes larger with increasing bias [3]. The coercivity HC decreases with increasing the target bias and hence increasing grain size. The film grown at –990 V shows HC of 16 Oe, which is comparable with that for a highly ordered Co_2MnSi film [4]. Since the measured magnetic moment per formula unit is much larger than the theoretically calculated value from a generalised Slater-Pauling curve (5 μ_B/f.u.) [5], the sample grown at –500 V with smaller grain sizes may contain segregated phases as well as the Co_2MnSi crystallites. These results suggest that the two regions in the films, grain boundary and bulk, evolve different magnetic properties after annealing: the films with smaller grains have their magnetic behaviour dominated by the grain boundaries, while those with larger grains exhibit bulk properties. Grain-size analysis by TEM structural characterisation by XRD further supports this finding.

[1] I. Galanakis and P. H. Dederichs (Eds.), *Half-Metallic Alloys* (Springer, Berlin, 2005).

[2] Y. Sakuraba, J. Nakata, M. Oogane, H. Kubota, Y. Ando, A. Sakuma and T. Miyazaki, *Jpn. J. Appl. Phys.* **44**, L1100 (2005).

[3] M. Vopsaroiu, M. J. Thwaites, S. Rand, P. J. Grundy and K. O'Grady, *IEEE Trans. Magn.* **40**, 2443 (2004).

[4] L. J. Singh, Z. H. Barber, Y. Miyoshi, W. R. Branford and L. F. Cohen, *J. Appl. Phys.* **95**, 7231 (2004).

[5] A. Hirohata, M. Kikuchi, N. Tezuka, K. Inomata, J. S. Claydon, Y. B. Xu and G. van der Laan, *Curr. Opin. Solid State Mater. Sci.* **10**, 93-107 (2006).

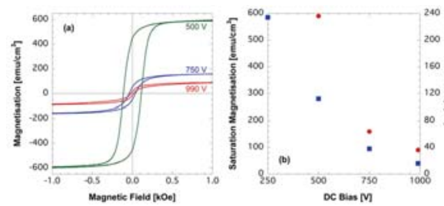

Fig. 1 (a) Magnetisation curves for a series of sputtered Co_2MnSi films. (b) Saturation magnetisation and coercivity for the corresponding DC bias.

AN-10

Effect of Nd doping on the spin polarization of Co_2MnSi Heusler alloy.

A. Rajanikanth[1,2], Y. K. Takahashi[2], K. Hono[2,1]
1. International Center for Young Scientists, NIMS, Tsukuba, Japan; 2. Magentic Materials Center, NIMS, Tsukuba, Japan

Giant tunneling magetoresistance (TMR) value has been achieved with half metallic Heusler alloys as the ferromagnetic electrodes[1]. One of the problems in achieving higher TMR values is the temperature dependence of the half metallicity of the Heusler alloys which is attributed to the presence of the Fermi level near conduction band. Another possible reason for the degradation of the half metallicity of the Heusler alloys is the magnon effect on the spin polarization, which was theoritically explained by Bratovsky et. al. [2], where one mode of magnons is thought to degrade the spin polarization, whereas phonons enhance it.

One of the possible ways of solving this problem is to dope a rare earth element to Heusler alloys to suppress the magnons. Doping of rare earth elements in soft magnetic alloys for enhancing the magnetic damping is a well known phenomenon [3], which is already implemented in the ultrafast magnetic recording heads and MRAMs. In the present study we have not studied the magnon suppression effect in Heusler alloys directly; rather, we are interested in the direct measurement of spin polarization and the effect of rare earth doping on it. Hence in the present study we have chosen Nd as a dopent in the Mn site of Co_2MnSi. The spin polarizations (*P*) were measured using the point contact Andreev reflection (PCAR) method.

The alloys were prepared by induction melting in a quartz tube and then wedge casted. These were annealed at 800°C for 48 h in a quartz tube. The phase characterization was carried out by using x-ray diffraction (XRD). The spin polarizations were measured with the PCAR technique at 4.2K. Thin Nb wire was electropolished and used as a superconducting tip for observing the Andreev reflection. The obtained conductance curves were then fitted with the modified BTK model to extract the spin polarization. The fitting parameters were, spin polarization (*P*), superconducting gap (Δ) and interfacial scattering parameter (Z) [4].

From Figure 1(a), in the XRD pattern the presence of the (111) and (200) superlattice peaks indicates that the annealed $Co_2Nd_{0.05}Mn_{0.95}Si$ alloy has the $L2_1$ ordered structure with some unidentified extra phase. However, Figure 1(b) is the XRD pattern of Co_2MnSi which was taken as a reference.

Figure 2(a), (b) and (c) shows the conductance curves obtained from the point contact measurements on a $Co_2Nd_{0.05}Mn_{0.95}Si$ alloy. Figure 2(d) shows a *P* vs *Z* curve, the intrinsic spin polarization was determined to be 0.58 by extrapolating the curve to $Z = 0.0$. From our previous results, the spin polarization obtained for Co_2MnSi was 0.56 using PCAR. Hence, we can conclude that the Nd addition has enhanced the spin polarization of Co_2MnSi. With in the point contact measurements regime, the values measured by several authors on thin films and single crystals of Co_2MnSi has shown only a spin polarization of 0.48~0.56 [5]. The values of spin polarizations obtained by the PCAR method are far from the ideal 100% spin polarization. The spin polarization reported by Sakuraba et al [1] is the only report which shows ideal half metallic nature measured from a tunneling magnetoresistance value of a magnetic tunneling junction. This is considered to be a tunneling spin polarization rather than the intrinsic spin polarization. But the PCAR method gives the intrinsic transport spin polarization of the conducting electrons, and the value of 0.58 for the Nd doped Co_2MnSi is a relatively higher value.

From our PCAR measurements we conclude that the spin polarization (P) value is enhanced with Nd doping in the Co_2MnSi alloy. Hence this alloy could be a potential material to enhance the TMR values if incorporated into a magnetic tunneling junction. It would be interesting to see the effect of rare earth doping in Heusler alloys theoretically.

1.Y. Sakuraba, et al Appl. Phys. Lett, 88, 19 192508 (2006).

2. A. M. Bratovsky, Appl. Phys. Lett, 72, 2334 (1998).

3. S. Ingvarsson, et al Appl. Phys. Lett 85 21 (2004).

4. G. J. Strijkers, et al Phy. Rev. B 63 104510 (2001).

5. E. Clifford and J.M.D Coey Appl. Phys. Lett 89 092506 (2006).

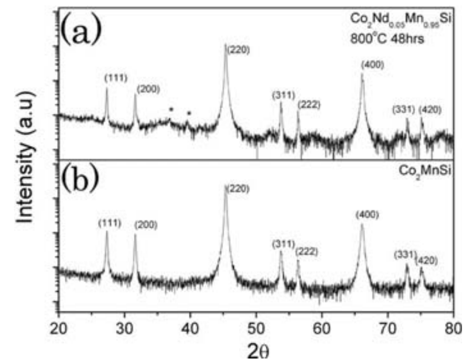

Figure1. XRD profiles of (a) $Co_2Nd_{0.05}Mn_{0.95}Si$. (b) Co_2MnSi bulk alloys

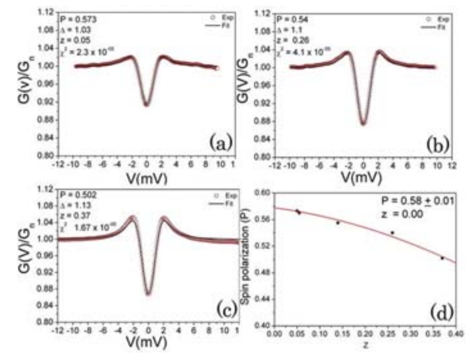

Figure 2(a), (b) and (c) Normalized conductance curves of $Co_2Nd_{0.05}Mn_{0.95}Si$, measured at 4.2K using four point ac lock-in techniques. (d) *P* values obtained at various Z values.

AN-11

Anisotropy and magnetic dynamic properties of Co_2MnGe Heusler compound.

M. Belmeguenai[2,1], F. Zighem[1], G. Woltersdorf[2], Y. Roussigné[1], S. Chérif[1], K. Westerholt[3], G. Bayreuther[2]
1. LPMTM Université Paris13, Villetaneuse, France; 2. Institut für Experimentelle Physik, Universität Regensburg, Regensburg, Germany; 3. Ruhr-Universität Bochum, Bochum, Germany

Half-metallic ferromagnets (HMF) are materials where one of the spin-channels is metallic and the second one is insulating at the Fermi Level. These materials show full spin polarization at the Fermi level and have triggered a lot of interest due to their potential use in spintronic applications. Several HMF have been predicted by means of electronic structure calculations, for instance, some Heulser alloys like Co_2MnGe. Co_2MnGe are considered as excellent candidates for such spintronic applications, since the Curie temperature is high (905 K) and there is a good lattice matching with the GaAs semiconductor family [1]. Despite the numerous works on such materials, few of them have been devoted to the magnetic properties. We have therefore studied the magnetic anisotropy and the dynamic properties of Co_2MnGe thin films with conventional ferromagnetic resonance (FMR) and microstrip line FMR spectroscopy (MS-FMR).
Co_2MnGe films of 30, 50, 75 and 100 nm in thickness were grown by RF-sputtering at an Ar pressure of 5×10^{-3} mbar on Al_2O_3 a-plane substrates at a growth temperature of 470°C. Before deposition of the Heusler film, a seed layer of V, 4 nm thick, was deposited in order to induce (110)-growth of the Heusler layer [2]. A final protective overlayer of gold, 4 nm thick, was grown on top of the film.
Magneto-optical Kerr effect (MOKE) was used at room temperature to obtain the hysteresis loops with the applied field parallel to the sample edges. For the dynamic measurements, our 22 GHz conventional FMR set-up is described in [4]. In the case of MS-FMR, the magnetic sample is mounted on a microstrip line used to excite its magnetization. This microstrip line is connected to microwaves generator (2-18.6 GHz) and to a Schottky detector used to measure the transmitted power. At each external applied field, the sample is swept through the resonance condition by varying the microwave frequency. When the magnetic sample undergoes a ferromagnetic resonance, the microwave losses are increased and the transmitted power changes slightly. In addition, the external magnetic field is modulated with amplitude of 4 Oe at a frequency of 170 Hz. This modulation allows lock-in detection to be used in order to increase the signal-to-noise ratio. The measured signal is proportional to the field derivative of the imaginary part of the rf susceptibility as function of the microwave frequency. The resonance frequencies and fields are obtained from the Lorentzian-derivative fit of the obtained results by MS-FMR and FMR, respectively. In contrast to the conventional FMR, MS-FMR allows dynamic measurements over a large frequency range and on low applied external fields not sufficient to hide the effect of the small magnetic anisotropies.
The study of spin wave frequencies in dependence of the in-plane sample orientation allows for the determination of anisotropy constants of thin magnetic films while the out-of-plane angular dependence gives the effective magnetization. These in-plane and out-of-plane angular dependencies of the different resonance frequencies (at 110 Oe) and fields for the 50 nm thick sample are represented on Fig.1a and Fig.1b, respectively. The sample exhibits a clear predominant four-fold magnetic anisotropy beside a uniaxial anisotropy along (110). This uniaxial anisotropy is most probably induced by the growth condition as far as the Co_2MnGe films are FCC. From the in-plane and the out-of-plane resonance field values (Fig. 1b), the effective magnetization ($4\pi M_{eff}$) and the g-factor are calculated (g=2.17)using the Kittel formula. These values are then used to fit both the in-plane angular- and the field-dependence of the resonance frequency (Fig. 1c) to determine the uniaxial ($H_u=2K_u/M_s$) and the fourfold anisotropy fields ($H_2=4K_4/M_s$) using the theoretical model presented in [4]. The obtained values for the different samples shows that the fourfold anisotropy is predominant for all the samples. Within the experimental ncertainties the effective magnetization seems to be independent on the samples thickness suggesting a weak out-of-plane anisotropy. The in-plane anisotropies and the effective magnetization are maximal for the 50 nm thick film. This is maybe due to the fact that the 50 nm sample was sputtered two months before the other samples. From the field separation between the perpendicular standing spin-wave mode and uniform mode FMR resonance fields, the exchange stiffness was estimated to be 0.98×10^{-6}erg/cm. The magnetization at saturation and exchange constant of this material are very closed to those of permalloy. Finally, a room-temperature resistivity of 110 μΩ cm has also been determined.

[1] S. Picozzi, A. Continenza, and A. J. Freeman, J. Phys. Chem. Solids 64, 1697 (2003).

[2] T. Ambrose, J. J. Krebs, and G. A. Prinz, J. Appl. Phys. 89, 7522 (2001).

[3] U. Geiersbach, K.Westerholt and H. Bach J. Magn. Magn. Mater. 240, 546 (2002).

[4] K. Lenz, E. Kosubek, K. Baberschke, and H. Wende, J. Herfort, H.-P. Schönherr, and K. H. Ploog, Phys. Rev. B 72, 144411 (2005).

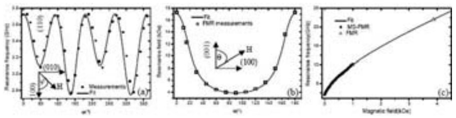

Fig. 1: (a) MS-FMR in-plane angular-dependence of the resonance frequency at 110 Oe applied field and (b) out-of-plane FMR angular-dependence of the resonance field at 22 GHz of 50 nm thick Co_2MnGe. (c) Resonance frequency of the uniform mode as a function of the magnetic applied field for ϕ=0°.

AN-12

The effects of annealing temperature on structural and chemical properties of the $Co_2Cr_{0.6}Fe_{0.4}Al$ surface and its relevance for the electron spin polarization at the surface.

J. Wüstenberg[1], J. Fischer[1], A. Conca[2], M. Jourdan[2], M. Aeschlimann[1], M. Cinchetti[1]
1. Institute of Physics, University of Kaiserslautern, Kaiserslautern, Germany; 2. Institute of Physics, Johannes Gutenberg University Mainz, Mainz, Germany

Co-based full Heusler alloys represent nowadays a class of materials with a high potential for application in the growing field of spintronics. This is due to their high Curie temperatures and their theoretically predicted minority-spin gap, resulting in a high spin polarization at the Fermi level. For spintronics applications, the spin polarization must be high not only in the bulk, but also at the surface region. This is not straightforward, since extrinsic as well as intrinsic mechanisms can reduce the spin polarization in the surface region. In fact, the highest spin polarization value measured so far with a surface sensitive technique at room temperature was reported by Wang et al. [1] for a single crystalline Co_2MnSi film, showing a spin polarization of 12% at the Fermi level.
In a recent paper, the highest Heusler surface spin polarization value of 45% was measured at the surface of a $Co_2Cr_{0.6}Fe_{0.4}Al$ (CCFA) sample by spin resolved photoemission with the 4th harmonic (50 fs FWHM, 5.9eV) of a pulsed laser oscillator system [2]. It has to be pointed out that these results were obtained at room temperature and in magnetic remanence. Though the preparation procedure leads to reproducible results, the systematic investigation of the morphology changes at the surface during annealing was still lacking.
In this contribution we present results of systematic LEED and Auger studies of the surface properties obtained after progressive annealing cycles. CCFA samples differing in substrate and/or buffer layer have been investigated. We conclude that no high spin polarization values can be measured unless the surface structure and relative composition of the alloy elements is stable and bulk-like. This can only be achieved above annealing temperatures of 400°C.
In this case, both LEED and X-ray diffraction show high geometric ordering in all samples. A typical LEED picture taken at E=73 eV after annealing up to 450°C is shown in figure 1. Also the chemical surface composition stabilizes at this temperature. Furthermore in samples with a Fe buffer layer, as used in [2], Auger spectra show that the iron content at the surface rises due to interdiffusion from the buffer layer. This can also be seen in Total Electron Yield X-ray absorption measurements and has positive influence on the functionality of GMR devices [4].
In the surface spin resolved electron spectra (figure 2) a peak in the minority electron channel evolves at 0.5 eV binding energy, as predicted in calculations by Wurmehl et al. [3]. The spin polarization at the Fermi level remains positive as a consequence of the reduced density of states for the minority carriers due to the predicted minority gap, which can be seen clearly for all samples above the proposed minimum annealing temperature.

[1] Wang et al., Phys. Rev. B 71 (2005), 144416

[2] M. Cinchetti et al., J. Phys. D: Appl. Phys. 40 (2007) 1544

[3] S. Wurmehl et al., J. Phys. D: Appl. Phys. 39 (2006) 803

[4] M. Jourdan, in print

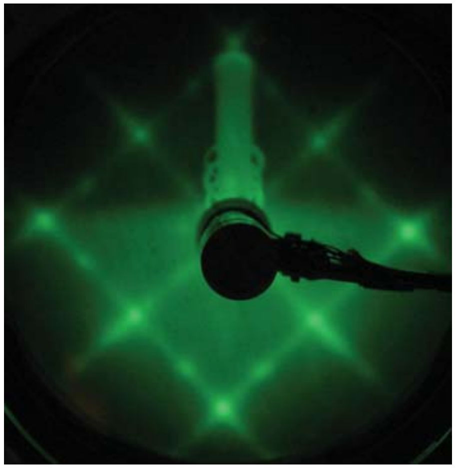

LEED taken at T=450°C. No LEED can be observed below 400°C. At T=550°C the superstructure vanishes and a very sharp fcc pattern appears.

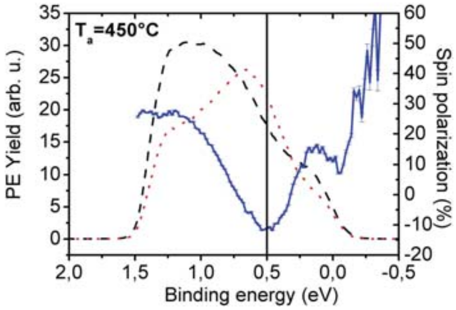

Spin resolved PE spectra. The dashed (black) and dotted (red) line represent majority and minority electrons, respectively. The resulting spin polarization is plotted in straight blue.

AN-13

The Different Capping Layer Influence on the Magnetic, Electronic and Structural Properties of the Co2MnGa/GaAs(100) Hybrid Structure.

S. Hassan[1], J. S. Claydon[1], W. Zhang[1], Y. Xu[1], C. D. Damsgaard[2], J. B. Hansen[2], C. S. Jacobsen[2], G. Van der Laan[3]
1. Electronics, University of York, York, United Kingdom; 2. Physics, Technical University of Denmark, Lyngby, Denmark; 3. Daresbury Laboratory, Warrington, United Kingdom

In order to design magnetic materials for specific applications, it is important to understand the effect of all the elements in the device. In this respect, it is essential to study the changes in the magnetic properties of the magnetic materials when capped with different types of materials. We report here the effect of the different capping layers, namely, Al and Au, on the magnetic, electronic and structural properties of Co2MnGa/GaAs(100) hybrid structure. Co2MnGa is a full Heusler alloy which is very promising for spintronic applications. It has an L21 structure, high Curie temperature and has been predicted to be half-metallic [1]. The combination of Co2MnGa with GaAs, due to the fairly low lattice mismatch [2-4], is very significant to integrate magnetic materials with the current semiconductor technology.
Two sets of samples with different thicknesses (4.7, 6.6 and 8.5nm) have been grown using MBE on top of GaAs(100) substrates and capped with 2nm layer of either Al or Au. The XAS and XMCD measurement have been carried out on station 1.1 of the SRS at Daresbury Laboratory.
From the XAS measurement, the Al-capped samples showed a pronounced shoulder after the Co L3 peak, which could be attributed to the photoelectron scattering from the ordered superlattice of the L21 structure[5]. However, this feature was absent in the Au-capped samples, which suggests that the Al- capped samples have more L21 ordered structure than the Au-capped samples. Also, the general shape of the Mn L2,3 edge of the Au-capped samples exhibited a fine structure, that could be explained by the localization of 3d electrons as a result of the strong hybridization between Mn and Au atoms at the interface. This hybridization has a tendency to localize the Mn electronic energy levels and leads to the observed structured absorption edges.
The XMCD measurements have been analysed using the Sum Rule and the total moment for Co and Mn have been calculated (as shown in table 1) and found to be generally very small compared with the experimental data of the bulk Co2MnGa, which might be attributed to a local atomic disorder either by interchange of Co and Mn atoms or by partial occupancy of the Mn sites by Co atoms. Interestingly, the total moment for the Co atoms in the Au-capped samples has been enhanced in comparison with that of the Al-capped films. This effect could be associated with the hybridization of Co and Au atoms at the interface, which gives rise to an out of plane magnetic anisotropy.[6]
The magnetic properties have been measured using AGFM along in plane and out of plane directions as shown in figure 1. While a fast in plane saturation has been observed for the Au capped samples, the Al capped samples didn't show this effect, which confirm that a possible hybridization of Au and Co atoms at the interface have happened especially that it becomes less pronounced along the out of plane direction, which means that we have out of plane anisotropy. This is correlated with the enhancement of the total magnetic moment of the Co atoms in the Au-capped samples.
In addition, the out of plane hysteresis loops showed an interesting double switching for both kinds of capped samples, which could be attributed to the independent switching of a possible intermixed layer at the film interface with the substrate. For a similar reason, the quenching of the fast magnetic saturation along the out of plane direction could be explained by the hybridization between Au and Co and Mn atoms could result in an interface layer saturated independently. This symmetry breaking could also be responsible for the less L21 structure observed by XAS in the Au capped samples compared to the Al capped samples.

1. P.J. Webster, J. Phys. Chem. Solids 32, 1221(1971).

2. S.N. Holmes, M. Pepper, Appl. Phys. Lett. 81, 1651 (2002).

3. S.N. Holmes, M. Pepper, J. Superconductivity 16, 191 (2003).

4. J.S. Claydon, S. Hassan, C.D. Damsgaard, J. Bindslev Hansen, C.S. Jacobsen, Y.B. Xu, and G. van der Laan, J. Appl. Phys. 101, 09J506 (2007).

5. N. D. Telling, P. S. Keatley, G. van der Laan, R. J. Hicken, E. Arenholz, Y. Sakuraba, M. Oogane, Y. Ando, T. Miyazaki, Phys. Rev. B, 74, 224439 (2006).

6. Brad N. Engel, Michael H. Wiedmann, and Charles M. Falco, J. Appl. Phys. 75, 6401 (1994).

Thickness (nm)	Au-Capped		Al-Capped	
	Mn mtot	Co mtot	Mn mtot	Co mtot
8.5	0.125-0.184 ± 0.004	0.340 ± 0.024	0.161 ± 0.001	0.160 ± 0.001
6.6	0.142-0.209 ± 0.002	0.357 ± 0.021	0.156 ± 0.003	0.157 ± 0.004
4.7	0.158-0.232 ± 0.002	0.377 ± 0.053	0.153 ± 0.005	0.144 ± 0.002
Bulk [1]	3.01	0.52		

Table 1. Total magnetic moments in μB per atom for the Co and Mn components for different film thicknesses capped with either Al or Au.

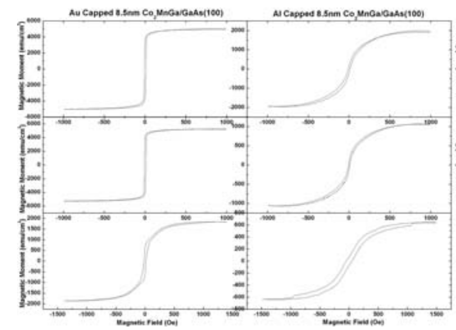

Fig 1. Hysteresis loops of the Au and Al-capped 8.5 nm Co2MnGa/GaAs along in plane ([0-1-1] and [0-11] and out of plane direction.

AO-01

Penetration depth of transverse spin current in ferromagnetic metals.

T. Tomohiro[1,2], Y. Satoshi[3], I. Hiroshi[1], A. Yasuo[3]
1. Nanotechnology Research Institute, National Institute for Advanced Industrial Science and Technology, Tsukuba, Japan; 2. Institute of Applied Physics, University of Tsukuba, Tsukuba, Japan; 3. Department of Applied Physics, Graduate School of Engineering, Tohoku University, Sendai, Japan

The field of current-driven magnetization dynamics (CDMD) [1] has drawn enormous attention because of its potential applications to non-volatile magnetic random access memory and microwave devices. CDMD is also important from a scientific point of view since it provides much information about non-equilibrium dynamics of the magnetization and physics of spin transport and spin relaxation. In the last decade much effort has been devoted to studying the physics and applications of CDMD both theoretically and experimentally [2].
The penetration depth of the transverse spin current is one of the most important quantities in CDMD, over which the travelling electrons transfer their transverse (perpendicular to the magnetization) component of the spin angular momentum to the magnetization and exert a spin transfer torque on it. There is a controversial issue regarding the penetration depth of the transverse spin current. One argument is based on the ballistic theory of electron transport [3], and the penetration depth is on the order of a few angstroms. The other is based on the Boltzmann theory of electron transport [4], and the penetration depth is on the order of a few nanometers. There are few experiments that measured the penetration depth of the transverse spin current. Urazhdin et al. analyzed the CPP-GMR of noncollinear magnetic multilayers and concluded that the penetration depth of the transverse spin current in NiFe is 0.8 [nm] [5]. Chen et al. analyzed the critical current of the CDMD in the Co/Cu/Co trilayer system and concluded that the penetration depth of the transverse spin current in Co is 3.0 [nm] [6].
We study the penetration depth of the transverse spin current in ferromagnetic metals by using the spin pumping [7] in magnetic multilayers both theoretically and experimentally. We consider the Cu/F1/Cu/F2/Cu five-layer systems, where the F1 and F2 layers are made of different ferromagnetic metals and their magnetization vectors are aligned to be parallel each other. When we apply the oscillating magnetic field whose frequency is the same as the resonant frequency of the F1 layer, the magentization of the F1 layer precesses and the spin current is pumped into the other layers. Since the magnetization vector of the pumped spin current is perpendicular to the magnetization vector of the F1 layer and the precession angle is very small (about 1 [deg]), the dominant component of the pumped spin current is perpendicular to the magnetization vector of the F2 layer. Therefore, it would be possible to determine the penetration depth of the transverse spin current in the F2 layer if we could analyze the dependence of the enhancement of the Gilbert damping constant on the thickness of the F2 layer. We measured the FMR spectrum line width of the F1 layer as a function of the thickness of the F2 layer, and observed the clear increase of the line width with increasing the thickness of the F2 layer as shown in Fig.1. To analyze the experimental results, we extend the conventional theory of spin pumping [7] by taking into account the finite penetration depth of the transverse spin current. In Fig.1 (a)-(c), the theoretical fits are shown by solid lines. The estimated values of the penetration depth of the transverse spin current in NiFe, CoFe and CoFeB are 3.7 [nm], 2.5[nm] and 12.0 [nm], respectively [8]. We will report the details of our study and analysis of the penetration depth of the transverse spin current in other ferromagnetic materials.

[1] J. C. Slonczewski, J. Magn. Magn. Mater. 159, L1 (1996); L. Berger, Phys. Rev. B 54, 9353 (1996).

[2] J. Z. Sun, Phys. Rev. B 62, 570 (2000); S. I. Kiselev et al, Nature 425, 380 (2003).

[3] M. D. Stiles and A. Zhangwill, Phys. Rev. B 66, 014407 (2002); A. Brataas et al, Phys. Rep. 427, 157 (2006).

[4] S. Zhang et al, Phys. Rev. Lett. 88, 236601 (2002).

[5] S. Urazhdin et al, Phys. Rev. B 71, 100401(R) (2005).

[6] W. Chen et al, Phys. Rev. B 74, 144408 (2006).

[7] Y. Tserkovnyak et al, Rev. Mod. Phys. 77, 1375 (2005).

[8] T. Taniguchi et al, cond.mat.0708.3528 (2007).

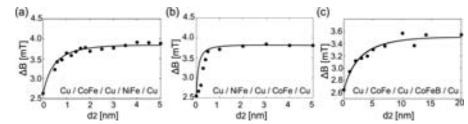

AO-02

Effect of Spin Memory Loss at Interfaces of Ferromagnet/Normal Metal on Spin-Transfer Torque.

S. Lee, K. Lee
Korea University, Seoul, South Korea

The spins of conduction electrons are polarized when an electrical current passes through a ferromagnet (FM) because the conductivities of FM are spin-dependent. The spin-polarized current exerts a torque on the noncollinear magnetization of the neighboring second FM, i.e. spin-transfer torque (STT), resulting in a new class of magnetization dynamics [1, 2]. The STT attracts a considerable interest because of its rich physics and potential for possible applications using current-induced magnetization switching, high frequency precession, and domain wall motion. Both from the fundamental standpoint and, in view of application, it is important to *quantitatively* estimate the magnitude and angular dependence of STT for a spin valve structure.
The drift-diffusion theory [3-6] is one of the theoretical approaches to calculate spin torque term (in-plane torque, a) and field-like term (out-of-plane torque, b) of the modified Landau-Lifshitz-Gilbert equation. Although this theory provides an analytic result, which is a great merit, it has several demerits such as idealization of the Fermi surfaces, impossibility to distinguish electrons propagating in different directions, and ignoring the spin-flip scattering at interfaces. However, the drift-diffusion theory was found to be successful in at least *qualitatively* predicting the angular dependence of STT, verified in the recent experiment corresponding to the so-called "wavy STT" [7, 8].
In spite of the *qualitative* agreement between the experimental result and the present drift-diffusion theory, a *quantitative* estimate of STT is highly desired for the application of the current-induced magnetic excitation. To realize this, the demerits listed above should be resolved. In this work, we relaxed one of the demerits of the present drift-diffusion theory related to the spin-flip scattering at interfaces, i.e. spin memory loss. In our model, the spin memory loss is considered by replacing an interface as a virtual bulk layer with a finite spin-flip length. We verified our model by comparing with the model used for the "wavy STT" in Ref. [8] assuming no spin memory loss at the interfaces, and found perfect agreement when we also ignored the spin memory loss.
In this work, we investigated the effect of spin memory loss on the STT. We found the spin memory loss significantly affects the magnitude and angular dependence of STT. One striking result is that the STT is not perfectly diminished although the spin memory loss is 90%, i.e. most spins are flipped when passing through the interface. The STT at the parallel magnetic configuration (P) is smaller than that at the anti-parallel configuration (AP) when the spin memory loss is negligible, resulting in the well-known asymmetric switching current density J_C, i.e. $J_C^P > J_C^{AP}$. The STT^P increases or slightly decreases and STT^{AP} significantly decreases with increasing the spin memory loss because of a different role of the spin memory loss on the transverse component of the spin accumulation (Fig. 1). When the spin memory loss is high, STT^{AP} is smaller than STT^P, i.e. $J_C^P < J_C^{AP}$. We compared the J_C^P/J_C^{AP} obtained from our model with the experimental results using Cu/Co/Cu/Co [9] and Cu/Py/Cu/Py [10] spin valve structures at 4 K. Best fits were obtained at the spin memory loss of about 30% which is in good agreement with experimentally determined spin memory loss by using giant magnetoresistance (GMR) measurement [11]. Our results evidence the close relation between GMR and STT.

[1] J. C. Slonczewski, J. Magn. Magn. Mater. 159, L1 (1996).

[2] L. Berger, Phys. Rev. B 54, 9353 (1996).

[3] L. Berger, IEEE Trans. Magn. 34, 3837 (1998).

[4] M.D. Stiles et al., Phys. Rev. B 69, 54408 (2004).

[5] A. Fert et al., J. Magn. Magn. Mater. 272-76, 1706 (2004).

[6] J. Barnas et al., Phys. Rev. B 72, 024426 (2005).

[7] O. Boulle et al., Nat. Phys. 3, 492 (2007).

[8] M. Gmitra and J. Barnas, Phys. Rev. Lett. 96, 207205 (2006).

[9] J. Grollier et al., Appl. Phys. Lett. 78, 3663 (2001).

[10] S. Urazhdin et al., Phys. Rev. Lett. 91, 146803 (2003).

[11] K. Eid et al., J. Appl. Phys. 91, 8102 (2002); J. Appl. Phys. 93, 3445 (2003).

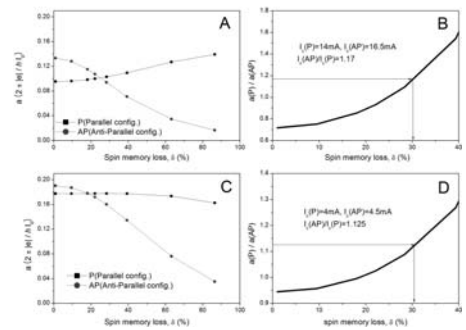

Fig. 2. The effect of spin memory loss on spin-transfer torque. (A) in-plane torque and (B) a^P/a^{AP} for Co/Cu/Co. (C) in-plane torque and (D) a^P/a^{AP} for Py/Cu/Py.

AO-03

Magnetic and structural properties of fully epitaxial Fe_3O_4/MgO/GaAs(100) for spin injection.

P. Wong[1], W. Zhang[1], Y. Xu[1], S. M. Thompson[2]
1. Spintronics and Nanodevice Laboratory, Department of Electronics, University of York, York, United Kingdom; 2. Department of Physics, University of York, York, United Kingdom

We report on successful growth of epitaxial Fe_3O_4 on GaAs(100) with an epitaxial MgO tunnel barrier by a combined technique of molecular beam epitaxy (MBE) and post-growth annealing of epitaxial Fe in an oxygen atmosphere. The quality of the magnetite films fabricated by our approach has also been confirmed with XPS, XMCD, RHEED and MOKE[1]. From the in-situ RHEED pattern shown in Fig. 1(a), a sharp (1 x 1) reconstructed GaAs surface was identified. The MgO layer was then grown by e-beam evaporation at a rate of 2 Å/min, while the substrates were kept at 673 K. A 3 nm thick epitaxial magnetite film was then fabricated by post-annealing of Fe grown at RT. Fig. 1(b) shows that the RHEED images of the MgO layer epitaxially grown on the GaAs(100) were streaky with several elongated spots indicating the presence of some small crystalline islands on the smooth surface of the MgO film. This could be explained by the fact that there is a large lattice mismatch (25.5%) between GaAs and MgO with an epitaxial relationship of MgO(100)[001]//GaAs(100)[001]. This is consistent with the findings from other groups[2-4]. It also suggests a cube-on-cube orientation of MgO on GaAs. The RHEED patterns in Fig. 1(c) also indicate that the epitaxial Fe film rotated 45° respect to the MgO lattice giving a small mismatch of 3.8% and an epitaxial relationship, Fe(100)[011]//MgO(100)[001]. After annealing the Fe film in an oxygen partial pressure of 5×10^{-5} mbar at 500 K for 10 mins, identical RHEED patterns in Fig. 1(d) of Fe_3O_4 were obtained as in the case of Lu *et al*[1]. However, it is noteworthy that the magnetite cell in this experiment is rotated 45° relative to the MgO because it gives an extremely low lattice mismatch (~0.33%) with the MgO layer and thus the final epitaxial relationship, Fe_3O_4(100)[001]//MgO(100)[001]//GaAs(100)[001].
Figure 2 shows the magnetic hysteresis loops for samples with t_{MgO} of (a) 0 nm and (b) 2.0 nm by MOKE. The magnetic field was applied along the major axes of the GaAs(100), i.e. [011], [001], [0-11] and [010]. Both samples showed magnetic anisotropy. A uniaxial anisotropy with its easy axis along the [0-11] direction was clearly defined for t_{MgO}= 0 nm. Two distinctly different mechanisms associated with "unidirectional chemical bonding" and "magnetoelastic coupling" respectively have been put forward to explain the unaxial magnetic anisotropy in hybrid magnetic metal/semiconductor system such as Fe/GaAs[5,6]. These two mechanisms might be responsible for the uniaxial magnetic anisotropy observed here as for the sample without the MgO interlayer. The 3 nm Fe_3O_4 with t_{MgO}= 2.0 nm also gave magnetic anisotropy which was different. In Figure 2, the MOKE observations show a predominant in-plane four-fold cubic magnetocrystalline anisotropy giving rise to global easy axes along <001> of the GaAs. Another interesting effect of inserting the MgO barrier is the increase of the cubic anisotropy. Such increase can be accounted by the nearly perfect lattice match between Fe_3O_4 and MgO (~0.33%) compared to that between Fe_3O_4 and GaAs (5%). To quantitatively compare and evaluate the change in the magnetic anisotropy in the samples, we are modeling the MOKE loops with a combined cubic anisotropy and uniaxial anisotropy, which will be presented in the full paper.

1 Y. X. Lu, J. S. Claydon, Y. B. Xu, S. M. Thompson, K. Wilson and G. v. d. Laan, Phys. Rev. B 70, 233304 (2004).

2 C. Martinez Boubeta, E. Navarro, A. Cebollada, F. Briones, F. Peiro and A. Cornet, J. Crystal Growth 226, 223 (2001).

3 K. Nashimoto, D. K. Fork, T. H. Geballe, Appl. Phys. Lett. 60, 1199 (1992).

4 W. Y. Hsu and R. Raj, Appl. Phys. Lett. 60, 3105 (1992).

5 O. Thomas, Q. Shen, P. Schieffer, N. Tournerie and B. Lepine, Phys. Rev. Lett. 90, 017205 (2003).

6 Y. B. Xu, D. J. Freeland, M. Tselepi and J. A. C. Bland, Phys. Rev. B 62, 1167 (2000).

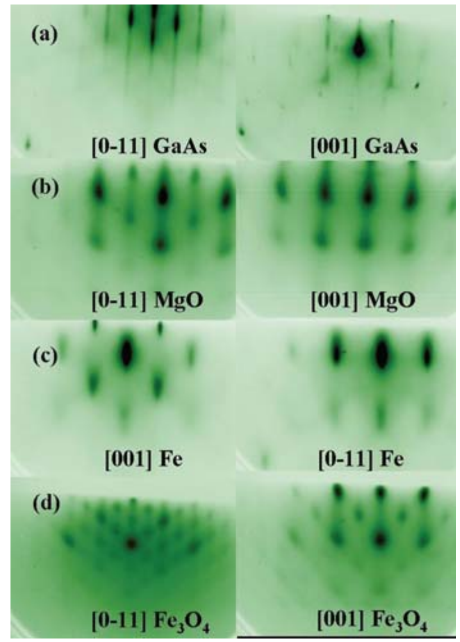

Figure 1(a)-(d), RHEED patterns of (a) GaAs(100) along [0-11] and [001] respectively, (b) MgO/GaAs, (c) Fe/MgO/GaAs and (d) Fe_3O_4/MgO/GaAs.

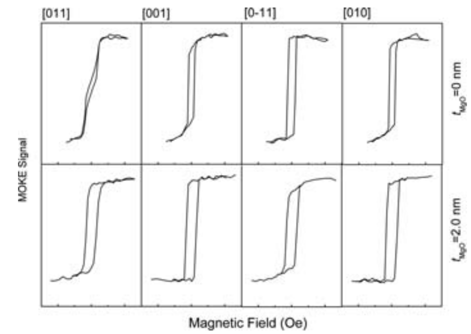

Figure 2, MOKE loops of 3 nm Fe_3O_4/MgO(t_{MgO}=0, 2.0 nm)/GaAs(100) along different crystallographic directions of the GaAs(100). The magnetic field range was -600 to +600 Oe.

AO-04

The effect of screening on extracted tunneling barrier parameters.

S. Bonetti, J. Persson, J. Åkerman
Microelectronics and Applied Physics, Royal Institute of Technology (KTH), Kista-Stockholm, Sweden

The electronic transport across a tunneling barrier is one of the most studied problems in modern physics. Among the various approaches, the possibility of extracting barrier parameters (thickness and potential heights) from a simple and non-destructive transport measurement is of particular interest and utility. For this purpose, different models have been introduced [1,2], based on the Wentzel-Kramers-Brillouin (WKB) approximation. In particular, the Brinkman-Dynes-Rowell (BDR) [1] model, which treats the case of generally asymmetric barriers has been cited widely in literature. Its usefulness comes from the proposed analytical quadratic expression, which in a straightforward way allows the extraction of the barrier parameters, instead of relying on numerical simulations.

In recent years, it has been possible to grow extremely thin (few atomic layers) barriers. In particular magnetic tunnel junctions have attracted attention, due to possible applications in spintronics. On these barriers, the quadratic BDR approximation fails to predict the correct barrier parameters when the fit with experimental data is obtained, and, with the same parameters, the full BDR simulation fails to follow the quadratic trend of the experimental data at high bias voltages.

It has been proposed that the roughness of the barrier can explain the discrepancies [3]. However, with this approach one can recover the correct functional shape of the conductance curve, but not its absolute value. Here we propose that field penetration into the electrodes can explain, at least in part, the discrepancies at high bias voltages, and produce barrier parameters that are closer to the correct ones. The effect of field penetration on tunneling conductance was already introduced by Simmons [4], but his treatment was not extended to asymmetric barriers, and not to atomically thin junctions at high bias voltages.

The starting point is the observation [5] that the capacitance of thin dielectric films has an extra contribution to the geometrical capacitance, which could be explained fairly well by assuming that the applied potential was partially screened due to the finite conductance of the electrodes [6]. In free electron approximation, for barriers thicknesses around 10 Å, and for Fermi energies between 2 and 10 eV (i.e. for most of metals), 20% - 30% of the applied potential drops in each of the electrodes.

In Fig. 1 it is possible to understand the effect of introducing field penetration into the electrodes in the model. If one plots the conductance as a function of the bias squared, the parabolic trend (which is a line with such axis) is preserved to higher bias the larger the screening. This is expected, since the effect of introducing screening is for the barrier to experience a smaller bias, where the standard BDR simulation is still in the region of quadratic trend.

One can now check which is the effect of screening on fitting experimental data, taken from Ref. [3]. To estimate the goodness of the fit, we used a combined figure of merit, the product of χ^2 times the value of the fourth derivative. Since odd powers are smaller compared to even ones, we expect the fourth order terms to be the dominant ones in determining the discrepancies from the quadratic trend. Free parameters are the two potential heights and the barrier thickness, fixed the screening ratio. By this criterion, setting a screening of 30% of the bias, we found that the best fitting (shown in inset) parameters are: ϕ_1 = 0.9 eV, ϕ_2 = 1.1 eV, d = 10 Å. The extracted barrier thickness is closer to the experimental one (d = 13 Å), compared to the value d = 7.3 Å in Ref. [3].

Recently, it has been proposed that the band structure of the insulator in the tunneling junction must be considered in the problem [7], and this is probably the fundamental factor that lies behind the failure of the BDR model. However, while band structure is a property of the barrier, screening is related to the electrodes, and we believe it is therefore a complementary part of the problem, and probably the full solution requires considering both effects. It is interesting to note that if the band structure is approximately introduced into the model by using an effective mass m* = 0.4 m_e, where m_e is the free electron mass, we get a best fitting with ϕ_1 = 1.5 eV, ϕ_2 = 1.9 eV, d = 13.1 Å, when the screening is set to 20% of the applied bias, in an even better agreement compared to the previous case.

[1] W.F. Brinkmann et al., J. Appl. Phys. 41, 1915 (1970).

[2] J.G. Simmons, J. Appl. Phys. 34, 1793 (1963).

[3] C. W. Miller et al., Phys. Rev. B 74, 212404 (2006).

[4] J.G. Simmons, Brit. J. Appl. Phys. 18, 269 (1967).

[5] C.A. Mead, Phys. Rev. Lett. 6, 545 (1961).

[6] H.Y. Ku et al., J. Appl. Phys. 35, 265 (1964).

[7] W.H. Butler et al., IEEE Trans. Magn. 41, 2645 (2005).

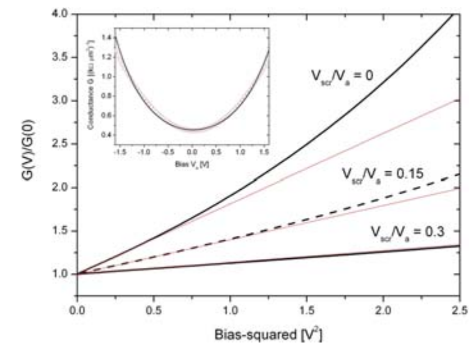

Fig. 1. Normalized conductance as a function of bias voltage squared. The curve is linear up to higher bias if higher screening is introduced. Inset: best fitting (line) of experimental data (symbols) when screening is considered.

AO-05

Rectification effect in the medium with noncoplanar magnetic structure.

O. G. Udalov, A. A. Fraerman
Institute for physics of microstructures RAS, Nizhny Novgorod, Russian Federation

The interplay between the spin and spatial degrees of freedom of electrons is of great interest from both a theoretical and a practical point of view [1]. Investigations into this interplay are based on two well-known effects: spin-orbit coupling and Zeeman splitting. When hamiltonian contains Zeeman term (for example, ferromagnetic metals in the frames of s-d approximation) the electron energy spectrum depends on a magnetic field (or magnetization) spatial distribution. Up to date, there are a lot of works dealing with systems with collinear and non-collinear but coplanar magnetization distribution. Systems with non-coplanar magnetization distribution are poorly investigated. However, the later has essential peculiarity: momentum-reversal symmetry is broken there. It is easily can be seen from Schrodinger equation with Pauli term included. Such an equation is not invariant with respect to complex conjugation if magnetization distribution is non-coplanar. Broken symmetry can lead to the peculiarities in transport properties of crystals.

One of the consequences of momentum reversal symmetry breaking was considered theoretically in works [2,3]. A mesoscopic metal ring with a magnetic texture was studied there. It was shown that, when the distribution of magnetization in the ring became non-coplanar, persistent electrical current occurred in the ring. The magnitude of this current is proportional to the degree of non-coplanarity of the magnetization distribution. The effect viewed in [2,3] is originated from the spectrum quantization in the ring. Therefore, it decreases to zero with the increase of the ring size (even in the absence of inelastic scattering).

This work is devoted to investigation of macroscopic effects arising due to momentum-reversal symmetry breaking in systems with non-coplanar magnetization distribution. In our work it is theoretically demonstrated that rectification (diode effect) should occur in the systems with non-coplanar magnetization distribution.

Phenomenological theory is built for rectifying effect occurring due to exchange interaction in the ferromagnetic medium. It is shown that third rank rectification tensor is non-zero only for the mediums with non-coplanar magnetization distribution.

Microscopic theory of rectifying effect is built for particular case of non-coplanar system - magnetic spiral. Formalism of Boltzman equation is used for calculations. It is shown that in the region of low frequency of external electric field there are two mechanism of diode effect. First is asymmetry of group velocity, which arises due to spectrum asymmetry. Second mechanism is scattering asymmetry. It arises due to non-trivial form of electron wave function in non-coplanar magnetic spiral. In the region of resonant frequencies, corresponding to energy gap between two spin subbands, one more mechanism of diode effect occurs. This mechanism connected with transitions of electrons from one spin subband to another spin subband under the impact of alternative external field. Note that these transitions are caused by electric field because of heterogeneity of magnetization distribution. Similar rectifying effect was considered in work [4], but for the system with spin-orbit interaction. Resonant mechanism is stronger than two mechanisms mentioned above, but it exists only in the narrow frequency range.

Results of microscopic theory are in agreement with phenomenological one’s.

[1] I. Zutic, J. Fabian, S. D. Sarma, Rev. Mod. Phys. 76, 323 (2004)

[2] D. Loss, P. Goldbart, A.V. Balatsky, Phys. Rev. Lettt. 65, 1655 (1990)

[3] G. Tatara, H. Kohno, Phys. Rev. B, 67, 113316 (2003)

[4] S. D. Ganichev, E. L. Ivchenko, S. N. Danilov, J. Eroms, W. Wegscheider, D. Weiss, and W. Prettl, Phys. Rev. Lett., 86, 19, 4358 (2001)

AO-06

Physical and electrical study of Permalloy/Al2O3/Si diodes for spin injection into silicon.

N. Bruyant[1], R. Benabderrahmane[1], M. Kanoun[1], C. Baraduc[1], H. Achard[2], A. Bsiesy[3]
1. SPINTEC, CEA CNRS, Grenoble, France; 2. LETI-Minatec, CEA, Grenoble, France; 3. SPINTEC, Université Joseph Fourier, Grenoble, France

The extension of spintronics into the field of semiconductor devices has generated much interest recently. Due to the absence of ferromagnetic semiconductors at room temperature, ferromagnetic metals have been used to inject spin polarised electrons into semiconductors. Several research groups have demonstrated the injection of efficient spin-polarized electrons from a ferromagnetic metal into a semiconductor by using either a reverse-biased Schottky ferromagnetic metal/semiconductor diode [1] or a ferromagnetic Metal/insulator/semiconductor (FMIS) diode [2]. In the last case, spin injection takes place by tunnelling across an interfacial insulating layer. This tunnel barrier avoids the so called conductivity mismatch between the ferromagnet and the semiconductor which was identified as a fundamental limit to spin injection [3]. The insulating layer may act both as an electrical barrier and as a barrier against ferromagnetic atoms diffusion and therefore avoid semiconductor contamination. A further promising step in this field is the use of silicon to build a spintronic device, due to the straightforward integration in the CMOS technology. The spin polarized current injected in the silicon channel via the tunnel barrier is then analysed by a second ferromagnetic electrode (collector). The resistance between these two ferromagnetic electrodes should depend on the relative orientation of their magnetization, parallel or anti-parallel. This effect would pave the way towards a spintronic memory on silicon.
Coherent spin propagation is a necessary condition to device functionnality, however it can be highly sensitive to the electrical properties of the structures such as interfacial defects, current transport mechanisms and recombination centers. So, it is necessary to avoid recombination via defects that may be induced by Ni or/and Fe diffusion either at Insulator/Si interface, in the oxide or in the substrate bulk. The presence of such defects in the oxide could induce trap assisted tunnelling (TAT) that would eventually flip the spin by spin orbit coupling. Furthermore, at the collector, the polarised electrons can be trapped by the interface defects, and, if the capture time exceeds the spin lifetime, spin polarisation can be lost. For these reasons, we have focused our study on the electrical and physical properties of the Permalloy/Insulator/Si stack which could be used as a spin injector and collector.
Samples with either thermal silicon dioxide or ALD (Atomic Layer Deposition) alumina were fabricated. To determine the contamination of silicon with ferromagnetic atoms, Time of Flight Secondary Ions Mass Spectrometry (TOF-SIMS) was performed. Two samples NiFe/SiO2 (4nm)/Si and NiFe/Al2O3 (2nm)/Si were studied. The contamination level by different ferromagnetic atoms (Ni60, Ni58, Fe56) reported in Fig. 1 (left) shows different behaviours for the two samples. The sample with alumina oxide shows a lower contamination level (1E18atm/cm3) than the silicon oxide sample. From these measurements, we can conclude that the alumina is a better diffusion barrier than the silicon oxide.
A detailed electrical study is necessary in order to verify if this structure is satisfying conditions of an injection collection and detection of spins. In order to investigate interfacial defect density (Dit), well known Capacitance-Voltage analyses at high and low frequency (CHF-LF-V) were performed. We compared the interfacial defect density between two samples NiFe/Al2O3 (2nm)/Si. In one of them, Al2O3 was exposed to a densification annealing at 700°C under O2 during 15mn. The value of Dit extracted for Al2O3 with densification (2E12) is more than one orders of magnitude smaller than the extracted value for Al2O3 without densification (5E13) and close to those reported in the literature.
In order to investigate the transport mechanism, current-voltage characteristics were performed for the sample NiFe/Al2O3 (with densification)/Si at temperature ranging from 80K to 300K. These characteristics show no temperature dependence which is consistent with tunnel transport. Another indication in favor of direct tunnelling is the good agreement between our experimental data and a direct tunnelling model on more than 4 orders of magnitude of current density (Fig. 1 right).
In this work, we have demonstrated that alumina is a better diffusion barrier than silicon dioxide. TOF-SIMS analysis shows a lower contamination level in NiFe/ Al2O3/Si sample. This observation is consistent with the electrical characterisation of the alumina barrier which allows a defect free transport mechanism thanks to good diffusion barrier properties. We conclude that Al2O3 might be a good candidate for spin injection into silicon.

[1] S.A. Wolf et al, Science 294 (5546) (2001) 1488–1495.

[2] B. T. Jonker et al, Nat Phys, 2007, 3, 542-546

[3] A. Fert et al, Phys. Rev. B 64 (2001) 184420.

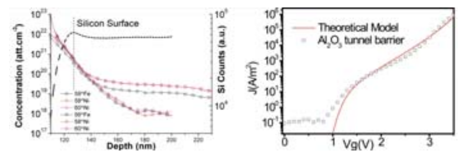

Left: TOF-SIMS Spectrum of NiFe/Al2O3(2nm)/Si(triangles) and NiFe/SiO2(4nm)/Si (circles). Right: Comparison of direct tunnelling model with experimental data.

AO-07

Efficient spin injection and spin filtering in semiconductors by utilizing the k^3-Dresselhaus spin-orbit effect.

T. Fujita[1,2], M. Jalil[1], S. Tan[2]
1. Electrical and Computer Engineering Department, National University of Singapore, Singapore, Singapore; 2. Data Storage Institute, Singapore, Singapore

Semiconductor (SC) spintronics is an emerging technology which promises to deliver devices that are faster and consume less power than electronic devices. The production of spin-polarized current in SC materials is, however, non-trivial and is presently the subject of much research interest. Some proposed methods of achieving this include direct current injection from ferromagnetic contacts, and utilizing the spin-Hall effect. An alternative method is to induce spin-current via spin-dependent tunneling of electrons through SC barriers in the presence of spin-orbit coupling (SOC) [1,2]. Specifically, the SOC spontaneously breaks spin degeneracy into two spin-split eigenstates, which are transmitted across the barrier with different probabilities. As a result, the transmitted current has a finite spin polarization. However, this proposed method inherently operates at low electron energies relative to the barrier height. It therefore suffers from extremely low electron transmission probability, rendering it impractical for real device applications.
In this work, we propose a means of overcoming this problem by injecting electrons across bulk zinc-blende semiconductor barriers with k^3-Dresselhaus SOC in the band structure [3], where the Fermi level exceeds the conduction band offset at the contact-SC interfaces (Fig. 1(a)). This regime is realizable through appropriate engineering of gate electrodes and SC doping concentrations. We theoretically analyze the spin polarization in two SC materials, GaSb and InSb, with the respective material parameters: effective mass m^*/m_0=0.041 and 0.013 (m_0 is the free electron mass) and Dresselhaus SOC strength β=187 and 220 eV Å^3. The electronic barrier height was fixed at U=10 meV. Figs. 1(b) and (c) respectively show the predicted spin polarization and electron transmission probabilities as a function of the injected electron energy E, for a barrier of width 85 nm. It can be seen that although an appreciable spin polarization is achieved in the low-energy tunneling regime (i.e. for E < U), the practicality of utilizing this result in an actual device is unlikely, given the extremely small tunneling current (Fig. 1(c)). For higher energies beyond the tunnel barrier height, one observes vastly different transmission characteristics, in particular: (1) a resonant behaviour with sharp peaks, (2) a high transmission (> 20% for GaSb and > 5% for InSb) across all energies, with peak values approaching 100%, and (3) an increasing divergence in the transmission of the two eigenstates with increasing energy. The last trend explains the increasing amplitude of the polarization curve with E in Fig. 1(a). For the range of energies considered, the polarization peaks at around 12% for GaSb and 5% for InSb. Unlike the tunneling scheme, however, there are certain energies for which the spin polarization vanishes. Thus, a careful tuning of the electron energy is required when using the structure as a source for spin-polarized current. Alternatively, the sharp modulations in the spin polarization indicate a potential use of the structure as a highly sensitive spin filter. For example, the height of the electrostatic barrier U may be modulated by a gate bias, causing a horizontal shift in the polarization spectrum as shown in Fig. 2 for GaSb. As a result, the polarization of the transmitted current can be changed significantly by inducing small variations in the barrier height. The inset of Fig. 2 shows the polarization as a function of barrier height U for a fixed electron energy of E=55 meV. Evidently, one can readily modulate the polarization between its maximum and minimum values, resulting in a highly tunable spin filter. The ability to flip the spins by application of a gate bias also enables the device to function as a spin transistor; in which case, a ferromagnetic contact should be used as the collector.

In summary, we have investigated a trilayer semiconductor structure with resonant polarization behaviour and high current transmission. Our analysis indicates a potential use of the structure as a source of spin current in an SC-based spintronic device, either as a sensitive spin filter, or a novel spin transistor.

[1] V.I. Perel', S.A. Tarasenko, I.N. Yassievich, S.D. Ganichev, V.V. Bel'kov, and W. Prettl, Phys. Rev. B 67, 201304(R) (2003).

[2] David Z.-Y. Ting, X. Cartoixa, Phys. Rev. B 68, 235320 (2003).

[3] G. Dresselhaus, Phys. Rev. 100, 580 (1955).

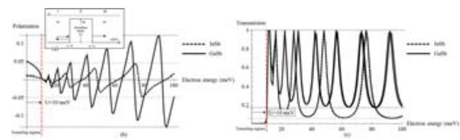

(a) Energy cross-section of device, (b) spin polarization and (c) transmission probabilities of the two spin-split Dresselhaus SOC eigenstates, as a function of injected electron energy for an electronic barrier height of U=10 meV and width 85nm.

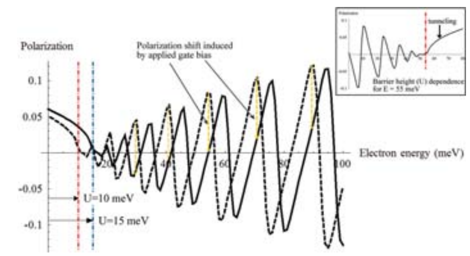

Spin polarization shift illustrated for U=10 meV (dashed) and 15 meV (solid) cases for GaSb barrier of width 85nm. Small changes in U (e.g. via gate bias) result in a large modulation of polarization (see inset, for E=55 meV fixed).

AO-08

Electric field effect on spin diffusion in a semiconductor channel.

J. Kwon[1], H. Koo[1], J. Eom[2,1], J. Chang[1], S. Han[1]
1. Center for Spintronics Research, Korea Institute of Science and Technology, Seoul, South Korea; 2. Department of Physics, Sejong University, Seoul, South Korea

The spin transport characteristics at a ferromagnet-semiconductor interface are important factors that give rise to the critical issues in the development of spin-FETs. Previous works [1-3] have reported spin injection into a metal or a semiconductor channel for systems in which the transport mechanism can be described by the spin diffusion models. In the diffusive regime, the accumulated spins evenly diffuse out in every direction and the spin signal (ΔR) decays exponentially with increasing distance between the injector and detector, L. However, if we wish to take into account spin drift induced by an electrical field (E), the spin diffusion model should be modified.
To clarify the spin drift effect, we fabricated a lateral spin valve device on a micron-sized InAs quantum well channel. In this system, the InAs channel was inserted between $In_{0.52}Al_{0.48}As/In_{0.53}Ga_{0.47}As$ double cladding layers. Figure 1(a) shows a conventional non-local measurement geometry (Geometry A) in which the charge current does not flow between the voltage probes. This geometry provides a robust method for measuring spin injection and detection without spurious effects. Figure 1(b) shows a modified non-local geometry (Geometry B) in which the voltage probe detects part of the current path but the bias current does not directly flow into the ferromagnet-semiconductor junction of the detector. If we subtract the constant charge-current-induced voltage drop from the measured voltage, we obtain the spin dependent resistance change. As shown in Fig. 1 (a), in Geometry A the current flows from the injector (FM1) to the left end of the channel which is the opposite side of the channel from where the detector (FM2) is located. Therefore the spin distribution is biased toward the opposite side of the FM2 as described by the distribution of spin polarization, P. In Geometry B, however, the spin drift occurs towards FM2 and the spin distribution slowly decays on the side of FM2. From the experimental results, we found that ΔR of Geometry B is larger than that of Geometry A by 3.3 mΩ at T = 60 K.
Figure 2 shows the temperature (T) dependence of the drift effect on spin transport. At room temperature, the spin signals for Geometries A and B are clearly observable and their magnitudes are almost identical. As temperature is reduced below room temperature, the spin signals increase but the signal for Geometry B increases at a faster rate such that at T = 20 K, the difference between ΔR values for Geometries A and B is 5.6 mΩ. In the experiments performed to obtain the data in Fig. 2, a constant bias current of 1 mA was used. This behavior occurs because the spin diffusion effect is much stronger than the drift effect at high temperature. The diffusion constant (D) and electron mobility (μ_e) are functions of temperature and decide the critical electric field which is expressed as $E_C = D/\mu_e\lambda_0$ [4], where λ_0 is the spin diffusion length in the absence of the drift effect. Since the diffusion constant is only weakly dependent on the temperature for our InAs quantum well [1], E_C is mostly determined by μ_e and λ_0. The magnitude of E_C is the required field at which the spin drift effect becomes the dominant factor in the spin transport; thus to determine the strength of the spin drift effect, we need to examine E/E_C. In our quantum well system E_C rapidly increases with temperature because μ_e and λ_0 decrease with increasing temperature. Therefore, E/E_C decreases with increasing temperature for a constant electric field (E).
In conclusion, we have shown experimentally the spin distribution asymmetry by measuring the spin signal of a lateral spin-valve structure in a semiconductor channel system. The magnitude of the spin signal difference due to the bias-current-induced drift effect diminishes from 5.6 mΩ at T = 20 K to close to zero at T = 300 K.

[1] H. C. Koo, H. Yi, J.-B. Ko, J. Chang, S.-H. Han, D. Jung, S.-G. Huh, J. Eom: Appl. Phys. Lett. 90, 022101 (2007).

[2] X. Lou, C. Adelmann, S.A. Crooker, E.S. Garlid, J. Zhang, K.S.M. Reddy, S.D. Flexner, C.J. Palmstrøm and P.A. Crowell: Nature Physics 3, 197 (2007).

[3] P. R. Hammar and M. Johnson: Phys Rev Lett. 88, 066806 (2002).

[4] Z. G. Yu and M. E. Flatté: Phys. Rev. B 66, 235302 (2002).

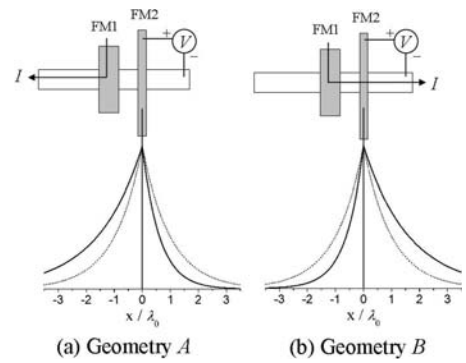

Figure 1 Measurement geometry and distribution of spin polarization. (a) Geometry *A*. (b) Geometry *B*.

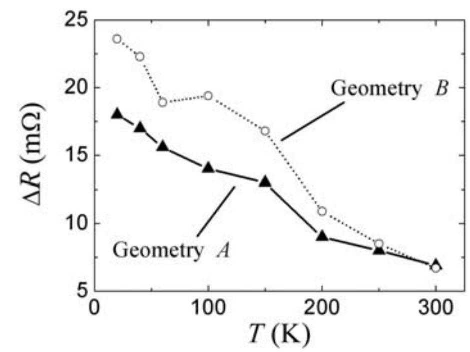

Figure 2 Temperature dependence of the spin drift effect. The bias current is 1 mA.

Effect of dynamical nuclear polarization on the transport through double quantum dots.

J. Inarrea[1,2], G. Platero[2]
1. Fisica, Universidad Carlos III, Leganes, Spain; 2. CSIC, Madrid, Spain

J. Inarrea1, G. Platero

Recent transport experiments in double quantum dots show that Pauli exclusion principle plays an important role [1-5] in current rectification. Thus these devices could behave as externally controllable spin-Coulomb rectifiers with potential application in spintronics as spin memories or transistors.

We analyze the electronic transport through a double quantum dot in the regime where spin blockade occurs as a function of a DC magnetic field. We have developed a model where the Overhauser interaction between both electronic and nuclear spins and their interplay with the external magnetic field are proposed to lift spin blockade regime. Our results indicate that the current leakage experimentally observed in the spin blockade region [1], occurs mainly due to the latter spin-flip processes, affecting the electrical response and properties of the potential current rectifying device.

Triplet states, in the double quantum dot, are responsible for spin blockade. This blockade is lifted by a electron spin flip to a singlet state generating a leakage current. In our model we consider both, interdot (1,1) and intradot(0,2) singlet states, which hybridize due to singlet-triplet exchange interaction. In this scenario, two opposite flip-flop processes can occur, one gives rise to a nuclear magnetic field which supports the external one, meanwhile the other counteracts the external magnetic field. Thus the leakage current obtained strongly depends on the external magnetic field and also on the Coulomb interaction, the interdot tunneling and the level detuning between the two dots. Transport experiments at the spin blockade region show strongly non linear behavior of the leakage current as a function of the applied magnetic field including instabilities and hysteretic behavior [2-5].

Our model consists on rate equations for the charge occupations and nuclei spin polarizations in the quantum dots in the presence of Hyperfine interaction assisted by phonons, which are self-consistently solved. We analyze the current through a double quantum dot in a static magnetic field at different level detunings. The external field produces singlet-triplet crossings which increase abruptly the current due to electron-nucleus spin flip flop, giving rise to abrupt steps in the current, as experimentally observed [2,4]. The calculated current as a function of magnetic field, presents hysteresis (see Figure) which is explained in terms of the induced dynamical nuclear polarization by Hyperfine interaction.

References:

[1] K. Ono, et al., Science, 297, 1313 (2002).
[2]K. Ono et al., Phys. Rev. Lett., 92, 256803 (2004).
[3] F.H.L. Koppens et al., Science, 309, 1346 (2005).
[4] S. Tarucha et al., Phys. Stat. Solid (b) 243,14, 3673, (2006).
[5]A. Pfund et al., cond-mat 0701054.

References:

[1] K. Ono, et al., Science, 297, 1313 (2002).

[2]K. Ono et al., Phys. Rev. Lett., 92, 256803 (2004).

[3] F.H.L. Koppens et al., Science, 309, 1346 (2005).

[4] S. Tarucha et al., Phys. Stat. Solid (b) 243,14, 3673, (2006).

[5]A. Pfund et al., cond-mat 0701054.

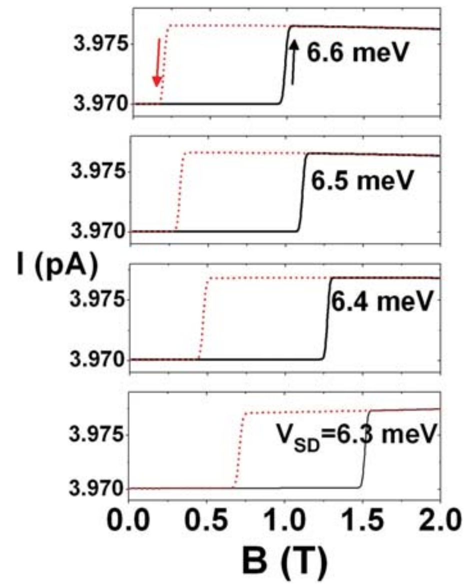

AO-10

Spin Current Characteristics in a Quantum Dot- Ferromagnetic Contacts Sandwich Structure.

W. Chen[1], M. Jalil[1], S. Tan[2]
1. Electrical & Computer Engineering, National University of Singapore, Singapore, Singapore; 2. Data Storage Institute, Singapore, Singapore

The injection and detection of spin-polarized current in a ferromagnetic-semiconductor-ferromagnetic (FM-SC-FM) trilayer structure has been studied intensively in recent years [1,2]. The current flowing through the system is spin-polarized due to the spin degenerate density of states (DOS) in the FM region, providing spin dependent scattering. The electrochemical potential μ becomes spin-split because of spin accumulation. For macroscopic analysis, spin current can be adequately modeled by the spin-drift-diffusion (SDD) model, a semiclassical approach based on the Boltzmann equations. Meanwhile, spintronics in the mesoscopic regime, eg. the quantum dot (QD) devices is also being actively studied. To account for the electron correlation in the central dot region and the dot-leads coupling, only the Green's function approach based on the equation of motions has been widely used [3].
Here we present an accurate theoretical treatment of spin current transport in a FM-QD-FM system, which integrates macroscopic spin transport in the FM leads with the microscopic effects of the QD in a self-consistent manner. Our model consists of a QD sandwiched between two FM bulk contacts. The spin current components $J_\uparrow$ and $J_\downarrow$ in the contacts are modeled by the spin-drift-diffusion equations. When electrical bias is applied, the electrochemical potential μ_σ in the FM contacts was assumed an exponential profile (Fig. 1), which splits within the spin-diffusion length of the dot-contacts interfaces and converges at the semi-infinite ends of the contacts. The QD is coupled to the FM contacts through the double tunneling barriers. The spin-polarized current flowing through the QD is calculated with the Keldysh nonequilibrium Green's function approach. We consider a single level QD with coulomb interaction energy U in the dot, so there are two conducting channels at ε_d and ε_d+U. When the electrochemical potential splits at the FM-dot interface, there is a discontinuity in μ_σ at the left and right interfaces due to the QD's resistance. We assume the spin currents at the interface are continuous, i.e. no spin flipping at the interface, therefore spin current in the QD and the contacts needs to be calculated self-consistently. We showed in Fig. 2 the total charge current over the two conducting channels of the FM-QD-FM device.
The current magnitude is sensitive to the dot-contact coupling energy Γ. An increase in Γ will result in the suppression of the interfacial resistance, allowing more electrons to tunnel through the dot over a wider energy range, thereby increasing the current magnitude. The increased admixture of contact and QD states with larger Γ will also result in the broadening of the resonant current peaks, as shown in Fig. 2(a). In the self-consistent calculations, it was found that the spin asymmetry arising from the intrinsic polarization of the leads itself is insufficient to generate an appreciable spin polarization of current. This is due to the inherently large resistance of the QD. An appreciable spin polarization requires a spin asymmetric Γ, which will lead to an imbalance in the tunneling rate for spin-up and spin-down electrons. Fig. 2(b) shows a steady increase of the spin-polarization of current with the contacts polarization p, which in turn enhances spin asymmetry of the coupling strength Γ_σ. In conclusion, our self-consistent integration of the FM-QD-FM device makes it realistic for high efficient spin filters or low power spin valves in spintronic applications.

[1] G. Schmidt, D. Ferrand, and L.W. Molenkamp, Phys. Rev. B, **62**, R4790 (2000).

[2] D.L. Smith and R.N. Silver, Phys. Rev. B, **64**, 045323 (2001).

[3] Y. Meir and N.S. Wingreen, Phys. Rev. Lett. **68**, 2512 (1992).

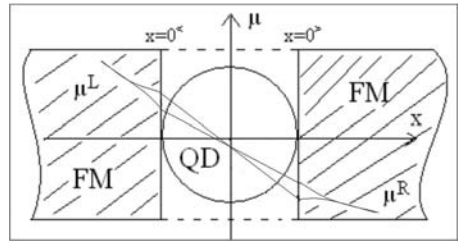

Fig. 1: Model schematic diagram and potential profiles.

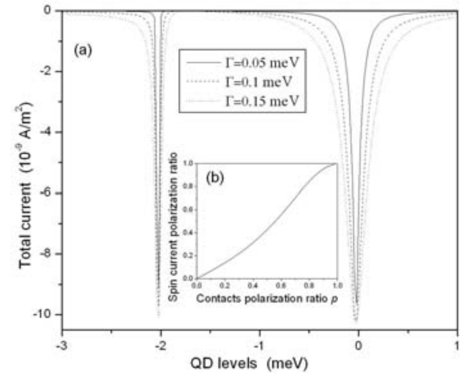

Fig. 2: (a) Total current in the two QD channels calculated via a self-consistent model involving SDD approach in the FM contacts, and Keldysh Green's function model for transport through the QD; (b) Spin polarization of current as a function of contacts polarization ratio *p*.

AO-11

Transport of carbon nanotubes coupled to ferromagnetic electrodes.

S. Sun
Department of Applied Physics, National university of Kaohsiung, Taiwan, Kaohsiung, Taiwan

In this work, same types of magnetic electrodes are connected to both sides of carbon nanotube (CN) with zigzag heads [1], as displayed in Fig. 1. The difference between the currents in parallel and anti-parallel alignments of magnetic polarization for the electrodes in various ratios of density of states between different spins is calculated. The Hamiltonian of the system in tight-binding model through the Fourier transformation in periodic circular-direction exhibits the form,

$$H=\Sigma_{k,\sigma,\alpha\in L,R}\,\varepsilon_{k,\sigma,\alpha}c^{+}_{k,\sigma,\alpha}c_{k,\sigma,\alpha}+\Sigma^{N}_{i}e_{p}d^{+}_{i}d_{i}+\Sigma^{N}_{i}\Sigma_{kx}t(kx)(d^{+}_{i}d_{i+1}+h.c)+\Sigma_{k,\sigma,\alpha\in L,R}\Sigma_{kx}V_{\alpha}c^{+}_{k,\sigma,\alpha}d_{\alpha}+h.c, \quad (1)$$

where N is the number of atomic sides in length and N=12 in this study; L and R index the left and right electrodes and σ is the spin index; the first term describes the kinetic energy of both magnetic electrodes indexed by L and R for the left and right sides, respectively; the second term means the orbital energy levels, e_p, for every atomic sides; the third term represents the kinetic energy of a CN by means of the hopping energy t(kx), and two hopping values tcos(kx a/2) and t are alternative in hopping sites; the final term describes the coupling interaction between the magnetic electrodes and the CNs by means of the coupling constant, V_α. The discrete kx is quantized in kx=2π/a (n/m), n=0,1,2,…m-1, where m is the chiral number, C_h, of the zigzag CNs C_h=(m,0)and in this study m=10. By means of non-equilibrium Keldysh Green's function theory, the formula of the tunneling formula has the form [2],

$$I=-2e/h\int d\varepsilon\,\Sigma_{kx}[f_L(\varepsilon)-f_R(\varepsilon)]\,\Sigma_\sigma\{[T_r(\Gamma^L_\sigma(\varepsilon)\,\Gamma^R_\sigma(\varepsilon)/(\Gamma^L_\sigma(\varepsilon)+\Gamma^R_\sigma(\varepsilon))\mathrm{Im}G^r_{\sigma\sigma}(kx,\varepsilon))]\} \quad (2)$$

The spin-dependent spectral function is $\Gamma^{\alpha}_{\sigma}(\varepsilon)=V^2_{\alpha}D_\sigma(\varepsilon)$ and the spin-dependent density of states in linear band approximation, $D_\sigma(\varepsilon)=1/W\,(1\pm\sigma r)$, for majority and minority spins are chosen + and -, respectively, where W is the bandwidth of the electrode and the polarization ration, r, has the form, $r=|(D_\uparrow-D_\downarrow)/(D_\uparrow+D_\downarrow)|$; $f_\alpha(\varepsilon)$ is the Fermi-Dirac function for left and right electrodes; and $G^r_{\sigma\sigma}(kx,\varepsilon)$ is the retarded Green's function for an individual spin of CN.

Based on the concept of Spintronics, we calculate the magnetoresistance (MR) in various at room temperature, T=300K, where MR is defined as $MR=I_p-I_A/\ I_p+I_A$, and I_p, I_A are currents between both electrodes with parallel and anti-parallel magnetic polarization, respectively [3-5]. Our result shows the MR is remarkable at large r. In other words, electrode with small r has no application in Spintronics of CN, as shown in fig. 2. Particularly, the MR increases rapidly at initial bias then reach its saturation at a little higher bias, as shown in fig. 3. This rapid bias response for MR exhibits potential application in Spintronics.

[1] R. Saito, G. Dresselhaus and M. S. Dresselhaus, Physical Properties of Carbon Nanotubes, Imperial Cpllege Press (1998)

[2] H. Haug, A. –P. Jauho, Quantum kinetics in transport and Optics of semiconductors, Springer-Verlag Press (1998)

[3] B. W. Alphenaar, K. Tsukagoshi, H. Ago, Physica E, 6, 848 (2000)

[4] L. W. Liu, J. H. Fang, L. Lu, H. F. Yang, A. Z. Jin, and C. Z. Gu, Phys. Rev. B 74, 245429 (2006);

[5] Ane Jensen, Jonas R. Hauptmann, Jesper Nygard, and Poul Erik Lindelof, Phys. Rev. B 72, 035419 (2005)

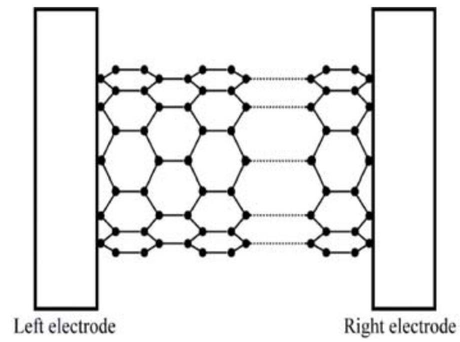

Fig. 1. Schematic illustration of zigzag carbon nanotube is connected by two magnetic electrodes.

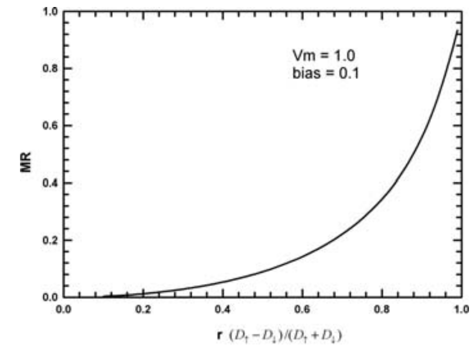

Fig. 2. Magnetoresistance (MR) in various r at bias 0.1 V, MR is defined as $MR=I_p-I_A/\ I_p+I_A$, and I_p, I_A are currents between both electrodes with parallel and anti-parallel magnetic polarization, respectively. The coupling interaction V_α is 1.0 eV.

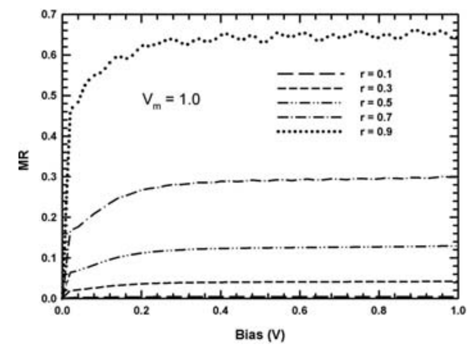

Fig. 3. Bias dependence of the Magnetoresistance (MR) in various r at the coupling interaction V_α = 1.0 eV. MR increases rapidly at initial bias then reaches its saturation at a little higher bias.

AO-12

The Effects of Cotunneling and Spin Flip on The Spin Polarized Transport in A Ferromagnetic Single Electron Tunneling Transistor.

M. Ma, M. Jalil
Department of Electrical and Computer Engineering, Information Storage Materials Laboratory, Singapore, Singapore

We study the spin-dependent transport in a ferromagnetic single electron tunneling(FM-SET) transistor consisting of an island weakly coupled to two ferromagnetic leads, and a gate electrode. We consider the contribution to the spin transport from sequential tunneling as well as higher-order cotunneling process, the latter of which has been of interest in recent experimental and theoretical research[1,2]. The cotunneling contribution becomes significant in the Coulomb blockade(CB) region, where the source-drain bias falls below a certain threshold value. In the CB region, the charging energy of one electron in the island exceeds the Fermi energy in the lead, and the resulting energy barrier renders it energetically unfavorable for sequential tunneling to occur; however, cotunneling transport is still possible since the electron exists as a virtual state in the island while tunneling from one lead to the other. Thus, in the CB region, cotunneling constitutes a major source of leakage current in a SET transistor and needs to be minimized. Luo *et al*. and Ohkura *et al*. have reported the suppression of cotunneling by using a granulated metal film island and multiple island electrodes, respectively[1].

In this work, we study the spin dependent transport through a FM-SET, specifically on the interplay between the inelastic cotunneling and spin flip processes. We consider the collinear configuration of the two symmetrical FM leads, i.e., the lead magnetizations are either parallel or antiparallel, and $p_1=p_2=p$, $R_{01}=R_{02}=R_0$,where p (R_0) is the polarization (tunnel resistance) of the lead, $R_0=(R^{\uparrow}+R^{\downarrow})/2$, $R^{\uparrow}=R_0(1-p)$,$R^{\downarrow}=R_0(1+p)$,$\uparrow(\downarrow)$ stands for up(down) spin. The sequential tunneling current is calculated based on the orthodox theory and the master equation method, while the cotunneling contribution is obtained by applying the well-established approximation of Jensen *et al*.[2], which eliminates the unphysical divergence in cotunneling current at the threshold voltage. The calculated sequential tunneling and cotunneling currents are plotted as a function of source-drain bias (I-V) and gate voltage (I-V_g) in Figs. 1(a) to (d), for both parallel(I^P) and antiparallel (I^{AP}) cases. For both cases, there are small but significant cotunneling contributions, especially near the threshold voltage for sequential tunneling. For the antiparallel case, both sequential tunneling and cotunneling currents are suppressed, reflecting the higher overall tunneling resistance compared to that in parallel case. However, the decrease is proportionately greater for cotunneling, so that the relative contribution of cotunneling current is smaller in antiparallel case.

We then focus on the effects of spin-related phenomena on the tunneling current in the SET transistor, namely the intrinsic spin polarization p of the leads, and the extent of spin flip (represented by spin flip rate Γ) in the island. We study the antiparallel case, which has the desired property of having a lower cotunneling contribution. We find that both sequential tunneling and cotunneling currents decrease monotonically with increasing p, as shown in Figs.2(a) to (c). The decrease of cotunneling current is more pronounced, i.e., when p changes from 0 to 0.8, the cotunneling current is reduced by about 90%, compared to a corresponding reduction of only 43% for sequential tunneling current.

Finally,we investigate whether the suppression of the relative cotunneling contribution at high lead polarization p still holds in the presence of spin flip process [see Fig.2(d)]. We find sequential tunneling is much more sensitive to spin flip in the island, while the cotunneling current hardly varies with Γ. Thus, we can utilize the spin mixing due to spin flip process to enhance the sequential tunneling current, while avoiding a similar increase in the undesired cotunneling current. By optimizing the spin-related properties of a FM-SET transistor, i.e., by choosing leads with high spin polarization, and by inducing high spin flip probability within the island, one can achieve a suppression of the cotunneling current relative to sequential tunneling in the FM-SET transistor. The utilization of these spin phenomena holds a distinct advantage over existing means of suppressing cotunneling by means of a multi-junction structure. The latter suffers from a lack of control and reproducibility inherent in the fabrication of multiple nanoscale junctions, as well as an excessively high resistance in the‘ON’state.

1.Xiangning Luo *et al*., Appl.Phys.Lett. 89, 043511 (2006); Kensaku Ohkura *et al*., Appl.Phys.Lett. 89, 183520 (2006).

2. H.D.Jensen *et al*, Phys.Rev.B 46, 13407(1992).

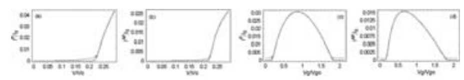

Fig.1 (a,b):I-V;(c,d): I-V_g. Dashed (solid) line: sequential tunneling (cotunneling) current components. Parameter values: $V_0=V_{g0}$=8mV,p=0.7,Γ =0,$V_{th}=0.22V_0$, $I_0=6.4\times10^{-7}$A,R_0=2.5 MΩ,V_g=0mV in (a) and (b), V=0.18V_0 in (c) and (d).

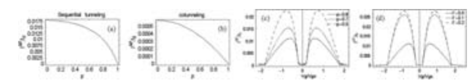

Fig.2 (a)(b):Tunneling current as a function of polarization p in sequential tunneling regime(a) and CB regime(b); (c)(d):I-V_g with various p values (c) or spin flip rate Γ(d). Parameters: $V_g=0.4V_{g0}$ in (a), V_g=0 mV in (b),Γ=0 in (c), p=0.9 in (d), V=0.18V_0,other parameters are the same as in Fig.1.

AO-13

Self-sustained spin-polarized current oscillations in diluted magnetic semiconductor superlattices.

R. Escobedo[1], M. Carretero[2,3], L. L. Bonilla[2,3], G. Platero[4]
1. Matemática Aplicada, Universidad de Cantabria, Santander, Spain; 2. G. Milan Institute of Modeling, Simulation and Industrial Mathematics, Universidad Carlos III de Madrid, Leganés, Spain; 3. Unidad Asociada al Instituto de Ciencia de Materiales de Madrid, CSIC, Madrid, Spain; 4. Instituto de Ciencia de Materiales, CSIC, Madrid, Spain

Among the challenges in spintronics, electrical injection of spin polarized current in semiconductor nanostructures is important because such nanostructures may find potential applications as spin-based devices. Different spin injectors have been proposed, including ferromagnetic or semimagnetic semiconductor contacts. The efficiency of ferromagnetic/semiconductor junctions has shown to be very small due to the large conductivity mismatch between the metal and the semiconductor.
Diluted magnetic semiconductors (DMS) are much more efficient as spin injectors, as it has been shown for contacts based in Mn. Compared to conventional semiconductor nanostructures, DMS's present an additional degree of freedom: the spin, which plays an important role in electron dynamics. In particular, in II-VI based semiconductor SL's doped with Mn carrier-ion exchange spin effects dominate the magneto-transport, producing spin polarized transport and large magnetoresistance. Exchange interaction between the spin carrier and Mn ions results in large spin splittings. Nonlinear transport through DMS SL's has been recently investigated [1]. In fact, the interplay between the non-linearity of the current as a function of the DC voltage and the exchange interaction produces interesting spin dependent feature: multi-stability of steady states with different polarization in the magnetic wells, time-dependent periodic oscillations of the spin-polarized current and inducedspin polarization in non magnetic wells by their magnetic neighbors, among others.
In this work we analyze nonlinear electron spin dynamics of a n-doped dc voltage biased semiconductor II-VI multi-quantum well (MQW) having one or more of its wells doped with Mn. Even if normal contacts have been attached to this nanostructure, we show that spin polarized current can be obtained provided one well has been doped with magnetic impurities [2]. We have analyzed under which conditions the system exhibits static electric field domains and stationary current or moving domains and time-dependent oscillatory current. For our sample configuration, there are self-sustained current oscillations for nanostructures with three or more QWs. Moreover, current self-oscillations may appear or not depending on the spin splitting induced by both, the exchange interaction and the external magnetic field. We calculate the critical spin splitting needed to have self-oscillations. From our results we propose how to design a device which can behave as spin-polarized current oscillator.

[1] D. Sanchez et al., Phys. Rev. B 65, 035301 (2001); M.Bejar et al., Phys. Rev. B 67, 045324 (2003).

[2] L.L. Bonilla et al., Appl. Phys. Lett., 91, 092102 (2007).

AO-14

Modeling of Spin-Transfer Torque in Magnetic Multilayers with Noncollinear Magnetizations.

H. Morise, S. Nakamura
Corp. R&D Ctr., Toshiba Corp., Kawasaki, Japan

The spin-transfer torque in magnetic multilayers[1, 2] can lead the magnetizations of nanomagnets to various types of dynamics such as excitaiton of spin waves[3], switching[4], and precessional motion[5]. These phenomena are expected to play key roles for realizing nanoscale spintronic devices such as MRAMs and microwave generators. The spin-transfer torque, whose origin is the interaction between the spin angular momentum of the conduction electrons and the local magnetic moments, can be estimated by the amount of the absorption of the transverse spin current in the magnetic layer. The transport of the transverse spin current across the interfaces[6] and that in the bulks[7, 8] have been investigated so far. However, the spin transport in the systems with many layers should be treated by taking both effects into consideration.

In the present work, we develop a theoretical modeling method to estimate the magnitude of the spin-transfer torque in a noncollinear magnetic multilayer based on such motivation. For the purpose, we employ a transfer-matrix technique which makes it easy to calculate the spin current in the system with many layers. We incorporate the chemical potential, the spin accumulation, the charge current, and the spin current into a location-dependent vector and relate the adjacent two vectors with the transfer matrix. With this method, we obtain the one-dimensional distribution of the spin accumulation and the spin current and as a result the magnetoresistance and the spin-transfer torque.

We calculate the spin-transfer torque in three kinds of multilayer structures by use of the above method. First, we consider the normal structure typified by Co/Cu/Co, which consists of a fixed layer and a free layer separated by a nonmagnetic spacer. Our special interest is on the roles of parameters characteristic to the noncollinear transport. Fig. 1 shows the critical switching current, which is inversely proportional to the spin-transfer torque, as a function of the transverse spin relaxation length l_J and those as functions of the normalized mixing conductances η^r and η^{t}. The result that the dependence on the mixing conductances is larger than that on the transverse spin relaxation length implies that the ballistic transport is ascendant over the diffusive transport in the system.

Second, we consider the synthetic antiferromagnet (SAF) structure, where the pinned layer consists of two magnetic sublayers antiferromagnetically coupled via a normal metal layer. A typical example of SAF is a multilayer composed of Co/Ru/Co. In this structure, the spin-transfer torque is reduced compared with that in the normal structure. However, the mechanism of the reduction has not been understood well yet. We consider two candidates for the mechanism, that is, the scattering of majority-spin electrons at the interface Co/Ru and the spin diffusion in the Ru layer. Fig. 2 shows the spin-transfer torque as a function of the relative angle between the magnetization of the pinned layer and that of the free layer. We find that short spin diffusion length of Ru layer is necessary to explain the P→AP switching. In other words, the diffusive effect is important for the spin transfer in this structure.

Third, we consider several types of the dual pinned layers (DPL) structure which includes an additional pinned layer in the opposite side of the first pinned layer from the free layer. Ref.[9] reported that some type of DPL structure produces much larger spin-transfer torque than that by the normal structure while another type of DPL structure does not. Our calculation on the enhancement factor agrees with this experimental result.

[1] J. C. Slonczewski. J. Magn. Magn. Mater., 159, L1 (1996).

[2] L. Berger. Phys. Rev. B, 54, 9353 (1996).

[3] M. Tsoi et al. Phys. Rev. Lett., 80, 4281 (1998).

[4] E. B. Myers et al. Science, 285, 867 (1999).

[5] S. I. Kiselev et al. Nature, 425, 380 (2003).

[6] A. Brataas et al. Phys. Rev. Lett., 84, 2481 (2000).

[7] S. Zhang et al. Phys. Rev. Lett., 88, 236601 (2002).

[8] M. D. Stiles et al. Phys. Rev. B, 66, 014407 (2002).

[9] S. Nakamura et al. Jpn. J. Appl. Phys., 45, 3846 (2006).

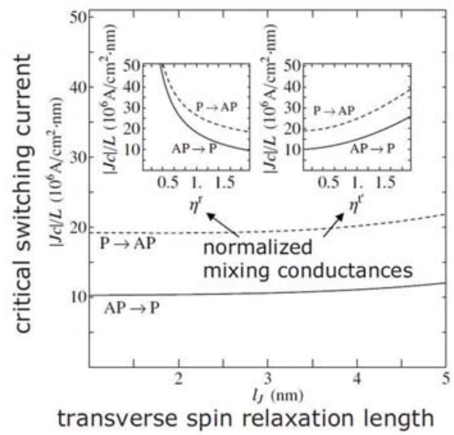

The dependence of the critical switching current divided by the thickness of the free layer on the transverse spin relaxation length and the normalized mixing conductances.

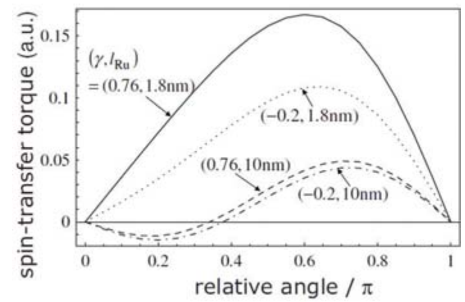

The spin torques for the SAF structure as functions of the relative angle between the magnetization of the pinned layer and that of the free layer. The spin asymmetry at the interface Co/Ru γ and the spin diffusion length of Ru layer l_{Ru} are changed.

AO-15

FMR studies of single permalloy layers sandwiched by Al.

H. J. Hurdequint[1], N. Sergeeva[1], J. Ben Youssef[2]
1. Laboratoire de Physique des Solides, CNRS-Universite Paris-Sud, Orsay, France; 2. Laboratoire de Magnetisme de Bretagne, CNRS-Universite de Bretagne-Ouest, Brest, France

Systematic investigations [1,2,3] of the spin resonance in magnetic films corresponding to purely metallic systems that we performed previously had revealed various remarkable phenomena that we associated to the specific nature of the interfacial coupling [2] between a ferromagnetic and a normal metal, which implies the *diffusion* of the microwave magnetization of the **conduction electrons** from one metal to the other. We have recently reported results of FMR studies of single permalloy (**Py**)layers sandwiched by **Ag**[4] and by **Au**[5].The FMR results have been systematically compared to the ones obtained on 'control' Py layers sandwiched by Al2O3[6].We report here the main results we have obtained in a detailed FMR investigation of three (**Py/Al**) films deposited by sputtering.We study (at X-band) the angular variation of the resonance spectrum (angle θ_H of the dc field with the film normal). The detected signal [5] is characterized by an A/B ratio which is a unique function of the signal 'phase'[1].We highlight the most **remarkable** phenomena observed in the angular variation of the resonance spectrum.

SampleA:thick Py(40nm), sub/Al40/Py40/Al10). The linewidth ΔH presents(around θ =10deg) a very *pronounced* peak (ΔHmax = 1.15 kOe), much larger in amplitude than the maximum(0.15 kOe)observed and well understood [6]of a Py(43nm) control film.

SampleB:thin Py(12nm), sub/Al6/Py12/Al8).As displayed in Fig.1,the linewidth presents a peak at a specific orientation (θmax= 9.7deg) around which a concomitant modification of the lineshape occurs.It is characterized by a rapid variation of A/B and hence of the signal ***phase***.

SampleC:thin Py(3.5nm),sub/Al6/Py3.5/Al8).Continuously with the orientation θ the resonance spectrum is here composed of **two** lines.The main intense line corresponds to the **FMR** line of the Py layer.A second partially resolved peak is observed: in higher field in parallel geometry and in lower field in the perpendicular one. We identify this second peak to the **CESR** line of the conduction electron spin accumulation of the metallic film[5].As displayed in Fig.2,a large variation of A/B is observed around the *crossing* orientation (27 deg),corresponding to a large (132 deg) variation of the signal phase when going from the parallel to the perpendicular geometry .This observation corresponds to the **first evidence** of the spin accumulation CESR signal in a single magnetic layer metallic film.

The ensemble of observed phenomena may be well understood and analyzed in terms of the theory of the signal (sketched briefly in ref[5]) we have developed to describe analytically the resonance spectrum observable in a **bimetallic** film (ferro/normal).Taking appropriate boundary conditions[7] at the metallic interface, the essential result obtained is that the resonance spectrum corresponds to the superposition of **two** sources of signal, associated respectively to the two eigenmodes(the'current' and 'spin-diffusion' modes[8])of propagation of the microwave magnetization in a metal.The crucial point is that these two sources of signal resonate at two distinct frequencies,the FMR frequency of the magnetic layer and the CESR frequency of the conduction electrons of the bimetallic film,respectively.Quite generally in a bimetallic film the two distinct Hres curves [H_{FMR} and H_{CESR}] will cross, the effect of the demagnetizing field being much weaker on the normal metal spin accumulation.

[1] H. Hurdequint, J.Magn.Magn.Mater. 93, 336 (1991).

[2] H. Hurdequint and G.Dunifer,J.de Phys. 49, C8-1717 (1988).

[3] H. Hurdequint and M.Malouche, J.Magn.Magn.Mater. 93, 276 (1991).

[4] H. Hurdequint, extended abstract p118-119, ICMFS 2003,July 22-25, Madrid (2003).

[5] H. Hurdequint, J. Magn.Magn. Mater. 310, 2061 (2007).

[6] H. Hurdequint, J. Magn. Magn. Mater. 242-245,521 (2002).

[7] M.Stiles et al., Phys.Rev.B 69, 054408 (2004).

[8] J.I.Kaplan, Phys.Rev. 115, 575 (1959).

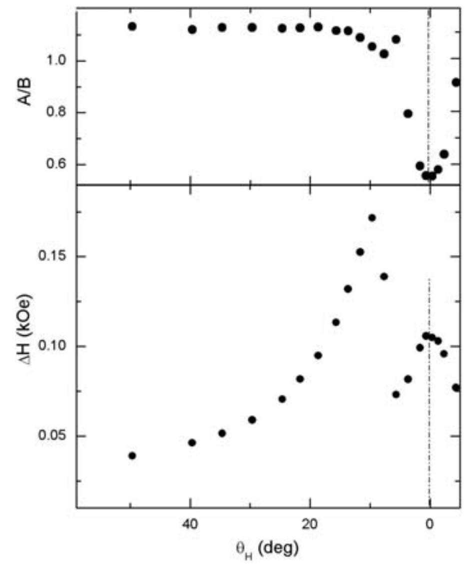

Fig.1: variation with θ_H for sampleB (Py12nm) of: a) the A/B ratio b) the line width ΔH

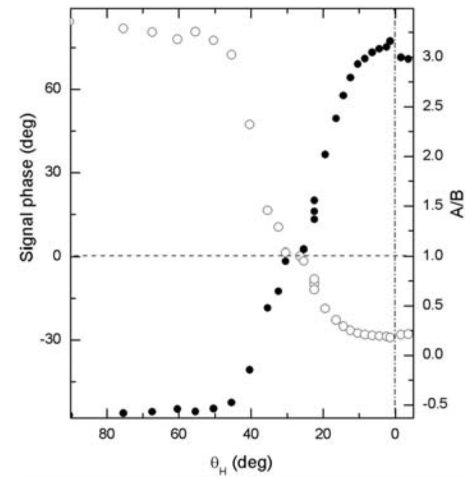

Fig.2: variation with θ_H for sampleC (Py3.5 nm) of: -the signal phase (black dots,left scale) -the A/B ratio (open circles,right scale)

AO-16

Verifying a sole effect of tunnel barrier on spin transport by spin-polarised photoexcitation.

K. Lee[1], T. Trypiniotis[1], H. Kurebayashi[1], S. N. Holmes[1,2], W. S. Cho[1], J. A. Bland[1], K. I. Lee[3], K. H. Shin[3]
1. Physics, Cavendish Laboratory, Cambridge, United Kingdom; 2. Toshiba Research Europe Limited, Toshiba Cambridge Research Laboratory, Cambridge, United Kingdom; 3. Center for Spintronics Research, Korea Institute of Science and Technology, Seoul, South Korea

Spin filtering effect has been studied in ferromagnetic material (FM) / semiconductor (SC) hybrid structures and is recognised as a fundamental building block of spintronic devices. In such a simple structure, understanding both the transport characteristics and the scattering mechanisms of the spin-polarised carriers is prerequisite for developing more useful structures. In order to solve the conductivity mismatch problem [1], which occurs at the FM/SC interface, it has been referred that the tunnel contact between them could be appropriate for efficient spin injection/detection [2].
Here we present the results of the electron spin filtering effects across the tunnel barrier using the optical excitation of spin-polarised electrons in n- and p-doped GaAs. Al/NiFe(5nm)/AlOx(1.6nm)/GaAs structures were deposited by DC/RF sputtering in ultrahigh vacuum. As seen in regular TMR devices, the plasma oxidation method allows the formation of well defined alumina tunnel contacts with relatively high resistance, as evidenced by conventional IV characteristics. After film deposition, the active mesa was defined by conventional photolithography and electrically isolated from the adjoining region by subsequently depositing a 25 nm TaOx films. Conventional current-voltage measurements reveal that the devices show clear Schottky diode characteristics, and thus tunnelling transport is expected to be the dominant process for the filtering of spin-polarised electrons [3]. As Pierce and Meier had performed in 1976, the circularly polarised photons are possible to make spin-polarised carriers inside the GaAs, which will move to the interface adjacent to the FM detector via applied bias. The measured helicity-dependent photocurrent (HDPC) reveals that the degree of spin filtering depends on the magnetic alignment of the FM layer while the initial injection efficiency into the FM layer is determined by the alignment of the magnetic layer with respect to the photon helicity. Furthermore, the HDPC, corrected for MCD, shows the expected behaviour for a single FM/barrier structure. Since the external magnetic field was applied along the perpendicular to the plane, a polar geometry, one can observe the maximum spin filtering currents are varied and proportional to the degree of the magnetisation of the FM layer. In case of p-GaAs, the HDPC is purely dependent on the property of the tunnel barrier since the band bending at the interface is totally different with the one of n-doped SC. We discuss these results by considering spin dependent transmission across the interface, supported by the results of local electrical measurement.

[1] G. Schmidt, D. Ferrand, L. W. Molenkamp, L. T. Filip and B. J. van Wees, Phys. Rev. B, 62, R4790 (2000)

[2] E. I. Rashba Phys. Rev. B 62 R16267 (2000); J. D. Albrecht and D. L. Smith Phys. Rev. B 68 035340 (2003)

[3] A. Hirohata, S. J. Steinnmueller, and J. A. C. Bland et al. Phys. Rev. B 66 035330 (2002)

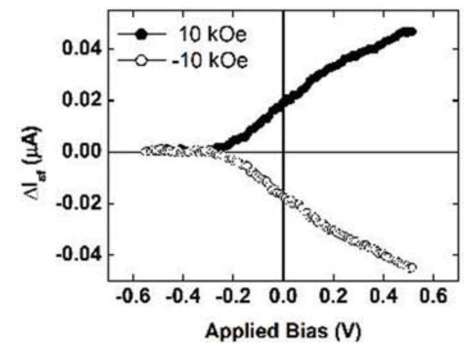

Spin filtering currents in [NiFe(5nm)/AlOx(1.6nm)/n+-GaAs] structure.

AO-17

Polarization dependence of phonon replica peaks in spin-LEDs.

R. Mansell[1], J. Laloë[1], S. N. Holmes[2], A. Petrou[3], I. Farrer[1], G. Jones[1], T. Bland[1]
1. Department of Physics, University of Cambridge, Cambridge, United Kingdom; 2. Toshiba Cambridge Research Laboratory, Cambridge, United Kingdom; 3. Department of Physics, SUNY, Buffalo, NY

Injection of spin polarized currents from thin ferromagnetic films into semiconductor light emitting diode (LED) structures has been used to study both the injection and transport of spin polarized electrons as part of a drive towards spintronic devices. In this study we look at LEDs with Fe films using both the Faraday and the oblique Hanle geometries. The magnetic injector films were 5 nm Fe, deposited by MBE on AlGaAs, which displayed the characteristic uniaxial anisotropies for this system [1]. Optical polarization spectra were detected in both geometries. These show a rich spectrum of peaks due to phonon-assisted recombination of light and heavy hole excitons (figure 1). The phonon replica peaks can be identified by their energy as LO, TA and LA phonon mediated showing that transport occurs in the X and L band minima in the semiconductor. The high electric field experienced by the electrons as they are injected through the Schottky barrier promotes electrons to these higher energy band minima. Transport in the X and L minima leads to rapid spin dephasing as shown by the theoretical work of Saikin et al [2]. This shows that optimisation of the semiconductor emitter for practical devices calls for in-depth understanding of the precise mechanisms of both transport and recombination in the entire structure. For example, in the case of the spectrum shown in figure 2, we observed a significantly larger optical polarization of the LO-phonon replica peak compared to that of the heavy hole exciton. This unexpected result shows that optimisation only for the exciton recombination wavelength does not lead in all structures to the highest polarization.

Furthermore, we have observed stronger phonon-assisted recombination and polarization in devices grown under continuous vacuum, than in samples transferred under an arsenic cap in air. This indicates that the clean interface may promote tunnelling to the X and L states, leading to a reduction of the net spin polarization of the injected current, therefore setting an upper limit for the efficiency of spin-injection through the Fe/GaAs interface separate to the models of Schmidt [3] and Rashba [4].

[1] Y. B. Xu et al. Phys. Rev. B 58 890 (1998)

[2] S. Saikin et al., J.Phys.:Cond.Mat. 18 1535 (2005)

[3] G. Schmidt et al., Phys. Rev. B 62 R4790 (2000)

[4] E. I. Rashba, Phys. Rev. B 62 R16267 (2000).

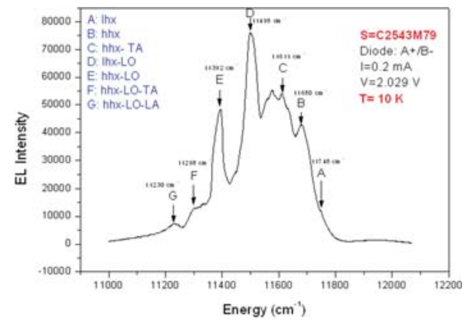

Emission spectrum from an InGaAs quantum well, showing various phonon-assisted recombination peaks.

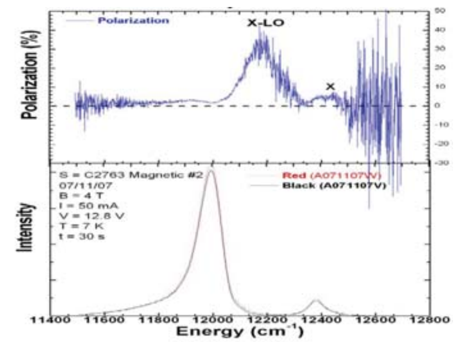

Example of emission and polarization spectra from a GaAs/AlGaAs spin-LED, showing different optical polarization values for the exciton, and phonon-assisted exciton recombinations. The data was collected in the Faraday geometry (field out of plane).

AO-18

Comparison of room temperature polymeric spin-valves with different organic components.

D. Dhandapani[1], N. A. Morley[1], A. Rao[1], A. Das[2], M. Grell[2], M. R. Gibbs[1]
1. Engineering Materials, University of Sheffield, Sheffield, United Kingdom; 2. The Department of Physics and Astronomy, University of Sheffield, Sheffield, United Kingdom

Introduction:
Organic spintronics is an exciting new research area, as it combines electron polarised spin transport with organic semiconductors. The long spin coherence length due to the weak spin orbit interaction in organic materials makes them potential candidates for spintronic devices. An organic spin-valve is a layered structure of two ferromagnetic electrodes with different coercive fields separated by a organic spacer layer[1, 2]. This research focuses on the further development of organic semiconductor spintronic devices consisting of magnetic/organic spacer/magnetic trilayers. The hole transporting polymers regio-regular[3, 4] and regio-random poly (3-hexylthiophene) were used as the spacer material; the choice was motivated by several factors, which included the highest occupied molecular orbital (HOMO) energy of P3HT (5.1eV) being close to the work function of the electrode material. Efficient carrier injection was therefore expected. Also P3HT has two different structures, with RR-P3HT being more conductive than RRa-P3HT. This is useful for the study of spin transport, as the spacer layer has the same chemical formula, but different electronic structure.
Experiment:
The organic spin-valves were $Fe_{50}Co_{50}$/RRa (RR)-P3HT/$Ni_{81}Fe_{19}$ on glass substrates. The bottom electrode $Fe_{50}Co_{50}$ was dc sputtered at 25kW/m^2 target power density at an Ar pressure of 7μbar, to a thickness of 40nm. The P3HT films were spin coated on top of $Fe_{50}Co_{50}$ electrode at around 1250rpm, and then heated at 50°C for 10 min. The thickness, d, was varied by varying the toluene solution and ranged from 50nm to 300nm. Finally the top electrode $Ni_{81}Fe_{19}$, was thermally evaporated at a base pressure of 1x10^{-7}mbar, to a thickness of 20nm. Magnetoresistance (MR) measurements were carried out by applying a current perpendicular to the film plane with the field parallel to the film plane, at room temperature.
Results and Discussion:
The $Fe_{50}Co_{50}$ which has harder magnetic properties was chosen as the bottom electrode and the top electrode was $Ni_{81}Fe_{19}$ which has very soft magnetic properties. The magnetization loops of the FeCo and NiFe layers were measured using magneto-optic Kerr effect (MOKE) magnetometer (Fig .1). Thus there is a large difference in the switching fields of the two electrodes. For the RRa-P3HT devices, we observe both anisotropic magnetoresistance (AMR) and spin MR for 50nm (Fig.2). We observed only the spin MR at room temperature in the RR-P3HT devices[3], with spacer thicknesses less than 100nm. Above 150nm RR-P3HT thickness, the superposition of AMR with spin MR was observed. For the RRa-P3HT devices, a negative spin MR was measured, while a positive spin MR was measured in RR-P3HT devices. This will be discussed further in relation to the response of the polymer.

[1] Z. H. Xiong, D. Wu, Z. V. Vardeny, and J. Shi, Nature. 427, 821 (2004).

[2] F. C. Wang, Z. H. Xiong, D. Wu, J. Shi, and Z. V. Vardeny, Synthetic Metals. 155, 172 (2005).

[3] N. A. Morley, A. Rao, D. Dhandapani, M. R. J. Gibbs, M. Grell, and T. Richardson accepted by Journal of Applied Physics (2008).

[4] S. Majumdar, R. Laiho, P. Laukkanen, I. J. Väyrynen, H. S. Majumdar, and R. Österbacka, Appl. Phys. Lett. 89, 122114 (2006).

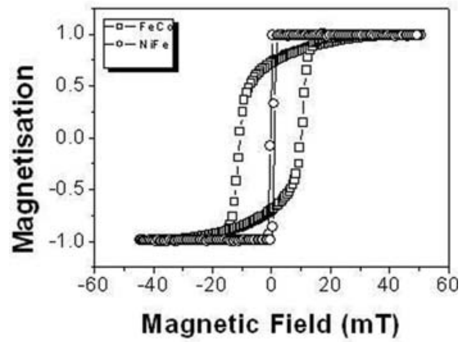

Fig. 1. Magnetization of the $Fe_{50}Co_{50}$ and $Ni_{81}Fe_{19}$ electrodes as a function of field.

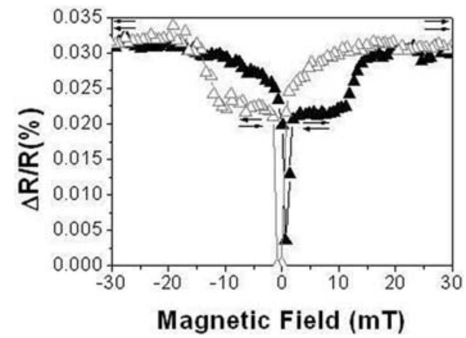

Fig. 2. Magnetoresistance of the $Fe_{50}Co_{50}$ /RRa-P3HT (50nm)/ $Ni_{81}Fe_{19}$ device. The arrows represent each layer's magnetization direction

AO-19

Measurement of the spin polarization of rare earth – transition metal Laves phase compounds by point contact Andreev reflection.

C. G. Morrison[1], K. N. Martin[1], G. J. Bowden[1], P. A. de Groot[1], R. C. Ward[2]
1. School of Physics and Astronomy, University of Southampton, Southampton, United Kingdom; 2. Clarendon Laboratory, University of Oxford, Oxford, United Kingdom

Spin electronics, or spintronics, is currently a very active field of research. Spin effects in devices and systems are dependent on the splitting of the electron current into spin sub-bands, or the spin polarization of the device. Devices improve in performance as spin polarization tends toward 100% or complete conduction through one spin sub-band. As such it is important to be able to accurately characterise the spin polarization accurately in materials. Ferromagnetic materials are of particular interest as these find wide applications in magnetoelectronic devices.
Previous research into the electron transport and magnetic properties of rare earth – transition metal Laves phase compound superlattices, in particular DyFe2 and ErFe2 layered with YFe2, has demonstrated the formation of an exchange spring configuration [1,2]. Further studies resulted in the discovery of giant magnetoresistance (GMR) in these superlattices [3]. Laves phase rare earth – transistion metal materials are excellent model systems in which to explore magnetic structures, switching and stability of exchange spring media.
Following on from these investigations, this digest focuses on the determination of the spin polarization of these Laves phase materials through point contact Andreev reflection (PCAR). It is hoped that characterisation of the spin polarization will lead to increased understanding of GMR in these Laves phase materials and superlattices.
Andreev reflection is a well studied effect discovered by A. Andreev [4]. At a metal-superconductor interface, conversion of normal current (single isolated electrons) to supercurrent (Cooper pairs) requires by conservation laws the creation of a hole travelling antiparallel to the electron current. Thus a second current channel is created and the conductance of the junction is doubled.
In ferromagnetic materials with a spin polarization this effect is suppressed, dependent on the degree to which the material is spin polarized. Research has been undertaken to determine the contact spin polarization Pc by PCAR in Ni, Fe, Co and alloys, including CrO2 [5], FePt films [6] and the potential half-metal LaSrMnO35 [5,7].
A mechanical point contact technique was used as described elsewhere [8]. Differential conductance (dI/dV = G(V)) of the junction was detected using standard ac lock-in techniques at 2kHz frequency [9]. A point contact spectra for a 4000Å Laves phase DyFe2 grown by molecular beam epitaxy is presented in figure 1. This spectra shows a clear peak in conductance below the superconducting gap of niobium at $\Delta = 1.5$meV.
Following the methodology of R J Soulen et al.[5] it is possible to extract a value for the
contact spin polarization PC. Their method is based on a modification of the Blonder-Tinkham-Klapwijk (BTK) model of metallic-superconductor microconstrictions. The
spin polarization may be extracted by decomposing the current through the point contact into two parts: a non-polarized part that obeys standard BTK theory and a polarized part that carries all the contact spin polarization PC. From this it follows that

$G(V)/G_n = 2(1 - P_C)$

Using this expression a value of PC = 36.5 ± 5% is obtained for Laves phase DyFe2.
It may also be noted that, by fitting the data to the modified BTK model, the value of Z, the interfacial scattering parameter, is low [10]. This may be seen from the absence of a dip at zero bias, which increases in magnitude as Z increases. Low Z implies a good quality point contact and a small contact radius.

Conclusions

Through use of point contact Andreev reflection a value of PC = 36.5 ± 5% has been determined. This value is close to that of iron, and closely resembles that of iron compounds such as NiFe published elsewhere5. It may be concluded that the spin polarization of these compounds is dominated by that of the Fe atoms, with the Dy atoms having a small modifying effect on the spin transport properties of the material.

[1] J. –M. L. Beaujour et al., *J. Mag. Magn. Mat.* **226**, 1870 (2001)

[2] K. N. Martin et al., *App. Phys. Lett.* **89**, 13 (2006)

[3] S. N. Gordeev et. al., *Phys. Rev. Lett.* **87**, 186808 (2001)

[4] A.F. Andreev, *Sov. Phys. JETP* **19**, 1228 (1964)

[5] R. J. Soulen Jr. et al., *Science* **282**, 85 (1998)

[6] K. M. Seemann et al., *Phys. Rev. B* **76**, 174435 (2007)

[7] Y. Ji et al., *Phys. Rev. B* **66**, 012410 (2002)

[8] A. G. M. Jansen et al., *J. Phys. C: Solid St. Phys.* **13**, 6073 (1980)

[9] J.G. Adler and J.E. Jackson *Rev. Sci. Instr.* **37**, 8 (1966)

[10] G. J. Strijkers et al., *Phys. Rev. B* **63**, 104510 (2001)

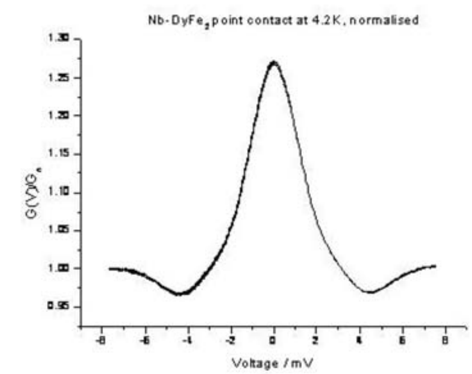

Figure 1: PCAR spectra of DyFe2 showing a clear peak at low bias voltages.

AP-01

Vapor phase synthesis of $L1_0$ FePt nanopowders and their magnetic properties.

J. Yu[1], D. Lee[1], B. Kim[1], T. Jang[2]
1. Department of Powder Materials Research, Korea Institute of Materials Science, Changwon, South Korea; 2. Dept. of Electronic Materials Engineering, Sunmoon University, Asan, South Korea

FePt nanoparticles are promising in magnetic materials for high density magnetic data storage media, since the FePt has a very high magnetocrystalline anisotropy, a high coercivity, and a high chemical stability [1].
In a bulk FePt, it needs to anneal at 1273 K to obtain the ordered tetragonal $L1_0$ structure from the disordered FCC structure through the order-disorder transformation. However, such annealing frequently leads to crystal growth and thereby concurring agglomeration of the separated nanoparticles. In order to avoid such agglomerations, we employed a new technique that allows preparation and annealing of FePt nanoparticles at the same time in the gaseous state prior to condensation. In this paper, therefore, we fabricated the $L1_0$-ordered FePt nanoparticles by the chemical vapor condensation (CVC) process and then investigated the microstructural characteristics and magnetic properties of the FePt nanoparticles.
The basic setup for CVC process is similar to that described in literature elsewhere [2]. To produce FePt nanoarticles, Ar carrier gas was fed through a heated evaporator (~230 °C) containing a solid precursor mixture of iron acetylactonate and platinum acetylactonate. The carrier gas entrained precursor vapor and passed through the heated furnace in which the precursor pyrolyzed and condensed into particles. The tubular furnace was uniformly heated at a temperature between 800 °C and 1000 °C and the FePt particles were attempted to synthesize at various mixing ratio of the precursors. Finally, the synthesized particles were collected from the chamber. And the characteristics of synthesized FePt nanopowders were analyzed by using TEM, XRD, XRD and VSM.
Chemical compositions of the FePt nanopowder synthesized at various mixing ratio of Fe and Pt precursors are summarized in Table 1. The Fe content in the synthesized powder increases monotonically with the increase of the amount of Fe precursor. $Fe_{50}Pt_{50}$ compound nanopowder is obtained only when the mixing ratio of Fe(acac.) and Pt(acac.) precursors is 2.5:1. This is simply due to more volatile property of Pt(acac.) than Fe(acac.).
Fig. 1 shows X-ray diffraction patterns of the FePt nanoparticles synthesized at various mixing ratio of the precursors. For the conditions of higher Pt contents (Fig. 1(a,b)), the peaks of PtO_2 are observed with typical cubic phase of FePt alloy. This is due to the excess amount of Pt metal vapor decomposed from Pt(acac.), which is left over after the formation of FePt and then oxidized. On the other hand, as shown in Fig. 1(c), the diffraction pattern of ordered $L1_0$ FePt phase is obtained at a higher Fe precursor mixing condition. It shows the (001) and (110) superlattice lines, indicating that a significant degree of $L1_0$ ordering phase, without any post annealing process. This result is confirmed by the selected area diffraction (SAD) result.
Fig. 2 shows TEM micrographs of the FePt nanoparticles synthesized at different reaction temperatures. The particles have spherical shapes and slightly agglomerate each other, yielding the average particle size of ~ 5 nm at 800 °C, ~ 7 nm at 900 °C, and ~ 10 nm at 1000 °C, respectively. It indicates that the particle size increases with the increase of reaction temperature, mainly due to the accelerated sintering effect at higher temperature. The collision of condensed nanoparticles occurs more actively at higher temperature, leading to easy growth and agglomeration of the nanoparticles as can be seen in Fig. 2(c).

A room temperature magnetization curves not exhibit superparamagnetism, unlike the particles of Sun et al. [1]. However, the coercivity of the powder in an isotropic state has quite lower value (~ 570 Oe). The details of magnetic properties will be discussed with the morphological and microstructural aspects of synthesized FePt nanopowders.

[1] S. Sun, C. B. Murray, D. Weller, L. Folks, and A. Moser, Science, 287, 1989 (2000).

[2] J.-H. Yu, D.-W. Lee, B.-K. Kim and T. Jang, J. Magn. Mag. Mater., 304, e16 (2006).

Elements (at%)	Mixing ratio of precursors, Fe(acac.) : Pt(acac.) in weight					
	1 : 3	1 : 2	1 : 1.5	1 : 1	2 : 1	2.5 : 1
Pt	79.6	78.0	76.5	66.7	54.9	50.6
Fe	20.4	22.0	23.5	33.3	45.1	49.4

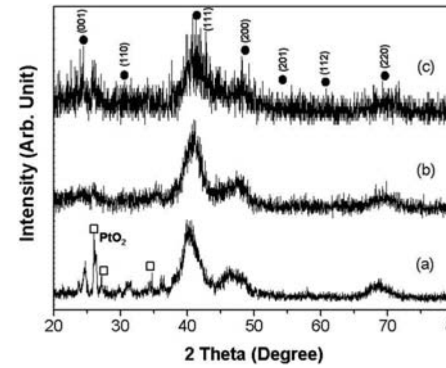

Fig. 1. X-ray diffraction patterns of FePt nanopowders synthesized with the mixing ratio of precursors, (a) Fe(acac.) : Pt(acac.) = 1 : 3, (b) 1 : 1 and (c) 2.5 : 1.

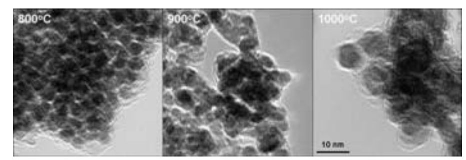

Fig. 2. TEM micrographs of FePt nanopowder synthesized with different reaction temperatures (a) 800°C, (b) 900°C and (c) 1000°C by chemical vapor condensation process.

AP-02

Two easy axes effect on nanosized spherical particles for advanced tape storage.

Y. Wang, J. Zhu
Electrical and Computer Engineering, Carnegie Mellon University, Pittsburgh, PA

INTRODUCTION
For advanced tape media, nanosized composite advanced particles (NanoCAP) [1], developed with spherical shape and high coercivity, have produced potential for spherical particles to replace their acicular counterparts in high density tape recording due to smaller size, higher packing fraction and stronger anisotropy. It was also demonstrated [2] that spherical particles should yield superior recording performance with an appropriate writer. The measurement of the hysteresis loop indicates that the particles have uniaxial crystalline anisotropy. However, it is extremely difficult to produce perfectly spherical particles, which introduces significant parasitic shape anisotropy. The combined effect of the two anisotropies is studied by micromagnetic modeling. Possible improvements are also discussed.
MODELING AND PARAMETERS
A micromagnetic model is developed to simulate spherical particles with a core-shell structure. Landau-Lifshitz-Gilbert equation is employed to fully study 3D micromagnetic behavior. The particle locations are random and the packing fraction can be up to 45%.
The two easy axes of the particle are illustrated in Fig 1. The diameter of the particle and its inner magnetic core is 17nm and 10nm, respectively. The particle aspect ratio is set to 1.5 estimated from the TEM picture in [1]. Damping constant is assumed to be 0.1 in the simulation. Packing fraction of the tape is usually around 40%. Other parameters will be discussed later.
RESULTS AND DISCUSSIONS
Coexisting with uniaxial crystalline anisotropy, the parasitic shape anisotropy degrades the hysteresis loop show in Fig 2(a). In the simulation, the easy axes of both crystalline and shape anisotropies are totally random in 3D space. It is important to note that the random angle θ between the two easy axes causes the more incoherent switching behavior among particles.
Fitting with experimental data is performed in Fig 2(b). Excellent agreement with experimental data is observed. Magnetization is obtained at 2500emu/cc and crystalline anisotropy constant 10^7erg/cc. It indicates that the material exhibits high saturation magnetization and anisotropy, which is coherent with [1]. For the rest of the results presented here, these parameters are used for all calculations.
Recording simulations are also performed shown in Fig 3. Two transitions are written at the linear density of 150 KFCI. With the increase of aspect ratio from 1.0 to 1.5, the recording transition profile continues to suffer from the parasitic shape anisotropy. A deep gap field of 7000 Oe and gap width 200 nm is assumed in the simulation. The direction of effective easy axes of the two anisotropies is set to have a standard deviation of 15 degrees with respect to the downtrack direction. Transition noise is boosted as well which will be included in full paper.
Further improvements are also feasible. One possible improvement is to align the particle long axes to the vicinity of downtrack direction. This may help the effective easy axes to align closer to the desired direction. The other option is to reduce the saturation magnetization of the particle. Since the strength of shape anisotropy is proportional to the square of magnetization, the negative influence will be greatly reduced. And high packing fraction of spherical particles ensures sufficient strength of the readback signal. More details will be presented in full paper.

[1] Y. Sasaki, N. Usuki, K. Matsuo and M. Kishimoto, Development of NanoCAP Technology for High Density Recording, IEEE Trans. Magn., Vol 41, No. 10, p. 3241 (2005)

[2] T. Inoue, K. Nakiri, H. Mitsuhashi, M. Fukumoto, T. Doi, Y. Sasaki and M. Kishimoto, Playback Performance of Ultrahigh-Capacity Tape Media With Nanosized Composite Advanced Particles (NanoCAP), IEEE Trans. on Magn., Vol 42, No. 3, p. 465 (2006)

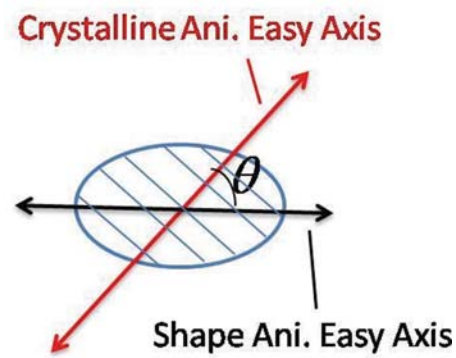

Fig 1. Illustration of two easy axes. The angle θ between the two is usually random and difficult to control.

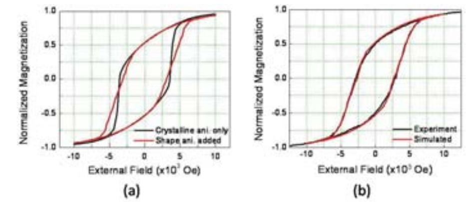

Fig 2. Hysteresis loop simulation. (a) is the comparison between crystalline anisotropy only and two easy axes. (b) is the curve fitting result.

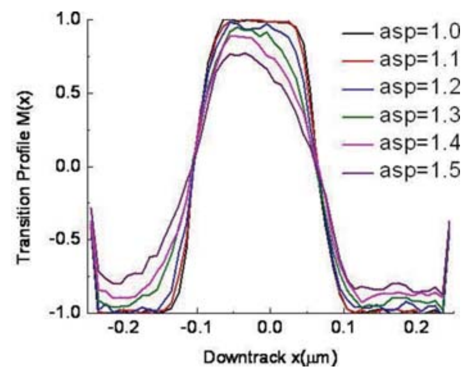

Fig 3. Transition profile in recording simulation.

AP-03

Synthesis and self-assembly of phase-, size- and shape-controlled $L1_0$-FePt nanorods by a modified polyol process.

L. C. Varanda[1], M. Jafelicci Jr.[2]
1. Físico-Química, Instituto de Química de São Carlos - USP, São Carlos, Brazil; 2. Físico-Química, Instituto de Química de Araraquara - UNESP, Araraquara, Brazil

FePt nanoparticles with controlled size, shape, chemical composition and magnetic alignment has become an important goal in developing nanocrystal arrays for applications in information storage, high performance permanent-magnets, biomedicine and catalysis.[1,2] This alloys are chemically stable and their magnetic properties tuned by controlling the Fe/Pt atomic ratio and by nanocrystal size. Most of previous work has focused on the synthesis of spherical FePt nanocrystals, mainly based in the polyol (volatile and toxic $Fe(CO)_5$ uses)[3] or polyol-derivate (using $Fe(acac)_3$)[1,4,5] processes. Despite these synthetic progresses, aligning these spherical nanoparticles magnetically has constantly been a problem for practical applications, and the magnetic easy axes of the assembled nanocrystals are randomly oriented in 3D. [1,2] This controlled alignment is essential for the fabrication of single-particle recording media with ultrahigh density, magnetic nanocomposites with maximum energy product, and magnetotransport devices[2]. Thus, 1D FePt nanorods (NRs) or nanowires are more interesting because they are expected to have magnetic and structural anisotropy with unique magnetic properties To this end, few efforts were recently made on the synthesis of Pt-based (NRs) and generally using the problematic $Fe(CO)_5$ compound. [6,7] Preview reported procedure[3] was modified in this work and the synthesis and self-assembly of FePt (NRs) with controlled shape, size and composition in the chemically ordered fct phase using a modified polyol process were reported. Typical synthesis of $L1_0$-$Fe_{55}Pt_{45}$ NRs following: in a three-necked round-bottom flask under gentle nitrogen flow and stirring, $Pt(acac)_2$ (0.5 mmol), oleylamine (OAm) and octadecene (OD) -OAm/OD of 2:1 (v/v)- and total volume of 20 mL were mixed and heated at 60 °C. 1,2-hexadecanediol (1.5 mmol) and $Fe(acac)_3$, (0.61 mmol) were added into the solution and the temperature slowly increased at 120°C, which was kept for 30 min. The temperature was then slowly raised to 180°C. After 3 hours, the suspension was cooled down to room temperature and the resulting NRs were separated by adding hexane and ethanol and centrifuging. NRs were self-assembled by droplet a dispersion of the particle in a 50:50 mixture of hexane/octane and slowly evaporated at room temperature. Length and composition of the NRs can be realized by tuning the volume ratio of OAm/OD and the Fe/Pt molar ratio, respectively. TEM results (Fig 1a-b) indicate that synthesized NRs are a monodisperse system with 60±5 nm in length and diameter of 2-3 nm and the controlled evaporation of the 60-nm $Fe_{55}Pt_{45}$ NRs in hexane/octane dispersion led to an $Fe_{55}Pt_{45}$ NR array with the NRs parallel to each other (Fig. 1b). According to the HRTEM image (Fig 1c) the NRs present a single nanocrystals structure and the lattice fringes are oriented ~90° from the rod-growth direction with interplanar distance found to be 0.284 nm, closed to the lattice spacing of the (110) planes (0.276 nm) in the fct ($L1_0$) FePt structure. This result suggest that the [001] direction is parallel to the rod-growth direction and that the fct phase was directly obtained during the synthesis, in contrast with the previews reported synthesis of the FePt NRs where the as-synthesized particles present the fcc phase. [2,6,7] The presence of the fct phase was confirmed by the XRD patterns (Fig 1d) and agrees with the direct fct structure related for spherical FePt nanoparticles[5] when the reaction kinetic was enhanced by using the slow heating rate, low temperature and the gentle stirring. The fast reaction kinetic favor the size decrease, but also favor the unstable fcc phase, in contrast with the condition used in this work, which the reaction rate is slow and the most stable phase (fct) was realized. Therefore, the XRD pattern of the assembly shows a stronger (001) peak relating to the (111) peak, indicating a partial structural alignment with the (001) planes parallel to the substrate. In-plane magnetic hysteresis loop of the assembly shows the better squareness with the coercivity reaching 10 kOe (Fig 1e).

1. Varanda, L.C., Jafelicci Jr., M., *J. Am. Chem. Soc.* **128**, p. 11062, 2006

2. Wang, C. et al., *Angew. Chem. Int. Ed.* **46**, p. 1, 2007.

3. Sun, S. Et al., *Science*, **287**, p. 1989, 2000.

4. Varanda, L.C. et al., *J. Appl. Phys.* **101**, p. 123918, 2007.

5. Jeyadevan, B. et al. *Jpn. J. Appl. Phys.* **42**, p.L350, 2003.

6. Hou, W. et al., *Small*, **2**, p. 235, 2006.

7. Chen, M. et al., *J. Am. Chem. Soc.* **129**, p. 6348, 2007.

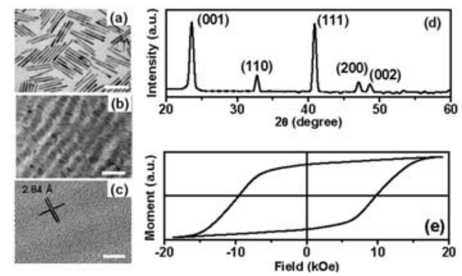

Fig 1. TEM images of the $L1_0$-$Fe_{55}Pt_{45}$ NRs obtained by a modified polyol process (a) as-synthesized (scale bar 50 nm), (b) after self-assembly procedure using a 50:50 mixture of hexane and octane (scale bar 60 nm), (c) HRTEM image of the NR showing the texture along the (110) planes and indicating that the [001] direction is parallel to the rod growth direction (scale bar 3 nm), (d) XRD pattern indicating the $L1_0$ phase formation and a strong increases in the (001) intensity reflection, and (e) the magnetic hyteresis loop showing a strongly ferromagnetic behavior with H_C ~10 kOe.

AP-04

Playback performance of facing targets sputtered tape media on moving tape substrate with a high speed.

S. Matsunuma[1], T. Inoue[2], T. Doi[2], T. Matsuu[3], A. Hashimoto[3], H. Fujiura[3], K. Hirata[3], S. Nakagawa[3]
1. R&D Division, Hitachi Maxell, Tsukubamirai, Japan; 2. Advanced Tape Division, Hitachi Maxell, Oyamazaki, Japan; 3. Department of Physical Electronics, Tokyo Institute of Technology, Meguro, Japan

Introduction

Sputtered tape media is a promising candidate for advanced storage tape with over 10 TB capacity per cartridge. By facing targets sputtering (FTS)[1], a nanometer-sized granular CoPtCr-SiO_2 film for longitudinal recording can be formed on a thin plastic substrate at room temperature with no damage[2]. In this paper, preparation of CoPtCr-SiO_2 film by FTS on a moving substrate is demonstrated, and moving speed effect on playback performance and microstructure is investigated.

Experimental

CoPtCr-SiO_2 granular magnetic film for longitudinal recording was formed by a multi-gun FTS system with a moving substrate apparatus at room temperature without cooling. Cross-sectional structure of sputtered media is C(5 nm)/CoPtCr-SiO_2 (20nm)/Ru (20nm)/Aramid substrate(4.5 µm). Argon pressure for sputtering for magnetic layer was 0.8 Pa. Microstructure was observed by 200 kV transmission electron microscopy (TEM). Playback performance was evaluated by a drum tester with anisotropic magnetoresistive (AMR) reader (track width=5.5 µm, shield-to-shield length=170nm)/writer (track width=12 µm, gap length=170nm) heads at tape speed of 3 m/s. Medium noise was measured in a range of 0 to 20 MHz.

Results and discussion

Two samples at different moving speed of substrate were named as sample L (slow moving speed, 5.8 cm/min) and sample H (high moving speed, 100 cm/min). In-plane coercivity and squareness were measured as 308.8 kA/m and 0.74 for sample L, 318.3 kA/m and 0.69 for sample H, by a vibrating sample magnetometer. XRD measurements showed epitaxial growth of *hcp*-CoPtCr(100)/*hcp*-Ru(100) planes. Figure 1 shows in-plane TEM images of sample L and H, which have similar microstructure of clear boundary and grains with uniform sizes. Vertical direction in Fig. 1 corresponds to moving direction of substrate during sputtering. Grain shapes and sizes of sample L and H are independent on the moving direction and speed. Average grain sizes were estimated at 8.0 nm for sample L and 7.8 nm for sample H. Segregations of Cr and Si to boundary regions of both samples were confirmed by point energy dispersive X-ray spectroscopy (EDS).

Cross-sectional TEM image of sample H are shown in Fig. 2, which indicates that straight columnar grains were grown and unaffected by the moving direction. So, it is concluded that moving speed of substrate does not affect the microstructure of the media by FTS.

Figure 3 shows the signal-to-noise ratio (SNR) dependence on linear recording density for both samples, measured by a drum tester. In Fig. 3, MP indicates commercial particulate tape media as a reference with coercivity of 214 kA/m and 0.5 Gb/in^2 areal density. SNR values for sample L and H are almost same in all densities, and over 8 dB higher from that of MP as well. PW50s, a pulse width of an isolated signal, for MP, sample L, and H were measured 361, 236, and 235 nm,respectively. Shorter PW50s than that of MP by 125 nm indicate resolution of sputtered tape by FTS on moving base film is better than that of particulate media. From these comparisons on playback performance and microstructure of sputtered tape media by FTS on moving substrate at slow and high moving speed, it is suggested that FTS process is suitable for efficient mass production of granular media.

In addition, we have successfully achieved deposition even on moving PEN and PET film, which are less thermally-resistant than Aramid, thanks to damage-free sputtering by FTS.

Conclusion

Moving speed of plastic substrate didn't affect on microstructure and playback performance of nanometer-sized granular media made by FTS. These results show that FTS process has great capability for mass-production of sputtered tape media with high throughput.

Acknowledgements:
Part of this work has been supported by a fund of "Collaborative Development of Innovative Seeds, Potentiality Verification Stage" of the Japan Science Technology Agency (JST).

[1] S. Akiyama, Y. Furuto, S. Nakagawa, and M. Naoe, *J. Appl. Phys.,* Vol. 67, pp. 5181-5183, 1990.

[2] S. Matsunuma, T. Inoue, T. Doi, T. Matsuu, A. Hashimoto, H. Fujita, and S. Nakagawa, *Digests of PMRC 2007,* pp. 84-85, 2007.

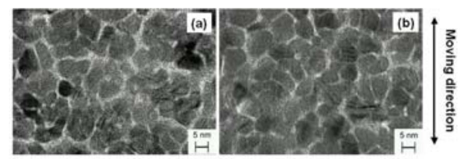

Fig. 1 In-plane TEM images. (a) Sample H, (b) Sample L.

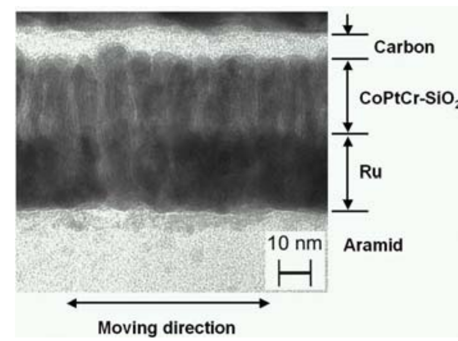

Fig. 2 Cross-sectional TEM image of sample H.

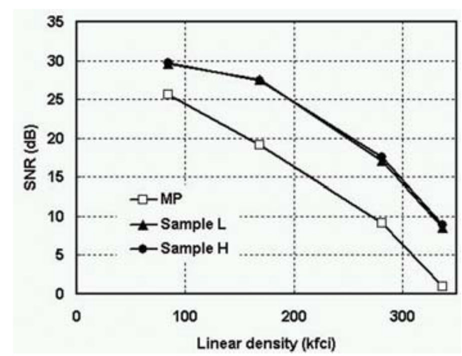

Fig. 3 SNR dependence on linear recording density.

AP-05

A possibility of >15Gbit/in2 recording density system with fine MP tape and GMR head.

N. Sekiguchi, M. Terakawa, T. Akasaka, T. Fukuda, Y. Kamoshita, H. Ohnuma, K. Maeshima, M. Yamaga
CDG, SONY, Tagajo, Japan

Abstract
The possibility of realizing the linear magnetic recording system over 15Gbit/in2 recording density has shown in our test with our newly developed MP (metal particulate) tape using 35 nm size fine metal particles and GMR head for HDD (hard disk drive).

Introduction
In order to obtain a high recording density, advanced magnetic recording media for tape systems using GMR head have been investigated. 1) 2) 3) It is necessary to use very low noise media to realize high recording density. For the particulate magnetic recording media, very fine particles, uniform dispersion of the particles and an extremely thin and smooth magnetic layer are required. We have reported a recording density of 3 Gbit/inch2 with MP tape using 45 nm size fine metal particles and GMR head. This paper reports the experimental results of the developed particulate tape using 35 nm size fine metal particles, which shows the capability of more than 15 Gbits/inch2 recording density with a narrow track GMR head.

Measurement & results
An MP tape sample using 35 nm size fine metal particles with the smooth surface and the thin magnetic layer was prepared. Table1 shows the tape structure and the characteristics of this sample. Abrasivity and electronic resistance of this tape were optimized for GMR head application. In order to prevent ESD, we adjusted the electronic resistance of this sample to a few mega ohm/sq. The electromagnetic property of this sample was measured by a drum tester with a MIG write head and a narrow track GMR read head (track width: 0.14 um) for HDD. Table 2 shows the measurement condition and the head property of this test. Under this condition with optimum write current, DSNR (Digital Signal to Noise Ratio) of this MP sample was calculated using eye diagram of the output signal of the pseudo-random pattern at 30MHz data clock.(minimum recording wave length 1T: 0.23 um). The DSNR of this MP sample was 18.7 dB when we used PR4 channel. Fig.1 shows the eye diagram of the test result. No ESD of GMR head were occurred during this test.

According to the test results with the assumption that 18 dB of DSNR meets the system requirement, this MP sample has enough SNR at this test recording density, which is 39.5G physical bit per inch2 (218 kfci and 181 ktpi). Considering that the read track width is narrower (about half) than the track pitch for linear tape systems and the coding efficiency, this test conditions correspond to more than 15 Gbit/inch2 recording density for linear tape systems.

Our newly developed MP tape sample with 35 nm size fine metal particles has the capability for realizing the linear tape system of more than 15 Gbit/inch2 recording density with a narrow track GMR head.

[1] T.Ozue et al.,"11.5-Gb/in2-Recording Using Spin-Valve Heads in Tape Systems",IEEE Trans. Magn.,vol.38,pp.136-140,January 2002. [2] H.Tetsukawa et al.,"Recording Characteristics on Thin Metal Evaporated Media in a Helical-Scan Tape System With a Spin-Valve Head",IEEE Trans. Magn.,vol.38,pp.1910-1912,Sept. 2002. [3] N.Sekiguchi et al.,"Examination of Newly Developed Metal Particle Media for >3Gb/in2 Recording in GMR-based Tape Systems ",IEEE Trans.Magn.,vol.41,pp.3235-3237,Oct. 2005

Mag. layer thickness (nm)	60
Under layer thickness (um)	1.1
Base thickness (um)	6.0
Base type	PET
Back thickness (um)	0.5
Total thickness (um)	7.6
Electric Resistance of mag. Side (ohm/sq)	5.3e+6
Electric Resistance of back side (ohm/sq)	6.3e+4
Magnetic particle size [nm]	35
Surface roughness of Mag side : Ra (nm)	2.1
Coercive force : Hc (kA/m)	215
Mrt value (mA)	11
Squareness : Rs (%)	89

Write head condition	
Head type	MIG
Head track width (um)	20
Head gap length (um)	0.2
Read head condition	
Head type	GMR
Head track width (um)	0.14
Shield to shield gap (um)	0.066
Measurement system	
Test unit	drumtester
H/M relative speed (m/s)	3.5

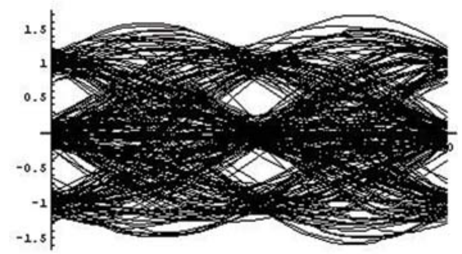

Eye diagram of the new MP media

AP-06

Investigation of thermal de-magnetization effects in data recorded on barium ferrite recording media.

M. L. Watson, T. W. Feebeck, R. A. Beard, S. M. Kientz
Storage Group, Sun Microsystems, Louisville, CO

It is very evident that, to remain competitive with alternative storage technologies, future tape based storage systems must have very significantly increased data rates and cartridge capacities. To achieve single cartridge capacities of many terabytes the volume of the recorded bits must be reduced to less than 10 $x10^6$ nm^3. Realizing viable recording channel signal to noise ratios (SNR) with these bit sizes requires that the number of magnetic particles per bit will have to be at least maintained compared with today's media. This will require particles with dimensions as small as 10 nm – 20 nm (with corresponding particle volumes of 1000 – 3000 nm^3 respectively).

Recording media fabricated using barium ferrite particles has been investigated for a number of years. Very recently advanced media of this composition has been demonstrated to have excellent recording performance with ultra-narrow read widths and at high linear densities [1]. The barium ferrite particles have a diameter of ~ 21 nm and a hexagonal platelet shape and can be manufactured to have a relatively high intrinsic magnetic coercivity due to their high crystalline magnetic anisotropy. However the reduction in particle size could, potentially, affect the archival storage capability of this type of media due to thermal demagnetization [2]. This paper reports the results of experimental studies undertaken to determine if such effects are present in this type of media.

To determine the thermal stability of the media time dependent coercivity measurements were performed, using a standard vibrating sample magnetometer (vsm), and a previously well described technique [3]. Several different media samples were investigated and, due to the inherently low moment of these samples, the vsm measurements were made using a 6.27-mm diameter disk laminated from ten sections of each media sample. Up to 12 different applied fields were used for each measurement and in each case the data could be fitted extremely well using a logarithmic trendline. The estimated time to reduce the magnetic moment to zero and the applied field (H_{cr}) for each data set was then used as an input to the equation [4]

$H_{cr} = H_o \{1 - [(K_uV/k_bT)\ln(fo\ t / \ln(2)]^n\}$

and the values of K_uV/k_bT and H_o were obtained using a Matlab non-linear optimization routine to fit this equation to the data. A typical data set, and the fit to the data, is shown in Fig. 1. From these measurements a value of $K_uV/k_bT \approx 100$ is obtained, indicating acceptable archival thermal stability for this media.

To determine if data recorded in this media is thermally stable, tapes were pre-written with random encoded data at various linear densities. The tapes were then baked alternately at 37 C, 49 C and 59 C for times up to 10^6 seconds and read back after each bake cycle using a nominally 1.0 µm read width GMR read head. The data was captured and processed using a sophisticated recording channel model which performs read equalization, timing recovery and Viterbi channel detection. The model has been found to very effectively replicate actual channels and recording systems and outputs several critical recording channel performance parameters, including the SNR of the sampled and equalized signal at the channel detector (D-SNR). Fig. 2 shows the D-SNR of tracks written at several linear densities immediately after writing and after baking multiple times. As can be seen there is no statistical difference between the two data sets, indicating that this media does indeed have good archival thermal stability. As can also be seen from Fig. 2, the D-SNR is very acceptable indeed (> 17 dB) at linear densities up to at least 360 kbpi, enabling very practicable bit error rates using advanced decoder and ECC systems.

The authors very gratefully acknowledge FUJIFILM Corporation for providing the media samples used in this investigation.

[1] A. Matsumoto, Y. Endo and H. Noguchi, IEEE Trans. Mag. vol. 42, no. 10, pp. 2315 - 2317, Oct. 2006.

[2] D. Weller and A. Moser, IEEE Trans. Mag. vol. 35, no. 6, pp. 4423 - 4439, Nov. 1999.

[3] L. He, D. Wang and W. D. Doyle, IEEE Trans. Mag. vol. 31, no. 6, pp. 2892 - 2894, Nov. 1995.

[4] M. P. Sharrock, IEEE Trans. Mag. vol. 35, no. 6, pp. 4414 - 4422, Nov. 1999.

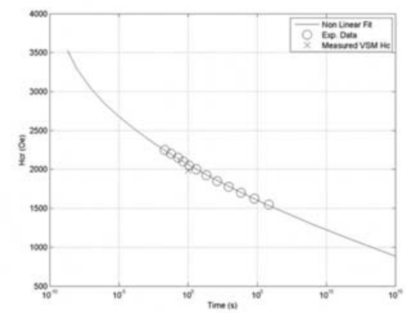

Figure 1. Data showing fit to time dependence data of advanced barium ferrite media assuming n = 0.5. The value of K_uV/k_bT from this fit is ≈100 indicating acceptable thermal stability.

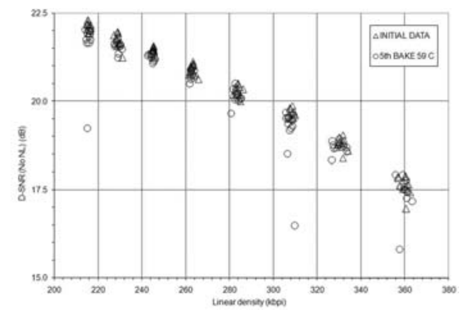

Figure 2. Detector SNR measured immediately after writing and after baking the media five times at 37 C, 49 C and 59 C for up to 10^6 seconds.

AQ-01

Influence of the capping molecule on the magnetic behavior of thiol capped gold nanoparticles.

P. Crespo[1], E. Guerrero[2], M. Muñoz-Márquez[2], A. Hernando[1], A. Fernández[2]
1. Instituto de Magnetismo Aplicado, Universidad Complutense de Madrid, P.O. Box 28230 Las Rozas,Madrid, Spain; 2. Instituto de Ciencia de Materiales de Sevilla, CSIC-US, Av. Américo Vespucio 49, 41092-Sevilla, Spain

Metallic nanoparticles (NPs) have been extensively studied, since they exhibit novel electronic, optical and magnetic properties. In particular, the experimental observation of ferromagnetism in gold NPs (with sizes below 2,5 nm) up to room temperature after appropriate functionalization of the surface is promoting a huge number of studies focused on the mechanisms that could account for ferromagnetic-like behavior. Alkanethiol-capped gold NPs [1] have shown a permanent magnetism which is currently not understood. Recently,
Hernando et al. [2] proposed spin–orbit coupling as the origin of orbital ferromagnetism in these systems.
From the experimental results obtained up to date, it is clear that the apparition of the magnetic behavior, in spite of the diamagnetism exhibited by bulk gold, is closely related with the interaction between the surface of the gold NPs and the protective molecule. In this work, gold nanoparticles (NPs) have been stabilized with a variety of thiol-containing molecules in order to change their chemical and physical properties. It is shown that NPs capped with alkanethiol chains have a marked ferromagnetic behavior which might be also dependent on the chain length. Moreover, the structural and magnetic characterization performed on the polymer-like Au(I) phase, which is formed as a precursor during the synthesis of the thiol-capped gold NPs, clearly indicates that the appearance of a ferromagnetic-like behavior is not only associated with the charge transfer that takes place upon Au-thiol group bonding but also with the formation of a metallic nanostructure, being necessary the simultaneous coexistence of Au-Au and Au-S bonds[3].
Moreover, as will be shown in this work, the geometry of the molecule also plays an important role on the magnetic behavior. Besides using alkane chains with different lengths as capping agents, gold nanoparticles stabilized with a thiol-containing biomolecule (tiopronin) have been also synthesized. While alkane chains are linear molecules and have a high tendency for self assembly, tiopronin molecules exhibit non-linear geometry. In both cases, the organic molecules are linked to the sulphur atom that bonds to the nanoparticle surface. X-ray absorption spectra (XAS) studies, magnetic characterization and surface plasmon resonance studies have been carried out for these two types of thiol-capped gold nanoparticles (NPs) which have similar size. In addition, Au NPs capped with tetraoctyl ammonium bromide have also been included in the investigation since such capping molecules weakly interact with the gold surface: this system will be used as a model for standalone-Au NP.
Regarding the magnetization, dodecanethiol-capped NPs have a ferromagnetic-like behavior, while the NPs capped with tiopronin exhibit a paramagnetic behavior and tetralkylammonium-protected NPs are diamagnetic (as correspond to bulk gold) across the studied temperature, see figure 1. These differences indicate that the modification of the surface electronic structure of the Au NPs depends on the geometry and the self-assembling capabilities of the capping molecules. Moreover, the lack of self assembling capabilities could avoid the appareance of orbital momenta in the conduction electrons of the nanoparticle, this mechanism has been proposed, along with high values of spin-orbit at gold surfaces, as to be responsible for the high local anisotropy field that blocks the magnetic moment.

In addition to the magnetic behaviour, regarding the plasmon resonance, it can be said that it is non-existent for tiopronin-capped NPs, whereas a trace of such a feature is observed for NPs covered with dodecanethiol molecules and, a bulk-like feature is measured for NPs capped with tetralkylammonium salts. These results are additional data which indicate that optical, electrical and magnetic properties of gold nanoparticles are related to several factors including charge transfer, geometry of the capping molecule and, in general, size and surface structure effects.

[1] P. Crespo, et al. Phys. Rev. Lett. 93 087204 (2004)

[2] A. Hernando et al. Phys. Rev. B 74 052403 (2006)

[3] E. Guerrero et al, Acta Materialia 55 1723, (2007)

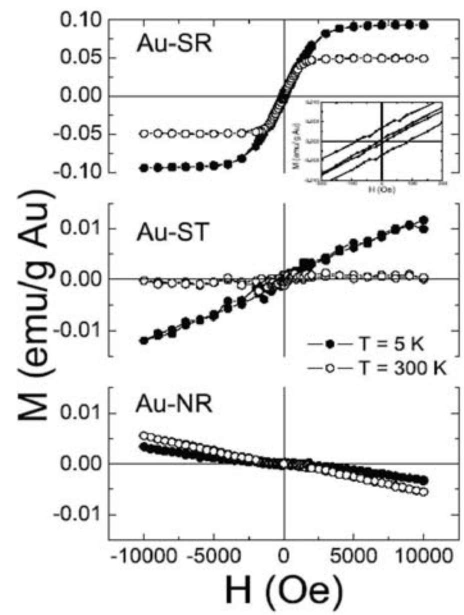

Figure 1: Magnetization curves for Au-SR (dodecanethiol); Au-ST (tiopronine) and Au-NR (tetraoctyl ammonium boride) samples

AQ-02

XMCD study of thiol capped Au nanoparticles.

V. Bouzas[1], *M. Garcia*[1], P. Andrea[4], D. Haskel[2], G. Ruggeri[4], C. de Julian Fernandez[3]
1. Dpt. Materials Science, University Complutense, MAdrid, Spain; 2. Advanced Photon source, Argonne National Laboratory, Argonne, IL; 3. Molecular Magnetism Laboratory, University of Florence, Florence, Italy; 4. Dpt. of Chemistry and Industrial Chemistry, University of Pisa, Pisa, Italy

It is well known that the physical properties of the materials are modified when the size is reduced to the nanoscale. An example of this nanoscale induced magnetism is the appearance of ferromagnetic-like behaviour in thiol capped Au nanoparticles (NPs) [1]. The bond between the sulphur atoms at the end of the thiol chain and the Au atoms at the NPs surface induces a charge transfer (as measured by XANES) from the Au to the S atom [2]. This transfer creates an open 5d electronic configuration in the surface of Au NPs needed for magnetism. While the effect has been reproduced in different samples and by different groups independently, the origin of this magnetism is still under discussion. XMCD can be a key tool to elucidate the origin of this magnetism due to its unique features as element sensitivity, the possibility to determine the orbital holding the magnetic moment and to separate orbital and spin contribution to the magnetization. The aim of this work is to study the origin of the magnetic ordering in thiol capped Au NPs by XMCD measurements.

Dodecanethiol-capped Au NPs were prepared as described in the literature following the bottom-up approach [3]. Briefly, polymeric Au nanocomposites were prepared by casting a solution of 4 wt. % of Au NPs and ultra high molecular weight polyethylene (UHMWPE) in p-xylene at 125 C, and recovering the film after solvent evaporation at room temperature.

Bright-field transmission electron microscopy (TEM) shows mostly spherical shaped particles with a mean size of about 3-4 nm (Figure 1). Au NPs are well dispersed inside the polymer matrix thanks to the dodecanethiol protecting layer that prevented particle aggregation during film preparation at high temperature.

SQUID measurements previously reported [4] showed that the sample exhibit a diamagnetic behavior with a ferromagnetic-like contribution. This ferromagnetic-like contribution is thermally independent in the 5-300 K range, and has a saturation value of 0.05 emu/g(Au), being saturated for a 0.5 T field.

XANES and XMCD measurements were performed at the L3 edge of Au. Figure 2 presents the results after 66 scans (33 with field H=+4T and other 33 with H=-4T, measured reversing the field each 3 spectra). Since field-reversal is equivalent to helicity switching measurements with opposite field direction can be combined to remove any spurious signal of non-magnetic origin. No XMCD signal was found in the sample, with resolution of 5×10^{-5}. Therefore if the XMCD signal exists, its value is below this limit.

Previous XMCD experiments on Co/Au multilayers [5] and Au NPs protected with polyallil amine hydrochloride [6] shown a ratio 0.23 XMCD/(emu/gAu) between the SQUID and XMCD signals. In our samples the MS value (0.06 emu/gAu) correspond to 2.11×10^{-3} μ_B/atom Au. Based on the ratios from the previously mentioned works, if this magnetization were localized in the 5d orbital of the Au atoms, the XMCD signal should be 4.7×10^{-4}, about one order of magnitude larger than the sensitivity of our experiment. Therefore, our results demonstrate that the magnetization of thiol capped Au NPs is not fully localized in the 5d orbital of Au atoms.

[1] P. Crespo,et al Phys. Rev. Lett., 93 (2004) 087204.

[2] P. Zhang, T. K. Sham, Phys. Rev. Lett. 90 (2003) 245502.

[3] A. Pucci, et al J. Mater. Chem. 14 (2004) 3495

[4] J. de la Venta, et al Adv.Mat. 19 (2007) 875.

[5] F. Wilhelm, et al Phys. Rev. B 69 (2004), 220404(R)

[6] Y. Yamamoto, et al, Phys. Rev. Lett. 93, 116801 (2004)

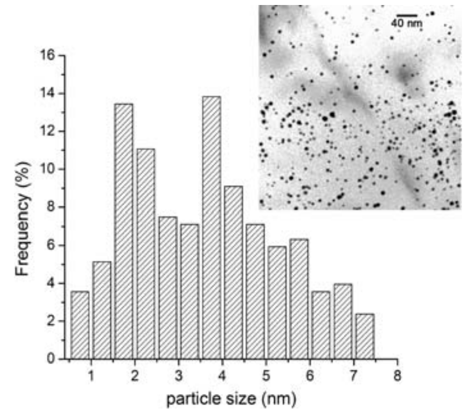

Figure 1. Bright-field transmission electron micrograph (a) and particle size distribution (b) of 4wt% Au NPs-PE film.

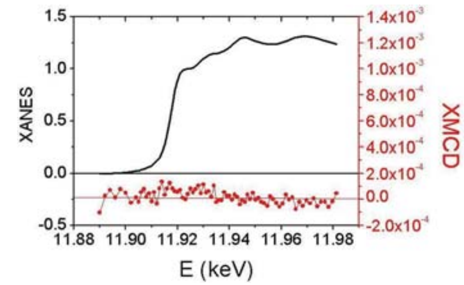

Figure 2. XANES and XMCD spectra for the thiol capped Au NPs embedded in the polyethylene matrix

AQ-03

Local structure, optical and magnetic studies of Ni nanostructures embedded in SiO_2 matrix by ion implantation.

S. K. Sharma[1], R. Kumar[2], M. Knobel[3], P. Kumar[4], P. Thakur[5], K. H. Chae[6], W. K. Choi[7], D. Kanjilal[8], R. Kumar[9]

1. DFMC, Unicamp, Campinas, Brazil; 2. Materials Science Division, IUAC, New Delhi, India; 3. DFMC, Unicamp, SP, Brazil; 4. Materials Science Division, IUAC, New Delhi, India; 5. Materials Science and Technology Research Division, KIST, Cheongrang, Seoul, South Korea; 6. Materials Science and Technology Research Division, KIST, Cheongrang, Seoul, South Korea; 7. Thin Film Materials Research Center, KIST, Cheongrang, Seoul, South Korea; 8. Materials Science Division, IUAC, New Delhi, India; 9. Physics, Ch. Charan Singh University, Meerut, India

The present work reports the formation of Ni nanostructures, their growth and saturation to form oxides by using ion implantation and subsequent thermal treatment in air at 600°C. Quartz (SiO_2) matrix was implanted with 100 keV Ni^+ ion beams to doses in the range 5×10^{15}-2×10^{17} ions/cm^2. The formation of Ni nanoclusters were observed by high resolution X-ray diffraction (HRXRD), UV-visible optical spectroscopy, dc magnetization, AFM/MFM and X-ray absorption spectroscopy (XAS). The cluster size distribution is narrow with an average size of ~25 ± 0.5 nm for the implanted sample at a dose of 1×10^{16} ions/cm^2, but increases with implantation dose. Optical absorption spectra also show a clear signature of a surface plasmon resonance (SPR) peak at around 388 nm in accordance with the theoretical Mie`s spectra. Temperature dependent zero-field cooled and field-cooled magnetization measurements clearly indicate a superparamagnetic behavior, which is properly analyzed considering the size distribution of the magnetic nanostructures. The results show that the magnetic properties of the nanoparticles can be controlled by the implantation dose. A detailed investigation of the local structure using Ni K-edge XANES/EXAFS suggests that the size of the Ni nanostructures is altered with implantation dose, reaching saturation in the form of oxides/silicates of Ni at a dose of 2×10^{17}ions/cm^2.

In the ZFC curves for 1×10^2ions/cm^2 (Fig.1), a characteristic superparamagnetic (SPM) peak confirms the nanoscale nature of Ni clusters. Also, the separation of ZFC and FC curves at a certain irreversibility T_{IRR} temperature is one of the characteristic features of superparamagnetism (SPM). We have seen that there is a sharp maximum in ZFC magnetization curve at about 18 K, which indicates the mean blocking temperature of the nanoclusters of Ni. However, with further increase in the fluence value the ZFC curves becomes broader. The broadening in the ZFC magnetization peak may be due to various reasons such as (i) broad particle size distribution, (ii) magnetic dipole-dipole interaction and (iii) some oxide formation. However, the reason (iii) can be ruled out as there is no formation of Ni oxide at a dose of 5×10^{16}ions/cm^2 in agreement with the XRD results. We have found that the magnitude of the magnetization also did not vary linearly with the increase of Ni ions in the system, which is less than the calculated value, may be due to the dipole-dipole interaction or some oxide formation (only at dose greater than 5×10^{16}ions/cm^2.

In order to understand the local structure of Ni nanostructures, we have performed the near edge X-ray absorption fine structure at O K-edge and Ni $L_{3,2}$-edge of all samples along with NiO nanoparticles. Figure 2 shows the normalized spectra of O K-edge all the samples along with SiO^2 and NiO nanoparticles. NiO nanoparticles show two major structures at 531.58 eV and 537.36eV with broad hump at higher energy range. These two structures may be due to the O 2p weight in states of predominantly Ni 3d character[1-2]. In the case of SiO^2, one structure at 535.42 eV and broad hump at higher energy are observed. In the implanted samples up to the dose value 1×10^{17} ions/cm^2 the O K-edge NEXAFS show spectra that are almost similar to the ones of SiO^2, which indicates that is no oxidation of Ni nanostructure taking place, but at the dose of 2×10^{17}ions/cm^2 the spectrum is well matched with the spectra of NiO nanoparticles. Such results also support our above mentioned results. The results of Ni K-edge suggested that the size of the Ni nanoparticles changes with the dose, reaching saturation in the form of NiO nanoscopic structure at a dose of 2×10^{17}ions/cm^2.

[1]G. Van der Laan, J. Zaanen, G.A. Sawatzky, R. Karnatak, and J.M. Esteva, Phys. Rev. B33, 4253 (1986).

[2] M. Medarde, A. Fontaine, J.L. Garcia-Munoz, J. Rodriguez-Carvajal, M. De Dantis, M. Sacchi, G. Rossi, and P. Lacorre, Phys. Rev. B46, 14975 (1992).

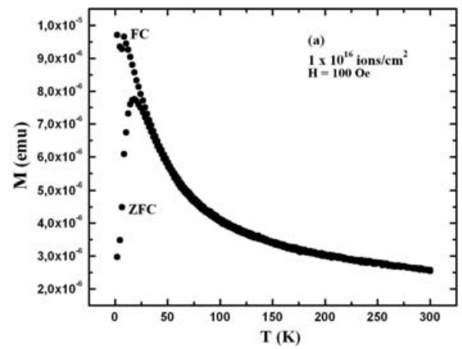

Figure 1 Magnetization versus temperature curves in zero-field-cooled (ZFC) and field-cooled (FC) modes for Ni implanted samples at a dose of 1×10^{16}ions/cm^2.

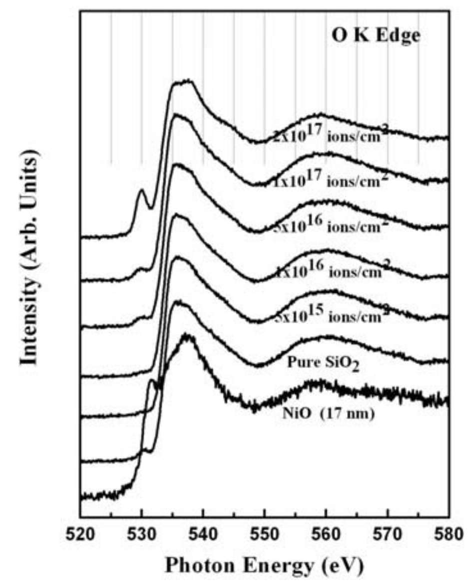

Figure 2. Normalized spectra of O K-edge near X-ray absorption fine structure (NEXAFS) spectra of Ni implanted samples at different doses along with SiO_2 and NiO nanoparticles.

AQ-04

Surface contribution to magnetic anisotropy energy in Fe_3O_4 nanoparticles.

N. Pérez[1,2], P. Guardia[1,2], A. G. Roca[3], M. P. Morales[3], C. J. Serna[3], F. Bartolomé[4], L. M. García[4,5], A. Labarta[1,2], X. Batlle[1,2]

1. Física Fonamental, Universitat de Barcelona, Barcelona, Spain; 2. Institut de Nanociència i Nanotecnologia IN2UB, Universitat de Barcelona, Barcelona, Spain; 3. Instituto de Ciencia de Materiales de Madrid, CSIC, Madrid, Spain; 4. Instituto de Ciencia de Materiales de Aragón, CSIC, Zaragoza, Spain; 5. Física de la Materia Condensada, Universidad de Zaragoza, Zaragoza, Spain

Nowadays, fine magnetic particles [1] are routinely used in many technological applications, such as magnetic recording and non-linear optics, and they are considered promising materials for various biomedical applications. Consequently, the study of their magnetic properties have attracted many efforts along the last decades, in particular because considerable deviations from bulk behavior have been widely reported for particle sizes below about 100 nanometers [3]. In particular, magnetic properties at the particle surface are governed by the breaking of the lattice symmetry associated with several chemical and physical effects leading to a site-specific surface energy, usually taken as a local uniaxial magnetic anisotropy normal to the surface. In the nanometer range of sizes, the contribution of the surface anisotropy to the total effective anisotropy of the particle may be larger than that of the core, which highly increases the characteristic switching time of the particle magnetization as a result of the increase of the effective energy barrier. Here, we study the magnetic anisotropy barrier distribution in a magnetite Fe_3O_4 nanoparticles in a colloidal suspension, in the framework of the $T\ln(t/\tau_0)$ scaling method of the time-dependent thermo-remanent magnetization data. The particles are synthesized by the high-temperature decomposition of an organic Fe precursor in the presence of a surfactant (oleic acid molecules covalently bonded to the NP surface) [2]. Transmission electron microscope images reveal a narrow size distribution with mean diameter $\langle d \rangle = 5$ nm. The Zero Field Cooling–Field Cooling (ZFC–FC) curves at 50 Oe show superparamagnetic behaviour down to ca. 50 K and a maximum in the ZFC curve at 15 K, while the irreversibility between the ZFC and FC curves confirms that our sample is a colloid of non-interacting particles. These two facts make the system suitable for a study on individual particle properties. Thermo-remanence experiments and $T\ln(t/\tau_0)$ scaling enable to obtain the effective distribution of anisotropy energy barriers [4]. We have developed an analytical model to account for the surface contribution to that effective energy barrier distribution. Furthermore, assuming a bulk anisotropy constant for the volume of the particle, $K_V = 1.3\times10^5$ erg/cm^3, we obtain analytically the surface anisotropy constant, $K_S = 2.9\times10^{-2}$ erg/cm^2. Besides, the K_S value obtained applying a Née-type relaxation mode to both the in–phase and out-of-phase components of the ac susceptibility gives is in excellent agreement with the value obtained from the scaling. Summarizing, thermo-remanent magnetization data and the $T\ln(t/\tau_0)$ scaling method enable to analytically account for the surface anisotropy contribution of an ensemble of nanoparticles in a colloidal suspension in absence of interparticle interactions.

The funding from the Spanish MEC (NAN2004-08805-CO4-02, NAN2004-08805-CO4-01, CONSOLIDER CSD2006-12 and MAT2006-03999), and from the Catalan DURSI (2005SGR00969) is acknowledged.

[1] X. Batlle and A. Labarta, 'Finite-size effects in fine particles: magnetic and transport properties', J. Phys D **35**, R15 (2002).

[2] A. G. Roca, M. P. Morales, K. O'Grady and C. J. Serna, 'Structural and magnetic properties of uniform magnetite nanoparticles prepared by high temperature decomposition of organic precursors', *Nanotechnology* **17**, 2783, (2006).

[3] P. Guardia, B. Batlle-Brugal, A.G. Roca, O. Iglesias, M.P. Morales, C.J. Serna, A. Labarta, X. Batlle, 'Surfactant effects in magnetite nanoparticles of controlled size', *J. Magn. Magn. Mat.* **316**, e756–e759, (2007).

[4] O. Iglesias, F. Badia, A. Labarta, Ll. Balcells, '$T\ln(t/\tau_0)$ scaling in small–particle systems: low temperature behaviour',*J. Magn. Magn. Mat.* **140–144**, 399–400, (1995).

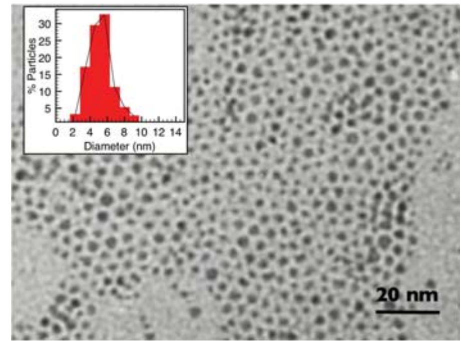

Transmission electron microscope image showing magnetite Fe_3O_4 nanoparticles of 5 nm mean diameter, synthesized by high temperature decomposition of organic precursors, and coated with oleic acid. Inset shows diameter histogram.

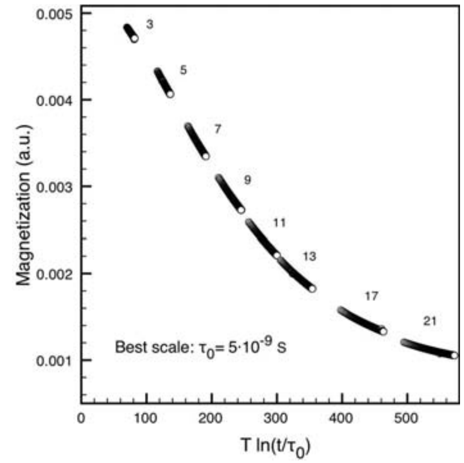

Time dependent thermo-remanent magnetization curves scaled with the $T\ln(t/\tau_0)$ method. Temperature is indicated besides each individual relaxation curve.

AQ-05

Microscopic, structural and magnetic investigation of polymer-encapsulated iron oxide nanoparticles.

A. R. Rodriguez[1], J. H. Coaquira[2], J. G. Santos[1], L. B. Silveira[1], E. M. Marmolejo[1], W. Tennpohl[1], J. P. Sinnecker[3], M. A. Novak[3], D. Rabelo[4], P. C. Morais[2]
1. Physics, Fundação Universidade Federal de Rondônia, Ji-Paraná, Brazil; 2. Physics, Universidade de Brasília, Brasília, Brazil; 3. Physics, Universidade Federal de Rio de Janeiro, Rio de Janeiro, Brazil; 4. Chemistry, Universidade Federal de Goiás, Goiânia, Brazil

Nanotechnology has spurred researcher efforts to design and produce nanoscale materials for incorporation into devices. Magnetic nanocomposites are an important class of functional materials, possessing unique magnetic properties associated to their reduced size (below 100 nm) with potential for use in devices with reduced dimensions. In special, due to high saturation magnetization, high magnetic susceptibility and low toxicity, ferrimagnetic iron oxide nanoparticles are promising candidates for applications as contrast agents in magnetic resonance imaging [1], material platform for DNA extraction [2] and gene and drug delivery [3]. On the other hand, as far as the size and size-dispersity control are concerned, the tendency of isolated magnetic nanostructures to aggregate (which is driven by particle-particle interaction and/or reduction in energy associated to the high surface-to-volume ratio) into bigger clusters during the synthesis process, has represented a critical obstacle. A general approach to overcome this obstacle and tailor particle surface properties for technological applications can be achieved by surface-coating or encapsulation [4]. Magnetic polymer-based spheres (micron-sized and nanosized) have been considered as an important material in the biotechnology industry [5]. In particular, mesoporous polymeric templates could be produced as micron-sized spheres allowing in-situ chemical synthesis of nanosized ferrite particles with adjustable magnetic properties and mass density [6]. The fine-tuning of physical parameters such as the net magnetic moment and composite density can be realized using chemical methods.
In this study, stable and size-controllable magnetite (Fe3O4) nanoparticles were prepared using mesoporous sulfonated styrene-divinylbenzene (Sty-DVB) copolymer as the hosting template. Several cycles (N) of chemical synthesis were used in order to increase the amount of encapsulated iron oxide and in order to tune the magnetic nanoparticle size [7]. The nanoparticle size distribution of the hosted magnetic phase was determined by Transmission (TEM) and Scanning (SEM) Electron Microscopies Figure 1 shows a typical SEM of micron-sized magnetic nanocomposite hosting magnetite nanoparticles. X-ray diffraction (XRD) was used to determine the magnetite phase (see Fig. 2) and also to estimate the particle size.
The magnetic characterization of the samples was carried out using DC and AC magnetic measurements in a broad range of temperatures (4-300K). The estimated effective anisotropy constant (Keff) is slightly above the values reported for bulk magnetite which suggests that the effect of other kind of anisotropy (surface or exchange) has less influence in the magnetic behavior of our magnetite nanoparticles. From DC magnetic isotherms, obtained by applying external magnetic fields up to 5T, it was observed higher coercive fields values for samples obtained with minimal chemical cycles (N). The hyperfine properties of the nanoparticles were investigated by Mössbauer Spectroscopy (MS). 77K and room temperature MS data reveal hyperfine parameters with a strong dependence on the number of chemical cycles (N).

[1] K.A. Hinds, J.M. Hill, E.M. Shapiro, M.O. Laukkanen, A.C. Silva, C.A. Combs, T.R. Varney, R.S. Balaban, A.P. Koretsky, and C.E. Dunbar, Blood 102 (2003) 867.

[2] B. Yoza, M. Matsumoto, and T. Matsunaga, J. Biotech. 94 (2002) 217.

[3] C. Bergemann, D. Müller-Schulte, J. Oster, L.A. Brassard, and A.S. Lübbe, J. Magn. Magn. Mater. 194 (1999) 45.

[4] P.C. Morais, R.B. Azevedo, D. Rabelo, and E.C.D. Lima, Chem. Mater. 15 (2003) 2485.

[5] P.C. Morais, V.K. Garg, A.C. Oliveira, R.B. Azevedo, D. Rabelo, and E.C.D. Lima, Eur. Cells and Mater. 3 (S2) (2002) 173.

[6] D. Rabelo, E.C.D. Lima, A.C. Reis, W.C. Nunes, M.A. Novak and P.C. Morais, Nano Lett. 1 (2001) 105.

[7] S.S. Andrade, D. Rabelo, V.K. Garg, A.C. Oliveira, and P.C. Morais, J. Magn. Magn. Mater. 289 (2005) 25.

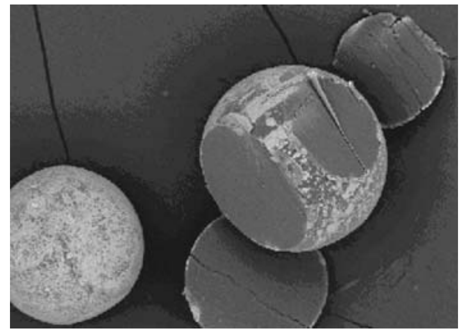

Fig 1: Typical SEM of 200 micron average diameter magnetic nanocomposite hosting magnetite nanoparticle.

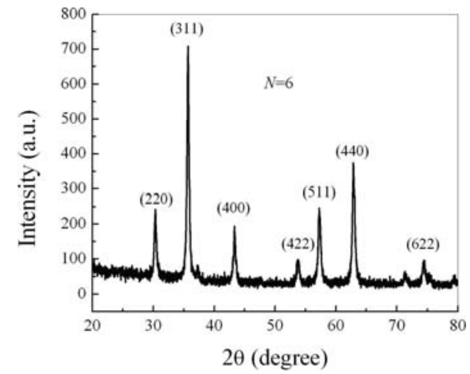

Fig 2: Typical XRD of polymer-hosted magnetite nanoparticle prepared after N=6 and using a 30 mmolar solution of ferrous-iron.

AQ-06

Magnetite Nanoparticles With No Surface Spin Canting.

A. Roca[1], D. Niznansky[2], M. González-Fernández[1], M. Morales[1], C. Serna[1]

1. Instituto de Ciencia de Materiales de Madrid (CSIC), Madrid, Spain; 2. Department of Inorganic Chemistry, Charles University, Prague, Czech Republic

When magnetic nanoparticles sizes cross the multidomain-monodomain limit, surface and finite size effects become more important and cause the appearance of many interesting physical properties [1]. In particular, spin canting at the surface have been observed to take place and to be the responsible for the reduction in saturation magnetisation and the increase in anisotropy and therefore in coercivity of the nanoparticles at low temperature[2].

New methods have been developed recently for the preparation of high quality nanoparticles in terms of size and shape monodispersity and high crystal order. That is the thermal decomposition of iron organic precursors in organic media and in the presence of oleic acid. This method have been used in this work for the preparation of magnetite nanoparticles of 6 nm in diameter and the surface spin canting effect has been analysed by different techniques, including magnetic measurements and Mössbauer spectroscopy at low temperature and in the presence of a magnetic field. Mössbauer is a powerful tool for studying structural, physical and magnetic properties and the best for iron oxide nanoparticles [3]. Magnetite nanoparticles of similar size prepared by coprecipitation and subsequently coated with a thin silica layer to reduce dipolar interactions and prevent from aggregation, have been used for comparison.

TEM images show that iron oxide nanoparticles synthesized by thermal decomposition are more uniform than those prepared from coprecipitation[4]. Magnetic measurements show superparamagnetic behaviour for the three samples at room temperature and higher saturation magnetization for the nanoparticles synthesized by thermal decomposition . Also, it has been shown that these nanoparticles saturate its magnetization at lower applied magnetic field than the coprecipitation ones. At low temperatures, the three samples show ferromagnetic behaviour with the lowest coercivity value for nanoparticles coated by oleic acid. Mössbauer measurements with and without field also reflects that the crystallinity degree is higher for nanoparticles synthesized by thermal decomposition and coated by oleic acid. Moreover, surface spin canting is neglected for these particles probably as a consequence of the oleic acid molecule covalently bond to the surface. The coprecipitation nanoparticles are less crystalline and spin canting exists in both the particles as prepared and those coated with silica.

[1]Battle, X.; Labarta, A., J. Phys. D: Appl. Phys. 2002 35 R15.

[2]Morales, M. P.; Veintemillas-Verdaguer, S.; Montero, M. I.; Serna, C. J.; Roig, A.; Casas, L. I.; Martinez, B.; Sandiumenge, F., Chem. Mater. 1999 11 11 3058.

[3]Murad, E.; Johnston, J. H. "Iron oxides and oxyhydroxides in Mössbauer Spectroscopy Applied to Inorganic Chemistry" 1987 (G.J. Long, ed. Plenum Press, New York-London)

[4]Roca, A. G.; Morales, M. P.; O'Grady, K.; Serna, C. J.; Nanotechnology 2006 17 11 2783.

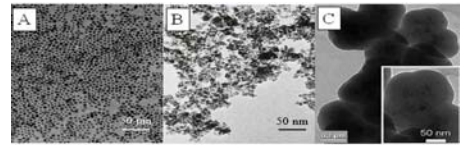

Figure 1: TEM images of a) magnetite nanoparticles coated by oleic acid (MO); b) Magnetite nanoparticles made by coprecipitation (M); c) Magnetite nanoparticles made by coprecipitation and coated by silica (MSi)

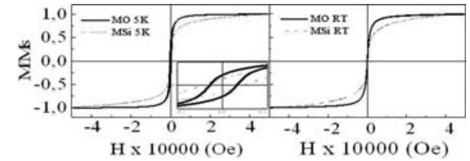

Figure 2: Normalized magnetization curves at 5 K (left side) and at RT (right side) of MO and MSi.

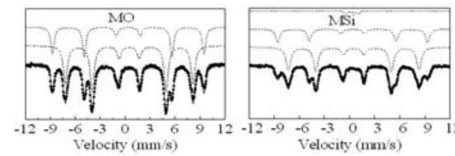

Figure 3: In-field Mössbauer spectra of samples MO (left side) and MSi (right side) at 4 K

AQ-07

Synthesis and characterization of anisotropic magnetic nanoparticles for lab-on-a-bead applications.

N. Kataeva, J. Schotter, H. Brueckl
Nano-System-Technologies, Austrian Research Centers GmbH, Vienna, Austria

Introduction

Traditionally, surface-based transducers are employed as biosensors for biomedical diagnostics. However, issues like limited diffusion and steric hindrance at flat surfaces complicate analyte molecule binding for those sensor designs. In contrast, binding process of analyte molecules to nanoparticles (NPs) immersed within the bulk sample solution are far more effective, but the possibilities to remotely sense those binding events are still quite limited. In order to enable remote sensing, a measurable property of the NPs has to change on the adhesion of analyte molecules. In the case of immunological detection, the two main methods of this kind include relaxation detection of magnetic NPs and sensing of the plasmon resonance peak shift of noble metal NPs. However, both of these methods require detection of rather small signals and are, therefore, limited in sensitivity.

A promising approach to overcome these limitations could be offered by optically detect relaxation processes of NPs. A suitable NP type for this purpose would consist, for example, of an elongated magnetic core and a noble metal shell. Here, the magnetic core allows alignment of the nanoparticle by an external magnetic field, while the spectral separation of the longitudinal and transverse plasmon mode of the noble metal shell allows the optical detection of the orientation of its long axis by measuring the adsorption at those two characteristic plasmon excitation wavelengths in linearly polarized light. Here, we present our progress in fabricating and characterizing such elongated core-shell NPs.

Methods

Monodisperse spindle-shaped iron-oxide NPs are fabricated by forced hydrolysis of ferric chloride solutions. The method consists of precipitating ferric hydroxide from a ferric chloride solution with subsequent addition of hydrochloric acid and phosphate ions and aging at 100°C [1]. The NPs are centrifuged and washed several times with distilled water and ethanol. The surface of the spindle-shaped NPs is functionalized with organosilane molecules (APTMS or MPTMS) by incubation in ethanol solution to generate an amine or sulfide moiety coated surface.

Citrate-capped gold NPs (diameter around 4 nm) are prepared by the reduction of chloroauric acid with sodium borohydride. For adhesion to the iron-oxide spindles, the gold NPs are also modified with MHDA or MPTMS by incubation in ethanol solution.

Finally, the Au-NPs are coupled to the functionalized iron-oxide spindles by the gold-amine or the gold-sulfide interaction by incubation in ethanol solution [2].

Results

The shape of the iron-oxide spindles is characterized by atomic force microscopy (AFM) after spreading the NPs from solution onto a flat mica substrate. They are about 50-70 nm in diameter, while the length varies from 350 to 400 nm (see Fig. 1).

Adsorption spectra of pure and Au-NP coupled iron-oxide spindles are shown in Fig. 2. Here, the Au-NPs are modified by an MPTMS layer in order to enable coupling to the iron-oxide spindles, which causes an increase of the plasmon resonance adsorption maximum to about 560 nm due to the larger refractive index of the MPTMS layer as compared to the pure ethanol solvent. The presence of Au-NPs for the coupled sample can be deduced by the increased absorbance around the plasmon resonance frequency of the Au-NPs. As unbound Au-NPs are easily separated from the spindles by centrifugation, the absorbance spectrum is indicative for successful chemical coupling of the two nanoparticle types.

[1] M. Ozaki, S. Kratohvil, E. Matijevic, J. Colloid Interface Sci. 1984, 102, 146-151

[2] M. Spuch-Calvar, J. Perez-Juste, L.M. Liz-Marzan, J. Coll. Inter. Sci., 2007, 310, 297-301

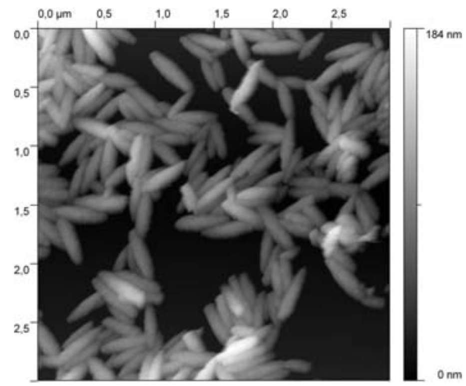

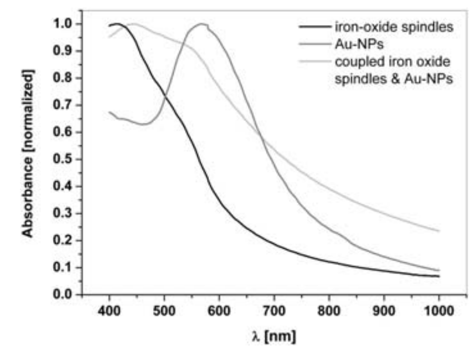

AQ-08

Magnetic Properties of γ-Fe_2O_3 Nanoparticles Precipitated in Alginate Hydrogels.

L. E. Wenger[1], G. M. Tsoi[1], P. P. Vaishnava[2], R. Naik[3], U. Senaratne[3], E. C. Buc[3], V. M. Naik[4]
1. Physics, University of Alabama at Birmingham, Birmingham, AL; 2. Physics, Kettering University, Flint, MI; 3. Physics & Astronomy, Wayne State University, Detroit, MI; 4. Natural Sciences, University of Michigan-Dearborn, Dearborn, MI

A study of the magnetic properties of γ-Fe_2O_3 nanoparticles precipitated inside alginate hydrogels has been undertaken. Alginate hydrogels are polysaccharides composed of α-L-guluronic and β-D-mannuronic acid subunits arranged in homopolymorphic and alternating blocks. When divalent cations such as Ca^{2+} and even trivalent cations are added to an alginate solution, the ions become bound between the guluronic acid subunits of the adjacent alginate chains, and thereby produce the so-called egg box structure and ionic interchain bridges. These bridges then result in the gelation of the aqueous alginate solution. Moreover, since alginate gels are highly biocompatible and hydrophilic, an alginate-based system with bound magnetic ions that are subsequently oxidized to form magnetic nanoparticles may be very suitable for biomedical applications such as drug delivery where an external magnetic field can be used for control and manipulation. Correspondingly magnetic nanoparticles were synthesized by cross-linking sodium alginate with Fe(II) or Fe(III) chloride salts in a methanol-water solution and then were oxidized at room temperature under alkaline conditions during which the Fe ions form γ-Fe_2O_3. The iron oxide alginate gels were subsequently recycled through multiple loadings of the salts followed by the oxidation process to determine the effect on the size and concentration of iron oxide nanoparticles. (See table below.) The average particle size D_{XRD} as determined from powder X-ray diffraction spectra was found to range from 2.3-to-3.3 nm with the larger particles resulting from the Fe(II) starting chloride salts and from the greater number of loadings. As expected the weight percentage of iron oxide also increased with the number of loadings and oxidation processes. Moreover, Mössbauer spectroscopy confirmed that the Fe in the resulting nanoparticles existed only as Fe(III) ions and that γ-Fe_2O_3 was the only phase present regardless of the initial Fe valence state of the chloride salt. The ^{57}Fe Mössbauer spectra at room temperature displayed simple quadruple doublets with isomer shifts of 0.141(4) mm/s and quadruple splittings of 0.690(8) mm/s, values typically associated with the presence of superparamagnetic γ-Fe_2O_3. The values of the saturation magnetization M_{sat} at 5 K were also found to be dependent upon the initial Fe valence state and to a lesser degree on the number of loadings as M_{sat} values of 129-142 emu/cm^3 of Fe_2O_3 were measured for the Fe(II) starting materials and 79 emu/cm^3 of Fe_2O_3 for the Fe(III) materials. In any case, these saturation magnetizations are significantly smaller than the bulk value (408 emu/cm^3) for γ-Fe_2O_3. As expected, the nanoparticles exhibited superparamagnetic behavior with the magnetic moments becoming frozen with decreasing temperature as evidenced by the appearance of a bifurcation in the zero-field-cooled (ZFC) and field-cooled (FC) magnetizations and an opening in the M_V *-vs.-H* hysteresis curves below 40 K. The values of magnetic anisotropy constant (1.0-3.5 x 10^6 ergs/cm^3) determined from the differences between the ZFC and FC magnetizations were found to be significantly higher than the bulk value (1.1 x 10^5 ergs/cm^3) for γ-Fe_2O_3, and are probably due to surface effects. Likewise, the nanoparticle size distributions as deduced from the blocking temperature distribution function $f(T_B)$ based on fits to the differences between the ZFC and FC magnetization curves as well as from fits of the M_V *-vs.-H* curves in the superparamagnetic regime with a Langevin function indicate fairly broad distributions of particle sizes with the corresponding particle sizes D_{TB} and D_{mag} being comparable to those deduced from XRD measurements as shown in the accompanying table. Not surprisingly the broadness of the distributions also increased with the number of loadings. The smaller saturated magnetization values found for these γ-Fe_2O_3 nanoparticle alginate composites as compared to the bulk saturated magnetization of γ-Fe_2O_3 combined with the non-zero slope of the high-field magnetization M_V *-vs.-H* data suggest that these magnetic nanoparticles have a non-negligible surface layer of non-collinear spins of a few tenths of nanometers surrounding a ferrimagnetically ordered γ-Fe_2O_3 core.

Sample	Wt.% Fe	XRD	ZFC & FC *M/H-vs-T*		M_V*-vs-H*	
		D_{XRD} (nm)	T_{peak} (K)	D_{TB} (nm)	M_{sat} (emu/cm^3) at 5 K	D_{mag} (nm) at 100 K
3rd loaded-Fe(II)	29.7	2.7±0.3	23	3.5±0.70	129	3.5±0.89
6th loaded-Fe(II)	41.2	3.3±0.3	37	4.3±0.68	142	3.9±1.19
3rd loaded-Fe(III)	26.2	2.3±0.3	15	-	79	3.7±0.37
6th loaded-Fe(III)	35.1	2.3±0.3	25	3.0±0.45	79	3.6±0.65

AQ-09

Intermatrix synthesis of magnetic nanocrystals by frontal polymerization and subsequent pyrolysis on iron containing monomer.

E. D. Maciejewska[1], M. Leonowicz[1], A. Pomogailo[2], G. Dzhardimalieva[2]
1. Faculty of Material Science and Engineering, Warsaw University of Technology, Warsaw, Poland; 2. Institute of Chemical Physics RAS, Chernogolovka, Russian Federation

Magnetic nanocrystals stabilized in a matrix attract substantial scientific and technological interest. Individual nanocrystals exhibit unique physical properties resulting from size effects and highly developed surface. Such materials can exhibit either superparamagnetic or ferromagnetic properties. The former can find medical applications in targeted drug delivery therapy and as contrast in NMR body screening, whereas the latter is aimed at high density magnetic recording systems. A significant problem arising in the preparation and application of the nanocrystals is their stabilization. Among the methods ensuring stabilization and conservation of the physicochemical properties is synthesis in a polymer matrix, using frontal polymerisation, which enables conversion of monomer to polymer in localized reaction zone 1970s [1,2].

In the current study the nanocomposites containing either Fe or Fe_3C nanocrystals were prepared by frontal polymerisation of iron containing acrylamide (FeAAm) monomer and subsequent pyrolysis of the polymer. The starting monomer, as well as the product of frontal polymerisation had amorphous structure without any trace of iron crystallites. The pyrolysis was carried out at higher temperatures: 643, 773 and 873 K.

All the pyrolysis products were in a form of coarse, irregular powder particles exhibiting broad size distribution, ranging from 50 to 500 μm. The magnetic nanocrystals were distributed within the volume of the powder particles.

The nanocomposites obtained at different pyrolysis temperatures exhibited different structure and microstructure. The product processed at 643 K was amorphous, which means that the pyrolysis temperatures, necessary for fabrication of nanocrystals, have to substantially exceed those recorded in a DSC during dynamic heating. The materials pyrolysed at 773 K and higher temperatures contained nanocrystals. However, composition of the crystallites depended on the pyrolysis temperature (Fig.1). Pyrolysis at 773 K resulted in formation of elementary iron, whereas higher temperatures produced iron carbide (Fe_3C). Moreover, the crystallite morphology was substantially different. The crystallites were embedded in a carbon matrix. Each crystallite is protected by a shell of several graphite layers.

Mossbauer spectroscopy gave more detailed information on the phase constitution. Analysis of the acrylamide complex as well as the polymer after frontal polymerisation revealed the existence of two paramagnetic phases. The polymerisation changes only the amount of these phases, remaining the other parameters unchanged. After pyrolysis the spectra change dramatically showing the existence of ferromagnetic phases. For the material pyrolysed at 773 K the spectra showed coexistence of α-Fe (86.87%) and the remaining paramagnetic phase (31.19%), which correlates with the XRD data. The analysis of the spectra for the material pyrolysed at 873 K proved a coexistence of Fe_3C (86.87%) and some amount of α-Fe (3.17%). The remaining paramagnetic phases amount to 10.96%.

The polymeric material is paramagnetic. The magnetic properties appear after pyrolysis. The phase constitution of the obtained nanocomposites affects their magnetic properties (Fig. 2). For the nanocomposites containing iron room temperature saturation magnetization and coercivity were 100 emu/g and 15.3 kA/m, respectively. The rather high coercivity, about twice the value measured for Armco iron, suggest that some amount of carbon went into solution with Fe. For the iron carbide containing material the magnetization and coercivity values were 40 emu/g and 48 kA/m, respectively. The loops were closed and symmetrical, and their shape was characteristic of ferromagnetic material. Low temperature magnetic studies confirmed that the materials did not show superparamagnetic behaviour.

Concluding, iron or iron carbide nanocrystals can be processed by frontal polymerisation of acrylamide iron nitrate complex, followed by pyrolysis. Application of this procedure forms nanocrystals, stabilizes the nanostructure and enables processing of nanocrystals within a narrow window of sizes.

Composition of the nanocrystals, their size, morphology and magnetic properties can be tailored by pyrolysis temperature.

In this study iron (10 nm) and iron carbide (10-80 nm) nanocrystals were produced. The material exhibits ferromagnetic properties.

[1] E.I. Maksimov, Dokl. Akad. Nauk SSSR 191 (1970) 1091.

[2] N.M. Chechilo, R.Ya. Khvilitskij and N.S. Enikolopyan, Dokl. Akad. Nauk SSSR 204 (1972) 1180.

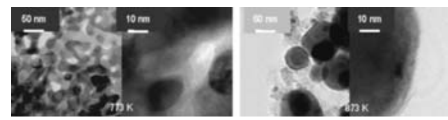

Figure 1. TEM microstructures of the material pyrolysed at temperatures: 773 and 873 K, for 150 min.

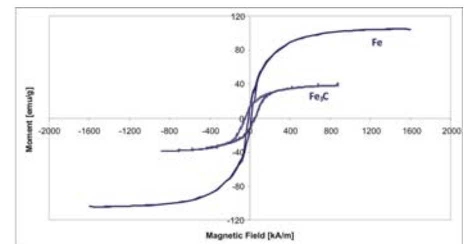

Figure 2. Room temperature hysteresis loops for materials pyrolysed at 773 (Fe) and 873 K (Fe_3C).

AQ-10

Synthesis of L10 (FePt)1-xAux Nanoparticle Monolayer on Polyimide Substrate.

J. Kim, R. Kim, N. Oh, H. An, C. Yoon, Y. Kim, C. Kim
Materials Science and Engineering, Hanyang University, Seoul, South Korea

L10 FePt nanoparticles are often considered for future high density magnetic recording medium because of the large coercivity resulting from the high magnetocrystalline anisotropy [1]. In fabricating the FePt nanoparticles, wet chemical methods, in general, produce superior quality nanoparticles in terms of size distribution and composition. Chemical methods, however, typically involve organic surfactants to drive the self-assembly of prefabricated nanoparticles so that monolayer configuration cannot be easily achieved on a large scale. In present study, we demonstrate that monolayer of ordered L10 FePt nanoparticles can be produced on a polyimide (PI) film for possible applications in flexible magnetic data storage. In addition, we show that the size distribution of the nanoparticles can be further improved by alloying the nanoparticles with Au.

In order to synthesize (FePt)1-xAux nanoparticles on a PI film, the PI precursor (p-phenylene biphenyltetracarboximide type polyamic acid) dissolved in N-methyl-2-pyrrolidinone was spin-coated on a Si substrate. The PI precursor was imidized at 400 °C for 1 hour under vacuum to produce 40-nm-thick PI film. A thin layer (0.2 – 0.8 nm thick) of Au was deposited by thermal evaporator on the PI film. On top of the Au layer, 3.2-nm-thick Fe-Pt layer was deposited using dc magnetron sputtering. To form the L10 structure, the deposited film stack was annealed in vacuum (10-3 Pa) at 800 °C for 1 hour. Initial and post-annealed compositions were verified using energy-dispersive x-ray spectroscopy.

Transmission electron microscopy (TEM) image of the Fe52Pt48 nanoparticles without Au is shown in Fig. 1(a). In order to obtain nearly equi-atomic ratio of Fe and Pt, the initial composition of the Fe-Pt film was deliberately enriched in Fe to compensate for the preferential etching of Fe by the PI film during annealing. Discussion on the nanoparticle formation mechanism was detailed elsewhere [2]. The average particles size for the Fe52Pt48 nanoparticles was 5.1 ± 1.8 nm. Introduction of the Au into the FePt particles as seen in Fig. 1(b) drastically changed the particle morphology as well as the particle density. While the average particle size for (FePt)91Au9 decreased to 3.8 ± 1.1 nm, the size distribution became considerably tighter. The size distribution curves in Fig. 1(c) clearly illustrate improved particle size distribution incurred by alloying the FePt particles with Au. Moreover, the particle number density increased from 4 x 109 particles/mm2 to 1 x 1010 particles/mm2 with Au. The inset in Fig. 1(b) verifies that the particles were formed in a monolayer. It was previously shown that Au deposited on the PI film formed finely dispersed nanoparticles due to the minimal wettability of Au on the polymer film [3]. It is conjectured that the Fe-Pt film tended to heterogeneously nucleate and grow on the preexisting Au nanoparticles, resulting in improved particle size distribution.

Electron diffraction patterns in Fig. 2 demonstrate that both Fe52Pt48 and (FePt)91Au9 nanoparticles were converted from the as-deposited fcc structure to the ordered face-centered tetragonal structure by annealing at 800°C. Lattice parameters estimated from the diffraction patterns were a = 0.39 nm and c = 0.38 nm, closely matching the literature values. Figure 2(b) also indicates that the (FePt)91Au9 nanoparticles formed single-phased solid-solution. Au at 27 at. %, however, led to additional peaks corresponding to metallic Au. The result agrees with the report by Hono and co-worker who estimated the solubility limit of Au in FePt to be around 20 at. % [4].

We demonstrated that monolayer of well-dispersed FePt nanoparticles, potential candidate for high-density magnetic date storage medium, can be formed on a polymer film by physical deposition. It was also shown that particle density and size distribution can be substantially improved by alloying the magnetic nanoparticles with Au.

This work was supported by Grant No. 04K1501-01210 from the Center for Nanostructured Materials Technology under the “21st Century Frontier R&D Programs” of the Ministry of Science and Technology, Korea.

[1] J. A. Christodoulides, Y. Huang, Y. Zhang, G. C. Hadjipanayis, I. Panagiotopoulos, and D. Niarchos, J. Appl. Phys. 87, 6938 (2000).

[2] S. K. Lim, C. S. Yoon, C. K. Kim, and Y.- H. Kim, J. Phys. Chem. B 108, 18179 (2004).

[3] J. H. Kim, J. Kim, N. Oh, Y-H. Kim, C. K. Kim, C. S. Yoon, Sungho Jin, Appl. Phys. Lett. 90, 023117 (2007).

[4] C. Y. Yoo, Y. K. Takahashi, and K. Hono, J. Appl. Phys. 100, 056105 (2006).

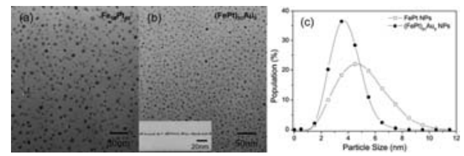

Figure 1. TEM image of the nanoparticles produced from Fe52Pt48 and (FePt)91Au9 annealing at 800°C

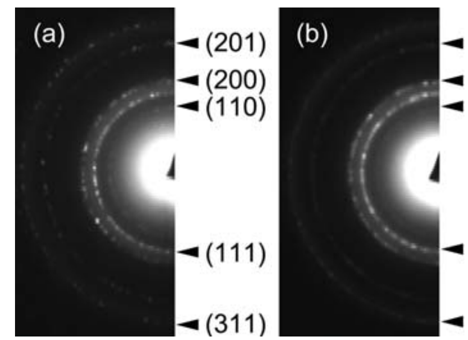

Figure 2. Indexed electron diffraction patterns from :(a) Fe52Pt48 (b) (FePt)91Au9 nanoparticles annealed at 800°C (fct L10 structure)

AQ-11

Co-CoO Nanoparticles Prepared by Reactive Gas Phase Aggregation.

J. A. De Toro, J. P. Andrés, J. A. González, P. S. Normile, T. Muñoz, P. Muñiz, A. J. Barbero, J. M. Riveiro
Departamento de Fisica Aplicada, Universidad de Castilla-La Mancha, Ciudad Real, Spain

The technique of gas phase aggregation [1] has been used to prepare partially oxidized Co nanoparticles by allowing a controlled flow of oxygen gas into the aggregation zone. This method is clearly different from the oxidation in a secondary chamber of a beam of preformed particles [2] The sputtering gas (Ar) pressure was 0.1 mbar. The nanoparticles were deposited on glass substrates positioned perpendicular to the beam in a secondary chamber. Preliminary transmission electron microscopy characterization shows that the mean size of the particles is about 5 nm. Two series of samples (thin films), corresponding to two different high-purity Co cathodes, were prepared as a function of oxygen pressure (P_{ox}) in the aggregation chamber. Figure 1 shows the saturation magnetization of the two series (black and red data points) normalized by the amount of deposited material. It exhibits the expected decreasing trend with increasing oxygen pressure. In fact, this synthesis technique may be used to prepare pure fcc CoO nanoparticles by employing adequately selected oxygen pressures, as it points out the absence of any other crystallographic phases in the x-ray diffraction pattern of the sample prepared with Pox=3.3x10^{-3} mbar (series B).

The magnetic behaviour of the samples was characterized measuring hysteresis loops and the thermal dependence of the magnetization (at 100 Oe) after conventional field (FC) and zero-field cooling (ZFC) protocols. For samples prepared under a sufficiently high oxygen pressure, the room temperature magnetic response showed neglectable coercivity and high saturation fields, suggesting superparamagnetism. (Note that the reference sample grown without oxygen did not show such behaviour, i.e., the strong direct exchange and dipolar interactions between the touching particles stabilizes them in the case of essentially pure Co nanoparticles [3]). As an example, Fig. 2 shows the FC and ZFC magnetization curves measured in the sample marked with a blue arrow in Fig. 1 (P_{ox} = 10^{-3} mbar). The curves show that the sample is certainly superparamagnetic at room temperature, with a blocking temperature of about 240 K. The room temperature instability of our partially oxidized particles can be explained by two factors: (i) the reduction of the magnetic moment (or ferromagnetic particle size), and, probably more importantly, (ii) the inhibition of direct exchange coupling between oxide-surrounded ferromagnetic regions. The question of whether the morphology of the partially oxidized particles is core-shell-like or a more disordered one remains to be investigated.

There is also another characteristic temperature, signalled with the symbol T_O, in the ZFC curve shown in Fig. 2. The magnetization is constant up to this temperature, but increases rapidly above it. This feature is interpreted as stemming from the disappearance of an anisotropic exchange coupling between the Co and CoO phases, which would pin the moment of the Co regions in their originally frozen directions [4], i.e., T_O is the exchange-bias onset temperature. In fact, a large shift was observed in the hsyteresis loop measured at 80 K after cooling in a field of 10 kOe. An account of the exchange-bias properties of the samples will be given elsewhere.

In short, a method to synthesize metal-oxide composite films with properties controlled at the nanoscopic level is proposed: reactive gas phase aggregation. It may also prove to be useful in the synthesis of pure CoO nanoparticles.

1. C. Binns, K. N. Trohidou et al., J. Phys. D: Appl. Phys. 38, R357 (2005).

2. V. Skumryev, S. Stoyanov et al., Nature 423, 850 (2003).

3. C. Binns, M. J. Maher, New J. Phys. 4, Art. No. 85 (2002).

4. P. S. Normile, J. A. De Toro et al., Phys. Rev. B 76, 104430 (2007).

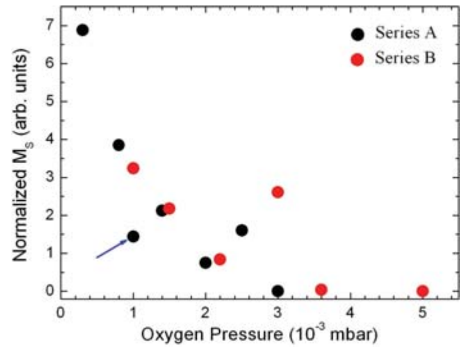

Fig. 1. **Saturation magnetization of the nanoparticle films as a function of the oxygen pressure in the aggregation zone.**

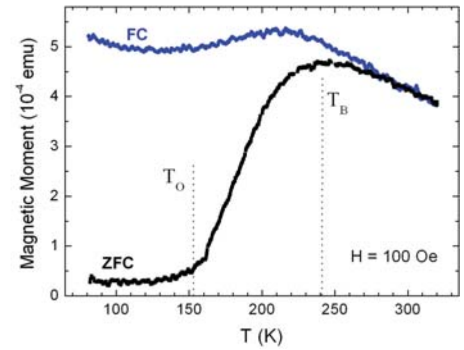

Fig. 2. **Field-cooled (FC) and zero-field cooled magnetization curves measured for a film of partially oxidized nanoparticles (sample marked with a blue arrow in Fig. 1).**

AQ-12

Magnetism of ε-Fe_2O_3 nanoparticles modified by Al and Ga substitution.

J. Poltierova Vejpravova[1], P. Brazda[2], D. Niznansky[2], S. Danis[1], S. Burianova[1], V. Sechovsky[1]
1. Faculty of Mathematics and Physics, DCMP, Charles University Prague, Prague 2, Czech Republic; 2. Faculty of Science, DIC, Charles University Prague, Prague 2, Czech Republic

A metastable ε-Fe_2O_3 phase attracts much attention owing to enormous room-temperature coercivity, H_c (up to 2 T in some reports)[1]. In spite of investigations by in-field Mössbauer spectroscopy [2] and neutron diffraction [3], the real microscopic mechanism leading to the huge coercivity observed is still unclear. So far, effects of the shape of nanoparticles or their possible core-shell structure yielding additional magnetic exchange interactions in the interface were not much considered [4]. In order to inspect the effect of substitutions on the ε-phase stability, and modifications of the magnetic properties, a series of samples doped by Al and Ga was prepared. Magnetic properties of the obtained materials were studied by magnetization measurements in the temperature range 2- 1000 K and magnetic in fields up to 14 T.
The ε- $X_{1/2}Fe_{3/2}O_3$, X = Al or Ga samples were fabricated using a technique based on the solid-state synthesis developed by Hutlova [5] (for details, please see [6,7]). In the first step, we obtained a composite of the $X_{1/2}Fe_{3/2}O_3$ nanoparticles embedded in an amorphous SiO_2 matrix. The composite powders were annealed at 1000°C for 9, 10 and 15 hours, respectively, in order to study the effect of the heat treatment time on the particle size and phase composition. The silica matrix was subsequently removed by a leaching procedure [3]. Final products (both the composites and the isolated nanoparticles) were characterized using powder X-ray diffraction (XRD), Mössbauer spectroscopy, and high-resolution transmission electron microscopy (HRTEM).
The characterization procedure confirmed single-phase materials (no sign of presence of hematite or maghemite phases). The Al and Ga atoms, respectively, substitute the Fe atoms preferably as revealed by Mössbauer spectra analysis and XRD pattern refinements. Magnetic properties of the substituted materials differ significantly from the binary ε-Fe_2O_3 phase. The low-field temperature dependence of zero-field cooled (ZFC) and field-cooled (FC) magnetization, respectively, measured in the temperature range 2 – 350 K show a furcation at the highest-reached temperature (350 K) for the Al- and Ga- substituted samples, in contrast to the pure ε-Fe_2O_3 (as demonstrated for the Al sample in the Figure 1, left panel). The series of order-to-order magnetic phase transitions exhibited by the pure ε-Fe_2O_3 in the 80 – 150 K range lacks; only a broad decay below ~ 100 K may be attributed to the relics of the ε-Fe_2O_3 magnetism. The high-temperature magnetization measurements revealed a shift of the para-to-ferrimagnetic magnetic phase transition in the pure ε-phase (480 K) to lower temperatures for the Al- and Ga- substituted samples (Figure 1, right panel). The evolution of the coercivity with temperature deviates significantly from the trend observed for the the ε-phase; the transition from the large coercivity state to the magnetically soft state below 100 K was not observed. In contrast both the Al and Ga substituted samples show continuous decrease of the coercive field with increasing temperature. The observed decrease of the absolute value of the coercivity at room temperature (typical hysteresis loops of two composites are shown in Figure 2) can not be directly attributed to the substitution effects [4], however, we may conclude, that the Al and Ga insertion on the Fe sites causes a dramatic change of magnetic properties keeping the same crystal structure.

<p>

[1] J. Jin et al, J. Magn. Magn. Mater.: vol 15, p. 1067, 2005.

[2] E. Tronc et al, J. Appl. Phys.: vol. 98, p.053901, 2005.

[3] M. Gich et al, Chemistry of Materials: vol. 18, p. 3889, 2006.

[4] J. Poltierova Vejpravova et al, submitted to Phys. Rev. B.

[5] A. Hutlova, Doctotal Thesis, Universite de Strasbourg, 2003.

[6] P. Brazda, Diploma Thesis, Charles University Prague, 2005.

[7] P. Brazda, unpublished.

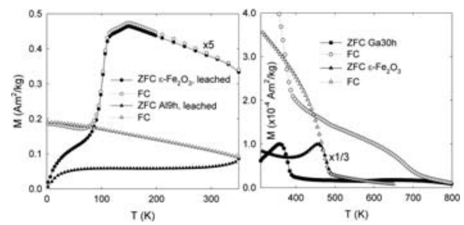

Figure 1: Temperature dependencies of the zero-field cooled and field cooled magnetization (measured at 5 mT). Left panel: comparison of the leached ε-Fe_2O_3 and ε-$Al_{1/2}Fe_{3/2}O_3$ in temperatures 2 - 350 K. Right panel:comparison of the composites ε-Fe_2O_3 and ε-$Gal_{1/2}Fe_{3/2}O_3$ in temperatures above 310 K.

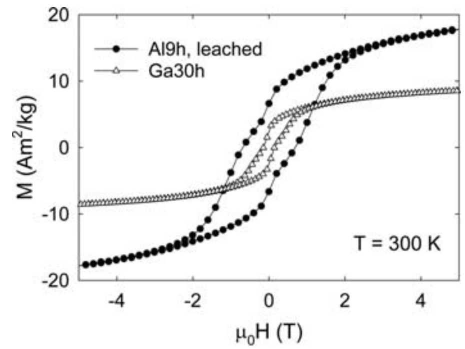

Figure 2: Room-temperature hysteresis loops of the silica composites: ε-$Ga_{1/2}Fe_{3/2}O_3$ annealed for 30 hours and the ε-$Al_{1/2}Fe_{3/2}O_3$ annealed for 9 hours, respectively.

AQ-13

The first ternary intermetallic Heusler nanoparticles: Co2FeGa.

L. Basit[1], A. Yella[1], S. A. Nepijko[2], V. Ksenofontov[1], G. H. Fecher[1], W. Tremel[1], C. Felser[1]
1. Chemistry, Inst. for Inorganic & Analytical Chemistry, Mainz, Germany; 2. Physics, Institute of Physics, Johannes Gutenberg - University, Mainz, Germany

Synthesis of materials with controlled particle size in nanometer regime is an active area in the field of materials research. With the control over particle size the electronic and magnetic properties of material can be tuned. To study the effect of nanometer dimensions on the properties of Heusler alloys, a first example of Co2FeGa Nano-Heusler is presented. So far only few publications have appeared [1,2] and some alternative strategies are in preparation [3,4]. Since Heusler compounds have a similar potential as Perowskite, this achievement becomes even more sparkling. We have manufactured the targeted monodisperse nanoparticles of Co2FeGa with size between 5 and 20 nm. Adjusting accurate stoichiometry is important for the properties of these compounds, which in case of Co2FeGa nanoparticeles was determined with EDX and EXAFS and the exact structure was determined by appropriate superstructure reflexes. Beside the HRTEM investigations, XRD (for cobalt and iron k-edges), NMR, Moessbauer spectroscopy, XMCD investigations were accomplished. The 111 and 200 superstructure reflexes of the L21 structure refers to a high order of the nanoparticles of 16-20 nm. Figure 1 shows the HRTEM images of a Co2FeGa Heusler nanoparticle.The nanoparticles of 20 nm show the moment expected from the Slater Pauling and a high curie temperature. The moment of 5μB per formula unit corresponds also to the bulk moment and permits the conclusion that the particles are half metallic ferromagnetic.Moessbauer investigations of 5nm large particles show, in accord with magnetic measurements, superparamagnetism, while larger nanoparticles (20 nm) show ferromagnetism up to high temperatures. The superparamagnetic nanoparticles are of great importance for the biotechnology, since they do not show agglomerate formation below the blocking temperature, if they are separated by appropriate spacer ligands.
First attempts with Co2FeGa show that these can not only be coated with carbon layer as a protection against corrosion but can also be functionalised. Heusler nanoparticles permit therefore most varied applications, far beyond the well-known applications of CoFe and FePt.
Somewhat larger nanoparticles are suitable because of their magnetic characteristics for the data storage and as halfmetallic ferromagnets their employment in spin electronics is of great importance.
In summary, we have synthesized and characterized Co2FeGa Heusler nanoparticles of different sizes. The synthesized Co2FeGa Heusler nanoparticles were characterized by HRTEM, XRD and Mossbauer. All peaks of XRD patterns can be attributed to a L21 Heusler structure with the lattice constant a0=0.537 Å. The size of the particles, as determined by transmission electron microscopy, is between 5-20 nm. Ferromagnetic behaviour of the particles as determined by the SQUID is presented and compared with the bulk Co2FeGa Heusler alloy.

[1] Spectroscopic and microscopic study of Vanadium oxide nanotubes, A. Gloskovskii, S.A. Nepijko, G. Schönhense, H.A. Therese, A. Reiber, H.C. Kandpal, G.H. Fecher, C. Felser, W. Tremel, M. Klimenkov J. Appl. Phys. 101 (2007) 084301. [2] Time-of-flight photoelectron spectromicroscopy of single MoS2 nanotubes, A Gloskovskii, S. A. Nepijko, M. Cinchetti, G. Schönhense, G. H. Fecher, H. C. Kandpal, C. Felser, H. A. Therese, N. Zink, W. Tremel and A. Oelsner J Appl. Phys. 100 (2006) 084330.

[3] Structure and magnetic properties of iron-platinum particles with iron oxide shell.

Lubna Basit, Ibrahim Shukoor,Vadim Ksenofontov, Wolfgang Tremel, Gerhard H. Fecher,

Claudia Felser, Sergei A. Nepijko, Gerd Schönhense, and Michael Klimenkov

[4] The first ternary intermetallic Heusler nanoparticles, L. Basit, A. Yella, S.A. Nepijko, M.Klimenkov, V. Ksenofontov, G.H. Fecher, G. Schönhense, W. Tremel and C. Felser in preparation

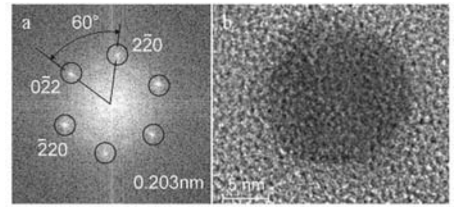

Fig. 1: HRTEM image of Co2FeGa nanoparticles (a) Fourier Transformation and highly resolved image of particle (b).

AQ-14

Giant diamagnetism in AuFe nanoparticles.

J. Wu[1], M. Jung[2], J. Min[3], H. Liu[1,4], J. Cho[3], Y. Kim[3]
1. Institute for Nano Science, Korea University, Seoul 136-713, South Korea; 2. Quantum Materials Research Team, Korea Basic Science Institute, Daejeon 305-333, South Korea; 3. Department of Materials Science and Engineering, Korea University, Seoul 136-713, South Korea; 4. College of Chemistry and Chemical Engineering, Henan University, Kaifeng 475001, China

Introduction

Smart nanoparticles (NPs) of multiple components offer thrilling opportunities in fundamental studies and multidisciplinary-interweaved nanotechnology that has rapidly grown with tremendous success in many areas including medicine, life science, materials science, environment, electronics, and energy [1]. Since metallic alloy NPs have been extensively investigated for various purposes, particularly the integration of magnetic and optical elements in one single entity promises multifunctionality for potential applications, we have prepared magnetic-optical AuFe alloy NPs via a one-pot polyol process [2]. In this work, we report the giant diamagnetism observed in the zero-field cooled (ZFC) curve of the Au0.5Fe0.5 NPs, as great interest is stimulated with shrinking dimension that giant diamagnetism ensues in such nanosystems, which is an omnipresent property of matter screening an external magnetic field by the electrons in the matter [3].

Experiment

The monosized AuFe NPs were synthesized by a polyol process from mixed precursors, gold acetate and iron (III) acetylacetonate. A typical synthesis was carried out in a flask, mixing Au(OOCCH3)3 and Fe(acac)3 in 1:1 in octyl ether with 1,2-hexadecanediol and a surfactant [2]. The reaction mixture was first heated and refluxed at a lower temperature and then rapidly raised to a high temperature to complete the reaction. Ethanol was added to the reacted mixture to precipitate the nanoparticles. The synthesized AuFe NPs were characterized by various tools, including XRD, TEM, UV-Vis, XPS, VSM and SQUID.

Results and Discussion

From the characterization, the fusion of the two elements into one nanostructure entity retains the optical and magnetic properties of the individual components. The XRD and TEM analysis confirms the formation of the alloy nanostructure with a narrow distribution of particle sizes and provides the detailed structural arrangements. Fig. 1(a) shows that the nanoparticles are spherical in shape and indicates that single NPs comprise several distinct sectors, as corroborated by high resolution imaging in Fig. 1(b) that reveals high crystallinity and some disorder. The UV-Vis measurements display an absorption band at ~560 nm and the AuFe nanoparticles can be rendered water soluble after thiolation. The magnetic investigation shows the superparamagnetic behavior of the nanoparticles at room temperature. Fig. 2(a, b) is the M~T curves of the AuFe NPs in the FC and ZFC modes under two different applied fields. Under the field of 100 Oe (Fig. 2(a)), the curves reflect typical behavior of a nanoparticles system. However, magnetic anomaly occurs when the field is 5 Oe. According to Fig. 2(b), the susceptibility in the ZFC curve initially, with decreasing temperature, increases to a maximum at ~175 K, and then reduces to become negative at ~100 K. Below the temperature, the susceptibility continues to progress to a large negative value of -1.5x10^–2 emu/gOe, though the FC curve remains positive over the whole temperature range. Fig. 2(c) sums up the ZFC curves under the fields upwards from 5, 20, 50, 100, 500 to 1000 Oe, respectively. The finding of the giant diamagnetic susceptibility on the order of -10^-2 emu/gOe is fascinating, as a giant negative magnetic susceptibility is associated with superconductors where the paired electrons expel all the external magnetic flux to achieve perfect screening. The mechanism leading to the giant diamagnetism in the AuFe NPs may incorporate the response of spin glass in AuFe systems, mediation by the coexistence of order-disorder in the individual NPs, induced large diamagnetism in nanostructured Au and/or possible superconducting state [3].

[1] A. S. Arico, P. Bruce, B. Scrosati, J.-M. Tarascon, and W. Schalkwijk, Nat. Mater. 4, 366 (2005).

[2] H. L. Liu, J. H. Wu, J. H. Min, Y. K. Kim, J. Appl. Phys., accepted.

[3] A. Hernando, E. Herreo, M. Vazquez, J. Alonso, A. Gonzalez, G. Rivero, J. M. Rojo, M. Vallet-Regi, and J. Gonzalez Calbet, Phys. Rev. B 56, 7800 (1997); A. Hernando, P. Crespo, and M. A. Garcia, Phys. Rev. Lett. 96, 057206 (2006).

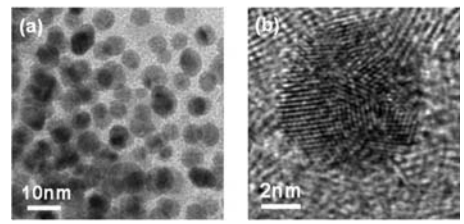

Fig. 1. TEM analysis of the AuFe NPs. (a) TEM image; and (b) high resolution lattices.

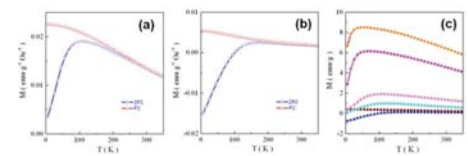

Fig. 2. M~H curves of the AuFe NPs under various applied fields. (a) FC and ZFC curves under the field of 100 Oe; (b) FC and ZFC curves under the field of 5 Oe; and ZFC curves under the fields upwards from 5, 20, 50, 100, 500 to 1000 Oe, respectively.

AQ-15

XMCD studies of core-shell FeRh nanoparticles.

A. Smekhova[1], D. Ciuculescu[2], F. Wilhelm[1], C. Amiens[2], A. Rogalev[1], B. Chaudret[2]
1. European Synchrotron Radiation Facility, Grenoble, France; 2. Laboratoire de Chimie de Coordination du CNRS, Toulouse, France

The nanoparticles (NPS) are the subject of intense research activities in the last decade [1]. Progress in chemistry made it possible to synthesize nanoparticles in the wide range of sizes down to several nanometers [2,3], but at the same time NPS exhibit large varieties of structural and, therefore, of electronic and magnetic properties. So, the further experimental investigations aimed at establishment of a correlation between structure and properties of NPS are highly desirable.
Here, we concentrate our attention at core-shell bimetallic FexRh1-x nanoparticles (x = 50, 80) that could be considered as a good target to explore the relation between the chemical distribution and an order inside NPS and their magnetic properties [4]. FexRh1-x nanoparticles were synthesized by simultaneous decomposition of stoichiometric quantities of Fe[N(Si(CH3)3)2]2 and Rh(C3H5)3 in mild conditions of temperature and hydrogen pressure.
Magnetic properties of FexRh1-x nanoparticles have been studied with X-ray absorption spectroscopy and X-Ray Magnetic Circular Dichroism (XMCD) near the K edge of Fe and the L2,3 edges of Rh. Whereas the former technique is sensitive to the local electronic structure and charge at the absorbing atom, the latter provides unique information about magnetic moments carried by the absorbing atom.
The XMCD measurements reveal different values of the spin and orbital magnetic moments at Rh atoms depending on Fe concentrations and on the way of NPS have been prepared. On the other hand, the magnetic moment at Fe atoms monitored via multielectron excitations and magnetization of the 4p states is found to be nearly the same for all samples. The influence of NPS structure on orbital and spin contributions of magnetic moment at Rh atoms are discussed.

[1] S.Sun, C.B.Murray, D.Weller, L.Folks, A.Moser, Science 287, 1989 (2000)

[2] S.Stappert, B.Rellinghaus, M.Acet, E.F.Wassermann, J.Cryst.Growth 252, 440 (2003)

[3] D.Li, N.Poudyal, V.Nandwana, Z.Jin, K.Elkins, J.P.Liu, J.Appl.Phys. 99, 08E911 (2006)

[4] D. D. Ciuculescu, C.Amiens, M.Respaud, P.Lecante, A.Falqui, B.Chaudret, Modern Phys. Lett. B 21, 1153 (2007)

[5] J. B. Kortright, D. D. Awschalom, J. Stöhr, S. D. Bader et al., JMMM 207, 7 (1999)

AQ-16

Surface-induced magnetic anisotropy of impurities.

A. Szilva[1], L. Szunyogh[1], G. Zarand[1], C. Muñoz[2]
1. Department of Theoretical Physics, Budapest University of Technology and Economics, Budapest, Hungary; 2. Instituto de Ciencia de Materiales de Madrid, Consejo Superior de

Investigaciones Científicas, Madrid, Spain

In order to explain the thickness dependence of the amplitude of the Kondo resistivity in thin films of dilute magnetic alloys [1], the role of the spin-orbit (SO) coupling has been outlined theoretically that in the presence of a surface gives rise to a level splitting of an impurity spin, decreasing thus the freedom for spin-flips needed to obtain a sizable Kondo effect [2]. By using a suitable fit to the measured amplitude of the Kondo resistance, in the case of thin films formed by a dilute *Au(Fe)* alloy Újsághy *et al.* estimated a spin-blocking depth of about 180 Å, where the level splitting should be higher than, or at least comparable to, the energy-scale fixed by the Kondo temperature, T_K = 0.3 K ~ 0.03 meV.
In this contribution we present detailed numerical studies of the magnetic anisotropy energy of an atomic-like impurity near the surface of a metallic host (Au and Cu), the valence band of which is described in terms of a realistic tight-binding surface Green's function technique. Two models are discussed and compared, namely, *(i)* when spin-orbit coupling is taken into account for the *d*-band of the host [2] (HSO model) and *(ii)* when the impurity's *d*-level experiences strong spin-orbit splitting due to Hund's rule coupling [3] (LSO model). The level-splitting of the impurity's spin-states is calculated within Abrikosov's pseudofermion representation using Green's function perturbation technique in leading order of the exchange interaction between the impurity and the host atoms. For large distances, *d*, from the surface an asymptotic analysis implies that in both cases the magnetic anisotropy constant is an oscillating function of *d* with a period determined by the extremal vectors of the host's Fermi Surface and with an amplitude decaying proportional with $1/d^2$.
In figure 1 the magnetic anisotropy constant, *K*, as calculated within the HSO model is shown for the case of a (001) surface of Au metal. As seen, despite of the large spin-orbit coupling in the host's *d*-band (~ 0.7 eV) the range of the magnitude of *K* is well below 0.1 μeV. In figure 2 the level splitting of a d^1 impurity with large on-site spin-orbit coupling, described thus in terms of a $J_{3/2}$ multiplet, is displayed for the case of (001) surfaces of Au and Cu. Noticeably, the magnitude of *K* is of order of 0.1-0.01 meV even for quite large distances. Since in this case the anisotropy is due by the orbital structure of the spin-states that couples to the tetragonal crystal field induced by the surface, it is not surprising that *K* is larger for a Cu metal host than for Au.
Our numerical results, thus clearly suggest that in the asymptotic regime the host-induced magnetic anisotropy energy is by several order of magnitude smaller than that raised by the strong local spin-orbit coupling. In the latter case it is even large enough to explain the thickness dependence of the Kondo resistance observed experimentally [3]. We also explore, in particular, the LSO model to study the magnetic anisotropy distribution of impurities in metallic clusters.

[1] Guanlong Chen and N. Giordano, Phys. Rev. Lett. 66, 209 (1991); J.F. DiTusa, K. Lin, M. Park, M.S. Isaacson, and J.M. Parpia, Phys. Rev. Lett. 68, 1156 (1992); M.A. Blachly and N. Giordano, Europhys. Lett. 27, 687 (1994); Phys. Rev. B 49, 6788 (1994); N. Giordano, Phys. Rev. B. 53, 2487 (1996); T. M. Jacobs and N. Giordano, Phys. Rev. B 62, 14145 (2000).

[2] O. Újsághy, A. Zawadowski, and B.L. Györffy, Phys. Rev. Lett. 76, 2378 (1996); O. Újsághy and A. Zawadowski, Phys. Rev. B 57, 11598 (1998); O. O. Újsághy, L. Szunyogh, and A. Zawadowski, Phys. Rev. B 75, 064425 (2007).

[3] L. Szunyogh, G. Zaránd, S. Gallego, M. C. Muñoz, and B. L. Györffy, Phys. Rev. Lett. 96, 067204 (2006).

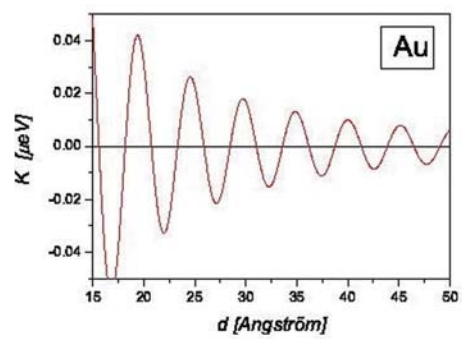

Calculated magnetic anisotropy constant induced by *spin-orbit coupling in the host* of an impurity as a function of the distance from the (001) surface of Au.

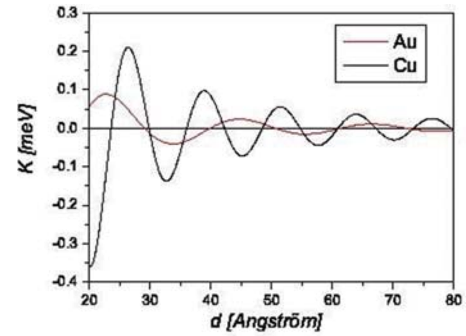

Calculated magnetic anisotropies induced by *strong local spin-orbit coupling* as a function of the distance from the (001) surface of Cu and Au.

AQ-17

Exchange bias in inverted AFM-core|FiM-shell nanoparticles.

G. Salazar-Alvarez[1], A. López-Ortega[2], J. Sort[3], S. Suriñach[2], M. D. Baró[2], J. Nogués[4]
1. Institut Catala de Nanotecnologia, Bellaterra, Spain; 2. Departament de Física, Universitat Autònoma de Barcelona, Bellaterra, Spain; 3. Institució Catalana de Recerca i Estudis Avançats (ICREA) and Departament de Física, Universitat Autònoma de Barcelona, Bellaterra, Spain; 4. Institució Catalana de Recerca i Estudis Avançats (ICREA) and Institut Català de Nanotecnologia, Universitat Autònoma de Barcelona, Bellaterra, Spain

The interest in bi-magnetic core-shell nanoparticles is steadily increasing due to the possibility to obtain enhanced magnetic properties. Particularly, since the report on the use of exchange bias to overcome the superparamagnetic limit [1], the amount of experimental and theoretical work on passivated ferromagnetic (FM) nanoparticles coated with the corresponding antiferromagnetic (AFM) oxide layer has increased in the recent years [2]. Here we present the study of inverted AFM-core|FiM-shell systems, as opposed to the typical FM-core|AFM-shell obtained from oxidation of transition metal nanoparticles. The inverse core|shell particles have been prepared by thermolysis of metal salts in organic solvents to produce the monooxide cores (MnO and FeO) with their subsequent passivation under air yielding the shell (Mn_3O_4 and Fe_3O_4). Such preparation allows us to study for the first time the dependence of the magnetic properties as a function of the antiferromagnetic core size, as opposed to the archetypical ferromagnetic metal-core| AFM metal oxide-shell configuration in which the dependence of magnetic properties on the size of the ferromagnet is studied. The first presented system is composed of narrowly sized distributed MnO|Mn_3O_4 particles with average particle sizes of 5 – 60 nm [3] whereas the second system is composed of monodispersed FeO|Fe_3O_4 particles with particle size of 11 nm, both systems have been prepared by chemical routes. The former system may be considered as a double inverted system since it is composed of an MnO AFM core with a bulk T_N~122 K and a Mn_3O_4 FiM shell with a bulk T_C~43 K (i.e., $T_C < T_N$ as opposed to conventional exchange biased systems). The latter system is composed of FeO|Fe_3O_4, with T_N~200 K < T_C~600 K. Transmission electron microscopy and x-ray diffraction studies reveal that the MnO|Mn_3O_4 particles are composed of a roughly constant 5 nm Mn_3O_4 shell with a varying MnO core size (0–50 nm). As can be seen in Fig. 1, for the FeO|Fe_3O_4 particles a roughly constant 3 nm Fe_3O_4 shell with a 5 nm FeO core is obtained. The exchange-coupling between the AFM cores and FiM shells give rise to a number of magnetic effects such as enhanced coercivity and loop shifts (exchange bias), or increased thermal stability of the ferrimagnetic component. These properties can, in fact, be controlled the AFM core size, as can be seen in Fig. 2 for the MnO|Mn_3O_4 particles. Remarkably, in the case of MnO|Mn_3O_4 particles the exchange coupling effects vanish at T_C of the Mn_3O_4 shell, whereas for FeO|Fe_3O_4 they disappear at about T_N.

[1] V. Skumryev et al. Nature 423 (2003) 850.

[2] J. Nogués et al. Phys. Rep. 422 (2005) 65.

[3] G. Salazar-Alvarez et al. J. Am. Chem. Soc 129 (2007) 9102.

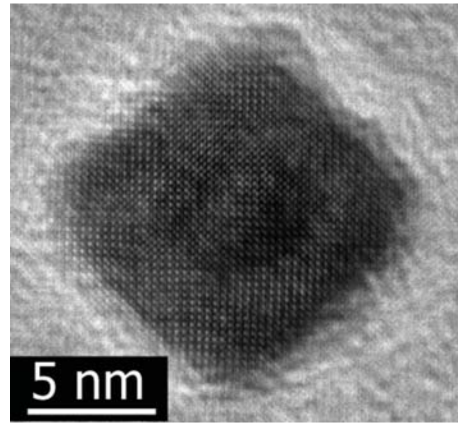

Figure 1 – TEM micrograph of FeO|Fe_3O_4 particles exhibiting a core-shell structure.

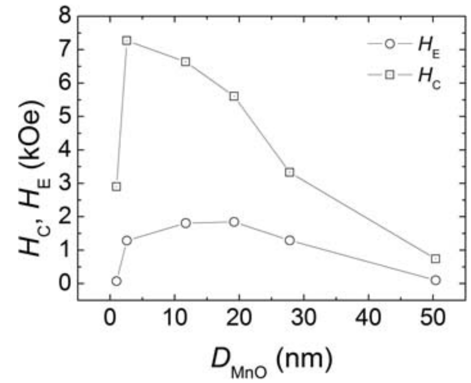

Figure 2. Dependence of the exchange bias, H_E, and the coercivity, H_C, on the diameter of the MnO core, D_{MnO}

AR-01

Analysis of Conduction Noise Attenuation by Magnetic Composite Sheets on Microstrip Line by Finite Element Method.

S. Kim, S. Kim, G. Ryu
Materials Engineering, Chungbuk National University, Cheongju, South Korea

Ferromagnetic metal particles or thin films have been proposed as the near-field noise absorbing materials in miniaturized RF circuits or devices [1]. Microstrip or coplanar lines are typically used to determine their noise absorbing capability by measuring reflection and transmission parameters (S_{11} and S_{21}, respectively). Absorption loss of those magnetic materials (in the form of thin composite sheets or films) is influenced by many factors such as material parameters, frequency, and sample dimension. It is, therefore, recommended to use a simulation technique in the determination of noise absorbing capability by modeling the actual system. In this study, Conduction noise attenuation by composite sheets of high magnetic and dielectric loss has been analyzed by using electromagnetic field simulator (Ansoft HFSS 9.0) which employs finite element method (FEM) and adaptive meshing. The simulation model consists of microstrip line with planar input/output ports and noise absorbing materials (polymer composite sheets of iron flake particles with high magnetic and dielectric loss [2]) as shown in Fig. 1. Modeling parameters are dimension and material constants (conductivity, permeability, permittivity, loss tangent) of the microstrip line and noise absorbing sheet. Input port is excited by TEM-mode wave with characteristic impedance of 50 Ω. S_{11} and S_{21} parameters are calculated as a function of frequency and their dimension (sheet size and thickness). Attaching a noise absorbing sheet with a dimension (width = 50 mm, length = 25 mm, and thickness = 1 mm), almost constant value of S_{11} (about -12 dB) is estimated and S_{21} is decreased with frequency from 0 dB (at 0.5 GHz) to -25 dB (at 6 GHz). The calculated power absorption is almost the same as the measured value as shown in Fig. 2. The power loss increases with frequency in the lower frequency region below 2 GHz and then saturates to a maximum value of about 90%, which is due to material loss (magnetic and dielectric) of the composite sheet. The attenuation of conduction noise (both electric and magnetic field) by the magnetic composite sheets is visually shown in the microstrip line model. The power absorption increases with sheet length (along the microstrip line) and thickness as shown in Fig. 3, since the power dissipation by material loss (magnetic and dielectric) is proportional to the sheet volume covering the strip conductor. On the while, the influence of sheet width (at a fixed length) on the power absorption is not so significant as shown in Fig. 4, since the electromagnetic field is concentrated along the microstrip line. The estimated frequency and size dependency of power absorption is well consistent with experimental results published in the previous study [2]. It is concluded that the proposed simulation technique can be effectively used in the design and characterization of noise absorbing materials in the RF transmission lines.

[1] S. Yoshida, M. Sato, E. Sugawara, and Y. Shimada, J. Appl. Phys. 85, pp. 4636-4638 (1999).

[2] S. T. Kim, H. S. Cho, and S. S. Kim, IEEE Trans. Mag. 41, pp. 3562-3564 (2005).

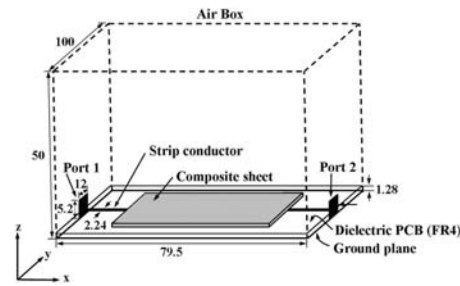

Fig. 1. Microstrip line model for FEM analysis.

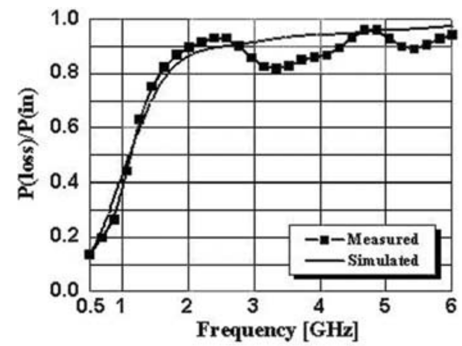

Fig. 2. Simulation and measured values of power absorption.

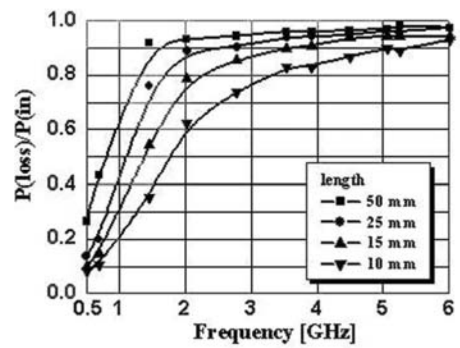

Fig. 3. The variation of power absorption with sheet length.

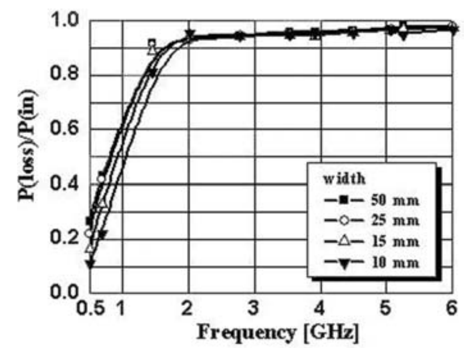

fig. 4. The variation of power absorption with sheet width.

AR-02

Microwave Absorbers of Two-layer (Dielectric/Magnetic) Composite Laminates for Wide Oblique Incidence Angles.

S. Kim, J. Kim
Materials Engineering, Chungbuk National University, Cheongju, South Korea

Advanced microwave absorbers for wide oblique incidence angles are required in many applications including wireless communication or vehicle identification in ITS (Intelligent Transport System) where 5.8 GHz DSRC (Dedicated Short Range Communication) system is applied. Multiple reflection or non- specular scattering of electromagnetic wave from pavement, sidewalls, overbridge, canopy in toll-gate, and other nearby structures deteriorates electromagnetic environment and results in undesired communication outside a specified region [1]. In this study, two-layered (dielectric/magnetic) microwave absorbers are designed for the achievement of low reflection coefficient over wide incidence angles at 5.8 GHz. The absorbing layer of composite sheets containing magnetic iron flake particles and the surface layer of low dielectric constant containing small amount of carbon black (and hence leading to impedance matching) have been made by conventional composite fabrication process. The complex permeability and complex permittivity of the composites were determined by reflection/transmission technique. The reflected power was measured by free-space arch test with variation of incident angle for both TE (transverse electric) and TM (transverse magnetic) polarization [2]. On the basis of transmission line theory, reflection loss has been calculated with variation of incident angles. Fig. 1(a) shows the reflection loss for normal incidence of plane wave determined in the single-layer composite (with thickness 1 mm) of iron flake particles terminated with metal. A high value of reflection loss (less than -1 dB) is predicted in GHz frequencies. Most of the power is reflected due to its high value of permeability and permittivity. Impedance matching layer is required to minimize wave reflection from such a highly reflecting surface. Fig. 1(b) shows the reflection loss determined in the two-layer composites laminate where the carbon black composite (thickness = 7 mm) is attached on the absorbing layer of iron flake particles. The minimum reflection loss (-30 dB) is predicted at 6 GHz. At this optimum thickness of the composite laminates, a low value of reflection loss (less than -10 dB) is predicted for wide incidence angles up to 55° for both TE and TM polarization as shown in Fig. 2. The measured value of reflection loss by free-space measurement is in good agreement with the theoretical value. The two-layer composite laminates consisted of magnetic absorbing layer with high magnetic loss and surface impedance matching layer of low dielectric constant can be proposed for the high potential microwave absorbers for electromagnetic radiation of oblique incidence.

[1] R. A. Pokharel, M. Toyota, and O. Hashimoto, IEEE Trans. MTT. 53(9), pp. 2726-2731 (2005).

[2] I. S. Seo, W. S. Chin, D. G. Lee, Compo. Struct. 66(1-4), pp. 533-542 (2004).

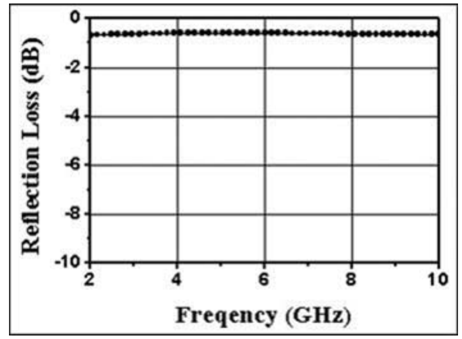

Fig. 1(a). Reflection loss for normal incidence: single layer of iron flake composite.

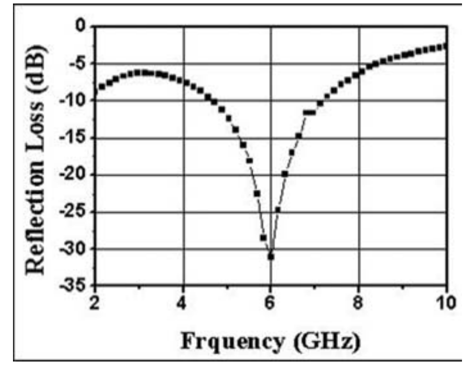

Fig. 1(b). Reflection loss for normal incidence: two-layer composites laminate of carbon black and iron flake particles.

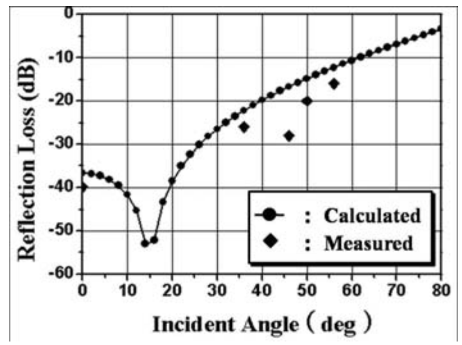

Fig. 2(a). Reflection loss determined in two-layered composite laminates for oblique incidence angles: TE polarization.

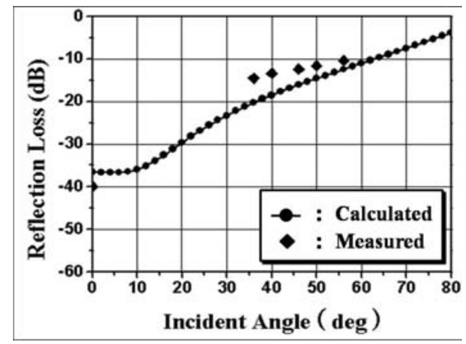

Fig. 2(b). Reflection loss determined in two-layered composite laminates for oblique incidence angles: TM polarization.

AR-03

Left-handed properties in the combined structures of cut-wire pair and continuous wire.

V. Dinh Lam, J. Kim, N. Thanh Tung, S. Lee, Y. Lee
Hanyang University, Seoul, South Korea

Recently, left-handed materials (LHMs) have attracted great attention because of their fascinating electromagnetic properties. Based on the Pendry's suggestion [1] and the Veselago's original prediction [2], a large number of both theoretical and experimental reports confirmed the existence and the main properties of LHMs. In this study, we experimentally studied the LH behavior of the combined structure of cut-wire pair and continuous wire. The cut-wire pair structure consists of a pair of finite-length wires, is separated by a dielectric layer. To achieve the LH properties, the cut-wire pairs were combined with continuous wires.

The samples were fabricated by using the conventional printed circuit board (PCB) process with copper patterns (36 μm thick) on both sides of a dielectric PCB (0.4 mm thick) with a dielectric constant of 4.8. These structures were designed and fabricated, and their transmission spectra were measured in the microwave frequency regime. The periodicity along the x and the y directions was achieved by printing the 2-dimensional array of patterns on the planar PCB. The periodicity along the z direction was obtained by stacking a number of pattern boards with a lattice constant of az = 1 mm.

Figure 1 shows the measured transmission spectra of the cut-wire pair structure with different numbers of layer. Evidently there is a band gap between 13.4 and 14.8 GHz in the transmission spectrum. This band gap becomes more evident when the number of layers increases, as expected. Another band gap begins to be formed at ~ 17 GHz. The observed results are similar to those in Ref. 3. Hence, it is confirmed that the first band gap in 13.4 – 14.8 GHz is due to the magnetic resonance, providing a negative magnetic permeability, and the second band gap starting at ~ 17 GHz is due to the electric resonance, providing a negative electric permittivity. This result reveals that the cut-wire pair structure exhibits both a magnetic and an electric resonance as the split-ring resonator. By combining the cut-wire pairs with continuous wires, one can get a combined structure that exhibits the LH behavior.

Figure 2 presents the photograph of fabricated combined structure and the measured transmission spectra of cut-wire pair, continuous wire and combined structures. For the comparison, all the structures here consist of three layers. The cut-wire pair structure displays a stop band between 13.4 and 14.8 GHz, corresponding to the magnetic resonance frequency range where $\mu < 0$, while the combined structure exhibits a pass band between 13.4 and 14.8 GHz, this pass band exactly coincides with the stop band of the cut-wire pair structure. Based on these results and the previous study [3], it is understood that the pass band between 13.4 and 14.8 GHz in the transmission spectrum of the combined structure indicates a clear evidence for the appearance of LH behavior.

There exists another pass band between 15.3 and 17.3 GHz in the transmission spectrum of the combined structure, and in this pass band both the permittivity and permeability are positive. Thus, this is a right-handed transmission band. The LH behavior of a combined structure can still be observed as the width of cut-wire pair increases until the cut-wire merges with the continuous wire, the so-called fishnet structure as shown in Fig. 3.

[1] J. B. Pendry, A. J. Holden, D. J. Robbins, and W. J. Stewart, IEEE Trans. Microwave Theory Tech. 47, 2075 (1999).

[2] V. G. Veselago, Sov. Phys. Usp. 10, 509 (1968).

[3] K. Guven, M. D. Caliskan, and E. Ozbay, Opt. Express 14, 8685 (2006).

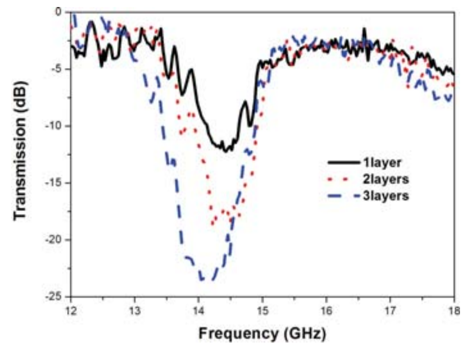

Measured transmission spectra of the cut-wire pair structure with different numbers of layers.

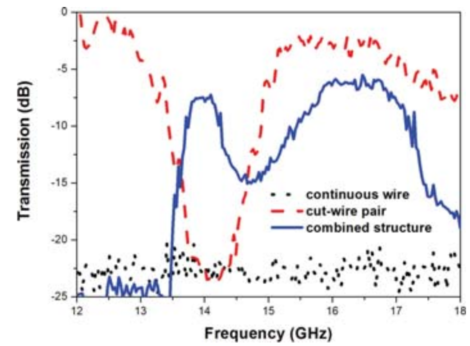

Measured transmission spectra of the cut-wire pair, the continuous wire, and the combined structures.

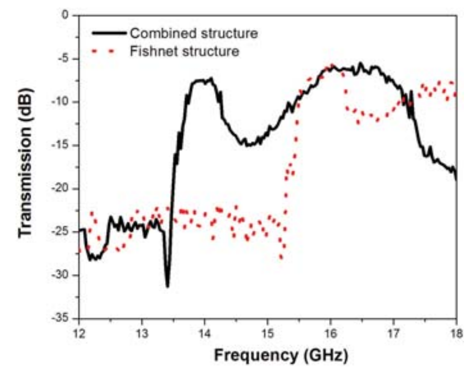

Comparison of the measured transmission spectra between combined and fishnet structures.

AR-04

Electromagnetic interference and shielding of valve hall in HVDC converter station.

C. Gao[1], Z. Zhao[1], S. Wang[2]
1. North China Electric Power University, Baoding, China; 2. Northeast Electric Power Design Institute, Changchun, China

Abstract—Radiate electromagnetic interference (EMI) from valve hall fires is analyzed by numerical method and measurement. According to the character of EMI, the practical shielding technique is discussed to satisfy the relative standards.

1. Introduction

For the widely use of HVDC, the EMI of HVDC converter station are paid more attention [1]. In this paper, we analyzed the radiated EMI of ±500 kV converter station by both the electromagnetic field numerical method and measurement. Based on the results obtained, the shielding technique must be used to the valve hall is discussed to satisfy the relative standards

2.EMI of valve halll

In general, EMI noise from the valve hall includes radiation and conducted propagation. Here we focus on the radiated noise due to the valve fires. EMI induced by corona discharges is ignored because it can be held to acceptable levels by proper electrical design of the bus bars and the hardware of the stations.

As the radiated noise may interfere the instruments around and the radio, some standards limit the level of EMI. The electric field intensity can not exceed 10 V/m to ensure the instruments around or in control room work properly according to IEC-6100-4. And the radio interference level (RIL) shall not exceed 40 dBμV/m at the locations under concern as shown in Fig.1.

Due to the complexity of the metal structures in valve hall, electromagnetic field numerical method must be used to analyze its EMI problem accurately. Here we use moment method [2] to compute the EMI level of valve hall by building an antenna model for valve tower as shown in Fig. 2. In our model, the metal structures are treated as wires and patches. The impedances of the valve are set as frequency independent according to the test results. And then EMI level for different frequencies are computed. It should be mentioned that the wall of valve hall is not considered in our model. So the results computed are those ignored the shielding effectiveness of wall.

Both the electric field intensity and RIL level are analyzed. Fig.4 shows the electric field intensity at the edge of valve. It decreases with the frequency increasing and is higher than 10 V/m when the frequency is lower than 100 kHz.

Fig. 4 shows the RIL level at the locations under concern. They are the directional diagrams of RIL level for 1 MHZ and 20 MHz when the distances to the valve hall are 450 m. We can see at frequency of 20 MHz, RIL level exceed 40 dBμV/m remarkably.

3.SHIELDING TECHNIQUE

Based on the relative standards and according to results computed, the EMI must be attenuated. Shielding is the useful method to decrease the RF noise and the shielding effectiveness of the wall should not be less than 40 dB. As only metal sheet can supply such high shielding effectiveness for RF, the wall of the valve hall must be built with metal sheet. In practice, the cladding of the wall should be consist of steel sheets with a thickness which is not thinner than 0.5 mm, and the distance between electrical contacts of sheets should not be larger than 35 mm. The shielding effectiveness of a real hall is measured and the results show that its SE is higher than 40 dB.

Here we represent some results measured and compare them with those computed by our method after the real shielding effectiveness of wall is considered. At the edge of hall, the electric field intensity measured by lower frequency sensor are 100-200 mV/m at the frequencies are several decades KHz. The corresponding results computed are 10-20V/m at the same positions, considering the real SE of wall is about 40 dB at this range of frequency, we can say that our method is accurate and the SE of wall is practical.

[1]DeVore, R.V., Kimball, D.F. etal., RF analysis of a 12-pulse HVDC converter, Generation, Transmission and Distribution, IEE Proceedings C Volume 135, Issue 3, May 1988 Page(s):210 - 218.

[2]Roger F. Harrington, Field computation by moment methods, New York: Macmillan, 1968.

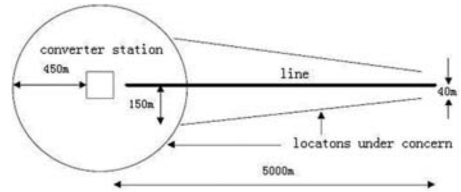

Fig.1 Locations under concern for RIL

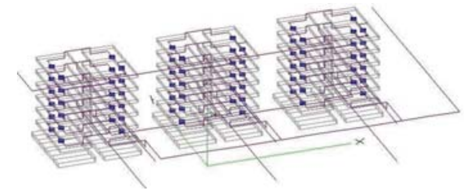

Fig.2 Model of valve tower

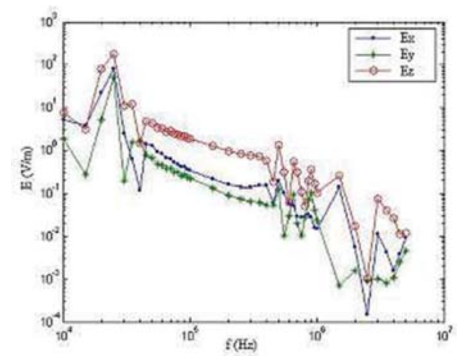

Fig.3 Electric field intensity at the edge of valve hall

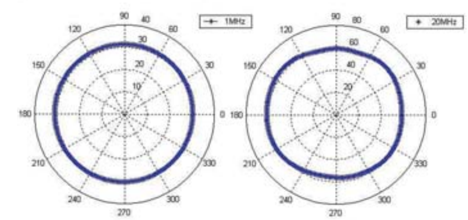

Fig.4 RIL level with distance is 450 m

AR-05

Study of coupling on parallel microstrip lines due to magnetic absorber sheet.

V. B. Bregar, J. Koselj, B. Drnovsek
Nanotesla Institute, Ljubljana, Slovenia

Absorber sheets based on magnetic-loaded composite are currently used as near-field absorbers for suppression of metal casing resonances, RFID enhancement and conducted noise suppression [1]. On dense electric circuits, single absorber sheet can cover large number of circuit connections. However, we observed significant coupling between the parallel microstrip lines even for line separation larger than line width. Signal coupling between transmission lines can present a significant problem [2] and can be increased by magnetic absorber sheets since these materials have relatively large permeability and permittivity. This could have negative effect on the application possibilities of the magnetic absorber sheets on the dense high-frequency circuits. On the other hand, it could lead to new uses in the microwave devices as the coupling effect between parallel lines is exploited for use in various devices like directional couplers or phase shifters [3], and in ferrite-coupled microstrip lines with magnetized ferrite substrate [4].
The aim of this study was to experimentally and numerically investigate the effect of coupling between parallel microstrip lines with applied magnetic-loaded absorber sheet. Numerical models allow us to examine parametrically the effect and identify key parameters of effective coupling, whereas experiments are used as a validation and examination of the effect with actual absorber sheets. The results will enable optimization of the magnetic-loaded absorber sheet for minimum coupling on PCBs, but also evaluation of potential for coupling devices.

For the experimental study microstrip circuits with two parallel lines were used. Lines are 1.6 mm wide with distance between lines 0.8, 1.6 and 3.2 mm. Parallel section is 50mm long, with absorber sheet applied in the middle of this section.Set-up was calibrated to eliminate coaxial cable characteristics from the measurements. Scattering parameters (S11, S21, S31 and S41) were measured in pairs, with 50 Ω terminations on the other ports, and were measured both without and with absorber sheet over both microstrip lines. Numerical modeling was done with Comsol Multiphysics software, RF module, and geometry of the model was identical to the experimental set-up.
From the experimental results, shown in Fig.2, it is clear that the application of the absorber sheet greatly enhances the S31 coupling at lower frequencies, but at the same time introduces large suppression of the through signal (S21). At lower frequencies the coupling is 10-15dB larger than without absorber sheets on microstrip lines, but in contrast to empty lines after broad peak falls with increasing frequency. Similar curves for S21 and S31 at higher frequencies indicate that the fall of coupling is due to the damping of the signal and not in change of the coupling itself. The difference in thickness of the absorber sheet affects much more the suppression than the coupling itself (linear effect), but affects also S11 and S41.
Further, we numerically analyzed the effect of permeability and permittivity of idealized absorber sheet. Numerical models show changed distribution of magnetic and electric field lines, that gives enhanced coupling between the microstrip lines. The results on Fig.3 show that the real part of the permittivity has the largest effect on the coupling S31, while permeability shows smaller, but still significant effect. In contrast, permeability does not affect much S41, whereas permittivity exhibits large effect. Imaginary parts of permeability and permittivity have an effect mostly on the signal suppression (S21), with permittivity again having larger effect. In addition, we examined both numerically and experimentally the effect of air gap between microstrip lines and absorber sheets and the dimensions of the absorber sheet. Results show that any gap significantly reduced the coupling efficiency and also suppression of S21, whereas change of length gives only proportional change in S21 and S31.

1. S. T. Kim, H. S. Cho, S. S. Kim, IEEE trans. on magnetics, vol. 41, pp. 3562 - 3564, 2005

2. B.R. Archameault, PCB Design for Real-World EMI Control, Kluwer Academic Publishers, 2002

3. JH Cho, HY Hwang, SW Yun, IEEE Trans. Microw. Theory Tech., vol.15, pp.113-115, 2005

4. MRML Albuquerque, AG d'Assuncao, IEEE Trans. on Magn., vol.34, pp. 1402-1404, 1998

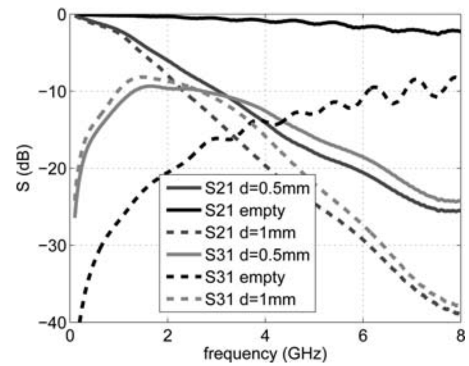

Measurements of S21 and S31 with two absorber sheets having thickness d=0.5mm and d=1mm.

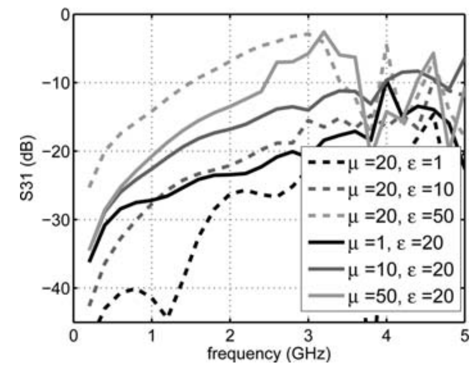

Numerical results for absorber sheets having only real permeability and permittivity.

AR-06

The influence of the construction of secondary reaction plate on the transverse edge effect in Single-sided linear induction motor.

S. Lee[1], H. Lee[2], S. Go[1], K. Kim[1], D. Jung[1], J. Lee[1]
1. Hanyang university, Seoul, South Korea; 2. Korea Railroad Research Institute, Uiwang, South Korea

The SLIM with aluminum-on-iron secondary has been favored for ground transportation. The performance of the SLIM depends markedly on the construction of the secondary or reaction rail[1]. Especially, the construction of the secondary reaction plate have a big influence on the transverse edge effect. The early analysis of transverse edge effects in linear induction motors is generally based on an idealized mathematical model[2]. Preston and Reece[3], Oberretl[4] and Lang[5] propose the analytic method and all of these methods allow for a 3-dimensional flux density distribution. These analytic analyses have not only some restriction such as iron to be extended to infinity or iron height and yoke flux distribution but also an impossible thing which is considering a detailed geometry of secondary reaction plate. On the other hand, 3D Finite Element Method can analyze without this restriction and fully consider a detailed secondary geometry data. But So far, there is no paper considering in detail the influence of the construction of secondary reaction plate on the transverse edge effect by using 3D FEM. In this paper, the influence of the construction of secondary reaction plate on the transverse edge effect is fully considered by 3D FEM. Fig 1 shows the analysis model for 3D FEM. this model is only 1 pole model. Both end effect and edge effect can be simultaneous considered by using 3D FEM analysis of full model. But 3D full model FEM analysis using by the present computer resource is impossible so that this paper takes only account edge effect with 1 pole model. Figure 2 (a) shows the 3D analysis result; the distribution of eddy current on the secondary reaction plate has both non-uniform current densities with a transverse component Jz and non-zero current densities with a longitudinal component Jx. Figure 2 (b) represents the transverse component Jz along center line of secondary plate and it is used for the use of an indicator to the transverse edge effect in this paper. Ten analysis models are selected to consider the influence of secondary construction and each model has only a difference in the construction of secondary reaction such as semi-cap or full-cap. Figure 3 shows the results of all models. Figure 4 shows the comparison between the result of 3D FEM analysis and the result of analytic analysis. Since considering a detailed construction of secondary by using analytic method is so difficult, there is a considerable difference between them. But a trend of the result of 3D FEM analysis and the result of analytic analysis is the same. As a result 3D 1pole FEM analysis is a very useful tool for considering the influence of the complex construction of secondary reaction plate on the transverse edge effect. Also it can be used in finding optimal construction of secondary reaction plate.

[1] A. J. Ellison and H. Bahmanyar, “The application of linear electric motors to the proposed surface-guided transport sys terns of the future”, lEE Conference Publication No. 120, October 1974, pp. 124-130.

[2] H.May, H.Mosebach, And H.Weh, “Numerical treatment of transverse edge effects in linear induction motors”, Electric Machines and Electromechanics: An International Quarterly, No. 4, May 1979, pp. 321-330

[3] T.W. Preston and A.B.J. Reece, “Transverse edge effects in linear induction motors,” Proc. lEE, Vol. 116, No.6, June 1969, pp. 973-979.

[4] K. Oberret I, “Three-dimens i onaI theory of linea r induct ion motors considering end-effect and winding distribution,” Arch. f. Elek., Vol. 55, April 1973, pp. 181-190, (in German).

[5] A. Lang, “The effect of stray fields on the design and performance of linear induction motors,” Ph. D. dissertation, Technical University of Braunschweig, June 1973, (in German).

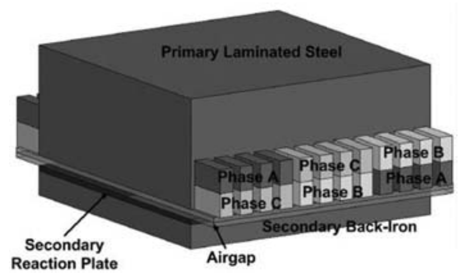

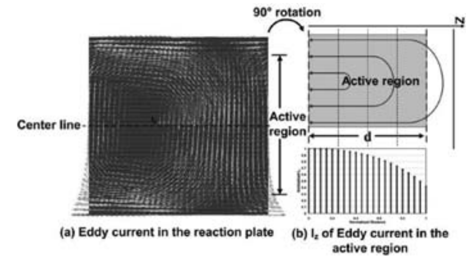

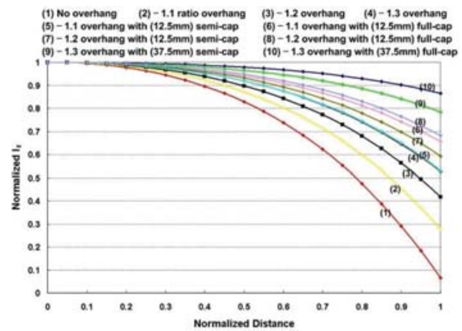

Results of FEM analysis

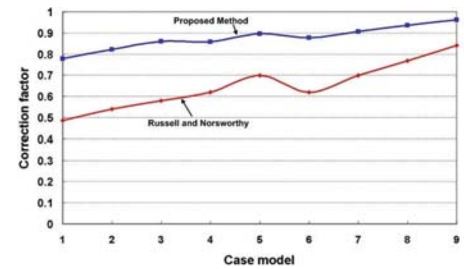

The comparison between 3D FEM and analytic method

AR-07

RF conduction in-line noise suppression effects for the NiFe and Fe magnetic composite.

K. Kim[1], J. Ryu[2], S. Lee[2], S. Lee[2], Y. Choa[3], S. Oh[4]
1. Physics, Yeungnam University, Gyeongsan, South Korea; 2. Composite Materials, Korea Institute of Materials Science, Changwon, South Korea; 3. Dept.of Chemical Engineering, Hanyang University, Ansan, South Korea; 4. Dept. of Materials Science and Engeering, Seoul National University of Technology, Seoul, South Korea

In oreder to enhance the signal integrity, the loss generation of ferromagnetic composite films is one of good countermeasure for the suppression of EM noise emission on transmission line [1, 2]. Therefore, to reduce the eddy current loss and to utilize the high frequency, we evaluated the RF EM noise suppression using the epoxy composite sheet combined with magnetic nanoparticles on transmission line.
The magnetic nanoparticles were fabricated by conventional Electric Explosion Wire (EEW) method. Fe and NiFe pure wires of 0.4 mm in diameter were used. Explosions were carried out in argon at a pressure 1.5×10^5 Pa. One of the main parameters influencing the properties of the produced nanopowder is the specific energy input into the wire W/Ws (where W is the energy input into the wire, Ws is the sublimation energy of the wire). A metal wire was installed between the ground and a high-voltage electrode that was connected to a capacitor bank through a triggered spark gap switch. The wires were fed by a feeding roller installed on the exploding vessel and were guided by a nozzle into the vessel. The electrical energy is deposited in the wire and is heated, vaporized, and turned into plasma. The vaporized metal vapor collide each other and condensed to form a metallic Fe and NiFe nanoparticles with around 100 nm in size. Composites containing metallic particles (NiFe, Fe) were fabricated with the different concentrations of fillers. Metallic particles and resin with net concentrations of 50 wt.% NiFe and 50 wt% Fe were mixed by a homogenizer for well dispersion, respectively and then they were cured at 120oC. In order to measure the complex permittivity and permeability at the radio frequency region, Agilent N5230A and 7 mm coaxial airline with electrical calibration module (Agilent N3696A) were used. Complex electromagnetic property data were obtained using Agilent 85071E (Material Measurement Software), in which the Nicolson-Ross-Weir method is implicated, from scattering parameters for reflected and transmitted waves over 0.5 GHz ~ 10 GHz. Fig. 1 shows the hysteresis loop of composite sheet for the Fe 50 wt.% epoxy composite and NiFe 50 wt.% composite and the images of magnetic powder, respectively. In magnetization curves, it can be deduced the amount of magnetic NiFe and Fe in composite sheet, which is about 50wt. % by comparison with those of values magnetization in bulk materials. In order to characterize the conduction in-line noise, the transmission line was prepared on printed circuit board by IEC standard (IEC 62333-2) as shown in Fig. 2 (a). The measured s-parameters by network analyzer were converted to power loss, which can be defined by $P_{loss}/P_{in}=1-(|S_{11}|^2+|S_{21}|^2)$. Figure 3 shows the permittivity, permeability (a), (b), the measured and simulated power loss (c), (d) for the Fe 50 wt.% epoxy composite and NiFe 50 wt.% composite, respectively. The signal attenuation of the composite sheet with Fe 50wt.% is a little bit higher than that of NiFe 50wt.%.The power loss was simulated by 3D model using the commercial HFSS v.11 program, which the simulated results were a good agreement those of experimental data. When the materials have similar permeability behaviors, the power loss could be dominant with the permittivity values. In same materials, the power loss is proportional to the magnetic moment and loss tangent (this result is not shown here for page limitation). As results, the magnetic powder composite sheet by EEW method is one of good candidate materials for RF noise suppression.

[1] Ki Hyeon Kim, S. Ohnuma, M. Yamaguchi, IEEE Trans. Magn. 40(4), 2838, (2004)
[2] Ki Hyeon Kim, Masahiro Yamaguchi, Phys.Stat. Sol.(b), 241(7), 1761 (2004)

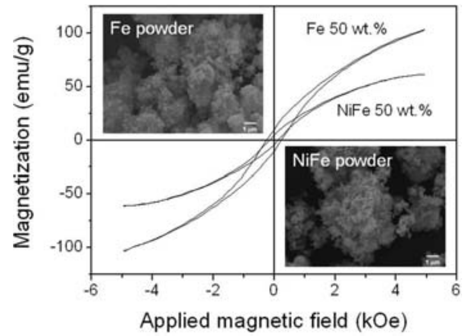

Fig. 1 A comparison of hysteresis loop of composite sheet and magnetic powder for the Fe 50 wt.% epoxy composite and NiFe 50 wt.% composite, respectively.

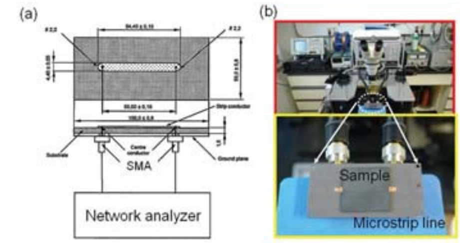

Fig. 2 A schematic of microstrip line zig (a) and measurements (b) for measuring in-line conduction noise.

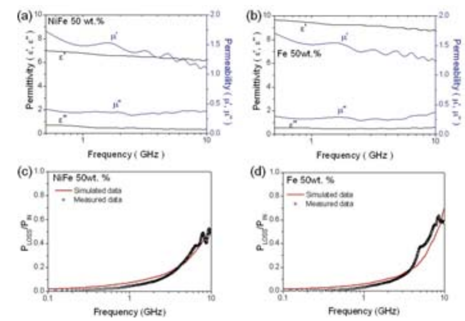

Fig. 3 The permittivity, permeability profiles (a), (b), the measured and simulated power loss (c), (d) for the Fe 50 wt.% epoxy composite and NiFe 50 wt.% composite, respectively.

Optimal bulk content of sulfur for high magnetic induction in inhibitor-free 3% Si-Fe strips.

S. Kim[1], J. Soh[1], J. Oh[1], S. Cho[1], S. Han[2], N. H. Heo[1]
1. Advanced Materials Group, Korea Electric Power Research Institute, Daejon, South Korea; 2. Chungnam National University, Daejeon, South Korea

The 0.15mm-thick 3%Si-Fe alloy strips containing 11, 29, 58, and 92 ppm sulfur were prepared through a vacuum induction melting, hot-rolling and double-stage cold-rolling process with a lubricant. Between each cold-rolling process, an intermediate annealing was performed at 800°C for 20 min under a high vacuum of 7×10^{-6} Torr. Final thickness reduction was 60%. The number of final cold-rolling passes was 9. Prior to vacuum-annealing at 1200°C for 12 h, the strip samples (10 mm × 100 mm in dimension) were heated to the temperature with a heating rate of 400°C/h or directly isothermal-annealed (approximately 35000°C/h) at the temperature under the flowing hydrogen of 3 liter H_2/min.
The correlation between bulk content of sulfur, area fraction of grains, magnetic induction and heating rate is shown in Fig. 1. Here, the area fraction is nearly equivalent to a volume fraction, because final-annealed strips showed a bamboo-structure. At 400°C/h, a sharp {110}<001> texture was obtained from the strip containing 58ppm sulfur, resulting in an excellent magnetic induction of 1.96 Tesla. A poor magnetic induction was obtained from the other alloy strips showing no or a limited {110} texture. The surface-energy-induced selective growth is mainly governed by the interfacial segregation kinetics of sulfur which forms a convex profile [1]. The convex segregation concentration decreases overall with decreasing bulk content of sulfur. This results in the shortened time or temperature range for {100} or {111} selective growth. It is therefore expected that {110} texture will be much more easily obtained from the alloy strips with a lower sulfur content. However, the anomalous final texture of the 11 ppm strips in Fig. 1 can be explained by the following selective growth kinetics [1],
$G(t)=M(t)\times[(\gamma_G/r(t))+(2\Delta\gamma_S/d)+C(t)]$,
where, $M(t)$ is the grain-boundary mobility, γ_G is the grain-boundary free energy, $r(t)$ is the average radius of grains excluding the selectively growing grains, $\Delta\gamma_S$ is the difference in surface energy between the growing grain and the grain which is consumed, d is the strip thickness, and $C(t)$ is the concentration of interface-segregated sulfur that has a strong grain-boundary pinning effect as the negative driving force term.
At a lower bulk content of sulfur, a weak grain-boundary pinning effect can enhances the growth of {100} or {111} grains during the selective growth. This hinders the final selective growth of {110} grains due to the size disadvantage. At a higher bulk content of sulfur, {110} grains are not easy to survive due to the enlarged time period of {100} or {111} selective growth. Therefore, a moderate bulk content of sulfur (i.e., 58ppm sulfur in this study) exists for obtaining the final {110} texture. As shown in Fig. 1(b), the area fraction of {110} texture increased with increasing heating rate. Also the total number of {110} grains increased in the strips containing 58ppm sulfur. In order to obtain an excellent magnetic induction even in the other strips, a much faster heating rate is required [2]. Additionally, the drastic increase in the total number of {110} grains with increasing heating rate is due to the larger {110} grains arising from the selective growth of the initially formed {110} grains which results in the increase in the number of the surviving {110} grains.

[1] N.H. Heo, K.H. Chai, and J.G. Na, Acta mater., vol. 48, 2901-2910, 2000.

[2] S.B. Kim and N.H. Heo, J. Appl. Phys., vol. 97, 10F914, 2005.

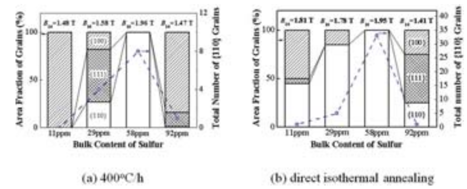

Fig. 1. Correlation between bulk content of sulfur, area fraction of grains, magnetic induction and heating rate.

AR-09

Performance Improvement of PM Synchronous Motor by Using Soft Magnetic Composite Material.

G. V. Cvetkovski, L. B. Petkovska
Faculty of Electrical Engineering and Information Technologies, Ss. Cyril & Methodius University, Skopje, Macedonia

Abstract— The paper is presenting some aspects of soft magnetic composite (SMC) material application in electrical machines. The stator core of the analyzed permanent magnet synchronous motor (PMSM), is made of magnetic iron sheets. Three types PMSM stators are analysed: laminated with open slots, laminated with closed slots using SMC and SMC stators. The comparative analysis is based on the magnetic properties and the calculated parameters of each motor model. The studied electromagnetic and electromechanical parameters are flux densities in various sections of the magnetic circuit and electromagnetic and cogging torque. The parameters' values for the three types of stators are calculated using Finite Element Method (FEM).

I. INTRODUCTION

The investigated object is a brushless three phase synchronous permanent magnet Koncar motor type EKM 90M-6 has 36 stator slots and a rotor with 6-skewed SmCo5 surface mounted permanent magnets. The rated data is I=18 A, T=10 Nm and n=1000 rpm@50 Hz.

The complexity of the magnetic circuit and the fact that the stator slots in the original design are opened influences the distribution of the magnetic field in the air gap as well as the electromagnetic and cogging torque.

Torque quality is very decisive issue for variable speed drive applications. There exist two undesired pulsating torque components in PM machines which affect the machine performance, one of which is ripple torque arising from harmonic content of the machine voltage and current waveforms and the other is cogging torque caused by the attraction between the rotor magnetic field and angular variations of the stator reluctance. These components not only affect the self-starting ability of the motor but also produce noise and mechanical vibrations.

Therefore, the investigation was focused on the design improvement of the PMSM by using SMC material as stator slot closure as well as for the stator cores in whole. The comparative analysis of the three stator topologies is based on magnetic field distribution in the motor.

II. SOFT MAGNETIC COMPOSITE MATERIALS APPLICATION

The basis for the material whose utilisation is the subject of this paper is bonded iron powder. The most important property of the SMC material, which is the ability to be easily shaped in complex forms. Although the soft magnetic composite materials have low permeability and high specific iron loss at low frequencies in the recent years they became very attractive for use as magnetic core parts or for manufacturing the whole cores in general. Another valuable property of the SMC material is the isotropy of the material and the rather good iron losses at high frequencies. This property makes the SMC material very attractive for producing a stator slot closure for the PMSM. The very fast development of new soft magnetic composite materials with improved magnetic properties goes in favour of the application of this material as stator core magnetic material. In this paper three models of the PMSM are going to be analysed. The laminated stator is made of grain oriented silicon steel with thickness of 0.5 mm, while the SMC material stator cores are made of SOMALOYTM500.

III. MAGNETIC FIELD ANALYSIS

In order to be able to analyse the two models of the PMSM with different stators accurately, a calculation of the magnetic field has to be performed for the three-stator topologies. After the motor has been properly modelled, a 2D FEM magnetic field calculation of the three models of motors at no load and at rated current load (Iph=18A) is performed. The distribution of the magnetic field at rated load, the air gap flux density at no load and the electromagnetic torque for the three models is presented in Fig.1, Fig.2 and Fig.3, respectively.

The calculated data form the FEM magnetic field analysis in the postprocessor mode could be also used to calculate some other magnetic and electric parameters necessary for the complete and complex analysis of the three PMSM models. The calculated values of these parameters (air gap flux, air gap flux density, back iron flux density, stator teeth flux density, slot closure average flux density, iron loss in the stator, iron loss in the slot closure, total iron losses, electromagnetic torque and cogging torque [1-2]), are going to be presented and comparatively analyzed in the full version of the paper.

[1] C. Studer, A. Keyhani, T. Sebastian, S.K. Murthy, Study in Cogging Torque in Permanent Magnet Machines, IEEE Industry App. Society Annual Meeting, 1997, New Orleans, pp. 42-49.

[2] T. Li, G. Slemon, Reduction of Cogging Torque in Permanent magnet Motors, IEEE Trans. on Magn., Vol. 24, No. 6, Nov. 1988, pp. 2901-2903.

Fig.1

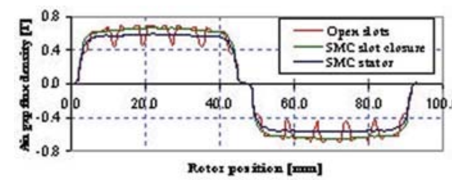

Fig.2

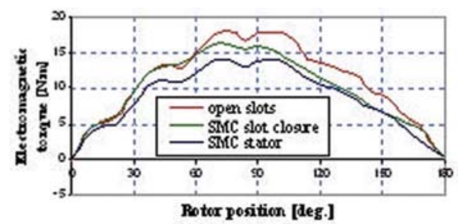

Fig.3

AR-10

Magnetic entropy change of V substituted Ni-Mn-Ga Heusler alloy.

S. Min[1], Y. Zhang[1], K. Kim[2,3], Y. Kim[2,3], S. Yu[1], K. Lee[4], Y. Kim[5]
1. BK21 Physics Program and Department of Physics, Chungbuk National University, Cheongju, South Korea; 2. School of Electrical & Computer Engineering, Chungbuk National University, Cheongju, South Korea; 3. CBNU BK21 Chungbuk Information Technology Center, Chungbuk National University, Cheongju, South Korea; 4. Superconductivity Lab., Korea Research Institute of Standard and Science, Taejon, South Korea; 5. Engineering, Korea Institute of Science and Technology, Seoul, South Korea

The temperature change of a magnetic material associated with an external magnetic field change in an adiabatic process is defined as the magnetocaloric effect (MCE), which was discovered in iron by Warburg[1]. It can be measured directly (adiabatic temperature change, ΔT_{ad}) or it can be calculated indirectly from the measured magnetization (magnetic entropy change, ΔS_M). Recently, a large magnetic entropy change has been found and intensively studied in Ni-Mn-Ga alloys, due to the possibility to use these materials as active magnetic refrigerants in the magnetic refrigeration technology[2].

The $Ni_{54}Mn_{21-x}V_xGa_{25}$ (x=0, 2, 4) samples were prepared by conventional arc melting method in argon atmosphere. For homogeneity of samles, ingot was melted several times. And then, the heat treatment was carried out at 110 K in a sealed quartz tube for 9 days and quenched in ice water. Quenching is believed to be important to obtain a high chemical order for this kind of alloys. The samples were examined by the X-ray diffraction and showed the single phase. The magnetic characteristics were performed with a Quantum Design superconducting quantum interference device (MPMS mode) magnetometer in the fields up to 20 kOe. The magnetic entropy change is calculated by the isothermal magnetization measurements.

Fig. 1 shows the temperature dependence of low-field magnetization for the samples. The Curie temperature, Tc was found to be 325, 300 and 265 K and the austenitic transition temperature, TA was found to be 315, 217 and 124 K for x=0, 2 and 4 of $Ni_{54}Mn_{21-x}V_xGa_{25}$, respectively. With an increase of the concentratioin of V for $Ni_{54}Mn_{21-x}V_xGa_{25}$ systems, the Curie temperature and austenitic transition temeprature decrease due to the dilution of the magnetic subsystem[3].

The magnetic entropy change as a function of temperature for the samples at the external magnetic fields of 20 kOe were calculated and plotted in Fig. 2. As shown in Fig. 2, the magnetic entropy change ΔS_M reaches a maximum value of about 2.49, 1.92 and 1.81 J/kg K for x=0, 2, 4 at 325, 300 and 265 K, respectively. With increasing V content, the magnetic entropy change decrease.

[1] E. Warburg, Ann. Phys. 13, 141(1881)

[2] Feng-xia Hu, Bao-gen Shen, and Ji-rong Sun, Appl. Phys. Lett. 76, 3460(2000)

[3] V. V. Khovailo, V. A. Chernenko, A. A. Cherechukin, T. Takagi, T. Abe, J. Magn. & Magn. Mater. 272-276, 2067 (2004)

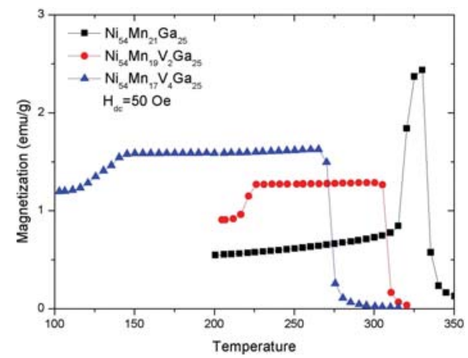

Fig. 1 Temperature dependence of magnetizations for $Ni_{54}Mn_{21-x}V_xGa_{25}$ (x=0, 2, 4)

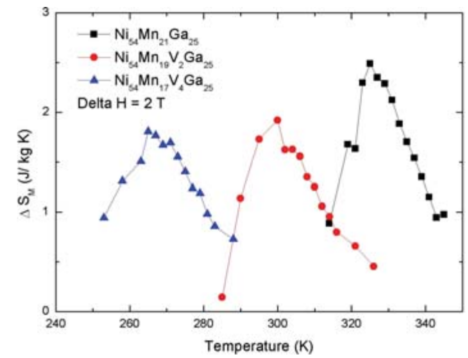

Fig. 2 The magnetic entropy change as a function of temperature for $Ni_{54}Mn_{21-x}V_xGa_{25}$ (x=0, 2, 4)

AR-11

Ferroresonance phenomena in electric circuits including amorphous cores.

N. Banu[1], E. Barbisio[1], O. Bottauscio[2], *M. Chiampi*[1], G. Crotti[2], D. Giordano[2]
1. Ingegneria Elettrica, Politecnico di Torino, Torino, Italy; 2. Electromagnetics, Istituto Nazionale di Ricerca Metrologica, Torino, Italy

The steady state behaviour of circuits and systems under ferroresonance conditions can be classified into four different types (fundamental, subharmonic, quasi-periodic and chaotic mode) [1]. The determination of the ferroresonance mode depends on many factors, such as the circuit parameters, the supply voltage and frequency, the shape of the nonlinearity (that is, usually, the magnetization curve or the hysteresis loop of the core of a saturable inductor) [2].
This paper investigates the influence on the ferroresonance mode of the nonlinear behaviour of a ferromagnetic inductance in a RLC circuit, supplied by a controlled voltage generator. The analysis is carried out both by experiment and simulation.
A core constituted by an amorphous ribbon, having small thickness (7 µm), is found to be well suited for the investigation. First, the amorphous alloys present very narrow hysteresis loops and negligible classical losses, making the ferroresonance arising easier [3]; in addition, the application of different field annealing to the same material can sensibly modify the shape of the magnetization curves; this behaviour is shown in Fig. 1 which compares the hysteresis loops of the same amorphous ribbon ($Co_{67}Fe_4B_{14.5}Si_{14.5}$) obtained after a longitudinal and a transverse field annealing respectively.
Since the presence of the unavoidable circuit resistances (winding resistance, resistance for current measurement) can reduce or prevent the development of the ferroresonance phenomena, an operational amplifier is series connected to the RLC electric circuit. It compensates the drop on the resistive component, removing partially or totally the Joule losses. The importance of this compensation is made evident in Fig. 2, which presents two current waveforms obtained under the same supply conditions with and without the insertion of the operational amplifier. A good agreement between the measurements and computations is found.
The investigations are developed considering different supply conditions, where the amplitude, frequency and waveform (sinusoidal, triangular, rectangular) of the controlled generator voltage are varied. Some amorphous or nanocristalline ribbons, with different chemical compositions and annealing treatments are characterized under controlled sinusoidal flux with digital hysteresisgraph and used in the experiments. As an example, Fig. 3 reports the measured and computed current evolution in a circuit including an amorphous ribbon inductor $Co_{67}Fe_4B_{14.5}Si_{14.5}$ with longitudinal field annealing) supplied by a rectangular voltage at 1 kHz; the chaotic mode ferroresonance is well evident. A detailed analysis about the influence of the magnetization curve shape on the ferroresonance phenomena will be reported in the full paper.

[1] P.Ferracci, "Ferroresonance", Group Schneider: Cahier n. 190, pp 1-28, 1998.

[2] D. M,. Scoggin, J. E. Hall, "Ferroresonance", IBM J. res. Develop, Vol 31, n. 6, 1987.

[3] E. Barbisio, O. Bottauscio, M. Chiampi, G. Crotti, D. Giordano, "Experimental and Modelling Analysis of Ferroresonant Electric Circuits", J. of Magnetism and Magnetic Mater., Vol. 316, n. 2, Sept. 2007, pp. e299-e301.

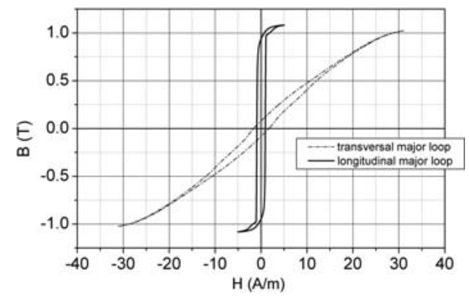

Hysteresis loops of an amorphous alloy ($Co_{67}Fe_4B_{14.5}Si_{14.5}$) respectively obtained after a longitudinal and a transverse field annealing

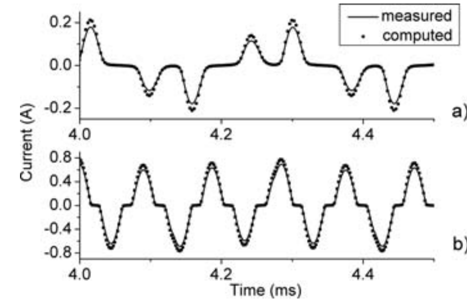

Measured and computed evolution of the current in a RLC circuit with a non linear inductance ($Co_{67}Fe_4B_{14.5}Si_{14.5}$ with longitudinal field annealing) supplied by a rectangular voltage at 3.5 kHz; a) without resistance compensation (total resistance = 2.8 Ω), b) with partial resistance compensation (equivalent total resistance ≈ 0.91 Ω)

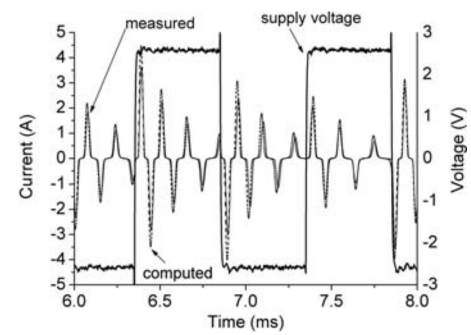

Measured and computed current evolution in a RLC circuit supplied by a rectangular voltage at 1 kHz (amorphous core $Co_{67}Fe_4B_{14.5}Si_{14.5}$ with longitudinal field annealing)

AR-12

Harmonic Distortion of Magnetizing Current in Combined Wound Toroidal Cores.

J. Chojnacki[1], P. Liszewski[1], *M. Soinski*[2], W. Pluta[2], R. Rygal[2], S. Zurek[3], P. Pinkosz[4]
1. ABB Sp. z o.o., 04-713 Warsaw, Poland; 2. Czestochowa University of Technology, Faculty of Electrical Engineering, 42-200 Czestochowa, Poland; 3. Wolfson Centre for Magnetics, School of Engineering, Cardiff University, Cardiff, United Kingdom; 4. Magneto Ltd, 42-224 Czestochowa, Poland

I. INTRODUCTION

Polycrystalline strips 80%Ni-Fe [1] have very good magnetic properties, but they are relatively expensive due to high content of Ni. As an alternative to the Ni-Fe alloys (permalloys) the nanocrystalline materials [2] can be used. Nanocrystalline toroidal cores are cheaper and often more useful in instrument transformers [3].

The aim of this paper is the comparison between the total harmonic distortion of the magnetizing current (THD_I) in wound toroidal cores combined from two sub-cores (with the same dimensions) made of grain-oriented electrical steel (SiFe) [4] and polycrystalline Ni-Fe (NiFe) or SiFe and nanocrystalline ribbon (Nano).

II. DESCRIPTION OF COMBINED WOUND TOROIDAL CORES

To increase the intensity of the output signal of an instrument transformer excited with low magnetic fields, the magnetic circuit can be made as a combination of SiFe and another, magnetically softer material, for instance NiFe or Nano.

The magnetic measurements were carried out on toroidal cores with dimensions d_1 = 145 mm, d_2 = 105 mm and h = 20 mm under sinusoidal voltage excitation and frequency of 50 Hz according to the international standard [5].

III. MAGNETIC PROPERTIES OF COMBINED TOROIDAL CORES

According to the measured data (Fig.1 a) magnetic materials can be characterized by different values of peak flux density (B) and also different relative permeability(Fig.1 b). Core made of nanocrystalline strip has significantly higher relative permeability than the NiFe, which can be utilized in low magnetic fields, i.e. in a range from 1 to 2 A/m.

In the case of a magnetic core combined from SiFe and NiFe, the resultant values of peak flux density are lower for the same values of magnetizing field than for the SiFe+Nano.

IV. HARMONIC DISTORTION OF MAGNETIZING CURRENT IN COMBINED WOUND TOROIDAL CORES

A distortion of a current waveform can be measured by a coefficient called "total harmonic distortion" [6], which is defined as in equation (1),

$$THD_I=(\sqrt{(I_2^2+I_3^2+I_4^2+\ldots)}/I_1)\times 100\% \qquad (1)$$

where: THD_I - total harmonic distortion of magnetizing current (%), I_1 – magnitude of the fundamental frequency of the current (A), I_2, I_3, I_4… – magnitudes of higher harmonics (A).

Comparison of the THD_I value for various combined cores is presented in Fig. 2.

The single SiFe core offers the lowest harmonic distortion in a magnetizing current (for the same values of flux density). The highest distortion occurs in the single NiFe. For the combined cores SiFe+NiFe and SiFe+Nano, the THD_I remain in a similar level, but at different flux densities. However, within the range of flux density 0.1 T ≤ B ≤ 1.1 T, the THD_I of magnetizing current for both combined cores are comparable but the magnetizing current for B > 1.1 T in the case of combined SiFe+Nano core is less distorted than for the SiFe+NiFe core.

V. CONCLUSIONS

For the combined core SiFe+Nano the peak flux density values in magnetization curve are higher for the same values of magnetizing field than for the SiFe+NiFe core and this reduces the measurement errors in middle voltage current transformers. The bulk relative permeability of combined SiFe+Nano core is much higher than in the case of SiFe+NiFe magnetic circuit, which increases the output voltage of current transformers.

The selection of materials for combined magnetic circuits of middle voltage current transformers should be based not only on the magnetization curve and relative permeability values, but also on total harmonic distortion of magnetizing current.

Total harmonic distortion in relation to peak flux density values indicate that the cores combined from SiFe and Nano offer best applicability in terms of the distortion, range of operational flux density, and price.

[1] Carpenter Technology Ltd., Catalogue "Magnetic Alloys", UK, 2004

[2] Nanocrystalline soft magnetic material – Finemet, Internet (01 Jan 2007): http://www.hitachimetals.co.jp

[3] ABB Outdoor Instrument Transformers Application Guide, 1HSE 9543 Edition 2.1, 2005-09

[4] EN 10107:2007 "Grain-oriented electrical steel sheet and strip delivered in the fully processed state"

[5] EN 60404-6, 2003"Method of measurement of the properties of magnetically soft metallic and powder materials at frequencies in the range 20 Hz to 200 kHz by the use of ring specimens"

[6] IEEE 1495-2000 Power Engineering Society, "Harmonic Limits for Single-Phase Equipment"

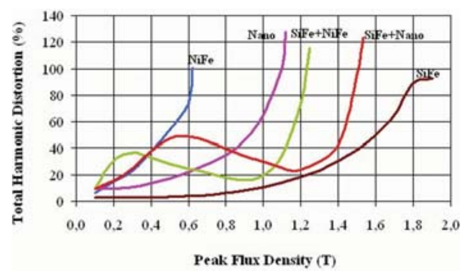

Fig. 1. Magnetic properties of single and combined toroidal wound cores: a) magnetization curve, b) relative permeability

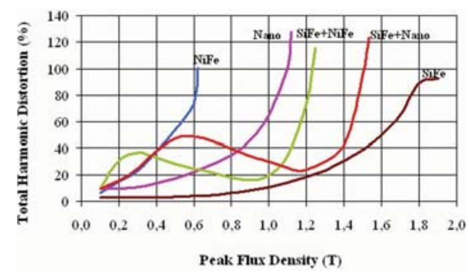

Fig. 2. Total harmonic distortion of magnetizing current for various cores

AR-13

The Characterisation of NiFe Cores for High Current Micro-inductors.

B. Jamieson, T. O'Donnell, N. Wang, J. Godsell, S. Roy
Microsystems Centre, Tyndall National Institute, Cork, Ireland

There is considerable interest in the integration of micro-inductors either on-chip or into the package, for application in switch mode power supplies for use in hand held electronic applications. For micro-inductors which are to be used in power converters, the inductor excitation current typically consists of a triangular waveform superimposed on a dc current. To increase the power handling of these inductors it is therefore important to understand their operation under dc-bias currents. In recent years there has been significant research into the integration of micro-inductors [1 - 3], however the majority of these were confined to low dc currents of less than 1 A. A few other devices with 'V' groove conductor and magnetic core design, have been demonstrated with current-carrying capabilities from 2.1 A up to 10 A [4, 5], although the width of the conductor which directly contributes to current handling ability has been increased for the higher current rating at the cost of inductances achieved. These 'V' groove inductors employ Co-Zr-O film as core materials deposited in a magnetic field using RF sputtering technique. While sputtering is a slow deposition technique which works well for deposition from nanometer up to a micrometer length scale on a relatively flat surface, we have demonstrated [6] deposition of a particular ferromagnetic alloy composition with uniform thickness even on a vertical side-wall using pulse-reverse electroplating technique. In this work we investigate the extension of the current handling to currents above 1 A for an one turn inductor structure with a wrapped around Ni45Fe55 core deposited in an uniaxial magnetic field of 200 Oe by pulse-reverse (PR) electroplating and the role which the shape of the inductor core play in increasing the maximum current. We are investigating the shape anisotropy effect on current handling capability further using micro-magnetic simulation of our fabricated inductor core structure.

Various inductors have been fabricated with the aim of characterizing the performance of the magnetic core under different dc bias conditions. The cross-section of a single turn inductor is shown in fig. 1. These inductors consist of a single copper conductor, 200 µm x 33 µm in cross-section and surrounded by a layer of magnetic material to form a closed core. The core consists of a 6 µm thick layer of Ni45Fe55, which is deposited by PR plating. The inductance was measured as a function of dc-bias current in the range from 0 A to 3 A. The graph in figure 2 shows a typical measurement of these devices normalized to zero bias fields.

It is well known that the shape can contribute to the anisotropy field of the core [7]. According to the analysis where the film is assumed to be homogenous the demagnetizing field is assumed to be affected by the shape of the device. As a result, the saturation field in the measured devices is much larger than the saturation of as-deposited Ni45Fe55. The effects of core shape are studied to determine the extent of the saturation enhancement and its effects on bias current capacity in the devices, in order to suggest designs to enhance bias capacity for next generation power inductors.

[1] Donald S. Gardner et al., IEEE Trans. On Magnetics, Vol. 43, NO. 6, June 2007

[2] S. Prabhakaran et al, J. Magn. & Mag. Mat. 290-291, 1343 (2005).

[3] N.Wang, et al; J. Magn. & Mag. Mat. 316, e233-e237, (2007)

[4] S. Prabhakaran et al., IEEE Trans. On Magnetics., Vol. 39, No. 5, Sept. 2003, pp. 3190.

[5] S. Prabhakaran et al., IEEE 36th Power Electronics Specialists Conference, 2005. PESC '05, pp. 1513

[6] S. Roy et al; J. Magn. & Mag. Mat. 290-291, 1524 (2005)

[7] S. Tumanski, Thin Film Magnetoresistive Sensors, IOP Publishing Ltd, 2001, pp 84.

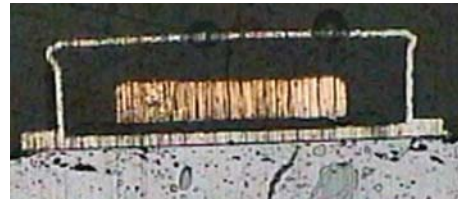

Figure 1: Cross-section of fabricated single turn inductor.

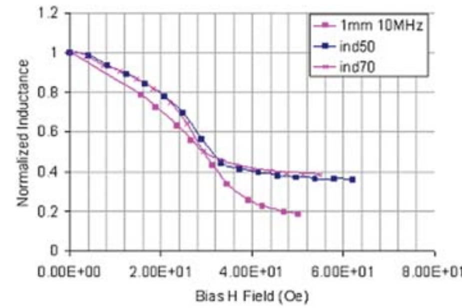

Figure 2: Effect of DC bias current on inductance

AS-01

FABRICATION OF 8X8 ARRAY OF SPIN VALVE PILLARS AND MR CHARACTERIZATION.

A. Lyle[1,2], Y. Hong[1,2], B. C. Choi[3], J. Rudge[3], G. S. Abo[1,2], S. Gee[1,4], H. Han[1,2], J. Jalli[1,2], G. W. Donohoe[5]

1. Electrical and Computer Engineering, University of Alabama, Tuscaloosa, AL; 2. MINT Center, University of Alabama, Tuscaloosa, AL; 3. Physics and Astronomy, University of Victoria, Victoria, BC, Canada; 4. Seagate Technology, Bloomington, MN; 5. Electrical and Computer Engineering, University of Idaho, Moscow, ID

Closed magnetic flux configurations such as vortices have been studied to achieve higher density by limiting interaction between elements [1, 2]. Waeyenberge et al. have already experimentally observed switching of vortex core magnetization using a magnetic field [3]. However, controllable switching of the vortex chirality, which refers to the counter-clockwise (CCW) or clockwise (CW) rotation of the in-plane magnetization, is desirable. The authors have previously simulated spin-polarized current switching of vortex configuration in a 100 nm diameter Co/Cu/Py spin valve pillar [4]. An 8x8 spin valve array based on the simulated spin valve structure was fabricated to experimentally prove the simulated results. In this paper, the 8x8 spin valve array was characterized for MR signal using magnetic field switching.

Electron beam (e-beam) evaporation was used to deposit the following stack onto a SiO_2 wafer: Ti(10)/Py(10)/FeMn(10)/Co(20)/Cu(4)/Py(6)/Ti(2) thickness in nm. Photolithographic patterning and ion milling were used to shape the entire stack into the bottom electrode. Once the bottom electrode was formed, e-beam lithography and ion milling were used to pattern 8 x 8 array of Py/FeMn/Co/Cu/Py/Ti pillars into the spin valve structure on top of the bottom electrode. Then, the structure was planarized using SiO_2 deposited with an e-beam evaporator and a liftoff process. Finally, e-beam evaporation, e-beam lithography, and ion milling were used to shape the top Cu electrode. After fabrication of the array, the array was characterized using a four point probe MR tester.

The fabricated 8x8 array consists of thirty eight 100 nm pillars, eight 200 nm pillars, eight 300 nm pillars, eight 400nm pillars, and two 5 µm pillars as shown in Figure 1. Inset in Figure 1 represents a typical SEM of two 5 µm pillars. Figure 2 shows examples of magnetic field switching MR signal observed from a 100 nm pillar. In Fig. 2(a), one finds that the magnetoresistance decreases by applying in-plane external magnetic field, while a maximum MR value is found at zero field. This result implies that the initial vortex configurations in Py and Co layers have opposite chiralities, in which the in-plane magnetizations in both layers are antiparallel at their remanent state. With increasing magnetic field strength the vortex configuration with antiparallel chiralities in Py and Co layers is distorted, and this leads to decrease of the magnetoresistance. We note that for about half of the pillar structures MR measurements reveal the curves with the minimum value of the magnetoresistance at zero applied field (Fig. 2(b)), while the application of external magnetic field leads to the increase of MR. This is attributed to the same chiralities of the in-plane magnetization of he initial vortex configuration in Py and Co layers. For these pillar structures the initial in-plane magnetizations of NiFe and Co layers are parallel, and it leads to a minimum magnetoresistance at remanence. In this case the application of external magnetic field leads to small changes of the magnetoresistance.

In conclusion magnetoresistance experiments are conducted with arrays of multilayered NiFe/Cu/Co nanopillars with varying diameter as small as 100 nm. The results imply that the chirality in the NiFe layer effectively changes the magnetoresistance values. The result suggests a new way to implement the vortex chirality in memory device applications, in which vortex states with controllable chirality switching in a layer of magnetic nanoelement may be used as memory bits

Acknowledgements

This research was supported by AFRL F29601041206.

1.J.G. Caputu, Y. Gaididei, F.G. Mertens, and D.D. Sheka, Phys. Rev. Lett., 98, 056604 (2007).

2.Q.F. Xiao, J. Rudge, B.C. Choi, Y.K Hong, G. Donohoe, Appl. Phys. Lett. 89, 262507 (2006).

3.B. Van Waeyenberge, A. Puzic, H. Stoll, K. W. Chou, T. Tyliszczak, R. Hertel, M. Fahnle, H. Bruckl, K. Rott, G. Reiss, I. Neudecker, D. Weiss, C. H. Back, and G. Schutz, Nature (London), 444, 461 (2006).

4.B. C. Choi, J. Rudge, E. Girgis, J. Kolthammer, Y. K. Hong, and A. Lyle, Applied Physics Latters, 91, 022501 (2007).

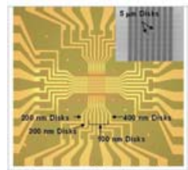

Fig. 1. Optical image of 8x8 spin valve pillar array. Inset shows two 5 um pillars.

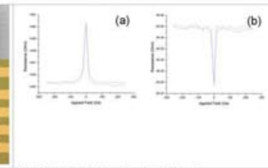

Fig. 2. MR signal of 100 nm diameter spin valve pillar.

AS-02

Two-dimensional imaging of giant magnetoresistance with improved sensitivity.

R. A. Armstrong[1], S. M. Stirk[1], R. T. Mennicke[1], A. F. Lee[2], J. A. Matthew[1], S. M. Thompson[1]
1. Physics, University of York, York, United Kingdom; 2. Chemistry, University of York, York, United Kingdom

The first 2 dimensional (2D) images of Giant Magnetoresistance (GMR) using an infra red (IR) camera in the wavelength regime 8-12µm are presented, demonstrating a factor of 3 improvement in sensitivity of the technique compared to previous work in the 3-5µm regime.
In the far IR, the dielectric response of a metal is directly related to its d.c. electrical conductivity with the result that the refractive index is a function of the electrical resistivity. This is exploited in remote techniques for measuring GMR by sensing a change in reflection, transmission or emission in an applied magnetic field. Emissivity lends itself to spatial resolution using an IR camera to generate images of a material's apparent temperature. A change in emissivity due to an applied magnetic field results in a change in IR power radiated from the material's surface, which is observed as a change in the temperature. IR imaging techniques thus allow 2D images of GMR to be constructed. This has been demonstrated for GMR and spin-valve multilayers down to a resolution of 30µm [1,2].
Assuming perfect thermal coupling between sample and detector, in the long wavelength Hagen Rubens region the GMR is proportional to the fractional change in emissivity, ε, i.e. $(\Delta\varepsilon/\varepsilon)=\gamma\times$GMR with a correlation factor γ=0.5. This dielectric model breaks down at shorter wavelengths where interband transitions become possible. This is seen in the magnetorefractive effect (MRE) spectrum in Fig. 1 in which the percentage change in the reflected intensity in an applied magnetic field is plotted as a function of wavelength. At long wavelengths the MRE tends to the Hagen Rubens value, whereas at short wavelengths the effect becomes smaller and changes sign. The wavelength regimes of the 2 cameras are indicated, showing a larger effect and different sign for the 8-12µm band. Further improvement is expected due to better matching of the spectral sensitivity of the camera and the Planck radiation curve. Over the reduced wavelength band, Stefan's Law must be modified to: $I\approx\varepsilon_{avg}\sigma'(T^x-T_0^{\ x})$, where I is the radiated intensity, σ' is a modified Stefan-Boltzmann constant, T is the sample temperature (typically 320K), T_0 the temperature of the environment and x the power to which T is raised, 4 when integrating over the entire spectrum. New values of σ' and x are found by simulation. The value of σ' does not affect the measurement, but the reduction in x from 9.4 in the 3-5µm range to 4.4 in the 8-12µm range improves the sensitivity. In practice, the sensitivity is reduced relative to its ideal value by ambient radiation which is field-independent, but the response remains proportional to the GMR.
A NiFeCr/[($CoFe_{1.5nm}$/$Cu_{1.2nm}$]$_{25}$/TaN_{7nm} antiferromagnetically coupled multilayer exhibiting 28% GMR in an applied field of 0.87T (provided by Seagate (Ireland)), was used to compare the 2 wavelength regimes. The correlation factor, γ, was found to increase in magnitude from 0.064 with the 3-5µm camera to 0.2 with the 8-12µm camera, with the sign of the effect reversing as expected. This corresponds to an apparent temperature drop of 0.6K in the applied field, easily detectable with the IR camera (resolution: 30mK). Fig. 2 shows the change in colour of the 2D temperature image as the magnetic field is applied giving a very visual image of the spatial variation of GMR across the sample. Note that this image has not been optimised for spatial resolution, but provides an indication of the potential of the technique for whole GMR wafer scanning.

[1] S.M. Stirk et. al., J. Magn. Magn. Mater. 316(2) e953 (2007)

[2] S.M. Stirk et. al. J. Appl. Phys. 99(8) 08T101 (2006)

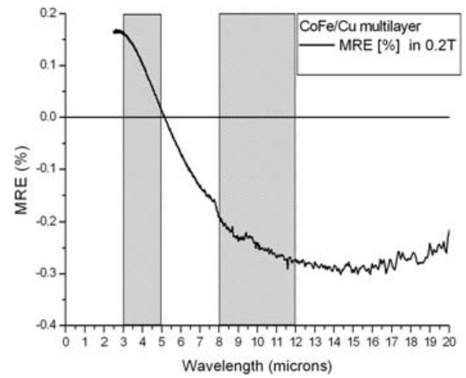

The change in reflected intensity for a NiFeCr/[($CoFe_{1.5nm}$/$Cu_{1.2nm}$]$_{25}$/TaN_{7nm} multilayer in an applied magnetic field of 0.2T. The shaded wavelength bands correspond to the wavelength sensitivity ranges of the two IR cameras under test.

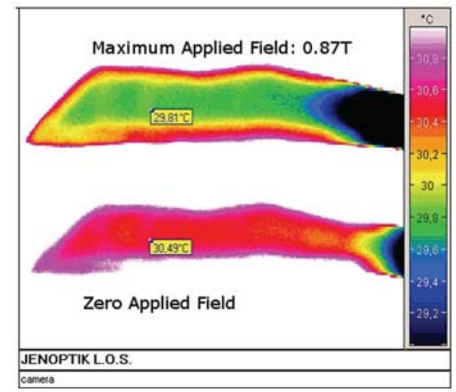

Thermal images of the giant magnetoresistive 5cm wide NiFeCr/[($CoFe_{1.5nm}$/$Cu_{1.2nm}$]$_{25}$/TaN_{7nm} multilayer showing the apparent temperature change as the magnetic field is reduced from 0.87T to 0T. This apparent temperature rise results from the increase in emissivity as the electrical resistivity is increased. The images are taken using an InfraTec/Jenoptik Varioscan 3021 IR camera sensitive to wavelengths from 8-12µm, the sample was heated to T=315K.

AS-03

Magnetic degradation of GMR spin-valve multi-layers due to electromigration induced failures.

J. Jiang[1], S. Bae[1], H. Ryu[2]
1. Electrical and Computer Engineering, National University of Singapore, Singapore, Singapore; 2. IT Convergence & Components Laboratory, ETRI, Daejon, South Korea

Introduction

Ferromagnetic(FM)/Cu spacer/FM GMR spin-valve multi-layers have been paid a great deal of attractions in the various spintronic devices such as magnetic recording read sensors and magnetic random access memories (MRAMs) due to their technical promises. The most important consideration in designing such spintronic devices is the magnetic stability of spin-valve multi-layers[1]. In this study, magnetic degradation of GMR spin-valve multi-layers was investigated for the first time by considering the electromigration(EM) induced inter-diffusion between the magnetic layer and Cu spacer. In order to clearly verify the physical nature for the magnetic degradation of GMR spin-valve multi-layers caused by EM, a Co diffusion barrier was used to control the Ni-Cu intermixing through NiFe/Cu interfaces in the NiFe/(Co)/Cu/(Co)/NiFe multi-layer based spintronic devices. In addition, diffusion behavior of Cu and its physical effects on the magnetic degradation in the spin-valve multi-layers with or without Co diffusion barrier were characterized by using a EDX(Energy Dispersive X-ray) and a cross sectional TEM(XTEM).

Experiment

All the NiFe(3.0)/Cu(x)/NiFe(3.0)[nm] and NiFe(2.5)/Co(0.5)/Cu(x)/Co(0.5)/NiFe(2.5)[nm](x=1.8~3.2nm) spin-valve multi-layers were sputtered at the base pressure around 2×10^{-8}Torr. Ar working gas pressure for NiFe,Co and Cu thin films was fixed at 2 mTorr. To study the effect of EM-induced failures (EIFs) on the magnetic stability of NiFe/(Co)/Cu/(Co)/NiFe multi-layers, M-H loops before and after applying DC constant electrical stress were measured by using a vibrating sample magnetometer(VSM). All the samples were stressed under $J=1\times10^{6}$ A/cm^2 for 12 hours and their resistance change(ΔR) was measured using a computer-controlled probe station. The Ni-Cu interdiffusion at the NiFe/Cu interfaces was qualitatively analyzed using a nano-beam EDX with a nominal beam size of 2 nm and XTEM.

Results and Discussion

Figure 1 shows the M-H loops of NiFe/(Co)/Cu/(Co)/NiFe spin-valve multi-layers before and after electrical stress. As clearly shown in Fig.1-a and b, NiFe/Cu/NiFe showed an obvious change of magnetic moment and interlayer coupling field, while there was no magnetic degradation in NiFe/Co/Cu/Co/NiFe mutli-layers. Fig.1-c shows ΔR during 12-hour electrical stress time. For the NiFe/Cu/NiFe tri-layers, resistance-time(R-t) curve showed a very serious oscillation characteristics (alternant electrical open and short), but in contrast, R-t curve showed continuous and smooth increase without any oscillation for the NiFe/Co/Cu/Co/NiFe multi-layers during electrical stress. By considering the relatively lower activation energy of Cu compared to that of NiFe and Co[1] and "current sinking effects"[2] describing 2/3 of applied current flows through Cu spacer due to film resistance difference, EIFs can be supposed to be first occurred in Cu spacer and then the melted Cu atoms would disperse through NiFe/Cu interfaces for intermixing with Ni atoms to form a Ni-Cu alloy (or non-magnetic Ni-Cu dead region) due to the high solid solubility between Ni and Cu atoms[3]. This would cause the decrease of magnetic layer thickness and accordingly result in the increase of "effective" spacer layer thickness. As a result, for the NiFe/Cu/NiFe, the interlayer coupling oscillation curve was seriously changed to shift toward the increasing direction of Cu spacer thickness after electrical stressing and the magnetization of NiFe/Cu/NiFe was dramatically reduced due to the decrease of magnetic moment in NiFe magnetic layer. EDX analysis shown in Figure 2 apparently demonstrates that the inter-diffusion of Cu through the NiFe/Cu interfaces in the NiFe/Cu/NiFe spin-valve multi-layers is quite serious, while the insertion of Co thin film between NiFe and Cu layer shows a significant diffusion barrier effect. In conclusion, it was clearly verified that the control of Cu spacer inter-diffusion due to electromigration is the most crucial factor in determining the magnetic stability in GMR spin-valve multi-layer based spintronic devices.

[1]S. Bae, et. al., IEEE Trans. Magn., vol.38, 2655, (2002).

[2]B. A. Gurney, et. al., J. Appl. Phys., vol. 81, 3998, (1997).

[3]Binary alloy phase diagrams, edited by Thaddeus B. Massalski, et. al., p.1444, (1990).

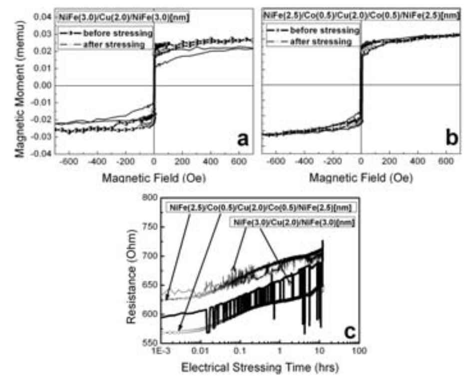

Fig.1.a~b) M-H loop comparison for tri-layer and multi-layers;c) Resistance vs. stressing time curves after stressing at J=1×106 A/cm2 for 12 hours, R.T..

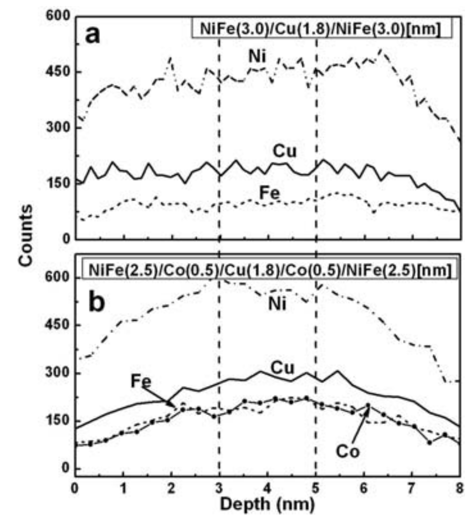

Fig. 2. EDX line-profile analysis across the tri-layer and multi-layer, respectively.

AS-04

High spin polarization of epitaxial films with artificial alternate monatomic $[Fe/Co]_n$ superlattice.

I. Chu[1], A. Rajanikanth[2], Y. Takahashi[2], K. Hono[2], *M. Doi*[1], M. Sahashi[1]

1. Department of Electronic Engineering, Tohoku University, Sendai, Japan; 2. National institute for materials Science, Tsukuba, Japan

[Introduction]

The point-contact Andreev reflection (PCAR) enables the direct measurement of the spin polarization in electron transport, which is one of important factor responsible for the magnetoresistance effect in various layered magnetic structure. The study on spin polarization is not only essential for better understanding of magnetic transport physics, but the wide application range of magnetoresistive devices makes it technologically relevant as well [1, 2)]. We tried to develop a suitable ferromagnetic material for CPP-GMR. Full metals system is needed because it is so important in application for MR heads sensor to obtain large change of resistance in the active area, while maintaining a low resistance in the total system. Moreover, in the case of an epitaxial system, more ideal surface is able to be obtained than in the case of a polycrystalline one. Therefore one would expect it to be easier to investigate the physical origin of spin scattering in the active area than in that of a polycrystalline one in which the moment direction exerts various effects in the unit area. We attempted to prepare samples incorporating an artificially AML $[Fe/Co]_n$ epitaxial film with ordered structure and to confirm the magnetic and structural properties of AML $[Fe/Co]_n$ epitaxial films on MgO (001) substrate by PCAR, STM and RHEED[3)]. For the sake of comparison, we also prepared the pure Fe, and $Fe_{50}Co_{50}$ alloy epitaxial films.

[Experimental]

We prepared ordered phase Fe50Co50 by the alternate monatomic deposition method, in which monolayer of Fe and Co is alternately deposited at suitable substrate temperature[4, 5)]. The samples were prepared on MgO substrates with orientation (001) by the EB evaporation technique. To examine the structure of the deposited epitaxial films, we used in-situ STM to observe their topology and in-situ Reflective High Energy Electron Diffraction (RHEED) technique to investigate epitaxial property of their surface. We prepared the samples with ordered or disordered epitaxial phase Fe50Co50 epitaxial layer on MgO (001) substrate by the alternated monatomic deposition of Fe (99.99 %) and Co (99.99 %) targets or the normal deposition of $Fe_{50}Co_{50}$ alloy target. The growth of an epitaxial film with 71 MLs (Monolayers) of [Fe/Co] on MgO (001) was performed at the substrate temperatures of 75 and 250 ^{o}C and a typical base pressure of less than 10^{-7} Pa. The disordered $Fe_{50}Co_{50}$ and pure Fe were fabricated at a substrate temperature of 75 ^{o}C, with thickness of 10 nm corresponding to that of the 71 MLs of AML [Fe/Co] epitaxial film. We present the PCAR measurements of X/Nb contacts, where X = bcc-Fe, $Fe_{50}Co_{50}$, and alternate monatomic $[Fe/Co]_n$. The PCAR measurements were done using an Nb tip, pressed into the metal films by a differential screw mechanism. A 0.3 mm diameter Nb wire was electropolished to a sharp needle with a tip diameter of approximately 100 nm, which was used to obtain the superconducting point contacts with the samples. The tip and film were enclosed in a jacket and immersed in a liquid helium bath. All measurements were performed at a temperature of 4.2 K. The normalized conductance curves were fitted with the modified Blonder-Tinkham-Klapwijk (BTK)[6)] model to estimate the spin polarization P using a multiple parameter fitting. The dimensionless interfacial scattering parameter Z, superconducting gap Δ, and P were the parameters used for the fitting.

[Result and discussion]

The Andreev reflection at the $[Fe/Co]_n$ /Nb point contact was used to determine the spin polarization of single-crystal films made by electron beam evaporation. From these measurements an intrinsic transport spin polarization P values of 0.48, 0.50 and 0.60 were obtained for pure Fe, $Fe_{50}Co_{50}$ alloy and alternate monatomic $[Fe/Co]_n$ epitaxial film, respectively (Table 1). Moreover we confirmed that the spin polarization is affected by the substrate temperature (0.60 for 75 ^{o}C, 0.57 for 250 ^{o}C) and is higher for AML [Fe/Co] epitaxial film than for $Fe_{50}Co_{50}$ alloy, due to the increase in the degree of ordering for $Fe_{50}Co_{50}$ afforded by the monatomic deposition method. It should be noted that the P of 0.60 is equivalent to the value obtained by PCAR for half metallic heusler alloys[9)]. These results are of importance in understanding the physical origin of spin transport in all metal CPP epitaxial systems.

[1] T. Valet, and A. Fert, Phys. Rev. B, 48, 7099 (1993)

[2] Michael Ziese Martin J. Thornton, Spin Electronics (2001)

[3] I. C. Chu, Y. Saki, S. Kawasaki, M. Doi, and M. Sahashi, Jpn. J. Appl. Phys. (submitted)

[4] I. C. Chu, M. Doi, and M. Sahashi, J. Magn. Magn. Mater., Vol. 304, Issue 1, e121-e123 (2006)

[5] I. C. Chu, M. Doi, and M. Sahashi, HB-09, INTERMAG SANDIEGO

[6] G. J. Strijkers, Y. Ji, F. Y. Yang, C. L. Chien, and J. M. Byers. Phys. Rev. B 63, 104510 (2001)

[7] D. J. Monsma and S. S. P Parkin, Appl. Phys. Lett. 77, 720 (2000)

[8] C. H. Kant, O. Kurnosikov, A. T. Filip, P. LeClair, H. J. M. Swagten, and W. J. M. de Jonge, Phys. Rev. B 66, 212403 (2002)

[9] S. V. Karthik, A. Rajanikanth, Y. K. Takahashi, T. Okubo, and K. Hono, Appl. Phys. Lett. 89, 0525505 (2006)

Ferromagnetic material	Spin Polarization	Measurement Temp.
Alternate monatomic [Fe/Co], Ts : 75 ℃	0.60	4.2 K
Alternate monatomic [Fe/Co], Ts : 250 ℃	0.57	4.2 K
$Fe_{50}Co_{50}$, Ts : 75 ℃	0.50	4.2 K
Fe, Ts : 75 ℃	0.48	4.2 K
$Fe_{50}Co_{50}$ [7]	0.50	0.25 K (STS)
Fe [8]	0.47	4.2 K

Spin polarization P of FM relative to reference. (FM : alternate monatomic [Fe/Co] grown at 75, 250 ^{o}C, $Fe_{50}Co_{50}$ alloy, Fe)

AS-05

Microstructure, magnetoresistance and interlayer coupling studies in FePt/Os/FePt thin films.

C. Shih-Yuan[1], Y. Yeong-Der[2], W. Jenn-Ming[1], Y. Chin-Chung[3]
1. Materials Science and Engineering, National Tsing Hua University, Taipei, Taiwan; 2. Materials Engineering, Tatung University, Taipei, Taiwan; 3. Applied Physics, National University of Kaohsiung, Kaohsiung, Taiwan

The antiferromagnetic coupling of the moments is due to the oscillatory exchange coupling phenomenon which reported by Parkin [1]. Several non-magnetic transition metals spacer layer such as Cr, Cu and Ru have stimulated considerable interest [2-4]. Because Os has very high melting and boiling point, which is predicted to have good effect on preventing interdiffusion between layers, and the disordered FePt is a very soft ferromagnetic material. In this investigation, we attempt to study on the effect of the Os layer to the FePt layers. The FePt/Os/FePt thin films were deposited on Si(100) substrates with a 5 nm Ta buffer layer by dc-magnetron sputtering system. The thickness of the ferromagnetic layers was 100 Å in all cases and a series of trilayers with Os spacer varied from 0 Å to 9 Å. The crystal structures were characterized by X-ray diffraction and high resolution transmission electron microscopy. Magnetic properties of the films were measured by a vibrating sample magnetometer. The magnetoresistance were measured with a standard dc four-point probe technique. We dealt with the FePt multilayer thin films without post annealing on purpose to achieve that the magnetism of FePt/Os/FePt thin films could be tend to appear an antiferromagnetic exchange coupling (AFC) behavior. Fig. 1(a) shows the hysteresis loops vs Os spacer thickness varied from 0 to 9 Å. As the thickness increased from 1 to 3 Å, it appeared an AFC behavior. The ferromagnetic behavior observed in samples with Os spacer layer of 0, 4, 5, 7 and 9 Å. In general, the AFC in multilayer system shows the first maximum of AFC peak occurring at spacer thickness between 8 and 11 Å for most spacer materials [5]; however, in FePt/Os/FePt films, it appeared at 2 Å. In our investigation, a clear AFC behavior of the FePt/Os/FePt system could be observed at 2 Å. From the M-H loops, the coercive force (Hc) of about several tens of oersteds was found which indicated that the FePt has a disordered structure. The results showed the squareness value decreased from 0.77 to the minimum value of 0.04 at 2 Å, and then increasing and dependence of saturation field on Os spacer layer thickness showed a maximum value of 2614 Oe at 2 Å as shown in Fig. 1(b) and 1(c), respectively. The anisotropic magnetoresistance is always existed in FePt multilayer system, even for samples with the Os thickness of 2 Å, i.e. for sample with strongest anti-ferro-magnetic coupling. Fig. 2(a) shows the variations of the ΔMR ratio with Os layer thickness. The measurements have been made with the magnetic field in the film plane and parallel to the current direction. The ΔMR ratio was defined as shown in the inset figure (ΔMR ratio = 100(Rp-Ro)/Ro), that Rp is the peak value of resistance due to interlayer exchange coupling. From the MR study, ΔMR ratio increased from 0.01 % to the maximum value 0.14 % at 2 Å and then decreasing. The peak field of MR figures increased from 10 Oe to the maximum value 250 Oe at 2 Å and then decreasing as shown in Fig. 2(b). The FePt/Os/FePt thin films with Os layer varied between 1 and 9 Å were investigated. This is the first time that a clear AFC behavior of the FePt/Os/FePt system could be observed for samples with Os at 2 Å. The microstructure and details of the FePt/Os/FePt thin films will be discussed.

[1] S. S. P. Parkin, N. More, K. P. Roche, Phys. Rev. Lett. 64 (1990), p. 2304.

[2] S. S. P. Parkin, Phys. Rev. Lett. 67 (1991), p. 3598.

[3] S. S. P. Parkin, R. Bhadra, K. P. Roche, Phys. Rev. Lett. 66 (1991), p. 2152.

[4] Y. Wang, P. M. Levy, J. L. Fry, Phys. Rev. Lett. 65 (1990), p. 2732.

[5] U. Hartmann, Magnetic Multilayers and Giant Magnetoresistance, Springer-Verlag, Berlin (2000).

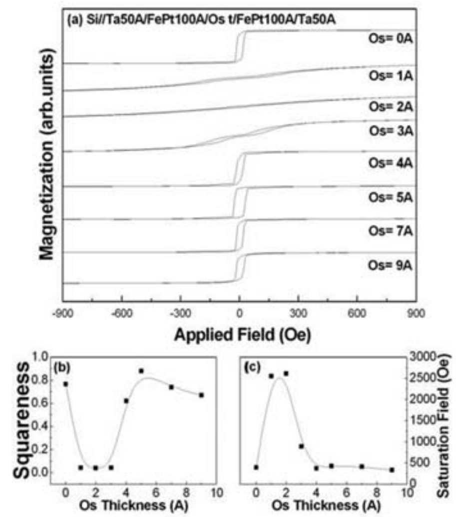

Fig. 1 The M-H loops of Si//Ta/FePt/Os/FePt/Ta thin films with various Os spacer thickness (a). The squareness (b) and saturation field (c) versus various Os thickness are plotted, respectively.

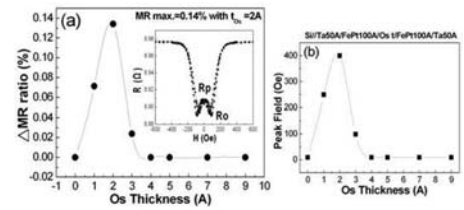

Fig. 2 Relationship between ΔMR ratio and Os thickness (a) and the peak field strength versus various Os thickness of Si//Ta/FePt/Os/FePt/Ta thin films (b).

AS-06

Novel Granular Thin Film Device Structure.

S. Regunathan, V. Ng
Information Storage Materials Laboratory, Dept of Electrical and Computer Engg, National University of Singapore, Singapore, Singapore

Granular thin films consist of nanometer size magnetic particles dispersed in non-magnetic insulating material[1]. The magnetic particles are super-paramagnetic with low coercivity(Hc) and their electrical properties are characterized by the phenomenon of Tunneling Magnetoresistance(TMR)[2].Though many works have been carried out,the research on granular film devices is very limited,most common being the Granular in Gap structure [3].
In this paper a novel granular film device structure is proposed which consists of a insulating HfO_2 layer sandwiched between two granular film layers.The granular film used in our experiment consists of Co particles embedded in HfO_2 matrix. This structure is fabricated and investigated for possible tunneling of electrons between the top and bottom layer which may enhance the magnetoresistance (MR)properties.
The thin films are fabricated on Si and glass substrates by sequential sputtering of discontinuous layers of Co and HfO_2.A thickness of 19nm (Fig.1a) is found to be optimum for the granular film in terms of Hc and MR ratio.Fig.1b shows the proposed structure whereby 2 layers of granular film are separated by a HfO_2 layer(9.3nm) and fig.1c shows the 38nm granular film reference.The granular film sputtered on Si and glass substrate are used for VSM and MR measurements respectively. Shadow mask technique is used to deposit Al contacts on the the glass substrate to facilitate MR measurements.The distance between the two contacts is 8mm.
Table 1 shows the Hc, saturation magnetization (Ms),magnetic retentivity(Mr) and squareness(S) obtained for the various structures.The proposed structure has a effective thickness of 38 nm for the granular film, but the Hc value is closer to that of the 19nm thick structure. This clearly indicates that, there is minimal magnetic coupling between the top and bottom granular film in the proposed structure.
Fig.2 shows the MR measurements for all the three structures. A constant dc current of 1μA is sourced and the corresponding voltage is measured in order to get the resistance.This measurement is carried out while sweeping the DC magnetic field from +4.2 KOe to -4.2 KOe and then back to + 4.2 KOe.The MR ratio is calculated as (Rmax–Rmin)/Rmin.It can be seen that the 38nm thick structure has the highest resistance(697.71KΩ),followed by the 19nm thick film(322.94KΩ)and the proposed structure(55.24KΩ).As far as the MR measurement is concerned the 19nm structure gives the highest MR ratio for the entire range followed by the proposed structure and then the 38nm structure.
However,closer analysis of the graph shows that the change in gradient is the highest for the proposed structure.In order to get a clear picture and to eliminate the confusion caused by the different resistance ranges for the 3 structures, MR ratio vs. Magnetic field graph has been plotted(Fig 3).It can be clearly seen that the proposed structure is more sensitive to the magnetic field variations in the range 0–3000 Oe,whereas for fields greater than 3000 Oe,the 19nm structure gives a better sensitivity. This variation could be due to the fact that there is tunneling occurring between the top and bottom layer of the proposed granular film structure and its contribution is more apparent at lower fields than at higher fields.Currently,lateral devices based on this structure are being fabricated,the dimensions of which are in the nanometer regime. The results for the same will be included during the final article submission.

[1]S Mitani et al.,J.Magn. Magn. Mater.,165:141,1997.

[2]I S Beloborodov et al.,Rev. Mod. Phys.,79:469, 2007.

[3]H Fujimori et al.,Mater. Sci. Eng. A,267:184, 1999.

Granular Film	Hc(Oe)	Ms(emu)	Mr(emu)	S
Proposed Structure	2.25	4.85e-04	2.20e-6	0.004536
38nm thick film	11.25	9.60e-04	1.10e-04	0.114583
19nm thick film	2.5	4.10e-04	8.5e-07	0.002073

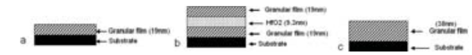

Fig 1 :Granular film a) 19nm thick b)Proposed structure c)38nm thick

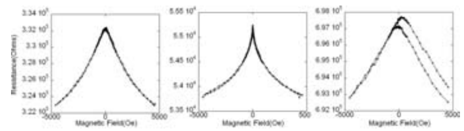

Fig 2: MR graph a) 19nm file(2.86 % MR) b) proposed structure(2.69%MR) c) 38nm film(0.72% MR)

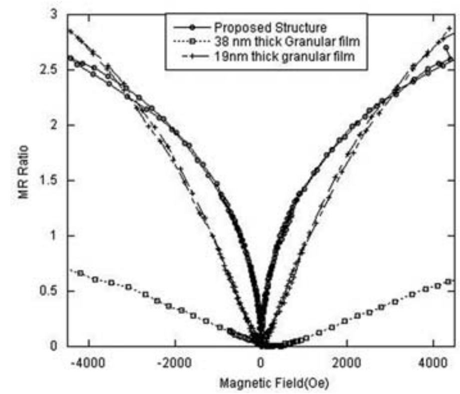

Fig 3:MR ratio versus Magnetic Field graph

Nature and entropy content of the magnetic transitions in pure and pseudo-binary Laves phases RCo_2

M. Parra-Borderías[1], F. Bartolomé[1], J. Herrero-Albillos[2], L. M. García[1]
1. Instituto de Ciencia de Materiales de Aragón, CSIC-Universidad de Zaragoza, Zaragoza, Spain; 2. Department of Materials Science, University of Cambridge, Cambridge, United Kingdom

RCo_2 Laves phases compounds (R= rare eath ion) are potential candidates for magnetic cooling [1] in the 30-150 K temperature range, due to their abrupt magnetization change in a narrow temperature range. As compounds displaying first-order phase transitions are more interesting for magnetocaloric applications, the determination of the thermodynamic order and the entropy content of RCo_2 magnetic transition is of great interest.
The first aim of this work is the systematic study of the nature of the magnetic ordering in five RCo_2 pure compounds (R = Er, Dy, Ho, Nd, Pr) [2] and in the pseudo-binary solid dilution $Er_xPr_{1-x}Co_2$ (x = 0.9, 0.8, 0.7, 0.6, 0.4) by using the Banerjee criterion [3], and analysing its application limits at the same time. According to this criterion, developed in the framework of the Landau-Lifshitz theory, one can distinguish first- and second-order phase transition analysing the parameters sign in the expression that relates magnetization and magnetic field [3]:
$\mu_oH=a(T)\times M+ b(T)\times M^3+ c(T)\times M^5$ (1)
To do so, we have systematically measured M(H) isothermal curves in all studied systems, as shown in Fig. 1 for R = Er and Dy. The application of Banerjee criterion to M(H,T) measurements on RCo_2 Laves phases, by fitting the curves as shown in Fig. 2, confirms the second-order character of the transition in $PrCo_2$ and $NdCo_2$, which was recently questioned [4]. Moreover, this study shows a *"weakening"* of first-order character in $Er_xPr_{1-x}Co_2$ (x = 0.9, 0.8, 0.7) solid dilutions as we diminish x, in the same way as $DyCo_2$ is *weakly* first-order, i.e. the discontinuity of first derivatives of thermodynamic potentials are very small. We will show that the thermal dependence of the Landau-Lifshitz parameters near the transition allows to define a new parameter, Δ, that quantifies the "strength" of the transition first- order character; this parameter can be phenomenologicaly related to the entropy change in the transition.
For $Er_xPr_{1-x}Co_2$ (x = 0.6, 0.4) a competition between ferromagnetic Pr-Co interaction and antiferromagnetic Er-Co interaction is observed as low-field reorientations in M(H,T) measurements. This process is studied by means of calorimetric and susceptibility measurements.
Finally, we present magnetocaloric parameters of RCo_2 compounds obtained applying Maxwell relations. The interest of pseudobinaries is mainly to combine the high critical temperature of some members of the series (as $GdCo_2$) and the very high entropy content of the first order transition of others (as $ErCo_2$) in order to tune the properties of the final system. We will present our results on the expectable results on this strategy.

[1] E. Gratz y A.S. Markosyan. Physical properties of RCo_2 Laves Phases. *Journal of Physics.: Condens. Matter*,**13**, R385, (2001).

[2] J. Herrero-Albillos, F. Bartolomé, L. M. García, F. Casanova, A. Labarta, and X. Batlle, Phys. Rev. B 73, 134410 (2006).

[3] S. K. Banerjee, Phys. Lett. 12, 16 (1964).

[4] M. Forker, S. Müller, P. de la Presa and A. F. Pasquevich, Phys. Rev. B 68, 014409 (2003)

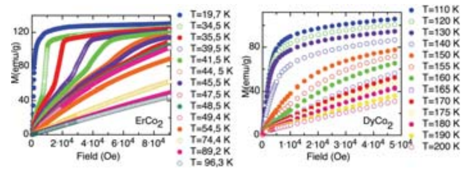

Figure 1: Magnetization of $ErCo_2$ and $DyCo_2$ as a function of magnetic field at constant temperature.

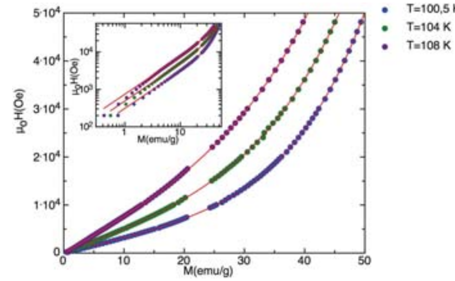

Figure 2: μ_oH as a function of Magnetization of $NdCo_2$ at three different temperatures (full circles). The solid lines represent the fit to Eq. 1.

AT-02

Estimating magnetic entropy change by a mean-field scaling method and the effect of magnetic irreversibility in first-order transitions.

J. S. Amaral[1], N. O. Silva[1,2], V. S. Amaral[1]
1. Physics and CICECO, Universidade de Aveiro, Aveiro, Portugal; 2. Materia Condensada, Facultad de Ciencias, Zaragoza, Spain

Magnetic refrigeration is an ecologically friendly alternative to vapor-cycle refrigeration. A magnetic refrigeration device is based on cycles of magnetizing and demagnetizing a magnetic material, making the study of the magnetocaloric effect of materials a very active field of research [1].
The magnetocaloric effect can be characterized from two distinct thermodynamic values, the adiabatic entropy change, ΔT_{ad} (from calorimetric measurements) and ΔSM (from calorimetric or magnetization measurements) [3]. The standard method for estimating ΔSM from magnetization measurements is to numerically integrate a Maxwell relation.
In a recent work [3], we presented a method based on mean-field theory, where directly from magnetization data, the mean-field exchange parameter λ and the state function f, from the equation of state M=f((H+λM)/T), are determined.
Having determined λ and f, magnetic entropy change can be estimated from numerically integrating the inverse f function in M, if λ does not explicitly depend on T. Taking experimental measurements from second- and first-order manganite systems, magnetic entropy estimations from the Maxwell relation integration were found to be comparable for both systems:
In the case of the first-order manganite, we found that if the if M versus H data generated by the mean field method was used to estimate ΔSM via integration of the Maxwell relation, an extra peak would appear near TC, very similar to experimental results obtained in first-order magnetic transition systems, and generally attributed to numerical errors [4]. However, the extra ΔSM peak from integrating the Maxwell relation persists even with arbitrarily small steps in T and H, which would minimize the numerical error, indicating that its presence has another origin. On the other hand, integrating the inverse f function produced curves with no extra ΔSM peak.
In order to better understand this effect, we modeled the results of measuring M(H) in non-equilibrium conditions in 1st order phase transitions, by the mean field model. The non equilibrium solutions correspond to situations of measurements in decreasing and increasing fields near the phase transition. The calculated values (together with the equilibrium solution) of M(H) at each temperature were used as input for the determination of the magnetic entropy change using the Maxwell relation. The state function used was the Brillouin function with S=2, and the exchange parameters chosen where a λ value corresponding to a $\theta_P \sim 300$ K, and $\lambda^3 = 1.5\ (\mathrm{Oe.g.emu^{-1}})^3$ (Figure 1).
Estimating the magnetic entropy change from the inverse Brillouin function for the three curves produced similar results, while using the Maxwell function for the three solutions gave far different results, whereas only in equilibrium are the two methods in agreement (Figure 2).
The amount of overestimation of ΔSM by Maxwell relation integration in out-of-equilibrium conditions depends on the how strongly first-order is the character of the transition, and can clearly exceed the limit of Rln(2S+1) for a large value of λ^3. For the same set of data, estimating ΔSM by the inverse Brillouin integration never exceeds this limit.
We acknowledge the financial support from FCT, (POCI/FP/63953/2005 and POCI/CTM/61284/2004) and PhD. grant SFRH/BD/17961/2004.

[1] Amaral, J. S., N. J. O. Silva, et al. (2007), Appl. Phys. Lett. 91(17): - 172503.

[2] Gschneidner, K. A., V. K. Pecharsky, et al. (2005), Rep. Prog. Phys. 68(6): 1479-1539.

[3] Pecharsky, V. K. and K. A. Gschneidner (1999), J. Appl. Phys. 86(1): 565-575.

[4] Wada, H. and Y. Tanabe (2001), Appl. Phys. Lett. 79(20): 3302-3304.

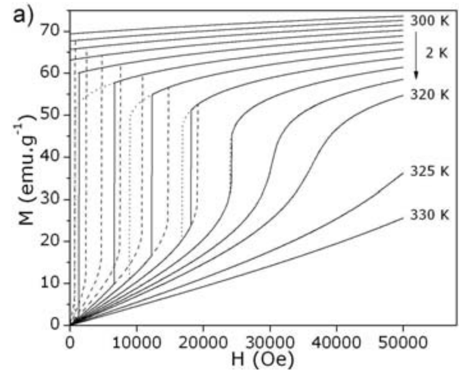

Magnetization versus field curves from mean-field model, with equilibrium and out-of-equilibrium solutions shown, as described in text.

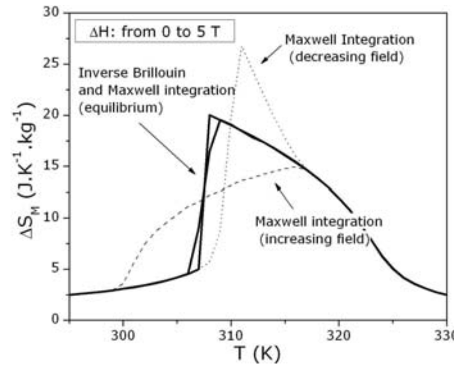

Magnetic entropy change estimation from Maxwell relation integration and from inverse Brillouin integration, for equilibrium and non-equilibrium solutions, as described in text.

AT-03

Magnetic and structural phase transitions in magnets with a NaCl structure.

F. A. Kassan-Ogly[1], B. N. Filippov[2]
1. Department of Theoretical and Mathematical Physics, Institute of Metal Physics, Ekaterinburg, Russian Federation; 2. Lab. of Micromagnetics, Institute of Metal Physics, Ekaterinburg, Russian Federation

A vast experimental material is available now for magnetic structures and properties of ferromagnets and antiferromagnets with a NaCl structures called monopnictides and monochalcogenides (UN, HoP, CeBi, EuS, UTe, GdSe and others). These antiferromagnets possess very peculiar features that did not obtain the adequate explanation within the framework of existing theoretical models and approaches. In particular, a wide variety of changing magnetic structures with varying temperature and magnetic field, coincidence of magnetic and structural phase transitions (of the first order, as a rule), very strong anisotropy, very special diffuse magnetic neutron scattering above phase transition points, and so on. The main aims of the present paper are the derivation of possible magnetic structures in an fcc lattice with the nearest-neighbor and next-nearest-neighbor interactions taken into account, and the development of a theory of magnetic and other properties of such antiferromagnets. As the initial point, we use not the conventional Heisenberg model, but rather the models of utmost strong anisotropy, modified 6-state and 8-state Potts models [1]. Figure 1 shows possible directions of a magnetic moment in these models. For both models we constructed the sets of interrelated equations for multicomponent order parameter that connect the magnetic and structural properties of the system, and proposed algorithm for their numerical solution.

A revised derivation scheme of possible magnetic structures in an fcc lattice with the nearest and next-nearest-neighbor interactions taken into account is proposed.

Two new types of antiferromagnetic ordering are obtained in an fcc lattice (Fig.2) that can be useful to improve the identification of conventional and new magnetic structures in monopnictides and monochalcogenides. On the base of exchange energy minimization it is shown that some antiferromagnetic structures considered earlier are impossible to exist.

We also showed that at some values of the ratio of cation and anion radii magnetic ordering is impossible in magnets with a NaCl structure.

We derived the expressions for correlations functions and carried out numerical calculations of temperature evolution of neutron magnetic scattering in entire temperature region. It is shown that transformation of the high-temperature diffuse scattering into magnetic Bragg reflections in the Curie or Neel point is the mechanism of magnetic phase transition (Fig.3), and that detailed study of the high-temperature diffuse scattering allows one to get information on the forthcoming phase transitions and low-temperature magnetic structures.

The applications of the developed theory can be found in [2—5].

1. Kassan-Ogly F.A., Modified 6-State and 8-State Potts Models in Magnetic Field, Phase Transitions, 2000, vol. 72, pp. 223—237.

2. Kassan-Ogly F.A. and Filippov B.N., Phase Transitions and Magnetic Scattering of Neurons in UAs. The Physics of Metals and Metallography. V. 100, No. 2, pp. 108—115.

3. Kassan-Ogly F.A. and Filippov B.N., Phase transitions in Antiferromagnets with a NaCl Structure. JMMM, v.300, no.1, pp. e559—e562, 2006.

4. Kassan-Ogly F.A. and Filippov B.N., Magnetic and Structural Phase Transitions in Crystals with a NaCl structure. The Physics of Metals and Metallography(in print).

5. Kassan-Ogly F.A. and Filippov B.N., Magnetic and Structural Phase Transitions in Uranium Chalcogenides. The Physics of Metals and Metallography. (in print).

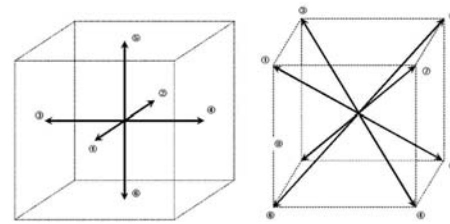

Modified 6-state and 8-state Potts models

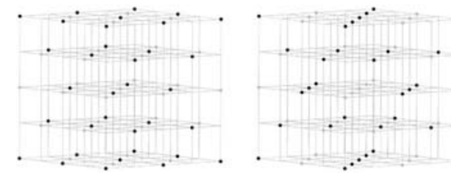

New types of antiferromagnetic ordering in an fcc lattice.

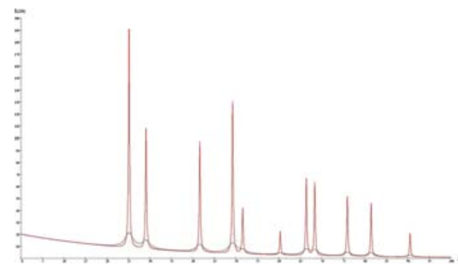

Typical neutron magnetic diffraction pattern.

AT-04

The magnetic phase transition and electronic properties of CoS2-xSex.

M. Otero-Leal[2], F. Rivadulla[1], J. Rivas[2]
1. Depto. Química-Física, Universidad de Santiago de Compostela, Santiago de Compostela, Spain; 2. Fisica Aplicada, Universidad de Santiago de Compostela, Santiago de Compostela, Spain

A first-order ferromagnetic-to-paramagnetic (FM-PM) phase transition is an atypical phenomenon normally associated to strong coupling among different degrees of freedom. In a ferromagnetic system, coupling between the magnetization, M, and other order parameters (or between M and some other non-ordering variable) can renormalize TC, and under certain circumstances change the order of the magnetic phase transition.[1]
Interestingly, many of the most exciting electronic/magnetic phenomena (large magnetocaloric response in ErCo2, Mn1-xFexAs, field-induced structural transitions and magnetoresistance in MnAs, metamagnetism in CoS2, etc.) appear close to a first order FM-PM transition.
The case of the itienerant ferromagnet CoS2 is particularly interesting: TN is reduced with pressure, at the time that the transition becomes first order. However, replacement of S by Se causes a similar reduction of TN in spite of the volume increase; a first-order phase transition has also been suggested for a moderate amount of Se. These results indicate that Se is not just increasing the volume of the unit cell, but it is playing a more decissive role in the physical properties of the material.
In this work we will present experimental results of magnetization under pressure and magnetic fields at different temperatures to monitor the change in the nature of the magnetic phase transition. We derived the Landau coefficients of the phase transition and, contrary to previous suggestions, we found that the transition is first order (or nearly first order) in CoS2, but becomes continuous after Se doping. However, at high fields a metamagnetic transition is observed in Se samples, and this could be the source of previously interpreted as a first order phase transition.
This result will be interpreted on the basis of thermodynamic model applicable to itinerant ferromagnets with strong spin fluctuations.
We will present also electronic transport, magnetoresistance, thermoelectric power, electron paramagnetic resonance, and high-pressure x-ray diffraction results on carefully synthesized samples in order to propose a new phase diagram for this family of compounds.

[1] S. Smart, Phys. Rev. 90, 55 (1953); Y. Imry, et al., Phys. Rev. B 10, 2900 (1974); Y. Imry, J. Phys.; Solid State Phys. 8, 567 (1975); C. P. Bean, D. S. Rodbell, Phys. Rev. B 126, 104 (1962). B. A. Huberman, W. Streifer, Phys. Rev. B 12, 2741 (1975); F. Rivadulla et al., Phys. Rev. Lett. 96, 016402 (2006).

AT-05

Symmetry breaking effects in epitaxial magnetic thin films.

E. Jiménez[1], N. Mikuszeit[1,2], D. Ecija[1], J. Gallego[3], N. Sacristán[1,4], J. Vogel[5], J. Camarero[1], R. Miranda[1,6]

1. Departamento de Física de la Materia Condensada and Instituto de Materiales "Nicolás Cabrera", Universidad Autonoma de Madrid, Madrid, Spain; 2. Institut für Angewandte Physik, Universität Hamburg, Hamburg, Germany; 3. Instituto de Ciencia de Materiales de Madrid ICMM, CSIC, Madrid, Spain; 4. Escuela Universitaria de Informática, Universidad de Valladolid, Segovia, Spain; 5. Institut Néel, CNRS, Grenoble, France; 6. Instituto Madrileño de Estudios Avanzados en Nanociencia, IMDEA-Nanociencia, Madrid, Spain

Magnetic anisotropy is one of the most important properties of magnetic materials and one of the most deeply investigated. As a consequence, the magnetization orientation along certain directions becomes energetically favored and the reversal (hysteresis loop) behavior depends on the applied field orientation. Hysteresis is the central feature of ferromagnetic materials below the Curie temperature and is the property that engineers exploit in practically all applications. Magnetization reversal processes and hysteresis reflect the responses of magnetization to applied fields, and thus they are fundamental to understand reversal mechanisms in nanomagnetism. During the last decades, epitaxial artificial structures represent model systems to study the influence of reduced dimensionality and symmetry on magnetic properties. For instance, the broken symmetry at surfaces and/or interfaces creates contributions to the magnetic anisotropy, leading to alter both magnetization easy-axes directions and reversal processes. The fundamental understanding and control of the phenomena is thus required in order to improve production methods and material quality.

In this presentation we will give a general picture on the magnetic properties, including both characteristic magnetization axis directions and magnetization reversal processes, of epitaxial magnetic systems with broken symmetry.

We have chosen a well characterized system, γ'-Fe4N(100) thin films, in which the four-fold crystal symmetry of the film is broken by a two-fold contribution, originating from stress relaxation of the films. Iron nitride films were grown on Cu(100) single-crystals by molecular beam epitaxy of Fe in the presence of a beam of atomic N provided by a radio-frequency plasma source. The mechanisms of growth were studied from the early stages up to 50 nm thick films by scanning tunneling microscopy (STM), low energy electron diffraction (LEED) and Auger electron spectroscopy. Under the appropriate growth conditions, the films are epitaxial and single-phase γ'-Fe4N(100) [1]. The effects of symmetry breaking of magnetic anisotropy on magnetization reversal behaviour have been investigated by high resolution vectorial Kerr magnetometry. Angular dependent in-plane resolved hysteresis loops were acquired in the whole angular range every 1.8°, with 0.5° angular resolution. The magnetization reversal processes was determined by analyzing the loops by using both normal and vectorial representations (left and right graphs of Fig.1a). In general, the reversal depends on the applied magnetic field angle and on the anisotropies involved. As expected for a thin film with four-fold crystal symmetry, the results show the existence of two easy and two hard magnetization axes. But, in this case, the easy axes are not orthogonal [2], the hard axes are not equivalent, the magnetization reversal behaviour around the two easy axes is not symmetric (see Fig.1a), and the reversal behaviours of the two hard axes are not alike. As a consequence, the polar plot of the remanence displays a "butterfly" shape behaviour (see Fig.1 b).

Numerical simulations based on a simple model have been used to address all the aforementioned features[3]. These features depend on additional terms of the magnetic anisotropy. For instance, the competition between the biaxial (four-fold) anisotropy and the additional uniaxial (two-fold) anisotropy, is the key parameter which control these effects. On the basis of anisotropy balance, we show that the model is applicable to a variety of other symmetry-breaking systems, including other metals, semiconductors, and insulating magnetic materials, indicating why many of these effects were not reported before. The anisotropy constants (and thus the ratio between them) can be changed, for example, if another substrate, layer thickness, material, or temperature are employed. This fundamental understanding could be applicable in order to prepare magnetic materials with custom-chosen properties.

[1] J. M. Gallego et al, Phys. Rev. B **69**, 121404R (2004); Phys. Rev. Lett. **95**, 136102 (2005).

[2] Ecija et al., J. Magn. Magn. Mater. **316**, 321 (2007).

[3] Ecija et al., Phys. Rev. B. accepted.

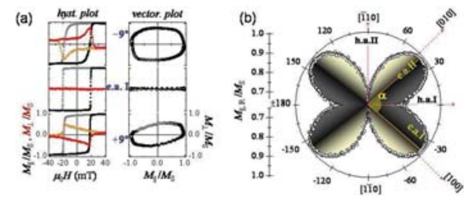

(a) In-plane resolved magnetization curves of a γ'-Fe_4N(100) film around one of the easy axes. Hysteresis (left graphs) and vectorial (right) plots reflect the non-symmetric behavior of the reversal around e.a.I. Upper (bottom) graphs show reversal governed by nucleation a propagation of 90° (180°) domain walls. (b) Polar plot of the remanence of the parallel component, i.e., $M_{\|,R}$= $M_{\|}$(0 mT). The range of angles where different reversal behaviors are found are marked with different shaded areas, e.g., brighter areas indicates the angles where the reversal proceeds by two irreversible transitions (around h.a.II).

AT-06

Cobalt doped β-peptide nanotubes: a new class of spintronic materials.

B. Sanyal[1], P. I. Arvidsson[2,3], O. Eriksson[1]
1. Department of Physics, Uppsala University, Uppsala, Sweden; 2. Department of Biochemistry and Organic Chemistry, Uppsala University, Uppsala, Sweden; 3. Discovery CNS \& Pain Control, AstraZeneca R\&D, S\"{o}dert\"{a}lje, Sweden

Novel materials for use in spintronics applications are continuously sought after [1]. The attention is caused by the potential of manipulating the electron spin in semiconducting devices, which may offer an improvement compared to conventional charge controlled devices. Currently most of the attention is paid to diluted magnetic semiconductors (DMS) for which applications in e.g. non-volatile memories and smaller electronic components have been suggested. The main goal which this research strives for is to develop a ferromagnetic semiconductor which is operational at room temperature. In addition to DMS materials, other groups of materials are currently being investigated [2]. For instance, organometallic molecular materials have recently been under focus. A class of materials which have potential in this field are peptide nano-tubes (PNTs), and they are the focus of this work. An isolated peptide ring has 15 H, 9 C, 3 N and 3 O atoms, as shown in Fig.1, where the infinite nanotube is shown by stacking the peptide rings.

We report a density functional theory based {\it ab-initio} investigation of protein nanotubes formed by a stacking of β-peptide rings. The calculations were performed using the Vienna Ab-initio Simulation Package (VASP) [3] within the projector augmented wave method. We have optimized the structure of β-peptide rings arranged in a nanotube geometry. The calculated inter-atomic bond distances both by local spin density approximation and generalized gradient approximation are found to agree with observations as is the equilibrium inter-ring separation (4.8 \AA). A significant energy gap of around 4 eV is present between the HOMO and LUMO (lowest unoccupied molecular orbital).

The electronic structure has been analyzed by calculating the density of states and band structures, which reveal wide bandgap semiconducting properties of the nanotube.

The possibility of doping β-PNT with transition metal atoms is found to be energetically possible, and Co doped β-PNT is found to be a strong ferromagnetic material with impurity states just below the conduction band edge. The interatomic exchange coupling for various transition metal atoms is shown in Fig.2. The important thing to note is that Co atoms couple ferromagnetically. The strength of the magnetic (exchange) coupling is quite strong for Co since the calculated energy difference between ferromagnetic and antiferromagnetic coupling is ~40 meV/atom. A mean field analysis, which is appropriate in the present case of strong neighboring magnetic atoms, reveal an ordering temperature of 350 K, which demonstrates an ordering temperature above room temperature. The total magnetic moment of the unit cell with 2 Co atoms is 2.00 μ_B, an integer value which is the signature of half-metallicity. From the analysis of the projected charge and magnetic moment inside the Co atomic spheres, one notes that Co has around 4 and 3 d-electrons in the spin-up and spin-down channels respectively yielding a magnetic moment of about 1 μ_B.

Finally, we have calculated the formation energy of the impurity Co atom in the β-PNT host. The calculated formation energy is around 3 eV signifying the fact that the energy cost of creating Co impurities in β-PNT is similar to the energy cost of impurity doping of conventional semiconducting materials. This makes Co doped β-PNT a very good potential candidate as an n-doped material in spintronics applications.

[1] S.A. Wolf {\it et al.}, Science {\bf 294}, 1488 (2001).

[2] For a review on spintronics based on organic materials, see W.J.M. Naber, S. Faez and W.G. van der Wiel, cond-mat/0703455.

[3] G. Kresse and J. Hafner, Phys. Rev. B {\bf 47}, 558 (1993); G. Kresse and J. Furthm\"{u}ller, Phys. Rev. B {\bf 54}, 11169 (1996).

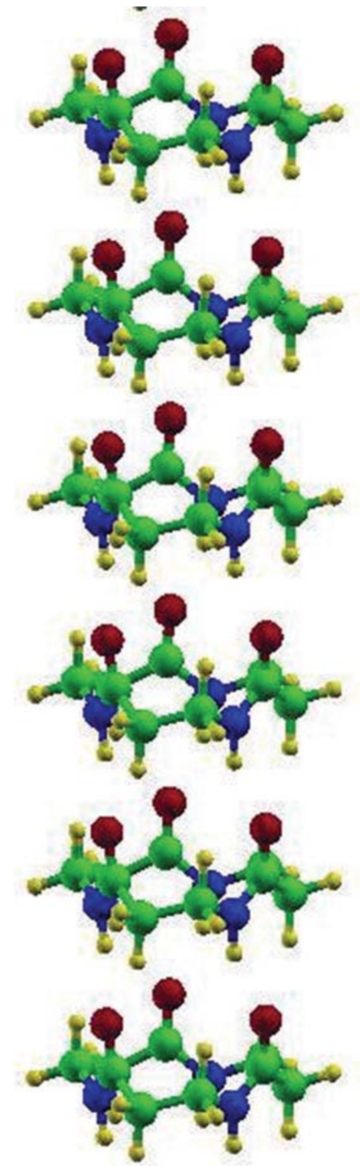

The infinite stacking of peptide rings. Red, blue, green and yellow colors indicate O, C, N and H atoms respectively.

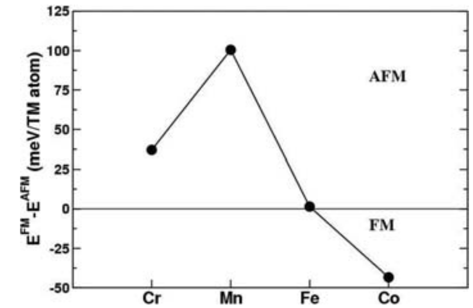

Calculated energy difference between ferromagnetic and antiferromagnetic alignments of transition metal atoms in β-PNT. Values below zero indicate that ferromagnetism is preferable.

AT-07

Magnetotransport Properties of $Y_2Fe_{17-x}Co_x$ Single Crystals.

J. Stankiewicz[1], K. P. Skokov[2], A. G. Khokholkov,[2], J. Bartolomé[1], Y. G. Pastushenkov[2]
1. Instituto de Ciencia de Materiales, CSIC - Universidad de Zaragoza, Zaragoza, Spain; 2. Faculty of Physics, Tver State University, Tver, Russian Federation

Fe-rich intermetallic compounds such as $Y_2Fe_{17-x}Co_x$ are attractive for use in magnetic cooling. Y_2Fe_{17} is a natural multilayer system in which the Fe layers (perpendicular to the *c* axis) are intercalated with dumb-bell Fe pairs. This weak ferromagnet shows a large planar anisotropy below its ordering temperature of 320 K. When Co is substituted for Fe in $Y_2Fe_{17-x}Co_x$ alloys, the easy-plane anisotropy prevails up to x≦8, where it changes to an easy axis one. There is experimental evidence for preferential site substitution of Fe by Co: Co atoms hardly substitute Fe at the dumb-bell sites till its content is over 60%.
In spite of the abundance of reports on the magnetic properties of $Y_2Fe_{17-x}Co_x$, we do not find any paper devoted to their electron transport properties. Here, we report results of electrical resistivity, Hall effect, and magnetization studies in single crystals of $Y_2Fe_{17-x}Co_x$ ($x \leq 4$). These measurements were performed in magnetic fields, up to 5T, and in a temperature range from 5 to 700 K. We find a large anisotropy in the Hall effect of $x \leq 2$ crystals that can likely be attributed to their layered structure and selective substitution.
The $Y_2Fe_{17-x}Co_x$ single crystals were grown using inductive melting. Their composition and orientation were checked by x-ray diffraction. All of the specimens show a hexagonal Th_2Ni_{17} crystal structure. The low-field Hall resistivity ρ_{xy} (Fig. 1) is almost one order of magnitude larger for the easy magnetization direction (H ⊥ c) than for hard magnetization direction (H II c) in Y_2Fe_{17}. It peaks close to T_c for both orientations. The temperature variation of magnetization is also shown in Fig. 1.
Phenomenologically, the Hall resistivity can be written as $\rho_{xy} = R_oB + R_s4\pi M$, where R_o and R_s are the normal and anomalous Hall effect (AHE) coefficients, respectively; *B* is the applied magnetic induction and *M* is the spontaneous magnetization. In ferromagnetic materials $\rho_{xy} \approx R_s4\pi M$. There is a simple relation between AHE and the longitudinal resistivity: $\rho_{xy}=a\rho_{xx}+b\rho_{xx}^2$. The first term represents the skew scattering component. The second term is brougth about either by side-jump or intrinsic, independent of scattering, contribution to ρ_{xy}. All terms follow from spin-orbit coupling. The intrinsic contribution, which is related to Berry phase effects on conduction electrons, can be quite large. Coefficients *a* and *b* are usually linear in the magnetization for the above mechanisms. To separate the various contributions to the AHE resistivity, we plot $\rho_{xy}/(M\,\rho_{xx})$ vs ρ_{xx} as shown in Fig. 2. Below $\rho_{xx} \approx 90\mu\Omega$cm ($T \approx 150$ K), this plot is linear for H II c and independent of ρ_{xx} for H ⊥ c. This clearly shows that skew scattering entirely dominates AHE resistivity for electrical current flowing along the *c* axis, but it has almost no effect otherwise. Similar behavior is observed for x=2 compounds but not in x=4 samples. The Kondo-Maranzana model (Maranzana67) of *d*-orbit-*s*-spin interaction accounts satisfactorily for such behavior if the layered structure and preferential substitution in $Y_2Fe_{17-x}Co_x$ is taken into account.
On the other hand, both side-jump scattering and intrinsic contributions to the AHE resistivity give a variation which is quadratic in ρ_{xx}. We find this for H II c in all compounds studied. Their separation is not easy and requires the application of very high magnetic fields. The AHE is usually attributed to side-jump scattering when ρ_{xx} is large, as it happens in concentrated magnetic alloys. However, our rough estimate for this effect shows that it may account only for 20% of the observed variation. For the intrinsic (Berry phase) conductivity we obtain a value of 680 Ω-1cm-1 which is not too different from the value (1032 Ω-1cm-1) found experimentally for bcc Fe.

We acknowledge support from the Ministerio de Ciencia y Tecnología of Spain through Grant No. MAT05/1272.

C. Zeng,*et al.*, Phys. Rev. Lett. 96, 037204 (2006).

F.E. Maranzana, Phys. Rev. 160, 421 (1967).

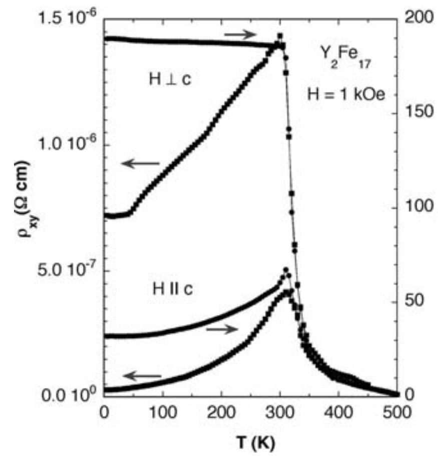

Fig.1 Hall resistivity ρ_{xy} and magnetization *M* as a function of temperature in Y_2Fe_{17}.

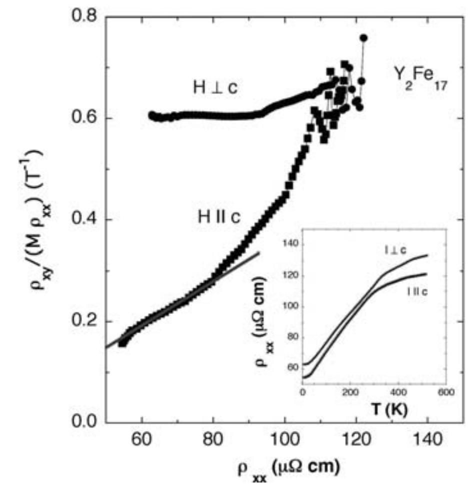

Fig.2 $\rho_{xy}/M\,\rho_{xx}$ as a function of ρ_{xx} for Y_2Fe_{17}. Inset shows ρ_{xx} vs *T*.

AT-08

Weiss oscillations modulated by microwave radiation.

J. Inarrea[1,2], G. Platero[2]
1. Physics, Universidad Carlos III, Leganes, Spain; 2. CSIC, Leganes. Madrid, Spain

J. Inarrea,1,2, G. Platero,1
2, Instituto de Ciencia de Materiales(CSIC), Cantoblanco, Madrid, Spain.
1, Escuela Politecnica Superior, Universidad CarlosIII, Leganes, Madrid, Spain.

In the last two decades, especially since the discovery of the Quantum Hall Effect, a lot of progress has been made in the study of two-dimensional electron systems, and very important and unusual properties have been discovered when these systems are subjected to external AC and DC fields. In the last years two experimental groups [1,2] have announced the existence of vanishing resistance in 2DES, i.e. zero resistance states, when these systems are under the influence of a moderate magnetic field (B) and microwave radiation simultaneously. In the same kind of experiments large resistivity oscillations have been observed [1,2]. In the same way, two decades ago a novel type of magnetoresistance oscillations, periodic also in 1/B, was discovered by D. Weiss et al.[3]. In this case these oscillations are observed in high-mobility ALGaAs/GaAs heterojunction with a holographic induced lateral periodic modulation in one direction. In other words a superlattices is grown on a two-dimensional electron system.

Experimental results about the effect of microwave radiation on the Weiss magnetoresistance oscillations are not available yet. However it would be very interesting to get to know that effect: for instance if these oscillation can be modulated, quenched or even if zero resistance states can be achieved. These novel experimental results would represent a real challenge for the theoretical existent models for the transport through these heterostructures.

In these scenario that represent the Weiss oscillations we have developed a theoretical model based in a previous one carried out by the authors to study the recent experimental results [1,2] on zero resistance states and microwave-induced resistance oscillations [4]. This novel extension of the model is based in the effect that microwave radiation is able to cause on the scattering that electrons suffer with charged impurities. We propose that the electron scattering jump is modulated by the presence of microwave radiation and the final electron jump presents an interference behaviour between the effect of the supperlattice and the effect microwave radiation. In our calculated results Weiss oscillations are modulated by microwave radiation presenting a pulse profile. The final profile presented by the magnetoresistance depends mainly on the spatial period of the superlattice and the frequency of the microwaves. Depending on the values of these parameters, the oscillations can reach zero resistance states (see Figure).

References:

[1] R.G. Mani, J.H. Smet, K. von Klitzing, V.Narayanamurti, W.B.Johnson, V. Umansky, Nature 240 646 (2002).

[2] M.A. Zudov, R.R. Lu, N. Pfeiffer, K.W. West, Phys. Rev. Lett. 90 046807 (2003).

[3] D. Weiss et al., Europhys, Lett., 8, 179, (1989) ; R.R. Gerhardts et al. Phys. Rev Lett. 62, 1173, (1989).

[4] J.Inarrea and G. Platero, Phys. Rev. Lett. 94, 016806,(2005).

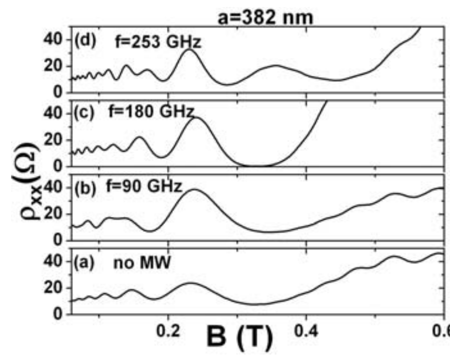

AT-09

Nonlinear modulation of spin-orbit interaction in a semiconductor channel.

H. Koo[1], J. Kwon[1], J. Eom[2,1], J. Chang[1], S. Han[1]
1. Center for Spintronics Research, Korea Institute of Science and Technology, Seoul, South Korea; 2. Department of Physics, Sejong University, Seoul, South Korea

Controlling spin-orbit interaction is essential part for the development of spin field effect transistor. The electric field generally induces the spin-orbit interaction in the high mobility system, while structural asymmetry of a quantum well shows the same phenomenon. If the quantum well asymmetry is linearly changed by electric field, the modulation of spin-orbit interaction is very simple. However, the electric field dependence of spin-orbit interaction shows non-linear relationship and it is determined by the structure of high mobility semiconductor system. Therefore, we have to decide the proper range of the gate voltage for an efficient modulation of spin-orbit interaction.

In this research, we utilize an inverted high electron mobility transistor (HEMT) structure with InAs channel [1, 2] to investigate the gate-controlled spin-orbit interaction. Figure 1 shows the vertical view and calculated energy diagram of the substrate. The inverted heterostructure, where the carrier supply layer is located below the quantum well, is grown by molecular beam epitaxy as shown in Fig. 1(a). In this system, the InAs channel is sandwiched by $In_{0.52}Al_{0.48}As/In_{0.53}Ga_{0.47}As$ double cladding layers. The quantum well shape is not symmetrical due to the carrier supply layer even without gate voltage as shown in Fig. 1 (b). Therefore the internal electric field arises and finally generate Rashba effect relative spin-orbit coupling.

Observing the Shubnikov-de Haas (SdH) oscillation at $T = 1.8$ K, we determined the gate voltage dependence of spin-orbit interaction parameter (α) and the carrier concentration (n_S). In order to measure SdH oscillation, the 2DEG strip is shaped by ion milling. The gate electrode was formed after depositing SiO_2 of which thickness is 100 nm. The channel resistance was measured in the external magnetic field perpendicular to the plane. As shown in Fig. 2, beat patterns arise because spin-up and -down electrons generate different oscillation frequencies, leading to beats when these two signals combine.Figure 3 shows that the spin-orbit interaction parameter decreases with increasing gate voltage but the gate voltage dependence of spin-orbit interaction parameter shows nonlinear relationship. When the minus gate voltage is applied, the slope of quantum well bottom becomes steeper and the more internal electric field is generated. In the case of applying plus gate voltage, the slope of quantum well tends to flat and the internal electric field becomes smaller. From our band calculation, however, for the same amount of applied voltage, the slope change induced by plus gate voltage is much smaller than that induced by minus gate voltage. The reason is that the carrier supply layer is located on the -z direction from the quantum well so that the slope of quantum well would not be flat and inversed. These simulation results agree with the experimental data of α in Fig. 3.

In conclusion, the spin-orbit interaction parameter is not linearly changed with gate voltage due to the non-linear quantum well reformation. This non-linear behavior is attributed to the asymmetric charge distribution of quantum well. From our experiment, the spin-orbit interaction strength is easily controlled in the range of $V_g < 0$ in an inverted heterostructure.

[1] J. Nitta, T. Akazaki, and H. Takayanagi, Phys. Rev. Lett. 78, 1335 (1997).

[2] H. C. Koo, H. Yi, J.-B. Ko, J. Chang, S.-H. Han, D. Jung, S.-G. Huh, J. Eom: Appl. Phys. Lett. 90, 022101 (2007).

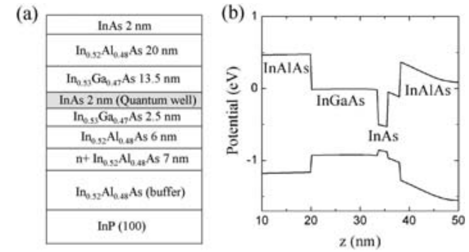

Figure 1 InAs channel heterostructure. (a) Vertical structure. (b) Energy diagram. The distance from the top surface is denoted by *z*.

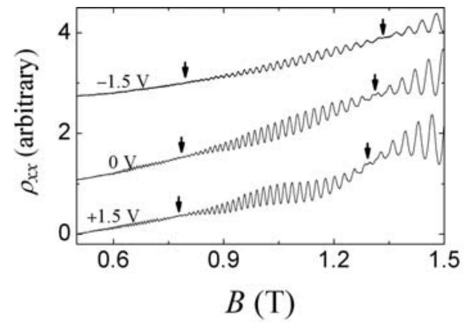

Figure 2 Gate voltage dependence of SdH oscillation at $T = 1.8$ K.

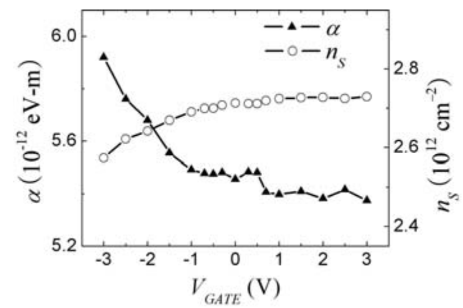

Figure 3 Gate voltage dependence of spin-orbit interaction parameter (α) and carrier concentration (n_S).

AT-10

Ordinary Magnetoresistance of Individual Single-Crystalline Bi Nanowires.

J. Ham[1], D. Kim[2], W. Shim[1], J. Kim[1], K. Lee[1], W. Jeung[2], W. Lee[1]
1. Department of Materials Science and Engineering, Yonsei University, Seoul, South Korea; 2. Division of Material Research, KIST, Seoul, South Korea

Semimetallic bismuth (Bi) has been extensively investigated over the last decade since it exhibits very intriguing transport properties due to their highly anisotropic Fermi surface, low carrier concentration, long carrier mean free path l, and small effective carrier mass m*. The magnetoresistance (MR) behavior and long carrier mean free path l in Bi thin films are of particular importance, since they can be exploited for spintronic device applications such as magnetic field sensors and spin-injection devices. With respect to "spintronics", it is expected that Bi can be used as a spin channel in a spin-injection device due to the very long spin diffusion length lsd of a few ten μm, following the relation $l_{sd}=(l\upsilon_F\tau_{\uparrow\downarrow})^{1/2}$, where, υ_F is the Fermi velocity and $\tau_{\uparrow\downarrow}$ is the spin relaxation time. In recent years, comprehensive studies have focused on Bi nanowires because of quantum confinement effect. Transport properties in Bi nanowires has been known to depend on the purity and the concentration of crystal defects since a distorted structure compromises the unusual electronic properties of Bi nanowires. Therefore, high crystal quality of Bi nanowires is crucial to investigate unique transport properties of Bi nanowires. In the present work, we report the magneto-transport properties of individual Bi nanowire grown by stress-induced method to prepare single-crystalline Bi nanowires.

Bi thin films were grown on a thermally oxidized Si substrate in a radio frequency (rf)-sputtering system with a Bi target of 99.999%. The deposition of Bi was carried out in a vacuum chamber with a base pressure of 5.0×10^{-7}Torr. Rf power of 100W and an Ar working pressure were utilized, yielding a growth rate of 32.7Å/sec. For growth of the Bi nanowires, the sputtered-Bi thin films were transferred to a furnace for heat treatment at 270 °C for 10 hours. A representative 400-nm-diameter individual nanowire device was fabricated by a combination of photolithography, electron-beam lithography, and a lift-off process (see Fig. 1A).

Measurements of current versus voltage (I-V) show that the contacts were highly ohmic at 300 K, corresponding to resistivity ρ of $1.29\times10^{-4}\Omega$cm. Fig. 1B and 1C shows the variation of the transverse and longitudinal ordinary magnetoresistance (OMR) of a 400-nm-diameter Bi nanowire. The largest transverse and longitudinal OMR of 2496 % at T = 110 K and –38 % at T = 2 K in the individual 400-nm Bi nanowire were observed, which is more than 4-times larger than the largest OMR (35 K) of polycrystalline 400-nm-diameter Bi nanowires array grown by electrodeposition. Therefore we are indicating that the Bi nanowire grown by stress-induced method shows the longest mean free paths l, and high-quality, single crystalline. The effect of wire-boundary scattering arising from the reduction of the cyclotron radius caused by a high magnetic field parallel to the axes of cyclotron resonance, occurring in only a single-crystalline nanowire [1, 2] was also observed.

Associated with the crystal quality of the Bi nanowire, mean free path is directly related to the observation of Shubnikov-de Haas (SdH) oscillations. The oscillations masked by impurity scattering is characterized by an exponential decay, $\exp(-1/w_c\tau)$, where relaxation time τ is defined $\tau=el/m^*$, and the observation of robust SdH oscillations (see Fig.2) proves that the Bi nanowire is the high quality, single-crystalline. Our results suggest the possibility of exploring the underlying physics in individual high quality single-crystalline Bi nanowires.

[1] J. Heremans, C. M. Thrush, Y. Lin, S. Cronin, Z. Zhang, M. S. Dresselhaus, and J. F. Mansfield, Phys.Rev.B 61, 2921 (2000).

[2] Z. Zhang, X. Sun, M. S. Dresselhaus, J. Y. Ying, J. Heremans, Phys.Rev.B 61, 4850 (2000).

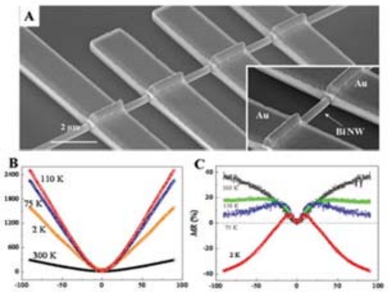

Fig. 1. (A) A SEM image of an individual Bi nanowire device. The OMR of the 400-nm-diameter Bi nanowire: (B) transverse and (C) longitudinal geometry.

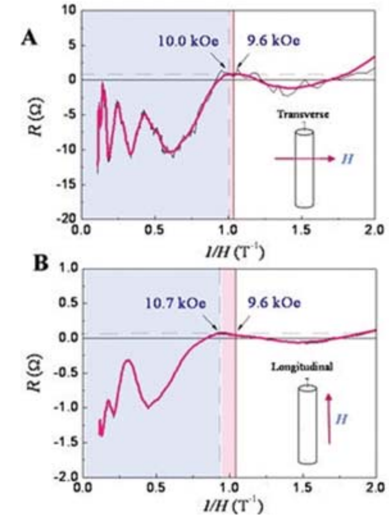

Fig. 2. Shubnikov-de Haas (SdH) oscillations obtained by the external field of (A) transverse and (B) longitudinal to the wire axis.

The effects of spin relaxation on spin transfer switching of a non-collinear giant magnetoresistance device.

N. Chung[1,2], M. B. Abdul Jalil[1], S. Tan[2], J. Guo[1], B. AL Sundaram[2]
1. Information Storage Materials Laboratory, Electrical and Computer Engineering Department, National University of Singapore, Singapore, Singapore; 2. Spintronics, Media and Interfaces Division, Data Storage Institute, Singapore, Singapore

Slonczewski[1] and Berger[2] pointed out that when a spin polarized current passes perpendicularly through a non-collinear giant magnetoresistance (GMR) device, a spin torque is resulted due to the interaction between the itinerant electron spin and the local magnetic moment of the free layer. Spin torque persists as long as the itinerant spin remains unaligned with the local moment, which implies that spin diffusion length might have a crucial impact on the spin torque and the switching behavior of a GMR device. In this article, we revealed that the spin diffusion length in both free and spacer layers have non-negligible effects on spin transfer switching in a GMR device. Based on the theoretical groundwork of Zhang, Levy and Fert[3], we investigated the effects of spin relaxation characterized by the spin diffusion length in these layers on the spin transfer torque (STT) and the areal resistance (RA) of a pseudo-spin-valve (PSV). We consider a typical $Co_{(pinned)}$-Cu-$Co_{(free)}$ PSV with non-collinear magnetization, and analyze its spin transport at varying angular deviation θ between the free and the pinned Co magnetizations. The layer thicknesses in the PSV are set as t_{Co1} = 10 nm for $Co_{(pinned)}$, t_{Cu} = 6.5 nm for Cu, and t_{Co2} = 2.5 nm for $Co_{(free)}$. Our calculations revealed that an increase of $l_{sf}^{(Cu)}$ in the spacer layer raises both the STT(Fig. 1a) and R(θ)(Fig. 1b) of the spin valve. However, a high probability of spin flipping in the spacer layer is found to be undesirable for spin transfer switching devices where a large spin torque is required, nor is it suitable for spin valve where a high MR ratio is required. The increase of STT and R(θ) with the increase of $l_{sf}^{(Cu)}$ is not indefinite, but begins to saturate when exceeds $l_{sf}^{(Cu)} > t_{Cu}$, so that the curves virtually coincide when $l_{sf}^{(Cu)} >$ 20 nm, as shown in Fig. 1. Next, the effects of the transverse ($l_{sf\perp}^{(Co2)}$) (Fig. 2) and the longitudinal ($l_{sf\parallel}^{(Co2)}$) (Fig. 3) spin diffusion length are analyzed at the free FM layer. It is found that $l_{sf\perp}^{(Co2)}$ is a critical component in determining the magnitude of the STT in the free FM layer. As shown numerically in Fig. 2a, the maximum STT drops sharply by around 30% when increases from 1 nm to 2 nm. Subsequently, there is a further drop of 30% in the maximum STT magnitude with every 1 nm increment in $l_{sf\perp}^{(Co2)}$. This suggests that $l_{sf\perp}^{(Co2)}$ is a very sensitive parameter and a small fluctuation in its value could severely degrade the performance of the spin transfer switching. A decrease in $l_{sf\perp}^{(Co2)}$ causes a stronger depolarization of the transverse spin accumulation ($m\perp$), which results in an increased transfer efficiency of the transverse spin angular momentum to the local moments in the free FM layer, and thus induces an increase in STT. In addition, we also noticed that as $l_{sf\perp}^{(Co2)}$ increases, the maximum STT is achieved at a larger θ. The total resistance change between the parallel and antiparallel configurations, i.e. R(π) - R(0) is not affected by $l_{sf\perp}^{(Co2)}$. However, the resistance R(θ) at an intermediate angle (0< θ <π) corresponding to non-collinear configuration, increases with increasing $l_{sf\perp}^{(Co2)}$, as shown in Fig. 2b. Numerical analysis of the effects of longitudinal spin relaxation (i.e. variation of $l_{sf\parallel}^{(Co2)}$) shows a significant degradation of both STT and R(θ) when $l_{sf\parallel}^{(Co2)} < t_{Co2}$, as shown in Fig. 3. A high degree of spin relaxation, i.e. a short $l_{sf\parallel}^{(Co2)}$ results in a stronger depolarization of the longitudinal spin accumulation ($m\parallel$) in the free FM layer, and hence a reduction of R(θ) and the overall MR ratio (Fig. 3b). The high depolarization of the $l_{sf\parallel}^{(Co2)}$ also causes an appreciable STT reduction, as shown in Fig. 3a.

1. J. C. Slonczewsky, J. Magn. Magn. Mater. 159, L1 (1996)

2. L. Berger, Phys. Rev. B 54, 9353 (1996)

3. S. Zhang, P. M. Levy and A. Fert, Phys. Rev. Lett. 88, 236601 (2002)

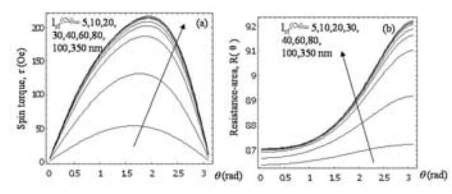

Fig. 1. (a) Spin transfer torque (STT), T(Oe), and (b) areal resistance, R(θ), as a function of magnetization angle, θ, with different spacer spin diffusion lengths, $l_{sf}^{(Cu)}$.

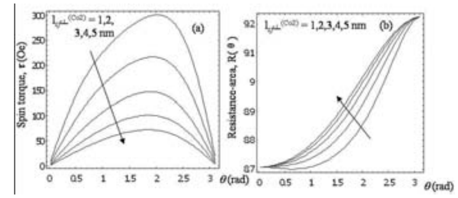

Fig. 2. (a) Spin transfer torque (STT), T (Oe), and (b) areal resistance, R(θ), as a function of magnetization angle, θ, with different transverse spin diffusion lengths, $l_{sf\perp}^{(Co2)}$.

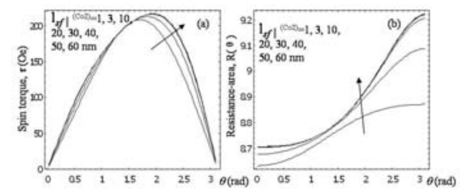

Fig. 3. (a) Spin transfer torque (STT), T (Oe), and (b) areal resistance, R(θ), as a function of magnetization angle, θ, with different longitudinal spin diffusion lengths, $l_{sf\parallel}^{(Co2)}$.

AT-12

Patterning of magnetic structures on austenitic stainless steel by ion beam nitriding.

E. Menéndez[1], A. Martinavicius[2], M. O. Liedke[2], G. Abrasonis[2], J. Fassbender[2], J. Sort[3], S. Suriñach[1], M. D. Baró[1], J. Nogués[4]
1. Physics, Universitat Autònoma de Barcelona, Bellaterra, Spain; 2. Institute of Ion Beam Physics and Materials Research, Forschungszentrum Dresden-Rossendorf, Dresden, Germany; 3. Physics, Institució Catalana de Recerca i Estudis Avançats (ICREA) and Universitat Autònoma de Barcelona, Bellaterra, Spain; 4. Institució Catalana de Recerca i Estudis Avançats (ICREA) and Institut Català de Nanotecnologia, Bellaterra, Spain

Nitriding of austenitic stainless steel (ASS) at moderate temperatures (~400°C) leads to the formation of the supersaturated nitrogen solid solution often called in the literature "expanded austenite" or γ_N phase [1,2]. This causes an enhancement of the microhardness and the wear resistance without loss of the corrosion resistance. Moreover, this phase shows ferromagnetic behavior, whose origin is linked to the expansion of the austenite (γ) lattice due to the incorporation of nitrogen atoms into interstitial positions [3,4]. Nitrogen depth profiles consist of quasi-linear decrease from nitrogen near surface concentration of ~25 at.% to ~15 at.% followed by a sharp leading edge. The onset of ferromagnetism is connected with nitrogen concentrations of ~15 at.%, thus the nitrided layer consists of two magnetically different parts (paramagnetic and ferromagnetic) determined by the obtained nitrogen concentration.

In this study, we report the influence of the nitriding temperature and time on the ASS ferromagnetic properties. AISI 304L ASS polycrystalline samples (discs of 10 mm diameter and 2 mm thickness) have been ion beam nitrided in the temperature range of 300-400°C. The ion energy and the ion current density were ~1 keV and 0.5 mA/cm^2 (the corresponding ion flux of ~510^{15} ionscm^{-2}s^{-1}), respectively. The processing times were 5 and/or 30 minutes. Periodic arrays of ferromagnetic structures in the micrometer range have been prepared at the surface of the samples using a 2000 mesh Cu transmission electron microscopy grid as a shadow mask (mesh size of 7.5 x 7.5 μm^2, 12.5 μm pitch, 20 μm thickness and 3.05 mm diameter). The structure was characterized by X-ray diffraction (XRD) and nuclear reaction analysis (NRA). The magnetic properties were determined by magneto-optical Kerr effect (MOKE) and magnetic force microscopy (MFM).

The XRD patterns of the nitrided ASS samples are presented in Figure 1. The XRD pattern consistent with the FCC lattice structure can be identified for the virgin ASS sample (not shown). For the nitrided samples, each austenite peak exhibits a satellite peak, located at lower diffraction angles which are related to the formation of the "expanded austenite". The amount of this "expanded" phase increases with the processing temperature, as it is evidenced by the increase of intensity of the γ_N XRD peaks in detriment to the γ ones.

This is consistent with NRA observations. For instance, a nitrided layer of around 1 μm depth is obtained in the sample nitrided at 400°C for 30 min, whereas ~15 at.% of nitrogen is obtained around 0.5 μm of depth.

MOKE measurement results of the virgin and the nitrided sample at 400°C for 5 min are compared in Figures 2(a) and 2(b) (patterned area).

It can be seen that the virgin sample does not show any hysteretic behavior, i.e. it is non-ferromagnetic. Conversely, the nitrided samples show clear hysteresis loops indicating the existence of ferromagnetic constituents in the nitrided layer. Figure 2(c) shows the AFM image of a patterned area of the nitrided sample which shows that a moderate sputtering process of the surface has taken place during nitriding resulting in the formation of the periodic array of squared pits. Figure 2 (d) is the corresponding MFM image in an applied magnetic field of 70 mT, where a magnetic dipolar contrast can be clearly seen in each entity, confirming the feasibility of the production of periodic arrays of isolated ferromagnetic structures. It is worth noting that the hysteresis behavior of the continuously nitrided areas and the patterned ones are quite similar due to the fact that the induced ferromagnetic structures are relatively large (micrometer range), leading to entities with magnetic multi-domain configurations.

[1] M.P. Fewell et al., Surf. Coat. Technol. 131, 300 (2000)

[2] G. Abrasonis, et al., J. Appl. Phys. 97, 083531 (2005)

[3] O. Öztürk and D.L. Williamson, J. Appl. Phys. 77, 3839 (1995)

[4] J. Baranowska, Vacuum 81, 1216 (2007)

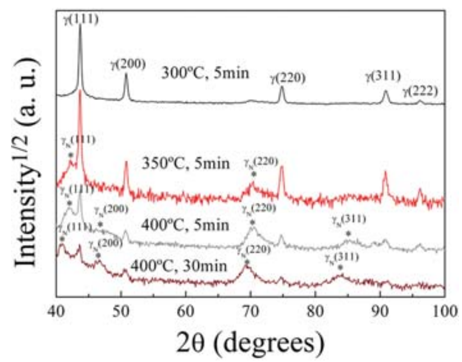

XRD patterns of the nitrided ASS samples (nitriding duration 5 min for 300 and 350°C and 5 and 30 min for 400°C)

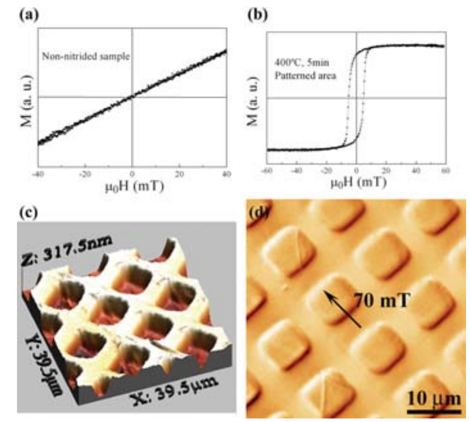

MOKE measurements of the non-nitrided sample (a) and of a patterned area of the ASS sample nitrided at 400°C during 5 min (b). 3D atomic force microscopy (AFM) image of a patterned area of the sample nitrided at 400°C during 5 min (c) and the corresponding MFM image (magnetic field of 70 mT) (d)

AT-13

Synthesis and characterization of particulate magneto polymer composite at microwave frequencies.

S. Borah, N. S. Bhattachyaryya
Physics, Tezpur University, Tezpur, India

The present day technology trends towards compact, cost effective, light weight integration of microwave passive and active devices with transmission lines. Although heavy wave-guide components are indispensable when there is handling of high microwave power but medium and lower power handling devices are considered miniaturized hybrid microwave integrated circuits (MIC's) are taking over. To design MIC's the substrate, which is the guiding media, plays the important role. The selection of substrate depends on frequency of operation, the type of planar line used, desired electrical, mechanical and thermal properties and fabrication. Particle-filled polymer composites are taking forefront in the present day applications as the properties can be altered simply by varying quantity, distribution and microstructure of the reinforcing phase. Magnetic particles reinforced in polymer matrices have excellent potential for electromagnetic device applications at microwave frequencies as nonreciprocal devices, tunable cavities, electromagnetic interference [EMI] suppression etc. Essential characteristic of the magnetic substrate material which determines its utility at microwave frequencies is its permittivity and permeability. In addition it should have low magnetic and dielectric loss. Determination of complex permeability and complex dielectric properties of any substrate material is very important. Different techniques have been used for successful measurements of the dielectric properties of materials [1-3]. Cavity perturbation technique is the simplest technique which provides a bridge between theoretical calculation and experimental observation and it does not have a special requirement for the geometry and size of the measured sample [4].

In the present investigation, the dielectric properties of a new composite material are studied using the cavity perturbation technique. Cobalt-nickel ferrite with average crystallite diameters ranging from 5.76-17.55 nm are prepared with stoichiometric formula Co1-xNixFe2O4 (x = 0, 0.2, 0.4, 0.6, 0.8, 1.0) using conventional chemical route. The substrate material is fabricated by reinforcing the ferrite in different volume fraction into low density polyethylene (LDPE) matrix [5,6]. Transmission Electron Microscopy (TEM), Scanning Electron Microscopy (SEM) and X-ray diffraction (XRD) patterns indicate the uniform particle indicate the uniform particle size, distribution and cubic spinel structure ferrite samples. The B-H loop study conducted at 10 kHz on the toroid shaped composite samples shows reduction in magnetic losses as compared to bulk sample.

The measurement of the dielectric constant of the sample is carried out in a TE103 mode rectangular waveguide cavity at 9.68 GHz with Q= 3226. The sample is placed at a point of maximum electric field. Permittivity of Co1-xNixFe2O4 – LDPE composite materials are found to be very high and the dielectric losses are found to be small as compared to the conventional bulk ferrites used for microwave passive devices Enhancement of permittivity value is observed with increase in % volume fraction of the reinforcer in the composite. The results are verified using Bruggeman's Theory [7].

[1] S. Li, C. Akyel, R. G. Bosisio, J. IEEE, MTT-29(10), 1041 (1981).

[2] B. G. Colpitts, J. IEEE, MTT-41(2), 229 (1993).

[3] W. Xi, W. R. Tinga, W. A. G. Voss, and B. Q. Tian, J. IEEE, MTT-40(4),

747 (1992).

[4] Z. Jian, Ch. Jiping, T. Yuling, and Q. Jinyu, J. MRS., 430, 263 (1996).

[5] S. Borah, N. S. Bhattacharyya, "Synthesis of Magnetic Material for Applications at High Microwave Power", International Conference on Magnetic Materials (ICMM-2007) (communicated).

[6] S. Borah, N. S. Bhattacharyya, "Development of Particulate Magneto-polymer Composite with Reduced Magnetic Losses", International Seminar on Frontiers in Polymer Science and Technology: POLY-2007 (communicated).

[7] D. A. G. Bruggeman, Ann. Phys. (Leipzig), vol. 24, pp. 63

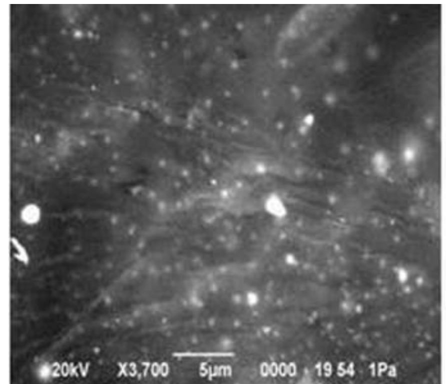

FIGURE 1. SEM image of LDPE-$Co_{0.6}Ni_{0.4}Fe_2O_4$ composite.

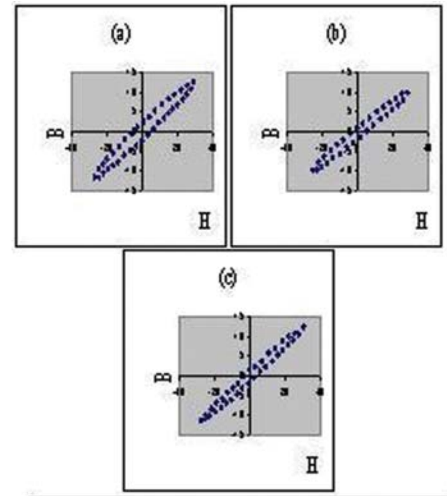

FIGURE 2. Hysteresis curves of $Co_{0.6}Ni_{0.4}Fe_2O_4$ particles annealed at (a)800°C, (b)600°C and (c)400°C temperature.

AT-14

Nanocrystals formation in $Ce_{100-x}Al_x$ (x=45, 50) ribbons by rapid solidification from the liquid state.

B. Idzikowski[1], Z. Sniadecki[1], D. Kaczorowski[2]
1. Institute of Molecular Physics, Polish Academy of Sciences, Poznan, Poland; 2. Institute of Low Temperature and Structure Research, Polish Academy of Sciences, Wroclaw, Poland

The heavy-fermion (HF) behavior is observed not only in a selected crystalline compounds but also in amorphous or nanocrystalline metallic matter. In conventional systems the strength of the exchange interaction between localized *f*-electrons and conduction electrons can be completely turned up by a specific stoichiometry, which create internal pressure (or also by external pressure), resulting in domination of either Kondo-type or the RKKY interactions. This is a consequence of the competition between the magnetic order and local Kondo resonance. HF behavior could be strongly enhanced by topological disorder, lattice defects or nanocrystalline structure. It is know that such kind of disorder cause substantial modifications of the low temperature properties of a HF materials resulting in a breakdown of the Fermi-liquid behavior. The interplay between structural disorder and strong correlations of electrons can be studied as a function of number and size of nanocrystalline grains embedded in an amorphous matrix.

Cerium shows variable electronic structure and dual valency states, because only low energy is sufficient to change the relative occupancy of its electronic levels. The interaction of RKKY-type decreases when the average distances between Ce atoms increases, *e.g.* by substitution of Ce by Al atoms in $Ce_{100-x}Al_x$ system. Usually amorphous HF alloys exhibit non-Fermi-liquid behavior at low temperatures. Topological disorder in these alloys is not so considerable as in mixed amorphous/nanocrystalline systems but due to the random substitution of constituent elements creation of the Kondo and/or Anderson lattices were observed.

In this paper the nanocrystalline state formation, crystallization processes, crystal structure of nanoparticles in $Ce_{100-x}Al_x$ are investigated. The master alloys with x=45, 50 were prepared by arc-melting of the Al and Ce elements with at least 99.9% purity under argon atmosphere on a water-cooled copper boat. Then the master alloys were rapidly quenched using a single roller melt-spinner with a Cu wheel. Cooling rates during melt spinning were controlled by the wheel surface velocity (v=40 m/s) or hole diameter in the quartz crucible. The ribbons are about 2 mm in width and 20-40 μm thick. For structural characterization x-ray diffraction (XRD) was used. Measurements were made on a diffractometer with Co Kα radiation in Bragg-Brentano geometry. The crystallization behavior of as-quenched samples was investigated by DSC measurements using Netzsch DSC404 apparatus between room temperature and 900°C with 20 K/min heating rate.

The XRD patterns for both compositions (Fig. 1) show Al_1Ce_1 nanocrystalline phase with the ClCs-type structure (Pm-3m space group) embedded in an amorphous matrix. This crystalline Al_1Ce_1 phase is known from A.A. Yakunin *et al.* [1] paper as a metastable one, without determined distribution of Ce and Al atoms in the lattice cell. The $Ce_{100-x}Al_x$ (x=45, 50) ribbons due to differences in Ce/Al ratio are in different nanocrytalline states, what suggests that amount of nanocrystals could be roughly controlled during rapid quenching process. The constant-heating DSC curves (Fig. 2) for $Ce_{50}Al_{50}$ and $Ce_{55}Al_{45}$ show two exothermal crystallization peaks at temperatures T_{x1} and T_{x2} with crystallization onset temperatures at T_{onset1} and T_{onset2}, respectively. For $Ce_{55}Al_{45}$ one can see third small event at about 350°C, which is not visible for $Ce_{50}Al_{50}$ at this heating rate. Summary enthalpy ΔH of first two peaks is about 20 J/g for both alloys. Endothermal effects associated with a glass transition below the primary crystallization peak T_{x1} are not visible against the other effects. This could indicate the presence of dispersed polyamorphous packings [2] with a wide range of local glass transitions, secondly the glass transition T_g is close or above T_{x1}, or finally $Ce_{100-x}Al_x$ (x=45, 50) system would be similar to Al-based metallic glasses where T_g is not visible in standard constant-heating DSC scans (as shown in our previous paper about Al containing pseudo-ternary rare earth – transition metal – metal/metalloid alloys [3]).

[1] A.A. Yakunin and G.V. Borisova, Izvestiya Vuz, Tsvetnaya Metallurgiya **7** (1979) 230.

[2] H.W. Sheng *et al.*, Nature Mater. **6** (2007) 192.

[3] P. Kerschl, U.K. Rössler, T. Gemming, K.-H. Müller, Z. Sniadecki, B. Idzikowski, Appl. Phys. Lett. **90** (2007) 031903.

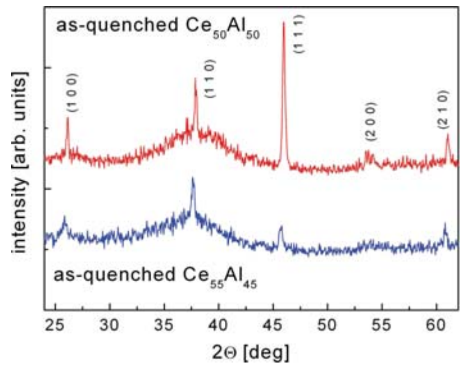

Fig. 1. XRD patterns of as-quenched $Ce_{100-x}Al_x$ (x = 45, 50) alloys.

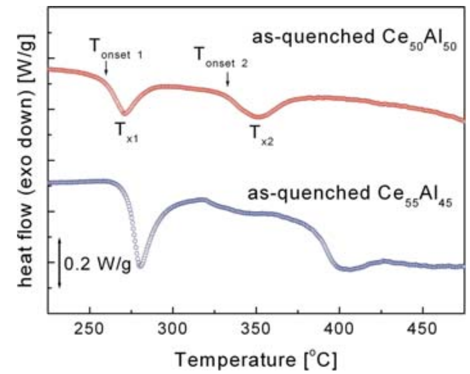

Fig. 2. Heat flow data from a DSC scan with a constant heating rate of 20 K/min as a function of temperature for melt spun $Ce_{100-x}Al_x$ (x = 45, 50) ribbons.

AT-15

Noise enhanced stability of magnetic systems.

M. Trapanese
Dipartimento di Ingegneria Elettrica, Elettronica e delle Telecomunicazioni, University of Palermo, Palermo, Italy

Escape from a metastable state is a phenomenon observed in several scientific areas. Among them there are the theory of diffusion in solids, chemical kinetics, and transport in complex systems.
The decay of magnetization with time (the aftereffect) can be interpreted as an escape from a metastable towards states closer and closer to the ground state and therefore studied with the theoretical means developed for diffusion processes. The rate of the decay of magnetization can be affected from applied fields and temperature. Even though at zero field and room temperature, aftereffect is unmeasurable, under particular conditions it becomes measurable leading to decay rates that can be seriously affect the working condition of a permanent magnet (i.e. the life span of a permanent magnet in electric machine can be seriously affected from temperature or a magnetic memory could shorten its life because of the presence of a reverse field). As a result, the study of the stabilization of magnetization could have a serious technological impact.
The study of mean first passage time (MFPT) is one of the parameters often considered in the theory of diffusive process. The mean first passage time of a Brownian particle moving in potential fields usually decreases with noise intensity according to the Kramers formula or some universal scaling function of the system parameters. The dependence on the noise intensity of the MFPT for metastable and unstable systems was revealed to have resonance character by Hirsch et al. [1] and then observed in different physical systems [2-7]. The most important conclusion of these studies is that the noise can modify the stability of the system in a counterintuitive way. The system remains in the metastable state for a longer time than in the deterministic case and the escape time has a maximum at some noise intensity. Noise-enhanced stability (NES) was originally found numerically by Dayan et al. [2], and ohserved experimentally in a tunnel diode by Mantegna and Spagnolo [4]. More recently, it was found that the noise induced slowing down [7] and the noise-induced stabilization are related to NES phenomenon.
NES in magnetic systems has not yet been fully investigated.
The main purpose of this paper is to study NES in magnetic systems. The magnetization of magnetic materials in zero field decays very slowly toward its ground state. This is due to the effect of large energy barriers. However, under the presence of a reverse field this effect can be accelerated. This field is named holding field.
In this paper NES in magnetic systems is studied by Preisach-Arrenius (PA) like model (8) and by dynamic simulation. In PA model a controllable fluctuating field is added to the usual thermal fluctuating field of PA model. In the dynamic simulation an external magnetic field (hext)applied to a magnetic material consisted of two components: one small asymmetrical periodical component added to a gaussian noise component. The value of h was computed at several time steps. As a result the history of the magnetization of the system could be computed by using Preisach Model. As a result the magnetization followed a history that resulted by the composition of a asymmetrical component and a gaussian component. The time needed to jump from the unstable part of the magnetization to the stable part was recorded as a function of the applied noise.
NES is studied for three systems: a toy model of a magnetic materials, a systems made from non-interacting hysterons and a Gaussian material.
First, a toy model of a magnetic material is considered. This toy model consists of very few hysterons. The decay rate of this model is studied as a function of the controllable fluctuating field. It is shown that NES occurs fo this system.
In the non interacting hysteron material hysterons are supposed to be placed in the Preisach plane along the line u=-v. The decay rate can be computed and it is shown that the it has a non monotonic behaviour as a function of the controllable fluctuating field. As a result NES occurs also in this case. The dynamic simulation confirmed the presence of NES by showing a non monotonic behaviour of the decay rate of magnetization from the unstable state to the stable state.
Finally, a Gaussian material is considered. In this case, the after effect and the effect of the controllable fluctuating field can be computed by integrating on the whole Preisach plane. The after-effect has been computed for several holding field as a function of the controllable fluctuating field. Also in this case a non monotonic behaviour of the decay rate as a function of the controllable fluctuating field is detected. This is the signature of NES. The dynamic simulation confirmed the presence of NES by showing a non monotonic behaviour of the decay rate of magnetization from the unstable state to the stable state.

[1] J. E. Hirsh, B. A. Huberman, and D. J. Scalapino, Phys. Rev. A 25, 519 (1982).

[2] I. Dayan, M. Gitterman, and G. H. Weiss, Phys. Rev. A 46, 757 (1992).

[3] N. V. Agudov and A. N. Maiakhov, Int. J. Bifurcation Chaos Appl. Sci. Eng. 5, 531 (1995).

[4] R. N. Mantegna and B. Spagnolo, Phys. Rev. Lett. 76, 563 (1996).

[5] F. Apostolico, L. Gammaitoni, F Marchesoni, and Santucci, Phys. Rev. E 55, 36 (1997).

[6] M. C. Mahato and A. M. Jayannavar, Mod. Phys. Lett. B 11, 815 (1997).

[7] R. Waekerbauer, Phys. Rev. E 58, 3036 (1998).

[8]E. Della Torre, L.H.Bennett, R.A.Fry and OA.Ducal, IEEE Trans. On Magnetics, 38, 5, 3409 (2002).

AU-01

Implementing mixture design to predict magnetic properties of hybrid bonded magnets.

J. Hsu[1], P. Sharma[1], A. Verma[2]
1. Physics, National Taiwan University, Taipei, Taiwan; 2. Moserbaer India Ltd, Greater Noida, India

Introduction

Hybrid bonded magnets exhibit variation in magnetic properties depending upon the blend i.e. weight fractions of magnetic powders, binder and the processing condition [1]. It is interesting to know the magnetic properties of each blend in order to tailor-made required magnetic energy. This study can be carried out by mixing the constituents in several proportions and measuring the magnetic properties. The major drawback of the said-approach is running a large number of experiments. On the other hand, the approach taken in the present study is to conduct only a few experiments and use the information to develop a mathematical model valid in the studied range of composition. In this study, a three-component constraint mixture design was implemented [2]. The focus was to fit the mathematical equations to model the response and to predict the magnetic property to any mixture over the studied composition range. In the present investigation, the compression moulded hybrid bonded magnets of strontium ferrite (SrFe12O19) and neodymium iron boron (NdFeB) rapidly solidified isotropic flakes with 10 different composition were made. Some design points are also replicated. The epoxy resin was used as a binder. The constraints applied on weight fraction of each component were: $0.25 \leqq W_{Ferrite} \leqq 0.72; 0.25 \leqq W_{NdFeB} \leqq 0.72; 0.03 \leqq W_{Binder} \leqq 0.07$, where $W_{Ferrite}$, W_{NdFeB}, and W_{Binder} are the weight fraction of SrFe12O19, NdFeB and binder respectively.

Results and discussion

The magnetic properties such as remanence (B_r),coercivity (H_c), and energy product $(BH)_{max}$of bonded magnets were measured. Using measured properties various regression model were fitted. Computer aided design D-optimal was used to fit the regression models [2, 3]. Full cubic model was found to be the most suitable model for each magnetic properties. The R square value is more than 95% which suggests that regression equations are adequate to fit the measured data. The produced equations for (B_r), (H_c) and $(BH)_{max}$are given in Eqs. (1), (2) and (3) respectively.

$$(B_r)=-2371.88W_{Ferrite}+869.89W_{NdFeB}+9.50\exp(+6)W_{Binder}+172.90W_{Ferrite}W_{NdFeB}-1.50\exp(+7)W_{Ferrite}W_{Binder}-1.50\exp(+7)W_{NdFeB}W_{Binder}+1.11\exp(+7)W_{Ferrite}W_{NdFeB}W_{Binder}+6834.69W_{Ferrite}W_{NdFeB}(W_{Ferrite}-W_{NdFeB})+5.54\exp(+6)W_{Ferrite}W_{Binder}(W_{Ferrite}-W_{Binder})+5.56\exp(+6)W_{NdFeB}W_{Binder}(W_{NdFeB}-W_{Ferrite}) \quad (1)$$

$$(H_c)=-8042.43W_{Ferrite}-2346.74W_{NdFeB}+4.33\exp(+7)W_{Binder}+1497.14W_{Ferrite}W_{NdFeB}-6.83\exp(+7)W_{Ferrite}W_{Binder}-6.83\exp(+7)W_{NdFeB}W_{Binder}+5.06\exp(+7)W_{Ferrite}W_{NdFeB}W_{Binder}+13620.12W_{Ferrite}W_{NdFeB}(W_{Ferrite}-W_{NdFeB})+2.53\exp(+7)W_{Ferrite}W_{Binder}(W_{Ferrite}-W_{Binder})+2.53\exp(+7)W_{NdFeB}W_{Binder}(W_{NdFeB}-W_{Binder}) \quad (2)$$

$$(BH)_{max}=-2.96W_{Ferrite}+0.49W_{NdFeB}+13704.07W_{Binder}-7.07\exp(-3)W_{Ferrite}W_{NdFeB}-215.84W_{Ferrite}W_{Binder}-215.92W_{NdFeB}W_{Binder}+1.60W_{Ferrite}W_{NdFeB}W_{Binder}+6.95\exp(-4)W_{Ferrite}W_{NdFeB}(W_{Ferrite}-W_{NdFeB})+0.80W_{Ferrite}W_{Binder}(W_{Ferrite}-W_{Binder})+0.807W_{NdFeB}W_{Binder}(W_{NdFeB}-W_{Binder}) \quad (3)$$

These regression equations can be directly used to predict the magnetic properties for any weight fraction of ferrite, NdFeB and binder. However, the sum of weight fractions of all component should be unity.

To check the adequacy of the fitted model equations, some experiments at specific design points were repeated in the same experimental condition and their magnetic properties were measured. Further the measured magnetic properties were compared with the predicted properties from the model equation. The deviation of actual magnetic properties of the bonded magnets from predicted one using mathematical model was shown in Fig. 1. It depicts that predicted magnetic properties are in agreement with the actual one. The difference in the magnetic properties is in acceptable limits.

Conclusion

The studies on the hybrid-bonded magnets of SrFe12O19 with NdFeB show that the constraint mixture design is adequate to predict the role of each component on the magnetic properties. In the present full study cubic model was found to be suitable for predicting (B_r),(H_c),$(BH)_{max}$. The present approach proposes a new methodology to develop mathematical equations for predicting properties of bonded-magnets and could be successfully implemented to the industry to design the properties of specific interest.

[1] John Ormerod, Steve Constantinides, Journal of Applied Physics. 81, 4816 (1997).

[2] John A. Cornell, *Experiment with Mixtures: Design, Model and the Analysis of Mixture Data*, New York, USA: John Wiley & Sons, 2002.

[3] F. Pukelsheim, *Optimal Design of Experiments*, New York, USA: Wiley, 1993.

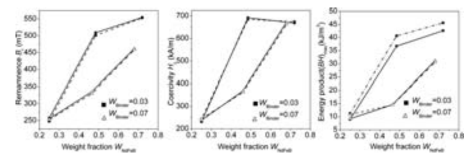

Fig. 1 Comparison between actual (dotted lines) and predicted (solid lines) magnetic properties

Establishment of multipole magnetizing method and apparatus using a heating system for Nd-Fe-B isotropic bonded magnets.

H. Komura, M. Kitaoka, T. Kiyomiya, Y. Matsuo
R & D, FDK Corporation, Kosai, Japan

[Introduction]
We examined multipole magnetizing method for Nd-Fe-B isotropic bonded magnets that contributes to the miniaturization of electromagnetic devices, and developed a new method using heating system. As it showed very strong magnetization characteristics, we called this method Ultra High Magnetizing (UHM) process. [1] The next problem is to contrive the way of adjusting magnetization characteristics. It is very important to apply this method to various industrial applications. Then, we did various examinations, and finally we devised it by using thermal demagnetization characteristics of magnets, and established the way of an adjustment of magnetization characteristics. In addition, we found the stability of magnetization characteristics with the thermal history than that of conventional technology. By these examinations, we were able to establish a magnetizing method and its apparatus.
[Experimental Procedure]
This method involves cooling the specimens in the magnetizing field using permanent magnets after rapid heating to temperatures above the Curie point of the Nd-Fe-B magnets. Furthermore, we installed a heater in the magnetizing field and enabled an adjustment of the temperature. We used three kinds of magnet powder and made ring-type bonded magnets with outside diameter=ϕ2.6 mm, inside diameter=ϕ1.0 mm, and length=3 mm. Figure 1 shows demagnetization curves of bonded magnets. Magnetization to 10 poles from outer of the bonded magnet was given. The temperature of the magnetizing field changed variously, and magnetization characteristics were evaluated. In addition, it is thought that initial demagnetization behavior of the UHM process is different from that of conventional technology because the heating history is given during magnetization. Therefore we compared the thermal flux loss with conventional technology.
[Results and Discussion]
Figure 2-a. shows the UHM magnetization characteristics with an adjustment of the temperature, and figure 2-b. shows the ratio of demagnetization on the basis of magnetization characteristics at 50 degrees centigrade in each magnet. The magnet with high coercivity shows higher magnetization characteristics and lower ratio of demagnetization. Figure 3 shows the thermal flux loss of the UHM process compared with conventional technology. The thermal flux loss of the UHM process, especially the magnet with lower coecivity, is smaller than that of conventional technology. It is thought that obtained magnetization characteristics contain initial demagnetization in the UHM process because the UHM process is including heating process. By the above, it became clear that an adjustment of magnetization characteristics is possible by an adjustment of the temperature in the magnetizing field of the UHM process. However, because the range that can be adjusted depends on the magnetic characteristics, it is necessary to select the magnet powder appropriately. As other advantages, it was clarified that the UHM process is excellent in the stability of magnetization characteristics with the thermal history compared with conventional technology.

H. Komura, M. Kitaoka, T. Kiyomiya and Y. Matsuo: J. Appl. Phys. 101, 09K104 (2007).

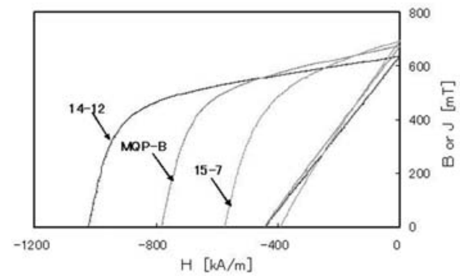

Fig. 1 Demagnetization curves of Nd-Fe-B bonded magnets.

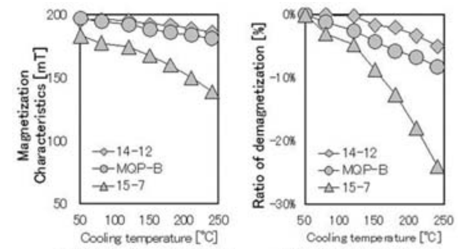

a) Magnetization characteristics. b) Ratio of demagnetization.

Fig. 2 Magnetization properties of the UHM process with an adjustment of the temperature.

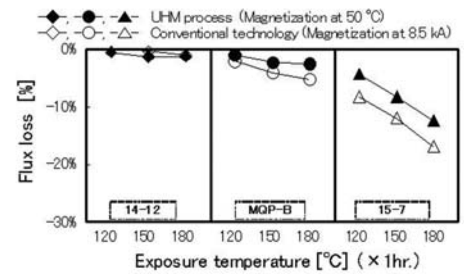

Fig. 3 Thermal flux loss.

AU-03

Investigation of eddy current loss in divided Nd-Fe-B sintered magnets for synchronous motors due to insulation resistance and frequency.

K. Yamazaki[1], M. Shina[1], M. Miwa[2], J. Hagiwara[2]
1. Dept. of Electrical, Electronics and Computer Engineering, Chiba Institute of Technology, Narashino, Japan; 2. TDK Corporation, Ichikawa, Japan

Owing to the progress of Nd-Fe-B magnets, permanent magnet synchronous motors are widely applied to the industry as highly efficient motors. On the other hand, as the resistivity of the magnet is relatively low, considerable eddy current loss is generated by the harmonic magnetic fields in the motor. It may cause the thermal demagnetization of the magnets. Accordingly, the magnets are often divided into several pieces to prevent the eddy currents.

There are several reports that investigated the eddy current loss in the divided magnets. Reference [1] reported the eddy current loss calculation of the permanent magnet in the synchronous motor. However, it did not compare the measured and calculated magnet eddy current loss, because the separation of the loss from the other losses in the motor is impossible in the measurement. Reference [2] investigated the effects of the magnet division by the simple experiment with the magnet specimen and an exiting coil. However, in the synchronous motor, the loss is generated by various kinds of harmonic magnetic fields. In addition, the critical insulation resistance between the divided magnets to obtain the loss reduction effect is also unclear.

In this paper, we investigate the loss reduction effect of the divided magnets from both results of the simple experimental apparatus and the synchronous motor, in order to clarify the effects due to the insulation resistance, frequency, and number of magnet divisions. First, the measured results of the simple experiment are compared with the 3-D finite element analysis to verify the validity. Next, the analysis of a permanent magnet synchronous motor is carried out.

Fig.1 shows the basic experimental apparatus to measure the eddy current loss of the divided magnets. The Nd-Fe-B magnets with thermal sensor are placed at the center of an exciting coil. The remanent flux density is 1.26T and resistivity is 1.3x10-6 Ωm. After surrounding the magnet by the heat insulation material, the coil is excited by AC current whose frequency is 1 to 30kHz. The eddy current loss is estimated from the increase of the temperature during 5 minutes.

Fig.2 shows the experimental and calculated eddy current losses due to the insulation resistance, when the frequency is 1kHz and the magnet is divided into 4-pieces as shown in Fig.1. The resistance is varied due to the surface treatment of the magnet. Although the calculated results underestimate the loss, the tendencies are agree well. Both results show that the loss much increases when the insulation resistance is less than 0.01 Ωm. On the other hand, it is almost constant over this region. The critical insulation resistance is clarified. Fig.3 shows the experimental and calculated loss due to the number of magnet divisions and frequency. it indicates that the loss reduction effect by the magnet division is weakened when the frequency is high.

The 3-D finite element analysis of the interior permanent magnet synchronous motor is carried out as shown in Fig. 4. The permanent magnet is affected by the various kinds of harmonic magnetic fields whose frequencies are kHz order. The loss reduction effect by the divided magnets shows same tendency as the basic experiment. It is also weakened, especially in the case of the high order harmonic fields.

[1]K. Yamazaki and S. Watari, “Loss analysis of permanent-magnet motor considering carrier harmonics of PWM inverter using combination of 2-D and 3-D finite-element method”, IEEE Trans. Magn., vol.41, no.5, pp.1980-1983 (2005)

[2]Y. Aoyama and K. Miyata, “Evaluation of the alternating magnetic losses in divided Nd-Fe-B sintered magnet”, The papers of Joint Technical Meeting on Static Apparatus and Rotating Machinery, IEE Japan, SA-06-83 (2006)

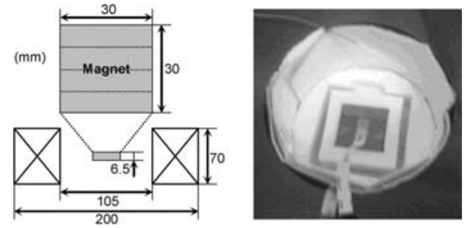

Fig.1. Basic experimental apparatus.

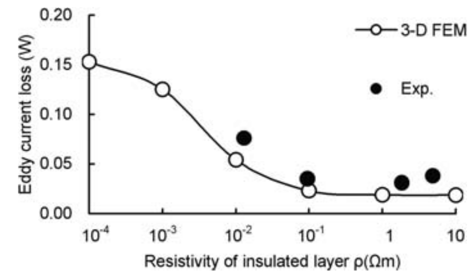

Fig.2. Experimental and calculated losses due to insulated resistance.

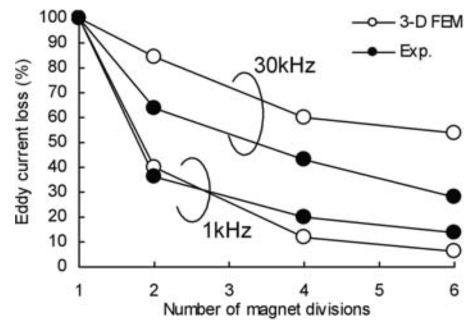

Fig.3. Losses due to number of magnet divisions and frequency.

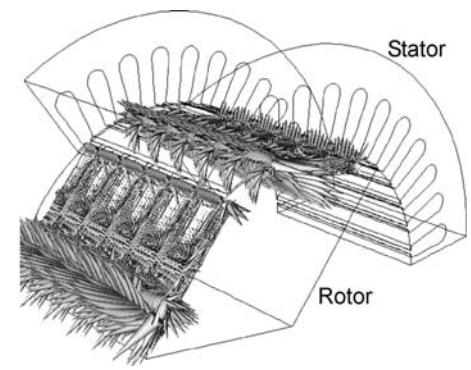

Fig.4. Eddy current analysis of permanent magnet synchronous motor.

AU-04

Outer Rotor Consequent-pole Bearingless Motor Improved Start-up Characterinstics.

T. Yamada[1], *Y. Nakano*[1], J. Asama[1], A. Chiba[1], T. Fukao[1], T. Hoshino[2], A. Nakajima[2]
1. Electrical Engineering, Tokyo University of Science, Chiba, Japan; 2. Japan Aerospace Exploration Agency(JAXA), Tokyo, Japan

I. INTRODUCTION
Magnetically suspended drives attract attentions by flywheel, pump and compressor drives. A bearingless motor combines functions of both non-contact magnetic suspension and torque generation together in a single motor. Therefore, the characteristics of magnetic bearing, no wear particles, less maintenance, and higher rotational speed are realized. In addition, a bearingless motor possesses the great advantages of downsizing, a simple structure and cost reduction, in comparison with a conventional tandem structure composed of magnetic bearings and a motor. Compact magnetically suspended bearingless motors are applicable for flywheel satellite posture regulation and home appliance energy storage system, and etc.[1]
The authors have proposed and fabricated a two-axis controlled noncontact bearingless drive system with passive magnetic bearings. This prototype machine is constructed by two-axis active position regulation having one unit of a bearingless motor with a consequent-pole permanent magnet (PM) rotor. The suspension and rotation tests were performed [2~3]. The rotor can be suspended, when it displaces within 0.1mm in radial direction. But touch down displacement of 0.3mm is requested in the point of view of mechanical process precision. The prototype machine was not able to start up at displacement of 0.3mm.
In this paper, an improved structure of a new prototype machine is proposed. The new structure is designed using three-dimensional Finite Element Method (3D-FEM). It is shown that start up is achieved from the touch down displacement of 0.3mm in experiment.
II. STRUCTURE OF BEARINGLESS MOTOR AND PASSIVE MAGNETIC BEARINGS
Fig.1 shows the x-z cross section of the proposed bearingless motor drive. A rotating part is in ring shape surrounding the stator part. In the stator part, a shaft is fixed to a base. Around the shaft, a stator core and windings are constructed. In the rotor part, there are three PM layers. The center PMs are radially magnetized, and are used for the bearingless motor functions generating torque and radial active forces. The PMs in the left and right are for axial-conical passive magnetic bearings. With the passive magnetic bearings, stiffness is enhanced in the three-axis movements, i.e., axial and conical directions. But unbalanced magnetic pull force is caused by PMs in the passive magnetic bearings. Then, negative stiffness is resulted in the two radial x- and y-axes. The magnetic pull force is mostly proportional to the rotor radial displacement. Thus, magnetic pull force is high at large displacement. Thus, a prototype bearingless motor was not able to start up at 0.3mm displacement.
To start up at 0.3mm displacement, high active suspension force of bearingless motor is needed. A design of rotor iron and PM structure is improved to enhance suspension force capability for start up using 3D-FEM. The detail of improved design will be included in presentation and 4-page paper.
III. EXPERIMENTAL RESULT
Fig.2 shows the displacement waveforms at start-up in developed prototype bearingless motor based on the proposed design. Before the suspension system is active, the x-axis rotor displacement is 0.3mm, and y-axis rotor displacement is 0.08mm. Thus, a rotor is touched down in x-axis. When the suspension system is activated, the displacements of x-axis and y-axis are moved to the center position. It is seen that successful magnetic suspension is achieved. The start-up is achieved from the touch down displacement of 0.3mm.
IV. CONCLUSION
In this paper, the design of an outer rotor consequent-pole type bearingless motor with passive magnetic was shown. The proposed motor design provides a start-up capability at displacement up to 0.3mm. In the experiment, it was shown that the proposed prototype machine is able to start up at 0.3mm displacement.

[1] Akira Chiba, Tadashi Fukao, Osamu Ichikawa, Masahide Oshima, Masatsugu Takemoto and David G. Dorrell "Magnetic Bearings and Bearingless Drives" Newnes Elsevier 2005 March 381pages ISBN 0 7506 5727 8

[2] Kazuyoshi Asami, Akira Chiba, Md. Azizur Rahman, Takeshi Hoshino, Atsushi Nakajima, "Stiffness Analysis of a Magnetically Suspended Bearingless Motor With Permanent Magnet Passive Positioning" IEEE Transaction on Magnetics, vol.41, no.10, pp.3820-3822,2005

[3] Tomohiro Yamada, Akira Chiba, Atsushi Nakajima, Takeshi Hoshino, Tadashi Fukao, Masatsugu Takemoto, Masahide Oshima, Osamu Ichikawa, "Basic Characteristics of an Outer Rotor Consequent-pole Bearingless Drive," the 10th International Symposium on Magnetic Bearings, Aug. 2006

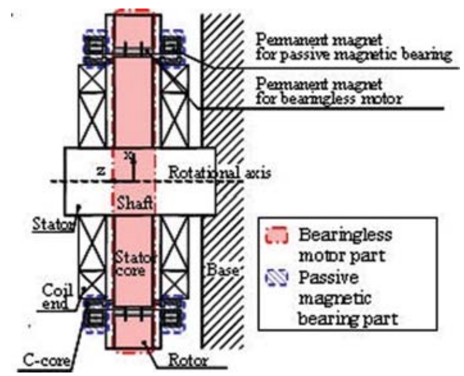

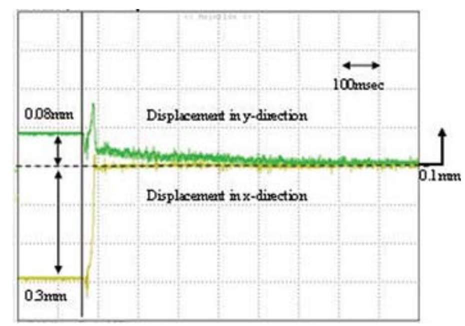

AU-05

Study of the Static Force by the Difference in the Winding Structure of Permanent Magnet Type Linear Synchronous Motor.

K. Suzuki[1], Y. Kim[2], H. Dohmeki[1]
1. Department of Electrical and Electronic Engineering, Musashi Institute of Technology, Tokyo, Japan; 2. Department of Electrical Engineering, Colleage of Engineering Chosun University, Gwangju, South Korea

I.INTRODUCTION

Recently, permanent magnet linear synchronous motor (PM-LSM) is used as a driving source in transportation systems. Usually, an initial cost of PM-LSM rises to employ a full-length armature-side-on-ground design. Thus our laboratory have proposed a discontinuous armature type PM-LSM (DPM-LSM) [1]. Fig. 1 shows the arrangement of proposed system. However, the armature has an outlet edge on structure [2]. From Fig. 1, a secondary mover advances into an armature gradually from free running. A generated thrust changes with numbers of magnetic poles of the secondary mover which overlaps the armature. Thus the armature structure of generated thrust sufficient also with a few magnetic poles is required. This paper compares the static force of each winding structure. The static force to measure is the thrust generated at the time of the secondary mover advancing into the armature. It is made comparison with the ratio of the static force produced from the magnetomotive force of the armature by winding structure. From this ratio, the winding structure of LSM used for discontinuous arrangement is determined.

II.WINDING STRUCTURE OF DPM-LSM

The structure of LSM compares two kinds. It is the distributed winding from which winding is distributed over two or more slots. Another structure is concentrated winding which winding concentrates on one slot. This distributed winding is short pitch winding in which the coil pitch of the armature is shorter than the secondary mover's pole pitch. The numbers of poles of an armature are 9 poles. And, the magnetic poles of a secondary mover are 8 poles. Next, the numbers of slots of the armature of this concentrated winding are 9 slots, and the numbers of magnetic poles of the secondary mover are 28 poles. The magnet which overlaps with the armature completely becomes 12 poles. Therefore, the magnetic pole and the slot are 4 poles 3 slots.

III.MEASUREMENT AND EXAMINATION OF STATIC FORCE

Measurement of the static force of each current and the cogging force in each winding structure uses a Push-Pull load cell, and pushes and measures the secondary mover by the draw gear. The position-static force characteristics of LSM are shown in Fig. 2. From Fig. 2, the static force is increasing because the secondary mover advances into the armature gradually. In the outlet edge, the magnetic pole which overlaps with the winding of the armature changes with a secondary mover's positions. Therefore, the armature which gives generated thrust sufficient also in the state with few magnetic poles is required. The thrust constant is computed from the static force when the magnetic pole of the secondary mover overlaps with the armature of LSM completely.

Table I shows each calculated parameter. Since each LSM differs in the size of equipment, or the permanent magnet and the number of winding, comparison is difficult for it. Therefore, the ratio of the magnetomotive force F at the time of the rated current produced per winding to the maximum thrust force Fmax compares. From Table I, it can be found with F/Fmax=2.082 A/N of the distributed winding LSM. Similarly, it can be found with F/Fmax=4.514 A/N of the concentrated winding LSM. The concentrated winding of the thrust produced per magnetomotive force of winding is larger.

IV.CONCLUSION

In this paper, each static force of the distributed winding LSM and the concentrated winding LSM was measured, and the ratio of the maximum thrust in the magnetomotive force of winding was computed. The result has checked that the thrust had occurred effectively from the structure of the winding to field system magnetic flux in the direction of the concentrated winding LSM. Therefore, an effective winding structure of LSM where the outlet edge exists is concentrated winding.

[1]K. Seki, M. Watada, S. Torii, and D. Ebihara:"Discontinuous Arrangement to Long Stator Linear Synchronous Motor for Transportation System", Proceedings PEDS97, pp.697-702 (1997)

[2]Y. Kim, and H. Dohmeki:"Cogging Force Verification by Deforming the Shape of the Outlet Edge at the Armature of a Stationary Discontinuous Armature PM-LSM", IEEE TRANSACTIONS ON MAGNETICS, Vol.43, No.6, pp. 2540-2542 JUNE 2007

Item	Distriduted Winding	Concentrated Winding
Ratesd Current Irms	0.919(A)	20.0(A)
Number of Winding Turn N	158(Turns)	36(Turns)
Magnetomotive Force F	145(A)	720(A)
Thrust Constant Kf	75.6(N/A)	7.98(N/A)
Maximum Thrust Force Fmax	69.8(N)	160(N)

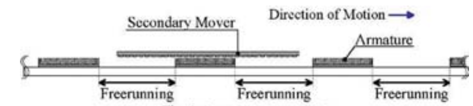

Fig. 1 Armature arrangment

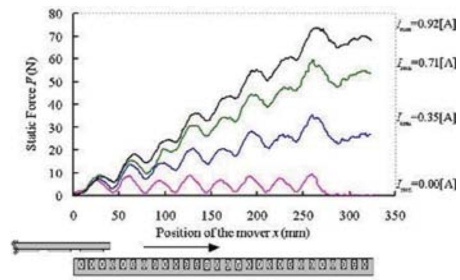

(a) The mover measured from 0 to 324(mm) of Distributed Winding LSM(g=5mm)

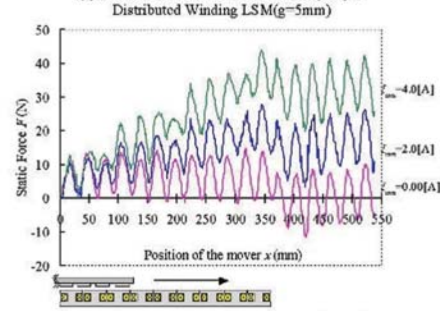

(b) The mover measured from 0 to 360(mm) of Concentrated winding LSM(g=8.0mm)
Fig. 2 Static force - Position characteristics

AU-06

Proposal of the Air-core Type Linear Synchronous Motor Using the Air Levitation System.

K. Suzuki[1], Y. Kim[2], H. Dohmeki[1]
1. Department of Electrical and Electronic Engineering, Musashi Institute of Technology, Tokyo, Japan; 2. Department of Electrical Engineering, College of Engineering Chosun University, Gwanju, South Korea

I.INTRODUCTION

The linear motor (LM) of direct drive has been produced and distributed mainly through factory automation (FA) transportation field focusing on high speed, low noise, simplification of driving apparatus and simplification of maintenance [1]. However, LM needs to contact and support a secondary mover. These linear motors cannot be used in a clean room by contamination of dust. Then, the mechanism which supports the secondary mover by non-contact is required for LM. We propose an air levitation system. This paper examines an air levitation type permanent magnet type linear synchronous motor (ALPM-LSM) which used porosity aluminum for the used support mechanism. Friction of this system is zero at the time of levitation. This motor can run by a low thrust. Then, the design of small PM-LSM of a low thrust which uses a air-core coil is described.

II.THE STRUCTURE OF ALPM-LSM

The air levitation system of this research uses porous aluminum material for the used support mechanism. Fig. 1 shows ALPM-LSM. From Fig. 1(b), air is sent to the cavity of a used machine style, and a secondary mover always levitates with the air which leaked from porosity aluminum. The secondary mover of ALPM-LSM levitates 98μm with air, and runs.

III.THE DESIHN OF ALPM-LSM

Friction of ALPM-LSM is zero at the time of levitation. Moreover, it is necessary to carry out the weight saving of the secondary mover's weight. This motor can be designed small by a low thrust force. The demand thrust is set to F*=0.447N, when it is made into secondary mover's weight M= 0.447kg and acceleration a*=1 m/s2. Next, the thrust force of LSM is generated according to the flux density Bg[T] in the air gap and the magnetomotive force of the coil of the armature. Thus the thrust force needs to calculate the flux density in the air gap. The flux density in the air gap is computed from the magnetic circuit in an air gap [2]. The concept of the magnetic circuit in the air gap is shown in Fig. 2. From Fig. 2, each magnetic reluctance Rml, Rg, and Rair in an air gap are computed. A magnetic circuit consists of magnetomotive force of the computed magnetic reluctance and a permanent magnet. The flux density in the air gap was computed with Bg=0.198T.

IV.MAGNETIC FIELD ANALYSIS BY FINITE ELEMENT METHOD

Magnetic field analysis of ASPM-LSM is conducted using the two-dimensional finite element method. Analysis asks for the static flux distribution in the air using the model of the secondary mover. Fig.3 shows the analysis result of the flux density of the finite element method. The value of the flux density of Fig. 3 is 4mm from the surface of a permanent magnet. This result is taking the thickness of the air gap and the coil into consideration. From Fig. 3, the analysis result of flux density is maximum Bmax=0.187T. Compared with flux density Bg=0.198T in the gap for which it asked from the magnetic circuit, the deflection as a result of magnetic field analysis is 5.65%. For the reason, the flux density for which it asks from the magnetic circuit is appropriate.

V.MEASUREMENT OF AN INDUCED VOLTAGE BY AN EXPERIMENTAL DEVICE

Induced voltage e[V] of an experimental device is measured and the flux density in the air gap is computed. As a result, the flux density was computed with Bg'=0.114 [T]. Compared with the flux density of a magnetic circuit and the finite element method, the deflection of flux density Bg' is 42.6%. This became small by the leakage flux which is not taken into consideration with the magnetic field circuit and the two-dimensional limited element.

VI.CONCLUSION

This paper described the design of the air levitation type PM-LSM. The design of LSM which uses the air core coil needs to constitute the magnetic circuit from three dimensions, and needs to compute the flux density in the air-gap.

[1]N. Corsi, R.Coleman and D. Piaget:"Status and new development of linear drives and subsystems",LDIA2007,pp.1-9 (2007)

[2]V.Karapetoff:"The Magnetic Circuit"McGraw-Hill, New York (1911)

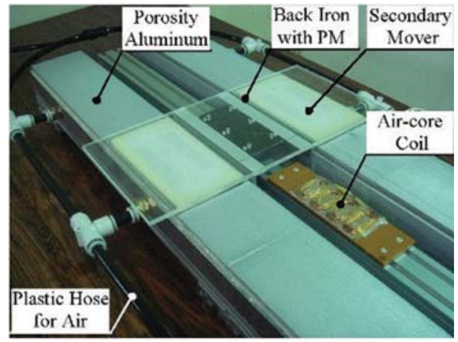

(a) Outline of ALPM-LSM

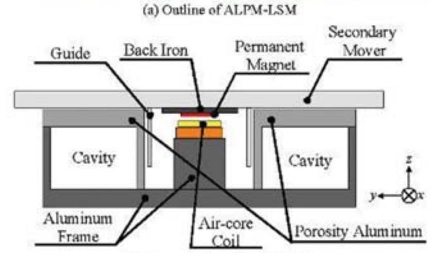

(b) Cross section of ALPM-LSM

Fig. 1. Structure of ALPM-LSM

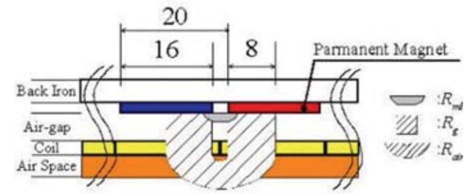

Fig. 2. The concept of the magnetic circuit in an air gap

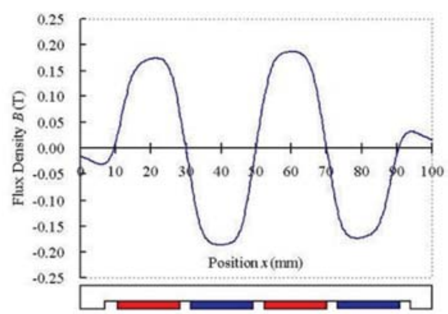

Fig. 3. The analysis result of the flux density of FEM

AU-07

Thrust Optimization of Linear Oscillatory Actuator Using Permeance Analysis Method.

M. Norhisam[1], F. Azhar[1], H. Hashim[1], M. Nirei[2], H. Wakiwaka[3], A. Razak J.[4]
1. Electrical & Electronic Engineering Department, Universiti Putra Malaysia, Serdang, Malaysia; 2. Faculty of Engineering, Nagano National College of Technology, Tokuma, Japan; 3. Faculty of Engineering, Shinshu University, Wakasato Nagano, Japan; 4. Research and Development, Malaysian Palm Oil Board, Kajang, Malaysia

I. INTRODUCTION

Nowaday, linear oscillatory actuator (LOA) are widely use in various application. It gives a rapid linear motion either in term of forward or backward direction. However, both directions or oscillatory motion can be achieved when AC power is supply to the LOA [1]. The purpose of the LOA development in this research is to work as a pruner. The LOA has been designed using FEM in [2] and mention as model A. However, the thrust produce is inadequate and need to improve. In this paper, the permeance analysis method (PAM) is use to optimize the thrust of LOA. The main constrain this research is to maintaining it weight below 2kg and size below 30mm diameter and 120mm length.

The PAM use magnetic equivalent circuit (MEC) approach that consists in building of a permeance network. By using PAM, it is necessary to assume magnetic path as a whole, and the analytical results are influenced by the assumption of air gap magnetic flux distribution [3]. The PAM technique also made effect of dimension of LOA structure to the thrust can be evaluate [4].

The optimization is done by varies the size of permanent magnet, rm and coil, Hc. To avoid magnetic saturation effect, high of slop, r2 and length between coils, lcc need to adjust at same value of rm and Hc. As a result, the high thrust of LOA has been designed with 450N of maximum thrust, the LOA weight is 2.0kg and overall size of LOA is 30mm diameter and 115mm length.

II. MAGNETIC EQUIVALENT CIRCUIT OF LOA

A. Structure of LOA

The structure and parameters of LOA is shows in fig. 1. These parameters will be use to develop the permeance equations in order to calculate the thrust of LOA.

B. Permeance and Magnetic Equivalent Circuit of LOA

The MEC was developed base on the permeance model of LOA. The permeance model is built depending on the estimated magnetic flux path at the air gap with following assumptions.

1)The permeability of the yoke is regarded as infinity.

2)The leakage flux is disregarded.

The permeance model and MEC of LOA are shows in fig 2. The permeance values are calculated using basic equation as equation (1).

P=(μOa)/l [H/m] (1)

Where P is the permeance value in (H/m), μO is the air permeability in (N/A2), a is the air gap area in (m2) and l is the air gap length in (m).

Magnetic energy and trhust value are expressed as equation (2) and (3).

Wm=NI(ØPM+ØC) [J]

Wm=NI(BkAm+NIPT) [J] (2)

F=δWm/δx [N] (3)

Where Wm is a magnetic energy in (J), ØPM is a permanent magnet magnetic flux in (Wb), ØC is a coil magnetic flux in (Wb), NI is a coil magneto motive force in (A), Bk is a magnetic flux density at operating point of permanent magnet in (T), Am is a cross area of permanent magnet in (m2) and PT is a permeance total for every magnetic equivalent circuit in (H/m).

III. THRUST CALCULATION

The thrust characteristic using PAM for this LOA has been calculated. The value of thrust calculated using PAM also has been compare to FEM and measured result using model A at same value of input power. As a result, difference about 15% of maximum thrust between these three methods. The optimized thrust with optimized parameter of LOA structure has been calculated. As a result, the LOA has been designed with having high value of thrust and optimum parameter. The thrust value is also compared to the FEM result. The comparison between the results is as shows in fig. 3.

IV. CONCLUSIONS

The thrust value of LOA has been calculated using PAM and compared with FEM and measured value. As a result, the LOA which is having high value of thrust has been designed. Increasing about 350N on the LOA thrust has been obtained by the optimized model compared to model A.

[1]Takano Y., Yeazaki S., Matsumoto K., Yamada H., “Thrust Simulation of Linear Oscillatory Actuator”, IEEE Trans of Magnetics, Vol. 33, No. 2. pp. 2085 - 2088, 1997

[2]Norhisam M., Alias K., R.N.Firdaus, S.Mahmod, N. Mariun, Abdul Razak J, “Comparison on Thrust Characteristic of Linear Oscillatory Actuators”, First International Power and Energy Conference PECon, Malaysia, pp. 470-475, 2006

[3]K.Hirata, Y.Kagami, M.Yanosaka, Y.Ishihari, T.Todaka, “Thrust Calculation Of Linear Pulse Motors Using A Combined Technique Employing The Finite Element Method And The Permeance Analysis Method”, IEEE Trans On Magnetics, Vol. 28, N0.2, pp. 1394-1397, 1992

[4]Mizuno T., Kawai M., Tsuchiya F., Kosugi M., Yamada H., “An Examination for Increasing the Motor Constant of a Cylindrical Moving Magnet-Type Linear Actuator”, IEEE Trans On Magnetics, Vol. 41, No. 10, pp. 3976 -3978, 2005

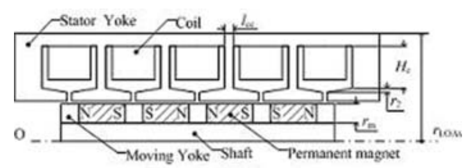

Fig. 1 : The LOA's structure

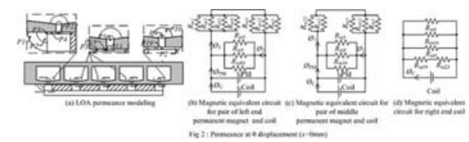

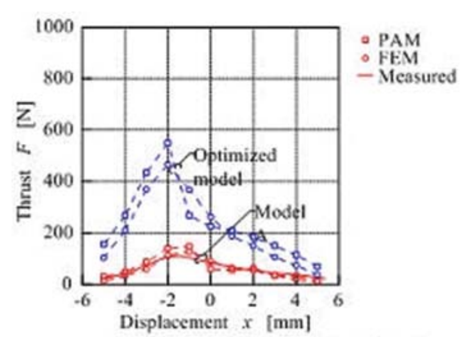

Fig 3 : Comparison result between PAM, FEM and measurement

AU-08

Optimal design of barrier shape improve torque of interior permanent magnet synchronous motor.

C. Jin, J. Lee
Hanyang University, Seoul, South Korea

The steady-state performance analysis and accuracy control of Interior Permanent Magnet Synchronous Motor (IPMSM) extremely depends on accurate determination of its parameters. The three important parameters of the IPMSM are magnet flux linkage, d-axis and q-axis inductances. Torque of IPMSM is divided into two parts. One is alignment torque and the other is reluctance torque.

Alignment torque depends on permanent magnet flux linkage, and reluctance torque relies on d-axis and q-axis inductance. Torque equation of IPMSM is shown (1).

T=P(ΨIq+(Ld-Lq)IdIq) (1)

One of the important factors of flux linkage, d-axis and q axis inductance is design shape of barrier. What is more, Shape of barrier is affected of length of rib.

This paper deals with proposal that optimal of barrier shape considering length of rib and q-axis inductance to improve torque IPMSM.

Design details for the IPMSM designed to operate constant torque 20Nm in the 45rpm(speed) / 12V(EMF) of constraint and to deliver 800W constant power over a 3:1 speed range extending from 400rpm to 1300rpm for washing machine. And this model has 8pole and 12slot. Fig 1 shows the model of IPMSM.

After design of the IPMSM for washing machine, the IPMSM test sample is manufactured on the basis of though verification of result of FEM. It progress to measure characteristic of test sample.

The agreement between amplitude of the predicted and measured of back-EMF is so good, but there is a serious difference between the amplitudes of the predicted and measured of torque. The amplitude of the measured torque is 17Nm while predicted torque is 20Nm.

Outcome of investigation about this problem, short length of rib cause rotor of IPMSM to increase reluctance torque with increasing q-axis inductance and current phase angle, to drop characteristic of magnetic torque. It is significant that magnetic torque is more effective than reluctance torque in constant torque region. Cause of magnetic torque drop is a part of magnetic flux linkage leak out through barrier and rib. And cause of reluctance torque's influence is extended increase of q-axis inductance and current phase angle.

But maybe it is not considered FEM analysis about above alluded to problem.

If that is the case, length of rib can not increase lack of definite view in mind. Because reluctance torque decrease under the influence decrease of q-axis inductance by saturation effect.

Consequently, it must design details of barrier shape considering length of rib and d- and q-axis inductance.

Fig 2 and Fig 3 show torque versus the angle of the current phase and torque versus current respectively.

It is verified improve the torque of IPMSM through manufacture of optimizing test sample.

[1]Dong-Hun Kim, Il-Han Park, Joon-Ho Lee, and Chang-Eob Kim, "Optimal Shape Design of Iron Core to Reduce Cogging Torque of IPM Motor" IEEE Trans. Magn., vol. 39, NO.3, MAY 2003

[2]Thomas M. Jahns, Seok-Hee Han, Ayman M. EL-Refaie, Jei-Hoon Baek, Metin Aydin, Mustafa K. Guven, and Wen L. Soong, "Design and Experimental Verification of a 50kW Interior Permanent Magnet Synchronous Machine" IEEE., pp 1941-1948, 2006

[3]T. Ohnishi and N. Takahashi, "Optimal Design of Efficient IPM Motor Using Finite Element Method" IEEE Trans. Magn., vol. 36, NO.5, SEPTEMBER 2000

[4]A. Kioumarsi, M. Moallem, and B. Fahimi, "Mitigation of Torque Ripple in Interior Permanent Magnet Motors by Optimal Shape Design" IEEE Trans. Magn., vol. 42, NO.11, NOVEMBER 2006

[5]Rukmi Dutta and M.F.Rahman, "A Comparative Analysis of Two Test Methods of Measuring d- and q-axis Inductances of Interior Permanent-Magnet Machine" IEEE Trans. Magn., vol. 42, NO.11, NOVEMBER 2006

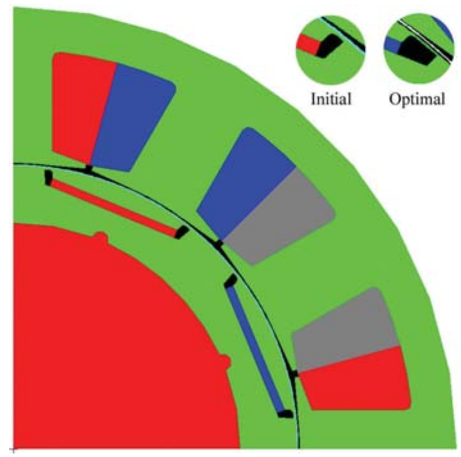

Model of IPMSM

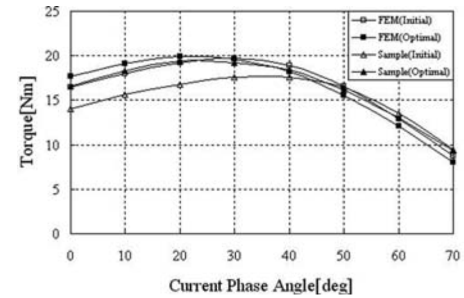

Torque versus the angle of the current phase

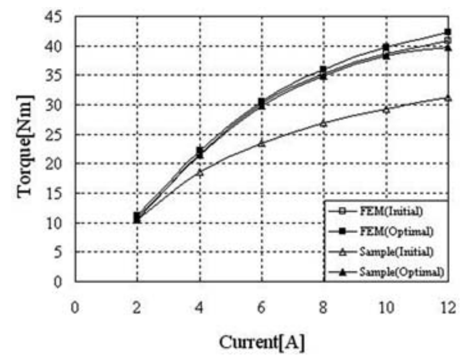

Torque versus the current

AU-09

Feasibility Study of a Passive Magnetic Bearing Using the Ring Sahped Permanent Magnets.

T. Azukizawa, S. Yamamoto, N. Matsuo
Kobe University, Kobe, Japan

1. Introduction

Magnetic bearings have the distinct features such as clean, noiseless, vibration free and maintenance free. However, high cost due to control apparatus for 5 degrees of freedom of the rotor, prevent their wide applications at present. It is expected to develop a cheap magnetic bearing system. A magnetic top consist of a couple of the ring shaped permanent magnets, abbreviate as PMs, seems to be a candidate for the passive magnetic bearing.
The purpose of this paper is to investigate the possibilities to build up a passive magnetic bearing composed of the ring shaped PMs, analytically.

2. Analysis of motion of a magnetic top

We had proposed a simple analytical method[1], instead of the previous precise analysis[2]. In this analysis, the ring shaped PMs, magnetized in axial direction, are simulated by the equivalent side current model. That is, a ring shaped PM is replaced by the set of circular coils located at the outer and inner surfaces of a ring shaped PM. The directions of currents in the outer and inner equivalent coils are inversed with each other, describing the axial magnetization of a PM. The magnetic forces acting on the levitating PM are calcurated as the interaction between the equivalent side currents of the levitating PM and the magnetic field generated by the equivalent side currents of the ground PM.
We had obtained the useful results about the relations between the 'levitating area' where a magnetic top can maintain levitating and the dimensions of the PMs, based on the static analysis. In this analysis, three dimensional layout of the PMs and the tilt angle of the levitating PM were considered, but the effects of rotation of a levitating PM were neglected[1].
In this paper, the characteristics of a magnetic top are discussed based on the dynamic analysis. Three dimensional layout of the PMs, the tilt angle of a rotating PM and the mechanical inertia of the rotating PM are considered, but aerodynamic damping effects are neglected. The motion of a rotating PM is simulated based on the equation of motions about the angular momentum of the rotating PM, using the 4th order Runge-Kutta argorithm.

3. Simulated behavior of a magnetic top

Figures show the simulated trajectories of the bottom of the axis of the levitating magnetic top for 5 seconds. The outer diameter, the inner diameter, the thichness of the PMs are 30mm/12mm/5mm for the levitatig PM, and 134mm/75mm/60mm for the ground PM, respectively. The mass of the levitating PM is 20.4g, and the equivalent currents are set as 286A/mm deducted by the measured magnetic field density at a surface of the PM. According to the previous analysis, the target point of the restoring magnetic force is (x, y, z)=(0, 0, 99.5)mm in this model. The initial position and the tilt angle of the rotating PM are (x, y, z)=(1, 0, 98.5)mm, 1 degree, respectively.
Figure (a), (b), (c) show the cases of rotating speed of 17, 1380 and 3240 rpm, respectively. The too low rotating speed is insufficient to maintain attitude of the top and results lack of levitation force as shown in Fig.(a). On the otherhand, the too high rotation speed generate the magnetic force larger than the restoring force resulting to fly out the top as shown in Fig.(c). The PM can maintain levitating in the levitating area as far as it rotates in a proper speed, as shown in Fig.(b).

4. Conclusions

In case of a magnetic top, it is difficult to repeat experiments in the same condition. However, the vertical and horizontal swaying frequencies, and size of the levitating areas are well in accordance with the analyzed values.
The following results can be obtained from the dynamic analysis in this paper:
1) A magnetic top, rotating in the axially symmetrical magnetic field, can be levitating by its precession.
2) The parameters to maintain levitation of a magnetic top are the tilt angle and the rotating speed.
3) In the model mentiond in this paper, the tilt angle should be about 1 degree, the rotating speed should be about 20 to 3200 rpm.
A magnetic top can be used as a rotating demonstration model in which some swaying motion can be permitted such as the toys or the relaxation items. The levitation area can be easily designed by the analysis proposed in this paper.

(1) T. Azukizawa, N. Matsuo, "Feasibility Study of a Magnetic Top As a Magnetic Bearing, LDIA 2007, Lille, France.

(2) A. San Miguel, "Numerical integration for the dynamics of the heavy magnetic top", Physics Letters A 335 235–244 (2005).

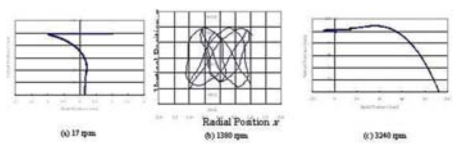

Figure: Trajectory of the bottom of the magnetic top in 5 sec

AU-10

Design Considerations of Axial Ring magnet.

C. Li, M. Devine, G. Hatch
Dexter Magnetic Technologies, Hicksville, NY

Ring is one of the basic geometries of permanent magnet. It is widely used in magnetic lenses, MRI devices, mechanical devices and sensors. Ring type magnets with transverse field have been discussed extensively due to their applications in MRI devices. For some applications such as Faraday Optical effect, magnetron guns, and klystron applications, an axial field is required. The requirement for this axial field can be a maximum possible field per given geometry; a sinusoidal type field with homogenous field along the axis or a field varies along the axis in a sinusoidal form. This article will discuss the relationship among the dimensions of a simple axial ring magnet.

Magnetic Field between the two poles of an axial ring magnet

In this discussion, we consider a ring magnet with radius of R_i and R_o and length L.

The orientation is along the length. We use polar coordinates in this discussion with the origin located at the center of the ring. By solving the Laplace equation, we can get the scalar potential for the region between the two poles. Expanding the scalar potential along the axis at the origin, we can show that the field along the z direction is in the form of equation 1.

We can see that we only need the field along the axis in order to obtain the field at any point. And the field along the axis is readily available by calculating the field from the surface charges on the pole faces.

So we have the general expression of the magnetic field between the two poles as in equation 2.

Optimum length of the ring to get uniform field

For a uniform field in the center region, we omit the high order terms with the condition of $r \ll L$ and obtain the optimum length to achieve a uniform field at the center region between the poles as shown in equation 3.

For example, If we have a ring magnet with OD of 2.00 cm and ID of one cm, from equation 3, we have 1.746 cm for the length in order to get a uniform field. Figure 1 shows the field plot along the axis with N35 material.

Optimum length for a peak field at the center

If the diameters of the ring are given, and a peak field at the center is required, then we can get the optimum length by taking the derivative of the field at the center. It is shown in equation 4.

We again using the above magnet as an example. From equation 4, we have the optimum length for maximum field at center to be 1.0 cm. By varying the length, we plot the field at the center of the ring in Figure 2. It shows that the field drops when the length increases to more than one cm.

$$H_z = \sum_{n=0}^{\infty} -\frac{1}{n!}\frac{\partial^n}{\partial z^n}\left(\frac{\partial \varphi_{axis}}{\partial z}\right) r^n P_n = \sum_{n=0}^{\infty} \frac{1}{n!}\left(\frac{\partial^n H_{axis}}{\partial z^n}\right)_{z=0} r^n P_n$$

equation 1

$$H_z = \frac{B_r}{2}\left(\left[\frac{1}{(\frac{1}{4}+\frac{R_2^2}{L^2})^{1/2}} - \frac{1}{(\frac{1}{4}+\frac{R_1^2}{L^2})^{1/2}}\right] + \frac{1}{2}\left[-\frac{3R_2^2}{L^2(\frac{1}{4}+\frac{R_2^2}{L^2})^{3/2}} + \frac{3R_1^2}{L^2(\frac{1}{4}+\frac{R_1^2}{L^2})^{3/2}}\right]\frac{r^2}{L^2}P_2(\cos\theta)\right.$$
$$\left. + \frac{1}{24}\left[\frac{45R_2^4 - 15R_2^2L^2}{L^4(\frac{1}{4}+\frac{R_2^2}{L^2})^{5/2}} - \frac{45R_1^4 - 15R_1^2L^2}{L^4(\frac{1}{4}+\frac{R_1^2}{L^2})^{5/2}}\right]\frac{r^4}{L^4}P_4(\cos\theta) + \ldots\ldots\right)$$

equation 2

$$L = 2\sqrt{\frac{R_1^{4/5}R_2^{\,2} - R_1^{\,2}R_2^{4/5}}{R_2^{4/5} - R_1^{4/5}}}$$

equation 3

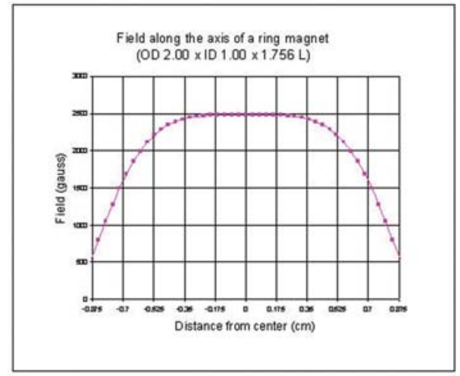

Figure 1: field plot along the axis for a N35 ring with OD=2 cm, ID=1 cm and Length=1.746 cm The magnet is oriented throught the 1.746 cm dimension.

$$L = \frac{2R_2^{2/3}R_1^{2/3}}{\sqrt{R_2^{2/3} + R_1^{2/3}}}$$

equation 4

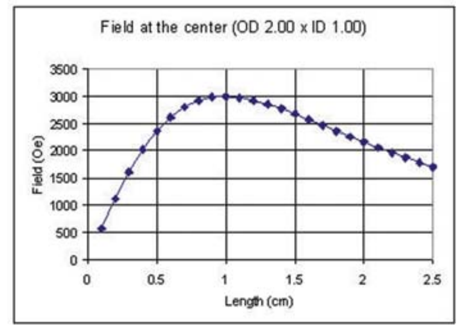

Figure 2: Field at the center of an axial ring with OD=2 cm, ID=1 cm and variable length

AV-01

Effect of microstructure refinment on magnetic properties of Fe-Pt thin films.

F. T. Yuan[1], H. W. Huang[2], W. M. Liao[4], H. W. Chang[1], D. H. Wei[1], S. K. Chen[2], Y. D. Yao[3], H. Y. Lee[4]

1. Institute of Physics, Academia Sinica, Taipei, Taiwan; 2. Materials Science and Engineering, Feng Chia University, Taichung, Taiwan; 3. Material Engineering, Tatung University, Taipei, Taiwan; 4. National Synchrotron Radiation Research Center, Hsinchu, Taiwan

Introduction

Ll_0 FePt has received many attentions in the field of permanent magnetism. The remarkable anisotropy and chemical stability makes it possible to be used as bio-compatible magnet. In order to enhance the magnetic performance, many efforts have been focused on the introduction of soft magnetic phase in FePt Ll_0 matrix. By the strong exchange coupling between magnetic hard and soft phase, the energy density, $(BH)_{max}$, can be significantly increased as predicted by the exchange spring model by Kneller and Hawig [1]. Very high value of $(BH)_{max}$ of larger than 40 MGOe has been reported in a nanostructured FePt-Fe_3Pt film prepared by multilayer deposition with ~60 nm in thickness [2]. For a single phase magnet, theoretical studies also have predicted that the $(BH)_{max}$ can also be enhanced by the reduction of mean grain size [3]. However, experimental investigation concerning this subject is not widely. In this study, the focus was placed on the relation between microstructure refinement and magnetic properties in single phase Fe-Pt films.

Experimental

Single layer films with composition of $Fe_{60}Pt_{40}$ with thickness of 100~300 nm were deposited at different temperatures of 400 and 800°C on quartz substrates to create significant different mean grain size. Generally, the low-temperature grown FePt films contain certain residual disordered region. However, in this study, the effects from the residual disorder phase must be ruled out. Therefore, after sputtering, the deposition temperature was maintained for different time; 400°C for 15 hours and 800°C for 1 hour to complete the ordering transformation and homogenize the film, forming single phase of Ll0 with uniform extent of ordering. The phase structure was analyzed by x-ray diffractometry (XRD). The mean grain size was measured from the transmission electron microscope (TEM) images. Magnetic properties were measured by using a vibrating sample magnetometer (VSM) with a maximum applied field of 2T at room temperature.

Results and discussion

Figure 1(a) show the x-ray diffraction patterns of the films with various thicknesses annealed at 400 and 800°C. The order parameter (S_{ord}) for each sample was measured from the intensities of peaks in the pattern and corrected by chemical composition. To further verify if the films annealed at different temperature are single phase, the slow scan of (220) peak group were performed. The results show clearly separated two symmetric peaks of (220) and (202) from Ll_0 phase as shown in Fig. 1(b) and 1(c). This confirms the films are with single phase of Ll_0. The relation between grain size and film thickness for the films annealed at 400 and 800°C is shown in Fig. 1(d). It indicates that the grain size in the 800°C-annealed films roughly equal to double of the film thickness; on the contrary, it only increases 23% while the film thickness was increased from 100 to 300 nm in the 400°C samples. Composition distribution across the grain boundaries was analyzed using energy dispersion spectroscopy (EDS) nanobeam line scan, no segregation was found in the the films. Magnetic properties are summarized in Table 1. Films annealed at 400°C exhibit higher coercivities and remanences than that of samples annealed at 800°C. A significant enhancement of $(BH)_{max}$ was obtained in the three different thickness films. The maximum $(BH)_{max}$ was 19.6 MGOe for the 300 nm-thick sample annealed at 400°C, which is 72% larger than that of 800°C annealed film with same thickness.

The magnetic data in Table 1 indicate that the enhanced energy density is mainly from the higher coercivities, remanences and coercive squareness ratio (S^*).

[1] E.F. Kneller and Hawig, IEEE Teans. Magn. 27, 3588 (1991).

[2] J.P. Liu, C.P. Luo, Y. Liu, and D.J. Sellmyer, Appl. Phys. Lett. 72, 483 (1998).

[3] T. Schrefl, J. Fidler, and H. Kronmuller, Phys. Rev. B 49, 6100 (1994).

[4] G.P. Zhao, C.K. Ong, Y.P. Feng, H.S. Lim, and J. Ding, J. Magn. Magn. Mater. 192, 543 (1999).

sample		H_c (kOe)	M_r (emu/cm^3)	M_{2T} (emu/cm^3)	S^*	$(BH)_{max}$ (MGOe)
100 nm	400°C	7.3	770	990	0.853	16.1
	800°C	7.8	670	850	0.657	13.7
200 nm	400°C	6.5	850	1110	0.855	19.1
	800°C	5.6	710	950	0.713	13.4
300 nm	400°C	6.3	880	1130	0.856	19.6
	800°C	4.7	680	920	0.691	11.4

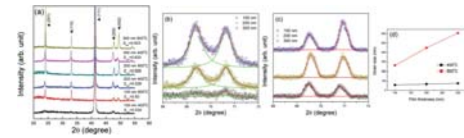

Fig. 1 (a)XRD patterns of the FePt films with various thickness annealed at different temperatures; (b) and (c) XRD slow scan of (220) group and fitting lines of the FePt films annealed at 400°C and 800°C, respectively; (d) relation between grain size and film thickness for the FePt films with various thickness annealed at different temperatures.

AV-02

Magnetization reversal mechanism and intrinsic properties of FePt (110) epitaxial thin films.

S. Fong[1,2], K. Cheng[1,2], D. Wei[1,4], C. Yu[3], C. Lin[2], F. Yuan[1], H. Chang[1], Y. Liou[1], T. Chin[2], *Y. Yao*[4]
1. Institute of Physics, Academia Sinica, Taipei, Taiwan; 2. Department of Materials Science and Engineering, National Tsing Hua University, HsinChu, Taiwan; 3. Department of Applied Physics, National University of Kaohsiung, Kaohsiung, Taiwan; 4. Department of Materials Engineering, Tatung University, Taipei, Taiwan

Ordered FePt phase with nanogranular/island-like structure is one of the most potential candidates for application in magnetic devices and permanent magnets due to its large magneto-crystalline anisotropy constant (Ku) to resist thermal fluctuation [1-4]. None work has been focused on the relationship between the magnetization behavior and surface morphology of FePt (110) films. In this present study, we fabricated Fe/Pt multilayers with different thickness (t) on MgO (110) substrates, and the thickness dependence of the magnetization reversal behavior and microstructure in FePt L10 epitaxial films was studied. The relationship between the surface morphology, magnetic domains, and the grain size of Fe/Pt multilayers were also discussed. We are the first to report the intrinsic properties and magnetization behavior of the FePt (110) epitaxial films by adjusting the thickness to control the microstructure. FePt films composed of [Fe(1 nm)/Pt(1 nm)] multilayers with different thickness ranged from 8nm to 40 nm were fabricated at 500 oC by molecular-beam epitaxy on Pt-buffered (10 nm)/MgO(110) substrates. Pt and Fe layers were deposited via e-beam evaporation at a deposition rate around 0.005 nm/s, respectively. The coercivity monotonically decreases from 9500 Oe to 2000 Oe as t changes from 8 nm to 40 nm and the easy magnetization axis lies in the [001] direction parallel to the film plane. The uniaxial magnetic anisotropy Ku increases with increasing t and shows a similar tendency following the slope of saturation magnetization (Ms). The Ku constant value ranged from 1.6 (t = 8 nm) to 2.8 × 107 erg/cm3 (t = 40 nm). If the growth temperature is higher, the Ku constant will close to the value of fully ordered FePt alloys (7 × 107 erg/cm3). With increasing thickness the isolated grains coalesce and connect to each other for t = 10~30 nm. When t is over 30 nm, the FePt films fully cover with the whole surface, and the film changes from the island-like to continuous morphology. Strongly faceted islands of FePt particles are observed with regular-shape distribution as shown in inset of Fig. 1. FePt L10 rectangular-like islands are aligned along the direction of MgO [001]. The major facet planes are (1 -1 0) and (001). It can be understood that with increasing film thickness, particles with multiple domain increases. The rotation of the magnetization is considered to be a dominating mechanism in the thinner films. The angular dependence profile of coercivity for the 34 nm thick FePt films shows a behavior closed to domain-wall motion. By reducing the thickness of FePt films, the angular dependence profile of coercivity becomes closed to the S-W rotation mode as shown in Fig. 1. The mechanism of the coercivity is associated with the surface morphology changed from isolated to continuous states. It indicates that strong exchange coupling exists in the thicker films and the disappearance of island structure causes the decrease of coercively. However, the average size of magnetic domains increases with increasing film thickness. The isolated grains are less magnetically coupled in the rotation mode and the reversal of magnetization is more independent. It is originated from the weakening of domain-wall motion, while domain rotation is enhanced depicting a decoupling of inter-grain interaction. The separated grains are less magnetically coupled in the rotation mode and the reversal of magnetization is more independent as identified with ΔM measurement and initial magnetization curves as shown in Fig. 2. This work clearly showed the effect of surface morphology of FePt (110) films via thickness control on their magnetic properties. The in-plane coercivity decreases with increasing film thickness, while uniaxial magnetic anisotropy, and average size of magnetic domains and grain size values increase with the thickness of FePt films.

[1] R. F. C. Farrow, D. Weller, R. F. Marks, M. F. Toney, David J. Smith, and M. R. McCartney J. Appl. Phys. 84, 934 (1998).

[2] S. Okamoto, N. Kikuchi, O. Kitakami, T. Miyazaki, Y. Shimada, and K. Fukamichi, Phys. Rev. B. 66, 024413 (2002).

[3] T. Seki, T. Shima, and K. Takanashi, J. Magn. Magn. Mater. 272, 2182 (2004).

[4] D. H. Wei, F. T. Yuan, H. W. Chang, K. L. You, Y. Liou, T. S. Chin, C. C. Yu, and Y. D. Yao, Nanotechnology 18, 335603 (2007).

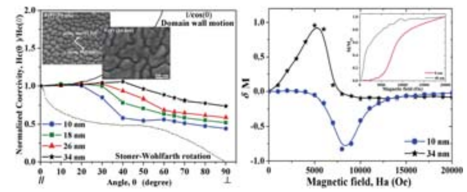

Fig. 1. Angular dependence coercivity and corresponding FE-SEM images for FePt films Fig. 2. ΔM plots and initial magnetization curves for FePt films

AV-03

Effect of Au underlayer on magnetic properties and ordering of CoPt thin films.

F. T. Yuan[1], H. W. Huang[2], A. C. Sun[3], D. H. Wei[1], H. W. Chang[1], S. K. Chen[2], Y. D. Yao[4]
1. Academia Sinica, Physics, Taipei, Taiwan; 2. Materials Science and Engineering, Feng Chia University, Taichung, Taiwan; 3. Physics, National Taiwan University, Taipei, Taiwan; 4. Materials Engineering, TaTung University, Taipei, Taiwan

Introduction
$L1_0$ CoPt and FePt thin films are commonly accepted as potential materials for future recording media with ultra high density exceeding 1 Tbit/inch^2 due to the very high Curie temperature and anisotropy. However, it remains limitations for manufacturing. One of the problems is the high processing (ordering) temperature (T_{ord}), which is necessary to form high anisotropy Ll_0 phase. Although Ll_0 CoPt exhibits higher anisotropic field, the Tord about 100°C higher than that of FePt constrains its potential on recording application. Lowering the ordering temperature of CoPt therefore becomes an important issue which many efforts have been devoted to. Alloying of several low-melting-point elements including Pb, Sn, Bi, Ag, and B has been reported to be effective in reducing Tord by creating defects or forming solid solution in CoPt grains [1]. Au/CoPt multilayer has also been reported to show lower T_{ord} than that of CoPt single layer [2]. However, the structural data and the mechanism is not discussed in details due to the intrinsically very strong (111) orientation which fails the monitoring of order transformation by the traditional θ-2θ scan. In this paper, the ordering process of Au-underlayered CoPt was studied by χ rotation method using synchrotron radiation light source which gives direct information of ordering. Additionally, magnetic properties and morphology evolution were studied in details.
Experimental
Thin film samples were deposited by radio frequency (rf) magnetron sputtering under a background vacuum better than 2×10^{-7} torr. Two series of sample were prepared: CoPt layer on Corning 1737 substrate and Au underlayer with thickness of 50 nm deposited at room temperature. A sequential annealing was performed at 400~700°C for 30 minutes after deposition. The thickness of CoPt layer is 20 nm. Exact composition of the CoPt films was $Co_{46}Pt_{54}$. Structural analysis were carried out at National Synchrotron Radiation Research Center (NSRRC) beamline 17B with energy of 8 keV (wavelength, λ= 1.55Å). In-plane magnetic properties were measured at room temperature using a vibrating sample magnetometer (VSM) with maximum applied field of 2 T. Surface morphology was investigated by scanning electron microscopy (SEM).
Results and discussion
Magnetic properties of the CoPt and Au/CoPt films are shown in Fig. 1(a) and 1(b). The coercivity (H_c) increased while the annealing temperature (T_a) exceeded 400°C for both CoPt and Au/CoPt films. As T_a reached 700°C, similar value of H_c (~12 kOe) were achieved for the two samples. Magnetization at applied field of 2T (M_{2T}) correspondingly decreased while T_a exceeded 400°C and reached a minimum at T_a=700°C. The temperature dependences of magnetic properties for the two films were similar, except a shift in T_a about 100°C. Figure 1(c) shows the x-ray diffraction pattern by χ-rotation method. It reveals that the CoPt film with T_a=500°C still remain disorder structure; on the contrary, a clear peak of (001) indicates that the Au/CoPt film at the same condition has begun to order. Figure 2 shows the hysteresis loops and the corresponding SEM images for the CoPt and Au/CoPt films annealed at 500 and 600°C. The loop of Au/CoPt films with T_a=500°C shows a stepwise shape indicating magnetic two-phase structure. This suggests the ordering is not complete. The SEM images show that the CoPt films remain continuous morphology even at T_a=600°C; however, the Au/CoPt film exhibits discontinuous phase separation structure (CoPt grain embedded in the gold matrix) at T_a=500°C. Comparing the SEM results with the XRD data, it is interesting to notice that in the CoPt films, the occurrence of ordering accompanies grain growth and surface roughening; but in Au/CoPt samples, it accompanies the phase separation. This suggests that the mechanism of ordering at lower temperature in Au/CoPt film may involve the relaxation of internal strain or stress. The further investigations are undergoing.
The findings of this study can be summarized as follows: (1) the insertion of Au underlayer was found to reduce the ordering temperature by about 100°C; (2) formation of L<l_0 phase can be successfully monitored by χ-rotation diffraction; (3) the phase separation between Au and CoPt was found to assist ordering transformation.

[1] O. Kitakami, Y. Shimada, K. Oikawa, H. Daimon, and K. Fukamichi, Appl. Phys. Lett. 78, 1104 (2001).
[2] T. Yokota, L. Gao, S.H. Liou, M.L. Yan, and D.J. Sellmyer, J. Appl. Phys. 95, 7270 (2004).

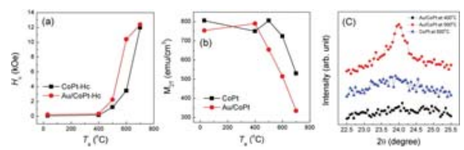

Fig. 1 Dependence of (a) coercivity, H_c, and (b) magnetization at applied field of 2T, M_{2T} on annealing temperature, T_a, for the CoPt and Au/CoPt films; (c) χ-rotation diffraction pattern for the CoPt film with T_a=500°C and Au/CoPt film with T_a=400 and 500°C.

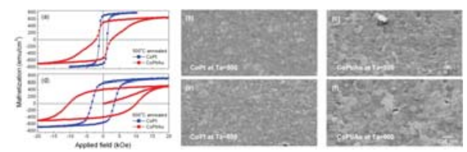

Fig. 2 Hysteresis loops and the corresponding SEM images for the CoPt and Au/CoPt films annealed at 500 and 600°C.

AV-04

Strain effect on the spin reorientation of epitaxial Nd-Fe-B films.

A. Kwon[1], V. Neu[1], V. Matias[2], J. Hänisch[2], R. Hühne[1], B. Holzapfel[1], L. Schultz[1], S. Fähler[1]
1. Institute for Metallic Materials, IFW Dresden, Dresden, Germany; 2. Los Alamos national laboratory, NM 87545, NM

While $Nd_2Fe_{14}B$ is already used in high performance bulk magnets, thin films are interesting for applications such as microactuators, motors and magnetic recordings. For technological applications, well textured $Nd_2Fe_{14}B$ films are available [1,2]. Nd-Fe-B has very high magnetocrystalline anisotropy, therefore, magnetoelastic anisotropy is usually neglected. However, in large external stress, especially spin reorientation transition at low temperature should be affected. Here a new approach to study the influence of huge strain on the intrinsic properties of Nd2Fe14B under uniaxial stress is presented.

Hastelloy, which has high ductility and cheap price, was used as a substrate to reach a strain up to 2% by conventional mechanical elongation which breaks the in-plane symmetry. In addition, this elongation gives uniaxial strain on the film. So one can expect with elongation direction, tensile stress is given and by poisson ratio the other directions have compressive stress (Fig.1). Prior to elongation, MgO(001) had been deposited by ion beam assistant deposition (IBAD). As a next step, Mo and $Nd_2Fe_{14}B$ are deposited at 450 °C by pulsed laser deposition. In fact, Nd-Fe-B films on Cr/Ta buffer layers shows perfect texture so that spin reorientation transition looks like in a single crystal (Fig.2 (a)). Below the spin reorientation temperature (T_{SR}), in-plane magnetization increases as the magnetization lies along an easy cone. By the tetragonal crystal symmetry the in-plane symmetry is broken and the [110] direction exhibited a higher polarization compared to the [100] direction. However, whereas films on Cr/Ta are discontinuous, a Mo buffer results in a smooth and continuous Nd-Fe-B film [1] which gives possibility to analyze strain effect. On top of the IBAD substrate, Mo grows epitaxially with a (001) orientation and Nd-Fe-B films on top of these buffers posses the desired (001) out-of-plane orientation with 3 different in-plane orientations. Before elongation, no distinguishable polarization is observed when measuring along different in-plane orientations (Fig.2 (b)). After elongation, lattice parameter along the elongation direction increases and lattice parameter of the other directions decrease. This was measured by 4 circle diffrectometry on the Mo buffers as the intensity of Nd2Fe14B is too low to analyze strain in the film itself. When hastelloy was stained plastically by 2%, a total ~0.9% of in-plane strain in Mo is observed. By this, Nd2Fe14B has distinguishably elliptical distortion of the cone shape below T_{SR} (Fig.2(c)), significantly higher compared to the influence of the 4-folded crystal symmetry (Fig.2 (a)). However, temperature for the spin reorientation does not change due to the strain.

* This work was supported by DFG as a part of SFB 463:"Rare earth transition metal compounds: structure, magnetism and transport".

[1] A. R. Kwon, V. Neu, L. Schultz, S. Fähler, J. Appl. Phys. 101, 09K506 (2007)

[2] A. R. Kwon, S. Fähler, V. Neu, L. Schultz, J. Magn. Magn. Mater. 302 252 (2006)

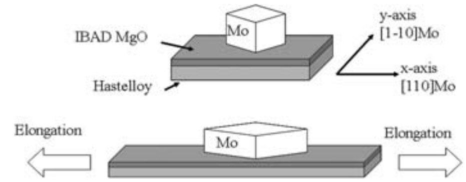

Fig.1 Schematic drawing of the investigation set-up

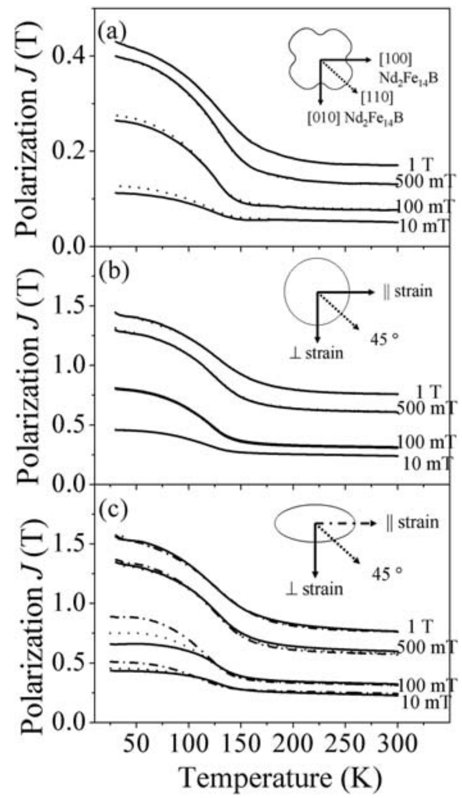

Fig.2 Spin reorientation transition behavior on (a) epitaxial films on a combined Cr/Ta buffer system (b) hastelloy as-deposited state and (c) hastelloy after elongation. Measurements had been made in different in-plane directions and applied fields marked in the graphs

AV-05

Magnetic properties and structure of Nd-Fe-B thin films with Ta buffer layer prepared on MgO(100) substrate.

H. Ishioka[1], T. Sato[2], H. Kato[1], H. Fujino[1], T. Shima[1]
1. Faculty of Engineering, Tohoku Gakuin University, Tagajo, Japan; 2. Toyota Central R&D Lab, Nagakute, Japan

$Nd_2Fe_{14}B$ alloy is a well-known material as a permanent magnet because of its high uniaxial magnetocrystalline anisotropy [1]. A lot of work has been extensively studied not only for bulk samples but also for thin film samples [2]-[4]. Since the easy magnetization axis of $Nd_2Fe_{14}B$ thin film is easily aligned to out of the film plane. It has opened up varieties of possibility for the applications in more efficient micromagnetic devices, such as actuators and motors. However, detailed magnetization mechanism of this material is still unknown so far. In this study, in order to clarify the coercivity mechanism, the microstructure and magnetic properties of $Nd_2Fe_{14}B$ films with Ta buffer layer has been investigated by changing the compositions and the film thicknesses.

The samples were prepared on a MgO(100) single crystal substrates using an UHV-compatible dc-sputtering apparatus. The base pressure is below 5×10^{-8} Pa. A Ta buffer layer of 20, 40 and 60nm were firstly deposited onto MgO (100) substrate at room temperature (RT). Then a Nd-Fe-B layer of 30nm was deposited at the substrate temperature in the range between 500 to 700°C. The magnetic properties were measured by a superconducting quantum interference device (SQUID) magnetometer. The structure characterization was performed by an X-ray diffraction with Kα radiation. The film composition was determined by an electoron probe micro-analysis (EPMA) to be $Nd_{15.2}Fe_{70.2}B_{14.6}$, $Nd_{14.3}Fe_{75}B_{10.7}$ and $Nd_{12.0}Fe_{83.3}B_{4.8}$ (at. %).

X-ray diffraction patterns of Nd-Fe-B thin films with various composition of Nd-Fe-B layer were shown in Fig. 1. The thickness of Ta buffer layer and Nd-Fe-B layer was fixed at 40 and 30nm, respectively. It is seen from this figure, the peaks from the c-plane of the $Nd_2Fe_{14}B$ phase, such as 004, 006 and 008 were clearly observed for all the samples. Among them, remarkable intense peaks of the c-axis of $Nd_2Fe_{14}B$ phase were observed for the samples with the composition of $Nd_{14.3}Fe_{75}B_{10.7}$. From the magnetization measurement, it is revealed that a maximum value of the coercivity H_c measured in the perpendicular direction was obtained for 11kOe at this composition.

This work was partly supported by Toyota Motor Corporation. The magnetization measurement was performed at Magnetic Material Laboratory at IMR, Tohoku University. The structural characterization was performed at the Hi-tech Research Center of Tohoku Gakuin University.

[1] M. Sagawa, N. Togawa, H. Yamamoto, and Y. Matsuura, J. Appl. Phys., 55, 2083 (1984).

[2] Y. Yamashita, J. Yamasaki, M. Ikeda, and N. Iwabuch, J. Appl. Phys., 70, 6627 (1991).

[3] H. Jiang and M. J. O'Shea, J. Appl. Phys., 87, 6131 (2000)

[4] D. J. Mapps, R. Chandrasekhar, K. O'Grady, J. Cambridge, A. Petford Long, and R. Doole, IEEE Trans. Magn., 33. 5, 3007 (1997).

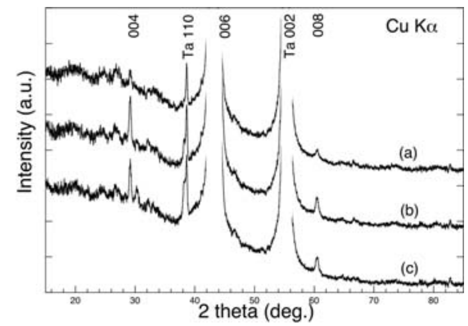

Fig. 1. XRD patterns of Nd-Fe-B thin films with different composition. All samples were prepared on MgO(100) substrate. (a) : $Nd_{12.0}Fe_{83.3}B_{4.8}$, (b) : $Nd_{14.3}Fe_{75}B_{10.7}$ and (c) : $Nd_{15.2}Fe_{70.2}B_{14.6}$ (at. %). The film thickness of Ta buffer layer and Nd-Fe-B layer is fixed at 40nm and 30nm, respectively.

AV-06

In field magnetic domain observation of Nd-Fe-B thin film by magnetic force microscopy.

T. Iwasa[1], H. Ishioka[1], H. Kato[1], T. Sato[2], T. Shima[1]
1. Faculty of Engineering, Tohoku Gakuin University, Tagajo, Japan; 2. Toyota Central R&D Labs., Nagakute, Japan

Among all permanent magnets, Nd-Fe-B based magnets are currently the most powerful ones with the highest maximum magnetic energy product $(BH)_{max}$ [1]. Nowadays, Nd-Fe-B magnets are used in a wide range of applications such as sensors, actuators and motors. The market for them is continuing to expand to hybrid vehicles as their magnetic characteristics. Also a lot of studies have been done not only for bulk samples but also thin films [2][3]. In order to develop high performance permanent magnets a detailed and fully understanding of the magnetization process of the rare earth based magnets are not only of fundamental interest, but also of technological significance. Magnetic force microscopy (MFM) is a convenient tool to observe the magnetic domain structure of the material [4]. Furthermore, in order to understand the magnetization process, in field magnetic domain observation is essential and important. In this study, detailed observation of in field magnetic domain structure of Nd-Fe-B thin film was performed by MFM equipped with an electromagnet which can apply in the direction perpendicular to the film plane.
The samples were prepared using a dc-magnetron sputtering system. The base pressure was less than 5×10^{-8} Pa. A Cr seed layer of 1nm and a Mo buffer layer of 20nm were deposited at the substrate temperature Ts of room temperature (RT). Nd-Fe-B layer was co-deposited with Nd, Fe and B at Ts = 300°C. A Mo (in some cases, Cr) capping layer of 10nm was finally deposited to avoid the oxidation and then it was annealed in the range between 400 and 700°C for 1 hour.
The coersivity (H_c) measured in the perpendicular direction of this sample was 18.8 kOe. Atomic force microscope (AFM) and MFM images of Nd-Fe-B thin film are shown in Fig.1. Bright and dark contrasts in MFM image represent an upward and a downward magnetization direction. Applied magnetic field during this measurement was performed at 3kOe. It was confirmed that a roughness of the surface of this sample was relatively flat and that was less than 1.5nm. A remarkable maze-like domain pattern was observed in MFM image. It is seem from MFM image, different behavior of the magnetic domain structure was observed at the center region of the image. With increasing an applied magnetic field, the magnetic domain was easily changed in this region. This behavior is thought to arise from the multiple phases of the Nd-Fe-B thin films.
This work was partly supported by Toyota Motor Corporation. The magnetization measurement was performed at Magnetic Material Laboratory at IMR, Tohoku University. The structural characterization was performed at the Hi-tech Research Center of Tohoku Gakuin University.

[1] M. Sagawa, N. Togawa, H. Yamamoto, and Y. Matsuura, J. Appl. Phys., 55, 2083 (1984).

[2] A.R. Kwon, U. Hannemann, V. Neu, S. Fähler, L. Schultz, J. Magn, Mater., 290-291, 1247 (2005).

[3] T. Shima, A. Kamegawa, K. Hono, H. Fujimori, J. Appl. Phys., 78, 2049 (2001).

[4] G.Q. Li, H. Takahoshi, H. Ito, H. Saito, S. Ishio, T. Shima, K. Takanashi, J. Appl. Phys., 94, 5672 (2003).

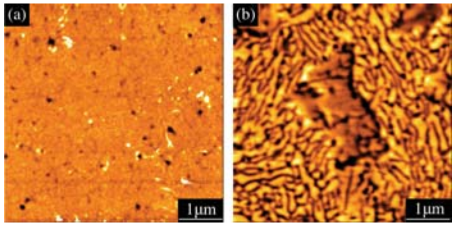

Fig.1 (a) AFM and (b) MFM images of Nd-Fe-B thin film. An in field applied magnetic field is 3kOe.

AV-07

Improvement in magnetic properties of PLD-made Nd-Fe-B thick film magnets.

M. Nakano[1], H. Takeda[1], F. Yamashita[2], T. Yanai[1], H. Fukunaga[1]
1. Electronics and Electrical Engineering, Nagasaki University, Nagasaki, Japan; 2. Matsushita Electric Industrial Co., Ltd., Osaka, Japan

We have already reported the fabrication of isotropic Nd-Fe-B thick film magnets, which have coercivity, remanence, and (BH)max values of approximately 1000 kA/m, 0.6 T, and 60 kJ/m3, respectively, prepared by the PLD method with a high deposition rate of approximately 90 microns/h[1]. In addition, an application of a 0.2 mm-thick Nd-Fe-B film on a Fe substrate to a milli-size motor was carried out as a practical usage. As the advancement in micro-machines such as small motors depends on magnetic properties of small size magnets, a further improvement in magnetic properties of film magnets is strongly required.According to the observation on microstructure for the previously reported films[1], the size of Nd2Fe14B grains ranged widely from 5 to 440 nm, and the average grain size was estimated at 150 nm, which suggests that refinement in grain size is a key technology to improve magnetic properties of the thick film magnets. It has also been reported that a use of additives such as Zr, Nb, Ga is effective to obtain homogeneous microstructure, and resultantly to increase remanence and coercivity for Nd-Fe-B based ribbons and HDDR powder[2][3][4], respectively.This contribution reports magnetic properties of the PLD-fabricated thick films prepared from Nd-Fe-B targets including Zr, Nb, Ga additives. Furthermore, the pulse annealing as a high-speed crystallization method was applied to the films including the additives. The targets with the composition of Nd2.6Fe14B + M0.5 at.% (M = Zr, Nb, Ga) and Nd2.0Fe14B + M0.5 at.% (M = Zr, Nb, Ga) and were prepared. They were ablated with a Nd-YAG pulse laser at the repetition rate of 30 Hz, and the films were deposited on Ta substrates. The distance between a target and a substrate was fixed at 10 mm, and the obtained thickness was larger than 20 microns. Before the ablation, the chamber was evacuated down to approximately 0.01 mPa with a molecular turbo pump. As-deposited films were amorphous, and, therefore, they were crystallized by annealing with an infrared furnace whose maximum output power was 8 kW. We set the annealing temperature, heating rate and holding time at 923 K, 400 K/min and 0 min, respectively, as the conditions of a conventional annealing (CA) method. In addition, we adopted a pulse annealing (PA) method, in which samples were instantaneously crystallized for 1.7-1.8 s as a high-speed crystallization method. After a sample was magnetized up to 7 T with a pulse magnetizer, magnetic properties were measured with a vibrating sample magnetometer which could apply a magnetic field up to approximately 1800 kA/m reversibly. All the post-annealed films were magnetically isotropic and, therefore, in-plane magnetic properties were shown in this article.
Figure 1 shows the coercivity values of PLD-fabricated Nd-Fe-B thick film magnets prepared from Nd2.6Fe14B + M0.5 at.% (M = Zr, Nb, Ga) targets followed by the CA and PA methods. It was clarified that an adoption of PA method as a high-speed crystallization one together with additives such as Ga showed the synergistic results for the enhancement in coercivity. As the cooperated effect of the PA method and additives causes a remarkable increase in coercivity, we can reduce the Nd content of a target. Therefore, we prepared the film magnets from Nd2.0Fe14B + M0.5 at.% (M = Zr, Nb, Ga) targets followed by the PA method. The obtained demagnetization curves are shown in Fig. 2. An increase in remanence by approximately 0.1 T could be achieved compared with those of samples prepared from Nd2.6Fe14B + M0.5 at.% (M = Zr, Nb, Ga) targets. It was also found that an addition of Zr, Nb and Ga is effective to increase the coercivity for the targets with stoichiometric composition. Resultantly, an enhancement in (BH)max was successfully achieved and obtained (BH)max value reached approximately 70 kJ/m3 for the both of Zr and Nb added films.

[1] M. Nakano et al., IEEE Trans. Magn. 43, 2672 (2007).
[2] H. Hashino et al., J. Magn. Magn. Mater. 278, 68-75 (2004).
[3] Z. Chen et al., J. Magn. Magn. Mater. 268, 105-113 (2004).
[4] S. Sugimoto et al., J. Magn. Magn. Mater. 239, 444-446 (2002).

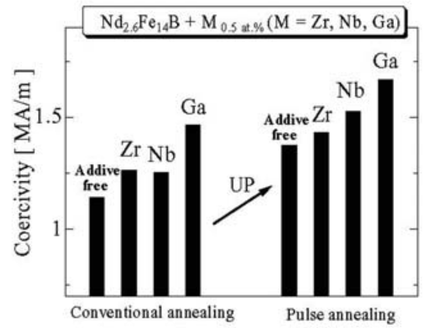

Fig.1. Comparison of coercivity values for samples prepared by two methods of CA and PA from $Nd_{2.6}Fe_{14}B + M_{0.5\ at.\%}$ (M = Zr, Nb, Ga) targets. It was clarified that an adoption of PA as a high-speed crystallization method together with additives showed the synergistic results for the enhancement in coercivity.

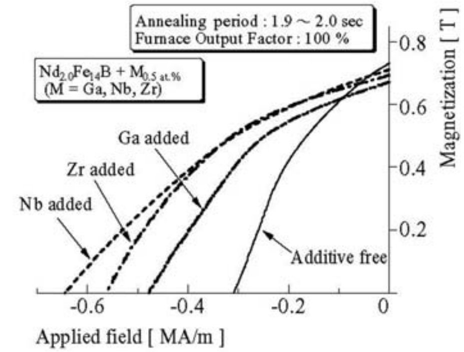

Fig. 2 Demagnetization curves of PLD-fabricated Nd-Fe-B thick film magnets prepared by a pulse annealing (PA) method from $Nd_{2.0}Fe_{14}B + M_{0.5\ at.\%}$ (M = Zr, Nb, Ga) targets. $(BH)_{max}$ value reached approximately 70 kJ/m^3 by reducing Nd content and add Zr or Nb.

AV-08

Electrodeposited Co-Pt-(P) thick films prepared by low temaperature process.

T. Tomimatsu[1], *M. Nakano*[1], T. Yanai[1], N. Fujita[2], H. Fukunaga[1]
1. Electronics and Electrical Engineering, Nagasaki University, Nagasaki, Japan; 2. Nara National College of Technology, Yamatokouriyama, Japan

The development of electrodeposited Co-Pt and/or Fe-Pt thick film magnets is expected to enable new applications such as micro-machines, because electrodeposition has a high material efficiency compared with a typical vapor deposition. In addition, a process in low temperature fabrication together with an increase in thickness for the deposited film is a key technology to advance electronic devices comprising with those films. Callegaro et al. have already reported the preparation of electro-deposited Co-Pt-(P) thin films for magnetic recording media and the coercivity of 438 kA/m without an annealing process [1]. This contribution reports a fabrication of electro-deposited Co-Pt films with P additive by low temperature process. We also achieved the increase in thickness up to 5 microns without deterioration of mechanical properties. Co-Pt films were prepared by electrodeposition using a plating bath, which contained 2 mM Pt(NH3)2(NO2)2, 3-5 mM Co(NH2SO3)2, 40 mM NaH2POH2O and 20 mM (NH4)2C6H6O7, respectively, together with the pH adjusted to 8 using NaOH at the fixed bath temperature of 333 K. Although the plating bath did not include NH2CH2COOH, the composition of the bath was similar to Callegaro's one [1]. ITO substrates, Pt sheets and Ag/AgCl electrodes were used as the cathode, anodes and reference electrodes, respectively. Electrodeposition was conducted potentiostatically at -1.0 V versus Ag/AgCl with a total charge ranging from 3 to 180 C/cm2 using a potentiostat. The as-deposited films were magnetized under a pulse magnetic field of approximately 7-8 T. The composition of deposited films was evaluated with an energy-dispersive X-ray analyzer (EDX). The magnetization curves were recorded with a vibrating sample magnetometer (VSM). Figure 1 shows the thickness of Co-Pt-(P) films as the function of the total charge. The thickness increased with increasing the charge, and the maximum thickness reached 5 microns at the charge of approximately 180 C/cm2. Evaluation on composition and magnetic properties for the as-deposited films were carried out. The content of Co could be controlled between 68 and 100 at. % by changing amount of Pt(NH3)2(NO2)2 in the bath and coercivity value of a film electrodeposited at Pt(NH3)2(NO2)2 = 3 mM, Co(NH2SO3)2 = 2 mM, and NaH2PO2 = 40 mM was approximately 250 kA/m(see Fig. 2). As shown in Fig.3, coercivity decreased with increasing exposure temperature, which indicated that inner stress of the films due to the P additive is one of mechanisms for the enhancement in coercivity.

[1] L. Callegaro et al, J. Mag. Mag. Materials 157/158 (1996) 190-192.

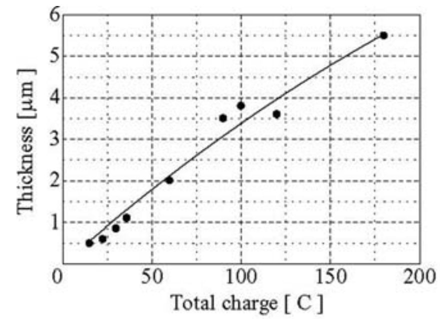

Fig. 1 Thickness of as-deposited Co-Pt-(P) films as a function of total charge. A sample thicker than 5 microns could be obtained.

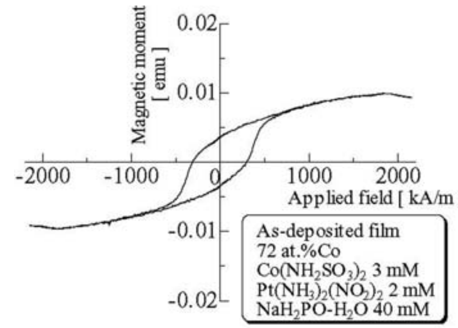

Fig. 2 M-H curve of an as-deposited Co-Pt-(P) film prepared by electrodeposition. The value of coercivity was approximately 250 kA/m.

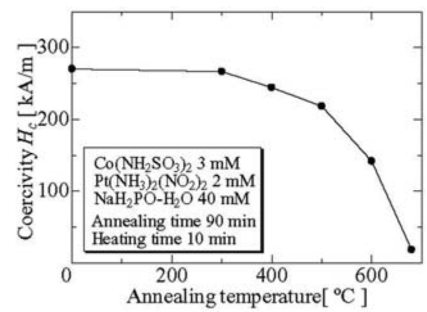

Fig. 3 Invetigation on the relationship between coercivity values of as-deposited samples and annealing temperature.

AV-09

Some magnetic properties of YTiFe11-xSixC carbides.

B. C. Cizmas[1], L. Bessais[2], C. Djega-Mariadassou[2]
1. Department of Physics, Transilvania University of Brasov, Brasov, Romania; 2. ICMPE, UMR7182 CNRS, Université de Paris XII, Thiais, France

The ThMn12 (S.G. I4/mmm) structure of R-Fe intermetallics exist only for the pseudobinary RFe12-xMx systems, where M is a structure stabilizing metal, either d transition metals (Ti, V) or p elements (Si, Ga). The solubility of M is limited, as example around x=1 for Ti and x=2 for Si. Due to the enthalpy value associated with the formation of the Fe-M bonds Ti occupies the 8i sites and Si preferentially occupies the 8f and 8j sites. Consecutively, it is possible to modify the Si content for early stabilized compounds with small amounts (x=1) of Ti element in 8i sites. The ThMn12 type structure shows interstitial sites in the 2b Wickoff position, which can be filled with carbon via solid-solid reaction. The Y(FeM)12 intermetallics play an important role in the determination of the Fe sub-lattice contribution to the magnetism of isomorphous R(FeM)12 intermetallics. This paper is devoted to the study of the structure and magnetic properties of YFe11-xSixTiC compounds. The effect of carbonation is analyzed using for comparison our previously results for noncarbureted system [1].
The polycrystalline YTiFe11-xSix alloys (x= 0 - 2) were prepared by induction melting method, annealed one week at 1273K and water quenched. The carbon insertion into the I4/mmm structure was performed by solid-solid reaction between the YTiFe11-xSix compounds ground to <36μm powder size and an appropriate over weight of C14H10 powders, two days at temperature above 673 K. X-ray diffraction analysis was carried out operating with Cu-K radiation by means of a Bruker diffractometer. The Curie temperature (Tc) was measured on a differential sample magnetometer in a relatively low magnetic field of 100 mT. Parallel and perpendicular isothermal magnetization data at low temperatures (8-300K) on magnetically aligned powders were obtained with PPMS-Quantum Design magnetometer, in external magnetic field up to 6T.
The cell parameters and the cell volume of ThMn12 structure increase after carbonation and decrease with Si content. For carbides, the a parameter decreases from 0.8577 nm down to 0.8488 nm and the c parameter from 0.4847 down to 0.4791 nm. It results that the unit cell volume Vo decreases linearly with x with ratio –5.70x10-3 nm3/Si at. The volume expansion ΔV/Vo induced by carbonation, related to the initial cell volume decreases linearly from 3.04%, for x=0 to 1.33%, for x=2. The Curie temperature Tc of carbides decreases nonlinearly with Si content from 698K, for x=0 up to 578K, for x=2 (Fig. 1a). It results, upon carbonation Tc increases around 30.7% for x=0 and 14.4% for x=2. For x>0.5, a quasi linear correlation with ratio +4.84 is observed between ΔTc/Tc and ΔV/Vo.
The saturation magnetization values, Ms of YFe11-xSixTiC at low temperature were determined by fitting the parallel magnetization isotherms Mpar(H) with the usual approach to saturation law. The saturation magnetization at 0K, Ms(0) was determined by fitting the Ms= Ms(T) curves. The average magnetic moment per atom, deduced from the Ms(0) values decreases with x from 1.66μB, for x=0 up to 0.94μB, for x=2. The comparison with calculated values in the rigid band assumption, using the magnetic valance approximation (MVA) shows a strong ferromagnetism induced by carbonation (Fig.1b).
The XRD patterns performed for magnetically oriented powder samples shows for YFe11-xSixTiC a uniaxial anisotropy with easy magnetization direction parallel to c axis. In order to determine the anisotropy constants K1, K2 and the recurrent anisotropy field Ba we have used the analytical interpretation, based on a statistical model of the perpendicular magnetization isotherms Mper(H) and applying a least-square numerical method. The obtained values at 8K are reported in Fig.1c, in function of Si content. The K2 values are very small around 0, but K1 and Ba decrease nonlinearly with x from 1.84MJ/kg and 3.76T for x=0, to 0.65MJ/kg and 1.97T, for x=2.
We consider that the competition between the change in electronic structure upon Si substitution for Fe and carbon insertion and the dilatation of the crystal lattice upon carbonation are responsible for the magnetic properties behaviors of YFe11-xSixTiC.

[1] C.B. Cizmas, C. Djega-Mariadassou, L. Bessais, "Influence of Si substitution on the structure and magnetic properties of YFe11-xSixTi (x<2)," J. Magn. Magn. Mater., vol. 242–245, pp. 823-825, 2002.

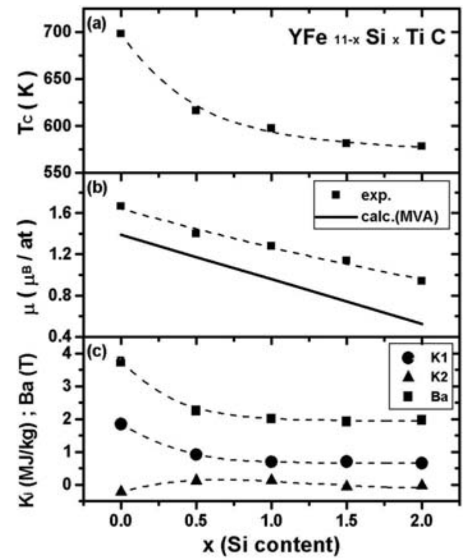

Fig.1 – Composition dependence of (a) Curie temperature (Tc), (b) magnetic moment / atom (μ) and (c) magnetocrystalline anisotropy parameters (K1, K2 et Ba) of YFe11- xSixTiC.

AV-10

A magnetic and Mössbauer spectral study of the $Lu(Fe_{1-x}Al_x)_2$ compounds.

C. L. Piquer[1], M. Laguna-Marco[1,2], J. Chaboy[1], R. Boada[1], F. Plazaola[3]
1. Instituto de Ciencia de Materiales de Aragón, 50009 Zaragoza, Spain; 2. Advanced Photon Source, Argonne National Laboratory, 9700 S, Cass Avenue, Argonne 60439, IL; 3. Departamento de Electricidad y Electrónica, Universidad del País Vasco (UPV/EHU), Apartado 644, 48080 Bilbao, Spain

In previous works we have performed a systematic x-ray magnetic circular dichroism, XMCD, study at the rare-earth $L_{2,3}$ edges in $R(Fe_{1-x}Al_x)_2$ compounds.[1-3] Our results indicate that Fe contributes to the L_2 R XMCD and this contribution is associated with the Fe molecular field acting at the R sites. These findings give rise to an experimental method of direct observation of the T(3d)-R(5d) hybridizations, which govern the R-T interaction. However, in the case of diluted $R(Fe_{1-x}Al_x)_2$ compounds a proper knowledge of the magnetic behavior of the Fe sublattice is necessary in order to make full use of this result. Within this framework we have carried out a ^{57}Fe Mössbauer study through the $R(Fe_{1-x}Al_x)_2$ series.
In this work we present the ^{57}Fe Mössbauer study performed on $Lu(Fe_{1-x}Al_x)_2$ (x = 0, 0.25 and 0.50) at T = 15 and 295 K (Figure 1). This study has been complemented with ac magnetic susceptibility, $\chi_{ac}(T)$, measurements between 5 and 350 K with an exciting field of 4 Oe, and with exciting frequencies of 1, 9, 90, 476, and 1.368 Hz. We have also measured FC/ZFC magnetization vs. temperature curves, M(T), between 5 and 350 K with an applied field of 4 Oe (Figure 2).
In $LuFe_2$, both Mössbauer spectra consist of two sextets with intensity ratio 3: 1 according to the presence of an easy magnetic axis along the [111] direction. [4] In the diluted compounds the Al atoms are randomly distributed over the 16d sites. The Mössbauer spectrum of $Lu(Fe_{0.75}Al_{0.25})_2$ at 295 K has been fitted with two symmetric doublets with relative intensities given by the binomial distribution. At T = 15 K, the $Lu(Fe_{0.75}Al_{0.25})_2$ Mössbauer spectrum shows the typical profile of a diluted compound. The spectrum has been fit with a model which considers that the Al atoms are randomly distributed over the iron sites. The $Lu(Fe_{0.50}Al_{0.50})_2$ spectra recorded at T = 15 K and T = 295 K are both a narrow paramagnetic doublet. In this case, due to the poorly structured profile of the spectra, they have been fitted with just one doublet.
In order to investigate the origin of the magnetic spectrum observed in $Lu(Fe_{0.75}Al_{0.25})_2$ at 15 K we have performed $\chi_{ac}(T)$ at different exciting frequencies and FC/ZFC M(T) measurements (Figure 2). At high temperatures (T ~ 300 K for x = 0.25, and T ~ 70 K for x = 0.50) a peak is observed in both ZFC M(T) and $\chi_{ac}(T)$ curves. Irreversible phenomena occur at temperatures below the maxima in M(T), and a clear dependence with the exciting frequency is observed in the $\chi_{ac}(T)$ curves. Similar behaviour is observed at lower temperatures (T ~ 45 K for x = 0.25, and T ~ 10 K for x = 0.50); however, the low temperature peak in $\chi_{ac}(T)$ is almost frequency independent, which seems to indicate the existence of a spin-glass state. These results are in agreement with the existence of magnetic clusters with different sizes and different magnetic responses.
Consequently, the magnetic spectra observed in $Lu(Fe_{0.75}Al_{0.25})_2$ at T = 15 K indicates that the magnetic iron moments are blocked at that temperature. In contrast, the paramagnetic spectra observed in $Lu(Fe_{0.50}Al_{0.50})_2$ at T = 15 K indicates that the blocking temperature is lower than 15 K. This results suggests that the lower temperature process, which takes place at T = 10 K in $Lu(Fe_{0.50}Al_{0.50})_2$, is at the origin of the freezing of the magnetic moments although further work is in progress to determine the exact nature of the phenomena observed.

[1] M. A. Laguna-Marco et al., Phys. Rev. B, 72(5), 052412 (2005).

[2] M. A. Laguna-Marco et al. AIP Conference Proceedings. X-ray absorption fine structure - XAFS13: 13th International Conference 882, 484-486 (2007)

[3] J. Chaboy et al., J. Phys.: Condens. Matter, 19(43), 436225 (2007)

[4] G. J. Bowden et al., Phys. C. (Proc. Phys. Soc.) 1, 1376 (1968).

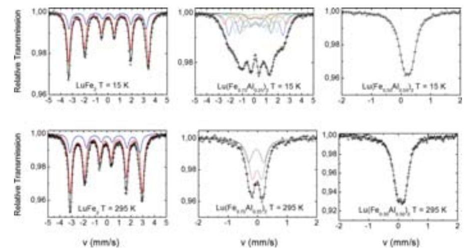

Mössbauer spectra of $Lu(Fe_{1-x}Al_x)_2$ obtained at the indicated temperatures.

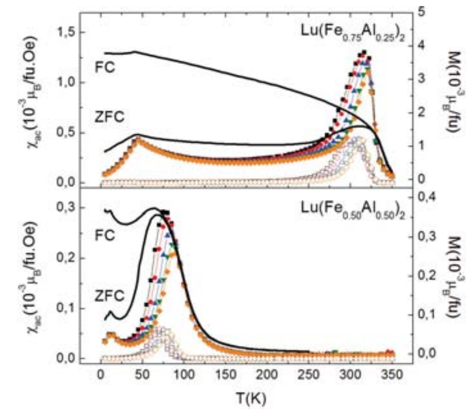

Left axis: temperature dependence of the ac magnetic susceptibility, $\chi_{ac}(T)$, between 5 and 350 K with an exciting field of 4 Oe, and with exciting frequencies of 1 (black), 9 (red), 90 (blue), 476 (green), and 1.368 Hz (orange). Dark symbols corresponds to the in-phase ac magnetic susceptibility, and open symbols to the out-phase ac magnetic susceptibility. Right axis: temperature dependence of the FC/ZFC curves measured with an applied field of 4 Oe.

AV-11

Magnetic properties of YCo_XNi_{3-X} compounds.

E. Burzo, R. Tetean, I. G. Deac
Faculty of Physics, Babes-Bolyai University, Cluj Napoca, Romania

The YCo_3 and YNi_3 compounds crystallize in a $PuNi_3$-type structure. In the above lattice the 3d transition metal atoms occupy three types of sites. The cobalt and nickel magnetic moments are dependent on the characteristic environment of a given site. The neutron diffraction studies show values of cobalt moments of 0.55(3), 0.79(4) and 0.04(1) μ_B [1]. Very weak nickel moments were reported in YNi_3, namely 0.057(3), 0.073(3) and 0.065(3) μ_B respectively [2].
The high field measurements performed on YCo_3 show the presence of two field induced successive transition at B_1=60 T and B_2=82 T [3]. These metamagnetic transition are believed to occur at different crystallographic Co sites and are considered to come from a special shape of density of state near the Fermi level.
By gradual substitution of cobalt by nickel in YCo_3 we expect that the magnetic behaviour of the pseudobinary compounds will be modified. The presence, in the same compound, of very weak nickel moments in addition to Co ones results in interesting magnetic properties.
The YCo_XNi_{3-X} compounds were prepared by arc melting the constituent elements in a purified argon atmosphere. The samples were heat treated in vacuum, at 950°C, for 10 days. The X-ray analysis shows the presence of one phase only, of $PuNi_3$ type. The lattice parameters are slighty dependent on composition due to nearly the same radius of Co and Ni ions.
The magnetic measurements were performed in the temperature range 5-900 K and external fields up to 9T. Above the Curie points, the susceptibilities were determined by using a Faraday type balance. Some magnetization isotherms, obtained for the compound having x = 2.4 are plotted in Fig.1. A transition towards a state having somewhat higher magnetization is induced by an applied field of 5-6 T, at low temperatures (5 K). The variation of magnetization above this transition is dependent on composition.
The increase of the magnetization at the critical field is of 0.012 μ_B (x=2.7), 0.07 μ_B (x=2.4) and 0.03 μ_B (x=1.8). We attribute these transitions to the nickel atoms whose magnetization's increase under the action of external field.
Similar transitions have been observed for cobalt in $ThCo_5$ where two states with different magnetizations are induced by an applied magnetic field [4]. In our case, the transition is not so sharp as in $ThCo_5$. We attributed the observed behaviour to a distribution of exchange fields and consequently of the critical fields during this ferromagnetic-ferromagnetic type transition determined by the presence of both Co and Ni atoms in the lattice.
There is experimental evidence that in observed metamagnetic transition nickel is involved. The high magnetization state in YCo_3 is observed in fields more than one order of magnitude greater than experimentally observed in the present study. In our system the critical field is little dependent on composition even the exchange interactions decrease strongly when cobalt is replaced by nickel. Also, the observed changes in the magnetization is of the order of magnitude of nickel moment induced when replacing yttrium by gadolinium in YNi_3 [5]. In this case the mean value of nickel moment increase from 0.07 μ_B (Y) up to 0.15 μ_B (Gd).
The neutron diffraction studies performed on $Er(Fe_XNi_{1-X})_3$ [6] show that Ni atoms prefer the 18 h sites. We suppose that a similar substitutional preference takes place in YCo_XNi_{3-X} compounds. We note that in $PuNi_3$ type structure the ratio of the atoms in h:c:b sites is 2:1/3:2/3.
In a first approximation we suppose that the nickel magnetic moment of h site in YCo_XNi_{3-X} is the same as that determined in YNi_3 (0.065 μ_B). In this case the nickel contribution to the magnetization will be 0.019 μ_B (x=0.3); 0.040 μ_B (x=0.6) and 0.078 μ_B (x=1.2). By comparing the induced nickel moment in $GdNi_3$, we expected an increase of Ni moment at the metamagnetic transition of the same magnitude as nickel moments in YNi_3.
These agree with experimental data, except for the compound with x=0.6. Probably that in this case the high decrease of the exchange interactions, as evidenced by changes in Curie temperatures, will influence significantly the nickel moments.
If we suppose that the decrease of the nickel moment is proportional to the exchange field, from the value evidenced in compound with x=0.3, the induced moment will be about half than that expected, in agreement with the experimental data. The compound with x=0.6 seems to be nonmagnetic. The above behavior is analyzed in correlation with band structures.

[1]E.Kren, et.al., Phys.Rev.B, 186,479 (1969) [2]D.Gignoux et.al., J.Magn.Magn.Mat., 21, 307, (1980) [3]T.Goto et. al., Physica B, 177, 255 (1992) [4]D.Givord et. al., J.Appl.Phys., 50, 7489 (1979) [5]E.Burzo, J.Laforest, Compte Rend.Acad.Sci. Paris B 274, 114 (1972) [6]D.Tharp et.al., J.Appl.Phys., 61, 4249 (1987)

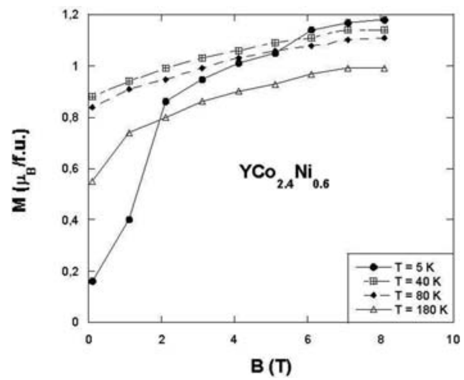

Magnetization isotherms for the compound with x=2.4.

Magnetostriction in Sm_2Fe_{17} before and after nitrogenation.

H. Chen, J. Xu, Y. Zhang, H. Du, C. Wang, Y. Yang
Physics School, Peking University, Beijing, China

Introduction

The interstitial $Sm_2Fe_{17}N_3$ compounds have excellent intrinsic magnetic properties for permanent magnet applications [1][2]. The high Curie temperature (750K), high saturation magnetization (1.56T, 300K), strong uniaxial anisotropy (12T, 300K), and the high theoretical value of (BH)max (59 MGOe) have attracted much attention. The fundamental and application researches were proceeded extensively, relating to the study of crystallographic strucure [3], substitution effects of Sm, Fe, or N by other elements, and different manufacture process to product SmFeN magnet, etc. However, no literature reported the magnetostriction in $Sm_2Fe_{17}N_3$. In this paper, we present a investigation of magnetostriction in Sm_2Fe_{17} and $Sm_2Fe_{17}N_3$.

Experiments

The investigated Sm_2Fe_{17} sample was produced by strip casting technique [4], similar to melt spinning, using a wheel speed of 1 m/s. The dimension of selected Sm_2Fe_{17} plate is $10\times10\times0.3$ mm^3. This sample was then annealed at 1323K for a week.

The investigated $Sm_2Fe_{17}N_3$ powder sample was bonded with epoxy resin, because the $Sm_2Fe_{17}N_3$ powders will decomposed into Sm nitride and α-Fe at temperatures above 873K. The dimension of bonded sample is $10\times10\times0.8$ mm^3. The strain gauges were sticking on the sample's surface, parallel or perpendicular to the magnetic field. The measurements were carried out using a Wheatston bridge; the data acquisition and processing were proceeded by a computer. To eliminate the magnetic resistor effect and temperature effect of the strain gauge, the compensation strain gauge was sticking on a copper plate, and placed together with the sample.

Results and discussion

Fig. 1 shows the $\lambda_{\|}$ - H hysteresis loop of Sm_2Fe_{17}. The $\lambda_{\|}$ is negative, the value of it increases with increasing field. The $\lambda s(\|)$ is -75×10^{-6} . The $\lambda_{\perp}$- H hysteresis loop of Sm_2Fe_{17} is shown in Fig. 2. The $\lambda_{\perp}$ is positive, the value of it increases with increasing field, and unable to obtain saturation at 2T field. The $\lambda_{\perp}$ (2T) is 78×10^{-6} .

Fig. 3 illustrates the $\lambda_{\|}$ - H hysteresis loop of $Sm_2Fe_{17}N_3$. The $\lambda_{\|}$ is also negative. The curve shows a magnetic hysteresis. Fig. 4 displays the comparison of magnetostrictions of Sm_2Fe_{17} before and after nitrogenation. It is obviously that the λs is lower after nitrogenation, because of the nonmagnetic epoxy composition. The lower value at low magnetic field can be attributed to the anisotropy increase dramatically after nitrogenation. The saturation field has increased very much.

The negative magnetostriction may result in compress anisotropy, due to the inverse effect of magnetostriction. The magnetostriction anisotropy can be used in the SmFeN bonded magnet fabrications [5].

[1] J.D.M. Coey, Hong Sun, J. Magn. Magn. Mater. 87 (1990) L251

[2] W.E.Wallace, M.Q. Huang, IEEE Trans.Magn. 28 (1992) 2312

[3] Y.C. Yang, et al., J. Appl. Phys. 70 (1991) 6018

[4] H. J. Zhi, Y. C. Yang, et al., J. Appl. Phys. 99 (2006) 08B517.

[5] Y. C. Yang, Patent: CN 1937110A, Sept. 19, 2006

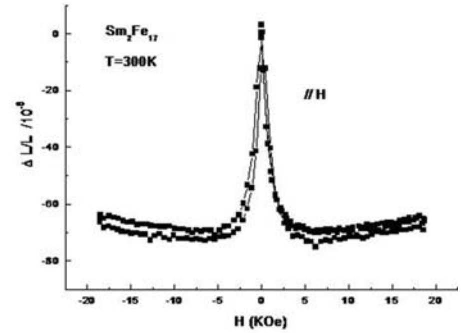

Fig.1 The $\lambda_{\|}$-H hysteresis loop of Sm_2Fe_{17}

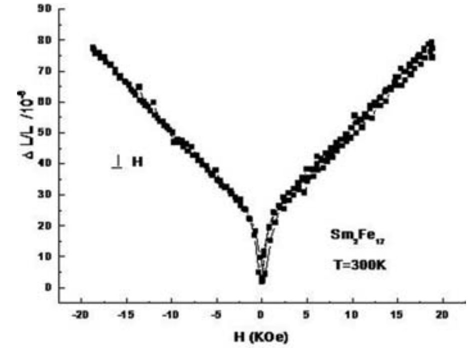

Fig.2 The $\lambda_{\perp}$-H hysteresis loop of Sm_2Fe_{17}

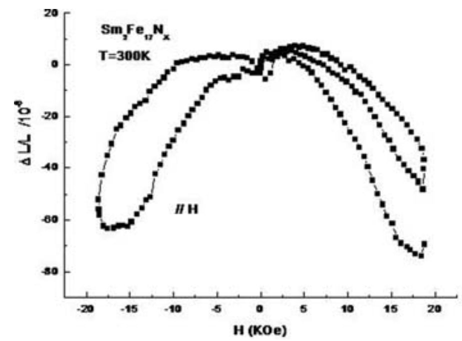

Fig. 3 The $\lambda_{\|}$-H hysteresis loop of $Sm_2Fe_{17}N_3$

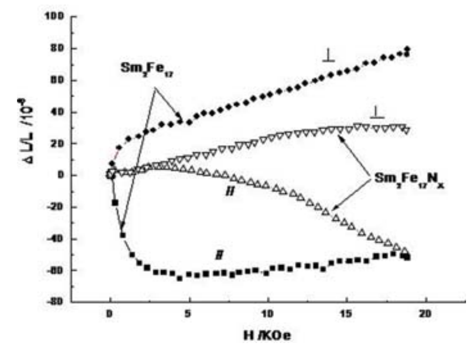

Fig. 4 Comparison of magnetostrictions of Sm_2Fe_{17} before and after nitrogenation.

AV-13

Magnetic properties of Zr-doped Lu_2Fe_{17} single crystal and its hydride.

E. Tereshina[1,2], A. Andreev[1], H. Drulis[3]

1. Institute of Physics of the Academy of Sciences of the Czech Republic, Prague, Czech Republic; 2. Department of Condensed Matter Physics, Faculty of Mathematics and Physics, Charles University, Prague, Czech Republic; 3. Institute of Low Temperature and Structure Research, Wroclaw, Poland

Lu_2Fe_{17} might be considered as the representative of the Fe-sublattice in a very interesting group of magnetic materials, R_2Fe_{17} (R - rare-earth metal), with extremely delicate balance of ferro- (F) and antiferro- (AF) magnetic interactions (because Lu is non-magnetic metal) [1, 2]. Different substitutions in the R and Fe-sublattices as well as introduction of the light atoms (hydrogen) can affect this balance and lead to a change of the type of magnetic ordering. Lu_2Fe_{17} is characterized by two types of magnetic ordering: ferromagnetic up to Curie temperature T_C = 130 K and incommensurate helical magnetic structure with the collinear arrangement of Fe moments in the basal plane below the Néel temperature T_N = 274 K. It was found that hydrogenation of Lu_2Fe_{17} leads to a suppression of antiferromagnetism and induction of the ferromagnetic state with T_C = 393 K [3]. In present work, we studied the effects of substitution (Zr for Lu) and interstitial (H) atoms on magnetic properties of $(Lu_{1-x}Zr_x)_2Fe_{17}$ compounds.
Alloys with $(Lu_{1-x}Zr_x)_2Fe_{17}$ (x = 0.2, 0.4) nominal compositions were prepared by melting pure elements and attempt to pull single crystals by means of modified Czochralski method in a tetra-arc furnace was done. The X-ray powder diffraction and thermomagnetic analyses showed that the alloy with x = 0.4 is multiphase. For the $(Lu_{0.8}Zr_{0.2})_2Fe_{17}$ compound, the hexagonal crystal structure of the Th_2Ni_{17} type was approved for the main (>90%) phase. Hence, the solubility range of Zr substitution for Lu in these compounds was determined as x = 0 - 0.2. Hydrogenation of $(Lu_{0.8}Zr_{0.2})_2Fe_{17}$ single crystal without powderization of the sample was successfully performed and magnetization along the principal axes of the initial compound and its hydride was measured in magnetic fields up to 5 T at 4.2 - 320 K.
Influence of substitution of Zr for Lu could be expected to be similar to the situation observed for a case of a substitution of the tetravalent Ce for Lu in $(Lu_{0.8}Ce_{0.2})_2Fe_{17}$ since Zr is tetravalent as well. In $(Lu_{0.8}Ce_{0.2})_2Fe_{17}$, ferromagnetism characteristic for Lu_2Fe_{17} at low temperatures was suppressed and the AF ground state was observed with T_N = 247 K [4], i.e. lower than in Lu_2Fe_{17}. However, we found a completely opposite effect for Zr substitution: the AF state present in Lu_2Fe_{17} at elevated temperatures is suppressed completely in $(Lu_{0.8}Zr_{0.2})_2Fe_{17}$. Zr-doped compound is found to possess a spontaneous magnetic moment of 34.1 μ_B/f.u. in the ground state and has an easy-plane type of magnetic anisotropy in the whole range of magnetic ordering. The values of magnetic moment and anisotropy field in the ground state of $(Lu_{0.8}Zr_{0.2})_2Fe_{17}$ are practically the same as in Lu_2Fe_{17}, however the temperature of magnetic ordering is increased from 274 to 325 K.
There are two important factors which influence strongly the magnetic properties of the compounds studied: change of interactomic distances and the additional electron from the substitution atoms. The fact of importance of the change of interactomic distances is confirmed by the dramatic effect of the hydrostatic pressure which is found to enhance AF. Since the lattice parameters of Lu_2Fe_{17}, $(Lu_{0.8}Zr_{0.2})_2Fe_{17}$, $(Lu_{0.8}Ce_{0.2})_2Fe_{17}$ do not differ considerably, both the 4th electron and the anisotropy of the change of the lattice parameters (change of the c-parameter is assumed to influence stronger than the change of the parameter a due to presence of the Fe atoms in the 4f position – "dumbbells" along the c-axis) are important and determine the particular changes of magnetism upon substitution. Hydrogenation as one of the methods of a significant increase of the interatomic distances leads to a similar development of magnetism of Lu_2Fe_{17}, $(Lu_{0.8}Zr_{0.2})_2Fe_{17}$, $(Lu_{0.8}Ce_{0.2})_2Fe_{17}$ compounds.
In $(Lu_{0.8}Zr_{0.2})_2Fe_{17}$, concentration of hydrogen content was determined by the volumetric method as 1.5 H at/f.u. Hydride $(Lu_{0.8}Zr_{0.2})_2Fe_{17}H_{1.5}$ has a spontaneous magnetic moment of 35 μ_B/f.u. in the ground state and ferromagnetic structure in the whole range of magnetic ordering with T_C about 370 K, i.e. considerably higher than in parent compound. Hydrogenation of Lu_2Fe_{17} and $(Lu_{0.8}Ce_{0.2})_2Fe_{17}$ crystals was also found to stabilize ferromagnetism in the whole range of magnetic ordering; and the ordering temperature was strongly increased.
The work is a part of the research project AVOZ10100520 and has been supported by grants GACR 202/06/0185 and GAUK 109-10/257015.

[1] D. Givord, R. Lemaire, IEEE Trans. Magn. MAG-10 (1974) 109.

[2] A.V. Andreev, D. Rafaja, J. Kamarád, Z. Arnold, Y. Homma, Y. Shiokawa, J. Alloys Compounds 361 (2003) 48.

[3] E.A. Tereshina, H. Yoshida, A.V. Andreev, I.S. Tereshina, K. Koyama, T. Kanomata, High Pressure Research 26 (2006) 485.

[4] A.V. Andreev, J. Kamarád, E.A. Tereshina, T. Komatsubara, I. Satoh, J. Phys. Conference Proceeding (2008) (in press).

AV-14

Crystalline and local structure of $SmCo_5$ based alloys.

V. P. Menushenkov[1], A. P. Menushenkov[2], R. V. Chernikov[2], V. V. Sidorov[2], T. A. Sviridova[1]
1. State Technological University "Moscow Institute of Steel and Alloys", Moscow, Russian Federation; 2. Moscow Engineering Physics Institute (State University), Moscow, Russian Federation

Synthesis of $SmCo_5$ compound has become a new advanced stage of development of hard magnetic materials. The highest coercive force (H_{ci}) was received for sintered Sm-rich ($SmCo_{5-x}$) magnets. Post sintering heat treatment (HT) including slow cooling from 1120 to 850°C and rapid cooling to room temperature increases H_{ci} from 0,1 to more than 3,5 T. According to X-ray diffraction data the changes of lattice parameters of $SmCo_5$ phase after aging at 1200–800°C revealed the increase of Sm content in $SmCo_5$ with decreasing temperature. The mechanism of Sm enrichment has not been determined yet. In recent years, the extended X-ray absorption fine structure (EXAFS) technique has been successfully applied to investigate the local atomic structure of alloys. In this work, we have investigated the local and crystalline structure of $SmCo_5$ phase in as-cast hypo- and hyper-stoichiometric $SmCo_{5\pm x}$ alloys after different heat treatment.

Ingots with nominal composition of $SmCo_x$ (x = 5, 4.5, 4, 3.5) were prepared by induction melting in Ar atmosphere followed by casting in an iron mould. The ingots were aged in a vacuum furnace in series at 1200°C for 2 h + 1000°C for 5 h + 900°C for 10 h. The phase identification was carried out by X-ray diffraction (XRD) using CuKα radiation. EXAFS spectra above the L_{III}-Sm and K-Co edges at 4 – 300 K were measured at the E4 beamline of HASYLAB (DESY, Hamburg, Germany) in transmission mode. EXAFS spectra analysis was performed with VIPER program.

Due to evaporation and oxidation process decreasing of Sm content takes place during HT. According to XRD data, after final aging the sample N1 (x=5) consists of the main $SmCo_5$ phase and minor rhombohedral Sm_2Co_{17} phase. Sample N2 (x=4.5) consists of only $SmCo_5$ phase. Samples N3 and N4 (x=4, 3.5) consist of a mixture of $SmCo_5$ and two crystalline modifications (rhombohedral and hexagonal) of Sm_2Co_7 phase. Table presents the unit cell parameters of $SmCo_5$ phase for samples N1-N4 after different aging.

It can be seen that unit cell parameters of $SmCo_5$ phase of the sample N2 do not change with reduction of the aging temperature. Therefore, it is assumed that the composition of N2 corresponds to the stoichiometric $SmCo_5$ compound. At 1200-1000°C the hyperstoichiometric alloy N1 is contained within the homogeneity limits and represents the solid solution $SmCo_{5+x}$, enriched with Co. Aging at temperatures lower than 1000°C results in formation of the Sm_2Co_{17} phase by decomposition of the $SmCo_{5+x}$ solid solution below the miscibility gap. Precipitation of Sm_2Co_{17} reduces Sm enrichment of solid solution, and after aging at 900°C the lattice constants of $SmCo_5$ phase are similar to those of sample N2. The unit cell parameters of $SmCo_5$ phase for samples N3 and N4 differ from those of N1-N2. The c value is below the stoichiometric one and does not change with decreasing temperature of aging, whereas a value exceeds the stoichiometric one and increases after aging at 900°C (see Table). These changes of lattice constants evidence the enrichment of $SmCo_5$ compound with Sm. Indeed, the changes in the composition from $SmCo_5$ to $SmCo_{5-x}$ via the formation of high-density crystallographic shear planes were observed by TEM.

EXAFS function $\chi(k)k^2$ Fourier transform moduli representing qualitatively the radial distribution curves F(r) are show on Fig. 1.

EXAFS data analysis demonstrates that reduction of aging temperature leads to the decrease of static local disordering in all samples. At the same time transition from monophase (N1-N2) to diphase (N3-N4) causes significant redistribution of samarium local environment (Fig. 1). The scale of changes reaches its maximum at N2-N3 transition. According to wavelet-analysis two nearest spheres of samarium local environment in all samples are formed by Co atoms only. Two-sphere model provides satisfactory quality of fitting in monophase samples (N1-N2) whereas we had to use 3-sphere Co-Co-Sm model for diphase alloys (N3-N4). This once again confirms Co atoms substitution with Sm in $CoSm_5$ lattice of Sm-enriched alloys (N3-N4).

In conclusion, EXAFS measurements and XRD study of the unit cell parameters of $SmCo_5$ phase in as-cast $SmCo_5$ based alloys after different heat treatment evidence the enrichment of the $SmCo_5$ phase with Sm by partial replacement of Co atoms by Sm.

This work was supported by RFBR (grant 05-02-16996-a).

Heat treatment	c (Å)	a (Å)	c/a	c (Å)	a (Å)	c/a
	N1			N3		
1 - 1200°C, 2 h	3,979	4,989	0,7976	3,969	5,001	0,7936
2 - 1 + 1000°C, 5 h	3,978	4,990	0,7972	3,968	5,003	0,7931
3 - 2 + 900°C, 5 h	3,973	4,996	0,7952	3,968	5,004	0,7930
	N2			N4		
1 - 1200°C, 2 h	3,973	4,998	0,7949	3,970	5,001	0,7938
2 - 1 + 1000°C, 5 h	3,973	4,998	0,7949	3,970	5,001	0,7938
3 - 2 + 900°C, 5 h	3,973	4,999	0,7948	3,969	5,003	0,7933

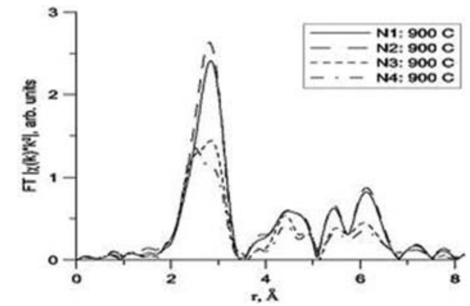

AV-15

Impact of Aluminium on the magnetic properties of RT2 compounds (R = rare-earth, T = transition metal) through the modification of the electronic structure.

R. Boada[1], J. Chaboy[1], M. A. Laguna-Marco[1,2], C. Piquer[1], F. Jiménez-Villacorta[3]
1. Física de la Materia Condensada, Instituto de Ciencia de Materiales de Aragón, Zaragoza, Spain; 2. Advanced Photon Source, Argonne National Laboratory, Chicago, IL; 3. SpLine / Spanish CRG (BM25), European Synchrotron Radiation Facility, Grenoble, France

The exact nature of the induced magnetic moments remains an open key problem into the understanding of the magnetic interactions in many magnetic systems. This is the case of the spin-polarization of the 5d states of the rare-earth in R-T intermetallic systems (where R denotes a lanthanide and T a 3d transition metal). The Laves phase compounds RFe2 and RAl2 exhibit ferromagnetic ordering. However, while the RAl2 systems show ferromagnetism (FM) below 150 K, the magnetic ordering temperature varies between 550 and 650 K through the RFe2 series. It is thought that the FM order in the RAl2 compounds is exclusively due to the rare-earth ions within a RKKY interaction framework. By contrast, the magnetism of the RFe2 results from the competition of the localized 4f magnetism of the rare-earth and the itinerant magnetism of the transition metal. The exact nature of the R-T interaction is not well accounted a priori by any theoretical model and only phenomenological descriptions addressing the critical role of the R(5d)-T(3d) hybridization have been reported [1-3]. The problem of characterizing the 5d states and of determining the exact nature of the R-T interaction becomes critical in the case of the R(FexAl1-x)2 compounds.
In addition, one of the most peculiar phenomenon occurring in the Laves phase RT2 compounds is the fact that in several cases the substitution of a magnetic T by a non-magnetic atom as Al induces ferromagnetic order [4]. This behaviour has been addressed to the modification of the 3d density of states (DOS) whose shape near the Fermi level, EF, is rather peculiar. Different hypothesis have been formulated to account for the impact of Al into the magnetic properties of RT2 [6-8]. However, these interpretations do not take into account the change of the DOS near EF due to the Al substitution. By contrast, theoretical band calculations suggest that the strong hybridization between the T(3d) and Al(3p) bands modifies the shape of the characteristic peak of the DOS in such a way that upon increasing Al content N(EF) increases and the magnetic properties of the system are modified.
Aimed to shed light on this debate, we report in this work a combined magnetic and XAS study of the (RyR'1-y)(FexAl1-x)2 compounds where R=Ho, Er and R'=Y, Lu. These new series of compounds have been tailored in such a way that the spin polarization of the 5d states due to the rare-earth and to the transition-metal is varied in a controlled way. Our main aim is to determine the relationship between the DOS modification induced by the substitution of Fe atoms by Al, and the change of the magnetic properties of these systems. To this end we have performed a detailed x-ray absorption spectroscopy (XAS) study of these compounds at the Fe K-edge and at the L1 and L3-edges of the rare-earth. Due to the element and shell selectivity of the XAS technique and the extreme sensitivity of the near-edge region of the absorption spectrum to the modification of the DOS, it is possible to address that differences in this energy region reflects the different magnetic state, as determined from a different DOS, while differences in the high energy region are linked to structural effects.
The analysis of the XANES spectra recorded at the Fe K-edge (see Fig. 1) indicates that when a magnetic rare-earth is substituted by a non-magnetic one (Y or Lu) for a fixed Fe content, no significant modification of the near edge region is observed. By contrast, the Fe K-edge is strongly changed upon substitution of Fe by Al. These results indicate that in the former case the modification of the magnetic properties of the systems is due to a simply dilution of the magnetic moment of the rare-earth. However, Al influences the magnetic properties of the compounds by modifying the DOS and then this effect has to be incorporated in order to account for the magnetic properties of the Al substituted systems. Similar results are found at the rare-earth L1-edge whose near edge region reflects the R-T hybridisation [7]. Consequently, the combined analysis of the XAS recorded at different edges indicates that the observed modification of the magnetic behaviour is due to the influence of Al into the peculiar DOS of the system. The expected results should gain insight into the origin of induced magnetic polarization in the 5d states and to assess the importance of RKKY interactions and R(4f)-R(5d)-Fe(3d) hybridisation in mediating the magnetic coupling.

[1] I.A. Campbell, J. Phys. F2, L47 (1972).

[2] H. Yamada et al., J. Phys. F14, 1943 (1984).

[3] M. S. S. Brooks et al., J. Phys.: Condens. Matter 1, 5861 (1989).

[4]K. Yoshimura and Y. Nakamura, Solid State Commun. 15, 767 (1985)

[5]H. Yamada et al., J. Phys. F: Metal Phys. 14, 1943 (1984)

[6]M. Aoki and H. Yamada, Physica B 177, 259 (1992).

[7] J. Chaboy et al., J. Phys.: Condens. Matter 7, 8197 (1995)

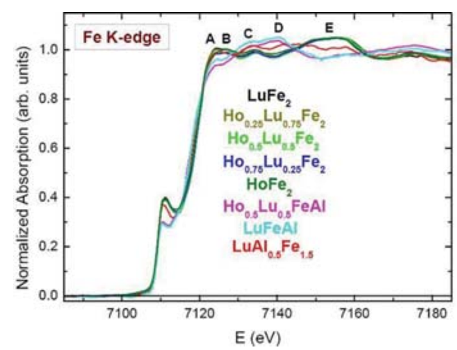

Figure 1. Normalized XAS spectra recorded at the Fe K-edge in the case of LuFe2 (black), Ho0.25Lu0.75Fe2 (dark yellow), Ho0.5Lu0.5Fe2 (green), Ho0.75Lu0.25Fe2 (blue), HoFe2 (olive), Ho0.5Lu0.5FeAl (magenta), LuFeAl (cyan) and LuFe0.5Al1.5 (red).

BA-01

A History of Magnetic Recording Areal Density Improvements — A Transducer Perspective.

R. Fontana
IBM Almaden Research Center (retired), San Jose, CA

Over the last 30 years, the areal density of magnetic recording disk products increased from 6 Mbit/in^2 (1978) to 200 Gbit/in^2 (2007) or a factor of 30,000. During this period, the transducer or head, i.e. the component that writes bits onto the disk surface and that reads the presence of these bits by detecting the stray fields from the written bit, evolved from a yoke structure with discrete wound coils and machined (i.e. sawed) and glued ferrite poles to today's lithographically intensive thin film processed devices with separate elements for reading and writing operations. This paper will describe the evolution of the magnetic recording head structure over these last 30 years and will discuss 1) how the introduction of MR and GMR films for sensing written bits with smaller area and 2) how the ability of the transducer to write bit cells having a sub-lithographic dimension along the written track, i.e. bit pitch, and a continuingly narrower dimension along the track pitch changed the areal density landscape for magnetic recording.

Table I illustrates the bit cell and head dimensions for magnetic recording in comparison to semiconductor processing minimum features over the last 30 years. Dramatic annual increases in magnetic recording areal density were achieved between the 1990 and 1996 time frame due to the introduction of MR films and even more dramatic changes in areal density were achieved between 1996 and 2002 due to the introduction of GMR films. These areal density increases were achieved because the high sensitivity of the GMR films allowed for the detection of smaller bit cells, in particular bit cells formed with successively narrower track pitches.

The impact of GMR films on magnetic recording areal density is better illustrated in Figure 1 where a history of the bit cell size for magnetic recording, DRAM. SRAM, and NAND flash is plotted. Note that in the early 1980's the bit cell area for magnetic recording, DRAM, NAND (or the EPROM equivalent) were essentially equivalent and remained comparable until 1991. Nine years later in 2000, after the introduction of first MR films (1991) and then GRM films (1998) for sensing the presence of bit cells, the area of magnetic recording bit cell was a factor of 6 – 7 smaller than comparable silicon based memory cells.

In sum, this paper traces the evolution of the read/write transducer used in magnetic recording over the last 30 years with particular emphasis on the impact of lithography and GMR films.

YEAR	1978	1990	1996	2002	2007
Areal Density (Gbit/in^2)	0.006	0.073	1.00	63	200
Bit Cell Area (um^2)	100	8.5	0.6	0.01	0.003
Track Pitch (um)	50	14	3.3	0.35	0.15
Bit Pitch (um)	2	0.6	0.18	0.043	0.02
Bit Aspect Ratio	25	23	18	8.0	7.5
Yoke Width (um)	40	11.2	2.6	0.28	0.12
MR Width (um)	NA	7.0	1.65	0.17	0.075
IC Minimum Feature (um)	3.0	0.6	0.22	0.08	0.05

Table I. Magnetic recording areal densities, bit cell dimensions, and head dimensions — 1978 to 2007

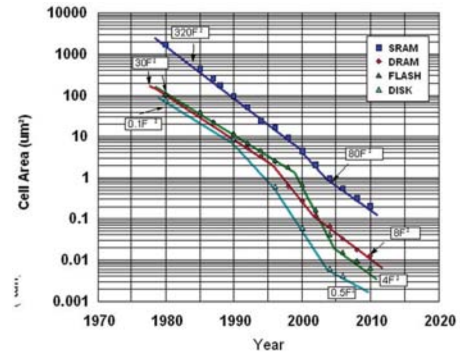

Figure 1. Bit cell areas for magnetic recording, DRAM, NAND flash, and SRAM — 1978 to 2007

The Spin Valve GMR Sensor.

B. Gurney
San Jose Research Center, Hitachi Global Storage Technologies, San Jose, CA

In this presentation I will discuss the spin valve giant magnetoresistance sensor that helped propel the hard disk drive industry to unprecedented areal density growth over the last decade. The advent of the spin valve sensor introduced a class of magnetic devices with a free and a pinned ferromagnetic layer that has become the standard for numerous sensor designs and a useful tool in many scientific investigations.

Around the time of the discovery of GMR by Albert Fert and Peter Grunberg the recording industry was on the verge of introducing a recording head with separate write and read elements where the reader used anisotropic magnetoresistance (AMR~1%). Could GMR (GMR~5-50%) be used instead? The ensuing flurry of research (that continues today) resulted in a much more sensitive recording sensor (Fig. 1) well suited to the 1-200 Gbit/in2 areal density where it has been used, and led to a much deeper understanding of transport in ferromagnetic and layered materials.

The spin valve structure grew out of studies of Fe/Cr and Co/Cu mulilayers when the origin of GMR was first being elucidated. These multilayers yielded high MR but required thick stacks and high saturation fields. What was needed was a sensor that would produce a high signal, low noise, a linear response in a few Oe field and also be compatible with the size and environmental constraints of recording. The spin valve successfully met those requirements and was introduced in products in 1997.

The basic structure (Fig. 2) derives its signal from the sharing of electrons between two ferromagnetic (F) layers separated by a conducting spacer. Spin dependent scattering in the bulk and at the boundaries of the F layers leads to an overall conductance that is different when the F layer magnetizations are parallel versus antiparallel. Control of the magnetization in the layers is an important feature of the structure where electrostatic, interlayer and current induced fields balance to properly orient the free layer and exchange anisotropy is used to fix the pinned layer direction. The need for strong pinning generated considerable research which led to the discovery of new antiferromagnets and a deeper understanding of exchange anisotropy.

Following the spin valve's introduction there was an explosive growth of new structures and improvements because layered structures provide many more degrees of freedom compared to a single alloy layer. Engineering of the interfaces by growth or by nanolayering with additional materials, control of scattering at the outer boundaries of the structure, improved pinning using a synthetic antiferromagnetic structure, and dual spin valves are a few examples. To investigate new structures significant changes in sputtering technology were needed including introduction of multiple target systems, higher quality vacuums and control of layers to the submonolayer level. The spin valve concept of responsive free layer and fixed pinned layer has been extended to other phenomena and devices, including tunneling magnetoresistance sensors that are now replacing GMR in disk drives and current perpendicular to the plane GMR structures.

More than 5 billion spin valve GMR heads have been used in hard disk drives. Along with other improvements in recording, they have made possible areal density increases between 60% and 100% per year (Fig. 3) bringing unprecedented storage capacity to customers, and helping to herald the age of the internet and pervasive digital video storage.

Ref [1]: "Spin valve GMR Sensor Materials for Hard Disk Drives", B.A. Gurney et al., in "Ultrathin Magnetic Structuress IV", B. Heinrich and JAC Bland, eds, Springer (2005).

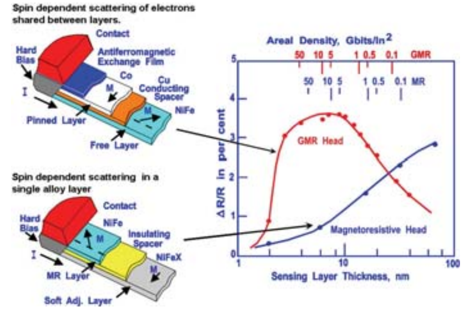

Fig. 1. Early results showed the spin valve GMR sensor could be extended to areal densities above 100 Gbit/in2.

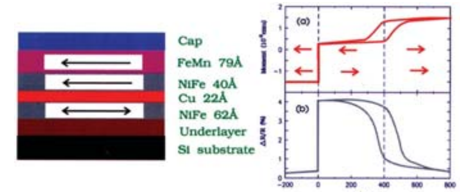

Fig. 2. The basic spin valve GMR structure with its corresponding magnetic and electrical response showing large magnetoresistance in small fields.

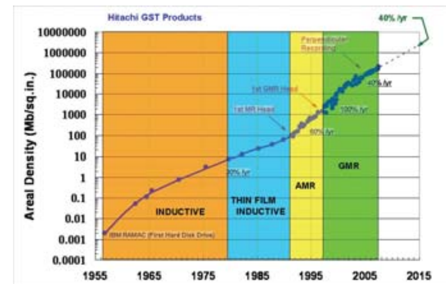

Fig. 3. The growth of areal density in hard disk drives showing when inductive, thin film inductive, AMR and GMR technologies were used to read back stored information.

BA-03

GMR spin valves, tunneling magnetoresistive devices, and beyond: transport, magnetism, and materials science.

O. Heinonen, E. W. Singleton, B. W. Karr, Z. Gao, H. Cho, Y. Chen
Seagate Technology, Bloomington, MN

The rapid increase in areal density storage capacity in magnetic hard disk drives over the past decade has, to a large extent, been enabled by advances in reader technologies. The discovery of giant magnetoresistance (GMR) [1] led to rapid development of current-in-plane (CIP) spin valve sensors [2] and directly resulted in an annual growth rate of areal density exceeding 100%. More recently, tunneling magnetoresistive (TMR) devices, with even higher signal than spin valves, have begun to replace GMR spin valves in disk drives.

In this presentation, we will review the underlying physics of spin valves and tunneling readers with an emphasis on the interplay between transport, magnetism, materials properties, and signal-to-noise ratio (SNR). For spin valves, we will examine the effects of bandstructure matching of the majority and minority spin channels of the ferromagnetic (FM) layers with the conduction bands of the normal metal (NM) spacer, and the effects of interfaces. Much improvement in the performance of spin valves came from carefully analyzing and engineering materials properties for optimal transport and magnetic performance, for example the use of synthetic antiferromagnets with Ru interlayers [3], surfactants for improved NM spacer and NM-FM interface properties [4], and specular capping layers [5]. All these impressive achievements in materials science brought the GMR ratio of sheet films up to about 20%.

The hard drive industry turned more recently to TMR devices for improved signal properties and because the heat dissipation in CIP spin valves became a problem as the devices were further scaled down in size. Initial efforts were focused on TMR devices with aluminum oxide barriers. In these devices Al is typically deposited on the CoFe electrode, and subsequently oxidized. The oxidation process both has to draw Al out from the CoFe electrode, and uniformly oxidize the Al without over- or under-oxidizing. Over-oxidizing leads to formation of Co oxides and the TMR signal rapidly degrades. Under-oxidizing leaves metallic Al pinholes which shunt current and degrade the TMR signal. For these reasons, it is difficult to achieve uniform Al oxide barriers with suitably low resistance-area product.

Other early barrier materials were HfO_2 and Ti oxide (non-stochiometric). HfO_2 barriers gave a relatively low TMR signal, about 12%, but provided a very uniform barrier with TMR ratio maintained down to thinner barriers than for Al oxide. A peculiar property of HfO_2 is also that at the thinnest barrier thickness at which TMR is observed, the inter-layer exchange coupling between the FM electrodes is anti-ferromagnetic. While this further pointed to excellent interface properties, it made for poor TMR devices, as the inter-layer exchange conspired with magnetostatic interactions to give the sensors poor symmetry properties. Ti oxide, on the other hand, provided a larger signal (~19%) for even thinner barriers than HfO_2 or Al oxide, with a weak ferromagnetic interlayer coupling. This paved the way for reliable, high-SNR devices, which were subsequently put in to production. More recently, MgO-based [6] TMR devices, with TMR ratios exceeding several hundred percent, have been developed for hard drive applications. Much of the physics and materials science developed for CIP spin valves and earlier tunneling readers could be leveraged for rapid development of functioning MgO-based tunneling devices.

Ultimately, TMR readers will have to be replaced by devices with lower resistance-area (RA) product. Even at an RA of 1 Ω-μm^2, the resistance of tunneling readers will become prohibitive. Furthermore, the noise in TMR readers – shot noise, thermal magnetic noise, as well as spin-dependent noise caused by spin-momentum transfer – scales poorly with diminished devices size and degrades the reader SNR. Currently under development are metallic current-perpendicular-to-plane (CPP) spin valves as well as current-confined-path CPP spin valves. These latter devices provide an RA product intermediate between all-metallic CPP spin valves and TMR readers, while maintaining high SNR.

1. M.N. Baibich et al., Phys. Rev. Lett. 61, 2472 (1988); G. Binasch, P. Grunberg, F. Saurenbach, and W. Zinn, Phys. Rev. B39, 4828 (1989)

2. B. Dieny et al., Phys. Rev. B43, 1297 (1991)

3. S.S.P. Parkin, N, More, and K.P. Rouch, Phys. Rev. Lett. 64, 2304 (1990)

4. W.F. Egelhoff et al., J. Appl. Phys. 82, 6150 (1997)

5. W.F. Egelhoff et al., J. Appl. Phys. 78, 273 (1995)

6. S.S.P. Parkin et al., Nature Materials 3, 862 (2004); S. Yuasa et al., Nature Materials 3, 868 (2004)

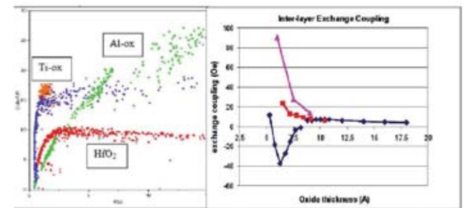

Figure Caption. Left panel: TMR ratio (Delta R/R) plotted as function of RA product (RXA) in Ω-μm^2 for Hf oxide, Al oxide, and Ti oxide. Right panel: Sheet film interlayer exchange coupling in Oe as function of oxide thickness for Hf oxide (diamonds), Al oxide (triangles), and Ti oxide (squares).

BA-04

GMR and TMR Sensors for non-storage applications.

M. Ruehrig, G. Rieger, J. Wecker
Corporate Technology MM1, Siemens AG, Erlangen, Germany

Less than a decade after the breakthrough discovery of the GMR effect by Grünberg and Fert [1] the new effect was sufficiently perfected and controllable to be introduced in most advanced commercially available products. Incorporating GMR spin valve sensors [2] and its technologically closely related counterpart TMR in cutting edge technology hard disk drives until today fuels the incomparable scaling law which keeps driving the magnetic recording industry towards ever higher recording densities.
Much less dramatic, though, was the influence of the GMR respectively TMR technology in other magnetic sensor applications. Although the potential to replace existing technologies like AMR or Hall sensors was soon realized after the discovery, GMR sensors until recently hardly gained significant market share in automotive and industrial applications.
Siemens started its GMR development for automotive and industrial applications soon after the breakthrough discovery as early as 1991. While focussing first on high signal exchange coupled multilayer systems, the potential of highly sensitive spin valve sensors was soon realized. In 1997 the first commercially available angular spin valve sensor in a crossed full bridge arrangement based on a proprietary reference layer system [3] was introduced to the market [4].
This system which is called AAF (artificial antiferromagnet) or SAF (synthetic antiferromagnet) reference system not only allowed a significant improvement of the thermal stability of the reference magnetization with enough rigidity against external disturbing magnetic fields, it also significantly reduced disturbing (magneto static) field interactions with the measuring layer due to the partially compensated net magnetic moment of the reference layer. Based on this concept a full sine-cosine Wheatstone bridge sensor was developed and marketed first by Siemens and afterwards by Infineon.
More recently the underlying concept was successfully transferred to the development of spin valve like TMR sensors [5] which are expected to gain significant importance due to the potential for higher MR signal, better thermal stability, improved sensitivity and beneficial scaling behaviour.
Today spin valve systems with exchange biased reference systems are state of the art. However, in many technologically relevant areas bridge arrangements are needed which are not so straightforward to be realized in exchange biased reference layer systems.
This paper will give an overview on non-storage GMR and TMR sensor applications by discussing the basic requirements for position, speed, angular, field and current measurements. For selected examples we will discuss options to tailor the sensor response curve by magnetic stack design with special focus on automotive and industrial applications.
New ideas for sensor bridge arrangements will we presented together with new readout schemes for TMR sensors.
The SIEMENS activities in GMR respectively TMR sensor development were partly funded my the German federal ministry for education and research (BMBF) and the European Union via RTN NEXBIAS, ULTRASMOOTH and SPINSWITCH

[1] M. N. Baibich, J. M. Broto, A. Fert, F. Nguyen van Dau, F. Petroff, P. Etienne, G. Creuzet, A. Friederich, and J. Chazelas, Phys. Rev. Lett. 61, 2472 (1988)

and G. Binasch, P. Grünberg, F. Saurenbach, and W. Zinn, Phys. Rev. B 39, 4828 (1989)

[2] B. Dieny V.S. Speriosu, S. Metin, S.S.P. Parkin, B. Guerney, P. Baumgart and D.C. Wilhoit, J. Appl. Phys 69 (8) 4774 (1991)

[3] H.A.M. van den Berg, German Patent DE 4243358 (1994), US Patent US 5.686.838 (1994) or H.A.M. van den Berg, W. Clemens, G. Gieres, G. Rupp, W. Schelter and M. Vieth, IEEE Trans. Magn. 32, 4624 (1996)

[4] W. Clemens, H. v. d. Berg, G.Rupp, W.Schelter, M. Vieth, J. Wecker, J.Appl.Phys. 81, 4310 (1997).

[5] M Rührig, R. Seidel, L. Bär, G. Rupp, M. Vieth and J. Wecker, IEEE Trans. Mag. 40, 101 (2004)

BA-05

Spintronic devices for memory and logic applications.

B. Dieny, R. Sousa, G. Prenat
SPINTEC, CEA/CNRS/UJF/INPG, Grenoble, France

Giant magnetoresistance[1]found its first application in magnetoresistive spin-valve heads for hard-disk drives[2]. Low field magnetic sensors for position encoders were also developed based on this technology[3] as well as MRAM using pseudo spin-valves[4].
Later on, the observation of large magnetoresistance at room temperature in magnetic tunnel junctions (MTJ)[5,6] opened new prospects of applications. Thanks to the current-perpendicular-to-plane geometry, new MRAM architecture could be conceived allowing reaching much higher density than in earlier spin-valve MRAM designs[7]. The first generations of MRAM design were based on field induced switching with its improved version named "toggle switching"[8]. Freescale launched a first 4Mbit MRAM product based on this technology in 2006.
The discovery of the possibility to manipulate the magnetization of magnetic nanostructure by a spin-polarized current constituted another major breakthrough in the development of spinelectronics. Berger already observed in 1982 that electrical currents could have a direct influence on the propagation of domain walls[9]. However, it is the prediction[10,11] and observation[12] of the possibility to switch the magnetic configuration of spin-valves or MTJ which triggered a considerable interest of the scientific community for these so-called spin-transfer effects. This effect provides a new way to write information in magnetic nanostructures and especially MRAM. The advantages of using spin-transfer writing in MRAM are a better scalability of MRAM design, lower power consumption and better write selectivity[13,14]. In addition, thermal assisted write schemes combined with either field or spin-transfer writing were proposed, offering the ultimate scalability in MRAM design[15]. Intense R&D efforts are in progress in large companies as well as start-ups to bring these advanced MRAM designs to production.
Besides memory applications, the combination of CMOS components with embedded MTJ in above-IC technology allows conceiving all sorts of innovative hybrid logic devices such as reprogrammable logic gates in which MTJs are used as variable resistance influencing the switching threshold of the CMOS circuits. Innovative architecture of complex electronic devices can also be conceived in which logic and memory are much more intimately intertwined than with CMOS only components.
In an historical perspective, the talk will review these present and future developments.
SPINTEC's activity of this topic was partly funded through ANR PNANO CILOMAG and European RTN SPINSWITCH.

1. Baibich, M., Broto, J.M., Fert, A., Nguyen Van Dau, F., Petroff, F., Etienne, P., Creuzet, G., Friederch, A. and Chazelas, J., Phys.Rev.Lett., 61 (1988) 2472.

2. Dieny, B., Speriosu, VS., Parkin, S.S.P., Gurney, B.A., Whilhoit, D.R., Mauri, D.. "Giant magnetoresistance in soft ferromagnetic multilayers" Phys. Rev.B.(Condensed-Matter) 43 (1991)1297-300.

3. H.Van den Berg et al, "GMR angle detector with an artificial antiferromagnetic subsystem (AAF)", Journal of Magnetism and Magnetic Materials, 165 (1), p.524-528, Jan 1997

4. Pohm, A.V., Beech, R.S., Bade, P.A., Chen, E.Y., and Daughton, J.M., "Analysis of 0.1 to 0.3 micron wide, ultra dense GMR memory elements", IEEE Trans.Magn., MAG-30, 4650 (1994).

5. Moodera, JS., Kinder, LR., Wong, TM. and Meservey,R.. "Large magnetoresistance at room temperature in ferromagnetic thin film tunnel junctions", Phys.Rev.Lett 74, (1995) 3273-6.

6. Miyazaki, T., Tezuka, N., "Giant magnetic tunneling effect in Fe/Al2O3/Fe junction", Journ.Magn.Magn.Mater.139 (1995), L231.

7. Tehrani, S., Slaughter, JM., Chen, E., Durlam, M., Shi, J., DeHerren, M., "Progress and outlook for MRAM technology", IEEE.Trans.Magn., 35, 2814, (1999).

8. Savtchenko, Leonid et al, "Method of writing to a scalable magnetoresistance random access memory element", patent US20030128603

9. S. Jen and L. Berger, " Dragging of stripe domains by a temperature gradient in Metglas 2826 MB (invited)", J. Appl. Phys. 53, 2298 (1982).

10. Slonczewski, J., "Currents and torques in metallic magnetic multilayers", J.Magn.Magn.Mater.159, L1 (1996).

11. Berger, L., "Emission of spin waves by a magnetic multilayer traversed by a current", Phys.Rev.B 54, 9353 (1996).

12. Katine, J.A., Albert, F.J ., Buhrman, R.A., Myers, E.B., and Ralph, D.C., "Current-Driven Magnetization Reversal and Spin-Wave Excitations in Co /Cu /Co Pillars ", Phys.Rev.Lett.84, 3149 (2000).

13. Slonczewski, J, "Electronic device using magnetic components", patent US 5,695,864 (1997).

14. O.Redon et al, "Magnetic spin polarisation and magnetisation rotation device with memory and writing process, using such a device", patent US6532164 (Nov.2001)

15.B.Dieny et al, "Magnetic device with magnetic tunnel junction, memory array and read/write methods using same", US 6950335(Nov2002).

BB-01

A dynamic scratch test to study read/write head degradation due to head disk interactions.

A. Wallash[1], H. Zhu[1], D. Chen[2]
1. Advanced Technology, Hitachi GST, San Jose, CA; 2. Mechanical Engineering Department, UC Berkeley, Berkeley, CA

As the head-disk spacing is reduced to increase areal density in hard disk drives, the likelihood of head-disk interactions increases. When these head-disk interactions involve direct contact to the read or write transducers at the air bearing surface, magnetic performance degradation is possible due to wear, mechanical deformation, or changes in stress induced magnetic anisotropy.

A dynamic scratch test is described to produce and study head degradation. Key features are the use of customized "nano-defects" on the disk, and a Guzik XY spin stand with a special *in situ* quasi static (QST) transfer curve measurement.

Disk indentations, scratches or embedded diamond or TiC particles were produced using a CSM NanoScratch tester with *in situ AFM*. Figure 1 shows examples of a progressive load scratch (left), an indentation (center) and an embedded diamond particle (right). The scratch and indentation were made using a Rockwell conical spherical diamond tip with a radius of 10µm. The height of the "pile-up" around the scratch or indentation is a function of the normal force, or load, of the diamond tip. The pile-up around the scratch/indentation is what hits the reader and writer while flying. To embed a particle into the disk, a single diamond particle, with a radius of 0.6µm, was pushed into the disk using a flat, 10µm x 10µm diamond tip until only 50nm protruded above the disk surface. Using these techniques, a large variety of defect shapes, heights and hardness can be made by varying the diamond tip radius, normal load profile, media substrate and particle size and type.

Magnetic head performance was measured before and after sweeping the read/write transducers repeatedly across the defect on the disk. Results are presented that compare the robustness of GMR and TMR head designs to head degradation caused by head disk interactions.

Figure 2 shows the QST transfer curves for a GMR read sensor after each sweep across the progressive load scratch shown in Fig. 1. Note the abrupt slope reversal, or "pin flip" after the 28th sweep across the defect, the flip back after sweep 43, and other dramatic changes in amplitude and asymmetry. The pin flip is explained by a reversal of the pinned layer in the GMR stack due to mechanical stress changes, and is remarkably similar to that caused by electrostatic discharge [1]. Other forms of read sensor head degradation, such as magnetic instability, will also be reported.

Figure 3 shows the resistance of a TMR sensor vs. sweep number over the hard, embedded diamond particle shown in Fig. 1. Failure analysis indicates that the abrupt resistance decrease after the 3rd sweep across the embedded particle is due to smearing/shorting of the tunneling barrier at the air bearing surface. Further sweeps "lap" away the smear and result in a partial recovery of the resistance. While no pinned layer flipping was observed in TMR heads, they were more easily degraded by head disk interactions that cut through the carbon overcoat on the head. In contrast, the GMR design exhibited pin flip but did not show the abrupt resistance decrease.

Figure 4 shows two Auger SEM images of the air bearing surface of two heads after the scratch testing. Brighter regions indicate wear of the carbon overcoat, confirming contact directly to the read/write transducers.

Changes in track averaged amplitude (TAA) and overwrite due to write head degradation, as well as wear of the carbon overcoat (COC) on the head and of the disk defects, will be discussed.

It is concluded that dynamic scratch testing provides valuable information about the strengths and weaknesses of the read/write transducers during head disk interactions, as well as wear characteristics of disk defects and the COC on the head.

[1] A. Wallash and Y.K. Kim, "Magnetic Changes in GMR Heads caused by Electrostatic Discharge", IEEE Trans.Magn.,Vol.34,No.4,1519,1998.

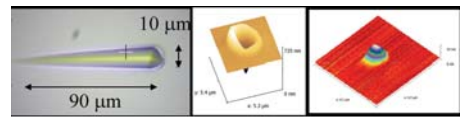

Fig. 1. Optical image of a progressive load scratch (left), and AFM images of an indentation (middle) and an embedded 0.6µm diameter diamond particle (right) on the disk surface.

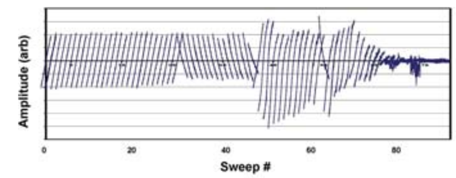

Fig. 2. QST transfer curves vs. sweep number for a GMR head swept repeatedly across a disk scratch. Note the dramatic changes in slope, amplitude, asymmetry and bias point caused by sweeping the read sensor across a disk defect.

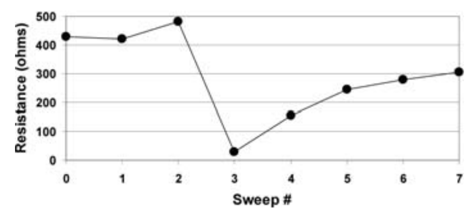

Fig. 3. Resistance of a TMR sensor vs. sweep across an embedded diamond particle.

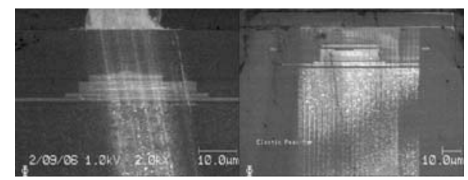

Fig. 4. Auger images showing COC wear (lighter regions) over two different read/write transducers after dynamic scratch testing.

BB-02

Effect of Segregant Surface Energy on PMR Media Roughness.

Q. Dai, H. Do, K. Takano, B. Marchon
Hitachi GST, San Jose, CA

Introduction

Recently the HDD industry has migrated to Perpendicular Recording (PMR)for higher areal density [1]. PMR technologies used thus far generally relied on media with small, well-segregated grains separated by amorphous oxide grain boundaries such as SiO2[2]. Up to now, however, the selection of the oxide for the grain boundary appears to be mostly empirical process. The materials choice and its implication on magnetic performance as well as on the tribological consequences are not well understood.

In the present paper, we will report detailed examinations of PMR media made with various oxides as segregants. The focus is the impact of the oxide property on resulting media roughness. We will demonstrate that oxides that facilitate the formation of small grains will also be more likely to form rougher media, leading to overcoat coverage difficulty.

Experiments

To study how oxides affect the PMR media grain growth and resulting media roughness, we have carried out experiments using a variety of oxides varying in surface energy as well as in heat of formation [3, 4]. The heat of formation gives an indication of the stability of the oxides. Surface energy of the oxides, on the other hand, may affect the overall grain structure. Table I shows the oxides used in the investigation, and the corresponding heat of formation and surface energy values. Disk samples were made such that all layers have the same thickness and composition, with the exception of the oxides.

Results and Discussions

Fig. 1 shows the corrosion susceptibility of media made with the oxides shown in Table 1, as a function of surface energy. The maximum anodic current of the media was used as a gauge of the overcoat coverage, which in the present experiment is affected only by the roughness. It is observed that as the oxide surface energy increased from V2O5 to ZrO2, the anodic current of the corresponding sample actually became lower. This indicates that the resulting media became smoother, and thus less likely to corrode. Although not reported here, we have observed that as the surface energy of the oxides decreased and the corrosion results deteriorated, the jitter noise actually decreased, possibly indicating smaller grains were achieved.

The inverted relationship between magnetic performance and the corrosion susceptibility is not surprising. It is likely that low surface energy oxides are better candidates for stabilizing small grains, analogous to the role of surfactants. At the same time, the low surface energy segregant may lead to media with higher roughness, leading to coverage difficulty.

AFM measurements shown in Fig.2 support the above hypothesis. The maximum valley depth of the finished media is captured and plotted against the surface energy of the oxides used in these samples. It is clear that the lower the surface energy, the deeper the valley between grains. The result is consistent with those shown in Fig.1, where as the valley depth increased, the anodic current also increased. In the full paper we will discuss in detail our understanding of the effect of segregant surface energy on the structure and how it might impact media roughness.

[1] Recording technologies for terabit per square inch systems, Wood, R.W., Miles, J., Olson, T. IEEE Trans Mag 38(5), 1977-1718, (2004)

[2] CoPtCr-SiO/sub 2/ granular media for high-density Perpendicular Recording, Uwazumi, H., Enomoto, K., Sakai, Y., Takenoiri, S., Oikawa, T., Watanabe, S., IEEE Trans Mag., Vol 39 (4), 1914-1918 (2003)

[3] Surface Composition of Binary-Systems - Prediction of Surface Phase-Diagrams of Solid-Solutions, Overbury S, Bertrand PA, Somorjai GA, Chemical Reviews 75 (5): 547-560 1975

[4] CRC Handbook

Oxide	Surface Energy (mJ/m^2)	Heat Formation (kCal/mol)
ZrO2	0.8	260
SiO2	0.6	220
Ta2O5	0.28	245
V2O5	0.1	180

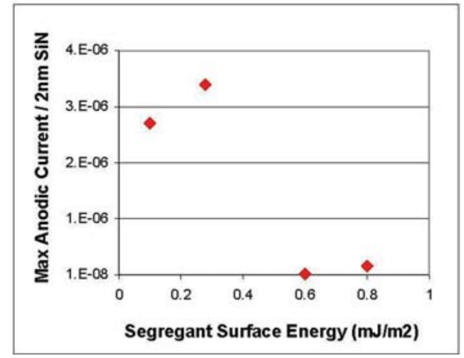

Fig.1. Maximum Anodic Current as a function of oxide segregant surface energy. The oxides with higher surface energy had lower anodic current, indicating improvement in overcoat coverage.

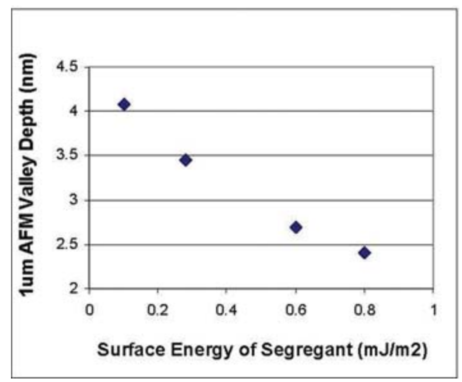

Fig.2. AFM roughness measured in valley depth (Rv) on finished media made with different segregants. The valley depth systematically increased with decreasing oxide surface energy.

BB-03

Stress Induced Permanent Magnetic Signal Degradation of PMR System.

S. Lee[1], S. Hong[1], N. Kim[1], J. Ferber[1], X. Che[1], B. D. Strom[2]
1. Samsung Information Systems America, San Jose, CA; 2. Apple Inc., Cupertino, CA

In the past, investigations of scratches have been notoriously difficult for lack of control in producing the scratches, and for the difficulties and finding and characterizing the micrometer scale scratches [1]. Both challenges have been overcome in this investigation. As a result, the study has revealed several important characteristics of the way media responds to scratch stress. Design guidelines for improved media designs follow from these revelations.
First, we found that PMR media is more sensitive to scratch stress than LMR media, both in its mechanical response and in the way that recorded magnetic patterns are affected. Fig. 1(a) shows the penetration depth of the tip measured while scratching and the residual scratch depth (measured after scratching) for PMR media using Hysitron nano-scratch system. Also shown in Fig. 1(a)) is the interface between DLC and the media layers before deformation. This Figure illustrates the relative elastic versus plastic response of the media at various loads. Of particular note is that the 20uN load produced penetration (residual) depth of 4.0nm (0.9nm), yet induced partial magnetic erasure. Both the severity of erasure and its width increased with load. Fig. 1(b) shows the residual depth after scratching for PMR and LMR media samples, as measured by AFM. Except at the highest loads, the PMR media shows greater residual depth, indicating greater plastic deformation of the media multilayer structure. The strength of this conclusion rests on the technique of applying the same stress to both media types, and analyzing the media in the same fashion. This conclusion raises serious concerns about PMR media reliability.
Second, we found that wherever residual "scratch" damage was observed, the magnetic patterns recorded on the media were damaged also. This observation is in contrast to earlier observations of magnetic patterns remaining undisturbed after mechanical "indentation" [2]. We attribute the difference to the material stresses and strains caused by friction during scratching; these friction stresses are absent during indentation. In particular, plastic strain in the ferromagnetic recording layer destroys its capacity as a memory medium. TEM cross section image of damaged PMR media was shown in Fig. 2 when 50µN load was applied during nano-scratch test. Damaged magnetic region turned out to be not re-writable possibly due to grain orientation change.
One more important observation is that the extent of permanent damage to magnetic patterns is broader than the apparent residual mechanical damage after scratching. This observation is consistent with the theory that plastic strains in the ferromagnetic layer result in magnetic degradation. These sub-surface strains are not always apparent from the surface morphology.
Finally, this investigation has led to a new development in media design. Rather than focusing on improving structural properties of protective overlayers (i.e. DLC and lubricant layers), the aforementioned observations suggest that strengthening the magnetic films would lead to greater scratch robustness for the media. Further improvements can be achieved by mechanically optimizing hardness of intermediate layer and soft magnetic underlayer so that mechanical stress cannot be concentrated on magnetic layer itself during head-disk interface contacts. Such approaches will facilitate the integration of PMR media while maintaining reliability of the HDD products.

[1] Suk, M. and Jen, D., "Potential Data Loss Due to Head/Disk Contacts During Dynamic Load/Unload,"IEEE Trans. Magn., 34, pp.1711–1713, 1998.

[2] Liew, T., Wu, S., Chow, S.K., Lim, C.T., "Surface and subsurface damages and magnetic recording pattern degradation induced by indentation and scratching,"Trib. Int., 33, pp. 611-621, 2000.

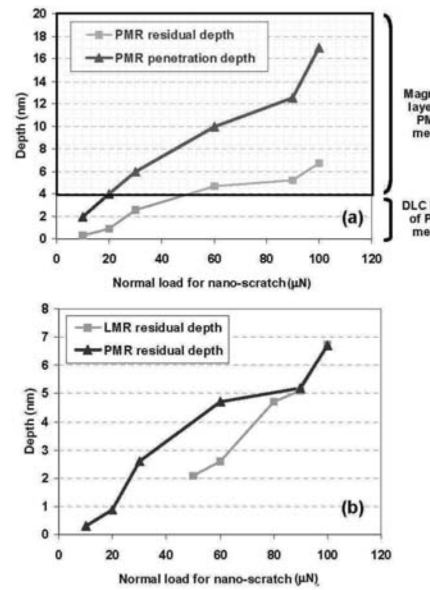

Fig. 1 (a) Penetration depth during nano-scratch vs. residual depth after nano-scratch with PMR media. Magnetic signal degradation was first observed when penetration depth was about 4nm with normal load of 20µN; (b) Comparison between LMR residual depth and PMR residual depth after nano-scratch tests.

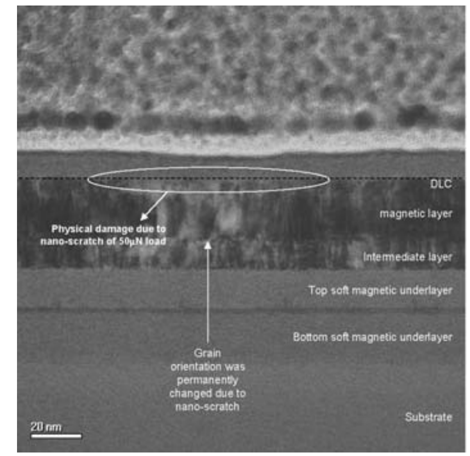

Fig.2 Cross section TEM (Transmission Electron Microscope) image of nano-scratched PMR media (50µN load)

Scratch Induced Demagnetization of Perpendicular Magnetic Disk.

M. Furukawa, J. Xu, Y. Shimizu, Y. Kato
Central Research Laboratory, Hitachi, Ltd., Fujisawa-shi, Japan

1. Introduction

The magnetic recording density of hard disk drives (HDDs) increases every year. To achieve this, HDD head/disk spacing has been reduced. In addition, perpendicular magnetic recording (PMR) was developed to surpass the super-paramagnetic limit of longitudinal disks for even higher recording density [1], and the stress induced demagnetizations are even more critical [2]. Therefore, the scratch resistance of PMR disks is an important issue. We analyzed the scratch performance of a trial PMR disk by focusing on scratch induced demagnetization.

2. Scratch Test

The scratch resistance of a disk can be evaluated at a drive level, e.g., an operation shock test [3]. However, a drive level test needs a magnetically capable head and disk and is usually time consuming. We instead proposed a component level scratch test method. The first, the disks whose magnetic pattern was randomly pre-written are used. Then, scratch mark was scribed using a stylus type scratch tester. The stylus was spherical, and had a 0.5 µm tip radius and 100-400 µN applied load. The scribing velocity was as slow as 0.1 mm/s to avoid any friction heating effects on the demagnetization [4]. The scratch depth was measured by an atomic force microscope (AFM) and the demagnetization was analyzed by a magnetic force microscope (MFM).

3. Results

The AFM and MFM images of the scratched areas at applied loads of 100 and 200 µN are shown in Fig. 1. The scratch was scribed in a circumferential direction on the disk, i.e., across the bit length direction. When the applied load was 100 µN, the scratch depth was about 1.1 nm, and no demagnetization was observed in the MFM image. However, when the applied load was increased to 200 µN, the scratch depth increased to about 3.8 nm, and demagnetization was observed in the scratched area.

A scratch scribed in a radial direction on the disk, i.e., along the bit length direction, was also investigated. A comparison with the circumferential direction, both the depth of the scratch and demagnetization showed similar behaviors. We conclude that the demagnetization is not related to bit orientation.

4. TEM Analyses and Discussion

For understanding scratch induced demagnetization, we conducted a cross-sectional analysis of the scratches by using transmission electron microscopy (TEM).

The TEM image of the scratched area of the trial PMR disk is shown in Fig. 2. The demagnetization observed disk was used. The carbon overcoat of the disk remains. It was not damaged by the scratch, but the grains in the recording layer tilted significantly, up to about 30°. From this observation, we believe that scratch induced demagnetization is closely related to the grain tilt of the recording layer. A simple schematic calculation (Fig. 3) shows that a grain tilt of 30°contributes about 2 nm to scratch depth. Therefore, dense and not easily tilted grains in the recording layer are important for scratch resistant PMR disks.

5. Conclusion

Scratch tests and a study of scratch induced demagnetization were conducted for a trial PMR disk. Scratch induced demagnetization happens when the scratch depth is up to 3.8 nm. After analyzing the structure of magnetic layer in disk with TEM, it was found that the grain of the recording layer, which is vertically orientated in a PMR disk, tilted under the scratch. A recording layer with a dense and not easily tilted grain structure is a must for a reliable hard disk drive.

Acknowledgments
The authors thank Mr. M. Okura, Mr. M. Honda, Mr. H. Tanaka, and Dr. T. Iwasaki.

[1] Tetsuya Osaka et al., IEEE. TRANS. ON MAGNETICS, Vol. 43, No .6, pp. 2109 (2007)

[2] Mike Suk et al., IEEE TRANS. ON MAGNETICS, Vol. 34, No. 4, pp. 1711 (1998)

[3] Brian H. Thornton1 et al., IEEE TRANS. ON MAGNETICS, Vol. 43, No. 6, pp. 2316 (2007)

[4] Akira Kikitsu et al., IEEE TRANS. ON MAGNETICS, Vol. 37, No. 4, pp. 1250 (2001)

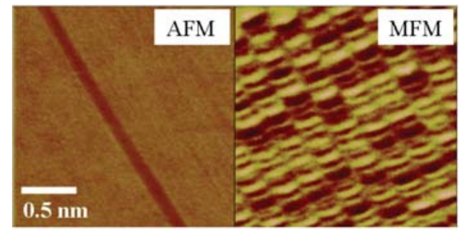

(a) Applied load: 100 µN; depth: 1.1 nm

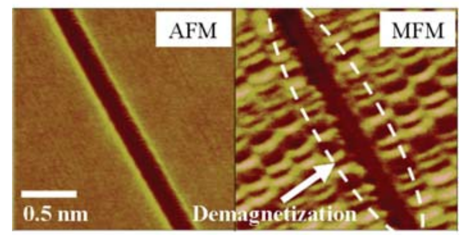

(b) Applied load: 200 µN; depth: 3.8 nm

Fig. 1 Scratch in circumferential direction of disk

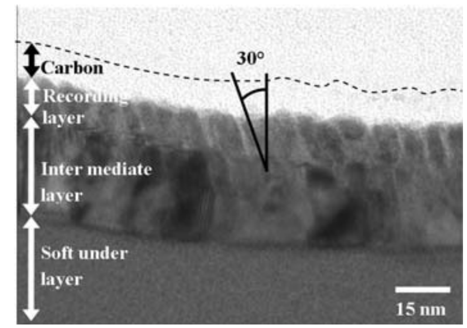

Fig. 2 TEM cross-sectional image of the scratched area

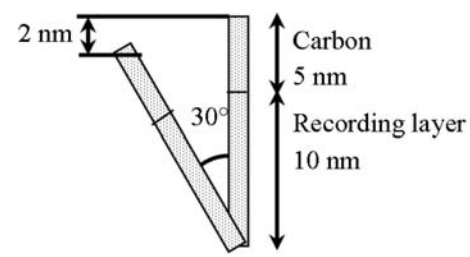

Fig. 3 Schematic of grain deformation

BB-05

Lubricant dynamics on a slider: "the waterfall effect"

B. Marchon[1], X. Guo[1], A. Moser[1], R. Kroeker[2], F. Crimi[2]
1. San Jose Research Center, Hitachi GST, San Jose, CA; 2. Server Business Unit, Hitachi GST, San Jose, CA

INTRODUCTION
As areal densities approach the Tb/in2 point, the requirement for ever lower head-medium spacing (HMS) is increasingly urgent. Conventionally, HMS has included fly-height, head and disk overcoat and head recession. More recently, it was deemed convenient to divide fly height into the sum of the disk touch-down height (TDH) and the head-disk clearance. Moreover, disk lubricant thickness, which had long been a negligible part of the HMS budget, cannot be ignored any longer [1], and it now amounts for about 10% of the total HMS. In addition to the static aspect of the lubricant contribution to spacing, dynamic aspects (i.e. moguls, ripples) stemming from slider interactions have to be taken into account as well [2]. Finally, some recent modeling work has been published that describes the evolution of a lubricant film on a slider surface. Such phenomenon is highly relevant to today's head-disk interface, as lubricant pickup from the disk to the slider is known to affect overall drive reliability.
In this paper, we will describe experiments and modeling aimed at better understanding lubricant dynamics on a slider air-bearing surface (ABS), both at rest and during flying. We will present recording data obtained on intentionally lubricated sliders, that suggest a slow removal of lubricant off the trailing ABS pad by air shear. An attempt will be made to reproduce experimental data with modeling calculations, using shear maps obtained from an air-bearing solver.
EXPERIMENTAL
Heads and Disks: Femto-long heads, designed to fly at a nominal 9nm at 15,000RPM, were lubricated with 2nm of fractionated ZTetraol (Mn=3010) using standard dipping procedures. Lube thickness was estimated from TOF-SIMS imaging. Sliders were flown on a standard commercial disk.
Recording Measurements: Immediately after loading the head, a servo pattern and a square wave bit pattern at 700 MFlux/s were written. The servo pattern ensured that the head stayed on track, thereby eliminating effects of thermal drift and minimizing the noise in the read-back signal. After applying a correction for thermal decay, the Wallace spacing loss formula was used to estimate the change in head-media spacing from the readback amplitude.
Modeling: Shear maps were calculated using the CML solver. Both Couette and Poiseuille shear maps were computed at the ABS surface, and added together. Shear flow was calculated assuming a no-slip boundary condition, using bulk viscosity values. Flow from diffusion was obtained using a constant diffusion coefficient obtained experimentally. We used a "free" lubricant layer of 1nm thickness with an effective viscosity equal to twice the bulk viscosity, on top of a "restricted" layer of 1nm thickness [4].
RESULTS AND DISCUSSION
Figure 1 shows lubricant maps obtained at various times. It is clear that the lubricant is generally being displaced downtrack from the pads towards the deposited end (DE). These maps also delineate areas of stagnation where lubricant accumulates. These specific ABS locations are typically where droplets are seen when present. Another important feature is the fact the lubricant flow seems to avoid the ABS trailing pad. This beneficial feature originates from the fact that the downtrack component of the shear stress is negative around this area, in effect pushing the lubricant away from it.
Figure 2 shows experimental magnetic spacing evolution from two different heads, as a function of time. As the lubricant film is displaced from the trailing pad, spacing decreases slowly by a total of 0.4-0.8nm in about 2 hours of continuous flying. This curves compare favorably with the model prediction, obtained by calculating the average lubricant film change on the trailing ABS pad as a function of time.
In the full paper, more experimental and modeling details will be described. In particular, the effect of viscosity will be probed by showing results obtained on sliders coated with Zdol. Also, the effect of diffusion constant of the lubricant on the etch cavity will be investigated.
REFERENCES
[1] X. Ma et al., IEEE Trans. Magn., 37, 1824 (2001)
[2] X. Ma et al., IEEE Trans. Magn., 38, 112 (2002); B. Marchon et al., IEEE Trans. Magn., 41, 616 (2005).
[3] L. Wu L, J. Appl. Phys., 99, 08N101 (2006); H. Kubotera et al. Source: IEEE Trans. Magn., 43, 3710 (2007).
[4] M. Scarpulla et al, J. Chem. Phys, 118, 3368 (2003).

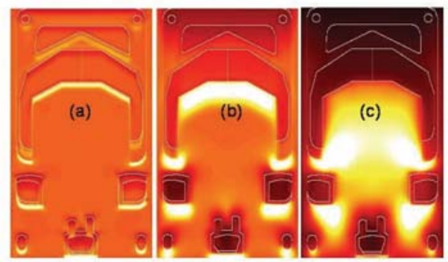

Figure 1: Lubricant maps calculated at (a) 1mn; (b) 10mn, and (c) 60mn

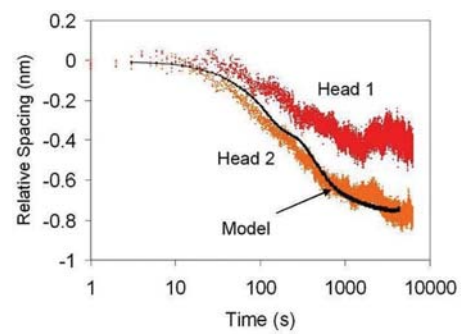

Figure 2: Magnetic spacing change as a function of time (solid line is model)

BB-06

Effect of Thermal Bonding on Frictional Properties of Monolayer Lubricant Films Coated on Magnetic Disk Surfaces.

H. Zhang[1], Y. Mitsuya[2], A. Fuwa[1], Y. Fujikawa[1], K. Fukuzawa[1]
1. Nagoya University, Nagoya, Japan; 2. Nagoya Industrial Science Research Institute, Nagoya, Japan

Monolayer perfluoropolyether (PFPE) films that are partially bonded to the disk surfaces are widely used for lubrication of magnetic disks. The bonding ratio (ratio of bonded thickness to total film thickness) may impact tribological behavior of lubricant films; however, studies so far are limited to conditions of heavy load and fast rotation that possibly damage bonded molecules. In this work, under lightly loaded and slowly rotated conditions, we measured the frictional properties of monolayer PFPE films that had different bonding ratios adjusted by thermal treatment. Friction mechanisms of mobile and bonded molecules are discussed by comparing the sliding-speed-dependent and molecular-weight-dependent friction properties.

Magnetic disks overcoated with 3-nm-thick amorphous-nitrogenated carbon films (average surface roughness: 0.45 nm) were used. The lubricants used were PFPE Zdol2000 and Zdol4000, functional polymers with different molecular weights of 2000 and 4000 g/mol, respectively. PFPEs films were dip-coated on the disk surfaces and were then annealed at 120°C. Anneal time was varied to adjust the bonding ratio. The total film thickness after thermal treatment was fixed at 2 nm. A self-developed pin-on-disk type tribotester [1] was used for friction measurements. A glass ball with a 1.5-mm diameter and an average surface roughness of 0.6 nm was used as the slider. The slider was loaded at a radius of 20 mm and the rotational speed of disks was set at 1 or 2 rpm. The external load from 0 to 1 mN was incrementally applied after one sliding revolution. At each external load, friction forces were measured at 60000 points during sliding and their average was taken.

Figure 1 shows the frictional properties of Zdol2000 films with different bonding ratios measured at 1 rpm. Friction of the 5%-bonded (non-annealed) film increased linearly with external load as described by Amontons' law. In contrast, friction forces of the annealed films increased with increasing bonding ratio and exhibited a nonlinear load dependency, which were well fitted by the Johnson-Kendall-Roberts model as plotted with solid curves in Fig. 1. Figure 2 compares the frictional properties measured at 1 and 2 rpm for the 5%-bonded and the 100%-bonded Zdol2000 films. With increasing speed, friction of the 5%-bonded film increased, whereas friction of the 100%-bonded film showed no obvious change. We thus speculate that mobile lubricant molecules show liquid-like frictional properties which are dominated by viscosity resistance, whereas bonded lubricant molecules exhibit elastomer-like frictional properties which are determined by energy dissipation during molecule deformation.

Figure 3 shows the frictional properties of Zdol4000 films measured at 1 rpm. Properties similar to Zdol2000 were observed. In contrast to Zdol2000, however, the dependency of friction on bonding ratio was weaker for Zdol4000. Compared with Zdol2000, Zdol4000 has a larger molecular weight, and thereby a higher viscosity and a longer chain length (equivalent to a higher flexibility of bonded molecules). Considering the liquid-like and elastomer-like properties of mobile and bonded molecules, these differences can rationally explain the larger friction of non-annealed Zdol4000 films and the lower friction of bonded Zdol4000 films as compared with Zdol2000.

[1] H. Zhang et al, Tribol. Lett., Vol. 28, pp. 163-170, 2007.

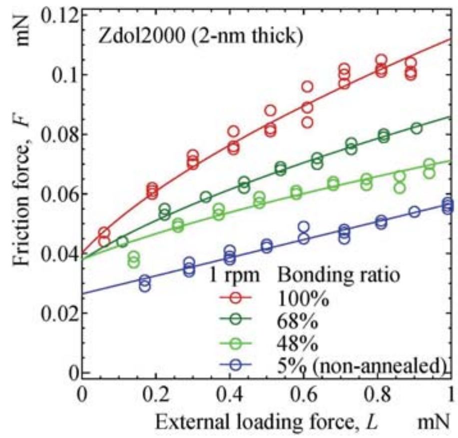

Fig. 1 Friction of Zdol2000 films with different bonding ratios.

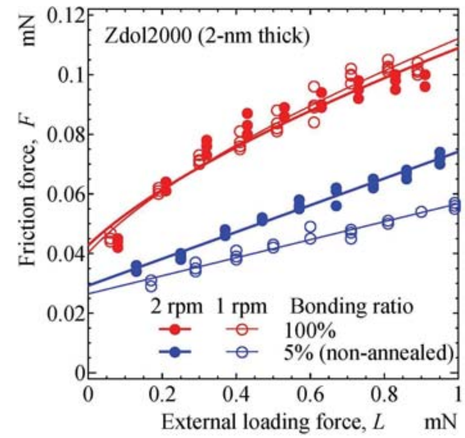

Fig. 2 Friction of Zdol2000 films measured at 1 and 2 rpm.

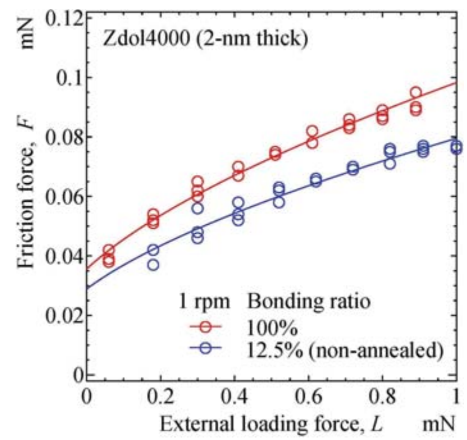

Fig. 3 Friction of Zdol4000 films with different bonding ratios.

Experimental Comparisons of Spreading and Replenishment Flows of Molecularly Thin Lubricant Films Coated on Magnetic Disks.

Y. Mitsuya[1], H. Zhang[2], J. Ohgi[2], K. Fukuzawa[2]
1. Nagoya Industrial Science Research Institute, Nagoya, Japan; 2. Micro-Nano Systems Engineering, Nagoya University, Nagoya, Japan

To ensure the reliability and durability of the head disk interface of magnetic disk drives, the lubricant film flow on the disk surface has become a significant concern since it is related to recovery performance when the film is damaged. So far, the flow characteristics of lubricant film have mainly been evaluated using the flow from the step-shaped lubricant boundary (step-boundary flow). This flow is categorized to that under ideal conditions, which is quite different from the sliding-induced depletion of lubricant film. In the present study, step-boundary and replenishment flows were compared for perfluoropolyether (PFPE) lubricant to clarify the similarities and differences between the two conditions.

2.5 inch-sized magnetic disks covered with hydrogenated diamond-like carbon and coated with Zdol2000, a polar lubricant, were used for flow measurements. The step-boundary and replenishment flows were measured through film profile changes with elapsed time using a scanning ellipsometor and an optical surface analyzer.

To measure the replenishment flow, lubricant depletion was made by in-contact sliding of a glass ball with a diameter of 1.5 mm. Gentle and mild sliding conditions were selected to avoid severe damage to the layering structure of the lubricant molecules. The conditions include a sliding velocity of 0.52 m/s, a loading force of 20 mN (2 gf), and disk turns of 30,000 passes. To accelerate depletion, the glass ball was driven oscillatorily in the disk radial direction at a frequency of 0.5 Hz and a seek distance of 0.2 mm. Typical lubricant profile changes for the two cases thinner than the monolayer (coated film thickness: h_0=2.0 nm) and nearly bilayer (h_0=4.6 nm) are demonstrated in Fig. 1 with elapsed time as a parameter. The monolayer case exhibits an ordinary recovery process, while the nearly-bilayer case exhibits a peculiar feature in three categories: i) a typical U-shaped valley appears as if the lubricant was peeling off; ii) reflow profiles from the peak toward the original lubricant surface and toward the valley are quite different; iii) the left bank of the valley moves forward, which means that the piled up molecules are flowing to the valley, while the right bank remains stationary, as if the lubricant molecules are frozen. The behavior of the right bank suggests that an unrecoverable phenomenon might occur under special conditions.

Depletion recovery rates for different initial coated film thicknesses are compared in Fig. 2, where the rate is defined as the area of the recovery cross section divided by the initial depleted cross section. The recovery rates for the monolayer and multiplayer cases are found to be roughly proportional to a logarithmic scale of time. However, for the nearly-bilayer case, the recovery rate exhibits saturation from the early stage.

The step-boundary flow was measured using the same lubricant/disk combinations as in the replenishment flow. Comparing these two flows, the unrecoverable phenomenon occurred when the bottom thickness of the valley, h_b, reached the monolayer thickness [1]. Using the spreading profiles, the diffusion coefficient distribution was calculated (Fig. 3). The diffusion coefficient, which became maximum around a thickness slightly thinner than the monolayer thickness, sharply decreased with thickness, which corresponds well to the recovery rate shown in Fig. 2. The unrecoverable phenomenon cannot be explained from the diffusion coefficient distribution obtained from the step-boundary flow, but it can be attributed to the unstable phenomenon peculiar to polar lubricants.

[1] Ma, X. et al, Physical Review E, 59, 1, pp. 722-727

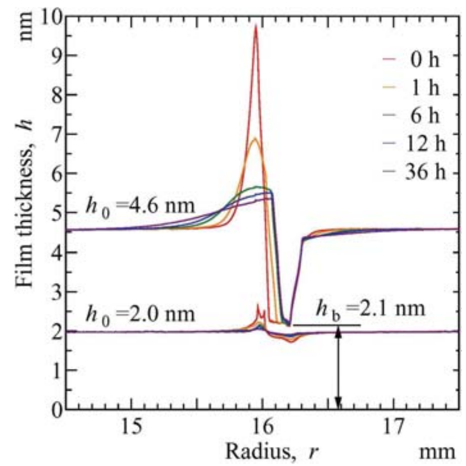

Fig. 1 Lubricant profile changes with elapsed time

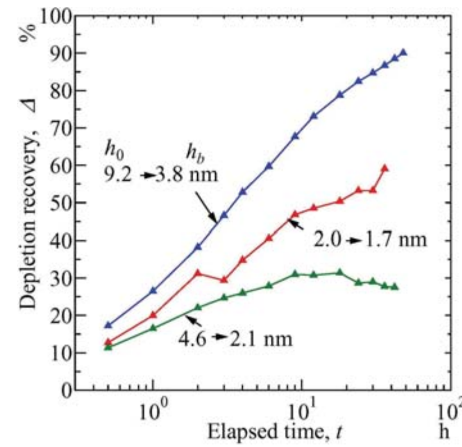

Fig. 2 Recovery rates of depleted lubricants

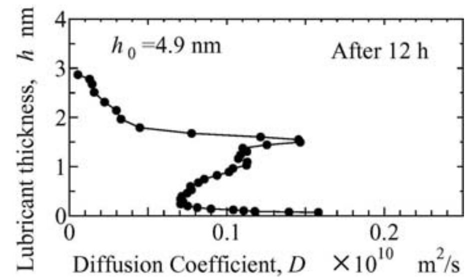

Fig. 3 Diffusion coefficient distribution along film thickness direction

BB-08

Coverage Analysis of Molecularly Thin Lubricant Films using Molecular Dynamics Simulations and CAICISS Measurements.

Y. Ikai, N. Nakamura, H. Chiba, T. Imamura
Fujitsu Laboratories Ltd., Atsugi 243-0197, Japan

Introduction

In recent HDD products, the flying height of head sliders has been reduced to less than 10 nm. For further reduction of the flying height, a lubricant film on a disk surface has to be thinned with maintaining the complete coverage over the surface. It was difficult, however, to precisely investigate the molecular-scale conformation of the lubricant films using conventional techniques.

A new method using coaxial impact collision ion scattering spectroscopy (CAICISS) was proposed to evaluate the coverage of thin lubricant films [1]. CAICISS can quantify chemical compositions on a surface by detecting the energy of the helium ions backscattered on the surface. In the proposed method, it was presumed that if a lubricant film of perfluoropolyether completely covers the surface, the flurine-to-carbon atomic ratio (F/C ratio) of the surface should become 2.

In this study, we calculated the conformation of molecularly thin lubricant films by molecular dynamics (MD) method, and investigated the validity of the coverage measurement method using CAICISS.

Simulations

Tanaka et al. [2] calculated coverage properties of Fomblin Z DOL on a disk surface by MD simulations. We carried out similar calculations to generate lubricant films of Fomblin Z TETRAOL 2500. The lubricant molecules were placed one after another at 6.0 nm height above the surface with an initial velocity toward the surface. Using this method, we generated four different lubricant films with randomly varying the initial position of each molecule. The generated films were separated into two groups in regard to the conformation. Figure 1 (a) is one of the high coverage results and Fig. 1 (b), the low coverage ones.

We then calculated the coverage and F/C ratio as a function of the film thickness. The coverage was simply calculated as a ratio of the covered area to the entire analysis area.

The F/C ratio was calculated assuming the CAICISS measurements. As Fig. 2 shows, we counted the numbers of F and C atoms considering the shadow cone radii [3] at an incident angle of 15 degrees from the surface. Figure 3 shows the calculated results for the high coverage group (a) and low coverage group (b). For both cases, the F/C ratio gives good agreement with the coverage at any film thickness. It shows that the coverage measurement method using CAICISS can evaluate the accurate coverage of lubricant films even with molecular-scale holes.

Experimental

We measured the F/C ratio of the samples prepared for different film thickness using CAICISS. The measurement parameters here were He for the incident ions, an acceleration voltage of 2 keV, and an incidence angle of 15 degrees from the surface.

Figure 4 shows the F/C ratio measured by CAICISS in comparison with the four calculated results. The high coverage results of the simulations gave good agreement with the measurements, and the low coverage ones were significantly lower than the measurements. It means that the high coverage group better expresses the conformation of the prepared sample.

Conclusions

We carried out MD simulations to generate lubricant films on a carbon protective film and calculated the coverage and F/C ratio for various film thicknesses considering the shadow cone radii. From the simulation results, we confirmed that the coverage measurement method using CAICISS can evaluate the accurate coverage of molecularly thin lubricant films. We also verified the MD simulation results in comparison with the CAICISS measurements.

[1] Y. Goto, N. Nakamura, A. Mizutani, H. Chiba, and K. Watanabe, FUJITSU Sci. Tech. J., Vol. 42, No. 1, pp. 113-121, 2006

[2] K. Tanaka, K. Iwamoto, and T. Kato, Microsys. Tech., Vol. 13, No. 8-10, pp. 1169-1174, 2007

[3] O. S. Oen, J. Surf. Sci., vol. 131, pp. L407-411, 1983

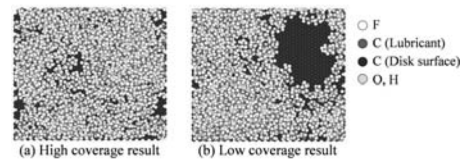

Fig. 1 Snapshots of MD simulation results for 1.6 nm average thickness films.

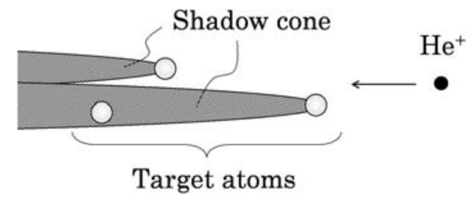

Fig. 2 Schematic of shadow cones.

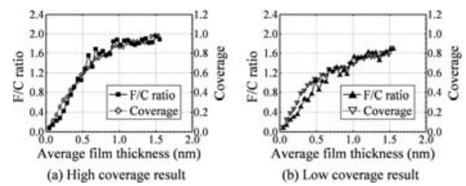

Fig. 3 In simulations, F/C ratio gives good agreement with coverage both for high and low coverage results.

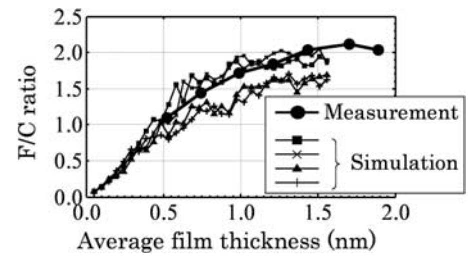

Fig. 4 Comparison between measured and calculated F/C ratios. High coverage group gave better agreement with measurements.

BB-09

Time Dependence of Head-Media Interference at Low Fly Heights.

J. He, J. Hopkins, S. Duan, K. Johnson
HGST, San Jose, CA

Touchdown height (TDH) is the fly height (FH) at which the head and disk start to make sustained contact. In the past, TDH had been found to correlate with disk roughness [1, 2]. However, the picture becomes significantly more complicated with the use of ultra smooth disks. Low roughness surfaces allow the head to fly much closer to the disk allowing forces that used to be negligible to come into play [3, 4, 5]. Lubricant film on the disk adds additional complication. The mobility of the lube allows the formation of lube moguls and/or ripples under the flying head that lead to head disk interference [6, 7]. All these effects make the head disk contact much more complicated than the simple picture of asperity or roughness induced contact.

In this paper, we describe a phenomenon that when a head is flying on a lubricated disk at FH values near the TDH, the onset of head-disk interference is a function of the FH and the flying time. The time to interference is called the Contact Free Time (CFT). We propose a lubricant migration mechanism to quantify CFT. A calculation based on this hypothesis agrees reasonably well with the data. Fig. 1 shows the plot of the quartic root of the CFT vs. FH and the result is seen to be extremely linear. The finite time needed for head-disk contact to develop reveals the subtle yet critical role of the lubricant. Lubricant dynamics under the influence of a flying head have been studied by others. One particular experiment shows that lube moguls form at the peaks of the substrate topography [6]. This result was not expected since the lube would be naturally pushed down from the top of peaks due to strong air shear. Nonetheless, the authors were able to make a convincing argument that lubricant flow would migrate to the peaks based on the disjoining pressure gradient originating from van der Waals forces. In this study, the head was flying on the order of 15 nm, much higher than the ~2.5 nm FH in our experiment. Because the van der Waals forces increase inversely with the cube of the head media separation, the disjoining pressure gradient should be an even greater effect for our work.

The mechanism of the formation and growth of lube moguls is illustrated in Fig. 2. Moguls grow in height with each pass of the slider until one or more of the lube moguls bridges the head and disk. The capillary force of a lube-bridged head-disk system is on the order of 5 mg-force for a 10 um x 10 um lube filled area [8]. This force is large enough to cause the head to hit the disk surface. We calculate lube flow from only the effect of the disjoining pressure gradient (Poiseuille flow) following the formulism and lubricant parameters from [5] and [8].

The flow of lubricant due to disjoining pressure gradient is:

$$q = h3 / 3\eta\ \partial\Pi/\partial x, \qquad (1)$$

where h is the lubricant film thickness with an average thickness h0 ~1nm, η is the effective viscosity ~ 1.0 Pa-sec, and Π is the disjoining pressure. The continuity equation is:

$$\partial h/\partial t = - \partial q/\partial x \qquad (2)$$

The change of disjoining pressure due to the head is:

$$\Delta\ \Pi = - A / 6\Pi\ (FH – h0)3, \qquad (3)$$

where A, the Hamaker constant, ~ 10-19 J

Combining the above equations, we derive the CFT as:

$$CFT = c4\ (FH – h0)4,$$

$$\text{where } c=(9\Pi\ \eta\ \delta a2\ \lambda\ /\ 2A\ h03\ \Delta t)1/4 \qquad (4)$$

δa is the length parameter characterizing the sharpness of the slider trailing pad edges (where the disjoining pressure gradient arises) and is taken to be 1um. Δt is the interaction time between the lube and the head can be expressed as the duty cycle, ~ 10-4 λ where λ the period of the rotation [6].

From eqn. (4), c is the slope of t1/4 vs (FH – h), ~ 6.1 (s1/4/ nm), quite close to the value of 8.3 in Fig. 1. c is proportional to η1/4 and inversely proportional to h03/4, and is amenable to verification with different lubricant types and thicknesses. We can also draw a conclusion from the expression that the head will be able to fly stably longer on disks with thinner and higher viscosity lubricants.

[1] A. H. Tan, J. S. Lin, C. M. Wang and C. Dong, IEEE Trans. Magn., vol. 35, pp. 2430-2432, 1999.

[2] D. Gonzalez, V. Nayak, B. Marchon, R. Payne, D. Crump, and P. Dennig, IEEE Trans. Magn., vol. 37, pp. 1839-1841, 2001.

[3] B. H. Thornton and D. B. Bogy, IEEE Trans. Magn., vol. 39, pp. 2420-2422, 2003.

[4] B. Marchon, Q. Dai, V. Nayak, and R. Pit, IEEE Trans. Magn., vol. 41, pp. 616-620, 2005.

[5] B. Marchon, Q. Dai, B. Knigge, and R. Pit, IEEE Trans. Magn., vol. 43, pp. 3694-3698, 2007.

[6] R. Pit, B. Marchon, S. Meeks, and V. Velidandla, Tribol. Lett., vol. 10, pp. 133-142, 2001.

[7] X. Ma, H. Tang, M. Stirniman, and J. Gui, IEEE Trans. Magn., vol. 38, pp. 112-117, 2002.

[8] C. M. Mate, J. Appl. Phys., vol. 72, pp. 3084-3090, 1992.

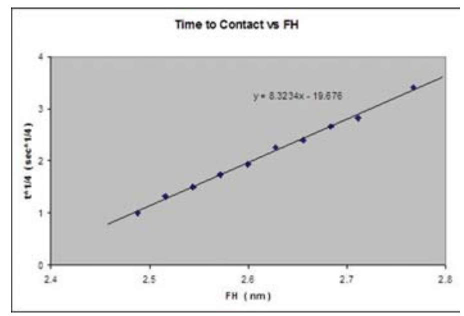

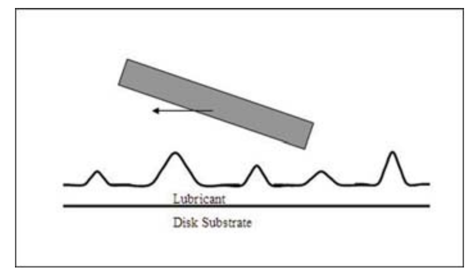

BB-10

Air bearing surface designs for less humidity sensitivity.

S. Zhang, G. Tyndall, M. Suk
Advanced Technology, Samsung Infromation Systems America, San Jose, CA

I. Introduction
In today's hard disk drives, air passing under the slider is typically compressed more than 10 times the ambient pressure. If the drives are running in a humid environment, the water vapor contained in the air can be easily compressed to reach super-saturation in the air bearing, which may cause the condensation of the vapor and thus the pressure drop in the air bearing. As a result, the air bearing is unable to support the slider with the existing flying attitude and needs to lower slider's flying height (FH) to regain the air bearing forces to balance the forces from the suspension [1, 2]. To minimize this humidity effect, one efficient method is to optimize the air bearing surface (ABS) to get it less sensitive to the humidity. In this paper, we present the concept of the air bearing's humidity sensitivity and strategies about how to reduce it through ABS optimization. Three ABS designs are proposed to illustrate the optimization approach. The simulation results indicate that the humidity sensitivity can be reduced significantly for optimized ABS than that not optimized.
II. ABS Designs for Less Humidity Sensitivity
Slider loss its FH in a humid environment and the amount of FH loss is related to both the relative humidity (RH) and temperature, the two parameters that determine the water content in the air bearing [1, 2]. We define the humidity sensitivity of an ABS as a ratio of FH at RH 70% and temperature 70 C divided by the FH under dry condition. The higher the ratio, the less sensitive of the air bearing to the humidity is.
The sensitivity ratio can be calculated by solving the FH under humid and dry conditions numerically. In brief, we solve the Reynolds equation for the FH under dry condition using the CML code [3] directly, and solve a humidity model that combines a solution of Reynolds equation with a pressure adjustment for the FH under a humid condition [2].
In order to reduce the humidity sensitivity, we have two methods in terms of ABS design: one is to optimize ABS to yield a smaller loss of air bearing force induced by vapor condensation. A derived equation indicates that a lower air bearing pressure can help to realize it [2]. But it is conditionally effective because when the pressure is lowered somewhere in the air bearing, it has to be increased somewhere else to maintain a constant air bearing force to balance the force from suspension unless a smaller suction force is preferred that may trade off air bearing's stiffness. Another method for reducing the humidity sensitivity is to optimize ABS to have a stiffer air bearing to resist the FH loss due to the vapor condensation. The air bearing stiffness is defined as the change of the air bearing force under a unit change of the slider's flying attitude such as FH, pitch or roll angles. A stiffer air bearing needs a smaller FH adjustment to compensate a given amount of change of air bearing force.
Based on the above discussion, we propose three ABS designs (Fig. 1) that have different humidity sensitivity. They are for 3.5" drives and fly at the same FH with a rotation speed 7200 rpm. Table 1 shows the simulation results of humidity sensitivity and air bearing stiffness for the three ABSs. The results indicate that Design 1 is the most sensitive to the humidity while Design 3 is the least. If look at the peak air bearing pressure, it does not show a direct relation with the humidity sensitivity explicitly because the loss of air bearing forces is not just a function of the peak pressure, but also a function of the pressure distribution over the whole integration area. The results in Table 1 also show that the air bearing stiffness has a major contribution in minimizing air bearing's humidity sensitivity. The higher the air bearing stiffness, the less humidity sensitive the air bearing is. Because design 3 has the stiffest air bearing, it therefore gets the least humidity sensitivity among the three ABS.
III. Conclusion
ABS optimization is an efficient method to minimize the humidity sensitivity of the air bearing. To illustrate the optimization strategy proposed, we design three ABS with different humidity sensitivity. The simulation results indicate that the humidity sensitivity can be reduced significantly for optimized ones than those not optimized.

1. Strom, B., et al, 2007, "Effects of Humid Air on Air Bearing Flying Height," IEEE Tran. Magn., 43(7), pp. 3301-3304.

2. Zhang, S., et al, 2008, "Simulating Air Bearing Pressure and Flying Height in a Humid Environment," J. Trib., 130(1).

3. Grisso, R., et al, 1999, "The CML Air Bearing Design Program (CMLAir32) Version 5 User Manual", CML, UC Berkeley.

	Units	Design 1	Design 2	Design 3
Hum. sens.	%	72.6	80.6	92.1
Peak pressure	atm	11	11	12.5
Stiffness by FH	gram/nm	-0.089	-0.090	-0.136
Stiffness by pitch	gram/µrad	-0.0147	-0.0208	-0.0425

Fig. 1 ABS designs with different humidity sensitivity

BC-01

Electroplated Co-rich CoPt thick films and patterned arrays for magnetic MEMS.

N. Wang[1,2], D. P. Arnold[1]

1. Interdisciplinary Microsystems Group, Dept. of Electrical and Computer Engineering, University of Florida, Gainesville, FL; 2. Materials Science and Engineering, University of Florida, Gainesville, FL

INTRODUCTION

Deposition of thick, high performance, permanent magnet(PM) materials is a critical enabling technique for the development of advanced magnetic microsystems. Recent approaches to fabricate thick PM films include sputtering of rare earth-transition metals or alternatively, electroplating of L10 CoPt or FePt alloys. However, both of these methods require high deposition temperatures and/or post-deposition annealing to achieve strong magnetization, which limits their compatibility within MEMS process flows. Co-rich CoPt films exhibit good magnetic properties in their as-deposited state due to the high anisotropy induced by the incorporation of Pt in the hexagonal phase of Co. Recently, Zana and Zangari electroplated Co80Pt20 thin films on textured seed layer of Cu (111) and Ru (0001) so that columnar growth and fine-grained microstructure were achieved [1, 2]. However, the previously reported films/arrays were limited to 2 µm in thickness. For MEMS device design, a large magnet volume is desired to achieve large magnetic forces and electromechanical energy exchange, so thicker films and patterned arrays are needed. In this work, Co-rich CoPt films/arrays with thickness around 10 µm are electroplated on both amorphous Cu and textured Cu(111) seed layers on silicon wafers.

EXPERIMENTS

Cu seed layers of 100 nm thickness were DC sputtered on silicon wafers by magnetron sputtering system without intentional heating [3]. Amorphous Cu seed layers formed on Si(100) wafers for which the native oxide had not been removed. In contrast, Cu (111) textured seed layers formed on H-terminated Si(110) wafers. After the seed layer preparation, AZ-4620 photoresist mask patterns with arrays of small magnets (150 µm x 150 µm) were defined by photolithographic techniques. Then, the CoPt was electroplated into the defined mask patterns from an amino-citrate bath [1]. The optimum electroplating conditions were found to be sensitive to the type of seed layers. Therefore, different sets of parameters were used for the two different seed layers [4]. The magnetic properties were measured by a VSM. In the analysis of the measured results, no demagnetization correction was performed.

RESULTS

After 90 min of electroplating, films with thickness of 8 and 10 µm were successfully fabricated on un-textured Cu and textured Cu (111) seed layers, respectively. The cross-sections clearly show that both films grew columnarly, as shown in figure 1. Figure 2 shows in-plane and out-of-plane hysteresis loops of magnetic films and arrays electroplated on un-textured and textured Cu seed layers. It can be seen that the coercivities reach as high as 260 kA/m (3300 Oe) and 330 kA/m (4100 Oe), respectively. The magnets on un-textured seed layers show perpendicular magnetic anisotropy with out-of-plane coercivity 260 kA/m much higher than in-plane coercivity of 130 kA/m. It is interesting to see that the magnets grown on textured seed layers did not show an out-of-plane anisotropy as reported in the previous investigations of thinner films [1, 2]. Instead, the magnets showed high coercivities of 330 kA/m and 320 kA/m for the out-of-plane and in-plane directions, respectively. In addition, in both cases, the patterned magnets arrays showed better squareness than that of films, due to the decrease of demagnetized field in the patterned arrays.

The magnetic properties of the magnetic arrays are listed in table 1.

1. I. Zana, et al, Electrochem. Solid-state Lett., 6 (12) C153-C156 (2003)

2. G. Pattanaik, et al, J. of Appl. Phys. 99, 08E901 (2006)

3. H. Jiang, et al, Thin Solid Films, vol. 315, pp. 13–16, 1998.

4. N. Wang, 214th

Electrochem. Soc. Mtg” (to be submitted)

Film thickness	Seed layer	Orientation	Hc (kA/m)	Br (T)	(BH)max (kJ/m3)	Squareness
8 µm	Un-textured Cu	Out-of-plane	260	0.28	8.8	0.26
8 µm	Un-textured Cu	In-plane	127	0.47	16.4	0.41
10 µm	Cu (111) textured	Out-of-plane	330	0.47	20.7	0.40
10 µm	Cu (111) textured	In-plane	321	0.36	14.6	0.30

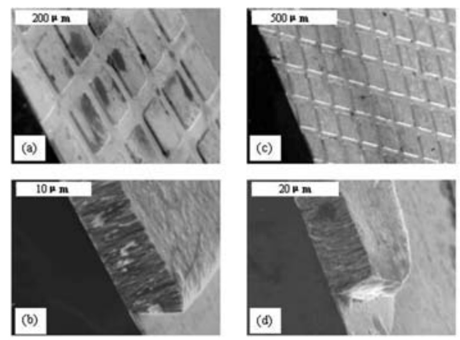

Figure 1 SEM images of CoPt micromagnets arrays and the corresponding cross-section, a) and b) show magnets on an amorphous Cu seed layer; c) and d) show magnets on a textured Cu (111) seed layer.

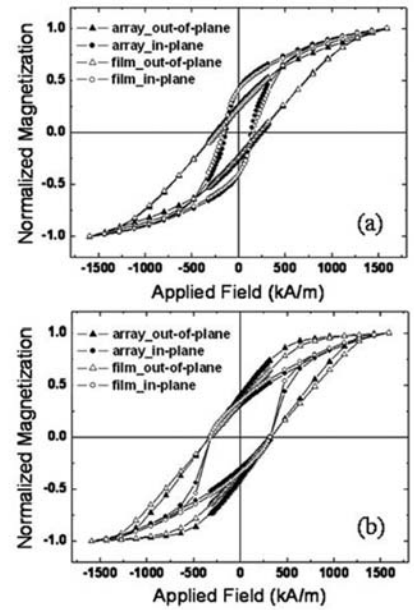

Figure 2. Hysteresis loops of thick magnetic films and arrays on a) amorphous Cu and b) Cu (111) textured seed layers

BC-02

Optical technique for measuring magnetic MEMS vibrations.

V. de Manuel[1], R. del Real[2], M. Díaz-Michelena[3], I. Arruego[4], I. Lucas[5], H. Guerrero[6]
1. Space Programs and Space Sciences, INTA, Torrejón de Ardoz, Spain; 2. Space Programs and Space Sciences, INTA, Torrejón de Ardoz, Spain; 3. Space Programs and Space Sciences, INTA, Torrejón de Ardoz, Spain; 4. Space Programs and Space Sciences, INTA, Torrejón de Ardoz, Spain; 5. Space Programs and Space Sciences, INTA, Torrejón de Ardoz, Spain; 6. Space Programs and Space Sciences, INTA, Torrejón de Ardoz, Spain

The in-situ measurements of magnetic properties, as magnetic susceptibility and gradient, are sometimes difficult tasks as there are no hand-held commercial devices. This kind of measurements are very important in mining and Magnetic Geology research both on Earth and in Space. At the Spanish National Institute of Aerospace Technology (INTA) it has been developed a magnetic susceptometer and gradiometer for measuring the magnetic properties of the Martian and Moon soil. As the magnetic signal is extremely low, a huge effort needs to be done to increase the Signal-to-Noise Ratio of the instrument. Thus, mechanical detection of the signal has been disregarded. Instead of it, we have developed an optical detection device based on optical fiber sensing techniques. In this work we report an optoelectronic device for the measurement of a vibrating magnetic Micro-Electro-Mechanical System (MEMS).

The scheme of the device (Figure 1) is very similar to [1, 2]. The light coming from a Light Emitting Diode (LED) is guided with a PolyMethyl-MethAcrylate (PMMA) optical fiber to a mirror on the vibrating MEMS. This light is reflected to the sensing fibers located around the emitting fiber ('Daisy' configuration). The light is then guided to a photodiode which will detect more or less light intensity depending on the distance of the mirror to the fiber extreme.

Figure 2 shows the voltage measured by the photodiode as a function of the distance by means of an EG&G photocurrent amplifier. In the figure it can be seen that the best sensing zone corresponds to the distances between 400 and 700 μm, the steepest part of the curve. The central part of this area is taken as the working point (WP) for further measurements.

Once the sensor is set in the WP we measure the sinusoidal variations of the voltage corresponding to the vibration of the magnetic MEMS. The amplitude of the signal produced by the vibrations of the MEMS is very small compared to that of the WP so to maximize the resolution of the device, a high pass filter (HPF) has to be added in the front-end electronics. In Figure 3 it is shown the schematic of the transimpedance amplifier and the HPF (cut-off frequency of the order of 10 Hz) used. The output of this circuit is directed to a lock-in amplifier.

The calibration of the 'Daisy' configuration fiber-optic sensor for a vibrating MEMS can be made with a piezoelectric loudspeaker with a well known amplitude to voltage characteristic curve. Figure 4 shows the locked-in signal versus the vibration amplitude of the loudspeaker. Every point is the average of 100 measurements. The calibration of the device by least squares method gives a slope of 1.8059 ± 0.0011 mV/μm. The standard deviation of every point was used to determine the uncertainty, which is of 4 nm in the 100-1000 nm range.

[1]- C. Prelle, F. Lamarque, P. Revel, Sensors and Actuators A 127 (2006) 139–146.

[2]- T. Oiwai and H. Nishitan, Meas. Sci. Technol. 15 (2004) 84–90.

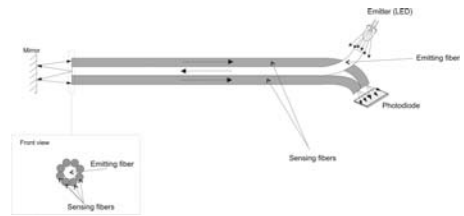

Scheme of the "daisy" fiber optic configuration.

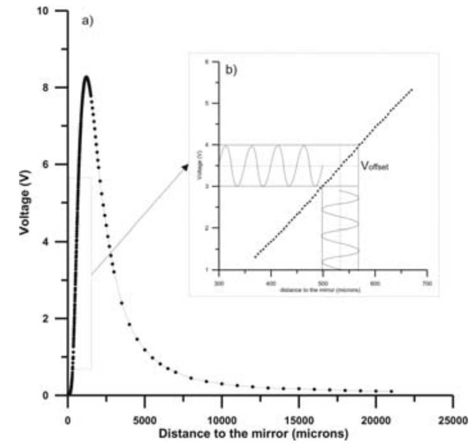

a) Response of the device depending on the distance to the mirror. b) Detail of the linear zone and hypothetical vibration of the MEMS with the corresponding response of the device.

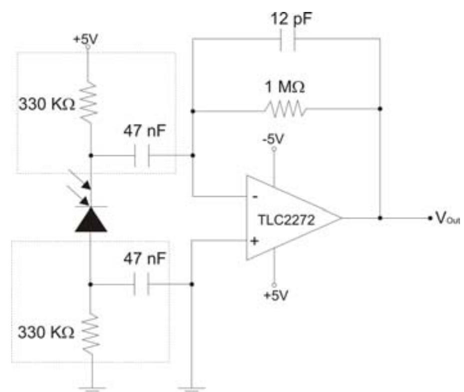

Electronics used for signal conditioning. The high pass filter is in the dashed lines boxes.

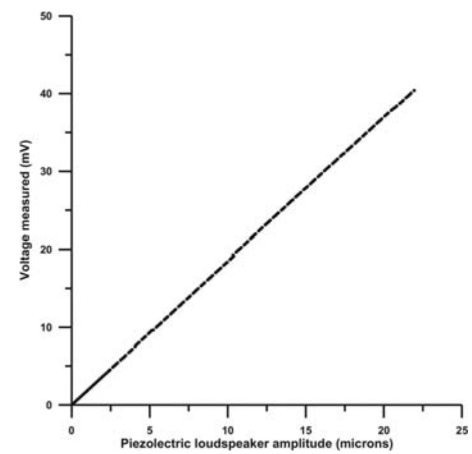

Response of the device for a vibrating piezoelectric loudspeaker.

BC-03

Design of Axial Flux Machine for Micro Flywheel Energy Storage System.

J. Yi[1], K. W. Lee[2], S. Jeong[2], *M. Noh*[1], S. S. Lee[2]
1. Mechatronics Engineering, Chungnam National University, Daejeon, South Korea; 2. Mechanical Engineering, KAIST, Deajeon, South Korea

The need for portable power generating devices is increasing rapidly, which spurred the research in micro electric power generation. In this paper, we present a design of micro generator attached to a flywheel that is passively supported by a high-temperature superconductor (HTS) bearing. The generator is in the form of the axial flux machine, which is also used as a motor to spin up the flywheel. We fabricated the stator coils using MEMS techniques. In this paper, we derived a mathematical model of the axial flux machine and verified the model against finite element analysis and experiments.

Fig.1 illustrates the schematic diagram of the system. The system consists of an electroplated planar stator, flywheel, and HTS bearing. The flywheel levitates above HTS when HTS is cooled and takes torque from the planar stator which consists of an axial flux type brushless DC motor/generator. The planar stator is fabricated with 5-lines, 100μm-width, and 50μm-height using MEMS techniques, as shown in Fig. 2. Fig. 3 shows the picture of the HTS bearing and the flywheel.

For the convenience of the analysis of the axial flux machine, we cut the motoring permanent magnets through an imaginary line at $r=R$, and unroll the axial surface as shown Fig. 4. Assuming the uniform field distribution in the radial direction, we can use 2D magnetostatic analysis to determine the field distribution. If we consider only the field by the motoring permanent magnets, the field is described by a potential equation $\nabla^2\psi=\nabla.M$ (1) where M is the magnetization vector representing the permanent magnets. The magnetization vector in eq.(1) is a periodic function for our case, and can be expressed as a Fourier series. If we consider only the first term of this Fourier series (space fundamental), eq.(1) can be solved analytically after applying appropriate boundary conditions. The axial field is obtained as $B_z=\mu_0 M_0 \sinh(qt_m) \exp(-q (t\_m+g)) \sin(qx)$ (2). Using this field equation, we can derived the torque and back-emf equation as $T=1.5\ n_c\ k_b\ F_0\ R_{avg}\ I_0$ (3) and $E_a=F_0\ R_{avg}\ \omega\ n_c\ k_b \sin\theta$ (4).

The analytical model is verified with a finite element analysis. The designed axial flux machine is built and tested in a prototype. The flywheel in the prototype rotates up to 51,000 rpm and stores the rotational kinetic energy of 337J. The complete spin down time is 3hr 20min inside a vacuum chamber. At maximum speed, the no-load three-phase electric output of the micro generator is 802mVrms, which matches with the model.

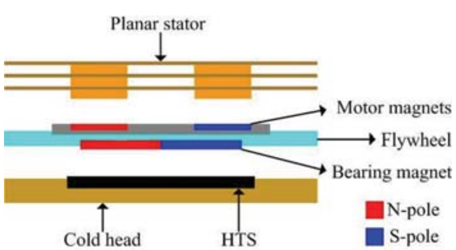

Schematic diagram of the micro flywheel energy storage system

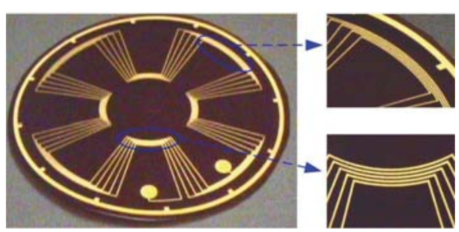

Fabricated planar stator

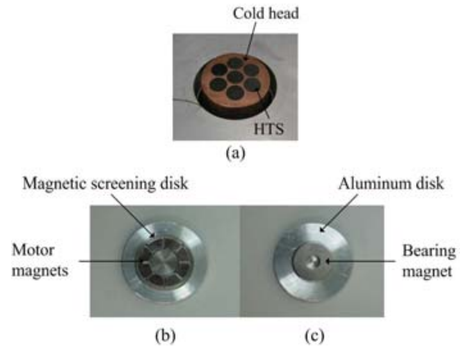

Fabricated HTS bearing and flywheel. (a) HTS on cold head, (b) eight motor magnets and magnetic screening, and (c) a ring type bearing magnet in the back side

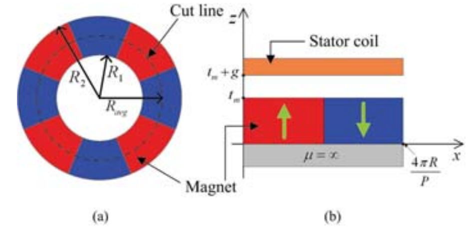

(a) Geometry of motoring permanent magnets and the imaginary cut line. (b) Unrolled axial surface. Only one electrical cycle is shown.

BC-04

Magnetic hysteresis loop micro sensor for wafer level testing of magnetic films.

E. Flick[1], K. Feindt[2], H. H. Gatzen[1]
1. Leibniz Universitaet Hannover, Institute for Microtechnology, Garbsen, Germany; 2. innomas GmbH, Ilmenau, Germany

Introduction

Achieving the desired properties of magnetic thin-films is a precondition for a successful fabrication of magnetic micro devices. Typically, these films are anisotropic, with a hard and an easy axis perpendicular to each other. In this case, it is necessary to measure the properties of such films along both axes to guarantee that the specified magnetic properties are met. Such a non-destructive in-situ measurement using micro sensors substantially increases the production efficiency [1]. This paper presents the development and fabrication of a hysteresis measurement system consisting of two independent sensors oriented at an angle of 90° to each other. This allows measuring the properties of anisotropic magnetic thin-films along the two desired axes. Each sensor represents a micro transformer, with the magnetic thin-film forming one leg. The measurements of the magnetic properties have to be carried out at exactly the same location. To fulfill this requirement, the sensors are designed to alternatively being engaged at the measurement spot. The sensors are intended for mounting in a micro actuator ultimately, which will perform the positioning [2]. The Leibniz Universitaet Hannover's Institute for Microtechnology (imt) carried out design and fabrication of the hysteresis loop micro sensor, while the innomas developed the measurement electronics executed the sensor evaluation.

Design and Fabrication

To achieve an optimal micro sensor design, a Finite Elements Method (FEM) analysis was carried out using ANSYSTM simulation software [3]. The induced voltage in the sensing coils is proportional to the change of magnetic flux in the magnetic layer.

The hysteresis loop micro measurement system was fabricated in thin-film technology. Each micro sensor consists of a NiFe81/19 ring core with air gap and two pairs of spiral coils. The core's gap orientation determines the measurement direction. Therefore, the two gaps are perpendicular to each other and this way covering both the easy and the hard axis of the magnetic thin-film. The magnetic core has a footprint of 400 µm x 400 µm, the air gap length is 30 µm. The total building height of the micro sensors is 62 µm. Each core carries a pair of six-turn excitation coils on top of two ten-turn sensing coils. The cross sections of the coils are 10 µm x 12 µm and 5 µm x 5 µm, respectively.

The micro sensor system was deposited on a glass wafer in five layers. For fabricating both the core components and the coil layers, electroplating NiFe81/19 and Cu, respectively, were applied. Photo masks were used for patterning micro molds for the deposition. As insulation material, photosensitive epoxy (SU-8™) was used [4]. Seed layers required for electroplating on insulators were created by sputter deposition and (in case of the coil seed layer) removed by Ion Beam Etching (IBE) after completing the electroplating process. The first and the last layer were planarized using Chemical-mechanical Polishing (CMP) [5, 6]. Figure 1 shows a micrograph of the fabricated hysteresis loop micro sensor chip.

Experimental Results

For an excitation sinus current of 31 mA, a frequency of 100 kHz, and a material film thickness of 20 nm, a measurement signal of about 6 mV was achieved. Comparing the results measuring without probe a significant increase of the induced voltage is shown. The difference between the measurement wave form with and without probe allowed to reconstruct the hysteresis loop.

Acknowledgment: This work is sponsored in part by the German Federal Ministry of Education, Research, and Technology (BMBF) within the framework of the program "MST Pruef" (project CHARMA).

References

[1] J.W. Judy: Microelectromechanical systems (MEMS): fabrication, design and application. Smart Materials and Structures 10, pp. 1115-1134, 2001.

[2] H. Gerdes, D. Dinulovic, H.H. Gatzen: Electromagnetic Dual-position Actuator for Measurement Applications. Actuator 2006, 10th International Conference on New Actuators, 14-16 June 2006, Bremen, Germany, pp. 824-827, 2006.

[3] H.H. Gatzen, D. Dinulovic, E. Flick, H. Gerdes, K. Feindt, M. Eccarius: Concept for a Wafer Level Test System for Measuring Magnetic Film Properties, Symposium on Magnetic Materials, Processes and Devices, 210th Meet. of The Electrochemical Society 2006, Cancun, Mexico, 2006, ecs transactions, Vol. 3, Issue 25, pp. 165-177, 2007.

[4] J. OBrian, P.J. Hughes, M. Brunet, B. ONeill, J. Alderman, B. Lane, A. ORiordan, C. ODriscoll: Advanced photoresist technologies for Microsystems. J. Micromech. Microeng. 11, pp. 353-358, 2001.

[5] C. Kourouklis, T. Kohlmeier, H.H. Gatzen: The Application of Chemical-Mechanical Polishing for Planarizing a SU-8/Permalloy Combination Used in MEMS Devices. Sensors & Actuators: A Physical, 106 (1-3), pp. 268-271, 2003.

[6] H.H. Gatzen, C. Morsbach, C. Kourouklis: Chemical-mechanical Planarization of a SU-8/Copper combination for MEMS. Proc. ASPE 18th Ann. Meet. 2003, Portland, Oregon, USA, pp. 575-578, 2003.

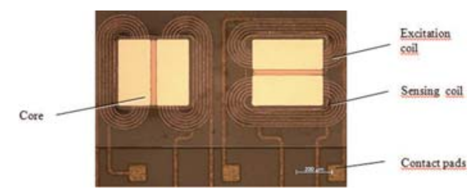

Figure 1: Micrograph of the fabricated sensor chip

BC-05

Thin Film Magneto-Impedance Sensor Integrated with L-10 FePt Thin Film Bias Magnet.

K. Ohmori[1], K. Tan[2], K. Itoi[1], K. Nagasu[1], Y. Uemichi[1], T. Aizawa[1], R. Yamauchi[1]
1. Microdevice department,Electron Device laboratory, Fujikura Ltd., Sakura, Japan; 2. Akita research institute of advanced technology(AIT), Akita, Japan

Magneto-Impedance (MI) sensor is very attractive as a highly sensitive magnetic field sensor. However, certain amount of bias field is required for operation because the sensor has only poor linearity and small sensitivity around zero magnetic field. To solve this problem, integration of SmCo thin film magnet with MI sensor has been proposed [1], where the magnet can generate only a fixed bias field. When we consider practical use, adjustability of the bias field after fabrication is desirable because dimensions and characteristics of the magnetic film can vary according to unintentional variations in fabrication conditions while precise setting of the bias field is essential to obtain high linearity as well as high sensitivity. In this paper, we propose an adjustment method of the bias field of a thin film magnet integrated with the MI sensor. We fabricated a CoNbZr thin film MI sensor with L-10 FePt thin film magnet, and showed that it is possible to adjust the bias field after fabrication.

Figure1 shows a top view of the fabricated sensor, where two Meander-type thin film MI sensors were arranged on FePt film side by side so that we can compose a Wheatstone bridge circuit by adding two resistors. Firstly, a 1.3um thick FePt film was RF-magnetron sputter deposited on a Si substrate, was patterned into a 0.6 mm-long and 2.4 mm-wide square by lift-off process, and then was annealed at 600 degrees C. After forming a 1um thick SiO2 layer, a 1um thick amorphous CoNbZr soft magnetic film was sputter deposited, then was patterned into 500 um-long and 30 um-wide meander lines by lift-off process. After forming Al electrodes, uniaxial anisotropy was induced in a transverse direction of the CoNbZr stripes by a rotational field annealing followed by a static field annealing of 3kOe at 400 degrees C. Finally we magnetized the FePt film with a static field of 10 kOe at RT.

We evaluated MI properties of the sample when various magnetizing angles were given in an in-plane direction with respect to the magnetizing field. Because the MI sensor has the sensitivity only along with its longitudinal direction, cosine components of the bias field generated by the magnet work as an effective bias field. In order to control the magnetization angle precisely, in-plane isotropy of the magnet film is required. The magnetization curve of the FePt film after the whole process that is shown in Fig.2 indicates good isotropy even after the field annealing of CoNbZr film.

Figure3 shows MI properties of the sample with magnetizing angles of 0-90 degrees. A bias field of 13.1 Oe was obtained when the magnetization is in the longitudinal direction, i.e., magnetizing angle is zero. We confirmed that the effective bias fields that can be estimated from the field shift in the Fig.3 coincide well with the cosine component of the bias field at zero degree as shown in the inset. We composed a Wheatstone bridge circuit and measured the bridge voltage induced by a pulse voltage as a function of externally applied field, which is shown in Fig.4. A linear sensor property was obtained.

In summary, we proposed the adjustment method of the effective bias field based on the magnetization-angle control of FePt bias magnet and achieved linear sensor characteristics in the fabricated sample.

[1] M.Takezawa et al., "Integration of high-frequency carrier-type thin-film magnetic field sensor with SmCo thin-film bias magnet," *IEEE Trans. Magn.,* vol.35, no.5, pp. 3682-3684, 1999.

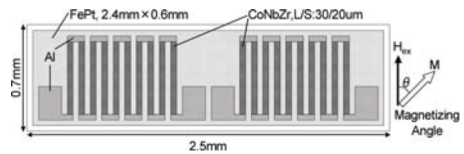

Fig.1. Top view of the fabricated sensor.

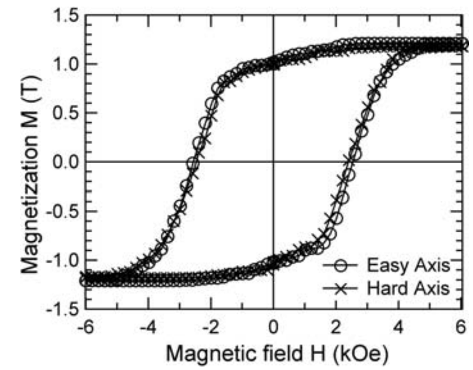

Fig.2. Magnetization curve of the FePt film.

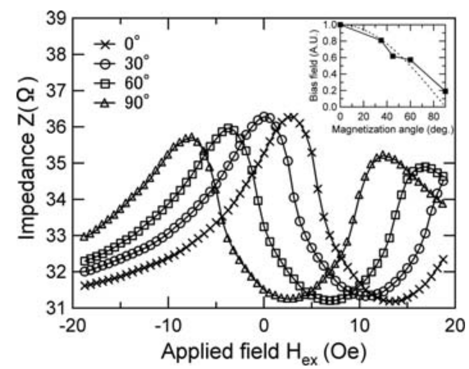

Fig.3. Magneto-Impedance properties with various magnetizing angle of integrated bias magnet.

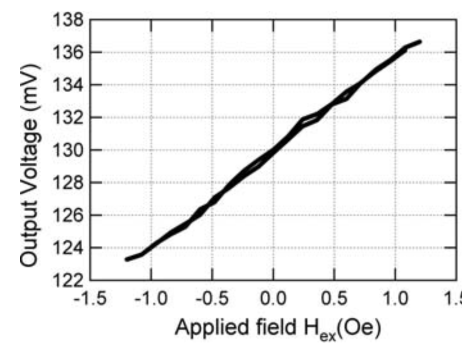

Fig.4. Output voltage of composed Wheatstone bridge circuit with two MI elements and two resistors.

BC-06

PWM Type Amorphous Wire CMOS IC Magneto-Impedance Sensor Having High Temperature Stability.

Y. Nakamura[1], T. Uchiyama[1], C. M. Cai[2], K. Mohri[3]
1. Nagoya University, Nagoya, Japan; 2. Aichi Steel Co., Tokai, Japan; 3. Aichi Micro Intelligent Co., Tokai, Japan

INTRODUCTION

We have presented a pulse frequency modulation (PFM) amorphous wire CMOS IC Magneto-Impedance (MI) sensor1, which enable to omit the analog-to-digital (A/D) converter in the electronic compass for mobile phone application2 by counting
the number of the microprocessor timing pulse in the multi-vibrator pulse width. Elimination of A/D converters is useful for downsizing, speed up and cost cutting in the mobile phone electronic compass. However, output stability of the PFM-MI sensor should be improved by canceling the fluctuation of sensor circuit parameter (R, C) with temperature variation.

We newly constructed a pulse width modulation (PWM) amorphous wire CMOS IC MI sensor on the basis of the PFM-MI sensor detecting the pulse duty ratio proportional to the applied magnetic field strength, in which the sensor circuit parameter (R, C) are canceled in the sensor output equation for improvement of the magnetic field sensing stability for temperature variation.

PWM-MI SENSOR CIRCUIT

Fig.1 represents a PWM-MI sensor circuit configuration modifying the PFM type
amorphous wire CMOS IC MI sensor.

Capacitor C1 begins to charge through resistor R1 toward Vdd. When the voltage across C1 reaches the threshold voltage Vth, the output of inverter Q1 goes LOW and that of Q2 goes HIGH, turning analog switch S1 ON and thereby discharging C1. The current from C1 is drawn the ground through r, an on-resistance of analog-switch. Two charge-discharge operations continue indefinitely, and the period of oscillation is therefore T = T1 + T2 (see Fig.2).

T is approximately to be the charging periods of T1charge and T2charge.

The sensor output is the pulse duty ratio expressed in equation (1) (see Fig.2), in which the sensor circuit parameter (R, C) is canceled, while R,C appear in the sensor output
(pulse frequency) of the PFM-MI sensor expressed as f = 1 / F(RC) 1).

Fig.2 shows dc magnetic field detection characteristics of the PWM-MI sensor.

A non-hysteresis detection characteristic is obtained for ±1 Oe, which is transformed to a highly linear characteristic in the microprocessor signal processing.

Fig.3 shows measured results of the output stability of the PWM-MI sensor for temperature variation (25 – 65 degrees centigrade). A highly stable characteristic is resulted in the PWM-MI sensor with the output variation less than about 0.1%/Celsius, while the output variation is large in the PFM-MI sensor of about 3 %/Celsius.

REFERENCES

1) C. M. Cai, K. Usami, M. Hayashi, K. Mohri, Frequency Modulation Type MI Sensor Using Amorphous Wire and CMOS Inverter Multi-vibrator, IEEE Trans. Magn., vol.40, no.1, pp.161-163, 2004.

2) K. Mohri, Y. Honkura, Amorphous Wire and CMOS IC Based Magneto-Impedance Sensors – Origin, Topics, and Future, SENSOR LETTERS, vol.5, pp.267-270, 2007.

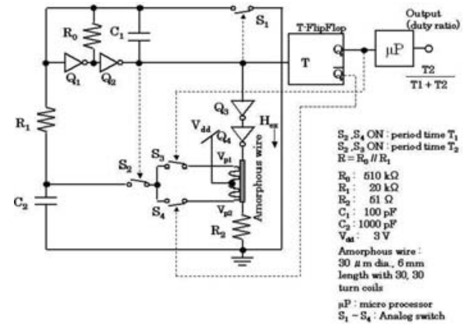

Fig.1 Configuration of PWM-MI sensor circuit.

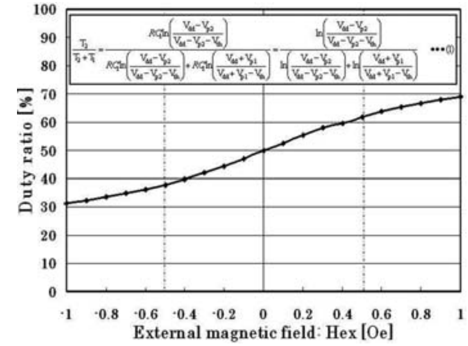

Fig.2 DC magnetic field detection characteristics.

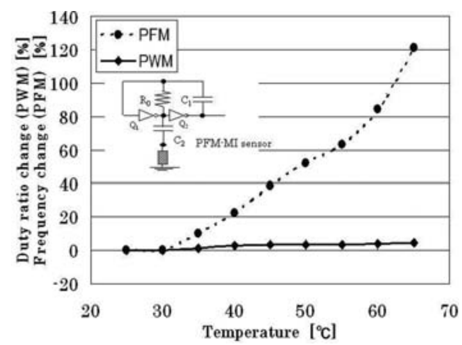

Fig.3 Sensor output stability for temperature variation.

BC-07

Microfabrication process and characteristics of thin-film noise suppressor integrated onto the re-wiring layer of a LSI chip.

M. Yamaguchi[1], T. Fukushima[1], T. Akiba[2], A. Nakamura[2]

1. Dept. of Electrical and Communication Engineering, Tohoku University, Sendai, Japan; 2. Division of Process & Device Analysis Engineering Development, Renesas Technology Corp., Kodaira, Japan

Ferromagnetic resonance (FMR) losses of soft magnetic thin film are useful for suppressing electromagnetic noise up to GHz range generated from a Large Scale Integration (LSI) chip. Basic researches for model transmission lines [1], [2] and preliminary demonstration for package-open LSI chip [3] are reported already. In this paper we proceeded to find out a practical need for magnetic film integration for a LSI chip, processed the film on the bare LSI chip, also processed hundreds of solder bumps for flip-chop bonding, and actually evaluated the magnetic near field emission.

The targeting application is for a re-wiring layer on a LSI chip. The re-wiring layer offers ever thick and long multilayer wiring which meet a need to increase the number of wires on a LSI chip having a fine design rule [4]. Typical thickness of the wire is more than a few microns and length is longer than a millimetre. These wires are processed at the final step of microfabrication process and the use of re-wiring layer is growing year by year. On the other hand, the power carrying and the information carrying electric currents flowing in the densely drawn re-wires often cause electromagnetic noise problem.

The test chip is a one-chip microprocessor with size of 10.8 x 10.4 mm2 and chip thickness of 725 um. The clock frequency is 40 MHz and the corresponding frequency spectrum reaches several hundred MHz and beyond. The close-up view of the chop is shown in Fig. 1. There are nominally 300 solder bump electrodes with diameter of 250-300 um. A 1.0 um-thick Co85Nb12Zr3 amorphous soft magnetic film with saturation magnetization of 1.1 T, anisotropy field of 845 A/m, relative permeability of 1000 and ferromagnetic resonance frequency of 1.1 GHz was sputter-deposited on top of the polyimide passivation layer, followed by 0.5 um-thick SiO2 deposition to make sure the insulation. After electrode opening by a lift-off process, the chip was annealed at 340 degree-C for 2 hours in a dc 0.3T field. Then solder bumps were formed by a screen-mask method. We also processed copper film instead of magnetic film as a reference. The completed chip is shown in Fig. 2 and was then bonded to a test printed circuit board to evaluate magnetic near field emission.

An electromagnetic near field measurement system (Type EMV-200, Hitachi display device, Inc.) with the probe size of 2.2 mm2 was used at a measurement distance of 3.85 mm in a frequency range of 10 MHz-1.44 GHz. The level of magnetic filed was successfully attenuated by the magnetic film, which was better than Cu film up to 360 MHz (9th harmonic). Attenuation of 3-7 dB was also seen up to GHz range. Maximum attenuation achievd was 6.7 dB at 774 MHz. These demonstrate the usefulness of magnetic film.

[1] Ki Hyeon Kim, Shigehro Ohnuma, Masahiro Yamaguchi, IEEE Trans. Magn. 40(4), 2838-2840 (2004).

[2] Jaecheon Sohn, S. H. Han, Masahiro Yamaguchi, and S. H. Lim, “Si-based electromagnetic noise suppressors integrated with a magnetic thin film,” Appl. Phys. Lett. 90, 143520 (2007).

[3] T. Fukushima, S. Koya, H. Ono, N. Masuda, M. Yamaguchi, “Evaluation of RF Magnetic Thin Film Noise Suppressor Integrated onto an Operating LSI Chip,” J. Magn. Soc. Jpn, 30, 531 (2006).

[4] T. Akazawa, “All about SiP Technology (in Japanese),” Kogyo-Chosakai (2005).

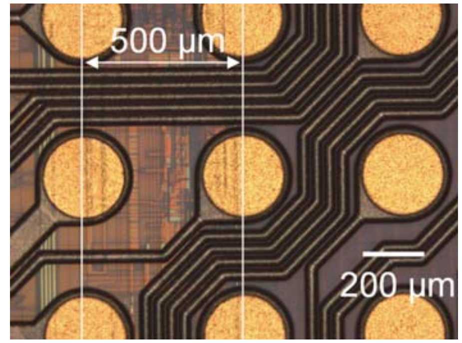

Fig. 1 Re-wiring wafer before magnetic film deposition.

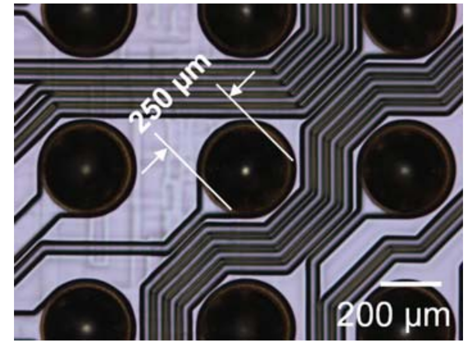

Fig. 2 Re-wiring wafer after magnetic film deposition and solder bump preparation.

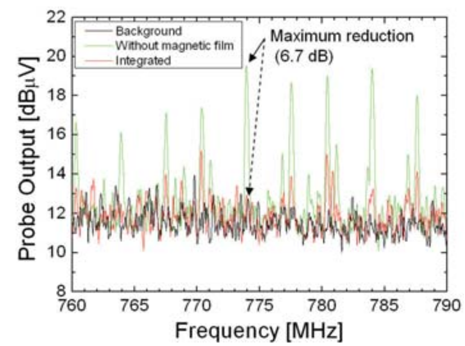

Fig. 3 Magnetic near field suppression by integrated magnetic film. The effect was maximum at 774 MHz (6.7dB).

BC-08

Investigation of Magneto Impedance Sensors in Micro Scale for an Application to Chip-cytometer.

D. Kim[1,2], H. Kim[1], D. Chun[1], W. Lee[2], W. Jeung[1]
1. Functional Materials Research Center, Korea Institute of Science and Technology, Seoul, South Korea; 2. Material Science & Engineering, Yonsei University, Seoul, South Korea

Magneto impedance (MI) effect, which implies sensitive change of impedance of soft magnetic materials with external magnetic field, has been attracted experimental and theoretical investigations because of its high sensitivity, resolution, and low power consumption. [1~3] In particular, the fact that the sensitivity of MI device is one of the highest of all magnetic sensors intrigued efforts to develop small field detection sensors such as magnetic particle detector.

However, conventional MI devices having millimeter dimension, despite their high MI ratio, cannot exploit the full capacity of MI effect because field measurement often involves spatially localized one. Moreover, since the MI effect is closely related to the magnetic permeability of the soft magnetic materials, impedance response to the external magnetic field shows basically non-linear and symmetric behavior which can be problematic for practical application. [4] In this work, we have fabricated calibrated Mi sensors with micro dimensions using $Co_{32}Fe_{32}Ni_{34}$ electroplated nanocrystalline wires which is expected to be adequate for localized magnetic field detection.

CoFeNi soft magnetic alloys with width: 30~70µm, length: 40~150 µm, and thickness: 1 µm were electroplated on silicon substrates. For electrical contacts, outer (inner) electrodes with 75 um (40 µm) in length were deposited on the wires by sputtering method. For ac measurement, we used a function generator as a signal source while the rms value of the device ac voltage was converted into dc value using Analog Devices AD8361 rf detector chip and then amplified in order to increase signal to noise ratio. This measurement technique is adequate for small ac signal measurement of which typical amplitude is less than a few hundreds of micro volts.

Figure 1. shows the MI profile of micro sized sensor. The maximum value of MI ratio of our devices with respect to external magnetic field was measured to be 22% as the ac current with the frequency of 22MHz and the power of 5dBm was applied. In order to obtain linear response, the device output was calibrated in the external field range of 0~10 Oe by numerically fitting sensor output to sigmoidal function and calculate inverse value from stored numerical coefficient. Figure 2. illustrates final output characteristic of the device. From linear fit, it was shown that the slope of the calibrated output is 1.00326 and has linearity of 0.7%FS. Futhermore, sensitivity of sensor output was found to be 4.1mV/Oe. Considering voltage detecting capability of conventional digital voltmeters, this result shows that the present device can detect magnetic field having magnitude less than 0.05Oe and spatial localization, in average, a few micro meters.

In summary, we have demonstrated that magneto impedance sensor can be miniaturized with retaining its macroscopic sensitivity. Although further work needs to be done in order to realize in-situ and dynamic detection of magnetic particle, it is expected that the calibrated sensor of this kind can be applied to the localized magnetic field detection such as chip-cytometer.

1. “Magneto-impedance effect in amorphous wires” L. V. Panina and K. Mohri Appl. Phys. Lett. 65, 1189 (1994)

2. “Giant magneto-impedance effect in nanostructured magnetic wires” M. Knobel, M. L. Sánchez, C. Gómez-Polo, P. Marín, M. Vázquez, and A. Hernando J. Appl. Phys. 79, 1646 (1996)

3. “Giant magneto-impedance effect in nanocrystalline glass-covered wires” H. Chiriac, T. A. Óvári, and C. S. Marinescu J. Appl. Phys. 83, 6584 (1998)

4. “Asymmetrical magneto-impedance effect in Fe-rich amorphous wires” C. Garcia, J. Gonzalez, A. Chizhik, A. Zhukov, and J. M. Blanco J. Appl. Phys. 95, 6756 (2004)

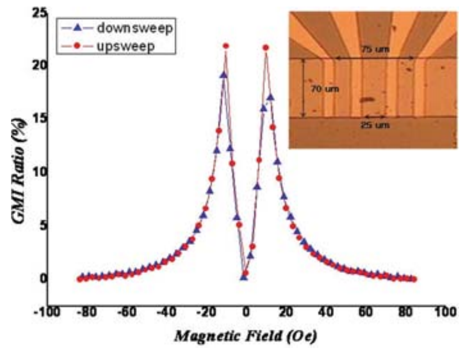

Figure 1. GMI profile of the micro scale particle detector. The inset shows the microscope image of the device.

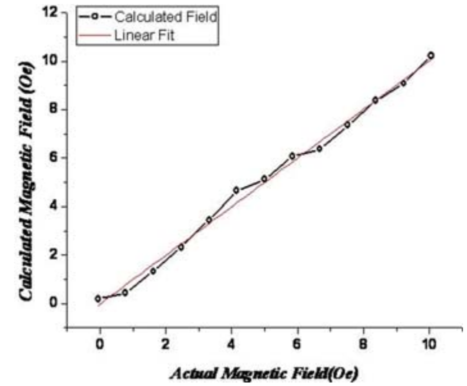

Figure 2. Calibrated sensor output characteristic.

BC-09

Development of Low Noise GMI Sensor and Its Applications.

H. Aoyama[1], M. Yamamoto[1], Y. Honkura[1], K. Sumi[2]
1. Electronic & magnetic product division, Aichi Steel Corporation, Tokai, Japan; 2. Toyota Central Research Laboratory, Nagakute, Japan

1. Background
Recently GMI sensors based on amorphous magnetic metal wire has been commercialized and is expanding its application fields. Major commercial applications include motion sensors for mobile phones and electronic compasses for automobile.
Although GMI sensor has potentiality to offer very high sensitivity of about 0.1nT resolution 1), commercialized products shows relatively low sensitivity, with the noise level of +/- 300-500nT. It is rather due to the cost/performance consideration for the nature of applications, which measures mainly geomagnetism. The authors tried to improve the sensitivity and attain lower noise level in order to expand the application field of the MI sensors.
2. Development
Low noise level of nano-tesla order was made possible by following 2 developments.
(1) Sensor element design
Special design is applied to achieve high sensitivity. Fig. 1 shows the magnified view of the element. Sensor coil is wrapped around the amorphous wire with the pitch of 50 microns with MEMS technology. The length of the wire is set to 4 mm, in order to reduce the demagnetizing field.
(2) Low noise electronic circuit (Fig. 2)
AC coupling is applied so that only the changing magnetic field can be effectively detected, and high resolution amplifier is selected. These measures create very high sensitivity with low noise level.
3. Results
Noise of the sensor output were observed in a magnetic shield tube. Fig. 3 shows the comparison of outputs between electronic compass product and developed sensor. Noise level were suppressed in +/- 0.5 nT. A photograph of the developed sensor is shown in Fig. 4.
4. Applications
Developed high sensitivity sensor enables new applications. One example is food inspection. This sensor was confirmed to detect an ferrous object as small as 0.3mm diameter in food. Second example is traffic counter. The sensor was able to detect minute magnetism that generated form an automobile even from the road side. From the detected signal, we can obtain passing car numbers, car speeds, and car lengths are calculated. Many other useful applications are expected.

1) K. Mohri et.al. IEEE Trans. Magn. Vol.38, No.5, SEPTEMBER, pp.3063-3068, 2002

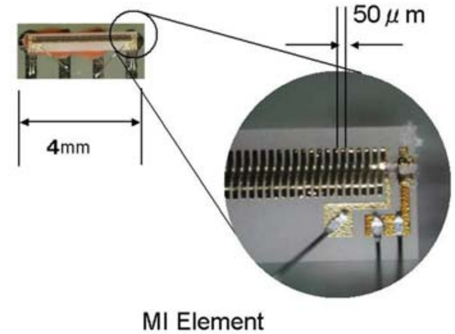

Fig. 1 Magnified view of MEMS MI element

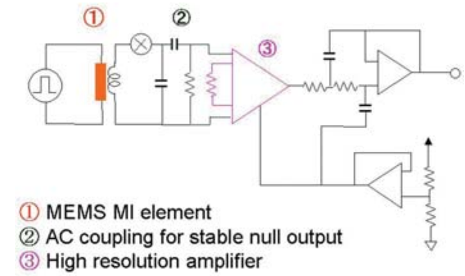

Fig.2 Low noise electronic circuit

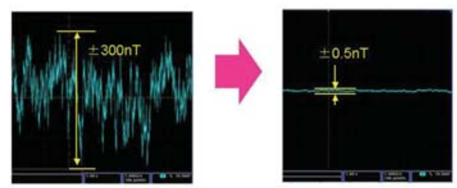

Fig. 3 Noise reduction

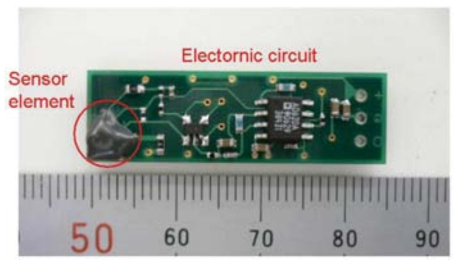

4. Developed MI sensor (35*11*6mm)

3-Axis Compact Electric Compass Using Maneto-Impedance Sensor.

M. Yamamoto, Y. Honkura
Aichi Steel Corporation, Aichi-ken, Japan

Introduction

Recently, the electronic compass used in the mobile phone is attracted in order to realize map heading up service. Various types of the electronics compass for mobile phone use such as FG sensor, MI sensor, Hall sensor and MR sensor had been developed and put into market. Only the 3-axis electric compass based on Magneto-impedance (MI) effect developed by Aichi Steel corp. successfully gave best performance to achieve most excellent azimuth accuracy and smallest size as well as low price and low current consumption1).

The performance of this 3-axis electronic compass has been greatly improved since MI element is much downsized2). Linearity is improved to 0.7%/FS, and hysterisis are much mininized. Accuracy of azimuth is improved from 5 degree to 2 degree.

MI type 3 axis compass3)

3-axis type of compact electronics compass has been developed and the internal structure is shown in Fig.1. Its size is 3.5 ×4.0×1.0mm. Different points of 3- axis type compass from 2-axis type compass is that its circuit has 3 MI elements, a switch alternating X, Y and Z type MI elements, 12 bit ADC and temperature sensor.

The downsized MI element shown in Fig. 2, has the size of 0.3 mm height, 0.6 mm length, 0.4 mm thickness, as small as one-third of previous one(0.93 mm length, 0.5 mm height, 0.28 mm thickness). Amorphous wire is also mininized from 20 m diameter to 10 m diameter. Hysterisis is much improved due to above improvements, so Linearity is improved.

When a pulsed current generated by the pulse generator circuit is run through the amorphous wire of 10 m diameter, the amorphous wire is magnetized. When external magnetic field is applied, an voltage is induced in the pickup coil of MI sensor element. The voltage is proportional to the external magnetic field strength.

Fig. 3 shows excellent 0.7%/FS linearity charateristics with 10 m diameter. Fig.4 shows the azimuth accuracy of 2 degree when measured from 0 to 360 degree of the direction against North due to linearity improvement and circuit noise improvement.

Applications

The compass with azimuth accuracy of 2 degree has been developed.Today the compass is widely used in mobile phone to make map heading up service with GPS. It also is used in the automobiles and boats to show the azimuth. In future, it is expected that map heading up service will be improved to move more smoothly and quickly.

[1] K. Mohri, Y. Honkura; Sensor Letters, Vol.5 No.2, pp.267-270 (2007)

[2] Y. Honkura, Electronic Journal 140th Technical Symposium, 2006.10.24, pp. 47-68 (2006)

[3] Aichi Micro Intelligent Corporation Profile.

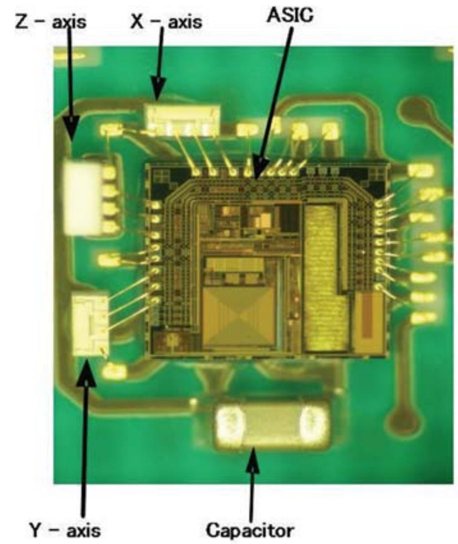

Fig 1. Configuration of 3-axis MI type Compass

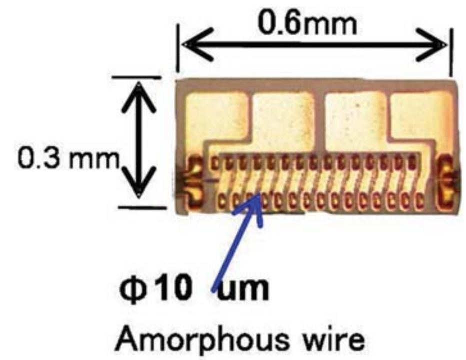

Fig. 2 Compact MI element with 10um amorphous wire

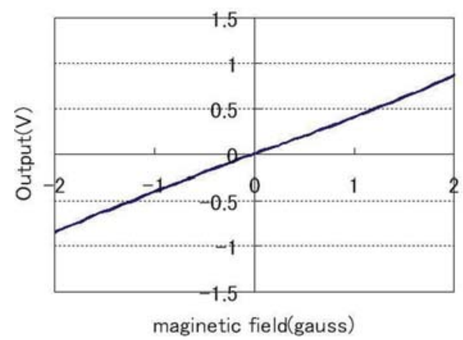

Fig. 3 Linearity Characteristics

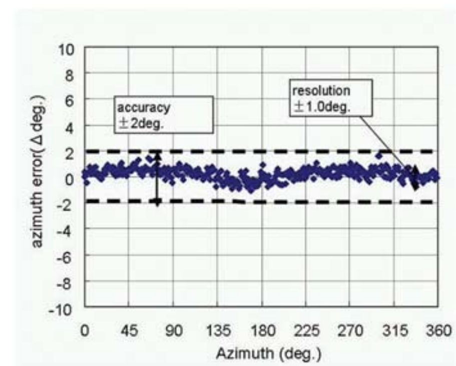

Fig. 4 Azimuth accuracy measured though whole angle

BD-01

Giant magnetoresistive sensors for DNA microarray.

L. Xu[1], H. Yu[2], S. Han[1], S. Osterfeld[1], R. L. White[1], N. Pourmand[2], S. X. Wang[1]
1. Materials Science and Engineering, Stanford University, Stanford, CA; 2. Stanford Genome Technology Center, Stanford University, Palo Alto, CA

Introduction

In recent years, Giant Magnetoresistive (GMR) sensors have shown a great potential as sensing elements for biomolecule detection[1-3]. GMR sensors are sensitive, can be easily integrated with electronics and microfluidics, and can generate fully electronic signals. The GMR detection system is also cheap and can be easily made portable. All these advantages make the GMR sensors attractive over the fluorescent sensors. In this work, we successfully deployed GMR sensors in a prototype DNA microarray. Prior researches[3] reported detection of DNA with concentrations above 1nM using GMR sensors. However, in order to be of use in most medical applications, the GMR sensors have to achieve a concentration sensitivity down to 1pM or less. With the help of "double modulation" detection technique and better surface chemistry, we accomplished detection of DNA samples down to ~10pM. Further research on microfluidics showed a great potential of improving the sensitivity to 1pM or below.

Materials and Methods

The principle of the GMR sensor is as follows: we coated the sensor surface with probe oligonucleotides. Target DNA sample was then applied onto the GMR sensor. Complementary target DNAs hybridized to the probe oligonucleotides and stayed on the sensor surface, while noncomplementary DNAs were washed away by rinsing. One end of the target DNA was modified to have a biotin group, which could bind to the streptavidin group attached to the magnetic nanoparticles. The stray field from the nanoparticles then generated the signal. A "double modulation" technique was used for signal readout. In this technique an AC magnetic field (frequency = 208Hz) was applied to excite the signal and an AC current (frequency = 500Hz) was passed through the sensor for signal readout. The interaction between the AC field and AC current generated a peak at 708Hz in the frequency domain. When the magnetic nanoparticles were at the vicinity of the GMR sensors, their stray field decreased the AC field sensed by the sensors, and therefore generated a signal change in the 708Hz peak. With this technique we could effectively reduce the 1/f noise, while eliminating electromagnetic interference at the same time.

Results

We performed DNA assays with various concentrations. The results are shown in Figure 1(a). The lowest concentration was 10pM, which gave signals of 2-4 uV. Scanning Electron Microscopy images of these assays were shown in Figure 1(b). The particle coverage corresponds well with the magnetic signal and the nominal DNA concentration.

One limiting factor for the sensitivity is the diffusion of target DNA to the sensor surface. To further improve the sensitivity, we are working on integrating microfluidics with the GMR sensors. Microfluidics can confine the DNA solution within the vicinity of the sensor surface. Therefore, the target DNAs do not need to travel a very long distance before binding to the probe oligonucletides. This can potentially improve the sensitivity and decrease the assay time. Figure 2 shows Scanning Electron Microscopy images of some preliminary experiments. The particle coverage of 10pM assay with microfluidics was higher than the corresponding 10pM assay without microfluidics, and the 1pM assay with microfluidics also showed decent particle coverage, indicating that microfluidic GMR sensors are very promising.

[1] M. Miller, et al, *"A DNA array sensor utilizing magnetic microbeads and magnetoelectronic detection"*, J. Magn. Magn. Mater. 225, 138-144 (2001)

[2] G. Li, et al, *"Spin valve sensors for ultrasensitive detection of superparamagnetic nanoparticles for biological applications"*, Sen. Actuators A, 126, 98-106 (2006)

[3] H. Ferreira, et al, *"Detection of Cystic Fibrosis Related DNA Targets Using AC Field Focusing of Magnetic Labels and Spin-Valve Sensors"*, IEEE Trans Magn, 41, 10, 4140-4142 (2005)

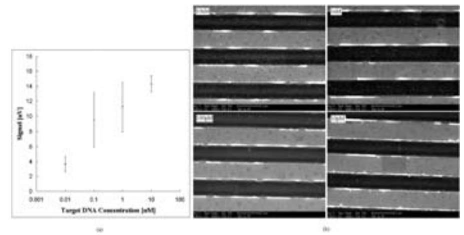

Fig 1 (a) Signals of DNA assays with various DNA concentrations; (b) Scanning Electron Microscopy images of the DNA assays.

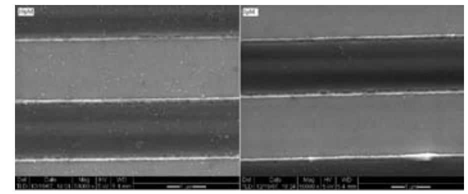

Fig 2 Scanning Electron Microscopy images of 10pM and 1pM DNA assays using microfluidics. Both assays finished within 45 minutes.

BD-02

Device for individualized detection of articles containing magnetic microwires based on ferromagnetic resonance.

P. Marín[1,2], D. Cortina[3], J. Calvo[3], *A. Hernando*[1,2]
1. Instituto de Magnetismo Aplicado, Universidad Complutense de Madrid, Las Rozas, Spain; 2. Departamento de Física de Materiales, Universidad Complutense de Madrid, Madrid, Spain; 3. Micromag 2000, S.L., Las Rozas, Spain

Glass coated amorphous microwires, show very interesting magnetic properties with a broadband range of applications. Among others, they present ferromagnetic resonance and therefore absorb electromagnetic energy on the microwave region of the spectrum. These microwires consist of an inner core of an amorphous metallic composition of typically tens of µm coated with glass. They are obtained by an extracting melt-spinning technique, based on Taylor's classical method [1]. The study of microwave properties is very promising technologically. At the microwave region (approaching GHz range), the ferromagnetic resonance occurs. As a rule, and using Kittel equation [2] for ferromagnetic resonance frequency, it is neccesary to apply a low frequency bias field to observe the effect.

The experiments realized show how a high frequency signal (1.28 GHz) can be modulated by the presence of a non bistable magnetic microwire. Figure 1 shows a draft of the set-up. A magnetic microwire of composition Fe2.25Co72.75Si10B15 is situated between Helmholtz coils conected to a low frequency (10 Hz) power supply. Simultaneously an electromagnetic wave (1.29 GHz), corresponding to microwire ferromagnetic resonance frequency, is generated by the emiting antenna. The modulated signal is received by the spectrum analyzer through the reception antenna.

The magnetization precesion at resonance frequency is only observed in a magnetically saturated microwire. So, the electromagnetic wave absorption occurs with bias field frequency.

Figure 2 shows the power level evolution with low frequency magnetic fiel intensity and the corresponding hysteresis loop. The temporal evolution of this signal is the consequence of high frequency signal modulation. The modulation effect can be modified by means of low frequency magnetic field intensity. The highest modulation is observed at microwire magnetic saturation. The modulation shape can be also modified by means of magnetic microwire low frequency hysteresis loop.

Based in this principle a device for individualized detection of articles containing magnetic microwires[3] has been developed. Figure 3 shows the electronic blocks diagramme. Each article to be identified has been tagged with a magnetic microwire characterised by certain hysteresis loop. The detection is based on high frequency signal modulation by means of ferromagnetic resonance. The signal detected my the reception antenna depends on microwire chacteristics.

[1]G.F. Taylor, Phys. Rev. 24 (1924)6555-6560

[2]C. Kittel, Phys. Rev.73 (1948)155 -161

[3] P. Marín, J. Calvo, D. Cortina, A. Hernando (ES200600336)

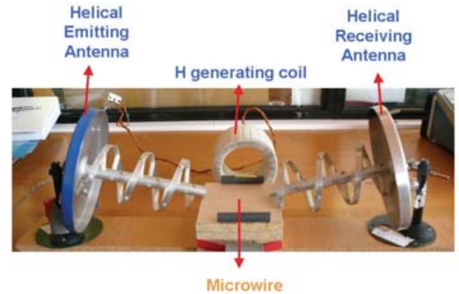

Experimental set-up for high frequency modulation

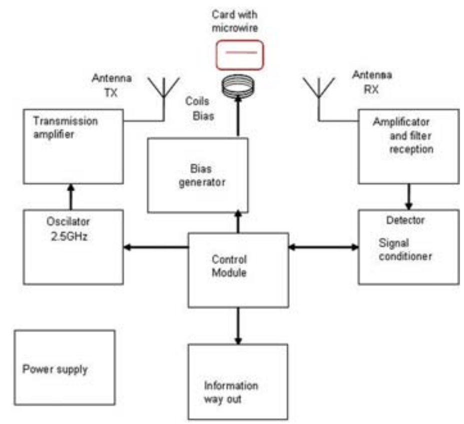

Block diagramme of identifier based on magnetic microwires ferromagnetic resonance

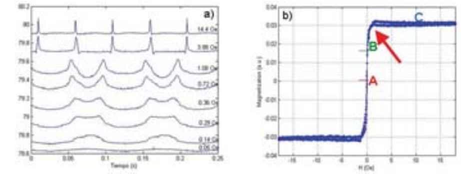

Influence of bias field intensity on power absorption level (a), hysteresis loop (b) for an FeCoSiB non bistable magnetic microwire

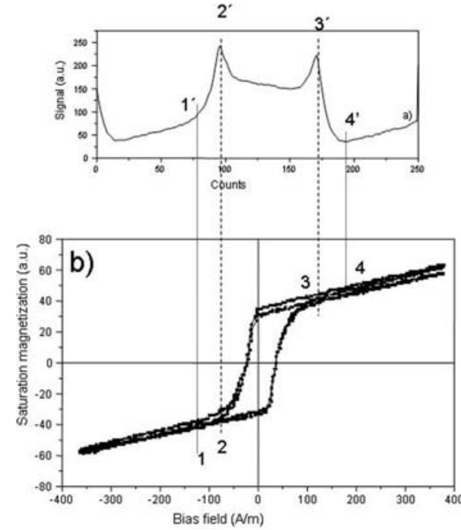

Corresponding detected signal for certain hysteresis loop

BD-03

Two-domain model for orthogonal fluxgate.

M. Butta, P. Ripka
CVUT v Praze - FEL - MagLab, Praha, Czech Republic

Orthogonal fluxgate has been patented in 1951; this principle was almost forgotten as the mainstream large-size parallel fluxgate has shown lower noise and better stability. Orthogonal fluxgates based on microwires and planar microstructures reappeared recently; these devices have a good potential for miniaturization as they need no excitation coil. The working mechanism of the orthogonal fluxgate has not been fully understood yet. In [1] Primdahl proposed a simple model describing the rotation of the magnetization M, due to the circumferential magnetic field HΦ. That model was based on the assumption of isotropy of the magnetic material; the first hypothesis Primdahl made, was the collinearity of B and H. Fundamental mode transverse fluxgate was later analysed by Sasada [2]; he has shown that this device cannot work without anisotropy.

Primdahl's model cannot be applied to the second-harmonic mode orthogonal fluxgates with electrodeposited magnetic wires. Measurement of the axial and longitudinal B-H loops (performed as explained in [3]) revealed significant anisotropy (as seen from Figs. 1 and 2). Moreover Primdahl's model cannot explain some typical features of the gating curves. Using this model we derived that the distance between the peaks in the gating curves depends linearly on the longitudinal field. We show that this is not true in the linear range of the fluxgate (Fig.3); the distance between the maxima changes only for high field values (i.e. comparable with the saturation field in circumferential direction). The observed distance between the peaks of the gating curve for small longitudinal field corresponds to the coercivity in circumferential direction (Fig.4).

We propose a new model for the mechanism of orthogonal fluxgates, suitable for electrodeposited magnetic wire. We assume the presence of easy axis of anisotropy in longitudinal direction, as typically found in these wires. Our model consists of two longitudinal domains with opposite direction of magnetization. The longitudinal field Hz causes domain wall movement from the central position: the domain with magnetization antiparallel to Hz becomes smaller (Fig.5). When we apply circumferential field HΦ, both the domains rotate in order to achieve the minimum energy direction between the easy axis and the orthogonal direction, where HΦ lies (Fig. 6). In the longitudinal direction we obtain net magnetization Mz due to the difference between the magnetic moments projected into the z axis. Mz is maximum when the domain magnetization has longitudinal direction, and decreases when HΦ rotates them towards circumferential direction. The resulting gating curve is shown in Fig. 7. If we take into the account also the hysteresis in circumferential direction, this gating curve must be modified: the magnetization vectors are aligned in longitudinal direction when the circumferential component zero, i.e. for HΦ equal to positive and negative coercivity. The resulting gating curve will have two peaks (Fig. 8), in correspondence to the coercivity in circumferential direction, as proven by the measurements (Fig.4).

We have performed experiments to validate the model, especially to verify difference in the roles between HΦ, which rotates the domains, and Hz, which moves the domain wall. The measurements were made on wires kindly supplied by S. Atalay [4].

This model can be also used to understand the coil-less fluxgate [5] mechanism, even if the detailed discussion about this topic is out of the scope of this paper.

[1] F. Primdahl: The fluxgate Mechanism, Part I: The Gating Curves of Parallel and Orthogonal Fluxgates. IEEE Trans. Magn. Vol. 6 (1970) pp. 376–383

[2] I. Sasada: Symmetric Response Obtained With an Orthogonal Fluxgate Operating in Fundamental Mode, IEEE Trans. Magn. 38 (2002) 3377-3379

[3] P. Ripka et al, Characterization of magnetic wires for fluxgate cores, Sens. Actuators A: Phys. (2007), in print, doi:10.1016/j.sna.2007.10.008

[4] S. Atalay et al, Magnetoimpedance effect in electroplated NiFeRu/Cu wire, J. Phys. D: Appl. Phys. 39 (2006) 431–436

[5] M. Butta et al, Fluxgate effect in twisted magnetic wires, Proc. SMM 18, 2007, p. 223

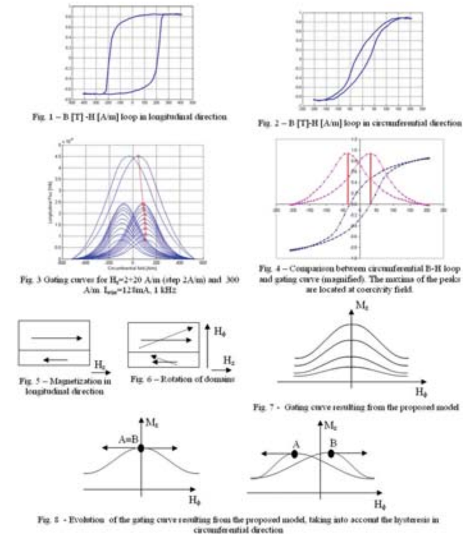

Figs.1-8

BD-04

Fabrication and characterization of magnetic tunnel junction field sensors with a Co_2MnSi thin film.

M. Masuda, T. Uemura, K. Matsuda, M. Yamamoto
Division of Electronics for Informatics, Graduate School of Information Science and Technology, Hokkaido University, Sapporo, Japan

Magnetic tunnel junctions (MTJs) with a Co-based full-Heusler alloy (Co_2YZ) thin film have attracted much interest as promising spintronic devices. We recently developed fully epitaxial MTJs with a Co_2YZ thin film and a MgO tunnel barrier, and demonstrated a relatively high tunnel magnetoresistance (TMR) ratio of 109% at RT (317% at 4.2 K) for $Co_2Cr_{0.6}Fe_{0.4}Al/MgO/Co_{50}Fe_{50}$ MTJs [1] and a TMR ratio of 90% at RT (192% at 4.2 K) for Co_2MnSi (CMS) /$MgO/Co_{50}Fe_{50}$ MTJs [2]. In these MTJs, the free layer of Co_2YZ was formed in the lower electrode. This is because the use of the Co_2YZ film as a lower electrode enables *in-situ* annealing at temperatures higher than 400°C for improving the film quality before growing both the MgO tunnel barrier and pinned upper layer. For field sensor applications, however, it is much more desirable for a free layer to be formed in the upper electrode so that the size and shape of the free layer can be easily controlled. In this study, we fabricated fully epitaxial MTJs with a CMS free layer for the upper electrode, and demonstrated relatively high TMR ratios by carefully optimizing the annealing temperature of the CMS upper electrode. Furthermore, shape-dependent TMR characteristics were obtained for field sensor applications.

The fabricated MTJ layer structure was as follow: (from the substrate side) MgO buffer (10 nm)/$Co_{50}Fe_{50}$ (40 nm)/IrMn (10 nm)/$Co_{90}Fe_{10}$ (2 nm)/Ru (0.8 nm)/$Co_{50}Fe_{50}$ (3 nm)/MgO barrier (2.5 nm)/CMS (50 nm)/Ru cap (5 nm)(CoFe/MgO/CMS-MTJ). The CMS and $Co_{50}Fe_{50}$ films were used as an upper free layer and a lower pinned layer, respectively. The magnetization direction of the lower $Co_{50}Fe_{50}$ layer was pinned through exchange biasing. All layers in the MTJ structure were successively deposited on a MgO(001) single-crystal substrate in an ultrahigh vacuum chamber (with a base pressure of about 8×10^{-8} Pa) through the combined use of magnetron sputtering and electron beam evaporation. The MgO buffer and tunnel barrier were deposited by electron beam evaporation at 400°C and RT, respectively. Other layers were deposited by magnetron sputtering at RT. After the deposition of the CMS layer, it was annealed *in-situ* at 300°C for 15 min. We fabricated MTJs with both memory and sensor configurations by controlling the shape of the CMS free layer. In the memory configuration, the easy axis direction of the magnetization of the CMS free layer is parallel to that of the $Co_{50}Fe_{50}$ pinned layer, while they are orthogonal each other in the sensor configuration. After the microfabrication, the MTJs were annealed at 325°C for 60 min in a vacuum of 5×10^{-2} Pa under a magnetic field of 5000 Oe to fix the magnetization direction of the $Co_{50}Fe_{50}$ electrode.

X-ray pole figure measurements for CMS111 diffraction revealed that the CMS upper electrode layer was grown epitaxially with the $L2_1$ structure. Figure 1 shows TMR major loops measured at RT and 4.2 K for a fabricated MTJ with a width (W) of 10 µm and length (L) of 50 µm. Here, the direction of L is defined along the pinned direction. The fabricated MTJs exhibited clear exchange-biased TMR characteristics with a relatively high TMR ratio of 94% at RT (209% at 4.2 K), a value comparable to that reported for MTJs with a CMS lower electrode and a $Co_{50}Fe_{50}$ upper electrode (90% at RT, 192% at 4.2 K) [2]. This result suggests that the annealing at 325°C improved the effective spin polarization of the CMS film without deterioration of the tunnel junction.

Figure 2 shows TMR minor loops at RT for MTJs with (a) W = 5 µm, L = 25 µm (memory configuration), and (b) W = 25 µm, L = 5 µm (sensor configuration). Anisotropic TMR characteristics, depending on the junction shape, were obtained. As shown in Fig. 2(b), inducing the shape anisotropy with the easy axis direction perpendicular to the pinned direction weakened the hysteresis nature. A field sensitivity of approximately 0.4%/Oe was obtained. Although a weak hysteresis nature remained mainly due to a formation of multiple magnetic domain structures, device-size reduction to a sub-micron length would lead to a hysteresis-free, linear response.

[1] T. Marukame, *et al*., Appl. Phys. Lett. 90, 012508 (2007).

[2] T. Ishikawa *et al*., Appl. Phys. Lett. 89, 0192505 (2006).

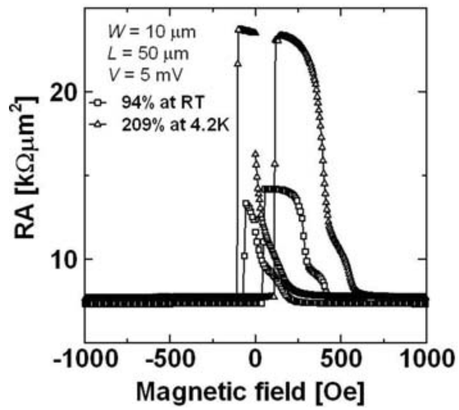

Fig. 1. TMR major loops at a bias voltage of 5 mV at RT and 4.2 K for a CoFe/MgO/CMS MTJ.

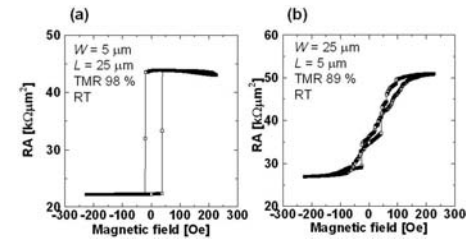

Fig. 2. TMR minor loops at a bias voltage of 5 mV at RT for a CoFe/MgO/CMS MTJ with (a) W = 5 µm and L = 25 µm (memory configuration) and (b) W = 25 µm and L = 5 µm (sensor configuration).

BD-05

High sensitive thin film wattmeter using magnetic thin film.

H. Tsujimoto, H. Toratani, Y. Deguti
Faculty of Engineering, Osaka City University, Osaka, Japan

Abstract
The new thin film wattmeter with the magneto resistance effect was proposed. The new magnetic thin film wattmeter has a three-layered structure (conductor film - insulation film – magnetic film). We could get the electric power consumption in the load from the voltage across the magnetic film along the current. We reported the circle shaped magnetic thin film wattmeter had the highest sensitivity by the results of computer simulation and the characteristic of the pre-production sample. We reported that the magnetic thin film wattmeter using the magnetic thin film was very useful as the embedded wattmeter into various electronic devices.

1. Introduction

Recently, the new energy such as the fuel battery is studying actively and the saving energy of the various electronic devices included household electric appliances are studying very much. The decrease of the electric power consumption is an important problem. The giant magnetic resistance effect (GMR) film has been applied to the magnetic recording head, the magnetic sensor, and so on, and those researches improve rapidly. We have reported that magnetic thin film device made by the magneto resistance effect film functions as a multiplier, a modulator and was used for the miniature wattmeter. The structure of the element is shown in the figure 1.
The characteristic when the form of the thin film wattmeter was made to change was analyzed. And the characteristic of the thin film wattmeter with a high sensitivity was studied with this paper.

2. Simulation and experiments

Fig.1 shows the basic structure of the thin film wattmeter by the magnetic thin film.
The thin film power meter has a three-layered structure. The top layer is a conductor film, the intermediate layer is an insulation layer and the bottom layer is a magnetic thin film with a magneto resistance effect. This power meter has two inputs and an output. One input is the current (I1) that flows through a load and another input is the current (I2) in proportion to applied voltage to the load. The current I1 flows the top layer of the thin film wattmeter and the current I2 flows in the magnetic film. The output is the voltage drop of the magnetic film along the current I2. The output voltage relates the electric power consumption in the load. The output characteristic of the thin film wattmeter was simulated and the output characteristic of the pre-production sample was measured.
The top layer of the pre-production thin film power meter is a conductor film (Cu: 25 um), the intermediate layer is an insulation film (Polyimide film: 25um) and a bottom layer is magnetic thin film (MR film:0. 1um). The width of the pre-production thin film power meter is 5mm and length is 21mm. When the electric power consumption in the load increased from 0 W to 70 W, the output of the wattmeter increased linearly from 0.32 V to 1.2 V. The frequency characteristic of the wattmeter was flat in the range of 2 kHz.
The changes of the resistance of the several wattmeters from the circle to the square were studied. Fig.2 shows the simulated characteristic of the resistance changes of the circle shaped wattmeter and the square shaped wattmeter when the input current I1 applied. The current I2 was 1mA. The diameter of circle wattmeter was 20 mm and the size of the square wattmeter was 20mm x 20m. The change of the resistance of the circle wattmeter was larger than that of the square wattmeter.
Fig.3 shows the characteristic of the resistance changes of the pre-production film wattmeter. The change of the resistance of the circle wattmeter was larger than that of the square wattmeter. As shown in Fig.1, the resistance change of the circle wattmeter of Fig.3 was about twice larger than B in the same as the result of Fig.2.

3. Summary

The new thin film wattmeter with the magneto resistance effect was proposed. We showed that we could get the electric power consumption in the load and that the circle shaped magnetic thin film wattmeter had the highest sensitivity. We reported that the new wattmeter was very useful as the embedded wattmeter.

1. H.Tsujimoto et.al,Technical report of IEE of Japan, MAG-98-218 (1998)

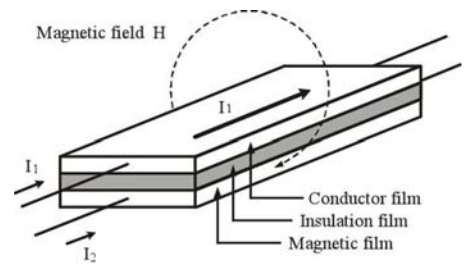

Fig.1 Basic construction of magnetic thin film watt meter

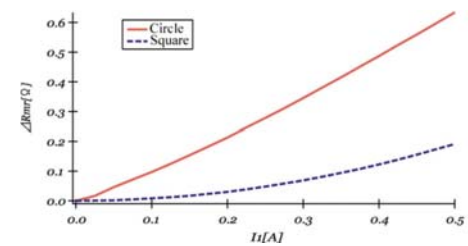

Fig.2 Simulated characteristic of the resistance changes of the circle shaped wattmeter and the square shaped wattmeter when the input current I1 applied. The current I2 was 1mA

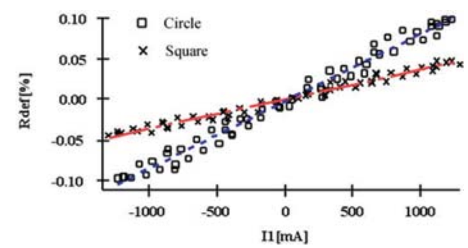

Fig.3 Characteristic of the resistance changes of the pre-production film wattmeter

BD-06

Acoustic Interferometer Based on Magnetostrictive Delay Lines.

C. Petridis[1], V. Vassiliou[1], M. Kollár[2], *E. Hristoforou*[1]
1. Mining and Metallurgy Engineering, National Technical University of Athens, Athens, Greece;
2. Electrical Engineering and Information Technology, Slovak University of Technology in Bratislava, Bratislava, Slovakia

This work presents an acoustic interferometer with absolute position measurement ability, based on the magnetostrictive delay line (MDL) technique actuated by sinusoidal elastic microstrains generated on the MDL. These microstrains produce a voltage output across a search coil, dependend on the position of this coil with respect to the excitation coil and being a superposition of the main propagating acoustic wave and the two reflected waves from the respective ends of the MDL. Determination of the position is accomplished by measuring the phase of individual harmonics of the voltage induced due to propagating magnetoelastic waves.
The position sensor is illustrated in Fig. 1. It comprises of a magnetostrictive $Fe_{77.5}Si_{7.5}B_{15}$ ribbon, to act as MDL and two coils made of enameled copper wire. Sinusoidal current is transmitted through the excitation coil. The sensing or search coil is connected with a lock-in amplifier for the output signal conditioning and processing.
The generated microstrains are governed by a Gaussian-type dependence on the applied field as was shown in [1]. Following our MDL model, it can be seen that the induced voltage is proportional to

$V_i \propto 1+k_0 \sin(2\omega t\text{-}2kl)-\sin(4\omega t\text{-}4kl)$ (1)

where k_0 and k are constants and l is the distance between the two coils.
Having set the excitation coil in a fixed position, then at a given excitation frequency, the change of the position x of the search coil results in a change of the induced voltage. Filtering particular harmonics one can record the amplitude or the phase of the 2nd or the 4th harmonic of the voltage induced in the sensing coil.
Change of the position of the search coil was checked by a laser interferometer during experiments. Figure 2 illustrates the 4th harmonic dependence on the distance in arrangement shown in Figure 1, at 30 kHz excitation frequency. The linear dependence as predicted by (1) can be observed, that is the proof of the absolute position ability measurement. The non linear behaviour at small displacements is due to the presence of ambient field caused by the excitation coil.
Figure 3 illustrates the phase dependence of the 2nd harmonic. A quazi-linear response can also be observed for this case. Figure 4 illustrates the dependence of the amplitude of the 4th harmonic, showing a non monotonic response (also qualitatively predicted by our model) that is clearly not suitable for measuring purposes. It is also evident that sensing of the 4th harmonic phase gives somewhat better results then that of 2nd. The sensitivity of the sensor, provided that the excitation coil is firmly fixed in position and well shielded, has been determined to be better than 5 μm. Such a sensitivity and the ability of measuring the absolute position of the search coil, makes the sensor able to operate in numerous applications.

[1] E. Hristoforou, P. Dimitropoulos, A new method for M-H and λ-H determination using the magnetostrictive delay line technique, J. Magn. Magn. Mater. 304 (2006) 164-167

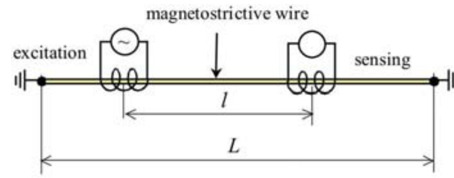

Fig.1. Magnetostrictive delay line (MDL) set-up

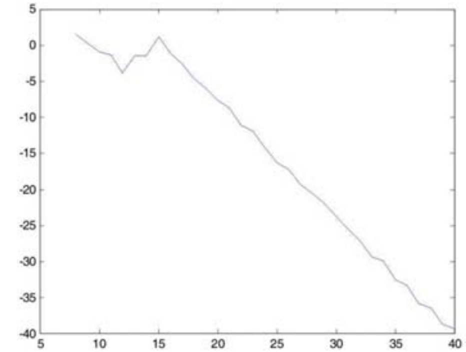

Fig. 2. The phase of the fourth harmonic at different positions of the search coil as a function of the distance *l*

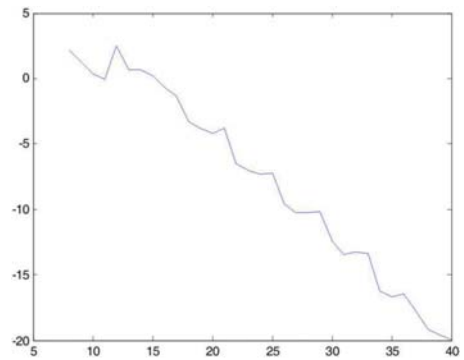

Fig. 3. The phase of the second harmonic at different positions of the search coil as a function of the distance *l*

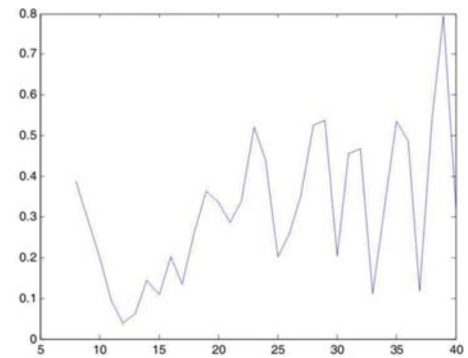

Fig. 4. Amplitude of the fourth harmonic at distance *l* of the search coil from the excitation spot

BD-07

2D magnetic sensor based on planar Hall effect and surface nano-structuration.

J. Briones, *F. Montaigne*, M. Hehn, G. Lengaigne, D. Lacour
Laboratoire de Physique des Matériaux, Nancy-University, CNRS, Vandoeuvre lès Nancy, France

A topological modulation of magnetic thin films can induce magnetic anisotropy originating from magnetostatic energy. The lateral modulation can be obtained by self-organization (ex. growth on step bunched substrates), either by a top-down approach (anisotropic chemical etching for V-grooves fabrication). The use of e-beam lithography allows us to achieve a better control of the modulation. Such a way, it is possible to change locally the periodicity and the direction of modulation. This can be used to elaborate 2D magnetic sensors based on the Hall planar effect. We will show that we have succeeded in realizing wavy shaped Si substrates with periodicities as low as 200 nm. An AFM picture recorded on a $Ni_{80}Fe_{20}$ thin film deposited on a prepared surface with a periodicity of 300 nm is presented in the figure 1 inset. First, we have investigated the magnetic properties of several magnetic mutilayers taking profit from their specific electronic transport properties. Indeed, the combination of anisotropy of magneto-resistance measurements (AMR) in different configurations with numerical simulations is a powerful tool to extract informations about the magnetic behaviour of our thin films. Without any modulation, our films always present an intrinsic anisotropy. We have demonstrated that patterning the substrate can counter this anisotropy and even impose a different easy axis of magnetization. AMR curves presented on the figure 1 show how we electrically determined the easy axis direction. The top and bottom AMR curves were obtained on NiFe films deposited on the same substrate but with orthogonal modulation directions. The black curves were recorded with a field applied along the current. On the contrary, the grey curves were obtained with a field applied in a direction perpendicular to the current. From this set of measurements, we can conclude without any ambiguity that the easy axes of magnetization are along the step direction in both cases. Moreover, the effect of thermal annealing under different field conditions has been studied. Once the control of local anisotropy by surface nano-structuration demonstrated, we have taken a step forward in designing and then developing a bidimensional magnetic sensor based on planar Hall effect. An optical photography of the magnetic sensor is presented in the inset of figure 2. The two active parts composing the sensor can be distinguished at center of macroscopic electrical leads paterned by a standard UV lithography process. The two active parts are composed of a thin NiFe layer deposited on wavy shaped substrate. The modulation directions are orthogonal for each part of the sensor thus, each of them has a sensitive direction perpendicular to the other. This allows to determined both the amplitude and the direction of an in-plan magnetic field. The figure 2 presents the eletrical response of one part of the sensor as a function of an magnetic field applied along its modulation direction. It can be noticed that the Hall planar effect delivers a linear reponse in the low field range as expected. More over the measure sentivity is as high as 75 V/T.A. To conclude, we have been able to demonstrate the concept of a high precision bidimentionnal magnetic sensor based on the combination of planar Hall effect and surface nano-structuration.

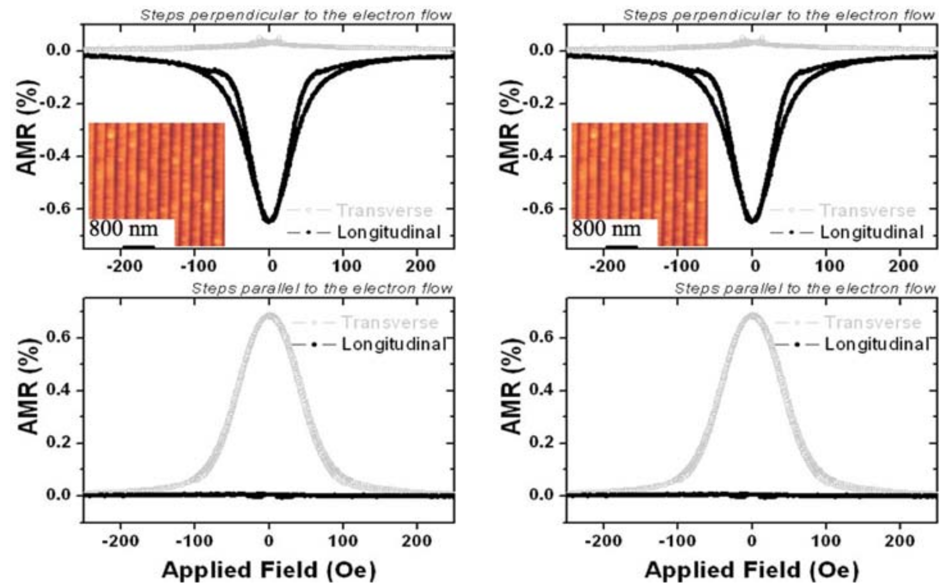

Fig. 1

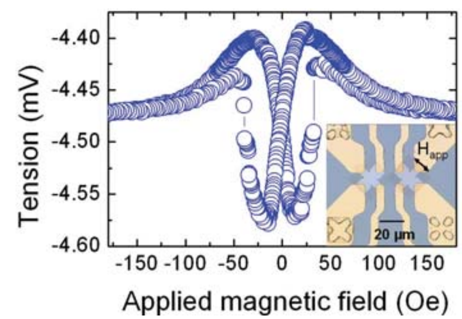

Fig. 2

Advanced Techniques for Modelling and Detection of Cracks in Hot Wire Steel.

R. Marklein, *M. Rahman*
Department of Electrical Engineering and Computer Science, University of Kassel, Kassel, Germany

Abstract
This paper presents innovative and advanced electromagnetic techniques for the in-line inspection of hot wire steel. The hot wire inspection procedure is performed with the eddy current (EC) sensor technique. Any type of crack on the upper surface of the steel wire disturbs the eddy current distribution, which can be detected by the eddy current sensors. However, the eddy current distribution is only weakly influenced by cracks, which are parallel to the wire, so-called longitudinal cracks. The conventional eddy current sensors cannot detect these cracks properly. To detect such longitudinal cracks a number of new EC sensors have been developed and successfully tested. Different numerical methods – the finite element method (FEM) and the boundary element method (BEM) have been used to model this NDT situation. The presented work is a part of the so-called INCOSTEEL project which is sponsored by the European Commission through the Research Fund for Coal and Steel (INCOSTEEL: In-line quality control of hot wire steel - Towards innovative contactless solutions and data fusion).

Statement of the Problem of Hot Wire Steel Inspection
The production of long steel products like steel wires, rods and bars within the steel market is subjected to very strict specifications, with regard to quality and reliability as well as in terms of increasing productivity. Non-destructive testing (NDT) techniques are widely used for quality assurance in steel manufacturing, e.g., for the detection and evaluation of all potential types of internal and surface defects. The goal of the project called INCOSTEEL is to optimise the in-line detection of transversal and longitudinal defects produced in the manufacturing process of hot wire steel of diameter D = 6 - 42 mm. Material assessment is carried out at a temperature of 1000°-1200° C at a rolling speed of up to 120 m/s. The aim of this presentation is to discuss the electromagnetic modelling techniques and to present the results of different EC sensors, developed for the INCOSTEEL project.

Simulation Results of Eddy Current (EC) Sensors
In this section the modelling of the detection of a crack with a point-coil (p-coil) sensor is reported (see Fig. 1). A p-coil sensor consists of a group of small elementary coils (see Fig. 1 a). Each element has the height of 3 mm and the diameter of 3.1 mm (see Fig. 1 b). 260 turns of copper wire is wound over a ferrite core to form a single element. In Fig. 1c the elements marked as 2 and 3 work as the receiving coils, while the other lone element works as the excitation coil. The simulations are performed by a 3-d eddy current simulation tool called Faraday, which is based on BEM technique.

Fig. 1c shows a snapshot of the detection process. 50 mm of a steel wire of the diameter D = 31 mm has been simulated here. The size of the crack is: length l = 10 mm, width w = 1 mm and depth d = 1 mm. The eddy current distribution on the steel surface is displayed in the bottom of Fig. 1c, where a excitation frequency of f = 74 kHz is used. The obtained voltage in the sensor coil is recorded and plotted on the top of Fig. 1c to determine the response of the sensor when a crack crosses the sensor.

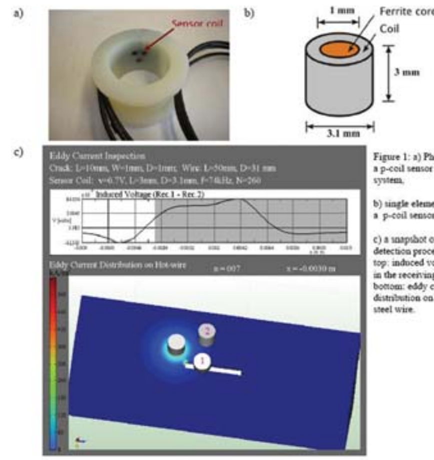

Figure 1: a) Photo of a p-coil sensor system.

b) single element of a p-coil sensor,

c) a snapshot of the detection process; top: induced voltage in the receiving coil, bottom: eddy current distribution on the steel wire.

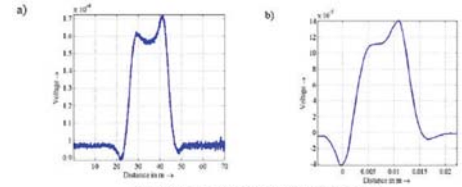

Figure 2: a) Experimental A-scan, b) synthetic A-scan.

Fig.2 shows the simulated A-scan (b) compared to the measured A-scan (a), which validates the predicted A-scan.

BD-09

Thermally modulated flux concentrator for minimizing 1/f noise in magnetic sensors.

W. Wang, Z. Jiang
Electrical Engineering, University of Wisconsin - Milwaukee, Milwaukee, WI

Magnetic Tunneling Junction (MTJ) based field sensor is a promising candidate for ultra-low field sensing [1-2]. However, MTJ's 1/f noise limits the low frequency sensing resolution, which is important in many medical and military applications. This impact can be minimized by modulating the field at 1kHz or higher frequency. Currently, the MEMS based modulation approach demonstrates the best results [1]. However, this approach suffers from low modulation efficiency and remaining magnetization in flux concentrator which impacts the sensing limitation. We propose a novel thermally modulated flux concentrator to overcome those two limiting factors.

The proposed approach is to replace the flux concentrator material from Permalloy or CoZrNb to magnetic materials with Curie points around sensing temperatures (room temperature in most cases). The field modulations can be achieved by modulating the flux concentrator's temperature around its Curie point, i.e. modulating the flux concentrator between ferromagnetic materials and paramagnetic material. Since the the flux concentrators are thin plates, their vertical thermal diffusion time is very short. If we take MnAs as an example, 20°C temperature range around Curie point (45°C) is enough for modulation purpose. The low frequency magnetic fields can be modulated at 1 kHz or higher frequencies, where the 1/f noise of magnetic sensors is greatly reduced.

The material selections are based on application temperatures. For the room temperature applications, MnAs (Tc at 45°C) and LaMn2Ge2 (Tc at 42°C) are the potential candidate materials.

Although MEMS based modulation approach has a much wider operation temperature range, the proposed approach has following advantages for the applications with predictable operation temperature, such as, medical applications.

(1)Higher Signal to Noise Ratio

Since there is no flux concentrator motion required, the gap between the flux concentrator and the magnetic sensor can be much smaller in the proposed approach. It's reported that 35% gain increasing was resulted from 0.5um gap reduction (5um to 4.5um) between magnetic sensor and the flux concentrator [3]. In contrast, the MEMS flux concentrator motion requires quite large margins on the minimum gap between magnetic sensor and flux concentrator. This margin inevitably leads to low modulation efficiency.

Since the downstream electronic measurement circuits filter out all signal components not at the modulation frequency, the final measured data are the modulated field components only. Higher modulation efficiency leads to higher signal level and signal to noise ratio.

(2)higher sensitivity

Although the easy axis of the flux concentrator is often designed in perpendicular to the field to be measured, there is still some hysteresis along flux concentrator's hard axis [3]. Similar hysteresis is expected in Permalloy based flux concentrator. Such hysteresis contributes to the sensitivity limit for low field sensing. In contrast, the proposed thermal modulation does not have such hysteresis. Magnetic domains are nucleated during each thermal modulation cycle.

(3)Less fringe fields from modulation driving sources

One possible implementation scheme for the proposed approach is to use laser beam to deliver the thermal energy and to remove the heat by passive cooling through substrate. Such implementation can separate the modulation driving source far from the magnetic sensor. Therefore, the fringe field from modulation driving source can be reduced significantly.

We've done a preliminary thermal analysis on the proposed thermally modulated flux concentrator. The flux concentrator is a pair of 50nm thick MnAs thin film trapezoids on 300μm thick GaAs substrate, whose bottom surface temperature is at 25°C. ANSYS thermal analysis results demonstrate successful field modulation with repeated heating and cooling cycles at 1kHz. The average heating power needed is 44mW for the flux concentrator with the same size of the MEMS based flux concentrator [1]. The cycle to cycle temperature repeatability is also simulated.

The left axis of Figure 1 shows the simulated temperature waveform within one cycle during stable operation. The stable operation condition is reached when the temperature difference between the start and end point of a given heating/cooling cycle is less than 0.01°C . The right axis of Fig. 1 shows the field amplification factor within one cycle under a constant external magnetic. The field amplification is completely lost when the temperature of the flux concentrator reaches Curie temperature (45°C for MnAs).

In summary, We presented a novel thermally modulation approach to reduce 1/f noise in MTJ based magnetic field sensor. The thermal analysis demonstrates the first order feasibility of the proposed approach.

(1)A. S. Edelstein, et al. Journal of Appl. Phys. 99, 08B317

(2) R. C. Chaves, et al. APPL. PHYS. LETT. 91, 102504

(3) A. Guedes, et al, IEEE Trans. on Magnetics, Vol. 43, No. 6,

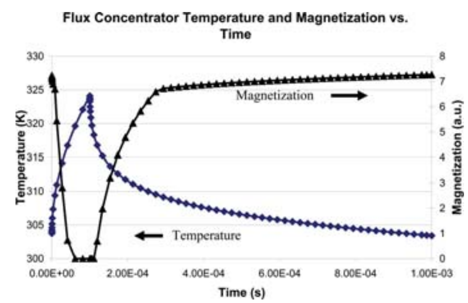

Figure 1. Flux concentrator temperature and magnetization waveform within one heating/cooling cycle

BD-10

Nanoscale InAs Hall Crosses Excited with Localized Magnetic and Electric Fields.

L. Folks[1], A. S. Troup[2], T. D. Boone[1], J. A. Katine[1], G. J. Sullivan[3], M. Field[3], E. Marinero[1], B. A. Gurney[1]
1. San Jose Research Center, Hitachi Global Storage Technologies, San Jose, CA; 2. Hitachi Cambridge Laboratory, Cambridge, United Kingdom; 3. Teledyne Scientific Company, Thousand Oaks, CA

We report scanning gate measurements that incorporate silicon probes coated with magnetic films to make the first measurements of the room temperature (RT) response of semiconductor Hall crosses to local applied magnetic fields under various local gate conditions [1-4]. The crosses consist of 400 nm and 100 nm wide shallow quantum wells of InAs (fig 1), and local gating was achieved by applying a voltage to the scanning probe. We have found that under certain small gate voltages (V_g) the devices are strongly responsive to the local magnetic field, and that the results may be described using a finite element model. This approach is useful for the design and optimization of local magnetic field sensors, such as those based on extraordinary magnetoresistance (EMR) effects.
The shallow AlSb / InAs / AlSb 2DEG used for these devices was 80 Å from the surface, and had a RT Hall mobility of 7,070 cm^2/Vs and carrier concentration of 1.9E12 /cm^2, as measured from mesoscopic van der Pauw samples. The RT mean free path of the electrons in the 2DEG is thus estimated to be around 160 nm. We have built Hall crosses with critical dimensions down to 100 nm (spanning the diffusive / ballistic transport transition) using electron beam lithography in combination with ion milling, and measured their response to uniform currents and magnetic fields, as well as to non-uniform magnetic and electric fields by scanning probe microscopy with both magnetic and non-magnetic probes.
In the 400 nm devices at low V_g we observe around 8 times higher Hall voltage signal when a magnetic probe rather than a non-magnetic probe is used. This magnetic signal is centered in the Hall cross, rather than having peaks at each of the corners as is observed for the non-magnetic probes, and reverses in sign when the magnetization of the probe is reversed. With the same magnetic probe, as V_g is increased the central signal peak elongates along the cross diagonal, changing orientation when V_g or magnetic probe field orientation is reversed (fig 2). These results are reproduced using a FEM model (fig 3) that incorporates the Lorentz force in the conductivity tensor and a standard parabolic semiconductor band structure with a band gap of 0.38 eV and Fermi level in zero bias at 0.15 eV above the conduction band. We also measure an asymmetry in the strength of the peak Hall voltage for positive and negative gate voltages, indicating that the resistance increase with negative bias is larger than the resistance decrease with positive bias.
In the 100 nm devices, in which we are entering the ballistic regime, we observe somewhat different behavior. At low V_g a single peak signal is observed at the center of the cross, as for the 400 nm devices. However, as V_g is increased in magnitude in either direction, the signal disappears from the center of the cross and flares instead in the voltage arms of the device (fig. 4), a behavior we have not observed in the 400 nm crosses. It appears that since the leads are now on the same length scale as the probe (probe diameter ~ 50 nm) we are able to scatter carriers into the voltage leads even when the probe is a considerable distance from the center of the cross.

1. H. Guillou, et al., J. Appl. Phys. 93 2746 (2003).

2. C. Cordier, et al., IEEE Sensors J. 5 934 (2005).

3. A. Baumgartner, et al., Phys. Rev. B 74 165426 (2006).

4. G. Papp and F. M. Peeters, J. Appl. Phys. 101 063715 (2007).

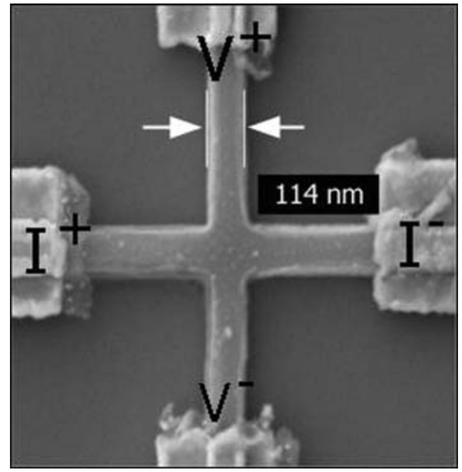

SEM image of a 100 nm Hall cross with current and voltage leads labeled.

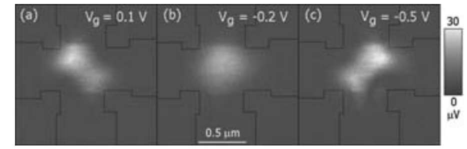

Maps of the absolute value of the local Hall voltage from a 400nm Hall cross with I = -0.2 mA scanned with a high moment magnetic tip, with V_g values as noted and the cross topography outlined in each panel.

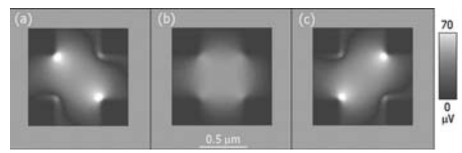

Computer model data for the absolute value of the local Hall voltage from a 400nm Hall cross under local magnetic and electric field conditions which match the experimental conditions in figure 2.

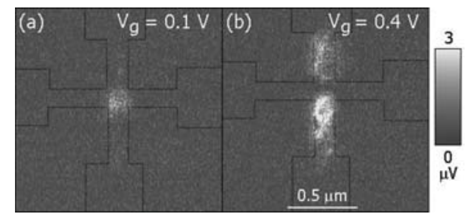

Maps of the absolute value of the local Hall voltage from a 100 nm cross with I = -0.15 mA scanned with a high moment tip, with V_g values as noted and the cross topography outlined in each panel.

BE-01

Field dependence of the magnetocaloric effect beyond the mean field approach: a universal curve for the magnetic entropy change.

V. Franco, A. Conde
Department of Condensed Matter Physics, Sevilla University, Sevilla, Spain

Currently, the field dependence of the magnetocaloric effect is being studied intensively for two main reasons. From a fundamental point of view, the analysis of this field dependence for different types of materials can give further clues of how to improve the performance of refrigerant materials for the magnetic field range employed in actual refrigerators (generally 10 to 20 kOe). From a practical point of view, the knowledge of the laws governing the field dependence of the magnetic entropy change can provide tools for making plausible extrapolations to magnetic field values outside the available experimental range in some laboratories.
The theoretical description of this field dependence has usually been made on the basis of a mean field approach, which corresponds to a power law of the field with an exponent 2/3. However, the authors have recently demonstrated that experimental data do not necessarily follow this $H^{2/3}$ law [1]. Instead, a relationship between the value of the exponent and the critical exponents of the material has been demonstrated.
The study of materials with a second order phase transition allowed finding a universal curve for the magnetic entropy change: not only the different magnetic entropy change curves of a material measured up to different maximum applied fields collapse onto a single curve, but also series of alloys with the same values of the critical exponent collapse onto the same curve [1,2]. This universal curve was initially derived in a purely phenomenological way using results of soft magnetic amorphous alloys. More recently, it has been applied to several crystalline rare earth alloys [3] and its existence can been demonstrated theoretically.
In this talk, the different procedures for constructing the universal curve will be described, outlining the demonstration of its existence and considering the particularities of different universality classes. This will be illustrated with experimental results from different types of materials, ranging from transition metal based alloys to rare-earth crystals and from bulk materials to nanoparticles. The practical applications of the universal curve (a tool for making extrapolations in temperature or field, and for enhancing the resolution of the experimental data close to the peak entropy change) will also be discussed.

[1] V. Franco, J.S. Blázquez, and A. Conde, Appl. Phys. Lett. 89, 222512 (2006).

[2] V. Franco, C.F. Conde, A. Conde, and L.F. Kiss, Appl. Phys. Lett. 90, 052509 (2007).

[3] V. Franco, A. Conde, V.K. Pecharsky, and K.A. Gschneidner, Jr., Europhys. Lett. 79, 47009 (2007).

BE-02

Isothermal and adiabatic measurements and modeling of sign switching magnetocaloric effect in NiMnSn.

L. Giudici[1,2], C. P. Sasso[1], M. Kuepferling[1], M. Pasquale[1], V. Basso[1]
1. Electromagnetism Department, INRIM, Torino, Italy; 2. Physics Department, Politecnico di Torino, Torino, Italy

Materials presenting Magnetocaloric Effect (MCE) are promising candidates for magnetic cooling technologies because they exhibit a first order magneto-structural phase transition induced by magnetic field which is accompanied by a large entropy change [1]. The accurate measurement of the entropy change as a function of temperature and field allows to classify an MCE material according to its refrigeration capacity. Materials presenting an inverse magneto caloric effect MCE effect have been recently discovered: the inverse MCE leads to an endothermal response under the application of field [2-4].
In this work we analyze a polycrystalline Ni-Mn-Sn sample which, depending on the initial sample temperature, presents both positive and a negative MCE features. Ni-Mn-Sn provides an ideal test for experimental and analytical methods used to estimate the MCE effect, since both endothermal and exothermal effects occur in a rapid sequence, in conjunction with a martensite to austenite magnetostructural phase transition.
In order to compare different experimental methods with a phenomenological model, direct isothermal entropy changes, $\Delta s(\Delta H)_T$, were determined using a calorimeter based on Peltier cells measuring the heat flux associated to an applied magnetic field up to $\mu_0 H = 2$ T [5]; the same experimental setup was used for calorimetric temperature scans in the presence of magnetic field to estimate Δs during heating/cooling at constant field. Adiabatic temperature changes $\Delta T(\Delta H)$ of the same sample were measured using a custom built cryomagnet insert under an applied field up to 7 T [6,7].
The phenomenological model used is based on the idea that the magnetic field changes the magneto-structural phase transition temperatures displacing the curves s(T;H) in the (s,T) plane. The s(T;H) curves are described by the following function (Fig.1):

$$s(T;H)=s_0 + c_{p0}\ln(T) + (c_{p1} - c_{p0})\int(1/T)x(T;H)dT + s_L(H)x(T), \qquad (1)$$

where c_{p0}/T and c_{p1}/T are the heat capacities of the martensite and austenite respectively, s_L is the entropy discontinuity at the first order phase transition and x(T) is the volume fraction of the sample occupied by the austenite. All these parameters can be determined fitting the integral of the specific heat in zero field measured by a calorimetry scan. The dependence from H and T of *x* gives the phase transition evolution. In the specific case: $x(T;H)=1/2\tanh[a(T-T_0(H))]+1/2$ and $T_0(H)$, the phase transition temperature, is inversely proportional to H in the case of the inverse magnetocaloric effect discussed here (Fig.1). The $\Delta s(\Delta H)_T$ and $\Delta T(\Delta H)$ can be predicted by comparing two s(T;H) curves made at two different fields, H_1 and H_2: $\Delta s(\Delta H)_T=s(T;H_2) - s(T;H_1)$; $\Delta T(\Delta H) = T(H_2;s) - T(H_1;s)$.
In order to achieve the same initial conditions, each $\Delta s(\Delta H)_T$ was measured after a zero field cooling to 270 K in order to completely transform back the sample to the low temperature martensite phase.
The comparison between isothermal entropy changes $\Delta s(\Delta H)_T$ and adiabatic temperature changes $\Delta T(\Delta H)$ measured at different temperatures T and field $\mu_0\Delta H = 2$ T shows that these two methods lead to results directly comparable in the framework of a simplified phenomenological model. The experimental $\Delta s(\Delta H)_T$ and $\Delta T(\Delta H)$ peaks in the temperature range of the inverse magnetocaloric effect, presented if Fig.2, can be predicted by the model assuming $T_0(\mu_0 H)= T_0 - [0.14\times(\mu_0 H)]$ K and $s_L(\mu_0 H) = s_L + [0.04\times(\mu_0 H)2]$ J kg^{-1} K^{-1} . The determined behavior of T_0, which shifts to lower temperatures as H increases, is in perfect agreement with temperature scan results performed at fields up to 2 T.

1)V. K. Pecharsky et al. Phys. Rev. B, 64, 144406, (2001)

2) J. Marcos et al., Phys. Rev. B 68, 094401 (2003)

3)T. Krenke et al., Nature Mat. 4, 450 (2005)

4)T. Tohei et al., J.App.Phys. 94, 1800 (2003)

5)M. Kuepferling et al.IEEE Trans. Magn. 43, 2764 (2007).

6)M.Pasquale et al., Phys. Rev. B 72, 094435 (2005)

7)M.Pasquale et al.,Appl. Phys. Lett. 91, 131904 (2007)

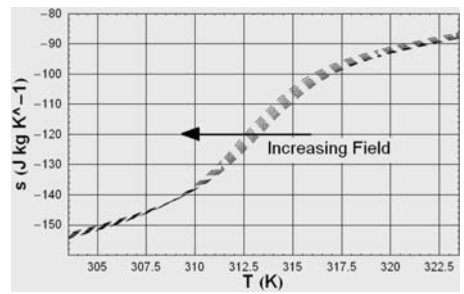

Model output of the s(T) curve in the martensite-to-austenite phase transition (increasing temperature). In the case of inverse magnetocaloric effect, the phase transition temperature is decreased by field application.

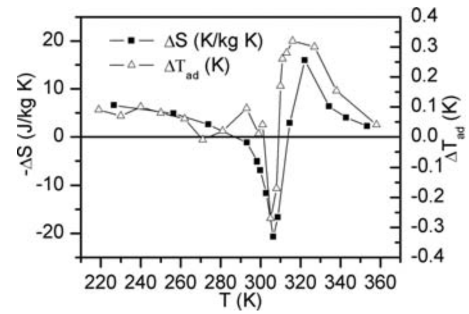

Isothermal entropy change ($\Delta s(\Delta H)_T$) and adiabatic temperature change ($\Delta T(\Delta H)_s$) measured during heating experiment for $\mu_0\Delta H$=2 T have been plotted together in order highlight their consistency.

BE-03

Magnetocaloric properties of $La(Fe,Co,Si)_{13}$ bulk material prepared by powder metallurgy.

M. Katter, V. Zellmann, G. Reppel, K. Uestuener
Vacuumschmelze GmbH & Co. KG, Hanau, Germany

Introduction:
The good magnetocaloric properties of intermetallic compounds based on $La(Fe,Si)_{13}$ make these materials very promising candidates as working materials for magnetic refrigeration at room temperature [1]. The preparation of bulk material by conventional casting is hindered by the very sluggish formation of the cubic $NaZn_{13}$ crystal structure which requires a long term homogenization heat treatment. The homogenization time can be reduced considerably by melt spinning or strip casting [2,3]. However, with these techniques no bulk material can be produced. It is the aim of this paper to describe an industrially applicable powder metallurgical production route to prepare fully dense bulk magnetocaloric materials with tightly controlled Curie temperatures based on $La(Fe,Co,Si)_{13}$.
Experimental:
Commercial powders of elemental Fe and Si were mixed with coarse powders of LaH_x as well as various La-Fe-Co-Si pre-alloys and milled in kg quantities in a jet mill under inert gas to a particle size of < 5 µm according to Fisher Sub Sive Sizer (F.S.S.S.). The powders were compacted either isostatically or in a die applying a pressure of 1.5 to 4 t/cm^2. The green parts were then sintered between 1333 K to 1433 K for 4 to 8 h under inert conditions. The density of the bulk samples was measured by the Archimedes principle. The magnetic properties were determined in a vibrating sample magnetometer for magnetic field strengths up to 17 kOe in the temperature range from 160 K to 370 K. The magnetic entropy change was deduced from these data according to the Maxwell relation $\Delta S = -\int(\partial M/\partial T)H dH$. For some samples also the adiabatic temperature change for a field variation of 17 kOe was measured directly in an electromagnet.
Results and Discussion:
Fig. 1 shows the magnetocaloric properties of ternary $La(Fe_{0,893}Si_{0,107})_{13}$ sintered at 1413 K to a density of 7.19 g/cm^3. The sample shows a strong first order type magnetocaloric effect. The magnetic entropy change for a field change of 16 kOe amounts to 21.9 J/kgK at a temperature of about 193 K. For this field change, the width of the entropy peak at half height, ΔT_{WHH}, is determined to be 6.6 K. The properties compare well with values reported in the literature for conventional cast, melt spun and strip cast material [1-3]. For a similar sample, a maximum adiabatic temperature change of 4.2 K was measured for a field change of 17 kOe. It is worth to mention that according to these results the $NaZn_{13}$ structure was obviously formed during reactive sintering out of the elemental starting powders without any melting and casting at all.
In order to increase the Curie temperature, the starting powders were blended with Co-rich powders, pressed in a rectangular die and sintered at 1353 K to a density of about 7.2 g/cm^3 and dimensions of about 23x19x13 mm. With the Co content increasing from 4.6 to 10.2 wt.%, the peak temperature increases from 254 to 336 K, the magnetic entropy change decreases from 9.4 to 4.5 kJ/kgK and ΔT_{WHH} increases from 13.7 to 31.5 K (all values for ΔH = 16 kOe), s. Fig. 2. The values are consistent with results reported for conventionally cast bulk samples [4]. The blocks can be machined by conventional techniques to the shapes required in magnetic refrigeration prototypes.
Conclusions:
Applying the powder metallurgical technique of reactive sintering, fully dense magnetocaloric bulk material based on La-Fe-Co-Si was produced in kg quantities. The Curie temperatures were tailored to the commercial relevant range from about 250 to 340 K. Such materials are available to be tested in magnetic refrigeration prototypes. The production process can be upscaled to industrial levels straight forward.

[1] A. Fujita, S. Fujidera, Y. Hasegawa and K. Fukamichi, Phys. Rev. B, vol. 67 (2003) 104416-1.

[2] O. Gutfleisch, A. Yan and K.-H. Müller, J. Appl. Phys., vol. 81 (2005) 036 102-1.

[3] S. Hirosawa, H. Tomizawa and K. Bekki, IEEE Trans. Magn., vol 42 (2006) 3608.

[4] F.X. Hu, J. Gao, X.L. Qian, Max Ilyn, A.M. Tishin, J.R. Sun and B.G. Shen, J. Appl. Phys., vol 97 (2005) 10M303-1.

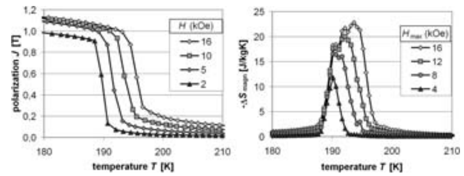

Figure 1: Temperature dependence of the polarization (left) and magnetic entropy change of sintered $La(Fe_{0,893}Si_{0,107})_{13}$ (right).

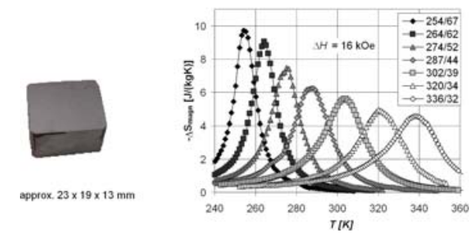

Fig. 2: Sintered La-Fe-Co-Si block (left) and magnetic entropy changes of various sintered La-Fe-Co-Si alloys (right). The inset lists the peak temperature in K and the maximum entropy change for a field change of 16 kOe in kJ/m^{3}K.

BE-04

Magnetocaloric Properties and Structure of the $Gd_5Ge_{1.8}Si_{1.8}Sn_{0.4}$ Compound.

V. Provenzano[1], T. Zhang[1,2], A. J. Shapiro[1], Y. G. Chen[2], R. D. Shull[1]
1. Magnetic Materials Group, NIST, Gaithersburg, MD; 2. School of Materials Science and Engineering, Sichuan University, Chengdu, China

In this paper we present the magnetic and microstructural results we obtained on the $Gd_5Ge_2Si_2$ compound doped with about 4.5 atom percent Sn; this doping level is 4 times that of our earlier studies [1, 2]. In the previous studies, we observed that doping the $Gd_5Ge_2Si_2$ compound with about 1% of either Fe, Al, Co, Cu, Ga, or Mn greatly reduced or completely eliminated its hysteretic losses as well as changing the characteristics of its magnetocaloric effect peak, whereas the same amount of Sn doping had instead negligible effect [1, 2]. The results of the present study provide valuable insight concerning the mechanism that different types of metal dopants have in both reducing the hysteresis losses and changing the characteristics of the magnetocaloric peak of $Gd_5Ge_2Si_2$.
The $Gd_5Ge_{1.8}Si_{1.8}Sn_{0.4}$ Sn-doped sample for this study was similarly prepared by arc melting as in the previous studies [1, 2]. Figure 1 shows respectively the room temperature x-ray powder diffraction spectra of the Gd_5Si_4 (A), $Gd_5Ge_2Si_2$ (B), and (C) $Gd_5Ge_{1.8}Si_{1.8}Sn_{0.4}$ compounds; the spectrum of the Gd_5Si_4 is analogous to that of $Gd_5Ge_2Si_2$ below its structural phase transition temperature of ~270 K. Thus, Figs. 1(A) and 1(B) respectively illustrate the typical orthorhombic and monoclinic structures of the undoped $Gd_5Ge_2Si_2$ below and above the phase transition temperature. Fig. 1(C), instead, shows that the spectrum peaks of the Sn-doped sample closely match those of the $Gd_5Ge_2Si_2$ monoclinic phase, with the exception of a slight shifting of the peaks to lower angles. This suggests that, at room temperature, similar to $Gd_5Ge_2Si_2$, the structure of the Sn-doped sample is monoclinic, except for a slight increase in the lattice parameters. These x-ray diffraction results are consistent with the corresponding microstructure and magnetic results. In fact, from the analysis of the SEM and EDS results, we concluded that about half of the tin atoms reside within the large grains of the main phase, while the other half segregated to the grain boundaries. This is different from what we had previously observed on $Gd_5Ge_2Si_2$ doped with either Fe, Al, Co, Cu, Ga or Mn, where the resulting microstructure consisted of a parent majority phase and a minority phase (rich in silicon and the respective doping element) [1, 2]. Consequently, the formation of the minority phase resulted in the partial depletion of Si from the majority phase [1, 2]. Figure 2 respectively show the M vs. H loops (A) and the entropy change, ΔS_m vs. T plot (B) for a ΔH=5 T of the $Gd_5Ge_{1.8}Si_{1.8}Sn_{0.4}$ sample. Similar to what we previously observed in $Gd_5Ge_2Si_2$ doped with about 1% Sn, the M vs. H loops shows the presence of hysteretic losses in the same temperature range where the ΔS_m vs. T plot exhibits a large magnetocaloric peak. Except for minor differences, the magnetocaloric properties (the hysteresis losses, Fig. 2A and magnetocaloric peak, Fig. 2B) of $Gd_5Ge_{1.8}Si_{1.8}Sn_{0.4}$ are basically the same as those of undoped $Gd_5Ge_2Si_2$.
To conclude, therefore, the present study conducted on $Gd_5Ge_{1.8}Si_{1.8}Sn_{0.4}$ re-enforces the previously stated hypothesis that the formation of a minority phase, rich in Si and the corresponding doping element is key for eliminating the hysteresis losses in $Gd_5Ge_2Si_2$ by suppressing the first-order orthorhombic-to-monoclinic field-induced phase transition. In fact, the x-ray diffraction spectra of the Fe-doped compound (taken both below and above the phase transition temperature, ~270 K) showed that it retained an orthorhombic structure in the 10-320 K temperature range. Consequently, the orthorhombic-to-monoclinic crystal phase transition did not occur [3], thereby preventing the reverse field-induced monoclinic-to-orthorhombic phase transition. Instead, for the present Sn-doped sample we showed that its magnetocaloric characteristics were similar those of the undoped $Gd_5Ge_2Si_2$. This finding, combined with the SEM and EDS results, showing that about half of the Sn atoms in $Gd_5Ge_{1.8}Si_{1.8}Sn_{0.4}$ reside substitutionally in the Ge-Si crystal lattice sites, while the other half segregated to the grain boundaries. This prevented the formation of a distinct minority phase (rich in Si) that is critical in both greatly reducing the hysteresis losses and changing the characteristics of the magnetocaloric peak of $Gd_5Ge_2Si_2$.

[1] R.D. Shull, et al., J. Appl. Phys. 99, 08K908 (2006).

[2] V. Provenzano, et al., Nature 429, 853 (2004).

[3] J.L. Her, et al., Mater. Trans., 46 2011 (2005).

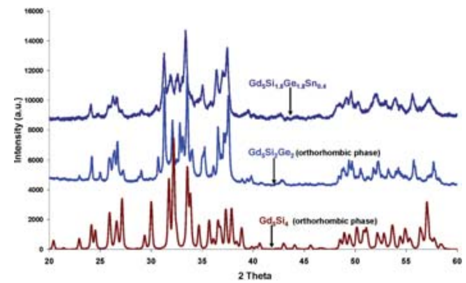

Figure 1 Room temperature x-ray diffraction spectra of: (A) Gd_5S_4, (B) $Gd_5Ge_2Si_2$ and (C) $Gd_5Ge_{1.8}Si_{1.8}Sn_{0.4}$.

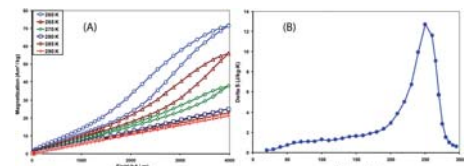

Figure 2 M vs. H loops (A) and -ΔS_m vs. T plot for ΔH=5 T (B) for $Gd_5Ge_{1.8}Si_{1.8}Sn_{0.4}$.

BE-05

Ferromagnetism in graphite induced by ion irradiation.

M. A. Ramos[1], A. Climent-Font[2], A. Muñoz-Martin[2], M. Garcia-Hernandez[3], A. Asenjo[3], P. D. Esquinazi[2,4]
1. Fisica de la Materia Condensada, Universidad Autonoma Madrid, Madrid, Spain; 2. Centro de Microanalisis de Madrid (CMAM), Universidad Autonoma Madrid, Madrid, Spain; 3. Instituto de Ciencia de Materiales de Madrid (ICMM), Consejo Superior de Investigaciones Cientificas (CSIC), Madrid, Spain; 4. Superconductivity and Magnetism Division, Institut für Experimentelle Physik II, Fakultät für Physik und Geowissenschaften, University of Leipzig, Leipzig, Germany

Pure graphite, the stable crystalline allotrope of carbon at room temperature and ambient pressure, is known to exhibit a strong and anisotropic "textbook" diamagnetism, due to its delocalized π electrons. Nevertheless, in the last two decades more or less clear evidences of ferromagnetic behavior in carbon at room temperature have been reported. And more recently [1-4], new findings of this kind have appeared in the literature, as the presence of ferromagnetic signals in proton-irradiated Highly-Oriented Pyrolitic Graphite (HOPG). In the latter experimental work, the analysis of possible magnetic impurities has been much more rigorous as to overcome the natural scepticism arose by the former experiments. Experiments employing x-ray magnetic circular dichroism [4] have demonstrated that the magnetic order in the investigated system originates only from the carbon π-electron system. Moreover, several theoretical works seem to support the importance of disorder [5] and/or of vacancy-hydrogen complexes [6] for the appearence of magnetic moments in graphite, though the true physical origin of these effects are unknown.
On the one hand, the possibility of intrinsic long range magnetic order in carbon is appealing from a fundamental scientific point of view because its existence in systems containing only s and p electrons is unusual and would demonstrate the importance of correlation effects between these electrons. On the other hand, the interest in producing organic materials with magnetic properties is obvious. Therefore, we have undertaken a joint research line to study this subject, by making use of the 5 MV tandem ion-accelerator hosted by the CMAM in the Universidad Autonoma de Madrid. At the same time of the ion implantation, the Particle-Induced X-ray Emission (PIXE) technique allows to determine in situ the amount of magnetic impurities in the sample, a crucial issue given the weakness of the reported ferromagnetic signals. The possible existence of ferromagnetism in HOPG samples has been studied [7] through SQUID magnetometry and Magnetic Force Microscopy (MFM).
In our first experiments [7] on this matter, we cut HOPG samples with a typical surface area of 17 mm^2 and 0.2 - 0.3 mm thick, using clean diamond wire. We conducted ion-beam irradiation of protons of 3 MeV energy, in high vacuum. Montecarlo SRIM simulations indicate a corresponding implantation depth of 75 micrometers for the H+ ions (protons). Spot size was here always about 1 mm^2. Total irradiated doses ranged 40 - 1000 microcoulomb. Using a SQUID magnetometer from Quantum Design, we have measured the magnetization of the samples, with magnetic fields applied parallel to graphene planes. After subtracting the linear (negative) diamagnetic background, in all cases a (weak) ferromagnetic curve was observed, with the sample of intermediate irradiation dose, 200 microcoulomb, exhibiting the higher ferromagnetic signal [7]. Nevertheless, we found somewhat surprisingly that also a non-irradiated HOPG sample exhibit some ferromagnetic signal, comparable with the samples of lesser magnetization. We discard the possibility of all this behaviour being due to magnetic impurities, since our PIXE experiments performed on some of these samples always gave concentrations below 10 ppm of Fe element, and indetectable for other magnetic impurities. Furthermore, a measurement performed under the very same conditions in a sample of powder graphite exhibited a perfect diamagnetic curve.
More recently, we have developed a specific sample holder, made of oxygen-free high-conductivity copper, appropriate to be employed both in the SQUID and in the ion-beam chambers, and to be transferred between them. So, the necessity is avoided of neither to touch the sample nor to add or remove any gluing substance, therefore assuring that one can really measure the net difference in magnetization of the graphite sample before and after ion irradiation, in these cases where the magnetic signals are so weak. Newly prepared HOPG samples present the same ferromagnetic curves as the former samples (with saturation magnetization around 4 10^-3 emu/g and coercive fields around 200 Oe) even before irradiation, likely due to the presence of defects and/or hydrogen already in the unirradiated samples. Finally, we have conducted experiments using protons, alpha particles and carbon as irradiating ions, under different conditions of energies and fluences, and discuss their effects on the magnetization curves of HOPG samples.

[1] P. Esquinazi, D. Spemann, R. Hohne, A. Setzer, K. H. Han, and T. Butz, Phys. Rev. Lett. 91, 227201 (2003).

[2] J. Barzola-Quiquia, P. Esquinazi, M. Rothermel, D. Spemann, T. Butz, and N. García, Phys. Rev. B 76, 161403 (2007).

[3] For a recent review, see P. Esquinazi et al., in Carbon-Based Magnetism, edited by T. Makarova and F. Palacio, Elsevier, Amsterdam, 2006, Chap. 19.

[4] H. Ohldag, T. Tyliszczak, R. Hohne, D. Spemann, P. Esquinazi, M. Ungureanu, and T. Butz, Phys. Rev. Lett. 98, 187204 (2007).

[5] M. A. Vozmediano, F. Guinea, M. P. Lopez-Sancho, cond-mat/0409567 (2004).

[6] P. O. Lehtinen, A. S. Foster, Y. Ma, A. Krasheninnikov, R. M. Nieminen, Phys. Rev. Lett.93, 187202 (2004).

[7] M. A. Ramos, A. Asenjo, M. Jaafar, A. Climent-Font, A. Muñoz-Martín, J. Camarero, M. García-Hernández, and M. Vázquez,

Progress in Industrial Mathematics at ECMI 2006, Bonilla, L.L.; Moscoso, M.; Platero, G.; Vega, J.M. (eds.), (Springer, Berlin-Heidelberg, 2007) 477-482.

BE-06

Magnetic properties of $TiO_2/\gamma\text{-}Fe_2O_3$ nanocomposites designed for photocatalytic applications.

V. Sechovsky[1], V. Tyrpekl[2], J. Poltierova Vejpravova[1], S. Danis[1], B. Bittova[1], D. Niznansky[2]
1. Department of Condensed Matter Physics, Charles University in Prague, Prague 2, Czech Republic; 2. DIC, Charles University Prague, Prague, Czech Republic

Photocatalysis is a fantastic way to clean facilities, living environments, and even reduce the spread of infections such as SARS in hospitals [1,2]. One of the most crucial tasks in water-works technologies is a separation of the photocatalyst from the liquid phase. Therefore we have designed a system constituted of a photoactive medium (nanocrystalline TiO_2 in the anatase modification) adsorbed on magnetic particles, which can be easily removed from the liquid phase by an applied magnetic field. In this work, we focus on magnetic characterization of the magnetically separable photocatalysts formed of maghemite nanoparticles coated by anatase. A series of samples was prepared by a novel synthetic technique described in [3] using a suspension of maghemite nanoparticles coated by citric acid (the final functional material was named after it: MagCit). The photoactive TiO_2 layer was subsequently adsorbed on the nanoparticle surface. The obtained products were dried and finally annealed at 100°C, 200 °C and 400 °C, respectively, to improve crystallinity of the originally amorphous anatase phase. The series of composites was characterized using powder X-ray diffraction (XRD), scanning electron microscopy (SEM), BET analysis, and transmission electron microscopies (TEM, HRTEM). The XRD patterns revealed maghemite phase (with C-type subcell) and anatase modification of TiO_2. The magnetite nanoparticles are covered by TiO_2 forming a needle-like microstructure (Figure 1, right panel) with high surface area, which is definitely more efficient for photocatalysis, than a compact monolayer. Magnetic properties of the prepared series were investigated by means of magnetization measurements in the temperature range 2 –350 K and magnetic fields up to 7 T. As an example, the room-temperature hysteresis loops are shown in Figure 2 (left panel). We observed no significant effect of the final heat treatment on the saturated magnetization value. The temperature dependence of the zero-field cooled (ZFC) and field-cooled (FC) magnetization (Figure 2, right panel), respectively, suggest a minor effect on the final particle size; the furcation point on the ZFC and FC curves appears at slightly lower temperatures for the MagCit sample annealed at 200 °C, probably caused by a slightly enhanced agglomeration rate in case of the higher annealing temperature.

In addition, an interesting feature was observed when comparing the maghemite particle size obtained from the XRD and magnetic measurements, respectively. While the characteristic scattering domain (equivalent to the mean particle size) in the XRD experiment is about 5 nm, results of the magnetic measurements suggest much larger particle size (20 nm). Detailed investigations by HR TEM method revealed, that the material consists of ~ 100 nm agglomerates of 3 – 5 nm maghemite nanoparticles, which are regularly coated by the anatase porous layer. Additional measurements of the a.c. magnetic susceptibility supported the idea of strongly interacting small magnetic particles (superferromagnetism [4]) with a typical range of the inter-particle interaction of about 25 nm.

<p>

[1] A. Fujishima and K. Honda, Nature: vol. 238, p. 37-8, 1972.

[2] A. Fujishima, K. Hashimoto, and T. Watanabe, TiO_2 Photocatalysis: Fundamentals and Applications. Tokyo: BKG, 1989.

[3] V. Tyrpekl, Diploma Thesis, Charles University Prague, 2008.

[4] S. Morup, J. Magn. Magn. Mater.: vol. 37, p.39, (1983)., S. Morup et al, J. Magn. Magn. Mater.: vol. 40, p.163, (1983).

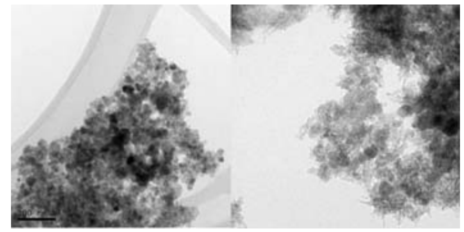

Figure 1: TEM images of the maghemite nanoparticles (left panel) and the final photoactive composite with anatase (right panel). The anatase (light grey) coats the magnetic nanoparticles (dark) in a form of needle-like, porous aglomerates.

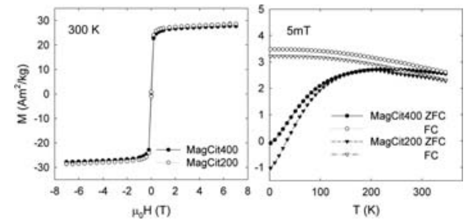

Figure 2: Magnetic properties of MagCit samples annealed at 400 °C and 200 °C, respectively. Left panel: room-temperature hysteresis loops, righ panel: temperature dependence of the zero-field cooled (ZFC) and field-cooled (FC) magnetization recorded at 5 mT.

BE-07

Elastic model for complex hysteresis in molecular magnets.

C. Enachescu[1], L. Stoleriu[1], A. Stancu[1], A. Hauser[2]
1. Department of Physics, Alexandru Ioan Cuza University, Iasi, Romania; 2. Department of Physical Chemistry, Universite de Geneve, Geneva, Switzerland

The spin transition solids [1] are molecular compounds belonging to the class of molecular magnets and are switchable between two states in thermodynamic competition: the diamagnetic low spin state (LS) and the paramagnetic high spin state (HS). The switch is accompanied by complex hysteretic processes that are fundamental for applications in information storage.
To understand this complex behavior, several models of the spin transition have been elaborated, involving short and long range interactions of elastic origin similar to the ones used in ferromagnetic materials [2]. The long range elastic interactions are due to the pressure which appears in the finite crystal as a consequence of the molecule volume and shape change. The short range interactions between two molecules depend on the distance between them and their orientation in the network.
In this paper we model the hysteretic behavior in a spin transition compound, considering the molecules situated in a bi-dimensional lattice and interacting with elastic connecting springs (fig. 1). The system size in the simulations is up to 4000 molecules.
At high temperature/low pressure the molecules are in the HS state; by changing the temperature or the pressure they can pass to LS state, if able to exceed the elastic force from closest springs. The switch of individual molecules is checked randomly with a Monte Carlo procedure. When a molecule changes its state, the new equilibrium positions of all molecules are calculated. The transition of a molecule from a state to another corresponds to a change of its volume and modifies the global interactions in the system and finally the position of each molecule (fig.2). The transition depends on random factors, but also on the status of the neighbor molecules.
In fig.3 we present experimental and simulated thermal hysteresis at various pressures, and we notice that they are in a good agreement. As expected, increasing pressure shifts the hysteresis loop in temperature.
In a previous work, we proved that the First-order reversal curves method provides valuable information on the interaction distributions in the sample [3]. In fig. 4, one can see simulated FORC curves for the thermal hysteresis at different pressures; we notice that the distribution is shifted towards higher temperatures but its shape does not change.
This model is able to correctly describe hysteresis in temperature and pressure. In the full paper, the role of interactions will be explained and a study concerning the size effects will be presented.
Acknowledgment: This work was supported by the European Network of Excellence MAGMAnet (FP6-515767-2)

[1]A. Hauser, Top. Curr. Chem., 234,155, 2004

[2]R. Tanasa, C. Enachescu, A. Stancu et al, Phys. Rev. B 71, 014431, 2005

[3]C. Enachescu, A. Stancu, et al. Phys. Rev. B, 72, 054413, 2005

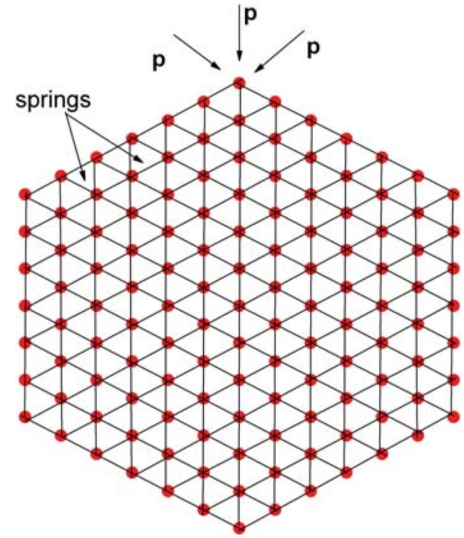

A hexagonal lattice with elastic connecting springs

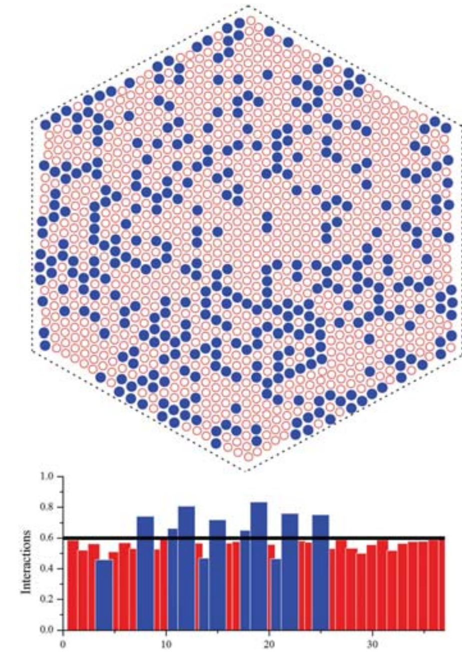

The position of molecules and interaction distributions during transition (full circles HS, open circles: LS).

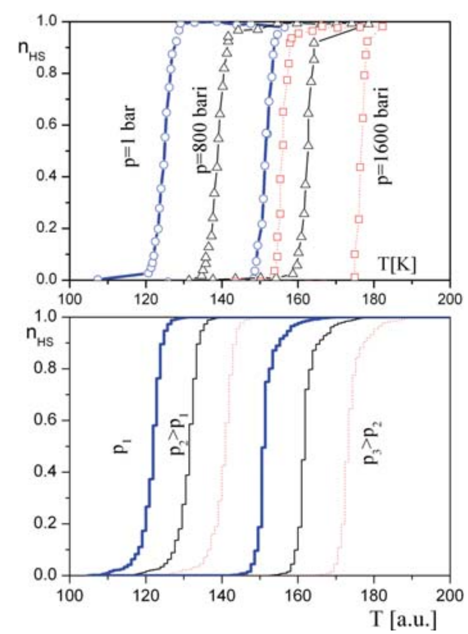

Thermal hysteresis at different pressures: experimental (up) and simulations (down)

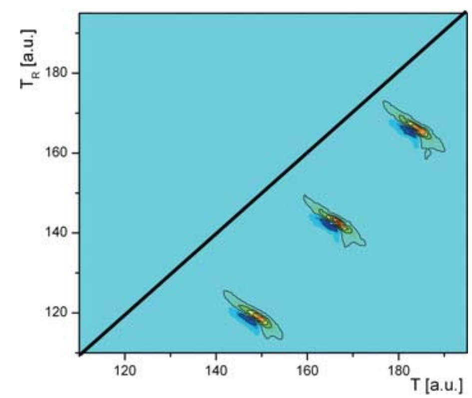

FORC distributions for thermal hysteresis at various pressures

BE-08

Various relaxation behaviors in one dimensional chain-like molecular magnet $[Fe^{II}(\Delta)Fe^{II}(\Lambda)(ox)_2(phen)_2]_n$ at low temperature.

J. Her[1,3], C. Sun[1,3], C. Chou[1,3], C. Chan[1,3], C. Lin[1,3], H. Yang[1,3], L. Li[2,4], K. Lin[2,4], S. Taran[1,3]
1. Department of Physics, National Sun Yat-sen University, Kaohsiung, Taiwan; 2. Department of Chemistry, National Chung-Hsing University, Taichung, Taiwan; 3. Center for Nanoscience and Nanotechnology, National Sun Yat-sen University, Kaohsiung, Taiwan; 4. Center of Nanoscience and Nanotechnology, National Chung-Hsing University, Taichung, Taiwan

Field-dependent (M(H)), thermoremanent (TRM) magnetization and AC susceptibility (χ'(T), χ''(T) and χ''(χ')) experiments of one dimensional chain-like molecular magnet $[Fe^{II}(\Delta)Fe^{II}(\Lambda)(ox)_2(phen)_2]_n$ have been performed.
The M(H) behavior of the sample measured at different temperatures has been shown in Fig. 1. The nature of M(H) loop is found to be varied with changing temperature. viz., i)for $T > T_m$(see the 10 K curve, T_m~8.6 K)[1,2], the M(H) curves behave like paramagnets; ii)for 7 K < T < T_m(see the 8 K curve), the magnetization value dramatically increases only with small applied field and shows no hysteresis loop, which is the characteristics of a soft magnet or superparamagnet (SPM); iii)for 2 K < T < 7 K(see the 2.5, 3 and 5 K curves), finite-size hysteresis loops have been observed, accompanied by a discontinuous step occurred at ~7000 Oe. The coercive field increases with decreasing temperature, however, the discontinuous step seems to be unchanged with varying temperature. iv)for T≦2 K(see the 2 and 1.7 K curves), the area of the hysteresis loop further increases and the discontinuous step becomes unobvious. In cases of i), ii) and iii), high field magnetization shows no hysteresis and no saturation even at our highest applying field 7 T. This behavior may be due to the presence of a paramagnetic region in our sample. In addition, the discontinuous step does not always present if we use different scanning interval. Since in most studies on molecular magnets, the field-sweeping rate is tuned to obtain different hysteresis loops[3], we achieve the same behavior by tuning the interval of scanning field. This is a strong evidence that our sample shows relaxation behavior.

TRM data of our sample measured at temperatures between 1.9~10 K can be quantitatively analyzed with stretched exponential[3,4].

$$m(t)=m_0\exp[-(t/\tau)^{\alpha}]+m_f$$

The relaxation of magnetization could be considered as a consequence of thermal activation between spin states. At low temperature, the temperature dependence of relaxation time, τ, can be fitted by Arrhenius law[5].

$$\tau=\tau_0\exp[E_a/k_BT]$$

Fig. 2 (solid square) shows the ln(τ) versus inverse T plot which represents Arrhenius law in form of straight line. The solid lines represent the Arrhenius law fitting results. From Fig. 2, two clear straight line portions are evident, signifying two distinguishable regions. The boundary between the regions is indicated by a gray square. The derived activation energies (E_a/k_B), comes out to be 70.9 and 47.1 K in high (I) and in low (II) temperature regions, respectively. The τ in the gray square region is too long to measure in laboratory, so that it is hard to determine the exact boundary temperature. Another approach to find out the boundary is the method used for SPMs. In SPMs, a characteristic freezing temperature (T_f) is of the order $E_a/25k_B$[5]. Although our sample is not SPM, the spin dynamics of most molecular magnets is quite similar to SPMs. Applying this relation to our results, gives T_f^I~2.8 K and T_f^{II}~1.9 K in region I and II, respectively. Therefore, we can propose a reasonable boundary temperature at 2.8 K, where the spins were frozen, leading to very long τ.

AC susceptibility is also a powerful tool to study the relaxation behavior. In χ'(T) and χ''(T) curves are found to be strongly frequency-dependent and the τ value has been calculated by oscillation frequency. In case of χ''(χ') (Cole-Cole plot), the τ value can be obtained by Debye model[6,7]. They're also plotted in Fig. 2 with open square and open triangle for temperature- and frequency-dependent magnetization curve, respectively.

Both DC and AC measurements show that there are at least three different phases below T_m. It might be caused by the structure frustration or presence of fractional cluster spin glass state.

[1] L. L. Li, K. J. Lin, C. J. Ho, C. P. Sun and H. D. Yang, Chem. Commun. 12, 1286 (2006)

[2] C. J. Ho, J. L. Her, C. P. Sun, C. C. Yang, C. L. Huang, C. C. Chou, L.-L. Li, K. J. Lin, W. H. Li, J. W. Lynn and H. D. Yang, Phys. Rev. B 76, 224417 (2007)

[3] J. Yoo, W. Wernsdorfer, E. C. Yang, M. Nakano, A. L. Rheingold and D. N. Hendrickson, Inorg. Chem. 44, 3377 (2005)

[4] C. Coulon, R. Clérac, L. Lecren, W. Wernsdorfer and H. Miyasaka, Phys. Rev. B 69, 132408 (2004)

[5] J. A. Mydosh, Spin glasses: an experimental introduction (Taylor & Francis, Inc., Bristol, 1993)

[6] K. S. Cole and R. H. Cole, J. Chem. Phys. 9, 341 (1941)

[7] R. Clérac, H. Miyasaka, M. Yamashita and C. Coulon, J. Am. Chem. Soc. 124, 12837 (2002)

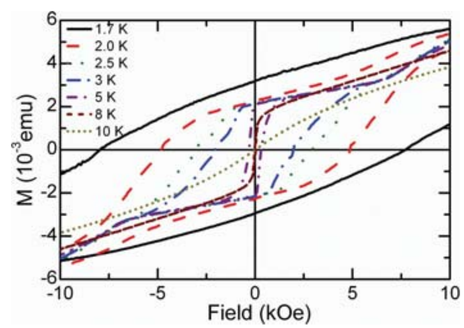

Fig. 1 Magnetic hysteresis

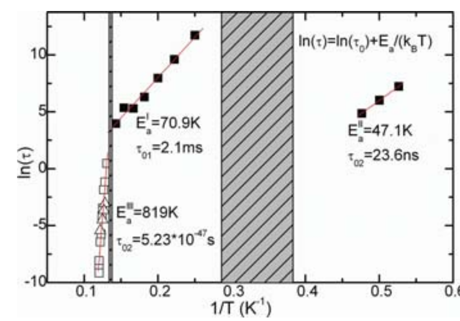

Fig. 2 Arrhenius law fitting results

BF-01

Study of the origin of the spin polarization in the Co-doped $(La,Sr)TiO_3$ diluted magnetic oxide.

O. Copie[1], G. Herranz[1], M. Bibes[1], R. Mattana[1], F. Petroff[1], K. Bouzehouane[1], H. Jaffres[1], E. Jacquet[1], J. Maurice[1], V. Cros[1], M. Basletic[2], E. Tafra[2], A. Hamzic[2], A. Barthelemy[1], P. Bencok[3]
1. Unité Mixte de Physique CNRS THALES, Palaiseau, France; 2. Department of Physics, Faculty of Science, University of Zagreb, Zagreb, Croatia; 3. European Synchrotron Radiation Facility, Grenoble, France

Spintronics applications require the use of highly spin-polarized current sources. For this purpose, half-metallic ferromagnets, such as various magnetic oxides, have been integrated in spintronic devices and high magnetoresistance values have been recorded. However, their Curie temperatures are too close to room temperature for technological applications. Another possibility to achieve high spin-polarized sources at high temperatures consists of doping the host materials with magnetic ions, as in diluted magnetic semiconductors [1]. We have followed this approach by doping metallic non-magnetic $(La,,Sr)TiO_3$ with 1,5% Co (CoLSTO) [2,3,4]. The samples were grown by pulsed laser deposition with a frequency-tripled Nd:YAG laser (λ = 355 nm) on $SrTiO_3$ (STO) (001) substrates.
In order to understand the origin of the magnetic properties of our CoLSTO samples (they revealed magnetic hysteresis cycles [2]), we have performed a broad study including micro- and nano-structural characterization, as well as the measurement of the spin-polarization through the analysis of the magnetotransport properties of tunnel junction devices using CoLSTO electrodes. Quite interestingly, we have found that growth conditions, such as oxygen partial pressure, have a relevant influence on the magnetic properties, probably revealing the role of defects, including oxygen vacancies, on the mechanisms leading to magnetic correlations.
It is well known that phase segregation is a major concern in these magnetic diluted systems [5]. Bearing this in mind, we have performed an extensive structural analysis of our samples combining X-ray diffraction, high-resolution transmission electron microscopy (HRTEM), electron energy-loss spectroscopy (EELS) and Auger spectroscopy. None of these experiments showed any direct evidence for the presence of Co-rich clusters.
To measure the spin polarization, CoLSTO tunnel junction devices with micro- and nanometric size have been fabricated either by optical lithography or by real-time resistance-controlled nanoindentation with a conductive AFM tip [6]. The measurements of the tunnel magnetoresistance (TMR) for the CoLSTO/LAO/Co junctions gave the TMR values up to 20%. (TMR is defined as TMR = $(R_p-R_{ap})/R_{ap}$, where R_p and R_{ap} are the resistances in parallel and anti-parallel configurations). Our TMR results enabled us to deduce that a spin polarization for the CoLSTO system is up to 80% [4]. We will address the dependence of the TMR and spin polarization on temperature and applied voltage bias, as well as the influence of growth conditions on the magnetotransport properties of these tunnel devices, with particular emphasis on the growth oxygen pressure.
Finally, in order to analyze better the origin of the ferromagnetism and spin polarization of CoLSTO films, we have carried out XMCD (X-ray Magnetic Circular Dichroism) experiments at the Co and Ti $L_{2,3}$ edges. These experiments have provided us with useful insights into the electronic states at the Co and Ti sites, which are relevant to understand the microscopic origins of the magnetic properties of the CoLSTO films. In particular, we will show that the spectral signature of both XAS (X-ray Absorption Spectroscopy) and XMCD indicates that cobalt is in ionic states.

[1] T.Dietl et al., Science 287, 1019 (2000)\\

[2] R. Ranchal et al., J. Appl. Phys. 98, 013514 (2005)

[3] G. Herranz et al., Phys. Rev. B 73, 064403 (2006)

[4] G. Herranz et al., Phys. Rev. Lett. 98, 216803 (2007).

[5] S.R Shinde et al., Phys. Rev. Lett. 92, 166601 (2004).

[6] K. Bouzehouane et al., Nanoletters 3, 1599 (2003).

BF-02

Ultrafast laser spectroscopy of GaMnAs.

E. Rozkotová[1], P. Horodyská[1], P. N ěmec[1], D. Sprinzl[1], F. Trojánek[1], P. Mal ý[1], V. Novák[2], K. Olejník[2], M. Cukr[2], T. Jungwirth[2]
1. Faculty of Mathematics and Physics, Charles University in Prague, Prague, Czech Republic;
2. Institute of Physics, AS CR, Prague, Czech Republic

Diluted magnetic semiconductors, with (Ga,Mn)As as a typical model material, have attracted attention for last few years due to the carrier-mediated origin of the ferromagnetism. This special feature enables to control the magnetization of the material also by changing the concentration of the carriers, which is very important property for future applications in semiconductor spintronics [1]. The carrier population can be modified by different methods, among which the optical injection of the carriers is the simplest one. The methods of ultrafast laser spectroscopy use a strong femtosecond laser pulse to inject the carriers and a second time-delayed laser pulse to probe the evolution of light-induced changes of material properties. Both carrier dynamics and magnetization dynamics can be investigated by these methods. In addition, the effects connected with the spin polarization of photoinjected carriers can be studied if the optical pumping is performed with circularly polarized light.

We measured simultaneously the dynamics of the sample reflectivity change and the polar Kerr rotation (KR) signal. The investigated samples were thin layers of ferromagnetic $Ga_{1-x}Mn_xAs$ (x = 0.058) grown by low temperature MBE. The experiments were performed both on as-grown and annealed samples. The easy axis of magnetization is in-plane for both samples. In Fig. 1 (a) we show the KR signal induced by linearly and circularly polarized laser pulses with no external magnetic field applied. The signal consists of two components. One part is strongly sensitive to the polarization of laser pulses and decays monotonously with the time delay. The second part is the same for linear and circular polarization of pump pulses and shows an oscillatory behavior. The polarization-independent part of the KR signal can be fitted well by a damped harmonic function superimposed on a time-dependent background for time delays above 50 ps. The deviation of the fit from the measured data in early stages of the dynamics indicates that ~ 50 ps is the time that is necessary for the oscillations to develop after the carriers are photoinjected. The duration of this transition region agrees well with the measured dynamics of the sample reflectivity change that reflects the (nonradiative) lifetime of the photoinjected carriers (electrons in particular). The dynamics of KR observed in the as-grown and the annealed samples are compared in Fig. 1 (b). The sample annealing resulted in an increase of both the oscillation angular frequency (21 GHz and 24 GHz in the as-grown sample and the annealed sample, respectively) and the oscillation damping time (0.4 ns and 1.1 ns, respectively) – those features are apparent in the Fourier transform of the oscillations as a small shift of the peak position and a considerable narrowing of the peak width (see Inset in Fig. 1 (b)). The frequency of oscillations is also strongly dependent on the laser intensity and the lattice temperature (not shown here).

The oscillatory behavior of the KR signal in (Ga,Mn)As was recently observed by two groups [2], [3]. The explanation of its origin was first proposed by A. Oiwa et al. [2]. They ascribed this phenomenon to the magnetization precession due to the change in magnetic anisotropy, which was induced by the presence of photoinjected carriers. On the other hand, J. Qi et al. [3] suggested that the reason for the anisotropy change could be the laser-induced temperature increase. In our case the estimated relative change of carrier concentration is only $\Delta p/p \sim 0.07$ %, which is highly improbable to cause any detectable change in the magnetic anisotropy. The observed relatively slow development of the oscillations also strongly favors the latter mechanism. Moreover, the duration of this transition region agrees well with the measured time when phonons were emitted by the nonradiative recombination of photoinjected carriers (i.e., when the lattice was heated up). The oscillation damping is connected with the Gilbert parameter in the Landau-Lifshitz-Gilbert equation [1]. Therefore, the suppression of the damping in the annealed sample reflects the improvement of sample magnetic properties by the annealing. This work was supported by Ministry of Education of the Czech Republic in the framework of the research centre LC510 and the research plan MSM 0021620834 and by the Grant Agency of the Charles University in Prague (Grants No. 252445 and FON/06/E002-FoNE-ERAS-CT-2003-980409)

[1] T. Jungwirth, J. Sinova, J. Ma šek, A. H. MacDonald, Rev. Mod. Phys. 78, 809 (2006).

[2] A. Oiwa, H. Takechi, H. Munekata, J. Supercond. 18, 9 (2005).

[3] J. Qi, Y. Xu, N.H. Tolk, X. Liu, J.K. Furdyna, I.E. Perakis, Appl. Phys. Lett. 91, 112506 (2007).

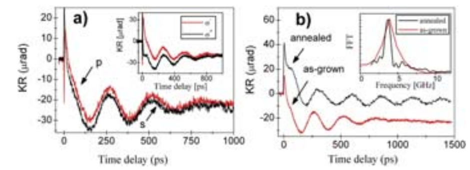

Fig.1: a) Dynamics of laser-induced Kerr rotation angle (KR) measured with linear polarization of pump pulses for the as-grown sample, T = 10 K, laser fluence 2.5 μJ.cm^{-2}, no external magnetic field applied. Inset: KR measured with circular polarization (CP) of pump pulses. b) Polarization-independent part of the KR signals for annealed and as-grown samples, which was defined as an average of the signals measured with opposite helicities of CP. Inset: Fourier transform of the oscillations.

BF-03

Preparation and properties of cobalt doped ZnO nanowires.

I. Enculescu[1], E. Matei[1], M. Sima[1], S. Granville[2], J. Ansermet[2], R. Neumann[3]
1. National Institute for Materials Physics, Magurele, Ilfov, Romania; 2. Institut de Physique des Nanostructures, EPFL, Lausanne, Switzerland; 3. Materials Research, GSI, Darmstadt, Germany

Nanowires are an important class of nanostructures with potential applications in a wide field of disciplines. Thus, such structures can be employed as building blocks for electronic or optoelectronic devices or as highly accurate sensors. This is the reason for which the field related to the preparation of nanowires of various materials increased strongly during the last decade.
The template approach represents one convenient method for obtaining nanowires with controlled morphology. As an example metallic nanowires with magnetic properties such as giant magnetoresistance or anisotropic magnetoresistance were prepared using electrochemical deposition in anodic alumina or ion track nanoporous membranes.
In this report we present our results on preparation of ZnO nanowires doped with cobalt. The templates employed were polycarbonate ion track templates, 30 micrometers thick, with cylindrical pores (diameters ranging from 50 to 600 nm).
Electrochemical deposition was employed to fill the pores with the desired material, cobalt doped ZnO nanowires being fabricated. The deposition was performed using a zinc nitrate bath (0.1 M) with the addition of cobalt nitrate (0.06 M). In figure 1 the electrochemical polarization and the chronoampermetric curves are presented for the cathodic processes employed in cobalt doped ZnO nanowire preparation.
As can be noticed from the figure 1(a) the deposition starts at a potential of approximately -600 mV with a plateau between -760 mV and – 900 mV followed by a strong increase of the current towards more electronegative potentials. We assume that a cobalt deposition takes place at more positive currents while the formation of ZnO becomes predominant at more negative potentials.
The results of SEM investigations and of the EDX analysis are presented in figure 2 for two deposition potentials, -800 and -1050 mV. As can be noticed the deposition at lower potentials leads to the formation of wires with a cobalt content of up to 5% while for more electronegative values of the deposition potential the cobalt content is almost negligible.

Magnetic measurements were performed up to this moment on two samples, one with highest Co concentration (5%) for a sample deposited at -760 mV and one with the lowest Co concentration (<1%) for a sample deposited at -1050 mV.

In figure 3 is shown the magnetic moment dependence as a function of temperature for the sample containing 5% Co, measured at 1 T, with the magnetic field aligned perpendicular to the length of the nanowires. This temperature dependence is typical for all the samples measured, at both perpendicular and parallel orientation of the magnetic field with respect to the nanowires' length, and at both 1 T and 50 mT field values. There are no magnetic transitions visible, no significant difference between the two curves at high or low temperatures, and the behaviour is as expected for a Curie or Curie-Weiss paramagnet.
In summary, arrays of ZnO nanowires doped with up to 5% Co were prepared. The approach allows an excellent control of dopant concentration by choosing the appropriate deposition potential. Thus, by this approach, one can tune the Co content in the nanowires by choosing the appropriate voltage of deposition. Such behaviour can led to the preparation of multisegment or multilayered nanowires in a similar manner in which multilayered metallic nanowires with GMR properties were obtained.The nanowire samples show paramagnetic-like temperature dependences. However, field loops at very low (2.5 K) temperatures suggest there may be a proportion of the Co moments that do not behave as purely paramagnetic J=9/2 ions, and this may indicate some weak interactions between them. Measurements are underway for samples doped with higher cobalt concentration.

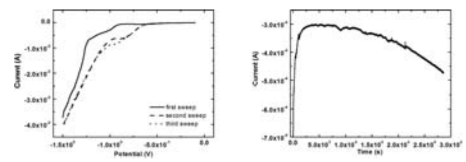

Figure 1. (a) Polarization curves for ZnO deposition. Pore diameter 600 nm, scan rate 5 mV/s. (b) chronoampermetric curve for Co doped ZnO nanowire preparation. Pore diameter 600 nm, deposition potential -760 mV.

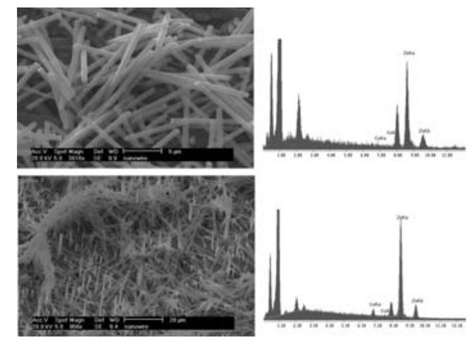

Figure 2. SEM and EDX data for (a) wires deposited at -800 mV and (b) wires deposited at -1100 mV.

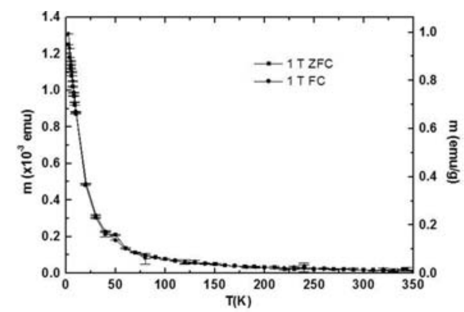

Figure 3. The magnetic moment dependence as a function of temperature for a sample containing 5% Co measured at 1T with the magnetic field aligned perpendicular to the length of the nanowire

BF-04

Room temperature ferromagnetism of FeCo-codoped ZnO nanorods prepared by chemical vapor deposition.

J. Chen[1], Y. Yan[2], J. Liu[1], M. Yu[1], A. West[1], *W. Zhou*[1]
1. Advanced Materials Research Institute, University of New Orleans, New Orleans, LA; 2. National Renewable Energy Laboratory, Golden, CO

.

INTRODUCTION

Spintronics is an emerging research field that tries to utilize electron spins as information processing media, which has attracted lots of attention due to its possibilities to enhance the performance of conventional electronic devices [1]. Diluted Magnetic Semiconductors (DMS) are among the most promising candidates for spintronics [2]. While low-dimensional DMS nanostructures are also highly pursued recently, attributing to their unique properties and the applications in nanodevices. Transitional-metal-doped ZnO nanowires or nanorods with room temperature ferromagnetism have been fabricated via various methods, though the origin of room temperature ferromagnetism is still being debated. In this article, room temperature ferromagnetic FeCo-codoped ZnO nanorods were fabricated by CVD and substitution of Fe and Co into ZnO lattice has been confirmed.

EXPERIMENT

The FeCo-codoped ZnO nanorods were synthesized following the procedures reported in previous experiments on Mn-doped ZnO nanowire arrays [3]. High purity Zn foil (Alfa Aesar, purity 99.998%, 0.25 mm thick), $CoCl_2\bullet 6H_2O$ powder (Alfa Aesar, purity 99.998%), and $FeCl_2$ powder (Alfa Aesar, 99.99%, ultra dry) with atomic ratio Zn:Fe:Co = 10:1:1 were used as source materials. Silicon wafers with 300 nm oxide layer were used to collect the products at the downstream and 10 mm away from the source materials. Different deposition temperatures have been used (in this report, 650°C, 750°C, 850°C). The morphologies of as-synthesized FeCo-codoped ZnO nanostructures were investigated by Carl Zeiss 1530 VP field-emission scanning electron microscope (FESEM). The transmission electron microscopy (TEM) and nanoprobe EDS were performed using a FEI Tecnai F20-UT microscope. The magnetic properties of the samples were measured by Quantum Design MPMS-5S superconducting quantum interference device (SQUID) magnetometer.

RESULTS AND DISCUSSION

Fig. 1(a) shows a low magnification TEM image of an (Fe, Co)-codoped ZnO nanowire prepared by CVD. Fig. 1(b)-(c) are the corresponding high resolution TEM images, which show that the nanowire is single crystalline with growth direction along the c-axis. The EDS spectra (Fig. 1(d)) reveal that both Fe and Co are detected at all sampling points and the concentrations of Fe and Co are about 0.8 at%. Fig. 2 is the M-H hysteresis loops of the nanorods at 300 K. The diamagnetic contributions from the silicon wafers have been subtracted from the data. The specimen grown at 850oC has the strongest room temperature ferromagnetic properties with a saturation magnetization ~0.012 emu/g and a coercive field ~100 Oe at room temperature. The results indicate that high deposition temperature will attribute to better magnetic doping and enhance the ferromagnetic ordering, however, once the deposition temperature exceeds certain level (in our case, 850°C).

.

[1] S. A. Wolf, D. D. Awschalom, R. A. Buhrman, J. M. Daughton, S. von Molnar, M. L. Roukes, A. Y. Chtchelkanova, and D. M. Treger, "Spintronics: A Spin-Based Electronics Vision for the Future," *Science*, vol. 294, pp. 1488, 2001.

[2] T. Dietl and H. Ohno,"Ferromagnetic III–V and II–VI Semiconductors," *MRS Bulletin*, vol. 28, pp. 714, 2003.

[3] J. J. Liu, M. H. Yu, and W. L. Zhou,"Well-aligned Mn-doped ZnO nanowires synthesized by a chemical vapor deposition method," *Appl. Phys. Lett.*, vol. 87, pp. 172505, 2005.

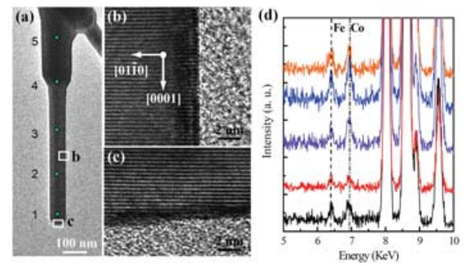

Fig. 1 (a) Low-magnification image showing the relative position of further HRTEM images and EDS sampling points. (b), (c) HRTEM images at the tip and side-wall areas of the nanowire. (d) Nanoprobe EDS spectra acquired at locations shown in figure (a).

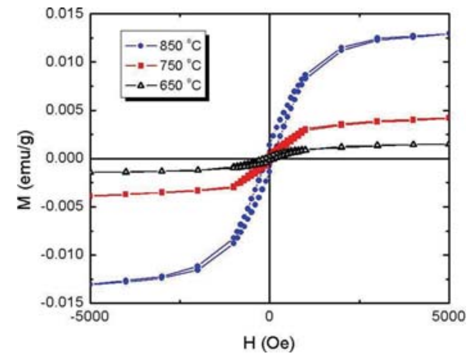

Fig. 2 Room temperature M-H hysteresis loops of FeCo-codoped ZnO nanostructures prepared by CVD at different substrate temperatures: 650°C, 750°C, 850°C.

BF-05

Magnetic interactions in (Zn,Co)O - effects of heat treatment and co-doping.

M. Wikberg[1], P. Svedlindh[1], V. Coleman[2,3], R. Knut[2], O. Karis[2], D. Iusan[2], B. Sanyal[2], G. Westin[3]
1. Engineering Sciences, Uppsala University, Uppsala, Sweden; 2. Physics, Uppsala University, Uppsala, Sweden; 3. Materials Chemistry, Uppsala University, Uppsala, Sweden

Diluted magnetic semiconductors have attracted interest both from theoretical and experimental standpoints. In particular transition metal doped ZnO has drawn much attention due to both theoretical predictions and experimental reports of high ferromagnetic transition temperatures (T_c). However, overall the reports have been inconclusive with results ranging from room temperature T_c to the absence of ferromagnetism even at cryogenic temperatures.
An extensive program has been set up to investigate magnetic interactions in Co-doped ZnO and its dependence on annealing conditions and co-doping. In this report we focus on (Zn,Co)O films with 5% Co and in some cases 0.8% Al, prepared by spin coating acetate-based solutions on quartz substrates. Subsequent heat treatments at 600°C or 800°C were performed for 1 hour in ambient or Ar atmosphere. The surface morphology and crystal microstructure of the films were investigated with scanning electron microscopy and grazing incidence X-ray diffraction. These investigations revealed uniform, polycrystalline, and most importantly phase pure films.
Electronic structure measurements were performed on beamline D1011 at MAX lab, Sweden, including X-ray absorption spectroscopy (XAS), X-ray photoelectron spectroscopy (XPS), resonant photoemission spectroscopy (RPES) and X-ray magnetic circular dichroism (XMCD). XMCD was recorded at remanence and showed no dichroism, which is consistent with magnetization results. We find that the Fermi level is located very close to the conduction band in all samples, indicating large amounts of intrinsic defects resulting in highly n-doped systems and also explains why Al co-doping does not affect the Fermi level. Occupied Co states can clearly be seen at the valence band (VB) edge by comparing ZnO and (Zn,Co)O XPS spectra. This conclusion is supported by the RPES results. Al co-doping does not significantly alter the VB of the pure ZnO but reduces the number of Co states at the VB edge for (Zn,CoAl)O. Increased absorption of Co 2p edges upon Al co-doping suggests that less Co 3d states are occupied. This leads to the conclusion that Al co-doping pushes the VB Co 3d states to higher energies.
Magnetic measurements were performed in a Quantum Design MPMS-XL Superconducting Quantum Interference Device (SQUID) magnetometer. Susceptibility (χ=M/H) vs. temperature (T) was studied between 375 K and 2 K, applying a field of 500 Oe. Magnetization (M) vs. field (H) measurements were performed at 2 K between 30 kOe and -30 kOe. The χ vs. T measurements reveal, for all measured samples, a paramagnetic behavior with no sign of a spin ordering even at the lowest temperature investigated. A clear difference in the magnetic response for different annealing conditions has been observed, with a higher magnetic moment for the samples annealed at 800°C (see inset Fig 1a) as well as an additional increase in magnetic moment if annealed in Ar flow instead of in ambient air, Fig 1b. Contrary to expectations, the carrier induced ferromagnetic behavior through Al-doping is not detected. Instead, a distinct decrease in magnetic moment is observed. The absence of magnetic hysteresis but a tendency of magnetic saturation for high applied fields, indicate that the dominating behavior is superparamagnetic and not ferromagnetic.
The electronic structure calculations have been performed using a Green's function Korringa-Kohn-Rostoker (KKR) method within the atomic sphere approximation (ASA). The local density approximation was used along with a spdf basis. In order to treat disorder, the Coherent Potential Approximation (CPA) has been employed. The Heisenberg pair-exchange parameters were calculated using the methodology of Liechtenstein et al.[1].
From calculations, values for the projected magnetic moment on Co atoms are $2.57\mu_B$ with short-range ferromagnetic Co-Co interaction. The calculated chemical interaction indicates a tendency for Co-clustering. The tendency for Co clustering is increased by co-doping with Al. If clustering is favored, some regions of the samples will contain a large concentration of Co. To simulate this situation, we have investigated the magnetic interaction for CoO in the zinc-blende and naturally occurring rock-salt structures. We have found that antiferromagnetic interaction between Co atoms is favored in both structures.
The absence of remanence in both XMCD and SQUID measurements together with the indication from calculations that cluster formation is favored, a tendency increasing with Al co-doping, lead us to the conclusion that the dominating magnetic behavior in (Zn,Co)O is superparamagnetic through the formation of randomly distributed Co-clusters. Although structural data indicates phase pure samples, regions rich in Co-content can not be excluded based on our structural and electronic characterizations. For clusters holding uncompensated spins at the surface, a small effective moment will be measured at low fields (Fig 1 b, moments derived from the low field slope of the M vs. H curves), well below the calculated value for Co atoms. The spins align with increasing field yielding the high magnetic moments detected at high fields (Fig 1b).

1. A.I. Liechtenstein, M.I Katsnelson, V.P. Antropov and V. A. Gubanov, J. Magn. Magn. Mater. 67, 65 (1987).

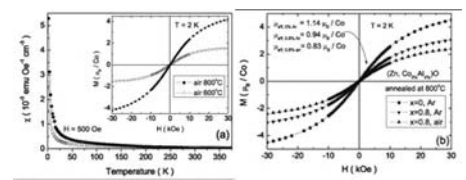

BF-06

Growth of $Zn_{1-x}Mn_xO$ nanorod arrays in aqueouse solution.

Y. Fang, J. Persson, M. Göthelid, J. Åkerman
Department of Microelectronics and Applied Physics, Royal Institute of Technology, Stockholm-Kista, Sweden

$Zn_{1-x}Mn_xO$ nanorod arrays have been grown in aqueous solution. The as-grown nanorods were characterized by scanning electron microscopy (SEM), X-ray energy-dispersive spectroscopy (XEDS) and X-ray photoelectron spectroscopy (XPS). The structure of $Zn_{1-x}Mn_xO$ nanorods is hexagonal and the arrays are uniform on the substrate. The incorporated Mn is around 5 at.% and the chemical state of the dopants is Mn^{4+}.

Dietl et al. have theoretically predicted that Mn doped p-type ZnO could show room temperature ferromagnetism [1]. To date, Mn-and Co-doped ZnO 1D nanostructures have been synthesized and room temperature ferromagnetism has been experimentally demonstrated by a number of research groups [2,3,4]. In this work, we use an aqueous solution method to grow $Zn_{1-x}Mn_xO$ nanorod arrays, which is novel, easy and energy saving.

$Zn_{1-x}Mn_xO$ nanorod arrays were grown on Si substrates coated with a magnetron sputtered ZnO seedlayer. The substrates were first cleaned by acetone, isopropanol and deionized water in an ultra-sonic bath. 100 ml of 0.025 mol/l zinc acetate dihydrate ($C_4H_6O_4Zn \bullet 2H_2O$) and 100 ml of 0.025 mol/l $Mn(NO_3)_2$ solution were mixed together with ammonia ($NH_3 \bullet H_2O$) slowly added into the solution until the pH value reached 10.8. The solution was heated to 90°C using a hot plate. Finally, the substrate was suspended in the solution for 3 hours with the sputtered surface facing down. As shown in Fig. 1, hexagonal nanorods with an average diameter of about 80~100 nm are clearly observed and the uniformity of the rods is good. Mn XEDS peaks in Fig. 2 indicate that the nanorods contain Mn and the atomic percent is about 5%. The nanorods also contain C about 5~6 at.%. One of the reagents in the aqueous solution is zinc acetate, which probably introduces the C contamination into the nanorods. In Fig. 3, the XPS data obtained for the wires can be observed both before and after annealing at 120°C and Ar sputtering for surface cleaning purposes. For Zn and O, the peaks are evident, and the only difference after sputtering and heating is that the intensity is increased and the water peak has disappeared. The sputtered lines show that the chemical state of the Mn is Mn^{4+}, according to the position of the peak at around 643 eV. The fact that the Mn has changed its state from 2+ (in the solution) to 4+ is evidence that points to the conclusion that the Mn has been incorporated into the ZnO lattice, and that it is not just residual Mn on the surface of the sample.

In summary, we have successfully grown uniform hexagonal $Zn_{1-x}Mn_xO$ nanorod arrays by using an aqueous solution method, which to the best of our knowledge has not yet been reported in the literature. XEDS and XPS spectra indicate that the Mn has diffused into the ZnO rather than it being residual Mn deposition on the surface. The investigation of the ferromagnetism of these $Zn_{1-x}Mn_xO$ nanorods is underway.

We gratefully acknowledge financial support from The Swedish Foundation for strategic Research (SSF), The Swedish Research Council (VR), The Göran Gustafsson Foundation and The Knut and Alice Wallenberg Foundation.

[1] T. Dietl, H. Ohno, F. Matsukura, J. Cibert, and D. Ferrand, Science 287, 1019 (2000).

[2] J.M. Baik and Jong-Lam Lee, Adv. Mater.17, 2745 (2005).

[3] U. Philipose and S. V. Nair, Appl. Phys. Lett. 88, 263101 (2006).

[4] A. Rahm et al., Microchim Acta 156, 21 (2007).

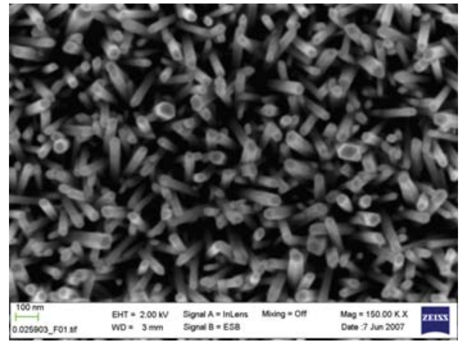

Fig.1. SEM image of the top veiw of the $Zn_{1-x}Mn_xO$ nanorods.

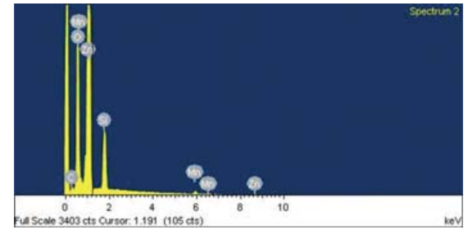

Fig.2. XEDS spectrum of the $Zn_{1-x}Mn_xO$ nanorods.

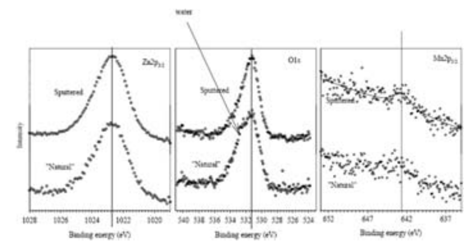

Fig.3. XPS spectrum of the $Zn_{1-x}Mn_xO$ nanorods.

BF-07

Investigation of ferromagnetism in N and Mn co-sputtered ZnO.

J. Persson[1], S. Bonetti[1], M. Göthelid[1], O. Tjernberg[1], J. Åkerman[1], M. Wikberg[2], O. Karis[2]
1. Material Physics, KTH, Kista, Sweden; 2. Departement of physics, Uppsala University, Uppsala, Sweden

ZnO is a promising material for new photonic applications due to its large bandgap (3.3eV) and exciton binding energy (60meV). It has also been predicted to be ferromagnetic at room temperature [1], providing a path to semiconductor spintronic applications. Several studies show that ferromagnetism is present in ZnO at room temperature: Ferromagnetic ZnO has been fabricated in bulk and in thin films with pulsed laser deposition [2] (a result disputed by [3]) and also by sputtering [4]. According to Dietls [1] theory the ferromagnetism in ZnO is mediated by holes in the case of Mn doping, thus co-doping with an acceptor species should increase the coupling between magnetic dopants and thus enhance the ferromagnetic behavior of the material. Room temperature ferromagnetism has indeed been shown by co doping where ZnO and Mn were sputtered in N_2 gas in order to introduce acceptors in the lattice [4]. Even though the majority carrier type was electrons, they argued that states introduced by the N acceptor mediated ferromagnetic coupling between the dopant atoms. It has been shown that the solubility of N is very low in ZnO even in a radical state [5], and that the presence of radical N species at the growth is important for an efficient doping. Therefore we propose to use a cyclotron resonance plasma source to enhance the number of N species present during sputtering growth.

The samples were prepared by co-sputtering of ZnO and Mn on Si substrates. The growth rates of each material was measured and adjusted to give a Mn concentration of 5at%. The sputtering gas was varied between Ar and N2, and a cyclotron plasma source was used in order to enhance the incorporation of N acceptors in the ZnO. The sputtering chamber was evacuated to $\sim 10^{-8}$ mTorr base pressure before sputtering. Temperatures were varied between RT and 450°C. The sputtering pressure was set to 2.5 mTorr. The flow rate was set to a maximum value of 20 sccm. This value was chosen to maximize the number of radical N species from the plasma source [6]. The samples where characterized with an XPERT high resolution x-ray diffraction (XRD) system and a Quantum Design SQUID magnetometer. The x-ray photoelectron spectroscopy (XPS) data was acquired in a custom made XPS system. X-ray magnetic circular dichroism (XMCD) data was taken at the European Synchrotron Radiation Facility (ESRF) in Grenoble. The XMCD signal was measured with the field perpendicular to the sample.

The films show a highly oriented growth, where the Mn doped samples show a small shift in the XRD spectra. It is evident that the incorporation of the Mn and N creates a small lattice distortion. The SQUID measurements show a hysteretic M-H loop at room temperature and at 10K, where samples grown with N_2 and specifically the samples grown with a plasma source enhancement of the N species show the strongest magnetic moment.

When the samples are investigated with XPS we find a shift in the N 1s and Mn2p peaks of the samples. The strongest N and Mn peaks correlate with the SQUID measurements.

XMCD measurements on the other hand show a paramagnetic behavior without any hysteresis.

The correlation between the strong N 1s peak in plasma grown samples and the strong magnetic moment of these samples would indicate that the N state has a strong influence on the ferromagnetism in ZnO, however the lack of XMCD data to support this theory will question similar results obtained where no magnetooptical measurement has been provided.

[1] Dietl et al Science 287, 1019 (2000)

[2] Sharma et al, Nature Materials 2, 673 - 677 (2003)

[3] Kundaliya et al, Nature Materials 3, 709 - 714 (2004)

[4] Xu et.al, Appl. Phys. Lett. 88, 242502 (2006)

[5] Fons et al, Phys Rev Lett 96, 045504 (2006)

[6] Weiler et al Appl Phys Lett 72, 1314 (1998)

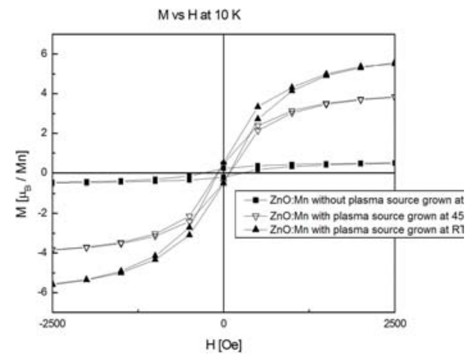

Squid measurements of ZnO:Mn at 10K

BF-08

Andreev and Optical Measurement of Spin polarisation in ZnO Based Dilute Magnetic Semiconductors.

J. R. Neal[1], K. Yates[2], A. J. Behan[1], D. S. Score[1], H. J. Blythe[1], A. M. Fox[1], L. F. Cohen[2], G. A. Gehring[1]
1. Physics and Astronomy, The University of Sheffield, Sheffield, United Kingdom; 2. Blackett Laboratory, Imperial College, London, United Kingdom

Recently there has been considerable interest into dilute magnetic semiconductors (DMS) since they were predicted[1] to exhibit ferromagnetism at room temperature. This has been driven by the aim of finding a material from which spin polarised currents may be injected, manipulated, usefully extracted and are also compatible with existing semiconductor technology.
ZnO based DMS materials have been shown to exhibit room temperature ferromagnetism[2,3]. However, progress has not been straight forward, as many of the techniques employed to characterise these materials are unable to distinguish between genuine DMS behaviour and secondary phases or ferromagnetic clusters within a semiconductor.
This study is concerned with the determination of the polarisation of the carriers, as devices may only be realised when there is a useful polarisation of the itinerant electrons within the DMS.
Here we report the use of Andreev reflectivity to directly measure the polarisation of the conduction electrons in doped ZnO. Andreev reflection occurs at a superconductor/conductor boundary where conduction across the boundary may occur. By measuring the differential conductance the polarisation of the conductor may be determined.
We also report the use of optical magnetic circular dichroism (MCD) to show that the room temperature ferromagnetism in these samples is associated with the ZnO lattice. MCD is a spectroscopic technique that is able to probe the band structure of the samples. When there is a splitting or unequal spin population of an energy band it leads to a differential absorption of circularly polarised light. Hence MCD can be used to identify where the magnetic moments reside in a material.
The thin film Zn(1-x)Co(x)O samples co-doped with up to 1% Al studied were grown by pulsed laser deposition (PLD) on Al_2O_3 (0001) substrates with Co concentrations of 5%. SQUID hysteresis loops of the doped films all show room temperature ferromagnetism, as has been observed previously [4,5,6]. By co-doping with Al, the number of carriers in the thin film was increased to produce carrier densities in the region of 10^21 cm-3 that exhibit metallic conductivity and large moments[7].
Figure 1 shows the Andreev spectrum for a 5% Co, 0.6% Al doped ZnO sample with a moment of 0.6μB/Co, grown at an oxygen pressure of 10^-5 Torr, measured at 4.2K . The data is fitted for the ballistic regime and due to the high contact resistance, the spreading resistance is negligible. From the inset, which shows the reliability of the fit, it can be seen that the polarisation in the sample is 44%.
In order to check that the observed polarisation was not due to metallic Co clusters[8] the signal was measured at many points and no variation was detected.
The 300K MCD spectra, measured in a field of 0.5T, for a 5% Co and 0.6% Al doped ZnO film 240nm thick, with a moment of 0.4μB/Co, grown at 10^-2Torr, is presented in fig 2. The large signal observed at the ZnO band edge (3.35eV) indicates that the ZnO band electrons are polarised and the observed ferromagnetism is intrinsic to the host ZnO and not due to defect phases.
Furthermore, the strength of the Co2+ d-d* feature at 1.95eV is larger than would be expected for paramagnetic Co2+ ions[9]. This indicates that the Co2+ ions experience a strong exchange field from the ferromagnetism and hence we can rule out the possibility of Co clusters as the primary source of the observed magnetism[10].
To conclude, we have demonstrated that when Co doped ZnO is co-doped with Al to produce a suitability high carrier density the thin films can exhibit large moments. Also, the splitting of the ZnO conduction band gives rise to a substantial spin polarisation of the conduction electrons which have the potential for exploitation in spintronic devices.

1.T. Dietl,Science,287,1019(2000)

2.P. Sharma,Nat. Mater. 2,673(2003)

3.J.R. Neal et al,PRL. 96,197208(2006)

4.M. Venkatesan,PRL. 93,177206(2004).

5.Ü. Özgür,JAP. 98,041301(2005).

6.A.J. Behan et al,PRL.In print(2008)

7.J.M.D. Coey,Nat. Mater.4,173(2005)

8.W. Pacuski et al,PRB73,035214(2006)

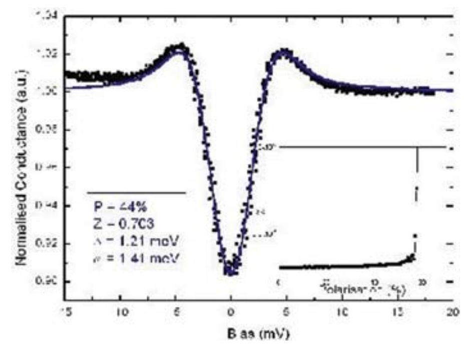

Figure 1: Andreev spectra for a Zn0.944Co0.05Al0.006O thin film. The solid line is a fit to theory for ballistic conductivity and yields a polarisation of 44% for the conduction electrons.

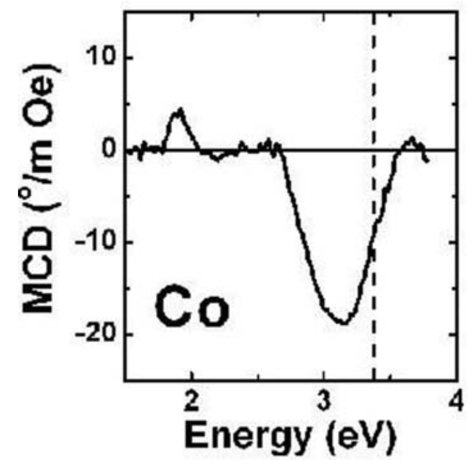

Figure 2: 300K MCD spectra for a Zn0.944Co0.05Al0.006O thin film. The vertical line indicates the ZnO band edge (3.35eV).

BF-09

Magnetic behaviour of Fe implanted TiO_2 thin films.

R. Sanz[1], M. Hernandez-Vélez[1,2], T. Kubart[3], D. Martin[3], J. Jensen[3]
1. Department of optical, magnetic and transport properties, Instituto de Ciencia de Materiales, CSIC, Madrid, Spain; 2. Fisica Aplicada, Universidad Autónoma, Madrid, Spain; 3. Department of Engineering Sciences, Ångström Laboratory, Uppsala University, Uppsala, Sweden

Ferromagnetic semiconductors, as obtained by doping semiconductors with magnetic impurities, are of great interest due to their potential application for future spintronics devices. Titanium dioxide, $TiO_2$is a wide band gap semiconductor. In addition it has a high refractive index and dielectric constant and excellent optical transmittance in the Vis-IR region. This is very suitable characteristics for electronic and optical applications. Adding to this the magnetic properties when doping with e.g. Fe may give rise to a suitable magnetic oxide such as transparent ferromagnetic semiconductor, which are appealing materials for magnetooptical devices. Depending on the fabrication technique, the magnetic properties may show strong differences ascribed to the different structures and magnetic ordering.

In this paper we present results on the magnetic properties of TiO_2 thin films implanted with ^{56}Fe ions. The films were grown by pulsed-dc magnetron sputtering in a argon/oxygen atmosphere using a titanium sputter target. The films were deposited onto silicon (100) wafers. Two sets of deposition were carried out; one with no external substrate heating (sample A), and one with the substrate heated to 573 K (sample B). The films thickness was about 400 nm in both cases. Structural analysis of the films was performed by means of grazing incidence X-ray diffraction measurements. The data revealed an essential amorphous TiO_2 film for sample A and a polycrystalline anatase film for sample B, see figure 1. The samples were implanted with 100 keV $^{56}Fe^+$ ions at room temperature to a total fluence of 1.3×10^{16} ions cm^{-2}. The implantation range is ~90 nm. The elemental depth profiles of the samples before and after implantation were analysed by ion beam analysis and XPS.

As a result of the ion implantation, the polycrystalline anatase film in sample B was modified, with a partial loss of crystallinity. The diffraction peaks reduced in intensity and even disappeared for some crystal planes. For the mainly amorphous film, ion implantation did not introduce any appreciable changes in the structure. There were no signals from the formation of Fe clusters or intermediate oxide phases nor was phase change appreciated in both types of implanted samples[1].

Magnetic measurements were performed of implanted and un-implanted samples, using a Super Quantum Interference Device (SQUID) at 4 and 300 K. Un-implanted samples did not show any ferromagnetic behaviour, only diamagnetic and paramagnetic signals ascribed to the Si substrate and the sputtered TiO_2, respectively. Hysteresis loops for the Fe implanted samples are shown in figure 2 at the two temperatures after subtracting the above mentioned linear magnetic contributions. A ferromagnetic characteristic is observed and summarized in Table 1, i.e., coercivity field (H_c), remanence (M_r) and saturation (M_s)moments normalized to Bohr's magneton per implanted Fe atom.

The results for the two films show similar values of the coercive field and magnetic remanence. However, the essentially amorphous sample (sample A) presented an enhanced value of magnetization. An amorphization also appears in the initial anatase film (sample B) as an effect of the implantation and may also be the origin of the ferromagnetism in this sample. Reported results on doping TiO_2 with Fe presented different magnetic responses depending on phase, type of carriers, and vacancies or interstitials[2,3]. Although stoichiometric TiO_{2+} contains only Ti^{4+} ions and is non-magnetic, unpaired 3d electrons in Ti^{3+} and Ti^{2+} ions, due to O defects, can potentially cause magnetism[4] in addition with the Fe ions by superexchange interactions. The conclusion of the preliminary result is that the degradation of crystalline order may be an important parameter in the magnetic response of these implanted, room temperature ferromagnetic materials.

1.A. R. Bally et al., J. Phys. D: Appl. Phys. 31 (1998) 1149-1154

2 A. Bernasik et al., Solid State Ionics 72, 12 (1994)

3. N. H. Honga et al., Journal of Magnetism and Magnetic Materials 281 (2004) 347–352.

4. S. Dae Yoon, et al. J. Phys.: Condens. Matter, 18, 27 (2006) L355-L361

Sample	4 K			300 K		
	H_c (Oe)	M_r/M_s	$M_s(\mu_B/Fe)$	H_c (Oe)	M_r/M_s	$M_s(\mu_B/Fe)$
A	206	0.098	1.6	108	0.198	0.75
B	237	0.106	1.4	116	0.198	0.41

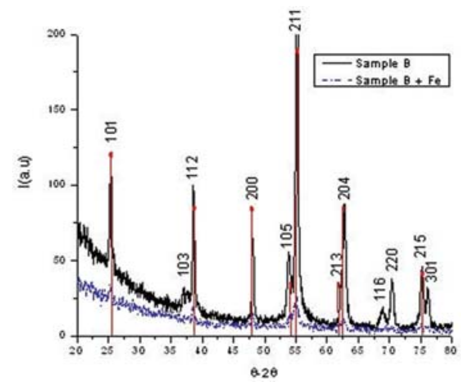

Diffractograms of virgin and Fe implanted sample B. Vertical lines indicated the remaining diffraction planes after implantation.

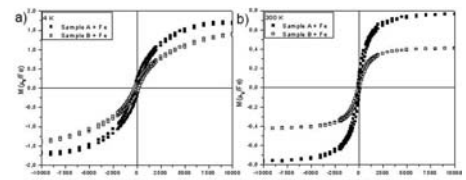

Hysteresis loops of Fe implanted samples at 4K a) and 300K b)

BF-10

(Ga,Mn)As ultrathin films with high Mn concentration.

J. Deng[1,2], W. Wang[1], L. Chen[1], J. Lu[1], Y. Ji[1], J. Zhao[1]
1. Institute of Semiconductors, Chinese Academy of Sciences, Beijing, China; 2. Department of Physics, University of Science and Technology of China, Hefei, China

In the past decade, diluted magnetic semiconductor (Ga,Mn)As films have attracted much attention for their potential application in future spintronic devices [1]. However, their Curie temperature Tc is much lower than room temperature, which hampers their practical applications. Recently, some groups studied magnetic properties of (Ga,Mn)As films with Mn concentration x larger than 0.1 and the thickness t less than 10 nm [2,3]. Although the Tc of 165~170 K of these ultrathin films is a little bit lower than the highest record of 173 K obtained in the thicker one [4], it is still widely accepted that the ultrathin thickness and high Mn concentration are key factors to increase TC of (Ga,Mn)As. So far, only few work has been carried out on (Ga,Mn)As ultrathin film with high Mn concentration. In this work, to comprehensively understand magnetic property of (Ga,Mn)As ultrathin film, we have grown a series of (Ga,Mn)As films with t = 7 nm and x = 0.14 at different growth temperature Ts by molecular-beam epitaxy, and investigated magnetization and magneto-transport property of them systematically.

All the samples were grown on GaAs (001) substrates and without GaAs cap layers. Reflection high energy electron diffraction (RHEED) patterns show clear streaky (1×2) surface reconstruction at Ts = 220 oC, and (1×1) surface reconstruction at Ts = 200 oC. However, RHEED pattern turned to a shadow when Ts = 170 oC. The second phase (hexagonal MnAs) segregation was observed when Ts was above 240 oC.

Temperature dependence of remanent magnetization measured by superconducting quantum interference device (SQUID) magnetometer shows that Tc of the sample grown at 220 oC (sample A) is 105 K before annealing, and can be enhanced up to 165 K after annealing at 160 oC for 16 h (Fig. 1). However, from Fig.1 we can also see that Tc appreciably decreases after annealing time being extended to 40 h, indicating the increase of Tc almost saturates when annealing time is up to 16 h. When annealing temperature is above 170 oC and annealing time is 20 min, a small quantity of the second magnetic phase can be found by SQUID measurements. From these data, we easily find that if the samples are thinner, annealing temperature and annealing time required for obtaining the saturation of Tc are higher and shorter, respectively. Usually, (Ga,Mn)As layer with a GaAs cap layer need longer annealing time to reach high Tc. The sample grown at TS = 200 oC is not a single phase, despite the fact that no obvious second phase can be observed from RHEED patterns. It is obvious that we can grow a single phase (Ga,Mn)As ultrathin films with high x at higher Ts. The effective Mn concentration of the annealed sample A can be deduced to be 0.09 from the magnetic field dependence of magnetization at 5 K (not shown here), lower than the nominal concentration of 0.14. The coercive field is about 25 Oe as much as that of (Ga,Mn)As films with typical thickness (x<0.1) grown on GaAs.

Magneto-transportation has been carried out. The hole density of as-grown and annealed sample A are estimated from Hall measurements to be about 8.4×10(20)/cm3 and 1×10(21)/cm3, respectively. The Tc obtained from temperature dependence of sheet resistance is consistent with that measured by SQUID. We also measured the relationship between the Hall resistance and the angle between the current direction and an applied in-plane field of 1 tesla by rotating the sample. As shown in Fig. 2, the in-plane magnetic anisotropy and the anisotropic magnetoresistance exist in as-grown and annealed ultrathin (Ga,Mn)As films, which is in agreement with the results obtained by SQUID measurements [2].

In summary, we have grown a series of (Ga,Mn)As ultrathin films with high Mn concentrations. Magnetization, magneto-transport measurements have been carried out systematically. The highest Tc is 165 K obtained by post-growth annealing. RHEED patterns and SQUID measurements show a narrow growth window for a single phase (Ga,Mn)As ultrathin films with high Mn concentration. The in-plane magnetic anisotropy and the anisotropic magnetoresistance exist in them.

[1] H. Ohno, A. Shen, F. Matsukura, A. Oiwa, A. Endo, S. Katsumoto, and Y.Iye, Appl. Phys. Lett. 69, 363 (1996).

[2] D. Chiba, Y. Nishitani, F. Matsukura and H. Ohno, Appl. Phys. Lett., 90, 122503(2007).

[3] Shinobu Ohya, Kenichi Ohno and Masaaki Tanaka, Appl. Phys. Lett., 90, 112503(2007).

[4] T. Jungwirth et al., Phys. Rev. B 72, 165204 (2005).

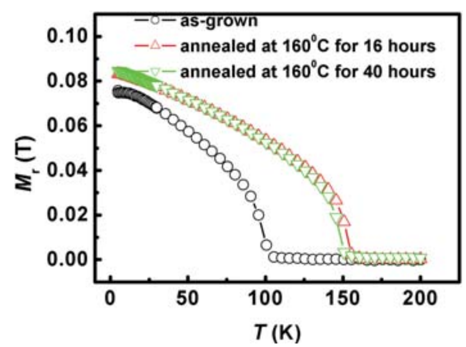

Fig. 1 The temperature dependence of remanent magnetization of annealed sample A

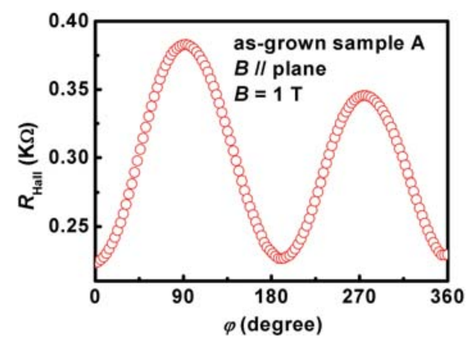

Fig.2 The Hall resistance vs the angle ϕ in as-grown sample A

BG-01

Non-resonant parametric recovery of spin-wave signals.

S. Schäfer, A. V. Chumak, A. A. Serga, B. Hillebrands
Fachbereich Physik and Forschungsschwerpunkt MINAS, Technische Universität Kaiserslautern, Kaiserslautern, Germany

Introduction :
The hybridized dipole-exchange magnonic dispersion spectra of thin magnetic films provide the grounds for storage and recovery of microwave signals by means of parametric interaction of spin waves with an longitudinal microwave magnetic pumping field [1]. Here we report on the non-resonant case of signal restoration when the pumping field frequency is not equal to twice the signal spin-wave pulse carrier frequency. This phenomenon reveals a logarithmic dependence of restored signal powers on the original signal intensity.

Experiment :
As shown in Fig. 1a, the experiment was realized using a thin ferrite Yttrium-Iron-Garnet film placed upon an input and an output antenna with a dielectric resonator between the antennae. A microwave pulse is applied to the input antenna, exciting a traveling spin wave within the ferrite film in the geometry of magnetostatic surface waves (MSSW). This traveling spin-wave pulse is partially converted into exchange dominated perpendicular standing spin waves (PSSW) where both dispersions cross as can be seen in Fig. 1b. After the traveling spin wave left the area between the antennae, a rf pumping field is applied via the dielectric resonator, amplifying the standing waves which transfer energy back to a traveling MSSW which is finally detected as a recovered microwave pulse (see Fig. 1).

Results and interpretation :
In Fig. 2, pulse powers against carrier frequency are depicted for the input pulse (theory, dashed line) as well as the experimental data (circles) and values according to the here presented theoretical interpretation (continuous line) of the recovered pulse. Considering the logarithmic scale, the strong non-linearity between the input signal and the recovered pulse powers is obvious. We interpret this behaviour using the so-called S-theory of parametric interaction[2]. The pumping field generates and amplifies both magnons from the thermal floor (including a so-called dominant magnon group with the highest gain of amplification) and PSSW modes excited by the traveling spin-wave pulse. After the dominant magnons exceed a certain critcal treshold, amplification for the other magnons is suppressed. This moment corresponds to the maximum of the recovered pulse. This process of suppression can be understood in terms of a mean internal pumping field generated by all magnon groups, compensating the external pumping [1]. In our interpretation of the experimental data we assumed that not only the intensity of PSSW modes but also the thermal floor level depends on the power of the input spin-wave pulse, since its relaxation provides energy to the magnonic system. Thus the dominant magnon group reaches the critical treshold faster in the case of stronger input signal. This is the reason for the non-linear relation between intensities of input and recovered pulse.
Comparing the input and output power of the experimental setup, it is evident that such a device is suitable for the compression of the input power range, thus increasing the accessible dynamic range of microwave spectral analysis devices.

[1] A.A. Serga, A.V. Chumak, A. André, G.A. Melkov, A.N Slavin, S.O. Demokritov, B. Hillebrands, Phys. Rev. Lett., **99**, 227202 (2007).

[2] V.S. L'vov, *Wave turbulence under parametric excitation*, in: *Applications to magnetics*, Springer, (1994).

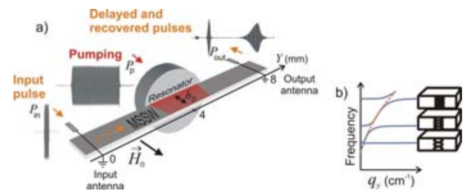

a) Experimental setup of experiments reported on, consisting of a single crystal YIG film, input and output antennae and a dielectric resonator for the aplication of the pumping microwave field. The waveforms depict the form of the input, pumping and restored pulse as can be seen on the oscilloscope. b) Section of the magnonic dispersion spectrum for a thin magnetic film showing the hybridization of the dipolar MSSW (dashed line) with the exchange dominated PSSW modes (cont. lines).

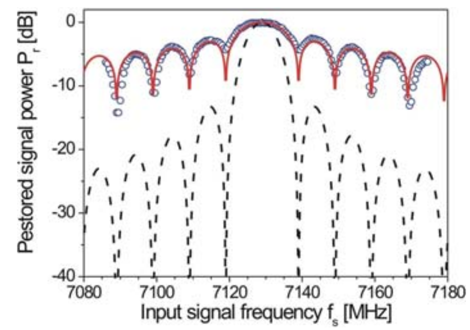

Arrangement of experimental data on the recovered pulse power (circles) as well as theoretical spectra of the input (dashed line) and recovered (continuous line) pulse against the signal frequency. The continuous line shows the restored pulse power as expected according to the phenomenological model proposed within this work.

BG-02

Reflectivity of microwave signal in ferromagnetic wires.

A. Yamaguchi[1,2], N. Higashio[1], K. Motoi[1], T. Kishimoto[1], H. Miyajima[1]
1. Department of Physics, Keio University, Yokohama, Japan; 2. PRESTO, Tokyo, Japan

Over the last years, various materials artificially fabricated have received considerable attention both in the fundamental physics and engineering applications. In ferromagnetic materials, their ferromagnetic properties in high-frequency region have attracted much attention since the applications in radio-frequency (RF) devices such as magnetic band pass filters and magnetic integrated inductors.

This study reveals the fundamental physical properties, reflectivity, as a function of frequency, and deals with a 1-D application of a novel concept inspired from a micron-scale line-shaped $Ni_{81}Fe_{19}$ wire and a magnetic domain wall (DW) in a boomerang-shaped wire.

The 30nm-thick line-shaped $Ni_{81}Fe_{19}$ wire and 50nm-thick boomerang-shaped $Ni_{81}Fe_{19}$ wire are patterned directly onto the MgO substrate by means of electron beam lithography and lift-off processing, as shown in Fig. 1 (a) and 1(b). The widths of the line-shaped $Ni_{81}Fe_{19}$ wire and the boomerang-shaped $Ni_{81}Fe_{19}$ wire were 5000 and 300 nm, respectively. A coplanar waveguide-shaped electrode is comprised of Cr (5nm)/Au (80nm). The device was contacted to a ground-signal-ground (GSG) typed microwave probe. There is no low-frequency cutoff because of the quasi-TEM mode of propagation in our devices. A vector network analyzer (VNA, frequency range: 200 MHz – 20 GHz) was used to inject the RF current into the samples and measure the reflectivity, S11, as a function of frequency. Here, an external magnetic field was applied at an angle of q from the longitudinal axis of the wires in plane to the substrate. All experiments were performed at room temperature.

Figure 2(a) shows the real part of the impedance ΔZ, which is calculated from the measurement result of the reflectivity, as a function of the frequency and external magnetic field at θ. As shown in Fig. 2(a), we found two ferromagnetic resonance structures. Each resonance frequency is plotted as a function of magnetic field shown in Fig. 2(b). The lower resonance frequency and the higher resonance frequency correspond to the lowest in-plane Damon-Eshbach mode and the lowest perpendicular standing spin wave mode, respectively.

Next, to clarify the reflectivity reflected the microscopic magnetization dynamics in magnetic domain wall in the boomerang-shaped wire. Figure 2(c) and 2(d) shows the simulated pattern of magnetization in the magnetic wire with DW and without DW calculated by OOMMF, respectively. The S11 signals with DW and without DW are displayed in Fig. 2(e). To remove the influence of cables, probes, etc., an on wafer calibration was done for the open-short-load calibration procedure using VNA measurement, the red dashed line corresponds to the calibrated S11 with DW at the absence of an applied magnetic field, which results in the no dip structure in the calibration line. After the magnetic field of 1 kOe was applied at direction in the substrate plane and it was decreased to zero, we measured S11 signal without DW. The black solid line corresponds to the S11 without DW. We find that two dips appear at 9.5 GHz and 10.5 GHz in the S11 signals without DW. This indicated that the precession of the internal magnetic moment within DW depended on the local magnetic effective field because of the internal spin structure of DW. In the other words, the intrinsic resonance of DW has effect on the reflectivity of the wire itself.

We have demonstrated that the reflectivity measurement of ferromagnetic resonance state in the straight line-shaped wire and the DW. We found the spin wave induced by RF signal produced the change of the reflectivity. These results can pave the way to new approaches of signal processing using 1-D spintronics devices.

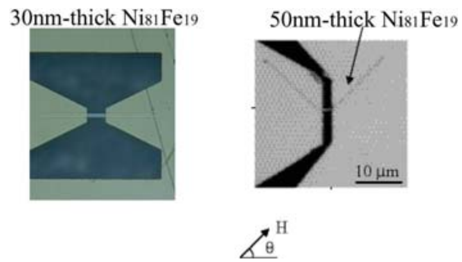

Optical micrograph (top view) of the system consisting of electrodes and (a) the straight line-shaped wire and (b) the boomerang-shaped wire. The magnetic field is applied in the substrate plane at an angle of θ to the longitudinal axis of the wires.

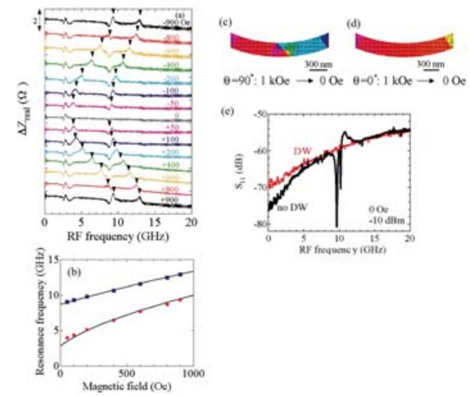

(a) The difference impedance ΔZ_{real} as a function of frequency and magnetic field in the straight line-shape wire. (b) The resonance frequency as a function of magnetic field. Simulated magnetization distribution (c) with and (d) without DW. (e) S11 with and without DW as a function of frequency.

BG-03

Ferromagnetic resonance on FeSiB thin films displaying spin reorientation transition.

M. Coisson, F. Celegato, P. Tiberto, F. Vinai
Electromagnetics, INRIM, Torino, Italy

The development of a perpendicular anisotropy in ferromagnetic materials is of great interest because of the perspective applications in data storage. However, even relatively soft magnetic materials that display perpendicular anisotropy are widely studied for fundamental investigations. Moreover, the ability to control a well defined anisotropy in a soft magnetic thin film makes it valuable for ferromagnetic resonance (FMR) studies having both theoretical and applied motivations. FMR studies allow to investigate anisotropy distributions in magnetic materials and magnetisation reversal and damping processes; devices based on such materials can be perspectively used as microwave tuners, absorbers or inductors.
In this paper, thin films of nominal composition $Fe_{78}Si_9B_{13}$ have been produced by rf sputtering on Si_3N_4 substrates. Films thickness varies from 25 to 600 nm; in all cases, the materials are amorphous and contain only a minority crystalline fraction, that increases with sample thickness.
Spin reorientation transition (SRT) is observed on the as-prepared samples: when thickness is below a certain threshold (samples 25 and 80 nm thick in our case) the magnetisation lies in the film plane, giving rise to soft magnetic properties characterised by a loop with small hysteresis and a fast approach to saturation. On increasing thickness (samples with thickness equal to 150 nm or above in our case), a perpendicular magnetic anisotropy develops that is clearly reflected in the magnetic force microscopy (MFM) images taken on all studied samples, and reported for a few selected specimens in figure 1. Thinner samples (80 nm thick in figure 1) don't show significant magnetic structures (MFM is sensitive only to the component of the magnetisation orthogonal to the film plane), whereas thicker samples (150 and 600 nm thick in figure 1) develop a clear stripe domain configuration, typical of materials displaying an out-of-plane magnetic anisotropy. The hysteresis loops of these samples, measured by means of a vibrating sample magnetometer, clearly mark the SRT with the appearance of a larger coercive field and a two-phase magnetisation process, with a fast magnetic switching near the coercive field and a slow and almost linear approach to saturation at higher fields. The thickest samples (as the 600 nm thick one) progressively reduce their out-of-plane anisotropy, as marked out by a more irregular stripe domain pattern detected by MFM and by a less pronounced two-phase behaviour of the hysteresis loop.
FMR has been studied on all as-prepared samples with a vector network analyser (VNA) in the frequency interval 40 MHz - 10 GHz. The specimens have been placed face down on a matched coplanar line connected to both ports of the VNA. A reference state is defined by submitting the sample to a saturating magnetic field H_{sat} applied in the film plane. For each applied static magnetic field value H, the ratio $S_{21}(H)/S_{21}(H_{sat})$ is calculated between the transmission parameters in the current state and in the reference state. Absorption peaks are then detected and their frequency is plotted against the applied magnetic field. Examples are given in figure 2.
SRT is marked by the appearance of a complicated FMR peaks pattern in the studied specimens: thinner films (80 nm thick sample, in figure 2) display a single FMR peak whose dependence on the applied magnetic field follows the Kittel law for thin films [1]. On thicker samples (150 nm thick film, in figure 2) multiple peaks appear, that evolve with the applied field in complicated ways: existing peaks may merge, and new peaks may appear. Whereas high frequency peaks can still be fitted with the Kittel law for thin films, low frequency ones can not. The thickest samples (600 nm thick specimen in figure 2) display again a single peak behaviour, although in this case it cannot be reproduced by the Kittel formula for thin films.

In conclusion, spin reorientation transition has been observed on FeSiB thin films that pass from an in-plane magnetic configuration to an out-of-plane one on increasing thickness, with a progressive reduction of the out-of-plane anisotropy on the thickest samples. Magnetic force microscopy and hysteresis loops evidence the appearance of stripe domain configurations with perpendicular magnetisation in all but the thinnest films. Ferromagnetic resonance, being dependent on the anisotropy of the material, is strongly affected by SRT: thin specimens with in-plane anisotropy are characterised by a single FMR peak; thicker films with out-of-plane anisotropy develop multiple FMR peaks; the thickest films return to a single FMR peak. The Kittel formula for thin films accounts only for FMR curves of the thinner films and for the high-frequency peaks of the thicker films.

[1] C. Kittel, Phys. Rev. 73 (1948), 155-161.

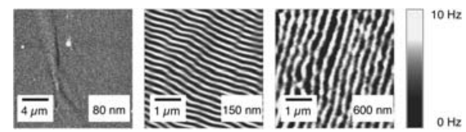

MFM images of 80 nm (left), 150 nm (middle) and 600 nm (right) thick samples.

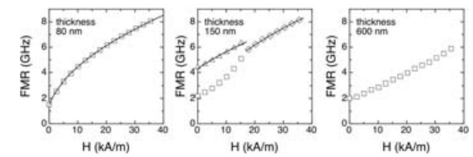

FMR peak(s) of 80 nm (left), 150 nm (middle) and 600 nm (right) thick samples. Symbols are experimental data. Lines are best fits according to the Kittel formula for ferromagnetic resonance in thin films.

Correlation receiver of below-noise pulsed signals based on the parametric interactions of spin waves in magnetic films.

G. A. Melkov[1], V. I. Vasyuchka[1], V. A. Moiseienko[1], *A. N. Slavin*[2]
1. Faculty of Radiophysics, Kiev National Taras Shevchenko University, Kiev, Ukraine; 2. Department of Physics, Oakland University, Rochester, MI

A correlation receiver capable of receiving pulsed microwave signals having amplitudes substantially below the noise level is proposed and experimentally realized. The device is based on the parametric interactions of spin waves propagating in an yttrium-iron garnet (YIG) film waveguide with dimensions 5.1 μm × 1 mm × 10 mm magnetized by the bias field $H = 941$ Oe along the waveguide length. Two wire antennae of the diameter 25 μm where situated near the opposite ends of the waveguide at a distance of 6 mm between them. The input pulsed signal of the carrier frequency f_s was supplied to the first antenna while the reference pulsed signal of the same carrier frequency was simultaneously supplied to the second antenna. The correlation signal of the frequency $2f_s$ was received by a dielectric resonator situated in the middle of the waveguide and coupled to an output transmission line [1].

First, we studied experimentally the general properties of the above described correlation receiver. The carrier frequencies $f_s = f_r = 4.715$ GHz and the powers $P_s = P_r = 20$ mW of both the input and reference signals were equal. Using the quadratic detector and oscilloscope we were able to observe the envelopes of both the input signal of the voltage U_s and the reference signal of the voltage $U_r \approx U_s$ (see Fig.1a and 1b, correspondingly). Both signals were rectangular pulses of the 100 ns duration modulated by a Barker code of the length $N = 3$ (see Fig. 1a, b). Using this code, the input and reference signals were subjected to a binary phase manipulation of 0 or π radians three times during the pulse duration. For instance, the input signal pulse in Fig. 1a during the first (0–33 ns) and second (34-67 ns) time intervals had the phase of the carrier equal to zero, while during the third (68-100 ns) time interval it had the carrier phase equal to π. The reference signal was inverted in time, i.e. modulated by the sequence (π, 0, 0). The small (≤ 0.8 dB) variations of the power of the input and reference pulses observed at the moments of phase manipulation are caused by the non-ideal performance of the phase modulators.

Fig. 1c shows the envelope of the output correlation signal having the carrier frequency of $f_{out} = 9.43$ GHz and peak power of 50 μW. The experimentally measured magnitude and shape of this output pulse agree well with the results following from the theory of nonlinear interaction of two contra-propagating spin wave packets developed in this work.

Second, we investigated the possibility of reception of a weak pulsed signal on the background of a strong noise using the above described correlation receiver. In this experiment we supplied to the first input antenna not only the pulsed signal of the power 1.4 mW modulated by the Barker code (see Fig. 1a), but, also, a continuous noise-like signal of the power 14 mW, so that the signal-to-noise ratio (SNR) was equal to 0.1. The noise-like signal had a Gaussian profile, and its spectral width was exceeding 200 MHz. The envelope of the combined input signal is shown in Fig. 2a, and it is clear from this Figure that, due to the small signal-to-noise ratio, the pulsed input signal is not noticeable on the noise background. The reference signal supplied to the second antenna had the shape similar to the one shown in Fig. 1b and power $P_r = 7$ mW. The envelope of the output correlation signal ($P_{out} = 3$ μW) is shown in Fig. 2b. As a result of correlation of the combined input signal with the pulsed reference signal the SNR in the output signal increased by more than 20 dB and became larger than 10.

[1] Yu. V. Koblianskiy *et al.*, Appl. Phys. Lett. **81**, 1645 (2002).

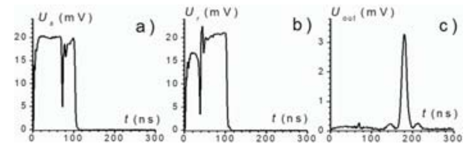

Oscillograms of the envelopes of the input pulsed signal (a), reference pulsed signal (b), and the output pulse (c); symbols 0 and π denote the phase of the microwave carrier in different time intervals.

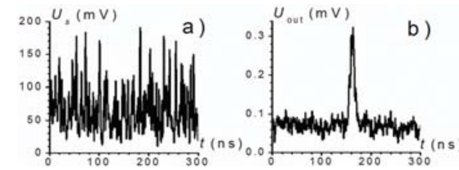

Envelopes of the combined (modulated pulse + noise) input (a) and convoluted output (b) signals for SNR = 0.1.

BG-05

Electronically Tunable Miniaturized Antennas on Magnetoelectric Substrates with Enhanced Performance.

N. Sun[1], G. Yang[1], A. Daigle[1], J. Lou[1], M. Liu[1], O. Obi[1], S. Stoute[1], C. Pettiford[1], J. Wang[1], K. Naishadham[2]

1. Electrical and Computer Eng., Northeastern University, Boston, MA; 2. RF communications Groups, Draper Laboratory, Cmabridge, MA

Antennas have been the critical components in radars, satellites, navigation systems, etc., which are crucial for the US Navy, DOD, as well as civilian applications. Compared to other components, antennas have been more resistant to orders-of-magnitude size reduction without drastic degradation in performance. Novel approaches are needed to improve the performance and reduce the size and signature of antennas with significantly enhanced bandwidth, high efficiency, and tunability for multifrequency and multiband operations. Smaller physical size, wider bandwidth, higher efficiency and tunability are desired characteristics of antennas for mobile systems. Antenna miniaturization can be achieved by printing a patch antenna over a high-permittivity substrate. However, the strong capacitive coupling between the antenna and the antenna's ground plane severely degrades its efficiency and bandwidth. To overcome this problem, antennas substrates with relatively permeability > 1 need to be used [1]. However, it has been challenging in achieving self-biased magnetic materials with a high permeability and low loss at RF and microwave frequencies suitable for antenna applications. There has been no report on self-biased magnetic antennas at GHz range.

Bulk ferrite materials, composites of ferrite particles in polymer matrix, metamaterials with embedded metallic circuits, etc., have been used as antenna substrates for achieving $\mu_r>1$. However, these antenna substrate approaches are too lossy to be used at frequencies > 500 MHz, and large biasing magnetic fields are needed for ferrite materials in antenna substrate. In order to be practically feasible in miniature antenna applications, it is important for antenna substrates to be comprised of self-biased magnetic materials, in which no external bias field is applied.

Microwave magnetic thin films provide a unique opportunity for achieving self-biased magnetic patch antenna substrates with $\mu_r>1$ at GHz frequency range. The strong demagnetization field of magnetic films allows for high ferromagnetic resonance frequencies up to several GHz and self-biased magnetization as well, which are essential for microwave magnetic devices. We propose to use novel magnetoelectric composite substrates for antennas with low-loss magnetic film materials and low-loss high permittivity dielectric materials.

Our research has led to new designs of electronically tunable self-biased patch antennas with magnetic metallic magnetic films and ferrite films. As shown in Fig. 1 and 2, we have achieved self-biased antennas at 2.1 GHz with a CoFeB film showing large tunability [2]. In addition, we have achieved self-biased antennas at 1.7 GHz and at 2.1 GHz with high quality self-biased ferrite films, as shown in Fig. 3 and 4. This is the first demonstration of electronically tunable self-biased magnetic patch antennas with enhanced performance at GHz.

Acknowledgements: This work is supported by the ONR YIP Award N00014-07-1-0761 managed by Dr. Colin Wood, and by Draper Laboratory.

1. Hossein Mosallaei and Kamal Sarabandi, "Magneto-Dielectrics in Electromagnetics: Concept and Applications" IEEE Trans. Antennas and Propagation, 52, 1558 (2004).

2. N.X. Sun, J.W. Wang, Andrew Daigle, Carl Pettiford, Hossein Mosallaei, and C. Vittoria, "Electronically Tunable Magnetic Patch Antennas with Metal Magnetic Films", Electronics Letters, 43, 434 (2007).

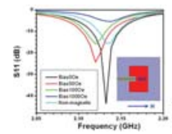

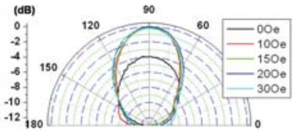

Fig. 1 (Left) Return loss of a magnetic patch antenna with different applied magnetic fields along feedline direction, showing large tunability of the radiation frequency. Fig. 2 (Right) The H-plane detected power of a magnetic antenna with different magnetic fields applied perpendicular to feedline, showing large tunability of the radiated field pattern with a magnetic field in the range of 10 Oe.

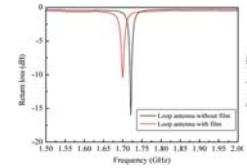

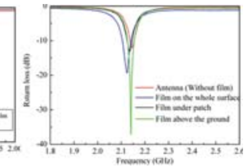

Fig. 3 (Left) Ring antennas with circular polarization with and without a self-biased ferrite film, showing self-biased magnetic antenna miniaturization effect with the ferrite film. Fig. 4 (right) Patch antennas with linear polarization with and without a magnetic film, showing self-biased magnetic antennas with miniaturization effects.

BG-06

On the study of left handed coplanar waveguide zeroth order resonator on ferrite substrate.

M. A. Abdalla, Z. Hu
School of Electrical and Electronic Engineering, University of Manchester, Manchester, United Kingdom

1-Introduction:
In the past few years, there has been a great interest in using left handed materials (LHMs) in microwave circuit applications due to their unique properties. The LHMs have been realized in different planar versions [1-3]. As a consequence, many novel planar LH microwave components have been proposed for various microwave applications. Ferrite medium has nonreciprocal and tunable properties. Therefore, tunable and nonreciprocal LH transmission lines (TLs) are expected on ferrite substrate as presented using microstrip TL [4] and using CPW TL [5].
In this paper, we propose a tunable and compact left handed gap coupled line resonator in coplanar waveguide configuration. The proposed resonator is studied analytically and its performance has been verified numerically for different DC magnetic bias.
2-Theory:
A novel LH transmission line resonator has been introduced as an application of the left handed transmission line theory. The principle of its operation is based on cascading a LH TL and a conventional one, right handed, and terminating them by either a short of an open circuit [6]. The total phase shift at the resonator end is the sum of phase shifts introduced by the two transmission lines. A zeroth order LH TL resonator has zero propagation constant due to the phase compensation of both sections. Thus, it can achieve zero electric length at a certain finite microwave frequency with small size. A gap coupled LH TL zeroth order resonator is introduced in [6].
In our work, the proposed resonator is designed by cascading a left handed unit cell transmission line by a right handed one on ferrite substrate in coplanar waveguide configuration. The two cascaded transmission lines are coupled to output and input ports through a small coupling air gap capacitor. An external DC magnetic bias (Ho) is applied horizontally to the ferrite substrate inducing an internal magnetic field. This magnetic field causes the ferrite substrate to have the substrate magnetization (Mo) in the same direction.
3- Numerical Results:
The proposed resonator has been analyzed numerically using the full wave electromagnetic simulation. The commercial software ANSOFT-HFSS is employed.
The performance of the proposed resonator in the case of a applying a dc magnetic bias of 1250 Oe is shown in figure 1 where the resonance frequency is at 3.9 GHz. The performance of the proposed resonator in the case of a applying a dc magnetic bias of 2000 Oe is shown in figure 2 where the resonance frequency is at 4.4 GHz. It is clear that the resonance frequency can be tuned by changing the applying DC magnetic bias. Also, the proposed resonator can suppress the higher order frequency harmonics.
4- Conclusion:
An air gap coupled line tunable zeroth order LH resonator on ferrite substrate has been presented. The results show that the proposed resonator has a tuning capability by varying the DC magnetic bias. The proposed resonator has the advantage of its compact size. Also, it can be applied in many filters and oscillators.

[1] F. Falcone, T. Lopetegi, J. D. Baena, R. Marques, F. Martin, and M. Sorolla, ‘ Effective negative ε stopband microstrip lines based on complementary split ring resonators’ IEEE Microwave and Wireless Components Lett., vol. 14, no. 6, pp. 280-282, June 2004.

[2] G. V. Eleftheriades, A. K. Iyer, and P. C. Kremer, ‘ Planar negative index media using planar L C loaded transmission line’, IEEE Trans. Microwave Theory and Tech., vol 50, no. 12, pp. 2702-2712, December 2002.

[3] C. Caloz, abd T. Itoh, ‘Transmission line approach of left handed (LH) materials and microstrip implementation of an artificial LH transmission line’, 2002 IEEE AP-S Int. Symp. Dig., vol. 1, pp. 412-415, June 2002.

[4] Tsutsumi and T. Ueda, ‘ Nonreciprocal left-handed microstrip lines using ferrite substrate’, 2004 IEEE MTT-S Int. Microwave Symp. Dig., vol. 1, pp. 249-252, June 2004.

[5] M. Abdalla, and Z. Hu, ‘ On the stud of CWP dual band left handed propagation with reciprocal and nonreciprocal characteristics over ferrite substrate,’ 2007 IEEE AP-S Int. Symp. Dig., vol. 1, pp. 2578-2581, June 2007.

[6] C. Caloz and T. Itoh, ‘ Electromagnetic metamaterials transmission line theory and microwave applications’, New Jersey: John Wiely & Sons, 2006.

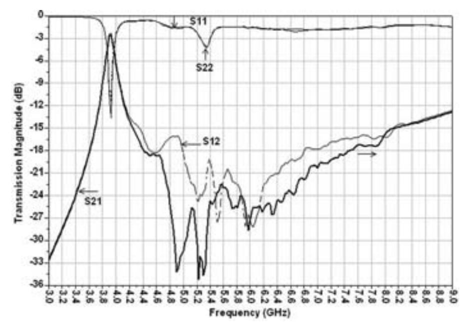

Figure 1: The full wave scattering parameters magnitude of the proposed resonator at Ho=1250 Oe

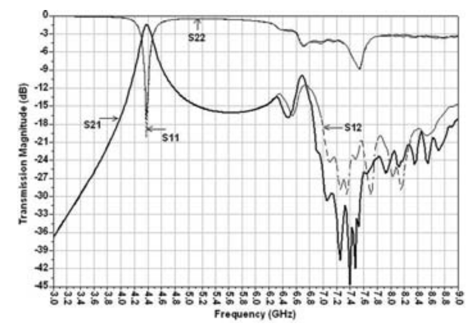

Figure 2: The full wave scattering parameters magnitude of the proposed resonator at Ho=2000 Oe

BG-07

Observation of bright and dark spin wave envelope solitons in periodic magnetic film structures.

A. Ustinov, N. Grigorieva, *B. Kalinikos*
Physical Electronics and Technology, St.Petersburg Electrotechnical University, St.Petersburg, Russian Federation

Periodic magnetic film structures (PMFS) first have attracted a close attention decades ago [1-3]. Recent years renewed interest to such structures that is stimulated by fundamental and applied investigations of nanostructures, magnonic crystals, and other metamaterials (see e.g. [4,5]). One of the focus areas for periodic structures is nonlinear wave dynamics, in particular, solitonic phenomena. Years ago, gap solitons have been theoretically predicted for "magnetically modulated" ferromagnetic films [6]. At the same time, solitonic effects in PMFS have never been experimentally studied.

This work reports the first observation of envelope solitons in PMFS. Two types of spin wave (SW) solitons, bright and dark, were generated through induced modulation instability (IMI) process [7]. Many ways could be exploited to fabricate planar PMFS. In this work, the PMFS was made utilizing metal strip grating placed onto a single-crystal yttrium iron garnet (YIG) film surface. The grating had a period of 171 µm and consisted of 16 copper strips, each one of 14 µm in width.

The experiments were done on a magnetostatic backward volume wave delay line made with a long and narrow 9.8 µm thick YIG film "waveguide". The in-plane bias magnetic field was 1220 Oe. The signals were excited and detected by input and output transducers separated by a distance of 10 mm. The grating was centered between the transducers. The soliton experiments were preceded with the measurements of the amplitude versus frequency characteristic (AFC) of the structure. The AFC recorded in a linear regime is shown in figure 1. Note that the position of the first stop-band ("gap") is well matched with the frequency of the main Bragg resonance that is due to the SW diffraction effect. It should be emphasized that the physical origin of this gap is quite different in comparison with the dipole-exchange gaps appearing in the ferromagnetic film spectrum where the first experiments on SW envelope solitons and modulational instability have been performed [8].

To study the generation process of solitons in detail, the carrier frequencies and amplitudes of the input microwave signals were systematically varied. The main attention was concentrated on the soliton formation in the vicinity of the gap. It turned out that bright solitons were formed on the left slope of the gap whereas dark solitons were formed on the right slope of gap. The frequency zones for bright-soliton and dark-soliton formation are indicated in Fig. 1 by arrows A and B, respectively. Figure 2 gives representative bright and dark soliton train profiles (left panels) together with their power spectra (right panels). Pairs of the input cw driving frequencies were set 5204 and 5206 MHz for bright-soliton generation, and 5211 and 5213 MHz for dark-soliton generation, respectively. The incident microwave power levels were 21.1 and 12 dBm, and 19 dBm and 16.3 for bright-soliton and dark-soliton cases, respectively.

In accordance with the IMI mechanism, time distance between the neighbouring solitons in each train was determined by the beat frequency of the two input cw signals. In both cases of the bright-soliton and dark-soliton generation it was possible to change the observed soliton train periods for about 10 % through adjusting the values of driving frequencies.

In order to give a physical interpretation to the experiment, a theory of SW spectrum for periodically metallized magnetic film was developed. On the basis of the obtained SW spectrum the dispersion and nonlinear response coefficients of the nonlinear Schroedinger equation (NLSE) were determined. Calculations showed that the NLSE theoretical model with a nonlinear damping term gives a good explanation of the experimental results.

This work supported by the Russian Foundation for Basic Research.

[1] C. G. Sykes, J. D. Adam, and J. H. Collins, APL 29, 388 (1976).

[2] R. L. Carter, at al, JAP 53, 2655 (1982).

[3] A. V. Voronenko, S. V. Gerus, and V. D. Haritonov, Sov. Phys. J. 31, 245 (1988).

[4] S. A. Nikitov, Ph. Tailhades, and C. S. Tsai, JMMM 236, 320 (2001).

[5] H. Puszkarski and M. Krawczyk, Solid State Phenomena 94, 125 (2003).

[6] Niu-Niu Chen, A. N. Slavin, and M. G. Cottam, Phys. Rev. B47, 8667 (1993).

[7] M. Remoissenet, Waves Called Solitons (Springer-Verlag, Berlin, 1999).

[8] B. A. Kalinikos, N .G. Kovshikov, and A. N. Slavin, Sov. Phys. JETP 67, 303 (1988).

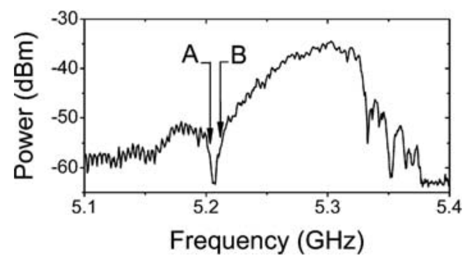

Fig. 1. Amplitude versus frequency characteristic of the experimental structure.

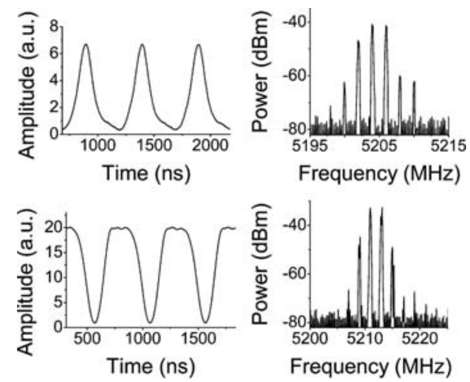

Fig. 2. Measured amplitude versus time profiles and power versus frequency spectra.

BG-08

Measurement System of FMR Linewidth ΔH_ω of Ferrite using a Shorted Stripline.

S. Takeda[1], H. Suzuki[2]
1. Magnontech, Ltd., Kumagaya, Japan; 2. KEYCOM Corp., Tokyo, Japan

Introduction

The measurement method of FMR (Ferromagnetic resonance) linewidth ΔH for microwave ferrite is specified in the international standard[1)] of IEC60556. This belongs to resonat method using cavity ans is based on perturbation theory. This has some advantages like having a high sensitivity and being suitable for smaller size of specimen. However, there are some drawbacks like; not suitable for narrower ΔH and large size of specimen due to collapse of perturbation approximation. Another big issue is a cost problem. If we want to cover wide frequency range, we have to prepare many cavities with different size because one cavity can measure it only at one frequency. The alternative non-resonant method using a shorted transmission line was already proposed by Bady[2)]. Unfortunately, this method is based on usage of analog network analyzer and contains several theoretical ambiguities. In this paper, we propose a new measurement system based on vector network analyzer, using a shorted stripline similar to Bady's method. This enables us to measure narrower ΔH for larger size of specimen over wide frequency range. And also the measurement of ΔH_ω is proposed sweeping frequency instead of current ΔH sweeping static magnetic field.

Measurement princple

Fig.1 shows a shorted stripline with a square slab shape of specimen. A disk shape is also available. The static magnetic field H_{ext} is applied perpendicularly to the plane of specimen. This situation is modeled by the equivalent circuit of Fig.2, where Lo is an air core inductance. When a specimen is loaded, it is considered that the portion of η of Lo is replaced by specimen's complex permeability μ=μ'-jμ" where η is a coupling coefficient. Here, Zio and Zil are input impedances of shorted stripline without and with specimen, respectively. Monitoring S_{11}s correspond to them, we can derive a value proportional to imaginary part ηωμ"Lo of impedance occupied by specimen even if η and Lo are unknown. A half linewidth is obatained from this FMR absorption curve. When frequency is contant, ΔH is measured sweeping static magnetic field H_{ext}. On the other hand, when H_{ext} is constant, Δω is measured sweeping frequency. If half linewidth Δω is enough smaller than resonant frequency ωr, the relationship of ΔH(Oe)=Δω(MHz)/2.8 will hold approximately. The value of ΔH obtained by sweeping frequency is different from current ΔH, so we'd like to call it ΔH_ω. On the same time, Gilbert relaxation constant α and relaxation time τ are calculated by α=Δω/(2ωr) and τ=1/(ωα).

Measurement system

We adopted to measure not ΔH but ΔH_ω under constant magnetic field of permanent magnet. In order to apply H_{ext} perpendicularly to the specimen plane accurately, this system has a fine tuning mechanism rotating a specimen plane and a field direction, monitoring FMR resonant frequency to get lowest. The situation without specimen, namely μ'=1, was realized by applying a strong magnetic field (5kOe) to specimen parallel to rf field. In case of slab specimen, a higher order (n>=3) MSW modes are always observed together with main peak. So the absorption curve of μ" of main peak is not symmetirical left and right. To reduce this influence, the half linewidth of Δω is derived by doubling a half value only at lower frequency side.

Measurement example

In Fig.3, the relationship between ΔH_ω and dimension ratio (t/L) is shown for 5mm square and 10mm square garnet measured at 2.24GHz, where t is thickness and L is side length of square slab. To be smaller dimension ratio tends to be slightly narrower ΔH_ω. Thus ΔH_ω is affected by shape and surface roughness of specimen.

Conclusion

By this system, any fine differences of ΔH_ω less than 50Oe of garnet can be measured. We believe this method would become a powerful tool to develop low loss garnet to improve insertion loss and intermoculation of circulator and isolator. Furthermore, saturation magnetization 4πMs of garne is also calculated by ω_r and H_{ext}. This is also available for quality control in garnet manufacturing line.

1)IEC60556 Ed.2 (2006), "Gyromagnetic materials intended for application at microwave frequencies- measuring methods for propwerties"

2)I. Bady, "Measurement of Linewidth of Single Crystal Ferrites by Monitoring the Reflected Wave in Shorted-Circuited Transmission Line", *IEEE Transaction on Magnetics*, vol.MAG-4 No.3 pp.521-526 (1967)

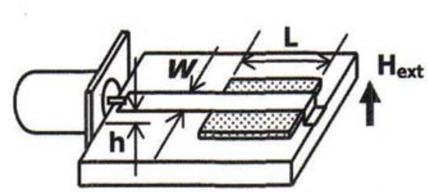

Fig.1 Shorted stripline with specimen

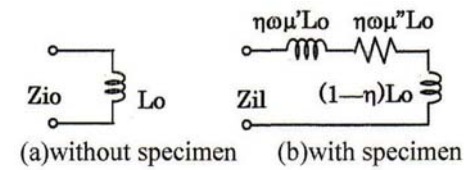

Fig.2 Equivalent model of a shorted stripline

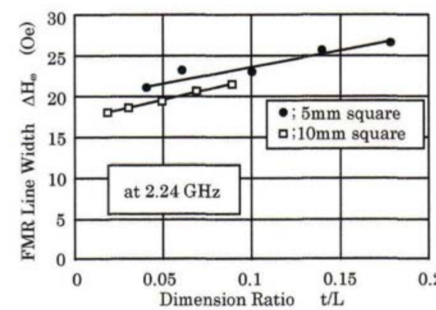

Fig.3 FMR linewidth ΔH_ω vs. dimension ratio of 5mm square and 10mm square slab at 2.24GHz

BG-09

On the study of ferrite coupled coplanar waveguide.

M. A. Abdalla, Z. Hu
School of Electrical and Electronic Engineering, University of Manchester, Manchester, United Kingdom

1- Introduction:
Recently, a pair of axially magnetized Ferrite Coupled Lines (FCL) structures has been used for nonreciprocal devices at millimetre wave frequencies. The FCL has been proposed experimentally for the first time in [1]. The analysis of the FCL was explained by using either the coupled mode approach [2] or the normal mode approach [3]. Later, novel microwave nonreciprocal devices such as circulators [4], gyrator, and isolator [5] based on the use of FCL sections were constructed. In all previous work, the FCL section was implemented using finline, microstrip, stripline, or slotline configurations. The coplanar waveguide structures have many attractive features in microwave applications.
In this paper, we introduce, for the first time, an FCL junction in coplanar waveguide configuration. The design of the proposed FCL section is done within the general FCL principles and the different performance properties of the proposed FCL have been verified numerically using full wave electromagnetic simulation results. Nonreciprocal CPW devices can be designed as applications of the proposed CPW FCL section.
2-Theory:
The proposed structure is realized by putting two closely spaced parallel lines on ferrite substrate which is longitudinally magnetized. The vertical cross section and the longitudinal cross section of the proposed CPW FCL structure are shown in figure (1-a and b) respectively.
In our work, the design objectives of the CPW FCL is to have centre frequency in the frequency band 5-11 GHz and its two input impedances at its ports matches to a 50 ohm
CPW feeding transmission lines. These design objectives are fulfilled by the full wave numerical solution of the proposed structure through the parametric studies of the different circuit geometry parameters to satisfy the propagation requirements of a typical FCL performance.
3- Numerical Results:
The proposed structure has been analysed using the full wave simulation. The commercial software ANSOFT-HFSS is employed.
The scattering characteristics of the proposed FCL CPW junction for excitation at port 1 are illustrated in figure 2. It is shown that the structure reacts as a forward coupler whose scattering transmission coefficients S21 and S41 are better than 5 dB level in the frequency band from 7-11 GHz. Similar results can be obtained for the case of excitation port is port 3.
The phase difference between the two outputs in both excitations at port 1 and 3 is illustrated in figure 3. For the case that the excitation is at port 3, the phase difference varies around 0 degree while for the case where the excitation is at port 1, the phase difference varies around 180 degree. In both cases, the maximum variation in the phase does not exceed few degrees.
The former power division results with the latter phase results of the forward coupler confirmed the even/ odd modes output on changing the excitation port of the FCL junction which is a unique property of the FCL junction.
4- Conclusion:
A novel CPW FCL has been proposed. The performance of the proposed FCL is optimized numerically. The unique features of the proposed FCL have been verified to agree with the theory of the FCL. The proposed FCL has a wide frequency band.

[1] L. E. Davis and D. B. Sillars, ‘ Millimetric nonreciprocal coupled slot finline components’, IEEE MTT Trans. vol, 34, pp. 804-808, 1986.

[2] J. Mazur and M. Mrozowski, ‘ On the mode coupling in longitudinally magnetized waveguiding structures’, IEEE MTT Trans. vol, 37, pp. 159-165, 1989.

[3] K. Xie and L. E. Davis, ‘ Nonreciprocity and the optimum operation of ferrite coupled lines’, IEEE MTT Trans. vol, 78, pp. 562-573, 2000.

[4] L. E. Davis, K. Xie, B. J, Climer, K. D. Newsome, and N. E. Periestley, ‘ Design and measurement of ferrite coupled circulators’, IEEE MTT-S Int. Symp. Dig., vol. 3, pp. 1153-1156, June 1999.

[5] J. Mazur, M. Solecka, M. Mazurm R. Poltorak, and E. Sedek, ‘ Design and measurements of gyrator and isolator using ferrite coupled microstrip lines, ‘IEE Proc. microwave, antennas & propagation, vol. 152, pp. 43-46, 2005.

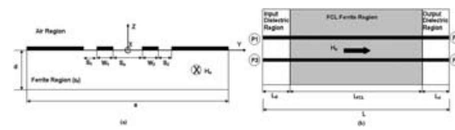

Figure 1 The CPW FCL (a) The vertical cross section, (b) The longitudinal cross section

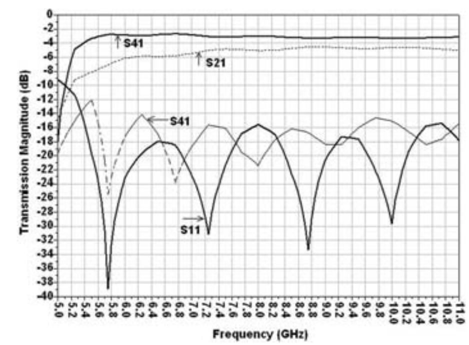

Figure 2 The full wave simulated magnitude of scattering parameters of the CPW FCL for input port 1

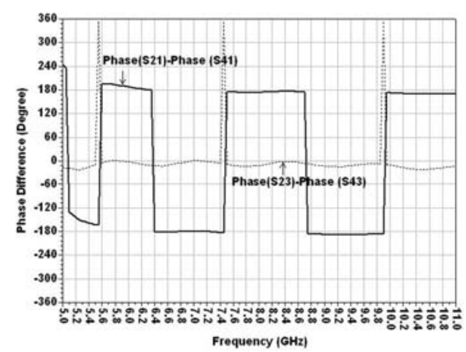

Figure 3 The full wave simulated phase difference for the two outputs for excitations at port 1 and 3

(110)-textured La2/3Ca1/3MnO3 thin films. Optimal electrodes in manganite tunnel junctions.

I. C. Infante[1], F. Sánchez[1], J. Fontcuberta[1], M. Wojcik[2], E. Jedryka[2], S. Estradé[3], F. Peiró[3], J. Arbiol[3,4], V. Laukhin[5], J. P. Espinós[6]
1. Magnetic Materials and their Applications, Institut de Ciència de Materials de Barcelona, Bellaterra, Spain; 2. Institute of Physics, Polish Academy of Sciences, Warszawa, Poland; 3. Dept. d'Electrònica, EME/CeRMAE/IN2UB, Universitat de Barcelona, Barcelona, Spain; 4. TEM-MAT, Serveis Cientificotècnics, Universitat de Barcelona, Barcelona, Spain; 5. Institució Catalana de Recerca i Estudis Avançats (ICREA), Barcelona, Spain; 6. Instituto de Ciencia de Materiales de Sevilla ICMSE (CSIC-USE), Sevilla, Spain

The application of manganite layers to functional devices, such as magnetic tunnel junctions (MTJs), has been hindered by the negligible room-temperature tunnel magnetoresistance (TMR) observed in the junctions fabricated so far. It is remarkable that the majority of manganite-based MTJs uses (001) pseudocubic substrates and, interestingly, much less attention has been devoted to other orientations. However, the drawbacks of (001) oriented electrodes are well documented and have been extensively studied and attributed to the intrinsic tendency of manganites to develop electronic inhomogeneities [1], which are localized in the proximity of the interface with the substrate [2]. Thus, the functionality of the (001) oriented MTJs is much affected by the high sensitivity of (001) electrodes. Although high values of TMR have been obtained at low temperature, the TMR temperature dependence decays at lower temperature than the Curie temperature (TC) of (001) manganite electrodes [3]. The occurrence of spin depolarization at the (001) interface has been argued to be the cause of this decrease in the TMR With the aim of contributing to better understanding and solving these problems, we have studied the effect of the atomic plane of growth in single manganite layers and heterostructures. With this purpose, we have used the same cubic substrate for the epitaxial growth but with two orientations: (001) and (110).
Epitaxial La2/3Ca1/3MnO3 (LCMO) films of different thickness have been simultaneously grown on SrTiO3 (STO) substrates with (001) and (110) orientation. From unit cell parameters of films in a wide range of thickness and from their magnetic properties we have investigated the effect of the crystal deformation on the TC. A first result signals the different magnetization dependence on temperature (Figure 1a) which appears at any given thickness, being the magnetization and the TC of (110) films always higher than that of (001) ones. Using the Millis magnetoelastic model [4] to analyze our data, we deduce that the TC of highly strained (001) films do not follow that model. On the contrary, less strained (110) film data fit nicely to the magnetoelastic model. Although the resulting dependencies of TC on strain can be partially related to biaxial strain, we conclude that the strong reduction of the TC on (001) films cannot be directed uniquely by this contribution but other causes may be at the origin. Thus, using 55Mn nuclear magnetic resonance (NMR), electron energy loss spectroscopy (EELS) and X-ray photoemission spectroscopy (XPS) we have investigated the electronic state of Mn ion through the films (by NMR) and the chemical composition of the films (by EELS) and that of film surface (by XPS). From these experiments, electronic phase separation and Ca segregation to the surface have been observed in (001) films, whereas (110) films are fully electronically and chemically homogeneous [5].
These experiments lead to conclude that LCMO layers could become better electrodes for MTJs and also serve to understand the physical origins of the observed electronic and chemical effects in bare films. We have also grown epitaxial bilayers of STO/LCMO//STO with (001) and (110) orientation and tuned the barrier thickness in the range of 2 to 5 nm, fixing the LCMO layer thickness to 25 nm. Structural characterization of these samples show that the STO capping layer does not contribute to change the strain of the LCMO unit cell for both (001) and (110) orientations. Magnetic properties of (001) and (110) bilayers present a different evolution when compared to their electrodes counterparts. Most remarkably, we observe (Figure 1b) an important decrease of the magnetization in (001) bilayers compared to that of (001) electrode, whereas the (110) bilayer magnetization remains almost unchanged as that of the (110) electrode. With NMR, EELS and XPS experiments we have found an evolution of the electronic phase separation and chemical redistribution in the (001) STO capped electrodes, whereas neither electronic nor chemical inhomogeneities are observed in (110) films.
We discuss these results on (001) and (110) LCMO electrodes and STO/LCMO bilayers in the framework of the promotion of carrier localization in (001) planes which can be related to the different polarity and elastic properties in (001) and (110) LCMO layers.

[1] E. Dagotto et al., Phys. Rep. 344, 1 (2001)

[2] M. Bibes et al., Phys. Rev. Lett. 87, 67210 (2001); M. Bibes et al., Phys. Rev. B 66, 134416 (2002)

[3] Moon-Ho Jo et al., Phys. Rev. B 61, R14905 (2000); V. Garcia et al., Phys. Rev. B 69, 052403 (2004)

[4] A. J. Millis et al., J. Appl. Phys. 83, 1588 (1998); K. H. Ahn and A. J. Millis, Phys. Rev. B 64, 115103 (2001)

[5] I. C. Infante et al., Phys. Rev. B 76, 224415 (2007)

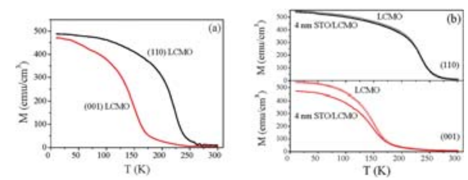

(a) Temperature dependence of the magnetization of 25 nm LCMO electrodes grown on (110) and (001) STO substrates. (b) Temperature dependence of the magnetization of 39 nm LCMO electrodes (symbols) and 4 nm STO capped LCMO electrodes (lines): (top panel) (110) samples and (bottom panel) (001) samples. Measurements shown in (a) and (b) were obtained with a magnetic field of 5 kOe applied in-plane of the samples.

BH-02

Observation of large tunneling magnetoresistance in Fe-MgO-Fe epitaxial multilayers using STM double tunneling experiments.

J. Lee[1,2], C. Krafft[2], R. D. Gomez[1,2]
1. Electrical and Computer Engineering, University of Maryland, College Park, MD; 2. Laboratory for Physical Sciences, Collegs Park, MD

Introduction

The theoretically predicted tunneling magnetoresistance (TMR) in coherent tunneling magnetic multilayers is over 1000% [1, 2]. However, the experimentally reported values are significantly lower. In particular for the Fe-MgO-Fe system, the highest measured TMR is 180% [3] at room temperature. Part of the difficulty in achieving the theoretical limit are factors such as contamination, interface roughness, pinholes, defects as well as the averaging effect from multiple magnetic grain boundaries. In this work, we report the results on epitaxially grown Fe-MgO-Fe structure on MgO (001) having nanometer sized topmost Fe islands, including measurements of TMR using an in situ scanned probe microscope in ultra high vacuum.

Experiment

All experiments were performed inside an Omicron surface analysis system at a base pressure less than 8 × 10-11 mbar. A polished MgO (001) substrate was cleaned by several cycles of sputtering and annealing (930~960°C) until the carbon peak in Auger spectroscopy was in the noise and the surface roughness (RMS) as measured by the AFM was less than 0.6 nm. A 35 nm thick Fe film was deposited on the MgO substrate at 400°C, which produced crystalline Fe islands with plateaus of up to several hundred nanometers wide. Next, 3 nm of MgO was deposited at a rate of 0.11 nm/min at room temperature and subsequently annealed at 450°C for 30 minutes. The STM images showed similar morphology as the underlying Fe grains and accompanied by some rounding at the edges. This indicated uniform, layer-by-layer coverage of the MgO film on the Fe grains. A Helmholtz coil was placed outside the system, which produced up to about ±10 Oe at plane of the sample for STM measurements.

Results and discussion

Figure 1a shows a schematic diagram of the structure and the STM wiring. Figure 1b is the STM image of a complete Fe(0.5nm)-MgO(3nm)-Fe(35nm)-MgO(substrate) structure. The top Fe aggregated into square nanoislands, some with single-atom step terraces. The base of the nanoislands was approximately 5-10 nm wide and capped with plateaus of about 2 nm wide. This is consistent with our result that showed the formation of ziggurat pyramid shaped islands of Fe on MgO [4]. The epitaxial growth of Fe is clearly exhibited by the alignment of the island edges along the MgO [110] direction. The magnetic structure of the system is shown by the MFM image in Figure 1c. Note that the MFM scale is more than 50 times larger than the STM image. It shows the magnetic ripples and domain walls emanating from the thick bottom ferromagnetic layer. The ripples are perpendicular to the local magnetization (along the easy axis of Fe) and from which we discern that the vertical line on the right center part of the image is a 90° Bloch wall that meets another 90° wall and a 180° wall oriented along the diagonal.

To measure the magnetic response of sample, we located a well-isolated Fe island on the flat plateaus of the bottom Fe structure, and measured the STM topography at various preset external magnetic field values. Since the STM is operated in constant current mode, any tunneling magnetoresistance change between the Fe layers will appear as a vertical displacement of the tip or an apparent change in the height of the surface features. Figure 2 is a series of line profiles for the island at 0 and ± 10 Oe. The measured height at zero field is 7.0 Å while for +10 Oe it is 2.1 Å and for -10 Oe, the apparent height is 10.5 Å. Clearly, there is a change of 8 Å between the positive and negative fields. We also check the response of the system with a non-magnetic sample and found no height differences introduced by the external field. Thus, this result suggests that a very large TMR, perhaps close to the theoretical limit, may be responsible for the observed height variation. Unfortunately, it is difficult to obtain a quantitative estimate of the true contribution to the MR for the moment. In order to calculate the real magnitude we need to establish the tunneling resistance based on the displacement, as well as develop a precise model for double junction tunneling. Also, we need to completely eliminate the effects due to the possible lateral shift of the tip due to the external field. These results, as well as progress for direct quantification will be presented in the paper.

[1] W. H. Butler et al. Phys. Rev. B 63, 054416 (2001)

[2] J. Mathon et al. Phys. Rev. B 63, 220403R (2001)

[3] S. Yuasa et al. Nature Mater. 3 (12), 868 (2004)

[4] J. Lee et al. J. Appl. Phys. 101, 09D123 (2007)

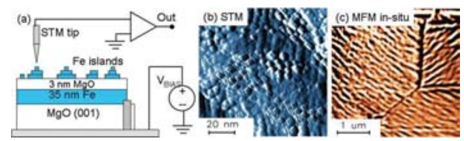

Figure 1. (a) Schematic diagram of double tunneling experiment on epitaxial Fe-MgO-Fe system with nanometer size top Fe islands, (b) STM image of the scheme, (c) MFM image of the sample but a larger scan area.

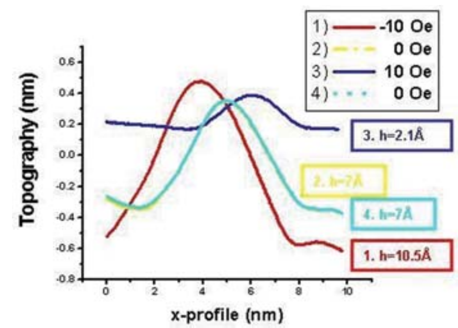

Figure 2. Line profiles across a single nanoisland taken at zero, ± 10 Oe external field.

BH-03

Multifunctional Ni/Au Multilayered Nanowires.

M. Cho[1], J. Cho[2,3], J. Wu[4], J. Min[2], J. Lee[2], B. An[2], Y. Kim[2]
1. Program in Micro/Nano System, Korea University, Seoul, South Korea; 2. Department of Materials Science and Engineering, Korea University, Seoul, South Korea; 3. Korea Electronic Technology Institute, Korea University, Gyeonggi, South Korea; 4. Institute for Nano Science, Korea University, Seoul, South Korea

Introduction
Nanowires are widely pursued one-dimensional nanosystems and promise immense opportunities in nanotechnology, ranging from nanoelectronic devices to cell-separation and magnetic labeling in biomedicine. Fabrication of multilayered nanowires with multiple functionalities is preferred from a single solution bath [1]. Synthesis of Ni/Au multilayered nanowires is appealing not only to magnetic devices but also to bio-applications as a result of magnetic and optical multifunctionality [2]. In this work, such Ni/Au multilayered nanowires were successfully prepared and characterized from a single solution bath [1].
Experiment
Multilayered Ni/Au nanowires were fabricated in anodized aluminum oxide (AAO) templates (200 nm and 80 nm in pore diameter) by pulse dc electrodeposition. The experiment was performed from a single solution bath of Ni and Au ions. The nanowires were characterized by SEM, TEM, optical microscopy, UV-Vis spectroscopy, and VSM.
Results and Discussion
In Fig. 1, the layered nanostructure of the Ni/Au multilayer nanowire was confirmed through TEM elemental mapping and line scanning. Alternative arrangements of the Ni and Au layers are distinctly separated, with respective individual layer thicknesses of ~70 nm for Ni layer and ~60 nm for Au layer. In experiment, the segmental lengths of individual Ni and Au layers can be tailored by adjusting deposition parameters. As shown in Fig. 2, various Ni/Au segmental aspect ratios were given, i.e., disk-shape of the Ni segments (Fig. 2 (a)), intermediate-shape of the Ni segments (Fig. 2 (b)), and rod-shape of the Ni segments (Fig. 2 (c)), compared to the rod-shape of the pure Ni nanowires (Fig. 2 (d)). Correspondingly, the magnetic properties of the multilayered nanowire arrays in AAO were investigated by VSM, exhibiting a clear dependence on the aspect ratio (Fig. 3). Fig. 3 (a) is the hysteresis of the disk-shaped Ni segments (aspect ratio < 1), showing the easy axis perpendicular to the nanowire axis. As the aspect ratio changes to ~1 (intermediate-shape of the Ni segments), the multilayered nanowire array becomes isotropic (see Fig. 3 (b)). When the rod-shaped Ni segments (aspect ratio > 1) were fabricated, the easy axis switches to parallel to the nanowire axis (Fig. 3 (c)), similar to that of the pure Ni nanowire array (Fig. 3 (d)). Thus, the easy-axis of the nanowire arrays was determined by the shape anisotropy, less than the small negative magnetocrystalline anisotropy of Ni. Moreover, the UV-Vis measurements give plasmon peaks characteristic of nanostructured Au in the Ni/Au multilayers. We shall discuss in detail the finite-size and proximity effects on the magnetic properties of the Ni/Au multilayers.

[1] J. H. Lee, J. H. Wu, H. L. Liu, J. U. Cho, M. K. Cho, B. H. An, J. H. Min, S. J. Noh, Y. K. Kim, Angew. Chem. Int. Ed. 46, 3663 (2007).

[2] B. Wildt, P. Mali, and P. C. Searson, Langmuir 22, 10528 (2006).

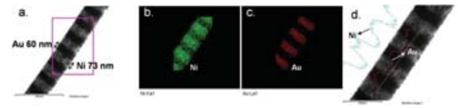

Fig. 1 TEM images of Ni/Au multilayered nanowire (Diameter: 200 nm) (a) Bright field image (b) Elemental mapping of Ni segment (c) Elemental mapping of Au segment (d) Line scanning of Ni & Au.

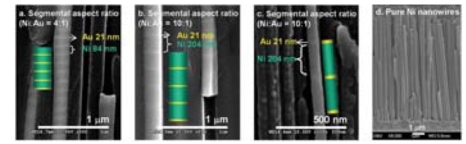

Fig. 2 SEM images of various segmental aspect ratio (a) Segmental aspect ratio (Ni:Au = 4:1, diameter = 200 nm) (b) Segmental aspect ratio (Ni:Au = 10:1, diameter = 200 nm) (c) Segmental aspect ratio (Ni:Au = 10:1, diameter = 80 nm) (d) Pure Ni nanowires (diameter = 230 nm).

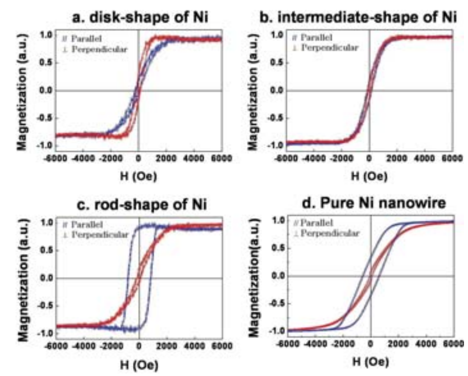

Fig. 3 VSM analysis of various Ni segment shape (a) disk-shape of Ni with 200 nm diameter (b) intermediate-shape of Ni with 200 nm diameter (c) rod-shape of Ni with 80 nm diameter and (d) pure Ni nanowire with 230 nm diameter.

BH-04

Novel phenomena in multi-layer composite structure observed by anomalous Hall effect measurement.

S. Das[1], T. Ichihara[1], H. Suzuki[1], Y. Matsuda[2]
1. Central Research Laboratory, Hitachi Ltd., Odawara, Japan; 2. Head Development, Hitachi Global Storage Technologies, Odawara, Japan

Introduction:
Application of anomalous Hall effect (AHE) measurement is helpful to investigate the magnetization processes in perpendicular magnetic anisotropy (K_u) thin films [1]. We employed AHE measurement on a multilayer thin film structure such as one generally used in the perpendicular magnetic recording medium, which is composed of a soft underlayer (SUL) with in-plane magnetization, a non-magnetic intermediate layer (IML), a hard magnetic Co-Cr based oxide layer and a soft magnetic metallic cap layer [2]. We observed that AHE measurement can selectively detect the magnetic properties of the topmost cap layer and the anomalous Hall voltage (V_{AHE}) from this layer increases with increasing cap layer thickness (t_{cap}). This is quite different from that of a single layer case where V_{AHE} decreases inversely with increasing film thickness. Based on the empirical results we developed a simple bi-layer model that suggests that such kind of phenomena could generally be observed in any stacked structure of magnetic thin films with different anomalous Hall coefficients.

Experiment:
A soft magnetic Co-Cr-Pt (CCP) cap layer (t_{cap} = 0 – 10 nm) was epitaxially grown on top of a magnetically hard Co-Cr-Pt-SiO_2 (CCPS) layer (thickness fixed at 13 nm) and both the layers possess perpendicular magnetic anisotropy (with $K_{u\_CCP} < K_{u\_CCPS}$). A stack of metallic seed layer (SL) deposited on glass substrate ensured the c-axis orientation of the CCPS layer. AHE measurement was performed using a standard four-probe method.

Results and discussions:
A CCPS layer without a CCP on it exhibited almost no V_{AHE} (Fig. 1), while a CCP layer directly deposited on the SL (i.e. without a CCPS layer underneath) exhibited comparatively large V_{AHE} (Fig. 1). Fig. 2 compares the magnetic hysteresis loops for a CCP(8 nm)/Non-magnetic spacer (2 nm)/ CCPS(13 nm) structure measured by the AHE method and a vibrating sample magnetometer(VSM). VSM loop exhibits two steps – one around 50 kA/m and another around 200 kA/m, indicating the individual magnetization reversal in the soft CCP and hard CCPS layer, respectively. This is due to the suppression of interlayer exchange coupling between these layers in presence of a comparatively thick non-magnetic spacer. However, the AHE loop reveals only one step around 50 kA/m suggesting that AHE measurement selectively detects the magnetization reversal only in the CCP layer. Measurement of the specimens without a CCP layer on the CCPS layer but with an SUL under the SL revealed large reversible V_{AHE} signal from the SUL, which implies that, though electro-conductive, CCPS does not produce any detectable V_{AHE}. This can be attributed to very small anomalous Hall coefficients (R_{CCPS}) of CCPS layer. Increase of V_{AHE} was observed with increasing t_{cap} as shown in Fig.3 for a series of CCP(0 – 10 nm)/CCPS(13 nm) specimens. This is quite different from the generally known phenomena where V_{AHE} decreases inversely with increasing thickness of a voltage producing layer [1]. In order to explain our empirical results, we considered a bi-layer model, consisted of a cap layer and the stack of other layers underneath with total thickness t_{others}. One V_{AHE} producing layer can be substituted by a voltage source and an electrical resistor connected in series and in a multilayer structure they are connected in parallel. In our bi-layer model the voltage sources are V_{cap} and V_{others}, which are characterized by the anomalous Hall coefficients, R_{cap} and R_{others}, respectively. Fig. 4 shows the change of V_{cap} and V_{others} with changing t_{cap} for $R_{cap} >> R_{others}$. V_{cap} increases with t_{cap} (for a fixed t_{others}), becomes maximum at $t_{cap} = t_{others}$ and decreases beyond that. In the region $t_{cap} >> t_{others}$, V_{cap} behaves the way similar to that of a single layer. Our model suggests a general conclusion: in a composite stacked structure composed of magnetic thin films with different anomalous Hall coefficients (R_{AHE}), there exists a region where V_{AHE} from a particular layer increases with increasing thickness, which is thinner than the total thickness of other layers.

[1] S. Nakagawa, A. Sato, I. Sasaki, and M. Naoe, "Observation of magnetization reversal processes in Co-Cr and Co-Cr-Ta ultrathin films under the canted magnetic field using anomalous Hall effect", J. Appl. Phys. Vol. 87, No. 9, p. 5705, 2000.

[2] S. Das and H. Suzuki, "Effects of SUL and cap layer thickness on the R/W performance of composite perpendicular media", presented in 52nd MMM conference (abstract ID: FQ-04, accepted for publication).

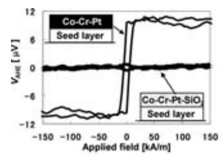

Fig. 1 Measured V_{AHE} from a Co-Cr-Pt and a Co-Cr-Pt-SiO_2 layer.

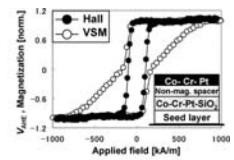

Fig. 2 Normalized V_{AHE} and VSM loop for a Co-Cr-Pt / spacer / Co-Cr-Pt-SiO_2 specimen.

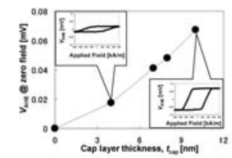

Fig. 3 Increase of V_{AHE} with increasing t_{cap}. Two measured V_{AHE} loops for t_{cap} = 4 nm and 10 nm are shown in insets.

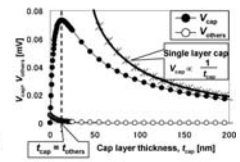

Fig. 4 Change of V_{cap} and V_{others} with increasing t_{cap}, calculated using a bi-layer model.

BH-05

Band and bubble domains in AF coupled [Co/Pt]/Ru multilayers.

C. Bran[1,2], O. Hellwig[3], U. Wolff[1], L. Schultz[1], V. Neu[1]
1. IFW Dresden, Dresden, Germany; 2. IMPRS "Dynamical Processes in Atoms, Molecules and Solids", Dresden, Germany; 3. Hitachi Global Storage Technologies, San Jose, CA

Introduction
Recently, [Co/Pt]/Ru multilayers have been developed, in which the influence of antiferromagnetic (AF) interlayer coupling on otherwise ferromagnetic (FM) films with perpendicular anisotropy can be studied [1]. The strong perpendicular anisotropy originates from the Co/Pt submultilayers which can be consider as a single FM layer. The separating Ru interlayer introduces an AF exchange between adjacent Co/Pt submultilayers [2].
Domain observations find two magnetic phases for this system, depending on the balance of exchange and dipolar coupling. The magnetization of each layer is either laterally correlated in AF configuration or vertically correlated, forming FM stripe domains and depend on the coupling strength via the details of the multilayer architecture.
The detailed study of the magnetization process in such samples is thus an important contribution to understanding the coupling mechanism.
Results and discussions
In this study we focus on $[(Co(4Å)/Pt(7Å))_8Co(4Å)/Ru(9Å)]_{18}$ multilayers which display a predominant dipolar coupling at room temperature, and we investigate the domain structure and magnetization process through the first quadrant of the hysteresis loop.
The average magnetic properties were determined by superconducting quantum interference device (SQUID) and the domain structure was characterized by MFM in magnetic field. For this, a Digital Instruments Dimension 3100 AFM/MFM has been upgraded for measurements with an external magnetic field up to 0.42 T, applied perpendicular to the sample.
A magnetic hysteresis loop with the field perpendicular to the film plane is shown in Fig. 1. Its behavior is very similar to that of simple Co/Pt multilayers with perpendicular anisotropy. In this ferromagnetic phase, the strong dipolar stray fields overcome the AF coupling between layers. The magnetization of each layer is vertically correlated from layer to layer, forming ferromagnetic band domains.
Fig 2 shows a series of MFM images for different magnetic fields applied perpendicular to the sample during the measurements. In a zero field state, due to the perpendicular anisotropy, band domains with average domain width of 180 nm are observed. By increasing the external magnetic field the domains which are aligned parallel to the field grow, while the oppositely aligned domains shrink. This process occurs gradually, until the domains transform into worms and, in the end, into a bubble domain structure at higher fields. This behavior is in principle understood by the so called bubble domain theory.
The theory was developed for single layer films by assuming a model in which the domains have cylindrical walls of zero width and it allows calculating the size and stability of the domains [3]. This leads to the prediction of a strip-out field (H_{SO}), the field in which the bubbles transform into band domains, and a collapse field (H_{CO}), the field in which the bubbles collapse. Approximating the [Co/Pt]/Ru as a thick single layer with perpendicular anisotropy, the values are H_{SO}= 0.4T and H_{CO} = 0.47 T, respectively.
A series of MFM images was recorded on the decreasing branch of the hysteresis loop in a narrow field range close to saturation (see Fig 3). By decreasing the field from 0.42 T to 0 T the bubbles diameter increases, until the bubbles transform into band domains. The MFM experiments show that this strip-out instability occurs at 0.36T. The collapse field lies above the accessible field of 0.42 T in the MFM experiment. It is estimated from the global magnetization measurements to be about 0.55T. In between these two field values, the bubble domain diameter shrinks with increasing field.
The discrepancies of these experimental values to the predicted values mentioned above reveal the influence of the layered structure with antiferromagnetic coupling and vote for an improved theory for these complex multilayers.

[1] O. Hellwig, T. L. Kirk, J. B. Kortright, A. Berger, and E. E. Fullerton, Nat. Mater. 2, 112 (2003).

[2] S.S.P. Parkin, Phys. Rev. Lett. 67, 3598 (1991).

[3] A.A. Thiele, J. Appl. Phys. 41, 1139 (1970).

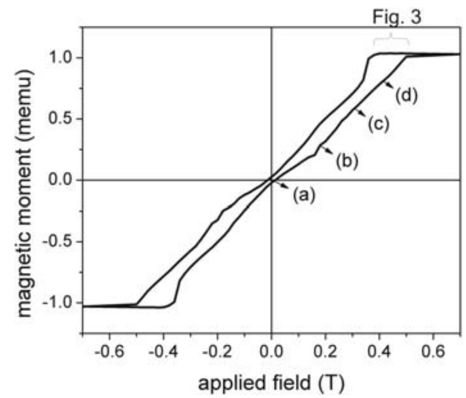

Fig. 1: Out-of-plane SQUID measurements of [(Co(4Å)/Pt(7Å))8Co(4Å)/Ru(9Å)]18 multilayers. The points a-d represent the magnetic field values of MFM images in Fig. 2.

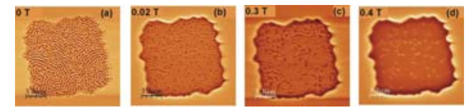

Fig. 2: Domain structure of [Co/Pt]/Ru multilayers recorded along the increasing branch of the hysteresis (see also Fig. 1).

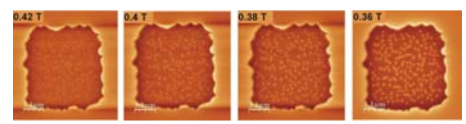

Fig. 3: Sequence of MFM images recorded on the decreasing branch of the hystersis loop.

BH-06

Exchange-spring behavior in Fe-FePt thin films studied via synchrotron radiation.

B. Laenens[1], N. Planckaert[1], J. Demeter[1], K. Temst[1], A. Vantomme[1], C. Strohm[2], R. Rüffer[2], J. Meersschaut[1]
1. Instituut voor Kern- en Stralingsfysica and INPAC, Katholieke Universiteit Leuven, Celestijnlaan 200D, B-3001 Leuven, Belgium; 2. ESRF, Rue Jules Horowitz 6, Boîte Postale 220 38043 Grenoble, France

The exchange-spring magnet, which is based on interfacial exchange coupled soft and hard ferromagnetic materials combines the high magnetisation of the soft phase with the high magnetic anisotropy of the hard phase. This kind of material is of interest for low-cost permanent magnets and other novel functional magnetic nanostructures. Fe-FePt bilayers are the prototypes of exchange spring magnets [1-3]. FePt in the $L1_0$-phase is a hard material with a high magnetocrystalline anisotropy [4-5] while Fe is a soft ferromagnetic material with a low anisotropy and high spontaneous magnetization. So far, experimental work has been performed on thin exchange spring bilayers with both the hard and the soft magnetic moments oriented in the film plane [3].
Nowadays, great interest goes to magnetic structures having their easy magnetization axis orthogonal to the film plane. Epitaxial FePt thin films stabilised in the $L1_0$ -crystal structure show this property when grown on MgO(100) [4-5]. Moreover, by depositing a thin Fe-film onto a $L1_0$ FePt layer, a new phenomenon emerges: while the hard FePt layer forces its magnetization perpendicular to the film plane, the soft Fe-layer prefers its magnetic moments to be in plane [1-2].
In this work we studied an Fe-FePt(30 nm) bilayer grown with molecular beam epitaxy of which the sample composition is illustrated in Fig.1. The soft Fe-layer consists of a wedged ^{56}Fe layer with a thickness ranging from 0 to 8.7 nm. Subsequently, an isotopically enriched ^{57}Fe layer with a thickness of 0.7 nm was grown onto the wedge. The sample was capped with 0.6 nm of ^{56}Fe and 3 nm of Ag. The isotopic enrichment has no influence on the electronic or magnetic properties of the bilayer, but allows us to selectively probe the magnetic structure of the ^{57}Fe layer as a function of the distance to the FePt-interface, using nuclear resonant scattering of synchrotron radiation (NRS). Synchrotron radiation, incident on the sample, will simultaneously excite the hyperfine-split nuclear energy levels of the ^{57}Fe atoms, giving characteristic beats in the temporal evolution of the subsequent nuclear decay signal. The analysis of this beat pattern, which is the time-based analog of classical Mössbauer spectra, allows a precise determination of the moment rotation through the ^{57}Fe-layer. The dependence on the distance t to the FePt-interface can be probed by moving the sample transversally with respect to the synchrotron beam.
Time spectra are recorded at 11 positions on the sample at the NRS beamline ID18 of the ESRF. Fig.1 shows a selection of the time spectra. The spectra are analysed using the fitting routine CONUSS [6]. From the analysis the angle θ, which is defined as the angle between the sample normal and the magnetic spins of the ^{57}Fe-layer, could be deduced. The right panel in Fig. 1 shows the rotation of the spins in the ^{57}Fe-layer as a function of the distance t. For a few monolayers of Fe, the magnetically hard FePt pins the magnetisation in the soft Fe layer to the out-of-plane direction. By increasing the Fe-layer thickness to 9 nm, the influence of the FePt diminishes and the magnetization cants to the in-plane Fe[001]-direction.
In addition, we performed magnetometry measurements at different positions on the wedge to investigate the strength of the exchange coupling. The external field was applied along an in-plane Fe[110] direction. From the time spectra we could deduce how the moments start to cant towards the external field as the field increases. A field of 4.5 Tesla was required to saturate the ^{57}Fe-spins in the middle of the wedge.

We thus were able to directly probe the magnetic properties of exchange-spring Fe-FePt bilayers by exploiting the isotope selectivity of NRS. Our results will be modeled in the framework of one-dimensional micro-magnetical calculations.

[1] G. Asti et al., Phys. Rev. B, 73, 94406 (2006).

[2] F. Casoli et al., IEEE Trans. Magn. 41, 3877 (2005).

[3] R. Röhlsberger et al., Phys. Rev. B, 899, 237201-1 (2002).

[4] A. Cebollada et al., Phys. Rev. B 50, 3419 (1994).

[5] R. F. C. Farrow et al., J. Appl. Phys. 79, 5967 (1996).

[6] W. Sturhahn et al., Hyp. Interact 125, 149-172 (2000).

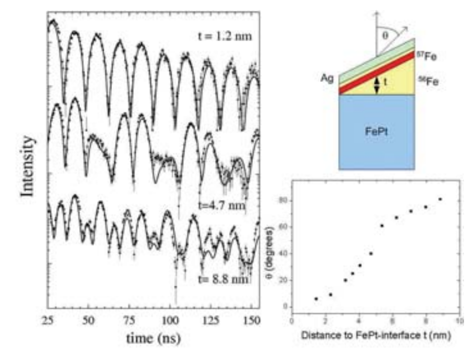

(left) Time spectra of the ^{57}Fe(0.7 nm)/^{56}Fe(t) /^{56}FePt-structure taken at zero field as a function of increasing distance t to the FePt-interface. The solid lines through the data are the fits obtained by the fitting program CONUSS [6]. (right) Illustration of the sample composition and depth dependence of the spin rotation in the ^{57}Fe layer.

BH-07

How to retrieve more information on magnetic films from microwave permeability measurements.

O. Acher[1], V. Dubuget[1,2], S. Dubourg[1]
1. Departement Matériaux, CEA, Monts, France; 2. UMR 6157 LEMA, Tours, France

INTRODUCTION

The growing interest in high frequency systems and ultrafast devices has boosted the investigation of the microwave permeability of ferromagnetic films in the GHz range. Efficient and reliable permeameters allow the determination of the microwave permeability of thin films with a good precision. Recently, it has been established that the integral of the imaginary part of the permeability multiplied with the frequency could be used to retrieve information on the magnitude and the orientation of the magnetization in thin films [1,2].

This paper provides experimental examples on information retrieval using this integral on soft amorphous CoZr films. This approach is compared to the conventional approach that relies on fitting the permeability spectra using the gyromagnetic equations for a uniformly magnetized thin film. It is shown that the integral approach provides a better precision, and can be used successfully even in cases where the uniform gyromagnetic model fails.

THEORETICAL APPROACH

The permeability tensor of a film with in-plane uniform magnetization is well known. In particular, the low-frequency permeability and the resonance frequency are related to the saturation magnetization $4\pi Ms$ by a generalization of Snoek's law to thin films (Eq. (1) in Fig. 1). In the case the magnetization is oriented at an angle θ with the direction z within the film plane (xz), Eq. (2) in Fig. 1 allows the determination of this angle. However, this holds only in the restricted framework of a uniform magnetization.

Recently, it has been established that though heterogeneities, magnetization dispersion, magnetic coupling, eddy current effects, can have large effect on the permeability, the integral of the imaginary part of the permeability μ" multiplied with the frequency f is not affected by this complexity. In order to retrieve information from the permeability of magnetic films with complex magnetization configuration, the efficient dynamic magnetization defined by Eq. (3) (Fig. 1) is a convenient quantity. At a sufficiently high frequency, it is equal to the saturation magnetization (Eq. (4)). It is also possible to retrieve information on the dispersion of the orientation of the magnetization through Eq. (5).

RESULTS

The permeability spectra of 6 amorphous CoZr films have been measured and processed using the equations on Fig. 1. Fig. 2 compares the numerical values of the saturation magnetization retrieved using different methods. It appears clearly that the dynamic magnetization defined by Eq. (3) provides the best estimates. The magnetization dispersion is found to be close to 10° using Eq. (5).

A bilayer manufactured by depositing two CoZr layer with their easy axis rotated by 90° in the film plane is also studied. The permeability of this sample along 2 directions is given in Fig. 3. There is no simple model available to account for this behavior, and Eqs (1) and (2) fail to account for the observation. Using the integral of the imaginary part of the permeability times frequency, a saturation magnetization of 11.2kG is retrieved, within 6% of the value obtained with a VSM. Quantitative indications on the dispersion of the magnetization are also obtained.

As a conclusion, microwave permeability measurements allow the retrieval of important information on the magnetization within thin films and multilayers, when the integral of the imaginary permeability times frequency is properly exploited. In contrast to other techniques, this technique is not restricted to very thin films or multilayers.

[1] O. Acher and A. L. Adenot, Phys. Rev. B 62, 11324 (2000).

[2] O. Acher and S. Dubourg, http://fr.arxiv.org/abs/0710.2980

$$\frac{F_0}{\gamma}\sqrt{\mu'_0-1}=4\pi M_s \quad (1)$$

$$\frac{\mu'_z-1}{\mu'_x-1}=\tan^2\theta \quad (2)$$

$$M_{\mu,x}(F)=\frac{1}{\gamma}\sqrt{\frac{2}{\pi}\int_0^F \mu_x"(f).f.df} \quad (3)$$

$$M_\mu=4\pi M_s \quad (4)$$

$$\frac{\sqrt{\langle sin^2\theta\rangle}}{\sqrt{\langle\cos^2\theta\rangle}}=\frac{M_{\mu,z}(F)}{M_{\mu,x}(F)} \quad (5)$$

Fig. 1. Equations relating static and dynamic (i.e. associated to the microwave permeability) magnetic parameters.

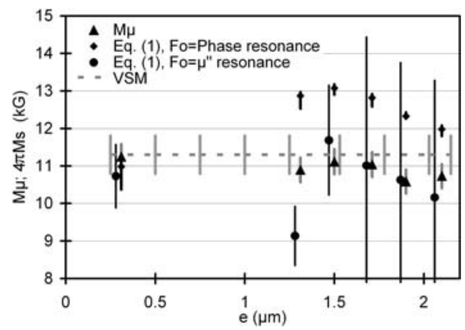

Fig. 2. Retrieval of the saturation magnetization through the integral quantity Mμ obtained from Eqs (3), (4). Comparison with the values retrieved from Snoek's law under the discrete form (Eq. 1), and taking for F0 either the phase resonance (corresponding to μ'(F0)=1), or the μ" resonance (corresponding to μ"(F0) maximum).

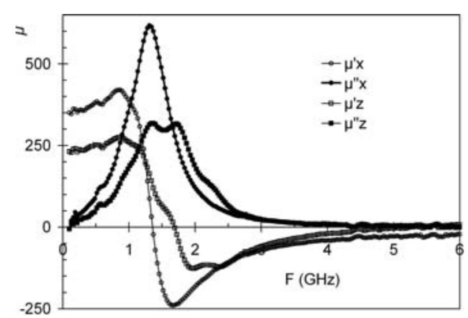

Fig. 3. Permeability spectra of the CoZr bilayer measured along two directions of its plane.

BH-08

The effect of FePt layer on the transition temperature of FeRh layer.

N. T. Nguyen, Y. Y. Hnin, T. Suzuki
Information Storage Materials Laboratory, Toyota Technological Institute, Nagoya, Japan

Recently, FePt/FeRh bilayers have attracted much attention because of their potential application. It is known that FeRh exhibits the first order transition from anti to ferromagnetic phase upon heating [1]. Thiele et al., showed the coercivity of a FePt/FeRh film decreased sharply at the transition temperature of FeRh layer [2]. However, there has been very little systematic study as to the detailed mechanism of the magnetization behaviors at around the first-order magnetic phase transition; Therefore, a systematic study has been carried out in order to understand their magnetization on temperature for FePt/FeRh.

Bilayers FePt/FeRh were deposited onto MgO(100) substrates by DC magnetron sputtering. Thin films of FeRh(300 nm) were first deposited onto MgO, then annealed at 700°C for 10 hours, followed by a successive deposition of FePt. As-deposited bilayers of FePt/FeRh thus fabricated were annealed for 5 min at 600°C.

Figure 1 shows XRD patterns of of the four different samples, as described in the figure. Strong peaks (001) of CsCl type FeRh are observed for all the samples while the (001) peak of FePt is seen only for the annealed FePt(300 nm)/FeRh.

Figure 2 shows M-T curves with different applied magnetic fields, H_{ap} during the heating and cooling processes of FeRh(300 nm) and FePt(30 nm)/FeRh(300 nm). It is seen that the transition temperature is shifted to the lower temperature as the H_{ap} is increased. The shift is about -0.70 K/kOe for the FeRh and -0.73 K/kOe for the FePt/FeRh. The total entropy changes associated with the transition are 186 mJ/K.cc and 172 mJ/K.cc, respectively. This observation is consistent with bulk measurements where the entropy change of 142 mJ/K.cc was observed [3]. This may presumably be interpreted in term of the stabilization of the FM phase by H_{ap} during the transition leading to a lower transition temperature [2].

Shown are in figure 3 M-T curves of the four different samples. The transition temperatures of FePt/FeRh are lower than that of a single layer of FeRh. This is believed due to an exchange coupling between FeRh and FePt[4].

The dependences of magnetization and coercivity on temperature for the annealed FePt(300nm)/FePt(300nm) are shown in figure 4. At the transition temperature, the coercivity in parallel directions decreases shapely from 3000 Oe to 350 Oe. However in perpendicular directions, the decrement in $H_{C\text{-}per}$ is not significant as compared with $H_{C\text{-}par}$.

[1] M. Fallot, Ann. Phys. 10, 291 (1938).

[2] S. Maat, J.-U. Thiele, and E.E. Fullerton, Phys. Rev. B, 72, 214432 (2005).

[3] J. S. Kouvel. Jour. Appl. Phys 37, 1257 (1966)

[4] Hnin Y.Yuko et al., be published in Jour. Mag. Mag. Mat 2008

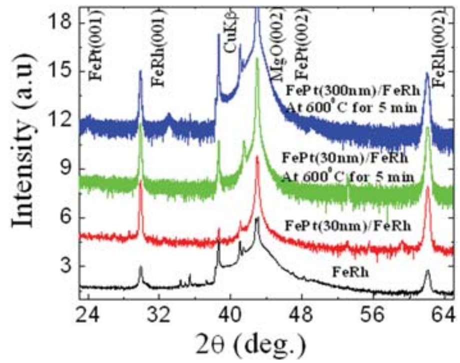

Fig.1. X-ray diffraction patterns of FeRh, FePt(30 nm) /FeRh as-deposited, FePt(30 nm)/FeRh, and FePt(300 nm)/FeRh, annealed at 600°C for 5 min.

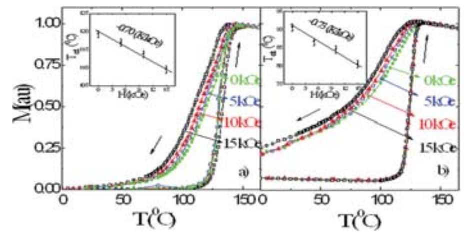

Fig. 2. M-T curves of a) FeRh(300 nm), and b) FePt(30 nm)/FeRh(300 nm) with various applied magnetic fields. Inset: The dependence of transition temperature on H_{ap} in the cooling process.

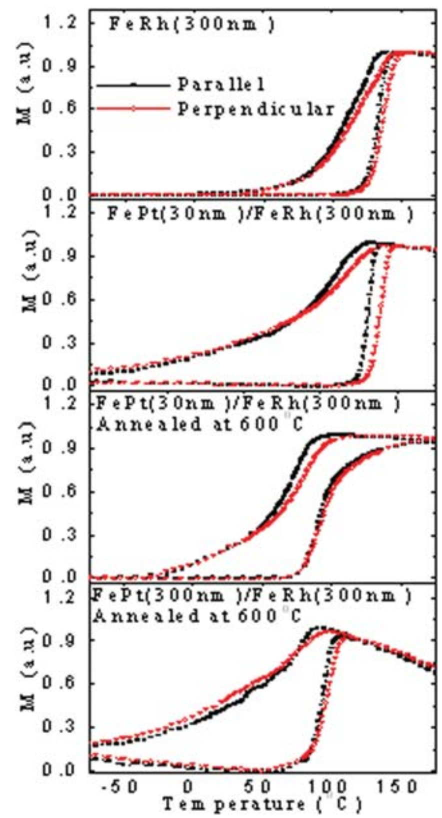

Fig. 3. M-T curves of FeRh, FePt(30 nm)/FeRh as-deposited, FePt(30 nm)/FeRh, and FePt(300 nm)/FeRh, annealed at 600°C for 5 min.

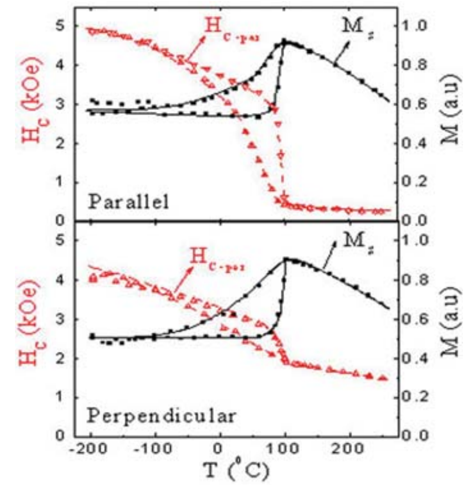

Fig. 4. The M-T and H_C - T curves of the annealed FePt (300 nm)/FeRh bilayer.

BH-09

Effects of perpendicular interlayer coupling on canting angles of TbCo sublattice magnetization by x-ray magnetic circular dichroism.

M. Lin[1], P. Huang[1], Y. Wu[1], H. Hou[1], C. Lai[1], H. Lin[2], F. Chang[2]
1. Department of Materials Science and Engineering, National Tsing Hua University, Hsinchu, Taiwan; 2. National Synchrotron Radiation Research Center, Hsinchu, Taiwan

Introduction:
The perpendicular interlayer coupling through oscillatory RKKY interaction has been reported between Co/Pt multilayers (MLs) and Co/TbCo bilayers with Ru spacer thickness [1]. In rare-earth and transition-metal (RE-TM) alloys, because of strong antiparallel exchange coupling between the TM and heavy RE moments, the orientation of Tb-sublattice moment was considered to be aligned in the opposite direction of Co-sublattice moment. However, the sublattice magnetizations of TbCo are not perfectly antiparallel, which depends on the competition between the exchange and the difference in the anisotropies of sublattices. Therefore, possible canting between the sublattice magnetization has been achieved by an external magnetic field [2]. In this work, we demonstrate that the canting angles between Tb and Co sublattices can be altered by the perpendicular RKKY interlayer coupling between Co/Pt MLs and Co/TbCo bilayers, the canting angle is directly measured by using x-ray magnetic circular dichroism (XMCD).
Experiment and Result:
The samples of Pt/ TbCo/ Co/ Ru(t_{Ru})/ Co/ $[Pt/ Co]_{n=5}$/ Pt/ Ta/Si were prepared by using UHV sputtering. All samples exhibited perpendicular anisotropy and showed oscillatory interlayer coupling with variation of the Ru spacer thickness. In Fig 1(a), the ferromagnetic (F) interlayer coupling at Ru=2 nm led to the clearly shifted minor loop of [Co/Pt] MLs. The schematic diagram in the inset showed the parallel magnetic moments in the remnant state between [Co/Pt] MLs and TbCo/Co bilayers.
In the XMCD measurement, the polarized x-ray was incident to the samples at an angle of 30 degree from the surface normal with P- and A-incidences as the schematic diagram shown in Fig 1(b). If the Tb- and Co-sublattice moments were perfectly perpendicular to the film surface, the XMCD intensity of the Tb M_5 and Co L_3 edge of P- and A-incidences should be equal (I_P=I_A) because the two incident X-rays had the same angle from the perpendicular moment. Therefore, the effective canting angle Φ_{Tb} and Φ_{Co} with respect to the surface normal direction can be calculated by using the equation $\tan\Phi=\cot 30*(I_A-I_P)/(I_A+I_P)$ where I_p and I_A represented the XMCD intensity of the Tb M_5 and Co L_3 edge of P- and A-incidences. [3]
The XMCD spectra of Tb $M_{4,5}$ and Co $L_{2,3}$ for the sample with Ru=2nm were shown in Figure 1(b). The XMCD results revealed the presence of the canting of Tb and Co moments in the TbCo film of Ru spacer at 2 nm with interlayer coupling strength of J=0.11 erg/cm^2. The canting angles of Tb and Co was determined to be close to Φ_{Tb}=10 and Φ_{Co}=5 degree. On the other hand, almost no canting effect was observed with a stronger coupling strength (J=0.38 erg/cm^2) when Ru was reduced to 1 nm. Since the Co/Pt MLs possessed perfectly aligned perpendicular magnetization, the strong interlayer coupling through RKKY interaction may align the sublattices of Tb and Co along the perpendicular direction so the canting angles were close to zero.

[1] M. S. Lin and C. H. Lai, J. Appl. Phys. 101, 09D121 (2007)

[2] S. Rinaldi and L. Pareti, J. Appl. Phys. 50, 7719 (1979)

[3] C. C. Lin, C. H. Lai et al., J. Appl. Phys. 95, 6846 (2004)

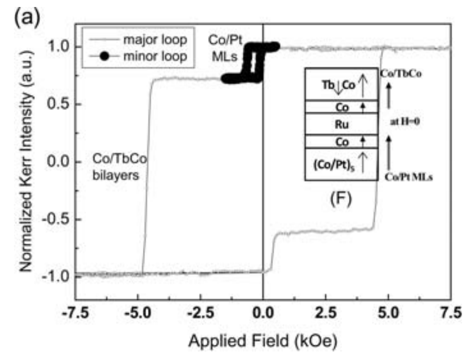

Figure 1 (a) Hysteresis loops, measured by polar-MOKE, of the $[Co(0.5)/\ Pt(2)]_{n=5}$/ Co(0.5)/ Ru(2)/ Co(0.5)/ TbCo(17) sample (unit: nm).

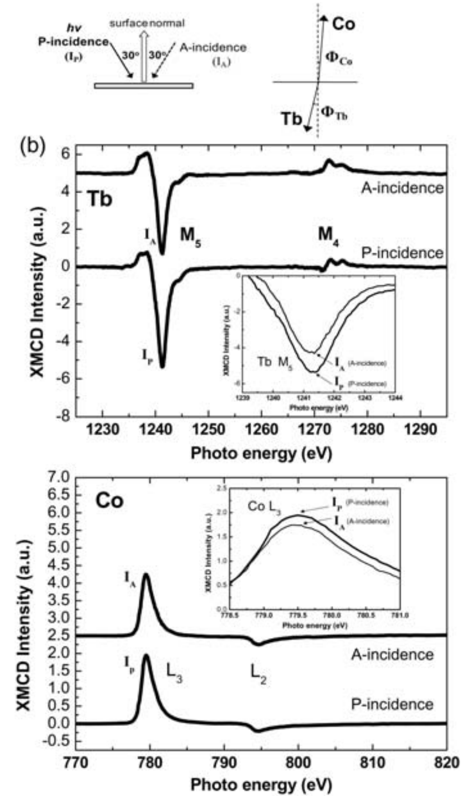

Figure 1 (b) The XMCD spectra of Tb edge and Co edge of P- and A-incidence in the $[Co(0.5)/\ Pt(2)]_{n=5}$/ Co(0.5)/ Ru(2)/ Co(0.5)/ TbCo(17) sample (unit: nm).

BH-10

Magnetization reversal in thermally processed Fe/SmCo spring magnets.

J. E. Davies[1], Y. Choi[2], J. P. Liu[3], J. S. Jiang[2], S. D. Bader[2], R. D. Shull[1], K. Liu[4]
1. Metallurgy/Magnetic Materials, NIST, Gaithersburg, MD; 2. Materials Science Division, Argonne National Laboratory, Argonne, IL; 3. Physics Department, University of Texas, Arlington, TX; 4. Physics Department, University of California, Davis, CA

Exchange spring magnets have been of intense interest due to their applications in permanent magnet,[1,2] thermally assisted magnetic recording,[3] and exchange coupled composite media.[4,5] Recently, it has been shown that the exchange coupling between hard and soft layers in thin film Fe/epitaxial-SmCo bilayer spring magnets can be enhanced through thermal processing of the material by varying the substrate temperature during deposition.[6,7] We perform first order reversal curve (FORC) measurements[8,9] on samples where the Fe layer was sputter-deposited at either 100°C or 400°C (referred to hereafter as T100 and T400, respectively) after depositing the SmCo layer at 400°C in order to better understand the effects of the thermal processing. We also use FORC to measure the irreversible magnetization present in each sample and relate this measurement to the different interfacial morphologies. The T100 sample has a sharp but jagged interface while the T400 interface is uniform but diffusive.
The FORC's [Figs. 1(a) and 1(b)] and FORC distributions [Figs. 1(c) and 1(d)] show reversal behavior characteristic of Fe/SmCo spring magnets.[9] The major loop delineated by the FORC's has two reversal steps with the first step following along the descending branch corresponding to Fe layer reversal. During Fe reversal the FORC's trace along the major loop and the FORC distribution (ρ) is zero [Figs. 1(c) and 1(d), above dashed line]. The second reversal step denoted in Figures 1(a) and 1(b) by the point labeled $\mu_o H_o$ corresponds to the reversal of the SmCo layer. Once the SmCo layer begins to reverse the FORC's deviate from the major loop and ρ becomes non-zero with two distinct features emerging. A negative/positive pair [Fig. 1(c) and 1(d), left of the solid vertical line] corresponding to the change in Fe reversal due to partial demagnetization of the SmCo layer and a high field peak [Fig. 1(c) and 1(d), right of the solid vertical line] corresponding to the SmCo reversal.
While qualitatively the same features occur for the two samples, there are clear differences. The features for T400 emerge at smaller reversal fields and are more localized. This is better illustrated in a FORC switching field distribution (FORC-SFD) obtained by projecting ρ onto the $\mu_o H_R$ (vertical) axis. The FORC-SFD for T100 [Fig. 2(a), filled symbols] is centered at $\mu_o H_R$ = -0.75 T and has a half width of 0.14 T. The T400 FORC-SFD is centered at $\mu_o H_R$ = -0.47 T with a half-width of 0.07 T. The smaller $\mu_o H_R$ magnitude indicates a stronger interlayer exchange coupling in the T400 sample. The narrowing of the FORC-SFD indicates smaller variations of interfacial properties. Both are results of the more uniform but diffusive interface due to the higher temperature deposition.
Integration over ρ yields the fraction of the magnetization that switches irreversibly (M_{irr} / M_s) for each sample. For T100 $M_{irr} / M_s \approx 0.37$, whereas for T400 $M_{irr} / M_s \approx 0.43$. Interestingly, the total SmCo layer contribution is only $M_{SmCo} / M_s = 0.24$. Thus the additional contribution to M_{irr} / M_s must originate from the Fe layer. In T100 this is most likely due to the jagged interface causing variations in exchange coupling. In T400 it is likely due to the interdiffusion resulting in a gradual increase in anisotropy across the interface. Also, the greater value of M_{irr} / M_s for T400 implies a thicker interfacial region is present compared to T100.
This work has been supported by ACS-PRF, DOE-BES, NRC Postdoctoral Fellowship (J.E.D.), DOD-MURI (Y.C.) and the Alfred P. Sloan Foundation (K.L.).

[1]E. F. Kneller, *et al.*, IEEE Trans. Magn. 27, 3588 (1991).

[2]R. Skomski, *et al.*, Phys. Rev. B 48, 15812 (1993).

[3]J. U. Thiele, *et al.*, Appl. Phys. Lett. 82, 2859 (2003).

[4]R. H. Victora, *et al.*, IEEE Trans. Magn. 41, 537 (2005).

[5]D. Suess, *et al.*, IEEE Trans. Magn. 42, 2357 (2006).

[6]J. S. Jiang, *et al.*, Appl. Phys. Lett. 85, 5293 (2004).

[7]Y. Choi, *et al.*, Appl. Phys. Lett. 91, 022502 (2007).

[8]C. R. Pike, *et al.*, J. Appl. Phys. 85, 6660 (1999).

[9]J. E. Davies, *et al.*, Appl. Phys. Lett. 86, 262503 (2005).

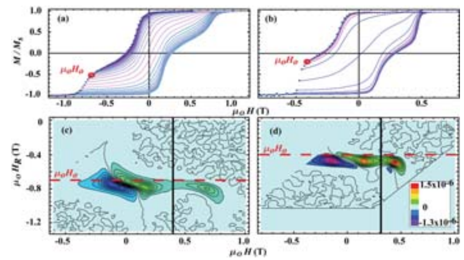

Figure 1- FORC's (top) and corresponding contour plots of the FORC distributions (bottom) for T100 [(a) and (c)] and T400 [(b) and (d)]. The onset of SmCo reversal is denoted by $\mu_o H_o$ corresponding to the dashed lines in the FORC diagrams. Both samples have FORC distributions consisting of a negative/positive pair of features at low fields corresponding to Fe reversal (left of solid line) and a single positive peak at high fields corresponding to SmCo reversal (right of solid line).

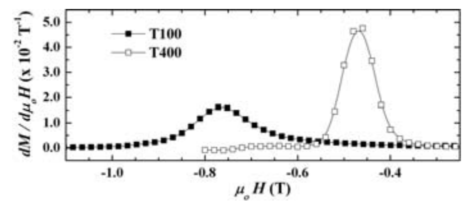

Figure 2 - The FORC-SFD's for T100 (filled symbols) and T400 (open symbols).

CA-01

Non-invasive Measurement of Tissue Iron Concentrations with Magnetic Resonance Imaging.

T. G. St Pierre
School of Physics, University of Western Australia, Perth, WA, Australia

There is a number of human diseases and disorders that result in excessive iron being deposited in tissues in the form of nanoparticulate iron oxyhydroxides. The effective clinical management of these diseases often requires measurement of tissue iron concentrations in order to be able to determine the type and extent of iron depletion therapy required. The majority of excess iron is deposited in the liver and there is evidence to indicate that in thalassemia and hereditary hemochromatosis, liver iron concentration can be used as a surrogate measure for the total body iron stores [1,2]. Until recently, the gold standard for liver iron concentration measurement was chemical assay of a needle biopsy specimen. However, the technique is subject to large sampling errors in addition to being invasive. Over the past few years we have developed a method for the non-invasive measurement of liver iron concentrations using magnetic resonance imaging. The method is based on the measurement of the rate of dephasing of proton spin precession in liver tissue [3]. The presence of clusters of iron oxide particles with a magnetic susceptibility significantly different from the surrounding water-containing tissue results in local perturbations of the static magnetic field generated by the magnetic resonance imager. The resulting increase in the range of fields experienced by the water protons in the vicinity of the iron oxyhydroxide particles yields a greater range of Larmor precession frequencies of the water protons and hence a greater rate of dephasing of the precession of the protons.

A calibration curve relating liver proton transverse relaxation rates (R_2) to liver iron concentration (LIC) has been determined though the in vivo measurement of R_2 by a series of single spin echo measurements and the measurement of LIC by chemical assay of biopsy specimens in 105 human subjects [4]. Figure 1 shows four example liver R_2-images together with their respective liver R_2-distributions for four human subjects. The R_2-distribution shifts to higher values as the liver iron concentration increases.

We have also demonstrated the ability of liver R_2-imaging to map liver iron concentrations [5]. Figure 2(a) shows an R_2 image of an array of tissue samples taken from a single iron loaded liver post-mortem. The mean values of R_2 for each sample are plotted against the chemically measured tissue iron concentrations in Figure 2(b) showing a high degree of correlation thus indicating that an R_2-image of the liver can be interpreted as an iron concentration map. Note the large variation in local LIC which leads to large sampling errors on the conventional biopsy method of measurement of LIC. The ability to measure the spatial variation of LIC may have applications in the detection of liver fibrosis or cirrhosis where the presence of scar tissue results in locally reduced iron concentrations.

This R_2 method of measuring liver iron concentrations has now replaced the needle biopsy method at many clinical centres. The method has been cleared by regulatory health authorities in Europe, USA, Canada, and Australia and is currently available in over 80 clinical centres worldwide with over 3000 patient measurements having been performed. It is being marketed under the commercial name FerriScan®.

[1] E. Angelucci, G. M. Brittenham, C. E. McLaren, M. Ripalti, D. Baronciani, C. Giardini, M. Galimberti, P. Polchi, and G. Lucarelli, New England Journal of Medicine. 343, 327-31 (2000).

[2] K.M. Summers, J.W. Halliday, L.W. Powell, Hepatology. 12, 20-25 (1990).

[3] T. G. St. Pierre, P. R. Clark, and W. Chua-anusorn, NMR in Biomedicine 17, 446-458 (2004).

[4] T. G. St. Pierre, P. R. Clark, W. Chua-anusorn, A. J. Fleming, G. P. Jeffrey, J. K. Olynyk, P. Pootrakul, E. Robins, and R. Lindeman, Blood 105, 855-861 (2005).

[5] P. R. Clark, W. Chua-anusorn, and T. G. St Pierre, Magnetic Resonance in Medicine 49, 572-575 (2003).

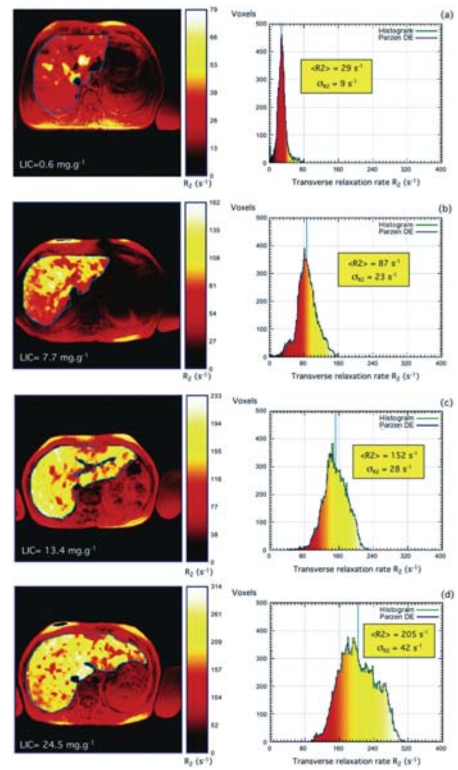

Figure 1: Liver R_2-images and R_2-distributions for 4 human subjects with liver iron concentrations ranging from normal at the top to highly loaded at the bottom (reproduced from [4]).

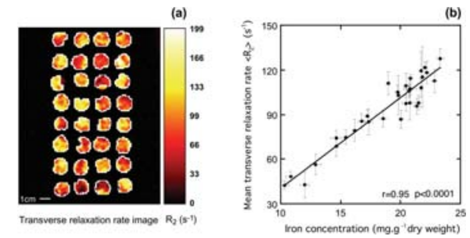

Figure 2: (a) R_2-image of an array of tissue samples from a single iron-loaded liver post-mortem. (b) plot of mean R_2 against tissue iron concentration for the samples (reproduced from [5]).

CA-02

Exploring the frontiers of magnetic nanoparticles prepared in microemulsions: from ferrofluids to biomedical applications.

J. Rivas[1,2], M. Lopez Quintela[2,1]
1. Laboratory of Magnetism and Nanotechnology(NANOMAG), University of Santiago de Compostela, Santiago de Compostela, Spain; 2. Laboratory of Magnetism and Nanotechnology(NANOMAG), University of Santiago de Compostela, Santiago de Compostela, Spain

The production of monodisperse magnetic nanoparticles (NPs) is nowadays one of the most important challenges in Nanotechnology. The microemulsion technique is a powerful method to prepare simple metallic and oxide NPs, as well as, core-shell and "onion-like" NPs . Although microemulsions cannot be considered as real templates, they constitute an elegant technique, which can provide a very good control of the final particle size. The reason for that is a complex interplay mainly between three parameters, namely, surfactant film flexibility, reactant concentration and reactant exchange rate. By adequately choosing these three parameters one can get a homogeneous distribution of particle sizes .
In the last years it has been shown that most of materials show a dramatic change in their properties at the nanometer/ subnanometer level. In particular, metallic clusters ("particles" formed by Natoms < 100 atoms) are one of the most promising and exciting research areas because they combine the scientific with the application interest. From the scientific point of view, there are many controversial points about the exact stability, structure/geometry and properties of these tiny nanoparticles. For example, according to theoretical calculations, different geometries –very different from the bulk- seem to be stable: for Natoms < 10/12, planar geometries are preferred, whereas for Natoms>10/12, 3D structures with compact, non-compact and five-fold symmetries are found to be the most stable ones, depending upon the conditions and approximations used for the theoretical calculations . A number of new fascinating properties seem to appear at these scales. As an example, fluorescence, catalysis, magnetism, and circular dicroism have been already reported. However, all these studies are very limited because of the procedures used for the cluster synthesis. Only very small amounts of highly polydisperse samples can be obtained after difficult separation procedures . We have recently developed a novel microemulsion-based method for the synthesis of clusters which allows their production in relatively large amounts, .
In this talk we will describe the microemulsion synthesis procedure showing preliminary results about the stability, structure, and properties of some magnetic clusters produced by this method . Biomedical applications of these "new" materials will be discussed.

(1)See e.g. López-Quintela, MA; Rivas, J. J.Colloid Interface Sci. 1993, 158, 446; Ibid, Curr.Opìnion Colloid Interface Sci. 1996, 1, 806; López-Quintela, M.A., Rivas, J. Blanco, M.C. Tojo, C. In "Nanoscale Materials", Ed. by L.M. Liz Marzán and P.V. Kamat. Kluwer Academic Plenum Publ., 2003, Chapter 6, pp.135-155.

(2)See e.g. López-Quintela, MA. Curr. Opin. Colloid Interface Sci., 2003, 8, 137.

(3)Häkkinen, H; Moseler, M; Landman, U. Phys.Rev.Lett. 2002, 89, 33401.

(4)Zheng, J.; Zhang, C.; Dickson, R.M. Phys.Rev.Lett. 2004, 93, 77402.

(5)Hurata, M.; Tsubota, S.; Kobayashi, T.; Kageyama, H.; Genet, M. J.; Delmon, B. J. Catal. 1993, 144, 175.

(6)Yamamoto, Y.; Miura, T.; Suzuki, M,; Kawamura, N.; Miyagawa, H.; Nakamura,T.; Kobayashi,K.; Teranishi,T.; Hori,H. Phys.Rev.Lett. 2004, 93, 116801.

(7)Schaaff, T.G.; Whetten, R.L. J.Phys.Chem.B 2000, 104, 2630.

(8)See e.g. Petty, J.T.; Zheng, J.; Hud, N.V.; Dickson, R.M. J.Am.Chem.Soc. 2004, 126, 5207; Negishi, Y.; Tsukuda, T. J.Am.Chem.Soc. 2003, 125, 4046.

(9)López-Quintela, M.A.; Rivas, J. Procedure for the synthesis of atomic quantum clusters. Spanish patent application No.P200502041, 2005.

(10)Guillén-Villafuerte, O.; García, G.; Anula, B.; Pastor, E.; Blanco, M.C.; López-Quintela, M.A.;

Hernández-Creus, A.; Planes, G.A. Angew.Chem.Int.Ed. 2006, 45, 4266.

(11)Ledo-Suárez A, Rivas J, Rodríguez-Abreu CF, Rodríguez MJ, Pastor E, Hernández-Creus A, Oseroff SB, López-Quintela MA. Angew.Chem.Int.Ed. 2007, 46, 8823.

CA-03

Spintronic biochips for biomolecular recognition detection.

P. Freitas[1,2], V. Martins[1,3], F. Cardoso[1,2], S. Cardoso[1], V. Chu[1], J. Conde[1,3], J. Loureiro[1,2], J. Germano[5,4], L. Sousa[5,4], M. Piedade[5,4]
1. INESC MN, Lisbon, Portugal; 2. Physics Department, Instituto Superior Tecnico, Lisbon, Portugal; 3. Chemical and Bioengineering Department, Instituto Superior Tecnico, Lisbon, Portugal; 4. Electrical Engineering Department, Instituto Superior Tecnico, Lisbon, Portugal; 5. INESC ID, LISBON, Portugal

Spintronic-based biomolecular recognition platforms use magnetic labels to tag biological targets (DNA strands, cells), and spintronic detectors to determine hybridization of the labeled biological targets to surface immobilized biological probes 1. The magnetoresistive detector (usually a spin valve or MTJ based sensor) senses the fringe field originating from the bound magnetic labels. In a spintronic biochip array, magnetoresistive detectors are fabricated on the substrate, with magnetic field guide lines (MFGs) being used to array labeled target biomolecules to the immobilized probes (magnetically assisted hybridization). DC and AC excitation fields are usually used, the DC field increasing the moment of the magnetic label, and the AC field modulating the bead moment to allow detection close to the sensor thermal background noise. For 130nm diameter magnetite labels, magnetized with 1.5kA/m fields, detection capability of the present platform runs from few labels up to few thousands. In order to allow scaling to hundreds of biological probes, a platform including a thin-film diode in series with a MTJ sensor at each probe site has been developed. The detection limits of this platform are compared with spin valve only or MTJ only based platforms. For point-of-care bioassays, a portable electronic platform was developed, allowing full control of the bioassay from a pocket PC. The noise level of this measuring platform is 140nV rms at 375 Hz, in fact determining the biological target lower detection limit. Control bioassays were done using spin valve based arrays (no diode), where e-Coli DNA strands were detected using 20mers oligo probes, immobilized on Au surfaces. Lower detection limits are at 1 pM target concentrations, and a linear response is obtained up to tens of nM (see Fig.1). Use of biomolecular target concentration using MFGs allows improving detection limit down to tens of fM. The possible integration of this biomolecular hybridization detection platform with other lab-on-chip modules is described.

References:

1-"Spintronic biochips for biomolecular recognition", P.P.Freitas and H.A.Ferreira, in Handbook of Magnetism and Advanced Magnetic Materials, vol. IV, (Ed. H.Kroenmuller and S.S.Parkin), Chap.XX, John Wiley Sons, 2007

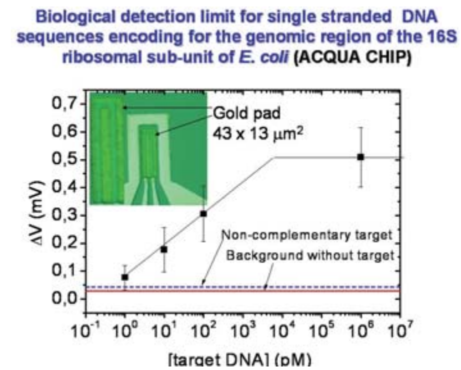

CA-04

In vivo sensing, moving and heating of magnetic nanoparticles in the human body.

Q. Pankhurst
London Centre for Nanotechnology, London, United Kingdom

The emerging field of 'endomagnetics' – the sensing, moving and heating of magnetic nanoparticles in the human body for diagnostic and therapeutic purposes - will be reviewed. Examples will be given for each of the modalities, including the following:
Sensing: A high-Tc SQUID based sensor system, with a room temperature hand-held probe, designed for use in a hospital operating theatre to detect breast cancer sentinel lymph nodes (Figure 1). The system is currently being evaluated in patients, and has been used successfully in seven operations.
Moving: A high field-gradient magnetic actuator designed to capture magnetic nanoparticle loaded haematopoetic stem cells for the treatment of atherosclerosis. Bench-top (Figure 2) and animal trials are under way to establish the efficacy of such a therapy, with promising results.
Heating: Magnetic field hyperthermia treatment for superficial and, as a long term goal, metastatic cancer, using antibody-targeted magnetic nanoparticles. Work is progressing on several fronts: the synthesis of improved magnetic particles for heat transduction (Figure 3), the engineering of new high-frequency drive circuits to produce rf fields in controlled geometries, and cell and animal studies of antibody-nanoparticle conjugation and tumour targeting.

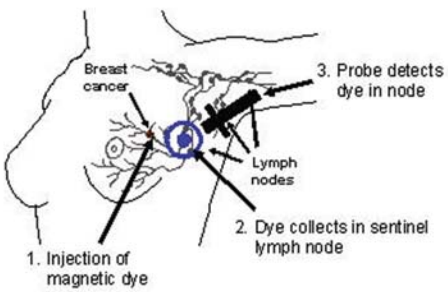

Figure 1: An intra-operative medical device for breast cancer surgery which uses a novel hand held probe with a high-sensitivity, high-Tc SQUID based sensor.

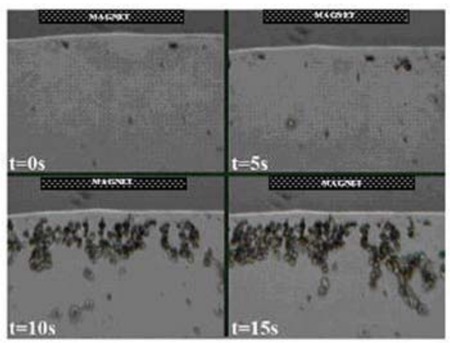

Figure 2: Microscope images showing the attraction of magnetically labelled CD133 stem cells towards a magnet placed at the top of a cells-in-water droplet. Scale: each cell is ca. 10 μm in diameter.

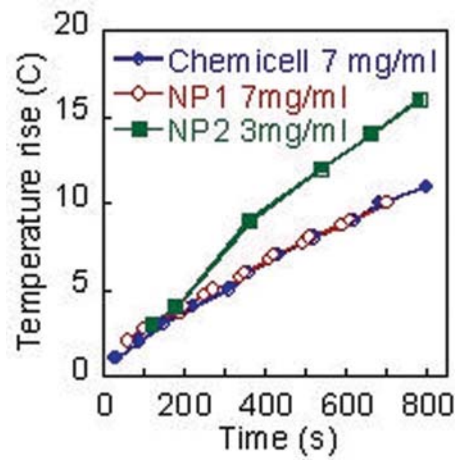

Figure 3: Magnetic field heating characteristics of a commercial nanoparticle suspension and two lab-synthesised samples – all are magnetite/maghemite based. Measurements recording in an rf field of magnitude 140 Oe and frequency 138 kHz.

CA-05

Room-temperature detection of single magnetic biomolecular labels with Hall devices*.

G. Mihajlovic[1], K. Aledealat[2], P. Xiong[2], S. von Molnár[2], M. Field[3], G. J. Sullivan[3], K. Ohtani[4], H. Ohno[4]
1. Materials Science Division, Argone National Laboratory, Argonne, IL; 2. Center for Materials Research and Technology (MARTECH) and Department of Physics, Florida State University, Tallahassee, FL; 3. Teledyne Scientific Company LLC, Thousand Oaks, CA; 4. Laboratory for Electronics Intelligent Systems, Research Institute of Electrical Communication, Tohoku University, Sendai, Japan

Superparamagnetic beads are becoming increasingly popular for labeling individual biomolecules in fundamental single-molecule biophysical studies as well as in biosensing applications. Since dimensions of such beads are typically of the order of a micrometer and smaller, the stray magnetic field distributions they generate are highly localized and often minute, thus imposing challenges on their detection. In this talk we will present our results on development of Hall devices, with sensing areas having lateral dimensions of ~1 μm and ~250 nm, fabricated from InAs/AlSb quantum well semiconductor heterostructures. In the first part of the talk we will focus on room-temperature device characterization, i.e. the frequency dependence of the magnetic field and magnetic moment resolutions obtained through Hall effect and electronic noise measurements. We will show that in the low frequency range, from 20 Hz to 1.6 kHz, the noise-equivalent magnetic moment sensitivities are of order 10^6 $\mu_B/\sqrt{\mathrm{Hz}}$ and 10^5 $\mu_B/\sqrt{\mathrm{Hz}}$ for 1 μm and 250 nm devices respectively. The sensitivity of the latter reaches the 10^4 $\mu_B/\sqrt{\mathrm{Hz}}$ range above ~ 1 kHz (Figure 1), corresponding to the detection limit of only 3 magnetite nanoparticles (16 nm in diameter)/√Hz at 1.6 kHz. In the second part of the talk a phase-sensitive measurement technique for detection of superparamagnetic microbeads and nanoparticles will be introduced. By using this technique and micron-sized Hall crosses we were able to achieve detection of a single 1.2 μm diameter bead with a signal to noise ratio (S/N) of ~ 33.3 dB (Figure 2), as well as detection of six 250 nm beads with S/N of ~ 2.3 dB per bead. The third part of the talk will focus on magnetic characterization of a single superparamagnetic microbead by phase-sensitive micro-Hall magnetometry. We will show the measured dependence of the bead's susceptibility on magnetic field, which can be explained quantitatively as due to the magnetic response of an ensemble of non-interacting magnetic nanoparticles with broad distribution of magnetic moments and a mean diameter of 8.6 nm. Overall our work demonstrates the efficacy of InAs quantum well Hall devices for applications in high sensitivity magnetic biomolecular detection.

*This work was performed at the Center for Materials Research and Technology (MARTECH) and the Department of Physics, Florida State Univerity, Tallahassee, FL, USA. Argonne, a U.S. Department of Energy Office of Science laboratory, is operated under Contract No. DE-AC02-06CH11357.

G. Mihajlovi ć et al., Applied Physics Letters 91, 172518 (2007).

G. Mihajlovi ć et al., Journal of Applied Physics 102, 034506 (2007).

G. Mihajlovi ć et al., IEEE Transactions on Magnetics 43, 2400 (2007).

G. Mihajlovi ć et al., Applied Physics Letters 87, 112502 (2005).

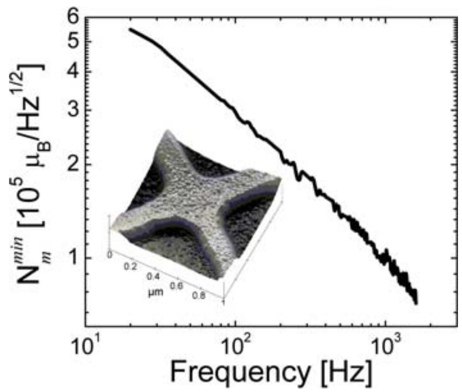

Fig. 1. Room-temperature noise-equivalent magnetic moment resolution of the 250-nm Hall sensor, shown in the inset, as a function of frequency.

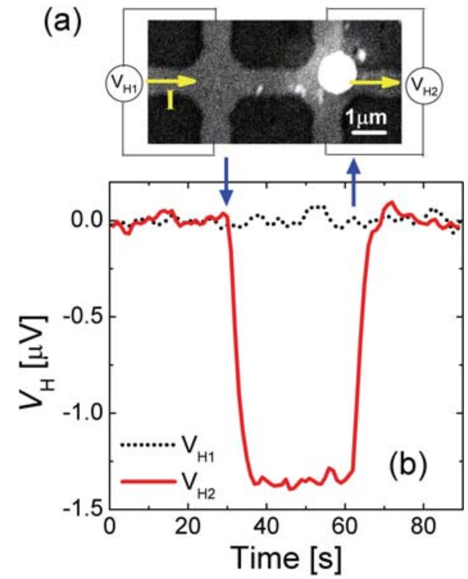

Fig. 2. (a) A SEM image of two adjacent Hall crosses with a 1.2 μm diameter superparamagnetic bead positioned on one of them. The image was adapted to show the actual detection measurement configuration. (b) Hall voltage as a function of time for the two crosses shown in part (a) of the figure. The drop in the signal from one cross upon applying the static field B_1 is due to the presence of the bead. The blue arrows indicate the moments of time when B_1 was applied (↓) and removed (↑), respectively.

CB-01

Spin transfer induced microwave emission and spin diode effects in MgO based magnetic tunnel junctions.

B. Georges[1], V. Cros[1], *J. Grollier*[1], A. Fert[1], A. Fukushima[2], H. Kubota[2], K. Yakushiji[2], S. Yuasa[2], K. Ando[2]

1. UMR CNRS-Thales, Palaiseau, France; 2. National Institute of Advanced Industrial Science and Technology (AIST), Tsukuba, Japan

Since the prediction by Slonczewski [1] and Berger [2] of magnetization dynamics induced by a spin-polarized current, many efforts have been focused on the understanding of the microwave emission features of a single spin-transfer nano-oscillator (STO) under magnetic field and current bias [3–7]. The challenge is now to increase the microwave emission power, which is typically a few hundred of pW/GHz for all-metallic pillars. Solutions to increase the power emission are to synchronize several STOs, to use magnetic tunnel junctions (MTJs) or to combine both approaches [8-10]. Indeed the development of MgO based tunnel junctions has made available MTJs with high MR ratios (more than 100 % at room temperature) and low RA ratios, required for the observation of spin-transfer effects in these systems. Spin-transfer induced magnetization precessions in MgO MTJs systems have been recently announced by a few groups [11,12]. However, it is difficult to discriminate between spin transfer induced emissions and thermal magnetization fluctuations because the latter are large in MTJs with large MR ratios, contrarily to all-metallic junctions.

We present some recent experimental results on microwave emission in MgO tunnel junctions. The junction stack is PtMn 15/ CoFe 2.5 / Ru 0.85 / CoFeB 3 / Mg0 1.075 / CoFeB 2 (nm). After sputtering, the junctions are etched with a 50x150 nm^2 elliptic section. The junctions deposition and processing are described elsewhere [13]. The RA and MR ratios of the junctions are typically 2 $\Omega.\mu m^2$ and 100%. We detect the microwave emissions by a spectrum analyzer after 32 dB amplification of the signal. In our convention, a positive current corresponds to electrons flowing from the thick to the free layer. The magnetic field is applied in the plane of the layers. Our results show distinct behaviours depending on the magnetic configuration of the junctions. In the parallel (P) state, the asymmetry of the emission as a function of the dc current is small, suggesting that the measured spectra are mainly due to thermal magnetization fluctuations (see Fig. 1(a)). On the contrary, in the antiparallel (AP) state, there exists a strong asymmetry between positive and negative current increasing with the current intensity. As can be seen on Fig. 1(b), for positive currents favouring the P configuration, the peak intensity peak increases with increasing current. The linewidth shows a minimum that could be attributed to the threshold current for spin transfer induced magnetization oscillations [6]. This behaviour is in agreement with the results of Nazarov et al. [11]. We will comment on these trends.

To gain further understanding of our results, we have performed spin diode experiments on similar junctions [14,15]. An external microwave current is injected in the MTJ nanopillar and we measure at the same time the dc rectified voltage and the microwave spectra (no dc current is injected in the sample). The bias field is applied along the hard axis. On Fig 2, we show at 200 Oe the frequency of the STO microwave emission as a function of the frequency of the source. The rectified voltage is presented in the inset as a function of the source frequency. From the dc voltage, we can see that at this field value, the intrinsic frequency of the STO is about f_0 = 2.3 GHz. By measuring the microwave spectra, we can detect the non-zero frequency components of the mixed signal $V(f) = R(f_0).I_{hf}(f_{source})$. Our measurement shows components at $f_0 \pm f_{source}$, confirming the mixing effect.

[1] J. Slonczewski, J. Magn. Magn. Mater. 159, L1 (1996)

[2] L. Berger, J. Magn. Magn. Mater. 278, 185 (2004)

[3] A. N. Slavin and P. Kabos, IEEE Trans. Magn. 41, 4, 1264 (2005)

[4] I. N. Krivorotov et al., Phys. Rev. B 76, 024418 (2007)

[5] M. R. Pufall, W. H. Rippard, M. L. Schneider, and S. E. Russek, Phys. Rev. B 75, 140404(R) (2007)

[6] J-V. Kim, Q. Mistral, C. Chappert, V. S. Tiberkevich and A. N. Slavin, cond-mat/0710.0495

[7] R. Bonin, G. Bertotti, I. D. Mayergoyz, C. Serpico, J.Appl. Phys. 99, 08G508 (2006)

[8] S. Kaka, M. R. Pufall, W. H. Rippard, T. J. Silva, S. E. Russek and J. A. Katine, Nature 437, 389 (2005)

[9] F. B. Mancoff, N. D. Rizzo, B. N. Engel and S. Tehrani, Nature 437, 393 (2005)

[10] J. Grollier et al., Appl. Phys. Lett. 78, 3663 (2001)

[11] A. V. Nazarov et al., Appl. Phys. Lett. 88, 162504 (2006)

[12] G. D. Fuchs et al., Appl. Phys. Lett 85 (2004)

[13] S Yuasa and D D Djayaprawira, J. Phys. D: Appl. Phys. 40, R337–R354 (2007)

[14] A. A. Tulapurkar et al., Nature 438, 339 (2005)

[15] J. C. Sankey et al., Phys. Rev. Lett. 96, 227601 (2006)

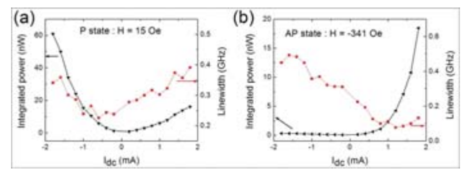

Integrated power and linewidth of the MgO tunnel junction as a function of the dc current in the P (a) and AP (b) states

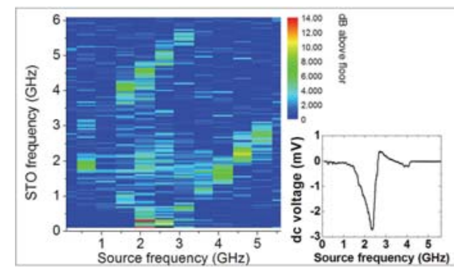

Spin diode experiments : Map of the emitted power of the junction (color scale) as a function of the STO and source frequencies. Inset : rectified voltage as a function of the source frequency.

CB-02

Quantized spin wave modes in magnetic tunnel junctions.

A. Helmer[1], T. Devolder[1], J. Hayakawa[2,3], K. Ito[2], H. Takahashi[2], S. Ikeda[3], P. Crozat[1], J. V. Kim[1], C. Chappert[1], H. Ohno[3]
1. Institut d'Electronique Fondamentale, Université Paris-Sud, Orsay, France; 2. Advanced Research Laboratory, Hitachi, Ltd, Tokyo, Japan; 3. Laboratory for Nanoelectronics and Spintronics, Research Institute of Electrical Communication, Tohoku University, Sendai, Japan

With GHz frequencies the operation speed of MRAM has reached the frequency range of the dynamic eigenexcitations of the underlying magnetic nanoelements (spin waves), whose energies are found to be quantized due to the lateral confinement [1]. Thus, the experimental observation and the understanding of spin wave modes in nanomagnets are prerequisites for the optimization of memory cells.
We have studied the magnetic field dependence of the mode frequency of thermally excited spin waves in MgO-based MTJs at 300K by analyzing the spectral density of the magnetoresistance noise. Our devices are rectangular shaped nanopillars of size 100x200 nm patterned from MTJs [2] of composition CoFeB (2 nm, free layer)/ MgO (0.85)/ CoFeB (3, pinned layer)/ Ru(0.8)/ CoFe(2.5)/ MnIr(8). The quasistatic properties of the free layer are consistent with the uniaxial anisotropy expected from the sample's elongated shape (Fig. A,B). Saturation of the synthetic antiferromagnet (SAF) is not reached for hard axis fields below 1.7 kOe (Fig.A), and spin-flop transition occurs typically at easy axis fields near 900 Oe (Fig.B).
For each external field we have measured the device voltage noise power for biasing currents +/- 0.5 mA. The noise spectra were obtained by subtracting simultaneously recorded zero-current reference spectra. The sweeping direction of the field was found not to affect the spectra, except for a marginal impact at low fields (below Hk). Similarly, for opposite current polarity the spectra show only minor deviations, also mainly at low fields.
For 6 devices of appropriate quasi-static properties we have measured the voltage power density versus hard axis fields from -1.4 to 1.4 kOe. One example of the resulting 2D density plots is shown in Fig. C.
Near zero field, the loops indicate the presence of several degenerate micromagnetic configurations (cf. inset in Fig. A). The corresponding noise spectra are strongly sample dependent, and will not be discussed here.
At slightly higher hard axis field (H below Hk), one or sometimes two modes are detected. The most intense mode has a frequency vanishing at Hk. The frequency of the less intense mode, when present, also vanishes at some field not corresponding to any characteristic point in the loop.
At fields saturating the free layer magnetization along the hard axis (H above Hk), we observed typically 5 to 10 peaks all below 12 GHz, none of them being a second harmonic of another. Surprisingly, the spectra were not symmetric with respect to zero field. Mode spacing was sample dependent, with modes appearing either in groups (Fig. C, positive H) or in an almost regular comb (not shown).
The mode whose frequency vanishes at Hk is generally also the most intense and the second lowest in frequency. The intensity of a mode does not systematically decrease with its index.
In some samples, modes of substantially weaker field dependence of the frequency were observed. In order to determine which of these modes may originate from excitations in the free layer or in the SAF, we have measured how the spectra are affected by a slight misorientation of the applied field. Only very few modes prove sensitive to the field misalignment.

In a first attempt to interpret the observed modes at large hard axis fields we have calculated the quantized mode frequencies of dipole-exchange spin waves propagating in a saturated single free layer of rectangular shape, following the approach of C. Bayer et al., formula (45) in [1], where we included an additional surface anisotropy to account for the considerably smaller layer thickness of only 2 nm in our samples. We have obtained qualitative agreement in the sense that the calculated modes were quantized and showed individually the observed field dependence. The effective magnetization was found to be 0.6 T.
To conclude, we have measured a large number of quantized spin wave modes in various MTJs and have obtained first insight into deterministic and statistical behaviour of the modes.
Acknowledgement: A. H. is supported by a PhD grant from the EU under the 6th Framework Program for the Marie Curie Research Training Network SPINSWITCH, contract n° MRTN-CT-2006-035327.

[1] C. Bayer et al., Spin-wave Excitations in Finite Rectangular Elements, in Spin Dynamics in Confined Magnetic Structures, vol. III, ed. by B. Hillebrands & A. Thiaville (Springer, Heidelberg 2006)

[2] S. Ikeda et al., Tunnel magnetoresistance in MgO-barrier magnetic tunnel junctions with bcc-CoFe(B) and fcc-CoFe free layers, J. Appl. Phys. 99, 08A907 (2006)

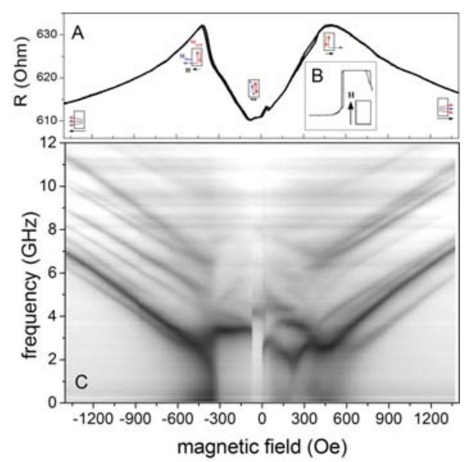

Voltage noise power density (a.u.) versus hard axis field (Panel C), and magnetorestistance hysteresis loops for applied hard axis (panel A) and easy axis field (panel B) for a device with anisotropy field $\mu 0$ Hk = 43 mT, and remanent resistances 605 and 705 Ohm.

CB-03

Low field spin-transfer induced precession in a pinned SAF layer for high frequency devices.

A. M. Deac[1,3], W. H. Rippard[1], J. A. Katine[2]
1. NIST, Boulder, CO; 2. Hitachi San Jose Research Center, San Jose, CA; 3. Institut fuer Festkoerperforschung, Forschungszentrum Juelich GmbH, Juelich, Germany

We have studied spin-transfer induced dynamics in the exchange-biased synthetic antiferromagnetic (SAF) reference layer of a spin-valve. Pillars with 150 x 50 nm^2 hexagonal cross-section have been fabricated from multilayers with the following structure: buffer layer /7 IrMn/3 CoFe/0.8 Ru/3 CoFe/4 Cu/6 CoFeB/ capping layer (where the thickness of each layer is given in nm). The long axis of the hexagons (which is the easy axis of the free layer) was oriented parallel to the pinning direction of the SAF. The static characterization of the samples was carried out via 2-point probe magnetoresistance and resistance versus current measurements. In our experimental configuration, positive fields are applied in the opposite direction with respect to the magnetization of the reference layer (thus favoring the AP state). For positive currents, the electrons flow from bottom to top. The coercivity of the free layer was about 700 Oe. The minor loop corresponding to the switching of the free layer was shifted from zero applied field with about 150 Oe, corresponding to the average magnetostatic field between the SAF pinned layer and the top CoFe layer. The magnetostatic interaction favors the antiparallel orientation between the free and the reference layer. The SAF layer starts to reverse around 1000 Oe.
The thick free layer acts as an very efficient polarizer, generating strong spin-transfer effects on the reference layer, especially considering the comparatively lower thickness of the top CoFe layer of the SAF (which translates into lower threshold currents). We have measured high frequency spectra at constant current and field, for fields between -3000 and 2000 Oe, varied in 100 Oe steps, and currents between -20 and 20 mA, with a 0.4 mA increment. The spectra exhibit strong precession signals even in 0 applied field, for currents above -10 mA. The signals are centered around 8 GHz in the absence of an external field, and shift down to less than 7 GHz as the applied field is increased to 800 Oe (Fig. 1). These peaks cannot be generated by free layer dynamics, as when the external field is increased, the total field acting on the magnetic moments of this layer increases and the precession frequency should increase as well. Consequently, we interpret these signals as the acoustic mode of the SAF pinned layer. If the field is kept constant, and the current is increased, the peaks exhibit a strong shift to lower frequency, which is typical of spin-transfer driven clamshell precession. At 700 Oe, for example, the signals red-shift with more than 1 GHz over the investigated current range (Fig. 2). Similar to simple layers not subject to exchange-bias, the peak amplitude registers an initial increase with the current (up to about -17 mA in this case), after which value the power drops suddenly and the peak width increases. Unlike free layers, which exhibit large 1/f noise with increasing current, the spectra corresponding to spin-transfer driven precession in the pinned SAF layer do not show any trace of 1/f noise, even in zero applied field, hence their potential interest for applications. In addition, spin-transfer driven precession in the SAF layer generates an optic mode as well at frequencies above 50 GHz, making theses structures potentially interesting for very high frequency spintronics devices.

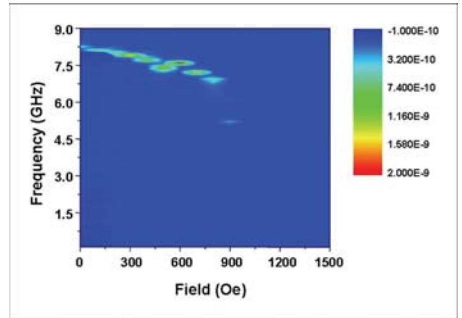

Fig. 1. Power (in Watt/Hz) of the acustic mode of the SAF layer, versus frequency and field, measured with a constant current (-14 mA). The 32 dB amplification has not been subtracted from the data.

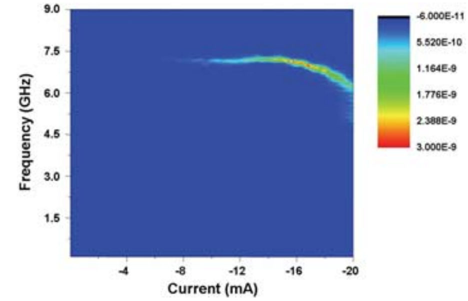

Fig. 2. Power of the SAF acustic mode, versus frequency and current, measured in a constant 700 Oe field. The power scale is the same as above.

CB-04

Spin-polarized current induced excitations in a synthetic antiferromagnet.

D. Gusakova[1,2], D. Houssameddine[1], U. Ebels[1], M. Cyril[2], B. Dieny[1], L. Buda-Prejbeanu[1]
1. SPINTEC URA 2512, Grenoble, France; 2. 2LIMN/DIHS/LETI CEA-Grenoble, Grenoble, France

In most applications of magnetic read heads or magnetic memories, the pinned layer is composed of a synthetic antiferromagnet (SAF), see Fig. 1a, in order to insure a rigid pinned layer alignment and to minimize the dipolar stray field on the free layer. This SAF consists of two ferromagnetic layers that are exchange coupled across a thin non-magnetic spacer whose thickness is adjusted to produce an antiferromagnetic coupling.

Recently, structures that are similar to CPP spin valve read heads containing an SAF pinned layer were used to study the spin transfer effect and in particular the microwave excitations [1]. In some studies [2] excitations have been observed that were attributed to the dynamics of the pinned SAF structure.

We therefore investigate here theoretically the conditions for which steady state oscillations may occur in the current-field plane of an SAF pinned layer, by keeping this time the free layer magnetization fixed and by considering a spin torque that acts only on the 'top' layer of the SAF structure, see Fig. 1a. For this one has to keep in mind that the hysteresis loop as a function of the applied field is quite different for an SAF structure than for a single free layer of a collinear planar structure. As illustrated in Fig. 1b, for a symmetric SAF structure, three regions can be distinguished. In the field range $-H_{SF} < H_{app} < H_{SF}$ the magnetization of the top and bottom SAF layers are well aligned antiparallel AP. We label the corresponding magnetization state in-plane stable state IPS_{AP}. When the applied field is larger than the spin flop field H_{SF}, but smaller than the saturation field H_{sat} ($H_{SF} < H_{app} < H_{sat}$) the magnetizations of both layers rotate in-plane, leading to the well known shearing of the magnetization, see Fig. 1b. We label this state as IPS_{SF}. The angle between both magnetizations decreases with increasing field until they align parallel (P) for $H_{app} > H_{sat}$. We label this state as IPS_P.

In order to obtain the critical current for which these static states become unstable, we consider in an analytic macrospin approach only the top SAF layer M_{top} which is exchange coupled to the bottom layer M_{bottom}, which itself is kept fixed. Applying general stability analysis [3] by linearization of the Landau-Lifschitz-Gilbert LLGS equation augmented by the Slonczewski spin torque term [4], we find analytic expressions for the critical boundaries in all three states. These are indicated by the blue and red bold lines in Fig. 1c, labelled J_{cP}, J_{cSF} and J_{cAP}. Here lines J_{cP} and J_{cAP} are very similar to those obtained for conventional collinear planar structures in the P and AP configuration [3], where the critical current J_c is dominated by the demagnetization field $J_c \sim \alpha 2\pi M_s$, with α the damping constant. The parameters for numerical evaluation are given in the figure caption. As a new result we find the critical current in the spin flop region which is inversely proportional to the applied field $J_{cSF} \sim \alpha/Happ$ and which joins the critical J_{cP} at the saturation field H_{sat}. In contrast at the spin flop field H_{SF} the critical current diverges.

In order to study the unstable regions for currents larger than the critical currents, we have solved the LLGS equation numerically. In difference to the analytic derivation, here we consider the evolution of both the top M_{top} and bottom layer M_{bottom}. Although a spin torque is included only for the top layer, for all three states coupled oscillations are obtained due to the relatively strong exchange coupling. Furthermore, for all three cases M_{top} and M_{bottom} oscillate around their respective static equilibrium position where the amplitude of the top layer, which feels the spin torque, is always larger than the one of the bottom layer. Typical trajectories are shown in Fig. 1d.

The simulations results are discussed in comparison to first experiments that have been preformed in our group recently which confirms the theoretical predictions.

[1] Q. Mistral et al., Appl. Phys. Lett. 88, 192507(2006) ; A. Deac et al., Phys. Rev. B 73, 064414 (2006)

[2] A. Deac, U. Ebels, Y. Liu, O. Redon, M. Li, P. Wang, B. Dieny, ICM2006, presentation TuP2-D4.

[3] J. Grollier et al., Phys. Rev. B 67, 174402 (2003).

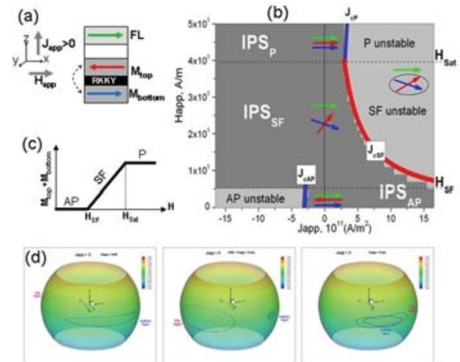

Fig. 1 : (a) Schematics of the spin valve structure, with a free layer and an SAF. The SAF is composed of a top layer of magnetization Ms_{top} and the bottom layer Ms_{bottom}. (b) Hysteresis loop of a symmetric SAF. (c) Current field state diagram for positive bias field. (d) trajectories for the spin flop state. The parameters for the numerical evaluation are: saturation magnetization $Ms_{top} = Ms_{bottom} = 1600$ kA/m, anisotropy energy constant $K = 8000$ J/m^3, top and bottom layer thickness t=2.5 nm, damping constant $\alpha = 0.02$ and exchange coupling constant $J_{RKKY} = -1$ mJ/m^2.

CB-05

Tuning the Coherence of Spin-Torque-Driven Dynamics in Nanomagnetic Oscillators.

K. Thadani[1], G. Finocchio[3], Z. P. Li[2], O. Ozatay[2], J. C. Sankey[1], I. N. Krivorotov[4], Y. T. Cui[2], R. A. Buhrman[2], D. C. Ralph[1]

1. Physics, Cornell University, Ithaca, NY; 2. Applied & Engineering Physics, Cornell University, Ithaca, NY; 3. University of Messina, Messina, Italy; 4. University of California-Irvine, Irvine, CA

In a magnetic multilayer sample, the spin-transfer torque from a spin-polarized DC current can excite steady-state magnetic precession at microwave frequencies [1]. This effect is of technological interest because it may allow the production of high-quality nanoscale frequency-tunable microwave sources and resonators. For applications, it is desirable that these magnetic oscillations have long coherence times, i.e. narrow linewidths in the frequency spectrum of the microwave signals. Therefore, understanding the role of thermal fluctuations and other mechanisms which may effect the coherence of these oscillators has generated considerable experimental [2, 3, 4] and theoretical interest [5]. The high-frequency dynamics of these oscillators have been studied previously in devices with nanopillar geometries [1, 2, 3] as well as point-contact geometries [4], and as a function of temperature [2] and the out-of-plane field angle [3, 4].
In this talk, we report measurements of how the linewidths depend on the in-plane angle of the applied magnetic field relative to the magnetic easy axis of nanopillar devices. We find that the most-commonly studied field orientation, in-plane and parallel to the easy axis, actually produces the broadest linewidths. As the field angle is rotated towards the in-plane hard axis, the linewidths can decrease dramatically, by almost a factor of 20-50 in some devices, thereby enabling a new and simple way to tune the coherence of the oscillations at room temperature. We also report the temperature dependence of the linewidths at the field angles giving the minimum linewidths, and compare our experimental results to macrospin and micromagnetic simulations. Micromagnetic simulations can reproduce our experimental results and help to explain the magnitude of the changes.
Our devices all have a nanopillar geometry, and we have measured two types of layer structures. In both kinds of samples, the free layer is the same material (Permalloy, Py) and it has the same thickness (4 nm). In the first type of multilayer the fixed layer (Py, 4 nm) is exchange-biased by an antiferromagnetic layer (IrMn, 8 nm), while in the second multilayer the fixed layer is thicker (Py, 20 nm) with no exchange bias. Our devices have an elliptical cross section, with a minor diameter of 50-70 nm and an aspect ratio of 2:1 or 3:1. We apply magnetic fields that are larger than the coercive fields of both layers, so that at I=0 the magnetizations of both layers are aligned approximately parallel along the field direction. We vary the field angle in-plane relative to the easy axis of the ellipse, and measure the frequency spectrum of the DC-current-driven resistance oscillations with a heterodyne mixer circuit [1].
As the applied magnetic field is rotated toward the in-plane hard axis, the linewidths of the osillation decrease by a large factor (20-50) in the exchange-biased fixed layer devices, while the decrease is only approximately a factor of 5 for the thick-fixed-layer devices. In the thick-fixed-layer devices, the dynamics are symmetric as a function of field angle relative to the hard axis, while they are not symmetric for the exchange-biased samples, indicating that the exchange-bias of the fixed layer still plays a role even though the applied magnetic field is larger than the exchange-bias field. Since the free layer is identical in both kinds of multilayer samples, we conclude that the configuration of the fixed layer affects the degree of coherence of the free layer. We have confirmed that the precessional mode that is excited is always predominantly a free-layer mode in both types of samples at all field angles, using spin-transfer-driven ferromagnetic resonance measurements (ST-FMR) [6, 7].
We have performed simple macrospin simulations and more detailed micromagnetic calculations in an attempt to understand our data. In the macrospin simulations, we found some narrowing in the predicted linewidths as a function of field angle, but only by a factor of 2-3, not by the much larger factor observed experimentally. Micromagnetic simulations, on the other hand, are in excellent agreement with our experimental results and can explain the large magnitude of the linewidth narrowing. They show that the oscillations are much more spatially uniform for an applied field along the in-plane hard axis than near the easy axis. They also show that the amplitude of the oscillations for a given current bias increases as the field angle is rotated from the easy axis to the hard axis, making the oscillations less susceptible to thermal fluctuations and giving enhanced coherence.

1. S.I. Kiselev et al., Nature 425, 380 (2003).

2. J.C. Sankey et al., Phys. Rev. B 72, 224427 (2005).

3. S.I. Kiselev et al., Phys. Rev. Lett. 93, 036601 (2004).

4. W.H. Rippard et al., Phys. Rev. B 74, 224409 (2006).

5. J.-V. Kim et al., cond-mat/0703317.

6. A.A. Tulapurkar et al., Nature 438, 339 (2005).

7. J.C. Sankey et al., Phys. Rev. Lett. 96, 227601 (2006).

CB-06

Phase locking of a Spin Transfer Oscillator to an external microwave current : a milestone for the synchronization of a large assembly of STOs.

B. GEORGES[1], J. Grollier[1], M. Darques[1], V. Cros[1], C. Deranlot[1], G. Faini[2], A. Fert[1]
1. Unité Mixte de Physique CNRS/Thales (CNRS-UMR137), Palaiseau, France; 2. Phynano team, Laboratoire de Photonique et Nanostructures, LPN - CNRS, Marcousis, France

STOs (Spin Transfer Oscillators) are non-linear oscillators very promising for applications in next generation telecommunication devices[1,2]. However the increase of the output power is a major challenge since the emitted power by a single STO is far too weak (< 1 nW). A solution is to achieve the synchronization in frequency and phase of an array of STOs [3]. Experimentally a first proof of synchronization of two close packed STOs has been given in 2005, independently by Kaka et al. and Mancoff et al [4,5]. In both cases, the coupling needed for synchronization was mediated by interacting spin waves generated by the spin transfer torque in a common magnetic layer However the spatial extension of the spin wave excitation,of the order of the µm, could be a strong drawback for its integration in large assemblies of STOs.

We have recently proposed an alternative scheme for the synchronization of STOs [6], that has the advantage to rely on a global coupling : each oscillator of the assembly is equally interacting with all the others. In fact, STOs are simply electrically connected to each others either in series or in parallel. The coherent emission of all STOs is governed by the coupling through the common self-generated (in each STO) microwave current that imposes a phase locking of the ensemble.

Here, we successfully demonstrate the phase locking of a single STO to an external source generated by a microwave source. As an example, we display in Fig 1 the map of the microwave emission in color scale of nanopillars without (Fig1a) and with injection of a microwave current (Fig1b) as a function of the dc current and frequency. These results are in agreement with experiments made by the NIST group in Boulder on STO nanocontacts [3].

To go further, we study in detail the influence of the intrinsic characteristics of the STO such as the linewidth, the agility in current or the power amplitude on the coupling efficiency. We clearly observe the major role played by the noise on the ability of STOs to phase lock to external signals. Moreover, we analyze our results in the frame of the model of weakly forced oscillators [7,8]. From our calculations, we extract the coupling parameter e, that determines the coupling strength between the STO and the external microwave signal. The predicted e depends on experimentally available parameters such as linewidth, agility, dc current etc. On Fig 2, we show the experimental variation of the coupling strength as a function of the amplitude of the microwave current (that is linked to the MR ration in STOs).We also observe that the coupling efficiency increases with the agility in current of the excitations. Our experimental results are in very good quantitative agreement with our calculations.

We believe that we gain through our study a clearer understanding of the conditions for successful synchronization of a large amount of STOs via a non local coupling such as the self emitted microwave current but also via a local coupling such as spin waves or hf dipolar field.

[1] W.H. Rippard et al Phys. Rev. B 70, 100406(R) (2004)

[2] S.I. Kiselev et al., Phys. Rev. B 72, 064430 (2005)

[3] W.H. Rippard et al, Phys Rev. Lett. 95, 067203 (2005)

[4] S. Kaka et al., Nature 437, 389 (2005)

[5] F.B. Mancoff et al, Nature 437, 393 (2005)

[6] J. Grollier, V. Cros, A. Fert, Phys. Rev. B 73, 1 R (2006)

[7] R. Adler, IEEE 61, 10 (1973)

[8] A. Slavin, IEEE 41, 4 (2005)

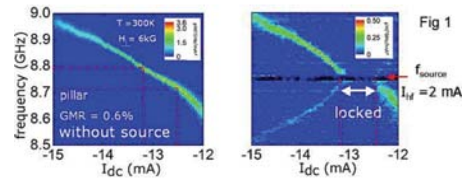

Fig 1

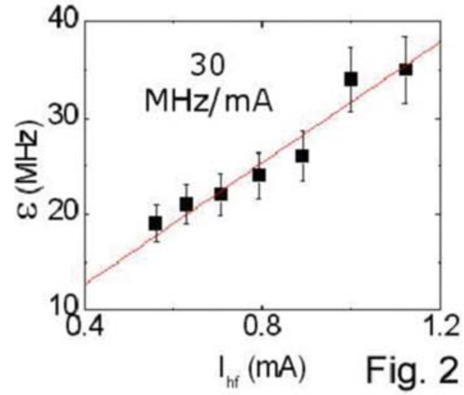

Fig. 2

CB-07

Magnetic point-contact precession frequency vs. magnetic field angle – The prospect for spin torque oscillator operation at 65 GHz.

S. Bonetti[1], J. Persson[1], F. B. Mancoff[2], *J. Åkerman*[1]
1. Microelectronics and Applied Physics, Royal Institute of Technology (KTH), Kista-Stockholm, Sweden; 2. Technology Solutions Organization, Freescale Semiconductor Inc., Chandler, AZ

Interest in Spin torque oscillators (STOs) [1–3] is rapidly increasing due to their potential use for microwave generation over large frequency ranges. In these devices, the transfer of spin angular momentum between a spin polarized current and a thin (on the order of few nm) magnetic layer generates a precession of the magnetization, and as a consequence oscillation of the device resistance, either through giant magnetoresistance (GMR) [4,5] or tunneling magnetoresistance (TMR) [6-8]. These devices are compact (~100 nm in lateral size), can be tuned in frequency in an approximately linear way by varying the applied current and magnetic field magnitude, and the tuning range is rather large, on the order of tens of GHz [9].
Besides current and field magnitude tunability, the frequency can also be tuned by varying the angle at which the magnetic field is applied [9]. In this work we study this dependence in GMR based magnetic point contacts and find that extrapolation of the angular dependence to entirely in-plane magnetic field predicts STO operation to frequencies as high as 65 GHz. Samples are point contact $Co_{81}Fe_{19}$(20 nm)/Cu(6 nm)/$Ni_{80}Fe_{20}$(4.5 nm) spin valves. The contact shape is elliptical, with minor axis a = 130 nm, and aspect ratio 3:1 between major and minor axes.
In order to perform measurements, samples are mounted, together with non-magnetic ground/signal/ground RF probes and *xyz* micromanipulator, on a turntable. The entire holder can be rotated, so that the direction between a fixed magnetic field and the sample can be varied from in-plane to out-of-plane. The RF signal detected by the probes is then amplified by a broadband (0.1 – 26 GHz) amplifier (+45 dB), and transmitted to a spectrum analyzer, capable of resolving power spectra up to a maximum frequency of 26.5 GHz. The magnetic field is kept constant at a value of 1.3 T in all measurements
Oscillation peak positions vs. field angle is presented in Fig. 1 for low current densities (close to the onset of oscillation). Since these samples have rather high oscillation frequencies to begin with and our spectrum analyzer is limited to 26.5 GHz, we only resolve the angular dependence some 25 degrees away from the film normal. In this angular range the frequency increases almost linearly with decreasing field angle. Assuming a ferromagnetic resonance (FMR) behavior [9], we can fit this behavior and extrapolate to an expected maximum operating frequency of about 55 GHz if the field were to be applied along the plane of the film. If we further increase the current and move away from the onset of oscillation towards an intermediate regime, we find oscillations at about 26 GHz (limit of our spectrum analyzer) when the field angle is 80°. FMR extrapolation from this point leads to a predicted frequency of 65 GHz for in-plane applied field. To the best of our knowledge, this is the highest estimated operating frequency of any STO to date and may open up for suggested high-speed consumer applications in the 57-66 GHz range [10].
We do not exclude that the magnetization dynamics may turn into complex regimes when such frequencies are approached. However, continuous single mode operation up to 35 GHz has been shown in earlier studies [9] when the typical frequencies for out-of-plane fields were around 5 GHz. Furthermore, we are not aware of intrinsic fundamental limits to the achievement of frequencies up to 100 GHz.
With more experimental data available, we also plan to present a study of the linewidth and of the integrated output power dependence on the applied field angle. Furthermore, we are in the process of extending the range of our experimental capabilities to 40 GHz, in order to investigate if the expected trend is followed up to that frequency. Final confirmation of actual oscillations at 65 GHz will be attempted by down converting the STO signal with an intermediate frequency generator.
We gratefully acknowledge financial support from The Swedish Foundation for strategic Research (SSF), The Swedish Research Council (VR), The Göran Gustafsson Foundation and The Knut and Alice Wallenberg Foundation.

[1] J.C. Slonczewski, J. Magn. Magn. Mater. 159, L1 (1996).

[2] L. Berger, Phys. Rev. B 54, 9353 (1996).

[3] S. I. Kiselev, Nature 425, 380 (2003).

[4] M.N. Baibich et al, Phys. Rev. Lett. 61, 2472 (1988).

[5] G. Binasch et al, Phys. Rev. B 39, 4828 (1989).

[6] M. Julliere, Phys. Lett 54A, 225 (1975).

[7] T. Miyazaki et al, J. Magn. Magn. Mater. 139, L231 (1995).

[8] J. S. Moodera, Phys. Rev. Lett. 74, 3273 (1995).

[9] W. H. Rippard et al, Phys. Rev. B 70, 100406(R) (2004).

[10] Proposed IEEE 802.15.3c protocol.

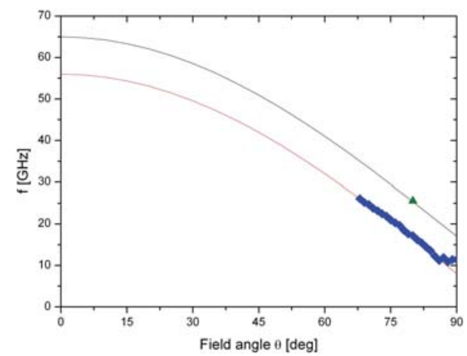

Fig. 1. Experimental (symbols) and extrapolated (lines) oscillation frequency of the STO vs applied magnetic field angle. Experimental points on the lower curve are at onset of oscillation, the single point on the upper curve is at an intermediate regime.

Asymmetric lineshapes in spin-torque nano-oscillators near threshold.

J. Kim[1], Q. Mistral[1], C. Chappert[1], V. S. Tiberkevich[2], A. N. Slavin[2]
1. Institut d'Electronique Fondamentale, CNRS / Univ. Paris Sud, Orsay, France; 2. Department of Physics, Oakland University, Rochester, MI

Thermal noise plays a defining role in the dynamics of auto-oscillatory systems. This is particularly relevant in nanoscale systems in which the thermal energy is comparable to the energy of the auto-oscillations. In such systems, there are two important consequences of noise. First, thermal noise leads to a broadening of the power spectrum. Second, thermal noise blurs the transition between the damped and auto-oscillatory states.

The spin-torque nano-oscillator (STNO) is an important auto-oscillatory system of present interest. In the context of nanomagnetism and spin-dependent transport, the auto-oscillations of magnetization in magnetic heterostructures are the result of the interplay between the intrinsic magnetic torques and dissipation, and an additonal torque furnished by spin-polarized currents. In a wider physical context, the oscillator represents a unique system in which the frequency nonlinearity is typically much larger than the intrinsic relaxation rate. As we will show, this last feature leads to significant qualitative differences between the power spectra of spin-torque nano-oscillator and other conventional oscillators, namely, significant line broadening and lineshape asymmetry occurs in STNOs.

We have developed a stochastic theory of spin-torque nano-oscillators [1,2] based on a classical Hamiltonian spin-wave formalism [3]. Based on a single-mode assumption in which the excited mode is the one which possesses the lowest relaxation rate, we derive a nonlinear oscillator equation from the Landau-Lifshitz equation of motion with Gilbert damping and thermal noise. From this stochastic nonlinear differential equation, the spectral power density of the STNO is computed with a Fokker-Planck formalism, and we demonstrate how to construct the necessary spin-wave correlation functions that are related to the voltage correlation functions measured experimentally from the Green's function of the Fokker-Planck equation [4].

We show that the power spectrum of the STNO near the generation threshold is broadened, non-Lorentzian, and asymmetric. This is a result of two important physical processes: (i) the large frequency nonlinearity of the oscillator; (ii) the coupling between phase and amplitude fluctuations, leading to a colored noise source for the oscillator phase. We argue that such line broadening and line asymmetry are key signatures of the threshold region, and give a simple means of determining the threshold in experiment. This point is especially significant for STNOs in which the influence of noise on device performance is of qualitative importance.

Our theory gives a good qualitative description of lineshape distortion measured in a recent STNO experiment. In the figure, we present a comparison between the calculated and measured power spectra for a spin-valve nanopillar system [5]. Dark solid lines represent fits to the experimental data (circles) using multiple Lorentzians, which are shown as shaded curves. Based on the linewidth and power variations, the critical current in the experimental system is estimated to be I_{th} = 5.2 mA. Below threshold (I = 5.0 mA), the experimental data (circles) are well described by a single Lorentzian curve, while for small to moderate above-threshold currents (I = 5.4, 6.0 mA) a second Lorentzian peak is required to account for the line asymmetry. The salient features of the measured lineshape distortion are well reproduced by the theory.

This work was in part supported by the MURI grant W911NF-04-1-0247 from the US Army Research Office, the contract W56HZV-07-P-L612 from the U.S. Army TARDEC, RDECOM, the grant ECCS-0653901 from the National Science Foundation of the USA, the Oakland University Foundation, and the European Communities program IST under Contract No. IST-016939 TUNAMOS.

[1] J.-V. Kim, Phys. Rev. B **73**, 174412 (2006).

[2] V. Tiberkevich, A. Slavin, and J.-V. Kim, Appl. Phys. Lett. **91**, 192506 (2007).

[3] A. N. Slavin and P. Kabos, IEEE Trans. Magn. **41**, 1264 (2005).

[4] J.-V. Kim, Q. Mistral, C. Chappert, V. S. Tiberkevich, and A. N. Slavin, arXiv:0710.0495v2 (2007).

[5] Q. Mistral *et al*., Appl. Phys. Lett. **88**, 192507 (2006).

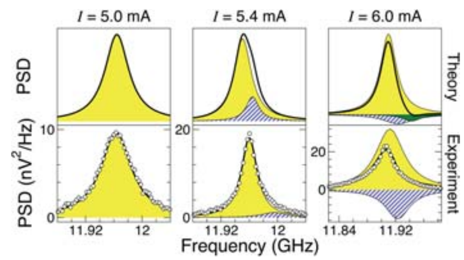

Comparison between theoretical and experimental STNO power spectra.

CB-09

Experimental and theoretical study of spin-torque microwave excitation linewidths in nanocontacts subject to out-of-plane external fields.

M. Pasquale[1], C. Serpico[2], P. Anzalone[3], G. Bertotti[1], M. Pufall[4], W. Rippard[4]
1. Divisione Elettromagnetismo, INRIM, Torino, Italy; 2. Dipartimento di Ingegneria Elettrica, Università di Napoli "Federico II", Napoli, Italy; 3. Dipartrimento di Ingegneria Elettrica Industriale, Politecnico di Torino, Torino, Italy; 4. Electromagnetics Division, NIST, Boulder, CO

Spin-polarized DC currents injected into nanoscale magnetic multilayers lead to spin-torque effects that can excite magnetization self-oscillations. Due to thermal fluctuations, experimentally observed self-oscillation power spectra always exhibit finite linewidth. The linewidth dependence on the exciting current can be rather complex, with non-monotone changes by orders of magnitude. In this paper, we compare analytical predictions for the linewidth dependence on applied field and current with measurements of the power spectrum of current-induced microwave magnetization oscillations.
Measurements were performed on a point contact (<40 nm in diameter) made at the top of a continuous 8 μm by 12 μm spin valve structure. The spin valve structure consisted of SiO2/Ta 2.5 nm/Cu 50 nm/Co90Fe10 20 nm /Cu 5 nm /Ni80Fe20 5 nm/Cu 1.5 nm /Au 2.5 nm. The Co90Fe10 layer plays the role of "fixed" layer for the spin-torque effect due to its larger volume and larger saturation magnetization relative to the "free" Ni80Fe20 layer. The device is current-biased so that current flows from the "fixed" into the "free" layer and changes in the relative orientations of the magnetizations of the two layers lead, via GMR effect, to voltage changes across the device. The device is contacted with a microwave probe, and a bias tee is used to separate the injected dc current from the high-frequency device response. The output is amplified and measured using a 23 GHz spectrum analyzer. The center frequencies f and linewidth of the excitations are determined from Lorentzian fits to the measured spectra. All measurements were performed at room temperature, subjecting the sample to an out-of-plane external magnetic field. In particular, the case where the field is at 60 degrees with respect to the film plane was investigated in detail in order to obtain data suitable for direct comparison with model predictions. A minimum linewidth of 10.6 MHz at 19.49 GHz was measured under a field of 0.75 T and a current of -6.43 mA In Fig.1, the power spectral density (PSD) of the measured voltage is reported for various values of the injected current. For intermediate current values (I = 8 mA) the PSD exhibits two peaks. In Fig.2 the linewidth of PSD peaks is reported as a function of the injected current. In the region around I = 8 mA, there are two distinct linewidth curves associated with the two peaks present in the PSD.In order to model the measured data, we assumed that the free-layer is uniformly magnetized and that the magnetization dynamics in the free layer is governed by the Landau-Lifshitz-Gilbert equation with the addition of the spin-transfer term in the form proposed by Slonczewski. Fluctuations are taken into account by adding a Gaussian white-noise term to the effective field. In this model, conservation of magnetization amplitude leads to stochastic magnetization dynamics on the unit sphere. The problem was studied without simplifying assumptions by solving the Fokker-Planck equation associated with the stochastic dynamics on the unit sphere. Solutions were obtained by using separation of variables and eigenfunction expansion techniques, along with appropriate numerical discretization techniques. From the solution of the Fokker-Planck equation, the autocorrelation function and the power spectral density of magnetization were computed.
By using the above theory, it is possible to explain the presence of multiple peaks in the PSD as a consequence of the presence of multiple attractors in the underlying magnetization deterministic dynamics. The non-trivial behavior of the linewidth as a function of the current is the consequence of the bifurcations the system undergoes under varying current. The ensuing richness of qualitative changes in the response of the system is captured well by the Fokker-Planck analysis, This would not be the case for simple classical oscillator noise models which cannot deal properly with the strong nonlinearity of the system dynamics.

Serpico et al., J. Appl. Phys., 101, 09A507 (2007)

Bertotti et al., Phys. Rev. Lett., 94, 127206 (2005

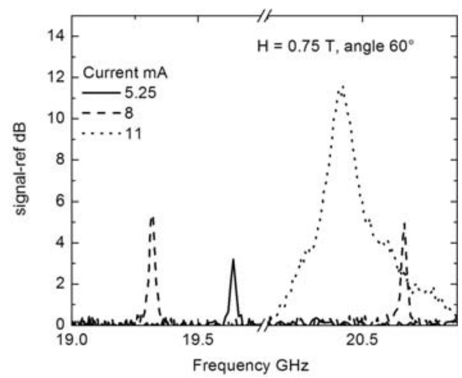

Power spectral density (PSD) of measured voltage for different values of injected current

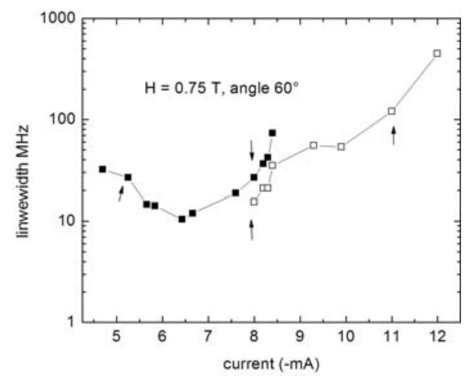

Linewidth of PSD peaks as a function of the injected current

CB-10

The frequency of microwave oscillation on domain wall magnetoresistance elements.

H. Endo[1], K. Shirafuji[1], H. Suzuki[1], M. Doi[1], M. Takagishi[2], H. N. Fuke[2], H. Iwasaki[2], M. Sahashi[1]
1. Department of Electronic Engineering, Tohoku University, Sendai, Japan; 2. Corporate Research & Development Center, Toshiba Corporation, Kawasaki, Japan

Magnetization dynamics has attracted much attention due to its potential for application in microwave oscillator. The microwave oscillation (MO) induced by spin polarized current has been observed in current-perpendicular-to-plane giant magnetoresistance (CPP-GMR) [1] and MgO magnetic tunnel junction structures [2]. At the same time, the magnetoresistance (MR) has been observed on CPP-spin valve (SV) structure which has $Fe_{0.5}Co_{0.5}$-AlO_x nano-oxide layer (NOL) as a spacer layer [3]. The NOL has metallic conductive channels with nano-meter size in an 1~2 nm oxide insulator. The origin of this MR can be attributed to confined domain walls in ferromagnetic metal nano-contacts in the NOL, which is called as domain wall MR (DWMR). Therefore, we proposed to apply our original nano-confined structure formed by NOL to the microwave oscillator [4]. In our previous work, we denoted that a peculiar MO was observed in DWMR elements, and the peak frequency was ~7 GHz at antiparallel (AP) configuration of free layer (FL) and reference layer (RL) magnetization. Here, we report another type of MO in DWMR elements, which shows higher MO frequency of over ~10 GHz.The SV films were prepared by the dc magnetron sputtering mehod. The design of SV film is underlayer/PtMn 15/$Co_{0.9}Fe_{0.1}$ 3.3/Ru 0.9/$Fe_{0.5}Co_{0.5}$ 0.5/$Fe_{0.5}Co_{0.5}$-AlO_x NOL/$Fe_{0.5}Co_{0.5}$ 2.5/cap layer (nm). The $Fe_{0.5}Co_{0.5}$-AlO_x NOL was formed by using the ion assisted oxidation (IAO) method [3]. We fabricated samples which had NOLs formed by different IAO conditions. One of them was formed by strong oxidation (sample S), and the other was oxidized weakly (sample W). The elements presented in our previous report belonged to sample S. The samples were fabricated into pillars with size of 0.3×0.3 ~ 0.6×0.6 μm^2 by the photolithographic method. The microwave spectrum was measured by spectrum analyzer from 0.1 ~ 18 GHz applying dc current (I) and magnetic field (H). The direction of I is defined as positive for current flow from FL to RL. The positive H denotes opposite direction to the magnetic aliment of RL.We measured MO spectra of some elements in both sample S and W, and estimated peak frequency (f) from highest peaks of each element. Fig.1 shows resistance area product (RA) dependence of f. f of sample S converged on 6 ~ 8 GHz. On the other hand, f of sample W was dispersed but higer than sample S in average. Here we focus on one of the elements in sample W. MR ratio, RA, and an interlayer coupling field between FL and RL (H_{in}) of the element was 3.7%, 0.73 $\Omega\mu m^2$, and 65 Oe, respectively. To confirm the magnetic configuration of FL and RL in high I, we measured R-H curves at I (Fig.2). With increasing I, intermediate state between parallel (P) and AP configuration was observed and shape of FL hysteresis got tilted. This state is considered to be due to the magnetic field induced by sense current and spin transfer torque. Fig.3 shows MO spectra at I = +33 mA. For H = +500 Oe, a small peak was observed at 8.2 GHz. As H was increased to +600 Oe, the peak jumped to 9.8 GHz and was sharpened drastically. As H was further increased, f increased slightly, and the peak height decreased. From Fig.2, FL magnetization was expected to be in the intermediate state below H = +500 Oe, and in AP configuration above H = +600 Oe. Therefore, the MO was considered to be separated into two modes according to the magnetic configuration. For sample W, f at AP configuration were mostly over ~10 GHz, but it gathered at ~7 GHz for sample S. This difference might be due to difference of an effective magnetic field on magnetic layers and nano-contacts.

[1] S. I. Kisele et al, *Nature* **425**, 380 (2003).
[2] A. A. Tulapurkar et al, *Nature* 438, 339 (2005).
[3] H. N. Fuke et al, *IEEE Trans. Magn.* **43**, 2848 (2007).
[4] K. Shirafuji et al, *J. Magn. Soc. Jpn.*, submitted.

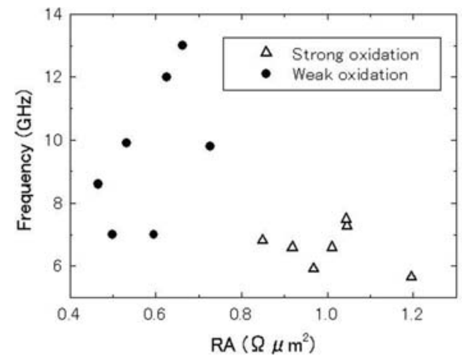

Fig.1 *RA* vs peak frequency of sample with strong and weak oxidation.

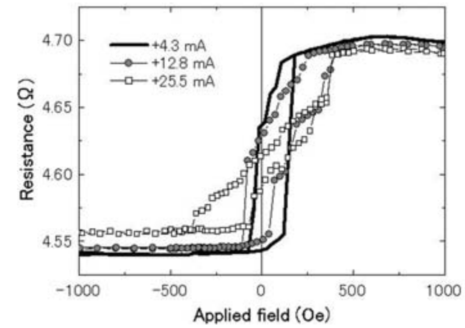

Fig.2 *R-H* curves at various sense currents.

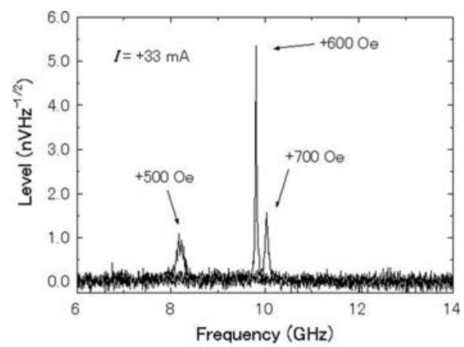

Fig.3 Microwave spectra at +33 mA under various applied magnetic fields.

CB-11

Spin wave Doppler shift.

V. Vlaminck, M. Bailleul
GEMME, IPCMS, Strasbourg, France

As recently predicted, forcing a DC current through a ferromagnetic metal could induce a change of its spin-wave spectrum [1, 2, 3]. A transfer of angular momentum is indeed expected when spin-polarized electrons flow through an inhomogeneous magnetization configuration, such as that occurring if a spin-wave is propagating in the medium. This transfer of angular momentum induces an additional torque acting on the magnetization. In the so-called adiabatic approximation, this simply results in a frequency shift for the spin wave modes [4]. The expected shift is proportional to the spin current Js and to the wave-vector k of the spin wave, (i.e. $\Delta \omega_{doppler} = k.Js / Ms$), which suggests an analogy with the well-known Doppler shift. Additionally it appears as a convenient way of measuring the polarization of the spin current in the bulk of the ferromagnet.
In this communication, we report an experiment dedicated to the observation of this "spin-wave Doppler shift". The experiment is based on the propagating spin wave technique [5]. Spin waves of wavelengths of the order of 800nm are emitted and detected inductively using submicrometer conducting patterns ("spin wave antennae"), which are connected to a network analyzer (10MHz-20GHz). The spin waves propagate along a thin permalloy micro-stripe (width: 1.5-7 µm, thickness: 20nm), subjected to a saturating out-of-plane field H0 and through which a large DC current density can be forced. Fig.1 is a scanning electron microscope image of our device showing the pair of antennae coupled to the ferromagnetic stripe.
Firstly, we demonstrate how the spin waves are emitted by an antenna by measuring its self-inductance $\Delta L11$. A typical curve obtained under a field µ0H0=0.869T is shown in Fig.2a (Re($\Delta L11$), Im($\Delta L11$)). Typical ferromagnetic resonance spectra is observed, from which the characteristic parameters of the ferromagnet can be estimated: the gyromagnetic factor g ~ 2.18, the Gilbert damping parameter α ~ 0.02 and the effective magnetization µ0Meff ~0.8 T.
Secondly we characterize the propagation of the spin waves between the two antennae by measuring the variation of mutual-inductance ($\Delta L12$). This is shown in Fig.2b where one recognizes clear oscillations arising from the phase delay accumulated along the propagation. We can extract the group velocity of the spin wave from the period of this oscillation: VSW ~ 1 µm/ns.
Finally we present our results of spin waves spectroscopy under a DC current, which constitute up to now the first experimental evidence of a Doppler shift for a spin wave. As can be seen in Fig.3 we perform spin wave propagation by measuring the mutual-inductances $\Delta L12$, $\Delta L21$ in conjugation with a large DC current flow along the stripe. We observe that the frequencies of the spin waves are shifted in accordance with the sign and the intensity of the current, namely toward higher frequencies when the propagation is in the same way as the electron flow and toward lower frequencies in the opposite direction. Additionally we show that a spin-torque term added into the Landau Lifshitz equation of motion of the magnetization gives a correct description of this phenomenon.

References :

[1] Y.B. Bazaliy et al., Phys. Rev. B 57, R3213 (1998)

[2] MD Stiles, A. Zangwill, Phys. Rev. B 66, 014407 (2002)

[3] J. Fernandez-Rossier et al., Phys. Rev. B 69, 174412 (2004)

[4] L.L.Hirst., Phys. Rev. 14, 503 (1965)

[5] M. Bailleul et al., Appl. Phys. Lett. 83, 972 (2003)

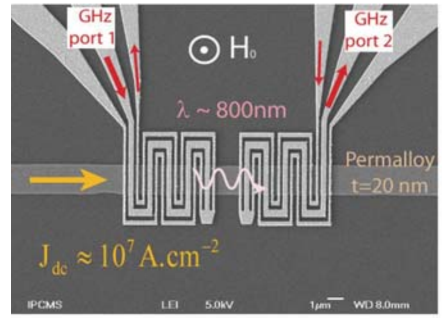

Fig.1: SEM picture of a typical device for the spin wave doppler shift experiment.

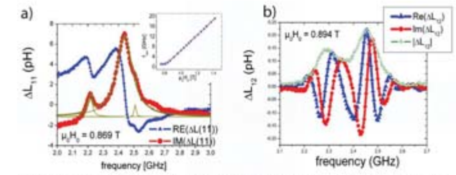

Fig.2: (a) FMR on a single antenna (auto-inductance ΔL11) under µ0H0 = 0.869 T, (framed) f0(H0). Lorentzian fits gives α ~ 0.02 and g ~ 2.18. (inset) Magnetic field dependence of the resonance frequency .
(b) Spin wave propagation (mutual-inductance ΔL12) on a permalloy stripe (w=3µm, t=20nm, L=15µm), under µ0H0 = 0.894 T.

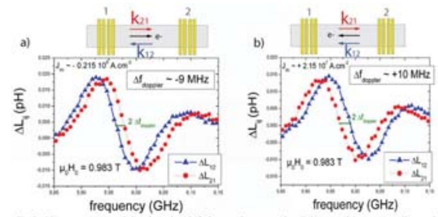

Fig.3: Measurements of the doppler shift for a spin wave (k = 7.84 µm-1) in a permalloy stripe (w=1.5µm, t=20nm, L=8µm). Wave vector k12 denoting a wave propagating from antenna 2 toward antenna 1 and vice versa. (a) Jdc < 0 and (b) Jdc > 0.

CC-01

Equilibrium and out-of-equilibrium spintronic phenomena in single crystal MgO based magnetic tunnel junctions.

C. Tiusan[1], F. Greullet[1], F. Bonell[1], M. Hehn[1], S. Andrieu[1], C. Bellouard[1], F. Montaigne[1], D. Halley[2], M. Bowen[2], W. Weber[2], E. Snoeck[3], F. Aliev[4], E. Popova[5], A. Schuhl[6,1]
1. Nancy Université- CNRS, Laboratoire de Physique des Materiaux - UMR7556, Vandoeuvre les Nancy, France; 2. Institut de Physique et Chimie des Matériaux, Strasbourg, France; 3. CEMES, Toulouse, France; 4. University of Madrid, Madrid, Spain; 5. Université de Versailles, Laboratoire de Magnétisme et d'Optique de Versailles, Versailles, France; 6. SPINTEC, Grenoble, France

The transport mechanisms in crystalline magnetic tunnel junctions (MTJ) attracted the interest of the international scientific community after the theoretical predictions of Butler et al [1] of giant tunnel magnetoresistance (TMR) effects, reaching several thousands of percents in single-crystal MTJ employing bcc ferromagnetic electrodes and MgO insulating barriers. In these model systems the electrons are classified with respect to the symmetry of their associated electronic Bloch wave function. The large predicted TMR ratio is related to a symmetry dependent attenuation rate within the MgO single crystal barrier combined with a half metallic property of a specific symmetry in the Fe electrode.

Within this topic, in 2001, our group started the experimental study of TMR in crystalline magnetic tunnel junctions, elaborated by Molecular Beam Epitaxy, combining single crystal bcc Fe, Co electrodes and MgO barriers. In 2002, we pointed out for the first time experimentally an intrinsic antiferromagnetic coupling effect in Fe-MgO-Fe tunnel junctions by spin polarized tunneling [2]. This effect, theoretically predicted by Slonczewski [3] can be explained today as a zero bias torque effect [4].

In 2004 we reported tunnel magnetoresistance effects whose amplitude overcame the expectations within the free-electron model. These results provided a first experimental evidence of the complex physics of tunneling in single crystal MTJs. A further deep understanding of fundamental aspects related to symmetry dependent tunneling [1] enabled us to gradually boost the TMR ratio at room temperature from 67% in 2003 [5] to 200% in 2006 (340% at 10K) [6]. Simultaneously, more and more spectacular results have been obtained in other laboratories [7]. Today, MTJs involving CoFeB electrodes show record TMR ratios approaching 1000% [8]. The MgO based MTJs represents nowadays the elementary brick either for data storage applications or fundamental physics studies concerning charge and spin transport by tunneling.

Over the last years, our research activity in Fe-MgO MTJs was mainly devoted to the engineering of new functionalities by playing with the electronic structure at the interface. In 2004 we demonstrated the role of the interfacial electronic structure on the tunneling [9] and subsequently that Fe/MgO interface engineering is a powerful tool to get high output voltage [10], large breakdown voltage and extremely low noise [11]. Detailed studies have been dedicated to carbon and oxygen [12] influence on tunneling when these impurities are located at the Fe-MgO interface.

Recently, we exploited the symmetry dependence of the tunnel conductivity to engineer novel MTJs functionalities. We demonstrated that, a suitably chosen Cr(001) epitaxial metallic spacer layer sandwiched in between the Fe ferromagnetic layer and the MgO, quenches the transmission of particular electronic states, therefore acting as an additional symmetry dependent tunnel barrier for electrons at the Fermi level [13]. Moreover, we show that this ultrathin Cr metallic barrier can promote quantum well states in an adjacent Fe layer.

In this presentation, we will give an overview of the experimental achievements of our group in parallel with advances on the same topics reported in literature. Within the framework of the symmetry filtering, we analyze in detail the difference in terms of TMR amplitude between the epitaxially grown MTJs and the sputtered CoFeB/MgO MTJs showing larger TMR ratios. The mechanisms of tunneling in our Fe-MgO MTJs will be discussed in detail, both in the equilibrium and the out-of-equilibrium regimes. Noise [11, 14] and ferromagnetic resonance experiments [15] will provide further evidence of direct tunneling. The influence of the interfacial electronic structure on the equilibrium coupling effect by spin polarized tunnel will be also addressed. Perspectives for out-of-equilibrium spin-torque experiments will be anticipated.

We strongly acknowlege M. Alnot and G. Lengaigne for technical support, J. Faure-Vincent and M. Sicot for their fundamental contribution in the initial stages of the project.

[1] Butler et al, Phys. Rev. B 63, 054416, (2001).

[2] Faure-Vincent et al, Phys. Rev. Lett. 89, 107206, (2002).

[3] J.C. Slonczewski, Phys. Rev. B 39, 6995, (1989).

[4] I. Theodonis et al, Phys. Rev. Lett. 97, 237205, (2006).

[5] Faure-Vincent et al., Appl. Phys. Lett. 82, 4507, (2003).

[6] Tiusan et al., J. Phys.: Condens. Matter 18, 941-956, (2006).

[7] S. Yuasa et al, Nat. Mater. 3, 868, (2004); S. Parkin et al., Nature Materials 3, 862, (2004).

[8] Y. M. Lee et al, Appl. Phys. Lett. 90, 212507, (2007).

[9] Tiusan et al, Phys. Rev. Lett. 93, 106602, (2004).

[10] Tiusan et al, Appl. Phys. Lett. 88, 62512, (2006).

[11] R. Guerrero et al, Appl. Phys. Lett. 91, 132504, (2007).

[12] M. Sicot et al, J. Appl. Phys. 99 08D301, (2006).

[13] F. Greullet et al, Phys. Rev. Lett. 99, 187202, (2007).

[14] F.G. Aliev et al, Appl. Phys. Lett. 91, 232504, (2007).

[15] E. Popova et al, Appl. Phys. Lett. 91 112504, (2007).

CC-02

Nature of Voltage Dependence of Spin Transfer Torque in Magnetic Tunnel Junctions.

M. Chshiev[1], I. Theodonis[2,3], N. Kioussis[2], A. Kalitsov[2], W. Butler[1]
1. Center for Materials for Information Technology, University of Alabama, Tuscaloosa, AL; 2. Department of Physics and Astronomy, California State University, Northridge, CA; 3. Department of Physics, National Technical University, Zografou, Greece

Current induced magnetization switching using spin transfer torque (STT) continues to generate interest for spin electronic applications such as MRAM, spin torque oscillators and detectors.[1,2] Among the most favorable candidates for realization of STT devices are epitaxial magnetic tunnel junctions (MTJ).[3,4] Thus, understanding the fundamental mechanisms that can affect the dependence of Tunneling Magnetoresistance (TMR) and STT on the applied voltage in MTJs is critically important.[5] Unlike fully metal-based nanostructures, at finite applied voltage, the total perpendicular (field like) component of the STT ($T_\perp$) in MTJs is not negligible[6] and in the ballistic regime exhibits quadratic behavior as a function of applied voltage[7] while the parallel STT term $T_\|$ could behave non-monotonically as a function of applied voltage.[7] Our predictions were recently confirmed experimentally.[8,9]

Here we provide a systematic study of the influence of majority and minority band filling on the applied voltage dependence of both the parallel ($T_\|$) and perpendicular ($T_\perp$) terms of STT in MTJs consisting of two ferromagnetic electrodes (FM and FM') separated by the insulator (Fig.1a). The calculations have been performed within the tight-binding model using the non-equilibrium Green function technique in the framework of the Keldysh formalism. The electrodes and the barrier are characterized by on-site energies $\varepsilon^\uparrow$, $\varepsilon^\downarrow$, ε^B with corresponding hopping parameters in each region as well as at the interfaces. The potential profile of the MTJ under applied voltage is shown in Fig.1b. For simplicity we put all hopping parameters t=-1eV and all calculations performed and presented here are for three monolayers of barrier thickness. The corresponding band width for both spin channels is therefore equal to 12*t*.

In order to show the effect of majority and minority band filling on the behavior of STT we fix the majority band by setting its on-site energy at three values corresponding to the ¼, ½ and ¾ filling, i.e. $\varepsilon^\uparrow$=+3, 0 and -3eV, and shift the minority band by changing $\varepsilon^\downarrow$ to trace the effect of the exchange splitting until ending up with the half-metallic case for which $\varepsilon^\downarrow-6|t|$ exceeds the Fermi level (which is set to zero and shown by dashed lines in Fig. 1b). The corresponding results for $T_\|$ and $T_\perp$ are shown in Figs. 2(a,b,c) and 2(d,e,f), respectively. For the case of ¼ majority band filling (Fig.2a) the parallel component of the STT exhibits a wide range of behavior from being a quadratic even function of applied voltage at $\varepsilon^\downarrow$=4.2eV to an odd one for the pure half-metallic case with $\varepsilon^\downarrow$=7eV. These are two limiting cases in the interplay between two collinear longitudinal spin currents Is(0) and Is(π) which define the parallel torque[5,7] since Is(0) and Is(π) are odd and even parity functions of applied voltage, respectively.[7] For the case presented in Figs. 2b and 2c the magnitude of $T_\|$ decreases and it is impossible to obtain a situation for which Is(0) vanishes, moreover, $T_\|$ is mostly defined by Is(0) and the odd parity voltage dependence dominates over even parity. It is interesting to note that in the half-metallic situation, the parallel torquance ($dT_\|/dV$) is negative for ¼ majority filling (Fig. 2a) and changes sign in case of ½ and ¾ filling (Figs. 2b and c). All of these curves can be explained in terms of the spin and charge current dependence on the interplay between evanescent states in the insulator and the Fermi surfaces of the ferromagnetic electrodes comprising the junction. In Figs. 2(d-f) we show the same effect of the band fillings on the voltage dependence of $T_\perp$. The zero voltage values correspond to the exchange coupling between FM and FM' through the barrier while the voltage induced part is always quadratic.

[1] J. C. Slonczewski, J. Magn. Magn. Mat. 159, L1 (1996); [2] L. Berger, Phys. Rev. B 54, 9353 (1996); [3] W. H. Butler et al, Phys. Rev. B, 63, 054416 (2001); [4] J. Mathon and A. Umerski, Phys. Rev. B, 63, 220403(R) (2001); [5] J. C. Slonczewski, Phys. Rev. B 71, 024411 (2005); [6] A. Kalitsov et al, J. Appl. Phys. 99, 08G501 (2006); [7] I. Theodonis et al, Phys. Rev. Lett. 97, 237205 (2006); [8] H. Kubota et al, Nature Physics 4, 37 (2008); [9] J. C. Sankey et al, Nature Physics 4, 67 (2008)

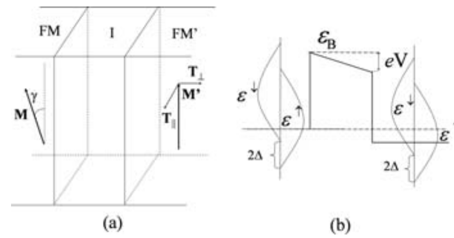

Figure 1. (a) Schematic representation and (b) corresponding potential profile of magnetic tunnel junction.

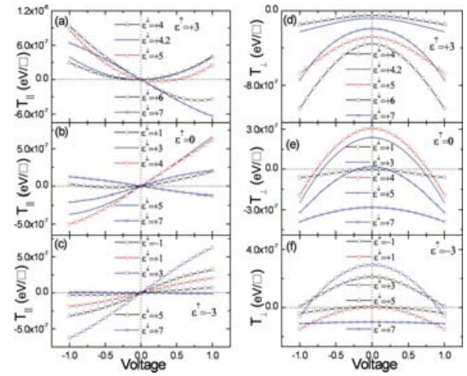

Figure 2. Parallel (a, b and c) and perpendicular (d, e and f) components of spin transfer torque as a function of applied voltage for different values of majority and minority on-site energies.

CC-03

Magnetic tunnelling junctions based on MgO(001) epitaxial barriers: from the interfacial spin dependent electronic structure to the ultimate TMR.

A. Cattoni, D. Petti, M. Cantoni, S. Brivio, R. Bertacco
Center LNESS - Department of Physics, Politecnico di Milano, Como, Italy

Since the discovery of spin dependent tunnelling, Magnetic Tunnel Junction (MTJs) have been widely investigated also in view of relevant applications like Magnetoresistive Random-Access-Memory (MRAM), magnetic sensors and novel programmable logic devices. Different class of materials, like half metals, have been tested in the past years. Nowadays it is well recognised that symmetry filtering in structures employing MgO barriers epitaxially matched with ferromagnetic electrodes FM(Fe, FeCo, FeCoB), provides better results in terms of stability and performances at room temperature. However, also in this case there is still a sizable gap in between theoretical predictions [1] of the TMR and experimental values,[2] probably to be ascribed to the non ideality of the interfaces.[3] In this spirit we have performed a detailed analysis and optimization of the formation of the FM/MgO interface with the aim of improving heteroepitaxy, reducing oxidation and maximizing the spin dependent properties of the interface electronic structure.
MgO/Fe and MgO/FeCo interfaces have been grown by MBE in a dedicated UHV system with different recipes for the growth of the MgO barrier, while monitoring in-situ the structural, chemical, electronic and magnetic properties of the interfaces via appropriate surface science techniques: low energy electron diffraction (LEED), photoelectron diffraction (PED), X-ray photoemission spectroscopy (XPS), ultraviolet photoemission spectroscopy (UPS), spin polarized inverse photoemission (SPIPE), absorbed current spectroscopy (ACS) and magneto optical Kerr effect (MOKE).
For both Fe and FeCo electrodes we found reliable recipes for the gowth of the MgO overlayer ensuring only the minimum surface oxidation inherent with the formation of a chemical bonding between the FM electrode and MgO, as seen by detailed analysis of the Fe 2p peaks in XPS. Epitaxial MgO layers with high crystallinity have been obtained by stoichiometric evaporation from MgO single crystals, as revealed by LEED and PED analysis. The electron spectroscopy investigation of valence band states via UPS gives the expected electronic structure of the MgO barrier, without sizable modification of the FM electronic structure. The same holds true for the unoccupied part of the electronic structure we have investigated also with spin resolution via SPIPE and ACS. In fig. 1 we report SPIPE spectra from 2 ML of MgO grown on Fe(001) (filled dots) and FeCo(001) (empty dots). The experimental features reflect transitions from Δ1 states to Δ5 states, whose splitting is connetcted to the exchange splitting of the bands and we assume as index of the quality of the interface.[4] The electronic structure of the two electrodes is inherently different due to the different symmetry and chemical composition. Fe(001) presents the well known doublet B1–B2, related to Δ5 final states close to H25' just above the Fermi level, with the good exchange splitting which is maintained upon MgO deposition as well as the splitting of C peak reflecting the exchange splitting of the bands at H15. D and E are characteristic peaks of the MgO overlayer, with E in particular related to the onset of the MgO conduction band. Q1 and Q2 are instead assigned to fully polarized majority resonance states localized at the interface. For FeCo the situation is quite similar, except for the B1 peak which is missing as the corresponding Δ5 state is now unaccessible to SPIPE being under the Fermi level. Also in this case we observe that the surface exchange splitting is unaltered upon MgO deposition.
According to the optimized procedures,complete Fe/MgO/Fe and FeCo/MgO/Fe MTJs have been realized first by shadow mask (with junction areas of 200x200 microns) and now by optical lithography at the micrometer scale. The bottom FM electrode (100 nm) is epitaxially grown on MgO and presents a very low defect concentration, as confirmed by a square hystheresys loop with a coercive field of only 0.8 Oe along the easy axis of the typical uniaxial anisotropy displayed by these films. The barrier thickness is 2 nm, while the top electrode is 10 nm thick with a coercive field of the order of 15 Oe. Preliminary transport measurements on Fe/MgO/Fe junctions shows state of the art values of the TMR at room temperature (of the order of 100 %), and high sensibility in the linear branch of the TMR (typically 3%/Oe).
In the paper we will give a complete comparison in between the performances of MTJs obtained employing different combinations of electrodes and interface preparation recipes, establishing a strong connection between the bias dependence of the TMR and the measured spin dependent electronic structure.

[1] W. H. Butler et al., Phys. Rev. B, 63, 054416 (2001)

[2] S. Yuasa et. al., Nature Materials, 3, 868 (2004)

[3] Heiliger et al. Journal of Magnetism and Magnetic Materials, 316, 478 (2007)

[4] R. Bertacco et al., Phys. Rev. B, 59, 4207 (1999)

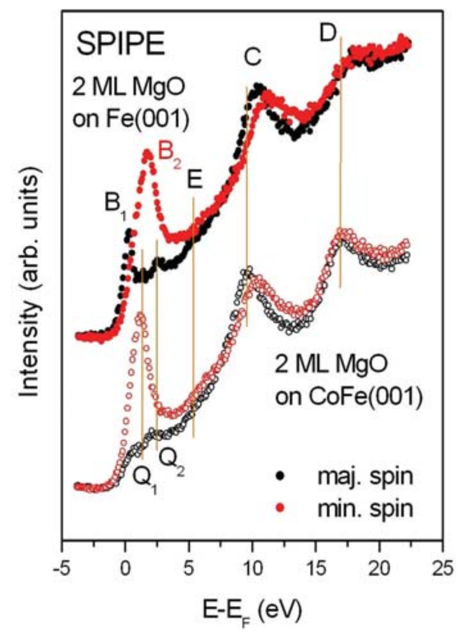

Fig. 1: SPIPE on 2 ML of MgO on Fe(001) (filled dots) and FeCo(001) (empty dots)

CC-04

Magnetic Tunnel Junctions with MgO Tunnel Barriers and NiFeSiB/CoFeB Hybrid Free Layers.

J. Cho[1], D. Kim[1], T. Wang[1], S. Isogami[2], M. Tsunoda[2], M. Takahashi[2], Y. Kim[1]
1. Department of Materials Science and Engineering, Korea University, Seoul, South Korea; 2. Department of Electronic Engineering, Tohoku University, Sendai, Japan

Introduction

The magnetic tunnel junctions (MTJs) consisting of MgO tunnel barriers are of great importance for MRAM application because they exhibit high TMR ratio. We employed NiFeSiB/CoFeB hybrid free layers to substitute traditionally used CoFeB layers with an aim to reduce switching field (Hsw) while maintaining high TMR ratio. Ni16Fe62Si8B14 has a lower saturation magnetization (Ms: 878 emu/cm^3) compared to CoFeB (Ms: 1170 emu/cm^3), and a higher anisotropy constant (Ku: 2,700 erg/cm^3) than Ni80Fe20 (Ku: 1,000 erg/cm^3) [1].

Experiment

The MTJs consisting of Si / SiO2 / Ta(5) / Ru(40) / hybrid free layer / MgO (1.0~1.9) / CoFeB (4) / Ru(0.85) / CoFe(3) / IrMn(7.5) / Ta(5) / Ru(50) (in nm) were prepared by dc magnetron sputtering under typical base pressure below 5×10^–9 Torr. The hybrid free layer consists of CoFeB(4), NiFeSiB(1.33) / CoFeB(3), NiFeSiB(2.66) / CoFeB(2), NiFeSiB(3.99) / CoFeB(1), or NiFeSiB (5.32). For all free layer structures, the Ms×t value was kept same. MgO tunnel barriers were formed by rf sputtering using a MgO target. All of MTJ samples were annealed in vacuum at 360°C for 1 hr with 3 kOe of magnetic field. TMR ratio was investigated by current-in-plane-tunneling (CIPT) measurement and two-probe method after fabricate junctions by a photolithographic patterning and ion beam etching. The junction sizes were varied from 10 μm×10 μm to 100 μm×100 μm.

Results and Discussion

Figure 1 shows the TMR ratio dependence on the MgO thickness for various free layer structures. The TMR ratio of the MTJ with a NiFeSiB-only was poor. To improve this, a CoFeB layer was placed between the MgO barrier and the NiFeSiB layer. When the thickness of NiFeSiB was 1.33 nm and CoFeB was 3 nm, the TMR ratio becomes 209%, which is comparable with that of the CoFeB-only free layer (204%). Moreover, the Hsw became 6 Oe which is lower compared to 12 Oe obtained form the MTJ with CoFeB-only free layer (not shown here). Figure 2 shows the in-plane XRD profiles of Si / SiO2 / Ta (5) / Ru (40) / hybrid free layer / MgO (10) films. The XRD peak intensity ratio of MgO (200) and MgO (220) should be 4 in case of (001) oriented MgO films [2]. The ratio of the MgO layer on the CoFeB layer was 3.6, whereas that of the MgO on the NiFeSiB was nearly 1. This means that the amorphous NiFeSiB layer located just below the MgO layer can not induce (001) orientation of MgO. The peak intensity ratio of the MgO layer on the hybrid NiFeSiB (1.33) / CoFeB (3) layer was 3.5.

Lately, an MTJ with a NiFe / CoFeB hybrid free layer was studied [3]. In this case, the CoFeB layer crystallized into the textured fcc (111) structure instead of bcc (001) after annealing, and as a result, the TMR ratio was reduced because the coherent tunneling of Δ1 electrons could not occur [3]. On the contrary, because the NiFeSiB layer maintained amorphous after annealing, the amorphous CoFeB layer could be crystallized into the bcc (001) following to the orientation of the MgO. As a consequence, the NiFeSiB / CoFeB free layer resulted in a high TMR ratio. In addition, since NiFeSiB has lower Ms compared to CoFeB, the NiFeSiB-containing MTJs exhibited lower Hsw values [1]. In summary, the NiFeSiB / CoFeB hybrid free layer approach was effective in terms of maintaining high TMR ratio and decreasing Hsw at the same time.

References

[1] B. S. Chun, I. S. Yoo, Y. K. Kim, J. Y. Hwang, J. R. Rhee, T. W. Kim, and W. J. Park, Appl. Phys. Lett. 87, 802508 (2005).

[2] K. Sunaga, M. Tsunoda, K. Komagaki, Y. Uehara and M. Takahashi, J. Appl. Phys. 102, 013917 (2007).

[3] S. Yuasa and D. D. Djayaprawira, J. Phys. D: Appl. Phys. 40, R337 (2007)

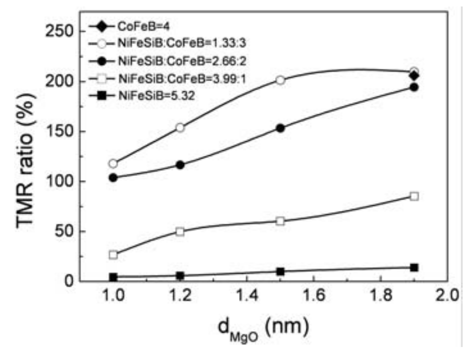

Fig. 1. TMR ratios of the MTJs as a function of MgO thickness. The net Ms value was kept same as that of the 4 nm thick CoFeB. The layer thickness scale is nm.

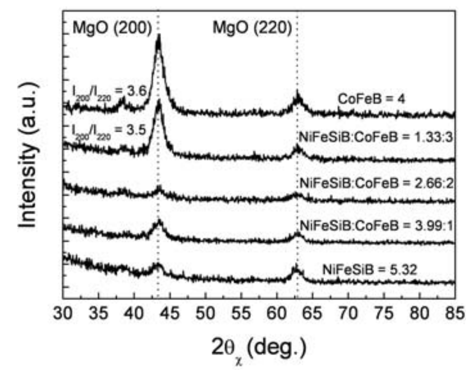

Fig. 2. XRD profiles of Ta (5) / Ru (40) / hybrid free layer / MgO (10) (in nm). Incident x-ray angle was fixed to 0.1°, and the penetration depth was 10 nm.

CC-05

The Surface Electronic Structure: a Key Parameter in Low Resistance Area Single Crystal Magnetic Tunnel Junctions.

P. Zermatten[1], M. Miron[1], G. Gaudin[1], A. Schuhl[1], F. Greullet[2], M. Hehn[2], C. Tiusan[2]
1. SPINTEC, CEA/CNRS, Grenoble, France; 2. LPM, CNRS/UHP, Nancy, France

We show experimental evidences of interface resonant states (IRS) tunnel transport in fully epitaxial Fe/MgO/Fe(001) magnetic tunnel junctions (MTJs). The presence of 100% spin polarized interface states in the energy gap of minority Δ1 states [1] has been theoretically predicted. Those states are coupled with the bulk Fe states and become available for conduction for small bias above the Fermi energy. When activated, their opposite spin-polarization with respect to the bulk Δ1 states of Fe, responsible on the large tunnel magneto-resistance (TMR) of Fe/MgO/Fe junctions, can drastically affect the TMR amplitude and sign.

Our Fe/MgO/Fe MTJs are grown by using ultrahigh vacuum MBE [2]. They present two different Fe/MgO interfaces. The annealing at 700K of the bottom Fe electrode provides a flat bottom interface with almost no defects. This atomically flat interface promotes IRS states. On the other hand, the top interface shows higher roughness, determined by the growth of the metallic Fe on the MgO insulator. Consequently, the IRS of the top Fe layer is expected to be quenched due to their high sensitivity to interface defects [2].

The transport measurements are done by conducting AFM tip after patterning mesa structure by e-beam lithography. By changing the bias voltage, the different density of states of top and bottom Fe/MgO layer is selectively probed. The d2I/dV2 characteristics measured on our samples point out two peaks: the first one at about 0.2eV [3] and the second one at 0.95V. These spectroscopic features are only present in the anti-parallel MTJ configuration being completely absent in the parallel one. Neither the observed peaks nor the asymmetry of the anti-parallel I(V) curve can be explain by the Fe bulk density of states. Therefore, we associate these peaks to the surface electronic structure of the bottom Fe. The IRS represent the stationary states in a quantum well (QW) where the minority spin Δ1 wave function is confined between the MgO insulator and the Fe Δ1 bulk gap. These surface states of the minority spin will provide a 100% negative polarization.

Moreover, our spectroscopic data show a significant increase of IRS-related conductivity when the thickness of the MgO is reduced from 3 to 2nm. Due to the opposite sign polarization of the IRS with respect to the 100% positive polarization of the bulk Δ1 Fe, it is obvious that their activation affects drastically the TMR amplitude.

Thus, the control of the IRS contribution to the tunneling in single crystal MTJ devices is a key parameter to control the TMR amplitude and sign in thin barrier Fe/MgO devices needed for low RA sub-micrometer MTJs in MRAMs.

[1] W. H. Butler et al, Phys. Rev. B 63, 054416 (2001).

[2] C. Tiusan et al., J. Phys.: Condens. Matter 19, 165201, (2007).

[3] C. Tiusan et al. Physical Review Letters 93, 106602 (2004).

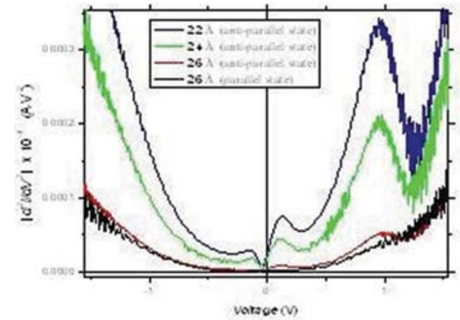

Second derivative of current in Fe/MgO(t)/Fe(001) MTJs for different thickness (t = 2.2, 2.4, 2.6) of the single crystal MgO barrier. We point out the peaks at about 0.2V and 0.9V in positive bias voltage when the electrons are flowing from the top Fe electrode towards the bottom atomically flat Fe/MgO interface.

CC-06

Transport characterization of the single and double magnetic tunnel junctions using point contact spectroscopy.

A. Iovan, S. Cherepov, A. von Bieren, S. Andersson, V. Korenivski
Nanostructure Physics, KTH, Stockholm, Sweden

The high potential of the magnetic tunnel junctions (MTJ) for microelectronic devices [1] justifies the intensive research efforts worldwide to understand and improve their properties. The studies of the transport properties of the junctions require a patterning process, which often is the standard multi-step lithography[2]. The junctions can be defined also by one-step lithography and measured with the aid of a conductive AFM [3]. However, if the number of junction to be measured increases the turnaround time of the AFM technique becomes long. Worledge et al. [4] developed a fast surface probe technique for measuring tunnel magnetoresitence of multilayered films, though the lateral geometrical aspects of the devices cannot be studied using this method.

In this report we discuss the use of the point contact spectroscopy (PCS) technique for the characterization of MTJ's using one step lithography for patterning nanopillars. The key of this technique is to produce a sample with a large array of tunnel junctions which are closely spaced on a substrate buffered with metallic layer for making the bottom electrical contact to the nanopillars. A top nano-contact is made mechanically using a conductive tip, at room temperature or in liquid helium. A large number of junctions can be measured just by moving slightly the tip on the surface of the sample. Single tunnel junctions were characterized using this method. However, the possibility of screening electrically a large number of junctions is particularly interesting for the study of coherent transport in double tunnel junction [5]. We observed such transport in our double magnetic tunnel junction (DMTJ) samples, where the measurements show that the magnetoresistence can increase by up to one order of magnitude.

Single tunnel barriers and double tunnel barriers were produced using sputtering. In order to pattern the samples, a 150-nm ZEP520A positive resist is spun on top of the multilayer samples and subsequently baked. A rectangular matrix can be drawn in the resist by e-beam lithography. The resist mask is then transferred to the stacks by using Ar ion beam etching. The process is finalized by removing the resist mask using oxygen plasma and the final structure is a large array of MTJ stacks, separated by trenches etched through the top electrode.

Figure 1(a) shows the measured I-V characteristics and the Brinkman fit [6] for a tunnel junction from the stack of SiO/NiFe(50nm)/MgO(3nm)/Co(10). The typical size for a single tunnel junction used in the design is 10 by 10 micrometers and the same value for the area is obtained from the fit curve. The barrier height extracted is 0.489 eV which is a reasonable value for MgO, where 0.3–1 eV barrier heights [7], [8] are expected. In addition the good matching between the deposited thickness of MgO (2nm) and fitted value (2.119 nm) indicate the measurement of a single tunnel junction.

This technique is very useful for the study of coherent transport in DMTJ's where typically a large number of samples must be screened to find the desired behavior. If the thickness of the intermediate layer is sufficiently small, effects of coherent transport can be observed. Figure 1(b) shows a staircase current voltage characteristics obtained for a double junction with the area of 170 nm by 800 nm. At the points of resonant transmission (steps in current) the magnetoresistence versus voltage (not shown) exhibits rapid changes in value as well as sign. We interpret this behavior as due to an activation of discrete transmission levels in the middle layer of the DMTJ caused by the magnetic transition in a sweeping external magnetic field. This activation is due to the changing potential in the intermediate layer caused by the change of the resistance of the magnetic tunnel junction.

In conclusion, in this work we use a novel method for a transport characterization of magnetic tunnel junctions including double barrier structures in the coherent transport regime. This study can be important for further development of magnetic nano-devices with new functionality.

1) S.P.P. Parkin et al, J. Appl. Phys. 85, 5828 (1999).

2)Yu Lu et al., Appl. Phys. Lett. 70, 2610 (1997).

3) H. Kubota et al, J. Appl. Phys. 94, 2028 (2003).

4) D. C. Worledge, P. L. Trouilloud Appl. Phys. Lett. 83, 84 (2003).

5) M. Chshiev et al, Europhys. Lett. 58, 257-263 (2002).

6) F. Brinkman, R. C. Dynes, and J. M. Rowell, J. Appl. Phys. 41,1915 (1970).

7) S. S.P. Parkin et al, Nature materials 3, 862 (2004).

8) S. Yuasa et al, Nature Materials 3, 868 (2004).

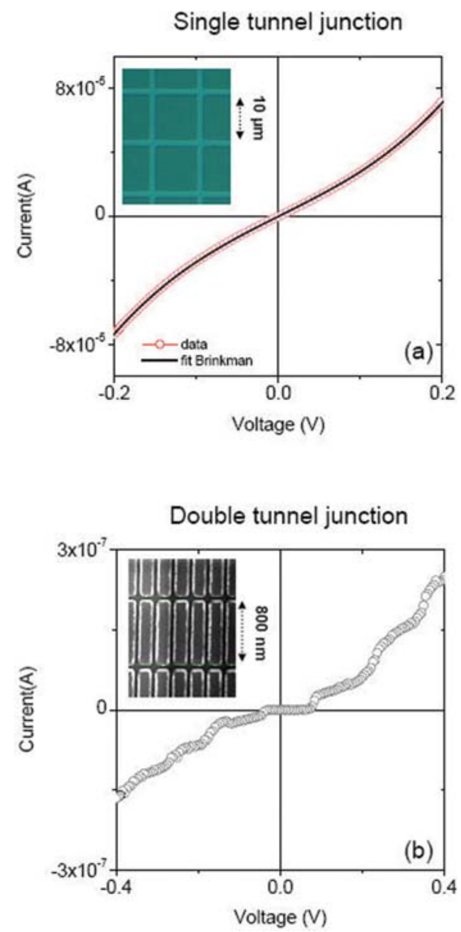

Figure 1 (a) Current voltage characteristic for a single tunnel junction and the Brinkman fit of this curve. The inset of the figure is the optical image of the measured array. (b) Current voltage characteristics measured at 4K for the DTJ: SiO/Fe(50nm)/MgO(3)/Fe(2nm)/MgO(2)/Au (20), the inset of the figure is the SEM image the measured DTJ's.

CC-07

Magnetotransport properties of MgO-based epitaxial magnetic tunnel junctions with a nonmagnetic electrode.

R. Matsumoto[1,2], A. Fukushima[1], T. Nagahama[1], Y. Suzuki[1,2], K. Ando[1], S. Yuasa[1]
1. Nanoelectronics Research Institute, National Institute of Advanced Industrial Science and Technology (AIST), Tsukuba, Japan; 2. Graduate School of Engineering Science, Osaka University, Toyonaka, Japan

First-principle theories predicted a giant tunneling magnetoresistance (TMR) in fully epitaxial magnetic tunnel junction (MTJ) with a crystalline MgO(001) barrier due to coherent spin-dependent tunneling [1,2]. We have experimentally achieved giant room-temperature MR ratios of 180%, 271% and 410% at in fully epitaxial Fe/MgO/Fe, Co/MgO/Fe and Co/MgO/Co MTJs, respectively [3-5]. In addition to the giant TMR effect, these fully epitaxial MTJs are a model system in studying novel phenomena such as an oscillation of MR ratio as a function of MgO barrier thickness (t_{MgO}) with a period (λ) of about 0.3 nm [3,6]. The theory proposed a model of interference between tunneling states, in which an oscillation of tunneling conductance with respect to t_{MgO} is expected [1]. In our previous study on fully epitaxial Fe/MgO/Fe–MTJs [6], both the tunneling resistance in the parallel magnetic state (R_P) and that in the antiparallel magnetic state (R_{AP}) exhibited short-period oscillations as a function of t_{MgO} with the same λ of 3.2 Å and different phases. R_{AP} also showed a long-period oscillation with λ = 9.9 Å. As a result, t_{MgO}-dependence of TMR is expressed as a superposition of the short- and long-period oscillations. However, the origin of the short-period oscillation is still unclear although this is an essential issue in understanding the physics of coherent tunneling. To clarify the origin of the short-period oscillation, we studied MgO-based epitaxial MTJs with a non-magnetic or a paramagnetic top electrode layer. In this study, we fabricated epitaxial Fe(001)/MgO(001)/Cr and Fe(001)/MgO(001)/Ru MTJs with various MgO thicknesses. Cr is antiferromagnetic (SDW) below about 300 K, while Ru is non-magnetic at any temperature. We performed high-precision measurements of the tunneling resistance as a function of t_{MgO} in these MTJs to investigate whether the tunneling resistance oscillates with respect to t_{MgO}.
We fabricated the 2 kinds of MTJ films with a wedge-shaped MgO layer on a single MgO(001) substrate by using molecular beam epitaxy growth except for sputter-deposited Ru layer. *In situ* RHEED observations showed that the Cr electrode layer grown on MgO is (001)-oriented single-crystalline while the Ru electrode layer on MgO is poly-crystalline. The growth conditions of the bottom Fe and MgO barrier layers were the same as in our previous studies [3,6]. The films were fabricated into MTJs using a high-precision micro-fabrication process which was also used in our previous study [6]. Tunneling resistance at a bias voltage of 10 mV was measured at 20 K, room temperature and 350 K with the dc 4-probe method.
The tunneling resistance per unit junction area (*RA* product) for both Fe/MgO/Cr–MTJs and Fe/MgO/Ru–MTJs exponentially increases with respect to t_{MgO}, which is a typical tunneling characteristic, as observed in our previous studies[3-6]. We tried to extract an oscillatory component in the $RA - t_{MgO}$ relationship by removing the exponential t_{MgO}-dependence from the $RA - t_{MgO}$ relationship (*i.e.*, by dividing *RA* by $C\exp(\alpha t_{MgO})$ which is obtained by fitting $RA - t_{MgO}$ relationship). The t_{MgO}-dependences of $RA/\ C\exp(\alpha t_{MgO})$ for the 2 kinds of MTJs at 20 K are shown in Fig. 1. The tunneling resistance of the Fe/MgO/Cr–MTJs exhibited the short-period oscillation with λ = 3.0 Å. The same oscillation was also observed at 350 K, where Cr is paramagnetic. In Fe/MgO/Ru–MTJs, on the other hand, no oscillatory feature was observed. This indicates band structure of electrode rather than spin angular momentum is responsible for the short-period oscillation. The results contain an important clue in clarifying the detailed mechanism of coherent spin-dependent tunneling.
This study was supported by New Energy and Industrial Technology Development Organization (NEDO).

[1] W. H. Butler, X.-G. Zhang, T. C. Schulthess, and J. M. MacLaren, Phys. Rev. B **63**, 054416 (2001).

[2] J. Mathon and A. Umersky, Phys. Rev. B **63**, 220403R (2001).

[3] S. Yuasa, T. Nagahama, A. Fukushima, Y. Suzuki, and K. Ando, Nature Mater. **3**, 868 (2004).

[4] S. Yuasa, T. Katayama, T. Nagahama, A. Fukushima, H. Kubota, Y. Suzuki, and K. Ando, Appl. Phys. Lett. **87**, 222508 (2005).

[5] S. Yuasa, A. Fukushima, H. Kubota, Y. Suzuki and K. Ando, Appl. Phys. Lett. **89**, 042505 (2006).

[6] R. Matsumoto, A. Fukushima, T. Nagahama, Y. Suzuki, K. Ando and S. Yuasa, Appl. Phys. Lett. **90**, 252506 (2007).

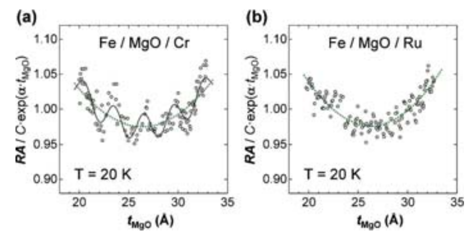

Fig.1 MgO thickness (t_{MgO})-dependence of oscillatory component in tunneling resistance for (a) epitaxial Fe/MgO/Cr–MTJs and (b) Fe/MgO/Ru–MTJs.

CC-08

High bias tunneling magnetoresistance and low frequency noise in fully epitaxial Fe/C/MgO/Fe(001) magnetic tunnel junctions.

D. Herranz[1], R. Guerrero[1], R. Villar[1], *F. G. Aliev*[1], F. Greullet[2], C. Tiusan[2], M. Hehn[2]
1. Fisica Materia Condensada, CIII, Universidad Autonoma de Madrid, Madrid, Spain; 2. Laboratoire de Physique des Matériaux, Nancy Université, Nancy, France

Magnetic tunnel junctions (MTJs) are nowadays one of the most active areas of material science and spintronics. Our recent studies have demonstrated that combined measurements of conductance and noise as a function of applied bias could be a powerful tool to investigate electron tunneling in MTJs [1-3]. We have also recently found that carbon-doping of the bottom Fe/MgO interface leads to strongly asymmetric TMR vs. bias, providing new root to create high-output voltage MTJ devices [4]. Present contribution reports on study of high bias (above 2V) dynamic conductivity, shot noise (10K) and room temperature 1/f noise in epitaxial Fe(100)[45nm]/Fe-C/MgO(100)[2.6 and 3nm]/Fe(100)[10nm] MTJs as a function of the magnetic state.

Our junctions show large tunnel magnetoresistance (up to 185% at 300K and above 300% at 4K). Multiple sign inversions of the magnetoresistance are observed for bias polarity when the electrons scan the electronic structure of the bottom Fe-C interface (Fig.1). Reduction of the barrier thickness mainly affects negative TMR by reducing TMR inversion bias voltage. These experiments demonstrate the role of the minority spin Fe interface resonance state (IRS) to the tunneling.

The experiments on shot noise (Fig.2) clearly indicate absence of electron correlations and/or sequential tunneling phenomena for negative bias when the electrons are injected from the top Fe/MgO toward the bottom Fe-Fe-C/MgO interface in carbon doped MTJs. This proves that both parallel (P) and anti-parallel (AP) spin-dependent conductance and the shot noise are due to direct tunneling between electron bands, as expected for a coherent tunneling. When electrons are injected from bottom to upper electrodes, the shot noise also shows Fano factors close to 1 except the bias voltage close to 0.5V when resonant tunneling (presumably through asymmetrically situated oxygen vacancies) weakly suppresses the shot noise (Fig.2, AP state). In general, our shot noise measurements validate the high quality of our epitaxial MgO barriers. The high MTJs quality is furthermore confirmed by the large breakdown voltage of the MTJs (up to 3 V) [2].

The low frequency noise analysis performed on our MTJs show extremely low 1/f noise levels at 300K [3]. We have found that the normalized noise (Hooge factor) asymmetry between parallel and antiparallel states may strongly depend on the applied bias and its polarity. Fully epitaxial Fe/C/MgO/Fe(001) MTJs exhibit record low Hooge factors being at least one order of magnitude smaller than previously reported (Fig.3).

[1] R. Guerrero, et al., Phys. Rev. Lett., 97, 0266602 (2006).

[2] R. Guerrero et al, Appl. Phys. Lett. 91, 132504 (2007).

[3] F.G. Aliev, et al., Appl. Phys. Lett. 91, 232504 (2007).

[4] C. Tiusan et al, Appl. Phys. Lett. 88, 062512 (2006).

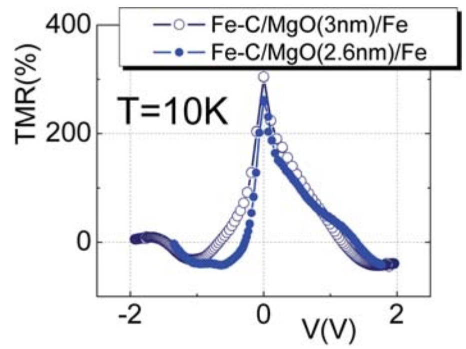

FIG. 1. Comparison of the high-bias TMR measured at 10K for MTJs with two different MgO thicknesses.

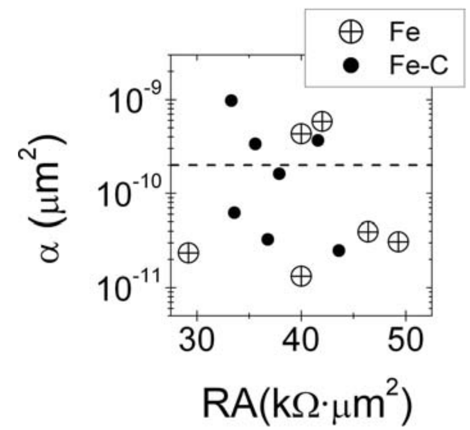

Fig.3 Room temperature normalized noise measured in Fe(100)[45nm]/MgO(100) [2.6nm]/Fe(100)[10nm] MTJs at +200mV as a function of Resistance by Area (RA) product. The dashed line indicates the lowest Hooge factor value previously reported for the MTJs.

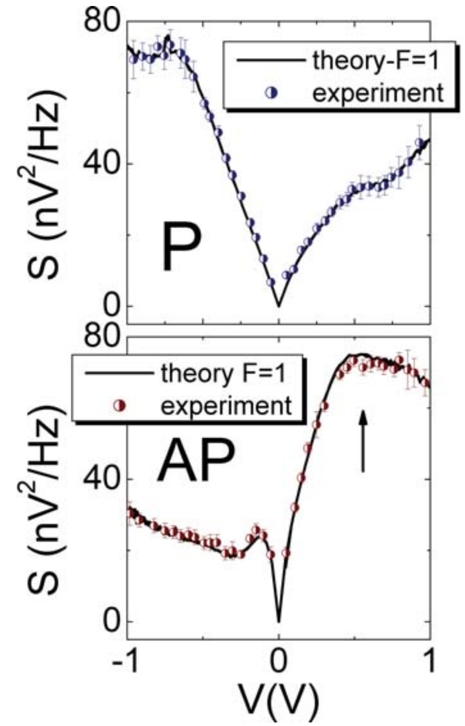

Fig. 2 Shot noise measurements in the P and AP states at 10 K in Fe/C/MgO(2.6nm)/Fe MTJ. Negative bias corresponds to electrons injected from the top Fe/MgO toward the bottom. For comparison, the solid curves show the theoretical expectation for the shot noise with electron tunneling having Poissonian character. Arrow indicates bias interval with suppressed shot noise.

CC-09

1/f magnetic noise dependence on free layer thickness in linear MgO magnetic tunnel junctions.

P. Wisniowski, J. M. Almeida, P. P. Freitas
INESC-MN, Lisbon, Portugal

Utilization of MgO based magnetic tunnel junctions as low field sensors requires besides high sensitivity, low noise level that ultimately determines sensor detection limit. The noise level of junction is the highest in the most sensitive region of transfer curves, which is usually a working region, and is dominated by 1/f magnetic noise. A reduction or cancellation of the noise is of primary importance in view of developing low field MgO based sensors. It was shown that thinning CoFeB free layer in MgO magnetic tunnel junctions allows to obtain linear junctions with sensitivity as high as 7.7 %/Oe [1]. The use of these high sensitive junctions as low frequency field sensors is determined by their noise spectra, which is a topic of this study.

Magnetic tunnel junctions with varying thickness of CoFeB(t_F) free layer from 14.5 Å to 30 Å with structure glass/Ta(50)/Ru(180)/Ta(30)/PtMn(160)/CoFe(22)/Ru(9)/CoFeB(30)/MgO13.5/CoFeB(t_F)/Ru(50)/Ta50 (thickness in Å), were deposited by magnetron sputtering (Nordiko 2000 system). The nominal layer thickness is given in angstrom. The easy axis of the magnetic layers was set by applying 20 Oe field during deposition. Before microfabrication, the films were passivated with 150 Å of Ti10W90(N2) deposited in another magnetron sputtering system. The samples were patterned by direct write laser lithography and ion beam milling with areas ranging from 4.5 μm^2 to 144 μm^2. Patterned samples were annealed in high vacuum at 330 °C, for 1 h in a magnetic field of 5 kOe applied along the easy axis, and furnace cooled in the field. The electrical properties were measured using a dc four-probe setup. Noise measurements were made in a magnetically shielded system.

Figure 1 shows dependence of TMR on CoFeB free layer thickness and corresponding transfer curves. TMR decreases gradually as free layer decreases and the junctions show linear response for CoFeB(t_F) ≤ 15.5 Å. For CoFeB(t_F) = 14.5 Å junctions present sharp drop in sensitivity as compared to thicker free layers and 40 % TMR. The junctions with CoFeB(t_F) =15.5 Å and CoFeB(t_F) = 14.5 Å show up to 7.7 %/Oe and 0.2 %/Oe sensitivity respectively. The change in the response of the free layer and drop in sensitivity for CoFeB(t_F) = 14.5 Å is due to onset of its superparamagnetic behavior.

To evaluate noise of the linear junctions noise spectra were measures along transfer curves. The extracted noise power density and detection limits show Fig. 2. The noise power of the two junctions is distinctive different at all frequencies and is essentially flat along transfer curve for CoFeB(t_F) = 14.5 Å. This is contrast to junctions with CoFeB(t_F) = 15.5 Å and thicker (not shown here) that exhibit sharp increase in noise power in the sensitive region. The absence of 1/f magnetic noise in junctions with CoFeB(t_F) = 14.5 Å is attributed to stabilizing effect of demagnetizing field of the pinned layer on magnetic fluctuations in the free layer.

The results show that reduction of three layer thickness can be used as an effective way to cancel 1/f magnetic noise in magnetic tunnel junctions, at the expense of sensitivity. In terms of field detection limit, the junctions with thin and thick free layer show the same detection limit of 25 $nT/Hz^{1/2}$ at low frequency (500 Hz). At high frequency (100 kHz), however, junctions with thicker free layer show detection limit of 1.5 $nT/Hz^{1/2}$, which is three times better than for thin free layer.

[1] P. Wisniowski, J. M. Almeida, S. Cardoso, N.P.Barradas, and P. P. Freitas, to be published in J. Appl. Phys.

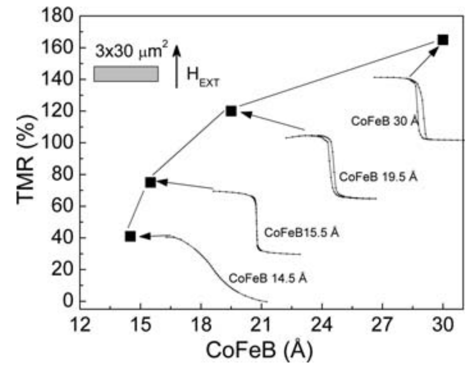

Fig. 1. Change in TMR and evolution of transfer curves with varying thickness of CoFeB free layer of junctions annealed at 330 ^{0}C.

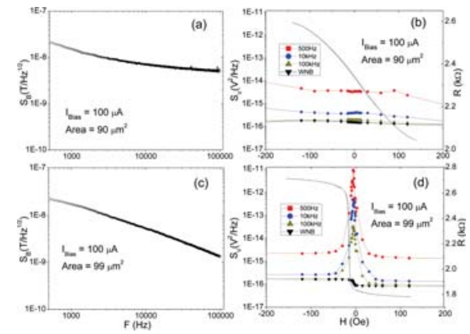

Fig. 2. Detection limit and noise power density for 14.5 Å (a), (b) and 15.5 Å (c), (d) thick CoFeB free layer. The noise power was measured along transfer curves and detection limit was determined for most sensitive point on transfer curves. WNB stands for white noise background.

CC-10

Hybrid Magnetic Tunnel Junction-MEMS device for 1/f noise supression.

A. A. Guedes[1,2], S. B. Patil[1], P. Wisniowski[1], V. Chu[1], J. P. Conde[1,2], P. P. Freitas[1,2]
1. INESC-MN, Lisbon, Portugal; 2. Instituto Superior Tecnico, Lisbon, Portugal

It was previously shown that it is possible to suppress 1/f noise in spin valve (SV) sensors, by modulating an external DC magnetic field at high frequency through the movement of a MEMS cantilever with an incorporated magnetic flux guide. This shifts the operating frequency and enables the detection of DC magnetic fields in the high frequency thermal noise regime, where the 1/f noise is typically 2 orders of magnitude lower. This past work presented a dc detection limit of 0.54 $\mu T/Hz^{1/2}$, being limited by the low cantilever magnetic field modulation efficiency, which was only 0.11 % . [1]
In this digest a major improvement is presented, where MgO based magnetic tunnel junctions (MTJ) and MEMS torsionators are now used, allowing a DC field detection limit of 27 $nT/Hz^{1/2}$ and an improved MEMS magnetic field modulation efficiency of 20 %.
MgO based MTJ sensors were deposited in an automated sputtering machine with the following structure: Glass/ Ta[50] / Ru [180] / Ta [30] / MnPt [200] / CoFe [20] / Ru [9] / CoFeB [30] / MgO [15] / CoFeB [15.5] / Ru [50] / Ta [50] / TiW(N_2) [150], (thickness in Å). The TMR ratio was 30 %, lower than the expected 60 % found in standard samples. This decrease can be explained by the use of an alternative annealing (flash annealing). The MTJ sensors were patterned down to a dimension of 1.5x15 μm^2. A 4000 Å thick CoZrNb flux guide concentrator was patterned close to it, to convey and focus the external field to the sensor area. Finally, after passivating the sensor with an oxide layer, a 30x20 μm^2 MEMS torsionator was fabricated with a double layer of a-Si:H (4000 Å)/Al (1000 Å) and an additional 2000 Å thick CoZrNb flux guide. The MEMS torsionator is actuated by a gate electrode at frequency f, causing it to oscillate at 2f. This oscillation produces a 2f AC magnetic field, which is read by the MTJ in a spectrum analyzer. Fig.1 shows a SEM micrograph of the integrated device and a cut view diagram.
Noise measurements in the 2 kHz – 500 kHz range were performed in the MTJ sensor. For a bias current $I = 10^{-5}$ A and at 500 kHz (close to the thermal noise background) the magnetic field detection limit is $B_{detect} = 4\ nT/Hz^{1/2}$ (Figure 2).
With this MTJ-MEMS hybrid device the minimum detectable DC field (B_{detect}) is given by:
$B_{detect} = S_B / e_{tors}$ (1)
where S_B is the MTJ noise in $T/Hz^{1/2}$ at the modulated frequency, and e_{tors} the magnetic field modulation efficiency of the MEMS torsionator.
Figure 3 shows the MTJ output, when the MEMS gate is actuated by a 20 V_{pp} AC signal at 230 kHz . The MEMS torsionator oscillates at 460 kHz. For a DC external field $B_{ext} = 0.36$ mT entering the flux guide, the MTJ sensor detects the generated AC field at 460 kHz, showing a magnetic output of 240 $\mu V/Hz^{1/2}$.
The total MTJ output is given by 2 contibutions, one magnetic - resulting from the AC detected magnetic field, and one electric – coming from direct capacitive coupling between the gate electrode and the MTJ sensor:
$\Delta V_{MTJ} = \Delta V_{magnetic} + \Delta V_{electric}$ (2)
$\Delta V_{magnetic} = S\ I\ e_{tors}\ B_{ext}\ \mathrm{Sin}\ (2\pi(2f)t)$ (3)
where S is the sensitivity of the MTJ sensor (Ω/mT), I the MTJ biasing current, e_{tors} the MEMS torsionator modulation efficiency of the external static field B_{ext} and f the frequency of the signal applied to the torsionator.

Using Eq. (3), the MEMS torsionator modulation efficiency (e_{tors}) was calculated and found to be 20 %. Putting this together with the noise of the MTJ sensor at the modulated frequency – S_B (4.4 $nT/Hz^{1/2}$ at 460 kHz) we can estimate from Eq. (1) the DC detection limit of this hybrid-device, $B_{detect} = 27\ nT/Hz^{1/2}$.
Further work is being developed, mainly to improve the intrinsic detection limits of the MTJ sensors, so that its further integration in this hybrid-device would lead to pT DC field detection.

[1] A. Guedes, S. Patil, S. Cardoso, V. Chu, J. P. Conde, P. P. Freitas, Hybrid magnetoresistive/MEMS devices for static field modulation, and sensor 1/f noise cancellation, J. Appl. Phys. in press.

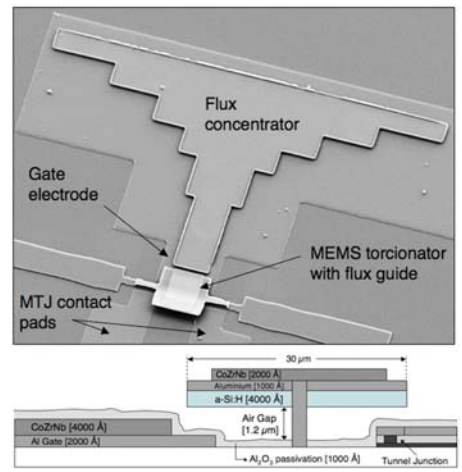

SEM picture of the device and a cut view diagram

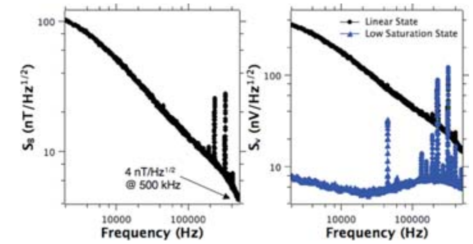

MTJ sensor noise spectrum

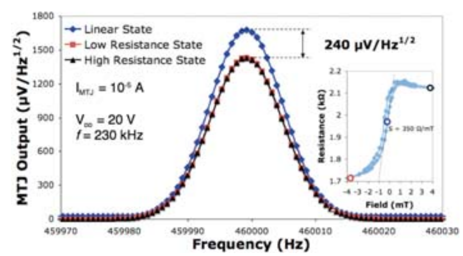

MTJ output (electric + magnetic) in linear and saturated state. The magnetic output is 240 $\mu V/Hz^{1/2}$

CD-01

Field driven ferromagnetic phase evolution originating from the domain boundaries in antiferromagnetically coupled perpendicular anisotropy films.

T. Hauet[1], C. M. Günther[2], O. Hovorka[3], A. Berger[3], M. Im[4], P. Fischer[4], O. Hellwig[1]
1. Hitachi Gst, San Jose, CA; 2. BESSY mbH, Berlin, Germany; 3. CIC NanoGUNE Consolider, Donostia, Spain; 4. Center for X-Ray Optics, Lawrence Berkeley National Laboratory, Berkeley, CA

Strong perpendicular anisotropy systems consisting of Co/Pt multilayer stacks that are antiferromagnetically coupled via thin Ru or NiO layers have been used as model systems to study the competition between local interlayer exchange and long-range dipolar interactions [1,2]. Magnetic Force Microscopy (MFM) studies of such systems reveal complex magnetic configurations with a mix of antiferromagnetic (AF) and ferromagnetic (FM) phases. However, MFM allows detecting surface stray fields only and can interact strongly with the magnetic structure of the sample, thus altering the original domain configuration of interest [3,4].
In the current study we combine magnetometry and state-of-the-art soft X-ray transmission microscopy (MXTM) to investigate the external field driven FM phase evolution originating from the domain boundaries in such antiferromagnetically coupled perpendicular anisotropy films. MXTM allows directly imaging the perpendicular component of the magnetization in an external field at sub 100 nm spatial resolution without disturbing the magnetic state of the sample [5,6]. Here we compare the domain evolution for two similar [Co(4Å)/ Pt(7Å)]x-1/ {Co(4Å)/Ru(9 Å)/[Co(4Å)/ Pt(7Å)]x-1}16 samples with slightly different Co/Pt stack thickness, i.e. slightly different strength of internal dipolar fields. After demagnetization we obtain AF domains with either sharp AF domain walls for the thinner multilayer stacks or “tiger-tail” domain walls (one dimensional FM phase) for the thicker stacks. When increasing the external field strength the sharp domain walls in the thinner stack sample transform into the one-dimensional FM phase, which then serves as nucleation site for further FM stripe domains that spread out into all directions to drive the system towards saturation (Fig. 1). Energy calculations reveal the subtle difference between the two samples and help to understand the observed transition, when applying an external field.
This work was partially supported by Lavoisier fellowship. The soft X-ray microscope was supported by the Director, Office of Science, Office of Basic Energy Sciences, Materials Sciences and Engineering Division, of the U.S. Department of Energy.

[1] O. Hellwig et al., Nat. Mater. 2, 112 (2003)

[2] O. Hellwig et al., J. Magn. Magn. Mater. 319, 13 (2007)

[3] A. Baruth et al., Appl. Phys. Lett. 89, 202505 (2006)

[4] Y. Fu et al., Appl. Phys. Lett. 91, 152505 (2007)

[5] P. Fischer, Current Opinion in Solid State and Materials Science, 7, 173 (2003).

[6] P. Fischer et al., Materials Today 9 (1-2), 26 (2006).

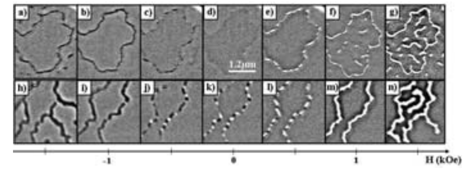

Fig. 1. MXTM images of [Co(4Å)/ Pt(7Å)]x-1/ {Co(4Å)/Ru(9 Å)/[Co(4Å)/ Pt(7Å)]x-1}16 magnetic domain configuration in the X = 6 (a-g) and X = 7 (h-n) cases, under -1.5 kOe (a,h), -1 kOe (b,i), -0.5 kOe (c,j), 0 Oe (d,k), 0.5 kOe (e,l), 1 kOe (f,m) and 1.5 kOe (g,n).

CD-02

Magnetization indicator film for Lorentz transmission electron microscopy measurements of perpendicularly magnetized nanostructures.

J. W. Lau
Metallurgy Division, National Institute of Standards and Technology, Gaithersburg, MD

Lorentz transmission electron microscopy (TEM) has been invaluable towards understanding the relationships between material properties and magnetic behavior in magnetic nanosystems. Samples magnetized orthogonal to the electron beam (in-plane magnetization) generate magnetic contrast by causing electrons to deflect, due to the Lorentz force. However, in the case of samples magnetized parallel to the electron beam direction (perpendicularly magnetization), no magnetic contrast is possible, because the Lorentz force, F, as in F=qV X B is zero. Here, q is the electron charge, V is the electron velocity, and B is the magnetic induction of the sample. One way to solve this problem is by tilting the sample. However, even for the best-case scenario where the nanostructures are magnetized in-plane, obtaining Lorentz contrast is a challenge at best for nanostructures below 100 nm. For similarly sized perpendicularly-magnetized nanostructures, the signal would be indistinguishable from noise even with modest tilts.
This work is driven by the need for in situ magnetic and microstructure characterization of perpendicularly magnetized nanostructures. Such systems are under scrutiny for bit-pattern media and magnetic sensor applications. In order to visualize magnetization orthogonal to the electron beam, we propose using a single-layer magnetic indicator film to detect such magnetization. We use micromagnetic simulations to demonstrate the feasibility of such an indicator film for an array of 100-nm nanodots consisting of a perpendicularly magnetized material such as Co/Pd multilayers. Fig. 1a shows the top-view of the simulation geometry and Fig 1b shows the side-view. White dots are magnetized out-of-plane while black dots are magnetized into the plane. The nanodots rest on a 30-nm thick non-magnetic layer. The perpendicular-magnetization indicator film, PMIF, rests on the opposite surface of the non-magnetic layer. Experimentally, such geometry can be achieved by first, fabrication of the nanodots on an electron transparent silicon nitride membrane window, followed by the deposition of a uniform film Permalloy film on the underside of the nitride membrane. For the layer containing the nanodots, we assume equal thicknesses in Co and Pd multilayers, and so the saturation magnetization of the nanodots, Ms(dot), is 850 kA/m, the uniaxial anisotropy strength, Ku(dot), is 530 kJ/m3, and an exchange coupling constant, A(dot) as 1.0e11 J/m. For the PMIF layer, we assume the saturation magnetization of Permalloy, Ms(PMIF), is 800 kA/m, the uniaxial anisotropy strength, Ku(PMIF), is 0, and an exchange coupling constant, A(PMIF) as 1.0e11 J/m. Elsewhere the material is taken to be non-magnetic.
Each of the nanodots within the dotted square of Fig 1a is switched in turn and the subtracted Lorentz images are shown in Fig. 2. The subtracted image is the difference between the before-switch image and the after-switch image followed by a low-pass filter. The dots outside of the dotted square of Fig. 1 were not switched in order to avoid aperiodic artifacts. The circle outlines in Fig.2 shows the original positions of the nanodots. We see in Fig.2 that the PMIF can clearly distinguish the nanodot that had switched from the ones that had not.
In summary, we have devised a method of observing magnetization orthogonal to the path of the electron beam in Lorentz TEM by the means of an indicator film. PMIF will allow us access to in situ perpendicular magnetic information that is not previously possible within in the TEM.

FIG. 1a

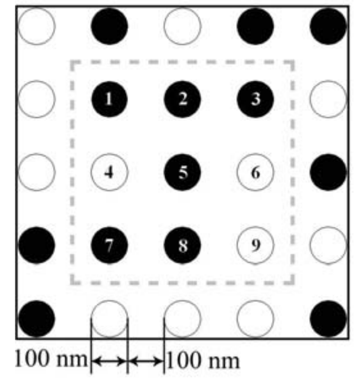

FIG. 1b

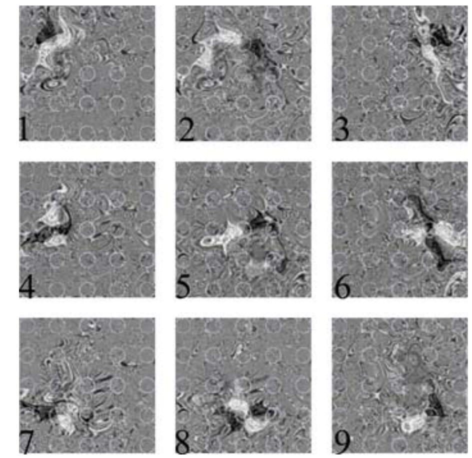

CD-03

Effect of in-situ FIB trimming on the spin configurations of hexagonal shaped ferromagnetic elements.

S. Y. Lua[1,3], S. S. Kushvaha[2], Y. Wu[2], K. Teo[2], T. Chong[3]
1. NUS Graduate School for Integrative Sciences and Engineering, National University of Singapore, Singapore, Singapore; 2. Department of Electrical and Computer Engineering, National University of Singapore, Singapore, Singapore; 3. Data Storage Institute, Singapore, Singapore

Spin configurations of micron and nanometer sized ferromagnetic elements are being studied intensively due to their fundamental importance in nanomagnetism [1, 2] as well as potential data storage applications [3, 4]. The spin configuration of magnetic nanostructures with negligible anisotropy has been demonstrated to be largely determined by their geometrical shape, lateral size and thickness [5]. In the work reported so far, generally, the variation of thickness was realized by fabricating different structures with a pre-determined thickness. Here, we explore the effect of successive in-situ focused ion beam (FIB) milling on the spin configurations of hexagonal shaped ferromagnetic elements at remanent state. The advantage of this approach is that the results obtained will be based on same structures, reducing the influence of irregularities caused by the fabrication processes.

The hexagonal shaped NiFe elements, with a thickness of 30 nm, a diagonal length of 2 μm and in 10×5 hexagonal array arrangement with an edge to edge spacing of 200 nm, were fabricated by electron-beam lithography and liftoff techniques. The sample was first saturated in-plane and then the magnetization configurations were imaged at remanent state using scanning electrons microscopy with polarization analysis (SEMPA). The SEMPA imaging experiments were performed in an ultra-high vacuum system consisting of a SEMPA and a FIB, which allows us to perform in-situ surface cleaning and thickness reduction by FIB prior to each SEMPA measurement. Micromagnetic simulation using the OOMMF code was carried out to obtain the remanent state magnetization configurations of individual elements at different thicknesses.

Figure 1 shows the in-plane magnetization configurations of the same dot arrays with different FIB trimmed thicknesses, obtained from SEMPA imaging: (i) longitudinal and (ii) transverse, as well as (iii) the topographic images captured simultaneously with the magnetic configurations. Panels (a) to (d) correspond to thicknesses of 30 nm, 20 nm, 12 nm and 8 nm, respectively. The images in panel (d) were obtained at a higher magnification as compared to those shown in (a) to (c). As can be seen from the images shown, panels (a) to (c), a single vortex state is observed in all elements with thicknesses of 12 nm, 20 nm and 30 nm. Interestingly, the elements from second to eighth columns were found to exhibit column-wise alternate sign of sense of rotation whilst the elements at the two side columns show random signs. This indicates that there is a strong magnetostatic coupling between the adjacent elements. As the thickness is reduced further to 8 nm, a double vortex structure was observed, as shown in panel (d). The slight distortion in both the magnetic and topographic images is due to the drift caused by long imaging duration. Unlike the previous report [5] on circular dots with diameter smaller than 500 nm showing a single domain state below a critical thickness, our results of the micron size elements show a multi-domains state. As the FIB milling could also cause alteration of the magnetic properties of the ferromagnetic elements, micromagnetic simulation has been performed for elements with different saturation magnetizations and thicknesses. Figure 2 shows the simulated magnetization configurations of the hexagonal elements with different thicknesses and magnetizations. The simulated results show a flux closure state with six regions of different contrast for elements with larger thickness, Fig. 2(a), but a double vortex structure for elements with much reduced thickness, Fig. 2(c), agreeing well with the SEMPA images. Work is on-going to modify the structures in-situ by FIB and study their magnetic configurations using SEMPA.

[1] L. Giovannini, F. Montoncello, R. Zivieri, F. Nizzoli, J. Phys.: Condens. Matter 19, 225008 (2007).

[2] B. Hillebrands, A. Thiaville (Eds.), Spin Dynamics in Confined Magnetic Structures III (Springer, Berlin, 2006).

[3] C. A. Ross, Annu. Rev. Mater. Res. 31, 203 (2001).

[4] K. Bussmann, G. A. Prinz, S. F. Cheng, D. Wang, Appl. Phys. Lett. 75, 2476 (1999).

[5] R. P. Cowburn, J. Phys. D: Appl. Phys. 33, R1 (2000).

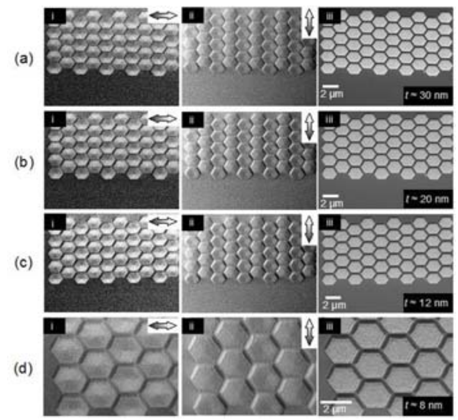

Figure 1. SEMPA images of the in-plane magnetization components: (i) longitudinal (x) and (ii) transverse (y), as well as (iii) topographic images, of the hexagonal elements acquired simultaneously.

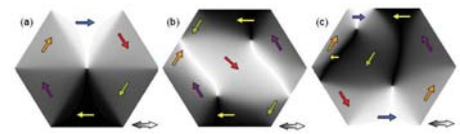

Figure 2. Simulated magnetization configurations (horizontal component) of the hexagonal element with (a) Ms = 860 KA/m and t = 30 nm, (b) Ms = 400 KA/m and t = 10 nm, and (c) Ms = 860 KA/m and t = 5 nm, respectively.

CD-04

Ballistic electron magnetic microscopy on Co/Cu/NiFe spin valves.

A. Kaidatzis, S. Rohart, A. Thiaville, J. Miltat
Laboratoire de Physique des Solides, Orsay, France

The advent of hot electron devices like the spin-valve transistor (SVT) [1] and the magnetic tunnel transistor (MTT) [2] creates the need for locally probing the spin dependent ballistic transport. Moreover, the research of magnetic systems with reduced dimensions implies the capability of imaging magnetic structures down to the nanometer scale. In this context, using a Scanning Tunneling Microscope and realizing a three terminal device sample structure, we have performed Ballistic Electron Magnetic Microscopy (BEMM) [3,4] measurements on Co/Cu/NiFe spin valves. Hot electron transport through Cu/Co/Cu and Cu/NiFe/Cu stacks was similarly studied by Ballistic Electron Emission Microscopy (BEEM).

Multilayers were deposited in a UHV chamber (base pressure <10^{-9} mbar) using an e-gun evaporator. The hydrogenated Si(111) surface was used as a substrate. Initially a 7 nm Au layer was deposited to form a homogeneous Schottky interface (barrier height > 0.8 eV). Afterwards, a 1.5 nm Cu seed layer was deposited, before the growth of the Co/Cu/NiFe spin valve. Then the film was covered by a 1.5 nm Cu and a 3 nm Au capping layers for ex-situ transfer. For the present study, the spin valve consisted of a 2 nm Co and a 2 nm $Ni_{80}Fe_{20}$ layers, separated by a 6 nm Cu spacer. For BEEM study, instead of the trilayer stack, single Co or $Ni_{80}Fe_{20}$ layers having various thicknesses were deposited (t_{Co}=1, 2, 3.5 and 4.5 nm, t_{NiFe}=1.4, 2, 4, 6 and 8 nm). All the experiments were performed at room temperature using a UHV-STM.

The spin independent hot electron attenuation length λ in Co and NiFe was determined by studying the variation of the transmission as a function of magnetic layer thickness. For both metals λ remains relatively invariable in the range 1 to 2 eV above the Fermi level, with a value 2.3±0.2 nm for Co and 3.4±0.1 nm for NiFe (see figure 1)

Spin dependent ballistic transport was studied in Co/Cu/NiFe trilayers. The Co and NiFe layers have coercive fields sufficiently different to reverse their magnetization independently. BEEM spectra in the parallel (P) and anti parallel (AP) configurations revealed a significant difference of ballistic electron transmission. A magnetic contrast of up to 70 % was measured (see figure 2). Finally, imaging of magnetic domains during the magnetization reversal process was achieved. The magnetic contrast switches from bright (magnetic saturation) to dark (anti parallel configuration). This study shows the non homogeneous reversal of the NiFe layer, which occurs by nucleation and propagation of domain walls (see Figure 3).

In conclusion, the spin independent attenuation length was determined for Co and NiFe layers. Ballistic transport in a Co/Cu/NiFe spin valve was shown to strongly depend on the relative orientation of the two magnetic layers. A magnetic contrast up to 70% was achieved and enables imaging the magnetic reversal of a NiFe thin film at few tens of nanometer scale.

1. D. J. Monsma, J. C. Lodder, Th. J. A. Popma, and B. Dieny, Phys. Rev. Lett. 74, 5260 (1995).

2. K. Mizushima, T. Kinno, T. Yamauchi, and K. Tanaka, IEEE Trans. Magn. 33, 3500 (1997)

3. W.H. Rippard and R. A. Buhrman, Phys. Rev. Letters 84, 971 (2000).

4. T. Banerjee, E. Haq, M. H. Siekman, J. C. Lodder, and R. Jansen, Phys. Rev. Letters 94, 27204 (2005).

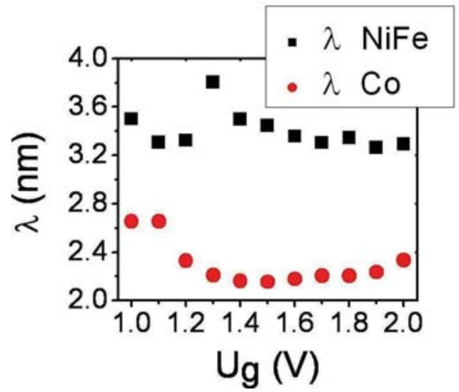

Figure 1: Variation of the attenuation length λ versus tunnel voltage for Co and FeNi films.

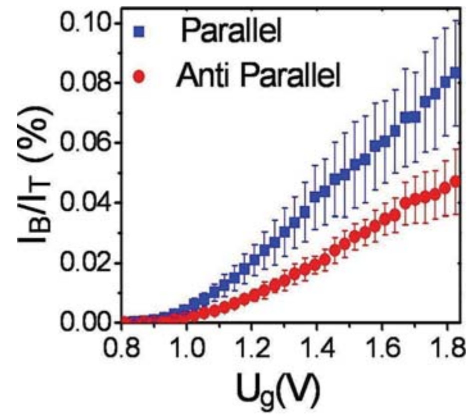

Figure 2: BEEM spectra taken on a Co/Cu/FeNi spin valve in the parallel and anti-parallel magnetization state. A magnetc contrast of 70% is shown at tunnel voltage 1.8V.

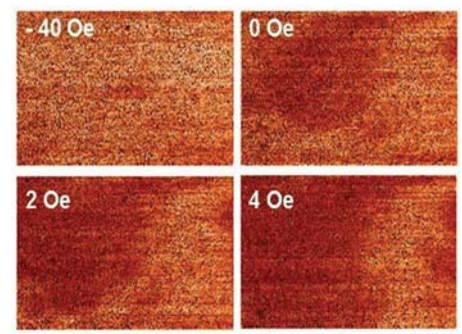

Figure 3: Successive BEMM images of the magnetization reversal in the spin valve. The sample was first saturated at -40 Oe. The images at 0, 2 and 4 Oe show the nucleation and growth of a magnetic domain (black area) in the FeNi layer. The images are 0.6 x 1 μm²

CD-05

Mapping Atomic-Scale Spin Structures on Insulators by Magnetic Exchange Force Microscopy.

R. M. Wiesendanger
Institute of Applied Physics, University of Hamburg, Hamburg, Germany

A fundamental understanding of magnetic and spin-dependent phenomena requires the determination of spin structures and spin excitations down to the atomic scale. The direct visualization of atomic-scale spin structures [1-4] has first been accomplished for magnetic metals by combining the atomic resolution capability of Scanning Tunnelling Microscopy (STM) [5, 6] with spin sensitivity, based on vacuum tunnelling of spin-polarized electrons [7]. The resulting technique, Spin-Polarized Scanning Tunnelling Microscopy (SP-STM), nowadays provides unprecedented insight into collinear and non-collinear spin structures at surfaces of magnetic nanostructures and has already led to the discovery of new types of magnetic order at the nanoscale [8]. More recently, the detection of spin-dependent exchange and correlation forces has allowed a first direct real-space observation of spin structures at surfaces of antiferromagnetic insulators [9]. This new type of scanning probe microscopy, called Magnetic Exchange Force Microscopy (MExFM), provides a powerful new tool to investigate different types of spin-spin interactions based on direct-, super-, or RKKY-type exchange down to the atomic level. By combining MExFM with high-precision measurements of damping forces [9] localized spin excitations in magnetic systems of reduced dimensions now become experimentally accessible.

In contrast to magnetic force microscopy (MFM) which probes the magnetic dipole forces between a magnetic sample and a ferromagnetic tip at a typical tip-to-surface distance of 10-20 nm [10, 11], MExFM combines the technique of non-contact atomic force microscopy (NC-AFM) [12, 13] with atomic-scale spin resolution by making use of an atomically sharp magnetic probe tip with a very well defined spin state at its apex. Based on the knowledge gained during the development of SP-STM in preparing such tips we have recently succeeded in resolving the surface spin structure of the antiferromagnetic insulator NiO(001) [9]. Atomic-resolution topographic NC-AFM images reveal chemical contrast between the oxygen atoms (bright sites) and the Ni atoms (dark sites) which results from a different total charge density above O- and Ni-sites. No contrast is observed between magnetically non-equivalent Ni sites, i.e. Ni atoms with a different orientation of their magnetic moments. By approaching the out-of-plane magnetized Fe-coated tip closer to the surface atoms, the spin-dependent exchange interaction between the rather localized Ni d-states of the sample and the Fe d-states of the tip leads to a different force or force gradient above Ni atoms with a different orientation of their magnetic moments. As a result, a superperiodicity corresponding to an antiferromagnetically ordered state of the NiO(001) surface is observed in the MExFM image. The apparent height difference between the magnetically non-equivalent Ni-sites only amounts to 1.5 pm, corresponding to the different magnitude of the spin-dependent quantum-mechanical forces felt by the tip above the different Ni atoms. To resolve such tiny signals, the AFM instrument has to be operated at low temperatures in order to reduce the thermal excitations of the AFM cantilever (force sensor).

More recently, MExFM has been applied to the antiferromagnetically ordered ground state of a single atomic layer of Fe on a W(001) substrate [14] for which a direct comparison with SP-STM results [3, 4] could be made.

[1] R. Wiesendanger, I. V. Shvets, D. Bürgler, G. Tarrach, H.-J. Güntherodt, J. M. D. Coey, and S. Gräser, Science 255, 583 (1992); R. Wiesendanger, I. V. Shvets, D. Bürgler, G. Tarrach, G. Güntherodt, H.-J. Güntherodt, and J. M. D. Coey, Europhys. Lett. 19, 141 (1992)

[2] S. Heinze, M. Bode, O. Pietzsch, A. Kubetzka, X. Nie, S. Blügel, and R. Wiesendanger, Science 288, 1805 (2000)

[3] A. Kubetzka, P. Ferriani, M. Bode, S. Heinze, G. Bihlmayer, K. von Bergmann, O. Pietzsch, S. Blügel, and R. Wiesendanger, Phys. Rev. Lett. 94, 087204 (2005)

[4] M. Bode, E. Y. Vedmedenko, K. von Bergmann, A. Kubetzka, P. Ferriani, S. Heinze, and R. Wiesendanger, Nature Materials 5, 477 (2006)

[5] G. Binnig and H. Rohrer, Rev. Mod. Phys. 59, 615 (1987)

[6] R. Wiesendanger, “Scanning Probe Microscopy and Spectroscopy: Methods and Applications”, Cambridge University Press, Cambridge 1994

[7] R. Wiesendanger, H.-J. Güntherodt, G. Güntherodt, R. J. Gambino, and R. Ruf, Phys. Rev. Lett. 65, 247 (1990)

[8] K. von Bergmann, S. Heinze, M. Bode, E. Y. Vedmedenko, G. Bihlmayer, S. Blügel, and R. Wiesendanger, Phys. Rev. Lett. 96, 167203 (2006)

[9] U. Kaiser, A. Schwarz, and R. Wiesendanger, Nature 446, 522 (2007)

[10] Y. Martin and K. Wickramsinghe, Appl. Phys. Lett. 50, 1455 (1987); J. J. Saenz, N. Garcia, P. Grütter, E. Meyer, H. Heinzelmann, R. Wiesendanger, L. Rosenthaler, H. R. Hidber, and H.-J. Güntherodt, J. Appl. Phys. 62, 4293 (1987)

[11] A. Schwarz, M. Liebmann, U. Kaiser, R. Wiesendanger, T. W. Noh, and D. W. Kim, Phys. Rev. Lett. 92, 077206 (2004)

[12] F. J. Giessibl, Science 267, 68 (1995)

[13] S. Morita, R. Wiesendanger, and E. Meyer (eds.), Non-contact Atomic Force Microscopy, Springer (2002)

[14] R. Schmidt, C. Lazo, H. Hölscher, U. H. Pi, V. Cacius, A. Schwarz, R. Wiesendanger, and S. Heinze, submitted.

CD-06

120° antiferromagnetic Néel structure of Mn monolayer on Ag(111).

C. Gao[1], W. Wulfhekel[1,2], J. Kirschner[1]
1. Max Planck Institute of MicrostrcutrurePhysics, Halle (Saale), Germany; 2. Physikalisches Institut, Universität Karlsruhe (TH), Karlsruhe, Germany

In magnetic materials, the competing exchange interactions between neighboring atoms often lead to frustrated spin structures. Magnetic frustrations are not only responsible for noncollinear antiferromagnetism, but also play an important role in determining the exchange bias effect at the interface between ferromagnets and antiferromagnets. The letter is of essential technological relevance. Magnetic frustrations may have chemical or topological origins. A classical example of a topological frustration is a 2-dimensional triangular lattice of antiferromagnetic atoms in which a non-collinear 120°Néel structure stabilizes as shown in Fig. 1a. Experimentally, the Néel structure has not been observed in real space because traditional magnetic imaging techniques have limited resolution. Only with the development of spin-polarized scanning tunneling microscopy (Sp-STM), it has become possible to resolve antiferromagnetic spin structure on the atomic scale [1].
In this contribution, we resolved the 120°Néel structure of a Mn monolayer on Ag(111) using Sp-STM with magnetically coated tungsten tips operating in the constant current mode. Sp-STM operating in the constant current mode has demonstrated its atomic resolution in 2-dimensional antiferromagnetic systems, such as Mn/W(110), Fe/W(001). The presence of a magnetic super cell lowers the translational symmetry resulting in a much slower decay of surface magnetic corrugation than the atomic corrugation. Thus, a constant current image taken with a magnetic tip reflects the magnetic superstructure rather than the atomic unit cell. The magnetic contribution in the Sp-STM image is proportional to the projection of the magnetization of the sample on the magnetization direction of the tip such that collinear and non-collinear antiferromagnetic spin structures of an antiferromagnetic monolayer on a fcc(111) surface can be distinguished experimentally as has been proposed by Wortmann et al [2]. In the case of a non-collinear spin structure, for example the 120°Néel structure, the relative magnitudes of the projection of the sample moments on two orthogonal directions are strongly different (cf. Fig. 1 (b) and (c)) which results in different Sp-STM images when the spin sensitive axis of the STM tip is rotated by 90°[2].
The first layer of Mn grows pseudomorphically on Ag(111) forming monolayer heigh islands in triangular shapes. Two kinds of islands are found distinguished by the orientation of the triangles which correspond to fcc and hcp stacking as identified by atomically resolved STM images. Using a Cr coated W tip which has an in-plane spin sensitivity, the Néel structure was demonstrated. The existence of at least two different magnetic domains of the structurally equivalent Mn islands is observed. The fcc and hcp islands are found to have the same 120°Néel structure but with different orientation of the moments which means the fcc and hcp islands have different magnetic anisotropy.

[1] S. Heinze, M. Bode, A. Kubetzka, O. Pietzsch, X. Nie, S. Blügel, and R. Wiesendanger, Scince. 288, 1805 (2000).

[2] D. Wortmann, S. Heinze, Ph. Kurz, G. Bihlmayer, and S. Blügel, Phys. Rev. Lett. 86, 4132 (2001).

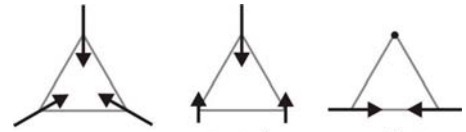

Fig. 1 The 120° Néel structure (a) and the projection of the spin polarization on the spin sensitive axis of the STM tip (b: tip magnetization parallel to one of the moments and c: tip magnetization perpendicular to one of the moments)

CD-07

The role of the spin-orientation of the tip in spin-polarized scanning tunneling microscopy in external magnetic fields.

D. Sander, G. Rodary, S. Wedekind, J. Kirschner
Max Planck Institute, Halle, Germany

Spin-resolved scanning tunneling microscopy (spin-STM) exploits the dependence of the tunnel current and of the differential conductance on the relative spin orientation between tip apex and sample to image spin structures, even with atomic resolution
[1]. A change of the spin orientation of the tip apex and/or that of the sample
induces a corresponding change of the tunnel current and of the differential conductance, which is the basis of the spin contrast. This entanglement between the spin orientation of sample and tip for the observed magnetic contrast is cumbersome for measurements in field, as it interferes with a clear identification of sample and tip contributions to the spin contrast.
We resolve the contributions of both a Co-sample and a Cr-covered W-tip to the contrast of spin-STM by spin-polarized STM measurements of the differential conductance during a complete magnetization cycle of Co-nanoislands on Cu(111).
The differential conductance is measured by applying a small AC voltage (10 mV, 4 kHz) to the gap voltage of the STM, and we detect the resulting modulation of the tunnel current with a lock-in amplifier. To obtain a spin contrast, we cover the electrochemically etched and subsequently flashed (2100 C) W-tip of the STM with 100 layers of Cr at 300 K. Spin-polarized STM measurements are then performed on double layer high Co islands at 8 K and in fields of up to 6 T, which are oriented normal to the sample surface. The Co islands were produced by the deposition of sub-monolayer quantities of Co onto the atomically clean Cu(111) surface at 300 K.
We measure the differential conductance during a scan of the magnetic field from 0 T, to -4 T, to +4T, and back to 0 T. We observe symmetric differential conductance curves with respect to the magnetic field. The differential conductance measurements during a cycle of the magnetic field show a hysteretic behavior, e.g. at +/- 1 T we observed two different values for the differential conductance, depending on the magnetic field history. These plots resemble a shape which is well known from the so-called butterfly curves of tunnel magnetoresistance (TMR) measurements. For fields smaller than a critical value, we observe a gradual change of the differential conductance with increasing field. At a critical field, the signal changes abruptly. This critical field depends on island size, and it is larger for larger islands. Its magnitude of appr. 1.5 T suggests that it is due to the magnetic switching of the Co islands along the sample normal in response to the external magnetic field [3]. We have performed dozens of tip preparation with a Cr-coverage between 40 and 100 ML and find consistently symmetric hysteresis cycles of the differential conductance. We conclude that the gradual change of the differential conductance at fields smaller than the switching field, which is similar for all islands, is due to the field-induced change of the spin orientation of the Cr-tip apex.
This result indicates that both Cr-covered W-tip and Co-island change their spin orientation in response to the applied magnetic field. A sudden switching of the magnetization direction of the Co-island and a reversible change of the spin orientation of the tip are extracted from the measurements. A change of the spin-orientation of the Cr-covered tip in response to the external field comes as a surprise, as usually one of the electrodes of a spin-STM experiment, be it the tip or the sample, has been assumed to exhibit a fixed spin orientation. This assumption is not valid in general, as our results suggest that the spin-orientation of the tip follows the external field. We can exploit this finding to rigorously identify the parallel (P) and anti-parallel (AP) states of our tunnel junction composed of a Cr-tip, a vacuum barrier and the Co-sample.

[1] K. von Bergmann, S. Heinze, M. Bode, E. Vedmedenko, G. Bihlmayer, S. Blügel, R. Wiesendanger, Phys. Rev. Lett. 96 (2006) 167203; C. Gao, U. Schlickum, W. Wulfhekel, J. Kirschner, Phys. Rev. Lett. 98 (2007) 107203.

[2] O. Pietzsch, A. Kubetzka, M. Bode, R. Wiesendanger, Phys. Rev. Lett. 92 (2004) 057202.

CD-08

Theoretical description of the high-frequency magnetic force microscopy (HF-MFM) technique.

M. R. Koblischka, U. Hartmann
Institute of Experimental Physics, University of the Saarland, Saarbruecken, Germany

In this contribution, we present a theoretical description of the high-frequency MFM (HF-MFM) technique [1-4]. HF-MFM is a further development of the MFM technique, enabling the measurement of (i) high-frequency currents via their stray field and (ii) the stray fields emanating from hard disk writer poles. For the measurement of high-frequency magnetic fields, an amplitude-modulation technique is employed. Figure 1 shows a schematic view of the HF-MFM setup.
The description of the measurement of a HF current is the simpler case as there is a direct relation between the amplitude-modulated current and the HF field. To calculate the force acting on the cantilever, we employ the dipole model for the cantilever and assume a point-shaped conductor. As the cantilever can only carry forces in z-direction, we can simplify the resulting equation. Regrouping and taking all parts depending on position but being independent of the current together, yields $F_z = c_1 I - c_2 I^2$.
The quadratic dependence of the force acting on the cantilever on the flowing current enables the use of the modulation technique. Both constants c_1 and c_2 contain geometry factors, c_2 the initial susceptibility of the magnetic coating of the cantilever, $\chi(\omega)$. This implies that the ideal HF-MFM cantilever material should have a large χ, which is also reasonably high in the high-frequency range. This condition could e.g. be fulfilled by the head material itself. However, to avoid skin effects, an ideal candidate for such a material are ferrites, which can be prepared in form of thin films onto the cantilevers [5].
The current is characterized by its carrier frequency, ω_c. The modulation current has a lower frequency, ω_m, and their relation is the modulation depth, $m = \omega_m/\omega_c$. Inserting the current into eq. (1), we obtain the force acting on the cantilever. The cantilever is acting like a low-pass filter, so that all components comprising a high-frequency part can be disregarded as illustrated in Figure 2.
The optimum frequency to achieve the maximum force on the cantilever is to chose the modulation frequency like the cantilever resonance frequency, ωres.
In the case of the HF-MFM measurements of hard disk writer poles, the situation is somewhat different: The amplitude-modulated current being sent into the coil of the writer pole is then transferred into a high-frequency magnetic field via the magnetic core material. As a consequence, there is another modulation step due to the non-linear relation between the gap field and the applied current. This means that the effective frequency components are not known a priori. Using the description given in [3], we can calculate again the forces acting on the cantilever for an amplitude-modulated current. As a result, we find that the optimum frequency to operate the HF-MFM in this case is always smaller than the resonance frequency of the employed cantilevers. This explains the earlier finding that a maximum HF-MFM signal is obtained at a modulation frequency corresponding to about 1/3 of the cantilever resonance frequency [6].
We would like to thank A. Cazacu and A. D. Johnston (SEAGATE, U.K) for the writer poles and valuable discusions.

[1] R. Proksch, P. Neilson, S. Austvold and J. J. Schmidt, Appl. Phys. Lett. 74, 1308 (1999).

[2] M. Abe and Y. Tanaka, J. Appl. Phys. 89, 6766 (2001).

[3] S. Li, S. Stokes, Y. Liu, S. Foss-Schrader, W. Zhu, and D. Palmer, J. Appl. Phys. 91, 7346 (2002).

[4] M. R. Koblischka, J. D. Wei, M. Kirsch, and U. Hartmann, Jpn. J. Appl. Phys. 45, 2238 (2006).

[5] M. Kirsch, M. R. Koblischka, J. D. Wei, and U. Hartmann,, J. Vac. Sci. B 25, 1679 (2007).

[6] M. R. Koblischka, J.D. Wei and U. Hartmann, J. Phys. Conf. Ser. 61, 591 (2007).

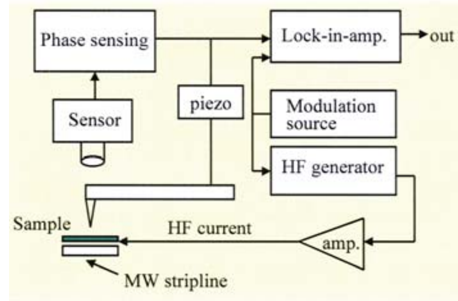

Fig.1 Schematical drawing of the HF-MFM setup.

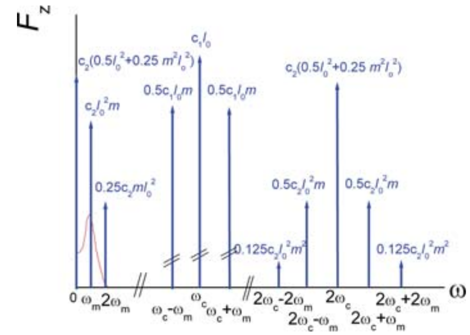

Fig.2 Low-pass filter effect of the cantilever and the individual components of the force.

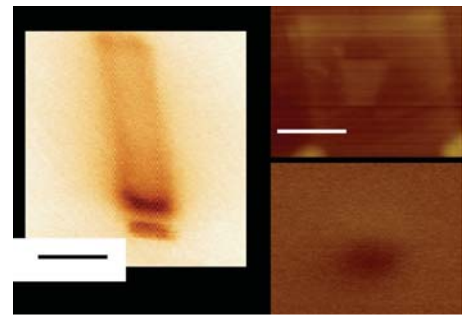

Fig.3 HF-MFM images (left: longitudinal writer pole, right: perpendicular writer pole). In both cases the carrier frequency is 1 GHz, and the modulation frequency 1 kHz. The scale bar on the left side is 500 nm long, on the right side 300 nm.

CD-09

Imaging a single domain wall position by Extraordinary Hall Effect in nanostructured thin films with perpendicular anisotropy.

M. Miron, P. Zermatten, G. Gaudin, S. Alain
SPINTEC (CNRS/CEA), Grenoble, France

The recent experimental evidence of the effect of current on domain wall (DW) motion opens the possibility of acting locally on a single DW. Lately, several types of device using this effect were proposed for magnetic mass storage and magnetic logic. They all use [1], [2], materials with in plane magnetic anisotropy. An alternative to this kind of materials would be to use thin films with out of plane anisotropy exhibiting at the same time a strong Extraordinary Hall Effect (EHE) [3]. This would allow a simple detection of the DW motion by a simple EHE measurement. For studying the effects of current and field on such a DW it is important to be able to control and to know precisely its position.

We propose a technique that allows pinning a DW at a stable position as well as, in certain conditions imaging it with a better precision than a typical MFM image.

We use a thin film that has an out of plane magnetic anisotropy, and in addition, a high EHE. The film is patterned to obtain a shape like the one depicted in figure 1. By passing a current through the central line and measuring the voltage between the side wires, magnetization reversal can be detected due to the EHE. If the magnetization is switched by DW motion, the displacements of the DW are evidenced by changes in the measured voltages. Due to the fact that the spatial sensitivities to DW position are different for the four voltage measurements, the movement of the DW will cause four different voltage changes. We will show how, based on these differences and knowing precisely the sensitivities, it is possible to find the position and shape of the DW.

We make a precise SEM image of our sample. Then this image is divided into cells. By simulating the current flow into the sample, we compute the contribution of the magnetization switching of each cell δVi for the four different EHE voltages. Afterwards, using a minimizing algorithm we find the combination of cells that need to be switched to fit simultaneously the four measurements.

In order for this method to work, several conditions must be fulfilled:

i. The DW must have a negligible volume compared to the sensitive volume.

ii. The sample has to be magnetically and electrically homogenous.

iii. The magnetic switching of any pack of cells will not significantly change the current lines.

This imaging technique has the particularity of being size independent. The fact that only the proportions are important allows two methods of testing: one uses a real sample large enough to be imaged easily by MFM, and the other one uses only simulations done with COMSOL.

We applied this technique for sample to small to be imaged by MFM with a good resolution (typically 100nm line width). The sample was prepared with a DW geometrically pinned between the two crosses. The displacements of the DW under an applied field were imaged. Evidence is found that the intrinsic pinning sites dominate the DW motion for small displacements.

We have developed a method that enables us to find the shape of a single DW trapped in an artificial pinning center, just by EHE measurements and electrical simulations. The main advantage of this method over classical imaging techniques like the MFM is that its absolute resolution is, to a certain limit (see the imposed conditions), increasing when decreasing the size of the sample. This is a consequence of the fact that the method is size-independent. The observation of DW displacements as small as 100nm are then possible in samples of comparable size (100nm).

[1] Del Atkinson, Dan Allwood, Gang Xiong, Michael Cooke, Colm Faulkner & Russell Cowburn - Nature Materials 2, 85–87 (2003)

[2] SSP Parkin - US Patent 6,834,005,

[3] F. Cayssol, D. Ravelosona, J. Wunderlich, C. Chappert, V. Mathet, J. -P. Jamet and J. Ferré - Journal of Magnetism and Magnetic Materials 240 30–33(2002)

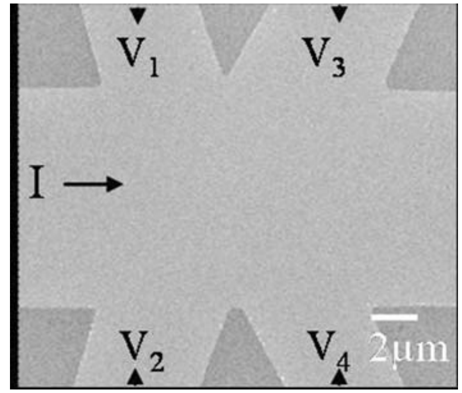

FIG. 1: SEM image and schematic picture of the measurement: the current passes through the central wire. Voltage are measured in between electrodes 1-2 2-3 1-4 and 3-4. If a DW would be pinned on the constriction it would be in the sensitivity area of all the measurements.

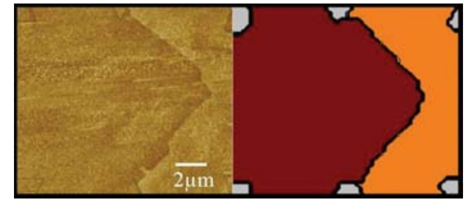

FIG. 2: Example of test performed on a 10x10 μm sample. On the left is the MFM image, and on the right the image obtained after voltage measurement and simulations.

CD-10

Hall imaging of the history dependence of the magneto-caloric effect in Gd5Si2.09Ge1.91.

M. Kuepferling[1], J. Moore[2], V. Basso[1], C. P. Sasso[1], L. Giudici[1], L. Cohen[2]
1. Department for Electromagnetism, National Institute of Metrological Research, Torino, Italy;
2. The Blackett Laboratory, Imperial College of Science, London, United Kingdom

Although materials with Giant Magneto Caloric Effect (GMCE) have been investigated intensively with respect to their performance as magnetic refrigerant, it is still a controversial matter of how to evaluate correctly the cooling power [1,2]. In general a magneto-caloric material is characterized by the entropy change Δs(T,H) as a function of magnetic field and temperature [1,3]. While in thermodynamic equilibrium Δs(T,H) is a unique function, a first order magneto-structural phase transition (as in GMCE materials) exhibits hysteresis in field and in temperature and so the value of Δs(T,H) depends on the history. Therefore it is indispensable for the correct evaluation of the performance of a material to carefully control the sequence of changing T and H when preparing for or during a measurement. Otherwise results cannot be compared.

In this paper we show Δs(T,H) obtained by different field and temperature sequences. The sample is polycrystalline Gd5Si2.09Ge1.91 undergoing a first order magneto-structural phase transition at 288.5K from orthorhombic ferromagnetic (FM) to monoclinic paramagnetic (PM). In sequence A we start from the FM low temperature phase, increase the temperature up to 292K (slightly above the transition temperature) and then apply a field of 1.8T and remove it (field rate 23mT/s). In sequence B we start again from the FM low temperature phase, apply first a field of 1.8T, increase then temperature up to 292K and remove the field. The entropy change Δs(μ0ΔH=1.8T-0T)|T=292K is measured directly during the field removal at constant temperature using a laboratory Peltier cell calorimeter [4]. Sequence A gives an entropy change of ΔsA= -4.6J/kgK while sequence B gives ΔsB= -7.1J/kgK. The different results can be explained qualitatively by the difference in phase fractions involved in the transition. In sequence A good part of the sample is transformed during heating in the PM phase and applying a field transforms back to the FM phase. If the applied field at the given temperature was not sufficiently high to complete the transformation to the FM state (saturation) only a small phase fraction takes part at the transformation to the PM state when removing the field (minor loop). In sequence B the field applied during heating stabilizes the FM phase and the material remains in the saturated FM state up to higher temperatures. Removal of the field reverses the transformation along the saturation loop and therefore the maximum entropy change is obtained.

This picture can be experimentally evidenced by using magnetic imaging techniques. The difference in FM and PM fractions after the different preparation sequences was observed by hall imaging [5] (see Fig.1). The magnetic moments over the imaged area have been integrated and gave a ratio of the total moment after sequence B to the one after sequence A as 1.64:1. This agrees well with the ratio of the entropy changes obtained by the direct measurement of ΔsB/ΔsA =1.54:1.

A quantitative comparison can be obtained by employing a Preisach type hysteresis model for thermodynamic transformations, which accounts for hysteresis in field and temperature [6]. The phase fractions and entropy changes can be calculated and qualitatively observed in the Preisach plane.

This study demonstrates the importance of hysteresis for the correct determination of the magneto-caloric effect in first order phase transition materials. Different measurement methods expose the sample to different field and temperature histories. Two common indirect measurement methods of Δs(T,H) serve as example: the magnetization curve at constant temperature by using Maxwell`s relations (first increasing temperature then field) and the heat capacity at constant field (first applying field then increasing temperature). It is known from literature that these methods lead to different results, due to errors in the data evaluation [2]. We show that in addition there are also inherent properties, as hysteresis, leading to difficulties in comparison of the methods if the state of the material and its history is not well specified. This result is of special importance for a typical thermodynamic cycle, which is always performed as in sequence A, so that a much lower effective efficiency than predicted by the maximum available entropy change may be obtained.

[1] V.K. Pecharsky et al., Phys. Rev. B 64, 144406 (2001).

[2] G.J. Liu et al., Applied Physics Letters 90 (2007) 032507.

[3] V.K. Pecharsky et al, Journal Magnetism and Magnetic Materials 200 (1999) 44.

[4] M. Kuepferling et al., IEEE Transactions on Magnetics 43 (2007) 2764.

[5] J.D. Moore et al., Applied Physics Letters 88 (2006) 072501.

[6] V. Basso et al., Journal Magnetism and Magnetic Materials 316 (2007) 262.

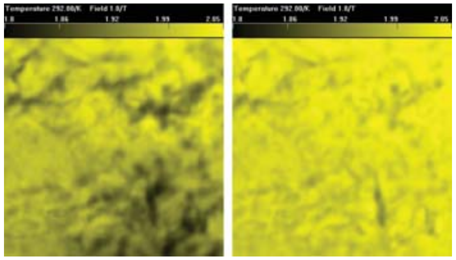

Fig.1 Hall images at 292K and H=1.8T (magnetic field applied normal to the sample surface) after applying sequence A (left) and sequence B (right). The same scale is used in both images where black is 1.8T and bright yellow is 2.05T. These values are the magnetic induction at the surface which includes the constant background applied field of 1.8T. The image window was 1.2mm x 1.2mm with a resolution of ~0.01mm.

CD-11

Imaging perpendicularly recorded data with servo feedback control.

C. Tseng[1], P. McAvoy[1], *I. D. Mayergoyz*[1], C. Krafft[2]
1. Department of Electrical and Computer Engineering, University of Maryland, College Park, MD; 2. Laboratory for Physical Sciences, College Park, MD

Recently, a spin-stand-based magnetic imaging technique has been developed for high-speed massive imaging of bit patterns recorded on hard disk media [1, 2]. This imaging technique provides a much faster imaging rate than that of MFM and has been recognized as a useful tool for detailed evaluation of bit patterns on perpendicular recording media [3]. However, for track densities above 100 kilo-track-per-inch (ktpi), non-repeatable run-out (NRRO) due to spindle vibration can result in appreciable distortion of spin-stand images acquired from commercial disks removed from their native environments. The purpose of this paper is to demonstrate that the NRRO distortion of the spin-stand image can be removed by using servo feedback control to drive a piezoelectric transducer (PZT) as a positioning actuator.

In spin-stand imaging, along-track scanning is performed by means of the rotation of the disk, while cross-track scanning is performed by stepping the head to progressively increasing or decreasing radii with the PZT. While the hysteresis exhibited by the PZT itself can be compensated [4], the presence of NRRO creates a situation in which cross-track steps cannot be made with a constant desired magnitude. Therefore, the spin-stand image resulting from a scan without using any feedback is corrupted to some extent by this irregular cross-track scanning step size. However, by using the position error signal (PES) generated from servo patterns already present on the disk, the actual position of the head (corrupted by NRRO) can be ascertained with respect to the target position. This PES can then be used to control a PZT, which displaces the read head in the cross-track direction toward the target position. By iteratively seeking on this target position (a given offset from the track center), a constant cross-track step-size can be achieved by rejecting measurement iterations whose computed offset PES is above some small predetermined bound. Once the desired accuracy is achieved for a particular radius, the measurement is kept and the next scanning step attempted.

Experiments have been performed to illustrate this technique in which two-dimensional images of commercial perpendicular media hard disk platters with an average track pitch of 145 ktpi are acquired on a Guzik spin-stand. In these experiments, a platter is first pre-written with data and servo patterns in its native drive, and then removed and mounted on a spin-stand. For a particular experiment of this kind, Figures 1a and 1b show the position error signals with respect to scanning steps in the cross-track direction before and after the servo feedback control is implemented. A total of 20 cross-track steps are made for each track. It can be observed (see Figure 1a) that the scanning step size is irregular without servo feedback control due to NRRO because the PES extracted from the image deviates from linearity. Therefore, the spin-stand image resulting from this scan without using servo feedback is corrupted by its irregular cross-track scanning step size. Conversely, the PES extracted from the spin-stand image produced by using servo feedback control is shown in Figure 1b. This PES approaches the ideal linear form desired, which illustrates the positioning accuracy of the cross-track steps in the spin-stand image. The spin-stand image of the servo data corresponding to the PES in Figure 1b is shown in Figure 1c. Figure 2 illustrates the result of imaging with servo feedback for user data written on a similar recent commercial perpendicular disk. It is apparent that significant distortion (due to intersymbol interference and cross-track interference) is present in Figure 2 as a result of the high density of user data. This contrasts with the clear two-level image of lower density servo data in Figure 1c. The image in Figure 2 thus demonstrates the necessity of powerful PRML-type signal processing algorithms to recover the binary information recorded in the depicted user data tracks.

[1] I. D. Mayergoyz, C. Serpico, C. Krafft, and C. Tse, "Magnetic imaging on a spin-stand," J. Appl. Phys., vol. 87, pp. 6824-6826, May 2000.

[2] I. D. Mayergoyz and C. Tse, Spin-stand Microscopy of Hard Disk Data, Elsevier, Amsterdam, 2007.

[3] A. S. Chekanov, E. N. Abarra and G. Choe, "Perpendicular recording media imaging using dynamic readback microscopy," IEEE Trans. Magn., vol 42, pp. 2345-2347, Oct 2006.

[4] C. Tseng, I. Mayergoyz, P. McAvoy, and C. Krafft, "Iterative compensation for hysteresis effects in magnetic recording," J. Appl. Phys., to appear April 2008.

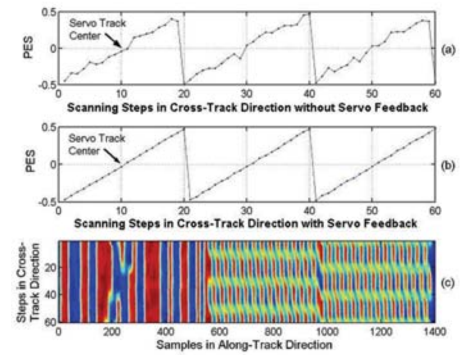

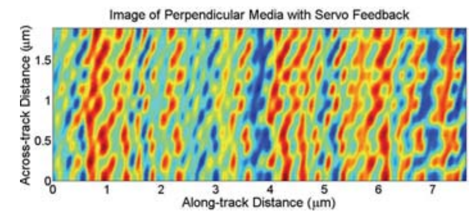

CE-01

Reversible exchange bias in ideal antiferromagnetic alloys.

D. Lederman, M. Cheon
Department of Physics, West Virginia University, Morgantown, WV

Most exchange bias (EB) theories rely on uncompensated spins in the AF to have a AF/FM coupling mechanism [1]. Uncompensated spins have been detected at the AF/FM interface in oxide and metallic AFs [2]. In dilute AF/FM bilayers an enhancement of EB can occur as a result of uncompensated spins that naturally form at AF domain boundaries [3]. The AF magnetic anisotropy is also important because 1) a weak AF anisotropy can cause a low blocking temperature (T_B); and 2) the direction of the cooling and measurement fields with respect to the AF anisotropy axis alter significantly the EB [4,5] and the domain reversal mechanism in the FM [6,7].
In order to address these issues we have studied EB using $Fe_xNi_{1-x}F_2$. NiF_2 and FeF_2 share the rutile crystal structure, but the localized Ni^{+2} spins lie in the (001) plane, in contrast to FeF_2, where spins align along the [001] direction. NiF_2 is also a weak ferromagnet with T_N=73.2 K [8] in bulk and 80 K in films [9]. FeF_2 is a classic AF with T_N=78.4 K. Because of the perpendicular magnetic easy axes of NiF_2 and FeF_2, the $Fe_xNi_{1-x}F_2$ alloy has a variable magnetic anisotropy that depends on x, thus providing an ideal system to probe the effects of AF magnetic anisotropy on EB.
$Fe_xNi_{1-x}F_2$ (110)/polycrystalline Co bilayers capped with Al or Pd, were grown via molecular beam epitaxy. The typical thickness of the AF, Co, and capping layers were 44, 17, and 2.5 nm, respectively. The roughness values were ≈ 0.7 nm for the MgF_2/AF, 1.0~nm for the AF/Co, 0.7~nm for the Co/cap, and 1.0~nm for the cap/air interfaces. A commercial SQUID magnetometer with the magnetic field H applied along the [001] direction was used to measure hysteresis loops.
Figure 1(a) shows the hysteresis loops measured at T = 30 K, after cooling from T=95 K to T = 5 K with H_{CF}= 2 kOe along the [001] direction. The loops were measured between $H = \pm10$ kOe for $Fe_xNi_{1-x}F_2$ samples with x = 0.05, 0.21 and 0.49. They had $H_E < 0$ and an uncompensated magnetization (defined as the shift of the hysteresis curve along the magnetization axis M) $\Delta M_S > 0$ at $T < T_B$ = 50 K (40~K) for x= 0.05 (0.21). For the x = 0.49 sample, $H_E < 0$ and $\Delta M_S < 0$ for $T < 20$ K and $H_E > 0$ and $\Delta M_S > 0$ for $T > 20$ K. When M was measured in the $H = \pm70$ kOe range as shown in Fig. 1(b), there were two superimposed loops: one had a relatively small coercivity H_C, corresponding to the Co layer, and the other had a large H_C with M corresponding to ΔM_S. Therefore, the uncompensated magnetization measured in the small field range was reversible at high fields and confined to the AF, as determined from micromagnetic calculations [10]. Because the EB was correlated with the "pinned" magnetic moments which are reversible at high fields, it was possible to reverse the sign of H_E at T = 5 K after field-cooling by performing asymmetric hysteresis loops. ΔM_S disappeared close to the T_N [Fig. 1(c)], indicating that it originated within the bulk of the AF. We believe that H_E can be reversed in all EB systems at low T (compared to T_B) if high enough fields are available. The magnitude of this field depends on the magnitudes of ΔM_S, the anisotropy of the AF, and T. For example, with a $Fe_{0.36}Zn_{0.64}F_2$ dilute AF sample, at T = 5 K it was impossible to reverse H_E in fields up to 70 kOe despite a large ΔM_S. However, at T = 20 K (T_N = 28 K), the effective anisotropy of the pinned magnetization was weak and the sign of H_E could be reversed in fields of only 10 kOe [Fig. 1(d)]. A reversible EB in magnetoelectronic devices could be achieved by creating an antiferromagnetic alloy with unpinned moments and a random anisotropy.

1. M. Kiwi, J. Magn. Magn. Mater. 234, 584 (2001).

2. H. Ohldag, A. Scholl, F. Nolting, E. Arenholz, S. Maat, A. T. Young, M. Carey, and J. Stöhr, Phys. Rev. Lett. 91, 017203 (2003).

3. P. Miltényi, M. Gierlings, J. Keller, B. Beschoten, G. Güntherodt, U. Nowak, and K. D. Usadel, Phys. Rev. Lett. 84, 4224 (2000).

4. A. P. Malozemoff, Phys. Rev. B 35, 3679 (1987).

5. H. Shi and D. Lederman, Phys. Rev. B 66, 094426 (2002).

6. A. Hoffmann, Phys. Rev. Lett. 93, 097203 (2004).

7. J. Olamit, Z. P. Li, I. K. Suller, and K. Liu, Phys. Rev. B 73, 024413 (2006).

8. A. S. Borovik-Romanov, A. N. Bazhan, and N. M. Kreines, Sov. Phys. JETP 37, 695 (1973).

9. H. Shi, D. Lederman, K. V. O'Donovan, and J. A. Borchers, Phys. Rev. B 69, 214416 (2004).

10. M. Cheon, Z. Liu, and D. Lederman, Appl. Phys. Lett. 90, 012511 (2007).

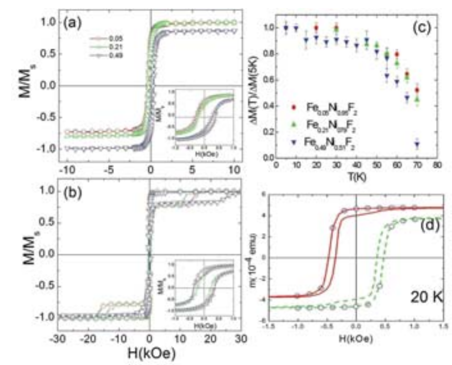

Figure 1 Hysteresis loops measured at T=30 K, after cooling down from T=95 K to T=5 K with H_{CF} = 2 kOe along the [001] direction, (a) between $H = \pm10$ kOe and (b) between $H = \pm70$ kOe for $Fe_xNi_{1-x}F_2$ with the values of x indicated in the legend. Insets: Same data for small fields. (c) Temperature dependence of ΔM_S. (d) *M-H* measurements of $Fe_{0.36}Zn_{0.64}F_2$ sample measured between $H = \pm10$ kOe (o), between +10 kOe and -3 kOe (solid line), and between -10 kOe and + 3 kOe (dashed line).

CE-02

Role of anisotropies on the asymmetric magnetization reversal behavior in exchange-biased systems.

E. Jiménez[1], *J. Camarero*[1], J. Sort[2], J. Nogués[3], N. Mikuszeit[1,4], J. García-Martín[5], A. Hoffmann[6], B. Dieny[7], R. Miranda[1,8]

1. Departamento de Física de la Materia Condensada and Instituto de Materiales "Nicolás Cabrera", Universidad Autonoma de Madrid, Madrid, Spain; 2. Departament de Física, Institució Catalana de Recerca i Estudis Avançats (ICREA) and Universitat Autònoma de Barcelona, Bellaterra, Spain; 3. Institució Catalana de Recerca i Estudis Avançats (ICREA) and Institut Català de Nanotecnologia, Bellaterra, Spain; 4. Institut für Angewandte Physik, Universität Hamburg, Hamburg, Germany; 5. Instituto de Microelectrónica de Madrid CNM-CSIC, Tres Cantos, Spain; 6. Materials Science Division and Center for Nanoscale Materials, Argonne National Laboratory, Argonne, IL; 7. SPINTEC, URA2512, CNRS/CEA, Grenoble, France; 8. Instituto Madrileño de Estudios Avanzados en Nanociencia IMDEA-Nanociencia, Madrid, Spain

An important issue in exchange-biased ferromagnetic-antiferromagnetic (FM/AFM) systems is the intrinsic asymmetric behavior of the magnetization reversal [1]. Around the easy direction there is a range of angles in which the evolution of magnetization shows an asymmetric behavior in the descending and ascending branches of the hysteresis loop. In general, magnetization reversal via rotation processes is more relevant in one of the two branches of the hysteresis loop, in which a larger density of domains during the irreversible processes is also observed. This manifest in the magnetization hysteresis loops by the occurrence of more rounded transitions of the parallel component of the magnetization ($M_{\|}$) and/or by larger values of the transverse component of the magnetization ($M_{\perp}$). Experimental data do not, however, agree on the pathways dominating the reversal in each of the two field branches. For some of the systems, rounded $M_{\|}$ transitions and/or larger $M_{\perp}$ values are found in the descending branch, where the field is applied parallel to the bias direction, while for other systems the opposite behavior was found.

We have studied the influence of the anisotropies on the magnetization reversal in exchange biased Co/IrMn and FeNi/IrMn bilayers and shed light on the aforementioned discrepancy on the asymmetric reversal phenomena, by pursing a detailed magnetization reversal study of exchange biased thin films with well defined uniaxial anisotropy. Our findings show that the competition between the uniaxial K_U (FM) and unidirectional K_E (interface) anisotropies and the interfacial spin frustration play the main roles that explain such behavior.

Angle dependent measurements have been performed with high resolution vectorial Kerr magnetometry for the two FM/AFM bilayers with different thicknesses. Reference FM samples present a well defined uniaxial magnetic anisotropy, promoted by a Ta buffer layer deposited at oblique incidence. The effective anisotropy of the Co films is about one order of magnitude larger than the one of the FeNi films with similar thickness. The FM/AFM samples were field cooled simultaneously with the external field aligned parallel to the easy-axis of the FM layer to render samples with collinear anisotropies, i.e., parallel K_U and K_E.

In general, the reversal is governed by irreversible (sharp) and/or reversible (smooth) transitions, which are correlated with nucleation and propagation of magnetic domains and rotational processes, respectively. Close to the easy axis, the reversal is asymmetric in the descending and ascending branches of the hysteresis loop (see Fig.1). The angular range where the asymmetry is found is much smaller in the FeNi case, as expected by its low intrinsic anisotropy. However, the asymmetry is different when comparing the Co/IrMn and FeNi/IrMn systems. For the Co/IrMn bilayers, larger $M_{\perp}$ values and rounded $M_{\|}$ transitions are always found in the descending branch of the hysteresis loop (see upper graphs of Fig.1). For the FeNi/IrMn bilayers, these features can be found in both descending and ascending branches, depending on the sign of the angle between the applied magnetic field and the easy axis (see bottom graphs of Fig.1). Additionally, when the field is applied along the easy direction, i.e., at 0°, $M_{\perp}$ is negligible during the whole loop for the Co case, which indicates nucleation of domains parallel to the field orientation during the irreversible transition of $M_{\|}$. However, for the FeNi case a clear hysteresis is found, indicating that the domains are not parallel to the easy axis of magnetization.

All these features are well reproduced with a Stoner-Wohlfarth model by considering collinear anisotropies for Co/IrMn and, surprisingly, non collinear anisotropies for FeNi/IrMn. The origin of this non-collinearity is given with a model which combines a three-dimensional lattice of spins and spin disorder (generated by a random interface roughness) to elucidate the spin configuration of the FM/AFM bilayer as a function of the anisotropy. The anisotropy balance and the interfacial spin frustration, leading to a rotation of the FM axis for small FM anisotropies, are the keys which control the asymmetry of the magnetization reversal in FM/AFM systems. [2].

[1] Camarero et al., Phys. Rev. Lett. **95**, 057204 (2005).

[2] Jiménez et al., submitted for publication.

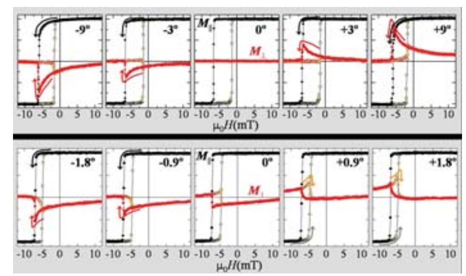

Fig.1: In-plane resolved magnetization Kerr hysteresis loops of 14 nm Co/5 nm IrMn (upper graphs) and 14 nm FeNi/5 nm IrMn (bottom graphs) films with the field applied at different angles respect to the magnetic easy axis direction. To clarify the evolution of the magnetization, the two branches of the hysteresis loops are depicted with different filled symbols. The arrows indicate the magnetic field branch with larger $M_{\perp}$ values and rounded $M_{\|}$ transitions.

CE-03

Asymmetric magnetization reversal behavior in exchange-biased multilayers in different antiferromagnetic thickness ranges.

D. Spenato, V. Castel, S. P. Pogossian, C. Le Graët, D. T. Dekadjevi, J. Ben Youssef
Laboratoire de Magnétisme de Bretagne, CNRS/FRE 2997, Université de Bretagne Occidentale, Brest, France

Exchange coupling between a ferromagnet and an antiferromagnet, called exchange bias, has been extensively studied due to its key role in applications such as giant magnetoresistive heads for high density recording. Among all the properties observed in exchange-bias systems, the asymmetry in the magnetization reversal is intriguing, since most of magnetic materials reveal symmetric reversal. The origin of asymmetry reversal is still contreversial and may be attributed, depending on the nature of the bilayers, to different magnetization processes.Moreover, the asymmetry depends on the angle between the external field and the exchange bias direction [1-3] A method to probe the magnetization reversal processes is to use experimental techniques that provide information on the vectorial character of the magnetization . In such experiments, the existence of transverse magnetization is interpreted as coherent magnetization rotation [2, 3] while the flatness of the transverse magnetization indicates that there are no net rotation of the F moments in the direction perpendicular to the applied field during the magnetization reversal (i.e. incoherent rotation or domain wall propagation).

In this digest, we study the magnetization reversal processes in NiFe/MnPt bilayers by tuning the ratio between the anisotropy (H_K) and exchange (H_E) fields especially on either side of a critical value $H_K=2H_E$ where a strong change in the hysteretic behavior is observed. Earlier works focus the effect of the competition between anisotropies on the magnetization reversal in F/AF bilayers with $H_K < 2H_E$ [2] or in lithography-induced high shape anisotropy in order to obtain $H_K > 2H_E$ [4]. We now extend these measurements to non-patterned thin films with intrinsic anisotropies $H_K < 2H_E$ and $H_K > 2H_E$. The static measurement is based upon vectorial vibrating sample magnetometry (VVSM). Both longitudinal magnetization (M_L), the component parallel to H and transverse magnetization (M_T), the component in the film plane but perpendicular to H have been measured with four detection coils. The samples are polycrystalline NiFe/MnPt bilayers of 35 nm Nife thickness and different MnPt thicknesses grown on Corning Glass substrate by conventional RF diode Sputtering. The MnPt thickness dependence of both the exchange field (H_E) and the coercivity (H_c)is shown in Fig.1. The shift of the hysteresis loop appears at a critical AF thickness t_{crit} of 7.5 nm. The inset in Fig.1 represents typical M_T (H) and M_L (H) loops for 10 nm MnPt measured for an applied magnetic field at 15 degrees with respect to the depositing field direction.

Since H_E depends on the AF thickness, changing MnPt thickness should result in different $H_K /2H_E$ ratios. In this study we have carried out a systematic study of the angular dependance of the magnetization reversal to probe the contribution of the coherent rotation to this reversal for two NiFe/MnPt samples, one with 10 nm MnPt thickness ($H_K > 2H_E$, Fig.2 (a))and for 40 nm MnPt thickness ($H_K < 2H_E$ Fig.2 (b)). The results are presented on Fig 3. Depending on the balance between these two anisotropies the magnetization reverses either in the opposite or the same semicircles during the ascending and descending branches of the hysteresis loop. These results show an experimental evidence that, the balance between the uniaxial and unidirectionnal anisotropies in NiFe/MnPt bilayers rules the asymmetric magnetization reversal [5]. We have compared our experimental data with numerical calculations based on a Stoner-Wohlfarth type model (solid line Fig.2). As one can observed on this figure, this model provides a relevant description of the behavior of the hysteresis loops in these bilayers. We are extending at the moment our study to NiFe/MnPt/NiFe trilayers, and the experimental results will be discussed.

[1] D. T. Dekadjevi, A. Suvorova, S. Pogossian, D. Spenato, and J. Ben Youssef, Phys. Rev. B 74, 100402(R) (2006).

[2] J. Camarero, *et al*, Phys. Rev. Lett. 95, 057204 (2005).

[3] J. Olamit and K. Liu, J. Appl. Phys. 101, 09E508 (2007).

[4] S. Chung, A. Hoffmann, and M. Grimsditch, Phys. Rev. B. 71, 214430 (2005).

[5] D. Spenato, V. Castel, S.P. Pogossian,, D.T. Dekadjevi, and J. Ben Youssef, Appl. Phys. Lett 91, 062515 (2007)

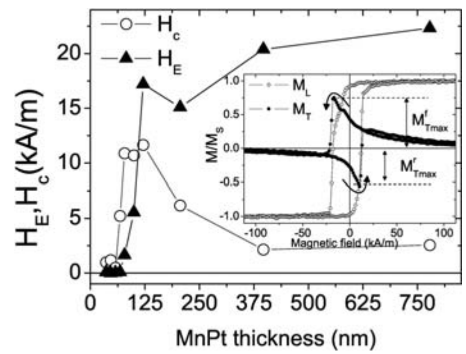

Fig.1 : MnPt layer thickness dependence of H_E and H_c for a NiFe layer thickness of 35 nm

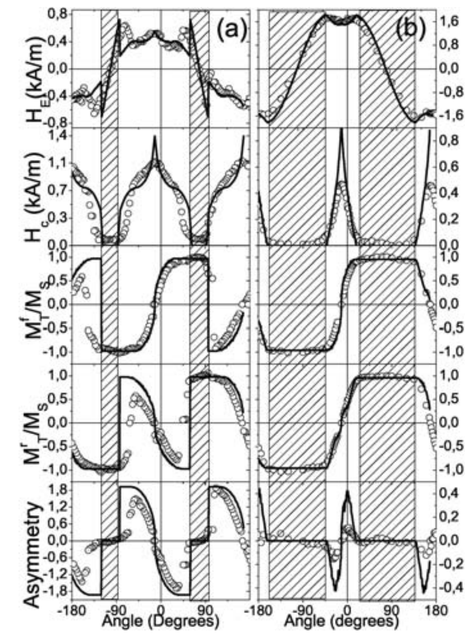

Fig.2

Tailoring of dynamic magnetic properties of ferromagnetic thin films by ultra-thin IrMn layers.

J. McCord[1], R. Kaltofen[2], L. Schultz[1]
1. Institute for Metallic Materials, IFW Dresden, Dresden, Germany; 2. Institute for Integrative Nanosciences, IFW Dresden, Dresden, Germany

The dynamic response of magnetoelectronic devices in the GHz regime relies on the dynamical response of the magnetization. The two key parameters which control the response of soft magnetic thin films are the magnetic anisotropy that determines the precessional frequency f_{res}, and the effective damping parameter α_{eff}.
One way to tailor the dynamic magnetic properties is to dope ferromagnetic thin films with rare earth elements. On the other hand it has been shown that exchange biased ferromagnetic/antiferrromagnetic (F/AF) systems exhibit an increase α_{eff} due to an inhomogeneous magnetization distribution within the AF layer and to a two-magnon scattering contribution. Here we demonstrate, how ultra-thin IrMn layers can be used to alter f_{res} and α_{eff} of $Ni_{81}Fe_{19}$ layers in a controlled manner and over a wide range.
The influence of an AF layer thickness t_{IrMn} as part of a $Ni_{81}Fe_{19}$ (10 nm)/IrMn/$Ni_{81}Fe_{19}$ (10 nm) structure on the static magnetic properties is displayed in Fig. 1. For the given system, adding a thin IrMn layer, the effective uniaxial anisotropy field $H_{k,AF}$ can be increased by an order of magnitude. The overall dependence of the static unidirectional and uniaxial anisotropy field H_{eb} with t_{IrMn} is shown in Fig. 2(a). The change of f_{res} and α_{eff} is displayed in Fig. 2(b). By adding a layer of IrMn, α_{eff} of the surrounding $Ni_{81}Fe_{19}$ layers can be significantly increased from 0,008 to 0,054. Congruently, the gain in f_{res} is by a factor of 4 from 0,8 GHz to 3 GHz, which corresponds to an increase of the effective field by a factor of 16. One selected example showing how the dynamic magnetic properties vary with the ferromagnetic film thickness t_{NiFe} is displayed in Fig. 3. Comparing the shown data from the sandwich structures and data from additionally prepared F/AF multilayers we were able to derive simple general expressions for a constant AF layer thickness below the onset of exchange bias:
(i) $f_{res} \sim (K_{u,F} + J_{u,AF}*(1/t_F))^{0,5}$
(ii) $\alpha_{eff} \sim \alpha_F + \alpha_{AF}*(1/t_F)$
In (i) (a modified form of Kittel's equation) the precessional frequency depends on the F film's uniaxial anisotropy constant $K_{u,F}$ and AF induced uniaxial coupling constant $J_{u,AF}$. α_{eff} can be described by the F layer's damping parameter α_F together with a AF induced coupling damping parameter α_{AF}.
Using Eq. (i) and (ii) for a given system, the essential dynamic magnetic properties can be adjusted easily by more than an order of magnitude. The use of thin AF layers allows for controlled tuning of effective magnetic properties of exchange coupled F layers independent and without modifications of the F layer's intrinsic properties.

[1] S.G. Reidy, L. Cheng, W. E. Bailey, Appl. Phys. Lett. 82, 1254 (2003)

[2] J. McCord, R. Mattheis, D. Elefant, Phys. Rev. B 7094420/1-8 (2004)

[3] J. McCord, R. Kaltofen, T. Gemming, R. Huehne, L. Schultz, Phys. Rev. B 75, 134418/1-8 (2007)

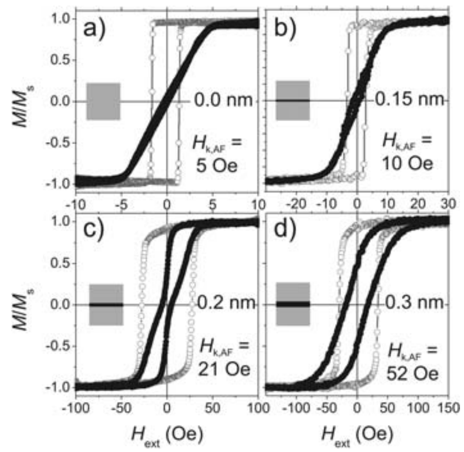

Fig. 1. Hysteresis loops along the easy and hard axis of magnetization for different AF layer thickness t_{IrMn}. Note the different magnetic field amplitude. The effective anisotropy field values $H_{k,AF}$ and t_{IrMn} are indicated.

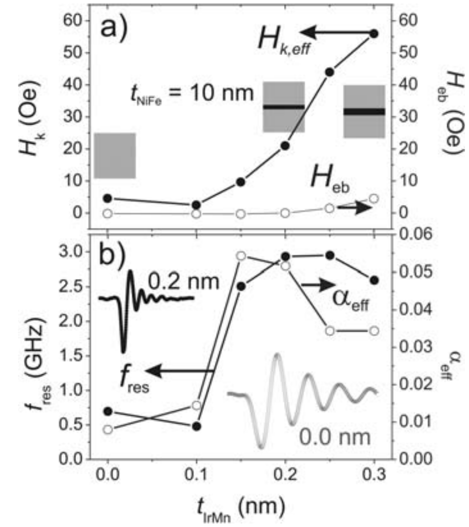

Fig. 2. (a) Change in $H_{k,AF}$ and exchange bias field H_{eb} with t_{IrMn}. (b) Variation of precessional frequency f_{res} and damping parameter α_{eff}. Two exemplary pulsed inductive microwave magnetometry (PIMM) curves together with the corresponding values of t_{IrMn} are shown (b).

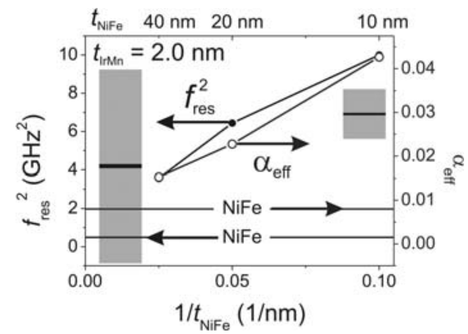

Fig. 3. (a) Change of f_{res}^2 and α_{eff} with the reciprocal NiFe thickness $1/t_{NiFe}$.

CE-05

Local magnetization studies by Magnetic Force and Kerr microscopy of exchange bias in Co/CoO patterned dots.

U. Wolff[1], S. Suck[2], D. Givord[2], J. Mc Cord[1], L. Schultz[1], V. Neu[1]
1. IFW Dresden, Dresden, Germany; 2. Institut Neel, Grenoble, France

Introduction

Exchange-bias (EB) is known to originate from symmetry breaking at the interface between a ferromagnet (FM) and an antiferromagnet (AFM). Due to the presence of complex disordered structural and magnetic configurations at the FM/AFM interfaces, a clear description of this phenomenon is still missing. The role of structural and magnetic defects is expected to be considerably reduced at nanosizes when the single crystalline and single domain state is entered [1]. Thus, the present study focuses on the magnetization behaviour of arrays of Co/CoO dots (120x360 nm<2>) observed by magnetic force (MFM) and Kerr microscopy at low temperatures, T = 50 K, and an applied in-plane field. When imaged with MFM the dots behave as magnetic dipoles where the reversal occurs mainly in a single switching event, as known for a Stoner-Wohlfarth process in a small uniaxial element. Nevertheless, in some dots multidomain formation is observed. In order to clarify the difference between microscopic and macroscopic reversal mechanism these results are compared with Kerr microscopy measurements on a mesoscopic length scale.

Magnetization behaviour

Patterned Co/CoO samples were prepared by electron beam lithography with a subsequent lift-off technique and characterized by global magnetic measurements using SQUID magnetometry. Fig. 1 shows a square shaped hystersis curve (Hc = 95 mT and Hb = 17 mT) after cooling the sample through the Néel temperature in a positive field along the long axis of the rectangular elements. The first and second loop reversals (measured by SQUID) are very similar, revealing a rather small training effect. This could also be expected due to the small sized dots (120x360 nm<2>).

Fig. 2 shows the AFM topography consisting of well structured rectangles as well as the MFM images at different applied fields. The sample was again cooled through the Néel temperature in a positive in-plane field. In zero field, the fully in-plane magnetized rectangles show up as rows of black and white contrast arising from the magnetic charges building up at the element edges. When negative fields are applied, the elements individually switch their magnetization direction which is observed as a sudden reversal of the MFM contrast. After applying a magnetic field of -130 mT a few dots have already switched and by increasing the field more and more dots switch until we have the exactly opposite state (H = -175 mT) as in zero field. As a whole, the sample reverses magnetization in a rather small field range of ΔH = 75 mT around -150 mT. Evaluating the total magnetization of the imaged area throughout a full cycle we can construct the hysteresis curve plotted in Fig. 1. There is a good agreement with the globally measured curve. Nevertheless, some deviations from the perfect dipolar switching can be found. Examples are elements with more than two poles, or dipoles which are tilted away from the long element axis (see encircled areas). The latter can be explained by coherent rotation processes before the switching occurs and the existence of several poles must be due to a multidomain configuration during switching event.

SQUID and MFM measurements are giving global as well as very local information about the structuring, e.g. defects, of the sample. Looking on a mesoscopic scale by Kerr measurements allows to differentiate between microscopic and macroscopic reversal. The reconstructed hysteresis curve (Fig. 3) shows a shoulder at negative magnetic fields compared to the curves in Fig. 1. These deviations dependent on sample homogeneity and the quality of the structuring and their study and control is of great importance for future applications.

[1] J. Nogués, J. Sort, V. Langlais, V. Skumryev, S. Surinach, J.S. Munoz, M.D. Baro, Phys. Rep. 422 (2005) 65

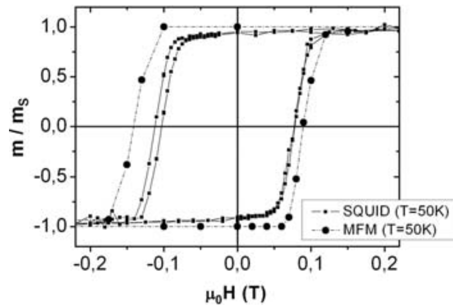

Fig. 1: Hysteresis cycles of a patterned Co/CoO sample

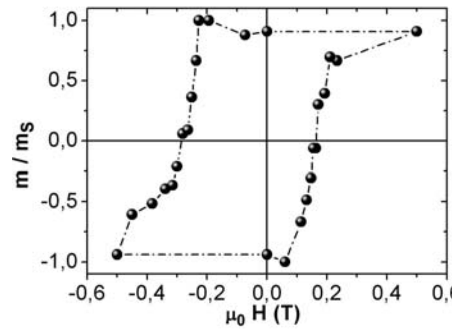

Fig. 3: Reconstructed hysteresis curve from Kerr measurements at 40 K

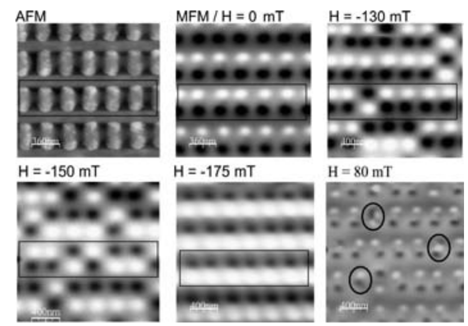

AFM and MFM images of a patterned Co/CoO sample at different in-plane fields

CE-06

Control of crystallographic orientation in IrMn/CoFe exchange bias systems.

N. Aley[1], G. Vallejo-Fernandez[1], K. O'Grady[1], B. Lafferty[2], J. Agnew[2], Y. Lu[2]
1. Physics, University of York, York, United Kingdom; 2. Seagate Technology Ltd., Derry, United Kingdom

Previous studies have shown that a (111) texture of IrMn parallel to the interface is important to give a large exchange bias eg.[1]. Other studies have found that optimising seed layer, composition, and the ordering of the IrMn leads to an enhanced exchange bias effect eg.[2]. NiFe seed layers have been shown to induce a (111) texture when used to seed IrMn growth leading to an enhancement of the blocking temperature, T_B [3]. We report on the origin of the increase in the average blocking temperature$\langle T_B\rangle$by varying the crystal structure of the IrMn/CoFe system using seed layers. We find that a (111) texture of the IrMn leads to an enhancement of the anisotropy constant of the antiferromagnet (AFM), thereby increasing$\langle T_B\rangle$.

Samples with structure Si <100> / Seed (5nm)/$Ir_{23}Mn_{77}$ (10nm)/CoFe (3nm)/ Ta (10nm) were prepared by DC sputtering using a HiTUS sputtering system. The seed layers used were Cu, Ru, and $Ni_{60}Cr_{40}$. The samples were deposited at ~ 120°C and then annealed for 30 minutes at 225°C in a 3kOe field. Structural characterisation of the samples was carried out by X-ray diffraction (XRD) using $\theta/2\theta$ and grazing incidence (GIXRD) scans. Thermal activation measurements were performed with a temperature controlled VSM to determine the blocking temperature distribution, using our well established measurement protocols [5]. The grain size distributions were determined from TEM images measuring 600 grains per sample.

Figure 1 shows a $\theta/2\theta$ scan for a sample with NiCr seed layer showing that the IrMn(111) peak is dominant. This indicates that the IrMn (111) planes in this sample are highly orientated parallel to the interface. GIXRD scans (not shown) confirmed this texture with the absence of the (111) peak for the NiCr seed sample. Thermal activation measurements are shown in figure 2 indicating a large increase in $\langle T_B\rangle$ for the NiCr sample (see table 1). The grain size analyses for the three samples are shown in figure 3. The distributions are log-normal with the NiCr showing the smallest grain size, and Cu the largest. The anisotropy of the AFM, K_{AF}, was then calculated using $K_{AF}V = k_BT_B.\ln(\tau.f_0)$, where V is the grain volume, τ the activation time, f_0 the attempt frequency ($f_0=10^9$ s^{-1}), and k_B is the Boltzmann constant [6]. From this equation the high T_B and small median grain size (D_m) for the NiCr sample indicates that the K_{AF} has increased due to the texture of the IrMn.

[1] M. Pakala, Y. Huai, G. Anderson, L Miloslawsky, J. Appl. Phys. 87 6653 (2000)

[2] M. Tsunoda, K. Imakita, M. Naka, M. Takahashi, J. Magn. Magn. Mat. 304 55 (2006)

[3] M. Fecioru-Morariu, G. Guntherodt, M. Ruhrig, A. Lamperti, B. Tanner, J. Appl. Phys. 102 053911 (2007)

[4] M. Vopsaroiu, M. J. Thwaites, G. V. Fernandez, S. Lepadatu, K. O'Grady, J. Optoelec Adv Mater 7 2713 (2005)

[5] L. E. Fernandez-Outon, K. O'Grady, M. J. Carey, J. Appl. Phys. 95, 6852 (2004)

[6] G. Vallejo-Fernandez, L. E. Fernandez-Outon, K. O'Grady, Appl. Phys. Lett. 91 212503 (2007)

Seed	D_m (nm)	$\langle T_B\rangle$ (K)	K_{AF} (erg/cm^3)
NiCr	3.8	477	$(2.9\pm0.4)\times10^7$
Ru	6.0	386	$(6.8\pm0.6)\times10^6$
Cu	10.7	367	$(1.9\pm0.2)\times10^6$

Table 1. Summary of Results.

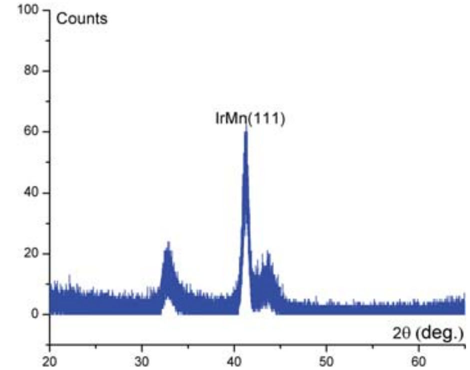

Figure 1 shows a $\theta/2\theta$ scan for a sample with a NiCr seed.

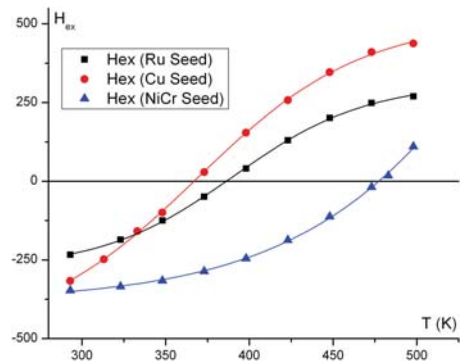

Figure 2 shows the grain size distributions for samples with Ru, NiCr and Cu seed layers.

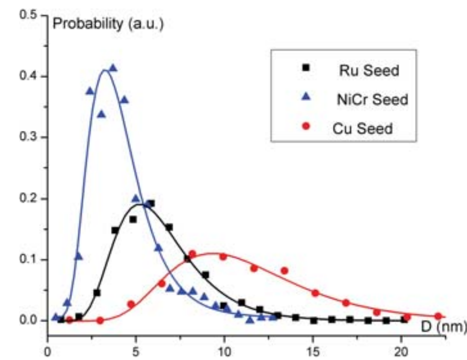

Figure 3 shows the variation of the exchange field H_{ex} with temperature.

Magnetoresistance in positive and negative exchange bias Ni/FeF_2 bilayered 200 nm anti-dots.

M. Kovylina[1,2], R. Morales[3,4], J. Villegas[4], M. Erekhinsky[4], I. V. Roshchin[4], A. Labarta[1,2], I. K. Schuller[4], X. Batlle[1,2]
1. Fisica Fundamental, Universidad de Barcelona, Barcelona, Spain; 2. Institut de Nanociència i Nanotecnologia (IN2UB), Barcelona, Spain; 3. Departamento de Física, Universidad de Oviedo, Oviedo, Spain; 4. Physics Department, University of California-San Diego, San Diego, CA

Despite the experimental and theoretical investigations, the exchange bias phenomenon (EB) in nanostructured systems remains poorly understood [1]. We used focused ion beam (FIB) lithography to prepare a series of samples of antidots of the same size and different distances in x-y directions. All of the fabrication has been performed on bilayered samples prepared by electron beam evaporation and consisted of antiferromagnetic (AF) FeF_2 (70nm), ferromagnetic (FM) Ni (50nm) and Al (4nm) as a protective layer. The square antidots with antidot size of 200 nm and x and/or y distance of 120-900 nm have been fabricated using an ion current of 30 pA (Fig.1). It is well known that magnetoresistance (MR) measurements can be used to determine exchange bias in thin films and nanostructures. MR was measured with the standard four terminal dc techniques in a He4 flow cryostat equipped with a superconducting solenoid. All measurements were carried out with the field applied parallel to the easy axis of the AFM and transport data were taken with the current in plane and perpendicular to the field. The resistivity was measured at 4.2 K in various field cooling conditions. The measuring field was applied along the same axis as the cooling field.

We observed three different types of behaviour (Fig.2): for small cooling fields, MR displays a shift towards negative field values (negative EB), while for large cooling fields the shift is positive (positive EB). In the intermediate case, we observed two MR peaks with different height and area. In the first and second case (small and large cooling fields) the reversal is sharper in the opposite field direction to the resulting shift of MR data. It is worth stressing that the switching from positive to negative EB depends on the density and/or relative x/y distances among antidots. The positions of the MR peaks are mostly independent of the cooling field, which suggest the AF domain size is comparable to or larger than the FM domain size and that each FM domain couples only to one AF domain with a particular direction of the EB [2]. For small/large cooling fields we have only one EB direction while two appear for the intermediate cooling cases.

The funding from the Spanish MEC through a FPU grant, Spanish CICYT project MAT2006-03999 and from the Catalan DURSI (2005SGR00969) are acknowledged.

[1] O. Iglesias, A. Labarta, X. Batlle, Journal of Nanoscience and Nanotechnology

(Invited Review paper), arxiv:cond-mat/067716(2007).

[2] O. Petracic, Z.P. Li, Igor V. Roshchin, M. Viret, R. Morales, X. Batlle,and I. K. Schuller, Appl. Phys. Lett. 87, 222509, (2005).

I. Roshchin, O. Petracic, R. Morales, Z.P. Li, X. Batlle and I.K. Schuller, Euro. Phys. Lett. 71, 297, (2005).

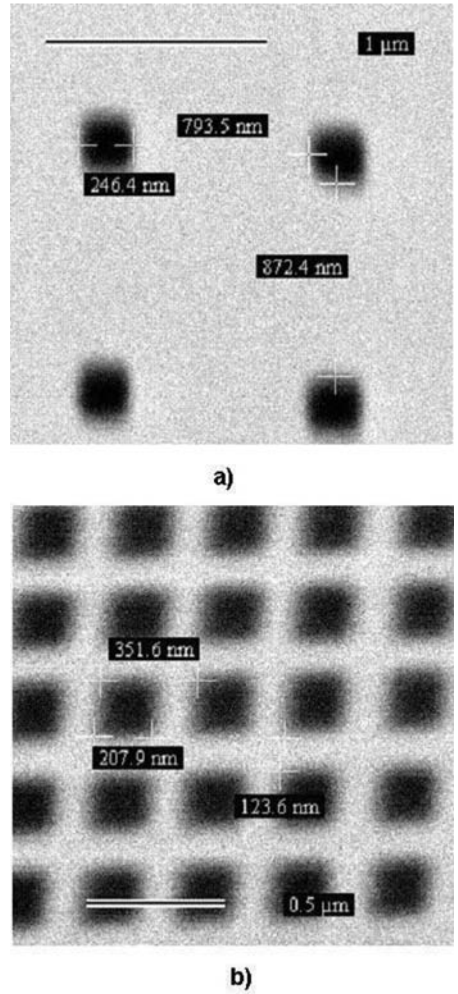

Fig. 1. SEM images of antidots with the size of 200 nm and antidot density (antidot area / total area): a) 0.06; b) 0.53.

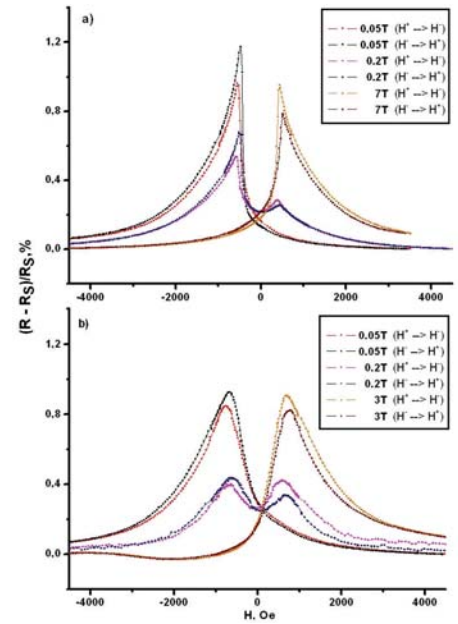

Fig. 2. MR data for antidot density: a) 0.06; b) 0.53.

CE-08

Exchange coupled IrMn/CoFe networks on mesoporous alumina.

N. N. Shams, M. Rahman, C. Lai
Materials Science and Engineering, National Tsing-Hua University, Hsinchu, Taiwan

Introduction

Some theoretical models dealing with exchange bias (EB) attribute such effects to the formation of domain and pinning of domain wall either in the ferromagnetic (FM) or in antiferromagnetic (AFM) layer. Therefore, the size of magnetic domain in both FM and AFM are crucial to the EB. Recently the EB nanostructure is widely studied for their technological importance in spintronics or other application as well as for an additional tunable source of anisotropy to stabilize the magnetization[1]. But fabrication of such structure is quite challenging. In this study, a mesoporous anodized aluminum oxide (AAO) is used as a prepatterned susbtrate to deposit IrMn/CoFe film. The EB is increased by 2 times on AAO compared to that of the continuous film due to pinning of the pores.

Experimental procedure

At first, 50 nm Al film deposited on a Si wafer by sputtering, is anodized to get AAO with a pore density of ~1 $x10^{11}cm^{-2}$. The pore diameter and the interpore distance is 10-12 nm and ~40 nm, respectively. Then Ta(3nm)/$Ni_{80}Fe_{20}$8nm)/$Ir_{20}Mn_{80}$(12nm)/$Co_{90}Fe_{10}$(10-20nm)/Ta(3nm) films are deposited on both Si/AAO and SiO_2 substrate by sputtering at room temperature. A Ta/NiFe seed layer is used to promote IrMn(111) texture and Ta overcoat is resists surface oxidation. Finally, the films are annealed at 210°C for 30 min in a magnetic field of 1.5kOe to promote EB. The morphological characteristic is observed by SEM and magnetic properties are measured by a VSM.

Result and discussion

The plane-view SEM image (Fig.1) of Si/AAO/Ta/NiFe/IrMn/CoFe film reveals that the magnetic material is deposited mainly on top of the AAO network [2]. The M-H loops of AAO/Ta/NiFe/IrMn/CoFe network structure and continuous SiO_2/Ta/NiFe/IrMn/CoFe film are shown in Fig. 2(a) and 2(b) respectively. The exchange field, H_{ex} and the coercivity, H_c of network structure exhibit larger magnitude than those of continuous film irrespctive to the thickness, t_{CoFe} of CoFe; i.e. the H_{ex} of network nanostructure is 275Oe, while it is 137 Oe in continuous film for a thickness of t_{CoFe}=10 nm. The anisotropy field also increases 2.4 times in the network IrMn/CoFe film. The kink in the M-H loop for t_{CoFe} =10 nm, is due to the presence of NiFe seed layer. The value of H_{ex} for NiFe/IrMn is 295 Oe and 145 Oe in network and continuous film respectively. The H_c of CoFe is 3 times larger in network strucutre (H_c = 47 Oe) than that of continuous (H_c = 13.5 Oe) film. Fig.3 shows the angular dependence of the EB nanostructure measured as described [3]. Both H_{ex} and H_c exhibited the expected unidirectional and uniaxial symmetry respectively. The increase of EB and H_c can be attributed to the pinning of domains caused by the AAO pores. The FM domain size is determined by the competition between the random field due to the interfacial AFM-FM interaction and FM-FM exchange interaction [1,4]. Therefore reducing the FM-FM interaction or decreasing the AFM domain size, EB can be increased. In our study, the presence of pores in network IrMn/CoFe may reduce the FM-FM interactions, or may favor the formation of smaller AFM domains, leading to a larger H_{ex}. The increase of both EB and H_c is presumably related to the network. So the H_{ex} of network EB structure may be tuned by controlling the pores of the mesoporous AAO template.

Conclusion

A feasible and convenient method is demonstrated to tune EB by pinning the domains of AFM/FM nanostructure. This kind of structure may be very useful in different applications and in addition, it provides a useful template to study different EB-related phenomena.

[1] K.Liu etal.,Phys.Rev.B 63,060403(2001).

[2] M.T. Rahman, etal.,Appl.Phys.Lett.91,132505(2007).

[3] J.W. Cai, K.Liu, and C.L.Chien, Phys.Rev.B,60,72(1999).

[4] Z.Li and S.F.Zhang,Phys.Rev.B,61,14897(2000).

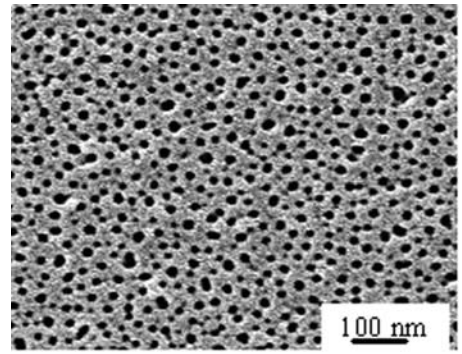

Fig. 1. SEM plan view image of AAO/IrMn/CoFe.

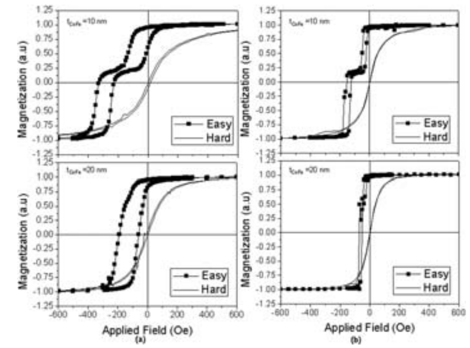

Fig. 2. M-H loop (a) AAO/IrMn/CoFe (b) SiO_2/IrMn/CoFe continuous film.

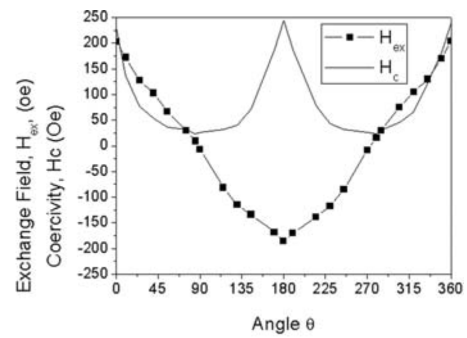

Fig. 3. Angular dependence of H_{ex} and H_c of AAO/IrMn/CoFe.

CE-09

Effects of nonmagnetic additives in metallic antiferromagnets on exchange bias.

M. Fecioru-Morariu[1], S. Ali[1], C. Papusoi[2], M. Sperlich[1], G. Güntherodt[1]
1. Physikalisches Institut (IIA), RWTH Aachen University, Aachen, Germany; 2. SPINTEC, CEA/CNRS, Grenoble, France

The phenomenon known as exchange bias (EB) refers to the shift of the hysteresis loop along the magnetic field axis originating from the interfacial exchange coupling between a ferromagnet (FM) and an antiferromagnet (AFM). Many aspects of exchange bias are not yet fully understood. This refers also to the role of nonmagnetic additives (dilution) in metallic AFMs with respect to the strength of the shift field or EB field (H_{EB}).

In insulating AFMs it has been shown both experimentally [1] and by Monte Carlo simulations [2] that it is possible to enhance H_{EB} by replacing magnetic atoms in the AFM by nonmagnetic ones not at the interface but rather throughout the volume part of the AFM. The enhancement of H_{EB} in exchange-biased insulating CoO was attributed to uncompensated AFM magnetic moments using a domain state (DS) model [1,2].

Here we analyze the effect of substitutional nonmagnetic defects in *metallic* exchange-biased AFMs on EB. As a model system we have chosen Cu as nonmagnetic dilution in the metallic intermediate-anisotropy AFM IrMn exchange biased to CoFe [3]. Atomic-force microscopy scans of samples with different Cu dilutions showed that the average grain size in the AFM IrMn decreases significantly with increasing Cu dilution in IrMn.

Magnetic characterizations were performed by SQUID magnetometry. Dilution by Cu atoms throughout the volume of the AFM IrMn gives rise to an enhanced H_{EB} of the CoFe/$(IrMn)_{1-x}Cu_x$ bilayers for 5 K ≤ T ≤ 350 K. Samples containing sole AFM layers with different Cu dilutions in IrMn showed also an enhancement of their thermoremanent magnetization (M_{TRM}) with Cu dilution. An evident resemblance in the behavior of M_{TRM} and H_{EB} with increasing dilution was observed.Also the temperature dependence of H_{EB} (of FM/AFM bilayers) shows a strikingly good qualitative agreement with that of M_{TRM} (of sole AFM) [3]. We conclude that the dilution and temperature dependence of H_{EB} has its origin in the M_{TRM} of the AFM itself [3,4].

Monte Carlo (MC) simulations based on a Heisenberg model were performed for FM/AFM bilayers [3,4] as well as for sole AFM layers [4] using the DS model for EB. A DS throughout the volume of the AFM is stabilized when the diluted AFM is cooled below the Néel temperature in an external magnetic field. In this context, the DS magnetization (M_{DS}) is related to the M_{TRM} measured for the sole AFM samples. For a realistic simulation of the CoFe/$(IrMn)_{1-x}Cu_x$ bilayers we considered their granular structure and assumed temperature dependent uncompensated moments of the AFM grains through an Arrhenius-Néel law. In the simulations we used a time-quantified MC algorithm which is based on a Heisenberg model and thus capable of describing the three-dimensional rotation of the spin moments. Figure 1 shows the simulated normalized EB field heb ($h_{eb} = \mu H_{eb}/|J_{AFM}|$) of an FM/AFM bilayer for different dilutions in the AFM as a function of temperature normalized by $|J_{AFM}|$. The experimental temperature dependence of H_{EB} of CoFe/$(IrMn)_{1-x}Cu_x$ bilayers is shown for some selected dilutions in the inset of Fig. 1. The experimental temperature and dilution dependence of H_{EB} is well confirmed by our MC simulations.

Moreover, our MC simulations clearly corroborate that the simulated temperature and dilution dependence of M_{TRM} [4] determines the corresponding dependence of H_{EB}. Our work demonstrates the extension of the adapted DS model to metallic intermediate-anisotropy exchange-biased AFMs.

The financial support received in the framework of the NEXBIAS EU Research Training Network (Contract No. HPRN-CT-2002-00296) is gratefully acknowledged.

[1] J. Keller, P. Miltényi, B. Beschoten, G. Guntherodt, U. Nowak, and K. D. Usadel, Phys. Rev. B 66, 014431 (2002).

[2] U. Nowak, K. D. Usadel, J. Keller, P. Miltényi, B. Beschoten, and G. Güntherodt, Phys. Rev. B 66, 014430 (2002).

[3] M. Fecioru-Morariu, S. R. Ali, C. Papusoi, M. Sperlich and G. Güntherodt, Phys. Rev. Lett. 99, 097206 (2007).

[4] C. Papusoi, J. Hauch, M. Fecioru-Morariu and G. Güntherodt, J. Appl. Phys. 99, 123902 (2006).

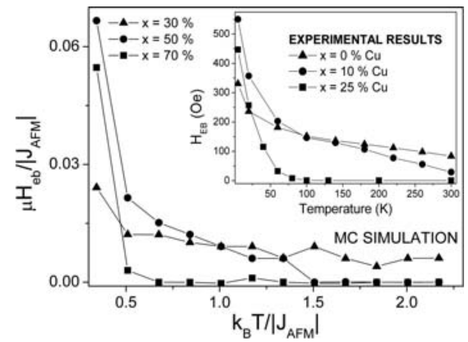

Figure 1: Simulated and experimental temperature dependence of the exchange bias field for different dilutions in the AFM.

CE-10

Negative and positive exchange bias in polycrystalline Ni/FeF_2 thin films.

R. Morales[1,2], J. Alameda[1], I. Schuller[2]
1. Dpto. de Fisica, Universidad de Oviedo, Oviedo, Spain; 2. Physics Department, University of California San Diego, La Jolla, CA

The exchange bias (EB) phenomenon appears in ferromagnetic/antiferromagnetic (FM/AF) thin films after cooling through the Néel temperature of the AF in an external magnetic cooling field (H_{FC}). The main feature of EB is the shift of the hysteresis loop along the magnetic field axis. The magnitude of this shift is known as exchange bias field H_{EB}.

The sign of EB, negative or positive, is defined by the relative sign of H_{EB} respect to the H_{FC} direction. If the loop is shifted in the direction opposite to H_{FC}, then EB is negative. Otherwise, EB is positive if the loop is shifted in the same H_{FC} direction.

All EB systems exhibit negative EB, but only few of them show the positive case. In this work we investigate the transition from negative to positive EB in polycrystalline Ni/FeF_2 bilayers as a function of H_{FC} and AF thickness. Fig. 1 shows the data for a Ni (50 nm)/FeF_2 (400 nm) bilayer. Three main features can be extracted from these data.

First, the transition from negative to positive EB occurs by gradual shift of the hysteresis loop from negative to positive values. This result is in contrast to the transition found in epitaxial FeF_2 [1] where double hysteresis loops were observed, and can be explained in the averaging regime of EB [2].

Second, the magnitude of positive EB is larger than the negative one. Previous works on epitaxial FeF_2 always obtained the same absolute value of H_{EB} for both positive and negative case [1,3]. Unlike epitaxial AF, high H_{FC} can increase the density of pinned uncompensated moments in polycrystalline FeF_2 yielding larger positive EB.

Third, the magnitude of H_{EB} is very low for thick FeF_2. The AF thickness dependence of EB demonstrates that the density of pinned uncompensated moments in polycrystalline FeF_2 is very sensitive to the AF thickness, proving the important role of the AF bulk on this EB system.

Work supported by the US Department of Energy and European Marie-Curie OIF.

[1] O. Petracic, Zhi-Pan Li, Igor V. Roshchin, M. Viret, R. Morales, X. Batlle, and Ivan K. Schuller. Appl. Phys. Lett. **87**, 222509 (2005).

[2] I. V. Roshchin, O. Petracic, R. Morales, Z.-P. Li, X. Batlle, and I. K. Schuller. Europhys. Lett. **71**, 297 (2005).

[3] M. R. Fitzsimmons, B. J. Kirby, S. Roy, Zhi-Pan Li, Igor V. Roshchin, S. K. Sinha, and Ivan K. Schuller. Phys. Rev. B **75**, 214412 (2007).

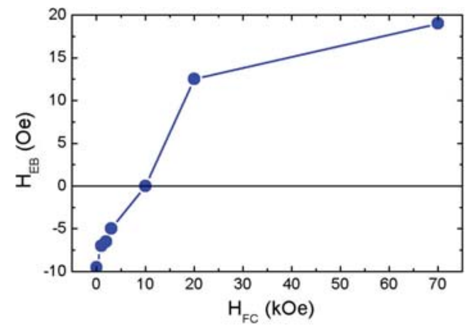

FIG. 1. Cooling field dependence of the exchange bias field of a polycrystalline Ni (50 nm)/FeF_2 (400 nm) bilayer.

CE-11

Large exchange bias IrMn/CoFe for magnetic tunnel junctions.

L. E. Fernandez-Outon[1], K. O'Grady[1], M. Zhou[2], M. Pakala[2]
1. Physics, The University of York, York, United Kingdom; 2. Western Digital Fremont Inc., Fremont, CA

INTRODUCTION/EXPERIMENT

Exchange bias systems are of interest due to their applications to pin one layer of spin-valves and magnetic tunnel junctions in read heads and MRAM devices. Thermal annealing processes for MgO based MTJs decrease the exchange field due to interlayer interdiffusion. Also the reduction of stack thicknesses to give higher areal densities reduces the thermal stability of the exchange biased system and its blocking temperature. Hence it is necessary to use high anisotropy AFs, such as $L1_2$-$IrMn_3$ [1], and grain size control to improve thermal stability and the blocking temperature,(T_B). In this paper we report on probably the largest value of exchange field measured with a low H_C of <5%(H_{EX}) in IrMn/CoFe multilayers at room temperature.

The samples, were sputtered onto a range of seed layers with the structure: Si/Seed layer/ IrMn (t_{AF})/CoFe(t_F)20/Ta(50) Å, with t_{AF} = 85 and 70 Å, and t_F = 25 and 10 Å. Measurements were made using an ADE Model 10 VSM, with a noise resolution of $1x10^{-6}$ emu. H_{EX} can be controlled by thermal activation [3]. In order to obtain uniform and reproducible data it is essential that measurements are made at a temperature (T_{NA}) where thermal activation of the AF does not affect the measurement. The samples studied are stable at RT and T_{NA} = 20°C. Prior to each measurement the AF must be set by heating to a temperature (T_{SET}) for a fixed period of time with the ferromagnet saturated by a setting field, (H_{SET}). T_{SET} = 225°C was found to be optimum, as it was the highest temperature at which no degradation of H_{EX} was observed.

RESULTS

Above T_{NA} thermal activation produces changes in the AF that increase with time according to a series expansion of ln(t) on an order that depends on the distribution of energy barriers to reversal within the AF [4-6]. The dependence on time of the setting process has been measured and proved to be linear with ln(t), indicating that there is a wide distribution of energy barriers within the AF [6].

The distribution of blocking temperatures was studied following the measurement procedure described in [3] and measured at T_{NA}. In this process the effect of thermal activation with a negative activation field (H_{ACT}), produces the shift of H_{EX} to positive values, progressively reversing the order in the AF, see fig.1. At the mean blocking temperature, T_B, half of the AF order has been reversed. This procedure allows for the assessment of the stability of the AF at different temperatures, and particularly at the working temperature of the MTJs.

The dependence of the H_{EX} on the magnitude of the setting field, H_{SET}, is shown in fig.2 for each of the samples studied. Table 1 shows the percentage difference in the measured value of H_{EX} for H_{SET} = 20 kOe relative to that for H_{SET} = 4 kOe. The interfacial spins are aligned at small fields less than 0.5 kOe. The application of higher H_{SET} increases H_{EX} due to an improved interfacial spin alignment at the interface. Alignment at both interfaces H_{EX} increases up to 37% when H_{SET} is increased from 4 kOe to 20 kOe. The H_C values are less than 10% of the value of H_{EX}, see table 1, which is indicative of the good quality of the interface. The variation of H_C with H_{SET} is very small compared to the error in H_C of 1%, this is consistent with data published elsewhere [2].

[1] K. Imakita, M. Tsunoda, M. Takahashi, Appl. Phys. Lett. 85 3812 (2004)

[2] L.E. Fernandez-Outon, G. Vallejo-Fernandez, K. O'Grady, J. Appl. Phys. In Press

[3] L. E. Fernandez-Outon, K. O'Grady, M. J. Carey, J. Appl. Phys 95 6852 (2004)

[4] P. Gaunt, J. Appl. Phys. 59, 4129 (1986)

[5] R. Street, J.C. Woolley. Proc.Phys. Soc. Jpn. A62, 562 (1949)

[6] M. El-Hilo, K. O'Grady, R.W. Chantrell, D.P.E. Dickson, J. Magn. Magn. Mat.123, 30 (1993)

$H_{EX}(H_{SET})$	S2	S3	S4	S5
H_{EX}(4kOe)	-1.796	-2.188	-3.537	-2.887
H_{EX}(20kOe)	-1.936	-2.922	-3.700	-3.292
ΔH_{EX} (%)	8	37	14	14
H_C(kOe)	0.055	0.540	0.200	0.130

Table 1 H_{EX} measured after application of a range of setting fields and average H_C

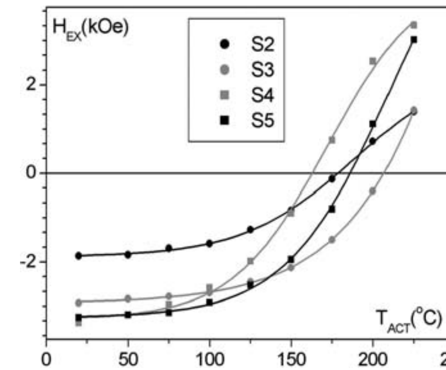

Figure 1 Variation of H_{EX} with the temperature of thermal activation for the set of samples measured

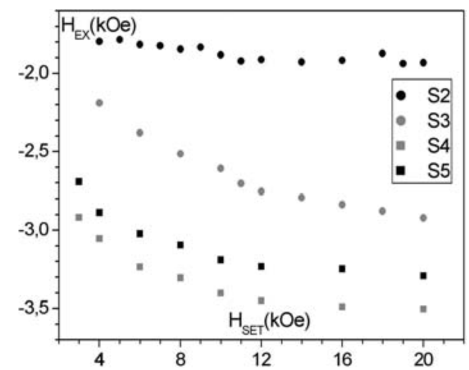

Figure 2 Variation of H_{EX} with the setting field for the set of samples measured.

CE-12

Observation of Metastable Remanence States in Pinned Antiferromagnetically Coupled Ferromagnetic Layers.

K. Srinivasan, S. Wong, S. N. Piramanayagam, R. Sbiaa
*Spintronics, Media and Interface Division, Data Storage Institute, A*STAR, Singapore, Singapore*

Soft magnetic layers of films that are synthetically antiferromagnetically coupled through Ru layers have applications in read sensors as well as perpendicular recording media. In read sensors, one of the soft magnetic layers is also pinned by an antiferromagnetic layer, such as MnPt, IrMn, or IrMnCr. Hysteresis loops and magnetoresistance properties of such soft magnetic layers have been reported by several researchers in the past. However, there have been few in-depth studies on the magnetization reversal characteristics of such structures. It was observed from our experiments that the minor hysteresis loops of such pinned and antiferromagnetically coupled structures exhibit systematic properties that point towards an unique magnetization reversal behaviour. This report discusses the interesting observations and a model to describe the behaviour.
<p>
Soft magnetic layers of the type FeCo(30 nm)/Ru(0.8 nm)/FeCo(x nm, x=30, 40) were deposited by sputtering on AlMg substrates used in hard disk media. Prior to the deposition of the sandwich, a sequence of underlayers such as Ta(5 nm)/Ru(10 nm) and an antiferromagnetic IrMn(5 nm) layer were deposited. All the layers were deposited at room temperature and there was no post-deposition annealing or intentional magnetic field to induce bias direction for the IrMn layer. However, it is likely that there is a magnetic field from the magnetron during the deposition. The films were characterized by vibrating sample magnetometer (VSM), and alternating gradient magnetometer (AGM).
<p>
Figure 1 shows selected minor hysteresis loops superposed on the major or full loop of the IrMn/FeCo(30)/Ru/FeCo(30) sandwich. For the minor loops which begin from a positive saturated state, it can be noticed that the structure along the return path shows a systematic dependence on the return field point. In addition, the minor loops carried out from the positive and negative saturation (not shown here) looked different, suggesting that the remanence states, although having M_r of almost zero, are different. In order to verify if this is true, the second sandwich IrMn/FeCo(30)/Ru/FeCo(40) was investigated. Figure 2 shows the full loop and selected minor loops. It can be noticed from the full loop that not only are the two remanence states different, but also the remanence is negative after positive saturation and vice versa.
<p>
In order to understand this interesting behaviour, a phenomenological model was developed. Figure 3 shows the full loop, a minor loop, and a schematic description of the magnetization states at various stages of reversal. It was assumed that the antiferromagnetic IrMn layer has random in-plane easy directions, half of which point to the right and the other half to the left, when projected on to a one-dimensional line. The model suggests that the top (free) FeCo layer always flips ahead of the bottom (pinned) FeCo layer, leading to the numerous and distinguishable remanence states. Despite this, based on the competition or co-operation of the pinning (induced by IrMn layer) and RKKY type coupling (Ru layer), only one of the remanence states has the lowest energy. While fundamentally interesting, such a sandwich has to be avoided for application as soft underlayer in perpendicular magnetic recording media in order to reduce the noise from the soft underlayers.

[1] S.S.P. Parkin et al., Phys. Rev. Lett., 64, 2304 (1990).

[2] H.S. Jung et al., J. Appl. Phys., 99, 08Q901-1 (2006).

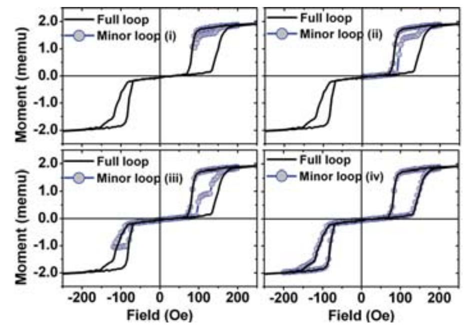

Fig. 1. Major and minor loops for IrMn(5nm)/FeCo(30nm)/Ru(0.8nm)/FeCo(30nm) structure. Curves (i), (ii), (iii) and (iv) are minor loops measured from positive saturated state to return field values of +85, 0, -120 and -200 Oe, respectively.

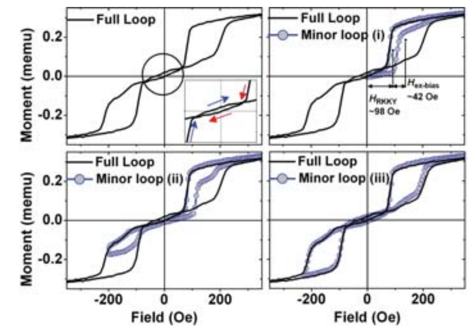

Fig. 2. Major and minor loops for IrMn(5nm)/FeCo(30nm)/Ru(0.8nm)/FeCo(40nm) structure. Curves (i), (ii) and (iii) are minor loops measured from positive saturated state to return field values of 0, -200 and -250 Oe, respectively.

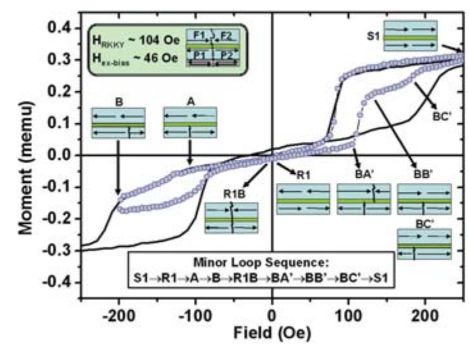

Fig. 3. Major and minor loop for sample shown in Fig. 2 with a phenomenological description of the magnetic states at various stages along the minor loop.

CF-01

Effect of hot and cold rolling on grain size and texture in FeSi strips with a Si-content larger than 2 wt%.

P. R. Calvillo[1], H. Hermann[2], J. Verstraete[1], *J. Schneider*[1,2], Y. Houbaert[1]
1. Metallurgy and Materials Science, Universiteit Gent, Gent-Zwijnaarde, Belgium; 2. Institut für Metallformung, Technische Universität Bergakademie Freiberg, Freiberg, Germany

The magnetic properties of electrical steel such as magnetization behaviour and specific magnetic losses are related to the microstructure and texture of the steel. The micro structural parameters having a strong influence on the magnetic properties are: grain size, inclusions, internal stresses and surface defects. They depend sensitively on the conditions during hot and cold rolling as well as on the final annealing treatment. Low values of the magnetic losses demand for large grain sizes and a large intensity of the cube texture is favourable for improved magnetization behaviour.
While the development of grain size and texture in conventional steels is already well understood, the knowledge for FeSi-alloys is far-off from complete. The interest in the case of FeSi-alloys is different from the case of conventional steels, where a high intensity of the {111} fibre and a small grain size is desired. In this paper we present and discuss some results of our recent studies on FeSi-alloys without phase transformation. Hot rolled samples of FeSi2.4 with a thickness of 2mm were fabricated using the four stand high speed hot rolling mill in Freiberg. The width of the hot rolled material is 80mm and the thickness is 2mm. The finishing temperature TF at hot rolling and the conditions for the following cooling down to 200°C have been varied in a wide range: 600 °C〈 TF〈 1100°C; rapid cooling down to 400°C〈 T〈 750°C followed by slower cooling down to 200°C. The samples have been cold rolled to a final thickness of 0.50mm. Finally a thermal annealing comparable with the continuous annealing was used in a specially designed laboratory furnace. The maximum temperature was 950°C.
In addition to metallographic investigations, the EBSD-technique is used for micro structural and texture characterization. The resulting grain structure and the relevant magnetic texture components for non-grain oriented electrical steels: eta-, theta-, zeta- and Cube-fibres before and after cold rolling as well as after annealing were analyzed. According to the shape of the grains these were classified as equiaxed, pancake or bands in the deformed states. The homogeneity of the grain size and texture across the thickness, which is favoured to reach optimum magnetic properties, is also analyzed in the different states.
The resulting grain structure and texture was found to be rather inhomogeneous across the thickness for all realized and quite different hot rolling conditions. The re-crystallization takes place heterogeneously through the thickness. The intensity of the magnetically relevant textures, especially of cube and rotated cube texture in the hot strips can be increased by a slower cooling after hot rolling. Cold rolling does not destroy the obtained favourable magnetic texture components in the hot strips. Nevertheless, cold rolling results in a general, but moderate decrease of the relevant magnetic textures and in an increase of the alpha-fibre. Rapid cooling after finishing the hot rolling down to about 400°C gives bands in the material, only at the surface re-crystallization takes place. The intensities of the relevant magnetic texture components depend sensitively on the hot rolling conditions. Preliminary studies indicate that there is a large impact of the (Si,Al)-content and of the realized deformation in the different passes at hot rolling on the grain size and its distribution as well as on the resulting magnetic texture.
Finally present models for the development of texture after cold rolling and thermal annealing in steels are regarded with respect to their relevance for the FeSi alloys. It is pointed out that the understanding and modelling of the development of grain structure as well as of magnetic texture and their interaction needs further investigations.

CF-02

Magnetization processes of Fe(Si,Al)-steels with homogeneous and inhomogeneous distribution of (Si,Al).

J. Schneider, J. Verstraete, K. Verbeken, *Y. Houbaert*
Metallurgy and Materials Science, Universiteit Gent, Gent-Zwijnaarde, Belgium

Recently there has been a lot of activity trying to produce steel with an increased concentration of Si and/or Al (over 3-wt%). Materials with homogeneous as well as inhomogeneous spatial distribution of (Si,Al) have been obtained. We will discuss in the paper aspects of the magnetization processes in these new types of materials. We will compare the resulting structure properties and magnetization behavior for samples with homogeneous and inhomogeneous distribution of (Si.Al) across the width of the strips.
A concentration increase of (Si and/or Al) may be obtained by surface deposition of Si and/or Al by hot dipping followed by a diffusion annealing, whereby homogeneous or inhomogeneous distributions of (Si,Al) across the width of the strips like for CVD followed by diffusion annealing are obtained. Normally the substrate is an Fe(Si-Al)-alloy without phase transformation. It was demonstrated by us that these techniques may also be applied to substrates with low, medium and high (Si-Al)-content to obtain materials with higher (Si,Al) content and homogeneous or inhomogeneous distributions of (Si,Al) across the width. It was found that the material after dipping may be cold rolled to get the desired final thickness, especially thin electrical steels with thickness smaller than 0.35mm.
In the following the structure and the magnetization behaviour of dipped and diffusion annealed samples using FeSi-substrates without phase transformation will be regarded. To discuss the magnetization processes in these materials with homogeneous or inhomogeneous (Si,Al) distribution across the with we have to take into account that there are spatial fluctuations of the value of the fundamental parameters exchange energy (exchange constant A), anisotropy energy (anisotropy constant K), and magnetostriction (magnetostriction constant λ). This will affect the domain wall energy (ED $\approx$ AK) and the domain wall width (dW $\approx$ A/K). In addition, the roughness of these samples is relatively large, which gives additional local demagnetizing fields in the surface region. These facts are reflected in the shape of the hysteresis loops for the same samples and in the unintegrated hysteresis loops, which indicate the distribution of the critical fields for domain wall motion at lower fields and domain wall rotation processes at higher values of the applied external field, respectively.
The B vs. H loops at low frequencies indicate low values of the remanence, that means a more or less isotropic behaviour, and a broad range of the field for the approach to saturation. The broad range of critical fields for domain processes appears in the samples with homogeneous as well as inhomogeneous (Si,Al) distribution across the width. The behaviour of the investigated samples is similar to that of amorphous samples. The unintegrated hysteresis loops for homogeneous as well as inhomogeneous samples are rather similar, which point to similar magnetization processes in samples with homogeneous as well as inhomogeneous distribution of (Si.Al) across the thickness. There appears no double peak in the distribution of the critical fields for domain processes of the samples with quite different (Si.Al)-content in the surface region and in the middle of the samples, which would indicate a superposition of two magnetically different materials.
The frequency dependence of the coercive force may be used to characterize the dynamic magnetic behaviour. Regarding the domain wall spacing L the dynamic coercive force Hac is proportional to $L^{1/2}$ and to the frequency $f^{1/2}$. If L is a function of frequency, deviations from the fact that Hac is proportional to the square root of f may be observed. The observed behaviour for the investigated samples indicates a variation of L with f, which means a variation of the number of moving walls with f.
With respect to the magnetic properties in the range up to 1000Hz it was found that the magnetization behaviour B vs. H as well as the magnetic losses P vs. B are practically the same for samples with homogeneous and inhomogeneous distribution of (Si,Al). The permeability exhibits the typical dependence as a function of the applied magnetic field and frequency. At much higher frequencies of 10kHz or higher the permeability is small and may be regarded as a constant like in the classic formulae for the skin depth. In this case the values of the permeability are finally determined mainly by the magnitude of order of the electrical resistivity, which is increased by increasing the (Si,Al) content, and the thickness of the material.
This brief discussion may indicate that the magnetization behaviour of the dipped and diffusion annealed samples may be well understood on the basic of the known relations between the parameters for the magnetization behaviour and the fundamental magnetic parameters A, K, and λ as well as the structure sensitive properties L (domain spacing), dW (domain wall width), and surface roughness. There appears no difference in the behaviour of samples with homogeneous or inhomogeneous (Si.Al) distribution across the width of the strips. The spatial fluctuations of the (Si,Al) content seem to be not remarkably relevant for the magnetization behaviour.

CF-03

Effects of Si content on the magnetic properties of Fe-Si alloy powder cores.

P. Jang[1], B. Lee[1], I. Jeong[2]

1. Div. of Applied Science, Cheongju University, Cheongju, South Korea; 2. R&D Center, Changsung Corp., Incheon, South Korea

I. Introduction

Despite of the excellent magnetic properties of the famous Fe-6.5% Si alloys, Si content in Fe-Si alloys has been mostly limited below 3 % because workability of the Fe-Si alloys decreases drastically beyond 3 % Si. Powder compressed cores can partly overcome the poor workability of the Fe-Si alloys. Even in the powder cores, however, poor workability of the Fe-Si alloys can decrease compaction ratio and density of core, leading lower permeability and higher core loss. In this study effect of Si content on the properties of Fe-Si alloy powder cores were investigated with an emphasis on optimum Si content.

2. Experimental procedure

Gas-atomized Fe-3%, 4.5% and 6.8%Si powders were annealed at 1000oC in vacuum, and then cooled to room temperature. The annealed powders were re-annealed at 900oC. The final powders with mean particle diameters of 49-56 um and a similar size distribution were mixed with 0.5% insulation agent and then compressed into toroid, the inner and outer diameters of which were 7.6 and 12.7 mm, respectively. The compressed cores were annealed at 800oC for 1 hr in 99.999% N2. The above annealing procedure is a condition for lowest total core loss in Fe-6.5%Si powder cores [1,2]. To reduce an experimental uncertainty five cores were fabricated at a time.

3. Results and discussion

Figure 1 shows a variation of total loss (Ptotal), hysteresis loss (Ph) and eddy current loss (Pe) of the Fe-Si cores as a function of Si content under a condition of 0.1 T and 50 kHz. Ph is larger than Pe in all cores. Pe decreases with increasing Si content while Ph slightly increases with increasing Si content. With increasing Si content workability decreases while resistivity increases as shown in Fig. 2. Resistivity of the cores increases with Si content. Compaction ratio(=density of core/density of bulk) decreases with Si content due to poor workability. As a result, 4.2%Si powders can have a moderate resistivity and workability. Ptotal shows a minimum value of 744 mW/cm3 in 4.2% cores. In Fe-Si alloys an abrupt decrease of ductility is due to the formation of FeSi(B2) and Fe3Si(DO3) ordered phases which appear as Si increases beyond around 5%. Lower compaction ratio of 6.8% cores in Fig. 2 is due to ordered phases as shown in Fig. 3. In Fig. 3, there is no trace of ordered phases in 3% and 4.2% cores. However, in 6.8% cores, the (111) and (200) characteristic lines of DO3 and (B2+DO3) phases are clearly seen. In Fig. 3, all indices of the diffraction lines are referred to the DO3 unit cell. AC permeabilities of 3%, 4.2% and 6.8 %Si cores at 50 kHz are 84, 96 and 87, respectively. Shapes of DC hysteresis loops of 3% Si and 4.2% Si cores are very similar when loops were measured under a maximum field of 400 Oe as shown in Fig. 4. High AC permeability and high magnetization loop of 4.2% cores are due to both relatively good workability and higher resistivity. In conclusion, lowest core loss could be obtained in Fe-4.2%Si alloy powder compressed cores when resistivity and magnetic properties are compromised with workability.

[1] Pyungwoo Jang, Bonghan Lee and Gwangbo Choi, Phys. stat. sol. (a), 204, 4108 (2007).

[2] Pyungwoo Jang, Bonghan Lee and Gwangbo Choi, J. Appl. Phys., to be published May, 2008.

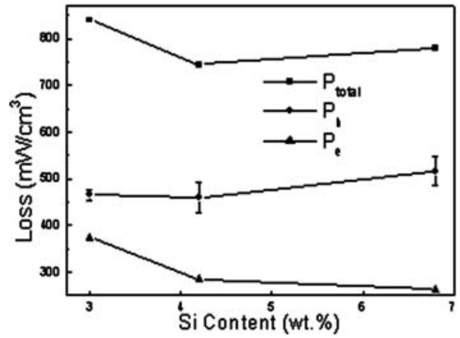

Variations of Ptotal, Ph and Pe of the Fe-Si cores as a function of Si content.

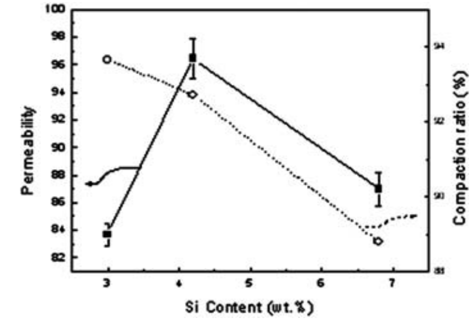

Variations of resistivity and compaction ratio as a function of Si content.

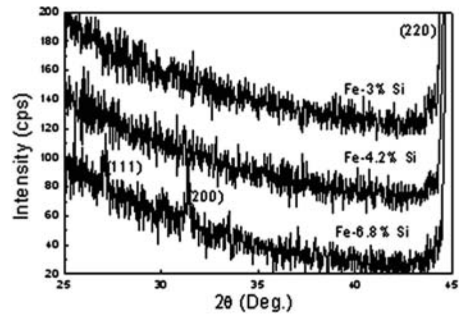

XRD diffraction patterns of Fe-Si powder cores.

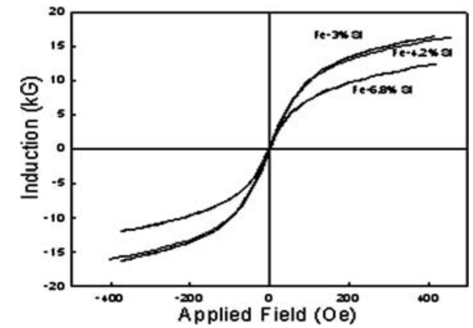

DC hysteresis loops of Fe-Si powder cores.

An In-depth Study of the Barkhausen Emission Signal Properties of the Plastically Deformed Fe-2%Si Alloy.

L. Piotrowski[1], B. Augustyniak[1], M. Chmielewski[1], F. J. Landgraf[2]
1. Dept. of Appl. Phys. and Math., Gdansk University of Technology, Gdansk, Poland; 2. Dept. of Met. Eng., University of Sao Paulo, Sao Paulo, Brazil

The digest presents the results of the in-depth study of the Barkhausen effect signal properties for the plastically deformed Fe-2%Si samples. The set of 10 samples having deformation levels up to ε = 8% has been investigated. The previous studies have shown that the rms-like signal envelope steadily increases with the increasing deformation level. However one can not tell whether the Barkhausen noise pulses are grater in number or rather their amplitude is higher. Being so we have undertaken the task of the time domain resolved pulse and frequency analysis of the Barkhausen noise signals. In Fig 1 the results of the time domain resolved FFT analysis for the non-deformed sample are presented. One can observe two, clearly separated maxima practically for all the frequency components of the signal – up to about 270 kHz. In order to facilitate the comparison of the results the contour maps obtained for all the samples have been intersected at various frequencies, the results of such intersection for the frequency f = 10 kHz are shown in Fig. 2. As can be seen the two maxima observed for the non-deformed sample disappear for the intermediately deformed sample (ε = 2%) and then an additional maximum appears for the highly deformed samples (ε = 8%). The intersection at the higher frequency (f = 250 kHz) gives different results (not shown). For all the investigated samples the two maxima envelope is present, though the observed minimum is somewhat less pronounced for the more deformed samples. In both cases the overall signal intensity is higher for the deformed samples but the difference is bigger for the lower frequency.
The complementary study consisted of the time resolved pulse count analysis as well as total pulse count. It turned out that the overall pulse number increases for the deformed samples, yet for the lower threshold levels the difference between deformed and non-deformed samples is not very important and the different deformation levels are practically non-discernible. The important difference is that for the non-deformed sample two clearly separated (in time domain) maxima are visible whereas for the deformed ones the maxima are weekly marked. Much bigger difference can be observed for the higher threshold levels (see Fig 3). Now two deformation stages (namely ε = 2 and 8%) are easily discernible and the difference between the deformed and non-deformed samples is more pronounced. The difference in the dynamic of the pulse count change for various threshold levels suggests usefulness of the pulse height distribution calculation. Such calculations have been performed for varying both the threshold level and time duration of the pulses. In order to show clearly the difference between the samples, the difference between the distributions obtained for the deformed samples and the one obtained for the non-deformed one has been calculated. The result of such calculation for the most deformed sample (e = 8%) have shown that the most useful region for comparison of the samples is the region of the relatively high threshold level (approx. about 1V), and pulse duration up to 10ms. For the higher pulses the total number of counts steadily decreases for all the samples and even though the rate of change of the relative pulse count as a function of deformation may be quite high the results become less certain.
Concluding one can say that the observed changes in results of both the time resolved FFT analysis and pulse distribution suggest that the increase in the Barkhausen noise signal as a function of deformation level is mainly due to the increase in the number of bigger pulses.

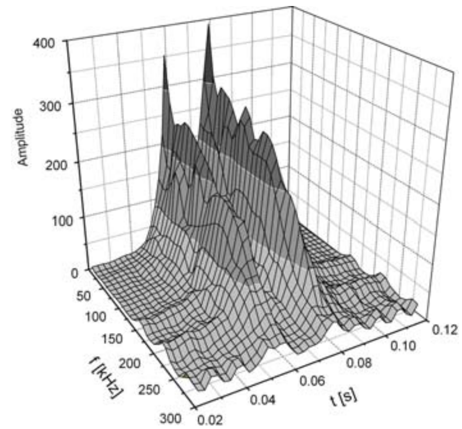

Fig. 1 The time resolved FFT analysis results for the non-deformed sample

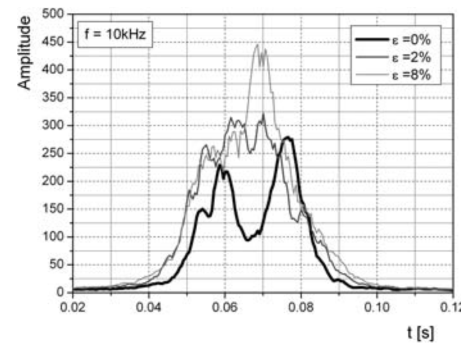

Fig. 2 The time resolved FFT amplitude for low frequency component of the measured Barkhausen noise signals for samples with different deformation levels.

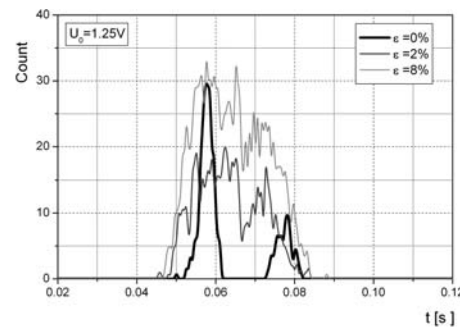

Fig. 3 The time distribution of the pulse count (high threshold voltgae) for the measured Barkhausen noise signals for samples with different deformation levels.

CF-05

Correlation between core loss and microstructure for Fe-Si powder cores.

S. Takemoto, T. Saito
R&D Center, Daido Steel, Nagoya, Japan

[Introduction]
Soft magnetic powder cores are widely used for choke coils and reactors of switching regulators and DC-DC converters as power supplies. They demand magnetic cores with high magnetic performance and miniaturization as well as with the ability to fabricate in various geometries. Recently powder cores have been used replacing the conventional soft ferrite for smoothing and boost choke coils of these power supplies in high frequency 50kHz to 1MHz.
In previous report [1][2][3], we have studied eddy current loss for Fe-Si powder cores and suggested that magnetic domain configuration should contribute to eddy current loss.
In this study we have examined the eddy current losses by decomposing into classical eddy current loss and excess loss. The correlation between excess loss and both magnetic domain configuration and crystal grain size was discussed.
[Experimental procedure]
Fe-3mass%Si powders were made by atomizing process. Powders were sieved to make various particle distributions. After annealing at 1223K in H2 atmosphere, silicone resin of 0.5mass% was added for the purpose of insulation between particles. Ring shaped specimens with outer diameter of 28mm and inner diameter of 20mm were press formed under 1.96GPa. The cores were heat treated between 1023K and 1273K in Ar atmosphere.
Core loss, Pc, was measured up to 100kHz at fixed magnetic flux density of 0.1T, and separated into hysteresis loss, Ph, classical eddy current loss, Pcl, and excess loss, Pexc.
[Results and discussions]
Figure1 shows the losses at 0.1T 100kHz decomposed into hysteresis loss, classical eddy current loss and excess loss. When particle size is large, main loss is classical eddy current loss, which is determined only by particle size. On the other hand, when particle size is small in terms of reduction of core loss, excess loss and hysteresis loss are significantly large. These losses are considered to have strong connection with microstructure.
Figure2 presents the dependencies of crystal grain size on hysteresis loss and excess loss. It is considered that both hysteresis loss and excess loss have an explicit dependency of crystal grain size for various particle sizes. As crystal grain size becomes larger, hysteresis loss decreases.
To discuss excess loss mechanism, paying a lot of attention to the magnetic domain configuration is of importance in terms of considering magnetising process for soft magnetic materials. We observed domain configuration in the Fe-3mass% Si powder core by means of Kerr effect microscope. The averaged crystal grain size and the averaged domain width were measured and the correlation between them was investigated. To compare the data with theoretical ones, calculation of domain width was carried out using following equation [4].
$L = (8\, \gamma\, r\, \mu_0 / N_d I_s^2)^{0.5}$
L :domain width, γ: domain wall energy, r: crystal grain size, Nd: demagnetising factor
Figure3 represents the averaged domain width from experiment along with the data calculated by the equation. The averaged domain width and crystal grain are 8μm and 33μm. The experiment data shows the increase in domain width as the crystal grain size increases.
It is concluded that wider domain with larger crystal grain makes excess loss larger.
These results is consistent with the data discussed for grain- oriented steels.[5]
More over we calculated excess loss for Fe-3Si powder core using equation described as follows [6]. Average particle size is 54μm.
$P_{exc} = 8(G\, S\, V_0 / \rho)^{0.5}(B\, f)^{1.5}$
B: excited magnetization, f: frequency, G: dimensionless geometrical factor 0.1356,
S: cross-sectional area, V0: phenomenological parameter, ρ: electrical resistivity of material.
Figure4 shows that calculated excess loss has a good agreement with measured data.

[1] T.Saito, S.Takemoto and T.Iriyama, IEEE Transactions on Magnetics, Vol.41, No.10, 2005, p3301

[2] S.Takemoto and T.Saito, Materials Science Forum Vols. 534-536, 2007, p1313-1316

[3] S.Takemoto and T.Saito, Proceedings of the 2004 WORLD CONGRESS OF POWDER METALLURGY & PARTICULATE MATERIALS, 2004

[4] H. Shishido, S. Goto, T. Kan and Y. Ito, IEEJ Technical Committee on Magnetics, MAG-85-13, 1985, P13

[5]R. H. Pry and C. P. Bean, Journal of Applied Physics, vol29,No.3, p532(1958)

[6]Giorgio Bertotti, Hysteresis in Magnetism, p428, 1998, (by Academic Press, Inc.)

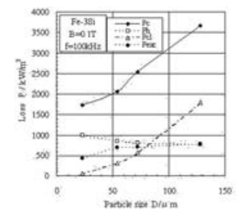
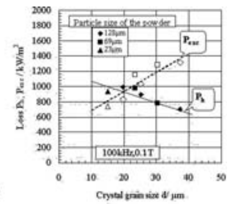

Fig.1 Losses decomposed into Ph, Pcl and Pexc in various particle size. Fig.2 Correlation between hysteresis loss and excess loss and crystal grain size.

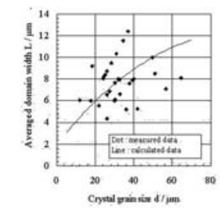
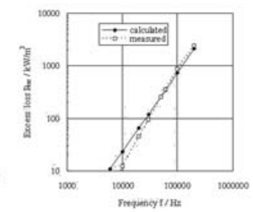

Fig.3 Correlation between crystal grain size and averaged domain width. Fig.4 Comparison of calculated excess loss with measured data

CF-06

Effect of surface magnetic domain structure on iron loss of thin-gauged 3% si-fe sheets.

H. Jung[1], J. Kim[1], S. Kim[2]

1. Metallurgy and Material Science, Hanyang University, Ansan, South Korea; 2. Machinery and Materials Group, Korea Electric Power Research Institute, Taejeon, South Korea

Introduction

Fe-3% Si grain-oriented silicon steel with {110}<001> Goss texture has been widely used for transformer cores. Currently, reducing the iron loss of the silicon steel is one of the most important industrial issues because of high oil price. Up to now, many methods regarding the reduction of iron loss have been developed including improvement in {110}<001> Goss alignment, reduction of sheet thickness and refinement of magnetic domain wall spacing. [1,2] In particular, thin-gauged 3% Si-Fe sheets with excellent Goss texture were recently developed through a tertiary recrystallization method, which was induced by the surface energy difference between (110) and other grains.[3] Through this recrystallization process, the thickness of the thin-gauged sheets was down to 0.1 mm, which effectively reduced the eddy current loss. However, few researches have been conducted on domain structures related to iron loss in the thin-gauged sheets. In this paper, we investigated the effects of domain structure on the iron loss of thin-gauged 3% Si-Fe sheets using a MOKE microscope and Bitter patterns.

Experimental Procedures

Thin-gauged 3% Si-Fe sheets with a thickness of 150 μm were prepared by hot and multistage cold rolling process including an intermediate annealing followed by conventional vacuum induction melting. The detailed procedure was in other literature. [3] After fabricating the thin-gauged sheets, the orientation of each grain was identified by an etch-pit method. Magnetic induction under an external magnetic field strength of 800 A/m, which was referred to as B10(T), was measured using a DC flux meter and an open-circuit method. Iron loss was measured by an H-coil method. In this H-coil method, the maximum magnetic-flux density, Bm, was 1.7 Tesla and the frequency of AC field was 50Hz. The domain patterns was observed by a Bitter method and the dynamic domain behaviors were observed by a MOKE microscope. For domain observation, the surfaces of the thin-gauged sheets were prepared by electrical polishing at 1 A in mixed perchloric and acetic acid (3:1). In order to observe Bitter patterns, magnetite (Fe3O4) particles with a size of 20 nm were prepared by a sol-gel process and an optical microscope was used. An observation of domain patterns using MOKE microscopy was performed after applying an AC field of the 8 kA/m along the rolling direction of the thin-gauged sheet.

Results and Discussions

Table 1 shows magnetic induction and iron loss values of four different thin-gauged 3% Si-Fe sheets. As indicated in the table, the magnetic induction values of four sheets are closed to a theoretical value of 2.05 Tesla. This indicates that Goss texture is well developed in all sheets. Despite of these analogous magnetic induction values, four sheets show the very different iron loss values. Figure 1 shows the schematic diagrams of microstructures and corresponding magnetic domain images of four sheets. In all samples, 180o strip domains are well developed and lancet domains are also formed inside the strip domains. The presence of the lancet domains indicates that the sheet normal direction, <110>, is tilted to <001> direction. Compared with Table 1, the domain images clearly show that the formation of tilted 180o strip domains result in high iron loss. Although several small disoriented grains to Goss texture are developed and have closure and spike domains, the iron loss of Sample 3 is very small, which results from low Eddy current loss. These results suggest the desirable microstructure of the thin gauged sheets for low iron loss.

[1] E. T. Stephenson, J. Appl. Phys. 55, 2142 (1984).

[2] J. L. Walter and C. G. Dunn, Trans. AIME. 215, 465 (1959).

[3] N. H. Heo, K. H. Chai, J. G. Na. Acta Mater. 48. 2901-2910(2000).

	B10(T)	Iron loss (W/kg)
Sample 1	1.94	1.94
Sample 2	1.97	1.37
Sample 3	1.94	1.23
Sample 4	2.00	1.21

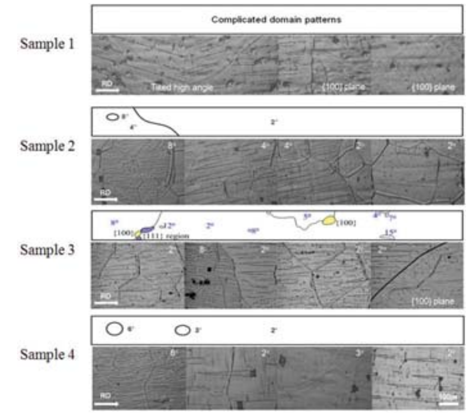

Figure 1 Disorientation of grains and corresponding Bitter patterns of thin-gauged 3% Si-Fe sheets

CF-07

Specific total loss components under axial magnetization in electrical steel sheets with different degree of Goss texture.

W. Pluta
Electrical Engineering Faculty, Czestochowa University of Technology, Czestochowa, Poland

1. Introduction
The efficiency of electrical machines is improved in between by the improve of electrical steel sheets quality [1]. Several years ago the specific total loss was measured at peak flux density equal to 1.0 T, later at 1.5 T and presently more and more the value 1.7 T is used for classification. This increase from 1.0 to 1.7 T also confirms both material and instrumentation improvements, particularly specific total loss decrease in electrical steel sheets.
The aim of the paper is to provide a contribution to the better understanding of specific total power loss in electrical steel sheets with different degree of Goss texture.
2. Measurement procedure
The experiment was carried out on grain-oriented (GO) and non-oriented (NO) electrical steel sheets with different texture degree κ. The texture degree was defined as a ratio of the volume of (110) [001] oriented crystals to the total volume of the sample and determined by using the anisometric method [2, 3].
The measurements of specific total power loss were carried out in a standard Epstein frame on samples magnetized along RD at 20, 50 and 150 Hz to allow separation of the specific total power loss into three components by the use of Bertotti's model [4].
3. Experimental data
The specific power loss P_S for GO (grades M140-27S, M150-30S and M165-35S) do not significantly differ – from scientific point of view - from each other. GO sheets posses degree of Goss texture 96%, 85% and 59%, respectively. The NO electrical steel sheets (grades: M300-35A and M470-50A) with lower Goss texture (15% and 10%) posses significantly higher specific total loss. The specific total loss of electrical steel consists of three components: hysteresis loss component and both classical and additional eddy current loss components. It was found that all three components are dependent on anisotropy i.e. degree of Goss texture and the dependencies show different trends as the magnetic flux density increases. The sum of eddy current losses increase nearly linear above 1.1 T as the maximum permeability was reached. The dependency of the additional loss on flux density shows also that the electrical resistivity has smaller influence on loss than the thickness of the sheets. This is also shows the nature of additional loss on which higher influence has the domain structure.
The relative additional loss factor η describes the ratio of the sum of classical and additional eddy current loss components to the value of classical eddy current loss component. The additional loss factor η for non-oriented electrical steel M470-50A is changing slightly with flux density but together with increase of grain orientation the dependence of the factor η on flux density become more non-linear. The non-linearity is higher at low flux densities and for GO steel.
Often in electrical machines design is used the loss separation factor Γ, which is the ratio between hysteresis and eddy current losses (considered together: classical and additional components). According to the practical knowledge, the loss separation factor Γ = (20 : 80)% in GO electrical steel and Γ = (60 : 40)% in NO electrical steel sheets [5]. The values of the additional loss factors η and ratio Γ are not commonly presented in literature and the assumption of constants ratio Γ for non and grain-oriented steel sheets is practically to simple.
The ratio Γ changes significantly from grade of electrical steel sheets according to texture degree κ and value of flux density. As the texture increases the ratio Γ increases faster, the hysteresis loss become less important and the eddy current loss opposite. In GO steel the ratio Γ changes significantly with high flux density opposite to the NO sheets. as the domain structure is reduced importance of eddy current loss components decreases and the hysteresis loss become more significant. In low texture degree k steels hysteresis loss is dominant and the ratio Γ do not change significantly with flux density in comparison to grain-oriented sheets.
5. Conclusion
The specific power loss separation was performed by means of Epstein frame measurement at three frequencies. The specific total power loss components in electrical sheets (with orientation 10, 15, 59, 85 and 96 percent) are strongly dependent on texture degree. In NO electrical steel sheets the hysteresis loss is the main component of specific total loss and in GO steel the eddy current loss components are more significant. The the additional loss factor η is strongly dependent on both flux density and the texture degree. The loss separation factor Γ differs significantly from the values most often mention in literature. Factor Γ depends on the texture degree and flux density and it could be about 50% to 50% in steel with grain orientation about 50 %. The changes of factor Γ with flux density is wider range in GO steel.

[1] Kubota T. et.al., J. Magn. Magn. Mater. vol. 215-216, pp.69-73, 2000

[2] Pluta W.A.,Influence of the magnetic anisotropy on rotational power loss in electrical steel sheets with Goss texture. PhD Thesis, Technical University of Lodz, Lodz 2001 (in Polish)

[3] Moses A.J., Pluta W.A., Steel Research International, nr 06, pp. 450-454, June 2005

[4] Berttoti G.: Hysteresis in magnetism. Academic Press, 1998

[5] Soinski M., Moses A.J.: Handbook of Magnetic Materials, vol. 8, Elsevier Science B.V., 1994

CF-08

Three Dimensional Polycrystal Magnetic Field Analysis of Electrical Steel.

K. Fujisaki
1. Technical Development Bureau, Nippon Steel Corporation, Futtsu-city, Japan; 2. Graduate School of Environmetal Studies, Tohoku University, Sendai, Japan

Introduction
Electrical thin steel plate is used for electrical equipment such as a motor core or transformer [1], since it has a high permeability. Usually, electrical steel is selected by its magnetic property so as to obtain the high performance of the electrical equipment. Then the magnetic property is important for the electrical steel design as well as the electrical equipment design. To estimate the magnetic property, numerical calculation method is useful for the evaluation. Though micromagnetics calculation method based on Landau-Lifshitz-Gilbert equation is researched in magnetic domain [2], only a single crystal grain or a few numbers of crystal grains are possible to calculate. However, since the electrical steel consists of a lot of numbers of crystal grains, the micromagnetic calculation method is impossible to be applied to. To obtain the magnetic characteristics of polycrystal steel, three dimensional polycrystal magnetic field analysis is proposed and applied to the GO steel in this paper.
3D Polycrystal Magnetic Field Analysis
The polycrystal steel consists of a lot of numbers of crystal grains which are separated in crystal grain boundaries. In the proposed 3D polycrystal magnetic field analysis, it is assumed that each crystal grain has the same magnetized characteristics as the magnetized characteristics of a single crystal grain, which are given by the measurement of a single crystal or the calculation of micromagnetics. The crystal grains have their own different crystal orientations from each other. Therefore, each crystal grain is considered to have its own orthogonal local coordinates which is based on the crystal orientation and the polycrystal steel is considered to have its own total coordinates as shown in Fig.1. Then the coordinate transformation from the local coordinates to the total coordinates is introduced as equation (1) in this case.
Equation (1) : $[T]=[Rz(\alpha)][Ry(\beta)][Rx(\gamma)]$.
Here, α, β, γ are an angle around Z-direction (normal axis), Y-direction (hard axis), X-direction (easy axis) respectively from the total coordinates. By the coordinate transformation, the magnetic flux density from a point of view of the local coordinates is related to the one of the total coordinates. In the local coordinates, the magnetic flux density is decided in the given single crystal magnetic characteristics and the crystal orientation. Then the Maxwell equations are introduced from a point of view of the total coordinates. By solving the Maxwell equations in finite element method, the magnetic flux density distribution in the polycrystal steel is obtained in the condition that the total electromagnetic energy is minimized.
Calculation results
Fig.2 and 3 are calculation results of the GO (Grain Oriented steel) materials with 56 crystals in 80mm square obtained by the proposed calculation method. The GO materials has the strong crystal orientation near (110)[001] [3]. Each crystal has its own crystal angle of α, β, γ as shown in Fig. 2 and 3. The α angle distribution of the GO materials shows that magnetic flux density gathers in the #4 crystal grain, since the α angle of #1 crystal grain is almost zero and the one of #2 crystal grain is plus and the one of #3 crystal grain is minus. The calculated magnetic flux density distribution shows that the #4 crystal grain has large magnetic flux density as shown in Fig.2. In supplying external magnetic field in easy axis direction, the angle difference of the magnetic flux density is expected to be the same as the α angle of each crystal grain. They are in good agreement as shown in Fig.3.

[1] K. Fujisaki, S. Satoh, IEEE Trans. on Magn., Vol. 40, No.4, pp.1820–1825, (2004)

[2] D. R. Fredkin and T. R. Koehler, J. Appl. Phys. 63, 3179, (1988).

[3] T. Yamamoto, S. Taguchi, A. Sasakura and T. Nozawa, IEEE Trans. on Magn., vol.8, pp.677-681, (1972).

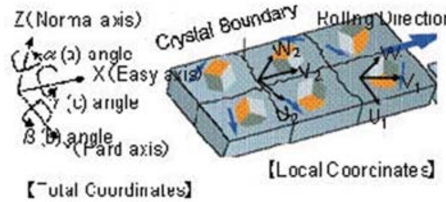

Fig.1. Total coordinates and local coordinates in each crystal.

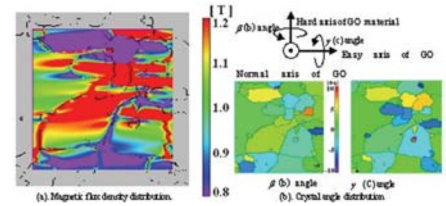

Fig. 2 Magnetic flux density distribution in GO materials (electrical steel) in supplying external magnetic field in easy axis direction.

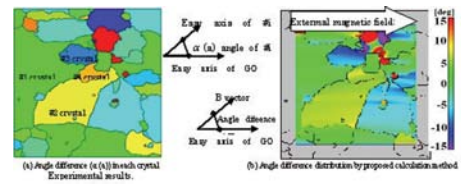

Fig.3. α angle distribution in each crystal grain of the GO material and angle difference of magnetic flux density vector distribution by proposed calculation method (35ZH,, Crystal grain number :56, Size :80mm2).

CF-09

Improvement of the Bertotti's formula for energy loss in soft magnetic materials.

K. Sokalski, J. Szczyglowski
TU Czestochowa, Czestochowa, Poland

The paper presents the application of the scaling theory to the description of energy loss in soft magnetic materials. The

postulated generalized description of energy loss has the form of series, dependent only on two exponents α and β. On the basis of measurement data it has been proved, that only two first terms of the series are relevant. For a wide class of soft magnetic materials, a universal linear dependence between α and β was obtained. The data collapse of energy loss, which confirms definitively the scaling hypothesis in the analyzed phenomenon, was also revealed. The Bertotti's formula of energy loss has been criticized in the light of the scaling theory.

The contemporary approach to energy loss phenomenon in soft

magnetic materials assumes that the total loss P_{tot} is the sum of described above contributions[1,2,3]

$P_{tot}=C_1 f B_m^{\gamma} +$
$C_2(f B_m)^2 +$
$C_3(f B_m)^{3/2}$ (1)

where: C_1,C_2,C_3 are constants.

The approach to energy loss, which assumes their additive character, allows for their separation and consequently for the independent analysis of the obtained components in different scales. However the results obtained in the

case of the modern materials of amorphous and microcrystalline structure reveal discrepancies between the theoretical and experimental values [4,5]. In the seventies of the past century the aforementioned approach to energy loss was criticized as being oversimplified. It was pointed out, that the energy loss phenomenon ought to be considerated as a total [4]. In order to find whether the discrepancy and the separation are correlated one should reconsider *ab initio* the source of separation in

(1). Following this line we focused our attention on the formula for the total density current $\mathbf{j}(\mathbf{r},t)$ being a result of the Barkhausen jumps at different random points $\mathbf{r}_i$ and at different random times t_i, presented in [1]

$\mathbf{j}(\mathbf{r},t)= \Sigma_{i=1}^{N}\mathbf{j}(\mathbf{r},t,\mathbf{r}_i,t_i)$,

where $\mathbf{j}(\mathbf{r},t;\mathbf{r}_i,t_i)$

is the contribution to $\mathbf{j}(\mathbf{r},t)$resulting from the Barkhausen jump at $(\mathbf{r}_i,t_i)$. This formula is a too rough approximation, because it does not correlate the events at $(\mathbf{r},t)$and $(\mathbf{r}_i,t_i)$.In order to improve (2) one should write down the following expression

instead of the aforegiven one

$\mathbf{j}(\mathbf{r},t)= \Sigma_{ti < t}$
$\mathbf{j}(\mathbf{r},t;\ \mathbf{r}_i,\ t_i)$
$\delta((\mathbf{r}-\mathbf{r}_i)^2-c_m^{\ 2}$
$(t-t_i)^2)$,

where c_m is the electromagnetic wave velosity in the considered material. The relationship (3) disables the derivation of the separation formula, whereas (2) leads to (1), which in general case for any given γ is not a homogeneous function, even though all its terms are homogeneous.

This contradiction results from the fact that all energy terms of this formula were derived independently of the others and next "artificially" summarized. This approach does not take into consideration the influence of these terms each other. We suspect that this contradiction in the Bertotti's formula is a reason of often observed discrepancy between the experiment and theory. Recently, an attempt to the application of the scaling theory in phenomenological description of energy loss in soft magnetic materials was made [6]. The obtained results pointed out on the validity of the assumptions and usefulness of the proposed

formula in practical applications, as well.

A heuristic argument has been developed into a coherent approach to understanding the ubiquity of scale invariance in a wider range of considered systems. By the scale invariance we mean a hierarchical organization that results as the homogeneity in generalized sense of functions describing properties of the considered complex system.

On the basis of the scale invariance of the considered system, it can be assumed, that the total energy loss in soft magnetic materials $P_{tot}=F(f, B_m)$

is given by a generalized homogenous function, where

P_{tot} - total energy loss, B_m - maximum magnetic induction, f - frequency of magnetizing field. This assumption leads to the following formula for energy loss [6]

$P_{tot} \approx B_m^{\ \beta}\ (\Gamma^{(1)}\ f/B_m^{\ \alpha} + \Gamma$
$^{(2)}\ (f/B_m^{\ \alpha})^2)$
(4)

where α, β, $\Gamma^{(1)}$ and $\Gamma^{(2)}$ are free parameters to be determined from the experiment. Measurement values of total energy loss for chosen magnetic materials and values of energy loss obtained from the scaling theory have been compared. The measurement and theoretical

data agree well, which confirms the expected improvement of the Bertotti formula.

On the basis of measurement data for all analyzed materials a relationship between the exponents α and β

was obtained in the following form

$\beta = 1.35\ \alpha + 1.75$. (5)

On the basis of presented results it could be stated, that the abovegiven relationship (5) is universal, whereas the exponents are not. The exponent values are dependent on the chemical composition of the material and the sample geometry.

[1] G. Bertotti, *Hysteresis in magnetism,* Academic Press, 1998.

[2] G. Bertotti, J. Magn. Magn. Mater. **112**, 253 (1984).

[3] G. Bertotti, IEEE Trans. Magn. **24**, 624 (1988).

[4] B. D. Cullity, *Introduction to magnetic materials,* Addison-Wesley, 1972.

[5] G. E. Fish, C.-F. Chang and R. Bye, J. Appl. Phys. **64**, 5370 (1988).

[6] K. Sokalski, J. Szczyglowski, M. Najgebauer and W. Wilczynski, *Losses scaling in soft magnetic materials* , COMPEL, **26**, 640 (2007).

CF-10

Influence of improving efficiency using Fe-P-B-Nb type ultra low loss glassy metal dust core on inductor for large-current.

H. Matsumoto, Y. Yamada, A. Urata
RESEARCH AND DEVELOPMENT UNIT, NEC TOKIN, Sendai, Japan

Introduction

As a result of the evident advancement of ubiquitous technology, information equipment applications, including those for notebook PCs are making significant progress and their power consumptions are increasing more and more. Following this trend, the supply of a high-speed, high-quality energy and the control of power consumption become big problems along with it in CPU. The achievement of a high level of power efficiency in the power supply circuit has become a high-priority issue. We observed the loss characteristic of metal inductors as well as their high-current compatibility and have developed Fe-P-B-Nb type soft magnetic material which is a new low-loss metallic glass composite material that can compactly achieve high-efficiency inductors for low-voltages and high-current power supplies. Fe-P-B-Nb type soft magnetic material is a metallic glass dust powder that features both a high saturated magnetic flux density (Bs=1.3T) that is proper to metallic materials and a stable amorphous structure proper to metal glass composite materials. There is no magnetic saturation under a high-current supply and it can therefore significantly reduce magnetic loss resulting from the effect of the core material. This paper reports the effect when applying to the loss characteristic and the inductor of Fe-P-B-Nb ultra low loss glassy metal dust core.

Experiments

Metallic glass powder that made Fe-based composition element was made by the water atomaiz method. The obtained metallic glass powder was observed particle shape by SEM, analyzed amorphous condition by XRD and metallic glass condition by DSC. Next, the made Fe-P-B-Nb metallic glass powder was mixed with the resin binder, and after granulation, the pressurizing molding was done to a constant particle size. The molding body of ring core (ϕ13mm×ϕ8mm×6.5mm) and the SMD choke coil (10mm×4mm and inductance 0.56 uH) was made. Permeability (1mA, 100kHz) and core loss (50mT, 300KHz) were measured in the made ring core.

Moreover, the SMD choke coil was mounted on voltage step down DC/DC converter evaluation board (MAXIM 1717 Evolution Kit), and power load efficiency was evaluated. Additionally, the rise in heat of the inductor according to the change of the current by the SMD shape was simulated based on the loss characteristic in the core.

Results and discussion

Fig.1 shows the results of a loss comparison between Fe-P-B-Nb type glassy metal and Fe-type amorphous dust material. It shows that the loss of Fe-P-B-Nb type glassy metal is 1/2 compared with iron powder, is 1/3 and a very low loss compared with Fe-type amorphous material. Fig.2 shows the improvement of the power load efficiency confirmed by the use of Fe-P-B-Nb glassy metal for the core of SMD choke coil. The graph shows that the use of Fe-P-B-Nb glassy metal has improved the effective efficiency all over the load current range from 0.1A to 10A. In particular, in the low-current range below 5A where the hysteresis loss has occupied an important share, the efficiency has been improved by more than 1.5%.

Fig.3 shows the results of the simulation of change of inductor surface temperature in SMD choke coil that used glassy metal and iron powder. The graph shows the possibility that generation of heat of the inductor can be controlled compared with iron powder by using Fe-P-B-Nb glassy metal.

Conclusion

We succeeded in the decrease of the loss of the core material by using Fe-P-B-Nb glassy metal, and the improvement of the inductor loss. Additionally, the possibility that it becomes easier to design the temperature in the power supply circuit was confirmed by generated heat about the inductor being suppressed.

[1] Y. Yamada, A. Urata and H. Matsumoto, Japan Society of Powder and Powder Metallurgy, 194, 2006.

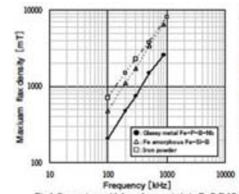

Fig.1 Comparison with loss characteristic in Fe-P-B-Nb glassy metal, Fe amorphous and Fe powder

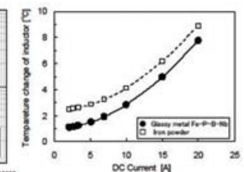

Fig.3 Temperature change of inductor in Fe-P-B-Nb glassy metal and Fe powder

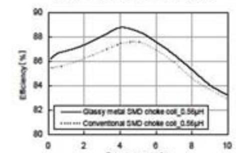

Fig.2 Power load efficiency characteristic

CF-11

Soft-magnetic Fe-based nanocrystalline thick ribbons.

M. Lee[1], C. Lin[1], *S. Wang*[1], T. Chin[2]
1. Department of Materials Science and Engineering, National Tsing Hua University, Hsinchu, Taiwan; 2. Department of Materials Science and Engineering, Feng Chia University, Taichung, Taiwan

Introduction

Since 1974, (Fe, Co)-Si-B, (Fe, Co, Ni)-(Cr, Mo, W)-C, (Fe, Co, Ni)-(Zr, Hf) and (Fe, Co, Ni)-(Zr, Nb, Hf)-B amorphous alloy systems were developed and they exhibited superior soft magnetic properties[1]. These have been widely used in the transformer cores that were wound from ribbons with the thickness around 30 μm[2]. Subsequently, Fe-based alloys with nano-crystalline structure were developed, such as FINEMET and NANOPERM, which exhibited much superior soft-magnetic properties their amorphous counterparts.

Recently, amorphous ribbons with thickness up to 220 μm exhibiting low core loss and good soft magnetic properties was developed in Fe-Al-Ga-P-C-B-Si[3]. This remarks a great improvement in developing "thicker" amorphous ribbon. In this study we intended to develop nano-crystalline thick ribbons from compositions modified from ternary Fe-B-Y BMG compositions by substituting Y with Ta and Ag. Our target was to obtain thick ribbons at thickness up to at least 100 μm, in which Ta was to replace the highly oxidative Y while Ag served as the nucleation agent to induce nano-crystalline structure. Structural, thermal and magnetic properties of the nano-crystalline thick ribbons were investigated and are disclosed in the article.

Experimental

$Fe_{71}B_{22}Ta_xY_{6-x}Ag_1$ (x= 1 ~ 5) ribbons with different thickness were prepared by the melt-spinning technique under Ar atmosphere. The ribbons were then post annealed at a temperature upon which proper crystallization occurred. The properties of ribbons were analyzed by XRD, DTA, VSM, and TEM.

Results and Discussion

DTA result of $Fe_{71}B_{22}Ta_xY_{6-x}Ag_1$ amorphous ribbon showed glass-transition temperature (T_g) and crystallization temperature (T_x) are 565 °C and 605 °C, respectively. $Fe_{23}B_6$ becomes the main crystalline phase as the annealing temperature is increased as shown in Fig. 1. According to the Scherrer equation, the grain sizes of the bcc-Fe and $Fe_{23}B_6$ can be calculated from the FWHM and found to vary from 20 - 36 nm and 16 - 24 nm in properly annealed samples, respectively. From TEM observation of the ribbon annealed at 615 °C, the structure consists of nano-crystalline mixture of bcc α-Fe and $Fe_{23}B_6$ phases. The average crystallite size of α-Fe and fcc $Fe_{23}B_6$ is around 19 nm, being typically the same for the two nano-crystalline phases. At higher annealing temperatures, the major crystalline phase becomes $Fe_{23}B_6$. In Fig. 2, the ribbons show good soft magnetic properties that saturation magnetization and coercivity are around 1.44 T (152 emu/g) and 35 A/m, respectively. By annealing for a longer time, the crystallite consists of the major $Fe_{23}B_6$ phase, however the ribbons still show good soft magnetic properties such as high saturation magnetization ~ 140 emu/g (1.31 T) and low coercivity ~ 46 A/m, respectively. Table 1 indicates a comparison in soft magnetic properties of our thick ribbons with some other ribbons. The effective permeability of our thick ribbon is superior. It is concluded that a new nano- crystalline thick ribbons have been developed in Fe-B-Ta-Y-Ag system with good thermal stability, glass forming ability and sound soft magnetic properties. These thick Fe-B-Ta-Y-Ag nano-crystalline ribbons show great potential in future applications.

[1] A. Inoue, A. Makino, T. Mizushima: J. Magn. Magn. Mater. 215-216, 246 (2000)

[2] T. Masumoto (Ed.): Materials Science of Amorphous Metals, Ohm, Tokyo, (1982)

[3] T. Mizushima, A. Makino, S. Yoshida, A. Inoue: J. Appl. Phys. 85, 4418 (1999)

Alloy system	Saturation magnetization (Tesla)	Coercivity (A/m)	Thickness (μm)	μ_e (at 1kHz)
$Fe_{71}B_{22}Ta_5Y_1Ag_1$	1.44	35	150	28000
$Fe_{77}Al_{2.14}Ga_{0.86}P_{8.4}C_5B_4Si_{2.6}$ [3]	1.5	3	30 ~ 220	12000
$Fe_{78}Si_9B_{13}$ [1]	1.56	3.5	50	10000

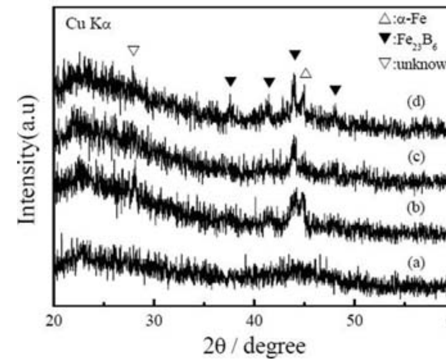

Fig. 1 XRD patterns of $Fe_{71}B_{22}Ta_5Y_1Ag_1$ ribbons, (a) as-quenched, (b) annealed at 615 °C for 5 minutes, (c) annealed at 630 °C for 3 minutes, (d) annealed at 630 °C for 5 minutes

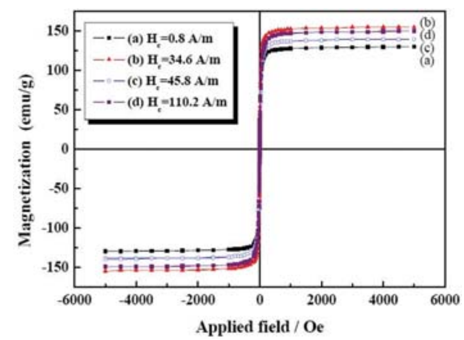

Fig. 2 M-H loops of $Fe_{71}B_{22}Ta_5Y_1Ag_1$ ribbons after different annealing conditions

CF-12

Gas flow effects to the magnetic properties of current annealed Vitroperm samples.

V. de Manuel[1], R. Pérez del Real[2]
1. Space Programs and Space Sciences, INTA, Torrejón de Ardoz, Spain; 2. Space Programs and Space Sciences, INTA, Torrejón de Ardoz, Spain

Current annealing of Finemet-like samples has many advantages compared with furnace annealing: it is a faster technique [1] and samples show smaller grains [2-4] together with better mechanical properties [5].

Other interesting results have been found when current-annealed samples were 'over-annealed', that is, when harder phases (FeB and big FeSi crystals) appear at temperatures over 650 C. After this kind of annealing the hysteresis loops reported were sometimes constrained (making them useful for fabricating magnetic labels [6]). These exotic results come from the fact that this technique is very sensitive to environmental conditions. In this work, it is presented how the effect of gas flow during current annealing can critically affect the magnetic properties of the sample.

Three Vitroperm® ($Fe_{73}Si_{16}B_7Nb_3Cu_1$) samples ($100\times8.3\times0.023$ mm^3) were annealed during 60 s with a computer-controlled Agilent® 3634 power source. The current density was $J=36.67\times10^6$ A/m^2 DC.

All samples were placed in a sealed chamber during annealing with a controlled overpressure of Ar. A valve at the inlet of the system, a manometer and a second valve at the outflow were used to control the flow of Ar escaping the chamber. The pressure inside the chamber, with the outflow valve completely opened, was set to 4 mbar (A), 10 mbar (B) and to 20 mbar (C) (initial presure P_0) controlling the opening of the inlet valve, which connected the Ar bottle with the system. Once set, the outflow valve was closed until reaching a value of 40 mbar. Thus, the Ar flow inside could be indirectly controlled during the annealing process, being proportional to P_0. The pressure during annealing was kept constant at 40 mbar in order to keep all annealing conditions of every sample constant except for the Ar flow.

The hysteresis loops are shown in figure 1.

Sample A had the lowest flow, and almost no heat exchange between the sample and the surrounding gas occurred. That is why the temperature of the sample was very homogeneous and the heat was enough to create FeB and big FeSi crystals showing the typical hard loop.

Sample C had the highest flow and therefore the heat exchange during annealing was enough to create only FeSi nanocrystals distributed homogeneously over the sample surface showing a soft hysteresis loop.

Sample B had enough gas flow to create such a temperature gradient that the sample got nanocrystallized creating FeSi nanograins (which corresponds to the softer phase) at the borders and crystallized creating FeB and big FeSi crystals at the center (which corresponds to the harder phase). For this reason it shows a constrained loop.

In order to prove this hypothesis, two pieces of sample B were taken: one from the center (sample B1) and the other from one edge (sample B2). Both hysteresis loops were measured with a VSM, obtaining the results in figure 2. A hard hysteresis loop for sample B1 with a coercive field of 14.97 Oe and a soft loop for sample B2 with a coercive field of 0.05 Oe are obtained demonstrating that a gradient existed during the annealing. As a conclusion, the magnetic properties of the samples can be tailored just by changing the gas flow during annealing.

[1]- P. Allia, P. Tiberto, M. Baricco, F. Vinai, dc joule heating of amorphous metallic ribbons: experimental aspects and model, Rev. Sci. Instr. 64 No. 4, 1053-1060 (1993).

[2]- R. Houssa, V. Franco, A. Conde, Microstructure of a FeSiB-Cu-Nb alloy submitted to Joule heating, Jour. Magn. Mag. Mat. 203, 199-201 (1999).

[3]- A. Gupta, N. Bhagat, G. Principi, A. Maddalena, N. Malhotra, B.A. Dasannacharya, P.S. Goel, H. Amenitsch, S. Bernstorff, Nanocrystallisation of amorphous alloys: comparison between furnace and current annealing, Intermetallics 8, 287-291, (2000).

[4]- Z. H. Lai, H. Conrad, G. Q. Teng, Y. S. Chao, Nanocrystallization of amorphous Fe-Si-B alloys using high current density electropulsing, Mat. Sci. Eng. A 287, 238-247 (2000).

[5]- P. Allia, P. Tiberto, M. Baricco, M. Knobel, F. Vinai, Nanostructured Materials for Soft Magnetic applications produced by Fast dc Joule Heating, IEEE Trans. Mag. 30, No.6 4797-4799 (1994).

[6]- P. Gupta, A. Gupta, V. Franco, A. Conde, Joule heating as a technique for obtaining uncoupled soft and hard magnetic phases in a Finemet alloy, Jour. App. Phys. 101 (2007).

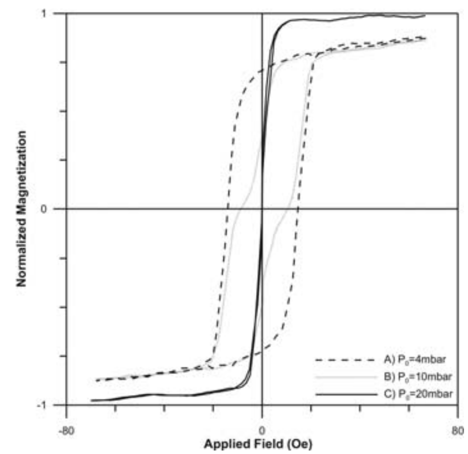

Hysteresis loops of the entire annealed samples.

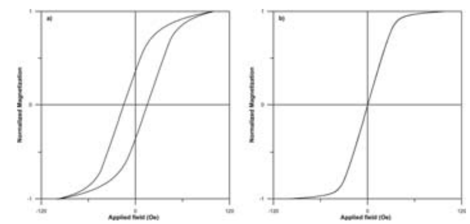

Hysteresis loops measured with a VSM for a) a piece of B taken from the center (B1) and b) a piece of B taken from one edge (B2).

Routes to Create Ultrathin Co Films with Perpendicular Magnetic Easy Axis.

S. Gallego, C. Muñoz
Inst. Ciencia Materiales Madrid, Madrid, Spain

The characteristic length scales governing the processes of magnetic reorientation and exchange in Co [1] make Co nanostructures specially appealing. Recently we have proved the existence of a double magnetic reorientation transition (MRO) in ultrathin Co films of 1-3 monolayers (ML) thickness grown on Ru(0001) substrates [2]. The uniqueness of such MRO is based on the correlation between magnetic orientation and ML completion, and on the ultrathin thickness of the film. Our ab-initio calculations of the magnetic anisotropy energy (MAE) demonstrate the fundamental role of the structural distortions on the MRO: there exists a 8% mismatch between the in-plane lattice parameters of Ru and Co, and it is the tendency of both elements to recover their own atomic volume which lies at the origin of the MRO.
The apparent simplicity of the Co/Ru(0001) ultrathin films hiddens in fact a complicated structure. Stacking faults at the Co/Ru interface altering the perfect hcp sequence have been observed [3]. The effect of stacking faults on the MAE has never been analyzed previously. In a pioneering work, we have investigated the MAE of the ultrathin Co films considering the existence of the experimentally observed stacking faults, both in the very low thickness regime (1-3 ML) and for larger thicknesses up to 7 ML. A different behaviour appears for both regimes, as evidenced in figure 1. In the lower thickness limit, the existence of a stacking fault altering a perfect hcp (AB/AB) or fcc (ABC/ABC) sequence doubles the MAE, improving the low values obtained in [1] where the stacking faults were not included. For thicker films, the magnetic easy axis varies depending on the global fcc or hcp structure of the Co film, with almost no influence of the stacking fault at the Co/Ru interface. While the magnetization lies in the surface plane at the fcc films, a perpendicular magnetization can be obtained for hcp structures.
The stabilization of Co films with perpendicular (to the surface plane) magnetic easy axis is of technological interest. Our investigations show that the key ingredient to obtain such structures is to stabilize hcp structures with an expanded in-plane lattice parameter (figure 2). The usage of Ru(0001) substrates achieves this goal for 2 ML thick films. However, the tendency of the Co film to distort towards a Co lattice upon increasing thickness makes necessary the search of additional routes to maintain the expanded two-dimensional (2D) Co lattice. A promising mechanism is the use of capping layers. On one side, a capping layer enhances the MAE of the Co film, expanding the range of thicknesses for which the MRO occurs (see figure 3 and ref. [4]). On the other, the adequate choice of the capping element helps to stabilize the expanded Co structure, thus favouring the perpendicular magnetic easy axis.
In this talk we will show all these results with detail, justifying the microscopìc origin of the obtained MAE and quantifying the interplay between strain, stacking and hybridization effects which allow to tune the magnetic properties of ultrathin Co films and, in particular, their magnetic anisotropy.

[1] Y. Shiratsuchi et al., Progress in Surface Science 82, 121 (2007).

[2] F. El Gabaly et al., Phys. Rev. Lett. 96, 147202 (2006).

[3] F. El Gabaly et al., New Journal of Physics 9, 80 (2007).

[4] J. de la Figuera (private communication).

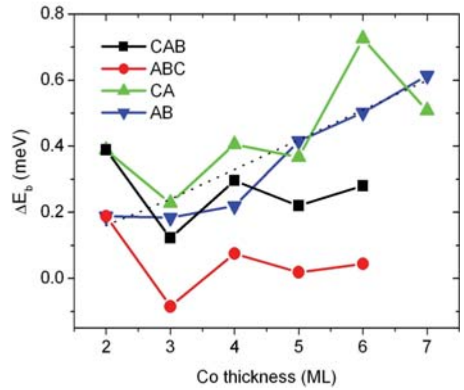

Evolution of the band energy contribution (Eb) to the MAE versus Co thickness for different stacking sequences of the Co/Ru(0001) system. The dotted line represents the dipole energy contribution (Edd), so that a perpendicular easy axis corresponds to the structures where Eb is larger than Edd.

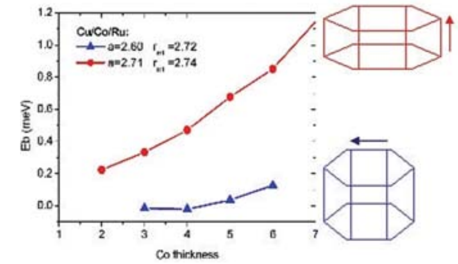

Band energy contribution vs. Co thickness for Co/Ru(0001) capped with 1 ML of Cu. The two curves correspond to two different hcp lattices with the same atomic volume.

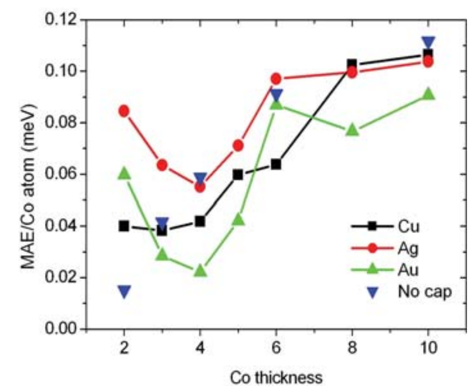

MAE per Co atom of the Co/Ru(001) system for different Co thickness in the presence of 1 capping layer of different noble metals.

CG-02

Perpendicular magnetic anisotropy at Co/Oxide interfaces.

Y. Dahmane, S. Auffret, U. Ebels, B. Rodmacq, B. Dieny
CEA Grenoble, Grenoble, France

For many spintronics applications, it is of increasing interest to use magnetic materials with perpendicular magnetization. We are currently developing new materials with exceptionally large perpendicular magnetic anisotropy (PMA) for various applications such as magnetic electrodes of tunnel junctions (MTJ) or perpendicular polarizers for RF oscillators [1].

Most of MTJ based on Al or Mg oxides require relatively high temperature annealing treatments (up to 350°C for magnesium oxide) in order to reach the largest possible TMR ratio. For such high temperatures, classical (Co/Pt) multilayers can no longer be used since, due to intermixing, PMA properties rapidly degrade with increasing annealing temperature and vanish for temperatures as low as 200 to 250°C. A similar problem due to recrystallization takes place with rare earth transition alloys.

Following previous investigations on oxygen-induced PMA in Pt/Co/oxide trilayers [2], we present here a study of the evolution of PMA in similar structures as a function of both Co thickness and thermal treatments.

Samples of the form substrate/Ta3/Pt20/Cot/AlOx/Cu2/Pt2 (in nm) were prepared by conventional dc-sputtering at room temperature. The oxide layer was obtained by natural oxidation (10 min, 170 mbar oxygen pressure) of a metallic aluminium layer. Annealing treatments were performed in a vacuum furnace at increasing temperatures from 150 to 350°C. Magnetic measurements were performed after annealing using Hall Effect, the magnetic field being applied either perpendicular to the plane, or in-plane for anisotropy field measurements.

Figure 1 shows, for the complete structure given above, with Al thickness of 0.5 nm, the hysteresis loop obtained in the as-deposited state for a Co thickness of 0.4 nm, the magnetic field being applied in the perpendicular direction. We obtain a square loop with 100% remanence, characteristic of a single domain perpendicular magnetization. The perpendicular magnetic anisotropy is quite large for this sample, since an in-plane field of 20 kOe is necessary to saturate the magnetization in plane.

The effective anisotropy per unit volume of Co film was derived from the saturation field measured with field applied in-plane for samples with out-of plane anisotropy and with field applied out-of-plane for samples with in plane anisotropy (Keff=MsHsat/2). Figure 2 shows the Co thickness (tCo) dependence of Keff*tCo for the as-deposited and 350°C annealed samples. Bulk and interfacial anisotropy can be separated by writing Keff*tCo=Kv*tCo+KsCo/Pt+KsCo/AlO. Fig 2 shows that whereas the bulk anisotropy almost does not vary with annealing temperature, the interfacial anisotropy dramatically increases upon annealing. Since it is well known that the interfacial anisotropy at the Pt/Co interface decreases with annealing and vanishes after annealing at 200°C, this implies that the very large anisotropy observed at 350°C is entirely due to the Co/AlOx interface. Interfacial anisotropy as large as 1.6 erg/cm2 has been observed (Fig.2). This is larger than all interfacial anisotropy ever reported in polycrystalline or epitaxial (Pt/Co) multilayers in as-deposited state and a fortiori after annealing [3].

As a consequence of this very large interfacial anisotropy, the reorientation transition between out-of-plane and in-plane anisotropy now occurs for a Co thickness of 2.7 nm which is exceptionally large in such structure.

[1] D. Houssameddine, U. Ebels, B. Delaët, B. Rodmacq, I. Firastrau, F. Ponthenier, M. Brunet, C. Thirion, J.-P. Michel, L. Prejbeanu-Buda, M.-C. Cyrille, O. Redon, and B. Dieny, Nature Materials 6, 447-453 (2007)

[2] B. Rodmacq, S. Auffret, B. Dieny, S. Monso, P. Boyer, J. Appl. Phys. 93, 7513 (2003)

[3] M.T Johnson, P.J.H. Bloemen, F.J.A. den Broeder, J.J. de Vries, Rep. Prog. Phys. 59, 1409 (1996)

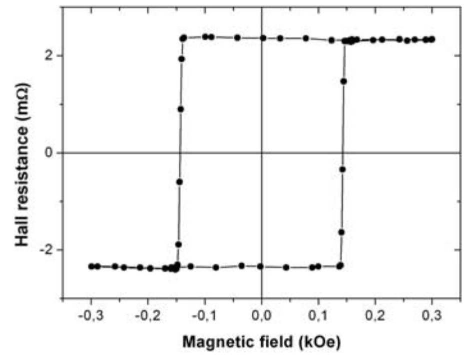

Figure 1: Hall Effect loop for a sample of composition Ta3/Pt20/Co0.4/AlOx/Cu2/Pt2 in the as-deposited state. The applied magnetic field is perpendicular to the layer plane

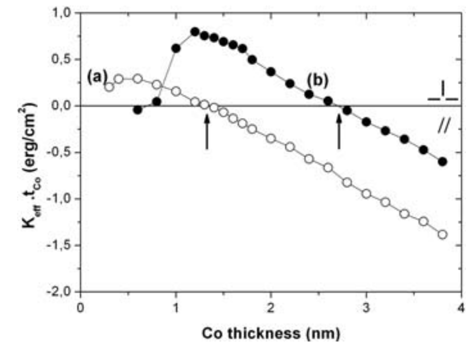

Figure 2: Variation of the product of the anisotropy energy by the Co thickness versus Co thickness for the as-deposited samples (a) and after annealing at 350°C (b). The slope is related to the bulk anisotropy whereas the intercept with vertical axis gives the interfacial anisotropy

CG-03

Giant magnetic anisotropy of Fe_3Pt alloy thin films with various crystallographycal orientations.

H. Yamamoto, *T. Suzuki*
Information Storage Materials Laboratory, Toyota Technological Institute, Nagoya, Japan

It was reported that the "quasi" $L1_2$ ordered phase of Fe_3Pt alloy thin films deposited onto MgO single crystal substrates exhibits huge magnetic anisotropy constants (K_1=-4×10^6, K_2=2×10^7 erg/cc)[1]. Theoritical calculation also predicted that Fe_3Pt alloy thin films could possese a large in-plane magnetic anisotropy in deforming fcc to fct or m-DO_{19}[2]. However, the origin of this giant magnetic anisotropy of Fe_3Pt alloy thin films is still open to question. Therefore, the purpose of this study is to elucidate the origin of such a giant magnetic anisotropy.

Alloy thin films of Fe_3Pt were fabricated by electron beam evaporation onto MgO(100), (111) and (110) substrates held at various deposition temperatures, T_s. The film thickness for all the samples was about 500 Å. The structural analyses were carried out by a XRD (Cu-K_α). Magnetization, M_s were measured by using a VSM. K_1 and K_2 were evaluated by torque magnetometer. K_1, K_2 and M_s of Fe_3Pt alloy thin films were investigated as a function of temperature, T for various crystallographical orientations.

From both the high angle and low angle X-ray diffraction analyses, the Fe_3Pt alloy thin films grown onto MgO substrates are found to be single crystalline films. Fig.1-(a) shows K_1 and K_2 of Fe_3Pt alloy thin films fabricated at various T_s. The maximum K_1 and K_2 values of the Fe_3Pt alloy thin films fabricated onto MgO(110) are 3×10^7 and -6×10^7 erg/cc, respectively. These values of K_1 and K_2 are larger than the values of the Fe_3Pt alloy thin films fabricated onto MgO(100) and MgO(111)(K_1 and K_2 are -4×10^6 and 2×10^7 erg/cc, respectively). Furthermore, the signs of K_1 and K_2 are oposite to those of the Fe_3Pt alloy thin films on MgO(100) and MgO(111). Fig.1-(b) shows the degree of ordering, S of Fe_3Pt alloy thin films. The Fe_3Pt films start to be ordered at about T_s=200 ^{o}C, increasing with T_s. Fig.1-(c) shows lattice constant ratio, c/a which changes with T_s. This variation of K_1 and K_2 with S suggests that there exists a strong relationship between the magnetic anisotropy and S.

The $L1_2$ phase and the m-DO_{19} phase are shown in Fig.2. In the bulk phase, *l* of the Fe_3Pt alloy is 2.64 Å. It is predicted that an 2% expansion of *l* reduces the energy difference between the $L1_2$ phase and the m-DO_{19} phase by theoritical calcultion[3]. Fig.3 shows K_1 and K_2 increase with *l*. Furthermore, the maximum expansion of *l* is 1.8%. This result might suggest that the m-DO_{19} phase stablized by the expansion of *l* is responsible for the giant magnetic anisotropy of the Fe_3Pt alloy thin films.

Fig.4 shows the relation between K_1, K_2 and $[M_s(T)/M_s(R.T.)]^2$. It is observed that the temperature dependences of K_1 and K_2 are very close to the curve of $[M_s(T)/M_s(R.T.)]^{1.8}$. The dependence for Fe_3Pt is, within the accuracy of experiment, consistent with the theoritical prediction of M^2 for the two-ion model put forward by O.N.Mryasov et al. for the case of $Fe_{50}Pt_{50}$[4].

[1]M. A. I.Nahid and T. Suzuki, J. Mag. Magn. Mat,286, 315(2005).

[2]J. M. MacLaren, et al., IEEE Trans. Magn. 41, 12, 4374(2005)

[3]R. R. Duplessis, et al., J. Appl. Phys., 95, 6589(2004)

[4]O. N. Mryasov, et al., Europhys. Lett. 69, 805(2005)

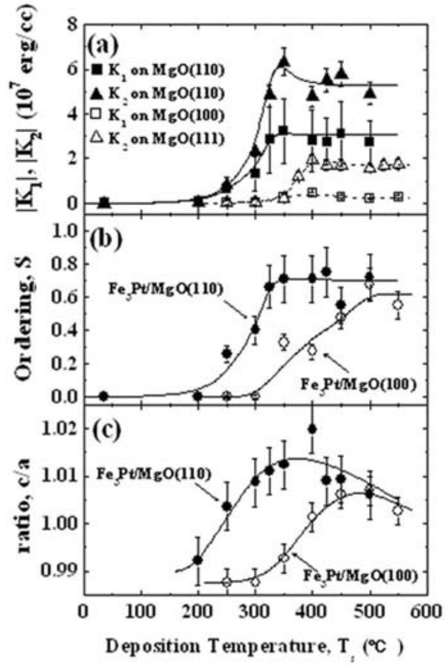

Fig.1 (a)K_1 and K_2, (b)S, and (c)c/a of the Fe_3Pt alloy thin films grown onto MgO(100),(111),(110)substrates at the various T_s.

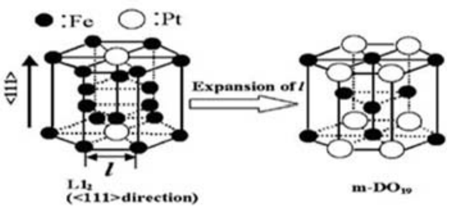

Fig.2 $L1_2$ and m-DO_{19}.

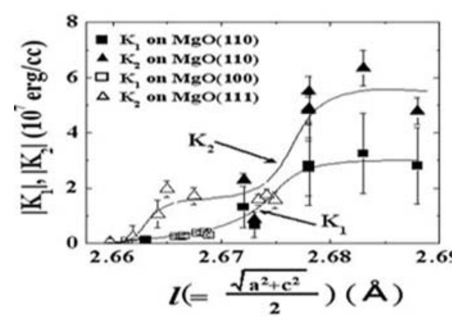

Fig.3 *l* vs K_1 and K_2 of the Fe_3Pt alloy thin films grown onto MgO(100), MgO(111), MgO(110) substrates.

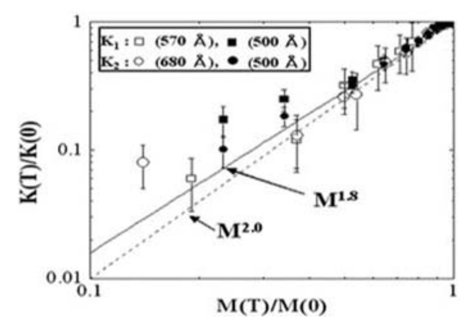

Fig.4 Temperature dependence of K_1, K_2 and $[M_s(T)/M_s(R.T.)$ of the Fe_3Pt alloy thin films grown onto MgO(100) and MgO(111) substrates.

CG-04

Uniaxial anisotropy and temperature driven magnetization reversal of Fe deposited on a MnAs/GaAs(001) magnetic template.

R. Breitwieser[2], *M. Marangolo*[1], M. Sacchi[2,3], C. Spezzani[4], L. Coelho[5], J. Milano[6], V. Etgens[1], J. Lüning[2], N. Jaouen[3]
1. INSP, Université Pierre et Marie Curie, Paris, France; 2. Laboratoire de Chimie Physique - Matière et Rayonnement, UPMC - Univ.Paris 6, Paris, France; 3. Synchrotron SOLEIL, Paris, France; 4. Sincrotrone Trieste S.C.p.A, Trieste, Italy; 5. Universidade Federal de Minas Gerais, Minas Gerais, Brazil; 6. Centro Atómico Bariloche and Instituto Balseiro-UNCuyo, CNEA, Bariloche, Argentina

The potential for semiconductor applications utilizing charge and spin of the conducting electrons has spurred significant interest in ferromagnetic MnAs layers grown epitaxially on GaAs. Recently, our group has explained transport measurements on epitaxial MnAs/GaAs/MnAs tunnel junctions by a resonant tunneling model through a band of localized states (played by As antisites) in GaAs.1 Potential applications include the technologically important areas of spin injection into GaAs-based devices, non-volatile memory devices, and optical control of ferromagnetism in semiconductor devices. It is well-known that MnAs bulk samples exhibit a first order phase transition at about 40°C from the ferromagnetic hexagonal α-phase to the paramagnetic β-phase. A more complex magnetic ordering has been found for MnAs epitaxially grown on GaAs substrates which exhibits a temperature region with coexistence1-4 of the α-phase and β-phase. Well ordered stripes alternating the two crystallographic phases are observed for MnAs/GaAs(001) (see STM image in figure 1) over a rather wide temperature range (~10°C to 40°C). Structural and magnetic properties of this transition phase have been studied extensively by, among others, AFM/MFM,1,3 XRD,2 and PEEM.5
When capping MnAs/GaAs(001) with a ferromagnet like Fe a complex coupling between the two magnetic systems is expected in the temperature range of the α-β-phase coexistence due to the stripe formation. We have recently confirmed this expectation by recording element selective hysteresis curves, which were obtained by resonant x-ray magnetic scattering at the Fe and Mn L3 absorption edge at three representative temperatures below (0°C, MnAs in the ferromagnetic α-phase), within the α-β-phase coexistence regime (22°C, stripe formation) and above the phase transition (70°C, paramagnetic β-phase). The temperature dependence of the dichroic signals6 (see figure 2) suggest that the formation and disappearance of the stripes is accompanied by a reorientation from parallel to antiparallel and then back to parallel coupling of the magnetization directions. This indicates a complex magnetization behavior in the coexistence of the α and β phase. Recently, we have confirmed this finding by X-ray PhotoEmission Electron Microscopy (X-PEEM at SLS Synchrotron), which allows imaging of the magnetic domain structure of the ferromagnetic Fe film and of the surface of the underlying MnAs film. The comparison of these images reveals unambiguously the coupling between the two magnetic domain patterns.
We note that typically an antiferromagnetic coupling between two ferromagnetic materials requires the presence of a non-magnetic spacerlayer, whose structural thickness actually defines the coupling. For the system studied here, on the contrary, we find a relative coupling between two layers in direct contact, which in addition can be reveresed by temperature variation. Potentially, this makes it a technologically attractive system for which we intend to measure magneto-resistance and other macroscopic properties.
REFERENCES

1. V. Garcia et al. Physical Review B 72, 081303(R) (2005) ; Phys. Rev. Lett. 97, 246802 (2006); Phys. Rev. Lett 99, 117205 (2007).
2. V.M. Kaganer et al., Phys. Rev. Lett. 85 85, 341 (2000).
3. L. Daeweritz et al. J. Crystal Growth 227-228 228, 834 (2001)
4. T. Plake et al., Appl. Phys. Lett. 80 80, 2523 (2002)
5. R. Engel-Herbert, Appl. Phys. A 84 84, 231 (2006).
6. M. Sacchi et al., to be published
7. A. Ouerghi et al., Phys. Rev. B 68, 115309 (2003)
8. N. Mattoso et al., Phys. Rev. B 70, 115324 (2004)

CAPTIONS.
Figure 1. Room temperature STM image of the MnAs/GaAs(001) template, prior to Fe deposition. Stripes form parallel to the c-axis of MnAs (y direction in the figure), alternating α (bright) and β (dark) phases. Shorter period troughs are visible normal to the stripes. X-ray scattering measurements give an average period of 924nm and 115nm for stripes and troughs, respectively.
FIGURE 2. (a) Specular reflectivity vs. temperature, measured at remanence after a magnetic pulse of 600 Oe. Top: asymmetry ratio. Bottom: magnetization averaged reflectivity. Open and solid symbols refer to cooling down and warming up, respectively. (b) Specular reflectivity vs. applied magnetic field at T = 22 °C (α-β phase coexistence). Photon energy is tuned to the Mn 2p resonance (640 eV, bottom) and to the Fe 2p resonance (707 eV, top). Vertical dotted lines locate the coercive field for the Mn curve (Hc ~ 75 Oe).

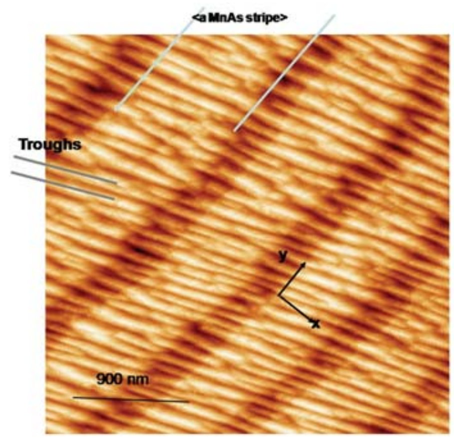

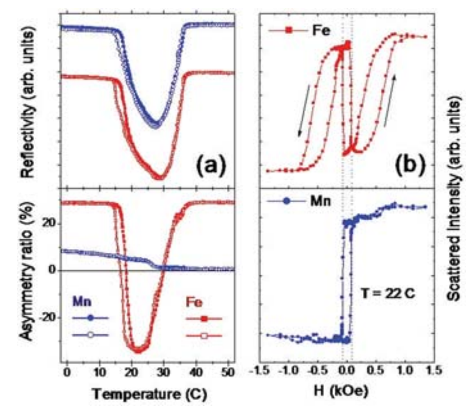

CG-05

Magnetic anisotropy control by ion irradiation.

A. Mougin[1], H. Cruguel[2], C. Beigné[3], A. Marty[3], J. Ferré[1], Y. Samson[3], O. Plantevin[2], F. Fortuna[2], H. Bernas[2]
1. LPS, Univ. Paris Sud, UMR CNRS 8502, Orsay, France; 2. CSNSM, Univ. Paris-Sud, UMR CNRS 8609, Orsay, France; 3. DRFMC/SP2M, CEA, Grenoble, France

The chemical ordering of thin FePt layers using light ion irradiation was analyzed in regards of their magnetic properties. Thin FePt(001) films grown layer by layer by Molecular Beam Epitaxy exhibit unique features of interest. First, a huge magnetocrystalline anisotropy can be obtained through uniaxial chemical ordering of the alloy within the L_{10} structure. Second, it was shown in thicker FePd films [1] that the combination of He ion irradiation and thermal mobility may control the transformation from the fcc chemically disordered phase to the tetragonal chemically ordered L_{10} one.
Films of thickness ranging from 2 to 30 nm were investigated and next irradiated at a temperature T=300°C with 30 keV He^+ ions at doses, starting from $2x10^{13}$ ions/cm^2.
For the thinnest films, the initial chemical order within the layer was revealed by a combination of Kerr magnetometry and microscopy experiments. In a 5nm FePt film, 2 magnetic contributions were evidenced by comparing the polar in-field and remnant hysteresis loops. The usual polar in-field hysteresis loop (Fig. 1a) shows a lower remanence than the remnant hysteresis one (Fig. 1b), obtained from Kerr microscopy. In the latter, after saturating the sample, magnetic field pulses were applied to trigger the magnetization reversal but cancelled to perform imaging. The remnant hysteresis loop was obtained from the magneto-optic intensity after switching off the magnetic field for each value. States of the reversal process frozen by the field cancellation can be observed and a fully remnant out-of-plane magnetic contribution accounts for the polar signal (Fig. 1b). A magnetic contribution with no significant perpendicular remanence at zero field must enter the in-field hysteresis loop (Fig. 1a). To confirm the existence of both contributions, we relied on polar Kerr magnetometry but applying the magnetic field at angle α of the sample plane. Like in anisotropy experiments, the magnetization is dragged towards the sample plane, requiring a larger applied field range. The loops and their angular dependence (Fig. 2a) confirm the existence of 2 magnetic contributions. Those are i) an out-of-plane component M_1 fully remnant and ii) a component M_2 without remanence. The M_2 behavior is assumed as being that of systems exhibiting stripes domains, well known from chemically disordered alloys. In each field configuration, signatures of M_1 and M_2 were simulated. A combination of the two contributions can reproduce the experimental loops (Fig. 1c and Fig. 2b). So, in thin FePt films, magneto-optical techniques appear as a unique tool to characterize and evidence the coexistence of magnetic components corresponding to local inhomogeneities between ordered or disordered phases.
Finally, as a clear signature of the L_{10} phase growth after irradiation, the usual polar Kerr hysteresis loops of films of increasing thicknesses are reported Fig. 3. The thinnest films that were initially partly disordered exhibit now a fully remnant loop. So, the combined use of ion irradiation with moderate heating could possibly lead to the L_{10} structure within nanometric size particles, without particle sintering. We are now exploring this opportunity.
We thank support by the french ANR-PNANO-CAMAIEU

H. Bernas et al, Phys. Rev. Lett. 91 77203 (2003)

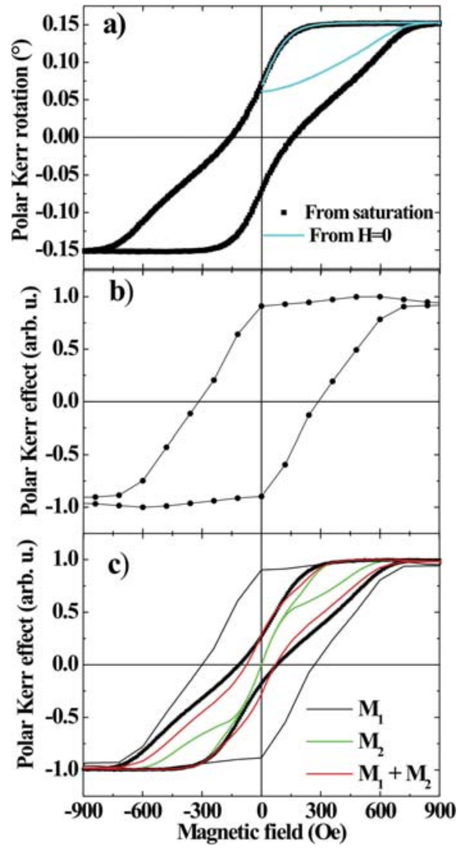

Fig 1: Polar in-field (a), remnant (b) and simulated (c) hysteresis loop of a 5 nm FePt layer.

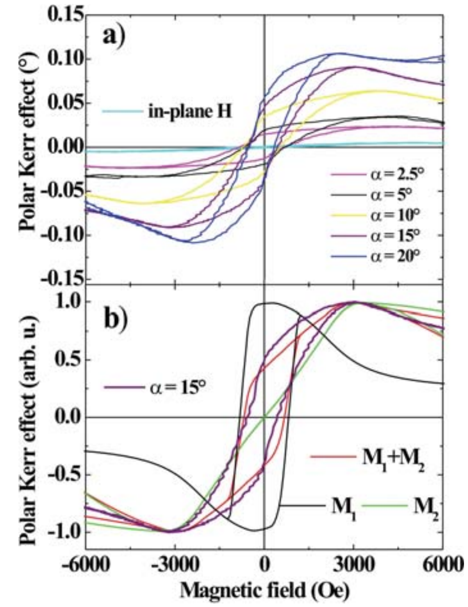

Fig 2: (a) Polar hysteresis loops of a 5 nm FePt layer as a function of the angle α between H and the sample plane. (b) Simulated loop compared with the α=15 experimental one.

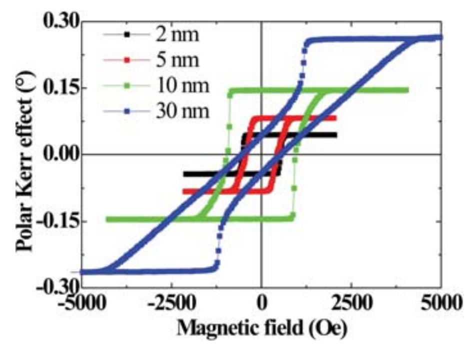

Fig 3: Polar in-field hysteresis loops for FePt films irradiated with 2 10^{14} He/cm^2.

CG-06

Study of magnetic structures on the nanoscale: a multiscale approach based on first principles calculations.

L. Szunyogh[1], L. Udvardi[1], A. Antal[1], B. Lazarovits[2,1], B. Újfalussy[2]
1. Department of Theoretical Physics, Budapest University of Technology and Economics, Budapest, Hungary; 2. Research Institute of Solid State Physics and Optics, Hungarian Academy of Sciences, Budapest, Hungary

During the last two decades, investigations of magnetic properties in confined geometries such as multilayers and clusters have led to discoveries of exciting new magnetic properties like giant magneto-resistance (GMR), exchange biasing and spin-dependent tunneling which have attracted much attention because of their importance in magnetic storage technologies. The development of nanoscale devices based on electron spin requires both a fundamental understanding of magnetic interactions and practical solutions to a variety of challenges.
In this contribution we present a multiscale study of the formation of magnetic patterns in various thin film systems. We derive the parameters of an extended classical Heisenberg Hamiltonian consisting of tensorial exchange interactions and on-site anisotropy terms derived from relativistic spin-polarized first principles calculations [1]. By using these parameters we then perform Monte Carlo simulations to explore the low-temperature (ground-state) spin structures.
The interplay of the different anisotropic exchange interactions and the on-site anisotropy can influence the formation of domain walls and lead to nanometer sized magnetic patterns. It is well-known that thin films may exhibit a large magnetic anisotropy, while it has also been recently shown [2] that the Dzyaloshinskii-Moriya (DM) interactions, $\boldsymbol{D}_{ij}$ $(\boldsymbol{S}_i \times \boldsymbol{S}_j)$ [3], can be especially strong at magnetic surfaces.
In case of an Mn monolayer deposited on a W(110) surface the DM interactions give rise to a formation of a cycloidal spin-spiral pattern modulating the underlying antiferromagnetic structure [3,4]. This is clearly seen in figure 1 that shows the spin-structure from our multiscale approach. We obtained a length of about 7.6 nm for the period of the spin-spiral that nicely compares the measured period of 12 nm [3].
Moreover, we present an extensive study for several ultrathin systems such as Mn, Cr and Fe monolayers deposited on W(001) and W(110) surfaces. In figure 2 displayed is the calculated ground-state spin-structure of a ferromagnetic Fe bilayer on W(110). It should be stressed that the domain wall formation here is the consequence of strong DM interactions, too, as switching them off the simulations result in a normal-to-plane ferromagnetic ground state.
We also investigate magnetic nanoparticles deposited on surfaces. In general, the form of the on-site anisotropy term can not be deduced from symmetry constraints, therefore, we invented a new strategy of the parametrization of the spin-Hamiltonia in terms of a least-square fit of the calculated (total) energies. It turned out that for the case of Cr trimers on Au(111) fourth-order spin-spin interactions play a crucial role. In order to find the ground-state spin-structure we solved the corrresponding Landau-Lifshitz-Gilbert equations. Figure 3 shows two configurations with different (±1) chirality that are degenerate in the absence of DM interactions. DM interactions, however, lift this degeneracy and state a) becomes the ground state. We confirmed this result in terms of ab-initio spin-dynamics simulations. We shall present new results on Cr trimers in equilateral and isosceles triangle as well as in linear chain geometries.

[1] L. Udvardi, L. Szunyogh, K. Palotás, P. Weinberger, Phys. Rev. B 68, 104436 (2003).

[2] I.E. Dzyaloshinskii, J. Phys. Chem. Solids 4, 241 (1958); T. Moriya, Phys. Rev. 120, 91 (1960).

[3] M. Bode, M. Heide, K. von Bergmann, P. Ferriani, S. Heinze, G. Bihlmayer, A. Kubetzka, O. Pietzsch, S. Blügel, and R. Wiesendanger, Nature 447, 190 (2007).

[4] L. Udvardi, A. Antal, L. Szunyogh, A. Buruzs, P. Weinberger, Physica B in print (2008).

Image of the ground state spin-structure of a Mn monolayer on W(110) as obtained from Monte-Carlo simulations displaying a cycloidal spiral modulation of a row-wise antiferromagnetic arrangement.

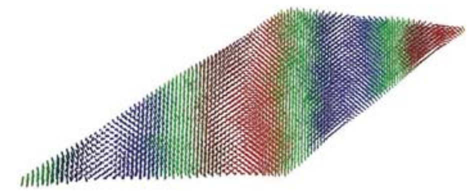

Image of the ground state spin-structure of an Fe bilayer on W(110) obtained from Monte-Carlo simulations. Due to DM interactions the ferromagnetic stripes (green arrows) and wide domain walls (red and blue arrows) are formed.

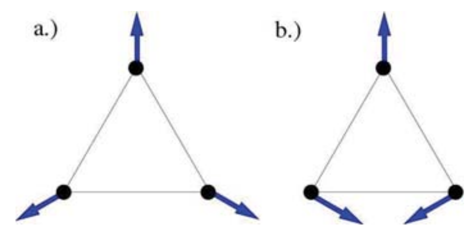

Spin-states with different chirality of a Cr trimer forming an equilateral triangle on Au(111) being degenerate in the absence of DM interactions. The DM interactions lift this degeneracy and state a) becomes the ground state.

CG-07

Magnetooptic sensing using ultrathin ferromagnetic films.

E. Liskova, S. Visnovsky
Institute of Physics, Charles University, Prague, Czech Republic

Magnetooptic (MO) reflection in ultrathin ferromagnetic films can be enhanced by embedding the films into multilayer systems. The effect can be exploited in sensors of magnetic fluxes. The media sandwiching ferromagnetic film must be chosen in a way which ensures the system chemical stability and favorable magnetic properties in addition to its optimal optical performance. The growth of ultrathin ferromagnetic films the thickness of which is typically ten nm requires the use of substrate with extremely flat surface. Often additional buffer layers are deposited on the substrate to achieve good interface quality. For an *ex situ* use, high purity Fe, Ni, and Co, as well as ferromagnetic alloys require the protection against oxidation which is best provided by Au capping layers. With the restriction to the normal light incidence and the magnetization perpendicular to interfaces, the optical characteristics of the system may be expressed in terms of the Jones 2×2 matrix, {{r_{xx}, -r_{yx}}{ r_{yx}, r_{xx} }}. This relates the incident and reflected electric field x and y components of the monochromatic plane wave. The propagation vector of the wave and the magnetization are set parallel to the z axis. There is an an approximate upper limit for $|r_{yx}|$, $|r_{yx}|_{max}=|\kappa_{xy}/\mathrm{Im}[2\kappa_{xx}]|$ where κ_{xx} and κ_{xy} are the diagonal and off-diagonal elements of the relative permittivity tensor in a ferromagnetic metal [1]. An optimal situation corresponds to a complete conversion of the incident x polarized wave to a MO reflected y polarized wave where $|r_{yx}|$ reaches its maximum value and $r_{xx}\rightarrow 0$. Any additional absorbing layers in the system reduce the value of $|r_{yx}|$. The optimum conditions are therefore approached by embedding the magnetic film into a Fabry-Perot like resonator made of dielectric layers. To avoid oxidation at inner interfaces of ferromagnetic films, oxygen free dielectrics, e.g., FeF_2 or AlN, are preferred. Nevertheless, these are also vulnerable to oxidation and may require capping with a noble metal (e.g., Au or Pt) layer. We are therefore led to study a layer sequence Au($d^{(Au1)}$)/AlN($d^{(AlN1)}$)/Fe($d^{(Fe)}$)/AlN($d^{(AlN2)}$)/Au. Here $d^{(X)}$, X=Au1, AlN1, AlN2, Fe, denotes the thickness of a layer. Then, the thicknesses, $d^{(X)}$, represent the variables in the design of a sensor with optimum MO performance. The relevant material parameters correspond to the radiation wavelength of 632.8 nm: $\kappa^{(Fe)}{}_{xx}$=-0.8845-17.938j and and $\kappa^{(Fe)}{}_{xy}$=-0.6676-0.08988j for Fe layer, $\kappa^{(Au)}$=-13.29-1.27j for Au and the AlN real index of refraction, $n^{(AlN)}$=2. Here, we focus on a single aspect of the sensor design. Figure 1 illustrates the effect of the Au capping on $|r_{yx}|$ and $|r_{xx}|$ as a function of $d^{(Fe)}$ for $d^{(Au1)}$=0, 5, and 9 nm. Despite the absorbing Au capping, there is a significant MO enhancement with respect to that on an air – Fe interface (marked by a dotted horizontal line) or in a Fe film on Au where AlN is absent. In the region of the $|r_{xx}|$ minimum, arg[r_{xx}] displays a steep change. The addition of the Au capping changes the conditions for the maximal $|r_{yx}|$ as well as those for the maximal amplitude of the ellipsometric parameter, $|r_{yx}/r_{xx}|$, and requires the readjustment of $d^{(AlN1)}$, $d^{(Fe)}$, and $d^{(AlN2)}$. Figure 2 shows the Au capping effect on $|r_{yx}/r_{xx}|$ as a function of $d^{(Fe)}$ for $d^{(Au1)}$=0, 5, and 9 nm. Surprisingly, the thickest Au (9 nm) gives the strongest $|r_{yx}/r_{xx}|$.
Supported by Czech Science Foundation grant #202-06-0531 and Czech Ministry of Education, Youth and Sports grant #0021520834.

[1] M. Mansuripur. Physical Principles of Magneto-optical Recording, Cambridge University Press, London, 1996, Chapter 6, pp. 206-211.

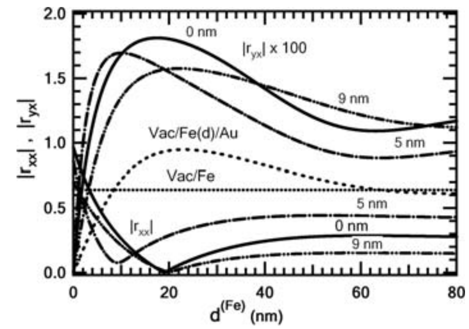

Fig1. Effect of Au capping on $|r_{yx}|$ in multilayers Au($d^{(Au)}$)/AlN/Fe($d^{(Fe)}$)/AlN/Au for $d^{(Au)}$ = 0, 5 and 9 nm as a function of Fe layer thickness. The figure show curves for $|r_{yx}|$ and $|r_{xx}|$ for structures (1) AlN1(58.9nm)/Fe($d^{(Fe)}$)/AlN2(30.4nm)/Au(substrate) (2) Au(5nm)/AlN1(62)/Fe($d^{(Fe)}$)/AlN2(24.7nm)/Au(substrate) (3) Au(9nm)/AlN1(86nm)/Fe($d^{(Fe)}$)/AlN2(154nm)/Au(substrate) Horizontal dotted line indicates $|r_{yx}|$ = 0.00641 at vacuum/Fe interface and dashed line is showing $|r_{yx}|$ in structure vacuum/Fe($d^{(Fe)}$)/Au.

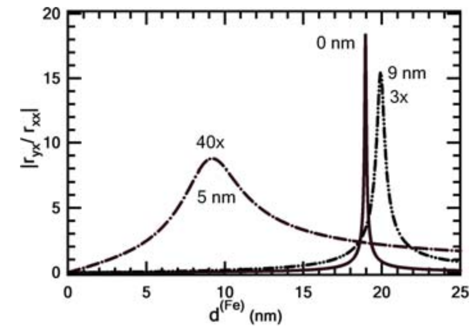

Fig2. Effect of Au capping on $|r_{yx}/r_{xx}|$ in multilayers Au($d^{(Au)}$)/AlN/Fe/AlN/Au for $d^{(Au)}$ = 0, 5 and 9 nm as a function of Fe layer thickness. The composition of multilayers are the same as in Figure 1.

CG-08

Nonuniform RKKY magnetism in nanosized films, wires and spheres.

E. Meilikhov, R. Farzetdinova
Kurchatov Institute, Moscow, Russian Federation

Indirect magnetic impurities' interaction of Ruderman-Kittel-Kasuya-Yosida (RKKY) type is considered as one of the basic mechanisms of the magnetic ordering in systems with free carriers of high concentration (e.g., degenerate semiconductors with magnetic impurities). Because every potentially interesting electronic device is characterized by nanosizes it is actual to consider how magnetic features of the relevant systems depend on their finite size [1,2]. The typical instances are thin films and wires of the thickness on the order of tens lattice constants *a*.

● Under considering the processes of ordering interacting magnetic moments in small systems one should take account of some new (as compared to "large" systems) circumstances associated with the surface and quantum-size effects. Firstly, with indirect interaction (of RKKY type) putting into effect with the aid of free charge carriers it is necessary to take into account the modification of the carrier energy spectrum connected with the system finiteness. Secondly, the non-uniformity of the effective field describing the spin interaction comes to be essential as those fields in the bulk and near the surface are differing. There are three parameters of the length dimension: the system size L by itself, the carrier de-Broglie wavelength $\lambda=2\pi/k_F$ defined by their concentration, and the characteristic interaction length l, coinciding, in the simplest case, with the carrier free path. Depending on the relation between those parameters, the following effects are possible and essential: (i) increasing the surface contribution - becomes apparent at $L<l$, (ii) the Fermi energy rise associated with the level quantization - appreciable at $L<\lambda$, (iii) shifting the lower boundary of the carrier wave number interval connected with the level quantization, as well, - comes to be essential at $L^2<l\lambda$.

● To obtain concrete results we use the mean-field theory extended over the case of the non-uniform effective magnetic field. The local effective field is defined by the relation $\mu H_{RKKY}(r)=n_\mu\int J(r-r')j(r')d^3r'$, where the integration is spread over the volume occupied by impurities, μ and n_μ are their moment and concentration, $J(r)$ is the energy of RKKY interaction between magnetic moments spaced at the distance r, and $0<j<1$ is the reduced magnetization in the point r'. Contrary to the infinite system, the value of that integral depends on the specific geometry of the system and the position of the considered point.

● The corresponding mean-field integral equation reads $j(h)=\tanh[(1/\tau)\int K(z,h)j(z)\,dz]$, where $\tau=kT/I_0$ is the reduced temperature (I_0 is the exchange energy), and the kernel $K(z,h)$ could be easily specified for films, wires and spheres. This nonlinear integral equation determines the spatial distribution of the magnetization in the system. To solve it we have used the method of successive approximations which turns to be rapidly convergent and stable.

● Calculations show that the magnetization of the considered objects is highly non-uniform. Results of calculating the spatial distribution $j(h)$ of the longitudinal magnetization in the wire of the diameter $2R=10a$ with the impurity concentration for which $4\pi n_\mu a^3=1$, and at the finite interaction length ($l=3a$) are represented in the Figure (insert, h is the distance from the wire axis): only the paraxial section of the wire has a significant magnetization, while its periphery is practically non-magnetic. Temperature dependencies of the average wire magnetization $\langle j\rangle$at $l=3a$ and $l=\infty$ are also shown in the Figure. The distinguishing feature of the dependence corresponding to the finite interaction length is its negative curvature.

● In conclusion, we have considered the mean-field continual model of the RKKY magnetism of thin films, wires, and small spheres under the condition of their essential non-uniformity. We succeeded in discovering the spatial magnetization distribution described with the nonlinear integral equation using some iterative procedure of rapid convergence. At temperatures close to the Curie temperature, the mentioned integral equation comes to be linear, the Curie temperature by itself is determined as the eigenvalue of the equation kernel, and the magnetization distribution over the film thickness is close to the parabolic one. As for the wire, its magnetization profile is much more nonuniform if the interaction length is comparable with the wire radius, and at temperatures close to the Curie temperature that distribution is near Gaussian. Magnetic properties of the sphere are more like those for the film than for the wire. The dependence of the Curie temperature on the film thickness has been found, along with the temperature dependencies of the average film, wire, and sphere magnetization. Results could be used for describing properties of nanosized system based on the diluted magnetic semiconductors.

1. E. Z. Meilikhov, R.M. Farzetdinova, Phys. Rev. B. 75, 052402 (2007). 2. T. Balcerzak, JMMM, 310, 1651 (2007).

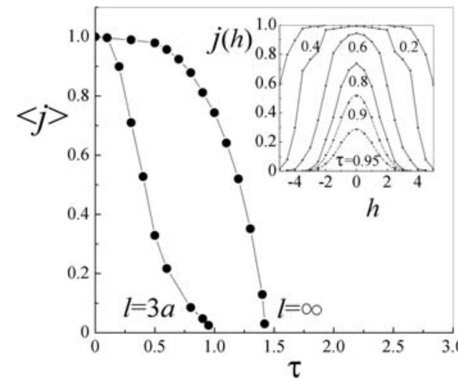

CG-09

Spin Dynamics of Ge:Mn Thin Films.

O. Kazakova[1], R. Morgunov[2], M. Farle[3], L. Ottaviano[4]
1. NPL, Teddington, United Kingdom; 2. IPCP, Chernogolovka, Russian Federation; 3. Universitat Duisburg-Essen, Duisburg, Germany; 4. Università dell'Aquila, Coppito L'Aquila, Italy

Modern electronics vastly relies on semiconductor heterostructures and rapidly develops towards high-speed digital circuits and use of diluted magnetic semiconductors (DMS) as a novel material solution[1]. To satisfy growing industrial needs, DMS should have high Curie temperature and be compatible with conventional silicon technology[2]. One of the most promising material solutions is to use germanium, which has higher electron mobility than silicon and, hence, is much more suitable for ultra-high-speed electronics. Magnetically doped germanium is also a particularly appealing candidate for spintronic applications.

We report a study of resonant and non-resonant microwave absorption in Ge thin films (t = 120 nm) implanted with manganese to a concentration of x = 2-8 at. %. The germanium matrix contains Mn_5Ge_3 ferromagnetic nanoclusters (Fig. 1 inset) and diluted Mn ions[3]. These two systems have considerably different Curie temperatures: T_{C1}(diluted Mn ions) ≈ 15 K, and T_{C3}(Mn_5Ge_3) = 290-295 K as revealed by SQUID magnetometry measurements. An additional transitional temperature, T_{C2} = 60 K, was found in Mn-implanted Ge samples and attributed to an additional type of clusters, for example, a fraction of amorphous GeMn precipitates, which become ferromagnetic below 60 K.

The electron spin resonant (ESR) spectra of Ge:Mn films exhibit a strong temperature dependence. Three main temperature intervals can be distinguished: low (T = 4-60 K), intermediate (T = 60–220 K) and high (T = 220–300 K) temperatures (Fig. 2). From the analysis of orientation and temperature dependencies of the resonances, we demonstrate that high-temperature resonant peaks correspond to the ESR in spatially separated ferromagnetic Mn_5Ge_3 clusters. On the other hand, low-temperature resonances can be interpreted as arising from spin wave excitations and obeying the dispersion law[4], $H_{res} \approx n^{2/3}$ (Fig. 2 inset). The appearance of spin-wave resonances at low temperatures indicates the presence of a cooperative magnetic response originating from long range spin ordering in the whole system.

We show that a strong non-resonant background observed at intermediate and high temperatures has a magnetoresistive origin and contains two components: a positive classic Lorentzian magnetoresistance and negative one arising from the Zeeman splitting. The orientation dependences of both components are explained by a superposition of the isotropic part of the magnetoresistance due to Zeeman splitting of the charge carriers' states and its anisotropic part caused by dimensional limitations in the thin film. Following the approach developed in Ref. 5, we show that the field-dependent magnetoresistance has a minimum at some characteristic magnetic field, H_ϕ, where phase coherence of carriers is destroyed. This field is related to the phase relaxation length of charge carriers, L_ϕ, as $H_\phi = hc/8\pi e L_\phi^2$. Based on this, we calculate L_ϕ, which is varied in the range 70-350 nm as the temperature decreases from 300 to 4 K (Fig. 1). Since this length exceeds significantly the cluster size, all observed features of the magnetoresistance are 'cluster-independent' and can be attributed to charge carriers in the Ge matrix.

In overall, we demonstrate a very good correlation between the ESR and SQUID magnetometry results. Combination of these techniques allow us to elucidate a complex magnetic structure of the Ge:Mn films, elucidate the different physical nature of resonances at high and low temperatures and distinguish contributions from several types of magnetically ordered clusters and diluted ions.

1 T. Dietl, J. Phys.: Condens. Matter. **19**, 165204 (2007).

2 S. Kuroda, et al., Nature Materials **6**, 440 (2007).

3 L. Ottaviano, et al., J. Appl. Phys. **100**, 063528 (2006).

4 B. Hoekstra, et al., J. of Appl. Phys. **48**, 382 (1977).

5 A. I. Veinger, et al., Semiconductors, **34**, 746 (2000).

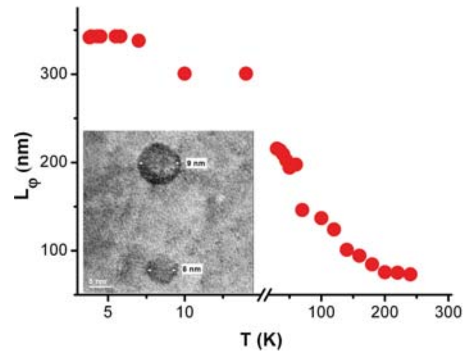

Temperature dependence of the phase relaxation length of the carriers in the Ge:Mn films doped with 2 % of Mn. Insets shows a high-resolution TEM image of Mn_5Ge_3 clusters with the size of 6 and 9 nm.

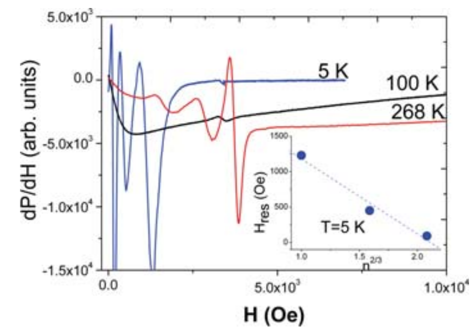

ESR spectra of the Ge film implanted with Mn concentration of 4 % at different temperatures. The inset shows dependence of the resonant field <it>H$_{res}$~~<\>> on the resonance peak number n in the Ge:Mn film (<it>x~~<\>> = 4 %) at <it>T~~<\>> = 5 K.~~

CG-10

Magnetoelastic coupling in epitaxial monolayers: The role of lattice strain.

D. Sander, Z. Tian, J. Kirschner
Max Planck Institute, Halle, Germany

Magnetoelastic (ME) coupling has been identified as a decisive contribution to the magnetic anisotropy of strained films [1]. However, experimental results [1] and theoretical work [2] of recent years clearly indicate that bulk magnetoelastic coupling coefficients do not apply to strained epitaxial monolayers. Rather, lattice strain induces a change of the effective magnetoelastic coupling, which can affect both magnitude and sign of the corresponding magnetoelastic coupling coefficient. Thus, bulk magnetoelastic properties are not suitable for the description of the impact of lattice strain on the magnetic anisotropy, and experimental and theoretical data on magnetoelastic coupling are required.

We compile in this contributions our recent results on the non-bulklike magnetoelastic coupling of Fe, Ni, and Co monolayers on Ir(100). We apply the crystal curvature technique [1] to measure both film stress during film growth and magnetoelastic stress during a reorientation of film magnetization. Whereas the former stress amounts typically to some GPa in epitaxially strained films, the latter is three orders of magnitude smaller of order MPa. Nevertheless, the resulting minute curvature changes are reliably detected, and allow direct measurements of the effective magnetoelastic coupling coefficients in films as thin as five monolayers. The in situ combination of both measurements on lattice-misfit induced stress and magnetization-induced stress is exploited to investigate the correlation between film stress, lattice strain, and magnetoelastic coupling coefficients for a film thickness from monolayers up to 10 nm.

We demonstrate how stress measurements are analyzed in conjunction with in situ low energy electron diffraction experiments to derive lattice strain and to detect structural transition in the growing film. Thus, subsequent in situ measurements of the magnetoelastic coupling coefficients are reliably correlated with the respective film strain. The epitaxial films are under large stress of the order GPa due to the mismatch between film and substrate in the percent range. For bcc Fe on Ir(100) we find a compressive strain ranging from -4.9% for pseudomorphic growth (2—10 layers), which relaxes to -2.4% at higher film thickness. Ni and Co grow as fcc films under tensile strain on Ir(100). We measure the difference of magnetoelastic stress along different crystalline axes by switching the external magnetic field along the length and width of the sample. ME coupling coefficients B1 and B2 are obtained according to the geometry of the sample and the magnetic field orientation.

Our results indicate that the ME coupling coefficients B1 and B2 of Fe, Co and Ni deviate from the bulk value. We show that lattice strain is an important factor which drives the deviation of the magnetoelastic coupling coefficients form the respective bulk values. The experimental results can be fitted with an effective strain-dependent ME coupling coefficient Beffi with Beffi=Bi+Deff. Our analysis shows that the nonlinear coefficient Deff is much larger than the first order coupling term Bi. We obtain for Fe: B1=-3.6 MJ/m3 and Deff=155 MJ/m3 (bcc Fe: B1 bulk: -3.4 MJ/m3), for Co: B1= 3.5 MJ/m3 and Deff= - 842 MJ/m3 (fcc Co: B1 bulk: -9.2 MJ/m3), and for Ni: B1= 1.3 MJ/m3 and Deff = 273 MJ/m3 (fcc Ni: B1 bulk: 9.4 MJ/m3). These results indicate that already a strain in the sub-percent range changes the ME coupling significantly [2].

The magnetic anisotropy of Fe, Co and Ni films on Ir(100) is well described by our experimental values of the ME coupling coefficients in calculating the ME anisotropy. We find an easy in-plane magnetization direction for Fe and Co. For Ni films on Ir(100) the easy axis is out-of-plane from 7 ML to 15 ML. With increasing film thickness a spin reorientation transition (SRT) is observed around 16 ML, and the easy axis turns back to in-plane. The thickness of 16 ML where this SRT is observed is well reproduced by our data on the strain dependence of B1 of Ni. The bulk value of B1 would favor a SRT back to in-plane at a much higher thickness in excess of 60 ML, in contrast to the experimental result.

[1] D. Sander, Rep. Prog. Phys. 62, 809(1999); J. Phys. : Condens. Matter 16 (2004) R603; G. Wedler, J. Waltz, A. Greuer, R. Koch, Phys. Rev. B 60 (1999) R11313.

[2] M. Fähnle, M. Komelj: Phys. Rev. B, 65, 212410 (2002); M. Fähnle, M. Komelj: Phys. Rev. B, 73, 012404 (2006).

CG-11

Spin-reorientation transitions induced by coinage-metal capping of Co/Ru(0001) studied by spin-polarized low energy electron microscopy.

F. El Gabaly[1,2], A. K. Schmid[2], K. F. McCarty[3], *J. de la Figuera*[4,1]
1. Centro de Microanalisis de Materiales, Universidad Autonoma de Madrid, Madrid, Spain; 2. Berkeley National Laboratory, Berkeley, CA; 3. Sandia National Laboratories, Livermore, CA; 4. Instituto de Quimica-Fisica Rocasolano, CSIC, Madrid, Spain

The control of the magnetic anisotropy in thin films is a topic of both applied and basic research. In particular it is of interest to achieve materials with perpendicular magnetic anisotropy. The anisotropy energy responsible for this effect arises from a delicate balance between competing effects, and it is influenced by the strain in the film, as well as the substrate and capping overlayer material. Although usually there is a single transition from perpendicular orientation to an in-plane magnetic easy axis as the magnetic film thickness is increased, the presence of sucesive easy-axis reorientation transitions in thin films have also been observed. In this case, the easy-axis is in-plane up to a critical thickness, then it turns to an perpendicular orientation, and back again to an in-plane orientation at a larger thickness, due to a complex interplay of magnetism and strain. It is uncommon to find magnetic materials where the easy axis changes orientation abruptly at consecutive atomic layers. Two systems which present consecutive spin-reorientation transitions at consecutive atomic layer thicknesses are Fe/W(110)[1] and Co/Ru(0001)[2]. In both systems the double spin reorientation transition takes place in films (or islands) one, two, and three atomic layers thick.
One crucial element to understand the behavior of such thin films is to have available a local determination of the magnetic properties as well as a simultaneous local characterization of the structure. The effect of roughness can be reduced or eliminated altogether if microscopic techniques allow to study the film on a single terrace or island. One technique that allows this level of detail in specific systems is spin-polarized low energy electron microscopy. The use of a source of spin-polarized electrons allows the determination of the 3-dimensional sample magnetization on a nm scale, even during the growth of the films themselves. Such a technique together with the growth of Co films in large substrate terraces in a perfect layer-by-layer mode for up to 10 monolayers[2] has been used successfully to understand the Co/Ru system[3].
Given that ultra-thin films of transition magnetic metals oxidize readily in air, capping the films with non-magnetic material such as gold or copper has become standard practice for measuring the magnetic properties ex-situ. This raises the issue of the possible effect of the capping layer on the magnetic properties of the magnetic film. Specially, capping layers have been observed to influence the magnetic anisotropy. Interface effects, a broad term that includes from the modification of the electronic structure of the magnetic material in direct contact with the capping layer to changes in the strain of the magnetic film, have been frequently detected. In particular it has been reported that the deposition of copper on cobalt films on W(110) produces an increase in the perpendicular magnetic anisotropy at around one monolayer [4]. But no consecutive complete reorientations of the magnetization, such as observed as a function of the thickness of the magnetic film itself [2] have been reported, to the best of our knowledge.
We report on SPLEEM observations of the easy-axis of magnetization of Co thin films on Ru(0001) during the growth of capping overlayers of coinage metals (Cu, Ag, Au), together with local area diffraction of selected combinations of materials. The different coinage metals present extremes in terms of lattice mismatch with the Co film, from a nearly lattice match for Cu/Co to a large mismatch that is accommodated by dislocations in Ag and Au/Co. For most of the capping layer and magnetic film thicknesses, there is no change in the easy-axis of the magnetization of the Co film although the Curie temperature may change. But for selected combinations of overlayer and magnetic film (1-2 ML Cu/ 3,4 ML Co/Ru, 1-2 ML Ag/ 3 ML Co/Ru, 1-3 ML Au/5,6 ML Co/Ru) we observe consecutive spin reorientation transitions by changing the capping -non-magnetic metal- overlayer thickness (from an in-plane easy-axis in bare films to perpendicular easy axis upon capping the film with a monoatomic capping layer, and to an in-plane orientation again for additional capping layers).

[1] K. Bergmann, PhD. thesis, Hamburg (2004).

[2] Farid el Gabaly et al., New J. of Phys. 9 80 (2007).

[2] Farid El Gabaly et al., Phys. Rev. Lett. 96 147202 (2006).

[3] T. Duden and E. Bauer, Phys. Rev. B 59 468 (1999).

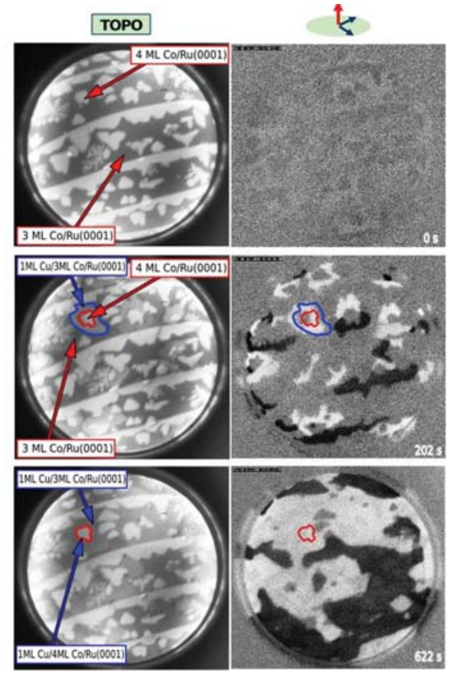

Sequence of spin-polarized images showing the topography of the film (left) and the out-of-plane component of the magnetization (right). A complete layer of copper is deposited on a film with 4 ML thick Co islands surrounded by a 3 ML thick Co film. The field of view of the images is 7 μm.

Magnetic Properties of Single-Crystalline FeRh Alloy Thin Films.

S. Inoue, Y. Y. Hnin, *N. T. Nguyen*, T. Suzuki
Information Storage Materials Laboratory, Toyota Technological Institute, Nagoya, Japan

Introduction

Thin films and nano-particles[1] of FeRh have drawn much attention from a basic point of view and also for possible applications, such as a HAMR. The CsCl type FeRh (bulk) exhibits the first-order magnetic phase transition.[2-3] However, the magnetic phase transition mechanism in films is quite complicated and is not well understood. In the present work, the effect of external magnetic field on AF-FM transition process in single crystalline Fe100-XRhX (26≦X≦56) films has been systematically investigated.

Experimental

Thin films of Fe100-XRhX were fabricated onto MgO(100) substrates by an electron beam co-evaporation. The substrates were kept at around 400deg. during deposition. As-deposited films were annealed at 700deg. for 4 hrs. Measurements of magnetic properties were carried out using a VSM. Magneto-optical properties were examined by a polar magneto-optical Kerr effect system

Results and Discussions

Figure 1 shows X-ray diffraction spectra (θ/2θ and ϕ) at 26≦X≦63. All the films are grown with FeRh(100) planes parallel to the substrate, and furthermore the ϕ-scan patterns confirms that the films exhibit the four-fold symmetry in the film-plane, indicating that the films are single crystalline films of the CsCl-structure. Figure 2 shows the temperature dependence of magnetization for different compositions. For 26≦X≦45 and X=63, the films do not undergo any transformation, behaving as ferromagnetic. However for 51≦X≦60, the films exhibit the AF-FM phase transition. A magnetic phase diagram for the films and bulk is shown in Fig.3 (a). It is found that the transition temperatures for films are higher than that of bulk, and the range for composition of which film exhibits the transition is expanded. Figure 3 (b) shows the composition dependence of total entropy change ΔS at the transition, together with the ones for bulk reported by Kouvel et al.[3] It is of great interest to note that ΔS decreases with increasing X. And it is found that ΔS=13.7 mJ/(deg g) in heating process and ΔS=14.3 mJ/(deg g) in cooling process at X=51, respectively, which are in reasonable agreement with the bulk value, ΔS=14.0 mJ/(deg g).[3] Magneto-optical polar Kerr spectra of the films under consideration are shown in Fig.4. The polar Kerr rotation for the AFM is nearly zero for the entire photon energy. However, upon the appearance of the FM phase, the polar Kerr effect becomes enhanced, showing a broad maximum at around 4 eV. The result of the polar Kerr effect upon heating and cooling is consistent with that for the magnetization behavior of the films.

1) H. Y. Y. Ko and T. Suzuki, J. Appl. Phys. 101, 09J103 (2007).

2)M. Fallot and R. Hocart, Rev. Sci. 77, 498 (1939).

3)J. S. Kouvel, C. C. Hartelius, J. Appl. Phys. 33, 1343 (1962).

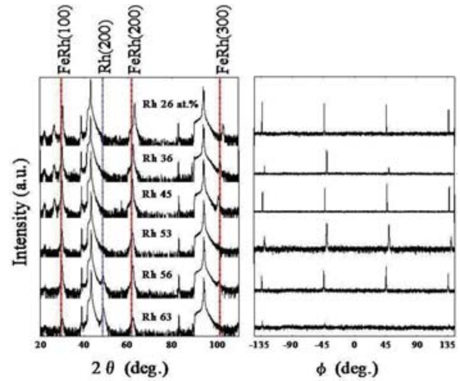

Fig.1 X-ray diffraction of diffrent compositions (26≦X≦63)

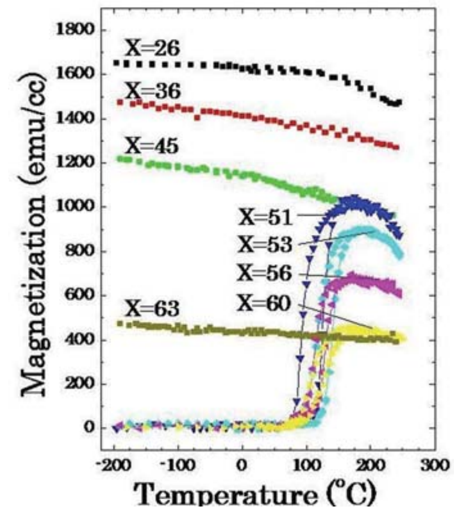

Fig.2 M-T curves at 26≦X≦63

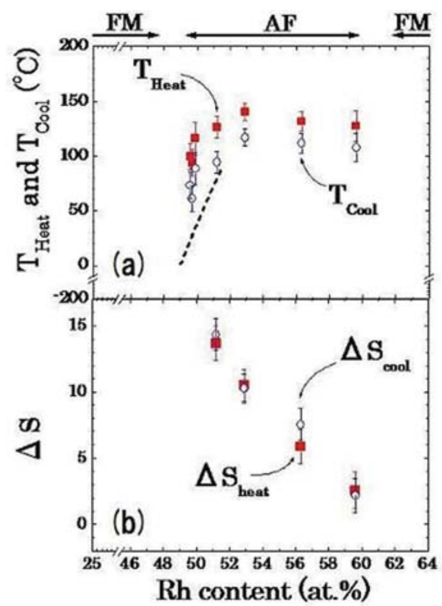

Fig.3(a) A magnetic phase diagram for films and bulk (dash-line), (b) The change of entropy at 51≦X≦60

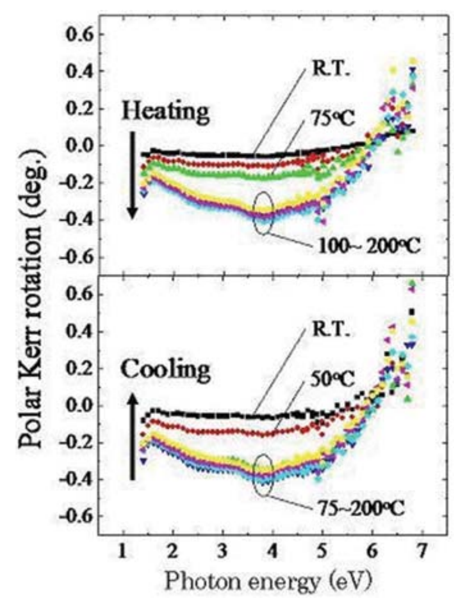

Fig.4 Polar Kerr rotation curves with different temperatures in heating and cooling process

CH-01

Controlling the microstructure in Ni-Mn-Ga alloys.

M. Pötschke, F. Thoss, U. Gaitzsch, C. Hürrich, S. Roth, B. Rellinghaus, L. Schultz
Institute for Metallic Materials, IFW Dresden, Dresden, Germany

Magnetic shape memory alloys show large strain when subjected to an applied magnetic field. This is due to the motion of twin boundaries in the martensitic phase. The effect was discovered in 1996 by Ullakko et al. [1]. Single crystalline samples of the off-stoichiometric Ni_2MnGa composition have recently been shown to produce strains of up to 10% [2]. Most of the investigations of magnetic field induced strain via twin boundary motion (MFIS) have been performed on single crystals, which show the largest MFIS effect.
However, the preparation of single crystals is a time and cost consuming process and there can be compositional changes along the axis of the crystal and segregations [3]. That is why from a technological point of view, polycrystals are of great interest. They are easier to produce. Unfortunately they usually exhibit lower strains because of the different orientations of the separate crystals and the presence of grain boundaries, which act as pinning centers and impede the twin boundary motion. A possible approach to improve the polycrystalline material is to have a coarse-grained and highly textured sample, because then it is nearest to a single crystal.
The attempt to achieve texture in polycrystalline Ni-Mn-Ga is by free directional solidification. The principle of the experimental set up is displayed in Fig. 1 (left). A hot mold is mounted on a cooling plate. To avoid heating of the cooling plate by the hot mold, an insulation ring is placed between the mold and the plate. When the melt is cast into the mold, a temperature gradient and thereby a heat flow through the melt towards the bottom is generated, which causes a directional solidification in opposite direction.
The texture of the sample was analyzed using EBSD. Fig. 1 (right) shows a typical EBSD-picture of one of the samples with an area of elongated grains at the bottom of the sample. The [100] direction seems to grow preferred in the direction of heat flow. In order to study the effect of various preparation conditions on the texture development, we have chosen the composition $Ni_{48}Mn_{30}Ga_{22}$, which is austenitic at room temperature and therefore easy to investigate via EBSD. For magneto-mechanical measurements we chose the compositions $Ni_{50}Mn_{30}Ga_{20}$ and $Ni_{50}Mn_{29}Ga_{21}$, which are martensitic (7M and 5M [4]) at room-temperature and therefore suitable for applications.
The casting process was performed in an Induret S investment cast machine. The as-cast samples were subjected to a thermal annealing at 1000°C for 48 h in an Ar / 5 % H_2 atmosphere. Variations in composition were ruled out by measuring the Austenite-Martensite transformation temperatures with a Perkin Elmer DSC. Since the transformation temperature depends strongly on the composition (50 K/ at. %) [5], variations of composition of less than 0.1 at. % can be resolved. All cuts of the samples were made electro-erosively to avoid mechanical impact and structural changes [6]. For visualization of the microstructure metallography by means of optical microscopy was used.
The mold temperature has a strong influence on the as-cast microstructure. The length of the zone of elongated grains depends on the casting parameters, especially the mold temperature. With increasing mold temperature the area of elongated grains grows. To increase the textured length an additional heater, which is wound around the hot mould, is used.
To study composition variations along the axis of the ingot samples were taken from different parts within the annealed ingot and DSC curves measured for these samples. DSC reveals chemical homogeneity along the sample of better than 0.1 at. %.
The annealing step (48 h, 1000°C, Ar/ H_2 atmosphere) causes a coarsening of grains, homogenization, stress relaxation, possible ordering during cooling and affects the texture. By cutting off the bottom grains of the sample the orientation of the as-cast state can be retained also after annealing.
The influence of different annealing parameters and a mechanical load on the texture development during annealing is investigated.
The superelastic behavior of textured austenitic samples with the composition $Ni_{48}Mn_{30}Ga_{22}$ is studied and compared to randomly oriented samples and theoretical values.
After a thermal treatment to adjust the right crystal structure and a mechanical training to decrease the stress, which is necessary for twin boundary motion, textured samples showed a magnetic field induced strain of 1%.

[1] K. Ullakko, J.K.. Huang, C. Kantner, R.C. O'Handley, V.V. Kokorin, Appl. Phys. Let. 69, No. 13 (1996) p. 1966

[2] A. Sozinov, A. A. Likhachev, N. Lanska, K. Ullakko, Appl. Phys. Lett. 80/10 (2002), p. 1746.

[3] D.L Schlagel, Y.L. Wu, W. Zhang, T.A. Lograsso, J. Alloys Comp. 321 (2000) p. 77

[4] J. Pons, R. Santamarta, V.A. Chernenko, E. Cesari, Mat. Chem. And Phys. 81 (2003) p. 457

[5] X. Jin, M. Marioni, D. Bono, S.M. Allen, R.C. O'Handley, T.Y. Hsu, J. Appl. Phys. 91/10 (2002) p. 8222

[6] U. Gaitzsch, M. Pötschke, S. Roth, N. Mattern, B. Rellinghaus and L. Schultz, J. Alloys Comp. 443 (2007) p. 99

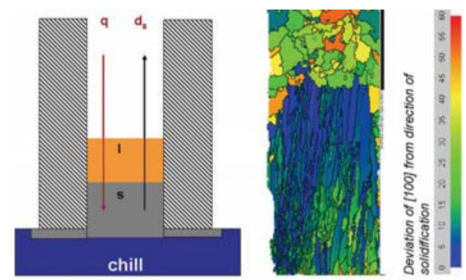

Fig. 1: Principle (left), EBSD-picture (right)

CH-02

Field, stress and temperature controlof the phase transitions in $Ni_{55}Mn_{20}Ga_{25}$ single crystal.

C. P. Sasso[1], M. Pasquale[1], L. Giudici[1,2]
1. Electromagnetics, INRiM, Torino, Italy; 2. Physics, Politecnico di Torino, Turin, Italy

Magnetic materials presenting field induced first-order structural phase transitions are attracting considerable interest due to their magnetocaloric, magnetoelastic or magnetoresistive properties [1-6]. In these systems temperature, stress and magnetic field can drive the transition and influence its hysteretic properties: a proper control of external parameters is then fundamental in the development of novel applications taking advantage of the multifunctional behavior of these materials.
In the present case we have investigated the combined effects of temperature-mechanical stress and magnetic field-mechanical stress on the martensitic phase transition occurring in the Heusler alloy with composition $Ni_{55}Mn_{20}Ga_{25}$. This composition presents a sharp first-order magneto-structural phase transition from a ferromagnetic-martensite phase to paramagnetic-austenite [7].
During heating the martensite-to-austenite (M-A) phase transition occurs in the temperature range A_s*=306 K≤T≤*A_f *=320 K* whereas the inverse transition (A-M) occurs in the temperature range M_f*=294 K≤T≤*M_s*=305 K*. At high temperature, T> A_f, the austenite presents a cubic symmetry lattice whereas the full symmetry is reduced in the martensite phase which presents a tetragonal unit cell with a *'c'* axis contracted by 6% [8,9].
The purely mechanical characteristics were studied performing stress-strain measurements on an oriented single crystal with {100} faces at different temperatures. (See fig.1) At temperatures above A_f = 320 K superelastic curves can be observed with large reversible strain. At temperatures around 315 K, a stress of the order of 32 MPa can induce the A-M phase transition. Decreasing the test temperature closer to M_s = 305 K we observe a decreasing of the stress necessary to activate the martensite growth. This reduction of the yielding stress is associated to a change of the A-M transition temperature under a compressive load. We observe that the M_s temperature is linearly reduced with a slope $dMs/d\sigma \approx -0.34$ K MPa^{-1}. On the other hand, at temperatures below M_f= 294 K stress strain-curves become superplastic, and a permanent 6% strain is retained after stress is released.
The effects of magnetic field and stress on the A-M phase transition were investigated using an electromagnet with one movable pole embedded in a two columns dynamometer. The movable pole was attached to the dynamometer crossbar and used to apply both a unidirectional compressive stress and a magnetic field up to 360 kA/m. In fig. 2, the stress-strain curves under applied field are presented. The applied field collaborates with the mechanical compressive stress promoting the growth of the martensite (the ferromagnetic phase) and hence we observe a general reduction of the yielding stress. When the material is already in the martensite phase the applied field has a smaller impact on the stress-strain curves whereas, at temperatures in the interval M_f≤T≤M_s, we have that the reversibility of the stress induced phase transition at zero field (superelastic behavior) is even cancelled, upon stress releasing, by the martensite stabilization due to the field. The reduction of the yielding stress at T=316 K allows to estimate that the magnetic field is equivalent to a corresponding stress of almost 10 MPa/T.

[1] E. M. Levin, V. K. Pecharsky, and K. A. Gschneidner, Phys. Rev. B, 60, p. 7993 (1999).

[2] J. Marcos, A. Planes, L. Mañosa, F. Casanova, X. Batlle, A. Labarta, and B. Martínez, Phys. Rev. B, 66, p. 224413 (2002).

[3] M. Han, D. C. Jiles, J. E. Snyder, T. A. Lograsso, and D. L. Schlagel, 95, p. 6945 (2004).

[4]V. K. Pecharsky and K. A. Gschneidner Jr., Phys. Rev. Lett., 78, p. 4494 (1997).

[5] M. B. Salamon and M. Jaime, Rev. Mod. Phys., 73, p. 583 (2001)

[6] Y. Tomioka, A. Asamitsu, and Y. Tokura, Phys. Rev. B, 63, p. 024421 (2000).

[7] V. A. Chernenko, E. Cesari, V. V. Kokorin, and I. N. Vitenko, Scr. Metall. Mater. 33, 1239 (1995).

[8] R. D. Tickle, R. James, Magnetics, IEEE Transactions on, 35, p. 4301 (1999).

[9] J. Murray, M. Marioni, S. M. Allen, R. C. O'Handley, and T. A. Lograsso, App. Phys. Lett., 77, p. 886 (2000).

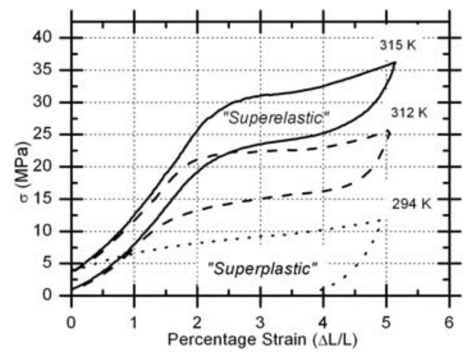

Stress-strain curves performed at different temperatures show either the *'superelastic'* or the *'superplastic'* behavior as temperature is decreased. Above M_s, the stress plateau after the yielding stress represents the stress induced A-M phase transition.

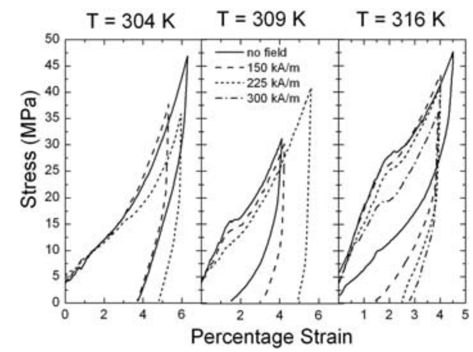

***'Superelastic'* and *'superplastic'* curves measured under different applied magnetic fields.**

CH-03

Effect of annealing conditions on the structure formation in NiMnGa shape memory alloys.

R. Wroblewski, M. Leonowicz
Faculty of Materials Science and Engineering, Warsaw University of Technology, Warsaw, Poland

Ferromagnetic shape memory alloys (FSMA) attract substantial scientific and technological attention due to a giant magnetic-field-induced strain (up to 10%) arising from rearrangement of martensitic variants. This effect was first reported for the Ni_2MnGa Heusler alloys [1]. The NiMnGa alloys undergo a martensitic transformation from parent, cubic $L2_1$ phase to martensite phase. The martensite phase may have different modulated or non-modulated structures, depending on the composition, represented by the electronic concentration (e/a) [2] and atomic order.
In this work we studied the effect of annealing temperature, chosen respectively below and above the ordering temperature, on the structure and transition temperatures for the $Ni_{50}Mn_{29}Ga_{21}$ polycrystalline alloy.
The alloy was induction melted and cast into an alumina die. Afterwards the alloy was homogenized at 1173 K for 72 hours and cooled with a furnace. The 25 mm diameter ingot was cut into 3 mm thick slices which were annealed at 873 K and 1073 K for 12 hours and subsequently either cooled slowly with a furnace or quenched in ice water. The X-ray diffraction analysis on bulk samples was done using Philips PW 1830 diffractometer, Cu Kα radiation. Magnetic measurements were done using LakeShore 7410 Vibrating Sample Magnetometer equipped with a cryostat.

The transformation temperatures, As (martensite-to-austenite transformation start temperature), Af (martensite-to-austenite transformation finish temperature) and Tc Curie temperature, for the specimens annealed at various conditions are shown in Table 1 and Figure 1. One can conclude from these data that the As temperature, 330 K, for the homogenized and for the annealed specimens is independent on the annealing and cooling conditions. However, different magnetization values, Af and Tc temperatures suggest differences in the magnetic anisotropy and structure of the specimens having various thermal history. Especially changes of the magnetization in the austenitic region, upon heating, for the specimen quenched from 1073 K, evidence structural inhomogeneities. The magnetization in the austenite region grows from 340 K up to 365 K. This suggests continuous evolution of the parent phase structure. These suggestions were confirmed by X-ray phase analysis (XRD), shown in Fig. 2. It is evident from this data that the homogenized specimen has a structure of non-modulated (NM) martensite. Both the specimens, slowly cooled and quenched from 873 K, exhibit broadly the same structure, characteristic of 5M modulated martensite. However, substantial differences are shown for the specimens slowly cooled and quenched from 1073 K, respectively. For the former 7M modulated martensitic structure was obtained, whereas for the later multiphase structure, showing reflections characteristic of both 5M and $L2_1$ phases is evident. It is clear from these studies that the order-disorder transformation in the austenite plays an important role in the formation of martensitic structure. Annealing at 873 K, irrespective of cooling rate, does not make any special change to the microstructure. However, quenching from 1073 K partially "freezes" the disordered B2 phase and consequently, at room temperature, a mixture of martensite and the parent phase is present. When slow cooling from 1073 K is applied the diffusion in the austenite enables ordering of Ga and Mn atoms and in consequence full transition from the B2 to $L2_1$ phase and formation of the martensitic phase. It is not clear in this stage why upon slow cooling from 1073 K the 7M modulated martensitic structure, very convenient for practical application, was formed.

1. K. Ullakko, J.K. Huang, C. Kantner, R.C. O'Handley, V.V. Kokorin, Appl. Phys. Lett. 69 (1966) 1966.

2. V.A. Chernienko, Scripta Mater. 40 (1999) 523.

Treatment	As	Af	Tc
Homogenized	335	345	375
873 K slow cooling	335	345	375
873 K quenching	335	340	365
1073 K slow cooling	335	345	370
1073 K quenching	335	340 - 365	365

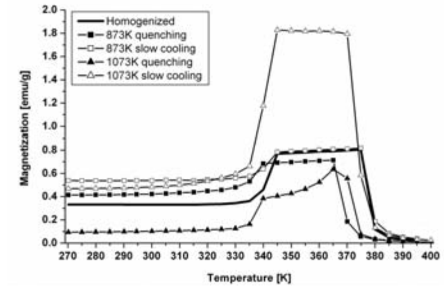

Fig. 1. Magnetization vs temperature for the specimens annealed at various conditions.

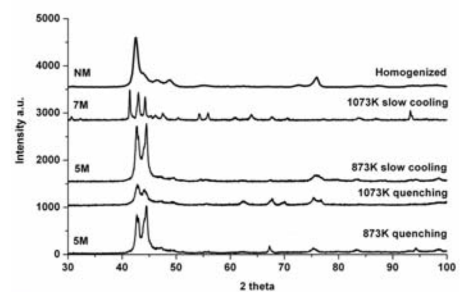

Fig. 2. XRD patterns for the specimens annealed at various conditions.

CH-04

Magnetic-field induced strain in 5M polycrystalline alloy.

U. Gaitzsch, C. Huerrich, M. Pötschke, S. Roth, L. Schultz
Inst metal mater, IFW Dresden, Dresden, Germany

Magnetic shape memory alloys show a unique coupling of magnetic and mechanical properties [Han00]. If twin boundaries move in the martensite phase, both the magnetisation and the shape changes. Therefore the magnetisation can be changed by application of an external stress (sensor mode) and the shape can be changed by an external magnetic field (actuation mode). If a sample shall be driven in the actuation mode, the twinning stress has to be smaller than the stress which is originated by an external magnetic field. The latter is defined by the crystal structure of the martensite phase. For the 5M structure the maximum stress is 2.6 MPa. This stress is reached in ideally oriented samples at the anisotropy field. If the external magnetic field exceeds the anisotropy field, the stress acting on a twin boundary stays constant. In contrast to that the twinning stress is a defect controlled property which is controlled by the microstructure of the martensite phase and can vary from sample to sample.

In single crystals, magnetic field induced strain of maximum 6 % can be seen in the 5M structure [Soz01]. The objective of this work is to achieve magnetic field induced strain in polycrystals. Investment casting is used in order to obtain directional solidification, which results in a [100] fiber texture [Poe07]. Once the samples are cast they have to be annealed for homogenization (1000 °C, 48 h) and stress relaxation (600 °C, 14 h) [Gai07a]. From these ingots cubic samples are cut for thermo-mechanical training. The first training step is cooling under load, which shall cause a variant selection during the martensitic transformation. However, by cooling under load the phase transformation is accompanied by a small strain only. Therefore additional compression cycles have to be performed to decrease the twinning stress and to increase the strain. These compression cycles have to be done along all three axis of the samples to activate all possible twinning systems, as it has been shown for 7M samples [Gai07b]. In contrast to that, a two axes compression can be applied, if the sample is properly oriented and trained before to decrease the twinning stress further. But, if the misorientation of the twin system is too large, a two axes compression will only lead to an accumulation of strain in the third, not compressed axis. Additionally the applied stresses must not be too large in the training process in order to avoid crack initiation or even brittle fracture in the samples. During the mechanical training the twin microstructure adopts to the deformation by simplification of the variant hierarchy and proper alignment of the twin boundaries. However, the exact mechanism is still under investigation. Therefore magnetic measurements are used as well as in-situ deformation in an SEM . Due to orientation contrast, twin variants can be observed in the BSE mode. Additionally, magnetic domains can be imaged by SEM [Ge07].

In a well-trained polycrystalline sample the magnetic field induced strain has been measured by relaxation in an external magnetic field after compression. This was done as well as the training experiments in an Instron mechanical testing machine, which is equipped with an home-made electromagnet. The whole setup can be operated in a temperature range of -25 °C to 100 °C. By changing the temperature the twinning stress can be lowered, which causes an increase of magnetic field induced strain to 1.5 %. But this strain has to be corrected for viscoelastic strain, which is caused by relaxation of the previously compressed sample. Therefore only 1.0 % can be related to the applied magnetic field. In fig.1 the relaxation curves with and without field are displayed.

[Han00] O'Handley, R. C., Murray, S. J., Marioni, M., Nembach, H. & Allen S. M. Phenomenology of giant magnetic-field-induced strain in ferromagnetic shape-memory materials. J. Appl. Phys. 87/9, 4712 - 4717 (2000).

[Soz01]Sozinov, A., Likhachev, A.A., & Ullakko K. Magnetic and Magnetomechanical Properties of Ni-Mn-Ga Alloys with easy axis and easy plane of magnetization. Proc. SPIE 4333, 189 - 195 (2001).

[Poe07] Pötschke, M., Gaitzsch, U., Roth, S., Rellinghaus, B. & Schultz, L. Preparation of melt textured Ni–Mn–Ga. J. Magn. Magn. Mater. 316, 383–385 (2007).

[Gai07a] Gaitzsch, U., Pötschke, M., Roth, S., Mattern, N., Rellinghaus, B. & Schultz L. Structure Formation in martensitic Ni50Mn30Ga20 MSM alloy. J Alloys Comp., 443, 99-104 (2007)

[Gai07b]: Gaitzsch, U., Pötschke, M., Roth, S., Rellinghaus, B. & Schultz, L. Mechanical training of polycrystalline 7M Ni50Mn30Ga20 magnetic shape memory alloy

Scripta Mater. 57 (2007) 493–495

[Ge07] Ge, Y., Heczko, O., Söderberg, O. & Hannula, S.-P. Mater. Sci. Eng. A (2007) doi:10.1016/j.msea.2006.11.183

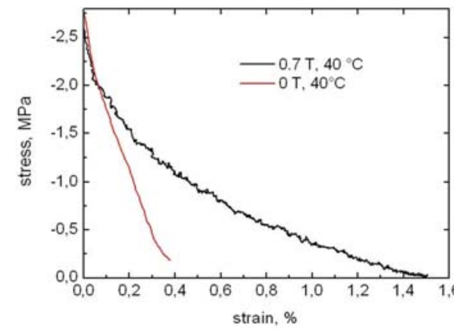

Relaxation of a polycrystalline sample after compression and unloading with and without magnetic field.

Angular dependence of magnetic shape memory effect – model and experiment.

O. Heczko
1. Institute for Metallic Materials, IFW Dresden, Dresden, Germany; 2. Laboratory of Materials Science, Helsinki University of Technology, Helsinki, Finland

Magnetic shape memory effect (MSME) is due to the redistribution of martensite twin variants in the magnetic field resulting in microstructure reorientation and giant strain [1]. The redistribution is driven by the difference of magnetic energy in differently oriented martensite variants. According the simple model [1-3] the MSME occurs, when the difference of magnetic energy ΔE_{mag} exceeds elastic energy needed for twin boundary motion.
$\Delta E_{mag} \geq \sigma_{tw}\, \varepsilon_0$ (1)
where σ_{tw} is twinning stress, and $\varepsilon_0 = 1 - c/a$ is tetragonal distortion of the lattice. The twinning stress describes the mobility of the martensitic twin boundaries. The magnitude of the twinning stress depends on the structure and the character of the obstacles in the material about which is known very little. Experimentally $\sigma_{tw}(\varepsilon)$, where ε is macroscopic strain, can be obtain from the stress-strain curve, i.e. from mechanical testing. This simple model describes reasonably well the observed MSM behavior in a single crystal with $\langle 100 \rangle$ orientation, i.e. in the orientation when magnetic field (or stress) is oriented along the a-axis of the crystal. In tetragonal 5M martensite, this axis is hard magnetic axis. In magnetic saturation in $\langle 100 \rangle$ orientation the difference of magnetic energy equals to $K_u \geq \sigma_{tw}\, \varepsilon_0$, where K_u is the magnetic anisotropy constant of tetragonal martensite. This value sets the largest difference and for other crystal orientations in the field the difference is smaller and thus it is expected that the MSME occurs in higher field. Although it is intuitively clear that the effect depends on crystal orientation in the magnetic field, the angular dependence of the MSM effect has not been studied rigorously. Here we calculate the difference of magnetic energy as a function of the angle between magnetic field and crystal axis and compare it with the experiment. The angular dependence is important for an application e.g. for the estimation of MSM effect in randomly oriented polycrystal.
The experiment was performed on single crystal close to stoichiometric Ni_2MnGa with Mn excess having 5M martensitic structure and exhibiting MSME at room temperature. The martensite-to-austenite transformation temperatures was 314 K. The MSME was evaluated from the magnetization curves measured in different angles to $\langle 100 \rangle$ crystal axis. The sharp magnetization change in the magnetization curve (Fig. 1) is a sign of the structural reorientation or MSME.
The model calculation was performed for idealized two variants microstructure assuming that the variants behave independently in the field, i.e. any mutual interaction is neglected. Additionally ideal uniaxial anisotropy behavior is assumed for each variant. Fig. 2 shows calculated difference as a function of the angle between magnetic field and $\langle 100 \rangle$axis.
The angular dependence of MSME is measured and observed behavior is compared with the prediction made from equation (1). However the prediction cannot be very precise as the angular dependence of the twinning stress is not yet known.

[1] O. Heczko, A. Sozinov, and K. Ullakko, IEEE Trans. Magn. 36, 3266 (2000)

[2] A.A. Likhachev and K. Ullakko, Physics Letters A 275, pp. 142-151 (2000)

[3] O.Heczko, J. Magn. Magn. Mat. 290-291, 787 (2005).

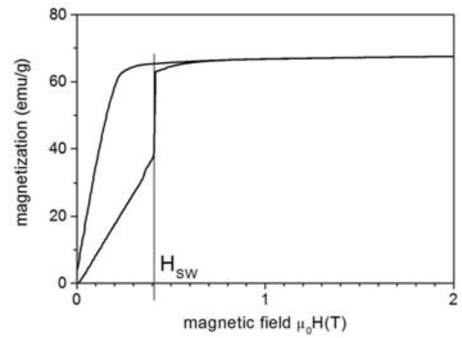

Fig. 1. Magnetization loop of Ni49.7Mn29.1Ga21.2 single crystal. The definition of switching field is marked in figure.

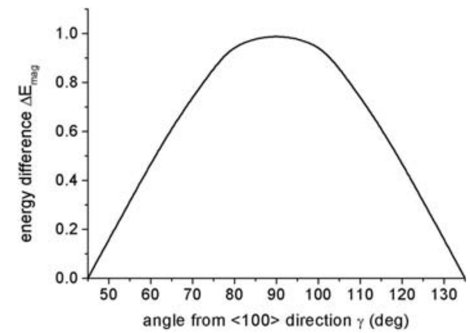

Fig. 2. Difference of the magnetic energy for different angles scaled to the maximum at <100> orientation.

CH-06

Magnetic properties of rapidly quenched Ni-Mn-Ga wires.

C. Gomez-Polo[1], J. Pérez-Landazábal[1], V. Recarte[1], V. Sánchez-Alarcos[1], G. Badini[2]
1. Dept. Fisica, Universidad Publica de Navarra, Pamplona, Spain; 2. Instituto de Ciencia de Materiales, CSIC, Madrid, Spain

Ferromagnetic shape memory alloys (FSMA) are characterized by the occurrence of large magnetic-field-induced strains as a result of the re-orientation of martensitic variants under applied magnetic field [1]. In particular, large magnetic field induced strains of around 10 % has been observed in Ni_2MnGa single crystals [2]. However, the analysis of production methods to obtain FSMA alloys to be applied as MicroElectroMechanical Systems (MEMS) elements constitutes one of the most interesting topics regarding the application of these new magnetostrictive alloys.
In this work, the magnetic properties of Ni-Mn-Ga FSMA in wire form is reported. Wires, with nominal composition $Ni_{2.10}Mn_{0.98}Ga_{0.92}$ and mean diameter 170 µm, were obtained by the rotating water bath melt spinning technique. Pieces of wire were annealed under vacuum at 400°C, 600°C and 800°C during 15 min.
The Scanning Electron Microscopy images show (see fig.1) that the as-cast wire displays a typical dendrite-like (cellular) structure of rapidly solidified alloys. The martensitic transformation, monitored through Differential Scanning Calorimetry, is mainly determined by the compositional heterogeneity associated to such cellular structures. The main effect of the low temperature annealings (annealing temperatures, $T_a \leq 600°C$) is to shift the broad martensitic transformation towards higher measuring temperatures as a consequence of the increase in the atomic order (i.e. atomic rearrangements associated to the annihilation of quenched-in vacancies and relaxation of quenched-in stresses). Once that the cellular structure disappears through thermal treatments leading to the recrystallization of the sample ($T_a = 800°C$), the martensitic transformation does not significantly differ from the transformation in the bulk sample.
With respect to the magnetic behavior of the alloy, a SQUID magnetometer was employed in the magnetic characterization of the samples. A remarkable decrease in the saturation magnetization is detected in the as-cast sample and correlated to the Mn-Mn antiferomagnetic interactions associated to structural defects (mainly antiphase boundaries, APBs). The recovery effect (mainly elimination of APBs) for low temperature annealings ($T_a \leq 600°C$), leads to an increase in the mean magnetization of the sample (see fig. 2), reaching similar values than those reported for the tetragonal phase (saturation value, $M_S \approx 81$ emu/g). The results indicate that a high temperature annealing (i.e. recrystallization of the sample) is required to optimise both the martensitic transformation and the magnetic characteristics of these rapidly quenched NiMnGa wires.

1.- K. Ullakko, J.K. Huang, C. Kantner, R.C. O'Handley, V.V. Kokorin, Appl. Phys. Lett. 69 (1996) 1966-1968.

2.- A. Sozinov, A.A. Likhachev, N. Lanska, K. Ullakko, Appl. Phys. Lett. 80 (2002) 1746-1748.

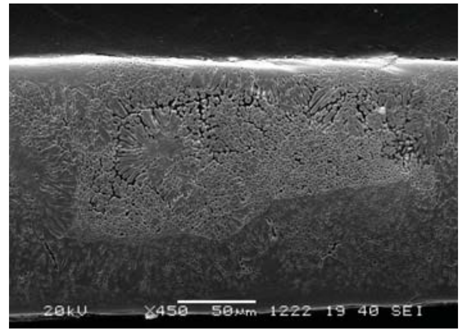

Fig. 1: Scanning Electron Microscope (SEM) images of the as-cast wire.

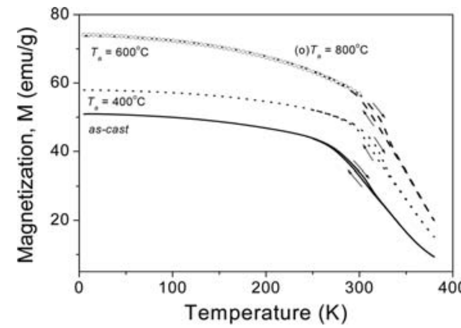

Fig. 2: Temperature dependence of the magnetization (6 T applied magnetic field) in the as-cast and annealed states.

CH-07

Comparative study of structural and magnetic properties of bulk and powder Ni52Fe17Ga27Co4 magnetic shape memory alloy.

J. Liu, N. Scheerbaum, D. Hinz, O. Gutfleisch
Institute for Metallic Materials, IFW Dresden, Dresden, Germany

Magnetic shape memory (MSM) alloys have attracted considerable attention within the last decade, owing to their capability to produce large magnetic-field-induced strain [1]. Ni-Fe-Ga-Co has been proposed as a new MSM system due to its wide martensitic and magnetic transformation temperature range [2]. We have shown recently that the martensitic transformation temperature Tm and the Curie temperature Tc can be tailored in a wide range by changing composition and heat treatment, Tm ~ 170 to 370 K and Tc ~ 280 to 400 K [3]. In particular, the alloy composition Ni52Fe17Ga27Co4 is more interesting for practical application due to its relatively high martensitic and magnetic transformation temperature (Tm = 363 K, Tc = 360 K).
Here, martensitic transformation, phase structure and magnetic properties of Ni52Fe17Ga27Co4 alloys in form of bulk and powder were studied. Bulk samples were prepared by arc-melting followed by annealing at 1473 K for 4 h, while powder samples were made from the bulk by filing and annealing at 673 K for different times (0 ~ 15 h). The martensitic transformation temperatures were determined using a differential scanning calorimeter (DSC, Perkin Elmer Pyris 1). The crystal structures were determined by X-ray diffraction at room temperature (XRD, Philip X'Pert, cobalt Kα radiation). Magnetic properties were analyzed using a high-temperature a.c. susceptometer (6 kHz), a SQUID magnetometer (Quantum Design MPMS-5S) and a vibrating sample magnetometer (VSM).
The peaks related to the martensitic transformation of the bulk sample, which are detected by DSC (Fig. 1), totally disappeared after powderisation. The Curie temperature of the powder sample is about 100 K lower than that of the bulk one (Fig. 2). The temperature hysteresis of magnetisation for the bulk sample is ascribed to a coupling of martensitic and magnetic transformations. Additionally, the saturation magnetisation (Msat = 54 emu/g) of the bulk sample is reduced significantly down to 35 emu/g by powderization, but increased again with increasing annealing time (Fig. 3). After the powders were annealed for 15 h, the Msat is up to 64 emu/g. This value is even above that of the bulk sample. However, after annealing, the martensitic transformation of the powder samples is still absent in both DSC and SQUID measurements. From XRD patterns (Fig. 4), it is found that the bct martensite in the bulk sample is completely transformed to a disordered fcc phase by filing, and then gradually changed into a bcc austenite phase during the subsequent annealing. The change of magnetic properties, e.g. Tc and Msat, of powdered samples is discussed in relation to the structural evolution.

[1] K. Ullakko, J.K. Huang, C. Kantner, R.C. O'Handley, and V.V. Kokorin, Appl. Phys. Lett. 69 (1996) 1966.

[2] K. Oikawa, Y. Imano, V.A. Chernenko, F.H. Luo, T. Omori, Y. Sutou, R. Kainuma, T. Kanomata, and K. Ishida, Mater Trans 46 (2005) 734.

[3] J. Liu, N. Scheerbaum, D. Hinz, and O. Gutfleisch, Acta Mat. submitted.

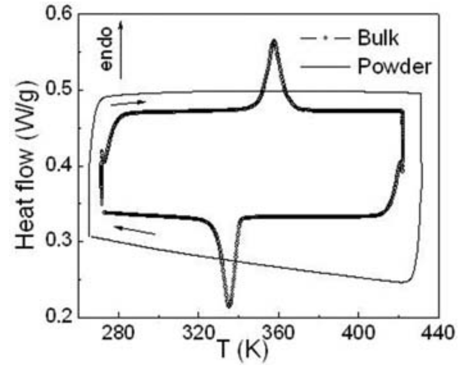

Fig. 1. DSC curves of bulk and powdered Ni52Fe17Ga27Co4.

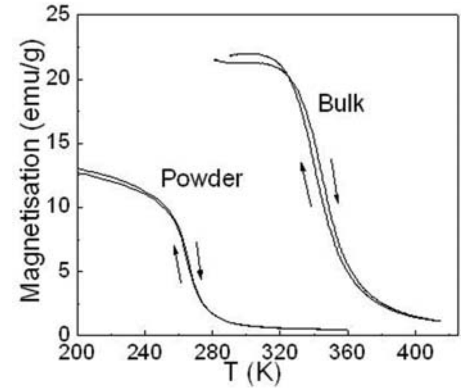

Fig. 2. Magnetisation vs. temperature curves of bulk and powdered samples.

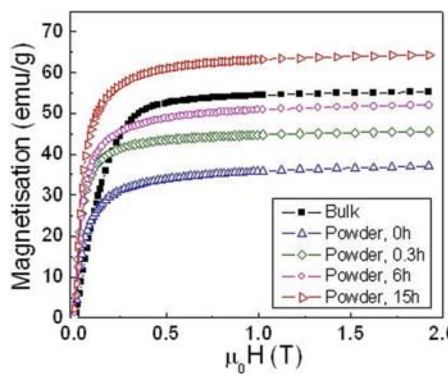

Fig. 3. Magnetisation curves of bulk and powder annealed for different times at 673 K samples at 10 K.

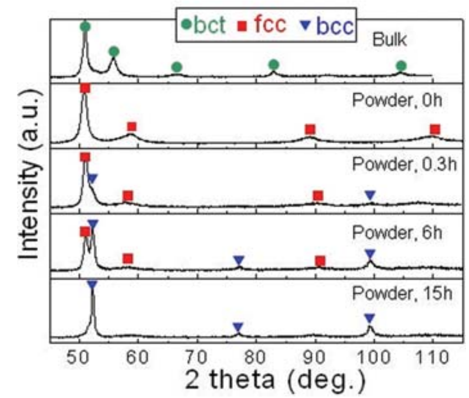

Fig. 4. XRD patterns of bulk and powder annealed for different times at 673 K samples.

CH-08

Magnetocaloric effect and martensitic transition in Ni-Mn-In alloys under hydrostatic pressure.

J. Lyubina[1], O. Gutfleisch[1], K. Nenkov[1], L. Mañosa[2], X. Moya[2], A. Planes[2], M. Barrio[3], J. Tamarit[3], S. Aksoy[4], T. Krenke[4], M. Acet[4]
1. Institute for Metallic Materials, IFW Dresden, P.O. Box 270116, D-01171 Dresden, Germany; 2. Facultat de Fisica, Dept. d'Estructura i Constituents de la Materia, Universitat de Barcelona, Diagonal 647, E-08028 Barcelona, Spain; 3. Dept. de Fisica i Enginyeria Nuclear, Universitat Politecnica de Catalunya, Diagonal 647, 08028-Barcelona, Spain; 4. Experimentalphysik, Universität Duisburg-Essen, D-47048 Duisburg, Germany

Near room-temperature magnetic refrigeration based on the magnetocaloric effect (MCE) is becoming a promising technology to replace the conventional gas-compression/expansion technique. Recently, several materials with a so-called giant MCE have been discovered, such as $Gd_5Si_2Ge_2$, $MnAs_{1-x}Sb_x$, $(Mn,Fe)_2(P,As)$- and $La(Fe,Si)_{13}$-type [1]. A first-order magnetic phase transition is common for all these materials that gives rise to an abrupt change of the magnetisation near the transition point. The large MCE in Ni-Mn-based Heusler compounds with compositions close to the stoichiometric Ni_2MnX (X = Ga, Sn, In, Sb) follows from a coupling between the martensitic transition and the magnetic order [2]. The magnetic properties of these alloys are sensitive to the distance between neighbouring Mn atoms and various types of magnetic behaviour are observed for various X elements [3,4].

In this work, we report the effect of hydrostatic pressure on the martensitic transformation and MCE in $Ni_{50}Mn_{34}In_{16}$ and $Ni_{49.5}Mn_{35.5}In_{15}$ alloys prepared by arc melting and subsequent heat treatment at 1073 K/ 2 h.

According to the Rietveld refinement of x-ray data (Cu Kα radiation, temperature range 40 - 350 K, ambient pressure), the high temperature austenite phase has the cubic $L2_1$ structure. The transformation to the martensite starts at about 240 K. At low temperatures, the modulated martensite structure is observed, presumably of 14M-type.

Figure 1 shows the temperature dependence of the magnetisation at a low magnetic field at selected applied pressures for $Ni_{50}Mn_{34}In_{16}$. The measurements have been performed using a SQUID magnetometer in a zero-field-cooled (ZFC), field-cooled (FC), and field-heated (FH) sequence. On cooling, the cubic $L2_1$ phase orders ferromagnetically at $T_c \approx 310$ K which causes a sharp increase of the magnetisation. At a lower temperature M_s, the sample transforms to the martensitic phase, and there is a sharp drop of the magnetisation. Upon further cooling the Curie temperature of the martensite is reached and the magnetisation rises again. The hysteresis in the FC and FH curves is a consequence of the first order character of the martensitic transition, while the splitting between the ZFC and FH curves is apparently associated with the presence of low temperature anisotropy. Whereas the magnetisation of the austenite and martensite phases is essentially unchanged on applying the pressure, all the characteristic temperatures associated with the martensitic transition shift to higher values as the pressure is increased (Fig. 1). The shift is also consistent with differential thermal analysis measurements under pressure [5]. It is observed that the transition temperature shift dT/dp varies with In concentration.

The magnetic entropy change ΔS_M has been calculated from the magnetisation versus field curves using the Maxwell relation [1]. Figure 2 shows ΔS_M for a field change of $\Delta H = (0 - 2)$ T for $Ni_{50}Mn_{34}In_{16}$. The sign of ΔS_M is positive in the temperature range near the martensitic transition, whereas negative ΔS_M values are observed near the Curie temperature of the austenite. As pressure increases, the positive $\Delta S_M(T)$ peak shifts to higher temperatures and the maximum entropy change ΔS_{max} increases from 225 to 265 kJ/m^3. However, the relative cooling power (RCP), integrated area under the $\Delta S_M(T)$ peak, remains essentially unchanged and is equal to 1.0(1) MJ/m^3. The analysis of the influence of pressure and magnetic field on the MCE and martensite transformation in the Ni-Mn-In alloys will be discussed in detail.

[1] K.A. Gschneidner Jr., V.K. Pecharsky, A.O. Tsokol, Rep. Prog. Phys. 68 (2005) 1479.

[2] T. Krenke, E. Duman, M. Acet, E.F. Wassermann, X. Moya, L. Manosa, A. Planes, Nature Materials 4 (2005) 450.

[3] J. Enkovaara, O. Heczko, A. Ayuela, R.M. Nieminen, Phys. Rev. B 67 (2003) 212405.

[4] T. Krenke, M. Acet, E. F. Wassermann, X. Moya, L.Manosa, A. Planes, Phys. Rev. B 73 (2006) 174413.

[5] L. Manosa, X. Moya, A. Planes, O. Gutfleisch, J. Lyubina, M. Barrio, J.-L. Tamarit, S. Aksoy, T. Krenke, M. Acet, Appl. Phys. Lett. (in press).

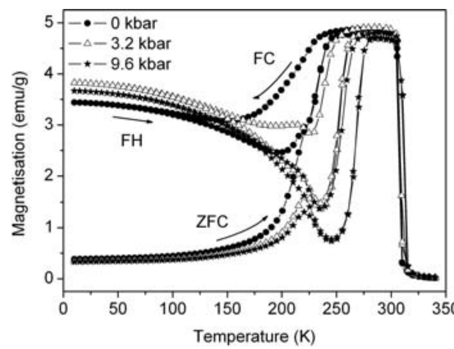

Fig. 1. Low field (H = 50 Oe) magnetisation versus temperature curves of $Ni_{50}Mn_{34}In_{16}$ for selected applied pressures.

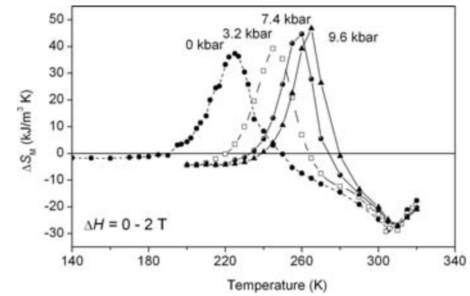

Fig. 2. Temperature dependence of the magnetic entropy change ΔS_M of $Ni_{50}Mn_{34}In_{16}$ under a magnetic field change of 0-2 T.

CH-09

Magnetic domain reorganization and twin boundary dynamics in magnetic shape memory alloys.

J. McCord
Institute for Metallic Materials, IFW Dresden, Dresden, Germany

Magnetic shape memory alloys (MSMAs) attract considerable research focus due to the exhibited magnetic field induced strain (MFIS, up to 10% for NiMnGa) for potential applications in e.g actuators. Under an external magnetic field, the twin variants with the easy axis parallel to the field grow by twin boundary motion. Investigating the performance during (fast) reorientation process provides vital information for the optimization of the properties for future devices. Using a unique dynamic actuation experimental set-up, the congruent magnetic field induced reorientation of crystallographic and magnetic domains could by imaged directly for the first time up to frequencies approaching the dynamic limit of MSMAs.
From static magnetic surface domain imaging, using a magneto-optical indicator film technique (MOIF), a clear picture of the volume domains of NiMnGa MSMA single crystals is derived. One example of domain images obtained separately from four different surfaces of the same crystal in the same state of magnetization is displayed in Fig. 1. With the occurrence of a twin boundary, also a hidden surface inside the bulk material has to be considered. Starting from this analysis, it is demonstrated that a reorganization of the magnetic domains is not required for the occurrence of twin boundary motion (Fig. 2). With the abrupt nucleation of the second variant sections of magnetically highly charged head-on domain structures at the twin boundaries are formed. The absence of interaction between magnetic and structural domains is different from currently proposed models, which assume domain wall movement under an external field.
Based on these results, the actuation performance of different MSMAs single crystals at various frequencies is presented. Reversible twin boundary motion activated in the frequency range up to 600 Hz is observed (Fig. 3). Strain hysteresis curves measured at different frequencies show similar onset of fields of strain. An average twin boundary mobility up to $2*10^5$ μm/s is found. The maximum field-induced strain increases with actuation frequency. Twin boundary mobility enhancement by fast twin boundary motion is proposed to explain the increase in MFIS.
Additional experimental data from temperature dependent measurements, from other MSMA bulk materials, and from thin films will be presented for comparison. The results provide significant information of twin boundary performance during static and high frequency actuation, and give important guidance to the refinement of already existing models of twin boundary motion.
Funding through the DFG Priority Program SPP1239 is gratefully acknowledged.

Y.W. Lai et al. Appl. Phys. Lett. 90 (2007) Nr. 19, S. 192504

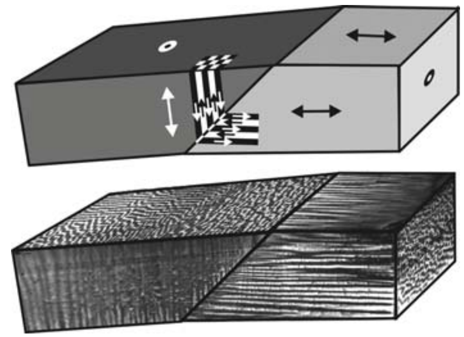

Fig. 1. (top) Scheme of MSMA crystal with two variants. The easy axis of magnetization corresponding to the crystallographic c-axis are indicated. (bottom) Magnetic domain images obtained from the sample surfaces of the crystal by MOIF imaging.

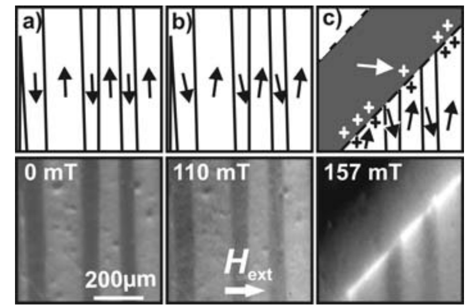

Fig. 2. Development of magnetic domain patterns imaged by MOIF technique together with an domain interpretation under an increasing field perpendicular to the initial easy axis of magnetization. The direction of the external field is indicated.

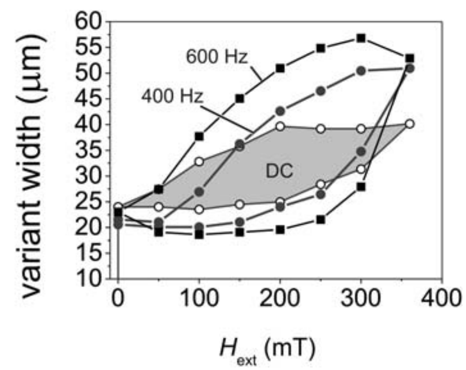

Fig. 3. Frequency dependence of hysteresis in variant width. A restoring mechanical compressive stress was applied to the sample.

CH-10

Exchange bias in Ni-rich ferromagnetic shape memory alloys Ni-Mn-Sn.

V. Khovaylo[1], V. Koledov[1], V. Shavrov[1], A. Korolyov[2], M. Ohtsuka[3], H. Miki[4], T. Takagi[4]
1. Institute of Radioengineering and Electronics, Moscow, Russian Federation; 2. Institute of Metal Physics, Ekaterinburg, Russian Federation; 3. Institute of Multidisciplinary Research for Advanced Materials, Tohoku University, Sendai, Japan; 4. Institute of Fluid Science, Tohoku University, Sendai, Japan

Recently, it was found that for ferromagnetic Heusler alloys $Ni_{50}Mn_{25}Sn_{25}$, $Ni_{50}Mn_{25}In_{25}$, and $Ni_{50}Mn_{25}Sb_{25}$, deviation from the stoichiometry results in appearance of martensitic transformation [1]. For these systems, the martensitic transformation temperature decreases upon substitution of Mn for Sn, In or Sb; an especially drastic decrease was observed in the NiMnIn system.
The stoichiometric $Ni_{50}Mn_{25}Sn_{25}$ has a Curie temperature T_C ~ 350 K and a saturation magnetic moment ~ 4.3 μ_B. Structural instability observed in $Ni_{50}Mn_{50-x}Sn_x$ has a considerable impact on magnetic properties of these compounds. The compositional dependence of the Curie temperature T_C of the austenitic phase was found to be small, while T_C of the martensitic phase strongly depends on the composition and drastically decreases with decreasing Sn content [1,2]. Magnetic properties of this system is quite interesting and has not been understood clearly yet. For example, it was reported [2] that different strength of exchange interactions in martensitic and austenitic phases of $Ni_{50}Mn_{37}Sn_{13}$ leads to an unusual sequence of magnetic transitions, namely, upon heating low-temperature ferromagnetic state transforms to a paramagnetic state at intermediate temperatures and then again to ferromagnetic state upon further heating. It has also been reported that in Co-substituted Ni(Co)-Mn-Sn highly magnetized austenite transforms to presumably antiferromagnetic martensite with negligible net magnetization [3]. Besides, very recently exchange bias behavior has been observed in $Ni_{50}Mn_{50-x}Sn_x$ alloys [4,5].
Motivated by the recent experimental results obtained for the Ni-Mn-Sn system, we studied low-temperature magnetic properties of Ni-Mn-Sn alloys with Ni excess by a SQUID magnetometer. Polycrystalline $Ni_{50+x}Mn_{37-x}Sn_{13}$ (A series) and $Ni_{50+y}Mn_{39-y}Sn_{11}$ (B series) ingots were prepared by a conventional arc-melting method. Since the weight loss during arc-melting was small (<0.2%) we assume that the real composition corresponds to the nominal one. The ingots were annealed at 1273 K for 24 h and quenched in ice water.
Field dependencies of magnetization $M(H)$ of the samples studied measured at liquid helium temperature indicate that in low fields $M(H)$ has a complex character. Specifically, when a sample is cooled down in zero magnetic field, the virgin magnetization curve differs significantly from subsequent full $M(H)$ loop. An example of these measurements is shown in Fig. 1 for the case of $Ni_{53}Mn_{34}Sn_{13}$ composition.
Solid experimental evidence for the existence of antiferromagnetic interactions at low temperature in Ni-Mn-Sn alloys with Ni excess can be obtained in the case when $M(H)$ loop is measured after field-cooling protocol. The shift of the hysteresis loop due to the exchange anisotropy is attributed to the coexistence of antiferromagnetic and ferromagnetic exchange interactions in the studied alloys. An example of these measurements is shown in Fig. 2 for the case of $Ni_{53}Mn_{36}Sn_{11}$ composition.
This work was partially supported by Russian Foundation for Basic Research Grants Nos. 06-02-16266, 06-02-39030 and 07-02-13629.

[1] Y. Sutou, Y. Imano, N. Koeda, T. Omori, R. Kainuma, K. Ishida, and K. Oikawa, Appl. Phys. Lett. 85 (2004) 4358.

[2] T. Krenke, M. Acet, E.F. Wassermann, A. Moya, L. Manosa, and A. Planes, Phys. Rev. B 72 (2005) 014412.

[3] R. Kainuma, Y. Imano, W. Ito, H. Morito, Y. Sutou, K. Oikawa, A. Fujita, K. Ishida, S. Okamoto, O. Kitakami, and T. Kanomata, Appl. Phys. Lett. 88 (2006) 192513.

[4] Z. Li, C. Jing, J. Chen, S. Yuan, S. Cao, and J. Zhang, Appl. Phys. Lett. 91 (2007) 112505.

[5] M. Khan, I. Dubenko, S. Stadler, and N. Ali, J. Appl. Phys. 102 (2007) 113914.

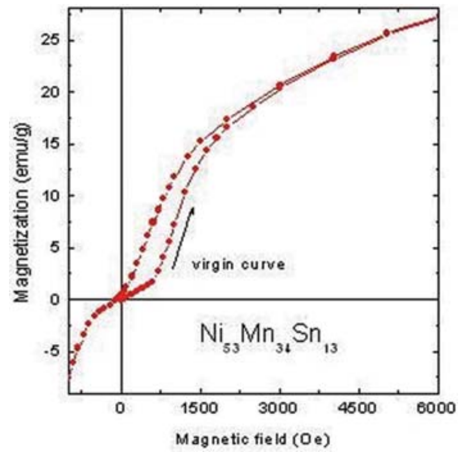

Fig. 1. Zero field cooled magnetization curve for $Ni_{53}Mn_{34}Sn_{13}$ alloy

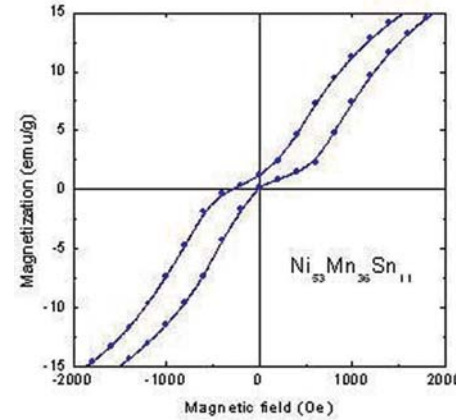

Fig. 2. Exchange anisotropy observed in $Ni_{53}Mn_{36}Sn_{11}$ alloy after field cooling protocol

CH-11

Magnetic and shape memory properties of FeMnSi-based glass-coated microwires.

H. Chiriac[1], *N. Lupu*[1], C. M. Craciunescu[2], S. Corodeanu[1], M. Grigoras[1]
1. Magnetic Materials and Devices, National Institute of Research and Development for Technical Physics, Iasi, Romania; 2. "Politehnica" University, Timisoara, Romania

Ferromagnetic shape memory alloys (FSMAs) belong to the class of smart materials whose physical properties depend on the interaction between thermal, magnetic and elastic energy. They are among the newest type of alloys that focused attention for use in actuators and transducers. The ferromagnetic Ni_2MnGa is the most well known and studied FSMA [1]. However, the occurrence of shape memory properties in Heusler-type alloys is limited to single crystal [1] and polycrystalline thin films and melt-spun ribbons [2,3]. More recently, it was reported the shape memory behavior in FeMnSi intermetallics [4]. In this work, we report the magnetic and shape memory properties of Fe-Mn-Si glass-coated microwires with additions of Ni and Cr, as an approach leading to new developments in the exploration of FSMAs prepared in different shapes.
(Fe,Ni)-Mn-(Si,Cr) glass-coated microwires have been prepared by glass-coated melt-spinning. The metallic nucleus of the microwires was ranging between 14 and 25 μm, whilst the glass coating varied between 15 and 40 μm. Mn has been substituted in the $Fe_{62}Mn_{33\text{-}x\text{-}y}Si_5$ master alloy with x = 8-12 at.% of Cr and y = 5 at.% Ni. $Fe_{62}Mn_{32}Si_6$ microwires have been also prepared. The structural studies indicated the formation of martensite-type $L2_1$ phase along with small traces of α-Fe. No other superlattice reflections have been observed in the as-quenched glass-coated microwires. The EDS spectra of the microwires after glass removal proven that the composition is very close to the nominal one, with slight differences for Mn content. No oxygen intakes have been detected.
The magnetic behavior of the as-quenched glass-coated microwires depends strongly on the composition and the ratio between the diameter of the metallic core and the glass thickness (Fig. 1).
Usually, FSMAs are paramagnetic in the as-cast state, their ferromagnetic behavior being induced by proper annealing [3]. On the contrary, for Fe-Mn-Si glass-coated microwires the ferromagnetic behavior is induced during the preparation process for certain compositions or/and ratios metallic core/glass thickness, as shown in Figs. 1 and 2.
It is worth noting that the character of martensite-austenite transformation in Fe-Mn-Si FSMAs is dramatically changing as a function of composition. The glass-coated microwires with additions of Cr and Ni exhibit premartensitic transformations to intermediate phase while for Fe-Mn-Si only direct martensite-austenite transformation is observed. One should notice also that the martensitic temperature (T_m) is shifted to higher temperatures (above 500 K) compared with already known Ni2MnGa FSMAs [1], indicating these novel materials suitable for different applications. All these aspects will be discussed in detail considering the electronic and the specific magnetic domains structure of Fe-Mn-Si-based glass-coated microwires.
Support from the Romanian CEEX Programme (Project Nano-4M) is highly acknowledged.

[1] C.J. O'Connor, V.O. Golub, A.Ya. Vovk, V.V. Kotov, P. Yakovenko, K. Ullakko, IEEE Trans. Magn. 38 (2002) 2844.

[2] H. Rumpf, C.M. Craciunescu, H. Modrow, Kh. Olimov, E. Quandt, M. Wuttig, J. Magn. Magn. Mater. 302 (2006) 421.

[3] V.A. Chernenko, E. Cesari, J. Pons, and S. Segui, J. Mater. Res. 15 (2000) 1496.

[4] A. Candini, O. Moze, W. Kockelmann, E. Brück, O. Tegus, J. Appl. Phys. 95 (2004) 6819.

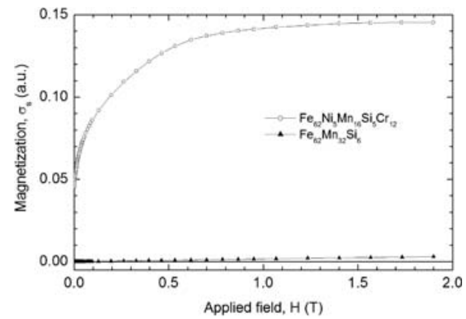

Fig. 1. First magnetization curves for Fe-Mn-Si and (Fe,Ni)-Mn-(Cr,Si) glass coated microwires with the metallic core diameter of 15 μm and the glass coat of 40 μm.

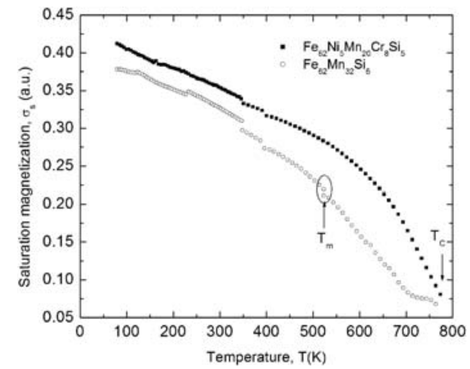

Fig. 2. Thermomagnetic curves for Fe-Mn-Si and (Fe,Ni)-Mn-(Cr,Si) glass coated microwires with the metallic core diameter of 20 μm and the glass coat of 20 μm.

CL-01

Analytical computation and experimental verification of magnetic core loss of permanent magnet generator considering the wind turbine speed.

S. Jang[1], *K. Ko*[1], J. Choi[1], H. Cho[2]
1. Chungnam Nat'l Univ, Daejeon, South Korea; 2. Korea Institute of Machinary & Materials, Daejeon, South Korea

Nowadays more attention is paid to the developing high efficiency electrical machines for energy saving and protection of natural resources. [1] In general, the electromagnetic losses appearing in electrical machines are widely classified into copper loss, core loss and rotor loss. In permanent magnet (PM) synchronous machines, core losses form a larger portion of the total losses than in another machine. So, satisfactory prediction of core loss at the design or analysis stage of PM machines is essential to active high efficiency and high performance.

Core loss in a magnetic material occurs when the material is subjected to a time varying magnetic flux. Traditionally, core losses consist of two components. The first component of core losses is the hysteresis loss which is the rate of change of the energy used to effect magnetic domain wall motion as the domain grows and rotates under the influence of an externally applied magnetic field. Hysteresis losses vary as a function of the frequency of the applied field. The second component of core losses is eddy current losses which flow in closed paths within the magnetic material. The eddy current losses are proportional to the square of the frequency of flux. [1]

For electrical machine designers, core loss data are usually provided in the form of tables or curves of total loss versus flux density or frequency. So, engineers normally use loss data obtained from the Epstein test as a basis on which to predict the core loss of each part of a particular machine with corresponding assumed flux density there. This method has been proved to have good precision in predicting core loss in transformers where the alternating field is dominant. However, complex flux distribution, flux density harmonics, and the rotational field in rotating machines bring great difficulties for the evaluation of core loss. [2][3]

This paper deal with core loss estimation of PM generator for wind power application using modified Steinmetz equation considered anomalous loss. Moreover, using the nonlinear finite element analysis (FEA), we applied separated rotating and alternating magnetic field to core loss calculation. Figure 1 shows the detail calculating process of core loss by proposed method. As shown in figure, in Step-1, the core loss data provided by manufacture are rearranged and plotted as a function of Pcore/f vs. B. In Step-2, the data of frequency vs. Core loss are plotted by curve fitting of Pcore/f vs. B plot and nonlinear curve fitting functions for core loss coefficient are derived. In Step-3, using the nonlinear FEA, the rotating and alternating magnetic field are separated. In Step-4, core losses are calculated using the obtained core loss coefficients.

In order to verify the core loss results by proposed method, the experimental system has been implemented with 3-ph induction motor, power analyzer (PM3300-Voltech) and manufactured PM generator. Figure 2 shows the experimental setup for no-load core loss measurement. The core losses data are obtained by subtract output power without stator core from output power with stator core.

From the comparison of between analysis results calculated using the obtained core loss coefficients and the provided core loss data, the deducted core loss coefficients have been validated, as shown in figure 3 (a). And, as shown in figure 3 (b), the analysis results with wind turbine speed agree extremely well with those obtained by nonlinear FEA and measurement.

[1] Y. Chen, and P. Pillay, "An improved formula for lamination core loss calculations in machines operating with high frequency and high flux density excitation," 37th IAS Annual Meeting. Conference Record, Vol. 2, pp. 759-766, 2002.

[2] L. Ma, M. Sanada, S. Morimoto and Y. Takeda, "Iron loss prediction considering the rotational field and flux density harmonics in IPMSM ans SynRM," IEE Proc.-Electr. Power Appl., Vol. 150, No. 6, Nov. 2003.

[3] M. Enokizono, T. Suzuki, J. Sievert, J. Xu, "Rotational power loss of silicon steel sheet," IEEE Trans. Magn., Vol. 26, No. 5, pp. 2562-2564, 1990.

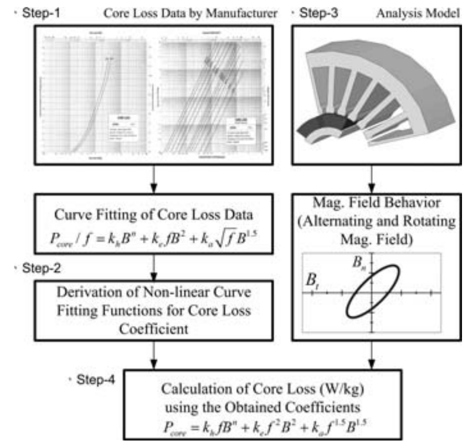

Fig. 1. The process of proposed core loss calculation method.

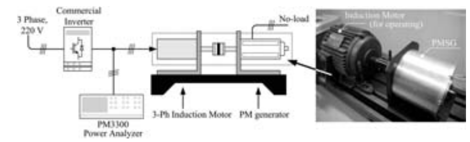

Fig. 2. The experimental setup for no-load core loss measurement.

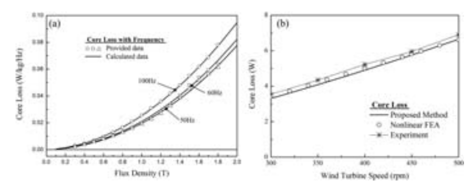

Fig. 3. (a) Analysis results and the provided core loss data, (b) Core loss with wind turbine speed

CL-02

Stator core loss prediction in large synchronous machines.

A. Knight, S. Troitskaia, Y. Zhan
Electrical and Computer Eng, University of Alberta, Edmonton, AB, Canada

A comparison between numerical and analytical approaches to calculate the stator core loss of large synchronous machines is presented. The approaches are implemented on machines with ratings above 1 MVA and skewed stators. The proposed approach allows the investigation of skew and inter-bar currents in the amortisseur circuits. The numerical approach used is a multi-slice 2D FEA model.
A multi-slice time-stepped FEA model is used to numerically predict the stator core losses [1]. This method is impractical for design use, but is used to provide a baseline prediction to evaluate the analytical method, due to the fact that it is impossible to segregate stator core loss during the test of a multi-MW machine. The analytical method predicts air gap flux density as the product of mmf and permeance functions [2]. Both sets of functions may be described using harmonic series that vary with time, angular position and axial position. The inputs to the analytical model are known mmf functions for the field and armature windings, the machine geometry, plus results from 4 magnetostatic FEA simulations. The magnetostatic FEA provides data on saturation level, plus harmonics to describe rotor and stator slot permeance harmonics. Both numerical and harmonic methods apply a bar-iron contact resistance interbar model to predict the amortisseur circuit currents [3]. A discrete number of axial loops are used to describe the currents: in the FEA model, these correspond to the number of FEA slices; in the harmonic model 5 slices are used, with discrete currents and mmf functions converted back to harmonic series.
In the harmonic method, the stator core flux is calculated by integrating the total air gap flux density over the surface of each tooth for each packet of laminations (between radial ducts). In order to do this, a number of assumptions are made: (1) if the angular period of a harmonic is less than one tooth pitch, λ, the flux harmonic will not penetrate down the tooth, skin effect must be considered (2) if the period is greater than λ, the flux penetrates down the tooth (3) all flux over λ enters the face of the tooth (4) flux density is uniform in a given region of the tooth or back iron. Each tooth is divided into 5 regions, increasing in distance from the air gap. The flux in each region allows the flux density to be calculated. If the flux passing through each tooth into the back iron is known, the back iron flux density can be calculated.
Core losses are calculated using traditional formulae for eddy, hysteresis and anomalous (or excess eddy current) loss. In both models, the core loss calculations require reconstruction of the flux density waveforms in the region of interest. In FE, the waveforms are constructed directly from the elemental vector potentials. In the analytical model the flux density harmonic series in each region of interest is summed to produce a time-domain signal. The number of flux density harmonics is typically in the range 2-5000.
Table 1 presents the predicted stator core loss values for three machines, for both open (OC) and short circuit (SC) test conditions. As mentioned earlier, direct measurement of stator core loss is not possible, however, the predictions are within the range of expectations based on measured total loss. It can be seen that the SC agreement is better than OC. This may be expected, as the SC condition is unsaturated, while OC tests are at a high flux level. OC predictions with the analytical method are consistently below FEA. Again, this may be expected as the analytical method assumes uniform back iron flux density between slots. It is well known that saturation causes uneven flux distribution in the back iron. The proposed method is consistent relative to FEA and provides the capability to rapidly analyze the impact of design changes. Future development of the method could involve adding a saturating reluctance network in the back iron.
Figure 1 illustrates the flexibility of the proposed method to analyze the impact of skew on SC stator core loss. It can be seen that total loss increases rapidly with increasing skew.

[1] McClay, C.I. and Williamson, S. Influence of rotor skew on cage motor losses. IEE Proc. EPA. 1998, Vol. 145, 5, pp. 414-422.

[2] Knight, A.M., Karmaker, H. and Weeber, K. Use of permeance model to predict force harmonics and damper winding effects in salient pole synchronous machines. IEEE Trans EC. Dec 2002, Vol. 17, 4, pp. 478-484.

[3] Dorrel, D.G., Holik, P.J. and Rasmussen, C.B. Analysis and effects of inter-bar current and skew in a long skewed-rotor induction motor for pump applications. IEEE Trans Magn. Jun 2007, Vol. 43, 6, pp. 2534-2536.

Rating (MVA)	1.28		14.1		7.0	
Simulation Type	FEA	Harmonic	FEA	Harmonic	FEA	Harmonic
OC Loss (kW)	5.1	4.0	32.9	24.2	21.4	15.5
SC Loss (kW)	1.1	1.6	8.4	8.4	6.2	6.2

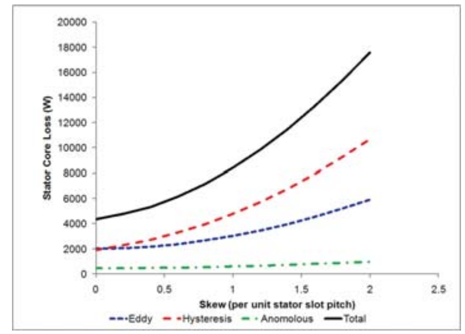

Figure 1. Effect of skew on short circuit stator core loss

Design and analysis of ultra high-speed permanent magnet generator driven by gas turbine for micro scale power generation.

S. Jang[1], *K. Ko*[1], J. Choi[1], Y. Lee[2]
1. Chungnam Nat'l Univ, Daejeon, South Korea; 2. Korea Institute of Science of Technology, Seoul, South Korea

Recently more attention has been paid to the development of a high-speed permanent magnet synchronous generator (PMSG) driven by gas-turbine. Since the generating system applying to PMSG do not have mechanical coupling such as gearbox, they have outstanding performances such as high efficiency, high power density, small size, low weight, simple mechanical construction, easy maintenance and good reliability, etc.[1][2] Since PMSG used in the portable or emergency power supplies, power generation using renewable energy resources, electric vehicles, and main generator for aircraft, are almost demanded good reliability, the design and accurate electromagnetic analyses of high-speed PMSG are essential.[3] However, it is quite difficult to design the high-speed PMSG because both mechanical and electromagnetic aspects should be considered owing to high rotor speed and high frequency in a stator.

Therefore, this paper deals with the design of an 870,000rpm class high-speed PMSG applied to micro turbine system. As shown in Fig. 1(a) and (b), since space where the high-speed PMSG coupled with the micro turbine occupies in the system is strictly limited, the work described in this paper is motivated by the desire to make maximum output power of the generator considering rotor dynamics, rotor structures, winding methods and bearing system under restricted space. First, we determine an axial active length and outer diameter of the rotor considering rotor dynamics. In particular, using simple open-circuit field solution obtained from space-harmonic method, we also determine the proper rotor structure by investigating the air-gap flux density due to PMs according to material (or permeability) of the rotor shaft. And then, since simple stator structure and compact winding method are required for our system due to restricted small space, slotless stator structure with an air-foil bearing and ring-wound method are employed for our work. Finally, we design and manufacture the high-speed PMSG shown in Fig. 1(c). The design procedure is shown in figure 2. As shown in figure, from solution by open-circuit and armature reaction filed of the determined model, we estimated electrical parameters such as back EMF constant, resistance and inductance. And, using the estimated electrical parameter, output characteristics of PMSG is obtained. As shown in figure 3, analysis results are validated by comparison with nonlinear FEA and experimental results. More detailed experimental and analysis results, discussion and design procedures will be presented in the final paper.

[1] Wang Fengxiang, Zheng Wenpeng, Zong Ming and Wang Baoguo, "Design Considerations of High-Speed PM Generators for Micro Turbines," PowerCon 2002, Vol. 1, pp. 158–162, Oct. 2002.

[2] W. L. Soong, N. Ertugrul, "Inverterless high-power interior permanent magnet automotive alternator," IEEE Trans. Energy Conversion, Vol. 40, pp. 1083-1091, 2004.

[3] T. F. Chan, L. L. Lai, Lie-Tong Yan, "Performance of a three phase AC generator with inset NdFeB permanent magnet rotor," IEEE Trans. Magn., Vol. 19, pp. 88-94, 2004.

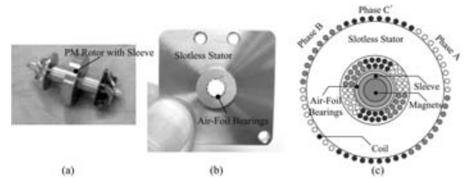

Fig. 1. (a) Rotor part of the high speed generator coupled with a blower and sleeve, (b) stator part of the high speed generator and (c) designed high speed generator.

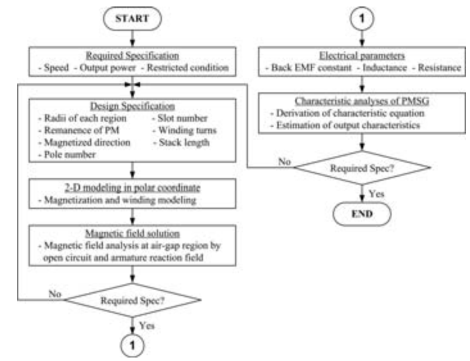

Fig. 2. The design flow chart of high-speed PMSG

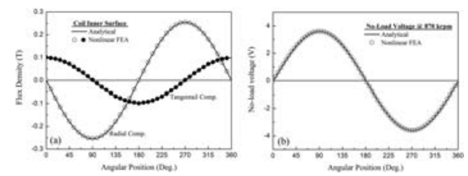

Fig. 3. The comparison between analytical method and nonlinear FEA; (a) Flux density at coil inner surface and (b) no-load voltage.

CL-04

Electromagnetic Performance Analysis and Vector Control of a Flux-Controllable Stator-PM Brushless Motor with Skewed Rotor.

M. Cheng[1], X. Zhu[1,2], W. Hua[1], H. Jia[1]
1. School of Electrical Engineering, Southeast University, Nanjing, China; 2. School of Electrical Information Engineering, Jiangsu University, Zhenjiang, China

Permanent magnet brushless (PMBL) motors are promising for electric vehicles (EVs)[1]. Among them, the stator-PMBL motor drive is most viable, since it inherently offers high efficiency, high power density and maintenance-free operation. Also, it takes the definite advantage that the PMs are located in the stator so that the thermal influence on the PMs becomes insignificant while the rotor becomes mechanically robust[2]. Recently, by incorporating both PMs and DC field windings, a flux-controllable stator-PMBL motor has been proposed, which not only remains the advantages of stator-PMBL motors, but also offers a unique field control capability [3]. However, similar to the switched reluctance (SR) motor, the flux-controllable stator-PMBL motor still suffers from severe torque ripples because of the nature of salient poles in both the stator and rotor. These torque ripples cause mechanical vibration and acoustic noise, which greatly affects its acceptability. To minimize the torque ripple, a current vector control strategy is applied to the proposed motor for the first time and the effectiveness is verified by both the simulation and experimental results in this paper.

Fig. 1 shows the structure and magnetic field distribution of the proposed flux-controllable stator-PMBL motor. It consists of two types of stator windings, namely the 3-phase concentrated armature winding and the DC field winding. The armature winding is the same as that of the doubly-salient PM motor[4], whereas the DC field winding is the key for airgap flux weakening above the base speed. Firstly, the electromagnetic performance of the motor with rotor skewing is obtained by 3D FEM. Fig.2 shows the measured three-phase back-EMF waveforms at 1500rpm. The total harmonic distortion (THD) of the waveforms is only 1.93% which are very close to sinusoidal waveform. Then, a mathematical model in rotor reference frame of the motor is built and the current vector control drive system is implemented by using Matlab/Simulink model. Thus, the feasibility of current vector control method is investigated. Furthermore, to verify the validity of the method, a 12/8-pole prototype is controlled with the current vector control strategy. The measured torque and current waveforms at different current control methods are shown in Fig.3. At the rated load, by comparing with torque ripple factor K_r=39.4% at the common rectangular current control method [5], the K_r= is only 14.1% at current vector control. Finally, the capability of flux control is investigated. Due to the existence of the additional DC field windings, the motor has a special capability of flux control. Above the base speed, by tunning the DC field current on line, the speed range is significantly extended form 2700rpm to 3600rpm, which is shown in Fig.4.

In this paper, a new flux-controllable stator-PMBL motor drive has been designed and controlled with a current vector control strategy. Both computer simulation and experimental results have confirmed that the operating torque ripple at the rated load can be significantly reduced by about 25.3%. Moreover, the DC field windings provide an additional degree of freedom with respect to the flux weakening operation. Hence, the proposed motor drive can offer lower torque ripple, fast speed response and wide speed range which makes the motor an interesting candidate for traction drive systems especially for EV operation.

[1]Z.Q. Zhu and D. Howe, "Electrical machines and drives for electric, hybrid, and fuel cell vehicles," Proceedings of IEEE, Vol. 95, No. 4, pp. 746-765, 2007.

[2]Y. Liao, F. Liang, and T.A. Lipo, "A novel permanent-magnet motor with doubly-salient structure," IEEE Trans. Ind. Appl., vol. 31, no. 6, pp. 1069-1078, 1995.

[3]Xiaoyong. Zhu and M. Cheng, "Design and analysis of a new hybrid excited doubly salient machine capable of field control," in Proc. IEEE IAS Annu. Meeting, 2006, vol. 5, pp. 2382–2389.

[4]M. Cheng, K. T. Chau and C.C. Chan,"Control and operation of a new 8/6 pole doubly salient permanent-magnet motor drive", IEEE Trans. Ind. Appl., vol. 39, no. 5, pp. 1363-1371, 2003.

[5]K.T. Chau, Q. Sun,Y. Fan and M. Cheng, "Torque ripple minimization of doubly salient permanent magnet motors," IEEE Trans. Energy Conversion, vol. 20, no. 2, pp. 352-258, 2005.

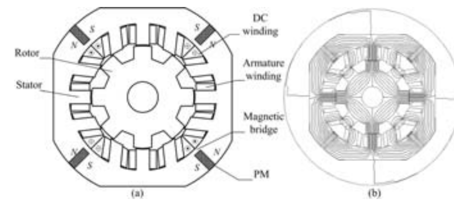

Fig.1 The proposed flux-controllable stator-PMBL motor.(a) Structure, (b) Magnetic field distribution

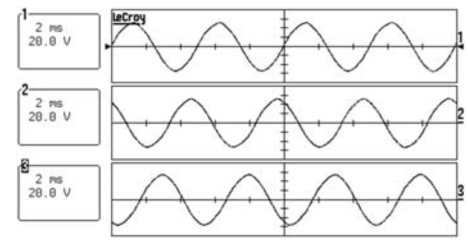

Fig. 2 The measured three phase back-EMF waveforms at 1500rpm

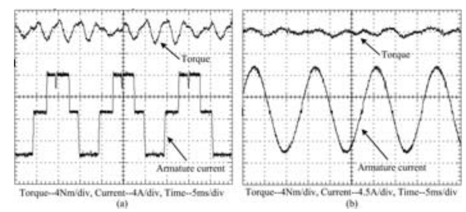

Fig. 3 The measured torque and current waveforms at 500rpm. (a) Rectangular current control, (b) Current vector control

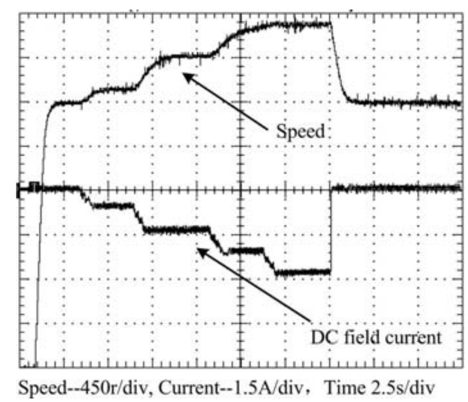

Fig. 4 The speed response at different DC field currents

CL-05

Permanent magnet optimization for reduction of cogging torque of BLDC motor using response surface methodology.

J. Lee, *H. Shim*, S. Wang
Mechatronics, Gwangju Institute of Science and Technology, Gwangju, South Korea

Abstract — This paper presents an optimization of permanent magnet (PM) in a brushless dc (BLDC) motor using the response surface methodology (RSM). Size and angle of the PM are optimized to minimize the cogging torque, while maintaining the magnitude of harmonic at a critical frequency and the operating torque. The optimized design is validated by carrying out nonlinear transient finite element analysis.

I. INTRODUCTION

Cogging torque is one of the main undesirable sources causing vibration and noise, which is magnetically induced in electric machines [1]. The cogging torque can be reduced by modifying the design of permanent magnet (PM). For a practical optimization technique, the response surface methodology (RSM) is used to minimize cogging torque. The design of experiment (DOE) is carried out on a basis of the nonlinear transient finite element analysis (FEA). For validation, in this paper, the optimized design is reanalyzed by the FEA to compare initial design.

II. INITIAL DESIGN AND VALIDATION OF ANALYSIS

A. BLDC motor

Fig. 1 shows a brushless dc (BLDC) motor with 6-poles, 9-slots, and 3-phases power sources. The 12 PMs and air holes next to the PMs are aligned in the rotor. The air holes are for reducing the cogging torque. The cogging torque of the initial design is 1.65e-4 [Nm] and the operating torque is 4.43 [Nm] at 1200 [rpm]. A fundamental frequence of radial magnetic force is 60[Hz]. Dominant harmonic is 2nd one occurring at 120 [Hz] and the magnitude is 6.17 [Nm], which is an interesting frequency in this paper.

B. Validation of FEM analysis

It is required to validate the finite element model with experimental data to confirm analysis accuracy. Fig. 1(b) depicts the analysis result of the flux line and the flux density. The maximum cogging torque is 0.19 [Nm] from the FEA and 0.19 [Nm] from experiment. Thus, the FEA is in good agreement with the experiment.

III. OPTIMAL DESIGN USING RSM

A. Construction of RSM

The DOE, as the major part of the RSM, is to determine sampling points for efficient construction of the RS model with less experiment. D-optimal design is used in this paper. Initial design values of the PM are shown in Fig. 1(a). The initial angle depicted in Fig. 1(a) is considered as 0°. The area of the PM is 26.25 [mm^2]. The number of sampling points is sixteen, which is determined by the D-optimal design with respect to design parameters. The nonlinear transient analysis is performed sixteen times in order to obtain the responses at each point. From a RS model equation the fitted second-order polynomials of three response functions are constructed, which will be revealed in a full paper.

B. Optimization

For optimization problem, an objective is to minimize the cogging torque. Constraint is three. The first constraint is that the PM area must be greater than 26.05 [mm^2] and less than 26.45. The second is that the operating torque is limited to maintain that of the initial design. The third is that the magnitude of 2nd harmonic is smaller than the initial design. From the purpose of minimizing the cogging torque and maintaining constraints, the estimated optimal design values are 1.46° for rotation, 10.35 [mm] for length, and 2.56 [mm] for thickness of the PM.

C. Reanalysis of optimal design

It is necessary to validate the estimated optimal design due to the fact that the responses in the RS model have nonlinearity. Fig. 2 shows the optimized design in which size of the PM is modified in accordance with arrows and the PM is rotated in the directions of circled arrows. The operating torque is decreased by 0.9[%], and the magnitude of harmonic is reduced by 0.49[%] comparing with the initial design. However, it is noted that the cogging torque is much reduced by 14.55[%] from the initial design, and the difference of the cogging torque performance between the initial and the optimized design is shown in Fig. 3.

[1] T. Yoon, "Magnetically Induced Vibration in a Permanent-Magnet Brushless DC Motor with Symmetric Pole-Slot Configuration", IEEE Transactions on Magnetics, VOL.41, NO. 6: 2173-2179, 2005.

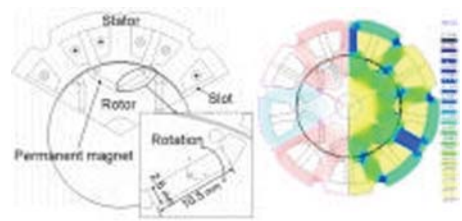

(a) BLDC Motor (b) plot of Flux line and flux density Fig. 1. BLDC motor and analysis result

Fig. 2. PM modification

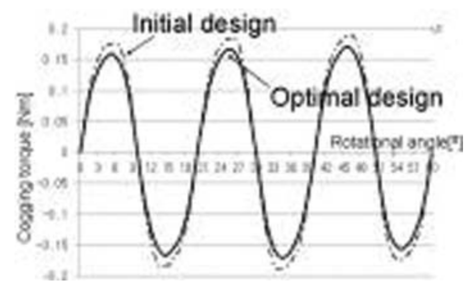

Fig. 3. Comparison of the cogging torque

CL-06

Design of Direct-Coupled, Small Scaled Permanent Magnet Generators for Wind Turbines.

S. Jang[1], H. Kim[1], *J. Choi*[1], D. You[1], S. Lee[2], B. Kim[3]
1. Chungnam National University, Dae-jeon, South Korea; 2. Korea Institute of Industrial Technaology, Kwangju, South Korea; 3. Korea Electric Power Research Institute, Daejeon, South Korea

Introduction

Recent study shows great demand for small-to-medium rating (up to 20kW) wind generators for stand-alone generation-battery systems in remote areas. The types of generator for this application is required to be compact and light so that the generators can be conveniently installed at the top of the towers and directly coupled to the wind turbines. A construction containing no gear box offers several advantages, namely higher overall efficiency and reliability, reduced weight and diminished need for maintenance. However, in order to produce a 60Hz frequency at such a low speed, a large number of poles required [1]. Potentially, the PMG displays uniqueness to meet requirements stated above.

Therefore, this paper deals with the design of a direct-coupled, small-scaled permanent magnet (PM) generator suitable for the wind power system shown in Fig. 1. With wind turbine characteristics presented in the Table I, the design of a wind turbine generator is performed as following steps: 1) Using the TRV method presented in [2], the outer diameter and axial length of the rotor is determined. 2) We derive the analytical open-circuit field solutions in terms of a magnetic vector potential and a two dimensional (2-d) polar coordinate system. On the basis of open-circuit field solutions and 2-d permeance function presented in [3], the analytical solution for the cogging torque is also derived. 3) Using the analytical solutions, the thickness and pole arc ratio of the PM and basic magnetic circuit of the stator are determined. 4) On the basis of initial design results, the detailed design satisfied with required specifications is achieved by non-linear finite element (FE) method.

Finally, the wind turbine generator based on final design results is manufactured, and we confirmed through non-linear FE calculations and measurements that its performance such as output power, node voltage, current are satisfied with required specifications under various load and speed conditions.

Design Results and Verification

Figure 2(a) shows the comparison of predictions with FE calculations for magnetic fields due to PMs considering slotting effect. Since the analytical results are shown in good agreement with FE results, we predict the proper magnet thickness using analytical field solutions, as shown in Fig. 2(b). Due to the design constraints that the starting torque should be smaller than 0.5Nm, we can select 0.77~0.8 for pole arc ratio which makes the cogging torque have the minimum value from the results of Fig. 2(c). Fig. 2(d) shows the schematic of the final design model with 8-pole parallel magnetized PM rotor and 3-phase, double-layer windings slotted stator. Design equations, more detailed design procedures and results used in this paper in order to obtain Fig. 2(d) will be given in the final full paper. Figure 3 (a) shows the actual manufactured PM generator for wind turbine. As shown in Fig. 3(b), experimental results for the performance of the manufactured PM generator are shown in good agreement with FE results under rated load and speed conditions. More detailed results and discussion for design verification will be made in the final full paper.

[1] Jianyi Chen, Chemmangot V. Nayar and Longya Xu, IEEE Trans. Magn., vol. 36, no. 5, pp.3802-3809, Sept. 2000.

[2] J. R. Hendershot and TJE Miller, Design of Brushless Permanent Magnet Motors, Magna Physics Publishing and Clarendon Press, 1994.

[3] Z. Q. Zhu and D. Howe, IEEE Trans. Magn., vol. 29, no. 1, pp. 143-151, Jan. 1993.

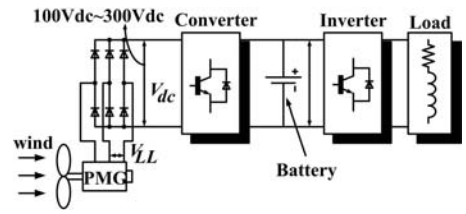

Fig. 1. The schematic of wind power systems with the PM generator.

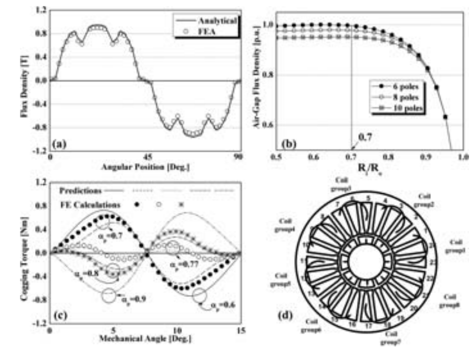

Fig. 2. (a) Comparison of predictions with FE calculations for the flux density due to PMs, (b) the variation of flux density due to PMs according to magnet thickness, (c) Comparison of predictions with FE calculations for the cogging torque, and (d) final design model.

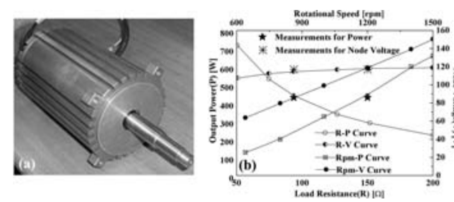

Fig. 3. (a) Manufactured PM generator and (b) FE calculations and measurements for the generator performance under rated load and speed conditions.

TABLE I
CALCULATED AND MEASURED TURBINE CHARACTERISTICS.

Wind speed	Nominal speed	Method	Torque [Nm]	Power [W]	Cp
12 m/s	1200rpm	Experiments	2.51	330	0.462
		Calculations	2.8	364 (+13%)	-
10 m/s		Experiments	2.16	260	0.459
		Calculations	1.67	210 (-19%)	-
8 m/s		Experiments	1.13	135	0.465
		Calculations	0.85	107 (-20%)	-

CL-07

Design and experimental evaluation of synchronous machine without iron loss using double-sided halbach magnetized permanent magnet rotor in high power fess.

D. You[1], S. Jang[1], K. Ko[1], S. Choi[2]
1. chungnam national univ., daejeon, South Korea; 2. Korea Institute of Machinery and Materials, Daejeon, South Korea

Introduction

Flywheel Energy Storage System (FESS) is environment-friendly energy storage equipment which can be supplying electrical energy when needed, after electrical energy is stored into mechanical rotational energy. Some applications such as bus and semiconductor production require high peak power output from the FESS to recover energy during regenerative braking and to protect the sensitive industrial process by momentary voltage sags or outages. Both these applications share the characteristic of high peak power requirements for only a short amount of time, so the total amount of energy required is small [1]. However, in the high power energy storage applications for distributed power source such as solar power or wind power, the important factor is to be continuously offering electrical energy from the mechanical rotation energy of flywheel for a long time. Thus, design of the high power FESS must be considered high power requirement for rotating the large and heavy flywheel in high speed and rotational loss reduction for supplying the electric energy for hours. Here, the rotational loss is defined as mechanical loss by mechanical friction including windage loss and iron loss by magnetic field parts including eddy current loss when flywheel is rotated.

In Fig. 1(a), a manufactured 5kWh-class FESS with the whole flywheel weights 215kg has the Active Magnetic Bearing (AMB) for elimination of mechanical friction and Floating Magnetic Bearing (FMB) for stable levitation of flywheel. And, the general PM Synchronous Motor/Generator (PMSM/G) with slotless iron-cored stator and 2-pole PM rotor is used for high power energy storage in dynamic range of flywheel speed 12000~18000rpm. These all parts are installed in vacuum chamber. As the experimental result for evaluation of the presented FESS, Fig.1 (b) shows the flywheel speed according to driving mode. In idling mode without generating load, the rotational loss of the FESS is mainly generated in the part of magnetic field such as AMB and PMSM/G. Also, the core loss of PM type motor/generator is much larger than that of AMB with zero power controllers. Therefore, to improve storage efficiency, the PM type motor/generator must be redesigned considering minimization of core loss in accordance with application object of the high power FESS.

Design and Evaluation of Invented PMSM/G

In our works for high power FESS, to design 30kW-class PM motor/generator without iron loss, we presents the invented PMSM/G with double-side PM rotor composed of Halbach magnetized array and coreless winding stator as shown in Fig. 2. Although the PM rotor with Halbach magnetized array has the disadvantage in complex analysis and fabrication, the Halbach array field has the excellent merits with non-saturation of rotor core by self-shielding property and with high flux density as well as the more sinusoidal waveform at the air gap as shown in Fig.2 (b) [2]. Also, the winding stator without core doesn't cause reduction of flywheel speed by the rotational loss in idling mode. For design approach of the invented PMSM/G, this paper offers analytical formulae and FEM verification for its magnetic field, force, inductance of the winding and back electromotive force in polar geometries [3]. And then, we have focus on design parameters estimation to satisfy the high power requirement according to PM size and winding turns. A manufactured PMSM/G through design process is evaluated from the required power and the core loss in motoring mode and idling mode as shown in Fig.3.

Reference

[1] R. Hebner, J.Beno, and A. Walls, "Flywheel batteries come around again," IEEE Spectrum,

vol39, p46, 2002

[2] Z.Q. Zhu and Howe, "Halbach permanent magnet machines and application: a review," IEEE Proc-Electr. Power Appl., vol.148, No.4, p299, 2001

[3] J. R. Melcher, "Continuum Electromechanics," Cambridge MA: MIT Press, 1981

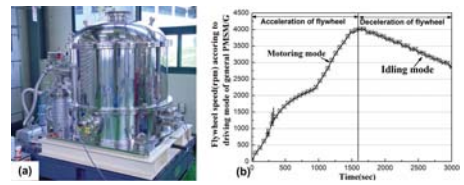

Fig.1. Experimental results of FESS with general PMSM/G: (a) photograph of 5kWh-class FESS with slotless iron-cored PMSM/G (b) Flywheel speed according to driving mode of general PMSM/G

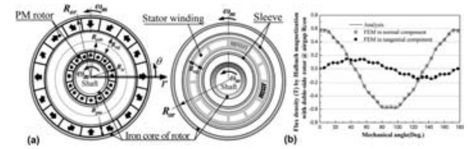

Fig.2. the invented PMSM/G with double-side Halbach array rotor: (a) magnetic field analysis model of PM rotor and coreless stator winding (b) flux density by Halbach magnetization with double-side rotor

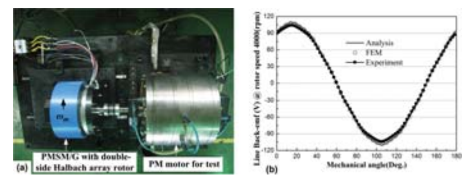

Fig.3. 30kW-class PMSM/G with double-side Halbach array rotor: (a) a manufactured PMSM/G (b) experimental verification for Back-emf estimation

CL-08

Experimental method for determining magnetically nonlinear characteristics of electric machines with magnetically nonlinear and anisotropic iron core, damping windings and permanent magnets.

G. Stumberger[1,2], T. Marcic[2], B. Stumberger[1,2], D. Dolinar[1]
1. Faculty of electrical engineering and computer science, University of Maribor, Maribor, Slovenia; 2. TECES, Maribor, Slovenia

This work focuses on experimental methods appropriate for determining magnetically nonlinear characteristics of electric machines that contain an iron core with magnetically nonlinear and anisotropic behavior, permanent magnets (PMs), damping windings in the form of a squirrel cage and a wye connected three-phase stator winding. The three stator currents are dependent due to the wye connection. Therefore, the magnetically nonlinear two-axis dynamic machine models with independent state variables are normally used to analyze dynamic behavior of such machines. However, before the analysis is performed, the magnetically nonlinear iron core characteristics, normally given in the form of current dependent characteristics of flux linkages, must be determined. A simple experimental method for determining magnetically nonlinear characteristics of iron core inductors and transformers by the DC excitation is proposed in [1]. Evaluation of different experimental methods appropriate for determining magnetically nonlinear characteristics of electromagnetic devices is given in [2], where each individual device coil is individually supplied by a current or voltage controlled source. However, in the case of machine discussed in this work the stator windings of individual phases are wye connected and cannot be supplied independently. An approach similar to that presented in [3], where the three-phase synchronous reluctance machine is supplied by a voltage source inverter (VSI) controlled in the d-q reference frame in order to determine magnetically nonlinear (machine's) iron core characteristics, could be applied. In this case, the current in one axis is closed-loop controlled in order to keep constant value, while the voltage in the other axis is changing in the stepwise manner. The characteristics of flux linkages are determined by numerical analysis of currents and voltages measured during the test. Unfortunately, in the case of machine discussed in this work, the aforementioned method gives incorrect results due to the currents induced in the squirrel cage. This problem can be effectively solved by applying a similar approach as that presented in [4], where it was used for determining mutual inductances of a three-phase squirrel cage induction machine. After the (voltage) change, the stator current reaches a steady-state value. If it stays in the steady state long enough, the squirrel cage currents die out. Thus, the squirrel cage currents influence the time response of the flux linkage calculated by numerical integration of current and voltage measured during the test, but they cannot influence final value of the flux linkage. If the test with closed-loop controlled current in one axis and with stepwise changing voltage in the orthogonal axis is performed with different amplitudes of applied values, the steady state values of the stator currents and flux linkages are different. This makes possible to determine current dependent characteristics of flux linkages of the machine discussed in this work.

In order to confirm the new, in this work proposed method for determining current dependent flux linkage characteristics, one stator and four different four-pole experimental rotors were manufactured. The rotor structures are shown in Fig. 1: a) reluctance rotor; b) reluctance rotor with squirrel cage; c) reluctance motor with inserted PMs; d) reluctance motor with inserted PMs and squirrel cage. The d-axis is defined with the direction of flux linkage vector due to the PMs (direction in which PMs are magnetized) while the q-axis is aligned with the direction of the lowest reluctance.

The flux linkage characteristics given in Fig. 1 show a very good agreement between characteristics determined for reluctance rotor with and without squirrel cage (curves a) and b)) as well as between characteristic determined for both aforementioned rotors with inserted PMs (curves c) and d)). In the last two curves the offset due to the flux linkage caused by the PMs is not present due to the integration, but it could be added in the form of integration constant. The results presented show that squirrel cage and damping windings do not influence the d-q axis flux linkage characteristics determined by the proposed method, thus confirming the method completely.

[1] S. Calabro, F. Coppadoro, and S. Crepaz, "The measurement of the magnetization characteristics of large power transformers and reactors through d.c. excitation," IEEE Trans. on Power Delivery, vol. 1, no. 4, pp. 224–232, 1986.

[2] G. Stumberger, B. Polajzer, B. Stumberger, M. Toman, and D. Dolinar, "Evaluation of Experimental Methods for Determining the Magnetically Nonlinear Characteristics of Electromagnetic Devices, " IEEE Trans. on Magn., vol. 41, no. 10, pp. 4030–4032, 2005.

[3] G. Stumberger, B. Stumberger, and D. Dolinar, "Identification of linear synchronous reluctance motor parameters," IEEE Trans. on Ind. Appl., vol. 40, no. 5, pp. 1317–1324, 2004.

[4] A. V. Stankovic, E. L. Benadict, V. John, and T. A. Lipo, "A novel method for measuring induction machine magnetizing inductance," IEEE Trans. on Ind. Appl., vol. 39, no. 5, pp. 1257–1263, 2003.

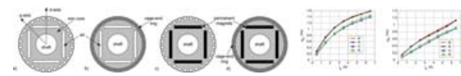

Fig. 1: Rotor structures and characteristics of d- and q-axis flux linkages determined for: a) reluctance rotor; b) reluctance rotor with squirrel cage; c) reluctance motor with inserted permanent magnets; d) reluctance motor with inserted permanent magnets and squirrel cage.

Detent force minimization of permanent magnet linear synchronous motor by means of two different methods.

Y. Zhu, Y. Cho
Electrical Engineering, Dong-A University, Busan, South Korea

Introduction

The thrust ripple in permanent magnet linear synchronous motor (PMLSM) is mainly generated by detent force, which is caused by the interaction between the permanent magnet (PM) and iron core without input current in armature winding. This paper proposes two different techniques to minimize the detent force in PMLSM. One is to choose an optimal constructive design; the other is the employ of a current compensator. In this paper, we investigate the performance of detent force minimization using both of them. The effectiveness is verified by both numerical and experimental results.

Analysis and Results

In this paper the structure of PMLSM model is shown in Fig. 1. The mover core of the prototype PMLSM is composed of the semi-closed slot iron core without auxiliary poles and the concentrated windings. The mover core is in a 9-slot/8-pole fractional-slot pitch structure [1], which is similar to the straightened rotary motor core being cut off on the middle point between two adjacent teeth. This structure not only reduces the back EMF harmonics, but also suppresses the detent force. The stator is the path with surface mounted permanent magnet.

The two-dimensional (2-D) FEM is used to calculated the detent force and the electromagnetic force. The results of the static force distribution with respect to the mover position are shown in Fig. 2. To minimize the detent force, we investigate the PMLSM system by two different techniques. The first technique is using to optimize the PMLSM structure. The detent force can be reduced to 6.9[N] by appropriately positioning the auxiliary poles shown in Fig. 1. The calculated and measured results with/without auxiliary poles are shown in Fig.3. They are in good agreement, which validates the 2-D FEM.

However, this remained detent force with auxiliary poles is still large for low velocity operation. The second technique is using current compensator to counteract the detent force [2]. The control block is shown in Fig.4. In this paper we test the PMLSM system on 0.1[m/s] using speed closed loop control based on general PID. The velocity and thrust responses are shown in Fig.5. We can see that the velocity and thrust responses are much better for involving the second technique, but the phase currents are distorted seriously and unbalance for only using the second technique shown in Fig. 6(a). The phase currents waveforms with the auxiliary poles and the current compensator are shown in Fig. 6(b), which is similar to sine wave. Therefore, the combination of these two techniques shows good performance of PMLSM.

[1] Thomas M. Jahns, and Wen L. Soong, “Pulsating torque minimization techniques for permanent magnet AC motor drives-a review,” IEEE Transactions on Industrial Electronics, vol. 43, no. 2, pp. 321-330, April 1996.

[2] Grcar B., Cafuta P., Stumberger G., and Stankovic A.M., “Control-based reduction of pulsating torque for PMAC machines,” IEEE Transactions on Energy Conversion, vol. 17, no. 2, pp. 169-175, June 2002.

Fig. 1. Structure of the prototype PMLSM.

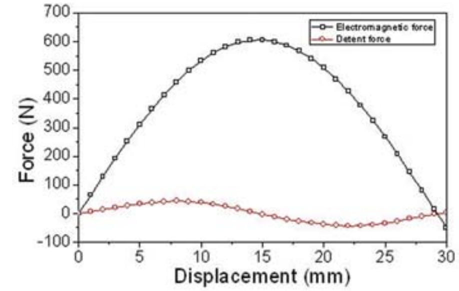

Fig. 2. Static force distribution according to mover position.

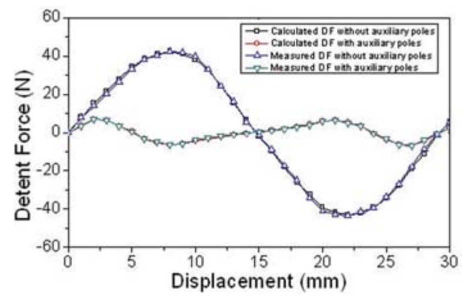

Fig. 3. Detent force with/without auxiliary poles.

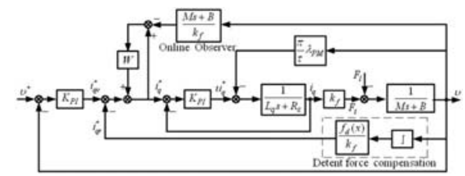

Fig. 4. Control diagram of PMLSM.

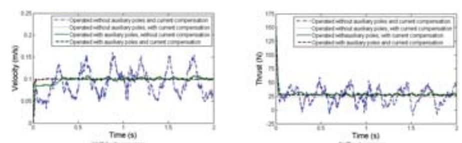

Fig. 5. Velocity and thrust responses for the general PID, the first technique, the second technique, and their combination.

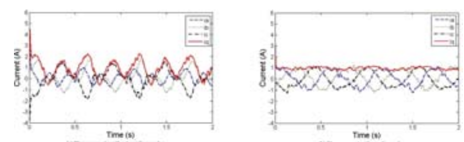

Fig. 6. Phase currents responses with/without auxiliary poles for the current compensation technique.

CL-10

A STUDY ON THE IRREVERSIBLE MAGNET DEMAGNETIZATION IN SINGLE-PHASE LINE-START PERMANENT MAGNET RELUCTANCE MOTOR.

J. Hong[2], H. Nam[3], *T. Kim*[1]
1. Electrical Engineering, Gyeongsang National University, Jinju, South Korea; 2. Hanyang University, Seoul, South Korea; 3. LG Electronics, Changwon, South Korea

I. Introduction

A single-phase line-start permanent magnet reluctance motor (LSPRM) is known to be capable of high efficiency and near unity power factor performance. These attributes make them an attractive choice for various high duty cycle applications. The LSPRM dose not need a driving system such as an inverter, because of the asynchronous starting torque by means of conductor bars in the rotor [1]. However, the large currents at a starting or locked rotor condition can cause severe irreversible demagnetizing in the permanent magnet. This demagnetizing field deteriorates the performance of the LSPMM such as phase peak-to-peak variation. Therefore, the demagnetization of the permanent magnet should be considered in the design of the rotor shape of the LSPMM. In this paper, we introduce the phenomena of the irreversible magnet demagnetization and propose design techniques which are effective to avoid irreversible demagnetization. To analyze the irreversible magnet demagnetization, two-dimensional finite-element method (2D FEM) is used. The nonlinear characteristic of the permanent magnet is considered as well as that of a magnetic core on each B-H curve.

II. Analysis Model

Fig. 1 shows the constructed proto-type LSPRM with two-layer rare-earth permanent magnet. It has a 24-slot stator and 2-pole rotor. The permanent magnet material is sintered Nd-Fe-B. The air gap was designed to be 0.5 mm to obtain a reasonable permeance coefficient value.

III. Analysis Results and Discussion

Fig. 2(a) shows the procedure of demagnetization. When operating P1 moves P2 due to the external demagnetization field, the residual flux density Br is decreased to B`r, and irreversible magnet demagnetization occurs. As a result, the magnetization M of the magnet is also decreased. Fig. 3 shows the demagnetization phenomena according to the increase of the stator magneto motive force (MMF). Firstly, the center part of the lower layer magnet is demagnetized as the MMF increases. And then, the overall regions of the lower layer magnet become demagnetized. Lastly, the regions of the upper layer magnet have an irreversible demagnetization. From these analysis results, we can know that more thick magnet in the lower layer compared to the upper layer is effective to avoid the irreversible demagnetization. It is also possible to use the magnet of a different material in the upper and lower layer. The experimental results will be shown to confirm the validity of the analysis results and the proposed design techniques in the full paper.

[1] G. H. Kang, J. Hur, H. Nam, J. P. Hong, and G. T. Kim, "Analysis of Irreversible Magnet Demagnetization in Line-Start Motors Based on the Finite-Element Method," IEEE Trans. Mag., vol. 39, no. 3, pp. 1488-1491, May 2003.

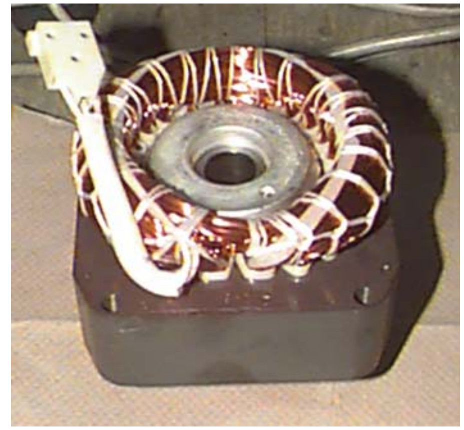

Fig. 1. The constructed LSPRM

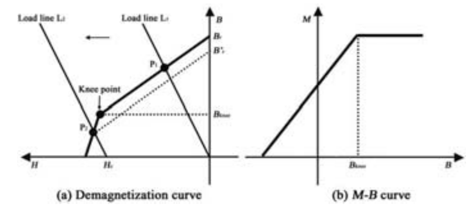

Fig. 2. Demagnetization curve of the permanent magnet

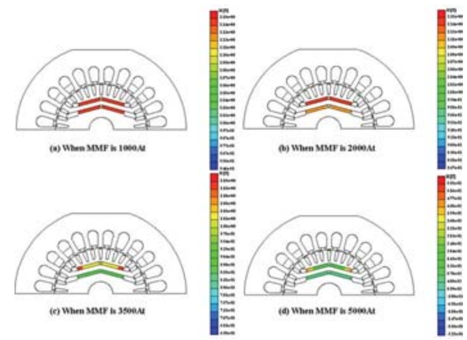

Fig. 3 Demagnetization phenomena according to the stator MMF

CL-11

Design of IPM type BLDC motor considering demagnetization characteristics.

B. Yang, S. Hong, B. Kwon
Hanyang Unv., Ansan, South Korea

Abstract
In this paper, a rotor is designed for the purpose of performance improvement of an Interior permanent magnet[IPM] type brushless DC motor with concentrated flux that takes into consideration demagnetization characteristics.

Introduction
The IPM type BLDC motors have been widely used in industrial appliances. But, the motor researched in this paper has a large leakage flux and a structure that is vulnerable to demagnetization. Methods exist to increase a thickness of magnet or to change a material of magnet to prevent leakage flux and demagnetization [1]. Cost is a factor in these methods due to increased use amount of magnet and material change. Therefore it is necessary to decrease leakage flux and to improve demagnetization performance of magnet without any change of usage amount and magnet material. This paper has designed a rotor for the purpose of performance improvement of an IPM type BLDC motor with concentrated flux that takes into consideration demagnetization characteristics. Through the optimum design of the rotor flux path, demagnetization characteristics are improved, counter EMF is increased, and magnetization is enabled after the inclusion of a permanent magnet.

Design of IPM type Motor
An IPM type BLDC motor with concentrated flux refers to a motor having a larger flux area than the pole area in the gap. The rotor is in the shape of a ferrite permanent magnet inserted into a round rotor core as shown in Fig. 1. Fig. 2 shows the flux distribution of the IPM type motor. Magnetization of the magnet is in a circumference as shown in Fig. 3. Since the leakage flux paths A and B are formed at both end areas on the structure of the rotor, a leakage flux is generated. The shape of the core inside the rotor is to be designed to minimize leakage flux in the IPM type BLDC motor with concentrated flux and to improve performance of the motor.
Fig. 4 represents briefly the distribution of the drag inside the rotor. Leakage flux path A is optimized to improve performance of the motor, and leakage flux path B is optimized to improve demagnetization factors. The limits in the design of the motor include a revolution speed of 1200rpm and peak current of 15A. Table I shows the motor shape and characteristic results following the improvement of leakage flux path B. As shown in Table I, as a result of the optimum design result for the motor characteristics by motor shape, the demagnetizing current of the proposed model is decreased about 25.9% comparing with the original. Since the allowable current of the inverter is 1.83 times to 15A, application is possible with the counter EMF improved by 14.5%.

Conclusion
This paper looks at the improvement of motor performance in consideration of demagnetization. As a result of an optimum design, this study enhanced the value of the counter EMF and enabled magnetization after assembly.

[1] Byoung-Kuk Lee, Gyu-Hong Kang, Jin Hur, “Design of spoke type BLDC motors with high power density for traction application”, 39th IAS Annual Meeting. Vol.2, pp 1068–1074, Oct. 2004.

	Original type	Proposed type
Core type	One-punched	Divided
Demagnetizing Current	37.1 [A]	27.2 [A]
Back-EMF (at 45RPM)	40.6 [V]	46.5 [V]
Magnetization current	3000 [A]	2800 [A]
Leakage flux	Low	Middle

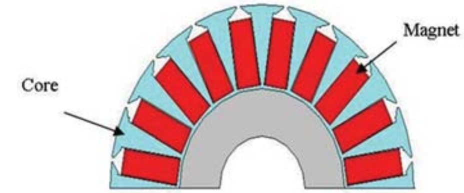

Fig. 1 The rotor structure (20 Pole 18slots)

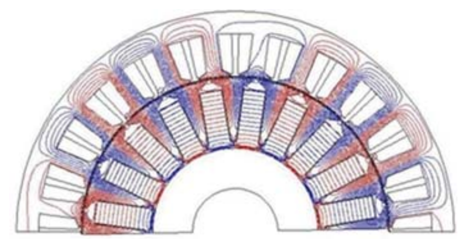
Fig. 2 The flux distribution

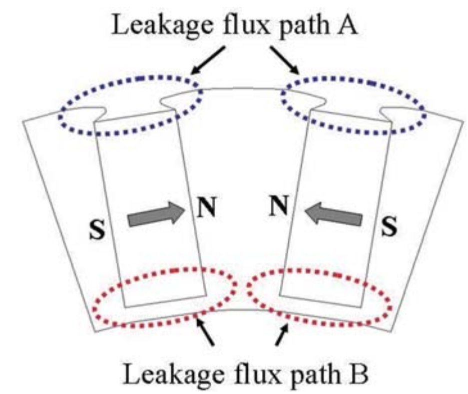

Fig. 3 The leakage flux path

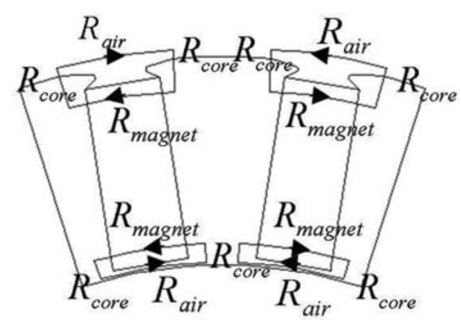

Fig. 4 Magnetic equivalent circuit

CL-12

Characteristic analysis of Permanent Magnet Motor Considering Anisotropic Characteristics of Electrical Steel Sheets.

S. Kwon[1], J. Lee[1], K. Ha[2], J. Hong[1]
1. Department of Mechanical Engineering, Hanyang Univeristy, Seoul, South Korea; 2. POSCO Technical Research Laboratories, Pohang, South Korea

I. Introduction

Finite Element Analysis (FEA) is generally used for the analysis and design of electrical machines. To improve its accuracy, more precise material data should be provided. Electrical steel sheets are classified into isotropic and anisotropic, and isotropic steel sheets are generally used for electrical motors and anisotropic steel sheets are used for transformer. Actually, isotropic steel sheets have anisotropic B-H and core loss characteristics reference to rolling direction, and the average value of rolling and transversal direction is provided by manufacturer. Therefore, using average material data leads to difference between experimental and FEA results. Measurement and analysis method considering anisotropic material characteristics are researched [1], however, it requires complex technique in measurements and large computation time to solve governing equation for FEA.

This paper focuses on the motor characteristics of permanent magnet motors considering anisotropic characteristics of electrical steel sheets. Motor characteristics of core loss, back Electro-Motive Force (EMF), and cogging torque are analyzed by FEA considering anisotropy of electrical steel sheets and compared to the results from experiment and general FEA; using single material data for the entire core region. For the analysis, rotating core lamination is not considered.

II. Measurement of B-H and core loss data

B-H and core losses are measured by Single Sheet Test (SST) reference to the angle from rolling direction and results are shown in Fig. 1 and Fig. 2, and angle is defined from rolling direction in the figures. As shown in Fig. 2, 7 samples are cut for the measurements. The size of the sample is 150×150 mm.

III. Analysis Method and Procedure

Measured B-H and core loss data are interpolated and prepared for 2-dimensional FEA. B-H data are consist of B, H, and θ (angle from rolling direction), and core loss data are consist of B, core loss (kW/kg), and θ. Using B-H data, FEA is conducted then core loss is calculated [2] with measured core loss data. Solving procedure of FEA is shown in Fig. 3. As shown in Fig. 3, governing equation is solved with the initial permeability of material then flux density and θ are calculated in each element. With the flux density and θ, new permeability is found from B-H data then governing equation is solved again.

IV. Results and Discussions

Analysis model is an Interior Permanent Magnet Motor of 4kW with 4-poles and 24-slots, and its analysis model(1/4 model) and fabricated appearance are shown in Fig. 4 (a) and (b). In Fig. 5, experimental and FEA results at no-load are compared. FEA results are from general FEA using single isotropic B-H data. For the back EMF and core loss, no significant differences are shown, however, flux distribution is not balanced and due to anisotropic B-H characteristics, therefore, core loss distribution should be unbalanced during one cycle of electrical angle. For cogging torque, significant difference exists. Cogging torque is the source of vibration of permanent magnet motors and supposed to be reduced by skew. However, considering anisotropic material characteristics, cogging torque will not reduced as expected. FEA results with anisotropic B-H and core loss and detailed comparison will be included in full paper.

[1]T. Nakata, N. Takahashi, K. Fujiwara and M. Nakano, ″Measurement of Magnetic Characteristics along Arbitrary Directions of Grain-oriented Silicon Steel up to High Flux Densities″, IEEE Trans. Magn., Vol. 29, No. 6, Nov. 1993.

[2] H. Nam, K. H Ha, J. P. Hong and G. H. Kang, ″A study on iron loss analysis method considering the harmonics of the flux density waveform using iron loss curves tested on Epstein samples″, IEEE Trans. Magn., Vol. 39, No. 3, May 2003.

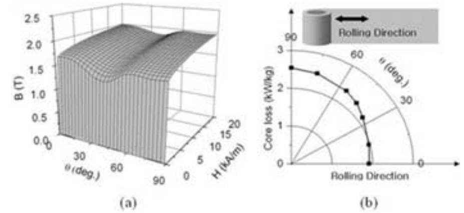

Fig. 1 Measured data of (a) B-H and (b) core loss(0.6T, 50Hz)

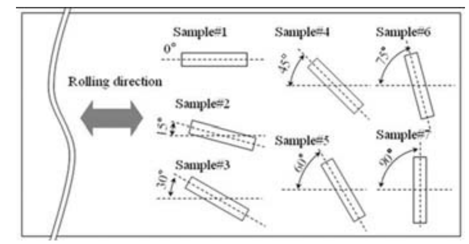

Fig. 2 Cutting of samples for SST

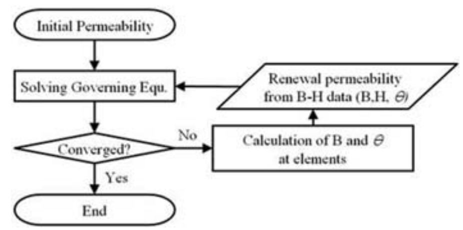

Fig. 3 Solving procedure of FEA

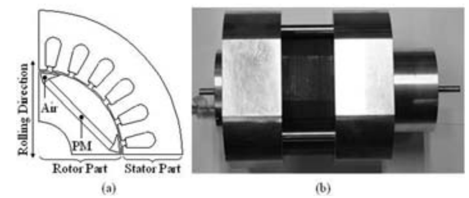

Fig. 4 Apperance of (a) analysis model(1/4) and (b) fabricated model

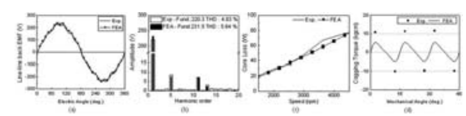

Fig. 5 Comparison of (a) line to line back EMF, (b) harmonic component of back EMF, (c) core loss, and (d) cogging torque

CM-01

Nonlinear eigenmodes of monodomain magnetic squares.

V. E. Demidov[1], U. Hansen[1], S. O. Demokritov[1], M. Kostylev[2]
1. Institute for Applied Physics, University of Muenster, Muenster, Germany; 2. School of Physics, University of Western Australia, Crawley, WA, Australia

Spin-wave eigenmodes in small magnetic elements have recently attracted growing attention due to their importance for the understanding of ultra-fast magnetization dynamics in such systems (see, e.g., [1-2]). Up to very recently these investigations were mainly conducted for the case of relatively small excitation amplitudes providing the linear response of the spin system of ferromagnetic films. At the same time, in magnetic nano-devices, e.g., spin-torque-tranfer nano-oscillators, the amplitudes of dynamic magnetization are essentially large (see, e.g. [3]), which makes the deep understanding of the nonlinear dynamics necessary for their technical applications.
It is extremely difficult to study nonlinear dynamics in nano-devices directly with a lateral resolution comparable to the device size. In this work we take advantage of the spatial scalability of the dipolar problem for experimental modeling of nonlinear magnetization dynamics of nano-devices on a larger scale [4]. The studied objects are squares with a side length w = 2 mm, patterned from low-loss dielectric films of yttrium iron garnet (YIG) films with a thickness of 5.1 μm. The excitation of dynamic magnetization was performed by means of a wire antenna with a diameter of 50 μm, attached to the square along its middle line. The power of the exciting microwave signal P was varied from 1 mW, providing the linear response of the system, to 200 mW. A static magnetic field of H=800-2000 Oe, creating a monodomain magnetization state of the square, was applied in the film plane perpendicularly to the antenna. The two-dimensional mapping of the dynamic magnetization was done by means of the space-resolved Brillouin light scattering spectroscopy in the forward scattering geometry.
Using the above technique we were able to record spin-wave intensity maps corresponding to different normal modes of the system. We also investigated how these modes change as the excitation power is increased and the magnetization dynamics becomes essentially nonlinear. An example of the experimental results is presented in Fig. 1, where the intensity maps and their spatial Fourier spectra are shown for the linear (P=1 mW) and the strongly nonlinear (P=200 mW) cases. The shown data were obtained for H=800 Oe, and the excitation frequency of 3.945 GHz which corresponds to the eigenmode (4,1). In the linear regime the spatial intensity distribution of this eigenmode represents a standing wave with four antinodes in the direction parallel to H and one antinode in the direction perpendicular to H. As the excitation power is increased, the spatial profile of the eigenmode demonstrates changes, which can be described as a widening and merging of the neighboring maxima of the standing waves, resulting in a flattening of the standing-wave profile. Similar modifications were also observed for other eigenmodes.
In order to understand the experimental findings a theoretical model based on the complex Ginzburg-Landau equation was developed. This model takes into account the nonlinear shift of the spin-wave spectrum as well as linear and nonlinear damping caused by the parametric excitation of spin waves. Numerical simulations based on this model have accurately reproduced the observed modifications of the eigenmode profiles (see Fig. 2), and have shown that they are caused by the nonlinear cross coupling between the eigenmodes. It was found that the dominating influence of nonlinear damping in the studied system leads to a generation of long-wavelength harmonics, which results in the energy channeling from higher-order eigenmodes to the lower-order ones.
Even though the experimental investigations were performed for millimeter-size squares, the above conclusions should also be valid for nano-scale monodomain square islands. The observed phenomenon of nonlinear mode coupling can be used in practice for nonlinear amplification and/or reduction of magnetic losses of the eigenmodes.
This work was supported in part by the Deutsche Forschungsgemeinschaft and the Australian Research Council (ARC).

[1] C. Bayer et al., Top. Appl. Phys. 101, 57 (2006).

[2] C.H. Back, D. Pescia, and M. Buess, Top. Appl. Phys. 101, 137 (2006).

[3] J.C. Sankey et al., Phys. Rev. B 72, 224427 (2005).

[4] V.E. Demidov, U.-H. Hansen, and S.O. Demokritov, Phys. Rev. Lett. 98, 157203 (2007).

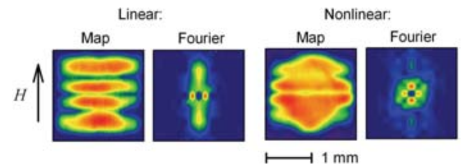

Fig. 1 Measured spin-wave intensity maps and their Fourier spectra for the eigenmode (4,1) in the linear and strongly nonlinear cases.

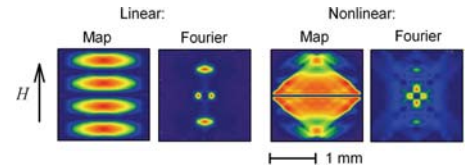

Fig. 2 Calculated spin-wave intensity maps and their Fourier spectra for the eigenmode (4,1) in the linear and strongly nonlinear cases.

CM-02

Synthesis and Magnetic Properties of Au Doped CoPt Nanowires.

J. Min[1], J. Wu[2], J. Lee[1], J. Ju[3], Y. Kim[1]
1. Department of Materials Science and Engineering, Korea University, Seoul, South Korea; 2. Institute for Nano Science, Korea University, Seoul, South Korea; 3. Cooperative Center for Research Facilities, Sungkyunkwan University, Suwon, South Korea

Introduction

Nanowires with enhanced surface functionalities and tailored surface morphology are of great interest owing to potential applications in surface reactions, catalysis, immobilizing molecules, nanomagnetics and nanomagnetoelectronics. Magnetic nanowires are promising for biological applications such as cell-separation and magnetic labeling. However, the implementation of such nanowires usually requires surface modification. Based on our previous study of Cu-doped CoPt alloy magnetic nanowires [1], we introduce Au composition in this work to fabricate CoPtAu nanowires, in which Au provides the optical properties and functioning with biological entities, such as immobilization.

Experiment

The CoPtAu alloy nanowires were constructed in anodic aluminum oxide (AAO) nanotemplates with pore diameters of 50 nm and 200 nm. All nanowires were dc electrodeposited at RT in various concentrations from solutions containing $HAuCl_4$, $CoSO_47H_2O$ and $PtCl_4$, in a single bath under a given constant current density. Their structure and properties were characterized by SEM, TEM, XRD, VSM and UV-Vis spectroscopy.

Results and Discussion

As shown in Fig. 1 (a)-(d), robust CoPtAu nanowires were acquired with homogenous distribution of the elements of Co, Pt and Au. Dependent on the deposition conditions (solution concentration and current density), the CoPtAu nanowires assume cubic or tetragonal structures and, thus, their magnetic properties are affected correspondingly. The XRD pattern (Fig. 1 (e)) shows that the CoPtAu nanowires prepared from the solution containing 0.28 M $CoSO_47H_2O$, 0.03 M $PtCl_4$ and 0.001 M $HAuCl_4$ under the current of 3 mA/cm^2 in AAO with a pore size of 200 nm possesses a tetragonal phase, with a = 2.682 Å and c = 3.675 Å. The magnetic measurements (Fig.1 (f)) indicate that the nanowires are ferromagnetic, showing the easy axis along the direction of the nanowires. In Table 1, the magnetic properties of the CoPtAu nanowires are compared to that of the CoPt, CoPtCu nanowire. It reveals that the Au doping has more significant effects than the Cu doping, both in coercivities and squareness. Particularly, the tetragonal CoPtAu nanowires show enhancement in magnetic properties. Their coercivity increases to 700 Oe for the easy-axis and 730 Oe for the hard-axis, compared to 560 Oe and 300 Oe for CoPt, 420 Oe and 270 Oe for CoPtCu, and 520 Oe and 290 Oe for cubic CoPtAu, respectively. The change in the squareness along the easy-axis is more impressive, from 0.24 for CoPt, 0.29 for CoPtCu, 0.44 for cubic CoPtAu to 0.51 for tetragonal CoPtAu, while the effects of doping on the squareness along the hard-axis is less sensitive. Using samples in ethanol, the optical measurements give plasmon peaks characteristic of nanostructured Au in the UV-Vis spectra. For the case of the nanowires with a nominal composition of $Co_{0.17}Pt_{0.51}Au_{0.32}$ by SEM-EDS, the plasmon manifests the unique optical property of the nanowires and the absorption feature peaking at ~720 nm and ~960 nm reflects the outcome of the shaped Au segments.

[1] J. H. Min, B. H. An, J. U. Cho, H. M. Ji, S. J. Noh, Y. K. Kim, H. L. Liu, J. H. Wu, Y.-D. Ko and J.-S. Chung, J. Appl. Phys. 101, 09K513 (2007).

Samples		CoPt	CoPtCu	CoPtAu (cubic)	CoPtAu (tetragonal)
H_c (Oe)	Parallel to wire axis	560	420	520	700
	Perpendicular to wire axis	300	270	290	730
M_r/M_s	Parallel to wire axis	0.24	0.29	0.44	0.52
	Perpendicular to wire axis	0.15	0.18	0.18	0.21

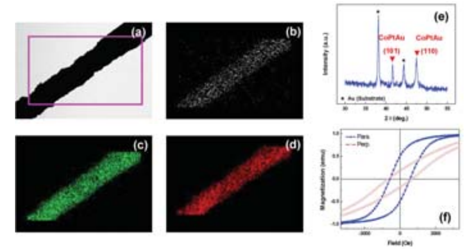

Fig. 1. Electrodeposited Au doped CoPt nanowires: (a) TEM image; elemental mapping of Co (b), Pt (c) and Au (d); and (e) XRD pattern of tetragonal CoPtAu nanowire array, and (f) hysteresis curves obtained parallel and perpendicular to the nanowire axis.

CM-03

FMR studies of interactions effects in magnetic nanowires arrays.

O. C. Trusca[1,2], D. Cimpoesu[1], A. Diaconu[4], I. Dumitru[4], J. Lim[1,3], X. Zhang[1,3], J. B. Wiley[1,3], A. Stancu[4], *L. Spinu*[1,2]
1. Advanced Materials Research Institute, University of New Orleans, New Orleans, LA; 2. Department of Physics, University of New Orleans, New Orleans, LA; 3. Department of Chemistry, University of New Orleans, New Orleans, LA; 4. Faculty of Physics, "Alexandru Ioan Cuza" University, Iasi, Romania

Nanostructured magnetic materials are the focus of many research efforts in the past few years, being very interesting not only from a theoretical point of view but mostly due to the wealth of their potential technological applications. Systems of magnetic nanowires are considered strong candidates for many technological applications as microwave filters, sensors or as materials for advanced data storage [1]. Characterization and understanding of the magnetic properties of nanowire arrays is still a challenging task, the complexity of the interactions among wires making difficult to interpret even the experimental results of classical characterization methods, like ferromagnetic resonace (FMR) [1-3].The magnetic anisotropy of such arrays is determined mainly by two contributions: the shape anisotropy with a magnetic easy axis parallel to the wire axis, and the magnetostatic coupling among wires, which can develop a magnetic easy axis perpendicular to the wire axis [4,5]. The main parameter that controls the frequency response of magnetic nanowires assemblies is the aspect ratio of the nanowires, i.e., the length to diameter ratio. The aspect ratio can be tuned by changing the length of nanowires keeping the same diameter of wires. In the case of template method for nanowires preparation this can be easily done using different electrodeposition times.
In the present work we chose to modify the aspect ratio of nanowires by keeping constant their length and modifying the nanowires' diameter. This approach is more challenging as it requires designing templates of different diameters but with the same average distance between the channels. Moreover, during the electrodeposition the constant length of nanowires for different samples of different diameters is controlled more difficult. The series of samples of different diameters, with the same length, and average distances between the centers of wires are ideal candidates for verifying the models recently proposed [5] to describe the interactions in such systems. Two series of Ni nanowire samples with diameters of 40, 60, 80 nm and constant lengths of 1000 and 500 nm were grown using standard electrodeposition technique in alumina templates. The templates were prepared by anodizing process with highly pure aluminium foils. In order to obtain templates with the same interpore distance of 100 nm and different pore sizes, the templates were etched in H3PO4 solution at room temperature using different etching times. The membranes produced following the above procedure have a much better quality than those commercially available, as it can be observed from the Scanning Electron Microscope (SEM) pictures displayed in Fig. 1.
The samples were studied using vibrating sample magnetometer and X-band ferromagnetic resonance experiments, at room temperature. Magnetization data (Fig. 1) confirm that the all magnetic nanowires with the length L=1000 nm have a uniaxial effective anisotropy along the wire's axis. However, for the nanowires with the length of 500 nm, depending on their diameter one can have an easy axis or easy plane anisotropic system. The FMR data shown in Fig. 2 substantiate this behavior which is intimately determined by the existence of magnetostatic interactions in these systems. In the full paper a comprehensive study of the magnetostatic interactions is presented explaining the different behavior of the FMR data in the two series of samples of different lengths.

1. A. Fert and L. Piraux, J. Magn. Magn. Mater 200, 338 (1999).

2. G. Han, B. Zong, and Y. Wu, IEEE Trans. Mag 38, 2562 (2002).

3 G. Han, B. Zong, P. Luo, and Y. Wu, J. Appl. Phys. 93, 9202 (2003).

4. A. Encinas-Oropesa, M. Demand, L. Piraux, I. Huynen, and U. Ebels, Phys. Rev. B 310, 104415 (2001).

5. I. Dumitru, F. Li, J. B. Wiley, D. Cimpoesu, A. Stancu, and L. Spinu, IEEE Trans. Mag. 41, 3361 (2005).

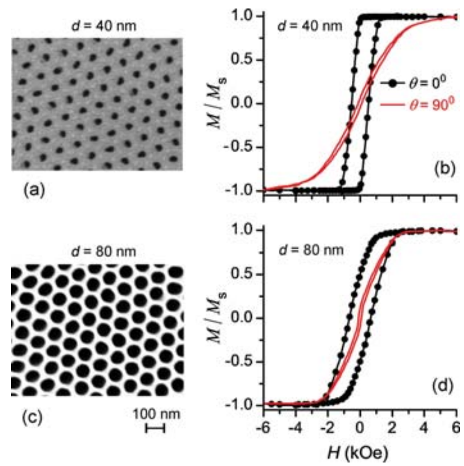

The top surface SEM image of the AAO template, and the hysteresis curves measured with the magnetic field applied parallel and perpendicular to the nanowires' axis, for samples with L=1000 nm and d=40 nm [(a) and (b)] and d=80nm[(c) and (d)].

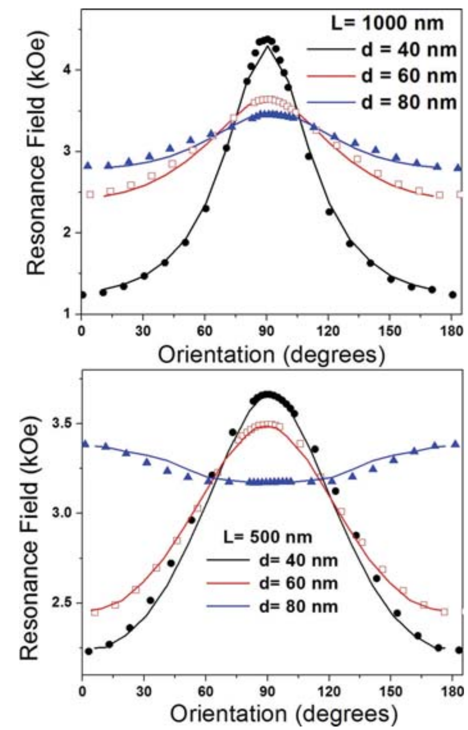

Experimental (symbols) and simulated (lines) angular dependences of the resonance field for samples with L= 100 nm (top) and L= 500 nm (bottom).

CM-04

Thermal coercivity mechanism in Fe nanoribbons and stripes.

F. Garcia-Sanchez, O. Chubykalo-Fesenko
POMT, Instituto de Ciencia de Materiales de Madrid, CSIC, Madrid, Spain

Recent advances in lithography and self-assembled techniques opened the possibility to prepare nanostripes and nanoribbons with the aim to study magnetisation dynamics in restricted geometry [1,2]. Alternatively, ribbon-shape objects can be created by extrusion technique [3], although with less control of particle orientations. The micromagnetic simulations have recommended themselves as a useful technique, capable to get insight into hysteretic processes in such nanostructures. It has been established that in thin nanostripes the magnetisation process occurs through nucleation and propagation of domain wall. The coercive field of long magnetic stripes and nanoribbons decreases as a function of their width, due to change of the character of the magnetisation reversal mechanism [4]. However, the coercivity values obtained through micromagnetic simulations rarely coincide to those obtained experimentally due to the exclusion of possipossible defects present in real experimental situations [5].
In the present work we evaluate the influence of thermally activated process on coercivity values on the timescale, characteristic for typical magnetometer measurement. Namely, as the widths of nanoribbons decrease, the energy barrier, separating the two magnetisation states, becomes comparable to this time scale for fields, below the values obtained through static micromagnetic approach. We have performed micromagnetic modelling of long Fe nanostripes with 4 nm x 30 - 250 nm x 400 nm dimensions. The cubic anisotropy easy axes were directed at 45 degrees to long wire dimension. The energy barriers have been calculated using the Lagrange multiplier technique [6]. Fig.1 represents energy barriers ΔE for zero applied field and various nanostripe widths. The change of the slope in this graph is associated with the change of the character of the saddle point configuration.
Fig.2 represents energy barriers for particles with different elongation as a function of the applied field. The typical magnetometer measurement time of the order of 0.1s gives an estimate of the thermally activated coercive field through the Arrhenius-Néel formula $\tau=\tau_0 \exp(\Delta E/k_BT)$. Finally, Fig.3 represents coercivity values obtained through micromagnetic simulations of nanostripes as a function of their widths. In this Figure we compare static (T=0K) coercivity values with those obtaned through the energy barrier evaluation. It can be clearly observed that the thermally activated coercivity values at 300K are smaller than those obtained through standard micromagnetic approach for particles widths below 100nm. Finally, Fig.3 represents coercivity values obtained through micromagnetic simulations of nanostripes as a function of their widths. In this Figure we compare static (T=0K) coercivity values with those obtaned through the energy barrier evaluation. It can be clearly observed that the thermally activated coercivity values at 300K are smaller than those obtained through standard micromagnetic approach for particles widths below 100nm.

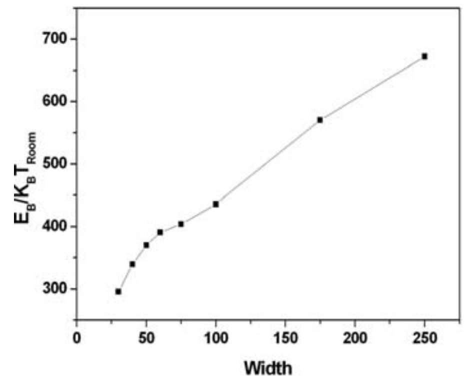

Fig.1 Energy barriers of elongated Fe nanoribbons as a function of their width at zero applied field.

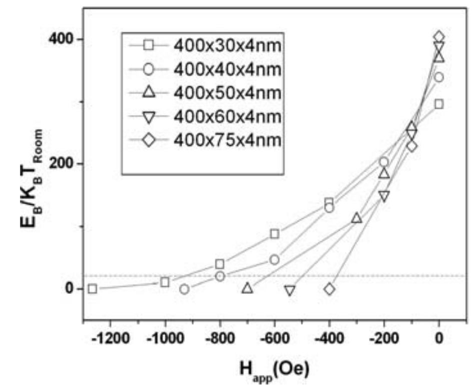

Fig.2 Energy barriers in Fe nanoribbons as a function of applied field. The dashed line corresponds to typical magnetometer measurements.

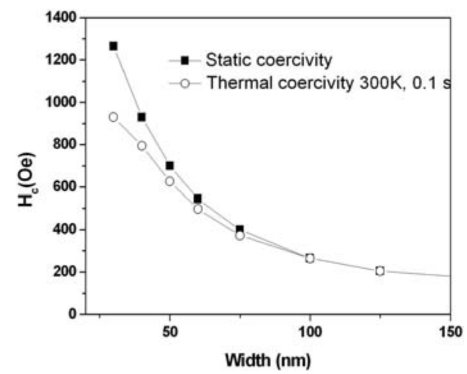

Fig.3 Comparison of the coercivity values obtained through static T=0K micromagnetic simulations with those obtained via energy barriers evaluation at T=300K and measument time 0.1s.

[1] M.Lezsek et al, J.Appl. Phys. 101 (2007) 09J110.

[2] V.M.Prida et al, Nanotechnology, 16 (2005) 2696.

[3] C.Biselli and D.G.Morris, Acta Materialia 44 (1996) 493.

[4] F.Garcia-Sanchez et. al J.Magn.Magn.Mat. 290-291 (2005) 479.

[5] F.García-Sánchez et. al. Physica B (2007)

[6] E.Paz et. al. Physica B 403 (2008) 330.

CM-05

Patterning of magnetic films by focused ion beam irradiation.

S. Tibus[1], D. Makarov[2], C. T. Rettner[3], T. Thomson[4], B. D. Terris[4], T. Schrefl[5], M. Albrecht[1]
1. Institute of Physics, Chemnitz University of Technology, Chemnitz, Germany; 2. Department of Physics, University of Konstanz, Konstanz, Germany; 3. IBM Almaden Research Center, San Jose, CA; 4. San Jose Research Center, Hitachi Global Storage Technologies, San Jose, CA; 5. Department of Engineering Materials, University of Sheffield, Sheffield, United Kingdom

Introduction
Magnetic patterning of continuous thin films has numerous applications within the field of magnetic recording [1]. The use of focused ion beam (FIB) irradiation opens new possibilities for magnetic pattern creation by tailoring the magnetic properties locally [2,3]. This technique is potentially useful in the creation of servo patterns for the purposes of high density magnetic recording [4].
Experiments
Nanometer-scale magnetic strip structures were made by patterning a Co/Pd multilayer medium using a focused Ga beam. The atomic force microscope (AFM) image (Fig. 1a) shows a small topographic contrast (0.9 nm) caused by the sputtering effect of the ion beam. After ac-demagnetization the magnetic force microscope (MFM) image (Fig. 1b) reveals typical magnetic domains, but the underlying strip pattern is not apparent. After saturation in a perpendicular field a well-defined strip domain pattern is observed in remanence (Fig. 1c). The irradiated, magnetically softer segments have reversed their magnetization direction due to the demagnetization fields of the adjacent unexposed medium.
The corresponding M-H loop and remanence curve were measured by polar magneto-optic Kerr effect (Fig. 2a). The M-H loop shows a well pronounced step in magnetization (arrow A), indicating the reversal of the soft, irradiated strips. At remanence a reduced magnetization is observed consistent with the MFM image. For reverse field values an additional stable domain configuration appears in remanence (arrow B). This domain configuration was imaged by MFM revealing an additional strip pattern (Fig. 1d).
Micromagnetic simulations
Micromagnetic simulations were performed using the freely available simulation package MAGPAR [5]. Using reduced values of 2/3 for the saturation magnetization and 1/8 for the anisotropy of the exposed strips, the simulation reproduces the experimentally observed features (Fig. 2b).
To follow the reversal process in more detail, the equilibrium spin configuration was extracted at various external field strengths (Fig. 3). Coming from positive saturation to remanence the change in magnetization is dominated by the reversal of the magnetically soft exposed strips. The driving force is a competition between the magnetostatic interaction and the exchange interaction between the hard and soft strips. When applying negative fields, the reversal is mainly due to domain wall motion in the hard magnetic strip material. In remanence a second stable domain configuration is observed where the hard strip splits, approximately, into a central domain pointing antiparallel to its outer parts while the soft parts reveal mainly an in-plane orientation of the magnetization pointing along the strip. This configuration is in qualitative agreement with the measured MFM image shown in Fig. 1d.
Summary
FIB irradiation was used to create strip patterns with modulated magnetic properties in a perpendicular Co/Pd film. Micromagnetic simulations were used to understand the nature of the magnetic domain configuration and their reversal in these periodic strip systems. The strip patterns reveal an antiparallel alignment of neighboring irradiated and unirradiated strips where the coupling strength can be tuned simply by varying the pattern period and/or exposure dose. The formation of such laterally coupled strips is determined by the competition between the magnetostatic interaction and the exchange interaction.
Acknowledgements
Financial support by the Deutsche Forschungsgemeinschaft through the Emmy-Noether program is gratefully acknowledged.

[1] A. Moser, K. Takano, D.T. Margulies, M. Albrecht, Y. Sonobe, Y. Ikeda, S. Sun, and E.E. Fullerton, *J. Phys. D: Appl. Phys.* **35**, R157 (2002).

[2] C. Chappert, H. Bernas, J. Ferré, V. Kottler, J.-P. Jamet, Y. Chen, E. Cambril, T. Devolder, F. Rousseaux, V. Mathet, and H. Launois, *Science* **280**, 1919 (1998).

[3] J. Fassbender, L. Bischoff, R. Mattheis, and P. Fischer, *J. Appl. Phys.* **99**, 08G301 (2006).

[4] M. Albrecht, C.T. Rettner, M.E. Best, and B.D. Terris, *Appl. Phys. Lett.* **83**, 4363 (2003).

[5] W. Scholz, J. Fidler, T. Schrefl, D. Suess, R. Dittrich, H. Forster, and V. Tsiantos, *Comp. Mat. Sci.* **28**, 366 (2003)

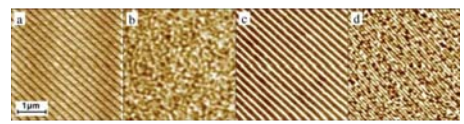

a) AFM and b) – d) MFM images

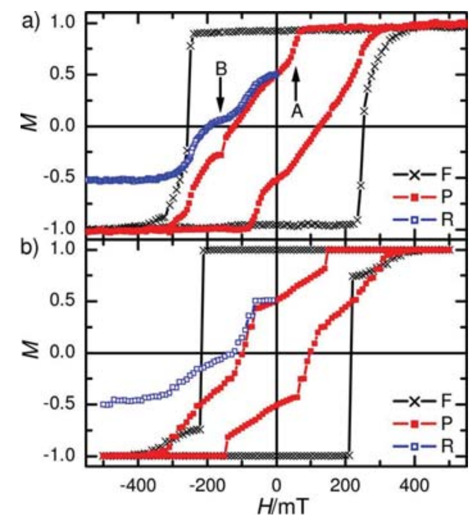

a) Experimental and b) simulated M-H-loop

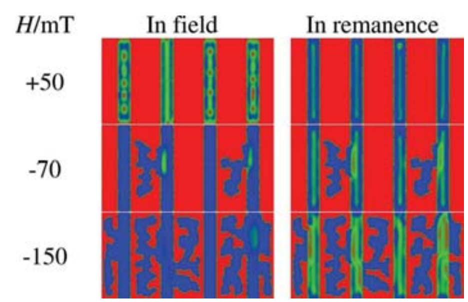

Simulated domain configurations

CM-06

A novel bottom-up fabrication process for controllable sub-100nm magnetic multilayer devices.

M. Kao, J. Ou, J. Wu
Physics, National Changhua University of Education, Changhua, Taiwan

Introduction:
Recently, nanostructured magnetic devices, such as spin valve and magnetic tunnel junction, have attracted much attention due to the great potential for developing practical and ultra-dense memory cells. For making nanometer-scaled current perpendicular to the plane (CPP) multilayer devices a standard subtractive fabrication process in combination of electron beam lithography and dry etching has been often used. Until the past few years, a bottom-up technique using a trilayer hole template was proposed [1-2] for fast and efficient way of testing nano-devices. The advantage of using this new technique is to avoid the etching process which commonly leads to edge shorting or distorted pattern. However, the cell size was strongly dependent on the lithography process only in the aforementioned new technique. Herein, we present a novel similar bottom-up technique for fabricating controllable sub-100nm spin valve and MTJ devices by tuning the thickness of the insulating layer and adding a buffer layer.
Experiments:
The template structure consisting of Si3N4-coated silicon substrate/Au 20/SiO2 x/Ge 20(thickness in nm and x is varied to be 100 and 200, respectively) was first prepared by thermal evaporation and sputtering method. A deep submicron hole was patterned into an electron beam resist spin-coated on the top of the template, followed by a dry etching to transfer the hole pattern to Ge layer. The sample was then dipped into a BOE etchant and the SiO2 underneath the Ge hole was etched out downward and laterally, giving rise to a very good undercutting profile, a hole template was then completed and ready for all sorts of metal films deposition. The controllable nano-devices can be fabricated through smaller hole template which can be achieved using lithography and a trick based on the fact that a buffer film growth vertically may narrow down the template hole at the same time, forming a more and more narrow neck during buffer film growth.
Results and discussion:
Figure 1 shows a SEM micrograph of the top-view of the hole array template. Notice that the grey circle around the hole reveals the laterally over-etched of SiO2 underneath the Ge film. Figure 2 (a) and (b) are the cross-sectional SEM images of two tested runs of multilayer deposition, in which the SiO2 layer in each case is 100 nm and 200 nm thick, respectively. The original hole diameter was 175 nm in each case and the multilayer were deposited with sequences of Cu 40/NiFe 10/Cu 5/NiFe 20/Cu 30 and Cu 140/NiFe 10/Cu 5/NiFe 20/Cu 30. With buffer layers of Cu 40nm and Cu 140nm deposited in the hole templates having 100nm and 200nm thick of SiO2 in each case, one can see the lateral dimension of the active layer, as arrows pointed, is 140 nm and 90 nm, respectively. A single hole template was fabricated for testing spin valve structure and a magnetoresistance was measured using an ac lock-in technique. Figure 3 shows the R-H loop measured on a spin valve device with 100 nm diameter and active layer sequence of NiFe 10/Cu 5/NiFe 20. The steps observed may have been due to local magnetization reversal. More details of fabrication process and electrical characterization will be presented.

[1]J.Z.Sun et al., APL, 81, 2202 (2002)

[2]J.Z.Sun et al., JAP, 93, 6859 (2003)

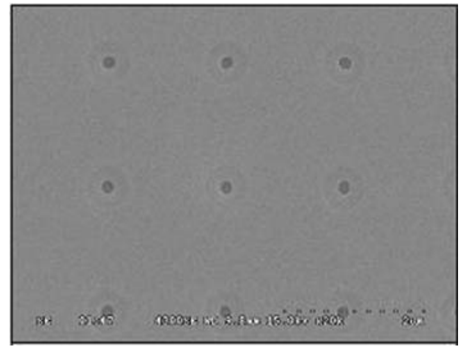

Fig. 1 The SEM micrograph of the top-view of the hole array template.

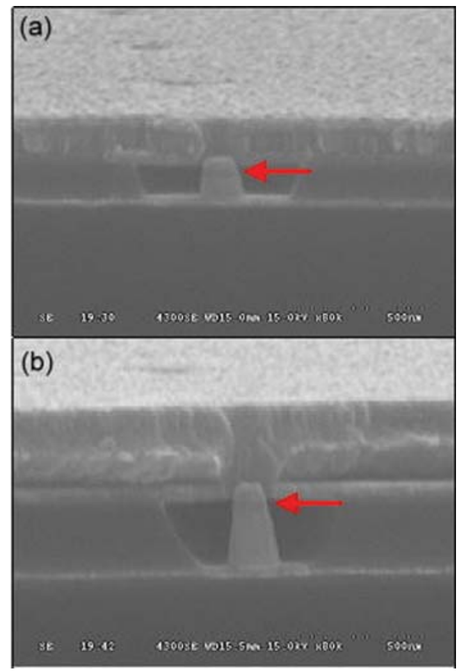

Fig. 2 Cross-sectional SEM images of test runs on the hole template with (a) 100 nm SiO2 insulating layer and multilayer of Cu 40/active layers/Cu30 and (b) 200 nm SiO2 insulating layer and multilayer of Cu 140/active layers/Cu30. The layers with arrows pointed are the active layers (NiFe 10/Cu 5/NiFe 20).

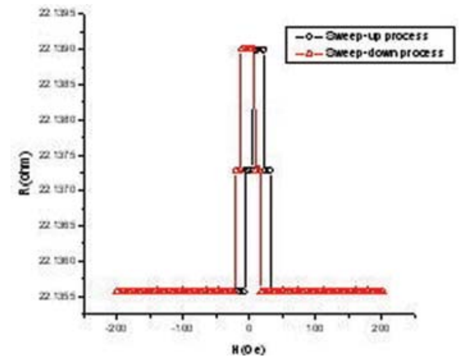

Fig. 3 Magnetoresistance curve measured on a spin valve with 100 nm diameter and layer sequence of NiFe 10/Cu 5/NiFe 20.

CM-07

Self-organised hexagonal patterns of independent magnetic nanodots.

T. Bobek[1], N. Mikuszeit[2], J. Camarero[2], S. Kyrsta[3], L. Yang[1], M. Niño[2], C. Hofer[4], L. Gridneva[5], A. Persson[5], D. Arvanitis[5], R. Miranda[2,6], *J. J. de Miguel*[2], C. Teichert[4], H. Kurz[1]
1. Institute of Semiconductor Electronics, RWTH-Aachen, Aachen, Germany; 2. Dept. Fisica de la Materia Condensada, C-3, Univ. Autonoma de Madrid, Madrid, Spain; 3. Materials Chemistry, RWTH-Aachen, Aachen, Germany; 4. Institut für Physik, Montanuniversität Leoben, Leoben, Austria; 5. Department of Physics, Uppsala University, Uppsala, Sweden; 6. IMDEA-Nano, Madrid Institute of Advanced Studies in Nanotechnology, Madrid, Spain

The formation of self-organized patterns on a semiconductor surface by ion erosion [1] has been taken advantage of to produce large-scale arrays of uniformly-sized, hexagonally-arranged magnetic nanodots. A special sample design has been used in which a magnetic layer was epitaxially grown by magnetron sputtering on a GaSb substrate; this film was subsequently covered with another GaSb layer, 1000 nm thick. The erosion of this sacrificial layer with Ar+ ions leads to the formation of a periodic dot pattern which eventually intersects the buried thin magnetic film. By interrupting this process at the appropriate moment, isolated magnetic nanodiscs can be generated. Different thicknesses and compositions of the intercalated metallic layer have been tested in order to optimize the morphology of the transferred dot pattern and to enhance the resulting magnetic properties. Here we report on the results using pure Co.
The best results were obtained using 400 eV Ar+ ions, resulting in dots of 15-20 nm in diameter, 5 nm thickness and 40 nm nearest-neighbor separation. Figure 1 shows the final surface morphology as determined by Atomic Force Microscopy after completing the erosion process.
The system's magnetic behavior was characterized by means of vectorial Kerr magnetometry. The saturation intensity for the dotted sample is approximately 3 times smaller than for the continuous film, confirming the partial removal of material during the patterning process. Furthermore, the coercive field increases by almost one order of magnitude upon patterning, up to ~15 mT. This effect can be explained by a change in the mechanism of magnetization reversal, which in the 2-dimensional film must be achieved by domain wall propagation. The dots, in contrast, have sizes of the order of the domain wall width and can therefore be expected to be single-domain. Their magnetization reversal must hence take place by coherent rotation.
Numerical simulations based on the Stoner-Wohlfarth model have been performed assuming that the sample consists of an array of particles with negligible coupling and randomly distributed 3-fold anisotropy [2]. The total system energy is calculated as a function of the angle between the applied magnetic field and the particles' magnetization; hysteresis loops are determined by total energy minimization. The experimentally observed zero overall anisotropy results from averaging over all field directions, which is equivalent to a random distribution of the easy axes directions among the particles. This calculation correctly reproduces the shape of the experimental hysteresis loops, as demonstrated by Figure 2. This fit could be achieved using only bulk Co parameters taken from the literature, with no adjustable ones. These results thus confirm that arrays of magnetically independent nanodots can be produced by this efficient patterning method; if used as a magnetic storage material, a density as high as 0.4 Tbit per square inch could be attained. Furthermore, the patterning process depends only on the semiconductor capping, and different intercalated magnetic materials can be used with the only limitation that their thickness remains below ca. 10 nm, so that the ordered pattern is preserved. This opens up the possibility to tailor the dots' magnetic properties, such as coercivity or anisotropy, to suit different applications.

This work has been supported by the European Commission through the NAMASOS STRP-NMP2-CT-2003-505854 contract.

[1] S. Facsko et al., Science 285, 1551 (1999).

[2] T. Bobek et al., Adv. Mater. 19, 4375 (2007).

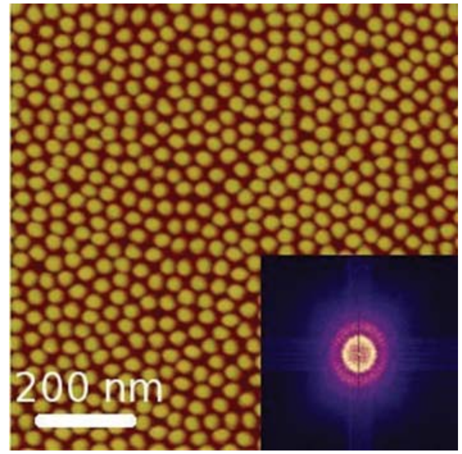

Figure 1

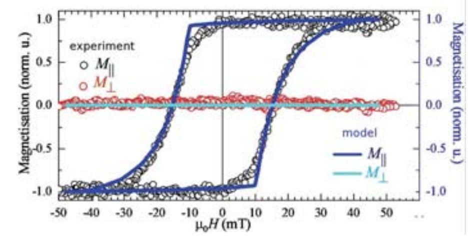

Figure 2

CM-08

Transverse Rectifier Based on Hybrid Magnetic/Superconducting Nanodevices.

D. Perez de Lara[1], E. M. Gonzalez[1], J. V. Anguita[2], J. L. Vicent[1]
1. Fisica de Materiales, Universidad Complutense de Madrid, Madrid, Spain; 2. Instituto Microelectronica, Madrid, CSIC, Tres Cantos, Spain

Villegas et al (1) reported a magnetic longitudinal rectifier device. This device is fabricated using thin superconducting films grown on top of arrays of periodic Ni nanotriangles. The rectification is due to the ratchet effect. Ratchet effect is the net flux of particles yielded by particle motion in asymmetric potentials when a zero average oscillatory driving force is applied to the particle set. This ratchet effect is relevant in many fields of research as molecular motors or dynamics of colloidal particles. In the hybrid magnetic/superconducting rectifier the particles are the magnetic vortex flux lines which are pinned by the Ni nanotriangles, which are the asymmetric potentials. In summary, in this device, injecting an ac input current yields an output dc voltage.

Recently, Gonzalez et al. (2) have reported a transverse nanorectifier which is based on superconducting thin films grown on top of array of non-magnetic asymmetric nanodefects. In the present work, we explore the properties of similar device based on arrays of magnetic nanocenters. In comparison with the non-magnetic rectifier the magnetic nanodevice shows larger output signal values for similar temperature and frequency ranges, besides the amplitude of the input signal, which is needed to yield rectification, is shifted to higher values in comparison with the non-magnetic rectifier.

In brief, the nanodevices are Nb films (100 nm thickness) on top of rectangular array (800 nm x 750 nm) of Ni nanotriangles (triangle side 600 nm and height 40 nm). These devices are fabricated on Si (100) substrates using electron beam lithography, magnetron sputtering, conventional lithography and ion etching techniques. The film is patterned with a cross-shaped measuring bridge that allows us applying, at will, currents and measure the output voltage parallel or perpendicular to the triangle basis. The sample is kept at constant temperature in the superconducting mixed state, close to the superconducting critical temperature. A small magnetic field (around 100 Oe) is applied perpendicular to the films to produce the vortex lattice. The magnetotransport experiments are done with a commercial He cryostat and ac current with frequency up to 10 kHz. Finally, the Ni triangles show a magnetic vortex state as has been published elsewhere (3).

Figure 1 shows the layout for the usual longitudinal (a) ratchet effect (1) and the layout (b) for the transverse ratchet effect (2).

In this work we show an enhancement of the transverse ratchet effect using magnetic traps for the vortices in comparison with the nonmagnetic device. In comparison with the non-magnetic rectifier the magnetic nanodevice shows larger output signal values for similar temperature and frequency ranges, besides the amplitude of the input signal, which is needed to yield rectification, is shifted to higher values in comparison with the non-magnetic rectifier. We will also show a comparison between the longitudinal and transverse ratchet effect for both cases magnetic and non-magnetic pinning centers.

(1) J. E. Villegas, S. Savel'ev, F. Nori, E. M. Gonzalez, J. V. Anguita, R. Garcia, J. L. Vicent, Science 302, 1188 (2003).

(2) E. M. Gonzalez, N. O. Nunez, J. V. Anguita, J. L. Vicent, Appl. Phys. Lett. 91, 062505 (2007).

(3) A. Asenjo, M. Jaafar, E. M. Gonzalez, J. I. Martin, M. Vazquez, J. L. Vicent, J. Magn. Magn. Mat. 310, e936 (2007)

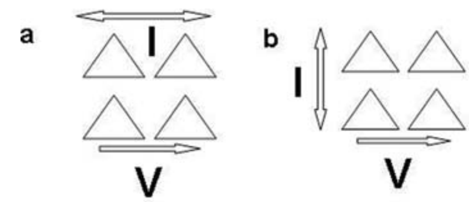

(a) Longitudinal ratchet measurement layout. (b) Transverse ratchet measurement layout.

CM-09

Electrical transport study of patterned lateral Niobium-Permalloy junctions.

S. R. Bakaul[1,2], K. Li[3], G. Han[2], Y. Wu[1]
1. Electrical and Computer Engineering, National University of Singapore, Singapore, Singapore; 2. Spintronic, Media and Interface, Data Storage Institute, Singapore, Singapore; 3. Industrial Materials Institute, Boucherville, QC, Canada

Recently there has been a renewed interest in investigating superconductor (S)- Ferromagnet (F) hybrid structures [1], in particular structures containing F layers with inhomogeneous magnetizations. So far most of the works have been focused on S-F multiple layers. In this paper, we study experimentally the electrical transport properties of an S-F-S lateral junction with a patterned F layer which exhibits a well-defined domain structure. The sample consists of a niobium (Nb) strip with a width of 2 µm and a gap of 150 nm. Centering on the gap and overlaid with the Nb layer at two sides is a 2 µm× 2 µm square of NiFe. Both the Nb and NiFe layers have a thickness of 60 nm. As a control, an S-normal metal (N)-S (Cu as N layer) sample with similar configuration as S-F-S sample was fabricated. The samples were characterized by both magnetic force microscopy (MFM) and electrical transport measurements. The latter was performed in a four-probe configuration as shown in figure 1a.

Fig.1b shows MFM image of the S-F-S sample at room temperature. A multi-domain structure is distinguishably observed in both the gap and overlaid regions. As the gap region is very small, the overlaid region is essential to create a multiple domain structure inside the gap which otherwise would be most likely in a single domain state. By cooling the sample from 20 K to 1.4 K, the resistance of the gap region decreases sharply from 440 ohm to 3.5 ohm in the temperature range of 5 K to 4 K, indicating that the critical temperature of this specific sample is about 4.5 K. From dI/dV curves at zero field and at 1.4 K, a superconducting gap of 0.6 meV was deduced which agrees well with the theoretically predicted value of 0.68 meV with a critical temperature of 4.5 K. The gap-related features disappear at about 3.5 T which can be considered as a critical field for the Nb film used in this sample. Fig.2 shows the dI/dV curves at 1.6 K and different applied field. The dI/dV curve shows a large fluctuation in the gap region at low field. Upon applying a small magnetic field (100 Oe) two conductance peaks appear at around 0.3 mV of bias voltage and these features disappear at a magnetic field above 0.4 T. Figure 3 shows the dependence of difference between these two peak positions (Vd) on magnetic field. Vd increases quickly at low field and saturate at higher field (> 0.3 T). In addition to these features, a slight reduction of zero bias conductance (ZBC) with magnetic field in the region between 0 to 0.2 T is observed; it then decreases linearly at magnetic field above 0.2 T. The ZBC at zero field is about 1.5%~ 8% higher than that at 0.2 T.

Although the underlying mechanism for the appearance of split peaks in the dI/dV curve is not well understood at the moment, judging from the Vd dependence on magnetic field, it is presumably caused by the annihilation of domain walls in the overlaid region. There is an exchange coupling between NiFe and Nb in the overlaid region. The effective exchange field increases with the degree of alignment of magnetization in the NiFe layer [2]. Due to this exchange coupling, the superconducting gap near the NiFe/Nb interface will be reduced as compared to that of the region which is further away from the interface. This may explain why additional conductance features appear in the gap region of Nb when a magnetic field is applied, which are not observed in the S-N-S sample. On the other hand, the presence of domain walls at the gap region allows the formation of Cooper pairs of opposite spin electrons stemming from neighboring domains magnetized in opposite directions, promoting the so-called crossed Andreev reflection (CAR) [3]. The CAR is known to contribute excess conductance in the gap region. As the field is increased, the magnetization in different domains become gradually aligned, resulting in a suppression of CAR and thus a decrease of conductance in the gap region. Above 0.2 T, Nb enters into a resistive mixed state due to the large exchange and applied field, causing a significant decrease of ZBC with the magnetic field. Further investigation is ongoing to understand quantitatively the experimental data using theoretical models. We are also fabricating and characterizing samples with NiFe of different lateral dimension and thickness. The results will be presented in the conference.

1. A. I. Buzdin, Rev. Mod. Phys. 77, 935 (2005).

2. B. Crouzy et al., Phys. Rev. B 76, 134502 (2007).

3. N. M. Chtchelkatchev and I. S. Burmistrov Phys. Rev. B 68, 140501(R) (2003).

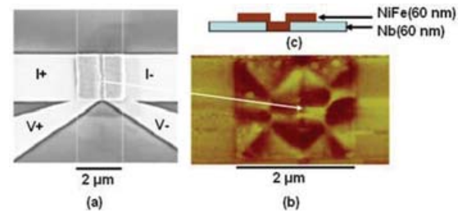

FIG. 1.(a) SEM image of SFS device. (b) MFM image of the magnetic region (c) Schematic cross-sectional view of SFS device.

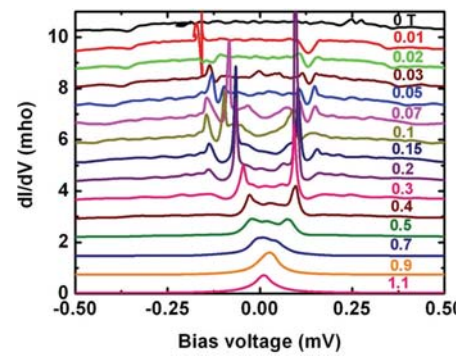

FIG. 2. dI/dV curves for S-F-S device at 1.6 K under different in-plane magnetic fields.

CM-10

Finite size effects in [Co(1nm)/Bi(2.5nm)]n line-structures.

C. Christides[1], T. Speliotis[2]
1. Department of Engineering Sciences, University of Patras, Patras, 26504, Greece; 2. Institute of Materials Science, NCSR Demokritos, Athens, 153 10, Greece

In the semimetal bismuth both, the electronic mean free path lmf and Fermi wavelength are large compared to conventional metals, making it an ideal material for studies on the nanoscale because classical and quantum size effects are expected [1,2]. Of particular interest [3] is the scaling of conductivity by the ratio lmf/D in granular conductors with average grain size D. In the present study we examine the artificial control of grain-boundary resistance and its contribution to magneto-transport properties of [Co/Bi]n multilayer line-structures. [Co/Bi]n and Bi lines were produced by a two-step micro-fabrication process. Scanning Electron Microscopy (SEM) was used to examine the granularity of these [Co/Bi]-line structures. Magneto-transport measurements have been carried out with a Quantum Design SQUID magnetometer.
Fig.1 shows the temperature dependence of resistance, R, at H=0 Oe (warming) and H=3 kOe (cooling) in [Co(1nm)/Bi(2.5nm)]n (n=10 or 20) and pure-Bi line structures. The decrease of R (that is normalized to RFC(5K) value in the FC curve of Bi and [Co/Bi]10 respectively) observed above 150 K in Fig.1A is due to finite size effects inside the granular microstructure of Bi. In addition, Fig.1B shows that a doubling of the total line thickness, from 45 nm in [Co(1nm)/Bi(2.5nm)]10 to 70 nm in [Co(1nm)/Bi(2.5nm)]20 line-structures, causes a slight increase of R below 150 K and a sharper drop of R above 150 K for the thicker lines, indicating that grain-size effects affect predominantly the electrical conductivity of these structures in the examined temperature range. Fig.2 shows the transverse magnetoresistance (MR) from a [Co(1nm)/Bi(2.5nm)]10 line structure at 10 K. The MR ratio: $\Delta R/R=80\%$, is much larger than that expected from the known anisotropic–MR (AMR) ratios, indicating that finite size effects are very important at low temperatures. This MR ratio decreases significantly above 100 K and becomes equal to about 1% at 280 K.
It is demonstrated that grain-boundary effects induce significant changes of the magneto-resistance, depending on the granularity of [Co/Bi]n-wires, which indicate that these multilayered structures might be potential candidates for applications in granular electronic systems [4].

[1] K. Liu, C.L. Chien, P. C. Searson, Phys. Rev. B 58 (1998) R14681.

[2] M.M. Rosario, Y.Liu, Phys. Rev. B 65 (2002) 094506

[3] G. Reiss, J. Vancea, H. Hoffman, Phys. Rev. Lett. 56 (1986) 2100.

[4] I. S. Belodorov et al, Rev. Mod. Phys. 79 (2007) 469.

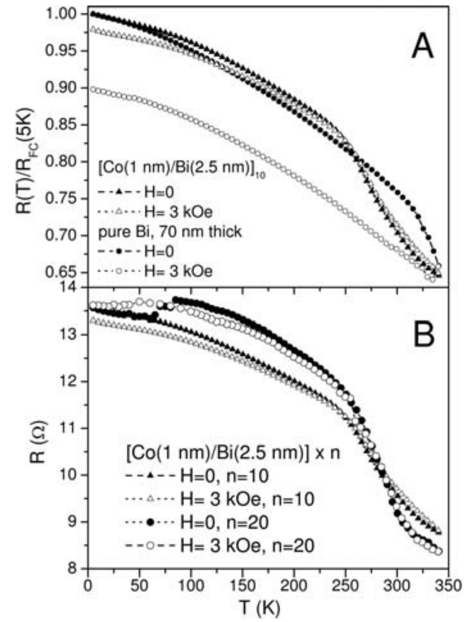

Fig.1 Temperature dependence of resistance at H=0 Oe (warming) and H=3 kOe (cooling) in (A) [Co/Bi]10 and pure-Bi line structures, (B) [Co/Bi]n line structures with n=10 and 20. The field is applied perpendicular to film.

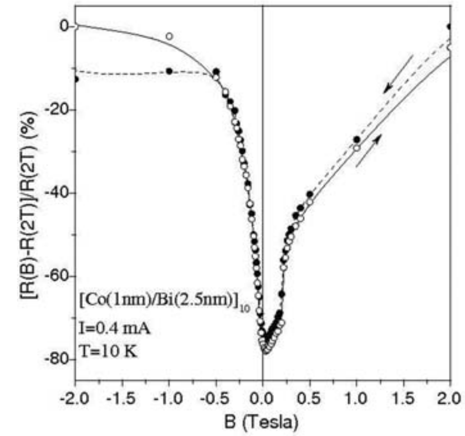

Fig.2 Transverse Magnetoresistance (MR) effec

CN-01

Dynamic and temperature effects in spin-transfer switching.

H. Pham[1,2], D. Cimpoesu[1,3], A. Stancu[3], *L. Spinu*[1,2]
1. Advanced Materials Research Institute, University of New Orleans, New Orleans, LA; 2. Department of Physics, University of New Orleans, New Orleans, LA; 3. Department of Physics, "Al. I. Cuza" University, Iasi, Romania

Recently, the current-induced spin-transfer torque [1] has been proposed as a convenient writing process in high density magnetic random access memory [2]-[4]. A spin-polarized current can switch the magnetization of a ferromagnetic layer more efficiently than a current induced magnetic field. In a typical spin-transfer memory cell, the current is sent along the *z* direction across a multilayer element with layers parallel to the (*x,y*) plane. The element consists of a "fixed" magnetic layer with magnetization pinned along the *x* axis, a nonmagnetic spacer, and a "free" magnetic layer exposed to the torque due to *x*-directed spin-polarization that the electrons acquire from fixed layer. A spin-transfer transmission mode [3] or a spin-transfer reflection mode [4] can be used to write the information. With increasing demand on the access time the current pulse shape becomes important. Also, with memory area density increasing and the memory cell size further shrinking the study of thermal fluctuations becomes of extreme importance for their recording thermal stability.

In this paper we have studied the dynamic switching in spin-transfer memory and its dependence on thermal effects. The model is based on stochastic Landau-Lifshitz-Gilbert equation [5], which is numerically integrated. As ferromagnetic material, Co with saturation magnetization $4\pi M_s$=12 kOe and damping constant α=0.01 was chosen. The free magnetic layer is assumed to be ellipsoid shaped, making the demagnetizing field uniform across the entire layer, and also it is assumed to be a single domain. The ellipsoid's principal axes are taken along *x*, *y* and *z*: long-axis length of 100 nm (along *Ox* axis), short-axis length of 75 nm (along *Oy* axis), and thickness *d*=2 nm, leading to demagnetizing factors N_x=0.014, N_y=0.022, N_z=0.964. The effective field consists of applied field, demagnetizing field, anti-ferromagnetic coupling between the fixed layer and free layer $\mathbf{H}_{ex}=-4\pi(N_y-N_x)M_s h_{ex}\mathbf{m}_p$ where the unit vector $\mathbf{m}_p$ gives the direction of the spin polarization (along *x* direction in our case), and thermal field.

At a given temperature the switching properties are discussed as a function of applied current pulse amplitude, duration and shape. Because an instantaneous change of the applied current from zero to some other value is not very realistic, sinusoidal time dependence for the current pulse rise and fall are assumed. The rise/fall time is a function of the pulse's amplitude so that the current sweep rate v_I, defined as the ratio between the amplitude and pulse's rise/fall time, is constant. If initially the magnetic moments of fixed layer and free layer are parallel aligned there is no torque acting on the free layer. However at finite temperature the thermal agitation assure that at no time this happens.

From Fig. 1 we can see that the switching diagrams have layer-like structures with switching/non-switching areas. A "comblike structure" of the switching diagram is experimentally obtained in Ref. 6 and it is explained taking into account the statistics of the possible initial states due to thermal fluctuations. In the full paper we present how the current sweep rate, damping constant, and also the thermal fluctuations affect the switching, the reliability, and the writing speed of spin-torque devices. Instead of a clear border between switching and non-switching areas we have a transition region where the final state is sensitive to thermal fluctuations.

Work at AMRI was supported by DARPA under grant No. HR0011-07-1-0031. Calculations were performed on computational facilities provided by Louisiana Optical Network Initiative (http://www.loni.org) which is supported by the Louisiana Board of Regents.

[1] J. C. Slonczewski, J. Magn. Magn. Mater. 159, L1 (1996); L. Berger, Phys. Rev. B 54, 9353 (1996).

[2] M. Hosomi, et al., IEDM Technical Digest 2005 (IEEE, Washington, 2005), pp. 459.

[3] Y. Huai, P. P. Nguyen, U.S. Patent No. 6,920,063 B2 (Jul. 19, 2005).

[4] F. B. Mancoff, B. N. Engel, N. D. Rizzo, U.S. Patent No. 7,149,106 B2 (Dec. 12, 2006).

[5] W. F. Brown Jr., Phys. Rev. 130 (1963) 1677.

[6] T. Devolder, et al., Phys. Rev. B 75 (2007) 064402.

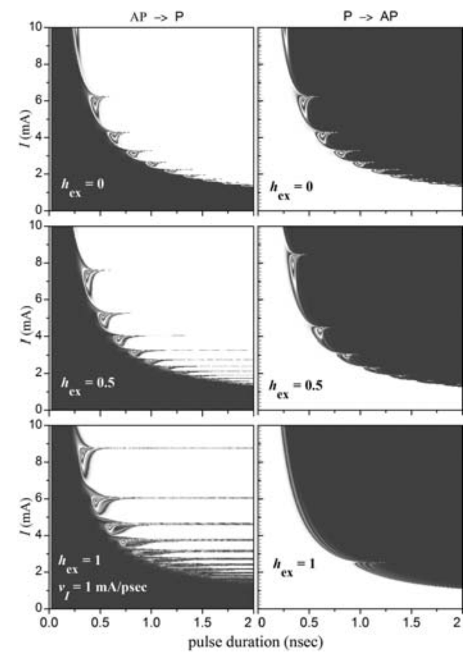

Fig. 1. Anti-parallel (AP) to parallel (P) (left) and P to AP (right) switching diagrams at *T*=0K, as a function of current pulse amplitude and duration, for a current sweep rate v_I=1mA/ps, and different values of the anti-ferromagnetic coupling h_{ex}. Initially the magnetization of the free layer is in the film plane, making an angle of 10^{-3} degree with the direction of the fixed layer. Black areas represent m_x=-1, white areas represent m_x=1, and the intermediate values of m_x are represented with shades of gray.

CN-02

Analysis of spin transfer switching speed in magnetic nano-structures.

J. Guo[1], T. Seng Ghee[2], *J. Mansoor Bin Abdul*[1], L. Lin[1]
1. National University of Singapore, Singapore, Singapore; 2. Data Storage Institute, Singapore, Singapore

Recent experimental evidence [1-2] of spin transfer switching at reasonably low current density (J) of 10^6~10^8 A/cm^2 in magnetic nanostructures has triggered keen interest in this research topic, which was initiated by the theoretical predictions of Slonczewski and Berger in 1996 [3]. However, the magnetization switching speed under the influence of spin transfer torque, which has far-reaching consequences to device operation has not been studied in depth. A long switching time poses a limit to the speed of device operation; while an underdamped "ringing" [4] switching behavior makes the device prone to radio-frequency (RF) noise. In this article, we investigate the effect of current density (J) and spin polarization of current (P) on the magnetization switching dynamics of an exemplary Co magnetic nanostructure of dimensions 50×50×50 nm^3. A three-dimensional dynamic micromagnetic model of the current-induced magnetization dynamics was developed, which incorporates the Slonczewski spin transfer torque term [3] and the damping effects of eddy current following the scheme by Torres *et al*. [5]. For the micromagnetic calculations, the magnetic nanostructure is discretized into cubic unit cells of length 10 nm. Figure 1(a) shows a significant improvement in the switching time (t_{sw}) to 2.5 ps for J of 2.3x10^9 A/cm^2, compared to t_{sw}≈3 ps for lower J values of 2.3x10^7 A/cm^2 and 2.3x10^8 A/cm^2. Figure 1(b) shows that, in general, a faster magnetic reversal can be achieved with a larger P for a specific J value. This may be explained by the fact that a higher P results in a larger transfer of momentum per conduction electron to the local moments, thus generating a larger effective field and a faster precessional motion. Additionally, we found that the effect of P becomes more significant as J increases. As shown in Fig. 1(b), when J=2.3x10^9 A/cm^2, t_{sw} is reduced by about a third when P is increased from 0.1 to 0.9, while at J=2.3x10^8 A/cm^2, the reduction in tsw is only ~ 5% for the same increase in P. The numerical results of our simulation indicates that the spin transfer switching time in the presence of eddy current can be optimized by a careful choice of J and P. The use of a large J to monotonically increase switching speed is not a viable option since a large J causes electromigration in metallic materials, while high spin polarization P which approaches 100% cannot be easily achieved, even with half metallic materials. However, with a suitable choice of J, the switching speed can be improved significantly while keeping to the experimentally observed range of P.

[1] J. A. Katine, F. J. Albert, and R.A. Buhrman, Phys. Rev. Lett. 84, 3149 (2000).

[2] Y. Jiang, T. Nozaki, S. Abe, T. Ochiai, A. Hirohata, N. Tezuka, and K. Inomata, Nat. Mater. 3, 361 (2004).

[3] J. C. Slonczewski, J. Magn. Magn. Mater. 159, L1 (1996); L. Berger, Phys. Rev. B 54, 9353 (1996).

[4] M. Covington, Science 307, 215 (2005).

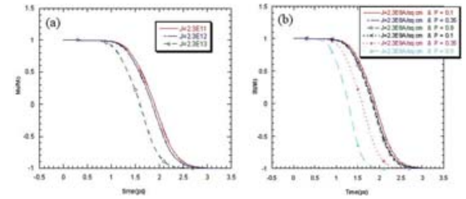

Fig.1 (a) Decrease in magnetization switching time t_{sw} with increasing J (in units of A/m^2); (b) Decrease in t_{sw} with increasing spin polarization of current at J=2x10^8 A/cm^2 and 2x10^9 A/cm^2.

CN-03

Current induced domain wall motion in ferromagnetic wires with out-of-plane magnetization.

H. Szambolics[1,3], J. Toussaint[1,3], A. Marty[4], I. Miron[2], L. Buda-Prejbeanu[2,3]
1. Department of Nanosciences, Institut Neel, CNRS, Grenoble, France; 2. Laboratoire SPINTEC, CEA-CNRS, Grenoble, France; 3. Institut National Polytechnique de Grenoble, Grenoble, France; 4. Laboratoire SP2M, CEA-CNRS, Grenoble, France

The possible applications of magnetic domain wall (DW) motion induced by spin-polarized current injection are rather numerous; this is why many efforts are invested in studying this phenomenon. Several theoretical approaches were developed, but even though all kind of systems can be described by them, experimental results refer mostly to systems with in-plane magnetization. In such a system the large width of the DWs makes them less sensitive to pinning and the current-generated Ampère field can be neglected. On the other hand, an out-of-plane magnetized system presents very narrow DWs and thus pinning plays an important role, but also increased DW velocities are expected [1]. We present here a study on such a system, a 120nm wide and 11nm thick Co/Pt nanowire where the DW width is around 10nm.
The modeling of DW motion induced by a spin-polarized current is based on the modified Landau-Lifschitz-Gilbert equation (LLG):
$\partial\mathbf{M}/\partial t=-\gamma_0(\mathbf{M}\times\mathbf{H_{eff}})+\alpha/M_s(\mathbf{M}\times\partial\mathbf{M}/\partial t)+(\partial\mathbf{M}/\partial t)_{ST}$ (1).
By γ_0 we denote the gyromagnetic factor, α is the Gilbert damping constant, M_s is the spontaneous magnetization and $\mathbf{H_{eff}}$ is the effective field summarizing the main contributions in a micromagnetic system: exchange, magnetocrystalline anisotropy, demagnetizing, Zeeman field and, in the case of perpendicularly magnetized nanowires, the stray field issued from the adjacent domains. The effects of the Ampère field are neglected in this paper.
To describe the effect of the current on the DW we used the approach proposed by Thiaville et al. [2]:
$(\partial\mathbf{M}/\partial t)_{ST}=-(\mathbf{u}.\nabla)\mathbf{M}+\beta/M_S\mathbf{M}\times[(\mathbf{u}.\nabla)\mathbf{M}]$ (2)
The first term is the adiabatic term, occurring when the spin current follows approximately the direction of the magnetization within the wall. This term is responsible for the distortion of the DW. The second term is the non-adiabatic contribution due to the mistracking of the electrons. It is responsible for the DW displacement. β is the non-adiabatic spin transfer parameter. The velocity **u** is a vector directed along the direction of electron motion, having the amplitude:
$\mathbf{u}=(g\mu_B PJ_{app})/(2eM_S)(1\ 0\ 0)$ (3)
Here g is the free electron's Landé factor (g=2), μ_B is the Bohr magneton, J_{app} is the current density, P is the current polarization rate and e is the charge of the electron.
For all the simulation reported below the material parameters used are the following:
μ_0M_S=0.32T, μ_0H_{anis}=1T, $A_{ex}=10^{-11}$J/m, α=0.01, P=1. Since the value of the parameter β is not well known and to analyze its effects, several values were considered.
The above mentioned equations were implemented in the micromagnetic solver WALL_ST® based on the finite differences approximation.
Walker already determined that in the case of field induced DW motion there are two linear regimes: a steady and a precessional regime [3]. These regimes are also observed in the case of current induced DW motion and a critical current density J_c can be determined. Two relations connect the wall velocity to **u**, β and α:
$\mathbf{v_{steady}}=(\beta/\alpha)\mathbf{u}$ (4)
$\mathbf{v_{prec}}=(1+\alpha\beta)/(1+\alpha^2)\mathbf{u}$ (5)

The simulations showed that β plays a very important role: it can lead to the presence or absence of one of the above mentioned regimes in a velocity versus current density curve. Indeed there are three possibilities:
Case β=0 For $J_{app} < J_c$ the magnetization in the DW tilts towards the hard axis reaching a maximal value of is 45° when $J_{app}=J_c$. Because the force exerted by the current on the wall is equilibrated by an internal restoring force the motion of the DW can not be maintained and the wall velocity goes quickly to zero. For high current densities, the internal force is defeated by the force from the current, the wall starts to precess becoming periodically Bloch/Neel and moves with a finite velocity in the direction of the current.
Case $\beta=\alpha$ leads to a new kind of motion: the DW motion occurs for all current densities, without any changes in the wall structure, the wall velocity being always equal to the velocity-like quantity **u**.
Case $\beta\neq 0$, α gives a "normal" behavior of the DW, where both the translation and oscillatory regime are present.
In Figure 1 a summary of the behavior of the DW under the influence of a spin-polarized current is shown. J_c is 20^{10} A/m^2; the corresponding highest possible value for the DW velocity is around 100 m/s (β=0.02). The transition region between the two linear motion regimes is quite narrow and one can remark that finally all the curves tend towards the $\beta=\alpha$ line.
The next step in our study is to determine the effect on pinning on the DW motion. Unfortunately this is a very controversial subject, as there is no proper definition of pinning centers. Thus several scenarios have to be taken into account: geometrical constrictions, anisotropy distribution, etc.

1. D. Ravelosona et al., Phys. Rev. Lett. 96, 186604 (2006).

2. A. Thiaville et al., Europhys. Lett. 69, 990 (2005).

3. N. L. Schryer, L. R. Walker, J. Appl. Phys. 45, 5406 (1974).

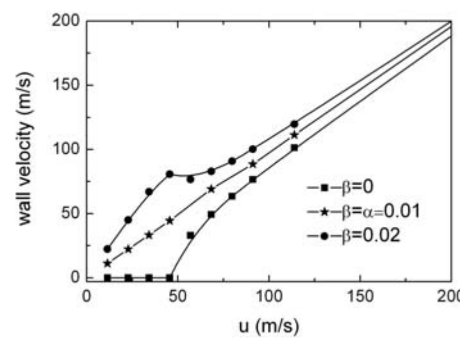

Fig. 1: Evolution of the domain wall velocity versus the velocity u representing the current density.

CN-04

Fast magnetization switching with short pulses.

W. Scholz[1], T. M. Crawford[2], T. W. Clinton[1], T. Ambrose[1], S. Kaka[1], S. Batra[1]
1. Research, Seagate, Pittsburgh, PA; 2. USC NanoCenter, Univ. of South Carolina, Columbia, SC

In this paper we study the magnetization reversal process of single domain Stoner-Wohlfarth particles subject to short pulses using analytical and numerical models. We investigate the effect of short unipolar and bipolar field pulses, which are applied perpendicular to the magnetocrystalline anisotropy axis, on the magnetization switching dynamics (cf. Fig. 1a). We find very fast precessional switching events (<100 ps) with field amplitudes down to about 1/4 of the Stoner-Wohlfarth switching field (cf. Fig. 1b), which is lower than the fast sub-Stoner-Wohlfarth switching described previously.[1,2] Our full micromagnetic simulations of nanodots confirmed that fast precessional switching with short field pulses is possible for technologically relevant magnetic nanostructures with sufficient margins for variations in the material parameters and timing.
This mechanism of fast precessional switching [3,4,5] with short pulses at low fields could find important applications in magnetic recording or magnetic random access memory devices. We show that (theoretically) even smaller switching fields are possible which are even independent of the anisotropy field.

[1] L. He, W. D. Doyle, H. Fujiwara, IEEE Trans. Magn. 30 (1994) 4086-4088

[2] D. Suess, T. Schrefl, W. Scholz, J. Fidler, J. Magn. Magn. Mater. 242-245 (2002) 426-429

[3] Z. Z. Sun and X. R. Wang, Phys. Rev. B 73 (2006) 092416.

[4] Z. Z. Sun and X. R. Wang, Phys. Rev. Lett. 97 (2006) 077205.

[5] K. Rivkin, J. B. Ketterson, Appl. Phys. Lett. 89, 252507 (2006).

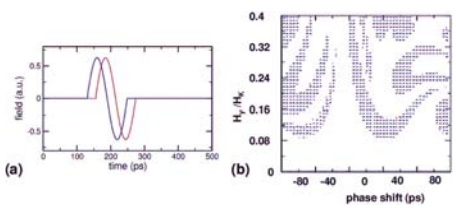

Fig. 1: (a) Field waveform of two bipolar pulses; (b) Switching phase diagram of a Stoner Wohlfarth particle as a function of phase shift between the pulses (blue: switched; white: not switched).

CN-05

Micromagnetic Simulations of Domain Wall Depinning Forced by Oscillating Fields.

O. Alejos Ducal[1], E. Martínez Vecino[2], L. López Díaz[3], L. Torres Rincón[3]
1. Electricidad y Electrónica, Universidad de Valladolid, Valladolid, Spain; 2. Ingeniería Electromecánica, Universidad de Burgos, Burgos, Spain; 3. Física Aplicada, Universidad de Salamanca, Salamanca, Spain

Notches in thin ferromagnetic strips may act as pinning centers for the domain walls (DW) existing in them, due to the locally lowering of the DW magnetostatic energy associated to the presence of the notch, that is, the formation of a pinning potential well. The analysis of DW depinning from notches has acquired a certain technological relevance due to its application to promising logic and storage devices [1].

The work presents the study of the DW dynamics under the application of an in-plane magnetic field directed along the largest dimension of the strip. The strip has a couple of symmetric notches placed on it, where a head-to-head DW has been pinned. The applied field is composed of two terms: a constant value plus a harmonically oscillating one. The constant part B0 is fixed to five different values lower than the required constant field to force the DW depinning. The amplitude Bz of the harmonic part is then investigated in order to produce this depinning for different frequencies.

As the theoretical model proposed in [2] predicts, a resonant behavior can be observed if the frequency of the harmonic field is near the DW natural oscillation frequency (see Fig.1). However, the resulting DW energy absorption peak is not centered at this natural oscillation frequency, and it shifts to lower frequencies.

This result can be explained if it is considered that the DW structure noticeably changes as the DW oscillates by the effect of the applied field. In fact, its width shrinks so that the DW equivalent mass increases. This increase is thought to be the responsible for the frequency shifting.

[1] S. S. Parkin, U.S. Patent No. 6834005 (2004)

[2] E. Martinez et al, Phys. Rev. Lett. 98, 267202 (2007)

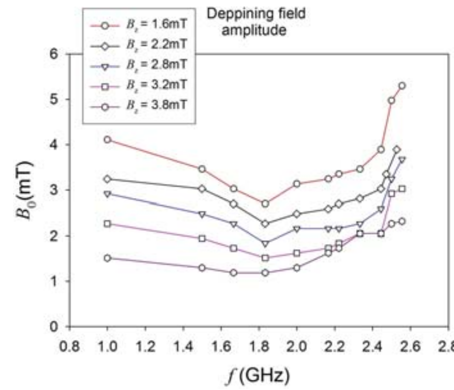

Figure 1. Depinning harmonic field for a DW as a function of the frequency. Five different constant fields have been considered. The natural oscillation frequency for this DW is of about 2.5GHz, while the absorption peak is around 1.8GHz.

CN-06

Effects of Shape Anisotropy on the Walker Breakdown Field in Field-Driven Domain Wall Motion.

W. Kim[1], S. Jung[2], H. Lee[2], K. Lee[1]
1. Korea University, Seoul, South Korea; 2. POSTECH, Pohang, South Korea

I. Introduction
Recently, the domain wall (DW) motion in nanowires has received a considerable interest because magnetic DWs can be used for logic [1] or information storage devices [2]. In the field-driven DW motion, DW velocity decreases with increasing magnetic field when the field magnitude is larger than a certain value, i.e. the Walker breakdown field (H_W) [3, 4]. The Walker breakdown is caused by DW precession around the in-plane easy axis. Because an out-of-plane tilting of DW costs energy due to shape anisotropy, it has been believed that the H_W increases with the shape anisotropy. In this work, using micromagnetic studies, we show that the H_W is almost independent of the shape anisotropy because of the anti-vortex injection during the DW precession.
II. Numerical and Theoretical Approaches
We performed 1-dimensional (1D) and 2-dimensional (2D) micromagnetic simulations and compared numerical results with theoretical ones. Micromagnetic simulations are based on the Landau-Lifshitz-Gilbert equation (Eq. (1)).
$\partial M/\partial t = -\gamma M \times H_{eff} + \alpha/Ms\ (M\times\partial M/\partial t)$, (1)
where the gyromagnetic ratio (γ) is $1.76 \times 10^7\ s^{-1}Oe^{-1}$, α is the Gilbert damping constant (= 0.02), Ms is the saturation magnetization (= 800 emu/cm^3), H_{eff} is the effective field including the external field applied along the in-plane easy axis of the nanowire, the magnetostatic field, and the exchange field (exchange constant = 1.3×10^{-6} erg/cm). A head-to-head transverse wall (TW) is initially placed in a rectangular-shaped $Ni_{80}Fe_{20}$ nanowire with cross-sectional area of 720 nm^2 and length of 5 μm. The unit cell dimension is $4 \times W \times T\ nm^3$ in 1D model and $4 \times 4 \times T\ nm^3$ in 2D model, where W is the width and T is the thickness of nanowire. The aspect ratio (= W/T) is varied to examine the effect of shape anisotropy on the H_W. We also performed a theoretical study through a use of the collective coordinate approach with variables of DW position, tilting angle, and DW width [5].
III. Results and Discussions
Fig. 1a (1b) shows numerical results of 1D (2D) micromagnetic simulations. In 1D model, the H_W clearly increases with the shape anisotropy whereas in 2D model, it does not vary much. Another interesting point is that in 1D model, the field (=H_{max}) for the maximum velocity is smaller than the H_W. In 2D model, however, the H_{max} is identical with the H_W.
All the results including theoretical ones are summarized in Fig. 1c. The H_W and H_{max} obtained from 1D model show excellent agreement with theoretical ones. From the collective coordinate approach, we obtained analytical formula of the H_W (Eq. 2) and H_{max} (Eq. 3).
$H_W = \alpha K_\perp/Ms$, (2)
$H_{max} = (\alpha K_\perp \sin 2\phi_{max})/Ms$, (3)
where $\sin\phi_{max}$ is $[\sqrt{(K^2+K\times K_\perp)}-K]^{1/2}/\sqrt{K_\perp}$, $K_\perp$ is the hard-axis anisotropy (= shape anisotropy) and K is the in-plane easy axis anisotropy which determines equilibrium DW width. The coefficient $\sin 2\phi_{max}$ appears in the Eq. (3) because the DW velocity is proportional to the DW width which varies with the external magnetic field. Because the $\sin 2\phi_{max}$ is smaller than unity, the H_{max} is always smaller than the H_W in case of rigid DW.
In 2D model, the DW shows the periodic oscillatory motion with cyclic transformation between the TW and the anti-vortex wall (AVW) at $H>H_W$ as reported in Ref. [6]. We attribute the disagreement between 2D model and theory (or 1D model) to the AVW formation. In 1D model, the tilting angle of DW measured from the wire plane at H close to H_W is almost 90°. In 2D model, however, the tilting angle is 90° at a vertex of triangular shaped DW, but is only 45° in other parts of DW. In case of uniform precession as in the theory or 1D model, the energy cost for the DW precession originates from the demagnetization energy and thus the shape anisotropy directly affects the H_W. In case of AVW formation as in the 2D model, however, the energy cost originates from the exchange energy, not the demagnetization energy. Therefore, the H_W in 2D model is almost independent of the shape anisotropy.
IV. Conclusion
We investigated the effect of shape anisotropy of nanowires on the Walker field through the use of the micromagnetic modeling and the collective coordinate theory. It was found that the Walker field is almost independent of the shape anisotropy in contrast to the theoretical prediction. It is because the DW precession occurs by the periodic transformation between a transverse wall and an anti-vortex wall.

[1] D. A. Allwood et al., Science 296, 5575 (2003).

[2] S. S. P. Parkin, U.S. Patent No. 6834005 (2004).

[3] N. L. Schryer and L. R. Walker, J. Appl. Phys. 45, 5406 (1974).

[4] G. S. D. Beach, C. Nistor, C. Knutson, M. Tsoi, and J. L. Erskine, Nat. Mater. 4, 741 (2005).

[5] S.-W. Jung and H.-W. Lee, J. Magn. 12, 1 (2007).

[6] Y. Nakatani, A. Thiaville, and J. Miltat, Nat. Mater. 2, 521 (2003).

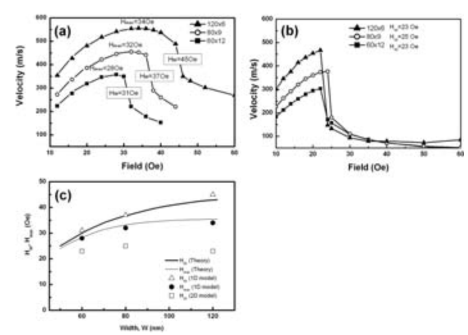

Fig. 1. Domain wall velocity versus external magnetic field with various nanowires obtained from (a) 1D model, and (b) 2D model. (c) Summary of H_W and H_{max} as a function of wire width.

CN-07

Testing the theory of nucleation in infinite square prism—micromagnetic simulations.

K. M. Lebecki
Institute of Physics, PAS, Warsaw, Poland

Analytical solutions are rare in micromagnetism, thus they are all the more valuable. Among them are theories of nucleation field of infinitely long structures. They are still popular due to recent interest in one-dimensional ferromagnetic samples. Infinite circular cylinder model is already well known and has been compared with many experiments and simulations. Less known theory of circular tube can also be helpful, as increasing number of authors report successful growth of ferromagnetic nanotubes. The case of infinite prism is more complicated, as no exact analytical solution is known. Brown has calculated the upper and lower bounds for the nucleation field of a square prism [1]. Aharoni suggests that theory of infinite circular rod can be employed in this case, if only an appropriate cross-section area factor is taken into account [2].
We compared these theories with simulations. We used publicly available micromagnetic simulations package OOMMF [3]. To account for infinite sample length we applied periodic boundary conditions (PBC) in one dimension. For that purpose, an algorithm implementing PBC with high accuracy was used [4]. The results of our modeling show qualitative agreement with the abovementioned theory, see Fig. 1.

[1] W.F. Brown, Jr., J. Appl. Phys. 33 (1962) 3026.

[2] A. Aharoni, J. Appl. Phys. 86 (1999) 1041.

[3] M.J. Donahue, D.G. Porter, Report NISTIR 6376, NIST, Gaithersburg, MD (1999). See: http://math.nist.gov/oommf.

[4] K.M. Lebecki, http://info.ifpan.edu.pl/~lebecki/pbc.htm.

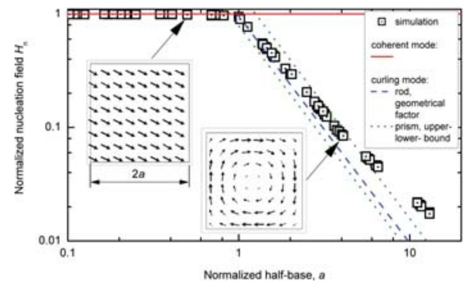

Fig. 1. Coercivity obtained by simulation (open points) and nucleation field predicted by the theory (lines) [1, 2], versus the square prisms half-base, *a*. Due to the rectangular shape of the hysteresis loop the coercivity and the nucleation field can be directly compared. Dotted- and dashed- lines concern the curling mode. Solid line represents the coherent mode. Insets show sample cross-sections of the simulated structure. Magnified in-plane magnetization component for two different cases is presented here, *a* = 0.5 and *a* = 4. These snapshots were taken just before abrupt change of the magnetization direction.

CN-08

Finite difference and edge finite element approaches for dynamic micromagnetic modeling.

A. Manzin[1], B. Van de Wiele[2], O. Bottauscio[1], M. Chiampi[3], L. Dupré[2], F. Olyslager[4]
1. Istituto Nazionale di Ricerca Metrologica, Torino, Italy; 2. Department of Electrical Energy, Systems and Automation, Ghent University, Ghent, Belgium; 3. Department of Electrical Engineering, Politecnico di Torino, Torino, Italy; 4. Department of Information Technology, Ghent University, Ghent, Belgium

The development of ultrahigh density storage media has led to an increasing attention towards the numerical integration of the Landau-Lifshitz (LL) equation [1]. However it is difficult to define validation procedures for establishing the accuracy of the computational codes. Analytical relationships can be obtained only under simplifying assumptions about geometry and physical properties. Moreover, the comparison with experiments is made difficult due to the nanometer dimensions of the samples and to the need of reproducing the exact working conditions. Hence, it is useful to define test bench problems as the ones proposed by the Micromagnetic Modeling Activity Group of NIST or to compare different numerical approaches. To this aim, this paper presents two 3-D micromagnetic algorithms, differing both for the space-time solution of the LL equation and for the magnetostatic field evaluation. In the first procedure (#1) the magnetic body is discretized using identical cubic finite difference cells, while the time integration is performed with a semi-analytical predictor-corrector scheme able to preserve the constraint on the magnetization amplitude [2]. To reduce the computational burden, the magnetostatic field is calculated by fast Fourier transforms, starting from the Green formulation of the Poisson equation. In the second procedure (#2) the spatial discretization of the LL equation is handled by a finite element method, employing tetrahedral elements and edge vector shape functions for the magnetization approximation [3]. The time evolution is handled by a finite difference scheme based on the middle point rule [4]. The magnetostatic field is obtained by solving the Poisson equation with a hybrid finite element/boundary element method, in order to treat the open boundary condition.
To evidence the accuracy of the numerical schemes, the simulation results are compared to the ones obtained using the NIST/OOMMF code, focusing the attention on switching phenomena in magnetic thin films.
As an example, Fig 1 reports the time evolution of the magnetization component subjected to reversal in the case of damping switching (α=0.02), considering only the magnetostatic and Zeeman terms. The rectangular film (500 nm x 250 nm x 5 nm) lies in the x-y plane. The reversal is obtained by applying an external field almost antiparallel to the initial magnetization state, which makes an angle of 10 degrees with the z-axis. With method #1 the film is discretized with cubic cells having side of 2.5 nm. With method #2 a coarser discretization is used, refining the mesh towards the edges (spatial step Δs = 10.8 nm) with respect to the sample centre (Δs = 21.6 nm) to account for demagnetizing fields. One subdivision is imposed along the film thickness.
In the fast precessional switching case (Fig. 2), the same film is subjected to an external field applied along the y-direction, and an initial magnetization along the x-axis. When accounting for the exchange contribution, algorithm #1 needs a small time step to ensure convergence (Δt = 7.5 fs). Method #2 requires the introduction of a regular mesh with spatial step Δs = 8.3 nm (smaller than the exchange length), in order to reach more accurate results. However, the mesh refinement leads to a high computational burden mostly in the evaluation of the magnetostatic field.
The comparison with the NIST/OOMMF code evidences how, with an appropriate choice of the space and time discretization parameters, both procedures give accurate results.

[1] J. Fidler and T. Schrefl, "Micromagnetic modelling – the current state of the art," J. Phys. D: Appl. Phys., vol. 33, pp. R135-R156, 2000.

[2] B. Van de Wiele, F. Olyslager, and L. Dupré, "Fast numerical 3D scheme for the simulation of hysteresis in ferromagnetic grains," J. Appl. Phys., vol. 101, pp. 073909, 2007.

[3] O. Bottauscio, M. Chiampi, and A. Manzin, "An edge element approach for dynamic micromagnetic modelling," To appear on J. Appl. Phys.

[4] M. d'Aquino, C. Serpico, and G. Miano, "Geometrical integration of Landau-Lifshitz-Gilbert equation based on the mid-point rule," J. Comp. Phys., vol. 209, pp. 730-753, 2005.

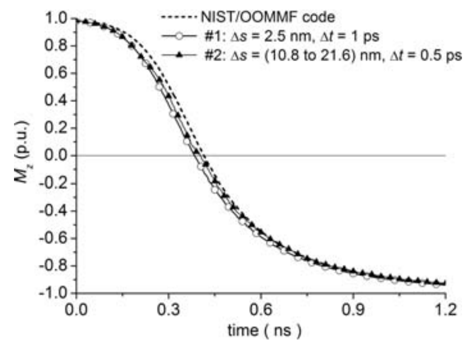

Damping switching. Time behaviour of the magnetization component subjected to reversal, when applying an external field H_a = 1.26 M_S (with M_S the saturation magnetization).

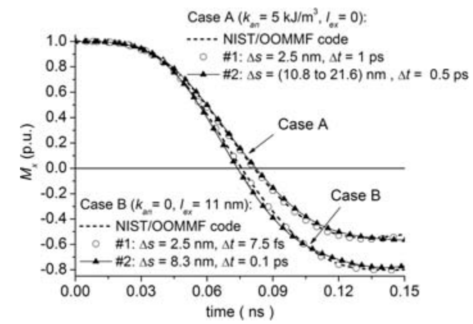

Precessional switching. Time behaviour of the magnetization component subjected to reversal, when applying an external field H_a = 0.025 M_S. In the anisotropic case (A) the easy axis is along x-direction.

CN-09

Computation of magnetization normal oscillations and resonant frequencies for ferromagnetic nanoparticles.

M. d'Aquino[1], C. Serpico[2], G. Miano[2], G. Bertotti[3]
1. Dipartimento per le Tecnologie, Università di Napoli "Parthenope", Napoli, Italy; 2. Dipartimento di Ingegneria Elettrica, Università di Napoli "Federico II", Napoli, Italy; 3. Istituto Nazionale di Ricerca Metrologica (INRiM), Torino, Italy

The determination of the resonances of ferromagnetic particles has great importance in the study of magnetization dynamics driven by microwave applied fields. In typical experimental situations, a small magnetic nanoparticle is saturated by applying a sufficiently strong DC magnetic field along a given direction. Small magnetization motions around this state are then excited by applying a small (compared to the DC component) radio-frequency (RF) applied field. In this condition, the ferromagnetic resonance curve is obtained by slowly varying the RF field frequency and measuring the power absorbed by the particle. From the observation of the peaks in this curve one determines the frequency values corresponding to the excitation of certain magnetization normal modes. In order to treat this problem from the theoretical point of view, analytical approaches limited to particles of special shapes were proposed by Brown and Aharoni[1]. Recently, numerical computations of normal modes for particles with generic shapes have been the focus of considerable research[2,3].
We propose a general formulation of the problem for arbitrarily shaped particles in terms of eigenvalue problem for suitable linear self-adjoint operators. This approach naturally leads to straightforward numerical computations of magnetization normal modes when a spatial discretization is introduced, for instance based either on finite difference or finite element methods.
From the theoretical point of view, magnetization dynamics is described by the Landau-Lifshitz-Gilbert equation (LLG). The effective field takes into account exchange, magnetostatic, uniaxial anisotropy and Zeeman interactions. We assume that the particle is saturated along the z-axis by the DC field. Therefore, the equilibrium configuration is aligned with the cartesian unit-vector along the z-axis. The small oscillations of the magnetization around the saturated state are studied by linearizing the LLG equation around the equilibrium configuration. The analysis is carried out in the frequency domain.
For a given applied field, the problem of finding the (normal) resonant modes of the ferromagnetic particle, usually referred to as exchange-magnetostatic modes, consists in determining the values of the frequencies for which the linearized LLG equation admits nonzero solutions.
We formulate this problem as an eigenvalue problem involving appropriate linear self-adjoint operators acting on vector fields in L^2. Details on these operators, their spectral properties and the orthogonality conditions for the normal modes will be given in the full paper.
This approach has several advantages as far as the numerical computation of the normal modes is concerned: i) particles of arbitrary shape can be considered; ii) the discretized operators can be assembled by using the classical exchange and magnetostatic operators implemented in both finite differences and finite elements micromagnetic codes; iii) the discretized version of the continuum eigenvalue problem is a standard self-adjoint matrix eigenvalue problem which can be efficiently solved with well-established techniques of linear algebra; iv) the solution of this problem gives directly all the resonant frequencies and the normal magnetization modes.
In order to test the effectiveness of the proposed technique, we have computed the normal oscillation modes and the resonant frequencies of a magnetic square thin-film subject to a saturating DC field along the z-axis. Here a spatial discretization based on finite differences has been used. Some results of the computation are reported in fig. 1. We observe that the first resonant mode is spatially (quasi) uniform. More numerical results will be reported in the full paper.

[1] W.F. Brown Jr, Micromagnetics, Interscience Publishers (1963).

Aharoni, Introduction to the theory of ferromagnetism, Oxford Press, New York (1996).

[2] M. Grimsditch et al, Phys. Rev. B 70, 054409 (2004).

[3] R.D. McMichael, M.D. Stiles, Journal of Applied Physics 97, 10J901 (2005).

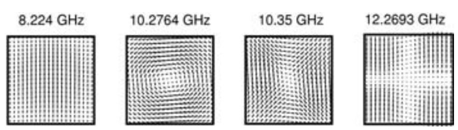

Numerically computed normal modes for a magnetic thin-film 100 nm x 100 nm x 3 nm. The saturation polarization is 1 Tesla, the exchange length is 5.71 nm, no uniaxial anisotropy is considered, the applied DC field is 1.2 Tesla. The normal modes are represented in the x-y plane.

CN-10

Micromagnetic modeling of magnetization switching mechanisms in high magnetoresistance tunnel junctions.

L. Torres[1], G. Finocchio[2], M. Carpentieri[2], E. Martinez[3], E. Jaromirska[1], O. Alejos[4], L. Lopez-Diaz[1]
1. Dept. Fisica Aplicada, Universidad de Salamanca, Salamanca, Spain; 2. University of Messina, Messina, Italy; 3. Universidad de Burgos, Burgos, Spain; 4. Universidad de Valladolid, Valladolid, Spain

Nanoscale time resolved images of magnetization dynamics induced by spin torque [1] have shown that the switching takes place through inhomogeneous magnetization spatial configurations. This fact points out the necessity of using full micromagnetic modeling to describe accurately the magnetization reversal mechanisms. In the last two years, magnetic tunnel junctions with high tunnelling magnetoresistance (MgO) have been one the most investigated systems due to their potential for device applications in magnetic storage [2].
In this digest, micromagnetic simulations of nanopillars of CoFeB(8nm, exchange biased fixed layer) / MgO(0.8nm) / CoFeB(4nm, free layer) with elliptical cross sectional area (90nm x 35nm) [2-4] are presented. Differently to previous works [3,4], we focus this study on the temperature dependence of the switching mechanisms. Furthermore, the effect of the non-uniform spatial distribution of the current density which depends locally on the resistance during the magnetization switching process is also considered. Temperatures from 50 K to 300K are analyzed in steps of 50K, computing for each case 50 stochastic realizations, in order to make reliable statistics. In Fig. 1 the average switching from the Anti Parallel State (APS) to the Parallel State (PS) is shown at both 50 and 300 K, while in Fig. 2 the PS to APS transition is presented. In both cases, an external field of 50 mT is applied along `x` direction (long axis of the ellipse) and positive or negative current densities of 10^7 A/cm2 are applied respectively. It can be observed how the effect of the temperature is higher in the PS to APS transition which indicates an asymmetry in the energy barrier. Finally, in Fig. 3 the dependence of the average switching time (defined as the time elapsed till the magnetization crosses zero) with temperature is depicted. The thermal activation helps the PS to APS switching producing a decrease of the switching time with temperature.

[1] Y. Acremann, J. P. Strachan, V. Chembrolu, S. D. Andrews, T. Tyliszczak, J. A. Katine, M. J. Carey, B. M. Clemens, H. C. Siegmann, J. Stöhr, Phys. Rev. Lett. 96, 217202 (2006).

[2] G. D. Fuchs, J. A. Katine, S. I. Kiselev, D. Mauri, K. S. Wooley, D. C. Ralph, and R. A. Buhrman, Phys. Rev. Lett., 96, 186603 (2006).

[3] G. Finocchio, M. Carpentieri, G. Consolo, A. Romeo, B. Azzerboni, L. Torres, L. Lopez-Diaz. Appl. Phys. Lett. 89, 262509 (2006).

[4] G. Finocchio, B. Azzerboni, G. D. Fuchs, R. A. Buhrman, L. Torres. J. Appl. Phys. 101 063914 (2007)

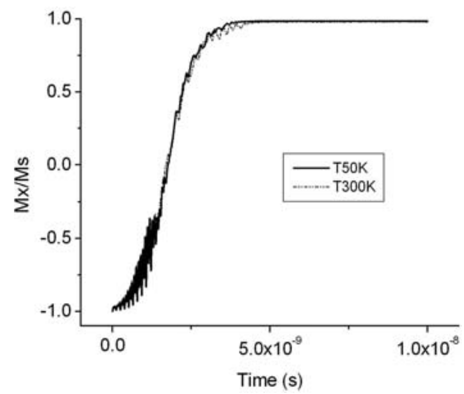

Averaged APS to PS transition

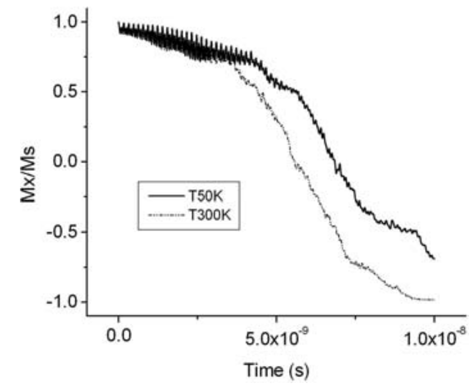

Averaged PS to APS transition

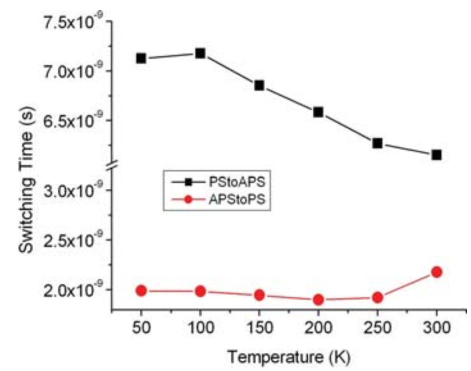

Temperature dependence of the switching time.

Effect of Sawtooth Shape on Switching Process of Write Head.

S. Wang[1], D. Wei[1], K. Gao[2]
1. Dept. of Materials Science and Engineering, Tsinghua University, Beijing, China; 2. Seagate Technology Seagate Technology, Bloomington, MN

Micromagnetic simulation is widely utilized to simulate magnetic recording read write process. Due to irregular shape of the write head, 3D micromagnetic simulation is required. Magnetostatic interaction is one of the most time and memory consuming aspects in micromagnetic simulation. Previously, there are two primary approaches [1,2]. The first is based on the regular mesh but utilize 3D FFT for magnetostatic field calculation. This approach in principle can be fast and accurate, but have issue to deal with arbitrary geometry and typically require extensive memory. Due to small discretization cell used in this approach, simulation time is also very significant. The other approach is based on irregular mesh; for the magnetostatic interaction, the simulation follows the same approach as FEM calculation. This approach in principle can be accurate and with reasonable speed since away from the point of interest, the mesh size can be large. However, it is arguable that too large size of the mesh may lead to incorrect results in dynamic simulation, especially for the region where domain wall motion dominates. Until now, there is no good approach to be both accurate and fast in simulation time. In addition, no appropriate method has been found to give accurate measure of the two previous approaches in term of accuracy. Thus, accurate study here will be extremely important for both recording simulation, especially for write head and Spin-RAM application due to irregular shape nature of the basic cell structure.

In this paper, we investigate the effect of sawtooth shape [3,4] on simulation results of switching based on micromagnetic simulation. The analytical calculation of demagnetization matrix for isosceles right-angle triangular prism has been done. In this work, static states of write head and reversal of magnetization in the direction perpendicular to medium (y-axis) are studied.

In simulation, the main pole of write head, with a total thickness of 40nm, is divided into 10nm×10nm×10nm clusters in Model A (all clusters are cubic) and Model B (clusters at hypotenuse are triangular prism). Magnetic parameters for material simulated are shown in table 1. Static states (with zero external field) in Model A and B are illustrated in Fig.1. The static states in Model A and Model B have slight difference.

The evolution of scaled averaged magnetization my(t) are demonstrated in Fig.2. The reversal properties of magnetization are studied with a 24,000Oe driving magnetic pole applied on the top surface of main pole. Several differences can be found for my(t) in Model A and Model B. Firstly, difference between two models is not very large but evident when my(t) is between -0.4 and -0.9. Secondly, reversal of magnetization is slightly swifter in Model A. Thirdly, the saturated domain pattern in Model A and Model B are similar. And finally, the averaged ultimate magnetization my(t) reaching the required error in Model A and Model B are also similar.

1. K. Z. Gao and H. N. Bertram, "Write Field Analysis and Write Pole Design in Perpendicular Recording", IEEE Trans. Magn., Vol 38, No. 5, pg. 3512, Sept. (2002).

2. Werner Scholz, Josef Fidler, Thomas Schrefl, Dieter Suess, Rok Dittrich, Hermann Forster and Vassilios Tsiantos, "Scalable parallel micromagnetic solvers for magnetic nanostructures", Computational Materials Science, Vol. 28, Is. 2, p. 366-83, Oct. 2003.

3. R. H. Victora, Xiao Shen and Stephanie Hernandez, "Feasibility of Recording 1 Tb/in2 Areal Density". Digests of TMRC, 2007(D3): 52-53

4. M.J.Donahue & R.D.McMichael, "Micromagnetics on Curved Geometries Using Rectangular Cells: Error Correction and Analysis", IEEE Trans. Magn. Vol. 43, Is. 6, P. 2878-80, June 2007.

4πMs/(Oe)	K1/(erg/cm3)	Hk/(Oe)	He/(Oe)
24,000	5,000	5.23	1000

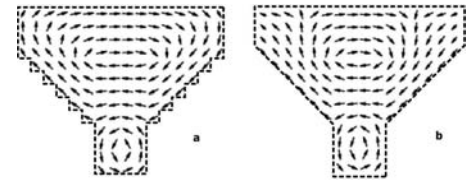

Fig.1 Static states (a) all clusters are cubic (b) clusters at hypotenuse are triangular prism

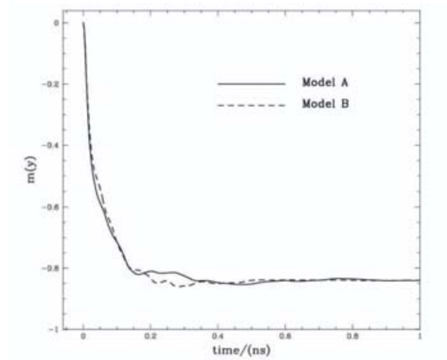

Fig.2 Reversal properties of averaged magnetization perpendicular to media (solid lines: all clusters are cubic, dashed lines: clusters at hypotenuse are triangular prism)

CN-12

Micromagnetic study of read sensitivity: Influence of curved hard bias and granular media.

L. Wang, G. C. Han, S. G. Wu, B. Liu
Spintronics, Media and Interface, Data Storage Institute, Singapore, Singapore

Hard biases (HBs) are indispensable to stabilization of free layers in various read heads. Transfer curve [1], [2], initial magnetization [3], and microtrack profile (read sensitivity) [4], [5] have been utilized to study stabilization properties and read performance. Almost all the HB shapes studied are non-curved with an exception in [4]. However, there have been other scopes in [4] and hence detailed examinations of curved hard biases by micromagnetics are lacking. Meanwhile, curved HBs are also of practical interest [6].

By using FEM micromagnetics, we here model curved hard bias with various shapes (see Fig. 1) and focus on their influences on microtrack profiles. Media is integrated in the simulation. For simplicity and speed-up, reference layer and shield layers are not considered. For comparison, rectangular HB and the case without HB have been simulated. Some typical parameters used are: free layer: track width (TW) x thickness x stripe height = 10 x 2 x 8 (nm^3); hard bias: width x thickness x height = 10 x 6.666 x 8 (nm^3); media: width x length x thickness = 1 x 10 x 6 (nm^3). The gap between FL and HB (FL and media) is 2 (1) nm. The damping constant is 0.2.

Fig. 2 shows the corresponding microtrack profiles. Important observations are: (i) The microtrack profile without HB is asymmetric. Such asymmetry has been identified that part of media field can act as forward or backward bias on the FL magnetization. (ii) The introductions of HBs result in better symmetry, compared to the case without HB. Thus, the symmetry of microtrack profile can be a signature of good HB stabilization. (iii) Case (e) – wall taper HB leads to better sensitivity, compared to cases (b), (d), and (c). (iv) Microtrack profiles of cases (b), (d) and (c) are nearly overlapped and approach that of case (c) (cf. the inset of Fig. 2). Normalized results also confirm such approaching trend. Geometrically (cf. Fig. 1), one may gradually transform from (b), to (d), and then to (c). (v) Symmetric and non-symmetric HBs respectively result in smooth and oscillatory profiles when the free layer in on track. Fortunately such oscillations are fairly small (see the inset of Fig. 2).

We have varied the position of the free layer along the HB thickness direction and found that generally speaking, the obtained profiles are smooth when the middle points of the FL and HB thicknesses are aligned. Note, however, that: (i) For case (d), the microtrack profiles can be still smooth with a larger variation range along the HB thickness direction, compared to other cases; (ii) For case (b), when the FL is near the upper-right corner, the profile is smooth and less sensitive due to shorter gap and hence larger stabilization.

Furthermore, for case (b), we have varied the base point of the curve along the HB width direction and found that hard bias with longer curve (with HB thickness unchanged) has larger signal. But this does not mean that the longer curve, the better the read performance. The tradeoff is that the microtrack profile may become asymmetric for the hard bias with very long curve (with HB thickness unchanged).

We have also performed MRW_{10} and MRW_{50} analyses and we conclude that curved hard biases, as long as they are properly designed, are capable of stabilizing free layers resulting in smooth, sensitive and symmetric microtrack profiles.

In above simulations, uniform medium were used. The effects of granular media on microtrack profile can also be considered. Some observations are: microtrack profile is sensitive (insensitive) to intergranular saturation magnetization (intergranular anisotropic and exchange constants).

[1] D. Z. Lu and J. G. Zhu, IEEE Tran. Magn., vol. 31, no. 6, p. 2615, 1995.

[2] O. Ertl, G. Hrkac, D. Suess, M. Kirschner, F. Dorfbauer, J. Fidler, and T. Schrefl, J. Appl. Phys. 99, 08S303-1, 2006.

[3] T. Suzuki, K. Ishihara, and H. Matsutera, IEEE Tran. Magn., vol 32, no. 5, p. 3383, 1996.

[4] K. Takano, N. Yamanaka, and M. Matsuzalu, IEEE Tran. Magn., vol 34, no. 2, p. 1516, 1998.

[5] K. Takano, IEEE Tran. Magn., vol 41, no. 2, p. 696, 2005.

[6] M. T. Krounbi, O. Voegeli, and P.-K. Wang, US Patent #5,018,037, 1991.

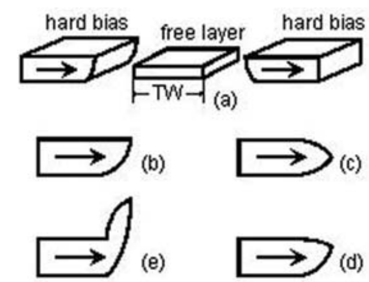

Fig. 1. Schematic drawing of curved hard biases. (a) modeling system (with free layer, media is not shown), (b) one-curve taper HB, (c) symmetric taper HB, (d) asymmetric taper HB, and (e) wall taper HB.

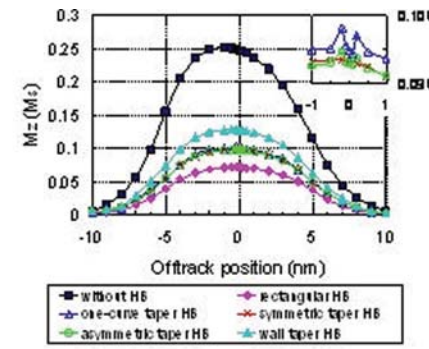

Fig. 2. Microtrack profiles without HB, for rectangular HB, and for one-curve [Fig. 1(b)], symmetric [Fig. 1(c)], asymmetric [Fig. 1(d)], and wall [Fig. 1(e)] taper HBs. Inset: large views for one-curve, symmetric, and asymmetric taper HBs.

Remanence analysis of nanocrystalline, epitaxial $SmCo_5$ films in high pulsed fields up to 35 T.

V. Neu, J. Freudenberger, A. Singh, L. Schultz
Institute for Metallic Materials, IFW Dresden, Dresden, Germany

The remanent magnetization as a function of the maximum applied magnetic field of a permanent magnet starts from zero for the fully demagnetized state, increases and then eventually saturates. The field required for this full saturation will depend on the anisotropy and easy axis distribution and can reach several ten Tesla in highly anisotropic Re-Co materials.

In this paper we study the magnetization process of nanocrystalline, $SmCo_5$ films, which are grown epitaxially such that the c-axes are oriented along two perpendicular in-plane directions of the single crystal MgO(100) substrate [1]. A typical $SmCo_5$ (11-20) pole figure measurement and an appropriate sketch of the easy axis distribution is seen in Fig. 1. Starting from the demagnetized state, the magnetization is measured in increasingly higher fields up to 7 T in a VSM along the MgO[001] direction. For even larger fields, the film has been additionally magnetized in the IFW High Pulse Field Laboratory at 10, 15, 25, and 35 T and after each field pulse the hystersis was measured in a field cycle of ±7 T. Minor loops are shown in Fig. 2a up to 10 T. For higher magnetizing fields the hysteresis is largely identical with the outermost curve. The coercivity and the remanent moment as a function of the maximum applied field show a rather modest increase until about 1 - 2 T, when the first irreversible magnetizing processes lead to a steep raise, and level off at about 5 T (Fig. 2b). Whereas coercivity reaches real saturation, there is a small but measurable increase in remanence for the highest fields (see Fig. 4).

We interpret the observed field dependent remanence as originating from a combination of the particular easy-axis distribution and a $1/\cos\theta$ angle dependency of the switching field as known for domain wall de-pinning. The idea is sketched in Fig. 3, where the easy axis distribution of the film is given as the superposition of two Gaussian distribution functions around the MgO[001] and MgO[010] direction. θ denotes the angle between the easy axis and the applied field. From previous angle dependent measurements, it is known, that the switching field closely follows a $1/\cos\theta$ law [2], which is scaled with the overall coercivity of $\mu_0 H_c = 3.4$ T. Due to the texture spread of a few degrees, grains with θ close to 90° will also switch magnetization (e.g. from I^- to III^+) if the applied field exceeds $H_c(\theta)$. This is exemplified by the shaded area under the distribution function. The effect on the remanence will be small due to the small projection of the magnetization vector onto the field axis, but will depend very sensitively on the width of the distribution function.

The increase of the remanence above the plateau is calculated by a spherical integration of the parallel moment component over the Gaussian distribution function up to a threshold angle θ_{max} determined from the applied field and the coercivity function. The result for a distribution width of 8° compares very well with the experimental data (Fig. 4). The performed remanence analysis after magnetization in high pulsed magnetic fields thus proofed to be a successful method to clarify the magnetization process and determine the angular distribution spread of these highly anisotropic, well textured $SmCo_5$ films.

[1] A. Singh, V. Neu, R. Tamm, K. Subba Rao, S. Fähler, W. Skrotzki, L. Schultz, B. Holzapfel, Appl. Phys. Lett. 87, 072505 (2005).

[2] A. Singh, V. Neu, K. Nenkov, S. Fähler, L. Schultz, B. Holzapfel, submitted to Phys. Rev. B (2008).

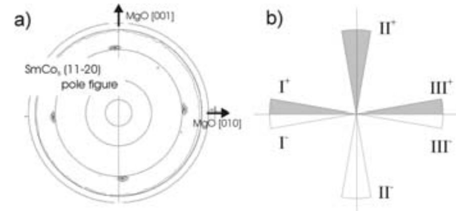

Fig 1: (a) $SmCo_5$ (11-20) pole figure of an epitaxial film grown on MgO (100); (b) sketch of the easy axis distribution.

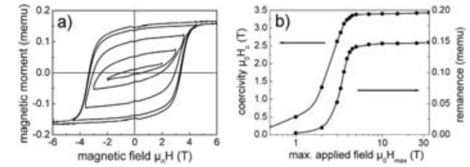

Fig 2: (a) inner magnetization loops along MgO [001]; (b) coercivity and remanence as a function of the maximum applied field.

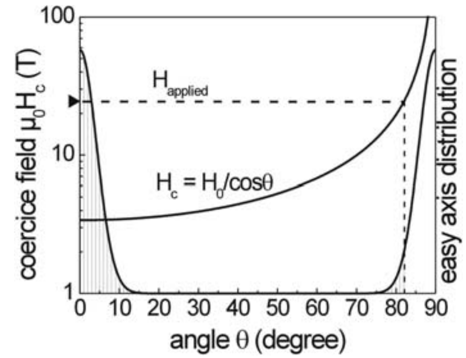

Fig 3: 4-fold Gaussian easy axis distribution together with the expected $1/\cos\theta$-coercivity dependency.

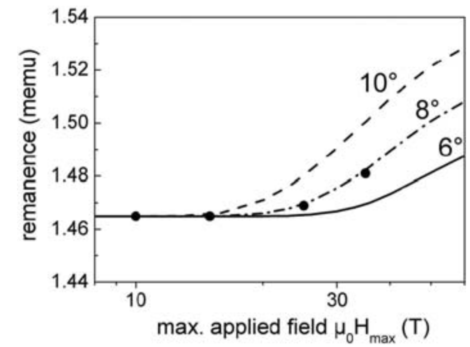

Fig 4: detail of remanent magnetic moment in comparison with calculation.

CO-02

Effect of Ga addition on the magnetic properties of $Nd_{60}Fe_{30}Al_{10-x}Ga_x$ alloy.

W. Kaszuwara, B. Michalski, M. Leonowicz, J. Latuch
Faculty of Materials Science and Engineering, Warsaw University of Technology, Warsaw, Poland

Effect of additional elements on the magnetic properties of Nd-Fe-Al alloys has been a subject of extended studies. It has been reported that partial substitution of Nd by Y stabilizes the RFe_2 (R – rare earth element) phase, which leads to decrease of the remanence. Substitution of Fe by Co, up to 5%, increases both the coercivity and remanence. However, for higher Co contents the remanence deteriorates. Similarly addition of Ni, up to 10%, leads to remanence growth, which for higher Ni contents abruptly decreases. On the other hand Ni addition does not affect the coercivity. All these elements, for some concentrations, improve the tendency for producing an amorphous-like structure. Substitution of Si for Al improves the coercivity of the magnets, which is, however, accompanied by small deterioration of the remanence [1]. Silicon addition is advantageous in rapidly solidified ribbon alloys only, because the Si deteriorates the ability for amorphisation; bulk material contains too large fraction of the crystalline phase. The ability for amorphisation decreases also with addition of boron [2]. On the other hand B, substituting Al, improves the coercivity and deteriorates the remanence.

The literature reports prove that addition of the fourth element in the Nd-Fe-Al system appears to be an effective method for improvement of the magnetic properties. In this study the effect of Ga for Al substitution in the $Nd_{60}Fe_{30}Al_{(10-x)}Ga_x$ (in at.%) system was analyzed.

The master alloy was prepared from elemental Nd, Fe Al and Ga with a purity of 99.9%, or better, by arc melting in a titanium-guttered argon atmosphere. The bulk samples were cylindrical in shape (rods) with a diameter of 1mm. They were prepared by casting the material into a copper die. The alloys were melted in a quartz crucible by induction and pushed into the die by helium overpressure.

Magnetic measurements were done using a Lake Shore vibrating sample magnetometer. As-cast rods were characterized by XRD. Thermal analysis was performed differential scanning calorimeter (DSC) at a heating rate 40K/min.

Substitution of gallium for aluminum leads to substantial growth of the coercivity up to 384 kA/m for x=8 (Fig.1). For higher Ga contents the coercivity decreases down to 104 kA/m. The remanence is constant up to x=8 and for higher Ga concentrations abruptly decreases. The saturation magnetization (measured in a filed of 1600 kA/m) changes in the similar way. Astonishingly the saturation magnetization and remanence for the alloy containing x=10 Ga is exceptionally high. The Ga addition also substantially affects the hysteresis loop shape (Fig.2). For the low Ga contents the shape of the initial magnetization curve points to the existence of domain walls pining centers; for x=0-8 the initial susceptibility changes in a range of 740×10^{-6}-380×10^{-6} emu/gGs. For x=10 the magnetic susceptibility equals to $4{,}6\times10^{-3}$ emu/gGs, and the initial magnetization Curie shows a shape characteristic of the demagnetization mechanism by nucleation of domain walls.

X-ray diffraction (XRD) (Fig.3), showed that growing Ga content results in a higher intensity of diffraction peaks and formation of new crystalline phases. Effect of Ga on the amorphisation ability is analogous to that presented in the literature for Si and B [1,2]. On the other hand, for the Ga contents in a range x=1-8, a remarkable increase of the coercivity, without loss of the remanence, is observed.

1. H.Chiriac, N.Lupu, Materials Science and Engineering, A304-306(2001)727.

2. Nguyen Chau, Nguyen Hoang Luong, Cao Xuan Huu, Nguyen Xuan Phuc, Nguyen Huy Dan, J.Magn.Magn.Mater., 242-245(2002)1314.

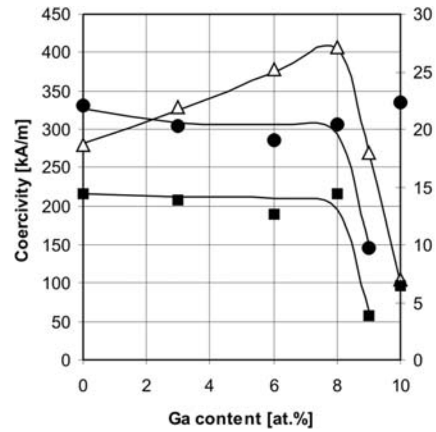

Effect of Ga content on the coercivity (△), remanence (■) and magnetization at 1600 kA/m (●) of Nd60Fe30Al(10-x)Gax alloys

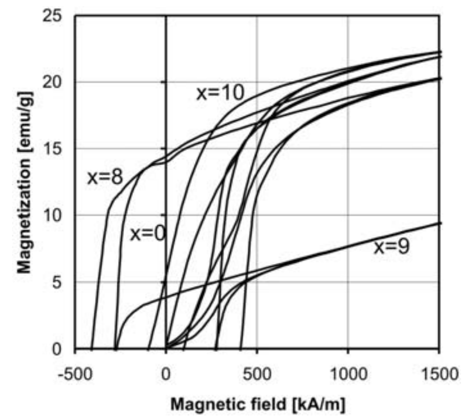

Hysteresis loops for the Nd60Fe30Al(10-x)Gax alloys

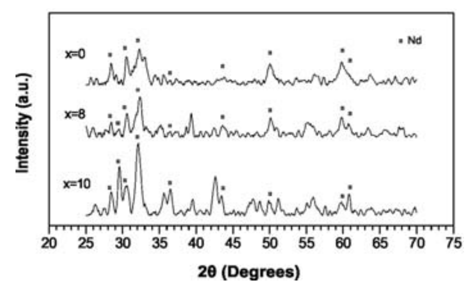

XRD patterns for the Nd60Fe30Al(10-x)Gax alloys

Ab initio calculation of the magnetic structures in $Nd_2Fe_{14}B$/α-Fe nanocomposite materials.

Y. Toga, H. Tsuchiura, A. Sakuma
Applied Physics, Tohoku University, Sendai, Japan

1) Introduction

Exchange-spring magnets are nanocomposite materials that are composed of hard- and soft-magnetic phases that interact by magnetic exchange coupling. These are promising systems for advanced permanent magnetic applications because they are expected to have a large energy product compared to conventional single-phase materials. The magnetic properties of these systems are significantly affected by the nanocomposite structure. This implies that the electronic structure of the system is susceptible to the grain boundaries. Thus it is crucial to have information on the electronic states near the grain boundaries in exchange-spring magnets. Here we study the electronic states near the boundaries between $Nd_2Fe_{14}B$(hard) and α-Fe(soft) multilayers, as a mock-up of exchange-spring magnets, by using ab-initio calculation based on the density functional theory (DFT).

2) Calculation method and model

In this work, DFT calculations have been used to determine all structural, energetic, and electronic results. The Kohn-Sham equations are solved self-consistently in a projector augmented-wave (PAW) method, in conjunction with the generalized gradient approximation (GGA) which describe the electron-ion interaction, as implemented in the Vienna ab initio simulation package (VASP) [3-4]).

The calculations were performed for two kinds of structures. The first structure is a multilayer film of $Nd_2Fe_{14}B$(100)/α-Fe(110) as shown in Fig. 1(a) where the commensurate structure is achieved by a lattice expansion of the Fe lattice as much as about 3% within the (110) plane. The second structure is a multilayer film of $Nd_2Fe_{14}B$(001)/α-Fe(001) shown in Fig. 1 (b), where the expansion of the α-Fe lattice is 3% within the c-plane. We investigate mainly the magnetic structure of each system in Fig. 1, varying the interfacial spacing between $Nd_2Fe_{14}B$ and α-Fe. The number of the α-Fe(110) layer we consider is 4 to 8, and for the $Nd_2Fe_{14}B$ layer we consider two unit cells both for (100) and (001) stacking systems

3) Results

Figure 2 shows the total energies of (a) $Nd_2Fe_{14}B$(100)/α-Fe(110) and (b) $Nd_2Fe_{14}B$(001)/α-Fe(001) multilayer systems as functions of the interfacial distance. The solid and dashed lines correspond to the parallel (P) and ant-parallel (AP) configurations, respectively, of magnetic moments of $Nd_2Fe_{14}B$ and α-Fe layers. In $Nd_2Fe_{14}B$(100)/α-Fe(110) structure, the total energy has minimum at an interfacial distance of 1.8Å for both the P and AP configurations, which is a little bit smaller value than the (110) interlayer distance of bulk α-Fe. We should stress here that the AP configuration is stable around the equilibrium spacing (1.8Å), whereas the P configuration is stabilized in rather large spacing. This result is robust against the number of Fe layers. The distribution of the magnetic moments at the equilibrium spacing (1.8Å) is plotted in Fig. 3. It is found that the moment in α-Fe reaches to that of bulk α-Fe (~2.2μB) in a few layers form the interface. At the equilibrium spacing, the interfacial exchange coupling of $Nd_2Fe_{14}B$(100)/α-Fe(110) is estimated to be -29erg/cm^2. In $Nd_2Fe_{14}B$(001)/α-Fe(001), on the other hand, we observe that the P configuration is always stable in the region of the realistic interfacial distance. The interfacial exchange coupling at the equilibrium spacing (~2.2Å) is about 120 erg/cm^2 which may be around 10 times larger than the values expected from measurements[2]).

1) R. Skomski and J. M. D. Coey, Phys. Rev. B 48, 812 (1993).
2) M. Shindo, M. Ishizone, A. Sakuma, H. Kato and T. Miyazaki, J. Appl. Phys. 81, 4444 (1997).
3) G. Kresse and J. Furthmuller, Phys. Rev. B 54, 11169 (1996); Comput. Mater. Sci. 6, 15 (1996).
4) G. Kresse and J. Hafner, Phys. Rev. B 47, R558 (1993).

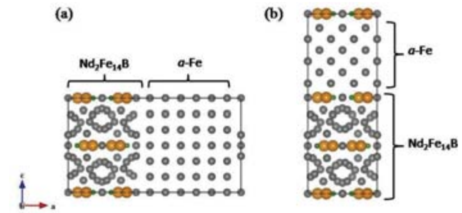

Fig.1 Models of composite system of NdFeB and α-Fe with a stacking of (a) NdFeB(100)/α-Fe(110) and (b) NdFeB(001)/α-Fe(001). The large spheres indicate rear-earth atoms.

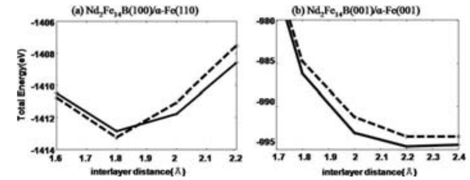

Fig.2 Total energies as a function of interfacial distance between NdFeB and α-Fe. Solid lines indicate the parallel (P) configuration of magnetization of NdFeB and α-Fe, and dashed lines the anti-parallel (AP) configuration.

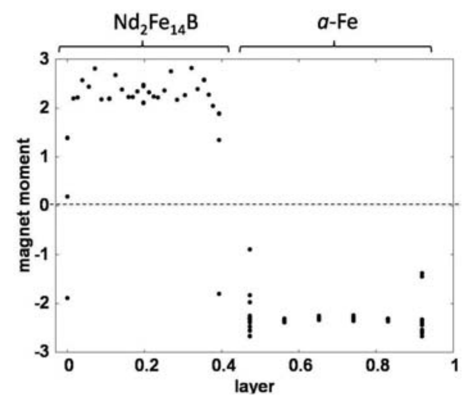

Fig.3. Distribution of magnetic moments of Fe atoms in NdFeB(100)/α-Fe(110) structure at the equilibrium spacing (1.8Å).

CO-04

Nanostructure and Magnetic Properties of Nd-Fe-B Thin Film Fabricated by UHV Sputtering.

D. Ogawa[1], T. Akiya[2], M. Oogane[1], H. Kato[2,3], Y. Ando[1]

1. Department of Applied Physics, Tohoku University, Sendai, Japan; 2. New Industry Creation Hatchery Center (NICHe), Tohoku University, Sendai, Japan; 3. Department of Applied Mathematics and Physics, Yamagata University, Yonezawa, Japan

Although exchange-coupled hard / soft nanocomposite magnets are predicted to exhibit remarkably high maximum energy product $(BH)_{max}$ beyond 100 MGOe [1], it is not easy to achieve such high values experimentally. However, recent progress in thin-film fabrication technique enabled us to obtain Sm-Co/Fe-Co multilayer films which exhibit $(BH)_{max}$ value of 32 MGOe, being larger than that of the commercially available bulk-type SmCo sintered permanent magnets [2]. In such multilayer geometry, however, the interface area between hard and soft phases is smaller and the exchange coupling become less effective than that for random dispersed geometry. Therefore, we have been fabricating nanophase-dispersed hard / soft thin films with crystallite orientation of hard phases [3]. Magnetization values of these films, however, were much smaller than the bulk values owing to the existence of non magnetic phases, resulting in low $(BH)_{max}$ values. In this paper, we tried to make a higher magnetization Nd-Fe-B thin film by using a UHV sputtering system, which is a first step of our project to realize the nanophase-dispersed $Nd_2Fe_{14}B/\alpha$-Fe thin films with high $(BH)_{max}$ values.

Thin films were deposited by dc-magnetron sputtering onto SiO_2 substrates in an Ar atmosphere. The base pressure of the sputtering system was below 2×10^{-6}Pa. Thin films have the form of SiO_2/Ta(t_{Ta} nm)/Nd-Fe-B(40 nm)/Ta(10 nm). In order to achieve higher orientation and magnetization, we adjusted various parameters such as substrate temperature during sputtering (T_s), Ar pressure (P_{Ar}), and Ta buffer layer thickness (t_{Ta}). Sputtering power was fixed at DC 150W. In order to obtain information about the degree of alignment, average grain size and volume fraction of each phase, we made a Rietveld analysis of X-ray diffraction patterns. Magnetization curves were measured at room temperature by using VSM and SQUID with the maximum applied field of 15 kOe and 50 kOe, respectively.

Fig.1 shows the example of an observed X-ray diffraction pattern. It should be noted that the Miller index l of strong reflections is large, such as (105) and (006). This indicates that the c-axis of $Nd_2Fe_{14}B$ grains are well oriented along the direction perpendicular to the film plane. The result of Rietveld analysis is shown by the solid line in Fig. 1, which tells us that the half width of distribution of c-axis directions, $\Delta\theta$, is about 7° along the normal of the film plane.

The reflections at 2θ = 30° and 62° could be indexed as those of fcc-type [4] Nd oxide. The volume fraction of NdO phase was estimated to be about 4% according to the Rietveld analysis. It is possible to roughly estimate the average grain size d_{cry} from the full-width with half maximum (FWHM) of reflections by using the Scherrer's formula. We found that d_{cry} increases with increasing substrate temperature T_s, and reaches about d_{cry} = 30 nm for T_s = 600°C.

We also found that the magnetization value depends strongly on the Ar gas pressure and takes a maximum at P_{Ar} =0.7 Pa. The maximum magnetization value is 15 kG, which is comparable with the bulk value. We then fixed the two parameters as P_{Ar} = 0.7 Pa and T_s = 600°C, and adjusted the Ta-buffer thickness. Fig. 2 shows the coercivity H_c and $(BH)_{max}$ as a function of Ta-buffer thickness, t_{Ta}. Both H_c and $(BH)_{max}$ exhibit a maximum around t_{Ta} = 5~7 nm. Magnetization curves shown in Fig. 3 are those for the film with t_{Ta} = 5 nm, which yields $(BH)_{max}$ of 36±7 MGOe.

[1] R. Skomski, et. al., Phys. Rev. B 48 (1993) 15812.

[2] J. Zhang, et. al., Appl. Phys. Lett. 86 (2005) 122509.

[3] H. Kato, et. al., J. Magn. Magn. Mater. 290 (2005) 1221.

[4] H. Sun, et. al., J. Magn. Magn. Mater., 164, 18 (1996).

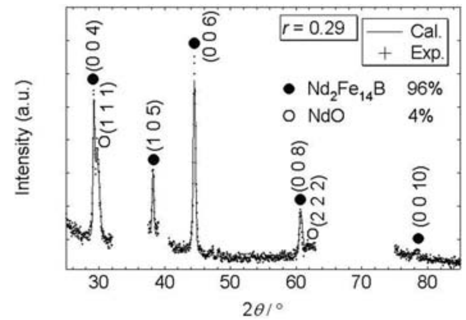

Fig. 1 Example of an observed X-ray diffraction pattern and the result of Rietveld fitting for a sample fabricated at T_s = 600°C, P_{Ar} = 0.85 Pa, and t_{Ta} = 10 nm.

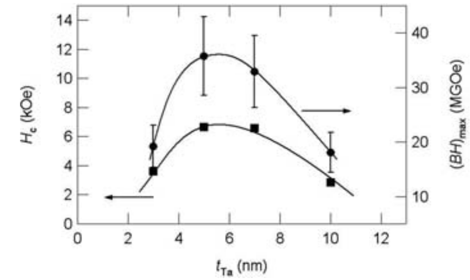

Fig. 2 Coercivity H_c and energy product $(BH)_{max}$ as a function of Ta buffer thickness.

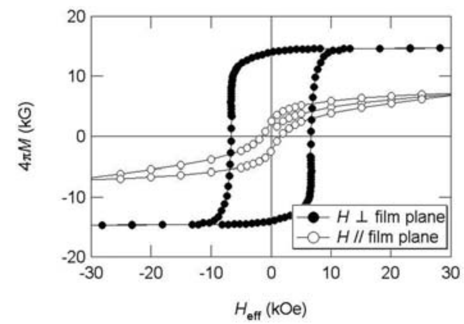

Fig. 3 Magnetization curves for the film of [SiO_2/Ta(5 nm)/Nd-Fe-B(40 nm)/Ta(10 nm)] sputtered at T_s = 600°C and P_{Ar} = 0.7 Pa.

CO-05

Effect of Nd and Nd_2O_3 layers on the magnetic properties for Nd-Fe-B thin films.

N. Oka[1], T. Sato[2], H. Kato[1], T. Shima[1]
1. Faculty of Engineering, Tohoku Gakuin University, Tagajo, Japan; 2. Toyota Central R&D Labs., Nagakute, Japan

Nd-Fe-B magnet is known as a permanent magnet, and it has been widely applied for sensors, actuators and motors [1]. Also a lot of studies have been done not only for bulk samples but also thin films [2][3]. Recently, a further improvement of magnetic properties of Nd-Fe-B magnet is required due to an increase of a number of hybrid vehicles by environmental situation. In order to improve the magnetic properties of Nd-Fe-B magnet at high temperature environment, heavy rare earth elements such as Dy and Tb have been necessary added. Furthermore, the effect of Nd rich phase or oxide phase existing at the grain boundary has not been cleared yet. In this study, in order to understand the coercivity mechanism, we have studied the effect of the introduction of heavy rare earth elements such as Nd and Nd_2O_3 to Nd-Fe-B film.
The samples were prepared using an ultra high vacuum sputtering system. The base pressure is below 5×10^{-8} Pa. Cr seed layer of 1 nm was deposited on MgO(100) substrate, and consecutively an epitaxial Mo buffer layer of 20 nm was grown at room temperature (RT). The Nd-Fe-B layer is co-deposited of Fe, Nd and B at the substrate temperature of 625°C. The thickness of Nd-Fe-B layer was changed from 2 to 50 nm. The heavy rare earth layers of 1 nm is deposited at RT and then the sample was heated up to 600°C. Finally, a Cr capping layer of 1nm was deposited at RT to avoid the oxidation. The magnetic properties were measured by a superconducting quantum interference device (SQUID) magnetometer. The film composition was determined by electron probe micro analyzer (EPMA). The structure was examined by the X-ray diffractometer (Cu Kα). The surface morphology was observed by an atomic force microscope (AFM).
Magnetization curve of Nd-Fe-B thin films with introducing rare earth layers, Nd layer (a), Nd_2O_3 layer (c) and without capping layer (b) are shown in Fig.1. The film thickness of Nd-Fe-B layer is fixed at 3 nm. The coercive force H_c of 17.4 kOe was obtained at the film without rare earth capping layer. With introducing a Nd layer, enhancement of H_c of 22.6 kOe was obtained. However, on the contrary, H_c was drastically decreased to 4.5 kOe for the film with Nd_2O_3 layer. From this results, Nd layer plays an important role for increasing the hard magnetic property.
This work was partly supported by Toyota Motor Corporation. The magnetization measurement was performed at Magnetic Material Laboratory at IMR, Tohoku University. The structural characterization was performed at the Hi-tech Research Center of Tohoku Gakuin University

[1] M. Sagawa, N. Togawa, H. Yamamoto, and Y. Matsuura, J. Appl. Phys., 55, 2083 (1984).

[2] A.R. Kwon, U. Hannemann, V. Neu, S. Fähler, L. Schultz, J. Magn. Mater., 290-291, 1247 (2005).

[3] T. Shima, A. kamegawa, K. Hono, H. Fujimori, J. Appl. Phys., 78, 2049 (2001).

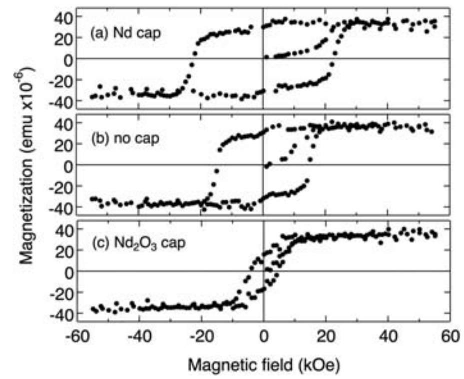

Fig.1. Magnetization curves for Nd-Fe-B thin films with introducing Nd layer (a) and Nd_2O_3 layer (c). For the reference, the film without rare earth capping layer (b) is also denoted.

CO-06

Refinement of surface morphology of Nd-Fe-B thin film by low temperature deposition.

H. Kato[1], I. Honda[1], T. Sato[2], T. Shima[1]
1. Faculty of Engineering, Tohoku Gakuin University, Tagajo, Japan; 2. Toyota Central R&D Labs., Nagakute, Japan

More than 2 decades have been passed since the discovery of $Nd_2Fe_{14}B$ compounds [1]. Since then, $Nd_2Fe_{14}B$ magnets have been widely used for many applications such as sensors and motors. Due to a high maximum energy product, a lot of studies have been performed for Nd-Fe-B sputtered films [2, 3] and it was found the crystal structure of $Nd_2Fe_{14}B$ is generated from the interface between substrate and/or buffer layers [4]. In particular, downward growth of strongly textured $Nd_2Fe_{14}B$ columnar grains can be prepared by triggering crystallization of sputter deposited amorphous Nd-Fe-B layer by the deposition of crystalline Cr overlayer [5]. Since hard magnetic properties and the microstructure of Nd-Fe-B films were strongly affected by a number of deposition parameters. In this study, in order to control the surface morphology of sputtered Nd-Fe-B films, two kinds of preparation methods were adopted. One is a low temperature deposition (LTD) procedure and post-annealing at high temperature after a capping layer was deposited at room temperature (RT). The other is a high temperature deposition (HTD)

Samples were prepared using a dc-magnetron sputtering system. The base pressure was under 5.0×10^{-8} Pa. A Cr seed layer of 1nm was deposited on a MgO(100) single crystal substrate, and consecutively an epitaxial Mo (001) buffer layer of 20nm was grown at RT. Nd-Fe-B layer was co-deposited at substrate temperature (T_s) in the range between RT and 700 °C. Also the samples were annealed at T_a in the range between RT and 700 °C for 1 hour. The nominal thickness t of Nd-Fe-B layer was varied from 10 to 100 nm. The magnetic properties were measured by super conducting quantum interference device (SQUID) magnetometer. The structure analysis was performed by X-ray diffractometer. The film composition was determined By electron probe micro analyzer (EPMA)

From the X-ray diffraction profiles, the peaks from the c-plane of the $Nd_2Fe_{14}B$ phase (such as 004, 006 and 008) were clearly observed at HTD samples. However, no remarkable peaks were also observed at LTD samples. Magnetization curves of LTD and HTD films are shown in Fig.1. The detailed procedure of LTD and HTD films are as follows, LTD: Nd-Fe-B film was deposited on Mo buffer layer at 300 °C and then the film was post-annealed at 625°C for 1 hour. HTD: Nd-Fe-B films was deposited on Mo buffer layer at 625°C. The coercivities measured in the perpendicular direction $H_{c\perp}$ of LTD and HTD film are 17.5kOe and 12kOe, respectively. It is confirmed from an atomic force microscope image, the surface of LTD film is flatter than that of HTD film. High $H_{c\perp}$ was achieved at LTD film. It is thought to due to the refinement of surface morphology.

This work was partly supported by Toyota Motor Corporation. The magnetization measurement was performed at Magnetic Material Laboratory at IMR, Tohoku University. The structural characterization was performed at the Hi-tech Research Center of Tohoku Gakuin University.

[1] M. Sagawa, N. Togawa, H. Yamamoto, and Y. Matsuura, J. Appl. Phys., 55, 2083 (1984).

[2] F. J. Cadieu, T. D. Cheung, and L. Wickramasekara, J. Magn. Magn. Mater. 535, 54 (1986).

[3] K. D. Aylesworth, Z. R. Zhao, D. J. Sellmyer, and G. C. Hadjipanayis, J. Magn. Magn. Mater. 82, 48 (1989).

[4] A.R. Kwon, U. Hannemann, V. Neu, S. Fähler, L. Schultz, J. Magn. Magn. Mater., 290-291, 1247 (2005)

[5] T. Shima, A. kamegawa, K. Hono, H. Fujimori, J. Appl. Phys.,78, 2049 (2001).

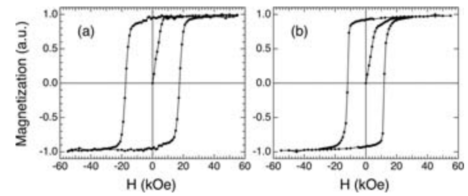

Fig. 1 Magnetization curves for Nd-Fe-B films prepared at different heat treatment procedure, (a) LTD and (b) HTD methods. (a) and (b) are prepared at low teperature deposition (LTD) and high teperature deposition (HTD), respectively. Initial magnetization curves are also denoted.

CO-07

Enhancement of coercivity for Nd-Fe-B thin films with Tb and Dy layer.

T. Sato[1], N. Oka[2], H. Kato[2], T. Shima[2]
1. Toyota Central R&D Labs., Inc., Aichi, Japan; 2. Faculty of Engineering, Tohoku Gakuin University, Tagajyo, Japan

$Nd_2Fe_{14}B$ alloy [1] has been practically used as a magnetomotive force for applications such as motors, actuators and sensors, because it has a large magnetocrystalline anisotropy and a high maximum energy product. In particular, the consumption of Nd-Fe-B sintered magnets has been increased by the expansion of hybrid vehicles' (HVs) market for environmental and energy issues. One of the problems for Nd-Fe-B sintered magnets is using heavy rare earth materials (Tb, Dy, etc.) to enhance of the coercivity H_c at high temperature use. Recently, another problem of the amount of material resources has been occurred and it urgs us to reduce the amount of these elements. Furthermore, the coercivity of Nd-Fe-B magnets is actually lower than the theoretical nucleation field [2] and the reason for the difference has not been clarified yet. In this study, in order to elucidate the mechanism of the coercivity of Nd-Fe-B magnets, we have investigated the magnetic properties of the Nd-Fe-B thin films covered with rare earth elements (RE) such as Tb and Dy layers.
The Cr (1 nm) / Mo (20 nm) / Nd-Fe-B / Tb or Dy (1 nm), w/o / Cr (10 nm) films were prepared onto single-crystal MgO(100) substrates using an UHV-compatible dc-sputtering apparatus (base pressure of $< 1 \times 10^{-8}$ Pa). The nominal thickness for Nd-Fe-B layer *t* was varied from 2 to 50 nm. The films were heated at 625 °C during the deposition of Nd-Fe-B layer, and then the films were annealed at 600 °C for 1 hr after depositing RE layer. The magnetization curves were measured in the applied magnetic field perpendicular to the film plane by using a superconducting quantum interference device (SQUID) magnetometer in the field up to 55 kOe (for some cases, 70 kOe). The structural analysis was performed by an x-ray diffraction with Cu-Kα radiation. All measurements were performed at room temperature.
The x-ray diffraction patterns from $Nd_2Fe_{14}B$ compound, $NdFe_4B_4$ compound, and Mo were observed for all films. The orientation relationship among the substrate and the layers is $(001)_{MgO}$ // $(001)_{Mo}$ // $(001)_{Nd2Fe14B}$. Fig. 1 shows the changes of H_c of Nd-Fe-B films by covering with Tb and Dy layers. For comparison, the film without a capping layer is denoted. For all films, H_c increases with decreasing *t* and shows a maximum at less than *t* = 8 nm. With further decreasing *t*, H_c decreases. The maximum value of H_c for the Nd-Fe-B film without RE layer was 21 kOe at *t* = 8 nm. The initial magnetization curve indicated that the film is a mixture of single-domain states and multi-domain states [2]. On the other hands, H_c was enhanced for the film with RE layer. The maximum value of H_c was 36 kOe for the film with Tb layer at *t* = 3 nm, and 30 kOe for the film with Dy layer at *t* = 5 nm. Since these initial magnetization curves increased slowly with the applied magnetic field, the magnetization process is mainly governed by a rotation of the magnetization. The enhancement of the coercivity of Nd-Fe-B films by covering with RE layer is thought to be due to the formation of $RE_2Fe_{14}B$ phase, whose anisotropy field is twice larger than the value of $Nd_2Fe_{14}B$ phase [4].
Support by Hi-tech Research Center of Tohoku Gakuin University and Toyota Motor Corporation are acknowledged.

[1] M. Sagawa, N. Togawa, H. Yamamoto, and Y. Matsuura, J. Appl. Phys., 55, 2083 (1984).

[2] H. Kronmüller, Phys. Stat. Sol., 144, 385, (1987).

[3] T.Shima, K. Takanashi, Y. K. Takahashi, and K. Hono, Appl. Phys. Lett., 85, 2571 (2004).

[4] S. Hirosawa, Y. Matsuura, H. Yamamoto, S. Fujimura, M. Sagawa, and H. Yamaguchi, J. Appl. Phys., 59, 873 (1986).

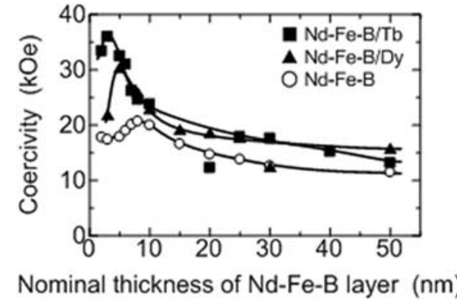

Fig 1. The effect of capping layers (RE: Tb and Dy) on the coercivity H_c for Nd-Fe-B films at different nominal thickness of Nd-Fe-B layer. Solid squares and triangles represent the results from Nd-Fe-B films with Tb and Dy layer, respectively. For the comparison, the films without a capping layer are denoted as open circles.

CO-08

FePt-based nanocomposite ribbons as exchange coupled magnets.

A. Crisan[1,2], O. Crisan[1], N. Randrianantoandro[2], I. Skorvanek[3]
1. National Institute for Materials Physics, Bucharest-Magurele, Romania; 2. Laboratoire de Physique de l'Etat Condense, Universite du Maine, Le Mans, France; 3. Institute of Experimental Physics, Slovak Academy of Sciences, Kosice, Slovakia

The interest for FePt based alloys increased recently due to their outstanding potential for technological applications as, for example, magnetic recording media, magnetic field sensors, and exchange spring magnets. In the form of nanocrystalline alloys, these nanocomposite spring magnets have high corrosion resistance and exhibit, upon appropriate annealing, the ordered hard magnetic tetragonal L10 FePt phase with a large magnetocrystalline anisotropy. In this study, we focus on the magnetic and crystalline microstructure of melt spun Fe51Pt27Nb2B20. The sample was prepared by melt spinning technique in Ar controlled atmosphere. The analysis of the crystal structure of sample and the phase composition was examined by X-ray diffraction (XRD) using a Bruker G8 diffractometer with Cu Kα radiation. The magnetic measurements were done with a superconducting quantum interference device (SQUID), with the applied field up to 5 T, parallel to the ribbons plane. Annealing of the as-cast sample has been done at 500°C for 30 minutes followed by another 30 minutes at 600°C. Other annealings were performed at 700°C for 40 minutes and 2 hours respectively. The annealings were done in an inductive furnace with strict control of the temperature under Ar atmosphere. It can be observed that the XRD spectra (Fig.1)of annealed samples exhibit sharp Bragg peaks, indicating the high degree of crystallinity in these samples. On the contrary, the as-cast state was found to be mainly a mixture of an amorphous state with a nanocrystalline solid solution of apparently cubic symmetry, as proven by the very broad lines in the diffraction spectrum and the indexation of their Bragg reflections that correspond mainly to the f.c.c. cubic FePt-rich solid solution. As the samples are annealed, the microstructure evolves into refining the width of the Bragg reflections, kept at the same angular position. This result proves that the incipient nucleation sites with a cubic symmetry from the as-cast state, evolve into larger nanocrystals but keeping the same crystal symmetry. The main phases that are indexed in the XRD spectra of annealed samples are mainly the f.c.t. L10 FePt and f.c.c. A1 FePt, together with small amount of boride, formed in later stages of annealing by polymorphic crystallization of the remaining amorphous phase. The average crystallite size in the as-cast state was 4.2 nm as determined by Scherrer's formula, corrected for instrumental broadening. Upon annealing, the grain size increases, since both tetragonal FePt and cubic FePt crystallizes from the initial solid solution. But the values, even at annealing temperatures as high as 700°C and for annealing times as great as 2 hours, are still below or around 15 nm. This shows that upon annealing the obtaining microstructure is formed by small enough grain so that the requirements for an exchange spring magnets to be fulfilled.
The magnetic measurements performed with a superconducting quantum interference device (SQUID) at 5K (Fig.2) show outstanding exchange spring behavior for the annealed samples, compared to the as-cast sample that is essentially a soft magnet with high saturation magnetization and virtually no hysteresis. The annealed samples show extremely high coercivity values of 14.5 kOe at 5K, that are comparable with the nanocomposite exchange spring magnets reported in the literature and important values of the remanent magnetization, which gives an extremely elevated energy product that makes the signature of a very performant exchange spring magnet.
In conclusion, an amorphous melt spun ribbons of the composition Fe51Pt27Nb2B20 has been synthesized by the rapid solidification technique and its microstructure and magnetic properties were studied. After appropriate annealing, an ordered L10 phase is formed and this produces magnetic hardening of the alloy. The annealed samples show co-existence of hard and soft magnetic phase, a two-phase behavior accompanied with a well-refined grain microstructure. These features are the key issues for the extremely high coercivity values that we have obtained here, values that are comparable with the best exchange spring magnets reported in the literature.

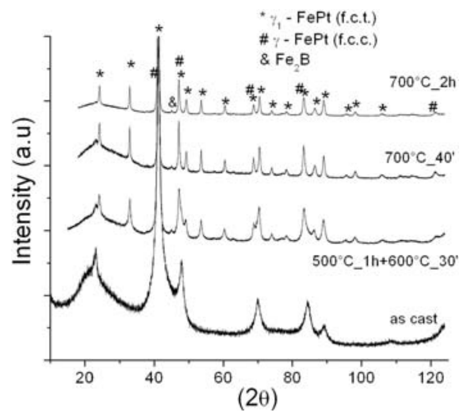

Fig. 1. XRD spectra of as-cast and annealed samples. The observed Bragg peaks are indexed on the figure and corresponds mainly to L10 FePt (or γ1 f.c.t.), A1 FePt (or γ f.c.c.) and Fe2B

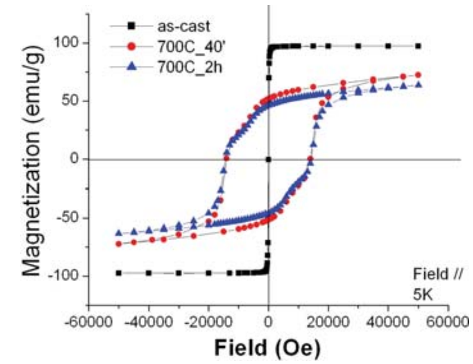

Fig. 2. Hysteresis loops at 5K recorded for as-cast and annealed samples in parallel applied field

CP-01

Genetic algorithm for Jiles-Atherton parameters optimization.

F. A. Cuéllar[1], A. Mendoza[2]
1. Physics Department, Universidad Nacional de Colombia, Bogotá, Colombia; 2. Grupo de Materiales Magnéticos y Nanoestructuras, Universidad del Quindío, Armenia, Colombia

The Jiles-Atherton Model (JAM) of Ferromagnetic Hysteresis[1], which expresses the magnetization process in soft-magnetic materials, based mainly on domain walls motion; has been used to analyze the pinning behavior depending on different materials characteristics[2,3]. The model parameters are coupled between them, and to the measurement temperature; besides, these parameters depend also on the particular characteristics of the samples. Mathematically, the JAM expresses the Magnetization in terms of Magnetic Field by means of the differential equation:$dM/dH=(M-M_{an})/[(\delta k/\mu_0)-\alpha(M_{an}-M)]$; the solution equation has a convergence condition expressed as an inequality between two parameters (a>k), and is a redundant in M derivatives summation[1]: $M=\Sigma[(-1)^n(k\delta)^n L^n((H+\alpha M)/a)]+\delta C(H_{max})$. Where k is the Pinning; δ is ± 1 depending on the field direction; L^n is the n-th derivative of the Langevin Function; α is the Mean Field Constant; a is the Thermal Fluctuation term and C is an integration constant. Jiles et al. purpose that some model parameters can be expressed not only as constants but as functions of other physical quantities; taking this into account, Fecioru-Morari et al. have purposed a Gaussian Function to stand for pinning[4]; this modification improves fitting of the H-M curves to the JAM, and was implemented in this work. To surpass the redundant characteristic, an iterative system was used to calculate the magnetization. The redundant characteristic makes more difficult to find the parameter values when fitting. Based on the above described characteristics of the JAM and the solution equation, it was necessary to implement a parameters optimization system to easily fit experimental curves. In a Genetic Algorithm (GA) each individual is represented by its chromosome, which is composed by its set of genes (in our case JAM parameters). The individuals are tested in their environment and their development is evaluated using the Fitness Function. GA's also include Mutation mechanisms. When the whole population has reached the convergence limit, the algorithm is ended and the solution individual is the best fitted among all of them. The GA here presented has the following characteristics: The Search Space is defined from characteristic values of the hysteresis experimental curve. The GA is real coded. The Fitness Function is a Least Squares (LS) calculation, made point by point between the experimental and simulated curves. Generation 0 is created randomly in the Search Space. Reproductive Trials are assigned using Fitness Ranking Technique. Population Size must be a multiple of four. Parents Selection is realized choosing two individuals to mate from different Ranks. Uniform Crossover was used to create the offspring, and total population replacement was adopted. The Crossover technique creates non valid individuals because they do not complain the solution's convergence condition (a>k); thus, the GA remaps them by mutating the non valid gen. Two mutation mechanisms were implemented, Random Mutation and Exploratory Mutation, the first one mutates a random gen into a random value; the second one mutates a decisive gen by changing it in a small quantity to obtain a finer adjust of parameters. The ending criterion was based on the population's convergence, when their mean deviation is lower than 0.5% the GA is ended. An experimental curve measured from a NiZn ferrite thin film, grown by RF sputtering technique at a deposition temperature of 600 K, is shown in Fig.1; inset shows the set of fitted parameters. Since it is not possible to know the individual parameters influence over the whole curve, the uncertainty is expressed as a percentage of curve deviation (C.U.). Pinning parameter k_0 is expressed in terms of the sample's volume. Acknowledgments: This work was partially supported by COLCIENCIAS under Research Project 1106-05-17612 and CENM, under contract 043-2005.

[1] D.C. Jiles and D.L. Atherton, J. Appl. Phys. vol. 55, pp. 2115-2120, 1984. [2] C. Calle et al., Phys. B., vol. 384, pp. 103-105, 2006. [3] V. H. Calle et al., Phys. Stat. Sol. C, vol. 4, pp. 4197-4220, 2007. [4] M. Fecioru-Morari and A. Stancu, J. Optoelectr. Adv. Mat., vol. 5, pp. 939-944, 2003.

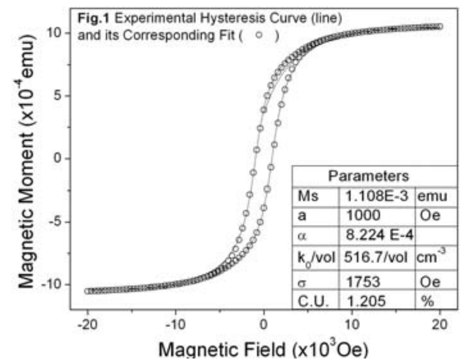

Angle Difference between B vector and H vector in Anisotropic Electrical Steel.

K. Fujisaki[1,2], S. Satou[3]
1. Technical Development Bureau, Nippon Steel Corporation, Futtsu-city, Japan; 2. Graduate School of Environmetal Studies, Tohoku University, Sendai-city, Japan; 3. N-Teck Ohita Corporation, Ohita-city, Japan

Introduction

Since electrical steel has superior magnetic property, it is used as a material of motor or transformer and then expected to be solving the environment and CO2 problem. When magnetic flux density B is related to magnetic field H as the magnetic property, the usual magnetic property is treated as though B vector was parallel to H vector. However, measurement data reported that B vector was not parallel to H vector and then there is an angle difference (θBH) between B vector and H vector [1]. Since it is expected to be important to clarify the mechanism of the angle difference (θBH) between B vector and H vector to design the electrical motor as well as electrical steel, numerical model is considered to obtain the angle difference (θBH) between B vector and H vector.

Numerical Magnetic Property Model

The angle difference between B vector and H vector is observed in measured magnetic property of grain oriented steel (GO) as well as non-oriented steel (NO) as shown in Fig. 1. In Fig. 1, where GO steel is used, B vector is controlled to be rotational as sinusoidal wave. Then the angle of B vector (θB) and the angle difference between B vector and H vector (θBH) is defined as Fig.2. Since the magnetic field is not sinusoidal, the angle difference (θBH) is clearly observed as shown in Fig. 1 (c). According to the measurement data [1], the angle difference (θBH) of GO changes from – 90 deg to + 50 deg as shown in Fig. 1 (c), though the one of NO changes from +10 deg to +45 deg. Then the strong anisotropic characteristics such as GO material seems to have large angle difference (θBH).

To express the strong magnetic anisotropic characteristics, we consider the finite element method model in which steel bars and air are arranged reciprocally in two dimensions plane as shown in Fig. 3. The longitudinal direction of the steel bar is considered to be in easy axis of this model and the orthogonal direction in which the steel bar and air are arranged reciprocally is considered to be in transverse axis. Outside the region arranged the steel bar and air, external magnetic field Hext is supplied by means of the four edge boundary conditions. At a center of the region, an equivalent area A is considered as shown in Fig. 3. The average magnetic flux density vector Bave and the average magnetic field vector Have are introduced from the average of B vector and H vector respectively in an equivalent area A. The external magnetic field Hext is controlled so as that Bave and Have are sinusoidal. The average Bave and Have are expected to have strong magnetic anisotropic property.

Calculation Results

The results are shown in Fig.4. The magnetic flux density at the center region A in Fig.4 is sinusoidal. The calculated angle difference (θBH) changes from -90 deg to +90 deg. This characteristic is the same as the measurement one. The difference between the calculation and the measurement is considered to be an effect of hysteresis which is ignored in the calculation model. The angle difference (θBH) is considered to be derived from the magnetic anisotropic characteristics.

[1] K. Fujisaki, Y. Nemoto, S. Sato, M. Enokizono and H. Shimoji, 7th International Workshop on 1&2-Dimensional Magnetic Measurement and Testing Proceeding, edited by J. Sievert (PTB-E-81). 159, (2002).

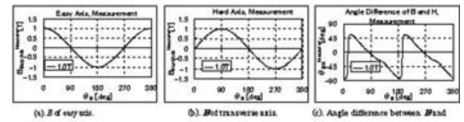

Fig.1. Measured magnetic property time series (measured steel: 35ZH135).

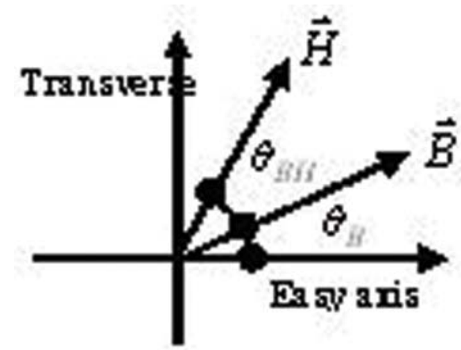

Fig. 2. B vector, H vector, angle of H and angle difference of B and H.

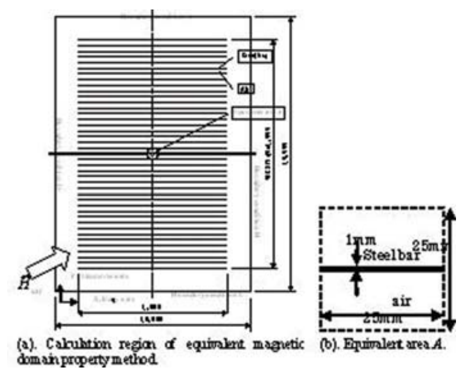

Fig.3. Calculation model of quivalent magnetic domain property method.

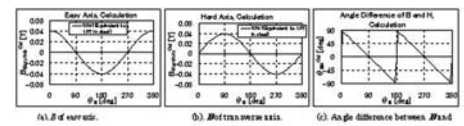

Fig.4. Calculated magnetic property time series by equivalent magnetic domain property method.

Data collapse and viscosity in three-dimensional magnetic systems.

A. Adedoyin, *A. Petru*
Electrical and Computer Engineering, Florida State University, Tallahassee, FL

Viscosity phenomena in magnetic systems have drawn much attention in the last decade mainly because of their negative implications in the magnetic recording industry. At temporally constant external conditions the total magnetization of a magnetic system exhibits a relatively slow but irreversible loss of its magnetic history, which is usually detrimental for the time reliability of recording information. The viscosity coefficient, generally defined as S(H,T) = dM/d(log t) (where t is time, H is the applied field, T is the temperature, and M is the magnetization) can be approximated as S(H,T) = S_0(T) * f(H/H*(T)), where f is a temperature independent function. The universality of the above scaling has been referred to as data collapse in magnetic viscosity. This scaling has been verified by both theoretical computations and experimental measurements [1] in isotropic materials by assuming that the direction of the magnetization is along the direction of the applied field (scalar models). In this work we investigate for the first time the validity of the above scaling technique to vector models of hysteresis for both the isotropic and anisotropic cases.
The generalization of scalar viscosity coefficient to vector magnetic systems [2] is challenging particularly because the trajectory of the magnetization in the case of vectorial relaxation phenomena (see Fig. 1) can deviate substantially from a straight line [3]. However, we show that the geometrical length of the magnetization "creep" (computed in integral form) depends approximately linearly on *ln*t . This observation allows us to define the vector magnetic viscosity coefficient in a way that is consistent with the generally accepted definition for scalar magnetization and investigate data collapse phenomena in vectorial systems. Sample simulation results for the vector viscosity coefficient as a function of the applied field are presented in Fig. 2. These simulations were performed for an isotropic system in which a strong magnetic field was first applied to saturate the sample, then decreased to some fixed value, rotated, and kept constant. After that the components of the magnetization vector were recorded as a function of time and the vector viscosity coefficient is computed. At t = 0 the magnetization vector is not align along the direction of the applied field, hence both the direction of the magnetization vector and its magnitude are changing slowly. Surprisingly, one can observe that the viscosity as a function of the magnetic field does not show the usual "bell-shaped" curves but has one or more peaks depending on the past magnetic history of the sample. The *multiplicity of these peaks is a pure vectorial effect* and their origin seems to be attributed to rotational changes of the magnetization during aftereffect. It is apparent from the figure that the data collapse phenomena fail for viscosities measured in multidimensional systems mainly because of the multiplicity of peaks on the viscosity curves.
A concise mathematical definition of the viscosity coefficient for vectorial magnetization processes will be presented at the conference. Simulation results for the vector viscosity phenomena in isotropic and anisotropic media will also be presented and discussed. The aftereffect phenomena are modeled by using the vector Preisach model of hysteresis in which thermal perturbations are modeled by a stochastic magnetic field superimposed over the external applied field [4]. The expected values of the magnetization as a function of time are computed by using the Monte Carlo method [3], which proves to be a computationally efficient approach that can be applied to any vector model of hysteresis such as the vector Jiles-Atherton, Energetic, or Della Torre models.

[1] I. Mayergoyz, Mathematical models of hysteresis and their applications. Academic Press, 2003.

[2] E. Cardelli and E. Della Torre, E., IEEE Trans. Magn., 42, 3126 (2006).

[3] P. Andrei and A. Ayodeji, J. Appl. Phys., to appear.

[4] W. F. Brown, Phys. Rev. 130, 1677(1963).

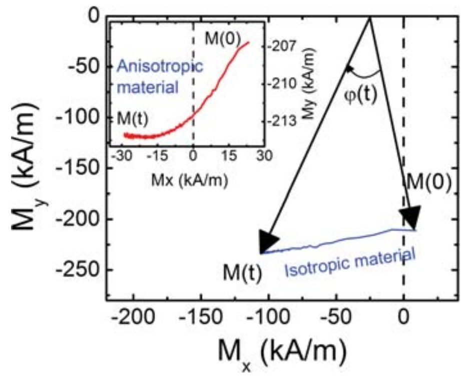

Fig. 1 Magnetization "creep" due to thermal relaxation in isotropic and anisotropic (see the inset) media.

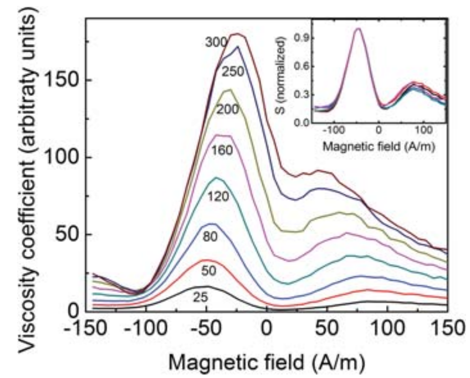

Fig. 2 Viscosity coefficient as a function of the magnetic field measured at different temperatures. The two peaks is a pure vectorial effect and their origin seems to be attributed to rotational changes of the magnetization during aftereffect.

CP-04

A Simplified Iron Loss Model for Laminated Magnetic Cores.

E. Dlala
Department of Electrical Engineering, Helsinki University of Technology, Espoo, Finland

The modeling of electromagnetic devices containing laminated cores requires an adequate description of the properties of the magnetic material. The shape of the dynamic hysteresis loop has to be modeled, and hence the power iron loss is predicted under arbitrary magnetization conditions. This means that an impeccable, systematic procedure that starts from a static hysteresis model must be embraced with Maxwell equations (diffusion equation). The excess loss related to the magnetic viscosity, which is also rate-dependent, needs to be included through the dynamization of the static model.
The diffusion equation of the lamination is non-linear, hysteretic, and time-dependent and thus requires an iterative time-stepping procedure. Moreover, when, for example, the 1D diffusion equation is integrated into the 2D finite-element analysis of electrical machines, convergence problems and complications are inevitably faced [1], [2].
On the other hand, the delay in the magnetic flux density *B* behind the field strength *H* resulting from the solution of the diffusion equation can be achieved differently and more efficiently without its solution. In the work of [3], an illustration of this idea was provided by considering a differential equation that delays its input with respect to the real value. Another similar method that is based upon two components, hysteresis and eddy currents, applied to grain-oriented materials has been introduced in [4].
In this article, we propose a methodology based on the procedure introduced in [5], and later refined in [6], to model, in a simple manner, the dynamic hysteresis loop, and hence the iron loss. The idea is to separate the magnetic field strength into three components, which are responsible for the static hysteresis, classical eddy-current, and excess losses. The drawback in [6] is that the *B*(*H*) relation is assumed to be linear in the calculation of the classical eddy-current loss, and thus the model is applicable only in the frequency range where the skin effect is negligible, or to magnetic cores with low conductivities or thin sheets.
This article aims to generalize model [6] in which the effect of the non-linearity on the classical eddy-current loss is considered. It is well known that the eddy-current loss is dependent on the *B*(*H*) relation, especially at saturation, where the skin effect becomes insignificant. Here, the dependency of eddy currents on non-linearity is achieved through the use of a non-linear function.
The proposed model can be applied to the prediction of core losses in non-oriented and grain-oriented materials. Here, numerical results of a non-oriented laminated steel of electrical machines are shown and compared with experiment. The simplified model has been identified for a soft magnetic steel of a thickness d = 0.5 mm and conductivity σ= 2.2×10^6 S/m. Figure 1 shows the model predictions of dynamic hysteresis loops compared with experiments. It is clear that when the effect of the non-linearity was considered, the model produced accurate results in good agreement with experiment.

[1] O. Bottauscio, M. Chiampi, and D. Chiarabaglio, “Advanced model of laminated magnetic cores for two-dimensional field analysis,” IEEE Trans. Magn., vol. 36, pp. 561-573, 2000.

[2] E. Dlala, A. Belahcen, and A. Arkkio, “Efficient magnetodynamic lamination model for two-dimensional field simulation of rotating electrical machines,” J. Magn. Magn. Mater., submitted for publication 25 August 2007, presented in SMM 2007.

[3] Fuzi, J., “Computationally efficient rate dependent hysteresis model,” COMPEL, vol. 18, pp. 44-45, 1999.

[4] T. Matsuo, and M. Shimasaki, “Simple modeling of the AC hysteretic property of a grain-oriented silicon steel sheet,” IEEE Trans. Magn., vol. 42, pp. 919-922, 2006.

[5] D. C. Jiles, “Modelling the effects of eddy current losses on frequency dependent hysteresis in electrically conducting media,” IEEE Trans. Magn., vol. 30, pp. 4326-4328, 1994.

[6] S. E. Zirka, Y. I. Moroz, P. Marketos, and A. J. Moses, “Measurement and Modeling of B-H Loops and Losses of High Silicon Nonoriented Steels,” IEEE Trans. Magn., vol. 42, pp. 3177-3179, 2006.

[7] G. Bertotti, “General properties of power losses in soft ferromagnetic materials,” IEEE Trans. Magn., vol. 24, pp. 621-630, 1988.

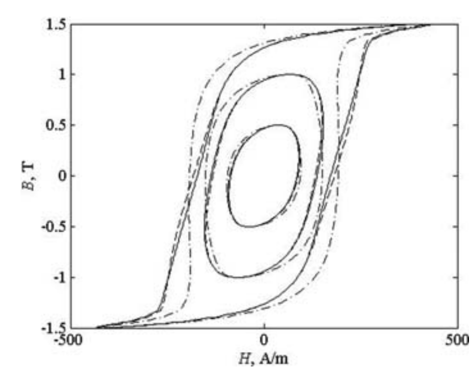

Figure 1. The iron loss predictions of the proposed model when eddy-currents were assumed to be independent of the non-linearity (dot-dashed), dependent on the magnetic non-linearity (dashed), and compared with experimental dynamic loops (solid) at a fundamental frequency of 400 Hz.

CP-05

Modeling of Vector Hysteresis of Soft Magnetic Composite Material.

Y. Guo[1], H. Lu[2], J. Zhu[1], Z. Lin[1], J. Zhong[1], S. Wang[3]
1. Faculty of Engineering, University of Technology Sydney, Sydney, NSW, Australia; 2. Faculty of Information Technology, University of Technology Sydney, Sydney, NSW, Australia; 3. Faculty of Electrical Engineering, Xi'an Jiaotong University, Xi'an, China

1. Introduction
Thanks to the unique magnetic properties, soft magnetic composite (SMC) materials and their application in electromagnetic devices have achieved significant development in the past decade [1]. A typical example of SMC application is the electrical machine with complex structure [2], in which the magnetic flux is basically rotating. To design and analyze such devices, vector magnetic properties of the core material should be properly determined, modeled and applied.
This paper presents the modeling of vector magnetic hysteresis of SMC based on a Stoner-Wohlfarh (S-W) elemental operator. A phenomenological mean-field approximation is used to consider the interaction between particles [3]. With the presented model, the magnetization processes of SMC under both alternating and rotating fluxes are numerically simulated. The simulations have been verified by experimental measurements.
2. Modeling of Vector Hysteresis
Under a magnetic field H, the magnetic moment ms of an S-W particle rotates to the orientation which results in a minimum energy. The position of ms changes with respect to H, and the domain rotation can be reversible or irreversible. The equilibrium orientation of ms can be evaluated by the asteroidal rule in the plane containing H and the easy axis as shown in Fig.1, where He and Hp are the H components along the easy axis and the perpendicular direction respectively, Hk=2K/(μ0ms), and K is the domain crystal anisotropy constant.
A mean field term is added to account for the macroscopic effect of interaction between S-W particles [4], Heff=H+kM, where k is a constant feedback coefficient and can be theoretically determined from experimental data [5]. The contribution of an S-W particle can be expressed by M=S(Heff), where S() stands for the S-W model.
The bulk material can be considered as a collection of many S-W single domain particles and the total magnetization is the vector sum of contributions of all these constitute domains. In numerical implementation, the magnetization is computed by the vector sum of ms of a group of magnetic particles.
3. Numerical Implementation
The magnetization processes of SMC with isotropic magnetic properties under both alternating and rotating magnetic fields have been simulated numerically. The results (Fig.2 and Fig.3) show that in an isotropic magnetic material M and H vector are collinear for an alternating magnetic field excitation, while for a rotating magnetic field excitation of constant magnitude M vector lags the H vector for a certain angle.
The detailed implementation process and more simulation results will be presented in the full paper.
4. Experimental results
The B-H relationships of SMC samples under various alternating and 2-D and 3-D rotating magnetic excitations have been measured by the authors[6]. The simulation and experimental results will be compared and analyzed.

[1] SMC Update 1997-2007, http://www.hoganas.com

[2] YG Guo, IEEE Trans Ind Appl, 39(6), 1696 (2003)

[3] JJ Zhong, IEEE Trans Magn, 41(5), 1576 (2005)

[4] DL Atherton, IEEE Trans Magn, 26(6), 3059 (1990)

[5] DC Jiles, J Magn Magn Mater, 61, 48 (1986)

[6] JG Zhu, ICEMS Proc, 2354 (2005)

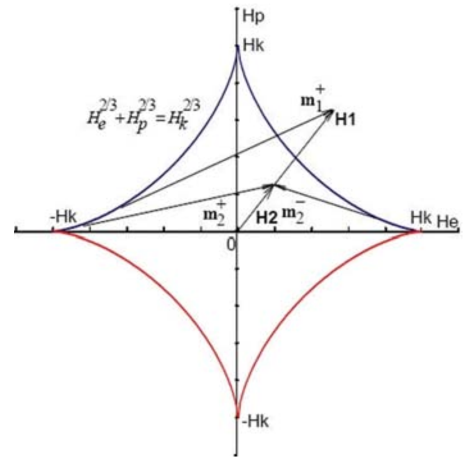

Fig.1 S-W elemental operator

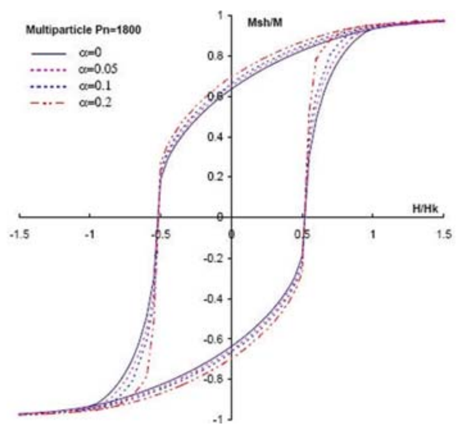

Fig.2 Hysteresis loops with mean interaction field

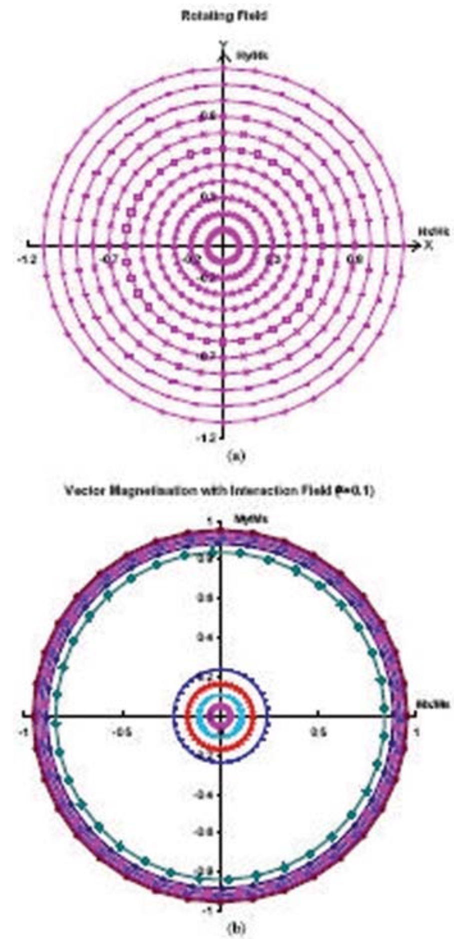

Fig.3 Loci of (a) rotating H and (b) M

Analysis of the local material degradation near cutting edges of electrical steel sheets.

G. Crevecoeur[1], P. Sergeant[1], L. Dupre[1], L. Vandenbossche[1], R. Van de Walle[2]
1. Departement of Electrical Energy, Systems and Automation, Ghent University, Ghent, Belgium; 2. Department of Electronics and Information systems, Ghent University, Ghent, Belgium

The introduction of stresses and strains caused by cutting processes on electrical steel, induces an alteration of the local magnetic properties of the material. Electrical machine manufacturers are often not aware of how the magnetic material is degraded quantitatively near the cutting edge. In order to be able to incorporate the material degradation into the design of electrical machines, it is necessary to characterize the local change of the magnetic properties in an accurate way.
The conventional way of performing local magnetic flux measurements on soft magnetic materials is the search coil method. This method however is destructive, while the method used in this paper – the needle probe method – is non-destructive, see [1]. The needle probe method enforces a certain magnetic induction in a steel sheet. Potential differences, which are dependent on the local material characteristics, are measured on the surface of the steel sheet, see Fig. 1.
This paper mainly deals with the interpretation of the measured needle potentials, i.e. the link between the measured needle signals and the local mechanical state of the material, and with the validation of the proposed method. The determination of the mechanical state uses a numerical 'forward' model of the material with the mechanical state as input and the needle potentials as outputs. As the inputs are unknown, the problem is an inverse problem. By using the numerical procedure, developed theoretically in [2], we are able to interpret the needle signals.
The numerical model is a 2D finite element model (FEM) with a material model, a Preisach distribution function (PDF), which fully characterizes the magnetic material. Two possibilities exist for building the PDF: propose an analytical expression for the PDF or build a so-called Everett PDF. Using an analytical Lorentzian expression of the PDF, discrepancies occur between calculated and measured hysteresis loops for plastically deformed samples. See Fig. 2, where a measured needle potential is compared with the closest calculated needle potential, using an analytical Preisach model. Therefore, we introduce the use of an Everett PDF, where the PDF is obtained directly from a set of measured hysteresis loops, following the Everett theory, see also [3]. This paper uses the local mechanical state, i.e. the plastic strain, of the material as material parameter. The link between the mechanical state (plastic strain) of the material and the magnetic material characteristics (Everett PDF) is made by macroscopically deforming the steel sheet for several levels of plastic deformation and to build the Everett PDF for these levels of plastic deformation.
A fully processed non oriented steel sheet designated as 800-50 A (thickness 0.5mm, 1.3% Si) was cut using a continuous C02-laser. Results of the locally recovered magnetic properties show that the degraded zone can extend to 3 mm from the cutting edge. The local peak differential permeability can be 5 times lower in the degraded zone and a local magnetic hardening is observed.
In order to validate the approach, proposed in the present paper, for the local identification of the magnetic properties, we numerically calculate the global macroscopic hysteretic characteristics of the steel sheet and compare these global characteristics with the macroscopic BH-loop measured on the strip. Indeed, differently cut steel sheets, have different macroscopic BH-loops. The local material degradation influences the global behaviour of the steel sheet. Loss increase, coercive field, etc., describe macroscopically the material behaviour and are used for making the comparison possible. The comparisons show that a fully characterized magnetic material (through an Everett PDF) is a better means for locally characterizing the magnetic material.

[1] G. Loisos, and A. Moses, "Critical evaluation and limitations of localized flux density measurements in electrical steels," IEEE Trans. Magn., vol. 37, no. 4, pp. 2755-2757, Jul 2001.

[2] G. Crevecoeur, L. Dupré, L. Vandenbossche, and R. Van de Walle, "Reconstruction of local magnetic properties of steel sheets by needle probe methods using space mapping techniques," J. Appl. Phys., vol. 99, no.8, Art. No. 08H905, 2006.

[3] L. Dupre, R. Van Keer, J. Melkebeek, "Modelling and identification of iron losses in nonoriented steel laminations using Preisach theory," IEE Proceedings – Electric power applications, vol. 144, no. 4, pp. 227-234, 1997.

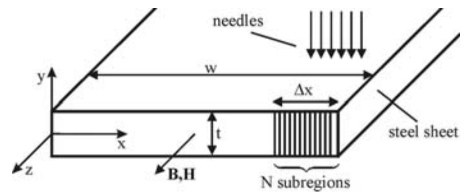

The needle probe method: the needle potentials are dependent on the local material characteristics, which spatially vary (different material properties in the N subregions).

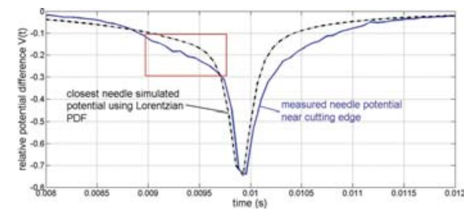

Measured relative needle potential near cutting edge of a steel sheet and closest simulated potential using a Lorentzian PDF (at 50 Hz). The needle potential can not be accurately simulated using the Lorentzian PDF, as indicated in the box. The correspondence between measured and computed signals is improved by using an Everett PDF.

CP-07

Modelling of magnetostrictive material and linear controling of nonlinear magnetostrictive drive system based on SVM.

J. An, *Q. Yang*, Z. Ma, H. Chen, L. Hou, W. Yang, F. Liu
hebei university of technology, Tianjin, China

Abstract—The disadvantages of the nonlinear dynamical system identification method based on neural networks are analyzed in this paper. A SVM method to construct inverse model of magnetostrictive material is presented. And the linear control of nonlinear magnetostrictive drive system is achieved. Simulative result indicates that the method presented in this paper can effectively construct the inverse model and well compensate for the hysteretic nonlinearity of magnetostriction actuator.

I.INTRODUCTION

Because of the needs of predicting and controlling the unknown system, system model identification[1-2] has become a very important topic. To a nonlinear system, there is not a standard method for system modeling yet, thus the study on identification methods and application of nonlinear system model has caused great attention of scientific researchers. At present, the researches of modeling black box system mainly concentrate on neural-networks-based method[1-2].

Support Vector Machine [3] is a new method based on statistical learning theory. we present a SVM method of modelling and controlling for magnetostrictive material. The better effects are obtained.

II. A practical control system of magnetostrictive material

Under the action of magnetic field, the magnetostrictive material can repeat stretching and shortening. For a magnetostrictive drive system, Fig.1 is the experiment data curve of the length change of magnetostrictive rod with the change of exciting coil current.

III.ON-LINE IDENTIFICATION OF NONLINEAR SYSTEM WITH SVM

To such a complicated multivalued function nonlinear system, how to get a better mathematical model quickly and how to apply it to prediction control at the same time, are very important to improve the precision of precise processing.

For such a complex nonlinear system, in this paper, we apply SVM to the identification and control of the black-box system.

A.Construction method of one-step prediction model.

To identify the nonlinear system of micro-shift driving that is introduced in this paper, two methods are used, which is SVM method presented in this paper and neural network method. The output error of SVM one-step prediction model is shown in Fig.2.. Fig.3 is the one-step prediction output error of model trained with RBF neural network.

B. Result of simulation.

We can see that the output of one-step prediction have very high accuracy from the error curves in Fig.2. The time each training needs is only 0.02s when a new sample is added, so it can be applied to on-line prediction control of many systems. Therefore whether from the training speed or from the accuracy of one-step prediction, the performance of the present method is far better than that of the RBF neural network method.

IV.CONTROL GIANT MAGNETOSTRICTIVE ACTUATOR WITH SVM

In the control of actual system, in order to improve control effect, we expect that the relation between the system input and output is linear even though most of the actual system is nonlinear.

In order to solve the problem, we utilize the nonlinear mapping and self-learning ability of SVM to construct online inverse model of giant magnetostrictive actuator.

To the SVM direct control system in Fig.4, from the simulation result in Fig.5 we can see that the inverse model constructed with SVM can compensate for the hysteretic nonlinearity of actuator and the SVM direct control system achieves the linear control of nonlinear system.

V.CONCLUSIONS

The performance of the SVM method presented in this paper is better than that of the RBF neural network method.

we compensate for the hysteretic nonlinearity of actuator and achieve the linear control of a nonlinear system.

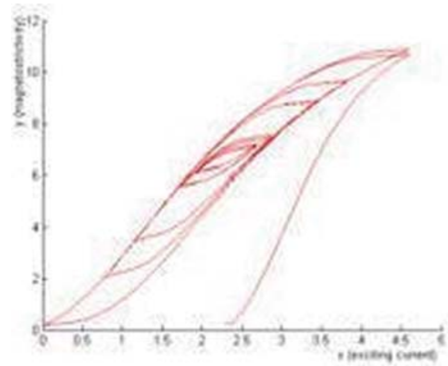

Fig.1 Experiment data curve of the length change of magnetostrictive rod with the change of exciting coil current.

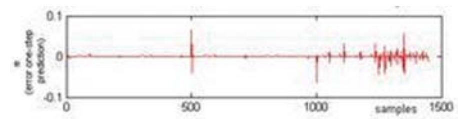

Fig.2 Output error of SVM one-step prediction model

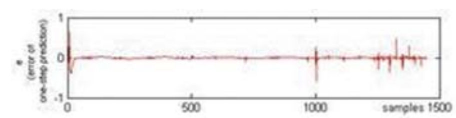

Fig.3 Output error of NN one-step prediction

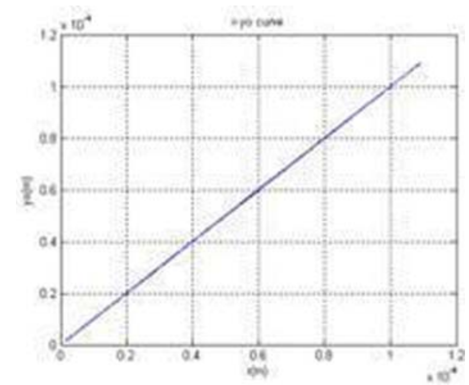

Fig.5 The output of controlled device with the system input

CP-08

Modelling hysteresis of a first order magneto-structural phase transformation.

V. Basso[1], M. Lo Bue[2], C. P. Sasso[1], M. Küpferling[1]
1. INRIM, Torino, Italy; 2. SATIE, ENS Cachan, CNRS, UniverSud, Cachan, France

Phase transitions where two or more interacting order parameters are involved have been the object of many theoretical studies since Bean and Rodbell paper of 1962 [1]. However the comprehension of hysteresis effect related to the presence of structural disorder remains a major problem
For example the evaluation of the magneto-caloric entropy change associated with magneto-structural phase transformations requires a detailed comprehension of the role played by hysteresis. We have recently introduced a phenomenological description of first order hysteretic phase transformations by means of a statistical distribution of independent bistable contributions [2]. The idea is that, in presence of several intensive variables, i.e. the temperature T and the magnetic field H, the driving force of the transformation is the difference of the Gibbs free energies g_0 and g_1 of the two metastable phases. Hysteresis is then given by to the superposition of bistable loops describing the phase fraction X as a function of the difference of the Gibbs free energies $Z = (g_0 - g_1)/2$. Each bistable change state at the thresholds g_u+g_c and g_u-g_c. g_u and g_c are parameters describing the local properties of the material modified by defects and impurities (Fig.1a). Then, while g_0 and g_1 are intrinsic properties of alloy, the statistical distribution of the bistables $p(g_c,g_u)$, takes into account the quenched disorder in the material.
This approach has been recently applied to describe the magneto-structural transformation of Gd-Si-Ge alloys [3] and to predict the entropy change and the entropy production of the material. For that material the magnetic field and temperature dependence of the functions $g_0(H,T)$ and $g_1(H,T)$ were extracted from a set of isothermal hysteresis loops and it was shown that a good agreement with the data was achieved by a distribution $p(g_c,g_u)$ independent of H and T.
This is however not the case for all materials with magneto-structural transitions. In this respect a good example is given by the behavior of the MnAs alloys [4,5]. Here the coercivity decreases when the temperature is increased and eventually disappears when the tricritical point is approached.
In order to describe MnAs one has to allow the distribution $p(g_c,g_u)$ to change with the temperature T. To do this we have to extend the model. Here we follow the approach of Ref.[6]: we introduce the temperature dependence in $p(g_c,g_u)$ by scaling functions. I.e. we limit to describe temperature dependence in which all the bistables rescale in the same way. Having two variables g_c and g_u, we have to introduce two scaling functions: $G_c(T)$ and $G_u(T)$. Normalized variables are $z_c = g_c/G_c(T)$ and $z_u = g_u/G_u(T)$. Normalized driving force is $z = Z / G_u(T)$ and the distribution is $p_z(z_c,z_u)dz_cdz_u = p(g_c,g_u)dg_cdg_u$.
The internal state of the system is due to the time history of Z(t). In Fig.1b it is shown an example of a borderline $b(g_c)$ separating in the (g_c,g_u) plane, the region of phase 0 from those in phase 1. With the normalized variables the line in the plane (z_c,z_u) is $b_z(z_c)= b(g_c)/G_u(T)$. The normalized line has to be always inside the triangular region of Fig.2c, i.e. $|b_z(z_c)-z|\leq z_c\, G_c(T)/G_u(T)$. In the normalized plane the distribution is temperature independent.
With this extended model we obtain a new expression for the entropy. We have an extra term that was not present in the expression for the constant distrubution. The expression for the out-of-equilibrium Gibbs free energy is Eq.(1) (see equations in Fig.2 right), where $A = (g_0+g_0)/2$. The entropy is Eq.(2). From that one obtains Eq.(3), where X is the phase fraction given by the model (Eq.(4)) and Y (Eq.(5)) is an integral in the (z_c,z_u) plane depending on the distribution. This is the new term appearing because the distribution depends on T. The importance of the term and its physical meaning will be clarified in the paper by the application of the model to the the literature data on MnAs of Refs.[4,5].

[1] C. P. Bean, and D. S. Rodbell, Phys. Rev. 126, 104-115, (1962)

[2] V. Basso, C. P. Sasso, and M. LoBue, J. Mag. Mag. Mater. 316, 262-268, (2007)

[3] M. LoBue, V. Basso, C. P. Sasso, G. Bertotti, J. Mag. Mag. Mater. 316, 361-363, (2007)

[4] A. Zieba, Y. Shapira, and S. Foner, Phys. Lett. 91A, 243-245, (1982)

[5] L. Tocado, Thermomagnetic study of materials with giant magnetocaloric effect, PhD thesis, Universidad de Zaragoza, 2007.

[6] G. Bertotti, V. Basso, M. LoBue, and A. Magni, Thermodynamics, hysteresis, and micromagnetics, in: Science of Hysteresis Vol. II (G.Bertotti and I. Mayergoyz eds.) Elsevier, (2006)

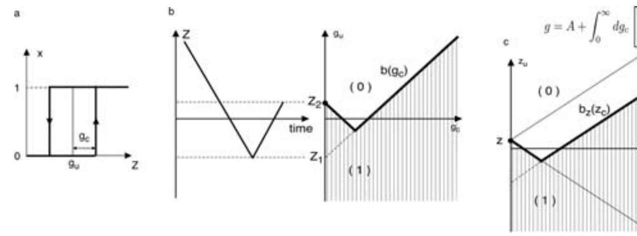

$$g = A + \int_0^{\infty} dg_c \left[\int_{-\infty}^{b(g_c)} (g_u - Z) p(g_c, g_u)\, dg_u - \int_{b(g_c)}^{\infty} (g_u - Z) p(g_c, g_u)\, dg_u \right] \quad (1)$$

$$s = - \left. \frac{\partial g}{\partial T} \right|_{H, b_z} \quad (2)$$

$$s = X s_1 + (1 - X) s_0 + \frac{dG_u}{dT} Y \quad (3)$$

$$X = \int_0^{\infty} dz_c \int_{-\infty}^{b_z(z_c)} p_z(z_c, z_u)\, dz_u \quad (4)$$

$$Y = \int_0^{\infty} dz_c \left[\int_{-\infty}^{b_z(z_c)} z_u p_z(z_c, z_u)\, dz_u - \int_{b_z(z_c)}^{\infty} z_u p(z_c, z_u)\, dz_u \right] \quad (5)$$

CP-09

The Preisach distribution and the symmetry of the local hysterons in strongly interacting nanoparticulate systems.

R. Tanasa, A. Stancu
Department of Physics, "Alexandru Ioan Cuza" University, Iasi, Romania

The Major Hysteresis Loop of a collection of magnetic nanoparticules is typically symmetric with respect to the origin. The Preisach model [1] starts from the hypothesis that every particle from this physical system is described by a rectangular local hysteresis loop shifted along the field axis (see Fig.1).

Recently, improvements in the experimental techniques, like Magnetic Force Microscopy or Magnetization induced Second Harmonic Generation opened the perspective to perform accurate measurements at the nanometer level in nanostructured systems like patterned media [2] or nanowires [3].

Actually, this type of measurement was already performed and essentially confirmed the validity of the existence of non-symmetric local hysterons [4]. However, when the experimental Preisach distribution calculated as a superposition of these local hysterons is used for the calculation of higher order magnetization curves the results are quite far from the experimental results.

In this paper we are analyzing the physical motivation of this disagreement by investigating the switching at fundamental level on others magnetization curves like the First order reversal curves. Our goal was to record the switching fields from negative to positive saturation H_α of a selected number of particles, like those who have H_β (positive to negative switch) the same with coercive field because in this case we have the biggest number of elements and our statistical results are significant.

We have simulated a nanostructured perpendicular medium (similar to patterned media) using an Ising type model in which each particle has an intrinsic anisotropy. The switching of particles was calculated with a typical Metropolis algorithm in which the energy barrier for each particle was evaluated with the Stoner-Wohlfarth model.

We have simulated a number of reversal curves with reversal field between minimum saturation ($-H_m$) and the coercitive field ($-H_c$) (see Fig. 2), to record H_α for selected particles and in the end to calculate the average value and the dispersion. We repeated the procedure for different values of the lattice parameter, *d*, and the results are presented in Figs.3 and 4. When interactions are negligible, *d=4*, all particles switch at the same positive field $H_\alpha=3$ regardless the reversal curve. The situation changes dramatically for the more interacting systems. For example, we observe that for *d=1* the same particles switches at a field H_α three times bigger than the absolute value of the negative switching field for the same particle. Their local hysteresis loop is strongly asymmetrical. One observes in this way that the same physical particle will not switch at the same fields on FORCs characterized by different reversal fields.

In the full paper we shall discusses how this analysis can provide new ideas for the proper interpretation of the experimental FORC diagrams for a number of typical nanostructured materials (longitudinal and perpendicular). The relation between the state dependent Preisach distribution and the FORC distribution is also discussed.

Acknowledgements: This work was partially supported by CEEX / AMCSIT MATHYS 324 program.

[1] I.D. Mayergoyz (Elsevier) 2003;

[2] H.J. Jang et al., J Appl Phys 93 (2003) 10143;

[3] T.G. Sorop et al., Phys Rev B 67 (2003) 014402;

[4] T.H. Wu et al., J Appl Phys 93 (2003) 7804.

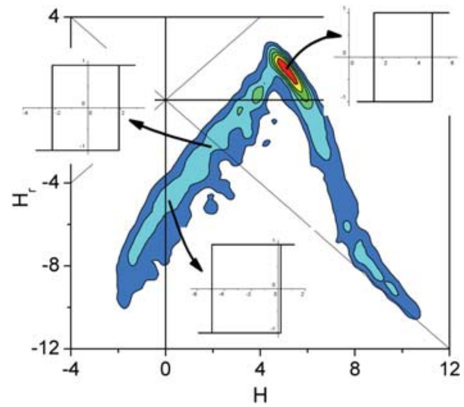

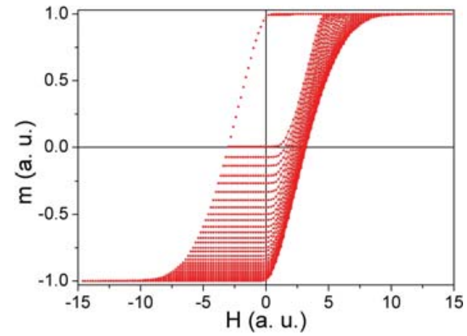

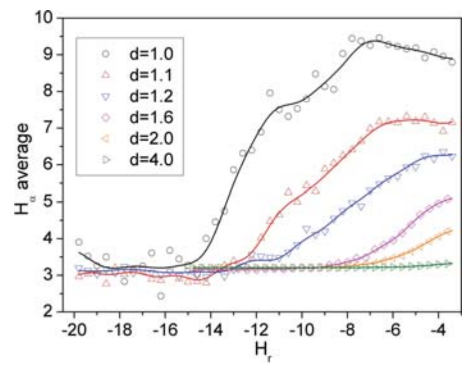

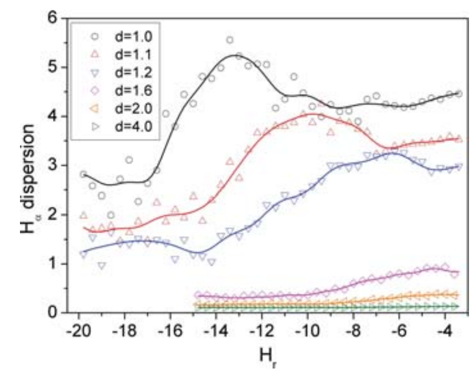

CQ-01

Magnetic and magneto-thermal properties of RFe4Ge2(R=Er,Dy) compounds.

P. Kumar[1], N. K. Singh[1], K. G. Suresh[1], A. K. Nigam[2]
1. Physics, IIT Bombay, Mumbai, India; 2. Tata Institute of Fundamental Research, Tata Institute of Fundamental Research, Mumbai, India

Magnetocaloric effect (MCE) in a magnetic material is an efficient tool to understand the correlations between its magnetic, structural and thermal properties [1,2]. MCE in a magnetic material is observed as the isothermal magnetic entropy change (ΔSM) or as the adiabatic temperature change (ΔTad) in the presence of an external magnetic field. The recent studies on the MCE of various materials have shown that a large value of MCE is the most important requirement for a magnetic material to be considered as a potential magnetic refrigerant. With the aim of identifying novel magnetic refrigerants, we have studied the magnetic and magnetocaloric properties of DyFe4Ge2 and ErFe4Ge2 compounds.

Both the compounds are antiferromagnetic with a Neel temperature of 65K for DyFe4Ge2 and 42K for ErFe4Ge2. They also undergo a structural transition at low temperatures. Furthermore, ErFe4Ge2 shows a spin spin-reorientation transition at 8 K. Both these compounds exhibit strong field-induced metamagnetic transitions at low temperatures as shown in the fig.1. The critical fields of the transitions in the case of DyFe4Ge2 are 1.6 kOe and 5.6 kOe, at 5 K. In the case of ErFe4Ge2, the critical fields are found to be 2.9 kOe and 3.8 kOe. The magnetocaloric effect has been measured in terms of the isothermal magnetic entropy change (ΔSM) using the magnetization isotherms obtained at temperatures close to the magnetic ordering and the structural transition temperatures. The maximum values of ΔSM are found to be 2.8 J/kg K and 2.1J/kg K for DyFe4Ge2 and 3.1 J/kg K and 1.2 J/kg K for ErFe4Ge2 near the structural transition and ordering temperatures respectively, for a field change of 60kOe as shown in the fig.2.

The refrigerating cooling power (RCP) values are found to be 213 and 162 J/kg for DyFe4Ge2 and ErFe4Ge2, respectively for a field of 60 kOe. The RCP values observed in the present case compare well with those of many potential materials [1,2], whose magnetic transitions are in the same range as in the present case. A detailed discussion of the magnetocaloric properties will be presented.

[1] V. K. Pecharsky and K. A. Gschneidner, Jr., J . Magn. Magn. Mater. 200, 44 (1999).

[2] A.M.Tishin and Y.I.Spichkin, The Magnetocaloric Effect and its Applications (IOP, New York, 2003).

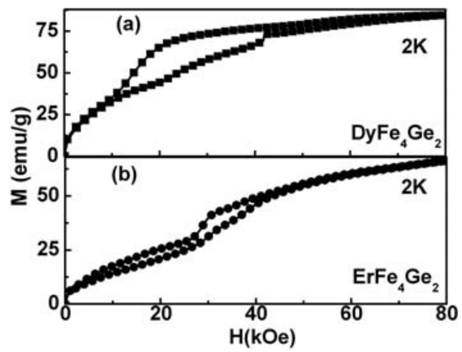

Fig.1 M-H isotherms at 5K for DyFe4Ge2 and ErFe4Ge2.

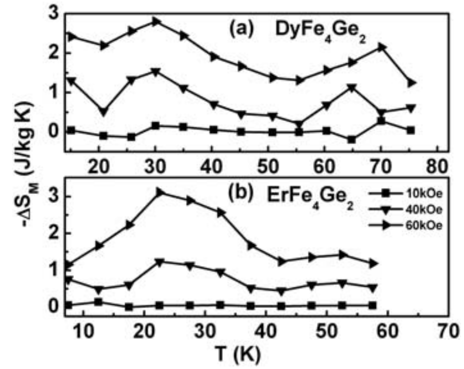

Fig.2. Temperature variation of isothermal magnetic entropy change, for a field change of 10, 40 and 60 kOe in DyFe4Ge2 and ErFe4Ge2

CQ-02

Capacity of magnetic inductive parameters on annealing characterization of cold rolled low carbon steel.

K. Gurruchaga[1,2], A. Martínez-de-Guerenu[1], M. Soto[1,2], F. Arizti[1,2]
1. CEIT, San Sebastian, Spain; 2. Tecnun, San Sebastian, Spain

ABSTRACT
The effect on magnetic measurements of dislocation density and texture changes during annealing of a cold rolled low carbon steel is analyzed. Low induction values are useful to characterize recovery whereas high induction values can be used to monitor recrystallization.

INTRODUCTION
The microstructure of cold rolled low carbon steels experiences recovery and recrystallization processes during the annealing treatment applied in industry. Recovery involves the annihilation and rearrangement of dislocations, while recrystallization leads to a new grain structure with a low dislocation density and different texture. The typical cold rolled low carbon steel texture intensity concentrates along α fiber (Φ Euler angle=[0-54.7]) with additional γ fiber. Recrystallized low carbon steel texture consists of an intense γ fiber and lower α fiber [1].
The evolution during annealing of the microstructure of a cold rolled extra low carbon steel was studied by metallographic and H_c measurements in [2]. The present paper researches into the use of other magnetic hysteresis loop parameters for the nondestructive characterization of the microstructural changes produced in this steel during the annealing.

RESULTS AND DISCUSSION
Samples from industrially produced low carbon steel, 76% cold rolled, were isothermally annealed in laboratory [2] to promote various degrees of recovery or recrystallization.
Figs 1-2 show, respectively, the evolution of B_r and B_{25} (induction when H = 2500 A/m) as a function of annealing time. During recovery at low annealing temperatures, B_r presents a progressive increasing tendency, which is attributed to the reduction of individual pinning site energies caused by the rearrangement of dislocations into lower energy configurations [3]. B_{25} only experiences a slight increase, which is explained by the low sensitivity to variations in the dislocation density at high magnetic fields [4].
During recrystallization both induction values are affected by texture changes [5]. The effect of texture evolution of these type of low carbon steels in terms of the magnetocrystalline energy (E_{crys}) will be discussed in the paper. The material is easier to magnetize when E_{crys} is smaller, so with the same applied magnetic field a higher induction level is reached.
Fig 3 presents the E_{crys} of α fiber calculated by the equation for a bcc crystal [6] when the magnetic field is applied in the transverse direction. The total energy decrease produced by the reduction of α fiber during recrystallization explains the observed higher induction values.
Fig 4 shows correlations between B_r and B_{25} with recrystallized fraction. Although both parameters are able to characterize recrystallization, B_{25} presents larger changes and is better correlated, which is explained because texture effects are usually more pronounced at higher induction levels [7].

CONCLUSIONS
- B_r can monitor the reduction in the dislocation density during recovery processes.
- High induction values are not useful to characterize recovery because the effect of changes in dislocation density is lower at high applied magnetic fields.
- B_r and B_{25} could be used to characterize recrystallization when the magnetic field is applied in transverse direction. B_{25} presents larger variations and better correlation with recrystallized fraction.

[1] E Novillo,MM Petite,JL Bocos,A Iza-Mendia,I Gutierrez,Adv Eng Mater,5,8,575,2003.
[2] M Oyarzabal,K Gurruchaga,A Martinez-De-Guerenu,I Gutierrez,ISIJ Int,47,10,1458,2007.
[3] SM Thompson,BK Tanner,J Magn Magn Mater,132,1-3,71,1994.
[4] K Eloot,A De Paepe,J Dilewijns,C Standaert,J Magn Magn Mater,157-158,459,1996.
[5] AD Rollett,ML Storch,EJ Hilinski,SR Goodman,Metall Trans A,32,10,2595,2001.
[6] BD Cullity,Introduction to magnetic materials. Addison-Wesley Publishing Company,1972.
[7] J Degauque,Mater Sci Forum,366-3,453,2001.

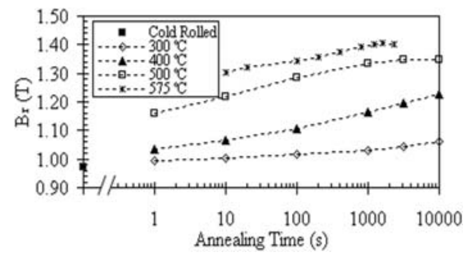

Fig 1 Evolution of B_r with annealing time

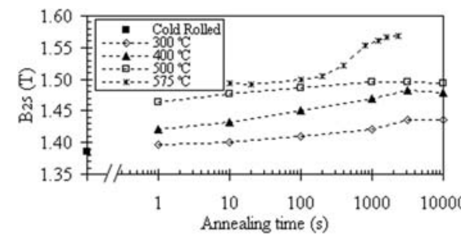

Fig 2 Evolution of B_{25} with annealing time

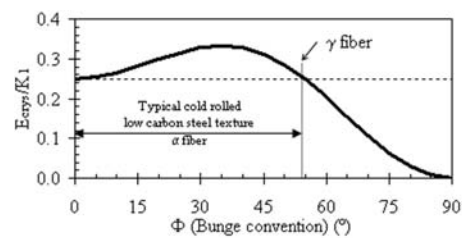

Fig 3 E_{crys} of α fiber as a function of the Φ Euler angle

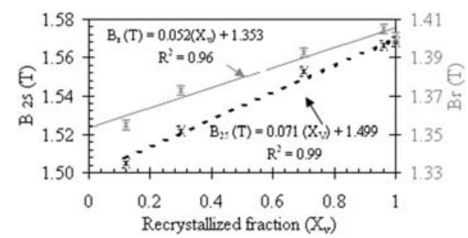

Fig 4 Correlations of B_r and B_{25} with recrystallized fraction

CQ-03

A fully digital magnetic property measurement system.

M. Soto[1,2], A. Martínez-de-Guerenu[1], K. Gurruchaga[1,2], F. Arizti[1,2]
1. CEIT, San Sebastian, Spain; 2. Tecnun (University of Navarra), San Sebastian, Spain

INTRODUCTION

Non-destructive evaluation techniques as magnetic hysteresis loop (B-H) and magnetic Barkhausen noise (MBN) are becoming of increasing interest for inspection of several material properties [1,2]. Depending on the aim of the measurements these techniques are applied in different excitation frequency ranges [2,3]. Most measurement systems have been developed using analogue electronics, which implies that they are restricted to a specific small range of frequencies. In most MBN measuring devices, the MBN signal is acquired after analogue filtering [1]. In this paper, the development of a new accurate, fully digital and configurable system, capable of performing simultaneous B-H loop and MBN measurements without changing any hardware, and in a wide band of frequencies (from 0.01 to 80Hz) is described. All the parameters related with B-H loops and MBN are obtained from only two signals.

PROPOSED SYSTEM

Fig 1 shows the schematic diagram of the hardware of the proposed digital system. The type, amplitude and frequency of the applied excitation waveform can be specified via a user interface. This signal is fed into a power amplifier and delivered to a coil wrapped around a U-shaped magnetic core. Two sensors are used: an encircling pick-up coil to obtain the induced electromotive force (EMF) and a Hall sensor, to detect the tangential field strength, placed next to the pick-up coil at the surface of the sample. The detected signals are acquired with a 24 bit A/D converter.

Fig 2 represents the digital processing of the acquired signals. The values of the magnetic flux density are calculated by numerical integration of the EMF, which allows us to integrate perfectly in a wide band of frequencies, opposite to analogue integration. Moreover, the offset introduced by the amplifier stage is removed by software. The MBN signal is obtained by digital filtering of the EMF signal. The use of digital filters provides the system with the flexibility required to do the measurements at different excitation frequencies for different applications.

Finally, several parameters are computed both from the B-H loop and from the MBN signal, which can be stored for further automatic batch data post-processing and comparison.

RESULTS

Next results present the capability of the system.

Fig 3 shows the B-H loop of two samples S1 (a cold rolled low carbon steel) and S2 (S1 after an annealing treatment at 500°C for 100s) at different excitation frequencies. As the excitation frequency increases, the B-H loops become wider due to the effect of eddy currents.

Fig. 4 shows the root mean square (RMS) envelope of these two samples at different excitation frequencies. The amplitude increases with the excitation frequency, but the shape of the RMS envelope of each sample is maintained.

CONCLUSIONS

- The proposed digital system presents a measurement system capable of performing B-H loops and MBN measurements in a wide band of frequencies acquiring only two signals, reducing significantly the time and the amount of data stored.
- The frequency, shape and type of the excitation signal, the specifications of the MBN filters and the sampling rate of the acquisition are configurable.
- The system stores the results for further post-processing.

[1]T.Liu,H.Kikuchi,Y.Kamada,K.Ara,S.Kobayashi,S.Takahashi,J Magn.Magn.Mater.,310,2,e989,2007

[2]V.Moorthy,B.A.Shaw,P.Mountford,P.Hopkins,Acta Mater.,53,19,4997,2005

[3]E.Carminati,A.Ferrero,IEEE Trans.Instrum.Meas.,41,6,1005,1992

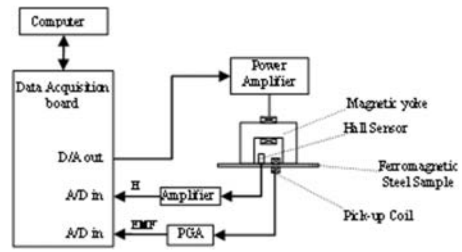

Fig 1. Hardware architecture of the system

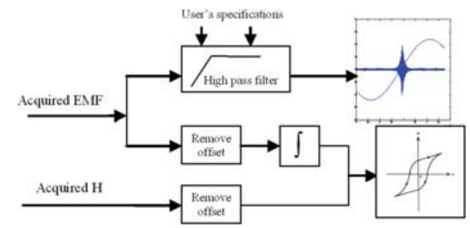

Fig 2. Digital processing of the signals (after acquisition)

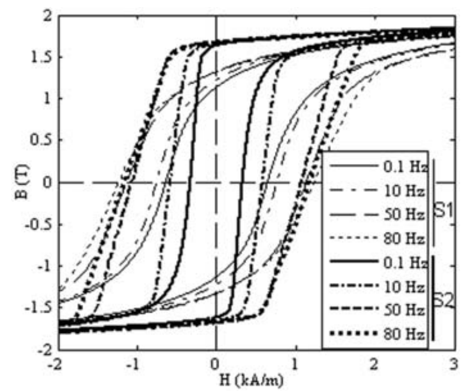

Fig 3. B-H loop of samples S1 and S2 at 0.1, 10, 50 and 80 Hz

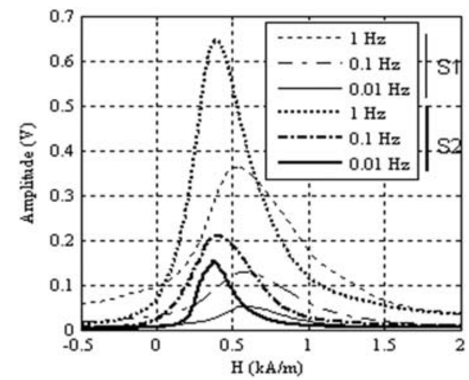

Fig 4. RMS envelopes of samples S1 and S2 at 0.01, 0.1 and 1 Hz

CQ-04

Preparation and magnetorheology of solvent-cast magnetite nanoparticle and poly(vinyl butyral) composite.

B. Park, J. You, F. Fang, H. Choi
Department of Polymer Science and Engineering, Inha University, Incheon, South Korea

Introduction

Iron oxide nanoparticles have been widely used because of their unique magnetic, catalytic, and biological properties which can provide potential applications in various areas such as biomedical engineering and magnetic storage device. Composite materials of the iron oxide and polymer have been also investigated for engineering application of the iron oxide nanoparticles due to their enhanced chemical resistance and dispersion stability. Thus the composites of iron oxide and polymer are recently introduced as dispersed particles for magnetorheological (MR) fluid, in which the MR fluid is a stable colloidal suspension composed of magnetic particles dispersed in a viscous or viscoelastic non-magnetic carrier fluid. MR fluids generally show rapid changes of rheological properties with external magnetic fields. The suspension becomes gel-like state under a magnetic field with enhanced both shear viscosity and viscoelastic characteristics.

In this work, the composite materials of poly(vinyl butyral) (PVB) and magnetite nanoparticles were prepared to be applied for MR fluid because of their proper magnetic characteristics and dispersion stability in a viscous medium. The composite was prepared via a solvent evaporation method using PVB and the synthesized magnetite nanoparticles, in which the magnetite nanoparticles were synthesized by a co-precipitation method using ferrous and ferric ionic aqueous solutions. Chemical and physical characteristics of the magnetite/polymer composite were investigated via various analysis methods. The MR characteristics of the composite particle suspensions were also investigated via a rotational rheometer by precisely controlling the magnetic field strength.

Experimental

The magnetite nanoparticles were prepared via a co-precipitation method with ferrous and ferric ionic aqueous solution using PAA as stabilizer. Both FeCl3 and FeSO4 were dissolved together in an aqueous medium. NH4OH was then added to the solution. After that, the PAA was added into the suspension and the mixture was stirred for 3h. In addition, PVB was dissolved in chloroform separately, and then the PVB mixture was added into the mixture of magnetite suspension. The mixture was stirred for 3days until the chloroform was completely evaporated. In order to examine their MR properties, the fabricated composite was dispersed in mineral oil.

Results and Discussion

Chemical structure of the synthesized PVB and magnetite nanoparticle composite was examined via an FT-IR, in which strong peak intensity of the iron oxide for the composite materials around 600 cm-1 was reduced compared to that for the pure iron oxide. The characteristic peaks for PVB were also observed for the composite with small shift due to the interaction and magnetic properties of particles. The composites were further confirmed by examining magnetic properties using VSM. Morphology and internal structure of the nanoparticle composite were also observed via SEM and TEM. Figure 1 shows TEM images of the fabricated composite particles which were sliced using an ultramicrotome. It was found that the magnetite nanoparticles were continuously dispersed in the PVB matrix. The particle size of the product was also determined to be 5~10 micron from the Fig. 1. MR fluids of magnetite-PVB hybrids dispersed in a mineral oil with a particle concentration of 25vol% were prepared and their steady shear properties under various magnetic fields were measured. Figure 2 shows increased shear stress for increased magnetic fields as a function of shear rate. As the magnetic field strength is increased, the yield shear stress of the MR fluid also increases, exhibiting typical MR effect.

[1] S. H. Sun, H. Zeng, D. B. Robinson, S. Raoux, P. M. Rice, S. X. Wang, G. X. Li, J. Am. Soc. Chem. M. S. Cabral, Biosens. Bioelectron. 126, 273 (2004).

[2] A. S. Lubbe, C. Bergemann, J. Brock, D. G. McClure, J. Magn. Magn. Mater. 194, 149 (1999).

[3] G. Bossis, P. Khuzir, S. Lacis, O. Volkova, J. Magn. Magn. Mater. 258–259, 456 (2003).

[4] S. T. Lim, M. S. Cho, I. B. Jang, H. J. Choi, J. Magn. Magn. Mater. 282, 170 (2004).

[5] S. T. Lim, M. S. Cho, I. B. Jang, H. J. Choi, M. S. Jhon, IEEE. Trans. Magn. 40, 3033 (2004).

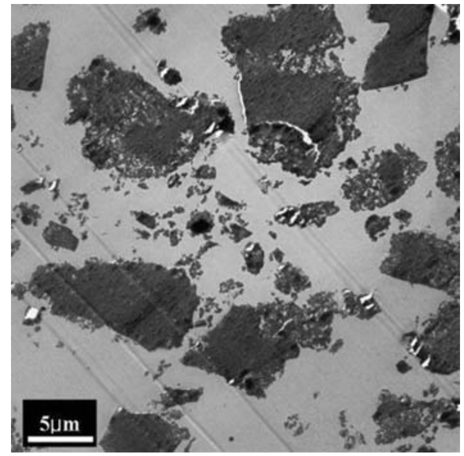

Fig.1 TEM image of PVB/magnetite composite nanoparticles

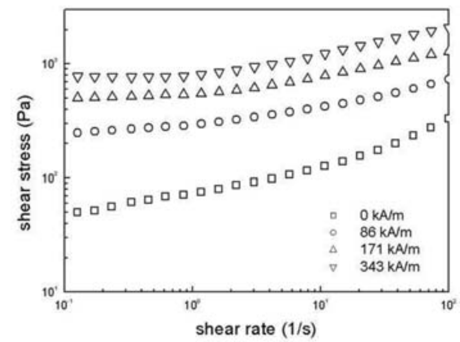

Fig.2 Shear Stress as function of shear rate for the composite based MR fluids

CQ-05

3D Magnetic Field Analysis by Homogenization Method for Thin Steel Plate of Magnetic Field.

K. Fujisaki[1,2], M. Fujikura[1], J. Mino[3], S. Satou[4]
1. Technical Development Bureau, Nippon Steel Corporation, Futtsu-city, Japan; 2. Graduate School of Environmetal Studies, Tohoku University, Sendai-city, Japan; 3. Nippon Steel Engineering Corporation, Tokyo, Japan; 4. N-Teck Ohita Corporation, Ohita, Japan

Introduction
Electrical thin steel plate is used for magnetic shielding in MRI coil as well as motor core [1], since it has a high permeability. To design and develop the shielding room, numerical calculation method is useful as well as experimental method. Usually shielding room has a size in a few [m] in length, though thin steel plate has a few [mm] in thickness. Since a large number of mesh divided in 3-dimensional space is necessary to calculate, shielding room calculation is almost impossible even by an up-to-date computer machine. Therefore, we propose a new calculation method so called equivalent B-H method, a kind of homogenization method, to reduce the number of calculation mesh, and to make clear the characteristics of magnetic shielding room. Especially in the equivalent B-H method, magnetic non-linear and isotropic characteristics which are important for the magnetizing materials are considered compared with the conventional homogenization method in magnetic field [2, 3].
Magnetic Shielding Room and Equivalent B-H method
A new type of magnetic shield room called open type has superior property such as high performance of shielding and transparent characteristics of shield room, which was invented by Kajima Corporation [4]. Since open type shielding room has a lot of thin steel plate, an equivalent element consisting of thin steel plate and air is considered as one mesh in numerical calculation, as shown in Fig.1. The open type magnetic shield room consists of inner shield (green color in Fig.1 (a)) and outer shield (red color in Fig.1 (a)).
From magnetic circuit theory in the equivalent element, equivalent permeability in each direction of equivalent element is expressed as the next equation (1). In the equivalent B-H method, magnetic characteristics of the equivalent element are directly introduced from electrical steel magnetic characteristics. Since several thousands of meshes in numerical calculation are necessary in the equivalent element, number of mesh extremely decreases. Since the permeability of the electrical steel and the one of the equivalent element are related analytically as in equation (1), the magnetic flux density in the electrical steel is introduced from the equivalent B-H calculation.
Analytical Evaluation
The equivalent B-H method is applied to the magnetic shield room, in which length is 5.8m, width is 3.3m, and height is 3.3m. The experimental leakage magnetic field distribution and the calculated one are almost same.
Since the exiting coil (MRI coil is simulated) is arranged in one-sided (A-side), the leakage magnetic flux density in A-side is larger than the one in C-side. The nearest position in side B and side D has also large leakage magnetic flux density.
The magnetic flux density in the shielding electrical steel is shown in Fig.3. The magnetic flux density in the A-sided electrical steel is larger than the one in the C-sided electrical steel. The nearest position in side B and side D of the electrical steel has also large magnetic flux density.

[1] K. Fujisaki, S. Satoh, IEEE Trans. on Magn,,Vol. 40, No.4, pp.1820–1825, (2004).

[2] H. Kaimori, A. Kameari and K. Fujiwara, IEEE Trans. Magn., vol.43, no.4, pp. 1405-1408, (2007).

[3] H. Waki, H. Igarashi, T. Honma, IEEE Trans. on Magn, Vol. 42, No.4, pp.847-850, (2006).

[4] T. Saito: JP 2002-164686A (2002).

$$\hat{\mu}_x = \frac{d\mu_e + (c-d)\mu_{air}}{c} \quad \hat{\mu}_y = \frac{d\mu_h + (c-d)\mu_{air}}{c} \quad \hat{\mu}_z = \mu_{air}$$

Here, μ_e、μ_h、μ_{air} is permeability of easy axis of electrical steel, hard axis of electrical steel and air respectively.

Equation (1).

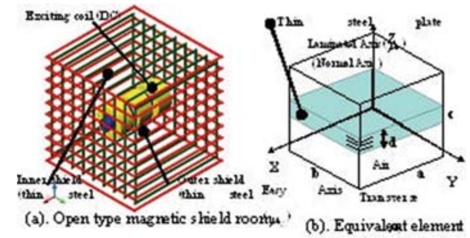

Fig.1. Equivalent element.

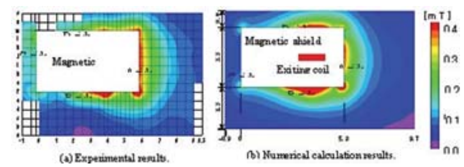

Fig.2. Leakage magnetic field in magnetic shield condition. (Center cross section of exciting coil)

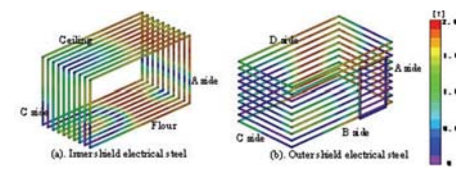

Fig. 3 Magnetic flux density distribution in shielding electrical steel.

CQ-06

Field Coil for Magneto-Optic Switching : Capacitance Considerations.

J. Tioh, M. Mina, R. Weber
Electrical and Computer Engineering, Iowa State University, Ames, IA

A tractable method for accurately predicting the parasitic capacitance of a field coil as part of an all-fiber Mach-Zehnder interferometric switch based on Faraday rotation is reported. The effects of the wire insulation layer, inter-turn air gap as well as capacitive coupling to the four nearest adjacent turns are considered in predicting the effective parasitic capacitance. The complex distributed capacitance network is resolved using Kron reduction to yield the equivalent shunt capacitance. Several coil configurations were designed and compared to experimental results. This new approach can be used in conjunction with existing expressions for inductance and loss to enable the complete and accurate a priori design of field generating coils.

The physical layer requirements of electro-optical as well as all optical networking were previously introduced [1] and a fiber-based switch based on the Mach-Zehnder interferometric configuration employing Faraday rotation was proposed to meet these requirements [2]. The switch has shown promising performance and interoptability with existing fiber networks, although the switching time could potentially be lowered to the order of several nanoseconds. Towards this end, detailed modeling and measurement of the coil impedance parameters have been performed in the process of investigating improved driver and coil configurations.

Attempts to realize field-generating elements inevitably results in at least two residual parameters - series resistance and shunt capacitance. Although the existence of this capacity is recognized, it is usually determined a posteriori, with design efforts concentrated on the inductance and loss parameters [3-4]. This paper presents an improved and tractable method for modeling the stray capacitance of field generating coils. The advantage of this approach (as compared to full numerical solutions of the electrostatic field equations) lies in the model simplicity, which affords simple and fast computations of the capacitance.

Winding dimensions of $\lambda/8$ or smaller are approximated as being electrically short. In following with the quasi-static assumption, the following expression (Figure 1) is developed for the turn-to-turn capacitance from one particular winding turn to any neighboring turn "k", where $|k| = 1$ is an adjacent turn :

The various capacitances form a distributed capacitance network (Figure 2) that can be expressed as an NxN admittance matrix, which gives the complete capacitive coupling between all nodes. This matrix is then reformed as a modified primitive impedance matrix and collapsed using Kron reduction [5] to yield the equivalent capacitance between the coil terminals.

Several test structures were fabricated using single-stranded copper wire and tested using an HP 8753C automated network analyzer. The predicted inductance values were calculated using the appropriate Wheeler formulas [6] with an inner coil diameter of 23mm. Good agreement between the predicted and measured parameters are obtained, generally within 8% (Figure 3). It is seen that the expression for the turn-to-turn capacitance is particularly accurate and the assumption of the electric field path to a turn's four nearest neighbors is reasonable. The equivalent capacitance tends to be underestimated as it does not account for fringing capacitance and coupling to nearby conductors on the test structure.

This paper proposes a tractable method for accurately predicting the parasitic capacitance of field generating coils. Six test coils were fabricated and tested. The predicted results are in agreement with the actual measured parameters, indicating the proposed method can be combined with existing inductance and loss parameter expressions for accurately predicting the circuit performance of field generating coils.

The research reported in this paper is partially supported by National Science Foundation grants 0087746, 0434872 and 0306007.

[1] J. Tioh, M. Mina, R.J. Weber, Magnetically Controlled Switches for Optoelectronics Networking: The Problem, Available Technology, New Implementations, IEEE. Trans. on Magnetics, Vol. 43, No. 6, 2698-2700, 2007.

[2] R. Bahuguna, M. Mina, R.J. Weber, Mach-Zehnder Interferometric Switch Utilizing Faraday Rotation, IEEE Trans. on Magnetics, Vol. 43, No. 10, 2680-2622, 2007.

[3] M. Bartoli, A. Reatti, M.K. Kazimierczuk, Modeling of iron-powder inductors at high frequencies, Proc. IEEE Industry Applications Conf., Denver, CO, 1994.

[4] M.K. Jutty, V. Swaminathan, M.K. Kazimierczuk, Frequency characteristics of ferrite core inductors, Proc. IEEE Electrical Manufacturing and Coil Winding Symp., Chicago, IL, 1993.

[5] G. Kron, Tensor Analysis of Networks, Wiley, New York, 1939.

[6] H.A. Wheeler, Simple Inductance Formulas for Radio Coils, Proc. I.R.E., 1398-1400, Oct. 1928.

$$C_{t_k} = 2\int_0^{\pi/2} \frac{\varepsilon_r \varepsilon_0 L (r_c + t)}{2(r_c+t)\left[\ln(1+t/r_c) + \varepsilon_r(1-\cos\theta)\right] + \varepsilon_r\left[|k|s + 2(|k|-1)(r_c+t)\right]} d\theta = A\tan^{-1}\left(\sqrt{\frac{B-C}{B+C}}\right)$$

$$A = \frac{4\varepsilon_r \varepsilon_0 L (r_c+t)}{\sqrt{B^2 - C^2}} \quad B = 2(r_c+t)\left[\ln(1+t/r_c) + \varepsilon_r\right] + \varepsilon_r\left[|k|s + 2(|k|-1)(r_c+t)\right] \quad C = -2\varepsilon_r(r_c+t)$$

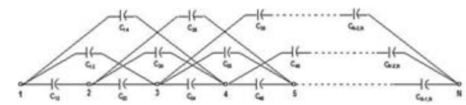

Coil	Predicted				Measured			
	C_{tt} (pF)	C_{eq} (pF)	L_{eq} (uH)	F_{res} (MHz)	C_{tt} (pF)	C_{eq} (pF)	L_{eq} (uH)	F_{res} (MHz)
1	10.60	1.882	1.317	101.08	11.03	2.006	1.519	91.18
2		0.642	5.778	82.63		0.690	6.632	74.40
3	11.79	2.053	1.802	82.75	11.89	2.027	1.923	80.61
4		0.699	9.317	62.37		0.741	10.415	57.29
5	11.61	2.028	2.101	77.12	11.27	1.998	2.155	76.70
6		0.691	12.199	54.82		0.724	12.893	52.09

Table 1 : Predicted and measured coil circuit parameters

CQ-07

Power loss measurement and prediction of soft magnetic powder composites magnetised under non-sinusoidal excitation.

P. Marketos[1], *J. P. Hall*[1], S. E. Zirka[2]

1. School of Engineering, Cardiff University, Cardiff, United Kingdom; 2. Department of Applied Physics and Technology, Dnepropetrovsk National University, Dnepropetrovsk, Ukraine

Introduction

This paper presents details of studies undertaken to measure the magnetic properties of soft magnetic powder cores and assess the applicability of a numerical modelling technique for the prediction of losses under a range of non-standard magnetisations. The modelling technique aims to allow prediction of magnetic properties under wide ranging conditions, including PWM magnetisation, based on obtaining limited information of the material's near-DC magnetic properties and electrical resistivity. This approach, based on a concept known as magnetic viscosity [1], offers significant advantages and has been shown previously to be accurate in its application with soft magnetic lamination materials.

Experimental Procedure and Results

Experiments were carried out on small toroidal powder cores, 45 mm inner diameter, 55 mm outer diameter, 5 mm core height and 29.21 g core weight, in order to measure their magnetic properties including power loss at frequencies ranging from 5 Hz to 200 Hz and different excitation waveforms. A computerised magnetic measurement system featuring digital feedback control [2] was used ensure that the shape of the excitation waveform was controlled at all times. Typical results under sinusoidal excitation are shown in figure 1.

Six BH loops, measured under 5 Hz sinusoidal excitation peak flux densities ranging from 0.5 - 1.5 T in steps of 0.2 T were used as inputs to the power loss prediction model in order to enable the prediction of loss under any excitation condition. The power loss Ploss of the toroid magnetised under sinusoidal excitation at 1.3 T, 50 Hz was also used as input to the model. Table 1 shows a comparison between measured and predicted Ploss values of the toroid magnetised under sinusoidal excitation for two different peak inductions 1.0 T and 1.5 T and three different frequencies 50, 100 and 200 Hz. Table 1 shows a very good agreement between measured and predicted Ploss values for the frequencies and flux densities tested.

Experiments were also carried out to assess the ability to measure and predict the Ploss of the powder core under non-standard, non-sinusoidal magnetisations. Figure 2 shows an example of such an excitation and the corresponding measured and predicted BH loops. The excitation was achieved by adding 30% of 7th harmonic component to a 50Hz sinusoidal excitation. The difference between measured and predicted Ploss was 2.2%.

Conclusions

Very good agreement was achieved between measured and predicted Ploss data for the range of frequencies and flux densities under test. The computerised measurement system was able to successfully magnetise the cores under different magnetisation conditions and under different frequencies and flux densities. The measurement system was able to measure and supply the input data required by the power loss prediction model which in turn was able to predict the losses of the powder core to within 2.5% of the measured values for all the excitation conditions under investigation.

Acknowledgement

This work was funded by the SPARK Award scheme of PowdermatriX Faraday, a node of the Materials Knowledge Transfer Network, which is a UK government Technology Strategy Board programme. The work was also supported by EPSRC Grant EP/C518616/1

[1] S.E. Zirka, Y.I. Moroz, P. Marketos, A.J. Moses, and D.C. Jiles,"Measurement and modeling of B-H loops and losses of high silicon non-oriented steels," IEEE Trans. Magn., vol. 42, no. 10, pp. 3177-3179,2006

[2] Zurek S., Marketos P., Meydan T. and Moses A. J., IEEE Trans. Mag., Vol. 41, NO. 11, Nov. 2005, pp. 4242-4249

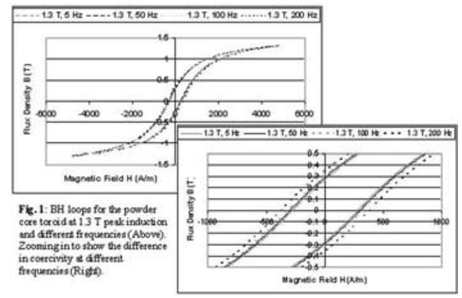

Fig. 1: BH loops for the powder core toroid at 1.3 T peak induction and different frequencies (Above). Zooming in to show the difference in coercivity at different frequencies (Right).

	Frequency (Hz)	P_{Loss} (J/m^3) measured	P_{Loss} (J/m^3) predicted	%difference
1.0 T	50	967.0	961.3	1.5
	100	1007.5	1017.5	1
	200	1127.3	1129.9	0.2
	Frequency (Hz)	P_{Loss} (J/m^3) measured	P_{Loss} (J/m^3) predicted	%difference
1.5 T	50	1856.0	1847.0	-0.5
	100	1989.6	1973.4	-0.8
	200	2257.5	2226.3	-1.4

Table 1. Measured and predicted values of Ploss under sinusoidal excitation.

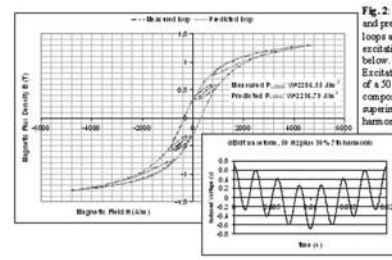

Fig. 2: Left: Measured and predicted BH-loops and P_{loss} for the excitation shown below. Below: Excitation comprising of a 50 Hz frequency component with a superimposed 30% 7th harmonic component.

CQ-08

Electromagnetic Wave Absorption Characteristics of Powder-Type Magnetic Wood Considering the Mixing Ratios of Two Types of Magnetic Powder.

H. Oka[1], Y. Yanagidate[1], H. Osada[1], K. Kubota[1], Y. Namizaki[2], F. P. Dawson[3]
1. Iwate University, Morioka, Japan; 2. Iwate Industrial Research Institute, Morioka, Japan; 3. University of Toronto, Toronto, ON, Canada

1.Introduction
The leakage of electromagnetic radiation or information security are of increasing concern given the increasing proliferation of wireless IT devices such as mobile phones, LAN and home robots. There is an increasing need to either to reduce the source of the unwanted radiation or to reduce its impact on the surrounding area. An electromagnetic wave absorber is one possible approach for solving such a problem. There are many approaches to absorbing radiation however in households it is important to use materials that preserve the ascetics. Moreover, it would be useful to use materials that reduce the carbon footprint. The use of powder-type magnetic wood is one such case in point. Powder-type magnetic wood retains the desirable wood and magnetic characteristics by combining waste wood and recycled magnetic materials. Because this composite material offers a woody texture and is very easy to process, the boards using this powder-type magnetic wood can be used as indoor electromagnetic wave absorbers[1]. In addition, the boards also offer moisture absorption characteristics and a diathermancy. Previously, we reported that a change in the mixing ratios of two types of magnetic powder can control the reflection loss of power-type magnetic wood. The purpose of this paper is to propose a method for calculating the material constants and estimating the reflection loss of a mix of two magnetic powders used to manufacture the magnetic wood from the individual material constants (complex permeability and complex permittivity) of the magnetic powder. Furthermore, the effect of moisture content on the reflection loss of the powder-type magnetic wood is reported.
2. Experiments and Calculations
Formulas <1>,<2> are the formulae for estimating the material constants from volume ratios of two types of magnetic powder.
$\varepsilon_{AB} = A\varepsilon_1/(A+B) + B\varepsilon_2/(A+B)$ <1>
$\mu_{AB} = A\mu_1/(A+B) + B\mu_2/(A+B)$ <2>
A : Mn-Zn powder volume ratio
B : Ni-Cu-Zn powder volume ratio
ε_1,μ_1 :material constants of powder-type magnetic wood using single Mn-Zn magnetic powder (A)
ε_2,μ_2 :material constants of powder-type magnetic wood using single Ni-Cu-Zn magnetic powder (B)
Table 1 shows the constitution of powder-type magnetic wood which is used for the experiments. Sample PMW indicates powder-type magnetic wood. Mn stands for simple Mn-Zn and Ni for simple Ni-Cu-Zn.
Fig.1 and 2 show experimental and calculated values of the reflection loss RL, respectively. The sample PMW-55 is used for the experiments and the Nicolson Ross method is used for the calculation. The thickness of the samples is 8mm and is associated with a center frequency of 2.45(GHz), which is the operating frequency of a microwave oven. The microwave oven is the strongest emitter of high frequency electromagnetic waves in our home.Table 2 shows calculated values of reflection loss characteristics.
3. Results
The simple calculation method to determine the material constants of powder-type magnetic wood is proposed. A two magnetic powder mixing type magnetic wood with zero moisture content shows the best reflection loss.
The results from our studies can be used to design powder-type indoor magnetic wave absorbers for their intended absorption frequency.

(1) H.Oka,H.Tokuta,et al: Effects of Humidity on the Magnetic and Woody Characteristics of Powder Type Magnetic Wood, J.Magn.Magn.Mat.,Vol.272-276, pp.1515-1517,(2004)

Samples	Mn:Ni Vol rate	Mn:Ni Vol%	Wood powder Vol%	Magnetic rate Vol%	Glue rate Vol%
PMW-Mn	10:0	30:0	54	30	16
PMW-73	7:3	21:9	54	30	16
PMW-55	5:5	15:15	54	30	16
PMW-37	3:7	9:21	54	30	16
PMW-Ni	0:10	0:31	54	30	16

		RLmax (dB)	Center frequency (GHz)	10dB over band (GHz)
PMW-55	Bone-dry	24.18	1.95	1.75
	RH20%	23.67	1.95	1.85
	RH50%	24.56	1.80	1.70
	RH80%	25.00	1.75	1.75

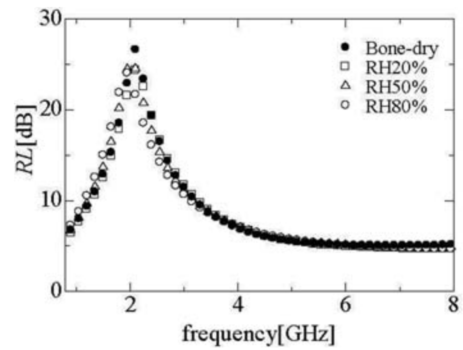

Fig.1 Experimental results of reflection loss characteristics of PMW-55 considering moisture content. RH:room humidity

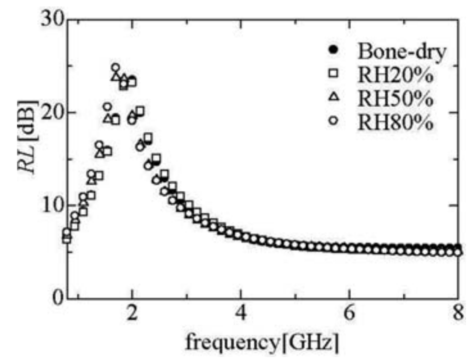

FIg.2 Calculated values of reflection loss characteristics of PMW-55 considering moisture content. RH: room humidity

CQ-09

Influence of asymmetry in stator geometry and magnetic circuit on cogging torque in PM brushless machines.

Z. Zhu, J. Chen, L. Wu, D. Howe
University of Sheffield, Sheffield, United Kingdom

Due to high efficiency and high torque density PM brushless machines are widely used in many applications, in which low torque ripple is often an important design consideration. However, PM machines with slotted stator have a common disadvantage that they exhibit cogging torque due to the interaction between PM mmf and airgap reluctance variation. As one of the sources of torque ripple, cogging torque should always be reduced as low as possible. Up to now, numerous methods have been proposed for analyzing and reducing the cogging torque. A comprehensive review may be found in [1]. However, existing analyses of cogging torque are based on the assumption of ideal design and perfect manufacture process [2]. But in practice, this may be not true, e.g. the outer surface of the stator may be not circular but exihibits asymmetries in the stator geometry, causing defects in the magnetic circuit of stator yoke and introducing high localized magnetic saturation. As a result, the amplitude and waveform of cogging torque may change significantly, as will be reported in this paper.

In this paper, the influence of asymmetry in stator geometry and/or magnetic circuit on cogging torque in PM brushless machines is investigated. The investigation is based on 6-pole, 18-slot machine having surface-mounted NdFeB magnet. The stator has flat-cuttings at both sides, one notch, and two diametrically opposite key-bar slots on the outer surface of the stator, its open-circuit equi-potential distribution being shown in Fig.1. The finite element predicted cogging torque waveforms with and without keybar-slots, notch, and flat-cuttings are shown in Fig.2. The influence of flat-cuttings and notch on the airgap field distribution and cogging torque is negligible. However, the deep keybar-slots cause significant changes in cogging torque, both amplitude and waveforms, Fig.2. The peak cogging torque is increased by approximately twice, while the waveform becomes non-periodic, as confirmed by experiment, Fig.3. For a 6-pole/18-slot PM machine, the least common multiple between the stator slots and rotor permanent magnets is 18. Hence the fundamental harmonic order of cogging torque waveform should also be 18 over 360 mech. deg., while its periodicity should be 360/18=20 deg. mech. Finite element analysis reveals that the maximum flux density in the stator yoke should be 1.4T if the keybar-slots do not exist. However, due to keybar-slots, the maximum localized flux densities in the stator yoke near the keybar-slots become as high as 2.3T, which is found to be responsible for the increase in amplitude and distortion in waveform of cogging torque. In this case, since there are 2 keybar-slots, their interaction (due to corresponding variation of permeance) with 6-pole rotor should produce a cogging torque component of order 6 over 360 deg. mech., i.e. its periodicity should be 360/6=60 deg. mech., since the least common multiple between 2 keybar-slots and 6-pole rotor is 6, as confirmed by both finite element analysis and measurement, Figs.2 & 3. Consequently, the resultant cogging torque waveform has a periodicity of 60 deg. mech. More finite element predicted and measured results when the machine is equipped with 1 or 2 magnets will be presented in full paper.

[1] Z. Q. Zhu, "Synthesis of cogging torque from a single stator slot in permanent magnet machines," IEEE Trans. Industry Applications, vol.42, no.3, pp.650-657, 2006.

[2] M. S. Islam, et al, "Issues in reducing the cogging torque of mass-produced permanent-magnet brushless DC motor," IEEE Trans. Industry Applications, vol. 40, no. 3, pp 813-820, 2004.

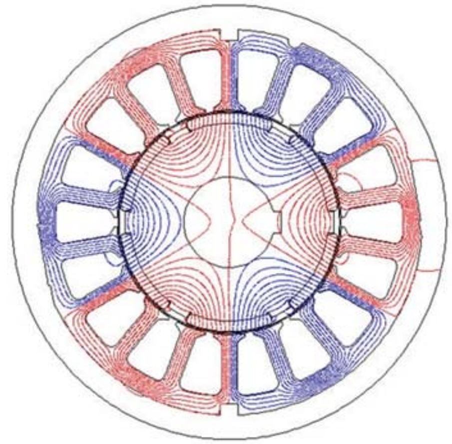

Fig. 1. Open-circuit equi-potential distributions with keybar-slots, notch, and flat-cuttings.

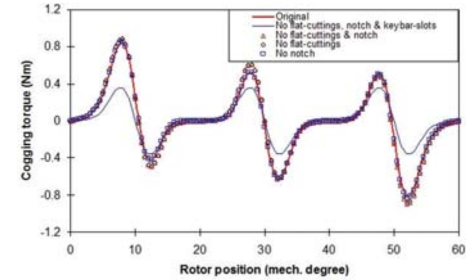

Fig. 2. Cogging torque with and without keybar-slots, notch, and flat-cuttings

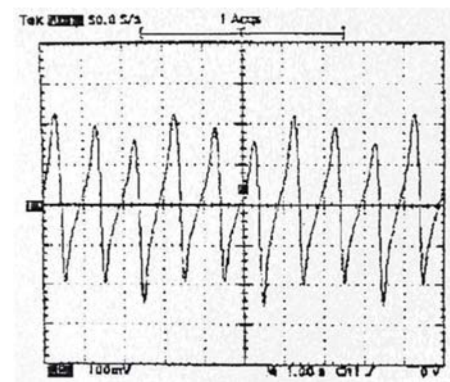

Fig. 3. Measured cogging torque with keybar-slots, notch, and flat-cuttings.

CQ-10

Electromagnetic modeling of a novel linear oscillating actuator.

Z. Zhu[1], X. Chen[1], D. Howe[1], S. Iwasaki[2]
1. University of Sheffield, Sheffield, United Kingdom; 2. IMRA UK Research Center, Brighton, United Kingdom

Linear oscillating actuators (LOAs) employing permanent magnets (PM) are being extensively exploited in industrial applications such as pumps, compressors and vibrators, because of their high efficiency and high power density. Of the various analysis methodologies, finite element method, both 2-D and 3-D, is widely used. An analytical model is proposed in [1] assuming the axial length of LOAs is infinite, and slotting and fringing effects being accounted for by introducing the Carter coefficient and repetitive models, while the magnetic saturation being considered only by introducing a fictitious air-gap. The lumped parameter magnetic circuit (LPMC) modeling is an attractive method to model the field leakage and non-linearity since it is essentially analytical method, but can account for the influence of magnetic saturation [2].
In this paper, axisymmetric finite element model, together with non-linear LPMC, is used to analyze the thrust force characteristics of a novel LOA. It is a tubular moving-magnet type actuator, Fig. 1(a), and consists of a Halbach array mover and two simple stator coils which are accommodated in the stator slots. The stator core may be laminated or employing soft magnetic composite (SMC) (In this paper, it is made of SMC due to its simplicity in manufacturing). In order to assess the merits of Halbach array mover, its electromagnetic performance is compared with that when axially magnetized magnet is removed, Fig. 1(b). The corresponding LPMC models are established, accounting for major flux components. It is worth to note that (1) for the Halbach array mover, each of radially magnetized magnet ring is required to be axially modelled by several parts, being 3 in the example, according to the relative axial position between the stator and the mover; subsequently (2) the central axially magnetized magnet ring is also subdivided radially into several parallel branches; and (3) the mover back-iron also provides the return flux path. Fig. 2 compares the per-turn flux-linkages versus mover axial displacement predicted by LPMC and finite element analysis for the prototype LOA, while Fig. 3 compares predicted and measured thrust force versus displacement for the prototype actuator with axially magnetized magnet in which the radially magnetized magnet ring consists of 8 sintered NdFeB magnets circumferentially. Good agreement is achieved. The full paper will discuss the predicted electromagnetic performance, e.g. thrust force, flux-linkage and back-EMF, by LPMC modeling and finite element analysis, the comparative study of LOAs with and without axially magnetized magnet and mover back-iron, as well as the design optimization.

[1] J. Wang, D. Howe, Z. Lin, "Comparative study of winding configurations of short-stroke, single phase tubular permanent magnet motor for refrigeration applications," Proc. of the 42nd IEEE IAS Annual Meeting (IAS'2007), pp. 311-318, Sep 2007, New Orleans, USA

[2] Z.Q. Zhu, Y. Pang, D. Howe, et al, "Analysis of electromagnetic performance of flux-switching permanent-magnet machines by nonlinear adaptive lumped parameter magnetic circuit model," IEEE Trans. on Magnetics, vol. 41, no. 11, pp. 4277-4287, Nov. 2005.

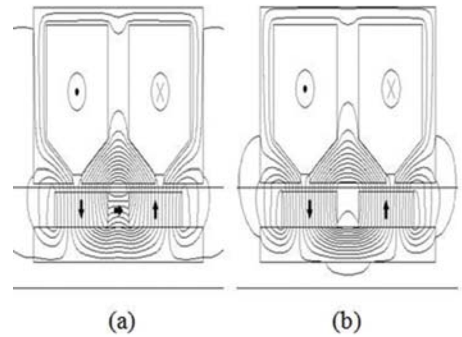

Fig. 1 Schematic tubular LOA. (a) with (b) without axially magnetized magnet

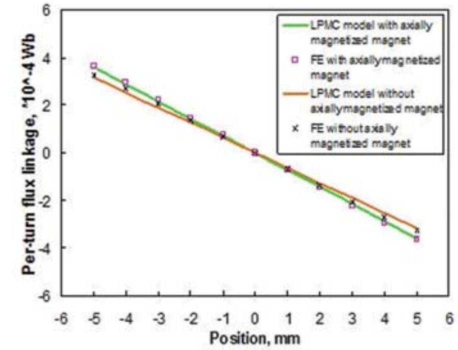

Fig. 2 Variations of per-turn flux-linkage with displacement with/without axially magnetized magnet

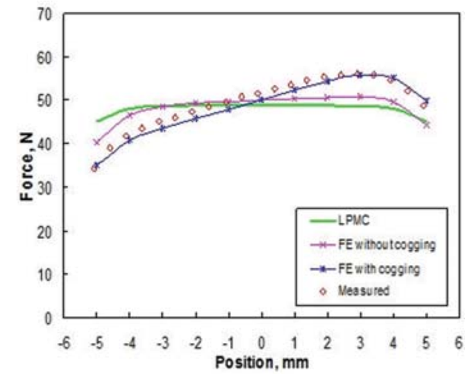

Fig. 3 Comparison of predicted and measured thrust force characteristics

CQ-11

Non-oriented electrical steel and magnetostriction: a review.

A. M. Severino
Departamento de Física - CCNE, Universidade Federal de Santa Maria, Santa Maria, Brazil

The magnetostriction of non-oriented electrical steels is receiving increasing attention because the need to reduce acoustic noise in many types of magnetic cores. In a magnetic material, the inter-atomic distances can vary with the intensity and the orientation of magnetization. With the study of magnetization processes it is possible to improve the magnetic properties of the steels, reducing the magnetic losses and, consequently, induce the rational use of electric energy. The idea is decrease the mechanical noise and the mechanical vibration in devices based on these materials. At the same time the growing development of technologies involving the miniaturization of magnetic materials, producing them in nano-dimensions and subjecting them to the presence of high magnetic fields induced, in the last years, an increment in the research of magnetoelastic effects in general [1].

In this work we will expand previous explanation about models for description of the magnetization mechanisms related to the variation of magnetostriction in electric steels. A nonlinear constitutive model was recently proposed for magnetostrictive materials by Liu and Zheng [2]. It is based in the fact that a nonlinear part of the elastic strain produced by a pre-stress is related to the magnetic domain rotation or movement and is responsible also for the change of the maximum magnetostrictive strain with the pre-stress.

This nonlinear model was used to compare some recent results obtained by Bohn et al. [3]. These results have shown that the reduction in magnetostriction at high frequencies would have important implications in the analysis and prediction of electrical machine noise. The magnetostriction results are also correlated results of Barkhausen noise and magnetic losses measured in the same sheets. Some of the models for magnetic losses uses the usual separation among component of losses in low induction, related to the movements of walls of magnetic domains and component of losses in high induction, associated the rotation of the magnetization. Though, experimental results shown that in general the component of high induction represents a larger amount than are predicted by the models. The magnetostriction results obtained by Bohn et al shows that the motion of 90 degrees domain walls and magnetization rotation occur at high magnetic induction region. So it is reasonable to associate the motion do domain walls to the process of nucleation, growth and annihilation of magnetic domains or, in other words, to the evaluation of the magnetic domain structure at high induction levels.

We also verified that not just there is a few number of experimental results in the literature for magnetostriction in steels but there is some controversy to explain its mechanisms. With this work we intended to demonstrate that the experimental determination of the magnetostriction, its confrontation with simulations obtained from analytic models and the correct understanding of the magnetization mechanisms are very important to design materials to new applications in the electrical steel industry.

[1] T.P.P. Phway and A.J. Moses, Journal of Magnetism and Magnetic Materials 316 (2007) 468-471

[2] X. Liu and X. Zheng, Acta Mech Sinica 21 (2005) 278-285

[3] F. Bohn, A. Gündel, F.J.G. Landgraf, A.M. Severino and R.L. Sommer, Journal of Magnetism and Magnetic Materials 317 (2007) 20-28

CQ-12

Optimization of Design Parameters for Ferrite Inductor for 10 MHz On-chip Power Module.

S. Bae[1,2], Y. Hong[1,2], J. Lee[1,2], J. Jalli[1,2], G. S. Abo[1,2], A. Lyle[1,2], H. Han[1,2], G. W. Donohoe[3]
1. Department of Electrical and Computer Engineering, University of Alabama, Tuscaloosa, AL; 2. MINT Center, University of Alabama, Tuscaloosa, AL; 3. Department of Electrical and Computer Engineering, University of Idaho, Moscow, ID

Introduction

Base-band processor voltage becomes lower to avoid overheat. Consequently, current needs to increase up to several amperes in smart phone. In order to achieve small ripple voltage, integrated and miniaturized on-chip power module has been intensively studied. On the other hand, an increase in switching frequency decreases L (inductance) and C (capacitance) in the power circuit, resulting in size reduction and integration of passive components. The switching frequency of commercial dc-dc converter has already been increased up to 5 MHz [1] and higher frequency [2,3]. A high Q inductor is an essential component for a high efficiency dc-dc converter. Therefore, a dc-dc converter with an air core chip inductor was proposed[3,4] to achieve high Q at high frequency. However, the air-core inductor Q is still below 20 in the 10 ~ 100 MHz range.

In this work, we report a design of ferrite planar inductor, which has Q over 50 at 10 ~ 100 MHz, for use in a 1 ~ 2 W buck type dc-dc converter module having 0.25 V and 5 A output. We used DOE (Design of Experiment) method to optimize copper coil, coil shape, ferrite film, thickness, and permeability.

Optimization of design parameters

In DOE process, input X's are Cu line space (2 ~ 500 µm), Cu line thickness (50 ~ 100 µm), ferrite thickness (2 ~ 500 µm), and permeability of ferrite (µ; 2 ~ 1000), and its response Y's are L (Inductance) at 10 MHz, Q at 10 MHz, and fr (Resonance Frequency). The copper line thickness is 50 µm which is 2 x the skin depth of copper at 10 MHz. Our proposed spiral inductor's coil area with 2.5 turns is 5 x 5 mm to meet the critical inductance of 125 ~ 30 nH at 10 ~ 100 MHz [5]. Cross sectional coil area is designed over 25,000 µm2 to withstand joule heating by maximum 5 A rated current [6,7]. Therefore, the coil width is fixed at 500 µm. Total, a 25 kind of test conditions is designed for a 4 X's, 3 level and 3 Y's DOE. Each Y is obtained by Ansoft HFSS simulation software.

Results and discussion

The weight of X's on the Y's is shown in Fig. 1. It is found that the most effective X for L is µ, X for Q is square of ferrite thickness, and X for fr is spacing of Cu lines. Correspondence of each X's to Y's is represented by contour plots in Fig. 2. From this optimizations, it is found that ferrite film and permeability need 100 ~ 300 µm thickness and high value, respectively, to achive high Q greater than 100.

The regression equations are given in Table I. These equations were derived as a result of DOE performance. From this, Y's of L is 125 nH, Q is 197.5 and fr is 316.3 MHz. These values are calculated from X's of A 127 µm, B 67.8 µm, C 130.3 µm 3 and D 156.5. Actually, there are some difficulties to fabricate 130.3 µm thick ferrite film below 400 °C. However, it is possible to select C of sputter deposited 3 µm of ferrite film to obtain Y's of L (66.1 nH), Q (74.6), fr (632.4 MHz) for X's of A (spacing of 210 µm), B (copper thickness of 64 µm), C (ferrite thickness of 3 µm), and D (permeability of 200). Deviations of the equations are found to be -9.1% in L, 2.8% in Q and 4.1% in fr. Therefore, there are confidence levels of roughly over 90% for L and 95% for Q and fr. However, loss tan δ = 0 is assumed in all the above estimations. Q will be decreased to 50% at loss tan δ = 0.01 and to 70% at 0.02.

In conclusion, we have successfully designed 5 mm x 5 mm high Q ferrite inductor which has above 50 of Q at 10 MHz. The following parameters are recommended to design the above high Q and high current ferrite inductor: 2.5 turns, copper thickness > 64 µm, copper width = 500 µm, loss tan δ of ferrite < 0.02, permeability > 157, and ferrite thickness > 3 µm.

[1] http://www.enpirion.com/Productdetails.aspx?pid=7

[2] Hazucha, et al., Solid-State Circuits, IEEE Journal of Volume 42, Issue 1, Jan. 2007 Page(s):66 - 73

[3] Hazucha, et al., Solid-State Circuits, IEEE Journal of Volume 40, Issue 4, April 2005 Page(s):838 - 845

[4] Schrom, et al., Applied Power Electronics Conf., APEC 2007 - Twenty Second Annual IEEE Feb. 25 2007-March 1 2007 Page(s):727 - 730

[5] P-L. Wong, et al., IEEE Trans. On Power Elec., Vol. 17, pp. 485-492, Jul. 2002

[6] I. Kowase, et al., IEEE Trans. On Mag., Vol. 41, pp. 3991-3993, Oct. 2005

[7] S. Prabhakaran, et al., 35th IEEE Power Electronics Specialists Conf., Vol. 6, pp. 4467-4472, 2004

	Uncoded Regression Equation	R^2
L at 10 MHz [nH]	= 13.293 + 0.09878A + 0.65555B + 0.53978C + 0.11109D - 0.0000426AB - 0.0000812AC + 0.0000558AD - 0.0001863BC - 0.0002656BD - 0.0001676CD + 0.0000008ABC + 0.0000005ABD + 0.0000023ACD + 0.0000121BCD - 0.0002668A^2 - 0.00487B^2 - 0.00101C^2 - 0.0000524D^2	0.9854
Q factor at 10 MHz	= -733.47 + 0.11895A + 21.957B + 1.216C - 0.17608D + 0.0005252AB - 0.0000352AC + 0.0000288AD - 0.0004287BC - 0.000311BD - 0.0000449CD - 0.0000008ABC + 0.0000018ABD - 0.0000017ACD + 0.0000027BCD - 0.0003453A^2 - 0.14519B^2 - 0.0023C^2 + 0.0002533D^2	0.7175
fr [MHz]	= -66.78 + 3.198A + 7.774B - 1.259C - 0.50797D - 0.00173AC - 0.00151AD + 0.0004264BD + 0.0000022ABC + 0.0000042ABD - 0.0000017BCD - 0.00214A^2 - 0.06075B^2 + 0.00252C^2 + 0.0004861D^2	0.9687

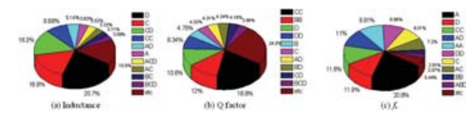

Fig. 1. Pie charts about weight of X's for Y's (L, Q factor and fr) ; A: Line space [µm], B: Cu thickness [µm], C: Ferrite thickness [µm], D: Permeability

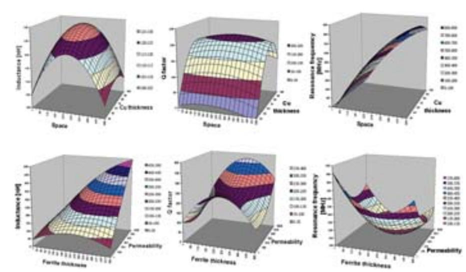

Fig.2. Effects of 4 X's on the 3Y's

CR-01

Magnetic properties of cobalt ferrite nanoparticles obtained by non-aqueous synthesis.

C. Vázquez-Vázquez[1], C. Mateo-Mateo[1], M. Buján-Núñez[1], M. López-Quintela[1], D. Serantes[2], D. Baldomir[2], J. Rivas[2]
1. Facultad de Química. Departamento de Química Física, Universidad de Santiago de Compostela, Santiago de Compostela, Spain; 2. Facultad de Física. Departamento de Física Aplicada, Universidad de Santiago de Compostela, Santiago de Compostela, Spain

Cobalt ferrite (CoFe2O4) nanoparticles were obtained by a non-aqueous procedure using acetophenone as reaction medium [1]. The particle size (determined by transmission electron microscopy) was tuned from 2 to 15 nm by changing the synthesis temperature from 120 to 200 C. These nanoparticles show a superparamagnetic behaviour. From the zero-field-cooling (ZFC) measurements at 100 Oe, it is observed an increase of the blocking temperature from 215 K to above 325 K with increasing particle size (Figure 1).
From the initial magnetization curves up to 50 kOe at 5 K it is observed that the saturation magnetization increases with the particle size. Additionally, the initial magnetization curves were measured at different temperatures from 5 to 320 K in order to determine the temperature dependence of the saturation magnetization and the anisotropy constant by means of the law of approach to saturation [2]. A decrease with temperature is observed for both properties; however, these changes are more important for the smaller nanoparticles compared to the larger ones (Figures 2 and 3). A large decrease of the saturation magnetization and the anisotropy constant is observed at low temperatures (below ~100 K), being more important for the smaller particles. This behaviour is related to the large surface/volume ratio observed for nanocrystalline particles and the larger amount of surface spins at smaller sizes [3]. Above this temperature, the decrease is less marked. For the smaller particles, an increase of the saturation magnetization and the anisotropy constant is observed around 150 K.
In order to get more insights about the magnetic behaviour, the isothermal magnetization curves as a function of the applied magnetic field were measured for both small and large particles (Figure 4). A large difference is observed at low temperatures (below ~100 K) compared to temperatures close and above the blocking temperature. It is possible to observe the different magnetic behaviour of the surface and core magnetic moments. The curves show a larger hysteresis at intermediate magnetic fields compared to the low-range ones. When approaching the blocking temperature, the hysteresis is reduced and finally disappears.
The magnetocaloric effect shown by these cobalt ferrite nanoparticles is reasonably high for nanomaterials.

[1] C. Vázquez-Vázquez, and M. A. López-Quintela, J. Solid State. Chem. 129, 3229 (2006).

[2] A. H. Morrish, The Physical Properties of Magnetism (Wiley, New York, 1965), 394.

[3] R. Aquino, J. Depeyrot, M. H. Sousa, F. A. Tourinho, E. Dubois, and R. Perzynski, Phys. Rev. B 72, 184435 (2005).

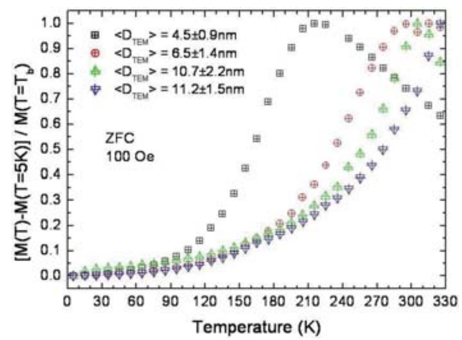

Figure 1. Zero-field-cooling (ZFC) magnetization curves as a function of the average particle size.

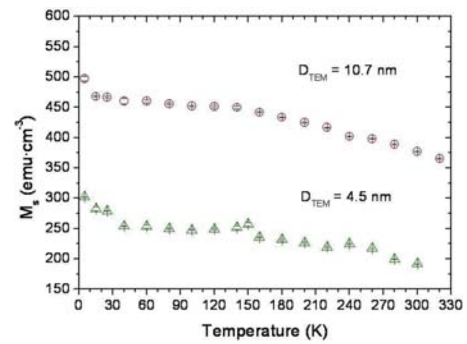

Figure 2. Temperature dependence of the saturation magnetization for cobalt ferrite nanoparticles.

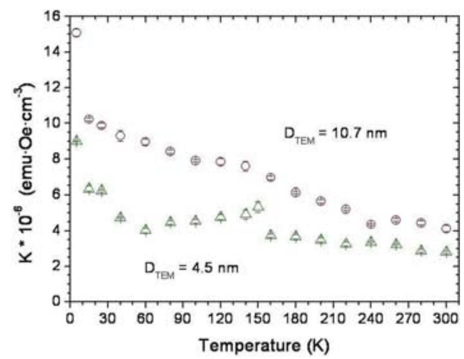

Figure 3. Temperature dependence of the anisotropy constant for cobalt ferrite nanoparticles.

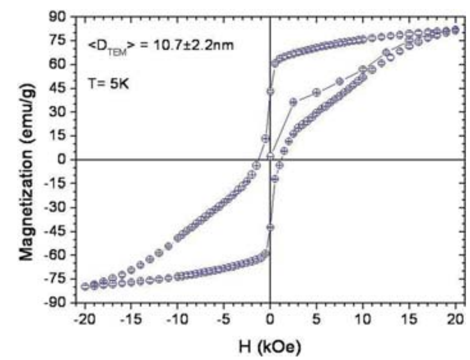

Figure 4. Magnetization curve at 5K as a function of the applied magnetic field for the 10.7nm-size sample.

Magnetic Properties of Nano-composite Particles of FePt/FeRh.

Y. Hnin[1], S. Inoue[1], N. T. Nam[1], T. Suzuki[1], Y. Hirotsu[2]
1. Information Storage Materials Laboratory, Toyota Technological Institute, Nagoya, Japan; 2. The Institute of Scientific and Industrial Research, Osaka University, Osaka, Japan

Magnetic nanoparticles has been attracting much interest for their fundamental properties and and also device applications [1]. A order b.c.c alloy FeRh undergoes a first-order phase transition from antiferromagnetic, AFM to ferromagnetic, FM state at around 100°C [2]. Using the temperature-dependent magnetic behaviour, an exchange coupled FePt/FeRh has been the subject for potential application to high-density magnetic recording media. Although the experimental and theoretical works are reported on the FePt/FeRh thin film system, the magnetic behaviours in the composite nano-particles of FePt/FeRh have not been found in literature. This study is carried out to understand the magnetic and structural properties on nanoparticles of FePt, FeRh and their composites.
Nanoparticles of FePt were synthesized by co-reduction of Iron (II) chloride tetrahydrate and Platinum acetylacetonate by super-hydride in the presence of oleic acid, oleylamine, 1,2-hexadecanediol and phenyl ether under the N2 atmosphere . In the case of FeRh particles, Rhodium (III) acetylacetonate was used as source material [3]. For the preparation of nano-composite FePt/FeRh, the solutions of pre-prepared FePt and FeRh were mixed simultaneously and stirred for a few hrs. The obtained solution was used as a source solution. Post-annealing of samples was carried out in the vacuum < 5×10-3 Pa. The structural properties were investigated with TEM, XRD (Cu Kα), and EDX. Magnetic properties were measured by VSM in fiels up to 15 kOe.
Figure 1 shows the x-ray diffraction patterns for the nano-particles of (a) as-deposited and annealed states (600°C-1h) of Fe64Pt34, (b) as-deposited and annealed states (600°C-6h) of Fe39Rh61, and (c) annealed state (600°C-6h) Fe64Pt34/Fe39Rh64, respectively. As-deposited nanoparticles of Fe64Pt36 show the fcc structure of (111) and (200) diffraction peaks. The ordered fct structure is observed in the annealed state showing the super lattice peaks of (001), (110), (311). For as-deposited Fe39Rh61 particles, a broad peak around 2θ=42° is observed, showing a characteristic of the disordered fcc structure of FeRh (111)γ phase. The annealed Fe39Rh61 particles exhibit a peak at around 2θ=43°, implying the coexisting of (111)γ and (110)α phases. Annealed nano-composites of Fe64Pt34/Fe39Rh61 show a broad peak at around 2θ=42°, it may be possibly due to the coexisting of FePt (111) and FeRh (110) peaks. Figure 1(d-e) show TEM images of nano-composite Fe64Pt36/Fe39Rh61 for (a) as-deposited and (b) annealed (600°C-6h) states, respectively. The uniform distribution of particles with a size of 3 nm is observed in the as-deposited state. However, single (about 3nm) and agglomerated (about 50 nm) particles are co-distributed in the annealed state. Figure 2(a) shows M-T curves for nano-composite of Fe64Pt36/Fe39Rh61 annealed at 600°C for 6 hrs under the applied filed 15 kOe during heating and cooling processes. The samples were cooled down from room temperature to -196 °C without the presence of an applied field. After that, measurements were carried out under the applied field. In the heating process, the magnetization decreases from -196 to 250°C showing ferromagnetic behaviour. In the cooling process, it exhibits a small increase with decreasing of temperature. Figure 2(b) shows the temperature dependences of coercivity, Hc and exchange bias field, HE on field cooling process for the nano-composite of Fe64Pt36/Fe39Rh61 annealed at 600°C for 6 hrs under the applied field. A significant decrease in Hc at around 30°C is observed with increasing temperature. This decrease is due to a strong exchange coupling between Ferro (FePt) and Anti-ferro (FeRh) phases. A unidirectional anisotropy constant, JK at T= -196°C is estimated to be 0.08-0.2 erg/cm2.

[1] T. Suzuki, Z. Zhang, A. K. Singh, J. Yin, A. Permal, and H. Osawa, IEEE Trans. Magn. 41(2005) 555.

[2] M. Fallot, Ann. Phys. 10, 291 (1938).

[3] H. Y. Y. Ko and T. Suzuki, IEEE Trans. Mag. 43 (2007) 885.

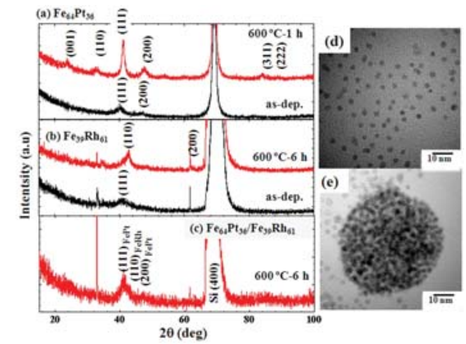

Fig. 1. XRD patterns for nanoparticles of (a) Fe64Pt36, (b) Fe39Rh61 (c) Fe64Pt36/Fe39Rh61 with as-deposited and annealed states, and TEM images for nano-composite of Fe64Pt36/Fe39Rh61 with (d) as-deposited and (e) annealed at 600°C for 6 hrs, respectively.

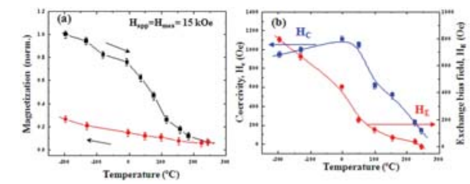

Fig. 2 (a) M-T curves for nano-composite of Fe64Pt36/Fe39Rh61 annealed at 600°C for 6 hrs under the field of 15 kOe during heating and cooling processes, (b) temperature dependences of Hc and HE on field cooling process, respectively.

CR-03

Synergic application of albumin nanoparticles: combination of Photodynamic Therapy with Cellular Hyperthermia.

M. M. Andrade Rodrigues[1], A. R. Simioni[1], F. L. Primo[2,1], M. P. Siqueira-Moura[2], Z. G. Lacava[3], P. C. Morais[4], *A. C. Tedesco*[1]
1. Departamento de Química, Grupo de Fotobiologia e Fotomedicina, Faculdade de Filosofia, Ciências e Letras de Ribeirão Preto, Universidade de São Paulo, 14040-901, Brazil, Ribeirão Preto, Brazil; 2. Faculdade de Ciências Farmacêuticas de Ribeirão Preto, Universidade de São Paulo, Ribeirão Preto-SP, 14040-903, Brazil, Ribeirão Preto, Brazil; 3. Universidade de Brasília, Instituto de Ciências Biológicas, Brasília DF 70910-900, Brazil, Ribeirão Preto, Brazil; 4. Universidade de Brasília, Instituto de Física, Núcleo de Física Aplicada, Brasília DF 70910-900, Brazil, Ribeirão Preto, Brazil

In this work, has been developed a new nano-drug delivery system (NDDS) associating biocompatible ionic magnetic fluid (MF) with a phthalocyanine drug (NzPc) in nanoparticles of bovine serum albumin (BSA). The samples were evaluated for synergic application that combines Photodynamic Therapy (PDT) with Hyperthermia [1]. The NzPc is a second generation of photoactive agents used in PDT that it is preferentially accumulated in the target tumor cells. Biocompatible magnetic fluids have been pointed out as a very promising nanosized-based magnetic material, applicable for tumor therapy. Considering that serum protein are by far the most abundant protein in blood vessels, as well as, they are extremely useful
as model systems for investigation processes, albumin-based beads were prepared containing or not maghemite nanoparticle associated with the NzPc according to the method of heat denaturation using mechanical stirring process at high-speed from an ultraturrax setup to optimize the preparation of the nanoparticles. The entrapped material, in this case NzPc and/or MF, was initially dispersed in the albumin aqueous phase after that the solution is added in a boiling flask containing sunflower oil and Span 80 with continuous stirring using ultraturrax at room temperature. Then, the mixture was emulsified by ultrasound at 150 W at room temperature through an ultra-sound device. In another boiling flask with mineral oil containing Span 80 was pre-heated under continuous agitation. The initial emulsion obtained as described above it was gently dropped directly to the preheated oil in the boiling flask with continuous agitation in a total time of 30 minutes. The final suspension was cooled down at room temperature under magnetic stirring. The obtained nanoparticles were washed with ethyl ether for oil separation, following centrifugation at 10.000 rpm for 30 minutes. After washing the “pellet” containing the nanoparticles were lyophilizated to remove any remaining water trace [2]. The morphology of the all particles (NzPc, MF and the complex NzPc/MF) was examined by scanning electron microscopy showed a spherical shape with average size of the 320 nm (Figure 1). The albumin-nanoparticles also were characterized for Zeta potential by photo-correlation spectroscopic from light scattering techniques. The Zeta potential was calculated from the electrophoretic mobility using the Smoluchowski equation. The time resolved analyses was obtained for the systems studied. The magnitude of the Zeta potential indicate the physico-chemical stability of the system. The Zeta potential of the particles was of -22.3 mV for NzPc, -22.6 mV for MF and of -24.0 mV for NzPc/MF. The fluorescence lifetime of the sample of NzPc/MF presented monoexponential decay of 4.78 ns with population of 100% and for sample of NzPc presented biexponential decay of 5.19 ns and 1.99 ns with population of 63.9% and 36.1%, respectively. It was evaluate the kinetic release of NzPC in human plasma serum from a comparative study between the nanoparticles associated to the NzPc and the nanoparticles associated to the complex NzPc/MF. It was observed that the albumin nanoparticles entrapped with of NzPc present a release profile showing small initial burst compared in the albumin nanoparticles entrapped with the complex NzPc/MF, both reaching the maximum at 1 h.

[1] D.M. Oliveira, P.P. Macaroff, K.F. Ribeiro, Z.G.M. Lacava, R.B. Azevedo, E.C.D. Lima, P.C. Morais, A.C. Tedesco J. Magn. Magn. Mater. 289 (2005) 476.

[2] A.R. Simioni, O.P. Martins, Z.G.M. Lacava, R.B. Azevedo, E.C.D. Lima, B.M. Lacava, P.C. Morais, A.C. Tedesco J. Nanosci. Nanotechnol. 6 (2006) 2413.

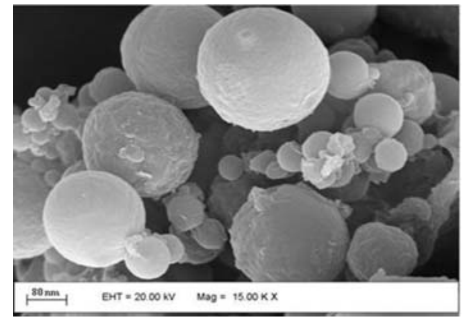

Fig.1: Scanning electron microscopy of the albumin-based nano-sized DDS loaded with ionic fluid

CR-04

Synthesis of Ni nanoparticles by dc magnetron sputtering.

H. Cui, *M. Sanz*, M. Maicas, C. Aroca
ISOM, Universidad Politécnica de Madrid, Madrid, Spain

Magnetic materials have been used with grain sizes down to the nanoscale for longer than any other type of material. The biomedical applications cover from magnetic separation of specific biological entities from their native environment to drug delivery, hyperthermia treatments or MRI contrast enhancement [1]. There are many synthesis methods depending on the final applications of the magnetic nanoparticles [2]. Sputtering methods are less extensively used, maybe due to the low efficiency of the process, however these methods have the advantage of a good control on the composition and size of the particles. Some works have already been done on Fe [3] and FeCo alloys [4]. In this work we apply the dc magnetron sputtering technique to the growth of Ni nanoparticles. Inert gas pressure and substrate temperature are the main parameters that control the morphology of the aggregates. High pressure promotes collisions in the gas phase and so the aggregation of atoms into particles while low temperature in the substrate reduces the tendency of joining those particles to become a continuous film. Figure 1 shows SEM images observed under direct sputtering using Ar as inert gas, Silicon substrates at 100K and a power discharge of 40 W. Results show how the porosity of the film increases with the Ar pressure. However, even for the highest pressures used and the low substrate temperature, isolated particles are not obtained but a dark porous film is grown instead. Similar results have been obtained for other temperature and power conditions. Figure 2 shows the early stages of the growing films at PAr=0.1 mbar. Ni nanoparticles with an average size of 4nm are found but they aggregate to make a film. Figure 3 shows the VSM magnetic response of the films. It is observed a decrease in both saturating and coercive fields with the increasing pressure.

A particle gun configuration avoids the mechanism of thin film growing and promotes further aggregation. Figure 4 shows a SEM image of a sample grown using a particle gun configuration like that described in [3]. The growing power was 40w, Ar pressure out of the chamber was 0.1 mbar and the substrate was at room temperature. The particle gun was placed at nearly 10mm of the substrate and had a pipe with a diameter of 1 mm and a length of 5 mm. Clear isolated particles were obtained. In figure 5 it is shown a high resolution SEM image that reveals the particles morphology in more detail. Their size is about 150 nm and some of them appear as aggregates of smaller particles (a), while others look like small crystals (b). No cooling was applied to the chamber during the growing so the increase in the temperature of the chamber at the end of the growing appears high enough to make some particles have a crystal structure.

In summary, nickel nanoparticles of a few nanometers can be obtained by dc sputtering growing at Ar inert gas pressures over 0.1 mbar. Those nanoparticles grow as a porous film even at Nitrogen cooled substrates. A particle gun configuration allows the growing of well isolated nanoparticles at room temperature substrates and can reach diameters over 100 nm.

[1] Q A Pankhurst, J Connolly, S K Jones and J Dobson. J. Phys. D: Appl. Phys. 36 (2003) R167–R181

[2] P. Tartaj, M. P. Morales, S. Veintemillas-Verdaguer, T. González-Carreño and C. J. Serna. J. Phys. D: Appl. Phys. 36 (2003) R182–R197

[3] P. Shah, A. Gavrin, J. Mag. Mag. Mat 301 (2006) 118

[4] Y. Hao, J. Bai, J.P. Wang, J. Mag. Mag. Mat. 311 (2007) 131

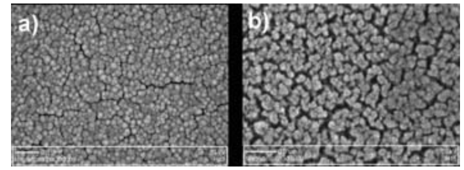

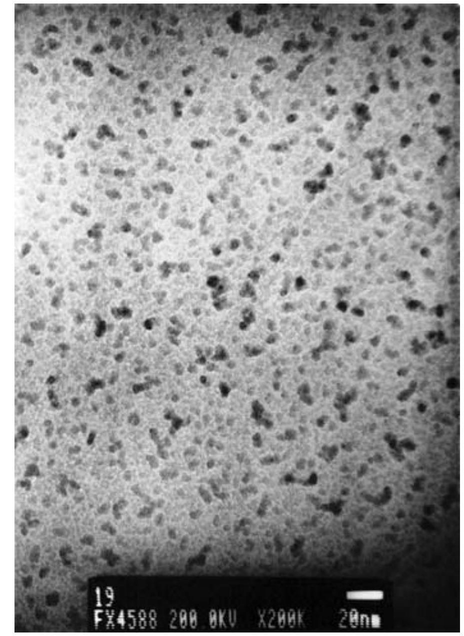

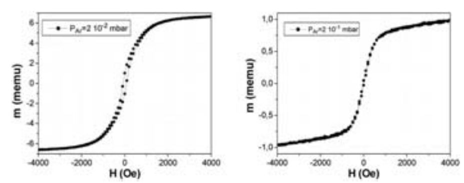

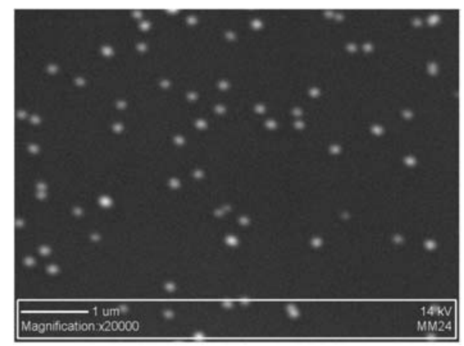

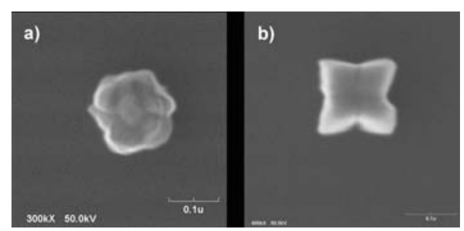

CR-05

Influence of the Si substrate on the transport and magnetotransport properties of nanostructured FeAg thin films.

J. Alonso[1], M. Fdez-Gubieda[1], J. Barandiarán[1], J. Chaboy[3], L. Fernández Barquín[4], I. Orue[2], A. Svalov[1], N. Kawamura[5]

1. Electricidad y Electrónica, Universidad del País Vasco, Bilbao, Spain; 2. SGIKER, Servicios Generales de medidas magnéticas, Universidad del País Vasco, Bilbao, Spain; 3. Instituto de Ciencia de Materiales de Aragón, CSIC-Universidad de Zaragoza, Zaragoza, Spain; 4. CITIMAC, Universidad de Cantabria, Santander, Spain; 5. Japan Synchrotron Radiation Research Institute, Kouto, Japan

In the last years, carrier transport mechanisms in magnetic thin films have been of great interest because of their applications in magnetic memories, spintronics, etc. In this context, metal/semiconductor structures play a fundamental role, and it is therefore essential to understand the influence of the substrate on the transport and magnetotransport properties of these magnetic thin films. We have prepared Fe_xAg_{1-x} thin films, with compositions in the range $0.3 \le x \le 0.85$, by sputtering and pulsed laser deposition (PLD) techniques. They were deposited simultaneously at room temperature onto a low resistivity (ρ~0.015 ohm-cm) 200 µm thick Si(100) substrate and a high resistivity (ρ~7-25 ohm-cm) 380 µm thick Si(100) substrate, both with native oxide layers (from now on, we will refer to them as Si1 and Si2, respectively). All the samples deposited onto Si1 present an anomalous thermal evolution of the resistivity, showing a dramatic drop in the range $200 < T < 300$ K. In a similar way, magnetoresistance (MR) also drops at the same temperature. This transition is completely reversible with temperature and independent of the applied magnetic field. Sveral hypothesis have been considered in the literature in order to explain this transition: the formation of a silicide in the interface which suffers an insulator-metal transition as the temperature increases [1], the formation of an inversion layer at the Si-SiO_2 interface which could provide a low resistive path for carrier transport [2] or the current switching to the whole substrate if its ρ is low enough [3]. In this work we report a systematic study of the transport and magnetotransport properties of one of the studied compositions: $Fe_{55}Ag_{45}$ in order to get a deeper knowledge of the transition.

The thermal evolution of the resistance and the MR was measured using a conventional six-point configuration.

In figure 1 (left) we present the thermal evolution of the resistance for PLD and sputtered $Fe_{55}Ag_{45}$ thin films deposited onto Si1 and Si2 substrates. Samples deposited onto Si2 present a typical metallic behaviour in all the temperature range, while the resistance abruptly drops at 200-300 K in those deposited onto Si1. The differences observed in the resistance values for the samples deposited simultaneously should be attributed to the different heat conductivity of each substrate that gives rise to different microstructures. As shown in figure 1 (right), this electronic transition also affects the thermal evolution of the MR: while the response of simultaneously deposited thin films is nearly the same before the transition, after this, the modulus of the MR decreases for the samples deposited onto Si1 substrate. On the other hand, magnetic measurements have shown no appreciable differences between films deposited onto different substrates.

To further investigate the role of the interface between the thin film and its corresponding substrate, we also deposited $Fe_{55}Ag_{45}$ granular alloys on Si1 substrate after being treated with fluorhidric acid in order to remove the native SiO_2 layer of the wafer. As it is shown in figure 1 (left), the resistance increases linearly with temperature, which clearly indicates that the presence of SiO_2 is essential for the manifestation of the current switch.

Finally, in order to study the electronic nature of this phenomenon, XAS measurements at the Fe-K edge on PLD samples were carried out at the beamline BL39XU of the SPRING-8 facility as a function of temperature (see figure 2). The spectra obtained are the typical of Fe-bcc, showing no formation of silicides or oxides. Important variations with temperature are observed in the XANES region which indicates clear changes in the electronic structure that should be associated to the anomalous resistivity drop.

In summary, at high temperatures a current switching happens related to the substrate employed during deposition. Based on our experimental results, we propose that some kind of interface layer is formed during deposition at SiO_2/Si, which "activates" above the transition point and allows the current transport switching.

[1]M.F. Li et al. J. Magn. Magn. Mater. 197, 31 (1999)

[2]J. Dai et al. Appl. Phys. 33, L65-67 (2000)

[3]S. Witanachchi et al. Appl. Phys. Lett. 90, 052102 (2007)

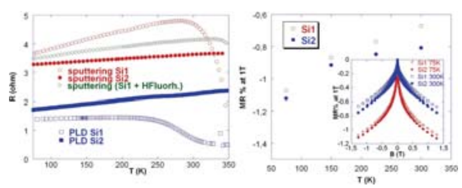

(Left) Thermal evolution of the resistance for sputtered and PLD $Fe_{55}Ag_{45}$, deposited on Si1, Si2 and sputtered on Si1 treated with HF; (Right) MR at 1 T vs temperature for $Fe_{55}Ag_{45}$ sputtered onto Si1 and Si2. In the inset: MR curves of the samples at 75K and 300K.

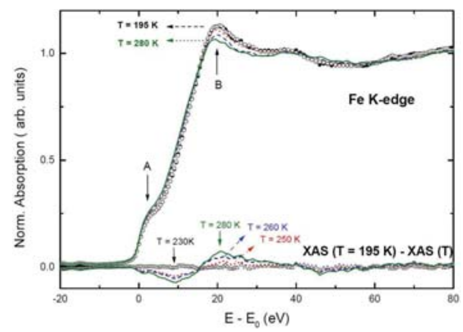

Fig 2: Comparison of the Fe K-edge XAS spectra of the PLD $Fe_{50}Ag_{50}$ alloy recorded at different temperatures.

CR-07

Characterization of nanocrystalline iron oxide powder modified by electroless nickel plating.

C. Lin[1], *C. Tsay*[1], T. Yang[1], R. Yang[2], D. Hung[3], Y. Yao[3]
1. Materials Science and Engineering, Feng Chia University, Taichung, Taiwan; 2. Dept. of Aerospace and Systems Engineering, Feng Chia Univ, Taichung, Taiwan; 3. Institute of Physics, Academia Sinica, Taipei, Taiwan

Electroless nickel plating has been used to prepare nanocrystalline powders or coatings and has attracted considerable R&D interests. It has been reported that nanocrystalline powders can be modified by electroless nickel plating to obtain nano-scale powders with unique structure and properties. In the present study, nanocrystalline iron oxide powders were modified by electroless nickel plating. The so-obtained nanocrystalline powders were characterized by X-ray diffraction, transmission electron microscopy, synchrotron X-ray absorption spectroscopy, and vibrating sample magnetometer. Experimental results show that initial nanocrystalline iron oxide powders remained Fe3O4 phase. The formation of a core-shell like nanoparticles was observed. Synchrotron x-ray absorption examination confirmed the structural and valence change after surface modification. A decrease in saturated magnetization and coercivity was observed after electroless nickel plating.

Nanocrystalline Fe3O4 powders was modified by electroless nickel plating treatment with various processing parameters. Though XRD patterns were not shown here, initial Fe3O4 phase can be observed and the relative amount of elemental nickel was different when prepared by solutions with different pH value. In general, the amount of nickel increased with increasing electroless processing time. Transmission electron microscopy was used to examine the particle size and morphology of the modified powders. It can be observed that the thickness of nickel increased with processing time. Fig. 1 shows the TEM image that was prepared with a pH =6 solution. It can be noted from Fig. 2 that the so-obtained powders exhibited a core-shell like structure where iron oxide powder was surrounded by a layer of Ni. The average grain size of initial nanocrystalline iron oxide powders was ~50 nm while the thickness of nickel was ~40 nm.

Synchrotron X-ray absorption technique was used to examine the local atomic environment and electronic state of the core shell powder. Figure 2 shows the variation in Fe valence state as a function of electroless nickel plating time. It can be noted that the initial Fe 3+ (indicated by the peak at 710 eV) was transferred into Fe 2+ (708 eV) at the early stage of electroless plating (say 15 minutes). No significant difference can be noticed thereafter. The magnetic properties of the corresponding nanopowders for those examined in Fig. 3 were evaluated by VSM and the magnetic hysteresis curves were shown in Fig. 3. Significant decrease in saturated magnetization (Ms) after electroless nickel plating was noticed. The original nanopowders possessed an Ms value of 53.8 emu/g and gradually decreased to 9.9 emu/g after electroless nickel plating for 45 mins. While the coercivity (Hc) only decreased slightly. It decreased from the initial 134.1 Oe to 122.4 with 5 mins. of electroless nickel plating and gradually increased back to 132.5 Oe with increasing processing time.

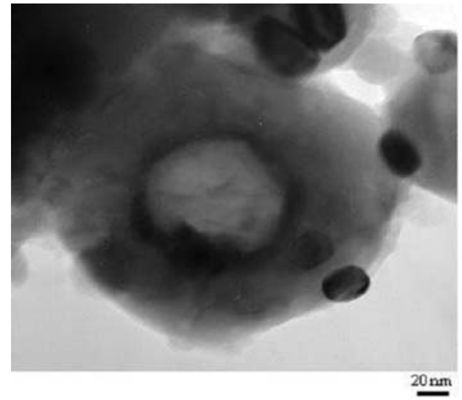

Fig 1 : TEM image of core-shell like Ni/Fe3O4 nanoparticle.

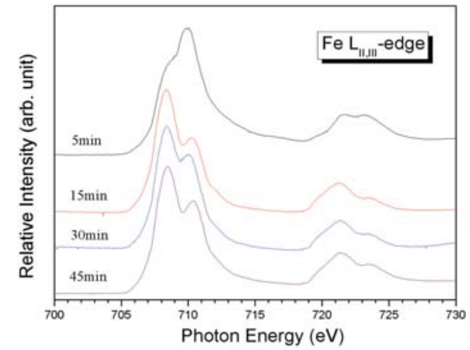

Fig 2 : XANES patterns of nanocrystalline powders after electroless nickel process

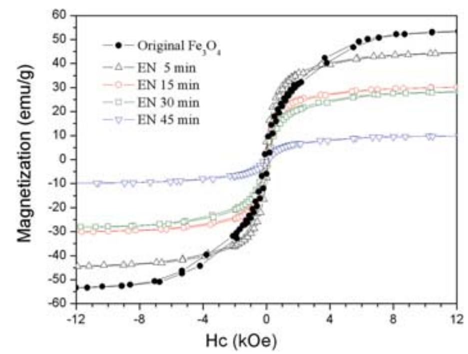

Fig 3 : VSM curves of nanocrystalline iron oxide powders before and after electroless nickel process

CR-08

Functionalized silica coated maghemite nanoparticles prepared by the microemulsion method for biomedical applications.

A. Drmota[1], A. Ko šak[2], A. Znidar ši č[1,2]
1. Kolektor Nanotesla Institute, Ljubljana, Slovenia; 2. Kolektor Magma d.o.o., Ljubljana, Slovenia

Monodisperse magnetic nanoparticles with unique properties which are dominated by superparamagnetism have a great potential to use in biomedical applications such as cell labeling and magnetic cell separation, drug delivery, hyperthermia and MRI contrast enhancement. Applications of nanoparticles in biomedicine impose strict physical, chemical and pharmacological properties, including chemical composition, crystal structure, magnetic behavior, surface structure, adsorption properties, solubility and low toxicity. In this field the main challenge is tailoring the surface of magnetic nanoparticles in order to functionalize and develop strong interactions with specific biological components (dye, drug or effector grafting). Therefore, chemical modification of the nanoparticle surface with biocompatible molecules, such as silica (SiO2), dextran, polyvinyl alcohol (PVA) and phospholipids, is an important issue that provides biofunctionality and resistance to physiological conditions such as pH and enzymes, binding sites between the particles and the target sites on the cell, cytotoxic drug attaching to a biocompatible magnetic nanoparticle carrier, etc. Superparamagnetic nature and a high degree of specific magnetization of the magnetic nanoparticles are demanded for their applications in drug delivery or magnetic separation to defeat hydrodynamic forces acting on the nanoparticles in the flowing solution and small sizes are required to allow the transport through the vascular system or tisular diffusion of particles [1,2].
Although there are many kinds of interesting magnetic nanoparticles, we have been focused our study on silica (SiO2) coated iron oxide (γ-Fe2O3) nanoparticles because of their non-toxic nature and lower susceptivity to physical and chemical changes.
Recently, a variety of synthesis methods such as coprecipitation in aqueous solutions, high-temperature decomposition, pyrolisis and hydrothermal synthesis were developed and improved to produce monodisperse nanoparticles. Among them, a precipitation in microemulsion has been shown as a perspective method for the preparation of magnetic nanoparticles of controlled size and morphology [3].
A microemulsion can be defined as a thermodynamically stable isotropic dispersion of two immiscible liquids consisting of nanosized domains of one or both liquids in the other, stabilized by an interfacial film of surface-active molecules. The surfactant molecules provide a confinement effect that limits particle nucleation, growth, and agglomeration.
In the present investigation, silica (SiO2) coated maghemite (γ-Fe2O3) nanoparticles were performed in-situ via the precipitation in two different microemulsion systems – water/CTAB,1-butanol/1-hexanol and water/SDS,1-butanol/cyclohexane – according to Schikorr`s reaction [4]:

$$Fe^{2+} + Fe^{3+} + 2OH^- + O_2 \longrightarrow \gamma\text{-}Fe_2O_3 + H_2O \qquad (1)$$

In this synthesis, the Fe(II) and Fe(III) hydroxides were precipitated during the reaction between two different microemulsions containing an aqueous solution of corresponding ions (µE-A) and precipitating reagent (µE-B). In the second step of the synthesis, the Fe(II) hydroxide is oxidized, resulting in the formation of the spinel maghemite (γ-Fe2O3) phase. The maghemite (γ-Fe2O3) particles obtained by this synthesis method were nanosized with a narrow particle size distribution of around (8 +/- 2) nm. The γ-Fe2O3 nanoparticles precipitated within the nano-sized microemulsion domains were surface coated with various thickness of silica (SiO2) shell, from 1 nm to 10 nm. The thickness of silica shell was carefully controlled by the amount of tetraethoxysilane (TEOS) added to the microemulsion after the precipitation step as well as with the size of microemulsion nanodomains affected by the water-to-surfactant molar ratio.
The influence of the microemulsion`s composition, the pH value after the precipitation of hydroxides, the concentration of reactants in aqueous phase, the temperature and the time of reaction and the type of surfactant, on the nature of the silica (SiO2) coated maghemite (γ-Fe2O3) nanoparticles were investigated.
Coated and uncoated magnetic (γ-Fe2O3) nanoparticles were characterized using transmission electron microscopy (TEM, HRTEM), X-ray diffractometry (XRD) and specific surface area measurements (BET). The specific magnetization (DSM-10, magneto-susceptometer) of the prepared samples was also measured.
The results showed a high specific surface area (BET) of around 105 m2/g corresponds to a small particle size with a narrow particle size distribution of around (8+/-2) nm for the prepared samples. The specific magnetization was relatively high and decreased from 59 emu/g for uncoated maghemite (γ-Fe2O3) nanoparticles to 17 emu/g for maghemite nanoparticles coated with 6 nm thickness of silica shell. The prepared samples did not show any coercitivity (Hc) or remanent magnetization (Mr), which is the characteristic of their supermagnetic nature.

[1] S. Mornet, F. Grasset, J.Portier and E. Duguet, European Cells and Materials Vol. 3 Suppl. 2, (2002) 110-113

[2] J. Vidal-Vidal, J. Rivas, M.A. López-Quintela, Colloids and Surfaces A: Physicochem. Eng. Aspects, 288 (2006) 44-51

[3] A.Ko šak, D.Makovec, M.Drofenik, Phys.Stat.Sol.(c) 1, 12, 3521 (2004)

[4] G. Schikorr, Z. allg. Chem., 212, 33 (1938)

CR-09

Magnetic nanoparticles obtained by ultrahigh vacuum glancing angle deposition technique at high temperature.

X. Bendaña, E. Ferreiro, G. Armelles, A. Cebollada, J. Garcia Martin
Instituto de Microelectrónica de Madrid IMM-CNM-CSIC, Tres Cantos, Spain

The successful application of magnetic nanoparticles in technological devices such as storage media or magneto-optical sensors requires that the nanoparticles preparation can be made at low cost and short processing time. Among the physical vapour deposition techniques, a relevant possibility is the glancing angle deposition (GLAD) method that employs oblique angle deposition and substrate motion [1]. We will show that such latter condition can be avoided in order to obtain naoparticles if the deposition is made using a substrate at high temperature.
Co nanoparticle films have been prepared onto glass substrates using magnetron sputtering in an ultrahigh vacuum chamber and GLAD with the off-normal deposition angle being 85°. The nominal thickness of Co was varied between 0.4 and 5 nm. Two series of samples have been prepared: one without capping to study the morphology of the nanoparticles, and another one with gold capping to avoid oxidation and to measure properly the magnetic properties. Two different substrate temperatures were applied during the Co deposition, RT and 400°C. It will be described that as the temperature increases not only the self-shadowing characteristic of GLAD but also the diffusion of the adatoms contributes to the formation of 3D nanostructures [2]: as a consequence, the uniformity is improved and as is shown in Figure 1 nanoparticles can be obtained. The magnetic and magneto-optical properties have been measured using Kerr magnetometry and spectroscopy, respectively, both in transversal (sensitive to the in-plane magnetization) and polar (sensing the perpendicular magnetization) configurations. As is shown in Figure 2, the magnetization reversal process depends on the in-plane direction, revealing a small uniaxial anisotropy with the easy axis perpendicular to the vapour flux direction, in agreement with previous results in ultrathin Co films grown by grazing-incidence molecular beam epitaxy [3].

[1] K.Robbie et al., Rev. Sci. Instr. 75 (2004) 1089. "Sulptured Thin Films: nanoengineered morphology and optics", A.Lakhtakia et al., SPIE. (2004).

[2] E. Navarro, Y. Huttel, C. Clavero, G. Armelles, and A. Cebollada, Appl. Phys. Lett. 84 (2004)2139.

[3] S. van Dijken, G. Di Santo and B. Poelsema, Appl. Phys. Lett. 77 (2000)2030.

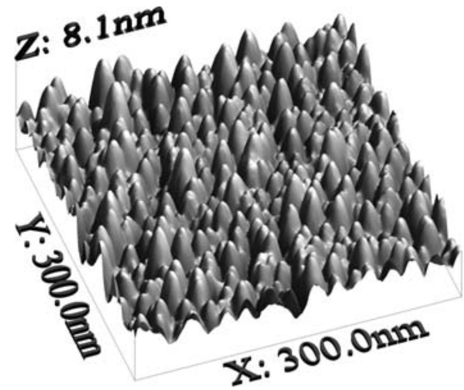

Atomic Force Microscopy image of Co nanoparticles obtained by glancing angle deposition sputtering at 400 °C.

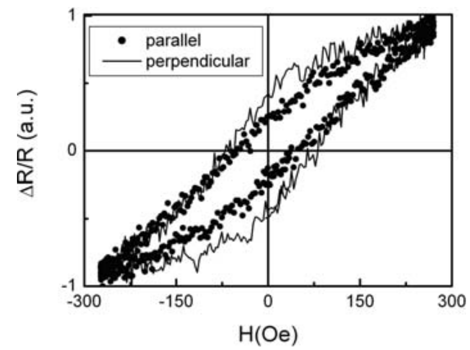

In-plane hysteresis loops, with the field applied parallel and perpendicular to the vapour flux direction during growth, of a Co nanoparticle film with 3 nm nominal thickness.

CR-10

Magnetic properties of nanocrystalline Co thin films grown on glass.

B. Presa[1], R. Matarranz[1], M. C. Contreras[1], J. F. Calleja[1], L. E. Fernandez-Outon[2], K. O'Grady[2]
1. Departamento de Física, Universidad de Oviedo, Oviedo, Spain; 2. Department of Physics, The University of York, York, United Kingdom

Introduction/Experiment

Thin films of Co metal and its alloys are of interest due to their application in TMR heads, MRAM and other applications [1,2]. In this work we report on an analysis of the evolution of the structural and magnetic properties of Co films with increasing thickness in the range 10 to 170 nm. The films were grown on glass substrates using a HiTUS sputtering system [3]. The base pressure achieved was 3×10^{-7} mbar and the process pressure was 3×10^{-3} mbar. The deposition rate was 0.6 Å s^{-1} for all films and a 3 nm Ta cap was also deposited on all samples to prevent oxidation. The structure of the films was determined using X-ray diffraction (XRD). The ultrafine nature of the grains was confirmed by TEM. The surface morphology of the films was imaged by AFM. Magnetic properties were measured by transverse MOKE giving the major hysteresis loops and the transverse susceptibility χ_T.

Results and discussion

Figure 1 shows the XRD pattern of Co films of 80 nm and 170 nm thick. The films are polycrystalline with a dominant hcp phase but with some fcc grains detected by a broad peak around θ = 51.6°. The peak at 44.5° is a combination of hcp (002) and fcc (111) reflections. It can be inferred from these spectra that the films develop the hcp <001> texture as the thickness increases. The crystallite size was estimated using the Scherrer formula and was found to increase from less than 2 nm for the thinnest sample to 24 nm for the thickest film. For fcc crystallites the size is always smaller than hcp varying from less than 2 nm up to 4 nm. This is in agreement with theoretical studies which suggest that the contribution from surface energy can stabilise the fcc phase below a critical size of 20 nm [4]. The ultrafine nature of the grains was confirmed by TEM. Figure 2 shows the 3D AFM images of the films for different thicknesses. Island-like features with a wide distribution of size are observed. The roughness (σ_H) and the average height (H) of the surface increase as the Co thickness increases. This fact is associated with the crystallite growth. Magnetic measurements reveal that the samples have an in-plane magnetization. Figure 3 shows the χ_T with the bias field applied along the easy and hard axis of magnetization. The magnetization reversal along the easy axis takes place in a wider range of applied magnetic field values as the thickness increases, involving more rotations as seen in Fig. 3(a). From Fig. 3(b) we can infer three important features: (i) the thinnest samples show two sharp peaks due to low anisotropy field dispersion, (ii) for thicker samples the anisotropy field, the anisotropy field dispersion and the coercivity increase [see Fig. 3(c)], and (iii) the samples become less magnetically anisotropic as the thickness increases, so higher values of the ratio between the coercivity of the hard (H_{CH}) and easy (H_{CE}) axis are detected [see Fig. 3(d)].

Conclusion

Nanocrystalline Co thin films were deposited by HiTUS. Structural analysis revealed that nanocrystals grow mainly in the hcp phase. Also the fcc phase was present but with much smaller crystallites. Soft magnetic properties and a well-defined uniaxial anisotropy were obtained for thicknesses below 50 nm. However, above this thickness the effective anisotropy begins to be controlled by the magnetocrystalline anisotropy of each crystallite due to the increase of its size. This fact gives rise to an increase in the coercivity, the anisotropy, and the dispersion.

[1] Y. T. Chen et al., IEEE Trans. Magn. 42, 278 (2006)
[2] I. J. Vera Marún et al., Phys. Rev. B 76, 064426 (2007)
[3] M. Vopsaroiu et al., J. Phys. D: Appl. Phys. 38, 490 (2005)
[4] O. Kitakami et al., Phys. Rev. B 56, 13849 (1997)

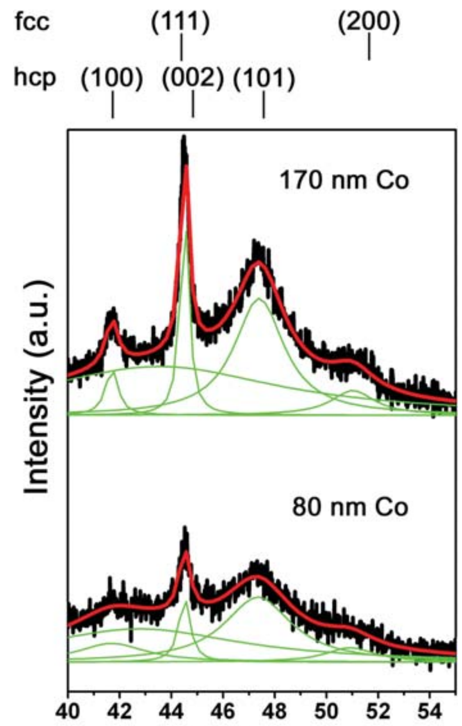

Fig. 1. XRD pattern of Co thin films.

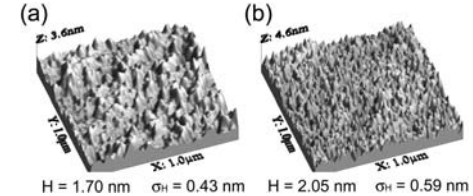

Fig. 2. 3D AFM images of Co thin films with thicknesses of (a) 50 nm and (b) 150 nm.

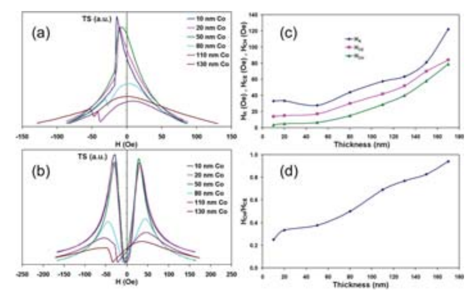

Fig. 3. χ_T with the bias field H along the (a) easy and (b) hard axis for different Co nominal thicknesses. (c) Evolution of the anisotropy field (H_K) and the coercivity of the easy (H_{CE}) and hard (H_{CH}) axis of magnetization. (d) Evolution of the ratio between H_{CH} and H_{CE}.

CR-11

Core-shell magnetic behaviour of iron ultrathin films prepared by sputtering at very low temperatures.

F. Jiménez-Villacorta, *R. M. Morillas*, E. Salas, E. Céspedes, C. Prieto
Instituto de Ciencia de Materiales de Madrid - CSIC, Madrid, Spain

Heterogeneous structures, formed by magnetic transition metal (TM) and its correspondent oxide (TMO), have raised great attention because of their unique properties. Besides other differences in magnetic features between bulk and nanostructures, a very fascinating effect is the interaction between the metal and the oxide, resulting in an overcome of the superparamagnetic effect, enhancement of the coercivity and, if the oxide component has a sufficiently large anisotropy, exchange bias[1,2]. Their microstructure plays a key role in the magnetic behaviour and changes the electrical resistivity and magnetorresistive properties[2]. TM/TMO structures have been largely investigated in several systems as magnetic particles in ceramic matrices[3], core-shell systems[4,5] and thin films[6]. Moreover, exchange-bias has been proposed as an appropriate mechanism to stabilize magnetization in nanostructures against thermal fluctuations[3]. Although the low blocking temperatures observed for TM/TMO systems can limit their potential applications, nanoparticles surface modification has been proposed for magnetic decoupling and consequently applications in magnetic recording[7]; for instance, passivating with an oxide layer. We have reported that partially oxidized Fe films prepared at low temperature consist essentially in granular core-shell magnetic systems, formed by ferromagnetic metallic iron grains surrounded by an iron oxide phase[8]. Samples prepared near TS = 200 K are especially remarkable because they present a magnetic behaviour typical from particle system with random anisotropy axes, in which nanocrystalline grains act as almost decoupled particles, surrounded by an oxide shell, forming exchange biased core-shell systems[9].
In this work, we present a structural and magnetic characterization of partially oxidized Fe ultrathin films with nominal thickness of 6 nm (capped with SiO2) obtained by sputtering on Si substrates at 200 K as well as the comparison with samples prepared at room temperature. Fig. 1 shows hysteresis loops obtained at different temperatures after cooling sample under an applied field of 20 kOe (FC cycles) and magnetization vs. temperature curves obtained after cooling sample with and without an applied magnetic field (FC and ZFC curves, respectively).
The obtained hysteresis loops as well as ZFC-FC magnetization curves of films prepared at low temperatures are similar to that obtained for thicker samples.8 All they are consistent with granular core-shell magnetic systems, formed by ferromagnetic metallic iron grains surrounded by an iron oxide phase. At lower temperatures, magnetization loops show that spins from the iron oxide shell (mainly consisting in FeO and Fe3O4) behave as a spin frozen system able to interact with the ferromagnetic core spins, leading to exchange anisotropy.
It can be concluded that from the magnetic characterization, ultrathin films prepared at TS = 200 K behave as ferromagnetic nanocrystalline grains acting as almost decoupled particles surrounded by an oxide shell forming exchange bias core-shell systems.

[1] J. Nogués, J. Sort, V. Langlais, V. Skumryev, S. Suriñach, J.S. Muñoz and M.D. Baró, Phys. Rep. 422, 65 (2005).

[2] J. Nogués and I.K. Schuller, J. Magn. Magn. Mat., 192, 203(1999).

[3] V. Skumryev, S. Stoyanov, Y. Zhang, G. Hadjipanayis, D. Givord and J. Nogués, Nature 423, 850 (2003).

[4] L. del Bianco, D. Fiorani, A.M. Testa, E. Sonetti, L. Savini and S. Signoretti, Phys. Rev. B, 66, 174418 (2002).

[5] S.A. Koch, G. Palasantzas, T. Vystavel, J.Th.M. De Hosson, C. Binns and S. Louch, Phys. Rev. B 71 (8) 5410 (2005).

[6] H.J. Kim, J.H. Park and E. Vescovo, Phys. Rev. B 61 (22) 15284 (2000).

[7] D.E. Speliotis, in: G.C. Hadjipanayis (Ed.), Magnetic Storage Systems Beyond 2000, Kluwer Academic Publishers, Amsterdam, 2001, p. 25.

[8] F. Jiménez-Villacorta, Y. Huttel, A. Muñoz-Martín, C. Ballesteros, E. Román and C. Prieto, J. Appl. Phys., 101,113914 (2007).

[9] F. Jiménez-Villacorta and C. Prieto, J. Phys.: Condens. Matter (submitted).

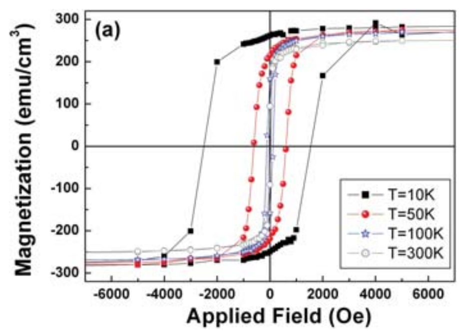

Fig. 1 (a) Magnetization loops.

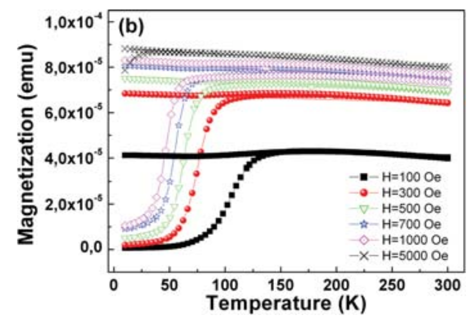

Fig. 1 (b) Zero field cooling - Field cooling magnetothermal curves.

Preparation and magnetic properties of disordered $CdFe_2O_4$ thin films.

H. Akamatsu, Y. Zong, Y. Fujiki, K. Kamiya, K. Fujita, S. Murai, K. Tanaka
Material Chemistry, Kyoto University, Kyoto, Japan

Cadmium ferrite ($CdFe_2O_4$) possesses a normal spinel structure in its stable phase, where Cd^{2+} ions occupy tetrahedral sites (A sites) and Fe^{3+} ions octahedral sites (B sites) in a face-centered-cubic closely packed oxide ion sublattice. It is well known that the normal spinel type of $CdFe_2O_4$ behaves like an antiferromagnet with a Neel temperature of 13 K, although, strictly speaking, spin freezing with only short-range correlation occurs at 13 K and no long-range order is observed down to 0.1 K. But a nonzero magnetization and high magnetic ordering temperature can be observed for $CdFe_2O_4$ nanoparticles fabricated by coprecipitation method and high-energy ball-milling. Large magnetization and high magnetic ordering temperature are attributed to such a structure that a site exchange between Cd^{2+} in the A site and Fe^{3+} in the B site takes place, and that strong superexchange interaction between Fe^{3+} ions in A and B sites leads to a ferrimagnetic order at least for localized magnetic moments even above room temperature. Our research group recently has fabricated sputtered $ZnFe_2O_4$ thin films, stable phase of which possesses a normal spinel structure, and is a frustrated antiferromagnet similar to $CdFe_2O_4$, and demonstrated that a ferrimagnetic behavior of the films is imposed to a site exchange of cations from the analysis of x-ray absorption near-edge structures (XANES).1)

In this presentation, we report on structural and magnetic properties of $CdFe_2O_4$ thin film prepared by the sputtering method. Sputtered $CdFe_2O_4$ thin films were deposited on silica glass substrates in an atmosphere of oxygen or argon by using a mixture of CdO and Fe_2O_3 powders as a target. The as-deposited and annealed thin films were subjected to an x-ray diffraction analysis with Cu Kα radiation to ascertain that the thin films were composed of a single phase of $CdFe_2O_4$.

Figure 1 illustrates dependence of magnetization on magnetic field of the sputtered $CdFe_2O_4$ films deposited in the oxygen atmosphere with or without heat treatment at 200 and 400 °C. Any films show ferro- or ferrimagnetic behavior even at room temperature. This may be due to the site exchange between Cd^{2+} in the A site and Fe^{3+} in the B site. The magnetization of $CdFe_2O_4$ thin film annealed at 200 °C is larger than the as-deposited thin film, and the film annealed at 400 °C has magnetization smaller than that of the as-deposited film.

Temperature dependence of magnetization for the present films is shown in Fig. 2. Cluster spin glass-like behaviors are observed for the as-deposited film and the film annealed at 200 °C, indicating that a ferrimagnetic order occurs for only localized magnetic moments. The magnetic behavior of the thin film annealed at 400 °C resembles that of bulk $CdFe_2O_4$. The annealing of the thin films at high temperatures such as 400 °C is apt to bring about the formation of $CdFe_2O_4$ with the normal spinel structure, leading to the magnetic behavior similar to that of bulk. In the presentation, we will also show results of analysis of XANES and Faraday effect measurements.

[1] Nakashima et al. Physical Review B 75, 174443 (2007).

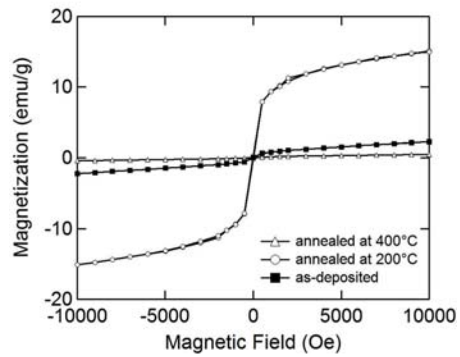

Fig. 1. Dependence of magnetization on magnetic field at 300 K for sputtered $CdFe_2O_4$ films deposited in an oxygen atmosphere with or without heat treatment at 200 and 400 °C.

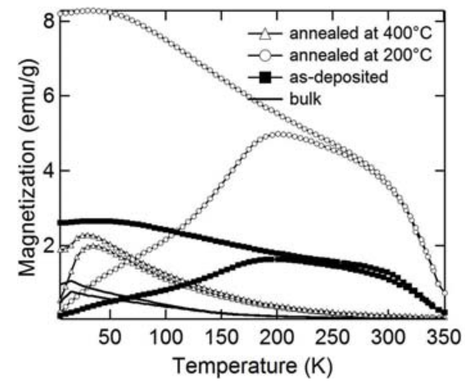

Fig. 2. Temperature dependence of magnetization measured at a magnetic field of 50 Oe for bulk $CdFe_2O_4$ and the sputtered $CdFe_2O_4$ films deposited in an oxygen atmosphere with or without heat treatment at 200 and 400 °C.

CR-13

Controlled synthetic conditions of FePt nanoparticles with high magnetization for biomedical applications.

D. Wei[1,4], D. Hung[2], C. Ho[3], P. Chen[3], Y. Yao[4]
1. Institute of Physics, Academia Sinica, Taipei, Taiwan; 2. Department of Information and Telecommunications Engineering, Ming Chuan University, Taipei, Taiwan; 3. Department of Chemical Engineering, Tunghai University, Taichung, Taiwan; 4. Department of Materials Engineering, Tatung University, Taipei, Taiwan

Nowadays magnetic nanoparticles (NPs) by using chemical synthesis have been received considerable attention due to their wide range research field such as bio-applications in marker or labeling material, separation, drug delivery, therapy, and sensors [1-4]. The aim of this work is to enhance the saturation magnetization (Ms) of the FePt nanoparticles (NPs) by controlling the initial mole ratio of Fe to Pt precursors and reaction conditions to effectively increase magnetization due to the size-dependent effect and with biocompatibility via surface modification. For a compositionally controlled synthesis with the reduction is as follows: 0.5 mmol for Pt(acac)2, Fe(acac)3 ranged from 0.5 to 1 mmol, 4.5 mmol 1,2-hexadecanediol were mixed with 30 ml of phenyl ether. The flask was heated up to 100 oC for 30 min with additive oleic acid (1~2 mmol) and oleylamine (0.5 mmol) stabilizers into flask at the same time. The initial mole ratio (Fe:Pt) of Fe to Pt precursors are varied from 1, 1.25, 1.5 to 2 (Fe):1 (Pt), respectively. And then they were heated up to 260 oC for 0.5~3 hr under the argon blanket. For all as-synthesized FePt NPs with different mole ratios are superparamagnetic at room temperature as shown in Fig. 1(a). The Ms of FePt NPs with reaction time for 0.5 hr increases from 1.5 emu/g (1:1) to 4.5 emu/g (2:1) with increasing Fe:Pt mole ratio due to the contribution of Fe atoms. The temperature dependence of the magnetization in an applied field of 50 Oe between 5 and 300 K using field cooling (FC) and zero-field cooling (ZFC) procedures was studied and showed a blocking temperature (TB) of about 18 K for FePt (2:1) NPs [Fig. 1 (b)]. The Curie temperature (TC) of FePt NPs is strongly composition dependent. It was also found that TC decreases with decreasing sizes of the FePt NPs. The FePt NPs with the disordered fcc structure could monodispersed in hydrophobic solvents without significant aggregation, and the average particle size was 2.5 nm with the narrow size distribution as shown in Figs.1 (c) and 1(d), respectively. It could be realized that the as-synthesized FePt NPs below critical particle size (Dp~ 3 nm) is at superparamagnetic state. The following analysis will be mainly focused on the ratio of 2 (Fe:Pt) with Fe58Pt42 composition as characterized by Nano-EDS, in order to enhance Ms effectively and investigate the effect with different reaction time. The variations of the XRD diffraction patterns and magnetization loops of the FePt (2:1) NPs with reaction time ranged from 1 to 3 hr are shown in Fig. 2. With increasing reaction time of the FePt NPs from 1 to 3 hr, the intensities of the FePt (111) and (200) diffraction peaks increased as shown in Fig. 2(a). It was found that the room temperature saturation magnetization increased from 11 emu/g (1 hr) to 18 emu/g (1 hr) with the increase of reaction time as shown in Fig. 2(b), and reached a maximum value of 36 emu/g while reacted temperature at 260 °C for 3 hr due to the increased size of FePt NPs. The FePt NPs were then transferred from oil- to water-soluble (bio-compatible) state and the covalent protein attachment was prepared by the mercaptoacetic acid (C2H4O2S). Streptavidin conjugation to FePt NPs which was used to cross-link free carboxylic acid groups on FePt NPs with amine-containing streptavidin. To examine the binding activity with antibodies, COOH- and EDC (1-ethyl-3-(3-dimethylaminopropyl) carbodiimide hydrochloride) modified FePt NPs were resuspended in PBS buffer and biotin-antibodies (goat polyclonal IgG) were added. FePt NPs attached with streptavidin-biotin as a bridge for binding selective protein/antibodies/DNA for functional nanoparticles were identified by using SDS/PAGE analysis as shown in Fig. 3. The further result shows that the binding activity of streptavidin-FePt NPs with antibodies increased in a sigmoidal saturated fashion along with increasing amount of biotin-antibodies. In this study, the high magnetization of water-soluble FePt NPs can be achieved by adjusting the molar ratio of Fe:Pt precursor and reaction time. It further confirms that FePt nanoparticles with high magnetization have been successfully conjugated to streptavidin protein and yet possess the ability to affinity bind to biotin-linked goat polyclonal IgG in aqueous solution as simulated in human body fluid. The potential usages of hydrophilic FePt NPs with high Ms conjugated with functional protein/antibodies/DNA have been attracted more interests in future biomedical development.

[1] K. E. Elkins, T. S. Vedantam, J. P. Liu, H. Zeng, S. H. Sun, Y. Ding, and Z. L. Wang, Nano. Lett. 3, 1647 (2003).

[2] W. S. Seo, J. H. Lee, X. M. Sun, Y. Suzuki, D. Mann, Z. A. Liu, M. Terashima, P. C. Yang, M. V. Mcconnell, D. G. Nishimura, and H. J. Dai, Nature Mater. 5, 971 (2006).

[3] J. H. Gao, G. L. Liang, B. Zhang, Y. Kuang, X. Zhang, and B. Xu, J. Am. Chem. Soc. 129(5), 1428 (2007).

[4] U. Queitsch, E. Mohn, F. Schäffel, L. Schultz, B. Rellinghaus, A. Blüher, and M. Mertig, Appl. Phys. Lett. 90, 113114 (2007).

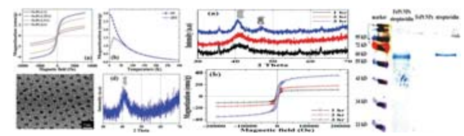

Fig. 1. (a) VSM data of the initial mole ratio (Fe:Pt) are varied from 1, 1.25, 1.5 to 2 (Fe):1 (Pt) for 0.5 hr; (b), (c), and (d) are the corresponding analyses of 2:1 ratio. Fig. 2. (a) XRD and (b) VSM data of FePt (2:1) Nps are reacted for 1~3 hr. Fig. 3. SDS/PAGE (polyacrylamide gel electrophoresis) analysis of FePt-streptavidin conjugation

CR-14

Properties of Co-HfO2 nanogranular magnetic thin films.

M. Chadha, V. Ng
ECE, National University of Singapore, Singapore, Singapore

Granular films comprise of well-defined nanometer size magnetic grains embedded in an insulating matrix has been a topic of active research [1]. Conduction takes place by electron tunneling through the insulator barriers between the magnetic grains giving rise to the spin dependent Tunneling Magneto Resistance (TMR) phenomenon. Owing to their nanometer size, the system also exhibits the coulomb blockade phenomena [2]. However, the most extensively studied Co-Al2O3 granular system shows a high content of cobalt oxide in the films [3-4] which results in a decrease in the TMR effect [4].

In the present work we investigate the effect of hafnium oxide (HfO2) used as a new insulating matrix in the cobalt granular film to decrease the possibility of formation of cobalt oxide during sputtering. Our motivation is related to the heat of formation of hafnium oxide being significantly higher than other oxides [5]. Besides introducing a new oxide material, we utilise a new sputtering method to control the properties of the system.

Granular films were sequentially sputtered on glass and silicon substrates using argon at 5 mTorr and a base pressure of ~10–8 Torr. A thin and discontinuous Co layer of nominal thickness T(Co) is first deposited, forming discrete Co grains. Then a discontinuous HfO2 layer of T(HfO2) gets deposited either in-between or as well above the Co grains. This is sequentially repeated to obtain a total thickness of 20 nm, followed by 8 nm of capping HfO2 layer. The Co grain size and the inter-particle oxide width can be independently adjusted with this method. T(Co) and T(HfO2) were varied while keeping the total thickness constant.

X–ray photoelectron spectroscopy on the as-prepared Co-HfO2 films show that the cobalt oxide peak is much smaller than that for Co-Al2O3 films. The magnetic properties were measured at Room Temperature (RT) using the vibrating sample magnetometer. Aluminum (Al) contact pads were sputtered by the shadow mask technique. The magnetoresistance (MR) of the samples were measured at RT by DC four-point probe setup with application of a maximum field of 4 kOe along the in-plane direction.

Fig. 1 (i) presents the hysteresis loops for films having T(HfO2) = 0.9 nm and T(Co) varying from 0.6 to 1.5 nm having 13 to 8 bilayers, referred as film A to F respectively. Fig 1 (ii) is the zoomed in of fig 1(i). Fig 2 (i) show the trends in coercivity (Hc) and Squareness (S) vs. T(Co). For films A-D, with small Co contents, the grains are superparamagnetic which is inferred from their low Hc and S values. With increase in T(Co) for fixed T(HfO2), the grain density and size increase. This increases the interaction between the grains giving rise to a gradual decrease in Hc and increase in S. Further increase of T(Co), in films E and F produces films of high Hc and S values, implying that of single domain ferromagnetic nature.

Fig. 3 shows the MR graphs. The TMR ratio is defined as $\Delta R/R0$ where R0 is the film resistance at zero field and ΔR is R0 - (film resistance at 4 kOe). Fig 2 (ii) shows the TMR ratio vs T(Co). The superparamagnetic film D shows the maximum TMR ratio. For superparamagnetic films having smaller T(Co) (i.e. films A to C) the spin diffusion length is smaller than the tunneling barrier for effective spin tunneling showing small TMR ratio and gradual MR curve. As the single domain grains have a small contribution to the spin dependent scattering [6], film E and F show low TMR ratio and sharper curves. Similar analysis was carried on films having T(Co)= 0.9 nm and T(HfO2) varying. The combined results will be presented in full paper. We found T(Co) = 1.0 nm and T(HfO2) = 0.9 nm, having 10 bilayers has a maximum TMR ratio of 3.92 % (±4 kOe, 300 K) and 5.81 % (±4 kOe, 10.4 K).

A device 200 nm by 200 nm by 20 nm (l by w by t) fabricated with the granular film deposited between the microscopic Al contact pads produced an enhancement in the TMR ratio (by 86% at RT). Devices with smaller dimensions are currently being fabricated.

In conclusion, by introducing a new insulator we have successfully reduced the amount of cobalt oxide content. Using the sequential sputtering method, properties varying with the microstructure were comprehensively studied and an optimum composition of Co and HfO2 layers thickness is achieved.

[1] Shihui Ge et al., J. Phys. D: Appl. Phys. 40 (2007) 3660 [2] K.Yakushiji, et al., J. Appl. Phys. 91 (2002) 7038 [3] Asami, et al., Surf. Interface Anal. 28 (1999) 250 [4] H.Fujimori, et al., J. Magn. Magn. Mater. 156(1996) 311 [5] Comprehensive Handbook of Chemical Bond Energies, CRC Press (2007) [6] Y. Asano, et al., Phys. Rev. B 49 (1994) 12831

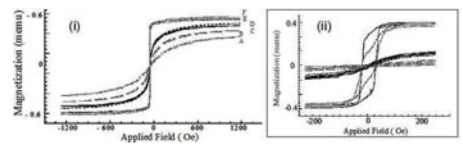

Fig 1: (i) Hysteresis loops for films A to F; (ii) zoomed in view of hysteresis loops

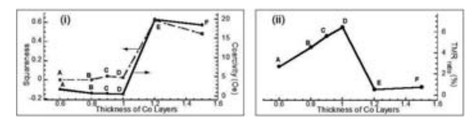

Fig 2: T(Co) vs. trends in (i) Hc and Ms; (ii) TMR ratio

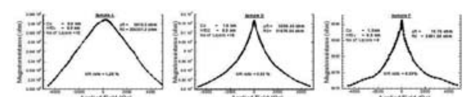

Fig 3: TMR curves for films with T(HfO2) = 0.9 nm and T(Co) = 0.6 nm (A), 1.0 nm (D) and 1.5 nm (F)

CR-15

Fe_3O_4 incorporated AOT-Alginate - composite nanoparticles for drug delivery.

C. Sudakar[1], A. Dixit[1], R. Regmi[1], *R. Naik*[1], G. Lawes[1], V. M. Naik[2], P. P. Vaishnava[3], U. Toti[4], J. Panyam[4]

1. Department of Physics and Astronomy, Wayne State University, Detroit, MI; 2. Department of Natural Sciences, University of Michigan-Dearborn, Dearborn, MI; 3. Department of Physics, Kettering University, Flint, MI; 4. College of Pharmacy, University of Minnesota, Minneapolis, MN

Biocompatible magnetic nanoparticles, such as magnetite (Fe_3O_4) and maghemite (γ-Fe_2O_3) have potential biomedical applications including contrast agents for magnetic resonance imaging, cell separation, targeted drug delivery, and localized hyperthermia. External magnetic fields can be used to deliver the magnetic particles in vivo to specific sites for targeted drug delivery applications. However, surface functionalization of these magnetic carriers is necessary for in vivo drug delivery. Liposomes, alginate, and other biopolymers have been commonly used for this purpose. Recently, Panyam *et al* [Pharmaceutical Res. **24**, (2007) 803] have reported a study on Aerosol OT™ (AOT)-alginate nanoparticles as a potential functional unit for enhanced and sustained cellular delivery of the water soluble drugs. This study demonstrated that encapsulation of doxorubicin in AOT-alginate nanoparticles resulted in higher and more sustained (>10 days) cellular delivery and cytotoxicity in tumor cells grown in culture.

Here we report the synthesis and characterization of AOT-alginate nanoparticles (25- 50 nm) loaded with rhodamine 6G (R6G), a water soluble molecule, and Fe_3O_4 nanoparticles (10 nm) using an emulsification-cross-linking process. R6G (1 mg) dissolved in aqueous sodium alginate solution (2% w/v; 0.5ml) was emulsified into AOT solution in chloroform (2.5% w/v; 2 ml) by sonicating for 1 min over ice bath. The primary solution is further emulsified into 15 ml of aqueous polyvinyl alcohol (PVA) solution (2% w/v) by vortexing for 1 min and sonicating for 5 min over ice bath to form a secondary water-in-oil-in-water emulsion. The emulsion was stirred using a magnetic stirrer, and 5 ml of aqueous calcium chloride or ferrous chloride solution (60% w/v) was added gradually to the above emulsion. The emulsion was stirred further at room temperature for ~ 24 hr to evaporate chloroform. Nanoparticles formed were recovered by ultracentrifugation at 30,000 rpm for 30 min, washed two times with distilled water to remove excess PVA and free R6G molecules, resuspended in water and lyophilized. We have prepared Ca^{2+} or Fe^{2+} cross-linked alginate-AOT-nanoparticles without and with incorporating Fe_3O_4 magnetic nanoparticles. For the latter, we added 5 % (by wt. of alginate) Fe_3O_4 magnetic nanoparticles, prepared by a soft chemical method, to the aqueous alginate solution during the processing.

The structural characterization of the R6G loaded alginate-AOT nanoparticles were carried out using transmission electron microscopy (TEM). For example, Figs. 1(a) and (b) show the TEM images of Ca^{2+} cross-linked Alginate-AOT nanoparticles without and with Fe_3O_4 magnetic nanoparticles. The alginate-AOT nanoparticles, varying in size between 25 to 50 nm, show an increased agglomeration due to incorporation of magnetic nanoparticles. It is clearly seen that the Fe_3O_4 nanoparticles are uniformly coated with a thin layer (~5 nm) of polymer as shown in the inset of Fig. 1(b).

The magnetic properties of the nanoparticles suspended in water were measured, using a SQUID magnetometer, with the results shown in Fig. 2. The bare Ca^{2+} cross-linked alginate-AOT nanoparticles are paramagnetic as can be seen in Fig. 2(a) from the M-H curves (inset) showing a linear dependence, and also from the temperature dependence of ZFC-FC curves. However, the composite Fe_3O_4-alginate-AOT nanoparticles show a superparamagnetic behavior at room temperature with a saturation magnetization of ~50 emu/g of Fe_3O_4. The ZFC-FC curves of this composite exhibits a blocking temperature of TB~ 100 K. Below TB, hysteretic behavior is observed with a coercivity ~ 250 Oe. The sharp drop observed in Fig. 2(b) ~ 270 K is due to blocking of brownian relaxation of magnetic nanoparticles caused by freezing of water. Similar results were observed in the case of Fe^{2+}-cross linked alginate-AOT nanoparticles, but with a two-fold increase in magnetization. The details of these results and the effect of magnetic nanoparticles on the R6G loading in AOT-alginate nanoparticles, as determined by HPLC analysis, will be discussed.

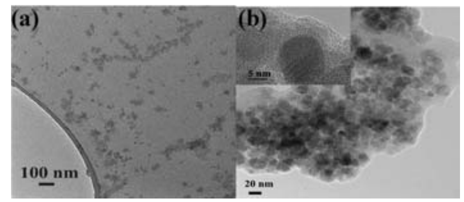

Fig. 1: Transmission electron micrograph (TEM) of Ca^{2+} cross-linked (a) alginate-AOT nanoparticles and (b) composite Fe_3O_4-alginate-AOT nanoparticles. Inset in (b) shows an individual Fe_3O_4 nanoparticle embedded inside AOT-alginate nanoparticles

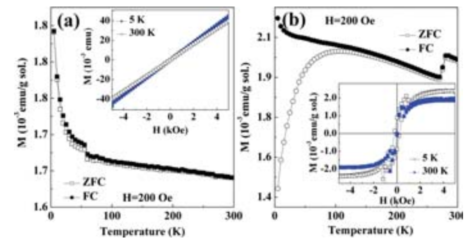

Fig. 2: Magnetic properties of Ca^{2+} cross-linked (a) alginate-AOT nanoparticles and (b) composite Fe_3O_4-alginate-AOT nanoparticles. The main panel shows the temperature dependence of the ZFC-FC curves measured using 200 Oe field. The insets show the field dependence of magnetization.

CR-16

Iron Oxide Nanoparticles Embedded in Thermoplastic Polymers for Magneto-optical Devices.

G. Carotenuto[2], *D. Davino*[1], A. Longo[2], V. Pagliarulo[1], G. Pepe[3], C. Visone[1]
1. Engineering Department, University of Sannio, Benevento, Italy; 2. Istituto per i materiali compositi, CNR, Napoli, Italy; 3. Coherentia INFM - Physics Department, Università di Napoli Federico II, Napoli, Italy

Optical plastics filled by nano-sized magnetic particles may have relevant applications in magneto-optics as for optical modulators and insulators and optical shutters, [1]. In this framework, the paper proposes the full characterization of ferromagnetic and superparamagnetic magnetite (Fe_3O_4) nano-particles embedded in polystyrene. These materials are generated by thermal decomposition respectively of iron (II) and iron (III) mercaptide in amorphous polystyrene.
Transparent plastics embedding nano-sized magnetic phases have unique physical features. Because of the small size of the guest phase (less than 50nm), these materials do not scatter visible light, so they are quite transparent in the VIS-NIR spectral region and, at the same time, they have relevant magnetic characteristics. Moreover, the Verdet's constant of a polymeric material filled with ferromagnetic nanoparticles is very large.
Recently, easy chemical method for the synthesis of polymer-embedded noble metal and sulfide clusters have been developed; this method is based on the thermal decomposition of homoleptic mercaptide molecules dissolved in polymers [2]. Thermolysis of mercaptide molecules takes place at temperatures compatible with polymer thermal stability, in addition normal alchyl mercaptides (i.e., $Me(SC_{12}H_{25})_x$) perfectly blend with most techno-polymers because of their non-polar nature. Because of the polymeric structures, mercaptides are hardly soluble in polar solvents (e.g., ethanol, etc.) and therefore they can be simply synthesized by adding the alcane-thiol to a metal salt solution in ethanol or an alkaline thiolate to a aqueous salt solution.
The nature of the inorganic phase generated by decomposition of iron (II) mercaptide and iron (III) mercaptide (i.e., $Fe(SC_{12}H_{25})_2$, $Fe(SC_{12}H_{25})_3$) dissolved in polymer was established by large angle X-ray powder diffraction (XRD). According to XRD data the inorganic phase generated by decomposition of iron mercaptide dissolved in polymer was magnetite (Fe_3O_4). The morphology of inorganic phase generated inside the polymer during the thermal annealing treatment was imaged by TEM. The magnetite/polystyrene nanocomposites obtained starting from iron (II) mercaptide gave aggregates of differently shaped particles (fig1a). The most prominent phase was made of acicular particles (10nm x 50nm) which exactly corresponded to the magnetite texture [3]. On the contrary, the magnetite/polystyrene nanocomposites obtained starting from iron (III) mercaptide showed only one isolated spherical nanoparticles, with an average size of 6 nm (fig. 1b).
The optical properties of the obtained films were analyzed by UV-Vis spectroscopy. The samples resulted quite transparent at wavelengths higher than 550nm (fig.2).
The magnetic characterization has been performed by a Vibration Sample Magnetometer. The results for the annealed iron (II) mercaptide/polystyrene blends are presented in fig.3. They show a ferromagnetic behavior depending on the different mercaptide amounts (down) and an an hysteretic behavior, just like bulk magnetite [4].
The characteristic magnetic parameters (i.e. saturation magnetization and remanence) of the magnetic plastics are strictly connected to the amount of magnetite dispersed in the polymeric matrix and present a dependence on the applied field orientation (fig.3 up).

[1] K.E. Gonsalves et al., J. Mater. Chem. 7(5)(1997)703-704.

[2] G. Carotenuto et al, Microw Opt Tech Lett, 48(12) (2006) 2505-2508.

[3] R. Vijaya Kumar et al, J. Appl. Phys. 89 (11) (2001) 6324-6328.

[4] X. Cao, et al, J. Mater. Chem. 7(6) (1997) 1007-1009.

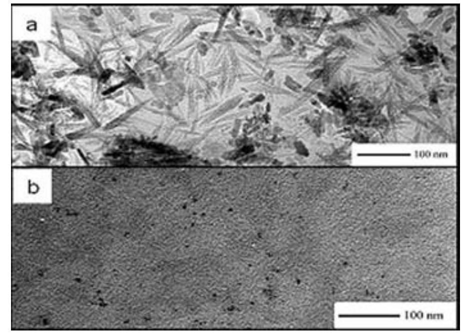

TEM-micrograph of magnetite/polystyrene nanocomposites obtained starting from: (a) iron (II) and (b) iron (III) mercaptides.

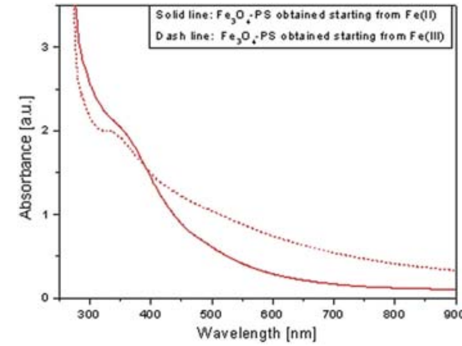

UV-Vis spectroscopy of magnetite/polystyrene nanocomposites.

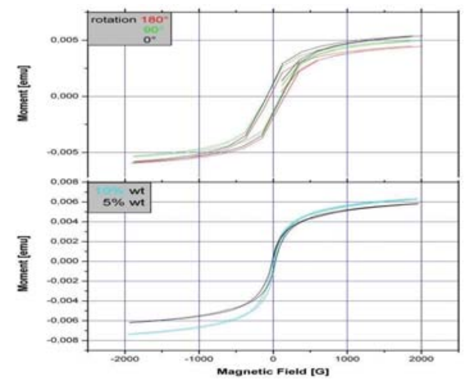

Magnetization curves of magnetite/polystyrene nanocomposites obtained starting from iron (II) mercaptide.

CR-17

Novel single-step synthesis of Fe1-xCox and MgO based core-shell structured nanospheres: High magnetization particles for biomedicine, catalysis and spintronics applications.

C. Martinez-Boubeta[1], L. Balcells[1], F. Sandiumenge[1], L. Casas[3], A. Calleja[1], V. Laukhin[1,2], C. Monty[4], B. Martínez[1]

1. ICMAB, Bellaterra, Spain; 2. Institut Catalá de Recerca i Estudis Avançats (ICREA), Passeig Lluís Companys 23, Spain; 3. Unitat de Cristallografía i Mineralogia, Dept. Geologia-UAB, Bellaterra, Spain; 4. CNRS/Procédés, Matériaux et Energie Solaire (PROMES), Font Romeu, France

In spite of encouraging progress in recent years, the development of magnetic nanoparticles that can be used as drug delivery vectors remains challenging. Among the multiple hurdles that must be overcome are the provision of a sufficiently high magnetic response and an adequate degree of biocompatibility. Here we synthesize alloyed nanoparticles in the iron-cobalt system through vapour-phase condensation and investigate their coating with magnesia shells to provide exceptional advantages such as environment stability, controlled interparticle interactions, enhanced magnetic moments and non-toxic hydroxyl surface groups that provides intrinsic hydrophilicity and allows surface attachment of drugs or biomolecules [1].

Namely, a target containing mixed powders of Fe, Co and MgO in the desired proportion is vaporized inside a vacuum chamber by focusing the sun heating power from a speculo ustorio as described in Ref. [2]. In the foregoing specification, the invention has been described with reference to specific embodiments. However, further modifications will be apparent to those skilled in the art. Moreover, effect of the process conditions on the synthesized powder, such as particle size, thickness of the shell, magnetic properties, etc., has not been studied systematically. For instance, the particles produced by this method can exhibit a size ranging from 5 to 200 nm, which depends mainly on the gas pressure during evaporation. With increasing argon pressure, a trend for increasing particle size was observed [3] as results from the decrease in the mean free path of the Fe atoms. Transmission electron microscopy (TEM) was used to study the crystal structure and particle morphology. Nearly spherical crystals with negligible shape anisotropy were obtained [Fig 1(a)]. Most likely because of the difference in surface energies, the metal clusters do not wet the MgO surface and therefore the MgO forms a continuous and epitaxial shell over the Fe islands [Fig 1(b)], as previously reported in Fe/MgO(001) thin films [4].

To investigate the magnetic properties of such well-defined and insulated Fe nanoparticles, they were mechanically compacted. In our case the particles thus obtained present a much stronger magnetic response than any composite material produced up to now involving magnetic nanoparticles encapsulated in inorganic matrices [Fig 2(a)]. The MgO capping might explain this behaviour due to the enhanced magnetic moment predicted for Fe atoms in the interface with a MgO layer [5]. According to the Mossbauer studies, 12 % of the iron atoms show a doublet that represents sites that are characterized by the broken translational symmetry at the surface of each particle [inset Fig 2(a)]. Magnetic measurements and TEM analysis were repeated on some of the samples in order to examine any aging effects, but no diminish of the properties was detected over several months' storage under ambience conditions.

Figure 2(b) shows the magnetic field dependence of the resistance for a MgO50Fe50 pellet at 150K. The value of the MR decreases with increasing field as may be explained by an increasing degree of alignment among magnetic moments in the samples. The absolute values of the magnetoresistive effect are small and decrease as the temperature rise, due to electron hopping between metallic grains in a process involving thermally activated tunnelling. Nevertheless, these core-shell formations constitute a model system for studying the physics of spin-dependent tunnelling because of their well-defined structure. On the other hand, an equivalent level of comprehension of the magnetoresistance effect in planar junctions has only recently emerged through the study of MgO(001) barriers with values of TMR that currently reach 1000% [6]. Also, the use of MgO and Fe makes the batch process cost-effective since the ferropericlase Mg1−xFexO and the (Mg,Fe)SiO4 silicate are the major constituents of the earth's mantle.

1 P. K. Stoimenov et al. J. Am. Chem. Soc. 125 (2007) 12907

2 B. Martínez et al. Phys. Rev. B 72 (2005) 165202

3 S. Gangopadhyay et al. Phys. Rev. B 45 (1992) 9778

4 C. Martínez-Boubeta et al. J. Crystal Growth 226 (2001) 223

5 C. Li et al. Phys. Rev. B 43 (1991) 780

6 S. Yuasa et al. J. Phys. D: Appl. Phys. 40 (2007) R337

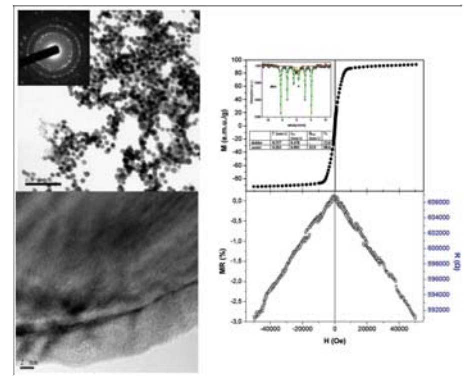

FIG. 1. (a) Low magnification TEM image of spheroidal NPs with average diameter close to 80 nm and corresponding to samples with MgO60Mg15Fe25 composition. (b) HRTEM image of a core-shell particle viewed along [110] Fe. These results show a cube-on-cube orientation relationship between MgO and the metal particle. The MgO layer thickness here amounts 3 nm. FIG. 2. (a) High-field hysteresis loops from a MgO61Fe39 [±3 % wt] sample at RT. Inset depict the Mössbauer spectrum at 300K (experimental points and numerical fits). (b) MR curve at 150K of a cold-pressed film with an isotropic granular structure consisting of 150 nm Fe particles and intergranular crystalline MgO.

CS-01

High Perpendicular Anisotropy Layers stacked Exchange Coupled Composite Media.

S. Oikawa, T. Maeda, A. Takeo
Hard Disk Drive Development Dept., TOSHIBA Corporation, Kawasaki, Japan

Introduction

There has been lots of calculation reports about Exchange Coupled Composite (ECC) media consisting of magnetically hard and soft(Ku=0) sub-grains, since the proposal by Victora et al [1]. Experimentally, it is difficult to make the soft sub-grain saturated in the perpendicular direction of the thin film media due to the demagnetizing field. However, the ECC media with Co-SiO2 as the soft layer is actually reported that shows a good perpendicular squareness with negative nucleation field Hn, and a excellent read/write performance [2]. In this study, the appropriate design of uniaxial magnetic anisotropy Ku of the soft layer were examined in the shape of thin film by LLG simulation. ECC media show excellent properties when relatively high Ku values are given to the soft layer.

Results and Discussion

The simulated results of one ECC grain magnetic behavior reproduced the study by Victora et al [1], such as the coercivity Hc reduction in a moderate interlayer coupling, and the flat angular dependence of switching field. Extending the simulated medium shape from one grain (8nm square) to thin film (192nm square), the slope of the magnetization curve in the part corresponding to the soft layer (thicker than the hard layer) became small due to the demagnetizing field and the perpendicular squareness Rs had fallen to about 0.6.

Smaller soft layer thickness ratio could improve the Rs. Fig. 1 shows the magnetization curve simulated at 300K condition. Ms and Ku in the hard layer(16nm) were set to 600emu/cc, 4E6erg/cc, respectively, assuming the present CoCrPt-oxide granular layer. Ku in the soft layer(4nm) was supposed as 0erg/cc. The shoulder of the curve seems to be round shape and the Rs is about 0.9 even in the direct coupling (no interlayer; A12=1.0uerg/cm). The ECC media with zero-Ku soft layer could not keep its magnetization in perpendicular saturated states under the thin film demagnetizing field, even if the soft layer was coupled directly with the hard layer.

As experimental comparison, the ECC media similar to that by Shimatsu et al. [2] was prepared using a sputtering system (CoPtCr-oxide hard layer / (interlayer) / Co-oxide soft layer). Rs=1, more than 2kOe of Hn and the Hc reduction in the ECC media were obtained successfully. Simulating the magnetization curve and the angular dependence of remanence coercivity Hcr with various Ku, Ms, A12 in the soft layer, the parameters had been investigated which could explain the experimental results most appropriately. As a result, calculated values in the combinations of Ms=900emu/cc and Ku=4E6erg/cc gave relatively good agreement with experimental results (Fig. 2). These results suggest the possibility that the experimental top Co granular layer has high Ku as the bottom CoPtCr granular layer. It is presumed that the unity of Rs in ECC media requires a large positive Ku of the soft layer (the order of 1E6erg/cc) enough to overcome the demagnetizing field, with the support of the interlayer coupling.

Even if the soft layer has as large Ku as the hard layer, high Ms of the soft layer provides lower anisotropy field Hk than that of the hard layer. The observation of the magnetization reversal process in the simulated ECC media with the high Ku soft layer displayed the prior rotation of the soft layer to that of the hard layer, which makes the switching filed of the ECC media reduced.

The additional simulations were performed about the case that the soft layer had a negative Ku [3]. The angular dependence of the normalized Hcr for the high Ku soft layer was close to that for single hard layer, different from that for the zero and negative soft layer. This property is similar to that of current perpendicular media.

Simply, higher Ku of the soft layer can increase the vKu/kT in one whole grain of ECC media. The result of thermal decay simulations indicated that the ECC media with positive Ku soft layer had higher thermal stability than that with zero and negative Ku soft layer, as expected.

The perpendicular anisotropy of the soft layer in ECC media are thought to need to take a positive large value in order to realize the ECC media type of magnetization reversal in the shape of thin film, which will lead to the above various advantages.

[1] R.H.Victora et al.: IEEE Trans. Magn., 41, 537 (2005).

[2] T.Shimatsu et al.: IEEE Trans. Magn., 43, 2103 (2007).

[3] A.Hashimoto et al.: J. Magn. Soc. Jpn., 30, 135 (2006).

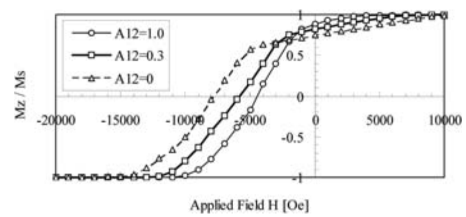

Fig. 1 Magnetization curves of the thin film ECC media with normal soft layer for various interlayer coupling A12.

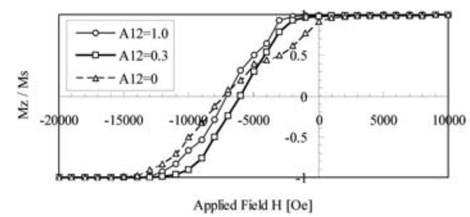

Fig. 2 Magnetization curves of the thin film ECC media with high Ku soft layer for various interlayer coupling A12.

CS-02

Segregation Mechanisms in Co-based Oxide Recording Media.

E. E. Marinero[1], D. T. Margulies[1], B. R. York[1], P. Rice[2]
1. Hitachi San Jose Research Center, San Jose, CA; 2. IBM Almaden Research Center, San Jose, CA

Introduction
A key requirement for ultra-high density recording is the development of a microstructure comprising uniform, small, thermally-stable and highly-oriented magnetic grains which are segregated and magnetically-decoupled by non-magnetic secondary phases. Species such as SiO2, TiO2 or Ta2O5 are incorporated into the target material employed to deposit the recording layer, and the segregation process is empirically controlled by optimizing the deposition parameters. This paper elucidates the mechanisms leading to the formation of the desired recording layer microstructure.

To derive a high degree of crystallographic and magnetic orientation, the use of a multi-layer stack employing seed layers such as NiW (fcc) directly deposited on the SUL followed by growth of hcp intermediate layers (IMLs) such as Ru are employed. Development of a highly oriented recording alloy is a necessary but not a sufficient condition for high density magnetic recording. Two critical processing steps have been found to be essential to yield the desired structural and magnetic properties: a) the optimized addition of oxygen into the sputter plasma for deposition of the magnetic layer and; b) the growth of said magnetic layer on an IML deposited under high pressure sputter conditions. We have used HRTEM combined with EELS analysis, XRD and magnetometry to elucidate the role each of these layers and processing steps play in the evolution of the optimum segregated microstructure.
Results and Discussion
Fig. 1 compares the microstructure of CoPtCr-TaOx grown on 18 nm thick Ru underlayers grown both at high and low pressure. A cursory inspection of the TEM images reveals little differences between them. However, as shown in (C), the magnetic properties are vastly different. Utilizing high angle annular dark field imaging (HAADF) and EELS analysis we note that growth of the magnetic alloy on low pressure Ru, leads to a high degree of bridging between magnetic grains. This leads to intergranular exchange coupling, resulting in coercivity losses. The high pressure regime, leads to interface roughness which drives the grain segregation and removes the bridging.

To verify the role of interfacial roughness in the segregation of the CoPtCr-SiO2, nanoscale layers were intercalated between Ru (RuCr) IMLs grown at low pressure and the magnetic layer. As an example, sub-nm Ta2O5 nucleation layers were deposited at high sputter pressures to generate a discontinous film at the interface. In Fig. 2 the layer sequencing, the evolution of interface roughness and the dependence of Hc on the nanolayer oxide thickness are given. A boost of ~ 1.5 kOe in Hc was measured when a 0.25 nm layer of the oxide was intercalated. Comparable film coercivity improvements as well as good SNR were obtained using high sputter pressure deposited nucleation layers (Ref 1). Note that as the layer thickness is incremented, the magnetic properties are negatively impacted due to loss of epitaxial growth.

The role of oxygen on the evolution of the CoPtCr-SiO2 microstructure was investigated by adding O2 to the sputter plasma during the CoPtCr-SiO2 growth. The results are given in Fig. 3, in which the influence of Oxygen addition on recording media grain size and film coercivity are given. Measurements were also made of the intergrain boundary zone dependency on oxygen content as well as changes in magnetic anisotropy.

In summary, results will be presented to elucidate the mechanisms driving the segregation process in recording media. These include interface roughness, the oxygen-mediated precipitation of the oxide phase at the grain boundaries, and the influence of the microstructural properties of both the IML and seed layers.

References: E.E. Marinero et al, US Patent Applications: 2007-0141400 and 2007-0042226.

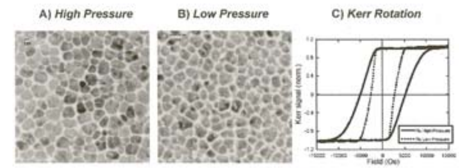

Fig. 1. HRTEM images of CoPtCr-TaOx: A) grown on a Ru IML deposited at high pressure; B) grown on Ru sputtered sputtered at low pressure; C) hysteresis loops of magnetic layers grown on Ru IMLs sputtered at 46 (solid) and 5 mTorr (dashed).

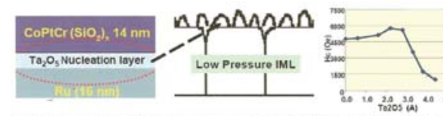

Fig. 2. Role of interface roughness: nanolayers of low mobility (high pressure deposition) nucleation layers are employed to drive the segregation process in the recording layer.

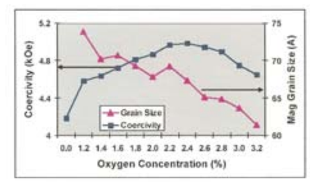

Fig. 3. Grain size and Hc vs. oxygen content in the magnetic layer sputter-plasma.

CS-03

Pseudo-hcp material and its evaluation for perpendicular recording media.

S. Saito[1], M. Takahashi[2,1]
1. Electronic engineering, Tohoku university, Sendai, Japan; 2. New industry creation hatchery center, Tohoku univ., Sendai, Japan

Pseudo-hcp structure (00.2-oriented hcp or 111-oriented fcc structure with stacking faults) and its structural evaluation will be introduced as showing its typical advantage in the texture control of overlying layer for a nonmagnetic intermediate layer (NMIL: alternatives to Ru) including a seed layer like as Ni-W alloy. Our newly proposed evaluation was also found to be effective in recording layer (RL) materials to clarify relationship between stacking order of atomic layers and uniaxial magnetocrystalline anisotropy (K_u) of Co based materials.

A NMIL plays an important role in controlling the structure of a RL by providing nuclei sites for the growth of magnetic grains in the RL, and by promoting epitaxial growth of the magnetic grains in the RL to afford a *c*-plane sheet texture. A precious metal Ruthenium (Ru) with a *c*-plane orientation and rough surface is widely used as an NMIL material. However, large Ru thicknesses (12–30 nm) sputtered under high P_{Ar} (enhancing the surface roughness) required greatly increase the cost of mass production of the media. From this view point, we propose new fcc materials with highly coherent stacking faults (pseudo-hcp materials) as alternative NMIL materials to replace hcp Ru, focusing on the conditions required for epitaxial growth. Fig. 1 shows the relationship between F_{NMIL}^{RL} and S_{NMIL}^{Co} for granular RL fabricated on various NMILs. Equivalue lines of K_u^{RL} (average value of K_u for CoPtCr-SiO$_2$ layer) are also shown. Here, F_{NMIL}^{RL} is the misfit defined as equ. (1), the distance between the nearest neighbor atoms in the close-packed plane of NMIL (d_{int}^{NMIL}), and the nearest neighbor atomic distance in the *c*-plane of CoPtCr magnetic grains (d_{int}^{RL} = 2.56 Å):

$F_{NMIL}^{RL} = (d_{int}^{NMIL} - d_{int}^{RL}) / d_{int}^{RL}$. (1)

While S_{NMIL}^{Co} is the spreading coefficient of the wettability of Co for NMIL, and is derived from Young-Dupré's equation:

$S_{NMIL}^{Co} = \gamma_{NMIL} - (\gamma_{NMIL-Co} + \gamma_{Co})$, (2)

where, γ_{NMIL} and γ_{Co} denote the surface energy for solid NMIL material and solid Co, respectively, and $\gamma_{NMIL-Co}$ denotes the interfacial energy between solid NMIL material and liquid Co. Remarkable feature is; 1) alloying fcc metals (Ni, Pd, Pt, Ir etc.) with bcc metal former (Cr, Mo, W, Ti, Nb, etc.), equivalent pseudo-hcp structure is obtained. The enhancement of the preferred epitaxial growth of hcp magnetic grains took place on only the specified (111) atomic terraces of the fcc NMIL with stacking faults, suppressing the equivalent variant growth (see ref. [1]), and 2) F_{NMIL}^{RL} < 6 % and S_{NMIL}^{Co} > 0.3 J/m^2 are essential requirements for the NMIL material to induce high K_u^{RL} of over 4.4 × 10^6 erg/cm^3 [2]. According to these guiding principles, not only binary alloys such as Pt-Cr, and Ir-Cr, but also ternary alloy systems with pseudo-hcp structure are suitable for alternative NMIL materials to replace Ru.

We also propose simple measure of the degree of stacking faults by using conventional laboratory-scale XRD. According to the in-plane XRD profile for pseudo-hcp materials, two diffractions can be seen; one originates from pure fcc (220) plane, I_H, which is very common and gives no information of the stacking faults. The other appears at low angle side, I_L, which can not be identified as the fcc structure but reflects the frequency of the stacking faults in the fcc lattice. Note that diffractions of I_H and I_L are equivalent to (11.0) and (10.0) diffractions of the hcp system (see fig. 2 (a-b)). Therefore, intensity ratio of I_L/I_H corrected by Lolentz and atomic scattering factors is defined as the degree of stacking order for pseudo-hcp materials. Theoretically, corrected I_L/I_H can be expressed by using structure factor of (11.0) and (10.0) diffractions, $E_{(11.0)}$ and $E_{(10.0)}$, as $|E_{(10.0)}/E_{(11.0)}|^2$, where $E_{(10.0)} = N_A + N_B \exp(-2\pi i/3) + N_C \exp(-4\pi i/3)$, $E_{(11.0)} = N_A + N_B + N_C = N$, and N, N_A, N_B, N_C correspond to the number of total and each atomic layer, respectively. Ideal values of this index are 0.25 for hcp stacking, while 0 for fcc stacking. Fig. 2 (c) shows corrected I_L/I_H for various pseudo-hcp materials as a function of additional material content. By adding various additional elements to host fcc materials, Ir and Pt based alloys are found to strongly enhance the hcp-like structure. In the presentation, relationship between I_L/I_H and K_u of Co based alloys are also discussed.

This study was partially supported by Industrial Technology Research Grant Program in 2006 from New Energy and Industrial Technology Development Organization (NEDO) of Japan.

[1] A. Hashimoto, et al., *Appl. Phys. Lett.*, **89**, 262508 (2006). [2] A. Hashimoto, et al., *J. Phys. D*, **41**, 012002 (2008).

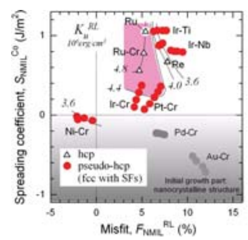

Fig. 1 The relationship between lattice misfit (F_{NMIL}^{RL}) and spreading coefficient (S_{NMIL}^{Co}) for granular RL fabricated on various NMILs. Isogram of K_u^{RL} is also shown in the figure.

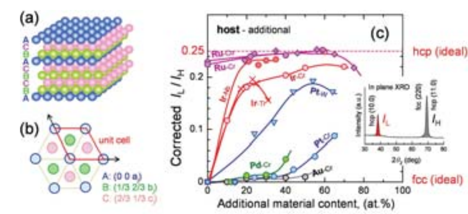

Fig. 2 (a) Schematic view of stacking structure, (b) unit cell of hcp system in the top view of the atomic plane (c-plane), and (c) corrected intensity ratio, I_L/I_H for various fcc-hcp materials as a function of additional material content.

CS-04

Magnetic interaction between recording layer and soft underlayer in granular-type perpendicular magnetic recording media with thin intermediate layer.

K. Shintaku
Akita Research Institute of Advanced Technology, Akita Prefectural R&D Center, Akita, Japan

Introduction

For high-density perpendicular recording, reduction of the film thickness of an intermediate layer between a recording layer and a soft underlayer (SUL) is important for saturation recording. A high-B_s soft underlayer is also needed to reduce the film thickness from the viewpoint of industrial production. To solve these problems simultaneously, I proposed CoPt-TiO_2 media with a highly oriented Fe-Co SUL with a high-B_s of 2.45 T and a thin Ru intermediate layer [1]. A CoPt-TiO_2 recording layer on a Ru intermediate layer of only 2 nm had a high crystal orientation, a high H_c, and a high squareness ratio (SQ) [2]. The medium had large reproduced output even for the Ru intermediate layer thickness of 2 nm. Although such an extremely thin intermediate layer thickness seems to influence magnetic interaction between a recording layer and a SUL, no experimental result was reported.

Experiment

Samples were prepared by DC and RF magnetron sputtering in an Ar gas atmosphere. Alloy targets of $(Co_{80}Pt_{20})$-(TiO_2) (CoPt : TiO_2 = 80 : 20 vol%), Ru, $Fe_{70}Co_{30}$, $Ir_{20}Mn_{80}$, Pt, and Ta were used. Substrates were ϕ 2.5-inch glass disks. A magnetic field of about 100 Oe was applied to induce an in-plane magnetic anisotropy in the radial direction of the disks during deposition. The base pressure is around 1 - 2 $\times 10^{-5}$ Pa. Substrate temperature was 20 °C. Magnetic properties were measured by a vibrating sample magnetometer (VSM) and a Kerr effect magnetometer.

Results and discussion

Figure 1 shows a schematic illustration of a prepared medium. Ru intermediate layer thickness was changed. IrMn was used as an fcc underlayer to obtain soft magnetic properties in an FeCo film, and an antiferromagnetic layer to pin the FeCo film. A Pt underlayer is effective in increasing the crystal orientation of the IrMn, which is necessary in order to enhance the exchange coupling energy between the FeCo and the IrMn films. Ta underlayer was greatly effective to enhance the crystal orientation of the whole film. As shown in Fig. 2, the minimum Ru layer thickness for obtaining the SQ of about 1 was 1.6 nm. Figures 3 and 4 show the Ru intermediate layer thickness dependence of H_c of the recording layer and H_{ch} (H_c in the hard axis direction) of the SUL, respectively. The H_c of the recording layer oscillated as a function of Ru intermediate layer thickness. The oscillation period was 0.6-0.8nm (2-3 atomic layer thickness). On the other hand, the H_{ch} of the SUL oscillated in inversely proportion to the H_c. A medium with Ru intermediate layers of larger H_c (peak position of oscillation) showed better soft magnetic properties than that of valley position of the H_c oscillation. This indicates that magnetic interaction between the recording layer and the SUL can be controlled by choosing an appropriate film thickness of Ru intermediate layer.

[1] K. Shintaku, IEEE Trans. Magn., 42, 2339 (2006).

[2] K. Shintaku, Digests of PMRC 2007, 15pD-28 (2007).

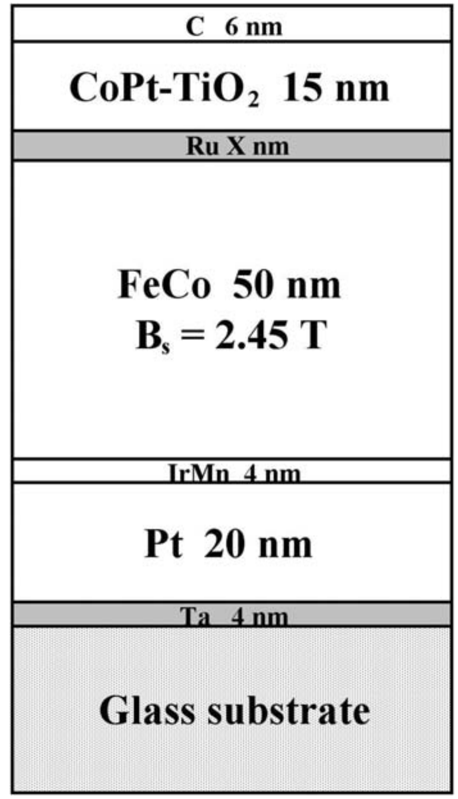

Fig. 1 Schematic illustration of a media.

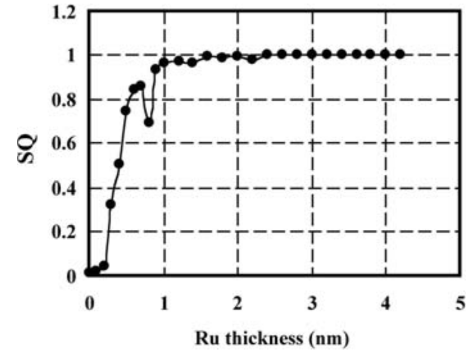

Fig. 2 Ru intermediate layer thickness dependence of SQ of the recording layer.

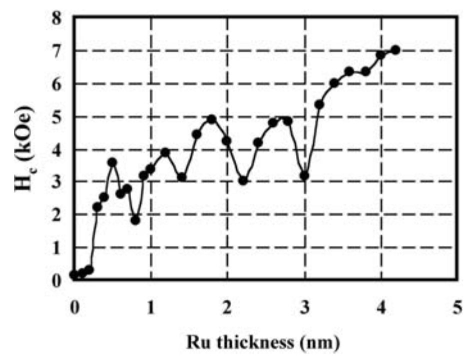

Fig. 3 Ru intermediate layer thickness dependence of H_c of the recording layer.

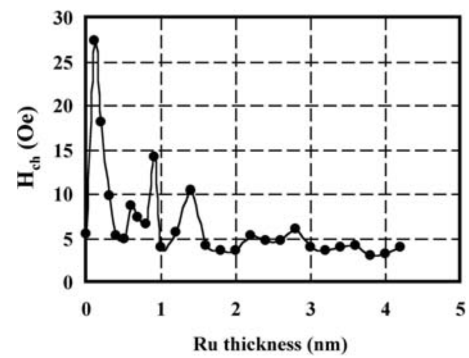

Fig. 4 Ru intermediate layer thickness dependence of H_{ch} of the SUL.

CS-05

A new method for controlling an exchange coupling of perpendicular recording media.

J. Ariake, N. Honda
AIT, Akita Prefectural R&D Center, Akita, Japan

Introduction

There are some proposals to control an exchange coupling of the recording layer in the perpendicular magnetic recording media in order to avoid trilemma difficulties (small grain size, high K_u material, difficult to write). However, many researchers pay attention on controlling it by adding so-called stacked layer such as a soft/soft stacked film. In such structure, the film thickness for two stacked layers is very important for precise control of the exchange coupling between two layers. For so-called "CGC" media (1), a continuous layer should be in the range of 1 to 3 nm in thickness to obtain good performance of the media.

In this paper, we propose a new method to control an exchange coupling of the perpendicular recording films by heat treatment of them.

Experimental

A Co-Pt-TiO_2 granular film was used as a recording layer of the perpendicular media. A Ru/Pt layer and CoZrNb were used as a underlayer and SUL, respectively. All films were deposited at room temperature. Heat treatment for the granular films was applied after depositing the films in a vacuum condition below $1x10^{-5}$ Pa. Temperature of the annealing (T_A) is from r.t. (no annealing) to 500°C for 30 min. After cooling down, a carbon protective layer was deposited on the Co-Pt-TiO_2 film.

Magnetic characteristics were evaluated by a Kerr effect magnetometer (Kerr: NEOARC, BH-M800UV-HD). Maximum applied field and a field sweep rate in Kerr measurement were 20 kOe and 0.38 ms/Oe, respectively. Magnetic structure was observed by a magnetic force microscope (MFM: Veeco, D3000) at ac-erased state. Surface images were also observed by an atomic force microscope (AFM) with MFM.

Results and discussion

Fig. 1 shows Kerr loops for Co-Pt-TiO_2 films with no annealing and annealed at T_A of 300°C. A Co-Pt-TiO_2 film is known to form separated grain structure in the media efficiently by TiO_2 grain boundary formation (2). Therefore, a very inclined M-H loop slope for the film was obtained as shown in Fig. 1(a). A Kerr loop slope of the annealed sample was steeper as shown in Fig. 1(b) than that of non-annealed one. In this experiment, a loop slope became steep with increasing T_A, indicating that the exchange coupling of the granular films became stronger with T_A. On the other hand, a magnetic cluster size for the annealed films became small in spite of a stronger exchange coupling than that for the non-annealed one as shown in Fig. 2. In the previous paper, there occurred no significant grain growth for the annealed Co-Pt-Cr-SiO_2 films (3). In our films, there seems also no significant grain growth from the AFM image. Furthermore, $\Delta H_c/H_c$ value (4) became small with increasing T_A as shown in Fig. 3. This indicates that the annealed film has a narrower switching field distribution compared with non-annealed one. Fig. 4 shows crystallographic properties of the films in this experiment. It was found that the crystallinity and crystal orientation of the annealed films became improved. This means that the film structure became uniform by annealing. This may bring about the improved magnetic characteristics such as a reduced $\Delta H_c/H_c$ value.

Summary

To summarize this report, it is obvious that the exchange coupling of the granular Co-Pt-TiO_2 films can be controlled by applying heat treatment of the film. The effect of the annealing was not only to control exchange coupling of the recording layer but also to uniform and reduce the film structure such as magnetic characteristics and crystal orientation.

(1) Y. Sonobe et al., J. Magn. Magn. Mater., vol. 235, 424, 2001.

(2) J. Ariake et al., IEEE Trans. Magn., Vol. 41, 3142, 2005.

(3) S. H. Park et al., IEEE Trans. Magn., Vol. 42, 2390, 2006.

(4) I. Tagawa and Y. Nakamura, IEEE Trans. Magn., Vol. 27, 4975, 1991.

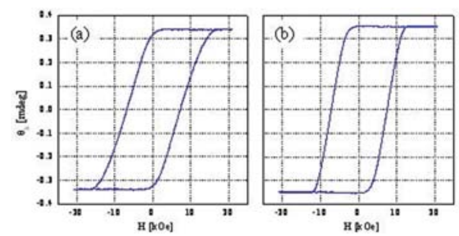

Fig. 1 Kerr loops for Co-Pt-TiO_2 films with (a) no annealing and (b) annealed at 300°C.

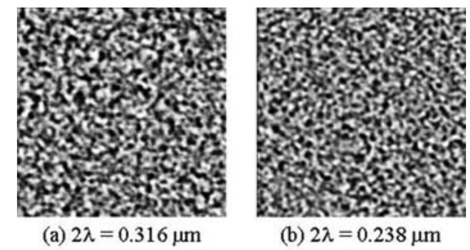

Fig. 2 MFM images for Co-Pt-TiO_2 films with (a) no annealing and (b) annealed at 300°C. (5 μm sq.)

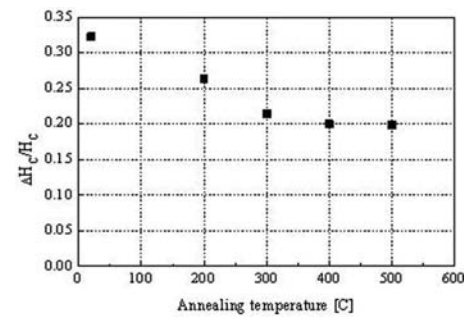

Fig. 3 ΔHc/Hc for Co-Pt-TiO_2 films with annealed at various temperature.

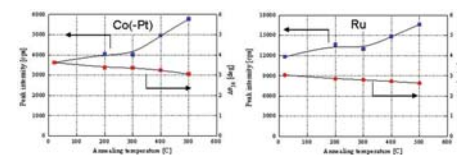

Fig. 4 Dependence of crystallographic properties on annealing temperature.

CS-06

A study of perpendicular magnetic recording media with an exchange control layer.

K. Tang, K. Takano, G. Choe, G. Wang, J. Zhang, X. Bian, M. Mirzamaani
Hitachi Global Storage Technologies, San Jose, CA

This paper is an experimental study of the hysteresis behavior and recording performance of ECC type media [1]. The magnetic recording layer structure in this study is comprised of a granular oxide magnetic layer, a cap magnetic layer and an exchange control layer (ECL) in between that reduces ferromagnetic exchange coupling strength between the granular oxide and cap layers. Fig. 1 plots saturation field (H_s) vs. ECL thickness (t_{ECL}) of such a medium. At t_{ECL}=0, the granular oxide and cap layers are strongly exchange coupled causing a pinning of the magnetic moment in the cap by the granular oxide that limits its role in assisting the switching of the granular oxide layer. This leads to a large value of H_s. As t_{ECL} increases, the exchange coupling strength between the granular oxide and cap decreases, allowing the magnetic moment in the cap to rotate more easily by an external field and thus to assist the switching of the granular oxide layer below resulting in an overall decrease of H_s. When t_{ECL} becomes very thick, the granular oxide and cap layers are so weakly coupled that the cap can only provide limited assistance in switching the granular oxide, resulting in an increase in H_s. These two regions define a minimum H_s point in the H_s vs. t_{ECL} curve. At very thick t_{ECL} values, weak exchange coupling leads to a two-stage switching mechanism where the cap and the granular oxide layers switch independently. Hysteresis loops at different t_{ECL} values are shown as inserts in Fig. 1. Smooth switching curves are observed at thin t_{ECL}, but hysteresis curves at thicker values of t_{ECL} show discontinuities.

Fig. 2 shows that media SNR and OW are improved with the incorporation of the ECL layer, and best performance is achieved near the t_{ECL} value that gives minimum H_s. In order to eliminate the effect of OW on media SNR, we compare an ECL medium with a non-ECL medium with similar OW. The two media use the same granular oxide and cap materials, and their OW's are matched by cap adjustment. The results indicate that the ECL medium offers a 0.5dB media SNR advantage. This suggests that the ECL plays a role in reducing noise introduced by the highly exchange coupled cap layer.

To study the effect of ECL properties on ECL media, we select a series of ECLs with different M_s values by varying the content of a non-magnetic element. In the case of high ECL M_s, no minimum H_s is observed suggesting that strong exchange coupling resulting from the high M_s of the ECL is enough to maintain one stage switching and therefore H_s decreases continuously with increasing t_{ECL} in the entire ECL thickness range studied. As M_s of the ECL decreases, two stage switching can occur at thick t_{ECL} and a minimum H_s point appears. Another study of varying M_s of the ECL is done on a second series, in which both ECL materials have low enough M_s so that minimum H_s point occurs. For the lower M_s ECL, the minimum H_s point shifts to thinner t_{ECL}, indicating that an ECL with lower M_s can sufficiently weaken exchange coupling between the granular oxide and cap and result in two-stage switching at a thinner t_{ECL} (Fig. 3). Optimum ECL thickness is closely related to magnetic properties of the ECL.

The coupling strength between granular oxide and cap layers also depends on M_s of the cap layer. Since lower M_s of the cap layer gives rise to weaker interfacial exchange coupling between the ECL and cap, two-stage switching behavior of the granular oxide and cap layer is reached at a thinner t_{ECL}. However, when the M_s of ECL is very low, the granular oxide-to-cap coupling strength is limited by the ECL layer, and the t_{ECL} at minimum H_s becomes less sensitive to M_s of cap layer. Accordingly, the optimum magnetic and recording properties of ECL media have to be designed with consideration of both ECL and cap properties, which will be discussed in more details in the full paper.

In summary, recording performance of perpendicular media can be improved with addition of an ECL. Thickness and magnetic properties of the ECL combined with magnetic properties of the cap layer are key factors to media optimization.

[1] R.H. Victora and X. Shen, IEEE Trans Mag, Vol. 41, No. 2, pp. 537-542 (2005)

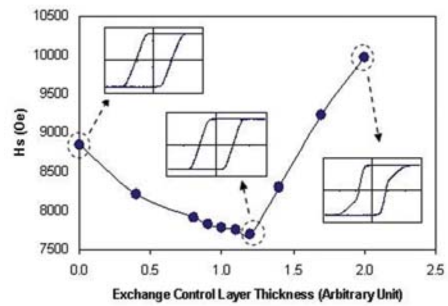

Fig. 1. Saturation field (H_s) as a function of exchange control layer thickness (t_{ECL}).

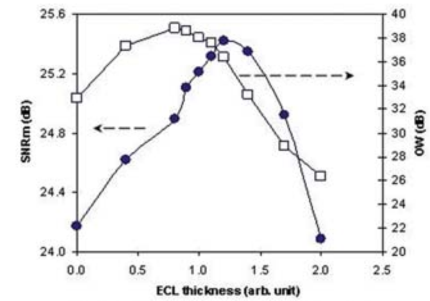

Fig. 2. Media SNR and OW as a function of exchange control layer thickness (t_{ECL})

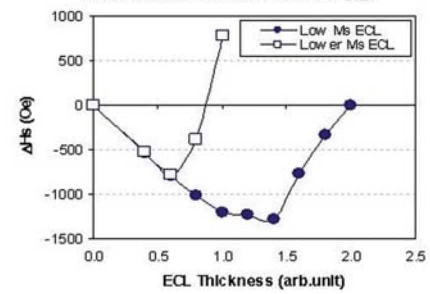

Fig. 3. H_s as a function of exchange control layer thickness (t_{ECL}) for two media with different ECLs. ΔH_s is the difference in H_s with respect to H_s at t_{ECL}=0.

CS-07

Al-N; a hexagonal-nitride seed layer underlayered Ru in granular-type perpendicular media.

S. Ishibashi[1], S. Saito[1], A. Hashimoto[1], M. Takahashi[2,1]
1. Dept. of Electronics Engineering, Tohoku University, Sendai, Japan; 2. New Industry Creation Hatchery Center, Tohoku University, Sendai, Japan

Introduction

Perpendicular magnetic recording media presently consist of a soft magnetic underlayer (SUL), a nonmagnetic intermediate layer (NMIL), and a recording layer (RL). Granular materials consisting of Co-base magnetic grains with oxide-rich grain boundaries are widely used for the RL, and the NMIL plays an important role in controlling the structure of such an RL by providing nuclei sites for the growth of magnetic grains in the RL, and by promoting epitaxial growth of the magnetic grains in the RL to afford a *c*-plane sheet texture. Ruthenium (Ru) with such a *c*-plane orientation and rough surface is widely used as an NMIL material. [1,2] However from the aspect of high density media, it is hard to realize further reduction of grain size retaining highly *c*-axis orientation and rough surface by only modification of Ru deposition process. As one of solutions of this problem, we think that it is important to achieve epitaxial growth of Ru grains on seed layer through the precise control of both the wettability and the lattice matching. In this presentation, we introduce hexagonal-nitride seed layers with covalent bond, AlN with Wurzite ($P6_3mc$) structure and Ta_2N with the L'3 ($P6_3/mmc$) structure. On these seed layers, Ru grains are expected to start from small initial nuclei due to not so good wettability nor lattice matching. The lattice miss fit ratios, $(a_{seed} - a_{Ru})/a_{seed}$ x 100, of AlN, Ta_2N to Ru are +14.8 %, +12.5 % respectively.

Experimental Procedure

All the samples in the present study were fabricated by dc magnetron sputtering under the total gas pressure of 0.6 Pa at room temperature onto amorphous glass substrate. The surface roughness of glass substrate was 0.3 nm. Film stacking structure is sub./ buffer (10 nm)/ seed (0-20 nm)/ Ru (0-20 nm)/ CoPtCr-SiO_2 (16 nm)/ C (7 nm). The Al-N and Ta-N seed layers were deposited by reactive sputtering using Ar and N_2 mixed gas with varying N_2 flow ratio. As the buffer layer, Ta, $Ni_{60}Zr_{40}$, $Ni_{60}Ta_{40}$, $Co_{91}Zr_4Nb_5$, $(Fe_{65}Co_{35})_{88}B_{12}$ were adapted. Crystallographic texture, grain dia. of Ru, GD_{Ru}, and *c*-axis direction distribution of Ru, $FWHM_{Ru}$, were analyzed using transmission electron microscope (TEM) and x-ray diffractometer (XRD) using Cu-Kα radiation. Magnetic properties were measured by the polar Kerr equipment.

Results and Discussion

At first, the fabrication condition, especially flow ratio of Ar and N_2 mixed gas, *f*, is optimized. As a result it was found out that the hexagonal AlN and Ta_2N films with *c*-plane sheet texture are realized under the condition of f = 40 % and 20 %, respectively. Fig. 1 shows a bright-field image obtained by cross-sectional TEM for a sub./ FeCoB/ AlN/ Ru/ C film. An enlarged view of the AlN layer is also shown on the right. Concerning the Ru layer structure, it is found that both highly oriented *c*-plane sheet texture and rough surface of over 2 nm in peak to valley are realized even though Ar gas pressure is as low value as 0.6 Pa. Furthermore, focused on the AlN layer, lattice stripes in the AlN grains representing the (00.2) plane are oriented parallel to the film plane from the initial growth region. Fig. 2 shows the Ru thickness dependence of grain dia. and *c*-axis direction distribution of Ru, GD_{Ru} and $FWHM_{Ru}$, in AlN/ Ru stacked film with various buffer layers. Focused on the buffer layer materials, the $FWHM_{Ru}$ decreases with changing in buffer structure from nano-crystalline to amorphous. As the results, both the low GD_{Ru} of 7 nm and low $FWHM_{Ru}$ of 3.5 deg. are obtained even for the sample deposited on glass substrate without special polishing. Fig. 3 shows the Ru thickness dependence of coercivity H_c for an AlN seed medium, together with that of a NiFeCr seed layer as a comparison. The H_c value of the AlN seed medium is larger than that of the NiFeCr seed medium in every Ru thickness. Note that the media plotted in fig. 3 show almost the same H_k of 14.7 kOe obtained from 625 emu/cm^3 and 4.6 x 10^6 erg/cm^3 in M_s and K_u. These results indicate that the AlN seed medium is more magnetically isolated than the NiFeCr seed medium. Therefore, it is concluded that the AlN seed layer has a great potential to realize magnetic isolation, low grain size, and highly *c*-plane orientation of granular-type perpendicular media through the control of Ru layer structure. The results of the Ta-N seed medium will be also discussed in the presentation.

1) T. Oikawa et al.: IEEE Trans. Magn. **38**, 1976 (2002). 2) R. Mukai, et al., IEEE Trans. Magn. **41**, 3169 (2005).

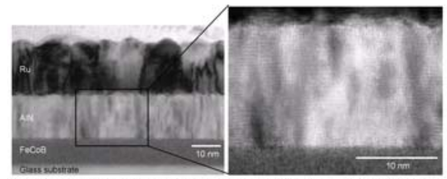

Fig. 1 Bright-field image obtained by cross-sectional TEM for a glass substrate/ FeCoB(10 nm) / AlN(20 nm)/ Ru(0.6 Pa, 20 nm)/ C(7 nm) stacked film. An enlarged view of an AlN layer is also shown.

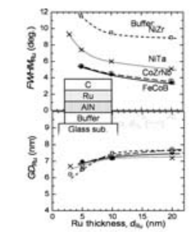

Fig. 2 Grain dia., GD_{Ru}, and *c*-axis direction distribution of Ru, $FWHM_{Ru}$, in Buffer/ AlN/ Ru stacked films.

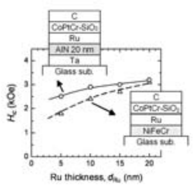

Fig. 3 H_c for a granular medium deposited on AlN seed layer and on a NiFeCr seed layer.

CS-08

Granular perpendicular soft layer with tunable anisotropy energy in exchange coupled composite media.

H. Hou[1], M. Lin[1], R. Liao[1], C. Lai[1], R. Chen[2], C. Lee[2]
1. Department of Materials Science and Engineering, National Tsing Hua University, Hsinchu, Taiwan; 2. China Steel Corporation, Kaohsiung, Taiwan

I. Introduction
Exchange coupled composite media (ECC) consists of both magnetic hard and soft layers, has been proposed to address the "trilemma effect" in perpendicular magnetic recording media [1-3]. The soft layer assists the reversal of main recording hard layer, and results in the reduced switching field, narrowed switching field distribution (SFD), and less-sensitive angular dependence when compared to the conventional perpendicular recording media. However, a granular structure and relatively low anisotropy field are crucial requirements for the soft layer. In this work, we developed a new type of soft layer, [CoPtCr-SiO_2/Pt] multilayers, which possessed tunable perpendicular anisotropy, and resulted in a low switching field and high thermal stability for the ECC media.
II. Experiment
All samples were prepared at room temperature using an 8-target magnetron sputtering system with the base-pressure of $1x10^{-7}$ Torr. The layer structure of conventional perpendicular media and ECC media were Ta 3/Pt 7/Ru 30/CoPtCr-SiO_2 17.5 and Ta 3/Pt 7/Ru 30/CoPtCr-SiO_2 17.5/Pt 0.75/[CoPtCr-SiO_2 1.1/Pt 0.75]$_5$ MLs (unit: nm), respectively. The magnetic properties of prepared samples were measured by a vibration sample magnetometer, and the microstructure was determined by transmission electron microscopy.
III. Results and Discussions
The conventional perpendicular media showed Hc~4600 Oe, M_S~380 emu/cm^3, and good grain isolation with an average grain size of 7nm. The Pt and [CoPtCr-SiO_2 1.1nm/Pt 0.75nm]$_5$ MLs were designed as the spacer and soft layer (SL) for novel ECC perpendicular media, which possessed perpendicular anisotropy and low coercivity ~200 Oe, as shown in Fig. 1. The ECC perpendicular media, substrate/Ta 3/Pt 7/Ru 30/CoPtCr-SiO_2 17.5/Pt 0.75/ [CoPtCr-SiO_2 1.1/ Pt 0.75]$_5$ (unit: nm), revealed the significant reduction of coercivity (Hc= 2900 Oe) and saturation field (Hs=6200 Oe), as shown in Fig 1, which may improve the writability. The [CoPtCr-SiO_2/Pt]$_5$ multilayer of full stack ECC media became granular due to the preferred segregation of SiO_2 at the grain boundaries of the recording layer (RL: CoPtCr-SiO_2). Therefore, this kind of media exhibited grain-to-grain epitaxial relationship between RL and SL, as shown in Fig. 2. In addition to the granular microstructure, the adopted [CoPtCr-SiO_2/Pt]$_5$ multilayer structure enabled us to tune the magnetic anisotropy energy K_U of SL by simply controlling the Pt layer thickness or the number of total layers. The measured K_U by the rotation method [4] were $1.33x10^6$, $7.19x10^5$, and $3.76x10^5$ erg/cm^3 when Pt thickness of [CoPtCr-SiO_2 1.1nm/Pt]$_5$ were 0.37nm, 0.75nm, and 1.13nm, respectively. The tunable anisotropy energy of the SL can be quite useful for advanced media, e.g. graded media [5].
In addition, remanent coercivity and angular dependence of ECC media showed the reduction of H_{cr}, 38%, and angular insensitivity, compared to the conventional PMR, as shown in Fig.3, which was considered to be helpful to improve writability and signal to noise ratio (SNR). Concerning about the thermal stability factor, K_UV/k_BT of the conventional PMR and the ECC was 100 and 129, respectively, which indicated that the ECC perpendicular media composed of a RL CoPtCr-SiO_2 and soft MLs [CoPtCr-SiO_2/Pt]$_5$ with perpendicular anisotropy led to enhancement of thermal stability.

In summary, this work demonstrated that [CoPtCr-SiO_2/Pt] MLs was a promising soft layer for ECC media, which showed the advantages of a granular microstructure and tunable anisotropy energy. In addition, the improvement of thermal stability, reduction of H_C, H_S, H_{cr} and less-sensitivity of angular dependence were also achieved when the perpendicular soft layer was employed in ECC media.

[1]R. H. Victora and X. Shen, IEEE Trans. Mag. 41, 537 (2005).

[2]R. H. Victora and X. Shen, IEEE Trans. Mag. 41, 2828 (2005).

[3]J. P. Wang et al., Appl. Phys. Lett. 86, 142504. (2005).

[4]G. Ju et al., J. Appl. Phys. 93, 7846 (2003).

[5]D. Suess, Appl. Phys. Lett. 89, 113105. (2006).

[6]Z. S. Shan, Y. F. Xu, J. P. Wang et al., IEEE Trans. Mag. 37, 1944 (2001).

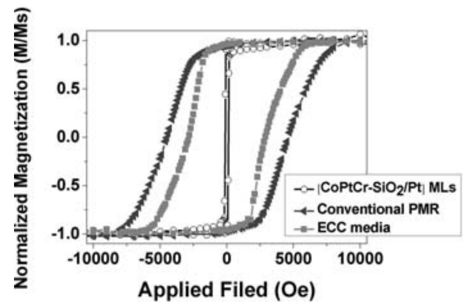

Fig1. Hysteresis loop of [CoPtCr-SiO_2/Pt] MLs, conventional PMR and ECC media.

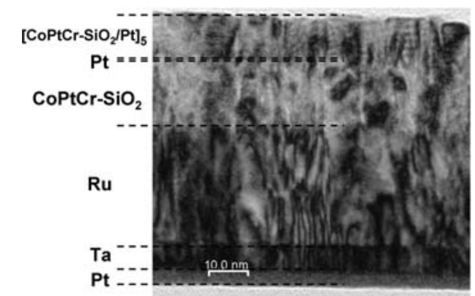

Fig 2. Cross sectional TEM image of ECC media

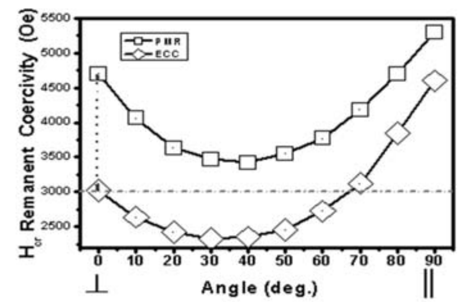

Fig 3. Remanent Coercivity of conventional PMR and ECC media.

CS-09

Effect of deposition condition of Ru-oxide/Ru bilayers on magnetic properties and orientation of CoPtCr-SiO_2 perpendicular recording media.

T. Matsuu[1], A. Hashimoto[1], K. Hirata[1], H. Fujiura[1], S. Matsunuma[2], T. Inoue[2], T. Doi[2], S. Nakagawa[1]

1. Dept. of Physical Electronics, Tokyo Institute of Technology, Tokyo, Japan; 2. Hitachi Maxell, Ibaraki, Japan

Introduction

CoPtCr-SiO_2 granular perpendicular magnetic recording media requires (001) texture of CoPtCr magnetic grains and well-isolated grain structures[1] to attain better playback performance. We prepared a Ru-oxide layer as a seed layer of Ru/CoPtCr-SiO_2 bilayer to attain (001) texture of the Ru underlayer which enhanced an epitaxial growth of CoPtCr (001) texture at room temperature. To attain the properties mentioned above, a Ru layer and a CoPtCr-SiO_2 layer were deposited at low gas pressure and high gas pressure, respectively[2]. In this study, we investigated the effect of a deposition condition of Ru-oxide layer. Some improvements of magnetic properties were attained by changing gas pressure for deposition of CoPtCr-SiO_2 layer.

Experimental

Ru-oxide/Ru/CoPtCr-SiO_2 thin films were deposited directly on glass substrates at room temperature using Facing Targets Sputtering (FTS) system. Ru-oxide/Ru/CoPtCr-SiO_2 films were prepared at 4 mTorr, 4 mTorr and 26 mTorr of gas pressure, respectively. Ru-oxide layers were prepared by reactive sputtering method using a gas mixture of 90 % Ar and 10 % O_2 as flow ratios into the sputtering chamber. Background pressure was 4.0×10^{-6} Torr. Magnetic properties were measured using a vibrating sample magnetometer (VSM). Crystallographic and microstructures were observed by X-ray diffraction (XRD) and a transmission electron microscopy (TEM).

Results and Discussion

In our previous study, it was found that a Ru-oxide layer was required to attain (001) texture of the top Ru layer. Coercivity of 3.0 kOe and squareness ratio of 0.92 in the perpendicular direction were obtained with Ru-oxide(8 nm)/Ru(15 nm)/CoPtCr-SiO_2(30 nm) thin films.

Fig.1 and 2 show XRD diagram and coercivity and squareness ratio in the perpendicular and in-plane directions of Ru-oxide(x nm)/Ru(15 nm)/CoPtCr-SiO_2(30 nm) thin films for various Ru-oxide layer thickness. When the thickness decreased below 5 nm, Ru (002) diffraction intensity decreased and perpendicular magnetic properties deteriorated. It indicated a Ru-oxide layer was required a certain amount of the thickness to improve the crystallographic orientation.

Fig.3 shows the cross-sectional TEM image of Ru-oxide(10 nm)/Ru(20 nm)/CoPtCr-SiO_2(30 nm) thin film. We observed the different crystal structures between a Ru-oxide layer and a Ru layer. Although the XRD patterns of a Ru-oxide layer with 15 nm did not show any diffraction lines, a Ru-oxide layer with 100 nm exhibited a diffraction peak corresponding to Ru (100) or RuO_2 (200) peaks which implies that a Ru-oxide layer has some crystallographic orientation.

Fig.4 shows the changes of saturation magnetization, coercivity and squareness ratio in the perpendicular and in-plane directions as a function of Ar gas pressure for a CoPtCr-SiO_2 layer. Although the higher Ar gas pressure causes the smaller saturation magnetization, because of a columnar grain structure caused by a high gas pressure condition, the higher Ar gas pressure condition promotes fine granulation of magnetic grains with grain boundaries and high perpendicular coercivity above 3.0 kOe and high squareness ratio.

Acknowledgements

Part of this work has been supported by a fund of “Collaborative Development of Innovative Seeds, Potentiality Verification Stage” of the Japan Science Technology Agency (JST).

[1] T.Matsuu, N.Nakagawa et al., Digests of PMRC 2007., 15pD-07(2007)

[2] J. Z. Shi, S. N. Piramanayagam et al., J. Magn. Magn. Mater.,20, 303 (2006)

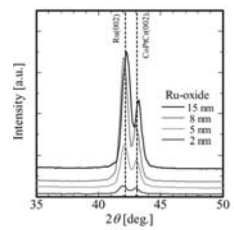

Fig.1 XRD diagram of Ru-oxide(x nm)/ Ru(15 nm)/ CoPtCr-SiO_2(30 nm) films for various Ru-oxide layer thickness.

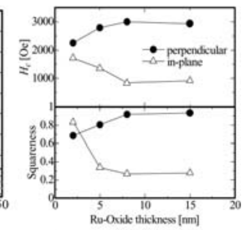

Fig.2 Changes of perpendicular coercivity and squareness ratio as a function of Ru-oxide layer thickness.

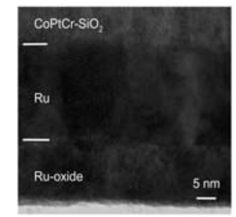

Fig.3 Cross-sectional TEM image of Ru-oxide (10 nm)/Ru(20 nm)/ CoPtCr-SiO_2(30 nm) film.

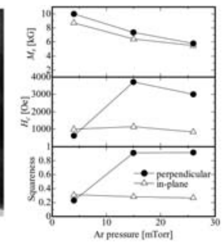

Fig.4 Saturation magnetization, coercivity and squareness ratio in the perpendicular and in-plane directions as a function of Ar gas pressure for a CoPtCr-SiO_2 layer.

CS-10

Remanence measurements of perpendicular recording media.

T. Deakin[1], C. Bunce[1], K. O'Grady[1], S. Z. Wu[2]
1. Department of Physics, The University of York, York, United Kingdom; 2. Seagate Media Research, Fremont, CA

Introduction and Experimental

Remanence measurements are important for the complete characterisation of magnetic materials, as they separate out the reversible and irreversible components of magnetisation. Also, information may be obtained from remanence data on the orientation of the easy axes, as the moment returns to the easy direction after saturation. The remanence can be measured from either a demagnetised (IRM) or saturated (DCD) initial state. Remanence measurements have been used extensively in the characterisation of longitudinal recording media due to the correlation to grain switching and the relationship to intergranular exchange, obtainable via ΔM measurements [1].

Following the paradigm shift to perpendicular recording in 2005, the issue of measuring the remanence and other parameters has had to be readdressed because of the strong demagnetising field, $H_D = -4\pi M$ [e.g. 2]. Recording media in general is specified in terms of the remanent coercivity, H_{cr}, determined from DCD curves. However, to measure H_{cr}, it is necessary to correct H prior to measuring the remanence and to measure the entire recoil loop so that the magnetisation when the total effective field, H_T, is equal to zero can be determined. As such, this is a time consuming process. In this work, we describe a technique for the direct measurement of a remanence curve, hence giving the value of H_{cr} and the SFD. Similar techniques can be used to measure the remanence in true zero field in order to determine the distribution of the easy axes.

We have studied a set of exchange-coupled composite (ECC) media. This type of media is composed of both hard and soft layers and was initially proposed by Victora [3]. The samples have a 12 nm CoPtO hard layer and a CoNiO soft layer with thicknesses, t_s, in the range 4 to 20 nm. All measurements have been performed on a PMC AGFM. DCD and IRM measurements have been made, both with and without a correction for H_D, the latter being made with custom-developed software that calculates the true effective applied field ($H_T = H_{appl.} - H_D$) at each field step [4]. For a field step of 160 Oe, this gives an error in H_T of ±80 Oe, but higher resolution measurements are possible with smaller field steps.

Results

An example of both uncorrected and corrected DCD curves for a sample of the ECC media with t_s = 8 nm is shown in Figure 1. It is clear that without the correction, a false value for H_{cr} is obtained, with the deviation in this case being 1.15 kOe or 20%.

It is also clear that the self-demagnetising field reduces the remanence determined at $H_{appl.} = 0$ for the uncorrected case making data interpretation difficult. The region of the change in H_{cr} is complex due to the presence of the hard and soft layers. A single layer film of the soft composition showed a single stage reversal with H_{cr} = 1.45 kOe. No separate reversal of the soft layer was observed in any of the composite films. This implies that the layers are exchange coupled and reverse as a single entity.

We also observe that as the thickness of the soft layer is increased the width of the switching region (SFD) decreases. However, a limiting value on the width of the SFD is reached corresponding to the width of the SFD for the soft layer itself. Hence it is the intrinsic properties of the soft layer that control the reversal of composite media. It is also noteworthy that the extrinsic SFD width due to the exclusion of flux closure at near saturation is more prominent in exchange decoupled layers.

[1] P. I. Mayo et al., J. Appl. Phys. 69 (8), 4733 (1991).

[2] R. J. M. van de Veerdonk, X. Wu and D. Weller, IEEE Trans. Magn. 38 (5), 2450 (2002).

[3] R. H. Victora and X. Shen, IEEE Trans. Magn 41 (2), 537 (2005).

[4] J. Wu et al., IEEE Trans. Magn. 38 (4), 1682 (2002).

t_s (nm)	H_{cr} (corr) (nm)	ΔH_{cr} (kOe)	SFD Width (kOe)
4	5.6	2.6	5.35
8	5.65	1.15	3.87
12	5.1	0.4	3.35
16	3.85	0.65	3.42
20	2.85	0.55	4.58
Single soft layer (12)	1.45	0.35	2.39

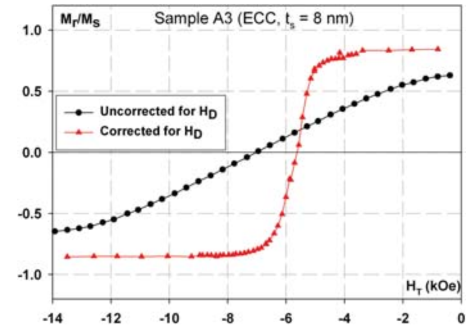

Figure 1. Example of uncorrected and corrected DCD curves, t_s = 8 nm.

CS-11

Microwave-assisted magnetization reversal in exchange spring media.

M. A. Bashir[1], J. Dean[1], T. Schrefl[1], A. Goncharov[1], G. Hrkac[1], S. Bance[1], D. A. Allwood[1], D. Suess[2]

1. Engineering Materials, University Of Sheffield, Sheffield, United Kingdom; 2. Solid State Physics, Vienna University of Technology, Vienna, Austria

The tremendous developments within data storage devices are leading researchers to think about areal density beyond 10Tbits/inch2. One key limiting factor for producing high areal density is the superparamagnetic effect [1] . An increase in anisotropy is favourable for small grains which can help increase the energy barrier restricting the effect of the superparamagnetic effect. However, limited write fields, directly proportional to anisotropy, is another limitation. In order to cope with this problem, numbers of other techniques are under consideration e.g. heat-assisted magnetic recording, composite media, and bit patterned media.. Recently, microwave assisted (MW) magnetization reversal in hcp-Co nanoparticle has been shown experimentally by Thirion et al[2]. We present micromagnetic simulations of microwave assisted switching of data-storage grains with a diameter of 5 nm and a thickness of 15 nm. Exchange spring media (ESM) having hard (Ku = 0.8MJ/m3) and soft (Ku = 0.2MJ/m3) magnetic material is compared with single phase media (SPM)(Ku = 0.42MJ/m3). where as Js = 0.6T, A = 1e-11J/m, $\alpha = 0.02$ are constant for both media. The use of exchange spring media, that is coupling a magnetically soft and hard layer together, allows switching fields to be reduced whilst maintaining a high thermal stability. Here we solve the Landau-Lifshitz equation for a single grain of either ESM or SPM media under the influence of a static magnetic field together with a rotating field perpendicular to the grain's easy axis. Temperature effects are not taken into account.

We investigated the full parameter space of microwave switching computing the switching fields of ESM and SPM grains for

(a) different frequencies of the rotating field,

(b) different amplitudes of the rotating field, and

(c) different field angles of the static external field.

Table 1 summarizes the effect of a microwave assist field on magnetization reversal. The switching field is normalized by the static switching field of the grain, Hstat. Without microwave assist the switching field are 1.24 T, 1.05 T, and 0.896 T for 10, 20, and 30 degree field angle and the ESM grain; and 1.32 T, 1.07 T, and 0.897 T for 10, 20, and 30 degree field angle and the SPM grain. Figure 1 shows the computed demagnetization curves for the two different media for a field angle of 10 degrees as function of the microwave frequency.

The results confirm that microwave assisted switching is highly effective in ESM. As compared to SPM, the maximum reduction of the switching field is found at lower values of microwave frequencies in ESM. For the ESM grain (10 degree field angle) a reduction of the switching field to 0.87 Hstat can be achieved at microwave field of only 15 GHz with an amplitude of 20 mT. The switching field is reduced to 0.82 Hstat for a microwave field amplitude of 40 mT. At an assist field of 20 mT no significant reduction of the field can be achieved for the SPM grain. For the SPM grain a reduction to a switching field 0.8 Hstat requires a microwave field of 20 GHz with an amplitude of 40 mT. For both type of media the maximum possible reduction of the switching field is found for a field angle of 20 degree. Whereas the minimum possible switching field of both media is comparable, the ESM grain shows an energy barrier that is 17 percent higher than the energy barrier of the SPM grains.

In summary, we showed that microwave assisted reduction of the switching field is possible in exchange spring media. As compared to single phase media a lower microwave frequencies are sufficient to achieve a similar reduction of the switching field. In exchange spring media a reduction of the switching field by 20 percent as compared to the non-assisted case can be achieved in a rotating field with frequency of 15 GHz and an amplitude of 20 mT.

[1] D. Weller and A. Moser, "Thermal Effect Limits in Ultrahigh Density Magnetic Recording," IEEE Trans. Magn. 35, 4423– 4439 (1999).

[2] C. Thirion, W. Wernsdorfer and D. Mailly, Nat. Mater. 2, 524 (2003)

			5 GHz	10 GHz	15 GHz	20 GHz	25 GHz	30 GHz
Exchange Spring Media	20mT	10 degree	0.976	0.944	0.871	0.992	1.000	1.000
	40mT	10 degree	0.960	0.919	0.823	0.968	1.000	1.000
	40mT	20 degree	0.962	0.943	0.884	0.810	0.990	0.990
	40mT	30 degree	1.003	0.987	0.936	0.849	1.008	1.023
Single Phase Meida	20mT	10 degree	0.985	0.962	0.917	1.000	0.992	1.000
	40mT	10 degree	0.955	0.947	0.894	0.803	0.985	0.985
	40mT	20 degree	0.955	0.946	0.936	0.854	0.765	0.974
	40mT	30 degree	0.963	0.952	0.931	0.880	0.819	0.991

Table 1: Switching field normalized by the switching field of the non-assist case for the exchange spring media (ESM) and the single phase media (SPM) for different rotating fields (amplitude, frequency). The numbers in degree give the field angle of the static field with respect to the grain's easy axis.

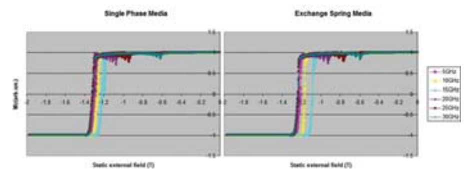

Fig. 1: The demagnetization curves for different frequencies of the rotating field. The amplitude of the rotating field is 20 mT. The external field is applied at an angle of 10 degree with respect to the film normal. Left: single phase media, Right: Exchange spring media.

CS-12

Micromagnetic Simulations of Cluster-pinned Recording Media.

C. Loke, S. Greaves, H. Muraoka
RIEC, Tohoku University, Sendai, Japan

To achieve high areal density recording in hard disks, grain sizes have to be reduced to maintain signal-to-noise ratio. However, this leads to a decrease of the energy barrier, which results in superparamagnetism. In perpendicular recording, the maximum anisotropy of the grains, which increases thermal stability, is limited by the write field of the head. To overcome this trilemma, a media in which domain wall pinning plays a role is proposed. The continuous/cluster-pinned media [1] is modeled with a continuous layer with high uniaxial anisotropy, exchange coupled to an adjacent layer of high anisotropy nanoscale clusters. The continuous layer facilitates easy nucleation and domain wall motion whilst the clusters act as pinning centres for the domain walls, controlling the coercivity and transition jitter. In this study, CPR media are investigated for the parameters determining the pinning field on domain walls.
A micromagnetic model based on the LLG equation was used. A 200nm wide × 300nm long continuous layer was modeled using regular, hexagonal cells with diameters of 3nm and height 4nm. The continuous layer was exchange coupled to a cluster layer which was modeled using grains of various sizes and shapes arranged on a square lattice with a pitch of 25nm. Both layers were 12 nm thick. The exchange coupling constant, A, between the two layers was 2.5 erg/cm^2. The other magnetic properties are listed in Table 1.
The two halves of the medium were initially magnetized in opposite directions, causing a domain wall to form between them in the continuous layer. An external field was then applied to move the domain wall, and the velocity of the domain wall was calculated for media with different cluster sizes to determine the parameters affecting the pinning field of the clusters. The pinning field was defined as the minimum field required to un-pin a domain wall.
Simulations with cubic clusters revealed that larger clusters exerted a higher pinning field on the domain walls, while a thinner continuous layer and increased cluster layer M_s also significantly increased the pinning field. The pinning fields for various cluster sizes are shown in Fig. 1. By altering the shapes of the clusters while keeping the total surface area in contact with the continuous layer constant, it was found that the pinning fields remained the same, but the location at which the domain wall was pinned changed depending on the shape of the cluster. For example, when the domain wall encountered a triangular-shaped cluster, first crossing the vertex of the cluster, the domain wall was pinned at the centre of the triangle. However, when the domain wall was parallel to the edge of the triangle then, depending on the field strength, it would become pinned at that edge. The pinning fields for various shapes and sizes of clusters are summarized in Fig. 2.
To test how the cluster density affected the pinning field, the cluster density was increased by creating smaller clusters at a pitch of 12.5nm, while maintaining a constant total surface area. It was found that a layer of dense, smaller clusters had a weaker pinning field of 1950 Oe, whereas a layer of larger, lower density clusters exerted a pinning of field 2250 Oe. Moreover, elongated clusters (20nm × 10 nm clusters) with lower density but the same surface area (9600nm^2) were found to have a larger pinning field of 3350 Oe.
In conclusion, the factors controlling the pinning fields of CPR media are: the cluster size, thickness of the continuous layer, cluster M_s and cluster density.
When recording on CPR media, the shape and density of the clusters plays a part in defining the sites where the domain wall is pinned.

[1] R. Skomski, M. L. Yan, Y. F. Xu, and D. J. Sellmyer, “Continuous/cluster-pinned recording media,” IEEE Trans. Magn., vol.43, pp. 2163-2165, June 2007.

	Continuous Layer	Cluster Layer
M_s (emu/cc)	400	
K_u (x10^6 erg/cc)	6.0	
A (erg/cm^2)	10	0
T (K)	300	

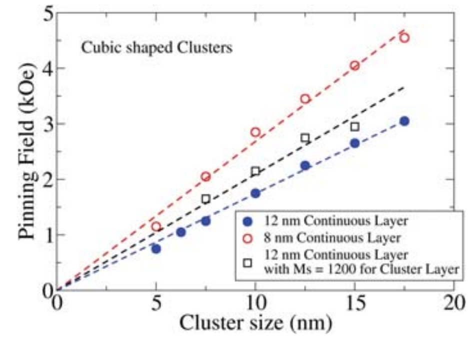

Fig. 1. Pinning fields in CPR media vs. cluster size (cubic clusters)

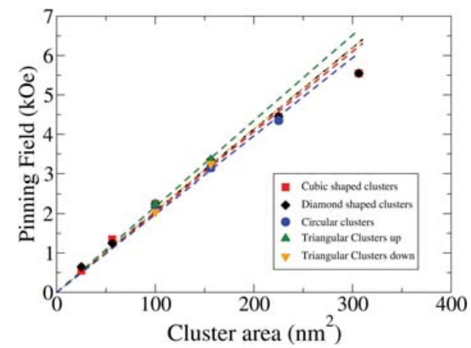

Fig. 2. Pinning Field vs cluster area for different cluster shapes.

CS-13

Effects of exchange and dipolar interactions on the determination of intrinsic switching field distributions in perpendicular recording media.

Y. Liu[1], K. A. Dahmen[1], O. Hovorka[2], A. Berger[2]
1. Department of Physics, University of Illinois at Urbana-Champaign, Urbana, IL; 2. CIC nanoGUNE Consolider, Donostia - San Sebastián, Spain

It is believed that perpendicular magnetic recording (PMR), which is nowadays the dominating hard disk drive technology, has the potential for a 10-fold increase of achievable storage densities [1]. Any progress in the development and optimization of PMR materials however relies on the availability of accurate characterization methodologies capable of extracting crucial material information such as the intrinsic switching field distribution of recording media, for example. One of the recently developed methods for this purpose is the ΔH(M,ΔM) method [2]. Among its main advantages is the fact that it relies only on a relatively simple set of macroscopic hysteresis loop measurements and that its reliability can be verified by a straightforward redundancy test of the experimental input data [3]. However, this methodology is based on a mean-field approximation of the inter-granular interactions, and its accuracy is considerably reduced in systems with pure exchange interactions [3,4]. A systematic analysis of the reliability of the ΔH(M,ΔM) method in the presence of both, the exchange and dipolar interactions, has not been done previously and is the main subject of the present work. Our computational study is based upon the coupled hysteron model [4,5]. In this model, PMR media are viewed as an assembly of bistable magnetic grains distributed on a two-dimensional square lattice. Magnetization reversal of each grain is described by a hysteron having a rectangular hysteresis loop with symmetric switching thresholds $\pm H_S$. The switching field magnitudes, H_S, vary randomly from grain to grain according to a probability distribution $D(H_S)$. In addition, every hysteron interacts with its nearest neighbors via ferromagnetic exchange J_{ex} and with every hysteron in the entire lattice via dipolar interactions J_{dp}. For the present analysis, we will assume a Gaussian switching field distribtion $D(H_S)$ having a mean of 5 and a standard deviation $\sigma=1$. Using this model, we now mimic the usual scenario for determining the switching field distribution $D(H_S)$ by the ΔH(M,ΔM) method. For a given set of parameters (J_{ex},J_{dp}), we first compute a set of recoil curves that start at various distances ΔM from saturation. Subsequently, we calculate the field difference ΔH between each recoil curve, classified by its corresponding ΔM-value, and the major hysteresis loop as a function of magnetization M. This ΔH(M,ΔM)-data set is then analyzed by means of a least-square fit to the corresponding mean-field approximation formula [2]. The quality of the fit for every (J_{ex}, J_{dp}) set is then determined by: a) calculating the square of the multiple correlation coefficient R^2 and b) calculating the difference P_d between the input value of σ and the 'recovered' variance σ_r extracted from the simulation data analysis. For an exact solution, we expect $R^2=1$ and $P_d=0$. The obtained results are shown as contour plots in Fig.1. As can be seen from these figures, in the absence of dipolar interactions the method remains accurate only for $J_{ex}<0.2$. The situation improves substantially for non-zero dipolar interactions. However, a simultaneous presence of both interaction types enhances the method's performance only for (J_{ex}, J_{dp}) sets inside the tilted-ellipse-like region embedded in the square $J_{dp}<1$ and $J_{ex}<1$. In this region $P_d\sim0$ and $R^2\sim1$, indicating that the method indeed remains accurate. This behavior results from a partial compensation between the opposite correlation tendencies of the short-range ferromagnetic and the long-range dipolar interactions (which are antiferromagnetic in nature). For example, when J_{ex} increases for a fixed J_{dp} of sufficient strength, the system gradually shifts from ferromagnetic to antiferromagnetic correlation dominated parameter space, proceeding via a nearly mean-field like regime when both competing tendencies mutually compensate. This cancellation, which we refer to as the 'correlation compensation effect', is responsible for an enhanced reliability of the ΔH(M,ΔM) technique for realistic values of dipolar interaction (illustrated by dashed lines in Fig.1). In addition, we find that due to this correlation compensation effect and the re-emergence of true mean-field behavior, inter-granular interactions are indeed removed from the data sets with very high accuracy. As a consequence, ΔH(M,ΔM)-data contain no or only very limited information about these very interactions and are therefore fundamentally unsuitable for determining the individual levels of simultaneously present interactions, independently of the type of approximation used for the data analysis. Fig.1: Contour plots of the fit quality measures as functions of J_{ex} and J_{dp}. (a) P_d. (b) R^2.

[1] Markoff, J., 2005, "Hitachi achieves storage record for disc drives", NY Times (April 4).

[2] A. Berger, Y. H. Xu, B. Lengsfield, Y. Ikeda, and E. E. Fullerton, IEEE Trans. Mag 41, 3178 (2005).

[3] A. Berger, B. Lengsfield, and Y. Ikeda, J. Appl. Phys. 99, 08E705 (2006).

[4] Yang Liu, Karin A. Dahmen, and A. Berger, accepted for publication in Phys. Rev. B

[5] Yang Liu, Karin A. Dahmen, and A. Berger, unpublished

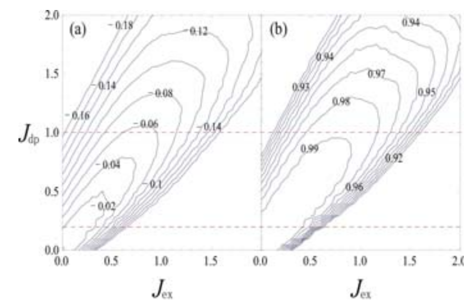

CS-14

Hybrid Soft Underlayer for Perpendicular Recording Media.

Y. Dong, R. Victora
Department of Electrical and Computer Engineering, The Center for Micromagnetics and Information Technologies (MINT), University of Minnesota, Minneapolis, MN

Introduction

An important issue in perpendicular recording is to reduce the spacing between the soft underlayer (SUL) and the recording layer while retaining an effective seed layer to promote good recording layer growth. Recently, new approaches have been proposed to reduce the effective magnetic thickness of this layer [1]. In an effort to quantify the benefit, a hybrid SUL media consisting [2] of an amorphous SUL, non-magnetic seed layer and crystalline SUL has been studied using micromagnetic simulation. By comparing the write fields and gradients in the hybrid SUL structure with those in the conventional structure, equivalent performance is obtained with a suitable combination of non-magnetic seed layers and crystalline SULs. Our simulation indicates that the hybrid SUL structure can support a thicker seed layer than conventional structure while maintaining high write field and gradient at the center of the recording media.

Hybrid Soft Underlayer Structure

The layer structure of the media in the micromagnetic modeling was amorphous SUL, seed layer, crystalline SUL, non-magnetic interlayer (non-MIL) and single-pole head. Fig.1 illustrates the conventional medium with amorphous SUL and the hybrid SUL structure. It is noticed that while additional intermediate layers such as Ru_1/Ta (15-20 nm) have to be deposited on the amorphous SUL in the conventional media, the hybrid structure is expected to need a thinner intermediate layer (5 nm Ru_2) owing to the presence of the crystalline SUL, thereby generating less reluctance in terms of a magnetic flux circuit.

Results and Discussion

Saturation magnetization of the write pole and amorphous SUL is 1910 emu/cm^3; Saturation magnetization of the crystalline SUL is 1170 emu/cm^3. The anisotropy field of the write pole and amorphous SUL is 10 Oe in plane, write pole width and length are 50 nm and 150 nm; Fly height is 5 nm; Recording media thickness is 15 nm; Crystalline SUL thickness is 20 nm; Non-MIL thickness is 5 nm. The seed layer thickness (t_{SL}) and crystalline SUL permeability ($\mu_{C\text{-}SUL}$) are varied to investigate their effect on effective field and gradient. The conventional structure with different non-MIL thicknesses ($t_{non\text{-}MIL}$) is also analyzed and compared with the new structure. For studying effects of underlayer on writability, computations were performed without any recording layers. The Landau Lifshitz Gilbert equation was used to calculate the vertical component of effective field and gradient at 12 nm below the air bearing surface of the head, i.e., middle of recording layer.

By varying the crystalline SUL permeability and seed layer thickness, field and gradients comparable to specific conventional seed layer thicknesses are obtained in the new structure. Comparative results are presented in Figure 2. When the $\mu_{C\text{-}SUL}$ is 24 and t_{SL} is 6 nm, the effective field and gradient in the hybrid SUL is comparable to those in a conventional structure with non-MIL 13 nm thick. Table 1 shows a variety of conventional structures and hybrid SUL structures. It is noted that when $t_{non\text{-}MIL}$ in conventional media is 15 nm, comparable field and gradient can be obtained in the hybrid SUL structure for t_{SL} from 6 nm to 18 nm and $\mu_{C\text{-}SUL}$ from 10 to 28, respectively. For $t_{non\text{-}MIL}$ of 10 nm, magnetic equivalence requires a permeability of 38 if the seed layer thickness is 18 nm. In other words, the hybrid structure can allow 43 nm of crystalline material to seed the recording layer yet be magnetically equivalent to 10 nm of seed layer in the conventional structure. From these results, it can be concluded that the hybrid SUL improves the writability of perpendicular recording media. With a suitable combination of crystalline SUL permeability and seed layer thickness, the hybrid SUL structure can reduce the effective magnetic spacing between SUL and recording head, or maintain comparable field and gradient with even thicker seed layer.

[1] S.N. Piramanayagam, H.B. Zhao, J.Z. Shi and C.S. Mah, Appl. Phys. Lett. 88, 092501 (2006).

[2] S. N. Piramanayagam, C. K. Pock, L. Li, C. Y. Ong, C. S. Mah, and J. Z. Sh, Appl. Phys. Lett. 89, 162504 (2006).

Conventional Structures	Hybrid SUL Structures		
$t_{non\text{-}MIL}$ (nm)	$\mu_{C\text{-}SUL}$ (t_{SL}=6 nm)	$\mu_{C\text{-}SUL}$ (t_{SL}=12 nm)	$\mu_{C\text{-}SUL}$ (t_{SL}=18 nm)
10	30	34	38
11	26	36	36
13	24	30	34
15	10	28	28

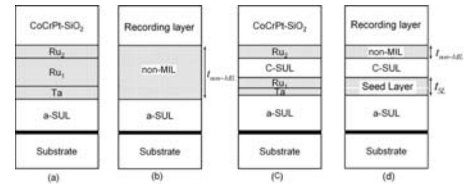

Fig. 1 Layer structure of perpendicular recording media with amorphous SUL in (a) and (b); with hybrid SUL in (c) and (d).

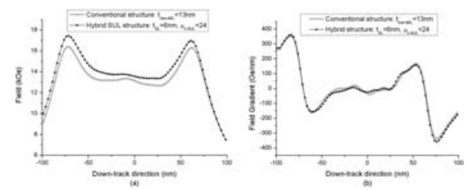

Fig. 2 (a) Effective field in down-track direction and (b) field gradient in down-track direction.

CS-15

Fast precessional switching in exchange spring media.

D. Suess[1], J. Fidler[1], J. Dean[2], T. Schrefl[2]
1. Institut of Solid State Physics, Technical University of Vienna, Vienna, Austria; 2. Department of Engineering Materials, The University of Sheffield, Sheffield, UK., Sheffield, United Kingdom

Recently composite media and exchange spring media were introduced to pospone the superparamagnetic limit to higher areal densities [1],[2]. It was shown that the required write field decreases by about a factor of two and four in composite media and exchange spring media, respectively. If the number of layers is increased the coercive field can be reduced even further.
The limits of the coercive field reduction mentioned above where investigated in a quasi static limit, where the external field is applied infinitely slow. However, the field rise times in magnetic recording are in the order of several hundred picoseconds. These fast field rise times together with small damping constants in the media allow for precessional switching in exchange spring media. The effect of precessional switching on switching times on exchange spring media was investigated in Ref [1]. It is shown that precessional switching is more pronounced in exchange spring media compared to single phase media. Reversal is reported for field pulses shorter than 25 ps [1]. Livshitz et al. investigated in detail the reduction of the switching field in exchange spring media due to precessional switching [2]. It is found that precessional switching occurs in exchange spring media for slower field rise times than in single phase media [1],[2]. Furthermore, due to precessional switching the angular dependence of the switching field is significantly modified [2].
In Fig.1 phase diagrams are presented which show the regimes of switching and not-switching for a magnetic trilayer. The phase diagram is plotted as a function of the external field pulse strength $\mu_0H_{max}$and the field pulse time τ. Within a field rise time t_r the field is increases linearly until the maximum field $\mu_0H_{max}$is reached. The maximum field is kept constant for a time τ. After this time the field is decreased linearly to zero within the time t_r.
In Fig 1 the phase diagrams are shown for different angles θ, which denotes the angle between the external field and the easy axis. Furthermore, the plots are done for different values of the field rise time t_r. The material properties of the investigated trilayer can be found in the figure caption of Fig 1. The dotted lines in the phase diagram show the static limit of the switching field, which is given by the coercive field of the trilayer if the external field is applied infinitely slow.
For fast field rise times of $t_r = 0.01$ ns and small angles $\theta = 10°$ it is interesting to note that the particle can reversed with the shortest field pulses if the external field is just large enough to reverse the particle et all. The trilayer can be reversed at a field of μ_0H_{max}= 1.15 T, whereas the static coercive field is μ_0H_c= 1.3 T. If the strength of the field pulse is increased, longer field pulses are required to guarantee switching. These fastest switching modes for small external fields was also found in single phase media as well [1].
If for a field rise time of $t_r = 0.01$ ns the angle $\theta = 10°$ is increased to $\theta = 45°$ precessional switching is more pronounced. The switching field (μ_0H_{max}= 1.4 T) is 30% smaller than the static coercive field (μ_0H_c= 1.9 T).
If the field rise time is increased to $t_r = 0.3$ ns precessional switching still occurs for $\theta = 10°$. Interestingly the switching process is faster than for the case of the fast field rise time of $t_r = 0.01$. This effect was also reported for magnetic single phase media and magnetic bilayers [1]. For $t_r = 0.3$ ns, $\theta = 10°$ and for external fields about μ_0H_{max} = 1.2 T the particle can even be switched with field pulses with a duration of $\tau = 0.49$ ns, whereas the switching time in the same field interval for the fast field rise time of $t_r = 0.01$ ns is 1.25 ns.
If the field angle is increased to $\theta = 45°$ no longer switching below the static coercive field occurs. However, the switching process occurs very fast. The particle can even be switched for $\tau = 0$. Hence, the particle is already reversed during the time when the field is increases from zero to μ_0H_{max} within the time t_r.
If the field rise time is increases to $t_r = 0.3$ ns the effect of reversal below the static coercive field also vanishes for for $\theta = 10°$.

[1] D. Suess, et al, Appl. Phys. Lett., 87 (2005) 012504.

[2] R. H. Victora et al, IEEE Trans. Magn., 41 (2005) 2828-2833.

[3] D. Suess, et al., IEEE Trans. Magn. 37 (2001) 1664.

[4] B. Livshitz, et al., Appl. Phys. Lett. 91 (2007) 182502.

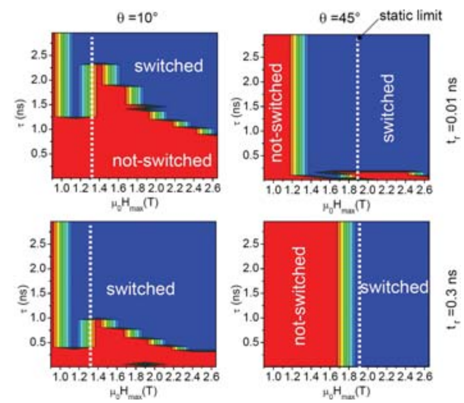

Phase diagram of the switching event for a magnetic trilayer with a total thickness of 25 nm. In all layers the same value of the intragranular exchange constant and the magnetization is assumed ($A=10^{-11}$ J/m, $J_s = 0.5$ T). The thickness of the softest layer is 11 nm with $K_1 = 0.125$ MJ/m^3. The layer in the centre has a thickness of 7 nm with $K_1 = 1$ MJ/m^3. The bottom layer with thickness 7 nm is the hardest with $K_1 = 2$ MJ/m^3. The damping constant is $\alpha = 0.02$.

CT-01

Co-rich Co-Pt films with low ordering temperature and high perpendicular hard magnetic properties for high-density magnetic recording media.

S. Chen[1,2], P. Kuo[3], C. Shen[3], Y. Fang[3], S. Hsu[3]
1. Department of Materials Engineering, MingChi University of Technology, Taipei, Taiwan; 2. Center for Nanostorage Research, National Taiwan University, Taipei, Taiwan; 3. Institute of Materials Science and Engineering, National Taiwan University, Taipei, Taiwan

Materials having high magnetocrystalline anisotropy constant (Ku) are generally attractive for ultrahigh density magnetic recording applications due to they allow smaller grains to keep thermal stability. Although Ku of L10 FePt and L10 CoPt films are as high as 7x107 erg/cm3 and 5x107 erg/cm3 respectively, the ordered temperature of FePt and CoPt films is usually higher than 500 °C [1, 2], which is too high for the manufacture process of hard disc. On the other hand, Ku of hcp Co3Pt alloy film is also as high as 2x107erg/cm3, and the temperature for obtaining high perpendicular magnetic anisotropy and high saturated magnetization (Ms) is only 300 °C [3], which is consistent with the current manufacture temperature of hard disc. Therefore, Co3Pt alloy film has significant potential to be applied in ultra high density magnetic recording media. In this study, the Pt underlayer with 200 nm thickness is deposited on corning glass substrates by conventional magnetron sputtering at ambient temperature. Co3Pt magnetic layer with thickness of 14 nm is deposited sequentially on the Pt underlayer. The as-deposited films are annealed at various temperatures for 30 min in a vacuum of 1 mTorr.

Figure 1 shows the dependence of (a) coercivity Hc and saturation magnetization Ms, and (b) squareness S on annealing temperatures for Co3Pt(14 nm)/Pt(200 nm) films. The perpendicular coercivity (Hc⊥) increases with increasing annealing temperature and reaches a maximum value at 300°C. The trend for perpendicular squareness (S⊥) is similar to that for Hc⊥.The HRTEM cross-sectional lattice image shows that a well epitaxial growth of hcp (002) Co3Pt on (111) Pt underlayer, which leads to present excellent perpendicular magnetic anisotropy of Co3Pt film at 300°C. When the annealing temperature is higher than 350°C, the transformation of hcp Co3Pt to fcc Co3Pt results in the drastically decrease of magnetic properties. Figure 2 (a) shows the perpendicular coercivity, perpendicular squareness and saturated magnetization of Co3Pt(14 nm)/Pt(200 nm) film annealed at 300°C are 3800 Oe, 0.93 and 650 emu/cm3 respectively. After depositing Co70Tb30 (85 nm) onto Co3Pt (14 nm) film, the Hc⊥ value increases from 3800 to 6560 Oe due to interfacial exchange coupling between Co70Tb30 and Co3Pt films, as shown in Fig. 2 (b). These magnetic properties obtained at low temperature of 300°C reveal its promising potential to be applied as magnetic recording media for high-density recording.

[1]T. Suzuki and K. Ouchi, IEEE Trans. Magn. 37, 1283 (2001).

[2]M. Yu, Y. Liu, A. Moser, D. Weller, and D. J. Sellmyer, Appl. Phys. Lett. 75, 3992 (1999).

[3]Shiro Mifuji, Hiroshi Sakuma, and Kiyoshi Ishii, J. Appl. Phys. 97, 10N102 (2005).

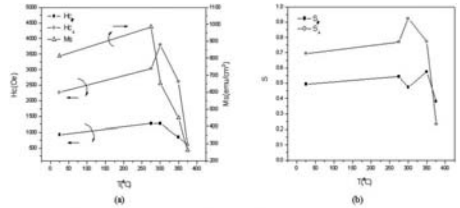

Fig. 1 (a) Coercivity Hc and saturation magnetization Ms, and (b) squareness S versus annealing temperatures in Co_3Pt(14 nm)/Pt(200 nm) films.

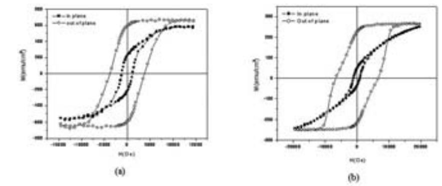

Fig. 2 M-H loops of (a) Co_3Pt(14 nm)/Pt(200 nm) bi-layer films, and (b) $Co_{70}Tb_{30}$ (85 nm) /Co_3Pt(14 nm)/Pt(200 nm) tri-layer films.

Microstructure and magnetic properties of FePt films on anodized aluminum oxide membranes.

C. Yu[1], S. Chen[2], Y. Yao[3], J. Wu[2]
1. Department of Applied Physics, National University of Kaohsiung, Kaohsiung, Taiwan; 2. Department of Materials Science and Engineering, National Tsing Hua University, Hsinchu, Taiwan; 3. Department of Materials Engineering, Tatung Universit, Taipei, Taiwan

Nowadays, the FePt with $L1_0$ phase has received significant attention owing to its excellent magnetic and magneto-optical properties, such as large saturation magnetization, high perpendicular magnetocrystalline anisotropy, high Curie temperature, and high environmental stability [1]. In pursuit of patterned recording media, magnetic nanomaterials fabricated through porous anodized aluminum oxide (AAO) have been widely investigated [2]. Recently, the percolated recording media has been investigated because of its high thermal stability[3,4]. In this study, FePt films were prepared on the AAO membranes with pore diameter of around 20nm and 200nm by a DC magnetron sputtering system. The thickness of FePt films was ranged from 15nm to 50nm. After deposition, a post annealing procedure with temperature ranged from 400^{o}C to 650^{o}C for one hour was taken to obtain the hard phase of FePt. In order to prevent the interdiffusion, a 10nm thick Au buffer was grown on AAO templates prior to FePt layers.

From x-ray spectrum, we found that the FePt films grown on both templates, with or without Au buffer, were polycrystalline after a high temperature annealing. Interestingly, the $L1_0$(001) phase was obtained while the FePt grown on the 20nm pore diameter AAO templates with Au buffer layers, as shown in Fig. 1(a). For the samples without Au buffer layers or grown on the AAO templates with larger pore diameter, one can not obtain the $L1_0$(001) phases, as shown in Figs. 1(b) and 1(c), respectively. Detail investigation on the XRD spectrum showed that the 20nm pore diameter AAO template can assist the formation of Au(100) phase that resulted in the formation of FePt $L1_0$(001) phases under 600^{o}C annealing. For all samples, the coercivity of FePt increased as increasing annealing temperature. However, the coercivity decreased while annealing temperature higher than 650^{o}C. A large perpendicular coercivity, namely 11000 Oe and 9000 Oe, was obtained in 600^{o}C annealed FePt samples grown on 20nm and 200nm pore diameter AAO templates with Au buffer layers, respectively, as shown in Figs. 2(a) and 2(b). It is in a good agreement with the observation of FePt $L1_0$(001) phases. And a relative lower perpendicular coercive value, namely 6500 Oe and 1000 Oe, was observed in FePt films directly grown on 20nm and 200nm pore diameter AAO templates, respectively, as shown in Figs. 2(c) and 2(d). That resulted from the interdiffusion between FePt and alumina. From these magnetic investigations, we concluded that a template with small pore diameter (or with large pore density) will enhance the coercive force (or domain wall pinning effect). For the experiments on thickness variation, the coercivity was almost the same for 15nm and 30nm thick FePt samples, as depicted in Figs. 3(a) and 3(b), respectively. But a relative lower coercivity was observed in 50nm thick FePt samples, as depicted in Fig. 3(c). The decreasing of coercivity in thicker films after annealing was probably due to the grain growth [5]. In summary, we have observed experimentally the first time the structure and magnetism of FePt on AAO template. The Au (100) buffer layers and AAO templates will enhance the coercive force of FePt films through assisting the formation of $L1_0$(001) phases and providing extra pinning sites, respectively.

[1] D. Weller et al., IEEE Trans. Magn. 36, 10 (2000).

[2] F. Y. Yang, K. Liu, K.M. Hong, D.H. Reich, P.C. Searson, C.L. Cien, Science 284, 1335 (1999).

[3] J. Zhu and Y. Tang, J. Appl. Phys., 99, 08Q903-1 (2006).

[4] M. Tofizur Rahman, Chih-Huang Lai, D. Vokoun, and Nazmun N. Shams, IEEE Trans on Mag., 43, 2133 (2007).

[5] K. Leistner, J. Thomas, H. Schlorb, M. Weisheit, L. Schultz, and S. Fahler, Appl. Phys. Lett. 85, 3498 (2004).

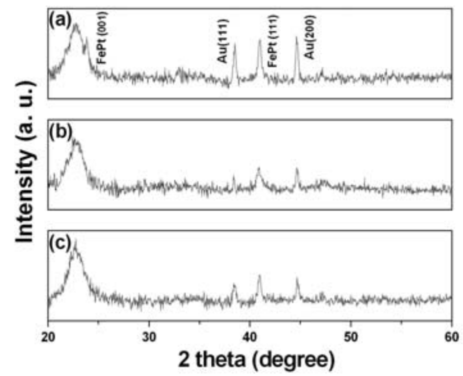

The θ-2θ XRD spectrum of 30nm thick FePt films.

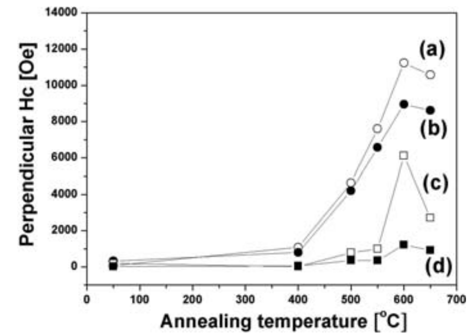

Coercivity vs.annealing temperature of 30nm thick FePt films.

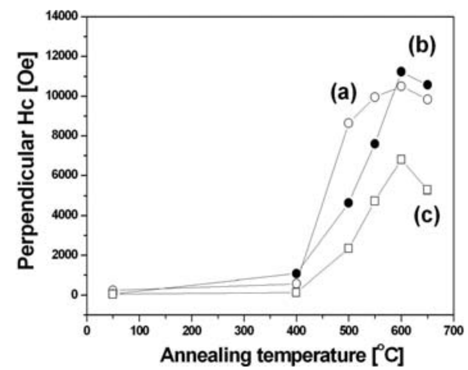

Perpendicular coercivity vs. annealing temperature of FePt films with Au buffer layers on 20nm pore diameter AAO templates.

CT-03

Effect of MgO addition on structural and magnetic properties of (001) textured FePt thin films.

A. Sun[1,2], Y. Tsai[3], F. Yuan[4], *J. Hsu*[1,2], P. Kuo[3]

1. Physics, National Taiwan University, Taipei, Taiwan; 2. Center for Nanostorage Research, National Taiwan University, Taipei, Taiwan; 3. Materials Science and Engineering, National Taiwan University, Taipei, Taiwan; 4. Physics, Academia Sinica, Taipei, Taiwan

Introduction

(001) textured Ll_0 FePt is commonly accepted as a promising material for perpendicular magnetic media with ultra high recording density exceeding 1 Tbit/inch^2. In order to enhance the recording performance, the medium with granular microstructure is necessary. In such a microstructure, magnetic grains or particles are surrounded and isolated with non-magnetic phase, which effectively decouple the grains and promote the independent magnetic reversal. Many attempts have been made to create this microstructure in Ll_0 FePt film using various non-magnetic materials. Among these isolation materials, MgO have received great deal of attention because it can induce strong (001) texture of Ll_0 FePt [1, 2]. It have been reported that large amount of MgO in the FePt-MgO two-phase mixture segregates and surrounds the Ll_0 grains uniformly after annealing [3]. A microstructure similar to currently used media has been achieved. Apart from the formation of granular film, the addition of MgO has been also reported to change the magnetic properties and domain structure of (001)-textured FePt film [4]. However, the effect of incorporating small amount of MgO is not extensively investigated. In this presentation, the effect of MgO doping on structural and magnetic properties in (001)-textured Ll_0 FePt grown on MgO underlayer will be discussed.

Experimental

Composite Magnetic $(FePt)_{100-x}$-$(MgO)_x$ films (x = 0~10 vol.%.) were magnetron sputtered on MgO(200) underlayer at 530 and 580°C with glass substrates in an ultra-high vacuum sputtering chamber. The thicknesses of the FePt-MgO film and MgO underlayer were set to 20 and 10 nm, respectively. The crystalline structure and microstructures of the films were identified by X-ray diffraction and transmission electron microscopy, respectively. The chemical composition of FePt analyzed by energy dispersive spectroscopy was $Fe_{48}Pt_{52}$. Since MgO is immiscible with the magnetic FePt phase, the MgO content of the magnetic FePt matrix was determined by calculating the formula $[R_{MgO}/(R_{FePt}+R_{MgO})]\times 100$ vol.%, where R denotes the sputtering rate. Magnetic properties were investigated with a vibrating sample magnetometer at room temperature with a maximum applied field of 1600 kA/m.

Results and discussion

Figure 1(a) shows the dependence of order parameter, S_{ord}, on the content of MgO. The samples with MgO less than 2 vol.% deposited at two different temperatures exhibit high S_{ord} value of 0.95~1. As MgO was increased gradually from 2 vol.% to 10 vol.%, the value of S_{ord} decreases to 0.67. Figure 1(b) displays the variation of lattice parameter of *c*-axis with MgO content. A compression of *c*-axis appeared in both 530 and 580°C deposited films. When the amount of MgO exceeds 2 vol.%, a drastic expansion was observed. At low MgO content region, the 580°C deposited films exhibit higher coercivity as indicated in Fig. 1(c), which can be related to its higher S_{ord}. The results of squareness ratio indicate that the 580°C film exhibit better alignment of *c*-axis as shown in Fig. 1(d). In Figs. 1(e) and 1(f), it is interesting to note that both samples present a peak in the dependence of anisotropic field (H_k) and anisotropic energy (K_u) on MgO content. The increament of H_k and K_u can be related to the lattice compression as shown in Fig. 1(b). The fact that MgO is immiscible to FePt implies that the shift of (002) peak is resulted from other origins such as internal strain or stress. It have been reported that in a fully ordered FePt film, the residual strain by phase transformation will elongate the *c*-axis and compress the *a*-axis of a $L1_0$ lattice [5]. The addition of small amount of MgO may facilitates the relaxation of residual tensil strain along *c*-axis and thus enhance the values of H_k and K_u. However, as MgO is overdoped, in-plane compressive stress/strain may increase rapidly, resulting in expansion of lattice parameter c and reduction of H_k and K_u. In summary, the addition of MgO with a small proper amount was found to improve the magnetic properties of the FePt $L1_0$ phase without degrading the ordering and alignment of (001)-orientation, helpful to employ FePt medium in the future magnetic recording.

[1] K.Kang, Z.G. Zhang, C. Papusoi, and T. Suzuki, Appl. Phys. Lett. 84, 404 (2004).

[2] T. Shima, K. Takanashi, Y.K. Takahashi, and K. Hono, Appl. Phys. Lett. 81, 1050 (2002).

[3] Y. Peng, J.G. Zhu, and D.E. Laughlin, J. Appl. Phys 99, 08F907 (2006).

[4] J.S. Chen, T.J. Zhou, Y.F. Ding, B.C. Lim, and B. Liu, J. Appl. Phys. 97, 3163 (2005).

[5] J.S. Kim, Y.M. Koo, and N. Shin, J. Appl. Phys. 100, 093909 (2006).

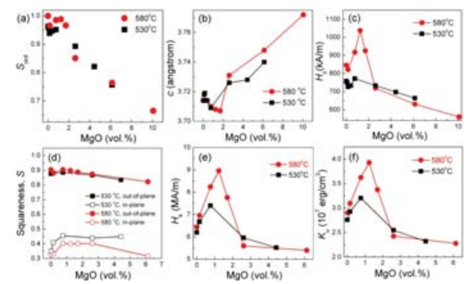

Fig. 1 Relation between (a) order parameter, S_{ord} ; (b) lattice parameter of *c*-axis; (c) coercivity, H_c; (d) in-plane and out-of-plane squareness ratio, *S* ; (e) anisotropic field, H_k; and (f) anisotropy energy, K_u and MgO content for the films deposited at 530 and 580°C.

CT-04

Thickness Dependence on (001) Texture Evolution and Magnetic Properties of Sputter-Deposited FePt:MgO Nanocomposite Films.

H. Kim[1], *K. Kim*[1], S. Lee[1], W. Jeung[2]
1. Materials Science and Engineering, Korea University, Seoul, South Korea; 2. Korea Institute of Science and Technology, P.O.Box 131, Seoul, South Korea

Introduction
(001) preferred orientation should be developed during $L1_0$ phase ordering reaction of FePt for perpendicular magnetic anisotropy applications. The (001) texture of $L1_0$ FePt is usually induced by sputter deposited on heated MgO (001) substrates [1], or using various composite materials [2,3], or using proper bufferlayers.[4] However, there is a thickness limitation of the films to develop the nearly perfect (001) texture of $L1_0$ phase during ordering reaction.[3,5] The reason for the dependence of film thickness on the (001) texture evolution is not clear yet. In this study, we analyzed the dependence of film thickness on the (001) texture development, degree of ordering reaction, and magnetic properties of the FePt:MgO nanocomposite films.
Experiments
$[\text{FePt } 2.8/\text{MgO } 3.2 \text{ nm}]_n$ multilayers were deposited at room temperature on thermally oxidized Si (100) substrates using a magnetron sputtering system with equiatomic FePt and MgO targets. The FePt and MgO sublayer thickness was varied from 2.4~3.4 and 0.4~3.2 nm, respectively. The samples were annealed in a vacuum furnace at 600 °C in a 4×10^{-6} Torr vacuum. The magnetic properties of the as-deposited and post-annealed samples were measured by using a vibrating sample magnetometer (VSM) in fields up to 12 kOe and a superconducting quantum interface device (SQUID) in fields up to 50 kOe at room temperature. The microstructures of the films were observed using transmission electron microscopy (TEM) and the crystal orientations were analyzed using X-ray diffractometer (XRD) in θ-2θ scan mode.
Results and Discussion
Figure 1 shows the variation of in-plane and out-of-plane coercivity (H_c), texture coefficient (T.C.) of (002) plane, ordering parameter (S), and tetragonality (c/a) of $L1_0$ phase as a function of number of bilayers (film thickness). Out-of-plane coercivity and ordering parameter approach the maximum value at n = 6, film thickness of 36 nm. However, T.C. of (002) and ordering parameter degraded from above 6 bilayers, and hence the coercivity decreased. Figure 2 shows XRD patterns of the $[\text{FePt } 2.8 / \text{MgO } 3.2 \text{ nm}]_n$ films with n varying from 4 to 9, corresponding to film thickness ranging from 24 to 54 nm. When the n is 6, only FePt (001) and (002) peaks can be clearly seen and any other peaks don't exist. This means that a heteroepitaxially grown nearly perfect $L1_0$ face-centered-tetragonal (fct) (001) texture were obtained for annealed $[\text{FePt } 2.8 \text{ nm} / \text{MgO } 3.2 \text{ nm}]_6$ films. As the number of bilayer (film thickness) increases, the relative intensity of (111) peak slightly increase and (00n) peak decrease. Compared with the T.C. in Fig. 1(b), it is obvious that (001) texture developed in thinner films. In Fig. 1(a), thicker films have small out-of-plane coercivity comparable to in-plane coercivity. This may be because randomly oriented fcc FePt grains are mixed in thicker films as can be seen in Fig. 2. Hence the ordering parameter S decreases as the film thickness increases [Fig. 1.(b)] and tetragonality slightly increases as can be seen in Fig. 1(c). The dependence of bilayer number (film thickness) on the texture evolution, degree of ordering, and the magnetic properties has a similar effect of the film thickness.[3,5] In the previous study [6,7], it was found that the anisotropic strain due to the $L1_0$ ordering was key factor to develop the (001) texture. Accordingly, we presumed that there should be a thickness limitation to satisfy the plane-stress condition [7] for the evolution of (001) texture and the $L1_0$ ordering.

[1] M. R. Visokay and R. Sinclair, Appl. Phys. Lett., 66, 1692 (1995).

[2] T. Yang, E. Ahmad, and T. Suzuki, J. Appl. Phys., 91, 6860 (2002).

[3] M. L. Yan, H. Zeng, N. Powers, and D. J. Sellmyer, J. Appl. Phys., 91, 8471 (2002).

[4] Y.-N Hsu, S. Jeong, D. N. Lambeth, and D. Laughlin, IEEE Trans. Magn. 36, 2945 (2000).

[5] B. C. Lim, J. S. Chen, J. P. Wang, J. of Magn. Magn. Mater., 271, 431 (2004).

[6] H. J. Kim and S. -R. Lee, J. Appl. Phys., 97, 10H304 (2005).

[7] J. –S. Kim, Y. -M Koo, B. –J. Lee, S. –R. Lee, J. Appl. Phys., 99, 053906 (2006).

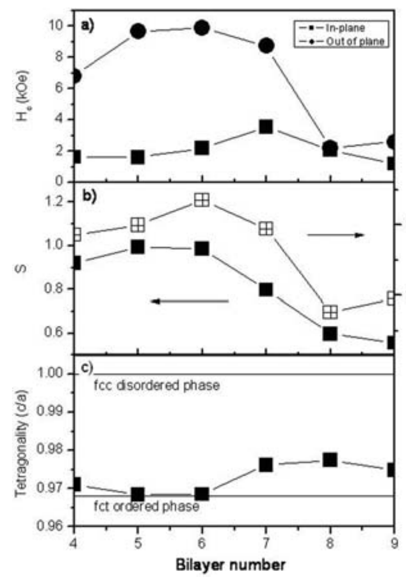

Fig. 1 The variation of magnetic properties and structural properties for $[\text{FePt } 2.8 /\text{MgO } 3.2 \text{ nm}]_n$ as a function of bilayer number. Samples were annealed at 600 °C for 30 min.

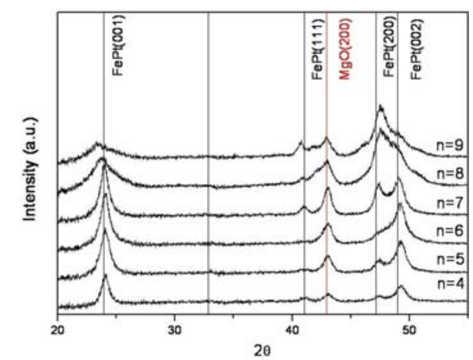

Fig. 2 XRD patterns for $[\text{FePt } 2.8 /\text{MgO } 3.2 \text{ nm}]_n$ as a function of bilayer number. Samples were annealed at 600 °C for 30 min.

CT-05

Dependence of ordering kinetics of FePt thin films on substrates.

C. Zha[1,2], S. He[1], B. Ma[1], Z. Zhang[1], F. Gan[1], Q. Jin[1]
1. Department of Optical Science and Engineering, Fudan University, Shanghai, China; 2. Department of Microelectronics and Applied Physics, Royal Institute of Technology, Stockholm, Sweden

$L1_0$ ordered FePt thin films have been intensively investigated in recent years for their potential applications for perpendicular magnetic recording. For practical use, it is necessary to obtain out-of-plane magnetic anisotropy with suitable crystalline orientation. There are two ways to get (001)-oriented $L1_0$ FePt films. One is the epitaxial growth [1-3], in which single crystal substrates (MgO and $SrTiO_3$, etc.) or assembled textured underlayers (CrRu, Pt etc.) have been used. The other is so-called non-epitaxial growth [4, 5]. The disordered (A1) FePt films which are soft magnetic, are deposited onto Si or glass substrates with or without underlayers at room temperature, and the $L1_0$ ordered structure is formed after post-annealing at a high temperature (T_A =550°C or above). Then it is interesting to investigate the ordering kinetics in the two cases.
We have prepared three kinds of $Fe_{51}Pt_{49}$ alloy films with nominal thickness about 8 nm, by dc magnetron sputtering. Sample A, B, and C are films which are deposited at room temperature on $SrTiO_3$ (100), MgO (100) mono-crystalline substrates and 2-nm-thick FeO_x covered Si wafer, respectively, and then annealed for 10 minutes at temperatures from 300 to 750°C in vacuum. The structure is studied by x-ray diffraction (XRD) with Cu K_α radiation. The magnetic property of the films is measured by vibrating sample magnetometer (VSM).
Fig. 1 is the chemical ordering parameter S and the *c*-lattice parameter of samples A, B, and C as a function of annealing temperature, which are calculated from the XRD data [6]. It can be seen that the chemical ordering parameter S of FePt thin films on the FeO_x underlayers is larger than that of films on the mono-crystalline substrates and the *c*-lattice parameter is smaller than that at the same annealing temperature. The FePt films on the FeO_x underlayer are completely ordered with perfect (001) orientation after 600°C post-annealing (XRD not shown here), while for the ones on MgO and $SrTiO_3$ substrates the chemical ordering parameter S is still 0.96, 0.95 even after 750°C post-annealing. Furthermore, the FePt film deposited on Si with FeO_x underlayers begin to order at 400°C, and finish at 600°C. On the contrary, the epitaxial films begin to order at 500°C, and nearly finish at 750°C. The difference of temperature of the $L1_0$ phase formation is about 150°C. Then the phase transition from fcc to fct phase of the epitaxial FePt thin films is more difficult than that of the non-epitaxial ones on the FeO_x layers.
Fig. 2 indicates the dependence of coercivity of FePt alloy films on annealing temperature. For the films deposited on MgO and $SrTiO_3$ substrates in Figs.2(a) and (b), the trends of coercivity are the same, increasing firstly and then decreasing with the annealing temperature. It is noticeable that the coercivities after 600°C post-annealing become smaller than those at 500°C. This may result from the decreasing of pinning sites of domain wall motion. On the other hand, for the FeO_x-FePt thin films in Fig. 2 (c), the out-of-plane coercivity increases with the annealing temperatue. This implies that its magnetization reversal is rotational mode.
In summary,the different ordering kinetics of FePt films is observed and the ordering temperature of non-epitaxial thin films on FeO_x underlayer is around 150°C lower than that of epitaxial ones on mono-crystalline substrates for the 8-nm-thick FePt alloy films.

1 R. F. C. Farrow, D. Weller, R. F. Marks, and M. F. Toney, A. Cebollada, G. R. Harp, J. Appl. Phys. 79, 5967 (1996)

2 T. Shima, T. Moriguchi, S. Mitani and K. Takahashi, Appl. Phys. Lett., 80, 288 (2002)

3 Y. F. Xu, J. S. Chen and J. P. Wang, Appl. Phys. Lett., 80, 3325 (2002); J. S. Chen, B. C. Lim, and J. P. Wang, Appl. Phys. Lett., 81, 1848(2002)

4 H. Zeng, M. L. Yan, N. Powers, and D. J. Sellmyer, Appl. Phys. Lett. 80, 2350 (2002); M. L. Yan, N. Powers, and D. J. Sellmyer, J. Appl. Phys., 93, 8292 (2003)

5 A. Yano, T. Koda, and S. Matsunuma, IEEE Trans. Magn. 41, 3211(2005)

6 B. E. Warren, X-Ray Diffraction, New York: Dover, 1990, pp. 208

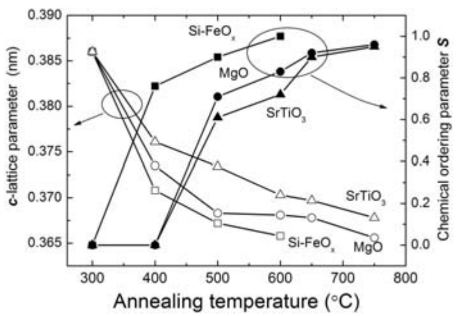

Fig. 1. Tthe chemical ordering parameter S and the *c*-lattice parameter of FePt thin films on MgO, $SrTiO_3$ and Si with FeO_x underlayer as a function of annealing temperature

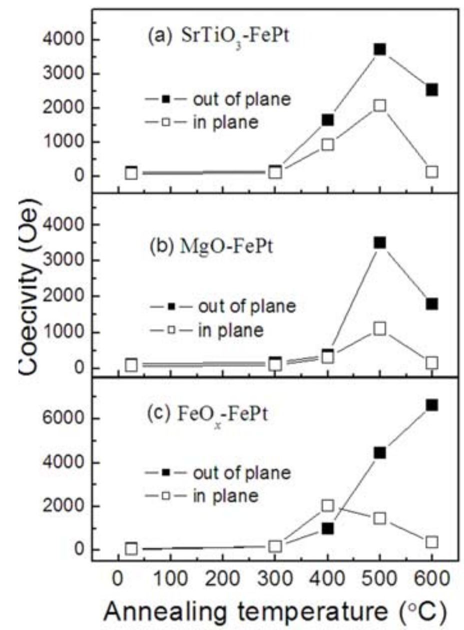

Fig. 2. The out-of-plan and in-plan Coercivity of FePt thin films on MgO, $SrTiO_3$ and Si with FeO_x underlayer as a function of the temperature.

CT-06

Domain reversal behavior of ultrathin FePt:C films.

H. Ko[1], P. Alagarsamy[1], S. Shin[1], W. Byun[2], S. Kim[2]
1. Physics, KAIST, Daejoen, South Korea; 2. Material Science, KAIST, Daejeon, South Korea

Introduction
Recently, researchers have attempted to solve various issues regarding the microstructural irregularities in ultrathin FePt films. Interestingly, Carbon doping in FePt thin films has been found to be one of the most effective ways to control L10 ordering and to reduce the average FePt grain size down to < 5 nm [1]. However, no detailed study has been reported on the magnetic domain patterns and domain reversal behavior of nanogranular FePt:C thin films. It is well-known that the domain patterns and domain reversal behavior of perpendicular recording media play an important role in the transition noise, and can be a serious limiting factor on the areal recording density. In this work, we report the study of time-resolved domain reversal patterns in the Carbon-doped equiatomic FePt films.
Experiment
7-nm thick FePt:C films were prepared on MgO(100) substrates using dc magnetron cosputtering of composite FePt and C targets. The volume concentration of the Carbon was varied up to 10 %. All the samples were prepared at a constant substrate temperature (350 °C). The crystal structure and microstructure of the films were characterized using X-ray diffractometry (XRD) and Transmission Electron Microscopy (TEM). Real time domain reversal patterns were obtained by means of a Magneto-Optical Kerr Microscope Magnetometer (MOMM) system capable of time-resolved domain observation with a spatial resolution of 0.4 μm and Kerr-angle resolution of 0.2°.
Results and Discussion
To reveal the effect of magnetic field and Carbon doping on the domain reversal behavior, direct observation of domain reversal patterns in real time was carried out in the MOMM system. The observed domain evolution patterns are illustrated in Figure 1 for various Carbon-doped FePt thin films. The areal expansion by domain wall-motion dominant process is clearly observed in the pure FePt film. As the amount of Carbon doping increases, time-dependent domain reversal pattern changes to nucleation-dominant reversal process at 10 vol. % Carbon-doped FePt film. To reveal the origin of domain reversal behavior with increasing Carbon doping in FePt thin films, we have considered the lowest energy state resulting from the sum of magnetostatic and domain wall energies. From the energy calculation, it was found that the change of the magnetostatic energy and the domain wall energy in our FePt:C films prefer wall-motion dominant process and nucleation-dominant process, respectively. Therefore, it would be difficult to clearly distinguish the actual contribution to the control of observed domain reversal patterns.
On the other hand, the effect of spatial anisotropy fluctuation coming from local structural variation on the domain reversal behavior was already simulated and proved as one of possible origin [2]. Therefore, to correlate the observed domain reversal behavior with the local structural variations in the Carbon-doped FePt films, TEM micrographs of the FePt:C films were obtained and analyzed. Figure 2 (a-c) shows the TEM micrographs of FePt:C thin films deposited at 350 °C with different Carbon concentration, while Figure 3(d) displays the average FePt grain size obtained from the TEM microstructure and calculated from the corresponding histogram, and the total number of available grains in the 150 ×150 nm2 area of TEM micrograph. With increasing Carbon concentration to 10 vol. %, the number of grains available in 150×150 nm2 was increased about 4 times with the average grain size of 4.3 nm. These results suggest that the Carbon doping plays an important role on building up the grain–grain boundary structure and leading to a uniform nanogranular structure from the continuous film structure. The increased number of grain–grain boundary pairs with increasing Carbon doping in FePt film leads to a large increase in spatial anisotropy fluctuation due to the separation of uniform FePt film into grain (magnetic)–grain boundary (non-magnetic) structure. Hence, such a large discrepancy of spatial anisotropy fluctuation is the main origin of different domain reversal behavior
This research work was supported by Korea Science and Engineering Foundation through the Basic Research Program and Ministry of Science and Technology of Korea through Leading Basic S&T Research Project.

1. H. S. Ko, A. Perumal, and S.-C. Shin, Appl. Phys. lett. 82, 2311(2003).

2. S.-B. Choe and S. -C. Shin, IEEE Trans. Magn. 36, 3167 (2000).

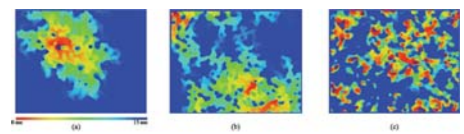

Fig.1 Time-resolved domain reversal patterns of FePt:C [(a) 0, (b) 5 and (c) 10 vol. %] thin films prepared at 350 °C substrate temperature

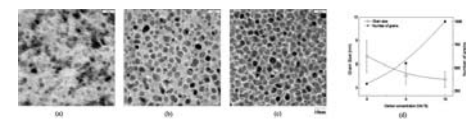

Fig. 2 TEM micrographs of FePt:C [(a) 0, (b) 5 and (c) 10 vol. %] thin films prepared at 350 °C substrate temperature and (d) the average grain size (△) and the number of available FePt grains (■) in the area of 150 ×150 nm2. The bar in the TEM micrographs scales 10 nm.

CT-07

Fabrication of easy-axis-aligned ultrahigh-density FePt nanoparticles.

Y. Wu, L. Wang, C. Lai
Materials Science and Engineering, National Tsing Hua University, Hsinchu, Taiwan

The ultra-high-density perpendicular recording media demand excellent thermal stability, good magnetic isolation, and a narrow-distribution of easy axis. Many researches focus on the fabrication of FePt nanoparticles (NPs), by chemical syntheses [1] or physical vapor deposition [2], to fit those requirements. Although well-separated fine FePt particles have successfully been fabricated, it is quite challenging to align the magnetic easy axis of those NPs. Highly ordered FePt NPs with well-aligned easy axis have been fabricated by alternate deposition of FePt (at 780 °C) and MgO (at R.T.) on a MgO (100) substrates [3]. However, MgO single-crystal substrates may not be suitable for commercial products. In our previous study, we demonstrated that the well-aligned (001)-oriented FePt NPs on SiO_2 substrates can be obtained by combining agglomeration and atomic-scale depositions of $[Fe/Pt/SiO_2]_n$ MLs [4]. In this work, we demonstrate the tunable particle size of FePt NPs by adjusting layer numbers of Fe/Pt/SiO_2. Eventually, fully isolated FePt NPs possessed a particle size of as small as 3.5 nm and a large out-of-plane coercivity ($H_{c,\perp}$) of 30 kOe were attained.
Sequential planetary sputtering of atomic-scale $[Fe/Pt/SiO_2]_n$ (n =3 to 18) MLs were performed on SiO_2||Si substrates at an ambient temperature. The corresponding thickness of Fe, Pt, and SiO_2 in each layer is 0.16 nm, 0.18 nm, and 0.28 nm, respectively. All samples were annealed in vacuum (1 x 10^{-5} Torr) at 700 °C for 2 s. The TEM plane-view images of samples (n = 3, 9, and 18) after annealing were shown in Fig. 1. All samples showed a clear particulate film structure, indicating that fully isolated FePt NPs were fabricated by agglomeration, a process that uncovering of a substrate or dewetting of an initially continuous film. The driving force of agglomeration was the divergence of surface/interfacial energy between films and substrates [5]. As the n value was equal to 18, all NPs presented an octagonal shape with the average particle size around 100 nm. The thickness of NPs was 22.5 nm, confirmed by TEM cross-section images, implying the particles were flatten-truncated octahedral shape. As reported in Ref. 4, the equilibrium flatten truncated octahedron shape of FePt NPs on an amorphous SiO_2 substrate was due to the lower interfacial energy of FePt/SiO_2 [4]. By reducing the n value to 9, NPs showed the reduced particle size of 10.1 nm and the clear octagonal shape in TEM plane-view image. In Ref. 2, it was reported that the equilibrium shape of FePt NPs tended to become an octahedron as the particle size was smaller than 10 nm, because the (111) surfaces were favorable in f.c.c/f.c.t system [2]. In our study, however, the flatten-truncated octahedral shape was kept even the particle size was reduced to 10 nm, which may be ascribed to the stabilizing effect on the particle shape due to the lower interfacial energy of FePt/SiO_2. Further reducing the n value to 3, NPs possessed the particle size of as small as 3.5 nm, and the areal density up to 1.4×10^{13} #/inch^2 were obtained. The shapes of these particles were sphere-like, implying the size may be too small to keep the flatten truncated octahedral shape of FePt NPs. The in-plane and out-of-plane hysteresis loops, shown in Fig. 2, were obtained by a superconducting quantum interference device. FePt NPs exhibited a well-aligned easy axis along [001] and possessed the high perpendicular anisotropy with a $H_{c,\perp}$ value larger than 45 kOe, which was attributed to the strong (001)-preferred orientation, confirmed by XRD, and high ordering factors as the particle size larger than 10 nm. In contrast, NPs with a size of 3.5 nm showed the poor perpendicular anisotropy and a small $H_{c,\perp}$ after annealing for 2s, which originated from the relatively low ordering factor due to the kinetic limit in small particles [6]. To beat the kinetic limit, these NPs were annealed at 700 °C for 6 hr. A large $H_{c,\perp}$ of 30 kOe was attained without obvious change of particle size. The coarsening of FePt NPs may be restricted by a large diffusion barrier due to the sinking of FePt NPs into SiO_2 substrates during annealing. The kink in the hysteresis loop implied the existence of a soft phase, which might result from some NPs with too small particle sizes.
In summary, the particle size of FePt can be controlled by tuning the n value of $[Fe/Pt/SiO_2]_n$ MLs. As decreasing the n value, the particle size reduces from 100 nm to 3.5 nm. The NPs show a flatten-truncated octahedral shape and well-aligned easy axis along [001] even as the particle size was reduced to 10 nm. The NPs with a size of 3.5 nm exhibit a large $H_{c,\perp}$ of 30 kOe after a 700 °C annealing for 6 hr.

[1] S. Sun et al., Science 287, 1989 (2000).

[2] J. M. Qiu and J. P. Wang, Appl. Phys. Lett. 88, 192505 (2006).

[3] T. Shima et al., Appl. Phys. Lett. 88, 063117 (2006).

[4] Y. C. Wu et al., talk BE-07 at MMM’07, Tampa.

[5] R. Saxena et al., Phys. Rev. B 72, 115425 (2005).

[6] R. V. Chepulskii et al., J. Appl. Phys. 7, 10J311 (2005).

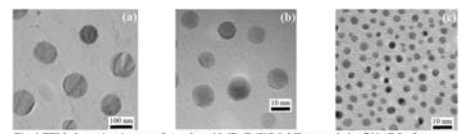

Fig. 1 TEM plane-view images of samples with $[Fe/Pt/SiO_2]_n$ MLs annealed at 700 °C for 2 s. The n values are (a) 18, (b) 9, and (c) 3. The scale bar of (a) is different from that of (b) and (c).

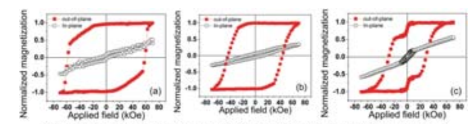

Fig. 2 In-plane and out-of-plane hysteresis loop of sample with $[Fe/Pt/SiO_2]_n$ MLs annealed at 700 °C. The n values are (a) 18, (b) 9, and (c) 3. (a) and (b) were annealed for 2 s. (c) was annealed for 6 hr.

CT-08

Structural and magnetic properties of textured Fe/FePt bilayer.

S. H. He, B. Ma, *C. L. Zha*, Z. Z. Zhang, Q. Y. Jin
Department of Optical Science and Engineering, Fudan University, Shanghai, China

Introduction

L10 ordered (FCT) FePt is a promising candidate for ultrahigh density recording media due to its high magnetocrystalline anisotropy. However, its coercivity is too high to be written by a real single pole head. New media designs are required. Recently, composite media and exchange spring media were introduced theoretically [1-3], and composite media effects were observed experimentally [4]. In exchange spring media a magnetic hard layer and a magnetic soft layer are strongly coupled. The switching field of the bilayer is far below the coercivity of hard magnetic layer due to the exchange interaction between them. Then a soft magnetic layer, such as Fe, can be utilized to promote the magnetization reversal of the ordered FePt layer.

We present here the structural and magnetic properties of Glass/Fe/(L10 FePt) bilayer. The Fe underlayer is a (002) textured film, on which an (001) textured FePt layer is prepared by epitaxial growth. The magnetic behavior of the bilayer has been studied.

Experimental

The Glass/Fe/FePt(7 nm) magnetic bilayers were fabricated in a dc magnetron co-sputtering system from individual Fe and Pt targets. The Fe layer was first deposited at room temperature, and then annealed at 600 °C in vacuum for 15 min. After that, perfect (002) textured Fe underlayer can be formed [5]. Then FePt layer was co-sputtered under the substrate temperature of 500 °C.

The crystallographic structure of the samples was examined by x-ray diffraction (XRD) with Cu Kα radiation. Magnetic properties were measured by a vibrating sample magnetometer (VSM) and magneto-optical Kerr magnetometer (MOKE).

Results and Discussion

Figure 1 shows the θ-2θ XRD patterns of the Glass/Fe/FePt samples as a function of the Fe layer thickness. For the sample with 6-nm-thick Fe layer, there is no Fe related XRD peak. The FePt (002) peak is clearly observed at 48.53°, an angle between the (200) and (002) peaks of bulk materials. This indicates that the film is still in the intermediate stage of an fcc-fct transformation. When the Fe thickness increases beyond 8 nm the Fe (002) peak shows up. Furthermore, both (001) and (002) peaks of FePt appear. Their intensities become apparent and the (002) peak approaches the very position with the increase of Fe thickness. FCT structure is formed. Simultaneously, the intensity of FePt (111) peak turns weak, and is invisible when Fe thickness increases up to 20 nm. This indicates that (001)-textured FePt layer are prepared on Fe underlayer with (002) orientation by epitaxial growth, since the mismatch between FePt (001)[100] and Fe (001)[110] lattice is 4.29% in our experiment.

The dependence of magnetic hysteresis and coercivity on the thickness of Fe layers is indicated in Fig. 2. Three kinds of magnetic behaviors can be observed. The first one is the Fe/FePt bilayer with 6-nm-thick Fe underlayer, which behaves as a single magnetic film as shown in Fig. 2(a). The second one is the exchange spring structure in which FePt and Fe layers interact in the way of exchange coupling as we can see in Fig. 4(b) and (c), when the Fe thickness is in the range between 8 – 12 nm. With further increasing of Fe layer thickness beyond 12 nm, there is a part of Fe layer which is uncoupled with FePt layer and keeps its own easy axis along film plane as the thickness is beyond the exchange length. This is the third kind. The hysteresis loops in Fig. 4(d)-(f) show the combination of soft magnetic phase and hard magnetic phase. This one is regarded as double-phase stage also.

[1] R. H. Victora and X. Shen, IEEE Trans. Magn., 41(10), 2828 (2005)

[2] D. Suess, T. Schrell, S. Fahler, M. Kirscher, G. Hrkac, F. Dorfbauer and J. Fidler, Appl. Phys. Lett., 87, 012504 (2005)

[3] A. Y. Dobin and H. J. Richter, Appl. Phys. Lett., 89, 062512 (2005)

[4]J. P. Wang, W. K. Shen, and J. M. Bai, IEEE Trans. Magn., 41(10), 3181 (2005)

[5] S. H. He, C. L. Zha, B, Ma, Z. Z. Zhang, and Q. Y. Jin, J. Magn. Magn. Mater. 310, 2656 (2007).

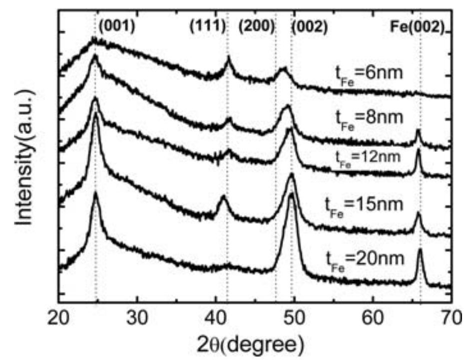

Fig. 1. The dependence of θ-2θ XRD patterns of the Glass/Fe/FePt bilayer on Fe thickness

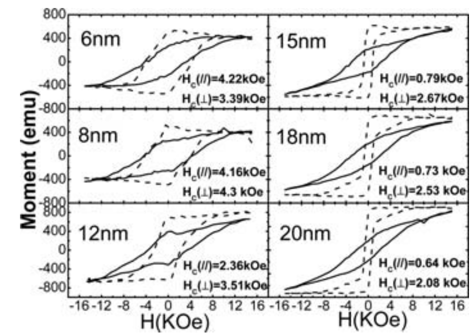

Fig. 2 The magnetic hysteresis loops for Glass/Fe/FePt bilayer with different Fe film thickness with out-of-plane loops in solid line and the in-plane loops in dash line.

CT-09

Control of Curie temperature of FePt(Cu) films prepared from Pt(Cu)/Fe bilayers.

J. Ikemoto, *Y. Imai*, S. Nakagawa
Dept. of Physical Electronics, Tokyo Institute of Technology, Tokyo, Japan

Introduction

$L1_0$ ordered FePt alloy thin films with (001) preferential orientation are regarded as hopeful candidates for future high density perpendicular magnetic recording media because of their high uniaxial magnetic anisotropy energy. Besides, FePt is the center of attention as heat assisted magnetic recording (HAMR) medium because of the controllability of Curie temperature by adding third element such as Cu[1]. Since the Curie temperature of FePt alloy is as high as around 500°C, it is required to control the Curie temperature around 250°C for application to HAMR medium applications. In our previous papers, we have found that Pt(100)[3nm]/Fe(100)[3nm] bilayered films deposited directly on crystallized glass disk substrates exhibited FePt highly ordered *fct* alloy with (001) preferential orientation after annealing at 600°C in hydrogen atmosphere for 120 min[2]. In this paper, we have attempted to controll Cu addition into Pt top layer in $Pt_{50-x}(Cu)_x/Fe_{50}$ bilayered films and fabricated Fe-Pt-Cu films by the annealing process described above. We evaluated the controllability of Curie temperature of FePt(Cu) ordered films with (001) preferential orientation.

Experimental

Facing targets sputtering (FTS) method was employed to prepare Pt/Fe and $Pt_{50-x}(Cu)_x/Fe_{50}$ bilayers. Cu was added to Pt layers by placing the composite targets consisting of Pt and Cu. Fe bottom layer and Pt(Cu) top layer were deposited directly on crystallized glass disk substrates (OHARA:TS-CZ) at room temperature in Ar atmosphere. The atomic ratio of Fe:Pt:Cu was determined by ICP-OES analysis. All the specimen bi-layers were annealed at 600 °C for 120 minutes in hydrogen (1 atm) to enhance inter-diffusion and ordering to *fct*-FePt. Crystallographic characteristics were evaluated by X-ray diffraction (XRD). Magnetic properties were measured by VSM at the maximum applied field of 15 kOe.

Results and Discussion

Prepared specimens can be categorized in 3-groups by the difference of Cu content, *i.e.* pure FePt(Pt[3 nm]/Fe[3 nm]), Cu-poor FePtCu($Pt_{42}Cu_8$[5 nm]/Fe[5 nm]) and Cu-rich FePtCu($Pt_{32.5}(Cu)_{17.5}$[4.5 nm]/ Fe[3 nm]). The atomic ratio of Fe:Pt:Cu of the Cu-poor and the Cu-rich FePtCu films were 50:42:8 and 37:41:22, respectively. Thickness of each layer was changed to maintain $L1_0$ crystalline structure, considering Cu atom was replaced in Fe site as described in later. All specimens indicated *fct*-FePt(001) preferential orientation. Lattice constant c calculated from *fct*-FePt(001) peak, magnetization of FePt, and Cu doped FePt films was plotted in Fig.1. Lattice constant c decreased as Cu percentile increases. This trend of c provided an evidence of the incorporation of Cu atom substituted for Fe or Pt in the *fct*-FePt lattice. Additionally Cu atom seemed to be located in Fe site since magnetization of Cu doped FePt films decreased with Cu addition[3]. Figure 2 showed changes of perpendicular coercivity and slope parameters $\alpha(=(d\boldsymbol{M}/d\boldsymbol{H})$ at $\boldsymbol{H}_c)$ at the coercivity. Domain wall pining effect by Cu addition resulted in large difference of α among pure FePt film and Cu doped FePt films.

Figures 3 and 4 showed the temperature dependence on saturation magnetization and perpendicular coercivity of FePt film and Cu doped FePt films, respectively. Pure FePt film held higher magnetization and coercitity at 300 °C than the Cu doped FePt films. By contrast with the pure FePt, the temperature dependence on the magnetization and perpendicular coercivity of Cu doped FePt films shifted lower. In particular, magnetization of Cu-poor FePtCu film, that is 8 at.% Cu doped FePt film, showed the steep decline at the temperature range from 150°C to 250°C and reached down on 0 at 300°C. This was suitable for HAMR medium. Meanwhile, magnetization of Cu-rich FePtCu film, that is 22 at.% Cu doped FePt film, vanished at 100°C. Consequently, Curie temperature of *fct*-FePt thin films was controlled from around 300°C to 100°C by adding Cu.

[1] D. C. Berrya and K. Barmak: J. Appl. Phys. Vol. 102, 024912 (2007)

[2] S.Nakagawa and T.Kamiki: J. of Magn. Magn. Mat. Vol. 287, 204-208 (2005)

[3] T. Kai *et al.*: J. Appl. Phys. Vol. 95, 609-612 (2004)

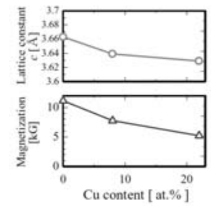

Fig.1 Changes of lattice constant c and magnetization of Cu doped FePt films as a function of Cu content.

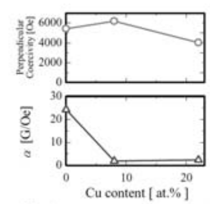

Fig.2 Changes of perpendicular coercivity and slope parameter α of Cu doped FePt films as a function of Cu content.

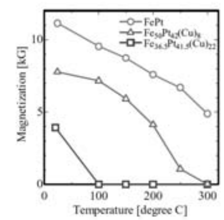

Fig.4 Temperature dependence of perpendicular coercitivity of FePt, $Fe_{50}Pt_{42}Cu_8$ and $Fe_{37}Pt_{41}Cu_{22}$ films.

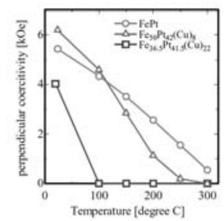

Fig.3 Temperature dependence of magnetization of FePt, $Fe_{50}Pt_{42}Cu_8$ and $Fe_{37}Pt_{41}Cu_{22}$ films.

CT-10

Exchange Coupling Assisted FePtC Perpendicular Recording Media.

J. Hu[1], J. Chen[2], Y. Ding[1], B. Lim[1], W. Phyoe[1], B. Liu[1]
1. Data Storage Institute, Singapore, Singapore; 2. Department of Materials Science and Engineering, National University of Singapore, Singapore, Singapore

I. INTRODUCTION
Exchange coupling assisted (ECA) perpendicular recording has been proposed to decrease the writing field, which allows the application of high anisotropy materials as recording media. Relative insensitivity to c-axis dispersion is another advantage of this kind of recording media. In this paper, FePtC based ECA media was fabricated and the magnetic properties of the films were investigated.
II. EXPERIMENTAL DETAINLS
FePtC based ECA perpendicular media with the structure of Glass/CrRu/MgO/$L1_0$ FePtC/fcc FePtC were prepared by an ultrahigh vacuum magnetron sputtering system. The CrRu and MgO act as the underlayer and buffer layer. Different deposition temperature was used to control the FePtC phases with soft (room temperature) and hard magnetic properties (350°C).
III. RESULTS AND DISCUSSIONS
The out-of-plane hysteresis loops of the ECA media and a single layer FePtC film were shown in Fig. 1. The coercivity H_c and saturation field H_s for the single FePtC layer (10 nm) were about 10 kOe and 24 kOe, respectively. After the introducing the top soft FePtC layer, the values of H_c and H_s reduced to be 8.3 kOe and 20 kOe (3 nm soft layer) and 7 kOe and 17.5 kOe (5 nm soft layer), respectively. No separated switching of soft and hard layers indicated that the two FePtC layers were exchange coupled with each other. Comparison of the loop steepness of the ECA media with that of the single hard layer indicated the increase of exchange coupling effect with the increase of the top soft layer.
The angle dependence of the coercivity and the remanent coercivity was measured for ECA media as shown in Fig. 2. To measure the angular dependence of the remnant coercivity, the sample was saturated at every angle by an applied magnetic field of –29 kOe, the field was then decreased to zero to measure the remanent moment. The remanent moment as a function of a magnetic field was measured for each angle by applying a positive magnetic field with a step of 400 Oe, until the applied field reached 29 kOe.
According to the Stoner-Wolfarth model, the switching field of the conventional perpendicular media is very sensitive to the angle between the easy axis and the applied magnetic field. In the ECA media in present work, the coercivity and the switching field demonstrated a less sensitivity on the angle between the easy axis of the hard layer and the external applied field, indicating by small variation when the angle increased from 0 to 15°. The insensitivity was attributed to the top soft layer. The angle dependences of coercivity and remanant coercivity are also consistent with the simulation results of Victora. [1]
Figure 3 shows the TEM images of the ECA media with different soft layer thickness. It can be seen that the ECA media was composed of two granular films. The grain size of the bottom hard FePtC layer is larger than that of the top soft layer. The grain size of top soft layer increases with the increasing layer thickness, which may explain the increase of the loop steepness with soft layer thickness. The grains of the soft layer located both on top of the bottom FePt grains and the grain boundaries.
IV. SUMMARY
In summary, the ECA media with structure of Glass/CrRu/MgO/FePtC (350°C)/FePtC (RT) were fabricated. The experimental results of angular dependence of the coercivity and the remnant coercivity are consistent with the simulation results.

[1] R. H. Victora and X. Shen, IEEE Trans. Magn. 41, 2828 (2005)

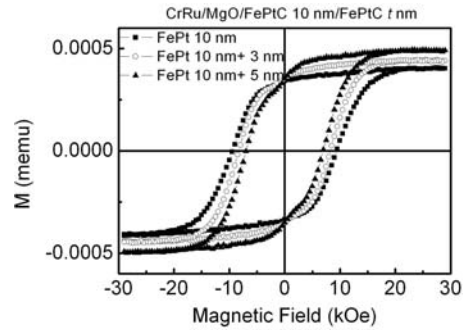

Figure 1 Hysteresis loops of ECA media and single FePtC layer

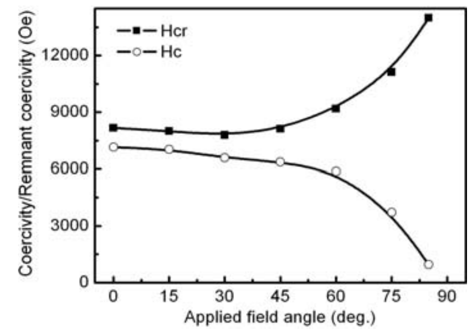

Figure 2 Angle dependence of the coercivity and the remnant coercivity of ECA media

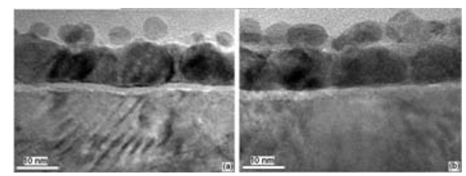

Figure 3 TEM images of ECA media, (a) CrRu/MgO/FePtC 10nm (hard)/FePtC 3nm (soft); and (b) CrRu/MgO/FePtC 10nm (hard)/FePtC 5nm (soft)

CT-11

Epitaxial thin $SmCo_5$ films with perpendicular anisotropy.

M. Seifert, V. Neu, L. Schultz
Institute for Metallic Materials, IFW Dresden, Dresden, Germany

Introduction

Hard magnetic thin films find important applications in nano and micro electromagnetic systems (NEMS, MEMS) and magnetic recording. $SmCo_5$ is a material with a high uniaxial magnetic anisotropy and therefore has the potential to be used as a high density recording media. Thus, in the last years, research focuses on the preparation of polycrystalline Sm-Co films with perpendicular anisotropy [1]. In our group we specialize on the realization of epitaxial growth and recent work led to $SmCo_5$ thin films with a perfect in plane texture [2]. Based on that knowledge, we developed epitaxial $SmCo_5$ films with strong perpendicular anisotropy by pulsed laser deposition, which can serve as test system for the study of perpendicular recording in high K_u materials.

Experiment

Films were prepared by pulsed laser deposition (PLD) at ultra high vacuum (UHV) conditions. At first, a buffer layer of 10 nm Ru was deposited onto an Al_2O_3 (0001) substrate, then 100 nm of $SmCo_5$ and finally 10 nm of Cr as an oxidation protection. The preparation temperature of the Sm-Co layer was varied systematically in a range between 550°C and 800°C. The texture of the films was analyzed with XRD and pole figure measurements. Magnetic properties were investigated using a vibrating sample magnetometer (VSM) and a magnetic force microscope (MFM). Additionally anomalous Hall Effect measurements were performed. Atomic force microscopy (AFM) was used to investigate the surface morphology. Thicknesses and composition of the layers were determined with EDX in a scanning electron microscope (SEM).

Results

Figure 1 shows the XRD pattern (CoKα) of the samples prepared at different temperatures. The (0006) peak of the Al_2O_3 substrate is clearly visible on which Ru grows with (0002) orientation. It can be seen that at 600°C the $SmCo_5$ (0002) peak appears for the first time and that the intensities increase up to 700°C. At higher temperatures additional Sm_2O_3 peaks are found.

To determine the orientation of the Sm-Co grains pole figure measurements were performed. We measured the (1 0 -1 4) pole of Al_2O_3 at $2\theta_{Cu} = 35.22°$ and the (1 0 -1 1) pole of $SmCo_5$ at $2\theta_{Cu} = 30.5°$. Because of the six-fold symmetry of the Sm-Co pole it was sufficient to measure a Φ range of 130°. The results of both measurements for the sample deposited at 700°C are displayed together in figure 2. It proves that the c-axis is oriented out of plane and reveals that there is an epitaxial growth with two different in plane orientations of the hexagonal unit cell, which are rotated 30° with respect to each other. The poles with the higher intensity (I) are rotated 30° with respect to the Al_2O_3 (1 0 -1 4) pole, the others (II) have the same orientation like the Al_2O_3. The peaks appear at a position of $\Psi = 44°$, which agrees well with the theoretical value of $\Psi = 42°$.

VSM measurements show, that already at low temperatures a SmCo phase with high uniaxial anisotropy is formed with coercivities of up to 2 T. However, these samples are macroscopically isotropic. Magnetic texture develops with increasing temperature. The sample prepared at 700°C possesses a square shaped out-of-plane hysteresis (squareness=0.81) with a coercivity of μ_0H_c=1.0 T. (Fig. 3 (a)). For higher temperatures the samples become isotropic again. VSM measurements contain small steps around μ_0H = 0T. To see if they arise from the film properties or are due to the substrate or measurement setup, additional Hall measurements were done. These measurements do not show any steps, but only the wanted square shape in the case of the 700°C prepared film (Fig. 3 (b)). For these films prepared at optimum temperature of 700°C the high uniaxial anisotropy of the Sm-Co phase is obvious from the largely different hysteresis loops measured in different directions. From the intersection of the flat in-plane (hard axis) loop with the out-of-plane loop the uniaxial anisotropy constant is deduced to K_u=10 MJ/m^3.

[1] Sayama,J.; Mizutani,K.; Asahi,T. APL 85 5640 (2004)

[2] Singh,A; Neu,V; Tamm,R.; Rao,K.; Faehler,S.; Skrotzki,W.; Schultz, L.; Holzapfel,B. JAP 99 (2006)

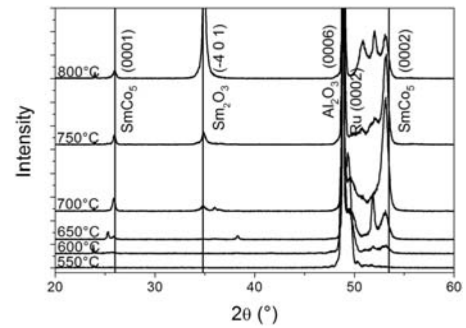

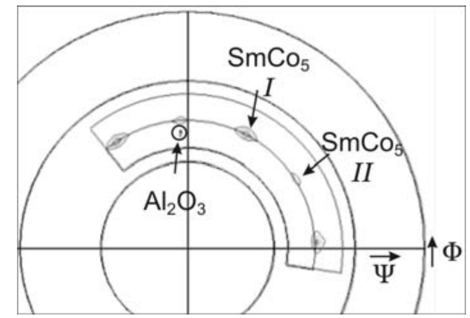

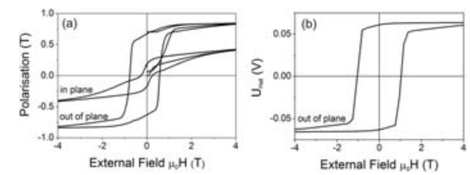

Studies on $Sm(Co,Cu)_5$ thin films with perpendicular anisotropy for extremely high areal density recording.

X. Liu[1], H. Zhao[1], Y. Kubota[2], J. Wang[1]
1. The Center for Micromagnetics and Information Technologies, Department of Electrical and Computer Engineering, University of Minnesota, Minneapolis, MN; 2. Seagate Research, Pittsburgh, PA

$SmCo_5$ is well known as a hard magnetic material for its ultrahigh uniaxial magneto-crystalline anisotropy (10^8 erg/cm^3). Recently it is considered a promising candidate for future high areal density perpendicular recording media because of the demand of media with extremely small but thermally stable grains. Until now, $SmCo_5$ films with perpendicular anisotropy were only obtained on Cu underlayer or Cu sub-underlayer.[1-4] While Cu underlayer could induce the perpendicular anisotropy in $SmCo_5$ at relatively low deposition temperature, it also leads to large grain size in $SmCo_5$ magnetic layer. In this study, we successfully fabricated $Sm(Co,Cu)_5$ film with perpendicular anisotropy on pure Ru underlayer (figure 1), instead of Cu underlayer, to control the grain size of SmCoCu film. And studies about the effect of deposition temperature, film composition and film thickness on the magnetic properties of SmCoCu films were performed.
The structure of SmCoCu films was Ta(3nm)/Sm-Co-Cu(10nm)/Ru(20nm)/Ta(4.2nm)/glass. The grain size of the $Sm(Co,Cu)_5$ layer was reduced to 17nm, which can be further reduced. The deposition temperature was reduced to a relatively low value, 350^{o}C. When the deposition temperature was lowered further to 250 ^{o}C and 150 ^{o}C, the perpendicular anisotropy in SmCoCu film could not be achieved (figure 2(a)). And the study of SmCoCu films' composition showed that the addition of Cu in the SmCoCu layer was another important factor for the perpendicular anisotropy (figure 2(b)). The SmCoCu film's out-of-plane coercivity was found to depend on film's thickness. A 2.2nm magnetic dead layer between SmCoCu and Ru layers was estimated by fitting the saturation magnetization vs. inverse of film thickness curve. The switching mechanism of the Sm-Co-Cu films was investigated by measuring the angular behavior of the remanent coercivity. A switching model involving the pinning sites that are related with Cu doping and grain boundaries was proposed and will be discussed in detail in the full presentation.

1. A. Singh, V. Neu, R. Tamm, K. Subba Rao, S. Fähler, W. Skrotzki, L. Schultz and B. Holzapfel, Appl. Phys. Lett., 87, 072505 (2005).

2. J. Sayama, T. Asahi, K. Mizutani, and T. Osaka, J. Phys. D 37, L1 (2004).

3. S. Takei, A. Morisako, and M. Matsumoto, J. Magn. Magn. Mater. 272-276, 1703 (2004).

4. I. Kato, S. Takei, X. Liu, and A. Morisako, IEEE Trans. On Magn. Vol. 42, No. 10 (2006).

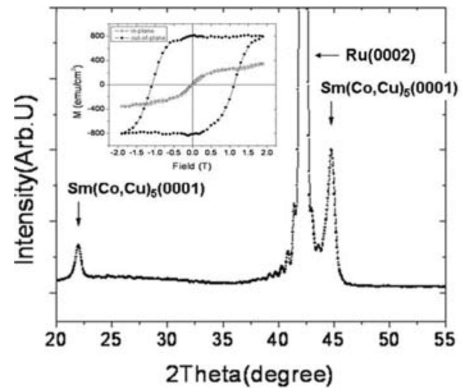

Figure1. XRD pattern of sample: Ta(3nm)/$Sm_{14}Co_{58}Cu_{28}$(10nm)/Ru(4nm)/Ru(16nm)/Ta(4.2nm)/glass. The inset shows its magnetic hysteresis loops in out-of-plane (black dots) and in-plane (white dots) directions.

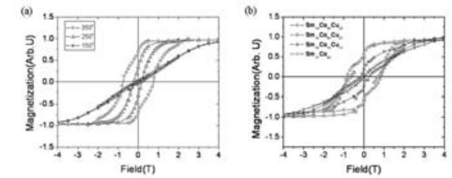

Figure2. (a) Out-of-plane magnetic hysteresis loops of SmCoCu films deposited at different temperature (film composition $Sm_{14}Co_{58}Cu_{28}$). (b) Out-of-plane magnetic hysteresis loops of SmCoCu films with different composition (all samples deposited at 350^{o}C).

CT-13

Second order anisotropy in exchange spring systems.

B. F. Valcu, A. Dobin, E. Girt
Seagate Technology, Fremont, CA

Exchange spring systems consist of a soft magnetic layer ferro-magnetically coupled to a hard magnetic layer [1]. When a reversal field is applied, the magnetization in the structure rotates incoherently, a partial domain wall being formed at the hard/soft interface. If the hard layer has large enough anisotropy, a relatively thin soft layer can be used as a write-assist, making the structure interesting for recording applications. The magnetic materials used for both the hard and soft layer have in general only first order anisotropy $Ku^{(1)}$. We report here experimental observation and micromagnetic studies of a change in the symmetry of the torque curve for exchange spring systems that leads to an apparent second order term $Ku^{(2)}$ in the anisotropy energy.

In torque measurements the magnetic film, whose moment was initially saturated, is rotated in a high field of constant magnitude. The magnetization direction deviates from the applied field, due to competition from the anisotropy field. The torque is proportional to the component of magnetization perpendicular to the field, measured for example using a vector VSM. When the applied field angle is varied, the torque follows a sinusoid curve, whose amplitude indicates the anisotropy energy constant.

The simplest way to analyze torque curves for a bi-layer system is to assume that the magnetic moments of the two layers are parallel with each other (rigid coupling). However, if one of the layers has much smaller anisotropy than the other –as it is the case with exchange spring systems-, the validity of the assumption must be questioned. We built a spin chain model in which magnetization is allowed to rotate from the bottom of hard layer to the top of soft layer. The exchange stiffness values of the two layers control the extent of magnetization non-uniformity.

Energy minimization leads to a second order differential equation for the magnetization direction as a function of the distance to the hard/soft interface [2]. Since in the torque measurement the deviation of the magnetization from the field direction is small, we can expand linearly the magnetization angle around the field angle and solve the equation analytically. We arrived at a closed expression for the torque, parameterized by the magnetic properties of the two layers. In case there is only one layer, the magnetization direction is constant through the film and the torque expression simplifies to:

$$m_y(\alpha_H)/m_{total}=-(\tfrac{1}{2}Hk^{(1)}\sin(2\alpha_H)+Hk^{(2)}\sin^2(\alpha_H)\sin(2\alpha_H))/(H+Hk^{(1)}\cos(2\alpha_H)+2Hk^{(2)}(\sin^2(2\alpha_H)-\sin^2(\alpha_H))).$$

In the above the perpendicular component of magnetization m_y is normalized by the total moment of the sample, α_H is the applied field angle, $Hk^{(1)}$ and $Hk^{(2)}$ are the first and second order anisotropy fields and H is the constant valued of the applied field.

For illustration, let us consider an exchange spring system in which the hard layer is 12 nm thick and the soft layer is 20 nm thick. The (effective) anisotropy field of the hard layer is 8 kOe, oriented perpendicular to the film surface, while the soft layer has no anisotropy. The largest deviation from the field direction is obtained when the external field (=16 kOe) is applied at 45 degrees with respect to the easy axis. In the case of rigid coupling, the magnetization is uniform through the film, and makes an angle of ~ 39 degrees with the easy axis (Figure 1). However, if the exchange constant in the film is finite, the magnetization in the exchange spring system rotates gradually from 33 degree to 45 degree. The resulting torque curves are also shown in Figure 1, for both rigid and non-rigid coupling cases. If we were to fit the two curves to sample-averaged $Ku^{(1)}$ and $Ku^{(2)}$, it is interesting to observe that in the non-rigid coupling case we would get a significant $Ku^{(2)}$ contribution. Allowing magnetization to rotate non-coherently changes the symmetry of the torque curve.

Experimentally we sputtered a series of exchange spring films, in which the thickness of the soft layer (denoted by t2 in Figure 2) was varied [3]. The torque curves were fitted using our micromagnetically-derived expression. The estimated anisotropy constant of the soft layer is independent of the film thickness. This ultimately proves the existence of the exchange spring effect.

[1] E. Fullerton et al, Appl. Phys. Lett., Vol. 72, No. 3,pp. 380-382 (1998). [2] E. Goto et al, J. Appl. Phys., vol. 36, No.9, pp. 2951-2958 (1965). [3] E. Girt et al, IEEE Trans. on Magnetics, vol. 43, Issue 6, pp. 2166-2168 (2007).

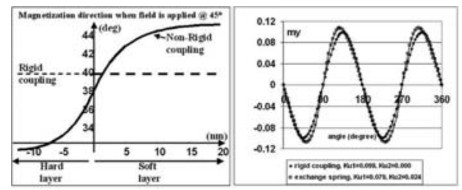

Torque curve for an exchange spring system has an apparent second order term in the anisotropy energy, due to the partial domain wall structure of the magnetization.

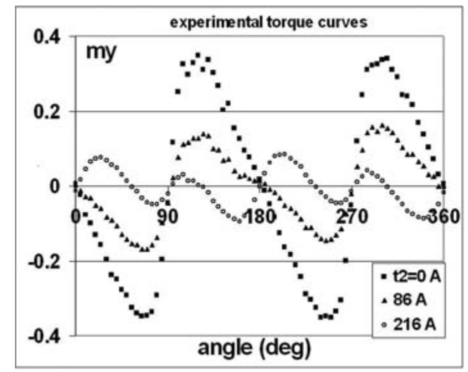

Experimental torque curves for various thickness values of the soft layer.

CU-01

Magnetic recording in patterned media at 5 - 10 Tbit/in^2

S. Greaves[1], Y. Kanai[2], H. Muraoka[1]

1. RIEC, Tohoku University, Sendai, Japan; 2. IEE, Niigata Instiute of Technology, Kashiwazaki, Japan

<p>**Introduction**

Bit patterned media (BPM) are expected to be able to support ultra-high recording densities well in excess of 1 Tbit/in^2. In this paper we describe how micromagnetic modelling was used to determine the areal density limit for a shielded, single-pole write head and single phase magnetic dots, without the use of thermal or microwave energy sources.~~<\>>~~

~~<p>**Models**~~

~~Head field distributions were calculated using a finite element model. The width of the main pole at the air bearing surface (ABS) was 10 nm and its length was 20 nm. Side and trailing shields were located 5 nm and 15 nm from the main pole, respectively. The ABS - soft underlayer (SUL) spacing was 8.5 nm and the recording layer was situated between the two.~~

~~The recording layer consisted of rectangular bit cells, with a single magnetic dot centered in each bit cell. The 10 Tbit/in^2 design was subject to the following constraints: Bit cell area = 65 nm^2, minimum non-magnetic boundary between dots = 2 nm, $K_u V / k T = 60$ and $H_d + H_{ATE} < H_k < H_{head}$, where H_d is the magnetostatic field in a saturated medium, H_{ATE} is the adjacent track erasure field, which is the head field in an adjacent track, H_k is the anisotropy field of the dots and H_{head} is the maximum head field.~~

~~Based on these constraints the magnetic dot size was chosen to be 11 nm × 3 nm × 7 nm in a 13 nm × 5 nm bit cell. A dot thickness of 7 nm gives a maximum head-medium spacing of 1.5 nm, i.e. contact recording if an overcoat is used. The maximum head field in the centre of the dots was 13300 Oe with a maximum head field gradient of 711 Oe/nm. Dots were discretised into 1 nm cubes and media contained 11 tracks of randomly magnetised dots to determine the effect of the magnetostatic field. The magnetic properties of the dots were M_s = 1380 emu/cm^3 and K_u = 10.85×10^6 erg/cm^3.~~<\>>

<p>**Results**

Using the parameters listed above, simulations of recording were carried out at a temperature of 300 K. The head-medium velocity was 10 m/s and the head field rise time (zero - 90\% of maximum field) was 0.12 ns. Even in the absence of geometric and material property distributions it was not possible to write error-free tracks, unless the temperature was reduced to zero. Despite the high head field gradient, the spacing between dots was too small to write to a selected dot without frequently over-writing the previous dot. Reducing the head-medium velocity to 5 m/s reduced on-track write errors, but increased adjacent track erasure.

Magnetostatic field distributions were calculated for media with randomly magnetised dots (up/down). The effective magnetostatic field distributions, taking account of the angle and assuming Stoner-Wohlfarth switching behaviour, are shown in Fig. 1. For a 13 nm × 5 nm bit cell the average value of H_d was 2570 Oe, with standard deviation, σ = 900 Oe. For a dot subject to $H_d + 3\sigma$, the average interval between thermally induced magnetisation reversal would be around 5 seconds. Writing schemes to limit the maximum magnetostatic field would be required to ensure data integrity in such a medium.

The areal density of the patterned media was reduced and the dot volume increased to determine the maximum areal density that could be used with the given write head. Bit cells of 15 nm × 8 nm and dots of 11 nm × 4 nm × 7 nm were found to permit reliable recording of data tracks without adjacent track erasure at a head-medium velocity of 10 m/s. The areal density of such a system is 5.38 Tbit/in^2 and long-term stability of dots is ensured. Fig. 2 shows a portion of such a medium. The central track was recorded with an alternating pattern and the magnetisation of the surrounding dots had a random up/down orientation.~~<\>>~~

~~<p>**Conclusions**~~

~~The head and medium design outlined here could support areal densities in excess of 5 Tbit/in^2, a tenfold increase on current demonstrations. To achieve 10 Tbit/in^2 requires an extremely high head field gradient; improved head designs are currently being investigated to meet this target.~~<\>>

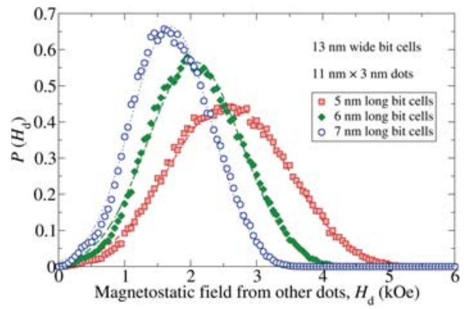

Fig. 1 Distributions of magnetostatic fields in media with randomly magnetised dots (up/down).

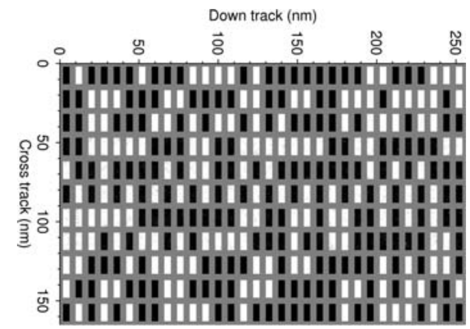

Fig. 2 A recorded track (the central track) in a 5.38 Tbit/in^2 patterned medium.

CU-02

Characterisation of a 2 Tbit/in^2 patterned media recording system.

N. Degawa[1], S. J. Greaves[1], H. Muraoka[1], Y. Kanai[2]
1. RIEC, Tohoku University, Sendai, Japan; 2. IEE, Niigata Institute of Technology, Niigata, Japan

Introduction

The potential and characteristics of bit patterned media with an areal density of 2 Tbit/in^2, for use in future storage devices, were investigated using micro-magnetic simulations based on the Landau-Lifshitz-Gilbert equation. The influence of dot size and position dispersions on the signal to noise ratio (SNR) was clarified. The head-medium synchronisation tolerance (write margin) for error-free writing was calculated, and the feasibility of achieving 2 Tbit/in^2 recording with bit patterned media was demonstrated.

The model

The region containing a single dot and its non-magnetic boundary is called the bit cell. The bit cell length (down-track direction) and width (cross-track direction) correspond to the bit length and the track pitch, respectively. In this research, the bit cell length in the patterned media was 13 nm and the width was 25 nm, giving an areal density of 2 Tbit/in^2. Rectangular, magnetic dots, formed from a number of 2 nm cubes, were centered in each bit cell. The dots in adjacent bit cells were never in contact. The dot dimensions were 16 nm × 8 nm and 10 nm thick and had a saturation magnetization, M_s, of 860 emu/cc. The exchange coupling constant, A, temperature, T, and easy axis dispersion were 10 erg/cm^2, 300 K and 0 degrees, respectively.

The simulated media contained seven columns (tracks) of dots in order to bring the maximum magnetostatic field close to the value predicted for an infinitely wide medium. A 1/0/1/0… pattern was programmed into the middle track of each medium. The polarity of bits in the remaining tracks was set at random. The sensitivity function of a 20 nm wide magneto-resistive (MR) head with a 25 nm shield-to-shield spacing was calculated and used to evaluate the SNR of tracks in an ideal patterned medium, and in media with random dot displacements and dispersions of dot areas.

Subsequently, write margins were determined for 2 Tbit/in^2 patterned media. The write fields of shielded, single pole heads were calculated using a finite element model. The main pole width was 20 nm and the length was 30 nm. The head to medium spacing was 6 nm, with a 2 nm thick seed layer between the bottom of the dots and the soft magnetic underlayer. Side shields were placed 10 nm either side of the main pole and a trailing shield was located 30 nm behind the main pole. The maximum write field in the uppermost layer of the medium was 9.4 kOe. The uniaxial anisotropy, K_u, of the media was 3.88×10^6 erg/cc and was chosen to give high thermal stability ($K_uV/kT = 120$) and anisotropy fields, H_k, slightly lower than the maximum head field. Multiple simulations of recording single bits were carried out, each with random media magnetization configurations. The probability of successfully writing a bit was calculated for different initial write head positions.

Results

Random variations in the dot positions of up to 2 nm did not have a significant effect on the SNR. Fig. 1 shows the effect on the SNR of introducing dispersions of dot areas. The bit cell length of 13 nm equates to a linear density of 1954 kfci, resulting in a small output signal from the read head. Dot area dispersions lead to large fluctuations in the amplitude of the readback signal, significantly reducing SNR. Fig. 2 shows the write margin, defined as the range of offsets between the trailing edge of the write head and the dot centers for which error free writing could be achieved. For these media, the write margin was 2 - 3 nm.

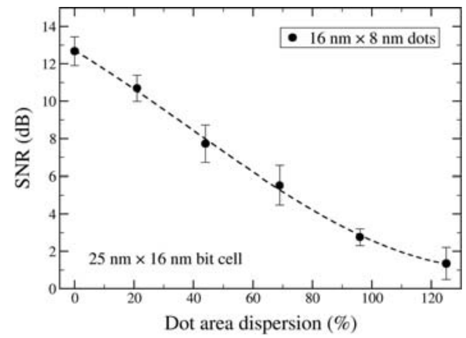

Fig. 1. Effect of dispersions of dot areas on SNR for 16 nm × 8 nm dots in 25 nm × 13 nm bit cells.

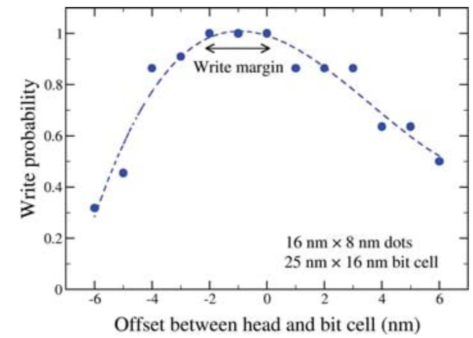

Fig. 2. Write margin for a 2 Tbit/in^2 patterned medium.

CU-03

Simulation Study of High Density Bit Patterned Media with Inclined Anisotropy.

N. Honda, K. Yamakawa, K. Ouchi
Research Institue of Advanced Technology, Akita Prefectural R & D Center, Akita-shi, Japan

1. Introduction
Bit patterned media is one of promising candidates which extend recording densities of perpendicular magnetic recording beyond 1 Tbit/in^2. However, when the packing density of the magnetic dots is increased towards 2 Tbit/in^2, some additional methods, such as use of exchange coupling [1] or in-plane anisotropy [2], should be introduced to reduce the enhanced effect of magnetostatic interaction between the dots. This paper proposes another simple technique of using inclined anisotropy, which is effective to realize high areal densities beyond 2 Tbit/in^2.
2. Simulation model of media and magnetic properties
Figure 1 shows modeled bit patterned media with an areal density of 2 Tbit/in^2 with an inclined anisotropy angle to the longitudinal direction, ϕ. The media consisted of three tracks with 51 dots for each with an analytic soft magnetic underlayer (SUL). Each 10x15x5 nm^3-dot was modeled with 48 exchange coupled 2.5 nm-cube elements with M_s=1000 emu/cm^3, $\langle H_k \rangle$=13-18 kOe with 15 % standard deviation, and an orientation deviation of 2 deg. The $\langle H_k \rangle$ values were determined so that the magnetic energy estimated from the minimum reverse filed in each easy axis satisfies the thermal stability condition. The smaller the angle, the smaller H_k is required. Figure 2 shows simulated anisotropy angle dependence of remanence properties of the media for perpendicular applied field. The switching field width, (H_{sr}-H_{nr}), reduced with decreasing the anisotropy angle, especially for angles less than around 50 degrees, which indicated change in the effect of the interaction field between the magnetic dots. Increased down track shift margins for recording were expected from the decreased switching field width [3].
3. Recording simulation
Although the anisotropy axes of the media were deviated from the perpendicular direction, a shielded planar pole head [4] was used for recording at 2 Tbit/in^2. Recording simulation was performed using the optimum magnetomotive force (MMF) for each medium. When the switching timing of the recording field was properly chosen, a 2 Tbit/in^2 pattern was successfully recorded on the center track without affecting adjacent tracks for all the media. The write error rates for 51 recorded bits were investigated for the media by shifting the switching timing in the down track direction, and the down track (DT) shift margins were estimated as no error shift width. The write rates at the adjacent track when the head filed was shifted in the cross track direction were also investigated for the media, and the cross track (CT) shift margins were obtained. The results are summarized in Fig. 3. It was found that the shift margins in the down and cross track directions were increased for media with inclined anisotropy and the effect was significant for media with angles less than about 50 degrees. The increased CT shift margins were also caused by the decreased switching field width. It is expected that an areal density of 2.6 Tbit/in^2 with a reduced track pitch of 20 nm would be realized with shift margins of 8 nm in DT and 7 nm in CT for media with an inclined anisotropy angle of 30 degrees.
We would like to thank Dr. S. Iwasaki for his stimulating guidance. This work was partially supported by Akita Prefecture CREATE, JST and SRC.

[1] N. Honda, K. Yamakawa, K. Ouchi, IEEE trans. Magn., vol. 43, pp. 2142-2144, 2007.

[2] N. Honda, K. Yamakawa, K. Ouchi, Digests of PMRC 2007, 16pE-06, pp.270-271, Tokyo, 2007.

[3] N. Honda, K. Yamakawa, K. Ouchi, IEICE Trans. Electron., vol. E90-C, pp. 1594-1598, 2007.

[4] K. Ise, S. Takahashi, K. Yamakawa, N. Honda, IEEE trans. Magn., vol. 42, pp. 2422-2424, 2006.

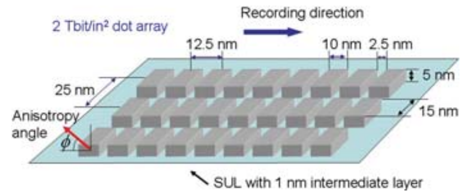

Fig. 1 Simulation model of bit patterned media.

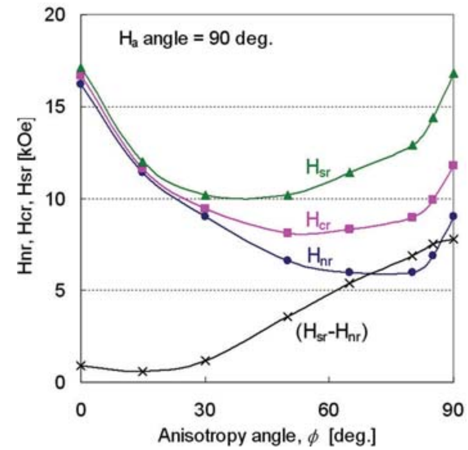

Fig. 2 Anisotropy angle dependence of remanence properties for perpendicular applied field.

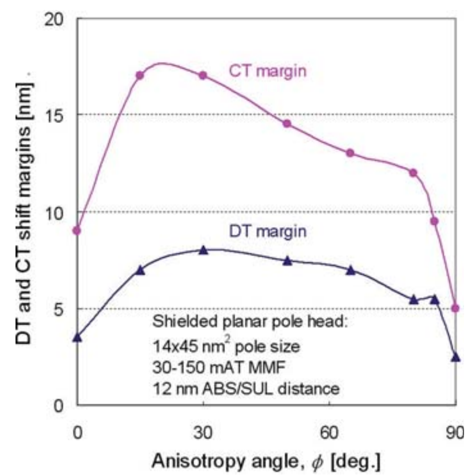

Fig. 3 Anisotropy angle dependence of shift margins in down track (DT) and cross track (CT) directions.

Writability in Discrete Track Media.

K. Moon[1], C. Che[1], Y. Tang[2], M. T. Moneck[2], J. Zhu[2], N. Takahashi[3]
1. Samsung Information Systems America, San Jose, CA; 2. ECE Department, Carnegie Mellon University, Pittsburgh, PA; 3. Fuji Electric Advanced Technology, Nagano, Japan

Discrete track media, based on conventional PMR media, were prepared to get grooves and lands in the magnetic layer, defined by e-beam lithography and ion-milling processes. The bottom of milled groove reaches the interlayer. The interlayer and soft under-layer are continuous under the patterned magnetic layer. Discrete track zones and continuous zones are alternatively positioned within a limited portion on a track with each zone being 50 μm long in the down-track direction. Both discrete track zones and continuous zones are repeated 10 times. The patterned recording tracks are designed to have 150, 100, and 50 nm widths with groove widths of 200 nm. Since these patterned zones are formed on a small scale in a given track, the flying of R/W head was minimally disturbed by the groove features. To secure a stable trigger on the Guzik spin stand, a number of Guzik servo signals are reduced to let the whole pattern area be in one sector. It was well recognized that discrete track media could effectively reduce adjacent track erasure (ATE) which would be a hurdle to high areal density of more than 500 Gbpsi [1]. The edge of the discrete track is supposed to have a stable magnetization configuration due to reduced self-demagnetization [1]. This stable magnetization at the edge may generate an issue in writing performance even if it could reduce ATE. In this study, writability of discrete track media as well as of continuous media with various write currents is discussed. Writability here is gauged by the amplitude of output signal which is the root-mean-square (rms) of the fundamental harmonics for LF writing frequency (53 Mf/s). Write track width of the head was 169 nm while read width was 89.5 nm. From separate experiments, the output of discrete zones and continuous zones became saturated at 12 mA. Therefore, writing current was changed from 6 mA to 12 mA with 0.5 mA step. An initial 2T writing part (200Mf/s) in a given track is saved from LF writing during experiments and used for triggering, by controlling the gate in the spin stand controller. It was found that the output signal in the discrete zone was smaller than the one in the continuous part at a certain range of current if current is less than 12mA when discrete zone becomes narrower (Fig. (1)). That indicated that the discrete zones are not fully magnetized at low writing current whereas continuous zones are already magnetized. But, no amplitude difference was observed between discrete zones and continuous zones when current were more than 12 mA. From cross-sectional TEM study and simulation, it is recognized that shallow wall angle after ion-milling could be one of root causes for this under-magnetization of discrete media (Fig (2)). In a conclusion, the writability of the discrete zone is not so different from that of continuous zone when current is more than 12 mA.

X. Che, Y. Tang, H. J. Lee, S. Zhang, K. Moon, N. Kim, S.Y. Hong, N. Takahashi, M. T. Moneck, J. Zhu, "Recording Performance Study of PMR Media With Patterned Tracks", IEEE Trans. Magn., vol. 43, no. 6, pp. 2293-2295, Jun. 2007.

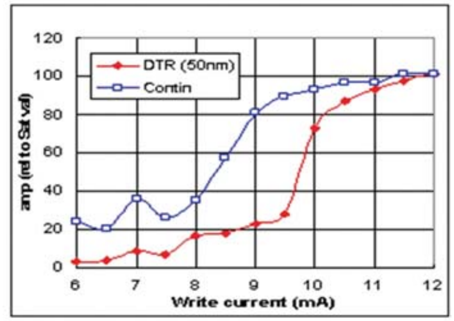

Fig. 1. Saturation test for a 50 nm line and a continuous track.

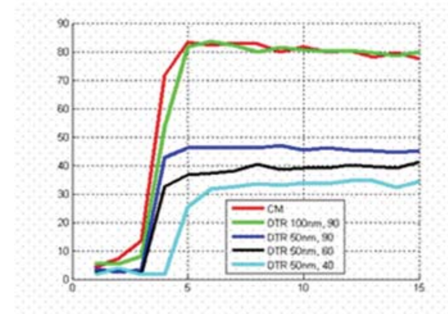

Fig 2. Simulation results with on different wall angles of 40, 60, and 90 degrees were used. Here CM signifies continuous media, whereas DTR does discrete track recording.

CU-05

Magnetization switching experiments on sub-micron Co/Pt multilayer dot with pulse field generator with nanoseconds duration.

N. Kikuchi, I. Atsuo, S. Okamoto, O. Kitakami
IMRAM Tohoku University, Sendai, Japan

I. Introduction

Bit patterned media (BPM) is one of the candidate solutions to overcome superparamagnetism limit of ultrahigh density magnetic recording. Understanding of dynamical switching behavior of the nanomagnet is one of the key issues to realize BPM, since the operation frequency is expected to be of the order of 1 G Hz and comparable with the timescale of magnetization reversal itself. However, investigation of dynamical switching behavior of individual hard nanomagnet in a timescale of nanoseconds is still challenging due to the difficulties of generating a large pulse field to switch magnetization, although a few works has been reported on continuous films [1, 2]. In this work, we have developed a nanoseconds pulse field generator with the maximum field of several hundred oersteds in submicron area. Magnetization switching behavior of a single Co/Pt multilayer dot with sub-micron diameter in the pulse field has been investigated by combining with anomalous Hall effect (AHE) detection [3].

II. Sample fabrication

A multilayer of $[Co(1.3\ nm)/Pt(2\ nm)]_3$ was deposited on a glass substrate with Pt (2 nm)/ Ta (2 nm) underlayers. The multilayer was patterned into a dot of 400 nm in diameter by means of e-beam lithography and Ar ion etching. A 10 nm-thick Pt film was deposited on the dot and subsequently patterned into cross-shaped electrode for AHE measurement. A Cu stripline of 10 µm in width and 200 nm in thickness for pulse field generation was deposited beside the Co/Pt dot. The distance was designed as 5 µm from the edge of the stripline to the dot center. A SEM image of the sample is shown as Fig. 1. The direction of pulse field is perpendicular to the film plane with this sample geometry.

III. Results

The developed pulse generator consists of a power supply, a coaxial cable as capacitor and two relay switches for charging and discharging. The amplitude of the pulse field is proportional to the charged voltage V_p and the estimated maximum field of 740 Oe on the dot was obtained with V_p = 400 V. The pulse duration is defined by the coaxial cable length with the rate of 10 nm/s and was fixed as 10 ns in this study. By careful adjustment of characteristic impedance of the whole system including the microfabricated sample, very rectangular shaped pulse with rise time of 0.4 ns was obtained. AHE measurement in a static field revealed that the switching field of the dot is 2.9 kOe. Since even the maximum pulse field is insufficient to switch the dot magnetization, all the measurements were carried out with the assistance of bias DC field H_{DC}. Figures 2 show switching probability after applying pulse field as function of H_{DC}. V_p was varied from 0 to 400 V. The direction of the pulse field was set to (a) anti-parallel and (b) parallel with the direction of H_{DC}. Significant reduction of required H_{DC} for switching (H^c_{DC}) is observed only when the pulse field direction is parallel to the direction of H_{DC}. H^c_{DC} depends on also V_p and decreases with increasing of V_p. These field amplitude and direction dependences indicate that the magnetization of the dot was switched by the generated pulse field, not by heating or eddy current. Moreover, these results suggest the possibility of real-time measurement of magnetization reversal of a single hard nanomagnets. The effect of pulse field becomes insignificant below V_p = 200 V. This threshold can be explained qualitatively by considering thermal relaxation process both of in timescales of the pulse field and measurement process, respectively. The origin of rather wide distribution of switching field found in Fig. 2 (b), which is apparently larger than experimental error, also will be discussed.

Acknowledgement

This work is partially supported by the "Research and Development for Next-Generation Information Technology of MEXT", Grant-in-Aid for Scientific Research from MEXT, the Storage Research Consortium in Japan, and Hatano foundation.

[1] M. Belmeguenai *et al*., J. Magn. Magn. Mater. **307**, 325 (2006). [2] M. Weisheit *et al*., IEEE trans. Magn. **42**, 3072 (2006). [3] N. Kikuchi *et al*. Appl. Phys. Lett. **82**, 4313 (2003).

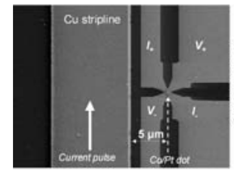

Fig. 1 SEM image of the device with Cu stripline and Co/Pt dot of 400 nm in diameter with four terminal electrode for AHE measurement. The dot distance from the edge of the Cu line to the dot center is 5 µm.

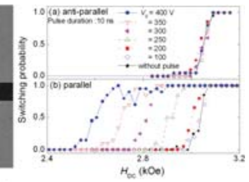

Fig. 2 Switching probability after applying pulse under static dc field H_{DC} of (a) anti-parallel and (b) parallel with pulse field. The probability is obtained by 20 times measurement at each point.

CU-06

Dot size dependence of magnetic properties in CoPt dot arrays fabricated using diblock copolymer.

K. Kimura, Y. Kamata, T. Maeda, Y. Isowaki, A. Kikitsu
Storage Materials & Devices Laboratory, Corporate Research & Development Center, Toshiba Corporation, Kawasaki, Japan

I. INTRODUCTION

Bit patterned media (BPM) is a promising candidate for high-density magnetic recording media because it can improve thermal stability and reduce media transition noise. We proposed the Artificially Assisted Self-Assembling (AASA) method a low-cost and large-area nanopatterning method for BPM [1]. For BPM applications, it is necessary to minimize the switching field distribution (SFD) of patterned dots. The origins of SFD in BPM are distributions of anisotropy, magnetization, exchange, magnetostatic coupling, dot size, and dot edge effects [2]. In our previous report, it is found that thick grain boundary and poor crystal orientation are the possible origin of the large Hc distribution [3]. In order to investigate the origin of the SFD, we made highly oriented CoPt dot arrays with different diameter and similar size dispersion using diblock copolymer.

II. EXPERIMENTAL METHODS

Highly oriented perpendicular magnetic films were fabricated by sputtering. Film stack was 2.5 in. glass disk/Ti seed layer 20nm/$Co_{80}Pt_{20}$ 15nm. These films were patterned by an Ar ion milling using self-assembled PS-PMMA diblock copolymer mask. PMMA dots were arranged in PS matrix with 45 nm and 60nm pitch. Each process step was optimized to give similar dot size distribution. Magnetic properties were measured by a vibrating sample magnetometer (VSM).

III. RESULTS AND DISCUSSION

Dot diameter and its dispersion were estimated from SEM images. Fig.1 shows the distribution of the dot diameter of (a) 60nm pitch and (b) 45nm pitch. The average diameter was 38nm and 24nm, respectively. However, one-sigma of the dispersion is similar for both samples (13-14%).

Fig.2 shows hysteresis loop (thick line) and DCD (dc-demagnetization) curve (thin line) for (a) 60nm pitch and (b) 45nm pitch. The hysteresis loop of 45nm-pitch has large amount of small coercivity region although the DCD curve is similar for both samples. This region is expected to correspond to the dots that have reversible magnetic property with relatively large anisotropy energy. Such dots could be damaged by oxidization at its side wall or physical etching process. This damage is emphasized for small dots in the 45nm-pitch sample.

From the hysteresis loops and the DCD curves, about a half of the 45nm-pitch dots changed into the reversible state. The critical diameter at which the accumulated area distribution reaches 50% is about 24 nm for the 45nm-pitch sample. This result indicates that dots whose diameter is less than 24nm are tend to have reversible nature.

In conclusion, it is found that smaller dot has large SFD even though the size dispersion is similar. The origin of the SFD is expected to be the change in the magnetic properties for small dots. The change seems to results in the reversible magnetic property and the critical size is around 24nm.

This work was partially supported in part by the IT Program (RR2002) of the Ministry of Education, Culture, Sports, Science and Technology (MEXT), Japan.

[1] K. Naito, H. Hieda, M. Sakurai, Y. Kamata, and K. Asawkawa, IEEE Trans. Magn., 58, (2002) 1949.

[2] T. Thomson, C. Hu, and B. D. Terris, Phys. Rev. Lett, 96, (2006), 257204.

[3] Y. Kamata, A. Kikitsu, H. Hieda, M. Sakurai, K. Naito, J. Bai, and S. Ishio, Jpn. J. Appl. Phys., 46 (2007), 999.

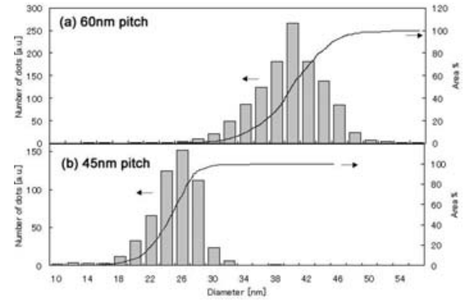

Fig. 1 Diameter dispersion and area % of patterned CoPt dot arrays. (a) 60nm-pitch. (b) 45nm-pitch.

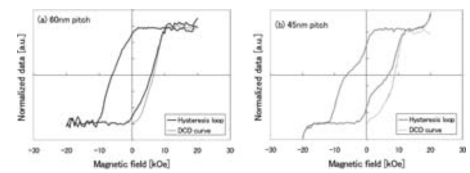

Fig. 2 Hysteresis loops and DCD curves for (a) 60nm-pitch. (b) 45nm-pitch.

CU-07

Study on ferro-antiferromagnetic transition in $L1_0$ FePtRh film for bit patterning.

T. Hasegawa[1], J. Miyahara[1], Y. Fu[2], T. Wang[2], H. Saito[1], S. Ishio[1]
1. Materials Science and Engineering, Akita University, Akita, Japan; 2. Venture Business Laboratory, Akita University, Akita, Japan

I. INTRODUCTION
Recently, with continually decreasing grain size, the magnetic thermal fluctuation has been one of the main problems for the high density magnetic storage. The $L1_0$ FePt film (fct structure) has a high magnetocrystalline anisotropy (K_u~$7x10^7$ erg/cm^3), which is considered to be suitable for a high recording density of more than 1Tbit/$in.^2$ due to its good thermal stability.
Bit patterned media which consist of the ferromagnetic (FM) dots regularly arranged in a nonmagnetic matrix have been proposed as a possible solution to overcome the superparamagnetic effect and medium noise of continuous media. For the fabrication of bit patterned media, lithographic patterning, ion irradiation and various chemical methods have been reported so far[1,2)]. In the lithographic patterning and self-organizing method, removing material between the dots or assembling particles leads to variations in the height of the storage medium which cause the tribology problems in the near-contact recording scheme. In the ion irradiation patterning, magnetic properties of continuous films are modified by local ion irradiation and a difference in the height between irradiated and nonirradiated areas was found to be about 2–3 nm. The resolution of patterning using local ion irradiation, however, depends on the distribution of ions in lateral direction and sharpness of FM-paramagnetic (PM) transition of films.
FePtRh bulk alloys are known to show a discontinuous FM-antiferromagnetic (AF) transition[3)]. A new type of bit patterned film which has sharp transitions between dots due to its discontinuous FM-AF transition could be realized by changing the composition locally by using ion irradiation or lithographic techniques. In this work, we report the influences of addition of Rh on the magnetic properties of a FePt film, and discuss the possibility of bit patterning by FM-AF transition.
II. EXPERIMENT
A function of $FePt_{1-x}Rh_x$-SiO_2(19vol%) (10nm) films were prepared by using a sputtering method onto SiO_2 substrates at room temperature. The films were annealed at 973 K for 2 hours by a rapid heating furnace. SiO_2 was added for improving the [001] orientation of FePt film. The composition and the crystalline structure were detected by the energy dispersive X-ray spectroscopy and the X-ray diffraction (XRD), respectively. The alternating gradient magnetometer were used for studying the magnetic properties.
III. RESULTS AND DISCUSSION
Figure 1(a) shows the 2θ-θ scans from the XRD measurements for the $FePt_{1-x}Rh_x$-SiO_2 films annealed at 973 K. The intensity of the superlattice (001) reflection peaks from the $L1_0$ phase are quite larger than that of fundamental (111) peaks in the films with 0<x<~0.40. These intensity differences indicate that a [001] crystalline texture normal to the film plane is obtained. The magnetic properties are shown in Fig.1(b). The films with 0<x<0.30 have the $L1_0$ structure and [001] crystalline texture normal to film plane with large coercivity (H_c) of 3.5< H_c<16.8kOe. The small magnetization (~300 emu/cm^3) is caused by the unsaturation due to its large H_c. At around x=0.30, an abrupt change from FM phase with high H_c to nonmagnetic phase appeared. This discontinuity seems to be caused by the FM to AF transition. In the case of $FePt_{1-x}Rh_x$ bulk alloy, it is known that the FM-AF transition is observed at around x~0.22 at room temperature[3)].
The FM-AF transition needs to occur easily during the bit patterning process, for instance by annealing or ion irradiation. To confirm this point, an experiment in which Rh was added into a FM FePtRh film to change the properties from FM to AF was carried out. Figure 2(a) and (b) show the magnetization curves of $FePt_{0.72}Rh_{0.28}$-SiO_2 film (10nm) and Rh(0.38nm)/$FePt_{0.72}Rh_{0.28}$-SiO_2(10nm) bi-layer film annealed at 973 K, respectively. The film shown in Fig.2(a) has a large H_c (~8kOe). In contrast, the film in Fig.2(b) shows nonmagnetic properties. It seems that the Rh/$FePt_{0.72}Rh_{0.28}$ bi-layer structure was mixed and changed to $FePt_{0.68}Rh_{0.32}$ within the AF region. These results suggest the possibility of realizing a bit pattern using a material with a critical composition of FM-AF transitions. The discontinuous FM-AF transformation between dots would make its boundary sharper than the FM-PM transformation, so local Rh or Pt addition into the $FePt_{1-x}Rh_x$-SiO_2 film (x<0.30) can realize the bit patterned film consisting of high H_c dots (x<0.30) and AF spacing (x>0.30).

1)Kusinski GJ et al. Scripta Mater 2003;48:949.

2)Hasegawa T et al. Acta Materialia(In Press).

3)Takizawa K et al. J Magn Magn Mater 2001;226:572.

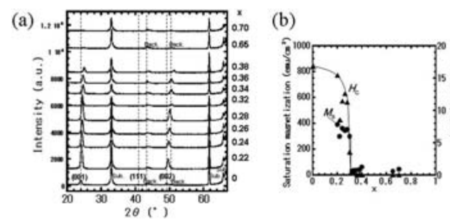

Fig. 1 XRD patterns (2θ-θ) (a) and magnetic properties (b) of $FePt_{1-x}Rh_x$-SiO_2(19 vol%) films (10nm) annealed at 973 K.

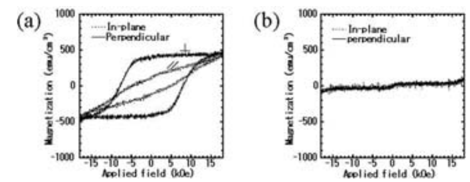

Fig. 2 Magnetization curves of $FePt_{0.72}Rh_{0.28}$-SiO_2(10nm) film (a) and Rh(0.38nm)/$FePt_{0.72}Rh_{0.28}$-SiO_2(10nm) bi-layer film (b) annealed at 973 K.

CU-08

$CoCrPt\text{-}SiO_2$ films on spherical SiO_2 particle arrays.

C. Brombacher[1], F. Springer[2], H. Rohrmann[4], M. Kratzer[4], M. Parlinska[3], S. Meier[3], P. Kappenberger[3], M. Albrecht[1]

1. Institute of Physics, Chemnitz University of Technology, D-09107 Chemnitz, Germany; 2. Department of Physics, University of Konstanz, D-78457 Konstanz, Germany; 3. Nanoscale Materials Science, Empa, CH-8600 Dübendorf, Switzerland; 4. Data Storage, OC Oerlikon Balzers AG, FL-9496 Balzers, Liechtenstein

$CoCrPt\text{-}SiO_2$ is a granular material consisting of small magnetically decoupled grains and is commonly used for perpendicular magnetic recording applications. In this study, the system was deposited onto SiO_2 spherical particle arrays with diameters down to 10 nm to form arrays of magnetic nanostructures following an approach by Albrecht et al. [1]. It was shown that the deposition of Co/Pt multilayers on Polystyrene spheres leads to single-domain and exchange isolated caps with a radial symmetric spatial variation of the anisotropy orientation [2]. Combining this approach with the advantages of CoCrPt-SiO2 is a promising way to realize "patterned media".

Densely packed arrays of monodisperse SiO_2 particles are formed in a self-assembling process by the method of Micheletto et al. [3]. These particle arrays serve as a topographic pattern for the subsequent depositions carried out in the commercially available RACETRACK hard disk fabrication system. Two layer stacks, Carbon(4 nm)/ $CoCrPt\text{-}SiO_2$(12%)(15 nm)/ Ru(12 nm)/ Ru(8 nm)/ Ta(5 nm) and Carbon(4 nm)/ CoCrPt-SiO2(12%)(10 nm)/ Ru(5 nm)/ Ta(5 nm) have been deposited onto SiO_2 particle arrays with diameters from 10 nm to 330 nm and for comparison onto planar SiO_2 substrates.

TEM studies reveal that the growth of $CoCrPt\text{-}SiO_2$ on the curved particle surface remains columnar with a substantial reduction of the lateral grain size down to 5 nm (Fig 1). The (0001) orientation of individual grains is pointing perpendicular to the particle surface.

By varying the growth conditions and the thickness of a Ru seed-layer, the degree of intergranular exchange coupling can be controlled, leading to pronounced differences in the magnetic domain structure and its magnetic reversal behavior.

A two-step Ru seed-layer with a thickness of 20 nm leads to magnetically exchange decoupled grains and strong perpendicular anisotropy. The variation of the orientation of the easy axis along the particle surface, as well as an increase in defects is leading to a reduction of the coercivity on particles compared to the coercivity on planar substrates (Fig 2 (a) and (b)). The domain structure remains nearly unaffected by the changes in topography, leading to multidomain magnetic caps (Fig 2 (c)).

Reducing the Ru thickness to 5 nm is leading to a substantial decrease in coercivity and to a narrow switching field distribution on planar SiO_2 substrates. On SiO_2 particles, however, single-domain magnetic caps are observed and the magnetic coercivity field is increasing for smaller particle sizes (Fig 2 (d) – (f)).

This work was supported by the European project MAFIN (contract No. FP6-26513).

[1] M. Albrecht, G. Hu, I.L. Guhr, T.C. Ulbrich, J. Boneberg, P. Leiderer, and G. Schatz, Nat. Mater. 4, 203 (2005).

[2] T.C. Ulbrich, D. Makarov, G. Hu, I.L. Guhr, D. Suess, T. Schrefl, and M. Albrecht, Phys. Rev. Lett. 96, 077202 (2006).

[3] R. Micheletto, H. Fukuda, and M. Ohtsu, Langmuir 11, 3333 (1995).

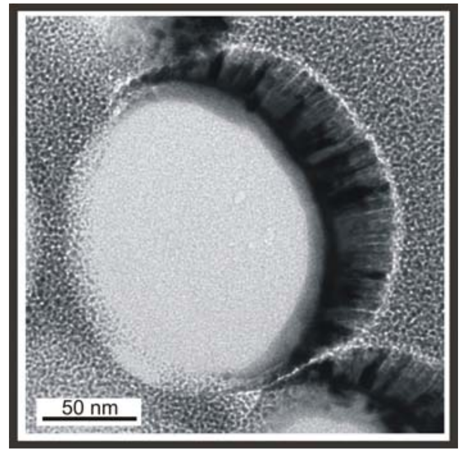

Fig 1: TEM image of Carbon(4 nm)/ $CoCrPt\text{-}SiO_2$(12%)(15 nm)/ Ru(12 nm)/ Ru(8 nm)/ Ta(5 nm) deposited onto SiO_2 particles with a diameter of 160 nm.

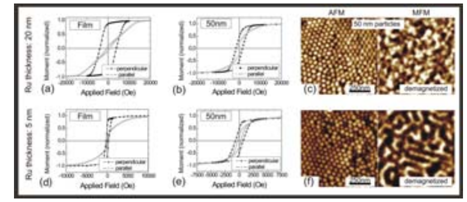

Fig2: SQUID loops of Carbon(4 nm)/ $CoCrPt\text{-}SiO_2$(12%)(15 nm)/ Ru(12 nm)/ Ru(8 nm)/ Ta(5 nm) on (a) planar substrate and (b) particles with a diameter of 50 nm and (c) corresponding AFM/MFM image after demagnetizing. SQUID loops of Carbon(4 nm)/ $CoCrPt\text{-}SiO_2$(12%)(10 nm)/ Ru(5 nm)/ Ta(5 nm) on (d) planar substrate and (e) SQUID loops and (f) AFM/MFM images on particles with a diameter of 50 nm.

CU-09

Fabrication of nanomagnet arrays by exfoliating thin films sputter-deposited onto molds.

H. Oshima[1,2], H. Kikuchi[1,2], H. Nakao[1,2], K. Itoh[1,2], T. Morikawa[3], H. Tamura[4], K. Nishio[5,6], H. Masuda[5,6]
1. Fujitsu Laboratories Ltd., Atsugi 243-0197, Japan; 2. Yamagata Fujitsu Ltd., Higashine 999-3701, Japan; 3. Fujitsu Laboratories Ltd., Akashi 674-8555, Japan; 4. Fujitsu Ltd., Kawasaki 211-8588, Japan; 5. Kanagawa Academy of Science and Technology, Sagamihara 229-1131, Japan; 6. Tokyo Metropolitan University, Hachioji 192-0397, Japan

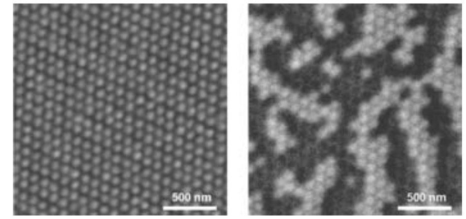

<P>Introduction
Fabrication of magnetic nanostructures has been of considerable interest both for fundamental studies of nanomagnetism and various applications such as bit patterned media [1]. Typically, lithographic patterning in a resist layer is subsequently transferred to a magnetic film in the nanofabrication process. However, especially when fabricating nanostructures on a scale of tens of nanometers, the process suffers from pattern distortion and edge roughness caused by etching and/or liftoff that are generally applied to the pattern transfer. In this study, we show a simple route to formation of perpendicular magnetic nanostructures without any etching or solvent by directly exfoliating magnetic thin films sputter-deposited onto molds.<\>>
<P>Experiments
We have prepared a Ni nanoimprint mold that has an array of cylindrical dots hexagonally arranged with 100 nm pitch in a macroscopically large circular patterned area of 18 mm in diameter. A thermoplastic polymer resist made of polymethylmethacrylate (PMMA) was spin coated on a Si substrate, and then the Ni mold was pressed onto the PMMA resist to create the pattern in the resist [2]. This nanoimprinted resist layer was utilized as a polymer mold for the following magnetic nanostructure formation.
Perpendicular Co/Pd multilayers were sputter-deposited onto the polymer mold at room temperature with the stacking structure of [Pd 1 nm/Co 0.2 nm]$_8$/Pd 50 nm. A flat glass substrate was then attached to the back surface of the deposited films using a liquid ultraviolet-curing adhesive agent. After ultraviolet curing, the front surface of the films was mechanically separated from the polymer mold.<\>>
<P>Results and discussion
The surface topography and magnetic domain structures of the sample have been investigated by atomic force microscopy (AFM) and magnetic force microscopy (MFM), respectively. The AFM image (left figure) shows the hexagonally arranged nanodots made of Co/Pd multilayers indicating high fidelity of the pattern transfer in this sputter-deposition/exfoliation method. The dimensions of the nanodots are about 60 nm in diameter and 20 nm in height and quite similar to those of the concaves in the polymer mold. The MFM image acquired in the same area in the as-prepared state (right figure) clearly demonstrates that each nanodot is in a single domain state and that its magnetization direction is either up or down. The image also suggests that the nanodots are exchange-isolated because of little magnetization at the boundaries between nanodots and trenches; the deposited Co/Pd multilayer probably has much thinner Co layers (below 1 ML) at the boundaries, which would greatly reduce their magnetization. Perpendicular coercivity measured by polar magneto-optical Kerr effect was 1.0 kOe in the patterned area of the sample, while that in the unpatterned area (flat film) is 0.6 kOe. The increase in the coercivity is also consistent with the nanodot formation in the perpendicular magnetic thin films [3].<\>>

[1] B. D. Terris and T. Thomson, J. Phys. D 38, R199 (2005). [2] H. Oshima et al., Appl. Phys. Lett. 91, 022508 (2007). [3] G. Hu et al., J. Appl. Phys. 97, 10J702 (2005).

CU-10

Design of Ni-Mold for Discrete Track Media.

K. Ichikawa[1], T. Usa[2], K. Nishimaki[2], K. Usuki[1]
1. Recording Media Research Laboratories, FUJIFILM Corp., Odawara Kanagawa, Japan; 2. Production Engineering & Development Center, FUJIFILM Corp., Odawara Kanagawa, Japan

Discrete track media (DTM) [1-3] has been promised as the media for the next generation HDD. For DTM production, Nano Imprint Lithography (NIL) must be the indispensable technology- and the NIL mold plays the most important role in it. But the nickel (Ni) mold has been hardly reported except the field of optical storage disks such as CDs and DVDs. Therefore, the DTM Ni-mold with narrower track pitch than present HDDs has been studied.
We designed and made two Ni molds with different patterns. One contains land-and-groove pattern for discrete track and servo pattern with 150nm track pitch (169kTPI) on 65mm whole area. This track density corresponds to the area density 100-150Gbpsi which is equivalent to that of the available HDD products. The other was designed for 300-450Gbpsi [2] and was fabricated discrete track and servo patterns with 90nm track pitch (282kTPI) in 200 to 500 um band at three radius positions (r=15mm, 21mm, 29mm). The ratio of land to groove is set as 1 to 2, and the height of pattern is 60nm.
The dimension of the pattern on Ni-mold should be designed with taking the change of line width in NIL process and magnetic property of finished DTM into consideration. [4] In particular, the fluidity of imprint polymer used in NIL process and the etching behavior may expand the line width of grooves. Therefore the land width of Ni-mold should be designed more narrowly.
Ni-mold was fabricated with the following process. 1) The EB resist was coated on Silicon wafer. 2) The designed patterns were drawn on the resist by electron-beam recorder with an R-theta stage. [5] 3) Silicon was patterned using reactive ion etching method. 4) Nickel was deposited on Silicon master by electroplating. 5) The Ni-mold was taken off.
Fig.1 shows SEM image of discrete track and servo area. The sample was tilted to show mold surface and the height. The defects were not found in observed surfaces. The unevenness of discrete patterns were replicated by electroplating.
Table.1 shows the result of measured line width and line width roughness (LWR). The line width and LWR of the trench pattern on etched Si were measured by Critical Dimension SEM. The measured position is full width at half maximum on Ni-mold. The line width is 30nm at 282kTPI, and is 44nm at 169kTPI. LWRs were a range from 6 to 7nm, and did not have the significant difference in each track pitch. It can be important to reduce LWR since the ratio of LWR to line width is increasing for a smaller pattern below 30nm line width. The difference of line width between each radius was within 10%.
Fig.2 shows AFM cross section at Ni-mold with 282kTPI.The pattern height is 60nm with standard deviation of 0.8nm.There is little height change.
We proved the feasibility to fabricate Ni-mold with the uniform line width and pattern height at 282kTPI.

[1]D.Wachenschwanz, et al.,"Design of a Manufacturable Discrete Track Recording Medium,"

IEEE. Trans. Magn. Vol.41, No.2, Feb.2005

[2]Y.Soeno, et al.,"Performance Evaluation of Discrete Track Perpendicular Media for High recording density,"

IEEE Trans., Mag. Vol.41, No.10, Oct.2005

[3]Xiaodong Che et al., "Study of Lithographically Defined Data Track and Servo Patterns" IEEE, Trans., Mag., Vol. 43, No.12 Dec 2007

[4] M.Hashimoto et al., "Influence of patterning fluctuation on read/write characteristics in discrete track and bit patterned media" Digests of PMRC 2007 pp146-147

[5] M.Nishikawa et al."Potential of Servo Pattern Printing on PMR Media With High Density Servo Signal

Pattern" IEEE. Trans. Magn., Vol.42, No.10, Oct., 2006

	90nm track pitch		150nm track pitch	
radius(mm)	Width(nm)	LWR(nm)	Width(nm)	LWR(nm)
15	31.9	7.4	46.2	7.2
21	29.8	6.5	44.8	6.3
29	29.9	7.1	42.5	6.0

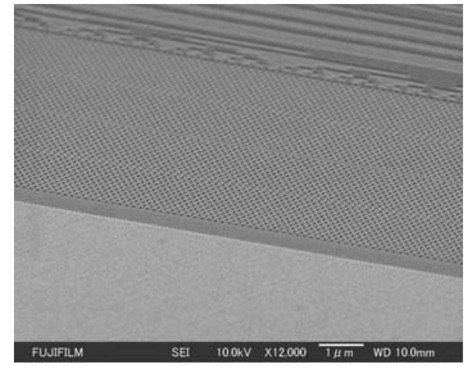

Fig.1 SEM image of the boundary between discrete area and servo area at 282kTPI

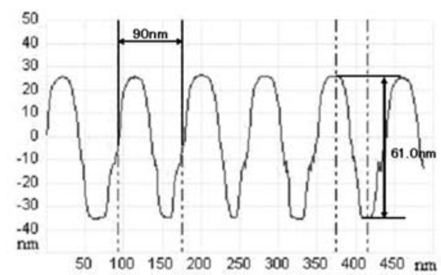

Fig.2 AFM cross section of Ni-mold with 282kTPI

CV-01

Integrated on-chip microstrip lines with Co-Ta-Zr magnetic films.

P. Khalili Amiri[1], B. Rejaei[1], Y. Zhuang[1], M. Vroubel[1], D. Lee[2], S. Wang[2], J. Burghartz[3,1]
1. Delft Institute of Microsystems and Nanoelectronics (DIMES), Delft University of Technology, Delft, Netherlands; 2. Department of Materials Science and Engineering, Stanford University, Stanford, CA; 3. Institute for Microelectronics Stuttgart (IMS CHIPS), Stuttgart, Germany

Introduction: Integrated passive devices such as transmission lines and inductors are indispensable components of contemporary radio frequency (RF) integrated circuits (IC's), being used for impedance matching, filtering, and RF signal transfer. These on-chip passives, however, typically suffer from high loss (low quality factor Q) and small inductance per unit area. In order to address those issues, monolithic integration of IC-compatible metallic magnetic films (e.g. Ni-Fe) has been increasingly studied in recent years [1-6]. Nevertheless, the high loss brought about by parasitic currents in the metallic magnetic films and the limited frequency range of operation due to ferromagnetic resonance (FMR) have thus far impeded the integration of magnetic RF devices in a practical setting. For example, while the use of thick magnetic films can bring about a significant increase in inductance, measurements for microstrip lines with Ni-Fe cores show that an increase of magnetic film thickness from 200nm to 500nm reduces the Q factor by a factor of ~2 due to enhanced eddy current loss, essentially rendering thicker Ni-Fe films useless [5, 6]. Moreover, for typical Ni-Fe layers, FMR limits the useful operation frequency to below 2GHz. Improved materials with higher resistivity (i.e. larger skin depth, thus enabling the use of thicker films) and increased FMR frequency (i.e. large anisotropy and saturation magnetization) are thus highly called for in order to better realize the potential benefits of integrated magnetic RF components. This work presents results on microstrip devices based on such a candidate material.

Experimental results: We deposited by RF diode sputtering a set of amorphous Co-Ta-Zr films with a resistivity of ~100μΩ-cm (~6 times higher than Ni-Fe), and an internal anisotropy field of ~18Oe (induced by an external field during deposition) [4, 7]. The films were patterned into 100μm-wide, 1mm-long stripes and incorporated into microstrip transmission line structures on a silicon wafer (fig. 1). When compared to non-magnetic control devices, microstrip lines with 50μm-wide aluminum signal lines and 1μm-thick Co-Ta-Zr magnetic cores showed an increase in inductance by a factor of ~11 which remained constant up to ~4.5 GHz. The Q factor was increased by a factor of ~6 at 0.7GHz and remained higher than that of the control lines up to ~3GHz (fig. 2). Propagation wavelength at 5GHz was shortened by a factor of ~4, leading to significant size reduction on the chip (e.g. when used in distributed elements such as quarter-wavelength transformers). The effect of shape-induced demagnetization fields in increasing the frequency range of operation was also studied. The fairly high resonance frequencies in our Co-Ta-Zr devices are attributed to a combination of internal and shape anisotropies, and can be further increased by moving the signal line towards the edges of the 100μm-wide magnetic stripe. In this way, one can take advantage of the nonuniform shape anisotropy profile (which is larger near the edges [8]), increasing the maximum frequency for inductance enhancement from 6 to beyond 7GHz. In conclusion, device characteristics of the Co-Ta-Zr lines are dramatically improved with respect to both non-magnetic control devices and previous results with Ni-Fe films [6]. The high resistivity of Co-Ta-Zr allows for the incorporation of a relatively thick (1μm) magnetic film without inducing excessive conductive loss. This results in an order-of-magnitude increase in inductance, while simultaneously maintaining a reasonable enhancement of Q factor and improving the high-frequency behavior of the line by realizing a fairly large (~150Oe) shape-induced anisotropy field.

[1] V. Korenivski, and R.B. Dover, IEEE Trans. Magn., vol. 34, pp. 1375-1377, 1998.

[2] M. Yamaguchi, K. Suezawa, K.I. Arai, Y. Takahashi, S. Kikuchi, Y. Shimada, W.D. Li, S. Tanabe, K. Ito, J. Appl. Phys., Vol. 85, No. 11, pp. 7919-7922, 1999.

[3] A.M. Crawford, D. Gardner, S.X. Wang, IEEE Trans. Magn., Vol. 38, No. 5, pp. 3168-3170, 2002.

[4] D.S. Gardner, G. Schrom, P. Hazucha, F. Paillet, T. Karnik, S. Borkar, IEEE Trans. Magn., Vol. 43, No. 6, pp. 2615-2617, 2007.

[5] M. Vroubel, Y. Zhuang, B. Rejaei, J.N. Burghartz, Trans. Magn. Soc. Japan, Vol. 2, No. 5, pp. 371-376, 2002.

[6] P.K. Amiri, B. Rejaei, Y. Zhuang, M. Vroubel, J.N. Burghartz, IEEE Trans. Magn., Vol. 43, No. 6, pp. 2630-2632, 2007.

[7] L. Li, D.W. Lee, M. Mao, T. Schneider, R. Bubber, K.-P. Hwang, Y. Min, S.X. Wang, J. Appl. Phys., Vol. 101, No. 12, pp. 123912/1-4, 2007.

[8] P.K. Amiri, B. Rejaei, M. Vroubel, Y. Zhuang, J.N. Burghartz, IEEE Trans. Magn., Vol. 43, No. 5, pp. 1880-1883, 2007.

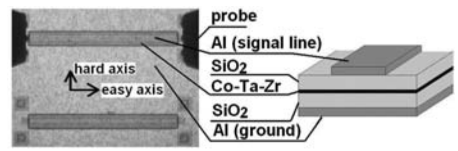

Fig. 1 Top view microphotograph (left) and cross section (right) of Co-Ta-Zr microstrips.

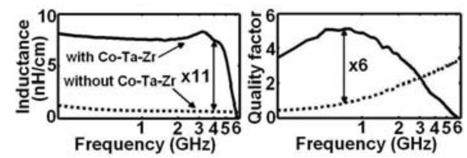

Fig. 2 Inductance and Q factor enhancement in microstrip with a magnetic film.

CV-02

Optimal Design of Microwave Absorbers Using Ferrite-epoxy and Iron-epoxy Composites.

R. Yang[1], S. Hsu[1], C. Lin[2], C. Tsay[2]
1. Aerospace and Systems Engineering, Feng Chia University, Taichung, Taiwan; 2. Materials Science and Engineering, Feng Chia University, Taichung, Taiwan

There has been a growing and widespread interest in radar-absorbing material (RAM) technology, e.g., radar-cross section reduction (stealth technology), electromagnetic interference reduction (EMI) and human health protection. These RAMs absorb microwave energy due to various interactive loss processes of magnetization and polarization in the materials. Polycrystalline ferrite is a class of material with appropriate complex permittivity and permeability which can be used for electromagnetic interference suppression and RAM coatings from centimeter to sub-millimeter spectrum. Iron powder is proved to be a suitable absorber and can be mixed with polymer to become an iron-epoxy composite. In this paper, the complex permittivity (ε'-jε") and permeability (μ'-jμ")as well as microwave absorbing properties of ferrite-epoxy and iron-epoxy composites were studied in the gigahertz range. Different absorbing powders (NiZn-ferrite, MnZn-ferrite, iron particles) are added to epoxy resin to manufacture the composites for the microwave absorbers. The X-ray diffraction(XRD)patterns of iron particle and NiZn-ferrite are shown in Fig. 1. The presence of peaks of iron particle confirms the formation of body-centric cubic(BCC)while the NiZn ferrites are spinel cubic structures. Epoxy resins are used as a matrix material (binder). The mixing ratio is varied form 50% to 80% in weight. For the investigation of the electromagnetic wave absorption properties, we prepared samples with toroidal shapes with an inner diameter of 3.04 mm and an outer diameter of 7.00 mm. The mixture was molded in a coaxial die with the same dimensions. The composite specimens were cured at room temperature for about 12 hrs before testing. The complex permeability and permittivity were measured and determined by using Agilent N5230A network analyzer (10Mhz~20GHz) with Agilent 85071E material measurement software. The frequency dependence of ε', ε", μ' and μ" for iron-epoxy with are shown in Fig.2 and Fig.3. Figure 4 shows the reflection loss in the X-band of microwave frequency as a function of frequency, composition and thickness of the composites adhered on the conducting plates. To obtain a broader frequency region of absorption, a genetic algorithm is adopted for the optimal design of wideband and multilayered radar absorbing coatings by using our own material database (not fictitious or adopted from other references). The synthesis of wideband absorbing coatings appears to reduce more than 20 dB in the frequency ranges of 8.0-12.0 GHz and the total thickness is less than 3 mm as shown in Fig. 5. The composition sequence of the muti-layered composite coating is Fe50%, MnZn, Fe80% and Fe60% with different thickness.

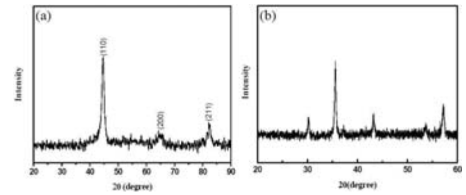

Fig.1 XRD patternsof iron oxide powder and NiZn ferrite.

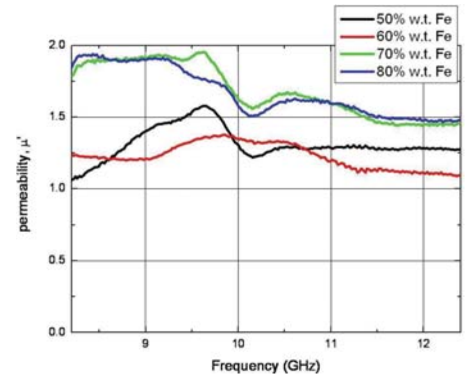

Fig.2 Dispersion spectra of real parts of permeability of iron-epoxy composites.

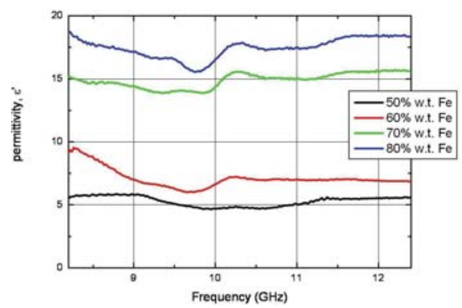

Fig.3 Dispersion spectra of real parts of permittivity of iron-epoxy composites.

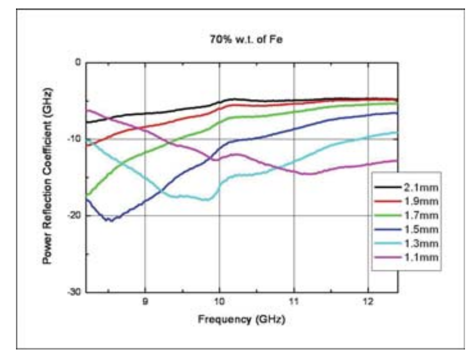

Fig. 4. Comparison on the reflection losses of iron-epoxy composits for different thickness.

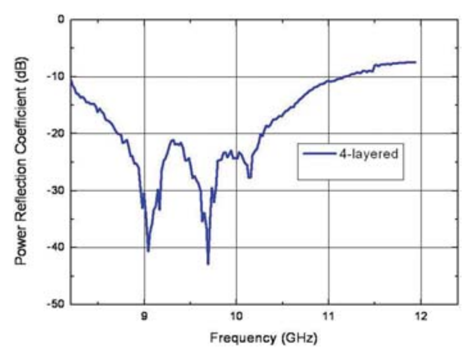

Fig. 5. The wideband absorbing muli-coating material optimally designed by the genetic algorithm.

CV-03

Strong Magnetoelectric Coupling at Microwave Frequencies in Metallic Magnetic Film / PZT Composites.

C. I. Pettiford, J. Lou, L. Russell, N. X. Sun
Northeastern University, Boston, MA

Magnetoelectric (ME) materials are the group of materials that are both ferro/ferrimagnetic and ferroelectric. Strong ME coupling has been successfully achieved in epoxy bonded bulk ME composite materials through a stress mediated ME coupling. These bulk ME composite materials and devices with strong ME coupling provide novel functionalities that are not able to be achieved by either magnetic materials or ferroelectric materials. Most recently a series of such electrostatically tunable microwave magnetic devices based upon glue bonded bulk ferrite/ferroelectric laminates [1-3]. These microwave ME devices provide great promise for electrostatically tunable microwave magnetic devices, which are much more energy efficient, compact, and light. However, all these demonstrated microwave ME devices use high quality yttrium iron garnet (YIG) single crystal as the magnetic phase in the ME composite materials and devices [1-3], which has a very low magnetostriction constant of 0.2ppm, which is not ideal for microwave ME devices. Plus the high cost and high process temperatures (>700°C) for YIG single crystals put severe limit on the YIG based microwave ME devices. An alternative is metallic magnetic films. In order to achieve strong ME coupling at microwave frequencies, these magnetic films need to have a large saturation magnetostriction constant and a high permeability, i.e. a low saturation magnetic field and high saturation magnetization, and a narrow FMR linewidth. Metallic magnetic films with excellent magnetic softness and low ferromagnetic resonance linewidth, however, typically have very low magnetostriction constants. We have developed FeCoN [6], FeCoB [7] and FeGaB [8] films for microwave ME devices with saturation magnetostriction >40ppm. Most recently, we developed the FeGaB films, and achieved FeGaB films with narrow ferromagnetic resonance linewidth of 15 Oe at X-band (10 GHz), a low saturation field of ~20 Oe, and a large saturation magnetostriction constant of 70 ppm [7]. These FeCoB and FeGaB films with the combination of excellent soft magnetic properties and large saturation magnetostriction constant provide great opportunities for applications in novel microwave ME composite materials with metallic magnetic films. Magnetoelectric coupling at microwave frequencies was studied in metal magnetic film/ Pb(Zr,Ti)O3 magnetoelectric composites. Both FeCoB/PZT and FeGaB/PZT multiferroic composite materials were studied (Fig. 1-2). Strong magnetoelectric coupling was observed in a FeGaB film / Pb(Zr,Ti)O3 multiferroic composite material, in which the FeGaB film has a narrow ferromagnetic resonance linewidth of 20 Oe at 10 GHz and a saturation magnetostriction constant of 50 ppm. Large electrostatically induced ferromagnetic resonance frequency shift of 110 MHz at ~2.3 GHz was observed (Fig. 2). This large ferromagnetic resonance frequency shift provides great opportunities for integrated microwave magnetoelectric devices.

1. A.S. Tatarenko, V. Gheevarughese, G. Srinivasan, "Magnetoelectric microwave bandpass filter" Electronics Letters, 42, 9, 540-541 (2006).

2. G. Srinivasan, Y. K. Fetisov, "Ferrite-Piezoelectric Layered Structures: Microwave Magnetoelectric Effects and Electric Field Tunable Devices", Ferroelectrics, 342, 65-71 (2006).

3. Y. K. Fetisov and G. Srinivasan, "Electric field tuning characteristics of a ferrite-piezoelectric microwave resonator", Appl. Phys. Lett., 88, 143503 (2006).

4. S. X. Wang, N. X. Sun, M. Yamaguchi & S. Yabukami, "Properties of a new soft magnetic material ", Nature, 407, 150, (2000).

5. G. A. Prinz, et al. "Growth of single crystal bcc -Fe on ZnSe via molecular beam epitaxy", Appl. Phys. Lett., 48, 1756 (1986).

6. N. X. Sun and S. X. Wang, "Soft high saturation magnetization (Fe0.7Co0.3)1-xNx thin films for inductive write heads", IEEE Trans. Magn, 36, 2506 (2000).

7. C. Pettiford, J. Lou, L. Russell, N. X. Sun, "Strong Magnetoelectric Coupling at Microwave Frequencies in Metallic Magnetic Film / PZT Composites", (unpublished).

8. J. Lou, R. E. Insignares, Z. Cai, K. S. Ziemer, M. Liu and N. X. Sun, "Soft magnetism, magnetostriction, and microwave properties of FeGaB thin films", Appl. Phys. Lett., 91, 182504 (2007).

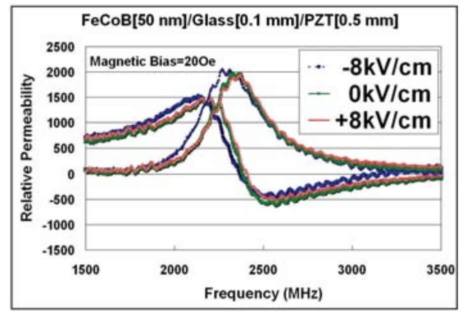

Fig. 1 Permeability spectrum of FeCoB/PZT composite versus electrostatic bias (+/-8kV/cm) at a fixed magnetostatic bias of 20 Oe (~2.3 GHz). A maximum shift in the permeability spectrum of 50MHz was observed.

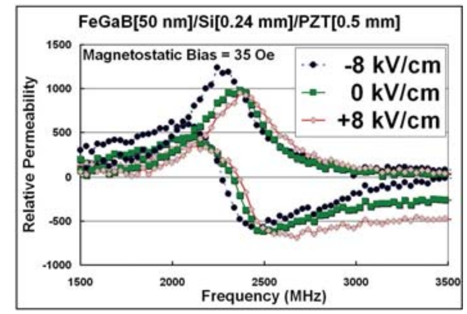

Fig. 2 Permeability spectrum of FeGaB/PZT composite versus electrostatic bias (+/-8kV/cm) at a fixed magnetostatic bias of 35 Oe (~2.3 GHz). A maximum shift in the permeability spectrum of 110MHz was observed.

CV-04

Nonlinear electrical tuning of ferromagnetic resonance in YIG film - PZT layered structures.

Y. Fetisov[1], G. Srinivasan[2]
1. Moscow State Institute of Radio Engineering, Electronics and Automation, Moscow, Russian Federation; 2. Physics Department, Oakland University, Rochester, MI

The ferromagnetic resonance (FMR) frequency f of a planar structure consisting of mechanically coupled ferrite and piezoelectric layers may be tuned by applying an elec-trical field E to the piezoelectric [1]. The field E creates a strain in the piezoelectric that is transmitted to the ferrite and resulting in a change in the internal magnetic field H in the ferrite and a shift in the FMR frequency. Past studies on a bilayer of yttrium iron garnet (YIG) film - lead-zirconium titanate (PZT) reveal a 25 MHz shift in FMR for E up to 8 kV/cm and a near-linear dependence shift on E [2].

Here we report results of investigations on nonlinear electric field tuning of FMR at high electrical fields E.

Figure 1 shows the bilayer structure used. An YIG film of dimensions 0.015x1x2.2 mm^3 grown on a gallium gadolinium garnet (GGG) substrate was bonded to a PZT plate of dimensions 0.5x4x4 mm^3 that was initially poled in an electric field. The bilayer was placed on a microstrip transducer of 50 µm width on an alumina ground plane. A bias magnetic field of H=1.15 kOe was applied parallel to the bilyer plane. The reflection coefficient S_{11} was measured in the frequency band of 3-8 GHz for voltages U up to 1000 V applied across the PZT plate.

Figure 2 shows FMR absorption profiles for U=0 V and 400 V. Figure 3 shows the dependence of the FMR frequency shift Δf vs U. For U<400 V, Δf is a near-linear function of U. The sign of the shift is reversed with the reversal of polarity of U. For U≈550 V (E≈11 kV/cm), a discontinuous jump and a reversal in the sign of Δf are observed in Fig.3, resulting in a butterfly-like dependence. The data in Fig.3 qualitatively tracks electrostriction vs U for PZT, which was measured using a strain gage. The discontinous changes in the frequency shift in Fig.3 are due to re-polarization of the PZT plate.

The research at Moscow was supported by a grant from Ministry of Education and Science of Russia. The work at Oakland University was supported by grants from ONR and ARO.

1. S. Shastry, G. Srinivasan, M. Bichurin et al, Phys. Rev.B 70, 064416 (2004).

2. Y.K. Fetisov, G. Srinivasan, Appl. Phys. Lett. 88, 143503 (2006).

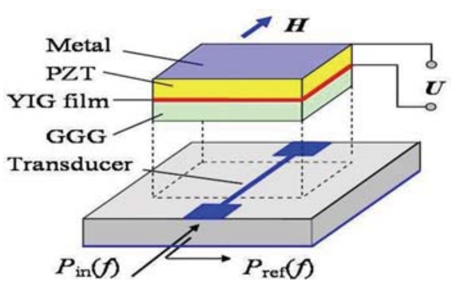

Fig. 1 Schematics of the YIG-PZT layered structure and the microstripline.

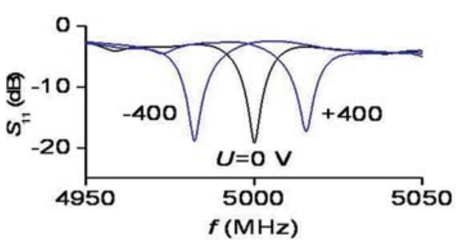

Fig. 2 FMR absorption profiles for the YIG-PZT structure

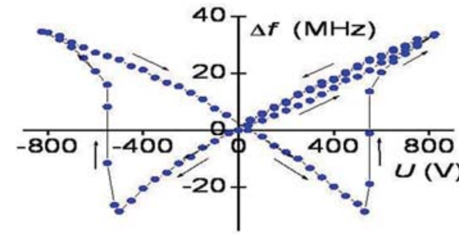

Fig. 3 The FMR frequency shift vs applied voltage

CV-05

Generation of chaotic spin waves in magnetic film active feedback rings through four-wave parametric processes.

A. Kondrashov[1], A. Ustinov[1], T. Stemler[2], *B. Kalinikos*[1,3], M. Wu[3], H. Benner[2]
1. Physical Electronics and Technology, St.Petersburg Electrotechnical University, St.Petersburg, Russian Federation; 2. Institute for Solid State Physics, Darmstadt University of Technology, Darmstadt, Germany; 3. Department of Physics, Colorado State University, Fort Collins, CO

Magnetic film active feedback ring systems (MFAFR) have proved to be useful in studies of nonlinear wave dynamics. For the previous work in MFAFR systems, there are two focus areas: (1) stationary spin wave (SW) soliton excitations and (2) chaotic SW dynamics. The processes responsible for these phenomena may involve only four-wave parametric interactions or both four-wave and three-wave interactions. For (1), the work was done at relatively high frequencies where the three-wave processes were prohibited and one observed the generation of SW solitons and soliton fractals through four-wave processes [1,2]. For (2), the work was done at relatively low frequencies where both three- and four-wave processes were allowed and interacted to produce chaotic SW signals [3,4].
This work reports for the first time the self-generation of chaotic spin waves in a MFAFR system that allows only the four-wave processes. The experiments have been performed for both magnetostatic surface wave (MSSW) and magnetostatic backward volume wave (MSBVW) configurations. With increasing the ring gain, one observed in turn the self-generation of a continuous SW, the breakup of the continuous wave into a breathing wave, the breathing of the breathing wave, and the development of chaotic SWs. In the frequency domain, one observed the development of the power-frequency spectrum from a single mode to a comb-like spectrum, a multiple frequency comb, and a broadband chaotic spectrum. The measured chaotic signals show typical signatures of deterministic chaos.
Consider in more detail the studies performed with MSSW. The MFAFR system consists of a 6.8 micrometer-thick yttrium iron garnet film strip with input and output microstrip transducers, a microwave amplifier, and an adjustable attenuator for gain control. Detailed information on the experimental setup is given in Ref. [4]. A static magnetic field of 1200 Oe was applied in the film plane and perpendicular to the main axis of the film strip.
Figure 1 shows representative power-frequency spectra that demonstrate the development of chaotic SWs with ring gain . In order to prove the deterministic origin of the observed chaotic signals, we recorded also the time-domain data. The time series analyzed below were taken for ring gains close to the critical value of =15 dB. A quantitative measure of the strength of deterministic chaos is obtained by evaluating the largest Lyapunov exponent, which describes the rate of divergence of neighboring trajectories in phase space. The evaluation was done with the standard analysis program TISEAN [5]. As a first test to distinguish between a stochastic process and a deterministic process, one applied the method of surrogate data [6]. The test clearly proved the deterministic origin of the observed dynamic behavior. The respective Lyapunov exponents were obtained from the experimental time series with time steps =6.5 ns by means of delay embedding. This method allows the reconstruction of the strange attractor from the time series of a single variable accessible in the experiment. The delay coordinates,, … are considered to be independent components of an -dimensional substitute phase space vector, where is called the embedding dimension. Using a delay time and an embedding dimension between 7 and 10 we obtained the following values for the largest Lyapunov exponent (in units of 1/): =0.0028, =0.0039, and =0.0032 for =11 dB, =15 dB, and =22 dB, respectively. These values result in a time limit of about 2 microseconds for reasonable predictions of the system dynamics. Similar experimental and numerical data have been obtained for the MSBVW configuration. A detailed comparative analysis of the MSSW and MSBWV regimes will be presented in the conference paper.
This work was supported in part by the Russian Foundation for Basic Research, the USA ARO, Grant W911NF-04-1-0247, USA NSF, Grant ECCS-0725386, and the Deutsche Forschungsgemeinschaft, Grant DFG 436 RUS 113/644/0-2.

[1] B. A. Kalinikos, M. M. Scott, and C. E. Patton, Phys. Rev. Lett. 84, 4697 (2000).

[2] M. Wu, B. A. Kalinikos, L. D. Carr, and C. E. Patton, Phys. Rev. Lett. 96, 187202 (2006).

[3] V. E. Demidov and N. G. Kovshikov, JETP Lett. 66 (4), 261 (1997).

[4] M. Wu, B. A. Kalinikos, and C. E. Patton, Phys. Rev. Lett. 95, 237202 (2005).

[5] R. Hegger, H. Kantz, and T. Schreiber, Chaos 9, 413 (1999).

[6] H. Kantz and T. Schreiber, Nonlinear Time Series Analysis (Cambridge University Press, Cambridge, 1997).

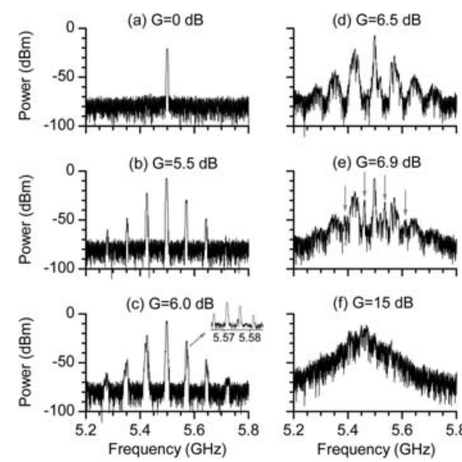

Fig. 1. Power-frequency spectra for different ring gains.

CV-06

Particle Effect of Electromagnetic Penetration in High Frequency in H Field and B Field application.

K. Fujisaki
1. Technical Development Bureau, Nippon Steel Corporation, Futtsu-city, Japan; 2. Graduate School of Environmetal Studies, Tohoku University, Sendai, Japan

Introduction
High frequency magnetic field (H) and high frequency electrical field (E) are used for applying the materials, because chemical phenomena often changes such as higher speed reaction and lower temperature reaction at the two points [1]. At the first point, bulk materials applied and particle materials applied in high frequency electromagnetic field are different in chemical reaction. At secondary point, chemical reaction in H field application only and E field application only is different especially in case of metal particle samples [2]. To make clear the chemical phenomena in electromagnetic field application, electromagnetic numerical calculation is often used. The chemical reaction difference is considered to be derived from the electromagnetic characteristics difference. However, calculation data are possible to explain the chemical reaction difference neither in H field application and E field application nor in bulk material applied and particle material applied by means of macro level (meter-size) calculation as well as nano-meter-size level calculation [3, 4]. To solve the problem, electromagnetic field calculation in micro-meter-size level is shown in this paper to make clear the particle effect of electromagnetic penetration in high frequency.
Numerical model of H field and E field application to conductive particle
To make clear the electromagnetic characteristics difference in H field application only and E field application only, the numerical models of H field only and E field only applied to conductive particles are used as shown in Fig.1. In case of H field application, exiting coil is considered to apply the external H field to the particles. 2D-model with conductive and magnetized particles is considered, where the induced eddy current flows in vertical direction of this paper. In case of E field application, 3D-model is considered. In both cases, every particle is insulated electrically each other. Particle diameter and frequency are considered to be that the diameter of the particle is several times larger than electromagnetic penetration depth of conductive particle materials. For comparison, bulk materials with the same electromagnetic material constants as the one of the particles are also calculated instead of the particles. Displacement current and eddy current are considered in the electromagnetic field calculation. Because of small size calculation such as micro-meter-size which is large enough for electromagnetic wave length in high frequency operation, finite element method is used for calculation.
Calculation results
Induced eddy current distribution is shown to evaluate the electromagnetic penetration in Fig.2 and 3 as calculation results. In case of bulk materials, electromagnetic field penetrates in only penetration depth in both bases of H filed only and E field only. In case of particles, electromagnetic field penetrates more deeply than the electromagnetic penetration depth in both cases of H field and E field. Induced current is considered to transmit to the near particles via induced magnetic field. The deep penetration of the electromagnetic field is expected to make increase the temperature of the particles which makes the chemical reaction of the particles increase. The penetration depth in case of E field application to the conductive particles is larger than the one of H field application. Therefore, chemical reaction change in particle application in high frequency electromagnetic field is considered to be derived from the deep penetration of electromagnetic field in particle application.

[1] H. Takizawa, T. Kimura, M. Iwasaki, K. Uheda, and T. Endo, "Microwave Processing of Advanced Ceramics Using 28 GHz Frequency", Ceramic Transactions,133,211-216,(2002).

[2] R. Roy, D. Agrawal, j. Cheng, and S. Gedevanishvili, "Full Sintering of Powdered-Metal Bodies in a Microwave Field," Nature, 399, 668 (1999).

[3] K. Fujisaki, Y. Kawazoe, H. Mizuseki, A.Jain, "Ab-initio and Electromagnetic Field Combined Calculation", The 4th International Conference on Intelligent Processing and Manufacturing of Materials, Sendai, PSB-6, (2003).

[4] K. Fujisaki, K. Umetsu, R, Hirayama, K. Yokota, H. Katou, H. Taira, S. Nishi, Y. Tomizawa, "Electromagnetic wave analysis of micro wave process by FDTD method", International symposium on micro wave effect and application, Nara, 2002-11, p.42-43, (2002) (Japanese)

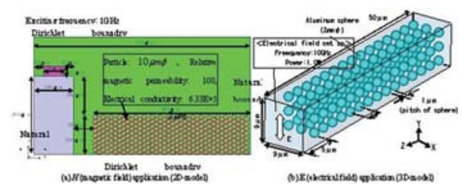

Fig.1. Numerical model of H (magnetic field) and E (electrical field) application to conductive particle.

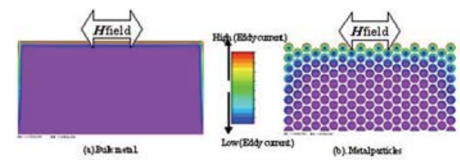

Fig. 2 Induced eddy current distribution of conductive materials in H field application (calculation results, imaginary part).

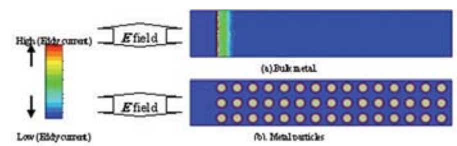

Fig. 3 Induced eddy current distribution of conductive materials in E field application (calculation results, imaginary part).

CV-07

The X-band permittivity of iron-epoxy composites under the magnetic field.

H. Dung Shing[1], S. Hsu[3], W. Liang[3], C. Lin[2], C. Tsay[2], Y. Yao[4], R. Yang[3]
1. Department of Information and Tele. Engineering, Ming Chuan University, Taipei, Taiwan; 2. Department of Material Science and Engineering, Feng Chia University, Taichung, Taiwan; 3. Department of Aerospace and Systems Engineering, Feng Chia University, Taichung, Taiwan; 4. Department of Materials Engineering, Tatung University, Taipei, Taiwan

Multiferroic, combined with an intrinsic coupling of magnetization and polarization via magneto-electric effect, has attracted a great deal of interest for novel applications in modern electronics. Up to date, some of studies on magnetic control of dielectric properties point to a high dielectric tuniability related to the external magnetic field. In 2003, Kimura et al., reported an 4% to 10% dielectric tuniability for TbMnO3 under 9 T magnetic field [1]. Hemberger et al., found a near 500% dielectric tuniability for CdCr2S4 in an external 5T magnetic field in 2005 [2]. Including these two reports, most of research focused on ferroelectric perovskites with magnetic orders and explained by a spontaneous polarization induced by magnetoelectric effect.
In this paper, we demonstrate the magnetic-control dielectric properties of micro-size iron particles dispersed in epoxy. The iron-epoxy composit is used to be a successful microwave absorption material. Comparing with research on ferroelectricity in a perovskite structure, the magnetic particles mixed with dielectric materials appealing attracted properties at microwave applications, provide a completely different aspect to the previous reports. In our study, the fraction of iron particles is fixed at 25 to 75 weight %, which means the 25g iron particles and 75g epoxy resin to make the 100g composite. In fabrication process, the iron particles and epoxy resin were mixed and stirred for 5-10 min and then poured onto a mold for 24 hour at room temperature. The 2 mm x 2 mm cylindrical samples are prepared for dielectric measurement.
A cavity resonator technique is utilized for permittivity measurements in the experiment. It is designed as a 7GHz to 13GHz resonator with a 6.5GHz cut-off frequency. In order to obtain a precise permittivity measurement, Teflon and Duroid/6010 materials are standard samples for calibration and adjustment in resonantor cavity before the measurement. The testing sample is then placed into the cavity and the resonant frequency is obtained by the Network Analyzed (Agilent 8510C). The permittivity functions as a frequency is then obtained by the perturbation method. The magnetic biasing effect in permittivity is measured by applied the external magnetic field while the frequency swept shown above.
The sample is also examined by SEM. As can be seen in Fig.1, the iron particle with a 20 micrometer in diameter is formed in the testing composite. The XRD date show that a clear iron signal is seen in the sample. In permittivity measurement, as can be seen in Fig. 2, the Teflon sample provides a permittivity around 2.1 between 7 GHz and 13 GHz. Its permittivity decreases as the frequency increases. The permittivity does not change while the external magnetic field is on. However, we found that the iron-epoxy composites present a dieelectric variation ranging from 2 to 5.4 by adding the iron particles in epoxy. The adding iron particles provide a more than 170 % enhancement in permittivity. Of interest are the permittivity is adjustable when the external magnetic biasing field is on. Comparing with Figs.3, 4 and 5, a clear dielectric tuniability is observed for the iron particles fraction more than 50% . As it can be seen in Fig. 5, the tuniability is up to 30% for iron was 75% in fraction at X-abnd(~12GHz) frequency. From our measurement, the iron-epoxy composites is tuniable after an iron particle adding and also a high tuniability is observed at high frequencies. In this paper, we will present the the experimental results and their details

[1]T. kimura et al., “Magnetic control of ferroelectric polarization”,Nature, Vol. 426, pp55-57, 2003

[2] J. Hemberger et al., “Relaxor ferroelectricity and colossal magnetocapactive coupling in ferromagnetic CdCr2S4”, Nature, Vol. 434, pp364-367, 2005

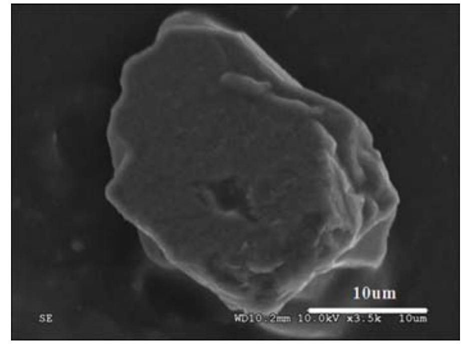

Fig. 1 The diemesion of iron-epoxy composite imagined by SEM

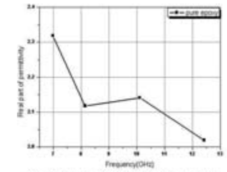

Fig. 2 The permittivity of Teflon sample

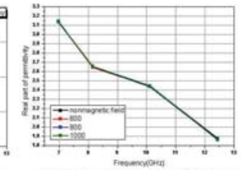

Fig. 3 The permittivity of iron (25%)- epoxy (75%) composite

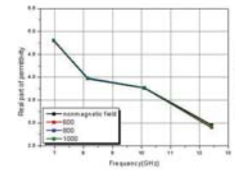

Fig. 4 The permittivity of iron(50%)-epoxy (50%) composite

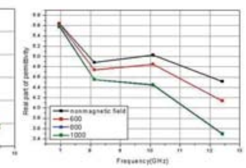

Fig. 5 The permittivity of iron (75%)- epoxy (25%) composite

CV-08

High-frequency Magnetic Properties and Attenuation Characteristics for Barium Ferrite Composites.

Z. Li, G. Lin, Y. Wu, L. Kong
Temasek Laboratories, National University of Singapore, Singapore, Singapore

<p>This is a comprehensive report on high-frequency magnetic properties and attenuation characteristics for barium ferrite composites, based on work on Temasek Laboratories of National University of Singapore in the recent years.
All barium ferrites were prepared using conventional ceramic technology. The composites were prepared by mixing 50 % (by volume) of the barium ferrite particles and epoxy. To achieve low reflectivity and broad bandwidth at microwave frequency of 2-18 GHz, the composites should have large μ' matching with relatively large ε', large imaginary permeability μ''_{max} to significantly attenuate the incident electromagnetic (EM) wave and the appropriate resonance frequency fr. ~~<>>~~

1. Control of resonance frequency fr:
Ion substitution can significantly modify the magnetocrystalline anisotropy of ferrites. For barium ferrites, Co^{2+} ions lead to a decrease in c-axis anisotropy or a modification of anisotropy from c-axis to c-plane. It is found that, to a good approximation, the resonance frequency fr is proportional to the out-of-plane anisotropy field H_θ for c-plane anisotropy or to Ha for c-axis anisotropy, as shown in Fig.1. Therefore, fr can be controlled by the anisotropy field, which is closely associated with the substitution amount of Co ions.

2. Increase in real permeability:
Doping with small amount of oxides is another method for improving the high-frequency magnetic properties. Additives of CaO, CuO, Bi_2O_3, MnO_2, RuO_2, IrO_2, Nb_2O_5 and V_2O_5 oxides can significantly increase μ'. Fitting to complex permeability shows that the increase is mainly attributed to an enhancement of wall resonance.
The combined doping of IrO_2 and V_2O_5 can greatly increase μ'_0 and μ''_{max} to 5.4 and 1.7, respectively, as compared to 3.0 and 1.2 for the undoped sample. The predicted frequency band for reflection loss RL<-10 dB covers from 3 to 12 GHz at the thickness of 0.35 cm. This is a potential EM attenuation material with low reflectivity and broad bandwidth at s, c and x microwave bands, as shown in Fig.2.

3. Enhancement of magnetic loss
In general, for natural resonance, μ''_{max} is related not only to μ'_0, but also to the effective damping coefficient λ by
$\mu''_{max}=(1/2)(\mu'_0-1)(1+1/\lambda^2)^{1/2}$.
For $Ba_3Co_{2+x}Ti_xFe_{24-2x}O_{41}$, λ is 1.43 for x=0 and decreases to 1.23 and 0.88 for x=0.5 and 1.0, respectively. The reduced λ leads to a significant increase in μ''_{max}, from 1.23 to 1.66 and 1.80, although μ'_0 remains almost the same for all composites. Due to the increase in μ''_{max}, the relative bandwidth W for RL<-10 dB expands from 2.3 to 3.4 for composites with x=0 and x=1.0. Also, the thickness of composites decreases from 0.30 to 0.22 cm.

4. The effect of particle size and shape
The permeability is closely related to the size and shape of particles. The experiments show that composites with micro-particles have much larger complex permeability than those with nanoparticles. The difference is attributed to multi-domain structures for micro-particles. Besides the rotation permeability from natural resonance, the wall permeability is an additional and significant contribution.
On the other hand, the experiments indicated that, after the doing of V_2O_5, the shape of particles is modified from cuboid-like to hexagonal-plate-like. Correspondingly, μ'_0 increases from 3.1 to 4.6 and μ''_{max} increases from 1.2 to 1.7, due to different demagnetizing factors N_d. Based on Maxwell Garnett mixing rule, the permeability of composite is closely associated with N_d.

5. Two types of dispersions
In general, barium ferrite composites with c-axis and c-plane anisotropy exhibit the resonance-like and relaxation-like dispersions, respectively. Most of composites involved in this paper are the relaxation-like dispersion.
However, the composites with resonance-like dispersion have some important characteristics: relatively high fr and low RL, as shown in Fig.3. For $BaMn_xTi_xFe_{12-2x}O_{19}$ composites, fr can be controlled from 9 to 15 GHz, depending on the substitution x. The composite with x=1.8 shows good attenuation characteristics. The band for RL<-15 dB can cover from 8.6 to 14.3 GHz at thickness of 0.23 cm. The materials are good for use as EM materials in higher microwave bands (x and Ku bands).

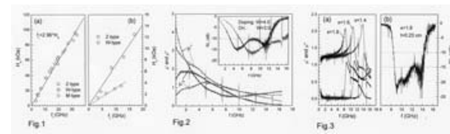

Fig.1 Linear relationship between resonance frequency and anisotropy field Fig.2 Complex permeability and (insert) reflection loss for W-type barium ferrite composites undoped (grey) and doped with IrO_2+V_2O_5 (black) Fig.3 (a) Complex permeability and (b) the corresponding RL-f curve for M-type barium ferrite composites with resonance-like dispersion.

CV-09

High frequency property of polyol-derived FeCo nanoparticles for EWA application.

D. Kodama[1], K. Shinoda[2], R. J. Joseyphus[3], Y. Shimada[4], K. Tohji[1], B. Jeyadevan[1]
1. Graduate School of Environmental Studies, Tohoku University, Sendai, Japan; 2. Institute of Multidisciplinary Research for Advanced Materials, Tohoku University, Sendai, Japan; 3. Department of Physics, National Institute of Technology, Tiruchirappalli, India; 4. Department of Electrical and Communication Engineering, Tohoku University, Sendai, Japan

Recent years, the popularization and use of various communication systems has begun to cause electromagnetic interference (EMI) to the electronic equipments. Though necessary measures are being taken on the side of electronic circuits to control the EMI, the measures on the development of electromagnetic wave absorber (EWA) materials have almost not advanced and new high frequency EWA is strongly required to absorb the interfering EM wave in the wide frequency range. On the other hand, the use of soft magnetic metal and alloy nanoparticles, which are well below the size that generates eddy current, has been proposed but yet to be tested. This paper reports the study undertaken to test the potential of polyol-derived FeCo nanoparticles with the particle size ranging between few hundred to few tens of nanometer as EWA.

The FeCo nanoparticles of various sizes have been synthesized by polyol process using the procedure described elsewhere [1]. The scanning electron microscope (SEM) image of FeCo particles used in the present study is shown in Fig. 1. The particles were cubic shaped and were about 100 nm in size. The magnetic properties of the particles such as saturation magnetization (M_s) and coercivity (H_c) were 209 emu/g and 193 Oe respectively. Though the M_s was lower and comparable to the bulk value of Fe, the H_c was larger.

The samples for high frequency property measurements were prepared as follows: First, the FeCo particles were colloid dispersed in isoparaffin and pasted on a glass substrate. Then, the specimen was heated to 373 K under an external magnetic field of 3 kOe to evaporate the solvent, which was used to assist the redistribution of the particles in the external magnetic field. Finally, an adhesive was introduced to inhibit the movement of the particles during measurements. The thickness of the sample ranged between 50 and 100 microns. The high frequency properties of plate-type FeCo samples were measured in the frequency range of 50MHz-9GHz using a shielded coil permeameter. Additional permeability measurements to obtain absolute values of real permeability were carried out using a ferrite yoke method.

The frequency dependence of real (μ’) and imaginary (μ”) parts of permeability for FeCo sample is given in Fig. 2. The permeability begins to show an increase before the frequency reached 1 GHz and exhibits plural number of peaks in the GHz range. Since the variation in physical properties within the sample has been found to be low from the Mossbauer spectroscopic measurements, the appearance of plural resonance peaks are considered due to the exchange resonance mode caused by surface effect or presence of very thin oxide or organometallic layers [2]. However, it should be noted that the absolute value of μ’ was low and practically demands a thicker layer.

Recently, appreciable enhancement in permeability has been reported through the formation of ferromagnetic particle composites formed of Fe and permalloy particles. The values obtained were larger than that of the individual components [3]. This has suggested that composites formed of ferromagnetic particles with different physical and magnetic properties could be a solution to develop EWA materials to suit the current demand. Thus, we attempted the preparation of a composite using submicron sized Fe particles and FeCo particles.

The high frequency properties of the composite synthesized by mixing Fe and FeCo particles in a weight ratio of 4:1 and that of Fe particles are also shown in Fig. 3. The composite exhibited a broad single peak as against the plural peak shown by FeCo alone. Though μ’ value dropped to 4.7 compared to 5.5 for pure Fe particle, the resonance peak shifted to 2.0 GHz as against 1.6 GHz for pure Fe. The above result is a consequence of the interaction between soft magnetic Fe and relatively hard (higher H_c) FeCo. Thus, it is speculated that varying the ratios between Fe and FeCo could control the resonance frequency of the composites. The resonance frequencies of composites with different Fe/FeCo ratio will also be reported and discussed.

[1] D. Kodama et. al., Adv. Mater., 18, 3154 (2006)

[2] G. Viau et. al., J. Appl. Phys., 81, 2749 (1997)

[3] Y. Shimada et. al., J. Appl. Phys., 101, 09M505 (2007)

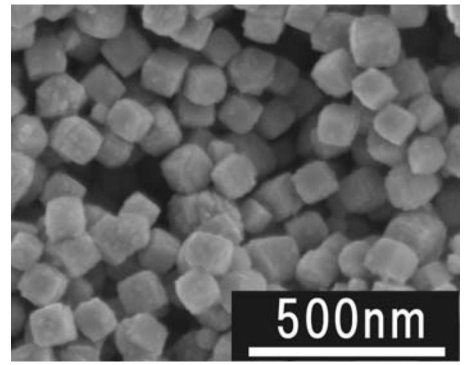

The SEM image of FeCo particles.

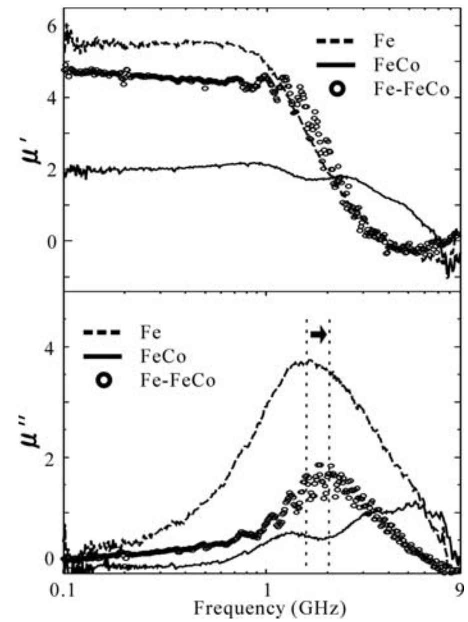

The frequency dependence of the permeability for FeCo, Fe and Fe-FeCo composite.

CV-10

Noise Suppression Effectiveness of Fe-Si-Al Magnetic Composite Thick Film on the Signal Transmission Cable.

K. Lee[1], D. Kang[1], I. Byun[1], I. Jeong[1], S. Kim[2]
1. R & D Center, Chang Sung Corporation, Incheon, South Korea; 2. Nano-Materials Research Center, Korea Institute of Science and Technology, KIST, Seoul, South Korea

Recently, in accordance with rapid progress of digital electronic equipment transmit high speed image data, the electro-magnetic interference (EMI) become a serious problem. Most of radiated emission noise is due to the common mode noise current in the data cables connected to digital equipment. To provide an effective solution for the problems, Mn-Zn or Ni-Zn soft ferrite bead cores are conventionally used as the common-mode noise filters.[1] As the ferrite core round data cable, magnetic wave caused by common-mode noise current in the MHz – GHz frequency range are absorbed by the bead core. However, permeability values of the ferrite materials are too small to fabricate a small bead core in quasi-microwave frequencies of gigahertz beyond Snoek's limit[2]. Several amorphous materials were proposed as a new material for EMI noise filter which is much smaller than ferrite core in the MHz - GHz.[3] This paper reports the higher permeability flexible thick film which is composite of Fe-Si-Al alloy flake and rubber to the noise filter.

The $Fe_{85}Si_{9.5}Al_{5.5}$ flake was fabricated by mechanical forging of spherical powders using an attrition mill. A soft magnetic paste made of Fe-Si-Al flakes and polymer solution was prepared. Magnetic composite thick film was fabricated by doctor-blade coating of the paste.

Fig.1 shows the noise current measurement system.[1] The current transmission characteristics of data cables were measured from 1 MHz to 1 GHz with network analyzer. We used 100cm twisted pair cables with a characteristic impedance of 100Ω. One end of the cable was connected to port 1 of a network analyzer via an impedance matching circuit and the other end was terminated with a resistance of 100Ω. A part of cable was wrapped with the magnetic composite thick film. The total volume of thick film was 0.187cc. A commercially available ferrite core (inner diameter 9.7mm, outer diameter 18.2mm, length 27 mm, volume 5.03cc) was also used for comparison. Common–mode noise current, which is equivalent to the transmitted power,S21, was detected with a micro loop antenna.

From SEM observation of Fe-Si-Al flakes and cross-sectional view of magnetic composite thick film, it was found that the thickness and aspect ratio of the flaky particles are ranged 1-3μm and 15-25, respectively and thin flakes are well aligned parallel to the film plane. The magnetic property of the flake was measured with VSM. The M_s and ${}_iH_c$ of the flake were 110 emu/g and 16.2Oe, respectively.

Fig. 2 shows the frequency dependence of permeability for magnetic composite thick film. As shown in Fig. 2, real part of permeability (μ_r') decreases with frequency above 30MHz and a high imaginary part of permeability(μ_r"≒8) is observed in range of 70MHz - 3GHz. The observed broad magnetic loss spectrum (70MHz - 3GHz) beyond Snoek's limit is attributed to the high saturation magnetization (110 emu/g) and low eddy current loss of the $Fe_{85}Si_{9.5}Al_{5.5}$ flake particles in magnetic composite film.

Fig. 3 shows the frequency dependence of S21 for the 100cm long cables on which the magnetic composite film and ferrite bead were wrapped, respectively. Because of the cable operates as an antenna for common mode noise current, the current power of S21 can be considered to radiation noise emission level. The radiated emission level increase in higher frequency range than 200MHz. Also, as shown Fig.3, it should be noticed that the emission noise level decrease average -4dB and -8dB in almost frequency of same range by attachment ferrite bead and magnetic composite thick film, respectively. These results show that the Fe-Si-Al composite thick film can be a good material as the common mode noise filter on high speed data transmission cable.

[1] Osamu Ishii, Masakatsu Senda, Koji Takei, Yasuhiro Koshimoto, Toshinori Mori, J. Appl. Phys. 79 (8), 15 (1996).

[2] J. L. Snock, Physica, 4, p.207 (1948)

[3] O. Ishii, M. Senda, K. Takei, and T. Mori, J. Appl. Phys, 34, L359 (1995).

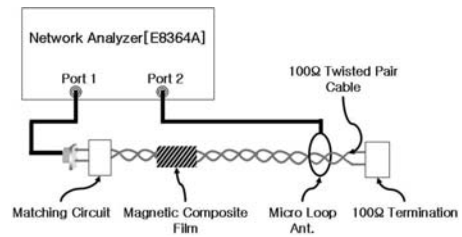

Fig. 1 Schematic diagram of the noise measurement

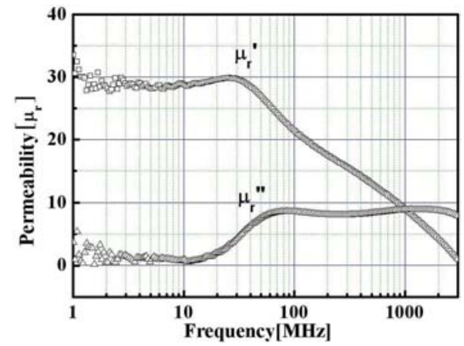

Fig. 2 Frequency spectrum of complex permeability(μ_r=μ_r'-jμ_r")of magnetic composite film

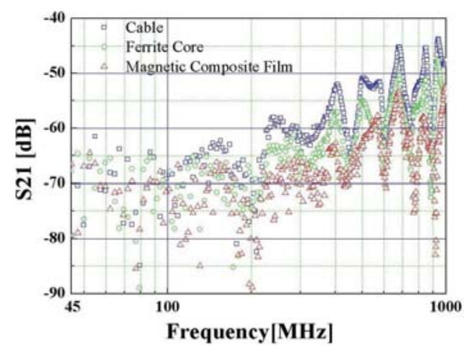

Fig. 3 Frequency spectrum of noise current power(S21) on signal transmission cable

CV-11

Microwave absorption properties in Bi-substitute Yttrium Iron Garnet.

D. Hung[1], Y. Fu[2], Y. Yao[3]

1. Information & Telecommunications Engineering, Ming Chuang University, Taipei, Taiwan; 2. Department of Materials Science and Engineering,, National Dong Hwa University, Hualien, Taiwan; 3. Department of Materials Engineering, Tatung University, Taipei, Taiwan

Introduction:

Yttrium iron garnet (YIG) materials possessing a high Q value over a broad-band frequency range make it to be widely used for various microwave components including magnetic filters, tunable oscillators, phase shifters etc., for years. However, from the past experience, YIG garnet is hardly used in multilayer communication chip, due to the sintering temperature is up to 1400oC that is higher than the melting temperature of most conductive metals. Bi-substituted YIG garnet has been known as the relevant ceramic materials that the sintering temperature is much lower than of pure YIG polycrystalline ceramics. In this study, Bi-substitute YIG was fabricated by sol-gel method. The experimental results show that the Bi-YIG sample allows a sintering temperature down to 900oC without change its garnet phase. Its microwave properties were examined by the FMR signal ranging from 45MHz to 20GHz. Of interest are that the FMR frequency is consistent to the different Bismuth contents in samples but its FMR absorption properties are modulated by substitution.

Sample preparation:

YIG:Bi having a stoichiometric composition of $Bi_xY_{3-x}Fe_5O_{12}$, where x=0.25, 0.5, 0.75, 1.00 were prepared by the sol-gel method. In order to obtain a uniform and successful substitution of Bismuth to Yttrium in YIG structure, a coprecipitation method was proceed by mixing the raw solution, The nearly atom-level mixing provides a uniform and high-quality power that was calcined in the air at 700oC for 2 hours and then milled again for 1 hours. The resulting power was pressed as a disk with 3000N/m2 and sintered in the air from 900-1200oC, respectively. All the samples have had at least 85% of theoretical density. Figure 1 shows the XRD patterns of successful samples for various Bismuth contents. From the XRD patterns, Bi-substituted YIG samples form a garnet phase at 900oC except the sample with x=1 substitute.

FMR absorption:

In this study, the YIG garnet substituted by the bismuth is concentrated on their FMR responses. Four different Bi-substitute samples (x=0.25, 0.50, 0.75 and 1.00) are fabricated by the sol-gel method and mold to 3mm x 4mm cylindrical shape. The samples are sintering to 900~1200 oC that is illustrated in section 2. A transmission line is designed for picking up the FMR signals in this experiment. The cylindrical samples are measured by the transmission line through the Network Analyzer (frequency from 45MHz to 20GHz). The magnetic field is applied along the microwave propagation. The FMR signals are observed by every 50Oe for a range from 50Oe to 3800Oe. Results demonstrate a series of FMR signals that are picking up from the $Bi_xY_{3-x}Fe_5O_{12}$ samples with x=0.25, 0.5, 0.75 and 1.0 substitution. In the experiment, the FMR signal is found when the external magnetic field is around 200Oe for all four different bismuth contents. Increasing the magnetic field, the signal is shifted smoothly from 2.5GHz to 18GHz. Of interest is that the results demonstrates the similar FMR frequencies no matter of the difference in bismuth substitution, even the bismuth substitution for yitrium is up to 1.00. It can be concluded that the YIG garnet does not change the spin-procession behavior that responses to the ferromagnetic resonance by the Bismuth substitution. But in results, the 3db absorption bandwidth are various to the four different samples.

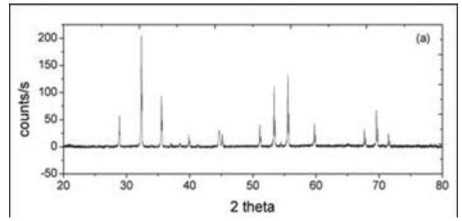

Fig. 1 XRD data for Bi-YIG (Bi=0.25)

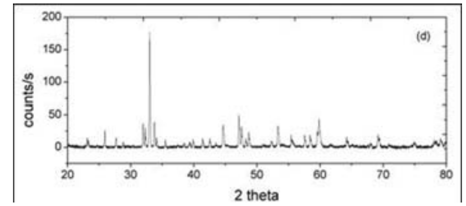

Fig. 2 XRD data for Bi-YIG (Bi=1.0)

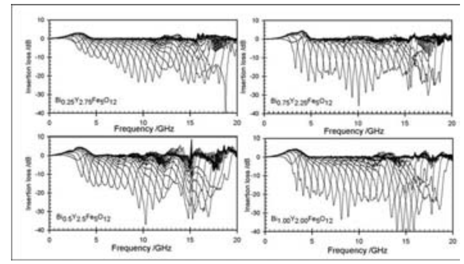

Fig. 3 The FMR signals of Bi-YIG (Bi=0.25, 0.5, 0.75, 1.0)

CV-12

Preparation and characterization of nano-fiber nonwoven textile for electromagnetic wave shielding.

M. Sonehara[1,2], T. Sato[2], M. Takasaki[1], H. Konishi[3], K. Yamasawa[2], Y. Miura[2]
1. Satellite Venture Business Laboratory, Shinshu University, Ueda, Japan; 2. Spin Device Technology Center, Shinshu University, Nagano, Japan; 3. Faculty of Textile Science and Technology, Shinshu University, Ueda, Japan

Introduction

The electromagnetic interference (EMI) has become extremely serious in various electronic equipments such as personal computers (a few GHz), cellular phones (0.8-2 GHz), electronic toll collection system (5.8 GHz), and others. Especially, the EMI at the medical equipment such as heart pacemakers is a hazardous problem because of the patient may have a risk of suffering severe damage when neglecting the EMI measures.

The authors developed a magnetic film for a noise filter in the electronic circuit [1]. In this study, a nanofiber nonwoven textile with an average diameter of about 600 nm spun by an electrospinning for electromagnetic wave shielding has been developed. Ni-Fe magnetic material was coated by sputtering unit on the textile surface for reflecting and absorbing electromagnetic wave. Because the functional textile is light, flexible and breathable, it will be versatile for the various electromagnetic wave shielding.

Fabrication

The raw material solution was made by stirring the mixture containing 12 wt.% of polyacrylonitrile (PAN) powder (Aldrich, mean molecular weight: 150,000) and 88 wt.% of N,N-Dimethylformamide (DMF) (Wako pure chemical industries) at 70 ^{o}C for 6 hours. The nanofiber nonwoven textile was prepared by an electrospinning system. A high voltage of 12 kV was applied to the nozzle which is separated at a distance of 100 mm from the grounded collector.

Metallic magnetic material, Ni-Fe, was coated on the nanofiber nonwoven textile with r.f. magnetron sputtering machine. $Ni_{83}Fe_{17}$ (at.%) was used for the metallic magnetic material at an Ar pressure of 0.5 Pa, and r.f. power of 100 W.

Measurement

EMI shielding effect defined as *SE* in the nanofiber shielding textile was measured using a vector network analyzer, a scatting parameters test set and waveguide components. When measuring, the nanofiber shielding textile was sandwiched between waveguide components.

SE was calculated with the following equations [2].

$$SE = (P_{ref} + P_{loss}) / P_{in} = 1 - 10^{(S_{21} [dB] / 10)} \quad (1)$$

$$P_{ref} / P_{in} = 10^{(S_{11} [dB] / 10)} \quad (2)$$

$$P_{loss} / P_{in} = 1 - (10^{(S_{11} [dB] / 10)} + 10^{(S_{21} [dB] / 10)}) \quad (3)$$

where P_{ref} is the reflective power, P_{loss} is the loss power, P_{in} is the input power, S_{11} is the input reflection coefficient and S_{21} is the forward transmission coefficient. Both S_{11} and S_{21} for the nanofiber shielding textile were obtained by the vector network analyzer and the scatting parameters test set.

Result and discussion

Figure 1 shows the frequency dependence of P_{ref} / P_{in}, P_{loss} / P_{in}, P_{thru} / P_{in} where P_{thru} / P_{in} means $1 - (P_{ref} + P_{loss}) / P_{in}$ in the nanofiber nonwoven textile (a) and the nanofiber shielding textile with Ni-Fe coating with sputtering time t_s of 15 min (b). In Fig. 1 (a), *SE* of the nanofiber nonwoven textile was about 10 % in measured frequency band. On the other hand, in Fig. 1 (b), *SE* of the nanofiber nonwoven textile with Ni-Fe coating was about 90 % in measured frequency band.

Figure 2 shows the relation between P_{ref} / P_{in}, P_{loss} / P_{in}, P_{thru} / P_{in} and Ni-Fe sputtering time t_s at 5.8 GHz. In Fig. 2, when increasing the Ni-Fe sputtering time t_s, both P_{ref} / P_{in} and P_{loss} / P_{in} increased. The nanofiber shielding textile with Ni-Fe coating showed sufficient reflection and absorbance of the electromagnetic wave.

[1] M. Sonehara, T. Sato, K. Yamasawa, Y. Miura, and M. Yamaguchi, Trans. Mat. Res. Soc. Jpn., 29, 4, 1735-1738 (2004)

[2] M. Yamaguchi, K.-H. Kim, T. Kuribara, and K.-I. Arai, IEEE Trans. Magn., 38, 5, 3183-3185 (2002)

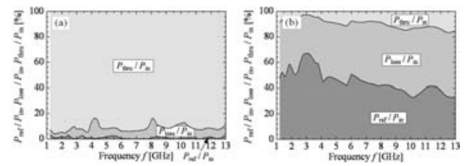

Fig.1 Frequency dependence of P_{ref} / P_{in}, P_{loss} / P_{in}, P_{thru} / P_{in} in the nanofiber nonwoven textile (a), and the nanofiber shielding textile with Ni-Fe coating with sputtering time t_s of 15 min (b).

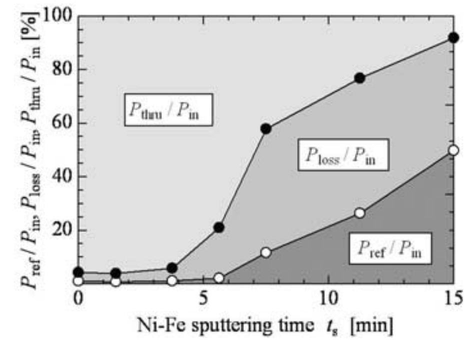

Fig.2 Relation between P_{ref} / P_{in}, P_{loss} / P_{in}, P_{thru} / P_{in} and Ni-Fe sputtering time t_s at 5.8 GHz.

CW-01

Characterization of iron magnetic nanoparticles by termomagnetogravimetry.

J. C. Aphesteguy[1], *S. E. Jacobo*[1], C. E. Rodriguez Torres[2], M. B. Fernández van Raap[2], F. H. Sanchez[2]
1. Chemistry, Universidad de Buenos Aires, Buenos Aires, Argentina; 2. Physics IFLP (CONICET), FCE, Universidad Nacional de La Plata, La Plata, Argentina

Along the last two decades we have witnessed considerable achievements related to the design of magnetic nanostructures, aiming both basic research and technological applications. Nanoparticles with super-paramagnetic properties have great potential to achieve such desirable properties. Various methods have been developed to synthesize iron oxide particles in nanometer size range [1-2]. These genuine improvements of fabrication techniques have not always been accompanied by a detailed comprehension of the relationships between structure, composition and magnetic properties in fine particle systems, even those composed of 'simple' materials as magnetite and maghemite whose bulk properties are well understood. Magnetite Fe_3O_4 is a ferrimagnet (T_N=860 K) with a cubic inverse spinel structure, that is, one third of the ions as Fe(III), occupies all the available A sites, one-third also as Fe(III), occupies half of the B sites, and one-third as Fe(II) occupies the other B sites. Maghemite γ-Fe_2O_3 has a nonstoichiometric spinel structure. There has been considerable controversy over whether Fe(III) occupies all the available tetrahedral sites with the vacancies being confined to the octahedral sites. For synthesis of magnetite initial molar ratios ranging from Fe^{3+}:Fe^{2+}=1:1 to 1.7:1 have been used by various researchers [3-5]. Frequently, the particles thus obtained have not been completely characterized with respect to the phase(s) present assuming that the only phase present is magnetite. Magnetite and Maghemite are isostructural, with nearly the same lattice parameter, then X-ray diffraction (XRD) cannot differentiate between them, especially in the nanophase. Although Mössbauer spectroscopy in bulk material can clearly identify the two oxides, owing to the presence of divalent iron in magnetite, in the case of nanophase state, the spectrum displays broadened and asymmetric lines due to the surface contribution making their identification difficult. Then additional techniques are necessary in order to characterize the oxide nanoparticles.

Here, we report on the preparation and characterization of iron magnetic nanoparticles, where besides XRD and Mössbauer spectroscopy, Thermogravimetric (TG) measurements performed in the presence of a magnetic field (Termomagneto-gravimetry, TMG) are used to identify the phases.

We have prepared iron oxide particles using various molar ratio of Fe^{3+}:Fe^{2+} 2:1. The solution was stirred for 15 minutes with nitrogen bubbling. The above mixture was poured in aqueous ammonium solution (50 % v) and the solution was stirred for 2 hours and dried in a vacuum oven during about 12 hours. The main purpose of using molar ratios smaller than 2:1 is to compensate for the oxidation of Fe^{2+} to Fe^{3+} during the preparation to obtain the magnetite phase.

Their XRD patterns (not shown) are typical of an inverse spinel structure, meaning the formation of either magnetite or maghemite. Their ME spectrum (see Fig.1) presents the main characteristics of γ-Fe_2O_3: a symmetric spectrum with a mean isomer shift value of 0.33 mm/s, corresponding to Fe^{3+}. However the TMG measurement of this sample (see Fig.2)displays a main feature at 273 C which was observed in commercial magnetite but not in maghemite. From these results a reinterpretation of the Mössbauer spectrum was attempted. A hyperfine field distribution was simulated using a discrete set of 5 Voigtian contributions, one of them constrained to bear the 0.67 mm/s isomer shift value of the 2+ site of magnetite (Fig. not shawn). The fit indicated that 13 % of the iron atoms could be in this environment. Assuming that magnetite 3+ Fe makes twice this contribution (26 %) to the spectrum, a maximum magnetite content of 39% of the nanoparticles phase composition is inferred.

[1] S.P. Sena, R.A. Lindley, H.J. Blythe, C.H. Sauer, M. Al-Kafarji and G.A. Gehring, J. Magn. Magn. Mater. 176, 111 (1997)

[2] F.C. Voogt, T.T.M. Palstra, L. Niesen, O.C. Rogojanu, M.A. James and T. Himba, Phys. Rev. B, 57, R8107 (1998)

[3] S.E. Khalafalla and G.W. Reimers, IEEE Trans. Magn. Mag-16 (1980), p. 178.

[4] K.T. Wu, P.C. Kuo, Y.D. Yao and E.H. Tsai, IEEE Trans. Magn. 37 (2001), p. 2651

[5] R.S. Molday, Magnetic iron-dextran microspheres, US Patent 4452773, 1984.

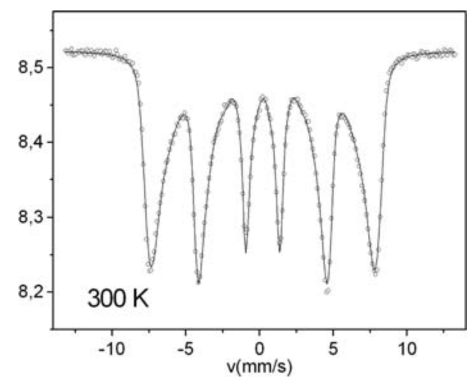

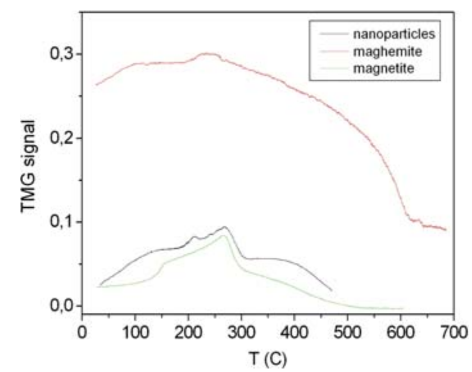

CW-02

Magnetization reversal study in a permalloy wire with 3 dissimilar trenches by using real-time magnetic force microscopy.

K. Cheng[1,2], C. Yu[1], S. Lee[1], Y. Liou[1], Y. Yao[3], J. Wu[3], J. Huang[2]
1. Institute of Physics., Academia Sinica., Taipei, Taiwan; 2. Department of Materials Science and Engineering, National Tsing-Hua University, Hsinchu, Taiwan; 3. Department of Materials Engineering, Tatung University, Taipei, Taiwan

During the last few years, patterned magnetic wires have attracted much attention in both fundamental research and applications in storage media because of their bulk and nanostructure properties. In particular, study of the domain structure in submicro ferromagnetic elements using magnetic force microscopy (MFM) has attracted growing interest because of the potential for developing spin electronic devices as well as magnetic storage media. In situ scanning of submicro scale permalloy (Ni80Fe20) wire with an applied magnetic field could provide detailed insight into magnetization reversals[1-3]. In this report, we design trenches of three different depths to study their magnetic structures and the magnetic pinning force[4]. We also provide quantitative MFM analysis of the different trenches.

The permally wires were fabricated by electron-beam lithography and lift-off process. Using dc magnetron sputtering with a base pressure of 5 x10-7 torr and a working pressure of 1x10-3 Torr. Figures 1a and 1b present atomic force microscopy (AFM) photographs of the wires and the AFM profiles of the three trenches. The width of the permalloy wire is 0.4 µm and the distance between the two extremities is 8 µm. The pattern thickness is 30 nm, and the depths of these trenches, from left to right, are 15nm, 10nm, and 5nm. The main goal of this investigation was to measure the magnetic behaviour by real-time magnetic force microscopy (real-time MFM) while applying an extra magnetic field. The magnetic field change range was from +300 Oe to –300 Oe. In the experiment, the positive and negative field were applied in the in-plane longitudinal direction.

The real-time MFM measurement can be used to analyze the phase-shift of the tip oscillation during MFM scanning, which is related to the tip-sample interaction energy[5]. The phase-shift value is proportional to the force gradient of the stray field from the trench. Figure 2a presents a diagram showing the average mean-phase value analysis method for the pattern wire. From Fig. 2a, it can be seen that as the ion-milling depth increased, the magnetic switching field also increased. The switching fields of part A, part B, and part C are 25 Oe, 15 Oe, and 10 Oe, respectively. The mean-phase variation is also proportional to the depth of the trench. Fig. 2a implies that a deeper trench has a larger pinning force. The ability of the pinning force is like the energy of the switching field.

If we can quantitatively determine the pinning force, we might be able to use it in magnetic storage media. Figure 2b shows the depth of permalloy film versus switching field and mean-phase change value. When the permalloy wire has no ion-milling effect, the rate of the Hsw near 0 Oe, is roughly 1.6 Oe per nm of thickness of the trench. The magnetic film thickness appears to influence the domain wall magnetization direction.

In summary, the magnetization reversal behaviour in a permalloy wire with trenches is a typical hysteresis curve. We observed that a deeper trench has a larger switching field. The mean-phase variation is proportional to the depth of the trench. The thicknesses of these trenches are 15nm, 20nm and 25nm, and the switching fields are 25 Oe, 15 Oe and 10 Oe. This means that the deeper trench has the larger switching field, and its rate is roughly 1.6 Oe per nm thickness of the trench. In the same magnetic pattern, we could use the mean-phase value analysis method to determine the local area reversal process and the pinning force.

[1]M. H. Park, Y. K. Hong, S. H. Gee, D. W. Erickson, and B. C. Choi, Appl. Phys. Lett. 83, 329 (2003).

[2]J. Lohau, A. Carl, S. Kirsch, and E. F. Wassermann, Appl Phys. Lett. 78, 2020 (2001).

[3]J. L. Tsai, Y. D. Yao, B. S. Han, S. F. Lee, C. Yu, T. Y. Chen, E. W. Huang, and D. J. Zheng, J. Appl. Phys. 93, 8424 (2003).

[4]M. Klaüi, C. A. F. Vaz, J. Rothman, J. A. C. Bland, W. Wernsdorfer, G. Faini, and E. Cambril, Phys. Rev. Lett. 90, 097202-1 (2003).

[5]Y.C. Chen, Y.D. Yao, S.F. Lee, Y. Liou, J. L. Tsai, and Y. A. Lin, Appl Phys. Lett. 86, 053111 (2005).

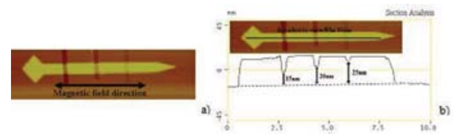

Fig 1〈a〉Atomic force microscopy〈AFM〉 image; arrow shows the external magnetic field direction. 〈b〉 The AFM profile of the three trenches.

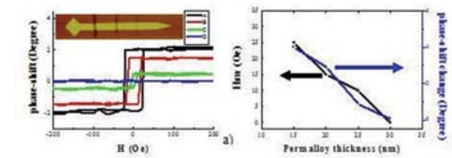

Fig 2〈a〉The phase-shift of MFM mean value at different magnetic field in A, B, C and D area. The hysteresis loops are from 200 to -200 Oe. 〈b〉Switching fields and phase-shift variation in different permalloy thicknesses.

CW-03

Diffracted magneto-optical Kerr effects of one-dimensional magnetic gratings.

J. Kim[1], G. Lee[1], Y. Lee[1], J. Rhee[2], C. Yoon[3]
1. Quantum Photonic Science Research Center and BK21 Program Division of Advanced Research and Education in Physics, Hanyang University, Seoul, South Korea; 2. BK21 Physics Research Division and Department of Physics, Sungkyunkwan University, Suwon, South Korea; 3. Division of Advanced Materials Science, Hanyang University, Seoul, South Korea

Magnetic photonic crystals (MPCs) are very interesting for the technical applications in information technology which requires the advanced solutions for heavy communication traffic, high-density storage and high-speed computing. By using external magnetic field, for instance, the properties of MPCs can be tuned [1]. The magneto-optical (MO) diffraction technique is a well-established method for the investigation on the micromagnetic properties of periodic structures based on magnetic/nonmagnetic media. There are several reports on the one-dimensional (1-D) array structures prepared by selective-area reactive ion etching or electron-beam lithography followed by ion milling. However, these fabrication methods for 1-D MPCs usually demand a great effort and time, and more simplified fabrication methods are required for the practical purpose. Recently, we have successfully fabricated 1-D MPCs by using a selective-area annealing of as-deposited Co_2MnSi film, and observed a great enhancement of the Faraday-like rotation of the first-order diffracted beam compared to the zeroth-order (undiffracted) one [2]. In this report, the MO properties of the 1-D magnetic-grating structure based on Co_2MnSi film were investigated. The longitudinal Kerr rotation of the first-order diffracted beam is also greatly enhanced, compared to the zeroth-order one.

Amorphous Co_2MnSi films were prepared by rf-magnetron sputtering on a glass substrate at room temperature. The as-deposited films exhibit no magnetic response at room temperature. By using the interference pattern of two femtosecond-laser beams, a selective-area annealing of the as-deposited Co_2MnSi film was achieved, and 1-D magnetic-grating structures were fabricated. The magnetic domain structure has been investigated using a magnetic-force microscopy system, which is basically a scanning-probe microscope (PSIA, XE-100) equipped with a magnetic tip (Nanosensors). The longitudinal Kerr rotation was measured at an incident angle of 45° by using a photoelastic-modulator method. A He-Ne laser light of 632.8-nm wavelength was used as a light source, and a detection system equipped with a photomultiplier tube was employed. For the polarizing optics, two MgF_2 Rochon polarizers were used. The external magnetic field was applied perpendicular to the incident plane using an electromagnet capable of applying a magnetic field up to ± 5 kOe.

Initially, the Co_2MnSi film was deposited onto a glass substrates at room temperature. The transmission-electron microscopy study revealed that the as-deposited film had a nearly amorphous structure and exhibited no magnetic response [2]. After the irradiation of interference pattern, the atomic-force-microscopy results showed regularly-spaced alternating lines with a periodicity of 2 μm, and the magnetic-force-microscopy images also revealed the similar periodic patterns of magnetic domains (not shown here). The hysteresis loops of the zeroth- and the first-order diffracted beams have been recorded by measuring the longitudinal Kerr rotation. The Kerr rotation was measured by using both p- and s-polarized incident beams. The magnetic field was applied perpendicular to the groove direction. The measured hysteresis loops imply that the sample is composed of magnetically inhomogeneous phases, which is indicated by a linear growth of the magnetization after a rather steep increase. It was also found that the longitudinal Kerr rotation of the first-order diffracted beam turns out to be nearly 28 times larger as compared to the zeroth-order one.

[1] I. L. Lyubchanskii, N. N. Dadoenkova, M. I. Lyubchanskii, E A Shapovalov, and Th. Rasing, J. Phys. D: Appl. Phys. **36**, R277 (2003).

[2] J. B. Kim, G. J. Lee, Y. P. Lee, J. Y. Rhee, K. W. Kim, and C. S. Yoon, Appl. Phys. Lett. **89**, 151111 (2006).

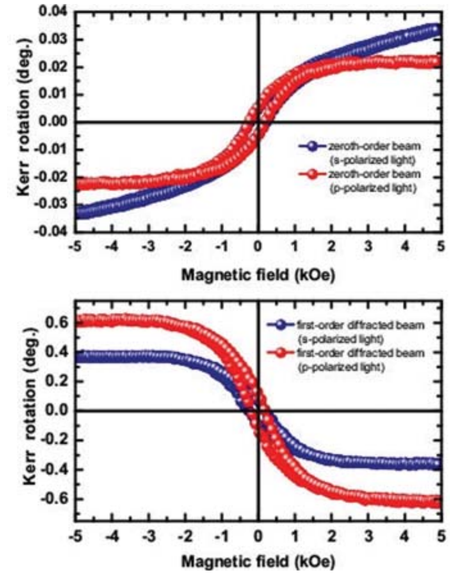

Fig. 1. Hysteresis loops of the longitudinal Kerr rotation.

CW-04

Strain induced ferrimagnetism in Mn2As and Fe2As thin films.

J. Kim, Y. Hwang, J. Choi, S. Cho
Univ.of Ulsan, Ulsan, South Korea

Epitaxial ferromagnetic or ferrimagnetic(FIM) thin films on semiconductor have attracted much interests for spintronic devices [1]. The tetragonal Mn2As, Mn2Sb, Fe2As, and Cr2As materials had antiferromagnetic (AFM) orderings at 573, 550, 325, and 393 K, respectively. Here, we present that MBE-grown Mn2As and Fe2As films exhibited a ferrimagnetic orderings above room temperature, strongly supported by the hysteric magnetization, anisotropic magnetoresistance, and anomalous Hall effect data. However, the tetragonal Cr2Sb thin film, which is newly synthesized, showed AFM ordering. The observed FIMs in Mn2As and Fe2As films were attributed to the strains due to the lattice mismatch and the difference in thermal expansion coefficients between the film and substrate, which will be discussed in detail. We have grown 1,000 Å-thick Mn2As and Fe2As thin films on Si(001) using a molecular beam epitaxy (MBE). The epitaxial growth was monitored by in-situ reflection high-energy electron diffraction (RHEED). The crystal structure and the growth direction of Mn2As and Fe2As thin films were tetragonal structures and (001) direction determined by x-ray diffraction (XRD) measurements. The c-axis lattice constant determined from the position of miller indices were c=6.211 (Mn2As) and 6.168 Å (Fe2As); this is smaller than that of bulk Mn2As (c=6.278 Å) and larger than that of bulk Fe2As (c=5.973 Å) lattice constant, which means that the strain due to difference of thermal expansion coefficients and lattice mismatch exists, which is consistent with the results of magnetic features for the Mn2As and Fe2As films observed by the magnetization measurements.

We have investigated the magnetic properties using SQUID measurements. The magnetic hysteric loops at different temperatures were obtained under the magnetic filed parallel to the film surface. Figure 1(a) shows the temperature-dependent magnetization (M) of Mn2As and Fe2As film between the 10 and 380 K in the magnetic field of 1,000 G. The magnetization curve shows a long tail and an incline between 200 and 350 K, which is a typical FIM ordering rather than FM one. Figure 1(b) and (c) show the magnetic field dependence of the magnetization of the Mn2As and Fe2As films. The magnetizations and coercive fields were (b) 412 and (c) 72 emu/cm-3; 803 and 1176 G at 10 K, respectively. The average magnetic moments per Mn and Fe atom determined from the saturated magnetization were 0.51 and 0.10 μB at 10 K for Mn2As and Fe2As films. In order to investigate the correlation between the magnetization and charge carrier transport, we have performed the magnetoresistance (MR) and Hall effect measurements.

Figure 2 shows the temperature dependence of the zero-field resistivity for Mn2As and Fe2As films. The distinct reisistivity anomalies could be observed around 230 and 300 K. Moreover, for Fe2As film has a slope change around 70 K. Figure 3(a) and (b) show the MR versus magnetic field curves of Mn2As and Fe2As films at 15 and 250 K. The applied field is perpendicular to the film plane. For Mn2As film, at low temperatures below 250 K, MR was decreased with magnetic field due to the spin-related scattering. This negative MR was larger for the applied field parallel to the current, so called anisotropic magnetoresistance (AMR) effect [2]. However, for Mn2As film, below 70 K, a monotonous resistivity increase with magnetic field is observed for all MR curves, which is due to the ordinary MR effect due to bending of the electron trajectories by the Lorentz force. We also observed the clear hysteresis and remanence of Hall resistance were observed below TC, which is consistent with the results of magnetization features observed by the SQUID measurements.

[1] G. A. Prinz, Science 282, 1660 (1998).

[2] A. P. Malozemoff, Phys. Rev. B 32, 6080 (1985).

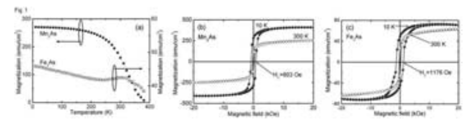

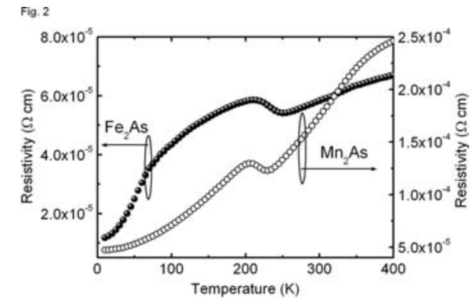

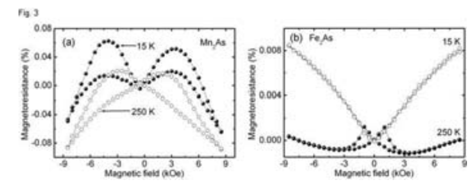

CW-05

Electron paramagnetic resonance studies of diluted magnetic semiconductors $Si_{1-x}Mn_xTe_{1.5}$ crystals.

Y. Hwang[1], Y. Um[1], J. Choi[1], S. Cho[1], S. Na[2], J. Kim[2]
1. Physics, University of Ulsan, Ulsan, South Korea; 2. Physics, Pusan National University, Pusan, South Korea

Recently much effort has been devoted to achieve the ferromagnetism in IV-VI based diluted magnetic semiconductors. In this work, we have investigated the electron paramagnetic resonance (EPR) of the diluted magnetic semiconductors $Si_{1-x}Mn_xTe_{1.5}$ ($0.1<x<0.4$) as a function of temperature ($77<T<300$ K). The samples exhibited a ferromagnetic ordering about 80 K, strongly supported by the hysteric magnetization and EPR lineshape data. The EPR experiment was performed using a spectrometer (Bruker, EMX-300) operating with X-band microwave frequency. The X-ray photoemission spsectroscopy (XPS) spectra of Mn 2p core levels measured from samples were shown in Fig. 1. The main peaks of the Mn $2p_{3/2}$ and Mn $2p_{1/2}$ doublet are located at 640.8 and 652.4 eV, repectively. These peak relative intensities were increases with increasing x. Since the Mn $2p_{3/2}$ core level spectra for elemental Mn is peaked at 639.0 eV, the present result reveals that the Mn atoms are bonded with other elements in our samples. This indicates that a portion of the Mn atoms chemically reacted with the host materials and become Mn^{2+}.
Fig. 1 XPS spectra of the Mn 2p core levels for the various Mn composition x.
Figure 2 show the EPR spectra for samples (a) at 300 K and (b) at 77 K. For the 300 K, main signal was observed at around 3480 G, those were the paramagnetic resonance signals. In addition, the effective g-factors were measured at the center of the resonance line. The g-factors at 3480 G were 1.98, 1.98, 1.99, and 1.99 for x=0.05, 0.11, 0.20, and 0.31, respectively. However, for the 77 K data, the other signals were observed between the 500 ~ 900 G. This change in line shape starts around 80 K. Since, considering the T_C of these samples have at around 80 K, this signals may corresponds to ferromagnetic resonance, which is consistent with the results of magnetic features of $Si_{1-x}Mn_xTe_{1.5}$ crystals observed by the magnetization measurements. The effective g-factors about 600 G were 4.92, 6.64, and 12.30 with x=0.11, 0.20 and 0.31, respectively. The magnetic structure for $Si_{1-x}Mn_xTe_{1.5}$ crystals shows a ferromagnetic transition at x=0.20 and 0.31 for low temperatures and a paramagnetic state for high temperatures where the g-factor shifts the most. In Fig. 2(b), the EPR lineshape was changed from fig 2(a) for x>0.2. This indicates that the spin-spin interaction is enhanced with the addition of Mn, which is consistent with the above behavior of the magnetic moment[1].
Fig. 2 EPR lineshapes of $Si_{1-x}Mn_xTe_{1.5}$ crystals measured at (a) 300 and (b) 77 K.
Figure 3(a) shows the EPR linewidth of the main signals (H~3480 G) as a function of temperature for x=0.11, 0.20 and 0.31. The linewidth was measured from peak to peak in the first derivative curves of the EPR absorption. The linewidth increased with the decrease of temperature. Webb et al. proposed the EPR linewidth increased with decreasing temperature because of the resonances due to inhomogeneously broadening [2]. Sayad and Bhagat described the unusual temperature dependence of the EPR linewidth in DMS [3] by the following relation; $\Gamma=\Gamma_0+\Gamma_1[\exp(-T/T_0)]$, where Γ_0 is the high-temperature linwidth and Γ_1 & T_0 are the empirical parameters associated with the freezing spins. Figure 3(b) shows the linewidth parameters (Γ_1, T_0) obtained from the fit to the above relation. The EPR lineshape were broadened symmetrically and the linewidth increase with increasing Mn composition.
Fig. 3 (a) EPR linewidth of the main signals (H~3.48 KG) as a function of temperature for x=0.11, 0.20 and 0.31. (b) The linewidth parameters from the fit to Eq. for $Si_{1-x}Mn_xTe_{1.5}$

[1] Y. H. Hwang, H. K. Kim, S. Cho, and Y. H. Um, J. Korean Phys. Soc. 48, 1432 (2006).
[2] D. J. Webb, S. M. Bhagat, and J. K. Furdyna, J. Appl. Phys. 55, 2310 (1984).
[3] Z. A. Sayad and S. M. Bhagat, Phys. Rev. B 31, 591 (1985).

Fig. 1

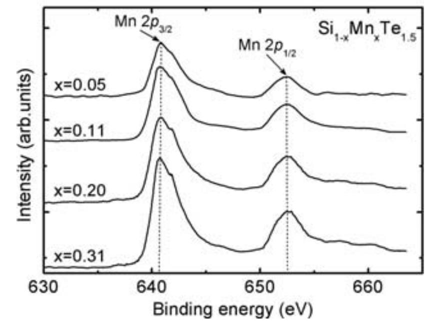

Fig. 2

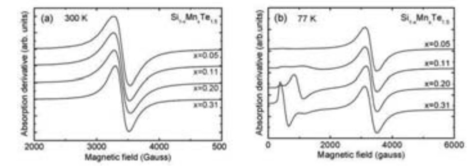

Fig. 3

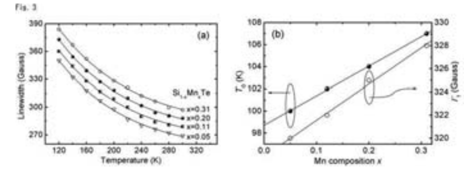

Metallographic Investigations of $Co_2FeAl_{1-x}Si_x$ Heusler-Compounds.

C. G. Blum, G. H. Fecher, B. Balke, C. Felser
Institut für Anorganische und Analytische Chemie, Johannes Gutenberg-University, Mainz, Germany

To get a deeper insight in the crystallisation process in $Co_2FeAl_{1-x}Si_x$ Heusler compounds, metallographic investigations were performed. Therefore discs were cut out of polycrystalline bulk samples (ingots), with respect to the cooling gradient applied during the preparation process. Each resulting ingot was cut in discs with cuts parallel to the cooling gradient and perpendicular. These discs were polished by hand in a multi-step process using 1 µm diamond-polishing paste in the final step.
After polishing, the surfcae of these discs were etched with 2 mol/L $FeCl_3$ in 10% HCl for 6-8 min, followed by washing with water and Toluene. The etched discs were examined with a light-microscope. The etching process was used to make the crystallite structure within each disc apparent. Different crystallites appear to be coloured after the etching process in different colours as green, red and grey scales. Using X-ray diffraction, it was found that single crystals within the polycrystalline disc show a surface of only one colour, when polished and etched this way. Thus, etching can be used as a first test to find single crystals.
Using this metallographic technique, the $Co_2FeAl_{1-x}Si_x$ Heusler compounds were found to exhibit two different types of crystallites: needle-like ones for x>0,8 (fig1) and block-like ones for x<0,5 (fig2). In the samples with x between 0,5 and 0,8 no crystallite structure was apparent using this technique.
As-melted $Co_2FeAl_{1-x}Si_x$ samples with x<0,8 form immediatly needle shaped crystallites, which are almost as long as the complete ingot and between 0,1 and 1 mm thick. They grow parallel to the cooling-gradient.
Figure 1a) shows the crystallites after etching. The disc was cut parallel to the cooling gradient. Figure 1b) shows a PEEM-Picture of a piece of the same ingot which was cut perpendicular to the cooling gradient.
These PEEM-images showed, that the needle shaped crystallites are surrounded by a Co-rich region, which is about 2 µm thick, as shown in Figure 1b). The structure, size and shape of these crystallites was not affected by annealing while small inhomogenities inside the crystallites vanish.
In the as-melted $Co_2FeAl_{1-x}Si_x$ Heusler-compounds with x>0,5 only a fine grain-structure was apparent using the etching process. Some of these grains grow while annealing at 1273 K, while some vanish. Figure 2 shows the growth process of the crystallites of a Co_2FeAl sample induced by annealing. No preferred orientation of these block shaped crystallites was observed.
Studies of the $Co_2FeAl_{1-x}Si_x$ Heusler-compounds with x<0,5 lead to comparable results, but the crystallites found here were smaller for increasing Si content.

[1] B. Balke, G. H. Fecher, C. Felser, Appl. Phs. Lett. 90 (2007) 242503

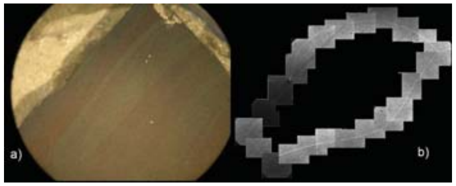

Figure1: a) Crystallites made apparent by an appropriate etching process in Co_2FeSi cut parallel to the cooling-gradient. The figure shows an area with 1 cm diameter; b) PEEM-Images taken at the Co-edge in Co_2FeSi. The Co-rich lines are 1,5-2,5 µm wide.

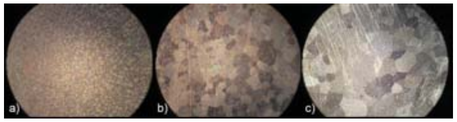

Figure2: Co_2FeAl; a) as cast and annealed at 1273 K for b) two, c) three weeks. All images show an area with 1 cm diameter.

CW-07

Magnetic entropy change in $La_{0.5}Nd_{0.2}Sr_{0.3}MnO_3$ peroveskite.

J. Cho[1], S. Ko[1], Y. Ahn[1], E. Choi[2]
1. Chemistry, Konyang University, Nonsan Chungnam, South Korea; 2. Opthalmic Optics, Konyang University, Daejeon, South Korea

Background

Conventional gas-compression refrigeration offers low efficiency and the working with a harmful refrigerant such as freon leads to environmental concerns. In contrast, magnetic refrigeration offers considerable energy savings, mechanical stability, light weight, high efficiency and environment safe [1, 2].

Magnetic refrigeration is based on the magnetocaloric effect (MCE). The magnitude of this effect is given by the field-induced magnetic entropy change, ($-\Delta S_M$). That is, when an external magnetic field is applied to a material, the magnetic spins in the material attempt to align with the magnetic field, there by reducing the magnetic entropy of the spin systems. If the process is carried out adiabatically so that the total entropy of the system is conserved, then the magnetic entropy reduction is compensated by an increase in the lattice entropy of the system by the creation of phonons, resulting in a temperature increase. The reverse takes place when the field is removed [3, 4].

In this paper, we present the study of magnetic entropy change in $La_{0.5}Nd_{0.2}Sr_{0.3}MnO_3$ for magnetic refrigeration around room temperature.

$La_{0.5}Nd_{0.2}Sr_{0.3}MnO_3$ perovskite was prepared by a conventional solid state reaction method.

Results and discussion

Thermal property of raw materials of $La_{0.5}Nd_{0.2}Sr_{0.3}MnO_3$ have analyzed by TGA-DSC. The DSC curve shows one endothermic peak at around 587 K. The endothermic peak is related to the thermal decomposition of La_2O_3, into intermediate oxide phases. The endothermic peaks at around 1219 K can be related to the thermal decomposition of $SrCO_3$. The endothermic peak can be considered as corresponding to the reaction forming a crystal structure of the perovskite at 1473 K.

The structural study was performed on an X-ray powder diffractometer. There is no evidence of an extra crystalline or amorphous phase being present. Each peak in the pattern can be indexed on a perovskite crystal structure.

Temperature dependence of magnetic moments was measured under zero-field cooled (ZFC) under 50 Oe. The magnetic ordering temperature, defined as the temperature at which the |dM/dT| curve reaches a maximum, is found to be about 336 K.

Fig. 1 shows the magnetization curves measured at various temperatures of $La_{0.5}Nd_{0.2}Sr_{0.3}MnO_3$. A positive slope in the isotherm plots of H/M versus M^2 is a clear indication of a second-order magnetic transition from a ferromagnetic state to a paramagnetic one.

The magnetic entropy change in a magnetic system can be calculated from the M-H curves of $La_{0.5}Nd_{0.2}Sr_{0.3}MnO_3$ using the following equation :

$\Delta S_M(T)_{\Delta H}=\int_{HI}^{HF}\{\partial M(T,H)/\partial T\}_H dH$ — (1)

Equation (1) can be transformed into numerical integration form using the trapezoidal rule as follows [5]:

$\Delta S_M(T_{av})_{\Delta H}=\delta H/2\delta T\{\delta M_1+2(^{n-1}\Sigma_{k=2})\delta M_k+\delta M_n\}$ — (2)

Fig. 2 shows the results of numerical integration of magnetization data in Fig. 1 using Eq. (2). This figure shows the temperature dependence of magnetic entropy change ($-\Delta S_M$) under an applied field of 10 kOe for $La_{0.5}Nd_{0.2}Sr_{0.3}MnO_3$. The maximum magnetic entropy change ($-\Delta S_M$) is 0.53 J/kgK for $La_{0.5}Nd_{0.2}Sr_{0.3}MnO_3$ sample in the field of 10 kOe. The maximum of magnetic entropy change ($-\Delta S_M$) of $La_{0.5}Nd_{0.2}Sr_{0.3}MnO_3$ sample is at the around the magnetic ordering temperature. The maximum magnetic entropy change ($-\Delta S_M$) of $La_{0.5}Nd_{0.2}Sr_{0.3}MnO_3$ increases with the increase of the applied field. This property indicates that it could be a suitable candidate as working materials in magnetic refrigeration technology around room temperature.

[1] E. Bruck, O. Tegus, D.T.C. Thanh, K.H.J. Buschow, J. Magn. Magn. Mater. 310, 2793 (2007).

[2] Y. Xu, M. Meier, P. Das, M.R. Koblischka, U. Hartmann, Cryst Eng. 5, 383 (2002).

[3] V. Provenzano, J. Lia, T. King, E. Canavan, P. Shirron, M. DiPirro, R.D. Shull, J. Magn. Magn. Mater. 266, 185 (2003).

[4] K.A Gschneidner Jr, V.K Pecharsky and A.O Tsokol, Rep. Prog. Phys. 68, 1479 (2005).

[5] J. S. Lee, Phys. stat. sol. (b). 241(7) 1765 (2004).

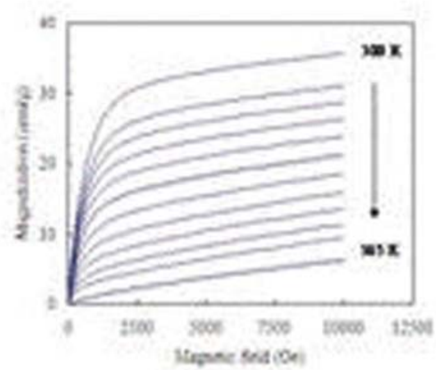

Fig. 1. Magnetization isotherms of $La_{0.5}Nd_{0.2}Sr_{0.3}MnO_3$ at various temperatures.

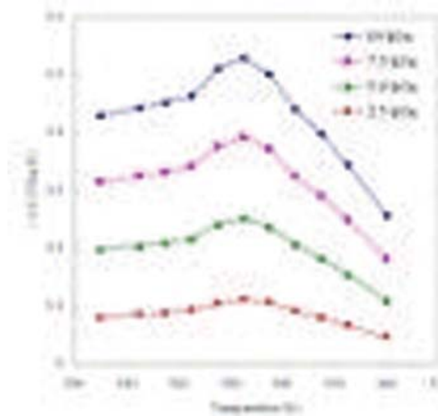

Fig. 2. Temperature dependence of magnetic entropy change of $La_{0.5}Nd_{0.2}Sr_{0.3}MnO_3$ under various magnetic fields.

CW-08

Magnetic behavior and magnetoimpedance effect in Cobalt-based ribbons.

A. Rosales-Rivera[1], M. Gomez-Hermida[1], A. Velasquez[1], D. Muraca[2], H. Sirkin[2]
1. Laboratorio de Magnetismo y Materiales Avanzados, Universidad Nacional de Colombia, Manizales, Colombia; 2. Física, Universidad de Buenos Aires, Buenos Aires, Argentina

Cobalt-based amorphous magnetic alloy ribbons have attracted considerable attention since 1980, because of its applicability in electronic devices. Interest is also associated with the presence of GMI effect, as detected in the middle 1990s [1-4]. Cobalt-based amorphous magnetic alloy ribbons have interesting properties, among them high magnetic permeability and vanishing magnetostriction constant, which become them suitable to obtain high MI responses. In this paper a systematic study of the dc magnetization, ac susceptibility and giant magnetoimpedance effect, in amorphous alloy ribbons Co80-xFexB10Si10 with x = 6, 8 and 10, is presented. The experiments were performed on samples of as-cast ribbons Co80-xFexB10Si10, prepared by the melt spinning technique. The dc field dependence of the magnetization, at room temperature, for all samples, for $-1 \leq H \leq 1$ kOe, is illustrated in Fig. 1. The curves in Fig. 1 are typical of an ultrasoft magnetic material, i.e., the loop is square shaped, having low coercivity; in addition, the saturation magnetization increases from 80 to 137 emu/gr with increasing x values. The dc field dependence of the real χ'ac part of the susceptibility, at room temperature, for the x = 10 sample at f = 1000 Hz is illustrated in Fig. 2. The χ'ac curve shows a peak at $H = \pm Ho \neq 0$ which could be associated with the transverse anisotropy field. No observable shift in the peak field occurs as a function of frequency. The amplitude of these peaks increases with increasing frequency. It could be related with the soft magnetic character of the sample. Similar characteristics were observed in the χ"ac curve (not shown here). The dc field dependence of the GMI ratio for the x = 6 sample, at room temperature, for the $0.5 \leq f < 10$ MHz is shown in Fig. 3. At low frequencies, f < 2 MHz, a single-peak (SP) behavior appears, typical for materials with vanishing magnetostriction [5]. For $2 < f \leq 10$ MHz, GMI results are no longer consistent with SP behavior. A two-peak (TP) behavior would be expected to occurs for large f, as previously reported from magneto-impedance measurements in Co-based and Fe-based amorphous ribbons [5]. In our case, the TP behavior is also observed (GMI vs. H curves in Fig. 3, at $H = \pm Hk \neq 0$ where Hk is the transverse anisotropy field). The χ'ac peak at Ho coincides quite well with the GMI peak at Hk, where GMI reaches its TP behavior.
In conclusion, all samples exhibit ultrasoft magnetic behavior, especially giant magneto-impedance effect, GMI. This behavior is consistent with the field dependences of the magnetization and ac susceptibility.

1. V.E. Makhotkin, B.P. Shurukhin, V.A. Lopatin, P. Yu. Marchukov and Yu. K. Levin, Sensors and Actuactors A, 25-27 (1991) 759.

2. F.L.A. Machado, B. Lopes da Silva and E. Montarroyos, J. Appl. Phys. 73 (1993) 687.

3. K. Mandal and S.K. Ghatak, Phys. Rev. B 47 (1991) 14233.

4. For recent reviews on the GMI effect, see for instance: M. Vázquez, J. Magn. Magn. Mater. 226-230 (2001) 693; M. Knobel and K.R. Pirota, J. Magn. Magn. Mater. 242-245 (2002) 33-40; M. Knobel, M. Vázquez and L. Krauss, Handbook of Magnetic Materials, Vol. 15, Ed. K.H.J. Buschow, North-Holland 2003, P. 497-563.

5. M. Vázquez, J.P. Sinnecker, G.V. Kurlyandskaya, Mater. Sci. Forum 302-303 (1999) 209.

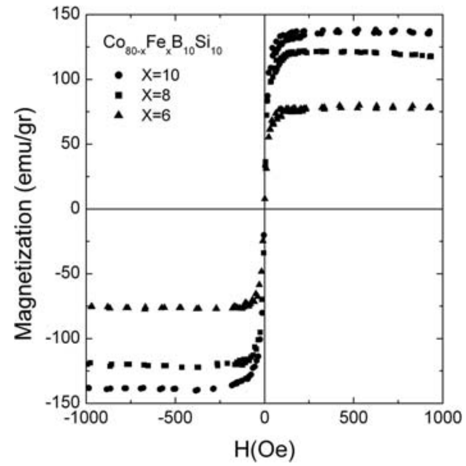

Fig. 1 – M vs. H measured on Co80-xFexB10Si10 with x = 6, 8 and 10 at room temperature.

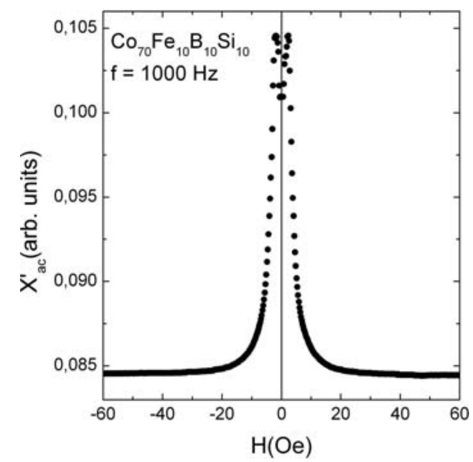

Fig. 2 – χ'ac vs. H measured on Co70Fe10B10Si10 at room temperature using a frequency f = 1000 Hz.

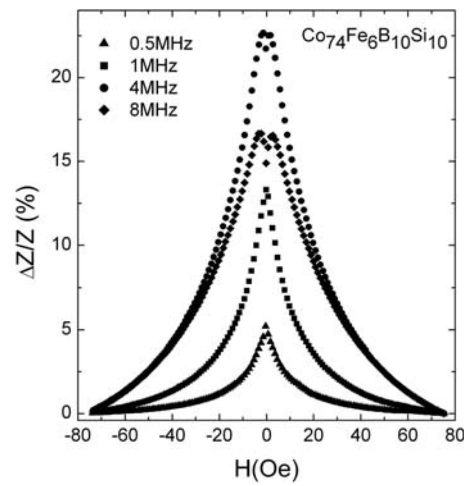

Fig. 3 – GMI ratio vs. H measured on Co74Fe6B10Si10 at room temperature for different frequencies f = 0.5, 1, 4 and 8 MHz.

CW-09

Correlation between surface magnetic field and Barkhausen noise in grain-oriented electrical steel.

S. Zurek[1], P. Marketos[1], S. Tumanski[2], H. V. Patel[3], A. J. Moses[1]
1. School of Engineering, Cardiff University, Cardiff, United Kingdom; 2. Institute of Electrical Theory and Measurements, Warsaw University of Technology, Warsaw, Poland; 3. Industry and Innovation Division, National Physical Laboratory, Middlesex, United Kingdom

Introduction

This paper shows a comparison of surface field and Barkhausen noise measured on the same grain-oriented (GO) sample. A single Epstein strip of conventional GO electrical steel, was tested at the Warsaw University of Technology (WUT) and the Wolfson Centre for Magnetics, Cardiff University (WCM). Prior to measuring, the domain structure was investigated with a static domain viewer to note the location of the grains (Fig. 1). The central part of the sample (40 mm x 20 mm) was examined with the use of two systems. The WUT used the Magnetivision system [1], which comprises a permalloy magnetoresistive sensor for the surface field investigation.

The surface of the sample was scanned in steps of 0.25 mm. The HS was measured at various values of peak flux density (Bpeak) as measured by means of a search coil wrapped around the sample.

The WCM used a similar system, in which the surface of the sample was scanned with a BN sensor. The sensor comprised a ferrite rod (3 mm in diameter) with a 1000 turn enwrapping coil close to the surface of the sample. The sensor was positioned with spatial resolution of 1 mm. Figure 2 shows the distribution of peak values of HS acquired with the WUT system at 50 Hz and two levels of sinusoidal Bpeak: 1.0 T and 1.5 T. The measured area is 140 mm x 30 mm and the values for each flux density shown in Fig. 2 were normalised to an arbitrary scale. A rectangle shows the area used for further analysis. Fig. 2 shows that the distribution of HS changes with B. It also shows that the overall topography remains similar at any B. However, this surface field activity does not seem to be directly connected to the grain structure, shown in Fig. 1 and Fig. 3. The comparison of results scanned for BN and HS from the two systems is shown in Fig. 3. The central area 40 mm x 20 mm (rectangle in Fig. 2) of the sample was scanned with the WCM system. The resultant rms Barkhausen noise distribution measured at 1.0 T, 50 Hz is shown in Fig. 3a. The results shown in Fig. 3a (BN) and Fig. 3b (HS) have a number of points with strong correlation. Lines A-A' and D-D' intercept at a grain over which there is very little activity for both BN and HS. On the right end of the D-D' line there is elevated activity (light grey or white) visible again in both cases. The intensity of HS and BN activities is clearly linked over around 50% of the tested surface area. However, this does not seem to be linked with the grain boundaries. It is therefore possible that the presented surface activity results from the grain-to-grain misorientation, which can take place at angles parallel to the surface of the sample, but also perpendicular to it. Such a misorientation would result in local demagnetising field, which would be dependent not only on the direction of a given grain, but also on the grains surrounding it.

Elevated HS and BN values are recorded in the vicinity of certain grains, whilst within other grains there is very little activity. Similar behaviour was observed at various flux density levels (from 0.5 T to 1.5 T) and magnetising frequencies (25 Hz and 50 Hz).

Conclusions

The measurements of the surface field and Barkhausen noise on the surface of a grain-oriented electrical steel sample show some correlation. On the other hand, there is a lack of clear link between the grain boundaries and the surface activity, which seems to be more affected only by certain grains. If Barkhausen noise is closely associated with hysteresis loss the results infer that this component varies spatially possibly independently of grain structure. More experimental work is required in order to understand and confirm the practical implications of these phenomena.

Acknowledgements

Dr. Zurek, Dr. Marketos and Prof. Moses are grateful for support from the UK EPSRC grant GR EP/C518616/1.

[1] Tumanski S., Stabrowski M., The magnetovision method as a tool to investigate the quality of electrical steel, Meas. Sci. Technol. 9 (1998), pp. 488–495

Fig. 1. Static domain structure aligned with rolling direction (RD) showing grain orientation in 40 mm x 30 mm GO sample (grade M4)

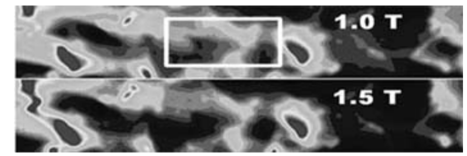

Fig. 2. Typical HS patterns at various B (arbitrary scale was used for each pattern)

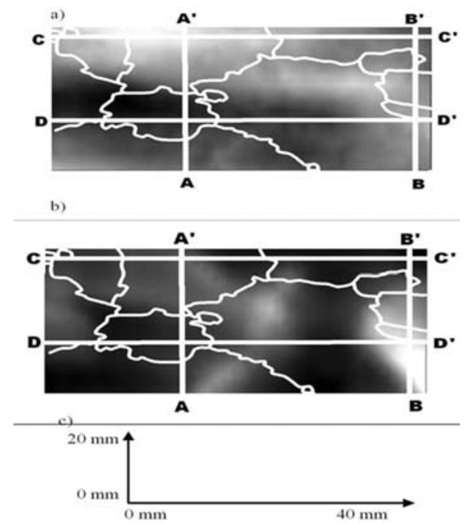

Fig. 3. Distribution of BN (a) and HS (b) measured at 1.5 T, 50 Hz, (c) corresponding diagram of dimensions used for further analysis

CW-10

Comparison of properties of magnetoacoustic emission and mechanical Barkhausen effects for P91 steel after plastic flow and creep.

B. Augustyniak[1], M. Chmielewski[1], L. Piotrowski[1], Z. Kowalewski[2]
1. Gdansk University of Technology, Gdansk, Poland; 2. Polish Academy of Science, IPPT, Warsaw, Poland

Magnetoacoustic emission is introduced now as a new nondestructive technique of assessments of damage stage of ferromagnetic steels exploited at high temperature under stress [1]. This effect is closely related with abrupt displacement of mainly 90-deg magnetic domain walls [2,3]. The mechanical Barkhausen effect (MBN), the analogue of classical Barkhausen effect, deals with voltage pulses induced at pick-up coil when sample is loaded mechanically. This effect was used to evaluate internal stress distribution function [3]. It is thus not trivial existence of correlation between MAE intensity and MBE because both are due to displacement of the same type of DW. We like to test this correlation in the case of P91 steel at different stage of microstructure due to or plastic flow or due to creep performed at high temperature. The samples are plane specimens, as reported at [4]. Uniaxial tension creep tests was conducted under stress 290 MPa at temperature 773K. The tests were interrupted at certain times (up to 445 h) and the samples have the following creep plastic strains (%): C1 - 0.85, C2 - 1.85, C3 - 3.15, C4 - 4.6, C5 - 5.4, C6 - 7.9 and C7 – 10.0. Plastic flow was also applied at room temperature and the next set of samples had the following plastic strain levels (%): P1 – 2.0, P2 – 3.0, P3 – 4.5, P4 – 5.5, P5 – 7.5, P6 - 9,0, P7 – 10.5. There was also tested 'new' sample labeled as N. Magnetisation was made with coil using triangular like current (with frequency of 0.1 Hz). The MAE signal was detected with resonant PZT transducer, amplified and transformed to Ua voltage with rms integral circuit. The MBN signal was induced at the pickup coil wound directly on the specimen during free torsion like oscillation with frequency 2 Hz. The rms like value Um of MBN intensity was also evaluated. The four representative plots of Ua and Um (in function of driving current (denoted as H) and torsion strain (denoted as X), are shown in Fig. 1 and in Fig. 2, respectively. There is evident an decrease of MAE and MBN activities for all damaged samples. This effect is compared by means of integrals plotted in Fig. 3 as function of resulting plastic strain. These four plots reveal two main properties: analogous type of decrease of MAE and MBN effects (abrupt from the first stage of plastic strain) and much higher decrease of intensity of both effects for the case of plastic flow. There is also evident close correlation between MAE and MBN dependence on modification of the microstructure. It proofs the thesis about common source of these effects. Without detailed microstructural analysis one can argue, using the as presented MAE and MBN results, that effective internal stress level - for the same plastic strain - is higher at the case of plastic flow than of creep damage. These results roof again that the MAE technique is very suitable for nondestructive assessment of damage state of ferrite-pearlite as well as martensite steels.

[1] B. Augustyniak, L. Piotrowski, M. Chmielewski, M. J. Sablik;; J. of Magn. and Magnet. Mater.; 304 (2006) s. e555-e557

[2] B.Augustyniak, L.Piotrowski, M.Chmielewski, M.J.Sablik, F.J.G.Landgraf, D.C.Miles, A.J.Moses; Luck of MAE in iron with 6,5% of Si; SMM18, Cardiff, to be published

[3] B. Augustyniak.;,J. Magn. Magn. Mater.; 196-197 (1999) pp. 799-801.

[4] B. Augustyniak, M. Chmielewski, L. Piotrowski, Z. L. Kowalewski, S. Mackiewicz, J. Szelazek; Proc. of the 4th Int. Conf. on Barkhausen Noise and Micromagnetic Testing, Petten, (2005) 293-304

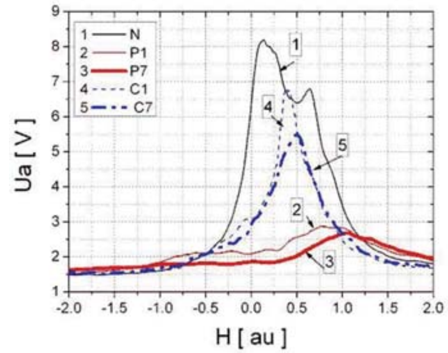

MAE intensity for new sample (N) and for samples after plastic flow (P1, P7) and after creep (C1, C7)

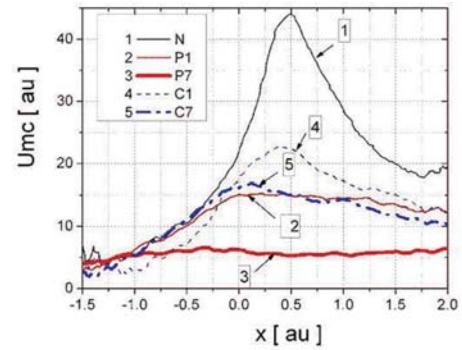

MBN intensity for new sample (N) and for samples after plastic flow (P1, P7) and after creep (C1, C7)

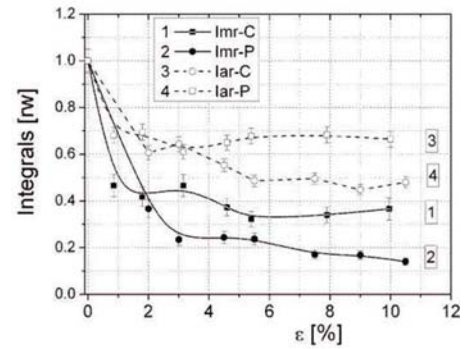

Integrals of MBN (Imr) and MAE (Iar) intensities in function of plastic strain after creep (C) and after plastic flow (P)

CW-11

Magnetic and microstructural investigation of pipeline steels.

G. Roland[1], E. Jose[2], A. Jose[3], K. Franz[4], M. Nasir[1], E. Chistian[1], P. Karin[1], H. Jose[3]
1. Inst. of Solid State Physics, Techn. Univ. Vienna, Vienna, Austria; 2. ESIME-Zacatenco, Instituto Politécnico Nacional, Mexico City, Mexico; 3. ESIQIE, Instituto Politécnico Nacional, Mexico City, Mexico; 4. Techn Univ Vienna, Inst. f. Sensor u. Atuatorsysteme, Vienna, Austria

The mechanical integrity of oil and gas pipelines is of major importance for the oil industry. The most effective method to detect local stresses and size defects in pipelines applies magnetic flux leakage (MFL) tools. The MFL signal is dependent, among other things, on the pipe wall magnetic properties and pipe wall stress. There exist several papers characterising the stress-state of pipeline steels [1–3], however, a systematic investigation correlating the microstructure with intrinsic magnetic properties of the material has not been reported. Therefore, in this paper three different types of steels API 5L (X52, X56, X60) obtained from out of service pipeline sections are investigated with respect to their microstructure, magnetic properties and magnetostriction.

The chemical compositions of the three steels under investigation were determined using the method included in the standard API-5L-2000. The microstructure was investigated using optical microscopy. As an example, Fig.1 depicts the typical microstructure in the longitudinal direction of two studied steel samples. The steel X52 exhibits a ferrite/pearlite microstructure with both phases banding along the rolling direction. The mean planar grain diameter (dm) was determined to be 22.5 µm. The microstructure of the steels X56 and X60 consist also of ferrite/pearlite with incipient banding and dm = 11.5 µm. The inclusion level of sulphurs, aluminates, silicates and globular oxides from the three studied steels were determined using the method in the standard ASTM E 45 [4]. The microstructure as well as the local composition of grains was studied also using a raster electron microscope (Quanta 3D 200) with EDX.

Two different sample geometries, rods and window-frames, were made of all steels taken from longitudinal and transverse directions. Fig. 2 shows minor hysteresis loops in the longitudinal and transverse direction of the steels X52 and X56, as obtained from the window-frame samples. The magnetic anisotropy is clearly visible, even though the materials are not fully saturated. This indicates that the bulk magnetic easy axis lies parallel to the rolling direction.

Using magnetic Barkhausen noise measurements Clapham et al. determined that the bulk magnetic easy axis in samples from steel API X70 is due to the strain induced during the cold-deformation stages of the pipe fabrication. They claimed that the presence of crystallographic texture and also the microstructure play no role in the origin of the bulk magnetic easy axis [1]. Magnetostriction is the most important intrinsic parameter of magnetic materials reflecting the stress influence on the shape of the hysteresis loop. Therefore, additionally magnetostriction measurements using strain gauge method and laser Doppler vibrometry were applied on all samples. The domain structure of the steel materials was observed using Magnetic Force Microscopy.

Pulsed field measurements were performed applying a maximum field of 5T in order to saturate the materials. However, in general stress states influence only the coercivity but not the saturation magnetization of ferromagnetic materials [5].

[1] L. Clapham, C. Heald, T. Krause, L. Atherton, P. Clark; J. Appl. Phys. 86 (1999) 1574.

[2] S. Takahashi, L. Zhang, S. Kobayashi, Y. Kamada, H. Kikuchi, K. Ara; J. Appl. Phys. 98 (2005) 033909.[3]O. Perevertovs; J. Phys. D 40 (2007) 949.

[3] O Perevertovs; J.Phys D 40 (2007) 949

[4] Designation: E45-05, Standard test methods for determining the inclusion content of steel. ASTM International, Edition approved Nov. 1, 2005.

[5] H. Hauser, R. Grössinger, F. Keplinger, M. Schönhart; J. Magn. Magn. Mat. (2007) in print.

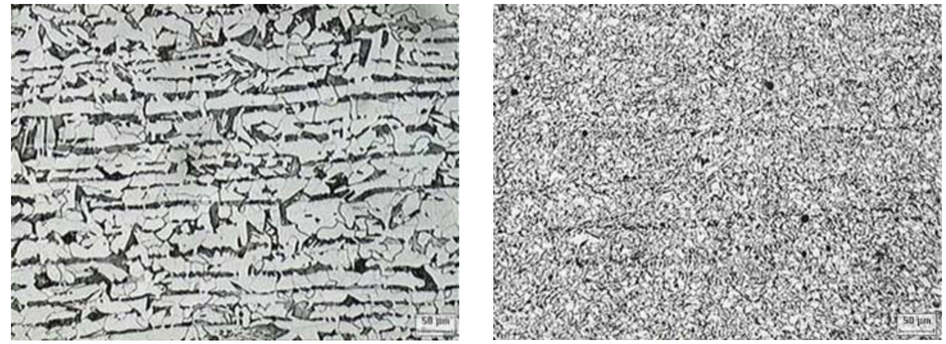

Fig. 1: Typical microstructure of a longitudinal section of steel samples (left) X52 and (right) X56.

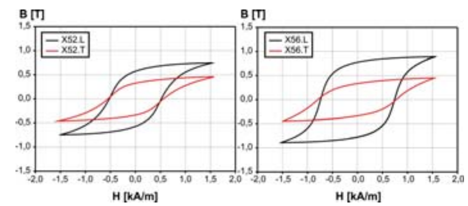

Fig. 2: Room temperature hysteresis loops measured on steels X52 (left hand side) and X56 (right hand side) in the longitudinal (L) and transverse (T) directions. The longitudinal direction is the rolling direction of the steel sheets and is parallel to the tube axis. The transverse direction is the direction of the bending process for the tube formation before welding.

A Pulsed Field Magneto-optic Kerr Effect Magnetometer for Studying Magnetic Thin-Films and Nanostructures.

D. Atkinson, J. A. King
Physics, Durham University, Durham, United Kingdom

A magnetometer is presented that brings together highly-sensitive focused magneto-optic Kerr effect detection [1] with a pulsed field capability that allows the study of a magnetization switching behaviour in thin-film and nanostructured magnetic samples. Figure 1 shows a schematic overview of the system. The magneto-optics are based upon a high stability, low power diode laser. The laser beam is polarised with a high quality prism, collimated and focused on to a sample to a spot with a diameter of 5 micrometers (FWHM) as determined by scanning the laser spot across a 200 nm wide nanowire, see figure 2. The reflected light passes through a ¼ wave-plate and an analysing polarising prism and is focused onto a photodiode detector.

Low frequency magnetic fields are generated with a small electromagnet driven by a bipolar amplifier. Pulsed fields are generated by passing current pulses through micro-strip lines onto which thin-films and nanostructures are fabricated. Pulses of current are generated by a simple pulse-forming network that is rapidly switched using either a mercury-wetted relay at low voltages or a spark-gap switch at higher voltages. The duration of pulses is determined by the length of the pulse-forming network, with a shortest pulse width of 800 ps.

The time resolution of the system is currently limited to microseconds and therefore is suitable for investigating switching behaviour such as the stochastic behaviour of thin-films and nanostructures as a function of pulse duration rather time resolved GHz magnetization measurements. As an example, figure 3 shows the amplitude of the MOKE signal measured as a function of pulsed field amplitude for pulse lengths ranging from 1 microsecond down to 1 nanosecond. The sample consists of 20 nm thick permalloy (nominally Ni81:Fe19) deposited on top of a 30 nm thick aluminium strip-line. For a given pulse length the MOKE signal increases rapidly over a small field range. The field amplitude needed for switching increases for shorter pulse lengths as expected for thermally activated behaviour, and interesting when the switching curves are offset with respect to the field amplitude the curves follow a the same field dependence indicating that the switching process is similar across three orders of magnitude from 1 microsecond down to 1 ns, see figure 4. A further point of interest in the switching of this sample is that with increasing field the MOKE signal reaches a peak and then reduces smoothly to a constant value as the field increases further. Further details of the MOKE system and example results will be presented.

[1] D.A. Allwood et al. J. Phys. D: Appl. Phys. 36, 2175 (2003)

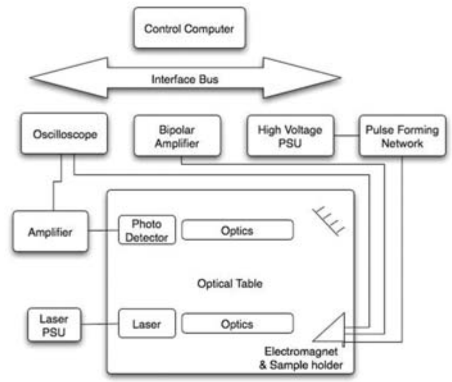

Figure 1. Schematic overview of pulsed MOKE system

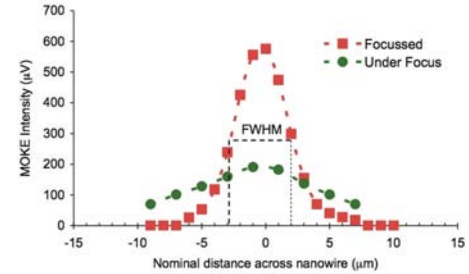

Figure 2. Data showing the variation of MOKE intensity obtained across a 200 nm wide nanowire - used to determine the laser spot diameter.

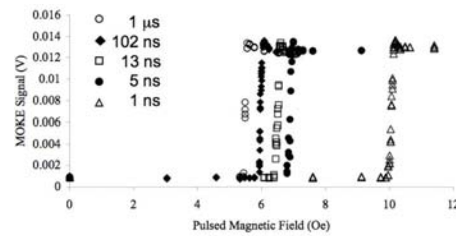

Figure 3. Examples of the field dependence of the switching behaviour obtained with different pulse lengths applied to a 20 nm thick permalloy film.

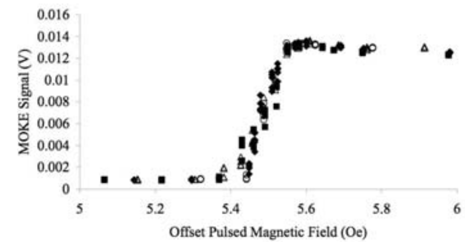

Figure 4. The switching behaviour of a 20 nm thick permalloy film measured with different pulse lengths - the data have been offset in field to show that the form of the field dependence of the switching is independent of the timescale of the applied field pulse length.

A novel application of high resolution scanning electron microscopy for perpendicular recording media characterization.

E. T. Yen[1], L. Lee[1], B. Lu[1], O. Mryasov[2]
1. Seagate Technology, Fremont, CA; 2. Seagate Technology, Pittsburg, PA

One of the apparent challenges in designing perpendicular recording media (PRM) includes complexity in correlation between characteristics of multilayer PMR and recording performances[1]. Thus, recording performance gain or loss due to a given change in media layer is generally difficult to identify and rationalize. However, there is a number of magnetic, microstructure and materials characterization means that can be used to guide PRM development by studying correlations between given building block properties and recording performances. Currently, the most prevailing microstructure analysis tool is the high resolution transmission electron microscopy. However, the sample preparation difficulties, long turn around time and high capital expenses makes this tool not as desirable in industrial research environment. In the meanwhile, key inventions such as field emission gun and the in-lens secondary electron detector make today's high resolution SEM (HRSEM) to attain fine feature resolution of about 1nm and thus becomes a meaningful development tool for high resolution topography images but still is not enough to resolve the state of art PRM media's sub-nanometer grain boundary width as well as fine features such as precipitates, stacking faults and crystal orientation of which HRTEM can do.

Nevertheless, In this paper, we describe a novel characterization approach based on combination of high resolution scanning electron microscopy (HRSEM) and automated image analysis at interlayer of PRM. We demonstrate that HRSEM can be quite useful to characterize interlayer topography which in all considered samples can be successfully correlated with observed recording performances. Interlayer is known to be critical to grain size control of recording layer and which, in turn, tunes the magnetic performances as described in [1]. As a matter of fact, the lack of crystal orientation contrast in SEM micrograph actually turns into an advantage for automated high throughput quantitative IL grain size image analysis as described below. Besides, the lack of grain boundary width resolution does not affect the determination of the center to center distance (d) which is one of the major contributors in media SNR [2].

As illustrated in HRSEM pictures below, clear grain topography with rather uniform gray level can be achieved for a typical interlayer (see Fig. 1) while, for comparison, grain topography of recording layer is much less clear (see Fig. 2). The latter can be attributed in part to recording layer planerization effect rather than to SEM resolution artifact. The crisp HRSEM image in Fig. 1 can then be analyzed quantitatively with highly automated software procedure implemented based on a special image analysis software. This image analysis procedure features background equalization, noise filtering, defect removal, grain image separation and Voronoi polyhedra statistical construction [3]. Voronoi grain size and the center to center distance histograms (not shown here)can be obtained easily and accurately with a sample size of about thousand grains and done within in a minute using a desktop PC. The microstructure characterization using Voronoi construction help to minimize uncertainties due to lack of grain boundary contrast. Interestingly, the lack of grain crystal orientation contrast in Fig. 1 reduces grain to grain gray level variations and as we find here overall helps accurate grain image separation within the automated analysis procedure. Note, that this is in contrast with painful and time consuming efforts in obtaining similar grain size histograms by HRTEM plane view micrograph analysis.

With such innovative, powerful and convenient characterization method at hand, we proceed to investigate perpendicular media performance as a function of grain size changes in a series of thickness ladder experiment. We observe strong media SNR and KuV/kBT dependencies upon variations in the center to center interlayer grain size. Due to space limitation, details will be discussed in the full paper.

REF[1] S.N. Piramanayagam, "Perpendicular recording media for hard disk drives", Journal of Applied Physics, Vol 102,011301(2007). REF[2]H.N. Bertram and M. Williams,"SNR and density limit estimate", IEEE Tran on magnetics, pp.4,Vol.36, No.1,2000. REF[3] Jin J. Chou,"Voronoi Diagrams for Planar Shapes," IEEE Computer Graphics and Applications, pp 55, Vol. 15, No. 2, Mar.,1995.

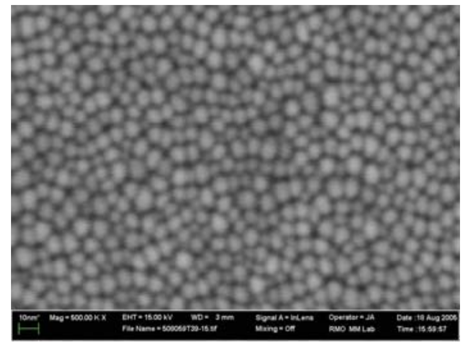

Fig. 1 Interlayer plane view HRSEM micrograph

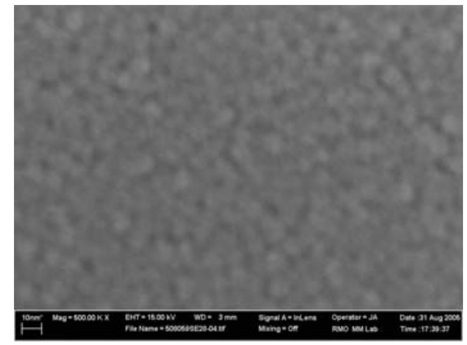

Fig 2 Recording layer plane view HRSEM micrograph

CW-14

Magnetic image detection of the stainless-steel welding part inside the multi-layered tube structure.

T. Hayashi[1,2], H. Yamada[1], T. Kiwa[1], K. Tsukada[1], M. Tamazumi[3]
1. Graduate School of Natural Science & Technology, Okayama University, Okayama, Japan; 2. Pulstec Industrial Co., Ltd, Hamamatsu, Japan; 3. Uno Kogyo Co.,Ltd, Okayama, Japan

For the non-destructive evaluation of the weld, detection of the stainless-steel welding part inside the multi-layered tube was demonstrated by low frequency magnetic imaging. The magnetic images were obtained by a developed measurement system, which consists of the exposure coil, magnetoresistive (MR) sensor, measuring circuit, and lock-in amplifier, moving stage and personal computer (Fig. 1). A wide area of the stainless-steel sample was exposed to the magnetic field via an induction coil. The diameter of the induction coil was 0.8m, which was comparable to the sample size. The MR sensor measured the vector components of the generated magnetic field from the sample within the range of the low frequencies between 20Hz and 1kHz. The vector components of the generated magnetic field from the sample were measured by scanning the MR sensor on the sample surface. A cylindrical stainless-steel sample was fabricated as a tube by rolling a stainless-steel sheet (SUS304) and welding each edge by an arc welder with argon gas. The welds were made with a tungsten electrode (TIG308). The diameter of the cylindrical sample was 150mm, and the height was 500mm. The multi-layered tube was fabricated by putting one tube inside another. The distance between the sensor and the sample surface was kept to 3 mm during the scanning.

The obtained vector components were divided into normal components (B_z) and tangential components (B_x and B_y) to the sample surface. Each magnetic field vector was calculated from two parameters, signal amplitude and phase, obtained from the lock-in amplifier at the same frequency of the applied magnetic field. From the tangential magnetic field components, the induced current in the sample was reconstructed using formula $I_{xy}(t)=K(-B_y(t)e_x+B_x(t)e_y)$ where K is constant, and e_x and e_y are respective x and y unit vectors. Fig. 2 shows the obtained current images of the single and double layer tube sample. These maps were the contour plot of tangential magnet field strength ($B_{xy} = (B_x^2 + B_x^2)^{(1/2)}$) and superposed with the current I_{xy} by using arrows at each measuring point. The tangential magnetic field strengths of both sides of the welding part were stronger than that of the welding part, and the direction of the current was inversed across the welding area. Additionally, the welding part inside the multi-layered tube, which was not optically observed from the surface, was successfully imaged. Fig. 3 shows the normal component images of the single and double tube sample. The normal magnetic field strength was inversed across the welding part, which denoted the same tendency of the direction of the current images.

In summary, the magnetic imaging of the stainless-steel welding part was obtained by the developed system, which detects the normal magnetic field strength and the current distribution of the sample. By using a low frequency exposure magnetic field, detection of the stainless-steel welding part inside the multi-layered tube became possible.

[1] K. Tsukada, et al., Rev. Sci. Instrum. Vol. 77,063703 (2006)

[2] K. Tsukada, et al., IEEE Trans. Magn. 42,3315 (2006)

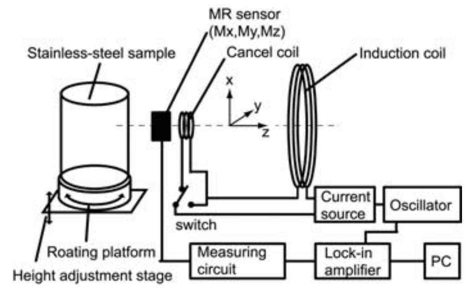

Fig. 1 Schematic diagram of the low frequency magnetic imaging system.

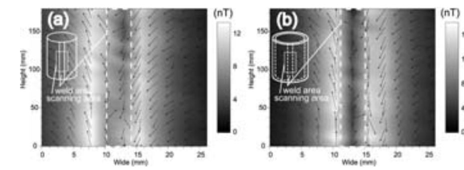

Fig. 2 Eddy current images of the stainless-steel welding sample (a) welding part is on the surface (single layer), and (b) the welding part is inside the stainless-steel tube (double layer). The frequency of the applied magnetic field is 20Hz.

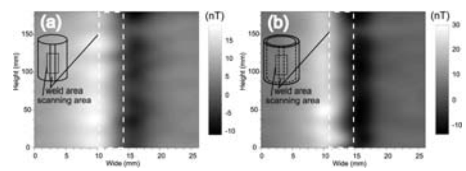

Fig. 3 Contour plots of the normal magnetic field strength of the stainless steel welding sample (a) the welding part is on the surface (single layer), and (b) the welding part is inside the stainless-steel tube (double layer). The frequency of the applied magnetic field is 20Hz.

Transient Eddy Current Measurement for the Characterization of Depth and Conductivity of a Conductive Plate.

W. Cheng
NDE Center, Japan Power Engineering and Inspection Corporation, Yokohama, Japan

Transient eddy current measurement rivals conventional single or multi-frequency eddy current technique for many of the common applications in non-destructive evaluation, such as the detection of defects, the estimation of thickness of a specimen itself or the coating, the measurement of electrical conductivity, and etc. Since the transient eddy current measurement signal is affected by both the plate thickness and the electrical conductivity, the interpretation of signal for the estimation of thickness and conductivity is studied. 3D transient eddy current simulation is carried out, and an optimization method to determine the conductivity and the thickness of a conductive plate is presented. A cylindrical air-cored coil is utilized for transient eddy current measurement. The coil is excited by transient current [1], and the normal component of the transient induced magnetic field flux density is detected by magnetic field sensors located on the coil axis. The period of the pulse wave is T, and current I0 is turned off at time t0. Ideally the turn-off time should be 0. However, practically there is a time delay for current turn-off. The 3D transient eddy current problem is solved in three steps correspondently: a static study is carried out for t<t0; the current is turned off at t0 and a transient procedure starts, during which the current drops from I0 to 0. The initial condition of the transient procedure is given by the solution of the static procedure. The eddy current, which concentrates in a small skin depth area close to the surface of the plate penetrates into the plate and decreases because of Joule dissipation, even after the current in the excitation coil is completely turned off at t0|+. The current in the excitation coil is described in Fig. 1. The normal component of magnetic flux density (Bz) along coil axis is calculated and the difference between two measurements, dBz = Bz1-Bz2, is utilized for depth and conductivity characterization.

The plate thickness is assumed to be 5, 7, 8, 9, 10, 15, and 20 mm respectively. And the conductivities used in simulation are respectively 0.5, 0.7, 0.9, 1.0, 1.1, and 1.5MS/m. The current is 15 Ampere and turned off in 5 µs.

The magnetic flux density at Z=2mm and Z=15mm above testing plate is calculated and dBz is obtained. Fig. 2 shows the responds of magnetic field flux density with respect to time in the transient procedure, when the plate thickness changes. The conductivity is keep constant as 1MS/m. Logarithm is taken for both time t and signal Bz. Signal of a thinner plate decreases faster than that of a plate with larger thickness. Fig. 3 shows the signal of 5, 8, 10, and 20 mm thick plate when the conductivity are respectively 0.5, 0.7, 0.9, 1.0, 1.1, and 1.5MS/m. It is clear that, for plates with same thickness, the larger the conductivity, the slower the decrease of signal Bz.

The conductivity and plate thickness affects signal Bz simultaneously. In order to determine the thickness and conductivity respectively, an optimization approach, which ensures the lowest sensitivity to thickness and highest sensitivity to conductivity, when conductivity is required; and vice versa for thickness, is adapted and the result will be reported in full paper.

[1] F. Thollon, "Eddy current NDT and deep flaws", http://www.lmn.pub.ro/team/problema27.html

excitation current

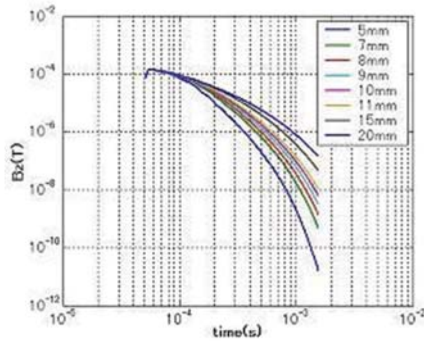

Bz of 1MS/m conductivity plate with different thickness

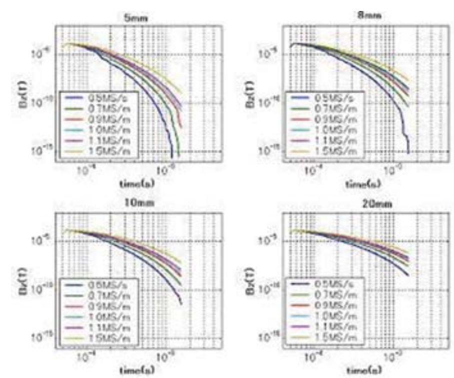

Bz of 5, 8, 10, 20 mm thick pate, conductivity changes

CW-16

Multidirectional Remanent Flux Leakage Transducers for Evaluation of Stress and Fatigue Loaded Steel Samples.

T. Chady, *G. Psuj*
Department of Electrical and Computer Engineering, Szczecin University of Technology, Szczecin, Poland

Abstact.In this paper stress and fatigue loaded ferromagnetic samples made of SS400 and S355J2G3 steels were evaluated using three different remanent flux leakage transducers. GMR sensors were used as the pick-up elements. Each transducer has its own integrated local magnetizing section which allows to magnetize the tested material in different direction. The performance of the transducers was verified using steel plate (S355J2G3) with EDM notches.

1.Introduction

The magnetic flux leakage method finds widespread use in a number of industries. It is based on a detection of leakage fields, caused by a change in the reluctance of ferromagnetic materials, which are magnetized in a DC field. The leakage magnetic fields are then measured by scanning a surface of the specimen with a flux density sensitive transducer. Observations confirm that this method is useful in evaluation the stage of degradation of stress loaded samples [1], [2]. However, obtaining uniform magnetization of the material in many practical cases can be a complicated task. Therefore, utilization of a local magnetizing coil seems to be an interesting alternative. In this paper three transducers with integrated magnetizing sections, which allow to magnetize in different directions will be presented. The minimization of the defect detection dependency on angle was achieved by integration of the data from different transducers.

2.Transducers

Figure 1 shows the view of the proposed transducers. Each transducer consists of two elements: a pick-up section and an integrated magnetizing section. The configuration of sections was different in each transducer. The magnetizing section of the TMAG_X transducer consists of two excitation coils wounded on the C-shaped ferrite core. The magnetization field was parallel to the scanning direction (x axis). The pick-up section was made of two absolute GMR elements differentially connected with the sensing axis parallel to the scanning direction. The first GMR was placed close to the specimen surface. The second one was placed above, so that it measured only unwanted interfering signals. In case of the TMAG_Y transducer, magnetizing section is rotated by 90° in order to magnetize the material in perpendicular direction to the scanning direction.

The magnetizing section of the TMAG_Z transducer consists of an excitation coil wounded on the rod ferrite core. In this case the magnetization was perpendicular to the sample's surface. The pick-up section consists of two absolute GMR elements connected differentially and placed one over another. The sensitivity axis of the GMR elements was parallel to the magnetization axis.

3.Selected Results of Experiments

Each sensor presents different range of angles, for which it is possible to detect the defect. To verify the performance of the measuring system the preliminary experiment was carried out using steel plate (S355J2G3) with EDM notches (depth 80%, width 0.2 mm, length 5 mm) manufactured at different angles (0, 30, 60 and 90 degrees) to the scanning direction. The results obtained for TMAG_X and TMAG_Y were presented in Figure 2. In order to enhance the performance of the measuring system, the results obtained from all transducers were combined using signal level data fusion algorithm. The results of the data fusion achieved for TMAG_X and TMAG_Y were presented in the Figure 2c. It can be observed that the fused results enable to detect all defects. The final tests were carried out on planar specimens made of steel (SS400, S355J2G3) stress or fatigue loaded in longitudinal direction. Figure 3 shows selected results of the measurements. Other results as well as the details of the fusion algorithm will be presented in the final version of the paper.

4.Acknowledgement

This work was supported in part by the State Committee for Scientific Research, Poland, under the Grant no: N N510 0861 33 (2007-2009).

[1] V. Babbar, L. Clapham, "Residual Magnetic Flux Leakage: A Possible Tool for Studying Pipeline Defects", Journal of Nondestructive Evaluation, Vol.22, No. 4, 2003, pp.118-125

[2] Y. Tsuchida et al., "Evaluation of Strain Distribution of Austenitic Stainless Steels by Measuring Remanent Magnetization", Electromagnetic Nondestructive Evaluation VIII, L. Udpa and N. Bowler (Eds.), IOS Press, 2005, pp. 151-158.

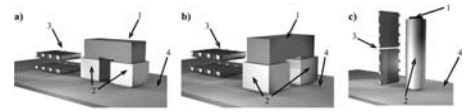

Figure 1. The view of the transducers used in the experiments: a) TMAG_X, b) TMAG_Y, c) TMAG_Z; 1) ferrite core, 2) magnetizing coil, 3) pick-up section, 4) sample;

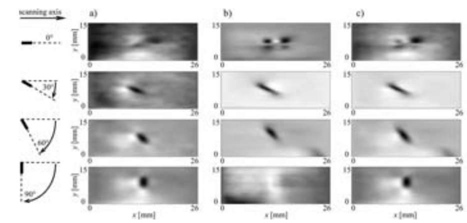

Figure 2. The results of the preliminary experiment and data fusion obtained for plate with EDM notches manufactured at 0, 30, 60 and 90 degrees to the scanning direction: a) TMAG_X, b) TMAG_Y; c) data fusion of TMAG_X and TMAG_Y results

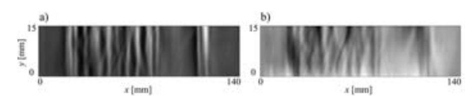

Figure 3. The results of the measurements obtained for stress loaded sample using transducer: a) TMAG_X, b) TMAG_Y

Understanding Adjacent Track Erasure in Discrete Track Media.

Y. Tang[1], X. Che[2], J. Zhu[1]
1. Electrical and Computer Engineering, Carnegie Mellon University, Pittsburgh, PA; 2. Samsung Information Systems America, San Jose, CA

Recently there are arising interests in the implementation of discrete track media (DTM) in perpendicular recording with drive level implementation demonstration by Toshiba and the recording areal density of 602 Gb/in2, highest area density in HDD demo, achieved by TDK. It is believed that with grooves separating data tracks magnetically and physically, higher recording track density can be achieved in DTM mainly due to the improved adjacent track erasure (ATE) performance in recording1,2, which is the key factor preventing today's continuous disk medium from achieving higher track density. This paper presents a micromagnetic modeling analysis that is performed on both continuous media (CM) and DTM with same magnetic properties for understanding the underlying physics of ATE.

In simulation, coupled-granular-continuous (CGC) media is modeled with a two layers structure. The bottom layer is exchange decoupled with 10 nm thickness, and Hk = 10 kOe. The top capping layer is 4 nm thick with varied inter-granular exchange coupling A1, and Hk = 12 kOe. The saturation magnetization for both layers is Ms = 550 emu/cc. The etching wall angle effect is considered in modeling by reducing the top layer track width.

A trailing shielded head with 120 nm pole width and 50 nm write gap is used to simulate ATE in recording. First periodic patterns with 200 KFCI linear density are recorded on the center track. Then the head write 800 KFCI patterns with an offset from the center track. The ATE is obtained by measuring the on-track signal profile in frequency domain. Figure 1 shows the ATE in continuous media and DTM with/without exchange coupling in the capping layer. The track/trench width is 100 nm. The offset, i.e. squeeze, is 135 nm. In frequency domain (second row in figure 2), it is obvious that the on-track signal are erased by the adjacent track recording except DTM with exchange coupling. By varying the offset of adjacent track recording, the roll-off curves of on-track signals for DTM and continuous media are plotted in figure 2. Without exchange coupling in the capping layer, there is no obvious ATE improvement in DTM. When exchange coupling in the capping layer is 5×10-7 erg/cm, believed to be a typical value for today's media, the track pitch can be reduced by 20 nm compared to continuous media with same amount of ATE. The fact there is ATE gain in DTM is because of the existence of inter-granular exchange coupling in today's PMR media. Our simulation results shows the improved ATE performance monotonic increases with increasing inter-granular exchange coupling in the capping layer of the media.

[1] S.J. Greaves and H. Muraoka, J. of Appl. Phys., vol.99, pp. F903–F905, 2006.

[2] X. Che, K. Moon, Y. Tang, N. Kim, H. J. Lee, S. Zhang, M. Monneck, Y. Tang, J. Zhu, N. Takahashi, PMRC 2007, 17pB-04

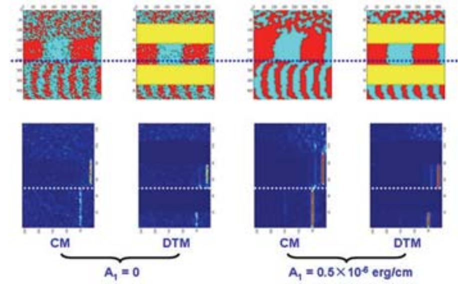

Figure 1. At 135 nm squeeze, comparisons of ATE performance on DTM and continuous media with/without exchange coupling A1 in the capping layer.

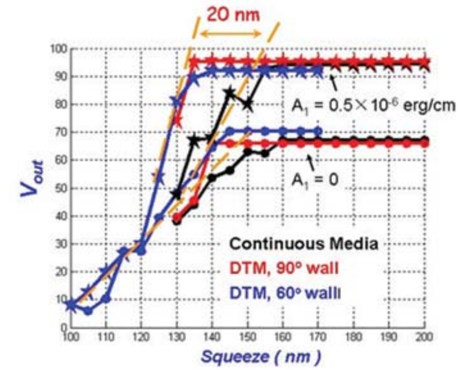

Figure 2. The on-track signals as a function of squeeze for DTM and continuous media.

DA-02

10 Tb/in^2 recording simulations on patterned domain wall assisted media.

A. Y. Dobin, H. J. Richter, J. Xue, D. Weller
Seagate Technology LLC, Fremont, CA

Magnetic recording on patterned media is predicted [1] to significantly increase the areal density owing to the ultimate reduction of the number of magnetic particles per bit of recorded information: from more than 20 grains per bit in current conventional perpendicular recording down to 1 dot per bit for patterned media. Domain wall assisted switching provides a means to reduce the size of magnetic particles without sacrificing their thermal stability and write-ability [2,3]. In this work we demonstrate theoretically that domain wall assisted patterned media can reach a record 10Tb/in^2 areal density.

We use a writer with a very small 10nm by 10nm pole tip at the ABS, and 45-degree flares and bevels in cross-track and down-track directions increase the write field. Side shields with 10nm gaps and trailing shield with 40nm gap are used to increase the down/cross-track field gradients to improve the bit-error rate and reduce adjacent track erasure. We chose aggressive values for the head-medium separation HMS=2nm and medium-SUL separation (interlayer)=1nm. The dot-to-dot spacing is 8nm, resulting in the areal density of 10Tb/in^2, and the dot diameter is 4.5nm. The composite hard/soft magnetic dots structure is shown in Fig. 1. The hard layer anisotropy and saturated magnetization are slightly below L10 FePt values, while the soft layer parameters are close to those of pure Co.

The contributions of different noise sources to the total write jitter are presented in Table 1. The standard deviations of the down-track dot position error (determined by lithography) and the timing synchronization (read/write electronics) were fixed at 5% of the bit length in our study. We calculated the jitter (see Fig. 2) owing to the hard layer anisotropy distributions (assuming $\sigma(H_k)/H_k$=5%) using 1D micromagnetic model for the domain wall assisted media [3] and FEM write fields. The demagnetization fields from neighboring dots produce fluctuations of the perpendicular field with $\sigma(H_{demag})$=210 Oe, the corresponding jitter is presented in Fig. 3. The jitter from both sources is found to be significantly reduced owing to the switching field distribution reduction in domain wall assisted media with optimized soft and hard layers [4]. The total jitter, calculated as a sum of variances of uncorrelated Gaussian distribution of all noise sources, has σ(jitter)=11% of the bit length, which corresponds to written-in BER of ~$10^{-5.3}$.

The energy barrier of the hard/soft structure (calculated using the recipe described in [3]) is E_b/k_BT_{300}~98 which is more than enough to keep the information thermally stable for more than 10 years. The energy barrier for the adjacent track erasure was calculated using a similar scheme with the FEM off-track write fields, yielding $E_b(ATE)/k_BT_{300}$~35. With the attempt frequency of 3000GHz and 1ns exposure time for each erasure cycle, we find the additional error rate of ~$10^{-5.7}$ after 1 million erasure cycles.

[1] H. J. Richter et al, Appl. Phys. Lett, 88, 222512 (2006); IEEE Trans. Mag., 42, 2255 (2006).

[2] D. Suess et al., Appl. Phys. Lett. 87, 012504 (2005).

[3] A. Yu. Dobin and H. J. Richter, Appl. Phys. Lett. 89, 062512 (2006); J. Appl. Phys., 101, 09K108 (2007).

[4] A. Yu. Dobin, to be published.

Noise source	σ_{jitter}/BitLength
Dot position error	0.05
Timing synchronization error	0.05
Hard layer anisotropy distribution	0.025
Demagnetization field fluctuations	0.08
Total	0.11

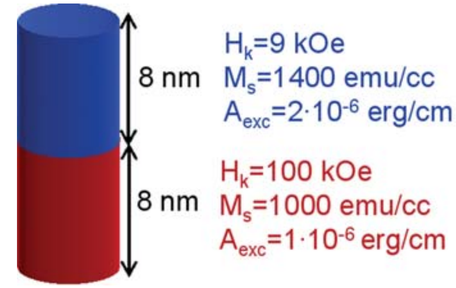

Fig. 1. Hard/soft composite dot

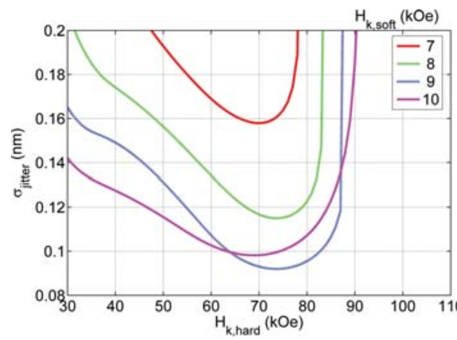

Fig. 2. Jitter due to hard layer anisotropy fluctuations vs. average hard/soft layers anisotropy fields

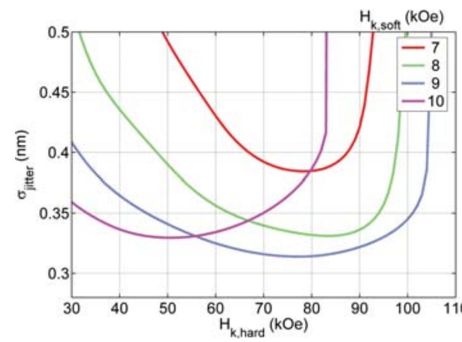

Fig. 3. Jitter due to fluctuations of the demagnetization field of the dots vs. average hard/soft layers anisotropy fields

DA-03

Patterned media for 10 Tbit/in2 utilizing dual-section “ledge” elements.

V. Lomakin[1,2], B. Livshitz[1,2], S. Li[1,2], A. Inomata[4], R. Choi[1], N. Bertram[2,3]

1. ECE, University of California, San Diego, La Jolla, CA; 2. Center for Magnetic Recording Research,, University of California, San Diego, La Jolla, CA; 3. Hitachi San Jose Research Center, San Jose, CA; 4. Storage Systems Laboratories, Fujitsu Laboratories Ltd., Kanagawa, Japan

Patterned media (PM) magnetic recording is envisioned for ultra-high recording densities. High density PM should utilize elements with high anisotropy to render a sufficient thermal stability, which can be reversed with sufficiently low head fields. Here, we introduce a new type of PM that utilize elements, referred to as “ledge” elements, and show that these PM can lead to recording densities of 10 Tbit/in^2 [1].

A ledge element is comprised of a magnetically hard and soft sections of dimensions w_x, w_y, t_h and a_x, a_y, t_s, respectively. The left corners of the sections are shifted with respect to each other by s_x and s_y in the x and y dimensions, respectively. Both sections have a damping constant α, saturation magnetization M_s, and exchange length l_{ex} (with A the exchange constant). The sections are coupled with energy per unit area J_s. A PM comprises an array of such elements with the pitch d_x and d_y. When $a_{x,y} < d_{x,y}$, both the soft and hard sections are physically separated. When $a_{x,y} = d_{x,y}$, the hard sections are separated whereas the soft sections form a continuous soft layer. An external magnetic field is $\mathbf{H}_{ext}=-H_a \mathrm{erf}(2t/\tau)(\mathbf{z}_0\cos\theta+\mathbf{x}_0\cos\theta)$, where θ is the field angle, H_a is the field magnitude, and τ is the field rise time. Reversal occurs when H_a is above a certain reversal field H_r.

Figure 2(a) shows the normalized reversal field H_r/H_K (with $H_K=2K_h/M_s$) versus a_x/w_x for small and large α in the cases of a “gamma” element with $s_x=0$, “mushroom” element with $s_x=(a_x-w_x)/2$, and “capped” structure with $a_x=d_x$. For all structures, H_r/H_K decreases substantially with increasing a_x/w_x. For large damping ($\alpha=1$), the reversal field saturates rapidly as a_x/w_x increases. The saturation is obtained due to a domain wall in the soft section. For smaller damping ($\alpha=0.1$), the decrease of H_r/H_K with a_x/w_x is much more pronounced with smallest values (H_r/H_K~0.07) obtained for the “gamma” and “mushroom” structures. These values are more than an order smaller than those for homogeneous elements, and ~5 times smaller than those for conventional composite elements (i.e. for $a_x/w_x=1$) [2-4].

The reduction of H_r/H_K~0.07 for small α is associated with precessional reversal [5-7], which occurs when α is small, θ is non-vanishing, and $\tau<\tau_{crit}$ with τ_{crit} being the critical rise time, i.e. the maximal τ allowing for precessional reversal. Figure 2(a) shows normalized τ_{crit} for the structures in Fig. 2(a). For the ledge elements, values of τ_{crit} are remarkably larger than those for homogeneous and conventional composite elements with largest values obtained for the “gamma” structure. For example, for H_K=72kOe, τ_{crit}=120ps for the ledge elements in Fig. 2, whereas it is τ_{crit}~16ps and τ_{crit}~2ps for the conventional composite and homogeneous elements, respectively. The τ_{crit} can be further increased significantly by optimizing the values of J_s. While τ_{crit}~100ps for ledge elements can be obtained in realistic recording heads, τ_{crit}~10ps for composite/homogeneous elements is hard or impossible to achieve.

Potential of the ledge structures for ultra-high density recording can be estimated based on the Neel-Arrhenius estimate. We require $(K_hV)/(k_bT)>50$, where $V=w^3/2$ is the hard section volume, T is the temperature, k_B is the Boltzmann constant, and the factor 50 is chosen to lead to sufficiently a long relaxation time. For recording at a density slightly above 10Tbit/in^2, a medium with $w=w_x=w_y$=4.2nm, $d_x=2w$=8.4nm, $d_y=1.6w$=6.72nm, M_s=1500emu/cc, $a_y=w_y$, $a_x=1.9w$=7.98nm, $t_s=t_h=w/2$=2.1nm satisfies the thermal stability criterion for T=300K. The reversal field and critical rise time are on the order of H_r=10kOe and 100ps, respectively (τ_{crit} increases to ~170ps for $J_s/(2K_ht_h)$=0.1 with a slightly stronger H_r). Such H_r and τ_{crit} can be obtained in practical recording systems. Moreover, these structures use elements of a small height. Therefore, recording heads with a small head-underlayer gap can be used thus allowing for strong head fields. Higher densities for thermally stable recording can be achieved with larger H_r.

Additional study is being conducted to characterize effects of various structure parameters, including interactions between the PM elements, and initial magnetization states.

[1] V. Lomakin at al, Appl. Phys. Lett., 92(1), 2008, accepted.

[2] R. H. Victora and X. Shen, IEEE Trans. Magn. 41, 537-42 (2005).

[3] E. E. Fullerton at al, Phys. Rev. B 58, 12193 (1998).

[4] D. Suess at al, Appl. Phys. Lett. 87, 12504-1-3 (2005).

[5] L. He, W. D. Doyle, and H. Fujiwara, IEEE Trans. Magn. 30, 4086-8 (1994).

[6] K.-Z. Gao, E. D. Boerner, and H. N. Bertram, J. Appl. Phys. 93, 6549-51 (2003).

[7] B. Livshitz at al, Appl. Phys. Lett. 91, 182502 (2007).

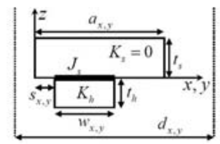

Fig. 1

Fig. 1: Central cross-section of the ledge element.

Fig. 2: (a) Normalized reversal field H_r/H_K vs. a_x/w_x for the “gamma”, “mushroom”, and “capped” structures with $t_h=2t_s$, $a_y=w_y$, $J_s/(2K_ht_h)=0.35$, and $\theta=45°$; (b) Normalized critical rise time $\tau_{crit}\gamma H_K$ for the structures in Fig. 2(a) (γ=1.76·10^7 Oe^{-1}s^{-1} is the gyromagnetic ratio).

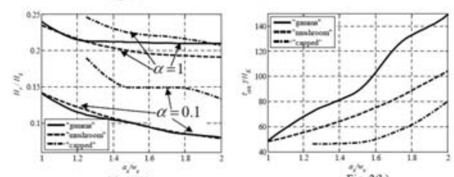

Fig. 2(a) Fig. 2(b)

DA-04

Characterization of timing jitter in synchronous writing of bit patterned media.

Y. Tang, X. Che
Samsung, San Jose, CA

One challenging problem in writing bit patterned media is synchronizing the write current reversal and the physical bit pattern location[1]. Since synchronizing signal is usually only available through averaging or interpolation, the relative jitter between bit pattern location and the write current reversal can have an important effect in synchronous writing. This paper characterizes two sources of jitter in a disk drive that can potentially affect write timing accuracy.

The first source is the jitter in disk speed. To correlate it to timing jitter, we wrote periodical isolated magnetic transitions on a PMR disk. One of the transition was used as the reference and other transistions were chosen for jitter measurement. Transitions with different distances from the reference were measured and the position jitter verses average transition distance is plotted in Fig. 1. Here jitter magnitudes of 5 heads in the same HDA are plotted in different symbols. It can be seen that the jitter increases with the transition distance. This is consistent with the effect of slow rotation speed variation. Also, the jitter for all heads increases at similar rate with distance, which suggests that the distance dependent jitter comes from the spindle speed variation. The jitter at near zero distance represents the jitter from electronics including the instrument itself.

While the spindle speed variation and electronics circuit are major sources of timing jitter during normal head flying, an addtional timing jitter can occur when a head is in or near in contact with disk. In this case, the slider may vibrate in the down track direction, which will cause write timing jitter. To characterize this effect, we wrote periodic signals over many sectors on a disk and recorded the readback signal. The read signal is digitally processed to calculate the frequency and magnitude of its vibration mode[2]. Fig. 2 showed that with high power applied to head heater, a 78KHz vibration mode with about 37nm in amplitude was observed.

To demonstrate the effect of this head/media interface induced jitter on writing, we wrote consecutive tracks in a disk drive with patterns derived from a bit map image of Samsung logo. Each row of the bit map was written onto one sector of one track with blue and white area coded in opposite magnetization directions on the disk. The writing was done with two different heater powers. In both cases, the signal was read back under the normal flying condition and recorded using a digital oscilloscope. The image is reconstructed by representing read signal level from each track in image brightness and pasting them together. Fig. 3 showed the reconstructed image under normal write condition and under high heater power during writing. The effect of down track jitter is manifested by the poorer image quality the image on the right side. In particular, the vertical lines in letters “M”,“U” and “N” showed clear difference in smoothness.

From these experiments, we have identified two sources of jitter in addtion to electronics noise that can potentially cause difficulty in writing bit patterned media: disk speed variation and head-media contact. In addition, the effect of write timing jitter is demonstrated with reconstructed images.

[1] H. J. Richter, A. Y. Dobin, O. Heinonen, K. Z. Gao, R. J. M. v. d. Veerdonk, R. T. Lynch, J. Xue, D. Weller, P. Asselen, M. F. Erden, and R. M. Brockie, “Recording on bit-patterned media at densities of 1 Tb/in and beyond,” IEEE Trans. Magn., vol. 42, no. 10, pp. 2255–2260, Oct. 2006.

[2] K.B. Klaassen, J.C.L. van Peppen, and R.E. Eaton, “Non-invasive take-off/touch-down velocity measurements,” IEEE Trans. Magn., vol. 30, no. 6, pp. 4164–4166, Nov. 1994.

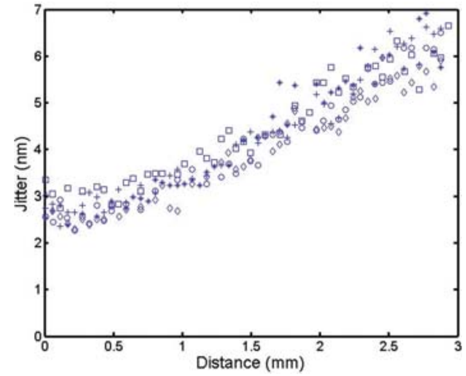

Fig. 1. Jitter as a function of transition distance.

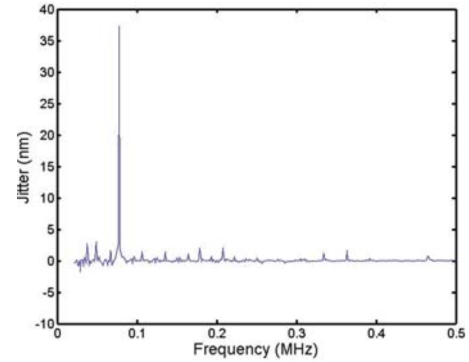

Fig. 2. Down track jitter with 116mW heater power.

Fig. 3. The reconstructed logo under normal write (left) and high heater power write (right).

DA-05

Formation of multilayered Co/Pd nano-dot array with an areal density of 1 Tb/in^2

J. Wi[1], H. Lee[1], K. Lim[1], T. Kim[2], K. Shin[3], K. Kim[1]
1. Department of Materials Science and Engineering, Seoul National University, Seoul, South Korea; 2. Department of Advanced Materials Engineering, Sejong University, Seoul, South Korea; 3. Future Technology Research Division, Korea Institute of Science and Technology, Seoul, South Korea

Many attempts have been made to form ordered magnetic nanostructures for scientific interest and practical use in magnetic devices. In particular, fabrication of patterned magnetic media is the important area due to ultimate data density of 1 Tb/in^2 and retardation of superparamagnetic limitation. We will show that the multilayered Co/Pd nano-dot array with an areal density of 1 Tb/in^2 which can be obtained by combination of the double development technique of HSQ resist [1] and the two-step plasma etching process [2]. Critical process issues and our solution will be described in view of the proximity effect in e-beam lithography and the redeposition problem in plasma etching.

10 Å Pd (top) /(3 Å Co / 8 Å Pd)10/50 Å Pd /40 Å Ta (bottom) multilayer was deposited on a 1000 Å SiO_2/Si(001) substrate, and a 300 Å thick amorphous Si layer was deposited as an etch mask and resist adhesion promotive layer. Afterwards, dot array patterns with pitches from 50 nm to 25 nm were defined by e-beam lithography using 100 keV accelerating voltage and 300 Å thick hydrogen silsesquioxane (HSQ). Resist development was carried out in tetramethylammonium hydroxide (TMAH) 25 % aqueous solution at 21 ^{o}C for 1 min. These resist patterns were transferred to the underlying metal layer by two-step etching. Amorphous Si and metal layers were etched successively using Cl_2 and Ar plasma.

Plan-view SEM images of the nano-dot array pattern with a 50 nm pitch are presented in Fig. 1 as following process steps. As presented in Fig. 1a, some material around nano-dot were appeared and built up during Ar plasma etching. These material might be a redeposit of Co or Pd. Non-volatile etch products are easily stuck on the sidewall or surface of pattern by back scattering from the Ar plasma [3,4]. The redeposit phenomenon could be solved by restriction of scattering event between sputtered material and Ar plasma. The morphology of nano-dot array was seriously altered by reducing of chamber pressure from 100 mTorr (Fig. 1a) to 10 mTorr (Fig. 1b). Inset of Fig. 1b clearly shows that redeposit around nano-dot array can be neglected. Using this plasma etching method, we successfully fabricate the Co/Pd nano-dot array with the pitch size of larger than 30 nm. However resist patterns below the 25 nm pitch, which corresponds to the areal density of 1 Tb/in^2, were not transferred to the underlying layer. The reason of process failure is that each dot in the resist patterns was not fully isolated after resist development due to the e-beam proximity effect. Interestingly, in addition, we found that development of HSQ stops at 1 min in a 25 % TMAH developer and the insoluble siloxane layer covers the resist surface. To continue the development, we introduced the siloxane layer removal step using a dilute HF solution between development steps [1]. Using the double development method (TMAH/dilute HF/TMAH), we could extend the development time and obtain fully isolated resist pattern with 25 nm pitch. These well defined resist pattern was transferred faithfully to the magnetic layer.

From the proposed method of resist development and plasma etching, we demonstrated of the patterned magnetic storage of the areal density from the 0.25 to 1 Tb/in^2 as shown in Fig. 2. More detail discussion on the fabrication process issues and magnetic properties of fabricated nano-dot array, will be given.

[1] H.-S. Lee, J.-S. Wi, S.-W. Nam, H.-M. Kim, and K.B. Kim, 2006 MRS fall meeting, O4.5 (J. Vac. Sci. Technol. B, submitted).

[2] J.-S. Wi, T.-Y. Lee, K.-B. Jin, D. H. Hong, K. H. Shin, and K.-B. Kim, J. Vac. Sci. Technol. B 24, 2616 (2006).

[3] H. W. Lehmann, L. Krausbauer, and R. Widmer, J. Vac. Sci. Technol. B 14, 281 (1977).

[4] L. Stafford, J. Margot, S. Delprat, M. Chaker, S. J. Pearton, J. Appl. Phys. 101, 083303 (2007)

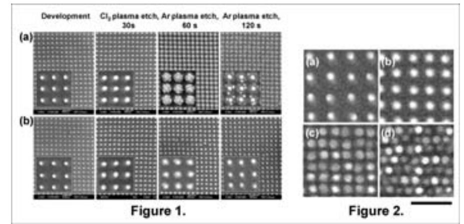

Fig. 1. SEM images of the dot array pattern with a 50 nm pitch as sequential process steps of resist development, Cl_2 plasma etch, and Ar plasma etch. Chamber pressure during Ar plasma etching is (a) 100 mTorr and (b) 10 mTorr. Fig. 2. SEM images of the fabricated Co/Pd nano-dot array with pitches of (a) 50 nm, (b) 40 nm, (c) 30 nm, and (d) 25 nm. Scale bar is 100 nm.

DA-06

SUB 100 nm FePt NANODOT ARRAYS FOR ULTRAHIGH-DENSITY MAGNETIC RECORDING.

H. Ko[1], P. Alagarsamy[1], K. Lee[1], S. Shin[1], J. Jung[2], H. Jung[2]
1. Physics, KAIST, Daejeon, South Korea; 2. Chemical and Biomolecular Engineering, KAIST, Daejeon, South Korea

Introduction

Numerous studies have been carried out to search suitable materials for perpendicular magnetic recording (PMR). FePt thin film has been found to be one of the promising candidates of PMR media because of their excellent magnetic properties [1]. However, there are many limitations to obtain high areal density with continuous recording media [2]. The other type of magnetic recording to obtain extremely high density beyond Terabits / in2 is patterned media. To achieve such ultra-high areal density, it is very much important to fabricate magnetic nanodot structure with dot size of few tens of nm. Recently, the use of scanning beam lithography method (conventional E-beam technique) helped to realize the regular pattern shape [3]. However, from the application point of view, one has to consider the simple and convenient method to fabricate the patterned nanostructure because high production cost and enormous preparation time are destructive features for the mass-production with large pattern area. So far, by bottom-up approach, there have been no detailed results to show regular dot shape and dot distance. Therefore, it is highly demanded both to develop new patterning technique and to get optimum magnetic properties from nanodot arrays with dot size of few tens of nm. In this work, we have successfully fabricated the patterned FePt nanodots with a regular dot size down to 80 nm using CFL (Capillary Force Lithography) imprint technique and studied the variation of magnetization state with changing the degree of ordering of the FePt nanodot arrays.

Experiment

FePt films were prepared on MgO(100) substrates using dc magnetron sputtering of FePt targets with a base pressure of better than 5*10-7 Torr. The film thickness was changed from 10 to 50 nm. Large area magnetic pattern was produced starting from the features of various dimensions made by CFL. The Si mold has a square shape with the size of 2.5 mm2. Each dot has a cylindrical shape with diameter (100 nm) and inter-dot distance (150 or 300 nm). After patterning nanodot arrays, all the samples were post-annealed at substrate temperature up to 600 oC. The crystal structure of the nanodots was characterized using X-ray diffractometry (XRD). The position and shape of the nanodots were confirmed with Atomic Force Microscope (AFM). Room temperature magnetic measurement was carried out using Superconducting Quantum Interference Device (SQUID). The magnetic domain patterns were observed using a Digital Instrument 3000 Magnetic Force Microscope (MFM).

Results and Discussion

Fig.1 shows the surface image of the patterned structures observed by AFM. A small variation of dot size comes from the different etching time. With more etching time, the dot size reduces. With as-made dot arrays, post-annealing has been carried out to obtain L10 ordered structure with a large magnetocrystalline anisotropy. Fig. 2 shows (a) the XRD patterns and (b) M-H loop of FePt nanodots annealed at various temperatures and 600 oC, respectively. The obtained results confirm the highly ordered L10 phase and the proper magnetic hysteresis loop for magnetic recording. Fig.3 shows the domain structures of low and high anisotropy dots. We could obtain the completely single domain structure in the higher anisotropy dot, which is in good agreement with our simulation results. Such a single domain structure makes it possible to realize more accurate writing and reading of recording bits. In addition, we have confirmed the presence of strong magnetic stray field around dots using electron holography method. However, it is found to be less than switching field of FePt nanodots. The coercivity change and switching field distribution of M-H hysteresis loops does not have any influence due to the magnetostatic interaction between neighboring dots, indicating that each dot works independently without any interference from the other dots.

This research work was supported by Korea Science and Engineering Foundation through the Basic Research Program.

References

1. H. S. Ko, A. Perumal, and S.-C. Shin, Appl. Phys. lett. 82, 2311(2003).

2. C. A. Ross, Annu. Rev. Mater. Res. 31:203-35 (2001).

3. C. Moutafis, et al. Phys. Rev. B 76, 104426 (2007).

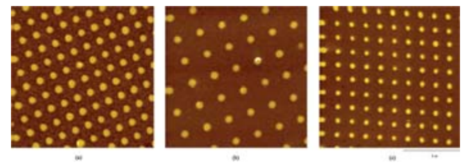

Fig. 1 AFM images of FePt nanodot arrays with dot size and interdot distance (a) 110 and 140 nm, (b) 110 and 290 nm, and (c) 80 and 170 nm

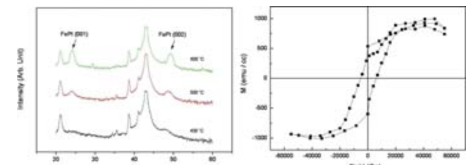

Fig. 2 (a) XRD patterns of FePt dot arrays with different annealing temperature and (b) M-H loop of FePt dot array annealed at 600 °C

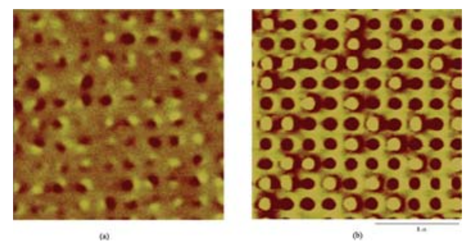

Fig 3. MFM images of FePt nanodot arrays annealed at (a) 400 °C and (b) 600 °C

DA-07

Dot size dependence of magnetization reversal process in $L1_0$ FePt dot arrays.

D. Wang[1], T. Seki[1], *K. Takanashi*[1], T. Shima[2]
1. Institute for Materials Research, Tohoku University, Sendai, Japan; 2. Faculty of Engineering, Tohoku-gakuin University, Tagajyo, Japan

The demand for ultrahigh density magnetic storage devices drives the bit size into a nanometer scale. One of the crucial issues for nanostructured magnetic materials is the thermal instability of magnetization due to the reduction of the magnetic volume. $L1_0$ ordered FePt alloy is one of the most promising materials for future ultrahigh density magnetic storage devices because the huge uniaxial magnetocrystalline anisotropy (K_u= 7×10^7erg/cc)[1] leads to excellent thermal stability of magnetization. For the application of FePt to storage devices, it is very important to understand the magnetization reversal process of nanostructured FePt, including the effect of the dimensions.
In previous papers, it was reported that nucleation-type magnetization reversal processes were observed in self-assembled FePt particulate films[2] and lithographically patterned FePt dot arrays[3]. In addition, the coercivity (H_c) depended strongly on the film morphology and the dot size. In order to understand the magnetization reversal process of nanostructured FePt, however, it is necessary to consider the effect of structural inhomogeneity on the magnetization reversal process. A phenomenological analysis, proposed by Kronmüller and his collaborators[4,5], described the magnetization reversal process of sintered permanent magnets such as Nd-Fe-B and Sm-Co from the viewpoint of the inhomogeneity of microstructure, and has been applied to a wide range of magnets to date. Such phenomenological analysis makes it possible to evaluate the defect region for magnetization reversal in nanostructured FePt and to classify it as the nucleation-type or the pinning-type reversal mode.
In this paper, the phenomenological analysis has been applied to the FePt dot arrays with different dot sizes fabricated by lithography technique. Their magnetization reversal processes are discussed in terms of structural inhomogeneity, and compared with that for self-assembled FePt particulate films. Furthermore, the micromagnetic simulation has been performed, and compared with the phenomenological analysis.
FePt films were prepared on a MgO (001) single crystal substrate using a UHV compatible magnetron sputtering system. A 1 nm-thick Fe seed layer and a 40 nm-thick Au buffer layer were first deposited at room temperature. A 50 nm-thick FePt (001) layer was epitaxially grown at 300 °C, and subsequently annealed at 500 °C for 15 minutes. FePt dots with a circular shape were fabricated through the use of electron beam lithography and Ar ion etching. The dot size (i.e., dot diameter, abbreviated as *d*, hereafter) was varied in the range from 250 nm to 5000 nm. The distance between two adjacent dots was designed to be the same as *d*. Post-annealing was performed at 500 °C for 15 min. Structural characterization was performed using x-ray diffraction (XRD) with Cu-Kα radiation. The magnetization curves of FePt dots were measured by a superconducting quantum interference device (SQUID) magnetometer.
The XRD measurement for a FePt continuous film indicates the formation of $L1_0$ ordered structure and the epitaxial growth with the (001) preferential crystallographic orientation normal to the film plane. The magnetization curves show that the easy axis of the film is perpendicular to the film plane. H_c is a small value of 0.8 kOe, in spite of a large K_u of 2.8×10^7 erg/cc. After patterning, however, H_c is enhanced up to 7.5 kOe for the dots with *d*=250 nm. Post-annealing after pattering leads to the further increase of H_c up to 10 kOe. The phenomenological analysis of magnetization curves gives the sizes of defect regions for *d*=250 nm to be 26 nm and 18 nm before and after annealing, respectively, suggesting that post-annealing promotes the recovery from the structural defects caused by Ar ion etching. Furthermore, this indicates that the structural defects play a key role for the value of H_c and H_c increases with decreasing the defect region. Micromagnetic simulations also show the reduction of H_c is caused by structural defects with a low degree of chemical order in a dot, which is consistent with the phenomenological analysis.
The defect regions of dots with different *d* have also been evaluated. H_c gradually increases with decreasing *d*, and the defect region also tends to decrease with decreasing *d*. Furthermore, the phenomenological analysis indicates that for *d*=250 nm and 1000 nm the magnetization reversal occurs through the nucleation of reversed domains. The minor loops starting from the demagnetized state show that the magnetic field required for the saturation of H_c is much smaller than H_c, which is characteristic of nucleation-type magnetization reversal. With increasing *d* to 5000 nm, in contrast, no characteristic behavior of nucleation-type magnetization reversal is seen, suggesting that magnetostatic energy and/or domain wall pinning are dominant factors.
All the dot arrays prepared show small effective demagnetizing factors compared with those for sintered permanent magnets. These small effective demagnetizing factors may result from with the high crystallinity of epitaxial films and/or the small dipolar interaction between dots with the well-defined geometry prepared by lithography technique.

[1] O. A. Ovanov *et al.*, Phys. Met. Metallogr., **35**, 81 (1973).

[2] T. Shima *et al.*, J. Appl. Phys., **99**, 033516 (2006).

[3] T. Seki *et al.*, J. Appl. Phys., **100**, 043915 (2006).

[4] H. Kronmüller, J. Magn. Magn. Mater., **7**, 341 (1978).

[5] H. Kronmüller *et al.*, **74**, 291 (1988).

DA-08

Separating dipolar broadening from the intrinsic switching field distribution in perpendicular bit patterned media.

O. Hellwig[1], A. Moser[1], A. Berger[1,2], T. Thomson[1,3], E. Dobisz[1], Z. Z. Bandic[1], H. Yang[1], D. Kercher[1], E. E. Fullerton[1,4]
1. San Jose Research Center, Hitachi Global Storage Technologies, San Jose, CA; 2. CIC Nanogune, Donastia, Spain; 3. University of Manchester, Manchester, United Kingdom; 4. Center for Magnetic Recording Research, University of California at San Diego, La Jolla, CA

A critical requirement for future bit patterned media (BPM) applications is the control and reduction of the magnetic switching field distribution (SFD) for reliably addressing single magnetic islands (bits) in the write process. Here, we use the DH(M,DM) method [1-3] to separate dipolar interactions due to neighbor islands from the intrinsic SFD by measuring a series of partial reversal curves of perpendicular anisotropy Co/Pd based multilayer films deposited onto pre-patterned Si substrates. For a 100-nm-period island array the dipolar broadening contributes 22% to the observed SFD. For a 45-nm-period array (318 Gbit/in2) this value increases to 31%. Corresponding experimental data from BPM fabricated by deposition of magnetic ML on pre-patterned substrates are shown in Fig.1. In Fig. 1a we show the full Micro-Kerr remanent reversal curve together with an MFM image after demagnetization. Figure 1c shows partial reversal curves obtained by setting initially 64%, 38%, and 22% of the islands into the positive magnetized state. In this magnetization plot we compare at any fixed horizontal level the reversal of different portions of islands in the same average dipolar environment i.e., the same average magnetization. The observed horizontal field displacements of the partial reversal curves with respect to the full reversal curve reflect the intrinsic SFD of the islands. If the intrinsic SFD were a delta function and the reversal were only broadened by dipolar interactions, then the partial reversal curves in Fig. 1c would show no horizontal displacement from the full reversal curve. In Fig. 1d we plot the same partial reversal curves after subtracting the initial magnetization values, such that the initial Kerr amplitudes match. Here we compare the reversal of the same islands in different dipolar environments. In the absence of dipolar interactions the partial reversal curves should follow the major reversal curve until saturation is reached. The observed horizontal displacements in reversal field for the different curves thus provide a direct measure of the dipolar interaction strength. While the plots in Fig. 1c and d provide a straightforward visualization of the intrinsic SFD and the dipolar interactions, a more quantitative determination is obtained by using the DH(M,DM) method [1-3]. Corresponding results are presented in Fig. 1b, where we compare the total SFD as obtained from Fig. 1a with the intrinsic SFD as extracted via the DH(M,DM) method from the partial reversal curves in Fig. 1c and d.
Our results highlight the importance of quantifying long-range dipolar interactions for determining the intrinsic SFD of patterned media [4,5]. In order to tighten the SFD in BPM it is necessary to address both the intrinsic SFD as well as the dipolar contribution. The intrinsic SFD can be tightened by optimizing pattern and media uniformity, but may also be influenced by tuning the reversal mechanism of the islands via more advanced media structures, such as for example exchange spring media. Dipolar broadening can be reduced by decreasing the magnetic moment of the media itself. However, there are limits to this approach, as it is the field from an island that generates the response in the read sensor and thus more sensitive read heads would be required as well.

[1] I. Tagawa and Y. Nakamura, IEEE Trans. Magn. 27, 45 (1991).

[2] A. Berger, Y. Xu, B. Lengsfield, Y. Ikeda, and E. E. Fullerton, IEEE Trans. Magn. 41, 3178 (2005).

[3] A. Berger, B. Lengsfield, and Y. Ikeda, J. Appl. Phys. 99, 08E705 (2006).

[4] O. Hellwig, A. Berger, T. Thomson, E. Dobisz, H. Yang, Z. Bandic, D. Kercher and E. E. Fullerton, Appl. Phys. Lett. 90 (2007) 162516.

[5] A. Moser, O. Hellwig, D. Kercher, and E. Dobisz, Appl. Phys. Lett. 91 (2007) 162502.

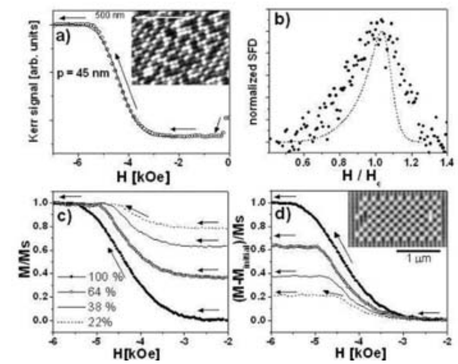

Figure 1: (a) Remanent island reversal curve for 30 nm islands on 45 nm pitch (318 Gbit/in2). The inset shows an MFM image of the corresponding pattern after demagnetization. (b) Total SFD as obtained from the reversal curve in (a) (solid dots) and corresponding intrinsic SFD as determined from the minor remanent reversal curves in (c) and (d) using the DH(M,DM) method [Berger papers] (dashed line). (c) and (d) show a set of partial remanent reversal curves for switching 64%, 38% and 22% of the islands and matching curves at the saturation level (c) and onset of the reversal (d) respectively. The inset of (d) shows a nearly perfect checkerboard pattern written and imaged via static read/write tester [4,5].

DA-09

Low Temperature Remanence Loop Measurements of Ion-Milled Patterned Media.

B. D. Belle[1], F. Schedin[1], T. V. Ashworth[2], E. W. Hill[1], P. W. Nutter[1], H. J. Hug[3], J. J. Miles[1]
1. School of Computer Science, The University of Manchester, Manchester, United Kingdom; 2. Institute fuer Physik, Universitaet Basel, Basel, Switzerland; 3. EMPA, Dübendorf, Switzerland

Introduction

One method which has been proposed in an attempt to delay the onset of the superparamagnetic limit in magnetic recording is the patterning of thin films into discrete islands each storing one bit [1]. Several fabrication techniques have been explored including Ar+ ion milling with a hard mask, which typically results in good pattern transfer with near vertical sidewalls [2]. However, as the island size is reduced, the effects of edge damage and ion implantation become more significant leading to a reduction in magnetic anisotropy and coercivity [3].

In this paper we show the effect of Ar ion milling on the coercivity of Co/Pt multilayer islands at low temperature. Here we present remanence loops measured at two discrete temperatures (9.3K and 21.5K). Studies at room temperature will follow to give a more complete temperature analysis.

Sample Fabrication and Measurements

A Co/Pt multilayer thin film, 100ÅPt + 15x (4ÅCo/10ÅPt), was deposited on a Si substrate using e-beam evaporation at 200C. A 7nm C overcoat (to act as a hard mask for milling) was then deposited by e-beam evaporation on the surface of the multilayer. Direct electron beam lithography (LEO 1530 Gemini FEG SEM and Raith Elphy Plus Lithography System with Laser Interferometer Stage) was then used to expose nanostructures in the resist. 15nm of Ti with a 5nm Au cap layer (required for SEM imaging) was deposited by e-beam evaporation. After lift-off, O2 plasma etch was used to transfer the Ti pattern into the underlying C layer. The combination of the Ti and C islands then acted as a hard mask for Ar ion milling (2keV, 18mA) which transferred the pattern into the magnetic layer.

Low temperature MFM experiments were then undertaken on several arrays of islands on square lattices with periods ranging from 200nm to 50nm using a custom built low temperature scanning force microscope at 9.3K [4]. The microscope is located within a superconducting magnet capable of producing fields of up to 7T perpendicular to the sample's surface. The sample was firstly saturated to -1.2T after which the field was reduced to zero. An MFM image was then taken at 0T using a Team Nanotec GmbH silicon cantilever with a 4nm Co coated oxidized tip. The field was then positively increased in small increments with MFM images taken at remanence after each field step. Remanence curves were later obtained by counting the number of dots which had reversed between successive scans. These experiments were then repeated on a subset of the arrays of islands (50nm to 100nm period) at 21.5K to observe the effect of temperature.

Results and Further Work

Figure 1a shows a typical MFM image for 60nm period islands. The islands are distinct with clearly discernable up and down states, which are readily countable, facilitating calculation of the SFD and remanence curves. The resulting remanence curves are shown in Figure 1b for the 50-100nm periods. Above 100nm coercivity is approximately constant with a slight peak around 150nm period. Below 100nm island period the coercivity falls steadily from ~5.5kOe to ~1.2kOe at 50nm island period. Although a more detailed study is required, this coercivity reduction indicates that milling does damage edges and that fabrication of smaller islands by this method will be challenging. However, the coercivity of the smaller islands is significantly higher than that achieved in our earlier work using Gold as a hard mask for ion-milling [3], showing that thin Carbon layers can be used successfully as a hard mask for ion-milling and that significant improvements in performance may be achieved by process optimisation. The temperature effect upon coercivity is clearly seen with the coercivity reducing when the temperature rises from 9.6K to 21.9K, the reduction being larger at higher coercivities as would be expected. Further measurements will be taken at room temperature to determine remanent coercivity across a wider range of temperatures. Analysis of size distributions will be presented and correlations between island size and switching field will be sought.

[1] A. Moser, K. Takano, D.T. Margulies, M. Albrecht, Y. Sonobe, Y. Ikeda, S.Sun, and E. E. Fullerton, J. Phys. D 35, R199 (2005)

[2] Y. Kamata, A. Kikitsu, H. Hieda, M. Sakurai, and K. Naito, J. Appl. Phys. 95, 6705 (2004)

[3] B.D. Belle, F. Schedin, N. Pilet, T.V. Ashworth, E.W. Hill, P.W. Nutter, H.J. Hug, and J.J. Miles, J. Appl. Phys. 101, 09F517 (2007)

[4] H.J. Hug, B. Stiefel, P.J.A. van Schedel, A. Moser, S. Martin, and H.J. Guntherodt, Rev. Sci. Instrum. 79, 3625 (1999)

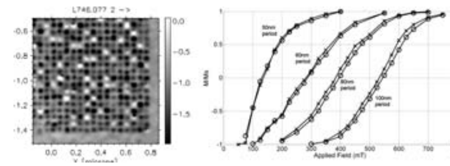

Figure 1a (left): MFM image of 60nm period islands during remanence curve measurement. Figure 1b(right): Remanence curves for islands with 50, 60, 80 and 100nm periods. Circles (O) denote measurements at 9.6K, crosses (X) denote measurements at 21.9K

DA-10

Magnetic properties of exchange-coupled composite nanoparticles and nanopatterns.

D. Goll, A. Breitling, S. Macke
Max-Planck-Institute for Metals Research, Stuttgart, Germany

Perpendicular magnetic recording on the basis of exchange coupled composite (ECC) media is currently considered to be the most straightforward method to realize ultrahigh recording densities of 1 Tbit/in^2 and more. ECC media are nanopatterns of magnetically isolated grains each consisting of a hard magnetic and a soft magnetic layer which are coupled by exchange interaction. The phase boundary between the two materials can be sharp or gradual. The composite system combines both high thermal stability of the stored information even for reduced grain dimensions close to the superparamagnetic limit and moderate switching fields which can be afforded by conventional write heads. Here, the first aspect is guaranteed by the magnetically hard component and the second aspect by the magnetically soft component. We have investigated the switching behavior and thermal reversal of composite particles and prepared different FePt/Fe composites.

The switching behavior of a composite particle is shown to be determined by the nucleation field of the soft component and the depinning field of a Neel wall at the phase boundary. Depending on the thicknesses of the layers the reversal process either takes place in two steps by nucleation and a following depinning of a Neel wall (Fig. 1), or in one unique step by an inhomogeneous rotation process. On the basis of micromagnetism analytical and numerical results for critical fields are determined as a function of the thickness of the layers (Fig. 2). Using the nudged elastic band method the minimum energy paths between equilibrium magnetization configurations of the hysteresis loop are calculated. From the minimum energy paths the minimum thermal activation energies for thermal reversal are determined as a function of the applied magnetic field and of the film thickness which is illustrated in Fig. 3 for a FePt/Fe ECC particle.

Composite FePt/Fe bilayers have been prepared by ion beam sputter deposition on MgO(100) substrates. Using electron beam lithography the bilayers have been nanopatterned into arrays of squared nanodots covering 3 mm x 3 mm. Fig. 4 shows for composite FePt/Fe elements the systematic decrease of the coercivity with increasing thickness of the soft magnetic Fe layer. The thickness of the hard magnetic FePt layer has been kept constant. The magnetic properties of the nanostructures are discussed within the framework of analytical and computational micromagnetism. The dependencies of switching fields, switching times and thermal stability of the composite nanoparticles on material parameters, shape, film thicknesses and character of the phase boundary are systematically analyzed. The results allow explicit predictions for the development of optimum high-density recording devices based on ECC media.

[1] D. Goll, S. Macke, H.N. Bertram, APL 90 (2007) 172506. [2] D. Goll et al., J. Iron and Steel Research International, Vol. 13, Suppl. 1 (2006) 97. [3] D. Goll, H. Kronmüller, Physica B (2008), doi: 10.1016/j.physb.2007.10.336.

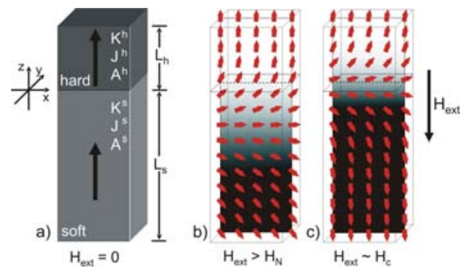

Fig.1: Spin distributions in a FePt/Fe composite particle at different fields (a) at zero field, (b) after nucleation in the soft magnetic layer and (c) before depinning of the Neel wall.

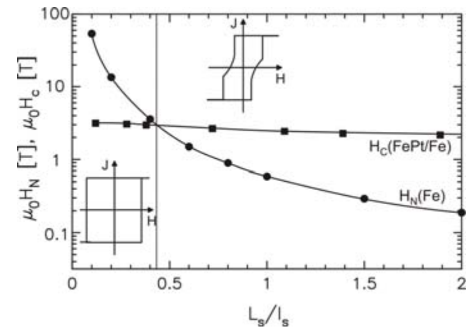

Fig. 2: Thickness dependence of the nucleation field in the soft magnetic part and the depinning field of a FePt/Fe ECC particle. The crossing point separates the one-step and the two-step hysteresis loop.

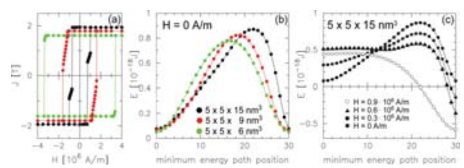

Fig. 3: (a) Hysteresis loops of a 5x5x15 nm^3 (black), 5x5x9 nm^3 (red) and a 5x5x6 nm^3 (green) FePt/Fe ECC particle. The FePt layer thickness is constant and amounts to 4.5 nm. (b) Minimum energy paths at zero field for the three particles in Fig. 3a. (c) Minimum energy paths for the 5x5x15 nm^3 particle as a function of the applied magnetic field.

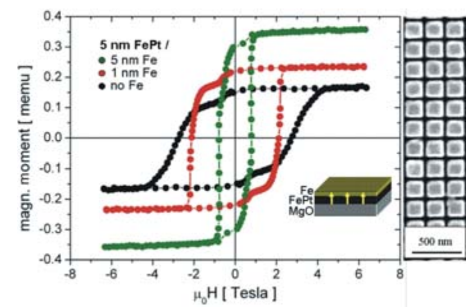

Fig. 4: Measured hysteresis loops of FePt/Fe composite elements produced by sputtering and lithography with different Fe layer thicknesses. The layer thickness of FePt is always 5 nm.

DA-11

Study of gas cluster ion beam planarization for discrete track magnetic disks.

K. Nagato[1,2], H. Tani[3], Y. Sakane[4], N. Toyoda[5], I. Yamada[5], M. Nakao[1], T. Hamaguchi[1]
1. The University of Tokyo, Bunkyo-ku, Japan; 2. Japan Society for the Promotion of Science, Chiyoda-ku, Japan; 3. Hitachi Global Storage Technologies Japan Ltd., Odawara-shi, Japan; 4. Western Digital Media Operations, San Jose, CA; 5. University of Hyogo, Himeji-shi, Japan

Magnetic disk recording is considered to be the most useful storage system in recent days. Discrete track media and patterned bit media are excellent candidates for achieving high density recording such as 1 Tbyte/in2 (1)-(5). Because the grooved surface of discrete track media makes head-slider flying instability, the media needs flat surface. To date, a flattening process that SiO2 is fulfilled into the grooves and extra materials were etched by ion milling has been reported (1). Recently, a gas cluster ion beam (GCIB) process has been proposed and investigated as a novel smoothing technique (6)(7). Gas cluster ions are aggregations of a few or several thousand atoms or molecules. These cluster ions have extremely low energy and show a unique characteristic of lateral sputtering. Thus, GCIB is expected to perform the planarization of discrete tracks in a dry condition. We studied GCIB planarization effect on discrete track carbon surfaces using test samples with fine grooves fabricated by focused ion beam (FIB). Figure 1 shows a schematic diagram of the GCIB apparatus. Ar gas clusters are generated through a skimmer and a nozzle from high pressure Ar gas source, then, ionized and accelerated. In this study, the cluster was formed from about 3000 atoms at maximum in the distribution. Acceleration energy for a cluster is 20 keV. The dose was set 5×10^11 ion/mm2. At first, we fabricated test samples with variant track pitch by FIB (Hitachi, FB-2000A). The discrete tracks were fabricated on magnetic record media disks with 30-nm-thick carbon overcoat. The track pitches were 100/150/200/300 nm, and the heights of peak-to-valley (P-V) were 15-20 nm. The surface roughness was measured by atomic force microscopy (AFM). At second, the test samples were irradiated by GCIB and the resultant surface roughness were measured by AFM. We compared the roughness before and after GCIB irradiation. Figure 2(a) shows the AFM comparison of the surface roughness of the test sample with the track pitch of 100 nm. The AFM measurements were carried out on the same areas. The discrete tracks with approximately 20 nm P-V were formed by FIB, and the tracks were clearly disappeared by GCIB. The surface after GCIB has peaks and valleys which are different from the initial surface. The decrease of Ra from 4.62 nm to 0.85 nm indicates that the tracks were smoothed by GCIB. The comparison of the power spectrum of the surface roughness (Fig. 2(b)) shows that the low harmonic cycles with 100 nm of the sample after FIB were high, but the sample after GCIB has no dependence on wavelength of 100 nm. We resulted that GCIB irradiation is effective for the planarization of discrete track disks.

[1] K. Hattori, K. Ito, Y. Soeno, M. Takai, and M. Matsuzaki, “Fabrication of Discrete Track Perpendicular Media for High Recording Density”, IEEE Trans. on Mag., vol. 40, no. 4, Jul. 2004, pp.2510-2515.

[2] Y. Soeno, M. Moriya, K. Ito, K. Hattori, A. Kaizu, T. Aoyama, M. Matsuzaki, and H. Sakai, “Feasibility of Discrete Track Perpendicular Media for High Track Density Recording”, IEEE Trans. on Mag., vol. 39, no. 4, Jul. 2003, pp.1967-1971.

[3] D. Wachenschwanz, W. Jiang, E. Roddick, A. Homola, P. Dorsey, B. Harper, D. Treves, and C. Bajorek, “Design of a Manufacturable Discrete Track Recording Medium”, IEEE Trans. on Mag., vol. 41, no. 2, Feb. 2005, pp.670-675.

[4] X. Che, Y. Tang, H. Jai Lee, S. Zhang, K. S. Moon, N. Y. Kim, S. Y. Hong, N. Takahashi, M. T. Moneck, and J. G. Zhu, “Recording Performance Study of PMR Media With Patterned Tracks”, IEEE Trans. on Mag., vol. 43, no. 6, Jun. 2007, pp.2292-2294.

[5] M. T. Moneck, J. G. Zhu, X. Che, Y. Tang, H. J. Lee, S. Zhang, K. S. Moon, and N. Takahashi, “Fabrication of Flyable Perpendicular Discrete Track Media”, vol. 43, no. 6, Jun. 2007, pp.2127-2129.

[6] I. Yamada, J. Matsuo, N. Toyoda, and A. Kirkpatrick, “Materials processing by gas cluster ion beams”, Mater. Sci. Eng. R 34 (2001) 231-295.

[7] S. Kakuta, S. Sasaki, T. Hirano, K. Ueda, T. Seki, S. Ninomiya, M. Hada, and J. Matsuo, “Low damage smoothing of magnetic material films using a gas cluster ion beam”, Nucl. Instr. Meth. B 257 (2007) 677-682.

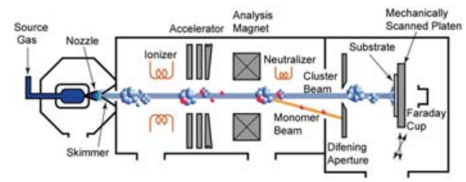

Fig. 1. Schematic diagram of GCIB apparatus.

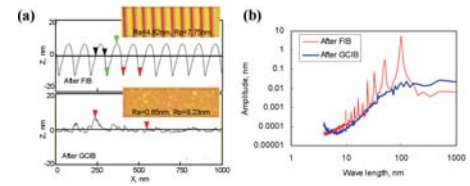

Fig. 2. (a) Comparison of surface roughness after FIB / GCIB, (b) Power spectra of surface profiles.

DB-01

Dynamic edge mode modeling and edge property measurements in magnetic nanostructures.

R. D. McMichael[1,3], B. B. Maranville[2,3], D. W. Abraham[4], C. A. Ross[5], V. P. Chuang[5]
1. Center for Nanoscale Science and Technology, NIST, Gaithersburg, MD; 2. Center for Neutron Research, NIST, Gaithersburg, MD; 3. Metallurgy Divison, NIST, Gaithersburg, MD; 4. IBM Thomas J. Watson Research Center, Yorktown Heights, NY; 5. Department of Materials Science and Engineering, Massachusetts Institute of Technology, Cambridge, MA

The material at the edges of a patterned magnetic thin film is different from the material away from the edges not only owing to the broken symmetry at the edge surface, but also because the patterning process exposes the edges to different conditions that may include high energy ion bombardment, different growth geometry and exposure to air. It seems likely, therefore, that the magnetic properties of the material at the film edge will be different from the magnetic properties in the interior of the structure.
In this talk, we will present recently developed measurement methods for the magnetic properties of the edges of thin films, describing the modeling that underpins the measurement method as well as example measurement results.
The primary method we have chosen for edge property measurements relies on detecting a "trapped spin wave" edge mode [1,2] in the magnetic resonance spectrum of a transversely magnetized, long, straight stripe. Figure 1 shows the modeled precession mode profiles in a stripe of Permalloy. The edge mode forms in the low-field region near the stripe edge with a precession frequency that is lower than the "bulk" modes. Because the edge modes are localized at the film edges, they can be used to monitor the properties of the edge material.
Modeled and measured edge mode frequencies have been found to closely follow a Kittel form:
$\omega = \gamma[(H_{appl} - H_{sat})(H_{appl} + H_2)]^{1/2}$.
The importance of this expression is that the two measurable parameters, H_{sat} and H_2, are properties of the film edge; H_{sat} is the field required to saturate the magnetization perpendicular to the stripe axis, and H_2 is an effective out-of-plane anisotropy for the edge mode.
The thickness dependence of H_{sat} for ideal edges is summarized by a simple approximate expression: $H_{sat} = 0.5M_s t/(t + d_e)$ where t is the film thickness an d_e is a characteristic distance that an edge mode extends into the interior of the film, approximately 27 nm for Permalloy. Surprisingly, the edge mode depth changes only by a factor of two as the film thickness spans three orders of magnitude [3]. Measurements of the thickness dependence of H_{sat} in real Permalloy stripes qualitatively follow the model predictions for ideal edges, except that the measured values are consistently lower, i.e. the real edges are easier to saturate than an ideal edge [4].
We have also modeled the effects of three types of edge defects on the magnetic edge properties [3]. Dilution of the magnetization near the edge, addition of a surface anisotropy term, and tilting of the edge each have the effect of reducing H_{sat}. At a microscopic level, each of these defects leads to a magnetostatic charge distribution that is less concentrated than the charges on an ideal edge.
The modeled effects of edge surface tilting have largely been confirmed by measurements on 20 nm-thick Permalloy stripes with edge surface angles that vary from 45° to 80° as the etch depth is varied [5]. Over this range, H_{sat} varies by nearly a factor of two. Here, as in the thickness dependence measurements, the measured values of H_{sat} are lower than the modeled values, suggesting that the edges have other non ideal characteristics beyond tilting of the edge surfaces alone.
Magnetic nanodevices of current interest often involve a multilayer stack, so we have recently begun modeling the behavior of interacting edge modes. For stripes of 10 nm Permalloy/ x spacer / 10 nm Co stacks, the dynamic modeling reveals two edge modes with two edge saturation fields that correspond to saturation of the Permalloy layer first, and the Co layer at higher fields. Both saturation fields are increased relative to their single-film values. While the saturation fields are clearly identifiable with one film or the other, above the saturation fields, the edge mode precession is not localized in one film or the other. The modes approximate an in-phase (acoustic) mode and an out-of-phase (optical) mode. At 20 nm spacer thickness the mode frequencies (and H_{sat} and H_2 values) are quite close to the single-film values, but the mode intensities show that there are still significant interactions.

[1] J. Jorzick, S. O. Demokritov, B. Hillebrands, M. Bailleul, C. Fermon, K. Y. Guslienko, A. N. Slavin, D. V. Berkov, and N. L. Gorn, Phys. Rev. Lett. 88, 047204 (2002).

[2] J. P. Park, P. Eames, D. M. Engebretson, J. Berezovsky, and P. A. Crowell, Phys. Rev. Lett. 89, 277201 (2002).

[3] R. D. McMichael and B. B. Maranville, Phys. Rev. B 74, 024424 (2006).

[4] R. D. McMichael, C. A. Ross and Vivian P. Chuang, J. Appl. Phys. In press.

[5] B. B. Maranville, R. D. McMichael, and D. W. Abraham, Appl. Phys. Lett. 90, 232504 (2007).

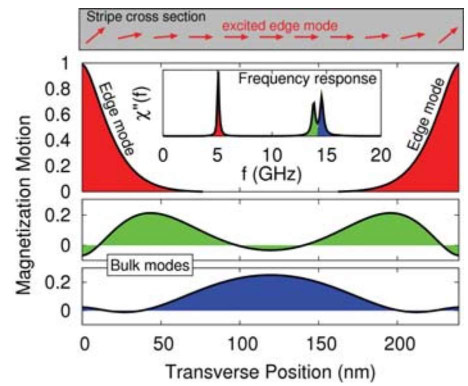

Fig1. Modeled precession mode profiles in a 250 nm-wide stripe of 25 nm-thick Permalloy. A 0.3 T field is applied perpendicular to the stripe axis.

DB-02

Spin injection driven magnetization dynamics: physical insights gained from numerical micromagnetics.

D. V. Berkov[1], J. Miltat[2]
1. Magnetic and Optical Systems, Innovent Technology Development, Jena, Germany; 2. Laboratoire de Physique des Solides, University Paris-Sud & CNRS, Orsay, France

If solely referring to magnetization distributions at equilibrium, it seems fair to state that the predictive power of numerical micromagnetics is now well established. In the dynamical regime, magnetization precession around the local and time dependent effective field provides a simple framework for picturing phase-coherent ballistic switching, both under the action of a pulsed field [1], or a pulsed spin-polarized current [2]. In some instances, mode analysis especially, a remarkable agreement has been obtained between cutting-edge experiments and micromagnetic simulations (see, e.g., [3-5]).
In this talk we present an overview of qualitatively important physical insights obtained from micromagnetic simulations of the spin-transfer induced magnetization dynamics. At present it is well established that spin transfer may lead to switching or sustained magnetiza-tion precession to be characterized by the power spectral density of one observable, usually the GMR or TMR response. First we focus on a specific nanopillar geometry that experimen-tally leads to remarkably narrow line widths and unique dispersion characteristics in GMR-type nanopillars [6-7], attempting to evaluate the relevance of numerical micromagnetics in forecasting the dynamic properties of these nano-magnetic Hopf oscillators. More precisely, the following issues will be addressed:
- Phase noise and line width,
- Dispersion in the micromagnetic regime and relevance to experimental data,
- Line width and power spectral density analysis.

In pillars, the main parameters entering the magnetization dynamics master equation may now be extracted from suitable experiments. It will nevertheless be shown that different work-ing hypotheses do lead to markedly different micromagnetic predictions, none of them yet really fitting experimental data and thus potentially raising fundamental physics issues [8].
In the second part of this talk we present a detailed discussion of the point contact experi-ments [9,10]. We show that in the point-contact geometry highly regular and strongly non-linear oscillation modes can be found immediately after the current exceeds the oscillation onset threshold and persist up to the highest current values for which microwave oscillations in a nanocontact persist [9,10]. Such a behaviour is in strong contrast to the nanopillar de-vices, where slightly above the threshold regular small-angle oscillations have been detected, and by increasing current quasi-chaotic magnetization dynamics can emerge.
Discussing the non-linear modes in point-contact devices [11], we show that only one of them - the so called 'bullet' - has a relatively homogeneous magnetization configuration of its core, thus enabling its analytical description [12]. For higher currents numerical simulations predict more complicated modes, where the core consist of one or more vortex-antivortex pairs which creation and annihilation governs the mode behaviour. We also show that the formation and mutual rotation of vortex and antivortex could be responsible for the low-frequency oscillations (frequencies ~ 200 MHz) observed in [10] for small external fields and point contacts with relatively large diameters (~ 80 nm).
We conclude this talk by emphasizing first, the importance of an exact knowledge of the Oersted field generated in each specific experimental setup and second, the absolute need for an accurate sample characterization.

[1] H. W. Schumacher et al., PRL, 90 (2003) 017201 and 017204
[2] T. Devolder et al., PRB, 75 (2007) 224430
[3] J. P. Park et al., PRL, 89 (2002) 277201
[4] V. Novosad et al., PRB, 72 (2005) 024455
[5] M. Buess et al., PRL, 94 (2005) 127205
[6] I. N. Krivorotov et al., Science, 307 (2005) 228
[7] I. N. Krivorotov et al., PRB, 76 (2007) 024418
[8] D. Berkov and J. Miltat, J. Magn. Magn. Mat. (2008), http://dx.doi.org/10.1016/j.jmmm.2007.12.023
[9] W.H. Rippard, et al., PRL, 92 (2004) 027201; PRB, 70 (2004) 100406(R)
[10] W.H. Rippard, et al., PRB, 75 (2007) 140404(R)
[11] D. Berkov and N.L. Gorn, PRB, 76 (2007) 144414
[12] A. Slavin and V. Tiberkevich, PRL, 95 (2005) 237201

DB-03

Hierarchical multi-scale model: application to FePt.

U. Nowak
Physics, University of York, York, United Kingdom

Well-established methods for the evaluation of magnetic material properties include spin density functional theory, spin models, and micromagnetics. Each of these methods covers only a certain range of time and length scales. In the present paper we introduce a multi-scale modelling approach, bridging the gaps between the three approaches above. The goal is to describe thermodynamic equilibrium and non-equilibrium properties of magnetic materials on length scales from the single atom reaching to micrometres, starting from first principles.

In the first step we model, as an example, bulk FePt in the ordered phase using an effective, classical spin Hamiltonian. This atomistic model [1] was constructed earlier on the basis of first-principles methods. The next step is to simulate this spin model using the stochastic Landau-Lifshitz-Gilbert (LLG) equation. Due to the atomic resolution, this approach covers only length-scales up to some nanometres. However, the thermodynamic equilibrium properties for the magnetisation, the parallel and perpendicular susceptibilities and the exchange stiffness [2] are then used to develop a micromagnetic approach [3,4], based on the Landau-Lifshitz-Bloch (LLB) equation [5]. With the latter approach, thermodynamic equilibrium and non-equilibrium properties of magnetic materials can be calculated for a temperature range from zero up to above the Curie temperature, enabling computer simulations of heat-assisted writing procedures.

As an example, the figure below shows the response of a 48nm x 48nm x 72nm FePt particle to a rapid heat pulse with varying peak temperature. The cell size for the simulation was 3nm. These curves successfully reproduce experimental results, including the times scales for the break down of the magnetisation and the recovery. Especially, even the slow recovery after complete demagnetisation [6] is reproduced.

[1] O. N. Mryasov, U. Nowak, K. Guslienko, and R. W. Chantrell, Europhys. Lett. 69, 805 (2005).

[2] D. Hinzke, N. Kazantseva, U. Nowak, O. N. Mrysaov, P. Asselin, and R. W. Chantrell, submitted to Phys. Rev. B.

[3] O. Chubykalo-Fesenko, U. Nowak, R. W. Chantrell, and D. A. Garanin,

Phys. Rev. B 74, 094436 (2006).

[4] U. Atxitia, O. Chubykalo-Fesenko, N. Kazantseva, D. Hinzke, U. Nowak, R. W. Chantrell, Appl. Phys. Lett., in press.

[5] D. A. Garanin, Phys. Rev B 55, 3050 (1997).

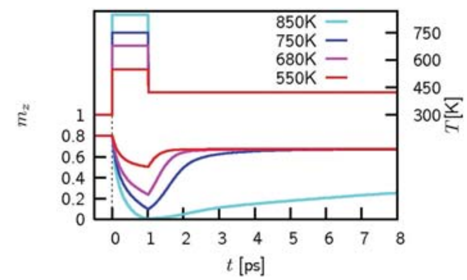

Magnetisation versus time following a 1ps heat pulse with different peak temperatures. The microscopic damping constant is assumed to be 0.1.

DB-04

Micromagnetics of Patterned Media Recording.

T. Schrefl, A. Goncharov, J. Dean, G. Hrkac, S. Bance
University of Sheffield, Sheffield, United Kingdom

Multiscale micromagnetic simulations are preformed for bit patterned magnetic recording. We solve the equation of motion for the magnetization in the head, the media, and the soft underlayer simultaneously. The input for the simulations are the detailed microstructure of the recording media, the geometry of the write head, the intrinsic magnetic properties and the current wave form of the write current. Macropscopic properties like current wave form or read back voltage are input/output of a multiscale simulation that treats the functional behavior of a recording system while taking into account the microscopic magnetization processes during recording and read back. A matrix compression technique is used for fast multiplication of matrices arising from the boundary element method, which is used to calculate the interaction fields between the write head and the storage media.

Recording on bit patterned media requires the synchronization of the write field with the predefined bit pattern. The write field rise time and the phase shift between the write field and the write current depend on fast magnetization reversal and fast changes of the domain configuration within the write head. Whereas the overall behavior is similar from write cycle to write cylce, the local magnetization configuration is not periodic. The domain configuration may change from one period to the next which causes rise time induced jitter. For a head velocity of 20 m/s the rise time jitter will translate into a position jitter of up to 1.5 nm.

Recording simulations on bit patterned media were performed using a standard single pole head with a trailing shield. The islands were of ellipsoidal shape with a length of 30 nm and a width of 7.5 nm. The center to center spacing was 8.98 nm. The island thickness was 3 nm, the air bearing surface (ABS) to media spacing was 3 nm and the ABS to soft underlayer (SUL) spacing was 8 nm. These dimensions lead to a recording density of 2 Tbit/in^2. For this head media combination we calculated the maximum write margins assuming a distribution of the magnetocrystalline anisotropy between the islands that is effectively zero. The simulations show that it is essential to including magnetostatic effects (interactions between the dots and head-media-head interactions). Using precomputed write fields for recording simulations reduces the write margins by 42 percent with respect to full micromagnetic simulations that take into account the mutual interactions between head and media.

To compute the write margins we were running the simulations several times with different initial positions of the head. The maximum possible write margin was found to depend on the write frequency. For writing at 1 bit per nanosecond the write margin was 3.5 nm and for writing at 2 bits per nanosecond the write margin was 1.75 nm. Moving the head out of phase a distance greater than the write margin leads to bit errors. Bit errors especially are found for bits where the stray field from the neighboring track is high. The non-uniform magnetization reversal of the dots and the magnetostatic interactions between the dots narrow the write margin. Most of the dots are multidomain for an extended time period before they reach their final magnetic state (up or down). A snap shot of the magnetization configuration during writing is shown in Figure 2. The switching field of an island can be reduced by about 20 percent appling a microwave assist field with an amplitude of 20 mT and a frequency of 14 GHz.

In order to estimate adjacent track erasure we calculated the energy barrier of bits in the neighboring track under the influence of the cross track head field and compare it with the energy barrier of an isolated single island. The calculated barriers are as follows in units of $k_B T$(T=300K): 52 for the isolated island, 37 for an island under the interaction field of neighboring islands, and 7.4 for an island under the interaction field of neighboring islands and the cross track head field. Without side shields adjacent track erasure might be a problem if the magnetostatic interaction field and the cross track head field add up.

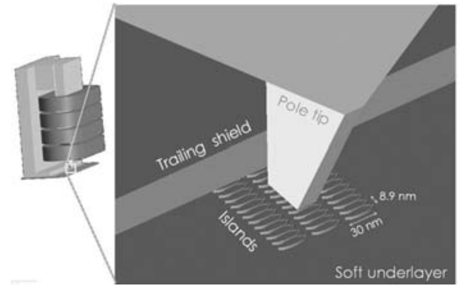

Figure 1: Multiscale simulation of bit patterned recording. The charcteristic length scale ranges form 10 micrometer (writer) to about 2 nanometer feature size in the data layer.

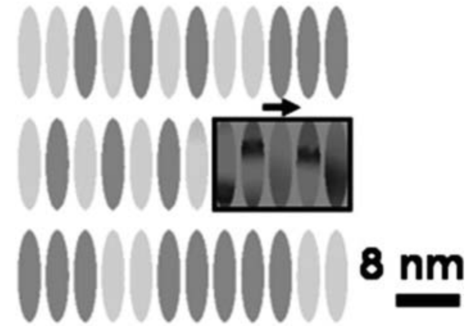

Figure 2: Magnetization reversal of the islands occurs by the nucleation of an reversed domain and successive domain wall motion. The shaded area denotes the position of the pole tip of head.

DB-05

MODELING THE MAGNETIC PROPERTIES OF NANOPARTICLES: FINITE-SIZE, SURFACE AND EXCHANGE BIAS EFFECTS.

O. Iglesias[1,2], X. Batlle[1,2], A. Labarta[1,2]
1. Dpt. Física Fonamental, Universitat de Barcelona, Barcelona, Spain; 2. Institut de Nanociència i Nanotecnologia de la UB (IN2UB), Barcelona, Spain

Magnetic nanomaterials present new magnetic and transport properties that arise due to a complex interplay between the intrinsic properties of the constituents (such as specifically tailored microstructure and finite size or surface effects) and the interactions among the entities forming them [1]. In particular, magnetic systems formed by nanosized particles have attracted increasing interest during the last decade because of their technological applications, ranging from magnetic recording to biomedicine. From the fundamental point of view, the computational approach to the modeling of the peculiar phenomenology of nanoparticle systems is an attractive challenge because, usually, it involves a wide range of time and length scales.
When reducing the size of magnetic particles to the nanoscale, surface and finite-size effects become fundamental in order to explain their unusual magnetic properties. As the size decreases, the magnetic properties of the particles depart from bulk behavior, resulting in reduced magnetization and different thermal dependence. In addition, the reduction in lattice symmetry caused by broken bonds at the particle surface, results in distinct local magnetic anisotropy and exchange interactions at the outer shells with respect to the core spins. Moreover, particle surfaces are exposed to environment and are, therefore, easily oxidized, resulting in compound structures with a ferromagnetic core surrounded by an antiferromagnetic. When cooling in the presence of a magnetic field the magnetic order established at the shell may result in a pinning of magnetic moments at the interface between the two phases giving rise to the so-called exchange bias (EB) effect.
In this contribution, we will review our recent work on the modeling of magnetic nanoparticles. We will focus on Monte Carlo (MC) simulation methods to study the phenomenology associated to finite-size and surface effects in models for a single nanoparticle [1], and to study the microscopic origin of EB effects in nanoparticles with core/shell structure [2,3].
Concerning the first point, we will present phase diagrams of the low temperature equilibrium configurations as a function of the surface anisotropy k_S for different particle diameters that have allowed us to identify a change in the magnetic ordering at high enough (but realistic) values of k_S. Through the simulated low temperature hysteresis loops, we have also identified a change in the magnetization reversal mechanism from quasi-uniform (induced by the core) rotation at low k_S values to a process in which the formation of surface hedgehog-like structures, like the ones displayed in Fig. 1, induce the non-uniform switching of the whole particle.
We will also report on results of MC simulations based on a model of individual core/shell nanoparticle with the aim to clarify the microscopic origin of the experimental phenomenology related to EB. The increase of the exchange coupling across the core/shell interface leads to an enhancement of exchange bias and to an increasing asymmetry between the two branches of the loops (as can be seen in the example shown in Fig. 2), which are due to different reversal mechanisms. A detailed study of the magnetic order of the interfacial spins shows compelling evidence that the existence of a net magnetization due to uncompensated spins at the shell interface is responsible for both phenomena and allows to quantify the loop shifts directly in terms of microscopic parameters with striking agreement with the macroscopic observed values.
Funding from the Spanish MEyC NAN2004-08805-CO4-02, CONSOLIDER CSD2006-12 and MAT2006-03999 projects, and Catalan DURSI (2005SGR00969) is acknowledged.

[1] X. Batlle et al., J. Phys. D 35, R15 (2002); A. Labarta et al. in Surface Effects in Magnetic Nanoparticles (edited by D. Fiorani, 2005).

[2] O. Iglesias et al., J. Nanosc. and Nanotech. (review article, in press) (2007) arXiv:cond-mat/0607716v2 ; J. Nogués, et al. Phys. Rep. 422, 65 (2005).

[3] O. Iglesias et al., Phys. Rev. B 72, 212401 (2005); Physica B 372, 247 (2006); J. Magn. Magn. Mater. 316, 140 (2007); J. Phys.: Condens. Matter. 19, 406232 (2007).

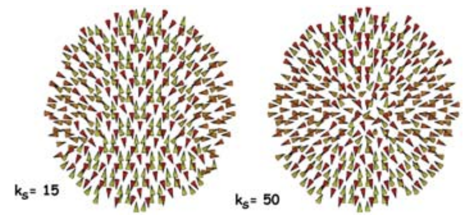

Magnetic configurations of maghemite particles with surface anisotropy k_S= 15, 50.

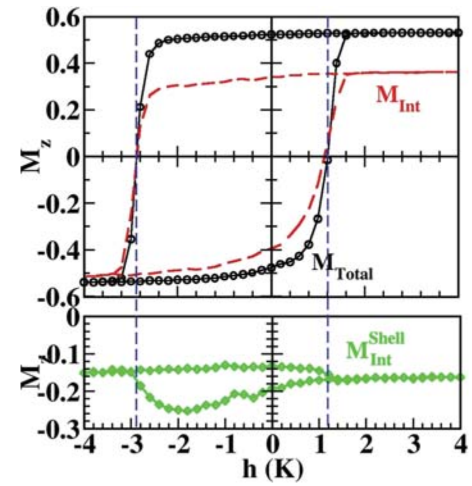

FC hysteresis loop of a core/shell nanoparticle (M_{Total}) displaying a shift in the applied field direction. Contribution of interfacial spins (M_{Int}) shown in dashed lines.

DB-06

Modeling the temperature dependent free energy barrier for magnetization reversal in nanomagnets.

T. C. Schulthess[1], C. Zhou[1], O. N. Mryasov[2], D. M. Nicholson[1], M. Eisenbach[1], P. R. Kent[1]
1. Oak Ridge National Laboratory, Oak Ridge, TN; 2. Seagate Research, Pittsburgh, PA

Over the past decade, magnetic nano-phased materials have been intensively investigated due to their great potential in many spintronics applications ranging from magnetic data storage to magnetic random access memory and other magnetoelectronic devices. These systems present unique challenges that often cannot be met with conventional simulation techniques. Due to the complex nature of atomic-scale interactions between both localized and induced moments that change drastically over short distances, the mechanisms governing nanostructure stability routinely differ between surface and interior, and are often dominated by entropic effects even at ambient temperatures. The magnetization dynamics close to the Curie point is governed both by transverse and longitudinal fluctuations, which requires accurate representation of the free energy as function of the magnetization. In this milieu, the physics can only be unraveled at the first principles level when combined with statistical methods to include entropy. Specifically, in nanomagnets such as FePt nanoparticles that are only a few nanometers in diameter and where the fraction of atoms within a lattice constant of the surface is large, complex non-collinear magnetic states and entropic effects will contribute significantly to the system's magnetic properties. Modeling the changes in the electronic structure and local magnetic properties requires ab initio electronic structure simulations. Such calculations can be done reliably within the zero temperature framework of the Local Spin Density Approximation (LSDA) to Density Functional Theory (DFT). However, due to the enhanced role of magnetic fluctuations in nanoparticles at finite temperature, the energy of an individual magnetic state is not as useful as in the study of bulk magnetic systems. Rather, it will be necessary to configurationally average over all states accessible at a given temperature using a stochastic sampling technique.

In this talk I will review a generalization [1] of the Wang-Landau method [2] with which we can efficiently compute the density of states and from it the temperature dependent free energy in nanoscale systems with a few thousand microscopic degrees of freedom. I will discuss its application to a first principles based model [3] of FePt nanoparticles to compute the temperature dependent free energy barrier for magnetization reversal in the particles. Results obtained from this new method compare well with simulations using traditional Metropolis method and extrapolate to the correct zero-temperature limit that can be calculated exactly from the model. Interestingly, even in these simple model calculations, where we simply truncate the exchange interactions at the surface, we see deviations from the expected Stoner-Wohfarth behavior in small particles, as incoherent reversal modes that originate from “looser” spins in the surface regions become important.

Furthermore, I will present results of DFT based ab initio calculations for FePt nanoparticles with up to ~1000 atoms. These calculations indicate that there are significant deviations in the local atomic moments compared to bulk values that are not captured in the simple model of the nanoparticles. Finally, I will discuss preliminary results of full-blown hybrid simulations in which the DFT calculations are encapsulated in the stochastic sampling to compute the first principles based free energy of the nanoparticles.

Acknowledgement: This research used resources of the National Center for Computational Sciences and the Center for Nanophase Materials Sciences, which are sponsored by the respective facilities divisions of the offices of Advanced Scientific Computing Research and Basic Energy Sciences of the U. S. Department of Energy (DOE). The work was supported in part by the Laboratory Directed Research and Development program at ORNL and the Scientific User Facilities Division of DOE.

[1] Wang-Landau algorithm for continuous models and joint density of states, C.-G. Zhou, T. C. Schulthess, S. Torbrugge, and D. P. Landau, Phys. Rev. Lett. 99, 08H906 (2006).

[2] Efficient, multiple-range random walk algorithm to calculate the density of states, F. G. Wang and D. P. Landau, Phys. Rev. Lett. 86, 2050-2053 (2001).

[3] Temperature-dependent magnetic properties of FePt: Effective spin Hamiltonian model, O. N. Mryasov, U. Nowak, K. Y. Guslienko, R. W. Chantrell, Europhys. Lett. 69, 805-811 (2005).

DC-01

Effective resistance mismatch and magnetoresistance of a CPP-GMR system with current-confined-paths.

J. Sato, K. Matsushita, H. Imamura
Advanced Industrial Science and Technology, Tsukuba, Japan

Current-perpendicular-to-plane giant magnetoresistance (CPP-GMR) has attracted much attention for its potential application as a read sensor for high-density magnetic recording [1, 2]. In order to realize a high-density magnetic recording, we need MR devices with high MR ratio and low resistance area product (RA). Although the RA value of a CPP-GMR system is much smaller than that of a tunneling magnetoresistance (TMR) system, the MR ratio of a conventional CPP-GMR system still remains a small value of a few %. Much effort has been devoted to increasing the MR ratio of the CPP-GMR system.
Recently, Fukuzawa et al. reported that they achieved the MR ratio of 10.2 % by CPP-GMR spin-valve with a current-confined-path (CCP) structure made of a nano-oxide-layer (NOL) with a lot of small metallic channels [3]. They showed that the MR ratio increases with increasing the RA value, which means that the MR ratio is enhanced for the system with narrow metallic channels. The similar enhancement of the MR ratio due to the CCP structure containing a domain wall was also reported by Fukue et al. [4]. The enhancement of the MR ratio due to the CCP structure is theoretically explained by one of the author [5]. However, the analysis of Ref. [5] is based on the assumption that the thickness of the non-magnetic layer is zero.
In 2000, Schmidt et al. pointed out that the conductivity mismatch is a basic obstacle for spin injection from a ferromagnetic metal into a semiconductor. Spin polarization of the injected current is strongly suppressed by the conductivity mismatch between these materials. Since the CPP-GMR system is made of thin films of different materials, we also have the conductivity mismatch in this system. However all the materials of the usual CPP-GMR systems are metals, the effect of the conductivity mismatch is not important. In Fig.1 (a) we plot the MR ratio of the ferromagnet (F) / non-magnet (N) / ferromagnet (F) trilayer system as a function of the ratio of the effective resistance. One can see that the MR ratio takes the maximum value when the effective resistances of ferromagnetic layer and non-magnetic layer are the same, i.e., the effective resistance are matched to each other.
However, for the CPP-GMR system with current confined paths, the effective resistance of the contact region increases with decreasing the width of the contact. Therefore, it is intriguing to ask how the mismatch of the effective resistance affects the MR ratio of the CPP-GMR system with current confined paths.
We numerically solve the spin diffusion equation [7] by use of finite element method in the contact geometry shown in Fig. 1(b) and calculate the MR ratio due to spin accumulation. A narrow non-magnetic metallic contact is sandwiched in between two ferromagnetic electrodes. CoFe and Cu are adopted as the ferromagnetic layers and non-magnetic metallic contact, respectively.
In Fig. 1(c), we plot the MR ratio of the CPP-GMR system with current-confined-paths against the radius of the narrowest cross section of the contact region. We use five values for resistivity of non-magnetic metallic contact, which corresponds to the variety of the purity of Cu in the NOL. Decreased resistivity of non-magnetic metallic contact means increased purity of Cu in the NOL. As is seen in Fig. 1(c), MR ratio increases with increasing the purity of Cu, which is consistent with the experimental results [3].
Moreover, one can see that the contact radius at which the MR ratio takes the maximum value decreases with decreasing the resistivity of non-magnetic metallic contact. This behavior can be understood as the concept of conductivity matching between ferromagnetic layer and non-magnetic metallic contact. In order to maximize the MR ratio of the system with the contact of low (high) resistivity, the contact should be narrow (wide) since the effective resistance is proportional to the resistivity over cross section.
As pointed out by Schmidt et al. [6] and Rashba [8], the large interfacial resistance can resolve the conductivity mismatch problem. Therefore, we are now studying the effect of the interfacial resistance on the MR ratio of the CPP-GMR system with a current confined path. We will present details of our analysis, effect of the interfacial resistance on the MR ratio and comparison with recent experimental results.

[1] W.P. Pratt et al, Phys. Rev. Lett. 66, 3060 (1991).

[2] A. C. Reilly et al., J. Magn. Magn. Mater. 195, L269 (1999).

[3] H. Fukuzawa et. al, Appl. Phys. Lett. 87, 082507 (2005).

[4] H.N. Fukue et. al, IEEE Trans. Magn. (2007).

[5] H. Imamura, Physica status solidi b 224, 4394 (2007).

[6] Schmidt et al., Phys. Rev. B 62, R4790 (2000).

[7] T. Valet and A. Fert, Phys. Rev. B 48, 7099 (1993).

[8] E.I. Rashba, Phys. Rev. B 62, R16267 (2000).

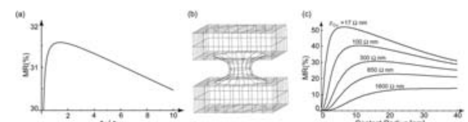

(a) MR ratio is plotted against the ratio of effective resistance for the spin polarization of conductivity in ferromagnetic layer is assumed to be 0.7. (b) Geometry of the 3D contact is schematically shown. In our numerical calculation, we assumed that ferromagnetic electrodes are cubes with side of length 45nm and the thickness of the contact is 2nm. (c) MR ratio is plotted against the radius of the narrowest cross section of the contact region. The resistivity of Cu in the contact is varied from 17Ωnm to 1600Ωnm.

DC-02

Current-perpendicular-to-plane magnetoresistances of CoFeB-based exchange-biased spin valves and CoFeB/Ru multilayers.

C. Ahn[1], K. Shin[1], W. Pratt Jr.[2]

1. Center for Spintronics Research, Korea Institute of Science and Technology, Seoul, South Korea; 2. Department of Physics and Astronomy, Michigan State University, East Lansing, MI

The magnetization direction of the magnetic layers can be reversed by spin-polarized currents [1,2], and this current-induced magnetization switching (CIMS) at reduced critical current density (J_c) has been studied in various magnetic tunnel junction (MTJ) structures. In particular, giant tunnel magnetoresistance (TMR) ratios together with CIMS have been expected theoretically and observed experimentally as well in the CoFeB/MgO/CoFeB MTJs. In a recent study, CIMS with synthetic ferrimagnetic (SyF) free layers of $Co_{40}Fe_{40}B_{20}$/Ru/$Co_{40}Fe_{40}B_{20}$ has been investigated, and J_c has been found to be reduced without losing thermal stability [3]. In order to elucidate the underlying physical mechanism for the use of antiferromagnetically coupled CoFeB/Ru/CoFeB trilayer systems as a free layer, knowledge of magneto-transport properties of both CoFeB and CoFeB/Ru interfaces is required. In this work, CoFeB-based exchange-biased spin valves (EBSVs) and CoFeB/Ru multilayers were fabricated to examine the spin diffusion length l_{sf} and the bulk spin-scattering asymmetry β of CoFeB and extract the interfacial specific resistance $2AR^*$ and spin-scattering asymmetry γ of CoFeB/Ru interfaces, respectively. The [FeMn(8)/CoFeB(t_F)/Cu(20)/CoFeB(t_F)] EBSVs (the numbers in the parentheses indicate the thickness of the layers in nanometers) were made by DC magnetron sputtering, and the MR measurement (at 4.2 K) has been done in the current-perpendicular-to-plane (CPP) geometry using a bridge circuit with a superconducting quantum interference device (SQUID) null detector. The hysteresis curve for the CPP specific resistance AR (area times resistance) of a $Co_{40}Fe_{40}B_{20}$-based EBSV with $t_{Co}40_{Fe}40_{B}20$ = 7 nm is shown in Fig. 1 (see the inset). We found almost ideal CPP-MR behavior for the EBSV samples with $t_{Co}40_{Fe}40_{B}20 \geq 5$ nm which show the well-separated pinned (solid arrows) and unpinned (dashed arrows) loops, giving well-defined parallel (P) and antiparallel (AP) states. For the samples with $t_{Co}40_{Fe}40_{B}20 < 5$ nm, the strong exchange-biasing effect exists and only the pinned loop is observed. We also tried the experiment with a $Co_{56}Fe_{24}B_{20}$, and the overall trend of AΔR (the difference in the specific resistance between the P and AP state) with various CoFeB thicknesses remains unchanged except that AΔR in $Co_{56}Fe_{24}B_{20}$ is smaller than one in $Co_{40}Fe_{40}B_{20}$ for the same CoFeB thickness partly due to the smaller saturation magnetization (M_s) of $Co_{56}Fe_{24}B_{20}$. AΔR versus t_{CoFeB} for a series of EBSVs is summarized in Fig. 1 (solid circles for $Co_{40}Fe_{40}B_{20}$ and open circles for $Co_{56}Fe_{24}B_{20}$, respectively). The data in Fig. 1 saturate in value beyond t_{CoFeB} ~ 15 nm and the saturation value of AΔR, AΔR(sat), is given by a Valet-Fert (VF) [4] extension to finite spin diffusion length as, $A\Delta R(sat) = 4(\beta_F \rho^*_F l^F_{sf} + \gamma_{F/N} AR^*_{F/N})^2/ (2\rho^*_F l^F_{sf} + \rho_N t_N + 2AR^*_{F/N})$, where β_F and l^F_{sf} are the spin-scattering anisotropy and the spin diffusion length of the ferromagnetic layer F, respectively, and the resistivity $\rho_F = \rho^*_F(1-\beta_F^2)$ can be measured independently by Van der Pauw (VdP) measurement. The saturation of AΔR requires a short spin diffusion length of the ferromagnetic layer, and makes the numerical VF fit indispensable. In this experiment with EBSVs, the important parameters to be extracted are the spin diffusion length l^F_{sf} and β. For both CoFeB concentrations, we thus ignored the interfacial resistance $2AR^*$ and spin-scattering asymmetry γ of CoFeB/Cu interfaces, and we have found that those parameters have negligibly small effect on the fitting results. It should be noted that VF theory with β = 0.26 ~ 0.3 and l^F_{sf} = 4.5 ~ 4.8 fits well to our experimental data. By comparing the obtained l^F_{sf} with that of $Co_{91}Fe_9$ [5], it is easily seen that the mean distance electrons diffuse between spin-flipping collisions is much shorter in CoFeB, which may be an evidence of increased spin accumulations at CoFeB/Ru interfaces in the SyF free layer which would lead to the efficient spin-transfer-torque exerting on the magnetization of the free layer. In summary, the magneto-transport properties of CoFeB have been carefully studied to give a useful clue for J_c reduction in MgO-based MTJs with CIMS. The spin diffusion length for $Co_{40}Fe_{40}B_{20}$ and $Co_{56}Fe_{24}B_{20}$ is found to be 4.5 ~ 4.8 nm while the spin-scattering anisotropy β is about 0.3.

[1] J. C. Slonczewski, J. Magn. Magn. Mater. 159, L1(1996).

[2] L. Berger, Phys. Rev. B 54, 9353(1996).

[3] J. Hayakawa, S. Ikeda, Y. M. Lee, R. Sasaki, T. Meguro, F. Matsukura, H. Takahashi, and H. Ohno, Jpn. J. Appl. Phys. 45, L1057(2006).

[4] T. Valet and A. Fert, Phys. Rev. B 48, 7099(1993).

[5] A. C. Reilly, W. Park, R. Slater, B. Ouaglal, R. Loloee, W. P. Pratt, Jr., J. Bass, J. Magn. Magn. Mater. 195, L269(1999).

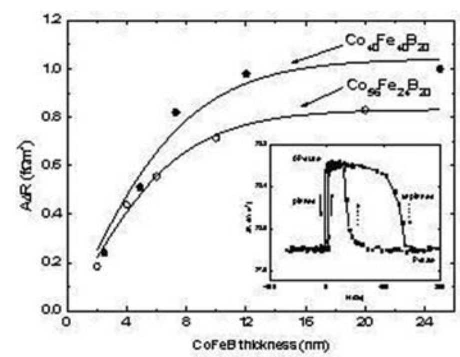

AΔR versus t_{CoFeB} for a series of EBSVs. The inset shows the typical hysteresis curve for the sample with $t_{Co}40_{Fe}40_{B}20$ = 7 nm.

DC-03

Magnetoresistance and switching properties of Co_xFe_{100-x}/Pd-based perpendicular anisotropy single and dual spin valves without exchange bias.

R. Law[1,2], R. Sbiaa[1], T. Liew[1], T. Chong[1]
*1. Data Storage Institute, A*STAR (Agency for Science, Technology and Research), Singapore, Singapore; 2. NUS Graduate School for Integrative Sciences & Engineering, National University of Singapore, Singapore, Singapore*

Magnetoresistive devices based on layers with perpendicular magnetic anisotropy (PMA) have been receiving increasing interest as they do not suffer from magnetization curling at the edges of patterned elements, which causes switching field fluctuations and cell instability. Recently, exchange-biased spin valves [1] and spin transfer switching in all-metal current-perpendicular-to-plane pseudo-spin valves with PMA have been demonstrated [2]. We report high current-in-plane giant magnetoresistance (CIP-GMR) of 9.7% and 13.0% in single-spin valves (SSV) and dual-spin valves (DSV) with PMA based on Co_xFe_{100-x}/Pd bilayers, respectively, a significant improvement over previous work [3]. Good separation and large coercivity difference in the magnetic layers was achieved without exchange biasing.

Perpendicular anisotropy spin valves were deposited using UHV dc magnetron sputtering onto thermally oxidized (100) Si wafers. The film structures of Ta/Pd/Soft layer/Cu/Hard layer/Pd/Ta and Ta/Pd/Hard layer1/Cu/Soft layer/Cu/Hard layer2/Pd/Ta were realized for SSVs and DSVs, respectively. The soft and hard magnetic layers were based on $(Co_xFe_{100-x}/Pd)_n$ bilayers, with layer thicknesses optimized for PMA and MR performance. In our spin valves, we have studied the effect of seed layer, crystalline orientation, annealing and various Co_xFe_{100-x} alloy compositions on PMA and GMR. Ta seed layers and the fcc (111) orientation were shown to be necessary to obtain good perpendicular anisotropy and sharp switching in the MR curves. As shown in Fig. 1, annealing improved the PMA of the magnetic layers but at the same time significantly depressed the MR ratio. This irreversible reduction of MR with annealing temperature was attributed to interdiffusion and alloying of CoFe and Pd within the magnetic layers, resulting in increased film resistance and reduced spin polarization.

Fig. 2 shows the maximum MR achieved for Co/Pd-, $Co_{90}Fe_{10}$/Pd- and $Co_{65}Fe_{35}$/Pd-based SSVs by optimizing Pd layer thicknesses while keeping Co_xFe_{100-x} and Cu spacer thicknesses constant. The highest MR of 9.7% was achieved for both Co and $Co_{90}Fe_{10}$ due to their similar compositions and identical critical Pd thicknesses required to maintain PMA. However, we note that the Co/Pd layers exhibited significantly larger coercivities than the $Co_{90}Fe_{10}$/Pd layers due to the lower saturation magnetization and better fcc (111) orientation of Co compared to $Co_{90}Fe_{10}$. On the other hand, the weaker PMA in $Co_{65}Fe_{35}$/Pd bilayers required thicker Pd within the bilayers to maintain perpendicular anisotropy, resulting in a lower MR of 7.0% due to increased current shunting and spin depolarization of conduction electrons.

We also describe the switching behavior of a Co/Pd-based perpendicular DSV with four distinct resistance states, as shown in Fig. 3, confirming that a DSV structure behaves as a simple additive/subtractive combination of two single spin valves. Such a DSV structure has potential for reducing spin transfer switching current densities as well as for multi-state storage devices.

[1] F. Garcia, F. Fettar, S. Auffret, B. Rodmacq, and B. Dieny, J. Appl. Phys. 93, 8397 (2003).

[2] S. Mangin, D. Ravelosona, J. A. Katine, M. J. Carey, B. D. Terris, and Eric E. Fullerton, Nature Mater. 5, 210 (2006).

[3] R. Law, R. Sbiaa, T. Liew, and T. Chong, Appl. Phys. Lett. 91, 242504 (2007)

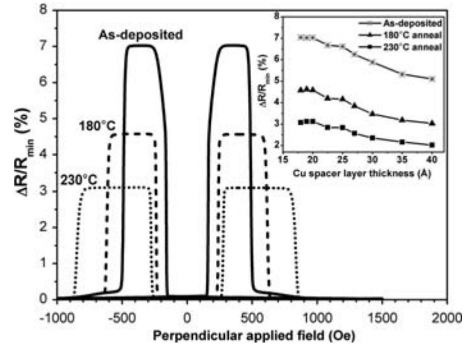

Fig. 1. MR curves of $Co_{90}Fe_{10}$/Pd-based perpendicular spin valves with a Cu 20 Å spacer layer for different post-anneal conditions. Inset: Cu spacer layer thickness and postanneal temperature dependence of MR ratio.

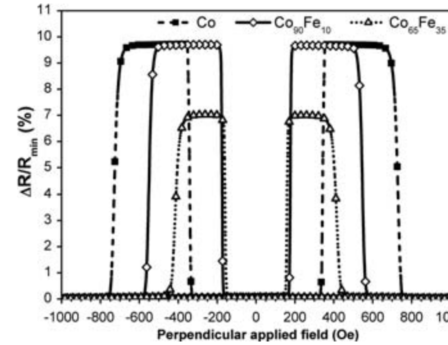

Fig. 2. Highest GMR achieved in CoFe/Pd-based perpendicular spin valves with different CoFe alloy compositions.

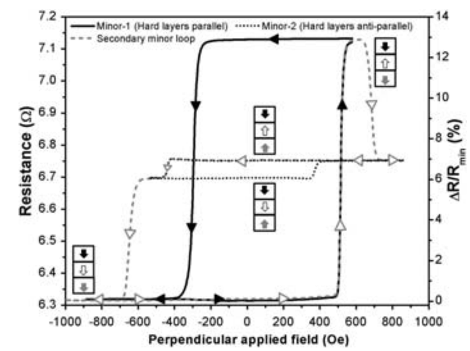

Fig. 3. Minor loops for Co/Pd-based dual spin valve for different hard layer configurations: Parallel hard layers (13.0% GMR, solid curve); Anti-parallel hard layers (1.0% GMR, dotted curve); Secondary minor loop which includes switching of the first hard layer (dashed curve).

DC-04

Magnetic structure of domain walls confined in a nano-oxide layer.

K. Matsushita, J. Sato, H. Imamura
Nanotechnology Research Institute, AIST, Tsukuba, Japan

Geometrically confined domain walls of nano-meter size contacts have drawn enormous attention because of its potential applications to future spintoronic devices [1]. In the last decade much effort has been devoted to study the magnetoresistance of atomic wires. One of main obstacles to applications of the atomic wires is mechanical stability. For example, Chopra et al. [2] reported that a Co atomic wire that shows 300% magnetoresistance (MR) ratio is stable for periods of up to as short as 2-3 min.

Recently, Fuke et al. fabricated the spin-valve with a current-confined-path structure made of a nano-oxide-layer (NOL) with a lot of fine holes filled with ferromagnetic metal [3]. Structures of domain walls confined in an NOL are very stable and typical size of the holes is as small as a few nano meters. They showed that the MR ratio increases with increasing a value of the resistance area product, which means that the MR ratio is enhanced for the system with narrow metallic channels. Doi et al. reported that a microwave oscillation of the domain wall in the NOL is induced by applying current perpendicular to the plane [4]. In order to understand these experiments, it is important to study magnetic structures of the domain walls and its effect on the MR ratio and on the current induced microwave oscillation. Since the domain walls are confined in an NOL, it is very difficult to observe the magnetic structure directly. The micromagnetics simulation technique provides a powerful tool for studying the magnetic properties of such domain walls in an NOL.

We study size dependence of magnetic structures in three-dimensional contacts as shown in Figs. 1 (a)-(c). The systems are divided into 2365 elements and dynamics of local magnetization of these elements are calculated numerically by solving the Landau-Lifshitz-Gilbert equation. Magnetic field due to the dipole-dipole interaction is evaluated by a finite-element-method and boundary-element-method (FEM-BEM) hybrid method [5]. For simplicity, we consider permalloy contacts, the crystalline anisotropy of which can be ignored. The material parameters are taken as $A = 1.3\times10^{-11}$ J/m and $M_s = 8.0\times10^5$ J/m^3. The characteristic length of magnetic structures in the contacts is Bloch line width defined as $(2A/\mu_0 M_s^2)^{1/2} \sim 2.2$nm.

Figures 1(a) and 1(b) shows typical magnetic structures of the nano contacts. When the contact is much larger than the Bloch line width the vortex-like magnetic structure shown in Fig. 1(a) is favored. As we decrease the size of the contact the Neel-wall-like structure shown in Fig. 1(b) becomes more stable than the vortex-like structure. For the contact with 20nm height, the vortex-like structure shown is a meta-stable magnetic structure and the other meta-stable magnetic structure is the Neel-wall-like one. For the contact with 2nm height, which is comparable small to the Bloch line width, the Neel-wall like structure shown in Fig. 1(b) is the only stable magnetic structure.

The typical thickness of the nano-oxide-layer studied by Fuke et al. and by Doi et al. [3,4] is about 2 nm. In the case, the magnetic structure of the domain wall should be Neel-wall like as shown in Fig. 1(b). Figure 1(c) shows the stiffness energy distribution on a cross section of the contact. One can see that the domain wall is well confined in the contact region and the stiffness energy. Absolute values of a gradient of local magnetization rotation angles are almost uniform in the contact region. Since magnitude of spin transfer torque is proportional to the absolute values of the gradient of the local magnetization rotation angle, the spin transfer torque is uniformly distributed in the whole of the contact. We will report details of our study and comparison of the calculated interlayer coupling field with the recent experimental results.

This work has been supported by NEDO.

[1] P. Bruno, Phys. Rev. Lett. **83** (1999) 2425; R. P. van Gorkom et al., Appl. Phys. Lett. **74** (1999) 422; H. Imamura et al., Phys. Rev. Lett. **83** (2000) 1003; N. Garcia et al., Phys. Rev. Lett. **82** (1999) 2923; Y. Ohsawa, IEEE Trans. Magn. **43** (2007) 3007.

[2] H.D. Chopra, Nature materials **4** (2005) 832-837.

[3] Fuke et al., IEEE Trans. Magn. **43** (2007) 2848.

[4] M. Doi et al., CE-15, 52nd MMM conference (2007).

[5] D. R. Fredkin and T. R. Koehler, IEEE Trans. Magn. **26** (1990) 415.

[6] A. Hubert, *"Magnetic Domains"*, Springer (2000).

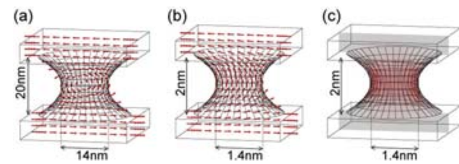

Figure 1. Typical magnetic structures for the contacts with 20nm and 2nm height are shown in the panels (a) and (b), respectively. Stiffness energy distribution in corresponding to the magnetic structure of (b) is shown in the panel (c).

MICROMAGNETIC STUDY ON DOMAIN WALL SIZE FOR NANOCONTACT MAGNETORESISTANCE IN SPIN VALVE STRUCTURE.

M. Takagishi, H. N. Fuke, S. Hashimoto, H. Iwasaki
Corporate R&D Center, TOSHIBA Corporation, Kawasaki, Japan

Introduction

New MR technologies are expected with both a high dR/R of more than 100% like TMR and a low RA of less than 0.5Ωμm2 like CPP-GMR. Recently it has been reported that FeCo nanocontacts (NCs) in CPP spin valve shows an MR ratio of about 10% [1], which MR origin is considered to be domain wall MR with a theoretical dR/R of more than 100% because of NCs of 1-3nm in diameter observed by a conductive AFM technique and large interlayer coupling, compared to CCP-CPP-GMR using Cu metal paths. It is expected that the smaller nanocontact size with the smaller domain wall increases MR ratio. Fig 1 shows the MR ratio dependency on domain wall size by using the theory of reference [2], with a spin asymmetry as a parameter. The theory indicates that FeCo NC with 2nm domain wall length shows an MR ratio of 160% . If nanocontact size is roughly equivalent to domain wall size, the experiment MR ratio can not be explained by the theory. In this paper, we report the relation between nanocontact size and domain wall size by using micromagnetic simulation and discuss about the discrepancy between experiment and theory

Simulation model

Fig 2 shows the model geometry of the nanocontact. Periodic boundary conditions are set on the four surfaces of this model. We have investigated domain wall size when changing NC size and Nano-Oxide-Layer (NOL) thickness in this figure, which are corresponding to NC width and NC length respectively. The contour of Fig 2 shows magnetization component in the direction of y-axis when Hy(external field)=500Oe.

Result and Discussion

Fig. 3 shows domain wall size dependency on NOL thickness and NC size. The domain wall size is defined as the span from +90% to -90% magnetization changing points. Domain wall size decreases with reducing NC size and NOL thickness. The domain wall size of our experimental film is estimated to be about 3nm from figure 3 because the experimental NC size is around 2nm and the NOL thickness is 1.2nm. Note that figure 1 shows an MR ratio of around 72% for 3nm NC size. This theoretical MR ratio is still larger than that of experiment.

There could be two reasons of the MR ratio discrepancy. One is impurity in NCs area. dR does not change clearly for zero field cooling, while it clearly changed at 150~200 degree C for 10kOe field cooling to the PtMn exchange-biased direction, as shown in Fig.4. Furthermore, interlayer coupling between pinned and free layers also change as dR changes for field cooling. Not that some Fe(Co) oxides have a magnetic transition at low temperature. This implies that magnetic oxides exist around NCs and cause a change of MR characteristic.. Another possible reason is that the NCs size might be too small to apply the Levy and Zhang theory for diffusive bulk scattering[3]. We will try to apply the more ballistic theory for our NCs.

Acknowledgement

This work was partly supported by NEDO program.

[1] H. N. Fuke, et al. IEEE Trans Magn. **43**, 2848 (2007)

[2] P. M. Levy and S. Zhang, Phys. Rev. Lett. **79**, 5110 (1997)

[3] J. B. A. N. van Hoof, et al. Phys. Rev. B **59**, 138 (1999)

[4] Y. Yuasa, et al. J. Appl. Phys., **92**, 2646(2002)

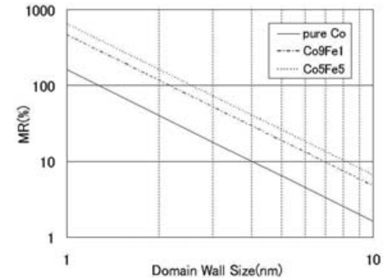

Fig.1 MR ratio vs. domain wall size calculated by using the theory of the reference[2]. We used spin asymmetry coefficient values of 0.35, 0.55 and 0.62 for Co, Co9Fe1 and Co5Fe5 respectively[4].

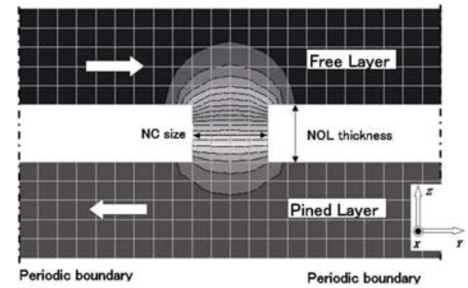

Fig.2 The model geometry of nanocontact. The contour shows magnetization component in the direction of Y-axis.

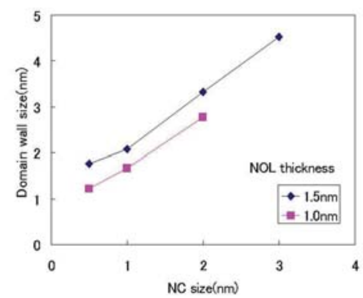

Fig.3 The relation between NC size and domain wall size by using micromagnetic simulation

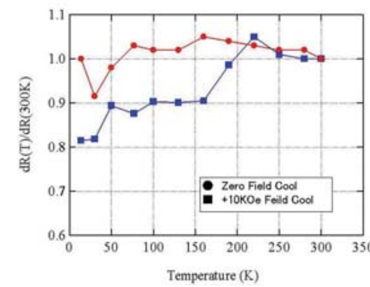

Fig.4 Temperature dependence of dR for SV with Co5Fe5 NCs. The sample was cooled under a field of 0 or 10kOe.

DC-06

Effect of surface scattering on magnetoresistance.

X. Chen[1], *R. H. Victora*[2]
1. Department of Physics, University of Minnesota, Minneapolis, MN; 2. Department of Electrical & Computer Engineering, University of Minnesota, Minneapolis, MN

Introduction

The magnetic and transport properties in magnetic nanowires have become an interesting topic in recent years, partly due to the need for a nanometer-scale magnetoresistance (MR) device in spintronic and high density magnetic recording applications. The advance in nano technology has made fabrication of magnetic multilayer structure in nanowires possible. As the dimensions of the device shrink to hundreds of atoms, many unexpected phenomena related to quantum size effect appear [1]. Previously, we have shown that in metallic nanowires, surface roughness plays an important role that can substantially increase the resistivity beyond the bulk value. In this work, we explore the effect of surface scattering on the magnetoresistance in a multilayered nanowire. It is found that even without any spin-flip scattering, the MR is significantly reduced by surface roughness.

Model

We consider two segments of 3-dimensional ferromagnetic (FM) nanowire joined by a spacer with negligible thickness and attached to two clean semi-infinite leads on both sides, as shown in Fig. 1. The FM leads are modeled by a single band tight binding Hamiltonian with a hopping integral 1eV and exchange splitting is also chosen to be 1eV. The nanowire is embedded into an insulating surrounding environment serving as the template in which the wire is deposited. The commonly used template material is alumina with a scattering potential of 3eV [2]. The rough interface between the nanowire and template is assumed to follow a Gaussian distribution with a standard deviation of one atomic spacing. The Landauer formalism along with a recursive Green's function technique is employed to calculate the transport properties. The resistance of parallel (PA) and anti-parallel (APA) alignment of magnetization, as well as the MR, are numerically calculated as a function of wire length and diameter.

Results

Resistance of both PA and APA channels is first calculated as a function of wire length as shown in Fig. 2 (a) for a wire of 10 atoms by 10 atoms. The variation of the MR ratio is plotted in Fig. 2 (b). When length is zero, electron transport is ballistic and MR ratio is maximal. As L increases beyond the mean free path, the transport crosses over to the diffusive regime. In this regime the resistance scales linearly with wire length obeying a quantum version of Ohm's law. A key observation in Fig. 2 (a) is the resistance for PA and APA channels increases at similar rates. Therefore, the numerator in the usual MR definition ($MR=(R_{APA}-R_{PA})/R_{PA}$) remains a constant, but the denominator keeps increasing with L. Therefore the MR ratio drops with increasing length as expected (Fig. 2 (b)).

More interestingly, the resistance is calculated as a function of width for wires of equal length in Fig. 3 (a). As the wire becomes wider, the resistance of PA and APA channels decreases at approximately the same rate. As a result the MR increases as shown in Fig. 3 (b). Surface roughness beyond the minimal value (approximately 0.25nm) assumed here will greatly accentuate the effect. Therefore, surface scattering, which is inevitable in many fabrication processes, can significantly reduce the MR ratio. The MR can be recovered by increasing the sample width. As the size of MR devices shrink to a scale comparable to the mean free path, we expect this surface effect to seriously impact performance.

[1] Xi Chen and R. H. Victora, App. Phys. Lett. 91, 212104 (2007)

[2] J. S. Moodera, J. Nowak and R. J. M. van de Veerdonk, Phys. Rev. Lett. 80, 2941 (1998)

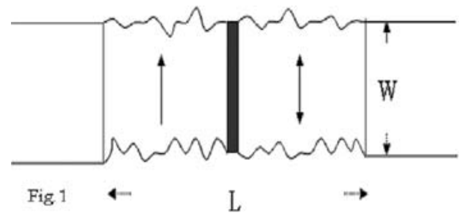

Fig 1

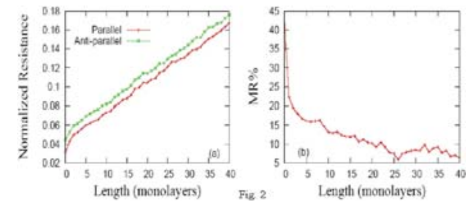

Fig. 2

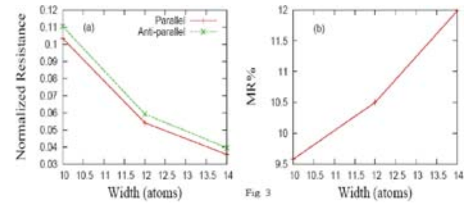

Fig. 3

DC-07

CPP-GMR characteristics of full epitaxial spin valves film with alternate monatomic $[Fe/Co]_n$ superlattice.

I. Chu, *T. Mano*, M. Doi, M. Sahashi
Department of Electronic Engineering, Tohoku University, Sendai, Japan

[Introduction]
In order to realize higher areal density magnetic recording, it is necessary to improve the sensitivity of read heads and to find a new Magneto-Resistance (MR) mechanism for sensing the weak signal from media with higher efficiency. MgO-TMR (Tunnel Magneto-Resistance), which is low resistance area product (RA) of around 0.5 $\Omega\mu m^2$, is most powerful to realize 1 Tbpsi magnetic recording in considering the areal density with lower RA. The read head with a lower RA than 0.5 $\Omega\mu m^2$ are preferable from the standpoint of a frequency response because RA of MgO-TMR is still high due to its oxide barrier. So, a full metal CPP (Current Perpendicular to Plane)-GMR is considered to be the candidate for over 1 Tbpsi. So far the body-centered-cubic (bcc) $Fe_{50}Co_{50}$ spin valve GMR is reported to show the large spin scattering asymmetry coefficients (β and γ) in CPP geometry[1)], which suggests that $Fe_{50}Co_{50}$ alloy has the advantage of a high spin polarization. When the ordered state with B2 structure is realized, how high is MR performance in comparison with the disordered $Fe_{50}Co_{50}$ alloy. So, the study of the alternate monatomic layer (AML) $[Fe/Co]_n$ epitaxial film system with artificially ordered B2 structure is very interesting from the view point of a spin conductance mechanism in CPP geometry. And moreover this B2 structure $Fe_{50}Co_{50}$ (001) has the property of a symmetry Δ_1 Bloch state at $k_{//}=0$ for only majority, where the symmetry based spin-filtering effect is most effective for $k_{//}=0$ [2)]. The ordered $Fe_{50}Co_{50}$ alloy is likely to be a suitable material for application to CPP-GMR and TMR devices in CPP system.

[Experimental]
The Epitaxial film stacks were prepared on MgO (001) substrates by Electron Beam (EB) evaporation technique. To examine the structure of the deposited epitaxial films, we used in-situ Reflection High-Energy Electron Diffraction (RHEED) technique for investigating the epitaxial property and in-situ STM for topography of the epitaxial film surface[3-5)]. Normally, the deposition using the $Fe_{50}Co_{50}$ alloy target was also performed as the reference. The growth of an epitaxial film with 21 MLs (1 Monolayer : 0.14nm) of [Fe/Co] on MgO (001) was performed at a substrate temperature of 75 ^{o}C and a typical base pressure of less than 10^{-7} Pa. The mismatch of lattice between the samples and MgO substrate is estimated as 4.1 %. The disordered $Fe_{50}Co_{50}$ alloy film with thickness of 2.94 nm was fabricated at a substrate temperature of 75 ^{o}C, corresponding to that of AML [Fe/Co] 21 MLs in alternate monolayer deposition. The Au electrode and spacer layer were selected for the full epitaxial system because of the small lattice mismatch around 1.0 % to the AML $[Fe/Co]_n$ layer. The seed Fe layer and Au epitaxial film for bottom electrode were performed at a substrate temperature of 300 ^{o}C. The full epitaxial trilayer on Au electrode was prepared with the design of Au 300 (nm)/ AML $[Fe/Co]_n$/ Au 5 (nm)/ AML $[Fe/Co]_n$. Finally, IrMn layer for pinning was deposited on the top of full epitaxial trilayer. The CPP-SVs elements were fabricated with the size from 1.5 to 4 μm by the conventional photo lithographic method.

[Results and discussion]
We confirmed the structural properties of trilayered epitaxial films with AML $[Fe/Co]_n$ (R_a : 0.18 nm) and $Fe_{50}Co_{50}$ alloy epitaxial film on Au electrode by RHEED before confirming the characteristic of CPP-GMR[3)].
The performance of CPP-GMR sensors that use spin-valves made of conventional materials with Cu spacer is limited by their less than 1.6 $m\Omega\mu m^2$ specific magnetoresistance change (ΔRA: resistance-change x area). This value is small because of the small change in film resistance that occurs when the relative angle between magnetizations of two magnetic layer materials is changed. The resistivity change ΔR originates from only functional parts in CPP-GMR. The specific resistivity change, ΔRA, were estimated to be 1.02, 1.59 $m\Omega\mu m^2$ for SVs with $Fe_{50}Co_{50}$ alloy and AML $[Fe/Co]_n$ respectively. If we assume the short distance of spin diffusion length of Au spacer compare to Cu, the observed ΔRA is fairly large value. The ΔRA of SVs with AML $[Fe/Co]_n$ is 1.5 times higher than that of SVs with $Fe_{50}Co_{50}$ alloy. We assume that high ΔRA results from high spin polarization of AML $[Fe/Co]_n$ due to increasing the degree of ordering by artificial AML [Fe/Co] deposition method.

[1] H.Yuasa, M. Yoshikawa, Y. Kamiguchi, K. Koi, H. Iwasaki, M. Takagishi, and M. Sahashi, J.Appl.Phys, 92 (5), 2646 (2002)

[2] X.-G. Zhang and W. H. Butler, Phys. Rev. B 70, 172407 (2004)

[3] I. C. Chu, Y. Saki, S. Kawasaki, M. Doi, and M. Sahashi, Jpn. J. Appl. Phys. (submitted)

[4] I. C. Chu, M. Doi, and M. Sahashi, J. Magn. Magn. Mater., Vol. 304, Issue 1, e121-e123 (2006)

[5] I. C. Chu, M. Doi, and M. Sahashi, HB-09, INTERMAG SANDIEGO

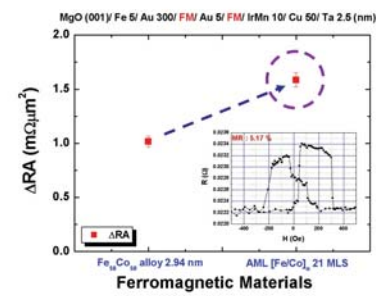

The relation of ΔRA and ferromagnetic materials. (FM : AML [Fe/Co], $Fe_{50}Co_{50}$ alloy grown at 75^{o}C). Inset shows R-H curve of SVs with AML$[Fe/Co]_n$

DC-08

Spin transfer magnetization dynamics in ultra small nanocontacts elaborated by CT-AFM nanolithography.

M. Darques, B. Georges, A. Ruotolo, *V. Cros*, S. Fusil, J. Grollier, R. Guillemet, K. Bouzehouane, C. Deranlot, A. Fert
Unite Mixte de Physique CNRS/Thales, Palaiseau, France

Generating a microwave signal by the pure electronic way using the spin transfer effect has become an important axis of the present evolution of spintronics. The physics of the interaction between a spin current and a magnetization is new and many questions remains. Especially it will be very important to get a deeper insight on the excited modes induced by spin transfer depending on the dc current or the applied field as well as the relaxation process that govern the linewidth of the emission. This new type of microwave oscillators also called STOs (Spin Transfer Oscillators) are non-linear oscillators very promising for applications in next generation telecommunication devices[1,2]. However the increase of the output power is a major challenge since the emitted power by a single STO is far too weak (< 1 nW). Some solutions have to be found to increase the amplitude of the spin torque and also to find some mechanisms to achieve the synchronization in frequency and phase of an array of STOs [3-6].
In the present work, we have focussed our study on spin valve nanocontacts. In fact, up to now, these are the device geometry that have yield the best microwave characteristics (agility, linewidth etc..). We have elaborated ultra small nanocontacts (less than 20 nm of diameter) using the original nanolithography process we have recently developped using a real time controlled nanoidentation technique [7]. On Fig 1, we present a scheme of the two types of structures we have studied : standard nanocontacts (a) and hybrid nanocontacts (b).
For standard nanocontacts, we have studied two configuration i.e. applied field in the plane and out of the plane. In the first case, we have detected some power emission only at high field and very low frequency (50-100 MHz). Moreover, the power amplitude remains always very weak. De plus, les niveaux de puissance sont relativement faibles. In Fig.2, we show the results obtained for an out of plane field of –2740Oe. Like for the in plane field, we have detected only some low frequency oscillations (around 50 MHz) that can however achieve 2GHz. As it can be seen, several orders of harmonics can be observed. The power emission is much higher in this configuration and can be as high as 50 pW/mA^2/GHz. The frequency of the emission are much lower than the ones expected for FMR resonnances of the uniform mode. Thus, we believe that these microwave emissions are probably associated to non uniform dynamics created by both the spoin transfer torque and the Oersted field. These recent results we want to extend are in very good agreement with the latest results of Puffall et al from NIST, Boulder [8].
For the hybrid structures, some very interesting and promising results have been obtained in this geometry. It is important to note that we have identified that we detect indeed some excitations inside the Co nanocontacts (50nm thick) and not in the extended NiFe layer.On Fig. 3a, we present one of the most intense peak that has been ever measured in STOs about 1 nW/mA^2/GHz. Moreover, These sub-GHz oscillations present an hysteretic character as a function of the injected current. As shown in Fig.3b, the onset of the oscillations is around 420 MHz and –4,2 mA for increasing current whereas they exists down to -4 mA with frequencies down to 300 MHz. These results are compatibles with some translationnal motion of a vortex or any other type of non homogenious magnetic configuration. In fact, sevral groups express a big interest for these types of oscillations since they present very thin linewidth [9].

[1] W.H. Rippard et al Phys. Rev. B 70, 100406(R) (2004)

[2] S.I. Kiselev et al., Phys. Rev. B 72, 064430 (2005)

[3] W.H. Rippard et al, Phys Rev. Lett. 95, 067203 (2005)

[4] S. Kaka et al., Nature 437, 389 (2005)

[5] F.B. Mancoff et al, Nature 437, 393 (2005)

[6] J. Grollier, V. Cros, A. Fert, Phys. Rev. B 73, 1 R (2006)

[7] K. Bouzehouane et al. Nanoletters, 3, 1599 (2003)

[8] M. Pufall et al, Phys. Rev. B 75, 104404 (2007)

[9]V.S. Pribiag et al, Nature Physics 3, 498 (2007); Q. Mistral et al, unpublished

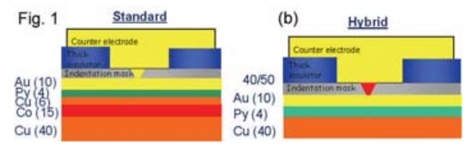

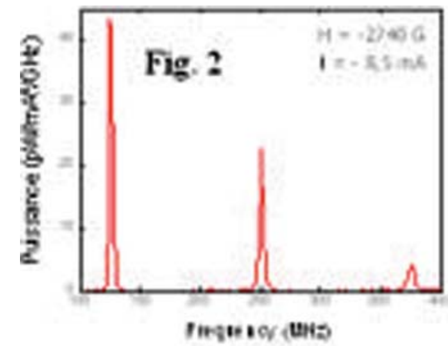

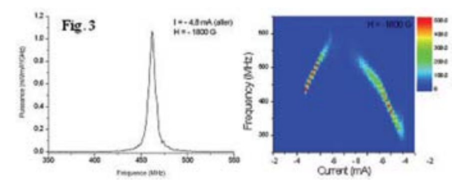

DC-09

Layered annular magnetic bridges for storage and logic applications.

F. J. Castano, B. G. Ng, C. H. Nam, C. A. Ross
Depart. of Material Science and Engineering, MIT, Cambridge, MA

The magnetotransport response of magnetic elements patterned from hard layer/ non-magnetic spacer/ soft layer structures is dominated by giant magnetoresistance (GMR) and results in distinct resistance levels depending on the relative alignment of the magnetization in the hard and soft layers. The ability to electrically discriminate these non-volatile magnetic states in elliptical structures has already been exploited commercially in magnetic random access memories and has recently been proposed to create logic devices [1]. On the other hand, ring-shaped layered elements have been recently shown [2] to display multiple resistance levels due to the existence of vortex-like configurations in both the hard and soft layers, which may be utilized to store more than one bit-per-element in storage applications. The present work explores the magnetotransport response of annular NiFe/Cu/Co structures using Wheatstone bridge (WB) contact configurations. Such bridges became unbalanced as each layer transitions into a vortex-like state, giving large changes in voltage. This behaviour is observed even for annular structures with deep-sub-micron dimensions and offers the possibility of operating these devices as non-volatile logic gates that do not require reprogramming after each operation.

Prototype devices (Fig.1) consisting of elliptical, circular and rhombic NiFe/Cu/Co ring-shaped elements with up to six Ta/Cu electrical contacts were fabricated using lift-off processing and a combination of optical and electron-beam lithographies.

(Fig 1)

The magneto-transport response was investigated using a 4-point technique with a 0.01mA current at 1kHz. The results from two different measurement configurations will be presented. In the first one the current in injected using two diametrically opposed leads and the voltage measured using two leads located on one side of the ring (Fig1.(a)-(d)). The highest resistance using this method (V13 in Fig.2 (a)) corresponds to both layers being antiparallel each in onion states, in agreement with previous work [2]. In the second configuration both current and voltage leads are located at diametrically opposed sites in the rings forming WB configurations, Fig.1(a)-(f). These measurements allow for the difference between both branches of the bridge to be measured. Interestingly, the greatest unbalance of the bridges corresponds to field ranges over which each ring is in a vortex configuration.

(Fig 2)

These results can be understood using micromagnetic modeling combined with an electrical model. Fig. 2(c) shows the calculated MR major half-loop for WB configurations. As the field is decreased from positive saturation, two 180deg domain walls form in the hard layer and their stray fields promote a reversal of the soft layer unlike that observed in single-magnetic layer rings. The soft layer reverses from both ends by the propagation of four 180deg domain walls. As these walls traverse the structure, they form intermediate configurations stable at remanence, such as state [1] shown in the inset in Fig.2c, which corresponds to the soft layer peak resistance in the WB model. As the reversal of the soft layer proceeds the four 180deg domain walls form metastable 360deg walls (state [2]), which collapse at higher fields. The hard layer transitions into a vortex-like state with multiple 360deg walls, which results in parallel and antiparallel orientation between the soft and hard layers in each half of the ring (state [3]), creating an unbalanced bridged particularly for smaller and narrower rings. Further increase of the reverse field nucleates a bi-domain state in the hard ring (state [4]) and the soft and hard ring become parallel (except for small areas corresponding to residual 360deg walls). These magnetic configurations are shown in Fig. 2. We will compare this field-induced reversal with current-induced reversal in identical structures.

[1]A. Ney, C. Pampuch, R. Koch, and K. H. Ploog, Nature 425 (6957), 485 (2003).

[2]F.J. Castano D. Morecroft and C.A. Ross, Phys Rev. B, 74, 224401 (2006).

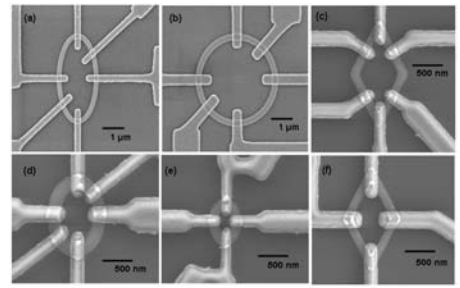

Fig.1. (a)-(f) Scanning electron micrographs of elliptical, circular and rhombic NiFe/Cu/Co annular devices with outer diameters ranging from 500 nm to 5μm and different contact configurations.

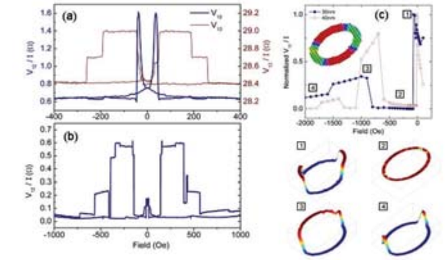

Fig.2. (a) Magneto-transport response using a standard 4-point contact configuration (V13) and a WB contact arrangement (V12) in the NiFe/Cu/Co bridge shown in Fig.1 (a). (b) WB response from a 100nm-wide, 1.9μm-long NiFe/Cu/Co bridge. (c) Modeled resistance for WB measurements on 300nm-long NiFe/Cu/Co elliptical rings with aspect ratio of 1.5 and widths of 30nm and 40 nm. The inset shows the magnetic configuration in the soft layer corresponding to the maximum unbalance of the bridge for a 40 nm-wide ring. Magnetoresistance configurations ([1]-[4]) corresponding to the different magnetization configurations in the soft and hard rings observed in the WB response (blue and red colors correspond to regions in which the magnetizations of the two layers are parallel and antiparallel, respectively).

DC-10

Investigation of strong biquadratic coupling in Co_2MnSi based trilayer structures.

Y. Sakuraba, S. Bosu, K. Saito, H. Wang, S. Mitani, K. Takanashi
Institute for materials research, Tohoku univ., Sendai, Miyagi, Japan

Half-metallic ferromagnets, which have perfectly spin-polarized conduction electrons, have attracted much interest in the spintronics field. One of full-Heusler alloys, Co_2MnSi(CMS), is expected as a promising half-metal because of its high Curie temperature well above RT (T_C = 985 K). Recent studies on magnetic tunnel junctions with CMS have showed extremely large TMR ratio of 570%, which clearly indicates half-metallic nature of CMS.[1] Although interlayer exchange coupling (IEC) behavior in FM/NM/FM nanostructures has extensively been studied in a wide variety of materials for a few decades, the knowledge of IEC in half-metal-based structure has been limited so far. Recently we have reported strong biquadratic coupling (H_s ~ 8KOe) with large oscillation period (3.3-3.5 nm) in epitaxial CMS/Cr/CMS trilayers. [2] The origin of this novel IEC behavior is still unclear. The electronic basis for the coupling between ferromagnetic layers through an intervening metal depends on the relative energy alignment of the spin-split bands. [3,4] Therefore it is interesting to investigate whether there is any relation between half-metallicity i.e. spin polarization and IEC or not.

The electronic structure of CMS was predicted to be sensitive to its chemical ordering [5]. Picozzi *et al*. reported that, Co-antisite creates in-gap state and causes a large depolarization effect. Therefore it is possible to examine the relation between IEC behavior and half-metallicity by fabricating CMS having different degrees of chemical ordering which can be controlled by annealing temperature. The purpose of this study is to clarify the relation between observed novel IEC behavior and half-metallicity of CMS by investigating the IEC behavior for CMS/Cr/CMS trilayers with different annealing temperatures for the bottom CMS. CMS(20 nm)/Cr(1.2 nm)/CMS(7 nm) trilayer samples were prepared by a UHV-compatible dc-sputtering method on MgO substrates. We annealed bottom CMS at different annealing temperatures (T_{ann}) to change the degree of the chemical ordering, i.e. to modulate the electronic structure. Top CMS was not annealed for all the samples to prevent inter-diffusion between Cr and CMS. The values of surface roughness (R_a) for top and bottom CMS measured by AFM are very small and almost the same upto T_{ann} = 400°C, as shown in Fig. 1(a), which means the IEC behavior is not affected by the interfacial roughness of trilayers. Long-range order parameter (S) of CMS single layer estimated from superlattice peak intensity in XRD is plotted against Tann in Fig.1(b). Almost perfect B2 ordered structure was observed even at as-deposited state, whereas $L2_1$-ordering appears from 300°C and takes maximum at 400°C. Magnetization curves in Fig. 2 show strong 90 degree coupling in CMS/Cr/CMS at different T_{ann}. (100°C-400°C). There is no significant change of strength and type of the coupling with T_{ann}. Explicitly, the IEC behavior does not depend on whether it is B2 or intermixing of $L2_1$ and B2 ordered structure in this case. Previous theoretical studies have showed that B2 structure is enough for CMS to have half-metallicity.[2] Therefore, if there is any realtion between half-metallicity and strong biqudratic coupling, this result does not contradict with theoretical predictions. Further study about Co-Mn-Si composition dependence of IEC behavior in CMS/Cr/CMS structure will also be shown in the presentation.

[1] Y. Sakuraba, M. Hattori, M. Oogane, Y. Ando, H. Kato, A. Sakuma, H. Kubota and T. Miyazaki, Appl. Phys. Lett., 88, 192508 (2006)

[2] H. Wang, A. Sato, K. Saito, S. Mitani, K. Takanashi and K. Yakushiji Appl. Phys. Lett., 90, 142510 (2007).

[3] D. M. Edwards, J. Mathon, R.B. Muniz and M.S. Phan, J. Phys. Condens. Matter 3, 4941 (1991)

[4] R. P. Erickson, K. B. Hathaway, and J. R. Cullen, Phys. Rev. B 47, 2626 (1993)

[5] S. Picozzi and A. Continenza, Phys. Rev. B., 69, 094423 (2004)

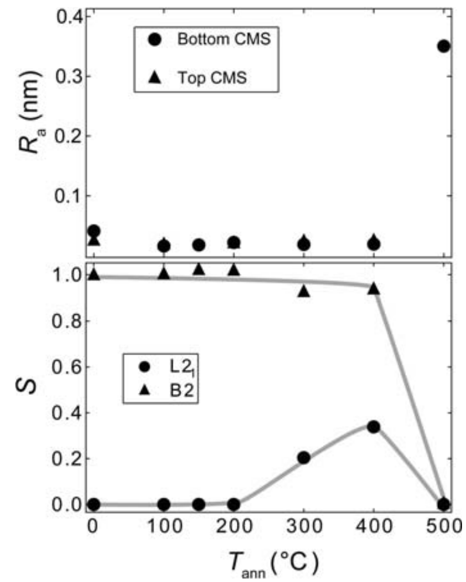

Annealing temperature (T_{ann}) dependence of surface average roughness (R_a) for top and bottom CMS (a) and long range order parameter (*S*) for single CMS layer (b).

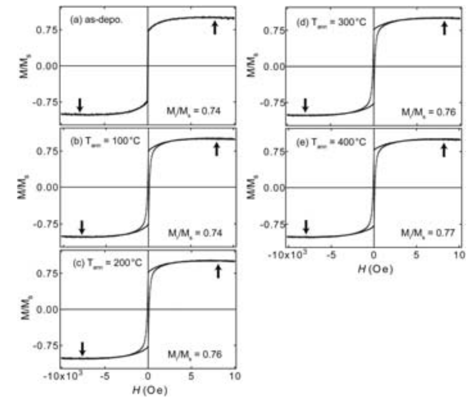

MH loops of CMS(20nm)/Cr(1.2nm)/CMS(7nm) trilayers for bottom CMS(20nm) annealing at (a) 100°C, (b) 200°C, (c) 300°C and (d) 400°C, respectively. Arrows indicate saturation field.

DC-11

CPP magnetoresistance effect through Graphene sheets.

E. W. Hill, T. G. Mohiuddin, D. Elias, A. K. Geim, F. Schedin, K. Novoselov, P. Blake, A. Zhukov
Centre for Mesoscience and Nanotechnology, The University of Manchester, Manchester, United Kingdom

Introduction

Single layer Graphene is a most remarkable material, consisting of a single layer of carbon atoms and was shown to be stable as a 2D crystal by Novoselov et al.[1] only a few years ago. Prior to that discovery Graphene had been something of a theoretical novelty, but in the last few years the material has been of great experimental interest particularly as its charge carriers can behave as a 2D gas of massless Dirac fermions [2] and it can support spin polarized conduction in the sheet plane [3], [4]. In this work we have looked at the conduction of spin polarized currents perpendicular to the plane of the sheet using the so-called CPP geometry.

Device Fabrication

Graphene flakes were prepared using the technique described by Novoselov et al. [1] on substrates which were covered with an array of patterned rectangular bars of 30 nm thick NiFe or NiFe30nm/Au10nm. Suitable single layer flakes which overlaid a NiFe bar were then identified using an optical microscope and their coordinated recorded. A PMMA resist layer was the applied and the upper electrode and contacts were patterned over the previously selected flakes. Some devices were also patterned in regions without flakes for comparison. An over-layer of 30 nm thick NiFe was then deposited by evaporation onto the patterned resist layer. Lift off was then employed to define the top electrode together with the contacts to the top and bottom electrodes. A schematic view of the final device is shown in figure 1a together with an optical micrograph of a device with a Graphene flake in place (figure 1b).

Results and discussion

Four probe measurements of the resistance of the crosses with and without the flake present were taken. Using NiFe without an overcoat of Au means that a thin oxide layer will form during the flake preparation stage. The measurements showed that this increased the contact resistance to the flake, but was not sufficiently continuous to magnetically uncouple the two NiFe layers when the flake was absent as shown in figure 2a. Thus, we observed only an AMR response without the flake, but there was a stable high resistance state at zero field indicating an anti-parallel magnetization state between upper and lower layers. We were concerned about the presence of the oxide layer which gave a high contact resistance and so we repeated the experiment with a thin Au capping layer on the lower NiFe electrodes. In this case we saw a spin valve response for both NiFe/Au/NiFe and NiFe/Au/Graphene/NiFe devices, but the response with the graphene present was larger by a factor of two. This is shown in figure 2b. We believe that the current is being channeled through the Graphene layer at what are effectively pin holes and the increase in the MR response is thus due to the CPP conduction as opposed to the CIP conduction in the devices without the graphene sheet.
Thus a single sheet of Graphene is sufficient to break the exchange coupling between two ferromagnetic layers and the presence of a Graphene sheet can give rise to current channeling and produce a good CPP response using simple cross electrode geometry.

1. Novoselov, K.S., et al., Two-dimensional atomic crystals. Proceedings of the National Academy of Sciences of the United States of America, 2005. 102(30): p. 10451-3.

2. Novoselov, K.S., et al., Two-dimensional gas of massless Dirac fermions in graphene. Nature, 2005. 438(7065): p. 197-200.

3. Hill, E.W., et al., Graphene spin valve devices. IEEE Transactions on Magnetics, 2006. 42(10): p. 2694-6.

4. Tombros, N., et al., Electronic spin transport and spin precession in single Graphene layers at room temperature. 2007. 448(7153): p. 571-574.

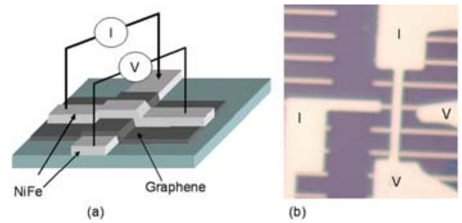

Figure 1. Schematic diagram of final device (a) with an optical micrograph (b) showing the cross geometry and the four probe measurement contacts.

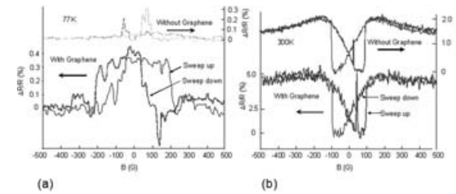

Figure2 (a) MR response of the device using only NiFe electrodes with and without the single layer Graphene spacer. (b) MR response of the device using NiFe/Au lower and NiFe upper electrodes with and without the single layer Graphene spacer.

DC-12

Magnetoresistance and energy model of Alq3-based spintronic devices.

L. E. Hueso[1,2], V. Dediu[2], I. Bergenti[2], A. Riminucci[2], P. Graziosi[2], F. Borgatti[2], F. Cassoli[3], Y. Zhan[2], C. Taliani[2], M. P. de Jong[4]
1. Department of Physics, University of Leeds, Leeds, United Kingdom; 2. ISMN, CNR, Bologna, Italy; 3. IMEM, CNR, Parma, Italy; 4. Nanoelectronics Group, University of Twente, Enschede, Netherlands

Spin transport in organic semiconductors has been receiving widespread attention since the first experimental demonstration of magnetoresistive effects (change in resistance under an applied magnetic field) in hybrid ferromagnetic/organic/ferromagnetic structures [1]. Continuous effort in the field has led to the realization, for example, of vertical organic spintronic devices with different organic semiconductor layers [2,3] or organic tunnel barriers [4]. However, there is still a lack of understanding on the mechanism that governs spin injection and transport in organics, leading to general disagreement even on the expected sign of the devices output magnetoresistance.

With the aim to clarify the spin transport behaviour in organic semiconductors, we present new results on hybrid inorganic/organic spin valves with the most successful up-to-date combination of materials [2-6]. The highly spin polarized manganite La2/3Sr1/3MnO3 and Cobalt have been used as ferromagnetic electrodes for spin injection into thick layers (up to 200 nm) of tris(8-hydroxyquinoline)aluminum(III) (Alq3). In a critical design improvement, we have for the first time introduced an artificial tunnel barrier (Al2O3 or LiF) between the organic and the Co top electrode to study its influence on spin injection into organic semiconductors and to improve the chemical stability and reproducibility of the devices.

In our manuscript we: explore the importance of artificial tunnel barriers for spin injection in organics, record room temperature magnetoresistance, demonstrate that only ferromagnetic electrodes and not organic semiconductor limit device output and, finally, sketch an energy diagram able to explain negative magnetoresistance in LSMO/Alq3/Co spin valves.

Our work is a new step forward in organic spintronics, as we prove that organic semiconductors do not have a clear limit for room temperature performance with the adequate ferromagnets, and we present a reliable model that could be easily extrapolated to predict the output of different materials combinations in hybrid spin valves.

[1] Dediu, V., Murgia, M., Matacotta, F.C., Taliani, C. & Barbanera, S. Sol. State Commun. 122, 181-184 (2002).

[2] Xiong, Z.H., Wu, D., Vardeny, Z.V. & Shi, J. Nature 427, 821-824 (2004).

[3] Majumdar, S., Majumdar, H.S., Laiho, R. & Osterbacka, R. J. Alloy & Compounds 423, 169-171 (2006).

[4] Santos, T.S., Lee, J.S., Migdal, P., Lekshmi, I.C., Satpati, B. & Moodera, J.S. Phys. Rev. Lett. 98, 016601 (2007).

[5] Xu, W., Szulczewski, G.J., LeClair, P., Navarrete, I., Schad, R., Miao, G., Guo, H. & Gupta, A. Appl. Phys. Lett. 90, 072506 (2007).

[6] Hueso, L.E., Riminucci, A., Bergenti, I., Zhan, Y. & Dediu, V. Adv. Mater. 19, 2639-2642 (2007).

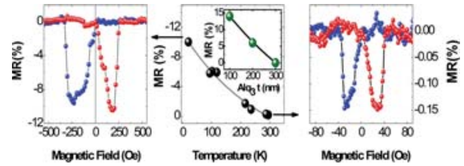

Figure 1. Magnetoresistance of a La0.7Sr0.3MnO3/Alq3(100 nm)/Al2O3/Co spin valve. a, Inverse spin valve effect at 20 K, showing a maximum value of 11%. b, magnetoresistance values with temperature, showing the decrease, but the persistence of the effect up to room temperature. c, room temperature inverse spin valve effect. The magnetoresistance of each individual electrode was carefully studied, enabling us to rule out anisotropic MR as the origin of our findings. A small background non-hysteretic signal, probably intrinsic to the organic semiconductor layer, was subtracted in every case to clearly show the hysteretic spin valve effect.

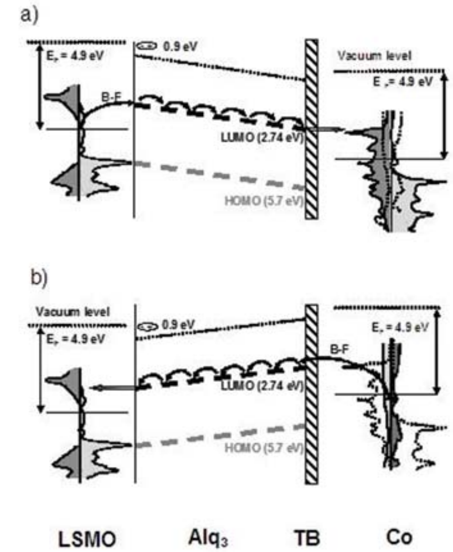

Figure 2. Energy diagram for a La0.7Sr0.3MnO3/Alq3/Tunnel Barrier/Co organic spin valve. a, Case when carriers are flowing from the LSMO to the d-states of Cobalt (continuous line, coloured plot). Cobalt s-states are also indicated by a dashed line b, Case when carriers are flowing from the s-states of Co (continuous line) to the LSMO. For the Cobalt DOS, d-states are also indicated by a dashed line. Light (dark) grey plots indicated spin up (down) polarization, respectively. Arrows indicate the carrier paths, including the resonance effect across the interfaces. B-F account for the multistep injection process proposed by Baldo and Forrest

DD-01

A novel 'pseudo' direct-drive brushless permanent magnet machine.

K. Atallah, J. Rens, S. Mezani, D. Howe
Electronic & Electrical Engineering, The University of Sheffield, Sheffield, United Kingdom

For low speed electrical machine applications, it is usually weight/size and cost effective to employ a high speed machine together with a mechanical gearbox. However, in many instances, the disadvantages associated with mechanical gearboxes, such as acoustic noise, mechanical vibration, the need for lubrication, concerns regarding reliability and maintenance requirements, make direct-drive solutions more functionally and/or economically attractive. Permanent magnet (PM) brushless machines exhibit relatively high torque densities, typically being ~30kNm/m3 for radial-field and ~50kNm/m3 for transverse-field liquid-cooled topologies [1-3]. However, although transverse-field machines exhibit the highest torque density, since their power factor is very low [4], typically between 0.3 to 0.5, the required inverter/converter VA rating is a factor of 2~3 times higher than that for an equivalent conventional brushless machine. This results in a significant cost penalty, which is limiting the take-up of transverse-field machine technology.

The paper describes a novel 'pseudo' direct-drive electrical machine, Fig. 1, in which a magnetic gear [5] and a radial-field PM brushless machine are mechanically and magnetically coupled. The machine combines the high power factor of a conventional brushless machine with the high torque density capability of a transverse-field machine. As can be seen in Fig. 2, which shows the harmonic spectrum of the radial flux density distribution due to the 2 pole-pair (ph) high-speed rotor permanent magnets, in the airgap adjacent to the outer 21 pole-pair (pl) permanent magnets (fixed to the stator bore), the 23 ferromagnetic pole-pieces (ns) on the low-speed rotor result in a large 21 pole-pair asynchronous space harmonic field, which interacts with the 21 pole-pair outer permanent magnets to achieve gearing, the gear ratio (Gr = ns/ph) being 11.5:1. However, a large 2 pole-pair fundamental field component still exists, which is employed to transfer power from/to the stator winding.

Fig. 3 compares the variation of the predicted geared electromagnetic torque and the measured output torque with the rms current density. It can be seen that, although the current density is less than 2Arms/mm2, a torque density in excess of 60kNm/m3 is achieved with natural cooling, at a power factor in excess of 0.9. In other words, whilst the stator winding is responsible for torque being developed by the high-speed rotor, since this is amplified by the magnetic gear action, the magnetic limit of the machine is reached before the thermal limit.

1. HARRIS M. R., PAJOOMAN G. H., ABU SHARKH S. M. : 'Comparison of alternative topologies for VRPM (transverse-flux) electrical machines', IEE Coll. New Topologies for PM Machines', Digest: 1997/090, 1997, pp. 2/1-2/7.

2. HARRIS, M. R., PAJOOMAN, G. H., ABU SHARKH, S. M.: 'Performance and design optimisation of electric motors with heteropolar surface magnets and homopolar windings', IEE Proc., Pt B, 143(6), 1996, pp. 429-436.

3. MITCHAM, A. J.: 'Transverse-flux motors for electric propulsion of ships', IEE Coll. on New Topologies for PM Machines', Digest 1997/090, 1997, pp. 3/1-3/6.

4 HARRIS M. R., PAJOOMAN G. H., ABU SHARKH S. M.: 'The problem of power factor in VRPM (transverse-flux) machines', 8th, IEE EMD Conf., 1997, pp. 386-390.

5. ATALLAH, K., CALVERLEY S. D., HOWE D.: 'Design, analysis and realisation of a high-performance magnetic gear', IEE Proc. Elec. Power Appl., 151, 2004, pp135-143.

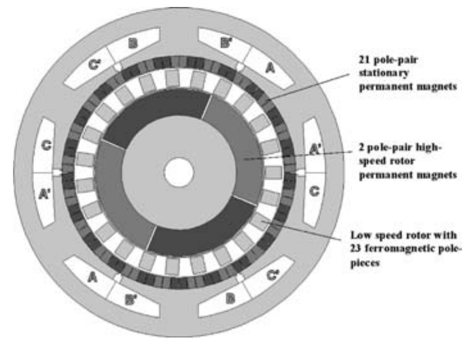

Fig. 1 'Pseudo' direct-drive, with magnetically & mechanically coupled magnetic gear & PM brushless machine

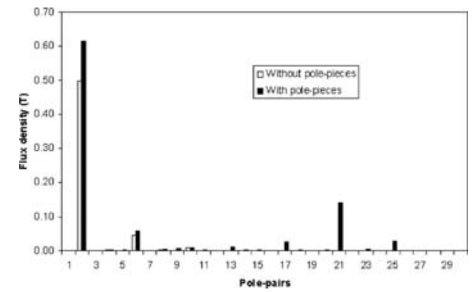

Fig. 2 Harmonic spectrum of radial flux density waveform due to the 2 pole-pair high speed rotor permanent magnets in the air-gap adjacent to the stationary permanent magnets

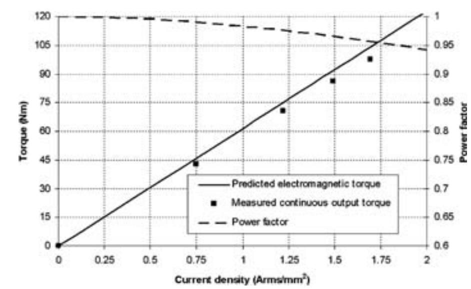

Fig. 3 Variation of low-speed torque and power factor with rms current density.

DD-02

Design optimization of a single-phase permanent magnet synchronous generator.

J. El Hayek[1], J. Brünisholz[2], P. Pittet[3]
1. Industrial Technologies, University of Applied Sciences Western Switzerland, Fribourg, Switzerland; 2. ATPS, ABB, Turgi, Switzerland; 3. Power Service, ALSTOM Ltd, Baden, Switzerland

This paper aims to present a study dealing with the design improvement of a single-phase permanent magnet synchronous machine used for distributed generation. It is a result of collaboration with a start up that is in phase of industrializing a Pico-hydroelectric power station, which answers a large request from developing countries where electrical supply networks do not reach the outskirts of large cities.
The investigation includes the permanent magnet reaction in short-circuit case, and the optimization of the maximum power that can be delivered by the generator. The heating and lifespan of the magnets, as well as the reduction in the harmonic distortions are also considered in this study.
1.Finite element (FE) magneto-dynamic model of the generator:
A model has been developed using the software Flux of Cedrat. Fig. 1 and Fig. 2 show respectively a part of the model with its meshing, and the associated electric circuit linked to the this model as well as the eventual load.
Simulation results are illustrated in Fig. 3. Voltage and load current present a certain harmonics rate, which can be minimized through a right choice of permanent magnets shape. Fig. 4 gives an optimized shape of the voltage, and Fig. 5 the temperature distribution in the machine.

2.Measurements and comparisons:
When Fig. 4 and 7 are compared, one can easily note the matching between simulation and reality.
3.Conclusion:
We could achieve an accurate model of the single-phase generator. Thank to this model the volume efficiency has been improved by a factor two; actually with same volume, the generator can deliver twice more power than before. In addition, the total harmonics distortion rate (THD) has decreased by a factor 5, from 15 % down to 3 %. And it is important to mention that these optimizations did not call any increase in terms of financial cost.

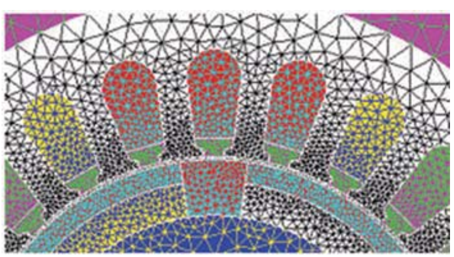

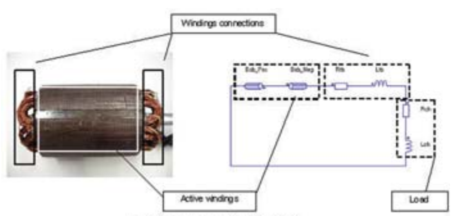

Fig. 2 Electric scheme linked to the FE-model

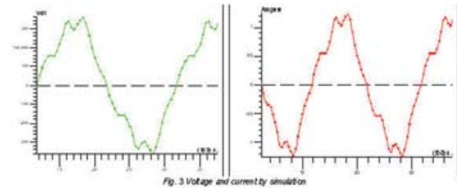
Fig. 3 Voltage and current by simulation

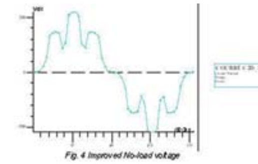
Fig. 4 Improved No-load voltage

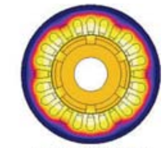
Fig. 5 Temperature distribution

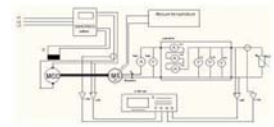
Fig. 6 Measurement layout

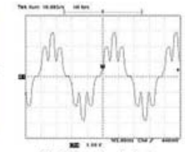
Fig. 7 Measured no-load voltage

DD-03

An Ultra-High Speed PM Motor for Small Milling Machine Applications.

J. Asama, *K. Maruyama*, Y. Yanagihara, A. Chiba
Electrical Engineering, Tokyo University of Science, Noda, Japan

I. Introduction

Small palm-sized milling machines, such as high precision machining grinders and dental milling tools, require an ultra-high rotational speed in its spindle. In these machines, an air turbine is often employed. However, the rotational speed decreases when a torque load is applied to the spindle. In addition, the air turbine produces high-frequency noises. An ultra-high speed electrical drive using a PM motor is expected for alternative drive sources. Many research groups have developed ultra-high speed PM motors [1]-[3]. However, these PM motors are relatively larger in size for palm-sized small milling tools. The objective of this paper is to design, fabricate, and test a small ultra-high speed PM motor. To achieve an ultra-high speed motor drive, a coreless stator with a magnetic yoke is fabricated. Basic motor characteristics are experimentally investigated with a comparison of calculated results by a computer simulation. The authors set a target of a few tens of watts in a shaft output at a rotational speed of 300,000r/min.

II. Design and Fabrication of Coreless PM Motor

Fig. 1 shows a configuration of a proposed coreless PM motor. Two motor units with a same design are built in tandem. One is used for a motor test, and the other is used for a torque load as a generator. An axial length and an outer diameter of a stator yoke is designed to be 5mm and 12mm, respectively. A rotor diameter including a sleeve is 6.1mm. Three-slot concentrated windings with non-magnetic teeth, *i.e.*, a coreless structure, are adopted. A low iron loss material, Super Core, is applied to the stator yoke. A fiber sensor is attached for a detection of a rotational angular position. The rated voltage and current are 24V and 2.3A, respectively. A forced air cooling is provided to remove heat generation. A fast controller with a FPGA device is fabricated for this ultra-high speed PM motor drive.

III. Basic Motor Characteristics

The fabricated motor was found to rotate up to 310,000r/min. By driving a motor, induced line-to-line emf is measured at a generator unit, as shown in Fig. 2. The measured induced emf is 20% smaller than the calculated values, which may be mainly caused by a flux leakage. Fig. 3 indicates measured copper loss of the motor, *Wcm*, and a sum of both mechanical and iron losses, *Wm* and *Wi*, at no load condition. *Wi* includes both the motor and generator losses. A rapid increase in losses may be caused by mechanical bearings because of both a coreless structure and a low iron loss yoke. By using these losses at no load condition and adjusting generator loads, a motor torque, *T*, is estimated from Eq. 1, where Pi is input power and *Wcg* is a generator copper loss at a load condition. Fig. 4 shows measured and calculated torques. At a speed higher than 250,000r/min, torque could not be measured because motor currents exceeded a rated value of 2.3A. The actual torque is below the calculation because the measured emf is smaller than the calculated one. The shaft output at 250,000r/min was 13W. In conference presentation and paper, more details in bearing and machine structures, measuring equipments, and test results of modified test motors will be included.

[1] C. Zwyssig et al., "Analytical and Experimental Investigation of a Low Torque, Ultra-High Speed Drive System," IEEE Trans. Power Delivery, vol. 3, pp. 549-557, Apr. 2006.

[2] J. Oyama et al., " The Development of Small Size Ultra-High Speed Drive System, " IEEE Trans. Power Conversion Conference-Nagoya.2007.PCC'07.

[3] L. Zhao et al., "A Highly Efficient 200000 RPM Permanent Magnet Motor System, " IEEE Trans on Magnetics, vol. 43, NO. 6, JUNE 2007.

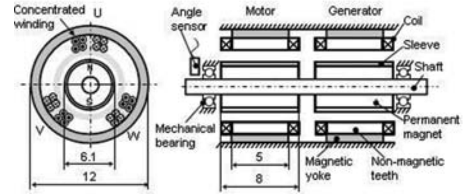

Fig.1

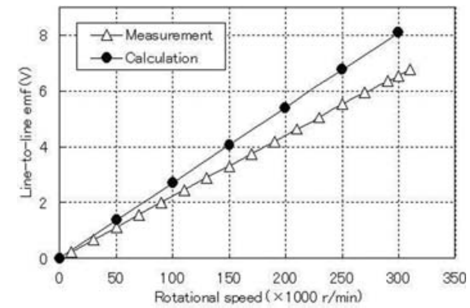

Fig.2

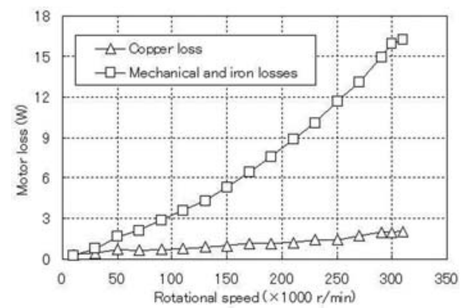

Fig.3

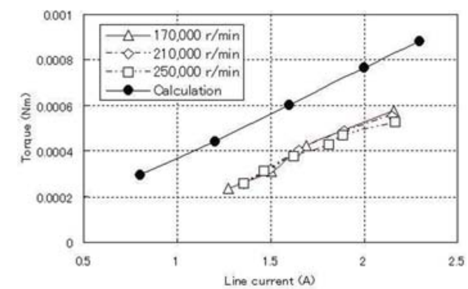

Fig.4

$$\omega T = Pi - (Wcm + Wcg + Wm + Wi) \ \ [\mathrm{W}] \qquad (1)$$

$$\eta = \omega T / Pi \times 100 \, [\%] \qquad (2)$$

DD-04

Design and analysis of a novel hybrid excitation synchronous machine with asymmetrically stagger permanent magnet.

Y. Chengfeng[1], *L. Heyun*[1], G. Jian[1], Z. Ziqiang[2]
1. School of Electrical Engineering, Southeast University, Nanjing, China; 2. Department of Electronic and Electrical Engineering, University of Sheffield, Sheffield, United Kingdom

There is an increasing tendency to study hybrid excitation machines for flux weakening operation recently. This kind of electrical machines combines the advantages of permanent magnet (PM) machines with the possibility of controllable flux by field windings [1-2]. Thus, it is easier to control the air-gap magnetic flux. A novel hybrid excitation synchronous machine with asymmetrically stagger PM (ASHESM) is developed in this paper. This machine combines the fixed excitation of PM with the variable flux produced by a toroidal field winding located on the inner stator. Besides, the PM pole and the solid iron pole are asymmetrically designed so that the flux of the prototype can be adjusted in a wide range with a relatively low field current. A set of design equations for ASHESM is derived. Three-dimensional (3D) finite element analysis (FEA) is employed to calculate the magnetic field distributions and to predict the flux adjusting performance of 1-kW ASHESM prototype. The predicted results are validated by experiments.

Fig. 1 shows the structure of the ASHESM, which consists of a rotor, an outer stator and an inner stator. The surface of claw-pole on rotor is divided into two sections, one is PM pole, and the other is a solid iron pole. PMs create a nearly constant flux, while the field winding currents generate a variable flux, both form the resultant flux in the air-gap. The flux generated by field windings may enhance (magnetize) or weaken (demagnetize) the PM flux according to the direction of field current, as shown in Fig. 2. If the flux generated by the field current flows in such direction that it is subtracted to the flux of the PM, the flux per pole closes its path in the same magnetic pole. Fig. 2(b) depicts this operating condition. In fact, in the air-gap, flux emanating from the PM and the iron pole cross the air-gap in opposite directions. As a result, the total flux per pole decreases as the field current increases. Flux essentially crosses the stator yoke axially. If the field current is reversed, the field flux uses the magnetic circuit as before, but flows in the opposite direction. Therefore, both components of the air-gap flux cross the air-gap in the same direction. Flux closes its path crossing the stator yoke essentially tangentially as is shown in Fig. 2(c).

The stator design for ASHESM is similar to that of the common PM synchronous machine. Due to the special design and control requirements of ASHESM, electric load, magnetic loading, machine sizing, field winding, rotor magnetic circuit structure and so on, all need to be specially designed. The electromagnetic design details will be given in the full paper. Based on the electromagnetic design method proposed for the ASHESM, a 1-kW 8-poles prototype is designed and manufactured as shown in Fig. 3. 3D Finite element method is used to analyze the static magnetic field of the ASHESM and to evaluate the field adjusting performance of the prototype machine. Fig. 4 shows the air-gap flux density with three different field currents. The resultant flux linkage and back EMF versus rotor position have also been obtained under different field currents and confirmed by experiments, as shown in Fig. 5. It shows that nearly 60% field control range can be achieved at no load and 55% at full load with a relatively low field current.

[1] J. A Tapia, F. Leonardi, T. A. Lipo. “Consequent pole permanent magnet machine with extended field weakening capability,” IEEE Transactions on Industry Applications, vol.39. no.6, pp: 1704-1709, 2003.

[2] Yacine Amara, JEAN Lucidarme, MOHAMED Gabsi, et al. “A new topology of hybrid synchronous machine,”. IEEE Transactions on Industry Applications, vol.37, no.5, pp. 1273-1278, 2001.

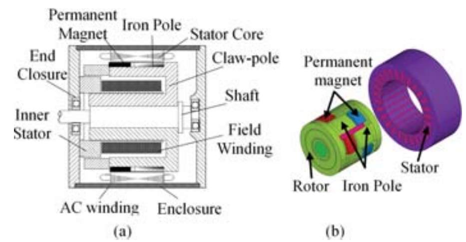

Fig.1 ASHESM. (a) Magnetic structure. (b) Stator and rotor model.

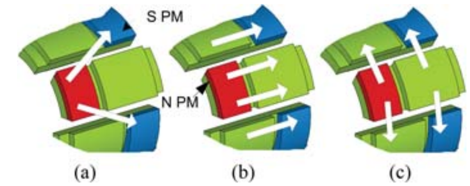

Fig.2 Field control principle of ASHESM. (a) PM flux. (b) Demagnetizing effect of field flux. (c) Magnetizing effect of field flux.

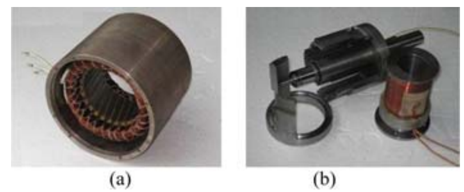

Fig.3 1-kW prototype assembly. (a) Stator. (b) Rotor.

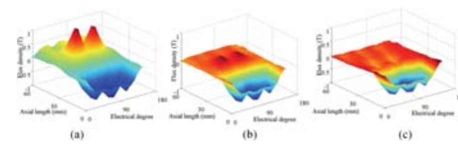

Fig.4 Air-gap flux distribution with different field currents. (a) -1.0A with field-weakening. (b) No field current. (c) 1.0A with field-enhancing.

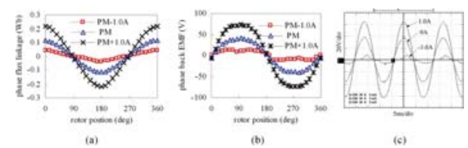

Fig. 5 Flux linkage and back EMF. (a) FE predicted flux linkage. (b) FE predicted back EMF. (c) Measured phase back EMF.

DD-05

Novel axial flux permanent magnet synchronous machines with segmented and laminated stator configuration.

W. Fei, P. Luk
Department of Aerospace Power and Sensors, DCMT Cranfield University, Shrivenham, United Kingdom

Axial flux permanent magnet (AFPM) machines have unique characteristics such as high aspect ratio, high torque density, and excellent efficiency that make them cogent candidates for electric propulsion. However, stator lamination fabrication is more difficult for AFPM machines when compared with their conventional radial flux counterparts. Recently, a new AFPM machine using soft magnetic composite (SMC) instead of laminated steel has been introduced [1,2], where a new yokeless and segmented armature (YASA) topology is also proposed to improve torque density. However, SMC machines are normally suitable for medium and high speed applications due to the poor core loss behaviour of the material under low frequencies (below 1 kHz) [3]. SMC is also much more expensive than laminated steel. This paper presents a novel AFPM for low speed applications utilizing steel laminated stator. In order to manufacture the steel laminated stator poles, an innovative stator pole structure is employed as shown in Fig.1 The machine stator poles with concentrated windings are segmented individually, and stacked together as an integrated stator by two high strength aluminium alloy ring holders. This structure thus possesses a number of advantages similar to the YASA configuration: (a) shortened end windings leading to higher power density, (b) ease of winding process and high winding fill factor, (c) reduced mutual inductance between the machine phases resulting in improved phase independency and fault tolerance, and (d) reduced stator core weight due to the absence of the stator yoke.
Generally, distributed integral-slot-windings are used for AFPM synchronous machines to produce sinusoidal or near sinusoidal back EMF waveforms. A high number of stator poles are essential for integral-slot-winding machines, which might make the proposed structure more difficult, or even impossible. In this paper, concentrated fractional-slot-windings are employed in order to achieve the proposed structure. To overcome the complexity in the modelling and analysis, an efficient yet accurate analytical model for AFPM machine is synthesized. Two typical fractional slot structures (12/10 and 12/8) with same stator pole number (twelve) and different magnet pole numbers (ten and eight) are studied first using the analytical model. It is found that, both non-triplen back EMF harmonics and cogging torque are much lower in the 12/10 structure. Consequently, a 5-kW 1000rpm AFPM synchronous machine with a 12/10 structure is designed, and the prototype machine is shown in Fig.1. To validate the analytical model, a comprehensive three-dimensional (3-D) finite element analysis (FEA) model of the prototype is developed. The cogging torque values from the analytical, 3-D FEA models and experimental measurements are compared in Fig.2. The results show close agreements, and the relatively low cogging torque of the proposed machine. The line back EMF values are compared in Fig.3, which also shows very close agreements. Noticeably, the line back EMF waveform is nearly sinusoidal, which can bring about excellent machine performance. From the results, it can be concluded that the proposed analytical model is efficient to be used for optimization and performance prediction of AFPM machines and the proposed 12/10 structure machine using the novel laminated steel stator is an eximious contender for electric propulsion.

[1] T. J. Woolmer, and M. D. McCulloch, "Axial flux permanent magnet machines: a new topology for high performance applications," IET Hybrid Vehicle Conference 2006, Warwick, pp. 27-42.

[2] T. J. Woolmer, and M. D. McCulloch, "Analysis of the Yokeless And Segmented Armature Machine," IEEE International Electric Machines & Drives Conference 2007, pp. 704-708.

[3] A. Parviainen, "Design of axial-flux permanent-magnet low-speed machines and performance comparison between radial-flux and axial-flux machines," PhD Thesis, Lappeenranta University of Technology, 2005.

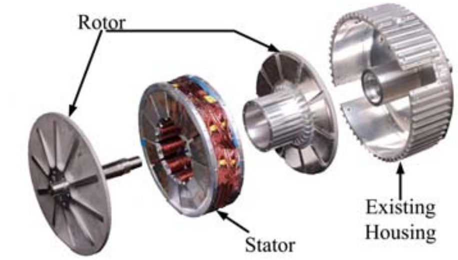

Fig.1. Exploded view of prototype

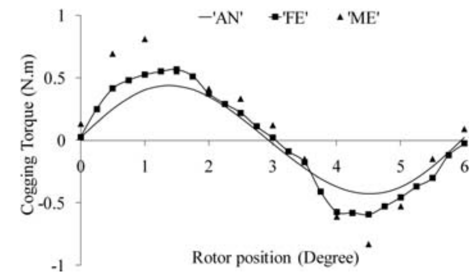

Fig.2. Cogging torque of the prototype ('AN'-analytical, 'FE'-3D FEM, 'ME'-measure)

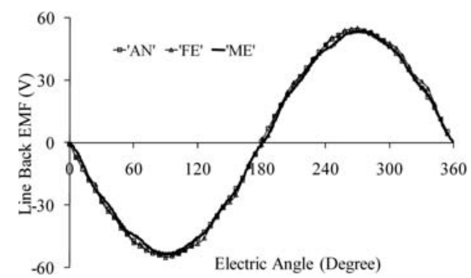

Fig.3. Line back emf of the prototype at rated speed 1000rpm ('AN'-analytical, 'FE'-3D FEM, 'ME'-measure)

DD-06

Modeling of a linear and rotative permanent magnet actuator.

G. Krebs[1], A. Tounzi[1], B. Pauwels[2], D. Willemot[2], F. Piriou[1]
1. L2EP-USTL, Villeneuve d'Ascq, France; 2. Psicontrol Mechatronics, Ieper, Belgium

Actuators with complex movements are of greatest interest [1]. In this paper, we study an open slot PM synchronous actuator which is aimed at implementing linear and/or rotary (l&r) movements simultaneously or independently. First, the actuator is described. Then, using a 3D-FEM code, calculations were carried out. The results are given as well as first measurements on a constructed prototype.

The actuator is constituted of two stators and a cylindrical rotor. Open slot PM synchronous machines were used for either the linear or the rotary movements where the PM are placed inside a non magnetic cylindrical support. Concentrated coils were chosen for the phase windings to simplify the construction. To ensure a dynamical behaviour, the numbers of the pole pairs have been chosen the lowest possible. Features of the designed actuator are given in table 1.

A prototype has been designed. The windings on the inner stator were omitted. Therefore, we used the inner part to put on the guidance system (Fig. 1).

To perform the study, we used a 3D-FEM code with a scalar potential formulation [2]. A special procedure was used to take into account both movements in different directions.

The actuator studied was meshed using hexahedron elements. To limit their number, the air parts on both sides of the actuator have been reduced. Periodical conditions have been imposed assuming an infinite rotor. The mesh is constituted of approximately 261,000 elements and 272,000 nodes. Each air-gap has two layers of elements. The linear displacement is 1 mm and the rotation angle is 1.5 degrees.

In Fig.3, we present the linkage fluxes, at no load, for a diagonal movement. As expected, the fluxes constitute a product of cosines.

Other calculations have been carried out to obtain the forces and thrust either at no load or at rated operating. In table 2, we give the maximal value obtained from the numerical calculations at rated operating points.

A prototype has been constructed further to the results obtained from numerical calculations. In figure 4, we give pictures of the rotor and the whole constructed l&r actuator.

First measurements have been carried out. In figure 5, we compare a linkage flux obtained by the simulation and measurement when the rotor is moved in rotation. The results are in good agreement.

[1]P.Bolognesi, O.Bruno, A.Landi, L. Taponecco "Electromagnetic actuator featuring multiple degrees of freedom: a survey", ICEM 2004, 5-8 september 2004, Krakow Poland.

[2]Y. Le Menach, S. Clenet, F. Piriou, "Numerical model to discretize source fields in the 3D finite element method", IEEE Trans. Mag., vol. 36, Issue: 4, July 2000 pp: 676 – 679

Parameter	
Number of slots or coils	18
Number of magnets	56
Rated frequency (Hz)	Up to 100
Rated rotary speed (rpm)	1200
Rated linear speed (m/s)	3

linear motion, thrust (N)	44.4
rotary motion, torque (Nm)	0.83
Helicoidal, thrust (N)/torque (Nm)	23 / 0.433

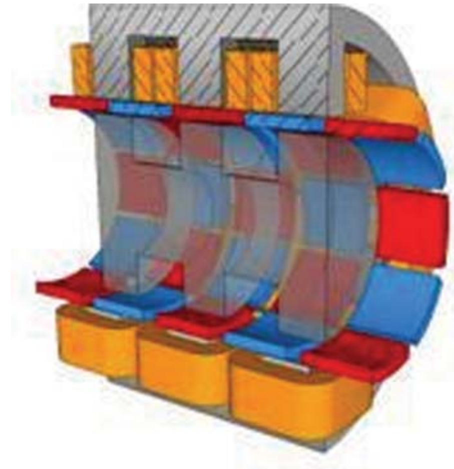

Fig. 1

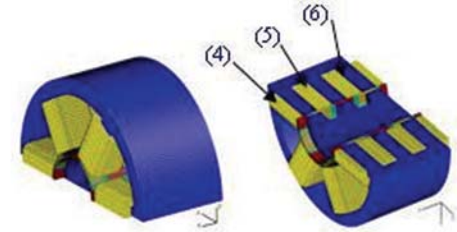

Fig. 2

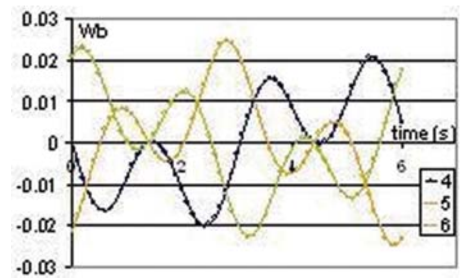

Fig. 3

Fig.4

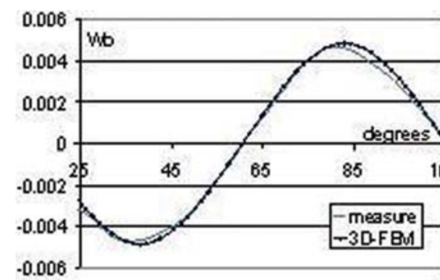

Fig.5

DD-07

Analysis and experimental verification of a single phase, quasi-Halbach magnetised tubular permanent magnet motor with non-ferromagnetic supporting tube.

J. Wang, T. Ibrahim, D. Howe
Electronic and Electrical Engineering, University of Sheffield, Sheffield, United Kingdom

Direct-drive linear reciprocating compressors offer numerous advantages over conventional counterparts which are usually driven by a rotary induction motor via crank shaft [1]. A novel design of single-phase, short-stroke, linear permanent magnet (PM) motor has recently been developed [2], and used in the linear compressor application. The moving-magnet armature of the motor employs quasi-Halbach magnetised magnets mounted on a mild steel supporting tube. While this design results in a great force capability it also leads to a heavy moving mass and hence greater spring stiffness, which will compromises the dynamic capability of the compressor system [3]-[4]. Further it has been shown [5] that eddy current loss incurred in the supporting tube will affect the efficiency of the compressor system.

The paper describes an alternative design in which the quasi-Halbach magnetised magnets are mounted on a non-ferromagnetic support tube, as shown in Figure 1, and analyses its performance. The open-circuit magnetic filed distribution is established analytically in terms of a magnetic vector potential formulated in the cylindrical coordinate system. The analytical field solution allows the prediction of flux linkage, back-emf and thrust force of the actuator in closed forms and facilitates design optimisation. The analytically predicted results are validated by finite elements analyses.

Figure 2 compares analytically predicted and finite element calculated variation of open-circuit radial flux density in the middle of airgap with axial position z. As will be observed, the analytical solution agrees broadly with the finite element prediction, the rms percentage difference is relatively small, being 5.09%.

A prototype has been constructed and its static performance evaluated. Figure 3 shows the test rig which was used to measure the static performance such as variation of flux linkage and thrust force with the armature position. The micrometer barrel was used to adjust the armature position, and the load cell, LVDT and flux meter (no shown) were employed to measure thrust force, axial position and flux linkage of the coil, respectively.

Figure 4 compares the variations of measured and finite element predicted thrust force with axial position of the armature. As will be seen, the experimental results agree reasonably well with finite element calculation.

Detailed analysis and design together with more experimental results such as flux linkage and cogging force will be included in the full paper. Comparative study in terms of efficiency and the cost of materials for two alternative tubular PM motor designs (with non-ferromagnetic or ferromagnetic supporting tube) will also be reported.

[1]K. Park, E. P. Hong, and K. H. Lee, "Development of a linear motor for compressors of household refrigerators", Proc. of 2001 Linear Drives and Industry Applications (LDIA'2001), Nagano, Japan, pp. 283-286, 2001

[2]J. Wang, D. Howe, and Z. Lin, "Comparative Studies on Linear Motor Topologies for Reciprocating Vapour Compressor", Proc. of IEMDC2007, Antalya, Turkey, 3-5 May, 2007, pp. 364-369.

[3]G. S. Choe, and K. J. Kim, "Theoretical and experimental analysis of nonlinear dynamics in a linear compressor", Trans. of ASME, J. of Vibration and Acoustics, Vol. 124, 2002, pp. 152-154.

[4]B. J., Huang, and Y. C. Chen, "System Dynamics and Control of Linear Compressor for Stroke and Frequency Adjustment", Trans. of ASME, J. of Dynamic Systems, Measurement, and Control, Vol. 124, 2002, pp. 176-182.

[5]J. Chai, J. Wang and D. Howe, "Evaluation of eddy current loss in tubular permanent magnet motors by three-dimensional finite element analysis", Proc. ICEM2006, Paper ID: PSA1-12, Chania, Greece, 2-5 September, 2006.

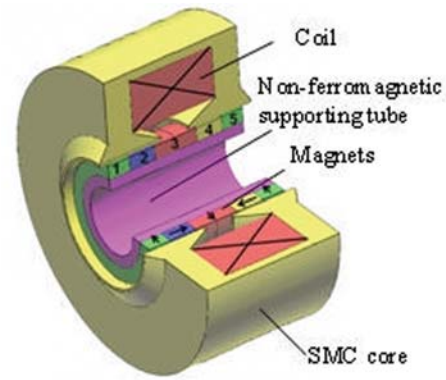

Figure 1 Schematic of single-phase, short-stroke, tubular permanent magnet motor

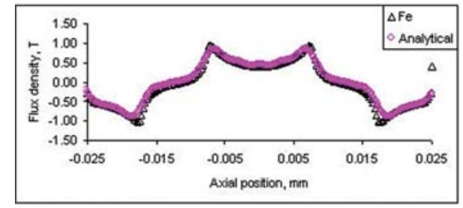

Figure 2 Comparison of radial flux density in air-gap

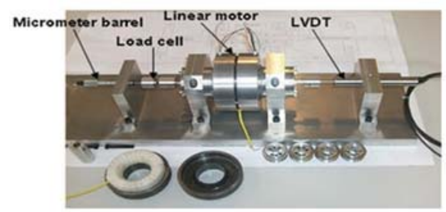

Figure 3 Static test rig for single-phase tubular PM motor

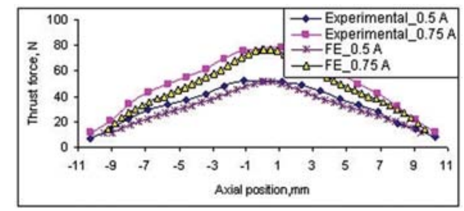

Figure 4 Variations of measured and predicted thrust force with armature position

DD-08

Optimization of a sea wave energy harvesting electromagnetic device.

M. Trapanese
Dipartimento di Ingegneria Elettrica, Elettronica e delle Telecomunicazioni, University of Palermo, Palermo, Italy

Current energy crisis and general concerns on environmental issues have triggered an ever increasing effort on harvesting renewable energies.
Amongst renewable energy sources, sea wave energy is definitely the one that has been less utilised. This is probably caused by three reasons: i) the low energy concentration in the sea waves, at least in the sites where it is technically possible to install conversion stations: ii) the strong technical novelties that are required to extract the energy that is contained in a highly and stochastically variable motion; iii) the difficulty to find a suitable electrical system able to convert the energy contained in the motion of the sea into electrical energy.
Several approaches to harvest sea wave energy have been proposed; almost all of them introduce a mechanical conversion device between the waves and the electromagnetic generator. This stage converts the mechanical energy contained in the waves into a more usable mechanical energy; it can be a hydraulic coupling device or a mechanical gear and, in any case, introduces additional losses and additional maintenance requirements. In order to reduce these losses a generator directly coupled to the sea waves should be used.
This paper presents the optimization of a permanent magnet linear generator directly coupled to sea waves.
Linear electrical generator has been recently studied for the exploitation of sea wave energy [1-2]. In order to maximize energy extraction, the stochastic features of the energy source must be included in the mathematical model of the system in order to satisfactorily tackle the problem. Moreover, they strongly influence the magnetic design. In order to study how to overcome the above said difficulties a PM linear electrical generator has been designed and built.
The principle of operation of the generator is shown in fig.1. The moving part of the generator is driven from the sea waves and induces and emf on the winding mounted on the armature.
The mathematical model includes the dynamic equations of the moving part of the generator and the electric equations of the winding. The coupling parameters (inductances, fluxes etc.) have been determined by a FEM analysis (which includes a careful analysis of the boundary conditions, because of the fact that the machine is working in a conductive medium).
The design has been optimized by including in the mathematical model used for the optimization the following aspects:

1. the dynamic and stochastic features of the waves;
2. a dynamic model of the hydraulic conversion system;
3. a parametric circuit model of the magnetic circuit as well as of the electric windings;
4. A circuit model of the power electronics converter used to connect the generator to the utility.

The main innovation of the optimisation approach proposed is that the speed of the machine is neither supposed known nor supposed fixed, but the stochastic features of the imposed movement are the factors that mostly influence the optimisation process.
The optimization has been performed by finding the maximum of an objective function that has been built on the basis of the mathematical model developed. The variables of the function were related to the magnetic circuit of the converter, the parameters to the stochastic features of the waves as well as to the characteristics of the hydraulic system and of the power electronics converter.
The results show several maxima that indicate several possible alternative designs. In order to verify the results, a reconfigurable machine has been built and tested in laboratory.
The tests have verified the value of the emf, of the magnetic induction as well as of the power production in several configuration of the machine.
In a scaled down version of the machine, it has been possible to generate almost 100 watt and to reach an output voltage of 200 V peak to peak. These values were in agreement with the design values within an error of 15%.

[1] Leijon, M.; Bernhoff, H.; Agren, O.; Isberg, J.; Sundberg, J.; Berg, M.; Karlsson, K.E.; Wolfbrandt, A. “Multiphysics simulation of wave energy to electric energy conversion by permanent magnet linear generator”, IEEE Transactions on energy conversion vol. 20, N.1, pp. 219- 224, 2005.

[2] Polinder H., Gardner F. and Vrisema V., “Linear PM generator for wave energy conversion in the AWS”, in Proc. ICEM 2000, Espoo, Finland, 2000.

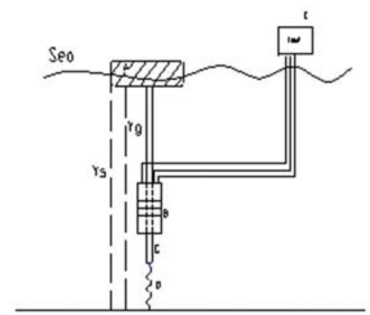

Fig.1 Schematic description of a conversion system based on a PM linear generator. A is the buoyant, B is the PM linear generator, C is the slider, D is the spring and E is the electrical load.

Design and characteristic analysis on the short-stator linear synchronous motor for high-speed Maglev propulsion.

H. Cho[1], H. Sung[1], S. Sung[1], D. You[2], S. Jang[2]
1. Maglev Research Team, Korea Institute of Machinery and Materials, Daejeon, South Korea; 2. Electrical Engineering, Chungnam National University, Daejeon, South Korea

Recently, the linear motors has been used in linear motion load without gears, screws or crank shafts. They are used widely in automation systems, manufacture, transportation, transfer system and military area, etc [1]. In particular, the linear synchronous motor (LSM) has many advantages, such as high efficiency, high power factor, high positional precision and so on. By reason of these remarkable advantages, German 'Transrapid' and Japanese 'MLX' chose the LSM as a propulsion device for their high-speed Maglev. This paper deals with the design and chacteristic analysis on the LSM for high-speed propulsion system. Important design criteria are established based on the two-dimensional (2-D) analytical method under several assumptions and the results are compared with the numerical solutions by the finite element analysis (FEA). An experimental system for SLSM propulsion was also constructed and tested to confirm the analytical design and high-speed operation.
In this study, in order to construct the experimental system for LSM, the short-stator linear synchronous motor (SLSM) has been employed. Fig. 1(a) shows the basic structure of SLSM. The primary member contains ployphase winding and is similar to its linear induction motor (LIM) counterpart. The secondary member requires a DC excitation winding. Interaction between the magnetic field and armature currents produces the thrust force. The speed of traveling magnetic wave depends on power supply's frequency. Fig. 1(b) shows the analytical model of SLSM. In order to establish analytical solutions for the magnetic field distribution in the machine, this study assumes that both the relative permeability of the core material and z-axis length is infinite. Letter (a)-(d) represent the surfaces at the indicated boundaries and y0 denotes the airgap length.
Figs. 2(a) and (b) show the flux density distribution in the airgap region and core material, respectively. The analytical solutions agree well with the finite element analysis (FEA) results. Fig. 3 shows the three-dimensional (3-D) drawing of SLSM experimental system. Figs. 4(a) and (b) show the manufactured 3-phase primary and 1.5 meter diameter secondary of SLSM, respectively. Acceleration tests were performed from 0 rpm to 1000 rpm which corresponds to 0 km/h and 283 km/h, respectively. Fig. 5 shows the acceleration characteristics of the SLSM when the machine works with vector control. The airgap length is fixed on constant uniform length of about 10 mm.
The LSM with short-stator running at rated speed of 400 km/h (max. 550 km/h) has been designed, manufactured, and tested. The experimental results from a SLSM test set confirmed the validity of the proposed design scheme.

[1]G.W.McLean, Proc. IEE, Electric Power Applications, 135, 380 (1988).

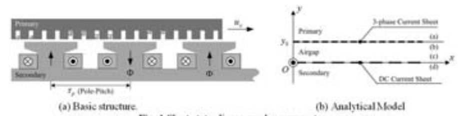

(a) Basic structure. (b) Analytical Model
Fig. 1 Short-stator linear synchronous motor.

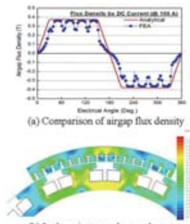

(a) Comparison of airgap flux density
(b) In the primary and secondary core
Fig. 2 Flux density distribution.

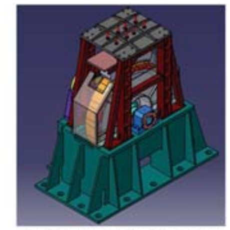

Fig. 3 3-D drawing of the SLSM test wheel construction.

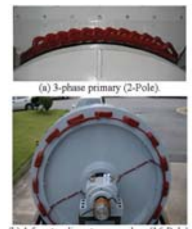

(a) 3-phase primary (2-Pole).
(b) 1.5 meter diameter secondary (16-Pole).
Fig. 4 Manufactured SLSM.

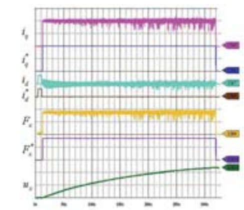

Fig. 5 Acceleration test results, $i_{d,q}$: d, q-axis current, $i_{d,q}^*$: d, q-axis current reference (100A/div.), F_x : thrust, F_x^* : thrust reference (266 N/div.), u_x : speed (115 km/h/div.).

DD-10

Eddy-current stator solid steel back-iron losses in small rotary brushless permanent magnet machines.

J. J. Paulides, K. J. Meessen, E. A. Lomonova
Technical university Eindhoven, Eindhoven, Netherlands

There is a growing interest in employing small slotless permanent magnet machines in direct-drive low-cost servo systems, i.e. demanding precision dynamic characteristics, due to their simple geometry, torque ripple reduction and possible self-bearing [1]. Albeit that the ever increasing necessity to miniaturize has placed severe constraints on the current slotless technology, since it inherently has a relatively large effective magnetic airgap which limits the magnetic loading that can be realised. However, even this reduced magnetic loading still results in considerable eddy-current losses, when a solid back-iron is implemented for costs purposes, which need to be reduced by selecting the most appropriate soft magnetic material for each application.
Considerable efforts have been devoted to analyze and improve the loss characteristics of laminated and solid soft magnetic materials [2]. These iron losses are a major roadblock in the efforts to miniaturize low cost slotless electrical machines, i.e. (0.1-1 watts). The classical approach to model iron losses are explained by the three well-known loss phenomena, namely, hysteresis loss, classical eddy-current loss, and the excess eddy-current loss [3]. In order to simplify the modelling of the eddy-current loss within the 2D finite element (FE) analysis (Fig. 1), the machine is assumed to be infinitely long. This means that instead of eddy-current loops, the induced currents are assumed to flow in the axial direction. It needs noting that 2D, compared to 3D, FE modelling provides a total eddy-current loss prediction that is overestimated, hence it is a useful approximation due to its ease of implementation. All the initial simulations, used to investigate the influence of different materials on the eddy-current loss, are performed at a fixed speed of 1200 rpm (470mW) and the hysteresis losses and excess losses in the back-iron are calculated to be 20 mW. To calculate the total eddy-current losses, the back-iron is split into 20 rings. In each ring, the current density is assumed to be constant in the radial direction. Fig. 2 shows the current density versus angle in the rings of the back-iron. The inner ring has the highest current density and the outer ring the lowest current density. The losses are calculated using the rms value of the current density in one ring, integrated over the surface of that ring. The current through the ring squared times the resistance of the ring gives the eddy current loss in each ring, which is summed to provide the total eddy current loss in the back-iron.
In most publications the iron loss analysis efforts are limited to making iron plates into thinner laminae or adding more silicon elements to steel boards to reduce iron loss. Although the benefits of employing higher electrical resistivity materials are indeed evident, viz. 1.4x10-7Ωm and 6.0x10-7Ωm give respectively 360mW and 80mW eddy-current loss this comes at a considerable premium in material costs. To validate the findings of the finite element study, iron losses under various speed conditions are measured on a prototype, as shown in Fig. 3. The measured iron losses include the hysteresis losses and excess losses, hence, it can be concluded that the prediction and the measurements provide a good clear perception of the eddy-current loss in the back-iron. Using the analysis and measurements it will be shown that the eddy-current loss, e.g. using the solid core material, causes a damping torque, which can be as high as the propulsion torque, and will initiate severe servo characteristic degradation.

[1] Z. Ren and L.S. Stephens, "Force Characteristics and Gain Determination for a Slotless Self-Bearing Motor," IEEE Trans. Magn., vol. 42, 1849-1860, 2006.

[2] G. Bertotti, Hysteresis in magnetism for physicists, Material Scientists, and Engineers (Academic, New York, 1998).

[3] R.M. Bozorth, Ferromagnetism (IEEE, New York, 2003).

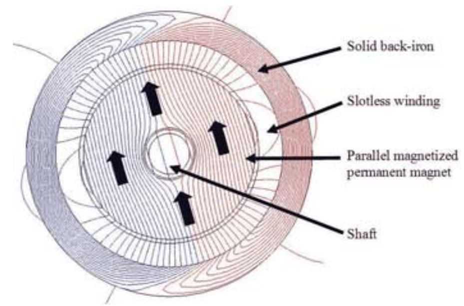

Equi-potential contours due to the eddy-currents in a two pole slotless permanent magnet machine (2D FEM).

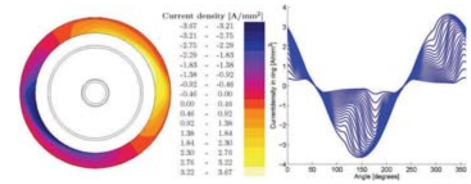

Eddy-current density within solid back-iron of the brushless permanent magnet machine at various radii.

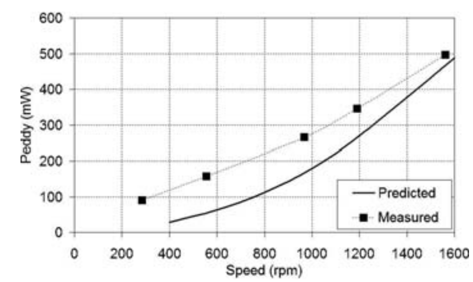

Measured total iron losses versus predicted eddy current losses.

DD-11

Experimental Method and Verification to Characterize the Unbalanced Magnetic Force in Electric Motors.

C. Lee, G. Jang
Dept. of Mechanical Engineering, PREM Lab., Hanyang University, Seoul, South Korea

Magnetically induced vibration is becoming common and serious in many electric motors since the advent of high grade permanent magnet (PM). Motor or supporting structures are excited by the traveling magnetic force or the torque between the rotating PM and the stator in case of a brushless DC (BLDC) motor. Many researchers investigated the characteristics of unbalanced magnetic force (UMF) in a BLDC motor theoretically or numerically [1, 2, 3]. UMF exists even in the rotationally symmetric design due to various manufacturing errors such as uneven magnetization of PM, rotor or stator eccentricity. However, an effective experimental device or even a publication to measure the UMF of an electric motor has not been reported. This research develops the experimental device to measure the UMF in electric motors directly. It also characterizes the UMF due to uneven magnetization of PM in a BLDC motor with the finite element analysis and the spectral analysis.

Fig.1 shows the developed experimental device to measure the UMF of electric motors. UMF of electric motors can not be measured in the assembled state of a rotor and a stator with bearings, because the UMF is exerted to the rotor and the stator to move the rotor to another equilibrium state by deforming the bearing. So this device measures the UMF once the rotor is taken apart from the motor assembly. The stator is fixed on the rotating stage, and the rotating stage is connected to a stepping motor through a belt. A load cell is attached to the separated rotor which is fixed to the xyz-table. The center of the rotor assembly is located at the rotational center of the stator assembly by moving the xyz-table. Then, the stator assembly on the rotating stage is rotated constantly by the stepping motor, and the variation of UMF exerted to the rotor is directly measured by the load cell of the rotor assembly.

The developed device is applied to a BLDC motor with 12 poles and 9 slots used in a computer hard disk drive. Once the rotor is taken apart, the magnetic flux density of PM's surface is measured with a Gauss-meter. It was found that PM is unevenly magnetized in such a way that maximum and minimum values of surface magnetic flux density are 142.7 mT and 130.9 mT, respectively. The peaks of magnetization of PM are uneven with 9 % difference. Then separated rotor and stator are fixed to the developed device to measure the UMF due to uneven magnetization of PM. Fig. 2 shows the measured and simulated UMF in the x directions, and their frequency spectra. Simulated magnetic force is calculated by using the finite element method and the Maxwell stress tensor once the B-H curves of PM are determined from the measured surface magnetic flux density of PM. It shows that the measured UMF matches well with the simulated one. Fig.2 (b) shows that the UMF has the dominant first harmonic, and the 9th harmonics, i.e. 8th and 10th, and 17th and 19th, etc. The second, third, and fourth harmonics existed only in the measured UMF are presumed to be experimental error. This phenomenon is effectively explained with the principle of the experimental device. Because the stator assembly rotates and the UMF is measured in the stationary rotor assembly in this experiment, the measured value is the UMF in the rotating coordinate and it repeats whenever a slot passes the load cell. It generates the slot effect so that the UMF in the rotating coordinate, i.e. F_r can be decomposed with Fourier series as follows:

$$F_r=\Sigma F_i \sin(ik\omega t+\phi_i) \quad (1)$$

where k and ω are the slot number and the rotational speed, respectively. It can be transformed to the fixed stationary coordinate, and the UMF in the x direction can be expressed as follows:

$$F_X=\cos\omega t\,\Sigma F_i \sin(ik\omega t+\phi_i)=1/2\,\Sigma F_i[\sin\{(ik-1)\omega t+\phi_i\}+\sin\{(ik+1)\omega t+\phi_i\}] \quad (2)$$

The above equation shows that the slot effect in the rotating coordinate, i.e. ik is transformed to the slot harmonics±1, i.e. $ik\pm1$ in the stationary coordinate [2]. The developed method is also performed to investigate the characteristics of UMF of electric motors due to rotor or stator eccentricity. This research will contribute to the reduction of the magnetically induced vibration and noise of electric motors by identifying the characteristics of UMF in electric motors.

[1] G.H.Jang, J,W,Yoon, N.Y.Park and S.M.Jang, "Torque and unbalanced magnetic force in a rotational unsymmetric brushless DC motor," IEEE Trans. Magn., vol. 32, no. 5, pp. 5157-5159, 1996

[2] Taeyong Yoon, "Magnetically induced vibration in a permanent-magnet brushless DC motor with symmetric pole-slot configuration," IEEE Trans. Magn., vol. 41, no. 6, pp. 2173-2179, 2005

[3] A. Hartman and W. Lorimer, "Undriven vibrations in brushless DC motors," IEEE Trans. Magn., vol. 37, no. 2, pp. 789-792, 2001

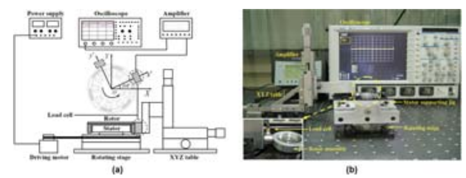

Fig. 1 Experimental setup to measure UMF in electric motors

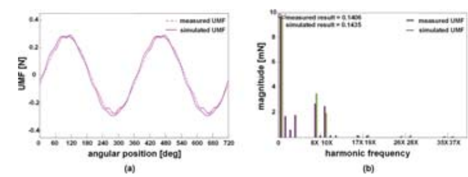

Fig. 2 Measured and simulated UMF in the x directions, and their frequency spectra (a) time domain and (b) frequency domain

DD-12

Study of an electromagnetic gearbox involving two PM synchronous machines using 3D-FEM.

M. Aubertin, A. Tounzi, Y. Le Ménach
L2EP - USTL, Villeneuve d'Ascq, France

An electromagnetic gearbox [1] has been designed for a combined automotive clutch and gearbox application. It is constituted of two PM synchronous machines with different rotation speeds. The system designed is presented and studied using 3D-FEM with the help of a procedure aimed to take account of two different speeds. Results are presented.

The designed system is a bell shaped device constituted of two open slot PM synchronous machines (Fig. 1). The rotor of the inner structure is linked to the source (i.e. the combustion engine) and rotates at high speed. The stator of the inner machine, which is also the rotor of the outer structure, is linked to the load (i.e. the wheel transmission). It rotates at a reduced speed. The stator of the outer machine is static. Both stators contain three phase windings but with different pole pair numbers. The stator of the inner part must be supplied through rotating rings.

The purpose of the system is to yield the combustion engine operating on constant power levels with a better efficiency. It only transfers power from the source to the load, thus its rated power is relatively low. Both windings are linked to a DC supply through converters. The supply of the inner stator windings allows varying the mechanical ratio of the gearbox through the frequency. The windings of the outer stator allow compensating the power between the one of the combustion engine and that of the load.

Using the locked step approach [2], slip surfaces, with regular meshes, are defined in each air gap. Thus, each of both displacements is modeled by a circular permutation of the unknowns by a mesh step or an integer multiple of this last according to the corresponding speed.

A prototype has been designed for a rated power of 5kW and the speeds related to the internal combustion engine and the wheels of a car, at 50km/h. A flux separator has been put to isolate magnetically both structures. Different features of the system are given in table 1.

In Fig. 2, a 3D view of the designed prototype is given with the different windings, magnets and magnetic separator.

The mesh of the whole modeled part is constituted of 610,200 elements and 177 000 nodes. Using a 3D-FEM code with the scalar potential formulation, calculations have been carried out at no load and rated operating taken into account the two speeds of both moving parts.

Fig. 3 shows the linkage fluxes at no load and rated speeds for both structures.

In Fig. 4, we present the electromagnetic torque, for both structures calculated at the rated supplying currents and speeds.

[1]Chau K.T., Dong Z., Jiang J.Z., Chunhua L., Yuejin Z.: "Design of a magnetic-geared outer-rotor permanent magnet brushless motor for electric vehicles", IEEE Trans Mag, Vol. 43, No 6, pp: 2504-2506.2007

[2]X. Shi, Y. Le Menach, J.P. Ducreux, F. Piriou, "Comparison of slip surface and moving band techniques for modelling movement in 3D with fem", COMPEL, Vol. 25, N°. 1, pp: 17-30, 2006

Parameter	Inner machine	Outer machine
Diameter of the rotor (mm)	144	250
Air gap (mm)	1	1
Number of slots	6	12
Number of magnets	8	16
Phase current (A)	29	22
Rated frequency (Hz)	100	60
Rated speed (rpm)	1500	450
Thickness of the magnets (mm)	3	4

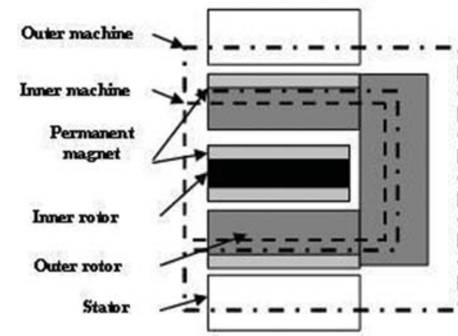

Fig1 : Scheme of the structure

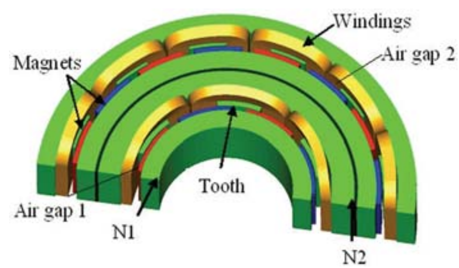

Fig2 : Geometry

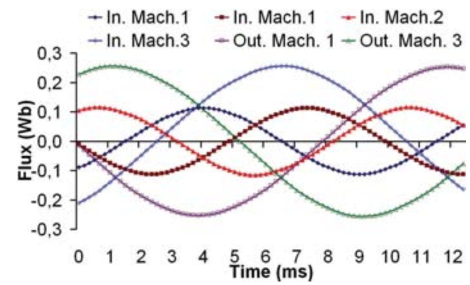

Fig3: Flux linkages

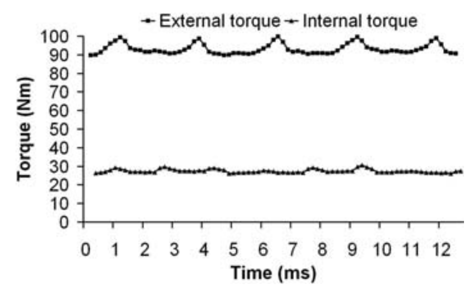

Fig4: Torque

DE-01

Domain wall propagation in thin magnetic wires.

R. Varga[1], K. Richter[1], A. Zhukov[2], V. Larin[3]
1. Institute of Physics, Faculty of Sciences, UPJS, Kosice, Slovakia; 2. Dept. Fisica de Materiales, Fac. Quimica, UPV/EHU, San Sebastian, Spain; 3. MFTI, Kishinev, Moldova

Domain wall propagation in thin magnetic wire is used to transport the information in modern magnetic devices [1,2]. Decreasing the dimensions of the wires leads us to the new phenomena, which could be successfully employed in such devices.

Amorphous glass-coated magnetic microwires are ideal material to study the single domain wall propagation [3-5]. Since the beginning of such study, the new effects appears like a negative critical propagation field [3], very fast domain wall propagation [4] that can even leads to the supersonic domain wall [5]. In the given contribution, we show the effect of the Ni content in amorphous glass-coated $Fe_{77.5-x}Ni_xSi_{7.5}B_{15}$ ($0 \le x \le 50$ at.%) magnetic microwire.

Typical fast domain wall dynamics in microwires consists of two regions [5]. Firstly, it is low field region with low domain wall mobility (fig.1). it is characterized by the transversal domain wall structure. At higher fields (above 850 A/m), the domain wall configuration changes to the vortex one and the domain wall mobility increases reaching the domain wall velocity up to 10 km/s. Such a change has been formerly confirmed theoretically [6] and experimentally [5]. In this range, the domain wall interaction with the phonons is recognized at 4200 and 5600 m/s as it was formerly found in ferrites [7].

The parameters that determine the high domain wall velocity will be treated and their effect will be shown by the measurements of the domain wall dynamics in magnetic microwires of different composotions.

[1] D. A. Allwood, G. Xiong, C. C. Faulkner, D. Atkinson, D. Petit, and R. P. Cowburn, Science 309 (2005), 1688.

[2] S. S. Parkin, “Shiftable Magnetic Shift Register and Method of Using the Same,” U.S. Patent 6834005, 2004; “System and Method for Writing to a Magnetic Shift Register,” U.S. Patent 6898132, 2005.

[3] R. Varga, K.L. Garcia, M. Vázquez, P. Vojtanik, Phys. Rev. Lett. 94 (2005), 017201.

[4] R. Varga, A. Zhukov, J.M. Blanco, M. Ipatov, V. Zhukova, J. Gonzalez, P. Vojtaník, Phys. Rev. B 74 (2006), 212405.

[5] R. Varga, A. Zhukov, V. Zhukova, J.M. Blanco, J. Gonzalez, Phys. Rev. B 76 (2007), 132406.

[6] E. Schlomann, Appl. Phys. Lett. 19 (1971), 274.

[7] S.O. Demokritov et al, J. Magn. Magn. Mater. 102 (1991), 339.

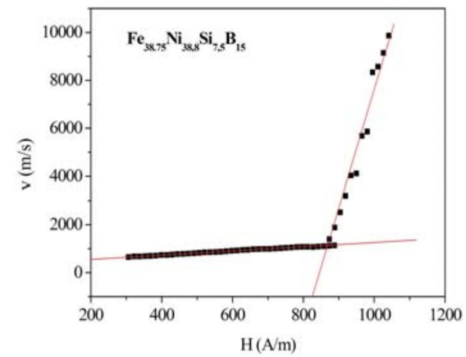

Fig.1.: Field dependence of the domain wall velocity of amorphous glass coated $Fe_{38.75}Ni_{38.8}Si_{7.5}B_{15}$ microwire.

DE-02

Domain wall propagation in nearly zero magnetostrictive amorphous microwires.

H. Chiriac, T. Óvári, M. Tibu
National Institute of Research and Development for Technical Physics, Iasi, Romania

Amorphous glass-coated microwires with positive magnetostriction ($\lambda > 0$), e.g. $Fe_{77.5}Si_{7.5}B_{15}$, exhibit a peculiar domain structure with an inner core (IC) that occupies most of the metallic core and an outer shell (OS) [1]. Such microwires display a bistable magnetic behavior, which is the result of this specific domain structure that originates in the minimization of the preponderant magnetoelastic term. A preexistent 180° domain wall is propagating within the IC when the applied field reaches to a certain value called the switching field, resulting in magnetization reversal. Studies of the domain wall velocity in such microwires have been recently performed [2, 3].
It has been recently shown that not only microwires with $\lambda > 0$ display bistable behavior, but also nearly zero magnetostrictive ones ($\lambda \approx 0$) [4], such as $Co_{68.15}Fe_{4.35}Si_{12.5}B_{15}$ ones with $\lambda = -1 \times 10^{-7}$, if their metallic nucleus diameter Φ is larger than 20 µm. In case of $\lambda \approx 0$, the axially magnetized IC appears as a result of the minimization of the preponderant magnetostatic energy term in their total free energy. In spite of the differences between the preponderant energy term in microwires with $\lambda > 0$ and those with $\lambda \approx 0$, they both display a similar mechanism of axial magnetization, i.e. the propagation of the 180° wall.
In this paper, the propagation of this wall within the IC of microwires with $\lambda \approx 0$ is investigated in order to study its mobility and damping mechanisms in correlation with the low anisotropy of these microwires.
Domain wall velocity has been measured in $Co_{68.15}Fe_{4.35}Si_{12.5}B_{15}$ microwires using a Sixtus-Tonks-like experimental set-up. Fig. 1 shows the dependence of wall velocity on applied field for a glass-coated microwire with $\Phi = 22$ µm and the glass thickness $\delta = 1.5$ µm. Bistable $Co_{68.15}Fe_{4.35}Si_{12.5}B_{15}$ microwires with $\Phi > 20$ µm display a wall mobility of the order of 10^2 m^2/A s, two orders of magnitude larger than the values reported in $Fe_{77.5}Si_{7.5}B_{15}$ amorphous glass-coated microwires.
This result opens up the way for employing microwires with $\lambda \approx 0$ as fast switching pulse generator elements, as well as in spintronic devices, subject to the significant reduction in the value of Φ. Therefore, the next step was to reduce the influence of the magnetoelastic energy term in microwires with $\Phi < 20$ µm, in order to enhance the importance of the magnetostatic term, and to induce bistability in the thinner samples. This has been performed by removing the glass coating through chemical etching. All investigated samples became bistable after glass removal, even those with very small values of Φ, e.g. $\Phi = 1.5$ µm. Fig. 2 illustrates the dependence of wall velocity on applied field for a microwire with $\Phi = 12$ µm, which became bistable after glass removal.
Wall mobility decreases after glass removal, whilst maximum velocity reaches over 2000 m/s. Annealing at 400°C for 30 min results in mobility values comparable to those observed in the thicker microwires which are bistable in the as-cast state.
The obtained results have been explained mainly considering the spin relaxation damping mechanism: the damping coefficient associated with spin relaxation is proportional to the anisotropy constant of the IC, and, as a result, it is very small in $Co_{68.15}Fe_{4.35}Si_{12.5}B_{15}$ microwires.
Summarizing, we demonstrated that domain wall velocities in microwires with $\lambda \approx 0$ are much larger than in microwires with $\lambda > 0$, that thinner microwires with $\lambda \approx 0$ become bistable after complete glass removal, and that wall mobility can be enhanced by annealing.

[1] H. Chiriac and T.-A. Óvári, Prog. Mater. Sci. 40 (1996) 333.

[2] R. Varga, K.L. Garcia, M. Vázquez, A. Zhukov, P. Vojtanik, Phys. Rev. B 70 (2004) 024402.

[3] R. Varga, K.L. Garcia, M. Vázquez, P. Vojtanik, Phys. Rev. Lett. 94 (2005) 017201.

[4] H. Chiriac, S. Corodeanu, M. Tibu, T.-A. Óvári, J. Appl. Phys. 101 (2007) 09N116.

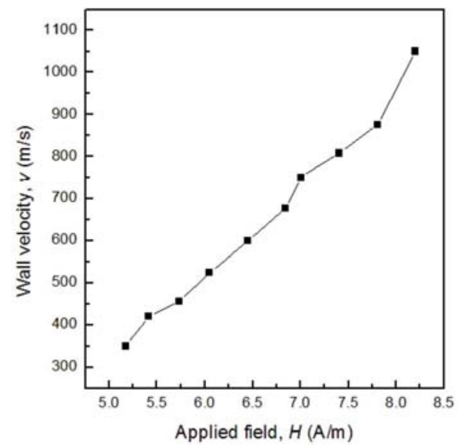

Fig. 1. Wall velocity vs. applied field for a $Co_{68.15}Fe_{4.35}Si_{12.5}B_{15}$ glass-coated microwire with $\Phi = 22$ µm and $\delta = 1.5$ µm.

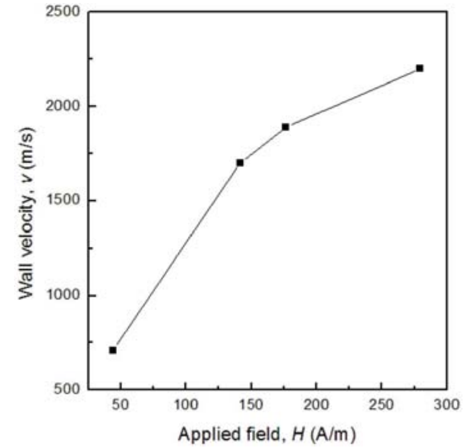

Fig. 2. Wall velocity vs. applied field for a $Co_{68.15}Fe_{4.35}Si_{12.5}B_{15}$ microwire after glass removal with $\Phi = 12$ µm.

DE-03

Electromagnetic wave absorbing material based on magnetic microwires.

P. Marín[1,2], D. Cortina[3], A. Hernando[1,2]
1. Instituto de Magnetismo Aplicado, Universidad Complutense de Madrid, Las Rozas, Spain; 2. Física de Materiales, Universidad Complutense de Madrid, Madrid, Spain; 3. Micromag 2000, S.L., Las Rozas, Spain

We present an experimental investigation related to an electromagnetic radiation absorbent sheet made up of a dielectric material containing amorphous magnetic microwires located such that, in the absorber use position, said electromagnetic radiation falls.
$Fe_{89}Si_3B_1C_3Mn_4$ microwires with positive magnetostriction constant of 2 10-5 and ρ between 0.2 and 0.6, were ρ is the ratio of the metallic core radius to the total radius of the microwire $\rho = Rm/R$ were cut in pieces of 1 mm length and imbibed in a sheet of dielectric permittivity, εr, between 5 and 6 located on a conductive base of the same dimensions. Two kinds of absorbent sheets were used. A first type (TI) consists in a sheet of 50 x 50 x 0.2 cm3 were microwires are distributed in all volume. Silicon resin has been mixed with 10 g. of 1 mm length Fe-rich microwires to prepare 50 x 50 x 0.5 cm3 sheets. A second type (TII), divided in three regions of thicknesses e1, e2 and e3 respectively where the microwires have been mixed in a paint with dielectric constant $\varepsilon r = 5$. The intermediate region of thickness e2 of 100 μm contains 1mm length magnetic microwires. The characteristic curves have been obtained in normal radiation incidence in anechoic chamber and hysteresis loops by a conventional induction method.
Hysteresis loop shape depends on the composition geometrical characteristic of the wires[1]. The high-frequency magnetic behaviour is connected with hysteresis loop. Fig 1a shows hysteresis loops, corresponding to the Fe-rich microwire, as a function of ρ. A higher longitudinal anisotropy due to thinner inner core is associated with a higher anisotropy field, Hk and lower remanence.
Ferromagnetic resonance (FMR) is connected with spin precession about magnetization vector at the effect of high frequency electromagnetic field applied such that magnetic component is perpendicular to magnetization vector and in a magnetic metal is characterized by a maximum in the absorbed power and a minimum in the penetration depth of the electromagnetic field. The precession of the microwave magnetization M is in phase with the microwave drive field h at FMR. Longitudinal anisotropy is strongly connected with ferromagnetic resonance. An increase in the anisotropy field should enhance the ferromagnetic resonance frequency [1].
Figure 1b shows the characteristic curves obtained for four TI silicon sheets prepared, each one with a different type of magnetic microwire from those shown in Figure 1a. It confirms the increase of the frequency associated to the maximum in the spectrum with microwire magnetic anisotropy field raise.
Although the maximum peak position can be understood by means of the microwires magnetic anistropy field the bandwidth associated to the spectrums should be further analysed. Malliavin et al [2] have shown that the shape of the ferromagnetic resonance peak associated to a unique microwire should be the result of relaxation mechanisms. The disipative effects include atenuation and relaxation terms in the magnetization movement equation. The high bandwith of Figure 1b should be understood as a result of microwires volume dispersion.
In order to clarify these aspects, several TII aborbent sheets with thickness e1 varying from 400 to 1050 μm have been prepared using in all cases 1mm FeSiBCMn magnetic microwires with anisotropy field Hk=5 Oe associated to hysteresis loop (c) on Figure 1a. These results are shown on Figure 2. An increase in e1 is associated to a decrease of the frecuency associated to the maximum absorption, fr.
The interpretation of the results, shown in Figure 2, related with the influence of e1 in the reflectivity requires a careful analysis of the interaction between the sample and both electric and magnetic fields of the wave.

[1]. D.P. Makhnovskiy, L.V. Panina, D.J. Mapps, Phys. Rev. B 63 (2001) 4424

[2] M.J. Malliavin, O. Acher, C. Boscher, F. Bertin, V.S. Larin, J. Magn. Magn. Mat. 196-197 (1999) 420

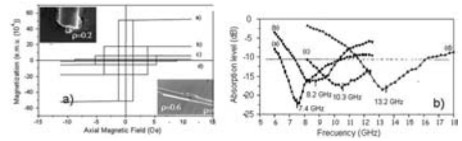

Hysteresis loops (a) and absorption spectrum (b) for silicon sheets of type TI of 2 mm thickness prepared with microwires of $Fe_{89}Si_3B_1C_3Mn_4$ with different ratio ρ=Rm/R between the radius of metallic nucleus, Rm, and the radius of the microwire, R for ρ=0.2 (a), ρ=0.25 (b), ρ=0.28 (c) and ρ=0.6 (c)

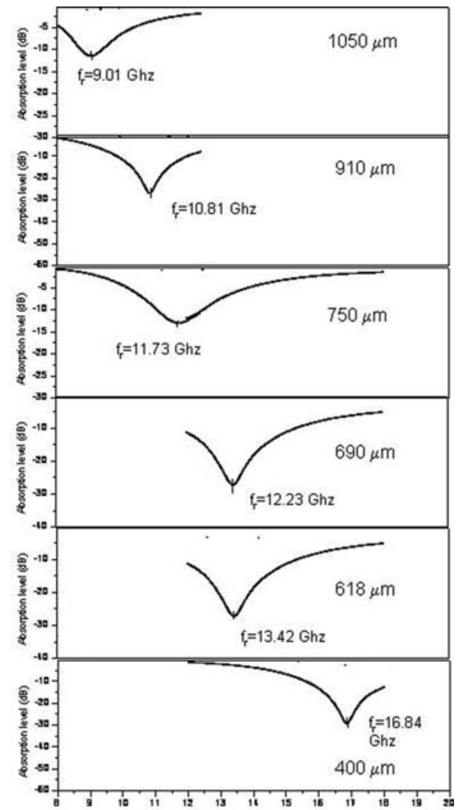

Influence of first layer thickness, e1, on absorption curves for absorbent sheets prepared using paint

Experimental determination of relation between helical anisotropy and torsion stress in amorphous magnetic microwires.

A. Chizhik[1], A. Zhukov[1], J. Blanco[2], J. Gonzalez[1], P. Gawronski[3], K. Kulakowski[3]
1. Dpto. Fisica de Materiales, Universidad del Pais Vasco, San Sebastian, Spain; 2. Departamento Física Aplicada I, EUPDS, Universidad del Pais Vasco, San Sebastian, Spain; 3. Faculty of Physics & Applied Computer Science, AGH University of Science & Technology, Cracow, Poland

The intensive studies of the magnetic properties of nearly zero magnetostriction Co-rich glass covered microwires attract considerable science interest in relation with the giant magnetoimpedance (GMI) effect observed in these microwires. The role of the helical anisotropy in GMI effect is well known. Up to now the value of the torsion angle, but not the value of the helical anisotropy, was brought in correspondence to the value of GMI effect. In the present work, we establish, for the first time, the correspondence between the value of the angle of the helical anisotropy and the value of the torsion stress.
Glass covered amorphous microwires exhibiting nearly zero negative magnetostriction, of nominal composition $Co_{69.5}Fe_{3.9}Ni_1B_{11.8}Si_{10.8}Mo_2$ (metallic nucleus diameter 19µm, glass coating thickness 2.6µm) were supplied by TAMAG Iberica S.L. The experiments have been performed using the transverse magneto-optical Kerr effect (TMOKE) in axial magnetic field. The intensity of the reflected light is proportional to the magnetization oriented perpendicularly to the plane of the light polarization, i.e. to the circular projection of the magnetization in the surface area of the microwire. The torsion stress have been applied to the microwire during the experiments.
The process of surface magnetization reversal in the presence of the torsion stress of different amplitude and directions has been studied. Figure 1 presents examples of the TMOKE dependencies on the axial magnetic field with the amplitude of the torsion stress as a parameter. Fig. 1 (c) shows the magnetization reversal in absence of applied torsion stress (τ=0). The surface magnetization reversal consists of two steps: the rotation of the magnetization from axial to circular direction in the outer shell of the wire and the jump between two states with opposite directions of surface circular magnetization.
The applied torsion stress induces strong transformation of the surface hysteresis loops. The most essential feature of this transformation is the stress induced change of the value and direction (sign) of the jump of the Kerr intensity ΔI (the circular magnetization ΔM_{CIRC}). For the torsion stress of $-2.2\ \pi\ rad\ m^{-1}$ value (Fig. 1(b)) the surface magnetization reversal consists only of the rotation of the magnetization from one axial direction to another and there is no jump of circular magnetization. The following increase of the applied stress of negative value causes the appearance and increase of the ΔM_{CIRC}) of the opposite sign.
The obtained results are related to the torsion induced change of the helical anisotropy, therefore, the analysis of the experimental results has been performed taking into account the existence of a helical magnetic anisotropy in the wire [1]. The comparative analysis of the experimental results and the results of the calculations permits us to determine and construct the dependence of the angle of the helical anisotropy on the applied torsion stress (Fig. 2). The obtained results are in agreement with the model [2] which considers the torsion stress as a interference of two tensile stresses of opposite signs (pressing and straining) directed at 45^O and 135^O relative to the longitudinal axis of the wire. Now we have the method which permits us to present the results of the experiments with torsion stress as a dependence on the angle of helical anisotropy.

[1] Chizhik A., et al. IEEE Trans. Magn., 42 (2006) 3889.
[2] Sablik M.J. and Jiles D.C., Phys. D: Appl. Phys., 32 (1999) 1971.

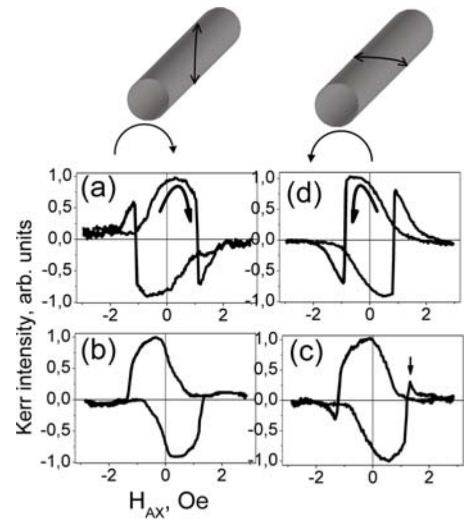

Fig.1 TMOKE dependencies in the presence of torsion stress. (a) $\tau = -22\ \pi\ rad\ m^{-1}$, (b) $\tau = -2.2\ \pi\ rad\ m^{-1}$, (c) τ=0, (d) $\tau = 8.9\ \pi\ rad\ m^{-1}$. Insets: schematically pictures of the inclination of the axis of helical anisotropy induced by the torsion stress.

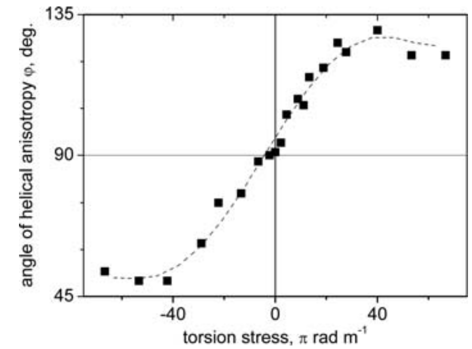

Fig. 2 Dependence of angle of helical anisotropy on applied torsion stress. Dashed line is a guide to the eye.

DE-05

Circular magnetoelastic anisotropy induced in the nucleus of FeSiB/CoNi soft-hard biphase microwire.

J. Torrejón, M. García-Hernández, G. Infante, K. J. Merazzo, G. Badini
Magnetism, ICMM (CSIC), Madrid, Spain

Bi-phase magnetic microwires have been recently introduced [1], whose main interests lay in the observed magnetostatic bias in the soft magnetic phase [2] and in their use as multifunctional sensing elements in magnetoelastic-based sensor devices [3]. Different families of biphase microwires have been introduced by adding an outer magnetic shell (hard CoNi or soft FeNi alloys) onto glass-coated microwires (soft FeCoSiB or hard FePtSi alloys) through combined sputtering and electroplating techniques. Depending on the relative magnetic character of nucleus/shell, bi-phase magnetic microwires can be tailored with different characteristics. The magnetic behaviour of each phase is determined by its intrinsic magnetic softness and by their magnetic interaction including magnetoelastic and magnetostatic contributions. The bias effect in soft/hard and hard/soft biphase microwires has been particularly investigated.
In this work, an analysis of the magnetoelastic interactions has been performed in a particular biphase system: a magnetically soft and bistable amorphous Fe-based nucleus plus a magnetically harder crystalline CoNi outer shell. The bistable character and the remagnetization process by a single domain wall displacement of the Fe-based nucleus is shown to be strongly modified by the presence of the CoNi shell.
The studied biphase system consists of a $Fe_{77.5}Si_{7.5}B_{15}$ nucleus (12 μm diameter), intermediate non-magnetic layers (Pyrex glass layer, 9 μm thick, and Au, 30 nm thick), and an external $Co_{90}Ni_{10}$ external layer which thickness is ranged up to 5 μm by control of the time and current density during electroplating. Magnetic measurements as a function of CoNi thickness and temperature have been performed in VSM and SQUID magnetometer, respectively.
Previously, the low-field behaviour of the soft nucleus was investigated under the remanent stray field of the hard shell to determine the magnetostatic bias effect. Here, the study is performed after demagnetizing the biphase system to identify the sole influence of the magnetoelastic interaction of the outer shell on the soft nucleus.
Figure 1a shows the low-field loops of the FeSiB nucleus for a range of CoNi thicknesses. As thickness, t_{CoNi}, increases the switching field and the remanence decreases. For t_{CoNi} of around 4-5 μm, bistability fully disappears and the remagnetization proceeds only by magnetization rotation denoting the presence of a strong circular magnetoelastic anisotropy. A similar effect is observed when reducing sufficiently the measuring temperature (see Figure 1b) for a biphase microwire with t_{CoNi}=1.5 μm. Magnetic bistability is no more observed below around 150 K measuring temperature because of the induced circular anisotropy, 1 kOe circular anisotropy field at 100K (no shown here), whose main origin is related to the different thermal expansion coefficients of different layers
A detailed study has been performed on the magnetoelastic anisotropy with circumferential easy axis induced in the nucleus of the biphase system by increasing the thickness of the outer shell and by reducing the measuring temperature.

[1] K.Pirota, M. Hernández-Vélez, D.Navas, A. Zhukov and M.Vázquez. Adv. Funct. Mater. 14 (2004) 266-268.

[2] J. Torrejón, G. Badini, K. Pirota and M. Vázquez. Acta Mater. 55 (2007) 4271-4276.

[3] M.Vázquez, K. Pirota, G. Badini, J. Torrejón and H. Pfützner. European Patent 2006; PCT/ES2005/070173.

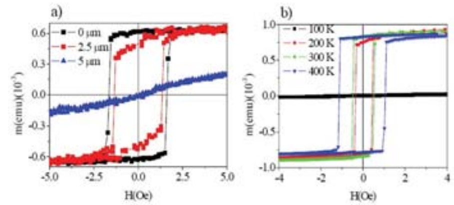

Figure 1.- (a) Room temperature low-field loops of FeSiB/CoNi microwires for selected thicknesses of CoNi outer shell (b) and low-field hysteresis loops at indicated measuring temperatures for a microwire with t_{CoNi}=1.5 μm.

DE-06

Temperature behaviour of magnetic anisotropy of nanocrystallized Finemet-based glass-coated microwires.

V. Dubuget[1,2], A. Adenot-Engelvin[1], F. Bertin[1]
1. CEA, Monts, France; 2. LEMA, UMR CNRS 6157, TOURS, France

Introduction

Glass-coated nanocrystallized microwires have already been studied by many groups owing to their excellent soft magnetic properties and good thermal stability [1]. These one are ascribed to the structural state, which consists of α-Fe(Si) crystallites with a grain size of about 15 nm, embedded in an amorphous residual matrix. The magnetic softness of these alloys is theoretically explained by the random anisotropy model [2,3]. As a feature of the glass coating, the magnetic properties seem to be strongly dependent on magneto elastic effects and engineering of the anisotropy has been achieved through the magnetostriction coefficient. However, in the case of nanocrystallized alloys, both composition and annealing procedure play on the magnetostriction value. The aim of this work is to determine which one is the best way from the study of the thermal behaviour of the effective anisotropy.

Experimental details

The microwires, with composition $Fe_{73.5}B_7Si_{15.5}Cu_1Nb_3$, were elaborated using a Taylor-Ulitovsky process. The diameter of the amorphous ferromagnetic core is 8.5 µm and the thickness of the Pyrex glass coating is 6.5 µm. The nanocrystalline state was obtained by conventional annealing at different temperatures from 830 K to 870 K during 1 hour to vary the magnetostriction coefficient. The temperature dependence of static magnetic properties was measured by means of a Lakeshore VSM from room temperature up to 970 K. The saturation magnetostriction (λs) was determined at room temperature from the experimental value of the anisotropy fields from various applied tensile stresses.

Results – Discussion

In figure 1, hysteresis loops are sketched from room temperature to 970 K for the microwires annealing at 870 K. The decrease of the saturation magnetization with temperature is observed up to the Curie temperature, Tc = 870 K, corresponding to the Tc of the α-Fe(Si) phase. From the magnetization curves, the magnetic anisotropy energy (K_{eff}) was calculated by $K_{eff} = 4\pi\int HdM$. A decrease in K_{eff} is also observed as shown on figure 2.

The dependence of the λs on the annealing temperature is presented in table 1. When the T_{an} increases, a decrease in λs is observed from -5.2 x 10^{-7} for T_{an} = 830 K to -1.6 x 10^{-6} for T_{an} = 870 K. The nanocrystalline fraction ν_{cr} induced by the various thermal treatments can be therefore deduced from the value of λs[2]. According to Herzer [2], the magneto-crystalline anisotropy can be estimated by $K_{m-c} = \nu^2D^6K^4/A^3$. For a given geometry of microwire (8.5-15 µm), the magneto-elastic anisotropy was calculated using a thermo-elastic model [4]: $K_{m-el} = 3/2\lambda s(\sigma_{zz}-\sigma_{\theta\theta})$. As shown in table 1, K_{m-el} is larger than to K_{m-c}.

A non-zero "residual anisotropy" is found, corresponding to the difference between the effective anisotropy and the sum of magneto-elastic and magneto-crystalline anisotropy. The residual anisotropy decreases with the annealing temperature and constitutes a non – negligible contribution of effective anisotropy.

Conclusion

The effective magnetic anisotropy of the nanocrystallized ferromagnetic glass-coated microwires determined from the magnetization curves at different temperatures is reported. This one is compared to the sum of the magneto-elastic anisotropy and the magneto-crystalline anisotropy. The thermal behaviour of these samples has to be compared with a microwire with the same magnetostriction coefficient but with a different composition, in order to determine which is the best way to engineer the effective anisotropy in nanocrystalline glass-coated microwires.

[1]C. Dudek, A.-L. Adenot, and O. Acher, IEEE Transactions on Magnetics 42, 2787-2789 (2006).

[2]G. Herzer, Handbook of Magnetic Materials; Vol. 10, edited by K. H. J. Buschow (Elsevier Science B. V., 1997), p. 415-462.

[3]A. Hernando, M. Vazquez, T. Kulik, and C. Prados, Physical Review B 51, 3581-3586 (1995).

[4]A. V. Torcunov, S. A. Baranov, and V. S. Larin, Journal of Magnetism and Magnetic Materials 196-197, 835 (1999)

T_{an} (K)	λs	Crystalline fraction	K_{eff} (J.m-3)	K_{m-el} (J.m-3)	K_{m-c} (J.m-3)	$K_{residual}$ (J.m-3)
830	-5.2 x 10^{-7}	0.79	1052	238	29	785
850	-1.1 x 10^{-6}	0.81	1181	526	31	624
870	-1.6 x 10^{-6}	0.83	1289	734	32	523

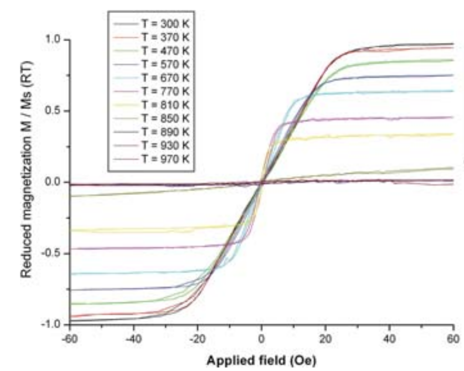

Temperature dependence of the hysteresis loops for microwires annealing at 870K

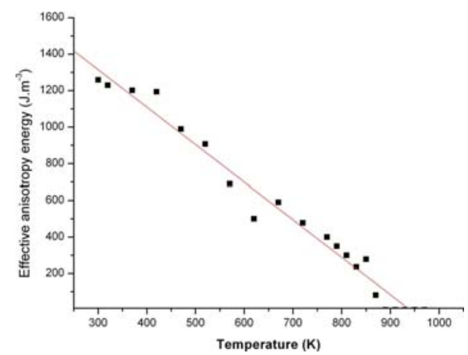

Variation of the effective anisotropy energy with temperature for microwires annealing at 870K

DE-07

Temperature Dependence of the Magnetization Reversal Process and Domain Structure in Fe77.5-xNixSi7.5B15 Magnetic Microwires.

J. Olivera[1,2], *M. Sánchez*[1], V. M. Prida[1], R. Varga[2], V. Zhukova[3], A. P. Zhukov[3], B. Hernando[1]
1. Fisica, Universidad de Oviedo, Oviedo, Spain; 2. Inst. Physics, Fac. Sci., UPJS, Park Angelinum, Kosice, Slovakia; 3. Dpto. de Física de Materiales, Fac. Químicas, Universidad del Pais Vasco, San Sebastián, Spain

The temperature dependence of the magnetization reversal process for a Fe77.5-xNixSi7.5B15 (x = 0-0.4) glass-coated microwires, with internal diameter 15 µm and total diameter 33 µm, has been systematically studied in the temperature range 4 –373 K. The magnetization reversal consists on the nucleation and propagation of a single-domain wall along the wire when certain value of the static magnetic field is applied (switching field)[1-3]. The hysteresis loops were measured by the VSM at room temperature in order to confirm the magnetic domain structure (see fig. 1), which has also been observed by means of Bitter technique, revealing a magnetic structure according to the core-shell model, with a surface radial domains having about 3 µm width, as it can be seen in fig. 2. The switching field dependence on temperature has been studied in amorphous glass-coated FeNiSiB by means of an induction method as a function of the nickel content and in the temperature range of 80-400 K, exhibiting a monotonous decreasing with temperature increasing for the microwire with 15% of Ni (inset of fig.1). The temperature dependence of both saturation and remanent magnetization was also measured for the different microwire Ni contents by using a Squid Magnetometer (Quantum Design), also shown in the inset of fig.1 for the above mentioned sample. The domain structure and therefore the magnetic behaviour of these microwires strongly depend on their composition, which is directly responsible of the sign and magnitude of their magnetostriction constant. It also depends on the value and distribution of internal stresses induced during the fabrication of the microwire, and the stresses produced by the difference in thermal expansion coefficient between the inner nucleus and the outer glass-coating. The observed switching field dependence on temperature is explained in terms of a simple model by considering two energy contributions of magnetoelastic pinning and structural relaxation [4]. The substitution of Ni for Fe creates new magnetostrictive interactions and this new short range order affects the effective anisotropy and magnetostriction. Different magnetization processes and magnetic structures can be obtained modifying the magnetostriction and the effective anisotropy in this way [5], and therefore different temperature dependence. The obtained results allow us to tailor the microwire magnetic properties for its application in magnetic sensors in different temperature ranges through the selection of their composition.

[1] J. González, N. Murillo, V. Larin, J. M. Barandiarán, M. Vázquez, A. Hernando, IEEE Trans. Magn. 33, (1997) 2362.

[2] M. Vázquez, A. Zhukov, K.R. Pirota, R. Varga, K.L. García, C. Luna, M. Provencio, D. Navas, J.L. Martínez, M. Hernández-Vélez, J. Non-Cryst. Solids 329, (2003) 123.

[3] M. Vázquez, A.P. Zhukov, K.L. García, K.R. Pirota, A. Ruiz, J.L. Martinez, M. Knobel, Mater. Sci. Eng. A 375–377, (2004) 1145.

[4] R. Varga, K. L. García, M. Vázquez, A. Zhukov, P. Vojtanik, Phys. Rev. B 70, (2004) 024402.

[5] J. Olivera, J. Gamcova, R. Varga, P. Vojtanik, V. Prida, B. Hernando, A. Zhukov, CSMAG'07 Conference, Ko šice, Slovakia (2007).

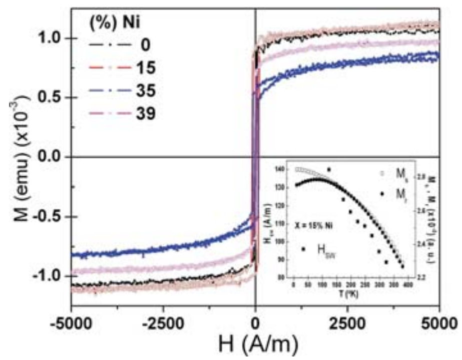

Figure 1: VSM room temperature hysteresis loops of FeNiSiB microwires with varying the Ni content. The inset shows the switching field (Hsw), saturation (Ms) and remanent (Mr) magnetization dependences on the temperature, for the Fe62Ni15.5Si7.5B15 microwire.

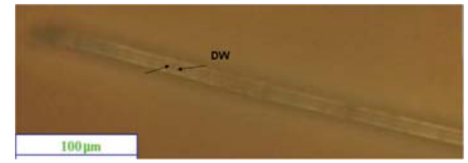

Figure 2: Magnetic domain structure of a Fe62Ni15.5Si7.5B15 microwire by Bitter technique. The arrows indicate the radial domain walls across the microwire surface.

DE-08

Synthesis and Characterization of Fe/FeOx Core/Shell Nanowires.

J. Lee[1], J. Lee[1], K. Jeon[2], J. Wu[1], H. Kim[1], J. Lee[1], Y. Suh[2], Y. Kim[1]
1. Department of Materials Science and Engineering, Korea University, Seoul, South Korea; 2. Fusion Biotechnology Research Center, Korea Research Institute of Chemical Technology, Daejeon, South Korea

Introduction
The one-dimensional nanostructure such as nanowire is an emerging nanomaterial both from fundamental and engineering standpoints. For example, magnetic nanowires are useful candidates for data storage and biomedical application [1]. In particular, Fe holds an important position because it possesses high saturation magnetization, and it can be easily converted to oxides where Fe-oxides are biocompatible. Fe can also be combined with Au to form a multifunctional nanowire in a barcode arrangement [2]. Compared to Fe/FeOx core/shell nanoparticles [3, 4], limited study has been carried out for core-shell nanowires. In the present study, we aim to achieve biocompatible surface (FeOx shell) while retaining high magnetization (Fe core).
Experimental
First, pure Fe nanowires were synthesized by dc pulse electrodeposition in nanopores of an anodized aluminum oxide (AAO) membrane using a FeSO4 aqueous solution. To obtain FeOx shell structure, the Fe nanowires embedded AAO membrane was annealed in air at elevated temperatures up to 700°C. Samples were characterized by SEM, TEM, XRD, nano-Raman spectroscopy, and vibrating sample magnetometry (VSM).
Results and Discussion
As shown in Fig. 1(a), the formation of the core-shell nanostructure (elemental Fe core and Fe oxide shell) was demonstrated by TEM. The oxidation was controlled by the annealing conditions. Fig. 1(b) shows a series of Raman spectra of the Fe nanowires thermally treated under different elevated temperatures in air, spatially resolved from a single nanowire using nano-Raman spectroscopy [5]. In the case of 400°C, the spectrum shows dominant α-Fe2O3, while Fe3O4 was formed at 500°C. The finding is further substantiated by XRD and magnetic measurements. Magnetization curves of the core-shell nanowires embedded in AAO were obtained by VSM (Fig. 2 and Table 1). At the as-deposited state, they showed soft magnetic property such as low coercivity. After annealing in air (Fig. 2(b) for the case of 500°C), the saturation magnetization was reduced as expected, but the coercivity increased from 55 Oe to 203 Oe (field parallel to the wire axis), and from 115 Oe to 239 Oe (perpendicular). This phenomenon appeared equally in all other annealing samples at different temperatures (Table 1). The enhancement in the magnetic properties of the nanowires is probably due to the grain growth, the formation of new species, and the core iron part of the nanowires prevented from further reaction with oxygen owing to spatial arrangements.

[1] A. Hultgren, M. Tanase, E. J. Felton, K. Bhadriraju, A. K. Salem, C. S. Chen, D. H. Reich, Biotechnol. Prog., 21, 509 (2005).

[2] J. H. Lee, J. H. Wu, H. L. Liu, J. U. Cho, M. K. Cho, B. H. An, J. H. Min, S. J. Noh, Y. K. Kim, Angew. Chem. Int. Ed., 46, 3663 (2007).

[3] S. Peng, C. Wang, J. Xie, S. Sun, J. Am. Chem. Soc., 128, 10676 (2007).

[4] A. Cabot, V. F. P., E. Shevchenko, Y. Yin, L. Balcells, M. A. Marcus, S. M. Hughes, A. P. Alivisatos, J. Am. Chem. Soc., 129, 10358 (2007).

[5] D. L. A. de Faria, S. Venancio Silva, M. T. De Oliveira, J. Raman Spectrosc., 28, 873 (1997).

		Ms (emu)		Hc (//) (Oe)		Hc (⊥) (Oe)	
Sample I	as deposited	0.105	41 % decrease	75	112% increase	121	50% increase
	annealed @ 400°C	0.062		159		182	
Sample II	as deposited	0.071	17% decrease	55	269% increase	115	108% increase
	annealed @ 500°C	0.059		203		239	

Table 1. Coercivity (Hc), saturation magnetization (Ms), and the corresponding change rate for the nanowire arrays in AAO as deposited and after annealing at 400°C and 500°C, respectively. The signs of // and ⊥ represent the external magnetic field applied parallel and perpendicular to the wire axis.

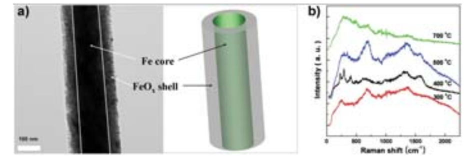

Fig. 1 (a) TEM image of one Fe/FeOx core-shell nanowire; and (b) nano-Raman spectroscopy under various heat treatments.

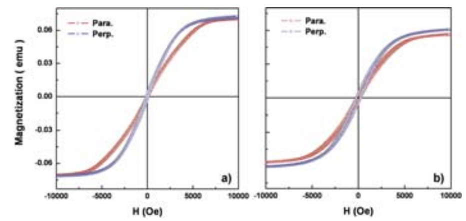

Fig. 2. Magnetization curves for (a) as-synthesized Fe nanowires in AAO and (b) after annealing at 500°C in air.

DE-09

Structure and Magnetic properties of electrodeposited cobalt nanowires in polycarbonate membrane.

S. r. Vishnubhotla[1], C. Kim[1], S. Yoon[2]
1. Chungnam National University, Daejeon, South Korea; 2. Andong National University, Daejeon, South Korea

Introduction:
In recent years nanoporous templates have been attracted by many researchers due to their potential use for fabrication of metallic nanowires. A promising method to obtain nanowires with large shape anisotropy is based on membrane technology [1]. It can be considered an alternative to conventional lithography methods. Arrays of nanowires are obtained by filling a porous template that contains a large number of straight cylindrical holes with narrow size distribution [2]. The use of nanoporous membrane increases the coercivity and squareness compared to that of a thin film or bulk material. Electrodeposition is of interest because it works under atmospheric pressure, does not require expensive equipment.
Experimental procedure :
Cobalt nanowires were grown into the resulting template by electrodeposition using three electrode cell configuration. The gold layer of 200 nm was sputtered on one side of the polycarbonate membrane which serves as a working electrode. The half cell potential, which was kept at -0.95 V throughout the experiment, for reduction of the metallic ions from the electrolyte, was monitored with respect to a standard calomel reference electrode. An 8-cm2 thin platinum sheet was used as a counter electrode. The room temperature electrolyte bath consists 80% by volume of 80 g/l of CoSO4.7H2O, 40 g/l of H3BO3, and 20% by volume of methanol to wet the nanopores prior to deposition in distilled water. The pH of the electrolyte was adjusted to 3.4. In order to understand the growth rate of nanowires during deposition, the current-time profiles were recorded and are shown in fig.6 along with their corresponding magnetic hysteresis profile. The deposition processes were accomplished under mild stirring of the electrolyte while monitoring the current-time profiles to derive information related to the deposition rate. The magnetic properties of the generated nanowires were investigated by vibrating sample magnetometry and their morphologies were observed by scanning electron microscope. The polycarbonate membrane was taken with 50 nm diameter and length ≤ 6 µm. The morphology of the nanowire arrays were investigated. Arrays of cobalt nanowires have been obtained by filling a porous polycarbonate membrane .
Results and Discussion:
Fig.1 shows the SEM images of the cobalt nanowires which were electrodeposited at -0.95 V relative to the Ag/AgCl reference electrode. Deposition was carried out for different times in order to grow 6- 11 µm long nanowires during the deposition. The samples were prepared by electrodeposition into the pores of commercially available track etched polycarbonate membranes with nominal pore diameter 50 nm and thickness 6 µm. A layer of gold with thickness 200 nm was sputtered on one side of the polycarbonate membrane to serve as a conducting electrode. The morphology of the nanowire arrays was investigated by SEM. Deposited membranes were fractured after immersion in liquid nitrogen, thus exposing the cross section for SEM studies. The SEM cross-sectional images of the nanowires (Fig. 1) show a dispersion of the wire axes with slight deviation with respect to the normal. In very few cases the wires are parallel.Fig. 2 shows the angular dependence of Coercivity (Hc) and remenant-saturation magnetization ratio. Here theta is the angle between the surface of the membrane and the applied magnetic field. It can be observed that the maximum Mr obtained for an applied field parallel to the nanowires while Hc of the array reaches the maximum when the field is applied perpendicular to the nanowires. The saturation magnetization and remanent magnetization were considered inorder to calculate the squareness ratio.
Conclusion:
Cobalt nanowires were successfully deposited into polycarbonate membrane. The track-etched polycarbonate membranes are commercially available .The deposition was done for few hours before structural and magnetic characterizations. The SEM images confirm growth of nanowires, but their alignment is disturbed due to fracture. The magnetic hysteresis loops of the samples are in support of the observations made structurally.

[1] A.Fert, L.Piraux, J.Magn.Magn.Mater. 200 (1999) 338

[2] A.Kazadi Mukenga Bantu et.al, J.Appl.Phys. 89, No.6, 2001

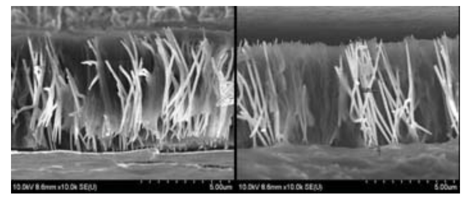

SEM images of the cobalt nanowires with 50 nm diameter and 6 micrometer length

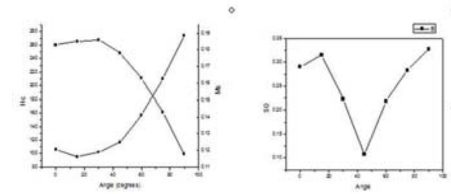

Comparison of Ms and Hc and squareness with respect to the angle

DE-10

Structural and thermal behaviour of nanocrystalline nanowires.

M. J. Vieyra, *T. Meydan*, F. Borza
Cardiff School of Engineering, Wolfson Centre for Magnetics, Cardiff, United Kingdom

Introduction

Electrodeposition of nanowires has been widely studied due to its advantage of controlling the deposition parameters to tailor the properties of the material. Thus, this method offers advantage for the fabrication of poles for write heads and for use in integrated microsystems. Previous work carried out has been on X-ray diffraction and magnetic study of FeCoNiB films and nanowires[1]. In this paper the study is on FeCoNiB nanowires with 10% boron in the electrolyte but the focus is on studying the effect of changing the deposition current, on the elemental percentage deposition in the nanowire and hence on the magnetic characteristics. **Experimental**

FeCoNiB nanowires of thickness 50 µm were deposited in the alumina template of different diameters (D = 20, 100 and 200 nm) using the electrochemical deposition method. The galvanostatic conditions used for the sample preparation were, time t_{on}/t_{off} = 12/380 (ms/ms) with the current density varying from 8 to 12 mA.

Results and Discussion

Effect of Diameter

Both Hc and squareness (SQ) decreased with the increase in the wire diameter. The coercivity values for FeCoNiB nanowires deposited in nanopore template of diameter 20 nm is comparable to the values obtained for CoFeB nanowires. The coercive values (H_c) for out-of-plane (o-o-p) measurements varied from 41 to 277 Oe for nanowire arrays of different diameters. It seemed to vary in the same manner for nanowires deposited at 8 and 9 mA pulsed current as can be seen from Figure 1. For nanowires of 20 and 200 nm the easy axis is in the o-o-p direction whereas it is the in plane (i-p) direction for nanowires of 100 nm. For most of the samples, the o-o-p plane coercivity was higher than the i-p coercivity suggesting lower magnetostatic interactions amongst the nanowires. It was observed that the o-o-p axis switched from easy to hard when the wire length increased beyond a critical value as observed for crystalline Co, but this was clearly not the case with the samples investigated here[2]. The variation in the $\triangle H_s$ (H_s^{oop}–H_s^{ip}) values were not large for the 100 nm pore diameter and for one of the samples with 200 nm pore diameter. This indicated an intermediate switching of the easy axis from out-of-plane to in-plane. EDX study showed that the atomic concentration of Fe and Co for the template diameter 20 and 100 nm did not vary as much as the change observed for 200 nm template diameter. This was attributed to the diffusion rate being higher in 200 nm diameter template leading to larger segregates compared to 20 and 100 nm diameter templates. From Figure 2a, the atomic concentration of Fe, Co and Ni deposits in nanopores diameter of 100 nm was higher than that of the deposits in the 20 nm nanopores diameter. . Simultaneously, it was also observed in Figure 2b that the increase in the pulsed current from 8 to 9 mA for the 200 nm nanowires allowed the deposition concentration to increase which indicated that pores of larger diameter did allow the formation of larger agglomerates with more ions concentration at higher currents.

Effect of temperature

The thermal stability of the FeCoNiB nanowires deposited at 9 mA pulsed current was studied over the temperature range 10-300 K. Figure 3 shows that the o-o-p coercive values increased from 45 Oe at 300 K to 76 Oe at 10 K. Similarly, the squareness increased from 0.01 at 300 K to 0.023 at 10 K. There was not a significant improvement in the coercive or squareness values. The results reported here for FeCoNiB sample are consistent with the values for CoNi nanowires obtained in the sense that the increase in coercivity and squareness occurs with the decrease in temperature[3].

M. Vieyra, et al, Journal of Applied Physics, Vol. 101, (2007), p. 1.

E. L. Silva et al, Physica B, 384, (2006), pp. 22–24.

X.Y. Zhang et al, Physica B 353, (2004), pp. 187–191.

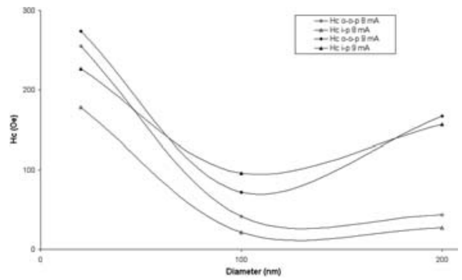

Coercivity variation with nanowire diameter.

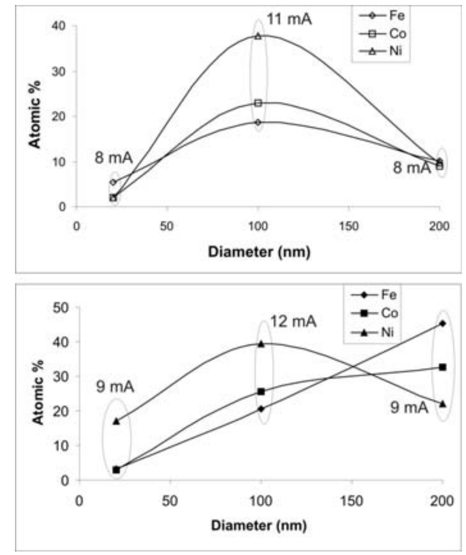

Variation of Fe, Co and Ni with the changing nanowire diameter.

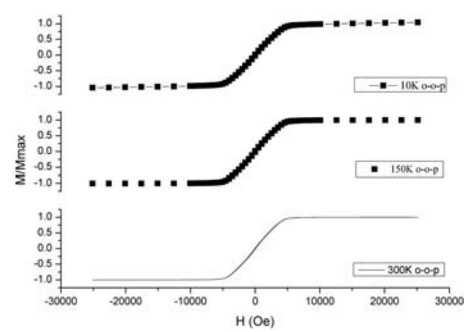

M/Mmax plot for FeCoNiB (10% Boron) nanowires at different temperatures.

DE-11

Silicon steel wire with low magnetic losses.

T. Yonamine[1], M. Fukuhara[1], N. A. Castro[2], F. G. Landgraf[3], F. P. Missell[1,4]
1. Divisão de Metrologia de Materiais, Instituto Nacional de Metrologia, Normalização e Qualidade Industrial-INMETRO, Duque de Caxias, Brazil; 2. Instituto de Pesquisas Tecnológicas-IPT, São Paulo, Brazil; 3. Departamento de Metalurgia e Materiais, Escola Politécnica da Universidade de São Paulo - EPUSP, São Paulo, Brazil; 4. Centro de Ciências Exatas e Tecnológicas, Universidade de Caxias do Sul, Caxias do Sul, Brazil

The aim of this work is to develop a process to produce silicon steel wire with the lowest possible magnetic losses, allowing its use as magnetic core material in a new type of transformer [1]. The technical feasibility of this patent strongly depends on the production of steel wires with magnetic losses similar to the grain oriented silicon steel sheets used in conventional transformers. The starting material was a wire with a diameter of 7.2 mm that was drawn down to 0.4 mm, in several steps. Heat treatments were performed in order to promote the stress relief and the recristalization of the deformed material. Magnetic losses can be reduced by increasing the grain size and by improving the crystallographic texture [2]. Our aim is to obtain a wire with a strong <100> texture component parallel to its length [3]. X-ray diffraction (XRD) and electron backscatter diffraction (EBSD) were performed for monitoring the evolution of texture.
The crystallografic texture of steel wires has received little attention in the international literature. The feature mentioned in all articles is the effect of plastic cold deformation which induces a strong <110> texture parallel to the length of the wire. Recrystallization does not seem to modify this texture. The absence of literature about recrystalization texture and/or grain size increase in low carbon steel wire encourages us to believe that processes may be developed, analogous to those used to control the texture of electrical steel sheets, which would achieve the desired <100> texture parallel to the wire length. In this work three wire drawing and annealing processes were investigated, which resulted in three lots of wire, each with a final diameter of 0.4 mm. Samples 7387, 7388 and 7402 correspond to the final stage of each process of wire drawing and annealing.

From EBSD analysis (Figure 1), it was possible to determine the orientation of each grain and thus to determine which directions are parallel to the wire length. Grains for which the easy magnetization direction <100> will be parallel to the wire length are red in Figure 1 (see Figure 2). From a comparison of the EBSD images of these samples, it was possible to confirm that sample 7402 had the greatest grain size, and that the grain size of sample 7388 was larger than that of sample 7387. Moreover, from the EBSD and DRX results it is possible to verify the decrease in the number of grains with {110} planes parallel to the transverse direction (green grains).

This result shows that one can modify the final texture to one completetly different from that commonly seen in the literature. Magnetic loss measurements are the most important yardsticks for electrical steels used with ac current, for motors, generators, transformers, energy meters, etc. The loss value is related to the inner area of the histeresis curve. In a preliminary test, whose objective was to obtain the wire smallest diameter (final diameter of 0.2 mm from the same starting material with diameter of 7.2mm) the magnetic losses were 12.4 W/kg. With greater control during wire drawing and heat treatment, as described in this paper, it was possible to reduce the magnetic losses to 4.81 W/kg, approximately 2.6 times lower, showing ours to be a promising technique. Magnetic field application during the heat treatment [4] is also being studied.

[1] Di Giulio, M.; Transformador com núcleo magnético de fios enrolados (Brazilian patent PI 9900223-0. Validation in other countries PCT/BR00/00005, Brazil, 1999).

[2] Ray, R. K.; Jonas, J. J. Transformation textures in steels. Int. Mat. Rev 35 (1990) 1-36.

[3] Haratani, T, Hutchinson, W.B., Dillamore, I.L. Bate, P. Contribution of shear banding to origin of Goss texture In silicon iron. Metal Science 18 (1984) 57-65.

[4] Bhandary V.S., Cullity B.D.; Texture and mechanical properties of iron wire recrystallized in a magnetic field; Trans. Metall. Soc. AIME 224 (1962) 1194.

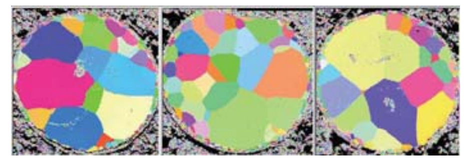

Figure 1. Orientation image map (OIM) of sample 7388

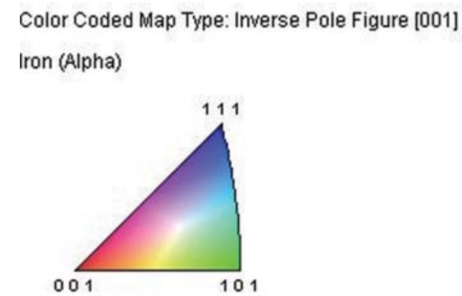

Figure 2. Color coded map

DF-01

A proposed "747" test to establish the areal-density capability of a magnetic recording system based only on data-block failure rate.

Z. Jin, M. Salo, *R. Wood*
HDD AdTech, Hitachi GST, San Jose, CA

The so-called '747' curve provides a well-accepted and convenient method of establishing the areal-density capability of a magnetic recording system [1]. The test and the imaginative naming can be attributed to two engineers, Earl Cunningham and Dean Palmer, working at IBM Rochester, Minnesota in 1978. The test is based on thresholds established for 'raw error-rate' measured prior to any error-correction. However the boundary between data detection (which transforms waveforms into bits) and error-correction (which operates at the level of bytes or symbols) is becoming increasingly blurred. In particular, the introduction of LDPC codes with powerful iterative detectors may obviate the use of conventional error-correction codes (ECC) altogether. To circumvent this problem, a '747' test is proposed that looks only at the rate of decoding failures of complete data-blocks after full ECC is applied.

The classical test traced out a curve resembling the profile of a '747' airliner. On the horizontal axis was plotted the distance between the 'home' track and the single encroaching or 'squeezing' track. On the vertical axis were plotted the distances that the head could be moved off-track, both towards and away-from the interfering track, before a certain threshold error-rate was exceeded. It has become more common to make the measurement by squeezing the 'home' track simultaneously from both sides (figure 1) and to report the average off-track capability (OTC). This yields similarly valuable information while avoiding problems associated with track-drift during the test.

The 747 test is traditionally based on raw error-rates, typically quoted as bit-errors per customer bit or sometimes symbol-errors per customer bit. A certain amount of ECC overhead is assumed. This ultimately has to be factored in as part of the format-efficiency calculation. The new proposal is to base the test on block failure rates after ECC and to quote areal-densities including the ECC overhead. This approach will enable the direct comparison of, for example, a system employing a conventional channel code with perhaps 10% ECC overhead vs. a system with only an LDPC code and no explicit error-correction overhead.

After error-correction or the application of a powerful iterative detector, the system will not have any measurable error-rate on-track or for significant amounts of off-track or squeeze. However at some critical displacement the failure-rate will rise rapidly from 0% to 100% over a short distance. To get the best discrimination and statistics, we set the threshold block failure rate to be 50%. A conventional test for areal-density capability usually also defines a certain on-track raw error-rate, for example, 1-symbol per 10^5 customer bits. The new proposal replaces the on-track error-rate criterion with a requirement for a certain margin before a linear-density 'push' would cause 50% data-block failures.

Figure 2 shows one example of a 747 curve with the new and the old critera for one particular read/write channel with 17 symbols (10-bit) of error-correction power (34 symbols of overhead). The new criterion offers much more margin, correctly reflecting the strength of modern ECC systems, and will allow considerably higher track-density and/or linear density to be quoted for given components. However, the net areal-density quoted will change little because the ECC overhead is now included into the areal density calculation.

It is hoped that this new criterion will in future allow more realistic and fairer comparisons of signal-processing systems that may have very different architectures.

[1] E.A.Cunningham and D.C. Palmer, "A Model for the Prediction of Disk File Performance from Basic Component Capabilities," Paper JE-3, 1988 joint MMM-Intermag Conference, Vancouver, BC, Canada, July 12-15 1988

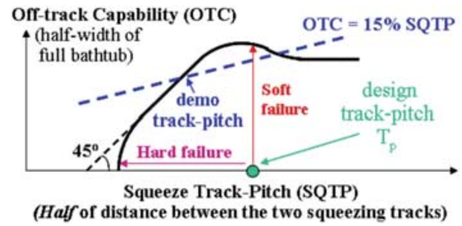

Figure 1. '747' with double-sided squeeze illustrating margins against failures caused by mistracking. The contour plotted corresponds to the distance that the reader can be moved off-track before a certain threshold raw error-rate is exceeded. The intercept between the 747 curve and dashed line at say 15% SQTP is a typical way of defining track-pitch in an areal density demonstration

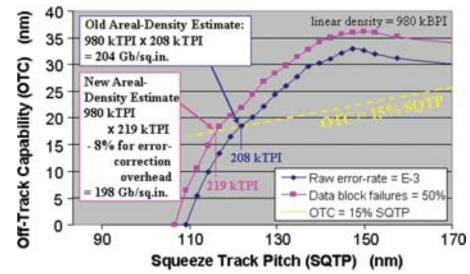

Figure 2. Example of 747 curves measured with the proposed 50% block failure criterion vs. a conventional raw error-rate threshold of 1-symbol (10-bit) per 1000 customer bits. The new criterion allows considerably more off-track and squeeze margin at a given linear density. This is consistent with the increased strength of modern error-correction systems. However, such error-correction systems add significant overhead. With the new criterion, this overhead is included into the calculation of areal-density. Thus the net areal-density quoted will not change greatly.

DF-02

Probabilistic Analysis of Off-track Capability for Higher Track Density Disk Drives.

K. Aruga, H. Ueno, T. Iwase, Y. Ogawa
HDD division (E3-333), Fujitsu Limited, Kawasaki, Japan

<u>Introduction</u>

The trend of track density(TPI) increase is larger than bit density(BPI) increase due to the difficulty of BPI improvement. However, the investigation of TPI increase is inadequate comparing to the BPI increase. This is because the track misresistration (TMR) budget is too complicated, and includes many area of technology, recording process, mechanical positioning, servomechanisms, read write channel etc.

In this paper, we will study TMR budget using probabilistic approach. The process from track misregistration to read write error will be simulated.

<u>Basic formulation</u>

The read MR head has a narrower core width (Cr) than write core width (Cw), shown in Fig.1. In the figure, mechanical track misregitration is displayed as a probability density pw, pr. Figure 2 indicates a typical 747 curve which shows the track density capability. To describe 747 characteristics, we introduce offset-margin and TPI-margin shown in Fig.2. According to the geometry model, we assume the signal output level is proportional to the width of overlapped section between write and read core. We define track offset as $\Delta x=xw-xr$, and the basic relation is described as,

$Sout=if\ (\Delta x<0,\ (Cr+\Delta x)/Cr\ pw(xw)pr(xr),\ else\ 1)$ (1)

$Nctk=if\ (\Delta x<0,\ -\Delta x/Cr\ pw(xw)pr(xr),\ else\ 0)$ (2)

$pw(x)=pr(x)=1/(\sqrt{2}\ \pi\sigma)\ exp(-x^2/(2\sigma^2))$ (3)

$ErrorRate(xroffset)=\int\int f(SN0)\ pw(xw)\ pr(xr)\ dxwdxr$ (4)

The precise formulation will be presented in the full paper.

<u>Comparing to experimental results</u>

We measured the offtrack capability using 15krpm, 140kTPI, 3.5inch drives. Figure 3 shows the offset value vs Viterbi Margin. The NRRO (Non Repeatable Run Out) 6sigma values in the calculation are 6nm, 30nm, 54nmm, respectively. In the case of NRRO6s 54nm, calculated result agrees experimental one very much. This indicates the probabilistic calculation is verified, and smaller NRRO can expand offtrack capability, of course.

Figure 4 shows the offset-margin correlation between calculated and measured value. The offset margin calculation was executed using by the measured data of Cr, Cw, and SN ratio at on-tracking, in every 500 heads. The both results correlate very well.

<u>Conclusion</u>

We tried probabilistic models of the track misregistration, and calculate from the offset probability to the error rate. The simulated results basically agree experimental value well. These results show the validity of these statistic modelling. We will be able to forecast the offset capability in future higher TPI recording by using this model.

(1) T.Yamaguchi et al, “Modeling and TMR Budget Design for Head-Positioning of High Track-Density Disk Drives”, IEEE Trans. MAG, Vol.35-2, pp892-897, March 1999

(2) K.Aruga et al, “Study on Positioning Error caused by FIV using Helium Filled Hard Disk Drives”, IEEE Trans. MAG, Vol.43-9, pp3750-3755. Sep. 2007

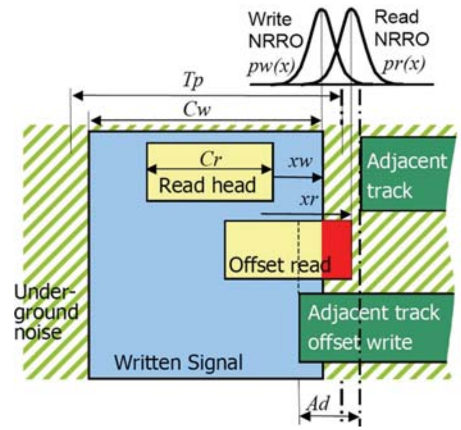

Fig.1 Geometry of write and read head

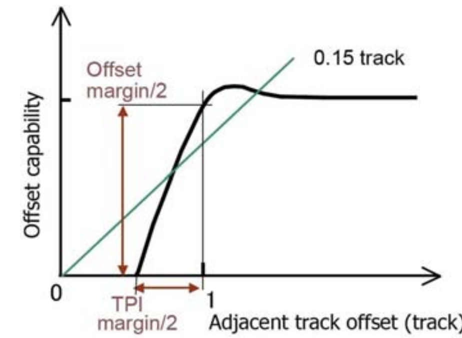

Fig.2 747 curve

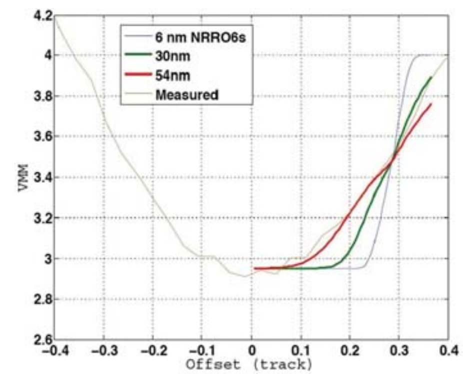

Fig.3 Calculated and measured offset capability

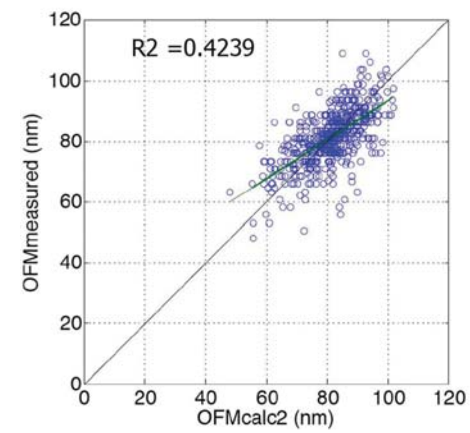

Fig.4 Calculated and measured offset-margin correlation

DF-03

Analysis of cross track response using a three dimensional model for Perpendicular Read Heads.

Z. Liu, B. Chen, S. Zhang
Data Storage Institute, Singapore, Singapore

The cross track response to perpendicular magnetization transitions are studied analytically and numerically. An analytical model for three dimensional reciprocity potential of perpendicular read heads has been developed for such studies. The model is able to predict efficiently the magnetic field and spectral response of the perpendicular read heads accounting to effect of the finite width of the read sensor element, the shields, and the soft underlayer magnetic properties. In contrast to previous analytical solutions [1-3], this model allows the effects of the skew angle and off track asymmetry to be considered. The 3d reciprocity potential and the spectral response function are verified using finite element simulations. Fig. 1 shows the field distribution of a read head. The spectral response function is represented in the form of 2d Fourier transform of the field intensity at the read sensor ABS, as shown in Fig. 2. The comparison of the analytical and finite element simulations is given in Fig.3. The response of the recorded transitions and pulses are obtained using the reciprocity principle. The influences of various head-media parameters on the read back signal and its distortions are investigated and discussed. It is noted that the property of the 2d Fourier transform is helpful when analyzing skew angle effects.

1. T. A. Roscamp, et al, Journal of Applied Physics, 91, 10, 8366(2002)

2. E. Champion, and H. N. Bertram, IEEE Trans. Magn., 31, 4, 2461(1995)

3. H. A. Shute, et al, IEEE Trans. Magn., 42, 5, 1661(2006).

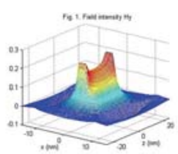

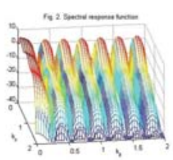

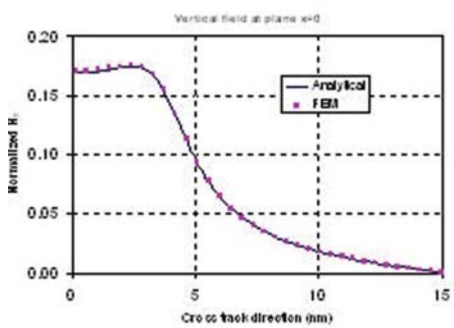

Fig. 3. Comparison of analytical and FEM simulations

DF-04

The reliability evaluation of piezoelectric micro actuators with application in hard disk drives.

Z. He[1], H. Loh[2], E. Ong[1]
*1. A*Star, Data Storagae Institute, Singapore, Singapore; 2. Mechanical Engineering Department, National University of Singapore, Singapore, Singapore*

In most cases, piezoelectric micro actuators/sensors will experience repeated load during their operations. The fatigue failure and the life cycles issues become important factors to be considered for researchers and engineers. So far a lot of research has investigated the fatigue behavior and mechanism of the piezoelectric actuators and the improvement methods [1~3]. However, the probability and statistics based reliability theory has not been well practiced in their applications. In this paper, a probabilistic design approach is presented to evaluate the reliability of piezoelectric micro actuators. The reliability evaluation of a disk drive dual stage positioning system using piezoelectric micro actuators are performed using the proposed approach.

Based on the relationship between the lifetime (number of cycles to failure) and degradation mechanism of piezoelectric actuators and the electric field strength, the concept of "electric strength" is proposed to indicate the electric field strength of the piezoelectric actuators at a specified lifetime. The lifetime of piezoelectric actuators, electric strength, and electric load are considered as the random variables and their probability distributions are discussed. A P-E-N curve, which described the relationship among the probability, electric strength, and lifetime are introduced for lifetime estimation for piezoelectric actuators. Based on the probability distributions of electric strength, E, and electric load, e, an interference model of electric load and electric strength is introduced to the reliability design of piezoelectric micro actuators. By this interference model, the relationship between the reliability and the usage lifecycles of the piezoelectric actuators can be obtained [4].

Furthermore the reliability model is expanded into two dimensional cases to take into account the effects of both driving voltage and temperature. Based on the relationships between the lifetime and degradation mechanism of piezoelectric actuators and the electric field strength, as well as the actuator working temperature, a two-dimensional probability model for evaluating reliability of piezoelectric micro-actuators is described. The concept of two-dimensional strength is proposed to incorporate the electric driving voltage, E, and the working temperature, T, of the piezoelectric actuators at a specified lifetime. The lifetime (number of cycles to failure) of piezoelectric actuator, electric load and temperature are considered as the random variables and their probability distributions are discussed. The P-N-E-T surface, which describes the relationship among the reliability, lifetime, electric driving voltage, and temperature, is presented. It is mathematically proven that there exists equivalence between the failure probability of electric driving voltage, temperature at a specified lifetime and that of the lifetime at a given electric driving voltage or temperature. Based on this equivalence, a two-dimensional strength probability distribution function is derived. A two-dimensional interference model between the two-dimensional strength and load is proposed to obtain the relationship among the reliability, lifetime, driving voltage and temperature [5].

A case study of a piezoelectric micro-actuator used for head positioning in a disk drive head positioning system demonstrates the application of the approach. The fatigue data of a piggyback piezoelectric micro actuator developed by Hitachi, Ltd. [1, 3] is collected. Firstly the electric load-strength interference model is applied to evaluate the reliability of the piezoelectric actuators and demonstrate the application of the reliability model. The quantified reliability versus usage lifecycles is obtained. With an assumption of 3 kHz drive of the piezoelectric actuators, the evaluated reliability is 96.70% with a 5 years operation in hard disk drives. By the two-dimensional model with taking into account both the electric driving voltage and temperature variation, the reliability of 96.32% is projected for the assumed 5 years operation. This verifies the validity of the electric load-strength interference model. Therefore, the proposed reliability evaluation method can be used to evaluate the reliability and estimate the lifetime of piezoelectric micro actuators or, in general, of mechatronics devices.

[1] S. Nakamura, H. Numasato, K. Sato, M. Kobayashi, I. Naniwa, "A push-pull mult-layer piggy PZT actuator", Microsystem Technologies 8(2002) pp. 149-154.

[2] J. Thongrueng, Tsuchiya, and K. Nagata, "Lifetime and degradation mechanism of multilayer ceramic actuator", Jpn. J Appl. Phys. 37 (1998) pp. 5306-5310.

[3] S. Nakamura, I. Naniwa, K. Sato, K. Yasuna, and S. Saegusa, "Life prediction method for piggyback PZT actuator", IEEE Transactions on Magnetics, 37 (2) (2001), pp. 940-943.

[4] Z. He, H.T. Loh, and E.H. Ong, "A probability approach to evaluating the reliability of piezoelectric micro-actuators", IEEE Transactions on Reliability, 54 (1) (2005), pp. 83-91.

[5] Z. He, H.T. Loh, and M. Xie, "A two-dimensional probability model to evaluate the reliability of piezoelectric micro-actuators", International Journal of Fatigue, 29 (2) (2007), pp. 245-253.

DF-05

A slider with an integrated microactuator (SLIM) for second stage actuation in hard disc drives.

H. H. Gatzen[1], P. J. Freitas[2], E. Obermeier[3], J. Robertson[4]

1. Institute for Microtechnology, Leibniz Universitaet Hannover, Garbsen, Germany; 2. INESC-MN, Lisboa, Portugal; 3. Microsensor & Actuator Technology, Berlin University of Technology, Berlin, Germany; 4. Department of Engineering, University of Cambridge, Cambridge, United Kingdom

Introduction

Preconditions for achieving an optimal recording density in Hard Disk Drives (HDD) are a minimal flying height and a perfect track registration. For accomplishing the first one, a dynamic flying height adjustment during writing and reading may optimize the head-to-disc spacing and was implemented into the latest generation of recording heads [1]. To achieve a perfect track registration, a second stage actuation is desirable for compensating to compensate the frequency limitations of the main actuator. Both flexure and Micro Electro-mechanical Systems (MEMS) based designs for second stage actuators were suggested [2, 3]. However, due to the price competitiveness of the industry, the extra costs required for such a device so far hindered its wide scale use. Nevertheless, the requirements are obvious: an optimal solution will provide both capabilities for flying height and track following adjustment and will be cost competitive.

SLIM Concept

To address the actuator requirements, the following approach was taken: an electromagnetic micro actuator was integrated into a pico form factor slider, resulting in a slider with an integrated micro actuator (SLIM) [4]. The integrated micro actuator activates a mounting block to which a chiplet containing the read-write element is attached. The actuator is capable of moving the read-write element on the chiplet both in vertical direction (adjusting the flying height) and in lateral direction (allowing second stage actuation). The cost competitiveness results from the fact that the slim components can be fabricated at lower costs than a present day HDD slider. The micro actuator is substantially less complex than a classic slider while the chiplet containing the read-write element takes up only one third of a pico slider's real estate on a wafer.

SLIM Design and Fabrication

SLIM pursues a two-wafer approach. The actuator magnetics reside in the bottom wafer and the actuator mechanics in the top wafer. Sandwiched between the two wafers is a spacer compensating for the magnetic actuator's building height. The actuator magnetics consist of a pair of variable reluctance (VR) micro actuators [5], the actuator mechanics of a mounting platform suspended by a pair of leaf springs. The mounting platform carries the chiplet containing the read-write element. Simultaneously exciting both actuators adjusts the chiplet's flying height, while alternatively exciting them causes a minute rotation of the chiplet, creating a lateral displacement of the read-write element. Therefore, this design allows both flying height adjustment and track following. A desired lateral displacement of ±625 nm results in a rotation of 0.18°. Due to the small rotational angle, the resulting change in flying height is only about one nanometer.

The SLIM fabrication is executed on a pair of Si wafers, creating both the actuator magnetics and mechanics in a thin-film batch fabrication process. Since the energy a microactuator is capable of transducing is proportional to its volume, high aspect ratio micro system technologies (HARMST) are applied for fabricating the actuator magnetics [5]. The microactuator mechanics are fabricated by applying silicon micromachining processes. At the wafer's back side, ultimately an ABS will be created by ion milling and will be covered by a DLC layer for sufficiently making the DLC slider wear resistant. However, for the first prototypes, this ABS will not be included, since the initial testing is performed on a static tester.

Experimental Investigations

To evaluate the actuation capabilities of SLIM, a static test stand was created. It allows for mounting a SLIM device in a position similar to its future application when flying on a data disc. A set of drive electronics is exciting the SLIM micro magnets, allowing for both a lowering of the chiplet and a rotation of the chiplet. For these experimental investigations, a special test chiplet is used featuring a permanent magnet. A GMR detection system is monitoring the chiplet motion.

[1] D.W. Meyer, P.E. Kupinski, J.C. Liu: Slider with temperature responsive transducer positioning, US Patent 5991113

[2] H. Du; G. K. Lau; B. Liu: Actuated suspensions with enhanced dynamics for hard disk drives. IEEE Transaction on Magnetics, 41 (10), 2005, pp. 2887-2889

[3] K. Suzuki, M. Kurita: A MEMS-Based Active Head Slider for Flying Height Control in Magnetic Recording. JSME International Journal, B 17, No. 3, pp. 453-458, 2004

[4] F. Chen, H. Xie, G. K. Fedder: A MEMS-based monolithic electrostatic microactuator for ultra-low magnetic disk head fly height control. IEEE Transaction on Magnetics Vol. 37, No. 4, pp. 1915-1918, 2001

[5] H.H. Gatzen: Schreib-/Lesekopf mit integriertem Mikroaktor (Read-Write head with integrated micro actuator) German Patent 10260009

[6] H.H Gatzen, D. Dinulovic, H. Saalfeld: Integrated electromagnetic second stage micro actuator for a hard disk recording head. Intermag 2008, Madrid (submitted)

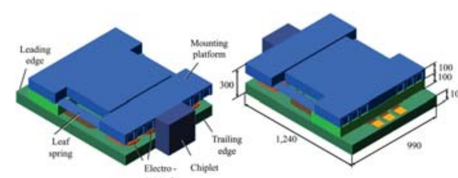

Figure 1: Slider with Integrated Microactuator (SLIM). Dimensions are in micrometer

DF-06

Integrated electromagnetic second stage micro actuator for a hard disk recording head.

D. Dinulovic, H. Saalfeld, H. H. Gatzen
Institute for Microtechnology, Leibniz Universitaet Hannover, Garbsen, Germany

Introduction

For advanced hard disc drive recording heads, both a flying height adjustment and a second stage track following capability for fine tracking is desirable. To fulfil these requirements in a cost competitive way, a Slider with an Integrated Micro Actuator (SLIM) has been proposed [1]. The dimensions of SLIM correspond to a pico-slider (1.240 µm x 990 µm x 300 µm). SLIM allows for both vertical (for head-to-disk spacing adjustment) and lateral (for fine tracking) motion of the read-write element. To do so, the integrated micro actuator contains a pair variable reluctance (VR) micro actuators. They activate a mounting block to which a chiplet containing the read-write element is attached. The actuator is capable of moving the read-write element on the chiplet both in vertical direction (adjusting the flying height) and in lateral direction (allowing second stage actuation). This paper describes the design and fabrication of the electromagnetic micro actuator.

Magnetic Core Properties

For accurately simulating a magnetic micro device, the magnetic material properties of the micro components have to be known. The most essential parameter is the relative permeability µr, which influences the system's reluctance. For thin film components, it is strongly influenced by the structure's shape. Vibrating Sample Magnetometer (VSM) measurements with arrays of the desired magnetic structures allow to estimate the respective permeability µr [2].

Micro Actuator Design

For establishing the SLIM electromagnets, a Finite Element Method (FEM) analysis was performed using the software tool ANSYSTM Multiphysics. 2-D and 3-D simulations were executed to determine the optimal dimensions of the magnetic core. For the chosen actuator design, a 2-D simulation predicted a magnetic force of about 355 µN at an air gap of 2.5 µm while exciting the coils with a current of 175 mA. A 3-D simulation resulted in very similar values: a magnetic force of about 340 µN for the same air gap. Figure 1 shows a 3-D FEM simulation result for the magnetic flux density for an excitation of 175 mA and an air gap of 5 µm. Based on the FEM results, the features and dimensions for the micro actuator were finalized. Each magnetic micro actuator (a complete system contains a pair) consists of a U-shaped soft magnetic core and of two double layered spiral coils for the excitation. The total size of one magnetic actuator is 460 µm x 300 µm x 62 µm. Two micro actuators are integrated in the slider. Therefore, a vertical motion of the chiplet with the read/write element as well as a rotational motion (resulting in a lateral displacement of the read-write element) are possible.

Micro Actuator Fabrication

The micro actuator was fabricated in thin-film technology. The wafer process to fabricate the actuator mainly uses High Aspect Ratio Micro Structure Technology (HARMST), combining UV depth lithography and electroplating. The materials employed are NiFe45/55 for the magnetic flux guides and magnetic poles, Cu for the coils, a photosensitive epoxy (SU-8™) for lateral insulation, and Si3N4 for insulating the two coil layers from each other. To achieve a constant magnetic layer thickness as well as flat surfaces, Chemical-mechanical Polishing (CMP) was applied. Figure 2 shows an SEM micrograph of a prototype.

Evaluation

For a functional evaluation, a first prototype was subjected to force and field measurements. Qualitative force measurements were conducted by allowing the micro actuator to exert forces on a NiFe45/55 stripe. Executing quantitative force measurements and field measurements includes involving the Physikalisch Technische Bundesanstalt in Braunschweig, Germany and the University of Göttingen, respectively.

[1] M. Kurita, K. Suzuki: Flying-height adjustment technologies of magnetic head. IEEE Transaction on Micro Electro Mechanical Systems, 40 (1), 2004, pp. 332-336

[2] H.H. Gatzen, P.J.P. de Freitas, E. Obermeier, J. Robertson: A slider with an integrated microactuator (SLIM) for second stage actuation in hard disc drives. Intermag 2008, Madrid (submitted)

[3] M. Bedenbecker, Z. Celinski, H.H. Gatzen: Directional permeability dependence in electroplated permalloy layers. ECS Trans. 3 (25), 2007, p. 123

Figure 1: Magnetic flux density of the micro actuator with 20 µm thick magnetic core

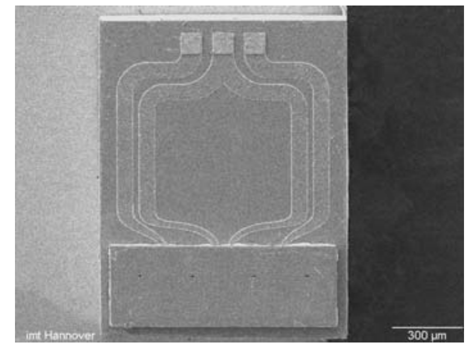

Figure 2: SEM micrograph of a SLIM micro actuator prototype

DF-07

Characterization of timing based servo signals.

G. Cherubini[1], *R. D. Cideciyan*[1], E. Eleftheriou[1], P. V. Koeppe[2]
1. IBM Research, Zurich Research Laboratory, Rueschlikon, Switzerland; 2. IBM Systems and Technology Group, San Jose, CA

The timing based servo (TBS) format [1] was first used in IBM tape drives with 8-mm cartridge that utilized bidirectional multi-channel serpentine linear recording. In TBS systems, recorded servo patterns consist of magnetic transitions with two different slopes corresponding to two different azimuth angles. The head position is derived from the relative timing of pulses generated by a narrow servo head reading the pattern. Furthermore, encoding of additional longitudinal position information can be provided by shifting specific transitions from their nominal pattern position without affecting the generation of the transversal position error signal. The TBS format including longitudinal position encoding was adopted by the linear tape open (LTO*) standard, where four data bands are straddled by five servo bands that are preformatted during tape manufacturing with a special TBS pattern at ± 6° azimuth [2]. Four generations of LTO tape drives have been supported by a single TBS format that enabled the doubling of cartridge capacity every two years and allowed scalability in conjunction with backward compatibility based on shingled tracks [3].
In this paper, an analytic expression for the transition response of TBS-based servo systems is introduced. In particular, a closed-form formula for the TBS transition response is given in the case of a Lorentzian response to magnetic transitions with 0° azimuth. Furthermore, an analytic expression for the pulse width at 50% amplitude of the TBS transition response is provided and a closed-form formula for the slope of the TBS dibit at the zero crossing is derived. The proposed analysis can be used to select the azimuth α and the minimum transition distance m of TBS servo patterns for future generations of LTO drives supporting higher track densities, and to determine the width W of the servo reader. Moreover, the characterization of the TBS transition response allows accurate simulations of the overall TBS servo channel.

The derivation of the servo transition response at a distance x from the transition measured in the longitudinal direction (parallel to the tape edge) is based on representing the servo stripe lines at an azimuth angle α by a staircase function with infinitesimal step size dy in the lateral direction. Then for a given reader width W all contributions of time-shifted micro-responses are added by linear superposition, i.e., by integration over the variable y, where y is the displacement across the track (lateral direction perpendicular to the tape edge). The general expression for the servo transition response is thus given by
$h(x;\alpha,W,f(.)) = \int_{[-W/2\ W/2]} f(x - y \tan \alpha)\, dy$
where f(x) is the transition response corresponding to a magnetic transition with 0° azimuth. In the following it is assumed that $f(x)=1/[1+(2x/P)^2]$ is the Lorentzian response, which is fully characterized by the pulse width at 50% amplitude P. In this case, the following closed-form formula for the TBS transition response is obtained
$h(x;\alpha,W,P) = (P/(2\tan \alpha))\ [\arctan((W \tan \alpha-2x)/P)-\arctan((-W \tan \alpha-2x)/P)]$.

Note that $h(x;\alpha,W,P)$ is the well-known Lorentzian function for α=0°. Figure 1 shows the TBS transition response for α=6°, W=8µm, and P=0.27µm, as well as the Lorentzian response.
The pulse width at 50% amplitude of the above transition response can readily be expressed by
$PW50(\alpha,W,P) = P\ [1+((W \tan \alpha)/P)^2]^{1/2}$.
Note that $PW50(\alpha,W,P)$ is an increasing function of α, with $PW50(\alpha,W,P)=P$ for α=0°. For the response shown in Fig. 1, $PW50(\alpha=6°,W=8\mu m,P=0.27\mu m)=0.87\mu m$.
Recalling that the minimum transition distance in longitudinal direction is m, the dibit response is given by
$g(x;\alpha,W,P,m) = h(x;\alpha,W,P) - h(x-m;\alpha,W,P)$.
For the TBS format used in LTO, the minimum distance between transitions in a dedicated servo band is m=2.1µm [2]. In general, the slope of the TBS dibit at the zero crossing can be expressed by
$s(\alpha,W,P,m) = [-8m\ W\ P^2] / [(P^2+(W \tan \alpha)^2+m^2)^2-4m^2(W \tan \alpha)^2)]$.
It is found that analytical and experimental TBS dibit responses are in good agreement.
* LTO is a trademark of HP, IBM and Quantum.

[1] R. C. Barrett, E. H. Klaassen, T. R. Albrecht, G. A. Jaquette, and J. H. Eaton, "Timing-based track-following servo for linear tape systems," IEEE Trans. on Magn., vol. 34, pp. 1872-1877, July 1998.

[2] Standard ECMA-319, "Data interchange on 12.7 mm 384-track magnetic tape cartridges – Ultrium-1 format," June 2001.

[3] G. A. Jaquette, "LTO: A better format for mid-range tape," IBM J. Res. Develop. 47, No. 4, pp. 429-444, July 2003.

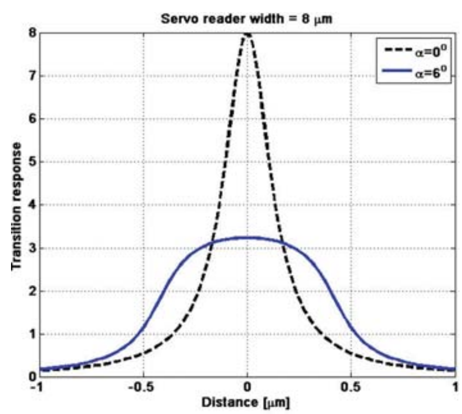

Fig. 1. Timing based servo transition response

DF-08

Evaluation of printed servo patterns.

B. Baker
Redwood Technology, Redwood City, CA

Printed servo patterns offer a significant decrease in the manufacturing cost of hard disk drives (HDDs). In 1998 Matsushita Electric Industrial (MEI) proposed printing the servo patterns of HDDs they manufactured for Quantum Corporation. Disks would be patterned in only a few seconds in special MEI machines [1, 2] before being inserted into the HDD.

Since initial feature sizes were two microns or greater, a final printed servo pattern would occupy too much of the disk surface. The author proposed[3] using the coarse but accurate printed pattern as a reference similar to the function of a traditional Servo Track Writer (STW). To accommodate the expected eccentricity, position information would be derived from phase measurements of nested chevrons. Heads of the drive would be used, as in STWs, to write the final pattern. HDDs would be assembled in a clean room, but the self-write process would be completed in a less expensive self-test rack.

Patterns were designed and sent to MEI for fabrication. First tests were done on a spin stand so features were added for consistent triggering of an oscilloscope at the pattern index. Scope data were analyzed with Discrete Fourier Transform (DFT) calculations, as in the channel chip[4], to measure accuracy of position derived from the difference of phases of A and B bursts of the chevrons.

Temperature variations of the lab air caused significant radial offsets of a test track. Spin stands were being modified to add servo capabilities in order to track the thermal expansion, but it was not practical to write the spin stand's reference bursts without erasing portions of the printed patterns. The solution was to capture a few successive revolutions of data to minimize thermal offsets.

The smooth, measured eccentricity could easily be followed or could be corrected by HDD firmware, so the interesting information was the small differences between the total position and the contribution of the known eccentricity. Those small differences, which might lead to track squeeze or incursions, were computed and found to be smaller than those of STW written drives.

Standard deviations of differences of position information derived from nearby radii were useful in optimization of parameters such as the separation between the permeable pattern and the DC driving magnet of the printing system[1]. The measurement software was transferred to partners at MEI and Fuji Electric for quicker verification of masters and sample disks.

A channel modification[5] enables use of the low-frequency coarse pattern in HDDs that turn at lower RPM. A decimation filter allows the clock of the output pattern to run 8 times faster than the frequency of the coarse input pattern. The write procedure was extended to allow output of the final pattern. Successor HDDs have those more capable channels. Continuation runs of two Quantum HDDs were completed by using SSW from a printed reference pattern. Yields were equivalent to those of STW written HDDs.

Subsequent measurements of patterns with finer features using better heads show continued improvements of the position information. Major deviations of measurements at nearby radii are nearly the same. By releasing and clamping the disk at a different angle relative to the spindle those major deviations were shown to be due to wobble of the air bearing of the spin stand. Hydrodynamic spindle bearings of HDDs are much better. Even with the consistent deviations a simple simulation of the actuator servo, with scaling for noise as the tracks narrow, shows ample protection against adjacent-track incursions. The present analysis also shows good tolerance of phase demodulation to worst case eccentricity of the pattern.

New compound phase patterns[6] eliminate the SSW process and its potential to introduce track squeeze. Position information would be derived from a master written in an e-beam system and reproduced by NIL (Nano-Imprint Lithography) with features smaller than 100 nm. These patterns have the same frequency for both coarse and fine position information and can be read with contemporary channel chips during a full-speed seek. They are well suited for perpendicular recording since it is not necessary to use Gray codes or other DC fields in the servo wedges. Printing of perpendicular media by horizontal fields has been analyzed and demonstrated[7].

[1] T. Ishida, K. Miyata, T. Hamada, and K. Tohma, "Printed Media Technology for an Effective and Inexpensive Servo Track Writing of HDDs", IEEE Trans. Magn., vol. 37, pp. 1875-1877, July 2001

[2] T. Ishida, K. Miyata, T. Hamada, H. Hashi, Y. Ban, K. Taniguchi, and A. Saito, "Magnetic printing technology – application to HDD", IEEE Trans. Magn., vol. 39, pp. 628-632, Mar. 2003

[3] B. Baker, S. Lambert, J. Lin, M. Moser, and S. Sun, Self-writing of servo patterns based on printed reference pattern in rotating disk drive, U.S. Patent 6304407, 2001.

[4] B. Baker and J. Fitzpatrick, Method and Apparatus for Spectral Analysis in a Disk Recording System, U.S. Patent 5784296, 1998.

[5] P. Moran, T. Everett, P. McEwen, M. Moser, S. Shepherd, E.Viega, M. Erkocevic, and B. Baker, Self-writing of servo patterns in disk drives, U. S. Patent 6738205, 2004.

[6] B. Baker, Compound phase encoding for printed servo patterns, U.S. Patent 7167329, 2007.

[7] A. Saito, T. Hamada, T. Ishida, Y. Takano, and E. Yonezawa, "A Novel Magnetic Printing Technique for Perpendicular Recording Media, IEEE Trans. Magn.", vol. 38, pp. 2195-2197, Sep. 2002.

DF-09

Overwrite performance change due to air-flow induced vibration of head stack assembly.

E. Jang, J. Chang

HDD R&D, Samsung Information Systems America, San Jose, CA

Overwrite (OW) performance of two types of head stack assemblies (HSA) were compared as a function of zone location of disk. They have the same types of head slider, suspension interconnect, and preamplifier but have different mechanical platform (Type A: 4 HGAs vs. Type B: 6 HGAs) and different arm structure. There is OW degradation by more than 2 dB at OD compared to ID for Type B HSA but not for Type A. This paper investigates the mechanism of OW degradation of Type B HSA at OD. It was found that the mechanical vibration of arm actuator is a key factor to the OW degradation.

Overwrite experiments were performed on a Canon RS-5220U spin-stand, RWA2003, at 7200 rpm, and in three zones (ID, MD, and OD) of 95 mm aluminum disks. Conventional OW test method was used with a narrow-band filter and LMR heads. The ratio of low frequency (LF) to high frequency (HF) is 1:7. The high frequency (1T pattern) of OD zone is 468.19 MHz and the linear density is 711.70 kfci. Testing was done with the same setup for both type HSAs except the number of disks (two disks for Type A and three disks for Type B). Fig. 1 shows typical OW performance for Type A HSA (2 disk platform) and Type B (3 disk platform). The sample size of HSA is 3 (12 heads for Type A and 18 heads Type B). As shown in the figure, the OD OW of Type B is worse than ID by 2.77 dB while OD OW of Type A is slightly better than ID by 0.91 dB. We also studied the variation of OW as a function of high frequency. Fig. 2 shows the test result for Type B at frequency of -15% ~ +45 % offset from the reference frequency. No OW degradation was observed up to 45% increase of the reference frequency. The better OW with increasing frequency may be due to thermal pole tip protrusion of the write head. These results indicate that the main origin of OW degradation of Type B at OD is of mechanical, rather than electrical.

In order to confirm mechanical vibration effect on OW, several experiments were performed. One of them is to monitor the OW performance at 3 different zones under only one disk test condition. Fig. 3 shows OW performance before and after removing the bottom disk for one HSA of Type A. There are no significant changes in OW between “Before” and “After” tests. Fig. 4 shows OW performance before and after removing the bottom two disks for one HSA of Type B. Originally, there were OW drops at OD compared to ID (by 5.7 dB for hd 4 and by 3.8 dB for hd 5). However, the OW of OD is higher than that of ID (by 3.8 dB for hd 4 and by 3.4 dB for hd 5) after removing bottom disks. Furthermore, there are increases in OW at OD compared to before removing the bottom disks (by 6.7 dB for hd 4 and by 7.1 dB for hd 5). Additionally, we investigated the arm damper effect on OW performance. There are remarkable increases in both OW and amplitude at OD/MD zones after attaching big size dampers, but there is still overwrite drop at OD compared to ID.

There are some differences between Type A and Type B – number of arm, number of disk, and thickness of arms. The arm thickness of HSA E-block is one of the critical factors for the off-track motion of the head slider during the spin stand testing. The experimental results indicate that both disk flutter and arm vibrations are root causes for OW drop of Type B HSA at OD. The followings are possible explanations. 1) Disk flutter caused by air disturbance due to disk rotation. 2) Interaction between head (or HSA) and disk results in flow-induced vibration. 3) Axial displacement is converted to radial track misregistration (TMR). Arm bending modes of HSA and servo bandwidth are also discussed.

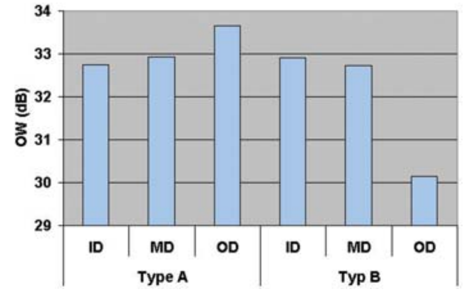

Fig. 1 Typical OW performance of two types of HSA

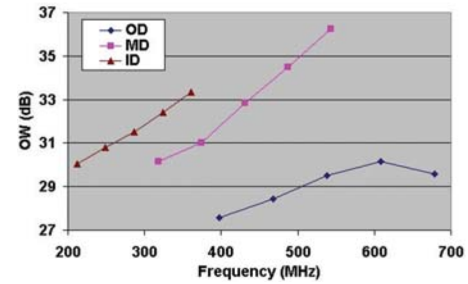

Fig. 2 OW versus high writing frequency for Type B

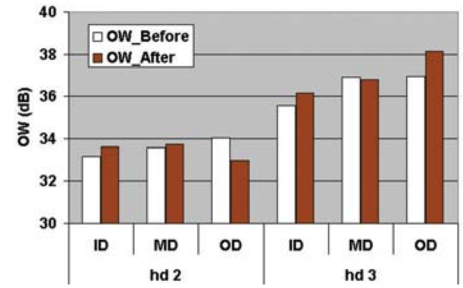

Fig. 3 OW before and after removing bottom disk for Type A

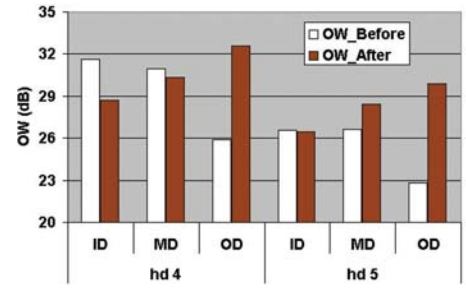

Fig. 4 OW before and after removing two bottom disks for Type B

DF-10

Reduced Order Models for Efficient Simulation of Hard Disk Drive Operational Shock Responses.

W. Lin[1], E. Ong[1], J. Mou[1], E. Ong[1], S. Hu[2]
1. Data Storage Institute, Singapore, Singapore; 2. Nitto Denko Corporation, Kameyama, Japan

The shock resistance of hard disk drive (HDD) under operational condition is one of the key challenges to the HDD industry with the increase applications of HDD in our daily life. Numerical study of HDD shock resistance will provide guidance to the designer in terms of design verification, performance prediction and optimization. However, due to the structural complexity of the HDD, inherent nonlinearity, as well as a large number of simulation in transient shock responses computed at sub-micro second time increment over a few milliseconds resulting in couple of ten thousand or hundred thousand time step computations; the traditional time-dependant fully meshed models, such as finite element method (FEM) which normally results in a large number of degrees-of-freedom (DOF), are usually computationally very intensive and time consuming or even prohibitive for designer to carry out the simulations. The remedy to this difficulty is the application of model order reduction techniques that allow the original problems with large number of DOF to be replaced with the models with substantially smaller DOF while capturing the behaviors of the original problems faithfully.

Projection-based model order reduction (MOR) uses the techniques of projecting the large DOF of the original system onto an orthogonalised subspace to form models with much smaller DOF. There are many research works in the area of projection-based model order reduction techniques. A well-known one is the Krylov subspace method which matches moments between the transfer function of the original system and that of the reduced order model to a given order. The Krylov subspace method has the advantages of numerical robustness and convenience in implementation. This paper presents the first time successful application of a projection-based Krylov subspace to generate accurate and efficient reduced order models for efficient and accurate simulation of HDD transient shock responses when the HDD is subjected to shock pulses. The reduced order models are generated directly from the HDD system structural matrices obtained from its finite element discretization and the Arnoldi algorithm to extract the subspace basis that spans the Krylov subspace from these structural matrices. Reduced order models are verified and validated with the commercial FEM software Ansys results and the experimental data in both time and frequency domains, as shown in Figs 1-4, for suspension shock transient dynamic responses when the HDD is subjected to half sine shock pulse of magnitude of 25G with the pulse width of 5 ms. It is also demonstrated in Table I that the reduced order model can achieve as high as significant four thousands computational speed up when compared with the traditional FEM simulations.

Model	DOF	Computation time (CPU second)	Root mean squared error
FEM (Ansys)	138,211	126,000	-
Reduced order model	50	32	2.1e-3

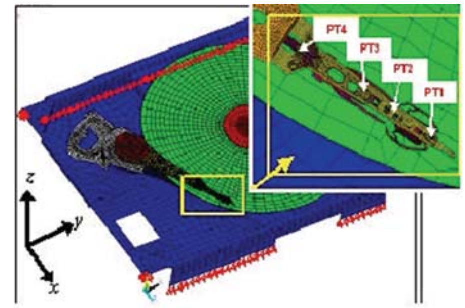

Fig 1. FEM discretization of a 1.8" HDD and the locations of the point of interest (P1, P2, P3 and P4) on suspension for shock response analysis.

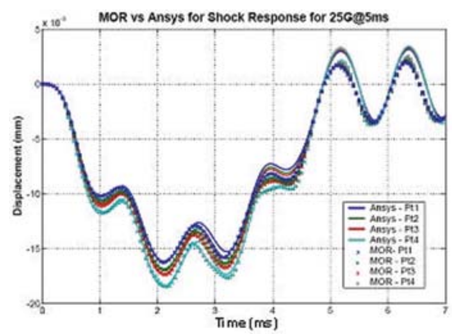

Fig 2. Reduced order model simulation results (indicated as MOR) compared with FEM results (indicated as Ansys).

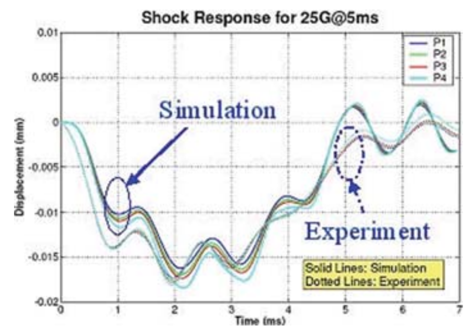

Fig 3. Reduced order model simulation results compared with experimental data.

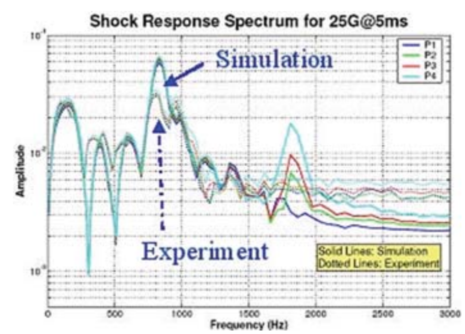

Fig 4. Shock response spectrum of reduced order model simulation results compared with experimental data.

DF-11

A Case for Redundant Arrays of Hybrid Disks (RAHD).

F. Wang[1], N. Helian[1], D. Deng[1], S. Wu[1], C. Liao[1], M. Rashidi[1], A. Parker[2]
1. Centre for Grid Computing, Cambridge-Cranfield HPCF, Cranfield, United Kingdom; 2. Cavendish Laboratory, Cambridge University, Cambridge, United Kingdom

1. Innovations & inheritance of prior work
Hybrid Hard Disk Drive was originally concepted by Samsung, which incorporates a Flash memory in a magnetic disk [1]. The combined ultra-high-density benefits of magnetic storage and the low-power and fast read access of NAND technology inspires us to construct Redundant Arrays of Hybrid Disks (RAHD, Fig.1) to offer a possible alternative to today's RAID (Redundant Array of Independent Drives) [2] and/or MAID (Massive Array of Idle Disks) [3]. We have designed two separable working modes for RAHD arrays: (1) High-Speed (HS) mode targeting at displaying the full potential speed of hybrid disks; and (2) Energy-Efficient (EE) mode targeting at reducing the energy consumption while maintaining acceptable performance.
2. High Speed (HS) Mode and internal management of hybrid disks
In the HS mode, the Flash memory always contains frequent data objects. We have designed two schemes to move the frequent data blocks into the Flash memory: (1) Using Decision Tree from Data Mining to predict the frequencies of data blocks (file attributes of a newly-generated file are used to predict its frequency). Blocks with high (predicted) frequency are then written onto the Flash memory [4]; (2) Tracking the frequencies of data blocks (when the disk is being used) and then migrating the most frequently-accessed data blocks into the Flash memory during the system idle periods [5]. Because of the high skew in common application loads, most of the requests are likely to be satisfied in the Flash memory without bothering the slower disks.
Three real-system traces (Cello-96, TPC-D, and Cello-99) [6] are used to investigate the data access patters. These traces capture all low-level disk I/O performed by the system at Hewlett-Packard Laboratories. Our simulator combines the modified DiskSim simulator [7] with an integrated Object Mover to simulate an array of hybrid disks. We use the above modified Disksim to configure an 8-hybrid-disk RAHD. Reads and writes in Flash are processed in terms of pages. The page size for the Samsung Flash memory used in the work is (2K + 64) Byte. Note that the page size is intended to fit a disk sector in size, hence a disk (Seagate Cheetah Ultra SCSI) in a RAHD is formatted to have a sector size of 2KB. Based on the observation that the majority of the disk I/O's (including both writes and reads) are probably going to less than 10% of the total disk space [5], a Flash memory is conservatively designed to occupy the first 10% of an enlarged disk space that is virtually continuous (inset of Fig.1).
3. Energy Efficient (EE) Mode
In the EE mode, some "active drives" remain constantly spinning whereas the remaining "passive drives" are allowed to spin-down following a period of inactivity. A request is directed to the Flash in the first instance. If the request is fulfilled by hitting the Flash memory, there is no need to awaken the sleeping disk. Otherwise, the request will be forwarded to the disk that is already active or needs to be awakened from sleep.
4. Real-system-trace-driven results
The trace-driven experimental results show: in the high speed mode, a RAHD outplays the purely-magnetic-disk-based RAIDs by a factor of 2.4 – 4; in the energy-efficient mode, a RAHD4/5 can save up to 89% of energy at little performance degradation. The highest performance comes from either Level 4 or Level 5. Considering that RAHD4 has an inherent bottleneck on the parity drive, Level 5 looks best in terms of the trade between the performance and the power-saving.

Hybrid disks are specially designed for personal and mobile applications whereas the proposed Redundant Arrays of Hybrid Disks (RAHD) can be used more broadly. It is found that a RAHD will provide improvements in performance, power consumption, and scalability. It is a conceptually simple technique for dramatically improving disk array performance, which is desirable for supercomputers and transaction processing.

[1] Samsung teams with Microsoft to develop first hybrid hard drive, physorg.com, 2007

[2] Patterson, David, et al, "A Case For Redundant Arrays Of Inexpensive Disks (Raid)", SIGMOD, 1988

[3] Dennis Colarelli, et al, Massive Arrays of Idle Disks for Storage Archives, 2002 Ieee

[4] Chen Liao, Accelerating File Systems By Predicting Access Frequency, UK e-Science All-Hand Meeting, Nottingham, November, 2007

[5] Frank Wang, et al, Evolutionary Storage: Speeding Up A Magnetic Disk By Clustering Frequent Data, IEEE Transactions On Magnetics, Issue.6, Vol.43, 2007.

[6] HP Storage Systems: Tools And Traces, hpl.hp.com, 2006

[7] Disksim 3.0 Manual, 2007

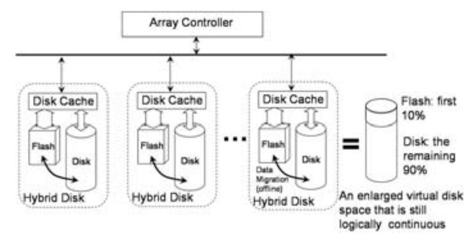

Fig.1 Redundant Arrays of Hybrid Disks (RAHD). Hybrid Disk schematic is also shown Based on the observation that the majority of the disk I/O's are probably going to less than 10% of the total disk space, a flash memory occupies the first 10% of an enlarged disk space that is virtually continuous. Accordingly, the most frequently-accessed data blocks are migrated into the flash memory periodically.

DF-12

What is the future of hard disk drive, death or rebirth?

Y. Deng[1], F. Wang[1], N. Helian[2]
1. School of Engineering, Cranfield University, Bedforshire, United Kingdom; 2. London Metropolitan University, London, United Kingdom

1.Introduction
Due to the thermal envelope, it is a challenge to further improve the performance of disk drives. There are many emerging Non-volatile Semiconductor Storage (NSS) techniques including flash memory [1], Magnetic Random Access Memory (MRAM) [2], and MicroElectroMechanical System (MEMS) [3]. Will the disk drive survive? The advances in the NSS techniques enable us to reconsider the disk architecture. This paper proposes a New Disk Architecture (NDA) which integrates a relatively small-size NSS into a traditional disk drive to boost disk performance.
2.Design and implementation
The NDA consists of a NSS module, a frequency tracker, a mapping table, and a data migration mechanism(Fig.1). The storage spaces of the NSS and the magnetic storage media are in the same linear space in terms of Logic Block Address.Many data access patterns indicate that a few blocks are frequently accessed, others much less often [4]. We used two fixed length Least Recently Used (LRU) lists including a hot list and a recent list to identify the most frequently and recently accessed data blocks. The mapping table contains a list of frequently accessed data blocks and their original locations and the locations after data migration. Newly incoming requests are compared against the list and redirected to the new location if the requested data resides there. A process runing in the background periodically migrates the frequently accessed data from the magnetic storage media to the NSS, and vice versa.
3.Performance Evaluation
We augmented Disksim [5] and employed real traces including Cello-96, TPC-D, and Cello99[6]to evaluate the NDA. A Quantum Atlas 10k disk is employed as a baseline system.We adopted NAND flash memory, MRAM, and MEMS as the NSS in the NDA. The parameters of flash memory are from Samsung K9F6408U0A . The random page read is 10µs and the page program time is 200µm. For simplicity, the garbage collection was calculated as a penalty: Penalty = (Page Size/Block Size) × Page Program time. The parameters (16 I/Os and 25ns cycle time) of MRAM are from [2]. The average access time of a MEMS device is 0.5 ms. Fig.2 shows the average response time of the baseline system and the NDA which employs different NSS. Fig.2 demonstrates that the performance speedup ranges from 2.85 to 3.03 with Cello99. By using Cello96, the NDA achieves performance speedup ranging from 2.30 to 2.53. However, the NDA only obtains performance speedup of about 1.1 for the three different NSS with TPC-D trace. We investigated the skews of the three traces. We found that Cello96 and Cello99 have skews of higher than 90%, whereas only 44% data accesses in TPC-D go to 10% storage capacity. The performance results indicate that the speedup is closely related to the skew. According to Fig.2, the NAND flash memory and MRAM have similar performance impact on the NDA. Compared with the NAND flash memory and MRAM, the MEMS has performance degradation of 9.76%, 1.10%, and 6.30% with the three different traces, respectively. This is reasonable because MEMS is slower than the NAND flash memory and MRAM. Fig.3 depicts the disk cache hit ratio of the baseline system and the NDA. It shows that the NDA achieves about 5.41% increase for the three different NSS with Cello99. For the Cello96, there is a negligible decrease (smaller than 1%) with three different NSS. The NDA incurs 0.30%, 3.57%, and 3.57% decrease of hit ratio for the three different NSS, respectively. The reason is that it is difficult to further improve the hit ratio with a small disk cache (Quantum Atlas 10k has a disk cache of 2MB) even though we attempt to accumulate the frequently accessed data into a relatively small NSS.
4.Conclusion
NSS such as flash memory is likely to replace disk drives in more and more systems where either size and energy or performance is important. We argue that the NSS cannot be used in the data intensive environments and is not suitable for large capacity storage (e.g. bigger than 100GB). By combining a traditional disk drive and a relatively small-size NSS, NDA achieves significant performance speedup and maintains large capacity.

[1].Samsung 32GB Flash-based HDD killer. http://www.reghardware.co.uk/2006/03/21/samsung_unveils_ssd/

[2].C. K. Subramanian, et al. Design Aspects of a 4 Mbit 0.18µm 1T1MTJ Toggle MRAM Memory, ICICDT, 2004, pp. 177–181.

[3].Steven W. Schlosser, et al. In Proc. of ASPLOS, 2000, pp.1–12.

[4].G.R.Ganger, et al. Disk Subsystem Load Balancing: Disk Striping vs. Conventional Data Placement. HICSS, 1993, pp. 40-49.

[5].DiskSim. http://www.pdl.cmu.edu/DiskSim/

[6].Storage Systems Program HP Laboratories. http://tesla.hpl.hp.com/public_software/.

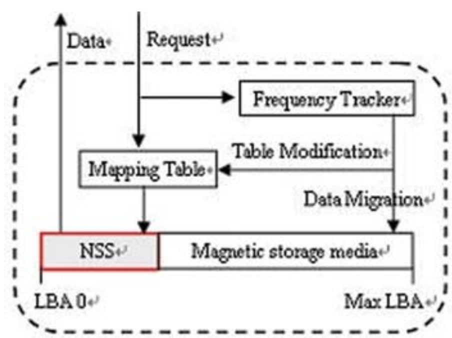

Fig.1 The NDA disk drive architecture

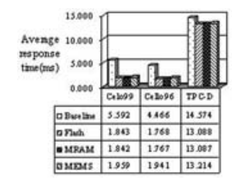

	Cello99	Cello96	TPC-D
Baseline	5.592	4.466	14.574
Flash	1.843	1.768	13.088
MRAM	1.842	1.767	13.087
MEMS	1.959	1.941	13.214

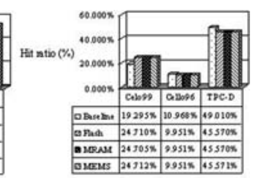

	Cello99	Cello96	TPC-D
Baseline	19.295%	10.968%	49.010%
Flash	24.710%	9.951%	45.570%
MRAM	24.705%	9.951%	45.570%
MEMS	24.712%	9.951%	45.571%

Fig.2 Average response time(Left figure)
Fig.3 Disk cache hit ratio (Right figure)

DG-01

Signal and Power Transmission in Real-time Internal Irradiation Dose Measurement System.

K. Shinohe[1], T. Takura[1], F. Sato[1], H. Matsuki[1], S. Yamada[2], T. Sato[3]

1. Graduate School of Engineering, Tohoku University, Sendai, Japan; 2. Graduate School of Medicine, Tohoku University, Sendai, Japan; 3. NEC Torkin Corp., Sendai, Japan

I Introduction

The radiation treatment is one of the cancer treatments and it is used together with other cancer treatments. Recently, the irradiation accuracy has improved by advance of the image diagnosis processors such as CT and MRI and the external irradiation machines. But the real-time data of the internal dose near the focus is required to treat the cancer effectively. Thus the implantable dosimeter and the wireless signal transmission system (Fig. 1) is needed. We use CdTe detector that is a semiconductor detector as the dosimeter. When X-ray is irradiated to CdTe detector, current flows in proportion to the irradiation energy and we can find out dose rate from the current. And the wireless signal transmission system is realized by a magnetic coupling with the structure of two coils located in the inside and outside body stable and is unique. We made the internal and external coil and examined the characteristic of communication area in communicating from the inside to the outside.

II Experimental methods and result

We made the solenoid coil as the internal coil, which is put into the focus by injector and the plane coil with ferrite core as the external coil. Our modulation method is PSK and the carrier frequency is 3MHz. We use the original signal data consisting of 10000 bits digital data prepared by PC and send them by the internal coil. The external coil receives the signal data and it is demodulated and input to PC again. It is compared with the original signal data and BER is measured. We defined successful communication as BER being 0. The transmission rate is 19200bps and we measured communication area in moving the external coil in the direction of X-axis or Y-axis and rotating the external coil. (Fig. 2) The result was shown in Fig. 3. When the external coil is located on the origin, communication distance is 300mm in the direction of Z-axis. When the communication distance is 200mm, which we need, the permissible dislocation is 90mm in the direction of X-axis and is 200mm in the direction of Y-axis. And communication is possible in any angle. The digital signal that we assume the irradiation dose information, the sending wave, the receiving wave, and demodulation wave are shown in Fig. 4.

We examined how communication area changes in the physiological salt solution where we assume inside the body when communication distance is 200mm. As a result, communication area is same as in air and it is not affected by the physiological salt solution. Then we confirmed that communication distance inside the body is 200mm.

III Conclusion

By using this wireless signal transmission system, we can transmit the data of the irradiation dose inside the body to outside the body. In the future, we will examine the influence of the linkage by the power transmission coil on the signal transmission coil.

[1]M.Takahashi, K.Watanabe, F.Sato and H.Matsuki, "Signal Transmission System for High Frequency Magnetic Telemetry for an Artificial Heart", IEEE Trans. Magn Vol.37 No.4 pp2921-2924 (2001)

[2]T.Somekawa, T.Takura, F.Sato, H.Matsuki, and T.Sato, "Prototype of Full-duplex Communication for Implantable Signal Transmission System of Magnetic Eight-Figure Coil", J. Magn. Soc. Jpn. Vol.31 No.4 (2007)

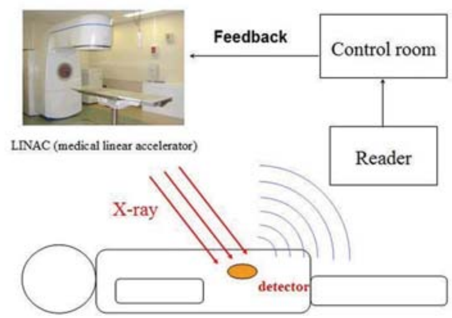

Fig. 1 The real-time irradiation dose measurement system

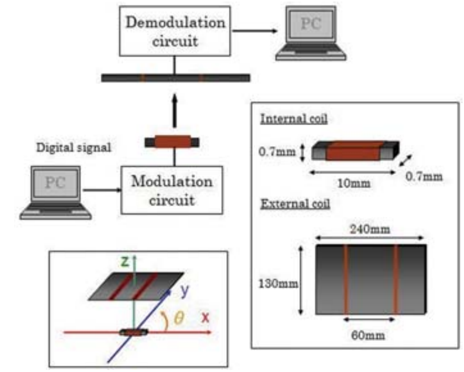

Fig. 2 Measurement circuit of Communication area

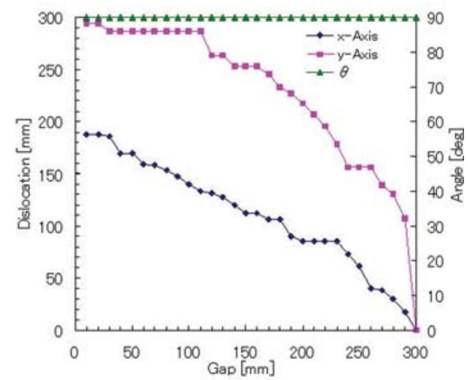

Fig. 3 Communication area(Characteristic by dislocation and rotation)

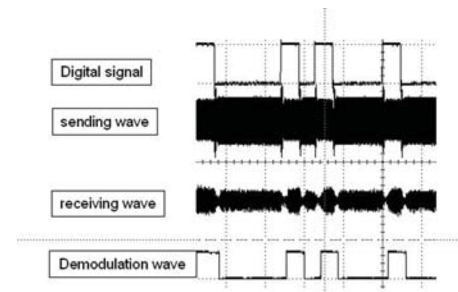

Fig. 4 Signal transmission waveform

DG-02

Imaging of electric permittivity and conductivity using MRI.

M. Sekino, S. Tatara, H. Ohsaki
Department of Advanced Energy, Graduate School of Frontier Sciences, The University of Tokyo, Kashiwa, Japan

Introduction

Imaging of electric permittivity and conductivity distribution in biological tissues gives valuable information on physiological and pathological parameters which are not obtained by anatomical imaging. Measurement of these properties is obviously important for numerical simulations of electromagnetic fields in humans and other living bodies. Electrical impedance tomography (EIT), in which surface potentials are measured during applications of currents via surface electrodes, has been applied to non-invasively obtain conductivity distribution. Some new methods use magnetic resonance imaging (MRI) to obtain conductivity distribution to achieve a high spatial resolution [1,2]. However, these conventional techniques only aimed at the imaging of conductivity. In the present study, we propose a method for imaging permittivity as well as conductivity using MRI.

Principle of permittivity and conductivity imaging

In addition to conventional MRI hardware, a radiofrequency (RF) transmitter is used to apply an electric current to a sample, as shown in figure 1(a). The current is applied to the sample from a pair of surface electrodes with the magnetic resonance frequency (Larmor frequency). Figure 1(b) shows an operational diagram for obtaining permittivity and conductivity images. While the transmitter (A) produces two RF magnetic fields in opposite directions via the RF coil, the transmitter (B) applies a current to the sample. The succeeding transmission and reception of signals are the same as in conventional spin-echo imaging. Two images, θ_{1x} and θ_{1y}, are generated from the phase angle of magnetic resonance signals with RF magnetic fields applied in the x and y directions to the sample, and with the application of current to the sample. In addition, two images, θ_{0x} and θ_{0y}, are obtained with the application of RF magnetic fields in the same directions, and without the application of current. We generated an image of $-\nabla^2(\theta_{1x}-\theta_{0x}-i(\theta_{1y}-\theta_{0y}))/(\theta_{1x}-\theta_{0x}-i(\theta_{1y}-\theta_{0y}))$. The real and imaginary parts of this image divided by $\omega^2\mu_0$ and $\omega\mu_0$ result in permittivity and conductivity images, respectively.

Methods

The proposed algorithm for calculating permittivity and conductivity was evaluated using numerical simulations and experiments. We assumed a cylindrical sample with a diameter of 30 mm, relative permittivity of 40, and conductivity of 0.14 S/m. In the simulation, the electromagnetic fields in the sample during an MRI acquisition were calculated by solving a wave equation of the magnetic vector potential. Magnetic resonance signals were estimated by solving the Bloch equation. The experiments were carried out using a 4.7 T MRI system. A cylindrical test tube was filled with a liquid consisting of an NaCl solution and ethanol to exhibit the above electric properties. Platinum electrodes were attached to the ends of the tube.

Results and discussion

Figure 2(a) shows the results of the numerical simulation. The images of permittivity and conductivity were generated by a pixel-by-pixel processing of the $\theta_{1x}-\theta_{0x}$ and $\theta_{1y}-\theta_{0y}$ images. The permittivity and conductivity values estimated by the proposed algorithm were in good agreement with those in the model at the center of the sample. The estimated permittivity and conductivity were 40 and -0.25 S/m, respectively. The inhomogeneity appearing at the edge of the sample was attributable to an inhomogeneity in the RF magnetic field, which is distinctive in a high-field MRI system. Our algorithm assumed that the RF magnetic field was homogeneous in the sample. Figure 2(b) shows the experimentally obtained phase images, permittivity image, and conductivity image. The permittivity and conductivity values were close to those in the liquid sample. We found errors in the bottom left part of the sample, which were caused by the lead wire used for injecting current to the sample. The results suggested that a reduction of error is necessary for practical applications. However, the proposed method has the advantage of noninvasively obtaining high-resolution images of the electric properties of a sample, and is easily applicable to biological tissues.

[1] M. Sekino, Y. Inoue, S. Ueno. IEEE Trans Magn, vol. 41, pp. 4203-4205, 2005.

[2] M. Sekino, K. Yamaguchi, N. Iriguchi, S. Ueno. J Appl Phys, vol. 93, pp. 6730-6732, 2003.

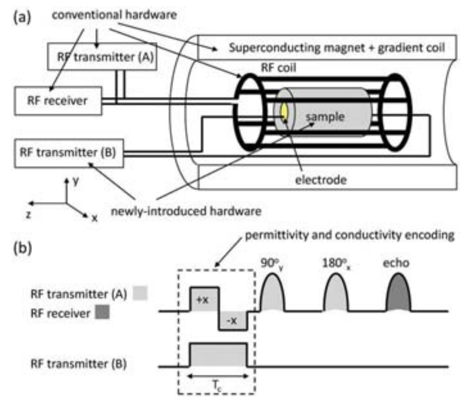

Figure 1: (a) Experimental setup for imaging of permittivity and conductivity. (b) Operational diagram of RF transmitter and receiver.

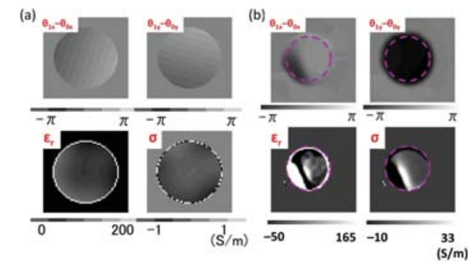

Figure 2: (a) Phase-angle images obtained from a numerical simulation, permittivity image, and conductivity image. (b) Experimental results.

DG-03

Optimization of coil structure in resonant circuit implant for hyperthermia using MRI.

J. Kunisaki, M. Shimizu, K. Kamio, S. Hiroe, T. Yamada, *Y. Takemura*
Division of Electrical and Computer Engineering, Yokohama National University, Yokohama, Japan

Hyperthermia is cancer treatment of raising the body temperature. It has an advantage that there are not major side effects as compared with various established treatments, such as surgical operation, radiotherapy and chemotherapy. The hyperthermia using implants, one of the warming methods in hyperthermia, has been reported in term of its ability to control the temperature and heat localized tissues [1]-[2]. A resonant circuit for the implant is heated efficiently by an external magnetic field [3].

We have reported preliminary results on a temperature rise of resonant circuits excited by a magnetic field from commercial MRI equipment [4]. A weak RF pulse of the magnetic field with a low duty ratio under normal diagnosis sequence of the MRI operation could raise the circuit temperature up to 13 deg. C. A combination of the hyperthermia using heated implants and diagnostic functions of MRI offers significant advantages such as human safety. At this point, size of the implants is dimension in 5-15 mm. In order to deliver them through catheter into the human body, miniaturization of the implant down to 1-3 mm is required. In this paper, the optimization of structure of the coil inductor in resonant circuits for implant hyperthermia is discussed.

Resonant circuits were heated by applying an ac magnetic field of 0.034 Oe as low as that of the RF pulse field of 1.5 T type MRI. The direction of the magnetic field was aligned as to penetrate the inductor coil. A temperature rise of the circuit was measured by an optical thermometer. The circuit was covered by polyurethane material as a thermal insulation. Three types of resonant circuits were fabricated from capacitor and different inductors in their coil structures. Two of the inductor coils were prepared with using a single wire (0.3 mm ϕ), and the other was with using a litz wire (15 strands with 0.08 mm ϕ). Effective cross section areas of these wires were same. Winding pitches of the single wire coils were 0 mm and 0.3 mm, and that of the litz wire coil was 0.3 mm. The diameter and turn of the coils were fixed at 6 mm and 10 turn, respectively. A resonant frequency of the resonant circuits was designed to 64.3 MHz, which was close to a RF field frequency of 1.5 T type MRI. Figure 1 shows a temperature rise of the resonant circuits measured at 40 min after applying the magnetic field. The frequency in the figure is indicated by a frequency shift from the resonant frequency. The temperature rise depended on the field frequency as shown in the figure. The maximum rise was obtained at lower frequency than the designed resonant frequency of the circuits. It was because that both of the inductance and the capacitance increased with increasing the temperature, and that the resonant frequency was decreased during the measurements [4]. The highest temperature rise among the three circuits was obtained from the circuit consisted of the litz wire coil. In order to obtain higher temperature rise from the circuit, a lower residual resistance and a higher induced electromotive force in the inductor are essential. However, resistance of the inductor is significantly increased by skin effect and proximity effect under the high frequency measurement. As the induced electromotive forces in the examined three inductors were equivalent, it was considered that the temperature rise was determined by the resistance of the coils.

Figure 2 shows frequency dependence of resistance of the coils used in the resonant circuits measured by using an impedance analyzer. It was found that the lowest resistance among the three coils was the litz wire coil, and the highest was the single wire coil wound closely. The effect of skin effect was suppressed by using the litz wire, and that of proximity effect was suppressed by using the coil wound with pitch.

The high temperature rise shown as Fig. 1 was achieved by the applied field strength and frequency within the reported guideline for human safety [5]. By optimizing the circuit structure, the circuit is expected to be miniaturized down to 1mm order, which is significant for realizing the hyperthermia treatment using MRI.

[1] I. Tohnai et al., Int. J. Hyperthermia, 12, 37 (1996).

[2] T. Takura et al., IEEE Trans. Magn., 43, 2454 (2007).

[3] Y. Kotsuka et al., IEEE Trans. MTT, 47, 2630 (1999).

[4] M. Morita et al., IEEE Trans. Magn., 41, 3673 (2005).

[5] W. J. Atkinson et al., IEEE Trans. Biomed. Eng., BME 31, 70 (1984).

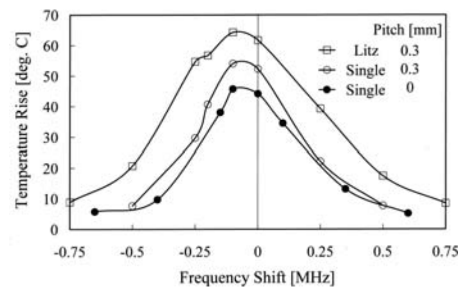

Fig.1. Frequency dependence of temperature rise of resonant circuits consisting of coil inductor with different structure. The center frequency was 64.3 MHz.

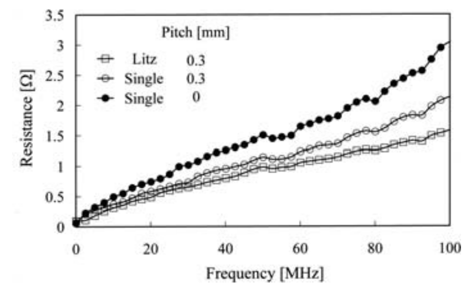

Fig.2. Frequency dependence of measured resistance of the coils used in the resonant circuits.

DG-04

Calculation of minimum parameters required for low-field low-size nano nuclear magnetic resonance (nanoNMR).

P. Gomez[1,2], S. Khizroev[2], D. Litvinov[3]
1. Electrical Engineering, Florida International University, Miami, FL; 2. Electrical Engineering, University of California Riverside, Riverside, CA; 3. Electrical Engineering, University of Texas, Houston, TX

Calculation of Minimum Parameters Required for Low-Field Low-Size Nano Nuclear Magnetic Resonance (NanoNMR)
ABSTRACT
This paper addresses the minimum parameters required to make Low-Field Low-Size NanoNMR a viable technology and potentially, one of the future Lab-On-Chip technologies. Low-field means an externally applied magnetic field less than 0.5 T and Low-Size means a magnet whose largest physical dimension does not exceed 5 cm. The goal is to develop adequately small and cost-effective NMR spectrometers that can be used at room temperature in a small office environment. In this study, tunneling magneto resistance (TMR) devices are used to sense the NMR signal. The parameters that are calculated are: minimum sample size and concentration required to obtain an adequate NMR signal, TMR sensor size and its distance to sample, RF coil size, RF frequency and RF power. The nanoscale TMR sensors designed in this research using in-house developed simulation software have an area of 100 nm x 100 nm [1] and the permanent magnet that was evaluated has a maximum dimension of 20 mm.
INTRODUCTION
Current NanoNMR technology makes use of ultra-high magnetic fields (> 7 T) that require excessively high frequencies (> 400 MHz). As a reference, the latest NMR Spectrometers from Varian® use frequencies of 500 and 600 MHz with magnets weighing 1 ton and 1.6 tons respectively [2]. These spectrometers need a special room with a minimum ceiling height of 3 m and several additional requirements such as unconventional cooling, power and shielding conditions.
The proposed technology, Low-Field Low-Size NanoNMR seeks the goal of downsizing the NMR Spectrometer to the point in scale when it is portable and cost-effective.
Figure 1 shows schematically the proposed NanoNMR sensor which was optimized throughout computer simulations using MATLAB®. The sensor consists of:
a) A permanent hollow cylindrical shaped magnet with uniform magnetic field in the hole
b) A sample container
c) A RF Helmholtz coil
d) TMR devices
Figure 1. NanoNMR Sensor
SUMMARY
In brief, to design a Low Field Low Size NMR Sensor, we need the following components with their respective characteristics:
a) A ring shaped permanent magnet made of Neodymium Iron Boron Grade N35 with an inner radius of 5 mm, an outer radius of 20 mm and a thickness of 16 mm to produce a homogeneous magnetic field of ½ Tesla at its center
b) A TMR sensor with pinned-layer (PL) and free-layer (FL) made of Fe50Co50 with a 0.3 nm Al2O3 barrier, an area of 100 nm x 100 nm and biased at 200 mV. This sensor was optimized using in-house developed software. A magneto resistance (MR) of 40% was obtained with this design with a resistance of 135 ohms at 1.5 mA.
c) A maximum distance between the TMR sensor and sample of 100 μm was obtained through MATLAB® simulations.
d) A minimum sample volume of 100 nL. The volume requirement is inversely proportional to the sample concentration
e) An operating frequency of 10.65 MHz
f) The RF coil is a Helmholtz pair with a coil radius of 5 mm made of copper 22 AWG. The coil radius and wire gauge are not critical, but the coil should fit in the hole at the center of the magnet
g) RF power < 100 mW
CONCLUSIONS
In this paper, the guidelines to design a Low-Field Low-Size NMR Sensor are developed through analytical calculations and numerical simulations. The results show that this is a feasible, economical and promising technology. Not only NanoNMR will make possible to measure NMR signals from relatively small samples but also the dramatic reduction in acquisition costs will make it affordable to every researcher in biochemistry.
Nanotechnology is rapidly emerging as a necessity in the biomedical industry and research and therefore, the right tools need to be provided for this purpose. Low-Field Low-Size NanoNMR is one such technology we have explored and found to be a realistic and cost-effective solution.

[1] Pablo Gomez, Dmitri Litvinov, and Sakhrat Khizroev, A method to design high SNR nanoscale magnetic sensors using an array of tunneling magneto-resistive (TMR) devices, Journal of Physics D: Applied Physics 40, 4396-404 (2007)

[2] Varian® Inc website: http://www.varianinc.com/image/vimage/docs/products/nmr/shared/nmr-magnets.pdf

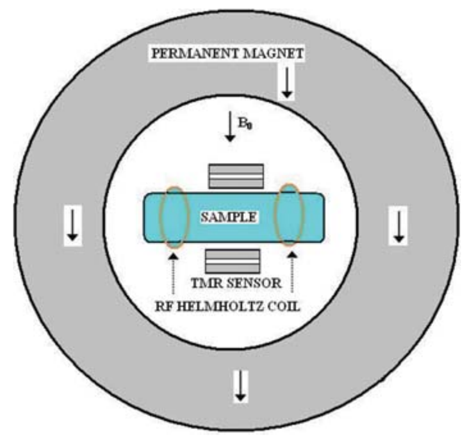

Figure 1. NanoNMR Sensor

DG-05

Microwave radiometry for early breast cancer detection.

M. P. Costin[1,2], O. Baltag[2]
1. Computer Science Institute, Romanian Academy, Iasi, Romania; 2. Faculty of Biomedical Engineering, University of Medicine and Pharmacy, IASI, Romania

Abstract — Noninvasive methods have already proven their usefulness in medicine, therefore new techniques are all the time researched. Our approach is using microwave radiometry in breast cancer detection. The technique is in order to be implemented in a national excellence research project.
Keywords — early cancer detection, noninvasive technique, microwave radiometry, microwave medical imagistic.

I. INTRODUCTION

The microwave radiometry is a measurement technique for inner temperature of biological structures. The interest for the microwave radiography [1], [2](also named microwave thermography), derives from the actual trend to find out, to innovate new noninvasive and without contact techniques [3]√[5], in order to monitor inner physiologic parameters. Regarding cancer detection, the actual research is directed towards new techniques discovery, other than mammography, which is using penetrating radiations, ionogen.
The paper presents the basic principles of microwave thermography, the radiation measuring technique for biologic structures, using very low microwaves receivers in the domain 1-10 GHz, applying the laws of worm body radiation, in the domain of microwaves.

II. MEASUREMENT AND EXPERIMENTAL RESULTS

The practical implementation used a radiometer that we designed on a schema similar to Dicke radiometer, in order to detect tumor tissues, breast abnormal developing structures. The measuring technique resides in applying a skin-contact dielectric antenna and measuring the electromagnetic radiation level in seconds over a specified time interval. The measured value constitutes an inner temperature indicia showing up the breast structure. The systematically data are cyclically taken, alternatively applying the antenna of the transducer on the same symmetrical positions on the right and on the left breast. The values corresponding to temperatures are represented on a diagram as a thermic map.

III. DEDICATED SOFTWARE FOR IMAGE PROCESSING

The processing is realized with special designed software that represents temperature level curves. The difference between these two kinds of thermo-images resides into the different depth of the site where we obtain the information from (the infrared thermography is sensitive to surface temperature, resulted both as effects to inner temperature and from temperatures close to surface).
Even if the image resolution, obtained by microwave thermography is relatively small, due to the imposed fan dimension of the antenna (which is not possible to be very small)–on one hand, and due to the wavelength on another hand, the advantages related to the other means of detection and diagnosis are pertinent. The images are transformed and a gradient computing relevantly plot and to illustrate the regions with high thermo-activity, often corresponding to breast cancer.
Fig. 1. Microwave medical diagnosis software
Fig. 2. Frame of microwave temperature-map image
Fig. 3. Microwave breast cancer images

[1] E. C. Fear, P. M. Meaney, M. A. Stuchly, Microwaves for Breast Cancer, IEEE Potentials, pp. 12–18, 2003.

[2] L. M. Burdina, E. G. Pinkhosevich, V. A. Hailenko, I. I. Burdina, S. G. Vesnin, N. N. Tikhomirova, Comparative analysis of inspection results in patients with breast cancer on the data of X-Ray Mammographical and radiothermometrical examinations, in Modern Oncology Journal, Nr. 1, Vol. 6, Moscow, 2004.

[3] K. Carr, Thermography: Radiometric Sensing in Medicine, New Frontiers in Medical Devices Technology, Editors A. Rosen, H. Rosen, pp. 311–342, John Willey & Sons, New York, 1995.

[4] A.F. Harvey, Microwave Engineering, Academic Press, New York, 1963.

[5] K. A. Butakov, S. V. Butakova and A. A. Ivanov, True temperature determination by irradiation in the microwave range, Springer New York, ISSN 0543-1972 (Print) 1573-8906 (Online), Collection: Physics and Astronomy, pp. 521-523, Volume 27, Number 6 June, 1984.

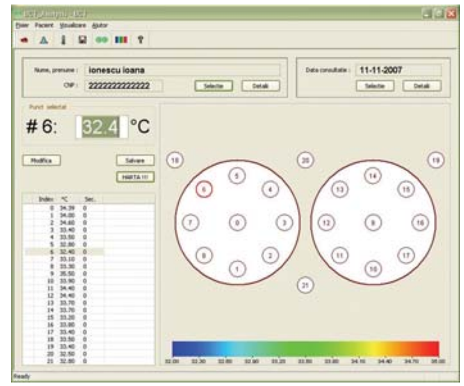

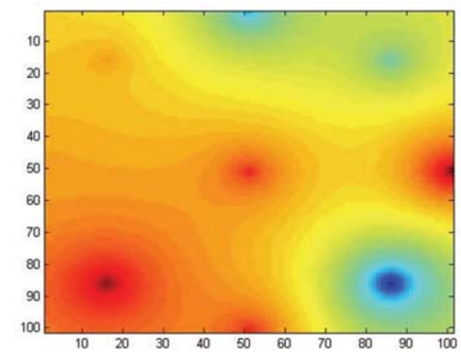

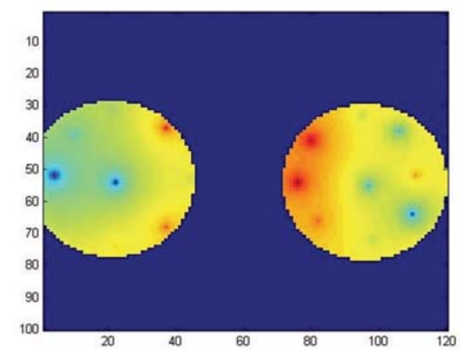

DG-06

Microwave resonator devices for ferromagnetic resonance detection of magnetic beads.

S. Ghionea, P. Dhagat, A. Jander
Department of Electrical Engineering and Computer Science, Oregon State University, Corvallis, OR

Immunosensors using magnetic beads for antigen labeling are being widely investigated for applications in medical diagnostics and monitoring the presence of bioterror agents [1-6]. In our previous work, we demonstrated the feasibility of ferromagnetic resonance (FMR) based inductive detection of beads immobilized in an immunoassay, using a slotline and a coplanar microwave waveguide as shown in Fig. 1 [7]. Here we present a new approach to FMR detection (Fig. 2a) using a resonant slotline excited by a microstrip. This design allows simultaneous excitation of two or more junctions using a single source. Multiple resonators can be added, allowing a single microstrip to drive several slotlines for detecting multiple antigens. Further, it can be used for differential measurement where one junction serves as the control.

In Fig. 2a, we illustrate the principle using a single slotline resonator. A radio frequency (RF) signal is applied to a microstrip on the bottom metallized layer of a dielectric substrate (Fig. 2a). The top metallized layer has the slotline resonator and coplanar waveguides (CPW), and additionally acts as a ground plane for the microstrip. A microstrip-slotline transition is formed between the top and bottom layer, with maximum signal coupling to the slotline resonator when the slotline electrical length is $\lambda/2$, where λ is the wavelength in the slotline [8]. The slotline resonator has an RF current node at the center and antinodes on the end. The ends of the slotline form short-circuited junctions, as shown in Fig. 2a, with CPWs as outputs. The surface metal at junction 2 is functionalized with antibodies specific to the antigen of interest and serves as the sensitive area. In the absence of a bead at the junction, no signal couples from the slotline to the CPW. When a magnetic bead is immobilized at the junction, FMR is excited in the bead when the RF frequency matches the FMR frequency as determined by a dc bias magnetic field. The precessing magnetization in the bead couples the signal from the slotline to the CPW. Thus an output signal is obtained only in the presence of a bead at the junction. Key advantages of the microwave resonator are compatibility with standard CMOS (complementary metal oxide semiconductor) processes, single source drive, and improved signal to noise ratio due to differential measurement.

Ansoft High Frequency Structure Simulator software was used to simulate S-parameters of a resonator device designed for 6 GHz frequency. A bead, with physical and magnetic properties modeled after a commercial Invitrogen M-450 Dynalbead, was placed at junction 2, as indicated in Fig. 2a. The dc field was applied along the out-of-plane axis. Plotted in Fig. 2b is the difference in the simulated S-parameter at each junction with and without the bead placed at junction 2. These data show signal coupling from the slotline to the CPW at junction 2 when there is a bead at junction 2. Due to the symmetry of the two junctions a differential measurement can be made by measuring the signal independently at the CPW of the two junctions, detecting beads at junction 2 using junction 1 as the reference. This eliminates any common-mode signal that may be present in the device, giving just the bead signal. This is an important technique in integrating the sensor within a lab on a chip platform.

The detected signal for varying resonator configurations will be detailed at the conference.

[1] P. Besse, G. Boero, M. Demierre, V. Pott, R. Popovic, Appl. Phys. Lett., 80, 22, pp.4199-4201, 2002.

[2] D. Graham, H. Ferreira, J. Bernardo, P. Freitas, J. Cabral, J. Appl. Phys., 91, 10, pp.7786-7788, 2002.

[3] D. Baselt, G. Lee, M. Natesan, S. Metzger, P. Sheehan, R. Colton, Biosensors Bioelectron., 13, 7, pp.731-739, 1998.

[4] G. Li, V. Joshi, R. White, S. Wang, J. Kemp, C. Webb, R. Davis, S. Sun, J. Appl. Phys., 93, 10, pp.7557-7559, 2003.

[5] A. Peruski, L. Peruski, Clin. Diagn. Lab. Immunol., 10, 4, pp. 506-613, 2003.

[6] E. Diamandis, T. Christopoulos, "The Biotin-(Strept) Avidin System: Principles and Applications in Biotechnology", Clin. Chem., 11, 5, pp.625-626, 2003.

[7] S. Ghionea, P. Dhagat, A. Jander, IEEE Sensors., accepted for publication, Sensors-02099-2007.R1, 2007.

[8] E. Mariani, J. Agrios, IEEE Trans. Microwave Theory Tech., MTT-18, 12, pp.1089-1095, 1970.

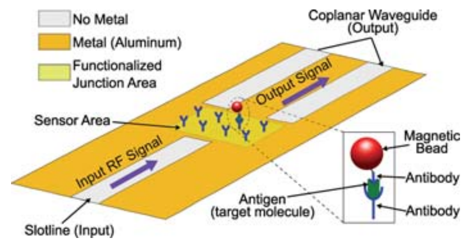

Fig. 1: Schematic of FMR detector junction.

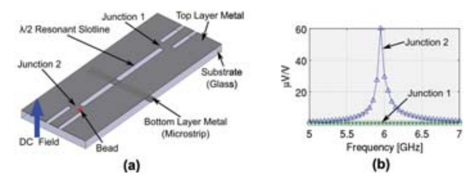

Fig. 2a: Schematic of microstrip-driven slotline resonator device. Two junctions are formed on either end of the slotline. Fig. 2b: Data showing signal at the junctions, with and without the bead as shown in Fig. 2a

DG-07

Magnetic Immunoassays – New Methods of Biochemical Diagnostics Based on Detection of Magnetic Nanoparticles by Non-Linear Magnetization.

P. Nikitin[1], P. Vetoshko[2], M. Nikitin[3], T. Ksenivich[1]
1. Natural Science Center, General Physics Institute, Russian Academy of Sciences, Moscow, Russian Federation; 2. Institute of Radioengineering and Electronics, Russian Academy of Sciences, Moscow, Russian Federation; 3. Department of Molecular & Biological Physics, Moscow Institute of Physics & Technology, Dolgoprudny, Moscow Region, Russian Federation

Recently using of superparamagnetic particles or magnetic beads (MB) as labels in biosensing has become very popular. We introduced a highly sensitive method of MB counting based on non-linear behavior of MB in magnetic field [1-3]. It consists in exposing MB to an alternating magnetic field at two frequencies f_1 and f_2. The response is measured at combinatorial frequencies $f= mf_1 + nf_2$, where m and n are integers (one of them can be zero). The integers can be varied in order to get the best signal-to-noise ratio, e.g. $f= f_1 \pm 2f_2$ [1]. The method allows very sensitive and robust detection of non-linear magnetic nanomarkers for different biosensing [2,3] and life science applications [4]. The Magnetic ImmunoAssay technology (MIAtek™) based on non-linear magnetization of MB is compatible with different assay formats (3D capillary and filter structures, lateral flow strips, biochips, etc) and with both heterogeneous and homogeneous immunoassays, where probe volumes with MB labels are formed, respectively, on a solid surface or by grouping of MB using inhomogeneous magnetic field or sedimentation directly in liquids or by filtration [1].

The first part of the present research is devoted to extension of 3D heterogeneous MIAflow™ format for detection of several biological agents simultaneously. For this purpose, a multi-channel BioMag readout device has been designed to count non-linear MB in several recognition zones with deferent capture antibodies. The threshold sensitivity of each channel is about 1 ng of total weight of magnetic nanoparticles. The sensing area per detectable magnetic particle is 3 orders larger than that reported for the other techniques. The first configuration for the multi-analyte assay shown in Fig. 1 consisted of several sequentially connected recognition zones with porous or multi-capillary structures. Different capture antibodies were immobilized on the large surface (up to 40 cm^2) of the structures. The antigens from large range of volumes (0.1 - 100 ml) of tested liquids were immunofiltrated by antibodies on these structures. Then blocking bovine serum albumin, second tracer antibodies, MB and washing buffer were pumped via flow channel forming sandwich immunocomplexes. The resulting number of magnetic labels in each zone was read by the BioMag device. Another multi-analyte setup was based on recording of parallel biochemical reactions in spatial syringes, where porous filters or multi-capillary structures were sealed as shown in Figs. 2,a-d. The antigens and reagents were delivered using an automated liquid handling system based on step motors.

The second part of the present paper is devoted to optimization of the MIAtek™ technology for homogeneous immunoassays to detect agglomeration of biomolecular complexes of antigens and antibodies with MB directly in liquids under test. Some of these assays do not require washing steps. As proposed in [1], three methods were tested for grouping of immunocomplexes in the probe volume, namely: by inhomogeneous magnetic field, by sedimentation directly in liquids and by filtration. It has been observed that separation of immunocomplexes by inhomogeneous magnetic field also accelerates binding of immunoreagents by active attraction of interacting particles and decreases assay time. An optical biosensor Picoscope™ [5] was used for measurements of kinetics at each step of reagent binding as well as for rapid selection of protocols, reagents, magnetic beads and buffers for highly sensitive detection of biochemical reactions. The magnetic immunoassays have been developed for detection of bacteria (*Salmonella typhimurium, Legionella pneumophila*) and soluble proteins (lipopolysaccharide of *Francisella tularensis* and F1 antigen of *Yersinia pestis*).

The developed magnetic biochemical diagnostic platforms and formats are promising for medical diagnostics, points of care, food pathogen detection.

The work was supported by Magnisense Company and RFBR grant.

[1]. P.I. Nikitin, P.M. Vetoshko, Patent RU 2166751 (2000), EP 1262766 publication (2001).

[2]. P.I. Nikitin, P.M. Vetoshko, T.I. Ksenevich. Sensor Letters, 5 (2007) 296.

[3]. P.I. Nikitin, P.M. Vetoshko, T.I. Ksenevich. J. Magn. Magn. Mater. 311 (2007) 445.

[4]. M.P. Nikitin, M. Torno, H. Chen, A. Rosengart P.I. Nikitin. JAP, 103 (2008) Issue 7.

[5]. P.I. Nikitin. Picoscopes, New Label-Free Biosensors, in: Handbook of Biosensors and Biochips, ed. R. Marks et al., Wiley (2007). ISBN 978-0-470-01905-4.

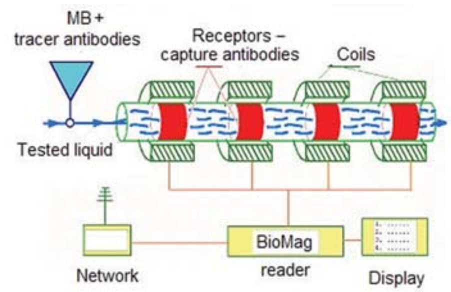

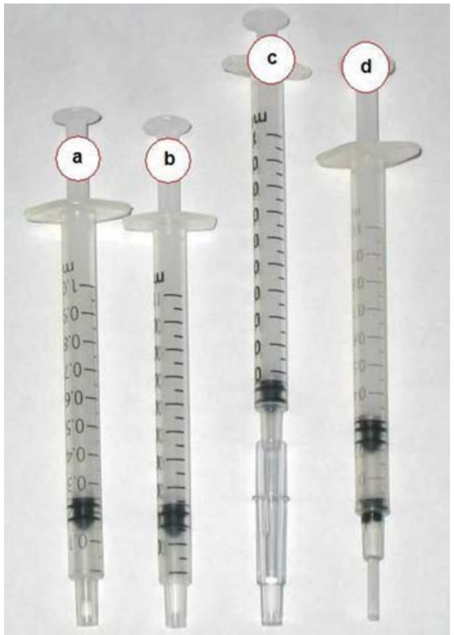

DG-08

Giant magnetoresistance sensors for lateral flow tests.

C. Marquina[1], J. M. De Teresa[1], J. Sesé[2], V. Grazú[2], B. Velasco[3], P. Freitas[4], R. Ibarra[1,2]
1. Instituto de Ciencia de Materiales de Aragon, CSIC-Universidad de Zaragoza, Zaragoza, Spain; 2. Instituto de Nanociencia de Aragon, Universidad de Zaragoza, Zaragoza, Spain; 3. CerTest Biotec, Zaragoza, Spain; 4. INESC, MN, Inst Engn Sistemas Computadores Microsyst & Nanot, Lisbon, Portugal

A great effort is currently being made in the research on lateral flow tests due to their wide use nowadays in Life Sciences. Their simplicity, low cost and the large variety of analytes that can be detected by means of this technique make them suitable for a large number of applications. However, the conventional tests based on immunorecognition and the use of coloured colloidal particles have still some drawbacks that limit their use: they do not provide a quantitative determination of the analyte, and their sensitivity is limited. Our strategy to overcome these disadvantages consists in the use of superparamagnetic core-shell nanoparticles to tag the analyte, instead of the coloured colloid. The use of these magnetic labels allows us to quantify the amount of analyte present in a problem sample with a very high sensitivity, detecting their magnetic response by means of the suitable magnetic sensor.

Our method is based on measuring the magnetorresistive response of a giant magnetorresitive (GMR) sensor placed in proximity to the magnetic nanoparticles present in the lateral flow strip. Our GMR sensors are of the spin-valve type, consisting of (6.5nm)NiFeCr/(4nm)NiFe/(2nm)$Co_{80}Fe_{20}$ as free electrode, (2.2nm)Cu as non-magnetic spacing, and (3.5nm)$Co_{80}Fe_{20}$/(30nm)MnNi/(5nm)NiFeCr as pinned top electrode, grown by ion-beam deposition. These sensors have a maximum magnetoresistance of 7% at room temperature and linear response around zero magnetic field. Laser lithography techniques are used to define the active part of the sensor and the contact pads. Besides the GMR sensor, our prototype consists of a permanent magnet to polarise the superparmagnetic nanoparticles, the electronic system to process the sensor output signal, and the mechanical system necessary to horizontally sweep the lateral flow strip containing the magnetic beads through the active region of the GMR sensor. This mechanical system allows also moving the strip vertically so that the sensor output is obtained by differential measurements, measuring the sensor resistance when strip and sensor are in soft contact and when they are separated a fixed distance in the vertical direction. In the figure we show the output signal of the magnetoresistive sensor corresponding to a test performed in a solution containing 25 mIU/ml of hCG hormone. Preliminary assays using our biosensor to detect the hCG pregnancy hormone in a solution show that the sensitivity of this method is thirty times higher than in the conventional pregnancy tests being able to detect tenths of nanograms. Several strategies to further increase the sensor sensitivity are currently being attempted.

The properties of the magnetic beads to be used in our test are also important to improve its performance. Therefore, different types of core-shell nanoparticles are being tested our group, in order to make a comparative study of their magnetic response at low magnetic fields, their agglomeration, etc. Other crucial aspect to take into account in order to increase the sensitivity is the proper functionalisation of the nanoparticle shell, in order to achieve an oriented immobilisation of the antibodies to be used in the immunorecognition process. Different functionalisation and immobilisation protocols are currently being studied in our group.

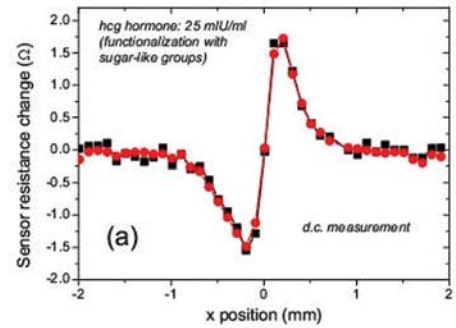

Output signal of the magnetoresistive sensor in d.c. configuration corresponding to a lateral-flow strip where a biorecognition test has been performed with a solution containing 25 mIU/ml of hCG hormone. The black curve corresponds to a single measurement and the red curve to the average of 5 measurements.

DG-09

Magnetic-Entasis Biorecognition Platform: Self Assembly of Magnetic Nanoparticles for Detection of Magnetically Labeled Biomolecules.

Y. Yamamoto[1], T. Yamanaka[1], *Y. Morimoto*[1], S. Sakamoto[3], Y. Mochiduki[3], M. Abe[4], H. Handa[3], A. Sandhu[1,2]

1. Quantum Nanoelectronics Research Center, Tokyo Institute of Technology, Tokyo, Japan; 2. Department of Electrical and Electronic Engineering, Tokyo Institute of Technology, Tokyo, Japan; 3. Graduate School of Bioscience and Biotechnology, Tokyo Institute of Technology, Tokyo, Japan; 4. Department of Physical Electronics, Tokyo Institute of Technology, Tokyo, Japan

Introduction

Biorecognition platforms based on the detection of magnetically labeled molecules are being developed for high speed, high sensitivity and inexpensive, point of care diagnosis of heart diseases, cancer and even for testing if drivers are under the influence of drugs [1-5]. Currently, GMR, spin-valve and Hall effect devices are widely used to detect 200-1000nm diameter superparamagnetic beads.

However, there is increasing demand for the detection of single, sub-100nm diameter particles in order to improve the resolution of biomolecular detection. The sensitivity of magnetoresistive devices may not enable the accurate and reproducible detection of single superparamagnetic labels of less than 100nm over large surface areas.

Here, we describe the main features of the 'magnetic-entasis platform'(MEP), a versatile approach for the rapid detection of single magnetic nanoparticle labels for large surface area biorecognition. Our method is based on inducing magnetic self assembly of columns of micrometer sized magnetic bead onto immobilized 'target' magnetic nanoparticles. We demonstrate that'magnetic-entasis' will enable the detection of single nano-magnetic particles immobilized over 5mmx5mm areas within several seconds.

Experimental

The nano-magnetic beads ('targets') were detected as follows (Fig.1):

(1) Optical photolithography was used to define gold thin film/silicon dioxide stripes with a five micrometer pitch on 5mm x 5mm sized silicon substrates.

(2) Functionalized 130nm diameter superparamagnetic beads ('targets') were selectively immobilized at differing concentrations onto the gold stripes. Scanning electron beam microscopy (SEM) was used to determine the areal density of the 'targets' immobilized on the gold stripes.

(3) The test substrate with the immobilized 'targets' was positioned under the objective lens of a digital microscope. The nanobeads were not visible even at x3000 magnification.

(4) A pipette was used to apply a drop of water containing micrometer sized superparamagnetic beads onto the test substrate. These 'columnar' micro-magnetic beads moved under the action of gravity over the sample.

(5) Magnetic field gradients were applied to the sample and the motion of the micro-magnetic beads monitored with the digital microscope.

Results

In the absence of the magnetic field gradient, the micro-magnetic beads moved smoothly across the gold/silicon dioxide patterned substrates. However, when the magnetic field was applied, the micro-magnetic beads were captured by the immobilized nanomagnetic 'target' beads and formed convex columns ('magnetic-entasis') estimated to be several tens of micrometers in height. The capture and formation of columns occurred within 30 seconds.

Approximately four, 130nm diameter nano-magnetic beads captured a single one micrometer columnar bead. In contrast, it required approximately 11 of the 'target' nanobeads to capture a single columnar bead with a diameter of 2.8 micrometers.

Conclusions

Magnetic self assembly of magnetic beads was used to detect 130nm 'target' nanobeads over large sampling areas. This method will find applications for monitoring biorecognition processes where detection of sub-100nm magnetic labels is a critical factor.

1. A. Sandhu, Nature Nanotechnology 2, 746, (2007)

2. ESF/EMBO Symp. Biomagnetism and Magnetic Biosystems Based on Molecular Recognition Processes (Sant Feliu de Guixols, Spain, 22–27 September 2007)

3. B.M. de Boera, etal., Biosens. Bioelectron. 22, 2366, (2007).

4. G. Li, et al. Sens. Actuat. A 126, 98, (2006).

5. A. Sandhu, etal., Biosensors and Bioelectronics 22, 2115, (2007)

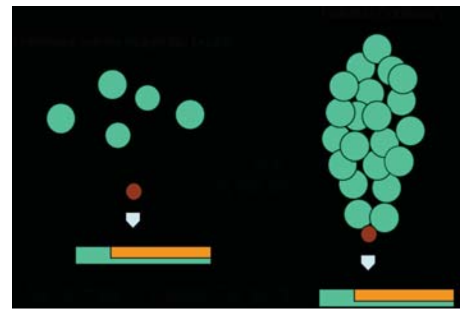

Magnetic-entasis for detection of nanomagnetic beads

DG-10

Magnetic bar array with linker technology for detection and investigation of non-magnetic molecules.

D. Lee[1], L. A. Roberts[2], E. Peroziello[3], R. Fontana[4], S. Maat[4], M. Nemat-Gorgani[2], S. Hoon[2], R. L. White[1]

1. Dept. of Materials Science and Engineering, Stanford University, Stanford, CA; 2. Stanford Genome Technology Center, Stanford University, Stanford, CA; 3. Center for Integrated Systems, Stanford University, Stanford, CA; 4. Hitachi Global Storage Technologies, San Jose, CA

Introduction:

For the detection and identification of biomolecules of interest, especially DNA fragments, a common technology is to generate an array of the target molecules on a microarray [1]. The dominant technology is to create an array of probe molecules with each node of the array having probe molecules matched to a particular target molecule. The array may be lithographically formed, as in the Affymetrix array, or by spotting, as in the Agilent array. These arrays are single-use and relatively expensive.

Arrays have also been generated in which paramagnetic beads, to which target molecules have been bonded, are ordered on a magnetic substrate [2, 3]. In these arrays the surface of the bead is typically covered with target molecules, fluorescently tagged. Here we report on a new variation of the paramagnetic bead technology. The target molecules are bonded to the paramagnetic bead using a "linker" molecule on the bead. The paramagnetic beads attach to the gaps of a micron-sized magnetic bars array (Fig. 1(a)). Under these circumstances the large molecules order in form of an array and can be observed for a substantial period of time for analysis and identification. In addition, the array can be reused after flushing away the magnetic beads with a high-velocity fluid.

Experiments:

The magnetic bar arrays were formed on 4" Si wafers with lithographic patterning technology common to the hard disk industry with a process sequence including (1) sputter deposition of a 150 nm SiO_2 base layer, (2) sputter deposition of a metallic multilayer comprising a hard magnetic material, (3) bi-layer photolithography, and (4) ion milling. The magnetic bars were arranged in rows, with bars typically 20 µm long and 2 µm wide with gaps between bars from 1.5 µm to 4 µm wide. The paramagnetic beads are captured by the fringing fields in the gaps between bars. The rows of bars were typically spaced by 20 µm (see Ref. [3] or Fig. 1(b) in this paper). The hard magnetic material for the bar structures was either formed by a single CoPt (70 nm) on a Cr seed layer or a $[Cr\ (5\ nm)/CoPt\ (10\ nm)]_7$ multilayer. The coercivities of these films were about 550 Oe and 670 Oe, respectively. After processing, the bars were magnetized parallel to the long axis of the bar geometry by applying an external 13 kOe magnetic field. Earlier experiments with bars of the soft magnetic material CoTaZr were less than fully successful since closure domains often formed at the bar ends due to demagnetization effects.

Microfluidic channels were then patterned on a 4" Pyrex wafer, and the glass wafer bonded to the silicon substrate through anodic bonding. The particles to be captured in the array were then flowed over the magnetic bar array through the microfluidic channels.

Results:

The capabilities of the system were demonstrated by creating an ordered array of immobilized yeast molecules. A group in the Stanford Genome Technology Center is studying the relationship between certain yeast DNA segments and the reproduction of the associated yeast molecules. The experiment requires observing specific yeast cells through a microscope for many hours, a very tedious task for mobile yeast cells. With the yeast cells immobilized in an array, time-lapse photography can be used to monitor a number of cells without continuous observer presence. For our experiment, we used streptavidin-coated paramagnetic beads 5 µm in diameter and Concanavalin A (Con A) as the linker molecule. Fig 1(b) shows the array of captured particles. Paramagnetic beads have been captured on nearly every gap in the array. The paramagnetic beads typically capture only one yeast molecule, though occasionally two or even three yeast cells bind to a single paramagnetic bead. The yeast cells can be pre-mixed with the paramagnetic beads and the binder, or flowed over the paramagnetic beads after capture. The pre-mixing is found to be more efficient.

Discussion:

We have demonstrated the capture of non-magnetic molecules of biological and perhaps medical interest in an ordered array. The technique is applicable to a wide range of molecules, and so is of general applicability. All that is required is a linker molecule like Con A which will bond the target molecule to the streptavadin-coated bead. For larger molecules, paramagnetic bead arrays can be made with trios (arranged in a triangle) or quads (arranged in a square) of paramagnetic beads, affording multiple capture sites for larger molecules. The magnetic array is inexpensive and reusable. We envision wide applicability for this technology.

[1] M. Schena, Microarray Biochip Technology. Westborough, MA: Eaton, 2002.

[2] D.R. Baselt et al., Biosensors and Bioelectronics, v. 13, pp. 731-739, 1998.

[3] L.A. Roberts et al., IEEE Trans. Magn., v. 40, pp. 3006-3008, 2004.

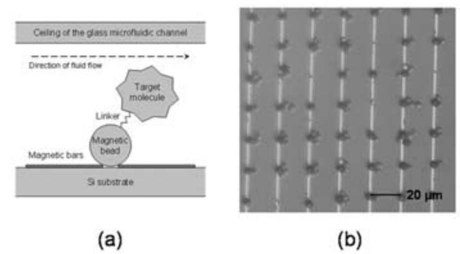

Fig. 1 (a) Schematic cross-section of magnetic bar array with linker technology and (b) optical microscope image of the microarray with 5 µm-diameter magnetic beads (dark-colored) and anchored yeast cells (light-colored).

DL-01

Voltage control of magnetic anisotropy in an ultrathin Fe film.

T. Maruyama, K. Ohta, N. Toda, T. Nozaki, T. Shinjo, M. Shiraishi, Y. Suzuki
Engineering science, Osaka university, Toyonaka, Japan

Recently, voltage controlled magnetization switching which has high potentiality for spintronic devices has started to attract a lot of attention because of its low energy consumption. Several kinds of approaches have been suggested so far, such as the voltage controlled interlayer exchange coupling [1, 2] and the electric field induced anisotropy change [3]. Very recently, Weisheit et al. reported that the coercivity of ultrathin FePt and FePd films can be changed by an applied electric field [4]. However, they used a liquid electrolyte to apply a large electric field. So as to apply this for practical spintronic devices, the effect should be realized in an all solid state device.

In this study, we focused on a structure which consists of a solid insulator and an ultrathin ferromagnetic layer (see Fig.1). All layers except for the top thick polyimide layer were prepared by a molecular beam epitaxy method. Since the influence of the electric field to the perpendicular anisotropy is effective only at the interface, the ferromagnetic layer should be composed of several monatomic layers. Besides, the ultrathin Fe layer deposited on an Au buffer layer exhibits a transition of magnetic anisotropy from in-plane to perpendicular depending on the film thickness [5]. This feature is suitable for the observation of the anisotropy change by the electric field. Therefore, we employed an ultrathin Fe film. The insulating layers consist of MgO, Al_2O_3 and polyimide. The polyimide was used to cover pinholes in the MgO/Al_2O_3 layers. A bias voltage was applied through the top ITO (Indium Tin Oxide) electrode. When a high voltage is applied to the system, the electronic state of the ultrathin Fe layer changes, leading to the change of magnetic anisotropy. From symmetry, a perpendicular magnetic anisotropy is expected to be induced/suppressed by an electric field. A change of the hysteresis loop induced by a voltage application was detected by the polar MOKE system shown in Fig.2.

In order to detect the small signal changes, a lock-in technique was used. A lock-in amplifier 1 is used to measure the Kerr ellipticity η, and a lock-in amplifier 2 is for the measurement of minimal change of lock-in 1 amplifier output caused by the voltage application. In the measurement, we needed to apply an ac high voltage to the sample, so the oscillation output from the lock-in 2 voltage (3.13V, 213Hz) was amplified up to 160V peak to peak by a high speed amplifier. Using this measurement system, we could observe a considerable modulation of magnetic anisotropy when the thickness of Fe was from 0.4 to 0.6nm. In the presentation, we will discuss about the Fe thickness and the bias voltage amplitude dependence of this effect. This result has a significant meaning from a viewpoint that we can control the magnetic anisotropy, which is commonly considered as a fixed material intrinsic constant, by an applied electric field even in the all solid state devices.

[1] C.-Y. You and S. D. Bader, J. Magn. Magn. Mater. **195** (1999) 488.

[2] C.-Y. You and Y. Suzuki, J. Magn. Magn. Mater. **293** (2005) 774.

[3] X. Nie, S. Blügel, Elektrisches, PCT/DE99/02840.

[4] M. Weisheit, S. Fähler, A. Marty, Y. souche, C. Poinsignon, and D. Givord, Science **315**, (2007) 349.

[5] C. Liu and S. D. Bader, J. Vac. Sci. Technol. A, **8**, (1990) 2727.

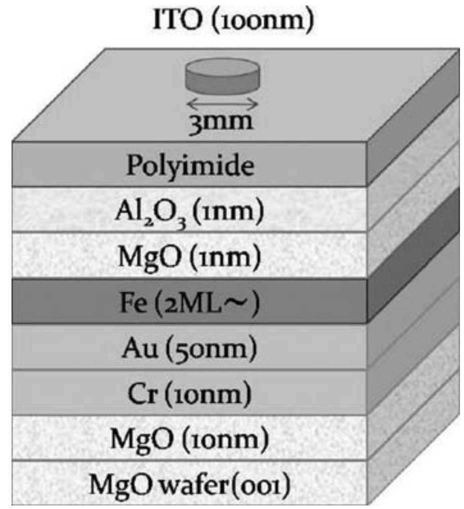

Fig.1 Sample structure

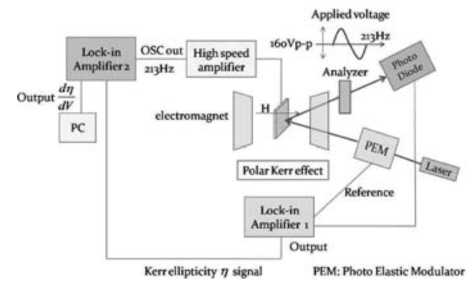

Fig.2 Experimental set-up (Lock-in method)

DL-02

Angular dependence of two magnon scattering in ultrathin ferromagnets.

P. Landeros[1], R. E. Arias[2], D. L. Mills[3]
1. Departamento de Física, Universidad Técnica Federico Santa María, Valparaíso, Chile; 2. Departamento de Física, Universidad de Chile, Santiago, Chile; 3. Department of Physics and Astronomy, University of California, Irvine, CA

We develope a theory to describe on a quantitative basis two magnon relaxation process in ultrathin ferromagnets. By extend an earlier formalism [1] to the case where the magnetization is tipped out of plane, one may extract information on the angular dependent time response of a system, as well as investigate the role of sample anisotropies or defects geometry in ultrathin films. It is know that surface or interface defects activate two magnon scattering and therefore we can manipulate the magnetic damping properties by controlling two magnon linewidth through defects. The nature of the damping of spin motions realized in such structures controls their response time and it is of interest to know whether the mechanisms well known in bulk materials are operative, and if there are new damping processes present unique to the nanoenvironment.
Our theory will be focused on the motion of the magnetization of ultrathin ferromagnetic films, under circumstances where the wavelengths involved are very long compared to the lattice constant, which is the domain probed by FMR spectroscopy and Brillouin light scattering. We provide explicit expressions for the two magnon contribution to the FMR linewidth and the two magnon induced frequency shift of the FMR line, in a form sufficiently general for application to a diverse array of defect structures. We also provide complete expressions for the frequency and wave vector dependent susceptibility tensor. This will allow the reader to analyze the influence of defect induced spin wave scatterings on Brillouin light scattering spectra as well, if desired. It is our view that to have the full form of the response functions in hand will prove useful in a variety of contexts. As an illustration of our results, we present in Figs. 1-3 numerical calculations of the angular and frequency dependence of the two magnon linewidth $\Delta H^2 = \Gamma^*\Phi^c$, for rectangular defects. It is interesting to note that both quantities (Γ and the critical angle Φ^c) depends on frequency, field angle, anisotropies and material parameters, and the defects details are contained only in Γ. This allow us to manipulate two magnon scattering rates by controlling defects geometry, in addition to the angular degrees of freedom. We see that the dependence of the two magnon contribution to the linewidth can show striking behavior, as the magnetization is tipped out of plane. It should be kept in mind that these calculations employ a particular model of the defect structure, and the behavior may change if the defect structure which activates two magnon scattering deviates substantially from the picture utilized in these calculations. The notion that the two magnon contribution to the linewidth cuts off when the angle between the magnetization and the film plane is greater than 45 degrees is supported nicely by the data reported in Ref. [2]. Of course, it will be of great interest to see detailed studies of the influence of tipping the magnetization out of plane. It is our hope that the results presented here will stimulate new and more detailed studies of the influence of tipping the magnetization out of plane on the response characteristics of ultrathin ferromagnets.

[1] R. Arias and D. L. Mills, Phys. Rev. B60, 7395 (1999); J. Appl. Phys. 87, 5455 (2000).

[2] R. D. McMichael et al., J. Appl. Phys. 83, 7037 (1998).

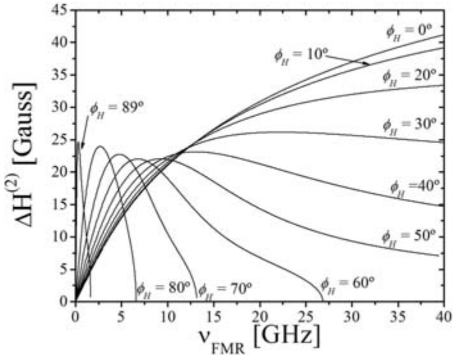

The frequency dependence of the two magnon contribution to the FMR linewidth, for the situation where the angle between the externally applied field and the plane of the film is held fixed, as the external field is increased. The parameters employed in these calculations are the same as those utilized in Ref. [1]

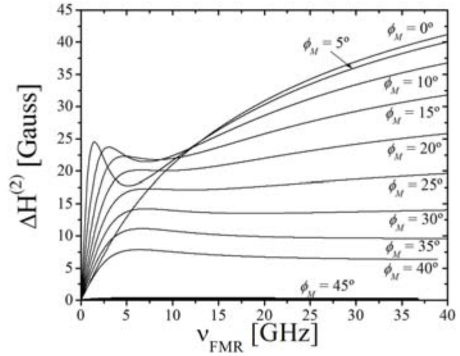

We illustrate the frequency dependence of the linewidth, as the angle between the magnetization and the film plane is kept fixed, as the external field is varied. The parameters are the same of Fig. 1

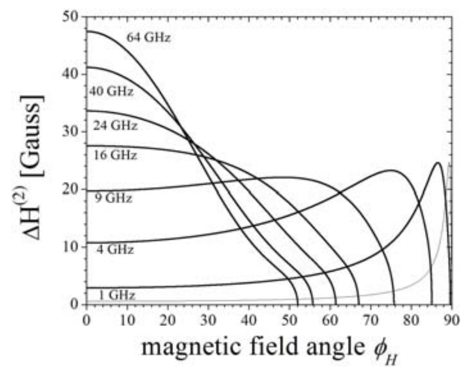

For various frequencies, we show the variation of the two magnon contribution to the FMR linewidth as a function of the angle between the external magnetic field and the plane of the film.

DL-03

CEMS study of epitaxial $Co_2Cr_{0.6}Fe_{0.4}Al$ thin films.

V. Ksenofontov[1], C. Herbort[2], M. Jourdan[2], C. Felser[1]
1. Institute of Inorganic and Analytical Chemistry, Johannes Gutenberg-University Mainz, 55099 Mainz, Germany; 2. Institute of Physics, Johannes Gutenberg - University, 55099 Mainz, Germany

The Heusler alloy $Co_2Cr_{0.6}Fe_{0.4}Al$ (CCFA) attracts large interest as a potential half-metallic ferromagnet [1]. In this compound a high tunelling magnetoresistance (TMR) is expected as a result of a high spin polarization at the Fermi level [2].
For the spin polarization the degree of structural disorder of Heusler compounds plays a crucial role. The preference of CCFA to grow in the *B2* structure with disorder on the Cr/Fe and Al positions instead of the fully ordered $L2_1$ structure is a known fact. Calculations predict that *B2* type of disorder has only a minor effect on the spin polarization, whereas additional disorder on the Co sites (*A2* structure) is predicted to strongly reduce the spin polarization [3].
Epitaxial thin films of the Heusler half-metallic compound CCFA were investigated using conversion electron Mössbauer spectroscopy (CEMS) in order to get insight into the structural and magnetic properties. Thin films of 100 nm thickness were deposited by rf magnetron sputtering on MgO substrates without and with 10 nm Fe buffer layer. CEMS spectra of non thermotreated samples with Fe buffer layer show distinguishable α-Fe and CCFA subspectra (Fig. 1a). The latter can be described as a broad distribution due to reduced crystalline quality. Subsequent thermal treatment improves the thin film crystallographic order and morphology and causes the diffusion of Fe atoms from the buffer layer into the CCFA (Fig. 1b). Apparently, the related diffusion of Cr atoms from the CCFA thin film into the Fe buffer layer also takes place. Thus the thermal treatment influences the Fe to Cr ratio of the CCFA, and obviously the position of the Fermi level. Increasing of treatment temperature intensifies a central peak in the Mössbauer spectra, which means enhancement of antisite Co/(Fe,Cr) disorder. Samples with Fe buffer layer prepared at the optimal annealing temperature of 550 °C, as determined by tunneling magnetoresistance measurements, reveal some degree of *A2* disorder (Fig. 1b). Thermal treatment at 600 °C reduces the magnetoresistance [2] and according to the CEMS data is associated with higher degree of *A2* disorder (Fig. 1c).
CEMS spectra of CCFA thin films without Fe buffer layer are presented in Fig. 2. A sample annealed at 450 °C indicates almost no Fe atoms occupying Co sites and consequently no *A2* disorder (Fig. 2a). Thermal treatment at 550 °C increases a degree of the antisite Co/(Fe,Cr) disorder (Fig. 2b). The *A2* disorder fraction in CCFA thin films without Fe buffer treated at 600 °C (Fig. 2c) is similar to the degree of disorder found in thin films with Fe buffer layer (Fig. 1c).
Hyperfine magnetic fields on iron atoms (H_{hf}) in CCFA thin films deposited on MgO substrates as a function of annealing temperature show the following trends. For samples without Fe buffer layer H_{hf} monotonously decreases with increasing of annealing temperature due to the *A2* disorder. For samples with Fe buffer layer similar decreasing of H_{hf} competes with increasing of H_{hf} due to an enrichment of Fe atoms which diffuse from the Fe buffer layer into CCFA. One can suppose that among others these two factors could determine the maximal value of magnetoresistance observed in CCFA films deposited on MgO substrates with Fe buffer layer after annealing at 550 °C [2].

1. S. Wurmehl, G. H. Fecher, K. Kroth, F. Kronast, H. A. Dürr, Y. Takeda, Y. Saitoh, K. Kobayashi, H.-J. Lin, G. Schönhense and C. Felser, J. Phys. D: Appl. Phys. 39 (2006) 803.
2. A. Conca, M. Jordan, H. Adrian, J. Phys. D: Appl. Phys. 40 (2007) 1.
3. Y. Miura, K. Nagao and M. Shirai, Phys. Rev. B 69 (2004) 144413.

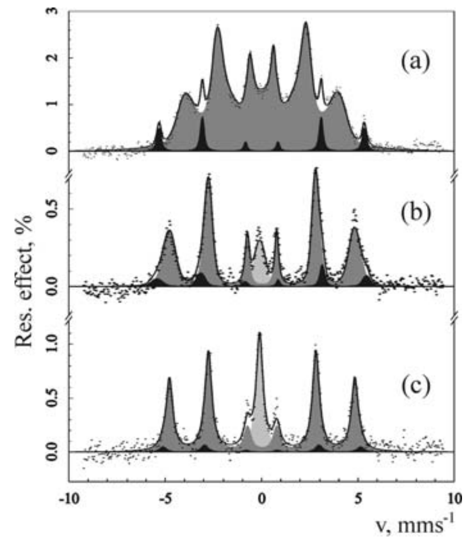

Figure 1 – ^{57}Fe CEMS spectra of 100 nm CCFA thin films (grey) deposited on MgO substrates with 10 nm Fe buffer layer (dark grey) without annealing (a), annealed at 550 °C (b) and 600 °C (c). The paramagnetic component (light grey) corresponds to Fe atoms occupying Co sites.

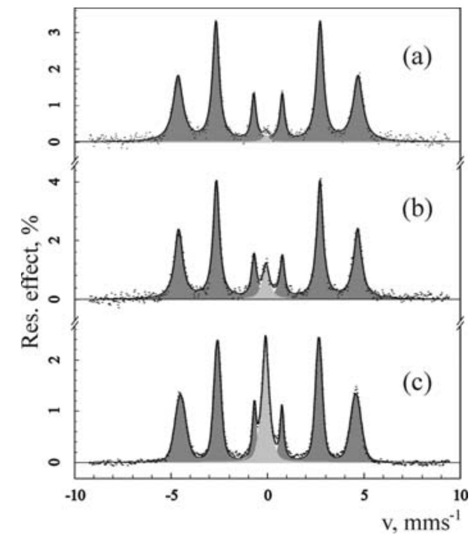

Figure 2 – ^{57}Fe CEMS spectra of 100 nm CCFA thin films (grey) deposited on MgO substrates annealed at 450 °C (a), 550 °C (b) and 600 °C (c). The paramagnetic component (light grey) corresponds to Fe atoms occupying Co sites.

DL-04

Morphology-induced oscillations of the electron-spin motion in Fe films on Ag(001).

L. Tati Bismaths[1], L. Joly[2], F. . Scheurer[1], W. Weber[1]
1. Institut de Physique et Chimie des Matériaux de Strasbourg,, Strasbourg, France; 2. Swiss Light Source, Villigen, Switzerland

It is well known that magnetic properties of thin films are inherently connected to the morphology and the structure of the films. It is in particular the strain arising from different lattice parameters of the film and the substrate which induces for instance additional magnetic anisotropy contributions. Here we report on spin-polarized electron reflection experiments in which the electron-spin motion, comprising an azimutal precession and a polar rotation around the magnetization direction of the ferromagnet, is studied in Fe films on Ag(001). Apart from quantum-size induced oscillations, the period of which depends on the electron energy, we observe also oscillations with a period of one monolayer independent of the electron energy. We assign the latter to oscillations of the surface lattice parameter when going from a filled to an incompletely filled Fe layer.

DL-05

Ferromagnetic Resonance of Disordered FePt Thin Films.

J. Gómez, M. Vásquez Mansilla, *A. Butera*
Centro Atomico Bariloche and Instituto Balseiro, Bariloche, Argentina

The intermetallic alloy FePt has received considerable attention in the last years due to the potential application as ultra high density storage media. Equiatomic FePt alloys have been intensively studied in the form of thin films and nanoparticles because of their unique magnetic and magneto-optical properties, especially the extremely large magnetic anisotropy, the very high coercivity, and the large polar magneto-optical Kerr effect. However, these properties are only observed when the alloy is atomically ordered in the L10 FCT crystalline phase, which is obtained after thermal treatment at high temperatures. Due to this fact, most of the research was devoted to the understanding of the physical properties of the ordered phase, while less attention was paid to the metastable disordered FCC phase which generally forms when films are fabricated at room temperature.
In this work we have analyzed the magnetic properties of a set of nominally equiatomic FePt films grown on oxidized Si (100) substrates. Samples of four different thicknesses (t = 10, 30, 60, and 100 nm) have been fabricated by dc magnetron sputtering at room temperature. The real atomic film composition was close 45% Fe, 55% Pt, as revealed by EDX studies. X-ray diffraction analysis confirmed the absence of atomic order and showed a moderate texture along the (111) direction. The dc magnetic response of the films was measured either in a VSM or a SQUID magnetometer. In Fig. 1 we present the in plane hysteresis loops for the four films. Loops perpendicular to the film plane show the typical linear variation of the magnetization due to the demagnetizing field of a planar sample. In all cases the in-plane loops show that the films are relatively soft, but we have observed a notorious change in the shape of the loops and an increment in the coercive field when the film thickness is increased. For t = 10 and 30 nm the coercive field is around 10 Oe, the remanence is almost equal to one and the magnetization reverses in a very narrow range of fields. On the other hand, the magnetization in the thicker films starts to decrease gradually at positive fields of 1kOe and the reversal occurs in a two step process. These measurements have been correlated with ferromagnetic resonance data (see Fig. 2) taken at both X-band (9.5 GHz) and Q-band (34 GHz). In the thinner films (10 and 30 nm) we have observed a single resonance absorption that can be related to the uniform precession of the magnetization. From the out of plane angular variation of this line we have deduced the effective demagnetizing field which is around 700 Oe for all films. This value correlates very well with the saturation field deduced from the perpendicular hysteresis loops. From Q-band measurements we obtained an average g-value of 2.09 which is coincident with the value of ferromagnetic iron. As expected, the linewidth of this resonance increases approximately by a factor of three with frequency and tends to be larger for thicker films. The two thicker films show an additional resonance line when the magnetic field is applied at, or very close to, the film plane normal. This line is shifted 400-700 Oe to lower fields from the main resonance and is observed at both X and Q-bands with approximately the same field separation from the uniform mode. These additional resonances, together with the change in the behavior of the magnetization, can be originated in the presence of stripe-like domains in the thicker films which are not present in the thinner ones.

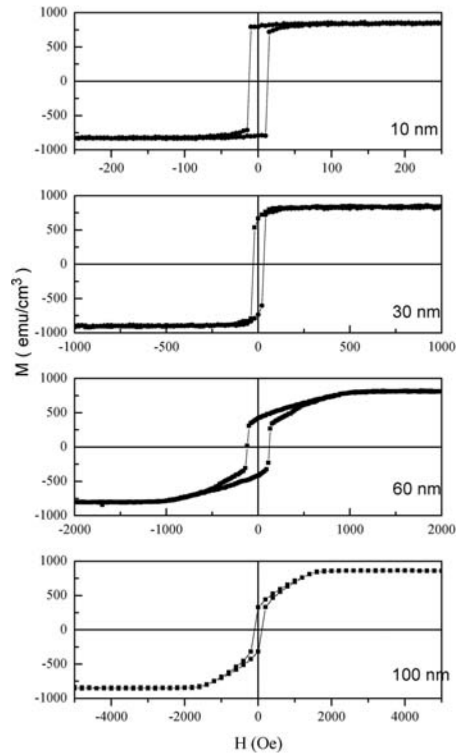

Magnetization per unit volume as a function of field with the applied field parallel to the film plane. The four loops correspond to the different thichnesses investigated.

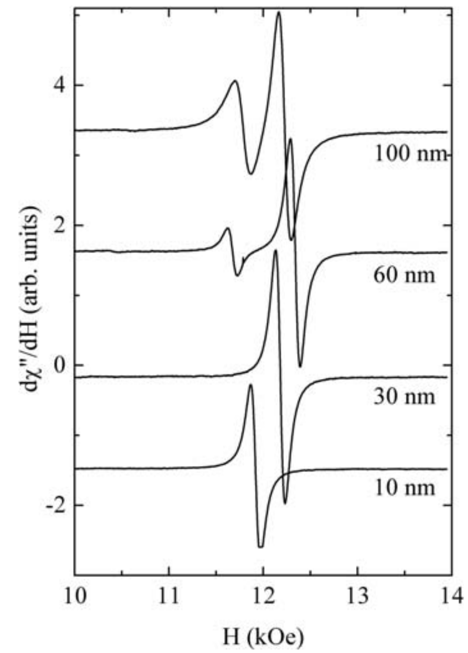

Ferromagnetic resonance spectra measured at X-band (9.5 GHz) with the applied field perpendicular to the film normal. The four spectra correspond to the different thichnesses investigated.

DL-06

Magnetization processes in ultrathin Co film grown on stepped Si(111) substrate.

A. Stupakiewicz[1,2], A. Fleurence[2], A. Maziewski[1], T. Maroutian[2], P. Gogol[2], B. Bartenlian[2], R. Mégy[2], P. Beauvillain[2]
1. University of Bialystok, Bialystok, Poland; 2. Institut d'Electronique Fondamentale, Universite Paris XI, CNRS, UMR 8622, Orsay, France

Self-organized ultrathin magnetic materials are the object of intensive investigations due to applications in magnetic storage media with perpendicular recording of the information. The magnetization reversal process of ultrathin Co film deposited on Au or Pt layer is strongly correlated with the film preparation. Especially, the domain wall (DW) propagation is sensitive to the magnetic anisotropy. In the present work, we demonstrate influence of periodical Si(111) stepped substrate surface on domain structure and magnetization processes in Au/Co/Au films.
Samples were prepared by molecular beam epitaxy in a ultra-high vacuum chamber. Substrates we used are 2° misoriented vicinal Si(111) misoriented toward the opposite [11-2] direction gives rise to an array of steps bunches alternated with 7×7 reconstructed terraces with about 80 nm length [1]. The in-situ STM images show the surface after the preparation of the substrate, Cu and Au buffers. The following structures were deposited on stepped Si(111) substrate: (i) a Cu buffer layer of 4 monolayer (ML) deposited at T=100°C; next layers were deposited at room temperature (ii) 30 ML thick Au(111) underlayer, (iii) d=3, 5, 7 and 15 ML thick Co layer and (iv) 30 ML thick Au cover layer. The hcp Co(0001) crystallographic phase is expected for cobalt deposited on Au(111) surface.
The magnetization reversal process were investigated at room temperature using the magneto-optical Kerr effect (MOKE) based magnetometer. Magnetization curves were registered as a function of perpendicular magnetic field $H_\perp$ or in plane H_{II} field applied along various azimuthal ϕ_H angles with respect to the [1-10] Si direction. L-MOKE loops were registered as a function of both H_{II} amplitude and ϕ_H angle.
The P-MOKE hysteresis loops for selected Co thicknesses are shown in Fig.1A. The thickness driven evolution of loops corresponds to spin-reorientation transition (SRT) from the out-of-plane to the in-plane magnetization and a decreasing of coercive field to zero with increase of Co thickness. Angular ϕ_H dependence L-MOKE hysteresis loops shows two fold symmetry. Easy and hard in-plane axis are parallel to [11-2] and [1-10] Si directions (perpendicular and parallel to the steps on the surface respectively), respectively. So, increasing d the spin reorientation undergoes from the axis perpendicular to in-plane. The SRT easy magnetisation axis – easy magnetization plane was discussed [2]. For d>7ML, the P-MOKE magnetization curve was observed (see Fig.1A) indicating the easy magnetization direction in-plane orientation known as the SRT in Au/Co/Au films on flat substrates [2]. The shape of the both P-MOKE and L-MOKE loops is an evidence for the uniaxial magnetic anisotropy. Figure 1B shows the in-plane hysteresis loops measured in the magnetic fields oriented at various directions in the sample plane by L-MOKE. Curves illustrating magnetization process when magnetic field is applied along hard and easy. Azimuthal L-MOKE symmetry is related to the presence of the uniaxial in-plane anisotropy induced by steps. The vectorial MOKE magnetometry allowed us the determination of the magnetic anisotropy constants in a phenomenological model, including an additional uniaxial anisotropy energy term related to the vicinal substrate [3].
Fig. 2A and B shows the remnant domain structure image registered for 3 ML and 5 ML thick Co film, respectively. Strong preference of domain wall orientation along the [1-10] Si is well visible. The preference could be explained by the step-induced in-plane magnetic anisotropy determined from L-MOKE measurements. The domain size decreases while approaching the SRT – compare Fig.2A and Fig.2B. Such decrease can be explained using the theory [4].
In conclusion, in this study it was shown that domain wall propagation and the perpendicular magnetic anisotropy in Au/Co/Au sandwich can be modification by morphology of the stepped substrates.
The work was supported by the Marie Curie Fellowships for "Transfer of Knowledge" (No. 2004-003177).

[1] A. Rota et al., Surface Science 600 (2006) 1207.

[2] M. Kisielewski et al., Phys. Rev. Let. 89 (2002) 087203.

[3] A. Stupakiewicz et al., phys. stat. sol. (b) 243 (2006) 202.

[4] M. Kisielewski, et al., Phys.Rev.B 69 (2004) 184419

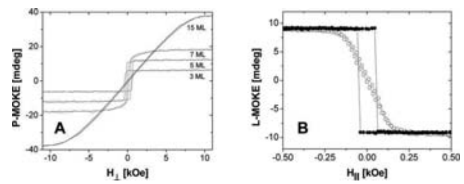

(A) - Polar Kerr rotation hysteresis loops for 3, 5, 7, 15 ML thicknesses of Co. (B) - Hysteresis loops measured by L-MOKE for 15 ML Co thickness in the easy (ϕ_H=0° – close points) and hard in-plane directions (ϕ_H=90° – open points), respectively.

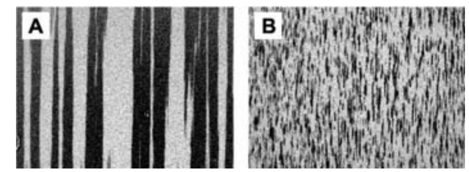

Remnant domain structure image observed for different Co thickness: (A) - 3 ML and (B) - 5 ML. Image size is 270x215 μm. Stripes of domains correspond to steps orientation along [1-10] Si. The sample was initially saturated by $H_\perp$>0 ("white" area) and then "black" domains were created by $H_\perp$<0 pulse magnetic field.

DL-07

Effects of Co/Sm composition on the ordered phase formation in Sm-Co thin films grown on Cu(111) single-crystal underlayers.

Y. Nukaga[1], M. Ohtake[1], F. Kirino[2], M. Futamoto[1]
1. Faculty of Science and Engineering, Chuo University, Tokyo, Japan; 2. Graduate School of Fine Arts, Tokyo National University of Fine Arts and Music, Tokyo, Japan

Thin films with high magnetocrystalline anisotropy have attracted much attention to the applications such as ultra-high density magnetic recording, micro-electro-mechanical systems, etc. $SmCo_5$ is a magnetic material with high K_u of 1.1×10^8 erg/cm^3 and it is one of the candidates as the recording layer in realizing such ultra-high density magnetic recording. Recently, $SmCo_5$ polycrystalline thin films with (0001) preferred texture have been prepared using Cu underlayers on glass substrates [1,2]. Formation of (0001) texture is interpreted to be favored by a small lattice mismatch with the Cu(111) plane. The lattice mismatch between $SmCo_5$(0001)[1-100] and Cu(111)[1-10] is -2.2%. In the present study, we fabricated Sm-Co thin films on Cu(111) single-crystal underlayers by changing the composition and the effects of Co/Sm composition on the ordered phase formation are investigated.
Thin films were prepared on α-Al_2O_3(0001) substrates at a substrate temperature of 500 °C using an MBE system under base pressures lower than 7×10^{-9} Pa. The film layer structure was Sm-Co(20 nm)/Cu(10 nm)/Co(2 nm)/Al_2O_3(0001). The Cu(111) single-crystal underlayer was prepared by hetero-epitaxial growth on the Al_2O_3 substrate [3]. Sm and Co were co-deposited on the Cu underlayer and the thickness of Sm-Co layer was fixed at 20 nm. The composition of Sm-Co layer was varied from Co-rich to Sm-rich region (12–35 at. % Sm) including the $SmCo_5$ stoichiometry (16.7 at. % Sm). The composition was confirmed by EDX. The surface structure during film deposition was studied by *in-situ* RHEED. The film structure was investigated by XRD with Cu-K_α radiation. $SmCo_5$ epitaxial thin films were obtained on Cu(111) single-crystal underlayers for all compositions. The epitaxial orientation relationship of $SmCo_5$(0001)[1-100] and $SmCo_5$(0001)[11-20]//Cu(111)[1-10] were determined from RHEED analysis. The $SmCo_5$ layer has two different types of domains whose orientations are rotated around film normal by 30 degrees to each other. Figure 1 shows the XRD patterns of $SmCo_5$ epitaxial thin films with different Co/Sm compositions. The superlattice (0001) peak of $SmCo_5$ ordered phase is observed in addition to the fundamental $SmCo_5$(0002) peak for all samples. The peak shift toward low angle direction is recognizable for the $SmCo_5$(0001) reflection with increasing the Sm composition, which indicates expansion of lattice constant, c_{SmCo5}. Cu atoms are known to substitute the Co site in the $SmCo_5$ structure forming an alloy compound of $Sm(Co,Cu)_5$ [4-6]. The $SmCo_5$ epitaxial thin films prepared in the present study are considered to include Cu atoms, since the thin films were grown at a high substrate temperature of 500 °C where Cu atom diffusion into the Sm-Co layer would take place. Figure 2 summarizes the change in the lattice constant estimated from the $SmCo_5$(0001) XRD peak. The lattice constant of $SmCu_5$ thin film was determined to be 4.08 nm from a $SmCu_5$ epitaxial thin film prepared under a similar experimental condition. The Sm-Co thin film with 16 at. % Sm which is close to $SmCo_5$ stoichiometry has a larger lattice constant than that of bulk $SmCo_5$ alloy. The measured lattice constant value indicates that the alloy composition is $SmCo_{2.6}Cu_{2.4}$. The lattice constant of Sm-Co thin film with 35 at. %, Sm is close to that of $SmCu_5$ alloy thin film. Large amount of Cu atoms are diffusing into the $SmCo_5$ epitaxial thin films forming alloy compounds of $Sm(Co,Cu)_5$. The Cu(111) underlayer and the Cu atom diffusion into the Sm-Co layer are considered to assist the formation of ordered structure.

[1] J. Sayama, T. Asahi, K. Mizutani, and T. Osaka: *J. Phys. D: Appl. Phys.*, **37**, L1 (2004).

[2] S. Takei, A. Morisako, and M. Matsumoto: *J. Magn. Magn. Mater.*, **272-276**, 1703 (2004).

[3] M. Ohtake, Y. Akita, F. Kirino, and M. Futamoto: *J. Appl. Phys.*, **101**, 09D122 (2007).

[4] F. Hofer: *IEEE Trans. Magn.*, **MAG-6**, 221 (1970).

[5] J. Sayama, K. Mizutani, T. Asahi, J. Ariake, K. Ouchi, and T. Osaka: *J. Magn. Magn. Mater.*, **301**, 271 (2006).

[6] Y. K. Takahashi, T. Ohkubo, and K. Hono: *J. Appl. Phys.*, **100**, 053913 (2006).

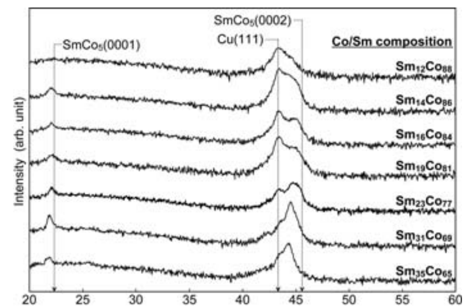

Fig. 1 XRD patterns of $SmCo_5$ epitaxial thin films grown on Cu(111) underlayers.

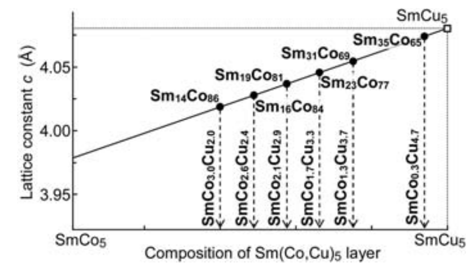

Fig. 2 Lattice constants of $Sm(Co,Cu)_5$ epitaxial thin films obtained by changing the Co/Sm composition.

DL-08

Analysis of the multiferroic properties in $BiMnO_3$ epitaxial thin films.

M. Grizalez[1,2], J. C. Caicedo[2], P. Prieto[3]
1. Universidad de la Amazonia, Florencia, Colombia; 2. Universidad del Valle, Cali, Colombia; 3. Centro de Excelencia en Nuevos Materiales, Cali, Colombia

The term multiferroic has been coined to describe materials in which two or all three ferroic properties ferroelectricity, ferromagnetism, and ferroelasticity coexist in the same phase [1]. It means that these materials have spontaneous magnetization. It also means that these order parameters can be regulated by the application of electric fields and/or magnetic fields, and/or using mechanical stresses. These compounds have gained renewed and ever increasing research interest in the last three years [2]. Especially those in which magnetic and ferroelectric orderings exist simultaneously, called magnetoelectric materials, it is possible to find a coupling between the magnetic and ferroelectric properties through the magnetoelectric effect that is the induction of an electric polarization using a magnetic field or vice versa [3]. Moreira dos Santos et al reported on the synthesis of $BiMnO_3$ thin films, which show the coexistence of ferromagnetic and ferroelectric properties [4].Recent theoretical calculations also suggest that it is likely to be both ferromagnetic and ferroelectric because of the covalent bonding between bismuth and oxygen atoms [5]. These properties make this material potentially interesting for both technological applications and for the study of magnetoelectrical interactions.

In this work, $BiMnO_3$ thin films were deposited by r.f. magnetron sputtering on single-crystal $SrTiO_3$ (001) and $Pt/TiO_2/SiO_2$ substrates. X-ray diffraction was used to analyze the crystal structure of the thin films, indicating that the films were monoclinic with two dominant orientation relationships along the substrate. The first is (111) $BiMnO_3$ ‖ (001) $SrTiO_3$; the second is (222) $BiMnO_3$ ‖ (002) $SrTiO_3$. Fig. 1 Film roughness was analized by AFM; quantitative values of grain size are in the range between 300 and 500 nm. Electrical measurements via R vs. T were taken from 450 K to 15 K. Magnetic characterization was carried out by using a Vibrating Sample Magnetometer (VSM) for magnetization versus temperature and for hysteresis loops at different temperatures. The saturation magnetic moment of $3.2\mu_B$ per Mn ion (still fairly smaller than that of the bulk, $3.6\mu_B$) was observed at 5 K, decreasing with increasing temperature fig. 2 .Ferroelectric characterization was carried out at low temperatures and at 300 K by using a cooling system, a temperature controller Cryodine model 22C of the LTS cryosystems series, the VISION™ software, and an RT66 test system from Radiant TechnologiesInc™. Hysteresis loops (Polarization v-s Voltage) were obtained and they show saturation polarizations of $1.51\mu C/cm^2$, $2.21\mu C/cm^2$, and $0.7\mu C/cm^2$ at 105 K, 122 K, and 300 K. Fig. 3

[1] N. Hill, A. Filippetti, Journal of Magnetism and Magnetic Materials, 242-245, 976-979 (2002).

[2] Z. H. Chi, C. J. Xiao, S. M. Feng, F. Y. Li, C. Q. Jin, X. H. Wang, R. Z. Chen, and L. T. Li, Journal of Applied Physics, 98, 103519 (2005).

[3] M. Grizalez, E. Delgado, M. E. Gómez, and P. Prieto; phys. stat. Sol. (c) 4, No. 11, 4203-4208 (2007).

[4] A. Moreira dos Santos, S. Parashar, A. R. Raju, Y. S. Zhao, A. K. Cheetham, and C> N. R. Rao, Solid State Communications, 122, 49-52 (2002).

[5] N. A. Hill, K. A. Rabe, Phys. Rev. B 59, 8759 (2000).

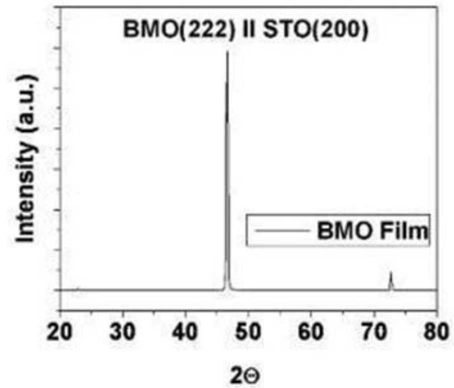

Fig. 1. X-Ray diffraction for a BMO/STO(100) thin film deposited at a pressure of $5x10^{-3}$ mbar.

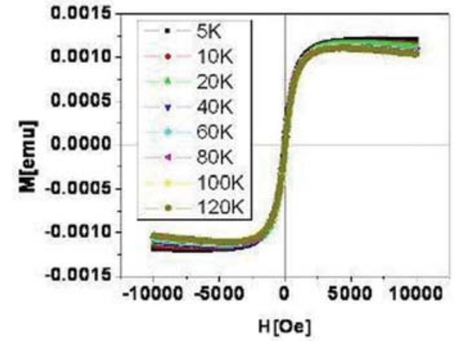

Fig. 2. Magnetic hysteresis loops of $BiMnO_3/SrTiO_3$ (100) thin films at different temperatures.

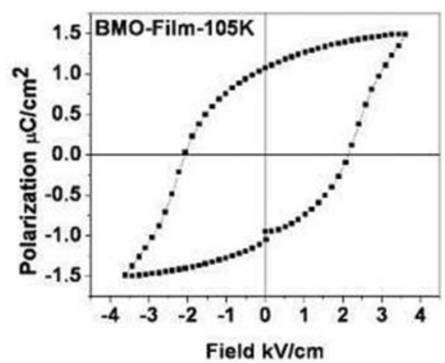

Fig. 3. P-V hysteresis loop of a BMO thin film on a $Pt/TiO_2/SiO_2/Si$ substrate at 105K.

DL-09

Electric and magnetic properties of multiferroic $BiFeO_3$ and $YMnO_3$ thin films.

J. A. Zapata[1], J. Narvaez[1], W. Lopera[1], *M. H. Gómez*[1], P. Prieto[2]
1. Physics, Universidad del Valle, Cali, Colombia; 2. Centro de Exelencia en Nuevos Materiales, Cali, Colombia

Multiferroic materials exhibit both ferromagnetic and ferroelectric polarizations along with coupling between them. The magnetic polarization can be switched by applying an electric field; likewise, the ferroelectric polarization could be switched by applying a magnetic field. Consequently, multiferroics offer rich physics and novel device concepts, which have recently become of great interest to researchers [1]. Perovskite $BiFeO_3$ (BFO) has attracted much attention given the coexistence of ferroelectric and magnetic orders. It possesses a rhombohedrally distorted perovskite structure at room temperature, with space group R3c [2] and an antiferromagnetic / ferroelectric phase with high Curie ($T_C \approx 1100$ K) and Neel ($T_N \approx 673$ K) temperatures, in bulk. Yttrium manganese oxide $YMnO_3$ (YMO) exhibits two stable crystallographic modifications – orthorhombic and hexagonal [3]; while magnetic ordering occurs in both phases, ferroelectric ordering occurs only in hexagonal, which belongs to systems without central symmetries with the P63cm space group, besides displaying a ferroelectric transition with Curie temperature, $T_C \approx 914$ K, and a rather low antiferromagnetic Neel temperature $T_N \approx 80$ K [4].
In the present work we report the preparation of BFO and YMO thin films grown on Pt/TiO_2 $/SiO_2/Si$ substrates by using a magnetron sputtering technique assisted by radio frequency in a pure oxygen atmosphere. $BiFeO_3$ and $YMnO_3$ targets were self-made by the usual solid-state reaction method. The presence of bismuth oxide ($Bi_2O_{2,75}$) impurity phase was detected in the X-ray diffraction (XRD) pattern in addition to the major $BiFeO_3$ phase, Also, we detected phases at trace levels of ($Bi_{24}Fe_2O_{29}$) and ($Bi_{25}FeO_{40}$). The presence of major yttrium manganese oxide (YMO) in hexagonal phase was detected in the X-ray diffraction (XRD).
We investigated the effects of deposition temperature and crystallization on morphology, magnetization, and polarization of BFO and YMO thin films.
The crystalline phases of the films were determined by X-ray diffraction (XRD). Surface morphology was obtained by atomic force microscopy (AFM), polarization electric field (P–E) measurements were performed by using the Ferroelectric Testing system (RT66a). We used a VSM technique on the Physical Property Measuring System (Quantum Design™)to measure magnetization of thin-film samples. Polarization as a function of electric field in capacitor structures based on our BFO films shows hysteretic behavior with a coercive field of 90 kV/cm and a remnant polarization of 37.2 $\mu C/cm^2$ (Fig. 1a). Magnetization measurements of the BFO samples evidence weak magnetization fig 2, corroborating the behavior of the magnetoelectric coefficient observed in a previous work for bulk material [5].
For YMO, we found an optimal deposition temperature of 850 °C. Surface morphology is improved when deposition temperature increases from 750 °C to 850 °C. Polarization as a function of electric field in capacitor structures based on our YMO films show hysteretic behavior with coercive field of -2.69 kV/cm, remnant polarization of 1.39 $\mu C/cm^2$, and saturation polarization of 4.17 $\mu C/cm^2$ (Fig. 1b).

[1] Fiebig M J. Phys. D: Appl. Phys. **38** R123 (2005).

[2] C. Michel, J.-M. Moreau, G. D. Achenbach, R. Gerson, and W. J. James, Solid State Commun. **7**, 701 (1969).

[3] C. Zhong, J. Fang / Solid State Communications **128**, 449–453,(2003).

[4] M. Qian, J Dong, Q Zheng / Physics Letters A **270**, 96–101,(2000).

[5] J. M. Caicedo, J. A. Zapata, M. E. Gómez, P. Prieto, Journal Appl Phys, to be published.

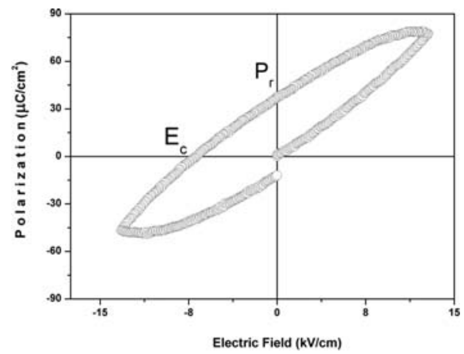

Fig 1a. Polarization as a function of electric field in capacitor structures for BFO films at substrate temperature 600°C

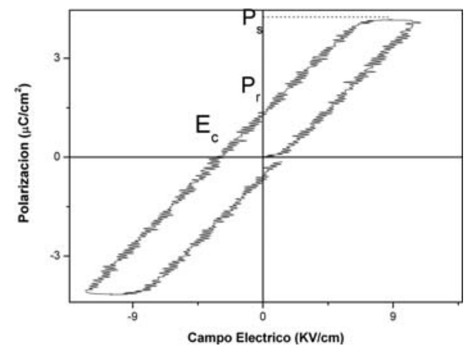

Fig 1b. Polarization as a function of electric field in capacitor structures for YMO films at substrate temperature 850°C

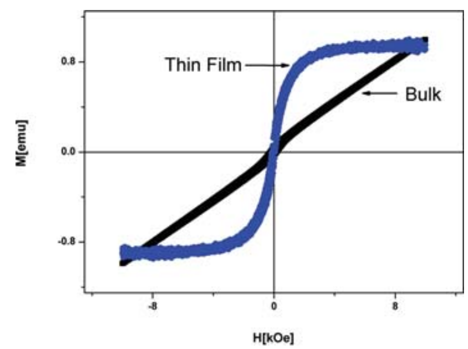

Fig 2. Magnetization as a function of magnetic field for BFO in bulk and Thin film, measured at 100K

DL-10

Graphene/Ni(111) system: Spin- and angle-resolved photoemission studies.

Y. S. Dedkov[1], *M. Fonin*[2], U. Rüdiger[2], C. Laubschat[1]
1. TU Dresden, Dresden, Germany; 2. University of Konstanz, Konstanz, Germany

The ability to manipulate a single-electron spin using external electric field is one of the long-sought goals in attempt to develop alternative device technologies. The control over electron spins would be invaluable for nanoscopic spintronics [1-3] and related applications, such as quantum information processing using individual electron spin qubits. The main paradigm for the researches in this field is a spin-based field effect transistor (spin-FET) device introduced by Datta and Das [4] where the spin of injected electron can be modulated via application of only electrical field without any additional magnetic field. An ideal spin-FET should combine an effective spin transfer with spin manipulation via electrical field.
However, a high efficient spin-FET device requires long spin relaxation time as compared to the mean time of transport through the channel combined with a sufficient difference of the spin rotation angles between two states ("0" and "1") as well as an insensitivity of spin rotation to the carrier energy. In the recent theoretical work [5] spin-FET was proposed on the basis of a single graphene layer, a novel material consisting of a flat monolayer of carbon atoms packed in a two-dimensional honeycomb-lattice, in which the electron dynamics is governed by the Dirac equation [6,7]. Long electronic mean paths [7] and negligible spin-orbit coupling of the carbon based system [8], i.e. large spin relaxation times, make graphene a best-choice material for the observation of near ballistic spin transport.
Here, we report on the first unambiguous experimental observation of a controlled spin-manipulation in a graphene layer epitaxialy grown on Ni(111) substrate [9] (Fig.1). We use photoemission spectroscopy of the electronic π states of epitaxial graphene layer on the Ni(111) surface to observe a strong dependence of binding energy of these states, E(**k**), on the direction of magnetization of the sample. Since the explanation of this effect is based on consideration of the system of three orthogonal vectors in the system: wave vector of electron, magnetization of the sample, and electrical vector perpendicular to the surface, we conclude that the observed extraordinary high "splitting" up to 225meV of the π band in the graphene layer is a manifestation of the Rashba effect which provides a direct possibility to a flexible control of an electron spin in a graphene-based spin-FET.
The inert properties of grapheme layer were studied by means of spin-polarized electron emission of secondary electrons from graphene/Ni(111) system before and after exposure to oxygen [10] (Fig.2). It is shown that the spin-polarization of secondary electrons at zero kinetic energy from graphene/Ni(111) system is reduced by about 1/3 with respect to one from the clean Ni(111) surface, but contrasting to the latter it remains practically unaffected upon oxygen exposure. These experimental observations open technical perspectives for application of graphite layers in spintronic devices.

[1] S. A. Wolf *et al.*, Science **294**, 1488 (2001).

[2] *Spin Electronics*, edited by D. Awshalom (Kluwer, Dordrecht, 2004).

[3] S. A. Wolf *et al.*, IBM J. Res. Dev. **50**, 101 (2006).

[4] S. Datta and B. Das, Appl. Phys. Lett. **56**, 665 (1990).

[5] Y. G. Semenov *et al.*, Appl. Phys. Lett. **91**, 153105 (2007).

[6] M. Wilson, Physics Today **59**, 21 (2006).

[7] A. K. Geim and K. S. Novoselov, Nature Materials **6**, 183 (2007).

[8] H. Min *et al.*, Phys. Rev. B **74**, 165310 (2006).

[9] Yu. S. Dedkov *et al.*, arXiv:0712.3149v1[cond-mat.mtrl-sci].

[10] Yu. S. Dedkov and C. Laubschat, arXiv:0710.2514v1[cond-mat.mtrl-sci].

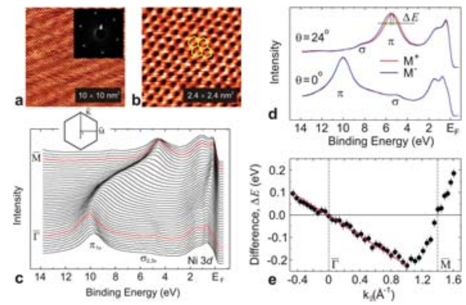

Fig.1. (a,b) Constant current STM image of the graphene/Ni(111) surface. The inset of (a) shows a LEED image obtained at 63eV. (c) Angle-resolved photoemission spectra measured with hν=40.8eV along Γ-M direction of the surface Brillouin zone. (d) Series of representative photoelectron spectra of the graphene/Ni(111) system for two different emission angles (marked in the plot) and two directions of magnetization, respectively. (e) Rashba "splitting" obtained from photoemission data as a function of the wave vector *k* along the Γ-M direction of the surface Brillouin zone.

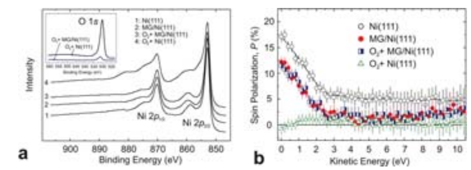

Fig.2. (a) Ni 2*p* core-level spectra of Ni(111), graphene/Ni(111), and systems obtained after exposure of the respective surfaces to oxygen. The inset shows O 1*s* XPS spectra obtained after exposure of Ni(111) and graphene/Ni(111) surfaces to large amounts of oxygen, respectively. (b) Spin-polarization of secondary electrons from Ni(111) (open circles), graphene/Ni(111) (filled circles), O_2+graphene/Ni(111) (half-filled squares), and O_2+Ni(111) (open triangles) systems after excitation with Al*K*α radiation.

Epitaxial growth of SrM(00*l*) film on Au(111).

A. Kaewrawang, G. Ishida, X. Liu, A. Morisako
Information Engineering, Shinshu University, Nagano, Japan

Introduction

For the preparation of hexagonal Sr-ferrite (SrM) thin films as a high density perpendicular magnetic recording medium, perpendicular *c*-axis orientation to the film plane has been concentrated. However, the *c*-axis oriented SrM thin films can be deposited at substrate temperature over 600°C [1]. Crystallographic and magnetic properties of SrM thin films can be improved by using the appropriate substrate or underlayer [2]. For *c*-axis orientation preparation of the film, Au underlayer with (111) orientation seems to be effective for promoting *c*-axis orientation because a misfit ratio between (111) plane of fcc Au and *c*-plane of hexagonal SrM is 2.1%. In this experiment, the SrM films on Au layer with various substrate temperatures were prepared by a DC magnetron sputtering system. Their crystalline and magnetic properties of SrM thin film deposited on Au(111) underlayer have been studied.

Experiments

The preparation of SrM/Au films deposited on thermally oxidized silicon wafers was performed at the base pressure below 2×10^{-6} Torr. For the sputtering of Au underlayer film, deposition was performed in an argon pressure of 2.0 mTorr, and 7 W of sputtering power. The underlayer substrate temperature, T_u, was varied in the range from room temperature (r.t.) to 500°C. For the sputtering of SrM film, the sintered target with stoichiometric composition of $SrFe_{12}O_x$ was used. The mixture gas of Ar and O_2 with ratio of 1.8 and 0.2 mTorr, respectively, was used as sputtering gas. The substrate was heated up to 525°C and the sputtering power was 20 W. In this study the thickness of SrM and Au was 95 nm and 75 nm, respectively. The crystal structure of the films was determined by X-ray diffractometer (XRD) with Cu Kα radiation. The magnetic properties were measured by vibrating sample magnetometer (VSM).

Results and Discussion

Fig.1 shows the X-ray diffraction diagrams of the film prepared on an underlayer at various T_u. When the film has Au underlayer without heating, strong (111) peak for Au. Consequently, the presence of the strong (00*l*) peaks for SrM indicates that the film has good perpendicular orientation. For the heated underlayer film, the intensity of Au(111) line becomes weak with increasing T_u. On the contrary, Au(200) becomes strong with increasing T_u. For T_u above 500°C, there are no obvious SrM peaks. The saturation magnetization, M_s, decreases with increase of T_u as shown in Fig.2a. Fig.2b shows the dependence of perpendicular and parallel coercivity, H_c, on T_u. $H_{c\perp}$ reaches a maximum of 3.6 kOe at T_u=300°C and $H_{c\parallel}$ increases with increasing T_u after T_u above 300°C.

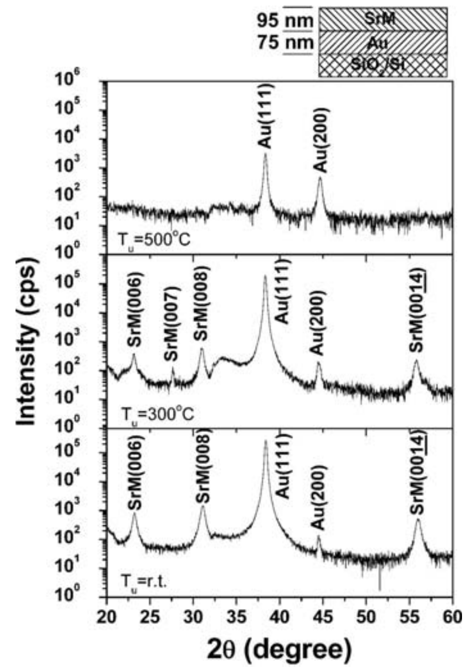

Fig. 1 XRD diagrams of SrM/Au films prepared for different T_u.

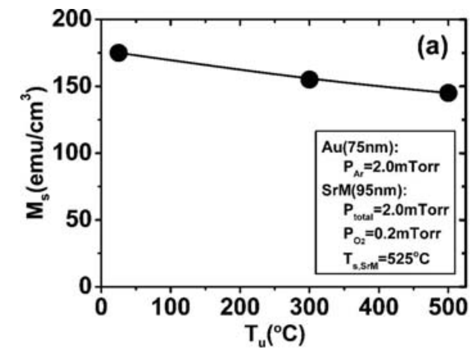

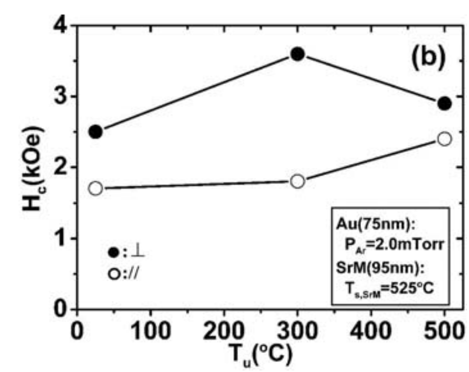

Fig. 2 (a) Dependence of M_s on T_u. (b) Dependence of H_c on T_u.

Conclusions

SrM thin films with apparent *c*-axis orientation were successfully prepared on Au(111) underlayer by epitaxial growth. The substrate temperature for Au underlayer has strongly effect on the (111) peak for Au and *c*-axis orientation for SrM which attains in the SrM films at substrate temperature for Au underlayer below 300°C.

[1] A. Morisako, et al., IEEE Trans. Magn., 33, 3100 (1997).

[2] S. Nakagawa, et al., J. Appl. Phys., 93, 8170 (2003).

DL-12

Surface characteristics of atomic-level Co-Cu thin film system : Molecular dynamics simulation.

B. Kim, K. Chae, Y. Chung
Department of Materials Science and Engineering, Hanyang University, Seoul, South Korea

1. Introduction

The understanding of thin film growth mechanism has been an essential issue to optimize device characteristics for technological application. For application in magnetic devices, ordered and uniform thin film is especially required for the coherency of the device [1]. In this paper, the growth behavior of the Co atoms on the Cu substrate for two different crystallographic orientations, (001) and (111), was extensively investigated by using molecular dynamics simulation.

Interatomic potentials were based on the Embedded Atom Method, and Zhou, et al. [2] were adopted to LAMMPS code. The size of the Cu(001) and Cu(111) substrates was (60×30×5) a_0 with the surface perpendicular to the z-axis. The temperature of substrates was isothermally maintained at 300 K. The incident energy of adatoms was set to 0.1 eV. The positions of the adatoms were randomly selected in the x, y-plane and the incident angles were set to be normal to the surface. The MD time step was fixed as 1 femto-second.

2. Results and Discussion

When the Co atoms are deposited on the Cu substrate at 300 K up to 20 monolayers (ML) with low incident energy of 0.1 eV, the tendency of growth behavior for the Co/Cu system turned out to be varied with the substrate orientation. The corresponding root-mean-square roughness W, during 20 ML deposition, was compared Co/Cu(001) with Co/Cu(111) (Fig. 1). The film roughness for the case of Co/Cu(111) was appeared to be significantly higher than the case of Co/Cu(001). The film roughness for the case of Co/Cu(111) was appeared to be significantly higher than the case of Co/Cu(001). To substantiate the differences of surface characteristics for Co films on Cu and Co surface, the net distance moved by Co adatoms from the release point in x-y plane for the deposition of 200 atoms was calculated and illustrated in Fig. 2. The degree of lateral displacement of Cu(001) and Co(001) was much less than that of Cu(111) and Co(111). Consequently, because of higher cohesive energy of Co ($E_{coh, Co}$ = 4.41 eV, $E_{coh, Cu}$ = 3.54 eV), high diffusivity of Co atoms on the Cu(111) or Co(111) substrate leads that Co atoms can be more agglomerated than the case of Cu(001) substrate.

The actual position of impact turned out to largely depend on the small distortions in the attractive potential due to the local acceleration [3] coming from the strong affinity between the Co adatom and substrate Cu atoms or between the Co adatom and surface Co atoms grown on the Cu substrate. The maximum value of locally accelerated energy of Co/Cu(001), Co/Co(001), Co/Cu(111), and Co/Co(111) was measured to be 2.3 eV, 1.9 eV, 1.6 eV, and 2.3 eV respectively. Consequently, in the initial stage of deposition for the Co/Cu(001) system, a Co adatom toward the Cu(001) substrate experiences larger locally accelerated energy than a Co adatom toward existing deposited Co atoms. When a Co adatom approaches to the vicinity of the edge between the Cu(001) substrate and deposited Co atoms, the Co adatom is affected by the steering effect caused by higher local accelerated energy from the Cu(001) substrate to fill the exposed Cu(001) substrate. Besides once a Co adatom is settled on the Cu(001) substrate, it hardly moves further due to the relatively lower diffusivity than the case of Co/Cu(111) (Fig 3(a)). On the other hand, for the Co/Cu(111) system, the behavior of approaching Co adatom seems to be steered to the deposited Co atoms. Moreover, it causes strong agglomeration of Co adatoms due to the high cohesive energy of Co atoms and the high diffusivity of Co/Cu(111). Eventually, the surface roughness of the Co/Cu(111) system increases rapidly and, consequently, the growth behavior follows the 3-D island growth mode (Fig. 3(b)).

[1] J. M. D. Teresa, et al., Science 286, 507 (1999).

[2] X. W. Zhou, et al., Phys. Rev. B 69, 144113 (2004).

[3] S.-P. Kim, et al., J. Korean Phys. Soc. 44, 18 (2004).

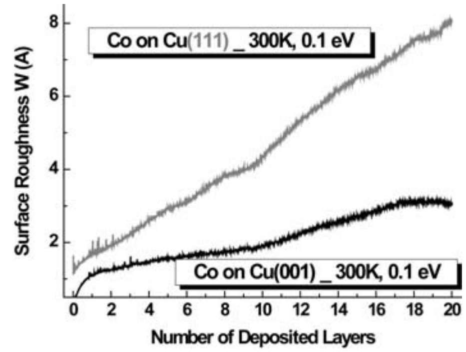

Fig. 1. Observed surface roughness of Co/Cu(001) and Co/Cu(111) during the deposition process.

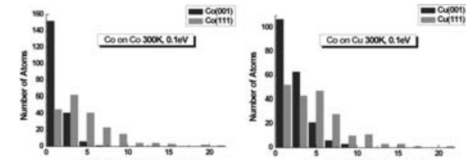

Fig. 2. Lateral displacement of Co adatom on (a) Co substrate, (b) Cu substrate with incident energy of 0.1 eV at 300 K.

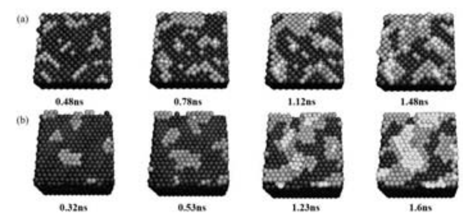

Fig. 3. Snapshots of surface morphology evolution during 1ML deposition; (a) Co on Cu(001) and (b) Co on Cu(111). A specific area was sampled for the illustration purpose. (Color legend: black for Cu, gray for Co in 1st layer, and white for Co in 2nd layer atoms)

Measurement of interface pinning at a metallic ferromagnetic thin film interface using inductive magnetometry.

K. J. Kennewell[1], M. Ali[2], M. Kostylev[1], D. Greig[2], B. J. Hickey[2], R. L. Stamps[1]
1. School of Physics, University of Western Australia, Crawley, WA, Australia; 2. Department of Physics & Astronomy, University of Leeds, Leeds, United Kingdom

Exchange pinning across a ferromagnetic interface has been studied using inductive magnetometry with frequencies up to 15 GHz in magnetic fields up to 4 kOe [1]. Two systems are reported. The first system is a Py/Co bi-layer where the magnetization in both films is assumed to lie in plane. These samples consist of permalloy films with thicknesses between 50 and 80nm directly coupled to Cobalt films with thicknesses between 0 and 5 nm. Secondly a Pt/Co multilayer with a strong out of plane anisotropy is coupled to a permalloy film through a thin Cu spacer layer. These samples have similar permalloy thicknesses as the first system with the Cu spacer layer varying in thickness from 0 to 4nm. All films were grown using DC magnetron sputtering on Si [100] substrates.
The resonant response at fixed frequency was determined by varying an externally applied magnetic field. Multiple peaks were obtained indicating excitation of standing spin wave modes in the bilayer geometry. The frequency of these high order spin wave modes were measured and values for interface induced pinning determined using a dipole-exchange theory for strip-line excitation of standing spin-wave modes (SSWM) [2]. The exchange mode frequencies are strongly dependent on film thickness and interface pinning from the Co layer. We show how this technique can provide sensitive estimates of interlayer exchange coupling and pinning parameters by exciting standing spin wave modes across the film thickness.
Shown in Figure 1 is a plot of the frequency versus field response of a single Py film where both the fundamental mode and the first exchange mode are observed. In the same figure it can be seen that in a Py/Co bilayer, two extra higher order exchange modes are also observed. The addition of Co to the Py film results in an asymmetrical excitation through the thickness of the film. This gives a nett magnetization which can be measured by the inductive technique. Interestingly, the intensities of these modes were found to vary dramatically with frequency as shown in Figure 2. Similar trends in intensity can be seen in our theory when the film is modelled with a weak interlayer coupling between the Py and Cobalt and a surface anisotropy present at the substrate. The surface anisotropy provides the necessary asymmetry to observe the first SSWM observed in the both the single and bilayer film. At higher frequencies the first SSWM of the Py overlaps the fundamental mode of the Cobalt. The weak interlayer coupling has the Py driving the Co increasing the observed intensity.
This work was supported by the Australian Research Council and the EPSRC.

[1] K. J. Kennewell, D. C. Crew, M. J. Lwin, R. C. Woodward, S. Prasad, and R. L. Stamps, Surface Science 601, 5766(2007)

[2] K. J. Kennewell, M. Kostylev, and R. L. Stamps, J. Appl. Phys., 101, 09D107 (2007)

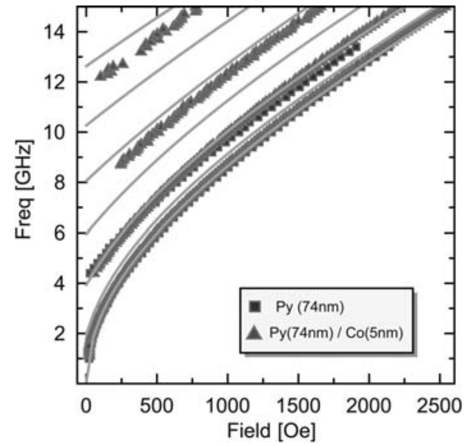

FIG 1: Measured resonance modes as a function of field for a Py single layer and Py/Co bilayer film. Two new modes are observed with the addition of Cobalt. Solid lines are calculated modes for a single Py layer for comparison.

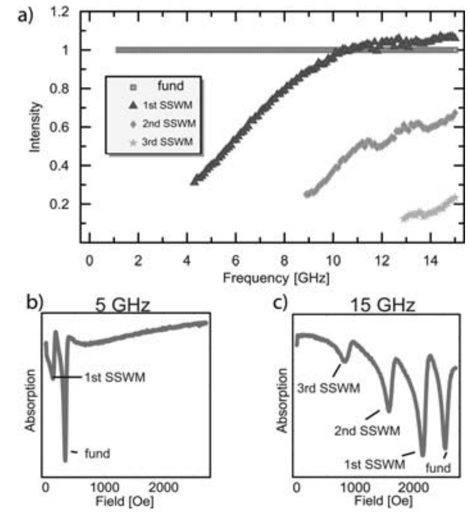

FIG 2: a) Intensities of all modes observed in the Py/Co bilayer normalized to the fundamental mode as a function of resonant frequency. As the frequency is increased the SSWM amplitudes increase relative to the fundamental. b) & c) Field sweep absorption curves at 5 and 15GHz from which the intensities in (a) were retrieved.

DL-14

Study of the magnetic properties of MnAs thin films as a function of the film thickness.

J. Milano[1,2], L. B. Steren[1,2], A. Repetto Llamazares[2], V. Garcia[3], M. Marangolo[3], M. Eddrief[3], V. H. Etgens[3]
1. CNEA-CONICET, San Carlos de Bariloche, Argentina; 2. Instituto Balseiro, UNCuyo, San Carlos de Bariloche, Argentina; 3. Institut des NanoSciences de Paris, INSP, Université Pierre et Marie Curie-Paris 6, Université Denis Diderot-Paris 7, CNRS UMR 7588, París, France

Since the earlier studies of MnAs epilayers grown over a GaAs substrates, the coexistence of two magneto-structural phases in a finite temperature range has been one of the most interesting topic of research. One of these phases is ferromagnetic (α phase) and the other one is non-magnetic (β phase). The bulk compound does not show such phase coexistence; on the contrary, it presents a magneto-structural first-order transition at 313 K from the low temperature α phase to the β one above this temperature [1]. In this contribution, we present results which were obtained for MnAs epilayers grown on GaAs(100). We have focused on the magnetization behavior as a function of temperature and the film thickness.
MnAs epilayers were grown by molecular beam epitaxy (MBE) as described in Ref. [2]. MnAs thin films of 66, 100 and 200 nm thick were grown on (100) GaAs substrates (with As termination), named M100-66, M100-100 and M100-200 respectively. The magnetometric curves were obtained through a SQUID magnetometer and the FMR ones were performed at $\nu \approx 9.45$ GHz (X-band) with the applied magnetic field perpendicular to the film surface.
In Fig. 1 we display the M vs. T curves for the three films and, for the powder sample which was taken as a reference of the bulk behavior. In that figure we can observe that all the films show a smoother loss of magnetization than the reference bulk. This behavior is the expected for the films that present the phase coexistence. However, among the studied films, the behavior is not exactly the same, i.e., for increasing thickness the transition becomes sharper as shown in Fig. 1. Then, the magnetization curve for the M100-200 sample is the most similar to the reference bulk.
In Fig. 2 we present the spectra obtained at different temperatures by FMR for the M100-200 sample. From that figure, we observe that all spectra have a complex structure. At 120 K, we can observe only a very wide mode. At 260 K, we can distinguish two modes, i.e., at higher fields the corresponding to the α phase and, at low fields, a wide mode that arises from the effect of the very small β phase regions [3] that remain within the α phase even at very low temperature [4]. At room temperature the low-field mode becomes narrower and better defined. For temperature greater than 303 K the two modes merge in only one.
By comparison with the FMR spectra shown in Ref. [3] of the M100-66 sample, in which the merging of the two mode occurs at 278 K, we can conclude that the FMR experiments present a similiar behavior to the SQUID measurement; it means that the magnetic transition temperature for thicker films are closer to the bulk one.
Summarizing, we have shown that the magnetic transition temperatures for increasing film thickness are closer to the bulk one. However, the magnetic anomalies, which are related with the presence of β phase regions at very low temperature, are present even for the thickest sample studied.

[1] L. Däweritz, Rep. Prog. Phys. 69, 2581 (2006).

[2] L. B. Steren, et al., Phys. Rev. B 74, 144402 (2006).

[3] A. Ney, et al., Phys. Rev. B 69, 081306(R) (2004).

[4] J. Milano, et al., Appl. Phys. Lett., in press.

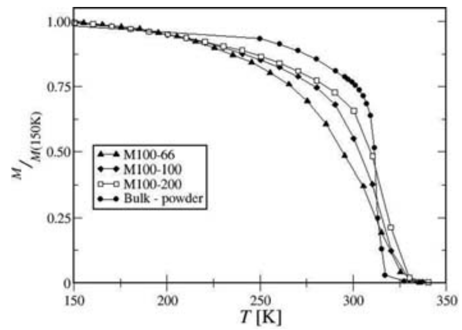

M vs. T curves for the three samples studied and for the powder taken as reference. The applied field during the film measurements was 1.5 T and 4 T for the reference bulk ones.

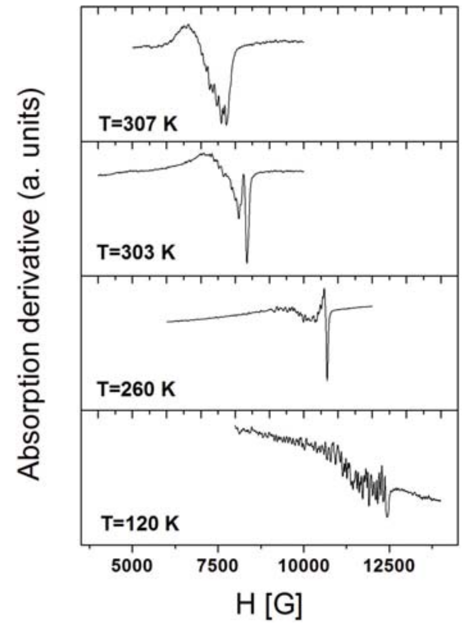

FMR spectra for the M100-200 sample at different temperatures. The magnetic field is applied perpendicular to the film surface.

DL-15

Fe-doping Effect on Morphologic and Magnetotransport Properties of La2/3Ca1/3Fe1-yMnyO3 thin films.

O. L. Arnache Olmos[1], A. Hoffmann[2], D. A. Giratá[1], M. E. Gomez[3]

1. Instituto de Física, Universidad de Antioquia, Medellín, Colombia; 2. Materials Science Division, Argonne National Laboratory, Argonne, IL; 3. Department of Phisics, Universidad del Valle, Cali, Colombia

In this work we have performed magnetotransport measurements as a function of temperature of La2/3Ca1/3Fe1-yMnyO3 (y = 0, 0.01 and 0.03) thin films, that present different morphologies depending on the 57Fe-concentration and the substrates. The morphology was studied by atomic force microscopy (AFM) at room temperature in air and the mean grain size were obtained. A series of thin films growth by dc magnetron sputtering on LaAlO3 (LAO) and SrTiO3 (STO) single crystal substrate at high O2- pressure (500mTorr), have been used as samples, with thickness between 50 and 80nm.

AFM images of the films shown a surface smoothing effect was noticed for undoped sample (rms between 1 and 3 nm), and a direct grain size (15 - 65nm) dependency regarding to Fe concentration was observed on doped films in both substrate. The films consists of numerous grains of rather rounded shape (see Fig. 1). This rounding effect is more pronounced in the 3% Fe doped sample on STO. During the Fe doping increase, the size and shape of the grains are changing (see Fig. 2).

On the other hand, the results of the magnetoresistance (MR) of LCMO, LCMFO-1% and LCMFO-3% films on STO and LAO, presented an increase of the MR in Fe doped samples regarding to the biggest Fe concentration and grain size (see Fig. 3). Probably, this increasing should be due to the fact that close to Curie temperature, the connectivity between grain, the disorder of spins and Fe doping effect at the grain surface, produces a significant increase of the resistance, but when a magnetic field is applied, this one suppresses the magnetic disorder causing in this way a decrease in the resistance, thus it is contributed that the MR reaches high values close to the transition metal-insulator temperature.

The maximum MR is still very sensitive to the substrate, even for the highest doping or grain size, although all magnetic properties are essentially similar. The maximum MR for the 3% sample is almost twice as high for sample grown on LAO compared to sample grown on STO.

In summary, we observed a direct grain size dependency and magnetoresistance vary non-monotonically with increasing of Fe concentration. This behavior can be understood in terms of competing influences from the strain relaxation, which enhance the tendency to order ferromagnetically, and reduce the double-exchange interaction.

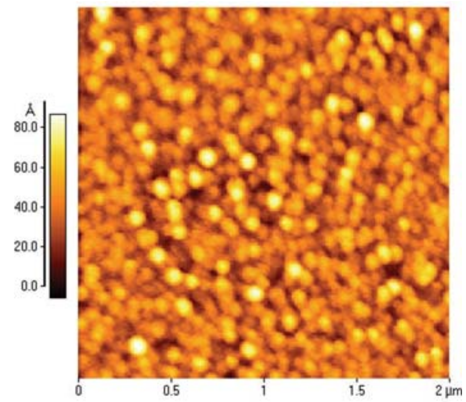

Fig. 1(a). AFM images of LCMFO-3% / LAO thin films

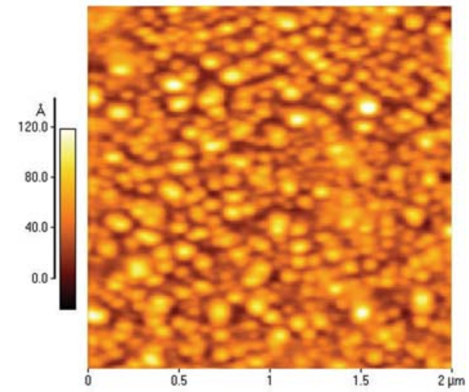

Fig. 1(b). AFM images of LCMFO-3% / STO thin films.

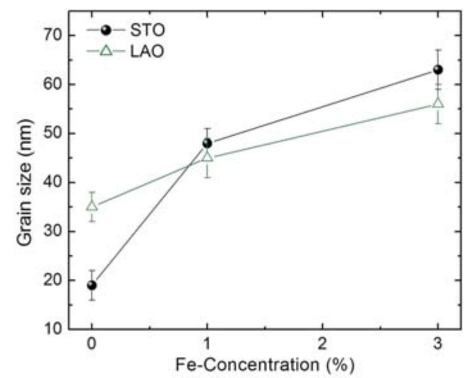

Fig. 2. Grain size as a function of Fe concentration of thin films on STO and LAO substrates.

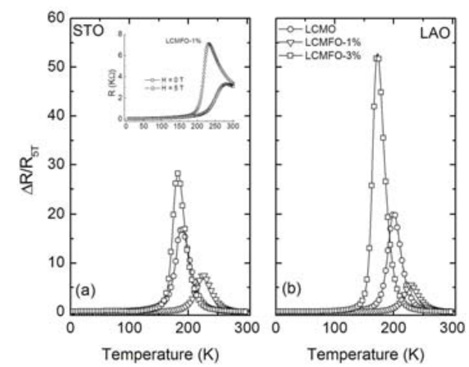

Fig. 3. Magnetoresistance (ΔR/R5T = [R(H=0)-R(H=5T)]/R(H=5T)) as a function of temperature for LCMO, LCMFO-1% and LCMFO-3% thin films grown on (a) STO and (b) LAO substrate.

DM-01

A study on surface magneto-optical Kerr effect of ultra thin Fe films on various GaAs substrates.

W. Guan, T. Shen, G. Jones
Joule Physics Laboratory, University of Salford, Salford, United Kingdom

Ferromagnetic thin films on semiconductors have attracted a lot of interest in recent years due to the potential applications in spin-based devices, such as spin-LED and MRAM and many more [1]. Amongst these ferromagnetic hybrid systems, although Fe on singular GaAs (001) has been relatively well studied [2], there is still a lot of work needs to be done to study Fe's behavior on other substrates. Ferromagnetic thin films' magnetic characterizations show clear substrate dependence [2,3], therefore we carry out the detailed study of the magnetic properties of Fe thin film on different GaAs substrates.

Ultrathin Fe films were epitaxially grown on various GaAs substrates. Apart from singular GaAs (001), three types of substrates were used, which were GaAs (311)B, vicinal (001) GaAs substrates with a 3 degree and 6 degree offcut angle towards the [111]A direction. All the substrates consist of a 500 nm n+ Si doped (2.0x10^18 cm^-3) GaAs epitaxial layer on an n+ GaAs substrate. Upon this epitaxial layer is a 350 nm undoped GaAs epitaxial layer, which was subsequently capped with a 1 nm of amorphous As as a protective layer. After decapping the As protective layer, Fe films were deposited at room temperature onto the GaAs substrates. The pressure during deposition was better than 4x10^-10 mbar. In order to compare the contribution to Fe films' magnetic properties that are more likely to be affected by the substrate, the thickness of Fe layer was kept to 7nm. The magneto-optical Kerr effect (MOKE) has been used to investigate the magnetic properties of ultra thin Fe films. Using our newly developed dual photoelastic modulator system [4], all MOKE measurements were carried out at room temperature in the longitudinal geometry.

The coercivity of Fe film on singular GaAs (001) substrate is 40 Oe. However from Figure 1b and 2b, which are the Kerr ellipticity of Fe on 3 degree and 6 degree offcut GaAs respectively, the coercivities are both about 32 Oe, and the one on 6 degree offcut substrate may be slightly bigger compared to that on the 3 degree offcut substrate. From Figure 3b, the coercivity of Fe on GaAs (311)B is only about 20Oe, which is much less than those of the films on singular and vicinal GaAs (001) substrates. The results indicate a clear substrate dependence for the in-plane magnetic property of Fe films.

The ultrathin Fe films epitaxially grown on singular GaAs (001) substrate have been observed to exhibit a remarkable in-plane uniaxial magnetic anisotropy (UMA) with the easy axis along the [110] direction and hard axis along the [1-10] direction - this result is basically in agreement with the finding of Gester et al [5]. As to the films on vicinal (001) GaAs substrates, we observed similar UMA, but unlike the singular substrate, we have not found the cubic magnetic behaviour of Fe on vicinal GaAs substrates. As the hysteresis loops along [100] and [010] directions have same coercivities as in [110] direction, this finding suggests that Fe on vicinal GaAs is dominated by the uniaxial magnetic anisotropy with the easy axis along the [110] direction superimposed on a cubic anisotropy with easy axes along [100] and [010] directions. For Fe on GaAs (311)B, it is clear to see that [0-11] direction is the hard axis. This is in agreement with the findings of Muduli et al [6] on (311)A GaAs substrate. But unlike (311)A GaAs substrate, it is not so obvious that [-233] direction is the easy axis. The magnetic anisotropy of Fe on this substrate seems to be the combination of a UMA with easy axis along [-233] direction and a four-fold magnetic anisotropy with the easy axes toward the [-130] and [10-3] directions. The asymmetric hysteresis loops alone hard axes (Figure 1a, 2a, 3a) can be explained by a 'mixing-in' of the transverse magnetisation contribution to the longitudinal measurement based on the second order magneto-optical effect, i.e. Voigt effect [7].

1.Wolf, S.A., et al., Science, 2001. 294(5546): p. 1488-1495.

2.Wastlbauer, G. and J.A.C. Bland, Advances in Physics, 2005. 54(2): p. 137-219.

3.Haque, S.A., et al., Physica B, 2001. 305(2): p. 121-126.

4.W. Guan, et al., J. Appl. Phys., 2008 (forthcoming).

5.M. Gester, et al., Thin Solid Films 1996. 275: p. 91.

6.P. K. Muduli, et al., J. Appl. Phys. 2005. 97: p. 123904

7.K. Postava, et al., Journal of Magnetism and Magnetic Materials, 1997. 172: p. 199

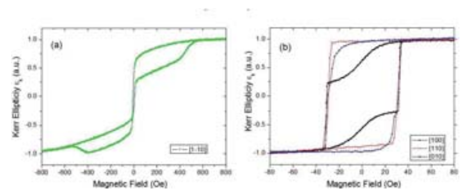

Figure 1: The Kerr ellipticity hysteresis loops of 7nm Fe on 3 degree offcut GaAs (001).

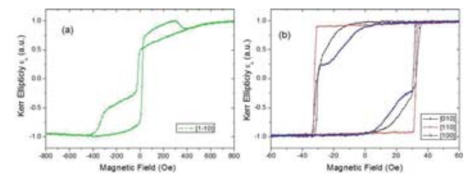

Figure 2:The Kerr ellipticity hysteresis loops of 7nm Fe on 6 degree offcut GaAs (001) along four major orientations.

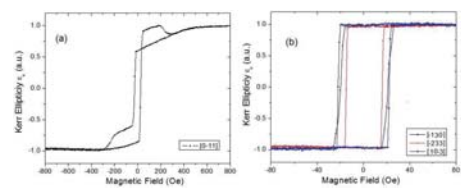

Figure 3: The in-plane ellipticity hysteresis loops of 7nm Fe on (311)B GaAs substrate along four major orientations.

DM-02

Composite oxide buffer layers for (002) Fe/MgO/Fe magnetic tunneling junctions.

H. Huang, P. Huang, C. Lai
Department of Materials Science and Engineering, National Tsing Hua University, Hsinchu, Taiwan

Recently, MgO-based magnetic tunneling junctions (MTJs) have been studied extensively due to the high tunneling magnetoresistance ratio (TMR ratio) of the fully epitaxial or highly textured (002) Fe/MgO/Fe MTJs [1], [2]. In this study, we proposed new composite oxide buffer layers (ZnO/MgO) with very thin thicknesses grown on Si/SiO_2 substrates rather than using expensive MgO single crystal substrates for the growth of (002) Fe/MgO/Fe structure. Furthermore, we introduced Cr as the bottom electrode. With the proper buffer layer thicknesses, a good Cr (002) crystal structure can be obtained and used as the structure template for the growth of (002) Fe/MgO/Fe structure due to the small lattice mismatch between Fe and Cr. The structural and magnetic properties of the top-type MgO (002)-based MTJs are discussed.

All samples in this study were fabricated by using an ion beam deposition (IBD) system. Buffer layers composed of ZnO and MgO were first grown on Si/SiO_2 substrates at room temperature. The crystal structures of the composite buffer layers were strongly dependent on the thicknesses of both ZnO and MgO. The XRD patterns of Si/SiO_2//ZnO x/MgO y/Fe 30/Ta 5 (nm) were shown in Fig. 1. Fe (110) and Fe (002) were both observed when the thicknesses of ZnO and MgO were relatively thick. As both thicknesses of ZnO and MgO were decreased to 2.5 nm, only Fe (002) was observed in the XRD patterns. Furthermore, the diffraction peak intensity of Fe (002) dramatically decreased when only 2.5 nm MgO was deposited as the buffer layer without any ZnO layer. When only ZnO of 2.5 nm was used as the buffer layer, Fe (110) would be the only diffraction peak observed. These results indicated that the existence of thin ZnO layer in the composite buffer layers was indeed very crucial for the growth of (002) MgO/Fe structure. Thinner ZnO layer exhibited better capability for the growth of MgO (002) layer, which might imply that the interface effects play an important role in the growth mechanism.

To integrate the ZnO/MgO composite buffer layers into devices, we introduced Cr as the bottom electrode due to its comparable electrical resistivity to that of Ta and the small lattice mismatch between Fe and Cr. All MTJ samples were deposited under a magnetic field of 100 Oe. The samples were then field-annealed at 250 ^{o}C for an hour under a magnetic field of 1500 Oe. The XRD patterns of Si/SiO_2//ZnO 2.5/MgO 2.5/Cr 30/Fe 3/MgO 2/Fe 3/IrMn 10/Ta 5 (nm) were shown in Fig. 2. The diffraction peak of IrMn (002) was observed, which implied that the (002)-oriented Fe/MgO/Fe trilayers were successfully fabricated. As shown in the insets of Fig. 2, MgO (002) diffraction peak can also be clearly observed for both the as-deposited and field-annealed samples, which indicated good crystallinity of MgO (002). After field-annealing process performed at 250 ^{o}C, enhancement of peak intensities and peak shifts toward high 2θ angles of MgO (002), IrMn (002) and Cr (002) were observed, which may result from the improvement of crystallinity and stress release. The magnetic properties of both as-deposited and field-annealed MTJ samples were shown in Fig. 3. The exchange bias fields were 225 Oe and 270 Oe for the as-deposited and field-annealed samples, respectively.

In summary, MgO-based MTJ samples with a strong (002) texture were successfully fabricated with the thin ZnO/MgO composite buffer layers. The Cr bottom electrode was introduced to keep (002) orientation and a top spin-valve (002) MTJ was obtained.

[1] J. Faure-Vincent et al., Appl. Phys. Lett. 82, 4507 (2003).

[2] S. Yuasa et al., Nat. Mater. 3, 868 (2004).

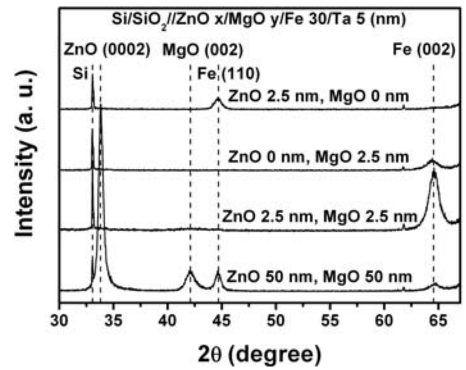

Fig. 1 The XRD patterns of Si/SiO_2//ZnO x/MgO y/Fe 30/Ta 5 (nm).

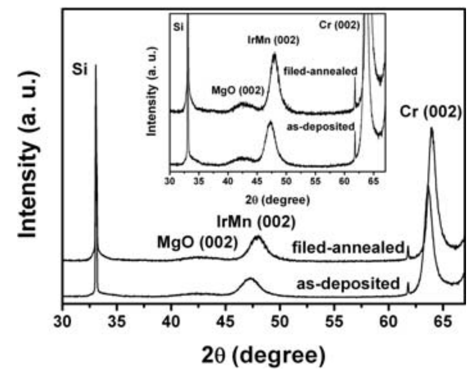

Fig. 2 The XRD patterns of Si/SiO_2//ZnO 2.5/MgO 2.5/Cr 30/Fe 3/MgO 2/Fe 3/IrMn 10/Ta 5 (nm). The insets show the enlarge patterns.

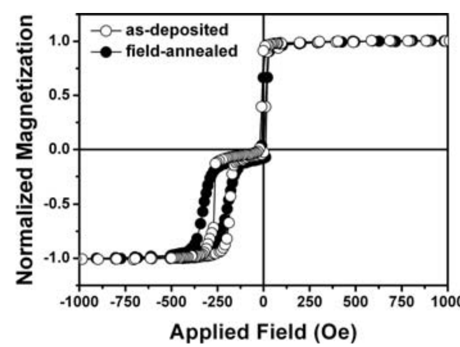

Fig. 3 The hysteresis loops of Si/SiO_2//ZnO 2.5/MgO 2.5/Cr 30/Fe 3/MgO 2/Fe 3/IrMn 10/Ta 5 (nm).

DM-03

Stripe magnetic domains in sputtered permalloy films.

D. Hrabovský[1], M. Rubio-Roy[2], J. Caicedo-Roque[1], E. Bertan[2], J. Fontcuberta[1]
1. ICMAB - CSIC, Bellaterra, Spain; 2. FAO, University of Barcelona, Barcelona, Spain

<p>Permalloy (Py) alloy (Ni_xFe_{100-x}) with Ni content of about 78 - 82 percent is prototype of soft magnetic material. Most studied Py films are those with x ≈ 81 because of the almost-zero magnetostriction and negligible magnetic anisotropy [1]. However, Ni rich films (x > 81%) quite commonly exhibit a weak perpendicular anisotropy, which originates from the film internal tensile stress [2] combined with a negative magnetostriction. A remarkable property of these films is that above a critical thickness (t_{cr}) the in-plane magnetization loops display characteristic features like increased coercivity and steeped magnetization curve [3]. These changes reflect the appearance of a dense stripe domain pattern in the film plane [4, 5] which originates from competition between the shape anisotropy, weak perpendicular anisotropy, and domain wall energy. However domains width observed by Saito [5] is $w \sim t^{1/2}$ (for $t > t_{cr}$) contrary to his model which predict $t^{1/3}$ (for $t > t_{cr}$) dependence on film thickness. Although there are numerous studies of this stripe domain structure, there are only few focused on the dependence of domains width in function of the film thickness - particularly in sputtered films [6].
Here we report on the characterization of permalloy films displaying a weak perpendicular anisotropy deposited by RF sputtering. We have grown series of Py films on Corning glass using a target of nominal composition $Ni_{81}Fe_{19}$ at various RF power and Ar partial pressures. Here we present films grown at 50 W of RF power and 0.05 Pa of Ar pressure. Films with thickness (t) ranging from 6.8 to 400 nm have been grown by varying the deposition time. Film thickness was determined from low-angle X-ray reflectometry experiments and estimated average growth rate of 6.7 nm/min. We have used X-ray photoemission spectroscopy (XPS) to verify that the metal stoichiometry of films matches that of target. The intensity ratio of 3p-Fe and 2p-Ni photoelectric peaks, after Shirley background subtraction, allowed to determine a Ni:Fe concentration of 81.2±0.3 : 18.8±0.3 which is closely coincident with that of the target.
Magnetization loops measurements were done at room temperature by magnetooptic Kerr setup (MOKE). Longitudinal MOKE loops (with magnetic field applied in-plane of the sample) were recorded for various sample orientations in order to identify the in-plane anisotropy. Polar MOKE loops (with field applied perpendicular to the sample surface) were also recorded.
In-plane magnetization loops of thinner films (t<100nm) displays a well defined uniaxial anisotropy (Fig. 1a) with a clear - square shaped - hysteresis loop along one (in-plane) direction and a closed loop along a perpendicular (in-plane) direction. In contrast, thicker films (t>200 nm) display magnetization loops identical in each in-plane direction (Fig. 1b). This property is an indication of stripe domain structure and therefore the existence of a weak perpendicular anisotropy. The critical thickness t_{cr} for appearing of stripe domains should be between 100 and 200 nm.
In the figure 2 we show MFM images of corresponding films. There is no visible domain structure on the 59 nm sample (Fig. 2 left) thus confirming that magnetization lies basically in the film plane. In contrast, the stripe pattern is well visible in the 200 nm film (Fig. 2 right) reflecting the occurrence of an out-of-plane magnetic anisotropy. Thicker films show similar properties with larger stripes and stronger magnetic contrast. This correlates with both the domain size and the strength of the out-of-plane anisotropy of the films.
We found that the domain width is closely proportional to $t^{1/2}$ as found by Saito [5]. In the following we will compare this result with existing models for stripe domains formation and we will discuss the possible effect of variation of internal film stress with film thickness.

<p>[1] E. Klokholm, J.A. Aboaf, J. Appl. Phys. 52, 2474 (1981)

[2] M.M. Yang and J.A. Aboaf, J. Appl.Phys. 66, 3734 (1989)

[3] E.E. Huber Jr., D.O. Smith, J. Appl. Phys. 30, S267 (1959)

[4] R.J. Spain, Appl. Phys. Letters 3, 208 (1963)

[5] N. Saito, H. Fujiwara, Y. Sugita, J. of the Phys. Soc. of Japan, vol 19, 1116 (1964)

[6] J. Ben Youssef, N. Vukadinovic, D. Billet and M. Labrune, Phys. Rev. B69, 174402 (2004)

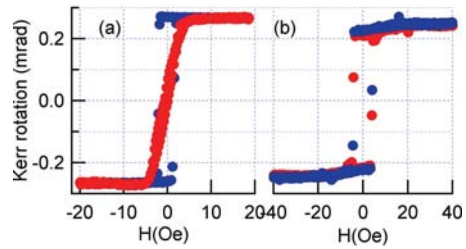

In-plane magnetization loops measured by MOKE in two perpendicular directions - a) 59 nm film b) 200 nm film

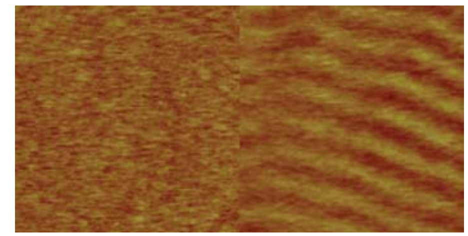

Magnetic domains structure observed by MFM - left 59 nm film, right 200 nm film. Vertical scale is 2.5 µm.

DM-04

Influence of capping layers on magnetic anisotropy in Fe/MgO/GaAs(100) ultrathin films.

P. Wong[1], W. Zhang[1], Y. Xu[1], Y. Fu[2], Z. Huang[2], Y. Zhai[2], Y. Xu[3], H. Zhai[3], S. M. Thompson[4]
1. Spintronics and Nanodevice Laboratory, Department of Electronics, University of York, York, United Kingdom; 2. Department of Physics, Southeast University, Nanjing, China; 3. Center for Materials Analysis, Nanjing University, Nanjing, China; 4. Department of Physics, University of York, York, United Kingdom

The effects of two different nonmagnetic covering layers, Au and MgO, on the magnetic anisotropy of epitaxial Fe on GaAs(100) with an epitaxial MgO interlayer grown by molecular beam epitaxy (MBE) have been studied by ferromagnetic resonance (FMR) and magneto-optic Kerr effect (MOKE). GaAs(100) substrates preparation prior to sample growth can be found elsewhere [1]. Growth of the films and their structural characterization were done by *in-situ* reflection high-energy electron diffraction (RHEED) and a crystal monitor calibrated with ex-situ atomic force microscopy (AFM). The substrate was annealed at 780 K for 45 mins until a sharp (1 x 1) reconstructed GaAs surface was identified. The MgO layer was then grown by e-beam evaporation at a rate of 2 Å/min, while the substrates were kept at 673 K. Then epitaxial Fe film with thickness t_{Fe} ranging from 7.1 to 42 ML, was grown at the same rate as that of MgO at room temperature (RT). The RHEED images of the 3 nm MgO layer epitaxially grown on the GaAs(100) were streaky with several elongated spots indicating the presence of some small crystalline islands on the smooth surface of the MgO film. This could be explained by the fact that there is a large lattice mismatch (25.5%) between GaAs and MgO with an epitaxial relationship of MgO(100)[001]//GaAs(100)[001]. This is consistent with the findings from other groups [2-4]. It also suggests a cube-on-cube orientation of MgO on GaAs. A 45° rotation of the epitaxial Fe lattice cell was identified respect to the MgO lattice giving a small mismatch of 3.8% and an epitaxial relationship, Fe(100)[011]//MgO(100)[001]. Before removing the samples from the chamber for *ex-situ* measurements, the samples were capped with either 3 nm Au or MgO epitaxially grown at RT.

The magnetic hysteresis loops, as shown in figure 1, for Au capped samples show that the uniaxial anisotropy dominates for the thicknesses from 7.1 to 21 ML. The MgO capped samples, however, exhibit strong cubic anisotropy with a weak contribution from the uniaxial anisotropy term. This is consistent with the FMR data with theoretical fitted curves derived from Landau-Lifshitz equation without damping. There are two interesting results found in this study. 1) The uniaxial anisotropy was still present with the MgO interlayer and Au capping layer. It is generally believed that the uniaxial anisotropy observed in the Fe/GaAs system comes from the Fe-GaAs interface. We would suggest that the presence of an overlayer might actually alter the electronic properties of the Fe film such that the spatial distribution and orientation of its bonding orbitals at the interfaces are changed, as suggested by Mc Phail *et al* [5]. 2) The MgO cover layer appears to suppress the uniaxial anisotropy in a more pronounced way than the Au cap. This might be accounted by the fact that the two different cover layers induced and provided different surface roughness and wetting effect which need to be further studied. The FMR experimental data also shows that the magnitude of the in-plane anisotropy varies with t_{Fe} for both series with the in-plane four-fold cubic anisotropy a more dominant term than the uniaxial one. As t_{Fe} increases from 7.1 to 42 ML, the data obtained from the FMR alongside with the MOKE observations confirms that the global easy axes slowly rotated to align with <011> for all the samples studied.

[1] Y. X. Lu, J. S. Claydon, Y. B. Xu, S. M. Thompson, K. Wilson and G. v. d. Laan, Phys. Rev. B 70, 233304 (2004).

[2] C. Martinez Boubeta, E. Navarro, A. Cebollada, F. Briones, F. Peiro and A. Cornet, J. Crystal Growth 226, 223 (2001).

[3] K. Nashimoto, D. K. Fork, T. H. Geballe, Appl. Phys. Lett. 60, 1199 (1992).

[4] W. Y. Hsu and R. Raj, Appl. Phys. Lett. 60, 3105 (1992).

[5] S. Mc. Phail, C. M. Gurtler, F. Montaigne, Y. B. Xu, M. Tselepi, and J. A. C. Bland, Phys. Rev. B 67, 024409 (2003).

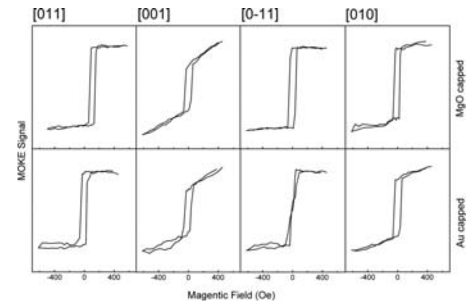

Figure 1, Hysteresis loops of 21ML Fe/MgO/GaAs(100) capped with either Au or MgO along the major axes of GaAs(100). The magnetic field range was from -700 to 700 Oe.

DM-05

Calculation of resonant standing spin wave mode response induced by a coplanar stripline.

K. J. Kennewell, M. Kostylev, R. L. Stamps
School of Physics, University of Western Australia, Crawley, WA, Australia

Planar waveguide inductive resonance methods are emerging as a common tool in the study of high frequency properties of metallic ferromagnetic films and multilayers [1-3]. The geometry and method of spinwave excitation in this technique are very different from that used in resonant cavity experiments, and correct interpretation of results requires an analysis which takes into account a number of features associated with the use of strip-line microwave experiments. We present a theory for resonance modes in ferromagnetic bilayers measured by a broadband inductive technique in a coplanar waveguide geometry. The effects of finite conductivity of the magnetic sample and the screening action of the coplanar ground-planes on the spin wave dispersion are included. The theory also includes contributions to the measured response from finite wavelength spin waves excited in this geometry.
Magnetostatic contributions to the spin wave frequencies in the planar waveguide geometry are described by a Green's function technique [4]. We derive a Green's function of the magnetic field of a spin wave for an arbitrary in-plane wave number which includes dipole and eddy current contributions. Exchange energy contributions to the spin wave modes are included with appropriate boundary conditions describing pinning at free surfaces and interfaces [5]. We derive a system of integro-differential equations which accounts for dipole and exchange coupling of the layers and the field screening by the metal of the coplanar line. Numerical solution of the equations results in a spectrum of acoustical, optical and higher-order modes and their eventual splitting.
Our theory is applicable to dipole exchange spin waves in single and bilayered ferromagnetic films with uniaxial magnetocrystalline anisotropies, and interlayer exchange interactions. Figure 1 shows a calculated response for a typical Py thin film 100nm thick for different pinning levels due to a surface anisotropy at one surface. It can be seen that the fundamental mode does not change drastically in frequency as a function of surface pinning. As pinning increases, higher order standing spinwave modes appear. These higher order modes require an asymmetry created by the pinning to give a nett measurable magnetization. It is also seen that the frequency of these modes is dependent on the pinning parameter. This dependence makes the model particularly useful for extracting quantitative pinning values for microwave frequency excitations in thin ferromagnetic films and multilayers.
Figure 2 demonstrates both the effects of sample conductivity and of the coplanar waveguide ground planes on wavevector dispersion in the film. It can be seen if the sample is excited with uniform resonance (k=0) then these effects disappear. However, the finite width of the coplanar transmission stripline dictates that k>0, and with narrow striplines, k can become appreciably large. The change in dispersion due to conductivity is dependent on film thickness, with ultra-thin films showing negligible change.
Support is acknowledged from ARC Discovery and Postgraduate awards.

[1] T. J. Silva, C. S. Lee, T. M. Crawford, and C. T. Rogers, J. Appl. Phys. 85, 7849 (1999)

[2] M. Covington et al., Phys. Rev. Lett. 89, 237202 (2002)

[3] G. Counil, J.-V. Kim, T. Devolder, C. Chappert, K. Shigeto, and Y. Otani, J. Appl. Phys. 95, 5646 (2004)

[4] K. J. Kennewell et al., J. Appl. Phys., 101, 09D107 (2007)

[5] R.F.Soohoo, Magnetic Thin Films (Harper & Row, New York, 1965)

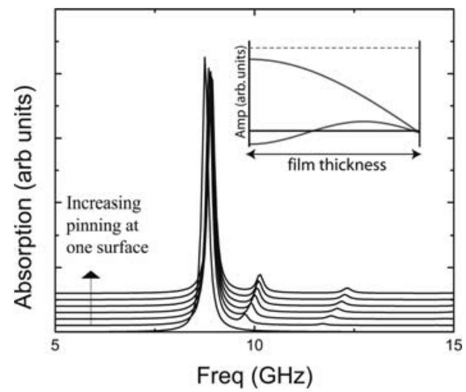

FIG 1: Absorption as a function of frequency calculated for 100nm Py film at a constant applied field of 1000 Oe. Stacked plot shows results for different surface pinnings, from zero pinning to complete pinning at one surface in the direction of the arrow. The inset shows the magnetization amplitude through the thickness of the film, with zero pinning only exciting the fundamental mode shown dashed, and strong pinning exciting the fundamental and higher order modes shown as solid lines.

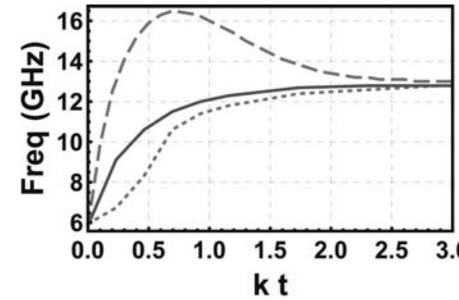

FIG 2: Dispersion in Py film 1μm thick. Solid line shows non-conductive dispersion in an isolated film for the Damon-Eshbach mode. Dotted line shows effect of including conductivity in calculation, whilst dashed line shows the effect of including the shielding effect of the coplanar ground planes.

DM-06

Ga^+ ion irradiation-induced out-of-plane magnetization in Pt/Co(3nm)/Pt films.

J. Jaworowicz[1,2], M. Kisielewski[1,2], A. Maziewski[1,2], I. Sveklo[1], J. Jamet[1], J. Ferré[1], A. Mougin[1], N. Vernier[1], J. Fassbender[3]
1. Laboratoire de Physique des Solides, Orsay, France; 2. Laboratory of Magnetism, University of Bialystok, Bialystok, Poland; 3. Institute of Ion Beam Physics and Materials Research, Forschungszentrum Dresden-Rossendorf, Dresden, Germany

Ion beam irradiation under weak or moderate fluence allows to modify and even control the magnetic properties of thin film structures [1–2]. So, this method stands now as an elegant technique for magnetic nanopatterning [3]. Moreover, irradiation at relatively high dose generates surface roughness and gives rise to surface etching, but also to a swelling effect [2].
In ultrathin film structures, ion irradiation produces essentially intermixing at interfaces. It usually reduces the Curie temperature, coercivity and anisotropy [1]. This can even induce an out-of-plane to in-plane spin reorientation transition (SRT) [2].
In this contribution we report on a new phenomenon, of a new type of in-plane to out-of-plane SRT under moderate Ga^+ irradiation, opposite to that happening usually in Pt/Co(x)/Pt films. This happens when considering a Pt(4.5nm buffer)/Co(3nm)/Pt(3.5nm overlayer) film with an in-plane easy axis, grown by sputtering on an Al_2O_3 (0001) substrate.
Limited 100 μm x 100 μm square areas were irradiated through a Cu mask by 30 keV Ga^+ ions at two different moderate doses of 0.5 x 10^{15} and 10^{15} ions/cm^2. This Cu mask was removed afterwards leaving non-irradiated zones between irradiated squares.
Topographic atomic force microscopy evidences a swelling of the film on irradiated square areas that increases with the dose, i.e. an effect similar to that found in Fe/Cr/Fe structures [2].
Polar magneto-optical Kerr (MOKE) microscopy, insensitive to an in-plane component of the magnetization, was used to reveal the spatial distribution of remnant perpendicular magnetization inside the irradiated areas and at their border (Fig. 1). The procedure was the following: a remnant MOKE image is first recorded after saturation of the sample under a large negative field. A second remnant image is obtained after submitting the sample to a positive field. The final MOKE image (Fig. 1) is deduced from the difference of the two previous ones. It shows a fine patchy domain structure with a partial perpendicular magnetization component.
More attracting is the presence of a sharp remnant highly magnetized out-of-plane ribbons at the boundary of irradiated squares (Fig. 1). The difference of images for two independent ac-demagnetized states (Fig. 2) clearly evidence the two opposite perpendicularly magnetized states in these sharp ribbon-like domains, meaning a non-reproducible reversal process in these ribbons.
Perpendicular remnant hysteresis loops of the irradiated squares and of their boundaries were deduced from remnant image snapshots recorded for increasing field values. Results are consistent with the coexistence of out-of-plane and in-plane magnetized small domains.
In ribbons at square boundaries, the magnetization reversal process occurs at a well defined coercive field value.
We will discuss about the possible origin of the ion irradiation induced out-of-plane magnetic anisotropy in Pt/Co/Pt films having an initial in-plane anisotropy. The swelling effect that relax strains into the film must give rise to an increase of the anisotropy. However strain relaxation can be non-uniform on the full square area providing the coexistence of small patches with in-plane and out-of-plane anisotropy. The presence of a rather huge perpendicular anisotropy and well defined coercivity in ribbons can also come in part from peculiar strain states at this boundary, but also from demagnetizing film limit conditions that tend to partly suppress the shape anisotropy term.

This work was partially supported by EU MC TOK project NanomagLab No MTKD-CT-2004-003177. J.J. has benefited of an EC Marie-Curie fellowship
(contract MEST CT 2004-51437).

[1] C. Chappert, H. Bernas, J. Ferré, V. Kottler, J.-P. Jamet, Y. Chen, E. Cambril, T. Devolder, F. Rousseaux, V. Mathet, H. Launois, Science 280 (1998) 1919

[2] J. Fassbender, J. McCord, J. Magn. Magn. Mat. 320 (2008) 579

[3] J. Ferré, J.-P. Jamet, in Handbook of Magnetism and Advanced Magnetic Materials, H. Kronmüller, S. Parkin (eds), (2007) John Wiley & Sons, Ltd, p 1710

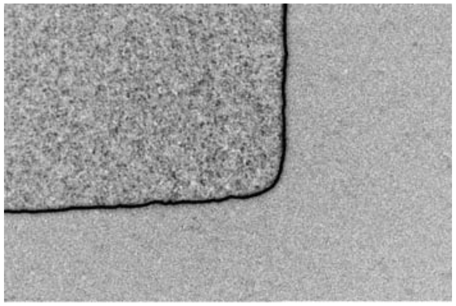

Fig.1 : Polar MOKE microscopy image obtained as the difference between the remnant image after applying a field of + 0.9 kOe and the remnant image after saturation in – 4 kOe. Size of the image is 58 μm x 39 μm.

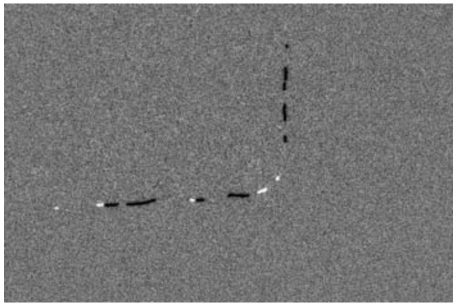

Fig.2 : Polar MOKE image, obtained from the difference between two independent ac-demagnetized states.

DM-07

Intermixing and spin-pumping effects on Gilbert damping of CoFeB.

S. Huang[1], C. Wang[1], J. Song[1], C. Lai[1], W. Chen[2], S. Yang[2], K. Shen[2], H. Bor[3]

1. Department of Materials Science and Engineering, National Tsing Hua University, Hsinchu, Taiwan; 2. Electronics Research and Service Organization, Industrial Technology Research Institute, Hsinchu, Taiwan; 3. Materials and Electro-Optics Research Division, Chuang-Shan institute of Science and Technology, Taoyoun, Taiwan

Introduction

CoFeB thin films have been widely used in MgO-based magnetic tunnel junctions (MTJs) to achieve a large tunneling magnetoresistance (TMR) ratio and low resistance-area (RA) spin-transfer devices [1]. In spin-transfer devices, how to reduce the switching current density is a challenging issue. According to the equation of intrinsic critical current density, $J_{C0}=\alpha M_S t_F(H+H_K+2\pi M_S)/\eta$ [2], J_{C0} can be tuned by altering the damping constant (α), the saturation magnetization (M_S) or effective anisotropic (H_K). In this study, we prepared CoFeB films with different capping layers and investigated the factors affecting the Gilbert damping constant.

Experiment results & discussion

The samples were fabricated in the form of half-MTJ stacks: Sub// SiO_2 /MgO (1 nm) /CoFeB (2.5 nm) /X (0-5 nm) /Ta (0-5 nm), where the capping layer X was Cu, Ag, Mg, or MgO respectively. We chose $Co_{72}Fe_8B_{20}$ as the material for the free layer due to its low magnetostriction. The damping constant (α) was obtained from the measurement of ferromagnetic resonance (FMR) by electron spin resonance (ESR) [3]. The magnetic properties were measured by vibrating sample magnetometer (VSM).

The damping constants of CoFeB with different capping layers of 5 nm are shown in Fig. 1. According to the spin-pumping theory [4], several metals such as Pt, Pd, and Ta were reported to enhance the damping constant of NiFe films when they were deposited on NiFe. In addition to spin-pumping effect, intermixing effect can be another important factor affecting the α value. To further understand how the damping constant was affected by the adjacent material, we changed the thickness of Ta (0-5 nm) and thickness of Cu and Ag in the composite capping layers (Cu/Ta (5) and Ag/Ta (5)). The dependences of M_S and damping constants of CoFeB on the capping layer thickness are shown in Fig. 2. Significant reduction of M_S was observed when the thickness of the capping layer Ta increased, which implied that the Ta capping layers caused the intermixing at the interfaces. On the other hand, the insertion of Cu and Ag effectively suppress the intermixing. Therefore, M_S increased with increasing the thickness of Cu and Ag. The damping constants showed opposite dependence on the capping layer thickness, that is, the damping constant decreased when M_S increased. These results suggest that the intermixing at the interface of CoFeB and capping layer may significantly increase the damping constants. From Fig. 2 (a), we observed almost the same trend of Ms vs. thickness of Cu and Ag, so we might expect to see the same variations of α values if the intermixing is only one dominant factor. However, the damping constants of CoFeB with the Cu/Ta capping layer are lower than those with the Ag/Ta in all thickness, as shown in Fig. 2(b). It was sufficiently indicated that the spin-pumping effect plays an important role on the damping constant in addition to the intermixing. Lower damping constants with Cu/Ta capping layers revealed that Cu exhibited a smaller spin-flip rate than Ag. Therefore, the spin electrons pumped out from CoFeB were easily accumulated at the CoFeB/Cu interface and then diffused back to CoFeB. The ferromagnetic precession can be preserved by the diffusion-back spins, which avoids the loss of angular momentum and reduces the damping constant. Consequently, the effective damping constant, α should be the summation of the intrinsic damping constant of α_0 and the spin-pumping or intermixing enhanced damping constant of α'. In summary, we can adjust α by selecting various capping layer, and take this advantage of modulate the switching current density in spin transfer devices.

[1] Zhitao Diao, M. Pakala, Alex Panchula, Y. Ding, D. Apalkov, Lien-Cang Wang, E. Chen, Y. Huai, J. Appl. Phys., 99, 08G501, 2006.

[2] Jonathan Z. Sun, Barbaros Özyilmaz, Wenyu Chen, Maxim Tsoi, Andrew D. Kent, J. Appl. Phys., 97, 10C714, 2005.

[3] Shigemi Mizukami, Y. Ando, T. Miyazaki, Jpn. J. Appl. Phys., 40, 580, 2001.

[4] Yaroslav Tserkovnyak, Arne Brataas, Gerrit E.W. Bauer, Phys. Rev. Lett., 89, 117601, 2002.

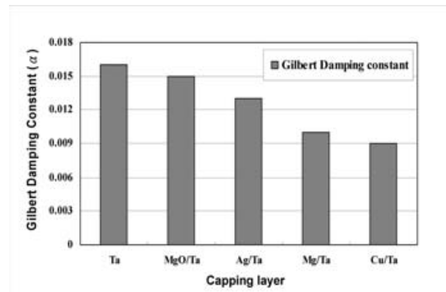

Figure 1. The Gilbert damping constant of CoFeB with different capping layer.

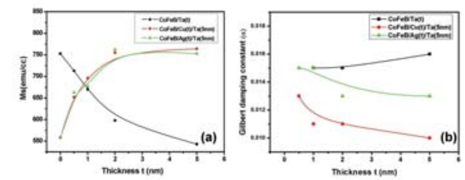

Figure 2. (a) Saturation magnetization, (b) Gilbert damping constant dependence on capping layer thickness.

DM-08

FMR Studies of $Ga_{1-x}Mn_xAs$ thin layers with x>0.1.

K. Khazen[1], M. Cubukcu[1], H. von Bardeleben[1], J. Cantin[1], S. Ohya[2,3], K. Ohno[2], M. Tanaka[2]
1. Institut des NanoSciences de Paris(INSP)Université- Paris 6, UMR 7588 au CNRS, Paris, France; 2. Electronic Engineering, The University of Tokyo, Tokyo, Japan; 3. Japan Science and Technology Agency, Kawaguchi-shi, Japan

The experimental data on the properties of ferromagnetic GaMnAs thin films doped with ≈7% of Mn are in good agreement with the Zener mean field theory [1]. This model predicts an increase of the critical temperature T_C with the magnetically active Mn concentration and the concentration of the charge carriers ($p^{1/3}$). According to this model, it should be possible to obtain a Curie temperature above 300°C by increasing the Manganese doping level to 10% and conserving a hole concentration of at least 10^{21} cm^{-3} [1].
Considering the solubility limit of Mn in the GaAs matrix, such high doping requires special growth conditions which are still a real challenge. Very recently the successful growth of such highly doped layers has been reported by Ohya et al. [2].They have also investigated the annealing procedure which avoid the formation of MnAs second phase. Nevertheless the layers did not show a significant increase in the critical temperature. This fact, considering the resistivity measurements of the annealed samples which present the samples as metallic systems, can be attributed to the existence of magnetic and charge compensating centers which are not out-diffused completely by low temperature annealing procedure [2].

In order to study in more detail the magnetic properties of such highly doped samples (15, 17 and 21%) we have performed ferromagnetic resonance measurements (FMR) on both as-grown and annealed samples and compared the results to those obtained for standard low doped samples with 7% of manganese.
From the angular variation of the resonance positions we have determined the anisotropy fields (H_i) as a function of the Mn concentration and the measuring temperature; using the relative magnetization values obtained from the intensity of the uniform mode spectrum, the magnetocrystalline constants (K_i) have been deduced from these values (fig.1). The anisotropy constants are known to vary with the strains and the hole concentration in the films. Although the low thickness (10 to 20nm) of the samples does not permit to measure the strain in the films by the XRD technique, the use of the mean field theory predictions [1,3,4] permits to separate the effect of each of these two parameters.

The numerical values of the static magnetization show that despite the magnetic homogeneity of the GaMnAs films, a large fraction of the introduced manganese ions is magnetically inactive probably due to a high concentration of interstitial Mn ions.

The hole concentration (relative) determined by a rough approximation: $T_c/x_{effective}$~$p^{1/3}$ for the annealed samples are shown in fig.1 as a function of $x_{effective}$. The three heavily doped samples show a gradual (nearly linear) increase in [p] with the effective Mn concentration. The hole concentration is nevertheless (about 4 times) higher than the one related to the reference sample with $x_{effective}$=0.043. The Curie temperatures determined from the FMR measurements are in good agreement with those reported formerly for these samples [2].

The variations of the uniaxial strain in these samples can be deduced by comparing the perpendicular uniaxial magnetocrystalline anisotropy constants (the dominant one in these structures) and the relative hole densities in each sample to those previously measured for a 7% doped reference sample (fig.1). We see that both the effective x and the strains increase at the same time. Although these results may seem normal at first glance, considering the absolute concentration values of Mn in the samples do not confirm the previous studies on the modification of the lattice parameter by the interstitial Mn ions (e.g. [5]). A more surprising aspect of the results is revealed when fitting this variation for samples with lower $x_{effective}$ (i.e. higher x) by a straight line. This line which well includes all three heavily doped samples passes by the origin point, yielding the absence of any parameter modifying the lattice constant other than the effective x.

In addition the variation of the linewidth of the FMR spectra and the Landé g-factors were studied.

[1] T. Jungwirth, REVIEWS OF MODERN PHYSICS, VOLUME 78, JULY–SEPTEMBER 2006

[2] S. Ohya et al. Appl. Phys. Lett. 90, 112503 (2007)

[3] Kh. Khazen, H. J. von Bardeleben, J. L. Cantin, L. Thevenard, L. Largeau, O. Mauguin, and A. Lemaítre, IEEE Trans. Mag., 43, 3028 (2007)

[4] Kh.Khazen et al., "FMR Investigation of GaMnAs Thin Films with Constant Mn and Variable free Hole Concentration", submitted to Phys. Rev. B, (2007)

[5] Zhao et al. Appl. Phys. lett. 86, 071902 (2005)

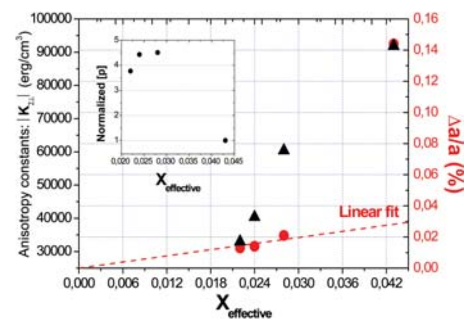

The variation of uniaxial anisotropy constants of the lattice parameter as a function of effective x (triangels). In order to demonstrate the progressive increase, the absolute values are mentioned. Circles show the deduced values of lattice parameter variation (uniaxial strain) as a function of effective x compared to the measured one for the reference sample as a function of effective x. inset: The free hole density normalized to the reference sample as a function of the effective x

DM-09

Large scale surface magnetic domains in magnetite thin films studied by spin-polarized scanning electron microscopy.

E. Kaji, A. Subagyo, K. Sueoka
Graduate School of Information Science and Technology, Hokkaido University, Sapporo, Japan

Introduction

Half metallicity and fully spin-polarization of magnetic thin films are essentially required characteristics to realize high performance spin related devices such as magnetic tunnel junctions spin valves and spin controlled transistors. Magnetite (Fe_3O_4) is one of the promising candidates for the materials of half metallicity [1]. Magnetite has high conductivity and high Curie temperature of 858 K [2], therefore, fabrication of high quality magnetite thin films have recently been of great increased interest for technological applications. Magnetic and crystallographic studies have performed on magnetite epitaxial films grown on MgO substrate and it has been reported that crystallographic symmetry introduces antiphase boundaries (APBs) in the epitaxial films that prevent the magnetite thin films from generating magnetic single domain structure. Reported low magnetoresistance ratio of magnetic tunneling junctions employing the magnetite thin films is due to the existence of the APBs [3]. APBs with antiferromagnetic coupling pin the magnetization of antiphase domains (APDs) nearby in opposite direction to reduced the magnetic domain structures down into 100-300nm scale. We have investigated APBs on surfaces by means of a scanning tunneling microscopy (STM) and obtained atomic resolution images revealed stoichiometry of magnetite thin films and detailed structure of APBs. We have been investigate correlation between the surface structure and macroscopic magnetic structures, and magnetic domains of a few tenths larger than that of APDs have been observed by means of STM and spin-polarized scanning electron microscope (Spin-SEM) or SEM with polarization analysis (SEMPA)[4]. The previous results suggested the annealing presses in UHV makes the spin configuration of the thin film visible using the Spin-SEM system and large fluctuations of magnetic domain are in the order of a few micro-meter [4]. In this paper, further Spin-SEM study is reported, that shows careful post annealing process offers clear magnetic domains of which domain boundary runs along <110> direction.

Experiment

The ultrathin epitaxial magnetite films were prepared by growth on a MgO (001) substrate by deposition of Fe in the presence of oxygen. The oxygen background pressure was set to 7.0×10^{-5} Pa. The flux of Fe was set to about 0.11 nm/min. The Fe was evaporated by an electron beam. The growth temperature was maintained at 523 K. This growth procedure gives a good stoichiometry of magnetite films. The surface cleanliness and stoichiometry were confirmed by X-ray photoelectron spectroscopy (XPS). Detained crystallographic structures were investigated by in-situ STM system [5]. Since our home made Spin-SEM system is independent instrument of the growth system equipped with XPS and STM, the sample should be transferred from the growth system to Spin-SEM via ambient condition in a short period. Experimental conditions and cleaning procedure with out ion sputtering of the sample surface are described in the reference [4]. Only an UHV annealing process at 573 K for 30 min was employed to produce clean surfaces.

Results

Figure 1 shows an SEM image and Spin image observed on the sample. The SEM image shows no surface morphology that suggested the surface is flat. In contrast to that, a clear spin dependent image is obtained. Due to the geometry of our Mott-type spin analyzer, the spin image reflects spin polarization components along 45 degree off plain and magnetic domain structure in an as-annealed remanent state. Stray magnetic fields around the sample were reduced below 0.01 mT by a magnetic shield attached over a pole piece of an SEM electron gun. Magnetic domain walls run along <110> direction and size of the magnetic domains is in the rage from a few hundred nm to a few micro meters. Since an easy axis of the film is expected along <111> direction, the magnetic domain structures are related to the crystallographic anisotropy. This result indicates that the large scale magnetic ordering similar to our previous observation exist in the magnetite thin films. Such ordering has not been reported in the transmission electron microscopy or magnetic force microscopy (MFM) studies. Although correlation of experimental condition of the UHV annealing process should be investigate in detail. This result suggests that the UHV annealing reduces the antiferromagnetic coupling at APBs to make the magnetic domain large and that the thin films of sub-micro meter may yield high spin-polarized electrode.

[1] W. Eerenstein, T. Palstra, S. Saxena, and T. Hibma, Phys. Rev. Lett. 88, 247204 (2002).

[2] R. J. Harrison and A. Putnis, Am. Mineralogist, 68, 375(1996).

[3] D. Margulies, F. Parker, M. Rudee, F. Spada, J. Chapman. P. Aitchison and A. Berkowitz, Phys. Rev. Lett. 79, 5162 (1997).

[4] E. Kaji, A. Subagyo and K. Sueoka, Phys. Stat. Sol. (C) 4, 4364 (2007).

[5] A. Subagyo and K. Sueoka, Jpn. J. Appl. Phys. 45, 2255(2006).

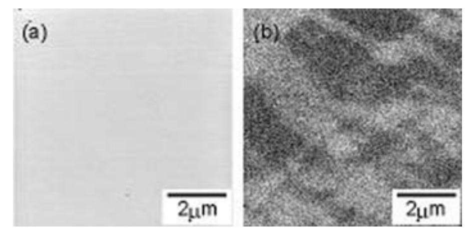

Fig. 1. The images are surface structure of the Fe_3O_4 taken with an Spin-SEM. (a) topographic image, (b) magnetic iamge.

DM-10

Determination of the Gilbert damping factor in $Ga_{0.93}Mn_{0.07}As$/GaAs Thin Layers.

K. Khazen[1], M. Cubukcu[1], H. von Bardeleben[1], J. Cantin[1], V. Novak[2], K. Olejnik[2], M. Cukr[2]
1. Institut des NanoSciences de Paris(INSP)Université- Paris 6, UMR 7588 au CNRS, Paris, France; 2. Institute of Physics AS CR, Praha, Czech Republic

The Gilbert damping factor is an important parameter for the characterization of the dynamic properties of the magnetization in ferromagnetic thin layers and is inversely proportional to magnetization relaxation time along the applied field. It can be obtained from ferromagnetic resonance measurements via the variation of the linewidth of the uniform mode spectrum with the measuring frequency. The FMR linewidths is generally decomposed into two parts: a homogenous broadened one ΔH_{homo} which increases linearly with the microwave frequency for a specific system and an inhomogenous one independent of the microwave frequency.

We report here the measurement of the damping factor by FMR spectroscopy in 50nm thick GaMnAs sample with 7% Mn, showing the critical temperature T_C=157K after annealing in air at 200°C for 30 hours. The measurements were performed at 9GHz and 35GHz in the 4K to 150K temperature range. We further investigated the anisotropy of the α-damping factor for different orientations of the applied magnetic field along the crystalline high symmetry directions and as a function of the measuring temperature (fig.1). Our results are compared to the very few previous reports on GaMnAs layers with similar Mn concentrations [1,2]. The values found in our high T_C samples are at least 10 times less than those reported previously. In this sample the damping factor is as low as metallic thin films (Fe) studied by Heinrich et al. [3].

The inhomogeneous linewidths are deduced, as well, for different directions of the film and different temperatures (fig.2)

In addition, the spectra are studied from the homogeneity point of view and the values of anisotropy constants and g-factors are measured as the reference values to be compared with other GaMnAs structures.

[1] Y.H. Matsuda et al., Physica B: Condensed Matter Volumes 376-377, 1 April 2006, Pages 668-671

[2] J. Sinova et al., PHYSICAL REVIEW B 69, 085209 (2004)

[3] R. Urban, G. Woltersdorf, and B. Heinrich, Phys. Rev. Lett. 87, 217204 (2001)

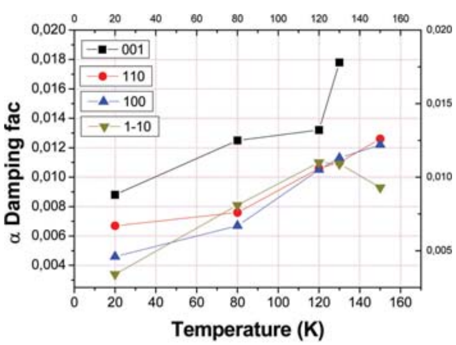

α damping factor as a function of temperature for high symmetry orientations of GaMnAs thin film

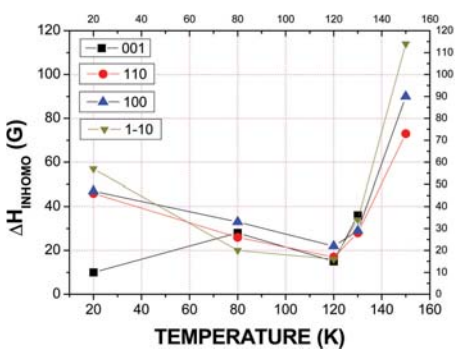

The inhomogeneous linewidth as a function of temperature

DM-11

Experimental evidence for bulk and interfacial contributions to static and dynamic properties of Py/Al_2O_3.

C. Le Graet, D. T. Dekadjevi, S. Pogossian, D. Spenato, *J. Ben Youssef*
Physics, LMB/UBO/CNRS, Brest, France

During the last decades, a phenomenon not yet understood is the damping mechanism in nanostructures. Saturated magnetization, anisotropic and structural properties should be considered to understand the damping mechanism. Moreover, the presence of interfaces in bilayers plays a keyrole in the damping. It is useful to distinguish the bulk and interfacial contributions to this mechanism [1-3]. We present an analysis of the static and dynamic magnetization properties of Si/Permalloy(t_{Py})/Al_2O_3(3nm) grown by rf sputtering as a function of the Permalloy (Py) thickness (t_{Py}). Py was chosen as the ferromagnet since it exhibits a very low anisotropy resulting in a small damping. Al_2O_3 was chosen since it is an insulator. We perform a study as a function of t_{Py} to discuss interfacial and bulk contributions. A dc magnetic field was used to induce an uniaxial anisotropy. Static and dynamic properties were studied at room temperature, using a conventional VSM and Ferromagnetic Resonance (FMR) at frequencies in the range 3-20GHz using a wideband resonance spectrometer with a non resonant microstrip transmission line. The keyrole of the interface in the static magnetic properties is demonstrated since the saturated magnetization (M_s) is proportional to $1/t_{Py}$. The anisotropic properties are also studied as a function of t_{Py}. Fig. 1 shows the normalized remanent magnetization versus t_{Py}. It reveals an inversion of the anisotropy axis at a critical thickness (t_{c}) of 7nm. Below t_{c}, the easy axis is in the plane but perpendicular to the direction of the applied field during growth (H_{d}) whereas above t_{c}, the easy axis is along this applied field. This effect on the anisotropy could be attributed to the bulk since no critical behaviour appears in Ms at t_{c}. The dynamic properties of our system should be influenced by these static properties. In the following, we measure the resonant field (H_{res}) as a function of the frequency (f) to determine: the gyromagnetic factor (γ), the effective magnetization (M_{eff}), the intrinsic and extrinsic contribution to the damping. γ and M_{eff} are deduced from the resonant condition. We find a negligible surface anisotropy. Also, a significant decrease in γ with decreasing t_{Py} is present. It suggests that an interfacial mixing results in a non negligible orbital moment altering the Landé factor, and consequently γ. Therefore, the interfacial structure does not bring a surface anisotropy but modifies the gyromagnetic factor. To understand the damping driving mechanism, we measure the evolution of the peak to peak parallel resonance linewidth (ΔH) as a function of f and t_{Py}: ΔH increases linearly with f in agreement with previous results. Two different contributions are then determined: the extrinsic and the intrinsic ones. Before t_{c}, the damping factor (α) is enhanced relatively to the refereed value of bulk NiFe. Above t_{c}, α values are in agreement with bulk NiFe. Concerning the extrinsic contribution, Figure 2 shows two different trends: one below t_{c} and one above t_{c}. Usually, this extrinsic contribution reflects the structural quality of the samples.

In this study, we have shown experimental evidence for the interface and bulk contributions to the Py/Al_2O_3 static and dynamic properties. The interface drives the gyromagnetic factor. However, there are no significant effects of the bulk structural properties (grain boundaries) on this factor. The bulk plays a keyrole in anisotropic properties and extrinsic part of the damping. A detailed structural analysis will also be presented.

[1] H. Hurdequint, J. Magn. Magn. Mater. 242-245 (2002) 521.

[2] Shigemi Mizukami, Yasuo Ando and Terunobu Miyazaki, Jpn. J. Appl. Phys. 40 (2001) 580.

[3] J. P. Nibarger, R. Lopusnik, Z. Celinski, and T. J. Silva, 83 (2003) 93.

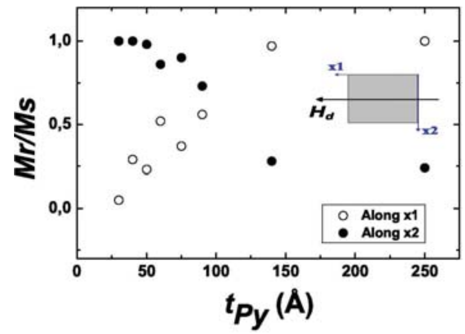

Normalized remanent magnetization as a function of t_{Py} along two different direction. In the insert: scheme of the sample direction.

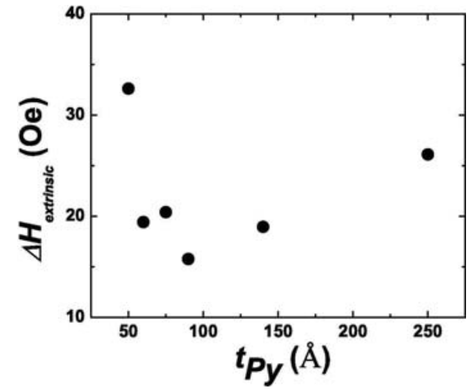

Thickness dependence of $\Delta H_{extrinsic}$.

DM-12

Asymmetry of polycrystalline Fe thin films showing bcc (110) growth orientation on glass substrates using second-harmonic generation.

F. Lee, J. Jeong, H. Lee, K. Lee, J. Kim, S. Shin
department of Physics, Korea Advanced Institute of Science, Daejeon, South Korea

Feel Lee, Jae-Woo Jeong, Hun-Sung Lee, Kyung-Dong Lee, Ji-Wan Kim
and Sung-Chul Shin
Department of Physics and Center for Nanospinics of Spintronic Materials, Korea Advanced Institute of Science and Technology,
Taejon 305-701, Korea

The effects of substrates on structural properties of Fe thin films are thoroughly studied for many years. In many previous reports, Fe thin film is believed to grow with isotropic polycrystalline structure on a glass substrate. However, recent study [1] reveals Fe thin film can have asymmetric polycrystalline structure even deposited on an isotropic glass substrate. In present work, we have studied asymmetry of polycrystalline Fe films of 5, 50, 200 and 300 nm thickness on glass substrate. For the investigation of thin film crystal symmetry, optical second-harmonic generation (SHG) has been used. SHG technique has intrinsic sensitivity to surface structure as well as crystal symmetry of thin film. We found that the surface structure of Fe thin film possesses asymmetric Cs crystal structure pretty close to C2v through considering SHG intensities. As a proof of Cs symmetry, it is presented one-fold intensity profile with one mirror plane in SHG intensity. Cs and C2v surface symmetry are usually showed at the (110) surface of cubic crystal. Therefore the surface structure of the polycrystalline medium would be related to bcc (110) growth orientation coinciding with XRD measurement, which is consistent with recent report [1]. Further we normalized SH in-plan asymmetries with various thickness. It is observed that SH asymmetry increased with increasing thickness. From these results, it is concluded that the surface structure of ultrathin polycrystalline Fe film below 5 nm is almost isotropic, while in the case of the thicker Fe thin films, surface structure possesses the symmetry closer to asymmetric Cs structure close to C2v.
Polycrystalline Fe thin films were fabricated on glass substrate in 300 K in DC magnetron sputtering system. Ar gas is used under 5 m Torr Under base pressure at 2x10-6 Torr in 500 Oe magnetic field. We covered Si3N4 on Polycrystalline Fe to keep the surface state.
We used a general SHG system setup to measure surface structure of ferromagnetic Fe films on glass substrate. We used femto-second terawatt Ti: sapphire laser, mode-locked at 780 nm, the center of wavelength as a pulse laser and 532nm Nd: YVO4 (Spectra, Millennia Vs J) continuous laser as pumping laser. Here we measured SH intensity from Fe sample at specified incident polarization at 80 mW and 0 mW~130 mW to get information on normalized SH asymmetry. Sample magnetization is fixed by external magnetic field 1kOe. The filter before sample is used for blocking unexpected SH wave from optical elements and the filter behind sample for blocking fundamental wave.
From previous report [1], Fe films have bcc (110) growth orientation would possess the symmetry class corresponding to (110) surface at its surface. We expected that the surface of the polycrystalline Fe showing (110) growth orientation would possess the lowest symmetry class Cs or C2v.
We measured SH intensity by azimuthal rotation of the sample on the sample stage. There are four selected configuration. Frequency-doubled s-pole output is almost comparable with the noise due to Dark current. The each data in Fig 1. shows one asymmetric mirror plane for frequency-doubled p-output. For sp configuration SH intensity have 65° mirror plane and for pp configuration have 120° mirror plane. There are only three crystal classes Cs, C3h and D3h including one mirror plane operator and except for inversion operator. The SH intensity profile shows a sine and only two symmetry classes, Cs and C2 can satisfy this condition in sp configuration. Therefore it is concluded that polycrystalline Fe on glass substrate showing (110) growth orientation possess Cs crystal class. For Fe films of various thickness, Cs asymmetry of SH intensity has been obtained and shown in Fig. 2. Normalized SH asymmetry is increased with increase of film thickness. Thus, it can be deduced that symmetry breaking in this system is closely related to bcc (110) growth of Fe with increasing film thickness.

[1] R. Sayed Hassam et. al. thin solid films 515 2943 (2007)

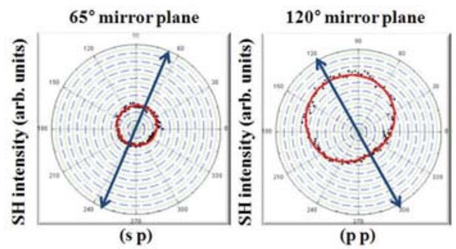

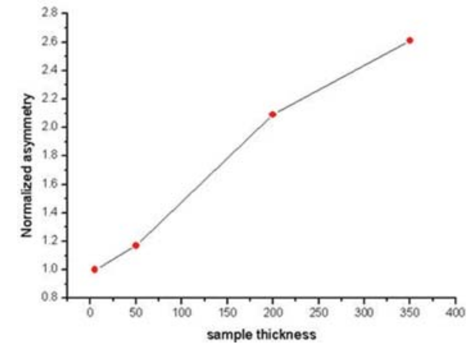

DM-13

Transition to antiferromagnetic interlayer coupling at the Cu spacer thickness of 2 nm in bottom spin valve films with $Co_{1-x}Fe_x$/Cr-NOL.

K. Sawada[1], K. Futatsukawa[1], M. Doi[1], N. Hasegawa[2], M. Sahashi[1]
1. Tohoku university, Sendai, Japan; 2. ALPS electric corporation, Niigata, Japan

Introduction
It is well known that there are several kinds of magnetic coupling, such as the exchange bias and interlayer coupling in SV films. However, nature of those magnetic coupling in SV films with the insertion of a nano-oxide-layer (NOL) have been not well discussed even though NOL plays a most important role in nano-constriction SV MR devices such as nano-contact MR, because the magnetism and structure of an ultra-thin NOL themselves were not clear, which NOL is formed by surface-oxidation of metal film layer such as $Co_{1-x}Fe_x$ alloy. Therefore, we have already reported the magnetism and structural consideration on $Co_{1-x}Fe_x$-NOL in pinned layer, where it is revealed that AFM CoO-FeO (T_B=~140 K) and Cr_2O_3-Fe_2O_3 (T_B=~220 K) are dominant component in $Co_{0.9}Fe_{0.1}$-NOL and the surface of $Co_{0.9}Fe_{0.1}$/Cr-NOL, respectively [1, 2].
In this paper, the interlayer coupling field (H_{in}) through Cu spacer for $Co_{0.9}Fe_{0.1}$/Cr-NOL SVs [x = 0.1, 0.3 and 0.7] with/without Cr are discussed for confirming NOL magnetism and structure in more detail.
Experimental
The sequential sputtering method was used for the sample preparation. The typical design of the SV sample was seed/IrMn 5.5/$Co_{0.9}Fe_{0.1}$ 1/$Co_{1-x}Fe_x$ 1 (x = 0.1, 0.3, 0.7)/Cr 0, 0.08/N.O. (0, 2, 10 kL)/$Co_{0.9}Fe_{0.1}$ 2/Cu 2/$Co_{0.9}Fe_{0.1}$ 2/Ta 3 [nm] on a thermally oxidized Si substrate (N.O.: the conventional natural oxidation process). 0 kL sample means the full metal SV. Oxygen exposure 1 L is oxygen partial pressure 1 μTorr × oxidation time 1 sec. All of the films were annealed at 270°C for 1.5 h under a magnetic field of 10 kOe. After the magnetic field cooling from room temperature to ~3 K under a magnetic field of 10 kOe, the R-H curves in each temperature were measured by using the conventional four-terminal methods under the temperature range of 5 K to room temperature. H_{in} was estimated as a central field of hysteresis loop at free layer.
Results and Discussion
It has been known the interlayer coupling is related to both RKKY like antiferromagnetic coupling and the Néel ferromagnetic coupling [2]. Table 1 shows H_{in} through the Cu spacer for each sample at R.T. Here, positive sign shows the ferromagnetic interlayer coupling. Large positive Hin was observed in the case of full metal SVs both Co-rich and Fe-rich, which suggests the presence of the Néel ferromagnetic coupling field along with the oscillatory RKKY coupling field because H_{in} shows the second RKKY antiferromagnetic maximum at near 2 nm. In contrast, H_{in} decreased by inserting NOLs, especially, in the case of the SVs with $Co_{0.7}Fe_{0.3}$-NOL and $Fe_{0.7}Co_{0.3}$-NOL, the interlayer coupling changed from ferromagnetic to antiferromagnetic coupling. It is considered that the influence of the Néel ferromagnetic coupling was weakened by the insertion of both $Co_{1-x}Fe_x$-NOL and $Co_{1-x}Fe_x$/Cr-NOL, which means that the interface between $Co_{0.9}Fe_{0.1}$ and Cu is more flat than without NOLs. The interfaces of the SVs with Fe-rich NOL were more flat than those with Co-rich NOL was also observed. In addition, from the results of the inserted $Co_{1-x}Fe_x$/Cr-NOL, it was obtained that the case of prepared by the stronger oxygen exposure had the more flat interface.
Figures 1 (a) ~ (c) show the temperature dependence on Hin for each sample at x = 0.1, 0.3, and 0.7. The positive H_{in} for full metal SVs increase with decreasing temperature. It is caused by the magnetic moment contributing to the Néel ferromagnetic coupling enhances with decreasing temperature. On the other hand, in the case of the SVs with NOL, the positive H_{in} decreases with decreasing temperature and the interlayer coupling of $Co_{1-x}Fe_x$/Cr-NOL SVs changed from ferromagnetic to antiferromagnetic coupling. It is considered that the RKKY like antiferromagnetic coupling also enhances with decreasing temperature and its influence contributing to the interlayer coupling is stronger than the Néel ferromagnetic coupling. In addition, although interesting results, the particular tendency of temperature dependence on H_{in} for $Co_{0.9}Fe_{0.1}$-NOL SV and $Co_{0.9}Fe_{0.1}$/Cr-NOL SV was observed at T_B of those CoO-FeO and Cr_2O_3-Fe_2O_3, respectively.

[1]M. Sahashi, K. Sawada et al, IEEE Trans. Magn., 43, 3668 (2007).

[2]K. Sawada et al, J. Magn. Soc. Jpn., submitted

[3]J. H. K. Aoshima et al, IEEE Trans. Magn., 36, 2629 (2000)

x in $Co_{1-x}Fe_x$	Full metal SV	$Co_{1-x}Fe_x$-NOL SV		$Co_{1-x}Fe_x$/Cr-NOL SV	
		N.O. 2 kL	N.O. 10 kL	N.O. 2 kL	N.O. 10 kL
0.1	26.6 Oe	24.6 Oe	22.4 Oe	21.3 Oe	17.5 Oe
0.3	19.4 Oe	–	−4.5 Oe	10.9 Oe	8.1 Oe
0.7	30.5 Oe	−1.7 Oe	–	3.9 Oe	0.9 Oe

Table 1 H_{in} for full metal SV, $Co_{1-x}Fe_x$-NOL SV, and $Co_{1-x}Fe_x$/Cr-NOL SV at R.T..

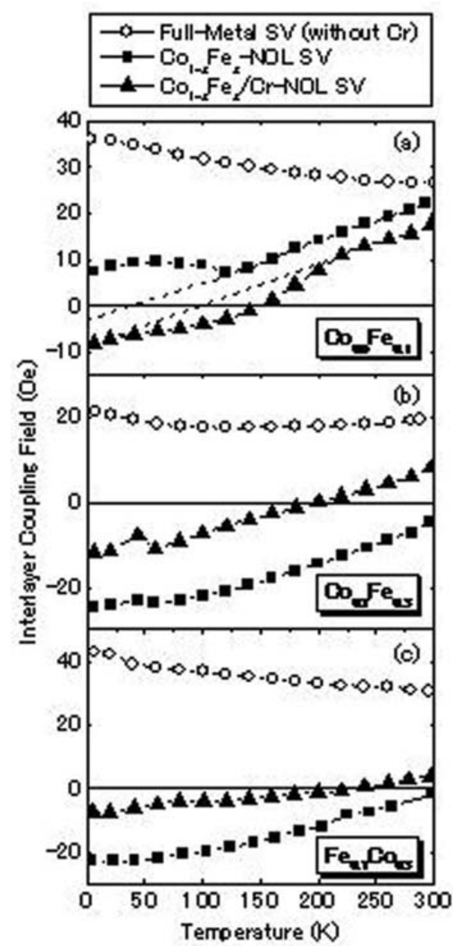

Fig. 1 Temperature dependence on interlayer coupling field for full metal SVs, $Co_{1-x}Fe_x$-NOL SVs, and $Co_{1-x}Fe_x$/Cr-NOL SVs at (a) x = 0.1, (b) 0.3, and (c) 0.7.

DM-14

The Effect of CoFe Surface Pre-Oxidation on Magnetic Tunnel Junctions.

P. Pong, W. F. Egelhoff
Magnetic Materials Group, National Institute of Standards and Technology, Gaithersburg, MD

Introduction
The ferromagnet/oxide interface plays a critical role in determining the tunneling magnetoresistance (TMR), the junction resistance, and the magnetic properties. Surface oxidation achieved by exposing the bottom ferromagnetic layer to oxygen before depositing the Al layer helps to suppress intermixing at the ferromagnet/Al interface [1, 2]. Initially, the deposited Al takes oxygen away from the ferromagnetic oxide to form Al2O3. After the oxygen is consumed and Al is deposited, the Al layer is oxidized in plasma to form Al2O3 barrier [1, 3]. This approach provides a very promising means of suppressing orange-peel coupling in magnetic tunnel junctions (MTJs) [4]. Further investigation illuminating the pre-oxidation effect on MTJ properties with a range of Al thicknesses is very important to the application of the technique.
Experiment
The thin films were deposited on thermally oxidized silicon wafers by dc magnetron sputtering in an ultrahigh vacuum chamber with a base pressure of 2x10-10 Torr. The metal films were deposited at room temperature in 2 mTorr argon. The oxide barrier layer was made by first depositing a thin Al metal and then oxidizing it in oxygen plasma (4 mTorr argon, 2 mTorr oxygen) for 2.5 minutes. The thicknesses of the Al metal cover a range from 4 to 18 angstrom. The sample structure is substrate\ 25 Ta \ 50 Au \ 100 IrMn \ 40 CoFe \ X Al: oxidized \ 50 CoFe \ 50 Ta \ 70 Ru. (X is shown next to the data, all units in Angstrom).
Results and Discussion
Figure 1 presents two sample sets with a range of Al thicknesses. One sample set was pre-oxidized with 1 mTorr oxygen for 30 seconds prior to the deposition of the Al layer while the other set was not pre-oxidized. The TMR of the pre-oxidized samples are all larger than the samples without pre-oxidation regardless of their Al thicknesses. Moreover, the RAs of the pre-oxidized samples are also in general higher. Thus pre-oxidation significantly improves the TMR, although it increases the RA of the junctions. We believe the improvement of the TMR is due to the fact that the pre-oxidation helps to suppress intermixing at the ferromagnet/Al interface, inhibiting the orange-peel coupling. This result shows that the pre-oxidation technique is applicable for Al2O3 MTJs regardless of their thicknesses. Further experiment involving a MTJ wafer with a wedge of Al2O3 characterized by current-in-plane-tunneling (CIPT) technique reinforced the validity of the usefulness of pre-oxidation. We have also studied the influence of the pre-oxidation time on the TMR and RA.
Conclusion
It was previously shown that pre-oxidation could suppress the orange-peel coupling and thus enhance the TMR in a series of MTJs with the same Al2O3 thickness. In this work, the technique was utilized on MTJs with a range of thicknesses and the result was compared with the MTJs without pre-oxidation. This study shows that the pre-oxidation technique is of general use and it is applicable on MTJs with various Al2O3 thicknesses.

[1] W. F. Egelhoff, Jr. et al., J. Appl. Phys., 89, 5209 (2001)

[2] J. Wolfman et al., J. Appl. Phys., 97, 123713 (2005)

[3] K. Sin et al., 2002 IEEE International Magnetics Conference, 2002. INTERMAG Europe 2002. Digest of Technical Papers, pp. ER10

[4] W. F. Egelhoff, Jr., et al., Appl. Phys. Lett. 88, 162508 (2006)

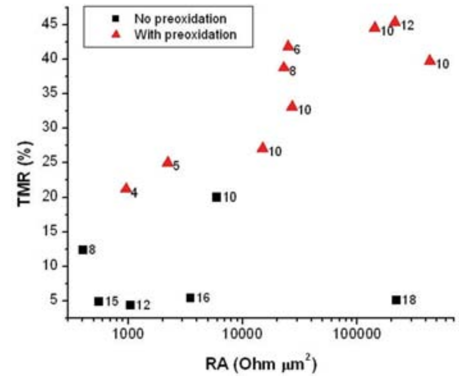

Figure 1. The effect of CoFe surface pre-oxidation on the TMR and RA of the samples with various Al thickness. The thickness is in Angstrom.

DN-01

Time-resolved magnetization dynamics in magnetic microstructures.

D. Bayer[1], J. Miguel[2], J. Sanchez-Barriga[3], J. Kurde[2], M. Piantek[2], F. Kronast[3], M. Cinchetti[1], B. Heitkamp[3], H. Dürr[3], W. Kuch[2], M. Aeschlimann[1]
1. University of Kaiserslautern, Kaiserslautern, Germany; 2. Freie Universität Berlin, Berlin, Germany; 3. BESSY GmbH, Berlin, Germany

For both fundamental and application points of view, the switching time and behaviour of a trilayer system consisting of a ferromagnetic/non magnetic/ferromagnetic trilayer (as used e.g. for magnetoresistive devices) is of utmost significance. In microstructured magnetic multilayer systems a clear view of the reversal dynamics has not been achieved experimentally because it needs a technique offering at the same time a high temporal and lateral resolution. Time-resolved XMCD-PEEM represents a state-of-the-art way of getting ultrafast time resolution (low picosecond regime) and simultaneously layer and spatially resolved information of the investigated magnetic multilayered structures. The magnetization can be excited by a short magnetic field pulse that can be achieved in principle through different pump-probe methods. In the actual applications we used a laser-induced electrical field pulse in a Au stripline.

The transient local magnetization dynamics was studied by time-resolved XMCD-PEEM in a stroboscopic pump-probe technique [1, 2]. Magnetic microstructures deposited on a Au stripline are magnetically disturbed by a short magnetic field pulse. The ultrashort magnetic field pulse is provided by an electric current pulse flowing through the stripline underneath the microstructure, triggered by an optical switch by means of a femtosecond laser pulse [3, 4]. This part of the technique, in combination with the length of the synchrotron bunch, is responsible for the time resolution of the experiment.

Fig. 1 presents the sample design (optical switch, stripline and magnetic microstructures) as well as static XMCD images of investigated Permalloy microstructures. To study reversible dynamics, the initial domain configuration has to be a Landau pattern. Therefore the domain configuration was characterized by high resolution static XMCD-PEEM measurements.

Time-resolved XMCD-PEEM measurement on the elongated Permalloy rectangle is shown in Fig. 2 . It is striking that the Landau pattern changes irreversibly from a two vortex state in a four vortex state after pulsing. The pump-probe series, depicted on the left of Fig. 2, shows the time evolution of the system. The difference images indicate the domain wall movement. Integrating different areas in the black, white and grey domain, as shown on the right side, image the dynamic magnetic response of the microstructure to the incoming field pulse. As the magnetization of the grey domains are perpendicular to the incoming field pulse, the changes in contrast are most obvious.

The dynamics observed for the rectangle shown in Fig. 2 will be discussed and compared to the dynamics of a permalloy square present on the same stripline. Correlations between shape and dynamics will be analysed as well.

Furthermore, we investigated the spinvalvesystem of Co/ Cu/ Py and will present first results.

[1] J. Stöhr, Y. Wu, B. D. Hermsmeister, M. G. Samant, G. R. Harp, S. Koranda, D. Dunham, and B. P. Tonner, Science 259, 658 (1993)

[2]W. Kuch, Appl. Phys. A 76, 665 (20039

[3] D.H. Auston, APL 26, 101 (1974)

[4] Th. Gerrits, H. A. M. van den Berg, J. Hohlfeld, L.Bär, and Th. Rasing, Nature 418, 509 (2002)

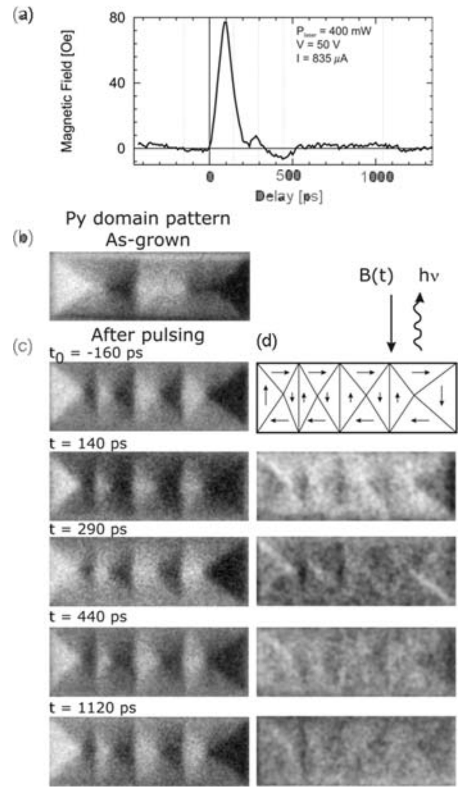

Fig 2.: (a) Shape of the magnetic field pulse. (b) Domain pattern before any pulsing. (c) XMCD PEEM images at several delays of the pump-probe scan. Difference images XMCD(t)-XMCD(t0). (d) Difference images XMCD(t)-XMCD(t0).

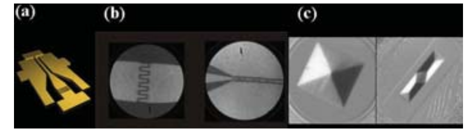

Fig. 1 (a) Sketch of the used switch and stripline combination used in the experiments. (b) PEEM images of the switch (finger length 10 μm, width 5 μm, gap 5 μm), the stripline including the magnetic microstructures in survey mode, and the magnetic structures is shown (from left to right, fields of view are ~ 100 μm, 250 μm). (c) XMCD images of a permalloy square (5x5μm) and a permalloy rectangle (5x15μm).

DN-02

Anisotropic x-ray magnetic linear dichroism at Fe, Co and Ni L edges: Interfacial coupling revisited.

G. van der Laan[1], E. Arenholz[2]
1. Diamond Light Source, Didcot, United Kingdom; 2. ALS, Berkeley, CA

The detailed knowledge of the spin arrangements in engineered magnetic nanostructures comprised of multiple magnetic species is essential to tailor their properties for device applications e.g. in information storage technology. Soft x-ray magnetic dichroism spectroscopies play a very important role in improving our understanding of complex heteromagnetic nanostructures since they provide elemental and chemical site-specific magnetic information with high sensitivity and tunable probing depth. X-ray spectromicroscopy techniques such as photoemission electron microscopy (PEEM), scanning transmission x-ray microscopy (STXM) or full field x-ray microscopy add spatial resolution down to a few nm.
We present the observation as well as theoretical description of anisotropic x ray magnetic linear dichroism (XMLD) on thin films at the Fe L3,2 edges in Fe3O4 [1], the Ni L3,2 edges in NiFe2O4 and NiO [2], and Co L3,2 in CoFe2O4 and CoO [3]. We show unambiguously that - contrary to current belief - spectral shape and magnitude of the XMLD is not only determined by the relative orientation of magnetic moments and x ray polarization but that their orientation relative to the crystallographic axes has to be taken into account for the accurate interpretation of the XMLD data.
The observed anisotropy of XMLD is a general phenomenon and is expected for any magnetic system. Consequently, conclusions based on the interpretation of XMLD spectra without accounting for the XMLD anisotropy have to be reconsidered. We will revisit some of the previous experimental results and reinterpret the experimental data based on our findings. Applying our results to Co/NiO(001) interfaces, we find perpendicular coupling between Ni and Co moments. The results are important considering the growing interest in understanding exchange-biased systems

[1] E. Arenholz, G. van der Laan, R.V. Chopdekar, Y. Suzuki, Phys. Rev. B 74, 094407 (2006)

[2] E. Arenholz, G. van der Laan, R.V. Chopdekar, Y. Suzuki, Phys. Rev. Lett. 98, 197201 (2007)

[3] G. van der Laan, E. Arenholz, R.V. Chopdekar, Y. Suzuki, Phys. Rev. B, accepted (2008)

DN-03

Topological hysteresis in superconductors and ferromagnets.

R. Prozorov[2,1], P. C. Canfield[2,1]
1. Physics and Astronomy, Iowa State University, Ames, IA; 2. Ames Laboratory, Ames, IA

Pattern formation in magnetic materials has been a subject of intense interest due to the desire to understand the behavior of complex systems where topological intricacy prohibits exact evaluation of the ground state. It is impossible to determine the equilibrium topology of magnetic domains in ferromagnets or the structure of the intermediate state in type-I superconductors from global free energy minimization. The pattern geometry has to be assumed and parameterized, and then the energy minimization can be used to find the best value of the free parameters. But is it the ground state pattern?
The situation is further complicated by magnetic hysteresis, which is usually caused by the imperfections and defects in the crystal structure resulting in pinning of magnetic flux in superconductors or domain walls in ferromagnets. The alternative cause of pinning is shape and surface - related energy barriers (e.g., geometric and Bean-Livingston) that result in a spatially nonuniform free energy and corresponding metastable states of the system. Yet, can there be magnetic hysteresis in perfect samples?
In this work we used Faraday and polar Kerr effects to conduct magneto-optical imaging of the flux distribution in a type-I superconductor (pure lead crystal, Fig.1) and a soft ferromagnet ($CeAgSb_2$ (Fig.2) with quite unusual spin structure and crystal electric field anisotropy). Kerr imaging was conducted directly by reflecting a linearly polarized light off the as grown surface of ferromagnetic crystal (see Fig.2). Imaging in superconductors was done by using bismuth - doped iron garnets with in-plane magnetization as magneto-optical indicators. By placing such indicator directly on top surface of the sample under study, we obtained real-time imaging of the magnetic induction (see Fig.1).
We find that tubular rather than lamellar structure corresponds to the equilibrium pattern in both systems. Although the microscopic physics is quite different, we find common points that determine pattern topology in these materials. The interplay between long-range and short-range forces as well as flux conservation play major role in determining the patterns geometry.
There are also results unique to superconductivity and to ferromagnetism.
In a type-I superconductor, evolution of the intermediate state can be mapped remarkably well onto coarsening of the conventional soap froth, but unlike it, the process is controlled by the reversible parameters – magnetic field and temperature rather than by the irreversible time.
In a ferromagnet on the other hand it is shown that apparent topological time-reversal symmetry breaking can be lifted on the scale of the entire sample by creating secondary dipolar magnetic domains.
Addressing the issue of magnetic hysteresis, we describe a novel type of magnetic hysteresis that is only observed in clean, pinning-free samples. Most importantly, this hysteresis cannot be annealed or removed by any sample improvement. We call this phenomenon *topological hysteresis* to indicate that the difference in the topologies of the intermediate state in type-I superconductors or ferromagnetic domains in soft ferromagnets upon cycling of the applied magnetic field can lead to a measurable hysteretic response of macroscopic magnetization.
Work at the Ames Laboratory was supported by the Department of Energy, Basic Energy Sciences under Contract No. DE-AC02-07CH11358. R. P. Acknowledges a support from the NSF Grant Number DMR-05-53285 and the Alfred P. Sloan Foundation.

[1] R. Prozorov, R. W. Giannetta, A. A. Polyanskii and G. K. Perkins, "Topological hysteresis in the intermediate state of type-I superconductors", Physal Review B, 212508 (2005).

[2] R. Prozorov, "Equilibrium topology of the intermediate state in type-I superconductors of different shapes", Physical Review Letters 98 257001 (2007).

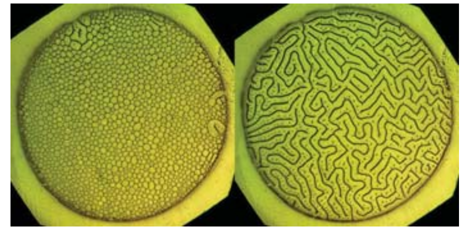

Fig.1 Structure of the intermediate state in Pb single crystal of 5 mm in diameter at 6 K and H=190 Oe. (left): increasing magnetic field (right) decreasing field.

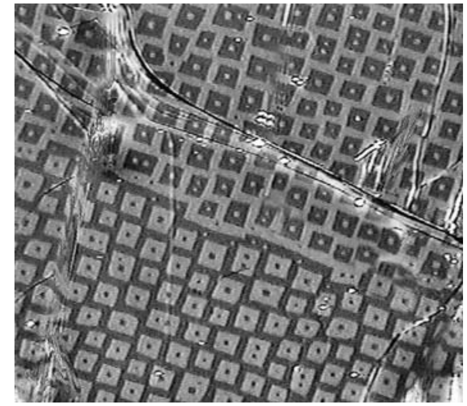

Fig.2 Equilibrium domain structure in CeAgSb2 single crystal at 4.8 K after compensation for the Earth magnetic field. Closed topology (tubular) structure is reversed in neighboring "dipolar" domains.

DN-04

Avalanches through windows: multiscale visualization in magnetic thin films.

G. Durin[1], A. Magni[1], S. Zapperi[2,3], J. P. Sethna[4]

1. Istituto Nazionale di Ricerca Metrologica, Torino, Italy; 2. Dep.of Physics, University of Modena and Reggio Emilia, CNR-INFM National Center on nanoStructures and bioSystems at Surfaces (S3), Modena, Italy; 3. ISI foundation, Torino, Italy; 4. Physics Department, LASSP, Cornell University, Ithaca, NY

The motion of domain walls in soft magnetic materials, a basic example of complexity in materials science, has been the subject of a long and continuing series of studies.In bulk systems, most of the statistical properties are understood in terms of a depinning transition [1]. In thin films, the motion is presumably dominated by depinning as well, but our understanding of the dynamics is still preliminary. Also, experimental data available are poor, although very promising. Puppin [2] found the critical exponent τ of the avalanche size distribution $P(S)=S^{\tau} f(S/S_o)$ in a Fe film is about 1.1, less than for bulk systems. Recently, Ryu et al. [3] argued that in MnAs films (Tc~45°C) there is a cross-over between two universality classes, as τ changes from 1.32 to 1.04 with T increases from 20 to 35°C. These experiments rely upon measuring avalanches optically, in a small sub-window of the entire sample, and often comparing windows of varying sizes.

Here, we explore two issues associated with extracting avalanche statistics from images: good methods for extracting avalanche distributions, and a proper scaling approach to address the finite-size cutoff in the avalanche sizes induced by the observation window.

The determination of avalanche size from images is not as simple as in fluxometric measurements because it is far more challenging to separate signal from noise in the richer space-time information provided. This is particularly important for size distributions, where small avalanches are crucial for estimation of the exponents. To address this question, we acquired images of domain walls on Py films using an high-resolution MOKE, with a slow varying longitudinal in-plane field.

After background subtraction and contrast enhancement, we tried to determine a reliable procedure to identify the domains in the images. Edge detection routines, for instance, are not useful in determining the position of the walls; by analyzing single images, we lose the useful information provided by the time sequence. Indeed, an effective point is to ignore the spatial information and consider only the evolution in time for each pixel. A significant jump in the measured intensity represents the switching time for the magnetization at that point. Spatial information must be then used to correct for the small number of pixels which appear to switch at a wrong time. While it is essential to make these corrections, these methods are pretty delicate. An example of avalanche visualization is shown in fig. In this case, we applied a procedure which significantly depleted small avalanches. We are exploring alternative methods which may perform better, to ensure a reliable estimation of the critical exponents.

We then consider the effect of the window size of images. Generally, the windows size both suppresses the largest avalanches and can add extra truncated avalanches at smaller sizes. Given that one can measure up to three decades of sizes for a given window, it is valuable to combine information from several window sizes; to do so we must understand the finite-size effects with windowed boundary conditions. We thus considered a realistic simulation of an elastic line moving in a random environment, and made distributions with/without avalanches that touch the borders of the window — including/avoiding the extra truncated avalanches. The fig. shows the results where only the avalanches that did not touch the sides of a LxL window are incorporated.

The tricky part of analyzing this data is that the large avalanches near depinning transitions are increasingly anisotropic: an avalanche with width W will have typical height $H \sim W^{\zeta}$. If $\zeta<1$, as in our case ($\zeta=0.63$), large avalanches become short and fat. This means that the main effect of large windows is to cut off the widest avalanches, while at small window sizes a substantial number of tall avalanches may also be removed. Thus, unlike isotropic finite-size scaling, the effects of larger windows are not similar to the small windows: they are similar to smaller windows *of a different shape*.

We can analyze the data using the finite-size scaling form

$P(S,L)=S^{\tau} P_W(S/L^{1/\sigma\nu})$, appropriate for systems with a strip geometry of width L and infinite height. Doing so, we find that the fitted exponents $\tau=1.14$, $1/\sigma\nu=1+\zeta=1.68$ are close to the theoretical expected values (1.13, and 1.63). In contrast, we found that the distribution including the avalanches touching the window borders has an exponent τ which continuously changes with window size, approaching the theoretical value only at the largest window sizes.This analysis enables us to conclude that the measurements at different window sizes must be take with care, but at the same time, when statistical distributions are properly rescaled, offer other critical exponents which can better characterize the dynamics domain wall in thin films.

[1]G.Durin and S.Zapperi, in “The Science of Hysteresis”, Academic, II, 181 (2005)

[2] E.Puppin, Phys. Rev. Lett., 84, 5415 (2000)

[3] K.-S. Ryu, et al., Nat. Phys. 3,547 (2007)

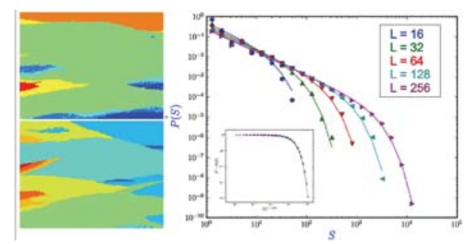

(left) Two avalanche sequences on a Py thin film. (Right) Distribution of avalanche sizes inside windows but not touching the borders. Inset shows the finite-size scaling collapse.

DN-05

Direct observation on a systematic change of the magnetic domain structure with temperature in 50 nm-MnAs/GaAs(001).

J. Kim[1], Y. Lee[1], K. Ryu[2], S. Shin[2], H. Akinaga[3]
1. Quantum Photonic Science Research Center and BK21 Program Division of Advanced Research and Education in Physics, Hanyang University, Seoul, South Korea; 2. Department of Physics and Center for Nanospinics of Spintronic Materials, Korea Advanced Institute of Science and Technology, Daejeon, South Korea; 3. Nanotechnology Research Institute, National Institute of Advanced Industrial Science and Technology, Tsukuba, Japan

Epitaxial ferromagnetic (FM) MnAs film on GaAs(001) has received considerable attention because of the potential for spintronic devices such as spin injection [1], magnetic tunneling junction [2], and magnetologics [3]. Apart from its technical aspect, there has also been a tremendous interest in the fundamental aspect. The MnAs system exhibits the coexistence of FM α-MnAs and non-FM β-MnAs stripes according to a systematic variation of the relative volume ratio in a temperature range of 10 - 45°C via the strain stabilization. In this study, we present the direct observation on a systematic change of the magnetic domain structure with temperature in the MnAs system with a film thickness of 50 nm, investigated by magnetic force microscopy (MFM).
A MnAs film of 50 nm thick was epitaxially grown on a GaAs(001) substrate in a molecular-beam epitaxy system. Ahead of the growth of MnAs, the substrate was heated up to about 600°C in the flux of As_4 for thermal cleaning, followed by the deposition of an undoped GaAs buffer layer of 350 nm thick. Subsequently, the MnAs film was grown at 270°C with a growth rate of about 0.05 nm/s. The longitudinal Kerr rotation was measured in an incident angle of 45° by using a photoelastic-modulator method. The magnetic domain structure has been obtained by using a MFM system, which is basically a scanning-probe microscopy equipped with a magnetic tip. In our measurements, the MFM images were obtained in the interleave mode at a lift scan height of 50 nm. The contrast of the observed MFM images illustrates the interplay between the stray fields above the film surface and the magnetic tip. We also added a special heating/cooling stage to the MFM. The stage yielded a sample temperature ranging from 0 to 180°C in a controlled manner with a negligible thermal drift. This stable performance was achieved by employing the independent configuration for the z scanner of the xy scanner.
Figure 1 presents the Kerr hysteresis loops of the 50 nm-thick MnAs/GaAs(001) film, measured at several temperatures. It should be noted that the saturation magnetization increases as temperature decreases, which is ascribed to the grown FM α-MnAs phase with decreasing temperature. It was found that the film revealed an in-plain easy axis (perpendicular to the stripe direction shown in Fig. 2). Figure 2 shows the temperature dependence of magnetic domain structure in the 50 nm-thick MnAs film, observed on a sample area of 4×4 μm^2 at several temperatures ranging from 20 to 45°C. As temperature decreases, the width of FM α-MnAs comes to be larger while that of the non-FM β-MnAs decreases, which coincides with the enhanced Kerr rotation with decreasing temperature, as in Fig. 1. It should be noted that the magnetic contrast at the surface of FM α-MnAs is due to the stray fields from the end parts of the in-plane magnetic domains. As the temperature decreases, the magnetic contrast becomes clear and the simple domain structures were formed at 35°C. The simple domain is defined as the spin configuration having a single spin direction along the width of FM stripe. As the temperature further decreases, the domains gradually collapse to form lager simple domains, and finally at 20°C the whole film turns to a nearly single magnetic domain except for small unstabilized regions.

[1] V. M. Kaganer et al., Phys. Rev. Lett. **85**, 341 (2000).
[2] V. Garcia et al., Phys. Rev. B **72**, 081303 (2005).
[3] C. Pampuch et al., Phys. Rev. Lett. **91**, 147203 (2003).

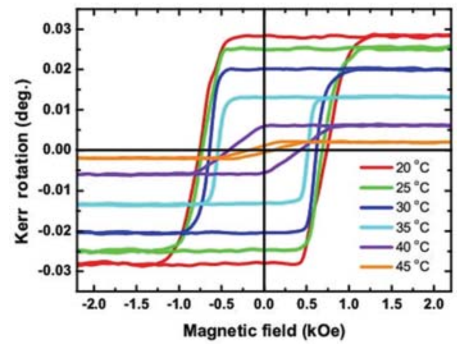

Fig. 1. Kerr hysteresis loops at several temperatures in a magnetic field along the easy axis.

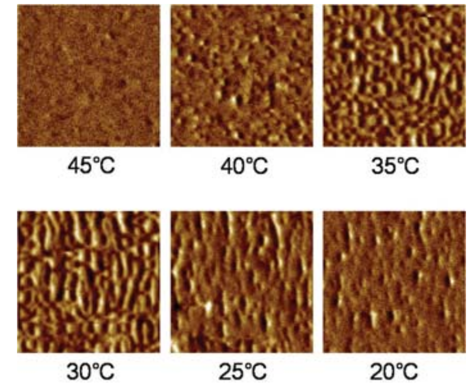

Fig. 2. MFM images of the 50 nm-thick MnAs film according to temperature. The observed scan area is 4×4 μm^2.

DN-06

Magnetic domain structure coupled with temperature and applied voltage in multiferroic $Bi_{0.7}Dy_{0.3}FeO_3$ thin films.

V. R. Palkar[1], P. Kovur[1], S. P. Dattagupta[1], S. Bhattacharya[2]
1. Electrical Engineering, Indian Institute of Technology Bombay, Mumbai, India; 2. Condensed Matter Physics, Tata Institute of Fundamental Research, Mumbai, India

Bismuth ferrite with coexistence of antiferromagnetic and ferroelectric ordering at room temperature has attracted many researchers all over the world. We were successful in inducing ferromagnetism in $BiFeO_3$ without disturbing its ferroelectric properties by doping with Tb/Dy at Bi site in thin films at room temperature [1-2]. In the present work multimode atomic force microscope (Nanoscope IV from Digital Instruments) configured to provide, simultaneously, both the magnetic (magnetic force microscopy-MFM) and the ferroelectric domain structure (piezo-response force microscopy-PFM) in thin film, tens of microns in lateral width and a resolution better than 50 nm is used to study the coexistence of two order parameters at microscopic level. The magnetic domain images are taken in situ at different temperatures and also at different applied voltages using MFM in order to determine the coupling behavior.

Figure 1 directly demonstrates the phase coexistence of magnetic and ferroelectric domain structures at microscopic level in same spatial area (20 μm) of pulse laser deposited $Bi_{0.7}Dy_{0.3}FeO_3$ thin films grown on $Pt/TiO_2/SiO_2/Si$ substrate. The effect of temperature on magnetic domain patterns is clearly evident from the figure 2. As the temperature increases zig-zag domains start getting aligned to form stripe domains. However, around 300°C magnetic domains are disturbed. This is obvious since it crosses the magnetic transition temperature which is of the order of 265°C as seen in DSC curve (Fig. 3). More interestingly the magnetic domain pattern also starts aligning with applied voltage of about 12 volts and remanence is seen even if the voltage is removed (Fig. 4). Due to instrumental limitations it is not possible to increase the voltage further which otherwise could have brought more clarity in the behavior.

The direct evidence of ferroelectric and magnetic domains in same spatial area of $Bi_{0.7}Dy_{0.3}FeO_3$ thin films helps to rule out the chemical phase separation of both the phases at microscopic level. The observed coupling of magnetic properties with temperature as well as with applied voltage in these films is tremendously important since it opens up the area for novel devices.

[1] V. R. Palkar, K.Ganesh Kumara & S. K. Malik,*Appl. phys. Lett.*. 84, 2856 (2004)

[2] V. R. Palkar, R. Anisha, R. Pinto & S. Bhattacharya, *Joul. Mater. Res.* , 22, 2068 (2007)

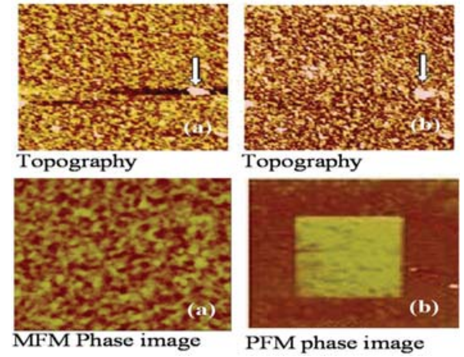

Fig. 1. Multimode scanning probe images of $Bi_{0.7}Dy_{0.3}FeO_3$ thin film (a) Topography and magnetic domain imaging using MFM (b) Topography and piezoresponse imaging using PFM. The image shows unambiguously the ferroelectric writing performed by the poling voltages and the existence of remanent polarization after the poling voltages were switched off. Scanned area for all images: 20 μm

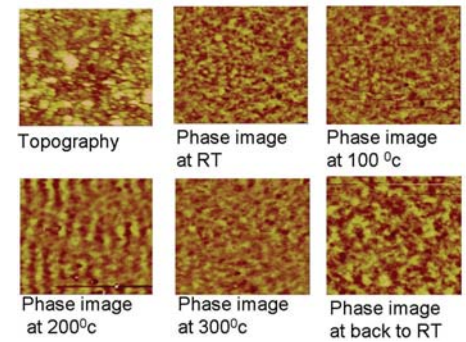

Fig.2. Topography at room temperature and magnetic domain imaging using MFM at different temperatures for $Bi_{0.7}Dy_{0.3}FeO_3$thin film Scanned area for all images: 20 μm

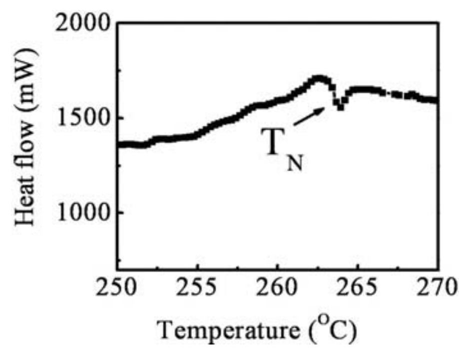

Fig.3. DSC curve for Bi0.7Dy0.3FeO3 thin film indicating transition at ~ 265°C

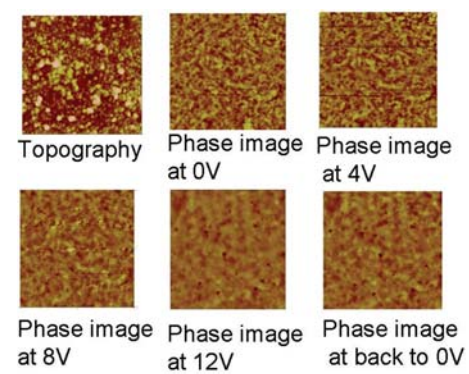

Fig.4. Topography and magnetic domain imaging using MFM at different applied voltages for $Bi_{0.7}Dy_{0.3}FeO_3$thin film Scanned area for all images: 20 μm

DN-07

A detailed magnetization reversal in a single Ni-Fe elliptical dot with several dot sizes.

Y. Endo[1], H. Fujimoto[2], R. Nakatani[2,3], M. Yamamoto[2]
1. Dept. of Electrical and Communication Engineering, Tohoku University, Sendai, Japan; 2. Dept. of Materials Science and Engineering, Osaka University, Suita, Japan; 3. Center for Atomic and Molecular Technologies, Osaka University, Suita, Japan

Introduction

Magnetic dots are much attractive as promising materials for practical applications, including non-volatile magnetic random access memory (MRAM), magnetic storage media and so on. In particular, the magnetization reversal in a single magnetic dot has been studied intensively from both fundamental and applied points of view. An experimental technique to directly observe the detailed magnetization reversal in a single magnetic dot is required.

Recently, we have proposed a new magnetization measurement method, the magnetic field sweeping (MFS)-magnetic force microscopy (MFM)[1-4], which uses a MFM tip as a detector while the magnetic filed is swept. In MFS-MFM, the MFM tip having low magnetic moment is fixed 10 nm above the surface at a point of interest within the dot, and then detects the phase changes (stray fields changes) in that point of the dot as the magnetic field is swept; That is, the precise magnetic state of a local point in a single magnetic dot can be directly observed at room temperature within one minute. We have successfully observed the magnetization reversal in a circular dot and the domain wall motion in a nanowire using MFS-MFM [1-4]. In this study, we report, using MFS-MFM, a detailed magnetization reversal in a single Ni-Fe elliptical dot with several sizes.

Experimental Procedure

Ni-20at.%Fe(Ni-Fe) elliptical dots were fabricated by electron-beam lithography, electron- beam evaporator, and a lift-off technique onto thermally oxidized Si (100) substrates. The thickness was 10 nm, the aspect ratio between the length of the major axis and that of the minor axis was 2 to 1, and the length of the major axis was varied from 200 to 1600 nm. The major axial distance between adjacent dots was 200 nm. The shape of the dot was observed by scanning electron microcopy (SEM). The magnetization process of dot arrays was investigated by magneto-optical Kerr effect (MOKE) magnetometry, while the magnetic state of a single dot was observed using our proposed measurement method, namely, MFS-MFM.

Results and Discussion

Figure 1 shows the curves of the phase vs. magnetic field (*H*) at various points in the 10-nm-thick Ni-Fe elliptical dots with the length of major axis of (a) 400 and (b) 1000 nm, as measured by MFS-MFM. The magnetic field is applied in the longitudinal direction of the elliptical dot. Here, Figs. 1(a-1) and 1(b-1) represent AFM image of each dot, and the position of each measurement is denoted in Figs. 1(a-1) and 1(b-1). Points 1-3 indicate measured points within each dot. For the dot with the length of major axis of 400 nm, points 1 and 3 [Figs. 1(a-2) and 1(a-4)] each displays a stepped hysteresis loop of the phase. These hysteresis loops are attributed to the change in the domain configuration at the dot edges with sweeping magnetic field. At point 2 [Fig. 1(a-3)], weak phase decreases are observed at approximately 100 and - 100 Oe. These phase decreases might be due to the core of a closure domain at the center of the dot. These results reveal that the magnetization reversal in the dot originates from the change in the domain configuration. On the other hand, for the dot with the length of major axis of 1000 nm, points 1 and 3 [Figs. 1(b-2) and 1(b-4)] each displays a hysteresis loop of the phase. These loops are attributed to the magnetization reversal taking place at the dot edge. At point 2 [Fig. 1(b-3)], sharp phase decreases are observed at approximately 50 and -30 Oe. These phase decreases are considered to be ascribed to the domain wall motion within the dot. These results reveal that the magnetization reversal in the dot originates from the domain wall motion within the dot. Thus, the magnetization reversal apparently differs according to the dot size. This difference is due to the fact that the magnetostatic energy is reduced with the increasing of dot size.

As a consequence, it is demonstrated that the detailed magnetization reversal in the elliptical dot with several dot sizes can be directly observed using MFS-MFM. From these results, it is concluded that the magnetization reversal changes from change in the domain configuration to domain wall motion with increasing dot size in the 10-nm-thick Ni-Fe elliptical dot.

[1] Y. Endo *et al*., J. Magn. Magn. Mater. **310**, 2436 (2007).

[2] J. Sato *et al*., Jpn. J. Appl. Phys. **46**, 4117 (2007).

[3] Y. Endo *et al*., Jpn. J. Appl. Phys. **46**, L898 (2007).

[4] Y. Endo *et al*., to be published in J. Appl. Phys. (2008).

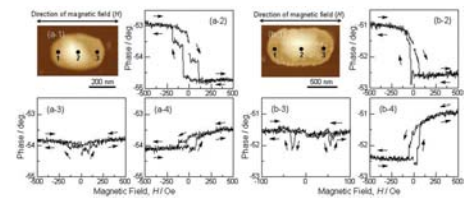

Fig. 1. AFM images of 10-nm-thick Ni-Fe elliptical dots with the length of the major axia of (a-1) 400 and (b-1) 1000 nm. Points 1-3 indicate measured points within the dot. Curves of phase vs. magnetic field (*H*) at various points in the Ni-Fe elliptical dots with the lengths of (a-2)-(a-4) 400 and (b-2)-(b-4) 1000 nm measured by MFS-MFM. The magnetic field is applied in the longitudinal direction of the dot.

DN-08

High-resolution MFM imaging of in-plane magnetic field using transient oscillation.

H. Saito[1], G. Egawa[1], S. Ishio[1], G. Li[2]
1. Faculty of Engineering and Resource Science, Akita University, Akita, Japan; 2. School of Physics Science & Technology, Southwest University, Chongqing, China

I. INTRODUCTION
Magnetic force microscopy (MFM) is a powerful tool to investigate microscopic magnetic domain structures and further improvement of spatial resolution is required. We recently proposed a new MFM imaging method of in-plane magnetic field gradient using the transient oscillation of a tip [1]. When a MFM tip moves to a next measuring position under a constant driven frequency of the tip, its oscillation frequency shifts from the driven frequency due to the transient oscillation of the tip. Measuring of the frequency change during tip scanning can image in-plane magnetic field gradient. Using a monopole type MFM tip, in-plane magnetic field gradient of $\partial^2 H_x/\partial z^2$ is imaged by this method, where x and z are the in-plane and perpendicular directions to a sample surface. On the other hand, conventional phase detection images perpendicular magnetic field gradient of $\partial H_z/\partial z$. Therefore, higher spatial-resolution is expected for the present method because of the higher order differential effect of magnetic field. In this study, we evaluate the spatial resolution of the present method and discuss the possibility of high resolution magnetic imaging.
II. EXPERIMENT
Figure 1 shows the block diagram of MFM measurement of in-plane magnetic field gradient. We used a phase detection MFM (JSPM-5400, JEOL Ltd.) with a frequency measurement apparatus (easyPLL, Nanosurf®) for detecting the phase and frequency during a lift-mode scanning with a constant tip-sample distance. The tip was driven at a constant frequency near the resonant frequency of the tip in vacuum atmosphere. CoCrPt-SiO_2 perpendicular magnetic recording media was observed by using high-coercivity FePt tips (H_c: 8kOe) made by NITTO OPTICAL CO., LTD. The magnetized direction of the tip is perpendicular to the sample surface.
III. RESULTS
Figure 2 (a), (c) show the MFM images of the perpendicular magnetic recording medium measured by conventional phase detection and the present frequency detection, respectively. These images ware observed at the same scan and the scanning direction was the horizontal direction of the image. The recording density of the media is 500 kfci and the mechanical quality factor Q is about 7000. Fig. 2 (a) is a conventional MFM image of perpendicular magnetic field gradient. Recorded bits and the track edges are observed. On the other hand, the frequency detection method images in-plane magnetic field gradient along the scanning direction and recorded bits are clearly observed without track edges in Fig. 2(c). The in-plane magnetic field gradient image was also obtained by making a differential picture of the phase detection image in the scanning direction. When the MFM tip is a monopole type tip, the signal of the phase image corresponds to $\partial H_z/\partial z$ and the signal of the differential picture corresponds to $\partial^2 H_x/\partial z^2$. This is the evidence that the present method can detect the higher order magnetic field gradient. The quality of the differential picture is worse than that of the present frequency detection image.
Figure 2 (b), (d) are the corresponding spectra of the recorded area of Fig. 2(a) and (c). These spectra were calculated by averaging the spectra of line profiles in the scanning direction. Here the peak signal corresponds to the recording signal of 500 kfci. For the conventional phase detection, the intensity of the spectrum decreases and takes a constant value with increasing spatial frequency k_x. Spatial resolution can be evaluated by the critical spatial frequency where the intensity of MFM signal equals to the noise [2]. The critical frequency is about 24 (1/µm) and the spatial resolution is about 20nm. On the other hand, for the frequency detection, the intensity of the spectrum takes a maximum and gradually decreases with increasing k_x. The frequency decay of the signal is smaller than that of the phase detection. The behavior of MFM signal is consistent with the transfer function spectra of $\partial H_z/\partial z$ and $\partial^2 H_x/\partial z^2$. In addition, the noise is not white and the intensity decreases with increasing k_x. This character is thought to be suitable for high-resolution imaging. The spatial resolution is almost the same as that of the phase detection. The origin of the noise and the possibility of high-resolution imaging of the present method will be discussed.

1. H. Saito, G. Egawa, S. Ishio, G. Q. Li, 52nd MMM Conference(2007)GR-02

2. H. Saito, R. Sunahara, Y.W. Rheem and S. Ishio, IEEE.Trans.,Mag., 41, 4394(2005)

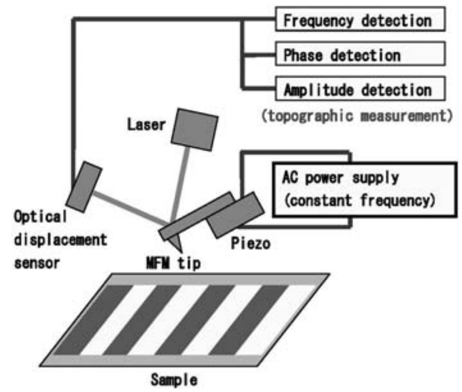

Fig. 1 Block diagram of MFM measurement.

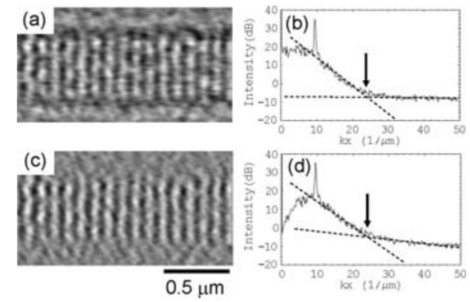

Fig. 2 Phase detection image [(a)] and frequency detection image [(c)] and the corresponding spectra [(b), (d)] for a CoCrPt-SiO_2 perpendicular magnetic recording medium.

DN-09

Characterization of coercivity of magnetic force microscopy probes.

M. Jaafar, A. Jacas, W. Rosa, A. Asenjo
Instituto de Ciencia de Materiales de Madrid, ICMM-CSIC, Madrid, Spain

Magnetic Force Microscopy (MFM) reveals as a useful technique to analyze the local magnetic behavior of the materials. Sometimes,the MFM data are complementary to the magnetic characterization performed by using standard macroscopic methods. So far, in the case of nanometric devices, only few techniques can supply valuable information about the behavior of individual nano-objects, and the MFM presents highest resolution. In this work a Nanotec Electronica S.L. microscope has been conveniently modified to apply magnetic fields in axial direction (up to 1.5 kOe) and in-plane direction (up to 2.0 kOe). The application of a magnetic field during the MFM operation modifies the magnetic state of the tip as well as the magnetic state of the sample. In this concern, previous MFM tip characterization can help to improve the quantitative MFM image interpretation.Notice that the evolution of the MFM signal versus the externally applied magnetic field can be used to obtain the local hysteresis loop of the sample or the hysteresis loop of the MFM probes. In this work, axial and transeverse hysteresis loops of the probes have been generated by measuring the changes in the standard MFM images observed when the magnetic field is applied. The variation of the MFM signal is adscribed to the modification of the magnetic state of the probes (Fig.1). This is enabled by the large coercitivity (1.7 kOe) of the checked longitudinal recording media. The properties of the probes depend on the coating material, the macroscopic tip shape and tip radius (Fig.2). In addition to the standard MFM images, we have performed the so-called “3Dmodes” measurements.This is possible thanks to the main advantage of the Variable Field Magnetic Force Microscope (VFMFM) which is its mechanical stability under variable external magnetic field for both in-plane and out-of plane directions that allows the observation of spin dynamic in real time.

In the “3D modes” a magnetic image is acquired along a surface scan as a function of the “in situ” applied magnetic field. Images (a) and (b) of fig. 3 correspond respectively to the characteristic topography and magnetic signal of a hard disk with parallel domains written along the track. The figures 3c and 3d correspond to the frequency shift measured along the black line marked in (a) and (b) images for increasing (c) and decreasing (d) magnetic fields. The vertical scale in 3c image is the external magnetic field that is decreased at each scan line from +60 mT at the upper line (position 1) to -60 mT at the lower scan line (position 2). In figure 3d the magnetic field increases from -60 mT at the lower scan (position 3) to +60 mT at the upper scan (position 4). The switching of the contrast when pass thorough the coercive field of the MFM probe (around 40mT) is observed in both “3Dmodes” images. Measuring the contrast along the dashed lines in the figures 3c and 3d the hysteresis loop of the MFM probe is obtained. We can observe the mechanical stability of the system since the position of the magnetic walls of the hard disk remains constant when varying the magnetic field. In conclusion, we can use this technique to performed local hysteresis loops of nanoelements in situ with the VFMFM thanks to the mechanical stability in the 3Dmodes and the previous characterization of the different probes.

[1]J.J. Sáenz et al.J.Appl.Phys.62(1987);[2]Y.Endo et al. JMMM 310(2007);[3] A. Asenjo et al.J.Appl.Phys. 100(2006);[4]M.Jaafar et al. 2007 IEEE Nano in press;[5]C.Gómez-Navarro et al.2002 Nanotechnology 13,314

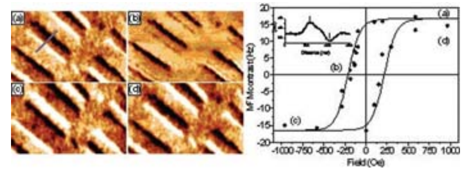

MFM images of a commercial longitudinal recording media after applying (a) +60mT, (b) -20mT, (c) -60mT (d) +60mT (e) MFM contrast measured across the bit transitions as a function of the applied axial field.

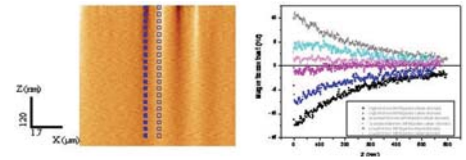

Evolution of the MFM contrast in a commercial hard disk as a function of the distance between tip and sample for some MFM probes. The profiles are measured from a 3D image (fast scan is Z and slow scan is X)

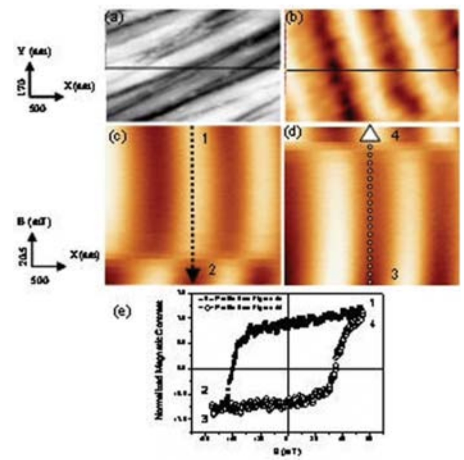

(a) Topography of a commercial hard disk (b) MFM image obtained in the same area (c) “3dmode” image where the horizontal x direction is the frequency shift (magnetic signal) for different out-of-plane magnetic fields; the acquisition direction is from top to down (d) similar “3dmode” image acquired increasing the field from the lowest scan to the top scan (e) Hysteresis loop of the MFM probe obtained from the marked lines in (c) and (d)

DN-10

Calibration of MFM probe tips for measurements in external in-plane magnetic fields.

A. Ehresmann[1], T. Weis[1], D. Engel[1], V. Höink[2], J. Schmalhorst[2], G. Reiss[2]
1. Institute of Physics and Centre for Interdisciplinary Nanostructure Science and Technology (CINSaT), University of Kassel, Kassel, Germany; 2. Thin Films and Nanostructures, Department of Physics, University of Bielefeld, Bielefeld, Germany

The analysis of MFM measurements carried out in external magnetic fields H_{MFM} parallel to the sample plane, i.e. perpendicular to the effective magnetization direction of commercial MFM probe tips, is difficult due to the influence of the magnetic fields not only on the sample but also on the tip's magnetic properties. In the simplest approximation an external in-plane magnetic field tilts the effective tip magnetic moment from the perpendicular direction by a certain angle. This means that not only the magnetic state of the sample, but also the alteration of the tip magnetic characteristics affects the MFM image.

To measure the effect of the in-plane magnetic field on the magnetization state of the MFM probe tip dedicated calibration samples were fabricated and a method was developed to extract the change in the magnetization state of the probe tip from the MFM images. This information can be used to analyse MFM images recorded by this tip and disentangle magnetization state changes of the probe tip and the sample by an external field. The calibration sample consists of an exchange biased thin film magnetic bilayer of a ferromagnet and a antiferromagnet. Preferably the layer system is chosen to have a large exchange bias field. After initialization of the exchange bias by, e.g., field growth or field cooling homogeneously over the whole sample, the sample is covered by a resist film (e.g. PMMA) thick enough to stop 10keV He ions. The resist is then patterned by lithography in stripes with their long axes perpendicular to the exchange bias direction. A subsequent 10keV He-ion bombardment in an external magnetic field H_{IB} antiparallel to the original exchange bias direction leads to an effective antiparallel exchange bias in the areas not covered by the resist mask with respect to the initial exchange bias direction. Finally the resist is removed. This results in a sample with lateral magnetic stripes with mutually antiparallel effective exchange biases without a topographic contrast [1–4 and refs therein]. Between the two exchange bias fields of the neighbouring stripes the magnetization state remains essentially uninfluenced by the magnitude and direction of the external in-plane magnetic field, therefore delivering a calibration sample without topography contrast and stable magnetic patterns for certain in-plane magnetic fields. Fig. 1(b) shows an MFM image of the topographically flat, but magnetically patterned sample with a MOKE hysteresis curve (Fig 1(a)) for applied in-plane fields.

The domain walls between the adjacent artificial antiparallely magnetized stripe domains may be modelled by an arctan function [5]. Then the magnetic force of the sample strayfields H_S on the MFM tip can be calculated when the following assumptions are made: 1.) The magnetic patterns of the sample are large compared to the MFM tip. 2.) The distance between the tip and the sample is large enough to allow the tip magnetization being modelled as a magnetic dipole moment. 3.) Applicability of the point-dipole approximation [6]. For MFM measurements in non contact mode the image contrast is not dependent on the force, but on the force gradient. If this is considered and with some further simplifications the response of the MFM for a measurement with a tip whose magnetization state is described by a magnetic dipole moment tilted by the angle θ between magnetic tip moment and the sample normal may be modelled by $R(H_{MFM}) \propto |\mu_{tip}|(\sin\theta(H_{MFM}) d^2H_{S,x}/dz^2 + \cos\theta(H_{MFM}) d^2H_{S,z}/dz^2)$

To calibrate a commercial non contact MFM tip by our calibration sample, MFM images have been taken at different values of the externally applied in-plane magnetic field H_{MFM}. The grey values of the MFM response along the stripe direction have been summed up for each image and the resulting profiles were fitted by a function corresponding to the above equation for the MFM response. With this fit the angle θ can be determined as a function of the externally applied in-plane magnetic field. This can be used to separate the influence of the external magnetic field on the tip magnetic moment from its influence on the magnetization state of real samples.

[1] A. Ehresmann et al., Phys. Stat. Sol (b), 243, 29 (2006)

[2] K. Theis-Bröhl et al., Phys. Rev. B 73, 174408 (2006)

[3] A. Ehresmann, Recent Res. Devel. Applied Physics 7, 401-21 (PartII) (2004)

[4] A. Mougin et al., J. Appl. Phys. 89 6606-8 (2001)

[5] D. Rugar et al., J. Appl. Phys., 68, 1169 (1990)

[6] U. Hartmann, Physics Letters A 137(9), 475–478 (1989)

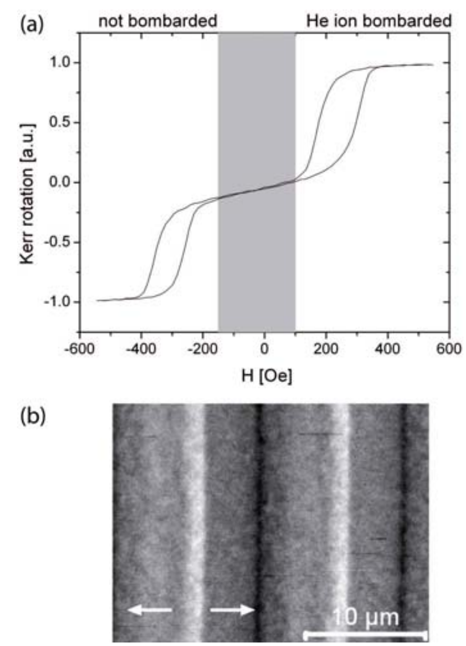

(a) Remagnetization curve of an IrMn(15nm)/CoFe(3nm) calibration sample with in-plane external magnetic field and with two antiparallel exchange bias directions. In the grey shaded region the sample magnetization changes only negligibly with applied external field. (b) MFM image of the above sample in remanence. Arrows denote the remanent magnetization directions in the stripes.

DN-11

An experimental investigation of the magnetically active volume in a magnetic force microscopy tip.

N. E. Mateen, *M. Gibbs*, M. Rainforth
Department of Engineering Materials, University of Sheffield, Sheffield, United Kingdom

The determination of tip active volume is a particularly long-standing problem for the quantitative interpretation of MFM images. Micromagnetic modeling has been used to estimate the image reproduced in MFM from different active volumes [1], but it has never been possible to confirm these calculations experimentally.
Using focussed ion beam milling, and a commercial pyramidal tip, we have explored changes in the fine scale resolution to be seen in atomic and magnetic force microscopy. On a single tip we have successively removed the magnetic coating, taking great care to avoid damage to the tip apex (see Fig.1). From this, using a reference sample (Veeco recorded tape) we have demonstrated that the active volume of magnetic material in magnetic force microscopy extends some distance beyond the immediate tip apex, and that when the effective diameter of material on the tip is reduced to be close to the critical dimension for single domain behaviour, there is a marked change in the amplitude of the tip response.
The AFM detail is not enhanced by the milling as the region at the tip apex was not involved during the milling process. In the MFM scans we demonstrate a slight increase in fine scale detail observed, but also a significant decrease in signal magnitude as the tip is milled (see Fig.2). We interpret this as changes in the micromagnetic configuration close to the tip apex, and ultimately to the removal of material decreasing the effective tip moment. This is the first time that there has been an experimental estimate of the magnetically volume in an MFM scan.

[1] Tomlinson SL, Farley AN. Micromagnetic model for magnetic force microscopy tips. Journal of Applied Physics 1997;81(8):5029-5031

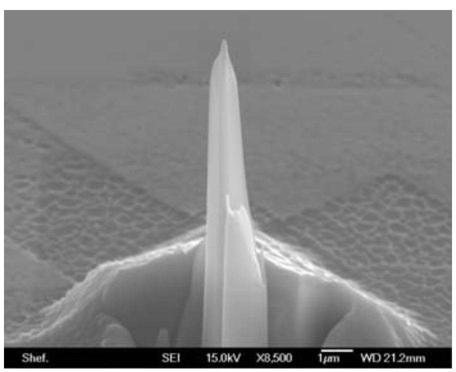

Fig.1 SEM image after the fourth step of FIB milling of a standard CoCr coated MESP MFM tip

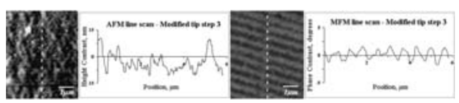

Fig 2 Correlated image pair of AFM/MFM images, with their associated pixel perfect line scans, after the same step of the FIB milling process as for tip in Fig. 1

DN-12

Plateau probes to enhance the capabilities of magnetic force microscopy.

N. Amos[1], R. Ikkawi[1], R. Fernandez[1], A. Lavrenov[1], A. Krichevsky[1], D. Litvinov[2], S. Khizroev[1]
1. Electrical Engineering, University of California, Riverside, Riverside, CA; 2. Center for Nanomagnetic Systems, University of Houston, Houston, TX

While magnetic devices were constantly scaled down, the spatial resolution achievable with commercially available magnetic force microscopy (MFM) probes remained almost the same, which makes it difficult to adequately study next-generation magnetic media. The state-of-the-art commercially available MFM probes promise an optimal spatial (or lateral) resolution of approximately 25 and 15 nm at ambient and ultra-high vacuum (UHV) conditions, respectively [1]. Our approach is to use silicon based plateau probes on which magnetic thin films, exhibiting magnetic properties similar to the ones found in various types of magnetic recording media, are effectively grown and then milled with focused ion beam (FIB) to fabricate high resolution magnetic force microscopy (MFM) tips [2]. The fabrication sequence is shown in Figure 1. Finally, the FIB-fabricated almost perfectly flat plateau-like tips with the radius ranging from 0.1 to several microns could be used as substrates for further thin film deposition with finely controlled deposition/growth properties. In this manner, not only the magnetic composition but also the orientation of the magnetization at the "tip" of the probe could be finely controlled. Such traditional thin films as CoCrPt based alloys, Co/Pd multilayers, and FePt L10 media were deposited on the plateau probes. Figure 2left shows an SEM image of CoCrPt granular media, which was sputter deposited on a plateau probe. Focused magneto-optical Kerr microscopy was used to directly compare the magnetic properties of media sputtered on a silicon substrate and on the plateau probes. Figure 2right shows a hysteresis curve for a FIB-fabricated MFM tip with Co/Pd multilayers with coercivity value of about 5000 Oe, which is an order of magnitude greater than the coercivity value of commercially available MFM probes. A detailed study will be presented to achieve MFM resolution of less than 10 nm at ambient condition.

[1] P. C. D. Hobbs, D. W. Abraham, H. K. Wickramasinghe, "Magnetic force microscopy with 25-nm resolution", Appl. Phys.Lett. 55, 2357 (1989)

[2] S. Khizroev, W. Jayasekara, J. A. Bain, R. E. Jones, Jr., M. H. Kryder, "MFM quantification of magnetic fields generated by ultra-small single pole perpendicular heads," IEEE Trans. Magn. 34 (4), 2030 (1998)

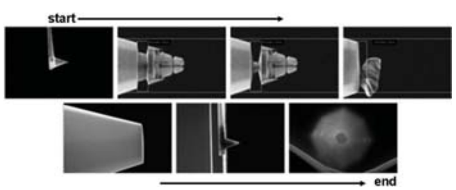

The main process flow for the FIB fabrication of MFM probes.

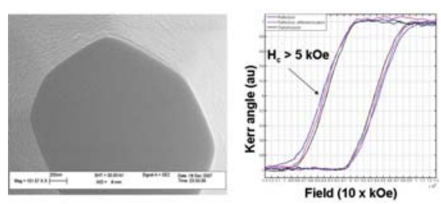

(left) SEM image of a plateau probe after the deposition of CoCrPt granular media, showing magnetic grains with a few-nanometer diameter. (right) Focused Kerr measurements indicating 5000 Oe coercivity.

DN-13

Fabrication of Magnetic Force Microscopy Tips via Electrodeposition and Focused Ion Beam Milling.

O. Cespedes, A. Luu, F. F. Rhen, J. D. Coey
Physics Department, Trinity College Dublin, Dublin, Ireland

Summary:
In this work we describe a method for the fabrication of magnetic force microscopy tips via electrodeposition and focused ion beam milling. Very high aspect ratios and interacting magnetic moments of order 0.1 to 1 pAm^2 (10^10 to 10^11 Bohr magnetons) are possible without altering significantly the tapping resonant frequency of the cantilever. These tips can achieve high resolution (5-10 nm) at room temperature and open atmosphere. They can also be fabricated into any shape, with applications for the patterning of nanostructures via atomic force microscopy.

Fabrication method and results:
Our method to fabricate magnetic force microscopy tips allows the deposition of relatively high amounts of magnetic materials without changing significantly the total mass of the tip. The process consists of four steps (see Figure 1 for schematics and images of the process):
1.- We deposit a 100 nm bi-layer Al/Ag on top of the tip. The aluminum layer is afterwards thermally oxidized / passivated.
2.- With a focused ion beam, we open a hole of some 100 nm where the deposition will be made (edge of the tip).
3.- An electric contact is made with the silver layer before the tip is put into a solution with the ions corresponding to the desired material. The only metallic area open to the solution is the gold layer where the hole has been opened. When an electric potential above the rest value is applied between the tip and the solution the ions flow into the previously milled hole.
4.- (Optional) Further patterning of the deposited material and increased aspect ratio is possible by using a focused ion beam as a sharpening tool (Figure 2).
With this fabrication method we have achieved the deposition of significant amounts of interacting magnetic material while avoiding big shifts and artifacts in the tapping resonant frequency. We must also emphasize that the geometry of the tip can be roughly controlled via the electrodeposition parameters at the step # 3. Electrodeposited materials from highly concentrated solutions at relatively low pHs and voltages give as result dense depositions of smooth surfaces and small grains [1]. As the applied voltage for electrodeposition is increased so does roughly the grain size. By decreasing the ionic concentration while working at low voltages we can also obtain elongated, thread-like or fractal-like structures.
The focused ion beam sharpening gives us the possibility to enhance the aspect ratio or to modify at will the tip geometry after the electrodeposition. This results into enhanced topographic images of samples with deep structures and high resolution magnetic images on smooth surfaces (Figure 3). Furthermore, the method allows the deposition and patterning of material in the desired position of an atomic force microscopy tip, which makes of them ideal tools for nano-stamp patterning.

[1] T. R. Ní Mhíocháin and J.M.D. Coey, Phys. Rev. E 69, 061404 (2004).

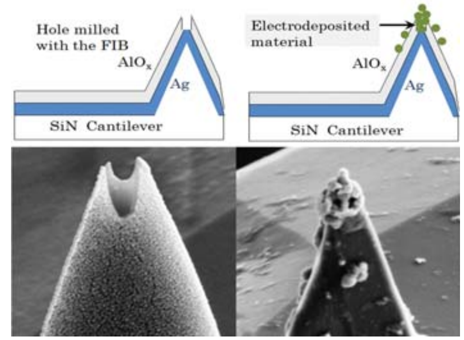

Figure 1: Top: Schematic of the fabrication method. Bottom left: 5 x 5 microm SEM image of a FIB milled hole on the edge of an AFM tip covered by an Al/Au/Ti multilayer. Bottom right: 10 x 10 microm SEM image of an electrodeposited CoPt nanoparticules inside the hole previously milled. The nanoparticle at the top of the tip (interacting material at usual lift heights) has a magnetic moment of about 0.1-1 pAm^2.

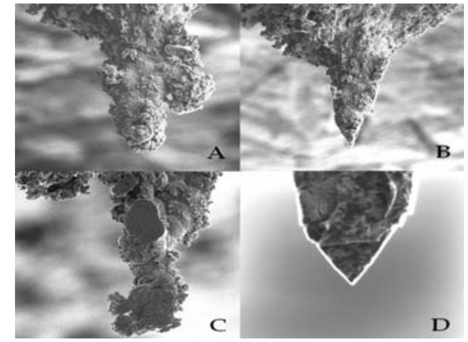

Figure 2 caption: Sharpening of an elongated nickel tip electrodeposited under low concentration-high voltage conditions. Sharpening is done in two different planes at 90 degrees (top-bottom). Images A to C are 10 x 10 microm and image D is 5 x 5 microm.

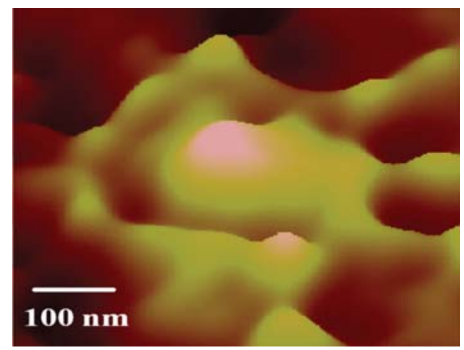

Figure 3: High resolution magnetic force microscopy image of a Co-doped SnO2 grain (thin film courtesy of Dr. Ciara Fitzgerald) obtained at room temperature and open atmosphere with a commercial scanning instrument and a tip fabricated following the method described.

DN-14

Contact Mode Scanning Hall Probe Microscopy.

T. Ohashi[1], H. Osawa[1], A. Sandhu[1,2]
1. Quantum Nanoelectronics Research Center, Tokyo Institute of Technology, Tokyo, Japan; 2. Electrical and Electronic Engineering, Tokyo Institute of Technology, Tokyo, Japan

Scanning Hall Probe Microscopy (SHPM) is valuable tool for monitoring localized magnetic fields at the surfaces of ferromagnetic materials and vortices in superconductors [1-2]. Safely lowering the Hall probe to the sample surface without damaging the sensor is a critical stage of the measurement procedure. High spatial resolution SHPM imaging is carried out using Hall sensors with scanning tunneling microscope tips (STM-tip) integrated adjacent to the probes. In these systems, the Hall probes are attached to piezoelectric actuators and lowered to the sample surface until a tunneling current is detected, when feedback circuitry is used to control the sample to probe separation. Hall probes with STM-tips can only be used for conducting samples. Further, such systems require complicated electronics to monitor tunneling currents and control the position of piezoelectric actuators. SHPM systems could be made more robust and easier to use if probe positioning and movement could be achieved without STM tips and piezoelectric actuators.
Here, we describe the features of a SHPM system where the Hall probe is attached to a flexible cantilever and the moment of contact with samples is monitored using a simple strain gauge embedded into the cantilever. This 'contact-mode' SHPM is a simple means of measuring non-conducting samples over large areas and wide temperature ranges.
Fig.1 is a schematic diagram of the Hall probe, strain gauge and flexible cantilever. The Hall probe was a 2 micrometer x 2 micrometer AlGaAs/InGaAs 2DEG sensor fabricated by conventional photolithography. A protective layer of silicon nitride was sputtered onto the probe. In contrast to our previous devices, there is no STM-tip adjacent to the sensor.
The cantilever was lowered towards the surface of a sample using a high resolution stepping motor and contact with the sample monitored by the output from a balanced bridge circuit with the strain gauge as one of its arms. The contact mode SHPM was used to measure domains at the surfaces of 50 micrometer thick garnets.
Fig. 2 is 50 micrometer x 50 micrometer contact mode magnetic image of the garnet. The difference between the black and white regions is 212 G and the domains have a width of 10 micrometers.
The contact mode SHPM can also be used at cryogenic and elevated temperatures.

[1] A.Oral etal: Appl.Phys.Lett., 69, 1324, (1996)

[2] A. Sandhu etal: Nanotechnology 15, S410, (2004)

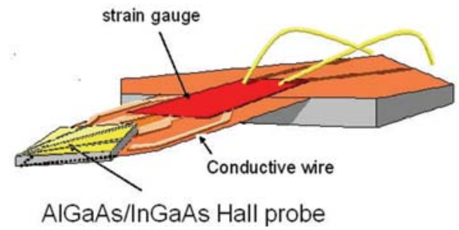

Schematic of Hall probe, strain gauge and flexible cantilever for contact mode SHPM

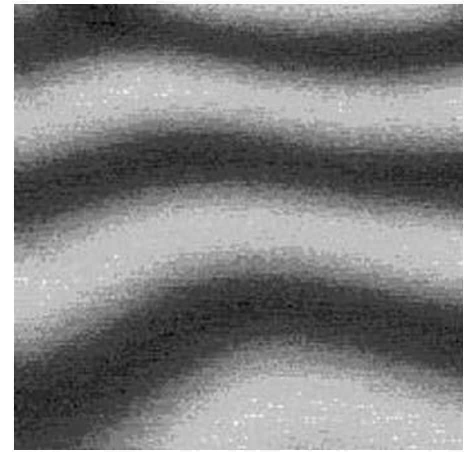

Magnetic image (50um x 50um) measured in contact with a garnet sample .

DN-15

Variable Temperature-Scanning Hall Probe Microscopy (VT-SHPM) with GaN/AlGaN Two-Dimensional Electron Gas (2DEG) Micro Hall Sensors in 4-400K range, Using Novel Quartz Tuning Fork AFM Feedback.

R. Akram, M. Dede, A. Oral
Department of Physics, Bilkent University, 06800, Ankara, Turkey

In this report, we present the fabrication and variable temperature (VT) operation of Hall sensors, based on GaN/AlGaN heterostructure with a two-dimensional electron gas (2DEG) as an active layer, integrated with Quartz Tuning Fork (QTF) in atomic force-guided scanning (AFM) Hall probe microscopy (SHPM)[1]. Physical strength and wide band gap of GaN/AlGaN heterostructure makes it a better choice to be used for SHPM at elevated temperatures, compared to other compound semiconductors (AlGaAs/GaAs and InSb), which are unstable due to their narrower band gap and physical degradation at high temperatures.

GaN/AlGaN micro hall probes were produced using optical lithography and reactive ion etching. The active area, Hall coefficient, carrier concentration and series resistance of the Hall sensors were ~1x1μm^2, 10mΩ/G, 6.3x1012cm^{-2} and 12kΩ at room temperature and 7mΩ/G, 8.9x1012cm^{-2} and 24kΩ at 400K, respectively.

A novel method of AFM feedback using QTF has been adopted. This method provides an advantage over STM feedback, which limits the operation of SHPM the conductive samples and failure of feedback due to high leakage currents at high temperatures. Figure 1 shows the assembly of GaN Hall probe on a 32kHz Quartz Crystal Tuning fork for AFM feedback SHPM. Simultaneous scans of magnetic and topographic data at various pressures (from atmospheric pressure to high vacuum) from 4.2K to 400K will be presented for different samples to illustrate the capability of GaN/AlGaN Hall sensors in VT-SHPM. Figure 2 shows the scan results of a hard disk sample at 77K.

Scanning Hall Probe Microscopy (SHPM) Using Quartz Crystal AFM Feedback, M. Dede, K. Urkmen, O. Girisen, M. Atabak, A. Oral, I. Farrer, and D. Ritchie, Journal of Nanoscience and Nanotechnology, accepted for publication

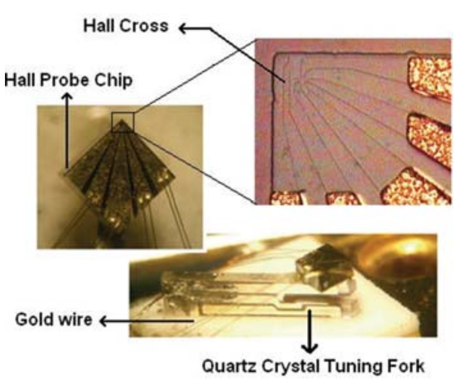

GaN/AlGaN 1μmx1μm Hall Probe mounted on a Quartz Crystal Tuning fork.

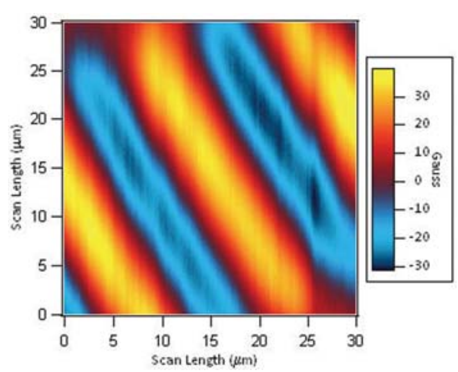

Scanning Hall Probe Microscope Image of a Hard Disk sample at 77K.

DO-01

Optical reading from videotapes using magnetic garnet film.

M. Kishida[1], N. Hayashi[1], K. Iwasaki[2], H. Umezawa[2], T. Nomura[3]
1. Science and Technical Research Laboratories, NHK (Japan Broadcasting corporation), Tokyo, Japan; 2. Research & Development Division, FDK Corporation, Sizuoka, Japan; 3. Department of Electrical, Electronics and Information Engineering, Shizuoka Institute of Science and Technology, Sizuoka, Japan

Introduction

In broadcasting stations, the recording media used to archive large volumes of content have mainly been magnetic videotapes. In the near future it will become necessary to transfer all this content from videotapes to new types of recording media. However, the time required to do so is prohibitive because videocassette recorders (VCRs) can only read data from videotapes at single (1x) speed. In order to greatly increase the speed at which videotape data are read, we propose an optical reading method using a magnetic garnet film; this will allow several data tracks to be read in parallel.

Magnetic garnet film

Bismuth (Bi)-substituted magnetic garnet films have a large Faraday coefficient and recorded patterns on a videotape can be transferred to the film simply by placing it in close proximity to the videotape.[1][2] Our trial films have a Faraday angle rotation of approximately 5 degrees per micrometer film thickness when a green laser (wavelength = 532 nm) is used. We observed the data pattern transferred from the videotape using a polarizing microscope. The thickness of the magnetic garnet film was 0.5 µm. A reflected film of thickness 50 nm and a protective film of thickness 20 nm were sputtered on the magnetic garnet film. A sample videotape in D-3 format was used and data were recorded using a D-3 VCR. The transferred data pattern, an example of which is shown in Figure 1, was clearly observed by the microscope. For the D-3 format (NTSC system), the track pitch is 20 µm and the bit length is between 0.385 and 1.3475 µm.

Reproduction of videotape data using laser and magnetic garnet film

We have designed an experimental setup to reproduce the signal from a videotape using a combination of a laser and a magnetic garnet film, as shown in Figure 2. The videotape is run using a VCR and is placed in contact with the magnetic garnet film. A linearly polarized laser beam is then directed onto the film. The plane of polarization of the reflected laser beam is rotated by the Faraday effect. Therefore, the data stored on the videotape can be reproduced using a polarizing beam splitter (PBS) and a differential amplifier. This data reproduction scheme is similar to the magneto-optical (MO) disk system.

In practice, the recording scheme adopted by VCRs involves a helical scan. However, in our demonstration we used videotape on which a data track was recorded horizontally. The tape speed was 1x with respect to the VHS system, which corresponds to 0.4x with respect to the D-3 system.

Figure 3 shows the spectrum of the reproduced signal at the bit length of 0.385 µm. A carrier-to-noise ratio (CNR) of over 30 dB was measured. At a speed of 4x with respect to the D-3 VCR system, the CNR was again more than 30 dB. We expect that at higher speeds, for example 40x, the CNR will be almost as high.

Conclusion

We have proposed a method to read data optically from a videotape using a magnetic garnet film. Our trial film of thickness 0.5 µm is able to induce a Faraday angle rotation of approximately 2.5 degrees when a green laser is used. We achieved reproduction of a videotape with over 30 dB of CNR at the minimum bit length of the D-3 format. We believe that this is sufficient to reproduce D-3 format videotapes optically. However, in order to apply this method to higher-density format videotapes, the resolution of the magnetic garnet film must be improved. It is also necessary to develop a parallel reproduction scheme for high-speed data reading.

[1] T. Nomura, "A new magneto-optic readout head using Bi-substituted magnetic garnet film", IEEE Trans. Magn., vol.21, pp.1545-1547, September 1985

[2] T. Terada et al., "A novel flying magnetic readout head based on magneto-optic transfer", IEEE Trans. Magn., vol.34, no.4, pp.2006-2008, July 1998

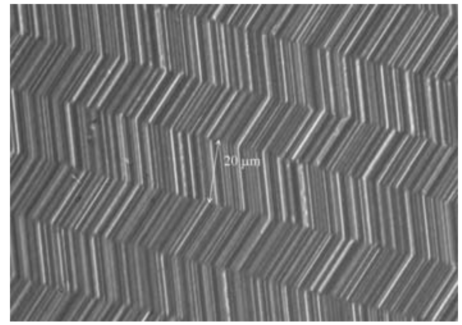

Figure 1 Example of transferred data pattern from videotape in D-3 format

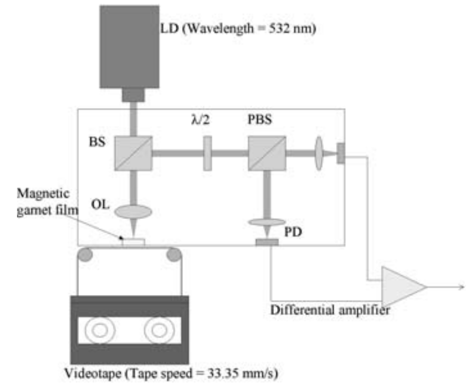

Figure 2 Experimental setup

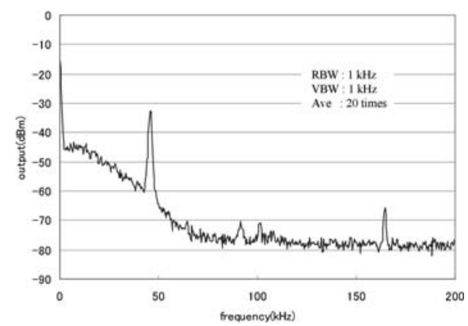

Figure 3 Spectrum of reproduced signal at the bit length of 0.385 µm

DO-02

The influence of the implantation on the magneto-optical properties of $(YBiCaSmLu)_3(FeGeSi)_5O_{12}$ surface.

L. Kalandadze
Batumi State University, Batumi, Georgia

We investigated the magneto-optical properties of the ion implanted $(YBiCaSmLu)_3(FeGeSi)_5O_{12}$ garnet films. The implantation process was carried out at the room temperature by Ne^+ ions with energy of 100 KeV and with various doses $(0{,}5\surd2{,}5)\times10^{14}$ ion/cm^2.
For investigating the magneto-optical properties of a garnet surface we have chosen the equatorial Kerr effect (EKE). The EKE consists in a change in the intensity of linearly polarized light reflected from the sample in the case of reversal of magnetization of the sample.
The research of the spectral dependences of the EKE for unimplanted and ion implanted with various dose garnet films has shown that the ion implantation significantly influences on the magneto-optical properties of the garnet films.
For examples, Figure 1(a) presents the dependences of the EKE on the quantum energy of incident light for the films before and after the implantation process with various doses. The angle of light incidence on the sample $\phi = 70^0$.
Fig.1.Dependences of the EKE on the quantum energy of incident light (a) and on the angle of light incidence (b) for the $(YBiCaSmLu)_3(FeGeSi)_5O_{12}$ films before (curve1) and after the process of implantation with various doses: 0,5 (curve 2), 1,5 (curve 3), and 2,5 (curve 4) $\times10^{14}$ ion/cm^2.
According to the Figure 1(a) the magneto-optical spectrum of the unimplanted garnet surface has the magneto-optical maxima in the region of light quantum energies 2,6; 3,4 and 4,5 eV. Most garnet films are characterized by the similar peaks (1). For the implantation with the minor doses the spectrum character of the EKE is practically the same. But it significantly changes when doses are $(1{,}5\surd2{,}5)\times10^{14}$ ion/cm^2. Specifically, an increase of the implantation dose causes a decrease of the magneto-optical maxima in the region of light quantum energies 3,4 and 4,5 eV, which may be connected with the split of FeO_4 and FeO_6 molecular complexes, where intensive electron transition takes place with energy more than 3 eV. But the increase of the implantation dose causes reduction of the negative magneto-optical maximum in the region of light quantum energy 2,6 eV with the effect reverse which gets in the end a new positive meaning.
Besides, the investigation of the dependences of the EKE on the angle in the region 2,6 eV (Figure1(b)) has shown that specific implantation dose $(1{,}5\surd2{,}5)\times10^{14}$ ion/cm^2 makes the change of sign of the effect but it hardly have any influence on the position of Brewster angle. This result has also been born out by the optical measurement which only proves the week relationship between the optical constants n and k and the implantation dose.
Present results in the region 2,6 eV might be explained by weakening antiferromagnetic ties between two iron sublattice and by turning over the magnetic moments of the iron ions which are responsible for the electronic transition in the external magnetic field.
In the proceeding, we have also researched the magneto-optical properties of ion implanted $(YBiCaSmLu)_3(FeGeSi)_5O_{12}$ garnet films after annealed at 270^{0}C for 2 hours. This kind experiment is particularly interesting in the matter of annealing process as it reduces the implantation defects and restores crystalline structure of ferrite-garnet (2). The experimental results showed that after annealing process in the region 2,6 eV, the sign of the effect remains same like unimplanted garnet films and the value of effect increases in ultra-violet region of spectrum.

We have also determined the spectral dependences of the component of the tensor of dielectric permittivity for the surface of the above-mentioned ferrite-garnet films before and after implantation process. These calculations let us evaluate the influence of the implantation on an electronic energy structure of the surface layer for the sample.

1. L.V. Nikitin and O. M. Nakashidze. Influence of the implantation on magneto-optical properties of ferrite-garnet films. In Abstracts of the VIIIth All-Union School-Seminar on New Magnetic Materials of Microelectronics, M, V.2, 1987, p.320 (in Russian)

2. P. Gerard, M. Delay. Ion implantation profiles in bubble garnets. Thin Solid Films, 88, 1, 1982 p.75

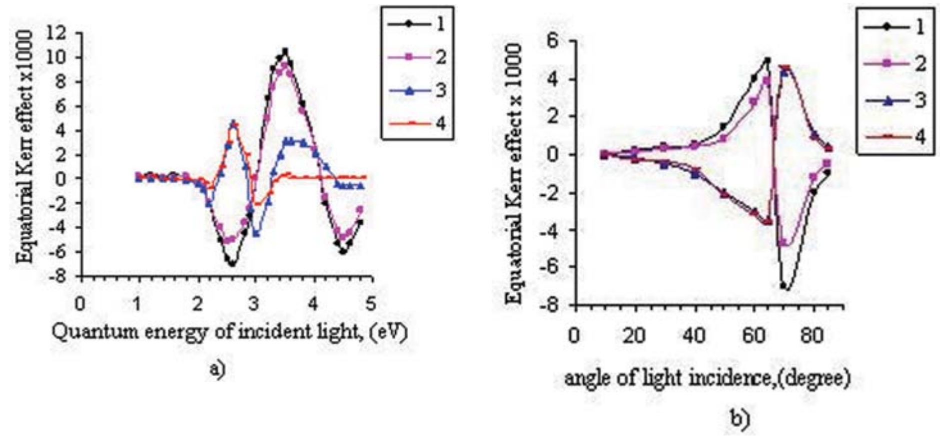

DO-03

On System Optimization for Magneto-Optic Switching: Material Considerations.

S. Kemmet, M. Mina, R. J. Weber
Electrical and Computer Engineering, Iowa State University, Ames, IA

Abstract
Optimization though material considerations of an all-fiber interferometric switch based on Faraday rotation is reported. The switch is a Mach–Zehnder interferometer (MZI) type. The interferometric action is controlled via Faraday rotation exhibited by magneto-optic (MO) material in the presence of an external magnetic field. To achieve optimal operation, domain behavior of the MO material is investigated. Results are presented that will lead to a switch with larger dynamic range with a low external magnetic field.

Introduction
As fiber optic and optical devices become increasingly utilized in high-speed communication networks, all-optical switching technologies have been proposed and developed.[1] A switch was proposed based on MO effect using bismuth substituted iron garnet[2]. The proposed fiber-based switch is based on a MZI setup utilizing Faraday rotation. The switch has shown promising ON-OFF dynamic range with reasonable applied external magnetic field. In this paper we investigate at the domain level the MO properties of bismuth substituted iron garnet [(Bi1.1Tb1.9)(Fe4.25Ga0.75)O12] samples[3] for optimization of a fiber-based MZI type optical switch. The MO Faraday rotator(MOFR) samples are 330µm thick and the refractive index is 2.344 at 1550nm. In the case of realizing the switch for single mode fiber (SMF), action of individual domains becomes the major contributing factor to the amount of Faraday rotation. Through domain level material investigation, switching with a greater ON-OFF dynamic range can be realized with significantly lower magnetic fields.

Switch Concept
The switch is a MZI type switch with a MOFR in each leg, shown in Fig 1. At the switch input a linearly polarized beam is split with a 3dB directional coupler, resulting in the state of polarization (SOP) in the upper and lower leg to be perpendicular. In each leg is a MOFR. The beams are recombined with a 3dB coupler. In the absence of an applied field, each beam is unaffected: an ON state. When the MOFRs are in an applied field Happ, the SOP is rotated by an angle θ due to Faraday rotation. The angle of rotation is described in the linear region by θ=θsat(Happ/Hsat) where θsat is the rotation at the saturation field Hsat. The output can be analyzed with use of simple matrix analysis and Jones matrices. If the SOP in one path is shifted 45° and the other by -45°, the output is 0, the OFF state.

Material Considerations
The relation θ=θsat(Happ/Hsat) holds when the diameter of the incident beam is large enough to sample many domains. However, when the beam size is smaller, contributions of individual domains affect the rotation of the SOP. The beam of a MMF, which has a diameter of about 62.5µm, samples many domains and generally obeys the above relation. However a SMF, which has a mode field diameter of approximately 10µm, passes through only a small number of domains. Individual domains align with an applied magnetic field at much lower field strengths than the bulk material. Therefore, by confining the beam to a single or small number of domains, switching can be accomplished at much lower fields.

Experimental Setup and Results
In order to determine the size of the beam on the face of the MOFR sample, the lateral offset method was used. With a separation of 1.25mm between the two fibers, the HPBW is approximately 16µm. Using magnetic force microscopy a domain width was determined to be approximately 20µm.
In Faraday rotators, if the beam width incident on the material is smaller than the domain dimensions then domains can be located in the material. By moving a sample between two aligned SMFs, one attached to a laser, with a polarization controller and power sensor, domains and domain walls can be identified as shown in Fig 2. Aligning the beam within a single domain, the Faraday rotation in the absence of a magnetic field was measured to be approximately 15°. A magnetic field was applied to the material. Individual domains aligned with the applied field as low as 10 Oe, well under saturation of 350 Oe.

Conclusion
Domain behavior of a magneto-optic Faraday rotator used in an all-fiber MZI type switch was investigated and reported. Domains within a MO thin film sample were differentiated and the rotation in the absence of a magnetic field was measured. Domain alignment with an external magnetic field was achieved at low field strength.

[1]G.Papadimitriou, C.Papazoglou, and A.Pomportsis, “Optical switching:Switch fabrics, techniques, and architectures,” J.Lightw.Tech., vol.21, no.2, pp.384–405, Feb.2003.

[2]R.Bahuguna,M.Mina,and R.Weber,“Mach–Zehnder Interferometric Switch Utilizing Faraday Rotation,” IEEE Trans.Magn.,vol.43,no.10,pp.2680-2622,June2007.

[3]V.Fratello,S.Licht,and C.Brandle, “Innovative improvements in Bismuth-Doped rare-earth iron garnet Faraday rotators,” IEEE Trans.Magn.,vol.32,pp.4102–4107,Sep.1996.

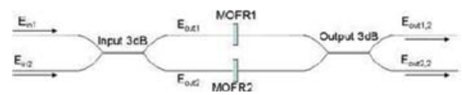

Fig. 1. Schematic of MZI with MOFR samples

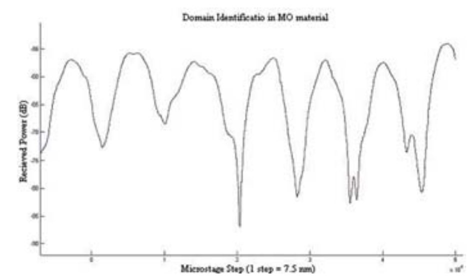

Fig. 2: Scan of sample - domains and walls are identifiable

DO-04

Practical magneto-optic spatial light modulator with single magnetic domain pixels.

K. Iwasaki[1], H. Mochizuki[1], H. Umezawa[1], M. Inoue[2]
1. Research and Development Division, FDK CORPORATION, 2281 Washizu, Kosai-Shi, Shizuoka, Japan; 2. Toyohashi University of Technology, 1-1 Hibarigaoka, Tennpakucho, Toyohashi-shi, Aichi, Japan

Spatial Light Modulators (SLMs) with a two-dimensional pixels array enable to modulate the intensity and the phase of light waves. Especially, Magneto-Optic Spatial Light Modulators (MOSLMs), which uses magnetization reversal for switching pixels, have advantages of high switching speed and non-volatility compared with other SLMs such as the liquid crystal type and the MEMS type. Therefore, the applications to the optical information processing like holographic storages using MOSLMs are developing [1].

J.Cho et al. reported the 128 by 128 MOSLM driving at 1 kHz frame rate in 1994 [2]. We have developed the improved 128 by 128 MOSLM to drive at higher frame rate and achieved to double the pixel density and to decrease the I2R losses in the metal drivelines by 70% [3]. In addition, we have enabled to operate without using external bias coil. This means that the pixels are switched in the state of a single magnetic domain by a magnetic field generated from the optimized drivelines on the pixel. Therefore our MOSLM is expected to drive faster than the one before.

In this study, we observed the magnetic domain structure of the pixel switched at high-speed drive condition and confirmed that there is a two-step process, the first step being pixel nucleation at the center of the pixel followed by a second step of pixel saturation. Then we measured the time of each step and estimated the frame rate under the optimized drive condition.

The pixels consist of Bi-substituted iron garnet film. As a polarized light ray enters the film, its polarization is rotated depending upon the orientation of the magnetization direction of the pixel. As a result, the pixels show up dark or light through an analyzer. Fig.1 shows the image of 128 by 128 MOSLM with checker pattern observed by polarization microscope. The pixel pitch is 16 micrometers. The magnetization direction is switched by the magnetic field generated from intersecting X and Y drivelines on the pixel as shown in fig.2. The dependence of domain structure on the pulse width of X and Y current was evaluated.

Fig.3 is a timing diagram to switch one pixel. Here, TX and TY denote the pulse width of X and Y current. TYD is the delay time of Y current from X current. Fig.4 shows the images of domain structure depending on various TYD under the condition of TY=1000nsec and TX=20nsec. When TYD=50nsec, there is a reversed domain at the center of the pixel where large magnetic field is generated from the X and Y drivelines. However, the pixel is not switched completely. The half of pixel area is magnetized oppositely when TYD=100nsec. Eventually, we confirmed that TYD should be longer than 200nsec to switch the pixel completely in the state of single domain. These results show that there is a two- step process, the first step being nucleation followed by a second step of domain wall motion. These steps need the time of 20nsec and 200nseconds respectively. We optimized the drive condition using these results and estimated the frame-rate of 128 by 128 MOSLM that repeats continuously between ON and OFF. As a results, it becomes 11kHz when 32 pixels are switched at the same time. It is ten times faster than conventional MOSLM. Furthermore, this MOSLM is able to turn the desired pixels on or off without external bias field. Therefore it would be expected to operate faster by using the best drive condition corresponding to writing pattern.

[1] T.Imura et al, Proc. SPIE, Vol. 6311-41(2006).

[2] Jaekyong Cho et al, J.Appl.Phys.76(3), 1910(1994).

[3] K. Iwasaki et al, Proc. SPIE Vol. 6311-42(2006).

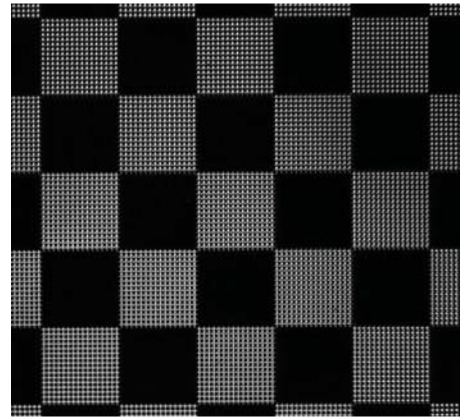

Fig.1 Image of 128 by 128 MOSLM

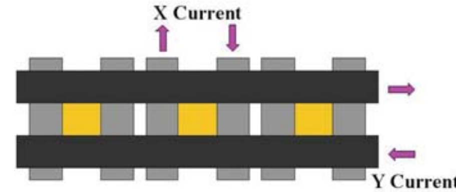

Fig.2 Drivelines structure

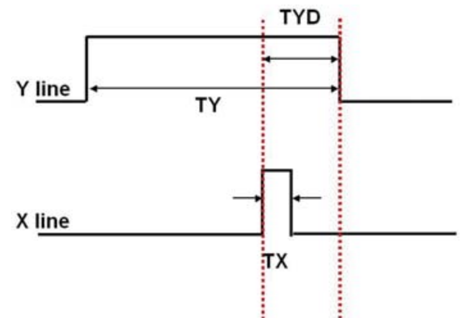

Fig.3 Timing diagram to switch one pixel

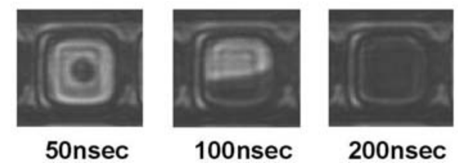

Fig.4 Images of domain structure depending on various TYD

DO-05

Enhanced magneto-optics in magnetic nanostructures, magnetophotonic crystals and semiconductors.

A. Granovsky[1], E. Ganshina[1], N. Perov[1], A. Vinogradov[2], A. Orlov[3], Y. Kalinin[4], A. Khanikaev[5], M. Inoue[5]

1. Faculty of Physics, Moscow State University, Moscow, Russian Federation; 2. Institute for Theoretical and Applied Electromagnetics, Moscow, Russian Federation; 3. State Research Institute for the Rare-Metal Industry, Moscow, Russian Federation; 4. Department od Solid State Physics, Voronezh State Technical University, Voronezh, Russian Federation; 5. Department of Electrical and Electronic Engineering, Toyohashi University of Technology, Toyohashi, Japan

Recently, there has been intense searching magnetic nanostructures and novel magnetic materials, which exhibit enhanced magneto-optic response [1-3]. It was shown that magneto-optic phenomena can be significantly enhanced in the case of resonant interaction of light with magnetic materials or in the vicinity of phase transitions [4,5]. But in the most cases enhanced magneto-optics is accompanied by a degradation of optical properties and therefore the problem is far from being solved. In the presentation we discuss our recent theoretical and experimental results on magneto-optic spectra of various magnetic nanostructures, semiconductors and magnetophotonic crystals, in particular: (i) magnetic nanocomposites $Co_x(TiO_2)_{1-x}$, $Co_x(Sm_2O_3)_{1-x}$, $Co_x(NbLiO_3)_{1-x}$, $Co_x(CaF)_{1-x}$, $(CoFeZr)_x(SiO_2)_{1-x}$, $(CoFeB)_x(SiO_2)_{1-x}$, and $(FePt)_x(SiO_2)_{1-x}$; (ii) discontinuous magnetic multilayers Co/SiO_2 and $Co_{0.45}Fe_{0.45}Zr_{0.1}/Si$; (iii) diluted magnetic oxides TiO_2:Co and semiconductors Si:Mn; (iv) the interface of magnetic and non-magnetic photonic crystals.

Magnetic nanocomposites were fabricated by ion-beam and rf-magnetron sputtering. A special compound target allowed us to get a wide range of metal-to-dielectric ratios x (depending on the target composition and the mutual arrangement of the target and substrates) in one deposition cycle. Diluted magnetic oxides $TiO_{2-\delta}:Co_x$ with x=0.5-8% were fabricated by magnetron sputtering. Mn-implanted silicon plates of both n and p types were obtained by implanting 195-keV manganese ions with doses from $1x10^{15}$ to $2x10^{16}$ cm^{-2}. Details of magnetophotonic crystals fabrication were described in [1]. The magneto-optic properties were investigated by studying the geometry of the transverse Kerr effect (TKE). The TKE spectra were meas-ured by the dynamic method in the 0.5–4.5 eV energy range in the applied magnetic field up to 2.5 kOe.

It is shown that magneto-optic response of magnetic nanocomposites with compositions close to the percolation threshold at some specific frequencies of light is much larger than that for bulk constituent ferromagnetic metal. The magneto-optic response is also enhanced for discontinuous multilayers when the volume fraction of metal in each layer is close to the metal-insulator transition. Using experimental data on optical parameters and the TKE spectra we found both diagonal and off-diagonal elements of the dielectric permittivity tensor for nanocomposites and compared them with theoretical calculations carried out in the framework of the effective medium approach. The calculated magneto-optic spectra for nanocomposites are in a qualitative agreement with experiment but it is not the case for discontinuous multilayers.

Ferromagnetism in Mn-implaned Si wafers was studied by means of VSM and SQUID-magnetometer, and Faraday effect. The Faraday rotation exists in Si:Mn at 80-305 K in the specrum range 1-6 mm and is mostly pronounced near the absorption edge, where the specific rotation is about 500 grad/cm. The positive sign of Faraday rotation indicates on p-type conductivity in Mn-implanted Si.

Magneto-optic spectra of thin films $TiO_{2-\delta}$:Co indicate on intrinsic ferromagnetism at room temperature both in anatase and rutile phases but in the limited range of charge-carrier concentration. The magneto-optic spectra are sensitive to the thin film thickness, Co volume fraction, annealing conditions. For small volume fraction of Co (<1%) the TKE spectra are characterized by 6 well-pronounced peaks, which are not typical for bulk Co and Co clusters. This fine structure disappears with increase of Co volume fraction up to 5-8% and magneto-optic response in reflection mode becomes larger than that for thick Co films. In combination with high transmittance at visible it opens up new avenues for the development of novel magnetophotonic crystals and advanced integrated magneto-optic devices.

Magnetorefractive effect [4] exists in a wide spectral range and is much larger than traditional magneto-optic phenomena. We discuss recent experimental results on magnetorefractive effect in magnetic nanocomposites and manganites in the framework of a simple theory of high frequency spin-dependent tunneling. It is predicted that magnetorefractive effect can be enhanced up to 60% in multilayered structures and magnetophotonic crystals.

We also propose the scheme of magnetophotonic crystals with simultaneosly high Faraday rotation and transmittance close to 100%.

[1] M.Inoue, A.Granovsky, O.Aktsipetrov, H.Uchida and K.Nishimura, “Magnetophotonic Crystals”, in Magnetic Nanosctructures, Springer Series in Materials Science, Vol. 94, 29, 2007.

[2] A.Khanikaev, A.Baryshev, A. Fedyanin, A. Granovsky, M. Inoue, Optics Express, 15, 6612, 2007.

[3] A.Granovsky, Yu. Sukhorukov, A. Orlov, N. Perov, A. Korolev, E. Ganshina, V. Zinenko, Yu. Agafonov, V. Saraikin, A. Telegin and D. Yarkin, JETP Lett., 85, 335, 2007.

[4] A.Granovsky, E. Ganshina, A. Yurasov, Yu. Boriskina, S. Erokhin, A. Khanikaev, M. Inoue, A. Vinogradov, Yu. Sukhorukov, J. Commun. Technol. Electron., 52, 1065, 2007.

[5] A. Vinogradov, A. Dorofeenko, C. Erokhin, M. Inoue, A. Lisyansky, A. Merzlikin, A. Granovsky, Phys. Rev. B, 74, 045128, 2006.

DO-06

Temperature properties of magneto-optic film and the non-destructive testing of a paramagnetic specimen.

J. Lee[1], *R. Wang*[2]
1. Department of Information and Communication Engineering, Chosun University, Gwangju, South Korea; 2. Department of Information and Communication Engineering, Graduate School of Chosun University, Gwangju, South Korea

Faraday rotation is a magneto-optical effect. The plane of a polarized light beam is rotated when the beam is transmitted to a magneto-optic (MO) film. The Faraday rotation angle (θ_F) and direction is affected by the strength and direction of the external magnetic field (H_E). Therefore, the strength and direction of the H_E can be estimated using an optical system which includes a polarizer and analyzer. It has been reported that non-destructive testing (NDT) with the use of the magneto-optical effect can detect cracks [1-3]. The magnetic field is leaked around a crack on the magnetized ferromagnetic specimen. These magnetic flux leakages (MFL) can affect the magnetic domain in the MO film, and a crack can be detected using a polarized lighting system to observe the magnetic domains. The small width of the magnetic domain of the MO film enables a small crack to be detected. The MO film needs to be thicker to permit a smaller domain width. However, the saturated magnetic field (H_S) increases with respect to increasing thickness of the MO film [4]. As a result, the MO film for inspecting cracks on a ferromagnetic metal with a high spatial resolution, i.e., small domain width, cannot be used for the NDT of a paramagnetic specimen.

This paper proposed an NDT technique that can detect a natural crack in a paramagnetic specimen by the use of an MO film and its temperature properties. The induced currents are distorted around the crack when a sheet type current is induced in a specimen. The eddy current, which appears as a result of the distorted current, is the cause of the magnetic field around a crack. The crack can be detected with the use of an MO film, which is positioned on the surface of a specimen. This is because the magnetic field around a crack affects the MO film. An MO film, which has a small H_S, is used for the NDT of a paramagnetic specimen because of the low magnetic field strength around a crack. Likewise, the MO film will be saturated when the H_E is larger than the H_S.

The crack can also be detected if the MO film and optical system are submerged in a transparent liquid which has a definite freezing point at a fixed pressure. In order to verify the effectiveness of the proposed NDT method, which uses a submerged MO film in a transparent liquid, the dependence of the domain width on the external magnetic field strength in 4~100 °C distilled water environments was investigated. The following results were obtained:

Fig. 1 shows the relationship between the magnetic domain width and the temperature. The domain width is approximately 65.8 µm at 4 °C, and almost three times the width at room temperature. As mentioned above, the width of the magnetic domain represents the spatial resolution in the NDT which uses the MO film, and a small crack can be detected using a magnetic domain with a small width. Therefore, the ability to detect a crack increases at high temperatures because the domain width decreases with increasing temperature.

Fig. 2 shows the domain ratio with respect to the strength of the H_E and the temperature. The domain ratio was approximately 50% at room temperature, when the external magnetic field was 0 mT, as shown in Fig. 2 (a). The bright area expanded with the external magnetic field, as shown in Fig. 2 (b), which was 1 mT at the room temperature. The domain ratio changed at approximately the boiling point of water, as shown in Fig. 2 (c) and (d). On the other hand, the MO film can be saturated in a small H_E at low temperatures, as shown in Fig. 2 (e) and (f). The magnetic field due to the distortion of the induced current around a crack can be used to detect a crack in a paramagnetic metal. However, the strength of the magnetic field due to the induced current is too weak to detect a crack with the use of an MO film, which has a relatively large saturated magnetic field. Therefore, a crack in a paramagnetic material can be detected with the use of an MO film at low temperatures.

[1] J. Lee, H. Lee, T. Shoji, D. Minkov, "Application of Magneto-Optical Method for Inspection of the Internal Surface of a Tube", Electromagnetic Nondestructive Evaluation (II); Amsterdam: IOS Press, 1998. p.49-57.

[2] J. Lee, J. Hwang, T. Shoji, "Numerical Analysis of Magneto-Optical Eddy Current Imaging Using FEM", Key Eng Mat 2006;306-308:235-240.

[3] J. Lee, T. Shoji, "Nondestructive Inspection for the Paramagnetic Materials using the Magneto-Optical NDI System", J. of the JSAEM 1998;6(4):337-342.

[4] M. Ishihara, T. Sakamoto, K. Haruna, N. Nakamura, K. Machida and Y. Asahara, "Advanced Magnetic Flux Leakage Testing System using Magneto-Optical Film" J. of the Japanese Society for Non-destructive Inspection 1996;45(4):283-289.

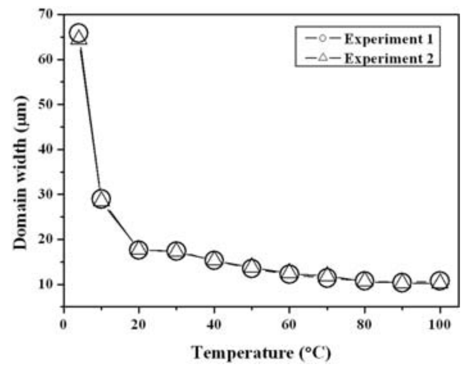

Fig. 1. The width of the magnetic domain at each temperature.

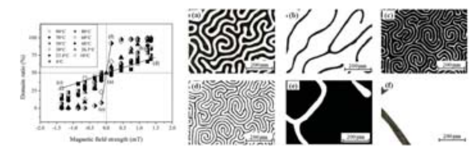

Fig. 2. The relationship between the magnetic field strength and the domain width.

DO-07

Enhanced magneto-optical diffraction by gyrotropic gratings.

Y. Lu[1], M. Cho[1], J. Kim[1], G. Lee[1], Y. Lee[1], J. Rhee[2]
1. Quantum Photonic Science Research Center and BK21 Program Division of Advanced Research and Education in Physics, Hanyang University, Seoul, South Korea; 2. BK21 Physics Research Division and Department of Physics, Sungkyunkwan University, Suwon, South Korea

Artificially fabricated magneto-photonic crystals can effectively lengthen the mean optical path of illuminated light thanks to the light localization in the vicinity of defect. An extraordinary magneto-optical (MO) effects in the bilayer system of a metallic film perforated with subwavelength-hole arrays and a uniform magnetic film can exhibit a MO enhancement, due to the coupling of surface plasmon polaritions with quasi-guided waves in the thin magnetic layer. The MO responses of diffracted beams are measured in the off-specular geometry, which is the so-called diffracted MO effect. This new technique has been utilized to analyze the magnetization reversal process. In addition, it can be used to change the amplitude and the sign of MO effects as illustrated by Antos et al. and Kim et al. [1-3] experimentally.
In this work, the rigorous coupled-wave approach implemented as Airy-like internal reflection series was employed to simulate the diffracted MO Kerr spectra presented in Ref. [1]. The simulation for the multilayered grating, as shown in Fig. 1, indicates a good consistency with the experiment in the zeroth- and the first-order diffractions for the polar magnetization. It was found that the magnitude of Kerr rotation in the zeroth order is one order smaller than that of the first one over a wide range of photon energy. In other words, it is likely to achieve the MO enhancement through the MO diffraction from gyrotropic gratings. In order to make it controllable, the comprehensive simulations on pure MO diffraction, excluding the dielectric layers, are carried out to elucidate the crucial influences upon it at a wavelength of a He-Ne laser. We found that this kind of MO enhancement is strongly dependent on the grating depth, and the ratio of Kerr rotation in the first order to that of the zeroth order monotonously decreases below unity with increasing the depth, as displayed in Fig. 2. This means that the shallow gratings give rise to the larger MO enhancement than the deep ones, which is of great advantage to the miniaturization and the integration of devices. Furthermore, it is believed that the absolute magnitude and the MO enhancement can be improved by designing the grating profile and selecting the gyrotropic materials elaborately.

[1] R. Antos, J. Mistik, T. Yamaguchi, S. Visnovsky, S. O. Demokritov, and B. Hillebrands, “Evidence of native oxides on the capping and substrate of Permalloy gratings by magneto-optical spectroscopy in the zeroth- and first-diffraction orders,” Appl. Phys. Lett. 86, 231101 (2005).

[2] J. B. Kim, G. J. Lee, Y. P. Lee, J. Y. Rhee, K. W. Kim, and C. S. Yoon, “One-dimensional magnetic grating structure made easy,” Appl. Phys. Lett. 89, 151111 (2006).

[3] J. B. Kim, G. J. Lee, Y. P. Lee, J. Y. Rhee, and C. S. Yoon, “Enhancement of magneto-optical properties of a magnetic grating,” J. Appl. Phys. 101, 09C518 (2007).

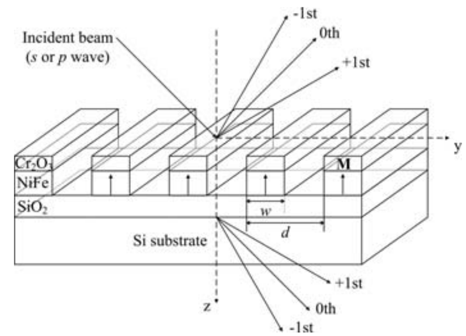

Fig. 1. Diffracted MO effects from a multilayered gyrotropic grating for the polar magnetization.

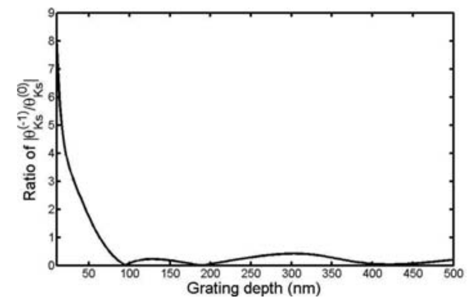

Fig. 2. Ratio of Kerr rotation in the first order to that of the zeroth one as a function of grating depth.

DO-08

Surface plasmon resonance effects in the magneto-optical activity of Ag/Co/Ag trilayers.

E. Ferreiro[1], X. Bendaña[1], J. González-Díaz[1], A. García-Martín[1], J. García-Martín[1], G. Armelles[1], A. Cebollada[1], D. Meneses[2], E. Muñoz-Sandoval[2]
1. Instituto de Microelectrónica de Madrid, IMM (CNM-CSIC), Tres Cantos, Spain; 2. Advanced Materials Department, IPICYT, San Luis Potosí, Mexico

A surface plasmon resonance is a collective excitation of conduction electrons at a metal-dielectric interface and is characterized by an electromagnetic wave strongly localized at this interface. This can be exploited in plasmonic systems made of noble metals, which can exhibit interesting light absorption, transmission and guiding properties.
One can incorporate this plasmonic character into magneto-optically (MO) active systems, by fabricating magnetoplasmonic structures made of ferromagnetic materials combined with noble metals. Here, the noble metal supports the plasmon resonance and the ferromagnet is responsible for the MO activity. This way, the MO response in such systems can be greatly enhanced when the plasmon resonance is excited, as has been shown in Au/Co/Au continuous trilayered structures [1,2,3] characterized by propagating or Surface Plasmon Polariton (SPP) resonances and nanoparticles [4], characterized by Localized Surface Plasmon (LSP) resonances. In both cases, the plasmon resonance endorsed by the presence of Au strongly affects the optical properties of the system and enhances the electromagnetic field in the spatial region where the MO active material (Co) is located, producing an enhanced MO effect that can be exploited practically in the development of surface magnetoplasmon resonance sensors of enhanced sensitivity [5].
Like gold, silver is another noble metal with even stronger and narrower plasmon resonances in the visible range [6] due to the optical properties of silver. In this work we have therefore carried out a systematic study on the MO properties of Ag/Co/Ag trilayers as a function of Co thickness when the SPP resonance at the air/trilayer interface is excited. Samples were grown by magnetron sputtering at room temperature on glass substrates. Co layers are sandwiched between a 16 nm thick buffer Ag layer and a 6 nm thick Ag top layer. Ag layer thicknesses were selected to optimize the SPP excitation. A 2 nm thick Pt capping layer was deposited to avoid any Ag deterioration, which is known to occur upon exposure to air after sufficient time. Co thickness was varied between 0 and 7 nm. Standard samples characterization included morphology studies by SEM and AFM, magnetic characterization by measuring polar and transverse Kerr loops, and MO characterization by measuring polar and transverse Kerr spectra in the visible range. Finally, both reflectivity and transverse Kerr effect were measured at 632.9 nm using the Kreschmann configuration [3], enabling SPP excitation at the air/trilayer interface. An example of these measurements can be seen in figure 1, where both reflectivity and transverse Kerr effect are shown to strongly depend on the light incidence angle, with intense resonances and specifically a large enhancement of the MO activity in the angular region where the SPP excitation occurs.
In figure 2 we have depicted a compilation of the experimental results (upper curve) and theoretical calculations (lower curve) of the Co thickness dependence of the transverse MO signal when the SPP is excited. A distinctive maximum in MO signal is observed both experimental and theoretically for a Co layer thickness around 2.5 nm, with decreasing values for lower and higher Co thickness. This clearly differs from the intuitively expected gradual increase of MO signal with magnetic layer thickness when no plasmon resonance is excited, and is due to the optimum reduction of the reflectivity and increase of the electromagnetic field at the Co layer for this specific thickness when the SPP is present. The differences in intensity and sharpness between theory and experiment are very likely due to the morphology of the actual samples originated by the tendency for a 3D growth of Ag on glass under the used deposition conditions. We believe that the optimization of layers planarity and interface sharpness will allow to experimentally reaching the theoretically expected values.

1.- C. Hermann et al., Phys. Rev. B 64 (2001) 235422.

2.- V. I. Safarov et al., Phys. Rev. Lett. 73 (1994) 3584.

3.- J. B. González-Díaz et al., Phys. Rev. B 76 (2007) 153402.

4.- J. B. González-Díaz et al. Small (2008) in press.

5.- B. Sepúlveda et al., Opt. Lett. 31 (2006) 1085.

6.- L. Novotny and B. Hetch, Principles of Nano-Optics, Cambridge: Cambridge University Press, 391-392 (2006)

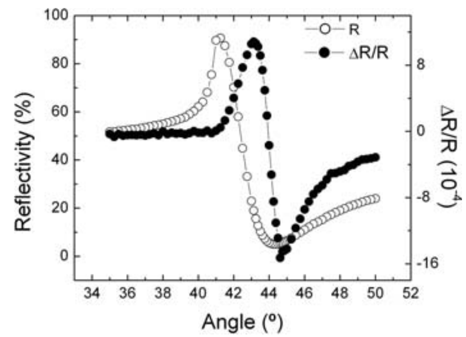

Figue 1: Reflectivity and variation of reflectivity due to Kerr effect for 2 nm Co thickness

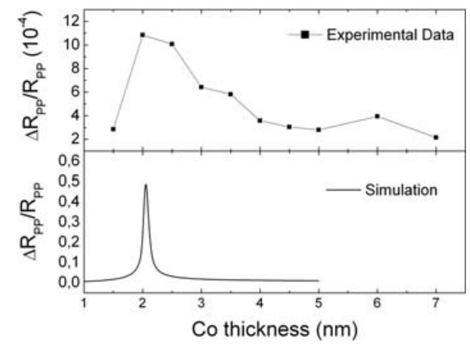

Figure 2: Relative variation of reflectivity maximum in transversal Kerr effect with SPP resonance

Magneto-optical properties of wider gap magnetic semiconductor ZnMnTe and ZnMnSe films.

M. Imamura[1], A. Okada[2], H. Higuchi[1]
1. Fukuoka Inst. of Tech., Fukuoka, Japan; 2. Mitsubishi Electric Corp., Amagasaki, Japan

(1)Introduction

II-VI based magnetic semiconductors (MSs) with a direct and wide optical band gap are expected to show high potential for optical applications utilizing short wavelength laser diodes (LDs), such as 532-nm green and 475-nm blue LDs. II-VI MSs $Zn_{1-x}Mn_xTe$ and $Zn_{1-x}Mn_xSe$ exhibit their absorption edges at 428-544 nm and 428-458 nm, respectively. The edge is not so influenced by the Mn concentration, as is typically observed in $Cd_{1-x}Mn_xTe$. We have confirmed that the Faraday rotation θ_F in the ZnMnTe films deposited on quartz glass (QG) substrates is large near the absorption edge [1]. This paper succesively reports the magneto-optical characteristics of ZnMnTe and ZnMnSe films synthesised on QG, and shows the result of a direct Faraday rotation observation sucessfully made for the ZnMnTe film under ac magnetic fields.

(2)Band gap energy and Faraday rotation of ZnMnTe and ZnMnSe films

Using molecular beam epitaxy, ~2-μm-thick ZnMnTe and ZnMnSe films were prepared on 0.5-mm-thick transparent QG substrates. Crystallinity was evaluated using an x-ray diffractometer. The preferred (111) growth reported previously for CdMnTe films on QG substrates [1] was also observed in the ZnMnTe and ZnMnSe films with weaker peak intensities. $A^{II}_{1-x}Mn_xB^{VI}$ MS alloys are direct-gap semiconductors whose band extrema occur at the Γ point, and a linear interpolation between $A^{II}B^{VI}$ and MnB^{VI} compounds gives a good first-order approximation of a value description of the dependence of E_g on x [2]. The interpolation on the energy gap of replacing the group II elements by Mn in $Cd_{1-x}Mn_xTe$, $Zn_{1-x}Mn_xTe$ and $Zn_{1-x}Mn_xSe$ is shown in Fig. 1. Values obtained from ZnTe-MnTe and ZnSe-MnSe interpolation are compared with those obtained from experimental $(\alpha h\nu)^2$-E_g plots in Table I. Figure 2 shows the variation of the Faraday angle with wavelength measured at room temperature in $Zn_{1-x}Mn_xTe$ and $Zn_{1-x}Mn_xSe$ films. Although a negative peak value of θ_F at room temperature is typical for $Cd_{1-x}Mn_xTe$ films over the wavelength range of 600-650 nm, for $Zn_{1-x}Mn_xTe$ films, a shift of θ_F dispersion to higher photon energies was observed as a result of the increase in band gap energy. The negative peak of the Faraday rotation in $Zn_{1-x}Mn_xTe$ films that have an absorption edge at 520-530 nm is near the edge.

(3)Green laser application for ZnMnTe films

We developed an equipment for observing the Faraday effect directly under ac magnetic fields generated by a ring magnet. Figure 3 shows the Faraday-effect signal observed for the $Zn_{0.82}Mn_{0.18}Te$ film using the equipment that has the ring magnet and a 532-nm green LD. The results saggest that $Zn_{1-x}Mn_xTe$ films are useful for green lights.

[1] M. Imamura et al., J.Appl.Phys. 99, 08M706 (2006). [2] M. Imamura et al., IEEE Trans. Magn. 42, 3078 (2006).

MS films on QG	E_g (eV) Interpolation values	E_g (eV) $(\alpha h\nu)^2$-E_g plots	Thickness (μm)
$Zn_{0.82}Mn_{0.18}Te$	2.38	2.38	2.16
$Zn_{0.80}Mn_{0.20}Te$	2.39	2.39	2.18
$Zn_{0.75}Mn_{0.25}Te$	2.42	2.42	2.36
$Zn_{0.84}Mn_{0.16}Se$	2.76	2.64	2.23
$Zn_{0.98}Mn_{0.02}Se$	2.74	2.69	1.40

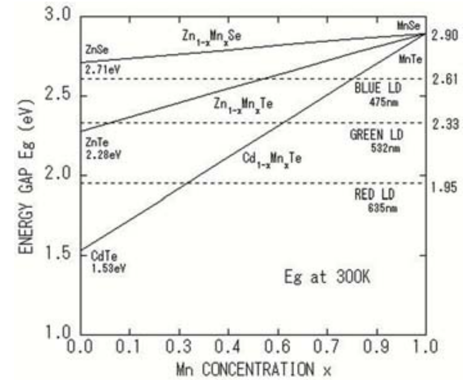

Fig. 1. Linear interpolation of E_g between the $A^{II}B^{VI}$ and MnB^{VI} compounds for $A^{II}_{1-x}Mn_xB^{VI}$ MSs.

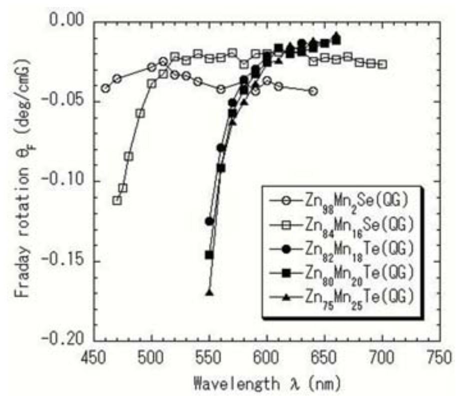

Fig. 2. θ_F vs. wavelength at room temperature in $Zn_{1-x}Mn_xTe$ and $Zn_{1-x}Mn_xSe$ films

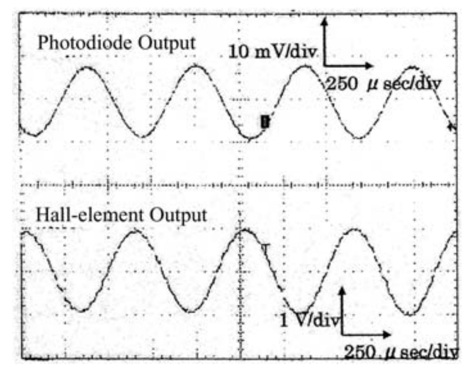

Fig. 3. Faraday-effect signal observed for the $Zn_{0.82}Mn_{0.18}Te$ film at a frequency of 1.6 kHz in an alternating magnetic field of 67 mT.

DO-10

Magnonic crystals-theory, experiment, parametric processes.

S. A. Nikitov, S. Bankov, Y. Filimonov, A. Kozhevnikov, S. Vysotsky
IRE, RAS, Moscow, Russian Federation

Magnetic films with magnetostatic spin waves (MSW) traditionally are considered as a perspective transmission medium that may be used for design of a wide class of miniature microwave electronic components. Application of periodic arrays combined with magnetic films opens new opportunities including creation of miniature bandgap structures so-called magnonic bandgap (MBG) crystals that have unique electromagnetic properties. The aim of this work is a rigorous analysis of different two-dimensional magnonic crystals, i.e. the structures with arrays of slots or strips or ethched holes of a finite length. The main ideas and approximations of the analysis are presented below. It was supposed that the thickness of metal screen with slots or thickness of strips is considered as equal to zero. Also we suppose that conductivity of these metal elements is infinite. Width of strips and slots is much smaller than the period of an array. Thus we may take into account only longitudinal currents flowing along strips and slots (electric and magnetic, respectively). All slots and strips in an array are considered as identical. Electromagnetic field is a superposition of electric and magnetic waves. It corresponds to the quasi-static situation in which the fields of electric and magnetic waves are almost uncoupled. We also describe magnetic material in a conventional way applying tensor of magnetic permeability. Loss in magnetic material can be taken into account. Slots in the two-dimensional array are tilted along the 0y axis. The angle of incidence of the MSW has an arbitrary value. Solving the boundary problem one finally obtains the dispersion dependencies of MSW propagating in 2D and 1D periodic structures representing surface magnonic crystals. The main feature of dispersion dependence is appearance of MBG.

Experimentally we studied linear properties and parametric instability of propagating MSW in a magnonic film consisting of yittrium iron garnet (YIG) film with 2D periodic arrays of etched holes with rhombic and quadratic symmetries. The film thickness was 16 µm, the holes depth was between 1 and 2 µm, their diameter – 32 µm and the structures period was 40 µm. We studied also the angular dependencies of dispersion and parametric instability threshold with respect to the angle between the axis of the structures and the applied external magnetic field and the MSW direction of propagation. The angle is the angle between the MSW wavevector and the lattice axis. It was measured that when the pair of antennas was located outside the YIG film with the 2D lattice neither amplitude and phase and frequency curves (AFC) nor (PFC) showed any distinct features. The dispersion obtained in this case is typical for the MSW. However, when one or both antennas were located within the YIG film the band gaps appeared in the spectra. This band appeared at some value of the angle for some range of the ratio between the areas of the etched and unetched parts of the YIG film located between the antennas. Increase in the portion of the etched area led to increase in the MSW losses within the whole frequency spectrum. This increase in propagation loss has made it impossible to register the band observed previously. When the band was registered at a given angle and the etched area between the pair of antennas was increased the depth of the band increased as well. It should also be noted that the shapes of the AFC and PFC plots were practically unchanged as the propagation direction of the MSW or the direction of the bias magnetic field was varied. The wavenumber of the propagating MSW was calculated to be k=860 CM-1. As the angle was varied the band was seen to move to the longer wavelength or the lower frequency of the MSW. The measured half-width of the minimum peak is equal to 16 MHz. The location of the minimum and its frequency width changed continuously as the angle increased. The above experimental results can be interpreted most simply for the angles and . In these cases due to the symmetry involved the MSW propagates normally to the 2D periodic structure and the Bragg condition was fulfilled. In view of the fact that the existence of the band was caused by the Bragg reflection we may conclude that in the vicinity of the Bragg resonance condition frequency bands that forbid propagation of the MSWs can be engineered. Reflection of the microwave power from the input antenna increases within these forbidden bands. We studied also the first-order parametric instability of the MSW. We found that the power thresholds which are necessary to develop the instability in 2D magnonic crystals exceed essentially (almost in two times) the analogous values for a YIG film without etched structure (i.e. without magnonic crystal). This increase is a result of increase of relaxation velocity of magnetostatic spin waves due to scattering by the nonuniformities of 2D lattice. It was also measured that the magnonic bandgap is not destroyed up to quite big levels of supercriticality of threshold power. It was also measured that the magnonic bandgap is not destroyed up to quite big levels of supercriticality of threshold power. It was also shown that at the conditions of effective hybridization of magnetostatic spin waves with exchange spin waves propagating at the right angle to the bias magnetic field the parametric instability threshold increased essentially.

This work is supported by RFBR, grant No. 08-02-00785.

DO-11

Enhanced magneto-optical activity in au/co/au nanodisks with localized surface plasmon resonances.

J. B. Gonzalez-Diaz[1], G. Armelles[1], A. García-Martín[1], A. Cebollada[1], J. M. García-Martín[1], B. Sepúlveda[2,1], M. Käll[2], L. Balcells[3]

1. Instituto de Microelectrónica de Madrid, IMM (CNM-CSIC), Tres Cantos, Spain; 2. Chalmers University of Technology, Göteborg, Sweden; 3. Institut de Ciència de Materials de Barcelona, Bellaterra, Spain

Hybrid noble metal-ferromagnetic heterostructures present optical and magneto-optical (MO) properties due to their individual constituents that, when combined, give rise to systems with enhanced optical and MO responses. For instance, it has been shown that the MO response of Au/Co/Au trilayered systems can be enhanced when its surface plasmon resonance is excited [1], enabling to develop new high sensitivity biosensors [2]. However, so far such enhancement has been only observed in continuous films that present simultaneously well defined propagating surface plasmon resonances and MO activity [1]. A discrete, nanostructured system exhibiting localized surface plasmon resonances (LSPR) may possess two advantages with respect to continuous structures: (i) the strong localization of the electromagnetic field associated to these resonances around the nanostructures can lead to a noticeable enhancement in the MO properties, and (ii) this spatial localization of the electromagnetic fields could be exploited to make such a system become a promising candidate for the development of high spatial specificity magneto-plasmonic sensing devices.

Even though complex onion-like nanoparticles made of noble metals and ferromagnets that exhibit LSPR have been obtained using different chemical methods [3], no MO activity has been reported in any of them. In this work we show that such active nanostructures exhibiting optical and MO properties can actually be obtained. The system analyzed consists of Au/Co/Au nanodisks prepared using a colloidal lithography procedure from continuous Au/Co/Au films grown onto glass by sputtering. This nanostructuration gives rise to strong changes in the optical absorption properties of the system. In figure 1 we show the absorption spectra of two samples with disk diameters of 60 and 110 nm, exhibiting a characteristic peak around 2 eV. The peak is due to the excitation of the LSPR of the Au/Co/Au nanodisks and its energy position depends on the nanodisk shape that is given by the trilayer thickness and the disk diameter. This resonance excitation in turn affects the MO response of the system. For example, figure 2 shows the Polar Kerr ellipticity spectra of the nanodisks (magnetic field applied perpendicular to the sample plane) compared to that of the continuous films. As it can be observed, the MO Kerr activity of the nanodisks shows an enhancement in the same energy region of the absorption peak. Its origin can be explained considering that the LSPR excitation induces a change in the complex reflectivity coefficients from which the MO Kerr activity is defined. The latter results are better seen in figure 3, where the Total MO activity (defined as the modulus of the complex Kerr rotation) of the d=110nm nanodisks normalized to that of the continuous layers is analyzed. The peak observed corresponds to that observed in the absorption spectra, illustrating the effect of the LSPR on the enhancement of the MO response. All these results will be finally understood with the help of theoretical simulations made with a scattering matrix formalism that takes into account the off diagonal terms of the dielectric tensor and consequently the MO activity.

[1] J.B. Gonzalez Diaz et al. Phys. Rev. B. 76,153402(2007)

[2] B. Sepúlveda et al. Oppt Lett.31,1085 (2006)

[3] N. S. Sobal et al. Nano Letters 2, 621 (2002); Z.Ban et al J. Mater. Chem 15, 4660 (2005); J. Zhang et al. J. Phys. Chem B 110, 7122 (2006); S. Mandal et al J. Mater. Chem 17, 372 (2007).

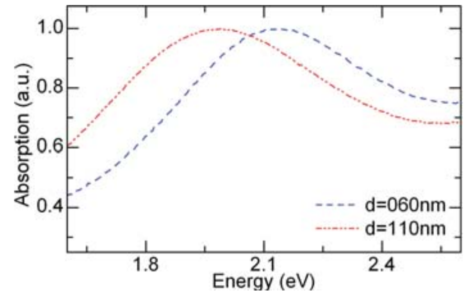

Figure 1

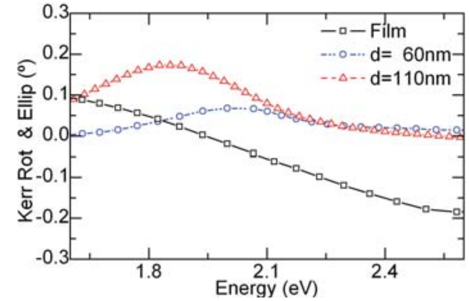

Figure 2

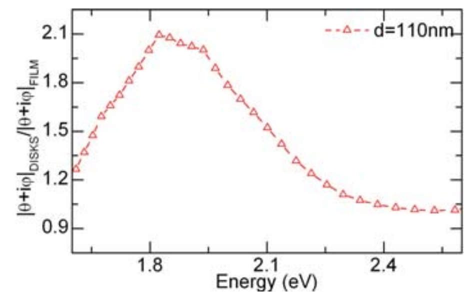

Figure 3

DO-12

Magnetic inverse opals.

D. Hrabovsky[1], E. Taboada[1], M. Lopez[2], J. Fontcuberta[1], C. Lopez[2], A. Roig[1]
1. Institut de Ciència de Materials de Barcelona (CMAB-CSIC), Bellaterra, Spain; 2. Instituto de Ciencia de Materiales de Madrid (ICMM-CSIC), Madrid, Spain

Photonic crystals (PCs) are dielectric microstructures with periodic modulation of the refractive index in one or several directions and with a period comparable to the optical wavelength. This internal organization confers them with a unique property: a photonic band gap structure (PBG) for electromagnetic waves. The photonic band gap represents the prohibition of the light propagation inside the PCs for some wavelengths. This characteristic makes the photonic crystals suitable for several applications such as sensors, lasers, optical fibers, photonic components in telecommunication devices and optical filters. Opals are 3-dimensional photonic crystals built up by dielectric spheres that self-assemble in ordered fcc crystalline arrangements. The PBG position will depend on the particle size and the difference in refraction index between the spheres (usually silica, titania or polystyrene, among others) and the air that fills the voids between the particles (1).
It has been observed that when a magnetic material is introduced into the structure of a PC, either as a defect or as a full component of the material, the new PC acquires novel magneto-optical properties such as a PBG tunability or an enhancement of linear and non-linear optical effects (2) that could lead to new magneto-optic components.
We will report on the synthesis, magnetic and magneto-optic characterization of inverse magnetic opals. Inverse opals are the result of filling the voids of a direct opal with another material, removing the spheres and leaving holes in their places. Briefly, the synthesis was as follows: direct opals of different sphere diameter -and thus different spectral position of the PBGs- were built up of polystyrene spheres of various sizes (380 and 467 nm), assembled by vertical deposition onto a hydrophilic glass substrate. Afterwards, silica was infiltrated between the spheres by chemical vapor deposition and then the original organic spheres were removed by dissolution with toluene. The corresponding PBGs of the inverse opals are centered at: 550 nm and 800 nm, respectively. Finally, an aqueous solution of superparamagnetic nanoparticles (NPs) of maghemite was prepared. The silica inverse opal was subsequently filled up with the magnetic NPs by soaking it into the magnetic dispersion and pulling the opal out of it using a vertical stepping motor. Following this procedure, inverse silica opals infiltrated with different amounts of maghemite NPs were obtained (see Fig. 1).
The maghemite NPs were synthesized in organic media by thermal decomposition of iron pentacarbonyl and transferred to water by using sodium citrate as the stabilizer (3). They are 10 nm in diameter, with narrow particle size distribution ($\sigma < 10\%$) and superparamagnetic at room temperature.
In order to study the properties of infiltrated opals, magnetization measurements were first conducted using an SQUID magnetometer with the applied magnetic field perpendicular to the sample surface. The measurements allowed us to confirm that magnetic infiltration was successfully achieved. Moreover, it was shown that the magnetic moment of the opals can be controlled by the infiltration process. On the other hand, these experiments revealed that the infiltrated opals were superparamagnetic at room-temperature, as observed in the raw maghemite NPs. This observation indicates that infiltration does not produce any significant aggregation of NPs.
Magnetization loops were measured by magneto-optical (MO) setup in transmission (Faraday configuration) and in reflection (Kerr configuration). In both configurations the light beam is normal (or close to normal) to the surface of the sample. Experiments with s- and p- polarization were conducted. The applied magnetic field was also perpendicular to sample surface. Experiments were done using low-power laser sources of different wavelengths (red 632.8 nm, 14 mW and green 542 nm, 1 mW). The incident laser beam was almost normal to sample surface and thus the polar component (parallel to the external field) of the magnetization was determined. Preliminary Faraday rotation experiments showed magnetization loops similar to those observed in the SQUID measurements, superimposed to a dominating diamagnetic contribution from the substrate.
Kerr measurements on the other hand, allowed observing magnetization curves also analogous to those extracted from SQUID. As expected, the Kerr rotation is found to increase with the NPs infiltration dose. Comparison of the values of the magnetic moment and Kerr rotation for samples with different NPs infiltration dose, suggest an enhancement of the magneto-optic response in the opals.
In summary, we have shown that magnetic inverse opals can be fabricated by a simple infiltration method. Measurements have revealed a strong Kerr rotation and available data may indicate a non linear magneto-optical response. Perspectives for further development will be discussed.

1. C. López, Adv. Mat. 2003, 15, 1679
2. M. Inoue et al. J. Phys. D: Appl. Phys. 2006, 39, R151-161
3. E. Taboada et al. Langmuir, 2007, 23, 4583

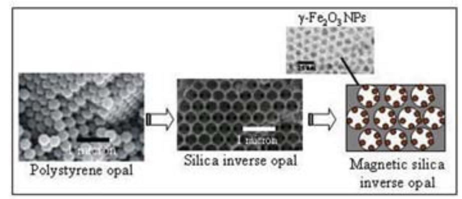

Controllability of growth-induced anisotropy of thin garnet films grown on (210)-oriented substrates.

S. Tkachuk[1], D. Bowen[1], C. Krafft[2], I. D. Mayergoyz[1,3]
1. Electrical and Computer Engineering, University of Maryland, College Park, MD; 2. Laboratory for Physical Sciences, College Park, MD; 3. UMIACS, University of Maryland, College Park, MD

It is well known that the sensitivity and magnetic field imaging range of garnet films as magneto-optical sensors are determined by the shape of the hysteresis loop which is controlled by the anisotropy properties. The anisotropy constants, in turn, depend on the chemical composition of a thin film, the crystallographic orientation of a substrate on which the film was grown and on the growth conditions, such as rotation rate or melt undercooling. In this respect, epitaxial films grown on (210)-oriented substrates are very attractive due to their unique anisotropy properties that allow for the existence of an easy plane of magnetization inclined to the film plane[1]. It turns out that if the following condition on the anisotropy constants
<p align="center"> $\kappa = -4K_{Ueff} K_i / K^2_{yz} = 1$ (1)~~<\>>~~
~~is fulfilled then the easy magnetization plane exists and the film will possess low saturation field and high magnetic field sensitivity. Here,~~ $\cancel{K_{Ueff}}$, $\cancel{K_i}$ ~~and~~ $\cancel{K_{yz}}$ ~~are the effective *out-of-plane* uniaxial, *in-plane* uniaxial and *canted orthorhombic* anisotropy constants, respectively.~~
~~<p>In this paper, we extensively study the dependence of the anisotropy properties of thin garnet films grown on (210)-oriented substrates on melt chemistry and growth conditions with the purpose to realize (albeit approximately) relation (1).~~<\>>
<p>Several garnet film samples of composition $(Bi, Pr, Lu, Gd)_3(Fe,Ga)_5O_{12}$ have been grown by liquid phase epitaxy onto (210)-oriented $(Ca,Mg,Zr)\text{-}Gd_3Ga_5O_{12}$ substrates. The anisotropy fields (anisotropy constants scaled by M_S) have been obtained through the ferromagnetic resonance (FMR) measurements using the appropriate equation for the resonance frequency[2]. The anisotropy fields along with growth rates, film properties and values of κ are given for each grown sample in Table I, where H_{Kueff} is effective out-of-plane anisotropy field, H_{Ki} is in-plane anisotropy field, H_{K1} is cubic anisotropy field, H_{Kyz} is canted othorombic anisotropy field, while H_S is the saturation field.~~<\>>~~
~~The design of the melts has been guided by the following requirements: crystallographic lattice matching between the film and the substrate, high Bi incorporation and canted magnetization. The epitaxial films were grown from a~~ $\cancel{PbO\text{-}Bi_2O_3\text{-}B_2O_3}$ ~~flux on substrates rotating at 196 rpm. The cation oxide percentages for the rare-earths are given in Table II. The Fe:Ga ratio was 5:1.~~
~~<p>It has been found (see Tables I and II) that by appropriately changing Pr content in the melt the desired control of anisotropy fields (constants) can be achieved. Indeed, the value of κ has been reduced almost by one order of magnitude and the clear correlation between the reduction in κ and saturation field has been observed. It has also been found that for κ=2.7 free energy deviations from energy values at κ=1 are relatively small and on the order of cubic anisotropy energy. Thus, the conclusion can be reached that by appropriate control of Pr content in the melt the garnet films with high magnetic sensitivity can be grown on (210)-oriented substrates.~~<\>>

[1] R.M. Mikherskii, and S.V. Dubinko, "Epitaxial garnet ferrite films with anisotropy of the inclined easy plane type", *Techn. Phys. Lett.,* vol. 26 (3), pp. 265-267, 2000.

<p>[2] L. Baselgia, M. Warden, F. Waldner, S. L. Hutton, J. E. Drumheller, Y. Q. He, P. E. Wigen, and M. Marysko, "Derivation of the resonance frequency from the free energy of ferromagnets", *Phys. Rev. B,* vol. 38, pp. 2237-2242, 1988.~~<\>>~~

-

Sample	Growth Rate (μm/min)	*d* (μm)	Δ*a* (A)	H_{Kueff} (Oe)	H_{K1} (Oe)	H_{Ki} (Oe)	H_{Kyz} (Oe)	H_S (Oe)	κ
A1	0.697	3.48	-0.001	958	-120	791	444	141	-15.3
B1	0.259	1.82	-0.008	-757	-99	981	-365	764	22.2
C1	0.307	2.15	-0.007	-422	-97	874	-328	325	13.7
D1	0.429	4.29	-0.011	-376	-237	1575	524	199	8.6
D2	0.334	2.67	-0.005	-285	-149	1098	487	198	5.3
E1	0.554	2.77	-0.014	-98	-220	1490	466	133	2.7

Table I. Anisotropy Fields in thin garnet films Table I. Anisotropy fields of (210)-oriented thin epitaxial garnet films, as determined from FMR measurements. The sample thickness is *d*, the lattice mismatch is Δ*a* and the easy plane ratio is κ.

-

Melt	Pr	Lu	Gd
A	0.0373	0.0932	0.5592
B	0.1724	0.0862	0.4310
C	0.1452	0.0907	0.4537
D	0.1335	0.0927	0.4635
E	0.1217	0.0811	0.4868

Table II. Cation oxide percentages for the melt iterations Table II. Cation oxide percentages for the designed melt iterations

DO-14

Adjustable Faraday rotation by using one dimensional magnetophotonic crystals.

M. Hamidi[1], A. Bananej[3], M. Tehranchi[1,2], M. Ghanaat Shoar[1]
1. laser and plasma resurch institute, Shahid Beheshti University, Tehran, Iran; 2. physics department, Shahid Beheshti University, Tehran, Iran; 3. Laser and Optics Research School, Tehran, Iran

During recent years there has been great tremendous progress on one dimensional magnetophotonic crystal (1D-PMC) as a compact isolator element in future nanophotonic circuits. Because of strong confinement of light in the defect magnetic layer, the interaction of light with material and as a consequence, the Faraday rotation can be enhanced dramatically. On the other hand, according to the different users' requirements, adjustable 1D-MPC in both of magnitude of magneto-optic effect and its wavelength dependent is the crucial bottleneck. In this paper according to our best of knowledge, for the first time, we propose a new method for overcoming these limitations. By using the symmetric periodic multilayer to determine the equivalent refractive index, the magnitude of the Faraday rotation in wide range of wavelength can be adjusted.

In the present work, we consider the basic structure as (Ta2O5/SiO2)m/Bi: YIG/ (SiO2/ Ta2O5)m which SiO2 is as low index layer with n=1.45 and Ta2O5 as high refractive index layer with, in the Bragg stack with optical thickness and Bi: YIG layer as the magnetic defect layer with optical thickness. Where = 720nm and m=6 is the repetition number. According to our simulation results, the Faraday rotation in this structure is 150 times greater than of a single layer of Bi: YIG.

It has been investigated the great dependence of Faraday rotation and transmission on the optical contrast ratio of dielectrics. But the choice of materials with refractive indices intermediate to those of the highest and lowest values is impossible in any spectral region; also, selection of materials is further limited by a number of other practical limitations. Now, in the case that, each of the low index layer replaced by a three symmetric multilayer as equivalent layer, the optical contrast ratio in the Bragg stack can be tuned continuously and as a consequence, the transmission property and Faraday rotation in the structure can be adjusted. Fig1.a shows the transmission of the 1D-MPC for different value of optical contrast ratio. It is evident by changing the optical contrast ratio from 1.43 to 1.09 by using the accessible and compatible a couple of materials, the light confinement in the defect point can be changed (Fig.1.a) and as a consequence, the magnitude of Faraday rotation vary from -3.35 to -0.74 in a wide range of wavelength (Fig.1.b).

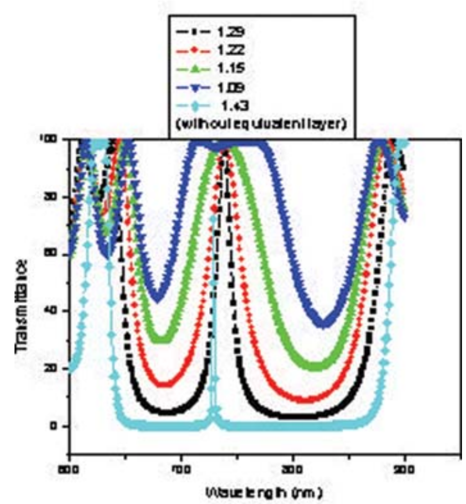

Figure 1. a

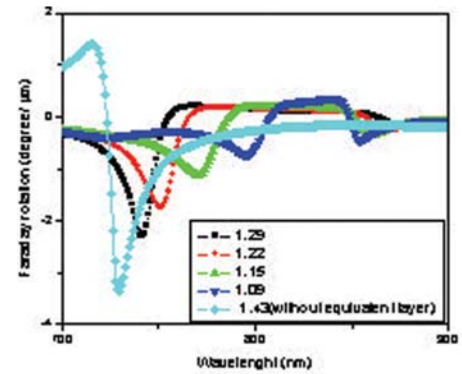

Figure 1. b

(1) H. Kalo, T. Matsushita, A. Takayama, and M. Egawa, "Theoretical analysis of magneto optical properties of one dimensional magnetophotonic crystals", J. Appl. Phys. 93(7), 3906(2003).

(2) M. Inoue, K. Arai, T. Fuji, M. Abe, "One dimensional magnetophotonic crystals", J. Appl. Phys. 85(8), 5768(1999).

(3) M. J. Steel, M. Levy, and R. M. Osgood, "Photonic band gaps with defects and the enhancement of faraday rotation", J. Lightwave. Tech. 18(9), 1297 (2000).

(4) A. Bananej, S. M. Hamidi, W. Li, C. Li and M. M. Tehranchi, "A flexible design for one-dimensional photonic crystals with controllable photonic bandgap width", In press, Optical Materials (2007).

DO-15

Optical Tamm states in 1D magnetophotonic crystals.

T. Goto[1], *A. Baryshev*[1,4], M. Inoue[1], A. Merzlikin[2], A. Vinogradov[2], A. Granovsky[3]
1. Toyohashi University of Technology, Toyohashi, Japan; 2. Institute for Theoretical and Applied Electromagnetics, Moscow, Russian Federation; 3. Moscow State University, Moscow, Russian Federation; 4. Ioffe Physico-Technical Institute, St. Petersburg, Russian Federation

Artificial structures composed of alternating dielectric materials with different refractive indices, known as photonic crystals (PCs), have been shown to affect the propagation of light, providing a new mechanism to control and manipulate the flow of light. Following the concept of photonic band gaps originating in light coupling to the spatially periodic structure and localization of light in the vicinity of defects introduced into the periodic structure [1], various one-, two- and three-dimensional PCs, photonic crystal fibers and waveguides, wave plates have been designed, and new fabrication technologies have been developed within the last two decades [2, 3].
Unique optical and magneto-optical properties are shown to exist when the constitutive materials of PCs are magnetic. For magnetophotonic crystals (MPCs), in which the constitutive elements are magnetic (or even only a defect introduced into the periodic structure is magnetic), there exists an additional degree of freedom to operate the photonic band structure, diffraction patterns, and the state of polarization of light, i.e., these characteristics can be influenced by the external magnetic field [4–6]. It is shown that MPCs enhance responses of known magneto-optical (MO) materials. Light confinement associated with the magnetic defect has been exploited to enhance and optimize MO responses and optical non-linearity of existing materials. In fact, the large enhancement of the Faraday rotation is demonstrated in one-dimensional (1D) MPCs composed of a magnetic garnet thin film sandwiched between dielectric Bragg mirrors [7]. The enhancement of the Faraday rotation can be also seen at the edges of photonic band gap appearing in multilayered magnetic structures [8].
In this work we present a new type of MPCs composed of two 1D PCs, namely, magnetic and nonmagnetic Bragg mirrors with slightly different photonic properties [6]. Such MPCs exhibit the resonant transmission and are experimentally shown to enhance the magneto-optical response of known materials (see figure). The surface state, so-called the Tamm state, is originated by the interface between two 1D PCs, and supports multiple propagation (localization) of light within magnetic layers. When magnetic field is applied, the difference of the wave vectors for left- and right-circular polarized localized Tamm modes, multiple propagation of these modes within the magnetic layer and the nonreciprocal character of the Faraday effect result in an enhancement of the polarization rotation by one order of magnitude. It is worth mentioning that the Tamm structures are of benefit for localizing light within (or at) any active material introduced at the interface (or built in between two PCs).

1. Joannopoulos, J. D., Meade, R., Winn, J.: Photonic Crystals. Princeton University Press, Princeton (1995)

2. Lopes, C.: Materials aspects of photonic crystals. Adv. Mater. 15, 1679 (2003)

3. Lourtioz, J,-M., Benisty, H., Berger, V., et al.: Photonic Crystals: Towards Nanoscale Photonic Devices. Springer, Berlin (2005)

4. Inoue, M., Fujikawa, R., Baryshev, A., et al., J. Phys. D: Appl. Phys. 39, R151 (2006)

5. Khanikaev, A. B., Baryshev, A. V., Inoue, M, et al., Phys. Rev. B 72, 035123/9 (2005)

6. Vinogradov, A. P., Dorofeenko, A. V., Erokhin, S. G., et al., Phys. Rev. B 74, 045128/8 (2006)

7. Inoue, M., Arai, K. I., Fujii, T., Abe, M., J. Appl. Phys. 83, 6768 (1998)

8. Inoue, M., Fedyanin, A. A., Baryshev, A. V., et al., J. Magn. 11, 195 (2006)

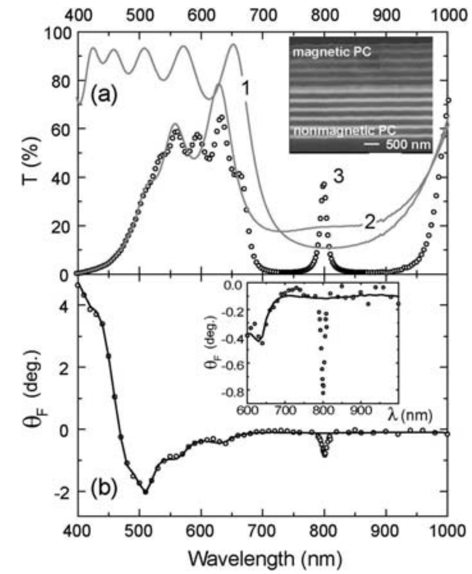

(a) Transmission spectra: (1) a quartz substrate/$(Ta_2O_5/SiO_2)^5/Ta_2O_5$ multilayer – the nonmagnetic PC, (2) a quartz substrate/$(Bi{:}YIG/SiO_2)^5$ multilayer – the magnetic PC, and (3) a quartz substrate/$(Ta_2O_5/SiO_2)^5/Ta_2O_5/(Bi{:}YIG/SiO_2)^5$ multilayer – the MPC supporting the Tamm state. (b) Faraday rotation spectra: the magnetic PC (solid line) and the Tamm structure (circles). Insets: SEM image of the Tamm structure, and a scaled-up plot showing the polarization rotation.

DO-16

Magneto-plasmonic nanostructures: a way to control surface plasmon excitation for Biosensor application.

D. Regatos[1], A. Calle[2], A. Cebollada[2], L. Lechuga[1], A. Armelles[2]
1. Nanobiosensor and Molecular nanobiophysics Group, Research Center on Nanoscience and Nanotechnology (CIN2: CSIC-ICN), Bellaterra, Spain; 2. Microelectronics Institute of Madrid (IMM-CNM), Tres Cantos, Spain

The use of surface plasmons (SP) in the development of optical components has drawn significant interest over the past decade, and the field is currently experiencing a dramatic growth. The future development of this field will depend on the ability to develop active devices whose optical response could be controlled applying an external agent such as, for example, a magnetic field. Very recently it has been shown that multilayers made of Co and Au has magneto-optical (MO) activity and well-defined plasmonic features [1]. These structures have been used to develop a new family of biosensors with enhanced sensitivity [2]. In this work, we analyse a new magneto-plasmonic nanostructure made of Fe and Au. A complete analysis of the Transversal Magneto-Optic Kerr Effect (TMOKE) in Au/Fe/Au trilayers will be presented. We will demonstrate how the Fe layer controls the propagation of the SP of the structure and we will analyse its implementation in biosensor devices.
Two sets of Au/Fe/Au trilayers have been grown on a glass substrate by magnetron sputtering at room temperature. The Fe thickness was 4.3 nm for one set and 2.7 nm for the other. For all the samples the thickness of the Au layer in contact with the glass substrate was 5 nm, whereas the thickness of the upper Au layer has been varied between 22 and 36 nm. In the inset of Fig. 1 we present a scheme of the experimental set up (Kretschmann configuration) .The upper Au layer was in contact with liquids of different refractive index. We have measured the reflectivity of the p-polarized light (Rpp) as a function of the incident angle and the relative variation of the Rpp induced by a magnetic field applied perpendicular to the incident plane (TMOKE signal). In Fig. 1 we show the Rpp and TMOKE signal for a 30nmAu/4.3nmFe/5nmAu/glass and for a liquid with refractive index of 1.3326. As can be observed, close to 71 degrees, due to the excitation of the SP (see Fig. 1a) the value of the Rpp decreases and, at the same time, the TMOKE signal experiments a sharp increase (see Fig. 1b). Moreover, in this configuration, the SP wave vector depends on the magnetization of the Fe layer and, therefore, the TMOKE signal can be related to the angular derivative of the Rpp multiplied by a factor (Δθmin) corresponding to the modification of the SP wave vector. This is clearly seen in Fig. 2, where we show the TMOKE signal and the angular derivative of Rpp for different samples multiplied, in each case, by the Δθmin. We also represent the theoretical simulation for each structure. The value of Δθmin as a function of the thickness of the Au upper layer is shown in Fig. 3 for the two sets of samples and their expected theoretical evolution. As can be observed the modulation factor of the 4.3 nm set samples is greater than that of the 2.7 nm set. Moreover, as we increase the thickness of the Au upper layer Δθmin decreases. This behaviour is due to the effective amount of magnetization seen by the SP, which is related to the integrated intensity of the electromagnetic field inside the Fe layer.
Finally, we will analyse the use of this structures as improved transducer for biosensor devices. We will study the sensitivity of the TMOKE signal to the changes of the liquid refractive index in a 30nmAu/4.3nmFe/5nmAu/glass sample and we have compared these, with the change of Rpp shown in a 48nmAu/2nmCr/glass structure (Rpp signal) for the same change of refractive index. The changes of the TMOKE signal are show to be a factor of two greater than the Rpp signal, which is due to the derivative character of the TMOKE signal as it was shown above.

[1] V.I. Safarov et al., Phys. Rev. Lett. 73 3584 (1994)
[2] B. Sepulveda et al., Optics Letters 31, 1085-1087 (2006)

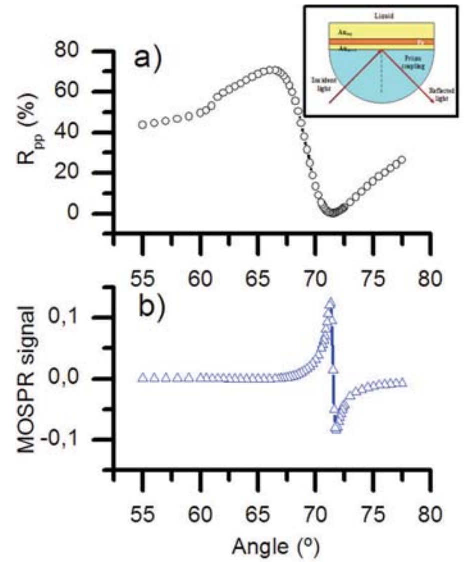

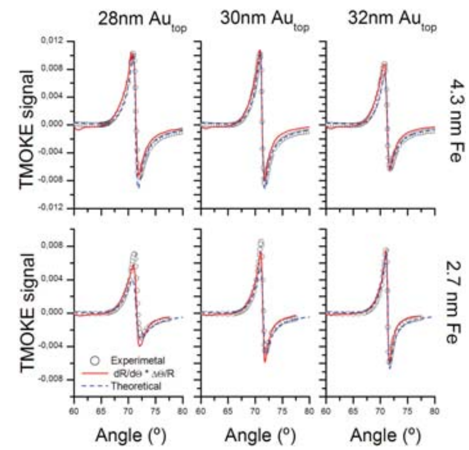

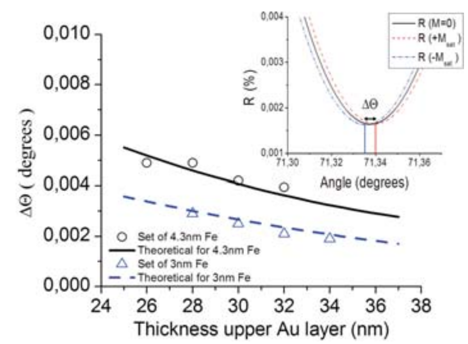

DO-17

Layered bismuth iron garnet films for magneto-optical applications.

M. Kucera[1], R. Gerber[2]
1. Faculty Math. & Physics, Charles University, Prague, Czech Republic; 2. School of Sciences, Salford University, Salford, United Kingdom

Bismuth substituted iron garnet (BiIG) is an attractive material for variety of magneto-optical (MO) applications due to its high angles of the Faraday rotation and rather low optical absorption in the visible and near infrared spectral range. These garnets can be considered to be used in optical communications (nonreciprocal devices such as optical isolators), MO imaging devices of stray magnetic fields (in superconductors or flaw detection in magnetic steels), or in magnetic photonic crystals (combining Bi garnets and dielectric mirrors).
Here we report on magnetic and MO properties of Bi iron garnet double-layer films produced by the pulsed laser deposition (PLD), in which an antiferromagnetic coupling is observed across the layer boundary. Such exchange coupled magnetic double-layers or multilayers have attracted considerable attention due to their direct overwrite capability and magnetically induced superresolution required in the MO high density recording applications.
The PLD garnet films were deposited onto (111) oriented GGG substrates using a KrF excimer laser. The best quality films were obtained at substrate temperatures between 550 and 600 °C and at oxygen pressure near 20 Pa. The films were characterized by the XRD, atomic force microscopy, magnetic, optical and MO measurements. The films exhibited an epitaxial growth, yielding samples of good crystalline and optical quality with fine granular structure and strong (111) preferred crystallographic orientation. The nominal film composition $Bi_{2.1}Dy_{1.0}Fe_{4.0}Ga_{0.9}O_{12}$ was close to that of the target. The typical average grain size was about 200 nm and the average r.m.s. surface roughness was from 3 to 9 nm depending on the deposition conditions. The Faraday and polar Kerr effects were measured in the spectral range from 250 to 900 nm and at temperatures from 20 to 500 K. Huge Faraday rotations up to 60 deg/µm are observed in the near ultraviolet region. The films exhibited square hysteresis loops and a strong perpendicular magnetic anisotropy. All the films had magnetic compensation temperature, which was strongly dependent on the deposition conditions.
To study the exchange coupling in such films a double-layer garnet system was prepared in which the individual layers differ in their compensation temperatures. This was achieved by the steep change of the oxygen pressure during the PLD process whilst the substrate temperature was kept constant. The growth process suggests that a layered garnet system comprising two layers of slightly different nominal composition was obtained. Due to different distribution of magnetic cations (Fe^{3+} and Dy^{3+}) over the three available garnet sites, the resulting layers differ significantly in their magnetic compensation temperatures. The Faraday rotation hysteresis loops of samples incorporating such double-layer systems revealed a complicated magnetic reversal process, Fig. 1. This behavior can be understood assuming that the layers couple antiferromagnetically across their boundary. Namely, in the BiDy-iron garnet, the rare earth Dy^{3+} magnetic moment is antiparallel to the resultant moment of the Fe^{3+} sublattices. Consequently in the layer with lower compensation temperature the magnetic moment originating from Fe^{3+} ions dominates, whereas the layer with higher compensation temperature Dy^{3+} moments dominates. Since the Fe^{3+} spin subnetwork in one layer is antiparallel to that in the second layer a domain wall is created between the individual layers and, as a result, a complicated magnetic reversal process is observed.
In summary, such granular garnet double-layer films represent a switching system that demonstrates the existence of a magnetic coupling between two insular layers of almost the same nominal composition, which differ in their compensation temperatures. By tailoring the PLD operational parameters, the layered systems of required compensation and Curie temperatures may be fabricated in a single fabrication step. Such garnet layered systems could have the potential as an alternative approach for magneto-optical recording media.
This work is a part of the research plan MSM 0021620834 financed by the Ministry of Education of the Czech Republic.

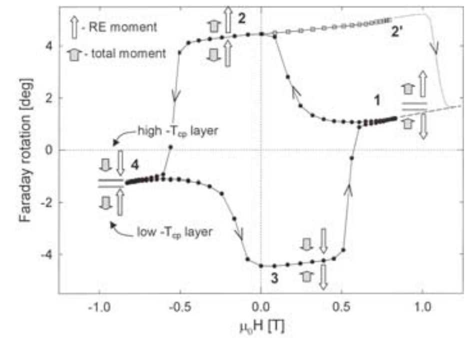

Fig. 1. Faraday rotation hysteresis loop of a double layer PLD garnet film at 500 nm. The arrows show rare earth (Dy) and total magnetic moments, respectively, the double line between arrows indicates the interface domain wall.

DP-01

Thermal properties of Spin Torque Oscillators: Singularity in Effective Energy.

P. B. Visscher, S. Wang
Department of Physics and MINT Center, University of Alabama, Tuscaloosa, AL

It is important to understand thermal fluctuations in spin torque systems, in order to predict oscillator linewidths, spin torque switching rates, and spin-torque MRAM stability. It has been found [1,2] that although the spin torque term in the Landau-Lifshitz equation is not conservative in the usual sense, it is possible to define an effective energy $E_{eff}(E)$ which describes the thermal behavior in the sense that the probability distribution of the magnetization vector **M** given by f(**M**) = $\exp(-E_{eff}(E(\mathbf{M}))/k_BT)$[1,2] is a steady-state solution of the Fokker-Planck equation.
The effective energy is computed from an integral η(E) of the spin torque over the orbit at energy E, as $E_{eff}(E) = \int^E[1-\eta(E')I/\alpha]dE'$, where I is proportional to the current and α is the Landau-Lifshitz damping coefficient. For the common case of in-plane anisotropy, in the past η(E) has been computed numerically and fit to a polynomial[1], but the fit is quite poor. We have found that this is because in general η(E) has a logarithmic singularity at the energy barrier. This arises physically from the fact that the energy landscape is very flat near its saddle point (the energy barrier), and the orbit period diverges. When this singularity is taken into account, the fit is extremely good, as shown in the figure, and it is possible to do semi-analytic calculations of the effective energy.
As a function of the magnetization vector **M** on the spherical surface |**M**| = M_s, the effective energy E(**M**) has a "Mexican hat" shape, with a central maximum (the parallel state) and a line of degenerate minima along the precessional orbit. As one increases the current, one can see the usual easy-axis energy minimum (a single value of M, at which the energy is concave upward) become very flat, and then concave downward (a local maximum) surrounded by a precessional orbit along which the energy is a (highly degenerate) minimum. The size of the precessional orbit increases until the barrier separating this minimum from the antiparallel minimum (which has become very deep) vanishes and switching occurs (at zero temperature). Before switching occurs, the shape of the precessional minimum determines the linewidth of the resulting microwave oscillations.
At nonzero temperature, switching occurs at a lower current. This current can be calculated by setting the experimental time scale equal to the reciprocal of the switching rate — within the transition-state theory, this is $f_0 \exp(-E_b/k_BT)$, where f_0 is the precession rate for small oscillations [3]. However, to compute a numerically accurate rate we have generalized to the case of spin torque switching a "bounce" algorithm [4] in which numerical simulations of slow processes are made possible by restarting the simulation ("bouncing") when the energy tries to dip below some cutoff value.
In the context of spin-torque switching, we will discuss Sharrock-like fitting of mean-switching-current vs. current-pulse-duration curves[5] — because this is sensitive to the form (the Sharrock exponent) of the dependence of the energy barrier on the current, the proper treatment of the logarithmic singularity is particularly important.

[1] P. B. Visscher and D. M. Apalkov, "Non-Boltzmann energy distributions in spin-torque devices", J. Applied Physics **99**, 08G513 (2006).

[2] Z. Li, J. He, and S. Zhang, "Stability of precession states induced by spin-current", Phys. Rev. B **72**, 212411 (2005).

[3] Shuxia Wang and P. B. Visscher, "Switching rate of MRAM element: verifying transition state theory", J. Applied Physics, **99**, 08G106 (2006).

[4] Shuxia Wang and P. B. Visscher, "Accelerated LLG simulation of magnetic stability: 'bounce' algorithm", IEEE Trans. Magn. **43**, 2893 (2007).

[5] J. Hayakawa, *et al*, Japan. Journal of Applied Physics **40** L1057-1060 (2006).

[6] D. M. Apalkov and P. B. Visscher, "Spin-torque switching: Fokker-Planck rate calculation", Phys. Rev. B **72**, 180405 (Rapid Communication), 2005.

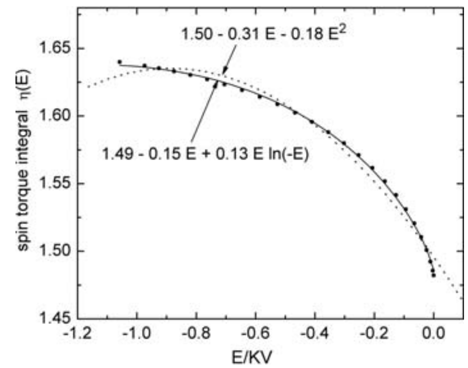

The spin torque integral η(E) [6] that determines the switching probability, with a three-parameter polynomial fit (dotted line) and logarithmic fit (solid line) to the numerical data from micromagnetic simulation (filled circles). The logarithmic fit is seen to be much more accurate.

DP-02

Spin torque induced RF-oscillations of the magnetic end domains in CoFeB/MgO/CoFeB nanopillars under subtreshold currents.

S. Cornelissen[1,3], M. van Kampen[1], G. Hrkac[2], T. Schreffl[2], L. Lagae[1]
1. NEXTNS, IMEC, Heverlee(Leuven), Belgium; 2. Department of Engineering Materials, University of Sheffield, Sheffield, United Kingdom; 3. EHSAT, K.U.Leuven, Leuven, Belgium

The spin torque effect, as predicted independently in 1996 by Slonczewski and Berger, has since been subject of lots of experimental research, which has shown that a spin polarized current can induce an oscillatory motion in a magnetization, yielding RF oscillations at GHz frequencies. These oscillations, which turn out to be very tunable, are very promising for future wireless communication devices. The use of MgO based tunnel junctions, as in this report, is a very promising route towards increasing output power, the bottleneck for integration of spin torque oscillators. Compared to spin valve multilayers (with typical MR ratios of 10%) MgO based tunnel junctions yield MR ratios up to 180% for a Fe/MgO system [1] and up to 500% at room temperature for a CoFeB/MgO system [2]. It was also shown that tunnel junctions can show spin torque oscillations [3] even under high bias voltages which shows the potential of MgO for oscillator applications.
Here RF-oscillations are described, measured on a nanopillar fabricated from a magnetic tunnel junction built up as follows (thickness in nm): Ta 3/CuN 40/Ta 5/PtMn 20/CoFe30 2/Ru 0.8/CoFe20B20 2/Mg 1.3/CoFe20B20 3/Ta 4, contacted with a (Au 100) top electrode, yielding an RxA product of $16\Omega\mu m^2$. A typical best measurement of the magnetoresistance measured on a $15x5\ \mu m^2$ tunnel junction device shows 300% TMR. The rectangular pillars of $100x200nm^2$ are created by means of e-beam lithography and dry etching.
Nanopillar RF measurements were performed with currents up to 4.5mA in varying external magnetic fields. RF oscillations were discovered in external magnetic fields close to the pillar's switching fields as shown in the left half of Figure 1. Large single peaks were observed for positive currents in the parallel configuration, and for negative currents in the anti-parallel configuration. Other configurations yield broader peaks of lower amplitude. The oscillations are reminding of earlier spin torque induced results near the switching fields of spin valves [4]. Output powers of these oscillations are very low compared to what can be expected from uniform spin torque induced oscillations.
Micromagnetic simulations have been performed to get further insight. The right half of Figure 1 shows the oscillations calculated from our model based on the Slonczewski spin torque term [5] in a solver that solves for local current densities. This simulator has previously shown quantitative agreement for point contacts [6]. In this case the simulations include the free layer under the influence of the magnetostatic fields from the entire layer stack and the oersted field. Temperature effects are not taken into account but nevertheless frequencies (4-4.5GHz) are calculated in a range very close to the experimentally found frequencies (6-8GHz) for similar currents (4 vs 3.5mA). Also it shows the experimentally observed trend of decreasing frequency for increasing external fields. A snapshot of the micromagnetic free layer magnetization vectors, as shown in the right of Figure 2 indicates that the measured oscillations are due to oscillations of the end domains of the free CoFeB layer. The model therefore suggests that the current destabilizes the end domains that are present because of magnetostatic fields. The spin torque induces oscillatory motions in these end domains only, which accounts for the rather low powers obtained from these oscillations. The left hand side of Figure 2 compares the experimentally found oscillatory modes with the simulated ones, which enforces the statement that spin torque is the driving force for the oscillations. In the two quadrants where the simulator predicts oscillations, large peaks are found in the experiment accompanied by some broader and less powerful peaks ascribed to thermal spin waves. In the quadrants where no oscillations are predicted (zero temperature model) only broad lower power peaks are observed, purely related to current induced thermal oscillations.
This work was supported by the European Communities programs IST STREP, under Contract No. IST-016939 TUNAMOS.

[1] Yuasa S. et al., Nat. Mater. **3**, 868 (2004)

[2] Lee Y.M. et al., APL **90**, 212507 (2007)

[3] Fuchs G.D. et al., APL **85**, 1205-1207

[4] T Devolder et al., PRB **71**, 184401 (2005)

[5] Sloncewski J.C., PRB **71**, 024411 (2005)

[6] Mistral Q. et al., arXiv:0710.5680v1

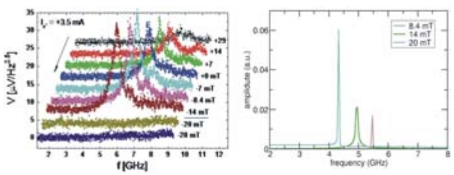

Figure 1: Left: RF oscillations (measured) of the free layer of the $100x200nm^2$ sized pillar in the parallel condition near the switching field (~18mT) for a current of 3.5mA. Right: RF oscillations as calculated by micromagnetic modeling for currents of 4mA.

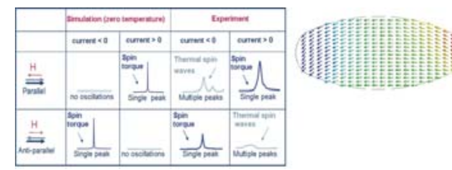

Figure 2: Left: table comparing the found (simulated/experimental) oscillations for positive and negative currents around the switching fields in both the parallel and anti-parallel configurations. Right: snapshot image of the state of the micromagnetic magnetization vectors of the free layer, showing the modes induced in the end domains.

DP-03

Experimental Study of Current-Driven Spin-Wave Excitations in GMR Nanopillars.

Q. Mistral[1], J. Kim[1], T. Devolder[1], P. Crozat[1], C. Chappert[1], J. Katine[2], M. Carey[2], K. Ito[3]
1. Institut d'Electronique Fondamentale, CNRS / Univ. Paris Sud, Orsay, France; 2. Hitachi Global Storage Technologies, San Jose, CA; 3. Advanced Research Laboratory, Hitachi, Tokyo, Japan

The spin transfer effect was first predicted theoretically in 1996 by L. Berger [1] and J. Slonczewski [2] and then observed experimentally in quasi-static magnetization reversal experiments [3]. At present, with MRAM and oscillator applications in perspective, the interest on spin transfer is focused on time resolved or high frequency measurements, in particular, for self-sustained oscillations [4]. Slavin et al. [5] have demonstrated that such oscillations are related to the magnetic excitations (spin-waves) of the system. In this picture each spin-wave mode is considered to be an independent oscillator and the observed signal corresponds to the spin-wave mode of the lowest damping. Such theory relies on parameters like the spin transfer efficiency σ and non linear damping Q [7] that are hard to obtain from first principles. We present an experimental study of current-driven magnetization oscillations in which good quantitative agreement with spin-wave theory is obtained. In addition, we show how σ and Q vary between different spin-wave modes.
The pillars we studied in experiment are made from magnetoresistive read head stacks with an exchanged biased synthetic antiferromagnet (SAF) and a sense (free) layer [6]. They are patterned to have a rectangular cross-section of various sizes, ranging from 100x200 nm^2 to 50x75 nm^2. To observe spin transfer excitations, a DC current ([-12,12] mA) is injected in the pillar and a magnetic field ([-1.5,1.5] kOe) is applied parallel to the easy axis of each device.
We observe high frequency excitations for positive magnetic fields (H), which favor an anti-parallel state, and positive currents, which favor a parallel state. In Fig. 1 we present a color-coded map of the power spectral density as a function of magnetic field for a current of 9 mA. We observe five excitations for which the field dependence of the frequencies qualitatively follows Kittel's law (dashed lines). The data are consistent with standing spin-wave modes propagating along the length of the device with dynamic magnetization being uniform across the width of the samples.
In Fig. 1 we show an example of fits based on spin wave theory. The spin transfer efficiency for this device is σ=55 GHz/A, and the non linear damping is Q=4 for uniform mode and Q=1 for all other spin-wave modes. The observed excitation between 600 Oe and 900 Oe is the uniform spin-wave mode (continuous lines on Fig.1). Around 900 Oe the high frequency signal stops when the SAF layers undergo a spin-flop transition (see hysteresis loop in the inset). After this transition, we observe two modes: the low frequency branch corresponds to the uniform mode and the higher branch is a nonuniform mode with a wave number of 1.
Using the same value of σ and Q, we are able to adjust the frequency versus current curves. In Fig. 2 we show the color-coded map of power spectral density versus the applied DC current for H=789 Oe (before spin flop) and H=1130 Oe (after spin flop). In both cases we observe the expected red shift associated with in-plane precession. For comparison we have plotted in Fig. 2 the expected frequency when non linear damping is neglected.
QM acknowledges support from a joint CNRS and STMicroelectronics PhD grant.

[1] L. Berger, Phys. Rev. B, **54**, 9353 (1996).

[2] J. C. Slonczewski, J. Magn. Magn. Mater., **159**, L1 (1996).

[3] J. A. Katine et al., Phys. Rev. Lett., **84**, 3149 (2000).

[4] S. Kiselev et al., Nature, **425**, 380 (2003).

[5] A. Slavin et al., IEEE Trans. Magn., **41**, 1264 (2005).

[6] Q. Mistral et al., Appl. Phys. Lett., **88**, 192507 (2006).

[7] V. Tiberkevich et al., Phys. Rev. B, **75**, 014440 (2007).

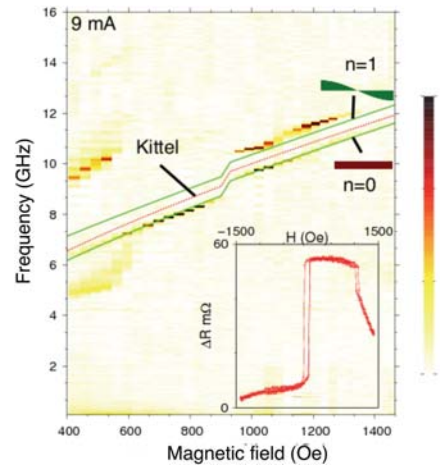

Color-coded map of power spectral density versus magnetic field for a 75x112 nm^2 GMR nanopillar device under 9 mA current. Inset: typical hysteresis loop. Continuous lines are calculated frequencies from spin wave theory.

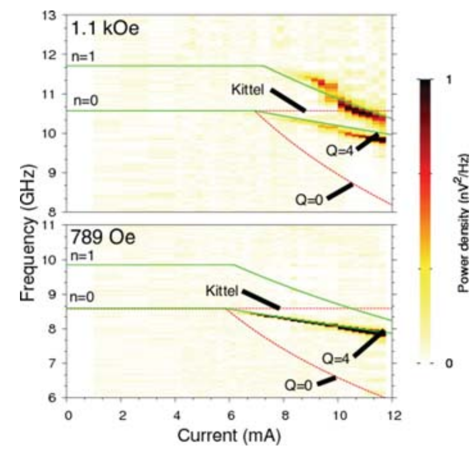

Color-coded map of power spectral density versus DC current for a 75x112 nm^2 GMR nanopillar device, above (1.1 kOe) and below (789 Oe) the spin-flop transition. Continuous lines are the calculated frequencies from spin wave theory with different non linear damping Q.

DP-04

Influence Of The Spin Current Polarization And Direction On The Current-Excited Spin Waves In A Nanopillar Spin Valve: A Micromagnetic Study.

A. V. Khvalkovskiy[1,2], B. Georges[1], J. Grollier[1], Y. V. Gorbunov[3], K. A. Zvezdin[2], V. Cros[1], H. Jaffres[1], A. Fert[1]

1. Unité Mixte de Physique CNRS/Thales, Palaiseau, France; 2. A.M. Prokhorov General Physics Institute of RAS, Moscow, Russian Federation; 3. Institute of Microtechnology – Spin MT ltd., Moscow, Russian Federation

This report presents results of a micromagnetic analysis of our experimental data on the current-induced spin-wave excitation in the free layer of a nanopillar spin valve. The measurements are made on a Py(30)/Cu(10)/Py(4) structure (in nm). The thin Py free layer (FL) is defined by electron-beam lithography and ion-milling, using a mask in a form of an ellipse with the axes of 150 nm and 50 nm. The thick Py reference layer (RL) is left unpatterned. The field dependence of the device resistance, for a field applied in the film plane along the FL axis, evidences that at zero field the FL and RL are magnetized antiparallel (AP) to each other. That is possibly due to a small demagnetizing field generated by the reference layer, which could be slightly etched. The measurements were performed at room temperature for static magnetic fields applied perpendicular to the ellipse plane. A coherent microwave signal is observed only when electrons flow from the FL towards the RL. Jumps in the frequency versus current curves indicate switching between different oscillating modes. The low-frequency mode (LFM) ranges from 1 to 3 GHz, the next mode (high-frequency mode, HFM) starts at about 4 GHz. All the modes have approximately the same power.

The simulations are performed using our home-made solver SpinPM by numerical integration of the Landau-Lifshitz equation, which includes an additional spin-transfer torque $-\gamma a_J \mathbf{M}\times[\mathbf{M}\times\mathbf{m}]$($\gamma$ is the gyromagnetic ratio, **M** and **m** are unit vectors along the magnetization direction of the free and reference layers accordingly, a_J is a spin-transfer parameter proportional to the current). A two-dimensional mesh is used and only the FL is actually taken into account in the simulations. We took M_s = 700 emu/cc for the saturation magnetization, α = 0.018 for the Gilbert damping parameter (yielded from SQUID and FMR measurements accordingly), A = 1.3×10^{-6} erg/cm for the exchange constant, anisotropy constant K = 0. The discretization step was 1.5 nm. The thermal fluctuations and the angular dependence of aJ are neglected.

Using a simple expression for the spin-transfer parameter a_J [1], we get for our device $a_J = 200\times p\times I$ (in Oe), where I is the current in mA and p is the current polarization. For each field, there is a critical value of for a_J for the onset of the oscillations. To define p, we compare the latter to the corresponding experimental critical current [2]. This procedure yields $p = 0.17 \pm 0.02$. This value is consistent with the value $p = 0.14$ for AP configuration, extracted according to the Ref. [3] from the spin accumulation distribution calculated for our device. A very careful derivation of p is important as it defines a balance between the Oersted field and the spin-transfer. Our calculations show indeed that the excited modes may be strongly affected by the spin polarization.

The field dependence of the out-of plane component of the vector **m** is calculated for a 1 μm × 1 μm × 30 nm plate. The direction of the in-plane component $\mathbf{m}_{\text{in-plane}}$ of this vector is arbitrary for ideally perpendicular field **H**. An unavoidable (and usually undefined) in experiments small misalignment of the field **H** from the perpendicular to the plane direction may influence the direction of $\mathbf{m}_{\text{in-plane}}$. The dependence of the spectral peak frequency on the direction of $\mathbf{m}_{\text{in-plane}}$ was thoroughly calculated for several values of H and I. We find that it is a key parameter, which defines the excited oscillating mode.

Our study reveals that the oscillatory state of the system is always a vortex. Three modes may be excited in our system (one LFM and two HFMs). The LFM is an oscillation of the vortex core around the ellipse center. The dependencies of the oscillator frequencies on the current show a quantitative agreement of the calculated LFM with the experimental one. If the simulations are performed assuming that the FL size is equal to the size of the lithography mask, there is a strong disagreement between simulations and experiments when the experimental mode switches to the HFM. The HFMs found in the simulations have frequencies above 10 GHz and very low emitted power (3 to 10 times less than the LFM); they have no correlation with the experimental data. We have studied the dependence of the excited modes on the FL size and aspect ratio, which may possibly deviate from the nominal values due to imperfections of the patterning process. This study shows that under quite realistic assumptions about the latter parameters, a good agreement with the experiments may be found.

1. J. Xiao, A. Zangwill, M. D. Stiles. Phys. Rev. B 70, 172405 (2004).

2. I. N. Krivorotov, D. V. Berkov et al., Phys. Rev. B 76, 024418 (2007).

3. A. Fert, V. Cros, et al. J. Magn. Magn. Mater. 272–276, 1706–1711 (2004).

DP-05

Angular dependence of generation linewidth of in-plane-magnetized anisotropic spin-torque oscillator.

V. Tyberkevych, A. Slavin
Department of Physics, Oakland University, Rochester, MI

The analysis of a stochastic dynamics of a spin-torque oscillator (STO) with the amplitude-dependent frequency was performed in [1], yielding the following expression for the generation linewidth $\Delta\omega$:
$\Delta\omega = \Gamma_0 (kT/E_0) (1 + (N/(Q\Gamma_0 + \sigma I)^2)$. (1)
Here Γ_0 is the ferromagnetic resonance (FMR) linewidth in the STO "free" layer, k is the Boltzmann constant, T is the absolute temperature, E_0 is the average energy of the STO auto-oscillations, N is the nonlinear frequency shift coefficient, $Q \sim 1$ is the dimensionless parameter characterizing the nonlinearity of magnetic damping, I is the bias current traversing the "free" magnetic layer, and σ is the coefficient that depends on the spin-polarization efficiency and geometrical sizes of STO. In this work we analyze the angular dependence of the generation linewidth of STO based on an *in-plane* magnetized *anisotropic* nano-pillar structure. In this case the dependence of the generation linewidth on the in-plane magnetization angle ϕ_0 is provided by the in-plane magnetic anisotropy H_A (see inset in Fig. 1) that can be caused both by the magnetocrystalline anisotropy of the magnetic material and by the shape anisotropy (non-circular shape) of the pillar "free" layer. The in-plane magnetization of an STO is more preferable than the out-of-plane magnetization, because the same oscillation frequency is achieved for a substantially lower bias magnetic field H_0. At the same time, it is known that even a small anisotropy substantially changes the nonlinear properties of spin waves [2], and, due to the above described nonlinear mechanism, can lead to significant variations of the generation linewidth $\Delta\omega$. Thus, in the practically interesting case of relatively small bias and anisotropy fields, H_0, $H_A << 4\pi M_0$, one can obtain simple expressions for N in the limiting cases of easy ($\phi_0 = 0$) and hard ($\phi_0 = \pi/2$) axis magnetization:
$N(\phi_0 = 0) \approx -(\omega_0/2)(H_0+4H_A)/(H_0+H_A)$, $N(\phi_0 = \pi/2) \approx -(\omega_0/2)(H_0-4H_A)/(H_0-H_A)$, (2)
where ω_0 is the FMR frequency for the given field orientation. It is clear, that the modulus of the nonlinear frequency shift coefficient $|N|$ for the hard-axis magnetization is always smaller than for the easy-axis magnetization. At the same time, linear damping rate Γ_0 and other parameters that determine the linewidth Eq. (1) depend on the magnetization angle ϕ_0 rather weakly. Therefore, the generation linewidth $\Delta\omega$ for the hard-axis magnetization is always smaller than for the easy-axis magnetization, as it is shown in Fig. 1 for the typical parameters of an STO. In the range of bias fields $4H_A > H_0 > H_A$ the sign of N changes as ϕ_0 rotates from easy $\phi_0 = 0$ to hard $\phi_0 = \pi/2$ orientation and, consequently, the nonlinear coefficient N vanishes ($N = 0$) for a certain intermediate magnetization angle. At this angle a clear minimum of the generation linewidth is observed (see curve 1 in Fig. 1). For larger magnetic fields, $H_0 > 4H_A$, the linewidth has minimum at the magnetization angle $\phi_0 = \pi/2$ and increases with the increase of H_0 (see curves 2 and 3 in Fig. 1). Recently, a qualitatively similar behavior of the generation linewidth $\Delta\omega$ has been observed in the experiments reported in [3].
Our results show that the performance of STOs can be significantly improved by using nano-pillar devices magnetized along the hard in-plane axis $\phi_0 = \pi/2$. For this direction of magnetization the generated frequency and threshold current remain almost the same as for the easy-axis magnetization $\phi_0 = 0$, but the generation linewidth is substantially reduced due to the lower value of the nonlinear frequency shift coefficient N (see Eq. (2)).

[1] J. Kim, V. Tyberkevych, and A. Slavin, Abstracts of the 52th MMM Conference (Tampa, FL, Nov 2007), CE-05; J. Kim., V. Tiberkevich, and A. Slavin, accepted to Phys. Rev. Lett. (2008).

[2] V. S. L'vov, *Wave Turbulence Under Parametric Excitation* (Springer-Verlag, N. Y., 1994).

[3] K. V. Khadani *et al.*, Abstracts of the 52th MMM Conference (Tampa, FL, Nov 2007), CE-02.

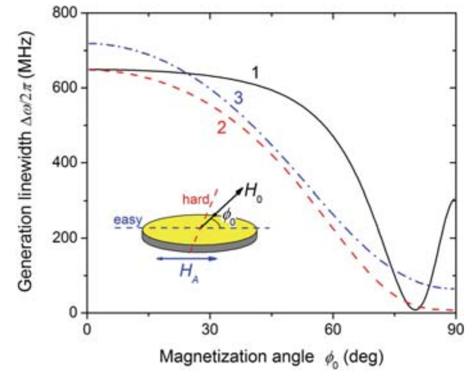

Dependence of the generation linewidth $\Delta\omega$ of an STO on the in-plane magnetization angle ϕ_0 for several values of the bias magnetic field H_0: 1 – $H_0 = 2H_A = 0.6$ kOe, 2 – $H_0 = 4H_A = 1.2$ kOe, 3 – $H_0 = 6H_A = 1.8$ kOe. Other parameters of STO: $4\pi M_0 = 8$ kOe, $H_A = 0.3$ kOe, $\alpha_G = 0.01$, $Q = 3$, "free" layer thickness 3 nm, shape of the nano-pillar – circular with the radius of 50 nm, spin-polarization efficiency 0.2, bias current $I = 3$ mA, temperature $T = 300$ K. The inset shows the "free" layer of the STO with the direction of the bias magnetic field and easy and hard magnetization orientations.

DP-06

Mutual phase-locking of two spin-torque oscillators: Influence of time delay of a coupling signal.

O. Prokopenko[1], *V. Tyberkevych*[2], A. Slavin[2]
1. Faculty of Radiophysics, Kiev National Taras Shevchenko University, Kiev, Ukraine; 2. Department of Physics, Oakland University, Rochester, MI

Spin-transfer-torque effect [1] opens a possibility for the development of a novel type of nano-scale microwave devices – *spin-torque oscillators* (STO). The practical application of STOs faces two main problems – low output power and large generation linewidth, both of which can be solved using the mutual phase-locking of several STOs [2, 3]. Using numerical simulations it has been demonstrated recently [4, 5] that the finite delay time of the coupling signal can lead to a substantial (~ 100 times) increase in the frequency band of phase-locking.
In this work we develop a theory of phase-locking of two STOs with account of the delay of the coupling signal. We consider the case of 2 nano-contact STOs coupled only by propagating spin waves. Our method and results, however, can be easily generalized to different types of coupling.
The dynamics of the two weakly-coupled STO can be described be the system of coupled nonlinear equations for the complex amplitudes $c_j(t)$ of spin wave modes, excited in j-th nano-contact [3]:
$dc_1/dt + i\omega_1(|c_1|^2)c_1 + \Gamma_{\mathrm{eff},1}(|c_1|^2)c_1 = \Omega_{1,2}\exp(i\beta_{1,2})c_2$, (1a)
$dc_2/dt + i\omega_2(|c_2|^2)c_2 + \Gamma_{\mathrm{eff},2}(|c_2|^2)c_2 = \Omega_{2,1}\exp(i\beta_{2,1})c_1$, (1b)
Here $\omega_j(p_j)$ and $\Gamma_{\mathrm{eff},j}(p_j)$ are the frequency and effective damping rate (that includes contribution from the positive natural damping and current-induced negative damping) of j-th mode, coupling frequencies $\Omega_{j,k}$ are defined by Eq. (6) in [3], and $\beta_{j,k} = \omega_k\tau_{j,k} = \omega_k a/v_k$ is the phase shift of the spin wave (radiated by the k-th nano-contact) acquired during its propagation to the j-th nano-contact ($\tau_{j,k}$ is the propagation time, a is the separation between the nano-contacts and v_k is the velocity of the spin wave). The system (1) without time delay ($\beta_{j,k} = 0$) was derived and analyzed in [3]. The description of the time delay by phases $\beta_{j,k}$ is valid for relatively small delay times $\Omega_{j,k}\tau_{j,k} << 1$.
In the absence of coupling ($\Omega_{j,k} = 0$), each of the Eqs. (1) has a free-running solution $c_j(t) = \sqrt{P_j}\exp[-i\omega_j(P_j)t]$, where the power P_j is determined by the condition of the vanishing of total damping $\Gamma_{\mathrm{eff},j}(P_j) = 0$. For the weak coupling ($\Omega_{j,k} << \omega_{j,k}$) it is possible to perform a perturbative analysis of Eqs. (1), and obtain criteria of phase-locking in a closed analytical form. Thus, in the case of almost identical oscillators (where all the parameters of two oscillators, except the free-running frequencies $\omega_{j,k}(P_j)$, are identical) the phase-locking occurs when $|\omega_1(P_1) - \omega_2(P_2)| < \Delta\omega$, where the phase-locking band $\Delta\omega$ is given by
$\Delta\omega = 2\,\Omega\,\sqrt{(1 + \eta^2)}|\cos(\beta - \arctan\eta)|$. (2)
Here $\eta = (d\omega/dP) / (d\Gamma_{\mathrm{eff}}/dP)$ is the dimensionless measure of the influence of the nonlinear frequency shift ($d\omega/dP$) compared to the influence of the nonlinear damping ($d\Gamma_{\mathrm{eff}}/dP$), and β is the phase difference between the oscillators caused by the delay of the coupling signal.
The optimum phase shift $\beta_{\mathrm{opt}} = \arctan\eta$ for which $\Delta\omega$ has a maximum value $\Delta\omega_{\max} = 2\,\Omega\,\sqrt{(1 + \eta^2)}$ changes from 0 for $|\eta| << 1$ (conventional oscillators) to $\pi/2$ for $|\eta| >> 1$ (STOs). The latter fact has been recently observed in numerical experiments [5].
The dependence of the phase-locking interval $\Delta\omega$ Eq. (2) on the distance a between the oscillators for typical STO parameters is shown in Fig. 1 (see curve 1). The overall decrease of the synchronization band (see curve 2 in Fig. 1) is caused by the decrease of the coupling coefficient Ω with the increase of the distance a.
Our results reveal the relation between the frequency nonlinearity of the STO and the optimum delay time (or, equivalently, phase shift) of the coupling signal, and allow one to calculate the parameters of the oscillator array (such as STO separation a) that are optimum for the STO synchronization.

[1] J. Slonczewski, J. Magn. Magn. Mat. **159**, L1 (1996); L. Berger, Phys. Rev. B **54**, 9353 (1996).

[2] S. Kaka *et al.*, Nature **437**, 389 (2005); F. B. Mancoff *et al.*, Nature **437**, 393 (2005).

[3] A. N. Slavin and V. S. Tiberkevich, Phys. Rev. B **74**, 104401 (2006).

[4] B. Georges *et al.*, Abstracts of the 52th MMM Conference (Tampa, FL, Nov 2007), CE-10.

[5] J. Persson Y. Zhou, and J. Akerman, J. Appl. Phys. **101**, 09A503 (2007); J. Akerman *et al.*, Abstracts of the 52th MMM Conference (Tampa, FL, Nov 2007), CE-10.

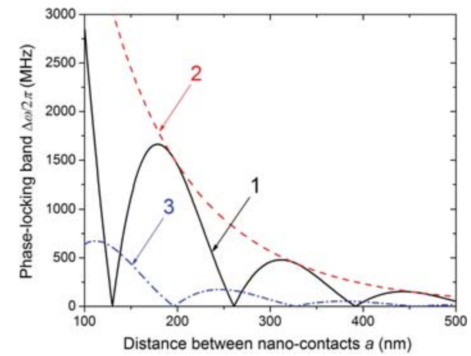

Dependence of the frequency band of phase-locking $\Delta\omega$ for two STO separated by a distance *a*: 1 – phase-locking band $\Delta\omega$ with account of time delay and frequency nonlinearity η, 2 – maximum possible band $\Delta\omega_{\max}$, 3 – phase-locking band $\Delta\omega$ for linear oscillators $\eta = 0$ multiplied by 10. Parameters of STOs: normally magnetized (magnetic field 15 kOe) circular nano-contacts of the radius 50 nm, saturation magnetization $4\pi M_0 = 8$ kOe, Gilbert damping constant $\alpha_G = 0.01$, nonlinear damping parameter $Q = 3$, exchange length 5 nm, supercriticality parameter $I/I_{\mathrm{th}} = 1.5$.

DP-07

Influence of the Demagnetizing Field in Spin Dynamics with A Perpendicular-to-Plane Polarizer.

C. Jui-Hang, C. Ching-Ray
Department of Physics, National Taiwan University, Taipei, Taiwan

It is known that a "perpendicular-to-plane polarizer (PERP)" used in spin-transfer torque device has many interesting results, and with potential application in spin-injected device [1][2]. In the device, the polarization of the
injected spin current is perpendicular to the easy plane of the free layer. As a result, the precessional frequency of a large-cone angle ($|\theta|\approx\pi/2$) steady state of the free layer moment can be tuned by changing the injected current in the absence of the external applied field. The first analytical results of the perpendicular-to-plane polarizer were given in Lee's paper [3]. In their paper, the critical current density is proportional to the uniaxial anisotropy field H_k. Since they assume the cancelation of the demagnetizing field and fringe field from the pinned layer, the critical spin-torque
amplitude for large-cone angle precession motion to start is independent of the damping constant α, demagnetizing field, and fringe field. In the article, we take an extra consideration of the effects of the demagnetizing and stray fields, and derive a rigorous form of the critical current density, which is sensitive to the damping constant, demagnetizing and fringe fields. The Landau-Lifshitz-Gilbert (LLG) equation of motion for the free layer moment including a Slonczewski's spin-transfer torque is $d\mathbf{M}/dt=-\gamma(\mathbf{M}\times\ \mathbf{H}_{eff})+(\alpha/M_s)\mathbf{M}\times(d\mathbf{M}/dt)+(\gamma a_J(\theta)/M_s)\mathbf{M}\times(\mathbf{M}\times\mathbf{p})$, where $\mathbf{p}$ is the unit vector of spin polarization direction along the z axis, and $\mathbf{H}_{eff}=H_k(\mathbf{M}\bullet\mathbf{x}/M_s)\mathbf{x}+(H_z-4\pi M_z)\mathbf{z}$ is the internal effective field, including the in-plane anisotropy field, stray field, and demagnetizing field. In spherical coordinates, the LLG equation can be written as a set of two first-order differential equations, $[(1+\alpha^2)/\gamma]d\theta/dt=h_1+\alpha h_2$, and$[(1+\alpha^2)/\gamma]\sin\theta(d\phi/dt)=-h_2+\alpha h_1$, where $h_1=-H_k\sin\theta\sin\phi\cos\phi+a_J(\theta)\sin\theta$, and $h_2=H_k\sin\theta\cos\theta\cos^2\phi-(H_z-4\pi M_s\cos\theta)\sin\theta$. To find the instability for the spin current at large cone-angle
precession motion, we have to average the rate of energy change, where the potential energy for the free layer magnetization is $U(\theta,\phi)=K(1-\sin^2\theta\cos^2\phi+h_D\cos^2\theta-2h_z\cos\theta)$. K is the uniaxial anisotropy constant, $h_D=4\pi M_s/H_k$, and
$h_z=H_z/H_k$. Taking time average for the energy variation, we obtain the stability threshold for spin-current-driven motion at the large cone-angle limit ($|\theta|\approx\pi/2$), $J_C^{PERP}=\alpha(4e/hbar)[Ms\bullet t/g(\theta\approx\pi/2)][(H_k^2/2+2\pi M_sH_k+H_z^2)/(3H_k^2/8+2\pi M_sH_k+2H_z^2)]H_z$, which depends on damping constant α, anistropy field, demagnetizing field, and stray field. Instead of the linear response of anisotropy field H_k [3], we find that the critical current density for the perpendicular-to-plane polarizer device depends on the anisotropy field nonlinearly as shown in Figure 1; and further, the
threshold current density can be reduced.

[1] Houssameddine, D. *et al.*, Nat. Mater. **6**, 447 (2007).

[2] A. D. Kent, Nat. Mater. **6**, 399 (2007)

[3] K. J. Lee, O. Redon, and B. Dieny, Appl. Phys. Lett.

86, 022205 (2005).

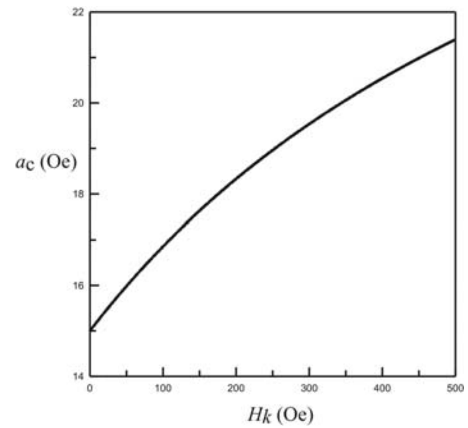

Figure 1: Threshold amplitude of spin torque a_J (labeled a_C) for magnetic switching in PERP device as a function of the anisotropy field of the free layer (α=0.01, M_s=1000 emu/cm^3, $H_z\approx$1500 Oe).

DP-08

Investigation of spin-wave radiation and current controlled three-magnon-scattering in spin-torque nanocontact devices.

H. Schultheiss[1], X. Janssens[2], M. van Kampen[2], S. Cornelissen[2], F. Ciubotaru[1], A. Laraoui[1], B. Leven[1], A. N. Slavin[3], L. Lagae[2], B. Hillebrands[1]
1. Fachbereich Physik and Forschungsschwerpunkt MINAS, TU Kaiserslautern, Kaiserslautern, Germany; 2. IMEC, Leuven, Belgium; 3. Oakland University, Rochester, MI

The magnetization dynamics of spin torque oscillators are of large interest for the fundamental understanding of the interaction between a spin polarized current and a magnetic thin film. A deeper understanding of the eigenmode spectrum of a nanocontact and the mechanism of spin-wave radiation is advantageous for technical applications.
Here we report on Brillouin light scattering microscopy investigations of the magnetization dynamics in spin-torque nanocontacts under the influence of an applied ac and dc current. The magnetic resonance frequencies of the nanocontacts are determined by Brillouin light scattering microscopy for different externally applied magnetic fields. For the observed resonance frequencies the spin-wave radiation patterns are studied with high spatial resolution. The spin-wave radiation patterns are studied for several applied microwave frequencies. Strong nonlinear effects are observed and discussed within the framework of three-magnon-scattering.
Intriguing is the shift of the power threshold for these nonlinear processes when a dc current is applied. Depending on the dc current direction the threshold and efficiency of the three-magnon-scattering can be strongly enhanced or reduced. This is a clear evidence that the internal damping due to magnon scattering can be tuned by a dc current.
Support by the DFG within the SPP 1133 and by the EC-MRTN SPINSWITCH (MRTN-CT-2006-035327) and EC-Dynamax (IST-033749) is acknowledged. MvK acknowledges the IWT Flanders for financial support.

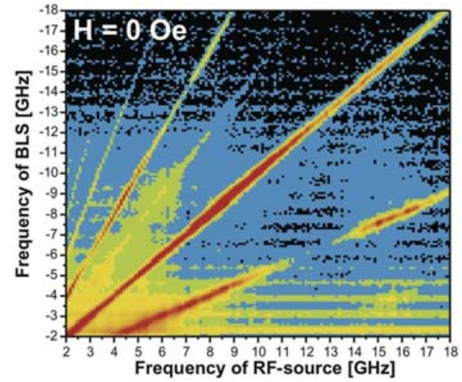

Spin-wave spectra in the vicinity of the contact area of the spin torque device measured with Brillouin light scattering microscopy for different applied microwave frequencies. The diagonal indicates the directly excited magnetic resonances whereas the signals above and below the diagonal show the intensities of spin waves created by nonlinear processes.

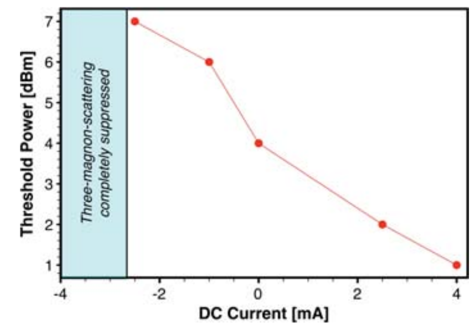

The power threshold for the appearance of spin waves with half the excitation frequency due to three-magnon-scattering can be tuned in a wide range if a dc current offset is applied. Below -2.5 mA the half frequency generation is completely suppressed.

DP-09

Mutual phase-locking in high frequency microwave nanooscillators as function of field angle.

G. Hrkac[1], T. Schrefl[1], S. Bance[1], A. Goncharov[1], J. Dean[1], D. Allwood[1], D. Suess[2], J. Fidler[2]
1. University of Sheffield, Sheffield, United Kingdom; 2. Vienna University of Technology, Vienna, Austria

We perform a qualitative analysis of phase locking in a double point-contact spinvalve system by solving the Landau-Lifshitz-Gilbert-Slonzewski equation using a hybrid-finite-element method. We show that the phase-locking behaviour depends on the applied field angle. Starting from a low field angle, the locking-current difference between the current through contact A and B increases with increasing angle up to a maximum of 14 mA at 30° and it decreases thereafter until it reaches a minimum of 1 mA at 75°. The tunability of the phase-lock frequency with current decreases linearly with increasing out of plane angle from 45 to 21 MHz/mA.
The model simultaneously solves the modified Landau-Lifshitz-Gilbert equation which is expanded with the asymmetric Slonczewski spin torque term and the Maxwell equations with a finite element/boundary element method.
The study was carried out on a spin valve structure consisting of Co90Fe10(20nm)/Cu(5nm)/Ni80Fe20(5nm). The Co90Fe10 layer is considered as the fixed layer meaning that the magnetization is pinned in terms of the spin torque driven magnetization processes due to a larger thickness, d, and higher saturation magnetization, Ms, compared to the Ni80Fe20 free layer. The spin valve system is contacted with two Cu point contacts (40nm in diameter) with a centre to centre distance of 500nm. The overall size of the simulation area was 1000 nm in diameter, with a discretization size of 4.5nm . We apply a fixed current through point contact A (Je,A = 7.16 x 1012 A/m2) and a varying current through point contact B at an external field of 740 mT at 15° out of plane.Starting with the same current density through both contacts two well distinguishable peaks can be observed (see figure1). Although the current through both currents is the same two different frequencies can be observed (one at 24.5 GHz and the other at 25.108 GHz). This is connected to the variation of the local change in magneto resistance, the direction of the applied field, the asymmetric Slonczewski term and the incoming spin waves from each point contact.Increasing the currentdensity to 1.67e13 A/m2 (21 mA) a phase-locking behavior can be observed, see figure 2, which originates from spin waves traveling through the device and synchronizing the individual oscillators at a frequency of 24.505 GHz. By increasing the currentdensity above 1.83e13 A/m2 (23 mA) the coherence of the individual oscillators breaks down and two separate oscillation frequencies of 24.5 GHz and 24.475 GHz can be distinguished. By increasing the applied field angle to 30° two things can be observed: a red shift in frequency and a shift of the locking regime to higher currents. The tunability changes to 31 MHz/mA and the locking current difference (difference between ccurrent through contact A and B)ΔIAB is increased to 14 mA. For an out of plane field angle of 45° the slope of the curve fB(IB) becomes smaller, so that the frequency decreases with increasing current at a rate of 21 MHz/mA; the locking current difference ΔIAB drops to 6 mA. For high out of plane field angles of 75°, the frequency of the magnetization oscillations near contact B first decreases and the one from A increases until they oscillate with the same frequency. The phase locking regime persists until the current in contact B is increased by 1 mA, where after two well distinguished frequency are observed, and show a blue shift in frequency with current. The average increase in frequency with current is 179 MHz/mA. ΔIAB is reduced to 1 mA. We show in this paper that the locking current difference is a function of applied field angle, which has its minimum of 1m A at high angles (75 degree) and reaches a maximum at low angles 15 degree. This value is similar to the locking-current difference found experimentally for a field angle of 75° [1] and shows that these results are in good agreement with the experiments published by Rippard [1} and Kaka et al [2].
This project is supported by the EU FP project 6 TUNAMOS (IST-16939).

[1] W. H. Rippard, M. R. Putfall, S. Kaka, T. J. Silva, and S.E. Russek, “Current-driven microwave dynamics in magnetic point contacts as a function of applied field angle”, Phys. Rev. B 70, 100406(R) (2004)

[2] S. Kaka, M.R. Pufall, W.H. Rippard, T.J. Silva, S.E. Russek and J.A. Katine, “Mutual phase-locking of microwave spin torque nano-oscillators”, Nature 437, 389 (2005)

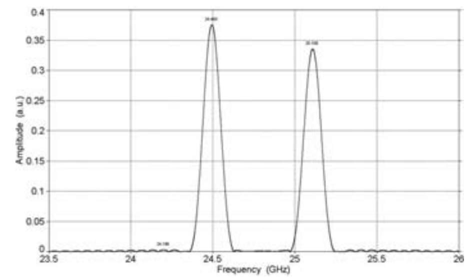

Fig. 1 Frequency as function of amplitude magnitude for a double point contact with a current of 9 mA through contact A and B.

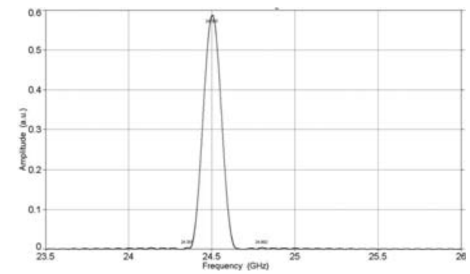

Fig. 2 Frequency as function of amplitude magnitude for a double point contact.The black graph represents a phase-locked regime with a current of 9 mA through contact A and 21 mA through contact B.

DP-10

Non-stationary analysis of large magnetization dynamics in nanoscale spin-valves.

G. Finocchio[1], L. Torres[2], M. Carpentieri[1], G. Consolo[1], B. Azzerboni[1]
1. University of Messina, Messina, Italy; 2. Universidad de Salamanca, Salamanca, Spain

The spin torque due to a spin polarized current in a nanomagnet can induce either magnetization reversal or several different king of magnetization dynamics (self oscillations)[1,2]. Recent time domain measurements of nanomagnet dynamics in exchange bias nanoscale spin-valves (IrMn/Ni80Fe20(Py)/Cu/Py) of elliptical cross sectional area (130nm x 60nm) show magnetization reversal and persistent dynamics excited in nanosecond scale[3]. Time domain measurements together to frequency domain measurements are able to explain completely the magnetization dynamics [4,5].
The frequency domain analysis gives information about the excited modes during all the measurement time with no information about the range of time where the mode is excited, this range can be determined by means of single shot storage oscilloscope measurements.
For the device employed in [3] those measurements show in the range of 20ns a frequency spectrum with two peaks, the same measurements in the range 0-4ns or 16-20ns show one the two peaks isolated.
Here we study in detail the same devices of ref[3] by means of the micromagnetic simulations and the micromagnetic spectral mapping technique (MSMT)[6]. We numerically solved the Landau-Lifshitz-Gilbert-Slonczewski equation [7] including the thermal field as an additive component to the effective field (we simulate a background temperature of 4.2K). For the spin torque, we use the formulation presented in [8] where shape of the torque has been computed by fitting experimental reversal data[5]. The pinned layer of the device is exchanged bias at 45 degrees with respect to the easy axis of the ellipse, the external field is applied at -45 degrees with respect to the easy axis. Here we report results related to an applied field of 68mT and current density of 0.5 10^8 A/cm^2. Fig. 1(a) shows the temporal evolution (60ns) of the x, y and z component of the average magnetization for that process, as can be noted from the spectrum of Fig. 1(b) the magnetization dynamics is mainly characterized by two excited modes (P1 at 6.4GHz and P2 at 7.35GHz, the insets of Fig. 1(b) show the spatial distribution of those modes computed by means of MSMT (power increases from white to black)). Performing the MSMT in different range of time we observe the magnetization dynamics governed by the P1 mode in the range (0-20ns) and a by the P2 mode in the range 40-60ns. Those results (also observed for other currents and fields) show the existence of jump between different dynamical modes in the nanosecond regime in agreement with experimental data. In the paper we will present a complete non-stationary study of the persistent magnetization dynamics and a generalization tool of the MSMT able to characterize the presence of those jumps systematically.

[1] J. Slonczewski, J. Magn. Magn. Mater. 159, L1 (1996); J. Magn. Magn. Mater. 195, L261 (1999).

[2] S. I. Kiselev, J. C. Sankey, I. N. Krivorotov, N. C. Emley, R. J. Schoelkopf, R. A. Buhrman, D. C. Ralph, Nature 425, 380 (2003).

[3] I. N. Krivorotov, N. C. Emley, J. C. Sankey, S. I. Kiselev, D. C. Ralph, R. A. Buhrman, Science 307, 228 (2005).

[4] I. N. Krivorotov, D. V. Berkov, N. L. Gorn, N. C. Emley, J. C. Sankey, D. C. Ralph, R. A. Buhrman, Phys. Rev. B 76, 024418 (2007).

[5] G. Finocchio, I. N. Krivorotov, L. Torres, R.A. Buhrman, D.C. Ralph, B. Azzerboni, Phys. Rev. B 76, 174408 (2007).

[6] R. D. McMichael and M. D. Stiles. J. Appl. Phys. 97, 10J901, (2005). G. Finocchio, et al, J. Appl. Phys. 91 08G507 (2006).

[7] L. Torres, L. Lopez-Diaz, E. Martinez, M. Carpentieri, G. Finocchio, J. Magn. Magn. Mat., 286, 381 (2005).

[8] J. Slonczewski, J. Magn. Magn. Mater. 247, 324 (2002).

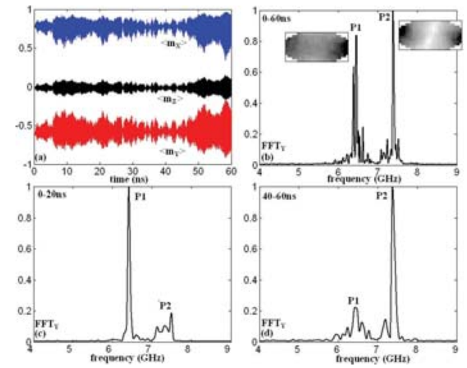

Fig. 1: (a) temporal evolution of the x, y, and z component of the average magnetization (H=68mT, J=0.5 10^8A/cm^2). Spectrum computed by means of the MSMT in the range (b) 0-60ns, (c) 0-20ns, (d) 40-60ns. Inset of Fig.1(b): spatial distribution of the modes P1 and P2 computed by means of MSMT (power increases from white to black).

DP-11

Magnetic Vortex Oscillators driven by Spin-Polarized Current and Perpendicular Anisotropy at Zero-Field.

V. Puliafito[1], B. Azzerboni[1], G. Consolo[1], G. Finocchio[1], L. Torres[2], L. Lopez-Diaz[2]
1. Dipartimento di Fisica della Materia e Tecnologie Fisiche Avanzate, University of Messina, Messina, Italy; 2. Departamento de Fisica Aplicada, University of Salamanca, Salamanca, Spain

It is well-known that a spin-polarized current can apply a torque on the local magnetization of a ferromagnet [1]. This effect provided a new technique for manipulating nanoscale magnetic systems. Experiments have demonstrated that spin-torque can be successfully used to build microwave oscillators which do not require the usage of external bias magnetic fields [2] as well as to excite steady-state magnetization oscillations in strongly non-uniform magnetic configurations, such as a vortex state [3]. The vortex-state is a three-dimensional spin structure whose magnetic moments are arranged in closed loops and tend to rise up within a small inner region (the vortex-core) to minimize the energy cost. The sense of flux-closure (counterclockwise or clockwise) is referred to as chirality, whereas the out-of-plane component of the vortex-core (positive or negative) determines the so-called polarity. This latter parameter acquires a fundamental role in gyrotropic vortex dynamics (and vortex-core reversal) because it determines the sense of gyration, independently of the chirality [4,5]. The earlier experiments demonstrated that a vortex-core reversal can be induced by applying either a static or a pulse of a relatively strong external magnetic field [5,6]. Later on, an analogous outcome has been obtained by using either an ac or a dc spin-polarized current [3,7,8]. In particular, it was recently demonstrated that a magnetic tri-layer nanocontact system, subjected to a dc spin-polarized current, can sustain a persistent magnetization precession without the usage of any bias field [8]. Moreover, it was predicted a strategy to increase the precession frequency by using a material with magnetocrystalline anisotropy in the thin magnetic “free” layer (FL) of the structure [8]. In that work, it was shown that the resulting oscillations correspond to a periodic gyrotropic motion of the vortex core, whose polarization and sense of gyration switch periodically. While the main goal of the work in Ref.8 was to demonstrate the feasibility of the so-called bias-field-free configuration, a detailed analysis of the properties exhibited by such oscillator as function of the anisotropy field strength was not carried out. With this in mind, in this work we present such a systematic study in order to gain a better understanding of the magnetization dynamics in nanocontact devices at zero-field driven by dc spin-polarized current and subjected to a perpendicular anisotropy field in the FL of variable strength. In detail, the anisotropy field strength is varied by acting on the anisotropy constant value (k_u) in order to perform a full-scale investigation: from the case of no anisotropy (k_u=0 J/m^3) to the one corresponding to a strong anisotropy (k_u=1x10^5 J/m^3). The study is carried out by using our 3D full-micromagnetic simulation framework, where the magnetization is assumed uniform in each cell and the Landau-Lifshitz-Gilbert-Slonczewski equation is solved by a fifth-order Runge-Kutta scheme [9]. The effective field carries the contribution of anisotropy, external, exchange, Oersted and magnetostatic fields. We have neglected the stochastic contribution arising from thermal noise. In all the analyzed cases, the output spectra are dense of harmonics, so that the corresponding time-domain signals are not pure sinusoids. Because it is well-known that spin-wave excitation in such devices exhibits a threshold character, our first investigation is devoted to the analysis of the dependence of the excitation threshold current I_{th} on the anisotropy field strength. Results summarized in Fig.1 (dashed line) reveal a linear dependence I_{th} vs k_u, with the threshold current which decreases with the increase of the anisotropy field. The calculation of the frequency generated at that threshold f_{th} allows to derive another intriguing property. In fact, a nonlinear dependence f_{th} vs k_u is found (see Fig.1, solid line), similar to the one obtained in Ref.8 in presence of a strong bias field. It shows that, at the excitation threshold, the precession frequency decreases with the increase of the anisotropy field strength. If a similar investigation is carried out at the same applied current value, the inclusion of materials with perpendicular anisotropy is always associated to higher generated frequency with respect to the case of no anisotropy. In such situation, the precession frequency exhibits a non-monotonic dependence on the anisotropy field, i.e. there exists a given value of anisotropy which determines a maximum of the output frequency.

[1] J.C. Slonczewski, J. Magn. Magn. Mater., 195, L261 (1999).

[2] X. Zhu and J.G. Zhu, IEEE Trans. Magn. 42, 2670 (2006).

[3] K. Yamada et al., Nature Materials 6, 270 (2007).

[4] A. Thiele, Phys. Rev. Lett. 30, 230 (1973).

[5] B. Van Waeyenberge et al., Nature 444, 261 (2006).

[6] T. Okuno et al., J. Magn. Magn. Mater., 240, 1 (2002).

[7] D.S. Sheka et al., Appl. Phys. Lett. 91, 082509 (2007).

[8] G. Consolo et al., Appl. Phys. Lett. 91, 162506 (2007).

[9] A. Romeo et al., Physica B 403, 464 (2008).

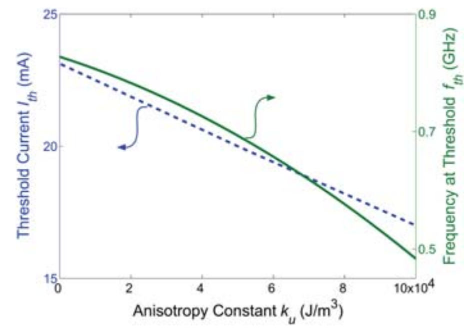

Fig.1

DP-12

Linear and Nonlinear Frequency Modulation of Nanocontact Spin-Transfer Oscillators: A Micromagnetic Study.

G. Consolo[1], V. Puliafito[1], L. Lopez-Diaz[2], B. Azzerboni[1]
1. Dipartimento di Fisica della Materia e Tecnologie Fisiche Avanzate, University of Messina, Messina, Italy; 2. Departamento de Fisica Aplicada, University of Salamanca, Salamanca, Spain

It has been theoretically predicted [1] and experimentally observed [2,3] that a dc current passing through a thin magnetic layer ("free" layer) of a magnetic layered structure can excite microwave magnetization oscillations in this layer. This phenomenon occurs because the bias current becomes spin-polarized in the direction of magnetization of a thicker ("fixed") magnetic layer, and then can transfer this induced spin angular momentum to the magnetization of the thinner free layer. One of the most efficient setup which has been used to sustain such steady-state precessions is the so-called nanocontact (or point-contact) geometry [1-3]. In these devices, the output frequency is tunable with both a static magnetic field and a dc current [2,3]. In addition, very narrow linewidths have been obtained as consequence of a large effective volume [4]. One of the most promising applications for communication systems was the experimental observation that the addition of an ac current to the dc bias current can be used to generate a frequency modulated (FM) output signal [3]. Moreover, since the excited output frequency in such devices is generally a nonlinear function of the input bias current [2,3], the possibility to build nonlinear spin-transfer modulators was opened [3]. While the experimental results were in agreement with theoretical models of nonlinear modulation [5], the corresponding numerical macro-spin simulations failed to describe the phenomenon accurately [3] and, to the best of our knowledge, a micromagnetic study has not been carried out so far. With this in mind, in this work we propose a full-scale micromagnetic investigation in order to get a better understanding of magnetization dynamics involved in modulation process as well as to get information about the spatial distribution of the excited spin-wave modes. To this aim, by using our micromagnetic framework [6], we take into account a setup very similar to the one proposed in Ref.3, where a nanocontact device is contemporary subjected to the combined action of a dc current, ac current and an out-of-plane bias field. When no ac current is applied, the output frequency vs. dc current dependence is a nonlinear function which can be partitioned into linear sub-intervals. This latter property allows us to carry out a detailed numerical investigation on both linear and nonlinear frequency modulators. To perform such study, we set a bias point I_{dc}=18 mA and we vary both magnitude (I_{ac}) and frequency (f_m) of the modulating signal. For I_{ac}<0.5 mA, a linear FM signal is derived whereas, for I_{ac}>0.5 mA, a nonlinear FM signal is observed. By acting on the modulation index, also, we analyze two cases of frequency modulation: narrow-band and wide-band.

Our results show that the frequency spectrum of a linear FM signal is composed by a central peak (f_c), corresponding to the carrier frequency, and equal-amplitude sidebands ($f_c \pm nf_m$), corresponding to the symmetric shift of the carrier at integer harmonics of the modulating frequency f_m. On the other hand, the spectrum of a nonlinear FM signal is composed by a central peak at a frequency (f_c'), which is shifted from the carrier frequency by an amount proportional to both the frequency sensitivity and the amplitude of the modulating signal, and nonequal-amplitude sidebands ($f_c' \pm nf_m$). An example is shown in the inset of Fig.1. In the case of a narrow-band modulation, a residual of amplitude-modulation (AM) also takes place (as shown in the main panel of Fig.1). We compare our numerical results to both experimental observations [3] and linear and nonlinear theoretical models of frequency modulation [5] deriving a satisfactory agreement.

Finally, by means of micromagnetic spectral mapping techniques [7], we also analyze the spatial distribution of spin-wave modes at each frequency. The latter investigation allows us to establish how an asymmetry in the frequency domain reflects in the spatial domain.

[1] J.C. Slonczewski, J. Magn. Magn. Mater. 195, L261 (1999).

[2] W.H. Rippard et al., Phys. Rev. B 70, 100406(R) (2004).

[3] M.R. Pufall et al., Appl. Phys. Lett. 86, 082506 (2005).

[4] J.V. Kim et al., arXiv:cond-mat/0703317 (2007).

[5] S. Haykin, Communications Systems (John Wiley & Sons) (2001).

[6] G. Consolo et al., Phys. Rev. B 75, 214428 (2007).

[7] R. D. McMichael and M. D. Stiles, J. Appl. Phys. 97, 10J901 (1999).

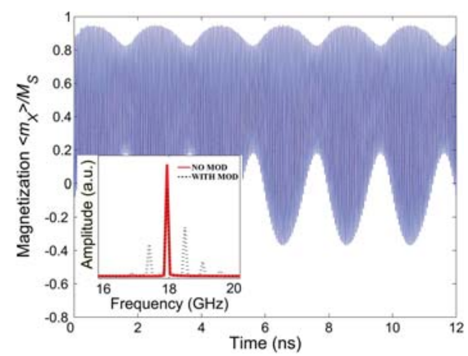

Fig.1 Main panel: time evolution of the normalized x component of the magnetization vector averaged over the contact area showing a nonlinear FM signal which exhibits a residual of AM. Inset: Frequency spectra related to the cases of no modulation (solid line) and nonlinear modulation (dashed line). In the latter case, the central peak is slightly shifted to the left and the amplitude of sidebands is different.

DP-13

Intrinsic Capacitance Effect on Microwave Power Spectra of Spin-Torque Oscillator with Thermal Noise.

B. Guan[1], Y. Zhou[2], F. Shin[1], J. Åkerman[2]
1. Applied Physics, The Hong Kong Polytechnic University, Hong Kong, China; 2. Institute of Microelectronics and Information Technology, Royal Institute of Technology, Stockholm-Kista, Sweden

Theory predicted that a spin-polarized current can exert a torque on a nano-scale magnet[1]. This torque can excite magnetization precessional motion with a steady microwave frequency ranging from 5 to 40 GHz that is tunable by adjusting current and applied magnetic field, and the quality factor as high as 18,000 [2]. The high Q value and the current tunability of these spin-torque oscillators (STOs) suggests their potential use in microwave signal processing applications.
However, there are also a number of discrepancies between the behaviors predicted by macro-spin simulation and the measured behaviors of the precessional dynamics in STOs. Experimentally, even at the temperature T=100K, the excitation has very narrow linewidth, leading to quality factors Q on the order of 10^4[3]. But the Q determined by both numerical simulation and analytical approach is much smaller [4]. As STOs have now been implemented in different materials and configurations, e.g. magnetic tunnel junctions (MTJs)[5], we believe that the intrinsic capacitance of the STOs structure will influence thermal stability of the system, and keep the Q factor of microwave power spectrum at a high level.
In our STOs model, a typical giant magnetoresistance (GMR) trilayer system has been adopted, with one fixed and one free ferromagnetic layer separated by a nonmagnetic spacer. The dynamics of the free layer magnetization is determined by the Landau-Lifshitz-Gilbert-Slonczewski equation, the details of which have been given by, e.g., Ref. [6].
The equivalent circuit of a spin-torque oscillator model is shown in Fig. 1. Here, an ideal capacitor C is connected in parallel with the STO to represent the intrinsic capacitance of the structure or that of connecting leads [7].
To study the temperature effects on spin valve behavior, we model the thermal fluctuations by adding a Langevin random field to the effective field, which consists the contribution of applied field, demagnetization field and uniaxial anisotropy field. The added thermal field is a fluctuating random field whose statistical properties obeys the Gaussian distribution [8]. In the presence of thermal fluctuations, the microwave power spectrum gets broadened with increasing temperature. The emitted power at a given frequency is derived by Fast Fourier Transform, and the data are fitted to a Lorentzian profile (dashed line), from which the quality factors Q are calculated.
Fig. 2 shows the power spectra at T = 30 with and without the added capacitance. The fitted Q values are 4200 and 1550 respectively. Fig.3 shows the same result at 100K where fitted Q values are 2300 and 1100 respectively. The addition of a small capacitance can hence enhance the quality factor about a factor of 2. Increasing the capacitance is also found to increase the quality factor even further.
In summary, the intrinsic capacitance effect does influence the stability of the system, and it can improve the Q factor value of the STO element even in the presence of thermal fluctuation. It is hence possible that some of the underlying reason for the high quality factors observed in experiments may be ascribed to either intrinsic or extrinsic sources of capacitance in parallel with the STO.

[1] J. C. Slonczewski, J. Magn. Magn. Mater. 159, 1 (1996).

[2] I. N. Krivorotov et al., Science 307, 228 (2005).

[3] M. R. Pufall et al., Appl. Phys. Lett. 86, 082506 (2005).

[4] J. V. Kim, V. Tiberkevich, and A. N. Slavin, J. Magn. Magn. Mater. Vol. 12, pp. 53 (2007).

[5] G. D. Fuchs et al., Phys. Rev. Lett. 96, 186603 (2006).

[6] J. Xiao, A. Zangwill, M. D. Stiles, Phys. Rev. B, Vol. 72, pp. 014446, (2005).

[7] A. V. Nazarov et al., J. Appl. Phys., accepted, (2007).

[8] E. B. Myers et al., Phys. Rev. Lett. Vol. 89, pp. 196801 (2002).

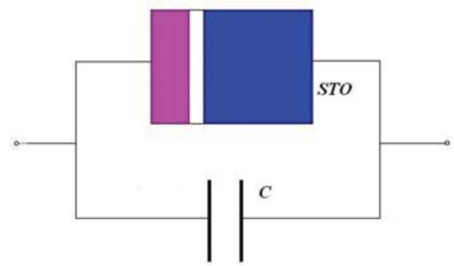

Fig. 1. The equivalent circuit of a spin-torque oscillator.

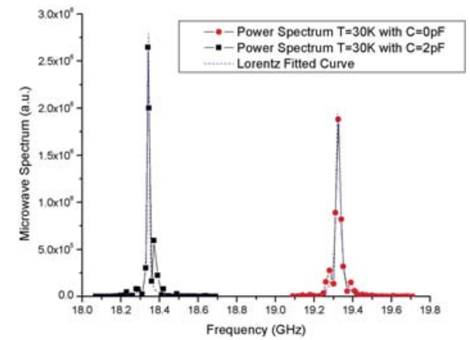

Fig. 2. The calculated power spectrum at T=30K with C=0 (red dot) and 0.2 PF (black square), individually.

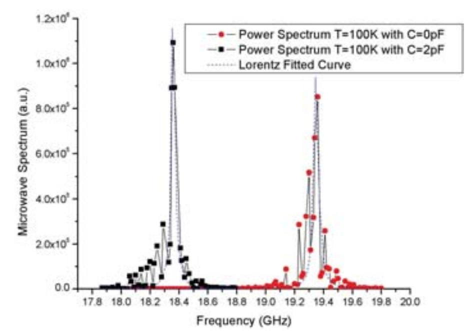

Fig. 3. The calculated power spectrum at T=100K with C=0 (red dot) and 0.2 pF (black square), individually.

DP-14

Spin torque oscillator phase locking to a noisy alternating current.

E. Iacocca, Y. Zhou, J. Persson, . Johan
Institute of Microelectronics and Information Technology, Royal Institute of Technology, Stockholm-Kista, Sweden

Recently, it has been experimentally demonstrated that a STO can lock to an injected alternating current [1]. In addition, recent numerical work has shown that there exists an unexpected intrinsic phase shift between the STO and the applied ac current. This phase shift can furthermore be utilized to improve the synchronization robustness of serially coupled STOs [2,3]. In this work we study the detrimental effects of current noise in the injected radio frequency current. We find that the STO will still lock to the injected current despite very large amounts of current noise. While the instantaneous phase difference between the STO and the injected current can be quite large, the average phase relation is still well defined.
A typical simulation with added white noise to the drive current is shown in Fig.1. The Stochastic Landau-Lifshitz-Gilbert- Slonczewski (LLG) equation, which is solved by the Ito calculus and a numerical method described by Milshtein [4], is used to determine the free layer motion. Before the ac current is turned on, the STO is allowed to settle into a steady state precession for about 30 ns. We then allow for an additional 10 ns of precession before analyzing the phase relation between the STO and the rf current.
Fig. 2 shows the intrinsic phase shift as a function of drive current for different noise levels. Despite the added noise, a well defined phase relation persists up to very high noise levels. Fig.3 shows the instantaneous phase relation over 10,000 precession periods for 3 different noise levels. While the average phase shift remains the same, the instantaneous values exhibit a Gaussian distribution with a width proportional to the added noise level.
We interpret the insensitivity to injected noise as due to the inertia of the precessing magnetization. The apparent Gaussian distribution originates from the phase noise of the rf current and not from that of the STO. We believe this insensitivity holds great promise to allow for STO synchronization even in the presence of inherent rf noise in existing Si CMOS technology.
We gratefully acknowledge financial support from The Swedish Foundation for strategic Research (SSF), The Swedish Research Council (VR) and The Göran Gustafsson Foundation.

[1] W. H. Rippard et al, Phys. Rev. B 70, 100406(R) (2004).

[2] Yan Zhou, J. Persson, and Johan Åkerman, J. Appl. Phys. 101, 09A510, (2007).

[3] J. Persson, Yan Zhou, and Johan Åkerman, J. Appl. Phys. Vol. 101, pp. 09A503, (2007).

[4] J. Xiao, A. Zangwill, M. D. Stiles, Phys. Rev. B, Vol. 72, pp. 014446, (2005).

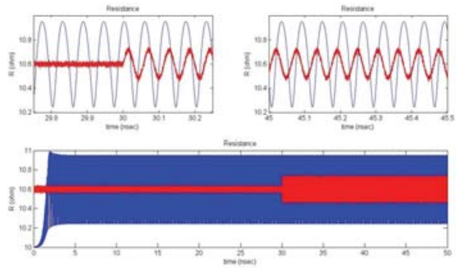

Fig. 1. A single simulation run showing the noisy drive current and the resistance of the STO.

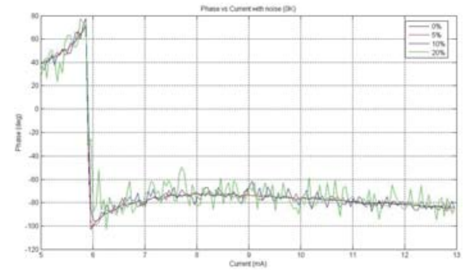

Fig. 2. Intrinsic preferred phase shift between the STO resistance and the injected rf current as a function of the drive current and for different levels of added noise.

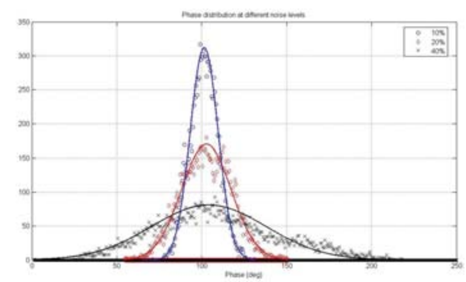

Fig. 3 Distribution of the instantaneous phase difference between the STO resistance and the injected rf current for different noise levels, with Gaussian fits.

DP-15

Point contact Spin Torque Oscillators at high magnetic fields: Non-monotonic field dependence of oscillation threshold current.

S. Bonetti[1], *J. Garcia*[1], J. Persson[1], F. B. Mancoff[2], J. Åkerman[1]
1. Microelectronics and Applied Physics, Royal Institute of Technology (KTH), Kista-Stockholm, Sweden; 2. Technology Solutions Organization, Freescale Semiconductor Inc., Chandler, AZ

Spin torque oscillators (STOs) [1–3] are one of the promising applications in spintronics. In these devices, a spin-polarized current can transfer its spin angular momentum to the magnetization of a thin magnetic layer and induce a precession in of the magnetization itself. Due to giant magnetoresistance (GMR) [4,5] or tunnelling magnetoresistance (TMR) [6-8] effects, one can detect an ac voltage with typical frequencies in the GHz range. These devices are compact (~100 nm in lateral size), can be tuned in frequency in an approximately linear way by varying the applied current and magnetic field magnitude, and the tuning range is rather large, on the order of tenth of GHz [9]. In this work we investigate the threshold of the oscillation region (in terms of applied magnetic field, driving dc current and frequency) when large magnetic fields (compared to the films coercive field) are applied normal to the film plane.

Samples are point contact $Co_{81}Fe_{19}$(20 nm)/Cu(6 nm)/$Ni_{80}Fe_{20}$(4.5 nm) spin valves. The contact shape is elliptical, with minor axis a = 130 nm, and aspect ratio 3:1 between major and minor axes. Results are presented in Fig. 1. The dependence of the threshold current on the applied field is plotted in Fig. 1a (symbols and continuous line). A clear minimum can be observed for a field value of approximately 1.25 T. In Fig. 1b, the relation between the magnetic field and the threshold oscillation frequency is shown. In this case the trend is monotonic, with a visible dip centered close to the same field value.

The first observation, the minimum in the threshold current at a certain value of field, can be explained by comparing it with the demagnetization field of a NiFe thin film [10], which is at about 1.1 T. The two values are close, and in the case when the applied magnetic field counteracts the demagnetization field, the energy needed for the magnetization to be pushed out of plane is a minimum. In STOs, the energy is provided by the continuous flow of dc current, and therefore one expects a minimum in the current needed to start oscillations.

The experimental behavior of the threshold current I_{th} can be fitted with the following empirical equation, quadratic in the applied field:

$I_{th} = I_{min} + \beta(H - H_d)^2$

where H is the applied field, I_{min} = 39 mA, H_d = 1.25 T (close to the theoretical value of 1.1T), and $\beta = 1.2\times10^2$ A/T^2. This expression is plotted as dashed line in Fig. 1a.

The second observation, the monotonic increase of threshold frequency with applied magnetic field, shows that field tunability is the dominant mechanism in determining the threshold frequency value. These devices show fairly linear frequency tunability both in current and field, as can be seen in Fig. 2. If current tunability had a larger effect than field tunability, one would expect the frequency vs field curve to be similar to the current vs field one (Fig. 1a). However, as clearly observed in Fig. 1b, when both current and field vary over a range which is approximately three times their minimum value (from Fig. 1a), the tuning due to the current just slightly influences (with the appearance of a central dip) the tuning due to the field.

With further experimental data available, we are also planning to perform a study on the linewidth and on the output power of the oscillation peak along the threshold

We gratefully acknowledge financial support from The Swedish Foundation for strategic Research (SSF), The Swedish Research Council (VR), The Göran Gustafsson Foundation and The Knut and Alice Wallenberg Foundation.

[1] J.C. Slonczewski, J. Magn. Magn. Mater. 159, L1 (1996).

[2] L. Berger, Phys. Rev. B 54, 9353 (1996).

[3] S. I. Kiselev, Nature 425, 380 (2003).

[4] M.N. Baibich et al, Phys. Rev. Lett. 61, 2472 (1988).

[5] G. Binasch et al, Phys. Rev. B 39, 4828 (1989).

[6] M. Julliere, Phys. Lett 54A, 225 (1975).

[7] T. Miyazaki et al, J. Magn. Magn. Mater. 139, L231 (1995).

[8] J. S. Moodera, Phys. Rev. Lett. 74, 3273 (1995).

[9] W. H. Rippard et al, Phys. Rev. B 70, 100406(R) (2004).

[10] J.A. Osborn, Phys. Rev. 67, 351 (1945).

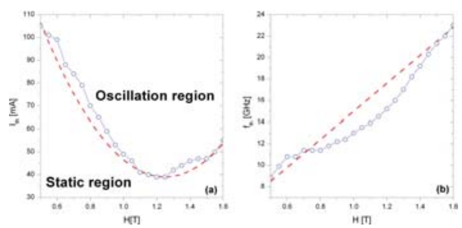

Fig. 1. Threshold current and frequency as a function of the magnetic field, applied close to the normal to the film plane (10° offset). (a) There is a clear minimum of the threshold current at about 1.25 T. (b) The frequency threshold is proportional to the applied field.

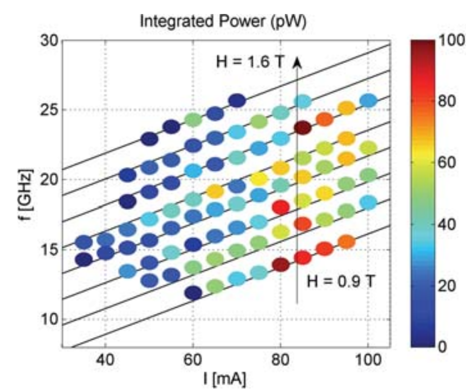

Fig. 2. Oscillation frequency as a function of the driving dc current, at different values of the field. Linearity in both quantities is readily noticed (tunability coefficient are 120 MHz/mA and 18.5 GHz/T). In color scale, the integrated output power.

DP-16

Time-dependent locking between a spin torque oscillator and an ac current.

Y. Zhou, J. Persson, J. Åkerman
Institute of Microelectronics and Information Technology, Royal Institute of Technology, Stockholm, Sweden

Using magnetodynamic simulations based on the Landau-Lifshitz-Ginzburg-Slonczewski equation, we study the detailed dynamics of the preferred intrinsic phase shift Spin Torque Oscillator (STO) and an alternating current. Depending on the details of both the STO and the applied current, this system can be overdamped, critically damped, or underdamped.

Recently, it has been experimentally demonstrated that a STO can lock to an injected alternating current [1]. In addition, recent numerical work has shown that there exists an unexpected intrinsic phase shift between the STO and the applied ac current. This phase shift can furthermore be utilized to improve the synchronization robustness of serially coupled STOs [2,3]. A typical simulation illustrating the existence of an intrinsic phase shift between the STO resistance and the external drive signal I_{ac} is shown in Fig.1. Before the ac current is turned on, the STO is allowed to settle into a steady state precession for about 24 ns. When the ac current Fig. 2 shows the temporal evolution of the relative phase shift $\Delta\phi$. From Fig. 2, we can see that $\Delta\phi$ gradually transits to the same steady state value $\Delta\phi_0$, regardless of the initial values. The underlying driving mechanism behind the preferred phase shift has been semi-analytically derived in a recent work by following the energy conservation law [3]. Depending on the ac current amplitude, the system can be under damped (I_{acamp} = 228 μA), critically damped (I_{acamp} = 57 μA), and over damped (I_{acamp} = 19 μA) as shown in Fig. 3 (I_{acamp} denotes the amplitude of the alternating current). For larger ac driving current, the system undergoes a under damped ringing transition before it finally settles down in the steady state. The ringing behaviour is expected to significantly affect the robustness of locking states of two serially connected STOs.

In summary, we have studied the detailed temporal locking characteristics of the STO under the interaction of an alternating current by using magnetodynamic simulations of the Landau-Lifshitz-Ginzburg-Slonczewski equations. It is found that the STO locks to the alternating current on a well-defined preferred phase shift regardless of the initial phase differences. The intrinsic $\Delta\phi_0$ and its temporal locking characteristics will impact any circuit design based on STO technology and will have direct consequences for phase locking in networks of serially connected STOs.

[1] W. H. Rippard et al, Phys. Rev. B 70, 100406(R) (2004).

[1] Yan Zhou, J. Persson, and Johan Åkerman, J. Appl. Phys. 101, 09A510, (2007).

[2] J. Persson, Yan Zhou, and Johan Åkerman, J. Appl. Phys. Vol. 101, pp. 09A503, (2007).

[3] Yan Zhou, J. Persson, S. Bonetti, and J. Åkerman, submitted to Appl. Phys. Lett.

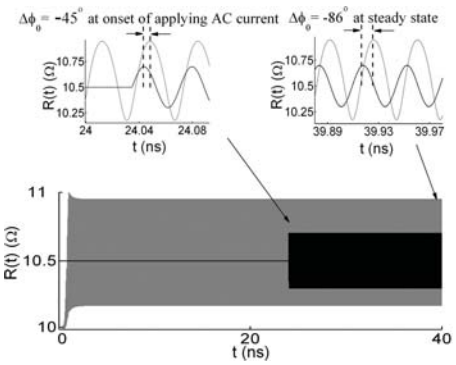

Fig. 1. A single simulation run to illustrate the preferred phase shift between STO and alternating current.

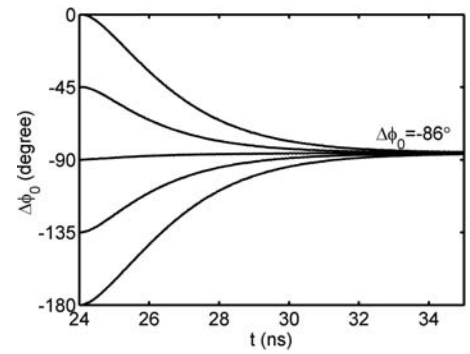

Fig. 2. The temporal evolution of relative phase shift $\Delta\phi$ between the ac current and the STO for different initial $\Delta\phi(0)$.

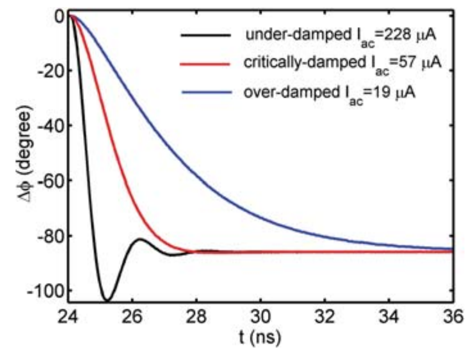

Fig. 3. The under damped, critically damped and over damped curves of the relative phase shift.

DQ-01

Estimation method on multiple sources of MEG based on columnar structure of the cerebral cortex.

H. Fukuda[1], M. Odagaki[1], O. Hiwaki[1], A. Kodabashi[2], T. Fujimoto[2]
1. Graduate School of Information Sciences, Hiroshima City University, Hiroshima, Japan; 2. Fujimoto Hayasuzu Hospital, Miyakonojo, Japan

1. Introduction

We propose a new method for estimating multiple electrical sources of brain activity by using magnetoencephalography (MEG) data.

The equivalent current dipole (ECD) method, which uses the moving-dipole model [1], has been generally employed for estimating electrical sources of MEG. There are several drawbacks for this method. First, the least squares algorithm does not ensure that the global optimum solution is obtained because the model has much redundancy. Second, operators have to separate multiple pairs of source and sink before the estimation of multiple dipoles. Third, the estimated position and orientation of the ECD do not necessarily reflect the columnar structure which is hypothesized as a minimum functional subunit of the cerebral cortex [2]. The first and third drawbacks are associated with not only this method but also other conventional methods [3].

In the proposed method, multiple dipoles can be estimated without selecting a pair of source and sink beforehand and employing any repeated algorithms in which a solution depends on an initial value. Moreover, the estimated dipoles reflect the columnar structure.

2. Method

Considering the columnar structure, the position and orientation of assumed current dipoles are limited to the surfaces of the cerebral cortex and along directions perpendicular to these surfaces, respectively.

The surfaces of the cerebral cortex are extracted from MR images of the head and represented by some voxels labeled "surface voxels." The assumed current dipoles are located at the surface voxels. For each surface voxel, unit vectors, which are oriented toward the adjacent voxels not labeled surface voxels, are calculated. Orientation of the surface vector at the surface voxel is defined as the total sum of the unit vectors. This step is similar to that adopted by Hayami et al. [4].

According to the Biot-Savart law, the relationship between the moment of the assumed current dipole located at the *j*-th voxel q_j and the magnetic field on the scalp surface reflects the activity of the *j*-th assumed dipole $\boldsymbol{b}_j = [b_{1j}, b_{2j}, ..., b_{Mj}]^{\mathrm{T}}$ can be expressed as $\boldsymbol{b}_j = \boldsymbol{L}_j q_j$, where M is the number of the MEG sensors, b_{ij} is the magnetic-flux density measured by the *i*-th sensor and vector $\boldsymbol{L}_j = [L_{1j}, L_{2j}, ..., L_{Mj}]^{\mathrm{T}}$ represents the sensitivity of the sensors to the *j*-th dipole. $\boldsymbol{L}_j$ is fixed in this step because the position and orientation of the *j*-th assumed dipole have been calculated in the surface extraction step mentioned above, while this vector must be detected by a repeated algorithm in the conventional methods.

Here, it is assumed that a single pair or spatially separated multiple pairs of source and sink observed in the N20m component of the somatosensory evoked field (SEF) or in the N100m component of the auditory evoked field (AEF) is/are targets to be analyzed. In these cases, the correlation between the measured field data $\boldsymbol{b}$ and $\boldsymbol{L}_j$ will be higher if the *j*-th assumed dipole is a real dipole. Hence, we consider the assumed dipole with spatially maximal correlation in the cortical surface as the real dipole.

3. Experiments

The proposed method was applied to estimate multiple electrical sources of the N20m SEF elicited by bilateral median nerve stimulation and the N100m AEF data elicited by bilateral pure tone stimulation.

From the SEF data, two dipoles were estimated in the postcentral gyri on both the hemispheres (Fig. 1). It was found that the value of each dipole almost agreed with the value estimated when the right/left median nerve was stimulated separately.

From the AEF data, two dipoles were estimated in the superior temporal gyri on both the hemispheres in many cases (Fig. 2). In some cases, the dipoles were estimated in the upper bank of the Sylvian fissure at a distance of 5mm from the superior temporal gyrus.

4. Discussion

The proposed method could estimate multiple dipoles when applied to the SEF an AEF data. These results indicated that our method can be used to estimate multiple dipoles in the cases where two pairs of source and sink are spatially separated. Moreover, our algorithm always leads to a unique solution once the assumed current dipoles are extracted form MR image. It is insisted that our method is used for analyzing brain activity.

[1] B. N. Cuffin, A comparison of moving dipole inverse solutions using EEG's and MEG's, IEEE Trans. Biomed. Eng., Vol. BME-32, No. 11, pp. 905–910, 1985.

[2] V. B. Mountcastle, Modality and topographic properties of single neurons of cat's somatic sensory cortex, J. Neurophysiol., Vol. 20, pp. 408–434, 1957.

[3] R. G. P. Menendez et al., Linear inverse solutions with optimal resolution kernels applied to electromagnetic tomography, Human Brain Mapping, Vol. 5, pp. 454–467, 1997.

[4] T. Hayami et al., EEG source estimation method considering the shape of the cortical surface, IEEE-EMBS 2005, pp. 1512–1515, 2005.

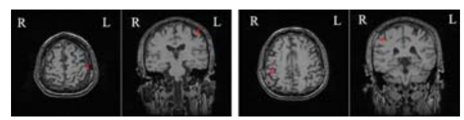

Fig. 1: Estimated current dipoles of N20m SEF.

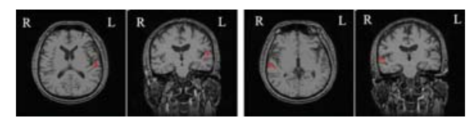

Fig. 2: Estimated current dipoles of N100m AEF.

DQ-02

Stochastic resonance in phase synchronization of auditory steady state responses in MEG.

K. Tanaka[1], M. Kawakatsu[2], I. Nemoto[1,2]
1. Research Center for Advanced Technologies, Tokyo Denki Universtiy, Inzai, Japan; 2. School of Information Environment, Tokyo Denki University, Inzai, Japan

1. Intoroduction
Auditory steady-state responses (ASSRs) to sinusoidal amplitude-modulated (SAM) waves have been studied extensively. The phase behavior of ASSRs has been used for determining hearing thresholds. However, the mechanisms of the generation of ASSRs are not known. We speculated from the result that synchronization of an ongoing 40 Hz component in MEG was at least partly responsible for the ASSR although the contribution of the superposition of evoked response to each cycle of the stimulus could not be excluded [1]. Possible synchronization of an ongoing process to the stimulus strongly suggested the presence of a nonlinear system, which then could give rise to stochastic resonance (SR). SR is often shown by nonlinear systems and refers to the decrease of noise to signal ratio (N/S) in the output obtained through an increase of the noise level in the input. We measured ASSRs to SAM tones which were presented with white noise of various intensities and examined the relationship between the N/S of the stimulus and the power and synchronization of the 40 Hz component of MEG.
2. Methods
The subjects were 5 males. A 1 kHz sinusoidal wave was amplitude modulated with modulation frequency 40-Hz and modulation depth 1.0 to obtain a SAM tone. A burst of the SAM tone lasting for 1.0 s was used as a stimulus for one epoch of MEG recording. The bursts of SAM were superimposed on white noise which lasted for one run consisting of 100 epochs. The intensity of the SAM tone was set at 40 dB above its threshold measured without the noise for each subject. The N/S used were 0, 0.02, 0.04, 0.06, 0.08 and 0.1. Stimuli were generated using a computer driven sound generator and delivered via ER2 transducers to ear inserts and then to the subject's right ear. MEG recordings were made with a 122-channel whole-head MEG system in a magnetically shielded room. For quantifying the degree of synchronization in ASSRs, we used the phase coherence. We estimated the phase coherence for the latter 500 ms period of the 1 s epoch.
3. Results
Fig.1 shows the power of ASSRs for the 6 N/S values in all the 5 subjects. Some subjects seemed to show 'positive' effect of noise.
Fig.2 shows the phase coherence of ASSRs for the 6 N/S values in all the 5 subjects. 4 out of 5 subjects were seen to demonstrate an increase in the phase coherence at some level of N/S compared to the noise-free condition. The position and shape of the peak differed much among the subjects. However, the peak of phase coherence in 4 out of 5 subjects were obtained for the N/S values for which the noise levels were their thresholds of hearing.
4. Disscutions
We measured ASSRs to stimuli consisting of SAM and white noise with various N/S values to see if there was any sign of SR. The optimum N/S to obtain strong coherence in ASSR varied among subjects and hence ASSR power nor phase coherence showed significant increase with addition of noise when averaged over the subjects. One may have to devise an appropriate statistical method to detect SR effect which would not be smeared out by the differences amog subjects. One method may be to employ the theory of extreme value distributions and treat the data as order statistics to get around the differences in optimum N/S values among subjects. Also, individual subject's data should also be statistically analysed so that any significant increase in power or phase syncrony at any N/S may be detected for each subject. We have tried some tentative methods and started to have preliminary results which seem encouraging [2]. Our result suggests that SR can be seen in phase synchrony of ASSR. It should be noted that most of the reported SR was seen for subthreshold stimuli. In our experiment three thresholds are relavant. One is for the amplitude of the carrier sound, secondly the modulation depth, and the other is for the noise level. SR was observed for suprathreshold stimuli with respect to the first two thresholds for the modulated sound and at around the threshold level of the noise.

[1] K. Tanaka, A model of phase synchronization of auditory the 40 Hz component in MEG, J Magn Soc Jpn, 30, pp.311–315, 2006.

[2] K. Tanaka, M. Kawakatsu, I. Nemoto, Stochastic resonance in auditory steady state responses in magnetoencephalogram, Clinical Neurophysiol, submitted for publication.

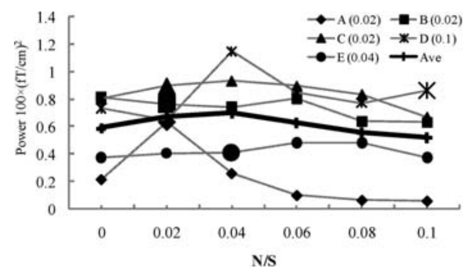

Fig. 1: The power of ASSRs as a function of the N/S in all the 5 subjects and their average. The bigger symbols indicate the N/S values which were obtained for hearing thresholds in noise levels.

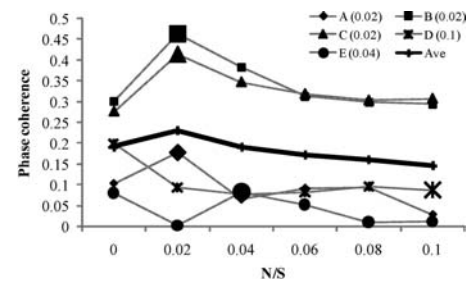

Fig. 2: The phase coherence of ASSRs as a function of the N/S in all the 5 subjects and their average. The bigger symbols indicate the N/S values which were obtained for hearing thresholds in noise levels.

DQ-03

Preparation, Characterization and Testing of Magnetic Carriers for Arsenic Removal from Water.

A. M. Estevez[1], J. M. Rodriguez[1], A. Alvaro[1], P. A. Augusto[2,1]
1. Department of Chemical Engineering, University of Salamanca, Salamanca, Spain; 2. DEQ, Faculdade de Engenharia da Universidade do Porto, Porto, Portugal

Abstract
To remove arsenic from water we developing a research project that applies magnetic separation methods. In order to increase the removal efficiency we are using magnetic aggregates. These magnetic aggregates are iron-based and were all (except for one) prepared by us. In this paper we report the preparation steps and some of the results of the characterization and absorption tests we have performed in order to conclude about its structure and efficiency in what concerns arsenic removal.

Arsenic Adsorption
Arsenic is found commonly in water under an inorganic form, mainly as arseniate (As V) in superficial waters and as arsenite (As III) in underground waters. As(III), for ordinary biological systems, is more toxic than As (V) [1,2].
In the present study we are aiming on the conjugation of the magnetic stabilized bed technique with adsorption of arsenic by ferromagnetic iron oxides.
Bearing in mind the above-described high adsorption capacity of the hydrated iron oxide FeOOH for the adsorption of As(III) and As(V) in water, as well as its magnetic properties, and the above-detailed problems in its practical application, we performing, in the present study, the conjugation of the magnetic stabilized bed technique [3,4,5,6] with adsorption of arsenic by ferromagnetic iron oxides, by applying some magnetic aggregate structures [7,8]. This will lead to a new process of arsenic elimination from water by its adsorption in a magnetic stabilized bed of hydrated iron oxide (FeOOH) particles, or, in the cases where these compound present less-adequate mechanical properties, in a magnetic stabilized bed of appropriated Fe-Si aggregates.
Preparation of Aggregates
One of the adsorbents used was purchased, but the rest of them was prepared as part of this work. The preparation of FeOOH is basically based on its precipitation from FeCl3 1M and NaOH 1N dissolutions. The magnetic aggregates of Fe-Si, were prepared by a co-precipitation from a dissolution of FeCl3 1M and also from a dissolution of Na2SiO3 plus NaOH 1N. The solid adsorbents were then dried at 105 ^{o}C and afterwards pulverized and filtered to make their size uniform.
The several aggregates and the ways they were prepared are detailed in Table 1.
Characterization and Adsorption Tests
Several test and analysis were performed concerning the aggregates structure and absorption ability and in Figure 1 we present one of the most important ones (concerning their arsenic adsorption efficiency), as an example.

[1] Ferguson JF, Davis J. A review of the arsenic cycle in natural waters. Water Res 1972;6:1259.

[2] Korte NE, Fernando Q. A review of Arsenic (III) in groundwater. Crit Rev Environ Control 1991; 21(1):1–39.

[3] E. Jaraíz, A.M. Estévez. Design concepts for a collar-type magnetic valve for small-size solids (mvs): theory and experiments. Powder Technology, 1987; 53:1-9.

[4] A.M. Estévez, J. Cuellar, E. Jaraíz, J.M. Rodríguez. Behaviour of magnetizable composites in a liquid-solid magnetofluidized bed. Potential use as a bioreactor. Chemical & Biochemical Engineering Quarterly, 1995; 9(2):67-77.

[5] C. Webb, Hong-Ku Kang, G. Moffat, R. A. Williams, A.M. Estévez, J. Cuellar, E. Jaraíz, M.A. Galán. The magnetically stabilized fluidized bed bioreactor: a tool for improved mass transfer in immobilized enzyme systems. The Chemical Engineering Journal, 1996; 61:241-246.

[6] J.M. Rodríguez, A. Macias Machín, A. Alvaro, J.R. Sánchez, A.M. Estévez. Removal of iron oxide particles in a gas stream by means of a magnetically stabilized granular filter. Industrial&Engineering Chemistry Research, 1999; 38(1):276- 283.

[7] J.R. Alvarez, A.M. Estévez, E. Jaraíz. Manejo de partículas sólidas mediante agregados magnéticos. Ingeniería Química 1984; 179:143-147.

[8] Wilkie JA, Hering JG. Adsorption of Arsenic onto Hydrous Ferric Oxide: effects of adsorbates/ adsorbent ratio and co-occurring solutes. Colloids Surf A: Physicochem Eng Aspects 1996; 107:97

Aggregate	Preparation
0	Commercial FeOOH
1	100 ml FeCl3 1M + 300 ml NaOH 1N
2	100 ml FeCl3 1M + 300 ml NaOH 1N
3	FeCl3 1M + excess of NaOH 1N
4	Fe-Si Complex. Si/Fe = 0.33 (2.9 ml Na2SiO3 + 300 ml NaOH 1N) + 100 ml FeCl3 1M
5	Fe-Si Complex. Si/Fe = 0.33 (2.9 ml Na2SiO3 + 300 ml NaOH 1N) + 100 ml FeCl3 1M
6	Second part of aggregate 5
7	Fe-Si Complex. Si/Fe = 0.1 (0.89 ml Na2SiO3 + 300 ml NaOH 1N) + 100 ml FeCl3 1M
8	Fe-Si Complex. Si/Fe = 0.6 (5.4 ml Na2SiO3 + 300 ml NaOH 1N) + 100 ml FeCl3 1M
9	Fe-Si Complex. Si/Fe = 0.6 (7.1 ml Na2SiO3 + 300 ml NaOH 1N) + 100 ml FeCl3 1M
10	Fe-Si Complex. Si/Fe = 0.6 (8.9 ml Na2SiO3 + 300 ml NaOH 1N) + 100 ml FeCl3 1M

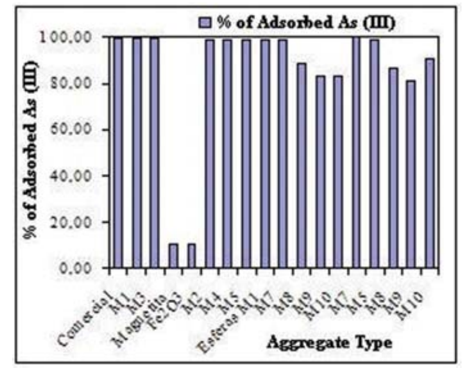

Figure 1 - Adsorption of the Aggregates

DQ-04

Synthesis of superparamagnetic nanoparticles by non conventional routes and their feasible application as contrast agents.

R. Costo, A. G. Roca, M. Morales, S. Veintemillas-Verdaguer
Materiales Particulados, Instituto de Ciencia de Materiales de Madrid, Madrid, Spain

Magnetic nanoparticles are of increasing technological and biomedical interest due to their unique properties [1]. A wide range of medical uses have been developed, from magnetic drug-targeting to hyperthermia and magnetic resonant imaging (MRI) [2]. In the last case, stable water dispersions of magnetic, small, rounded, hydrophilic particles at physiologic pH are preferred [2, 4] and not all methods to synthesize magnetic nanoparticles are suitable to prepare contrast agents for MRI with long blood circulating time [3].
Alternative synthesis routes have been developed in the last few years to improve the nanoparticles size distribution and the reaction yield. One of these new methods is the laser pyrolysis, which is a promising and versatile method that allows the continuous synthesis of various nanoparticles, with well defined chemical composition, size and structure [9]. On the other hand, thermal decomposition of organo-compounds in organic media allows the synthesis of superparamagnetic iron oxide nanoparticles with controlled size and shape, narrow size distribution and very good crystallinity [6, 7, 8]
In this work, aqueous suspensions stable at pH 7 have been prepared from nanoparticles synthesized by these two new methods. The as prepared particles were further modified by surface coating with carboxylic compounds to make them water stable. In the case of magnetite nanoparticles synthesized by laser pyrolysis, first they were subjected to a pretreatment with nitric acid and iron nitrate to improve their size distribution and then coated with phosphonoacetic acid (Sample L). In the case of the hydrophobic magnetite nanoparticles synthesized by decomposition, dimercaptosuccinic acid was used to remove the oleic acid making them hydrophilic (Sample O). A control sample consisting of a commercial iron oxide contrast agent was used for comparison.
All samples were stable in water in a wide pH range and, in particular at pH 7, they present a high negative charge which assures its stability [table 1]. Aggregate sizes smaller than 90 nm were measured by dynamic light scattering, which is an essential requirement for in vivo applications. Finally, magnetic and relaxometric characterization of these dispersions were carried out and it was concluded that particles with higher crystallinity, and therefore higher magnetization saturation and susceptibility, lead to relaxivity values that are almost three times higher than those measured for commercial MRI contrast agents with similar aggregate size.

[1] P. Tartaj, Curr. Nanosc, 2, 43 (2006)

[2] Mornet S., Vasseur S., Grasset F. and Duguet E. . Mater. Chem. 14, 2161 (2004)

[3] P. Tartaj, M.P. Morales, S. Veintemillas-Verdaguer, T. Gonzales-Carreño, C.J. Serna, 2006, Synthesis, properties and biomedical applications of magnetic nanoparticles. In: Handbook of Magnetic Materials Vol. 16, (K.H.J. Buschow Ed.), chapter 5, Pag. 403 - 482.

[4] C. Corot, P. Robert, J.M. Idée, M. Port, Adv. Drug Deliv. Rev., 58, 1471 (2006).

[5] J. Lee, T. Isobe, M. Senna, J. Colloid Interface Sci, 177, 490 (1996)

[6] Hyeon T, Lee S S, Park J, Chung Y and Na H B J. Am.Chem. Soc. 123, 12798 (2001)

[7] Shouheng Sun and Hao Zeng J. Am. Chem. Soc. 124, 8204 (2002)

[8] Shouheng Sun, Hao Zeng, David B. Robinson, Simone Raoux, Philip M. Rice, Shan X. Wang and Guanxiong Li J. Am. Chem. Soc. 126, 273 (2004)

[9] S. Veintemillas-Verdaguer, M.P. Morales, C.J. Serna, Appl. Organometal. Chem., 15, 365 (2001)

Sample	Particle size (TEM)	Particle size (XRD)	Aggregate size (PCS)	Z-potential at pH=7
Sample O	9.2 nm	12 nm	70 nm	-27 mV
Sample L	8 nm	9 nm	80 nm	-38 mV

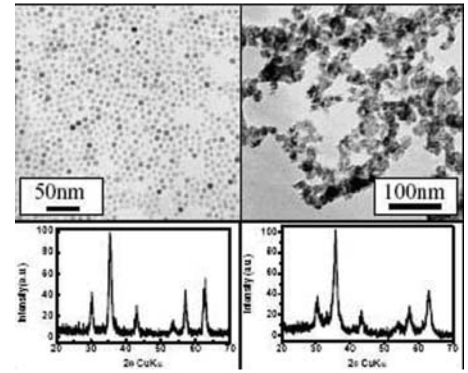

TEM images and X-ray diffraction patterns for samples O (left) and L (right)

DQ-05

Magnetic properties of iron oxyhydroxynitrate nanoparticles.

N. J. Silva[1], V. S. Amaral[2], L. D. Carlos[2], A. Millán[1], F. Palacio[1], B. Rodríguez-González[3], L. M. Liz-Marzán[3], T. Berquó[4], F. Fauth[5], V. de Zea Bermudez[6]
1. Fisica de la Materia Condensada, Instituto de Ciencia de Materiales de Aragón, CSIC/Universidad de Zaragoza, Zaragoza, Spain; 2. Departamento de Fisica and CICECO, Universidade de Aveiro, Aveiro, Portugal; 3. Departmento de Quimica Fisica, Universidad de Vigo, Vigo, Spain; 4. Institute for Rock Magnetism, University of Minnesota, Minneapolis, MN; 5. LLS, BM16-ESRF, Grenoble, France; 6. Departmento de Química, Universidade de Trás-os-Montes e Alto Douro and CQ-VR, Vila Real, Portugal

Iron oxyhydroxynitrate is an ordered precursor of 6-line ferrihydrite in the process of hydrolysis of an iron nitrate salt [1]. The iron(III) oxyhydroxynitrate with general formula $FeO(OH)_{1-x}(NO_3)_x$ ($0.2<x<0.3$) has been previously obtained in the form of a powder consisting of aggregated nanoparticles after freeze drying a Fe(III) nitrate water solution [1,2]. Here we report magnetic studies on iron(III) oxyhydroxynitrate nanoparticles with different average sizes grown in a organic-inorganic hybrid matrix. This allowed to access the magnetic properties of the isolated nanoparticles. These magnetic properties are compared to those of other iron oxides.
The first step of the nanohybrids preparation involves the synthesis of a cross-linked organic-inorganic hybrid precursor, similar to the one used in the synthesis of an undoped matrix, termed diureasil [3]. In the second step, a solution of iron(III) nitrate nonahydrate, water and ethanol was added to the non-hydrolyzed hybrid precursor. The resulting mixture was then stirred in a sealed flask for a few minutes at RT. After this, the solution was cast into a mould and transferred to an oven at ca. 40 °C for a period of 7 days. Samples were obtained after aging for 3 weeks at ca. 80 °C. Samples were labelled Ih(x), where x is the iron mass concentration.
The powder XRD patterns of the two most concentrated samples of Ih nanohybrids (Fig. 1) show that iron(III) oxyhydroxynitrate nanoparticles were efficiently stabilized in the matrix. Differences between patterns of iron(III) oxyhydroxynitrate and ferrihydrite are apparent: in the iron(III) oxyhydroxynitrate nanoparticles XRD patterns the relative intensity of the double peak at 60-65 °C is the opposite of that of ferrihydrite, and the shoulder appearing at 33 °C in the ferrihydrite nanoparticles is not present in the Ih nanohybrids. TEM images of the Ih(3.8) and Ih(6.5) nanohybrids show the presence of globular-shaped nanoparticles, with diameters of the order of 3 nm. The nanoparticles have nonfacetted and fuzzy edges and the nanoparticles/matrix contrast is low. SAXS patterns of Ih nanohybrids can be modelled as spherical isotropic and diluted Ih nanoparticles dispersed in a homogeneous matrix using GNOM [4]. The main conclusion of this analysis is that the particles size increases with the iron content.
The temperature dependence of the dc susceptibility χ shows that the Ih nanoparticles are superparamagnetic (Fig. 1): all zfc curves present a maximum at $T=T_B$ that increases with the iron content (Fig. 1, inset). This increase agrees qualitatively with the observed size increase, since the anisotropy energy E_a and therefore $T=T_B$ depend on size. Below $T\sim T_F$ the $M(H,T)$ curves of the Ih nanocomposites show irreversibility, that depends on the temperature and field history. Above $T\sim T_F$, the $M(H,T)$ curves of the Ih nanohybrids are reversible, and can be described has having linear and partial saturation components, associated to χ_{AF} and μ_{un}, respectively. We have considered a distribution of μ_{un}, with μ_{un} being described by a Langevin law. $<\mu>_{un}$ was found to decrease with temperature and corresponds to a mean number of fully uncompensated Fe^{3+} ions of 3, 4, and 9 in samples Ih(1.7), Ih(3.8) and Ih(6.5), respectively.

For $T>T_B$, a paramagnetic-like doublet in the Mössbauer spectra of the Ih nanohybrids is observed, as expected for unblocked superparamagnetic particles. For temperatures below T_B, the Mössbauer spectrum is magnetically split in a sextet. As observed in the susceptibility, T_B identified with Mössbauer increases with the iron content. In sample Ih(6.5), the magnetic hyperfine field B_{hf} at 4.2 K is similar to that previously found for iron(III) oxyhydroxynitrate powders (B_{hf} 450-460 kOe [2]), being lower than that of 6-line ferrihydrite. At the same time, the isome shift QS shows some differences when compared to that usually found in 6-line ferrihydrite (-0.06 mm/s), approaching for that fitted for schwertmannite (QS =-0.37 mm/s at 4.2 K).

[1] U. Schwertmann, J. Friedl, and H. Stanjek, J. Coll. Interface Sci. 209, 215 (1999);

[2] U. Schwertmann, J. Friedl, and G. Pfab, J. Sol. State Chem. 126, 336 (1996);

[3] V. de Zea Bermudez, L. D. Carlos, and L. Alccer, Chem. Mater. 11, 569 (1999);

[4] D. Svergun, J. Appl. Cryst. 25, 495 (1992).

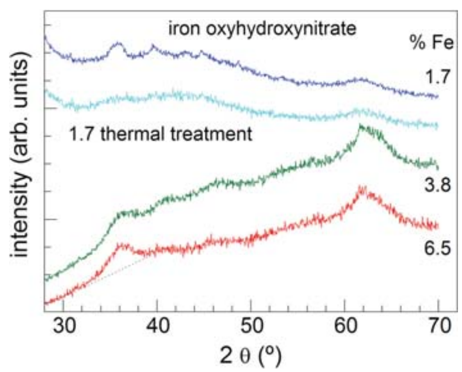

Fig. 1. X-ray diffraction (XRD) patterns of Ih samples and sample Ih(1.7) after a thermal treatment.

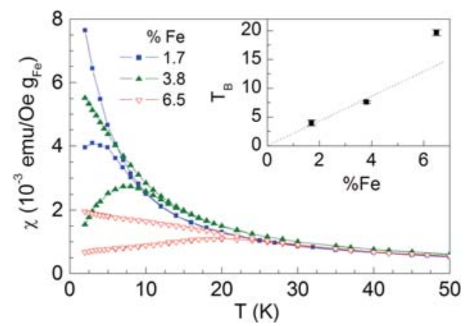

Fig. 2. Dc susceptibility χ of Ih hybrids as a function of temperature. Inset shows the dependence of T_B with the iron content.

DQ-06

Biosorption of Cu(II) ions by magnetically labeled yeast.

S. V. Gorobets, V. V. Lizunov, I. V. Dem'yanenko
National Technical University of Ukraine "Kyiv Polytechnic Institute", Kyiv, Ukraine

Last years in connection with the sharp increase in environmental contamination by ions of heavy metals, the interest to working out new and to improvement of existing ways of clearing of liquids has considerably increased. The yeast culture *S. Cerevisiae* 1968 [1] is one of the perspective and inexpensive biosorbents used for clearing of liquids from ions of heavy metals and represents a by-product of many fermentative manufactures. For removal of yeast, which sorbed the ions of heavy metals, in a high-speed mode, the high-gradient magnetic separation (HGMS) is applied [2]. For this purpose the yeast cells obtain the magnetic properties by joining to them of magnetic labels. The aim of the present work was the finding of optimal quantity of magnetic labels (magnetite Fe_3O_4) which are necessary for the most effective removal of yeast *S. Cerevisiae* 1968 from a solution after the sorption by them of ions of heavy metals (for example, Cu^{2+}).

The yeast *S. Cerevisiae* 1968 was grown up on the mineral Reader's medium which contained 1 % of glucose and 0.1 % of yeast autolysate in aerobic conditions at temperature 28 C. The daily culture was centrifuged and washed twice by a sterile physiological solution. The magnetite Fe_3O_4 was obtained by means of a method described in work [3]. To join the magnetic labels to yeast *S. Cerevisiae* 1968, the suspension of nanomagnetite in water was mixed with a yeast solution (concentration of cells was $3x10^6$ cells/ml). The initial concentration of copper ions Cu^{2+} was 100 mg/l. The measurements were performed at a room temperature in intervals of time 1, 3, 5, 10, 20 and 30 minutes. The finding of the concentration of copper ions was carried out with the help of spectrophotometer SF-46.

We made the ferromagnetic heads with the controllable characteristic sizes from 10 microns to 100 microns and with brachiate surface of a type similar to that described in the work [4] by the instrumentality of a new rather cheap electrolytic method. In the present work the efficiency of catching of yeast by a modeling ferromagnetic head of a spherical form with a diameter 100 microns was investigated at different relations of quantity of yeast cells with quantity of magnetic labels (from 5:1 to 100:1).

In Fig.1 the time dependences of mass of copper ions Cu^{2+} sorbed by yeast for various concentrations of magnetic labels in a solution are presented. The curve 1 corresponds to the relation of yeast and magnetic labels in proportion 10:1, and the curve 2 corresponds to the relation 100:1. The curve 3 describes the time dependence of mass of copper ions sorbed by yeast without the adding of magnetic labels. It can be seen that the most part of ions Cu^{2+} is sorbed during the first ten minutes from the beginning of the experiment. It is established that the solution in which yeast with magnetic labels is in the proportion 100:1 catches ions Cu^{2+} better than solutions with a large quantity of labels. At the same time the maximum quantity of sorbed copper ions after 10 minutes from the experiment beginning was observed for a solution of yeast cells without joining of magnetic labels to them. However in this case at the further carrying out of experiment the process of desorption and, as a consequence of this, the increasing of concentration of copper ions in a solution were observed. The similar effect was absent when magnetic labels had been added in a yeast solution. The obtained results are in good agreement with known from the literature experimental data [2,5].

Thus, for effective carrying out of process of biosorption of heavy metals ions by the method of magnetic separation the relation between the quantity of yeast and magnetic labels in solution should be equal to 100:1. I.e., as the results of the present work have shown, the increasing of the quantity of magnetite in the proportion (yeast:magnetite) leads to the reduction of the efficiency of biosorption of copper ions (see Fig.1). The further reduction of quantity of magnetite leads to impossibility of effective extraction of a yeast-magnetite conglomerate by the magnetic filter with a ferromagnetic head of type [4] after the finishing of the process of biosorption of cooper ions. We also note that the application for biosorption of copper ions the yeast-magnetite conglomerates even at small quantity of magnetite 100:1 gives an additional advantage in comparison with use of yeast without giving magnetic properties to them. Namely, in case of use of "magnetic" yeast the process of desorption is absent (Fig.1).

1. Wanga J., Chena C., Biotechnology Advances 24, 427 (2006).

2. Gorobets S.V., Gorobets O.Yu., Kasatkina T.P., Ukrainetz A.I., Goyko I.Yu., Journal of Magnetism and Magnetic Materials 272-276, 2413 (2004).

3. Massart R., Magnetics, IEEE Trans. on. 17, 247 (1981).

4. Worl L.A., U.S. Los Alamos National Laboratory The Actinide Research Quarterly Nuclear Materials Researchand Technology 2, 1 (1999).

5. Patzak M., Dostalek P., Fogarty R., Safarik I., Tobin J., Biotechnology Techniques 11, 483 (1997).

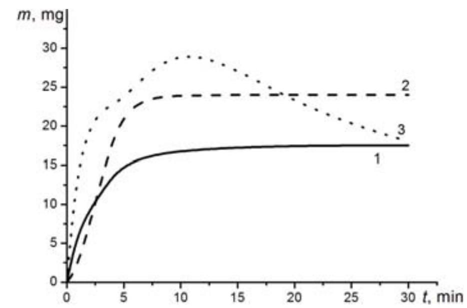

Fig.1.

DQ-07

COATING of cobalt ferrite nanoparticles with silica for an in-vitro gmr biosensor agent.

S. Tang[1], S. Bae[1], W. Lee[2]
1. Electrical and Computer Engineering, Biomagnetics Laboratory (BML), National University of Singapore, Singapore 117576, Singapore, Singapore; 2. Dept of Physics, Sookmyung Women's University, Seoul 140-742, Seoul, South Korea

Introduction

Ferrite nanoparticles are now widely noted in the biomedical field, one application being their use as a biosensor agent to detect biological information, such as in a DNA counter (BARC), and other disease diagnostic biosensors. However, the biological entities should be attached on the surface of ferrite nanoparticles via coating material to avoid problems of cytotoxicity and a probing problem with biological entities[1,2]. Accordingly, development of a new coating material, which can provide high biocompatibility and durability under a wide rage of physiological conditions, especially with no serious degradation of magnetic properties, are urgently required for the successful use of ferrite nanoparticles as biosensor agents. In particular, research interests on the investigations of the coating effects on the magnetic property changes during the coating process have increased significantly, because there has been no detailed report on the physical mechanism of magnetic property variation in coated magnetic nanoparticles so far.

In this study, effects of silica coating on the magnetic property in Co-ferrite nanoparticles[3] with high magnetic anisotropy were investigated in terms of coating treatment steps and coating thickness for an in-vitro biosensor agent application. In order to study the effects of magnetic anisotropy on the coating-induced magnetic degradation, Mg-ferrite nanoparticles, which have a softer magnetic property, were compared to that of Co-ferrite nanoparticles.

Experimental procedures

Co- and Mg-ferrite nanoparticles with different particle sizes synthesized by a sol-gel method were dispersed in oleic acid(OA) and oleylamine(OL) for separation. The dispersed samples were mixed with a solution of TEOS and ethanol and then left to stand for 1 hr for coating[1]. Coating status was confirmed by scanning electron microscope (SEM) and the magnetic properties for each coating step were measured by using a vibrating sample magnetometer (VSM).

Results and Discussion

Figure 1 and 2 show the M-H loops of 200 nm size Co- and Mg- ferrite nanoparticles treated at the different coating steps. As can be clearly seen in Fig. 1 and 2, the chemically isolated or silica-coated Co- and Mg-ferrite nanoparticles showed a change of coercivity and saturation magnetic moment compared to the original ones. Furthermore, as also confirmed by Figs. 1 and 2, the magnetic properties in the Co-ferrite nanoparticles for each coating step were not seriously changed as compared to that of Mg-ferrite nanoparticles. OA and OL-dispersed Mg-ferrite nanoparticles that were treated with TEOS showed a 50% increase in coercivity, while Co-ferrite nanoparticles, under same conditions, exhibited only 28% increase in coercivity (Tables 1 and 2). The saturation magnetic moment also showed the same trends as the change of coercivity for both Mg- and Co-ferrite nanoparticles under same conditions. There was a 45 % of decrease in saturation magnetic moment for TEOS-treated Mg-ferrite nanoparticles compared with only 4.5 % decrease for the Co-ferrite nanoparticles. The change of magnetic properties after each coating process step is supposed to be due to the reduced magnetic interaction among the nanoparticles (increased the inter-particular distances) caused by the introduction of silica and the chemically-induced isolation. In addition, it strongly implies that the magnetic anisotropy is directly relevant to the magnetic degradation of ferrite nanoparticles during coating process. In conclusion, all the experimental results shown in this study clearly confirmed that the change of magnetic properties during coating process is entirely evident at the first coating step - chemically-induced particle isolation by OA or OL. In addition, from the above results, ferrimagnetic Co-ferrite nanoparticles coated with silica can be considered to be a good candidate for an in-vitro biosensor agent due to its small magnetic degradation after coating caused by its large magnetic anisotropy.

[1] M.E. Park, J.H. Chang / Materials Science and Engineering C 27 (2007) 1232–1235

[2] D. Luo et al. / Journal of Controlled Release 95 (2004) 333–341

[3] Tung, L. D.; Kolesnichenko, V. L.; Caruntu, D.; Chou, N. H.; O'Connor, C. J.; Spinu, L. J. Appl. Phys. 2003, 93, 7486. (b) Hanh, N.; Quy, O. K.; Thuy

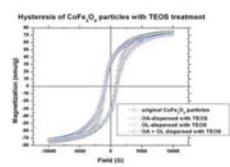

Fig 1: Hysteresis loops of cobalt ferrite nanoparticles treated differently

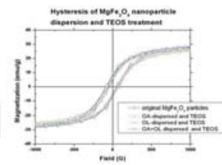

Fig 2: Hysteresis loops of magnesium ferrite nanoparticles treated differently

	H_c(G)	M_s(emu/g)
Original	788.54	75.57284
OA-dispersed	972.24	70.57024
OL-dispersed	889.09	72.33704
OA+OL-dispersed	898.02	67.25728
OA-dispersed, TEOS- treated	932.11	72.21522
OL-dispersed, TEOS-treated	999.83	72.15385
OA+OL-dispersed, TEOS-treated	1016.3	72.07692

Table 1: Coercivities and magnetizations of various cobalt ferrite nanoparticle samples

	H_c(G)	M_s(emu/g)
Original	50.244	32.32714
OA-dispersed	87.752	30.05333
OL-dispersed	76.75	30.37398
OA+OL-dispersed	73.204	28.89145
OA-dispersed, TEOS- treated	75.024	29.89481
OL-dispersed, TEOS- treated	75.293	30.44369
OA+OL-dispersed, TEOS- treated	76.088	32.25926

Table 2: Coercivities and magnetizations of various magnesium ferrite nanoparticle samples

DQ-08

Effect of Metallic-coating Thickness of Thermosensitive Magnetic Powder for Cancer Therapy.

T. Takura[1], F. Sato[1], H. Matsuki[1], T. Sato[2]
1. Dept. of Electrical and Communication Engineering, Graduate School of Engineering, Tohoku University, Sendai, Japan; 2. NEC Tokin Corp., Sendai, Japan

1. Introduction

Hyperthermia is a therapeutic method that necrotize cancer tumor by heating. Soft heating[1] has been proposed as one method of it. This is where the thermosensitive magnetic materials inserted into the tumor as a heater produces heat in a high-frequency magnetic field. Although the heater needs to be implanted in the tumor tissue, there are various advantages to soft heating, such as easy retreatment, localized heating of the tumor, and a low degree of invasiveness. So, in this work, we developed thermosensitive magnetic powder coated with Ag-paste. This powder composed of the Ni-Cu-Zn ferrite granules and Ag-paste is used as the heater for hyperthermia. We examined the difference of heating in terms of thickness of Ag.

2. Principle of Our Magnetic Powder

Our powder produces a higher heat due to losses of hysteresis and inductive current than magnetic powder alone. Fig.1 shows the characteristic of the powder in a high-frequency magnetic field. T represents the temperature of the powder and Tc the Curie-point in this figure. While T < Tc, the magnetic flux is concentrated in the effect of high permeability of ferrite, and the temperature of the powder rises as a result of the generation of short-circuit current in the metal. On the other hand, when T > Tc, the temperature rise is limited because the permeability decreases rapidly and the thermosensitive ferrite does not concentrate the magnetic flux. Since the temperature of the powder does not rise higher than that of the Curie-point, temperature control is achieved with the use of a Curie-point as criteria.

3. Experiment

Our magnetic powder has two heat sources. They are hysteresis loss and inductive current loss. We can examine the rate of heating by comparing magnetic powder alone with the powder with Ag-coating. Fig.2 shows the temperature profile of the magnetic powder. The temperature of the powder with Ag-coating rose near the Curie-point, while that of the magnetic powder without coating was below the Curie-point much. The heating by the loss of inductive current in the metal is the most of heating. Therefore, the thickness of Ag has a relationship to the heating of the powder. We examined heating value of magnetic powder of when Ag-thickness changed. In the experiment, the thermosensitive magnetic powder is Ni-Cu-Zn ferrite granules (150-350 µm in diameter) and the Curie-point is 90 Celsius degree. Our powder for cancer therapy is made by baking Ag-paste on the magnetic powder. The amount of the powder we used is 1.0 g. We used some powder changed Ag-thickness variously (5 µm, 10 µm, 15 µm, 20 µm). The powder, which is placed in the insulator, is thermally excited through the use of a solenoidal coil. The exciting condition is set to 200 kHz and 4 mT. Fig.3 shows the characteristic of the powder as a function of Ag-thickness. As a result, the powder of 15 µm showed the top of the temperature rise.

4. Conclusion

Our original powder achieved higher heating value than magnetic powder alone. It is confirmed that we can increase heating value of the powder by selecting optimal metallic thickness. Therefore, we can expect high effcet of cancer therapy.

[1] H. Matsuki and K. Murakami: High Quality Soft Heating Method Utilizing Temperature Dependence of Permiability & Core loss of Low Curie Temperature Ferrite, IEEE Transactions on Magnetics, Vol. MAG-21, No.5, pp. 1927-1929 (1985).

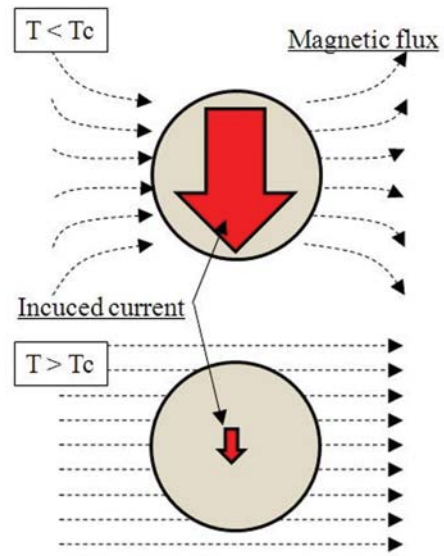

Fig.1 Heating principle of thermosensitive magnetic powder with Ag-coating. We define the Curie-point as Tc, and the temperature of the powder as T.

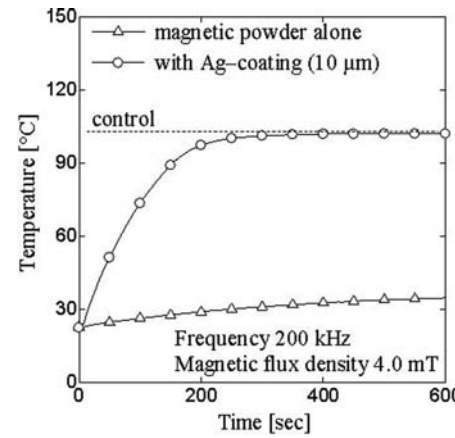

Fig.2 Temperature profile of the powder with Ag-coating and magnetic powder alone.

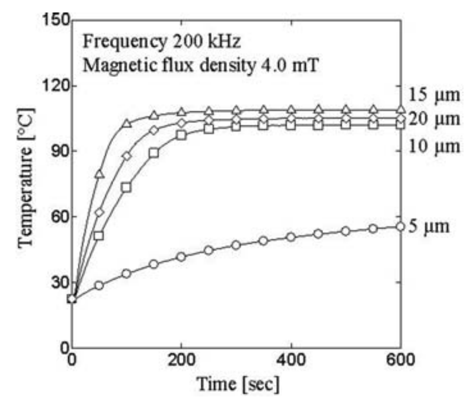

Fig.3 Temperature Characteristic of the powder as a function of Ag-thickness.

DQ-09

Fe Oxide Nanoparticles produced by laser pyrolysis for biomedical applications.

V. Bouzas[1], R. Costo[2], M. García[1], M. Morales[2], S. Veintemillas-Verdaguer[2]
1. Dpt. Material Science, Universidad Complutense de Madrid, Madrid, Spain; 2. Institute of Materials Science, CSIC, Madrid, Spain

Iron oxide nanoparticles are commonly used in biomedical applications as contrast agent for Magnetic Resonance Imaging [1]. The magnetic properties of the nanoparticles strongly depend on their features and small changes in shape and size can alter significantly the magnetic response of the nanoparticle. Therefore nanoparticle production methods with a narrow size distribution are required for these purposes. Among the different methods that can provide this kind of nanoparticles, laser pyrolysis has the advantage to produce homogeneous material in quantities fairly larger than other chemical methods, that requires a long time to produce few milligrams and results expensive. Here, we report on the preparation and magnetic characterization of Fe oxide nanoparticles by laser pyrolysis and the relationship between the preparation conditions and the magnetic response.
Iron oxide nanoparticles were prepared by pyrolysis laser (CO_2 laser W=79watts, P=400mbar) using the method described previously [2]. Table 1 summarizes the main preparation parameters.
XRD and TEM analysis confirmed the existence of Fe oxide nanoparticles (compatible with maghemite and magnetite) with size between 2 and 4 nm, except for BONFEX06 which showed bimodal size distribution with maxima at 3.7nm and 14.9 nm
The magnetization curves measured at 10 K are presented in figure 1
At this temperature, all the samples exhibit ferromagnetic behaviour and no one is saturated at a field of H=7T. Results are quite similar for samples BONFEX02, BONFEX03, BONFEX04 and BONFEX05 (all these prepared using the same flux of C_2H_4). For these particles is also observed that the magnetization under a 7T field increases as the particle size does as expected: it is well known that Fe oxide nanoparticles present a surface shell with a reduced magnetization [3], and the fraction of atoms in this surface shell increases as the particle size decreases.
Sample BONFEX06 has a very different behaviour. For this heterogeneous sample the curve presents an almost linear behaviour but the graph opens, indicating that, this is not paramagnetic. Although it is very tough to reach conclusions about this complex sample the presence of large and likely more crystalline particles could arise a higher anisotropy. Therefore a field of H=7T is far away to saturate the material and larger fields are required to saturate it. This also could explain the low magnetization of the sample.
Sample BONFEX08 present an intermediate behaviour between the others with the larger HC but the lower magnetization at 7T that, as well, can be understood as a large anisotropy (larger than for BONFEX02, BONFEX03, BONFEX04 and BONFEX05, but lower than BONFEX06).
Comparison of the magnetic measurements with the preparation conditions shown in table 1, it is inferred that that the magnetic features of the nanoparticles can be controlled in a wide range of values through the carrier flux during the preparation, while the addition of an air flux or the evaporation temperature of $Fe(CO)_5$ seems not to alter dramatically the magnetic properties of the nanoparticles. In particular, larger flux leads to smaller values of the magnetization of the samples under a 7T field.

[1] J. W. Jung and P. Jacobs, MAgne. Reson. Imag. 13 (1995) 661.

[2] S. Veintemillas-Verdaguer, M.P. Morales, C.J. Serna, Mater. Lett. 35 (1998) 227.

[3] A. E. Berkowitz, W. J. Schueleand P. J. Flanders J. Appl.Phys. 39 (1968) 1261

SAMPLE	GAS FLUX			EVAPORATION T(C°) $Fe(CO)_5$
	CARRIER	COAXIAL	WINDOWS	
BONFEX02	$9C_2H_4$+9Air	22 He	726 N_2	26
BONFEX03				10
BONFEX04	9 C_2H_4		726 N_2+40Air	10
BONFEX05				22
BONFEX06	18 C_2H_4	190 He	1517He+40Air	22
BONFEX08	$12C_2H_4$+6Air		1517He	10

Table 1 Main preparation parameters for the Fe oxide nanoparticles

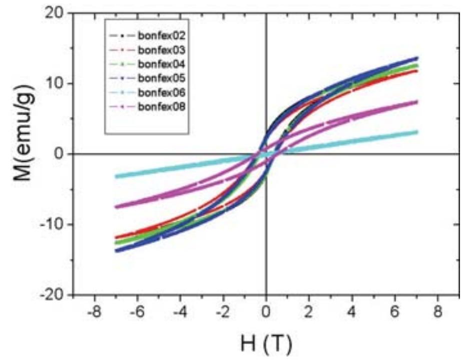

Figure 1. Magnetization curves measured at 10 K after zero field cooling

DQ-10

Magnetic properties and potential biomedical applications of CM-CL-SPIONs.

M. Lin[1], J. Gu[1], T. Veres[3], J. Dobson[1], H. Lee[2], M. Muhammed[4], D. Kim[1]
1. Institute of Science and Technology in Medidicine, Keele University, Stoke-on-Trent, United Kingdom; 2. Department of Materials Science and Engineering, Myongji University, Kyunggi-do, South Korea; 3. Industrial Materials Institute, National Research Council Canada, Boucherville, QC, Canada; 4. Materials Chemistry Division, Royal Institute of Technology, Stockholm, Sweden

Recently, we developed a novel versatile backbone nanocarriers carboxymethyl activated dextran crosslinked superparamagnetic iron oxide nanoparticles (CM-CL-SPIONs) for biomedical applications.[1] Due to their potent immovability in water and capability of additional conjugation of bioactive molecules, CM-CL-SPIONs are of particular concerned on biomedical applications, such as magnetic resonance (MR) contrast agents, magnetic targeted drug delivery system (DDS) and immunomagnetic cell separation etc.[2] In this study, we attempt to modify and optimize the procedure of SPION surface with crosslinked dextran layer for more functionaliztion with biocompatible molecules. The synthesis of SPION, introduction of carboxymethyl group after preparing the dextran coating on SPION, the magnetic properties of the sample at each stage by SQUID and their biocompatibility by MTT assay with MG 63 cell line are briefly summarized. Especially, the binding capacity is estimated on the basis of magnetic measurements as well as thermal and physiochemical analysis. Light microscopy was used to visualize MG 63 cell morphology. In addition, fluorescent observation of the cell cytoskeleton and intracellular clathrin localization has also been evaluated.

Fig.1 shows the ZFC/FC curves of CL-SPIONs and CM-CL-SPIONs measured in a field of 50Oe on a superconducting quantum interference device (SQUID) magnetometer. The temperature dependence of magnetization of both CL-SPIONs and CM-CL-SPIONs exhibit a sharp cusp around 17K and 30K in the zero-field cooled (ZFC) susceptibility, respectively. The blocking temperature (TB) was determined to be around 100K (CL-SPIONs) and 120K (CM-CL-SPIONs) from the divergence of ZFC and FC data. Above TB, the thermal fluctuation energy is larger than the uniaxial anisotropy energy. Carboxymethylation process increases the blocking temperature of the nanoparticles. As previously described, carboxymethylation of CL-SPIONs was achieved at hydrothermal condition at high pH, during which, some agglomeration of nanoparticles may take place.[1] In CM-CL-SPIONs, the agglomerated particles act as clusters, which increase the blocking temperature.

That magnetic data was also multi-parametrically fitted with a theoretical model. [3]Firstly by considering d0 = 9.4 nm (predetermined by TEM imaging) as imposed parameter, the intrinsic anisotropy constant Keff was determined to be 4200 J/m3 by fitting the measured ZFC curve with the theoretical curve. It was found that CL-SPIONs sample agree well with the model, while CM-CL-SPIONs sample. At high temperature, the magnetic moment of CM-CL-SPIONs seems to be frozen. This blocked state could be consistent with some agglomerations of strongly interacting nanoparticles in ferromagnetic clusters that drastically change the size distribution of the particles. In order to take into account of these effects, d0 and σ were adjusted to ZFC curves while keep Keff = 4200 J/m3 as imposed parameter.

MTT assay is a cell proliferation assay, based on the ability of a mitochondrial dehydrogenase enzyme in viable cells to cleave the tetrazolium rings of the pale yellow MTT and form a dark blue formazan crystal. The number of surviving cells is directly proportional to the level of the formazan product created, which can then be quantified by reading absorbance at 570 nm with a multiwell scanning spectrophotometer (ELISA reader). MG 63 cell line is a human osteosarcoma cell and selected for particle cytotoxicity test. Cell viability after 24 hours incubation with CM-CL-SPIONs was tested by a standard MTT assay with MG 63 cell line. Incubated with CM-CL-SPIONs for 24 hours, even up to 1000 μg/mL concentration, MG 63 cells showed good survival rate. (Fig 2) The cell morphologies were also observed under light microscope for up to 4 days. No significant cell morphologies changes were observed during the 4 days incubation.

1. Lin, M. M.; Li, S.;Gu, J. L.; Lee, H. B.; Muhammed, M.; Kim, D. K. Submitted to Intermag 2008.

2. Pankhurst, Q.A. ; Connolly, J. ; Jones, S.K. and Dobson, J., J. Phy. D: Appl. Phy.., 2003. 36: p. R167-R181

3. Sappey, R. Vincent, E., Hadecek, N. Phy. Rev. B., 1997. 56(22): p. 14551-14559.

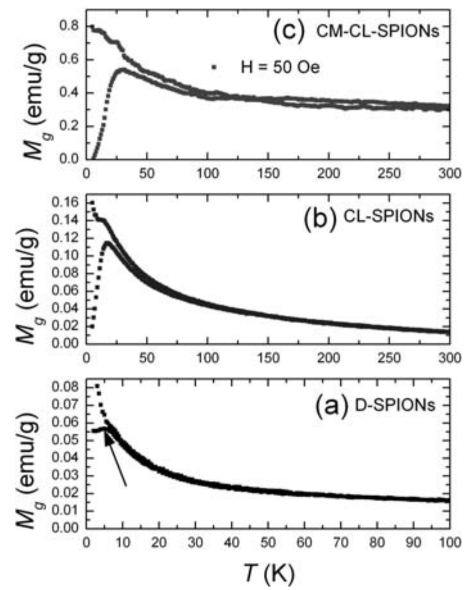

Figure 1. SQUID measurments of a) D-SPIONs; b) CL-SPIONs and c) CM-CL-SPIONs.

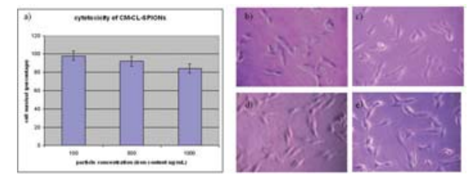

Figure 2. a) cytotoxicity of SPIONs; b)-e) microscopy images of MG 63 cells incubated with no particles as control, b) day 1and d) day 4; or CM-CL-SPIONs (iron content 100 μg/mL) at c) day 1 and e) day 4.

DR-01

Controlling vortex chirality in magnetic submicron dots by modulating the magnetic properties in lateral direction.

Z. Zhong, H. Zhang, X. Tang, Y. Jing, L. Jia, L. Zhang
State Key Laboratory of Electronic Thin Films and Integrated Devices, University of Electronic Science and Technology of China, Chengdu, China

Magnetically soft submicron dots have received considerable attention due to their tendency to support a stable vortex magnetization state, which may be applied in data storage and non-volatile magnetic random access memory. The vortex state can be described in terms of two quantities: (i) a core polarity that defines whether the out-of-plane component (vortex core) of the magnetization points up or down, and (ii) a chirality that defines the in-plane curling direction of the spins. However, due to the geometrical symmetry of the submicron dots, the chirality of magnetization rotation was statistically distributed clockwise or counterclockwise, but could not be controlled on purpose by application of magnetic in-plane fields. The application of magnetic vortex as device elements requires the perfect controllability of the chirality of the magnetization circulation at room temperature. For this reason, methods introducing the asymmetrical strucuture to achieve the required controlling over the chirality in the vortex state in ferromagnetic submicron dots are investigated [1,2].
Here, We try to introduce the lateral modulated magnetic properties in lateral direction in submicron dots to control the vortex chirality. The lateral modulated magnetic properties in submicron dots may be the magnetization, anisotropy, and exchange stiffness. In this work, numerical micromagnetic simulation using the 3-D OOMMF package is used to study the magnetization configuration and the reversal process of the sub-micron ferromagnetic dot shown in Fig.1 (a), where the submicron dot with a diameter of 200 nm and a thickness of 20nm is composed of two parts only with different magnetization orientated symmetrically to the y-axis in order to reduce the complexity of the analysis. The applied magnetic field is along the x axis. Based on the analytical resulsts, a novel strucutre based on gradient magnetization in lateral direction was proposed to control the chirality.
All the simulated submicron dots with lateral gradient magnetization are vortex magnetization configuration in ground state and show vortex-type magnetization reversal process. Comparing with the submicron dots with lateral uniform magnetization, there are two features for the submicron dots with lateral gradient magnetization. In one feature, the core of vortex of the submicron dots with lateral gradient magnetization is not in the center of the dots, and the off-distance increases with increasing the intensity of gradient magnetization. In the other, the one-step nucleation process changes to the two-stage nucleation process while increasing the intensity of gradient magnetization, although the magnetization reversal of all the dots is via vortex nucleation, displacement, and annihilation. Fig.1 (b-d) show the typical vortex-type hystersis loops corresponding to various intensity of gradient magnetization. The intensity of gradient magnetization is defined the difference magnetization between the two parts.
After carefully analyzing the spin arrangement in magnetization reversal process, we observe that a twisted "C" metastable state develops in the part with larger magnetization, which has relatively soft magnetic properties. The part with larger magnetization reverses firstly and then the part with lower magnetization does, so a two-stage nucleation process appears when the applied field decreases. If we introduce asymmetrical magnetization distribution in lateral direction, we may control the open direction of "C" metastable state, and then we can control the vortex chirality in remanent state. Based on the analysis of the magnetization reversal process, we propose a new structure to control the chirality of the vortex. Our proposed structure is composed of dot with a quarter lateral gradient magnetization parts, which locates at the upper or lower quarter part at the right of the dot. When the applied field along the x axis decreases from saturation, the dot with the quarter lateral gradient magnetization in the upper develops a CCW whirling, while for that in lower quarter, it develops a CW whirling. Results of micromagnetic simulation are consistent well with the analytical results. This new structure opens a new way to control the chirality of the vortex, it is important for the devices relating to the vortex's chirality.

Acknowledgement
This work is supported in part by the National Nature Science Foundation of China under Grant Nos. 60490296, 60671029, and 9030615, and by the key project of Chinese Ministry of Education under Grant No.105151.

[1] M.Schneider, H. Hoffmann, J.Zweck, Appl. Phys. Lett.79, 3113(2001)

[2] P. Vavassori, R. Bovolenta, V. Metlushko, B. Llic, J. Appl. Phys. 99, 053902(2006)

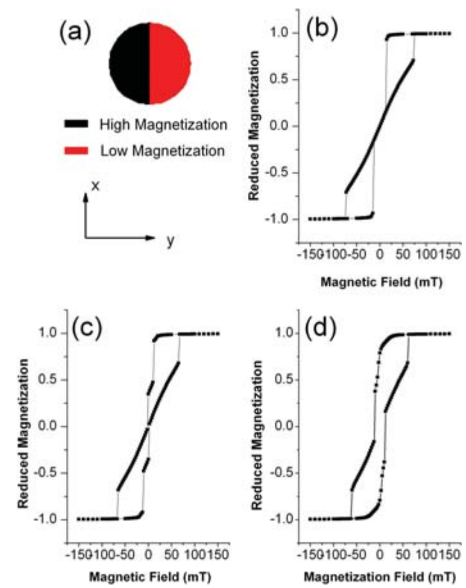

Fig.1 Schematic diagram of simulated ferromagnetic submicron dot (a) and the hysteresis loops of submicron dot for the intensity of Ms gradient magnetization for 0.2 Ms (b), 0.3 Ms (c), 0.4 Ms (d)

DR-02

Helical states in multilayer nanomagnets.

V. Mironov[1], A. Fraerman[1], B. Gribkov[1], S. Gusev[1], S. Vdovichev[1], B. Hjorvarsson[2], H. Zabel[3]
1. Institute for physics of microstructures RAS, Nizhniy Novgorod, Russian Federation; 2. Uppsala University, Uppsala, Sweden; 3. Ruhr-University, Bochum, Germany

The magnetic force microscopy was applied to investigate noncollinear helical states in multilayer nanomagnets consisting of a stack of three single domain ferromagnetic disks separated by insulating nonmagnetic spacers. The possible existence of helical states in tri-layer nanomagnets is based on the universal long-range interaction between layers through magnetostatic stray fields. The interaction between disks leads to frustration in magnetic moments orientation for the first and third disks. When the interaction between these disks is large enough $2E_{13} > E_{12}$ and $2E_{13} > E_{23}$ (where E_{ij} (i,j = 1, 2, 3) are the interaction energies between i and j disks) and the magnetic moments are free to rotate in the particle plane, then non-collinear helical state is realized as the ground state in this system. Note that helical state is doubly degenerate i.e. the energies for "left" and "right" helicoids are equal.

The Co/Si multilayer nanomagnets were fabricated by means of electron beam lithography and ion etching of a [Co/Si]×3 multilayer thin film structure grown by magnetron sputtering. The details of the lithography process are described in [1]. The electron microscopy and e-beam lithography were performed using a "JEOL – JEM 2000EX II" scanning electron microscope. The coercivity of the ferromagnetic Co films did not exceed 20 Oe. Si layers were used as spacers, effectively hindering any interaction except the magnetostatic interaction. The Co disk dimensions (diameter and thickness) were chosen according to the single domain requirements [2]. In our experiments, we used disks with diameters of 300 nm and thicknesses less than 20 nm.

The MFM investigations of the magnetic states in the multilayer nanomagnets were carried out using a vacuum scanning probe microscope "Solver HV" (manufactured by "NT-MDT" Company). MFM measurements were performed in the oscillatory noncontact (constant height) mode using home made Co-coated cantilevers. The amplitude of cantilever oscillations was about 30 nm and the average scanning height was 50-60 nm. The phase shift of cantilever oscillations caused by the gradient of the magnetic field was registered as the MFM contrast. All measurements were performed in a vacuum of 10^{-5} Torr, which increases the MFM signal due to increasing of the cantilever quality factor.

To register a helical state of magnetization in tri-layer nanomagnets by MFM we considered a structure where the thickness of Co layers increases with increasing distance between a layer and the MFM probe. Thus, the change of magnetic moment of the layers was used for compensation of the effects concerned with different distances between the disks and the tip. Our calculations and computer simulations showed that a stack with Co layers thicknesses of 16, 11, 8 nm and with 3 nm spacers has the helical state with $\theta_{12} = 109°$, $\theta_{13} = 257°$ (where θ_{ij} are the angles between i and j layers) and this structure is quite optimal for the observation of spiral peculiarities in MFM images of the helical state.

Taking into account the result of model calculations, tri-layer nanomagnets with Co layer thicknesses of 16, 11, 8 nm and with 3 nm Si spacers were fabricated and measured. The MFM image of this structure is represented in Fig. 1. (The dashed lines separate the regions with dark and bright contrast to emphasize the spiral symmetry of MFM contrast). As it is clearly seen the MFM image demonstrates "left" and "right" handed spiral contrast distributions corresponding to the helical states with different chirality.

In conclusion, the helical states in artificial multilayer nanomagnets consisting of three single-domain ferromagnetic disks separated by nonmagnetic spacers were investigated by magnetic force microscopy methods. For optimized tri-layer nanomagnets with Co layer thicknesses of 16, 11, 8 nm and with 3 nm Si spacers the spiral MFM contrast with different chirality was observed experimentally. The realization of helical nanomagnets is not only of interest for fundamental investigations but they could also be used in spintronics devices. In an external magnetic field perpendicular to the ferromagnetic layers, the magnetization distribution can be transformed from non-collinear into a non-coplanar cone magnetic spiral. In this case, we expect unusual transport properties along the magnetic field direction [3-5].

The authors are very thankful to A.Klimov, V.Rogov, D.Nikitushkin, I.Nefedov and I.Shereshevsky for assistance. This work was supported by the RFBR and by EC through the NANOSPIN project (contract NMP4-CT-2004-013545).

[1] A.A.Fraerman et.al. Phys. Rev. B, 2002, V. 65, P. 064424 1-5.

[2] R.P.Cowburn, et.al. Phys. Rev. Lett., 1999, V. 83, P. 1042–1045.

[3] G.Tatara, H.Kohno, Phys. Rev. B, 2003, V. 67, P. 113316 1-3.

[4] A.A.Fraerman, O.G.Udalov, http://arXiv:cond-mat/0612327, e-preprint 2006.

[5] A.F.Volkov, et.al. Phys. Rev. Lett., 2003, V. 90, P. 117006 1-4.

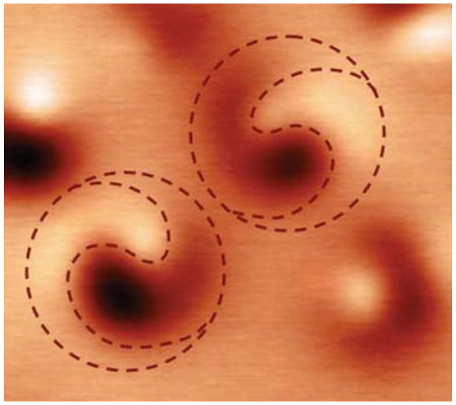

DR-03

Double vortex interaction of micron-sized elliptical Py element studied by real-time Kerr microscopy.

B. Hong[1], J. Bland[1], J. Jeong[1,2]

1. Cavendish Laboratory, Cambridge University, Cambridge, United Kingdom; 2. Department of Materials Science and Engineering, Chungnam National University, Daejeon, South Korea

Magnetic vortex dynamics in patterned magnetic elements is a fascinating issue from both fundamental and technological points of view [1]. In this work, different magnetization switching behaviors through double vortex interaction exhibited in micron-sized elliptical magnetic particles were investigated by using a full field Kerr microscopy. Both micromagnetic simulation and experimental measurements were carried out to determine the origin of this behavior. It was found that the direction of which the vortex core rotates largely depends on the edge spins which were not saturated by external field. It was also found that the switching field varies significantly depending on the relative direction of which vortices rotate.

The elliptical shaped magnetic thin film elements were defined by 220~240 nm DUV photolithography on PMMA photoresist, and magnetic thin film were grown by molecular beam epitaxy (MBE) in an ultrahigh vacuum (UHV) chamber with base pressure below 2×10^{-10} mTorr. Metal layers consisting 20 nm Py and 5 nm Cu were grown on silicon (100) substrate. The practical measurements were carried out using Kerr microscope with time resolution of 30 msec. Fig. 1 show the magnetic domain image observed by Kerr microscope when the applied field is parallel to the long axis of the elliptical pattern. As shown in Fig. 1 two very distinguishable switching states were observed. Magnetic elements in Fig. 1a shown two vortex cores each rotating positively (clockwise) and negatively (anti-clockwise), while the magnetic elements in Fig. 1b shown two negatively (anti-clockwise) rotating vortex cores. Furthermore, by comparing Fig.1c and 1d, it is noticeable that magnetic elements with two negatively rotating vortices shown higher magnetization under same field condition of 0.9 mT.

The micromagnetic simulation was carried out using OOMMF simulation package, with standard Py parameters and a cell size of 10 nm × 10 nm × 20 nm. In this simulation, small amount of edge spins were intentionally introduced to reproduce the practical scenario. The simulation results show strong agreement with the practical measurement. Fig. 2a shows the magnetic domain motion of one positive and one negative vortex cores and Fig. 2b shows the motion of two negatively (positively) rotating vortex cores.

Fig. 3 shows the total energy and magnetization versus applied field of two different switching states of (a) magnetization of non-competing vortices, (b) magnetization of competing vortices, (c) total energy of non-competing vortices, (d) total energy of competing vortices. It was observed that although the initial magnetization and total energy were identical for both configurations, the final values were significantly different. At an applied field of 2.25 mT, the relative magnetization of non-competing configuration reached >0.85 while the competing configuration only reached approx. 0.7. Under the same condition, the total energy was -2×10^{-15} J and -1.25×10^{-15} J respectively for non-competing and competing configurations. The higher total energy and lower magnetization was caused by the formation of a more stable state due to two competing vortex cores. An anti-vortex core was also formed in between two vortex cores in order to achieve 180 degree spin rotation; this vortex core also contributed to the total energy, and therefore increased the stability of this state.

[1] B. Van Waeyenberge, A. Puzic, H. Stoll, K. W. Chou, T. Tyliszczak, R. Hertel, M. Fähnle, H. Brückl, K. Rott, G. Reiss, I. Neudecker, D. Weiss, C. H. Back, and G. Schütz, Nature 444, 461 (2006).

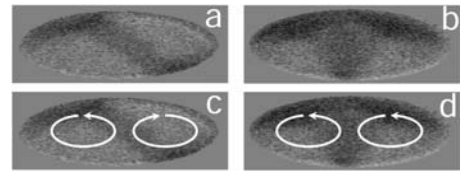

FIG. 1. (a), (b) Kerr microscope images of 20 μm × 8 μm elliptical elements at 0.9 mT with different magnetization states. Corresponding magnetization states (c) competing vortex cores (d) non-competing vortex cores.

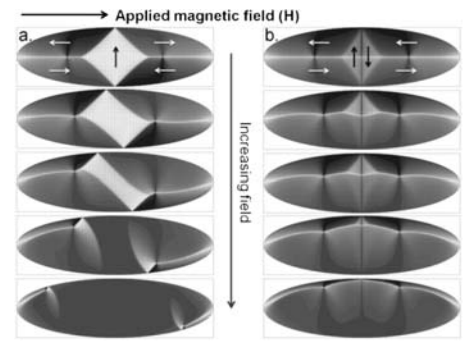

FIG. 2. OOMMF results of 20 μm × 8 μm elliptical elements of two switching states, (a) two non-competing vortices (b) two competing vortices.

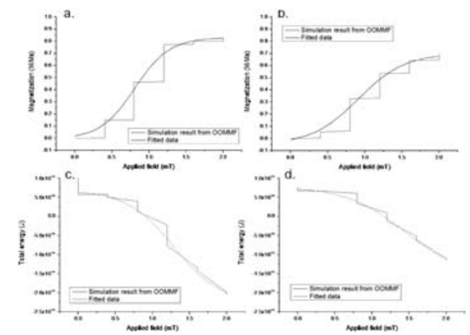

FIG. 3. OOMMF simulation results for magnetizations and total energies of two vortices configuration, (a) magnetization of non-competing vortices, (b) magnetization of competing vortices, (c) total energy of non-competing vortices, (d) total energy of competing vortices.

DR-04

Evolution of mixed states composed of vortex cores and anti-vortex cores in different helicities under external field.

Z. Wei, M. Lai, C. Lee, Z. San, Y. Hsieh, T. Ho
National Tsing Hua University, Hsinchu, Taiwan

Micromagnetic properties of magnetic patterned thin films have drawn a lot of attention because of the rapid development of magnetic sensors, whose dimensions are often in submicron. For submicron-sized thin films, in addition to single-domain state, many other magnetization states [1] compete energetically. In this article we numerically and experimentally investigate the field evolution of mixed states, each of which consist of the same number of vortex cores and anti-vortex cores [2], in a submicron-sized elliptical permalloy thin film.

Numerically, the 3D micromagnetic simulations of submicron-sized elliptical permalloy thin films are performed by the integration of the LLG equation [3], where the exchange field, magnetostatic field, Zeeman field, and anisotropy field are included in our simulation. The material parameters for permalloy thin films are as follows: the saturation magnetization is 800 emu/cm^3, the exchange constant is 2×10^{-6} erg/cm, and the uniaxial anisotropy constant is 10^3 erg/cm^3. Each ellipse is divided into many cubic unit cells, and the side length of each unit cell is set to be 7.5 nm, which is smaller than the exchange length of the permalloy to promise the accuracy in our calculation. When the largest magnetization angular variation between any two successive iterations is below 10^{-8}, we assume the system to have reached the equilibrium state.

Experimentally, the permalloy elliptical thin film array with different sizes and aspect ratios are fabricated by electron beam lithography and e-gun evaporation through lift-off process. First, elliptical patterns on the silicon-dioxide coated silicon substrate are exposed in polymethyl methacrylate (PMMA), the electron beam resist, and a commercial scanning electron microscope (SEM) is used for direct writing. The sample is developed followed by the formation of the elliptical trenches in the e-beam resist. After film deposition using e-gun evaporator, and the lift-off process in acetone, all resist is removed and the permalloy ellipse are obtained on the substrate. The magnetic force microscope (MFM) is used to image the magnetic pole density distribution on the film. The same MFM pattern corresponding to the one obtained from the simulation is adopted to research the magnetization process under field.

Figure 1 shows the numerically obtained remanent magnetization states with different combinations of vortex cores and anti-vortex cores in different helicities. There are totally 4 vortex cores and 2 anti-vortex cores in each case. In Fig. 1(a) the rhombic domain, which is composed of two neighboring vortex cores, is located in the center of the ellipse, and each pair of vortex core and anti-vortex core, which form the so-called Bloch line, is located in one the two sides of the rhombic domain. When the magnetic field is applied along the +x/-x direction, the rhombic domain is tilted, and the Bloch line in the left side of the rhombic domain moves down/up while the Bloch line in the right side moves up/down. When the magnetic field is applied along the +y/-y direction, the rhombic domain is contracted/extended, and each pair of the vortex core and anti-vortex core annihilates almost simultaneously, and in each of the two cases it transforms into two-vortex state eventually. In Fig. 1(b) the rhombic domain is located in one end of the ellipse, and the two pairs of vortex core and anti-vortex core are located in the other end of the ellipse in series, which form a long Bloch line. When the magnetic field is applied along the +x/-x direction, the rhombic domain is tilted, and the Bloch line moves up/down. When the magnetic field is applied along the +y/-y direction, the rhombic domain is contracted/extended, and each pair of the vortex core and anti-vortex core annihilates in sequence from right to left as the field is increased, and in each of the two cases it transforms into two-vortex state eventually. In addition, the mixed states composed of 6 vortex cores and 4 anti-vortex cores in different helicities are also investigated. In our study, the simulation result is in good agreement with the experimental result.

[1] D. Goll, G. Schutz, and H. Kronmuller, Phys. Rev. B 67, 094414 (2003).

[2] K. Shigeto, T. Okuno, K. Mibu, T. Shinjo, and T. Ono, Appl. Phys. Lett. 80, 4190 (2002).

[3] N. A. Usov and S.E. Peschany, J. Magn. Magn. Mater. 130, 275 (1994).

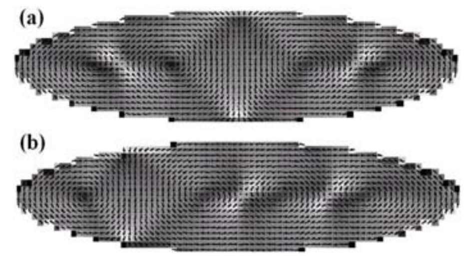

Fig. 1. Numerically obtained remanent spin configurations of the mixed states of crossties and vortex rhombic domain, which is in the center of the ellipse (a) and in one end of the ellipse (b). The long axis, short axis, and thickness of each ellipse are 480 nm, 120 nm, and 60 nm, respectively. The arrows represent the directions of the magnetization vectors in each cubic cell, and the grey scale represents the magnetic pole density distribution.

DR-05

Effect on the dipole-dipole interaction between adjacent dots in Ni-Fe elliptical dot arrays.

Y. Endo[1], H. Fujimoto[2], Y. Kawamura[2], R. Nakatani[2,3], M. Yamamoto[2]
1. Dept. of Electrical and Communication Engineering, Tohoku University, Sendai, Japan; 2. Dept. of Materials Science and Engineering, Osaka University, Suita, Japan; 3. Center for Atomic and Molecular Technologies, Osaka University, Suita, Japan

Introduction

Magnetic logic devices composed of magnetic dots or magnetic nanowires have been much of interest because they are one of candidates as a promising operation system in future computers[1-3]. We have newly proposed the magnetic logic gate (MLG) having the fundamental unit formed by four elliptical magnetic dots, and have successfully demonstrated that NAND and NOR operations can be performed in the MLG using the micromagnetics simulation[2]. Recently, Imre et al. have also observed NAND and NOR operations in the similar MLG using magnetic force microscopy (MFM)[3]. In these MLGs, the distance between the adjacent dots is one of the key parameters because the dipole-dipole interaction between the adjacent dots plays the important role in the logic operations. However, from the experimetal point of view, the optimal distance still remain unclear. Here, we investigated the effect on the dipole-diople interaction between the adjacent dots in Ni-Fe elliptical dot arrays with several distances between the adjacent dots, and optimized the distance at which the magnetization between the adjacent dots coupleed by the dipole-dipole interaction.

Experimental Procedure

Ni-20at.%Fe(Ni-Fe) elliptical dots were fabricated by e-beam lithography, e-beam evaporator, and a lift-off technique onto thermally oxidized Si (100) substrates. The thickness was 10 nm, the aspect ratio between the length of the major axis ($a1$) and that of the minor axis ($a2$) was 2 to 1, and $a1$ was varied from 200 to 1600 nm. The major axial distance (D) between adjacent dots was varied from 30 to 250 nm, while the minor axial distance (d) was fixed 1000 nm. The shape of the dot arrays was observed by scanning electron microcopy (SEM). The magnetization process of dot arrays was investigated by magneto-optical Kerr effect (MOKE) magnetometry, while the magnetic configuration of dot arrays was observed using MFM. Additionally, the effect on the dipole-dipole interaction between the adjacent dots was measured by our proposed measurement method, namely, magnetic field sweeping (MFS)-MFM[4].

Results and Discussion

Figure 1 shows the coercivity(Hc) in Ni-Fe elliptical dot arrays as a function of the distance (D) between the adjacent dots. The magnetic field is applied in the longitudinal direction of the dot. In each dot size, its coercivity increases as the distance becomes short below 30 nm. The reason for this might be that the magnetization between the adjacent dots couples by the dipole-dipole interaction at the distance below 30 nm.

In order to clarify the magnetic configuration of the Ni-Fe elliptical dot arrays in detail, we observed MFM images of these dot arrays at various magnetic fields [Fig. 2]. At the distance of 20 nm, bright and dark contrasts appear at each dot edge, and simultaneously reverse at the magnetic field of -30 Oe. This means that the magnetic configuration of each dot changes from a single domain (SD) state to an opposite SD state with a coherent rotation due to the dipole-dipole interaction between the adjacent dots. In contrast, at the distance of 110 nm, bright and dark contrasts appear at each dot edge, reverse in either upper or lower part of several dots, and further reverse completely at the magnetic field of -100 Oe. This reveals that the magnetic configuration in each dot changes from a SD state to a opposite SD state via a closure domain state as the magnetic field is varied, and that the magnetization of each dot randomly rotates. Furthermore, the curve of phase vs. magnetic field at both edges obtained by MFS-MFM changes from a stepped hysteresis loop to a square one with decreasing the distance between the adjacent dots. (They are not shown) These also reveal that the dipole-dipole interaction becomes stronger with decreasing the distance between the adjacent dots.

In summary, it is concluded that the optimal distance at which the magnetization between the adjacent dots couples by the dipole-dipole interaction is below 30 nm.

[1] D. A. Allwood *et al*., Science **296**, 2003 (2002).

[2] S. A. Haque *et al*., J. Magn. Magn. Mater., **282**, 380 (2004).

[3] A. Imre *et al*., Science **311**, 205 (2006).

[4] Y. Endo *et al*., J. Magn. Magn. Mater., **310**, 2436 (2007).

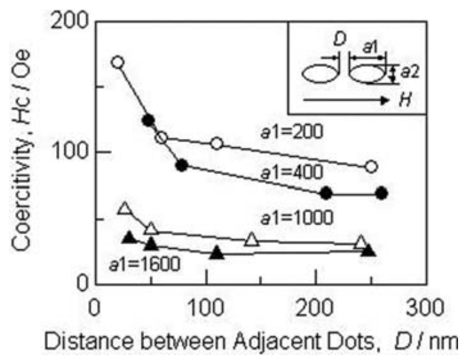

Fig. 1. Change in coercivity(Hc) in Ni-Fe elliptical dot arrays with the distance(D) between the adjacent dots.

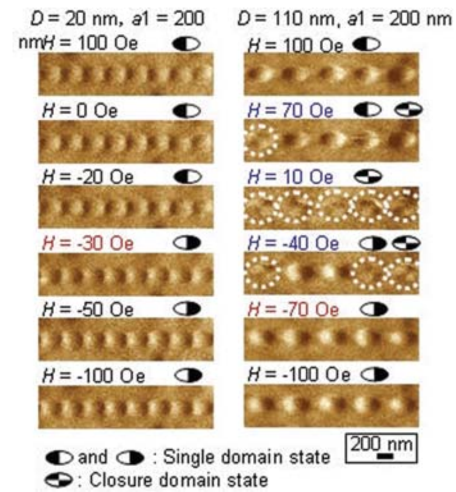

Fig. 2. MFM images at various magnetic fields(H) of Ni-Fe elliptical dot arrays($a1 \times a2$=200×100) with the distance (D) between the adjacent dots.

The effect of dipolar interaction on the magnetization reversal of nano-patterned permalloy dots array.

Y. Tsai, C. Chang, J. Wang, J. Wu, L. Horng
Taiwan SPIN Research Center, National Changhua University of Education, Changhua, Taiwan

Magnetic thin films in the small lateral length scales have provided a wealth of scientific interest and potential applications, such as magnetic field sensor and magnetic memory. For the memory application, ultra-high density and thus lager memory capacity is the main concern. Advanced nanofabrication techniques have enabled the realization of magnetic dots in few tens nanometers. However, the practical application for memory relies on how well one can control every single dot in the array. It is therefore that the influence on the magnetization reversal of each dot from adjacent dots needs to be understood. Namely, the interdot interactions may restrict the memory density in nature. Herein, millions of identical permalloy dots with various diameter and interdot spacing have been fabricated for the study of interdot interactions. A commercial SEM modified for direct writing system with auto-focusing technique was employed for the fabrication. Alternate Gradient Magnetometer (AGM) and Magnetic Force Microscopy (MFM) were used to investigate the magnetization reversal of these dots array.

The samples were fabricated by a standard electron beam lithography and thermal evaporation through a lift-off technique, the fabrication procedure is as follow. A SiN-coated silicon wafer is spun-coated with a bilayer electron resist (PMMA-MAA/PMMA). Millions of permalloy dots array with individual dot diameter of 250, 500, 750nm and the aspect ratio of spacing to diameter ranged from 0.2 to 2 were made, in which the total array size for each sample is around 3mm×3mm. The permalloy film was thermally deposited and the film thickness was controlled to be 30 nm monitored by a quartz crystal. AGM measurements and MFM imaging were used to study the magnetic configurations of these peramlloy dots array due to their excellent field sensitivity and high spatial-resolution.

Figure 1 shows the SEM micrograph of two samples, in which the size uniformity in the millions of dot is within few percent of variation. Figure 2 shows the M-H loops for dot arrays with diameter of 500nm and interdot spacing ranging from 100 to 625nm. Notice that single transition only happens in the array with 100nm spacing and two transitions happen in the others but having different nucleation/annihilation fields. Similar behaviors were observed in other dot arrays. Fig.3 summarizes the experimental data for nucleation field and annihilation fields. It is found that the nucleation and annihilation fields decrease with decreasing/increasing spacing/diameter. For the arrays with larger/smaller spacing/diameter, two transitions were occurred. Fig.4 shows a hysteresis loop and the corresponding MFM images taken in-situ in the present of external field applied, in which the vortex evolution is clearly seen. Such MFM images may provide a deep inside of how the magnetization reversal takes place in each dots array. The vortex nucleation/annihilation in densely dot arrays is influenced by the magnetostatic coupling between the dots. Details regarding to the inter-dot interaction in each sample will be presented.

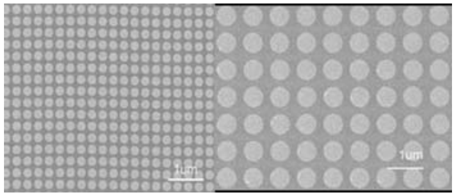

Fig. 1. SEM images of dot arrays with various diameter/spacing of 250/125 nm on the left and 750/375 nm on the right.

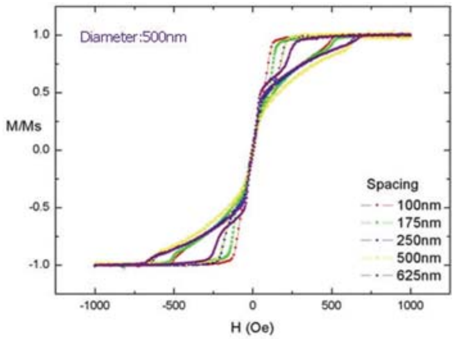

Fig.2. Hysteresis loops measured from dots array with diameter 500nm and different spacing, as specified. Notice that single transition only happens in the aray with 100nm spacing and two transitions happen in the others but having different nucleation/annihilation fields.

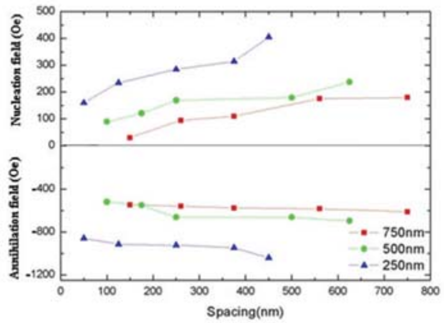

Fig.3. Nucleation and annihilation fields versus the interdot spacing for various arrays with diameter specified.

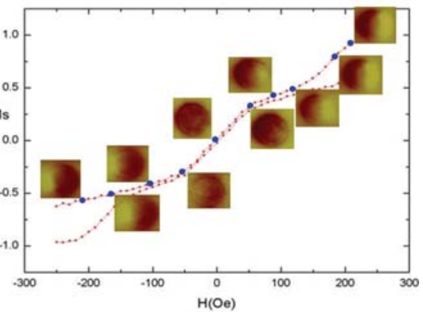

Fig.4. The hysteresis loop and the corresponding MFM images of dots array with diameter 500nm and spacing 500nm, showing the vortex evolution in the present of external magnetic field.

DR-07

Interaction in soft magnetic bilayers nanoscale arrays.

J. E. Davies[2], L. H. Bennett[1,2], E. Della Torre[1,2], B. C. Choi[3], S. N. Piramanayagam[4], E. Girgis[5]
1. George Washington University, Washington, DC; 2. National Institute of Standards and Technology, Gaithersbug, MD; 3. University of Victoria, Victoria, BC, Canada; 4. Data Storage Institute, Singapore, Singapore; 5. National Research Center, Dokki, Egypt

Magnetic bi-layers are becoming increasingly popular especially as a medium for perpendicular patterned media. In order to understand interaction between the layers and the nature of the effect of the spacing layer and of the interaction between adjacent magnetic dots, we measured a sample consisting of a buffer layer of 5 nm of Ta, on a nonmagnetic substrate, that is coated with two magnetically soft layers of 26nm thick FeCoTaZr, that are separated by an 0.8 nm Ru spacer layer, and finally coated with a 4 nm carbon protective layer. A description of the preparation of this type of material is given by S. S. N. Piramanayagam and J. P. Wang . The main idea of this research is to see the effect of the shape anisotropy on the coupling between the two layers of a patterned medium over a range of sizes and shapes of patterned samples. The purpose of this paper is to show that Preisach modeling of the hysteresis loop is an effective tool to analyze this coupling.

A microphotograph of this type of material that we measured is shown in Fig. 1. The perpendicular magnetization was measured using a vibrating sample magnetometer, VSM, and the hysteresis curve shown in Fig. 2, was obtained for the sample. The medium was found to be magnetically soft, that is, it has coercivity of the order of 5 G, and a squareness the order of 0.3. The coupling between the layers is magnetostatic rather than exchange due to the thickness of the separation layer. The observed hysteresis loop is wasp-waist, that is it is narrower near the demagnetized state than it is as saturation is approached. Wasp-waist hysteresis loops can be produced by a variety of effects, usually between two or more magnetic materials. For example, if two soft magnetic films are ferromagnetically coupled, they can be harder to demagnetize than to magnetize, giving rise to a wasp-waist behavior. This is consistent with our picture of this material.

We then modeled this sample with one of the coupled Preisach models that we previously presented [2]. The result is shown in Fig. 3. The model used consists of two cross-coupled Preisach models in order to obtain a net positive feedback to simulate magnetostatic antiferromagnetic coupling,. This computes the irreversible component of the hysteresis loop. If the coupling were negative, then we would have antiferromagnetic coupling. To this irreversible component, we have to add a reversible component. In the model, if the product of α and β is positive, this corresponds to ferromagnetic coupling. The fit was obtained using Gaussian Preisach functions for the irreversible component and an arctangent function of the applied field to simulate the reversible component. Due to the soft nature of the material, it was unnecessary to make the reversible component magnetization dependent.

We have concluded that the model accurately describes the material and that the two films are ferromagnetically coupled. Additional measurements show that the material is not isotropic in the plane, but is wasp-waist with little reversible component along the easy axis and conventional with a smaller squareness along the hard in-plane axis, as shown in Fig. 4. Further work will present the effect of different dot spacing and shape.

1. S. N. Piramanayagam and J. P. Wang, “Method of producing a magnetic recording medium”, U. S. Patent #6699332_B1_(2004).

2.L. H. Bennett and E. Della Torre, “Analysis of wasp-waist hysteresis loops,” J. Appl. Phys., 97, 10E502 (2005).

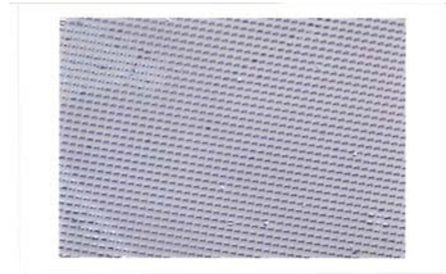

Optical microphotograph of the patterned sample that we measured,

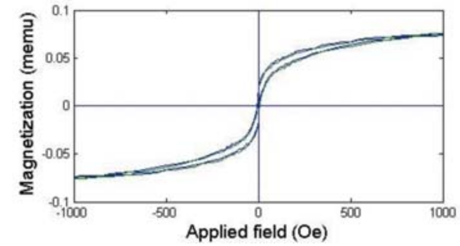

Measurement of the double magnetization perpendicular to the film.

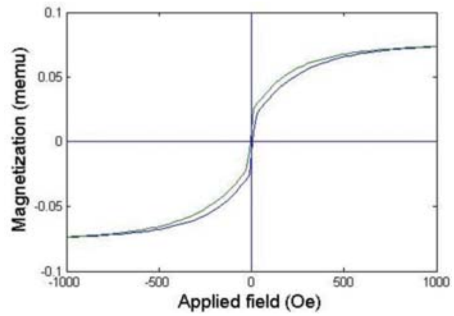

Wasp-waist model for the material shown in Fig. 2.

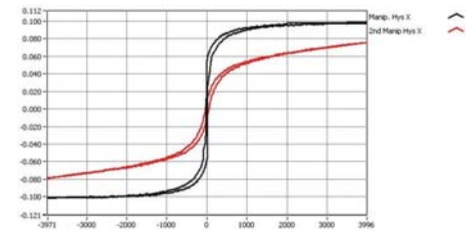

In-plane measurement of the patterned sample.

DR-08

Magnetic imaging and angle-resolved magnetoresistance behaviour of micropatterned films containing Co antidots.

E. Celasco[1,2], P. Martino[1], A. Chiolerio[1], F. Celegato[3], P. Allia[1]
1. Physics, Polytechnic of Turin, Turin, Italy; 2. Physics, Materials and Microsystems Laboratory (χ-lab)- LATEMAR Unit, Chivasso (TO), Italy; 3. INRIM, Torino, Italy

A pattern of Co anti-dots has been fabricated by optical lithography by means of an arc quartz lamp working in the UV range. Optical lithography has been selected in order to obtain a very good periodicity on the micrometer scale together with an extended total patterned area (1mm square).
The resist was spin-coated on Si(100) substrates. In order to obtain maximum resolution and optimum sharpness of the resulting features, the resist thickness has been reduced to 600 nm after specific dilution and the lithography has been performed in hard contact mode. Subsequent to resist developing, a high purity Co film of 65 nm was deposited by thermal evaporation in high vacuum (base pressure < 5×10-8 Torr). The Co anti-dot pattern has been obtained by lift off process. Removing the photoresist with his proper solvent, both complete adhesion of Co on the patterned zone and complete photoresist lift-off in the complementary zone were obtained.
Morphological analysis performed by Atomic Force Microscopy (AFM) indicates a periodic and regular shape Co anti-dots in an hexagonal matrix configuration forming a macroscopic square matrix.
Magnetic Force Microscopy (MFM) was exploited to obtain images of static magnetic structures existing within the Co anti-dot pattern. The samples were demagnetized before each MFM measurement, by applying a reducing alternate magnetic field, both in plane and out-of-plane. MFM images showed complex although well-defined magnetic domain structures related to the presence of the regular array of holes, which induce local stresses. Magnetic information derived from the MFM images was enhanced by means of a numerical procedure [1], which has been shown to compensate possible artefacts like instrumental distortions and to improve the signal to noise ratio.
MFM imaging does not allow for a precise determination of the magnetization orientation, although it is apparent that the magnetization vector lies predominantly in the film plane. In order to possibly clarify the equilibrium magnetic state of the anti-dot array, our results were compared to micromagnetic simulations concerning similar anti-dot systems [2] in the demagnetised state. Such a comparison makes it possible to deduce the presence of three different wedge-shaped like domains around each hole (see Fig.1a).
Angle-resolved magnetoresistance (MR) measurements were performed at room temperature of the patterned film in order to verify the pinning effect of the hexagonal antipillar lattice on the propagation of domain walls. An evaporated 15 nm-thick copper bridge was optically lithographed in a chevron shape directly above the patterned area, in order to realize a straight probe for electrical measurements, avoiding current density inhomogeneities which have been shown to seriously affect the measured MR [3]. The sample was submitted to the magnetic field of an electromagnet (maximum applied film: up to 3 kOe); the orientation of the current density vector with respect to H vector was varied in the film plane between 0° to 90° at steps of 30, and was also set perpendicular to it. As an example, the MR curve at 0° is reported in Fig. 1b.
Both high-field MR sloping behavior and an increase in coercivity with respect to the continuous film have been observed, as recently found in similar systems [4]. The magnetoresistance resulted to be strongly angle-dependent; MR curves were characterized either by an apparent low-field resistance dip, or by a resistance maximum; mixed behavior was observed also. In all cases were the measured MR curves hysteretic and asymmetric.

[1] Chiolerio A., Celasco E., Celegato F., Guastella S., Martino P., Allia P., Tiberto P., Pirri C.F., submitted to Journal of Magnetism and Magnetic Materials.

[2] Yu C.T., Jiang H., Shen L., Flanders P.J., Mankey G.J., Journal of Applied Physics, 87 (2000), 9

[3] Wang C.C., Adeyeye A. O., Y. H. Wu and M. B. A. Jalil, Journal of Applied Physics, 97 (2005) 023521

[4] Wang C.C., Adeyeye A. O., N. Singh, Y. S. Huang and Y. H. Wu, Physical Review B, 72 (2005) 174426

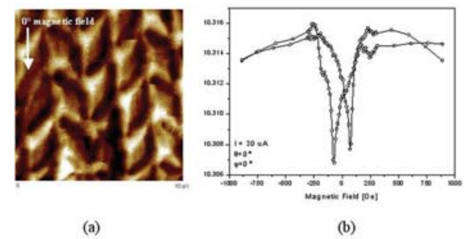

Fig. 1 : (a) MFM image of Co antidot array and (b) Magnetoresistance curve at 0°

DR-09

Analysis of the nucleation-propagation sequence in the magnetization reversal of antidot arrays.

F. García-Sánchez[1], E. Paz[1], O. Fesenko-Chubykalo[1], F. Palomares[1], J. González[1], F. Cebollada[2], J. Haba[2], R. Yanes[1], U. Atxitia[1]
1. Instituto de Ciencia de Materiales de Madrid, CSIC, 28049 Cantoblanco, Spain; 2. Física Aplicada a las Tec.de la Inf., Univ. Politécnica de Madrid, 28031 Madrid, Spain

Singlecrystalline Fe thin films usually exhibit soft magnetic properties, with characteristic square loops along their easy axes and low coercivity values, just a few or at most tens of Oersteds. Their magnetization reversal processes are based on the nucleation of one or a few walls that get unppined from their nucleation regions and easily propagate throughout the sample [1]. The patterning of these films allows the tayloring of their magnetic properties which is obviously important for technological applications but also, from a more fundamental point of view, to understand different reversal mechanisms occurring in systems including local anisotropies of magnetoelastic origin. In the particular case of ordered antidots arrays, the minimization of the otherwise high magnetostatic energy associated to the stray fields leads to substantial changes in the reversal processes with respect to those of continuous films: large changes in their coercivity and magnetoresistance are usually observed linked to new easy axes configurations and novel domain structures [2, 3].

We present in this work a micromagnetic analysis of the reversal processes of antidots arrays lithographed of single crystalline Fe(001) films by means of two different models, trying to cover both the behavior of an infinite array with periodic boundary conditions (model I, Fig. 1a) and that of a finite one partly covering the surface of a continuous film (model II, Fig. 1b). We have compared their main predictions with the experimental results [4] measured -by means of a magneto-optic Kerr effect device at room temperature- in an array with geometrical parameters equal to those employed in the micromagnetic calculations, lithographed on a Fe(001)/GaAs film, with the diagonals of the (square) array along the [100] directions.

For both models we have considered a square array of circular antidots of diameter D= 1 μm, separation λ= 1 μm (along the line joining their centres), with intrinsic parameters corresponding to Fe and their crystalline easy axes being parallel to the array diagonals, which are also easy axes from the point of view of the magnetostatic energy. The energy minimization was carried out by integrating the Landau-Lifshitz-Gilbert equation with a cubic discretization cell, 4 nm in size (roughly one tenth of the Fe exchange correlation length), and preserving the magnetization in the film plane. The 3D dipolar magnetic potential was evaluated by means of the DADI Method [5].

A common feature of both models is that the magnetization reversal takes place by means of two irreversible jumps when the field is applied out of the diagonal or the side of the (square) array and that they predict coercivities of the order of 100 Oe, which agrees with the experimental values. In the case of model I the reversal is governed by a nucleation-propagation sequence starting from the inhomogeneous magnetic moment structures present at the antidot surfaces and resulting from the magnetostatic energy minimization; Fig. 2a shows the calculated angular dependence of both switching fields according to this model, θ being the angle between the applied field and the array diagonal. In the case of model II the reversal is due to a wall artificially nucleated in a low anisotropy region of the external frame which propagates through the array; its angular dependence of the coercivity is presented in Fig. 2b and exhibits a very good agreement with the experimental results. Our micromagnetic simulations suggest that the reversal processes are determined by a nucleation-propagation process due to the existence of walls propagating from the continuous part of the film. The existence of walls propagating from the outer region may be a common feature of many experimental situations and will largely determine the character of the magnetisation reversal in lithographed films.

[1] F. Cebollada el al., Phys. Rev. B 66, 174410 (2002).

[2] L.J. Heyderman et al., Phys. Rev. B 73, 214429 (2006).

[3] F.J. Castaño et al., Appl. Phys. Lett. 85 (14), 2872 (2004).

[4] F. Pigazo et al., J. Appl. Phys. 99, 08S503 (2006).

[5] M.R. Gibbons, J. Magn. Magn. Mat. 186, 389 (1998).

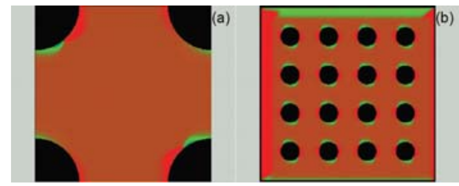

Fig. 1.- Sketch of the antidots corresponding to model I (a) and to model II (b).

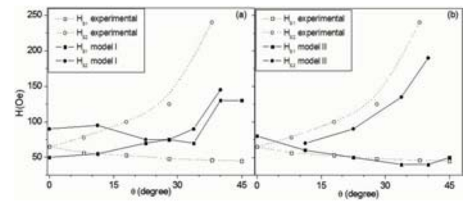

Fig. 2.- Angular dependence of the coercivity according to models I (a) and II (b) compared to the experimental measurements

DR-10

Magnetic behaviour of Ni antidot arrays on alumina nanoporous membranes.

P. Prieto[1], A. J. Chaves-Neto[3], K. R. Pirota[2], M. Knobel[3], J. M. Sanz[1]
1. Física Aplicada, Universidad Autónoma de Madrid, Madrid, Spain; 2. Instituto de Ciencia de Materiales de Madrid, CSIC, Madrid, Spain; 3. Instituto de Física" Gleb Wataghin", Universidad Estadual de Campinas, Campinas, Brazil

Theoretical and experimental studies have demonstrated that the magnetic properties of magnetic materials in the form of thin films, e.g. magnetoresistance, coercivity, permeability and magnetization reversal, can be controlled by artificially produced arrays of antidots. Most of the reported results correspond to magnetic antidot arrays obtained by different lithographic process. However, in this work we report on the magnetic behaviour of highly ordered arrays of Nickel antidots obtained by depositing Nickel on nanoporous alumina membranes (NAM) used as templates [1].

The NAMs with arrays of porous with a high order hexagonal symmetry were fabricated using the so called two steps anodization process in oxalic acid. After fabrication, the pore diameter can be modified by a heat treatment in phosphoric acid (5 % in volume) [1]. The Nickel antidot arrays have then been obtained by the deposition of nickel thin films on the NAM substrates, so that the film replicates the array of nanoholes of the substrate. The Nickel film was deposited by ion beam sputtering (deposition rate of ≈0.02nm/s) at room temperature. The substrates were NAMs with a distance between the centres of two adjacent pores of 105 nm and a pore diameter of 75 nm. The diameter of the antidots, keeping constant the antidot density, has been modified by changing the thickness of the Ni thin film grown on top of the NAM template.

The morphology and geometry of the antidot nanostrustures have been studied by SEM, while RBS and AES depth profiling have been used for elemental and chemical in-depth characterization. The magnetic behaviour of the Ni antidot arrays has been studied by vibrating sample magnetometry (VSM) at room temperature with a maximum magnetization field of 1T. Magnetization loops were measured with the applied magnetic field, both parallel and perpendicular to the plane of the array of antidots. In some cases, the magnetic properties were measured in a temperature range between 2 and 300K by MPMS using a Quantum Design magnetometer.

Figure 1 shows the in-plane hysteresis curves of 54nm thick continuous film of Ni grown on Si as compared with the same film grown on the NAM and forming an array of antidots. As expected, the coercive field is much higher in the nanostructured array of antidots than in the continuous film (i.e., 19.8 versus 3.1 mT), due to pinning effects. The saturation magnetization for the continuous film MS ≈ 0.5T is in good agreement with literature values for Ni [2]. On the contrary, the saturation magnetization of the antidots array is clearly enhanced with respect to that measured in the continuous thin film deposited on Si. This effect has been observed previously and is probably due to Ni/Al2O3 interface effects.

Figure 2 shows the coercive fields for both applied magnetic fields (i.e. parallel and perpendicular to the surface), as a function of the thickness of the Ni film grown on top of the NAM. The figure shows a clear decrease of the coercive field as the thickness of the Ni film increases, for both the in-plane and out-plane configuration of the applied magnetic field. Assuming that the coercivity is related with the pinning of the domain walls produced by the antidot, the observed decrease of the coercivity could be associated with the reduction of the antidot diameter as the thickness of the grown film increases.

Finally we have also studied the magnetic properties of the antidots array as a function of the temperature and we will show that it is possible to tailor the magnetic behaviour of the Ni antidot nanostructures by controlling its chatacteristic sizes, i.e. antidot diameter and interantidot distance.

[1] Z.L. Xiao et al., Applied Physics Letters 81(15) (2002) 2869

[2] J.B. Yi et al., Journal of Magnetism and Magnetic Materials 284 (2004) 303.

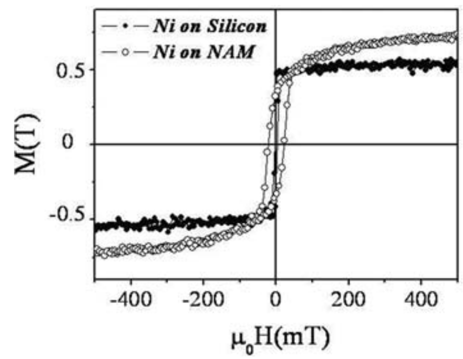

Fig.1 In-plane M-H loops for a 54nm thick Ni film grown on Si (continuous film) and grown on NAM (antidots array).

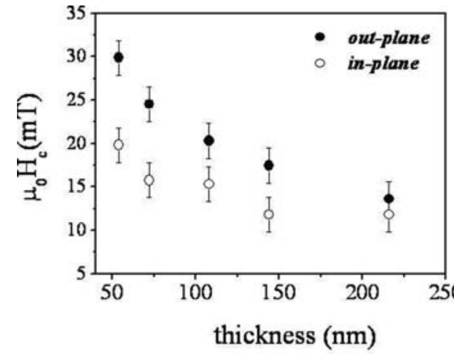

Fig.2 In-plane and out-plane coercive fields as a function of the thickness of the Ni film grown on NAM templates.

DR-11

TAILORING magnetization reversal mode and switching field of magnetic nanostructure with perpendicular anisotropy.

M. Rahman, N. N. Shams, Y. Wu, C. Lai
Materials Science and Engineering, National Tsing Hua University, Hsinchu, Taiwan

Introduction

Patterned magnetic nanostructures exhibit very different properties from those of continuous films and recently attracting great attention due to their technological importance in high-density magnetic recording media [1-3] and fundamental studies. However, fabrication of patterned structure with different feature geometry over large area as well as control of their magnetic properties are quite challenging. In the present study, we demonstrate a method to control the feature geometry and their switching characteristics of magnetization.

Experimental procedure

At first, a thin Al film deposited on a Si wafer by sputtering is anodized to get porous alumina with densities ~1 x10^{11}cm^{-2}. Two AAO/Si templates with aspect ratio, *A*(ratio of the hole height to diameter) of 2.3 and 1.1 are prepared by controlling the post treatment time in dilute phosphoric acid. Then {Co(0.5nm)/Pt(2nm)}5 multilayers (MLs) are deposited onto the AAO/Si templates and bare Si wafer by sputtering at room temperature. The morphological characteristics of this structure are observed by using scanning electron microscope (SEM) and transmission electron microscope (TEM) imaging. Magnetic properties are measured by using a vibrating sample magnetometer (VSM). Magnetization reversal process investigated by first order reversal curve (FORC) technique.

Results and discussion

Cross sectional TEM and plane view SEM observation (Fig.1) reveals that the magnetic material is deposited mainly on the top of the land and around the perimeter of the holes for the aspect ratio, *A* of 2.3, resulting a network structure or a continuous film with holes. When the *A* is reduced to about 1.1, significant amount of magnetic materials deposited inside the holes at the bottom but not completely filled. Though few magnetic materials are still deposited on the wall of AAO near the top, but the thickness is significantly thinner than that on the land and at the bottom. As the anisotropy of Co/Pt MLs is related to individual layer thickness and deposition direction, the magnetic materials at the top and bottom may be considered to be near isolated [4].

The films exhibit strong perpendicular anisotropy and squarness ratio,*S* of almost unity and negative nucleation fields for the samples deposited on Si and AAO/Si with the *A* of 2.3. The coercivity,H_c of MLs on AAO/Si is about 1550 Oe, more than one order magnitude higher than that on Si (140 Oe). The increase of H_c can be ascribed to the pinning effect imposed by the holes. The H_c and *S* are reduced to about 1250 Oe and 0.85 respectively, as the aspect ratio is reduced to 1.1. Fig. 2 shows the angular dependence of the switching field,H_s of Co/Pt MLs deposited on Si and AAO/Si as a function of the angle between applied field and easy axis. The magnetization reversal of Co/Pt MLs deposited on Si is dominated by domain-wall motion with negligible pinning, while the reversals of Co/Pt MLs deposited on AAO with *A* of 2.3 is governed by strong domain-wall pinning. The switching fields, H_s of (Co/Pt)/AAO/Si film is quite insensitive to the angular variation from the easy axis when the *A* is 2.3. The H_s remains constant for the angular deviation of about 45^o from the easy axis. Micromagnetic simulation confirms that this kind of behavior is due to the pinning effect induced by the holes [3]. This unique switching behavior is promising to address the problem of adjacent track erasure in high density magnetic recording. With a decrease of *A* to about 1, H_s follows Stoner-Wohlfarth (S-W) like angular dependence showing a minimum at 45^o that indicates rotation-dominated reversal. The switching behavior well corresponds to the microstructure shown in Fig.1 (b) and good in agreement with the result obtained from first order reversal curve (FORC) measurement.

Conclusion

A simple approach is demonstrated to tune the switching field and magnetization reversal process of magnetic nanostructure by controlling the feature geometry. The fabricated structure can be used for high density magnetic recording. Moreover, the approach may be promising for fabricating magnetic nanostructure for practical applications and understanding of nano-scale magnetic phenomena.

[1] R. P. Cowburn, A. O. Adeye and J.A. C Bland, Appl. Phys. Lett,. 70, 2309 (1997).

[2] A. Y. Toporov, R. M. Langford and A. K. Petford-Long, Appl. Phys. Lett. 77, 3063 (2000).

[3] M. T. Rahman, N. N. Shams, Y.C. Wu, C. H. Lai, and D. Suess, Appl. Phys. Lett. 91, 131205 (2007).

[4] G. Hu etal, J. Appl. Phys., 95, 7013 (2004).

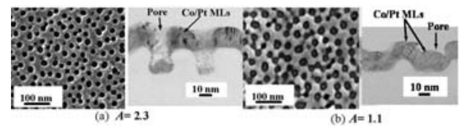

Fig.1. SEM plane view and TEM cross-section image of Co/Pt MLs deposited on AAO with aspect ratio; (a) 2.3, (b) 1.1.

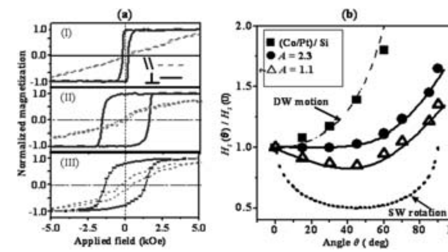

Fig.2. (a) M-H loops Co/Pt MLs deposited on (I) Si, and AAO/Si with aspect ratio (II) 2.3, (III) 1.1. (b) Switching field of Co/Pt MLs deposited on Si and AAO/Si with different aspect ratio as a function of angle θ between the applied field and the easy axis.

DR-12

Property variation in coupled permalloy nanostructures.

A. O. Adeyeye[1], S. Jain[1], N. Singh[2]
1. Electrical and Computer Engineering, National University of Singapore, Singapore, Singapore; 2. Institute of Microelectronics, Singapore, Singapore

Mesoscopic magnets consisting of networks of interacting ferromagnetic dots have drawn increasing attention due to its potential applications in digital computation[1]. It is well known that the magnetic switching of isolated nanomagnets can be drastically modified when they are in close proximity to each other due to the dipolar interaction field. These field-coupled magnetic elements function as the building blocks for the next generation of logic computation. Anti-dot structures (the reverse of isolated nanostructures), is another class of magnetic nanostructures in which arrays of holes are embedded into contiguous magnetic materials. They can be described as artificially engineered "defects" in an otherwise continuous film. The question of how these defects affect the macroscopic and microscopic magnetic properties of the continuous media is of great interest, and the switching mechanism during the magnetization reversal process is an important issue which is still being studied rigorously. With advance in lithographic and other control fabrication techniques, it is now possible to create regular array anti-dot structures in thin magnetic films. It has been found that the anti-dots can act as pinning centers inhibiting the movement of domain walls during magnetization reversal [2]. In this work we have systematically investigated the magnetostatic interactions in square lattice ferromagnetic dots and anti-dot structures. For the dot array the inter-dot spacing (s) was varied from 100nm to 1 µm while the dot diameter was fixed at 600nm. For the anti-dot structures, the hole diameter was 500nm while the inter-hole spacing was varied from 250nm to 1µm.
The periodic arrays of 25nm thick Ni80Fe20 dots and anti-dots were fabricated on silicon substrate using deep ultra violet lithography at 248nm exposure wavelength, electron beam deposition then followed by the lift-off process. 36 different patterns on a single 5x5mm2 sample were fabricated for direct comparison of the magnetic properties. Successful lift-off was determined by the color change of the patterned film and confirmed by examination under a scanning electron microscope (SEM).
Shown in Fig.1(a) is SEM micrograph of the dot array with s=100nm. The corresponding SEM for dot array with s=1µm is shown in Fig.1(b). Shown in Fig.1(c) is the SEM for the anti-dot array with s=250nm and the corresponding array with s=1.3µm is shown in Fig.1(d).
We systematically investigated the switching behavior of these structures using magneto-optical Kerr effect (MOKE) magnetometry, with magnetic field sweeping frequency of 1Hz and spot size of 20µm. Shown in Fig 2(a-c) are the representative M-H loops for the dot array with s=100nm, anti-dot array with s=250nm and the reference film deposited under the same process conditions. We observed marked changes in the magnetic properties due to different reversal mechanism in both the dot and anti-dot arrays compared to the continuous film. The large increase in the coercivity for the anti-dot array can be attributed to the pinning of domain walls in the vicinity of the holes.
A detailed analysis of the variation of the coercivity as a function of s is shown in Fig 2(d). As expected, for closely packed holes (s=250nm), the coercivity is larger compared with hole array of s=1.3µm due to the significant increase in the pinning sites for the domain walls. These results will be supported by magnetic force microscopy and micromagnetic simulations.
We have further investigated the effect of magnetic anisotropy in anti-dot structures by engineering the holes in various lattices. Shown in Fig.3 are the four variations of the anti-dot with neighboring holes positioned in a fixed pattern. The interaction between the holes significantly changes the dynamics of the reversal mechanism for the entire lattice.

[1] A. Imre, G. Csaba, L. Ji, A. Orlov, G. H. Bernstein, and W. Porod, 311, 205, Science (2006)

[2] A. O. Adeyeye, J. A. C. Bland and C. Daboo, Appl. Phys. Lett. 70,3164 (1997).

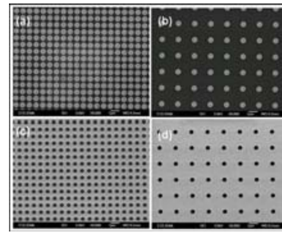

Fig.1SEM micrographs for dot array with (a) s=100nm, and (b) s=1µm, and anti-dot array with (c) s=250nm, and (d) s=1.3µm, respectively.

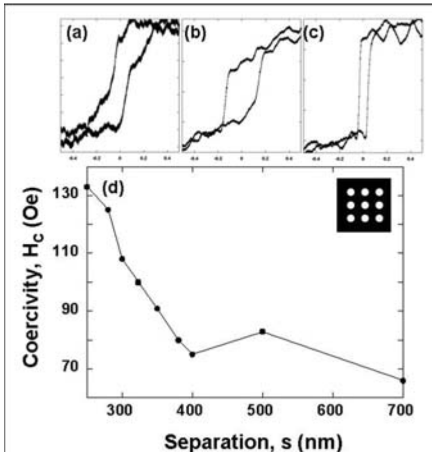

Fig.2Representative M-H loops for (a) dot, (b) anti-dot, and (c) reference film. (d) Coercivity variation as a function of s for anti-dot arrays.

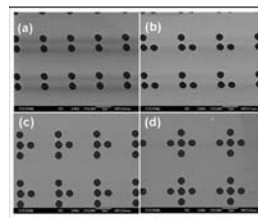

Fig.3 SEM micrographs of anti-dot arrays in various lattice geometries. Diameter of the hole=500nm, and spacing between the holes is 100nm, respectively.

DS-01

Double Ferromagnetic Resonance Absorption Of Non-Saturated States In Arrays of Bi-Stable Magnetic Nanowires.

J. De La Torre Medina[1], J. Olais-Govea[2], A. Encinas[2], L. Piraux[1]
1. Université Catholique de Louvain, Louvain-la-Neuve, Belgium; 2. Instituto de Física, San Luis Potosí, Mexico

In this work we present ferromagnetic resonance (FMR) measurements performed on arrays of single domain, bi-stable magnetic nanowires (NW). Arrays of CoFe NW have been grown by electrodeposition at a constant potential into the pores of a track-etched polycarbonate (PC) membrane with porosity P = 4.5 % and pores diameter d = 30 nm. FMR measurements are carried out in the frequency swept mode by the microstrip transmission line method[1]. The transmission coefficient between 0 and 50 GHz is recorded by applying a constant magnetic field in the direction of the wires axis. These measurements are then repeated at different magnetic field values between ±10 kOe. An important feature of low diameter high aspect ratio NW is that they present a behaviour close to that of ideal infinite monodomain cylinders with square hysteresis loops. In this way, our nanowires present a bi-stable magnetization along the wires axis, where the two equilibrium states are named here after positive m(+) and negative m(-) with respect to the wires easy axis[2]. However, the whole array of NW obeys a coercive field distribution, which arises from inhomogeneities such as wire length, interwire distance, misalignment of the wires, diameter dispersion, and specific microstructure of each wire[3]. An insight of the coercive field distribution is the successive reversal of the magnetization with the magnetic field of individual wires. This reversal of NW corresponds to intermediate non-saturated magnetic states containing a finite number of m(+) and m(-) NW as represented by the point A over the hysteresis loop of figure 1. In the resonance response of non-saturated states, groups of NW in the m(+) and m(-) states presses in opposite directions, which result in different resonance frequencies for each group of NW. In addition, transmission spectra have a double FMR absorption as long as both the m(+) and m(-) groups of NW are present. This is a consequence that wires with its magnetization oriented in opposite directions satisfy different dispersion relations. In figure 2 it is shown the recorded FMR signal at different points over the hysteresis loop and can be observed that the shape of the transmission spectra changes with the NW magnetic configuration. Indeed, at each point over the hysteresis loop the number of m(+) and m(–) wires depends on the value of the applied field. As can be seen in Fig. 2 the FMR signal does not changes if it is recorded during the (a) descending and (b) the ascending magnetization curves at the same absolute field value. In addition, the apparition of the double peak in the FMR signal takes place once the system goes out from saturation. In figure 2, for negative reverse fields the low frequency peak corresponds to the m(+) NW while the m(–) NW absorb at higher frequencies. Conversely, for positive reverse fields the FMR frequencies for the m(±) NW are reversed. The double absorption peak corresponding to non-saturated states changes in intensity as the reverse field is increased. Particularly, since the absortion or imaginary part of the susceptibility χ is proportional to the net magnetization, the intensity of each peak is proportional to the corresponding number of m(+) and m(–) NW[4]. For instance, in the descending part of the cycle, corresponding to a rotation of the magnetization from the positive to the negative direction, the intensity of the m(+) peak decreases while that of the m(–) increases. It is worth noting that the field dependence of each peak is opposite as the reverse field goes in opposite directions. Finally, this double absorption is reproducible and provides an interesting use for novel and more functional microwave devices.

[1] A Encinas-Oropesa, M Demand, L Piraux, I Huynen, and U Ebels, Phys Rev B 63, 104415 (2001)

[2] T G Sorop, C Untiedt, F Luis, M Kroll, . Rasa, J L de Jongh, Phys Rev B 67, 014402 (2003)

[3] D Grundler, G Majer, K-B Broocks, Ch Heyn, D Heitmann, J Appl Phys 85, 6175 (1999)

[4] A G Gurevich and G A Melkov, Magnetization Oscillations and Waves (CRC, New York, 1996), pp. 10-29

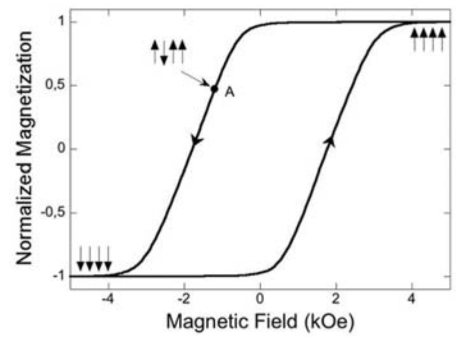

FIG 1. Hysteresis loop of the array of 30nm CoFe nanowires array measured with the field applied parallel to the wires. An intermediate non-saturated state corresponding to wires in the m(+) and m(-) states is represented by the point A over the major hysteresis loop.

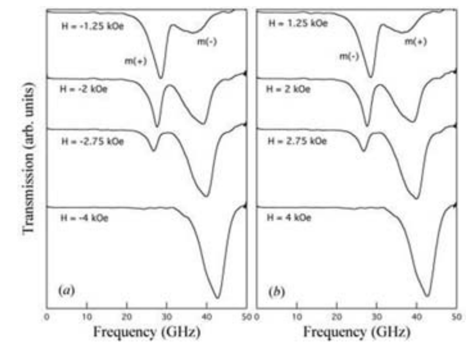

FIG 2. Transmission spectra recorded in the frequency swept mode at different reverse field values during the (a) descending and (b) the ascending parts of the hysteresis cycle.

DS-02

Soft magnetic properties and high frequency characteristics in FeCoSi/native-oxide multilayer films.

H. Zuo, *S. Ge*, Z. Wang, Y. Xiao, D. Yao
Key Laboratory for Magnetism and Magnetic Materials of Ministry of Education, Lanzhou University, Lanzhou, China

Soft magnetic thin films used in high frequency range are required to have high electrical resistivity (ρ) to minimize eddy current loss, and a large saturation magnetization ($4\pi M_s$) and in-plane anisotropy field (H_k) to increase ferromagnetic resonance (FMR) frequency. Although metal-insulator granular films have demonstrated soft magnetic properties and high resistivities, it is only at metal volume fractions approaching percolation threshold that soft magnetic properties are obtained [1]. But the effective saturation magnetization decreases in proportion to increasing the oxide fraction. Recently, a newly introduced discontinuous metal/native-oxide multilayer structure [2], which has been exposed in situ to oxygen to form oxide surface layers, can significantly improve the soft magnetic properties and high frequency characteristics.

In this study, magnetic multilayer films [FeCoSi (d)/native-oxide]$_{50}$ consisted of magnetic FeCoSi layers and in situ oxide layers were deposited on water-cooled glass substrates by DC magnetron sputtering. The dependences of soft magnetic properties and high frequency characteristics on FeCoSi thickness d and oxidation time t were investigated using a vibrating sample magnetometer (VSM) and a shorted microstrip transmission-line perturbation method [3], respectively.

Fig 1. shows H_c and H_k dependences on t for the films of d = 10 Å. The multilayer film shows a minimum H_c at an oxidation time of ~20 s where H_k is the largest. The H_c and H_k dependences on d show that H_c is almost constant and H_k increases with d. These results suggest that the appropriate thicknesses of the native-oxide layers and FeCoSi layers are very important in decreasing H_c of the multilayered films, which may be caused by the exchange coupling between the FeCoSi layers. Fig. 2 shows the easy and hard axis loops for the film of d = 20 Å. The easy axis loop is very square with H_c = 8.4 Oe. Importantly, this film exhibits large H_k of 130 Oe, which gives rise to a good high frequency performance. As can be seen in Fig. 3, the FMR frequency reaches a value as high as ~4.1 GHz, which is much higher than those of granular films.

It is concluded that the [FeCoSi (d)/native-oxide]$_{50}$ films studied here can be a better candidate for the application in GHz range.

[1] Shihui Ge, Dongsheng Yao, etc, J. Phys. D: Appl. Phys. 40, 3660 (2007).

[2] G. S. D. Beach and A. E. Berkowitz, IEEE Trans. Magn., 41, 2043 (2005).

[3] Yan Liu, Linfeng Chen, C. Y. Tan, H. J. Liu, and C. K. Ong, Rev. Sci. Instrum. 76, 063911 (2005).

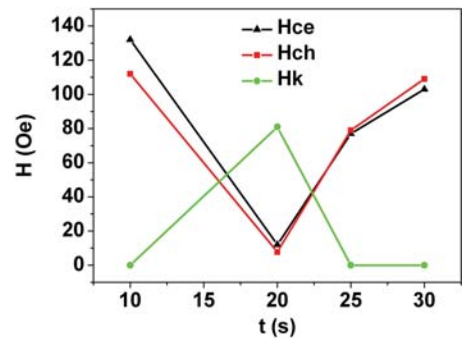

Fig. 1. H_c and H_k dependences on t for the films of d = 10 Å.

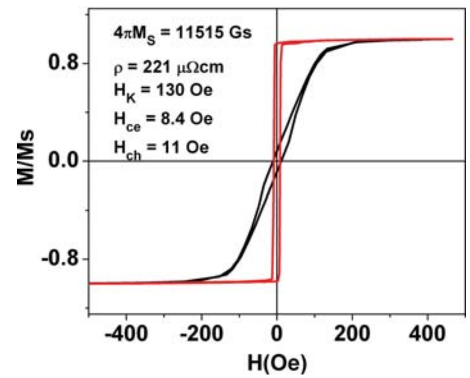

Fig.2. The easy and hard axis loops for the film of d = 20 Å.

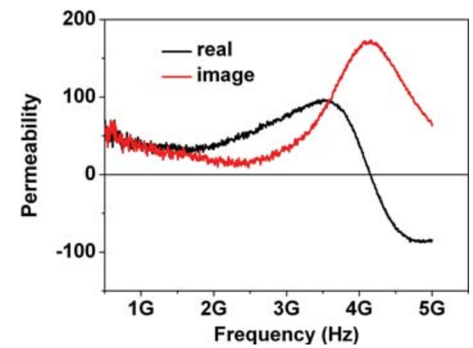

Fig.3. The permeability characteristic for the film of d = 20 Å.

DS-03

Excellent low loss performance of microwave permeability in high resistive CoFeHfO films by thermal annealing.

K. Dong Young[1], Y. Seok Soo[1], R. B. Parvatheeswara[2], K. CheolGi[2], T. Migaku[3]
1. Department of Physics, Andong National University, Andong, South Korea; 2. School of Nano-Science and Engineering, Chungnam National University, Daejon, South Korea; 3. Electronic Engineering, Tohoku University, Sendai, Japan

The ongoing demands for the microwave devices have stimulated the research on microwave magnetic materials with high real permeability, high ferromagnetic resonance frequency (f_r) and low losses altogether at operating frequencies up to GHz region. Recently, Ha et al. have successfully achieved the optimized composition of CoFeHfO, which possesses a high electrical resistivity (ρ = 3570 Ωcm) along with a large saturation magnetization ($4\pi M_s$ = 20 kG) and a good induced anisotropy field (H_k = 84 Oe)[1-2]. However, the microwave permeability performance of the as-prepared CoFeHfO thin films is not really good as it is characterized by their poor imaginary permeability properties in the GHz range.
In this work, we investigate the thermal field annealing effect of microwave permeabilities using the optimum composition of CoFeHfO thin films. The improved high real permeability and low loss properties in the microwave frequency range are explained in terms of the enhanced magnetic properties and the microstructural change after field annealing.
The CoFeHfO thin films with t = 220 nm were deposited by reactive rf-sputtering using an Ar+O_2 atmosphere with a base pressure of less than 2.0×10^{-7} Torr, onto Si(100) substrates at ambient temperature, and in a dc magnetic field of 100 Oe to induce an in-plane uniaxial anisotropy. The film composition was controllably modified by varying the aerial fraction of Hf chip on a $Co_{30}Fe_{70}$ target and the partial pressure of oxygen. The CoFeHfO films were annealed at various temperatures T_a for 1 hour under a magnetic field of 3 kOe. The microwave permeability spectra were measured using a one turn coil permeameter in the frequency range from 50 MHz to 9 GHz.
We investigated the annealing temperature dependences of the microwave permeability spectra in the frequency range from 50 MHz to 9 GHz. Figure 1 shows the real and imaginary permeability spectra of t = 220 nm sample at different annealing temperatures. The imaginary permeability (losses) shows a merged two peaks behavior in as-prepared and 100 ^{o}C annealed samples as shown in Fig.1 (a) and (b), which are located at nearly 1.5 GHz and 3 GHz frequencies, respectively. This result indicates that there are two different magnetic phases in as-prepared sample consisting of the minor and major parts of low and high induced anisotropy. Although the low anisotropy part is minor, imaginary permeability at near the corresponding ferromagnetic resonance frequency can be dominated. The minor part of the low anisotropy can degrade the overall loss behavior in the low frequency range.
However, the imaginary permeability of 150 ^{o}C annealed sample, as shown in Fig.1 (c), shows a sharp single peak behavior. The high real permeability of 185 and the negligible low losses are remained up to 2.0 GHz, and then shows a typical ferromagnetic resonance behavior with f_r = 3.35 GHz. The Gilbert damping constants are obtained by directly fitting the measured permeability spectra using the solution of the LLG equation. The low damping constant ($\alpha < 0.017$) is obtained with film thickness of 220 nm. This result confirms that there is a single magnetic phase and all the magnetization spins are highly aligned to the easy axis direction. The minor part of the low anisotropy is believed to be transformed into the major part of the high anisotropy by structural relaxation during the annealing at T_a =150 ^{o}C. Since the excellent performance of microwave permeability (high real permeability and low loss) is accompanied with improved magnetic properties for this sample. This material is very beneficial for magnetic devices operating in the microwave range. Further observation of microwave permeability spectra for samples with T_a > 200 ^{o}C results in degraded performance, as shown in Fig.1 (d)-(f), which may be caused by the formation of Co(Fe) precipitations with low induced anisotropy field and random magnetization orientation of nanograins. These results clearly demonstrate that the high resistive optimized CoFeHfO composition annealed at 150 ^{o}C exhibits superior magnetic performance apart from low Gilbert damping constant.

[1] N. D. Ha, M. H. Phan and C. O. Kim, Nanotechnology 18, (2007) 155707.

[2] N. D. Ha, C. G. Kim, C. O. Kim. M. H. Phan, Solid State. Comm. 33, (2007) 502.

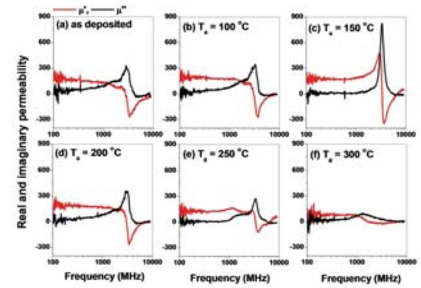

Fig.1. The real and imaginary permeabilities of CoFeHfO sample annealed under T_a = (a) as-prepared, (b) 100, (c) 150, (d) 200, (e) 250 and (f) 300 ^{o}C, respectively

DS-04

MAGNETOIMPEDANCE EFFECT IN SANDWICHED AND MULTILAYERED AMORPHOUS FILMS: SIMULATION AND EXPERIMENTS.

M. A. Corrêa[1], F. Bohn[2], A. Viegas[3], A. de Andrade[5], R. Sommer[4]
1. Centro de Ciências Exatas e Tecnológicas, Universidade Federal do Pamapa, Caçapava do Sul, Brazil; 2. Departamento de Física, Universidade Federal de Santa Maria, Santa Maria, Brazil; 3. Departamento de Física, Universidade Federal de Santa Catarina, Santa Maria, Brazil; 4. Centro Brasileiro de Pesquisas Fisicas, Rio de Janeiro, Brazil; 5. Universidade Federal de Santa Maria, Frederico Westphalen, Brazil

In recent years, amorphous thin films of soft ferromagnetic alloys have attracted considerable attention due to their soft magnetic properties and potential for technological applications. One of the most interesting phenomena observed in these materials is the magnetoimpedance (MI) effect which corresponds to the dependence of the impedance of a given magnetic material with an external magnetic field through the skin depth δ_m . In recent years, nanostructured amorphous magnetic were found to exhibit interesting magnetoimpedance properties. In particular we reported very high magnetoimpedance in a F/M/F multilayer, where F is a magnetic multilayered film and M is a non-magnetic metallic film [1]. The theory of MI for these structured samples has been developed by L. V. Panina et. al. [2], which takes into account the dimensionality and magnetic parameter of the system. The Panina's results are mainly based on the problem of the boundary conditions for a try-layer (F/M/F) and the main point of the theory is that the magnetic permeability description is a function of the magnetic field and frequency of the current. However, on the other side, L. Spinu, et. al. [3] has recently reported their results on the transverse magnetic susceptibility calculations by solving of the Landau-Lifshitz equation for a wide range of frequencies. In the present work we report our recent experimental results on the magnetization and magnetoimpedance in structured films produced by magnetron sputtering, together with the simulation data using a mix of the Panina and Spinu recipes. The samples studied were (i) FM/SiO_2/Cu/SiO_2/FM sandwiched layers (SW), where the FM layer is, in fact, a multilayered film [F(10nm) + Cu(1nm)] $\times$ 50 and F is the amorphous ferromagnetic alloy $Fe_{73.5}Cu_1Nb_3Si_{13.5}B_9$ [1] and (ii) a multilayer film (ML) in the form [F(10nm) + Cu(1nm)] $\times$ 50. The effect of both, the probe current frequency (in the range 10MHz - 1.8GHz) and the dimensions of the magnetic and non-magnetic layers were investigated.
The results are discussed within the frameworks of the models proposed in ref. 2 and ref. 3. Figure (a) below show the field dependence of Z of SW film at 530 MHz, where the points correspond to the experimental data, while the solid lines are the simulation results. Figure (b) below show the field dependence of Z of ML sample at 1.4 GHz, in the same way the points correspond to the experimental data while the solid lines are the simulation results. MI ratios of 220 % were obtained for this sandwich at 180MHz with a ferromagnetic and Cu layers of 2mm and 1mm, respectively, and sample length of 12mm.

[1] M. A. Correa, et. Al., J. Appl. Phys, **101**, 043905 (2007).

[2] L. V. Panina, et. Al., Sens. Actuators A, **81** 71 (2000).

[3] L. Spinu, et. Al., J. Magn. Magn. Mater, **296** 1 (2006).

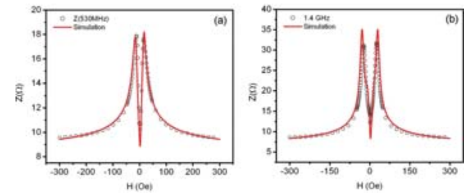

(a) Z × H simulation and experimental results of the SW sample at 530 MHz. (b) Z × H simulation and experimental results of the ML sample at 1400 MHz.

DS-05

Complex impedance and capacitance spectra characterizations of MgO-based MTJs with/without Mg doping.

J. Huang[1,2], *C. Hsu*[1,2], W. Chen[1], S. Chen[3], C. Liu[3]
1. Physics, National Cheng-Kung University, Tainan, Taiwan; 2. Institute of Innovations and Advanced Studies, National Cheng-Kung University, Tainan, Taiwan; 3. Materials Science and Engineering, National Cheng-Kung University, Tainan, Taiwan

Magnetic tunnel junctions (MTJs) of a highly textured MgO insulating layer recently attracts great attention due to the giant tunnel magnetoresistance (TMR) and accelerates the realization of magnetoresistive random access memory and related spintronic devices. In 2005, Anelva Corporation included a 0.4nm Mg layer at the bottom interface to reduce the resistance-area and enhance the TMR ratio of MgO-based MTJs for read head application in hard disk [1]. Then, several groups have attempted to probe the change of MgO layer texture or interfacial condition due to Mg doping and generally attribute the enhancement of TMR to improved texture of MgO layer or less oxidized surface of the bottom electrode [1-3]. Here, we fabricate MTJs with/without 0.4 nm Mg doping and the corresponding TMR ratios are respectively 4% and 0.76%. We utilize the complex-impedance (CI) and –capacitance (CC) spectra to characterize the texture of MgO layer and interfacial conditions of a MTJ [4]. The CC spectra of MTJs without and with 0.4nm Mg doping are shown in Figure 1(a) and (b). The Cole-Cole type CC spectra, [imaginary part of C* (C") in y-axis vs. real part of C* (C') in x-axis], of MTJs w/wo a 0.4nm Mg discontinuous layer consist of several arcs and a rising tail. We observe the capacitance contributions of arcs decline, but the arcs in high- and low- frequency region respectively are suppressed and grown up for MTJs due to 0.4 nm Mg doping. With the microstructure analysis by high-resolution transmission electronic microscopy (HR-TEM) images [the inset of Figure 1(a)], an equivalent circuit model (ECM) is utilized to analyze the CC spectra of MTJs w/wo 0.4 nm Mg doping. The ECM includes the Debye-type dielectric relaxation contributions (arcs in a Cole-Cole diagram) to describe the relaxation behavior of the textured and amorphous MgO layer as well as a resistance to represent the Schottky barriers at CoFe-MgO interfaces with imperfectly blocking property [5]. The analyzing results indicate the relaxation frequency of textured MgO contribution increases due to 0.4 nm Mg doping, which suggests the improved texture of MgO layer. Meanwhile, the analysis of corresponding CI spectra shows an increase and a decrease of the interfacial resistance and capacitance for 0.4nm Mg doping MTJs. Furthermore, the dc bias dependent CI spectra have also been performed. The CI spectra of MTJs with 0.4nm Mg doping show little sensitivity to dc bias, but the spectra of MTJs without 0.4nm Mg doping are very sensitive to dc bias. The result indicates the interfacial defects are also suppressed due to 0.4nm Mg doping. The results of CI and CC spectra are also consistent with the x-ray reflectivity and HR-TEM results. We conclude the CI and CC technique could be convenient and useful to understand the mechanism for enhancement of TMR due to the Mg doping.

[1] K. Tsunekawa, D. D. Djayaprawira, M. Nagai, H. Maehara, S. Yamagata, N. Watanabe, S. Yuasa, Y. Suzuki, and K. Ando, Appl. Phys. Lett., 87, 072503 (2005).

[2] J. C. Read, P. G. Mather, and R. A. Buhrman, Appl. Phys. Lett., 90, 132503 (2007).

[3] Y. Lu, C. Deranlot, A. Vaurès, F. Petroff, and J.-M. Georgea, Y. Zheng and D. Demailles, Appl. Phys. Lett., 91, 222504 (2007).

[4] J. C. A. Huang, C. Y. Hsu, W. H. Chen, and Y. H. Lee, IEEE Trans. Magn., 43, 911 (2007).

[5] J. C. A. Huang and C. Y. Hsu, Appl. Phys. Lett., 85, 24 (2004)

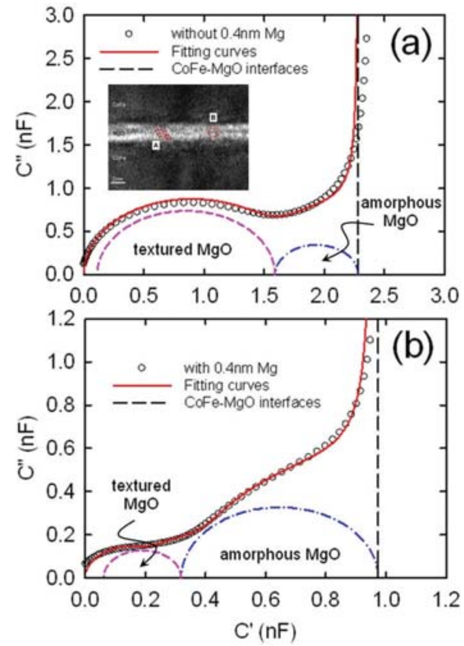

The complex-capacitance of MTJs (a) without and (b) with 0.4nm Mg doping. symbols are experimental data and curves are fitting curves by the equivalent circuit model.

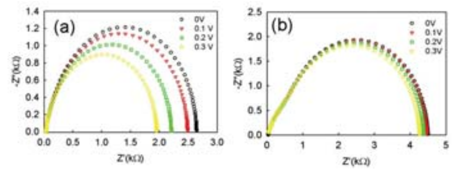

The dc bias dependent complex impedance spectra of MTJs (a) without and (b) with 0.4nm Mg doping.

DS-06

A modulated microwave absorption study of $FeNbO_4$

G. Alvarez[1], R. Font[2], J. Portelles[2], R. Zamorano[3], *R. Valenzuela*[1]
1. Instituto de Investigaciones en Materiales, Universidad Nacional Autonoma de Mexico, Mexico City, Mexico; 2. Fisica Aplicada, Universidad de la Habana, Havana, Cuba; 3. Ciencia de los Materiales, Instituto Politecnico Nacional, Mexico City, Mexico

We present an electron paramagnetic resonance (EPR) study in powder samples of the monoclinic phase of $FeNbO_4$, in the X-band (8.8-9.8 GHz). For all the temperatures, the EPR spectrum showed a single Lorentzian line attributable to Fe^{3+} ions. A contribution of Fe^{2+} ions in the EPR spectra was detected at low temperatures, originating a broadened signal as compared with the spectrum at room temperature, as shown in Fig. 1.
This behavior can be ascribed to a strong magnetic dipolar interaction between Fe^{2+} and Fe^{3+} ions, as proposed in a study [1] based on the effects of (Fe^{2+}/Fe^{3+}) mixed valence on the electrical conductivity of $FeNbO_4$, and confirmed by magnetic susceptibility measurements as a function of temperature.
In addition, we present in this work two techniques based [2-7] on modulated microwave absorption, to obtain further knowledge on this material: magnetically-modulated microwave absorption spectroscopy (MAMMAS) and low-field microwave absorption (LFA). In the MAMMAS measurement, the sample is subjected to a constant dc field, and its microwave absorption behavior is obtained as a function of temperature [2,5-7]. LFA refers to the microwave absorption around the zero DC field range (-1000 Oe $< H_{DC} < +1000$ Oe), in an otherwise typical electron paramagnetic resonance setup [2-4,7]. MAMMAS response suggests that the dominant magnetic exchange is antiferromagnetic at low temperatures ($T<140$ K), and has a paramagnetic behavior for high temperatures. The LFA spectra showed straight lines with positive slope and non-hysteretic traces. The profiles obtained by plotting the slope vs. temperature of the LFA line are similar to those detected by the MAMMAS technique, giving evidence that both types of measurement show the same processes of absorption. We conclude that both experiments are therefore a manifestation of the sample response to electromagnetic excitation, in which the same fundamental physical processes take place. The MAMMAS response has an experimental correlation d^2P/dH^2, with the derivative of the modulated microwave power absorption. A discussion on the usefulness of these techniques in the investigation of a wide range of magnetic materials is also presented.

[1] I. Gnanasekar, V. Jayaraman, E. Prabhu, T. Gnanasekaran and G. Periaswami, Sens. Actuators B 55 (1999) 170.

[2] Alvarez and R. Zamorano, J. Alloys Compd. 369 (2004) 231.

[3] Montiel, G. Alvarez, M. P. Gutiérrez, R. Zamorano and R. Valenzuela, J. Alloys Compd. 369 (2004) 141.

[4] Montiel, G. Alvarez, I. Betancourt, R. Zamorano and R. Valenzuela, Appl. Phys. Lett. 86 (2005) 072503.

[5] Alvarez, R. Zamorano, J. Heiras, M. Castellanos and R. Valenzuela, J. Magn. Magn. Mater. 316 (2007) e695.

[6] Alvarez, R. Font, J. Portelles, R. Zamorano and R. Valenzuela, J. Phys. Chem. Solids 68 (2007) 1436.

[7] P. Gutiérrez, G. Alvarez, H. Montiel, R. Zamorano and R. Valenzuela, J. Magn. Magn. Mater. 316, e738 (2007).

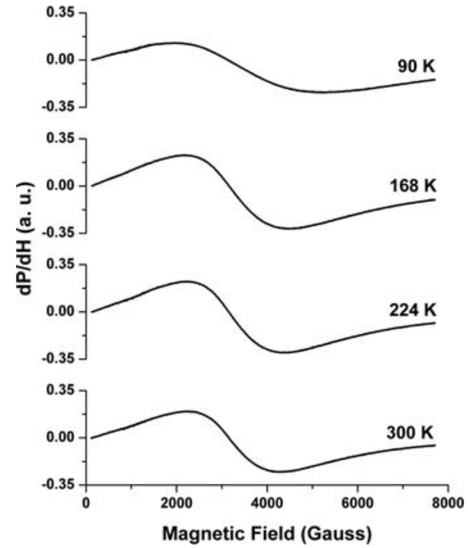

Fig. 1. EPR spectra of $FeNbO_4$ for selected temperatures

DS-07

$IrMn/CoFe-SiO_2/IrMn$ exchange coupled nanostrucutre for high frequency applications.

N. N. Shams, M. Rahman, Y. Wu, C. Lai
Materials Science and Engineering, National Tsing-Hua University, Hsinchu, Taiwan

Introduction

An approach to increase the performance of integrated inductor used in high speed electronics in the GHz regime is to apply a magnetic film on top of and/or below the RF coil to enhance and confine the magnetic flux. A combination of anti-ferromagnetic (AFM) and ferromagnetic (FM) with high anisotropy, K_u, exchange biased (EB) film is promising candidate as high magnetization ($4\pi M_S$) and large anisotropy field, H_k can be achieved due to exchange coupling[1]. But FM metallic films posses low electrical resistivity which increase the eddy current loss. To overcome this, granular film consisting of FM nanograins embedded in a nonmagnetic insulating matrix, is one of good options. However, the granular films deposited in the presence of oxygen environment causes lower magnetization due to the oxidation of the FM grains[2]. In this research, we introduced a novel AFM/FM-granular nanostructure to improve the magnetic properties of the granular film along with high electrical resistivity. Our EB system is CoFe nanograins embedded into the SiO_2 matrix, which is sandwiched by two IrMn layer. This kind of EB granular nanostructure may be interesting not only for exploring its application in high frequency but also for studying EB nanostructure.

Experimental procedure

The $IrMn/FeCo-SiO_2$ nanostructure is deposited by sputtering without any substrate heating. The film structure is $Ta(3nm)/NiFe(8nm)/Ir_{20}Mn_{80}(12nm)/Co_{90}Fe_{10}-SiO_2(50nm)/Ir_{20}Mn_{80}(12nm)/Ta(3nm)$. The $Co_{90}Fe_{10}-SiO_2$2 granular layer is deposited by co-sputtering of $Co_{90}Fe_{10}$ and SiO_2. A Ta/NiFe seed layer is used to promote IrMn(111) texture and Ta overcoat resists surface oxidation. Finally the samples are annealed at 210°C for 30 min in a magnetic field of 1.5kOe to promote EB. The magnetic properties are measured by VSM. The microstructure is characterized by TEM, and the resistivity at room temperature is obtained from a standard 4-point measurement. The resonance frequency is characterized by a network analyzer up to 3 GHz[3].

Result and discussion

The plane-view TEM image(Fig.1) reveals that the CoFe nanograins are separated by amorphous SiO_2. The average grain size is about 5-6 nm. M-H loop of $IrMn/CoFe-SiO_2/IrMn$, granular film without any AFM layer, $CoFe-SiO_2$ and the continuous, IrMn/CoFe/IrMn film has been shown in the Fig. 2(a), 2(b)and 2(c)respectively. It is found that both anisotropy field, H_k and exchange field, H_{ex} is increased in granular EB system. The value of H_k = 80 Oe and H_{ex} = 50 Oe for $IrMn/CoFe-SiO_2/IrMn$ nanogranular film which is even higher than the corresponding value of continuous IrMn/CoFe/IrMn film (H_k = 50 Oe and H_{ex} = 37Oe). The value of H_k of $CoFe-SiO_2$ is only 13Oe. The FM domain size is determined by the competition between the random field due to the interfacial AFM-FM interaction and FM-FM exchange interaction [4, 5]. The presence of nonmagnetic SiO_2 may reduce the exchange interaction between the FM-FM interaction, thus favoring the formation of smaller FM domain, larger net random field, and larger H_{ex}. Table.1 shows the high frequency data for the aforementioned three kind of films. The highest resonance frequency, f_{res} of 2.5 GHz is achieved for the $IrMn/CoFe-SiO_2/IrMn$ film which is even higher compared to the CoFe nanoparticles embedded in SiN matrix [2]. This high f_{res} originates from high H_k of EB granular system. The high quality factor (Q=μ'/μ") of $IrMn/CoFe-SiO_2/IrMn$ film may be due to the less eddy current loss as the EB granular film posseses a high resistivity of 132 μΩ-cm while it is 7.5 μΩ-cm for EB continuous film.

Conclusion

We have prepared the EB granular nanostructure simply by sputtering which is convenient to achieve nanostructures over large area compared to the self-assembled synthetic materials or lithography. The EB $CoFe-SiO_2$ system is found as a superior candidate to the ordinary granular films or continuous FM films. In addition, further modification of any characteristics can be possible by tuning the ratio of CoFe and SiO_2 in the EB $CoFe-SiO_2$ granular nanostructure.

[1] R.F.Jiang etal., IEEE.Trans.Mag.,43,3930(2007).

[2] Y.Liu etal.,Appl.Phys.Lett.,90,112506(2007),

[3] M.Yamaguchi etal.,IEEE.Trans.Magn.,36,5,4941,(1996).

[4] K.Liu etal.,Phys.Rev.B 63,060403(2001).

[5] Z.Li and S.F.Zhang, Phys.Rev.B61,14897(2000).

Film structure	$4\pi M_s$ (kG)	H_k (Oe)	H_c (Oe)	H_{ex} (Oe)	Q=μ'/μ"	f_{res} (GHz)	permeability, μ'
$CoFe-SiO_2$	15	13	25	0	28	1.6	700
$IrMn/CoFe-SiO_2/IrMn$	15	80	15	50	75	2.5	100
IrMn/CoFe/IrMn	17	50	20	36	6	1.7	1030

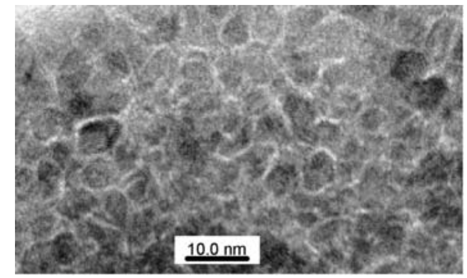

Fig.1. Plan view TEM image of $Ta/NiFe/IrMn/CoFe-SiO_2/Ta$ film.

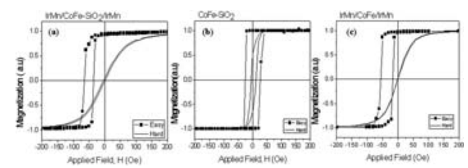

Fig. 2. M-H loop for (a) IrMn/CoFe-SiO_2/IrMn (b) CoFe-SiO_2(c) continuous IrMn/CoFe/IrMn film.

DS-08

Permeability of ferromagnetic microwires composites/metamaterials and potential applications.

L. Liu, L. Kong, G. Lin, S. Matitsine
Temasek Lab, National University of Singapore, Singapore, Singapore

1. Introduction

Glass-coated ferromagnetic microwires filled composites or metamaterials attract great interest recently due to high effective magnetic permeability and high loss in radio wave and microwave frequency, and negative permeability due to the ferromagnetic resonance [1, 2]. Since the conductive microwires are coated with a layer of glass which prevents induced current flow across microwires in contact, the materials with microwire inclusions are expected to have low effective permittivity as compared to composites with bare conductive wires. Such feature makes glass-coated ferromagnetic microwires suitable inclusions for many applications, such as EM shielding materials, high attenuation materials and double negative meta-materials (DNM), etc. The microwires fabricated with Taylor-Ulitovsky method comprised an inner metallic core covered by Pyrex-like coating [3].

The aim of this study is to investigate magnetic properties of microwires for high attenuation applications, and also to explore the possibility to use microwires to make Meta-materials of negative refraction index. Anisotropic static magnetic properties are first measured with vibrating sample magnetometer (VSM). Next, the high frequency permeability of composites with regularly distributed microwires is obtained by the impedance method and coaxial line method from 1MHz to 10GHz. Finally, the properties of proposed composite/metamaterials, such as reflectivity and effective permittivity and permeability are evaluated with the theoretical and numerical calculations.

2. Magnetic properties of microwires

CoFeNiSiB amorphous ferromagnetic microwire with various inner and outer diameters was provided by Microfir Tehnologii Industriale. The static magnetic properties along and perpendicular to the axis of microwire were measured with SMI/MEDIA 880 vibrating sample magnetometer (VSM). Both Agilent N5230A vector network analyzer (VNA) with APC-7 coaxial transmission line and Agilent E4991A impedance analyzer were employed to measure the permeability and permittivity. The coaxial line sample has an inner diameter of 3mm, outer diameter of 7mm, and a thickness of about 2mm. The same samples were use in the impedance measurement with impedance analyzer with 16454A magnetic materials test fixture. The measured permeability of composites with 14.2% by volume of microwire (D=13.3μm/d=9.4μm) is plotted in Figure 1.

3. Reflectivity and effective refraction index of microwire composites/metamaterials

Reflectivity of a layer of metal-backed composite is calculated using transmission line theory in VHF (Figure 2). Anisotropic composite of microwires oriented along the magnetic field achieves broadband attenuation (>10dB). The thickness of this composite is about 0.4% of the wavelength. However, only incident wave with H-field along the wire axis can be absorbed. The cross polarized component is totally reflected due to high conductivity of microwires.

Composites with regularly or randomly distributed long conductive fibers have negative effective permittivity when frequency is close to the resonance of the included fiber [4]. The negative effective permittivity of metamaterials with containing conductive fibers along E field is obtained from a unit cell by HFSS (a commercial finite element solver) calculation, and verified with free space measurement. Combing the long conductive fibers with microwires may result in metamaterials with both negative permeability and permittivity within certain frequency band. Negative refraction index may possibly be obtained from such kind of metamaterial. However, it is quite difficult to reduce the dielectric and magnetic loss of the metamaterial due to the intrinsic resonance phenomena of the inclusions.

[1] A. L. Adenot-Englvin, C. Dudek, O. Acher, JMM, Vol. 300, 33-37(2006)

[2] L. Liu, S. Matitsine, L. B. Kong, G. Q. Lin, C. R. Deng, Y. B. Gan and K. N. Rozanov, 83-86, Proc. of Symposium P: EM materials, ICMAT2007, World Scientific Publishing (2007).

[3] V. S. Larin, A. V. Torcunov, A. Zhukov, J. Gonzalez, M. Vazquez and L. Panina, JMMM, Vol. 249, 39(2002)

[4] L. Liu, S. Matitsine, Y. B. Gan and K. N. Rozanov, J of Appl. Phys., 98, 063512(2005).

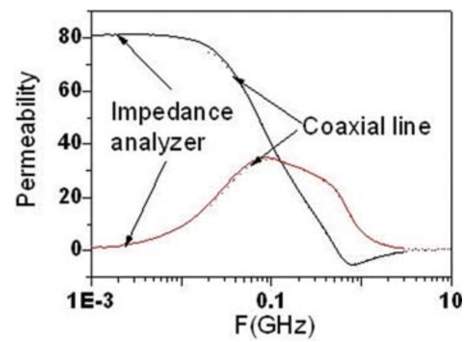

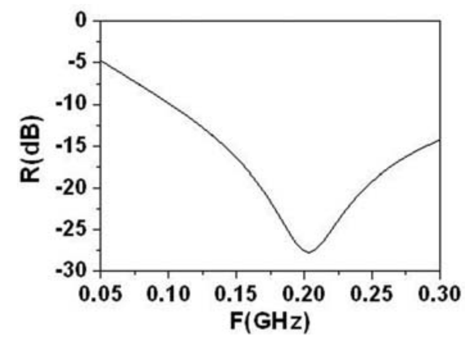

DS-09

Microwave permeability of amorphous FeCoSiB thin films on flexible substrates.

M. Han, Y. Ou, L. Deng, J. Xie, H. Lu
State Key Laboratory of Electronic Thin Films and Integrated Devices, University of Electronic Science and Technology of China, Chengdu, China

Soft magnetic thin films with high frequency permeability have found many applications, such as magnetic heads in magnetic recording industry, magnetic cores for planar inductors in power electronics [1], high frequency magnetic sensors [2], et al. However, most reported magnetic thin films were deposited on rigid substrates (silicon or glass), only few films have been deposited on flexible substrates[3]. Magnetic thin films on flexible substrates can find applications in electromagnetic devices, such as electromagnetic wave absorbers, RF noise filters. Compared to bulk magnetic materials, the permeability of magnetic thin films are much larger within GHz range if assuming they have same saturation magnetization and same anisotropy field [4]. The Landau-Lifshitz (L-L) equation is the one frequently used to describe the dynamic behavior of magnetization vector under the alternative changing magnetic filed. The solved L-L equation describing the intrinsic permeability dispersion of film with an in-plan anisotropy can be expressed as:

$\mu_i=\gamma M_s/(\gamma H_k+i\alpha\omega)\times\{1+\omega^2/[(\gamma H_k+\gamma M_s+i\alpha\omega)(\gamma H_k+i\alpha\omega)-\omega^2]+1\}$ —— (1)

, where γ is the gyromagnetic factor, α is the damping constant, ω is the angular frequency. When the effect of eddy current on permeability is considered and on the basis of the Maxwell Equations, the permeability dispersion should obey the following equation [5]:

$\mu_r=\mu'-i\mu''=\mu_i[(1-i)\delta/t]\times[e^{(1+i)t/\delta}-1]/[e^{(1+i)t/\delta}+1]$ ——- (2)

, where μ_i is the permeability from equation (1), t is the thickness of film, δ is the skin depth ($\delta = [2/(\omega\sigma\mu_0\mu_i)]^{1/2}$). If eddy current effect is ignored, then equation (1) applies. In this contribution, we will report the microwave permeability of amorphous $Fe_{66}Co_{17}Si_1B_{16}$ thin film deposited on the Mylar flexible substrates and show the difference when the eddy current is included or not.XRD technique has been employed to show the as-prepared films in amorphous state. The thickness of film was measured to be 610 nm by SEM. The morphology of film has been investigated by AFM. Magnetic hysteresis loop was taken on a vibrating sample magnetometer (VSM). The coercivity was found to be about 11 Oe, see Fig. 1(d). In order to measure the frequency dependence of permeability, the as-prepared film on flexible substrate had been cut into stripes and been wounded into a so-called laminated insulator ferromagnetic on the edge (LIFE) structure [6], see Fig. 1(a). The LIFE structure was then inserted into the coaxial line of an Agilent Vector Networks Analyzer (8720ET). If we assume that the eddy current effect on permeability is ignored for our samples, then the intrinsic permeability can be calculated from the measured effective permeability of thin film composites based on the following equation [6]:

$\mu_{fi} = 1+(\mu_{eff}-1)/V_f$ —-(3)

, where V_f is the volume fraction of film deposited, μ_{fi} is the intrinsic permeability of film, μ_{eff} is the effective permeability of thin film composites. The measurement frequency range is of 1 GHz - 10 GHz. After the intrinsic permeability (μ_{fi}) values have been extracted, then we use equation (1) and (2) to simulate the intrinsic permeability dispersion spectra to see whether the eddy current effect is playing a role. The measured spectra and the fitted spectra (the dotted lines) are shown in Fig. 1(b). The experimental data agree better with the ones with eddy current effect considered than the ones without considering eddy current effect, but their difference is not significant. More calculation results will be shown that when films thickness is larger than 2 μm, the eddy current effect on their permeability dispersion spectra will be significant, as the one shown in Fig. 1(c), and then Equation (3) can not be used for LIFE structures. According to the fitting results in Fig. 1(b), the ferromagnetic resonance (FMR) frequency is found to be about 3.2 GHz. The damping constant (α) is fitted to be 0.15.

Acknowledgement
This work is financially supported by National Natural Science Foundation of China (Grant No 60701016).

[1] Ki Hyeon Kim, Jongryoul Kim, Hee Jun Kim, Suk Hee Han, Hi Jung Kim, IEEE Trans. Magn. 38, No.5, (2002) 3162.

[2] Anh-Tuan Le, Wan-Shik Cho, Yong-Seok Kim, Jeong-Bong Lee, Chong-Oh Kim, Heebok Lee, Sensors and Actuators A 135 (2007) 547–551.

[3] Z. W. Li, Y. Liu, L. Yan, C. Y. Tan, C. K. Ong, J. Appl. Phys. 99, 043903(2006).

[4] D. J. Sellmyer, Y. Liu, D. Shindo, Hanbook of Advanced Magnetic Materials, Vol. IV, Tsinghua University Press, Beijing, 2005.

[5] E. van de Riet, F. Roozeboom, J. Appl. Phys. 81 (1), (1997), 350-354.

[6] O. Acher, J. L. Vermeulen, P. M. Jacquart, J. M. Fontaine, P. Baclet, J. Magn. Magn. Mater. 136 (1994) 269-278.

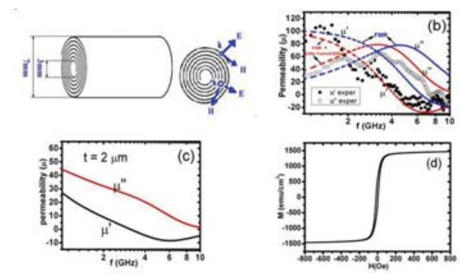

Fig. 1 (a)Laminated Insulator Ferromagnetic on the Edge (LIFE) structure; (b) the experimental spectra; the fitted spectra when considering the eddy current (EC) considered (the red dotted lines); the fitting spectra without considering the EC (the blue dotted lines); (c) the calculated value for thin films with thickness 2 μm; (d) the M-H loop of the as-prepared films.

DS-10

Magnetic damping in exchange-coupled IrMn/ CoFe multilayers for microwave applications.

R. Jiang[1], C. Lai[1], J. Lin[2]

1. Department of Materials Science and Engineering, National Tsing Hua University, Hsinchu, Taiwan; 2. Centre for Condensed Matter Sciences, National Taiwan University, Taipei, Taiwan

The antiferromagnetic/ ferromagnetic exchange-coupled multilayers (MLs), uniquely combining with ultimate saturation magnetization ($4\pi M_S$ up to 1.8-2.4 T), ultrahigh anisotropy field (H_K >200 Oe), enhanced ferromagnetic resonance frequency (f_{res}~5-10 GHz), and suitable real-part permeability (μ'~50-200), have been proposed to be promising candidates for the magnetic-integrated radio-frequency (RF) devices [1, 2]. Moreover, the importance of another phenomenological parameter, magnetic damping (α), which tends to broaden the FWHM of imaginary-part permeability (μ'') and results in the deterioration of quality factor ($Q=\mu'/\mu''$), in magnetic thin films for RF devices has been clarified [3]. In general, the magnetic damping can be split into two fundamentally different channels: (i) Gilbert-type damping, which leads to a dissipation of energy into the lattice, and (ii) two-magnon scattering, which leaves the energy in the spin subsystem by scattering into magnons with nonzero wave vector ($k\neq0$) [4]. From the viewpoints, understanding the magnetic relaxation processes in RF devices has become the essential challenges. In this work, the α-value and its effect on high-frequency characteristics of $\{IrMn/\ CoFe\}_N$/ IrMn MLs for RF devices were studied, by FMR technique and the Landau-Lifshitz-Gilbert (LLG) equation, for the first time.

The magnetic damping α, was extracted as a function of CoFe thickness (t_{CoFe}) in $Ir_{20}Mn_{80}$(8 nm)/ $Co_{50}Fe_{50}$(t nm) bilayers (BLs), Fig. 1(a). The observed $4\pi M_S$ of CoFe was 2.0 T. The H_K increased linearly with 1/ t_{CoFe}, implying a characteristic of the surface effect. The interfacial exchange strength was 0.35 erg/cm^2, obtained from the hysteresis loop shift ($J_{CoFe} = M_S \times t_{CoFe} \times H_{EX}$). The α-value was first decreased with decreasing t_{CoFe}, and reached the minimum value of 0.012 when t_{CoFe} was set to be 30 nm. Since the Gilbert-type damping was a material-dependence parameter and relatively small (one to two order of magnitude smaller than two-magnon scattering), the significant change of α-value was considered mainly resulting from two-magnon scattering, correlated to the lattice defects in the volume of CoFe. Therefore, it was reasonable to expect that the two-magnon scattering was decreased with decreasing t_{CoFe}, because the volume part of CoFe was the dominating contribution. However, the α-value increased again for further decreased t_{CoFe} (< 30 nm). This increase originated from the local fluctuations of exchange-coupling at the IrMn/ CoFe interface, which provided an extra mechanism for dissipation of the coherent precession mode, due to the increased ratio of interface/ volume at small t_{CoFe}. To tune the H_K and f_{res}, we prepared the $\{IrMn/\ CoFe(t\ nm)\}_N$/ IrMn MLs with different t_{CoFe} (t_{CoFe}=200, 100, 50, 25, 10 nm) and stacking number N (N=1, 2, 4, 8, 20), while keeping the total thickness of CoFe at 200 nm. The α-value in MLs showed the similar trend to the BLs: first decreased with decreasing t_{CoFe}, and then increased for further decreased t_{CoFe} (< 50nm), as shown in Fig. 1(b). Moreover, it was noticed that the minimum t_{CoFe} with the minimum α-value was shifted from 30 nm to 50 nm, and the minimum strength of α was varied from 0.012 to 0.049, which suggested that other energy dissipation mechanisms may exist, i.e., the local fluctuations of exchange-coupling at the extra CoFe/ IrMn interfaces, and interlayer-coupling between each CoFe, when compared to the IrMn/ CoFe BLs.

Table I summarized the main characteristics of $\{IrMn(8\ nm)/\ CoFe(t\ nm)\}_N$/ IrMn MLs for RF devices. The $4\pi M_S$, H_K, and H_{EX} were obtained by VSM. The α-value was determined by the out-of-plane angular dependences of the resonance field (H_R) and linewidth ($\triangle H_{PP}$) of a FMR spectra (9.53 GHz). The f_{res}, μ', and the frequency that satisfied the Q of 5 and 10 (f_{Q5} and f_{Q10}), were analyzed by the LLG equation. The relatively low f_{Q5} and f_{Q10} were observed, though the f_{res} and μ' were extremely high. These results suggest that the reduction of α-value in exchange-coupled MLs is the key factor in obtaining preferable properties for RF devices, in addition to high H_K, optimum combinations of different parameters are important to meet the GHz requirements.

[1] J. P. Michel et al., IEEE Trans. Magn. 42, 3368 (2006)

[2] R. F. Jiang et al., IEEE Trans. Magn. 43, 3930 (2007)

[3] T. Tanaka et al., IEEE Trans. Magn. 40, 2005 (2004)

[4] K. Zakeri et al., Phys. Rev. B. 76, 104416 (2007)

t_{CoFe} (nm)	stacking number (N)	$4\pi M_S$ (Tesla)	H_K (Oe)	H_{EX} (Oe)	f_{res} (GHz)	magnetic damping (α)	real-part permeability (μ')	f_{Q5} (MHz)	f_{Q10} (MHz)
200	1	2.0	40.0	5.5	2.5	0.079	500	280	140
100	2	2.0	66.6	20.2	3.2	0.062	300	580	300
50	4	2.0	105.1	42.1	4.1	0.049	190	1110	590
25	8	2.0	178.4	84.8	5.3	0.055	110	1640	880
10	20	2.0	387.4	239.9	7.8	0.060	50	3060	1700

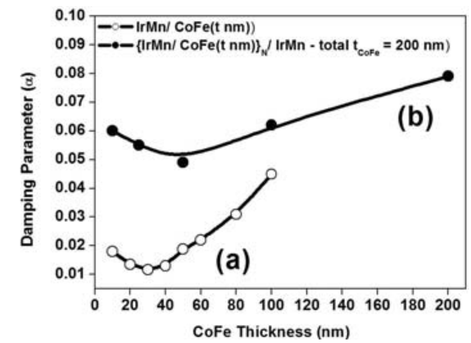

Fig. 1 Magnetic damping α of (a) IrMn/ CoFe(t nm) BLs and (b) $\{IrMn/\ CoFe(t\ nm)\}_N$/ IrMn MLs with various t_{CoFe} and N

DT-01

Synthesis of nano-crystalline barium hexaferrite using a reactive co-precipitated precursor.

M. Montazeri-Pour, A. Ataie
School of Metallurgy and Materials Engineering, University of Tehran, Tehran, Iran

Barium hexaferrite magnetic material has significant potential for applications such as permanent magnets and microwave absorbing coatings, because of the adequate combination of high Curie temperature, high coercivity and chemical stability. Fine $BaFe_{12}O_{19}$ (BaM) particles also exhibit suitable properties for perpendicular magnetic recording media. Among the non-conventional synthesis methods, co-precipitation is the most attractive due to simple operation and ease of mass production.

The use of a mixed solvent is a new approach in nano-materials synthesis and processing. Diethylene glycol ($O(CH_2CH_2OH)_2$) is a polar solvent which is miscible with water at any ratio, and the addition of diethylene glycol to water can easily change its physicochemical properties.

The objective of the present study is to investigate the influence of using 75% volume diethylene glycol as a co-solvent along with water on the characteristics of BaM processed by co-precipitation method.

$FeCl_3.6H_2O$ and $BaCl_2.2H_2O$ with Fe/Ba molar ratios of 11 and 12 were dissolved in water/diethylene glycol mixture with volume ratio of 1:3. Two prepared solutions were co-precipitated by the addition of NaOH with OH^-/Cl^- molar ratio of 2 at room temperature. The final PH value of solutions reached to about 11.3. The co-precipitated samples were washed by distilled water, dried and annealed at various temperatures for 1 h. The samples synthesized with Fe/Ba molar ratios of 11 and 12 are named for brevity “DEG11”, “DEG12”, respectively.

XRD, SEM, DTA/TGA, FTIR and TEM techniques were used to evaluate the products characteristics.

DTA/TGA traces for the DEG11 and DEG12 samples in Fig. 1 show the exothermic peaks attributed to the formation of barium hexaferrite at 695^{o}C and 614^{o}C, respectively. The temperature of 614^{o}C is one of the lowest temperatures has been reported for formation of barium hexaferrite via co-precipitation route. XRD patterns of the DEG11 sample after annealing at various temperatures showed that barium hexaferrite phase became the major phase at 700^{o}C, but some un-reacted intermediate phases like barium monoferrite and hematite still observed. Remaining of barium monoferrite phase up to 900^{o}C in this sample demonstrated surplus barium present in it. XRD results also showed that barium hexaferrite fully formed in DEG12 sample after annealing at 650^{o}C. It can be concluded that using diethylene glycol as a co-solvent along with water significantly lower the formation temperature of magnetic phase.

The presence of the characteristic absorption bands of diethylene glycol in the FTIR spectrum of DEG12 co-precipitated precursor indicated that diethylene glycol acted as capping agent and stabilizer, limiting particle growth and prohibiting agglomeration.

From SEM images, the mean particle size of the DEG12 sample annealed at 800^{o}C was measured as 70 nm. Barium hexaferrite crystallites with mean size of 35 nm, which is approximately consistent with size obtained from XRD line broadening technique, could be seen in TEM image of DEG12 sample annealed at 700^{o}C (Fig .2).

C. Feldmann, “Polyol-mediated synthesis of nanoscale functional materials”, Solid State Sciences, Vol.7, 2005, pp.868–873.

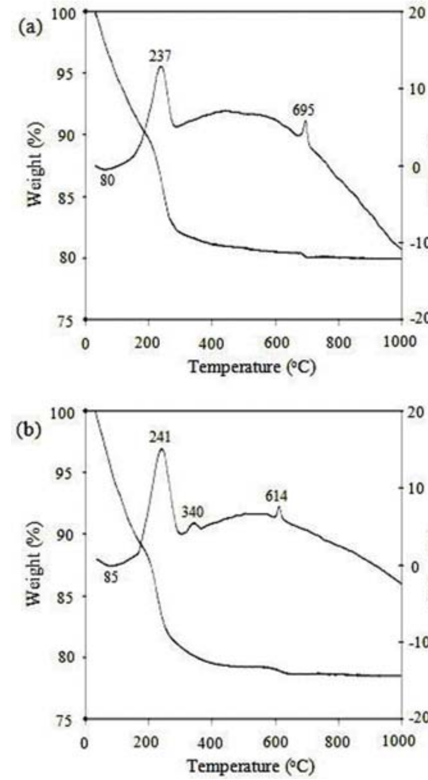

Fig. 1. DTA/TGA traces for the samples: (a) DEG11, (b) DEG12.

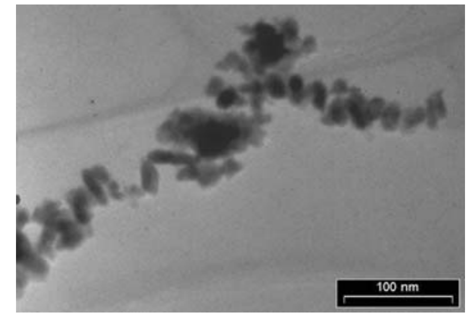

Fig. 2. TEM image of DEG12 sample annealed at 700^{o}C.

DT-02

Development of anisotropic NdFeB bonded magnet MAGFINE with high heat resistance for automobile use.

K. Noguchi, C. Mishima, H. Matsuoka, Y. Honkura
Aichi Steel Corporation, Tokai-shi, Aichi-ken, Japan

Anisotropic NdFeB bonded magnets called MAGFINE which has the possibility of the world's strongest bonded magnet with a maximum energy product of 199 kJ/m3 are interested in application for household appliance and automobile use[1]. Conventional small motor has been new designed to achieve down sizing of 50% and weight reduction of 40% by using MAGFINE magnet[2], and the new motor called MF motor has been launched in 2005. In the case of automobile use, the high stability under 150 – 180 deg.C is required for the magnet in the long term. To improve the durability properties, the authors have studied on the improvement of the coercivity force and rectangularity on the raw magnet material, and the additional magnet coating to avoid from oxidation.

The newly developed MAGFINE has higher coercivity force of 1,430 kA/m than that of 1,114 kA/m compared with conventional one with heat resistance of 100 deg.C. Moreover, the protection coating against oxidation by O2 and H2O under exposure atmosphere was newly developed. In the result of this additional coating, the newly developed MAGFINE showed the smaller flux losses than that of the conventional one on the exposure test under 150 deg.C after 1,000 hr. It is obvious that the newly developed MAGFINE has high heat resistance properties of 150 deg.C and has possibility for automobile use like as window motor, blower motor and so on.

[1]Y. Honkura, C. Mishima, N. Hamada, and H. Mitarai: Proc.17th Intl. Workshop on Rare-Earth Magnets and their Applications, (2002), pp. 52-61.

[2]Y. Hayashi, H. Mitarai, Y. Honkura.: abstract of the IEEE / Intermag 2003, in Boston, CS-17

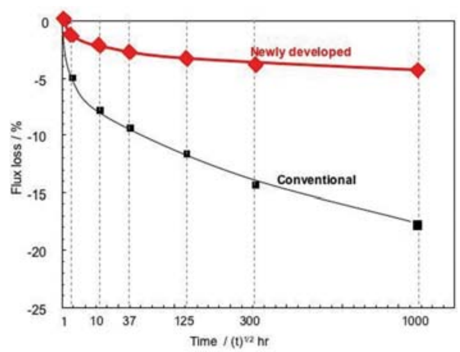

Fig. 1. Result of exposure test under 150 deg.C in air.

DT-03

Effects of conventional HDDR process and the additions of Co and Zr on anisotropy of HDDR PrFeB-type magnetic materials.

J. Han, C. Wang, H. Du, H. Chen, Y. Yang
School of Physics, Peking University, Beijing, China

The hydrogenation disproportionation desorption recombination (HDDR) process is well known as an effective way for producing anisotropic Nd2Fe14B-type magnetic powders. Pr2Fe14B-type alloys are comparable in terms of their intrinsic magnetic properties and phase relations with the advantages of a much lower spin reorientation temperature, so HDDR process is tried to prepare anisotropic Pr2Fe14B-type magnetic powders. It has been showed that both anisotropic ternary Pr-Fe-B and Pr-Fe-B powders with alloying additions can be prepared by appropriate solid-HDDR process. However, the origin of anisotropy is unclear till now. Gutfleisch et al. found that there exist intermediate phase Fe3B and Pr(Fe,Co)12B6 in the solid disproportionated products of Pr13.7Fe80.3B6 and Pr13.7Fe63.5Co16.7Zr0.1B6 alloys, respectively, and the amount of intermediate phase is related to the degree of anisotropy in the final products. However, they did not find the above two intermediate phases in the corresponding conventional disproportionated products. Cannesan et al. observed the intermediate phase Pr(Fe,Co)12B6 in the Pr13.7Fe63.5Co16.7Zr0.1B6 conventional disproportionated products processed at 860°C and above, and advanced the intermediate phase may play a role in inducing texturing on further treatment of the materials. The present authors also investigated the preparation of anisotropic ternary Pr13Fe80B7 powders using solid-HDDR process and mechanism on the formation of anisotropy. It is found that the degree of anisotropy in HDDR Pr13Fe80B7 materials is related to the disproportionation time, and the short disproportionation time is helpful for obtaining high anisotropy while long disproportion time will lead to isotropic powders. At the same time, according to investigation for the disproportionated products of Pr13Fe80B7 alloys, no other phases except PrH2, Fe and Fe2B are found, and the origin of anisotropy is found to be related to the early rod-like disproportionation microstructure.

To further understand the preparation of HDDR anisotropic Pr-Fe-B powders and how the anisotropy is formed. The effects of conventional HDDR process and the alloying additions on the anisotropic Pr-Fe-B magnetic powders are further investigated in the paper. The results show that the degree of anisotropy in conventional HDDR Pr13Fe80B7 materials decreases monotonically with the prolonging disproportionation time, and short conventional disproportionation time is helpful for preparing highly anisotropic Pr13Fe80B7 material. However, it is notable that the degree of anisotropy in conventional HDDR Pr13Fe80B7 materials is smaller than that in solid HDDR Pr13Fe80B7 materials under the same disproportionation time. At the same time, it is found that the addition of Co and Zr may make the HDDR PrFeB materials have higher anisotropy compared with the HDDR pure ternary PrFeB materials under the same HDDR process, but their degree of anisotropy will also decrease monotonically with the prolonging disproportionation time, and be close to zero when the disproportionation time is greater than 20 h. Based on this, the origin of anisotropy is discussed by XRD investigation for the disproportionated products of the above alloys. The results show that the origin of anisotropy in HDDR Pr-Fe-B materials with the addition of Co or Zr may differ form that in HDDR pure Pr13Fe80B7 materials, and the former maybe from the residual "Pr2(Fe,Co, Zr)14B" nucleus while the latter is not. Finally, it is also found that HDDR Pr-Fe-B materials with Co or Zr can obtain high magnetic properties even if the high desorption temperature is used, and this shows the addition of Co and Zr may make the HDDR process more relaxed.

1.T. Takashita, and R. Nakayama, Pro. 12th International Workshop on RE Magnets and their Applications, Kyota, Japan, P. 551 (1989)

2. W. Pan, L.Y. Cui, P. Wang and S. X. Zhou, Proc. 14th International Workshop on RE Magnets and Their Applications, Sao Paolo, Brasil, P.467 (1996)

3. O. Gutfleisch, A. Teresiak, B. Gebel, K. H. Muller, N. B. Cannesan, D. Brown and I. R. Harris, IEEE Trans Magn, 37(4), 2471(2001)

4.R. N. Faria, D. N. Brown and I. R. Harris, J. Alloys and comp, 296, 219(2000)

5. P. J. McGuiness, B. Podmiljsak, and S. Kobe, IEEE Trans Magn,39(5), 2956(2003)

6. F. D. Saccone, C. E. Rodriguez Torres, F. H. Sanchez and O. Gutfleisch, Physica B, 320, 312(2002)

7. N. Cannesan, D. N. Brown, A. J. Williams and I. R. Harris, J. Magn. Magn. Mater. 233, 209(2001)

8. N. Cannesan, J. M. Lereton, A. J. Williams and I. R. Harris, J. Magn. Magn. Mater. 242, 1372(2001)

9. L. P. Barbosa, H. Takiishi, and R. N. Faria. J. Magn. Magn. Mater. 268, 132(2004)

10. Jingzhi Han, Shunquan Liu, Honglin Du, Jinbo Yang, Yingchang Yang. J. Appl. Phys. 97(10), 10F305-1(2005)

DT-04

Magnetic properties and structure for bonded magnet using Dy-F coated NdFeB powder.

M. Komuro, S. Yuichi
Energy and Enviroment Laboratory, Advanced Research Laboratory, Hitachi, Japan

Introduction

Bonded and sintered NdFeB magnets are now commonly used for various magnetic circuits including motors, generators, medical instruments, hard disk drives and measuring devices because of their high magnetic performance. In the field of HEV motors, a high temperature resistance is necessary for the NdFeB magnet. One of the week points for the NdFeB bonded magnet is large temperature dependence of coercivity. In order to compensate the week point, large coercivity NdFeB bonded magnet has been produced for magnet motors by adding with Dy to NdFeB. Recently, the grain boundary diffusion process using Dy2O3 or DyF3 powders was reported for NdFeB magnets with 2mm thick1-3). According to the report3), the Dy distribution width around the grain boundary was almost comparable to the width of the Nd-rich grain boundary phase. In this paper Dy-F solution has been used for surface diffusion process instead of the Dy2O3 or DyF3 powders for NdFeB MQ powder. The magnetic properties and composition distribution was evaluated in this study.

Experimental

Rare-earth fluoride solution was synthesized from a rare-earth acetic acid and fluoric acid. An alcohol was used as the solvent for the Dy-F solution without corrosive elements. The MQ powders were mixed with the Dy-F solution. The Dy-F solution on the magnet powder was dried in a vacuum chamber, leading to the growth of the Dy-F layer with grain diameter of 20nm. The magnet powder coated with 2.6wt% Dy-F layer were heated at 973K for 2 hours for the diffusion. The Dy-F coated powder was compacted at 353K after mixed with resin. The size for bonded magnets was 10x10x7mm3. Demagnetization curves were measured by VSM (Vibration sample magnetometer) after magnetizing at the magnetic field of 3.2 MA/m. The temperature dependence of magnetic properties was measured by VSM under the air. SEM observation was performed for a cross-sectional specimen by S3500N with a wavelength-dispersive X-ray spectroscopy .

Results

The cross sectional view near powder surface was observed as shown in Fig. 1. The coated layer can be seen at the surface of powders shown in Fig. 1(a). The composition distribution was measured for F and Dy for the same position of Fig. 1(b) and (c), respectively. Both F and Dy were detected at the surface of powders, resulting Dy-F layer was grown on the surface of MQ powders. F and Dy were not seemed to exist homogeneously in the powders in Fig. 1.

The temperature dependence of residual magnetic flux density (Br) and coercivity (iHc) are shown in Fig. 2. The coercivity for Dy-F coated bonded magnet is larger than that for the non-coated bonded magnet between 293K and 473K. Coercivity difference between Dy-F and non-coated bonded magnets becomes larger with rising temperature. On the other hand, Br for Dy-F coated bonded magnet is slightly smaller than that for the non-coated bonded magnet below 373K. Above 423K, Br for Dy-F coated bonded magnet is larger than that for non-coated bonded magnet. The average temperature coefficients between 293K and 473K for iHc and Br were -0.22%/K and -0.08%/K for Dy-F coated bonded magnet. The corresponded values for non-coated bonded magnet were -0.30%/K and -0.16%/K, respectively. Compared these values, the temperature coefficient for iHc and Br were reduced by 26% in each 50% compared with these for the non-coated bonded magnet. The both values of iHc and Br for Dy-F coated bonded magnet showed higher than these for the non-coated bonded magnet above 423K. The higher magnetic properties for the Dy-F coated bonded magnet are thought to be caused by the oxidization prevention by the coated layer and increase of anisotropy by Dy.

1) H. Nakamura, K. Hitota, M. Shimao, T. Minowa, and M. Honshima, IEEE Trans . Magn., 41, 3844 (2005).

2) K. Hirota, H. Nakamura, T. Minowa, and M. Honshima, IEEE Trans. Magn., 42, (2006).

3) H. Nakamura, K. Hirota, T. Minowa, and M. Honshima, J. Magn. Soc. Jpn. 31, 6 (2007).

DT-05

Effect of grain size and hot-deformation temperature on texture in die-upset Nd-Fe-B magnet.

H. Kwon, J. Lee
Materials Science and Engineering, Pukyong National University, Busan, South Korea

1. INTRODUCTION Magnetic performance of a permanent magnet is determined by a combination of high coercivity and high remanence, together with a good squareness of the demagnetisation curve. For the high remanence and good squareness a good alignment of magnetic grain (good texture) is essential. One of the most common techniques being used to align the Nd2Fe14B grains in the Nd-Fe-B material is a die-upset or hot deformation technique. The die-upset technique is usually applied to the melt-spun Nd-Fe-B material. The melt-spun material is hot-pressed first in to a high density compact, and then the compact is subjected to the die-upset to cause a severe deformation. The die-upsetting leads to a good texture of the nanocrystalline Nd2Fe14B grains with their easy magentisation c-axis is parallel to the compression direction. The formation of texture is known to take place via the stress-induced preferential grain growth. Considering the texture formation mechanism, the grain size before the die-upsetting is believed to play an important role. In the present study, the hot-pressed compacts with various grain sizes ranging from several tens of nm to several hundreds nm were prepared, and then they were subjected to a die-upsetting. The effect of grain size in the hot-pressed compact on the texture in die-upset magnet was investigated. The effect of hot-deformation temperature on the texture in die-upset magnet was also investigated.

2. EXPERIMENTALS

Starting alloy of Nd13.5Fe80Ga0.5B6 was prepared by an arc-melting using high purity elements. The prepared alloy was melt-spun with surface velocity of 40 m/s. The obtained ribbon was briefly milled for 5 min using a mortar and pestle, and the powder was compacted by a hot pressing. The hot pressing was carried out under vacuum at various temperatures in a closed die for 2 min with pressure of 1 T/cm2. The hot-pressed compact was subsequently die-upset with strain rate of 5.8 x 10-3/sec in an open die at various temperatures to achieve height reduction of aroound 75 %. Texture in the die-upset magnets was evaluated by a magnetic means. A cube (2 x 2 x 2 mm3) was cut from the die-upset sample. Demagnetization curve was measured along the direction parallel and perpendicular to the pressing direction using a VSM at room temperature after pre-magnetizing with pulsing field of 50 kOe. The obtained demagnetization curve was corrected to compensate the demagnetizing field of the specimen using a proper correction factor. Texture in the die upset sample was evaluated using the ratio of M7(//)/M7(⊥), where, M7(//)and M7(⊥) are the magnetization at 7 kOe along the directions parallel and perpendicular to the pressing direction, respectively. Microstructure of the material at various conditions was examined using HRSEM and TEM.

3. RESULTS AND DISCUSSION

In order to prepare the hot-pressed compacts with different grain size, the powder material was hot-pressed at different temperatures. The compacts hot-pressed at 750 C, 770 C and 820 C had grain size of around 50 nm, 100 nm and 200 nm, respectively. These compacts with different grain size were die-upset at 750 C and the texture in the die-upset samples was examined. Fig. 1(a) shows the effect of grain size in the hot-pressed compact on the texture in the die-upset sample. It appears that the die-upset sample from the hot-pressed compact with fine grain size (50 nm) exhibited much higher texture with respect to the samples from the hot-pressed compacts with coarser grain size (100 nm and 200 nm). Meanwhile, the effect of die-upset temperature on the texture in the die-upset sample was investigated using the compact hot-pressed at 770 C, and the results were shown in Fig. 1(b). It appears that the sample die-upset at lower temperature of 700 C had lower texture, so did the sample die-upset at higher temperature of 900 C. The samples die-upset at modest temperature range from 750 C to 850 C showed much higher texture. The dependence of texture in the die-upset samples on the initial grain size and hot-deformation temperature is to be explained based upon the dissolution and precipitation mechanism.

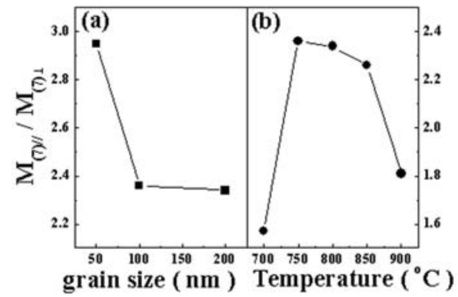

Fig. 1. Effects of (a) grain size and (b) die-upsetting temperature on the texture in the die-upset Nd13.5Fe80Ga0.5B6 sample.

DT-06

Boron enriched stoichiometric melt spun $RE_2(Fe,Co)_{14}B$-based alloys with enhanced coercivity.

I. Betancourt[1,2], T. Schrefl[1], H. Davies[1]
1. Department of Engineering Materials, University of Sheffield, Sheffield, United Kingdom; 2. Departamento de Materiales Metalicos y Ceramicos, Instituto de Investigaciones en Materiales, Universidad Nacional Autonoma de Mexico, Mexico, Mexico

Hard magnetic alloys are the precursor materials for fabrication of permanent magnets, which can be used for a very wide range of applications including: loudspeakers, levitation systems, actuators, motors and recently, biomedical devices (cardiac valves, magnetic catheters, dental care) [1,2]. In particular, nanograined hard magnetic rare earth (RE)-iron-boron-based alloys have attracted considerable scientific and technological interest over the past 20 years due to their outstanding combination of magnetic properties, which can be tailored by suitable control of phase constitution and its relative grain sizes. In this work we present B-enriched, stoichiometric, melt spun (NdPr)FeB alloys with intrinsic coercivity $_iH_c$ values above 1000 kA/m and energy densities between 120-140 kJ/m^3, studied by XRD, TGA, VSM and micromagnetic simulations.
The alloy series: $Nd_2Fe_{82}B_6$, $RE_{12}Fe_{82}B_6$, $RE_{12}Fe_{78}B_{10}$, $RE_{12}Fe_{76}Zr_2B_{10}$ and $RE_{12}(Fe_{0.9}Co_{0.1})_{76}Zr_2B_{10}$ (with RE=$Nd_{0.75}Pr_{0.25}$) was obtained by a devitrification annealing of initially fully amorphous alloy ribbons produced by chill block melt spinning technique with a roll speed of 30 m/s. X-ray diffractograms for all the alloy series indicated only 2/14/1 peaks. Magnetic Thermogravimetric Analysis (MTGA) was used to determine the Curie temperature (T_c) for the whole alloy series, showing the following results: $Nd_{12}Fe_{82}B_6$ (311°C, in accord with the reported value of 312 °C for the 2/14/1 phase [1]);$RE_{12}Fe_{82}B_6$(307 °C);$RE_{12}Fe_{78}B_{10}$ (307 °C); $RE_{12}Fe_{76}Zr_2B_{10}$ (282 °C)and $RE_{12}(Fe_{0.9}Co_{0.1})_{76}Zr_2B_{10}$ (350 °C).
Demagnetising J-H curves for all the compositions are shown in Fig.1, for which an increasing trend of $_iH_c$ is observed with the composition sequence showed in the Figure caption, starting at 713 ±7 kA/m for the reference $Nd_{12}Fe_{82}B_6$ alloy to a maximum of 1176 ±31 kA/m for the $RE_{12}(Fe_{0.9}Co_{0.1})_{76}Zr_2B_{10}$ ribbon sample. The remanen1ce J_r exhibited a monotonous diminishing tendency after Pr substitution, from 0.98 ±0.02 T down to a minimum of 0.83 ± 0.01 T for the Co-containing alloy. The energy densities values observed were > 120 kJ/m^3 for all the cases, with a maximum for the B-enriched alloys of 140 ±4 kJ/m^3 corresponding to the $RE_{12}Fe_{76}Zr_2B_{10}$ ribbon sample.
Micromagnetic simulated J(H) curves are shown in Fig.2 for the (a) $Nd_2Fe_{82}B_6$ (b)$RE_{12}Fe_{82}B_6$ and (c) $RE_{12}Fe_{78}B_{10}$ alloys. Although consistently higher $_iH_c$ values were obtained compared with the experimental curves (due to the Brown paradox), the coercivity enhancement after Pr substitution is clearly manifested, as a consequence of the higher anisotropy constant K_1 used (with K_1= $0.75K_1$(Nd) + $0.25K_1$(Pr)). On the other hand, a further increase in $_iH_c$ for the B-enriched alloy is observed by assuming the presence of small precipitates (presumably Fe_3B) in a volume fraction lower than the limit detection of the XRD analysis (i.e.< 4%). These small crystallites are afforded by the excess of B, which is segregating outside the 2/14/1 grains, as it is suggested by the constant T_c observed for the $RE_{12}Fe_{78}B_{10}$ alloy respect to the stoichiometric $RE_{12}Fe_{82}B_6$.
Therefore, considerable enhancement of $_iH_c$ in stoichiometric melt spun alloys is feasible by means of excess of B content (10 at%) preserving high J_r values and thus, energy densities > 120 kJ/m^3. High T_c values are also attainable by means of partial Fe substituion by Co.

[1] R. Skomski and J.M.D. Coey in "Permanent Magnetism", Taylor & Francis Group, New York 1999, pp 303-340. [2] E. du Tremolet de Lacheisserie and P.R. Ochette in Magnetism. Materials and Applications. Ed. E. du Tremolet de Lacheisserie, Springer, New York 2003, pp 433-439.

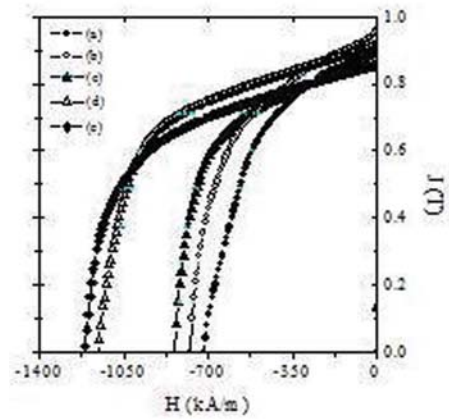

Fig.1. Demagnetising J(H) curves for (a) $Nd_2Fe_{82}B_6$ (b) $RE_{12}Fe_{82}B_6$ (c) $RE_{12}Fe_{78}B_{10}$ (d) $RE_{12}Fe_{76}Zr_2B_{10}$ and (e) $RE_{12}(Fe_{0.9}Co_{0.1})_{76}Zr_2B_{10}$ nanocrystalline alloys.

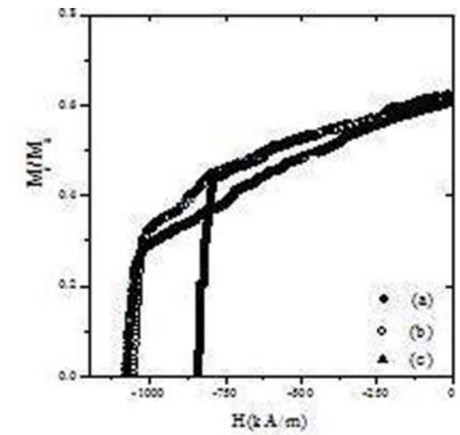

Fig.2. Micromagnetic J(H) curves for (a) $Nd_2Fe_{82}B_6$ (b) $RE_{12}Fe_{82}B_6$ and (c) $RE_{12}Fe_{78}B_{10}$ nanocrystalline alloys.

DT-07

The copper, titanium and carbon influence on properties of permanent magnets based on FeNdB alloy.

G. P. Brekharya[1], V. Vystavkina[2], K. Elena[1]
1. Solid State Physics, Dneprodzerzhinsk Technical StateUniversity, Dneprodzerzhinsk, Ukraine;
2. Materials Science, Zaporozhye State University, Zaporozhye, Ukraine

Abstract
A correlation between microstructure, phase composition, microhardness and magnetic properties of NdFeB magnets alloyed by carbon, titanium and copper has been investigated. Permanent magnets with nominal composition of Fe76Nd16B8 were produced and heat-treated according to standard technology. It was found that coercivity of magnets produced from alloy with Cu addition is considerably rise and reached value 15 kOe. It was shown that permanent magnets have considerable level of properties at minimum content of carbon fibre. The coercivity of 15,8 kOe and remanence of 10-11 kGs were reached after heat treatment. The bonded magnets were produced from rapid quenched ribbons with combined addition of powder carbon, copper and titanium. After heat treatment the obtained bonded magnets have higher microhardness and homogeneity with high coercivity of 18 kOe.

Experimental
High purity elements were induction melted under protective argon atmosphere to produce Nd16Fe76B8 master alloy. Master alloy were crushed in vibrating milling to obtain powder with particles size less then 10 μm. Before powder compacting the carbon fiber were introduced to alloy. For Cu- and Ti-containing magnets preparation powder copper and titanium were introduced together with carbon fiber during compacting stage. Sintered and bonded magnets of following types were produced: 1 – carbon fiber added, 2 – Cu-powder added, 3 – carbon fiber and Cu-powder added, 4 - carbon and copper powders added, 5 – powders of C, Cu and Ti added. Nominal compositions of produced magnets are listed in table.

2 Result and discussion
Magnets exhibit multiphase microstructure consisting of Nd2Fe14B grains, α-Fe, NdFe4B4 phase and Nd-rich grains. After minor addition of carbon fiber the gray-dark colored intergranular phase appeared in intergranular regions. It was found that with increasing carbon content the magnetic flux measured in search coil decreases and W=0 for xC=0,8 wt. %[1].

It was found that Cu-doping enhances magnetic properties substantially. The optimal for magnetic properties amount of Cu addition is 2 wt.%. The Cu-doped magnets exhibit multiphase microstructure. According to EDS data matrix phase represent Nd2Fe14B grains and occupy 90% of total amount. The NdFe4B4 phase, Nd-rich and Nd44,68Fe13,84Cu38,31 (at.%) phase were observed [1].

Negative effect of carbon fiber addition to Cu-doped magnets can be explained by presence of main magnetic phase grains of two different axis c orientations. During sintering carbon diffuse to matrix phase from the fiber. That part of grain that was in close contact with fiber is enriched with carbon, boron diffusion to intergranular region is occurred simultaneously. Carbon may dissolves in matrix phase by introducing ore displacement type. The matrix Nd2Fe14B is strongly oriented to applied field direction, but new Nd2Fe14(B,C) phase is randomly oriented during grain grows stage [2].

From the above data analyses it can be concluded that after diffusion to phase component carbon lead to critical point lowering on the phase diagram e.g. to eutectic with low melting point formation. The triple low-melting eutectic presence lead to Nd2Fe14(B,C) phase crystallization from liquid during cooling. Addition of Cu without carbon fibre lead to sharp increase of coercivity due to better isolation of main magnetic phase grains. Combine addition of Cu and C lead to arbitrary oriented Nd2Fe14(B,C) grains formation and residual textured Nd2Fe14B grains presented in the structure. As result of different oriented grains existence the demagnetization curves has platform part.

The next step for magnetic properties enhancement copper, carbon with Ti was introduced to master alloy in the powder form before sintering. Powders of C, Ti and Cu are located on Nd2Fe14(B,C) phase grain boundaries during compacting and favors to TiC carbides formation (fig.1). Paramagnetic carbides and Cu-containing phase formation at intergranular regions lead to better isolation of Nd2Fe14(B,C) grains and prevent Nd2Fe14(B,C) phase formation. It may be concluded that the main high coercivity state mechanism for investigated magnets is pinning of inverse domains nucleation. So, the negative effect of carbon must be suppressed by combine alloying with Ti. The minor carbon addition to Nd-Fe-B magnets may be one of the ways for coercivity enhancement due to metallo-ceramic system formation with unique physic-mechanical properties.

[1] O. Kharitonova, V. Vystavkina, G.Brekharya. Carbon fiber reinforced magnets of Nd-Fe-B system // Visnyc Lviv University. - 2006. – vol.39 – P. 127-134

[2] Brekharya G., Vystavkina, O. Kharitonova, Shpak A. The investigation of copper and carbon influence on properties of permanent magnets based on Fe76Nd16B8 alloy // Metalophysics and advanced technology. – 2006. - vol.28, #3. - P. 383-395

Alloys	Composition, wt. %						Hμ, kg/mm2	W, mWb	
	Nd	Fe	B	C	Cu	Ti		before HT	after HT
master	34,76	63,93	1,37	- 0,1÷0,7 - -	-	-	561,8	17	24
type 1	34.6	63.7	balance	0,1-0,7	-	-	553,8	14	18
type 2	34,08	balance	1,27	-	1÷4	-	605,0	58,5	58,5
type 3	34,07	balance	1,27	0,02÷0,2	2	-	587,0	56	56
type 4	33	balance	1,1	0,02÷0,2	2	-	547,7	2,65	2,67
type 5	33	balance	1,1	0,02÷0,2	1,5	1	-	-	-

DT-08

Effect of heat treatment on the magnetic property and microstructure of sintered Nd-Fe-B magnets.

W. Li[1], T. Ohkubo[1,2], K. Hono[1,2]
1. National Institute for Materials Science, Tsukuba, Japan; 2. CREST, JST, Japan

Introduction

Post sintering heat treatment has been known to be effective in enhancing the coercivity of sintered Nd-Fe-B magnets [1]. Since the coercivity is strongly influenced by the microstructure, it can be expected that important microstructure changes occur during the aging treatment. Although a lot of efforts have been made to study the microstructure change by aging, there is little information on the structure and chemistry of the grain boundaries which play a dominant role in the hard magnetic properties. In this work, we have focused the change of the grain boundary structure before and after the aging treatment of sintered Nd-Fe-B magnets. To study the microstructure of the grain boundaries, SEM,TEM and 3-dimensional atom probe (3DAP) have been employed.

Experimental details

Commercial sintered magnets with a (BH)max of 48 MGOe were provided from a manufacturer. The composition of the magnets were Nd11.7Pr2.8Fe76.8B6.0Al0.5Cu0.1O2.1, which were produced following the standard process of sintered magnets, i.e., strip casting - jet milling - magnetic alignment and pressing - sintering. After sintering, one was annealed, while the other was not. The microstructures have been investigated by SEM, LEO 1550 and CrossBeam 1540 EsB,TECNAI G2 F30 TEM equipped with energy filter and EDS, and laser assisted 3DAP.

Results and discussion

The coercivity of the magnet is increased from 9 kOe to 11 kOe by optimal post sinter aging. Figure 1 shows TEM energy filtered images of the as-sintered and aged samples. The zero loss images of the two samples clearly show the presence of a grain boundary in the center of the view. In both as-sintered and optimally annealed samples, Nd enrichment can be detected along the grain boundaries in the Nd jump ratio maps. The HRTEM image of the grain boundary in the as-sintered sample (Fig. 2(a)) does not show clear feature corresponding to the Nd-enriched phase along the grain boundary, and the Nd rich region does not appear to be continuous. Fragmented grain boundary phase of about 3 nm is seen. On the other hand, a thin continuous amorphous layer can be clearly seen in the grain boundary of the aged sample (Fig. 2(b)). The thickness of the amorphous grain boundary phase is approximately 5 nm, which is thought to be thick enough to cut the exchange coupling between the grains. Figure 3 shows the 3DAP composition profiles across a grain boundary of the aged sample. The composition variation near the grain boundary can be clearly detected. In the grain boundary, there is a Cu and Nd enriched layer of about 5 nm. The compositions are about 25% and 30%, respectively.

Also in this work, the compositions and structures of the Nd rich phases usually showing different contrast in SEM observation have also been determined by detailed TEM and EDX analysis. Eutectic lamellae of Cu enriched and depleted phases have also been found in the Nd-rich grains. It indicates the wetting of the Nd-rich phase along the grain boundaries may be due to the melting of the Nd-rich phase by the eutectic reaction with Cu.

Conclusion

The microstructure investigation shows that there is a systematic presence of continuous Nd rich layer in the grain boundaries in the optimally annealed sample. While in the as-sintered one, the Nd rich region in the grain boundary is not continuous, thus the Nd2Fe14B grains cannot be well decoupled. The 3DAP result indicated that a substantial amount of Cu is enriched along the thin grain boundary phase.

1. J. Strzeszewski, G.C. Hadjipanayis, A.S. Kim, J. Phys. Colloq. C-8(1988)633

This work was supported by Toyota Motor Co. Ltd. and the Ministry of International Trade and Industries.

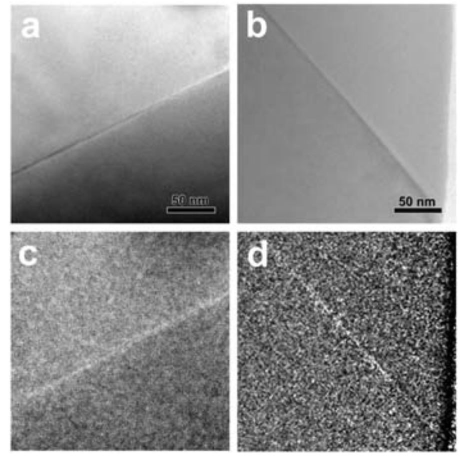

Fig.1 Elemental maps of the samples: Zero loss of the as -sintered sample (a) and optimally annealed sample (c); Nd map of the as-sintered sample (b) and optimally annealed sample(d);

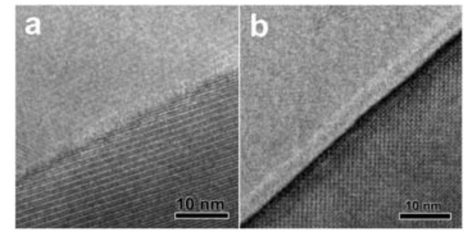

Fig. 2 HRTEM images of as-sintered (a) and optimally annealed (b) samples.

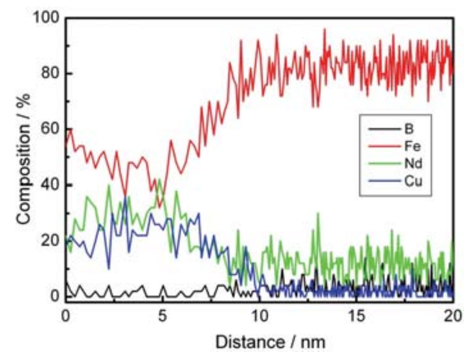

Fig.3. Concentration depth profiles for Nd, Fe, B and Cu determined from the 3DAP analysis.

DT-09

Field-induced coercivity enhancement phenomena in sintered Nd-Fe-B magnets.

H. Kato[1,2], T. Akiya[2], K. Koyama[3]
1. Department of Applied Mathematics and Physics, Yamagata University, Yonezawa, Japan; 2. New Industry Creation Hatchery Center, Tohoku University, Sendai, Japan; 3. Institute for Materials Research, Tohoku University, Sendai, Japan

These is an imperative need to develop a nature-friendly electric vehicle (EV) as an alternative transportation. Sintered Nd-Fe-B magnets are the most promising materials for a driving motor of the hybrid EV and the forthcoming pure EV. Since the operating temperature of magnets in these high-power motor applications reaches beyond 200°C, a very large value of coercivity H_c is necessary at room temperature. Current Nd-Fe-B magnets commercially available for such high H_c applications, therefore, contain a huge amount (~10 wt.%) of Dy to enhance H_c. But, this method has at least two crucial disadvantages. First problem is an estimated short supply of Dy in the EV mass-production stage owing to its low natural abundance as compared with that of Nd. The second inferiority in using Dy arises from the antiparallel coupling of Dy and Fe moments, which results in smaller magnetization and much-reduced energy product values. It is well known that a heat treatment around 600°C is indispensable to obtain a high coercivity in the sintered Nd-Fe-B magnets. This process is thought to cause some microstructural change in the grain boundary [1]. We have found that the coercivity in sintered Nd-Dy-Fe-B magnets can be further increased by applying a high magnetic field during the annealing [2]. In the Dy-free Nd-Fe-B magnets, we have found that such a coercivity enhancement phenomena occurs [3] only when a small amount of Cu is added, and when the annealing temperature is around 500°C or around 550°C. We have demonstrated [3] that these annealing temperatures are corresponding to eutectic points of Nd-Cu and Al-Cu phases, respectively. In this work, we report a more systematic study of the annealing-field dependence of coercivity for a series of Nd-Fe-B magnets with different amounts of Dy.

The heat treatments were carried out by using a furnace installed in a cryocooled superconducting magnet which generates magnetic fields of up to H_a =100 kOe. We modified the furnace system so as to enable a rapid quenching of the samples immediately after the field annealing. Magnetization measurements were performed after the induction method in fields of up to ±100 kOe.

When we fixed the annealing temperature at T_a=500°C, we observed a gradual enhancement of H_c as the field value during annealing, H_a, was increased. Figure 1 shows the room temperature values of H_c as a function of H_a for samples with Dy 2 wt.% and 6.8 wt.%. In spite of a slight scattering of data points, there is an apparent tendency for H_c values to increase linearly with H_a in both samples. The rate of increase in the Dy 6.8 wt.% sample is significantly larger than that in the Dy 2 wt.% sample. We made a least-squares fitting on these data by using a linear equation, $H_c = H_c(0) + \alpha H_a$, and deduced a slope α which corresponds to a coercivity enhancement factor. In Fig. 2, we plotted the α value against the Dy content. Although very small, the α has a positive finite value in samples with Dy 0 wt.% and 2 wt.%. It should be noted that, for higher Dy content, α increases rapidly and reaches about 0.05 for Dy 10.6 wt.% sample. It is natural to assume that Nd is partly replaced by Dy not only in the main $Nd_2Fe_{14}B$ phase but also in the Nd-rich intergranular phase. Since a Dy^{3+} ion has a larger single-ion anisotropy than that of a Nd^{3+}, the magnetic energy of intergranular phase during a field annealing becomes larger in Dy-containing samples. According to the field alignment model we proposed [1, 2], the critical grain size d_c of Nd(Dy)-rich intergranular phase therefore decreases with increasing Dy content. This would be the reason for the rapid increase in the α value with increasing Dy content. If the number of field-aligned Nd(Dy)-rich particles increases owing to the decrease of d_c, then a deterioration of surface magnetic anisotropy at the outermost Nd^{3+} ion of a main $Nd_2Fe_{14}B$ phase would be diminished, resulting in the coercivity enhancement.

Acknowledgments: This work was supported in part by TOYOTA Open Research Call Program.

[1] F. Vial, et al., J. Magn. Magn. Mater., 242-245 (2002) 1329.

[2] H. Kato, et al., Appl. Phys. Lett., 84 (2004) 4230.

[3] H. Kato, et al., J. Magn. Magn. Mater., 310 (2007) 2596.

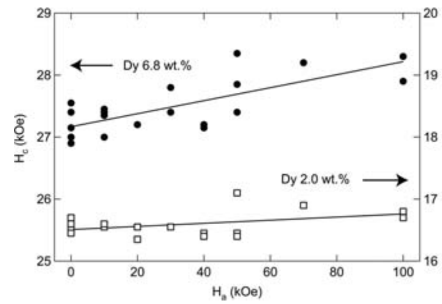

Fig. 1. Room temperature coercivity values plotted as a function of magnetic field value H_a applied during annealing at T_a = 500°C for Dy-containing Nd-Fe-B magnets. Solid lines are results of least-squares fitting.

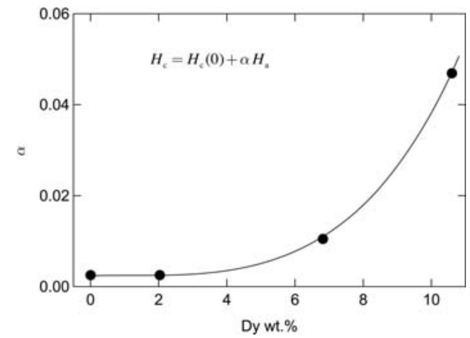

Fig. 2. Coercivity enhancement factor α derived from the fitting shown in Fig. 1, plotted against Dy contents.

DT-10

Small angle neutron scattering study of interface nanostructure in sintered Nd-Fe-B magnets.

T. Akiya[1], H. Kato[1,2], M. Takeda[3], J. Suzuki[3], D. Yamaguchi[4], S. Koizumi[4], M. Sagawa[5], K. Koyama[6]

1. New Industry Creation Hatchery Center, Tohoku Univ., Sendai, Miyagi, Japan; 2. Department of Applied Mathematics and Physics, Yamagata Univ., Yonezawa, Yamagata, Japan; 3. Quantum Beam Science Directorate, Japan Atomic Energy Agency (JAEA), Tokai-mura, Naka-gun, Ibaraki, Japan; 4. Advances Science Research Center, Japan Atomic Energy Agency (JAEA), Tokai-mura, Naka-gun, Ibaraki, Japan; 5. Intermetallics Co., Ltd,, Kyoto, Japan; 6. Institute for Materials Research, Tohoku University, Sendai, Miyagi, Japan

Sintered Nd-Fe-B magnets are the most promising materials for a driving motor of the hybrid electric vehicle (HV). In these kinds of application, a large value of the room-temperature coercivity as high as H_c = 30 kOe is required, because the operating temperature of the magnets reaches beyond 200°C. As a symptomatic treatment, Nd has been replaced partly by a heavy rare-earth element Dy to enhance H_c. But the problem is an estimated short supply of Dy in the HV mass-production stage due to its low natural abundance. Since the coercivity value in Dy-free Nd-Fe-B magnets is about 10 kOe, they are only applicable in low temperature circumstance such as MRI. However, it is possible, in principle, to achieve much higher coercivity without using Dy, since anisotropy field of $Nd_2Fe_{14}B$ main phase reaches H_A = 90 kOe at room temperature [1]. Therefore, it is very important to know the reason for a serious gap between H_c and H_A. It is widely accepted that the coercivity of sintered Nd-Fe-B magnets is highly dominated by the intergranular Nd-rich phase, which is reported [2] to change from discontinuous to continuous arrangement by annealing around 500~600°C. We have recently shown that the coercivity in sintered Nd-Fe-B magnet can be further increased by applying a high magnetic field during the annealing [3,4]. We found that such a coercivity enhancement phenomena occurs only when a small amount of Cu is added, and when the annealing temperature is around 500°C or around 550°C. We have demonstrated that these annealing temperatures are corresponding to eutectic points of Nd-Cu and Al-Cu phases, respectively [5]. In order to investigate the relation between the H_c increase and change of interface nanostructure, we started a small angle neutron scattering (SANS) study. SANS technique has an advantage over microscopic methods. That is, we can non-destructively obtain quantitative information averaged over a bulk sample. The pioneering SANS work by Fujii *et al*. was reported in 1987, stating that there are film-like precipitates along the grain boundaries where the thickness decreases from 6 nm to 4 nm by annealing at 600°C [6]. In this paper, we report SANS data for Dy-free Nd-Fe-B magnets annealed with and without high magnetic fields, and investigate a correlation between the interface nanostructure and the coercivity.

Two kinds of sintered Nd-Fe-B samples with and without Cu and Al additives were prepared. The 99% enriched ^{11}B isotope was used to avoid high neutron absorption of ^{10}B in natural boron. The samples were cut into plates with dimensions $15 \times 18 \times 1.5$ mm^3, in which the tetragonal *c*-axis of $Nd_2Fe_{14}B$ grains was aligned parallel to the 15 mm side. Samples were annealed at various temperatures between T_a = 450 ~ 650°C. External magnetic field applied during the annealing was 0 or 100 kOe. SANS experiments were performed with SANS-J and PNO apparatus of JRR-3 at the Japan Atomic Energy Agency (JAEA) in which the incident wavelength of neutrons were 0.65 and 0.2 nm, respectively. The incident beam was normal to the 15×18 plane of the sample. In order to separate the magnetic scattering contribution from nuclear one, all the samples were magnetized in 100 kOe field prior to the experiments. The two dimensional detector in SANS-J enabled us to obtain a whole set of SANS intensities $I(q_{//}, q_{\perp})$, where $q_{//}$ and $q_{\perp}$ are scattering vectors along the directions parallel and perpendicular to the *c*-axis of $Nd_2Fe_{14}B$, respectively.

The main results are summarized as follows. We found that, in all the samples examined, the intensity I of scattered neutrons was proportional to the q^{-4} for $q < 0.5$ nm^{-1}, irrespective of the direction of q. For $q > 0.5$ nm^{-1}, on the other hand, the intensity was markedly higher than that expected from the q^{-4} dependence. These results show that there exists a neutron scatterer with a dimension of less than 10 nm, which is considered to be a Nd-rich grain boundary phase in the matrix of $Nd_2Fe_{14}B$ phase. It should be noticed that, in the sample with Al and Cu additives, we observed a small but finite increase of intensity as compared with the sample without Al and Cu additives for the q range of $0.1 < q < 1$ nm^{-1}. Since Al- and Cu-containing samples have higher coercivity, this result suggests that there is a correlation between the density of neutron scatterer at a Nd-rich grain boundary and the coercivity. In order to investigate this correlation more systematically, we measured the SANS intensity in this q range for various Al- and Cu-containing samples, which have different H_c values ranging from 13 to 16 kOe owing to different field annealing conditions. We then analyzed the data with the $I = A\, q^{-4}$ equation. We found that the value of prefactor A increases with increasing H_c. Such an increase in the A value suggests a solid formation of the Nd-rich phase in the matrix of $Nd_2Fe_{14}B$ phase. Thus, this result is a direct evidence of correlation between interface nanostructure and coercivity in sintered Nd-Fe-B magnets.

Arcnowledgments: This work was supported in part by TOYOTA Open Research Call Program.

[1] Yamada *et al*., Phys. Rev. B, **38** (1988) 620.

[2] Vial *et al*., J. Magn. Magn. Mater., **242-245** (2002) 1329.

[3] Kato *et al*., Appl. Phys. Lett., **84** (2004) 4230.

[4] Akiya *et al*., J. Magn. Soc., **30** (2006) 447.

[5] Kato *et al*., J. Magn. Magn. Mater. **310** (2007) 2596.

[6] Fujii *et al*., IEEE Trans. Mag. **Mag-23, No.5** (1987) 3119.

DT-11

Reduction of sensitivity to sintering temperature for Nd-Fe-B magnets through co-doping Zr and Nb.

M. Yan, X. Cui, L. Yu, T. Ma
Department of Materials Science and Engineering, Zhejiang University, Hangzhou, China

Introduction

Sintered NdFeB magnets have been widely applied in various fields due to their outstanding magnetic properties. Further improvement of the magnetic properties is always the major objective of all researchers [1, 2]. It has been known that optimum magnetic properties are obtained when the average grain size is about 5~6 μm, which is primarily dominated by the sintering temperature [3]. Since the local temperatures in sintering furnaces are inhomogeneous, it is vitally important to decrease the sensitivity of green compacts to sintering temperature for production of magnets with high consistency of properties. In this work, an attempt has been made to decrease the sensitivity of green compacts to sintering temperature.

Results

Fig.1 shows the effect of sintering temperature on magnetic properties of Nd13.3Dy0.48FebalB5.75Al0.24Ga0.1 magnets. It can be seen that magnetic properties showed poor consistency of properties. The difference of maximum energy product (BH)m among the magnets sintered at each temperature exceeded 30 kJ/m3, and the difference of intrinsic coercivity iHc ranged from 65 to 140 kA/m, reflecting the high sensitivity to sintering temperature. The effect of sintering temperature on magnetic properties of magnets containing 0.07 at. % Nb and 0.07 at. % Zr is shown in Fig. 2. When the sintering temperature was 1373K, the energy product and coercivity difference of the magnets were only 9.4 kJ/m3 and 24.4 kA/m. It indicates that the Zr and Nb co-doped magnets possessed much better consistency of properties than Nd13.3Dy0.48FebalB5.75Al0.24Ga0.1 magnets. Moreover, both iHc and (BH)m of the Zr and Nb co-doped magnets increased with increasing the sintering temperature, and reached maximum values at 1373K. A high energy product with the value of 404 kJ/m3 was obtained.

The reduction of sensitivity to sintering temperature and the improvement of magnetic properties through Zr and Nb co-doping are explained as follows. Firstly, the addition of Zr is beneficial to inhibit abnormal grain growth. For the magnet without Zr, abnormal grain growth occurs at the sintering temperature of 1373K, as can be seen in Fig.3 a. For the magnet containing 0.07 at. % Zr, no abnormal grain growth is observed at higher sintering temperatures, as shown in Fig. 3b. Secondly, the addition of Nb can regularize grain shape and optimize microstructures, thereby improving the magnetic properties [4]. Moreover, it is considered that the formation of intragranular precipitates containing Zr or Nb is beneficial to enhance the pinning of the domain walls, resulting in the improvement of coercivity [5].

Figure captions

Fig.1 Magnetic properties of Nd13.3Dy0.48FebalB5.75Al0.24Ga0.1 magnets.

Fig. 2 Effects of sintering temperature on magnetic properties of (NdDy)13.32FebalB5.75Al0.24Ga0.1Nb0.07Zr0.07 magnets.

Fig.3 Microstructures of the magnets sintered at 1373K.
(a) base magnet and (b) Nd13.3Dy0.48FebalB5.75Al0.24Ga0.1Zr0.07.

[1] M.Yan, L.Q. Yu, J.M. Wu, and X.G. Cui, J.Magn.Magn.Mater., 306,176(2006)

[2] Y. Matsuura, J.Magn. Magn. Mater., 303, 344 (2006)

[3] N. C. Liu and A. S. Kim, J. Appl. Phys., 67, 4629 (1990)

[4] P. De-Rango, S. Rivoirard, A. Traverse, D. Fruchart, and F. N. Genin, J. Alloys Compd., 356-357, 579 (2003)

[5] S. Pandian, V. Chandrasekaran, G. Markandeyulu, K. J. L. Iyer, and K. V. S. Rama Rao, J. Appl. Phys., 92, 6082 (2002)

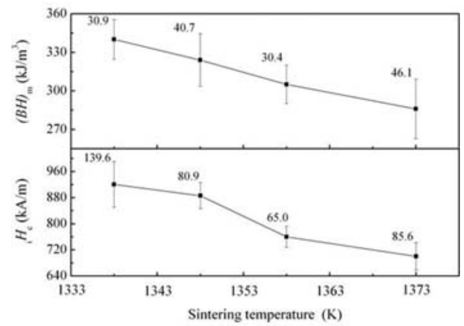

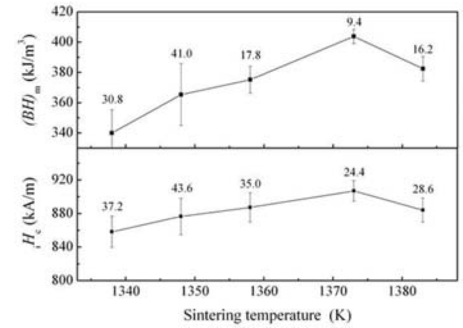

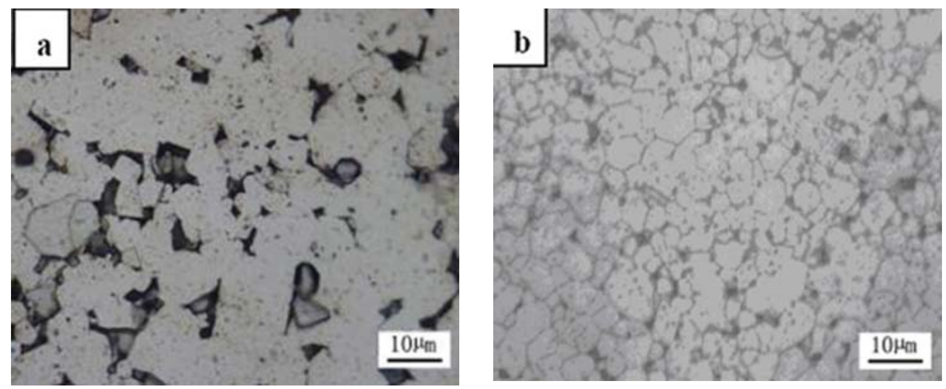

DT-12

Structure and magnetic properties of low neodymium magnets containing minor addition of molybdenum.

M. Spyra, M. Leonowicz
Faculty of Materials Science and Engineering, Warsaw University of Technology, Warsaw, Poland

Magnetic nanocomposites have been intensely studied since their developed in late 80-ties of the XXth century. They usually consist of a nanoscale mixture of hard and soft magnetic phases. According to the basic calculations, for optimal magnetic coupling between the both magnetic phases, the grain size should be 10 nm and 20 nm, for the hard and soft phase, respectively. Such a microstructure can be produced by rapid solidification of a molten alloy, however, the direct quenching requires application of a very narrow window of the process parameters. Thus, an alternative method is based on the processing of overquenched (amorphous) ribbon alloys with their subsequent annealing. We have been already published studies on the $Nd_9Fe_{77-x}B_{14}Ti_x$, x= 2,4,5 system in which we obtained, for the $Nd_9Fe_{73}B_{14}Ti_4$ alloy $_JH_c$ = 907 kA/m and $(BH)_{max}$ = 99 kJ/m^3 without loss of the remanence [1].

In this study the $Nd_9Fe_{77-x}B_{14}Mo_x$ ribbons (x = 0, 2, 3, 4, 5) were prepared by rapid solidification of molten alloys by melt-spinning with the roll speed 20 m/s. The overquenched ribbons were annealed at 983 K for 20 min. The phase constitution was evaluated using x-ray diffraction (XRD) (PHILIPS PW 1830, Cu – K^{α}) and Mössbauer spectroscopy. The magnetic properties were measured using a LakeShore 7410 vibrating sample magnetometer in maximum external field 3T.

The nanostructure in the alloys was produced by annealing the amorphous precursors. The onset of the crystallization temperature of the amorphous phase grew from 933 K for the Mo-free alloy up to 993 K for the 5 at% Mo alloy.

The XRD phase analysis revealed in the $Nd_9Fe_{77}B_{14}$ alloy the existence of magnetically soft α-Fe and magnetically hard $Nd_2Fe_{14}B$ phases, whereas in the alloys containing Mo, additionally the MoB_2 and Mo phase could be present (Fig. 1). This was broadly confirmed by Mössbauer spectroscopy.

Addition of the third element to the Nd-Fe-B alloys often leads to the increased coercivity, however, this effect is usually accompanied by a substantial decrease of the remanence, due to incorporation of a nonmagnetic element. In our case the remanence is close to 0.8T for the Mo-free alloy and decreases to 0.75 T for 4 at% Mo addition. The maximum energy product $(BH)_{max}$ increases for the alloys containing Mo, reaching maximum value 88 kJ/m^3 for 4 at% Mo. The hysteresis loops are smooth and the shape of the initial magnetization curves indicates a change of the coercivity mechanisms giving rise for pinning of domain walls for the Mo containing alloys (Fig. 2). The improvement of the magnetic properties we attribute to the, observed by TEM, substantial refinement of the grain size.

Concluding we can state that small addition of molybdenum ium, 2-4 at%, to the $Nd_9Fe_{77-x}B_{14}Mo_x$ alloys leads to increase of the coercivity and maximum energy product, without markedly affecting the remanence. The highest properties: J_r = 0.75 T, $_JH_c$ = 1013 kA/m, $(BH)_{max}$ = 88 kJ/m^3 have been achieved for the $Nd_9Fe_{73}B_{14}Mo_4$ alloy.

Improvement of the magnetic properties for the alloys containing Mo addition is caused by the change of the phase morphology of the Nd-Fe-B alloys, mainly by a formation of an uniform nanocrystalline microstructure.

[1] M. Spyra, M. Leonowicz: "Improvement of the magnetecic properties of low neodymium magnets by minor addition of titanium", J. Magn. Magn. Mater. – in print.

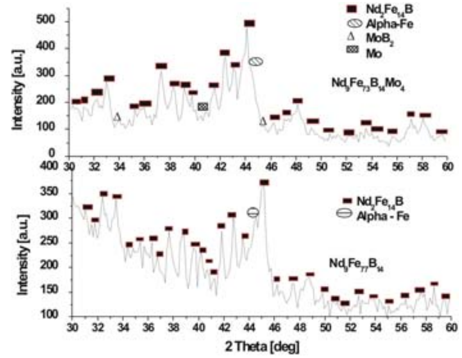

Fig. 1. X-ray patterns for the $N_9Fe_{77}B_{14}$ and $Nd_9Fe_{73}B_{14}Mo_4$ alloys.

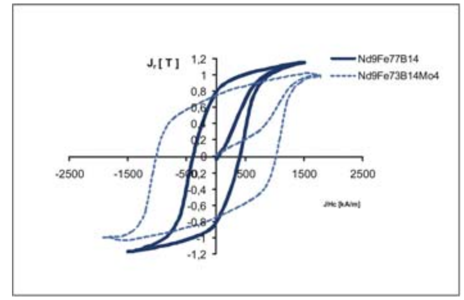

Fig. 2. Hysteresis loops for the $Nd_9Fe_{77}B_{14}$ and $Nd_9Fe_{73}B_{14}Mo_4$ alloys.

DU-01

Multi-tooth Flux Switching PM Brushless ac Machines for High Torque Direct-Drive Applications.

Z. Zhu[1], J. Chen[1], D. Howe[1], S. Iwasaki[2], R. Deodhar[2]
1. University of Sheffield, Sheffield, United Kingdom; 2. IMRA UK Research Center,University of Sussex, Brighton, United Kingdom

High torque density is one of the development trends of permanent magnet (PM) brushless machines, e.g. for aerospace and automotive applications. Multi-tooth structure is often employed to increase the torque / power density of the machines, such as hybrid stepping machines and multi-tooth switched reluctance machines [1][2] and a multi-tooth flux-switching machine which was briefly discussed in [3] as a stepping motor. A high electric loading may be required in order to achieve high torque density, especially for machines having magnets on the stator, such as flux-switching PM (FSPM) machines, in which the temperature rise of magnets may be more easily managed [4].
In this paper, multi-tooth FSPM brushless ac machines are investigated and compared with conventional FSPM brushless machines. As can be seen from Fig.1, in both machines, concentrated stator winding is employed, the stator core consists of modular "U"-shaped laminated segments between which are placed circumferentially magnetised permanent magnets, the rotor is similar to that of a switched reluctance machine, which is simple and robust. Their major difference is that there is more than one tooth of stator segments in the multi-tooth FSPM machine, Fig. 1. In this paper, the general stator and rotor slot/pole combinations will be derived, and the electromagnetic performance of a 2-tooth, 6-stator slot and 19-rotor pole FSPM brushless ac machine, in which the total number of stator small teeth and their width are equal to those in a conventional 12-stator slot and 10-rotor pole FSPM machine, is predicted by finite element analysis and validated by experiment. It is shown that (1) the number of magnets in 2-tooth FSPM machine is only half of that in the conventional machine; (2) predicted phase back-emf waveform of the 2-tooth machine is sinusoidal and ~40% larger than that of the conventional machine, Fig. 2(a); (3) the torque ripple are negligible in the 2-tooth FSPM machine and its electromagnetic torque is larger than that of the conventional machine at rated current; (4) the 2-tooth flux-switching machine exhibits higher torque density at light electric loading, but it becomes saturated more quickly with current than that of the conventional machine, Fig. 2(b), due to high armature reaction.

[1] B. C. Kuo, and G. Singh, "A dc-type hybrid step motor for large power application," IEEE Tran. Ind. Appl., vol. IA-11, No. 4, pp. 365-372, July 1975.

[2] J. Faiz, M. R. Harris, and J. W. Finch, "Two-dimensional finite element analysis of multi-tooth per stator pole switched reluctance motor-four teeth per stator pole," Proc. IEEE Industry Application Society Annu. Meeting, No. 1, pp. 234-240, Oct. 1990.

[3] A. Mailfert, H. Kubler, and J. Zhou, "Hybrid stepping motors comparative experimental results," Proc. International Conference on Electrical Machines, No. 1, pp. 781-783, Aug. 1987.

[4] Z.Q. Zhu, Y.Pang, D. Howe, S. Iwasaki, R. Deodhar, A. Pride, "Analysis of electromagnetic performance of flux-switching permanent magnet machines by non-linear adaptive lumped parameter magnetic circuit model," IEEE Trans. Magnetics, vol.41, no.11, November 2005, pp.4277-4287.

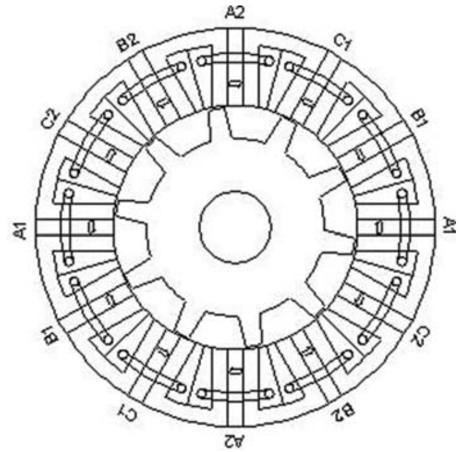

Fig.1(a) Conventional 12-stator slot and 10-rotor pole

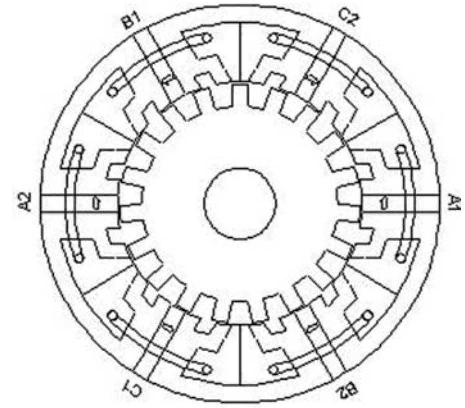

Fig.2(b) 2-tooth, 6-stator slot, and 19-rotor pole

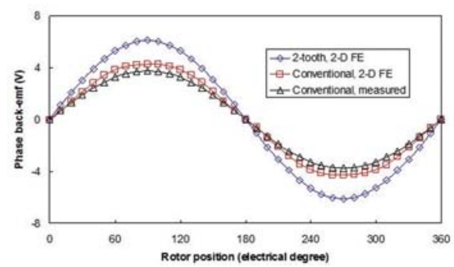

Fig.2(a) Comparison of phase back-emf

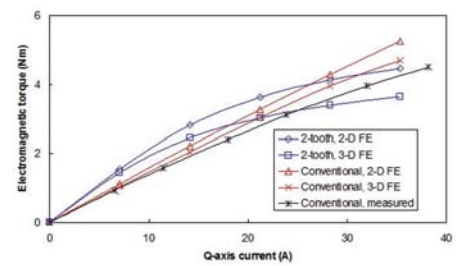

Fig.2(b) Comparison of torque-current

Optimum Design of Transverse Flux Linear Motor for Weight Reduction and Improvement Thrust Force Using Response Surface Methodology.

D. Hong, B. Woo, D. Kang
Korea Electrotechnology Research Institute, Changwon, South Korea

Linear motor has a few partial limitations. The major reason is the low power density due to the inherent large air gap. For the application of linear motors to high power system, therefore, Permanent Magnet (PM) type Transverse Flux Linear Motors (TFLMs) can be considered because this motors can develop high magnetic thrust and reluctance thrust in relatively small air gap [1-2].
TFLM has two important electromechanical components, a linear actuator and springs for refrigeration application. By controlling the operating frequency of the actuator around mechanical resonance frequency, it has higher efficiency than the conventional rotary type compressor.
This paper presents the shape optimum design of transverse flux actuator for linear compressor using Response Surface Methodology (RSM). Generally RSM is used with 2 or 3 design variables ; however, in this paper, Fig. 2 shows that eight design variables using the table of mixed orthogonal array are utilized. For each parameter combination, the response value is determined by 3-D Equivalent Magnetic Circuit Network (EMCN) method.
For this reference model, the comparison of the static force obtained from 3-D EMCN, 3-D FEM simulation and experiment is shown in Fig. 1. From the results the use of 3-D EMCN is validated as it can be observed, since 3D EMCN shows good agreement with experimental tests.
Table I shows the design variables and flux path. In order to determine the equations of the response surface, several experimental designs have been developed to establish the approximate equation using the smallest number of experiments. Equation (1) shows the two fitted second order polynomial of object functions for the eight design variables. Table II shows the adjusted coefficients of multiple determination R2adj for three responses are YW (99.9 %), YT (99.9 %), and YD (99.7 %). In Table III and IV, the optimal point is searched to find the point of less than 12.63 % of the weight and greater than 6.87 % of the thrust force maintaining the detent force of initially designed PM type TFLM. The simulation result of predicted optimum set is shown Table II with good agreement. The Pareto chart of thrust force, detent force and weight shows influential design variables in Fig. 3.
In this paper, The performance of optimized PM type TFLM is improved when compared with the initial model. Therefore, when this proposed approach is applied, it is more efficient to raise the precision of optimization and reduce the number of iteration of experiment in the optimization design by RSM.

[1] D. K. Hong, B. C. Woo, and D. H. Kang, "Application of Fractional Factorial Design for Improving Performance of 60W Transverse Flux Linear Motors," Proc. of MMM 2007 Conf., November, 2007.

[2] D. K. Hong, B. C. Woo, J. H. Chang and D. H. Kang, "Optimum Design of TFLM with Constraints for Weight Reduction using Characteristic Function," IEEE Trans. Magn., Vol. 43, No. 4, pp. 1613-1616, April, 2007.

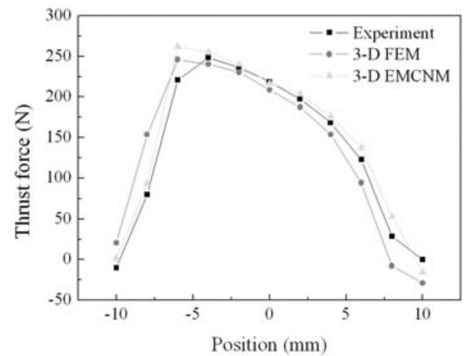

Fig. 1 Comparison of 3-D EMCNM, 3-D FEM and Experiment of reference model

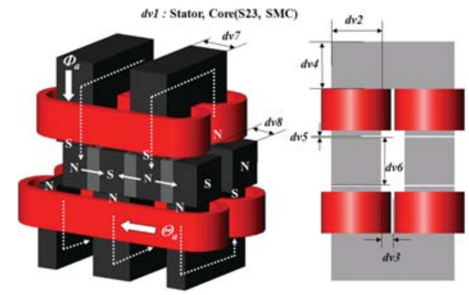

Fig. 2 Design variable of PM type TFLM

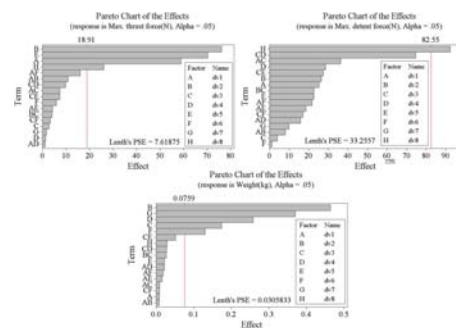

Fig. 3 Pareto chart

Level \ Design variable	C_{MAT}	S_{b1}	S_{b2}	S_{h1}	C_a	PM_h	S_{ls}	S_{lc}
1	*S23*(-1)	20(-1)	12(-1)	22(-1)	0.3(-1)	22(-1)	15(-1)	11(-1)
2	*SMC*(+1)	23(0)	15(0)	25(0)	0.5(0)	25(0)	17(0)	13(0)
3		26(+1)	18(+1)	28(+1)	0.7(+1)	28(+1)	19(+1)	15(+1)

Table I Design variable and level

Model	Weight[kg]	Thrust force[N]	Detent force[N]
Initial	2.178	302.59	45.98
RSM (predicted)	1.984	330.00	45.98
3D EMCN	1.903	323.4	47.4
Variation between initial and 3D EMCN model %	-12.63	6.87	3.09

Table II Comparison of initial and optimum model

$$\begin{aligned}
Y_T = {} & 279.79 - 26.61C_{MAT} + 38.89S_{b1} - 2.15S_{b2} + 3.5S_{h1} \\
& - 27.64C_a + 2.71PM_h + 1.24S_{ls} - 10.59S_{lc} - 1.04S_{b1}^2 \\
& + 0.77S_{b2}^2 - 7.16S_{h1}^2 + 4.04C_a^2 + 0.98PM_h^2 - 4.13S_{ls}^2 \\
& - 1.44S_{lc}^2 - 6.27C_{MAT}\,S_{b1} \\
Y_D = {} & 48.95 + 7.19C_{MAT} + 10.52S_{b1} - 19.42S_{b2} - 12.74S_{h1} \\
& - 2.37C_a - 0.24PM_h - 16.59S_{ls} - 33.88S_{lc} + 26.78C_a^2 \\
& - 9.82S_{ls}^2 + 6.74C_{MAT}\,S_{b1} - 11.57S_{b1}S_{ls} - 36.20S_{b1}S_{lc} \\
& + 26.49S_{b2}S_{h1} + 8.29S_{b2}C_a - 8.51S_{b2}PM_h \\
Y_W = {} & 2.145 - 0.009C_{MAT} + 0.23S_{b1} + 0.077S_{b2} + 0.125S_{h1} \\
& - 0.013C_a + 0.068PM_h + 0.176S_{ls} + 0.008S_{lc} \\
& + 0.01S_{b1}^2 - 0.009S_{b2}^2 - 0.01S_{h1}^2 + 0.0127PM_h^2 \\
& + 0.006S_{ls}^2 + 0.018S_{lc}^2 + 0.0065C_{MAT}\,S_{b1}
\end{aligned}$$

Equation (1)

DU-03

2D analytical calculation of the no-load induced EMF in an axial flux slotted permanent magnet machine.

J. Pérez[1], F. Frechoso[1,2]
1. Electrical Engineering, Universidad de Valladolid, Valladolid, Spain; 2. Member, IEEE, Valladolid, Spain

Introduction: Three methods are proposed and compared in order to obtain the induced electromotive force (EMF) in an axial flux slotted permanent magnet machine under no-load conditions. Each method solves the Laplace equation via magnetic scalar potential and, based on a two-dimensional approximation of the magnet geometry, takes into account the slotting of the machine.
An axial flux machine with three phases, eight poles, and 24 slots was chosen. The inner rotor has 8 permanent magnets surface mounted, which are axially magnetised. The two outer slotted stator cores have an infinite permeability. Looking radially inwards onto the machine and ignoring curvature, allows the machine to be represented as a lineal one, where the x-coordinate represents the circumferential direction and the y-coordinate the axial direction. This model assumes the radial direction to be infinite. By symmetry, only a half of the geometry is studied.
Analytical models: The two-dimensional Laplace equation for the magnetic scalar potential, v, is: $\delta^2 v/\delta x^2+\delta^2 v/\delta y^2=0$
The most general solution can be written as:
$v=\Sigma[A_n\cos(\beta_n x)\cosh(\beta_n y)+B_n\cos(\beta_n x)\sinh(\beta_n y)+C_n\sin(\beta_n x)\cosh(\beta_n y)+D_n\sin(\beta_n x)\sinh(\beta_n y)]$
where the constants A_n, B_n, C_n, D_n and β_n can be determined by imposing appropriate boundary conditions. Once the magnetic scalar potential is defined, other parameters, such us the magnetic flux crossing any given area or the induced EMF can then be computed.
1st method: Fourier series method:
This method consists on considered interconnected rectangular regions, where the solution can be obtained by applying the superposition theorem and defining several simpler problems. In the common boundary to two regions the magnetic scalar potential and its spatial derivate must be continues across the boundary [1]. The problem is solved in two steps: a)Assume an arbitrary potential distribution along the boundaries in terms of some unknown Fourier coefficients. Solve the field equations in the regions. b)Obtain the unknown coefficients by matching the normal derivate of the potential function along each boundary.
2nd method: magnetization profile in an even air-gap + slot permeance:
This method obtains the analytical expressions for the flux density distributions in the air-gap and in the magnets, solving the Laplace and Poisson equation respectively via the magnetic scalar potential, by taking into account the symmetry conditions, the boundary conditions and the magnetization profile [2]. The magnetization distribution is represented by its Fourier series expansion, as follows: $M_y=(B_r/\mu_0)\Sigma[b_n\sin(\beta_n x)]$ The expression of the magnetic scalar potential in the air gap,is: $v_g(x,y)=\Sigma(K_{yn}/\Delta\, \beta_n)\sin(\beta_n x)\sinh[\beta_n(l_s-y)]$ where $\Delta=\cosh(\beta_n g)+\mu_r\sinh(\beta_n g)\mathrm{tgh}(\beta_n l_m/2)$, $\beta_n=n\pi/\tau_p$, and $K_{yn}=0$ if n is odd and $K_{yn}=[4B_r\cos(n\pi)/\mu_0 n\pi]$ if n is even, being B_r the remanence, μ_r the relative recoil permeability, μ_0 the vacuum recoil permeability and τ_p the pole pitch.
The effect of slotting on the field produces by the magnets is incorporated by means of a slot permeance coefficient, which consist of evaluating the above expression with the air-gap modified so as to take into account that the magnetic field over the slot must travel further to reach the stator[3].
3rd method: magnetic scalar potential in an even air-gap + slot permeance:
In this third method, we have considered an even air-gap with fixed magnetic scalar potential in the magnet and stator surfaces ($+V_0$ in the north face, $-V_0$ in the south face and null in the stator surface), and the slot are take into account by the permeance coefficient. The expression of the magnetic scalar potential in the air-gap is: $v_g(x,y)=\Sigma[P_n/\sinh(\beta_n g)]\sin(\beta_n x)\sinh[\beta_n(l_s-y)]$ where $P_n=0$ if n is odd and $P_n=-4V_0/\tau_p\beta_n$ if n is even.
Results: In order to compare the proposed methods, we have calculated the flux linkage and the induced EMF in a coil with an span of 3 slots. Figure 1 shows the flux linkage and the induced EMF, respectively, obtained with each method.
Conclusions: Three different analytical methods are proposed and compared. The difficult of first method increasingly with the number of interconnected regions, although the technique is quite straightforward. In order to reduce this difficult, another two methods are proposed in whose the slotting effect is represented by a permeance coefficient. The flux linkage and the induced EMF calculated by the three methods show a good agreement.

[1] H. A. Toliyat and G. B. Kliman, "Handbook of Electrical Motors". New York, Marcel Dekker Inc, 2004.

[2] Z. Q. Zhu, D. Howe, E. Bolte and B. Ackermann, "Instantaneous magnetic field distribution in brushless permanent magnet dc motors, part I: open-circuit field", IEEE Trans. Magn., vol 29, no. 1, pp. 124-135, 1993.

[3] D. C. Hanselman, "Brushless Permanent Magnet Motor Design". Rhode Island, The Writers' Collective, 2003.

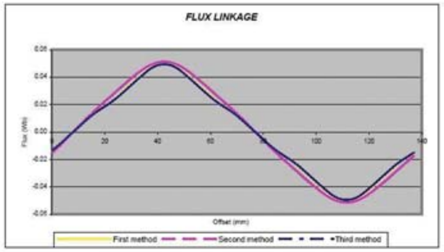

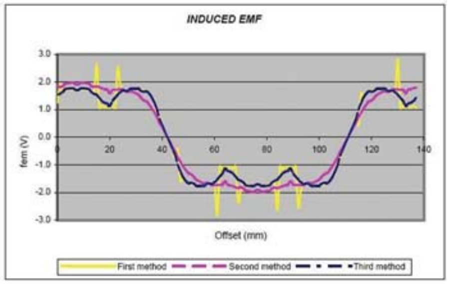

DU-04

Modeling permanent magnet axial flux machine with Lie's symmetries.

L. T. Loureiro[1], J. R. Zabadal[2], *A. F. Flores*[1], R. P. Homrich[1]
1. Electrical Engineering, Universidade Federal do Rio Grande do Sul, Porto Alegre, Brazil; 2. Nuclear Engineering, Universidade Federal do Rio Grande do Sul, Porto Alegre, Brazil

Abstract: A permanent magnet axial flux machine was designed, built and tested. Analytical model with Lie's symetries and numerical model were developed for the machine and comparisons were carried out. An analytical model and comparison results will be presented.
Key words: Electrical Machine. Torus machine. Permanent Magnets. Axial flux. Analytical model. Electrical Machine Testing. Lie's Symmetries.

Introduction

The axial flux machines tend to present a larger air gap than the radial ones, therefore they require higher excitation. The excitation can be provided by per-manent magnets. A machine with rated rotation 450 RPM, torque of 3 Nm and outside diameter of 0.16 m was built. A finite element software was used to carry out the numerical simulation. Analytical models for the windings and permanent magnets inductions were developed. Along with the permanent magnet induction were also calculated the electromotive force and the torque.

Description of Machine

The Torus machine, object of this paper, is an axial flux, disc-type machine, with a stator mounted between two external rotors. Its construction is rather simple, compact and has reduced axial length. This characteristic is interesting for applications that have space restrictions.

The machine has a stator with eighteen coils that are connected in three groups with six coils in series, which are energized sequentially. Each rotor has six permanent magnets that interact with the stator coils. The excitation of coils groups is carried out through a converter that energizes the coils sequentially. In this way, the stator magnetic induction moves along with the permanent magnet magnetic induction. The permanent magnets poles in front of the stator have the same polarity in corresponding positions.

Figure 1 shows the frame, cores, magnets and the complete machine.

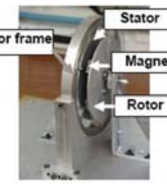

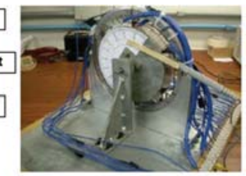

Figure 1a Frame, Cores and Magnets Figure 1b Complete Machine

The main characteristics of Torus machine are presented in the table:

rotation	450 RPM	poles number	6
torque	3 Nm	phases number	3
outside diameter	0,16 m	coils number	18
axial lenght	0,0545 m	coils per phase number	6

Analytical Model

The windings behavior is described by the following equation;

$$\nabla^2 \vec{A} = -\mu \vec{J} \quad (1)$$

The solution of this equation in air gap and winding region, along with applica-tion of boundary conditions and Lie's translation symmetry admitted by equation, results in winding magnetic induction:

$$\vec{B}_{ef} - \frac{1}{r}(\Gamma z + C_4)\vec{\theta} + (\Gamma \theta - C_6)\vec{z} + C_8 \quad (2)$$

The calculated and simulated values are shown in figure 2a.

The air gap scalar magnetic potential was modeled through gaussian curves, equation (3).

$$f_1 = \left(e^{-x^2/4k_1t}\right)/\sqrt{4\pi k_1 t} \qquad f_2 = \left(e^{-y^2/4k_1t}\right)/\sqrt{4\pi k_1 t} \quad (3)$$

The sum of these functions verifies the Laplace equation in long periods. The substitution x=x+Iz and y=y+Iz makes the combined function become function of x, y and z. The expression of permanent magnet induction is derived after carrying out some mathematical operations and application of a Lie's scale symmetry. The values of permanent magnet induction corresponding to the simulation, the analytical model and the measurements are shown in figure 2b.

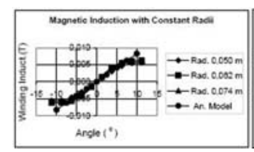

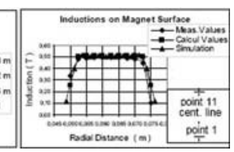

Figure 2a Winding Magnetic Induction Figure 2b Magnets Magnetic Induction

Conclusions

The comparison shows that analytical modeling produced results campatible with the numerical simulation and measurements. The utilization of Lie's symmetries is powerful method in electromagnetic systems and can have a wider application.

OLVER, P. J. Applications of Lie Groups to Differential Equations. 2nd Ed. New York. Springer-Verlag. 2000.

BLUMAN, G.W., KUMEI, S. Simmetries and Differential Equations. New York. Springer-Verlag.1989

BINNS, K.J.; LAWRENSON, P.J.;TROWBRIDGE, C.W. Electric and Magnetic Fields. Chichester, UK: John Wiley & Sons, 1992.

DU-05

Optimal Design of an SPM Motor Using Taguchi Method and Genetic Algorithms.

C. Hwang[1], L. Lyu[1], P. Li[1], C. Liu[2]
1. EE, Feng Chia University, Seatwen, Taichung, Taiwan; 2. EE, National Sun Yat-sen University, Kaohsiung, Taiwan

INTRODUCTION

This paper presents the use of the Taguchi method [1]and genetic algorithms-based (GAs) optimization techniques [2]in optimizing an surface-mounted permanent magnet (SPM) motor for use as a fan motor in air-conditioners. In this application, the SPM motor is designed to provide high efficiency and low cogging torque for the requirement of high EER and low noise operation.

DESIGN OF EXPERIMENT

There are eight factors, A, B, C, D, E, F, G and H, corresponding to eight design variables which are chosen as shown in Fig. 1, and each at three levels except factor A that has two levels. Where A is the magnetization of magnets (radial, r or parallel, p), B (lso) is the slot opening in mm (levels 2.0, 2.2 and 2.4), C (ηm) is the ratio of angular magnet pitch to angular pole pitch (levels 1.0, 0.96 and 0.92), D is the thickness of magnet in mm (levels 5.0, 5.5 and 6.0), E (g) is the air gap length in mm (levels 0.4, 0.5 and 0.6), F (lmcc) is the position for cutting the magnet in mm (levels 0, 1 and 2), G (θmcc) is the angle for cutting the magnet in electrical degrees (oE) (levels 20, 30 and 40), and H (lmc) is the distance from motor center used as the center of a circle for magnet in mm (levels 0, 1 and 2). To obtain the peak to peak values of cogging and efficiency for each case, two-dimensional FEA is conducted. Table I shows the values of three settings of three design parameters and the motor performance indexes.

ANALYSIS OF RESLTUS

After conducting the analysis of means and analysis of variance, average peak to peak values of cogging torque (Tcog)and efficiency (Eff) for all levels of all factors are tabulated in Tables II and III.

It is noted in Tables II and III that the best combination of design parameters for minimum cogging torque and maximum efficiency are determined to be (A2, B3, C2, D1, E1, F1, G1, H3). Finally, GAs is applied to find the optimal values of the design variables. They are B = 2.35 mm, C = 0.967, D = 4.96 mm, E = 0.412 mm, F = 0.12 mm, G = 19.85oE, and H = 1.95 mm. The final results are found using the FEM analyses. The peak to peak values of cogging torque and efficiency of the original, the Taguchi design, and Gas are 6.7846 mNm, 0.8497 mNm, 0.6626 mNm, and 66.30 %, 71.21 %, and 72.56 %respectively.

[1]S. X. Chen, T. S. Low, and B. Bruhl, “The Robust Design Approach for Reducing Cogging Torque in Permanent Magnet Motors,” IEEE Trans. Magnetics, Vol. 34, No. 4 pp. 2135-2137, July 1998.

[2]N. Bianchi and S. Bolognani, “Design Optimisation of Electric Motors by Genetic Algorithms,” IEE Proc.-Electr. Power Appl., vol. 145, No. 5, pp. 475-483, September 1998.

L18	A	B	C	D	E	F	G	H	Tcog(mN.m)	Eff(%)
1	p	2	1	5	0.4	0	20°	0	7.860	72.72
2	p	2	0.96	5.5	0.5	1	30°	1	1.100	69.99
3	p	2	0.92	6	0.6	2	40°	2	3.200	65.48
4	p	2.2	1	5	0.5	1	40°	2	0.991	68.69
5	p	2.2	0.96	5.5	0.6	2	20°	0	3.850	69.55
6	p	2.2	0.92	6	0.4	0	30°	1	2.529	70.45
7	p	2.4	1	5.5	0.4	2	30°	2	0.535	70.50
8	p	2.4	0.96	6	0.5	0	40°	0	0.449	71.21
9	p	2.4	0.92	5	0.6	1	20°	1	3.531	71.24
10	r	2	1	6	0.6	1	30°	0	8.025	62.33
11	r	2	0.96	5	0.4	2	40°	1	6.802	66.38
12	r	2	0.92	5.5	0.5	0	20°	2	0.058	61.91
13	r	2.2	1	5.5	0.6	0	40°	1	4.007	61.77
14	r	2.2	0.96	6	0.4	1	20°	2	2.275	63.90
15	r	2.2	0.92	5	0.5	2	30°	0	10.52	64.88
16	r	2.4	1	6	0.5	2	20°	1	4.418	64.62
17	r	2.4	0.96	5	0.6	0	30°	2	0.847	64.76
18	r	2.4	0.92	5.5	0.4	1	40°	0	11.05	66.46

Settings/Factors	Ai	Bi	Ci	Di	Ei	Fi	Gi	Hi
i=1	2.6717	4.5075	4.3060	5.0918	5.1752	2.6250	3.6653	6.9590
i=2	5.3336	4.0287	2.5538	3.4333	2.9227	4.4953	3.9260	3.7312
i=3	0	3.4717	5.1480	3.4827	3.9100	4.8875	4.4165	1.3177

Settings/Factors	Ai	Bi	Ci	Di	Ei	Fi	Gi	Hi
i=1	69.98	66.46	66.77	68.11	68.40	67.13	67.32	67.85
i=2	64.11	66.54	67.63	66.69	66.88	67.10	67.15	67.40
i=3	0	68.13	66.73	66.33	65.85	66.90	66.66	65.87

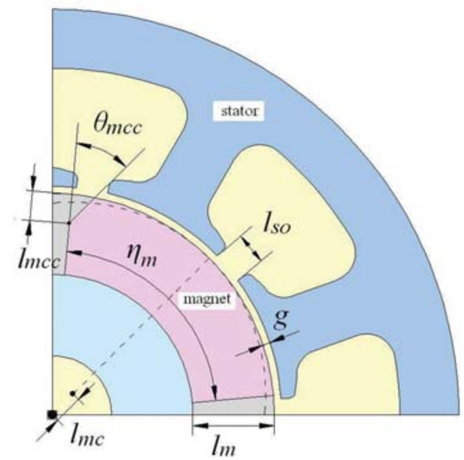

Fig. 1. A pole pitch of the SPM motor

DU-06

On the Material and Temperature Impacts of Interior Permanent Magnet Machine for Electric Vehicle Applications.

A. Wang[1], H. Li[1], C. Liu[2]

1. Electrical Engineering, North China Electric power university, Baoding, China; 2. Electrical Engineering, National Sun Yat-Sen University, Kaohsiung, Taiwan

1. Introduction

Due to its high efficiency, high torque density, lower torque ripple, and lower cogging torque features [1], [2], Interior Permanent Magnet (IPM) machine with neodymium-iron-boron (NdFeB) material has attracted increasing interests among researchers and designers in many high-performance applications such as traction motors used in hybrid electric vehicles [3]. However, with its different applications and operational environments, impacts of the overall machine system performance at various permanent magnet (PM) materials and temperatures have seldom been assessed. The objective of this paper is to present the detailed investigations on these impacts, such that the design and application guidance of selecting different PMs in an IPM motor for electric vehicles can be provided.

2. IPM Machine

As shown in Fig. 1, a 55 kW IPM machine has been designed with a single layer of buried rotor magnets, 6 slots per pole for possible hybrid electric vehicle application. The rotor pole contains V-shape buried magnets that are magnetized along the d-axis, while the stator slots are embedded with double layer distributed windings to produce the desired magneto-motive forces. The pilot design parameters are given in Table I and the transient model analyses have been performed at one pole by 2D finite element method (FEM). The resultant flux lines at one time instance with the rotor pole being 3 slots apart from the energized stator at a speed of 2000 rpm are depicted in Fig. 2 for illustration.

3. Investigations of the PM and Temperature Impacts

Table II provides the five NdFeB materials, namely HS_43EH, HS_36EH, HS_35EH, HS_40FH and HS_32GH, that are potential selections for the desired IPM applications. Based on these material information and 2D FEM, comparison system performance were thoroughly calculated and illustrated in Figs. 3~5. As can be observed, though the HS_43EH PM will provide the maximum averaged and minimum ripple torques at all temperatures, with at least 30% higher cogging torques than the others, such material will only be competitive for the low-cost large torque applications. While for the operating environments with higher temperature, though with higher cost, the HS_40FH PM will provide almost the same levels of maximum averaged and minimum ripple torques, and much lower cogging ones for the desired applications. Similarly, if cost and cogging effects are the main concerns, it can be seen that the HS_35EH PM will provide a relatively better solution.

[1] S. X. Chen, T. S. Low, and B. Bruhl, IEEE Trans Magn., 34, 2135 (1998).

[2] M. N. Uddin, T. S. Radwan, and M. A. Rahman, IEEE Trans. Energy Conv., 17, 79 (2002).

[3] T. M. Jahns, S. H. Han, A. M. El-Refaie, J. H. Baek, M. Aydin, M. K. Guven, and W. L. Soong, IEEE IAS Conf., 4, 1941 (2006).

Material	HS_43EH	HS_36EH	HS_35EH	HS_40FH	HS_32GH
Br (T)	1.14	1.04	1.0	1.1	1.0176
Hc (kA/m)	-840	-784	-733	-849.33	-786
Max. Temperature	140 C	140 C	140 C	180 C	200 C

rated power	rated voltage	# of pole	# of stator slot	stator outer radius	stator inner radius	stator axial length	rotor inner radius	air gap	magnet thickness	PM	Core	rated current
55kW	220V	12	72	125mm	95mm	85mm	65mm	0.6mm	5.5mm	HS_40FH	M19-Gage	200A

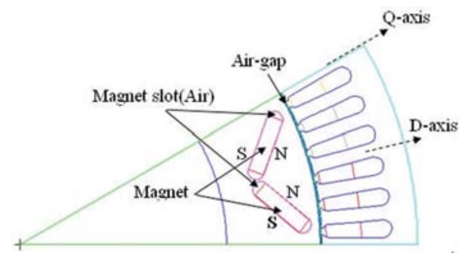

Fig. 1 Single pole view of the analyzed IPM machine

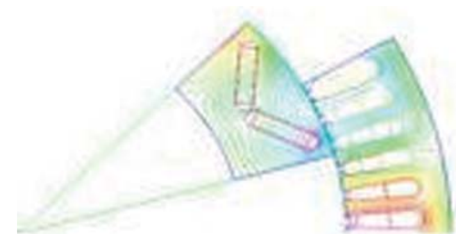

Fig. 2. Flux lines of the IPM machine

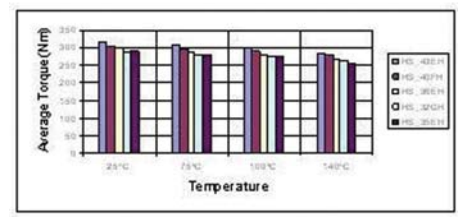

Fig. 3. Machine averaged torques

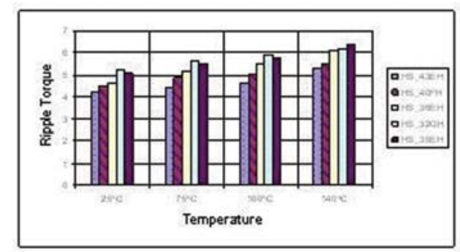

Fig. 4. Machine ripple torques

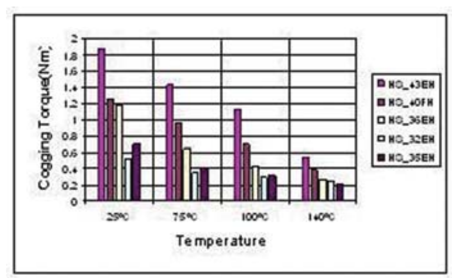

Fig. 5. Machine cogging torques

DU-07

Fabrication and properties of FePt thick films for micro-machine application.

P. Jang[1], B. Lee[1], K. Rhie[2], S. Choi[2]
1. Div. of Applied Science, Cheongju University, Cheongju, South Korea; 2. Department of display, semiconductor and physics, Korea University, Chochiwon, South Korea

1. Introduction
Due to their very high magneto-crystaline anisotropy energy(7x106 J/m3) and excellent chemical stability, FePt films are one of the potential candidates for future magnetic recording media and micro-machine application. However, FePt films should be thicker than several tens micrometer for some micro-machine applications such as micro-magnet, micro-undulators or wiggler. Because of very poor workability of ordered L10 FePt alloys, it is almost impossible to fabricate the FePt thick films with several tens micrometer by rolling FePt bulk materials directly. Recently multilayer technique was proposed, in which Fe and Pt foils were stacked on stainless tube to obtain nano-composite materials and then rolled by a reduction ratio of 10,000 followed by post-annealing [1]. In thin film processes it has been known that it is impossible to grow the films thicker than several tens micrometer because of very high residual stress. In this study we have successfully grown the FePt films thicker than ten micrometer on Fe substrates by sputtering with the help of HF surface treatment.
2. Experimental procedure
We had first proposed a probability of micro-undulator for T-Hz sources [2]. The structure of the micro-undulator is very similar to that of double layered perpendicular recording media, so that FePt films thicker than ten micrometer were sputtered at 400oC on 99.9% bulk Fe substrates with very smooth surface. For the 10 um FePt, Fe-Pt composite targets were sputtered for 11 hr with a sputtering power of 100 W. To improve adhesion between FePt and Fe substrates, 50 – 100 nm thick intermediate layers such as Ti, Hf, W, Fe and others were tried. And HF surface pretreatment was also tried because it is known that hydrogen termination forms on Si dangling bonds on the Si surfaces [3]. The films were annealed on a vacuum better than 2 x 10-5 torr in order to transform disordered FePt phase to L10 ordered phase.
3. Results and discussion
Ti is known as an element to improve adhesion between thin films and substrates. For films thinner than 3 um Ti was effective to increase adhesion. However, in films thicker than 10 um, Ti is not effective to increase adhesion between FePt and Fe. Other elements such as W, Hf, and Fe are less effective than Ti. Even though 10 um FePt thick films were successfully sputtered on the Ti layer, the FePt films were peeled off during annealing process. All the intermediate layers used in this study could not acquire a successful FePt film. It is known that hydrogen terminated H-Si bonds was kept for several minutes in the air and for several hours in ultrahigh vacuum when Si wafer was pre-treated in HF dilute aqueous solution by pull-dry method. Even though bond structure of Fe was different from Si, pull-dry dry method was tried. After treating the Fe substrate with HF solution, 11 um thick FePt films were successfully grown on Fe bulk substrate. Figure 1 shows XRD diffraction patterns of 11 um FePt films on Fe and Ti substrates. It can be shown that the formation of L10 phase was confirmed from the (001) super-lattice peak. The ordering parameter of the two samples was calculated to be around 0.82. XRD patterns of two samples are nearly same, which means that the growth or preferred orientation of the FePt thick films is not affected by the orientation of substrate surface. A low degree of (111) preferred orientation was confirmed in Fig. 1. In SEM observation very coarse and deep columnar structure was observed so that the film was not continuous and the surface was not reflective. Figure 2 shows VSM loops of the FePt films. From non-existence of kinks in the in-plane loop it can be seen that the film shows single-phase magnetic behavior. In-plane and perpendicular coercivities are 7.5 and 2.5 kOe, respectively, which are much higher than those of cold rolled FePt foils. The reason for the higher coercivity seems to be due to a deep columnar structure. In conclusion, FePt films thicker than ten micrometer was successfully sputtered on Fe substrates and the developed FePt thick films are thought to be applied to micormachine application.

[1] N. H. Hai, N. M. Dempsey, M. Veron, M. Verdier, and D. Givord, J. Magn. Magn. Mater., 257, L139 (2003)

[2] Pyungwoo Jang, Keungwon Rhie, and Byungcheol Lee, Phys. stat. sol. (a), 204, 4194 (2007)

[3] P. Dumas, Y. J. Chabal, and G. S. Higashi, Phy. Rev. Lett., 65, 1124 (1990)

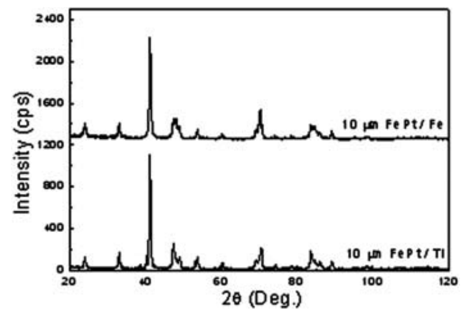

XRD patterns of 11 um FePt thick films on Fe and Ti substrates.

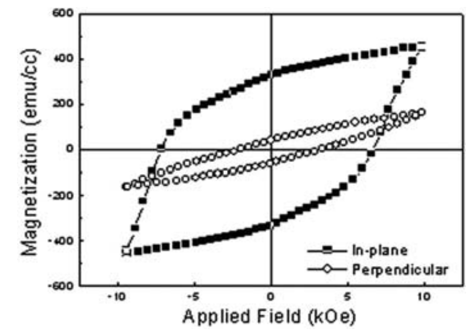

VSM loops of 11 um thick FePt thick films under a maximum field of 10 kOe.

DU-08

Optimum Design of 60 W Longitudinal Flux Linear Motor for Weight Reduction and Improvement Performance Using DOE.

D. Hong, B. Woo, D. Kang
Korea Electrotechnology Research Institute, Changwon, South Korea

In order to increase the power density, permanent magnet (PM) type longitudinal flux linear motors (LFLMs) can be considered for the application of the linear motors in high power density systems. Since LFLMs can produce high magnetic thrust and reluctance thrust with relatively small air gap. There are several practical examples of LFLM in [1-2]. Fig. 1 shows the structure of the developed LFLM. It has two important electromechanical components, a linear actuator and resonance springs for refrigeration application. By controlling the operating frequency of the actuator around mechanical resonance frequency, it has higher efficiency than the conventional rotary type compressor. Fig. 1 shows the prototype of PM type TFLM for compressor. Fig. 2 shows the flow chart of optimization procedure. Fig. 3 shows design variables of the PM type LFLM. The effective factors are DV1, DV2, DV3 by table of orthogonal array, Pareto chart and RSM. Table I shows the design variable and level of effective factors in central composite design (CCD). The CCD is used. CCD is frequently used for fitting second-order response model. The adjusted coefficients of the multiple determination R2adj for two responses are weight (100 %) and FThrust (100 %) in Equation (1). This paper presents the optimum design of longitudinal flux actuator for linear compressor using RSM. Its design goal is to reduce the weight of the machine with the constraints of thrust and detent force with respect to the initial machine. At first step, most influential design variables and their levels should be determined and be arranged in a table of orthogonal array. Each response value is determined by 2-D finite element method (FEM). With the use of reduced gradient algorithm (RGA), finally, the most desired set is determined, and the influence of each design variables on the objective function can be obtained. The weight can be reduced by 9.58 %, thrust force improved by 5.11 % and detent force maintained of initially designed PM type LFLM in Table II.

[1] H. Lee, S. S. Jeong, C. W. Lee and H. K. Lee, "Linear Compressor for Air-Conditioner," International Compressor Engineering Conference at Purdue, pp. 1-7, 2004.

[2] T. Mizuno, M. Kawai, F. Tsuchiya, M. Kosugi, and H. Yamada, "An Examination for Increasing the Motor Constant of a Cylindrical Moving Magnet-Type Linear Actuator," IEEE Trans. Magn., Vol. 41, No. 10, pp. 3976-3978, October, 2005.

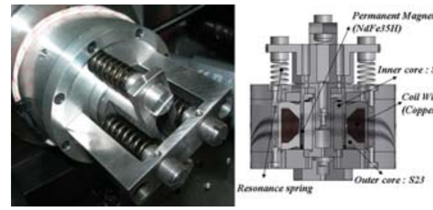

Fig. 1 PM type LFLM for compressor

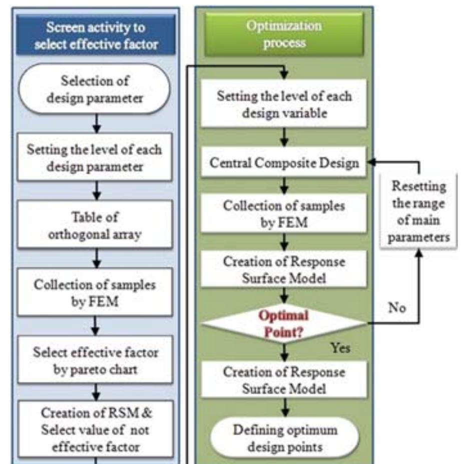

Fig. 2 Flow chart of optimization procedure

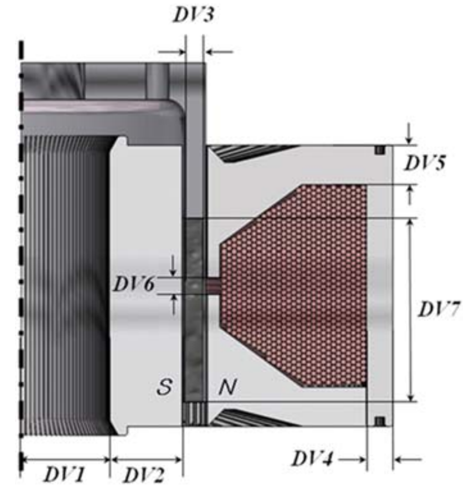

Fig. 3 Design variable of PM type LFLM

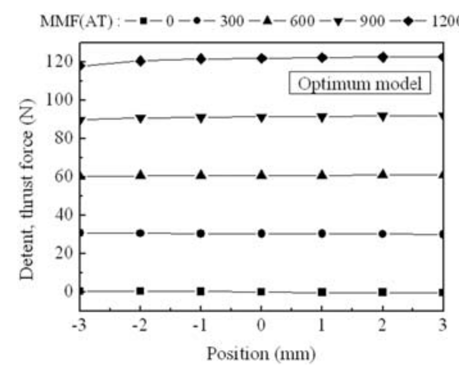

Fig. 4 Detent and thrust force profile of the optimum model by mmf

Design Variable	Level				
	-α(-1.216)	-1.0	0.0	1.0	α(1.216)
DV1	8.1269	8.449	9.94	11.431	11.7531
DV2	5.7232	5.95	7	8.05	8.2768
DV3	1.92136	1.9975	2.35	2.7025	2.7786

Table I Design variable and level of CCD

Model	Weight (kg)	Avg. thrust force (N)
Initial	1.4575	57.8900
Optimum predict (RSM)	1.3167	60.8000
Optimum simulation (2-D FEM)	1.3179	60.8477
Variation between initial and optimum simulation (%)	-9.58	5.11

Table II Comparison of initial and optimum model

$$
\begin{aligned}
F_{Thrust} = & -12.6886 + 2.0746DV1 + 2.3649DV2 + 11.6036DV3 \\
& - 0.0015DV1^2 - 0.0231DV2^2 - 2.054DV3^2 \\
& - 0.0029DV1DV2 + 0.4608DV1DV3 + 0.4785DV2DV3
\end{aligned}
$$

$$
\begin{aligned}
Weight = & \ 0.4278 + 0.0359DV1 + 0.359DV2 + 0.0366DV3 \\
& + 4.009E\text{-}10DV1^2 + 0.00084DV2^2 + 0.0005DV3^2 \\
& + 0.0017DV1DV2 + 0.001DV1DV3 + 0.001DV2DV3
\end{aligned}
$$

Equation (1)

DU-09

Optimal Design of a Small PM Wind Synchronous Generator for Wide Range of Winds Speed.

B. Ebrahimi[1], J. Faiz[1], M. Rajabi Sebdani[1], M. A. Khan[2]
1. Department of Electrical and Computer Engineering, University of Tehran, University of Tehran, Tehran, Iran; 2. Department of Electrical Engineering, University of Cape Town, Cape Town, South Africa

Due to the design introduced of permanent magnet synchronous generator (PMSG) in [1], the 12-blade turbine is replaced with a 3-blade one. So the torque, in new generator, is increased and the speed, voltage and frequency is decreased. In this paper, the generator presented in [1] is redesigned so that the voltage level of the generator output is increased considerably, while keeping the rated frequency of the generator output close to that of the grid. It's note worthy that this way, the volume of the PM used in generator is decreased and this will affect greatly on the find cost of the generator manufacture. This paper presents a multi objective optimization method to improve, terminal voltage, power factor and PM volume in use. For this purpose, the analytical model of the machine is utilized to calculate the excitation voltage, power factor and PM volume and Effects of them are investigated via this model. PMSG parameters and dimensions are then optimized using genetic algorithm incorporated with an appropriate objective function. The results show an enhancement in PMSG performance. Finally 2D time stepping finite element method (TSFE) is used to evaluate the analytical results in opera2d.10.5. The comparison of results validates the optimization method.

Some of the typical PMSG and dimensions are selected as design variables where values are determined through on optimization procedure. In this paper, design variables are axial length, remanent flux density of the PMs, specific electric loading, efficiency, power factor, terminal voltage and wind speed. To have a more realistic design, some constraints are applied to design variables listed in table I. The pole pairs, rated frequency, number of blades, the main fixed specifications in the design procedure are (250 rpm), 50 Hz and 3 respectively. In this paper roulette wheel method is used for selection and each step elite individual sent directly to the next population. Table II shows genetic algorithm parameters used in this paper. A three phase PMSG for handling materials application is chosen as the basis of design optimization. The minimum value of the terminal voltage, PM volume and power factor in the algorithm is chosen close to their initial values of the non-optimized generator. The results of optimization are summarized in table III. The variations of calculated terminal voltage (Ref. [1] and proposed design) with time, using TSFE, are illustrated in figs 1 and 2.

M. A. Khan, P. Pillay and K. D. Visser, "On adapting a small PM wind generator for a multi blade, high solidity wind turbine", IEEE Trans on EC, Vol. 20, No. 3, Sept 2005

Parameter	Unit	Minimum Value	Maximum Value
Terminal Voltage	Volt	180	240
Axial Length	Meter	0.04	0.08
Pole arc to Pole pitch ratio	-	0.556	0.9
Remanent of flux density	Tesla	0.8	1.4
Area of conductor	Square of milli meter	1.257	4.398
Specific electrical loading (SEL)	Ampere/meter	10000	40000
Efficiency	%	80%	100%
Power Factor		0.7	0.9
Wind speed	meter/sec	7	13

Parameter	Value
Probability of crossover	0.7
Probability of mutation	0.05
Population size	55
Number of Generations	600

Specification	Nominal Design	Initial Design Ref. [1]	Optimal Design
Excitation Voltage	262.18	51.27	255.2
Pole arc/Pole pitch	0.696	0.905	0.8657
Power Factor	0.7	0.7	0.8828
Current Density	2.65	2.037	1.502
Total Mass	67.067	85.93	77.2554
Wind Speed	-	10	8.62

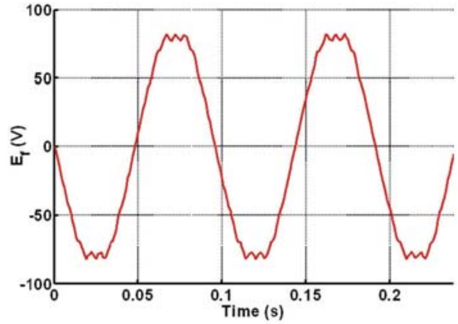

Fig. 1. Variation of terminal voltage with time using FEM in ref. [1]

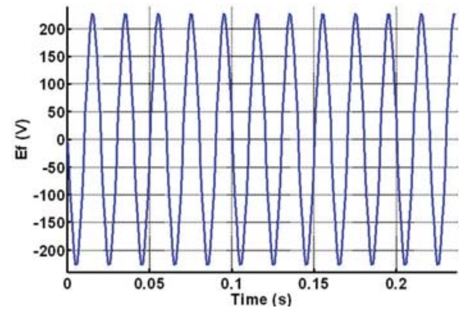

Fig. 2. Variation of terminal voltage with time using FEM proposed design

DU-10

Analytical analysis of magnetic field and back electromotive force calculation of an axial-flux permanent magnet synchronous generator with coreless stator.

P. Virti č[1], P. Pi šek[1], T. Mar či č[1], M. Hadziselimovi č[1,2], B. Štumberger[1,2]
1. TECES, Development centre for electrical machines, Maribor, Slovenia; 2. Faculty of Electrical Engineering and Computer Science, University of Maribor, Maribor, Slovenia

Introduction

This paper presents the analytical analysis of magnetic field and back electromotive force (back EMF) calculation in an axial flux permanent magnet synchronous generator (AFPMSG) without stator core. For the verification, the numerical calculation (finite element method (FEM)) of magnetic field is accomplished and comparison between analytical and numerical solution of magnetic field is presented.. The paper also presents the comparison between analytical and numerical (FEM) solution of back EMF using Faraday's law. The validity of the proposed analytical method is additionally confirmed with measurements of back EMF on prototype AFPMSG with coreless stator.

The prototype AFPMSG for wind energy application consists of internal stator and twin external rotor. Permanent magnets (PMs) are glued to the rotor steel discs and the coils are built in the non-magnetic stator using polypropylene and epoxy. The AFPMSG excitation is accomplished by 10 sectors of NdFeB magnets on the both parts of rotor, respectively.

The finite element method allows an accurate analysis of magnetic field considering geometric details and non-linearity of magnetic material, but they are time consuming and poorly flexible in the early design stages. On the other hand, the analytical methods of magnetic field analysis cannot consider geometric details, but can achieve time saving and flexible computation when performing magnetic field and back EMF calculation.

Methods of analysis

In this paper an analytical solution of Maxwell's equations and constitutive equation is used to evaluate magnetic flux density by PMs in the centre of air-gap region with central radius of PMs [1,2]. Due to the coreless stator, the final whole magnetic field (magnetic flux density) at constant radius can be obtained by the superposition of magnetic fields produced by PMs and armature current. Magnetic field densities produced by PMs (for each part of rotor) and armature current can therefore be calculated separately and analysis model can be replaced by three independent analysis models.

The back EMF of the AFPMSG at no-load condition has been calculated using Faraday's law of electromagnetic induction based on the time variation of magnetic flux: The magnetic flux can be obtained through the magnetic flux density ***B*** on the cross-section surface inside the each coil.. A detailed description of the proposed analytical method for the magnetic field distribution and EMF calculation will be presented in final paper.

Results and discussion

The comparison between analytical and FEM solution of magnetic flux density distribution under no-load condition calculated at the central radius of PMs in the centre of air-gap is presented in Fig.1. Analytical, FEM and measurement results of the back EMF under no-load condition according to displacement are presented in Fig.2. The final paper will also present the analytical calculation of magnetic flux density and back EMF in dependency on both, armature current and mechanical angle. EMF calculation will be verified by the FEM and measurements.

Conclusion

In order to obtain the analytical solution of magnetic flux density, the program environment Matlab is used. For the verification of the analytical solution of magnetic flux density the FEM is accomplished using Ansys program package.

Analytically calculated magnetic flux density is in very good agreement with the results obtained by FEM, while thee analytical solution of back EMF is in good agreement with measurements and FEM. Moreover, the FEM and measurements confirm the validity of the proposed analytical method. The main advantage of this method is more than 500 times shorter computational time and more flexible computation for the back EMF calculation in comparison to FEM.

The analytical method presented in this work is very convenient for comprehensive studies and have already been incorporated into design and optimisation processes of the coreless AFPMSG.

[1] J. Azzouzi, G. Barakat and B. Dakyo, "Quasi 3D analytical modeling of the magnetic field of an axial flux permanent magnet synchronous machine", IEEE Transactions on Energy Conversion, Volume 20, Issue 4, Dec. 2005, Page(s):746–752.

[2] D.L. Trumper, W.-j. Kim and M.E. Williams, "Design and analysis framework for linear permanent-magnet machines", IEEE Transactions on Industry Applications, Vol. 32, No. 2, March/April. 1996, Page(s):371–379.

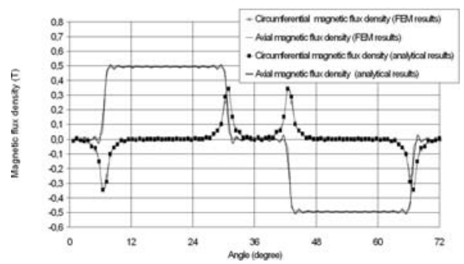

Fig.1 Analytical and FEM result of magnetic flux density distribution according to mechanical angle

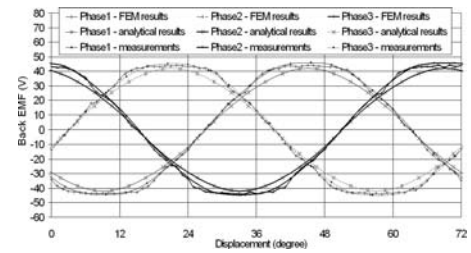

Fig.2 Comparison of analytical, FEM and measurement results of the back EMF under no-load condition according to displacement

DV-01

Theoretical and experimental studies of structural characteristics, magnetic response and electronic properties of Sr_2FeMnO_6 double cubic Perovskite.

J. A. Rodriguez, D. A. Landinez-Tellez, R. Cardona, F. E. Fajardo, J. Roa-Rojas
Physics Dept., Universidad Nacional de Colombia, Bogotá, Colombia

The aim of this work is to carry-out calculations in order to predict the main electronic and structural properties of Sr_2FeMnO_6. We have found that the Sr_2FeMnO_6 presents a metallic behavior. On the other hand, structural features were studied on polycrystalline samples synthesized by solid state reaction method. This study was carried through Rietveld analysis on X–ray diffraction (XRD)pattern. From the results, we conclude that it crystallizes in the FCC structure (space group #225).

Samples were synthesized by means of the standard solid state reaction method. Precursor powders of SrO, FeO and MnO_2 (Aldrich 99.9%) were stoichiometrically mixed according to the nominal composition Sr_2FeMnO_6. X-Ray diffraction was made by means a PW1710 diffractometer with $\lambda_{CuK\alpha}$=1.5406 Å. Rietveld refinement of the pattern was made by means of code GSAS. Magnetic response was investigated through DC magnetic susceptibility measurements by using a Quantum Design model 2000 MPMS SQUID system.

We use the wien2k [1], which is a program based on Density Functional Theory (DFT) [2,3] in the GGA approximation. The unitary cell volume was optimized by minimization of energy, but the internal parameter *x* (O-coordinate) was optimized by means of the minimization of global forces on the atoms. The minimum of force on the oxygen atom was about of 12.5 mRy/a.u. and the parameter *x* was equal to 0.250953. The muffin-tin radiuses used, in ua, were 1.87, 2.20, 1.86 and 1.69 for Fe, Sr, Mn and O respectively. Other parameters of wien2k were: RMT×Kmax = 8.0 and Gmax=14.0. We used 165 k-points over the irreducible Brillouin zone and the maximum angular momentum was l =10.

From the fitting to the Murnaghan's state equation of the energy as a function of volume, we obtain the value of 3656.585 ua^3 (541.850 $Å^3$) for the volume total cell, lattice constant equal to 15.406 ua (8.153 Å) and bulk modulus ~ 9 MBar. Rietveld analysis, reveals that Sr_2FeMnO_6 has the characteristic superstructure of a cubic perovskite type with $A_2BB'X_6$ formula. The matching between experimental and calculated results for the lattice constant parameter is 98.6%.

Figure 1 shows the spin-polarized total density of states (DOS) and DOS projected on the like-atomic orbitals of Fe, Mn and O. Fermi level is the reference for energies. It is observed that the material behaves as a metallic system. The metallic characteristic of the material is due to a little DOS above the Fermi level. That little DOS is due to the up-P_z-O, up-D_{eg}-Fe and dn-P_x+P_y)-O orbitals. The material exhibits a total magnetic momentum of ~7.6 μ_B in the cell. By chemical formula the magnetic momentum is ~1.9μ_B. That value is mainly due to Fe and Mn atoms with a contribution of ~43.7% and ~56.3% for Fe and Mn respectively. In the figure we observe that the contribution of the D-orbitals of Fe and Mn are the most important for the total magnetic momentum.

Magnetic response of Sr_2FeMnO_6 has been investigated by measuring the DC magnetic susceptibility in the temperature range 5 to 300 K and at an applied magnetic field of 5 kOe. Figure 2 shows the temperature dependence of the DC magnetic susceptibility. Experimental data of this picture can be fitted well with the Curie-Weiss law $\chi=\chi_0+C/(T-\theta_c)$, where $C=N\mu^2_{eff}/3k_B$ is the Curie constant, N is Avogadros's number, μ_{eff} is the effective magnetic moment, k_B is the Boltzmann constant, θ_c is the paramagnetic Curie temperature and χ_0 is the temperature independent susceptibility term. We obtain that χ_0 is 1.67 $\times10^{-3}$ emu/mol, C = 1.01289 emu K/mol, θ_c = 1.9995 K and the effective magnetic moment per unitary formula μ_{eff} = 2.80μ_B.

[1] P. Blaha, K. Schwarz, G. K. H. Madsen, D. Kvasnicka, J. Luitz, WIEN2k, An Aug-mented Plane Wave + Local Orbitals Program for Calculating Crystal Properties (Karlheinz Schwarz, Techn. Universität Wien, Austria, 2001), ISBN 3-9501031-1-2.

[2] P. Hohenberg, W. Khon, Phys. Rev. 136 (1964) B864.

[3] W. Khon, L. S. Sham, Phys. Rev. 140 (1965) A1133.

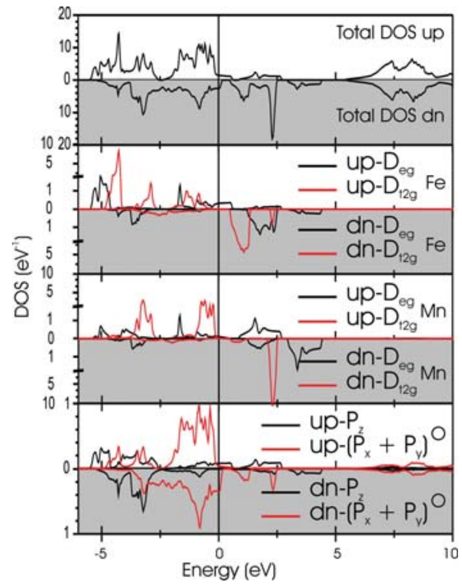

Fig 1. Total and projected density of states for the FCC complex perovskite structure of Sr_2FeMnO_6 material.

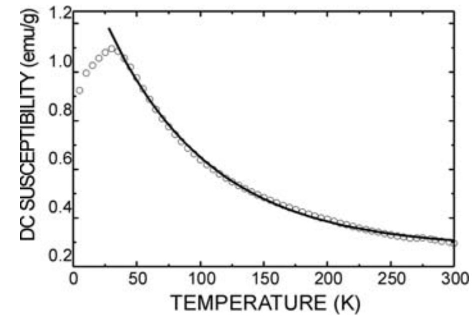

Fig. 2. Curie-Weiss fitting in DC susceptibility as a function of temperature for Sr_2FeMnO_6 double perovskite. Round points represent experimental data and line corresponds to fitting.

DV-02

Local probe studies on $Pr_{1-x}Ca_xMnO_3$ system.

A. M. Lopes[1,2], T. M. Mendonça[1,2], J. S. Amaral[3], A. M. Pereira[1], P. B. Tavares[4], Y. Tomioka[5], Y. Tokura[6], J. G. Correia[7,2], V. S. Amaral[3], J. P. Araújo[1]
1. Department of Physics and IFIMUP, Univ. of Porto, Porto, Portugal; 2. EP, CERN, Geneva, Switzerland; 3. Department of Physics and CICECO, Univ. of Aveiro, Aveiro, Portugal; 4. Department of chemistry and CQ-VR, Univ. of Tras-os-Montes e Alto Douro, Vila Real, Portugal; 5. CERC, National Institute of Advanced Industrial Science and Technology, Tsukuba, Japan; 6. Department of Applied Physics, Univ. of Tokyo, Tokyo, Japan; 7. Instituto Tecnólogico Nuclear, Sacavém, Portugal

Manganites, with a general formula of $T_{1-x}D_xMnO_3$, where T is a trivalent rare earth element and D is a divalent alkaline earth element still challenge our understanding. Much attention has been devoted to these perovskite compounds due to their peculiar magnetic and electronic properties. The entanglement between lattice, spin, charge and orbital degrees of freedom leads to phenomena like phase separation, polaron clusters and charge ordered (CO) states that occur not only at a macroscopic level but also appear at the nanometer scale. To achieve a better understanding on the small bandwidth manganites, where the mentioned phenomena tend to be more pronounced, a local probe study was performed in $Pr_{1-x}Ca_xMnO_3$. In order to obtain the desired local scale information on the different magnetic and electronic states along the system phase diagram a hyperfine field systematic study was carried out using Perturbed Angular Correlation spectroscopy (PAC) via the ^{111m}Cd probe. This nuclear hyperfine method is specially effective to sample atomic scale environments and its efficiency is temperature independent allowing to explore a wide range of temperatures. The measurement of the Electrical Field Gradient (EFG) tensor and the Magnetic Hyperfine Field (MHF) at the Ca/Pr site was performed in a series of samples ranging from x=0 to 1, in the 10 K to 1000 K temperature range.
The macroscopic characterization of the produced polycrystalline samples shows good agreement with the literature results. As expected, our structural analysis revealed that samples stabilize in an orthorhombic structure [1,2]. The study of the magnetic properties, also in good agreement with the literature [1,3,4], allowed to determine the characteristic Curie-Weiss, Néel(T_N), Curie (T_C), and charge-order (T_{CO}) temperatures.
The macroscopic information was correlated with systematic PAC measurements performed in the same samples. At room temperature the principal component of the EFG, Vzz, decreases with increasing Ca content, i.e., with the decrease of the orthorhombic distortion. Moreover we found that the CO region of the phase diagram delimits distinct regimes for the dependence of EFG parameters on Ca content. For samples that belong to the region of the phase diagram where CO effects occur (in the 151 K to 275 K temperature range) we found that the EFG parameters depend strongly on Ca content. As mentioned above, although a decrease of Vzz with Ca content could be expected in terms of the trend of the lattice parameters, a sharp decrease around x=0.32(where CO effects appear) was surprisingly found. This shows that at the Pr/Ca lattice site, contributions to Vzz other than the static lattice contribution become important. The observed sharp decrease around x=0.32 can be understood when the temperature dependence of the EFG of the whole system is considered. This study revealed that samples outside the CO region of the $Pr_{1-x}Ca_xMnO_3$ phase diagram have the expected increase of Vzz with decreasing temperature without any noticeable anomaly. On the other hand, for samples within the CO region, the common increase of Vzz with decreasing temperature is only observed for temperatures above T'>>TCO. Below T' a clear anomalous decrease of Vzz is found when decreasing temperature and this feature remains till the charge-order temperature is reached, showing that CO effects are preceded by anomalous lattice dynamic effects. It is also shown that this anomalous decrease of Vzz when decreasing temperature is responsible for the sharp decrease of Vzz vs Ca concentration, observed at room temperature in the CO region.
The study of the magnetic hyperfine field for the $Pr_{1x}Ca_xMnO_3$ system was also performed and the low T measurements on the end-members revealed the presence of a hyperfine magnetic field Bhf=1.2T at 10 K in $PrMnO_3$ compound while no mesurable MHF is present in $CaMnO_3$. Both systems are quoted in literature as having a pure antiferromagnetic arrangement of the Mn ions [5, 6], thus the MHF should vanish at the probe site. The MHF measured below 77 K for $PrMnO_3$ may be associated to the onset of magnetic order of Pr moments. This ordering is refereed in literature [7] as being responsible for a small canting of both the Pr and Mn magnetic sub-lattices yielding a non vanishing magnetic field at the probe site. For samples with low Ca concentrations (x<0.14) a small MHF (Bhf<0.7 T) was detected at 77 K in accordance with the spin canted magnetic state [6] whereas for x=0.95 no MHF was found, although some reports claim the existence of a small percentage of ferromagnetic domains embedded in an antiferromagnetic matrix [8]. Below T_C, in the x=0.25 compound, a Bhf=4.4 T at 11 K was measured, compatible with a fully ferromagnetic environment. In the CO x=0.35 compound we had to consider also the presence of a MHF. In literature either a canted AF-CE-type magnetic structure [4, 6] or a AF-CE/FM phase coexistence [4, 8] has been reported. To ascertain about the existence of a canted AF-CE-type magnetic structure or a AF-CE/FM phase coexistence we performed two distinct fits for spectrum at 11 K. Our MHF results suggest that the magnetic configuration of the Mn ions should be a canted AF-CE-type. Similar conclusions are drawn for the compound with x=0.32.

DV-03

Complex magnetic behaviour in anion deficient manganite superstructures R. Cortés-Gil1,2, J. M. Alonso2,3, A. Hernando2,4, M. L. Ruiz-González1, M. García-Hernández3, M. Vallet-Regí2,5, J. M. González-Calbet1,2,* 1Departamento de Química Inorgánica, Facultad de Químicas, Universidad Complutense, 28040-Madrid, Spain 2Instituto de Magnetismo Aplicado, UCM-CSIC-RENFE, Las Rozas, P.O. Box 155, 28230-Madrid, Spain 3Instituto de Ciencia de Materiales, CSIC, Sor Juana Inés de la Cruz s/n, 28049-Madrid, Spain 4Departamento de Física de Materiales, Facultad de Físicas, Universidad Complutense, 28040-Madrid, Spain 5Departamento de Química Inorgánica y Bioinorgánica, Facultad de Farmacia, Universidad Complutense, 28040- Madrid, Spain.

J. M. González-Calbet
Quimica Inorgánica, UCM, Madrid, Spain

Ever since Colossal Magnetoresistance was discovered in Ln1-xAxMnO3 systems (Ln = lanthanide and A = alkaline-earth)[1] an extensive research on compositional variations of manganese perovskite related oxides has been performed allowing a deeper knowledge of the intriguing composition-structure-properties relationship on these materials. In this way, compositional variations in the anionic sublattice of La0.5Sr0.5MnO3 have been introduced in order to stabilize a new manganite superstructure with La0.5Sr0.5MnO2.5 composition.[2] Structural characterization by means of X ray and electron diffraction confirms brownmillerite structure for La0.5Sr0.5MnO2.5, where oxygen deficiency is accommodated along [101] and in this sense, this material can be understood as an intergrowth of alternating octahedral and tetrahedral layers along b direction.
A neutron diffraction study was performed in order to know the magnetic structure. The analysis date reveals a G-type antiferromagnetic (AFM) structure at 5 K where the magnetic moments of Mn are AFM coupled not only in the Mn-O layers but also between them. The thermal evolution confirms this ordering is kept to 140 K where paramagnetic state is reached. However, a magnetometry study reveals an evident Ferromagnetic (FM) contribution to room temperature[2]. This behaviour would be related to double exchange interactions in the octahedral layers thanks to Mn4+ and Mn3+ presence. FM interactions are not detected by neutron diffraction probably due to the short range character which provides a too weak signal. Moreover, the AC susceptibility measurements show a cusp at temperature close to 70 K. The position of this cusp depends on the frequency of the AC magnetic field which could be related to spin glass behaviour.

[1] R. Von Helmolt, J. Wecker, B. Holzapfel, L. Schultz and K. Samwer, Phys. Rev. Lett., 76, 2331 (1993)

[2] R. Cortés-Gil, M. L. Ruiz-González, J. M. Alonso, M. Vallet-Regí, A. Hernando, J. M. González-Calbet, Chem. A Eur. J., 13, 4246, (2007)

DV-04

Anisotropic magnetoresistance in ferromagnetic manganites.

M. Granada, J. Rojas Sánchez, L. B. Steren, J. D. Fuhr, B. Alascio
Centro Atómico Bariloche (Comisión Nacional de Energía Atómica) and CONICET, San Carlos de Bariloche, Argentina

Magnetoresistive phenomena are of great interest due to their potential applications in spintronics devices. The anisotropic magnetoresistance (AMR), which describes the dependence of the resistivity with the angle between the electric current and the magnetization, is a general property of ferromagnetic (FM) materials. This dependence can be written as [1]
$\rho(\theta)=1/3\rho_{\|}+2/3\rho_{\perp}+(\cos 2\theta-1/3)(\rho_{\|}-\rho_{\perp})$, (1)
$\rho_{\|}$ and $\rho_{\perp}$ being the resistivity with the electric current **I** applied parallel and perpendicular to the magnetization **M**, respectively, and θ the angle between **M** and **I**. The AMR is defined as the ratio
$AMR=\Delta\rho/\rho_{ave}=(\rho_{\|}-\rho_{\perp})/(1/3\rho_{\|}+2/3\rho_{\perp})$, (2)
usually multiplied by 100 for the results to be expressed in percent.
This effect is also present in FM manganites and it has been studied by many authors [2]. However, the results are commonly discussed on the basis of an existing model that has been developed for transition metals [3], where the conduction mechanism is completely different from that of manganites. In this work we performed a study of the dependence of the AMR with temperature in manganite films and based on this results we envisage a model to describe the anisotropic transport in manganites.We deposited $La_{0.75}Sr_{0.25}MnO_3$ films of different thicknesses on $SrTiO_3$ (001) single crystalline substrates by dc sputtering. X-ray diffraction patterns show that the samples grow textured in the (001) orientation of the substrates. Magnetization curves indicate that the Curie temperature T_C of the samples is close to 300 K and the saturation is near the nominal one.
The electric transport measurements were performed in the standard four lead configuration with the electric contacts aligned in the (100) direction on the plane of the films. A magnetic field H = 10 kOe, well above the saturation field, was applied on the plane of the films during the AMR measurements. In this way we can ensure that the magnetization is oriented parallel to the magnetic field, an thus the angle θ can be measured as the angle between **H** and **I**. We measured ρ(θ) curves at different temperatures. Each curve was fitted with eq.(1), and from the parameters obtained we calculated the AMR for each temperature, using eq.(2).
In fig.1 the AMR, as well as the parameters $\Delta\rho=\rho_{\|}-\rho_{\perp}$ and $\rho_{ave}=1/3\rho_{\|}+2/3\rho_{\perp}$, are presented for three different samples. The behavior is similar in all the cases. At low temperatures, the AMR (fig.1.a) is nearly constant and negative, decreasing abruptly at temperatures close to T_C (magnetization curves are shown as an inset in fig.1.c). The ρ_{ave} curves (fig.1.b) reproduce the ρ(T) measurements; the metal-insulator transition is above room temperature and so, the resistivity increases monotonously below 300 K. The difference Δρ is negative (i.e. $\rho_{\|}<\rho_{\perp}$) in all the temperature range, presenting a minimum and then a drop at T_C (fig.1.c). This drop is to be expected since the magnetization, which is at the origin of AMR, disappears.
It is clear that the sign of the AMR and its decrease at T_C are related to the behavior of Δρ. We analyzed the dependence with temperature of the obtained parameters in order to get some insight on the origin of the anisotropy. We studied the particular case of the 20 nm thick film. At temperatures lower than 250 K, ρ(T) curves can be described by
$\rho(T) = A + BT^2 + CT^5$, (3)
corresponding A to scattering of electrons with impurities and deffects,BT^2 to electron-electron scattering and CT^5 to scattering of electrons with phonons. From fitting eq.3 to Δρ and ρ_{ave}, we obtained the parameters A, B and C for $\rho_{\|}$ and $\rho_{\perp}$. The contribution of the BT^2 term to the resistivity is larger than the CT^5 one for $0 < T < 200$ K. All of the coefficients of $\rho_{\perp}$ are larger than those of $\rho_{\|}$, but the difference is more important in the coefficient B. This indicates that the origin of the anisotropy lays on electron-electron interactions. Inspired in this idea, we propose a model that takes into account the effect of the spin-orbit interaction on the electronic states of the ferromagnetic manganite. Preliminary calculations performed at 0 K (half-metallic state), are in agreement with the experimental result $\rho_{\|}<\rho_{\perp}$. Work is in progress for introducing the temperature dependence in the calculations.

[1]I. A. Campbell and A. Fert, *Ferromagnetic Materials*, Vol.3, Chap.9: Transport properties of ferromagnets. North-Holland Publ. Comp. (1982).

[2]M. Ziese and S.P. Sena, J.Phys.: Condens. Matter **10**, 2727 (1998). V. S. Amaral *et al.*, *J.Appl.Phys.* **87**, 5570 (2000). E. Favre-Nicolin and L. Rano, *J.Magn.Magn.Mater.* **272**, 1814 (2004). I.C. Infante *et al.*, *J.Appl.Phys* **99**, 08C502 (2006).

[3]A. Fert, *J. Phys. C* **2**, 1784 (1969). I. Campbell *et al.*, *J. Phys. C* **3**, S95 (1977).

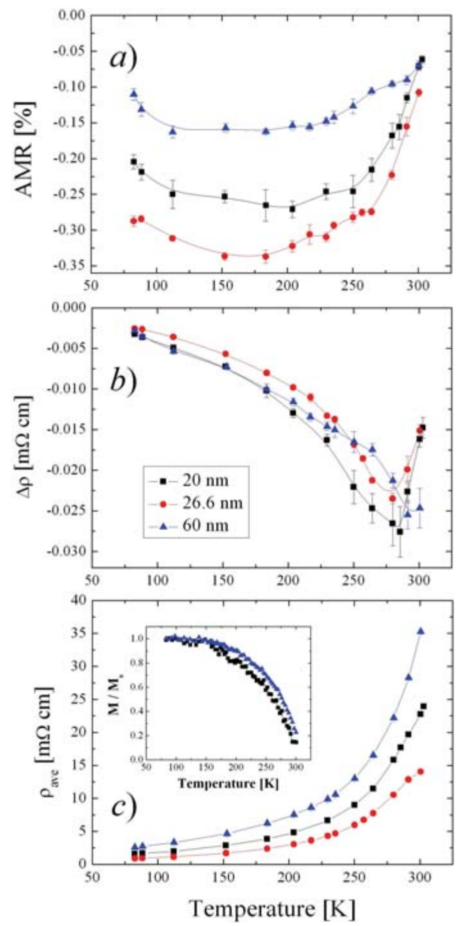

AMR (*a*), Δρ (*b*) and ρ_{ave} (*c*) measured at different temperatures for $La_{0.75}Sr_{0.25}MnO_3$ films of different thicknesses: 20 nm (■), 26.6 nm (●) and 60 nm (△).

DV-05

Comparative study of magnetic ordering in bulk and nanometer-sized $La_{0.4}Ca_{0.6}MnO_3$ manganite.

E. Rozenberg[1], M. Auslender[1], A. I. Shames[1], I. Felner[2], E. Sominski[3], A. Gedanken[3], A. Pestun[4], Y. Mukovskii[4]
1. Physics, BGU of the Negev, Beer-Sheva, Israel; 2. Physics, The Hebrew University, Jerusalem, Israel; 3. Chemistry, Bar-Ilan University, Ramat-Gan, Israel; 4. Moscow Steel and Alloys Institute, Moscow, Russian Federation

The magnetic ordering in electron-doped (x > 0.5) manganites $La_{1-x}Ca_xMnO_3$ shows a strong antiferromagnetic (AFM) component and a charge ordered (CO) state upon heating. In particular, bulk $La_{0.4}Ca_{0.6}MnO_3$ (LCMO) compound has the critical temperatures of such transitions $T_N \sim 150$ K and $T_{CO} \sim 260$ K [1]. Lu et al [2] claimed that the reduction of the LCMO samples dimension down to nanometer scale changes dramatically their magnetic ordering: ferromagnetic (FM) like ground state with spontaneous magnetization $M_S \sim 1\ \mu_B$/f.u. at 5 K appeared in LCMO powders with grain sizes of 60 and 20 nm. The AFM/CO state in bulk LCMO is known to be stable against external perturbations, so the data by Lu et al seems to be questionable.
To explore the size effect in LCMO, the dc magnetic and electron magnetic resonance (EMR) measurements were carried out on bulk and nano LCMO in the ranges 5 K $\leq$ T $\leq$ 350 K and 5 K $\leq$ T $\leq$ 600 K, respectively. Bulk samples were synthesized by solid state reaction at highest T = 1350^o C in an air. To check the influence of non-stoichiometry, two bulk samples with slightly different compositions: $(La_{0.4}Ca_{0.6})_{0.99}MnO_3$ and $La_{0.4}Ca_{0.6}MnO_3$ (labeled further as Cer1 and Cer2) were studied. The LCMO nano-powder with mean grain size of 17 ± 2 nm was prepared by the sonication-assisted co-precipitation [3] and subsequent crystallization at 900 K. The single phase nature of the samples structure being described by the P_{nma} space group, is shown by XRD. The lattice parameters are closed to each other, but demonstrate some compression of unit cell in nano LCMO, see Table.
The M versus T dependences measured at dc magnetic field H = 1 T reveal the maxima at critical $T_{CO} \sim 260$ K and ~ 267 K in Cer1 and Cer2, respectively. The low-T frustration of magnetic state - the difference between field-cooled (FC) and zero field-cooled (ZFC) curves is observed below ~ 200 K in both ceramics. The M vs. H hysteresis loops measured at T = 5 K and at H $\leq$ 5 T demonstrate that non-collinear magnetic ordering with non-saturated M and very small $M_S \sim 0.02\ \mu_B$/f.u. is characteristic of both Cer1 and Cer2 samples. The pronounced size effect is registered - for nano LCMO M vs. T curve shows the shoulder near 260 K and the broad maximum at ~ 200 K. The difference between FC and ZFC magnetizations is observed just below $T_{CO} \sim 260$ K and the low-T M_S increases up to ~ 0.05 μ_B/f.u. These results definitely contradict the data by Lu et al [2]. However, they agree with our EMR measurements.
E.g., the doubly integrated intensity of EMR signal (DIN) of bulk Cer1 and nano LCMO correlates pretty well with their M vs. T dependences – the maximum at $T_{CO} \sim 260$ K and the shoulder at this temperature together with maximum at T ~ 185 K are observed in these samples, respectively. Moreover, the sharp decrease of DIN vs. T (which is usually attributed to appearance of low-T AFM ordering [4]) is recorded for all samples studied upon cooling. However, such decrease is less pronounced in nano LCMO, which means that its low-T FM component, though small, is stronger comparing to the bulk samples.
The nature of magnetic correlations and magnetic ordering in bulk and nano LCMO was studied also by means of the model fittings [5] of electron paramagnetic resonance (EPR) parameters. It appears that DIN^{-1} vs. T (at PM state DIN is proportional to susceptibility) obeys a Curie-Weiss (CW) law with positive CW temperatures Θ_{CW}, see Table. Independent fitting of the PM line width vs. T with the Huber model [6] resulted in the Θ_{CW} values close to those obtained from the DIN^{-1} fits. The characteristic high-T asymptotes $\Delta H_{pp}(\infty)$ for the two ceramics are close to each other being smaller than this one for nano LCMO, see Table. Validity of the model [6] means that the ion-ion spin relaxation mechanism prevails in all samples studied.
In summary, the XRD data shows that both the cation composition and oxygen stoichiometry in bulk and nano LCMO are close. The AFM/CO order remains stable upon the reduction of the samples sizes. However the low-T FM component proves enhanced in nano LCMO as compared to its bulk counterparts, supposedly due to strong surface and inter-grain interaction effects. FM correlations in all LCMO samples are strong at PM state (large positive Θ_{CW}), which is an electron-doping effect. The domination of ion-ion spin relaxation at PM state and drastic fading of the FM correlations upon cooling mean that the excess electrons are localized – the lower T the deeper the localization. Even small changes of the oxygen stoichiometry notably influences magnetic ordering in LCMO that allows us to suppose that FM like order in nano LCMO reported by Lu et al [2] may be induced by a non-stoichiometry in their sol-gel prepared samples.

1. M. Pissas and G. Kallias, Phys. Rev. B 68, 134414 (2003).
2. C.L. Lu et al., Appl. Phys. Lett. 91, 032502 (2007).
3. G. Pang, et al, Mater. Res. Bull. 38, 11 (2003).
4. A.I. Shames et al, J. Magn. Magn. Mater., 290-291, 910 (2005).
5. M. Auslender et al., IEEE Trans. Magn., 43, 3049 (2007).
6. D.L. Huber et al., Phys. Rev. B 60, 12155 (1999).

Sample	Cer1	Cer2	Nano
a, b, c (Å) P_{nma} notation	5.395; 7.595; 5.402	5.394; 7.594; 5.402	5.382; 7.573; 5.395
Θ_{CW} (K) - DIN^{-1} fit	211 ± 5	228 ± 3	213 ± 3
Θ_{CW} (K) - ΔH_{pp} fit	208 ± 2	212 ± 1	205 ± 2
$[\Delta H_{pp}(\infty)]$(G) - ΔH_{pp} fit	2183 ± 17	2179 ± 14	2368 ± 18

DV-06

EMR probing of magnetic ordering in $Pr_{1-x}Sr_xMnO_3$ (x = 0.22, 0.24, 0.26) manganite single crystals.

A. I. Shames[1], E. Rozenberg[1], Y. M. Mukovskii[2], G. Gorodetsky[1]
1. Physics, Ben Gurion University of the Negev, Be'er-Sheva, Israel; 2. Moscow Steel and Alloys Institute, Moscow, Russian Federation

The $Pr_{1-x}Sr_xMnO_3$ (PSMO) compounds are known to mimic in many ways the behavior of the prototypical $La_{1-x}Ca_xMnO_3$(LCMO) system of doped manganites [1]. The two systems have the same sequence of magnetic phases upon doping, and comparable percolation threshold x_C, i.e., the critical doping level at which a crossover from a localized-type conductance to the itinerant one occurs [2,3]. This crossover is accompanied by transition from inhomogeneous to homogeneous ferromagnetic (FM) ground state. However, recent studies of magnetic and transport properties [4], as well as neutron diffraction (ND) measurements [5], carried out on PSMO single crystals with Sr-doping level in the vicinity of x_C = 0.24, reveal some notable differences between LCMO and PSMO, e.g., specific charge ordering of Mn^{4+} and Mn^{3+} ions, as well as low-temperature FM like order of Pr-subsystem in the PSMO.

To obtain a deeper insight into the nature of magnetic ordering in near-critically doped PSMO, the X-band (ν = 9.4 GHz) electron magnetic resonance (EMR) measurements were carried out in the temperature interval 5 K $\leq T \leq$ 600 K on single crystalline samples of PSMO (x = 0.22, 0.24, 0.26) grown by a floating zone technique, using radiative heating [6],labeled here as PSMO-22, PSMO-24 and PSMO-26. The T-dependences of the following EMR spectra parameters: the resonance field H_r, peak-to-peak line width ΔH_{pp} and the doubly integrated intensity (DIN, proportional to the EMR susceptibility χ_{EMR}) were analyzed. The results obtained were compared with those on dc/ac magnetic and transport properties reported for these PSMO crystals in Ref. [4]. The FM Curie temperatures T_C = 168 ± 1 K, 177 ± 1 K and 203 ± 1 K are characteristic for PSMO-22, PSMO-24 and PSMO-26, respectively.

In the paramagnetic (PM) region far above the T_C, the single Lorentzian like resonance line is observed. Its resonance field H_r is T-independent and close to 340 mT, corresponding to the PM g-factor of 1.98 ± 0.01 for all samples studied. At a certain temperature the low field shift of the signal occurs and the line distorts, which results in appearance of multiline spectra at low T. Namely, two signals with distinct low and high field H_r having different T dependences are observed in all samples below about 200 K. In addition, the third EMR signal becomes observable below ~85 K (PSMO-24) and ~100 K (PSMO-26).

The intensity of EMR absorption (DIN) increases upon cooling, shows maxima at T ~ 185 K in PSMO-26 and at T ~ 145 K in both PSMO-22 and PSMO-24 crystals. Further cooling results in vanishing of DIN in PSMO-22 below 30 K, whereas DIN in PSMO-24 and PSMO-26 remains observable down to the lowest temperatures. Moreover, the low-T shoulder is detected on DIN vs. T dependences of both PSMO-24 and PSMO-26, reflecting the appearance of the third low-T EMR signal. It is important to note that definitely non-linear dependences of inverse DIN vs. T are observed in wide interval of PM temperatures ~ 300 – 600 K in all samples studied. The line width ΔH_{pp} versus T shows minima at ~ 180 K, 200 K and 225 K in PSMO-22, PSMO-24 and PSMO-26, respectively and increases upon further heating.

Using our previous results regarding EMR in near-critically doped LCMO [7], we analyzed the data obtained in terms of specific ferromagnetic insulating (FMI) phase, appearing in PSMO below T_C. This suggestion is strongly supported by the outcomes of very recent ND studies carried out on PSMO (x = 0.22 and 0.24) crystals [5]. In particular, it was directly shown that specific quasi-static charge ordering of "1/4-type" occurs in these samples. This, in turn, means that the localization of charge carriers takes place in full agreement with the model of FMI phase appearance. It seems that the FM like order of Pr-subsystem, detected by magnetic measurements in Ref. [4], manifests itself in appearance of the third low-T EMR line in PSMO-24 and PSMO-26 crystals. Its absence in PSMO-22 may be connected with the enhanced effects of charge ordering and FMI state of Mn-subsystem in this sample, being in insulating like state within the whole T-interval of our measurements.

The non-linear dependences of inverse DIN vs. T at PM state agrees pretty well with the inverse ac magnetic susceptibility vs. T curves detected in Ref. [5] on PSMO crystals. This means that the strong short-range order persisting at PM state of PSMO leads to notable deviation of inverse DIN/susceptibility vs. T curves from a linear Curie-Weiss like dependence. E.g., the short-range charge ordering was observed in PSMO at least up to 350 K in Ref. [5]. Let us note that the line width ΔH_{pp} vs. T curves at PM state demonstrate increasing contribution of charge carriers spin relaxation mechanism [8] with increasing of Sr content. All these facts allow us to conclude that replacing of the lanthanum ions by the praseodymium ones weakens the double exchange and favors the persistence of localized nonmetallic states of charge carriers in both FM and PM states of near-critically doped PSMO.

[1] C. Martin et al., Phys. Rev. B 60, 12191 (1999).

[2] T. Okuda, et al., Phys. Rev. B 61, 8009 (2000).

[3] G.-M. Zhao et al., in Physics of Manganites, ed. by T. A. Kaplan and S. D. Mahanti (Kluwer/Plenum, N-Y, 1999), p.p. 221–241.

[4] V. Markovich et al, Phys. Rev. B 71, 224409 (2005).

[5] S. F. Dubinin et al, Phys. of Solid State 49, 739 (2007).

[6] D. Shulyatev et al, J. Cryst. Growth 237/239, 810 (2002).

[7] A.I. Shames et al, Phys. Rev. B 68, 174402 (2003).

[8] M. Auslender et al, IEEE Trans. Magn. 43, 3049 (2007).

DV-07

Magnetic and magnetoresistive properties of $Pr_{1-x}Ca_xCoO_3$ (x =0.3, 0.5) cobaltites.

I. G. Deac[1], R. Tetean[1], D. Andreica[1,2], E. Burzo[1]
1. Physics, Universitatea Babes-Bolyai, Cluj-Napoca, Romania; 2. Laboratory for Muon-Spin Spectroscopy, Paul Scherrer Institut, Villigen, Switzerland

Since the discovery of the "colossal" magnetoresistance MR effect in manganites, the search for the next MR materials has been widely conducted in various transition-metal oxides. Doped cobaltite perovskites $Ln_{1-x}A_xCoO_3$ (Ln= rare earth and A = Ca, Sr, Ba), have recently attracted much attention due to their unique feature to change the spin-state of the Co^{3+} ion. The spin-state of undoped $LnCoO_3$ exhibits a gradual crossover with increasing temperature, from the low-spin (LS) state ($t^6_{2g}e^0_g$) to the intermediate-spin (IS) state($t^5_{2g}e^1_g$) or to the high-spin (HS) state($t^4_{2g}e^2_g$) [1]. Upon doping A^{2+} ions into $LnCoO_3$, some of trivalent Co ions become tetravalent, and these also contain a mixture of low and higher spin sates. Both double and superexchange interactions are present in these compounds. The competition of different kinds of interactions leads to a highly inhomogeneous ground state characterized by the coexistence of FM regions, spin-glass regions, and hole-poor LS regions [2,3].

In the present work, the physical properties of perovskite cobaltites, $Pr_{0.7}Ca_{0.3}CoO_3$ and $Pr_{0.5}Ca_{0.5}CoO_3$ have been investigated. The polycrystalline samples were prepared by the conventional ceramic method. The samples were single perovskite phase of orthorhombic *Pbnm* symmetry. Electrical measurements were carried out by the four-probe method. The magnetization measurements were done in a cryostat by using DC extraction method. The μSR (muon spin rotation/relaxation/resonance) experiments were performed at the GPS spectrometer at the Paul Scherrer Institute.

Preliminary measurements of the magnetization in 1 T field for the samples, with x = 0.3 and x = 0.5, do not show distinct ferromagnetic transitions down to about 50 K and 70 K, respectively. There are some slight changes in the magnetization as a function of temperature, but these cannot be seen as genuine ferromagnetic transitions (Fig. 1.). The shape of χ – T curves is rather complex, not typical of normal ferromagnets. A paramagnetic Curie temperature (θ_p) can be estimated from the linear part of the reciprocal susceptibility, to be -25 K, while the effective paramagnetic moment is 3.71 μ_B for the sample with x = 0.3. The ac susceptibility measurements show a sharp, frequency dependent peak for both the real χ' and the imaginary χ" components of the complex susceptibility at 16 K, for the sample with x = 0.3 when H_{ac} = 1 Oe (Fig. 1.). For the sample with x = 0.5, a broad maximum was found in ac susceptibility at about 75 K. The μSR measurement showed a missing asymmetry below 55 K for $Pr_{0.7}Ca_{0.3}CoO_3$ indicating the presence of magnetic clusters. In the x = 0.5 sample a decrease of asymmetry occurs below 70 K, suggesting the onset of magnetic order. A paramagnetic insulating phase was found to develop and to coexist with the ferromagnetic one below 30 K [3]. Generally, the magnetic measurements indicate that these cobaltites are magnetically inhomogeneous, with small ferromagnetic clusters or domains being present in a paramagnetic and/or an antiferromagnetic matrix, as a consequence of the spin-state transition of Co^{3+}/Co^{4+} ions. The resistivity decreases with increasing temperature for both samples, in spite of their low "metallic" values. The sample with x = 0.3 has a low negative magnetoresistance MR, of a few percents, while for the sample with x = 0.5 we found MR ~ 22% (Fig. 2). The electrical behavior of the studied samples has the main features of conduction in a phase separated system: it shows negative magnetoresistance and it is controlled by grain-boundary effects.

[1] S. Tsubouchi, et al., Phys. Rev. B 66 (2002)052418. [2] T. Fujita, et al., J. Phys. Soc. Jpn. 73 (2004) 1987.[3] A. Chichev, et al.,J.Magn.Magn.Mat.316 (2007) e728.

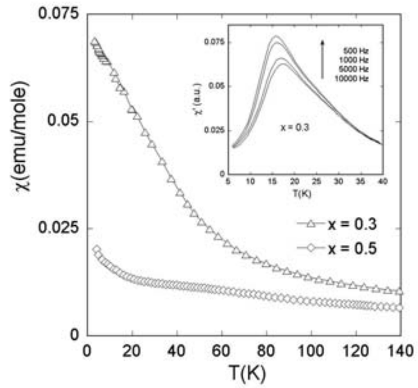

Fig. 1. Magnetic susceptibilities for the two samples. In insert, frequency dependence of the ac susceptibility for the sample with x = 0.3, H_{ac} = 1 Oe, f = 500 - 1000 Hz.

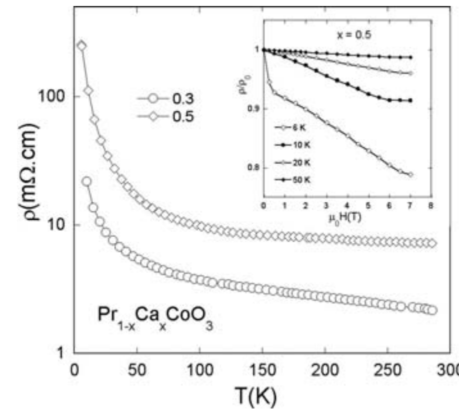

Fig. 2. Electrical resistivity for the two samples in 0 T . In inset: ρ(H)/ρ(0), at 6, 10, 20 and 50 K.

DV-08

Magnetism of LCMO/YBCO thinfilm epitaxial heterostructures.

N. M. Nemes[1,3], M. García-Hernández[1], Z. Szatmári[2], T. Fehér[2], F. Simon[2], J. García-Barriocanal[3], F. Y. Bruno[3], C. Leon[3], C. Miller[3], Z. Sefrioui[3], C. Visani[3], J. Santamaría[3]
1. Instituto de Ciencia de Materiales de Madrid, Consejo Superior de Investigaciones Cientificas, Madrid, Spain; 2. Institute of Physics, Budapest University of Technology and Economics, Budapest, Hungary; 3. GFMC, Dpto. Fisica Aplicada III, Universidad Complutense de Madrid, Madrid, Spain

The growth of heterostructures combining oxide materials is a new strategy to design novel artificial multifunctional materials with interesting behaviors ruled by the interface. In heterostructures involving oxide superconductors and colossal magnetoresistance (CMR) ferromagnets interfaces are especially complex, with ferromagnetic (F) and superconducting (S) properties at the interface depressed over nanometer length scales. Recently, F/S structures made of YBa2Cu3O7 (YBCO) and La0.7Ca0.3MnO3 (LCMO) have attracted considerable attention [1,2]. The critical temperature of the superconductor depends on the relative orientation of the magnetization of the F layers, giving rise to a new giant magnetoresistance (GMR) effect which might be of interest for spintronic applications. Large positive magnetoresistance peaks occur for antiparalel (AP) alignment of the manganite layers, much resembling the GMR in metallic superlattices, resulting from enhanced interface scattering in the AP configuration.
Detailed study of the magnetic properties of the ferromagnetic manganite thinfilm electrodes are necessary in order to gain a better understanding of the functioning of these F/S devices. Manganite monolayers as thin as 3 nm exhibit clear ferromagnetic hysteresis loops (Fig. 1, left panel). The saturation magnetization does not diminish in thin manganite films indicating a lack of a pronounced magnetic dead layer. The coercive field increases drastically in thinner films, indicating the possibility of fabricating trilayers with AP configuration. Nevertheless, the field of saturation is also larger in thinner films raising the possibility that the magnetization lies out of the film plane. Temperature dependent resistivity is shown in the right panel of Fig. 1. Films thicker than 6 nm behave metallically at low temperature with well defined metal insulator transition, although the thinnest films remain insulating at low temperature.
As the AP configuration in low external magnetic field is needed for the GMR effect, it is important to know the direction of easy axes of magnetization in the individual F layers. Using ferromagnetic resonance we map the direction of the in-plane easy axes in 5 and 15 nm thick LCMO films and find that both exhibit biaxial symmetry, similar to LSMO films [3]. Nevertheless, the symmetry direction in the two films is rotated by 45 degrees with respect to the crystallographic directions. In the 5 nm film the in-plane easy axes are the (100) and (010) while in the 15 nm film the easy axes are the (110) and (1-10), indicated by the minimum values of the resonance field (Fig. 2).
As the thickness of the manganite thinfilm is shown to be responsible for dramatic changes in the magnetic and metallic behaviour of the electrode, it is important to study the properties of manganite thinfilms as they form part of various F/S bilayer structures. The YBCO underlayer in particular may alter the magnetic properties of the manganite thinfilm. The coercive field of 15 nm thick manganite thinfilms grown on STO with YBCO on top are much smaller (around 50 Oe) than that of similar manganite thinfilms grown on YBCO (150-300 Oe). The saturation magnetization is reduced considerably in manganite thinfilms grown on YBCO (~320 emu/cm3) vs. those grown on STO (~580 emu/cm3).

[1] V. Peña, Z. Sefrioui, D. Arias, C. Leon, J. Santamaría, J. L. Martinez, S. G. E. te Velthuis and A. Hoffmann Phys. Rev. Lett. 94, 057002 (2005)

[2] C. Visani, V. Peña, J. Garcia-Barriocanal, D. Arias, Z. Sefrioui, C. Leon, J. Santamaría, N. M. Nemes, M. Garcia-Hernandez, J. L. Martinez, S. G. E. te Velthuis and A. Hoffman Phys. Rev. B 75, 054501 (2007)

[3] M. Mathews, F. M. Postma, J. C. Lodder, R. Jansen, G. Rijnders and D. H. A. Blank Appl. Pys. Lett. 87, 242507 (2005)

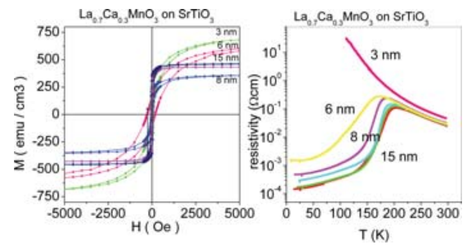

Magnetization (left) and resistivity (right) of LCMO thinfilms with various thicknesses between 3 and 15 nm.

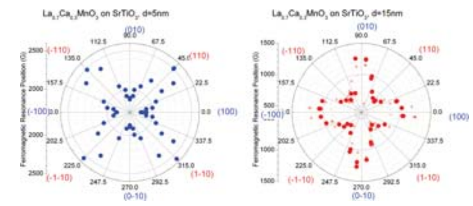

Ferromagnetic resonance in d=5 nm and d=15 nm LCMO thinfilms with the external magnetic field lying along various in-plane directions.

DV-09

In-situ strain effect on extrinsic electrical transport and magnetotransport in $La_{0.7}Sr_{0.3}MnO_3$ films.

R. Gangineni, L. Schultz, I. Mönch, K. Dörr
Institute for Metallic Materials, Leibniz Institute for Solid State and Materials Research Dresden, Dresden, Germany

In recent years, grain boundaries in conducting ferromagnetic manganites have been studied extensively for their spin-polarized electron tunneling associated with large magnetoresistance. In this work, we focus on the change of extrinsic electric transport and magnetotransport properties with respect to in-situ strain of epitaxial $La_{0.7}Sr_{0.3}MnO_3$ films grown on PMN-PT $(0.72Pb(Mg_{1/3}Nb_{2/3})O_3$-$0.28PbTiO_3)$ containing etched steps. Application of an electric field E along the substrate normal allows reversible control of the in-plane piezoelectric strain. A reversible strain of about 0.11% is acquired with an application of 10 kV/cm to the piezoelectric substrate [1,2]. The steps on PMN-PT substrate are defined by optical lithography and ion beam etching with a height between 300 and 600 nm and a step width of 25 µm. Films of 20 to 70 nm thickness are grown using off-axis pulsed laser deposition. The piezoelectrically induced biaxial in-plane strain can be compressive or tensile. With decreasing temperature (T), the electric coercive field (E_C) increases considerably, enlarging the field range $|E| < E_C$ available for the in-plane expansion. Strain-dependent loops of resistance (R) recorded during one cycle of the electric field for several temperatures are shown for sample A (20 nm) in Fig.1. The in-plane expansion reaches large values for E < 0. This is reflected in the extremely large R enhancements observed at 70 K and 90 K for negative E. Left axis of Fig.2 represents the temperature dependent R of a 20 nm film with respect to applied strain of 0.05% and in no applied strain. On right axis of Fig.2, temperature dependence of gauge factor Γ (defined as the ratio of the relative R change and the change in strain) is displayed. The change in resistance with respect to applied strain varies according to thickness of the film. The strain-induced R change of the film (20 nm) is large (20-25%) for 50 K < T < 300 K in contrast to the strain response of the film on the step free substrate [1]. The effect of strain in magnetic fields up to 5 T is shown in Fig.3 for sample A (20 nm). The high-field part of the grain boundary MR has been attributed to field-induced magnetic ordering of Mn spins in a magnetically less ordered layer at the grain boundaries [3]. The effect of strain on the magnetism of these layers is an interesting question, addressed in earlier work [4]. Decrease in MR (H = 5T) in the compressed state (E = 7.1 kV/cm) and increase in the expanded states (E = -1.8 to -7.1 kV/cm) in comparison with the piezo strain-free case (E = 0) is observed [2]. In summary, reversible strain variation in step edge junctions in spin-polarized $La_{0.7}Sr_{0.3}MnO_3$ films has been demonstrated utilizing piezoelectric substrates of PMN-PT. Both R and MR decrease (increase) significantly upon in-plane compression (expansion). Further, the results obtained from the effect of strain on polycrystalline films and films deposited on single steps of PMN-PT substrates are compared.

1. C. Thiele, K. Dörr, S. Fähler, L. Schultz, D.C. Meyer, A.A. Levin, P. Paufler, Appl. Phys. Lett. 87 262502 (2005).

2. R.B.Gangineni, L.Schultz, C.Thiele, I.Mönch and K.Dörr, Appl. Phys. Lett. 91, 122512 (2007).

3. R. B. Gangineni, K. Dörr, N. Kozlova, K.Nenkov, K. –H. Müller, L. Seethalakshmi and L. Schultz, J. Appl. Phys. 99, 053904 (2006).

4. Yeong-Ah Soh, G. Aeppli, C. -Y. Kim, N. D.Mathur, and M. G. Blamire, J. Appl. Phys. 93,8322 (2003).

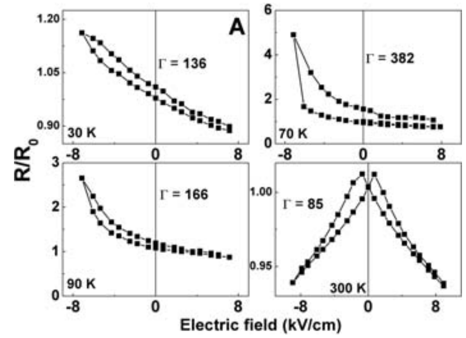

Resistance (normalized to the value at zero electric field) as a function of applied electric field at different temperatures of $La_{0.7}Sr_{0.3}MnO_3$ (20 nm) on a substrate containing steps.

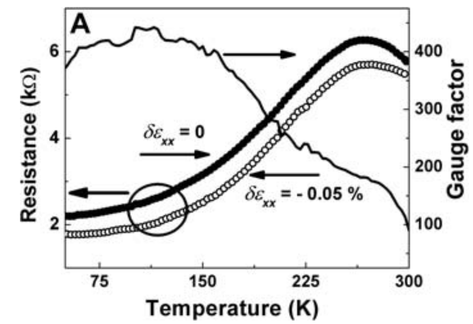

Temperature dependence of the resistance R (left axis) in two different strain states for 20 nm LSMO film deposited on PMN-PT. The gaugefactor Γ (right axis) is the relative resistance change to relative strain change.

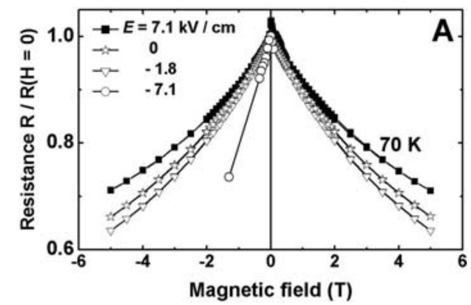

Resistance (normalized to the value at zero magnetic field) as a function of magnetic field at various strain states of sample A (20 nm).

DV-10

Effect of Cr Doping on the Magnetic Properties of $La_{0.3}Ca_{0.7}MnO_3$

L. E. Wenger[1], G. M. Tsoi[1], R. Suryanarayanan[2], T. Sudyoadsuk[3]
1. Department of Physics, University of Alabama at Birmingham, Birmingham, AL; 2. Laboratoire de Physico-Chimie de l'Etat Solide, CNRS, Université Paris-Sud, Orsay, France; 3. Department of Chemistry, Ubon Ratchathani University, Ubon Ratchathani, Thailand

Electron-doped manganites such as $La_{1-x}Ca_xMnO_3$ (x > 0.5) with Mn(IV)/Mn(III) ratios greater than one are typically insulators which exhibit several interesting properties including a charge-ordering (CO) transition followed by an antiferromagnetic ordering at lower temperatures.[1] Since this CO state is accompanied by a lattice stiffening, its formation and stability are very sensitive to how the spin, charge, and lattice degrees of freedom interact and compete. Thus the substitution of another 3d-element at the Mn-site can have a dramatic effect on the magnetic properties including the total suppression of the CO state and the appearance of a low-temperature ferromagnetic phase. Even an insulator-to-ferromagnetic metal transition accompanied by a colossal magnetoresistance (CMR) has been observed.[2,3] Moreover, recent investigations have shown that phase separation can occur at the local level in various doping regimes such that the appearance of a CMR effect might also arise from the coexistence of ferromagnetic metallic regions with these CO insulating domains.[4,5] Cr substitution is a particularly interesting substitution as Cr^{3+} is isoelectronic with Mn^{4+} and the magnetic interaction Cr^{3+}–O–Mn^{3+} is known to favor ferromagnetism through the superexchange mechanism. Hence, the effect of Cr substitutions on the structural, magnetic, and electrical transport properties of electron-doped $La_{0.3}Ca_{0.7}Mn_{1-y}Cr_yO_3$ (y = 0.0, 0.10, 0.15, 0.20, and 0.25) polycrystalline samples prepared by sol-gel technique have been investigated between 5 and 300 K in magnetic fields ranging from 0 to 5 Tesla. The CO transition at 260 K and the antiferromagnetic transition at 170 K observed in the parent manganite (y = 0.0) are gradually suppressed and occur at lower temperatures while the onset of a ferromagnetic remanence grows with the addition of Cr until only ferromagnetic-like behavior is observed in the y ≥ 0.20 manganites. These features along with a magnetic hysteresis and irreversibility indicate that ferromagnetic clusters coexist with an antiferromagnetic/CO phase for the lower Cr-doped manganites (y ≤ 0.15) as the magnetic hysteresis curves are offset from the origin for these Cr-doped samples. However, for the higher Cr-doped manganites (y ≥ 0.20), the antiferromagnetic/CO phase is completely suppressed as the hysteresis curves are not offset and only the ferromagnetic cluster glass phase is present. The electrical resistivity for the Cr-doped samples in zero magnetic field exhibit an exponential temperature dependence that is consistent with the small polaron hopping model above 100 K and the Mott's hopping mechanism at lower temperatures. Unlike the parent compound $La_{0.3}Ca_{0.7}MnO_3$, a small negative magnetoresistance is observed in all Cr-doped samples at temperatures below the onset of the magnetic remanence. The appearance and magnitude of this magnetoresistance are consistent with spin dependent hopping between spin clusters and/or between ferromagnetic domains, and not with any insulator-to-metallic transition typically associated with a colossal magnetoresistance effect.

[1] E. Dagotto, T. Hotta, and A. Moreo, Phys. Reports **344**, 1 (2001).

[2] R.-W. Li, J.-R. Sun, Z.-H. Wang, and B.-G. Shen, J. Appl. Phys. **88**, 5924 (2000).

[3] C. Martin, A. Maignan, F. Damay, M. Hervieu, B. Raveau, Z. Jirak, G. André, and F. Bourée, J. Magn. Magn. Mater. **202**, 11 (1999).

[4] S. Mori, C.H. Chen, and S.-W. Cheong, Nature **392**, 473 (1998).

[5] S. Mori, R. Shoji, N. Yamamoto, T. Asaka, Y. Matsui, A. Machida, Y. Moritomo, and T. Katsufuji, Phys. Rev. B **67**, 012403 (2003).

DV-11

1/f noise study of electron transport in $La_{0.82}Ca_{0.18}MnO_3$ single crystals.

X. Wu[1,2], G. Jung[2], B. Dolgin[2], V. Markovich[2], Y. Yuzhelevski[2], M. Belogolovskii[3,4], Y. M. Mukovskii[5], K. Suzuki[1], G. Gorodetsky[2]
1. Materials Engineering, Monash University, Clayton, VIC, Australia; 2. Physics, Ben Gurion University, Beer Sheva, Israel; 3. Donetsk Physical and Technical Institute, National Academy of Sciences of Ukraine, Donetsk, Ukraine; 4. Scientific and Industrial Concern 'Nauka', Kyiv, Ukraine; 5. Moscow State Steel and Alloys Institute, Moscok, Russian Federation

A fundamental interest in mixed-valence manganese perovskites arises from their strongly spin-dependent conductivity and pronounced manifestations of phase separation (PS). In a complex and rich phase diagram of $La_{1-x}Ca_xMnO_3$ (LCMO) manganites the critical doping level x_c=0.225 separates ferromagnetic (FM) insulating ground state at $x < x_c$ from FM metallic ground state above x_c. In the doping range 0.17< x <0.25 a mixed FM state composed of insulating and metallic FM phases with different levels of orbital ordering appears below Curie temperature Tc[1]. Therefore, physical mechanisms dominating transport properties of low-doped LCMO became remarkably different when the temperature is changing[2].
Interesting metastable resistivity states in low doped LCMO single crystal can be induced when current flow exceeds some threshold currents [2], depending on the history of the sample. Some of these metastable resistance states are relatively very stable and can only be removed by heat treatments at temperature much higher than Tc. Noise measurement is a well known technique to study the dynamical property of physical system. In such complex system as low-doped LCMO one expects that noise data will allow to get a deeper insight into the dynamics of dissipation processes associated with different transport mechanisms. In this report we use noise technique to probe the dynamical property of low-doped LCMO single crystals at three different states, i.e. pristine state and two current-induced metastable resistance states.
The experiments were performed with $La_{0.82}Ca_{0.18}MnO_3$ single crystals grown by a floating zone method. Two states were induced by two current-pulse treatments at 78 K, a pulse of 10 V and 5 seconds and a pulse of 30 V and 5 seconds. Resistance, Current-voltage characteristics, differential resistance, and noise spectra were measured at various temperatures in variable temperature cryostat using a standard four-point contact arrangement. 1/f low frequency noise is found in all experimental ranges.
Resistance measurements show that the current-pulse treatments shift the Resistance vs Temperature curves to higher resistance level. The induced high resistance states are stable within the experimental temperature range. When the resistance is normalized by the resistance at Tc, the resistance vs. temperature curves at three different states collapse together.
The noise measurment result at the pristine state is shown in Figure 1. Sv is I^2 dependant with exception at 77 K, which means that the observed noise is caused by current independent resistivity fluctuations. Noise intensity at 77 K initially increases as I^2 but around 1 mA starts to decrease. After a 10 V pulse treatment, the noise spectral density is enhanced, but the behavior of the noise is similar to the results at the pristine state, as shown in Figure 2. However, after the 30 V pulse treatment, deviation of Sv from I^2 dependence were observed at all temperatures below and around Tc.
The results were interpreted in terms of spin-polarized tunnel conduction mechanism, and current-induced modification of PS along the percolation path.
In summary, we have observed 1/f voltage noise at three different states of LCMO single crystals in a wide range of currents and temperatures corresponding to markedly different magnetic and transport properties of the system. Non-equilibrium noise appears and decreases with increasing bias at situation where transport is dominated by tunneling mechanism. The pulse treatments don't change the behaviors of the static transport property, but induce significantly change in the dynamical transport property.

1. Papavassiliou, M.Pissas, M.Belesi, M. Fardis, J. Dolinsek, C. Dimitropoulos, and J.P. Ansermet, Phys. Rev. Lett. 91, 147205(2003)

2. Y. Yuzhelevski, V. Markovich, V. Dikvosky, E. Ronzenberg, G. Gorodetsky, and G. Jung, Phy. Rev. B 64, 224428 (2001)

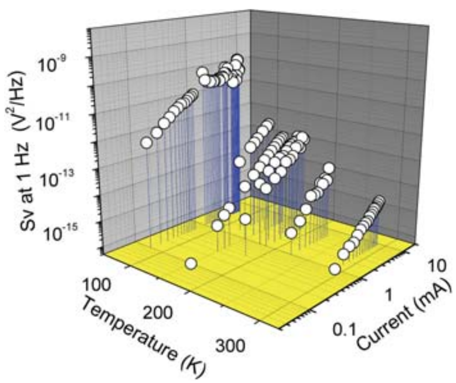

Fig. 1. Sv as a function of temperature and current at the pristine state

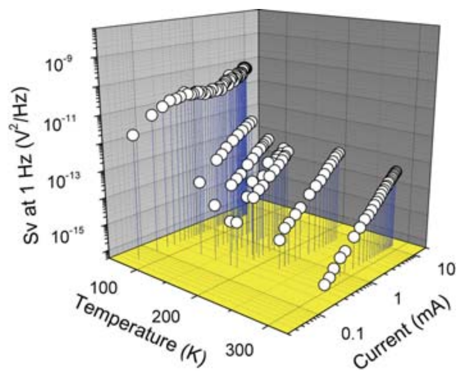

Fig.2. Sv as a function of temperature and current at the state after a 10 V pulse treatment

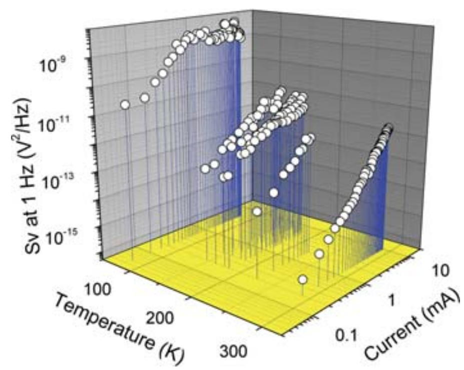

Fig.3. Sv as a function of temperature and current at the state after a 30 V pulse treatment

DV-12

Effect of substrate orientation on magnetic anisotropy and 1/f noise in La0.7Sr0.3MnO3 thin films.

L. Mechin[1], P. Perna[1,2], M. Saib[1], S. Flament[1], C. Barone[1,3], D. Fadil[1], J. Routoure[1]
1. GREYC-ENSICAEN, CNRS, Caen, France; 2. DiMSAT, University of Cassino, Cassino, Italy;
3. Dipartimento di Fisica "E.R. Caianiello", University of Salerno, Salerno, Italy

We report in this paper the effects of SrTiO3 (STO) substrate orientation on magnetic anisotropy and 1/f noise in La0.7Sr0.3MnO3 (LSMO) thin films. Films of various thicknesses have been deposited by pulsed laser deposition on STO (001), STO (110) and vicinal STO (001) substrates, where the vicinal angles were 2, 4, 6, 8 and 10° from the [001] direction towards [110]. The structural properties of the films were studied using X-ray diffraction in symmetrical and assymetrical X-ray configurations. Reciprocal space maps (RSM) of the regions around (002), (103) and (223) STO reflections were performed in order to measure the strain in the films. Atomic Force Microscopy (AFM) and Scanning Tunnelling Microscopy (STM) clearly revealed the effect of substrate orientation on the surface morphology of the films. 80 nm large terraces were typically observed on STO (001) substrates, whereas (100) elongated grains appeared on STO (110) substrates (fig.1) and terraces of variable width depending on the miscut angles appeared in the case of the vicinal substrates (fig.2). The root mean square roughness was found in the 0.132 – 0.328 nm range for all the investigated samples. SQUID magnetometer measurements revealed a Curie temperature of about 350K. Kerr Magneto-Optical microscopy was used to investigate the magnetic anisotropy, the magnetic domain arrangement and the magnetization reversal in the films. LSMO films on STO (001) showed an in-plane biaxial magnetic anisotropy along the [110] and equivalent directions. LSMO films on STO (110) and on vicinal substrates, if the miscut angle is higher than 4°, showed an uniaxial anisotropy with the easy axis along the [100] axis on STO (110) and along the step direction on vicinal STO, respectively. Finally, 1/f noise measurements, and resistivity versus magnetic field characteristics will be presented. Possible devices making use of the magnetic anisotropy will be discussed.

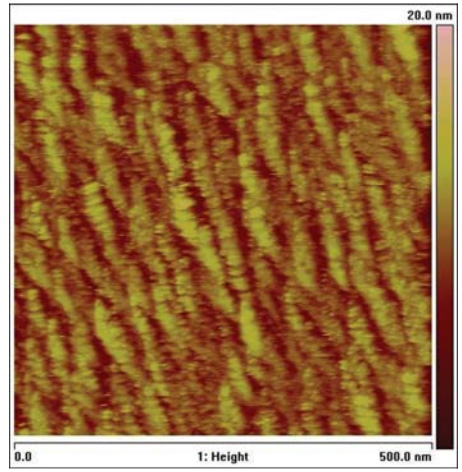

500 nm * 500 nm STM image of a 40 nm thick LSMO film deposited on a STO(110) substrate showing elongated grains along (100)

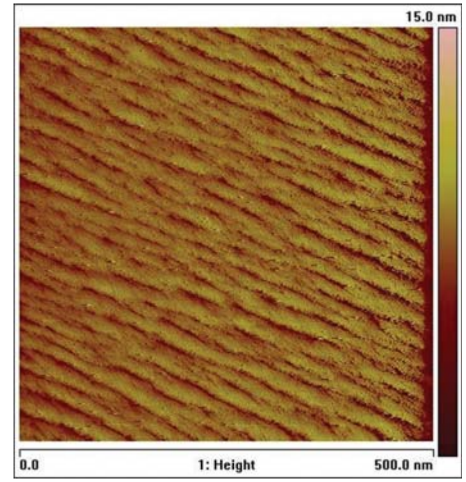

500 nm * 500 nm STM image of a 40 nm thick LSMO film deposited on a 10° vicinal STO substrate showing 30 nm large regular terraces.

DV-13

Room temperature giant magnetoimpedance in La0.67Sr0.33MnO3.

M. Ramanathan
Department of Physics, National Univeristy of Singapore, Singapore, Singapore

The discovery of colossal magnetoresistance (CMR) in manganites of the general formula R1-xAxMnO3 (R = trivalent rare earth ion, A = divalent alkaline earth ion) in early 90's stirred excitement among scientific community due to possible application of these materials in novel spintronic devices [1]. While several exotic electronic and magnetic phases exhibited by these oxides shifted recent interest in these materials towards more fundamental studies on strongly correlated electron systems, technological exploitation of the CMR effect at room temperature has been hampered by the need of magnetic field of H > 1 Tesla to induce more than 10 % magnetoresistance (MR). It was suggested that extrinsic MR arising from spin-polarized tunneling of charge carriers between misaligned ferromagnetic grains in polycrystalline materials can be exploited for practical applications at low magnetic fields (~ 0.5 T) compared to the intrinsic MR which peaks at the ferromagnetic Curie temperature but becomes negligible much below TC[2]. Though the extrinsic MR is large ≈ 30-35 % at 10 K and at 0.5 T, it decreases rapidly while approaching the room temperature[3,4]. Extensive efforts are underway in different laboratories to enhance the magnitude of magnetoresistance at low fields, particularly in milli and micro tesla range using techniques such as artificial grain boundary in epitaxial films, trilayer tunnel junctions and step edge junctions.
In this report, we explore the possibility of enhancing the magnetoresistance in mT range using a different approach. Although magnetoresistance in various manganites with dc current has been extensively studied during the past one decade, high frequency magnetotransport in these materials is hardly investigated.In this work, we have investigated the magnetic -field response of the ac impedance in La0.67Sr0.33MnO3 by directly passing r.f. current in the sample.
Our recent study of temperature dependence of high frequency electrical impedance (f = 100 Hz - 5 MHz) in La0.75Sr0.25MnO3 established that magnetic transition masked by scattering of charges can be detected with radiofrequency electrical impedance [5]. In this report we study the complex impedance Z (f, H) = Z′(f, H)+jZ″(f, H) of La0.57Sr0.33MnO3 over an extended frequency range(f = 0.5 MHz - 30 MHz) as a function of dc magnetic field (-100 mT ≤ ≤ 100 mT) at 300 K. We show that the ac magnetoresistance (ΔZ′/Z′(0)) in a small field of 100 mT is much larger (≈ 47 % at f = 2 MHz) than the dc magnetoresistance (< 1 %). It is also shown that the ac magnetoreactance, ΔZ″/Z″(0), as a function of magnetic field exhibits a transition from a single peak to a double peak behavior with increasing frequency beyond 20 MHz and even change of sign from negative to positive in contrast to the ac magnetoresistance which is negative and exhibits only a single peak centered around the origin for all frequencies (see figure 1). The observed magnitude and features of magnetoimpedance are shown to be strongly dependent on the length of the sample. We attribute the observed enhancement of ac magnetoresistance to the suppression of the transverse permeability under the external dc magnetic field. Our study suggests that radio frequency magnetotransport can be exploited not only for low-field magnetic sensing at room temperature but it can also be used to probe dynamical transverse permeability in these compounds.

[1]Y. Tokura (Ed.), Colossal Magnetoresistive Oxides (Gordon & Breach science publisher, Singapore, 2000).

[2] H. Y. Hwang, S-W. Cheong, N. P. Ong, and B. Batlogg, Phys. Rev. Lett. 77, 2041 (1996.

[3]A. Gupta, G.Q.Gong, G. Xiao, P. R. Duncombe, P. Lecoeur, P. Trouilloud, Y. Y.Wang, V. P. Dravid and J. Z. Sun, Phy. Rev. B 54, R15629 (1996).

[4]R. Mahendiran, R. Mahesh, A. K. Raychaudhuri, and C. N. R. Rao, Solid State Commun. 99, 149 (1996).

[5] S. K. Barik, A. Rebello, C. L. Tan, and R. Mahendiran, J. Phys. D: Appl. Phys. 41, 020019 (2008).

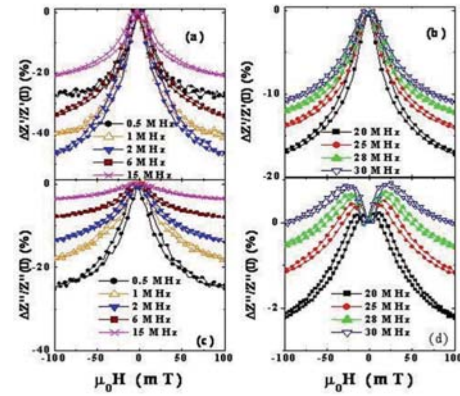

Figure 1: Magnetic field dependence of the ac magnetoresistance (ΔZ′/Z′ (0), top panel) and the ac magnetoreactance (ΔZ″/Z″(0), bottom panel) at various fixed frequencies for f = 0.5 – 15 MHz((a) & (c)), and f = 20 – 30 MHz ((b) & (d)). Note that the single peak in ΔZ″/Z″(0) transforms into double peaks at ±Hp and Hp shifts up in field with increasing frequency.

DV-14

Electroresistance in mixed valence manganites.

N. Biskup, A. de Andrés, M. Garcia Hernandez
ICMM, Madrid, Spain

Transition metal oxides, having strongly correlated electron systems, show unusually drastic phase transitions (Mott transitions) under external perturbation, including ferromagnetism, superconductivity, and others. Because of the strong coupling between spin, charge, and orbital degrees of freedom, the perovskite manganites (general formula: $R_{1-x}A_xMnO_3$, with 0<x<1; R=La, Pr; A=Ca, Sr). typically exhibit a rich variety of electronic and magnetic properties, such as ferromagnetism with metallic conduction, and charge/orbital ordering, depending on carrier concentration. Historically, the most studied phenomenon in manganites is magnetoresistance (MR), the magnitude of which ranges from "giant" 10%–20% to colossal 10^8% in charge ordered $Pr_{1-x}Ca_xMnO_3$, x=0.3–0.5 [1]. Recently, a more debated phenomenon is electroresistance (ER), i.e., nonlinear current-voltage (I-V) characteristics. Similar to MR, the magnitude of ER varies in different compounds, reaching equally colossal values in $Pr_{0.7}Ca_{0.3}MnO_3$ [2]. ER and MR are shown to be coupled, i.e., the voltage/current necessary to trigger insulator-metal transition decreases with magnetic field. Since this initial report in 1997, a significant number of publications report nonlinear I-V effects in manganites. Initially, investigations were limited to materials with charge order (CO) ground state. Different interpretations for these nonlinearities included depinning of CO state, depinning of charge density waves, or change in the orientation of orbital ordering (OO). Indeed, nonlinear effects were subsequently found in materials without CO and recent reports tend to interpret the nonlinear I-V characteristics in manganites as the consequence of Joule heating due to the large currents [3].

We have shown that all narrow-bandwidth (insulating) manganites show strongly nonlinear I-V characteristics, including negative differential resistance (NDR) [4]. NDR is always accompanied by heating which makes it difficult to extract its origin. However, in systems with CO/OO, we have observed the discontinuous transitions between low and high resistive states (LR→HR) that are caused by charge/orbital rearrangements and not by heating [5]. Moreover, in $La_{0.9}Sr_{0.1}MnO_3$ these discontinuous transitions are found only in the ferromagnetic state, thus linking the ER with magnetic order [6]. We will show that the magnetic ordering, i.e. LR→HR transitions are the cause of heating due to the transfer of entropy on the switch between ordered and disordered magnetic states.

In spite of the interconnection between magnetic order and electroresistance, magnetic field and electric field can induce different states. We show that, while the magnetic field enhances the orbital order in $La_{0.9}Sr_{0.1}MnO_3$ and concomitantly induces higher resistive state (larger electron gap), electric field is able to suppress the orbital order and the system enters into the metallic state. This leads to a colossal ER at low temperatures while MR is almost absent.

1 Y. Tomioka, A. Asamitsu, Y. Moritomo, and Y. Tokura, J. Phys. Soc. Jpn. 64, 3626 (1995).

2 A. Asamitsu, Y. Tomioka, H. Kuwahara, and Y. Tokura, Nature (London) 388, 50 (1997).

3 S. Mercone, R. Frésard, V. Caignaert, C. Martin, D. Saurel, C. Simona, G. André, P. Monod, and F. Fauth, J. Appl. Phys. 98, 023911 (2005).

4 N. Bi škup A. de Andrés, I. M. Ochando and M. T. Casais, Phys. Rev. B 73, 184404 (2006).

5 N. Bi škup and A. de Andrés, Phys. Rev. B 74, 184403 (2006).

6 N. Bi škup, A. de Andrés, N. M. Nemes, M. Garcia-Hernandez, K. V. Glazyrin and. Y. M. Mukovskii, Appl. Phys. Lett. 90, 222502 (2007).

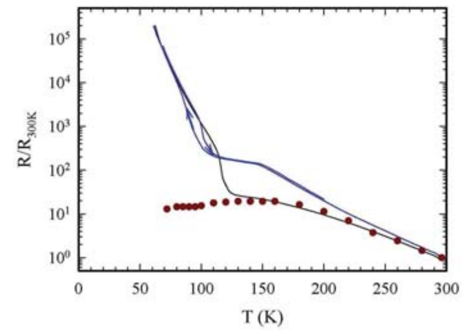

Temperature dependence of normalized resistance. Blue line, with hysteresis: B=0T, I«I_t (I_t is threshold current for HR→LR transition). Black line - magnetoresistance: B=8T, I«I_t. Points - electroresistance: B=0 T and I>I_t.

DV-15

Impedance spectroscopy of magnetoresistive manganite films exhibiting electric-pulse-induced resistance switching.

T. Nakamura, K. Homma, T. Yakushiji, K. Tachibana
Department of Electronic Science and Engineering, Kyoto University, Kyoto, Japan

Magnetoresistive manganites have been attracting considerable interest for their unique magnetic and electric properties such as half-metallicity and colossal magnetoresistance (CMR). Recently, a large resistance change by the application of an electric pulse was observed at room temperature in metal oxides such as $Pr_{1-x}Ca_xMnO_3$ (PCMO). This effect provides a possibility of a next-generation nonvolatile memory, called resistance random access memory (ReRAM). ReRAM is highly expected due to its low power consumption, small bit cell size, and fast switching speed. In this work, PCMO films were deposited on $Pt/SiO_2/Si$ and SiO_2/Si substrates by rf magnetron sputtering or by metalorganic chemical vapor deposition (MOCVD). The electrical-pulse-induced resistance switching behavior was investigated in the PCMO-based devices. In order to study the switching mechanism in the PCMO-based devices, the frequency response of complex impedance of the devices was measured under various DC biases.

PCMO films were deposited from $Pr_{0.7}Ca_{0.3}MnO_{3-\delta}$ targets using rf magnetron sputtering. The distance between the target and substrate was maintained at 70 mm. After the chamber was evacuated to a high vacuum of about 1×10^{-6} Torr, working gas of argon was introduced. Before the deposition, the target was pre-sputtered for 30 min to obtain a clean target surface. The process pressure was controlled at 20 mTorr during the sputter deposition. The rf power was 100 W. The deposition temperature was 600 °C.

Polycrystalline PCMO films were also deposited by liquid-source MOCVD. We used tris(dipivaloylmethanato)praseodymium [$Pr(DPM)_3$], bis(dipivaloylmethanato)calcium [$Ca(DPM)_2$], and tris(dipivaloylmethanato)manganese [$Mn(DPM)_3$] as the source materials. These source materials were dissolved in tetrahydrofuran (THF, C_4H_8O) at a concentration of 0.1 mol/l. After each dissolved source was introduced into a vaporizer by N_2 carrier gas at 200 sccm, the vaporized source was transported into the MOCVD reactor and subsequently mixed with O_2 oxidant gas. The optimal proportion of the flow rates of the liquid sources was determined using *in situ* infrared spectroscopic monitoring. The pressure in the reactor was maintained at 10 Torr.

The film thickness was obtained by cross-sectional scanning electron microscopy (SEM). All films were about 100 nm thick. The atomic composition of the PCMO films was evaluated by energy dispersion X-ray spectroscopy (EDS).

On top of films grown on SiO_2/Si substrates, two metallic electrodes of Al were deposited by thermal evaporation. We also prepared layered structures composed of PCMO sandwiched between Pt bottom electrode and top electrodes of Al. Electrical pulses were applied to the sample through the electrodes and the resistance was measured after each pulse. All the electric measurements have been done at room temperature.

We measured *I-V* characteristics in the Al/PCMO/Pt devices. The *I-V* characteristics exhibited nonlinear, asymmetric, and hysteretic behavior. The resistance switching of the PCMO films was measured by applying a single positive electric pulse and single negative electric pulse alternatively to the Al top electrode. The pulse amplitude was 5.0 V, and the pulse width was 500 ns. Positive or negative pulses reversibly switched the resistance of the PCMO films between the high resistance state and the low resistance state. The resistance switching ratio was between 100 and 1000.

The frequency response of complex impedance of the PCMO-based devices was measured under different DC biases. In order to reproduce observed spectrum by theoretical simulation, three sets of parallel RC components in series were required as an equivalent circuit. These three components can be assigned to grain bulk, grain boundary, and film-electrode interface. Therefore, impedance spectroscopy indicates whether the overall resistance of the device is dominated by bulk, grain boundary, or interface component. Figure 1 shows typical impedance spectra of the PCMO-based device as a function of dc bias. As dc bias increased, the interface component decreased. The bias dependence of the Cole-Cole plots suggested that the resistance switching in the PCMO-based devices was mainly due to the resistance change in the interface between the film and the electrode. Impedance spectroscopy is a promising technique for characterizing the resistance switching in magnetoresistive manganite films.

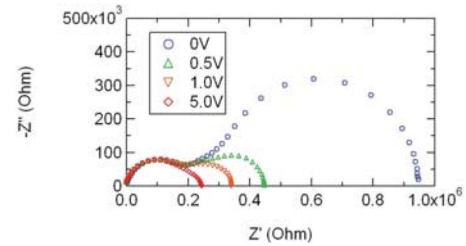

Figure 1. Impedance spectra of the PCMO-based device as a function of dc bias.

DV-16

Strain effect on MnO_6 octahedrons in the colossal magnetoresistance (CMR) films.

C. Wu, *H. Chou*, F. Yuan
National Sun Yat-sen University, Kaohsiung, Taiwan

The metal-insulator transition temperature(T_p)andthe ferromagnetic-paramagnetic transition temperature(T_C)of doped manganese CMR films can be altered by the strain effect [1-4]. The strain effect suppresses the T_C of LaMnO3 dopping Ca(or Sr) films with the decreasing films'thickness, whereas the T_C of $La_{1-x}Ba_xMnO_3$ films is found to increase for x ≦ 0.2 in thinner films. Up to now, the mechanism of the strain effect has not been fully understood.
$La_{0.67}Ca_{0.33}MnO_3$(LCMO)and $La_{0.8}Ba_{0.2}MnO_3$(LBMO) films with thickness of (200,50 and 20nm) and (150,45 and 15nm)were grown on $SrTiO_3$(100)(STO) substrates by a radio frequency magnetron sputtering system. The electric and magnetic properties were characterized by a four-point probe and a superconducting quantum interference device (SQUID), respectively. The crystal structures were studied by a X-ray diffraction (XRD)and an extended X-ray absorption fine structure (EXAFS). The Orbital structures were studied by X-ray absorption near-edge structure (XANES). The XAS measurements are taken by beam-line of the National Synchrotron Radiation Research Center in Taiwan.
The XRD confirms that the LCMO and LBMO thin films are epitaxial,and their(T_C)is very close to (T_p). The strain effect of the substrate on films suppresses the transition temperature of LCMO films while enhances that of LBMO films. The Mn K-edge EXAFS measured by the fluorescence yield mode at 11K is shown in Fig.1.Three structures can be identified as the distribution of : (A)O around Mn, (B)La(Ca or Ba) around Mn and (C)the multi-scattering from the Mn to the next Mn. For LCMO films, Fig. 1(a), the average distance dMn-O increases for the thinner film, the distribution of La(or Ca) for thinner film increases to a larger range and the scattering of (C) structure can barely be seen. This implies that the strain effect in LCMO does change the MnO_6 octahedron that increases the average bond length, dMn-O, in a way that opens up a wider space for smaller Ca cations to distribute. Within this strain effect, the MnO_6 octahedrons become more off-alignment that reduces the Double Exchange (DE) coupling and, thus, the transition temperature. For LBMO films, Fig. 1(b), the strain effect decreases the average bond length, dMn-O, and increase average bond length, dMn-La(sites), and exhibits stronger multi-scattering from the core Mn ion to the next Mn ions. This indicates that the MnO_6 octahedrons in LBMO thinner film is also changed according to the strain effect. The alignment of MnO6 octahedrons becomes better for the thinner LBMO film that enhances the multi-scattering of the structure (C). All these effects enhance the DE coupling and the transition temperature.XANES measured by a total electron yield mode at 78k which exhibits the hybridizations of the unoccupied O 2p and Mn 3d orbital. Due to the crystal field and the Jahn-Teller distortion effect, these states experience splitting into many states. The structure (D)and (E) are the hybridizations of O 2p and Mn 3d. The separations of these two structures can be corresponded to the splitting energy of Mn 3d (t_{2g}↓)and (e_g↓) bands due to the crystal field, which are 0.75eV for both thick films and then increases 0.1eV for LBMO thinner film and decreases 0.1eV for LCMO thinner films. The increasing of separation of (D) and (E) structure can be looked as the enhancement of crystal field on the Mn ion. This coincides with the observation in Fig. 1.
We found that the strain effect does affect the shape and the alignment of MnO_6 octahedrons, and, as a result of this, the DE coupling is suppressed for LCMO films and enhanced for LBMO films. By comparison with our earlier study which indicate the dopents at La sites are the matter of the strain effect, the correlation between the dopents, Ca and Ba in La sites, and the different response of MnO_6 octahedrons in LCMO and LBMO films is not clear at this stage.

1)S.Jin, T.H.Tiefel, M.McCormack, H.M.O'Bryan, L.H.Chen, R.Ramesh and D.Schurig, Appl.Phys.Lett.67,557(1995).

2)T.Kanki, H.Tanaka and T.Kawai, Phys.Rev.B 64,224418 (2001).

3)J.Zhang, H.Tanaka, T.Kanki, J.H.Choi and T.Kawai, Phys.Rev.B 64, 184404(2001).

4)H.Chou, M.H.Tsai, F.P.Yuan, S.K.Hsu, C.B.Wu,J.Y.Lin,C.I. Tasi and Y.H.Tang, Appl.Phys.Lett.89, 082511(2006).

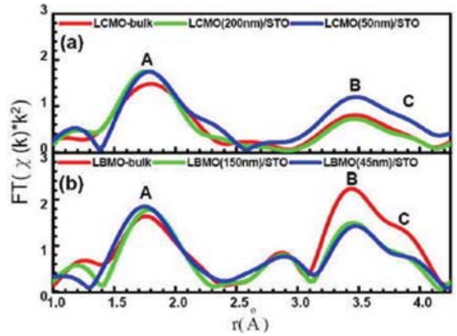

Fig.1: The Mn K-edge EXAFS. Structures A, B and C are the distance between the core Mn ion and 1st Oxygen shell, the 1st La (or Ca, Ba) shell and the 1st Mn shell, respetively.

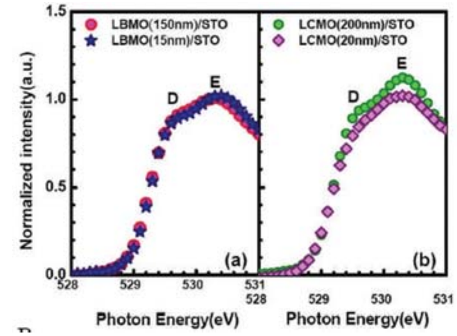

Fig.2:The pre-edge of O K-edge XANES. Structure A and B are the hybridizations of O 2p and Mn 3d(t2g↓) and Mn 3d(eg↓) obitals.

Pulsed current induced multi level resistivity switching in two magnetodielectrics: antiferromagnetic Nd0.5Ca 0.5MnO3 and ferromagnetic La2NiMnO6.

M. Ramanathan
Physics, National university of Singapore, Singapore, Singapore

Electrically addressable non volatile memory devices are currently attracting enormous attention due to their potential applications in compact data storage. In particular, recent observations of voltage polarity dependent resistivity switching, i.e., high resistance state (“OFF” state) for positive voltage pulses and low resistance (“ON” state) for negative voltage pulses found in Pr0.67Ca0.33MnO3 capacitor like structures deserves a particular attention [1].
The magnitude of electroresistance was found to depend on the polarity, amplitude and number of pulses. However, the effect of pulse width or period on the I-V characteristics and CER effect has been hardly investigated. We demonstrate pulse current induced bi-level and multi-level switching of electrical resistance triggered by variation in pulse width or period for a fixed low current in two magnetodielectric insulators with different grounds states: charge-orbital ordered antiferromagnetic Nd0.5Ca0.5MnO3 and charge disordered ferromagnetic LaNi0.5Mn0.5O3. It is found that resistance increases abruptly by as much as 50 % upon a sudden change of period from 0.2 s to 1s for a fixed pulse width (25ms) or decreases abruptly upon increase of pulse width for a constant period. It is shown that multiple resistive states can be induced by a sequence of controlled pulse width or period as shown in the figure and this approach can be exploited for non volatile resistive random access memory [2]. We discuss possible origins of the observed results. It is shown that multiple resistive states can be induced by a sequence of controlled pulse width or period and this approach can be exploited for non volatile resistive random access memory.

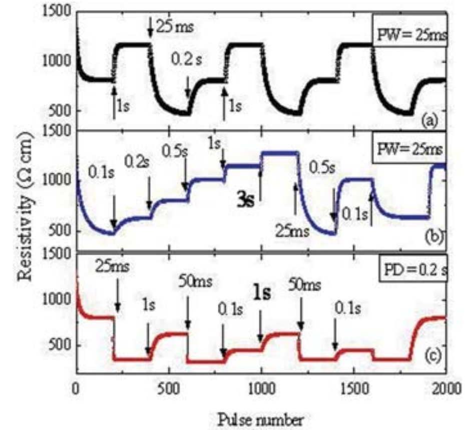

Figure 1: (a) Tri-level resistivity switching induced by variations three pulse periods (1s, 25ms, and 0.2s) for a fixed pulse width (PW = 25 ms) and current (2 mA) in Nd0.5Ca0.5MnO3 at 100 K. Each pulse train consists of 200 pulses. (b) Multilevel resistivity switching in response to a sequence of pulses width different periods for a (b) fixed pulse width and for (c) for a fixed period but with different pulse widths . The arrows indicate the stating of a new pulse train and the numbers represent different periods for (a) and (b) and pulse widths for (c).

References

[1] S. Q. Liu, N. J. Wu, and A. Ignatiev, Appl. Phys. Lett. 76, 2749 (2000); A. Baikalov, Y. Q. Wang, B. Shen, B. Lorenz, S. Tsui, Y. Y. Sun, Y. Y.Xue, and C. W. Chu, Appl. Phys. Lett. 83, 957 (2003);A. Odagawa, H. Sato, I. H. Inoue, H. Akoh, M. Kawasaki, and Y. Tokura, Phys. Rev. B 70, 224403 (2004); X. Chen, N. J. Wu, J. Strozier, and A. Ignatiev, Appl. Phys. Lett. 87, 233405 (2005).

[2] A. Rebello, C. Raj Sankar, and R. Mahendiran (to be submitted).

DW-01

Design optimization of a non-contact rapid charging inductive power supply system for electric-driven vehicles based on finite-element electromagnetic field analyses.

Y. Kamiya[1], Y. Daisho[1], R. Yokoyama[1], S. Takahashi[2]
1. Graduate School of Environment and Energy Engineering, Waseda Univ., Tokyo, Japan; 2. Showa Aircraft, Tokyo, Japan

A non-contact rapid charging type inductive power supply (IPS) system has been developed and tested as a charger for electric-driven vehicles (EVs). By using the developed system, EV charging can be carried out safely, easily, and in a short period. Optimizing the track and pick up design of the IPS achieved significant improvements in efficiency, weight, thickness, and air gap length. The results obtained are listed below.
a) The design optimization of the track/pickup part for an IPS having a plane core and round shape was conducted by means of finite-element electromagnetic field analyses in consideration of external drive circuit. Based on this study, we arrived at parameters such as drive frequency (22 kHz), inner core diameter (90-mm radius), and core thickness values (4.0 mm for the track side, 2.0 mm for the pickup side). In addition, with the objective of ensuring high-precision analyses, we devised a technique of separately evaluating the eddy current loss and the hysteresis loss in the magnetic material.
b) Based on the results of electromagnetic field analyses, an actual IPS was fabricated. Through non-contact power transmission experiments, the attainment of a 92% total efficiency was confirmed during 30 kW power transmissions. Also, slimming (33 mm), weight reduction (35 kg), and a long air gap (100 mm) were successfully accomplished.

Yushi KAMIYA, Takashi Onuki: 3D eddy current analysis by the finite element method using double nodes technique, IEEE transactions on magnetics, Vol. 32, No. 3, pp. 741- 744 (1996)

Size L×W×T	847×847×33mm
Weight of Pick up	35kg
Weight of Rectifier	30kg
Weight of Communication System	1kg
Magnetic Air Gap (Mechanical Clearance)	100mm (84mm)

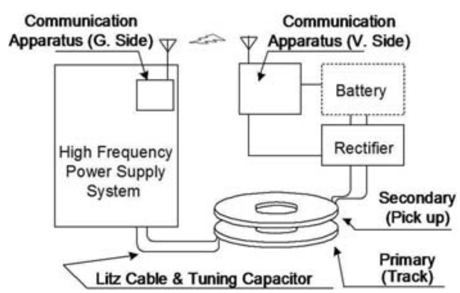

Schematic View of IPS System

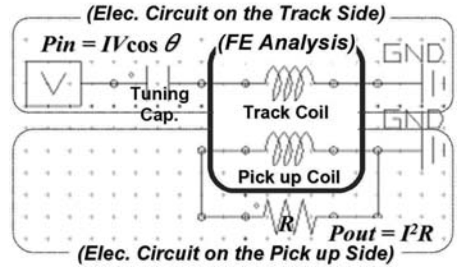

FE Electromagnetic Field Analysis in Consideration of External Circuits

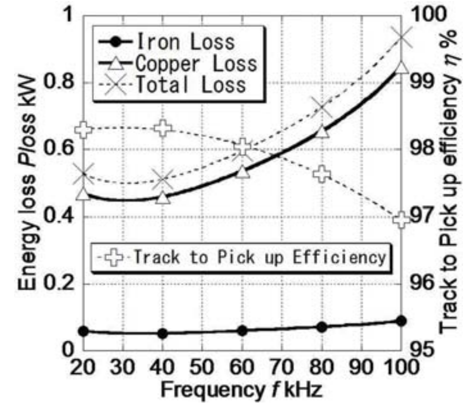

Loss & Efficiency from Track to Pick up@30kW

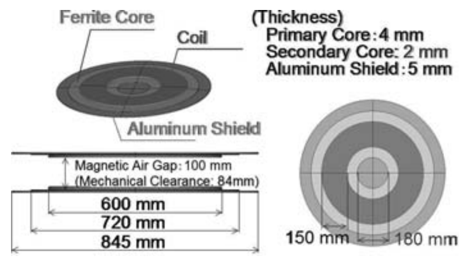

Final Shape of IPS

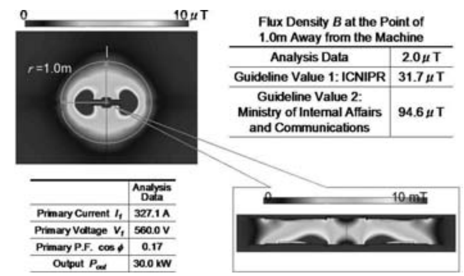

Leakage Flux @M. A. Gap: 100mm (30kW)

IPS on the Electric Micro Bus "WEB-1Advanced"

DW-02

An Analytical Model of the Electromagnetic Efficiency of Litz-Wire Windings for Domestic Induction Heating Systems.

J. Acero[1], R. Alonso[2], J. M. Burdio[1], L. A. Barragan[1], J. I. Artigas[1]
1. Electronic Engineering and Communications, University of Zaragoza, Zaragoza, Spain; 2. Applied Physics, University of Zaragoza, Zaragoza, Spain

Domestic induction hobs basically consist of a planar winding situated below a metallic vessel and supplied by a medium-frequency power source, normally operated between 20 kHz and 70 kHz. In Fig. 1 an induction system comprising the planar inductor and the load is shown. The inductor consists of n litz-wire concentric turns, each one of them having a_i radius. The litz wire comprises an isolated number of n_o strands, being Φ_o the strand diameter. The load is a semi-infinite medium characterized by its conductivity σ_l and its relative magnetic permeability μ_{rl}.
The induction efficiency of this system is defined as: $\eta_{ind}=\Delta R/(R_o+\Delta R)$, where ΔR is a resistance representing the power dissipation in the load for heating purposes; and, R_o is a resistance which represents the non-desirable warming-up of the windings. In its turn, R_o is further divided into the conduction resistance, R_{cond}, related with the *skin effect*; and the induction resistance, R_{ind}, which represents the losses by the called *proximity effect*, i.e. the currents induced in the wires by the alternating fields in which they are immersed, [1]. Note that ΔR and R_o are not independent; rather, they are related through the unique solution of the magnetic field of the system. This field depends on the electromagnetic and geometric parameters of the whole system.
Some models of the induction efficiency based on a Finite Element Analysis (FEA) calculation of the losses in both the work piece and the winding have been proposed [2]-[3]. However, the FEA calculations may become unpractical, specially for windings consisting of several turns of litz wire with a large number of strands and a small diameter, because they could involve high computational cost.
Recently, on the one hand it has been proposed an analytical model of the impedance for a planar circular induction system [4]; and, on the other hand, a frequency-dependent model of losses for litz-wire planar windings, [5]. Considering simultaneously both models, an analytical model of the induction efficiency is developed and experimentally verified. Thus, [4] provides the required ΔR. However, the main contribution of the present work is that from the equations of [4] it has been deduced the field at the positions of each turn, H_{oi}, which is needed to estimate the proximity losses in windings [5]. Besides, also through [5], R_{cond} is calculated, having therefore the terms of R_o. Thereby, the model includes the operating frequency, the properties of the load, the geometry of the windings, and several litz-wire parameters like the number of strands, the strand diameter and the packing factor.
An experimental setup was built to verify the model. Frequency-dependent tests have been performed based on resistance measurements by means of a precision LCR meter (Agilent 4284A). The tests were performed with a 23-turn litz-wire flat winding geometry, corresponding to the inductor currently manufactured to deliver up to 3500 W in a commercial induction heating appliance (a_1= 25 mm, a_{23}= 105 mm). The litz wire has been manufactured with strands of Φ_o=0.5 mm. Three different kinds of loads have been tested: aluminium copper, and ferromagnetic steel. Considering the ferromagnetic load operating at 25 kHz and using the developed model, the optimum number of strands of the litz wire has been calculated and results are shown in Fig. 2 (a). For this application we have selected n_o= 20. The experimental results of η_{ind} are also shown in Fig. 2 (b). It must be noted the lower efficiency achieved with non magnetic loads. As it can be seen, measured and calculated results exhibit a very good agreement.

[1] J. Lammeraner and M. Stafl, Eddy Currents, London: Hiffe Books, 1966.

[2] J-K. Byun, K. Choi, H-S. Roh, S-Y. Hahn, “Optimal design procedure for a practical induction heating cooker,” IEEE Trans. Magn., vol. 36, pp. 1390-1393, July 2000.

[3] O. Bíró, K. Preis, G. Buchgraber, I. Ticar, “Voltage-driven coils in finite element formulations using a current vector and magnetic scalar potential,“ IEEE Trans. Magn., vol. 40, pp. 1286-1289, Mar. 2004.

[4] J. Acero, R. Alonso, J.M. Burdío, L.A. Barragán, and D. Puyal, “Analytical equivalent impedance for a planar circular induction heating system,” IEEE Trans. Magn., vol. 42, pp. 84-86, Jan. 2006.

[5] J. Acero, R. Alonso, J.M. Burdio, L.A. Barragán, D. Puyal, “Frequency-dependent resistance in litz-wire planar windings for domestic induction heating appliances,” IEEE Trans. Power Electron., vol. 21, pp. 856-866, July 2006.

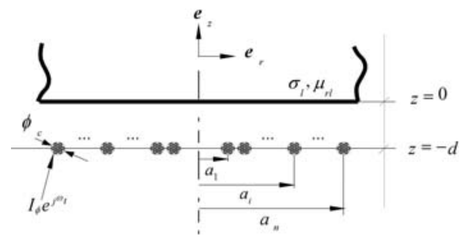

A litz-wire planar inductor of *n*-turns with a load consisting of a medium characterized by its conductivity σ_l and relative permeability μ_{rl}.

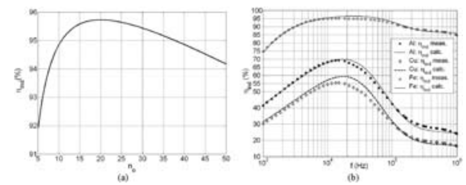

Calculated and experimental results: (a) optimum number of strands with ferromagnetic load at 25 kHz; (b) Calculated and measured frequency-dependent induction efficiency for different loads: aluminium (Al), copper (Cu), and ferromagnetic steel (Fe).

DW-03

High Frequency Coaxial Transformer for DC/DC Converter Used in Solar PV Systems.

J. Lu[1], X. Yang[2], F. Dawson[3]
1. School of Eng., Griffith University, Brisbane, QLD, Australia; 2. Province-Ministry Joint Key Laboratory of Electromagnetic Field and Electrical Apparatus Reliability, Hebei University of Technology, Tianjin,, China; 3. Department of Electrical and Computer Engineering, University of Toronto, Toronto, ON, Canada

Abstract—This paper discusses the design and analysis of a high frequency coaxial transformer (HFCT) for a DC/DC converter used in solar PV power systems. The experimental results demonstrate that the transformer voltage ratio is in good agreement with the turns ratio. The low leakage impedances measured for this transformer at various frequencies up to 500 KHz indicate the advantages of the coaxial transformer structure. This unique winding structure also provides a small capacitive coupling between the primary and secondary windings. The simulation results confirm the uniform distribution of magnetic flux in the magnetic core, and the uniform distribution of eddy current density in the windings.

Index Terms— High Frequency Coaxial Transformer, Eddy Current, Magnetic Flux,

I. INTRODUCTION

Photovoltaic arrays are coupled to the grid using a dc-ac converter and an isolation transformer. The isolation transformer is typically large given that the operating frequency is the utility frequency. A way of avoiding the use of a large transformer is to employ a dc-ac-dc converter with a high frequency (HF) link isolation transformer. In this event, the transformer is designed for HF operation and hence its size can be reduced significantly. Higher output power from multiple solar PV modules is achieved by connecting each PV array to its own resonant dc-ac converter and single phase transformer. The dc-ac resonant converter output signals are phase shifted with respect to each other by 120 degrees. The secondaries of the HF link transformers are connected in a three phase wye configuration and the output is connected to a three phase rectifier, as shown in Fig. 1. The transformers with small size and high power efficiency at high operating frequency are often required in DC/DC converter systems. Conventional transformer designs cannot perform well at HF because the insertion loss and eddy current loss are too high. The HFCT presented in this paper can address the aforementioned problems and provide a better performance in HF applications.

II. TEST RESULTS FOR THE COAXIAL TRANSFORMER

Figure 1 (a) shows the HFCT construction (right side at bottom) and the packaging of a three phase system (top image of right side). The solar PV system requires an isolation transformer therefore the number of turns on the primary and secondary windings is the same and equal to 6 at a frequency of 500 kHz and a voltage of 450 V. Each winding is comprised of 7 thin insulated wires that are used to form a litz wire. The turns ratio (a=6/6=1) is in good agreement with the voltage ratio (V1/V2) from 100 kHz to 1 MHz. The measured results from 100kHz to 1MHz indicate that the leakage inductance, Leq (0.689µH) is relatively small compared with a conventional transformer (3.53µH) at 500kHz, while Req increases slightly with frequency due to the skin depth effect. The leakage inductance decreases in a linear fashion over the frequency range of interest. The magnitude of the magnetizing inductance tracks the frequency response of the permeability, µ, which rises in the high frequency range. The coupling capacitance (20.9 pF) between primary and secondary windings is much smaller than the values (210pF) observed in conventional transformers with a similar rating. The coaxial transformer performed well over an extended frequency range (100 kHz to 1MkHz), while the leakage inductance and winding loss of a conventional transformer increase rapidly above a frequency of 200 kHz.

III. MAGNETIC FIELD ANALYSIS OF COAXIAL TRANSFORMER

A FEM-based numerical method was used to determine the magnetic flux and eddy current distributions. The excitation source is applied to the outer winding and the inner winding was open circuited. Figure 1 (b) shows the current distributions in both the primary and secondary windings, where the eddy current density in the outer (primary) winding is somewhat higher than the one in the inner (secondary) winding. The peak current density including eddy current was determined at the surface of the outer winding; 743A/cm2 for the open circuit case, and 810A/cm2 for the short circuit case. The maximum current densities in the inner (secondary) winding for both open circuit and short circuit cases were found to be less than 61.63A/cm2 and 60.7A/cm2 respectively.

IV. CONCLUSION

A HFCT using uniformly distributed litz wire winding structure has been investigated. The turns ratio and voltage ratio in the HF range of interest are in good agreement with each other. The minimum leakage inductance (0.689µH) and coupling capacitance (20.9pF) have been achieved by using such winding structure. The flux and eddy current distributions were uniform and the high current density appeared at the surface of the outer winding, and was 743A/cm2 for the open circuit case, and 810A/cm2 for the short circuit case. The current densities in the inner winding were over 10 times smaller than the outer winding.

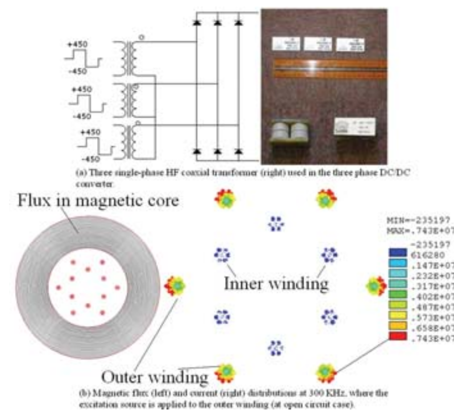

Fig. 1 HF coaxial transformer and its magnetic filed distribution.

DW-04

Novel EU core variable inductor.

M. Xianmin[1], L. Fengchun[1], W. Jianze[2], J. Yanchao[2]
1. Department of Electrical and Electronics Engineering, DaLian University of Technonlogy, DaLian, China; 2. School of Electrical Engineering and Automation, Harbin Instituted of Technology, Harbin, China

Introduction

Recently, many types variable inductor have been widely used in SVC system. Orthogonal-core, three legged core, and parallel-laminated core designs have been presented for variable inductors[1,2]. These devices worked in saturation state by a DC current control, so increases the harmonics of the AC current. Recent investigation indicated that the current distortion of an orthogonal-core variable inductor with partial gaps is decreased[3]. One configuration use tow orthogonal-core variable inductor worked in half wave of source can also be reduced[4].

In this paper, the authors propose an EU core variable inductor, which is a simple structure without partial gaps, designed to decrease current distortion. The operating principle is also described in this paper. The EU core variable inductor can configure to single phase and three phase application. We present their basic structure and basic characteristics and give an examples. The main characteristics were verified with a single phase and a three phase prototype.

Single phase EU core variable inductor

EU core variable inductor is made by one E-shaped core and one U-shape core assembled at 90° one from other and a winding wound on each core. Figure 1 shows the single phase configuration of the device. Linear reluctances in the magnetic equivalent circuit can be ignored because the non-linear reluctance is the major factor of effecting flux distribution. Figure 2 shows magnetic equivalent circuit. In the figure R1,R2,R3,R4,R5,R6 is the magnetic reluctance of E-core and U-core interface part. The magnetic equivalent circuit can be simplified to figure 3. This simplified magnetic equivalent circuit is same as presented in[5].

Divided the core to 68 parts employed 3-D reluctance network method proposed in[5], construct the simulation model of single phase EU core variable inductor. Experiment result indicated its harmonic component is small than convention orthogonal core variable inductor. Because the 6 interface parts of device worked in different saturation state, the single phase variable inductor can decrease the harmonic current output.

Three phase EU core variable inductor

Three phase EU core variable inductor use same core of single phase one. In the figure 4, mount one winding in the every lamb of E core. The configuration is simple used in the three phase motor starter neednot to single phase control. Same as single phase one, build the 3-D simulation model of three phase EU core variable inductor. Experiment result indicated the output current of AC winding not include 3rd harmonic component because of unique magnetic path.

Conclusion

In this paper EU core variable inductor has been verified by construct a single phase prototype and a three phase one. The novel EU core variable inductor has some important features. (a) Single phase variable has a lower harmonic component characteristic. (b) Three phase variable inductor simple topology, increased credibility of the system application.

[1]J. Tellinen and J. Jarvik, Minimization of higher harmonics in high power saturated reactors for AC power transmission lines, Power Quality '98, IEEE, 1998:133-138.

[2]Arturi, C.M, A thermodynamic approach to energy conversion in parametric transformers, Circuits and Systems, IEEE 39th Midwest symposium on, 1996(3):1079–1082.

[3]Nakamura, K. and Ichinokura, O., et al., Analysis of orthogonal-core type linear variable inductor and application to VAr compensator, IEEE Trans. on Magnetics, 2000,36:3565–3567.

[4]O. Ichinokura, T. Jinzenji, K. Tajima. A New Variable Inductor for VAR Compensation. IEEE Trans. On Magnetics. 1993, 29(6):3225–3227.

[5]Tajima, K.; Kaga, A.; Anazawa, Y.; Ichinokura, O.; One method for calculating flux-MMF relationship of orthogonal-core,IEEE Trans. on Magnetics, 1993, 29(6):3219 - 3221.

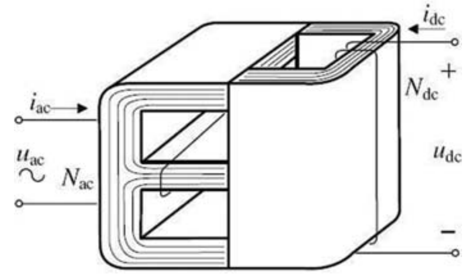

Fig.1 Single phase configuration

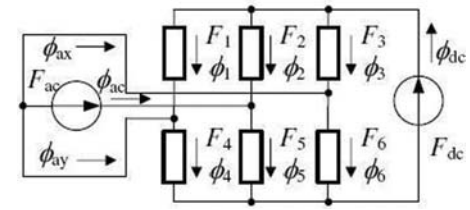

Fig.2 Single phase brief MEC

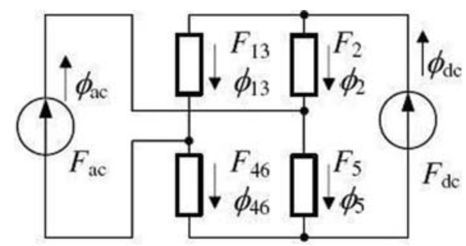

Fig.3 Single phase brief MEC

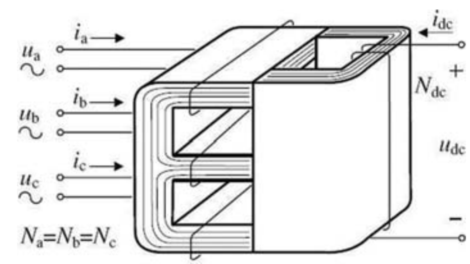

Fig.4 Three phase configuration

DW-05

Stability analysis of contact-less electrical energy detachable transformer.

H. Chen, *Q. Yang*, J. Li, S. Yang, S. Hou
Hebei University of Technology, Tianjin, China

I. INTRODUCTION

In many applications, the Contact-less Electrical Energy Transmission (CEET) technique has distinct advantages over the conventional energy transmission method which uses wires and connectors owing to the following reasons.

(1)An electric connector may not appropriate due to the dangerous environment (humidity, underwater, gas, dust).

(2)Energy has to be supplied to moving objects or to implanted medical devices through the intact skin.

(3)Reliability is improved by avoiding mechanical contacts in battery chargers.

A typical CEET system consists of primary converter, detachable transformer and secondary converter. The detachable transformers are difficult to design and optimize because of these variables: a): The distance between the windings cannot be considered as a constant b): Windings could not be facing to each other all the time. c): The loads are variable, depending on whether the electronic device that acts as a load is working or not.

II. SIMULATION MODEL AND RESULTS OF DETACHABLE TRANSFORMER

Mutual inductance model is applied to analyze the energy transmission behavior of detachable transformer.

The equivalent circuit of detachable transformer can be obtained as shown in Fig. 1 (a), (b).

The dimensions of E-E detachable former model are shown in Fig.2. The broken line is symmetry axis. The amplitude of voltage source is 100 V. The primary and secondary of detachable transformer consist of 54 turns of Litz wire.

A. The Influence of Displacement on Coupling Rate

This paper calculates the coupling rate of E-E type detachable transformer with gaps of 5 mm and 10 mm respectively. Fig. 3 shows the calculated coupling rate of detachable transformer as a function of horizontal displacement of secondary system. Overall, the coupling coefficient decreases rapidly as the displacement increases.

As shown in Fig. 3, the coupling rate has little change (about 0.85 and 0.94) when secondary winding displacement is smaller than 20mm (keep the detachable transformer gap unchanged during the simulation). In this case, the designed detachable transformer has a relatively stable ability.

B. Parameter Analysis

The structure of E-E type detachable transformer are optimized and the output voltage, power and efficiency at different transmission frequency are calculated.

Fig. 4 shows output voltage, power, and efficiency as a function of operating frequency. The efficiency strongly increases with the frequency nearly the same way as the output power. The optimized detachable transformer attains maximum results at about 60 kHz. But, if keep on to increase frequency, both of them decrease remarkably. This may due to increasing core loss caused by higher frequency and copper loss by increased alternating winding resistance

III. CONCLUSIONS

In this paper, a high-frequency, high-stability and high-efficiency detachable transformer suitable for applications with a wide input range and wide load range in CEET system is described. Through the study of coupling rate of transformers with horizontal and vertical displacement, an optimized structure of detachable transformer is obtained and the operational stability is improved. Finally, the performance evaluation results as a function of frequency are presented using a diagram in which the transformer achieved the optimum efficiency at the frequency of 60 kHz.

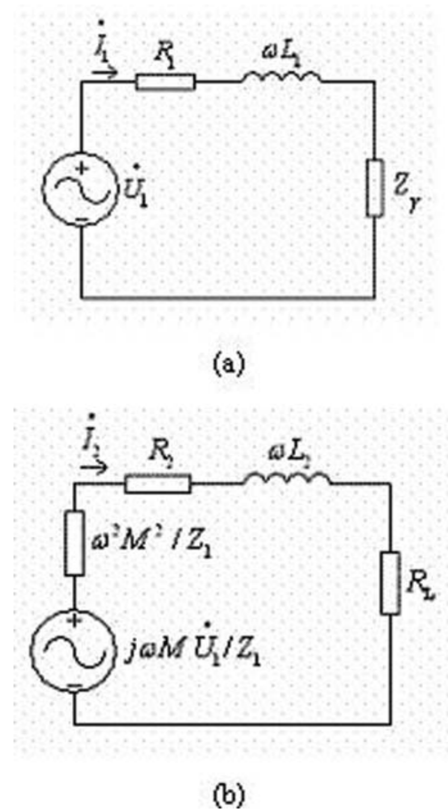

Fig.1. (a) Equivalent electric circuit of primary system (b) Equivalent electric circuit of secondary system

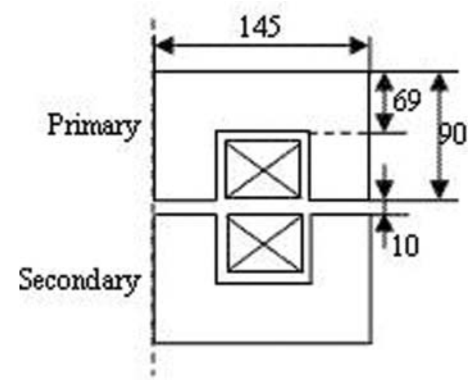

Fig. 2. E-E detachable transformer model (mm)

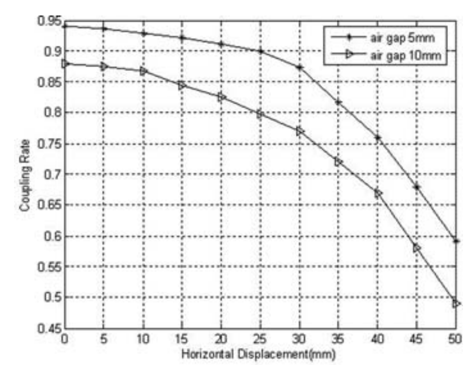

Fig. 3. Coupling rate as a function of horizontal displacement

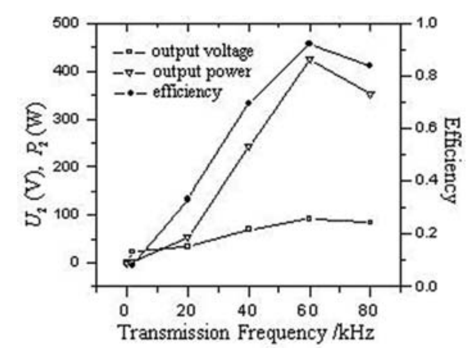

Fig. 4. Output voltage, output power and efficiency a as a function of transmission frequency

DW-06

A Forced Vibration Analysis of Cable-type Power Transformer Winding by the Pseudospectral Method.

J. Ha, *H. Chung*, S. Woo, P. Shin, J. Lee
Hongik University, Jochiwon, South Korea

Vibration analysis of high voltage power transformer is very important for design of the mechanical structure of the insulation system as well as for diagnostics of the power system. In this paper, the electromagnetic force generated by the interaction of short-circuit current with the leakage flux is calculated by the Maxwell stress method based on the finite element analysis of the equation: $\nabla\times(1/\mu)\nabla\times\boldsymbol{A}=\boldsymbol{J}-j\omega_e\sigma\boldsymbol{A}+\omega_e^2\boldsymbol{A}$, where $\boldsymbol{A}$ is magnetic vector potential, σ electrical conductivity, ω_e power frequency, μ permeability, respectively. And then the vibration forces of the windings are calculated by the pseudo spectral method[1,2], which is straightforward and it has novel advantages in its conceptual simplicity over other computational methods. The equations of the winding motion(circular helical systems) are based on the Timoshenko beam theory and are consist of 6 equations for internal forces(T) and moments(M) in the tangential(t), normal(n) and binormal(b) directions. To the binormal direction the two equations are given as $(dT_b/ds)+\tau T_n=-\omega^2\rho A U_b$, $(dM_b/ds)+T_n+\tau M_n=-\omega^2\rho I_b\Omega_b$ for a harmonic motion at the natural frequency ω, tortousity τ, and density of winding ρ. U represents the displacement and Ω is the rotation. The equations of motion are approximated by the series expansions of the Chebyshev polynomials and are collocated at the Gauss-Labatto collocation points[2,3].
The boundary condition is considered as the side constraint, which is merged into the governing equations to form the set of algebraic equations.
To verify the method a distribution power transformer of helical winding of cylindrical type, which is operated for 60 Hz, 6600V/380V and 100kVA, is analyzed for various boundary conditions. The short-circuit current and electromagnetic force are calculated by FEM program and the results are verified with theoretical formula and PSPICE program. The simulation results are fairly good agreement with the other verified methods within 5 % error rate. The turn-to-turn short-circuit current is 500 times of the rated current and the electromagnetic force is about 20-200 times.
For the forced vibration analysis of the cable-type winding, the calculated forces from FE analysis are put into the equations of the winding motion(see Fig.1). The equations are also solved by the proposed pseudo spectral method and analyzed the vibration modes and forces under the various boundary conditions. Figure 2 shows the cable-type winding model; the centerline radius, wire diameter and pitch of the winding are 404.5 mm, 4.37 mm and 26 mm, respectively. The number of collocation points required to achieve the convergence of the pseudo spectral solution was less than K=120, however, the ANSYS required about 8000 nodes for the same model. Table 1 describes the forced vibration mode frequencies of free-fixed boundary condition for 20 turns winding, which is compared with the results of ANSYS program. The computed results are in fairly good agreement with the simulated data of ANSYS. The methods presented in this study may serve as one of the useful tools in the electromagnetic force analysis of the transformer winding behavior as well as vibration forces under the short-circuit condition for design of the structure.
(* This work has been supported by ETEP(2006-0273) funded by MOCIE, Korea)

[1] J. Lee, Eigenvalue analysis of double-span Timoshenko beams by pseudospectral method, Journal of Mechanical Science and Technology, vol. 19, no. 9, pp. 1753-1760, 2005.

[2] J. Lee and W. W. Schultz, 'Eigenvalue analysis of Timoshenko beams and axisymmetric Mindlin plates by the pseudospectral method, Journal of Sound and Vibration, vol. 269, no. 3, pp. 609-621, 2004.

[3] P.S. Shin, J. Lee, and J.W. Ha, ' A Free Vibration Analysis of Helical Windings of Power Transformer By Pseudospectral Method", IEEE Trans. on Magnetics, vol.43. no.6, pp.2657-2659, June 2007.

Mode	Proposed Method	ANSYS Program
1st	3.20(Hz)	3.19(Hz)
3rd	7.35(Hz)	7.36(Hz)
5th	16.48(Hz)	16.56(Hz)
7th	30.67(Hz)	30.83(Hz)
9th	49.40(Hz)	49.64(Hz)

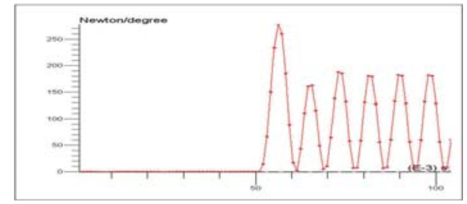

Fig.1 Simulated electromagnetic force during the internal winding fault.

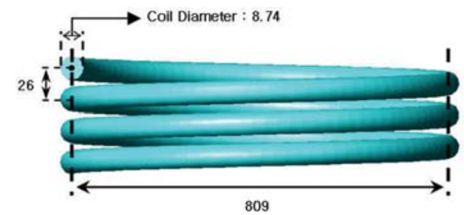

Fig. 2 Cable-type winding model of 100 kVA transformer

DW-07

Coupled three phase inductors for interleaved inverter switching.

A. Knight, J. Ewanchuk, J. C. Salmon
Electrical and Computer Eng, University of Alberta, Edmonton, AB, Canada

It can be shown that placing coupled inductors between switches in the output legs of three-phase inverters, as shown in Figure 1, can offer significant advantages in the output waveforms of the inverters. This topology is intended to produce multi-level PWM output voltage waveforms with each leg switching at $0, V_{dc}/2$ *and* V_{dc}. Hence PWM voltage harmonics are lowered by 50% while the load sees output current ripple at twice the switching frequency. In the case with ideally coupled inductors, operating the upper and lower switches with complementary modulating signals results in interleaved switching such that the output current divides into complementary ac inductor coil currents in each leg, with magnitudes equal to half the output current. An additional steady dc offset current also flows in both coils in a leg, with magnitude equal to half the peak output ac current. Considering the flux in each coil of a leg, $\psi_1 = L_{11}i_1 + L_{12}i_2 + L_l i_1$ and $\psi_2 = L_{12}i_1 + L_{22}i_2 + L_l i_2$. It can be seen that if the ac components of the coil currents in each leg are equal and opposite, the output ac current will effectively see half the leakage inductance of each coil. Conversely, DC offset current and high frequency switching current is common to both coils and these see effective inductance equal to four times the magnetizing inductance of each coil. A desirable set of coupled inductances for each leg have the following characteristics: (1) low leakage inductance; (2) high magnetizing inductance; (3) self inductance exactly equal to mutual inductance between coupled coils on the same core. This desirable performance may be achieved using three independent toroidal coupled inductors. This approach had been implemented in on a 6 switch inverter similar to that shown in Figure 1 and results in a 5-level output voltage, with very low current ripple, as shown in the experimental plots in Figure 2.

Use of three toroidal inductors requires an offset flux in each core. This creates some disadvantages: the core must be sized such that the sum of the dc flux and high frequency ripple does not drive the core into saturation; losses increase losses due to the higher total flux density; there is no flux reversal, increasing the risk of the core being driven into saturation. A preferred approach is to use a single three-limb core. The three-limb core eliminates the dc flux, but also introduces the risk of increased di/dt and switch damage. Let i_{au}, i_{al}, i_{bu} bethe currents in the upper and lower coils of leg a, i_{ao} the fundamental output currents, i_{ahf} the high frequency coil ripple. One may assume that $i_{au} = i_{dc} + i_{ao}/2 + i_{ahf}$; $i_{al} = i_{dc} - i_{ao}/2 + i_{ahf}$. If one assumes that the coils are closely coupled and that all three legs have equal impedances, then the total mmf, M in each limb of the core may be written as $M_a=2N(i_{dc}+i_{ahf})$, $M_b=2N(i_{dc}+i_{bhf})$, $M_c=2N(i_{dc}+i_{chf})$. Considering a simplified magnetic equivalent circuit for a three-limb core, it can be shown that the DC mmf components cancel and only high frequency fluxes are present in the core. It also becomes clear that if the high frequency currents are common in all three legs, the high frequency fluxes also cancel. This may becomes a critical mode of operation; cancelation of flux results in a collapse in the magnetizing inductance of an inverter leg, leading to shoot through and catastrophic device failure. In reality, this mode is only likely if all switches are on simultaneously (common if sinusoidal PWM is used). Use of an alternate modulation scheme, such as discrete PWM will alleviate this issue. Results of operation DPWM modulation of an inverter with a 3-limb core feeding an RL load are presented in Figure 3. The 5 level output voltage can clearly be seen. The coupled inductors with interleaved switching offer significant advantages over traditional filter inductors.

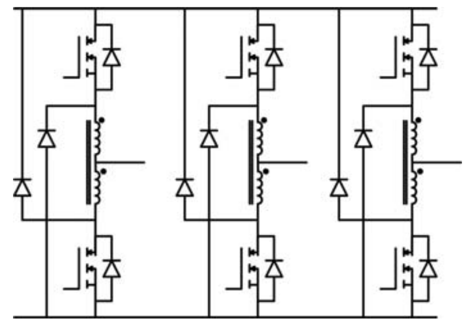

Figure 1. Coupled inductor inverter circuit

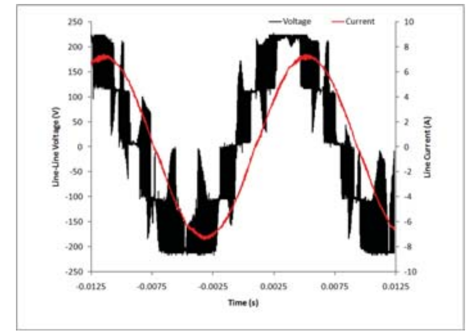

Figure 2. Measured line-line output voltage and output line current, using DPWM and toriodal cores

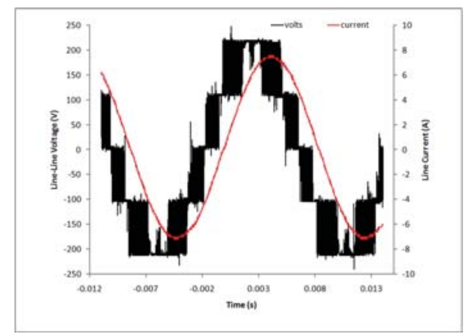

Figure 3. Measured line-line output voltage and measured line current using a three-limb coupled inductor

DW-08

A novel approach to extending the linearity range of displacement inductive sensor.

M. S. Damnjanovic, L. Zivanov, L. Nagy, S. Djuric, B. Biberdzic
Department of Electronics, Faculty of Technical Sciences, Novi Sad, Serbia

This paper presents a meander type displacement inductive sensor, usable for detection of small displacement in the plane (less than 0.5mm). Planar, low cost PCB technology was chosen for our prototype.

Previously we have reported measured characteristics of displacement inductive sensor consisting of two sensor elements, each having a pair of meander coils, faced one another [1]. In each pair, one of the coils is fixed (coil A) and between its terminals the input inductance L_{IN} was measured. Other coil (coil B in each pair) is short-circuited. Moving coil B above the coil A, in directions of x- and z-axes, coupling between coils will change, as well as input inductance, serving as a measure of displacement.

The first pair of coils, insensitive to displacement in x-direction, has width of conductive segments of coil A w_A=1.52mm and coil B w_B=0.51mm (Fig. 1). Near x=0, inductance variation for small displacement in x-direction is less than a few nH. This pair of coils is used for determination of distance between coils, i.e. z-coordinate. In order to achieve less x-sensitivity, gap g is inserted in the middle of each conductive segment of coil A. For sets of such sensor elements were made, with gaps 0, 0.25mm, 0.51mm and 0.76mm.

The second pair of coils consists of two equal width coils, w_A=w_B=0.51mm. If the coil B is arranged relative to coil A by one quarter of pitch p (near x=0.44mm), the slope of the input inductance L_{IN} has its maximum. It depends nearly linearly on displacement in the x-axis direction. Information about z-coordinate from the first pair of coils, in combination with the information from the second pair, will help us to determine the displacement in the x-z plane.

In this paper, we present an extended equivalent circuit model of inductive sensor (Fig. 2), as well as a calculation method based on the partial inductance method and comparison with measurement. Using this model, we have developed new simulation tool in MATLAB for evaluation of the input impedance of the sensor. This calculation method is previously verified in [2].

All sensors were tested using Impedance Analyzer HP4194A. Results of simulation and measurement are presented in Fig. 3 and Fig. 4. If the gap g=0.25mm is inserted, the linearity range is approximately 3 times wider than linearity range of structure without gap (Fig. 3).

The advantage of this displacement sensor is that the B-coils are short-circuited (so the sensor has one port, only). A possible application of such sensors is in robotics. Miniature version of such sensors could be incorporated into soft-covered fingertips of a robotic gripper. So, normal and tangential components of fingertips' deformation could be measured and corresponding forces could be calculated.

[1] S. Djuric, L. Nadj, B. Biberdzic, M. Damnjanovic, Lj. Zivanov, "Planar inductive sensor for small displacement," IEEE 26th International Conference on Microelectronics MIEL 2008,Nis, Serbia, 11-15. May 2008, to be published.

[2] G. Stojanovic, Lj. Zivanov, M. Damnjanovic: "Novel efficient methods for inductance calculation of meander inductor", COMPEL - The international journal for computation and mathematics in electrical engineering, Vol. 25, No. 4, pp. 916- 928, 2006.

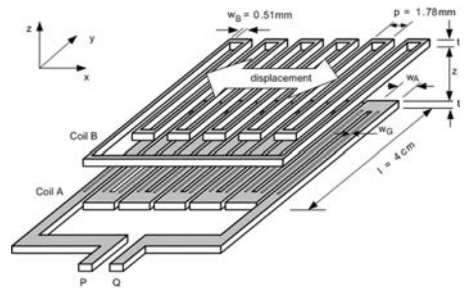

Fig. 1. Improved sensor element for z-direction.

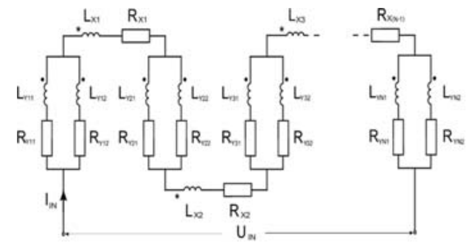

Fig. 2. Equivalent circuit model of the sensor element with gap g.

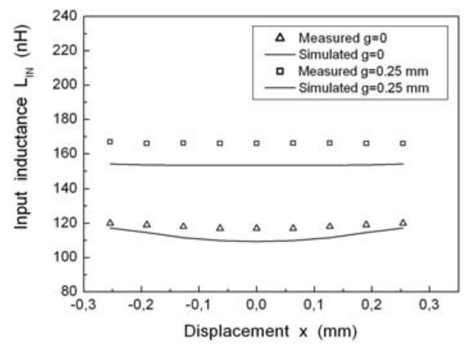

Fig. 3. Measured and calculated values of the input inductance L_{IN} for the first pair of coils, g=0 and g=0.25mm, z=0.1mm.

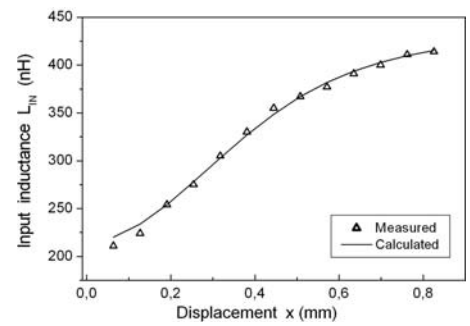

Fig. 4. Measured and calculated values of the input inductance L_{IN} for the second pair of coils, z=0.1mm.

DW-09

A New Technique for Measuring Ferrite Core Loss under DC Bias Conditions.

C. Baguley[1], U. K. Madawala[1], B. Carsten[2]
1. ECE, University of Auckland, Auckland, New Zealand; 2. Power Conversion Consulting and Research, Corvallis, OR

Introduction: Despite knowledge of the highly non-linear nature of ferrite core losses under DC bias conditions [1] there is a lack of comprehensive data on the phenomenon. This can largely be attributed to the difficulty of measuring core losses under DC bias conditions due to the very poor power factor, pf, of highly inductive core loss measurement circuits [1], [2]. The contribution of this paper is to propose a ferrite core loss measurement technique which overcomes this difficulty and which, to the authors knowledge, has not previously been used for the measurement of core losses under DC bias conditions.

The Measurement Technique: The proposed technique improves the pf of the core loss measurement circuit by neutralizing the mutual inductance of the core under test, CUT, using two coupled air cored windings. The improved pf reduces the ratio of excitation VA to core losses and thereby allows core losses to be accurately measured at high frequencies through the multiplication of the excitation current, I_{excite}, and winding emf, V_{sense}, waveforms. Fig. 1(a) shows the core loss measurement circuit, and Fig. 1(b) shows the resulting power factor for various ratios of equivalent core loss resistance, R_c, to CUT mutual reactance, X_{m_cut}. However the design and construction of the coupled air cored windings is difficult as it requires the "impurity" [3] of the mutual inductance between the windings to be minimized. The impurity causes the phase angle between the open circuit secondary winding emf and primary exciting current waveforms of the coupled air cored windings to deviate from quadrature, and therefore results in a significant core loss measurement error if it is not minimized. The impurity of two coupled air cored windings with a common connection point has been defined as [3]:

$$\sigma = \omega^2[C_1R_1M_0-C_{12}(R_1(L_2-M_0)+R_2(L_1-M_0))] \qquad (1)$$

where C_1, C_2, and C_{12} are coil 1 and 2 self and inter-capacitances, R_1 and R_2 are the winding resistances, L_1 and L_2 are the winding inductances, ω is the excitation frequency, and M_0 is the true (or geometric) inductance between the coils. To minimize impurity it is apparent from (1) that the self and inter-capacities between the coupled air cored windings must be minimized, as well as the winding resistances and thus the winding eddy current losses at high frequencies. To meet this requirement the coupled air cored windings are constructed using stranded wire, and two primary coils are used to sandwich the secondary to improve the coil coupling, with all coils being placed end to end to minimize inter-coil capacitance.

To measure core losses in the presence of a DC bias the measurement circuit is modified to that shown in Fig. 2. In this circuit I_{excite} and V_{sense} are measured and multiplied together to measure the total core losses of two ferrite CUTs at the same time. Two CUTs are used in order to allow DC bias windings to be placed on each with polarities such that, when connected in series, the DC bias windings are effectively decoupled from the AC windings in the circuit. Decoupling is necessary in order for the DC bias to be exact [1].

In the paper the results of core loss measurements made using the proposed measurement circuit are presented showing the effects of frequency, core shape, and temperature on ferrite core losses under DC bias conditions. Measurements are made with a Clarke and Hess model 2335 high frequency wattmeter at controlled core temperatures. An analysis of the impurity of the coupled air cored mutual windings is also presented.

[1]C. Baguley, B. Carsten, and U. Madawala, "An Investigation into the Impact of DC Bias Conditions on Ferrite Core Losses", IEEE Trans. Magn., 2008, in press for publication.

[2]J. Thotuvelil, T. G. Wilson, and H. A. Owen, "High Frequency Measurement Techniques for Magnetic Cores", IEEE Trans. on Power Elec., vol. 5, no. 1, Jan 1990, pp. 41-53

[3]S. Butterworth, "Capacity and Eddy Current Effects in Inductometers", Proc. Phys. Soc .of London, 33, 1921, pp. 312-354

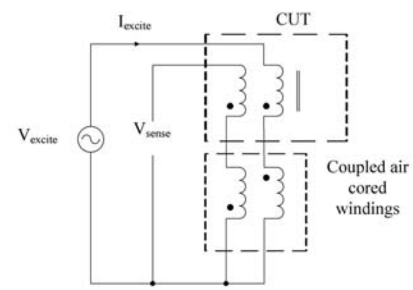

Fig. 1(a)

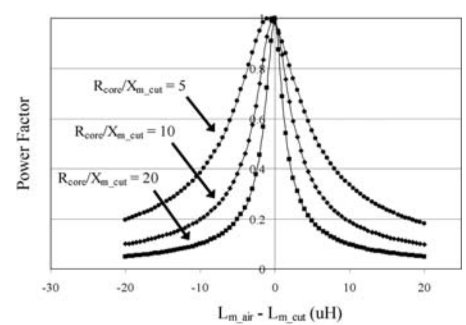

Fig. 1(b)

Fig. 1 (a) Core loss measurement circuit and, (b) variation of power factor with difference in mutual inductances

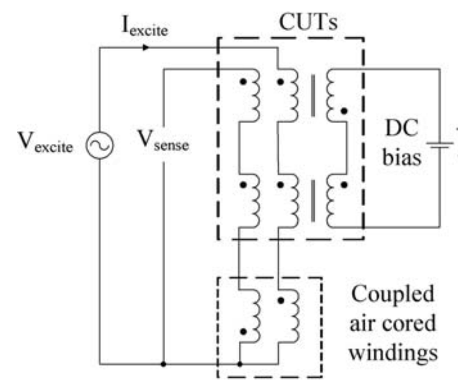

Fig. 2

Fig. 2 Core loss measurement circuit for DC bias conditions

EA-01

Spin-torque oscillator in the presence of thermal noise.

A. N. Slavin[1], J. Kim[2], V. Tiberkevich[1]
1. Department of Physics, Oakland University, Rochester, MI; 2. Institut d'Electronique Fondamentale, Universite Paris-Sud, Orsay, France

The passage of a spin-polarized current through a magnetic multilayer can lead to self-sustained magnetization precession [1]. This effect is interesting due to the potential applications in tunable nano-scale microwave auto-oscillators. Thermal noise plays an important role in the dynamics of nano-sized spin-torque oscillators (STO) in which the characteristic energy of oscillations is comparable with the thermal energy kT. In such nano-oscillators the presence of thermal noise not only determines the generation linewidth, but, also, blurs the threshold between the regime of sub-critical noise-induced damped oscillations and the regime of super-critical auto-oscillations. Also, in contrast with conventional quasi-linear oscillators, in STO the generated frequency demonstrates a strong shift with power, the sign of which depends on the orientation of the bias magnetic field [2].
The theory of a strongly nonlinear STO in the presence of thermal noise developed in this work is based on the nonlinear oscillator equation for the complex amplitude $c(t)$ of a spin wave excited by spin-polarized current [2]
$dc/dt + i(\omega_0 + N|c|^2)c + \Gamma_0(1 + Q|c|^2)c - \sigma I(1 - |c|^2)c = f(t)$, (1)
where ω_0 is the linear frequency of the excited spin wave mode, N is the nonlinear frequency shift coefficient, Γ_0 is the linear relaxation rate, Q is the dimensionless parameter describing the increase of damping with the increase of the spin wave power $|c|^2$, σ is the spin-polarization efficiency parameter defined in [2], I is the charge current passing through the magnetic layer, and $f(t)$ describes the influence of thermal noise. The function $f(t)$ is a stochastic Gaussian process with the correlator $\langle f(t)f^*(t')\rangle = 2\Gamma_0 n_T \delta(t - t')$, where n_T is the mean spin wave power in the state of thermal equilibrium (i.e., at $I = 0$).
In the framework of this theory the solution of the nonlinear stochastic equation (1) driven by the thermal noise is reduced to the solution of a corresponding linear and deterministic Fokker-Plank problem (FPP) for the probability density function describing the auto-oscillation process. Both stationary and non-stationary solutions of the FPP are obtained. It is demonstrated that the nonlinearity of the auto-oscillation frequency leads to the renormalization of the intensity of phase-noise and to a significant broadening of the auto-oscillator linewidth [3].
In substantially supercritical regime ($\zeta = \sigma I/\Gamma_0 \geq 1.2$) the main contribution to the linewidth of generation comes from the phase fluctuations of the spin wave amplitude $c(t)$. Analyzing Eq. (1) in this regime, we derived the following expression for the linewidth of the spin-torque-induced oscillations:
$\Delta\omega = \Gamma_0 (n_T/n_0) (1 + (N/\Gamma_0(\zeta + Q))^2)$, (2)
where $n_0 = |c_0|^2 = (\zeta - 1)/(\zeta + Q)$ is the mean dimensionless power of the auto-oscillation. Equation (2) clearly shows that the equilibrium relaxation rate of the excited mode Γ_0 determines the overall scale of the possible linewidth variations. Then, it demonstrates that the linewidth $\Delta\omega$ is proportional to the noise level (n_T/n_0), which is determined by the ratio of the population of thermal spin waves n_T to the population of driven spin waves n_0. Finally, Eq. (2) shows that the nonlinear frequency shift parameter N gives a measure of the contribution of the amplitude fluctuations to the phase noise far above threshold.
Fig. 1 demonstrates that the dependence of the spin-torque oscillator linewidth on the magnetization angle θ calculated from (2) for $Q = 3$ has a minimum at the angle θ ≈ 80 degrees, at which the nonlinear frequency shift coefficient N changes its sign. This result is in good quantitative agreement with the experiment [4].
The nonlinearity of STO is, also, responsible for the asymmetry, broadening, and non-Lorentzian shape of the generation line near the auto-oscillation threshold [5]. In addition, the Fokker-Plank formalism makes possible the calculation of the generation power in both sub-critical and super-critical regime, and provides a simple method for the experimental determination of the auto-oscillation threshold [6].

[1] J. C. Slonczewski, J. Magn. Magn. Mater. **159**, L1 (1996); L. Berger, Phys. Rev. B **54**, 9353 (1996).

[2] A. N. Slavin and P. Kabos, IEEE Trans. Magn. **41**, 1264 (2005).

[3] J.-V. Kim, V. S. Tiberkevich, and A. N. Slavin (2007), arXiv:cond-mat/0703317 (accepted by Phys. Rev. Lett.).

[4] W. H. Rippard *et al.*, Phys. Rev. B *74*, 224409 (2006).

[5] J.-V. Kim, V. S. Tiberkevich, and A. N. Slavin (2007), arXiv:0710.0495 (submitted to Phys. Rev. Lett.).

[6] V. S Tiberkevich, A. N. Slavin, and J.-V. Kim, Appl. Phys. Lett. **91**, 192506 (2007).

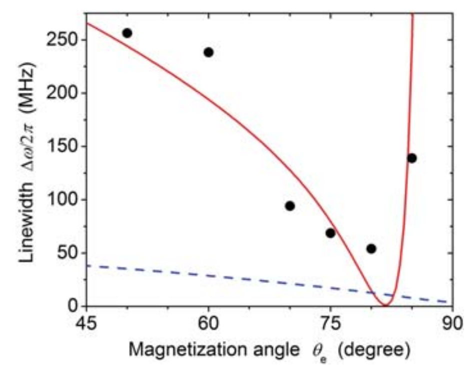

Angular dependence of the spin-torque oscillator linewidth calculated from Eq. (2) for Q = 3 (solid line) and measured experimentally in [5] (black dots). The dashed line represents the multiplied by ten result for the linewidth of a quasi-linear auto-oscillator calculated from Eq. (2) for N = 0.

EA-02

Frequency Pulling and Locking in RF Assisted Spin-Torque Switching.

S. H. Florez, J. A. Katine, M. Carey, O. Ozatay, L. Folks
Hitachi Global Storage Technologies, San Jose, CA

We demonstrate, at low temperature, that rf currents can dramatically alter the dc driven free layer magnetization reversal dynamics, as well as the dc switching level of current-perpendicular-to-plane spin valves. These effects are observed when the frequency of the rf current, f_{ext}, is tuned to be within a range around the dc driven magnetization precession frequencies, f_0^{dc}. For these frequencies, interactions between the dc driven dynamic excitations and the injected rf induce frequency locking and frequency pulling effects that lead to a measurable dependence of the critical switching current on the frequency of the injected rf.

Spin transfer torque (STT) can excite a broad variety of magnetization dynamics, including reversal and steady-state precessional states [1, 2]. While there has been much interest in the precessional dynamics appearing in the non-hysteretic regime, it has also been recognized that similar dynamics can exist in the hysteretic regime [3-7]. These pre-switching (PS) precessional modes play a key role in determining the spin-torque induced reversal mechanisms. Accordingly, our experiments focus on the unexplored PS dynamical regime as well as on the effects of additional rf current injection on the pre-switching and switching modes.

Figure 1a shows an (I^{dc},f_{ext}) phase diagram measured at 4.2 K, where the grayscale represents the dc resistance. The figure reveals the dependence of the direct critical switching current, I_c on f_{ext}. These data correspond to a 50 nm x 100 nm hexagonal pillar comprising an IrMn pinned antiparallel (AP) coupled bilayer $Co_{50}Fe_{50}$ (25 Å)/Ru(8 Å) /$Co_{50}Fe_{50}$(25 Å), a 40 Å Cu spacer, and 35 Å $Ni_{92}Fe_8$ as the free layer (FL). Measurements of the dc-only driven PS modes reveal that for currents increasing toward I_c, the resonance frequencies drop to a minimum $(f_0^{\ dc})^{min}$. For this sample the threshold is near 4.2 GHz, as marked on figure 1a. The locations of the dc-only driven peak frequencies, for $I^{dc} < I_c$ are also shown on this figure as white squares. For f_{ext} in this range, additional measurements (not shown here) show frequency locking between the dc driven resonance and the external rf. The region where this occurs is shaded and labeled in the diagram. From figure 1a we see that when this effect occurs near the switching boundary there is an increase in I_c. In contrast, for f_{ext} in the range below 4.2 GHz, there is a steady drop in I_c as the frequency of the external rf increases.

We have performed macrospin simulations based on the Landau-Lifshitz-Gilbert equation using Slonczewski STT [2], including combined dc and rf currents. Strictly speaking such a calculation is over-simplified since it does not take into account micromagnetic details such as non-ideal edge-effects, however, as shown in figure 1b, the model qualitatively captures the underlying physics for the reduction in I_c observed for f_{ext}, below $(f_0^{dc})^{min}$ (also obtained through simulation) and the increase in I_c for $f_{ext} \approx f_0^{\ dc}$, as well as the frequency-locking boundary.

In figure 2 (a) we plot M_y, M_z orbits at a fixed dc current of 1 mA and increasing f_{ext}. Each plot shows three orbits and the arrow indicates the direction of increasing f_{ext}. The labels indicate their corresponding location on the phase diagram in figure 1(b). The Fourier spectra of the M_y components corresponding to the orbits shown in figure 2(a) are shown in figure 2(b). An important conclusion we extract from
the macrospin simulations is that the precessional frequency and orbit are correlated such
that small (large) orbits correspond to high (low) frequencies (which is also the case for
dc-only driven PS precession). Therefore, when rf currents with $f_{ext} \approx f_0^{dc}$ are applied such that frequency pulling or frequency locking occur, effects on the magnetization precessional orbits also appear. Through this type of analysis we explore the nature of the dynamic excitations resulting from the interaction between the external rf and the dc driven precession and explain the origin of the effects of the rf on the critical switching boundary.

[1] L. Berger, Phys. Rev. B 54, 9353 (1996).

[2] J. Slonczewski, J. Magn. Magn. Mater. 195, L261 (1996).

[3] S. I. Kiselev et al., Nature 425, 380 (2003).

[4] T. Devolder et al., Phys. Rev. B 71, 184401 (2005).

[5] O. Ozatay et al., to be published.

[6] J. Z. Sun, Phys. Rev. B 62, 570 (2000).

[7] M. D. Stiles and J. Miltat, Spin Dynamics in Magnetic Structures III (Springer Berlin, 2006).

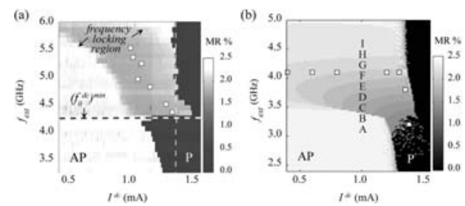

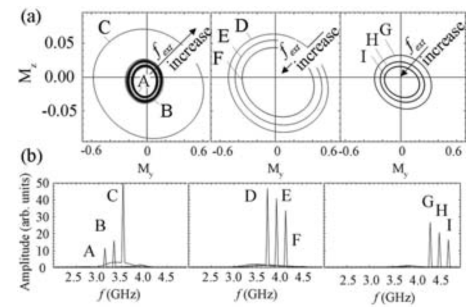

Time-Domain Studies of Nonlinear Magnetization Dynamics Excited by Spin Transfer Torque.

I. Krivorotov[1], N. Emley[2], J. Sankey[2], G. Finocchio[3], L. Torres[4], B. Azzerboni[3], R. Buhrman[2], D. Ralph[2]

1. Department of Physics and Astronomy, University of California, Irvine, Irvine, CA; 2. Cornell University, Ithaca, NY; 3. Dipartimento di Fisica della Materia e Tecnologie Fisiche Avanzate, University of Messina, Messina, Italy; 4. Departamento de Fisica Aplicada, Universidad de Salamanca, Salamanca, Spain

Spin transfer torque [1, 2] applied to a nanomagnet can either switch its magnetization between static magnetic states or induce steady-state magnetization precession. The primary experimental technique used for studies of spin-torque-driven magnetization dynamics is measurements of the spectra of persistent resistance oscillations excited by direct spin-polarized current. These frequency-domain measurements [3-6] yield ample information on quasi-periodic dynamics but give little insight into non-periodic dynamical processes. We have developed several new experimental approaches [7, 8] that employ time-domain electrical measurements (both stroboscopic and real-time) to probe the transient dynamics of spin-transfer-driven magnetic switching and persistent but non-periodic current-driven processes. We employ these techniques for detailed characterization of current-driven dynamics in Ir20Mn80/ Ni80Fe20/ Cu/ Ni80Fe20 elliptical nanopillar spin valves with misaligned magnetic moments of the free and the pinned layer. Our measurements provide new understanding of strongly nonlinear regimes of magnetization dynamics driven by spin transfer torque that cannot be obtained by conventional frequency-domain measurements.

In the current-induced switching regime, we observe GHz-range resistance oscillations prior to magnetization reversal and a step-wise dependence of the magnetization reversal time on the magnitude of an external magnetic field. These observations reveal a precessional character of current-driven switching in our samples. To understand the origin of the precessional reversal, we make micromagnetic simulation of the reversal process [9]. Our simulations demonstrate that the key factor determining the mechanism of magnetization reversal is the equilibrium angle between magnetizations of the free and pinned layers. We find that in the case of collinear magnetizations of the pinned and free layers, current-induced reversal proceeds via a vortex nucleation process. However, even relatively small misalignments of magnetizations of the pinned and free layers (> 5 degrees) lead to a dramatic change of the reversal mechanism, giving a coherent precessional reversal. Micromagnetic simulations of current induced switching in our samples are in good agreement with our experimental data as shown in Fig. 1.

Near the phase boundaries of the current-field phase diagram that separate different static and dynamic states of magnetization, our measurements reveal that the magnetization dynamics can become stochastic. In particular, close to the phase boundary between persistent oscillatory dynamics and current-driven switching, we find that the resistance signals due to the persistent dynamics evolve as a function of increasing current from a periodic sinusoidal oscillation to brief, randomly-timed, non-sinusoidal, large-amplitude swings in resistance as shown in Fig. 2. Simultaneously, the average frequency of the oscillations approaches zero. These measurements suggest that the magnetization dynamics are affected by thermal fluctuations in the neighborhood of the shallow local minimum of the magnetic energy landscape that exists near the static-dynamic phase boundary for a very large precession angle [7].

Our time-domain measurements also demonstrate that magnetization motion at boundaries of the dynamical phase diagram separating different modes of persistent oscillation can have a stochastic character [10], and can be described as random switching between two dynamical modes with different frequencies [7]. This switching can occur on a time scale of nanoseconds and it is the dominant mechanism limiting the linewidths of the dc-driven persistent oscillations near these phase boundaries.

1. J. C. Slonczewski, J. Magn. Magn. Mater. 159, L1 (1996).

2. L. Berger, Phys. Rev. B 54, 9353 (1996).

3. S. I. Kiselev, J. C. Sankey, I. N. Krivorotov, N. C. Emley, R. J. Schoelkopf, R. A. Buhrman, and D. C. Ralph, Nature 425, 380 (2003).

4. W. H. Rippard, M. R. Pufall, S. Kaka, S. E. Russek, and T. J. Silva, Phys. Rev. Lett. 92, 027201 (2004).

5. O. Boulle, V. Cros, J. Grollier, L. G. Pereira, C. Deranlot, F. Petroff, G. Faini, J. Barnas, A. Fert, Nature Phys. 3, 492 (2007).

6. D. Houssameddine, U. Ebels, B. Delaët, B. Rodmacq, I. Firastrau, F. Ponthenier, M. Brunet, C. Thirion, J.-P. Michel, L. Prejbeanu-Buda, M.-C. Cyrille, O. Redon, and B. Dieny, Nature Mater. 6, 441 (2007).

7. I. N. Krivorotov, N. C. Emley, R. A. Buhrman, D. C. Ralph, Phys. Rev. B, in press (2008).

8. I. N. Krivorotov, N. C. Emley, J. C. Sankey, S. I. Kiselev, D. C. Ralph, R. A. Buhrman, Science, 307, 228 (2005).

9. G. Finocchio, I. N. Krivorotov, L. Torres, R. A. Buhrman, D. C. Ralph, B. Azzerboni, Phys. Rev. B 76, 174408 (2007).

10. I. N. Krivorotov, D. V. Berkov, N. L. Gorn, N. C. Emley, J. C. Sankey, D. C. Ralph, R. A. Buhrman, Phys. Rev. B 76, 024418 (2007).

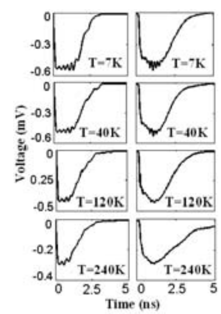

Fig. 1. A comparison between computed (left) and experimentally measured (right) voltage signals due to current-induced magnetization reversal from the low to the high resistance state for four different temperatures and applied current step current magnitude of 4.8 mA.

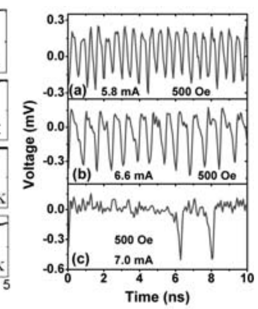

Fig. 2. Real-time signal due to persistent magnetization dynamics measured with a microwave storage oscilloscope at $H = 500$ Oe for three values of the current bias (a) $I = 6.0$ mA, (b) $I = 6.8$ mA, and (c) $I = 7.0$ mA.

EA-04

Current-driven vortex oscillations in metallic nanocontacts.

Q. Mistral[1], M. van Kampen[2], G. Hrkac[3], *J. Kim*[1], T. Devolder[1], P. Crozat[1], C. Chappert[1], L. Lagae[2]
1. Institut d'Electronique Fondamentale, CNRS / Univ. Paris Sud, Orsay, France; 2. IMEC, Leuven, Belgium; 3. Department of Engineering Materials, University of Sheffield, Sheffield, United Kingdom

Lateral confinement in magnetic nanostructures leads to the appearance of complex magnetic states. One important example concerns the magnetic vortex, which arises in patterned structures from competing exchange and dipolar interactions. The dynamics of such vortices is largely governed by the confining potential which defines them. Recent experiments have shown resonance phenomena to be possible with such vortices, including sub-GHz excitations, below the usual ferromagnetic resonance frequency, which involve the spiralling motion of the vortex core about its equilibrium position.
More recently, it has also been shown experimentally that magnetic vortices can be brought into a self-oscillatory state [1]. This is made possible with the spin-transfer effect, whereby spin-angular momentum is transferred between a spin-polarized current and magnetization in a multilayer. It is well-known that spin-transfer leads to an additional torque on magnetization, and it has been demonstrated that this effect can lead to steady-state vortex oscillations in nanopillars [1]. In this talk, we describe how current-driven vortex oscillations can also occur in the absence of any structural confining potential. We demonstrate that spin-polarized currents applied through metallic point-contacts on a continuous magnetic multilayer stack can also lead to vortex oscillations. Here, the Oersted field generated by the applied current provides an effective potential in which a magnetic vortex can oscillate.
The experimental system we study has the multilayer composition Ta/Cu/Ta/NiFe/IrMn/CoFe/Cu/NiFe/Pt, which is a sputter-grown laterally extended stack on which a Cu nanocontact (200 nm in diameter) is deposited. We have measured the electrical high-frequency power spectra through the point contact for external magnetic fields applied perpendicular to the film plane with a direct current flowing through the contact. An example of low-frequency power spectra obtained, for a field of H = 2.1 kOe, is presented in Fig. 1. These modes are consistent with vortex oscillations, as the peak frequencies are much lower than the ferromagnetic resonance frequency expected at these fields, hysteresis with applied currents is associated with the existence of these modes [2], and a frequency blueshift is observed with applied currents despite the large in-plane component of magnetization [3].
We have performed full micromagnetics simulations to study the sub-gigahertz oscillations in detail. We take into account the spatially inhomogeneous current distribution flowing through the magnetic free layer and consequently use the Oersted field generated by this current for the magnetization dynamics. The simulations reveal that the observed oscillations correspond to a large-amplitude translational motion of a magnetic vortex. In contrast to nanopillars in which the vortex core precesses within the spin-transfer region, the dynamics reported here corresponds to an orbital motion *outside* the contact region. This is a novel feature brought to light by our experiments. The simulated frequencies give a good quantitative agreement with the measured values, as shown in Fig. 2a. Furthermore, we have derived a modified form of the Thiele equation that includes spin-transfer, and we show that a rigid-vortex approximation can account for the observed variation in the frequency with applied field and currents, as shown in Fig. 2b.

This work was supported by the European Communities programs IST STREP, under Contract No. IST-016939 TUNAMOS, and "Structuring the ERA", under Contract No. MRTN-CT-2006-035327 SPINSWITCH, and by the Région Ile-de-France in the framework of C'Nano IdF. QM acknowledges support from a joint CNRS and STMicroelectronics PhD grant.

[1] V. S. Pribiag et al., Nat. Phys. **3**, 498 (2007).

[2] M. R. Pufall et al., Phys. Rev. B **75**, 140404(R) (2007).

[3] A. N. Slavin and P. Kabos, IEEE Trans. Magn. **41**, 1264 (2005).

[4] Q. Mistral et al., arXiv:0710.5680v1 (2007).

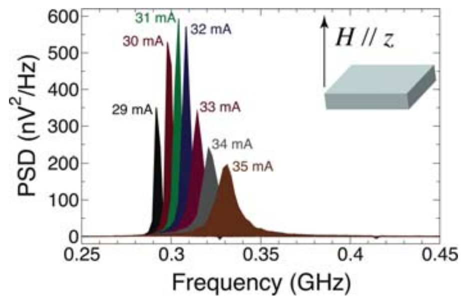

Fig. 1: Experimental power spectra of current-driven magnetization oscillations in metallic point contacts, for a perpendicular applied field of H = 2.1 kOe.

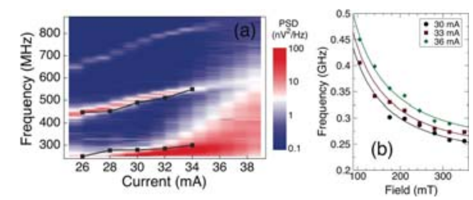

Fig. 2: (a) Color-coded map of experimental power spectral density for H = 3.5 kOe, with solid squares representing results from micromagnetics simulations. (b) Comparison of field dependence of oscillation frequency between analytical theory (lines) and experiment (dots).

EA-05

Self-Torque Induced by Local Spin-Transfer Effect and Lateral Spin Diffusion in Magnetic Layers with Inhomogeneous Magnetization.

K. Lee
Korea University, Seoul, South Korea

Initial spin torque theories derived the spin torque term within the macrospin assumption [1]. However, micromagnetic studies [2] and time-resolved imaging experiment [3], have revealed that the spin torque most often generates incoherent spin-waves and thus non-uniformities in the magnetization. Therefore it is essential to consider a possible feedback mechanism between the inhomogeneous magnetization and the spin-transfer torque.
Several authors proposed that the lateral diffusion of spin-dependent reflected electrons at a NM/FM interface (NM=non-magnetic metal, FM=ferromagnetic metal), can induce a stabilizing or destabilizing effect on the local magnetization of the F layer depending on the direction of the current due to local spin-transfer effects [4]. This effect can be named *self-torque* since it allows a single FM layer with inhomogeneous magnetization to exert spin transfer effects on itself.
In order to quantitatively study this phenomenon, we developed a 3-dimensional numerical model to *self-consistently* solve both Landau-Lifshitz-Gilbert and time-dependent spin transport equations. The study was carried out on 3-dimensional structure of Cu (10 nm) / Co (t nm) / Cu (80 nm) patterned to nanopillar of 60 x 30 nm ^{2} where t varies from 2 to 8 nm. The patterned part of Cu lead was also included in the numerical study. Magnetic excitation in this single ferromagnet has been calculated as a function of out-of-plane external field (Hz = 0~5T) and injected current (-15~+15mA). As in the experiment [5], magnetic excitations were observed only at negative currents (electrons from thick to thin Cu). The critical current for the excitation linearly depends on the out-of-plane field (Fig. 1(a)). Even when Hz > 4πMs we observed high frequency precession motions of magnetizations at negatively large currents instead of the out-of-plane saturation. Thickness-dependent slope of H_{crit}/I_{crit} is in good agreement with the experimental results especially for a thin Co layer (Fig. 1(b)).
Our result confirms the existence of *self-torque* effects and allows investigating the interplay between the lateral spin diffusion currents and the magnetic excitations in the FM. Numerical studies on spin-valve structures were also performed. The *self-torque* significantly changes the current-induced dynamic modes and more strikingly, can reduce the linewidth of microwave power spectrum. It indicates that the *self-torque* can serve an effective cooling of spin system by suppressing the magnon excitation. In the presentation, the current-induced magnetization dynamics affected by the *self-torque* will be presented in detail.

[1] J. C. Slonczewski, J. Magn. Magn. Mater. 159, L1 (1996); L. Berger, Phys. Rev. B 54, 9353 (1996).

[2] J. Miltat et al., J. Appl. Phys. 89, 6982 (2001); J. G. Zhu and X. Zhu, IEEE Trans. Magn. 40, 182 (2004); K. J. Lee et al, Nat. Mater. 3, 877 (2004); D. Berkov and N. Gorn, Phys. Rev. B 71, 052403 (2005); K. J. Lee and B. Dieny, Appl. Phys. Lett. 88, 132506 (2006).

[3] Y. Acremann et al., Phys. Rev. Lett. 96, 217202 (2006).

[4] M. L. Polianski and P. W. Brouwer, Phys. Rev. Lett. 92, 026602 (2004); M. D. Stiles, J. Xiao and A. Zhangwill, Phy. Rev. B 69, 054408 (2004)

[5] B. Ozyilmaz, A. D. Kent, J. Z. Sun, M. J. Rooks, and R. H. Koch, Phys. Rev. Lett. 93, 176604 (2004).

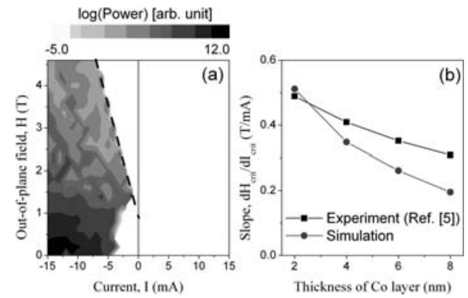

Fig. 1. (a) Contour of microwave power obtained for Cu (10nm) / Co (2 nm) / Cu (80 nm) structure. The white region indicates no magnetic excitation. The dotted line shows a linear dependence of the critical current for magnetic excitation on the out-of-plane field. (b) Thickness-dependent slope (dH_{crit}/dI_{crit}).

EA-06

Spin Torque Influence on the High Frequency Magnetization Fluctuations in Magnetic Tunnel Junctions.

S. Petit[1], N. de Mestier[1], C. Thirion[1], U. Ebels[1], Y. Liu[2], M. Li[2], P. Wang[2], *C. Baraduc*[1]
1. SPINTEC, CEA/CNRS, Grenoble, France; 2. Headway Technologies, Milpitas, CA

The observation of steady magnetization excitations induced by spin transfer torque has been reported by many groups in magnetic nanostructures traversed by a spin-polarized current of sufficient density. Here we show that far below this precessional critical current density, spin torque impacts also magnetization thermal fluctuations: in particular, we observed that the noise spectrum of TMR read-heads strongly depends on the direction and amplitude of the applied DC-current.
The electrical noise of 300 nm diameter TMR read-heads with alumina barrier was measured in a range of 1 to 10 GHz as a function of magnetic field, DC current bias and temperature. Measurements were performed both in the parallel and anti-parallel states. We observed several peaks in the noise spectra that shift with the applied DC field and DC current bias. These peaks are attributed to several modes of thermally activated ferromagnetic resonance excitations (FMR) in the free layer, each peak frequency following the Kittel law.
The most interesting feature of the noise spectra is a pronounced asymmetry with the sign of the current[1]. For positive current the normalized noise peak grows, while for negative currents the normalized peak amplitude is reduced. Finally for opposite magnetic field values, the effects of positive and negative currents are exchanged. In other words, symmetric points in the H-I phase diagram exhibit the same behavior. This observation indicates that spin transfer torque reduces or enhances the thermal fluctuations as a function of the DC-current direction, depending on whether it tends to favor or disfavor the equilibrium magnetic configuration.
The influence of spin-torque on magnetic fluctuations is modeled using the macrospin approximation in the framework of linear response theory[2], modified to take into account spin-torque effect. Magnetization dynamics is assumed to follow the Landau-Lifschitz-Gilbert equation modified with the two spin transfer terms: the Slonczewski torque and the inter-layer exchange coupling torque that we hereafter call the “field-like term”. The fundamental FMR mode is analytically calculated using the fluctuation-dissipation theorem. Our model shows that the evolution of the peak line width with the applied current is directly related to the amplitude of the Slonczewski torque while the shift of the resonance frequency is sensitive to the field-like term.
The experimental data are successfully compared with our model. The experimental spectra were first corrected from the noise induced by the experimental set-up itself and from the transfer function of the transmission line between the nanostructure and the spectrum analyzer. The noise spectra were carefully analyzed to take into account the variation with the applied current of both the conductance and the magneto-resistance ratio of the MTJ. From these measurements it was possible to extract the current dependence of the two spin-torque terms. In particular, we have shown that it is possible to extract the Slonczewski spin-torque term from the resonance peak line width in the near-equilibrium regime. Concerning the field-like term extracted from the resonance frequency variation, we must however stress that it is subjected to uncertainties due to the high sensitivity of the resonance frequency to magnetic field, Joule heating and thermo-electric effects.
A significant advantage of these measurements performed below the critical current is the possibility to extract the spin-torque amplitude for both current directions i.e. when the spin-torque tends to destabilize the magnetization equilibrium position as well as when it stabilizes it. Moreover the observed reduction of thermal fluctuations by spin transfer torque could lead to potential applications. Taking advantage of this effect could help to reduce the electrical noise in hard-disk read-heads especially when the multilayer structure is specifically designed.
In summary, we have studied power spectral density of the voltage noise of magnetic tunnel junctions with alumina barrier in the GHz frequency range and observed that thermal magnetic fluctuations are either reduced or enhanced by the DC-current bias depending on its sign. We ascribe this effect to the influence of spin transfer torque on ferromagnetic resonance excitations depending on whether it favors or disfavors the equilibrium magnetic configuration. Potential use of this effect to control electrical noise in read-heads is conceivable.

[1] S. Petit et al, Physical Review Letters 98 (7), 077203 (2007)

[2] N. Smith, Journal of Applied Physics 90 (11), 5768-5773 (2001)

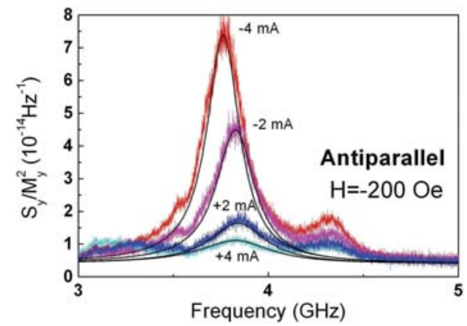

Magnetization fluctuations spectra of a MTJ in the anti-parallel state for different values of applied DC-current. The FMR excitations peaks evolve anti-symmetrically with the current sign consistently with the spin torque effect. Solid lines correspond to the susceptibility calculated within the linear response theory.

EB-01

Design considerations of tubular flux-switching permanent magnet machines.

J. Wang, W. Wang, K. Atallah, D. Howe
Electronic and Electrical Engineering, University of Sheffield, Sheffield, United Kingdom

This paper describes a tubular, 3-phase, flux-switching permanent magnet (PM) machine, as shown in Fig. 1, which combines salient features from switched reluctance with simple and robust mover structure and high force capability of permanent magnet machines with no end-windings and zero net radial force, and has the potential for low cost manufacture. Further, since the armature reaction field is essentially perpendicular to the axis of magnetisation, the risk of irreversibly demagnetising the magnets is low. This enables a high peak electric loading, and, hence, a high peak power density and force capability. The machine is, therefore, eminently suitable for a variety of applications which requires great mechanical robustness and the ability to operate in harsh environment, such as free-piston energy converters and active vehicle suspensions.
The paper derives feasible pole-slot number combinations applicable to both rotary and linear flux-switching PM machines, Table I, where Ns is the number of stator slots(modules)and Np is the number of active mover poles(teeth), and examines an alternative winding configuration which is unique to tubular machine topology. It is shown that various feasible pole-slot combinations exists for flux-switching machines, and that the alternative winding configuration yields ~10% higher thrust force capability as compared to the conventional design.
In conventional rotary brushless DC or flux-switching PM machines, a coil is usually wrapped around a stator tooth. This winding configuration results in the winding factor for the fundamental being equal to 0.866. For tubular flux-switching machines, however, there is an alternative winding configuration in which the two coils in one slot are connected in series to form a phase winding, as shown in Fig. 2. This gives rise to ~13% increase in fundamental winding factor and hence 13% higher force capability. Furthermore, the phase windings in this configuration are essentially physically, magnetically and thermally isolated from each other. This will lead to a high degree of fault-tolerance. Fig. 3 compares the variation of thrust force of the 12-slot, 10-pole flux switching machines with conventional and alternative winding configurations as functions of current density. Both machines are optimally designed with the same volumetric and thermal constraints for active vehicle suspension applications. As will be seen, the alternative winding configuration yields ~10% higher force capability as compared to the conventional design.
Detailed derivation and performance analysis of the feasible pole-slot number combinations and alternative winding configuration for tubular flux-switching machines together with the procedure for achieving optimal design for applications in active vehicle suspension will be described in the full paper.

1.J. Wang, W. Wang, R. Clark, K. Atallah and D. Howe, "A tubular flux-switching permanent magnet machine", Journal of Applied Physics, in press.

2.J. Corda and B. Ouhab, Proceedings of 9th International Conference on Electrical Machines and Drives, (1999), 276.

3.E. Hoang, A. H. Ben-Ahmed, and J. Lucidarme, Proceedings of 7th European Conference on Power Electronics and Applications, (1997), 903

4.H. Pollock, C. Pollock, R. T. Walter and B. V. Corti, Proceedings of IEEE Industry Applications Society Annual Meeting, (2003), 1451.

5.Z. Q. Zhu et al, IEEE Trans. on Magn., 41, (2005), 4277.

6.J. Wang et al., IEEE Trans. on Energy Convers., 22 (2007), 229.

7.J. Martins, et al, IEEE Trans. Veh. Technol., 55, (2006), 86.

Ns	Np	Ns	Np
3	2,4,5	12	8,10,14,16,20,22
6	4,5,7,8,10,11	15	10,20,25
9	6,12,15	18	12,15,21,24,30,33

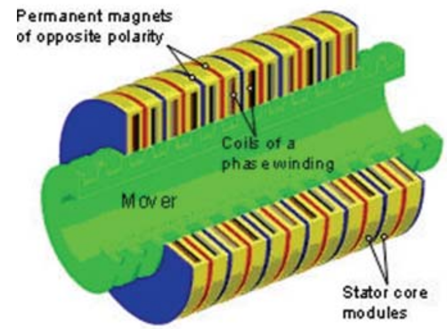

Fig.1 Schematic of tubular, 3-phase, flux-switching PM machine

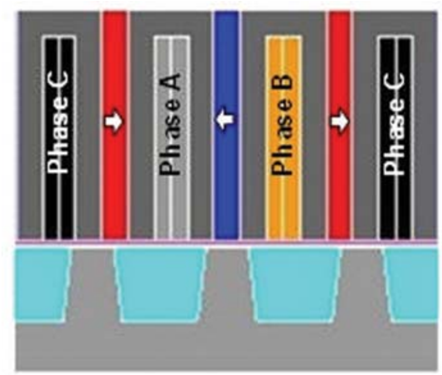

Fig. 2 Alternative winding configuration

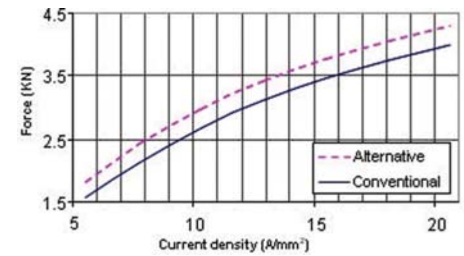

Fig. 3 Comparison of thrust force capability for two winding configurations

EB-02

Linear induction motors with modular winding primaries and wound rotor secondaries.

J. Eastham[1], T. Cox[1,2], J. Proverbs[2]
1. The University of Bath, Bath, United Kingdom; 2. Force Engineering, Shepshed, United Kingdom

Introduction
Linear induction motors commonly use conventional double layer stator windings. These provide an excellent travelling field with little harmonic content. However when applied to linear stators they must use either half empty slots or coils that overlap at the ends of the stack. In addition the end winding at the sides of the machine tends to be bulky.
Modular Windings
It is the objective of this paper to use modular windings [1][2] which have winding groups that are in a plane and do not overlap. This leads to machines that are inexpensive to wind, compact and can be stacked end to end since no overlapping coils or half filled slots are needed. This is a particularly useful feature when long stators for EM launchers or urban transport schemes are considered. Whilst the windings are excellent mechanically they have the drawback of a high harmonic content in the mmf wave. For example a 9 coil winding of coil configuration (R –R R B –B B Y –Y Y) has large 8 and 10 pole mmfs. Fig. 1 illustrates this showing the open circuit flux together with the 8 and 10 pole components. These components travel in opposite directions.
The windings are typically in use for machines with permanent magnet excitation [1]. For this duty either an 8 pole or a 10 pole magnet array can be provided to cooperate with either the 8 or 10 pole mmf wave respectively. If for example an 8 pole array is chosen then net force will result only with the 8 pole mmf. The 10 pole mmf merely produces air-gap flux which gives extra leakage reactance.
The situation is radically different for induction machines. If an inductive plate rotor is used both the 8 and 10 pole fluxes produce secondary eddy currents and force. The 10 pole force opposes the 8 pole and the net force is severely reduced. Fig. 2 illustrates this condition by comparing the response for an 8 pole short plate rotor first to a double layer winding with small harmonic content and secondly to the 9 coil modular winding described previously. It will be seen that the plate rotor performs poorly with a modular wound stator due to the backward going harmonic. These results were obtained using the MEGA package time stepped FE modelling.
New Principle
The situation can be improved by using an 8 pole double layer wound secondary. This, like the permanent magnet secondary, will respond substantially only to the pole number for which it is wound since the winding factor controlling the induced emf is small except for the fundamental. The response as shown in Fig. 2 is excellent; the peak force is closely the same as when a double layer stator and plate rotor is used but the peak is closer to the synchronous speed indicating a much better secondary efficiency (90% compared to 50%).
The new principle [3] of using wound secondaries so that simple modular primary windings may be used has been described with respect to a particular 9 slot 8/10 pole winding, but it will be appreciated that there are a large number of modular windings [1][2] with substantial harmonic content which can also be used.
An Experimental Machine
A test rig has been constructed to prove this principle using 9 slot 8/10 pole stator winding sections. This cooperates with a short wound rotor carrying a fractional slot double layer 8 pole winding designed so that standstill locking forces are small. Tests were performed using the standstill variable frequency principle [4] to estimate the dynamic response of the system and the results are plotted on Fig. 3 for comparison with FE standstill variable frequency results. It will be observed that the correlation is excellent.
Conclusions
Simple modular windings can be used for linear induction motor stators when wound rotors are employed. The new arrangement enables inexpensive stator modules to be used in EM launch and urban transport systems.

[1] J Wang, Z P Xia, D Howe, S A Long, "Comparative Study of 3-Phase Permanent Magnet Brushless Machines with Concentrated, Distributed and Modular Windings", PEMD 06, Mar. 2006, pp 489-493

[2] Libert F., Soulard J., "Investigation on Pole-Slot Combinations for Permanent-Magnet Machines with Concentrated Windings", ICEM 04, Sep. 2004

[3] J F Eastham, Force Engineering Patent "Improvements in and relating to Electromotive Machines" International Patent Application No PCT/GB2007/003849

[4] J F Eastham, P C Coles, M Benarous, J Proverbs, A Foster "Linear Induction Motor Variable Frequency Standstill Tests to Predict Operational Velocity Performance", LDIA 03, Sep. 2003, pp 81-84

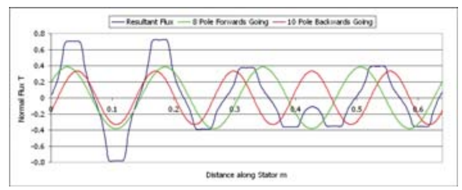

Fig. 1. Open circuit flux and principal components

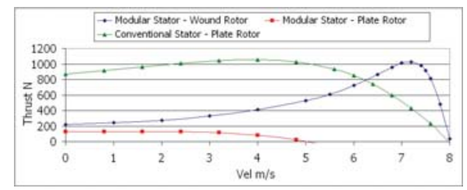

Fig. 2. Short rotor thrust speed curves

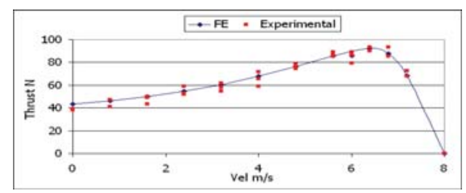

Fig. 3. Wound rotor experimental and FE results

EB-03

Magnetic Actuator Design using Level Set based Topology Optimization.

S. Park[1], *S. Min*[1], S. Yamasaki[2], S. Nishiwaki[2], J. Yoo[3]
1. Mechanical Engineering, Hanyang University, Seoul, South Korea; 2. Aeronautics and Astronautics, Kyoto University, Kyoto, Japan; 3. Mechanical Engineering, Yonsei University, Seoul, South Korea

Topology optimization which determines optimal distribution of material has been widely applied to design magnetic devices since the work by Dyck and Lowther[1]. The element based topology optimization method has resulted in mesh dependent boundaries and gray scale elements due to numerical instabilities[2]. These features have great influence on the performance of magnetic devices due to discontinuity of magnetic flux. Level set based topology optimization has emerged recently as an attractive alternative to overcome shortcomings of the conventional method. Level set method is a numerical technique for tracking interfaces and shapes using the implicit function, so called level set function[3]. Sethian and Wiegmann[4] firstly introduced level set method to topology optimization in order to represent material boundaries, and could design a cantilever beam with distinct boundaries free from mesh dependency and gray scale elements. Thus, the goal of research is to develop a novel design methodology for optimum structural design of magnetic actuators using a level set based structural optimization method where the level set method can represent the precise boundary shape of a structure and also deal with complex topological changes during the optimization process.

In this work, we focus on designing a yoke of magnetic actuators using level set based topology optimization in order to improve magnetic force on armature while reducing its weight. Level set method is introduced to represent material boundaries between a ferromagnetic material domain and another domain filled with air where level set function $\phi(\mathbf{x})$ is defined as shown Fig. 1. The magnetic quantities are calculated by linear magneto-static finite element analysis under the assumption that the material property has linear relationship between magnetic field intensity and flux density. To represent the distribution of ferromagnetic material, the magnetic reluctivity of each element can be defined using level set function as follows:

$\nu(\phi(\mathbf{x}))= \nu_0(\nu_{air}+(\nu_{mat}-\nu_{air})H(\phi(\mathbf{x}))$

where ν_0 is magnetic reluctivity in free space and H(x) is Heaviside function which has zero or one according to x. To formulate the optimization problem the objective function is set to maximize the magnetic energy in a domain between a yoke and an armature since the magnetic force on an armature becomes larger as it increases, and the amount of material used in the domain is constrained to limit its weight. The movement of the implicit moving boundaries of the structure is driven by a transformation of the objective and the constraint into speed functions that govern the level set propagation. The normal velocity is derived from optimality and convergence conditions of level set eqution and calculated using sensitivities of the objective function and the constraint where the adjoint variable method is employed since the objective function has implicit dependency with level set function.

The proposed method is applied to design a yoke of magnetic coupler shown in Fig. 2(a) which enables the transmission of mechanical energy through a magnetic field interaction. In order to maximize the magnetic force on the positioner, the design domain is considered as yokes and the positioner and the magnetic energy is calculated in an air gap domain. Fig. 2(b) shows the optimal layout of ferromagnetic material that has clear-cut boundaries and the exact shape extraction of the optimal design can be easily integrated with CAD/CAE systems. It is summarized in Table. 1 that the optimal design provides 10% higher magnetic force and 30% less material usage than the initial design.

[1] Dyck, D.N. and Lowther, D.A., 1996, “Automated design of magnetic devices by optimizing material distribution,” Magnetics, IEEE Transactions on, Vol. 32, No. 3 pt.1, pp. 1188-1193.

[2] Sigmund, O. and Petersson, J., 1998, “Numerical instabilities in topology optimization: A survey on procedures dealing with checkerboards, mesh-dependencies and local minima,” Structural Optimization, Vol. 16, No. 1, pp. 68-75.

[3] Osher, S. and Sethian, J.A., 1988, “Fronts Propagating with Curvature-Dependent Speed - Algorithms Based on Hamilton-Jacobi Formulations,” Journal of Computational Physics, Vol. 79, No. 1, pp. 12-49.

[4] Sethian, J.A. and Wiegmann, A., 2000, “Structural Boundary Design via Level Set and Immersed Interface Methods,” Journal of Computational Physics, Vol. 163, No. 2, pp. 489-528.

	Initial design	Optimal design
Volume in design domain (mm^2)	344	240 (30%↓)
Magnetic force on armature (N/m)	44.2	48.4 (9.5%↑)

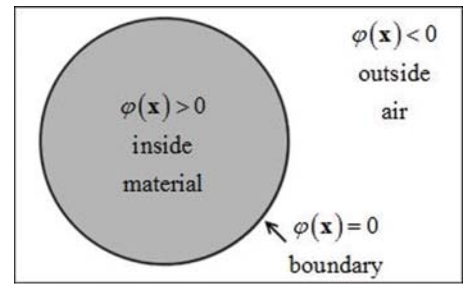

Fig. 1 Material boundary representation using level set function

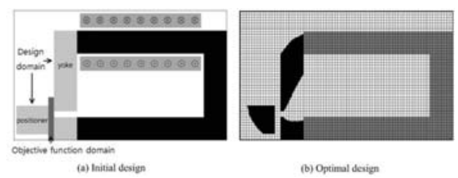

Fig. 2 Magnetic coupler design problem

EB-04

Comparsion of numerical and analytical simulation of saturated zig-zag flux in induction machines.

A. Binder, *T. Knopik*, R. Hagen
Institute for Electrical Energy Conversion, Technische Universität Darmstadt, Darmstadt, Germany

Iron saturation in induction machines (IM) is determined by (i) the main flux saturation kh, which is excited by the magnetizing current and is dominant at no-load, being clearly visible in the no-load characteristic, and decreases with increasing slip (Fig. 1a, b), and by (ii) the load dependent air gap zig-zag flux saturation kzk, which increases with increasing slip and dominates the iron saturation at stall, being clearly visible in the voltage-current-characteristic at unity slip s = 1 (Fig. 1c, d). Whereas the main flux saturates the iron teeth at full length and the iron back, the zig-zag flux along with the slot leakage flux saturates the tooth tips. The analytical calculation of the main flux saturation is well known and found in good coincidence with numerical solutions. The analytical non-linear calculation of the zig-zag flux still is matter of investigation. Here, the basic work of Weppler, Schetelig and Taegen is revisited and combined. It proves to be a very useful approach to calculate the saturated zig-zag flux and the corresponding tooth flux pulsation under load, along with the induced rotor cage harmonic currents. Hence it allows a satisfactory analytical prediction of the saturated stalled voltage-current characteristic and the stray load losses.
Fig. 1: Saturation in IM: a) Main flux path, b) No-load characteristic, c) Zig-zag leakage paths at s = 1, d) Locked rotor characteristic.
Weppler combined for induction machines the well-known main flux saturation factor kh with the rotor skew, leading to increased saturation due to the different superposition of the stator and rotor fundamental field in different radial machine cross sections. Further he introduced a method for calculating the air-gap zig-zag flux, which is not based on the conventional summing of stator and rotor field harmonics to arrive at a harmonic leakage inductance. He directly calculates the flux from simple lumped parameter magnetic circuits, defining the coefficients kzk for the zig-zag flux saturation in the tooth tip and kns1-2 for the stator and rotor slot leakage flux saturation. Schetelig improved this method by considering also the saturation in the stator tooth tip, which is caused by the slot harmonics of the rotor m.m.f. and the rotor slot fields, which amplify the slot harmonic field amplitudes due to the rotor slot openings, with the help of conformal mapping. For closed rotor slots a special iterative method for saturation of the tooth tips is used.
Taegen pointed out by careful measurement with tooth and yoke coils, that there is a different saturation for harmonic components of the zig-zag flux with low and high ordinal number. The saturation of harmonic field waves with small wave lengths in the range of a stator/rotor slot pitch is determined by tooth-tip saturation kzk. Harmonic fields with long wave lengths (so-called slot difference harmonics), hence with low ordinal numbers, magnetize in parallel to the main flux via the iron back, resulting in another higher saturation. Adding this effect to the Weppler-Schetelig theory, the harmonic leakage inductance, corresponding to the zig-zag flux, is determined for an equivalent magnetic circuit, which allows the calculation of the saturated locked voltage-current characteristic without any correction factors. Further, the sum of all field harmonics for a certain value g ≠ 0 cause a pulsation in the stator tooth.
Considering the harmonic content of leakage flux up to certain maximum ordinal number yields the time function of the flux pulsation in the stator teeth, and in a similar way, in the rotor teeth, along with the calculation of the cage harmonic currents, which are damping the flux pulsations considerably.

The above described methods were applied to several 4-pole, skewed aluminium cage induction machines with 36 stator slots and 28 rotor slots. The analytically calculated no-load and locked voltage-current-characteristics were compared with measurements (Fig. 2a). With the 2D FEM program package FLUX2D non-linear time stepping simulations for unskewed machines were performed and compared to the analytical results (Fig. 2b, Fig. 3).
The FEM and analytical result fit very well, showing a by ca. 10% bigger current in comparison to the skewed rotor due to the lack of skew leakage inductance.
As an example, for the same rated motor data of Fig. 2 the analytically calculated tooth flux density in the middle tooth is shown in Fig. 3a at no-load and in Fig. 3a at rated slip for an unskewed rotor. The increase of the tooth flux pulsation amplitude with increasing slip due to the increasing zig-zag flux is clearly visible and in good coincidence with the FEM result, which for clarity is shifted in Fig. 3a.
In the full paper the numerical solutions and further experimental work is given in more detail along with a description of the analytical calculation method.

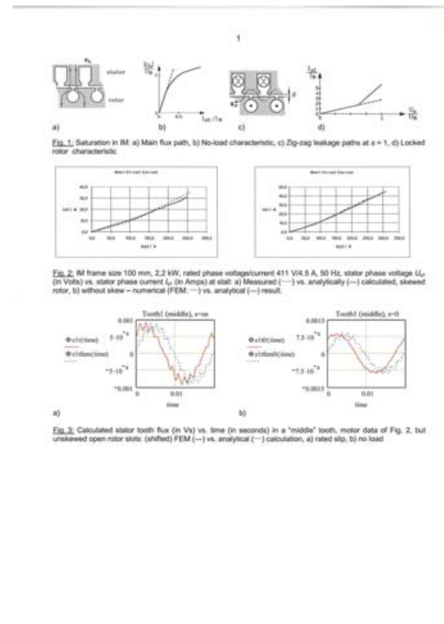

EB-05

Newly structured double excited 2-DOF motor for security camera.

J. Lee[1], D. Kim[2], S. Baek[1], B. Kwon[1]
1. Hanyang University, Ansan, South Korea; 2. Korea Electronics Technology Institute, Gwang-ju, South Korea

Introduction

Recently, the research of multiple degrees of freedom (DOF) motor has been extensively conducted without a dynamic transfer device [1-2]. The Multiple-DOF motor with only one joint is not necessary to use additional gears and links parts. Therefore, The Multiple-DOF motor can eliminate the combined effects of inertia, backlash, non-linear friction, and elastic deformation of gears. But it has a complicated control algorithm and difficult manufacture due to the spherical shape. Thus, it has not been put to practical use. However, the 2-DOF motor has the advantage of the 3-DOF Spherical motor in terms of practical use.

A few researchers have been concerned to develop 2-DOF motor. Hirata has suggested 2-DOF motor which consist permanent magnet rotor and 'E' type, 'C' type stator segment for linear/rotate motion [3]. Yano has suggested 2-DOF motor which consist inner sub-motor and outer sub-motor for horizon/vertical motion [4]. It is not suitable for a security camera application with pan-tilt motion. This paper has proposed the novel designed 2-DOF motor with pan-tilt motion to use in a security camera and also analyzed its performance by 3D FEM.

Design of a Double Excited 2-DOF

Fig. 1 and 2 show the proposed structure of 2-DOF motor and the operation principle. The proposed 2-DOF motor consists of the rotor and the stator. The Stator is designed as 'C' type to form closed loop to tilt direction. 'C' type stator is placed to 12 stator segments. Also Stator is placed to 90 degrees interval by 3 phases so that it react both main pole and auxiliary pole. Rotor is designed to form flux loop of symmetry via tilt rotating axis so that flux is not overlapped. The Rotor is placed to auxiliary pole, because it does not pan direction driving by only main pole. Tilt positioning is decided by main pole in 2-phase conduction. And pan positioning is decided by stator current excitation. The proposed model is following advantage. First, lamination is possible structure. Because two-dimensional core that is not third dimension processing was divided by several, processing is easy. Second, Encoder or hall sensor is not required. Third, it is not required for complex axis conversion and is available for independent control.

Result and Discussion

Fig. 3 shows torque simulation results which do tilt-pan direction by 3D-FEM. According to excite in each phase, the torque converges in position that is '0' by pan-tilt torque simulation. As a result, it can drive -33~+33 degree tilt to 5 degrees interval and 360 degree pan. Micro position drive is impossible by shortcoming of proposed 2-DOF motor. However, it is not required for security camera application which can be reserved visual field in some degree. Therefore, it is noted that the proposed 2 -DOF motor is suitable for security camera application. The experimental results will be perfomed in future.

[1] L. Martins Neto, R.M. Mendes, D.A. Andeade, "Spherical Motor - A Three-Dimensional Position Servo", Electrical Machines and Drives, 1995. Seventh International Conference on (Conf. Publ. No. 412) 11-13 Sep 1995 Page(s):227 - 231

[2] Y. Kaneko, I. Yamada, and K. Itao, "A spherical DC servo motor with three degrees-of-freedom", Trans. ASME Dynam. Syst. Meas. Contr., vol. 111, no. 3, pp. 398-402, Sept. 1989.

[3] Yano, T., Suzuki, T.,"Basic characteristics of the small spherical stepping motor" IEEE/RSJ International Conference on, Intelligent Robots and System, Vol2 Oct. 2002

[4] Hirata, K., Yamamoto, T., Yamaguchi, T., Kawase, Y., Hasegawa, Y., "Dynamic Analysis Method of Two-Dimensional Linear Oscillatory Actuator Employing Finite Element Method", IEEE Trans, Magnetics, vol. 43, no. 4, April 2007, pp. 1441-1444.

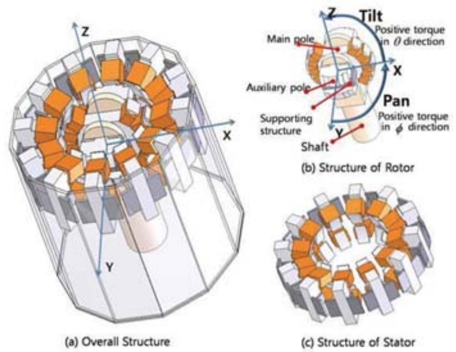

Fig. 1 Proposed Structure

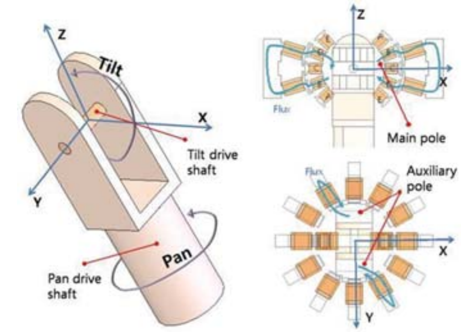

Fig. 2 shaft and flux flow

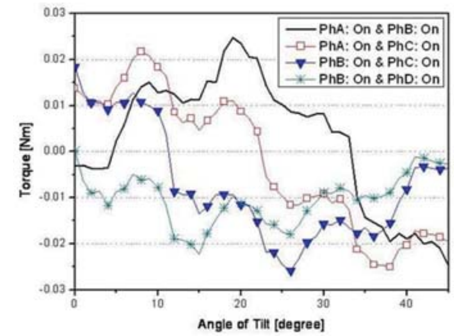

(a) Tilt simulation

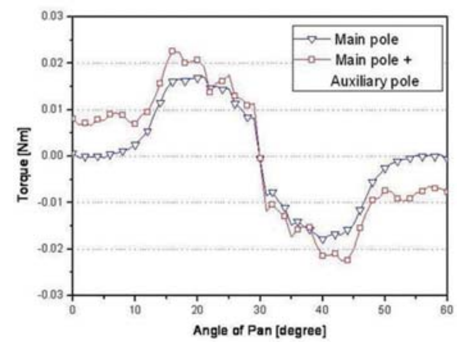

(b) Pan simulation

Fig. 3 2-DOF Simulation

EB-06

3-D Finite Element Analysis of Magnetic Forces Exerted on Stator End-windings of an Induction Motor.

R. Lin, A. Arkkio
Helsinki University of Technology, Espoo, Finland

I. INTRODUCTION
This paper studies the forces on the end-windings of a 1250-kW induction motor by 3-D finite element analysis.
II. MODEL AND METHODS
A. Model
The stator winding consists of two-layer chorded coils. The coil group of phase A is studied. The coil end is divided into 29 segments, as marked in Fig. 1.
B. Methods
A time-harmonic analysis is used. The equation to be solved is:
$\nabla\times[\boldsymbol{\upsilon}(\nabla\times\underline{\boldsymbol{A}})]+j\omega\boldsymbol{\sigma}\underline{\boldsymbol{A}}=\underline{\boldsymbol{J}}$. (1)
C. Magnetic Forces
The force $\boldsymbol{F}$ is calculated by
$\boldsymbol{F}=\int\boldsymbol{J}\times\boldsymbol{B}\,\mathrm{d}V$. (2)
The force consists of a constant time-average component and a periodic sinusoidal component with double frequency. Here, the time-average component is studied.
III. RESULTS
Figs. 2-4 and 5-7 plot the distribution of average volume density of forces at no-load and rated-load.
IV. CONCLUSIONS
At both no-load and rated-load, in the coil ends which are close to iron core, inner layer coils have larger radial force density than outer layer coils, as shown in Figs. 2 and 5. In the inner layer, coil 1 has stronger peripheral and axial force densities, but in the outer layer, those in coil 4 are stronger, as shown in Figs. 3, 4, 6 and 7. Besides, all the forces tend to enlarge the coil outward.

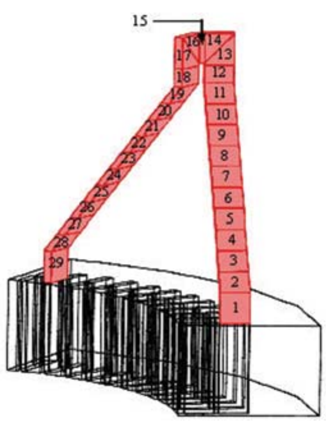

Fig. 1. The index of segments of one coil for forces.

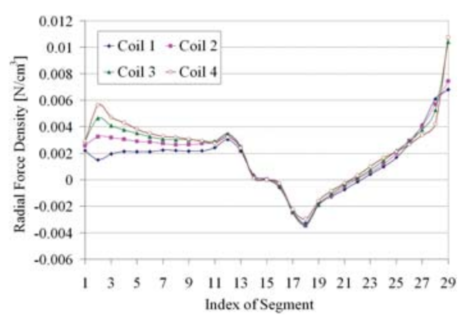

Fig. 2. The average density of radial force at no-load. The positive radial direction is outward. (Segment 1-14: outer coil; 16-29: inner coil)

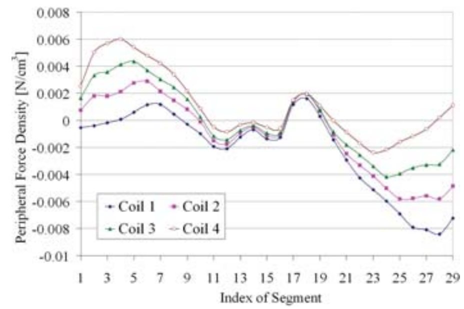

Fig. 3. The average density of peripheral force at no-load. The positive peripheral direction is clockwise. (Segment 1-14: outer coil; 16-29: inner coil)

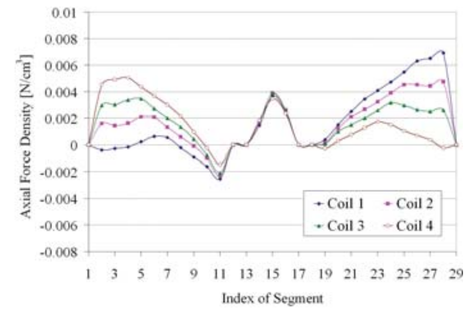

Fig. 4. The average density of axial force at no-load. The positive axial direction is upward. (Segment 1-14: outer coil; 16-29: inner coil)

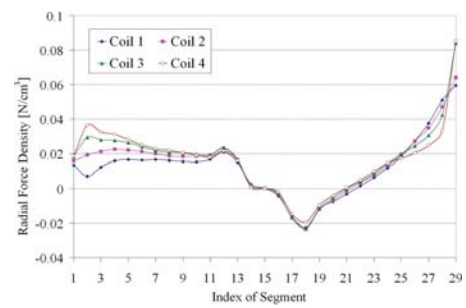

Fig. 5. The average density of radial force at rate-load. The positive radial direction is outward. (Segment 1-14: outer coil; 16-29: inner coil)

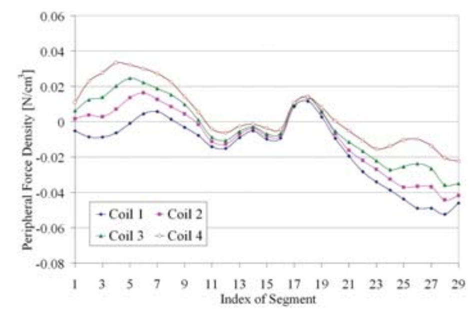

Fig. 6. The average density of peripheral force at rate-load. The positive peripheral direction is clockwise. (Segment 1-14: outer coil; 16-29: inner coil)

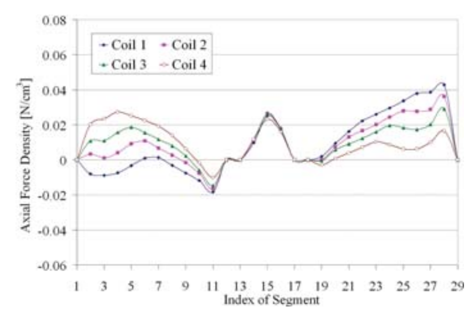

Fig. 7. The average density of axial force at rate-load. The positive axial direction is upward. (Segment 1-14: outer coil; 16-29: inner coil)

EB-07

Magnetoelastic Characteristics of the Multilayered Magnetostrictive Thin Film with Polyimide Substrate for Micro Actuator.

H. Lee, C. Cho
Mechanical Engineering, Inha University, Incheon, South Korea

Magnetostrictive materials have been studied for sensors and actuators using Joule effect, Villari effect, Wiedemann effect etc.[1-4] They introduced rod and thin film type designs and fabrication techniques for the applications.[5-7] Among them, thin film structures can be applicants for micro scale devices for their thin film characteristics and high magnetic-mechanical responses should be produced under the low magnetic field to be a micro actuator. During ten years, most magnetostrictive thin films for actuators were based on Si substrates of high brittle property, so it could not be used in impact or bent environment. The development of micro actuators based on magnetoelastic response requires highly magnetostrictive thin films with flexible substrates.

In this paper, we have suggested a TbFe/Ni/TbFe layered magnetostrictive film type actuator and investigated to the magnetoelastic characteristics of the actuator for micro application.

The schematic diagram of a multi body structure is illustrated in Fig. 1, which consists of array type cantilevers thickness of 127μm as polyimide substrate (Kapton, Dupont Corp.) with frame (size of a: 1.5mm, b: 1mm, c: 1.5mm). The back side of each cantilever is deposited with multilayer of TbFe/Ni/TbFe film thickness of 0.2/0.1/0.2μm and 0.2/0.1/0μm using selective DC magnetron sputtering.

When the magnetic field is applied to the film deposited structure along with longitudinal direction as Fig. 1, magnetic field creates magnetic moment and it leads to magnetization of the structure, and the magnetization in the deposited film that causes magnetostriction. As a result of the movement of the multi body structure, it can be used as a position drive actuator.

To fabricate a suggested thin film actuator design, the micromachining process and selective DC magnetron sputter techniques are combined.

The fabricated film thicknesses are measured by X-ray diffractometer (XRD). From XRD results, the film thicknesses can be calculated as follows:

$\Lambda = I\lambda/2(\sin^2\theta - 2\delta)^{1/2}$

Where I is the intensity of the upper peak point at each 2θ, λ is the wave length of the deposited film, Λ is the film thickness and δ is the real part of the refractive index and has a value of 10^{-5}.

The magnetic moments and the magnetostrictions are also measured to characterize the magneto-mechanical properties of the TbFe/Ni/TbFe films at each deposited film thickness. The magnetic moment is observed using vibrating sample magnetometer. 0.2/0.1/0.2μm has higher hysteresis and coercive force of 0.01T.

The magnetostrictions of each film are determined by measuring the differences of the curvature of the coated silicon substrates using the optical cantilever method. The curvatures of the length and width directions of the film due to external magnetic fields by the electromagnet are measured by detecting deflected the laser signals through a position sensitive detector. The calculated magnetostrictions can be expressed as deflections. The measured deflection results at each thickness are shown in Fig. 2.

In summary, polyimide substrate based TbFe/Ni/TbFe layered actuators are fabricated using micromachining process with selective DC magnetron sputtering technique. The actuator has cantilever arrays and its back side is deposited with magnetostrictive thin films at the thicknesses of 0.2/0.1/0.2μm and 0.2/0.1/0μm. The thickness is evaluated using XRD. Characterized results show the magnetic moments at the two kinds of substrate size. TbFe/Ni/TbFe of 0.2/0.1/0.2μm shows higher magnitude of magnetic moment, coercive force and hysteresis. Maximum deflection is about 60μm under 0.5T for 0.2/0.1/0.2μm as a micro-device application.

1 F. D. Smith, Proc. Phys. Soc. 42, 181 (1930).

2 J. P. Joule, Phil. Mag. III 30, 76 (1847).

3 E. Villari, Ann. Phys. Chem. Lpz. 126, 87 (1865).

4 I. R. Smith and K. J. Overshott, Br. J. Appl. Phys. 16, 1247 (1965).

5 R. J. Gibbs, E. W. Hill and P. J. Wright, J. Phys. D: Appl. Phys. 37, R237 (2004).

6 H. Janocha, Sens. Actuator A-Phys. 91 126 (2001).

7 O. Zivotsky, K. Postava, L. Kraus, M. Foldyna and J. Pi štora, J. Magn. Magn. Mater. 304, e534 (2006).

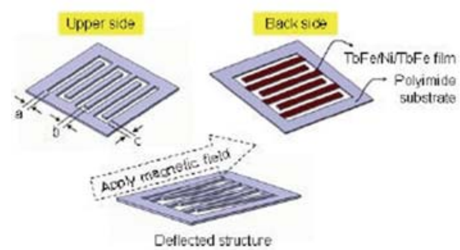

Fig.1 Schematic design and the princple of operation.

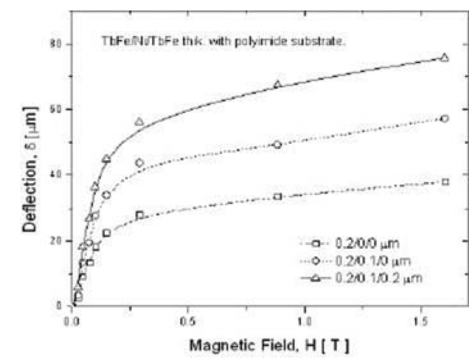

Fig.2 Deflection of the multi body actuator at each deposited thickness of TbFe/Ni/TbFe.

EB-08

Analysis of the force produced by speed-induced eddy currents in an xy-actuator.

A. F. Flores Filho[1], N. F. Baggio Filho[1], M. A. da Silveira[2]
1. Post-graduate Programme in Electrical Engineering, Federal University of Rio Grande do Sul, Porto Alegre, Brazil; 2. Post-graduate Programme in Engineering – Environment, Energy and Materials, Lutheran University of Brazil, Canoas, Brazil

The xy-actuator employs a slotless ferromagnetic slab as armature core and orthogonal planar windings with multiple phases, Fig. 1. Its mover comprehends a set of two permanent magnets, a back iron and a guiding system. The actuator presents a 3d distribution of the magnetic flux density throughout its magnetic structure[1][2]. The movement of the actuator can be established when the coils of the armature phases located under the permanent magnets are properly fed with currents. Induced currents will appear in the armature core due to the velocity of the mover and to the switched currents in the coils. This work will focus on the effect of the velocity only. That will produce a magnetic braking force that act on the mover. To reduce it and let the actuator benefit from the 3d distribution of magnetic field, the armature core should be made of a ferromagnetic material with magnetic isotropy and also high resistivity. Hence, the use of a magnetically isotropic and particle-insulated soft magnetic composite called Somaloy 500 [3] was considered. For comparison, two armature cores were employed: one is a slab of AISI 1020 steel; the other is a set of pieces of Somaloy 500 put together to resemble a solid slab. The electrical resistivity of the Somaloy 500 is much higher than that of AISI 1020 steel. BUt Somaloy 500 presents a lower maximum permeability than the AISI 1020. Yet, the 12-mm large air gap between the armature core and the mover of the actuator sets the operation point of the permanent magnets. A 3d finite element model allowed a dynamic simulation. That made possible to verify the distribution of the velocity-induced current density J in the armature core. Table 1 shows the velocity-induced current as a result. The analysis provided the current through a cross section of the armature core defined in between the projected center of the permanent magnets over that core and along the thickness of that core. The magnetic braking force was obtained by means of the displacement of the mover over the plane of the armature core at a velocity ν. A standard weight attached to the mover by means of a string pulled it by a force F, Fig. 2. That induced currents in the armature core, and they react by producing a braking force on the mover. Its dynamic relation to the system can be given by Eq. (1), $F_f=-k\nu=F_b+F_{mf}$ (1), where F_f is the total friction force, F_b is the braking force produced by the velocity-induced current, F_{mf} is the mechanical friction force, m is the mass of the mover and k is an overall friction coefficient. As it takes into account mechanical friction and the magnetic braking forces, k is related to both effects. When Somaloy 500 was employed, k= 0.382235 Ns/m, while k = 1.86564 Ns/m when an AISI 1020 core is used. With the figures obtained for k in each case, the magnetic braking force produced by the velocity-induced current was computed, Fig. 3. The mumerical results and experimental ones point to the differences between the use of both materials and, at the same time, favours a soft magnetic composite core to diminish the velocity-induced eddy currents and their effects.

[1]A.F. Flores Filho, A.A. Susin and M. A. da Silveira, An Analytical Method to Predict the Static Performance of a Planar Actuator, IEEE Transactions on Magnetics, v.39, no. 5, p.3364 – 3366 (2003) [2]M.A. da Silveira, A.F. Flores Filho, R.P. Homrich, Evaluation of the Normal Force of a Planar Actuator, IEEE Transactions on Magnetics, v.41, no. 10, p.4006 - 4008 (2005) [3]Höganäs AB: Soft Magnetic Composites from Höganäs Metal Powder, Höganäs (1999)

Velocity (m/s)	Induced current (A)	
	AISI 1020	Somaloy 500
0.10	2.37128	0.11274
0.15	3.24823	0.16762

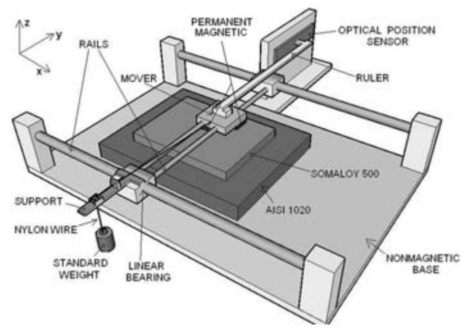

Fig. 2. Setup to measure the magnetic braking force

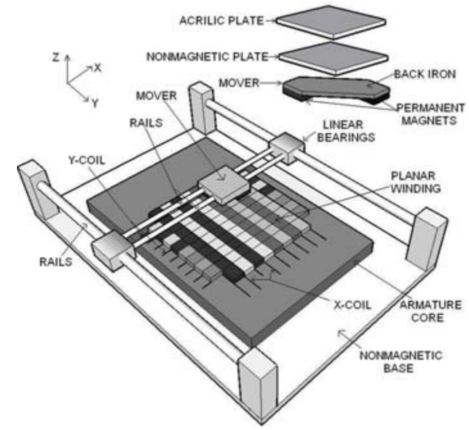

Fig. 1. View of the actuator and its parts

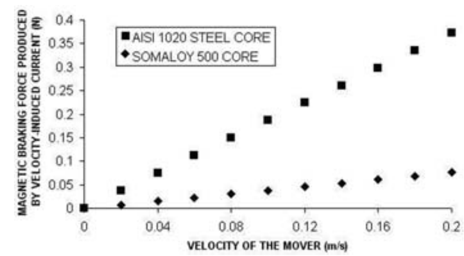

Fig. 3. Braking force vs. car velocity

EB-09

An Extension to Multiple Coupled Circuits Modeling of Induction Machines to Include Variable Degrees of Saturation Effects.

M. Ojaghi, *J. Faiz*
Department of Electrical and Computer Engineering, University of Tehran, Tehran, Iran

Multiple Coupled Circuit Modeling (MCCM) of Induction Machine (IM) [1], using winding function theory and its extension[2], has gained a broad application in the analysis of IM, mainly because of its ability to analyze faulty machines. However, neglecting magnetic saturation effects is a great weak-point of this model. Nandi took valuable steps on adding saturation effects to it[3] using a theory presented in[4], where the reluctance increasing effect of saturation is substituted by a proportional increase in the Air-Gap (AG) length as eq.1 where ϕ is the angle in the stator frame, ϕ_f is the angle of the peak value of the AG flux density(B_m), P is machine's pole pairs, g, ρ and g_s are the mean value of AG length, the peak value of its fluctuation and the AG function respectively in the presence of saturation(see Table 1 for eqations). Our contribution in this paper has the following advantages:

1.No approximation encountered in evaluating the inverse AG function P_s (see eq.2).

2.Introducing the saturation factor (K_{sat}) as a variable in the model:

K_{sat} is the ratio of fundamental components of the AG voltage for saturated and unsaturated conditions [4], so it obviously varies by varying the load. Thus introducing K_{sat} to the model as a variable is necessary. Using some definitions given in [4] we obtain eqs.3 where g_0 is the normal AG length of unsaturated machine.

3.Introducing a simple but precise technique to evaluate the angular position of B_m :

When simulating an IM using MCCM, flux-linkages of rotor meshes are evaluated. It is obvious that any time, B_m is within the arc of a mesh which has the most flux-linkage. Using flux-linkages of this mesh and the two adjacent meshes and a linear function, ϕ_f can be obtained precisely by eq.4 where θ_r is the angle of rotor in stator frame, θ_i is the angle of center of mesh i who has the most flux-linkage in rotor frame, λ_i is the flux linkage of mesh i and n is the number of rotor bars. In [3] the angle of time derivative of stator flux linkage space vector has been taken instead of $2P\phi_f+\pi/2$. Fig.1 represents these two angles on a simulated IM, where their high difference is notable.

4.Establishing analytical equations to calculate inductances and their derivatives:

MCCM needs all self and mutual inductances of stator phases and rotor meshes and their derivatives versus θ_r to be available [1]. The introduction of the AG function as eq.1 causes all of these inductances and derivatives to be time variant, so they must be updated by progress of the simulation. All users of MCCM till now have introduced look-up tables or approximate functions to update them, but in this paper, we established precise analytical functions. For this purpose we first determined the indefinite integral of P_s function (eq.2) with respect to ϕ as eq.5, then using winding function theory and its extension, we obtained simple equation for inductances and derivatives. Fig.2 represents the variation of self inductance of rotor mesh 1 and its derivative. When K_{sat} =1, L_{11} is constant and its derivative is zero. By increasing K_{sat}, L_{11} and its derivative fluctuate largely.

Using these equations, an 11kW, 380V, 50Hz, 4 poles, Δ connected IM was simulated using MCCM. Also experiments were done on IM while its currents and voltages sampled and saved on PC using PCI-1710HG card made by ADVANTECH. Using an estimation technique, we estimated the stator inductance (L_s) from simulation and experimental data(Fig.3a). As seen adding saturation effect to MCCM causes an oscillation of about 300Hz in the estimated inductance which is in accordance with experiments, although the amplitude of oscillations are different. This difference is partly due to some inherent abnormalities such as eccentricity in motor structure and partly due to dependency of (3) to core material. Fig.3b shows the normalized power spectral density of motor line current. As expected, saturation caused odd harmonic components to be present in the simulation results which are in accordance with experiment results.

[1]. X.Luo et al,"Multiple Coupled Circuit Modeling of Induction Machines",IEEE Trans.on IA,Vol.31,No.2,pp.311-318,1995.

[2]. J.Faiz & I.Tabatabaei,"Extension of Winding Function Theory for Nonuniform Air Gap in Electric Machinery",IEEE Trans.on Mag.,Vol.38,No.6, pp.3654-3657,2002.

[3]. S.Nandi,"A Detailed Model of Induction Machines With Saturation Extendable for fault Analysis",IEEE Trans.on IA, Vol.40,No.5 pp.1302-1309,2004.

[4]. J.C.Moreira & T.A.Lipo,"Modeling of Saturated ac Machines Including Air Gap Flux Harmonic Compon,nts",IEEE Trans.on IA,Vol.28,No.2, pp.343-349,1992.

$g_s=g[1-\rho\cos(2P\phi-2P\phi_f-\pi/2)]$ (1)	$P_s=1/g[1-\rho\cos(2P\phi-2P\phi_f-\pi/2)]$ (2)
$g=3K_{sat}g_0/(K_{sat}+2)$, $\rho=2(k_{sat}-1)/(3K_{sat})$ (3)	$\phi_f=\theta_r+\theta_i+\pi(\lambda_{i+1}-\lambda_{i-1})/n(2\lambda_i-\lambda_{i+1}-\lambda_{i-1})$ (4)
$f(\phi,\phi_f,K_{sat})=\cos^{-1}[(\cos(2P\phi-2P\phi_f-\pi/2)-\rho)/(1-\rho\cos(2P\phi-2P\phi_f-\pi/2))]/2Pg(1-\rho^2)^{0.5}$ (5)	

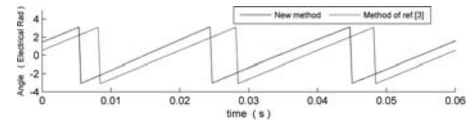

Fig.1. Angle of B_m.

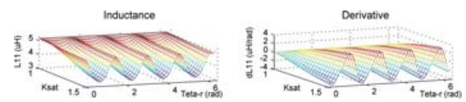

Fig.2. L_{11} & dL_{11}/dTetar.

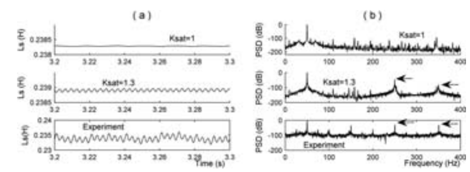

Fig.3 (a)- Estimated inductance of stator. (b)-Normalized power spectral density of motor current

EB-10

Switched Reluctance Motor with External Rotor for Fan in Air-condition.

H. Chen
College of Information and Electrical Engineering, China University of Mining & Technology, Xuzhou, China

Switched Reluctance external rotor motor had been developed to drive fan in air-condition directly. The electromagnetic design of the external rotor motor is implemented based on the Switched Reluctance internal rotor motor with the two dimensions finite element electromagnetic field calculation. The method is described with some examples, such as the electromagnetic design of the Switched Reluctance 3-phase 6/8 external rotor motor with six internal stator poles and eight external rotor poles could be implemented based on the Switched Reluctance 4-phase 8/6 internal rotor motor with eight external stator poles and six internal rotor poles, but the calculated period of the external rotor motor is 45 degree, and the calculated period of the internal rotor motor is 60 degree. The electromagnetic design of the Switched Reluctance 4-phase 8/12 external rotor motor with eight internal stator poles and twelve external rotor poles could be implemented based on the Switched Reluctance 3-phase 12/8 internal rotor motor with twelve external stator poles and eight internal rotor poles, but the calculated period of the external rotor motor is 30 degree, and the calculated period of the internal rotor motor is 45 degree.
Those had got three Chinese invention patent rights, such as Chinese Invention Patent 200710019552.7, Chinese Invention Patent 200710019638.X, Chinese Invention Patent 200710019705.8.
The design results of the Switched Reluctance 3-phase 6/8 external rotor motor were given, which is compared with that of the Switched Reluctance 4-phase 8/6 internal rotor motor.

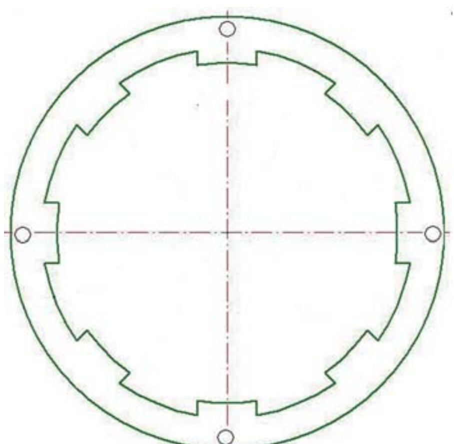

External rotor iron core

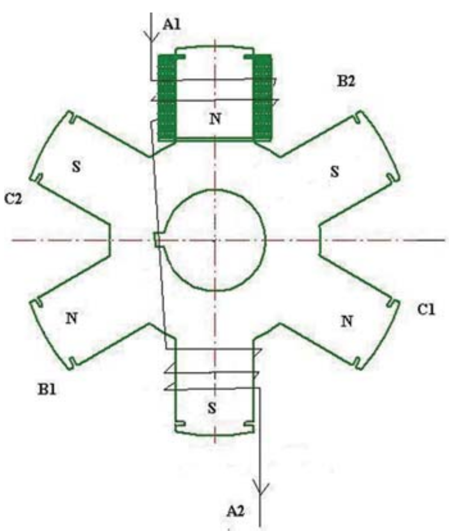

Internal stator iron core

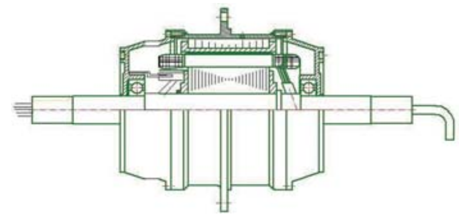

Switched Reluctance 3-phase 6/8 external rotor motor for fan in Air-condition

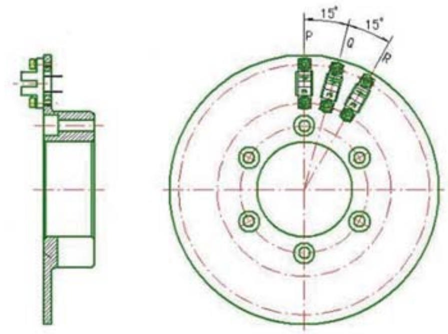

External rotor position detector

EB-11

End turn leakage reactance of concentrated modular winding stators.

T. Cox[1,2], J. Eastham[1], J. Proverbs[2]
1. The University of Bath, Bath, United Kingdom; 2. Force Engineering, Shepshed, United Kingdom

Introduction
The common method [1] for calculating end turn reactance involves removing the machine core from the problem and forming air-cored coils from the two end regions of the machine coils. The results of this calculation can vary considerably from experimental values due to the presence of the core iron. Lawrenson developed approximate methods for modifying the inductance to allow for the iron in the case of a turbogenerator [2]. It is the objective of this paper to use 3D & 2D finite element modelling to calculate the leakage inductance of concentrated and modular windings, including the presence of the core. These windings are in use for permanent magnet machines [3] and are proposed for special linear induction motors [4].
3D Finite Element Modelling Methods
The first finite element method using the MEGA package involved the use of several full 3D stator models of varying core widths [5]. For convenience these were linear in form. The stator reactance measured from the terminals comprises several parts including end turn, slot and magnetising reactance components. Whereas all other reactance components are directly proportional to core width, end turn reactance is constant. Therefore, if the terminal reactances of several otherwise identical machines of varying core width are plotted, referring this plot to zero core width will yield a value for end turn reactance of the machine Fig. 1.
This method and its results have been validated experimentally, by constructing 3 otherwise identical machines of reducing core width, and referring to zero core width. These results are also plotted on Fig. 1 for comparison with the FE values. It will be observed that the correlation between the results is excellent.
A simpler method has also been developed. A 3D FE model can accurately model all aspects of a stator. A 2D FE model can accurately model per metre depth all stator characteristics whose parameters can be described in two dimensions, and thus is able to account for all reactance effects except end turn reactance. Therefore, if both 2D and 3D FE models are produced based on the same machine, the difference in reactance between the two must be due mainly to end turn leakage reactance, and can therefore be calculated. This method gave a value within 10% of the 3 core experimental and full 3D results with significant saving in computation.
Differences
The main reason for the differences between experimental and FE results and the simple analytical method [1] is the presence of Iron [2]. The analytical method makes no allowances for the presence of iron, where this has been shown experimentally to have a significant effect on the measured end turn reactance. The three machines of varying core width have been tested experimentally with and without iron cores, and their reactance referenced back to zero Fig. 1. This shows an obvious and significant difference due to the presence of an iron core.
Analytical Parameterised Modelling Method
A new method of modelling end turn reactance of iron cored concentrated coils was now developed. The 2D and 3D comparison method used above was used to find values of end turn reactance over a useful range of coil depths, pitches & widths. These values were then used to develop the parameterised equation[6] for 12mm coil protrusion Fig. 2.
This equation is able to predict the end turn leakage inductance of a machine within 10%.

Conclusions
Simple analytical methods of end turn leakage reactance modelling have been found to be inexact when modelling concentrated iron cored coils. The equation developed is a fast and accurate method of calculating end turn reactance. The correlation between experimental results and 2D finite element results using this method of calculating end turn reactance is excellent.

[1] Henderson, J. R. Jr. and Miller T.J.R 'Design of brushless permanent-magnet motors' Magna Physics Publishing & Clarendon Press Oxford 1994.

[2] Lawrenson,P.J. 'Calculation of machine end-winding inductances with special reference to turbogenerators' Proc IEE Vol. 117, No.6, June 1970.

[3] J Wang, Z P Xia, D Howe, S A Long, "Comparative Study of 3-Phase Permanent Magnet Brushless Machines with Concentrated, Distributed and Modular Windings" IET Power Electronics, Machines and Drives, Mar. 2006 Page(s):489 - 493

[4] J.F Eastham, T Cox, H.C Lai, J Proverbs, "The use of concentrated windings for offset double stator linear induction motors", LDIA Lille Sep. 2007

[5] Barnes, E.C., 'An experimental study of induction machine end-turn leakage reactance', AIEE Trans., Vol 70, 1951, pp671-679

[6] Hamlaoui M.N., Mueller M.A., Bumby J.R., Spooner E., 'Polynomial modelling of electromechanical devices: an efficient alternative to look up tables', IEE Proc.-Electr. Power Appl., Vol 151, No. 6, Nov. 2004

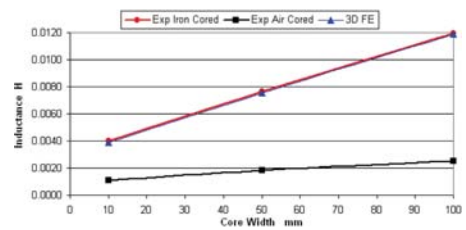

Fig. 1. Experimental with and without iron core and FE 3 core width inductance results

$$
\begin{aligned}
L = (& (8.190E{-}21 d^2 + 1.252E{-}18 d - 2.611E{-}17) w^4 + (-2.036E{-}18 d^2 - 2.824E{-}16 d + 2.217E{-}15) w^3 \\
& + (1.765E{-}16 d^2 + 2.207E{-}14 d + 2.380E{-}13) w^2 + (-7.875E{-}15 d^2 - 5.620E{-}13 d - 3.234E{-}11) w \\
& + (2.045E{-}13 d^2 + 3.095E{-}12 d + 2.581E{-}9)) p + ((-2.180E{-}18 d^2 + 2.430E{-}16 d + 6.477E{-}15) w^4 \\
& + (4.415E{-}16 d^2 - 6.377E{-}14 d - 1.006E{-}12) w^3 + (-2.495E{-}14 d^2 + 5.292E{-}12 d + 5.193E{-}11) w^2 \\
& + (5.600E{-}13 d^2 - 2.045E{-}10 d - 2.531E{-}9) w + (-1.079E{-}11 d^2 + 4.295E{-}9 d - 3.359E{-}8))
\end{aligned}
$$

Fig. 2. Inductance equation where L is inductance per turn, d is coil depth (30-50mm), w is coil width (10-120mm), p is coil pitch (40-260mm)

EC-01

X-ray and valence band photoemission microscopy of ultra-thin magnetic cobalt films on ruthenium.

A. Mascaraque[1], L. Perez[1], L. Aballe[2], T. Onur Mentes[2], J. F. Marco[3], F. El Gabaly[4,5], C. Klein[5], A. K. Schmid[5], K. F. McCarty[6], A. Locatelli[2], J. de la Figuera[3,4]
1. Dpto. de Fisica de Materiales, Universidad Complutense de Madrid, Madrid, Spain; 2. Elettra - Sincrotrone Trieste, Trieste, Italy; 3. Instituto de Quimica-Fisica Rocasolano, CSIC, Madrid, Spain; 4. Centro de Microanalisis de Materiales, Universidad Autonoma de Madrid, Madrid, Spain; 5. Berkeley National Laboratory, Berkeley, CA; 6. Livermore National Laboratories, Livermore, CA

Thin-film ferromagnetic materials are still a source of surprises. For example, consider the easy axis of magnetization, a property crucial for technological applications. Recently, spin-polarized low-energy electron microscopy [1] revealed that ultra-thin cobalt islands and films on ruthenium present consecutive spin-reorientation transitions: mono-atomic (ML) films present an in-plane easy-axis of magnetization, bilayer islands or films have an out-of-plane easy-axis, while thicker films have an in-plane easy-axis again. Furthermore, additional deposition of silver [2] produces also a magnetic easy-axis reorientation -at selected Co coverages- as a function of the silver coverage, again with atomic scale abruptness: depositing Ag on an in-plane magnetized 3 ML thick cobalt film produces an out-of-plane easy-axis, depositing additional Ag layers switches the easy-axis in-plane again.
To understand, and even predict the observed magnetic behavior, separating those different contributions becomes essential. Magnetic, structural and electronic measurements from uniform film regions with precisely known properties (such as structure and thickness) are needed. Such measurements are challenging in systems such as cobalt on ruthenium, where the film wants to form three-dimensional islands rather than remain flat. Here we use the imaging capability of photoemission microscopy coupled to a synchrotron radiation source (ELLETRA, Italy) to measure the properties of a few layers thick uniform cobalt regions on ruthenium. Photoemission microscopy performed by a low energy electron microscope with energy filtering -Spectroscopic Photoemission and Low Energy Electron Microscope, SPELEEM [3]- is a versatile technique capable of obtaining both spatially resolved X-ray absorption data -by imaging the secondary electrons emitted by the sample upon X-ray illumination-, or spatially resolved and angle-resolved photoemission data in normal incidence.
In the last mode we have performed valence band measurements of Ag films of several thicknesses, both directly on the ruthenium substrate as well as on 3 ML thick Co films in order to clarify the contribution that dominates the magnetic behaviour. We report on the surprising observation of a strong valence-band dichroism in the Ag-related d-bands of the films grown on 3 ML Co. Ab-initio calculations of the band structure to explain the experimental results are under way.
By using circularly polarized X-rays, the L-level dichroism from regions as small as a single Co island is detected, providing a direct image of the local structure's magnetization. We have also measured the dichroic difference between the L3 and L2 Co levels. In particular we have imaged both Co islands and films 3 ML thick using L-level dichroism (see Figures). The islands have a triangular shape with a common orientation, aligned along the high symmetry directions of the substrate[5]. After the application and removal of an external magnetic field prior to our photoemission microscopy observations, we detected that large islands (around one micrometer in size) present the same magnetization pattern which includes vortex-like structures, while smaller islands were observed to be single domain in remanence. Based of micromagnetic simulations based on the OOMMF code [4], we suggest that our observations can be explained by the interplay of in-plane shape anisotropy of the triangular islands coupled to the applied magnetic field direction.

[1] Farid El Gabaly et al., Phys. Rev. Lett. 96 147202 (2006).

[2] Farid. El Gabaly et al., unpublished.

[3] E. Bauer, Surf. Rev. Lett. 5 1287 (1998)

[4] M. J. Donahue and D. G. Porter, OOMMF Users Guide Version 1.1b2 (National Institute of Standards and Technology, Gaithersburg, MD, 2004).

[5] Farid el Gabaly el al., New J. of Physics 9 80 (2007).

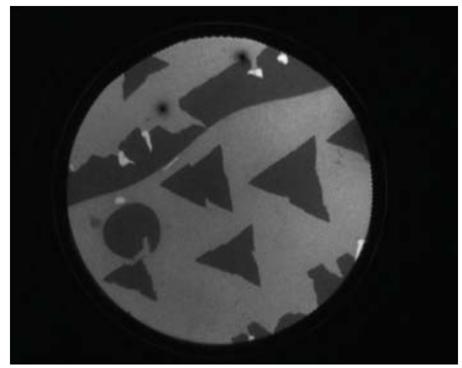

5 μm field-of-view low energy electron image showing 3 ML thick Co islands (dark gray) surrounded by a 2 ML thick film (light gray).

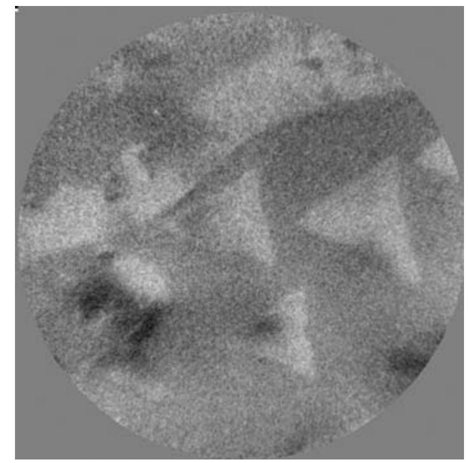

Same area as shown previously with electrons, but using X-ray magnetic circular dichroism with the L3 level. The black and white areas correspond to magnetization of the islands in the X-ray incidence direction (white) or magnetization in the opposite direction (black). Grey areas indicate no component of the magnetization in the X-ray incidence direction.

EC-02

Magnetostatic interactions in an artificial two-phase magnet.

S. Sievers[1], S. Schnittger[2], K. Braun[1], U. Siegner[1], C. Jooss[2]
1. Physikalisch-Technische Bundesanstalt, Braunschweig, Germany; 2. Institut für Materialphysik, Universität Göttingen, Göttingen, Germany

We report on the effect of magnetostatic interactions on the emergent magnetization pattern in artificial two-phase magnets, which are a model system for the study of collective effects in magnetic arrays. The structures consist of patterned hard magnetic CoPt squares with out of plane anisotropy embedded in a soft magnetic Permalloy (Py) matrix. In previous work [1] we have shown that the patterning introduces a long-range ordered symmetry breaking domain pattern in the matrix if the distance between the CoPt squares is equal to their size. At smaller distances the magnetostatic interaction between neighboring squares results in a correlated nucleation of reversal domains at opposing edges of the hard magnetic squares [1]. In this paper we address the following new aspects: (i) Long-range order in small arrays with only a few CoPt squares and in arrays with larger distances d between neighboring CoPt squares. (ii) The role of the matrix in the correlated nucleation of reversal domains in adjacent hard magnetic squares.
The arrays were fabricated as described in [1]. The CoPt squares and the matrix have a thickness of 50 nm and the size of the squares is 5x5 μm^2. Magnetic force microscopy (MFM) is used to image the structures.
Figure 1 shows MFM images of 1x1, 1x3, and 3x3 arrays for a distance d between adjacent CoPt squares of 5 μm. We find that single squares as well as one dimensional arrangements of squares influence the domain pattern in their proximity, but do not cause a breaking of the symmetry. Yet, in arrays with only 3x3 squares a symmetry breaking pattern appears. Here, in the area between four squares the magnetization of the Py is reorganized and the domain walls form large rhombs. One of these rhombs is marked by dotted lines. These large domains have diagonal magnetization, as previously observed in larger 7x10 arrays [1]. Both for 3x3 and 7x10 arrays, all of the rhombs are aligned over the whole array, i.e., they show long-range ordering. Moreover, this magnetization pattern is found to be very stable. Even though it disappears at a perpendicular field of 400 mT, for which the magnetization of the Py aligns with the field, the pattern reappears once the field is turned off. Our results indicate that the long-range ordered rhomb-shaped domain pattern is the ground state of two-dimensional arrays with d being equal to the square size. If the distance between the squares is doubled, d=10 μm, the domain pattern in the matrix becomes less regular and the rhomb shaped domains decompose into smaller domains, see figure (1d).
In order to obtain additional insight in the correlation of reversal domains in adjacent hard magnetic squares,
we analyze the interaction between the CoPt and the matrix close to the CoPt/Py interface. Figure (2a) shows a corner of a CoPt square. The CoPt square is in a multi domain state. The domains which are located directly at the edge of the square produce a stray field which, in turn, generates an out of plane component of the matrix magnetization opposite to the magnetization of the CoPt domains. Since the CoPt is in a multi domain state, the magnetization of the matrix is modulated along the square edge in the proximity of the interface, as can be seen from the line profile. The modulation in the matrix decays within several hundred nanometers (data not shown). If the distance between the squares is reduced to the decay length of the modulation of the matrix, the CoPt squares begin to interact via the Py matrix. An image of the matrix between two neighboring squares spaced by the distance d = 1μm is shown in figure (2b). At this short distance correlation of domains in the hard magnetic squares is found. Figure (2b) indicates that this correlation is strongly affected by the domain pattern in the matrix.

[1] S. Schnittger, S. Dreyer, Ch. Jooss, S. Sievers, and U. Siegner, Appl. Phys. Lett. 90, 042506 (2007).

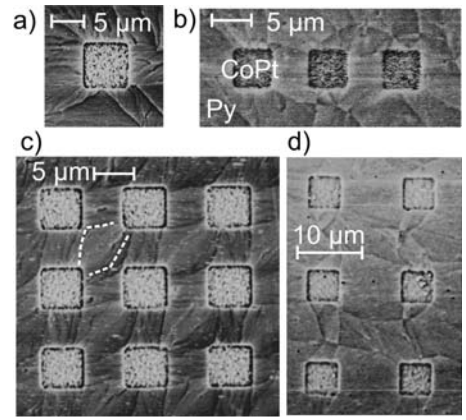

Figure 1: MFM images of CoPt/Py arrays with different numbers of elements (a): 1x1, b): 3x1, c)-d): 3x3) and element distances (b)-c): 5 μm, d): 10 μm).

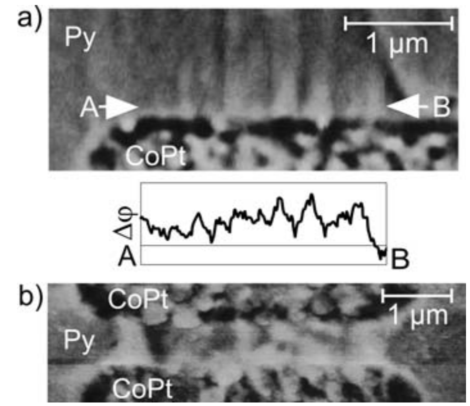

Figure 2: MFM images of the interfacial region between the CoPt squares and the Py matrix for d = 5 μm (a) and d = 1 μm (b). Visible are stripe domain patterns in CoPt and complex domain patterns in Py which are strongly modified by the stray field of the CoPt elements.

EC-03

360° domain wall generation in the soft layer of magnetic tunnel junctions.

F. Montaigne[1], M. Hehn[1], D. Lacour[1], J. Briones[1], R. Belkhou[2,3], S. El Moussaoui[2,3], F. Maccherozzi[2,3], N. Rougemaille[4]

1. Laboratoire de Physique des Matériaux, Nancy-University, CNRS, Vandoeuvre lès Nancy, France; 2. Synchrotron SOLEIL, Gif-sur-Yvette, France; 3. Synchrotron ELETTRA, Basovizza, Italy; 4. Institut Néel, CNRS & Université Joseph Fourier, Grenoble, France

Most studies concerning the micromagnetic properties of nanostructures are performed on single ferromagnetic layers. However, spintronics applications generally require structures with several magnetic layers, separated by a non-magnetic spacers. In these structures, magnetic couplings may appear between the ferromagnetic layers. This is emphasised in nanostructures having in-plan magnetizations for which an antiferromagnetic dipolar coupling originates from the stray fields at the nanostructure edges. An antiparallel alignment of the two layers can thus be observed in micron and submicron tunnel junctions and spin valves. We have used the chemical selectivity and the high spatial resolution of the X-ray photo-emission electron microscopy technique (X-PEEM) to study the influence of the dipolar coupling taking place between a FeNi (Py, soft layer) and a Co (hard layer) layer when inserted in a elliptical shaped magnetic tunnel junction (MTJ). The comparison of our experimental results to micromagnetic calculations sheds light on the previous observations of 360° domain walls (DW), on their formation conditions and on their statistics of occurrence (1). The MTJ multilayer stack has been grown by sputtering. 1x3 μm^2 ellipses have been patterned by electron beam lithography. To determine the onset of the magnetic structure within each layer of the MTJ, the samples were imaged using X-PEEM. Figure 1 shows images taken at zero field recorded at the Co and Ni edges after saturation with a 1 kOe field applied parallel to the ellipses long axis. Here, the observed contrast is due to the magnetization component parallel to the long axis. The Co magnetization is uniform and oriented along the saturating field (white contrast in Fig 1 a). Regarding the Py layer, some elements show a single domain state magnetized in the opposite direction. Other ellipses present an inhomogeneous Py layer magnetization. More insight in this domain structure is gained after a 90° rotation of the sample. Then, the magnetic contrast arises mostly from the magnetization component along the ellipses short axis. Figure 2 shows images recorded at the Ni edge for two ellipses exhibiting a non-uniform state. Black/white or white/black contrasts are signatures of clockwise (CW) and counter clockwise (CCW) 360° DW. Understanding the presence/absence of these 360° DWs requires a study of the Py magnetization reversal dynamics. Therefore, we have modeled our MTJs using the 3D OOMMF code. In silico experiences show that the dipolar field originating from the Co layer activates the nucleation and propagation of two domains at each extremity. They also reveals that the nucleation of the two domains by opposite curling direction is a mandatory condition to the formation of a 360° DW. Figure 2 c. shows a simulated DW. All the ellipses do not exhibit the same magnetic state at zero field. The statistic of DWs formation has then be studied. We observed that 82% have always the same magnetic configuration (DW or not). These ellipses are composed of three subgroups: 50% have a single domain state, 27% stabilize a CW DW, and 23% a CCW DW. As the presence of a DW is linked to the initial direction of curling, these statistics prove that for a majority of elements, the curling direction is determined uniquely for each ellipses extremity. Furthermore it appears that each curling direction is equally probable on the observed array. Local anisotropy sources related to the local structure of the ellipses and to their topology, can influence the curling direction and each ellipse extremity may have a specific anisotropy direction. Those local anisotropy sources (shape and/or magnetocristalline) break the symmetry of the system. For the 82% of the elements exhibiting always the same magnetic configuration, the initial curling direction determines the zero field state and the observed magnetic configurations are induced by the local magnetic anisotropy at the ellipses extremities. A significant number of ellipses (18% of ellipses) presents either a 360° DW or a single domain state. In this case, the curling direction is not uniquely determined by the local magnetic anisotropy at one ellipses extremity: the magnetization curling direction could be driven by a stochastic effect as thermal fluctuations. In conclusion, we show that the formation of 360° DWs in our system is mainly influenced by the local magnetic anisotropies existing at each extremity of the elements. Controlling the nucleation/propagation of such DWs is essential for magneto-transport measurements or for devices based on the switching of the two layers of a magnetic tunnel junction.

(1) M. Hehn et al. accepted in Appl. Phys. Lett.

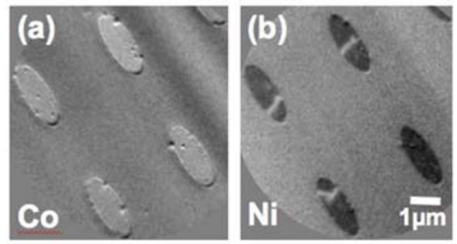

Fig 1

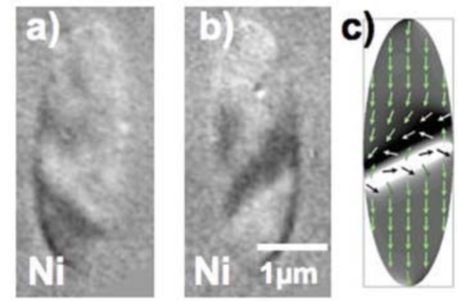

Fig. 2

EC-04

Magnetic reversal in patterned nanostructures with circular exchange-bias.

M. Tanase[1], A. K. Petford-Long[1], O. G. Heinonen[2], K. S. Buchanan[3], J. Sort[4], J. Nogues[4]
1. Materials Science Division, Argonne National Laboratory, Lemont, IL; 2. Seagate Technology, Bloomington, MN; 3. Center for Nanoscale Materials, Argonne National Laboratory, Lemont, IL; 4. Universitat Autonoma de Barcelona, Bellaterra, Spain

In this paper we report studies of the behavior of magnetic vortex structures in single layer Permalloy or CoFe ferromagnetic (FM) disks and in disks exchange-biased to an adjacent IrMn antiferromagnetic (AF) layer. 1 µm diameter disks were fabricated by electron lithography and lift-off, on 50 nm thick SiN windows set into a 300 µm-thick Si wafer frame. Four different configurations were sputter-deposited: Ta/$Ni_{80}Fe_{20}$/Cr (Py); Cr/$Co_{90}Fe_{10}$/Cr (CF); Ta/$Ni_{80}Fe_{20}$/IrMn/Cr (Py/IrMn); Cr/$Co_{90}Fe_{10}$/IrMn/Cr (CF/IrMn). t_{Py}=12nm and t_{CF}=10nm. An exchange-bias (EB) was imprinted in a vortex geometry in some of the bilayer disks by zero field cooling (ZFC) through the Neél temperature of IrMn from 240°C, as described previously by Sort et al. [1]. MOKE magnetometry data was used to confirm the vortex geometry of the EB. Images of the magnetization reversal process of the FM layer were obtained using Lorentz transmission electron microscopy (LTEM). Vortices were swept out of the disks and renucleated by changing the intensity of a magnetic field applied in-situ in the microscope, by tilting the sample around the holder axis and weakly exciting the objective lens. The Py and Py/IrMn disks spontaneously formed vortices at remanence, whereas the CF and CF/IrMn disks formed either vortices or domain walls but could all be set in a vortex state by an in-situ demagnetization procedure.
For the micromagnetic simulations the grain structure was simulated by seeding random nucleation sites which grew until their boundaries met, with an average grain size of 20 nm. This grain structure was propagated conformally through the film thickness. The exchange-bias coupling was modeled using an interfacial energy density ε_{eb} at the FM/AF interface, leading to an effective field H_{eb}. The FM magnetization was relaxed into an equilibrium vortex state, and the direction of H_{eb} in each AF grain was taken as an average of the direction of the magnetization in the adjacent FM grain. A random, in-plane uniaxial magnetocrystalline anisotropy was added to the CF grains.
The displacement of the vortex from the disk center as a function of the in situ applied field is plotted in Fig. 1 for Py and ZFC Py/IrMn and in Fig. 2 for CF, CF/IrMn and ZFC CF/IrMn disks. Filled data points indicate experimental data and empty data points indicate simulations. The simulations show that increasing the EB produces a flatter displacement vs field curve, such that a larger field is necessary for a given displacement of the vortex. Linear fits through the initial vortex displacement curve for the experimental data show a decrease in slope from 1.77 for the Py disks to 1.67 for the ZFC Py/IrMn disks. The simulated curve with an interfacial coupling energy ε_{eb}=0.1 erg/cm^2 gives the best fit to the experimental curve for the ZFC Py/IrMn disks.
In-situ magnetizing experiments show that for the Py disks the vortex nucleation occurs with random chirality, whereas in ZFC Py/IrMn disks the initial chirality in the FM layer is preserved throughout the magnetizing experiments indicating an EB vortex configuration. This is confirmed by the fact that the vortex nucleation field (H_n) and annihilation field (H_a) are insensitive to the applied field direction. H_n and H_a increase for the ZFC Py/IrMn disks with respect to the Py disks, indicating that the circular exchange bias increases the stability of the vortex state.

CF and CF/IrMn disks reverse by a mechanism involving domain walls at remanence that collapse into a vortex at higher fields. In ZFC CF/IrMn disks the reversal follows a regular pattern whereas in CF and CF/IrMn disks the reversal is randomized by microstructural pinning. By comparison between the experimental data and simulations, we conclude that the value of EB for ZFC CF/IrMn disks is larger than that for ZFC Py/IrMn disks (0.3 vs. 0.1 erg/cm^2 from best fitting simulation). In addition, pinning effects originating from nonzero magnetocrystalline anisotropy cause the vortex to move in a zig-zag motion about the ideal trajectory (in the absence of pinning).
Work carried out in part by UChicago Argonne, LLC, Operator of Argonne National Laboratory. Argonne, a U.S. Department of Energy Office of Science laboratory, is operated under Contract No. DE-AC02-06CH11357

[1] J Sort et al., APL 88, 042502(2006)

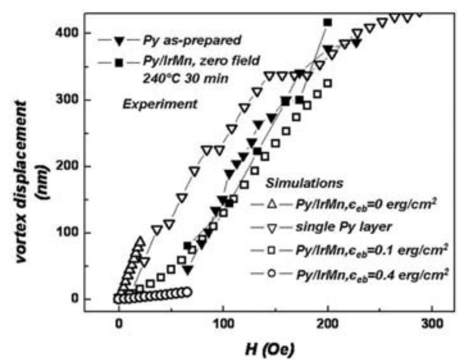

Fig.1 Displacement of vortex vs. applied field in 1µm diameter Py and Py/IrMn disks

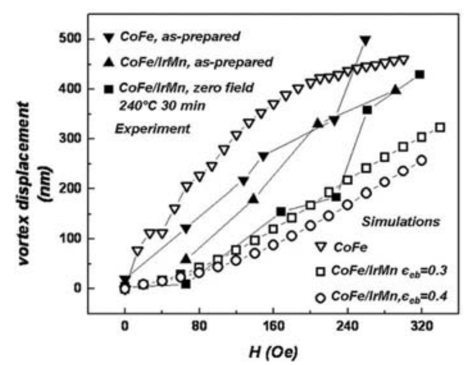

Fig.2 Displacement of vortex vs. applied field in 1µm diameter CF and CF/IrMn disks

EC-05

Static and dynamic properties of exchange bias modulated thin films.

C. Hamann[1], J. McCord[1], R. Kaltofen[2], I. Mönch[2], R. Schäfer[1], L. Schultz[1]
1. Institute for Metallic Materials, IFW Dresden, Dresden, Germany; 2. Institute for Integrative Nanosciences, IFW Dresden, Dresden, Germany

Due to the high demand on new magneto electronic devices, there is a steady search for new magnetic materials and preparation methods (1-3). Recently, to tailor exchange biased thin films properties, ion beam assisted patterning gains importance. As associated disadvantage, this method inherits sputter effects and may lead to an alteration of the magnetization saturation of the implanted area (4). As an alternative, we used local oxidation of the antiferromagnetic layer to prepare extended NiFe/IrMn films with laterally modulated unidirectional anisotropy.
The films were structured into 2-d arrays of alternating stripes with (NiFe/IrMn) and without unidirectional anisotropy K_{ud} (NiFe/IrMnO). Thereby, the stripes were either aligned parallel or perpendicular to the preset K_{ud}. The role of interfacial contributions between the magnetically different areas was addressed by varying the stripe dimension from 20 µm down to 2 µm.
Measuring the macroscopic properties, different reversal mechanisms for the two different stripe orientations have been detected. Stripes aligned parallel to the unidirectional anisotropy exhibit a two step hysteresis (Fig. 1a) similar to spin valves, those aligned perpendicular show a shifted but single step hysteresis loop (Fig.1b). Microscopic Kerr observations revealed for the parallel alignment separate switching of the two different stripe magnetizations (comp. Fig. 1a), 2a)). For the perpendicular stripe orientation the free and biased stripes reverse simultaneously along the forward and recoil branch of the loop (Fig. 1b), 2b)). Reducing the stripe width down to 2 µm both structure types exhibit quasi-domains (Fig. 2c), d)). Those quasi-domains appear as correlated reversal of a broad range of neighboring stripes.
The magnetic features are discussed in terms of lateral direct exchange coupling at the stripe interface and Néel wall interactions.
To investigate the dynamic behavior, pulsed inductive microwave magnetometry (5) was employed. Different to the quasi-static behavior, the parallel aligned stripes (Fig. 3a) above 10 µm show two resonant frequencies f_{res} originating from the bimodal magnetic properties. Below 10 µm the resonance frequencies merge to one intermediate frequency at about 1.5 GHz. The perpendicularly arranged stripes (Fig. 3b) maintain a dynamic behavior similar to the extended reference samples throughout the whole range of 2 µm to 20 µm. In addition, a third f_{res} similar to the merged frequency of the parallel stripes is observed. In both cases, the increasing f_{res} for all stripe dimensions below 10 µm are due to increased NiFe-IrMn contribution caused by the offset of the stripe width. The different dynamic performance for the two alignments is ascribed to the introduction of additional quasi-magneto-static coupling for the parallel stripes.
The presented observations demonstrate that by combination of different magnetic properties anisotropic magnetization reversal behavior and different dynamic properties can be created which are due to the direct exchange coupling of the magnetization at the stripe interfaces.

1 J. Kools, IEEE Trans. Mag. 32, 3165 (1996).

2 M. Miller, P. Lubitz, G. Prinz, J. Krebs, A. Edelstein, S. Cheng, and F. Parsons, IEEE Trans. Mag. 33, 3388 (1997).

3 G. A. Prinz, Science 282, 1660 (1998).

4 J. Fassbender, and J. McCord, J. Magn. Magn. Mat. 320, 579 (2007)

5 T. J. Silva, C. S. Lee, T. M. Crawford, and C. T. Rogers, J. Appl. Phys. 85, 7849 (1999)

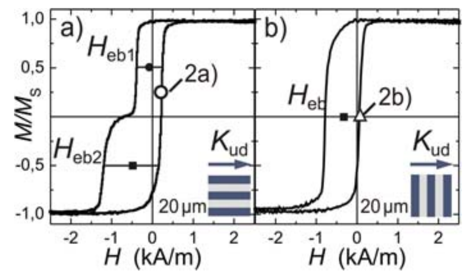

Fig.1 Magnetization loop for 20 µm stripes aligned a) parallel and b) perpendicular to K_{ud}.

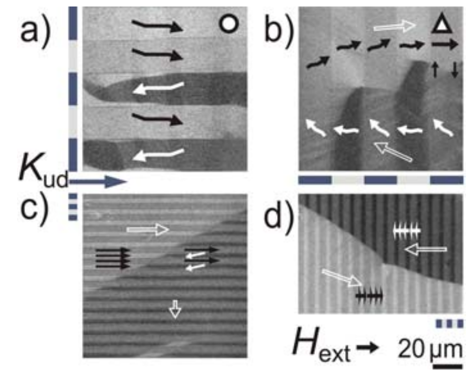

Fig.2 Kerr images for 20 µm stripes a) parallel b) perpendicular to K_{ud}. The field is indicated as open symbols in Fig. 1a) and b). Comparable domain states for 2 µm stripes c) parallel and d) perpendicular to K_{ud} along the recoil branch.

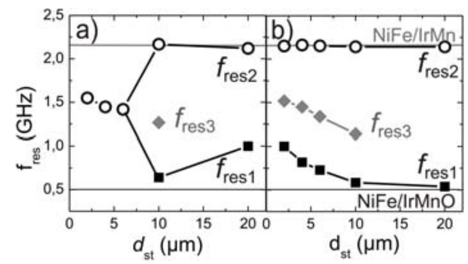

Fig. 3 Resonance frequencies f_{res} versus stripe width for a) parallel and b) perpendicular orientation to K_{ud} For comparison f_{res} of the single extended reference films are plotted as lines.

EC-06

Dynamic splitting of azimuthal spin wave modes in circular magnetic dot in vortex ground state.

K. Y. Guslienko[1], A. N. Slavin[2], V. Tyberkevych[2], S. K. Kim[1]
1. Research Center for Spin Dynamics and Spin-Wave Devices and Nanospintronics Laboratory, Seoul National University, Seoul, South Korea; 2. Department of Physics, Oakland University, Rochester, MI

Spectrum of spin wave excitations of circular magnetic dots in a vortex ground state consists of low-frequency gyrotropic (or translational) mode, that describes motion of the vortex core, and high-frequency spin wave modes, which describe excitations of the main part (far from the vortex core) of the dot [1]. It was shown both experimentally [2, 3] and numerically [2] that high-frequency spin waves with azimuthal indices $m = +1$ and $m = -1$ (i.e., the modes that propagate in opposite directions) demonstrate significant frequency splitting of the order of 1 GHz for typical dot parameters. It is clear, that the frequency splitting is caused by the spin wave interaction with magnetic core, since it vanishes after removing of small central "core" region of the dot [3]. This fact can also be proven rigorously by symmetry considerations, since magnetic dot without a core ("ring" magnetic structure) has an additional symmetry – reflection about the plane of the dot.
An attempt [4] to explain frequency splitting by spin wave interaction with the static dipolar field of the core (which breaks reflection symmetry of the system) produced frequency splitting that is several times smaller than experimentally observed one [2, 3]. Thus, at the present time the reason of significant frequency splitting of $|m| = 1$ modes remains unclear. It is also unclear, why other azimuthal modes with $|m| \neq 1$ have much smaller splitting.
In this work we develop a simple theoretical explanation of the splitting of $|m| = 1$ modes that quantitatively agrees with experimental data. The splitting is explained as a result of *dynamic hybridization* of $|m| = 1$ azimuthal modes with the gyrotropic mode. The gyrotropic mode can be considered as a mode with azimuthal index $m = 1$. Due to the same azimuthal behavior, this mode can hybridize with high-frequency $|m| = 1$ modes and shift their frequencies. As a result of hybridization, profile of the azimuthal mode $\boldsymbol{m}_V$ in the vortex ground state can be approximately written as $\boldsymbol{m}_V = \boldsymbol{m}_R + i\eta\boldsymbol{m}_G$, where $\boldsymbol{m}_R$ in the normalized profile of the azimuthal mode in a "ring" structure and $\boldsymbol{m}_G$ is the normalized spatial profile of the gyrotropic mode. The coupling constant η is determined by the condition of orthogonality of $\boldsymbol{m}_V$ and $\boldsymbol{m}_G$:
$\eta = \int \boldsymbol{M}(\boldsymbol{r})\,(\boldsymbol{m}_G^* \times \boldsymbol{m}_R)d\boldsymbol{r}$, (1)
where $\boldsymbol{M}(\boldsymbol{r})$ is the spatially-inhomogeneous equilibrium orientation of magnetization vector and integration is performed over the area of the dot.
It is clear from Eq. (1) that, for spin wave modes with other azimuthal dependence ($|m| \neq 1$), $\eta = 0$ (no hybridization with gyrotropic mode) and their splitting is caused solely by the interaction with a static dipolar field of the core, which is weak far from the vortex core.
The spin wave frequencies in the vortex ground state can be calculated as matrix elements of the spin wave Hamiltonian (that includes contributions from the magnetodipolar interaction and inhomogeneous exchange) with orthogonalized profile $\boldsymbol{m}_V$. Using the fact that both $\boldsymbol{m}_R$ and $\boldsymbol{m}_G$ are eigen-modes of the "ring" and "vortex" structures and neglecting influence of the static core field, one can derive simple expression for the frequency ω_V of the azimuthal mode, shifted by the hybridization with the gyrotropic mode: $\omega_V = (\omega_R - |\eta|^2\omega_G)/(1 - |\eta|^2)$, where ω_R is the unshifted frequency of the azimuthal mode (without the hybridization) and ω_G is the gyrotropic frequency.
For typical experimental parameters, the coupling constant $|\eta|^2$ is small and proportional to $\omega_G/\omega_R \sim \sqrt{(L/R)}$*, where* L *and* R *are thickness and radius of the dot, respectively. Then, the frequency splitting* $\Delta\omega = |\omega_V^{(+1)}| - |\omega_V^{(-1)}|$ *between the* m = +1 *and* m = -1 *modes than can be written approximately as*
$\Delta\omega \approx 2|\eta|^2\omega_R$. *(2)*
Fig. 1 shows the dependence of the frequency splitting Eq. (2) on the dot aspect ratio L/R. *One can see, that the developed here simple analytical theory of splitting of azimuthal modes gives a reasonable description of experimental data [2].*
The work of K.G. and S.K. was supported by Creative Research Initiatives (Research Center for Spin Dynamics & Spin-Wave Devices) of MOST/KOSEF.

[1] K. Yu. Guslienko *et al.*, Phys. Rev. Lett. **96**, 067205 (2006).
[2] J. P. Park and P. A. Crowell, Phys. Rev. Lett. **95**, 167201 (2005).
[3] X. Zhu *et al.*, Phys. Rev. B **71**, 180408 (2005).
[4] B. A. Ivanov and C. Zaspel, Phys. Rev. Lett. **94**, 027205 (2005).

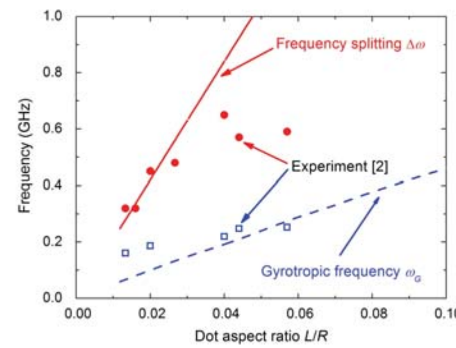

The dependences of the frequency splitting of azimuthal $|m| = 1$ modes $\Delta\omega$ (red solid line) and gyrotropic frequency ω_G (blue dashed line) on the dot aspect ratio L/R (thickness/radius). The symbols show experimental data taken from Ref. 2. Parameters of magnetic dot: saturation magnetization $M_0 = 770$ G, gyromagnetic ratio $\gamma/2\pi = 2.95$ GHz/kOe, thickness $L = 20$ nm.

EC-07

Enhancment of superconductive vortex pinning through formation of magnetic vortices.

A. Hoffmann[1,2], L. Fumagalli[3], N. Jahedi[3], J. C. Sautner[3], J. E. Pearson[1], G. Mihajlovi ć[1], V. Metlushko[3]

1. Materials Science Division, Argonne National Laboratory, Argonne, IL; 2. Center for Nanoscale Materials, Argonne National Laboratory, Argonne, IL; 3. Electrical and Computer Engineering, University of Illinois at Chicago, Chiacgo, IL

The pinning of superconducting vortices in type-II superconductors has been studied for a long time due to the wide variety of unusual flux flow phenomena and, more importantly, for its relevance in applications, since vortex pinning is one of the essential parameters controlling the enhancement of critical currents. A case of particular interest is the use of artificial magnetic pinning centers, since they can be fabricated to match well the characteristic length scales relevant for superconductivity and their magnetization offers another degree of freedom to influence the pinning properties. To this end, a lot of work has been focused on periodic arrays of magnetic structures, which give rise to commensurate pinning of superconducting vortices in adjacent superconducting films.

In our current work, we compare the pinning effects in Nb films due to magnetic permalloy dots with either single domain or vortex magnetization configuration. Magnetic vortices occur in small circular magnetic structures when magnetostatic energies become dominant. This may give rise to hysteresis loops characterized by two critical fields for the nucleation and annihilation of the magnetic vortices. The formation of a magnetic vortex minimizes the overall magnetic stray fields from the dot. However, at the center of the vortex, the so-called vortex core, there is a singularity, where the magnetization points out-of-plane resulting in a strong, but very localized magnetic field penetrating the superconductor.

We observe a clear correlation between the magnetoresistance in the superconductor [see Fig. 1(a)] and the magnetization configuration of the magnetic dots [see Fig. 1(b)]. Namely, while the magnetic dot is quasi-saturated (i.e., positive fields for the decreasing field branch) the resistance minimum due to the coherent pinning is higher than for the magnetic vortex state (i.e., negative fields of decreasing field branch). This indicates that the pinning of the superconducting vortices is strongly enhanced for the magnetic vortex state. The origin of this enhanced pinning is the presence of locally larger magnetic stray fields produced by the magnetic vortex cores. Furthermore, measurements of minor loops, where the vortex core polarity is constant, do not show any asymmetry between positive and negative applied magnetic fields. This absence of an asymmetry for parallel and anti-parallel orientation between the superconducting vortex flux and the magnetic vortex cores suggests that the enhanced pinning is not due to the magnetostatic interactions, but is rather due to the local suppression of superconductivity by highly localized, large perpendicular stray magnetic fields generated by the magnetic vortex cores. Thus this work shows that a careful tuning of the magnetic properties allows for a controlled manipulation of the superconducting vortex pinning.

This work was supported by the Office of Basic Energy Sciences, U.S. Department of Energy, under Contract No. DE-AC02-06CH1357.

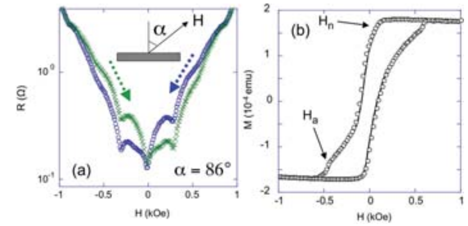

Fig. 1: (a) Magnetoresistance of the Nb film just below T_c with the magnetic field applied at 86° with respect to the surface normal (see inset). Open symbols are for decreasing fields, while crosses are for increasing fields. (b) Magnetic hysteresis loop of the permalloy dots measured at the same temperature as the magnetoresistance measurements in (a). There are two well-defined critical fields, indicative of magnetic vortex nucleation (H_n) and annihilation (H_a).

EC-08

Beams of spin waves guided by permalloy micro-stripes.

V. E. Demidov[1], S. O. Demokritov[1], K. Rott[2], P. Krzysteczko[2], G. Reiss[2]
1. Institute for Applied Physics, University of Muenster, Muenster, Germany; 2. Department of Physics, Bielefeld University, Bielefeld, Germany

Since the first observations of spin-wave quantization effects in magnetic micro-stripes [1] the interest to the high-frequency magnetization dynamics in confined ferromagnetic structures with sub-micrometer lateral dimensions has been continuously growing. Such investigations are of importance for the deep understanding of basic physics of magnetic phenomena on the microscopic scale, as well as for technical applications of magnetic nanostructures for high-speed signal processing and information storage technologies.
In this work we study propagation of spin waves in permalloy micro-stripes by means of a micro-focus Brillouin light scattering (BLS) technique [2] with the spatial resolution of 250 nm, which allows the direct space-resolved mapping of magnetization dynamics on the sub-micrometer scale. The experimental samples are 300 μm long micro-stripes with the widths w=2.1, 5.1, and 10.2 μm patterned from a 20 nm thick permalloy (Ni80Fe20) film deposited onto a glass substrate. At the top of the stripes 300 nm thick and 1 μm wide Au stripe antennae were manufactured. The antennae were oriented perpendicularly to the axes of the permalloy micro-stripes and were used for the excitation of spin waves by a microwave-frequency current. The samples were placed into a static magnetic field of H=300-2000 Oe oriented in the plane of the stripe perpendicular or parallel to its axis.
We experimentally show that the shape of the spin-wave beam propagating in micro-stripe waveguides significantly depends on the orientation of the static magnetic field H. In particular, if H is oriented along the stripe axis, the spin-wave intensity distribution in the transverse section of the stripe is nearly uniform and independent of the propagation coordinate. As a result, the spin-wave beam occupies nearly the entire cross-section of the stripe and is characterized by a constant width. These facts are illustrated by Fig. 1, where the intensity map is shown recorded in 2.1 μm wide stripe. The map was obtained for H=930 Oe and excitation frequency f=9.4 GHz. The scanned area has dimensions of 2.2 μm * 3.5 μm. Note that for the given propagation geometry the shape of the spin-wave beam is practically independent of the stripe width and the excitation frequency.
In the case of H oriented perpendicularly to the stripe axis, the spin-wave propagation was found to have completely different character. In contrast to the previous case, the transverse distribution of the spin-wave intensity changes periodically with the propagation coordinate, which is equivalent to a periodic modulation of the width of the spin-wave beam. This results in a periodic self-focusing of the spin-wave energy at the stripe axis appearing at the points, where the width of the beam has its minima. An example of the spin-wave intensity maps recorded in transversally magnetized permalloy stripe with w=2.1 μm is presented in Fig. 2. The map has dimensions of 2.2 μm * 7 μm. It clearly shows a periodic local increase of the intensity on the middle line. Further measurements have shown that the period of this focusing pattern depends strongly on the stripe width and the excitation frequency and can vary from several micrometers to fractions of a micrometer.
In our talk we will present further experimental data characterizing the above two types of spin-wave propagation in micro-stripes. We will also discuss a theoretical model explaining the experimental findings and allowing calculations of the self-focusing spatial period. As illustrated by Fig. 3, the results of the calculation using the model show very good agreement with the experimental data.

We believe that our findings can be of especial interest for the design and optimization of microscopic waveguides to be used for efficient transmission of spin waves and microwave-frequency signal processing in microelectronic magnetic circuits.

[1] C. Mathieu, J. Jorzick, A. Frank, S.O. Demokritov, A.N. Slavin, and B. Hillebrands, Phys. Rev. Lett. 81, 3968 (1998).

[2] V.E. Demidov, S.O. Demokritov, B. Hillebrands, M. Laufenberg, and P.P. Freitas, Appl. Phys. Lett. 85, 2866 (2004).

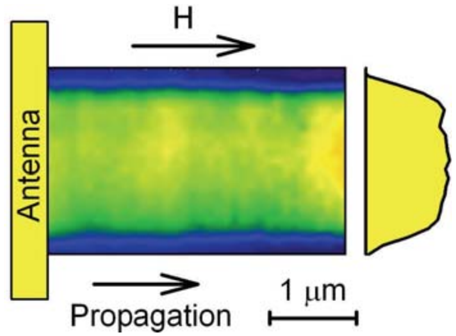

Fig. 1

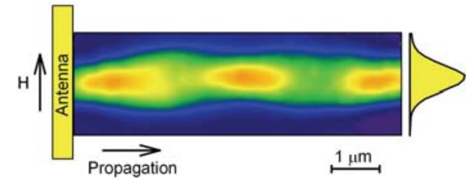

Fig. 2

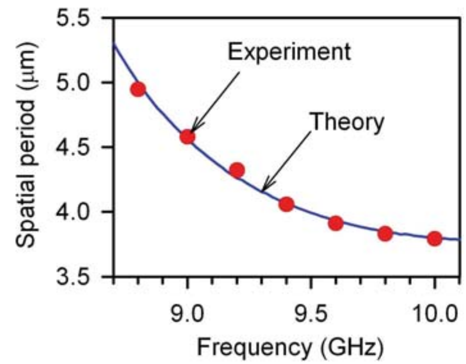

Fig. 3

EC-09

Direct magnetic patterning on paramagnetic FeAl sheets by ion irradiation through poly(methyl methacrylate) and porous alumina shadow masks.

E. Menéndez[1], j. sort[2], E. Jiménez[3], J. Camarero[3], O. Liedke[4], J. Fassbender[4], D. Baró[1], S. Suriñach[1], S. Deevi[5], K. Rao[6], A. Weber[7], L. Heyderman[7], J. Sommerlatte[8], K. Nielsch[8], J. Nogues[9]
1. Departament de Física, Universitat Autònoma de Barcelona, 08193 Bellaterra, Spain; 2. ICREA and Departament de Física, Universitat Autònoma de Barcelona, 08193 Bellaterra, Spain; 3. Surface Science Lab (LASUAM, Lab. de Física de Superficies), Dpto. Física de la Materia Condensada, Universidad Autónoma de Madrid, 28049 Madrid, Spain; 4. Institute of Ion Beam Physics and Materials Research, Forschungszentrum Dresden, 01314 Rossendorf, Germany; 5. Research Center, Chrysalis Technologies Incorporated, 23234 Richmond, WA; 6. Department of Materials Science and Engineering, Royal Institute of Technology, 10044 Stockholm, Sweden; 7. Paul Scherrer Institut, 5232 Villigen, Switzerland; 8. Max Planck Institute of Microstructure Physics, 06120 Halle, Germany; 9. ICREA and Institut Català de Nanotecnologia, Campus UAB, 08193 Bellaterra, Spain

At room temperature, atomically ordered $Fe_{1-x}Al_x$ alloys are paramagnetic for Al atomic contents, x, larger than 0.32. However, between x = 0.32 and x = 0.5, these alloys become ferromagnetic when being atomically disordered [1]. This effect has been systematically studied in ball milled powders [2] and can be used to generate arrays of ferromagnetic dots at the surface of a paramagnetic $Fe_{60}Al_{40}$ sheet by local deformation techniques, such as nanoindentation [3].
In this presentation we will show that a similar magnetic patterning, scaled down to the sub-100 nm regime, can be achieved by ion irradiation through lithographed poly(methyl methacrylate), PMMA, masks (90 nm thick) or porous alumina templates. Irradiation has the advantage over nanoindentation that, due to the low doses used, it does not induce any surface corrugation, avoiding eventual tribological problems. Moreover, the induced ferromagnetism is confined into the locally disordered regions, rendering isolated magnetic dots surrounded by a paramagnetic matrix, thus virtually free from the detrimental effects of interdot exchange interactions. Furthermore, contrary to nanoindentation or other types of irradiation (like focused ion beam), all magnetic nanostructures are obtained simultaneously (i.e., in an in-parallel process). Patterning of magnetic structures with several geometries can be performed in very large areas (several cm^2) and in a few seconds. Contrary to the PMMA masks, the use of alumina templates does not require sophisticated equipment for their fabrication and the membranes can actually be reutilized. However, in this case one is restricted to hexagonal arrays and the limited long-range order of this type of masks.
The fabricated entities exhibit a range of magnetic properties, depending on their size and shape. Hysteresis loops, recorded by magneto-optic Kerr effect, reveal magnetization reversal by coherent rotation (single domain states) for sizes smaller than 100 nm. Flux closure states (e.g. magnetic vortices) form at larger sizes in square or circular dots. The local character of the induced ferromagnetism and the magnetization reversal mechanisms were examined by magnetic force microscopy. As an example, shown in Figure 1 is the magnetic force microscopy image of a hexagonal array of circular dots (300 nm in diameter) obtained by ion irradiation through an alumina membrane. The corresponding hysteresis loop shows a central constriction, evidencing that magnetization reversal occurs via formation of a vortex state.
Remarkably, the structural effects induced by the irradiation (i.e., atromic disorder) are fully reversible. That is, by annealing the disordered (ferromagnetic) FeAl phase at 750 K, the ordered (non-magnetic) FeAl structure is completely recovered. Consequently, FeAl sheets can be re-patterned indefinitely. Contrarily, most of the other patterning methods, e.g. those based on intermixing, can only be patterned once.
Furthermore, it should be noted that the described procedures can be easily extrapolated to a variety of other systems, such as CoZr, CoAl, CoGa, CoV, NiSn, FeGe, $FePt_3$ and FeV intermetallics or even austenitic stainless steel, where local deformation causes a martensitic phase transformation [4].

[1] A. Taylor and R. M. Jones, J. Phys. Chem. Solids. 6, 16 (1958).

[2] X. Amils et al., Phys. Rev. B 58, R11864 (1998) ; X. Amils et al., J. Magn. Magn. Mater. 203, 129 (1999).

[3] J. Sort et al., Adv. Mater. 18, 1717 (2006).

[4] J. Sort et al., Appl. Phys. Lett. 89, 032509 (2006).

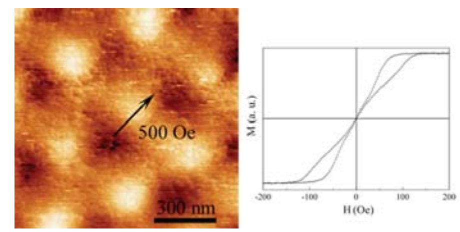

(Left) Magnetic force microscopy image (obtained applying a field of 500 Oe) of a pseudo-ordered array of magnetic dots obtained by ion irradiation of a paramagnetic $Fe_{60}Al_{40}$ paramagnetic sheet through an alumina membrane; (right) corresponding hysteresis loop, typical of magnetization reversal via formation of a vortex state.

EC-10

Transverse magnetization in Nickel nanowire arrays patterned from Cu/Ni/Cu epitaxial films.

M. Ciria[1], J. L. Diez-Ferrer[2], J. I. Arnaudas[2,1], B. G. Ng[3], F. J. Castaño[3], R. C. O'Handley[3], E. S. Friend[3], C. A. Ross[3]
1. ICMA, CSIC-Universidad de Zaragoza, Zaragoza, Spain; 2. Instituto de Nanociencia de Aragón, Universidad de Zaragoza, Zaragoza, Spain; 3. Department of Materials Science and Engineering, Massachusetts Institute of Technology, Cambridge, MA

The control of the domain configurations in lithographically defined magnetic elements with sub-micron lateral dimensions (nanomagnets) is of great current interest for a range of spintronic devices for both storage and logic applications. Most reported work to date has been focused on nanomagnets patterned from polycrystalline films, which typically display a magnetization reversal dominated by shape anisotropy. In the present work, we show that arrays of Nickel wires with sub-micron widths, patterned from epitaxial Cu (3nm)/Ni (4-15 nm)/Cu (100 nm) films, display transverse easy magnetization direction instead of the longitudinal easy axis expected from the increased shape anisotropy. On patterning the Cu/Ni/Cu stacks into nanowires, the strain in the film releases transversally to the long axis of the wires introducing a magnetoelastic anisotropy which is sufficient to overcome shape anisotropy and generate an easy axis magnetization direction transverse to the nanowires long axis.
Large area (~ cm2) arrays of Nickel nanowires were made using a subtractive fabrication approach combining interference lithography and ion-milling. Epitaxial Cu (3nm)/Ni (4-15 nm)/Cu (100 nm) were grown on Si(001) wafers at room temperature by e-beam evaporation in a chamber with a base pressure below 2 x 10^{-10} Torr. The nickel films exhibit out of plane magnetization for Nickel thicknesses between about 1.5 and 10 nm [1]. Arrays of Ta nanowires were first defined over the films using templates created by interference lithography (see Figs. 1a-b) and liftoff processing. Pattern transfer was achieved using Ne ion milling. Arrays of wires with widths from 200 nm and periods of 400 nm and above were investigated using AGM, VSM and MFM. For structures patterned from 4 nm-thick Ni films (see Fig. 1c), the magnetization lays out-of-plane for both the nanowires and the films, although the coercive force is larger for the nanowire arrays (290 Oe) than for the unpatterned film (215 Oe), and the magnetization reversal appears to include magnetization rotations. For structures made from 9nm, 10nm and 15 nm- thick Ni films, the magnetization for both the arrays and the films lays in-plane (see Figs. 1d - f). Most significantly, hysteresis loops applying magnetic fields transversally to the long axis of the wires saturate at lower fields than those measured on applying fields parallel to the wires.
We also observe that, compared with the film, become magnetically easier (⊥ lines) or harder (‖ lines) magnetize the structure after the patterning process (see in Figs. 1e for t_{Ni} = 10 nm) ; regarding the out-of plane anisotropy observed in the Ni films, we observe that for t_{Ni} = 9 nm the perpendicular to the plane direction is no longer easier than the in-plane transversal direction to the lines, although the difference in the magnetization process is small between both directions.
That kind of loops appear to agree with MFM images shown in figs 2a and d, taken at remanence after applying a field of 1 kOe perpendicular to the plane. The magnetic image has the same periodicity than the nanowire arrays, with maximum signal located at the borders and the center of the wires (Fig 2c), that contrast may be due to the in-plane components of the magnetization; while the remanence observed in the 9nm-thick film could be ascribed to the domain structure that can be observed on top of the periodic structure (see Fig 2d).

The reported behavior could be explained including an in-plane anisotropic magnetoelastic contribution in the magnetic anisotropy energy, due to an anisotropic relaxation of the strain [2] In this way, our finite element modeling indicates that the transverse line strain relief is largely a function of cross-section aspect ratio. The outer 1-1.5 thickness units of a given cross section relax their strain completely, while the center regions retain their biaxial strain state.

[1] R. Jungblut, M. T. Johnson, J. aan de Stegge, A. Reinders, and F. J. A. den Broeder, J. Appl. Phys. 75, 6424 (1994).

[2] E. S. Lyons, R. C. O'Handley, and C. A. Ross, J. Appl. Phys. 99, 08R105 (2006).

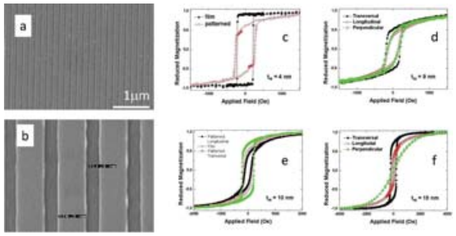

(a) and (b) SEM images of the patterned films with the Ta wires. (c)-(f) BH loops for structures with t_{Ni} =4, 9, 10 and 15 nm

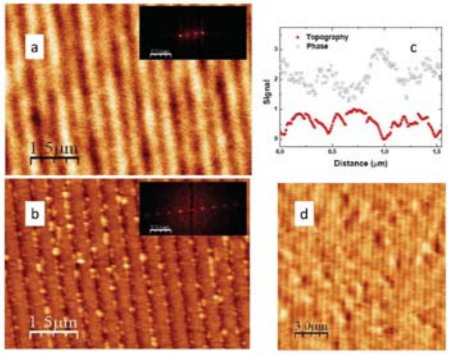

Simultaneous (a) MFM (phase) and (b) topographic images taken on the 9 nm thick nanolines. The insets are the Fourier spectra. (c) Selected profile taken from the same line from images (a) and (b); (d) MFM taken on a large area, showing clearly a perpendicular domain with a size larger than the nanolines width.

EC-11

Magnetostatic dipolar domain wall pinning in chains of Permalloy triangular rings micro-magnets.

P. Vavassori[1,2], D. Bisero[2], V. Bonanni[2], A. Busato[2], M. Grimsditch[3], K. Lebecki[4], V. Metlushko[5], B. Ilic[6]

1. CIC nanoGUNE, San Sebastian, Spain; 2. CNISM, CNR-INFM S3, and Dipartimento di Fisica, Universita` di Ferrara, Ferrara, Italy; 3. Materials Science Division, Argonne National Laboratory, Argonne, IL; 4. Institute of Physics, Polish Academy of Sciences, Warsaw, Poland; 5. Department of Electrical and Computer Engineering, University of Illinois at Chicago, Chicago, IL; 6. Cornell Nanofabrication Facility, Cornell University, Ithaca, NY

Manipulation of magnetic domain walls (DWs) in nanostructures has recently become the focus of intense research due to its great potential for application to spintronics. Magnetic nanorings are particularly apt geometry to such investigations [1]. If the magnetocrystalline anisotropy is negligible, only the geometry of the ring determines the microscopic spin structure of the magnetic states. The effects of geometrical constrictions, such as notches and corners, on DWs in nanorings have been intensively investigated [2].

In an earlier work we have studied the magnetization reversal in Permalloy (Py) triangular rings and we observed that head-to-head DWs can be positioned at selected corners and moved between corners by applying a magnetic field [3]. In this contribution we present the results of a combined experimental and numerical study with which we determined the details of the pinning of domain walls in isolated and interacting Py triangular rings (side 2 µm, width 250 nm and thickness 25 nm). In the former case the rings form a square lattice with a period of ~4.2 µm so that inter-element interactions are negligible; in the second sample the rings are arranged in chains with a corner tip of each triangle in proximity of the edge centre of the triangle above with inter-element spacing of 50 nm. Using the longitudinal and diffraction magneto-optics Kerr effect (L- and D-MOKE, respectively [4,5]), magnetic force microscopy (MFM), and micromagnetic simulations [6] we determined the field dependence of the spin structure in the rings. The results show that magnetization reverses from an onion state to the reversed state via the formation of a vortex. Each onion state is characterized by DWs (one head-to-head and the other tail-to-tail) geometrically pinned at two corners of the ring [see MFM image in Fig. 1 panel (a)]. We prepared each sample in a well defined onion state (monitored with D-MOKE) and determined the DW motion and pinning potentials recording the L-MOKE loops obtained by sweeping the wall with a field H1 applied along a branch of the ring. We studied this process as a function of a second fixed field H2 applied perpendicularly to the branch of the ring along with the DW is swept to prevent oblique segments from switching, as sketched in panel (b) of Fig. 1 for the chains of rings. In the case of isolated rings a DW moves freely between the geometric pinning potential wells determined by adjacent corners as the external field H1 reaches a critical value Hd and a single transition is observed in the loops at any value of H2 [solid line in Fig. 1 panel (c)]. For interacting rings, when the wall is swept in the branch closer to the corner tip of the nearest neighbor ring, the loops show an intermediate step for H2 above a certain value caused by the pinning of the wall by the magnetostatic dipolar field emanating from the corner of the nearest ring neighbor [see open symbols in Fig. 1 panel (c)]. Quite interestingly, the depinning of the DW from the starting corner is always (viz. at any value of H2) anticipated in the chains with respect to isolated rings [compare open dots (Hd) and open triangles (Hd1) in Fig. 1 panel (d)], due to the presence of the potential well created by the magnetostatic interaction. We observed that H2 affects appreciably only the depinning field Hd1 from the corner but not the depinning field Hd2 from the potential well due to the magnetostatic interaction [compare open and solid triangles in Fig.1 panel (d)]. Qualitatively, the process can be modeled as a domain wall in a triple potential well landscape with the depth of the two wells at the adjacent corners delimiting the branch, function of the vertical applied field H2. Micromagnetic simulations reproduce the behavior observed and provide additional details on the DW spin structure during its motion.

[1] P. Vavassori et al., Appl. Phys. Lett. 91, 093114 (2007); M. Kläui et al., Phys. Rev. Lett. 90, 097202 (2003); M. Kläui et al., Appl. Phys. Lett. 81, 108 (2002).

[2] P. Vavassori et al., Phys. Rev. B 67, 134429 (2003); A. Libál et al., J. Appl. Phys. 98, 083904 (2005); M. Kläui et al., Appl. Phys. Lett. 81, 108 (2002); J. Rothman et al., Phys. Rev. Lett. 86, 1098 (2001); M. Kläui et al., Appl. Phys. Lett. 78, 3268 (2001).

[3] P. Vavassori et al., J. Appl. Phys. 101, (2007).

[4] P. Vavassori, Appl. Phys. Lett. 72, 1600 (2000).

[5] M. Grimsditch and P. Vavassori, J. Phys.: Condens. Matter 16, R275 (2004).

[6] M. J. Donahue and D. G. Porter, OOMMF User's Guide, Version 1.2 alpha 3 (NIST, Gaithersburg MD, 2002).

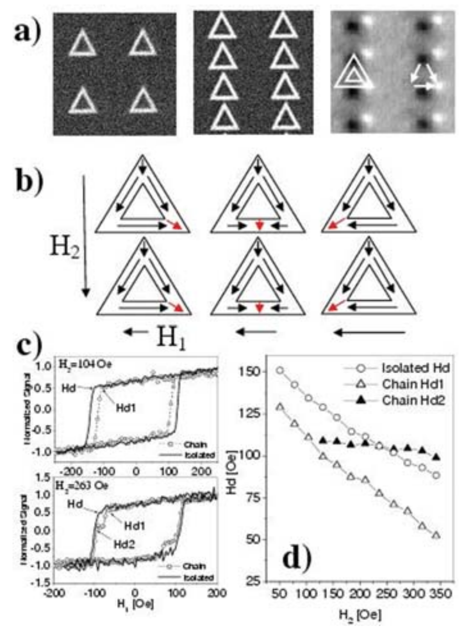

Fig. 1 Panel (a): SEM images of the two arrays and MFM image of the remanent state of the sample with chains of rings. Panel (b): schematic of the experiment described in the text. Panel (c): loops of the two samples recorded at two values of H2. Panel (d): domain wall depinning fields for the two samples.

EC-12

Partial frequency band gap in 1D magnonic crystals.

M. Kostylev[1], G. Gubbiotti[2], P. Schrader[1], G. Carlotti[2], A. O. Adeyeye[3], S. Goolaup[3], N. Singh[3], R. L. Stamps[1]

1. School of Physics, University of Western Australia, Crawley, WA, Australia; 2. CNISM, Dipartimento di Fisica, Universita di Perugia, Perugia, Italy; 3. Department of Electrical and Computer Engineering, National University of Singapore, Singapore, Singapore

The development of new magnetic recording technologies based on patterned media requires a deep understanding of the magnetic dynamics of laterally confined structures on a submicron length scale. We report results from experimental and theoretical investigation of spin-wave spectra of one-dimensional periodic arrays of interacting Permalloy ($Ni_{80}Fe_{20}$) stripes. Samples with different type of translational symmetry were fabricated on a silicon substrate using deep ultraviolet lithography with 248 nm exposure wavelength followed by a lift-off technique. Brillouin light scattering (BLS) technique was used to measure spin wave spectra as a function of the transferred wave vector, with the magnetic field applied along length and width of the stripes in a wide range of fields, as well as during hysteresis cycles.

Our previous theory [1] shows that propagating collective spin wave modes are formed due to magnetostatic interaction which couples the dynamical magnetization of adjacent stripes resonating into individual stationary states. Several discrete collective modes were obtained from light scattered within the plane normal to the major (longest) axes of the stripes (ϕ=90°), while experimentally studying wavevectors across several Brillouin zones of the periodic array. Different types of collective modes were identified for different geometries and at different applied fields.

In-plane angle resolved measurements were made by changing the relative orientation (ϕ) between the magnetic field (applied along the stripes length) and the scattering plane with a constant incidence angle of light θ=30°, corresponding to a value of transferred wavevector of 1.81×10^5 rad/cm. (Sample parameters: width is 350 nm, thickness is 30 nm; and edge-to-edge spacing is 55 nm.) We found that with the increase in the in-plane angle ϕ, the mode frequencies increased (Fig. 1, dots). We understand this as due to a change in group velocity of the collective modes with the change in ϕ. For ϕ=0 (propagation along the major stripes axis y) the modes represent *collective* backward volume magnestotatic spin wave excitations with negative group velocity. For larger angles (rotation towards the axis x) they transform into Damon-Eshbach surface wave *collective* excitations with positive group velocity.

To explain dependence of the spin wave eigenfrequencies on the wave number we constructed a theory of collective spin wave modes propagating at an arbitrary angle ϕ with the array major stripes axis. Our theory is based on the Bloch wave approach for collective modes developed in Refs. [1] and the Green's function of dipole field of guided spin waves with continuos wavevectors along the y axis [2]. The one-dimensional calculation of Ref. [1] was overcome here by the use of a two-dimensional Green's function which allows one to rigorously account for eventual nonuniformity of the out-of-plane profile of the dynamic magnetization. The lines in Fig. 1 show the results of our calculation. One sees a good agreement with the experimental data. To produce these results we used the following magnetic parameters of permalloy: saturation magnetization $4\pi M_0$=10100 G, gyromagnetic ratio $|\gamma|$=2.82 MHz/Oe, and exchange constant A=9 10^7 erg/cm. To obtain this good fit we had to assume that the coherence length of the Bloch waves is finite and equals to two structure periods.

To achieve a better understanding of the band structure of the one dimensional magnonic crystal under investigation, we performed a calculation of the full two-dimensional eigenspectrum of collective modes $\omega(k_x,k_y)$, shown in Fig. 2. This calculation was done for a value of the applied field H=0.5 kOe in order to compare the results of calculation with the experiments performed as a function of k_y for ϕ=0° and as a function of k_x for ϕ=90°. One sees a set of surfaces which do not cross each other. It is noticeable, however, that the spectrum does not show full stop bands: the stop bands existing for a fixed value of either k_y or k_x overlap with the permitted frequencies for other values of the two parameters, thus one concludes that the frequency gaps in this structure are partial.

Support by ARC (Australia) and MIUR (Italy) is gratefully acknowledged.

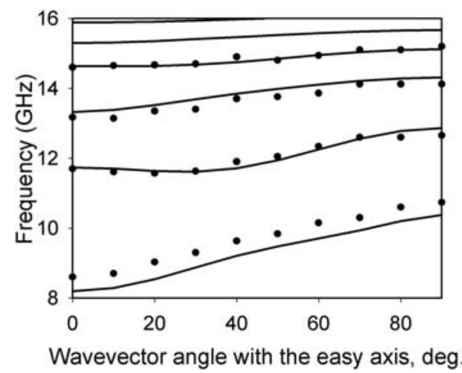

Fig. 1

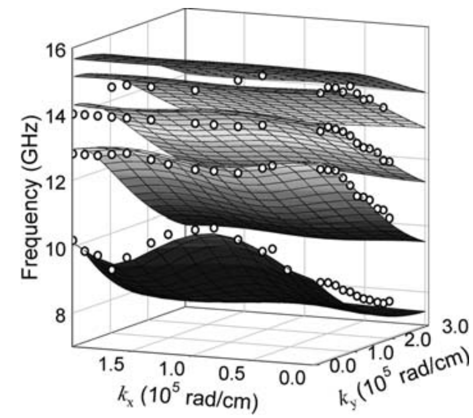

Fig. 2

ED-01

Head-to-SUL spacing reduction with a magnetic seed and the effect on perpendicular recording characteristics.

G. Choe, M. Minardi, K. Zhang, M. Mirzamaani
Hitachi GST, 5600 Cottle Road, San Jose, CA

In narrow track perpendicular recording system designs, reduction of write head-to-media SUL spacing has become a primary way to enhance media writeability. However, the crystallography of the Co-alloy recording layer was reported to degrade at reduced Ru underlayer thickness due to an increase in Ru (0002) c-axis dispersion[1]. Although many attempts using different seed layers such as Ta, Ti, Ni-alloys and AlN were made to improve Co c-axis orientation at reduced Ru underlayer thickness, it is difficult to retain good anisotropy of well-isolated Co grains when the Ru underlayer thickness varies. In this study, recording characteristics were investigated for a new underlayer structure using a magnetic seed used to reduce the recording layer-to-SUL (RTS) spacing without degrading the Co c-axis orientation.

The reference non-magnetic multi-underlayers consist of FCC(111) Ni-alloy (9nm)/BCC(110) Cr(9nm)/HCP(0002) Ru(11nm). The RTS spacing is varied by partially replacing the non-magnetic FCC Ni-alloy layer with a magnetic CoNiFe layer that acts as a part of the underlying SUL through magnetic exchange coupling. Fig.1 shows the change in the Ru and Co (0004) c-axis dispersion(XRD $\Delta\theta_{50}$) as a function of the CoNiFe-to-non-magnetic Ni-alloy thickness ratio at constant total thickness ~ 9nm. The $\Delta\theta_{50}$ values of Ru and Co decrease with increasing CoNiFe thickness, indicating that the Co c-axis orientation is further improved at lower RTS. As shown in cross sectional TEM image of the layered structure (Fig. 2), both magnetic CoNiFe and non-magnetic Ni-alloy have predominant FCC (111) planes growing in the perpendicular direction, which promotes epitaxial growth of the subsequent Cr BCC (110) and Ru HCP (111) layers.

In this study, we characterized the media magnetic performances using heads with trailing-shield (TS) and wrap-around shield (WAS) writer designs. For both heads, the magnetic write width (MWW) increases with decreasing RTS, indicating that the write field becomes stronger with lower RTS. However, the influence of side fringing fields on the nearest adjacent track erasure was highly dependent on the head type at different RTS spacing. As shown in Fig. 3-a, for the TS head, the erase band(EB) representing the magnitude of side fringing field erasure linearly decreases with decreasing RTS spacing, indicating that the side fringing field is better confined to on-track pole at lower head-to-SUL spacing. The WAS head, with a side shield to reduce the side fringing field, shows narrower EB than the TS head for a wide range of RTS spacing, and the EB is less sensitive to RTS spacing. Besides the head writeability, the change in RTS spacing also affects the read-back response, particularly at different linear densities. The track average amplitude (TAA) at low linear density is significantly higher at lower RTS, while the TAA at high linear density is similar for all the RTS ranges within 8 nm. Fig. 3-b shows the signal-to-media noise (SNRm) dependence on linear density for media with different RTS spacing. At low linear density(250 KFCI), SNRm is improved regardless of the amount of RTS reduction. By replacing the non-magnetic Ni-alloy layer with 4nm thick CoNiFe layer, the SNRm is enhanced at every liner density. However, as RTS spacing is further reduced, the SNRm begins to degrade and the decrease is more significant at higher KFCI conditions. This suggests that even though the magnetic seed containing FCC/BCC/HCP multi-underlayer enables RTS spacing reduction with enhanced Co c-axis orientation, it is also important to optimize the amount of spacing reduction and the head media integration to improve overall system performance.

[1]S. Oikawa, A. Takeo, T. Hikosaka and Y. Tanaka, IEEE Trans. magn. 36, 2393 (2000)

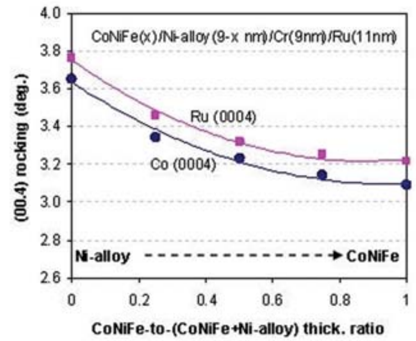

Fig.1 Change in XRD $\Delta\theta_{50}$ of Ru and Co (0004) with increasing CoNiFe thickness ratio of CoNiFe(x nm)/Ni-alloy(9-x nm)/Cr(9nm)/Ru(11nm)

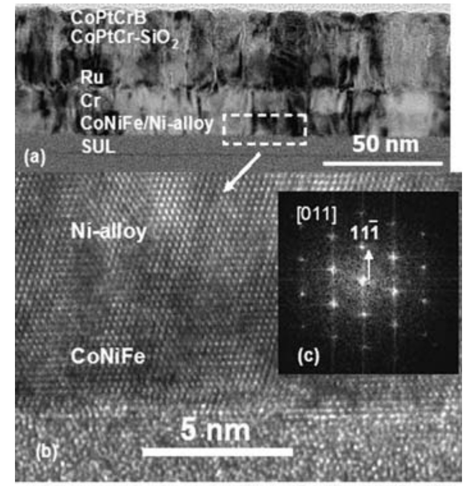

Fig.2 Cross sectional TEM view of the media with CoNiFe(2nm)/Ni-alloy(7nm)/Cr(9nm)/Ru(11nm) underlayers: (a) bright field image, (b) high resolution image of CoNiFe/Ni-alloy layers and (c) FFT pattern

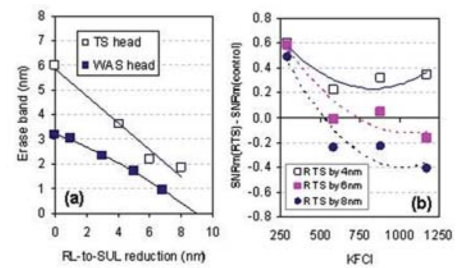

Fig.3 (a) Erase band and (b) ΔSNR_m [SNR_m(reduced RTS by x nm) $- SNR_m$(no RTS reduction)] for media with different RTS spacing

ED-02

Reduction of transition layer thickness showing incoherent switching behavior in single $CoCrPt\text{-}SiO_2$ perpendicular media.

H. Jung, M. Kuo, S. Malhotra, G. Bertero
Western Digital Media Inc., San Jose, CA

Perpendicular magnetic recording technology recently demonstrated high areal density of 520 Gb/in^2 [1]. For further improvement of media performance, advanced media structures with the concept of exchange-coupled composite [2] and exchange spring [3] media are currently in development. We recently reported the existence of highly exchange-coupled initial thin layer on top of Ru layer in $CoCrPt\text{-}SiO_2$ films [4], which should be removed ideally. This non-uniform microstructure caused significant incoherent switching behavior and high magnetic activation volume (V_{act}). The hard magnetic layer is particularly sensitive to microstructure of intermediate layer (IL). Good epitaxial growth of CoCrPtB films on top of Ta/RuCr IL with narrower crystallographic c-axis orientation ($\Delta\theta_{50}$) of 2 - 3° was reported. [5]. In this paper, the effect of two different types of Ta/Ru_1/Ru_2 (IL1) and Ta/RuCr/Ru_2 (IL2) on magnetic switching behavior and magnetic cluster volume in single $CoCrPt\text{-}SiO_2$ media is investigated. Here Ru_1 and Ru_2 indicate the Ru layer deposited at low and high pressure of Ar, respectively.
Fig. 1 shows the effect of t_{MAG} on coercivity (H_c) and coercivity squareness (S*) of the $CoCrPt\text{-}SiO_2$ films with two different IL types. Replacement of Ru_1 with RuCr provides superior $\Delta\theta_{50}$ of < 2.3°. As t_{MAG} in IL1 varies from 2 to 27 nm, H_c linearly increases, reaches a plateau, and then decreases. It reaches maximum value of H_c = 6.6 kOe at t_{MAG} = 18 nm. The use of IL2 achieves higher H_c at thinner t_{MAG}, H_c = 7.3 kOe at t_{MAG} = 12 nm. The H_c trend is similar to that in IL1. S* significantly decreases from 0.59 to 0.41 at $t_{MAG} \leq 8$ nm and become constant at $t_{MAG} > 8$ nm for IL1 while they continuously decrease from 0.61 to 0.40 with increasing t_{MAG} to 30 nm for IL2. Overall IL2 provides higher S* than IL1.
The short time switching field (H_o) and thermal stability (K_uV/k_BT) at room temperature are estimated by fitting time-dependent H_{cr} to Sharrock's equation using the attempt frequency = 1 GHz and n = ½. The plot of H_{cr}/H_o versus t_{MAG} is fitted with Sharrock's equation as used in Ref 6. Curve fitting is good at certain ranges, indicating that they follow coherent switching behavior. There exist incoherent switching behaviors at thin and thicker layers: $t_{MAG} \leq 6$ nm and $t_{MAG} > 21$ nm for IL1 and $t_{MAG} > 12$ nm for IL2. The critical thickness exhibiting superparamagnetic state decreases from 3.4 nm for IL1 to 1.6 nm for IL2. A similar incoherent switching behavior was reported in CoPt-O layers with $t_{MAG} > 21$ nm and the critical thickness was ~6 nm. [6]
Values of H_{cr} at 45° normalized by H_{cr} at 0° ($H_{cr\,45°}/H_{cr\,0°}$) in films with two IL types show similar trends in Fig. 2. The 4 nm-thick film with IL1 clearly exhibits that $H_{cr}/H_{cr\,0°}$ continuously increases with increasing the angle between the easy axis and applied field direction, close to domain wall switching behavior. Initial high values of $H_{cr\,45°}/H_{cr\,0°}$ significantly decrease with increasing t_{MAG} and then increase again. Interestingly, the value of t_{MAG} showing minimum $H_{cr\,45°}/H_{cr\,0°}$ decreases from 15 nm for IL1 to 9 nm for IL2. Compared to IL1, IL2 enhances coherent switching behavior at $t_{MAG} \leq 9$ nm but also increases incoherent switching behavior at $t_{MAG} > 9$ nm. The increase in incoherent switching behavior and the decrease in H_c at thicker layers with IL1 were understood by both lower K_u, caused by formation of sub-grains and higher stacking faults density, and stronger magnetoelastic effect at the top region containing higher oxide contents. [7] They will provide broader magnetic c-axis orientation. Values of V_{act} decrease with increasing t_{MAG}. IL2 provides considerably higher V_{act} than IL1.

It is concluded that IL2 achieves higher H_c at thinner t_{MAG} by both reduction of transition layer thickness showing incoherent switching behavior and the increase in V_{act}. Reduction of V_{act} by using a proper IL will further improve magnetic properties in the hard layer while maintaining higher H_c at thinner t_{MAG}.

[1] S. Mao, et al., 8th PMRC 2007, p. 15pA-01.
[2] R. H. Victora and X. Shen, IEEE Trans. Magn. 41, 537 (2005).
[3] D. Suess, et al., IEEE Trans. Magn. 41, 3166 (2005).
[4] H. S. Jung, et al., Appl. Phys. Lett. 91, 212502 (2007).
[5] K. W. Wierman, et al., J. Appl. Phys. 91, 8031 (2002).
[6] X. W. Wu, et al., J. Magn. Magn. Mater. 303, e261 (2006).
[7] H. S. Jung, et al., IEEE Trans. Magn. 43, 615 (2007).

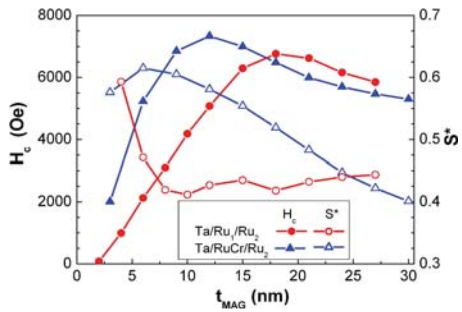

Fig. 1 Effect of t_{MAG} on Hc and S* in $CoCrPt\text{-}SiO_2$ films with two different IL types.

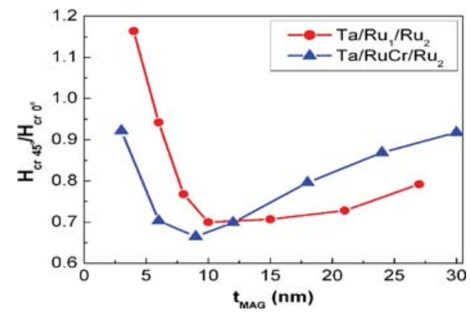

Fig. 2 Effect of t_{MAG} on angular normalized Hcr at 45° in $CoCrPt\text{-}SiO_2$ films with two different IL types.

ED-03

Compositional structure and magnetic properties of CoCrPt-SiO_X Perpendicular Recording Medium.

M. Futamoto[1], T. Handa[1], Y. Takahashi[2]

1. Faculty of Science and Engineering, Chuo University, Tokyo, Japan; 2. Central Research Laboratory, Hitachi, Ltd., Tokyo, Japan

INTRODUCTION For high density perpendicular magnetic recording, CoCrPt-SiO_X recording layer with isolated crystal grain structure is widely employed. Magnetic properties and the thermal stability depend on grain diameter, the crystal grain composition as well as the grain boundary composition [1]. In the present study, we investigated the distribution of grain diameter and the composition focusing on individual crystal grains by using a transmission electron microscope (TEM) equipped with an energy dispersive X-ray spectrometer (EDX). The grain boundary composition was also estimated from the average film composition including the boundary region and the average grain compositions. The K_u values of individual crystal grains were estimated from the grain compositions.

EXPERIMENTAL A perpendicular recording medium with a structure of protective-layer/[CoCrPt-SiO_X (12 nm)]/Ru/underlayer/glass substrate was used for TEM analysis. In the EDX measurement, an electron beam of about 2 nm in diameter was focused at the center of a crystal grain to measure the grain composition. Wider electron beam was used to measure the average film composition including the grain boundaries. Two types of crystal grain, with uniform TEM contrast and with irregular contrast, were recognized in the plan-view TEM image as shown in Fig. 1(b) and (c). We measured the grain compositions by classifying the two types of grain.

RESULT AND DISCUSSION Fig. 2(a) shows the dependence of composition on crystal grain diameter measured for uniform contrast crystal grains. The composition of individual grain depends little on the grain diameter. However, Co and Pt compositions slightly increases, while Si slightly decreases with increasing the grain diameter. Fig. 2(b) shows the relationship between grain diameter and K_u value estimated by citing the reference [2]. The K_u values increases slightly with increasing the grain diameter. Table I summarizes the compositions determined for the average film layer including the grain boundaries, the uniform contrast grains, the irregular contrast grains, and the grain boundaries. The grain boundary composition is calculated from the average film composition and the two types of crystal grains by referring the respective volume ratios estimated from the plan-view TEM observation. When the average composition is compared between two types of grain, the Co and Pt contents are decreased while that of Si is increased for the irregular contrast grain. The result suggests that oxides like SiO_X are incorporated within the crystal grain, which might be the reason for the brighter contrast in the TEM image. It is not possible to directly measure the grain boundary composition because the width is approximately 1.1 nm which is smaller than the electron beam diameter of 2 nm. The composition of the grain boundary estimated in the present study clearly indicates that the grain boundary includes a lot of Si atoms and not a small amount of Co, Cr, and Pt elements. Although Si and possibly other elements are expected to exist in the form of oxides, the oxygen content could not be determined in the present study due to a lack of sensitivity of the EDX analysis.

[1] N. Inaba *et al.*, *IEEE Trans. Magn.*, vol. 36, no. 1, pp. 54-60, 2000.

[2] T. Shimatsu *et al.*, *IEEE Trans. Magn.*, vol. 40, no. 4, pp. 2483-2485, 2004.

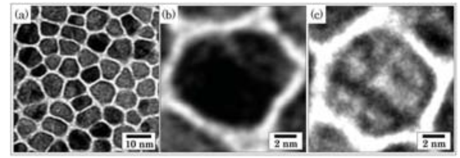

Fig. 1 Plan-view TEM image of CoCrPt-SiO_X magnetic layer (a) and examples of uniform contrast grain (b), and irregular contrast grain (c).

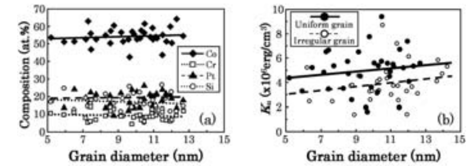

Fig. 2 Grain diameter dependence of uniform contrast grain composition (a) and K_u values estimated for the two types of crystal grain (b).

Table I Compositions of magnetic layer, crystal grain, and grain boundary.

Atomic %	Co	Cr	Pt	Si
(a) Magnetic layer	48.2	10.5	17.9	23.4
(b) Uniform contrast grain	54.2	9.4	19.4	17.0
(c) Irregular contrast grain	52.8	9.2	17.7	20.3
(d) Grain boundary	14.4	17.4	12.8	55.4

ED-04

Exactly Lattice Matched Novel Under Layers (LML) in Perpendicular Media.

A. Ajan, T. Sugimoto, T. Uzumaki
Magnetic Media Laboratory, Fujitsu Laboratories Ltd., 10-1 Morinosato-Wakamiya, Atsugi, Japan

Introduction: In order to enhance the perpendicular media [1] performance, good c-axis orientation of magnetic CoPt grains, lower grain size and smaller size distribution are necessary. Ruthenium (single or double layer) or its alloys stand out to be the best candidate as intermediate layer, which impart a good epitaxial growth, grain size control and high nucleation field for the CoCrPt-SiO2 type magnetic layer [1,2]. Since the seed layers (NiCr, NiFeCr or Ta)[2] have a lattice mismatch of >7% with Ru(0002), a thick Ru layer(~25-40nm) was needed. This reduces the writing capability and increases the cost of the media. Thus it is necessary to develop new seed layer materials, which has near perfect lattice match with Ru(0002), thereby reducing the Ru thickness (~5-10 nm). Here we describe the structural properties of the newly developed materials (alloys) with face centered cubic (fcc) structure, whose (111) textured plane can controllably be varied to make an exact lattice match with Ru(0002) plane.<p>

Experimental:

The materials for LML are chosen from a combination of one of Ni, Cu, Pt, Pd, Al such as NiPt, NiPd, PdCu etc.. In order to illustrate the LML concept, we have made the following structure on 2.5” glass substrates; Ta(3nm)/(Ni+Pt)(10nm)/C(3nm). The Ni and Pt (or other alloy combinations) are co-sputtered in various power ratios in order to obtain different alloy compositions. ICP analysis indicated that the expected and obtained atomic ratios are within the range of ±1at%. For the SNR evaluation, the following media structures were made; Anti-parallel soft under layer(APS_SUL)/PdNi(LML)/Double Ru layer (5-30 nm)/Magnetic recording layers(CoCrPt-SiO2/CoCrPtB)/protective layer(C). Media were studied using various techniques such as X-ray diffraction (XRD), TEM, SQUID magnetometer, Kerr magnetometer, Guzik spin-stand and UDT tester.<p>

Results and Discussion :

Figure 1A shows the X-ray diffraction (XRD) spectrum for various PtNi(x) composition in Glass/Ta/PtNi/C structure. The data indicates that for the entire composition range, the film contain grains which are fcc structured. The peak position of PtNi(x)(111) shift systematically towards the higher angle side as the Ni percentage increases from 0 to 100 at%. Fig. 1B shows the calculated lattice spacing of the alloy in the (111) plane. As the Ni content in the film increases, a continuous variation of lattice spacing is observed, which nearly follows the Vegards law [3]. The lattice mismatch of (111) plane with Ru(0002), is also shown in the same figure. The lattice matching of PtNi with Ru(0002) is nearly perfect when Pt content is ~60 at%. Similar variation of lattice spacing is observed with other LML layers such as PdNi, PdCu etc.. Moreover, the transverse TEM image of the interface between LML and Ru indicated a smooth interface and lattice packing across the thickness of the film. <p>

For studying the Ru (0002) growth, we have sputter deposited APS_SUL (FeCo alloy(25 nm)/Ru(0.5 nm)/FeCo alloy(25 nm))/Ta(3 nm)/PdNi or PtNi(5 nm)/Ru(8-26 nm))/C(4 nm) on glass substrates. The Δθ50 of Ru(0002), which is a measure of the distribution of c-axis orientation from the film normal, is estimated from the XRD rocking curve measurement. For comparison purposes, media with a conventional NiFeCr alloy seed layer of 5 nm thickness is used. It is clear from the Fig.2 that for obtaining the same Δθ50 of c-axis, a 15 nm thinner Ru could be used with PtNi or PdNi alloy than that of NiFeCr alloy. <p>

The SNR of the media with various Ru thickness were evaluated at a writing frequency of 990 kBPI. The results indicated that the SNR level (from a standard media) could be maintained until ~10 nm of Ru thickness (Fig. 3). For NiFeCr underlayer media, SNR decreases by more than 1dB at Ru thickness of 15nm in comparison to the media with Ru thickness of 25nm. This lartge difference of SNR variation with Ru thickness is attributed to the better lattice matched growth for the Ru layer on LML. <p>

LML alloys may also be used for the lattice match growth for CoPt layers. Since the lattice spacing of CoPt grain depends strongly on the Pt content, LML provide an ideal choice as an under layer. Further discussion on the structural, magnetic and SNR evaluation of media along with the performance of media with thinner Ru thickness will given in the detailed paper.

[1]Iwasaki et. al, IEEE Trans. Magn., vol. 11, p. 1173,1975; (For recent reviews), S. N. Piramanayagam, J. Appl. Phys., vol. 102, p. 011301, 2007.; J. H. Judy, J. Magn. Magn. Mater., Vol. 287,p. 16, 2005. <p>

[2]Shibamoto et. al., Intermag-2005 Digest, paper CQ-02,2005; Uwazumi et. al., IEEE Trans. Magn., vol. 37, p. 1595, 2001. <p>

[3]L. Vegard, Z. Phys. Vol. 5, p. 17, 1921, C.S. Barrett, Structure of metals, 2nd Ed., McGraw Hill, 1952.

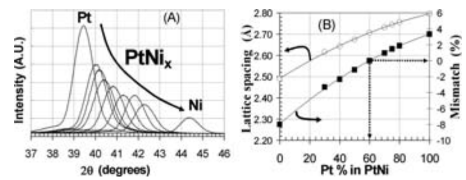

Fig.1 (A) X-ray diffraction spectrum, (B) Lattice spacing in (111) plane and lattice mismatch with Ru(0002), for various PtNi compositions.

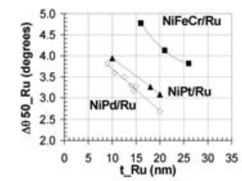

Fig.2 c-axis dispersion (Δθ50)of Ru(0002) on different seed layers for various Ru layer thickness (t_Ru).

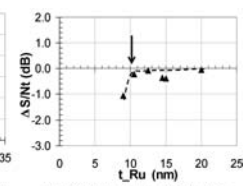

Fig.3 SNR changes of media with different Ru layer thickness on PdNi LML layer.

ED-05

Magnetic and Recording Characteristics of CoCrPt-Oxide Media with a Mixture of SiO2 and TiO2.

I. Tamai, R. Araki, K. Tanahashi
Central Research Laboratory, Hitachi,Ltd., Odawara-shi, Kanagawa-ken, Japan

CoCrPt-oxide granular films have been widely used as a recording layer in perpendicular recording media. The granular films have a well-isolated structure with oxide grain-boundaries, thereby leading to low noise properties. To further improve media performance in higher areal densities, we need smaller grains with narrower size distribution while maintaining the well-isolated structure. However, an increase in oxide content tends to hinder film growth with high quality, resulting in poor media performance. Various oxides such as Cr-O, Si-O, Ta-O, and Ti-O have been studied as a segregant to de-couple Co-alloy grains [1-3], but it is still unclear which oxide additive is suitable for use with future media with small grains. In this study, we prepared CoCrPt-oxide media with SiO2, TiO2, or a mixture of SiO2 and TiO2, and we investigated the capability of dual oxide by comparing the magnetic and recording characteristics of three types of media.
The media were deposited onto glass disk substrates using an Anelva C3010 sputtering system. Anti-parallel coupled FeTaCoZr layers through thin Ru were used as a soft magnetic underlayer (SUL), and Ru was used as an intermediate layer. The granular layer was deposited by reactive sputtering of CoCrPt alloy targets doped with SiO2, TiO2, or a mixture of SiO2 and TiO2. The O2 partial pressure (PO2) was varied by adjusting the flow rate of Ar-10%O2 gas. A CoCrPtB cap layer was deposited onto the granular layer, and its thickness was varied from 3 to 5 nm as a way of controlling media write-ability.
Figure 1 shows the magnetic properties of the CoCrPt-oxide granular films as a function of PO2. For the media with SiO2 (CCPS), coercivity (Hc) and nucleation field (-Hn) increase as PO2 increases up to 2.3 Pa, while for media with TiO2 (CCPT), Hc and -Hn increase up to a PO2 of 1.7 Pa, and then decrease as PO2 increases further. CCPS media have a higher achievable Hc than that of CCPT media. Media with a mixture of SiO2 and TiO2 (CCPST) have a higher Hc especially at a low PO2 than that of the CCPS or CCPT media. The recording characteristics of the three types of media with various PO2 and cap layer thicknesses were evaluated with a wrap-around-shield head. The recording performance for a PO2 of 1.3 Pa was optimum for the CCPT and CCPST media, and the performance for a PO2 of 1.7 Pa was optimum for the CCPS media. These optimal PO2 values are slightly lower than the PO2 values at which the highest Hc was obtained. Figure 2 shows the recording characteristics at the optimal PO2 as a function of cap layer thickness. For all the media, the magnetic core width (MCW) increases as the cap layer thickness increases, and it is correlated with the change in Hc. The CCPST and CCPS media exhibit a higher SNR than the CCPT media. Considering that the high SNR of the CCPST media is obtained on narrower MCW conditions than the CCPS media, we believe that the CCPST media have greater potential for areal density growth than the CCPS media. We clarified the reason for the difference in recording characteristics by conducting TEM analysis. As shown in Fig. 3, the CCPS granular film has well isolated grains, while the CCPT granular film has non-uniformly separated grains. In addition, many sub-grains, which are consistent with the lower Hc, were observed. The degraded performance of the CCPT can be attributed to the inhomogeneous microstructures. The CCPST granular film appears to have narrower and more uniform grain boundaries than the CCPS and CCPT films. These microstructures would lead to higher packing density, which is one possible reason for the improved performance of the CCPST media. To further explain the recording results, we will present a detailed compositional analysis of grain cores and grain boundaries.

[1] T. Chiba et al., J. Magn. Magn. Mater. 287, 167 (2005)
[2] J. Ariake et al., IEEE Trans. Magn. 41, 3142 (2005)
[3] G. Choe et al., IEEE Trans. Magn. 42, 2327 (2006)

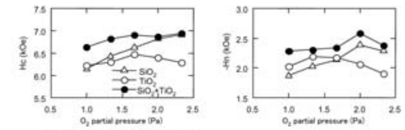

Fig. 1. Hc variation with O_2 partial pressure.

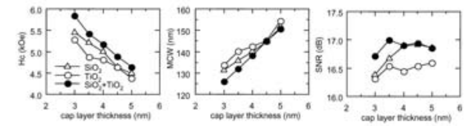

Fig. 2. Hc, MCW and media SNR variations with cap layer thickness.

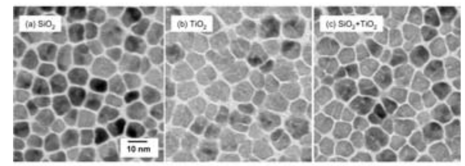

Fig. 3. Plan-view TEM images of CoCrPt-oxide films with (a) SiO_2, (b) TiO_2, and (c) a mixture of SiO_2 and TiO_2.

Investigation of high and low Mobility sputter conditions to enhance decoupling in oxide composite media.

H. Lee[1], S. Kong[2], H. Lee[2], H. Oh[2], V. W. Guo[1], J. Zhu[1], D. E. Laughlin[1]
1. Electrical and Computer Engineering, Carnegie Mellon University, Pittsburgh, PA; 2. Samsung Advanced Institute of Technology, Yongin-Si, South Korea

I. INTRODUCTION

Oxide composite perpendicular media has been shown to produce fine grains that are decoupled by oxide at the grain boundaries, leading to low noise performance in disk drive media. However, too large an increase in oxide content to decouple the grains can result in an interconnected or isolated network of magnetic volumes, rather than segregating completely to boundaries of columnar grains. In this work, we present an overview of our recent work on producing fine granular mixtures of magnetic media (either Co alloy or L10) and an oxide which acts to isolate the grains. Low and high mobility sputter conditions, which correspond to two very different regimes in Thornton's well-known film growth model [1], were investigated. High Ar pressure during deposition of recording layer was selected to achieve a well-separated film microstructure in the low mobility conditions whereas bias sputtering was utilized to modify a film microstructure in high mobility sputter conditions.

II. LOW MOBILITY SPUTTER CONDITIONS

In Fig. 1, a notable contrast in film morphology for different argon gas pressure is seen from the TEM micrographs of CoCrPt-SiO_2 media. A similar visual grain size of about 7 nm, however, much better defined SiO_2 on the thicker boundary was observed at higher Ar pressure. The magnetic measurements show that there is an optimum Ar pressure in order to have high squareness and negative nucleation (see Fig. 2). The CoCrPt-SiO_2 media fabricated with a high Ar pressure of 60 mT showed reduced squareness and positive nucleation field.

III. HIGH MOBILITY SPUTTER CONDITIONS

Another approach to enhancing this grain separation is to utilize bias sputtering [2]. One example (FePt-MgO) of bias-sputtered films where biasing aids in achieving decoupling is shown in Fig. 2. For unbiased FePt-MgO deposited at room temperature (RT), the length scale for the precipitation of oxide is 1-2 nm, and an interconnected network is seen, which is likely to produce a large switching volume. On the other hand, well-defined grains with boundaries are in evidence with biasing. See Fig. 3(b). There is no significant grain growth or coalescence in the biased films even at elevated temperatures of 400°C. Average grain size is 5 nm.

For CoCrPt-SiO_2 films, the grain size can be achieved by appropriate choices of sputtering pressure and substrate bias. The enhanced mobility of the adatoms by bias sputtering controlled the growth of the columar structure of the composite structure. The films were sputter-deposited at room temperature.

1) J. A. Thornton, "The microstructure of sputter-deposited coatings," J. Vac. Sci. Technol., A 4, 3059-3065, (1986).

2) H.-S. Lee, J. A. Bain, and D. E. Laughlin, Appl. Phys. Lett., 90, 252511, (2007).

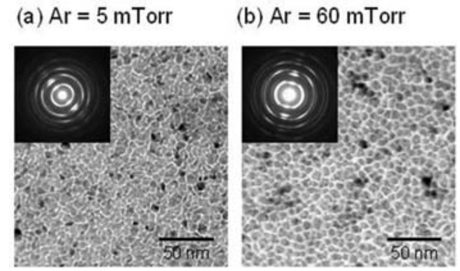

Fig.1. Plan-view TEM micrographs of CoCrPt-SiO_2 media for different Ar pressure.

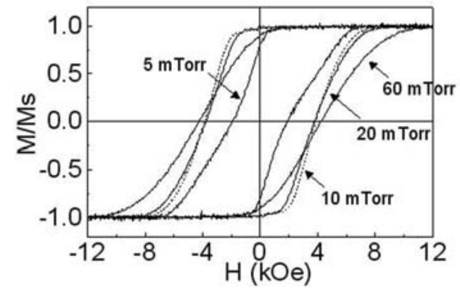

Fig. 2. Out-of-plane Hc as a function of Ar pressure.

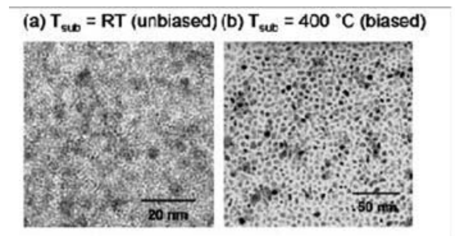

Fig. 3. Plan-view TEM micrographs of sputtered FePt-MgO media for different substrate temperature. Note the different scale bars.

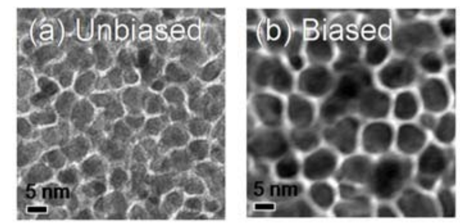

Fig. 4. Plan-view TEM micrographs of sputtered CoCrPt-SiO_2 media (unbiased and biased). Ar pressure and bias voltage were utilized to modify the film microstructure.

ED-07

High-Resolution TEM Analysis Of Perpendicular CoCrPt-SiO_2 Media.

R. Araki[1], Y. Takahashi[1], I. Takekuma[2], S. Narishige[2]
1. Central Research Laboratory, Hitachi Ltd., 1-280 Higashi-koigakubo Kokubunji-shi, Tokyo, Japan; 2. Central Research Laboratory, Hitachi Ltd., 2880 Kozu, Odawara, Kanagawa, Japan

Introduction For high-density perpendicular magnetic recording media, not only the grain size in a magnetic recording layer should be small, but also the grain boundary should be uniformly wide to reduce the medium noise [1]. As width of the grain boundary plays an important role in the exchange decoupling, it should be finely controlled. In this study, we have analyzed the relationship among the boundary width, the grain size, and the in-plane crystallographic orientation of grain in a CoCrPt-SiO_2 magnetic layer.

Experimental The media sample was analyzed and sputtered on a glass substrate at a room temperature was composed of the following layers: a CoTaZr soft magnetic one, seed ones, a Ru intermediate one, a CoCrPt-SiO_2 granular magnetic one and a protective one. The size structures and the crystal lattice directions of CoCrPt-SiO_2 grains were measured with a Hitachi HF-2000 high-resolution transmission electron microscope (TEM). The grain size was defined as the length of the dark contrast region on the line connecting between centroids of neighboring grains and the width of grain boundary was defined as the length of the bright contrast region. About 100 grains in a CoCrPt-SiO_2 layer were used to obtain the average values of grain size and of the grain boundary width. Although the grain size defined in this study was different from the diameter of a grain, we confirmed that the average and the dispersion of the grain size distribution was equivalent to the value defined by the conventional method. To analyze the correlation between the boundary width and the crystallographic orientation, the a-axis direction of each neighboring grain was measured.

Results and discussion A plan–view high–resolution TEM image of a CoCrPt–SiO_2 layer is shown in Fig.1. The average grain size and its dispersion were 7.5 nm and 18 %, respectively. The average width of the grain boundary was 0.68 nm. The dependency of the grain boundary width on the grain size in a CoCrPt–SiO_2 layer is shown in Fig. 2. We found that the grain boundary width increased with the grain size. This fact suggests that the inter-grain exchange coupling depends on the grain size. The a-axis direction is shown by a triangle-mark on each grain in Fig. 1. We defined the crystal grain cluster as a group of grains with an a-axis direction that ranged from 0 to 1 degree. A frequency histogram of the number of grains in a cluster is shown in Fig. 3. The dependency of the average width of grain boundaries on number of grain in a cluster (cluster size) is shown in Fig. 4. The grain boundary width tended to decrease as the cluster size increased.The dotted line shows the average of grain boundary width surrounding non-clustered grain. We also found that the grain size in a cluster decreased as the cluster size increased. These results suggest that the controlling of the size of a crystal grain cluster is a way to control the grain boundary width. To achieve a wider grain boundary for exchange decoupling, we need to reduce the size of the crystal grain cluster.

[1] I. Takekuma, et al., *J. Appl. Phys.*, 99, 08E713(2006)

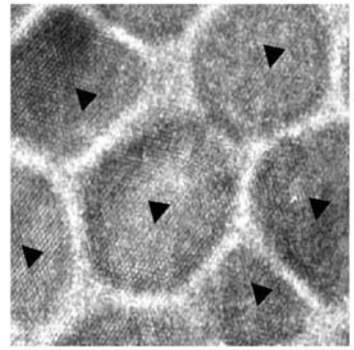

Fig. 1 High-resolution TEM image of CoCrPt-SiO_2 grains

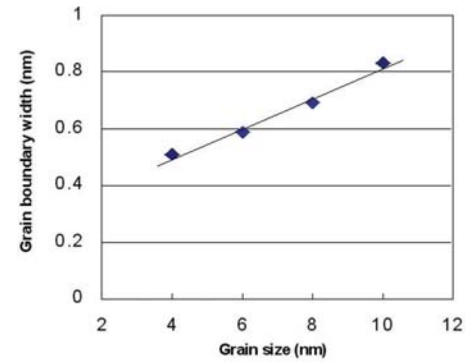

Fig. 2 Grain boundary width as function of grain size

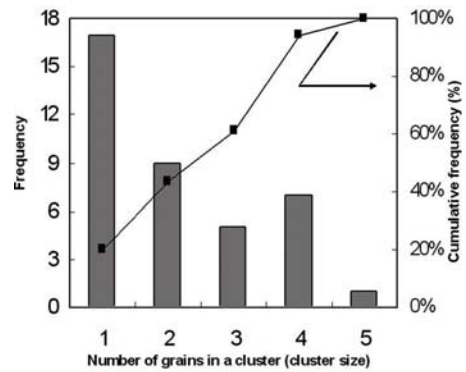

Fig. 3 Histogram of number of grains in cluster

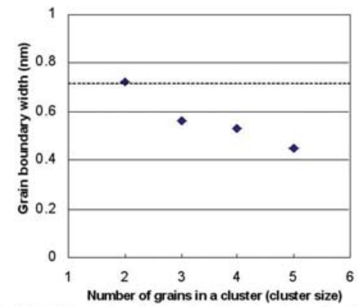

Fig. 4 Grain boundary width as function of number of grains in cluster

ED-08

Epitaxially grown FCC/BCC/HCP multi-underlayers for high performance perpendicular recording media.

G. Choe, X. Xu, K. Tang, X. Bian
Hitachi GST, San Jose, CA

Fabrication of a magnetically decoupled fine grain structure with high perpendicular anisotropy is necessary to achieve high density perpendicular recording. In a Co-alloy based recording layer that grows epitaxially onto a nonmagnetic underlayer, the nonmagnetic underlayer plays an important role in controlling the c-axis orientation of the Co crystals and the Co grain size and distribution. Ru underlayers with amorphous Ta [1] or crystalline Ni based seed layers [2] were reported to enhance the Ru and Co (0002) crystallography.

In this study, a new epitaxially grown FCC/BCC/HCP multi-underlayer structure is reported as a promising underlayer candidate to obtain well-isolated Co grains with good c-axis orientation. The multi-underlayers, consisting of FCC (111) Ni-alloy, BCC (110) Cr-alloy and HCP (0002) Ru layers, are grown epitaxially, resulting in preferred (0002) texture of Ru and Co grains, smooth surface morphology, excellent magnetic and read/write performance. Fig.1 shows a bright field cross sectional TEM view of a multi-layered media structure and a FFT of each layer component. As indicated by the FFT patterns, each underlayer grows in the perpendicular direction with the atomic plane of closest packing. A highly oriented Ru HCP <0002> c-axis is achieved through epitaxial growth onto the underlying Cr BCC (110) and Ni-alloy FCC (111) planes. The lattice matching of the Ni-alloy/Cr and Cr/Ru was analyzed by obtaining the FFT patterns (Fig.2) of enlarged HRTEM image at the interfaces. The lattice of the Ni-alloy layer matches well to that of Cr layer with ~0.3% lattice misfit ratio, while the lattice misfit ratio between Cr and Ru layers is relatively large at ~11%. The lattice parameter of Cr seemingly expands to the growth direction from 0.278 nm at Ni-alloy/Cr interface to 0.285 nm at the Cr/Ru interface.

The Co (0004) c-axis orientation dispersion was measured by XRD $\Delta\theta_{50}$ for bi-layered CoPtCr-SiO2/CoPtCrB recording layers deposited onto underlayers with varying thickness of Ni-alloy and Cr layers. The $\Delta\theta_{50}$ value sharply decreases with increasing Ni-alloy thickness for Ni-alloy(x nm)/Cr(9 nm)/Ru(11nm) and ~ 3 deg was achieved for Ni-alloy > 4nm thickness. For Ni-alloy(5nm)/Cr(x nm)/Ru(11nm) underlayers, an increase in the Cr layer thickness slightly improves the Co c-axis dispersion. Fig.3 shows the coercivity Hc of the recording layer as a function of Ni-alloy and Cr layer thicknesses. The Hc increases with increasing thickness of either Ni-alloy or Cr and appears to correlate well with the Co c-axis dispersion. Nucleation fields and saturation fields also increase with increasing Ni-alloy thickness and/or Cr thickness. Fig. 4 shows the change in signal-to-media noise ratio measured at two linear densities (457, 685 KFCI) with varying Cr thickness of Ni-alloy(5nm)/Cr(x nm)/Ru(11nm) underlayers. The SNRm continues to increase with increasing Cr thickness and the SNRm gain at thicker Cr layer is more obvious at higher linear density. The media jitter is significantly reduced with increasing Cr thickness. Improved recording performance is also achieved by optimizing head-to-SUL spacing with variation in each underlayer thickness.

[1] M. Zheng and G. Choe, US patent 7138196, [2] M. Shibamoto et. al., Intermag 2005 digest CQ-02

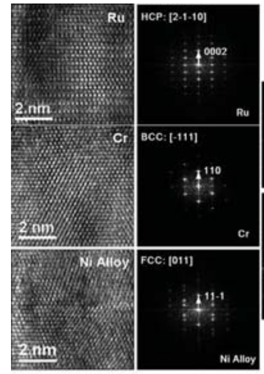

Fig.1 Cross-sectional TEM images of Ni-alloy / Cr / Ru multi-underlayer and FFT patterns

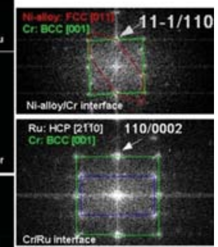

Fig.2 FFT patterns at Ni-alloy/Cr and Cr/Ru interfaces

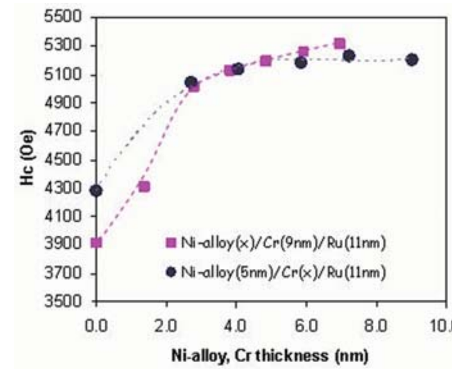

Fig.3 Change in Hc with increasing Ni-alloy or Cr layer thickness

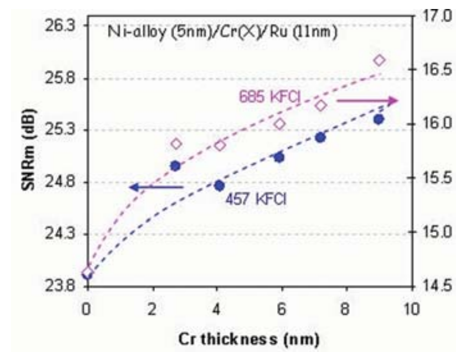

Fig.4 Change in SNRm with increasing Cr layer thickness in Ni-alloy(5nm)/Cr(x nm)/Ru(11nm) underlayer

ED-09

A General Method to Fabricate Exchange Coupled Composite Media with Graded Structure for Energy Assisted Magnetic Recording.

H. Zhao, H. Wang, J. Wang
ECE, University of Minnesota, Minneapolis, MN

Small and uniform grains and exchange-decoupling between grains in magnetic recording media are key requirements for high density magnetic recording. $L1_0$-FePt has been studied intensively as the future recording material. Unlike the current CoCrPt-type perpendicular recording media, preparation of $L1_0$-FePt media need either substrate heating or post-annealing to assist the $L1_0$-FePt phase formation, which is similar to that of the longitudinal recording media, but normally needs higher temperature (≥350°C). This difference, together with the intrinsic differences in material properties between FePt and CoPt alloys, demands innovative methods to achieve those key requirements, especially for exchange-coupled composite (ECC) media with graded structure (or so-called graded media).

In this paper, an atomic and nanoscale layer engineering process (capable for media production line) without involving post-annealing was proposed [1] and demonstrated to control grain size and grain isolation and to form the high-anisotropy phase at relatively low substrate temperature. As shown in Figure 1 (a), a particular underlayer that can generates small and uniform grains (e.g. RuAl) is deposited at first, and then followed by the multilayer consisting of alternating thin FePt layer and thin layer of grain boundary material. In this method, the underlayer (RuAl) serves as the template for columnar grain growth and therefore defines the grain size and size distribution of the whole recording media. A proper lattice misfit between (002) RuAl underlayer and the interlayer (e.g. Pt) above it provides a strain energy for the directly formation of L10 phase FePt at substrate temperature around 350°C or less. Grain isolation is achieved by surface diffusion of grain boundary materials (e.g. Ag, Cu) on top of previous FePt layer. Figure 1 (b) shows the typical structure for a FePt-type anisotropy graded media that can be made using this method. FM-M and FM-S are the ferromagnetic magnetic layers with medium and low anisotropy, respectively. FM-M and FM-S can be made from FePt with reduced process temperature to control the ordering of FePt (equivalently the anisotropy). The graded structure can also be achieved by varying the composition of FePt alloy in FM-M and FM-S layers. The key advantages of our proposed fabrication method for FePt media are: 1) clean interface for exchange-coupling control (especially for direct coupling between soft and hard region) in graded media structure with more than one magnetic region in grain vertically; 2) highly packed grains (in-plane) with narrow grain boundary – crucial for future energy assisted magnetic recording media.

Figure 2 shows the TEM plane-view, XRD spectrum and hysteresis loops of samples made with this method. Sample A shows typical grain size and size distribution, which is similar to that of the RuAl underlayer alone (not shown here). The FePt(001) peak in the XRD spectrum of sample B confirmed the existence of . $L1_0$-FePt phase. Anisotropy graded sample C (Glass\Ta(3nm)\AlO(5nm)\RuAl(20nm)\Pt(7nm)\[FePt(6nm)\Cu(2nm), 370°C] \. [FePt(2nm)\Cu(1nm), 200°C] \ [FePt(2nm)\Cu(1nm), <150°C]) was prepared by reducing the process temperature for the top two FePt layers. Figure 2 (c) shows the hysteresis loops of sample B and C. The coercivity of sample C was reduced significantly as expected. More details will be discussed in the full paper.

[1] H. Zhao and J. P. Wang, Information Storage Industry Consortium (INSIC) Quarterly Reports, 2006-2007

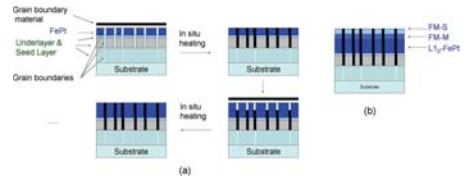

Figure 1. (a) The schematic drawing of the process for template-controlled and surface-diffusion-assisted grain isolation; (b) A typical structure of anisotropy graded media.

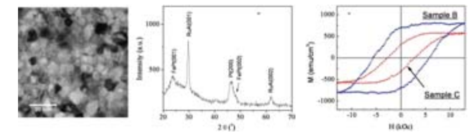

Figure 2. (a) TEM plane-view of sample A (Glass\RuAl(20nm)\Pt(1.3nm)\FePt(5nm)\Ag(1nm)\FePt(5nm)); (b) XRD spectra of sample B (Glass\Ta(3nm)\AlO(5nm)\RuAl(20nm)\Pt(8nm)\FePt(6nm)\Cu(2nm)); (c) Hysteresis loops of sample B ($L1_0$-FePt) and sample C (with graded anisotropy).

ED-10

Tuning pinning-site size of percolated perpendicular media (PPM) fabricated on pre-patterned substrates.

M. Rahman[1], C. Lai[1], D. Suess[2]
1. Materials Science and Engineering, National Tsing Hua University, Hsinchu, Taiwan; 2. Solid state physics, Vienna University of Technology, Vienna, Austria

<u>Introduction</u>

Recently, a new class of perpendicular media consisting of exchange coupled grains with non-magnetic pinning sites, termed as percolated perpendicular media (PPM), has been proposed theoretically for recording density of 1Tb/in^2 and beyond [1, 2]. Few experimental realization of PPM are also shown its promise in high density magnetic recording [3, 4].However, the ultimate success of PPM is limited by the control of pinning site size and density that is quite challenging.We have already reported the fabrication of PPM with wide range of pinning-site density [3]. Here, we demonstrate a simple method to fabricate pinning sites with a wide range of size from 5-30 nm and its effects on the magnetic properties of the Co/Pt mulitlayers (MLs). Furthermore, the thermal stability of such media is estimated by micromagnetic simulation.

<u>Experimental procedure</u>

At first, a thin Al film deposited on a Si wafer by sputtering is anodized to get porous alumina (AAO) with a density of ~ 1 x 10^{11}cm^{-2}. The pore diameter,*d* is tuned from 5- 30 nm by controlling the pore widening time at dilute phosphoric acid while the aspect ratio (pore height/diameter) is kept almost same at 5. Then {Co(0.5nm)/Pt(2nm)}5 MLs are deposited onto the porous AAO/Si by sputtering at room temperature.

<u>Results and discussion</u>

Fig.1 (a) – (d) show plane-view SEM images of Co/Pt MLs deposited on AAO with different pore diameters,*d*. The pores are clearly visible in all samples. The cross-sectional TEM image {inset of Fig.1 (b)} of sample with *d* of 10 nm reveals that the magnetic material is deposited mainly on the top of the pores. As a result, the Co/Pt MLs are percolated by columnar defects.

The media exhibit strong perpendicular magnetic anisotropy and negative nucleation fields as shown in Fig. 2 (a). As shown in Fig.2 (b), the out-of-plane coercivity, H_c of (Co/Pt) MLs increases from 140 Oe to 1300 Oe when it is deposited on AAO/Si with *d* of 5 nm. Then the H_c increases with increase in pore diameter and saturates at 1600 Oe for the *d* of 10-20 nm followed by a decrease for further increase in *d* to 30 nm. The variation of H_c as a function of pore diameter is due to the domain-wall pinning at the pores as evidenced by the initial magnetization curve shown in Fig. 2(a). The magnetization of initial curves for the all samples deposited on AAO irrespective of pore diameter, starts to increase when the applied field reaches a critical field to de-pin the domain walls. It can be concluded that the optimum pinning-site size for Co/Pt MLs is about 10-20 nm, which is 1 to 2 times of the domain wall width of the Co/Pt MLs. This result is good in agreement with the theoretically predicted optimum pinning site size for PPM[1].

We also investigate the switching behavior of the fabricated structures as shown in Fig. 2.c (I). Unlike the Stoner-Wohlfarth or domain-wall motion model, the switching fields, H_s of all samples deposited on AAO are quite insensitive to the angular variation from easy axis that may be beneficial to address the problem of adjacent track erasure. Micromagnetic simulation confirms that this kind of switching is due to the domain wall pinning at the pores as shown in Fig.2.c (I). Finally, thermal stability of a written bit in the proposed media with *d* of 10 nm is investigated using the nudged elastic band method as shown in Fig.2c (II). Fig.2c (II)-top shows the magnetization after applying the external field. After removing the field, the domain wall which separates the bit from the film moves towards the next pinning centers into a stable state S_1 shown in Fig.2c (II)-bottom. In order to de-pin the domain wall from the weakest pinning center of stable state S_1, an energy barrier of ΔE = 69 kBT300 has to be overcome. Thus, the investigated sample is thermally stable even though the H_c is small.

<u>Conclusion</u>

We introduced a simple and economic method to control pinning-site size over a wide range for percolated perpendicular media. Though the magnetic properties are shown for Co/Pt MLs, the approach is versatile to any magnetic materials to engineer the optimum pinning effect. Furthermore, the fabricated PPM is thermally stable and the angular insensitivity of H_s may ensure high signal-to-noise ratio.

[1]J.Zhu,and Y.Tang,IEEE Trans.Magn.43,687(2007).

[2]D.Suess, etal.,J.Appl.Phys.,99,08G905(2006).

[3]M.T.Rahman, etal.,Appl.Phys.Lett.91,131205(2007).

[4]D.E.Laughlin etal,IEEE Trans.Magn.43,693(2007).

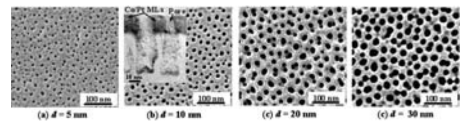

Fig.1. SEM plane-view images of Co/Pt MLs deposited on AAO with different pore diameters and TEM cross-sectional image with diameter of 10 nm (inset of 1.b).

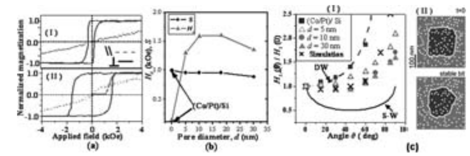

Fig.2. (a) M-H loop of (Co/Pt) MLs deposited on Si (I) and AAO with d of 10 nm (II), (b) Variation of H_c and S as a function of pore diameter and (c) Switching field, H_s as a function of angle θ between the applied field and the easy axis (I). The simulated H_s of the sample with *d* of 10 nm is also presented. (II) top: The reversed domain after applying an external field locally. bottom: Stable domain bit pattern pinned at the nonmagnetic defects.

ED-11

Effect of carbon cosputtering in the growth of ultra-thin FePt particulate films on oxidized Si substrates.

P. Alagarsamy[1], S. Tomoko[2], T. Yukiko K[1], K. Hono[1,2]
1. Magnetic Materials Center, National Institute for Materials Science, Tsukuba, Japan; 2. Graduate School of Pure and Applied Sciences, University of Tsukuba, Tsukuba, Japan

Granular-type L10 ordered equiatomic FePt alloy thin films are considered as one of the promising candidates for recording media with an areal density of Terabits/in2, since the large magnetocrystalline anisotropy (Ku) of this material provides a thermal stability of the FePt particles as small as 3 nm [1] For such large recording densities, the required lowest coercivity is 12–15 kOe and media thickness is below 5 nm [1]. The use of MgO single crystal substrates to obtain desirable properties in FePt films [2,3] is not suitable for practical applications because of their cost. In this work, we explore an appropriate way to obtain strong perpendicular anisotropy in FePt films using MgO polycrystalline underlayer that was sputter deposited on economically viable substrates such as glass or thermally oxidized Si wafer. To control magnetic isolation of particles, c-axis oriented L10 ordered FePt-C granular films were prepared by cosputtering FePt and carbon. The obtained properties are encouraging and desirable for the application of perpendicular recording.
FePt films of 1–10 nm and 3 nm thick FePt-C granular films were fabricated on thermally oxidized Si substrates with 10 nm MgO intermediate layers using sputtering with a base pressure of better than 10e-7 Pa and the sputtering Ar gas pressure of 10 mTorr. The MgO layer was deposited at a substrate temperature (Ts) of 100 oC by rf sputtering a MgO target. Subsequently, the FePt and FePt-C films were deposited at Ts=500 oC by dc sputtering a FePt target with carbon chips. The structure of the films was characterized by X-ray diffraction (XRD) patterns. The plan-view and cross sectional microstructures of the films were examined by Phillips CM200 and FEI Technai F30 transmission electron microscopes (TEM). Room-temperature magnetic properties of the films were investigated by a SQUID magnetometer with an applied field up to 55 kOe.
At first we carried out careful investigation of FePt(x nm)/MgO (10 nm) films with x=1,2,3,4,5,7, and 10 nm. The MgO underlayer has a polycrystalline nature with strong (200) texture. The FePt (1 nm) film has an average particle size of 4 nm and well separated from each other, but shows low degree of L10 order. With increasing FePt thickness up to 5 nm, the isolated FePt particles of 30 nm [Fig.1(a)] with a high degree of L10 order (~0.75) and large Ku (3.9×10e7 ergs/cc) was fabricated. The coalescence of the particles occurs at larger FePt thicknesses (> 5 nm) and eventually the particles are interconnected to form an island structure. In addition, we observed the development of randomly oriented FePt grains which leads to a rapid increase in in-plane coercivity with increasing FePt thickness. Perpendicular coercivity of the isolated FePt particles is controllable in the range from 15 to 20 kOe.
Fig.1 shows the plane view micrographs of FePt and FePt:C(4 %) films with 10 nm MgO(200) underlayer on oxidized Si substrate. The microstructures are found to be similar particulate structure for both films. However, the XRD results showed that the presence of fine FePt(111) reflection in the FePt film disappeared with carbon addition, indicating that the orientation of the FePt grains is controlled considerably. Room temperature M-H loops show that the remanence ratio increased from 90 % for the FePt film (Fig.2a) to 100 % for the FePt-C film (Fig.2b). Also, the tiny hysteresis loops observed in the in-plane loop is also reduced noticeably. This is because the small carbon addition helps to develop the strong (001) texture. In addition, the perpendicular coercivity increases from 21 kOe to 22.5 kOe for the low amount of carbon addition and decreases to 15 kOe for 30 % carbon content.

In summary, the carbon addition in ultrathin FePt particulate structure enhances the development of (001) texture of the grains. The obtained properties of FePt:C/MgO(10 nm) films deposited on economically viable substrates suggest that this system is promising to accomplish a magnetic recording medium capable of storage density beyond 1 Tb/in2, if a better method to obtain a finer monodisperse granular structure can be found.

[1]M.L. Plumer, J. van Ek, D. Weller, The Physics of Ultra-High-Density Magnetic Recording (Springer-Verlag Berlin Heidelberg 2001), Chap. 8, pp. 230.

[2]Z.L. Zao, J.S. Chen, J. Ding, Y.B. Yi, B.H. Liu, and J.P. Wang, Appl. Phys. Lett. 88, 052503 (2006).

[3]R. Maab, M. Weisheit, S. Fahler and L. Schultz, J. Appl. Phys. 100, 073910 (2006).

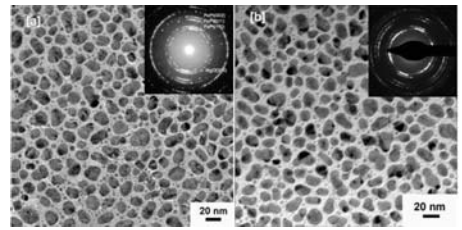

Fig.1. TEM bright field images and SAED patterns of 3 nm thick FePt:C(x vol.%)/MgO(10 nm) films with x=0 [a] and 4 [b].

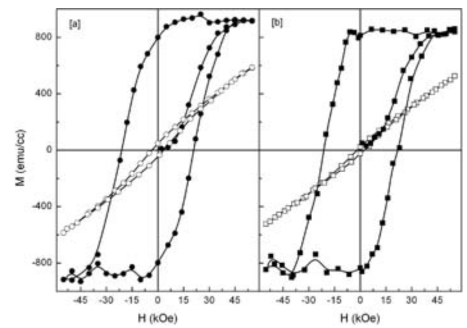

Fig. 2 Room temperature M-H loops of 3 nm thick FePt:C(x vol%)/MgO(10 nm) films with x=0 [a] and 4 [b] on oxidized Si substrate.

ED-12

Effect of carbon mixing on the perpendicular anisotropy of FePt thin film.

S. Lee, M. Kim, J. Park
Materials Science and Engineering, Korea Advanced Institute of Science and Technology, Daejeon, South Korea

The ordered (L10) FePt-based granular thin film has been known as a promising candidate for ultra high density magnetic recording media because of its high magnetocrystalline anisotropy energy. Numerous research efforts have been performed to fabricate FePt-based granular thin film showing a perpendicular magnetization and magnetically decoupled fine grain structure [1-5]. And it was shown that ordered (001) FePt films were, at elevated temperatures, easily growing epitaxially on (200) MgO single crystal substrate [1] to show a good perpendicular magnetization. However, the ordered (001) FePt films are prone to an excessive grain growth during elevated temperature deposition and are also susceptible to a strong magnetic coupling between grains leading to a low coercivity squareness. In order to solve these problems, we have studied the effect of the intercalation of carbon thin layer on the perpendicular magnetization of ordered FePt thin film on (200) MgO single crystal substrate. FePt film was DC-magnetron sputter-deposited on (200) MgO substrate at 600C using Pt chips placed on Fe target. Carbon was added to FePt film in a form of mutilayer of (FePt/C)4/FePt/MgO. The volume fraction of carbon was altered by varying the thickness of intercalated carbon film layer at a fixed thickness of FePt film layer. The measurement of the magnetic hysteresis curve using vibrating sample magnetometry showed that the FePt:C composite film showed a large perpendicular anisotropy. However, its magnitude was varying with the volume fraction of mixed carbon in FePt alloy (Figure 1), in agreement with the previous reports [2,5]. Unlike a general expectation, the result showed that the perpendicular coercivity was rather increasing with the carbon volume fraction before eventually decreasing at a large volume fraction, exhibiting a maximum at about 20 vol.% of carbon. This result was rather surprising in view of the fact that magnetic crystalline energy Ku was known to be continuously decreasing with the increase of carbon volume fraction [2]. In order to find out its reason, we have measured the variation of (001) FePt texture with carbon content using x-ray diffraction. The result showed that the variation of the intensity of ordered (001) peak was similar to the variation behavior of perpendicular coercivity with the carbon volume fraction, showing a maximum near about 20 vol.%. This was believed to be due to two factors, the enhancement of texturing and the increase of the ordering kinetics. The micromagnetic simulation using OOMMF was carried out to study the effect of texturing on the perpendicular coercivity. The comparison of simulation results on three different textures, (111), random, and perpendicular textures indicated that the perpendicular coercivity can be significantly enhanced as a result of perpendicular texturing. The ordering kinetics was believed to be increased not only because the intensity of (001) ordering peak was increased but also Ms was significantly reduced at 20 vol.% of carbon. The microstructure observation using TEM showed that the size of ordered FePt grains was greatly refined as a result of carbon mixing. More importantly however, the observation (Figure 2) showed that the FePt grains have begun to be completely encircled by amorphous carbon film at the carbon volume fraction of about 20 vol.%. Thus, the FePt grains became isolated from neighboring grains and became free from constraint due to transformation (disordering to ordering) strain. This will lead to a large increase of ordering kinetics. A further increase in the carbon volume fraction would slow down the ordering kinetics because of increasingly higher carbon supersaturation in the disordered phase.

The authors are grateful to the center for Nanostructured Materials Technology under the 21st Century Frontier R and D Program of the Ministry of Science and Technology, Korea, for the financial support of this research through Grant No 07K1501-01210

[1] J. U. Thiele, L. Folks, M. F. Toney, and D. K. Weller, J. Appl. Phys., vol. 84, p. 5686, 1998.

[2] A. Perumal, H. S. Ko, and S. C. Shin, IEEE Trans. Magn., vol. 39, p. 2320, 2003.

[3] T. Yang, E. Ahmad, and T. Suzuki, J. Appl. Phys., vol. 91, p. 6860, 2002.

[4] C. M. Kuo and P. C. Kuo., J. Appl. Phys., vol. 87, p. 419, 2000.

[5] M. L. Yan, R. F. Sabirianov, Y. F. Xu, X. Z. Li, and D. J. Sellmyer, IEEE Trans. Magn., vol. 40, p. 2470, 2004.

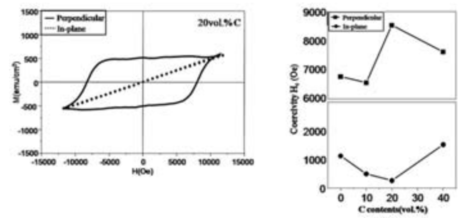

Figure 1. Magnetic hysteresis curve of FePt-20vol.%C and variation of perpendicular coercivity with the volume fraction of carbon.

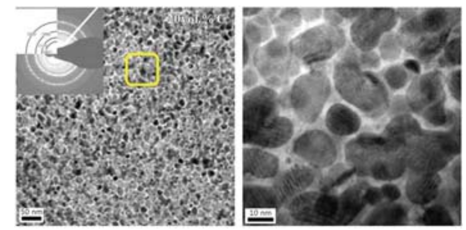

Figure 2. TEM image of FePt-20vol.%C film: (a) bright field image; (b) high resolution image of indicated area.

EE-01

Radio-frequency transverse susceptibility studies of effective magnetic anisotropy in nanoparticle assemblies.

H. Srikanth[1], P. Poddar[2,1], M. Morales[1], N. Frey[1]
1. Department of Physics, University of South Florida, Tampa, FL; 2. National Chemical Laboratory, Pune, India

Magnetic nanoparticles are considered basic building blocks of next generation spintronic devices as well as high density storage applications. Magnetism in nanoparticle assemblies and clusters is strongly influenced by particle shapes, intrinsic magnetocrystalline anisotropy, surfaces, interfaces and inter-particle dipolar interactions. It is often extremely difficult to decouple many of these effects from conventional experimental methods. Transverse susceptibility is an excellent tool for probing all these effects in nanoparticle assemblies. We use a very sensitive tunnel-diode oscillator (TDO) operating at 12-15MHz to measure the transverse susceptibility in different classes of ferrite nanoparticles. The main advantage of TS over conventional methods is that it uses singular point detection in directly measuring the most important parameters in magnetic materials such as the switching and anisotropy fields in a single experiment. We have established over the past few years that the TS method is very effective in studying anisotropy field distribution, inter-particle interactions and superparamagnetic relaxation that are inherent in nanoparticle aggregates [1-3]. Moreover, TS is versatile and could be applied to various geometries including thin films, multilayers and nanowires that form the basic components of spintronic devices.

Experimentally, in this technique both DC magnetic field H_{DC} (which can be varied) and a small perturbing AC field (H_{AC}) field from kHz to MHz range is applied. TS as a function of H_{DC} show two maxima at $\pm H_K$, which directly correspond to the anisotropy fields and are referred to as the anisotropy peaks. These peaks are highly sensitive to magnetocrystalline nature, particle size and shape distribution, as well as surface environment around particles, inter-particle interactions, and temperature.

An important problem in nanoparticle assemblies is to understand the influence of inter-particle dipolar/exchange interactions on the global magnetization as well as the effective magnetic anisotropy. To study the effect of varying strength of dipolar interaction on TS peaks in a reasonably controlled fashion, we used high quality, chemically synthesized, monodispersed manganese zinc ferrite (MZFO) nanoparticles as a model system and varied their concentration in paraffin wax matrix which is a non-magnetic host. The variation in coercivity, blocking characteristics as observed through DC susceptibility experiments were measured and compared with TS experiments. We were thus able to make a systematic study of the influence of interparticle interactions directly on the anisotropy peaks.

For magnetic property measurements, MZFO particles coated with excess surfactant and suspended in n-propanol were dispersed in varying concentrations in pure paraffin wax to alter the average interaction strength in a reasonably controlled manner with MZFO(conc) being the most concentrated dispersion resulting in the largest interactions. Samples labeled MZFO(50), 100 and 500 correspond to 50μl, 100μl and 500μl volume dispersion of nanoparticles in paraffin wax with MZFO(50) having the least contribution from dipolar interactions. The blocking temperatures for these samples varied from 27K to 32K as the concentration increases. The TS experiments were done using a sensitive RF coil that is part of a tunnel-diode oscillator with a resonant frequency around 12 MHz. The shift in resonant frequency is directly proportional to change in transverse susceptibility which can be monitored at varying fields and temperatures above and below the blocking transition. In the field-dependent TS data, two distinct peaks located at the anisotropy fields can be seen clearly at low temperatures in the blocked state. As the temperature is increased, when the system becomes superparamagnetic, the two TS peaks merge into a single peak centered at zero field. Our key result from TS studies on all the samples with varying interaction strengths is that the effective anisotropy fields (HK) increase with increasing interparticle interaction strength. Specifically, the HK values vary from 100 Oe for the most dilute sample to around 600 Oe for the most concentrated one. This large variation cannot be accounted for by the increase in blocking temperature alone or by taking a distribution of anisotropy fields. While the influence of interactions in nanoparticle assemblies have been investigated through DC and AC susceptibility experiments, our work reported here represents the first transverse susceptibility study that directly probes the influence of interactions on the effective anisotropy. We will also report on using transverse susceptibility as a probe of exchange bias in nanoparticles with enhanced surface spin disorder [4].
<p>
Work supported by NSF through grant CMMI 0728073

[1] L. Spinu, C. J. O'Connor and H. Srikanth, IEEE Trans. Magn. 37, 2188 (2001)

[2] P. Poddar, J. L. Wilson, H. Srikanth, D. Farrell and S. Majetich, Phys. Rev. B 68, 214409 (2003)

[3] P. Poddar, H. Srikanth, S. A. Morrison and E. E. Carpenter, J. Magn. Magn. Mater. 288C, 443 (2005)

[4] N. A. Frey, S. Srinath, H. Srikanth, C. Wang and S. Sun, IEEE Trans. Magn. 43, 3094 (2007)

Magnetic properties characterization of single IBICVD fabricated magnetic particles.

T. Suzuki, Y. Pogoryelov, A. Htoo
Information Storage Materials Laboratory, Toyota Technological Institute, Nagoya, Japan

Introduction

The research interest in nanoscale magnets is stipulated by their potential application for high-density recording media, so-called patterned media. The method of ion beam induced chemical vapor deposition (IBICVD), which was previously used to fabricate magnetic dot arrays of ferromagnetic (FM) materials [1-3], requires understanding of the physical processes, responsible for the magnetic properties of each low-dimensional particle in such arrays. In this view it is attractive to investigate magnetic behaviors of an isolated single particle fabricated by IBICVD in order to clarify the basic physics associated with size reduction. For these purposes the method based on the measurements of anomalous Hall effect, known for its high sensitivity [4-5], was selected to study magnetic properties of single FM particle (Fe).

Experiment, Results and Discussion

For experiment a 20 nm thick Pt cross electrode structure was fabricated through the specially designed mask in the e-beam deposition system onto glass and Si substrates. Then the intersection of the electrodes was further etched in the focused ion beam (FIB) system to form the electrodes of desired width. In this experiment the width of Pt electrodes was ~ 2 µm. A single particle of Fe was deposited by IBICVD to the center of electrodes intersection. An FIB system with liquid Ga ion source and equipped with three deposition nozzles was used for deposition. The base pressure of the deposition chamber was about 2×10^{-5} Pa. Precursors vapor pressure was controlled by heating nozzle during the deposition. All samples studied in this work were annealed at 600 °C for 5 hours before measurements. AHE measurements were performed on the improved setup at room temperature and the current I was set at 0.5 mA. Figure 1 shows the Hall loop for a single Fe particle (1.5 µm diameter and 700 nm thickness) for magnetic field applied perpendicular to the surface. The observed decrease of anomalous Hall voltage in the high-field region indicates the increase of the magnetization component along the in-plane direction. The asymmetry of the loop indicates the appearance of the contribution from the planar Hall effect [6]. This is presumably due to a misalignment of a particle structure with respect to the applied magnetic field direction. In order to check the existence of the inplane magnetization component measurements in the in-plane geometry were carried out by utilizing planar Hall effect (PHE). Results are presented in the inset of Fig. 1. The observed asymmetry is probably due to the slight deviation of the field direction from the sample plane. In that case the obtained loop is a combination of two effects – AHE and PHE [7]. These effects have different symmetries regarding to the applied magnetic field H [8]. Besides in order to confirm the effect of suppression of the perpendicular magnetization component by the in-plane one it is possible to utilize the characteristic property of the IBICVD method. The matter concerns the role of high energy Ga ions on the process of formation of a structure of single particle. As a result of the ion collision with the Fe metal-organic molecule the part of the momentum is transferred to the Fe atom after molecule decomposition. These will cause partial intermixing of the deposited Fe with the electrode material (Pt) and formation of some amount of FePt phase at the interface. It was possible to confirm these by studying the similar sample fabricated onto Si substrate. Hall effect studies of a single Fe particle on the sample with Si substrate showed the absence of perpendicular magnetization component (Fig. 2). Only component corresponding to the planar Hall effect was observed. Apparently due to the small thickness of the Pt electrode there also occurs partial implantation of Fe atoms into Si substrate with the formation of Fe-silicide. As it is known, such Fe-silicide possesses the in-plane magnetization [9], which possibly suppresses the perpendicular component in the detected signal.

The obtained results indicate the predominantly inplane orientation of the magnetization in the Fe particles fabricated by IBICVD. This is apparently determined by the formation of an appropriate material structure. Thus it was shown that the measurement method based on the anomalous Hall effect can be successfully applied for the studies of magnetic properties of single IBICVD fabricated particles and also for the indirect characterization of their structural features.

[1] A. Lapicki, E. Ahmad, and T. Suzuki, J. Magn. Magn. Mater. 240, 47 (2002).

[2] Q. Y. Xu, Y. Kageyama, and T. Suzuki, J. Appl. Phys. 97, 10K308 (2005).

[3] Ye. Pogoryelov, T. Suzuki, IEEE Trans. Magn. 43, 888 (2007).

[4] N. Kikuchi et al., J. Appl. Phys. Lett. 82, 4313 (2003).

[5] N. Kikuchi, R. Murillo, and J.C. Lodder, J. Appl. Phys. 97, 10J713 (2005).

[6] S. Das, H. Yoshikawa, S. Nakagawa, J. Appl. Phys. 93, 8098 (2003).

[7] S. Nakagawa, I. Sasaki, M. Naoe, J. Appl. Phys. 91, 8354 (2002).

[8] S. Haan, C. Lodder, and T.J.A. Popma, J. Magn. Soc. Jpn. 15, 349 (1991).

[9] Kläsges R. et al., Phys. Rev. B 56, 10801 (1997).

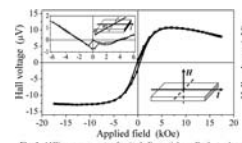

Fig. 1 AHE measurements of a single Fe particle on Pt electrode on glass substrate. Inset shows PHE measurement results.

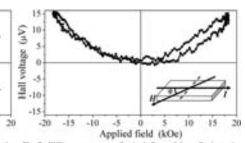

Fig. 2 PHE measurements of a single Fe particle on Pt electrode on Si substrate in the in-plane geometry.

EE-03

Ground states in ferromagnetic nanotubes.

P. Landeros, O. Suarez, A. Cuchillo, *P. Vargas*
Departamento de Física, Universidad Técnica Federico Santa María, Valparaiso, Chile

In this paper we present a theory to describe the magnetic ground states in ferromagnetic nanotubes. Our model enables us to investigate the size dependence of the ground states as a function of the tube geometrical parameters, by using a simple form characterizing the magnetic configuration. Geometrically, tubes are characterized by their external and internal radii, R and a respectively, and lenght L. It is convenient to define the ratio, β=a/R, so that β=0 is a solid cylinder and $\beta\rightarrow 1$ corresponds to a narrow tube. We adopt a simplified description of the system in which the discrete distribution of magnetic moments is replaced by a continuous one, defined by a function such that $\mathbf{M}(\mathbf{r})\delta v$ gives the total magnetic moment within the element of volume δv centered at point **r**. The total magnetic energy is composed by four contributions which are taken from the well known continuum theory of ferromagnetism. That is $E=E_x+E_d+E_K+E_z$ where E_x is the exchange energy, E_d is the dipolar contribution, E_K is the anisotropy energy and E_z is the Zeeman term. We then proceed to describe the magnetization of the mixed state which allow us to calculate the total energy of the system. The arrangement of magnetic moments in a tube [1-3] can be seen as a uniform state in the middle region of the tube, but with two deviations of the magnetization, like a incomplete vortex domain walls, located at the tube ends (see Fig. 1). We adopt a trial function for the magnetization with four minimizable parameters, where d and λ are the dimensions of the regions where the magnetization deviate from the z-axis. θ_0 and θ_L correspond to angles of the magnetization with the z-axis, evaluated at the tube ends. This set of model parameters enable us to investigate in detail the magnetic properties as a function of the geometrical parameters (R, β and L). The model parameters are such that they minimize the total energy for each set of geometrical parameters. It is worth to mention that the variational problem with four parameters can be simplified considerably if the tube is symmetric, that is, if there is no difference between both tube ends. Therefore, in some special cases, the four parameters model is reduced to a two parameters model, when d=λ and $\theta_0=\theta_L$. If we know the magnetization vector and the geometry of the ferromagnetic body, we can obtain the total energy, E, of a magnetic nanotube in the mixed state. With the energy expression it is easy to demonstrate that the uniform magnetization state is achieved when the cylinder radius is small enough, and that the mixed state configuration dominates for a wide selection of geometrical parameters. On the other hand the d parameter, half width of the domain wall, increases up to its maximum value d=L/2 when the vortex state is the ground state configuration. These results are shown in Figure 2.

If we only consider the Uniform (F) and Vortex (V) states, it has been shown recently [3] that the phase diagram depends on the topological form factor β. The critical line ($E^F = E^V$) that separates magnetic phases Ferro and Vortex (F and V) follows a very simple equation. Thus, to the left (right) of this curve we have $E^F < E^V$ ($E^F > E^V$)[3]. However, if we evaluate the energy of the mixed state in the symmetric case (d=λ and $\theta_0=\theta_L$) we find that the mixed states have lower energy than the two main states (F and V) over a wide range of geometrical parameters.

The phase diagram in the R-L plane contains three regions corresponding to the three ground states, as shown in Figure 3.

[1] Jehyun Lee et al., J. Magn. Magn. Mater. 310, 2445-2447 (2007).

[2] A.P. Chen et al., J. Magn. Magn. Mater. 316, e317-e319 (2007).

[3] J. Escrig et al., J. Magn. Magn. Mater. 308, 233-237 (2007).

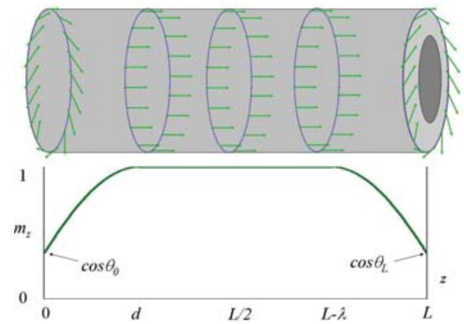

Mixed state in magnetic nanotubes. In the middle region the magnetization is uniform, and in the ends we have incomplete vortex domain walls.

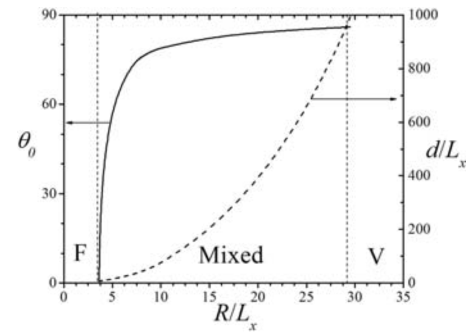

θ_0 and d as a function of R for a tube with β=0.5 and L=2000L_x

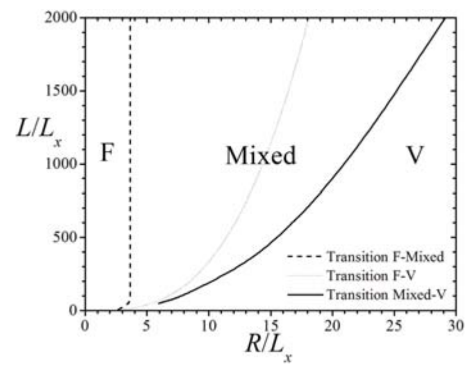

Magnetic phase diagram of independent ferromagnetic nanotubes with β=0.5.

EE-04

A study of the magnetic behavior of Ni/Cu multilayer nanowire arrays, using FORC diagrams.

F. Beron, L. Carignan, D. Menard, A. Yelon
Génie physique, École Polytechnique de Montréal, Montréal, QC, Canada

Multilayer nanowire arrays (alternation of ferromagnetic (FM) and non-ferromagnetic (NF) discs along a nanowire) are promising nanostructures, especially for the use of giant magnetoresistance (GMR) with current perpendicular to the plane (CPP). Their magnetic behavior depends upon a number of factors: nanowire diameter, length and interwire distance, disc thickness, ferromagnetic material, etc. The first-order reversal curve (FORC) method is an effective way to study and distinguish their magnetic behavior. With a standard magnetometer, it allows us to obtain information about the magnetization reversal of the magnetic entities.
A set of first-order reversal curves consists of several minor hysteresis curves beginning at different reversal fields H_r, the FORC distribution ρ is then calculated by applying a second-order mixed derivative of magnetization.[1] Using extrapolated FORC diagrams permits us to obtain only the signal coming from irreversible processes, while the reversibility percentage can be calculated from the slope of the first-order reversal curves at H_r.[2] The position of the peak of the distribution on the H_c axis (H_c^{FORC}) is related to the coercive field of the nanodiscs.[3]
Arrays of Ni/Cu multilayer nanowires were fabricated by electrodeposition into an alumina template (diameter = 175 nm), with Ni disc thickness between 20 and 50 nm, and Cu thickness between 10 and 35 nm.[4] Vector major hysteresis loops were measured both with out-of-plane (along the nanowire axis) and in-plane (perpendicular to the nanowire axis) applied field. During the magnetization reversal, we observed no net component of transverse magnetization (M_y), perpendicular to the applied field H_x. Extrapolated FORC diagrams were measured out-of-plane (Fig. 1) and in-plane (Fig. 2). While the major hysteresis loops of all arrays have similar shapes, their FORC diagrams reveal distinct patterns, suggesting different magnetic behavior.
In the out-of-plane direction, H_c^{FORC} values from multilayer nanowires (between 200 and 250 Oe) are considerably lower than the theoretical coercive field of an isolated nanodisc and the reversibility percentage increases with the thickness of Cu. We assume that this is caused by a small rotation followed by a spin flip magnetization reversal in the nanodiscs. This behavior is favored by the in-plane component of the interaction field due to the dipolar interactions between the discs in a nanowire. From the null M_y component of the vector plots, it is not possible to discriminate between a reversal by spin flip only, and an alternative rotation toward y-direction from disc to disc before the flip. The high H_c "tail" of the FORC distributions (Figs 1 b-c) is assumed to derive from some nanodiscs not subject to any in-plane field, such as those located at the extremities of the sample and the nanowires.
The interaction field in the nanowire axis direction depends predominantly on the FM thickness. We can see on the FORC diagrams that when the Ni thickness decreases, the elongation along the H_u axis, as well as the flatness of the H_u cross-section top, also decreases. These features are related to the maximum value and the distribution of interaction fields felt by the nanodiscs.[3] The central peak in the FORC distribution represents nanodiscs that are not subject to an out-of-plane interaction field.
In the in-plane direction, the FORC diagram shape can be explained by the creation and annihilation of vortices in the nanodiscs, which is theoretically predicted to be the predominant magnetic behavior for an isolated disc, especially when the disc thickness is large. We assume that the nanodisc distributions of thickness and diameter in the nanowire arrays disperse and widen the characteristic FORC distribution of the creation and annihilation of a vortex (i.e. two sharp peaks located at (H_c, H_u) and (H_c, -H_u), and a broad one around (H_c+H_u, 0)). We believe that the single peak visible on the experimental FORC diagrams (Fig. 2) is due to the small H_u values, which favor the convolution of these peaks in the numerical calculation. The presence of vortices in the nanodiscs is consistent with no M_y signal in the vector plots, because the magnetization perpendicular to the vortices in one direction is compensated by the vortices in the opposite direction.
The FORC diagrams of nanowire arrays with small spacer thicknesses exhibit some "wings" around the peak (Figs 2 a,c). They are thought to come from the antiparallel interaction field created by the dipolar interaction of a nanodisc with its neighbors along the nanowire.[4]

[1] C.R. Pike *et al.*, JAP **85**, 6660 (1999).

[2] F. Béron *et al.*, JAP **101**, 09J107 (2007).

[3] F. Béron *et al.*, J. Nanosci. Nanotechnol. **8**, in press (2008).

[4] L.-P. Carignan *et al.*, JAP **102**, 23905 (2007).

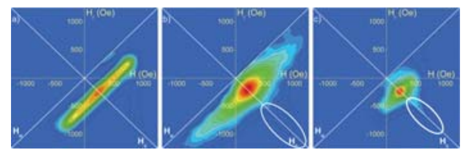

Figure 1 : Extrapolated out-of-plane FORC diagrams. t_{Ni}/t_{Cu} = a) 50/15 nm b) 30/35 nm c) 20/10 nm. The distribution "tails" are encircled.

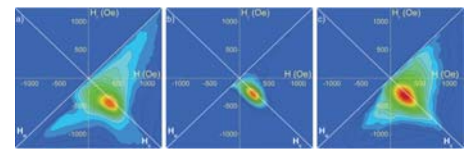

Figure 2 : Extrapolated in-plane FORC diagrams. t_{Ni}/t_{Cu} = a) 50/15 nm b) 30/35 nm c) 20/10 nm.

EE-05

Magnetic properties of metal/silicon nanocomposites tailored by specific metal precipitation.

P. Granitzer, K. Rumpf, H. Krenn
Institute of Physics, Karl Franzens University Graz, Graz, Austria

Summary:
Porous silicon (PS) is used as template for electrochemical deposition of distinct metals. The precipitation of different ferromagnetic metals (e.g. Ni, Co) under various process parameters leads to nanocomposites consisting of 3-D arrays of metal-structures embedded in the PS-templates. These arrays are tunable in their structure by the electrochemical parameters and due to the fact that the magnetic characteristics depend on the geometry and distribution of the incorporated metal it is possible to fabricate desired ferromagnetic nanocomposites with specific characteristics like coercivity, squareness or magnetic anisotropy.

Experiments and discussion:
PS-templates of different morphologies (pore-diameter adjustable between 30 nm and 100 nm, length up to 50µm) are filled by a pulsed galvanic process with Ni or Co. The geometry (spheres, ellipsoides, wires) of the embedded metal-structures and their spatial distribution within the pores is tunable by the fabrication parameters (deposition current density, pulse duration). Thus samples with specific magnetic characteristics (coercivity, squareness, magnetic anisotropy) can be prepared. In case of Ni the magnetocrystalline anisotropy is small (anisotropy constant K = -0.005 MJ/m3) and moreover the precipitations exhibit random orientation leading to a cancellation of the crystal orientations resulting in a dominantion of the shape anisotropy. The coercivity HC is always smaller for PS-membranes with a high amount of embedded Ni-wires than for those with preferentially deposited particles shown in fig. 1 for various temperatures. In both cases (wires, particles) HC shows a tempartyre dependence which follows an exponential law contradictory to some literature [1] where a linear relation is assumed.
Considering ZFC/FC (zero field/field cooled) measurements the broadness of the ZFC-curve of a sample containing mainly ellipsoidal Ni-particles (< 200 nm) depends on the size distribution as well as on the density of the spatial distribution of the particles which means on their interaction (fig 2a). Samples with metal wires (length of a few micrometers) show a gently increasing ZFC-magnetization and a flat FC-curve(fig 2b). Both indicate a strong dipolar coupling of the embedded nanostructures.
At typical pore-diameters of 60 nm Co tends more to precipitate as particles than Ni does and up to now the maximum length of the Co precipitations is 200 nm (Ni up to a few micrometers). Therefore Co-filled PS-membranes offer less magnetic anisotropy (below 10%) between easy axis and hard axis magnetization mainly due to the shape of the spherical and ellipsoidal particles (the greater magnetocrystallin anisotropy of Co: K = 0.53 MJ/m3 does not effect because it is averaged out due to random orientation of the precipitations). In contrast to Ni-particles the temperature dependence of the coercivity of Co-particles do not show a continous exponential curve. Between 4.2 K (HC = 500 Oe) and 100 K (HC = 470 Oe) the coercivity HC is nearly constant, whereas from 100 K to 250 K (HC = 260 Oe) the coercive field reduces almost of 50%.

Conclusion:
The fabrication of PS-templates with desired pore-arrangements and subsequent metal filling (Ni, Co) of the channels by a galvanic process leading to tailored precipitations yields to ferro-magnetic nanocomposites with tunable magnetic characteristics. The use of silicon as base ma-terial is of interest not only due to the capability of applications in today's micro and nanotech-nology but also because of the biodegradability of porous silicon in the human body which of-fers potential in medical and biological applications like destroying of tumor cells (hyperthermia).

[1] S. Wirth, M. Field, D. D. Awschalom, S. von Molnar, Phys. Rev. B 57, 14028, (1998).

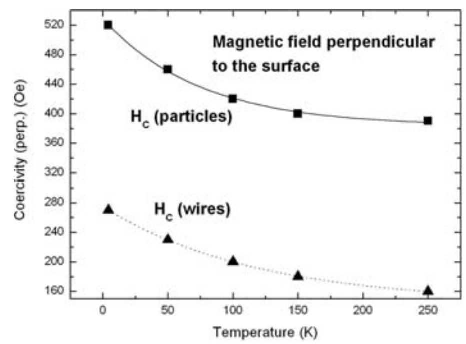

Figure1:Temperature dependence of HC of a specimen with preferentially embedded Ni-wires and of another one with mainly Ni-particles, respectively.

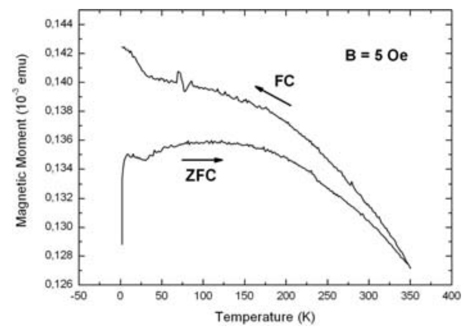

Figure2a:ZFC/FC magnetization curves of preferentially embedded Ni-particles (max. length 200 nm, diameter ~ 60 nm).

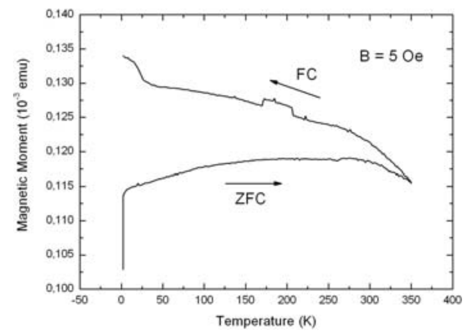

Figure2b:ZFC/FC magnetization curves of PS-template containing mainly Ni-wires (length about 2 µm, diameter ~ 60 nm).

EE-06

Polymer nanocomposites with embedded Cobalt nanoparticles.

S. N. Kale[1], S. H. Hatamie[1], S. D. Kulkarni[2]
1. Department of Electronics-Science, Fergusson College, Pune, India; 2. Centre for Materials Characterization, National Chemical Laboratory, Pune, India

In the last decade, one of the most interesting categories of materials which have been explored in their nanodomain are the magnetic materials. This is because of their potential applications in nanotechnology, typically in memory devices, nanomedicine, medical instrumentation and also in the novel area of Spintronics. A more focused area of magnetic nanomaterials is the polymer-embedded magnetic nanoparticles. Such configurations find applications as magnetic fillers (nanocomposite materials), electromagnetic device applications like electromagnetic interference suppression and in biomedicine as MRI contrast agents. Magnetic nanoparticles embedded in the polymer matrices are also providing a lot of new information about critical phenomena in the underlying structures [1-2]. In addition, such materials have made important contributions to fundamental studies in nanoscale physics such as quantum tunneling of magnetization, spin reversal mechanisms in single-domain particles and quantum size effects [3-4].
Out of many magnetic systems, including Fe-oxides, perovskite manganites, Nickel, Manganese, Cobalt is one interesting material which can be harnessed for variety of applications mentioned above [5]. Though Co exhibits ferromagnetism at room temperature, it has been less explored in nanoregime due to its rapid oxide formation, which is rather easy during the coating mechanism. The key requirement here is to develop a processing technique based on the idea of the encapsulation of the Co nanoparticles in an inert atmosphere to form a non-agglomerated and stable coating layer.
In this context we have synthesized Cobalt nanoparticles using wet chemistry route. Whole procedure is done in vacuum to ensure that there is no oxide formation. Using a combination of ultrasonication and vacuum drying Co nanoparticles were embedded in a matrix of Poly-Vinyl Alcohol (PVA). The processing conditions were optimized to achieve good uniform dispersion of the nanoparticles in the polymer matrix. The concentration and dispersion of nanoparticles were varied in a controlled way to yield self-supporting, flexible films. The films have been characterized and compared with bare nanoparticles using X-Ray Diffraction (XRD) technique, Vibrating Sample Magnetometry (VSM) and Transmission Electron Microscopy (TEM). Typical Co nanostructures show particle size ~ 20 nm using XRD and TEM data. VSM analysis show increased coercivity of the films (260 Oe) as compared to Co nanoparticles (120 Oe) at room temperature. As is known, magnetic nanoparticles precipitated from solution tend to aggregate thereby exhibiting larger cluster size. However, in the polymer matrix, inter-particle separation was seen to improve, which is also reflected in VSM results. In isolation these particles are envisaged to be single domain, thereby showing increased coercivity. The results have been understood on the basis of dipolar interactions and their influence on magnetic properties. Overall, the excellent dispersion coupled with reasonable control over magnetic properties achieved in our experiments is promising for electromagnetic applications of these materials.

[1] Yu. A. Koksharov, S. P. Gubin, I. D. Kosobudsky, G. Yu. Yurkov, D. A. Pankratov, L. A. Ponomarenko, M. G. Mikheev, M. Beltran, Y. Khodorkovsky and A. M. Tishin, Phys. Rev. B 63 (2000) 012407.

[2] E. Troc, A. Ezzir, R. Cherkaoui, C. Chaneac, M. Nogues, H. Kachkachi, D. Fiorani, A. M. Testa, J. M. Greneche and J. P. Jolivet, J. Magn. Magn. Mat. 221 (2000) 63.

[3] X.X. Zhang, J.M. Hernadez and J. Tejeda, Phys. Rev. B 54 (1996) 1.

[4] D.D. Awschalom, D.P. DiVincenzo and J.F. Smyth, Science 258 (1992) 414

[5] S.J. Lee, J.R. Jeong, S.C. Shin, J. C. Kim, Y. H. Chang, Y. M. Chang, J. D. Kim J. Magn. Mag. Mater. 272 (2004) 2432

EE-07

Temperature Dependence of Magnetic Correlations within a Magnetite Nanoparticle Assembly.

K. Krycka[1], C. Hogg[2], Y. Ijiri[3], R. Booth[2], J. Borchers[1], W. Chen[1], M. Laver[1], T. Gentile[1], B. Maranville[1], B. Breslauer[3], S. Majetich[2]
1. NIST Center for Neutron Research, Gaithersburg, MD; 2. Carnegie Mellon University, Pittsburgh, PA; 3. Oberlin College, Oberlin, OH

Single domain nanoparticles are of prominent interest for biomedical and data storage applications, as well as a means to directly probe the magnetization dynamics of interparticle correlations. Our samples are polycrystals of ferromagnetic monodisperse 7 nm diameter magnetite nanoparticles with an average edge-to-edge separation of 2.5 nm. They have blocking temperature below room temperature and strong interparticle magnetic correlations. Preparation techniques are described elsewhere [1]. Using small angle neutron scattering (SANS) we have examined these nanoparticles in order to determine the temperature dependence of their magnetic interparticle correlations. SANS is a technique well suited for nanoparticles because it covers length scales from single particles up to long-range correlations and probes a whole ensemble at once. Both of these features are absent when using local probes such as TEM.

While a typical magnetic SANS experiment observes the convolution of nuclear and magnetic scattering terms which cannot be uniquely resolved, we have used polarization analysis in order to provide an unambiguous separation and independent measurement of magnetic and nuclear contributions. An FeSi supermirror array was used to polarize the incident neutrons, while a polarized 3He cell was used as a spin analyzer with coverage over the entire angular range of the scattered beam. Polarization efficiencies range from 0.75 to 0.88. Using the formalism of Moon, Riste, and Koehler [2] we have implemented and further developed an algorithm to extract all four polarization-corrected spin scattering cross-sections (i.e. ↑↑,↑↓,↓↓, and ↓↑). The polarization analysis was conducted on a pixel-by-pixel basis from position sensitive detector scans, and it reproduces the corrected spin dependent scattering in 2D. Additionally, the 3He polarization decays during the period of data collection so we have also explicitly included its time dependence within our algorithm. Using a transmission geometry, the direction of the incident beam is denoted the x-axis, while the z-axis corresponds to the perpendicular neutron polarization axis. Here ↑↑ and ↓↓ (non-spin flip) corrected cross-sections along Qz provide nuclear information, while ↑↓ and ↓↑ (spin flip) cross-sections also along Qz yield information about pure magnetic moments oriented along the x and y axes. ↑↓ and ↓↑ cross-sections along Qy, however, give information about magnetism oriented along only the x-axis. Finally, magnetic scattering along the third direction, z-axis, may be obtained from (↑↑+↓↓)_Qy - (↑↑+↓↓)_Qz. Assuming that magnetic scattering is nearly isotropic in the absence of an applied magnetic field, the scattering from the combined x and y directions should be twice as much from either the x direction or the z direction. This is observed experimentally and displayed in Figure 1 at 50 K (same trends also observed for 100, 200, and 300 K). The inset taken at 300 K shows a pronounced peak at 0.085 inverse angstroms consistent with the interparticle spacing.

Within the framework outlined above, we can isolate and probe directly the magnetic evolution of interparticle correlations with temperature. Figure 2 illustrates that the magnetic correlation lengths change not only at the bulk magnetic blocking temperature of 65 K, but substantially vary up to 300 K. The curling over feature near low Q indicates a loss of long range magnetic correlations with increasing temperature. The inset shows that the corresponding nuclear scattering does not significantly vary, as expected. Additionally, at all temperatures saturation from an applied field of 1.3 Tesla (not shown) shifts the magnetic scattering to longer length scales and lower Q than was observable in our current set-up.

Unpolarized SANS (not shown) shows a similar temperature dependent reduction in the low Q combined nuclear plus magnetic scattering. As with the polarized data, this demonstrates a decrease in the long-range magnetic correlations with increasing temperature. Further decrease upon application of a saturating magnetic field indicates that even at the highest temperature (300 K) long range magnetic correlations are non-negligible. While the polarized and unpolarized data are in agreement, the interpretation of polarized SANS is more straightforward.

[1] J. Am. Chem. Soc. 2002, 124, 8204-8205.

[2] Phys. Rev. 1969, 181, 920-931.

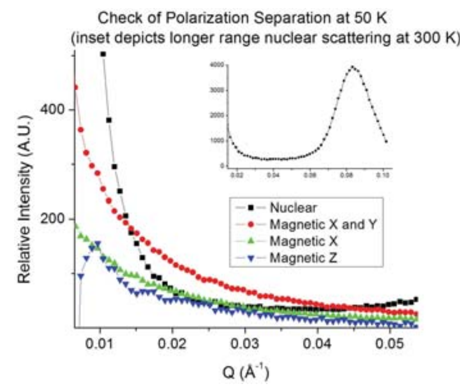

Figure 1

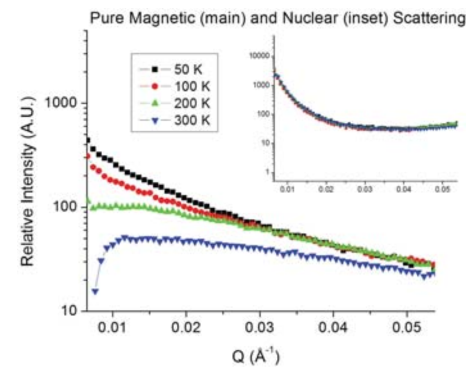

Figure 2

EE-08

First-order Magnetic Phase Transition in Manganese Phosphide Nanorods.

R. Booth, *S. Majetich*
Physics Department, Carnegie Mellon University, Pittsburgh, PA

Manganese phosphide is an interesting material to investigate in nanoparticle form because it has a Curie point near room temperature. In most of the commonly studied nanoparticle materials, such as Co, Fe, and iron oxide, the blocking temperature where the particle moments decouple is well below the Curie temperature where the atomic moments disorder. In MnP there is a first order ferromagnetic-to-paramagnetic phase transition near room temperature associated with a concurrent hexagonal to orthorhombic structural phase transition. MnP is also an interesting material for the study of nanoparticle interactions because it has a sizeable saturation magnetization (636 emu/cc at low temperature, greater than that of Ni). The strength of the magnetostatic interactions between nanoparticles can therefore be tuned over a wide range with small changes in the sample temperature.

MnP nanoparticles were synthesized by high temperature solution chemistry methods [1, 2]. Comparison samples of bulk MnP were prepared by arc melting mixtures of elemental powders. Transmission electron microscopy images of the nanorods as-synthesized show a broad and bimodal size distribution (Figure 1). There are large numbers of small nanorods 15 nm in length or shorter, plus larger nanorods with typical dimensions of ~ 60 nm length and ~20 nm width. The large and small nanorod fractions can be separated by size-selective precipitation.

Small, spherical MnP nanoparticles (< 8 nm) have blocking temperatures below 100 K [1], and are therefore become superparamagnetic long before they reach the Curie temperature, which is 291 K for the bulk alloy. In contrast, the field-cooled magnetization of nanorod samples shows an abrupt drop in the magnetization just below room temperature (Figure 2). The zero field-cooled (ZFC) magnetization is sharply peaked at this temperature. With a blocking transition the ZFC peak is usually much broader and varies with particle size. In the MnP nanorods. We associate the peak near 280 K with the Curie temperature of the nanorods. This is confirmed by magnetization curves as a function of the applied field.

Because the MnP nanoparticles have a first-order magnetic phase transition near room temperature, there is a large change in magnetic entropy in this range. Ball-milled MnFePAs [3] showed large values of magnetic entropy due to an analogous phase transition, but this required a large applied field and the behavior was less than optimal due to irreversible magnetic losses. Melt-spun MnFePGe ribbons [4] also show significant irreversible losses. Nanocomposite materials have the advantage of reduced saturation fields, and with good structural order the irreversible losses may be less than those for ball-milled materials. Magnetic entropy and irreversible losses for bulk, large, and small nanorod samples near their Curie temperature.

1. J. Park. B/ Koo, K. Y. Yoon, Y. Hwang, M. Kang, J.-G. Park, and T. Hyeon, J. Am. Chem. Soc. 127, 8433 (2005).

2. K. A. Gregg, S. C. Perera, G. Lawes, S. Shinozaki, and S. L. Brock, Chem. Mater. 18, 879 (2006).

3. O. Tegus, E. Brück, K. H. J. Buschow, and F. R. de Boer, Nature 415, 150-152 (2002).

4. A. Yan, K.-H. Mueller, L. Schultz, and O. Gutfleisch, J. Appl. Phys. 99, 08K903 (2006).

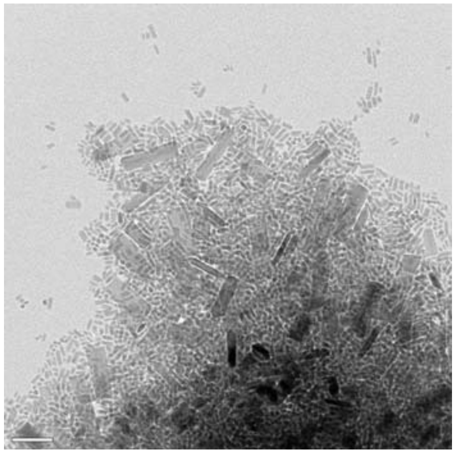

Figure. 1. (a) TEM image of MnP nanorods prior to size selective precipitation.

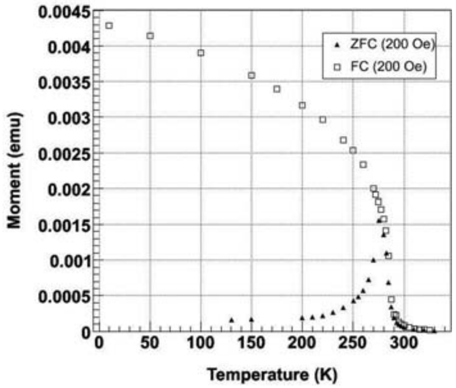

Fig. 2. Field-cooled and zero field-cooled magnetization of chemically synthesized MnP nanoparticles showing a phase transition near 280 K.

Self-assembly Nanoscale Triangular Shaped Fe64Ni36 Dot Arrays.

D. Niu[1], X. Zou[2], J. Wu[2], Y. Xu[1]
1. Spintronics and Nanodevice Laboratory, Department of Electronics, The University of York, York, United Kingdom; 2. Department of Physics, University of York, York, United Kingdom

Self-assembly fabrication techniques such as nanosphere lithography (NSL) have attracted much interest because of their low cost and high throughput. The challenge is to fabricate large area and well defined structures with feature sizes approaching the superparamagnetic limit.
In this paper, we report the fabrication and magnetic properties of FeNi dot arrays with ultrafine, large-area, well-ordered periodic nanostructures fabricated on silicon substrate by nanosphere lithography (NSL). We have achieved well-defined triangular shaped dots with lateral size of about 30nm (as shown in Fig.1) with the thickness of 10nm. The composition of the elements was determined by Nano EDAX. The ordered magnetic dot arrays have a large enough uniform area for magneto-optic Kerr effect (MOKE) measurements.
The hysteresis loop of the triangular shaped Fe64Ni36 dot arrays were achieved at room temperature by focused MOKE, as shown in the figure 2. The MOKE loops from the continuous thin films have also been measured to compare the magnetic properties of both the dot arrays and the thin film. The coercivity Hc of the dot arrays was found to increases to approximately 200Oe while the Hc of continuous thin film is around 50 Oe. This may be due to the fact that in the continuous films the coercivity is controlled by the nucleation and depinning of domain wall, and in the nanoscale structures by magnetization rotation as the exchange energy is too high to form domain wall.
To gain an insight into magnetization reversal process, we have performed micromagnetic calculations using the object-oriented micromagnetic framework (OOMMF). We found that the magnetization process follows two steps, the rotation of the top corner and then a switching of the bottom base
Both these processes show the effect of the local shape anisotropy. The easy–axis of the bottom base of the triangle is along the direction of the applied magnetic field. For the top corner, however, the magnetization reversal might be similar to that of the hard axis. We think that the competition of these two local shape anisotropies lead to the two step reversal process.
These results suggest that the magnetization reversal process in sub-50nm magnetic dots can be controlled by the local shape anisotropies related to the detailed shape of the dots, which should be significant for the development of ultrahigh-density patterned media.

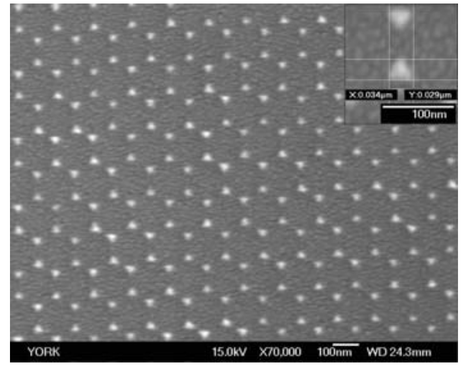

Fig. 1 SEM image of the Fe64Ni36 dot arrays made by NSL

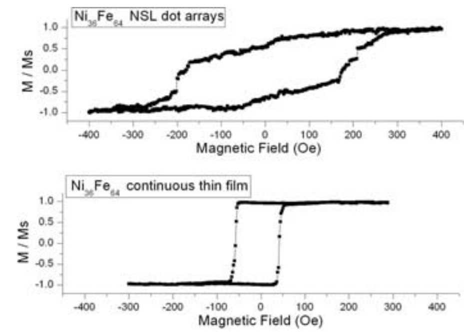

Fig. 2. The hysteresis loops of the triangular shaped dot arrays with the enhanced coercivity of 200 Oe and the continuous thin film with the coercivity of 50 Oe.

EE-10

Monodispersive doped iron core-shell nanoclusters: synthesis, transport and magnetic properties.

Y. Qiang, A. Sharma, D. Meyer
Physics, University of Idaho, Moscow, ID

Iron naturally occurs in oxidation states that range from Fe0 (for example, at the core-mantle boundary) to Fe3+ (at the Earth's surface). Recently, core-shell structured iron nanoparticles have drawn great attention for potential application in biology, enhanced NMR imaging, information storage, and reduction of carbon dioxide and ground water remediation [1-5]. However, as common as what we have experienced in our daily life on the oxidation of metals, a pristine surface of Fe0 exposed to air or oxygen-including atmosphere will be oxidized instantly, a process normally called initial oxidation. This initial oxidation will lead to an instant formation of an oxide layer on the metal surface. Nanometer-sized iron particles exposed to oxygen including environment show no exclusion to this rule. This leads to the Fe nanoparticles covered by a thin layer of oxide, which was termed as core-shell structured Fe nanoparticles. The typical thickness of this oxide layer is ~ 2-3 nm. Although the core may have the types of quantum effects characteristic of metal nanoparticles, the whole particle will involve the core and properties of the outer shell. Therefore, the properties of the core-shell nanoparticles may significantly depend on details of the shell structure and properties. For example, the biocompatibility of the Fe may be mediated by the oxide layers. It has been observed that cancer cell can absorb a large amount of Fe-iron oxide core-shell structured nanoparticles, thus enhancing the NMR imaging. Reduction of carbon chloride by Fe is also completed through the surface oxide layers. Most recently, it has been suggested that iron nanoparticles may be the next generation clean fuel for engine, incuring the questions of a clear picture on oxidation-reduction of Fe-iron oxide nanoparticle system.

In particular, the behavior of Fe-based alloys has been extensively studied for the scientific interest and potential technological applications such as thermostat, sensors, semiconductors, biomedical and environmental applications [2-5]. We present here synthesis, characteristics, magnetic properties and magnetoresistance (MR) of Cu, Ni, and Pd doped DxFe100-x (D=Cu, Ni, Pd and x = 2, 5, and 15) core-shell nanoclusters deposited on Si substrate, which are prepared by a third generation sputtering-gas-aggregation cluster source. The average nanocrystllite size of DxFe100-x nanoclusters is about 12 nm. XRD and TEM observed the presence of dopants and iron in core, Magnetite (Fe3O4) in shell. The resistance-temperature curves shows exponential behavior till 70-90 K and proportionality is observed with further increase in temperature. Zero field cooling (ZFC) and field cooling (FC) curves indicate a jump in magnetic moment between 70 and 90 K. These phenomena are similar to Verway type transitions6. The shifts in Verway transition observed in resistance, ZFC and FC can be due to interionic coulomb interaction between spinel structures of Fe3O4, and dopant oxides such as CuFe2O4. Magnetic properties and Verway transitions of the core-shell nanoclusters are doping concentration dependent. Verway transition temperature decreases from 90 K to 70 K when increasing doping concentration. For example of Cu doped iron nanoparticles, the magnetization is from 81 emu/g for x = 2 to 53 eme/g for x = 15. The maximum positive MR observed 1.52 % at 5 K for x = 2 when magnetic field of ±7 T is applied. MR decreases with increasing Cu concentration.

*: this work is supported by DOE-BES and DOE-EPSCoR

1. Kenji Ueda, Hitoshi Tabata, and Tomoji Kawai, App. Phy. Letters, 79, 988 (2001).

2. Jiji Antony, You Qiang, Donald R. Baer and Chongmin Wang, J. of Nanoscience and Nanotechnology, 6, 568 (2006).

3. Z. G. Yu, Jun He, Shifa Xu, Qizhen Xue,O. M. J. van't Erve, B. T. Jonker, M. A. Marcus, Young K. Yoo, Shifan Cheng and Xiao-dong Xiang, Phy Rev. B 74, 165321 (2006).

4. Y. Qiang, J. J. Antony, A. Sharma, J. Nutting, D. Sikes, and D. Meyer, J. Nanoparticles Res. 8, 489 (2006).

5. C. B. Wang and W. X. Zhang, Environ. Sci. Technol. 31, 2154 (1997).

6. M. Ziese and H.J. Blythe, J. Phys: Condens. Matter. 12, 13 (2000).

Porous Silicon/Metal Hybrid System with Ferro and Paramagnetic Behaviour.

K. Rumpf, P. Granitzer, H. Krenn
Institute of Physics, Karl Franzens University Graz, Graz, Austria

Summary:
Fabricated ferromagnetic hybrid systems consisting of a porous silicon (PS) matrix with incorporated metal-nanostructures exhibit magnetic properties which can be distinguished in two ranges. A first one is related to magnetic fields below the saturation magnetization of the deposited metal and a second one to higher magnetic fields. Considering the low field region the samples show magnetic characteristics due to the metal-precipitations (geometry, distribution, kind of metal) tunable by the deposition parameters. At higher fields an additional non-saturating term is ob-served which is dependent on the temperature and differs in strength between Ni and Co. In the frame of this work this additional paramagnetic term is investigated.

Experiments and discussion:
Magnetization measurements performed on the semiconductor/metal nanocomposite have been carried out in a field range between +7 T and -7 T and the temperature has been varied from 4.2 K up to 310 K. Considering a PS-membrane with precipitated Ni-structures at applied fields greater than 1 T the non-saturating term decreases with increasing temperature (figure 1a). This behaviour is independent of the geometry and distribution of the embedded Ni-structures within the chan-nels of the PS-template. The field dependence of the suszeptibility shows an exponential decay (figure 1b).
The decay of the magnetization with increasing temperature shows a paramagnetic-like behav-iour which follows the Curie-Weiss law very well, illustrated in figure 2a and 2b for an applied magnetic field of 7 T. Considering PS-membranes filled with Co-particles a non saturating behav-iour is also observed but is less developed than for Ni-filled samples (not shown here). In this case at a magnetic field of 7 T the enhancement of the magnetization above the saturation of the spin-magnetism is about 20% in contrast to Ni structures where the increase amounts about 130% of the ferromagnetic saturation of the low field behaviour.

Conclusion:
The fabricated semiconductor/metal nanocomposite system offers not only a ferromagnetic be-hav-iour (which is tunable by the deposition parameters) at magnetic fields below the saturation magnetization MS of the embedded metal but it exhibits also an additional paramagnetic-like term at magnetic fields above MS, following the Curie-Weiss law. This additional term depends on the kind of metal which is deposited within the template offering a stronger contribution in case of Ni than of Co. For both metals the mentioned high field behaviour is temperature de-pendent.

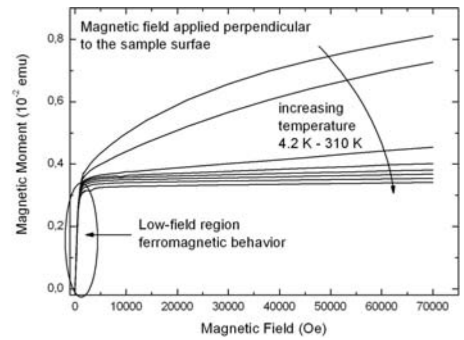

Figure 1a:Magnetization curves of a Ni-filled sample exhibiting a non-saturating bahaviour which decreases with increasing temperature between 4.2 K and 310 K.

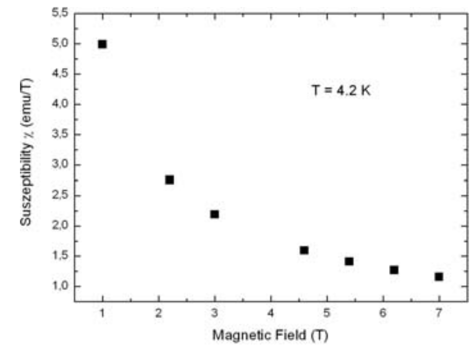

Figure 1b: Field dependence of suszeptibility measured at T = 4.2 K shows an exponential decay.

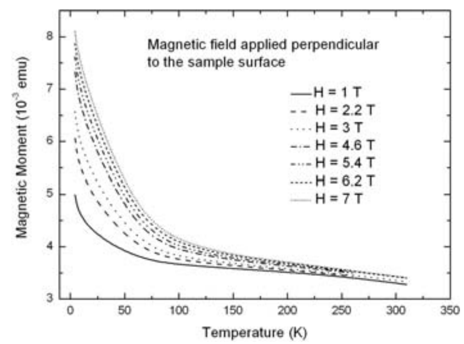

Figure 2a: Temperature dependence of the magnetization of a Ni-filled specimen measured at magnetic fields between 1 T and 7 T.

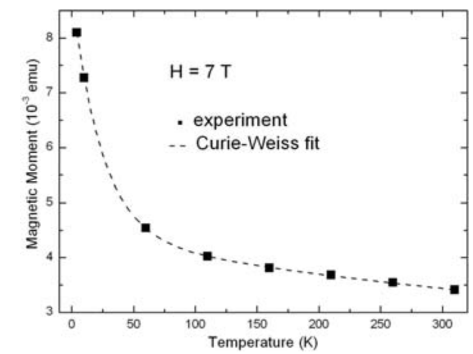

Figure 2b: The graph shows a Curie-Weiss fit for measurements carried out at 7 T.

EE-12

Electrical Resistance and Magnetoresistance of Glass Ceramics Containing Magnetite Nanoparticles.

P. Allia[1], F. Celegato[2], M. Coisson[2], P. Tiberto[2], F. Vinai[2], O. Bretcanu[3]
1. Politecnico di Torino, Torino, Italy; 2. INRIM, Torino, Italy; 3. Imperial College, London, United Kingdom

Magnetite nanoparticles less than 100 nm in size embedded in bio-compatible glass-ceramic matrix have been considered for specific biomedical applications such as bone cancer therapy [1]. We report on the electrical resistivity and magnetoresistance of three ferrimagnetic glass-ceramics prepared at different melting temperatures (1500 and 1550 °C), both as-cast and annealed (T_{ann} = 600 °C for 14 hours). The electrical resistivity was measured between 60 K and room temperature by means of the 4-point method. Isothermal magnetoresistance (MR) curves were measured in the same temperature interval and up to a maximum field of 70 kOe. In our glass-ceramics, magnetite nanoparticles give rise to a percolating network [2].
The electrical resistivity of all samples is dominated by activated processes; the Verwey transition separating the activation regime from the variable-range hopping regime occurs around 110 K. The transition has been independently observed by measuring the sample magnetization as a function of temperature under constant field. A magnetization jump is observed at exactly the same temperature where the resistance vs. T curve exhibits a change in slope. The Verwey-transition temperature T_v is lower than the standard value observed in bulk magnetite (about 120 K) and could be related to either imperfect stoichiometry or to frozen-in stresses. A negative, unsaturating MR is observed in all samples up to 70 kOe. When the temperature is decreased from RT down to T_v, MR_{max}=|[R(H=70 kOe)-R(0)]|/R(0) is observed to increase; below T_v, MR_{max} is increasingly and markedly reduced.
The effect is interpreted as follows: the MR observed at high fields mostly arises from spin disorder at magnetite grain-grain interfaces. The electrical current is carried through hopping processes within the percolating magnetite network. The hopping range is much less than the average grain size, even in the variable-range hopping regime. Both intra-grain and inter-grain hopping processes exist. At large fields, intra-grain hopping does not contribute to the MR because the magnetization at the atomic sites involved in the hopping process is substantially aligned by the field, and therefore is almost the same. Therefore, the MR effect is dominated by inter-grain hopping, which occurs between atomic sites whose magnetization can be substantially misaligned even at high fields. It is well known that the magnetization of magnetite grains is highly disordered at grain-grain boundaries [3]. Such a disorder is not suppressed by an applied field as high as 70 kOe. Above T_v, the hopping is short-ranged and all electrons do probe the surface magnetic disorder; in the variable-range hopping regime below T_v, the fraction of electrons hopping between sites located deeper in each grain increases. These electrons do not appreciably contribute to the MR signal, because they involve sites exhibiting the same magnetization direction. Therefore, the overall MR is increasingly reduced below T_v.

[1] K.M. Spiers et al., Key Engineer. Mater. 254-256, 213 (2004)

[2]O. Bretcanu et al., Acta Biomater. 1, 421 (2005)

[3] J.M.D. Coey et al., Appl. Phys. Lett. 72, 734 (1998)

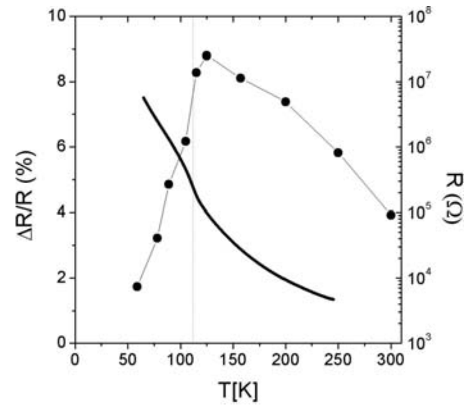

Symbols: temperature behavior of the maximum magnetoresistance of a glass ceramic material containing magnetite nanoparticles. Full line: electrical resistance as a function of temperature.

EF-01

Switching field distribution reduction and effective write gradient enhancement in domain wall assisted media.

A. Y. Dobin
Seagate Technology LLC, Fremont, CA

Domain Wall Assisted Magnetic Recording has been extensively studied as a means to overcome the super-paramagnetic limit of the magnetic recording. In previous work [1-3], the main benefit of the DWAMR was attributed to the increase of the energy barrier without increasing the switching field. Then the grain diameter can be reduced without sacrificing thermal stability or write-ability, which allows to increase the areal density. In this work we will demonstrate that in optimized domain wall assisted media, in addition to the aforesaid effect, the switching field distribution is reduced and the effective write gradient is enhanced.

For simulations below we use a hard/soft composite media structure with 8nm-thick soft and hard layers, saturation magnetization 1000emu/cc, exchange stiffness 1microerg/cm. The field is applied at 10deg off the easy axis. For large enough soft layer anisotropy the dependence of the switching field on hard layer anisotropy (Fig. 1) becomes flat, which leads to a significant reduction of the switching field distribution (SFD) caused by the fluctuations of the hard layer anisotropy. In Fig. 2, the relative SFD normalized to relative hard layer anisotropy distribution is shown. Note, that for coherent "Stoner-Wohlfarth" switching this normalized SFD is equal to 1. We can see that for optimum values of soft and hard layer anisotropies the normalized SFD for domain wall assisted switching can be reduced by a factor of 10.

Next we studied the domain wall assisted switching under realistic write fields, using FEM write head fields.

The maximum anisotropy of a coherent (Stoner-Wohlfarth) particle that can be written with this head is ~18kOe. The gradient of the maximum switchable anisotropy ("effective write gradient") reaches 0.25 kOe/nm. Maximum switchable anisotropy of the hard layer in the 8/8nm hard/soft layer structure, calculated using the 1D micromagnetics [3], is shown in Fig. 3. Optimizing soft layer anisotropy allows switching hard layers with extremely high anisotropy of ~55kOe, 3-fold increase with respect to the single layer media. The "effective write gradient" (Fig. 4), reaches 8kOe/nm for the composite media. To compare the effective write gradient with that of the single layer media, it has to be normalized with the maximum switchable anisotropy. At optimum soft layer anisotropy, the normalized gradient is enhanced by a factor of ~10 compared to that of the single layer media, which will result in sharpening of the transitions, reduction of the transition jitter, and hence significant media SNR improvement. We will also present the full micromagnetic recording simulations which confirm our findings, and discuss the underlying physics of the SFD reduction.

[1] R. H. Victora and X. Shen, IEEE Trans. on Magn. 41, 537 (2005).

[2] D. Suess et al., Appl. Phys. Lett. 87, 012504 (2005).

[3] A. Yu. Dobin and H. J. Richter, Appl. Phys. Lett. 89, 062512 (2006); J. Appl. Phys., 101, 09K108 (2007).

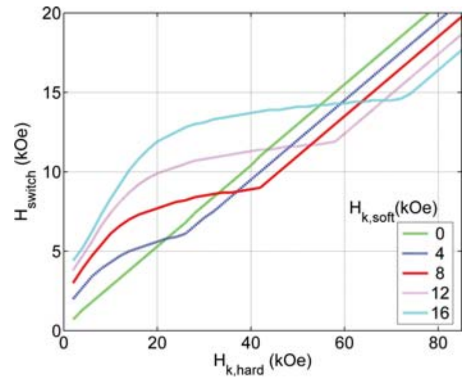

Fig. 1. Switching field vs. hard layer anisotropy for several soft layer anisotropies.

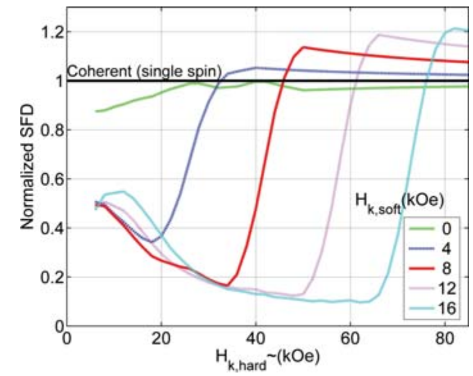

Fig. 2. Normalized SFD≡($\delta H_{switch}/H_{switch}$)/($\delta H_{hard}/H_{hard}$) vs. average hard layer anisotropy field.

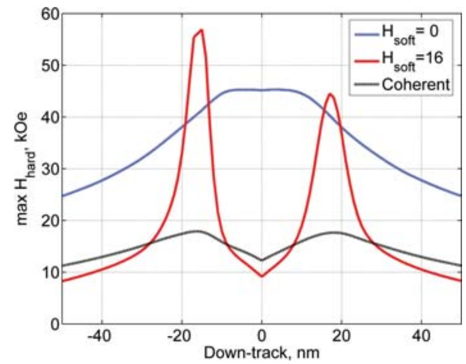

Fig. 3. Maximum hard layer switchable anisotropy in write field vs. down-track position, for composite media with 0 and 16kOe soft layer anisotropies, as well as coherent ("Stoner-Wohlfarth") medium.

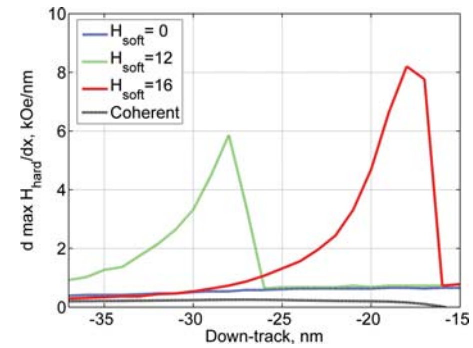

Fig. 4. The gradient of the maximum switchable hard layer anisotropy (a.k.a. "effective write gradient") vs. down-track position.

EF-02

A Simple Model for Optimal Read Width due to Finite Write Width and Off-track Interference.

Z. Jin[1], H. N. Bertram[1,2]
1. Hitachi GST, San Jose, CA; 2. CMRR, UCSD, La Jolla, CA

For a written track of infinite width a wider reader is always preferred because the signal to noise ratio (SNR) varies as the square root of the read width [1]. However, with current areal densities in the range of 300-500Gb/in2 [2], extremely narrow written track widths are needed. Because the reader reads beyond the geometric read width, for finite written track width, an optimal read width will occur. Here, in order to estimate the optimal read width, a simple model is used that includes the effect of the finite widths of both the reader and the written track. In addition the effect of off-track interference is included in the SNR estimate.
A reader microtrack profile is assumed of the form h(z) = exp(-c0z^3), where z is the cross track direction. c0=8ln2/WR^3, WR is the read width defined by the half height locations of h(z). Assuming uniform writing over a write width Ww, the SNR including off-track interference is given by:
$(\int_{-WW/2}^{WW/2} h(z-z0)dz)^2/(\alpha\int_{-WW/2}^{WW/2} h^2(z-z0)dz + (2\int_{WW/2}^{\infty} h(z-z0)dz)^2)$ (1)
In (1), the reader is centered at position z0 and α is the media noise scale factor independent of the read width. The effect of off-track interference is estimated from a tail integral of the signal profile.
In Fig. 1, the on-track (z0 = 0) SNR is plotted versus WR/WW with and without the adjacent track interference term. Also included is a dashed curve of the simple “basic” variation of the SNR with read width WR (assuming uniform reading only over a finite read width). The vertical axis is calibrated from a measurement at WR/WW = 0.73 that yields α = 3.2 for an on-track SNR (2T) of 18.8dB. For low values of WR/WW and all cases, the SNR varies as the square root of the read width WR. The simple case of a uniform reader exhibits an SNR reduced by 1dB due to the specific form of h(z). At higher values of WR/WW, the SNR saturates due to the finite write width without the adjacent track term and maximizes including the adjacent track term. With the adjacent track interference term a maximum occurs: for a value of α = 3.2, this maximum occurs at WR/WW ~ 0.7 with a SNR of 18.9dB. Note that near the maximum, the SNR is approximately independent of read width (within a 10% WR/WW variation). Even without including the off-track interference term the noise variation with read width is significantly reduced from the simple form (dashed).
Equation (1) can be used to calculate SNR versus off-track position. As shown in Fig. 2, experimental measurements (circles in Fig. 2) agree reasonably well with the curve calculated with a WR/WW of 0.73. This value of WR/WW was determined experimentally for the head been used. The off-track capability (width at a threshold SNR) increases with decreasing read width until the on-track SNR becomes lower than the threshold SNR.
In Fig. 3, SNR is plotted versus write width WW for two values of read widths. Note that the smaller reader is less sensitive to variation in the written track width WW. The plots are scaled so that WW = 1 corresponds to any chosen value of write width. For example, if WW =1 -> 100nm, WR -> 63nm and 73nm, respectively.

[1]. H. N. Bertram, Theory of Magnetic Recording. Cambridge, U.K.: Cambridge Univ., 1994.

[2] Sining Mao et. al., “Reader Technology for 1 Tbpsi Recording,” Paper 15pA-01, PMRC 2007, Tokyo, Japan

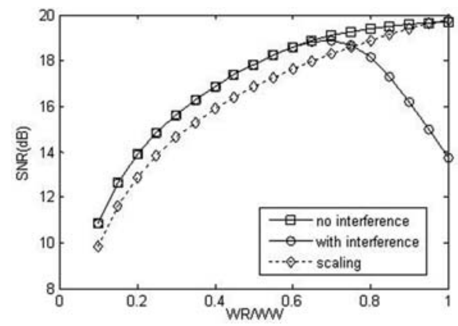

Fig. 1 Calculated SNR versus the ratio of read width to written track width (WR/WW) with side interference (circle), without interference (square) and from scaling (dashed).

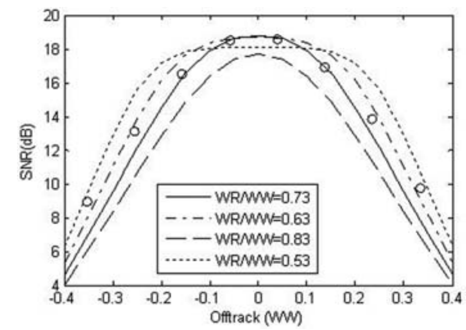

Fig. 2 SNR versus off-track position for various read width WR/WW from 0.53 to 0.83 with α=3.2. Calculated (solid) and experimental (Circles) SNR agrees reasonably well within 15% written track with.

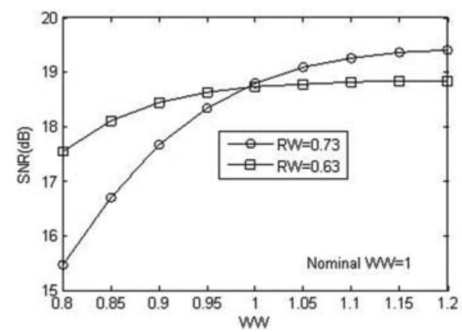

Fig. 3 SNR versus WW for read width WR = 0.63 and 0.73. With almost identical SNR at nominal WW of unity, narrower WR at 0.63 has much less sensitivity (more tolerance) to WW than wide wider WR at 0.73.

EF-03

Micromagnetic Study of Short and Long Yoke PMR Head Trailing Shield.

A. F. Torabi[1], D. Bai[2], T. Pan[2], S. Li[2], S. Song[2], L. Zhong[2], L. Wang[2], K. Stoev[2], S. Mao[2]
1. Western Digital Corporation, San Jose, CA; 2. Western Digital Corporation, Fremont, CA

Introduction

Higher data rate recording requires faster head switching rise time. In order to improve the head switching time and reduce the time delay between write current and write field, shorter yoke length is considered. In this paper, Finite Element Micromagnetic Model [1-2] has been used to study the writer dynamics in perpendicular magnetic recording (PMR) trailing shield head design. In particular, frequency roll off of head field vs. dibit frequency and simulation of nonlinear transition shift (NLTS) are studied.

Results and Discussions

Figure 1 shows the cross section view of the head design that was used in this work. Shorter yoke length about half of long yoke length of 13 um has been used to compare the write dynamics of recording head. In particular, study of write dynamic and effect of PMR yoke length in high frequency response of the recording head.

Figure 2 shows the normalized head field for a dibit response as a function of data rate for both short yoke and long yoke as well as the effect of write current overshoot amplitude (OSA). Short yoke has much better frequency response and slower roll off as compared to long yoke.

To quantify the effect of yoke length on data rate in terms of head media performance, modeling of nonlinear transition shift was performed. Micromagnetic media model was used to study the recording process using the simulated head field that was calculated using micromagnetic finite element model. Fifth harmonic elimination technique was used to model the NLTS. Figure 3 shows a comparison of NLTS for short vs. long yoke. Assuming a minimum requirement of 14dB NLTS (20%), short yoke can push the data rate up to 1.9Gbs. and long yoke up to 1.25 Gbs. The write current overshoot (OSA) was 100%. Model shows qualitative agreement with experimental with better performance for the shorter yoke.

[1]W. Scholz, S. Batra, "Micromagnetic simulation of head field and write buble dynamics in perpendicular recording",IEEE Trans. Magn., Vol. 41, No. 10, pp 2839-2844, Oct 2005

[2]D. Suess, T. Schrefl, Micromagnetic Finite Element (femme) software

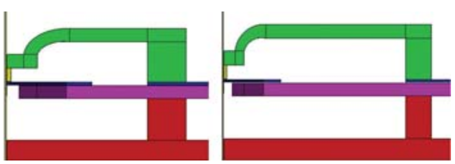

Fig 1: Schematic drawing of short (left) and long yoke (right) used in the modeling

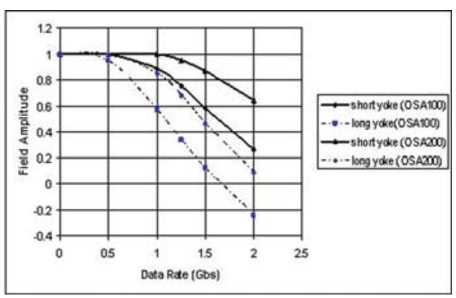

Fig 2. Frequency roll of head field vs. data rate for short and long yoke and effect of write current overshoot amplitude (OSA)

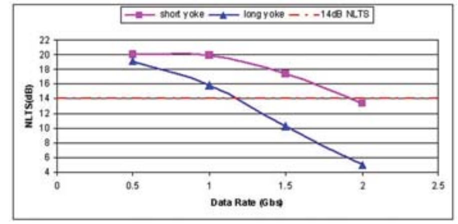

Fig 3. Modeling of NLTS vs. data for short and long yoke

EF-04

Reduction in Switching Field for a Granular Perpendicular Medium Using Microwave Assisted Magnetic Recording.

S. Batra, W. Scholz
Seagate technology, Pittsburgh, PA

Recently, there is a renewed interest in ECC media [1,2] and microwave assisted switching [3] both of which offer the potential of reducing switching field thereby allowing writeability on higher HK medium needed to reduce grain size and increase areal density. We use micromagnetic simulations to study the write-ability improvements in a perpendicular recording system due to microwave (RF) assist field. In presence of an in-plane RF field, all the grains in the medium undergo a coherent precession when the medium grains are assumed to be uniform with identical magnetic properties and thermal fluctuation fields are not included (T = 0 K). A typical switching event is shown in Fig. 1, where Mz reverses from –1 to +1 in 1 ns while in-plane component undergoes coherent precession. The medium parameters chosen are HK = 22 kOe, and Ms =400 emu/cm3, he = 0.037, LLG damping value α = 0.02 and grain size of 6 nm with medium thickness of 15 nm. For an applied in-plane RF field of 0.068 HK at a frequency of 28 GHz, we observe that medium can be switched with a uniform field (DC) of 0.31 HK applied at an angle of 20°, a significant reduction in the DC field compared to Stoner Wohlfarth (SW) switching field of 0.45 HK. The phase space of switching is a function of RF field magnitude, RF frequency and applied uniform field magnitude and direction. For the case of medium with uniform grain size and T = 0 K, switching results are consistent with the single spin results [4, 5]. As medium damping is increased, a higher value of uniform field is required, implying that the reduction in switching field is less compared to the case of lower damping value and is plotted in Fig. 2.

Next, we consider a realistic granular medium where grains are no longer uniform. In addition to medium parameters listed above, we assume σ(HK) ~ 5%, angular dispersion sigma of 2°, and grain size volume sigma of 20%. For this case, a uniform field of 0.37 HK applied at an angle of 20° is required to switch medium. Next, we turn on the thermal fluctuation by setting temperature of 300 K in addition to the distributions assumed in magnetic medium properties. For this case, we need to apply still a larger uniform field of 0.39 HK applied at 20° and the optimal RF frequency is increased to 34 GHz. An in-plane RF field of 0.068 HK at the optimal RF frequency requires a uniform switching field of 0.39 HK compared to Stoner Wohlfarth switching field of 0.45 HK applied at the 20° to the anisotropy direction. This is a significant reduction in switching field. We will show that this reduction is by microwave assist field lowering the switching field for the granular medium and not by the coherent precession of individual grains. Next, we comment on the RF frequency needed to observe reduction in switching field. We observe reduction in switching field over a broad frequency range, however, a frequency of 34 GHz gives a maximum reduction in switching field as shown in Fig. 3. This reduction in switching field depends on the damping in the medium and the magnitude and direction of microwave and DC bias field.

[1] D. Suess, "Micromagnetics of exchange spring media: Optimization towards the limits," J. Magn. Magn. Mat., 308 (2007) 183-197.

[2] R.H. Victora, X. Shen, IEEE Trans. Magn. 41 (2005) 537.

[3] J. G. Zhu, "Microwave assisted magnetic recording", Paper B6, TMRC Conference, Minneapolis, 2007.

[4] W. Scholz and S.Batra, "Micromagnetic Modeling of Ferromagnetic Resonance Assisted Switching", MMM 2007, paper CC-10, to appear in J. Appl. Phys.

[5] G. Bertotti, C. Serpico, I. Mayergoyz,, Phys. Rev. Lett. 86, 724-727 (2001).

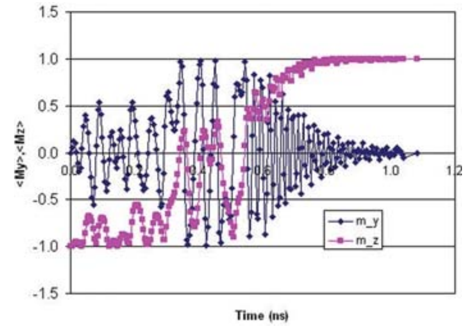

Fig. 1: Coherent precession of magnetization leading to switching in 1ns.

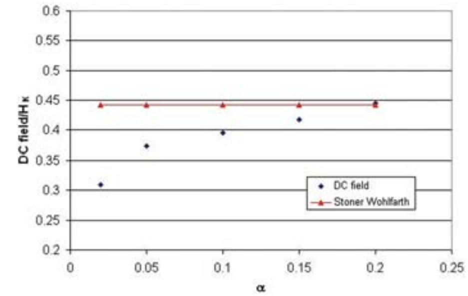

Fig. 2: DC Field needed to switch medium as a function of damping value α. An in-plane RF field of magnitude 0.068 HK at 28 GHz is applied in addition to the uniform DC field.

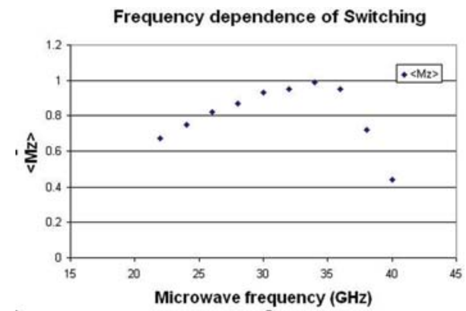

Fig. 3: Frequency dependence of switching for the medium. Head field of 0.39 HK and a microwave field of 0.068 HK were applied to get complete switching of grains in the medium. For this case, medium damping value α of 0.05 is assumed.

EF-05

A Trailing Shield Perpendicular Writer Design with Tapered Write Gap for High Density Recording.

L. Guan[1], J. Smyth[1], M. Dovek[1], S. Chan[2], T. Shimizu[2]
1. Headway Technologies, Milpitas, CA; 2. SAE Magnetics (H.K.) Ltd, Hong Kong, China

Today's commercial PMR products are universally using a trailing shield for the write head design [1]. Key parameters for delivering sufficient write field and field gradient include the ABS dimensions, the main pole neck height (NH) and the trailing shield throat height (TH). With the continuous push for higher areal density, the main pole ABS area decreases ~ 1/ TPI^2, as both pole width (PW) and pole thickness (PT) reduce linearly with TPI, resulting in a proportional loss to the write field strength. Typically, to compensate for the large field drop due to the scaling of the ABS area, the main pole neck height and shield throat height are reduced correspondingly. The effort of reducing NH or TH, however, has drawbacks on nominal performance and the controllability of dynamic performance (DP) parameters, such as magnetic write width (MWW) and reverse (LF over HF) overwrite (OVW). In particular, short TH may cause the saturation of trailing shield and result in poor field gradient. The sensitivity of DP parameters on NH/TH also increases with decreasing NH/TH, resulting poorer DP sigma for the same wafer/back-end process tolerance.

In this work, we investigated a new PMR writer design with tapered write gap [2][3] by finite element analysis (FEA) and experiments. Fig. 1 shows the ABS and cross-sectional schematics of taper write gap design. Two new design parameters are introduced: taper angle a and taper distance d. By tapering main pole at the trailing edge, larger trailing edge field and field gradient are achieved. Fig. 2 shows the down-track field profile of two designs: conventional design with TH = 0.1um and taper write gap design with TH = 0.2 um, a =15deg, d = 0.2um. Taper write gap design shows the same leading edge field, but enhanced trailing edge field magnitude and field gradient, even with much longer TH. Thus superior SNR performance can be expected from better field properties of taper write gap design.

In addition to better SNR performance, another advantage of taper write gap design over short NH/TH design lies in the fact that there is a self-compensating mechanism in such design. In general, the write field is a function of multiple variables: H(A1, A2, NH, TH) = f1(A1) x f2(A2/A1) x f3(NH, TH), where A1 and A2 are the cross-sectional area of main pole at ABS and behind ABS respectively. The larger ratio of A2/A1, i.e. larger taper angle a or taper distance d, the better is flux concentrated. When taper angle a or taper distance d varies due to wafer process or back-end process, A1 will increase or decrease, but A2/A1 will change in the opposite way. So the two terms, f1(A1) and f2(A2/A1), compensate with each other, leaving the write field less affected. Fig. 3 shows the calculated OVW as a function of ABS area A1 for conventional trailing shield and tapered write gap designs. As one can see, taper write gap design shows much weaker OVW dependence on ABS area. Due to the same self-compensating mechanism, the NH/TH sensitivity, f3(NH, TH), is also reduced for taper write gap design. Overall, less DP sigma caused by wafer/back-end process can be achieved with tapered write gap design.

We have fabricated PMR writer with both conventional trailing shield and tapered write gap designs. Two lapping processes are applied to make HGA samples: (1) normal lapping process to study the nominal DP performance and (2) tilted lapping process to study the sensitivities of DP parameters to ABS position for two designs. The results will be discussed in details.

[1] M. Mallary, A. Torabi, and M. Benakli, IEEE Trans. Magn., vol. 38, pp. 1719-1724, Jul. 2002.

[2] Y. Kanai, Y, R. Matsubara, H. Watanabe, H, H. Muraoka, Y. Nakamura, IEEE Trans. Magn., vol. 39, pp. 2405-2407, Sept. 2003

[3] Published US Patent Application 2005-0219743 (Oct. 6, 2005)

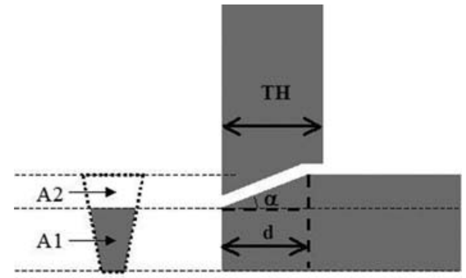

Fig. 1 ABS and cross-sectional schematics of taper write gap design

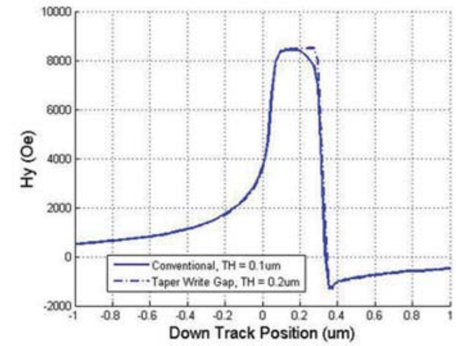

Fig. 2 Down-track field profiles of conventional and taper write gap design

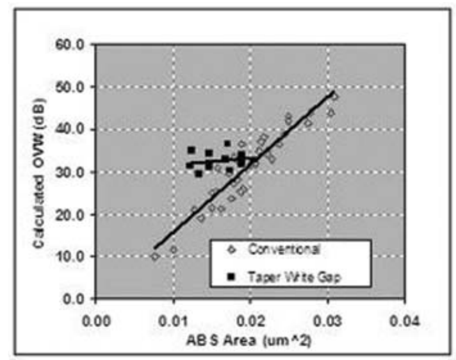

Fig. 3 Calculated OVW as function of ABS area for conventional and taper write gap designs

EF-06

Time-dependent fields and anisotropy dominated magnetic media.

K. Rivkin, N. Tabat, S. Foss-Schroeder
Seagate Technology, Edina, MN

Recently there has been a significant interest in using the r.f. field to facilitate magnetization reversal.In the present work we will explore both analytically and numerically the optimal parameters of constant frequency microwave assisted magnetization reversal (MAMR) based on a single dipole model. We consider a magnetic sample with uniaxial anisotropy subjected to circularly polarized r.f. field H1 oriented in the plane perpendicular to the easy axis, with the frequency ω, as well as the d.c. field Hdc which is oriented parallel to the easy axis and opposite to the initial direction of the sample's magnetization. By solving the Landau-Lifshitz equation in spherical coordinates[1] we discover that for a range of effective anisotropy fields Hani given by Eq.1 such solutions become unstable, with an exception of the solution which corresponds to the reversal of the magnetization. Maximal switchable anisotropy is Hdc+8Hrf.
We then solve Landau-Lifshitz equation numerically for two configurations: in the first case, the 3ns exposure of the media to the RF field precedes the application of the DC field, in the absence of the RF field, so called "pre-assist" configuration; in the second case the RF and DC field are applied simultaneously, so called "assist" configuration. A random noise introduced into the system. We measure the probability by calculating how many out of 10 calculations result in a switched state. The damping parameter β is assumed to have a value of 0.01. The amplitude of RF field in all numerical experiments is 2000 Oe. In the "pre-assist" configuration (Figure 1.) we see that circularly polarized fields are capable of reliable magnetization reversal, with results being almost independent from the value of the DC field applied after the RF field. Switching shows good correspondence to the analytical solution given. Linearly polarized fields are not performing as well jitter-wise. Results for the "assist" configuration are shown in Figure 2. With an exception of the operating frequencies shift, numerical results for circularly polarized field fit rather well the analytical model.

K. Rivkin and J. B. Ketterson "Magnetization reversal in the anisotropy-dominated regime using time-dependent magnetic fields", Applied Physics Letters 89, 252507 (2006).

G. Bertotti, A. Magni, I. Mayergoyz, C. Serpico, "Bifurcation analysis of Landau-Lifshitz-Gilbert dynamics under circularly polarized field," J. Appl. Phys. 89 (2001) 6710-6712

$$H_{DC}+\sqrt{3}\left[\frac{\omega}{\gamma}+f(H_{DC},H_1)-\frac{H_1}{\sqrt{2}}\right]\le H_{ani}\le H_{DC}+\left[H_1^{\frac{2}{3}}+\left(\frac{\omega}{\gamma}+f(H_{DC},H_1)\right)^{\frac{2}{3}}\right]^{\frac{3}{2}}$$

Eq.(1)

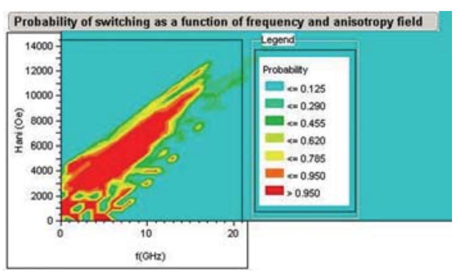

Figure 1.b. Pre-assist, circularly polarized R.F. field, 1000 Oe DC field.

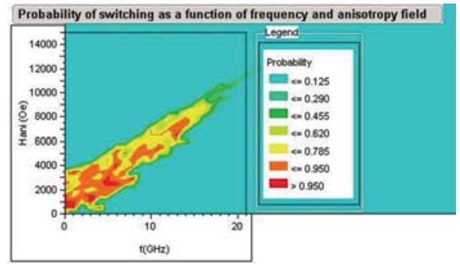

Figure 1.b. Pre-assist, linearly polarized R.F. field, 1000 Oe DC field.

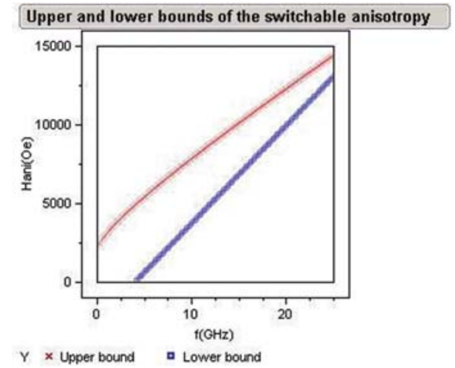

Figure 1.c. Pre-assist, analytical results.

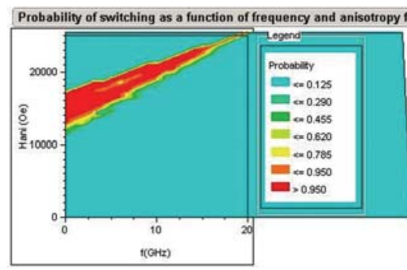

Figure 2.a. Probability of switching as a function of the media anisotropy field and applied frequency, assisted configuration, 10000 Oe DC field, circularly polarized R.F. field

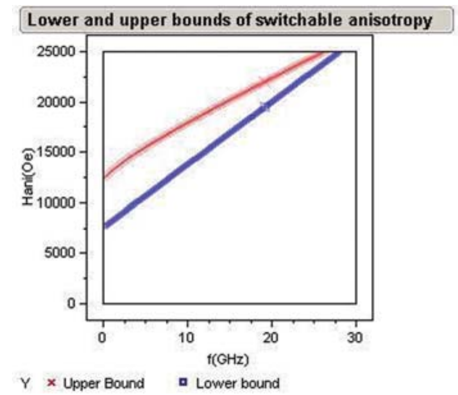

Figure 2.b. Assist, analytical results.

EF-07

Effect Of Interlayer on Read Write Process in Perpendicular Recording.

K. Gao[1], V. Sapozhnikov[1], A. Zheng[2], O. Heinonen[1]
1. Seagate Technology, Bloomington, MN; 2. Seagate Technology, Fremont, CA

Interlayer in perpendicular recording affects the distance between the head and the soft under layer (SUL, or keeper) and thus plays an important role in recording performance. In this paper, we investigate the effect of interlayer thickness on read write process in perpendicular recording. We show that depending on different head media combinations, different responses in the read write process can be expected and several previously well-known arguments may have its own limitation. In the write process, we use finite element method (FEM) to generate write field profile for a given recording head design, then use micromagnetic media simulation to provide media magnetic response. To validate the results, the M-H loop of the media was simulated and compared to the experiment measurement. A good agreement is obtained. For the same media, we determine write process transition quality using 4 different metrics, the total effective field at trailing edge of the head, the effective field gradient at transition region, the field profile change in the vicinity of the transition and transition curvature.

We show that the transition quality response is highly depending on the head media combination. Different choices of media designs have big impact on the transition quality. For conventional single layer media, with Stoner-Wohlfarth (S-W) type of switching, reduction of interlayer thickness will cause the peak effective field to be reduced. However, with ECC type of media, a monotonic increase in the peak effective field can be expected as the interlayer thickness is reduced.

For current media with ultra small writer dimension, we show that there exists a design space where reduce the interlayer thickness, the peak effective field, the effective field gradient, the write field profile at trailing edge and the transition curvature are all kept approximately same. A unique example is shown that for a particular combination of head media design, we observe that the measured media overwrite improves as the interlayer thickness is reduced. However, no SNR / BER gain is observed. Thus the model prediction is in good agreement with the spin-stand measurement.

In playback process, the spatial resolution of a reader is usually characterized by transition half-width T50, an important factor in head performance. We show that interlayer thickness reduction brings the mirror image of the recording layer closer to the reader. As illustrated in Figure 1, this affects T50 in two ways. First, because the effective HMS of the mirror image decreases, "T50" of the mirror image decreases (the mirror of the read back signal gets sharper). This decreases the total T50. Second, the amplitude of the mirror read back signal increases. Therefore, the contribution of the mirror T50 to the total T50 increases. This increases the total T50.

Due to the complexity of many different interaction terms in the playback process, we use micromagnetic simulation to study the subtle detail in addition to the analytical formula to see which of the two effects prevails by computing the sensitivity of T50 to the interlayer thickness. The sensitivity is obtained based on the media samples we used for the write process study, where a possible identical transition can be written. The design space in the simulation is enlarged to reflect the general response.

The parameters for the modeling exercise are: reader HMS = 8-20 nm, media transition parameter a = 4-10 nm, media record layer thickness = 15-25 nm, interlayer thickness IL=10-30 nm, and reader shield to shield spacing is chosen to match the experiment parts. The results show that DT50 = -0.086DIL which predict that in this particular playback process, a finite penalty is seen in the playback process. We show that this result is also consistent with the measurement for the given head media combination.

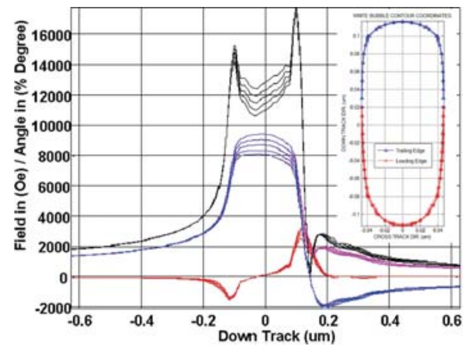

The write field profile for a particular head medium combination in perpendicular recording which has the same peak effective field, same effective field gradient, same field profile at trailing edge and same transition curvature for different interlayer thickness.

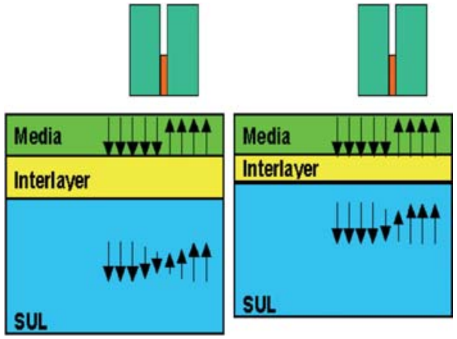

Illustrate the impact of interlayer thickness on playback process where both spacing loss and impact of resolution due to magnetic image of the reader are included.

EF-08

Infulence of negative field on media noise in combination of capped medium and shielded pole head.

T. Ichihara[1], H. Kashiwase[1], H. Nakagawa[1], H. Nemoto[1], M. Mochizuki[2]
1. Central Research Laboratory, Hitachi Ltd., Odawara, Japan; 2. Hitachi Grobal Storage Technologies, Fujisawa, Japan

By using a shielded pole head and a capped medium, high area density could be obtained with improvement of write-ability [1]. On the other hand, optimization of field distribution from shielded pole writer and that of exchange coupling in the cap layer of the medium were major issues for improvement of total R/W performance. In this study, it was found that the media noise increased drastically at particular linear density in some combinations of shielded pole heads and capped media. Furthermore, the phenomenon was investigated by MFM observation. Schematic illustration for a structure of the capped medium was shown in Fig. 1. Two antiferromagnetically coupled Fe-Co-Ta-Zr alloy layers were used for the SUL. Total SUL thickness was varied as 0, 10, 20 and 30 nm. A Co-Cr-Pt-SiO2 granular layer with thickness of 13 nm and with Ms of 400 emu/cc, was used as a recording layer. A Co-Cr-Pt alloy with thickness of 8 nm was used as a cap layer on top of the granular layer. Ms of the cap layer was varied from 330 to 500 nm. Shielded pole writers and GMR readers were used to investigate the R/W performance over a linear density range of from 50 kfci to 1300 kfci. Fig. 2 shows linear density dependences of normalized media noise power for the capped media with various Ms of cap layer. As increasing Ms of the cap layer, media noise of the linear density of around 550 kfci increased drastically. Since the increase of media noise was suppressed by increasing SUL thickness or decreasing write current, it was considered that the phenomenon came from the negative field around the edge of trailing shield [2]. Fig. 3 shows MFM images of written pattern with various linear densities on the capped media. When Ms of the cap layer was 500 emu/cc, maze-like domains were formed at AC erased region between each written pattern because of the larger exchange coupling in the cap layer with higher Ms. Furthermore, the width of the domain was comparable to the transition period of 550 kfci pattern, 46.2 nm. Fig. 4 shows crosstrack distributions of transition jitter estimated from MFM image in Fig. 3. For the medium in which Ms of the cap layer was 500 emu/cc, the transition jitter of 550 kfci pattern increased drastically. It was considered that the magnetization relaxation by field around trailing shield was enhanced at the 550 kfci pattern of which the transition period was comparable to the magnetic cluster size. These results indicated that optimization of field at the edge of trailing shield and optimization of magnetic cluster size for the capped media were important for improvement of total R/W performance. In conclusion, it was observed that the media noise of the pattern around 550 kfci increased drastically in combinations of shielded pole head and capped media with higher Ms cap layer and thinner SUL. MFM observation indicated that the phenomenon was correlated with the domain width at AC erased region and it was considered that the magnetization relaxation by the negative field around trailing shield was enhanced when the transition period of the pattern was comparable to the magnetic cluster size.

[1] Y. Hsu et. al, IEEE Trans. Magn., vol. 43, No. 2, pp. 605 - 608

[2] K. Takano et. al, IEEE Trans. Magn., vol. 43, No. 2, pp. 594 - 599

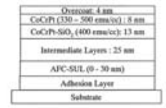

Fig. 1 Schematic illustration for structure of capped medium

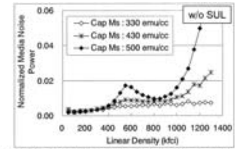

Fig. 2 Linear density dependences of normalized media noise power for capped media with various M_s of cap.

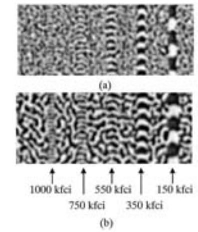

Fig. 3 MFM images for written patterns with various linear density on capped media without SUL.
(a) Cap M_s : 330 emu/cc, (b) Cap M_s : 500 emu/cc.

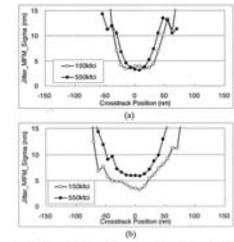

Fig. 4 Crosstrack distribution of transition jitter estimated from MFM.
(a) Cap M_s : 330 emu/cc, (b) Cap M_s : 500 emu/cc.

EF-09

Investigation on magnetic fields from field genarating layer in MAMR.

K. Yoshida[1], E. Uda[1], N. Udagawa[1], Y. Kanai[2]
1. Information and Communications Engineering, Kogakuin University, Tokyo, Japan; 2. Niigata Institute of Technology, Kashiwazaki, Japan

Introduction

Several kinds of technology have been proposed to be as the break through to overcome super-paramagnetism limitation in magnetic recording. HAMR(heat assisted magnetic recording) and BPM(bit patterned media) are thought to be promising candidates to realize ultra-high recording density over 2 Tb/in2. They, however, require the drastic changes from the conventional fabrication technologies for a writing head and a recording medium. Recently, MAMR(Microwave assisted magnetic recording) was proposed by J. G. Zhu which utilizes the ferromagnetic resonance phenomenon that dramatically decreases magnetic switching field in writing process, enabling us to use the recording medium materials with extremely large magnetic anisotropy constant[1],[2]. MAMR might be also added as one of the candidates for the future technology. However, many physical aspects should be clarified to put practical technology. In this paper the characteristics of the magnetic fields from the field generating layer in MAMR are investigated with micromagnetic simulations.

Calculation procedures

Fig.1 shows a schematic diagram of a microwave field oscillator which comprises a field generating layer and a perpendicular anisotropy layer[2]. The polarization layer that supplies a polarized spin to the field generating layers was neglected for simplicity. The lengths of the perpendicular layer and field generating layer are 20 nm and 6 nm, respectively. The cross section of the x-coordinate is square with a length of 60 nm. The saturation magnetizations (Ms) and the anisotropy constant (K) of the perpendicular layer are 0.377 T and 5×105 J/m3, respectively. The Ms and K of the field generating layer are 2 T and 2×105 J/m3, respectively. The stiffness constant between the perpendicular and field generating layers is varied from 2 pJ/m to 10 pJ/m. The magnetization vectors are calculated with the Landau-Lifshitz-Gilbert equation with a spin torque term,

$(1+\alpha^2)dM/dt=-\gamma M\times(H_{eff}+\alpha H_{st})-\gamma/M_S M\times(\alpha M\times H_{eff}-M\times H_{st})$ (1)

$H_{st}=ajM_p=h\eta JM_p/(4\pi eMsd)$,

where H_{st} is the effective field due to spin torque, M_p is the unit vector of the magneization of the polarization layer, J is the injected current density, η is the polarization factor of spin current, Ms and d are the saturation magnetization and thickness of the field generating layer, respectively. The aj was set to be from 10 to 100 kA/m. A damping factor of 0.02 was used in the calculations. All the region was desretized into cubic cells of a 2nm length. The generated AC fiield were observed on the dashed plane(the x-y plane) with a distance of 15 nm from the down side of the generating layer.

Calculation results

Fig.2 represents the snap shots of the y-component of the magnetizations in the field generating layer in gray scal. The magnetizations rotate counterclockwise around the center of the square. The rough image of the magnetization directions are depicted in the picture at T=0 sec. The magnetizations do not rotate in unison. Fig.3 shows the trajectory of the generated AC field averaged in the observing plane that corresponds to a recording medium plane. The field oscillates in the x-y plane with a frequency of ~20 GHz. The oscillation amplitude is about 10 kA/m that is not sufficient to assist magnetization switching. This is because of the non-unison rotation of the magnetizations in the generating layer. The amplitude can be increased by preventing the magnetizations of the field generating layer from rotating in non-unison.

[1] X. Zhu and J-G. Zhu, IEEE Trans. Magn. Vol 42, No.10, pp.2670(2006).

[2] J-G. Zhu, X. Zhu, and Y. Tang, Digest of PMRC 2007, 15pA-05(2007).

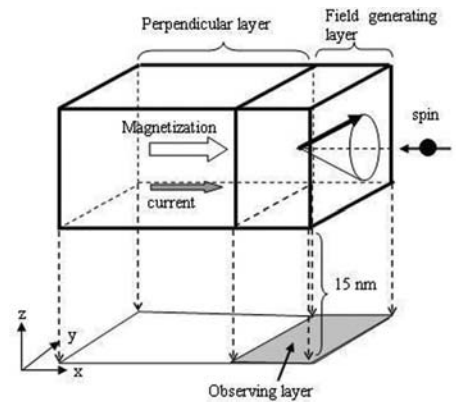

Fig. 1 Schematic diagram of microwave field oscillator.

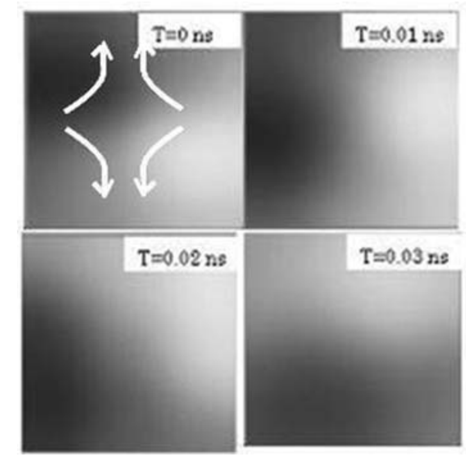

Fig.2 Snap shots of th magnetization configurations in the field generating layer.

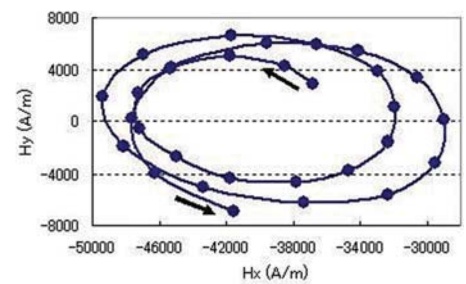

Fig.3 AC magnetic field trajectory generated by the field generating layer in the x-y plane.

Effect of media reversal mode on head footprint.

B. F. Valcu[1], B. Allimi[2], A. Dobin[1], R. Lynch[1], R. Brockie[1]
1. Seagate Technology, Fremont, CA; 2. Department of Materials Science and Engineering, University of Connecticut, Storrs, CT

The magnitude of the applied field needed to reverse magnetization in a thin film with perpendicular anisotropy depends on the field angle: the field is minimum at 45 degrees and doubles when the angle is either 0 or 90 degrees, following the Stoner-Wohlfarth (SW) asteroid. Recording heads used for writing on thin film media have a non-uniform spatial distribution of the field: under the pole the magnetic flux is perpendicular to the surface of the media, while at the pole edge there is a significant longitudinal component and thus the field is tilted with respect to the perpendicular easy axis. If magnetization reversal follows the SW curve, then it must be significantly easier to write on the medium at the pole edge compared to the region under the middle of the pole. Consequently the footprint of the recording head on such a medium should have a 'doughnut' shape. Micromagnetic simulations of the perpendicular recording system predicted the 'doughnut', however there is little direct experimental evidence [1]. When the experiment is performed in the spinstand, the disc is rotating under the head: the portion of the media that is not well written by the field from the center of the pole will ultimately travel under the pole edge where there is enough field angle to switch it.

We used a stationary 'drag' recording tester to measure the footprint of the recording head. The head is in direct physical contact with the medium. Initially a wide region on the disc is DC erased, by 'dragging' the head on the disc. Subsequently the head position is fixed in the middle of the erased region and the head is energized with a write current, such that media magnetization is reversed in the opposite direction. The head is then moved quasi-statically and the playback signal maps out the recorded footprint. Fig. 1 reveals that the shape is indeed that of a 'doughnut'.

There is a direct connection between the angular dependence of the switching field of the media and the recording head footprint. To experimentally prove that the footprint changes shape when media has a different reversal mode, we employed a bi-layer exchange spring film [2]. In this structure one layer has large perpendicular anisotropy, while the other layer is very soft. If the soft layer is thick enough, under the action of a reversal field the magnetization reverses incoherently, with a domain wall propagating from the soft layer inside the hard layer. The switching field (i.e. remnant coercivity Hcr) dependence on field angle deviates considerably from SW (see Fig. 2): at small angles the switching field is almost independent of field orientation.

The flat dependence of media switching field on angle, convolved with the spatial decrease in the magnitude of the write field as the distance to the pole center is increased, results in an effective field experienced by media that has a 'dome-like' profile. In Fig. 3 we show the experimental footprints for two bi-layer structures: for the one in which the soft layer is only 4 nm thick the reversal mode is coherent rotation (SW), thus the footprint has a 'doughnut' shape; for the other in which the soft layer is 22 nm thick the switching mode is non-coherent rotation and the footprint has a 'dome-like' shape.

[1] Yuchen Zhou, and Jian-Gang Zhu,IEEE Transactions on Magnetics, vol. 41, No. 12, pp. 4449-4453 (2005).

[2] Erol Girt, A.Yu. Dobin, Bogdan Valcu, H. J. Richter, Xiaowei Wu, Tom Nolan, IEEE Trans. on Magnetics, vol. 43, Issue 6, pp. 2166-2168 (2007).

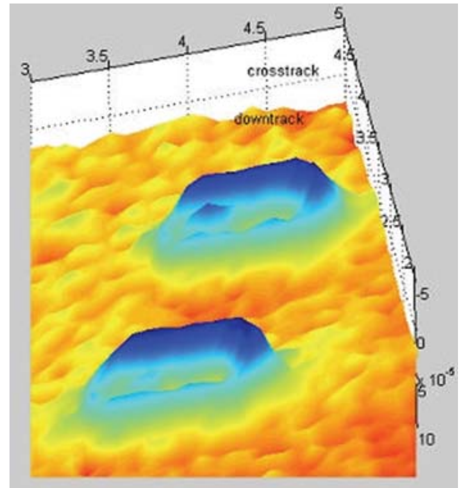

Head footprint on perpendicular media.

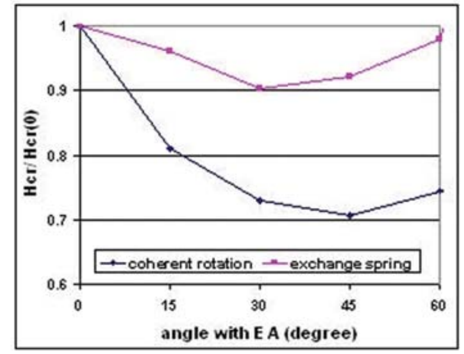

Figure 2 Switching field dependence on applied field angle for various reversal modes.

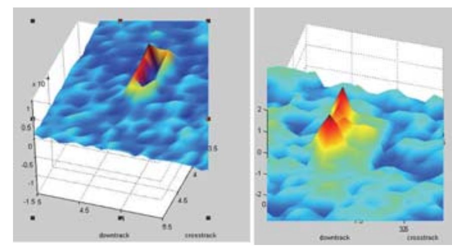

Figure 3 Head footprints for exchange spring systems with the magnetic hard layer 12 nm thick and the magnetic soft layer 4 nm (left) and 22 nm (right). The structure with thick soft layer reverses non-coherently, as opposed to the Stoner-Wohlfarth behavior of the film with thin soft layer.

EF-11

Magnetic recording readback responses in three-dimensions for multi-layered recording media configurations.

R. Wood[1], D. T. Wilton[2]
1. HDD AdTech, Hitachi GST, San Jose, CA; 2. School of Mathematics and Statistics, University of Plymouth, Plymouth, United Kingdom

In the past, simple two-dimensional (2-D) approximations have generally been adequate to represent the on-track response from a magnetic recording system. However, in the push to achieve ever higher storage densities two important factors have changed. First, the bit aspect ratio (track-width over bit-length) has decreased significantly. Second, the advent of perpendicular recording now means that there is a soft magnetic underlayer (SUL) included as part of the recording medium. Under these circumstances, 2-D analyses of head fields and head response functions, which assume infinite head and track widths, are no longer accurate. This is especially true at long wavelengths (low spatial frequencies) where the SUL renders the 2-D approximations totally inaccurate. A three-dimensional (3-D) analysis is thus necessary for getting good estimates of the 'on-track' response and is also essential in examining any side-reading/writing effects.

The approach taken here relies on an initial transformation into the 2-D spatial frequency domain and then the use of transmission matrices to relate the fields in the different layers. The general approach allows for complex structures with any set of 3-D magnetic sources and with an arbitrary number of layers. Each layer can have any anisotropic permeability, however, a linear B-H relationship must hold since the analysis is based on breaking down the magnetization into its Fourier components.

We apply this approach to the analysis of magnetic recording readback signals. For simpler configurations it is possible to write analytic expressions in the frequency domain. This is true, for example, for the system comprising a single recording layer, an anisotropic soft-underlayer (thickness d_s, permeability μ_{sx}, μ_{sy}, μ_{sz}) and suitable spacer layers giving a total separation from head to SUL of d_{sh}. This system is the subject of much of the discussion here. We examine in particular the low-frequency response associated with flux-flow in the soft underlayer and also the behavior of the main response for finite read- and write-widths. This work leads to an understanding of the nature of the "DC-null" and the related low-frequency side-reading phenomena. For example, the depth of the DC-null can be approximated by taking the larger of the write- or read-width, $\max(W_W,R_W)$, and dividing by twice the characteristic cross-track propagation-length, $\sqrt{(d_s d_{sh} \mu_{sz})}$. Also the Signal-to-Interference power ratio (rms bit response to rms low-frequency side-reading interference level) for random data can be approximated by $W_W b/[4\pi d_s d_{sh}.\sqrt{(\mu_{sx}\mu_{sz})}]$, where b is the bit-length. Another useful contribution that will be presented is an analytic expression that approximates the 3-D on-track readback frequency response without involving an inverse transform along the cross-track, z-axis.

The figure below shows an example of the analysis where, to aid visualization, we have translated back to the spatial domain. Here, a track of W_W=150 nm is written with an elliptical curvature (semi-axis = 50 nm) and a circularly-symmetric a-parameter (a=10 nm). The reader is 100 nm wide and the gap between the high-permeability shields is 30 nm.

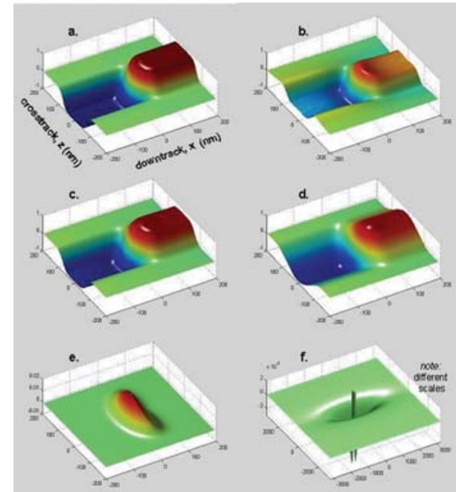

Figure. Although the analysis of this example proceeds entirely in the frequency-domain, here we take the inverse-FFT and view the results as solid surfaces in the spatial domain: a) Magnetic transition as written in the recording layer (thickness δ=15 nm, a=10nm) b) Normalized field at head surface but *with SUL absent* (magnetic spacing = 15nm) c) Same as b) but with SUL introduced (d_{sh}=45nm, d_s=100nm, μ_{sx}=μ_{sy}=100, μ_{sz}=10) d) Readback signal as a function of down-track and off-track position (R_W=100nm) e) Readback impulse response as a function of down-track and off-track position f) Same as e) but with the in-plane scales zoomed out and with vertical scale greatly exaggerated in order to illustrate the 'negative disturbance' caused by the return flux Note: the units on the horizontal axes are nanometers. The vertical axis is normalized magnetization (a) or vertical field (b, c) or reader response (d, e, f).

EG-01

Direct observation of magnetocaloric effect with pulsed-field magnet.

T. T. Nguyen[1], E. Brück[1], C. D. T[1], O. Tegus[2], J. Klaasse[1], J. Buschow[1]
1. Faculty of Science, Universiteit van Amsterdam, Van der Waals-Zeeman Institute for Experimental Physics, Amsterdam, Netherlands; 2. Inner Mongolia Normal University, Key Laboratory for Physics and Chemistry of Functional Materials, Hohhot, China

Most studies devoted for room temperature applications of magnetic refrigeration are now focused on materials showing giant magnetocaloric effect (MCE). However, as being a common feature of compounds with first-order field-induced magneto-structural transition, large MCE observed in these materials comes often with large thermal hysteresis which could make them unsuitable for applications because a real refrigerator is expected to be operated at rather high cycle frequencies [1].
After the discovery of giant MCE on MnFeP1-xAsx compounds [2], it was found that the MnFe(P,Ge) alloys also exhibit magnetocaloric effect in the same order of magnitude with tunable Tc in a large range of working temperatures. In the present work, samples of MnFe(P,Ge) were prepared by high energy ball milling and melt-spinning technique at 40 m/s speed- of-the-wheel. Shown in Fig.1a, the isothermal magnetic entropy change recorded for Mn1.2Fe0.8P0.75Ge0.25 melt-spun ribbon is 20 J/kgK under the field change of 2 T. Note that for this sample thermal hysteresis is only 1 K.
The fast magnetic measurements are performed on the 20T pulsed field magnet in the field up to 15 T at different starting temperatures (Fig.1b). The field vs. time profile is a half sinus with duration 100 ms. The magnetization process is close to being adiabatic at the field sweep rate of about 3×10^2 Tesla/s. At an ambient pressure of less than 10^-3 mbar the heat exchange with the surrounding can be neglected and the contribution of eddy current heating due to field increase (and decrease) is also small. On the other hand, magnetocaloric effect makes the sample to be heated with increasing applied field. This heat amount is then totally compensated when the field decreases from 15 Tesla to zero-field. Because of intrinsic inertia of thermocouples, the monitoring of temperature during the field sweep can not be accomplished by just reading a thermocouple. Instead we exploit fact that the magnetization becomes lower with increasing temperature (Fig.1c). Based on the comparison of magnetization curves obtained either in adiabatic or isothermal process, we can calculate the adiabatic temperature change with respect to an equivalent field change. This elegant method was first introduced by Levitin et al [3]. In this way, the adiabatic temperature change of Mn1.2Fe0.8P0.75Ge0.25 ribbon is calculated to be approximately 3 K/Tesla (Fig.1d).

In summary, the pulse field technique is a good approach for directly monitoring the MCE in adiabatic condition even for very fast field-sweep rates. The experimental results observed with fast magnetic measurements confirm that the compounds of MnFe(P,Ge) can be used as refrigerants working at high frequency. The excellent magnetocaloric properties of MnFe(P,Ge) bring practical magnetocaloric cooling a step closer.

[1] Brück E, J. Phys. D: Appl. Phys. 38, R381–R391 (2005)

[2] Tegus O, Brück E, Buschow K H J and de Boer F R, Nature 415, 150 (2002)

[3] R.Z. Levitin et al, J. Magn. Magn. Mater. 170, 223-227 (1997)

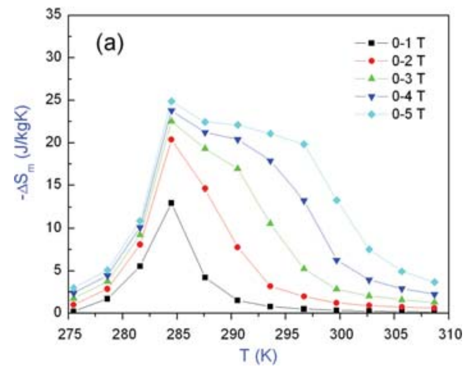

Isothermal magnetic entropy changes of Mn1.2Fe0.8P0.75Ge0.25 ribbon (Fig.1a)

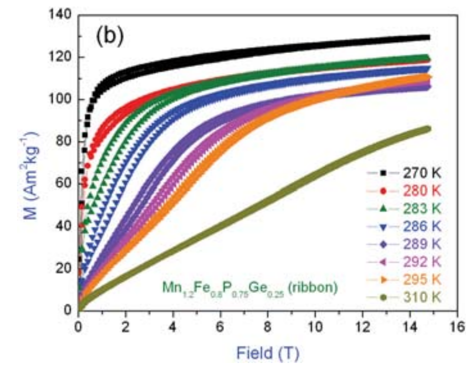

Magnetization loops measured in 20T pulsed-field magnet at different starting temperatures in the field up to 15 Tesla (Fig.1b).

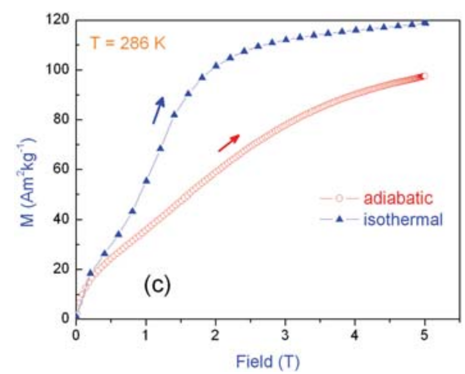

Adiabatic and isothermal magnetization curves measured in the vicinity of Tc in the field up to 5 T (Fig.1c)

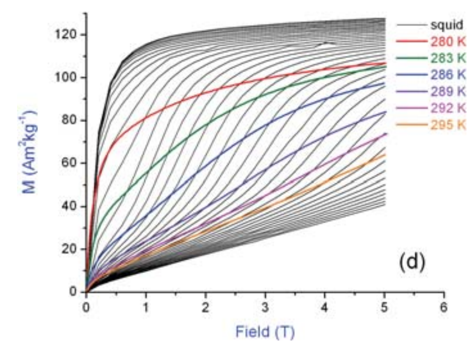

Field dependence of adiabatic temperature change is derived from the comparison of isothermal and adiabatic measurements (Fig.1d).

EG-02

The dc & ac properties of soft magnetic materials for the operational conditions found in novel electrical devices.

H. V. Patel, M. J. Hall, O. Thomas, S. C. Harmon
Industry & Innovation Division, National Physical Laboratory, Hampton Road, Teddington, United Kingdom

The increased use of electromagnetic devices in strategic areas such as environmentally friendly transport places demands on the supply chain. To achieve more efficient modelling predictions and reliable devices, a study of the behaviour of soft magnetic material properties for operational conditions needs to be performed. Modelling of electrical machines requires reliable data if the specification is to be met without too many costly development cycles. The conditions of interest include operational magnetic flux density waveforms, mechanical stress and temperature.
Existing standards [1] are essential for purchase and sale of electrical steel as well as other soft magnetic special alloys, however they are not easily adapted for operational conditions such as temperature and the application of mechanical stress. These conditions are common to many applications of magnetic materials and so techniques to determine the properties will benefit many users. In addition, material suppliers will be able to provide data that better matches the conditions of use and so material selection will be improved. If electrical machines are to replace heavy and high maintenance hydraulic and pneumatic systems (MORE electric concept) then they need to operate in extreme conditions [2]. Researchers involved in the development of embedded starter/generators for MORE electric transport estimate that the temperature would be 450 °C and the stress 450 MPa. For the automotive industry, these will probably be 200 °C and 200 MPa. A measurement technique is required that can produce these stress levels and temperatures simultaneously as well as the magnetic flux density waveforms encountered in use.
To determine the effect of stress on dc properties, it is possible to place a permeameter (in accordance with IEC 60404 part 4 [3]), in an Instron machine. In electrical machines it is the ac properties that are most important. When measuring specific total loss the standard methods require the flux density waveform to be sinusoidal, however actual waveforms for an electrical machine are not sinusoidal (figure 1 shows an actual waveform in a switch reluctance machine). It is necessary to know the specific total loss for this operational waveform. The generation and control of such waveforms is not possible using the analogue approach of IEC 404 parts 2 and 3, [2] and [4], and digital techniques are required.
The test specimen needs to have free ends for clamping in the jaws of an Instron machine and along with placing the material in an oven has made it necessary to move to an open circuit design. This removes the fundamental measurement principle of using a closed magnetic circuit. Figure 2 shows that demagnetization has an immediate effect and alters the measured BH curve.
This paper will discuss the specification of the measurement system, how this has been achieved in practice and how the presence of demagnetization has been considered. Materials under test were conventional grain-oriented electrical steel and Rotalloy 3. Due to the poor mechanical properties of Rotalloy 3, a Rotalloy 3 metal matrix composite re-enforced with carbon fibre has been developed, and the magnetic properties of this material will be discussed in the paper.

[1] IEC Standard 60404 part 2, "Methods of measurement of the magnetic properties of electrical steel sheet and strip by means of an Epstein frame."

[2] M. J. Hall, M. A. Gonzalez-Fernandez, "Measurement of magnetic properties for conditions of use and how to get there from the comfort of the laboratory", IET Seminar on Challenges in the Modelling and Measurement of Electromagnetic Materials, p.39-44, 2006

[3] IEC Standard 404 part 4 "Magnetic materials - Methods of measurement of d.c. magnetic properties of magnetically soft materials."

[4] IEC Standard 60404 part 1, "Methods of measurement of the magnetic properties of electrical steel sheet and strip by means of an Epstein frame."

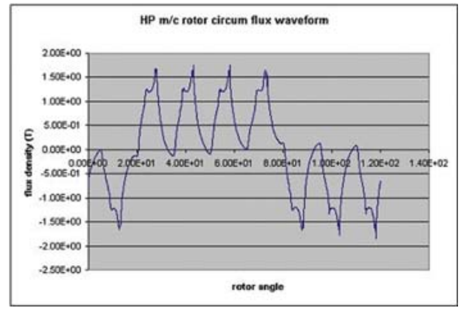

Figure 1. Actual waveform for a switch reluctance machine

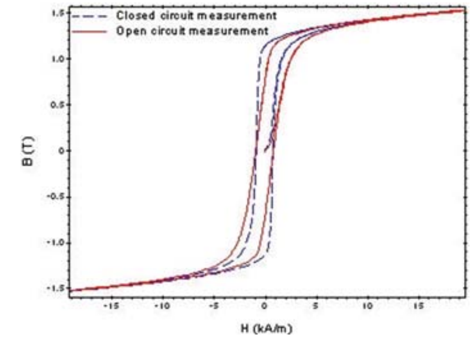

Figure 2. Effect of removing the magnetic yoke on the measured BH curve of a soft magnetic material

Eddy current effects and pinning effects in Fe and Ni single crystals with low defect densities.

S. Takahashi, S. Kobayashi
Faculty of Engineering, Iwate University, Morioka, Japan

Magnetic hysteresis loops reflect the domain wall displacement as well as the rotation of magnetic moments. The domain wall displacement is dominated by the pinning effect due to lattice defects and the eddy current effect. As the domain walls displace by the external field, the local magnetic moments within the domain wall change during the displacement and eddy current is induced in the domain wall. The force due to eddy current acts as frictional force in the domain wall displacement. The eddy current effect becomes predominant in the low temperature where the electrical conductivity increases. Dislocations act as obstacles when the domain walls move under the external field. In this study, the two effects have been studied in Fe and Ni single crystals with low defect densities by the minor hysteresis analysis discovered recently.[1,2] The seven magnetic properties and seven scaling rules are represented by a set of minor hysteresis loops. The scaling rules include
$W_F^* = W_F^0(M_a^*/M_s)^{nF}$,
$W_R^* = W_R^0(M_R^*/M_R)^{nR}$,
$H_c^* = H_c^0(M_R^*/M_R)^{nC}$,
where W_F^*, M_a^*, W_R^*, H_c^*, and M_R^* are minor-loop hysteresis loss, minor-loop magnetization, minor-loop remanence work, minor-loop coercive force, and minor-loop remanence, respectively, and M_s and M_R are saturation magnetization and remanence, respectively. The parameters of a minor loop depend on microstructures and the magnetic-field amplitude. W_F^0, W_R^0, and H_c^0 are minor-loop coefficients, which have a linear relation with coercive force and are more sensitive to lattice defects than coercive force.

The minor-loop coefficients increase by plastic deformation at room temperature in both metals. But the temperature dependence of the coefficients is quite different in Fe and Ni metals. The coefficients increase with the increase of true stress in Fe metal above $T = 200$ K and they increase remarkably with the decrease of temperature below $T = 200$ K as is seen in the temperature dependence of W_R^0 in Fig. 1(a). The increasing rate of the coefficients at low temperature is the largest in the sample without plastic deformation. While in Ni metal, the coefficients increase, take a maximum and decrease with decreasing temperature as shown in Fig. 1(b). The maximum point moves towards a lower temperature with increase of true stress.

The remarkable increase of minor-loop coefficients below $T = 200$ and 430 K in Fe and Ni metals, respectively can be explained by the appearance of eddy current effect, due to the increase of electrical conductivity with the decrease of temperature in both metals. The decrease of the coefficients below $T = 200$ K for Ni metal is due to the decrease of domain wall thickness associated with a rapid increase of magneto-crystalline anisotropy. Such anomalous increase of the coefficients below $T = 200$ K and in the medium temperature range from 200 to 430 K for Fe and Ni single crystals were found to be associated with the constriction of hysteresis loops with very low remanence and low permeability around coercive force.

[1] S. Takahashi, L. Zhang, J. Phys. Soc. Japan, 73 (2004) 1567.

[2] S. Kobayashi, T. Fujiwara, M. Tsunoda, S. Takahashi, H. Kikuchi, Y. Kamada, K. Ara, T. Shishido, J. Mag. Mag. Mater. 310 (2007) 2638.

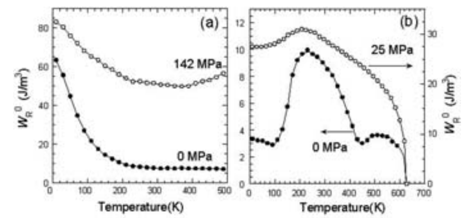

Fig. 1: Temperature dependence of minor-loop coefficient W_R^0 for (a) Fe and (b) Ni single crystals, taken before and after plastic deformation.

EG-04

Experimental Prediction of Iron Losses in Electromagnetic Devices.

G. Almandoz[1], E. Ritchie[2], J. Poza[1], A. Gonzalez[3]
1. University of Mondragon. Faculty of Engineering, Arrasate, Spain; 2. Aalborg University. Institute of Energy Technology, Aalborg, Denmark; 3. ORONA Elevator Innovation Center, Hernani, Spain

The performances of electromagnetic devices such as transformers or electrical machines depend strongly on the iron losses. The overall efficiency, the thermal behaviour or the compactness are some of the design aspects which are influenced by this phenomenon. So, it is necessary to predict these losses accurately if an optimum design of the device is required. Iron losses phenomenon in soft magnetic materials is described by the well known loss separation method in which the overall iron losses are divided into three components: hysteresis, eddy and excess losses [1]. This method can be applied with sinusoidal or arbitrary flux density waveforms [2]. The drawback of this analytic method is that it depends on a set of experimentally estimated coefficients so its accuracy is subject to a precise estimation of these coefficients. Furthermore it does not consider the effect of minor loops so that it may not be suitable for iron loss calculation in electric machines or transformers. In these devices minor loops might appear due to the geometry of the core or due to pulse width modulation (PWM) supply voltages. In this work an experimental method for iron losses prediction in electromagnetic devices is proposed. The main goal is to predict accurately the iron losses in the design process before building any prototype. This method is based on experimental tests performed using a Single Sheet Tester (SST). Fully automated SST with a closed loop control makes possible to analyze iron losses in soft magnetic materials with non sinusoidal flux density waveforms. Iron losses are computed integrating the area enclosed by the hysteresis loop so that possible minor loops are taking into account and the results don't depend on any coefficients. As example specific iron losses in the teeth and the yoke of a permanent magnet synchronous machine (PMSM) have been computed. Flux density waveforms in these parts of the stator core have been obtained from Finite Element Analysis (FEM) of the machine. The laboratory equipment comprises a SST, a wide bandwidth linear amplifier, an analog PI controller, two sensors and a Data Acquisition (DAQ) system based on a personal computer equipped with a multifunction DAQ card of National Instrument. The equipment is completely automated so that the user can perform different tests in an easy way thanks to the interface built in LabView. The proposed methodology consist in driving a magnetic material sample using a SST with the flux density waveforms calculated in FEM or experimentally measured in different parts of the magnetic core of a device. The magnetic core is divided in different parts so that the magnetic field distribution is approximately uniform in each of them. This way the specific iron losses measured using the laboratory equipment are the iron losses in this part of the magnetic core of the device. Then assuming that the magnetic field distribution in each part is homogeneous the overall iron losses can be calculated.In this digest the most relevant results are shown. In the full version more results will be included. Temporal flux density waveforms in two different points of the stator core when the motor works in open circuit mode have been calculated in FEM. These points are situated in a tooth and in the above part of a slot. In Fig1 calculated flux density waveforms in a tooth and in the yoke are shown. In Fig2 experimentally measured hysteresis loops are presented. In Fig3 experimentally determined iron losses are presented. These curves have been obtained driving the M80065D sample with the described flux density waveforms at different frequencies.

[1]G.Bertotti, "General properties of power losses in soft ferromagnetic materials," Magnetics, IEEE Transactions on, vol. 24, no. 1, pp. 621-630, 1988.[2]A. Boglietti, A.Cavagnino, M.Lazzari, and M.Pastorelli, "Predicting iron losses in soft magnetic materials with arbitrary voltage supply: an engineering approach," Magnetics, IEEE Transactions on, vol. 39, no. 2, pp.981-989,2003.

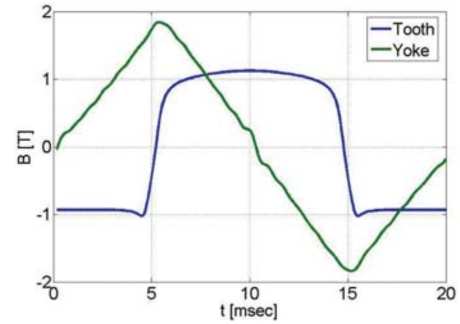

Temporal representation of magnetic fields

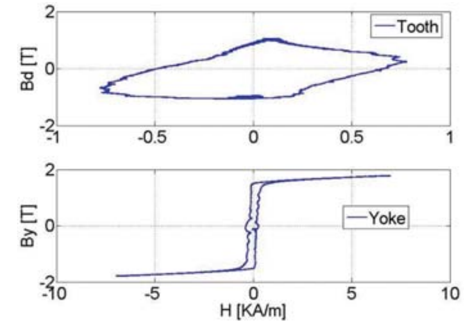

Experimentally measured hysteresis loops

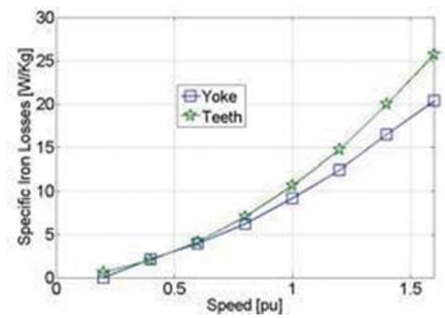

Specific iron losses when the motor works in open circuit mode

EG-05

Miniature iron-gallium actuator with displacement magnifying mechanism.

M. Ghodsi[1], T. Ueno[1], C. Sze Keat[2], T. Yano[2], T. Higuchi[1]
1. Precision Eng. Department, The University of Tokyo, Tokyo, Japan; 2. Mechano Transformer Corporation, Kawasaki, Japan

1. Introduction
In the last two decays, the requirements for precision and micro-displacement actuators have been increased. For example, these actuators are used for micropositioning [1] and vibration controls [2]. In most applications, piezoelectric (PZT) is used as an actuation element. However, the PZT has low Young's Modules, needs high voltage source and because of its brittleness property, miniature size or arbitrary shape cannot be obtained easily. On the other hand, to increase the performance of the equipments especially in the space applications, it is required to make actuators smaller, lighter and with low power consumption. Because of these requirements, magnetostrictive seems a good candidate for miniature actuator. In 1999 large magnetostriction material made of iron-gallium alloy was developed. Although strain of iron-gallium is small (160-250 ppm), it is strong (large Young's Modulus ≈ 70~90 Gpa) [3] and has high flux density saturation (1.7 T). Furthermore, it will be saturated by low magnetic field (30 kA/m) [4] and its high permeability (≈200) makes it suitable for close magnetic circuits. These specifications combined with high ductility (easy machining) and operation in different temperatures [5] promise wide range of industrial applications for recently developed magnetostrictive material, iron-gallium alloy. In this research, iron-gallium bar is combined with a magnifying mechanism to make a high efficiency miniature actuator. Static and dynamic behaviours of the actuator are investigated.
2. Principle of Actuator
Figure 1(a) shows a schematic configuration of iron-gallium actuator. This actuator consists of two main parts that make a close magnetic circuit. First part is an iron-gallium bar and second part is a magnifying mechanism to amplify strain of the iron-gallium. To enhance the performance of magnetic circuit, the magnifying mechanism is made of high permeability magnetic steel. The length of iron-gallium bar is 10 mm and its cross section is square by 1 mm width (Fig. 1(b)). The maximum strain of annealed iron-gallium is 250 ppm. Thickness of magnifying system is 0.8 mm and energized coil is ϕ=0.05 mm, 240 turns. Iron-gallium displacement is transmitted to the head by phosphor-bronze elastic arms. By energizing the coil, generated magnetic fluxes pass through the iron-gallium bar and increase its length. Similar to lever mechanism this enlargement is magnified and large vertical displacement is achievable by head.
3.Results and discussion
As shown in Fig. 1(b), the actuator is fixed on a brass fixture. By energizing the coil, a vertical displacement can be realized in the aluminium head. Photonic sensor (14.7 µm / V in front slop) is used for the vertical displacement measurement. Figure 2, shows the displacement of actuator when the coil is energized by sinusoidal signal with different amplitudes. Although the maximum expected displacement of iron-gallium is 2.5 µm, a large displacement of 23 µm is achievable. It means that, this actuator can magnify the displacement about 9 times. It is obvious that small hysteresis makes this actuator suitable for real applications.

1.F.E.Scire, E. C. Teague,Review of Scientific Instrument, Vol. 49, no. 12, pp. 1735-1740, 1978.

2.W.Zhang, G.Meng, H.Li, International journal of Advanced Manufacturing Technology, Vol. 28, no.3,4, pp. 321-327, 2006.

3.P.R. Downey, A.B. Flatau, Journal of Applied Physics, Vol. 97,10R505, 2005.

4.M.Ghodsi, T.Ueno, T.Higuchi, and E.Summers, The 18th Symposium on Electromagnetics and Dynamics, pp. 445-448, 2006.

5.M.Ghodsi, T.Ueno, H.Teshima, H. Hirano, T. Higuchi, E. Summers, Sensors and Actuators Phys. A 135, pp. 787-791, 2007.

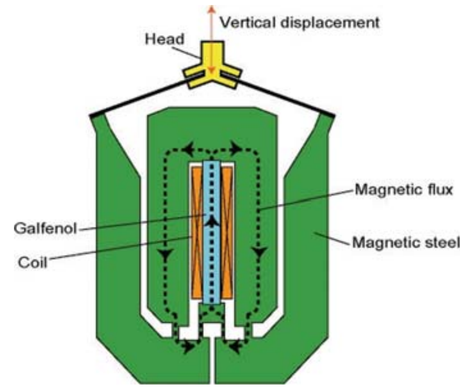

(a)

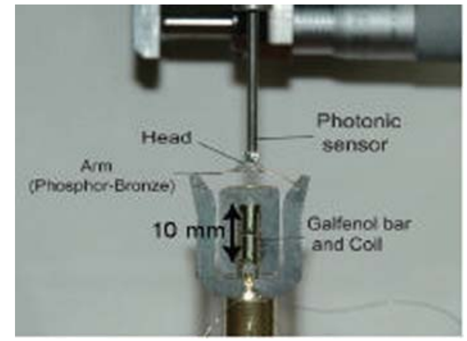

(b) Figure 1: (a) Schematic (b) manufactured prototype of miniature iron-gallium actuator

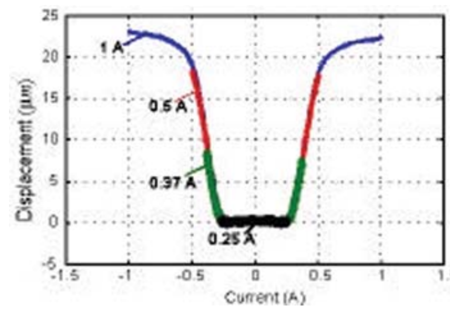

Figure 2: Relationship between the applied current and displacement of miniature actuator

EG-06

Application of magnetoelastic sensors for monitoring of the combustion process in diesel engines for locomotives.

A. Bienkowski[1], R. Szewczyk[1,2], J. Salach[1]
1. Institute of Metrology and Measuring Systems, Warsaw University of Technology, Warsaw, Poland; 2. Industrial Research Institute for Automation and Measurements PIAP, Warsaw, Poland

Monitoring of the combustion process in diesel locomotive engines is very important from the practical point of view. The commonly used strain-gauge sensors are not well suitable for this application, due to high temperature and corrosive environment of sensor operation. Moreover, in the case of this application the sensor should be as flat as possible, to reduce problems during the installation of it.
This paper presents a novel solution of utilizing ring-shaped magnetoelastic sensors with amorphous alloy cores in monitoring of the combustion process in diesel locomotive engines. Sensor is mounted on the binding screw of the head in a diesel engine. Special cylindrical backings enable uniform stress distribution, as well as protect the sensing element from twisting during the installation. Results of the tests of functional properties of developed sensor are also presented. These results indicate that sensor sensitivity, as well as its resolution, is sufficient for monitoring of combustion process.

EG-07

Longitudinal and transverse magnetoimpedance in FeNi/Cu/FeNi multilayers with longitudinal and transverse anisotropy.

D. de Cos[1], J. M. Barandiaran[1], A. Garcia-Arribas[1], V. O. Vas′kovskiy[2], G. V. Kurlyandskaya[1,2]
1. Electricity and Electronics, Basque Country University UPV-EHU, Leioa, Spain; 2. Physics of Magnetic Phenomenon, Ural State University named under A.M.Gorky, Ekaterinburg, Russian Federation

Magnetoimpedance (MI) consists in the change of the impedance of a ferromagnetic conductor under an external magnetic field [1-2]. Special efforts have been made recently for the development of thin film miniature MI sensors compatible with semiconductor electronics [1, 3-4]. A typical MI multilayer consists of two magnetic layers separated by a nonmagnetic conductive lead [1, 5]. Up to now most studies have concentrated on MI devices with transverse magnetic anisotropy, i.e. with the in-plane easy magnetization axis perpendicular to the direction of the current. This type of the anisotropy usually results in higher MI ratio and sensitivity for the longitudinal MI effect (external field is parallel to the current). In this work both longitudinal and transverse MI is studied for multilayered structures of FeNi/Cu/FeNi with either longitudinal or transverse magnetic anisotropy, at relatively low frequencies up to 500 MHz, convenient enough for technological applications.

The NiFe(150nm)/Cu(500 nm)/NiFe(150 nm) multilayered structures were prepared at room temperature by rf sputtering using metallic masks and glass substrates. Each multilayer has 50 µm(Permalloy) and 5 µm (copper) wide stripes. The length of the MI stripes was 12 mm. A constant field of about 100 Oe was applied in plane of the multilayeed structure during deposition. Such an external field was either parallel to the Cu-leads, creating a longitudinal anisotropy (sample L), or perpendicular to it (sample T), creating a transverse anisotropy. The anisotropy field values were estimated from the shape of the M(H) curves obtained by MOKE studies.

The MI was measured as described in ref. [5]. MI ratio ($\Delta Z/Z$) is usually defined with respect to the saturated sample or the maximum applied field where Z is a minimum: $\Delta Z/Z = (Z(H)-Zmin)/Zmin$. MI sensitivity (s) is defined as $s = (\Delta Z/Z)/\Delta H$, where 0.1Oe field increments were taken in the calculation in order to avoid excessive noise.

Figure (a) shows the frequency dependence of the maximum longitudinal MI ratio for samples of L and T type. It is clearly seen that the longitudinal $\Delta Z/Z$ ratio is higher for T multilayers than for L multilayers in all frequency range under consideration. The maximum sensitivity for T samples was about 31%/Oe (at about 100 MHz) while for the L samples was only about 5.5%/Oe (at about 200 MHz) (see Table, Figure (b,c)). Transverse MI ratio for T samples is negligibly small below 100 MHz and only 1 % for higher frequencies (Figure (c)). However, transverse MI for L samples is much higher ($\Delta Z/Z$(f= 300 MHz)= 70 %). Relatively high value of the longitudinal MI ratio (($\Delta Z/Z$(f= 300 MHz)= 54 %) was also observed for L samples (Table, Figure (b)). In a frequency range of 90 to 300 MHz the longitudinal and transverse $\Delta Z/Z$ sensitivities of L samples are higher than typical sensitivities of giant magnetoresistance detectors (of about 2%/Oe). One can therefore propose a design with a single sensitive element detector with enhanced functional parameters for 2 way detection of magnetic field in the plane of the MI multilayer, instead of using two different MI elements.

G.V. Kurlyandskaya acknowledges a “Ramon y Cajal” Fellowship of the Spanish MEC. This work was partially supported by The Plan Nacional de Materiales under MAT2005-06806 grant.

[1] L.V. Panina, K. Mohri, T. Uchiyama, M. Noda, K. Bushida, IEEE Trans. Magn. 31 (2) (1995) 1249.

[2] A. Antonov, S. Gadetsky, A. Granovsky, A. Diachkov, M. Sedova, N. Perov, T. Furmanova, A. Lagarkov, Physica A 241 (1997) 414.

[3] Y. Nishibe, N. Ohta, K. Tsukada, H. Yamadera, Y. Nomomura, K. Mohri, T. Uchiyama, IEEE Trans. Veh. Technol. 53, (2004) 1827.

[4] Kurlyandskaya, G.V., Muñoz, J.L., Barandiaran, J.M., García-Arribas, A., Svalov, A.V., Vas′kovskiy, V.O. J. Magn. Magn. Mater., 242-245 (2002) 291.

[5] D. de Cos, A. García-Arribas, J. M. Barandiarán Sens. and Act. A, 115 (2004) 368.

Sample (anisotropy)	Longitudinal MI (s (%/Oe)				Transverse MI (s (%/Oe)			
	f= 15 (MHz)	f= 90 (MHz)	f= 210 (MHz)	f= 300 (MHz)	f= 15 (MHz)	f= 90 (MHz)	f= 210 (MHz)	f= 300 (MHz)
L (longitudinal)	0.6	5.0	5.5	4.0	0.5	9.0	16.0	14.0
T (transverse)	15.8	28.2	24.6	21.7	0	0	1.3	2.0

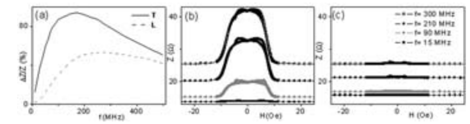

Figure. Frequency dependence of longitudinal ΔZ/Z ratio (a); transverse Z(H) variation for L (b); and transverse Z(H) variation for T (c) FeNi/Cu/FeNi MI multilayers.

EG-08

Magnetorheological characteristics of carbonyl iron embedded suspension polymerized poly(methyl methacrylate) microbead.

J. You, B. Park, *H. Choi*
Department of Polymer Science and Engineering, Inha University, Incheon, South Korea

Introduction

Magnetic microspheres have attracted much interest in past decade due to their various potential applications in such as biosensor and specific molecular recognition areas [1, 2]. Among these magnetic microspheres, soft magnetic materials such as carbonyl iron (CI) have been investigated due to their reversible changes in their magnetic properties in response to external magnetic fields. The CI with these changeable magnetic properties has been considered as a good candidate material for magnetorheological (MR) fluid application with great attentions as promising damping materials [3], in which the MR fluid is a magnetic particle suspension dispersed in a viscous non-magnetic carrier fluid. Rheological properties such as yield stress and shear viscosity of the MR fluid can reversibly and instantly be changed as a result of dispersed magnetic particles building up chain-like structure under a magnetic field due to magnetic dipole-dipole interaction between particles [4, 5]. However, both sedimentation of the CI particles due to the large density mismatch with the carrier liquid and difficulties in re-dispersion after caking in the pure magnetic CI based MR fluid systems have been regarded as serious disadvantages. The magnetic microspheres of CI and poly(methyl methacrylate) (PMMA) composite was prepared to reduce the density mismatch in this study. The microsphere was prepared via in-situ suspension polymerization using poly(vinyl alcohol) and triblock copolymer as stabilizer and co-stabilizer, respectively. As a result, a core-shell structure of the microsphere was obtained, and then MR characteristics of the CI embedded suspension polymerized PMMA microbeads were investigated.

Experimental

The microsphere was fabricated via suspension polymerization of styrene in the presence of CI. The CI was dispersed in aqueous solution in which both poly(vinyl alcohol) and PEG-PPG-PEG triblock copolymer were dissolved. Purified styrene monomer, in which benzoyl peroxide was dispersed as an initiator, was added into the CI suspension. The polymerization was held at 80 degree C for 12hr. The dried product particles were dispersed into mineral oil for the MR application. The fabricated microsphere was examined using both SEM and TEM. In addition, MR properties of the product particle based MR fluid were measured in a steady shear mode using a rotational rheometer. The density and MR properties of the product particle were compared with those of pristine CI particles.

Results and Discussion

SEM image given in Fig. 1 represents surface morphology and shape of the product microspheres showing a round shape with porous surfaces and 10micron of average particle diameter. The surface of microsphere was observed to be constituted by many grains of PMMA, and the density of the composite particles was lowered to be 3.27 g/cm3 compared to the density of pristine CI with 7.89 g/cm3. From the change of surface morphology and reduced density, it was determined that the magnetic microsphere of composite was successfully fabricated.

Volume concentration of the product particles was fixed at 25 v/v % for MR suspension. Both shear stress and shear viscosity responses under steady shear condition were investigated as a function of shear rate for different magnetic field strength ranging from 0 to 343 kA/m. Figure 2 shows that shear stress was found to increase with applied magnetic field strength, resulting yield behavior, and suggesting that the product microsphere of CI and PMMA composite could be well applicable into the MR fluid.

[1] D. L. Graham, H. A. Ferreira, P. P. Freitas, J. M. S. Cabral, Biosens. Bioelectron. 18, 483 (2003).

[2] J. Connolly, T. G. St Pierre, J. Dobson, Bio-Med. Mater. Eng. 15, 421 (2005).

[3] S.T. Lim, M.S. Cho, I.B. Jang, H.J. Choi, M.S. Jhon, IEEE. Trans. Magn. 40, 3033 (2004).

[4] I. Bica, J. Magn. Magn. Mater, 241, 196 (2002).

[5] S.T.Lim, H. J. Choi, M. S. Jhon, IEEE. Trans. Magn. 41, 3745 (2005)

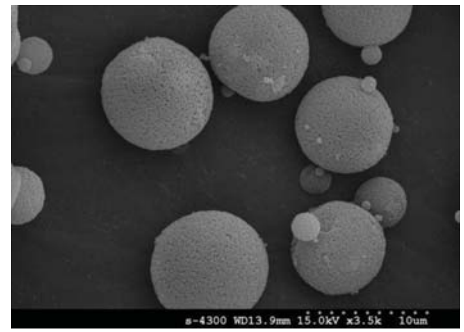

Fig. 1 SEM image of PMMA/CI microspheres

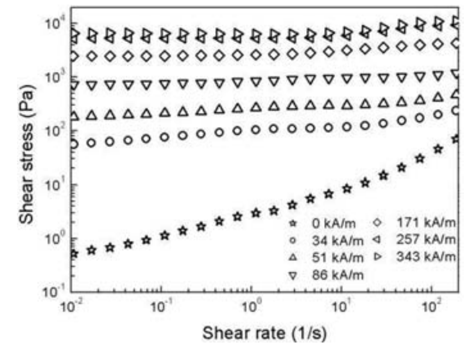

Fig. 2 Flow curve of PMMA/CI based MR fluids

EG-09

Effect of Slit Patterning Perpendicular to Magnetic Easy Axis In Thin Film Inductors.

T. Masai[1,2], Y. Kitamoto[2]

1. TDK, Minami-alps city, Yamanashi pref., Japan; 2. Innovative and Engineerd Materials, Tokyo Institute of Technolgy, 4259 Nagatsuta, MIdori-ku, Yokohama, Japan

[1. Introduction]
The demand of utilizing magnetic thin films in power inductors and high frequency inductors(1) is increasing. In spiral inductors using magnetic films with uniaxial anisotropy, low permeability in easy axis direction in MHz range reduces inductance. In order to improve the characteristics of magnetic thin film inductors in MHz range, it is important to control domain-wall displacement and increase its resonant frequency in magnetic easy-axis direction. Thus, we fabricated magnetic wire arrays by slit patterning perpendicular to easy axis in magnetic thin films and discussed the influence of the wire width on magnetic characteristics.

[2. Experimental]
CoZrTa soft magnetic thin films were prepared using dc magnetron sputtering. Thickness of the magnetic films was 500 nm. Slit patterning was made by lithography and wet etching as shown in Fig. 1. The longitudinal direction of magnetic wires is perpendicular to easy axis in the magnetic films. The wire width (L) was 0.02, 0.05, 0.1, 0.2, 0.5, 1.0, 2.0, 5.0, and 6.0 mm. The gap length (S) between magnetic wires of all the samples was 0.02 mm. Permeability was measured using an impedance analyzer.

[3. Results and discussion]
Fig. 2 shows frequency dependence of real part of relative permeability in the directions parallel and perpendicular to the magnetic wires. The perpendicular direction to the magnetic wires corresponds to magnetic easy axis in the thin films.

The permeability in the perpendicular direction decreases in the low frequency range below 100 kHz, but the resonant frequency originated from domain-wall displacement (the first drop of the frequency dependence in the perpendicular direction as seen in Fig. 2) increases with the decrease of the wire width. On the other hand, the permeability is kept at around 1000 in the range below 100 MHz and the resonance related to domain-wall displacement is not observed in the parallel direction, suggesting that the magnetic behavior in the parallel direction is based on magnetization rotation in the magnetic hard axis.

In order to investigate effects of the slit pattering in practical devices, we fabricated inductors shown in Figs. 3 and 4. A spiral coil was fabricated on a substrate by Cu-electroplating, and the magnetic wire array sample was bonded onto it. The magnetic field induced by the coil penetrates the patterned magnetic film. Therefore, it is expected that the influences of the patterned magnetic films appear in frequency characteristics of their inductance. The dependence of the inductance at 1 MHz on the magnetic wire width L is shown in Fig. 5. The inductance takes the maximum at L=0.5 mm. This behavior is explained by the shift of the resonant frequency in the magnetic easy-axis direction.

[4. Conclusion]
We fabricated the magnetic wire arrays by slit patterning perpendicular to magnetic easy axis in magnetic thin films with uniaxial anisotropy. The resonant frequency was shifted to higher frequency range. Moreover, we fabricated inductors using patterned magnetic thin films. The inductance at 1 MHz was increased by the slit patterning, and took the maximum at the wire width of 0.5 mm. These results show that the slit patterning perpendicular to the magnetic easy axis is effective to improve characteristics of inductance in the easy axis.

1) S. Ohnuma, K. Shirakawa, S. Murakami, and K. Masumoto: J. Magn. Soc. Jpn. 23 p.1633-1636 (1999)

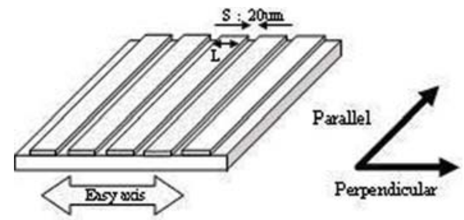

Fig. 1 Patterned magnetic thin film

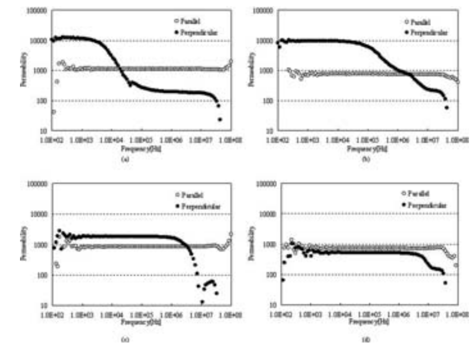

Fig. 2 Frequency dependence of permeability for patterned films. (a) L= 6.0mm (b) L= 2.0mm (c) L=0.5mm (d) L= 0.2mm

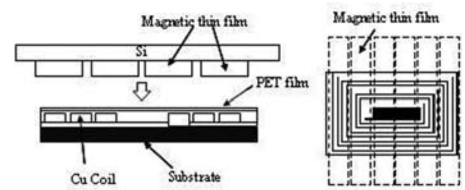

Fig. 3 Cross sectional view of the inductor with patterned magnetic films. Fig.4 Top view of the inductor

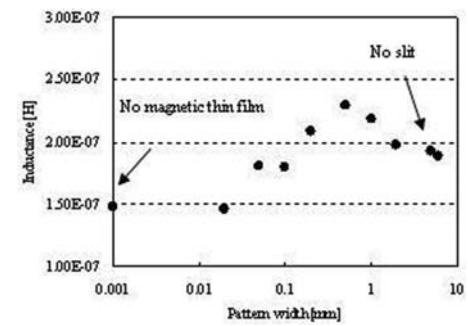

Fig. 5 Dependence of inductance at 1MHz on wire width for the inductor with patterned magnetic films

EG-10

Miniaturization of antenna using Y-type hexagonal ferrite.

K. Kawano, Y. Okamoto
Product Development HQ, TAIYO YUDEN CO.,LTD., Takasaki-shi, Japan

The demand for the miniaturization of antenna, which is used for the mobile telephone, has been increased along with the downsizing of the mobile. Especially for the digital broadcasting services such as DMB and DVB-H, the miniaturization is one of key issues because the antenna size is inversely proportional to the frequency, which was assigned from 170 MHz to 800 MHz for these services. These frequency ranges are relatively lower and it indicates that the antenna will need the larger size.

It is well known that the size of the antenna can be miniaturized by the effect of wavelength shortening using the material with the permittivity and/or permeability. Generally, the dielectric material is widely used for the antenna application. On the other hand the soft magnetic material has been not used because there is not suitable material having the enough performance in the required frequency range. However, there might be possibilities to apply the magnetic material for antenna of the digital broadcasting services because the operation frequency is lower than 1GHz.

In this study, the possibility of the Y-type hexagonal ferrite is investigated for the effect of the miniaturization of the antenna. Y-type hexagonal ferrite with the chemical composition of $Ba_2Co_2Fe_{12}O_{22+x}$ is fabricated by the conventional ceramic sintering method. XRD measurement shows that the fabricated sample has the single phase. Figure 1 shows the frequency dependences of both permittivity and permeability of the material. As we can see, the imaginary parts of both are relatively small up to 1GHz, indicating the small material losses. Figure.2 shows the inversed F antenna designed for this study. This antenna has the size with 30mm length, 5mm width and 1mm thickness and the pattern of silver is screen-printed on the ferrite substrate. Voltage Standing Wave Ratio (VSWR) is calculated by high frequency structure simulator (HFSS) and it is found that the resonance frequency is ~1.085GHz. Experimental result of VSWR is shown in figure.3 and the resonance frequency is ~1.09GHz, which is very similar to the simulation result. The resonance frequency is shifted to ~0.84GHz when the upper side antenna is covered by other substrate of the ferrite. This result indicates that the wavelength shortening is going to be effective when the antenna pattern is covered by the magnetic material as much as possible, and the volume of the antenna can be reduced to ~50%. The antenna gain at 1.09GHz is shown to be –2.7 dB, which might need to be improved.

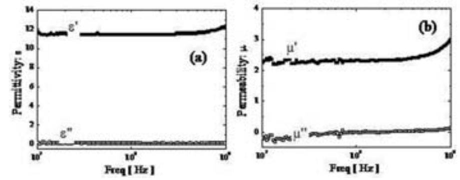

Fig1: Frequency dependences of (a) permittivity, (b) permeability of Y-type hexagonal ferrite.

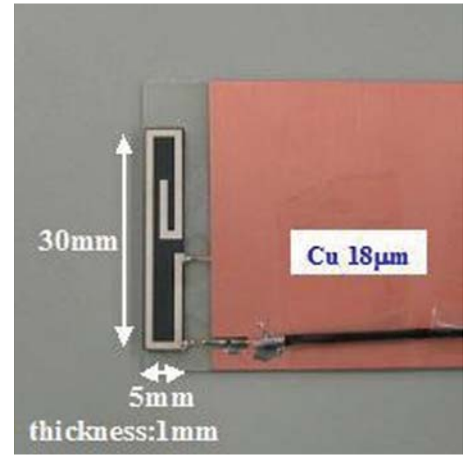

Fig2: Designed inversed F antenna

Fig3: Experimental result of VSWR of the antenna shown in fig2.

EG-11

Development of Axial Flux Permanent Syncrnous Motor by using High-Density Magnetic Composites.

H. Nakai[1], T. Arakawa[1], K. Hiramoto[1], S. Tajima[1], Y. Inaguma[2]
1. Toyota Central R&D labs., INC., Aichi, Japan; 2. Daido Institute of Technology, Nagoya, Japan

1. Introduction
The electric motors of electrical hybrid vehicles require a high torque/volume ratio. We have paid an atttention to an axial flux permanent magnet synchronous motor (AFSM) to be able to generate a high torque, compared with a radial flux permanent magnet synchronous motor. The flux in the stator of an AFSM is distributed in three dimensions. Therefore, the use of a powder magnetic core was attempted, namely a high-density soft magnetic composite (HDMC) with a low core loss and three dimension isotropy. The aim of this paper is to confirm the performance of the AFSM with an HDMC.
2. Structure of the motor
The structure of the AFSM is shown in Figure 1. Torque is generated in the gap between the rotor and the stator, and a torque increase becomes possible because this gap area can be expanded. Therefore, the AFSM having double gaps has the capability for increased torque. The development target of the motor was set to the max torque 100 Nm and highest rotational speed 8000 rpm.
The HDMC has bending strength and resistivity in the relation of contradiction [1]. Efficiency decreases because the eddy current increases due to the decrease in resistivity when the necessary strength is secured for a maximum torque. Then, the tooth and the yoke are designed to be a division structure in order to achieve both a low loss and the necessary strength (Table 1 and Figure 2). The tooth material was selected in order to ensure an adequate bending strength, while the yoke material was selected in order to minimize the core loss.
The rotor core is composed of rolled magnetic steel sheets. The surface of the core has alternating magnets and silent poles. The purpose of this structure is to generate a reluctance torque in addition to a magnet torque.
3. Performance verification by prototype
Figure 3 shows a photograph of the prototype. The current-torque characteristics of the prototype are shown in Figure 4. The results indicate that the prototype falls below the calculated value though the torque target value was almost satisfied. Because the loss grew as shown in Figure 5, it is assumed that the disadvantageous eddy current of the stator is larger than the predicted value. It is thought that this loss increase is due to the PWM.
4. Conclusion
This examination was able to confirm that an AFSM with an HDMC as a stator core can achieve a high torque/weight ratio.

[1] S.Tajima et al., Materials Trans., Vol.45, no.6, pp.1891-1894,2004

	resistivity	bending strength
tooth	0.3 p.u.	180 MPa
yoke	1.0 p.u.	110 MPa

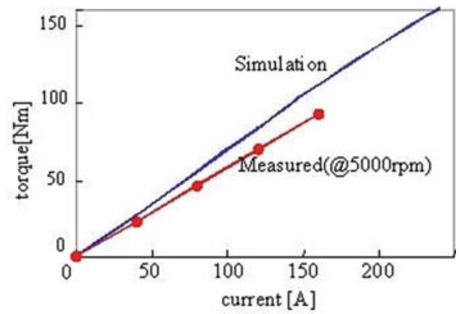

Comparisons between measured and calculated values of torque vs. current

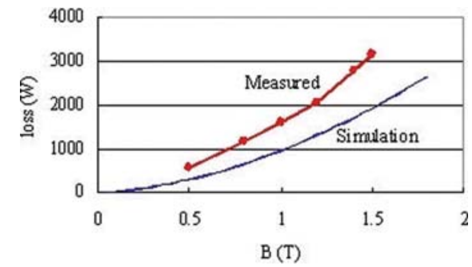

Comparisons between measured and calculated values of stator loss (300Hz)

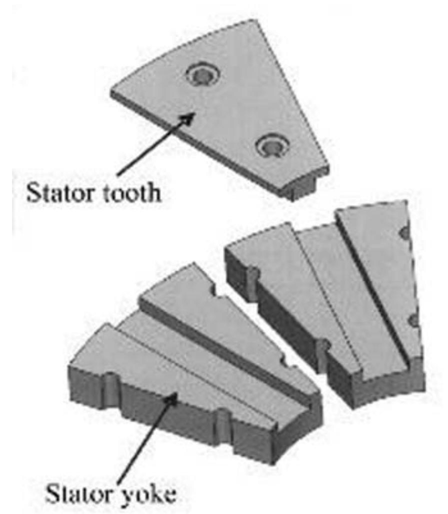

Structure of stator

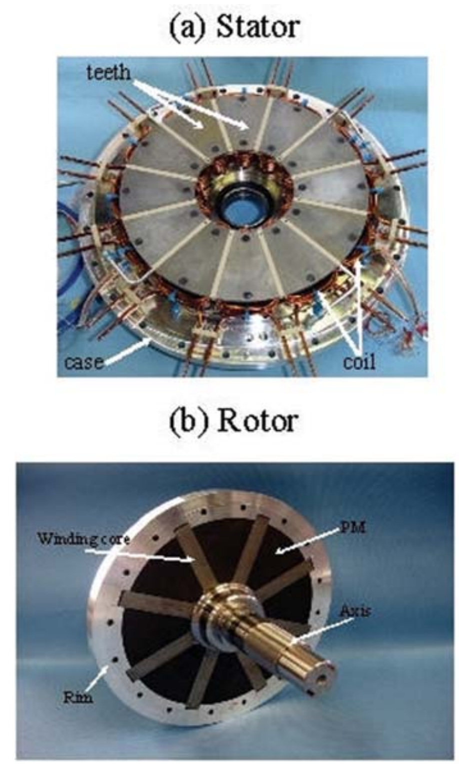

Prototype motor

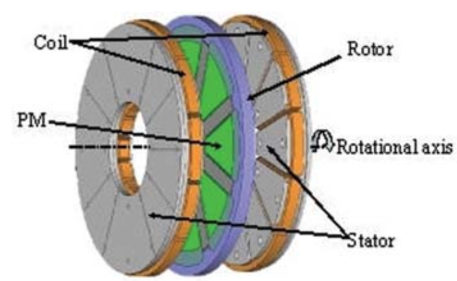

Structure of the AFSM

EG-12

Validation of Voltage and Current Waveforms of Nonlinear Inductors Computed with a Novel Finite Element Methodology.

R. Salas, J. Pleite
Tecnologia Electronica, Universidad Carlos III de Madrid, Leganés, Spain

MnZn soft ferrite cores are widely used as inductors and transformers in power electronic converters with switching frequencies between 10 kHz to 1 MHz [1]. In the design and simulation of magnetic components a model for the nonlinear behavior of the magnetic material is required [2]. The nonlinear effects in cores are saturation, hysteresis, and eddy currents.
In two previous papers [3-4] we proposed a modeling procedure for magnetic components based on FEA techniques. In this paper we extend the analysis of Refs. [3-4] and explore the applicability of our method to an RM shaped-soft ferrite core inductor which is included in a DC/DC converter operating at 40 kHz and 100 kHz. To do so we present a theoretical-experimental comparison of the voltage and current versus time waveforms of the inductor. As in Refs. [3-4] we will assume that the core exhibits saturation.
Theoretical voltage and current waveforms of the inductor vmod(t), imod(t) were obtained as follows [3-4].
First, we assigned the BH curve of the material to the modeled core to be tested to take into account the saturation effect. The BH curve was experimentally measured using a two-winding ferrite-core transformer (FERROXCUBE TN23/14/7 ring core, 3F3 material [5]). The number of primary and secondary turns was 60.
Next we computed the flux versus current i, Φmod(i), using the Maxwell field simulator's magnetostatic solver [6]. Then the inductance versus i, Lmod(i), is computed by differentiating Φmod with respect to i. Finally, Lmod(i) is introduced into a buck converter designed in the PSIM circuit simulator [7] to obtain vmod(t), imod(t) by transient simulation.
To illustrate how our method works we have applied it to a buck converter at 40 kHz and 100 kHz containing a resistor R = 3.1 Ω, two capacitors Cfv = Cb = 450 μF, a mosfet transistor (IRF530A), a diode (BYW29F), and a 10-turn soft ferrite core inductor (FERROXCUBE RM14/I core, 3F3 material [5]).
To experimentally check the accuracy of our method we computed Φmod(i) and compared the results to measurements, Φexp(i), Fig. 1(a). The experimental inductance Lexp(i) and Lmod(i) are shown in Fig. 1(b). Lexp(i) was computed by differentiating numerically Φexp with respect to i. Finally, we compared vmod(t), imod(t) to experimental waveforms vexp(t), iexp(t), Figs. 2-3. Time dependence of the instantaneous power v×i computed both from vmod(t), imod(t) and from vexp(t), iexp(t) are also shown, Figs. 2(c)-3(c). As Vin (DC input voltage) increases, imod(t) takes a more curved shape, Figs. 2(b)-3(b). This curved shape would not exist in the case of a linear model. Agreement between our theory and the experimental results is seen to be quite good. More detailed experimental results will be reported in a more detailed paper.

[1] N. Mohan, T.M. Undeland, W.P. Robbins, Power Electronics: Converters, Applications, and Design, John Wiley & Sons, 2003.

[2] P. R. Wilson, J. N. Ross, and A. D. Brown, "Simulation of magnetic component models in electric circuits including dynamic thermal effects," IEEE Trans. Power Electron., vol. 17, pp. 55-65, 2002.

[3] R. A. Salas, J. Pleite, E. Olías, A. Barrado, Nonlinear saturation modelling of magnetic components for circuit simulation, IEEE International Magnetics Conference, Intermag 2006. San Diego, California, USA.

[4] R. A. Salas, J. Pleite, C. González, V. Valdivia, Saturation Core Modeling Procedure for Magnetic Components using Finite Element Analysis, IEEE International Symposium on Industrial Electronics, ISIE 2007, Vigo, Spain.

[5] FERROXCUBE, Data Handbook Soft Ferrites and Accessories, 2004.

[6] Ansoft Corporation, Maxwell Software, Version 10, Pittsburgh, 2001.

[7] PSIM Version 6.0, Powersim Inc.

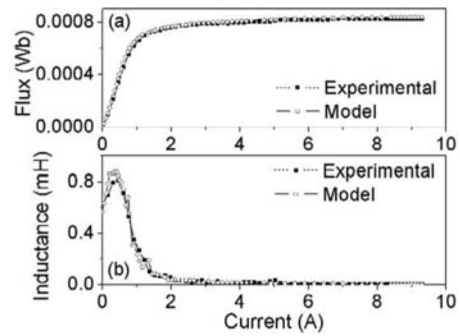

Fig. 1: (a): Plot of Φexp(i) and Φmod(i). (b) Plot of Lexp(i) and Lmod(i).

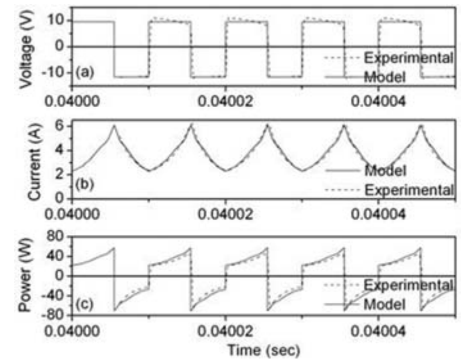

Fig. 2: Experimental and modeled waveforms at 100 kHz, Vin = 21.04 V, and duty cycle = 0.5482: (a) Voltage. (b) Current. (c) Power.

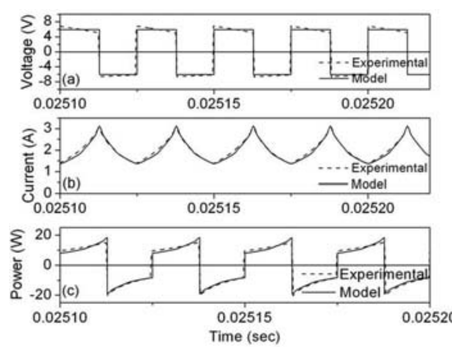

Fig. 3: Experimental and modeled waveforms at 40 kHz, Vin = 12 V, and duty cycle = 0.51: (a) Voltage. (b) Current. (c) Power.

EH-01

Spin control by doping non-magnetic ions in magnetic ordering type of multiferroic materials.

K. Choi[1], S. Kim[1], B. Lee[2], C. Kim[1]
1. Physics, Kookmin Univ., Seoul, South Korea; 2. Hankuk University of Foreign Studies, Yongin, South Korea

Introduction

Recently, numerous researches have been focused on the magnetic ordering type of multiferroic materials, RMn_2O_5, orthorhombic $RMnO_3$(R=rare earth), delafossite $CuFeO_2$, spinel $CoCr_2O_4$, $MnWO_4$, and hexagonal ferrite $(Ba,Sr)_2Zn_2Fe_{12}O_{22}$[1]. These materials are reported showing 'frustration magnet' due to canted spiral magnetic spin. These phenomena bring about incommensurate spin behavior and ferroelectricity by spin current model. Especially, $CoCr_2O_4$ materials have been investigated for multiferroic property and dielectric anomalies have been explained by spin current model. But $CoCr_2O_4$ materials have very small polarization (*~2μC/m*^{2}) [2]. Here, we control spin behavior by substituted non-magnetic ions in $CoCr_2O_4$.

The objective of the present research is to elucidate the role of the Cr ion in the multiferroic effect by replacing the Cr ion in the multiferroic material with a similar transition metal ion Fe. The similar ionic radii of Fe^{3+} and Cr^{3+} mean that lattice distortion effects of the substitution may be ignored, and the electronic structure can be studied.

Experiment and results

The spinel $CoCr_{1.98}{}^{57}Fe_{0.02}O_4$ (CCO), $Co_{0.9}Zn_{0.1}Cr_{1.98}{}^{57}Fe_{0.02}O_4$ (CZCO), $CoCr_{1.88}Al_{0.10}{}^{57}Fe_{0.02}O_4$ (CACO) powders were prepared by wet chemical solution process. Weighted amounts of cobalt acetate, zinc acetate, aluminum acetate, chrome nitrate, and ^{57}Fe isotope were dissolved in acetic acid, ethanol, nitric acid, and distilled water. For doping ^{57}Fe to facilitate Mössbauer measurement, iron isotope was dissolved in a diluted HNO_3 and then the proper amount of ^{57}Fe added into the solution. The solution was refluxed at 80 oC for 12 hours to allow the gel formation and then dried at 120 °C in a dry oven for 24 hours. The dried powder was grounded and annealed at 1000 °C for 3 hours in air. The crystal structures of the samples were examined by x-ray diffraction with Cu Kα radiation (λ = 1.5406 Å). Magnetic properties were characterized by the vibrating sample magnetometer (VSM). The Mössbauer spectra were recorded using a conventional spectrometer a electromechanical with a ^{57}Co source in a rhodium matrix.

The crystal structure was found to be single-phase cubic spinel with space group of *Fd3m*. The lattice constants a0 were determined to be CCO = 8.340, CZCO = 8.328, and CACO = 8.305 Å, respectively. These results are due to that Co^{2+}(0.72 Å) and Zn^{2+}(0.74 Å) have the similar ionic radius and they occupies A (tetrahedral) sites and Cr^{3+}(0.63 Å) and Al^{3+}(0.51 Å) have the different ionic radius and they occupies B (octahedral) sites. The Bragg factor RB and RF were below 5 %, respectively.

The zero field cooled (ZFC) magnetization curves taken at 100 Oe for various temperatures are shown in Fig. 1. The ferrimagnetic transition were observed at around 90 ~ 97 K, which was determined as Néel temperature. ZFC curves showed an abnormal magnetic transition (T_S) at 28 K(CCO), 18 K(CZCO), 20K (CACO), which are associated with spiral magnetic order in the systems. With Al ions substituted in B site, the magnetic transition temperature decreases, but the magnetization increase. Mössbauer spectra of CACO were taken at various temperatures ranging from 4.2 to 93 K as shown in Fig. 2. Two magnetic phases were developed and showed two sharp sextets of spectra below T_S. The isomer shifts at all temperatures range are about 0.3 mm/s relative to Fe metal, which means that both Fe ions are Fe^{3+} states. The electric quadrupole splittings(ΔE_Q) were found to be nearly zero values below T_N. The magnetic hyperfine fields of outer and inner sub-spectrum were H_{hf} = 480 and 462 kOe, respectively. These effects can be explained by Al substitute specification B site. These results bring forth the decreasing Néel and spin-reorientation temperature and increasing magnetic moments.

[1] S-W Cheong and Maxim Mostovoy, Nature, **6**, 13 (2007).

[2] Y. Yamasaki, S. Miyasaka, Y. Kaneko, J.-P. He, T. Arima, and Y. Tokura, Phys. Rev. Lett., **96**, 207204 (2006).

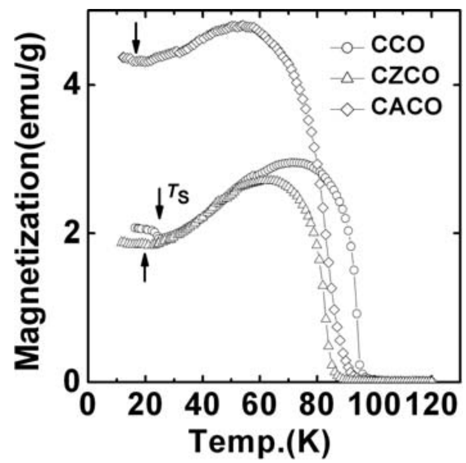

Fig. 1 Magnetization for CCO,CZCO,CACO at various temperatures at 100Oe.

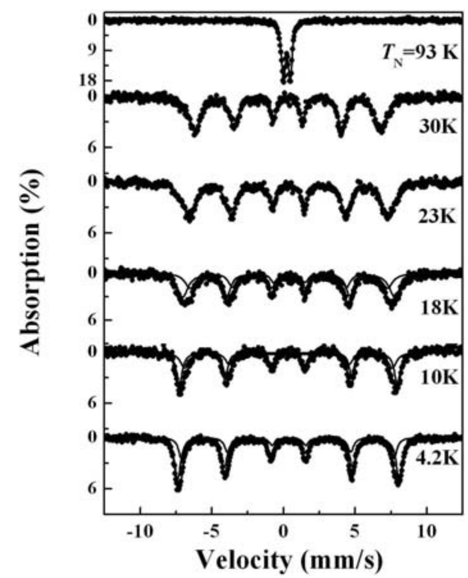

Fig. 2. Mössbauer specta of CACO at various temperatures.

EH-02

Dielectric and magnetic properties of low-temperature sintered $Ni_{0.24}Cu_{0.21}Zn_{0.55}Fe_{1.96}O_4$+x$Pb_{0.95}Sr_{0.05}(Zr_{0.52}Ti_{0.48})O_3$ composites.

L. Jia, H. Zhang, S. Bao, Z. Zhong
university of electronic science and technology of China, chengdu, China

Introduction

Recently the magnetoelectric materials prepared by combining together the ferroelectric and ferromagnetic materials in which the coupling interaction between two phases could produce interesting effect and provide opportunities for potential applications, such as compact electrical filters for suppressing electromagnetic interference (EMI) and magnetic electric sensors have dawn significant interest due to their multifunctionality [1-2]. In the present work, $Pb_{0.95}Sr_{0.05}(Zr_{0.52}Ti_{0.48})O_3$ (PZTS) was chosen as a ferroelectric phase because of its superior ferroelectric characteristics and $Ni_{0.24}Cu_{0.21}Zn_{0.55}Fe_2O_4$ was chosen as a ferromagnetic phase because of its high permeability at low sintering temperature. A series of the new co-fired composites which process both inductive and capacitive properties were synthesized. The relationships between the microstructure evolution and electromagnetic properties of the composite materials with various amounts of PZTS were presented.

Experimental detail

The composites with composition of $Ni_{0.24}Cu_{0.21}Zn_{0.55}Fe_{1.96}O_4$+x$Pb_{0.95}Sr_{0.05}(Zr_{0.52}Ti_{0.48})O_3$ (where x=0-25 wt%) were prepared by a standard solid-state reaction method. The highly active $Pb_{0.95}Sr_{0.05}(Zr_{0.52}Ti_{0.48})O_3$ (PZTS) powders with average grain size of about 150 nm were synthesized by a self-propagating method [2]. The raw materials, NiO, α-Fe_2O_3, ZnO and CuO, of high purity, were mixed and milled. The mixed powders were calcined at 850 oC for 2 h in the air. Then the powders were mixed with ultrafine PZTS powders and a small amount of flux, and milled, dried and pressed. The pressed disc-shaped pellets and toroidal samples were sintered at 900 oC for 3 h in the air and then cooled in the furnace. The phase composition of the samples was identified by a means of X-ray diffraction using CuKα radiation. A scanning electron microscopy was used to observe the microstructures of the samples. The complex permeability and the complex permittivity of the samples were measured by an HP4291B impedance/materials analyzer in the frequency range of 1 MHz-1.8 GHz. Saturation flux density (Bs) and coercive force (Hcb) values were measured by an IWATSU SY-8232 B-H analyzer. The bulk density was determined by the Archimedes method.

Results and Discussion

The peaks in the XRD patterns are identified to be characteristics of both spinel phase and perovskite phase in all samples with PZTS. It was confirmed that there is no visible chemical reaction between two phases. The main results are shown in Table 1. In the undoped PZTS sample, abnormal grain growth was observed clearly. On the contrary, all samples with PZTS have compact microstructures without huge grains, the grain size decreases with the increasing x.

The variation of complex permittivity of the composites with frequency confirmed that when x varied from 0 to 25 wt%, the dielectric constant at 1MHz increased from 11 to 31, the ferroelectric resonance peaks shifted toward a low frequency, and the dielectric loss was improved. The increase of dielectric constant is mainly attributed to the introduction of PZTS, which raises the amount of dipoles in the composite materials. As a result, the increase of dipoles leads to the increase of local displacements (dielectric polarization) in the direction of external applied electric field for electrons, and the increased polarization causes a significant enhancement of the dielectric constant. The variation of complex permeability with frequency showed that the initial permeability decreased with PZTS content. As the PZTS content increased from 0 to 25 wt%, the μi decreased from 218 to 70, while the imaginary part of permeability decreased from 3.7 to 0.3. The resonance frequency (fr) shifted toward a high frequency with the increase of PZTS content. It is probably the main reason attributed to the decrease of magnetic moment per unit volume. In addition, the presence of weak magnetic PZTS in the composites pins the domain wall motion, which lead to a decrease of initial permeability. And the addition of perovskite component observably inhibits the grain growth, so, and thus causes a decrease of domain wall contribution, which is mainly determined by grain size. From Snoek's formula, the natural resonance frequency shifts toward higher frequency with the decrease of initial permeability. From Table 1 we can also see that, as the PZTS content increases, the Q-factor increase markedly. Combining the previous microstructure analysis, we conclude that mainly be caused by the increase of dispersive air gaps [3] and the decrease of eddy current loss, which is accompanied by the addition of PZTS. According the measured data, it can be concluded that the composites have excellent performance in wide frequency rang and can be used for embedded inductors either embedded capacitors.

[1] D. R. Patil, S. A.Lokare, S. S. Chougule, B.

PZTS content (wt%)	Bulk density (g/cm3)	Avarage grain size (μm)	Initial permeability	Q-factor (1MHz)	Resonance frequency (MHz)	Dielectric constant (1MHz)	Saturation flux density (mT)	Coercive force (A/m)
0	5.28	1.8	218.03	49	26.2	11.382	226.51	170.18
5	4.95	0.39	166.36	119	34.1	14.141	144.88	267.73
15	5.16	0.36	115.04	172	59.2	22.353	80.853	278.30
25	5.19	0.34	70.56	236	83.3	30.552	44.706	287.54

EH-03

Processing related magneto-dielectric properties of Ni-Zn-Co ferrite ceramics.

L. Kong, Z. Li, G. Lin
Temasek Laboratories, National University of Singapore, Singapore, Singapore

1. Introduction

It is well known that reduction of antenna size has always been a challenge to the designer, especially for HF (2-30 MHz) and VHF (30-300 MHz) bands where conventional antennas have rather large physical sizes. For practical reasons, the physical dimensions of an antenna should be compatible with the radiation performance, which requires materials for antenna applications to have specific magneto-dielectric properties. These properties include high refractive index and impedance-matched to free space, together with low dielectric and magnetic loss tangents. However, such materials are rarely found in nature [1, 2]. Hence, exploration of this class of materials is of scientific and technological significance.

In this paper, we present our recent study on the effect of processing on the magneto-dielectric properties of Ni-Zn-Co ceramics ($Ni_{0.88}Zn_{0.07}Co_{0.05}Fe_{1.90}Mn_{0.02}O_4$). Three methods, one-step sintering, one-step sintering with high-energy ball milling and two-step sintering, were used to prepare the ferrite ceramics. The ceramics were characterized in terms of phase composition, grain growth, microstructure development, DC resistivity, relative complex permeability and relative complex permeability over 1 MHz - 1 GHz.

2. Phase formation and densification

For one-step processing, it is found that the ferrite phase formation seemly started at 600°C. However, reaction is not complete after calcining at 900°C. The large temperature span for ferrite phase formation is attributed to the nonhomogeneity of the mixture. In contrast, the reactivity of the mixture is greatly enhanced as a result of the high-energy ball milling. Ferrite phase formation also started at 600°C, but ferrite is already the main phase at this temperature and single phase ferrite is obtained at 700°C. It means that the high-energy ball milled powder requires a phase formation temperature at least 200°C lower than that required by the one-step sample. The enhanced reactivity of the high-energy milled powder is due to the refinement of the oxide grains/particles.

The mixture milled by high-energy ball milling also had a better densification behavior, by showing that the samples derived from the milled powder possessed higher measured densities than those prepared by other two methods. The samples prepared via two-step processing were of the highest porosity.

3. Dielectric and magnetic properties

The samples derived from the high-energy ball milled powders had better dielectric properties than other samples, in terms of dielectric loss tangent. The better dielectric properties of the samples can be attributed to their higher densities, because lower porosity is a key to achieving low dielectric loss tangent.

Similarly, the high-energy ball milling processing led to samples having higher static permeability. The magnetic properties of the ferrite ceramics, as a function of sintering temperature, can be described by the magnetic circuit model.

Several samples prepared by different means have been found to possess promising magneto-dielectric properties (matching permeability and permittivity and low loss tangent) over 30-90 MHz, as shown in the figure attached, which might be potentially useful for miniaturization of VHF antennas.

1. H. Mosallaei and K. Sarabandi, Magneto-Dielectrics in Electromagnetics: Concept and Applications, IEEE Trans Antennas Propagat. 52 [6], 1558-67 (2004).

2. K. Buell, H. Mosallaei and K. Sarabandi, A Substrate for Small Patch Antennas Providing Tunable Miniaturization Factors, IEEE Trans. Microwave Theory Tech., 54 [1], 135-46 (2006).

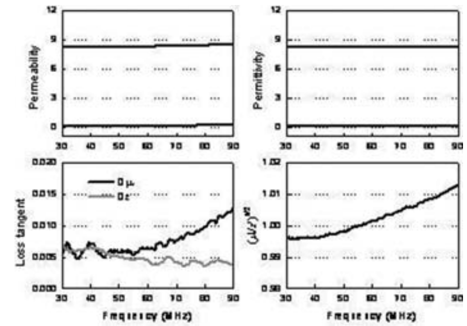

Representative magneto-dielectric properties of the Ni-Zn-Co ferrite ceramics over 30-90 MHz.

EH-04

Dielectric properties of the charge-ordered oxyborate Fe_2OBO_3

M. Sanchez-Andujar[2], *J. Mira*[1], B. Rivas-Murias[2], S. Yanez-Vilar[2], N. Biskup[3], J. Rivas[1], M. Senaris-Rodriguez[2]

1. Fisica Aplicada, Universidade de Santiago de Compostela, Santiago de Compostela, Spain; 2. Quimica Fundamental, Universidade da Coruna, A Coruna, Spain; 3. ICMM, Consejo Superior de Investigaciones Científicas, Madrid, Spain

Isostructural A_2OBO_3 (A= Mn, Fe) compounds display, within the same structure, charge, magnetic and orbital ordering at different orbitals. As for the charge order in these mixed-valence materials (A^{2+}/A^{3+}), the origins of this phenomenon are different when comparing both compounds: whereas Mn_2OBO_3 shows it through Jahn-Teller distortions [1] (i.e., electron-lattice interactions) the mechanism in Fe_2OBO_3 is of electrostatic origin [2] (electrostatic repulsions between charges). This has allowed attributing the differences to the role of t_{2g} vs. e_g interactions in both compounds [3]: Fe^{3+} and Mn^{2+} present the same electronic configuration but there is an extra t_{2g} electron in Fe^{2+} and an extra hole in the e_g orbital of Mn^{3+}).

Recently Angst et al. [4] have completed the picture of Fe_2OBO_3 by finding integer valence states of the Fe ions in the charge-ordered phase, awarding this compound the honor of being the clearest example of ionic charge order so far.

Concerning the search of new dielectric materials, there has been a recent surge of interest in exploring alternative strategies beyond the typical structural approach. Among them we have been focusing on materials that display condensation of electronic charges [5]. It is therefore obvious that, within this approach, Fe_2OBO_3 becomes highly appealing.

For this purpose we have synthesized this material in polycrystalline form by a ceramic method [3] and we have measured the dielectric permittivity of the raw sample. The values of dielectric permittivity are very high, suggesting the presence of Maxwell-Wagner effects. In fact, the data are fitted to a Maxwell-Wagner expression.

In order to understand the dielectric behavior of this compound an impedance spectroscopy analysis was carried out. Via this method it is possible to estimate whether the dielectric response corresponds to the material bulk response or not. Different regimes are found depending on the temperature: for $T<200$ K the values are associated to the material bulk response, in the range $200 \text{ K} < T < 300$ K there is a mixed regime and for $T > 300$ K the response cannot be associated to the response of the bulk material, i.e., it is of extrinsic nature.

The presence of such extrinsic effects is masking the intrinsic dielectric response of the material. In order to observe it, the sample was sandwiched between mica layers in order to eliminate the contributions of free charge carriers and the formation of Schottky barriers at the contact-sample interface.

When measuring the sample prepared in this way (results shown in the figure) it is observed a plateau in the dielectric permittivity above 150 K, at a value around 45 (with a slight increase at higher temperatures, see inset).

The charge order is observed in this oxyborate below 320 K, but the order is of short range. At around 150 K this charge order becomes long-range with a clear consecuence on the dielectric behavior. In this context, it is worth mentioning that this step observed at around 150 K in the dielectric response versus temperature is also coincident with the onset of antiferromagnetic ordering, pointing to a coupling of dielectric and magnetic properties.

[1] R. Norrestam, M. Kritikos, A. Sjoerdin; J. Solid State Chem. **114**, 311 (1995).

[2] J. P. Attfield, A. M. T. Bell, L. M. Rodriguez-Martinez, J. M. Greneche, R. J. Cernik, J. F. Clarke, D. A. Perkins; Nature **396**, 655 (1998).

[3] B. Rivas-Murias, F. Rivadulla, M. Sanchez-Andujar, A. Castro-Couceiro, M. A. Senaris-Rodriguez, J. Rivas; Chem. Mater. **18**, 4547 (2006).

[4] M. Angst, P. Khalifah, R. P. Hermann, H. J. Xiang, M.-H. Whangbo, V. Varadarajan, J. W. Brill, B. C. Sales, D. Mandrus; Phys. Rev. Lett. **99**, 086403 (2007).

[5] J. Rivas, B. Rivas-Murias, A. Fondado, J. Mira, M. A. Senaris-Rodriguez; Appl. Phys. Lett. **85**, 6224 (2004).

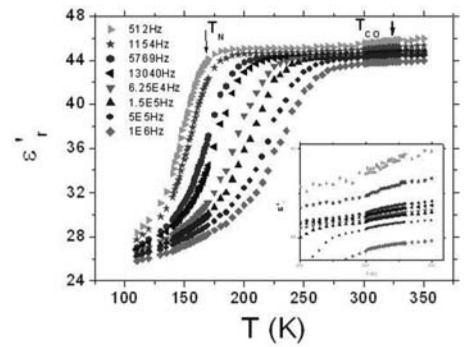

Dielectric constant versus temperature at different frequencies in a sample sandwiched between mica layers. Inset: detail at high temperatures.

EH-05

Magneto-electric Effects in Single Crystal Hexaferrite-Piezoelectric Bilayers.

V. Mathe, *G. Srinivasan*
Physics, Oakland University, Rochester, MI

Abstract: Ferrite-piezoelectric heterostructures show strong magneto-electric (ME) interactions that are mediated by mechanical forces [1]. The first measurements of low-frequency ME effects have been reported for bilayers of single crystal hexagonal M, Y, and Z-type ferrites and lead zirconate titanate (PZT). Studies were performed on bilayers of Ba-Al-M, Sr-Al-M, Zn_2Y, or Co_2Z and PZT. Bilayers with M-ferrites show the weakest ME coupling and the strongest coupling is measured for samples with Y-type ferrites. In M-type ferrites, ME voltage coefficients increase with increasing Al-substitution. Theoretical estimates of ME coefficients are in good agreement with data.

Introduction:Ferrite-piezoelectric layered structures exhibit an ME effect that is related to the interaction between magnetic and electric subsystems mediated by elastic deformations [2]. When a bilayer is subjected to a bias field H and ac magnetic field dH, magnetostriction induced mechanical strain is transferred to PZT and manifests as an ac voltage dV due to piezoelectric effects. The strength of ME effect is defined as the voltage coefficient α_E = dV/dH t, where t is the thickness of PZT in the bilayer. Studies in the past reveal a giant low-frequency ME effect in bilayers with ferrite, terfenol-D or shape memory alloys and PZT or PMN-PT [3]. But the ac ME effects would vanish when the magnetostriction saturates. Since hexaferrites have high, non-saturating magnetostriction at high bias fields, one can accomplish strong high-field ME effects. Here we present the data and theoretical estimates of ME coupling in hexagonal ferrites and PZT.

Results:Bilayers were made with Al-substututed M-type, $Ba(Sr)Fe_{12-x}Al_xO_{19}$ (x = 0-2.0), Zn_2Y, and Co_2Z. The ferrite was bonded with a thin layer of epoxy to a 1 cm dia, 0.5 mm thick PZT disc that was poled in an electric field of 30 kV/cm. The magnetostriction was measured with a strain gage. Data on H dependence of α_E was obtained by measuring dV across PZT in an ac field dH at 100 Hz. The measurements were made for two field orientations, transverse (T) when H and dH were parallel to each other and to the sample plane and longitudinal (L) for the fields perpendicular to the sample plane.

Figure 1 shows data for bilayers of Sr-Al-M and PZT. For the M-type, the longitudinal ME coefficient is quite small, on the order of 1 mV/cm Oe, whereas the transverse coefficient is quite high, as seen in Fig.1. The coefficient α_E(T) shows a gradual increase with increasing H and tracks the variation in magnetostriction with H. When Al is substituted, there is an increase in α_E(T) with x up to 0.8. Further increase in x results in weakening of the strength of ME coupling. Samples of Ba-Al-M showed weaker ME coupling than for Sr-Al-M.

Figure 2 shows the H-dependence of α_E (T) for bilayers of Zn_2Y-PZT and Co_2Z-PZT. Both hexaferrites have easy plane anisotropy, and α_E (T) is much higher than for α_E (L), similar to the case for M-type ferrites The data in Fig.2 indicates the strongest ME coupling for the bilayer with Y-type ferrite. The ME coefficient increases with H up to a bias field of 10 kOe, a value close to the in-plane anisotropy field, and then decreases for higher H.

Theoretical estimates of α_E(T)using our model in Ref.2 are in good agreement with the data in Figs. 1 and 2.

The research was supported by a grant from the National Science Foundation (DMR-0606253).

1. G. Srinivasan, E. T. Rasmussen, and R. Hayes, Phys. Rev. B. 67, 014418 (2003).

2. M. I. Bichurin, V. M. Petrov, and G. Srinivasan, Phys. Rev. B 68, 054402 (2003).

3. Ce-Wen Nan, M. I. Bichurin, S. Dong, D. Viehland, and G. Srinivasan, J. Appl. Phys., in press, 2007.

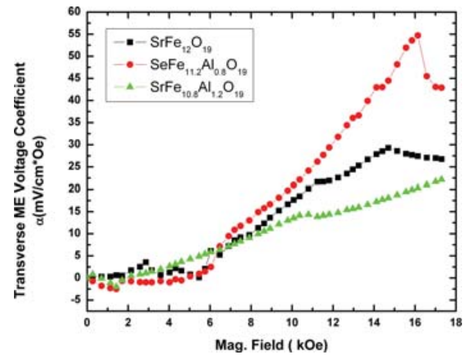

Fig.1: Bias magnetic dependence of the transverse magnetoelectric coefficient for bilayers of single crystal M-type hexagonal ferrites and PZT.

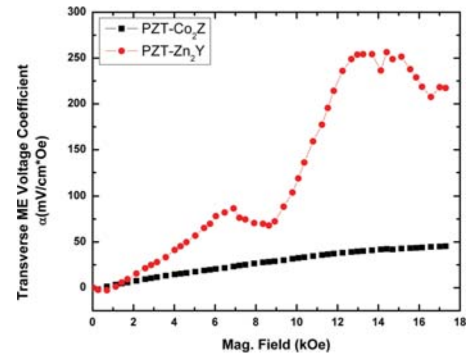

Fig.2: similar data as in Fig.1, but for bilayers of single crystal Z and Y-type hexaferrites and PZT.

EH-06

Anisotropic Susceptibility and Weak Magnetic Moment of $YbMnO_3$ Single Crystal.

J. Fontcuberta[1], M. Gospodinov[2], V. Skumryev[3]
1. Institut de Ciència de Materials de Barcelona, CSIC, Campus UAB, 08193 Bellaterra, Spain; 2. Institute of Solid State Physics, Bulgarian Academy of Sciences, 1784 Sofia, Bulgaria; 3. Institut Català de Recerca i Estudis Avançats (ICREA), and Departament de Física, Universitat Autònoma de Barcelona, 08193 Bellaterra, Spain

After the high temperature superconductivity, the revival of giant magnetoresistance and more recently the magnetoelectric phenomenon have further fuelled the interest in rare-earth oxides. In the hexagonal family of the $RMnO_3$ oxides [1] long range magnetic and polar orders could coexist. The magnetic order of the Mn moments is determined by antiferromagnetic in-plane Mn-O-Mn superexchange, which is much stronger than the interplane Mn-O-O-Mn exchange. As a result, at T_N, Mn orders in a typical for frustrated antiferromagnets 120^0 arrangement within the *ab* basal plane. The R-ions magnetic moments eventually order at much lower temperatures, however they could influence the magnetic structure at higher temperatures. In order to approach the mechanisms behind the intriguing properties of this highly anisotropic compounds and employ them in possible applications, studies on single crystals are required.
Here we report the anisotropic magnetic response of $YbMnO_3$ single crystal. We will limit our discussions to the high temperature region, where the Yb moments are in paramagnetic state. $YbMnO_3$ platelet-like single crystals have been grown by flux method as described elsewhere [2].
The low dc-field cooled, FC, and zero field cooled, ZFC, susceptibility in a field applied along the *c*-axis is given (at an expanded scale) on Fig 1. It clearly shows a peculiarity at $T_N \approx 81$ K, which signals the onset of long range order between Mn moments. An important feature of this transition is the difference between FC and ZFC susceptibility measured at low magnetic field, which sets right below T_N. The temperature at which the two susceptibilities split decreases with increasing the applied field and the difference between the two susceptibilities diminishes at high enough fields. Such behaviour is not a characteristic of an ideal antiferromagnetic structure, for which the Mn moments are supposed to compensate below T_N, but signals the existence of net magnetic moment and coercivity. Unlike the *c*-axis case, no any peculiarity at T_N is observed on the susceptibility measured with a field applied within the basal *ab*-plane and the FC and ZFC susceptibilities coincide for all temperatures down to 2 K. The above observations are in agreement with the measured ac-susceptibility response. As seen from Fig.3, both the real and the imaginary components of ac-susceptibility along the *c*-axis exhibit frequency dependent maxima just below T_N (unambiguously identified by the onset of magnetic losses). No peculiarity at T_N is observed on the ac-susceptibility measured with field applied within the basal *ab*-plane. This behaviour is reminiscent to the one observed for $LnMnO_3$ single crystal, which exhibits weak ferromagnetism attributed to canting of the antiferromagnetic moments due to antisymmetric Dzyaloshinskii-Moria interaction [3]. From the value of magnetic moment measured along the *c*–axis at 8 K and assuming that this moment results from canting of Mn^{3+} moments, one could estimate a canting angle of about 0.35^0 from the *ab*-plane.
The inverse susceptibility (Fig.2) along the hexagonal *c*-axis obeys Curie-Weis law at temperatures above 150 K. When the field is applied within the basal *ab*-plane it deviates from the linear dependence until temperatures as high as 350 K. From the Curie constant $Cg = 2.1\times10^{-2}$ K.emu/g an effective paramagnetic moment $\mu_{eff} = 6.8\ \mu_B$ is estimated in a good agreement with the theoretical value of $\mu_{eff} = 6.7\ \mu_B$ calculated from the Yb^{3+} free-ion and the spin-only value for the Mn ion. Linear fit of the data along the *c*-axis gives paramagnetic Curie temperature $\theta_c = -170$ K, while the high temperature approximation of *ab*-plane susceptibility yields $\theta_{ab} = -257$ K. The strongly anisotropic value of θ is in contrast to negligibly small difference in the susceptibility along different crystallographic directions measured in $RMnO_3$ with non-magnetic R (as it has been demonstrated for $YMnO_3$ [4] as well as revealed by our unpublished data on $LuMnO_3$). This points to the decisive role, which the R ion plays in determining magnetic anisotropy and also warns that the widely used $T_N/|\theta|$ criterion as a measure for the degree of frustrations should be applied with precautions for such highly anisotropic systems.
The existence of uncompensated components of magnetization leading to weak ferromagnetism, eventually coupled to polar order, may have important consequences for occurrence of magneto-electric response and hence for applications.

[1] E. F. Bertaut, F. Forrat, P.-H. Fang, Compt. Rend. 256 1958 (1963)

[2] F. Yen et al., Phys. Rev. B 71, 180407 (2005)

[3] V.Skumryev et al., Eur.Phys.J. B. 11, 401 (1999).

[4] S.A.Kizhaev, V.A.Bokov, O.V.Kachalov, Soviet Physics – Solid State 8, 215 (1966); F.Bertaut, F.Forat, P.Fang, Compt.Rend. 256, 1958 (1963).

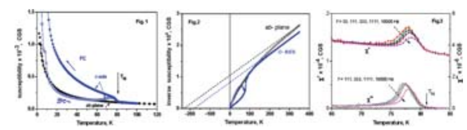

Fig.1 Temperature dependence of dc-susceptibility along the *c*–axis (circles) and the *ab*-plane (rhombs) measured at field 100 Oe (note that the susceptibility axis has been expanded to see the peculiarity at T_N). Fig.2 Temperature dependence of inverse dc-susceptibility along the *c*–axis (circles) and the *ab*-plane (diamonds) measured at field 100 Oe. Fig.3 Temperature dependence of the real and imaginary components of the ac susceptibility along the *c*–axis at different frequencies.

EH-07

Pressure effect on the magnetic ordering in $BiMnO_3$

C. Chou[1,2], C. Lin[1,2], S. Taran[1,2], C. Huang[1,2], J. Her[1,2], C. Sun[1,2], C. Chan[1,2], H. Sakurai[3], E. Takayama-Muromachi[3], H. Yang[1,2]
1. Department of Physics, National Sun Yat-Sen University, Kaohsiung, Taiwan; 2. Center for Nanoscience and Nanotechnology, National Sun Yat-Sen University, Kaohsiung, Taiwan; 3. National Institute for Materials Science, Tsukuba, Japan

Pressure-effect on the ac susceptibility($\chi(T)_P$) has been performed for the polycrystalline $BiMnO_3$. The multiferroic materials that combine ferroelectric and ferromagnetic(FM) ordering are of fundamental and technological interest as coupling between different order parameters such as pressure, electric, and magnetic fields[1-4], enables several ways to interact with these materials. One of the well known multiferroic material, $BiMnO_3$, has two structural phase transitions. At ~770 K, the Pbnm orthorhombic structure is turned to the C2 monoclinic, but, at ~450 K, where it shows ferroelectricity, the structure is changed from monoclinic(1) to monoclinic(2)[2,3]. It is also a FM insulator with the FM Curie temperature, T_C, at 99~105 K[2-4]. In general, the long range ferromagnetism, such as in $La_{1-x}Ca_xMnO_3$ manganites is due to the double exchange interaction(DE), is associated with metallicity. However the magnetism of the $BiMnO_3$ having insulating state is rather unusual. As one knows that pressure can control the overlap between the cation and anion orbital, thus it will be interesting to study the effect of pressure on the FM phase of $BiMnO_3$.
<p>
In order to check the quality of our sample, ac susceptibility($\chi(T)$) and magnetization(M(T)) have been measured. The $\chi(T)$ in three different frequencies shows maximum χ' at T_{max} = 98 K, indicating the FM Curie temperature[4]. The field-cooled dc M(T) (H = 100 Oe, Fig. 1) shows the FM ordering at around same temperature, and the result agrees with recently published papers on this system[2-4]. It is interesting to see that with increasing magnetic field the FM ordering temperature shifts towards higher temperature (see the Fig. 1).
<p>
The M-H hysteresis loop of $BiMnO_3$ taken at T < T_C shows weak ferromagnetism indicated by small coercive field[2-4]. Because $BiMnO_3$ is an insulator, RKKY and DE are not suitable to explain its FM ordering. Recently, several publications[3,5,6] have pointed out that the superexchange interaction is applicable to elucidate the FM-insulating behavior in $BiMnO_3$. Earlier in a similar system $LaMnO_3$, having superexchange interaction, the pressure effect has been found to show some interesting properties[7]. It is a hint that pressure effect on the magnetic ordering of present system would be interesting.
<p>
Figure 2 shows the $\chi(T)_P$ of $BiMnO_3$ under several external pressures ranging from 0 to 15 kbar. Under no pressure the curve shows one hump at around T_{C1}. With increasing pressure up to 11.3 kbar, the position of T_{C1} goes on decreasing. It is interesting to note that beyond this pressure, an additional hump appears at lower temperature (defined by T_{C2}). This hump becomes more obvious and shift toward lower temperature as the pressure is increased, following with a simultaneous suppression of the original T_{C1} peak (see inset of Fig. 2). Above 14 kbar, T_{C1} peak disappears. Since the structure is unchanged below 450 K and undistorted under pressure (even at 27 GPa)[1-3], the magnetic behavior may not be associated with structure. The possible reason for the appearance of the additional peak and the suppression of T_C under pressure may be due to the competition of two different exchange processes which can be tuned by the external pressure. Along this line, detailed neutron diffraction under high pressure is in planning and will be much helpful to solve the magnetic structure.

[1] Z. H. Chi, S. J. You, L. X. Yang, L. C. Chen, C. Q. Jin, X. H. Wang, R. Z. Chen, L. T. Li, Y. C. Li, X. D. Li, and J. Liu, J. Electroceram., 10832 (2007).[2] T. Kimura, S. Kawamoto, I. Yamada, M. Azuma, M. Takano, and Y. Tokura, Phys. Rev. B 67, 180401 (2003).[3] Z. H. Chi, C. J. Xiao, S. M. Feng, F. Y. Li, C. Q. Jin, X. H. Wang, R. Z. Chen, and L. Y. Li, J. Appl. Phys. 98, 103519 (2005).[4] Alexei A. Belik and Eiji Takayama-Muromachi, Inorganic Chemistry 45,

10224 (2006).[5] T. Atou, H. Chiba, K. Ohoyama, Y. Yamaguchi, and Y. Syono, J. Solid State Chem. 145, 639 (1999).[6] A. Moreira dos Santos, A. K. Cheetham, T. Atou, Y. Syono, Y. Yamaguchi, K. Ohoyama, H. Chiba, and C. N. R. Rao, Phys. Rev. B 66, 064425 (2002).[7] J.-S. Zhou and J. B. Goodenough, Phys. Rev. Lett. 98, 087201 (2002).

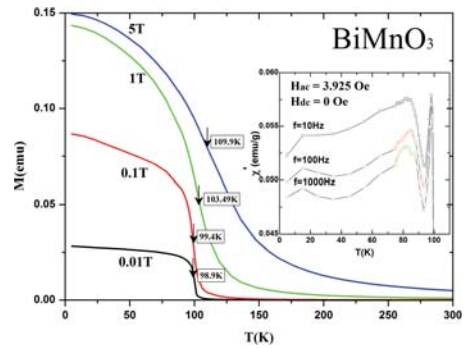

Fig. 1 M(T) in different fields; inset : $\chi(T)$ in different frequency.

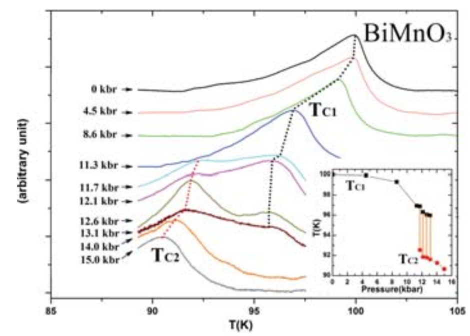

Fig. 2 $\chi(T)_P$ under high pressure; inset : T_{C1} and T_{C2} vs. pressure.

EH-08

Magnetic properties of Ga substituted $NiCr_{1.9-x}Ga_xFe_{0.1}O_4$

G. Ahn[1], S. Park[1], S. Park[2], C. Kim[2]
1. HANARO Utilization Technology Development Center, Korea Atomic Energy Research Institute(KAERI), Daejeon, South Korea; 2. Dept. of Physics, Kookmin University, Seoul, South Korea

I. INTRODUCTION

The ferrimagnet chromites (ACr_2O_4; A=Co, Zn, Ni, etc) are cubic normal spinel, in which A ions occupy the tetrahederal sites and Cr ions occupy the octahedral sites. Recently, many researchers have been interested in the properties of chromite material with multiferroic effects[1,2]. The $NiCr_{2-x}Fe_xO_4$ system, there is a cubic to tetragonal (c/a < 1) transition for the Fe concentration x≤0.2 under room temperature.
In this work, we have studied the $NiCr_{1.9}Fe_{0.1}O_4$ with Ga doping, and evaluated the impact on magnetic properties by x-ray diffraction, neutron powder diffraction, magnetization, and Mössbauer spectroscopy measurements.

II. EXPERIMENT

Polycrystalline samples of the $NiCr_{1.9-x}Ga_xFe_{0.1}O_4$ (x=0.0, 0.45, 0.95) were prepared with the solid state reaction method. The ultimate single phase samples were obtained by annealing for 12 h in atmosphere at 1200 °C. The crystalline structure was analyzed using a Philips x-ray diffractometer with Cu $K\alpha$ radiation and neutron diffraction at Korea Atomic Energy Research Institute Reactor HANARO HRPD (High Resolution Powder Diffractometer, λ = 1.8348 Å). The temperature dependence of magnetization curves were also obtained with a vibrating sample magnetometer (VSM). The hyperfine magnetic property of samples was measured by using Mössbauer spectroscopy.

III. RESULT AND DISCUSSION

The crystalline structure of $NiCr_{1.9-x}Ga_xFe_{0.1}O_4$ (x=0.0, 0.45, 0.95) were found to be a cubic spinel with space group of *Fd-3m* at room temperature. Figure 1 shows some of the neutron diffraction patterns for $NiCr_{1.45}Ga_{0.45}Fe_{0.1}O_4$ at various temperature ranges. The neutron diffraction patterns for $NiCr_{1.45}Ga_{0.45}Fe_{0.1}O_4$ above 4 K showed that the magnetic peaks were overlapping on the nucleus peaks. The magnetic peaks decreases when temperature increases and it disappears at Néel temperature.
The temperature dependence of zero field cooled (ZFC) curves for the $NiCr_{1.9-x}Ga_xFe_{0.1}O_4$ (x=0.0, 0.45, 0.95) were taken under low external field of 100 Oe. The ferromagnetic transition of $NiCr_{1.9-x}Ga_xFe_{0.1}O_4$ (x=0.0, 0.45, 0.95) were observed at 150 K, 125 K, and 90 K, respectively.
Figure 2 shows the Mössbauer spectra of $NiCr_{1.9-x}Ga_xFe_{0.1}O_4$ (x=0.45, 0.95) at 4.2 K. Mössbauer spectra of the Ga substituted $NiCr_{1.9-x}Ga_xFe_{0.1}O_4$ (x=0.45, 0.95) were measured at various temperatures ranging from 4.2 to 295 K. The Mössbauer spectrum of $NiCr_{1.45}Ga_{0.45}Fe_{0.1}O_4$ indicates that there are two magnetic phases, which are due to the two different sites of the Cr3+ state.[1] However, in case of the Mössbauer spectrum of $NiCr_{0.95}Ga_{0.95}Fe_{0.1}O_4$ indicates that there are three magnetic phases. As well-known, $NiGa_2O_4$ has an inverse spinel structure at room temperature. Therefore, the increasing of the Ga substitution, Ga ions enter into both octahedral (B) and tetrahedral (A) sites; simultaneously the same amounts ratio of Fe ions occupied to the B and the A sites.

[1] K. Tomiyasu, J. Fukunga, and H. Suzuki, Phys. Rev. B **70**, 214434, 2004.
[2] L. G. Antoshina, A. N. Goryaga, and D. A. Chursin, Phys. Solid State **44**, 747, 2002.

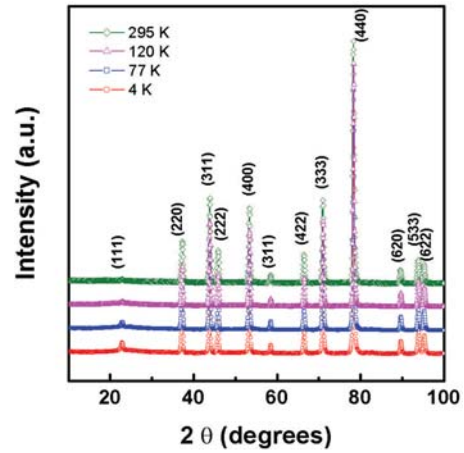

Fig. 1. The neutron diffraction patterns for $NiCr_{1.45}Ga_{0.45}Fe_{0.1}O_4$ at various temperature ranges.

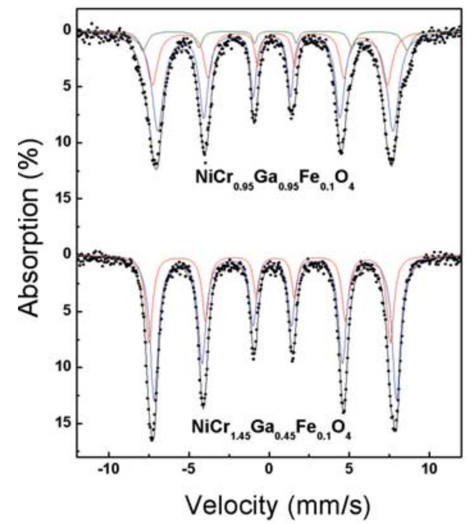

Fig. 2. The Mössbauer spectra of $NiCr_{1.9-x}Ga_xFe_{0.1}O_4$ (x=0.45, 0.95) at 4.2 K.

EH-09

Synthesis and magneocaloric effect of functional perovskites by sol-gel reaction.

K. Jeongju[1], A. Yangkyu[1], *C. Eun Jung*[2]
1. Chemistry, Konyang University, Nonsan, Chungnam, South Korea; 2. Opthalmic Optic, Konyang University, Nonsan, Chungnam, South Korea

In recent years, interest in research on the magnetic refrigeration technology has been considerably enhanced because of its potential impact on energy savings and environmental concerns [1]. Magnetic refrigeration utilizes the magnetocaloric effect (MCE), which is the characteristic of magnetic materials to heat up when magnetized and cool down when demagnetized [2].

Perovskite-type lanthanum manganese oxides have been of considerable interest in the last decade due to their colossal magentoresistivity effect (CMR). From the view point of application in the magnetic refrigeration, a material that exhibits a flat MCE versus magnetic field H response over the desired operation temperature range is needed [3]. Perovskite-type lanthanum manganese oxides are usually prepared by conventional solid state reaction method that needs temperature (1273–1873K) and longer annealing time to obtain homogeneous composition and desire structures [4].

In this paper, we present the study of magnetic entropy change in $La_{0.75}Ba_{0.10}Sr_{0.15}MnO_3$ for magnetic refrigeration around room temperature by sol-gel reaction.

Fig. 1 shows the X-ray diffraction pattern of the perovskite compound obtained by sol-gel reaction. The results are consistent with the data of perovskite crystal structure. The perovskite particles show spherical shapes and have the average diameter of about 1micrometer as shown in Fig. 2. Fig. 3 shows the low-field magnetization as a function of temperature in zero-field-cooled (ZFC) process for the samples calcinated at 1273 K for 12h. The Curie temperature T_c is 342K, which is determined by a minimum of dM / dT curves shown in Fig. 3. Fig. 4 shows the isothermal magnetization curves of perovskite particles.

The magnetic entropy change can be calculated from the magnetic field variation using the following equation:

$$\Delta S_M(T)_{\Delta H}=\int_{HI}^{HF}\{\partial M(T,H)/\partial T\}_H dH \text{ — (1)}$$

Eq. (1) can be rewritten as following:

$$\Delta S_M(T_{av})_{\Delta H}=\delta H/2\delta T\{\delta M_1+2^{n-1}\Sigma_{k=2}\delta M_k+\delta M_n\} \text{ — (2)}$$

From magnetization isotherms we calculated the change in entropy near the ordering temperature using Eq. (2). The results are shown in Fig. 5. Under a magnetic field of 1 T, the maximum entropy change is 0.41 J/kgK at T_c = 342 K.

This feature suggests that it could be a suitable candidate as working substance in magnetic refrigeration technology near room temperature.

[1] Y.I. Spichkin, A.M. Tishin, Int J Refrig. 290, 700 (2005).

[2] Farhad Shir, Catherine Mavriplis, Lawrence H. Bennett, Edward Della Torre, Int J Refrig. 28, 616 (2005).

[3] K.A. Gschneidner Jr, V.K. Pecharsky J. Appl. Phys. 85, 5365 (1999).

[4] R.D. Sanchez, J. Rivas, C.V. Vazquez, A.L. Quintela, M.T. Causa, M. Tovar, S.B. Oseroff, Appl. Phys. Lett. 68, 134 (1996).

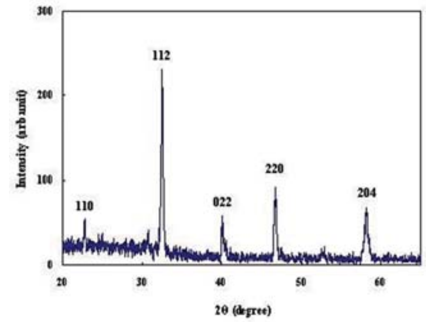

Fig. 1. X-ray diffraction pattern of $La_{0.75}Ba_{0.10}Sr_{0.15}MnO_3$.

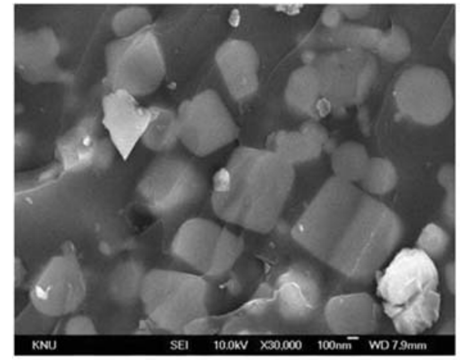

Fig. 2. SEM image of $La_{0.75}Ba_{0.10}Sr_{0.15}MnO_3$

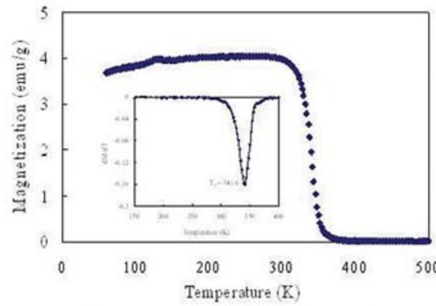

Fig. 3. Temperature dependence of magnetization in zero-field cooled(ZFC) process with applied field 100 Oe for d*M*/d*T* as the function of temperature.

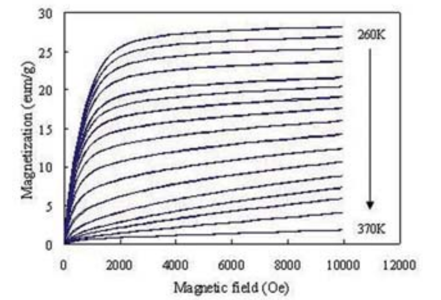

Fig. 4. Magnetization isotherms of $La_{0.75}Ba_{0.10}Sr_{0.15}MnO_3$ at various temperatures.

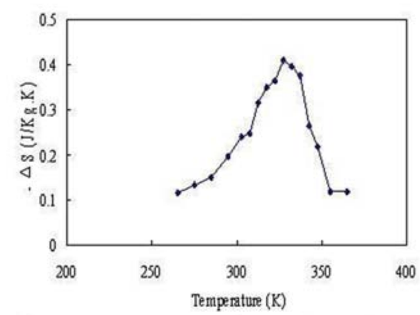

Fig. 5. Temperature dependence of magnetic entropy change for $La_{0.75}Ba_{0.10}Sr_{0.15}MnO_3$.

EH-10

Ferrimagnetic $Ba_{0.5}Sr_{1.5}Zn_2Fe_{12}O_{22}$ (Zn-Y) single crystal barium ferrites.

J. Jalli[1,2], Y. Hong[1,2], S. Gee[1,3], J. Lee[1,2], S. Bae[1,2], G. S. Abo[1,2], A. Lyle[1,2], H. Han[1,2], J. Kim[4], H. Lee[4], S. Lee[4]

1. Electrical and Computer Engineering, University of Alabama, Tuscaloosa, AL; 2. MINT Center, University of Alabama, Tuscaloosa, AL; 3. Seagate Technology, Bloomington, MN; 4. Pohang Superconductivity Center, Pohang University of Science and Technology, Pohang, South Korea

Introduction

The study of the magnetoelectric (ME) effect, namely, the induction of electric polarization (magnetization) by applying magnetic (electric) fields, has attracted perpetual interest for more than four decades because of its potential for advanced ME devices [1]. However, the ME effect studied to date has been too small at low magnetic fields and/or the working temperatures are too low for practical device applications. One of the most important requirements for ME material used in practical applications is a magnetic insulator having a high magnetic ordering temperature. In this sense, ferrites, which are magnetic oxides containing iron as the major metallic component, are prominent candidates [2]. These materials combine room temperature ferromagnetic and insulating properties and have long been used in technological applications such as magnetic recording and high-frequency devices. Recently, hexagonal barium ferrites of the composition $Ba_{0.5}Sr_{1.5}Zn_2Fe_{12}O_{22}$ (Zn-Y) were found to posses a strong electric polarization and magnetization which is also an insulator in the zero-field ground state [3]. In this paper we report the growth and characterization of Zn-Y single crystals for their magnetoelectric studies.

Experimental

Single crystals of the composition $Ba_{0.5}Sr_{1.5}Zn_2Fe_{12}O_{22}$ were grown in platinum crucible using a high temperature furnace. The primary mixtures of $BaCO_3$,$SrCO_3$, ZnO, Fe_2O_3, and Na_2CO_3 in the required mol ratios was blended and thoroughly ground together in a pestle for 1 hour. The finely blended powder is filled in a platinum crucible with approximately three-fourths of the volume. The platinum crucible is then placed in a top-lift enclosed furnace and fired at the temperature of 1450 °C for 12 hours to homogenize the melt. After completely homogenizing the melt for 12 hours, it is slowly cooled at the rate of 2.5 °C/hr to 1000 °C, and then cooled more rapidly in the furnace to room temperature. The, thus obtained, crystals were slowly separated by leaching in hot dilute nitric acid from the platinum crucible.

Results and Discussion

The obtained crystals exhibited the typical hexagonal ferrite growth habit with a plate like geometry. Figure. 1 (a) shows the hysteresis loop measured in the perpendicular and in-plane directions of the Zn-Y single crystal. The saturation magnetization was measured to be 21.9 emu/g and the uniaxial anisotropy of 10 kOe respectively. Figure 1 (b) shows the x-ray diffraction spectrum of the Zn-Y single crystal. The x-ray diffraction pattern confirms that the structure is an extended single crystalline array of Zn-Y with in-plane crystallographic orientation. The microwave properties of the single crystal will be presented.

Conclusions

$Ba_{0.5}Sr_{1.5}Zn_2Fe_{12}O_{22}$ single crystals have been successfully grown from melts using a flux system of $BaCO_3$ - $SrCO_3$ - Na_2CO_3. The obtained crystals exhibited the typical hexagonal ferrite growth habit with a plate like geometry and are of 2-3 mm in thickness. Saturation magnetization, anisotropy field, and coercivity values are close to the bulk values. The control of electric polarization by using magnetic fields in these ferrites will be presented.

Acknowledgements

This work was supported by the Office of Naval Research under grant number N00014-06-1-0416.

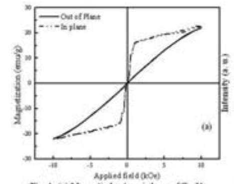

Fig. 1. (a) Magnetic hysteresis loop of Zn-Y single crystal.

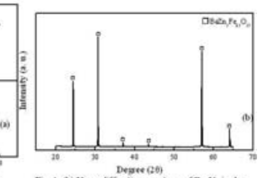

Fig. 1. (b) X-ray diffraction spectrum of Zn-Y single crystal.

EH-11

Increment of saturation magnetization and reduction of electric coercive field in multiferroic Bi ferrite films by adding cobalt.

H. Naganuma, J. Miura, S. Okamura
Department of Applied Physics, Tokyo University of Science, Tokyo, Japan

Multiferroic $BiFeO_3$ materials have attracted much interest as ferroelectric materials because first-principle calculation predicted that the $BiFeO_3$ films possess the extremely large spontaneous polarization of 100 C/cm^2. In fact, in experiments, high remanent polarizations of 50 - 150 C/cm^2 were reported. However, the electric coercive field as well as the leakage current density of these films was quite large. Therefore, the dielectric breakdown of $BiFeO_3$ films occurred at below the electric field of domain switching. One of the candidate ways to improve the high electric coercive field (domain switching field) as well as high leakage current density is adding the additives. Actually, both the electric coercive field and the leakage current density of $BiFeO_3$ films were reduced by adding La. On the other hands, $BiFeO_3$ showed small spontaneous magnetization due to its antiferromagnetic spin configuration, which hinders the multiferroic property of $BiFeO_3$. In present study, we suggest that a local ferrimagnetic spin configuration can expect to form by substituting the iron atoms at the *B*-sites with other 3*d* transition atoms because of the differences in magnetic moment between the *B*-sites. Indeed, the magnetic moment increased by adding a manganese atom to bulk $BiFeO_3$.[1)] Additives can anticipate reducing electric coercive field as well as leakage current density, and enhancing magnetic moment.

Figure 1 shows the x-ray diffraction patterns for the 5 at.% Co-added $BiFeO_3$ film and pure $BiFeO_3$ film. Both films showed many diffraction peaks due to $BiFeO_3$ structure, and no other secondary phases could be observed.

Figure 2 show the ferroelectric hysteresis loops measured at room temperature (a), (b) and 90 K (d), (d). At room temperature, the expanded ferroelectric hysteresis loop was observed for the pure $BiFeO_3$ film. By contrast, ferroelectric hysteresis loop with relatively high squareness was obtained for the Co added $BiFeO_3$ film. Improvement of the squareness of the ferroelectric hysteresis loops in the Co added $BiFeO_3$ film is due to reduction of the leakage current density (not shown here). At 90 K, leakage current density was sufficiently suppressed according to leakage current property (not shown here), therefore the electric coercive fields can compare. The electric coercive field dependence of the remanent polarization was shown in Fig. 2(e) and 2(f). It can be clearly seen that the electric coercive field of $BiFeO_3$ film was reduced by adding the cobalt without the reduction of remanent polarization.

Figure 3 shows the magnetic curves for the 4 at.% Co-added $BiFeO_3$ film and pure $BiFeO_3$ film measured at room temperature. Although weak ferromagnetism was observed for pure $BiFeO_3$ film, the spontaneous magnetization as well as coercive field was appeared by adding cobalt. Father more, the saturation magnetization increased by adding cobalt. These results suggest that the cobalt addition might induce a local ferrimagnetic spin configuration by substituting the iron atoms at the *B*-sites to cobalt.

In conclusion, we investigated Co additional effect on ferroelectric and magnetic properties in $BiFeO_3$ film. It was revealed that cobalt addition affects not only reducing electric coercive field and leakage current density but also increasing saturation magnetization and magnetic coercive field. This is the first report about the additive which was able to simultaneously improve these multiferroic characteristics.

1) M. Azuma *et al.*, J. Mag. Mag. Mat., **310**, 1177 (2007).

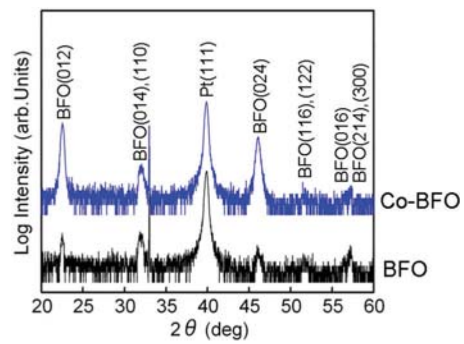

Fig 1 X-ray diffraction patterns for the 5 at.% Co-added $BiFeO_3$ film and pure $BiFeO_3$ film

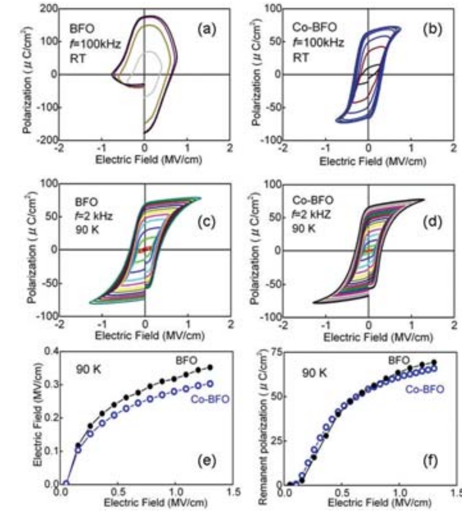

Fig 2 Ferroelectric hysteresis loops measured at room temperautre (a), (b) at 90 K (c), (d), and electric field dependece of E_c and P_r at 90 K (e), (f).

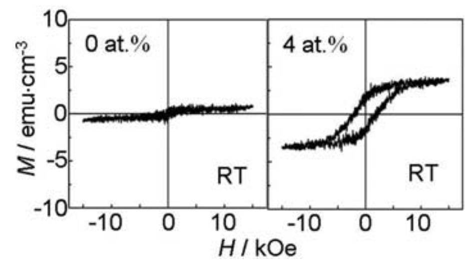

Fig 3 Magnetization curves measured at room temperature

Influence of oxygen and nitrogen on magnetic properties of soft magnetic CoFeZr nanoparticles embedded in alumina dielectric matrix.

A. Fedotov[1], J. Fedotova[1], Y. Kalinin[2], A. Sitnikov[2], V. Fedotova[3], Y. Ilyashuk[1]
1. Belarusian State University, Minsk, Belarus; 2. Voronezh State Technical University, Voronezh, Russian Federation; 3. Joint Institute of Solids and Semiconductors Physiscs, Minsk, Belarus

The influence of reactive gases addition in a gas mixture during ion-beam sputtering procedure on magnetic properties of the $(Co_{45}Fe_{45}Zr_{10})_x(Al_2O_3)_{100-x}$ nanocomposite films has been investigated.The films with metallic alloy ratio $20 < x < 65$ at.% were sputtered in the chamber evacuated either with pure Ar under pressure P_{Ar} of $6.7\text{x}10^{-2}$ Pa (set 1 films) or Ar + O_2 with partial pressure $P_O = (1.3\text{-}5.0)\text{x}10^{-3}$ Pa (set 2) or Ar + N_2 with $P_N = (1.31\text{-}2.13)\text{x}10^{-2}$ Pa (set 3) gas mixtures. Magnetization, permeability at 20-200 MHz, atomic force microscopy (AFM) in AC MFM regime and Mössbauer spectroscopy (MS) studies were performed at 300 K. The presence of nanoparticles with sizes of 2 - 10 nm was confirmed by transmission electron microscopy and phase contrast AFM microscopy.

Comparison of Figs 1-3 shows that for set 2 and 3 films the region of superparamagnetic state was expanded far beyond the percolation threshold $x_C \approx 41\text{-}45$ at.% observed for the set 1 films [1,2]. The last became apparent in a lack of sextet in MS [2], conservation of non-hysteresis behavior of magnetization curves (see, Fig. 1) and lowering of real μ′ and imaginary μ″ parts of complex magnetic permeability μ(see, Figs. 2 and 3) far beyond x_C in comparison with the films of set 1. MS have shown that such peculiarities were due to the formation of oxide or nitride shells around nanoparticles preventing magnetic interaction between them even at the direct electric contacting of nanoparticles covered with these shells [1].

Analysis of Figs 1-3 and earlier results [1-3] allows for the conclusion that the values of μ and magnetic state of the composites under study are strongly dependent on the chemical composition of gas mixture in the sputtering chamber. In this connection we should like to underline two main features that are characteristic for the nanocomposites studied.

Firstly, at room temperatures the low-x composites display low values of μ (compare Figs. 2 and 3), great values of DC resistivities [1-2], lack of hysteresis for the magnetization curves (Fig. 1) and of sextet componet in MS [2] that is characteristic for the superparamagnetic state. The presence of this feature in the samples far below x_C is not generally dependent on the the composition of gaseous atmosphere during film deposition, although the x region where the superparamagnetic state is observed was shifted to higher x values with the addition of reactive gases into the vacuum chamber.

Secondly, for the studied nanocomposites with $x > x_C$ their magnetic state, including the AC MFM response [1,3] and values of high-frequency μ′ and μ″ (Figs. 2 and 3), is strongly dependent on the composition of gaseous atmosphere in the sputtering chamber. Specifically, the superparamagnetic state and labyrinth-like AC MFM contrast (see, [3]) were conserved even beyond the percolation threshold.

[1] A.M. Saad, V.A. Kalaev, J.A. Fedotova, K.A. Sitnikov, A.V. Sitnikov, Yu.E. Kalinin, A.K. Fedotov, A.I. Svito. Rev. Adv. Mater. Sci. 14 (2007) 14-21

[2] A.M. Saad, A.K. Fedotov, J.A. Fedotova, I.A. Svito, B. V. Andrievsky, Yu.E. Kalinin, V.V. Fedotova, V. Malyutina-Bronskaya, A.A. Patryn, A.V. Mazanik and A.V. Sitnikov, Phys. Stat. Solidi (c) 3 (2006) 1283-1290.

[3] J. Fedotova, A. Larkin, A. Fedotov, V. Kalaev, A. Sitnikov, Yu. Kalinin, B. Andrievsky, A. Patryn, Physics, Chemistry and Nanostructures: Reviews and Short Notes to NANO-MEETING-2007, Minsk, Belarus 22-25 May 2007, pp.62-65.

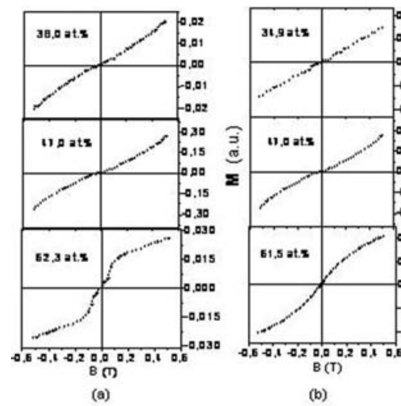

Fig. 1. Magnetization curves recorded for nanocomposites sputtered in pure Ar (a) and Ar+O2 (b) ambient.

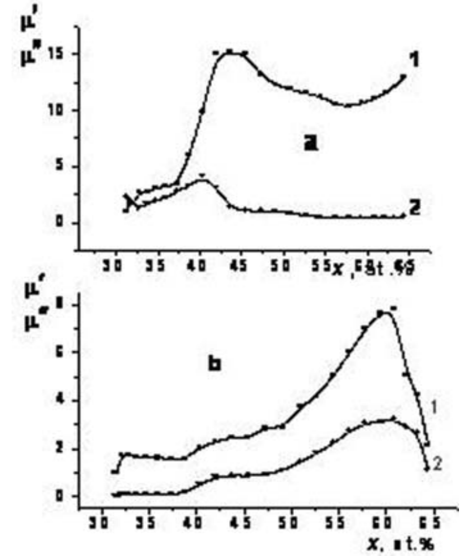

Fig. 2. Dependences of real (curves 1) and imaginary (curves 2) parts of permeability for f = 25 MHz vs x ratio for nanocomposites deposited in Ar (a) and Ar + O2 (b) ambient.

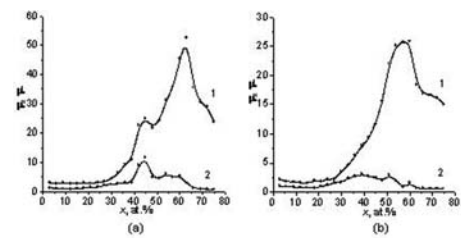

Fig. 3. Dependences of real (curves 1) and imaginary (curves 2) parts of permeability for f = 25 MHz vs x ratio in nanocomposites of set 3 deposited at $P_N = 1.31\text{x}10^{-2}$ Pa (a) and $P_N = 2.13\text{x}10^{-2}$ Pa (b).

EL-01

Determining parameters of a line-start interior permanent magnet synchronous motor model by the differential evolution.

T. Mar či č[1], G. Štumberger[2,1], B. Štumberger[2,1], M. Hadziselimovi ć[2,1], P. Virti č[1]
1. TECES, Research and Development Centre for Electrical Machines, Maribor, Slovenia; 2. University of Maribor, Faculty of Electrical Engineering and Computer Science, Maribor, Slovenia

Introduction

The line-start interior permanent magnet synchronous motor (LSIPMSM) presents an interesting and energy-high-efficient alternative for induction motors widely used in low-cost electric drives, where the usage of a voltage-source inverter is too expensive. Even in these drives the dynamic behavior is important. To evaluate it, a reliable dynamic model of the motor is required. However, the presence of a squirrel-cage and rotor saliency because of magnetic flux barriers, which have to accommodate the magnetic segments of permanent magnets below the squirrel-cage, present serious obstacles for determining model parameters by the finite element method or experimental method. Thus, determining LSIPMSM dynamic model parameters presents an engineering challenge, which is in this work effectively solved by applying a stochastic search algorithm [1], called differential evolution (DE) [2]. DE has been previously used in optimization of magnetic bearings [3] and for determining magnetically nonlinear characteristics of power transformers [4].

In this work a magnetically linear lumped parameter dynamic model of LSIPMSM is discussed. Its parameters, which are constants, are determined by DE, while the optimization objective is the best possible agreement between the measured and by the model calculated time-behavior of model variables. As far as the authors of this paper are aware, the proposed paper for the first time proposes the usage of DE for determining parameters of LSIPMSM dynamic model.

Lumped parameter dynamic model of the LSIPMSM

The two-axis dynamic model of a three-phase LSIPMSM is used, which is presented in Fig. 1. The voltage balance in the stator and rotor windings of the discussed LSIPMSM is described by equations (1a), (1b), and (1c), (1d), respectively. They represent the electrical subsystem of the LSIPMSM and are written in the d-q reference frame, where the d-axis is aligned with the permanent magnet flux linkage vector. The mechanical subsystem is described by the torque equation (2) and equation (3) describing motion.

Determining model parameters by the DE

The stator resistance R_s can be directly measured on the motor's terminals, while the flux linkage due to permanent magnets ψ_m can be determined from the measured back-emf. All other model parameters in (1a) through (3) have to be determined in the optimization process. The DE searches for model parameters in the optimization process providing minimal value of squared difference between measured and calculated currents and motor speed. In order to prevent model parameters from being adjusted for one transient only, measured response from more than one transient should be used in the optimization process. In the given case the tested LSIPMSM was first fed with 25 Hz and then with 50 Hz voltage supply, thus causing two transients. Parameters determined by the DE were used in the dynamic model to calculate time-responses of currents and motor speed. The comparison of calculated and measured currents and motor speed is presented in Fig. 2. More details will be provided in the full paper.

[1] P. G. Alotto, C. Eranda, B. Brandstätter, G. Fürntratt, C. Magele, G. Molinari, M. Nervi, K. Preis, M. Repetto, and K. R. Richter, "Stochastic algorithms in electromagnetic optimization," IEEE Trans. Magnetics, vol. 34, no. 5, pp. 3674–3684, 1998.

[2] K. V. Price, R. V. Storn and J. A. Lampinen, Differential evolution: a practical approach to global optimization, Springer, 2005.

[3] G. Štumberger, D. Dolinar, U. Pahner, and K. Hameyer, "Optimization of Radial Active Magnetic Bearings Using the Finite Element Technique and the Differential Evolution Algorithm," IEEE Trans. Magnetics, vol. 36, pp. 1009-1013, July 2000.

[4] G. Štumberger, S. Seme, B. Štumberger, B. Polajzer, and D. Dolinar, "Determining Magnetically Nonlinear Characteristics of Transformers and Iron Core Inductors by Differential Evolution," Accepted for publication in IEEE Trans. Magnetics, pp. 4.

$$u_d = R_s i_d + L_{sd}\frac{di_d}{dt} + L_{md}\frac{di_{kd}}{dt} + \frac{d\theta}{dt}\left(-L_{sq}i_q - L_{mq}i_{kq}\right) \qquad (1a)$$

$$u_q = R_s i_q + L_{sq}\frac{di_q}{dt} + L_{mq}\frac{di_{kq}}{dt} + \frac{d\theta}{dt}\left(L_{sd}i_d + L_{md}i_{kd} + \psi_m\right) \qquad (1b)$$

$$0 = R_{kd}i_{kd} + L_{rd}\frac{di_{kd}}{dt} + L_{md}\frac{di_d}{dt} \qquad (1c)$$

$$0 = R_{kq}i_{kq} + L_{rq}\frac{di_{kq}}{dt} + L_{mq}\frac{di_q}{dt} \qquad (1d)$$

$$t_e = p\left(\left(L_{sd} - L_{sq}\right)i_d i_q + L_{md}i_q i_{kd} - L_{mq}i_d i_{kq} + \psi_m i_q\right) \qquad (2)$$

$$J\frac{d^2\theta}{dt^2} = p\left(t_e - t_l\right) - f\frac{d\theta}{dt} \qquad (3)$$

Fig. 1. Voltage equations, torque and motion equation of the LSIPMSM model.

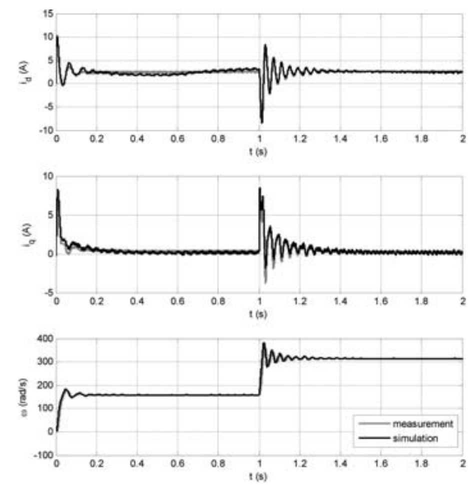

Fig. 2. Comparison of calculated and measured currents and motor speed; where the motor was fed with 25 Hz and 50 Hz voltage supply.

EL-02

Design and performance measurement of high speed permanent magnet synchronous motor with full-ring magnet for axial-flow turbo fan.

S. Jang[1], *J. Park*[1], K. Ko[1], J. Hwang[2]
1. Electrical Engineering, Chungnam National University, Daejeon, South Korea; 2. MAGPLUS, Daejeon, South Korea

Introduction

In recent high speed electrical machines became more attractive in many industrial applications such as machine tools, centrifugal compressors, vacuum pumps, turbine generators, and so on. Due to their high efficiency, small size and light weight, high speed electrical machines are likely to be the key technology for many future applications of motion control and drive systems. A system can be made much smaller and lighter at the same power level by increasing the operation speed [1]-[3].

So far, in most of high speed technology applications, a mechanical gearbox has been utilized to couple a conventional electric motor and the high speed mechanical load. Using a mechanical gearbox has the obvious disadvantages of reducing efficiency and reliability of the system, occupying a large space and increasing cost. Another way to achieve high rotational speed is to use an inverter. The inverter transforms the 60 Hz frequency and voltage into a desired high frequency and voltage [4]. This output can be produced with a high speed machine, eliminating the need for a gearbox and greatly reducing the size, complexity, and weight of the machine by trading speed for torque. A direct drive system in which a machine is coupled directly to a load is much more compact and highly efficient and requires much less maintenance.

This paper deals with design and experiment of high speed permanent magnet synchronous motor (PMSM) for axial-flow turbo fan supplying compressed air into the burner of industrial boiler. Usually, air fed into combustion of a boiler is supplied by a belt driven conventional fan, that has many disadvantages such as big noise, big size, less efficiency due to a fixed speed, and so on. However, the boiler with an axial-flow turbo fan using high speed PMSM has many advantages over the one with belt driven conventional fan. First, we designed high speed PMSM for axial-flow turbo fan using electromagnetic analysis method in this paper. Second, the analytical results are compared with those obtained from a finite element method (FEM). Finally, we manufactured and performed experiment of high speed axial-flow turbo fan with designed high speed PMSM.

Design specifications and constraints

High speed PMSM consists of 2-pole permanent magnet rotor and 24-slot stator corresponding with rotor. As stated above, we designed high speed PMSM using electromagnetic analysis method in this paper. The analytical results are compared with those obtained from a FEM. Table 1 shows the design specifications and constraints.

Results and discussion

Fig. 1(a) shows the magnetic flux line distributions due to permanent magnet predicted by FEM results obtained from the commercial package ANSOFT MAXWELL. Fig. 1(b) and 1(c) show the comparison of between analytical and FEM results for the flux density distributions and back-EMF. The analytical results are shown in good agreement with those obtained from FEM results. In our manuscript paper, we will present driving performance.

[1] B.H.Bae, S.K.Sul, J.H.Kwon and J.S.Byeon, “Implementation of sensorless vector control for super high speed PMSM of turbo compressor,” IEEE Trans. Indust. Appl., vol.39, no.81, pp.811-818, May/June 2003.

[2] Z.Q.Zhu, K.Ng, and D.Howe, “Design and analysis of high speed brushless permanent magnet motor,” 8th IEE International Conference of Electrical Machines Drives, pp.2573-2575, Sep. 1997.

[3] S.M.Jang, H.W.Cho, S.K.Choi, “Design and analysis of a high speed brushless DC motor for centrifugal compressor,” IEEE Trans. Magn., vol.43, no.6, pp.2573-2575, June 2007.

[4] Jussi Lahteenmaki, “Design and voltage supply of high speed induction machines,” Acta Polytechnica Scandinavica, Electrical Engineering Series No.108, Helsinki, Flnland.

Parameter	Unit	Value
Power	kW	13
Speed	rpm	16000
Stator outer diameter	mm	107
Back-EMF constant	V/rad/sec	0.147

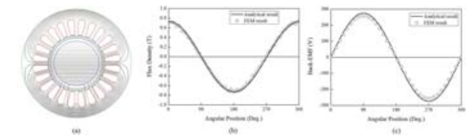

Fig. 1. Analytical results: (a) flux path, (b) flux density and (c) back-EMF.

Fig. 2. Manufactured high speed PMSM with full-ring magnet: (a) rotor, (b) stator and (c) housing.

EL-03

Finite element analysis of stator winding faults in permanent magnet brushless AC motors.

J. A. Farooq, T. Raminosoa, A. Djerdir, A. Miraoui
Electrical Engineering and Control Systems, University of Technology Belfort Montbeliard, Belfort, France

Abstract—The paper presents an investigation of various stator winding faults in permanent magnet synchronous motor by finite element simulation analysis. Finite element method (FEM) was chosen to take into account most of the physical phenomenon and because its results are generally close to real machines. The satisfactory results of FEM simulations thus eliminate the need to realize high cost prototypes. The different studied faults include: phase inter turn short circuit, phase to phase fault and three phase short circuit fault. The simulation results can serve as step towards development of fault diagnosis algorithms.
Index Terms—Fault diagnosis, Finite element method, Permanent magnet machine, Stator faults.

I. INTRODUCTION

Permanent magnet motors (PMSM) are now widely used for their attractive features like compactness and high efficiency. Thus to improve their reliability, research on fault modeling, simulation and detection is demand of the day. Most of the earlier work in this respect has been done on induction motors [3-5]. Dai et al. [2] have studied some stator winding faults for permanent magnet brushless DC machines by finite element (FEM) simulations. Gerada et al [1] uses reluctance network to simulate stator winding faults for permanent magnet brushless AC machines, but none of them have treated the important case of an internal phase to phase winding fault.

In this work we have simulated most of the possible stator faults that can really occur. FEM approach was adopted since it is well known to give results close to real machines.

II. SIMULATION RESULTS AND DISCUSSION

The machine analyzed in this paper is a 3 phase, 12 pole with distributed winding and external rotor configuration. The windings are star connected with isolated neutral point. Fig. 1 shows its cross section view with a modified stator winding scheme to introduce various internal faults.

For the case of inter-turn short circuit in one phase, 3rd harmonic appears in the faulty phase current (Fig. 2 and 3), whereas 2nd and 4th harmonic appear in the torque and speed (Fig. 4 and 5).

For the case of phase to phase short circuit, 3rd harmonic appears in the current of the two faulty phases (Fig. 6 and 7). Depending on the severity of the fault 2nd harmonic may also appear in these currents (Fig. 8 and 9). Moreover it is noted that the phase currents flowing in the winding after the fault point are in negative sequence. This will create a rotating field in the opposite direction and can produce high eddy currents in the magnets which can lead to their demagnetization.

In addition for the case of phase to phase fault (Fig. 6) the current amplitudes in the faulty phases are approximately twice the rated value, so the classical protection systems may not react immediately. Therefore, the obtained results can be used to develop an efficient diagnosis algorithm to prevent further propagation of the fault.

[1] C. Gerada, K. Bradley, and M. Sumner, "Winding turn-to-turn faults in permanent magnet synchronous machine drives," IEEE Ind. Appl. Conf., vol. 2, pp. 1029- 1036, Oct. 2005.

[2] M. Dai, A. Keyhani, T. Sebastian, "Fault analysis of a PM brushless DC motor using finite element method," IEEE Trans. Ener. Conv. Vol. 20, pp. 1-6, Mar. 2005.

[3] C. R. da Silva, M. B. R. Corrêa, C. B. Jacobina, A. M. N. Lima, E. R. C. da Silva, R. N. Andriamalala, H. Razik, "A new approach for inter turn short circuit detection in six phase induction motor," IEEE Ind. Elect. Conf., pp. 4969-4974, Nov. 2006.

[4] S. M. A. Cruz, A. J. M. Cardoso, "Stator winding fault diagnosis in three phase synchronous and asynchronous motors, by extended park's vector approach," IEEE Trans. Ind. Appl. vol. 37, pp. 1227-1233, Sep.-Oct. 2001.

[5] O. A. Mohammad, N. Y. Abed, S. C. Ganu, "Modeling and characterization of induction motor internal faults using finite element and discrete wavelet transform," IEEE Inter. Magn. Conf., pp. 769-769, May 2006.

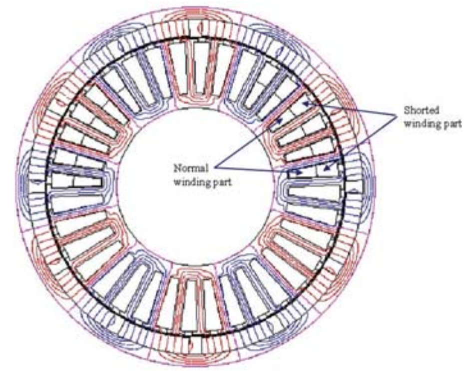

Fig. 1. Cross section view of studied machine

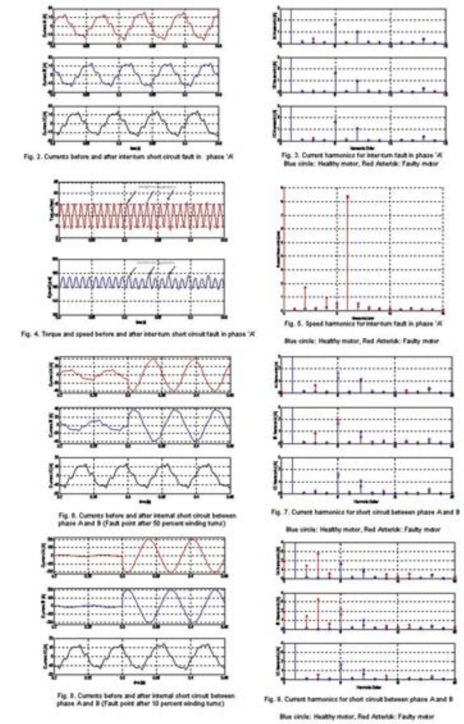

EL-04

Analysis method for considering the effect of magnetic cross saturation of IPMSM.

Y. Kim[1], I. Jung[1], J. Hur[1], J. Hong[2]
1. KETI, Bucheon, South Korea; 2. Hanyang University, Seoul, South Korea

1. Introduction

Recently, interior permanent magnet synchronous motors (IPMSM) are widely used in industrial applications, which require high power density [1]. Several control methods have been proposed in order to reduce the loss of IPMSM and improve their performance. One of the control strategies is the maximum torque-per-ampere (MTPA) control. The possibility of operating methods depends on parameters of IPMSM. Specially, the d- and q-axis inductances vary depending on the d- and q-axis current respectively, and as a result the control performances are affected by the magnetic cross saturation. This paper presents a simulation method to decide correct the current vector of IPMSM. It is important that permanent magnet flux, resistance of stator iron loss, and d- and q-axis inductances are evaluated at the nonlinear equivalent magnetic circuit model. Especially, the d- and q-axis inductances vary depending on the d- and q-axis current and as a result the control performances are affected by the magnetic cross saturation. In this paper, these parameters are calculated by finite element analysis (FEA).

2. Description of Proposed Analysis Method

The MTPA control of IPMSM, previously, has been developed by using the voltage equation of that, and the voltage equation is derived as if the magnetic cross saturation is ignored and Ld and Lq are assumed to be constant parameter [2]. It seems that the operating performances become worse and the control system may become unstable. Therefore, in order to improve the operating performances, the decision method of the current vector should be considering the effects of magnetic cross saturation. In this paper, the proposed computation method is based on the iteration algorithm shown in Fig. 1. Also, the iteration method can be solved by using a numerical optimization algorithm. In order to choose a proper current vector that satisfy condition of the MTPA control, the proposed analysis method uses the inductance, which is obtained from the FEA, that consider the magnetic cross effect. In each iteration step, the inductances, which correspond to the current vector, are replaced to the voltage equation.

3. Results and Discussion

The motor is in the employment of the compressor of the air conditioner. The simulation results of the torque and the current vector trajectory controlled by the constant power and torque (MTPA) control are shown in Fig. 2. and Fig. 3. The d- and q-axis inductances are used in the analysis considering the effect of the magnetic cross saturation.

In Fig. 2, the black solid-symbol curves represent results without the effect of the magnetic cross saturation, and the MTPA trajectories shown as the white open-symbol, in which the proposed analysis method is used. The MTPA trajectory from the proposed analysis method is that smaller armature current amplitude, thus this current vector decision may conduct the efficiency improvement of the IPMSM as shown in fig. 3. In final full paper, experimental results and discussions will be provided, and analysis results are compared with experimental results for verification of the analysis method.

[1] S. Morimoto, Y. Tong and Y. Takeda, "Loss Minimization Control of Permanent Magnet Synchronous Motor Drives," IEEE Trans. on Industry Electronics, IE-41, 5, pp. 511-517, 1999.

[2] Oct. H., Wentzloff, D.D., Jahns, T.M., Wai, J., McCleer, P.J., "Optimization Technique for Improving Torque Performance of Concentrated Winding Interior PM Synchronous Motor with Wide Speed Range," in Proc. IEEE IAS Annual Meeting, vol. 4, pp. 2486 – 2492, Oct. 2002

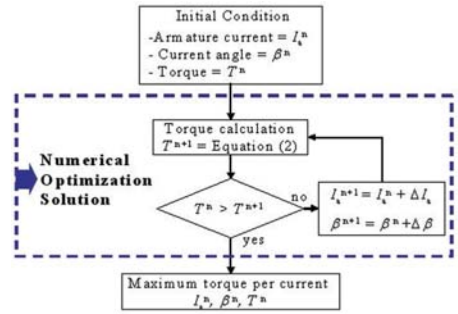

Fig. 1 Flow-chart of the proposed simulation method

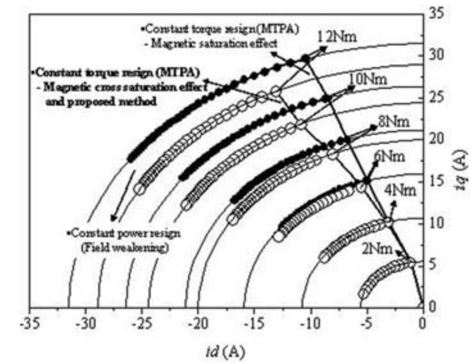

Fig. 2 Trajectory of MTPA control

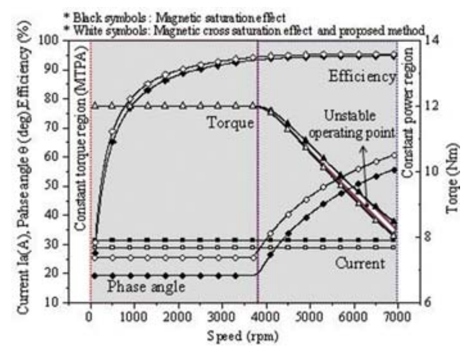

Fig. 3 Torque characteristics of prototype IPMSM

EL-05

Design and finite-element analysis of interior permanent magnet synchronous motor with flux barriers.

B. Stumberger[1], G. Stumberger[1], M. Hadziselimovic[1], T. Marcic[2], P. Virtic[2], V. Gorican[1], M. Trlep[1]
1. University of Maribor, Faculty of EE&CS, Maribor, Slovenia; 2. TECES, Development centre for Electrical Machines, Maribor, Slovenia

Introduction
Interior permanent magnet synchronous motors (IPMSMs) are used for variety of industrial applications. In traction and spindle drives, constant output power operation and wide speed range are desirable. In order to extend the speed range of IPMSM, the magnetic field, due to the permanent magnets (PMs), is at the increase of the speed weakened by phase advance of stator current in order to exert a demagnetizing component of armature reaction field. The great disadvantage of such motor drives is the rapid decrease of motor output torque with the increase of the level of flux weakening (FW).
IPMSMs can offer high-efficiency drive by properly utilizing magnet and reluctance torque components. The reluctance torque components of the IPMSMs can be increased only by increasing the saliency ratio. It has been reported that the proper adding of weak permanent magnet material into the rotor structure of synchronous reluctance motor (SRM) can improve motor performance [1]. Such a motor is then usually called permanent magnet assisted synchronous reluctance motor (PMASRM) or interior permanent magnet synchronous motor with flux barriers (IPMSMFB). Leakage flux between barriers and saturation in the core increases pretentiousness of such motor design [2, 3].
The aim of the paper is the design and analysis of PMASRM which will exhibit similar maximal torque per current density and higher output power capability and efficiency than the existent IPMSM. Both motors, the existent IPMSM and PMASRM should have the same rotor and stator diameter, the same stator construction, the same axial length, the same number of poles, the same active electrical steel material and the same amount of NdFeB magnet material.
Method of analysis and results
The calculation of motors` performances was carried out on the basis of the FEM calculations of magnetic conditions. The influence of iron losses on the output power capability and constant-power speed range was included in the analysis by the posterior iron loss calculation [4]. Various parameters of PMASRM rotor structure were taken into account at determination of suitable rotor contruction. These parameters are: thicknesses of flux barriers, number and angular locations of flux barriers, width of the tangential and radial rotor ribs, location and number of PM segments per pole and residual flux density of used PM material. On the basis of FEM analysis the rotor of PMASRM with three-flux barriers was built. Rotor lamination of IPMSM and rotor lamination of PMASRM are presented in Fig. 1a and Fig 1b. For PMASRM the PM material was placed only in the flux barriers closest to the rotor shaft (Fig. 1c), while the air was accounted for in the flux barriers closest to the rotor surface. The calculated performance of the conventional IPMSM was confirmed with the measurements in the range of speed 3000-10000 rpm, while the calculated performance of the PMASRM was confirmed with the measurements at speed 1500 rev/min only, due to the low voltage winding arrangement and due to the temporary measurement equipment limitations. Some calculated and measured results are presented in Fig. 2. Efficiency of the PMASRM versus speed (Fig. 2b) was calculated for the same current densities as for IPMSM current densities, obtained from the measuremens of the load conditions.

Conclusion
Results of the output power capability comparison between IPMSM and PMASRM (measured and calculated) show that PMASRM exhibits higher output power capability and better efficiency than the existent IPMSM for the same level of flux weakening. At the same current density level and at the same level of flux weakening, the total iron losses of the PMASRM are similar to the iron losses of IPMSM. PMASRM exhibits higher iron losses than IPMSM in rotor and lower iron losses than IPMSM in stator.

[1] S. Morimoto, M. Sanada, and Y. Takeda, "Performance of PM-Assisted Synchronous Reluctance Motor for High-Efficiency and Wide Constant –Power Operation,"IEEE Transactions on Industry Applications, vol. 37, pp. 1234-1240, Sept./Oct. 2001.

[2] K. C. Kim, J. S. Ahn, S. H. Won, J. P. Hong and J. Lee, "A Study on the Optimal Design of SynRM for the High Torque and Power Factor,"IEEE Transactions on Magnetics, vol. 43, pp. 2543-2545, June 2007

[3] P. Niazi, H. A. Toliyat, D. H. Cheong and J. C. Kim, "A Low-Cost and Efficient Permanent-Magnet-Assisted Synchronous Reluctance Motor Drive,"IEEE Transactions on Industry Applications, vol. 43, pp. 542-550, March/April 2007.

[4] B. Štumberger, V. Goričan, A. Hamler, M. Trlep, and M. Jesenik, "Accuracy of Iron loss Calculation in Electrical Machines by Using Different Iron Loss Models,"JMMM, vol. 245-255, pp. 269-271, 2003.

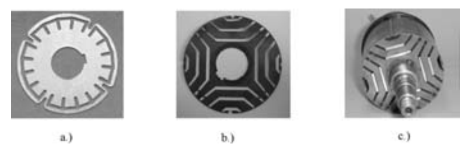

Fig. 1. a.) Rotor lamination of IPMSM; b.) Rotor lamination of PMASRM; c.) Rotor of PMASRM

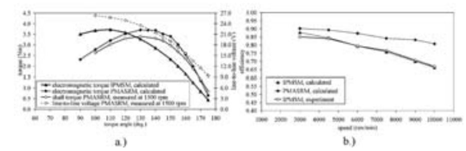

Fig. 2. a.) Measured flux-weakening performance of PMASRM and electromagnetic torque capability of IPMSM and PMASRM in dependency on torque angle at current density 7.35 A/mm2; b.) Efficiency versus speed for IPMSM and PMASRM for the same level of flux-weakening

EL-06

Performance of IPMSM for Electro-Hydraulic Power Steering with Electric Driven Pump Unit.

Y. Kim[1], S. Rhyu[1], J. Hur[1], J. Hong[2]
1. KETI, Bucheon, South Korea; 2. Hanyang University, Seoul, South Korea

1. Introduction
As the needs of motorization in automobile system increase, the electro-hydraulic power steering (EHPS) system is in the spotlight. Because EHPS system does not need a drive belt, takes up very little space and easy to position in the car, additionally, energy consumption is lowered, which leads to reduced fuel consumption [1].
The electric driven pump unit for EHPS system is consisted of a hydraulic pump, a pump motor and an electric control unit (ECU), and the hydraulic pump is run by electric motor. The electric motor is controlled by the ECU. The ECU adapts the power of the pump motor based on both the speed of the car and the turn speed of the steering wheel. Moreover, ECU, electric motor and hydraulic pump are all in one unit-which is also a replacement part. This paper will describe the development of the interior type permanent magnet synchronous motor (IPMSM) controlled by ECU, introduce the equivalent magnetic circuit method to analyze and design for the IPMSM, and finally provide the experimental results of the IPMSM.
2. IPMSM for EHPS system
IPMSM is expanding the application extent for commercial applications, such as electric vehicles, pumps, compressors. Because that it is possible to employ both relructance and magnetic torque and to drive a motor over a wider speed range through the use of field weakening control. Specially, the motor for EHPS system is needed to have low torque ripple and cogging torque as well as high efficiency of that. In the paper, first, optimal shape design for reducing the cogging torque is acomplished by using the response surface method. Fig 1 show design variables to minimize the cogging torque. Second, the torque charateristics is presented by considering the nonlinear electromagnetic characteristic of this IPMSM [2]. For the characteristic analysis, 2-D FEM and equivalent magnetic circuit method are used and analysis results are compared with the experimental results for verification of the analysis method.
3. Results and Discussion
Fig. 2 shows the analysis result of the cogging torque. The optimization of design variables are accomplished by using the response surface method. Fig 3 shows the experimental devices for the proto type IPMSM.
Fig. 4 and Fig 5 show the experimental results of the dynamo-test. When the speed command is 4000 rpm, performances of the motor is shown in Fig. 4, When the Torque command is 3.4 N-m, performances of the motor is shown in Fig. 5. From these results, motor efficiency is about 90% at the 1 kW point and the efficiency of including the ECU is about 85%. Finally, the more detailed results and discussion will also be given fully in full paper.

[1] Tomy Sebastian, Mohammad S. Islam and Sayeed Mir, " pplication of Permanent Magnet Synchronous Machines in Automotive Steering Systems" KIEE Trans. on Electrical Machinery and Energy Conversion Systems, Vol. 5-B No. 2, pp. 111~117, 2005

[2] Fernandez-Bernal, F.; Garcia-Cerrada, A.; Faure, R, " Model-based loss minimization for DC and AC vector-controlled motors including core saturation," IEEE Trans. on Industry Applications., Volume 36, Issue 3, pp. 755-763,, May-June 2000

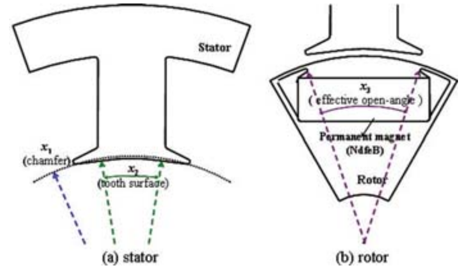

Fig. 1 Set of design variables

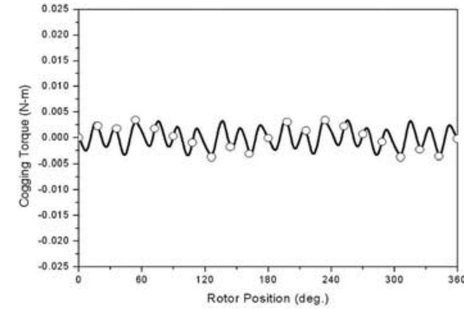

Fig. 2 Analysis result of cogging torque

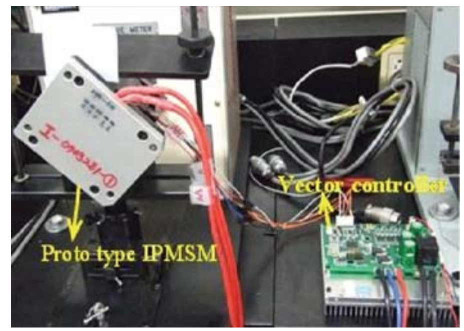

fig. 3 Test set of proto type IPMSM

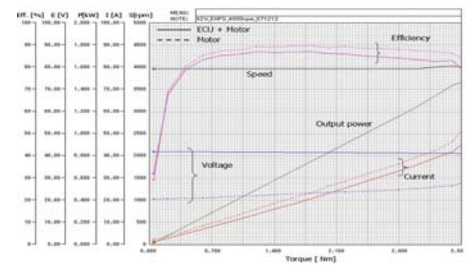

Fig. 4 Experimental results of speed 4000 rpm

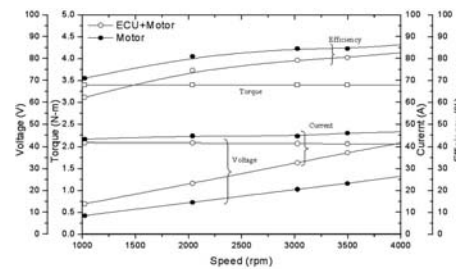

Fig. 5 Experimental results of torque 3.4 N-m

EL-07

Influence of driving methods on dynamic torque characteristic of high-speed permanent magnet synchronous motor with hall sensor.

S. Jang[1], *U. Lee*[1], D. You[1], J. Park[1], T. Sung[2]
1. Chungnam National University, Daejeon, South Korea; 2. Korea Electric Power Research Institute, Daejeon, South Korea

Introduction

High-speed motors are becoming attractive in applications such as micro-turbine generators, pumps, and fans [1]. Especially, due to the feature such as high efficiency, small volume and high power density, high-speed Permanent Magnet Synchronous Motor (PMSM) has gained the increasing popularity in many fields [2-4]. In PMSM with the various applications, driving method has generally two types. One is six-step drive by hall sensors and the other is sinusoidal drive by encoder type sensors. The six-step driving method is based on the feedback of rotor position obtained at fixed points from typically every 60 electrical degrees for commutation of the phase current. This driving method has the advantage of self-starting by absolute position and the rapid acceleration by quasi-rectangular shape currents with various harmonics. However, the current harmonics created by the difference between the discrete reference voltage and sinusoidal back EMF by PM rotor speed increase torque ripple at high-speed. The sinusoidal driving method with continuous sinusoidal reference voltage has a few current harmonics in relation with the sinusoidal Back-EMF. This means that dynamic torque is produced with very little ripple at the high speed. In spite of these merits, sinusoidal drive is not generally used for industry applications because of the dynamic range restriction of encoder at the high speed. Therefore, to improve dynamic characteristics and efficiency in PMSM operation, this paper presents the sinusoidal drive by the estimated rotor position obtained from hall signals and clock of controller over the specific speed. In our analysis, the dynamic torque is estimated by electromagnetic field with space harmonics and time harmonics generated from current and PM magnetization. And verification of analysis is performed by Finite Element Method (FEM) and the experimental results.

Experimental results according to driving mode

Fig. 1(a) shows the cross-section of 4-pole, 3-phase surface-mounted PM machine with a parallel magnetized PM rotor and a slotted stator core. Fig. 1(b) presents an eddy current type dynamometer as mechanical load. It is coupled to the manufactured high-speed PMSM to measure current harmonics. Fig. 2(a) shows phase back EMF and the phase reference voltage waveform by the continuous current (180 electrical degree) mode under six-step drive. Here, one sector has 60 electrical degrees. Fig. 2(b) shows the sinusoidal reference voltage obtained by estimated rotor angles based on hall sensor signals and the back EMF waveform under sinusoidal drive. As shown in figure, the sinusoidal reference voltage corresponds with the back EMF. Fig. 2(c) shows that the initial driving method under six-step mode is replaced by sinusoidal mode at specific speed. The torque of six-step driving method is higher than that of sinusoidal driving method at low speed and the torque ripple of six-step method is higher than that of the sinusoidal method. Therefore, the changing driving method has the advantage of rapid speed response at initial drive and reduces vibration and loss characteristic of PMSM at high speed.

Fig. 3 shows experimental result of current harmonics to recognize influences from mode change. There are district differences between the two consequences. While the current harmonics has multiple components at the six-step mode due to nonlinear of switching as shown Fig. 3(a), there dominate the first harmonic component at sinusoidal mode as shown Fig. 3(b). The more detailed results and discussion will be given in final paper. The mathematical expressions related to analytical results will also be given fully in final paper.

[1]B. H. Bae, S. K. Sul, J. H. Kwon, J. S. Byeon, IEEE Trans. Indust.Applicat.,39, 811(2003).

[2] J. B. Ahn, Y. H. Jeong, D. H. Hang, and J. H. Park, IEEE Trans. Elect,. 2879(2004)

[3]M.A Rahman, A. Chiiba, T. Fukao, IEEE Power Engineering Society Meeting.1272(2004).

[4] M. Mekhiche, s. Nichols, J. L. Kirtley, D, Boudreau, R. Jodoin, IEEE international Electric Machines and Drives Conference,658(2001)

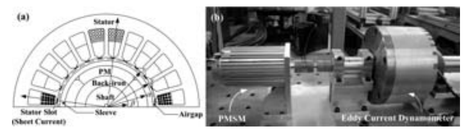

Fig. 1. 2kW-class high-speed PMSM: (a) analysis model for torque estimation (b) manufactured PMSM with eddy current dynamometer

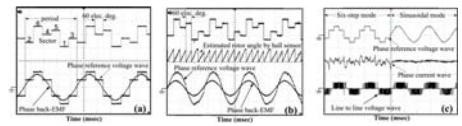

Fig. 2. Input voltage according to drive mode: (a) six-step drive (b) sinusoidal drive (c) change of driving mode at the specific rotor speed

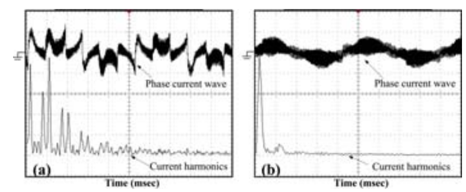

Fig. 3. Experimental results of current harmonics according to driving method: (a) six-step method (b) sinusoidal method

EL-08

Thrust Ripple Minimization of Permanent Magnet Linear Synchronous Motor by the Notch and the Auxiliary-teeth.

D. Lee, K. Jang, G. Kim
Electrical Engineering, Changwon National University, Changwon, South Korea

A slot type permanent magnet linear synchronous motor(PMLSM) is used widely as the driving source for factory and office automation because it has the advantages of high-efficiency and high-energy density. But, there are the disadvantages that a noise and a vibration of the apparatuses are induced and the control ability of the instruments is curtailed because of thrust ripple[1]. Therefore, thrust ripples reduction is an essential requirement in slot type PMLSM.
The thrust ripples of the slot type PMLSM can be classified into categories: (i) the ripple due to the detent force caused by magnetic reluctance difference of slot-teeth structure, (ii) the ripple due to the detent force caused by end-effect, (iii) the ripple due to the harmonic components of permanent magnet.
So, in this paper, the notch and auxiliary-teeth are installed on armature core to reduce the detent force caused by magnetic reluctance difference of slot-teeth structure and end-effect. And, the permanent magnet shape is changed to reduce the thrust ripple due to the harmonic components of permanent magnet.
Table 1 shows the specifications. Fig.1 shows the armature of notch model and measurement equipments of the PMLSM.
Fig. 2, Fig. 3 and Fig.4 show the detent force and the thrust characteristic. As shown in table II, the peak values of detent force are decreased remarkably by notch and auxiliary-teeth. Also, the thrust is decreased. PM shape changing is ignored because the effect of it is very small to reduce detent force. So, in this paper, the optimum model is proposed, notch and auxiliary-teeth are applied at the same time.
As the results, the peak-value of detent force of optimum model is 10.27[N] which is 14.7[%] of basic model. The peak value of thrust is decreased from 898.9[N] to 847.9[N]. But, the distortion ratio of thrust is decreased from 7.52[%] to 1.93[%] because the 2nd, 5th and 6th harmonics components of optimum model are decreased remarkably in comparison with that of basic model by notch and auxiliary-teeth. Therefore, the vibration and noise are decreased and operating characteristic of PMLSM is improved as distortion ratio is reduced remarkably.

[1] Ki-Chae Lim, Joon-Keun Woo, Gyu-Hong Kang, Jung-Pyo Hong, Gyu-Tak Kim,, “Detent Force Minimization Techniques in Permanent Magnet Linear Synchronous Motor”, IEEE Trans. on Magnetics, Vol. 38, No. 2, pp. 1157-160, 2002

TABLE 1. THE SPECIFICATIONS OF ANALYSIS MODEL

	Items	Values [unit]		Items	Values [unit]
Stator (PM)	Material	Nd-Fe-B	Mover (Armature)	Turns	304
	Residual induction	1.32 [T]		Height of teeth	16.95 [mm]
	Height of PM	9.0 [mm]		Width of teeth	14 [mm]
	Length of PM	93 [mm]		Slot pitch	40 [mm]
	Width of PM	26.5 [mm]		Rated current	6.53 [A]
	Pole pitch	30[mm]		Mechanical air-gap	1.4 [mm]

TABLE 2. DETENT FORCE, THRUST & DISTORTION RATIO

Model	Detent force	Detent force (experiment)	Thrust	Thrust (experiment)	Distortion ratio
Basic model	69.8[N]	53.3[N]	898.9[N]	907.97[N]	7.52[%]
Notch model	40.86[N]	33.4[N]	881.5[N]	885.4[N]	4.74[%]
Auxiliary-teeth model	38.57[N]	-	867.8[N]	-	6.01[%]
Optimum model	10.27[N]	-	847.9[N]	-	1.93[%]

(a) Armature of notch model (b) The measurement equipment and prototype machine

Fig. 1 the armature of notch model and measurement equipments of the PMLSM

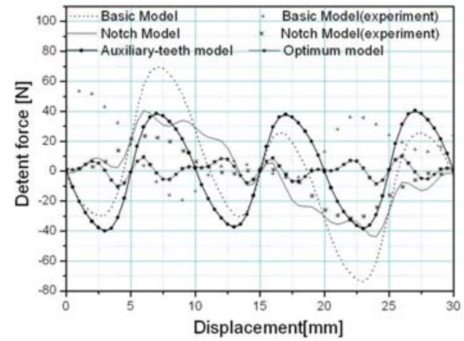

Fig. 2 Detent Force

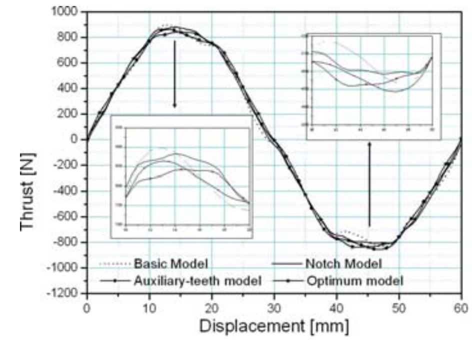

Fig. 3 Thrust

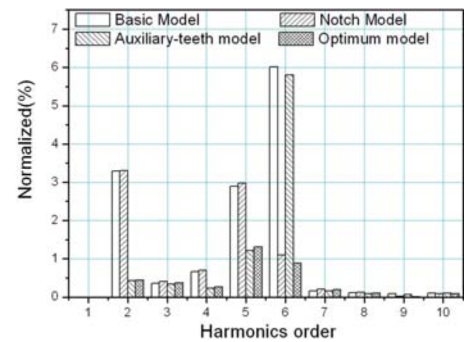

Fig. 4 Harmonics components of thrust

A Study on the Vibration Characteristic According to PM Arrangement in PMLSM.

D. Lee, S. Lee, K. Jang, G. Kim
Electrical Engineering, Changwon National University, Changwon, South Korea

A slot type Permanent Magnet Linear Synchronous Motor(PMLSM) has high efficiency, high energy density and high control ability. But, detent force is always produced by the structure of slot teeth and end effect. As detent force is acted as noise and vibration of the apparatuses, it is decreased the control ability because it acts as thrust ripple[1].
Generally, the best part of researches in PMLSM is to reduce detent force. But, the research of PMLSM does not exist about the vibration. So, the vibration characteristic of PMLSM according to PM arrangement is experiment and analysis in this paper.
Fig. 1 shows the PM arrangement on the stator. The basic model, a general skew model and the V-skew model are shown. The structure of stator and mover except the PM arrangement are same.
Fig. 2 shows developed forces of skew model. The detent force, thrust, normal force, and lateral force are operated in the PMLSM. Usually, the detent force, normal force, and the lateral force act as negative effect in the PMLSM.
Table 1 shows detent force, thrust, distortion factor of thrust and lateral force. The detent force of general skew and V-skew model decreased remarkably than No-skew model. The peak-value of lateral force of general skew model is 31.95 [N]. The other side, the lateral force of No-skew and V-skew model becomes 0[N] because they have symmetry structure about Z-axis direction.
Fig. 3 shows the accelerometer and location of acceleration sensor for vibration experiment.
Fig. 4 shows the mechanical vibration frequency when the impact hammer is hit to x-direction.
The vibration is measured according to the velocity changing. Fig. 5 shows experimental results of vibration.
Fig. 6 shows the vibration frequency by FFT at 2[m/s]. The vibration of x-direction is generated greatly because mover is free operated in the x-direction. But, the vibration of y-direction and z-direction are smaller than it of x-direction because the movement is limited owing to upholding for LM guide in the y-direction and z-direction. So, that is meaningless to measure the vibration dimensions of y-direction and z-direction.
Therefore, the vibration of x-direction according to the velocity is shown in Fig. 7. In the Fig. 7(a), the vibration of basic model is generated greatly at 50[Hz] as the effect of detent force. The vibration of detent force for other models must be generated at 16.66[Hz] because the periodic of detent force is different by skew. That is very smaller to because detent force is reduced. But, the vibration of detent force is reduced by increasing inertial force according to increasing velocity. When the velocity is under 1.0[m/s], the vibrations of all models are similar. But, the vibration of skew model is increased greatly in case of velocity at 1.5[m/s] and 2.0[m/s] because the lateral force is increased.

[1]Ki-Chae Lim, Joon-Keun Woo, Gyu-Hong Kang, Jung-Pyo Hong, Gyu-Tak Kim,, "Detent Force Minimization Techniques in Permanent Magnet Linear Synchronous Motor", IEEE Trans. on Magnetics, Vol. 38, No. 2, pp. 1157-160, 2002

TABLE 1. DETENT FORCE, THRUST, DISTORTION RATIO AND LATERAL FORCE

Model	Detent force	Detent force (experiment)	Thrust	Thrust (experiment)	Distortion ratio	Lateral force
Basic	68.3[N]	53.3[N]	903.03[N]	907.97[N]	4.67[%]	0[N]
Skew	23.3[N]	19.2[N]	900.12[N]	869.2[N]	2.42[%]	31.95 [N]
V-skew	25.3N]	26.4[N]	903.89[N]	904.9[N]	2.45[%]	0[N]

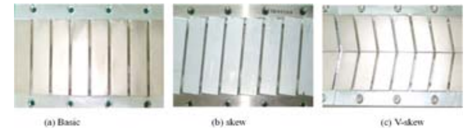

Fig. 1 PM arrangement

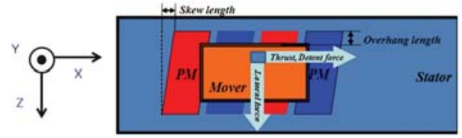

Fig. 2 Developed forces of skew model

Fig. 3 Vibration experiment

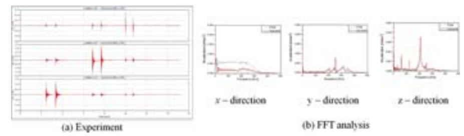

Fig. 4 Mechanical vibration (hitting point: x-direction)

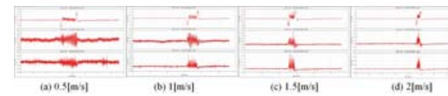

Fig. 5 Vibration according to velocity

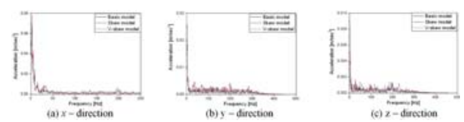

Fig. 6 Vibration at 2[m/s]

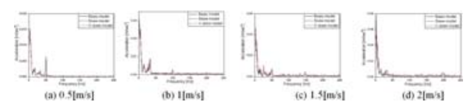

Fig. 7 x-direction vibration according to velocity

EL-10

Flux Barrier Design to Improve Torque Characteristics of Double-layer Interior Permanent Magnet Synchronous Motor.

S. Kim[1], J. Jung[1], J. Hong[1], S. Lee[2]
1. Department of Mechanical Engineering, Hanyang University, Seoul, South Korea; 2. Research Center, Korea Institute of Industrial Technology, Gwangju, South Korea

I. Introduction
Interior permanent magnet synchronous motor (IPMSM) is widely used for many industrial applications such as electric vehicles and home appliances due to its high power density and wide speed range. From the torque performance point of view, however, the IPMSM has two drawbacks. That is, torque ripple and cogging torque are relatively large as compared with a surface mounted permanent magnet motor. These problems are produced mostly by the discontinuous reluctance variation because of the slotted structure of stator core and saturation of magnetic circuit [1]. In particular, the magnetic saturation of IPMSM operated in wide speed range through flux weakening control greatly varies according to load condition. Therefore, the shape optimization of IPMSM is demanded to improve torque characteristics, but it is very complex and difficult work, because a lot of design variables and the interactions between them must be considered. However, this paper shows it is possible to enhance torque performance by the optimal design of flux barrier without considering other design parameters. At that time, response surface method (RSM) is applied as an optimization method [2]. In the end, the more details on the optimization and RSM will be given fully in final paper.
II. Prototype Model and Specifications
Fig. 1 shows the configuration of prototype model for driving air-conditioning compressor in hybrid electric vehicle. The specifications given in the model are listed in Table I.
III. Flux Barrier Design Optimization
A1, A2 and A3 displayed in Fig. 2 are design variables selected in this paper. The objective function and constraint condition for the optimal design of flux barrier are as follows:
Objective function:
- Torque ripple at the base speed less than 10%
- Torque ripple at the maximum speed less than 30%
- Peak value of cogging torque less than 0.1Nm
- Total harmonic distortion (THD) of back-EMF less than 4%

Subject to:
- Average torque at the base speed more than 5.5Nm
- Average torque at the maximum speed more than 2.55Nm

Fig. 3(a) and (b) show the flux barrier and fabricated configuration of Final model.
IV. Results and Discussion
Fig. 4(a) displays the torque waveforms of final model obtained by finite element analysis (FEA) at the base and maximum speed. At this time, input current is 15.95A and 12.5A, and current angle is 32.5o and 63.6o respectively. In Fig. 4(b), test and FEA result of cogging torque are compared. Fig. 5(a) and (b) show the back-EMF waveform measured at 3500rpm and harmonic analysis of the waveform respectively. The more detailed test results and discussion will be included in final paper.

[1] M. Sanada et al., "Torque ripple improvement for synchronous reluctance motor using an asymmetric flux barrier arrangement," IEEE Trans. Ind. Applicat., vol. 40, no. 4, pp. 1076-1082, July/August 2004.

[2] S. I. Kim et al., "Optimization technique for improving torque performance of concentrated winding interior PM synchronous motor with wide speed range," in Conf. Rec. IEEE-IAS Annu. Meeting, vol. 4, pp. 1933-1940, 2006.

Items	Value
Number of poles	6
DC link voltage	155V
Rated output power	2kW
Base and max. speed	3500, 7500rpm

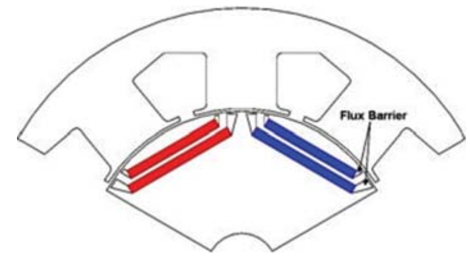

Fig. 1. Configuration of prototype model

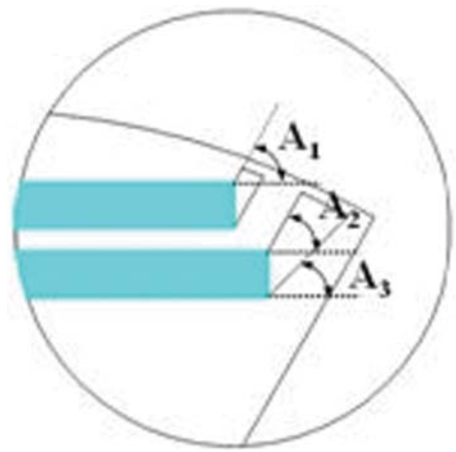

Fig. 2. Design variables

(a) flux barrier (b) Fabricated configuration

Fig. 3. Final model

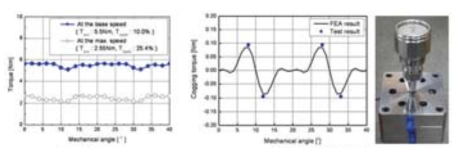

(a) Torque (b) Cogging torque

Fig. 4. Torque characteristics

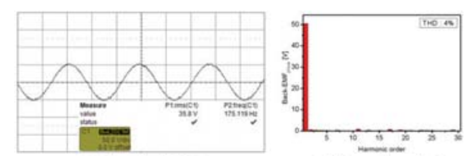

(a) Phase back-EMF (b) Harmonic analysis

Fig. 5. Back-EMF @ 3500rpm

EL-11

Study on High Efficiency Performance in Interior Permanent Magnet Synchronous Motor with Double-layer PM Design.

L. Fang, J. Jung, B. Lee, J. Hong
Department of Mechanical Engineering, Hanyang University, Seoul, South Korea

-Introduction-
The interior permanent magnet synchronous motors (IPMSM) have wide applications to household goods, industrial use, and electric and hybrid vehicle propulsion. Compared to DC motors and AC induction motors, the IPMSM have superior performance characteristics, that including high efficiency, high torque density, and wide constant power operating range[1]. In this study, a high efficiency IPMSM used as a traction motor in vehicle propulsion system is introduced firstly to be a prototype model, and then double-layer design is applied to the IPM rotor for improving the motor efficiency performance further.
The double-layer structure is created by splitting the single-layer PM into two pieces, and forming double flux barriers. From the rotor structure point, the double-layer IPMSM has the beneficial attributes of both the synchronous reluctance motors(SynRM) and the PM motors. Taking advantage of SynRM attributes, the high rotor saliency can be achieved by increasing split layer, which is benefit to the reluctance torque production. In the case of generating specific torque rating, the increasing of reluctance torque production lower the dependency on magnet torque production. Correspondingly, the copper loss decreases with the reducing of armature current relating to magnet torque production. In this study, the introduced prototype single-layer model is optimal designed into double-layer structure with the help of a coupled optimization method that design of experiment(DOE) and response surface methodology(RSM)[2]. An optimum double-layer structure is quickly determined and the advantages of double-layer IPM design on the efficiency improvement are verified through the motor performance comparison. The torque production and efficiency performance are calculated by using the equivalent circuit method(ECM)[3] and finite element method(FEM).
-Equivalent Circuit Method (ECM)-
Equivalent circuits for IPMSM based on the synchronous d-q reference frame including core loss consideration are presented in Fig. 1. The mathematical model is built from the equivalent circuit. The d-axis and q-axis voltages and hybrid torque equations are given as (1), (2) and (3) respectively. In the equivalent circuit, Ra is armature winding resistance per phase, Rc is equivalent iron loss resistance, ψa is flux linkage of PM per phase(rms), Ld and Lq are d-axis and q-axis inductance, Pn is number of pole pairs, β is the lead angle of phase current (=arctan(-id/iq)).
-Prototype Model and Optimum Model-
A 15-kW high efficiency IPMSM used as traction motor is given as prototype model. It has 16-pole and 24-slot, with concentrated windings arranged in stator part, as Fig. 2(a) shows. Using the same amount of magnet, an optimum structure of double-layer IPM is designed with the object of high efficiency at constant torque range. Fig. 2(b) shows the optimum double-layer IPMSM model.
-Results Comparison-
Fig. 3 shows the results comparisons between the prototype single-layer model and the optimum designed double-layer model. The same torque performance along all the speed range is restricted, as Fig. 3(a) shows. The improving of efficiency performance is observed from Fig. 3(b). The hybrid torque production that reluctance torque and magnet torque are compared separately in Fig. 3(c). The copper loss existing in armature windings is reduced when the magnet torque decreased, which is verified in Fig. 3(d). In general, the motor efficiency improving is achieved by enhancing reluctance torque production to compensate the reducing of magnet torque production.

[1] SHIGEO MORIMOTO, YOJI TAKEDA. "Machine Parameters and Performance of Interior Permanent Magnet Synchronous Motors with Different Permanent Magnet Volume," Electrical Engineering in Japan, vol. 131, No. 4,2000.

[2] Raymond H. Myers, Douglas C. Montgomery, "Response Surface Methodology: Process and Product Optimization Using Designed Experiment", A Wiley-Interscience Publication John Wiley & Sons, INC.

[3]Ji-Yong Lee, Sang-Ho Lee, Geun-Ho Lee, Jung-Pyo Hong, Jin Hur, "Determination of Parameters Considering Magnetic Nonlinearity in an Interior Permanent Magnet Synchronous Motor," IEEE Transaction on Magnetics, vol. 402, no. 4, APPRIL 2006.

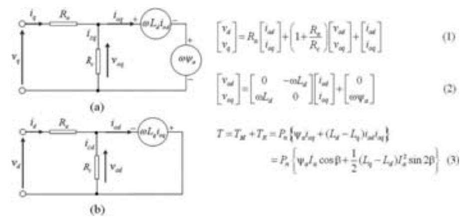

Fig.1. Equivalent circuits and mathematical model of IPMSM in synchronous d-q reference frame (a) d-axis circuit, (b) q-axis circuit. In addition, d-axis and q- axis voltages and torque equations (1), (2), (3).

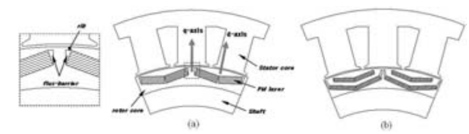

Fig.2. Cross-section of IPMSM models (a) prototype single-layer model, (b) optimum double-layer model

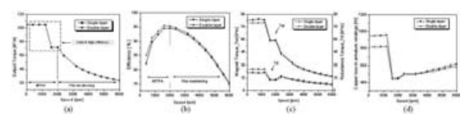

Fig.3. Results comparison between single-layer model and double-layer model (a) output torque performance, (b) motor efficiency performance, (c) reluctance torque and magnet torque characteristic, (d) copper loss characteristic

A new PMLSM having 9 pole 10 slot structure and its shape optimal design for detent force reduction.

C. Koh, I. Hwang, H. Yoon
School of Electrical & Computer Engineering, Chungbuk National University, Cheongju, South Korea

A permanent magnet linear synchronous motor (PMLSM) having conventional structure of $4\tau_p=3\tau_s$ (or $2\tau_p=3\tau_s$) where τ_p and τ_s are PM pole and winding slot pitches, respectively, has quite big detent force, and applications to a place requiring precise position and speed control have been limited [1]. In this paper, a new PMLSM having structure of $9\tau_p=10\tau_s$(*9 pole 10 slot structure*) is suggested to reduce the cogging force, and the detent force is minimized by optimizing both armature core length and shape of the exterior teeth simultaneously.

A cogging force from one slot of armature core can be represented, using Fourier series expansion, as follows:

$f_c(x)=\Sigma A_n \sin(n\omega x+\alpha_n)$ (1)

where the summation is over the harmonic components($1\leqq n\leqq\infty$), A_n and α_n are the magnitude and phase angle of the n-th harmonic component, respectively. Using (1), the total cogging force of a PMLSM having 12 poles and 9 slots, as an example of $4\tau_p=3\tau_s$ structure, can be proven to consist of only 3n order harmonic components as follows:

$F_{12p9s}(x)=3\Sigma A_n \Sigma \sin(n\omega x+n\theta_i+\alpha_n)=9\Sigma A_{3n}\sin(3n\omega x+\alpha_{3n})$ (2)

where the first and second summations are for the harmonic components($1\leqq n\leqq\infty$), and winding slots($1\leqq i\leqq 3$), respectively, θ_i is the position of the i-th slot. In the same way, the suggested PMLSM having *9 pole 10 slot structure* can be proven to have only 10n order harmonic components in its cogging force as follows:

$F_{9p10s}(x)=\Sigma A_n \Sigma \sin(n\omega x+n\theta_i+\alpha_n)=10\Sigma A_{10n}\sin(10n\omega x+\alpha_{10n})$ (3)

where the first summation has the same meaning as in (1) and the second is for the winding slots($1\leqq i\leqq 10$). Comparing (3) with (2), it is clear that the suggested PMLSM reduces the cogging force very much because the magnitudes of the 10n harmonic components are, in general, much smaller than those of the 3n harmonic components.

On the other hand, the detent force of the suggested PMLSM is reduced by optimizing both armature core length and shape of the exterior teeth. In the optimization, the detent forces are approximated to a response surface using Multi-quadric radial basis function with pareto-optimal sampling points obtained by using Latin hypercube design employing *MinMax* and *MaxMin* criteria and the corresponding detent forces calculated from finite element analysis[2].

Fig. 1 and Table I compare the optimized design of the suggested PMLSM with that of convectional one having 12 poles and 9 slots where the overall lengths of armature core are 206.8(mm)and 185.6(mm), respectively. For the optimized designs, the finite element analysis gives the detent forces of 1.95[N] and 12.56[N], as shown in Fig. 3(a), and the thrust forces of 246.53[N] and 230.81[N], as shown in Fig. 4(a), at the same armature current of 709.37(AT)/phase for the suggested and conventional PMLSMs, respectively.

In order to validate the performance of the suggested PMLSM, a sample PMLSM is constructed as shown in Fig. 2. While driving the PMLSMs using ADAX-08LL2 servo system, the detent and thrust forces are experimentally measured by using load cell. Fig. 3(b) shows the suggested PMLSM reduces the detent force to 14.42[N] from 24.9[N] of the conventional one. Fig. 4(b) shows a comparison of the thrust forces. As the armature current increases, the suggested PMLSM gives bigger thrust force than the conventional one. At the armature current of 3.8[A], the suggested PMLSM gives 6.7% bigger thrust force than the conventional one.

[1] M. Inoue, et. al., "An approach to a suitable stator length for minimizing the detent force of PMLSM," IEEE Trans. on Magn., Vol. 35, No. 4, pp. 1890- 1893, July 2000

[2] Y. Zhang, et. al., "A robust optimal design algorithm using adaptive RSM," Proceedings of COMPUMAG 2007, Aachen, Germany, June 24-28, 2007, pp.973-974

Item	Suggested	Conventional
Mechanical structure	$9\tau_p=10\tau_p$	$12\tau_p=9\tau_p$
Phases/Lamination(mm)	3/50	3/50
Armature winding(turns)	132	132
Slot width/pitch(mm)	12.45/18.45	12.5/20.0
PM width/pitch/height(mm)	14.8/20.5/4.0	12.5/15.0/4.0

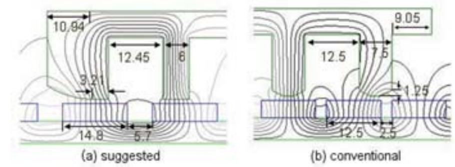

Fig. 1 Comparison of the optimized shapes

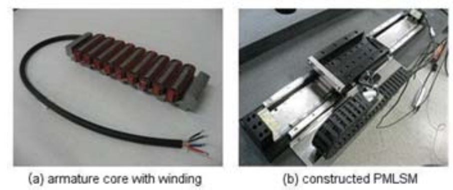

Fig. 2 Construction of the suggested PMLSM

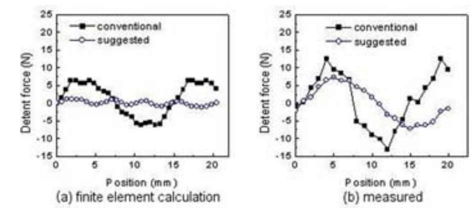

Fig. 3 Comparison of the detent forces

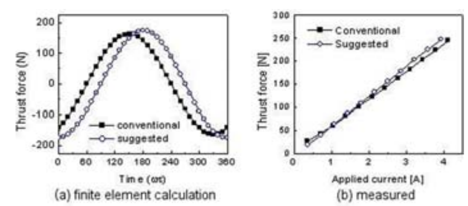

Fig. 4 Comparison of the thrust forces

EM-01

The role of uncompensated spins in exchange biasing.

H. J. Hug[1,2], I. Schmid[1], P. Kappenberger[1]
1. Nanoscale Materials Science, Empa, Duebendorf, Switzerland; 2. Institute of Physics, University of Basel, Basel, Switzerland

The origin of the exchange bias (EB) effect has been traced back to the existence of pinned uncompensated spins (UCS) in the antiferromagnet (AFM) or at its interface. However, the understanding of the underlying mechanism is still clouded by contradictory reports: Ohldag et al. [1] used XMCD to extract the direction and density of pinned UCS from the vertical shift of element specific magnetization loops. In their interpretation, the positive vertical shifts reflects a parallel coupling of the UCS to the spins of the ferromagnet (FM). Tsunoda et al. [2] used a similar experimental method but did not find any vertical shift. Furthermore, Kappenberger et al. [3] (magnetic force microscopy) and Eimüller et al. [4] (XMCD PEEM) reported an antiferromagnetic coupling between the UCS and the FM spins.
In this work different perpendicular exchange-biased AFM/FM multilayers were prepared. The FM layers consisted of CoPt and CoPd multilayers. For the AFM layers either CoO (sample S1) or MnIr (sample S2) was used. These samples were then studied by vibrating sample magnetometry (VSM) and high resolution low-temperature magnetic force microscopy (MFM).
The VSM-loops obtained after field-cooling in 1T showed positive vertical shifts for all samples that arises from pinned UCS aligned parallel to the FM spins. For the MFM experiments, the samples were set into an up/down stripe domain state at room temperature (RT) and zero-field cooled to 8.3K. The MFM images of samples S1 (fig. 1(a)) and S2 (fig. 1(b)) reveal regular stripe patterns due to domains in the FM layers. Figs 1(c) and (d) show MFM data acquired after saturation of the FM layers. Then, weak and more granular stripe patterns remain visible even in the highest field we could apply (7T). Surprisingly, the comparison of figs. 1(a) and (b) with figs. 1(c) and (d) reveals an inverted contrast. In conclusion, the pattern visible after saturation of the FM layers is due to a pattern of pinned UCS, that are aligned antiparallel to the spins of the FM.
Our VSM and MFM results prove the existence of two distinct groups of pinned UCS. Thus, one such group (called “p”) aligns parallel to the FM while the other group (called “ap”) aligns antiparallel to the FM. In the VSM experiments performed after field cooling in 1T the total magnetic moment of the p-group dominates that of the ap-group. In the MFM experiments the uncompensated AFM spins are cooled in zero external field but are still subjected to weaker field generated by the FM domains (about 200mT). The MFM clearly reveals that the ap-group dominates over the p-group. It is noteworthy that the ap-spins align antiparallel to the (local) cooling field generated by the FM domain pattern. From this we conclude that the ap-spins are exchange coupled to the FM spins and thus are responsible for the EB-effect. To study the dependence of the p-moment on the cooling field, an EB-sample with a high RT remanence was fabricated, saturated at RT and then cooled in various fields ranging from zero to 7T. After zero-field cooling a negative vertical shift of the M(H)-loop was found. The vertical shift became positive for moderate cooling fields and remained constant up to 7T. The EB-effect did not change sign and became slightly smaller in high cooling fields. These results confirm that a saturated FM generates pinned ap-spins in the AFM via exchange coupling, while the p-spins are generated by the cooling field. Hence, only the ap-spins are responsible for the EB-effect.
Given that most experimental techniques (including those used in our work [5]) measure the sum of both spin groups indiscriminately, contradictory results can arise. Our work may provide guidelines for the design of experiments which can correctly determine the densities of those UCS that do contribute to the EB effect .

[1] H. Ohldag et al., Phys. Rev. Lett., 91 (2003) 17203.

[2] M. Tsunoda et al., Appl. Phys. Lett. 89 (2006), 172501.

[3] P. Kappenberger et al., Phys. Rev. Lett., 91 (2003) 267202.

[4] T. Eimueller et al., J. Appl. Phys. 85 (2004) 2310.

[5] I. Schmid et al., Euro Phys. Lett. 81 (2008) 17001.

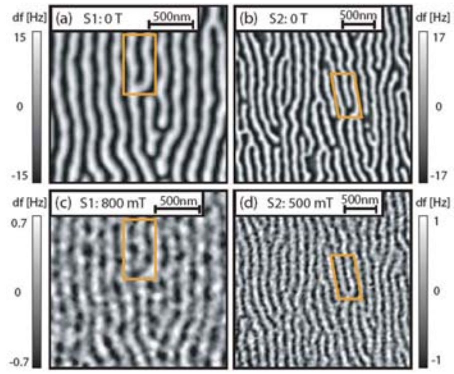

Fig.1: MFM images: domain pattern of the FM layers observed after zerofield cooling the samples containing CoO (a) and MnIr (b) as an antiferromagnet to 8.3K. After saturating the FM layers the weak and grainy contrast of the MFM images (c) and (d) arises from pinned UCS of the AFM layers. A comparison of (a) with (c) and (b) with (d) clearly reveals the existence of pinned magnetic moments of the AFM that are antiparallel to the magnetic moments of the FM layers.

EM-02

Measuring exchange anisotropy in Fe/MnPd using inductive magnetometry.

K. J. Kennewell[1], X. Ji[2], J. Hu[1], K. M. Krishnan[2], R. L. Stamps[1]
1. School of Physics, University of Western Australia, Crawley, WA, Australia; 2. Materials Science and Engineering, University of Washington, Seattle, WA

Measures of exchange bias determined from resonance differ significantly from those obtained using conventional magnetization experiments [1]. Quasi-static magnetization measurements of M(H) infer values of exchange anisotropy from coercivity and magnetization loop shifts [2]. Coercivity and other features of magnetization loops are averaged over entire samples, and typically involve a variety of history dependent magnetization processes. Because of these complications, actual magnitudes of exchange anisotropy are difficult to extract from magnetization measurements. By way of contrast, ferromagnetic resonance measurement instead characterizes the curvature of the free energy, which is dictated by the effective fields acting on a magnetization near equilibrium [3]. Analysis of the frequencies as a function of field strength and orientation can provide measures of local fields created by the exchange anisotropy.
In this work [4], we present results from investigations using an inductive ferromagnetic resonance technique [5, 6] of exchange anisotropy and exchange bias in epitaxial Fe/MnPd. A 13.5GHz network analyzer (Agilent 8719ET) is used as both the excitation and measurement device, coupling to the sample through a mutual inductance with a coplanar stripline. The stripline and sample are placed in an externally applied field up to 900 Oe, and the sample can be rotated in-plane. The sample was grown on a single crystalline MgO substrate oriented along the [001] direction using ion beam sputtering [6] in an ultrahigh vacuum at less than 10^-8 Torr.
Fig. 1 shows data obtained from resonance experiments in which the field is applied along different in-plane directions at a constant 10.8GHz. The results are interpreted in terms of effective anisotropies acting on the Fe films [7, 8]. The fourfold anisotropy of the Fe thin film layer has effective fields with roughly the same magnitude as the maximum applied field range, so a complete field profile as a function of frequency is not seen. However, the fourfold behaviour is clearly visible and the unidirectional exchange anisotropy is seen as a difference in resonance between $\theta=\pi$ and 2π.
Fig. 2 shows measurements of the resonance frequency aligned along the samples hard axis. The frequency lowers as the magnetization is pulled into the hard direction, reaching a minimum at the same field where the magnetization aligns with the applied field. Note two resonance branches are modelled in the figure for each applied field direction. Only one branch is observed experimentally due to the symmetry breaking nature of the exchange anisotropy. Interestingly, there is a jump in frequency for the transition to the hard direction for field values near the frequency cusp. We propose these anomalous frequencies are evidence of dispersion of the unidirectional magnitudes and directions about the field cooling direction.
Support is acknowledged from ARC Discovery and Postgraduate awards.

[1] Xi and R. M. White, Phys. Rev. B 61, 80 (2000)

[2] J. Nogués and I. K. Schuller, J. Magn. Magn. Mater. 192, 203 (1999)

[3] A.H. Morrish, The Physical Principles of Magnetism. Wiley-IEEE Press, (2001)

[4] K.J. Kennewell, X. Ji, J. Hu, K. M. Krishnan, R. L. Stamps, J. Appl. Phys. 101, 09E518 (2007)

[5] T. J. Silva, C. S. Lee, T. M. Crawford, and C. T. Rogers, J. Appl. Phys. 85, 7849 (1999)

[6] G. Counil, J.-V. Kim, T. Devolder, C. Chappert, K. Shigeto, and Y. Otani, J. Appl. Phys. 95, 5646 (2004)

[6] N. Cheng, J. Ahn, and K. M. Krishnan, J. Appl. Phys. 89, 6597 (2001)

[7] M. J. Pechan, D. Bennett, N. Teng, C. Leighton, J. Nogués, and I. K. Schuller, Phys. Rev. B 65, 064410 (2002)

[8] R. D. McMichael, M. D. Stiles, P. J. Chen, and W. F. Egelhoff, Phys. Rev. B 58, 8605 (1998)

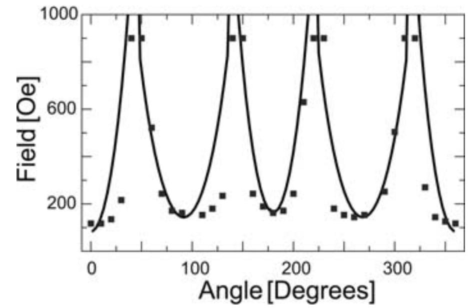

FIG 1: Resonant field as a function of angle at a constant frequency. Evidence for fourfold anisotropy is clearly seen. The solid line is a theoretical fit derived from the free energy.

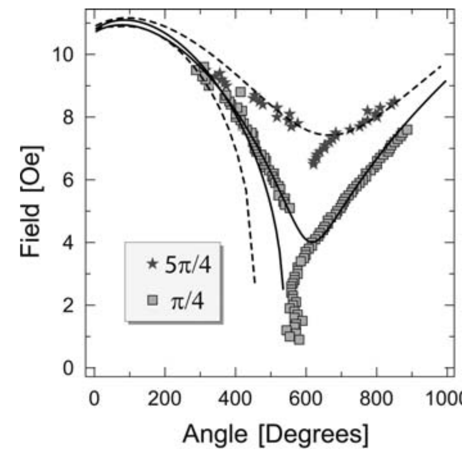

FIG 2: Response as a function of field in the exchange bias sample with the applied field aligned along the hard axis at $\pi/4$, results shown from field applied along both directions. A best fit overlayed from calculation.

EM-03

Dependence of the training effect on the antiferromagnet structure in the domain state model for exchange bias.

A. G. Biternas, U. Nowak, R. W. Chantrell
Department of Physics, University of York, York, United Kingdom

The application of giant magnetoresistance spin valve read head is wide-spread in high-density magnetic recording and draw a great deal of attention in exchange-coupled systems of ferromagnetic-antiferromagnetic (AFM) bilayers. These so called exchange bias systems exhibit unidirectional anisotropy, where a horizontal shift of the hysteresis loop is observed in the ferromagnet after an initial cooling process in a field. After a sequence of consecutive hysteresis cycles, a reduction of this effect is observed at constant temperature. This reduction is called the training effect. In the present paper, Monte-Carlo simulation techniques are used to investigate the training effect of the exchange bias field using the domain state model [1,2]. The behavior of the training is investigated for different values of antiferromagnet thickness and dilution with defects.

The data for each AFM dilution and thickness value were fitted to two different laws, firstly, the empirical power law $H_{eb}(n)= H_{eb}^{e-p}+\kappa/\sqrt{n}$ for n>1, where n the number of consecutive hysteresis loops and H_{eb}^{e-p} the equilibrium exchange bias field, and secondly, the recursive sequence : $H_{eb}(n+1)=-\gamma(H_{eb}(n)-H_{eb}^{e-rs})^3+H_{eb}(n)$, derived from a discretized Landau-Khalatnikov equation by Binek *et al.* [3,4].

According to Zhang *et al.* [5], training effect changes from one type to another with decreasing antiferromagnet thickness. They considered Type I training effect to be when the two branches of the hysteresis loop move to opposite directions, shrinking it from both sides. Type II training effect is when the two branches move to the same direction with a smaller shrinkage of the hysteresis loop.

As shown in Fig. 1 increasing the thickness of the antiferromagnet changes the type of training effect from Type II to Type I. Also, the exchange bias field and the training effect magnitude decreases with increasing thickness. This is due to the fact that it is harder to form domain walls which are perpendicular to the interface.

Figure 2 shows the dependence of the training effect on the dilution of the antiferromagnet. The exchange bias field increases as a function of AFM dilution up to the value of 50%, where it has its maximum. For low dilutions the field is close to zero. Also, the training effect is more intense at dilutions greater than 20%. Below that the training effect is weak. These results are found to be in qualitative agreement with the experimental data of Keller *et al.* [6] in epitaxially grown Co/CoO bilayers systems diluted with nonmagnetic substitutions ($Co_{1-x}Mg_xO$). The dilution dependence of both exchange bias field and magnitude of the training effect are related in the sense that for high and low dilutions the exchange bias decreases as well as the training effect. These results can be interpreted within the domain state model for exchange bias where the magnetization reversal of the ferromagnetic layer causes irreversible changes in the antiferromagnet domain structure.

[1] U. Nowak, K. D. Usadel, J. Keller, P. Miltenyi, Beschoten and G. Güntherodt, Phys. Rev. B 66, 14430 (2002)

[2] P. Miltenyi, M. Gierlings, J. Keller, B. Beschoten, G. Güntherodt, U. Nowak and K. D. Usadel, Phys. Rev. Lett. 84, 4224(2000)

[3] C. Binek, Phys. Rev. B 70 (2004)

[4] C. Binek, X. He, and Polisetty, Phys. Rev. B 72 (2005

[5] K. Zhang, T. Zhao, H. Fujiwara, J. Appl. Phys. 91, 6902(2002)

[6] J. Keller, P. Miltényi, B. Beschoten, G. Güntherodt, U. Nowak, and K. D. Usadel, Phys. Rev. B 66, 014431 (2002)

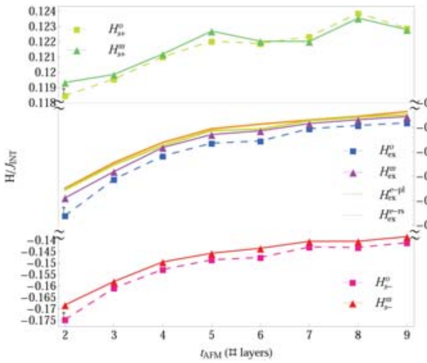

Figure 1. AFM thickness dependence of first and subsequent cycles mean value of exchange bias and coercive fields. H_{s+}^{o},H_{s-}^{o}: Positive and negative switching field of the first loop; H_{s+}^{m},H_{s-}^{m}: Mean value of positive and negative switching field of the 9 subsequent loops; H_{ex}^{o} : Exchange bias field of the first loop; H_{ex}^{m}: Mean value of exchange bias field of the 9 subsequent loops; H_{ex}^{e-p}: Exchange bias field equilibrium produced using power law fit; H_{ex}^{e-rs}: Exchange bias field equilibrium produced using recursive sequence.

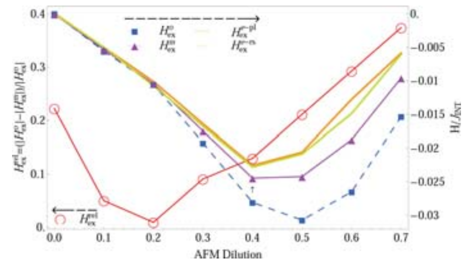

Figure 2. AFM dilution dependence of first and subsequent cycles mean value of exchange bias field. Abbreviation as above. H_{ex}^{rel}: Relative training effect calculated as noted on the label.

EM-04

Temperature Dependence of IrMn Pinning: Single Crystal versus Polycrystalline Effects.

P. Pong, C. L. Dennis, W. F. Egelhoff
Magnetic Materials Group, National Institute of Standards and Technology, Gaithersburg, MD

Introduction

Recently it has been found that the instability of the antiferromagnet against thermally activated changes is the reason of the difficulty to study the exchange bias phenomenon [1]. Extreme caution is necessary when studying the antiferromagnet behaviour because the actual state of the antiferromagnet can only be inferred from the ferromagnet behaviour with careful design of field sequence and temperature cycling. Fernandez-Outon et al. investigated the possible origins of thermal instabilities of antiferromagnet and they suggested that large increase in coercivity for polycrystalline IrMn at 10K is due to the freezing spins at the grain boundaries [1]. In this paper, we have investigated both single crystal and polycrystalline IrMn in order to verify the model of Fernandez-Outon et al.

Experimental Methods

The thin films were deposited on thermally oxidized silicon wafers by dc magnetron sputtering in an ultrahigh vacuum chamber with a base pressure of 2x10-10 Torr. The metal films were deposited at room temperature in 2 mTorr Argon. The oxide barrier layer was made by first depositing a thin Al or Mg metal and then oxidizing it in an oxygen plasma (4 mTorr Argon, 2 mTorr Oxygen) for 2.5 minutes. The magnetic hysteresis loop measurements were carried out with a SQUID magnetometer (MPMS, Quantum Design, USA) at the temperature of 300 K, 200 K, 100 K, and 10 K. The crystalline structures of the thin films were studied with RHEED.

Results and Discussion

Three magnetic tunnel junction film structures were made: (1) sample A – substrate / 100 Cu (100) / 10 IrMn / 5 Co / 0.5 Al / 2 Al2O3 / 20 Conetic (Ni77Fe14Cu5Mo4) / 10 Cu / 10 Ta, (2) sample B – substrate / 20 Conetic / 1 CoFeB / 1.5 MgO / 2.5 Co / 10 IrMn / 10 Au, (3) sample C – substrate / 20 Conetic / 0.5 Co / 1 Al2O3 / 0.5 Co / 2.5 Conetic / 0.5 Co / 10 IrMn / 10 Cu (all units in nm). The RHEED study shows that the IrMn on top of the Cu of sample A is single crystal structure while the IrMn of sample B and C are polycrystalline structures. The coercivities of the pinned layer loops were measured from the centers of the loops to the zero field in the hysteresis measurements at four different temperatures. The results are shown in Figure 1. All three samples show increases in their coercivities of their pinned layer loops from room temperature to 10 K. These increases are due to the stronger pinning strength of the IrMn at lower temperatures. In Figure 2 the coercivities are expressed as percentages in reference to the coercivities measured at room temperature. Comparatively speaking, the coercivities of the pinned layer loop (Hpin) of sample A which contains single crystal IrMn did not increase with the lower temperatures; however, the Hpin of both sample B and sample C increased considerably to about 1000 % and around 10000 % respectively as the temperature decreased from room temperature to 10 K.

Conclusion

The large increase of coercivity in polycrystalline IrMn was reproduced; however, no remarkable increase of coercivity was observed in single crystal IrMn. The coercivity of the single crystal IrMn showed very little change upon cooling to 10 K. These results provide strong evidence for the model of Fernandez-Outon et al.

[1] Fernandez-Outon et al., J. Opto. and Adv. Mater., 9, 1127 (2007)

[2] M. Tsunoda, K. Imakita, M. Naka, and M. Takahashi, J. Magn. Magn. Mat. 304, 59 (2006).

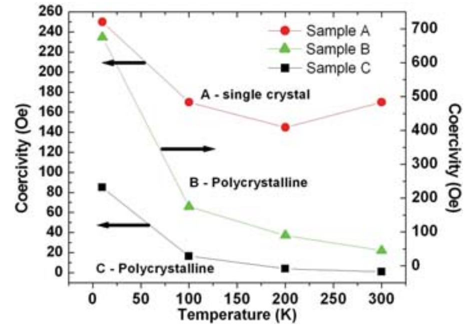

Figure 1. SQUID hysteresis measurement of sample A, B, and C from 300 K to 10 K.

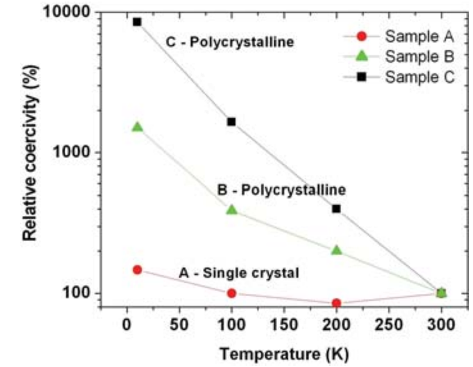

Figure 2. The changes of the coercivities with temperature relative to the coercivities at 300 K of samples A, B, and C.

EM-05

Exchange coupling between an amorphous ferromagnet and a crystalline antiferromagnet.

M. Fecioru-Morariu[1], G. Güntherodt[1], M. Rührig[2], A. Lamperti[3], B. Tanner[3]
1. Physikalisches Institut (IIA), RWTH Aachen University, Aachen, Germany; 2. Corporate Technology, CT MM 1, Innovative Electronics, SIEMENS AG, Erlangen, Germany; 3. Department of Physics, Durham University, Durham, United Kingdom

The exchange bias (EB) effect refers to the shift of the hysteresis loop along the field axis direction in ferromagnetic/antiferromagnetic (FM/AFM) bilayers. This is the consequence of the unidirectional anisotropy induced in the FM layer which results from the exchange coupling across the FM/AFM interface. The exchange biasing of amorphous soft ferromagnetic materials is important both for a fundamental understanding as well as for various applications including giant magnetoresistance (GMR) sensors.

Here we investigate the EB effect in bilayers of an amorphous FM (CoFeB) and a crystalline AFM (IrMn) in a top-pinned configuration [1]. When the crystalline IrMn layer is deposited on top of the amorphous CoFeB layer, no EB is observed.

On insertion of a thin crystalline FM layer of NiFe between the amorphous CoFeB and the crystalline IrMn, exchange coupling appeared and it was dependent on the thickness of the NiFe layer. The dependence of the absolute value of the EB field H_{EB} and of the coercivity H_C on the thickness x of the NiFe layer is plotted in Fig 1(a). We observe that the appearance of EB occurs when the thickness of the NiFe layer is about 2 nm or thicker. By further increasing x the H_{EB} rises to a maximum and then decreases for larger x values. At the same time, H_C increases with increasing x and stays almost constant at larger x values.

We demonstrate by X-ray diffraction that the appearance of EB in the CoFeB/NiFe/IrMn system is directly related to the appearance of the (111) texture of the IrMn layer [1]. This can be easily observed by comparing Fig. 1(a) with Fig. 1(b), the latter showing the dependence of the integrated intensity under the (111) IrMn peak on the thickness of the NiFe layer. In other words, the (111) texture of the IrMn layer is associated with the AFM state of the IrMn layer, which in contact with the FM layer gives rise to EB.

A significant enhancement in the blocking temperature of the CoFeB/NiFe/IrMn layers was observed on increasing the thickness of the NiFe layer [1]. This effect is also directly correlated with the (111) texture responsible for the antiferromagnetic phase of the IrMn layer, which developed progressively with increasing thickness of the NiFe layer. The blocking temperature was found to vary linearly with the intensity under the (111) X-ray diffraction peak of IrMn.

The above system can be used to induce a controllable EB anisotropy or pinning of the amorphous FM. It can serve as free-layer part of a magneto-resistive sensor with a strongly pinned FM (reference) layer. This sensor would allow to easily align the two FM layers (free and reference) orthogonal to each other, giving rise to a linear response of the sensor's electrical resistance with respect to the applied magnetic field.

A detailed magnetic and structural analysis of the correlation between the EB, blocking temperature and the (111) texture of IrMn will be given. Moreover, the effects of replacing the NiFe layer by a CoFe layer on EB as well as the resistance measurements of a GMR sensor with two orthogonal anisotropy directions will be presented.

The financial support provided through the European Community's Marie Curie actions (Research Training Networks) under contracts HPRN-CT-2002-00296, NEXBIAS and MRTN-CT-2003-504462, ULTRASMOOTH is gratefully acknowledged.

[1] M. Fecioru-Morariu, G. Güntherodt, M. Rührig, A. Lamperti and B. Tanner, J. Appl. Phys. 102, 053911 (2007).

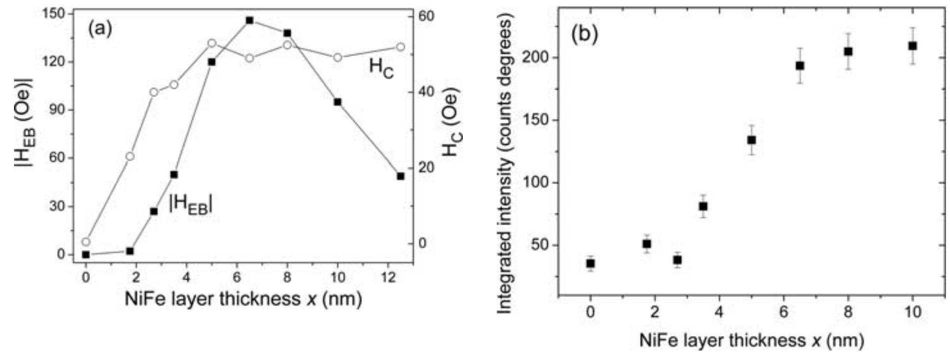

Figure 1: (a) Dependence of absolute value of the exchange bias field H_{EB} and coercive field H_C of CoFeB / NiFe (x nm) / IrMn on the thickness x of the NiFe layer and (b) integrated intensity under the IrMn (111) diffraction peak as a function of the NiFe layer thickness x.

EM-06

Local exchange anisotropy of epitaxial and polycrystalline MnIr/CoFe bilayers.

H. Kato[2], *T. Kato*[1], S. Tsunashima[2], S. Iwata[1]
1. Department of Quantum Engineering, Nagoya University, Nagoya, Japan; 2. Department of Electrical Engineering and Computer Science, Nagoya University, Nagoya, Japan

Exchange coupling between an antiferromagnetic (AF) layer and a ferromagnetic (F) layer plays an important role in spin valve heads and magnetic random access memories (MRAM). Even though the extensive experimental and theoretical investigations have been carried out [1], detailed mechanism of exchange biasing at AF/F interface is still unclear. In this study, we report a comparison of the magnetic force microscope (MFM) images between microstructured epitaxial and polycrystalline CoFe/MnIr bilayers to throw a light on the exchange biasing in microscopic scale.

(001) oriented epitaxial bilayers composed of Ir (5 nm) / $Co_{90}Fe_{10}$ (10 nm) / $Mn_{80}Ir_{20}$ (30 nm) / Au (30 nm) / Cr (10 nm) / MgO (001) were prepared by a molecular beam epitaxy (MBE) method. A static magnetic field of 200 Oe was applied along [100] direction during the deposition of MnIr and CoFe layers. The bilayers were annealed at 330 °C in a field of 850 Oe after the deposition. Polycrystalline bilayers were prepared in the same way as the epitaxial bilayer, except for the film construction of Ir (5 nm) / $Co_{90}Fe_{10}$ (10 nm) / $Mn_{80}Ir_{20}$ (30 nm) / Au (30 nm) / surface oxidized Si substrate. Magnetic properties of the sheet films were measured by alternating gradient field magnetometer and torque magnetometer. The structure of the film was characterized by *in-situ* RHEED and *ex-situ* X-ray diffraction. The films were micro-patterned by using e-beam lithography followed by Ar^+ ion etching. The shape of the microstructured bilayers was checked by atomic force microscopy (AFM) and the magnetic domain structure was investigated by magnetic force microscopy (MFM).

RHEED observations and XRD profiles showed that the epitaxial bilayer has (001) orientation and grows on MgO(001) with the crystallographic relationship of $Co_{90}Fe_{10}$ [100] // $Mn_{80}Ir_{20}$ [100] // Au [100] // Cr [110] // MgO [100]. While the polycrystalline bilayers was confirmed to have (111) preferred orientation. Figure 1 shows torque curves for (a) (001) oriented epitaxial and (b) polycrystalline bilayers. Both bilayers exhibited almost the same exchange anisotropy (unidirectional anisotropy) of 0.2–0.3 erg/cm^2. Even though the field was applied along [100] direction for the epitaxial bilayer, the easy direction of exchange anisotropy deviated about 15 deg from the [100] direction. On the other hand, the easy direction of the polycrystalline bilayer is parallel to the direction of the applied field during the post annealing.

Figure 2 shows the MFM images of circular patterned CoFe/MnIr elements with 500 nm and 300 nm diameters. As shown in Fig. 2 (a), each epitaxial element has its own easy direction (exchange bias), while the mean direction of the exchange bias was confirmed to be consistent with the corresponding torque curve (Fig. 1 (a)). The distribution of easy direction was found to be significant for the 300 nm diameter elements (Fig. 2 (b)). In the case of the polycrystalline elements, the distribution of the easy axis was also found as shown in Fig. 2 (c), however the distribution for the 500 nm elements seems to be narrower than that for the epitaxial elements with 500 nm diameter. These results imply that the distribution is related to the crystal grain size and the magnetocrystalline anisotropy of the antiferromagnetic MnIr layer.

[1] J. Nogués and I. K. Schuller, J. Magn. Magn. Mat., **192**, 203 (1999).

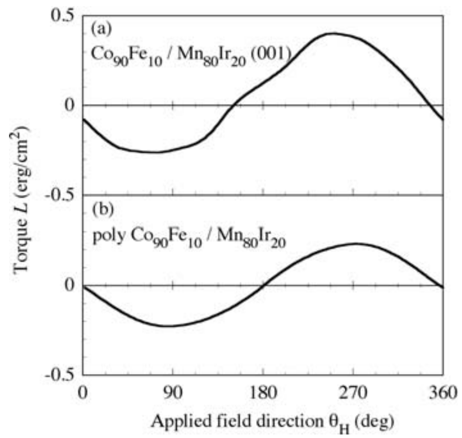

Fig. 1 Torque curves for (a) (001) oriented epitaxial and (b) polycrystalline bilayers.

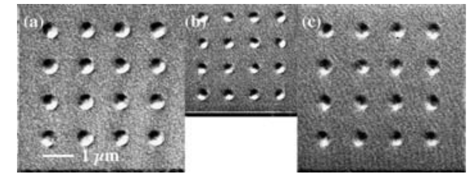

Fig. 2 MFM images of circular patterned epitaxial CoFe/MnIr (001) elements with (a) 500 nm and (b) 300 nm diameters, and (c) polycrystalline CoFe/MnIr elements with 500 nm diameter.

EM-07

The significant enhancement of the thermal stability in Co/Cu/Co/IrMn spin valve through insert 1nm FeMn layer.

L. Wang, Q. Q. Qin, *H. X. Wei*, X. F. Han
Institute of Physics, Beijing, China

The Ta(5nm)/Co(4nm)/Cu(2.5nm)/Co(4nm)/ Ir22Mn78 (10nm), Ta(5nm)/Co(4nm)/Cu(2.5nm)/Co(4nm)/ Fe50Mn50 (10nm), Ta(5nm)/Co(4nm)/Cu(2.5nm)/Co(4nm)/ / Ir22Mn78 (1nm)/ Fe50Mn50 (9nm) and Ta(5nm)/Co(4nm)/Cu(2.5nm)/Co(4nm)/ Fe50Mn50 (1nm)/ Ir22Mn78 (9nm) spin valve were fabricated, after half hour annealed at 473 K, we found that the GMR ratio with IrMn-based decreased dramatically while FeMn-based spin valve still kept the same value. Through inserting 1nm FeMn layer into the IrMn/Co interface, we found that the thermal stability of the IrMn-based spin valve can be improved greatly. Hysteresis loops and other microstructure analyse show that the inserting 1nm FeMn layer not only can increase the coupling energy of the Co/IrMn at the interface, but more important, due to the less content of the Mn in FeMn alloy than that of IrMn, it can also effectively reduce the Mn diffusion into the Co/Cu/Co interface which have a greatly influence on the GMR ratio. Since in MRAM and other TMR device, it is necessary to anneal at high temperature to improve the oxide layer, as a mostly common used AFM materials, the tunnerling junction suffer from the Mn diffusion of the IrMn layer which greatly damaged the insulator interface, this work will give more choices for fabricating high quality spin valve devices for different applied field.

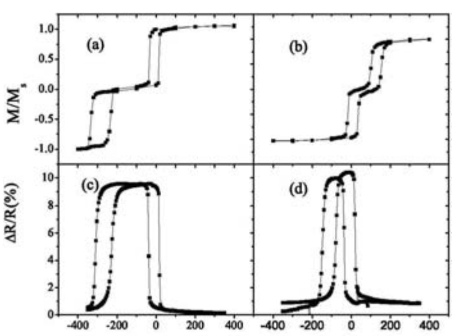

Fig.(1) hysteresis loop and R vs H curves at room temperature for (a),(c) Ta(5nm)/Co(4nm)/Cu(2.5nm)/Co(4nm)/FeMn(10nm) and (b),(d) Ta(5nm)/Co(4nm)/Cu(2.5nm)/Co(4nm)/IrMn(10nm)

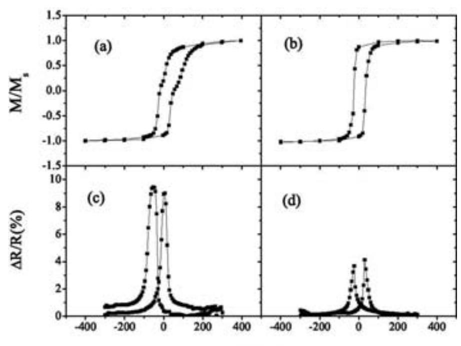

Fig.(2) hysteresis loop and R vs H curves at room temperature after annealed for (a),(c) Ta(5nm)/Co(4nm)/Cu(2.5nm)/Co(4nm)/FeMn(10nm) and (b),(d) Ta(5nm)/Co(4nm)/Cu(2.5nm)/Co(4nm)/IrMn(10nm)

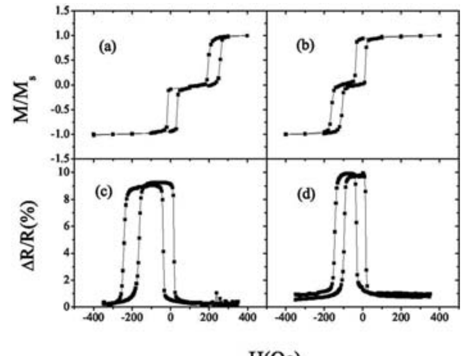

Fig.(3) hysteresis loop and R vs H curves at room temperature for (a),(c) Ta(5nm)/Co(4nm)/Cu(2.5nm)/Co(4nm)/FeMn(1nm)/IrMn(9nm)/Ta(5nm) And (b),(d) Ta(5nm)/Co(4nm)/Cu(2.5nm)/Co(4nm)/IrMn(1nm)/FeMn(9nm)/Ta(5nm)

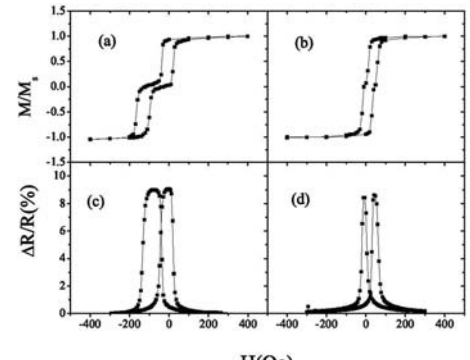

Fig.(4) hysteresis loop and R vs H curves at room temperature after annealed for (a),(c) Ta(5nm)/Co(4nm)/Cu(2.5nm)/Co(4nm)/FeMn(1nm)/IrMn(9nm)/Ta(5nm) and (b),(d) Ta(5nm)/Co(4nm)/Cu(2.5nm)/Co(4nm)/IrMn(1nm)/FeMn(9nm)/Ta(5nm)

EM-08

Exchange bias in Cu/Ni/FeMn trilayer with perpendicular magnetic anisotropy.

L. T. Tu, C. Kim
Department of Materials Science and Engineering, Chungnam National University, Deajeon, South Korea

I. Introduction
The exchange bias phenomena in ferromagnetic(FM)/ antiferromagentic (AFM) typically exhibits a shift of the hysteresis loop for the bilayer film. Usually, the exchange bias is observed in (FM-AFM), with the magnetization of the FM film oriented in the film plane. However, recently, the exchange bias effect has been induced along the perpendicular magnetic anisotropy direction in bilayer and multilayer [1]. The perpendicular exchange bias was reported in [Co/Pt], [Co/Pd], [Pt/FeCo] multilayer with FeF2, CoO, FeMn and IrMn.
In this paper, we study about perpendicular exchange bias in Cu/Ni bilayers with a FeMn film deposited on the top of Ni[5].
II. Experimental
Several series of trilayers with compositions Cu(100nm)/N(4nm)/FeMn(tFeMn nm)/Cu(5nm) were deposited on Si(001) wafers by dc-magnetron sputtering with base pressure of 2x10-7 Torr and Ar working pressure of 0.4 mTorr. During the deposition, a magnetic field of 250 Oe was applied perpendicular to the film plane. The values of tFeMn from 2 to 12 nm. Hysteresis loops, with the magnetic field applied normal to the film plane, were measured using vibrating sample magnetometry (VSM). The epitaxial orientation relationships and microstructural characteristics of the films were studied by X-ray diffraction (XRD).
III. Results and discussion
The dependence of FeMn thickness on the exchange bias field and coercivity in the Ni(4 nm)/FeMn(tFeMn nm) samples were showed in Fig. 1. The Hex is zero for below antiferromagnetic critical thickness of 2 nm, then rapidly increases to maximum at tFeMn =5 nm (Hex=305 Oe) and reached to near saturation value at tFeMn = 8nm. The exchange bias field is decreasing in range from 5 to 8 nm of FeMn. Because the FeMn is antiferromagnetic but insufficiently pinned by magnetocrystalline anisotropy. As the FeMn thickness increases further, the Ni magnetization becomes more and more pinned and totally pinned above 8 nm. This is the reason for the exchange bias near saturation value [2]
The FeMn thickness dependence of coercivity in the Ni/FeMn system is also shown in Fig.1. The maximum coercivity resulted when tFeMn is 2nm[2,3].
The exchange bias field and coercivity are also studied as a function of angle. The angle θ is the angle between the magnetic field and normal to the film. The angle θ changes in sample rotation with respect to an axis lying in the film plane. Fig.2 showed when the field applied parallel with the film normal, the exchange bias field is obtained maximum value. The Hex = 0 when the field applied in plane with film plane. The XRD pattern of Cu(100nm)/Ni(4 nm)/FeMn(5nm)/Cu(5nm) sample shows the (001) orientation for the Si and Cu layer (fig. 3) [3].
IV. Conclusion
The thin film of Cu/Ni/FeMn with perpendicular exchange bias has been investigated.The exchange bias field and coercivity were studied as a function of thickness. The maximum exchange bias field is obtained around 305 Oe at 4 nm of Ni and 5 nm of FeMn. The dependence of exchange bias field Hex and coercivity Hc are also measured with maximum value when the field applied normal with film plane.

[1] J. Sort, V. Baltz, F. Garcia B. Rodmacq and B. Dieny., Phys. Rev. B 71, 054411 (2005).
[2] F. Garcia, G. Casali, S. Auffet, B. Rodmacq, B. Dieny, J. Appl. Phys. 91, 6905, (2002).
[3] Haiwen Xi, T.F. Ambrose, T.J. Klemmer. R. van de Veerdont, Phys. Rev. B 72, 02447 (2005).
[4] J. Nogues, Ivan K. Schuller, J. Magn. Magn. Mater. 192, 203 (1999).
[5] R.C. O'Handley, Oh-Sung Song, C.A. Ballentine, J. Appl. Phys. 74, 6302 (1993).

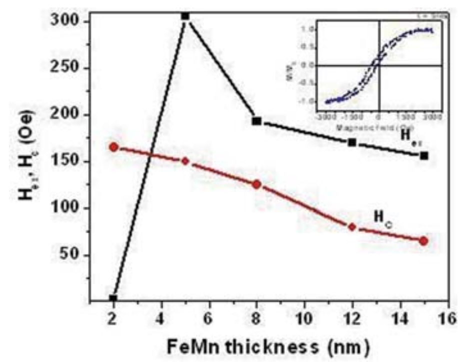

Fig.1

Dependence of exchange bias field Hex and coercivity Hc with the FeMn thickness for Cu(100nm)/Ni(5 nm)/FeMn(tFeMn nm)/Cu(5nm)

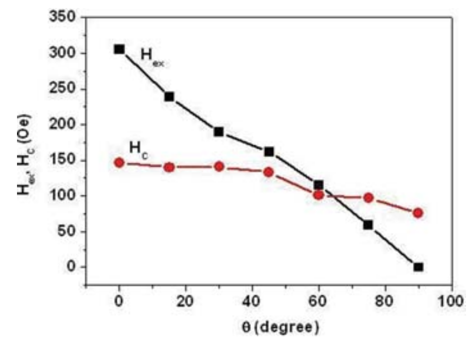

Fig.2

The Hex and Hc as a function of the angular in Cu(100nm)/Ni(4 nm)/FeMn(5nm)/Cu(5nm) films.

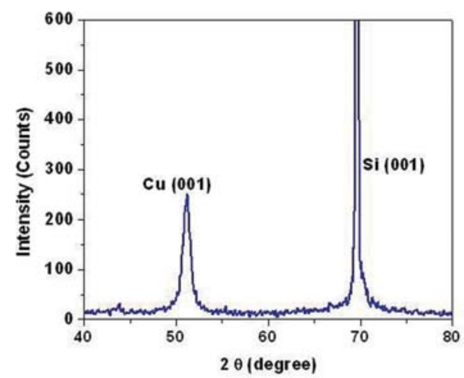

Fig.3

XRD data for Cu(100nm)/Ni(5nm)/FeMn(5nm)/Cu(5nm) film

EM-09

Parallel and perpendicular exchange biases in epitaxial FePt-FeMn multilayers with different crystalline orientations.

N. N. Phuoc, *T. Suzuki*
Information Storage Materials Laboratory, Toyota Technological Institute, Nagoya, Japan

Although perpendicular exchange bias has recently received much attention, its physical origin is still in controversy. In particular, the question that the AF spin structure at the interface, which is assumed to be important to the mechanism of perpendicular exchange bias, follows the AF bulk structure [1] or has a random canting distribution [2, 3] remains unclear. The present work is therefore motivated to study systematically the correlation between parallel and perpendicular exchange bias and the crystalline orientations to clarify that point.
Samples with the stacks of [FePt (x nm)/FeMn (10 nm)]$_{10}$ were fabricated onto MgO(100), MgO(110) and MgO(111) substrates using the ion beam sputter-deposition system with the base pressure better than 2×10^{-6} Pa. An X-ray diffractometer and a vibrating sample magnetometer were employed to characterize the structural and magnetic properties of the samples.
Figure 1-(a), (b) and (c) show the θ-2θ XRD patterns for [FePt(10 nm)/FeMn (10 nm)]$_{10}$ multilayers deposited onto MgO (111), MgO (110) and MgO(100) substrates, respectively. The observation of the strong FePt and FeMn peaks corresponding to the crystalline orientations of the substrates indicate that samples are in fcc phase. The Φ-scans shown in Fig. 1-(d), (e), and (f) unambiguously demonstrate that the present samples are epitaxially deposited thin films. The rocking curves in Fig.1-(g), (h), and (k) show that the sample grown onto MgO(100) has a narrower c-axis orientation than that deposited onto MgO(110) and MgO(111).
The dependences of parallel and perpendicular exchange biases (H_E), unidirectional anisotropy constants (J_K) and blocking temperatures (T_B) for [FePt(x nm)/FeMn (10 nm)]$_{10}$ multilayers deposited onto MgO (100), MgO (110) and MgO(111) are shown in Fig. 2. It is of interest to see that for the FePt thickness small, the value of exchange bias for samples grown onto MgO(111) is significantly higher than that grown onto MgO(110) and MgO(100) and consequently the J_K value in the case of MgO(111) is nearly independent of FePt thickness, presumably attributed to the role of the spin structure of the AF bulk, which may favor to be stable in (111) direction. Another interesting point is the discrepancy between parallel and perpendicular blocking temperatures, which can be interpreted in terms of the spin canting at the interface, thus causing the ordering in parallel direction is higher than that in perpendicular direction [3]. The ratio of parallel and perpendicular exchange biases (not shown here) is not only dependent on the crystalline orientation but also on the thickness of FePt, which will be further discussed in details in the presentation.
In summary, a systematic study of FePt-FeMn multilayers grown onto MgO substrates with different orientations has been carried out with some interesting results. In particular, the fact that the ratio of parallel and perpendicular exchange biases is strongly dependent on FePt thickness and crystalline orientation tentatively suggests that the role of interface anisotropy, random fluctuations of AF spins at the interface and the spin structure of AF bulk should be carefully taken into account for the study of perpendicular exchange bias mechanism.

[1] S. Maat, K. Takano, S.S.P. Parkin, and E.E. Fullerton, Phys. Rev. Lett. 87, (2001) 87202.

[2] C.H. Marrows, Phys. Rev. B 68, (2003) 12405.

[3] N.N. Phuoc and T. Suzuki, J. Appl. Phys. 101 (2007) 9E501.

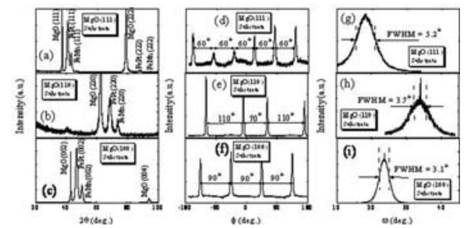

Fig. 1. XRD patterns for: θ-2θ scans (a, b, c), Φ-scans (d, e, f) and rocking curves (g, h, i) for [FePt(10 nm)/FeMn (10 nm)]$_{10}$ multilayers deposited onto MgO (100), MgO (110) and MgO(111).

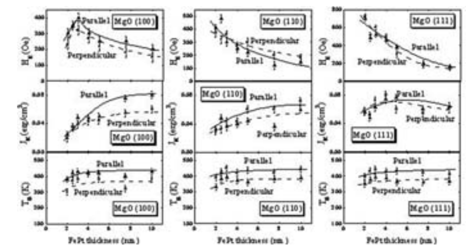

Fig. 2. Thickness (FePt) dependence of parallel and perpendicular exchange biases H_E (measured at T = 80 K), unidirectional anisotropy constants J_K and blocking temperatures T_B for [FePt(x nm)/FeMn (10 nm)]$_{10}$ multilayers deposited onto MgO (100), MgO (110) and MgO(111).

EM-10

Enhanced Exchange Anisotropy by ultra-thin Co_xFe_{100-x} (x > 80) Layer Insertion at the Interface of $L1_2$-ordered $Mn_3Ir/Co_{65}Fe_{35}$ Bilayers.

K. Komagaki[1], M. Tsunoda[2], K. Noma[1], H. Kanai[1], K. Kobayashi[1], Y. Uehara[1], M. Takahashi[2]
1. Advanced Head Technology Department, Head Division, FUJITSU LIMITED, Nagano, Japan;
2. Department of Electronic Engineering, Tohoku University, Sendai, Japan

Large exchange anisotropy is indispensable for an ultra-high density recording in hard disk drives, because the decreasing element dimensions causes a decline of exchange bias properties in spin-valve devices. $L1_2$-ordered Mn_3Ir can induce large exchange anisotropy in spin-valve tunnel magnetoresistance head elements [1], and possibly has a potential to further enhance the exchange anisotropy. Referring the case of disordered Mn-Ir, it was reported that the unidirectional anisotropy constant, J_K, shows a remarkable compositional dependence in Co_xFe_{100-x} /MnIr bilayer system. The J_K takes a maximum value at x = 70 and rapidly decreases with further increase of Co content as shown in Fig. 1 [2]. The rapid decrease of J_K at x > 70 might be due to a bcc-fcc phase transformation in Co_xFe_{100-x} [3]. We can thus expect to enhance the J_K when the Co_xFe_{100-x} (x>80) maintains bcc structure. In this study, we successfully achieved the enhancement of the exchange anisotropy with the technique of ultra-thin Co_xFe_{100-x} (x>80) layer insertion at the interface of $L1_2$-$Mn_3Ir/Co_{65}Fe_{35}$ bilayers. Bilayer samples in a stack sequence of substrate/Ta(5)/Ru(10)/$L1_2$-Mn_3Ir(10)/Co_xFe_{100-x} (0.5)/$Co_{65}Fe_{35}$(4)/Ru(0.9)/Ta(3) (thickness in nm unit) were prepared on thermally oxidized silicon wafer with a magnetron sputtering apparatus. The substrates were held at room temperature during the deposition, except for that of the MnIr layer. The MnIr layers were deposited at the substrate temperature of 200°C and with the Ar sputtering gas pressure of 2.0Pa in order to obtain the $L1_2$-ordered phase [1]. The Co_xFe_{100-x} insertion layers with various compositions were prepared by co-sputtering of Co and $Co_{65}Fe_{35}$ targets, and the Co compositions were ranged from 65 to 98 at.%. Thermal annealing was performed in vacuum at 320°C for 4hrs under applied field of 15kOe. The composition of insertion layer and thickness of each layer were determined with X-ray fluorescence analysis. The microstructure of the bilayers was examined with X-ray diffraction and grazing incident X-ray diffraction (GID) with Cu-Kα radiation source. M-H loops were measured with a vibration sample magnetometer. The J_K was calculated with the equation of $J_K = M_s d_F H_{ex}$, where $M_s d_F$ is the areal saturation magnetization of Co_xFe_{100-x} /$Co_{65}Fe_{35}$ bilayers, and H_{ex} is the exchange bias field. Fig.2 shows the change of J_K as a function of the Co composition in Co_xFe_{100-x} insertion layer. The J_K of the bilayer without insertion layer is 0.93erg/cm^2 as shown by open circle in Fig. 2. In the bilayers with insertion layer, the J_K increased with increasing the Co composition of the insertion layer and the maximum value of J_K was obtained at the range of 85 to 98 at.% of Co. Fig.3 shows GID profiles of $L1_2$-$Mn_3Ir/Co_{65}Fe_{35}$ bilayers (a) without and (b) with the $Co_{90}Fe_{10}$ insertion layer. Thin and thick solid lines provide the profiles for as-deposited and annealed bilayers respectively. The peak at $2\theta_\chi$ = 44.7° is asigned as bcc-CoFe(110) diffraction and fcc-CoFe does not contribute to this diffraction peak. In Fig.3 (a), there is no remarkable difference of the diffraction peak between the as-deposited and annealed bilayers. On the other hand, in Fig3 (b), we can observe the increase of diffraction intensity in the annealed bilayer. These results mean that crystal structure of the ultra-thin $Co_{90}Fe_{10}$ insertion layer was transformed to bcc structure by thermal annealing, following the bcc structured $Co_{65}Fe_{35}$ layer. Therefore, we can conclude that the enhancement of exchange anisotropy with ultra-thin Co_xFe_{100-x} (x>80) insertion layer is owing to the bcc phase formation in the insertion layer.

[1] K. Komagaki, K. Yamada, K. Noma, H. Kanai, K. Kobayashi, Y. Uehara, M. Tsunoda and M. Takahashi, IEEE Trans. Magn., vol. 43, pp. 3535-3537, 2007

[2] M. Tsunoda, K. Nishikawa, T. Damm, T. Hashimoto and M. Takahashi, J. Magn. Magn. Mater., vol. 239, pp. 182-184, 2002.

[3] M. Hansen and K. Anderko, Constitution of Binary Alloys (McGraw-Hill, NewYork, 1958), P.472

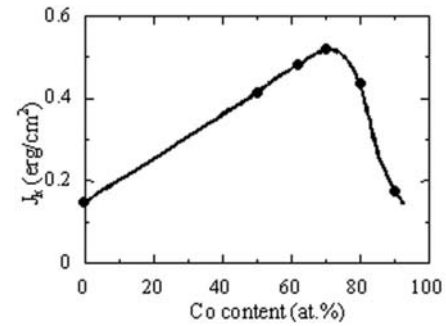

Fig.1 Compositional dependence of exchange anisotropy in disordered Mn-Ir (10 nm)/Co_xFe_{100-x}(4 nm) bilayers. (from Ref.2)

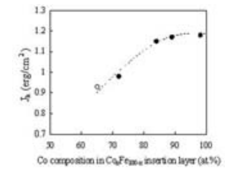

Fig 2 The change of J_k in $L1_2$-$Mn_3Ir/Co_{65}Fe_{35}$ bilayers as a function of the Co composition in Co_xFe_{100-x} insertion layer at the interface.

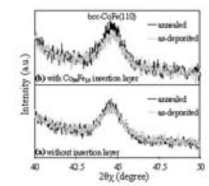

Fig.3 GID profiles of $L1_2$-$Mn_3Ir/Co_{65}Fe_{35}$ bilayers (a) without and (b)with the $Co_{90}Fe_{10}$ insertion layer at the interface .

EM-11

Lateral grain size effect on exchange bias in polycrystalline FeNi/FeMn bi-layer films.

P. Sharma, T. Huang, A. Sun, *J. Hsu*
Physics, National Taiwan University, Taipei, Taiwan

Introduction

In this work the lateral grain size effect on exchange biased ferromagnetic (FM)/antiferromagnetic(AFM) polycrystalline bi-layer films has been investigated. In the past various investigations on grain size effect have been carried out [1-3]. The adopted approaches for altering grain size were the FM/AFM thickness, and deposition conditions etc. However, considering exchange bias as an interface phenomenon then only lateral grain size would play a part rather than its thickness. Indeed varying FM/AFM thickness changes the lateral grain size but to some certain extent the texture, grain orientation and interface roughness also changes. Therefore, the effect of varying FM/AFM thickness on exchange bias could be the combined effect of all parameters. In order to separate out the grain size effect, if by some means variation of lateral grain size is imparted without varying FM and AFM thickness and deposition conditions, its effect can be well understood. In this work, lateral grain size variation was achieved by depositing identical NiFe/FeMn bi-layer on the varying Ta buffer layer thickness, assuming that larger Ta grains would promote greater lateral grain area and so the coupling.

Experimental

In the present investigation, Ta(t nm)/NiFe(5 nm)/FeMn(20 nm) film with varying Ta thickness (t = 5, 10, 15, 20, 25, 30, 35, 40, 45 and 50 nm) were deposited on glass substrate by dc magnetron sputtering. During deposition process the base pressure was less than 7×10^{-6} Pa and Ar gas pressure was maintained at 0.27 Pa. The deposition rates for all layers were set at 0.1nm/s. In order to produce unidirectional anisotropy, a magnetic field of the order of 24 kA/m was applied during deposition. No field cooling was carried out after deposition.

Results and discussion

The variation of exchange bias field (H_{eb}) and coercivity (H_c) with Ta thickness is shown in Fig.1. It show that exchange bias is monotonically increased from 6.4 kA/m (t_{Ta}=5nm) to 18.7 kA/m (t_{Ta}=35 nm). Further increasing Ta thickness up to 50 nm, H_{eb} is slightly decreased. H_c is also found to increase gradually with Ta thickness. To understand this surprising increase in H_{eb} with identical NiFe and FeMn thicknesses, we have systematically investigated the influence of crystallographic texture, roughness and lateral grain size of FeNi/FeMn bi-layer from XRD, AFM and TEM studies respectively.

In the X-ray studies it was found that Ta thickness as well as its texture does not affect (111) texture and so the exchange bias field. Cumulative macroscopic roughness was found constant for all Ta thickness. Therefore, the contribution from roughness to H_{eb} is identical for all samples. Since we did not observe the texture and roughness effect, the increase in H_{eb} might be due to its grain structure. The cross-sectional TEM images of FeNi/FeMn bi-layer film deposited on t_{Ta} = 5 and 35 nm are shown in Fig.2 (a, b). The lateral grain sizes at the interface with t_{Ta} = 5 nm and 35 nm underlayer are nearly 3-5nm and 10-12 nm respectively. Ta underlayer grain structure clearly influences the growth of top FeNi and FeMn layers since large grains extend through interface to FeNi and FeMn layers. High-magnification images on the right hand of Fig. 2 show the columnar growth through grain-to-grain epitaxy mechanism, which confirms that lateral grain size of NiFe is also increased, even with the constant FM/AFM thickness. Since no texture and roughness effect were identified in identical bi-layer systems, we ascribe such increase in H_{eb} to the increase in lateral grain size area, which consequently increases the interface coupling. The detailed description of all parameters will be presented in the full paper.

[1] Koichi Nishioka, Chunhhong Hou, Hideo Fujiwara, and Robert D. Metzer, Journal of Applied Physics 80, 4528 (1996).

[2] G. Choe and S. Gupta, IEEE Transaction on Magnetics 33, 3691 (1997).

[3] Sadia Manzoor, M. Vopsaroiu, G. Vallejo-Fernandez, and K.O'Grady, Journal of Applied Physics 97, 10K1181 (2005).

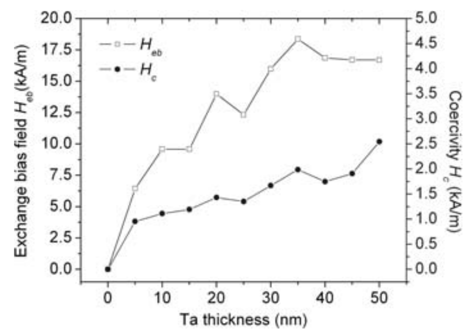

Fig. 1 Variation of H_{eb} and H_c with Ta thickness

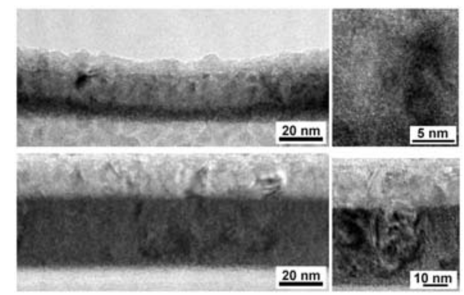

Fig. 2 Cross-sectional TEM images of FeNi(5)/FeMn(20) deposited on (a) t_{Ta}=5 nm (b) t_{Ta}=35 nm. Right-side images are with high magnification revealing the columnar growth through grain-to-grain epitaxy.

EM-12

The influence of different Mn-oxide structures on the exchange bias field in NiFe/Mn-oxide bilayers.

J. Guo[1], T. Chen[1], Y. Chiu[1], H. Ouyang[1], *K. Lin*[1], E. Vass[2], J. van Lierop[3]

1. Department of Materials Engineering, National Chung Hsing University, Taichung, Taiwan; 2. Institut for Experimentalphysik, University of Innsbruck, Innsbruck, Austria; 3. Department of Physics and Astronomy, University of Manitoba, Winnipeg, MB, Canada

I. INTRODUCTION

The shift of a magnetic hysteresis loop away from zero field in a system composed of a ferromagnet (FM) coupled to an antiferromagnet (AF) when the FM/AF bilayer is field-cooled below the Neel temperature (T_N) of the AF is called exchange bias [1]. It is known [2] that the AF Mn (T_N~ 100 K) can form different stoichiometric oxides such as AF MnO (T_N~ 119 K) and ferrimagnetic Mn_3O_4 (T_c~ 42 K), depending on the method of preparation and oxygen content during Mn-oxide deposition. In this work we investigate the exchange bias behavior in NiFe/Mn-oxide bilayers by incorporated different %O_2/Ar ratios during the bottom Mn-oxide layer deposition by ion-beam bombardment. The results indicate the metallic Mn layer provides stronger exchange coupling than the Mn-oxide layers when they are in contact with the top NiFe layer. Annealing the different Mn-oxide compositions results in a sudden decrease in Hex that is attributed to the formation of the MnO phase. The structural evolution of the Mn and the Mn-oxide by ion beam bombardment and annealing is in good agreement with magnetic properties of the respective films.

II. EXPERIMENTAL METHOD

A dual ion-beam deposition technique [3] was used to prepare the NiFe (10nm)/Mn-oxide (20nm) bilayers. A Kaufman source was used to focus an argon ion beam onto a commercial $Ni_{80}Fe_{20}$ (at%) or the Mn target surface while the End-Hall source was used to clean or in situ bombard the substrate during deposition with mixture of O_2/Ar that was varied from 0% (Mn) to 41% (Mn-oxide) O_2/Ar. No external field was applied during deposition. Bottom Mn-oxide layers were annealed at 700 °C for 10 minutes using a rapid thermal annealing (RTA) method and then capped with the top NiFe layer. The crystal structures of the NiFe/Mn-oxide bilayers were characterized with x-ray diffraction (XRD) using a Rigaku D/MAX2500 diffractometer. A JEOL (JEM-2010) transmission electron microscope (TEM) operating at 200 kV was used for microstructural analysis. Magnetic measurements were performed in a commercial SQUID magnetometer (Quantum Design MPMS-7) where the thin film was field cooled (20 kOe) with magnetic field applied parallel to the film plane from 300 K down to 5 K. In these measurements, the exchange bias field, H_{ex}, is defined as the shift in the hysteresis loop along the field axis with respect to zero field.

III. RESULTS AND DISCUSSION

A smooth interface between the top NiFe layer and the bottom Mn-oxide layer was revealed via the cross-sectional TEM. The bottom Mn-oxide film layers prepared with 0% O_2/Ar consisted of the b.c.c. Mn (a= 8.87 Å) phase whereas composite Mn and rock-salt MnO (a= 4.84 Å) phases were found in films prepared with 8%O_2/Ar. However, increasing the % O_2/Ar to 41%O_2/Ar resulted in the formation of the tetragonal Mn_3O_4 (a= 5.81 Å, c= 9.55 Å) phase.

Magnetometry results have shown larger 5 K exchange bias fields (H_{ex}) in NiFe/metallic Mn bilayers compared to NiFe/Mn-oxide (8% to 41%O_2/Ar) bilayers. The NiFe/Mn bilayers exhibit the largest H_{ex}~ -310 Oe amongst all samples. In addition, the decrease of H_{ex} with increasing % O_2/Ar (8 to 21 % O_2/Ar) was attributed to the in-situ oxidation reaction of the metallic Mn into MnO due to ion-beam bombardment [3]. Further, the larger H_{ex} when the bottom Mn-oxide layer was prepared with higher % O_2/Ar (21 to 41 % O_2/Ar) was attributed to the formation of the ferrimagnet Mn_3O_4. Surprisingly, a sudden drop in both the H_c and the H_{ex} was observed when annealing these Mn-oxide layers before being capped with a NiFe layer. The presence of the AF MnO phase after annealing seems to be the origin of the decreased H_{ex} and H_c due to weaker exchange coupling between the NiFe and MnO that is a result of the lower magnetocrystalline anisotropy of the MnO (K~ 280 erg/cm^3), compared to that for the Mn_3O_4 (K~10^7 erg/cm^3).

*Research was supported by the National Science Council of Taiwan (NSC 96-2221-E-005-056) and by the Natural Sciences and Engineering Research Council of Canada.

[1] J. van Lierop, B. W. Southern, K.-W. Lin, Z.-Y. Guo, C. L. Harland, R. A. Rosenberg, and J. W. Freeland, Phys. Rev. B, in press (2008).

[2] P. Z. Si, D. Li, J. W. Lee, C. J. Choi, Z. D. Chang, D. Y. Geng, and E. Bruck, Appl. Phys. Lett. 87, 133122 (2005).

[3] K.-W. Lin, P.-H. Ko, Z.-Y. Guo, H. Ouyang, and J. van Lierop, J. Nanosci. Nanotech. 7, 265 (2007).

EM-13

Effect of the ferromagnetic layer thickness on the blocking temperature in IrMn/CoFe exchange couples.

G. Vallejo-Fernandez, L. E. Fernandez-Outon, B. Kaeswurm, K. O'Grady
Physics, The University of York, York, United Kingdom

The exchange anisotropy across a ferromagnetic/antiferromagnetic *F*/*AF* interface is of great importance both from the fundamental and technological point of view. In order to achieve high recording densities in hard disk drives (HDDs), the reduction of the total thickness of the spin-valve stack is crucial [1]. Since the *AF* is the dominant layer in the total thickness of the sensor, most studies in the literature are focused on how to implement the thermal stability of the *AF* layer while reducing its thickness. Usually, the thermal stability of a given system is quantified in terms of the blocking temperature at which the exchange bias H_{ex} goes to zero. Factors such as the ordering parameter S, the *AF* grain size, seed layers, dilution concentration and the crystallographic orientation of the *AF* layer have been reported to have a dramatic effect [e.g. 1]. However, there is a lack of data in the literature regarding the effect of the *F* layer on the thermal stability of exchange bias systems [2]. In this work we present a detailed study on the thermal stability of IrMn/CoFe exchange couples as a function of the thickness of the *F* layer t_F.

Samples with composition Si/Ru(5nm)/IrMn(10nm)/CoFe(t_F)/Ru(10nm) where t_F= 3,4,5,8 and 12nm were prepared using a HiTUS sputtering system [3]. Magnetic measurements were carried out using an ADE model 10 VSM fitted with a continuous flow cryostat enabling temperature control to better than 0.5K/hour. Bottom-biased structures were preferred to avoid changes in the microstructure of the *AF* layer ensuring that any changes in the magnetic measurements are due entirely to the *F* layer. Hysteresis loops were measured following a detailed measurement procedure where thermal activation is used to probe the state of order of the *AF* layer [4]. By increasing the temperature T_{ACT} at which the exchange couple is thermally activated with the *F* layer in negative saturation, the hysteresis loop of the *F* layer can be shifted along the field axis from negative to positive values. All the measurements are done in thermal activation free conditions. Examples of the hysteresis loops obtained following this protocol are shown in Figure 1a. Figure 1b shows the dependence of the exchange field on the thickness of the *F* layer showing the well known $1/t_F$ behaviour.

Figure 2a shows the distribution of blocking temperatures for the systems studied while the variation of the median blocking temperature $<T_B>$ with t_F is shown in Figure 2b. For small *F* thicknesses, $<T_B>$ decreases within error. However, for thicker *F* layers (12nm) a reduction of ~17% is observed.

In recent work we have described a method to calculate the anisotropy constant of metallic polycrystalline *AF* materials based on a measurement of $<T_B>$ and a careful knowledge of the grain size distribution within the system studied [5]. In that work, the effect of the exchange field from the *F* layer H^* was neglected. By studying samples with different *F* thicknesses we can now quantify that effect. Preliminary data show that neglecting H^* induces a small deviation (<4%) in the measurement of K_{AF} when t_F<4nm. However, for thicker *F* layers (12nm) this deviation can be as big as 30%. This estimate is based on the extrapolation of the curve shown in Figure 2b, i.e. the case H^*=0.

[1] K. Imakita, M. Tsunoda, M. Takahashi, J. Appl. Phys. 97, 10K106 (2005).

[2] H. Xi, J. Magn. Magn. Mat. 288, 62 (2005).

[3] M. Vopsaroiu, G. Vallejo-Fernandez, M. J. Thwaites, J. Anguita, P. J. Grundy, and K. O'Grady, J. Phys. D: Appl. Phys., 38 p.490 (2005).

[4] L. E. Fernandez-Outon, K. O'Grady, and M. J. Carey, J. Appl. Phys. 95, 6852 (2004).

[5] G. Vallejo-Fernandez, L. E. Fernandez-Outon, and K. O'Grady, Appl. Phys. Lett. 91 212503 (2007).

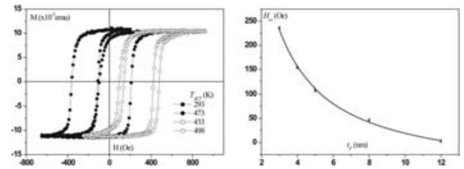

Figure 1. a) (left) Hysteresis loops obtained after thermally activating at different temperatures T_{ACT} for an IrMn(10nm)/CoFe(3nm) bilayer and b) Ferromagnetic thickness dependence of the exchange bias at room temperature after resetting the system at 498K for 90 minutes (right).

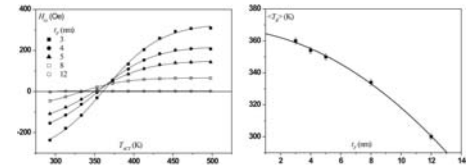

Figure 2. a) (left) Distribution of blocking temperatures for the samples studied and b) (right) Variation of the median blocking temperature $<T_B>$ with the thickness of the *F* layer.

EM-14

Probing the influence of in-plane roughness on magneto-resistance in spin-valves using off-specular reflectivity techniquestechniques.

J. Park[1], C. Furjanic[1], D. Draganova[1], C. Chen[1], S. M. Watson[2], J. A. Borchers[2], M. Carey[3], P. Sparks[1], J. C. Eckert[1]
1. Physics, Harvey Mudd College, Claremont, CA; 2. NIST Center for Neutron Research, Gaithersburg, MD; 3. Hitachi Global Storage Technologies, San Jose, CA

In recent studies of exchange-coupled multilayers, off-specular neutron reflectivity has played a key role in characterizing the field-evolution of in-plane magnetic domains and revealing local ordering between adjacent magnetic layers [1-3]. To investigate the effect of roughness on magneto-resistance in spin-valves (SV), we have used off-specular x-ray and neutron reflectivity to study two series of SV's with Si/SiO_2/5 nm Ta/3 nm $Co_{50}Fe_{50}$/1 nm $Ni_{98}Fe_2$/3 nm Cu/X $Co_{65}Fe_{35}$/1.6 nm IrMn/1 nm Cu/5 nm Ta with X = 11 or 15 nm produced by DC magnetron sputtering. Though the two series were produced during the same run, they have different structural roughness.
Specular x-ray reflectivity measurements indicate that the interfacial roughness for one of these sample series is larger as the fall-off of the scattering with increasing Q is much faster. Fits to the specular reflectivity of the "smooth" X = 11 nm sample suggest that the average roughness of the interface in the sample is ~1.2 nm, while the average roughness of the "rough" 11 nm sample is > 3 nm. Diffuse background measurements also show evidence of correlated in-plane roughness through the depth of the "rough" samples.
This roughness difference translates into significant contrast in magneto-resistance (MR) of the samples. The MR loops of the smooth sample (red line) and a rough sample (black line) measured at 6K are shown in Fig. 1. The most notable difference is the shift in the coercive switching field of the free layer. The coercive fields are estimated to be ~11.8 mT and ~16.1 mT for the smooth sample and the rough sample, respectively.

Previous specular PNR studies of these samples [4] revealed that domain walls parallel to the interfaces develop in the pinned layer upon field cycling in samples for X > 9 nm. To search for complementary perpendicular domain walls that give rise to magnetic diffuse scattering, we performed transverse Q_x scans for the X = 15 nm sample at fields of 32 mT and 670 mT at 5 K, corresponding to the antiparallel and saturated states respectively. The (++) and (- -) non-spinflip cross sections for a Q_z of 0.046 A^{-1}, shown in Fig. 2, reveal a sharp peak at the specular position on top of a broad diffuse peak. The width of the diffuse peak does not change with field, and the splitting of the diffuse peak tracks that of the specular. The diffuse scattering thus seems to arise from structural in-plane roughness, consistent with the x-ray results. From the inverse of the full-width-at-half-maximum of the diffuse peak [1,3], we approximate an in-plane structural correlation length of 100 nm.

The characteristics of the off-specular scattering change with field, and a diffuse, magnetic spin-flip peak seems to emerge in the canted magnetic state [3] associated with the MR maximum during the second field cycle. Additional measurements are planned to determine if this scattering arises from the formation of in-plane magnetic domains.

From our current measurements, we thus far conclude that in-plane structural roughness (possibly induced by subtle differences in substrate surface preparation) leads to increased coercivity of the free layer in a rough SV sample. Future work will provide a detailed analysis of the transverse scans in order to separate diffuse scattering from structural roughness, magnetic roughness and magnetic domain formation.

[1] J.A. Borchers, et al., Phys. Rev. Lett. **82**, 2796 (1999).

[2] Sean Langridge, et al., Phys. Rev. Lett. **85**, 4964 (2000).

[3] C.H. Marrows, et al., Phys. Rev. B 66, 024437 (2002).

[4] J. Park, et al., J. Appl. Phys. (in press).

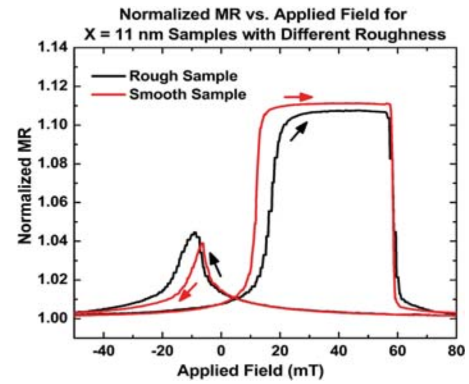

Fig. 1 Normalized MR vs. field for X = 11 nm spin valves with different roughness: rough (black) and smooth (red) obtained after field cooling in H=-0.65T. MR trends for 15 nm SV's are similar.

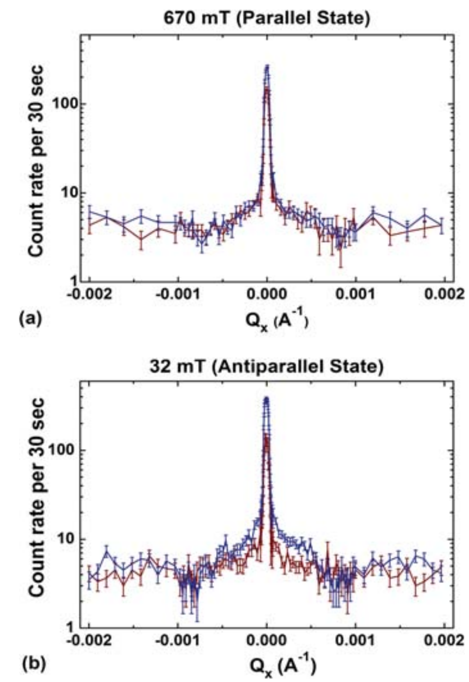

Fig 2. Transverse Q_x scan has been measured around Q_z = 0.046Å^{-1} for rough X = 15 nm sample at (a) 670 mT and (b) 32 mT. Red and blue lines correspond to two non spin-flip cross sections, (++) and (- -), respectively.

Intuitive operation of magnetically driven fish-type microrobot using smart interface.

T. Honda, K. Ono, J. Yamasaki
Department of Applied Science for Integrated System Engineering, Kyushu Institute of Technology, Kitakyushu, Japan

Introduction

Since a microrobot including a magnet can be operated by external magnetic fields, it would be suitable for difficult applications in industrial and biomedical fields. Based on this concept, some attempts have been made on microrobots working for pipeline inspection and treatment inside a human body [1,2]. On the other hand, we have proposed a new type of magnetically driven microrobot for amusement and educational use. In our previous paper, we demonstrated that a fish-type microrobot could swim like a real fish in water tank wound with a coil [3]. In order to improve its controllability, we have developed a turning control system using a smart interface. This paper describes its principle and testing results.

Structure and actuation principle

Fig. 1 shows a fish-type microrobot. It consists of a body balanced with a float and a weight, and a propulsive mechanism including an oscillator and a bending part. The oscillator is composed of a NdFeB magnet with a rotary axis and a pair of arms. The bending part is composed of a polyimide cantilever and a polyethylene caudal fin. The arms of the magnet and the both sides of the caudal peduncle are linked by means of two threads. Fig. 2 shows the actuation of the propulsive mechanism. When a magnetic field is applied perpendicular to the water surface, the magnet rotates due to magnetic torque and then one side of the arms pulls the thread, which causes the cantilever to deflect to one side. In alternating magnetic fields, therefore, two arms pull the threads alternatively. Thus the caudal fin oscillates and generates a thrust. In case of turning, the fin oscillation is biased to right or left side by applying the alternating magnetic field biased with DC magnetic field.

Smart interface

In our previous paper, the waveforms of the magnetic field were programmed beforehand [3]. Therefore, the operation feeling was poor. To solve this problem, we have proposed a smart interface that provides intuitive operation. Fig. 3 shows an interface, which consists of a plastic card with one end fixed by a gripper and other free. A strain gauge is attached to the fixed end, and connected to an amplifier supplying power to the coil. When the free end of the interface is manually bent, the magnetic field corresponding to the strain is generated in the water tank.

Testing results

Fig. 4 shows the waveform of the magnetic field in the drive coil while the microrobot was operated by the interface. To begin with the robot turned right by oscillating the interface biased right, and then turned left by switching the bias of the interface to the opposite side. The operation feeling was intuitive because the movement of the caudal fin synchronized with that of the interface.

[1] T. Honda, T. Sakashita, K. Narahashi, and J. Yamasaki: J. Mag. Soc. Jpn., 25, 1175(2001).

[2] K. Ishiyama, M. Sendoh, A. Yamazaki, and K.I. Arai: Sens. & Act., A91, 141(2001).

[3] M. Tomie, A. Takiguchi, T. Honda, and J. Yamasaki: IEEE Trans. Magn., 41, 4015 (2005).

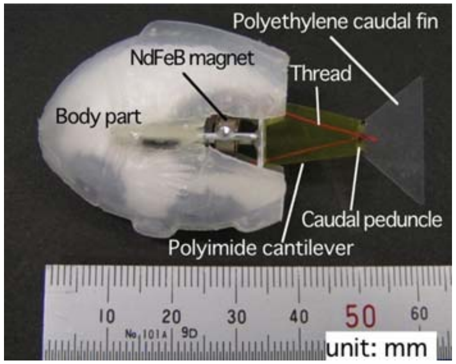

Fig. 1 Side view of fish-type microrobot.

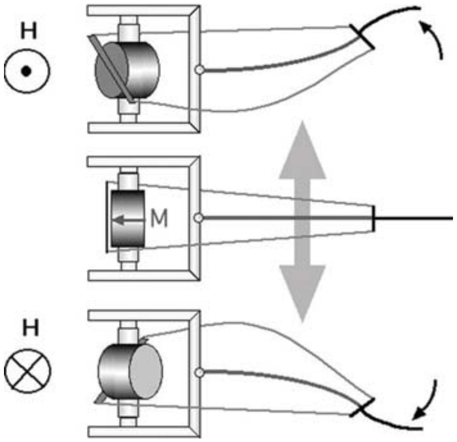

Fig.2 Actuation behavior of propulsive mechanism.

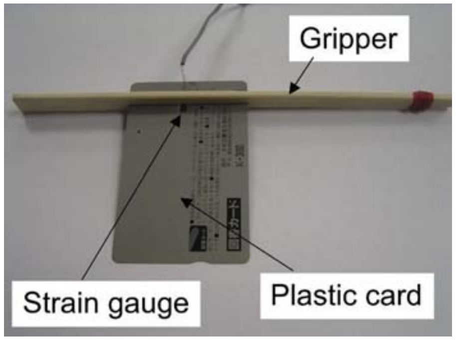

Fig. 3 Photograph of interface.

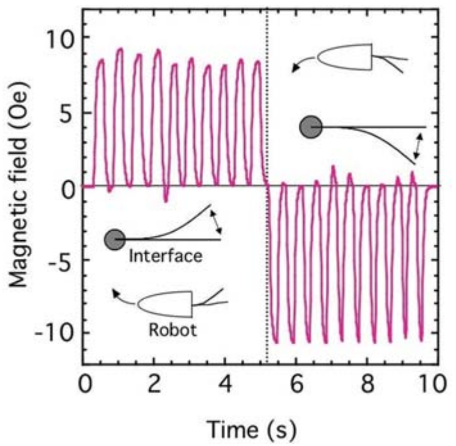

Fig. 4 Waveform of magnetic field during operation by interface.

Three-dimensional motion of a small object by using a new magnetic levitation system having four I-shaped electromagnets.

T. Ohji, H. Hara, K. Amei, M. Sakui
University of Toyama, Toyama, Japan

Introduction

In a common active magnetic levitation system, a floating object is controlled stably by an electromagnet with a narrow air-gap to reduce leakage flux. However, in order to move a floating object dynamically, it is necessary to arrange electromagnets for horizontal motion and to make an air-gap wide for vertical motion at the expense of leakage flux. Magnetically levitated micro-robot system enabling three-dimensional motion using a large-scale electromagnet with a pole-piece is reported[1]. We propose a new magnetic levitation system having a compact electromagnet, which composes of four I-shaped electromagnets.

Configuration and features

Fig. 1 shows the configuration of the controlled electromagnet, the floating object, and the control system. The controlled electromagnet comprises top iron plate, four NdFeB magnets, and four I-shaped electromagnets (EM1-4). The volume of the electromagnet is around 360 cm3. Permanent magnets magnetized in same direction generate bias magnetic flux and contribute to a power-saving and an air-gap increase. The floating object is composed of two NdFeB magnets and a light non-metal body. The mass of the object is around 50 g. Three displacement sensors detect the object position, and the information is fed to the control system through an A/D converter. Control signals calculated in a DSP are supplied to each I-shaped electromagnet through a D/A converter and a power amplifier. In order to control each x-, y-, and z-direction, four I-shaped electromagnets are divided into three sections as shown in Fig. 2. Four I-shaped electromagnets are regarded as a parallel connection in case of z-direction control. In case of x- direction, they are regarded as the parallel circuit of EM1 and EM3 and the parallel circuit of EM2 and EM4, and an inversed current is applied to each circuit. By this way, each controller for stabilizing the object can be designed separately. Finally, calculated three control signals are allocated to four input signals through a V-converter.

Experimental results of three-dimensional motion

By using model-following servo control technique, the stable levitation and three-dimensional motion were achieved. Fig. 3 shows the trajectory of the floating object. The deviation of the actual position from the desired position in continuous motion is less than 0.8 mm. Fig. 4 shows the input voltage change of each I-shaped electromanget. It turns out that the electromagnet controls the behavior of the object while creating the magnetic field for the circular motion.

Conclusions

The proposed magnetic levitation and translational motion system having simple and compact controlled electromagnet is fabricated in our laboratory. Smooth and wide-ranging three-dimensional motion was achieved experimentally.

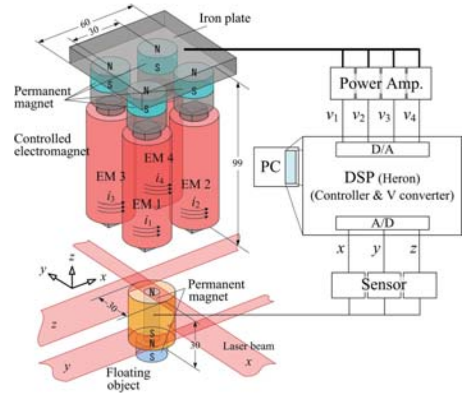

Fig. 1 Proposed magnetic levitation system.

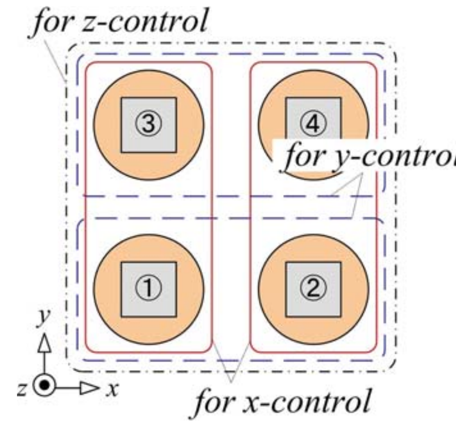

Fig.2 Selected electromagnets for each direction control.

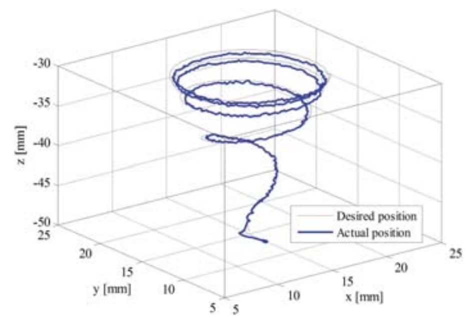

Fig. 3 Trajectory of the floating object.

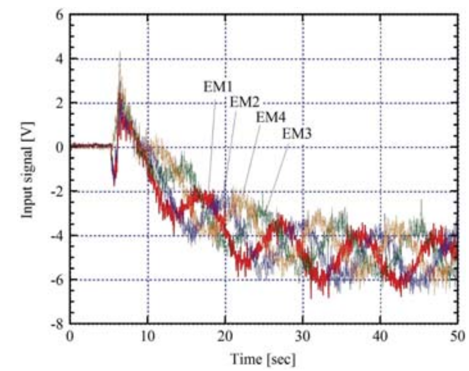

Fig. 4 Input voltage of each electromagnet.

[1] Khamesee M.B., Shameli S.E., IEEE Transaction on Magnetics, Vol. 43, No. 2, pp. 533-542 (2007)

A Novel Design of a Disk-Shaped Bearingless PM Motor for Artificial Hearts.

J. Asama, *Y. Kishi*, A. Chiba
Electrical Engineering, Tokyo University of Science, Noda, Japan

I. Introduction

A centrifugal pump type of artificial heart supports a blood circulation of patients from serious heart disease. For no blood contamination, a long term use, and low blood damages, mechanically frictional parts, such as ball and slide bearings, should be eliminated in an artificial heart. To meet these demands, magnetic bearings and bearingless drives are applied [1]-[3]. Furthermore, a physical structure of the artificial heart should be as thin as possible because these devices are often implanted vertically in the lower side of the patients. In this paper, a novel design of a disk-shaped bearingless permanent magnet (PM) motor is proposed for implantable centrifugal artificial hearts. The height of the proposed bearingless PM motor is designed to be 10mm. The objective of this paper is to demonstrate the effectiveness of the proposed bearingless PM motor using the finite element method (FEM).

II. Principle of Bearingless PM Motor

Fig.1 shows the exploded view of the proposed bearingless PM motor. The stator consists of twelve U-shaped magnetic cores. Two independent motor and suspension windings are wound around these cores. End windings expand in the radial directions. In this way, this bearingless motor can be thin.

The rotor consists of two disks (upper and lower) and a PM ring. In the disk, PMs are magnetized in the radial direction (radial PM) and inset into the rotor disks. In Fig.2, the PM ring is magnetized in thrust direction (thrust PM) and inserted between these disks. Suppose the magnetized direction of the thrust PM is upward, those of the upper and lower radial PMs are inner and outer directions, respectively. The thrust PM flux flows in the rotor and stator cores through air-gaps. Therefore, this bearingless PM motor works as an eight-pole synchronous motor.

The radial rotor motion is actively controlled. By exciting the suspension windings, unbalanced magnetic field is generated at the air-gaps, and then, the radial suspension force is generated. Thrust and tilting motions of the rotor are passively restricted by the bias PM flux. Thus, the rotor can be levitated.

III. FEM Analysis Results

It is noted that the height of the bearingless PM motor is 10mm. The rotor diameter is 45mm. Other analysis conditions are omitted in this paper. First, radial suspension force was calculated when the current is applied so as to produce the force in the X-axis. Although the suspension force was larger than the PM attractive one, the direction of suspension force does not correspond to the X-axis at a certain rotating angular position, θ_z. This error is evaluated by using an angle between the force direction and the X-axis, ϕ_e. In the case of the winding configuration shown in Fig.3a, the error angle ϕ_e was large, as shown in Fig.4. To decrease it, both an angle of radial PM arc,ϕ_{pm}, and a winding configuration are changed. As a result, ϕ_e was minimized. In addition, thrust and tilting stiffnesses under this analysis condition are high enough for magnetic levitation. It is concluded that the disk-shaped bearingless PM motor is feasible.

[1] D. J. Farrar, et al., ASAIO Journal, Vol. 53, pp.310-315, 2007.

[2] J. Asama, et al., Artificial Organs, Vol. 30, No. 3, pp.160-167, 2006.

[3] C. Nojiri, et al., ASAIO Journal, Vol. 46, pp.117-122, 2000.

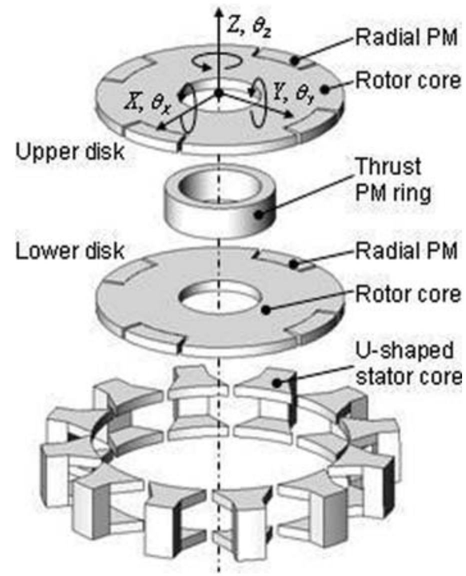

Fig.1.

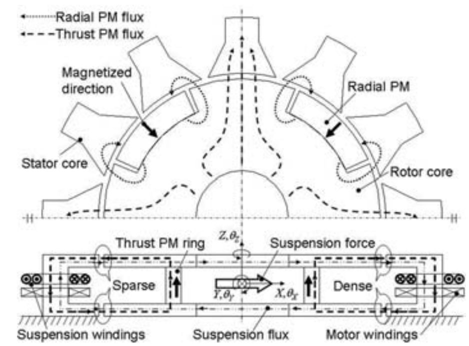

Fig.2.

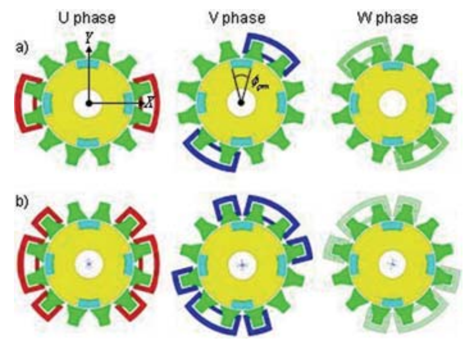

Fig.3.

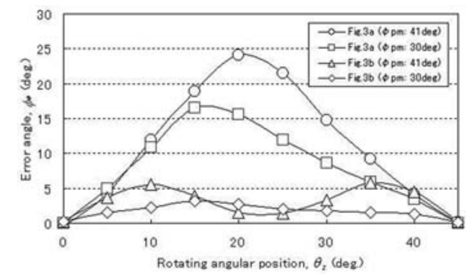

Fig.4.

EN-04

Effect of the active damper coils of the superconducting magnetically levitated bogie in case of acceleration.

S. Ohashi
Electrical and Electric Engineering, Kansai University, Osaka, Japan

A superconducting magnetically levitated (JR Maglev) transportation system has been developed in Japan. Fig.1 shows a cross section of the system. This system which is based on the side wall electrodynamic suspension (EDS), keeps the air-gap length at about 10 cm. Although the EDS system has the advantage of stable levitation without active control, the result of the numerical simulation shows that the damping factor of the levitation system is small. So the active damper coil system has been proposed.
Levitation forces is generated by passing the SC coils on the bogie[1]. The eight-figure null-flux connection is used for the levitation coil on the ground. If the bogie passes under the center of the eight-figure coils, levitation force is generated. Levitation force is calculated by the virtual displacement method. Current induced in the levitation coils is calculated as follows[2];the EDS system is given as an air-core coil system, and modeled as electric circuits. Then solving the electric circuit equations, we can calculate the current of the levitation coils. The motion of the bogie is calculated by putting these electromagnetic forces. Iterating these procedures, the transient motion of the bogie is given. Fig. 2 shows the arrangement of the active damper coils. They are set in front of the SC coils. Voltage is applied on them to control the vibration of the bogie. Fig.3 shows method for control against vertical oscillation. Because eight-figure connection is applied on the levitation coils, the polarity of the voltage applied on the upper and lower damper coils are different. The calculated results show that the active damper coils works effectively when the voltage in proportion to the vertical acceleration of the bogie is applied [3]. Their dimension is defined as follows; the energy consumed in them is calculated when the bogie oscillates vertically for the natural oscillation. The damper coils when the energy takes maximum value is defined as the optimal one.
Running simulation of the bogie is shown. Vertical oscillation of the bogie when the bogie runs at first v=120 m/s and accelerates up to 140 m/s. As velocity of the bogie is changed, vertical position of the bogie is changed. Thus vertical oscillation of the bogie occurs. Fig.4 shows without damper coils, 5 with passive damper coils and 6 with active damper coils (as shown in Fig.3). Effect of the damper coils are clearly shown. Effect of the damper coils under other bogie condition and characteristics against the bogie acceleration will be shown in the final paper.

[1] S.Ohashi, K.Higashi, H.Ohsaki and E.Masada, "Running Simulation of the Superconductive Magnetically Levitated System", in Proceedings of EPE'95, 1995, Vol.3, pp650-655.

[2]S.Ohashi"Improvement of the damping using the active damper coils system in the superconducting magnetically levitated bogie", IEEE Trans. on Magnetics Vol.35, No.5, pp4001-4003, 1999.

[3]S.Ohashi,"Improvement of the damping using the active damper coils system in the superconducting magnetically levitated bogie", Proceeding of Maglev conference 2002,PP08201

(in CDROM)

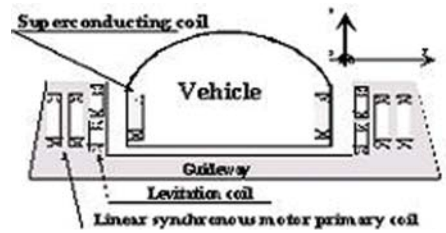

JR Maglev system

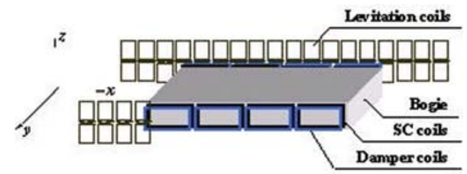

Arrangement of the active damper coils

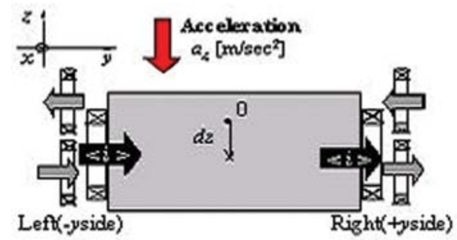

Control method for vertical oscillation

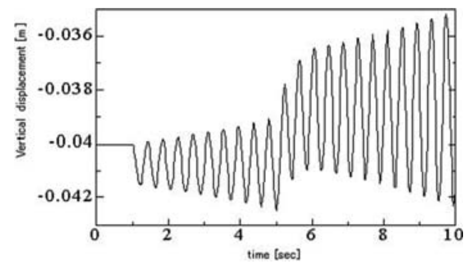

Vertical displacement without damper coils

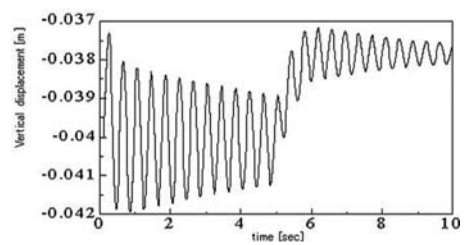

Vertical displacement with passive damper coils

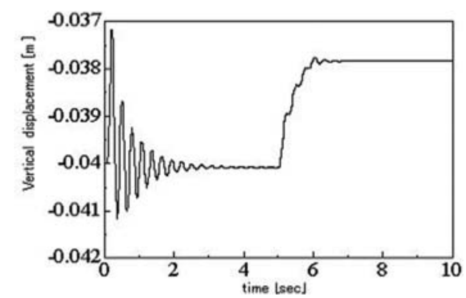

Vertical displacement with active damper coils

EN-05

Assessing the Maglev Force Capabilities of Two Passive Flat Guideway Topologies when using Electrodynamic Wheels.

J. Bird

1. Advanced Technology Center, General Motors Corporation, Torrance, CA; 2. Electrical and Computer Engineering, University of Wisconsin-Madison, Madison, WI

Despite high-speed magnetic levitation vehicles (maglev) being commercial available, intercity urban planners world-wide continue to balk at the immense capital cost associated with installing currently available maglev designs. This is unfortunate since maglev has some unique characteristics,such as low pollution and high-speed. If the maglev guideway construction costs could be brought radically down then perhaps maglev would be more frequently used. In order to minimize the guideway costs the guideway needs to be passive (non-electrified) and preferably horizontally flat. Flat passive guideways will also be more easily integrated into the existing transportation infrastructure. Flat guideways can also make use of electromagnetic directional switching [1] rather than mechanically moving guideways, and are less likely to accumulate debris and snow; they also create less aerodynamic drag forces. Two flat passive guideway topologies shown in Fig 1a & 1b are assessed in this paper. Using these guideways a vehicle would create the suspension and thrust forces by electromechanically rotating the magnetic rotors, also called electrodynamic wheels, shown in Fig 1a, 1b, above the split and dual split-sheet guideways. The forces are created by the induced eddy currents in the guideway, thus there is a slip speed defined as s=ω-vr (w=rotor mechanical angular velocity,r=outer radius, v=translational velocity). A lateral re-centering force is created when the magnetic rotors are offset from the center. Numerous such wheels are needed for a full size vehicle and dynamic control is essential. An onboard power source or power transfer to the vehicle will be needed and the vehicle will need to run on wheels at very low speeds. High efficiency is possible when using multiple electrodynamic wheels in series[2]. This paper focuses on assessing the ability to create sufficient lateral re-centering guidance forces when the wheels are laterally off-center. The 3D A-Φ steady-state convective diffusion model presented in [3] is used to calculate the forces. The 4 pole-pair Halbach rotor shown in Fig 1c has been used. The re-centering split-sheet guideway force shown in Fig 1a is dependent on the split sheet current difference, as seen in Fig 2a and 2b. In contrast, the dual rotor and dual split-sheet topology create re-centering forces when offset onto the guidance sheets located on either side of the guideway (see Fig 2c). The full paper shows that the dual design creates greater re-centering guidance force. Due to limited space only an example of the split-sheet guideway forces are shown. The iso-field plot for the A-Φ model used to obtain the results is shown in Fig 3a and the resulting lift, thrust and lateral restorative forces are shown in Fig 3b-3d. The forces are small because the experimental setup parameters have been used (ie: Halbach rotor OD=0.1m, width=0.05m, guideway width=77mm etc). The results show that relatively high lateral forces can be created albeit at the expense of a reduced lift and thrust force. The lift and thrust force can be improved by using a greater rotor width (Fig 3e). More results given in the full paper.

[1] J.L.He & D.M.Rote,Double-row loop-coil configuration for EDS maglev suspension, guidance, and electromagnetic guideway directional switching,IEEE Trans.on Magn., vol. 29,pp.2956-2958,Nov 93

[2] J. Bird and T. A. Lipo,Characteristics of an electrodynamic wheel using a 2-D steady-state model,IEEE Trans. on Magn.,vol. 43,pp.3395-3405,Aug.2007.

[3] Bird J.,T.A. Lipo,Modeling the 3D Rotational and Translational Motion of a Halbach Rotor above a Split-Sheet Guideway,Intermag 08,Submitted (InterMag Id# 455646)

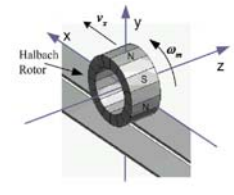

Fig 1a. A Halbach rotor rotating and translationally moving above an aluminum split-sheet guideway.

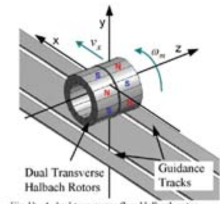

Fig 1b. A dual transverse flux Halbach rotor rotating and translationally moving above an aluminum split-sheet guideway.

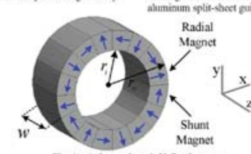

Fig. 1c. A four pole-pair Halbach rotor

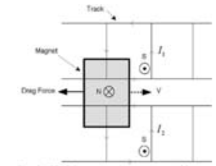

Fig 2a Vehicle magnets at center position, no guidance force ($I_2=I_1$)

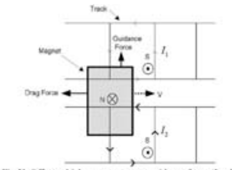

Fig 2b Offset vehicle magnets create guidance force ($I_2>I_1$)

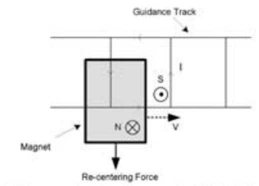

Fig 2c Illustration showing the re-centering guidance force created by the dual-split sheet when the transverse magnetic rotor is offset onto the guidance track. A ladder track has been used in these figures so as to more clearly show the induced eddy-current paths and re-centering forces.

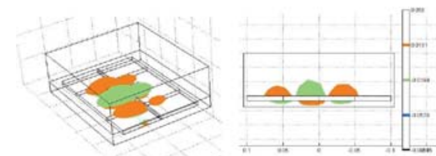

Fig 3a. Perspective and side view of a B_y magnetic flux density iso-surface plot in the non-conducting region due to the induced guideway currents

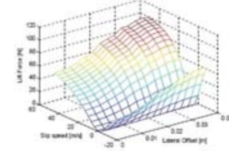

Fig 3b. Lift force vs. slip velocity and lateral rotor offset for a 5 ms^{-1} translational velocity

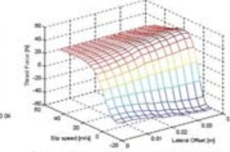

Fig 3c. Thrust force vs. slip velocity and lateral rotor offset for a 5 ms^{-1} translational velocity

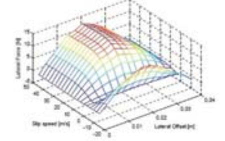

Fig 3d. Lateral re-centering force vs. slip velocity and lateral rotor offset for a 5 ms^{-1} translational velocity.

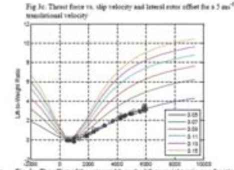

Fig. 3e. The effect of the rotor width on the lift-to-weight ratio as a function of RPM for the case when the Halbach rotor is at the center of the split-sheet guideway. A 5ms^{-1} translational velocity and 9.5mm air gap was used. Experimental measurements are also shown. The lift-to weight ratio is defined as: $L_w = F_y/(m.g)$ where F_y is the lift force and $m.g$ is the mass and gravity of the Halbach rotor.

EN-06

Magnetic levitation with minimum power consumption using disturbance compensation.

J. Ahn[1], S. Kim[2], J. Lee[1], J. Choi[3]
1. Electrical Engineering, Hanyang University, Seoul, South Korea; 2. Electrical Engineering, Yuhan College, Buchon, South Korea; 3. Industry Application Researh Division, Korea Electrotechnology Research Institute, Changwon, South Korea

In the super clean process as semiconductor or LCD manufacturing process, magnetic levitation and transportation system without external power supply is suitable because there is no mechanical coupling between stator and mover, then it doesn't make any dust. However there is no external power supply, the power consumption has to be kept in its minimum, the zero-power levitation control must be adopted.[1] The internal non-linearity of magnetic levitation system makes itself unstable, the conventional control method cannot sustain its stability with disturbances. Luenberger observer, robust levitation controller and other non-linear control theories had been adopted for compensating its non-linearity. They were effective but difficult to implement because they had complex structure. Disturbance Observer(DOB) has been focused because of its simplicity and characteristics of frequency response which is suitable for electro-mechanical system.[2] Therefore the zero power controller with DOB is proposed in this paper. The disturbance is considered as load variance. The system non-linearity and parameter uncertainty are compensated by DOB, it is possible to implement relatively simple and robust zero power levitation controller. The proposed method is verified by simulation and experiment.

[1] Y. H. Kim, K. M. Kim, and J. Lee, "Zero Power Control with Load Observer in Controlled-PM Levitation," IEEE Transactions on Magnetics, Vol. 37, No. 4, pp. 2851~2854, July 2001.

[2] D. L. Trumper, S. M. Olson and P. K. Subharmanyan, "Linearizing Control of Magnetic Suspension Systems," IEEE Transactions on Control Systems Technology, Vol. 5, No. 4, pp.427~438, July 1997.

Part	Item	Value
Stator	Teeth height	30[mm]
	Teeth width	5[mm]
CPM	Weight	3.91[kg]
	Coil turn	334[turns]
	Magnet height	2.7[mm]
	PM area	629.35[mm^2]
	Core length	57.7[mm]
	Stack length	16.7[mm]

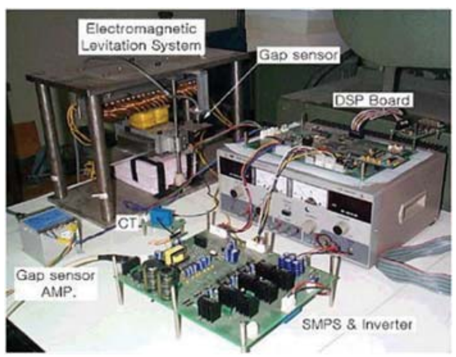

Experiment set-up of magnetic levitation

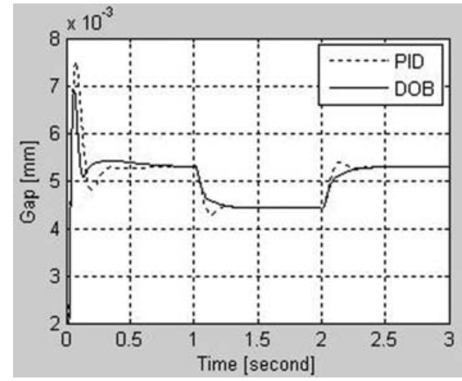

Simulation result: gap control response

EN-07

Design and Dynamic Analysis of Rectangular-Surface Electromagnets for Levitation Applications.

S. Jang[1], *J. Choi*[1], J. Park[1], H. Sung[2], S. Sung[2]
1. Chungnam National University, Dae-jeon, South Korea; 2. Korea Institute of Machinery&Materials, Daejeon, South Korea

Introduction

The magnetic levitation (Maglev) train is one of the best candidates for new-generation transportation system because they are environment-friendly, compact, light-weight and suited to mass-transportation [1]. Therefore, the study on propulsion, levitation and guidance system for the Maglev train has been developed. Especially, in order to improve their reliability, particular attention to design and control of the levitation systems has been increased.
Typically, there are three types of levitation technologies: electromagnetic suspension (EMS), electrodynamic suspension (EDS), hybrid electromagnetic suspension (HEMS). The EMS is inherently unstable due to the characteristics of the magnetic circuit. Therefore, precise air-gap control is dispensable in order to maintain the uniform air-gap. However, EMS is easier than EDS technically and it is able to levitate by itself in zero or low speeds. Also, EMS requires a much smaller variation of the current's amplitude as compared with HEMS because the permeability of permanent magnet (PM) is unity [1-3].
Therefore, this paper deals with design and dynamic analysis of electromagnets having rectangular cross-section for levitation applications. First, by applying equivalent magnetic circuit (EMC) method to analysis model shown in Fig. 1(a), initial design for electromagnets is performed. And then, on the basis of the initial design results and 3-D finite element analysis (FEA) model shown in Fig. 1(b), detailed design for those is also accomplished. Second, as shown in Fig. 2, the testing apparatus including the electromagnet and a driver is manufactured. Finally, in order to confirm the validation of the designed electromagnet, this paper investigates using control concept of 1-axis suspension system shown in Fig.3 that the uniform airgap is maintained under required load weight conditions, and required levitation force is produced under rated current. In particular, the influence of temperature of windings on levitation control is investigated in detail.

Results and Discussion

Figure 4 shows the measured results for temperature of windings, current of the electromagnet and maintained air-gap in levitation system. It can be seen that current of the electromagnet is much affected by the temperature of windings, which results in the failure of the precise air-gap control due to variation of magnetic levitation force. It can be judged that this phenomenon is caused by the variation of the winding resistance according to temperature of windings. In order to solve this problem, the block diagram shown in Fig.3 should be modified to make the gain (Kp and Td) have not fixed but flexible value considering windings temperature. More detailed results and discussion will be given in final paper. The mathematical expressions related to the EMC methods, state and output equation used in Fig.3 will be also given in final paper.

[1] H. W. Lee, K. C. Kim and J. Lee, IEEE Trans. Magn. vol. 42, no. 7, pp.1917-1925, 2006.

[2] H. Weh and M. Shalaby, IEEE Trans. Magn., vol. 13, no. 5, pp.1409-1411, 1977.

[3] Y. K. Tzeng and T. C. Wang, IEEE Trans. Magn., vol. 30, no. 6, pp.4731-4733, 1994.

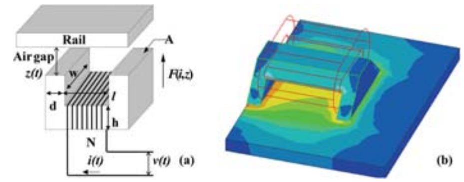

Fig. 1. Analysis model: (a) EMC analysis model and (b) 3-D FEA model.

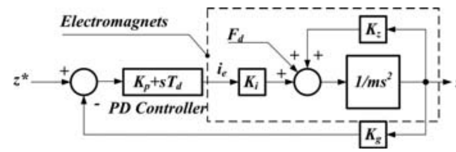

Fig. 3. Control concept of 1-axis suspension system for levitation of the electromagnets.

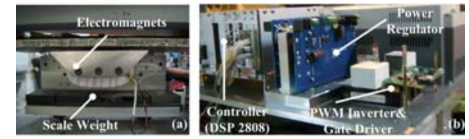

Fig. 2. Testing Apparatus: Manufactured (a) Electromagnets and (b) driver and power devices.

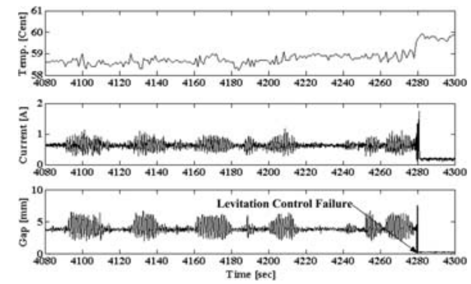

Fig. 4. Measured results for temperature of windings, current of the electromagnet and maintained air-gap in levitation system.

Basic Characteristics of an Active Thrust Magnetic Bearing with a Cylindrical Rotor Core.

K. Hijikata[1], S. Kobayashi[1], M. Takemoto[1], Y. Tanaka[1], A. Chiba[2], T. Fukao[1]
1. Mechanical Systems Engineering, Musashi Institute of Technology, Setagaya-ku, Japan; 2. Electrical Engineering, Tokyo University of Science, Noda-shi, Japan

Magnetic bearings (MBs) can suspend rotor shafts by electromagnetic force without mechanical contacts or lubrication. Therefore, the MBs have advantageous features such as high rotational speed, maintenance free, using in specific environments and low acoustic noise. Accordingly, the various types of MBs have been developed and commercialized for application to special blowers, LNG pumps, turbo-molecular pumps and all that [1-5]. In these MBs, thrust magnetic bearings (TMBs) with thrust disks are generally used for active suspension control of thrust direction [2-4]. However, the thrust disks, which have large diameter, have caused various problems such as worsening performance to assemble or to disassemble and limiting rotational speed. Accordingly, this paper proposes a novel structure of an active thrust magnetic bearing using a small cylindrical rotor core without the large thrust disk. It is shown with 3D-FEA and experiment that the proposed TMB with the cylindrical rotor core is effective in producing characteristic features.

Fig. 1 shows the structure of the proposed TMB. The proposed TMB has the simply cylindrical rotor core. The stator is composed of an E shape core and permanent magnets. In addition, suspension windings in two slots of the E shape core are wound in the same direction and are connected in series.

Fig. 2 shows the principle of the thrust force generation. The excitation flux ψmag is generated by permanent magnets. The cylindrical rotor core is magnetized at 3 pole of N-S-N by the ψmag. If the suspension current flows in the suspension winding, the suspension flux ψs is generated as shown in Fig. 2. It is evident that the flux density in the left-side air gap is increased. On the contrary, the flux density in the right-side air gap is decreased. Therefore, this superimposed magnetic field results in the thrust force acting on the rotor core toward the left direction.

Fig. 3 shows the relationship between the thrust force and the suspension current analyzed with 3D-FEA. The dimensions of the proposed TMB are shown in Table. 1. It is seen that the thrust force is almost linearly increasing according to the suspension current. In addition, when the current density of the suspension current is 6A/mm2, the thrust force is 163.4N which is 2.5 times larger than the rotor-shaft weight of the experimental machine. Thus, it is found that the proposed TMB with the cylindrical rotor core is effective in producing the thrust force. In the full paper, other analysis results and experimental results of the experimental machine will be provided in order to make clear the basic characteristics of the proposed TMB.

[1] A.Chiba, T.Fukao, O.Ichikawa, M.Takemoto, and D.G.Dorrell, "Magnetic Bearings and Bearingless Drives," Newnos, 2005.

[2] F. Matsumura, and T. Yoshimoto, "System modeling and control design of a horizontal-shaft magnetic-bearing system," IEEE Trans. Magn., Vol. 22, pp. 196-203, May 1986.

[3] C. Redemann, P. Meuter, A. Ramella, and T. Gempp, "Development and prototype of a 30kW bearingless canned motor pump", in Proc. IPEC-Tokyo 2000, Tokyo, Japan, 2000, pp.377-382.

[4] Zuoxing Yang, Lei Zhao, and Hongbin Zhao, "Global linearization and microsynthesis for high-speed grinding spindle with active magnetic bearings," IEEE Trans. Magn., Vol. 38, pp. 250-256, Jan. 2002.

[5] Xu Yanliang, Dun Yueqin, Wang Xiuhe, and Kong Yu, "Analysis of hybrid magnetic bearing with a permanent magnet in the rotor by FEM," IEEE Trans. Magn., Vol. 42, pp. 1363-1366, Apr. 2006.

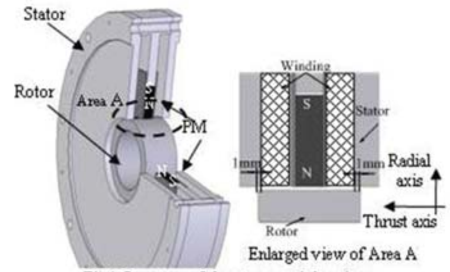

Fig.1 Structure of thrust magnetic bearing with cylindrical rotor core

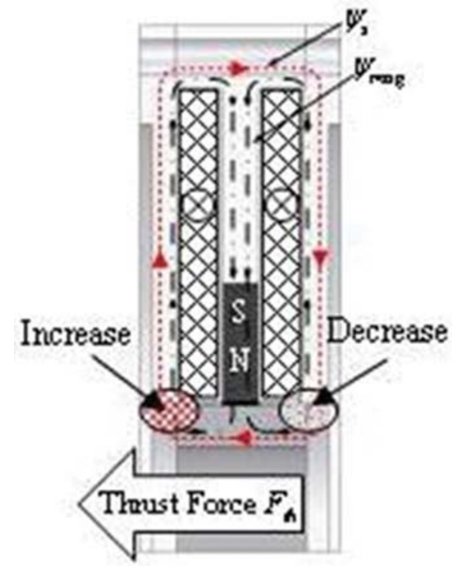

Fig.2 Principle of thrust force generation

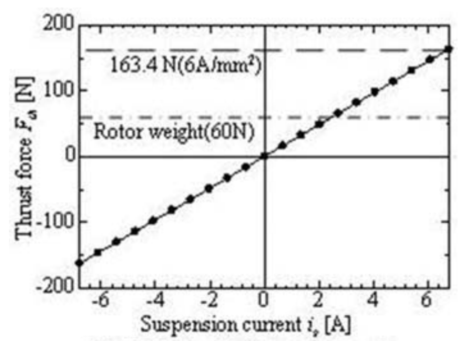

Fig.3 Relationship between F_A and i_s

Table.1 Dimensions of Thrust magnetic bearing

Rotor weight	60 N	Stator diameter	180 mm
Touch down(thrust)	0.7 mm	Rotor diameter	50 mm
Touch down(radial)	0.1 mm	Stator length	30 mm
Gap length	0.8 mm	Rotor length	22 mm
Coil packing factor	39.7 %	Opposed length	1 mm

EN-09

Magnetically-Levitated Steel Plate Conveyance System Using Electromagnets and a Transverse-Flux Linear Induction Motor.

J. Choi, Y. Baek
Mechanical Engineering, Yonsei University, Seoul, South Korea

To maintain high-quality steel plates is very important to such processes as painting and coating in the steel industry. However, a roller-based steel plate conveyance method widely used is difficult to ensure the high quality of steel plates due to its scratches by friction. One of the solutions for this problem is to use magnetic levitation in conveying steel plates.
Magnetic levitation can maintain the high quality of steel plates during processes because of its noncontact characteristics. As a study on steel plate conveyance and magnetic levitation, Hayashiya et al.[1],[2] proposed two combined lift and propulsion systems using electromagnets and transverse-flux linear induction motors (TFLIMs). Their experimental results are focused on the effects of the levitation force of a TFLIM on the levitation behaviors of the systems, so the conveyance behaviors are not shown.
This study presents a novel-concept noncontact steel plate conveyance system. The novel concept is to use an unbalanced force generated by the deviation of the center-of-mass of a steel plate from the origin of a reference frame and a thrust force generated by a TFLIM for steel plate conveyance. These two forces are summed and used as a total thrust force in our conveyance system to enhance its conveyance performance. And also its experiment results are presented to show the behaviors during levitation and conveyance.
Fig. 1 shows the components of the system and its photograph. Also, the system responses during levitation and conveyance are shown in Fig. 2. Fig. 2(a) presents the z-axis position of the steel plate used in this study. After a conveyance experiment starts at 0.7 sec, the levitation forces by the TFLIM affect the levitation position of the steel plate to a constant level. We observed that the z-axis stability of the system is maintained. Figs. 2(b) and 2(c) are the roll and pitch motion data of the steel plate, respectively. The roll motion is bounded within the stable limit cycle and the pitch motion is changed due to the conveyance experiment right after 0.7 sec. The pitch motion at the initial state is negative because of the deviation of the initial position of the steel plate from the origin of the reference frame. So, this phenomenon affects the conveyance motion at a small movement of about -0.2 mm in the x-axis direction as shown in Fig. 2 (d). However, during the period of the conveyance motion, the pitch motion is changed to the positive direction and also the conveyance motion is directed to the positive x axis. We observed that the conveyance motion can be generated from a combined force of the thrust by the TFLIM and also the force due to the deviation of the center-of-mass of the steel plate. Fig. 2(d) has a lower-level position resolution due to the measuring resolution of the laser displacement sensor compared to Figs. 2 (a), (b) and (c) collected from the capacitance-type gap sensors.
This study proposed a noncontact steel plate conveyance system. The presented method to improve the ability of the conveyance movement of the system is to use the effect of the moment generated by the deviation of the center-of-mass of a rigid-body steel plate. This method was integrated with magnetic levitation and a transverse-flux linear induction motor. A prototype of the conveyance system was built and its experimental results were presented to verify the feasibility of the proposed concept.

[1] H. Hayashiya, D. Iizuka, H. Ohsaki, and E. Masada, "A novel combined lift and propulsion system for a steel plate conveyance by electromagnets," IEEE Trans. Magn., vol.34, no.4, pp. 2093-2095, July 1998.

[2] H. Hayashiya, H. Ohsaki, and E. Masada, "A combined lift and propulsion system of a steel plate by transverse flux linear induction motors," IEEE Trans. Magn. Vol. 35, no. 5, pp. 4019-4021, Sept. 1999.

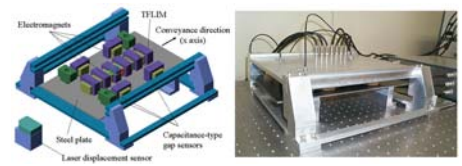

Fig. 1. System components and its prototype photograph.

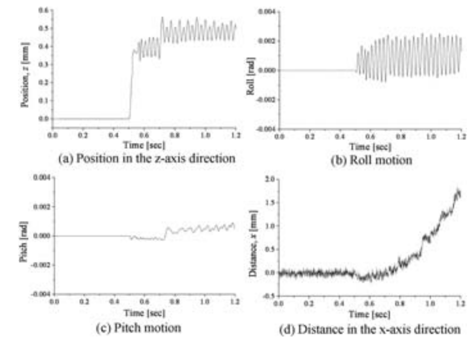

Fig. 2. Levitation and conveyance experimental results.

EN-10

Combination resonance of a rigid body levitated above a diamagnetic slab.

T. Sugiura, T. Hosono

Mechanical Engineering, Keio University, Yokohama, Japan

According to recent research, permanent magnet can be levitated stably in a static magnetic field by using a diamagnetic material[1]. This method of levitation has am advantage over other ones: intrinsic stability without control under room-temperature condition. Thus its industrial applications such as efficient rotary bearings or mass transportation can be expected. So far there have been some researches on static stability of diamagnetic levitation, but its dynamics has not been treated so much. This research investigates nonlinear dynamics of a rigid body levitated over a diamagnetic slab.

In our model shown in Fig.1, the rigid body consists of a bar and two permanent magnets attached at its both ends. This rigid body can be stably levitated without any control, only by an attractive force from a lifting magnet placed over the levitated body and also by a repelling force from a diamagnetic material placed under the levitated body. Now we consider that the lifting magnet is externally excited in the horizontal direction sinusoidally.

First, the equations of motion describing translation and rotation of the rigid body have been derived, using an analytical expression of nonlinear magnetic force. This expression can be obtained by magnetic dipole approximation of the attached magnets and by the mirror image method for evaluating diamagnetic response. These equations show nonlinear coupling between two eigenmodes: vertical translation and one of two modes caused by coupling of horizontal translation and rotation. This nonlinear coupling can lead to combination resonance of these eigenmodes.

Numerical results of motion of the rigid body have been obtained by the Runge-Kutta method. Figure 2 shows horizontal motion of the lifting magnet shaken externally and vertical motion and rotation of the levitated body, displaying their time histories and their spectra. It can be found that the nonlinearly coupled two eigenmodes mentioned above show their resonance at their eigenfrequencies, respectively, at the same time when the excitation frequency of the lifting magnet is the sum of those eigenfrequencies. This resonance is what is called combination resonance. Numerical results of frequency responses show that this combination resonance occurs only when the excitation frequency is in the neighborhood of the sum of those eigenfrequencies. Frequency responses also show a soft-spring tendency of this resonance.

Experiments have also been carried out, using a high-speed camera. Figure 3 shows experimental results of combination resonance, corresponding to Fig.2. Experimental results have verified our theoretical and numerical predictions.

[1] M.D.Simon, L.O.Heflinger, A.K.Geim, Diamagnetically Stabilized Magnet Levitation, Am.J.Phys., 69-6, (2001), 702-713.

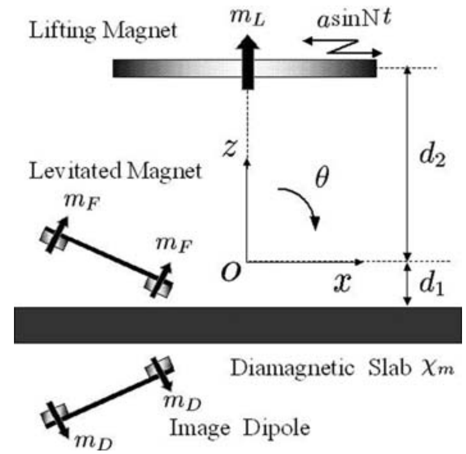

Fig.1 Analytical model of diamagnetic levitation

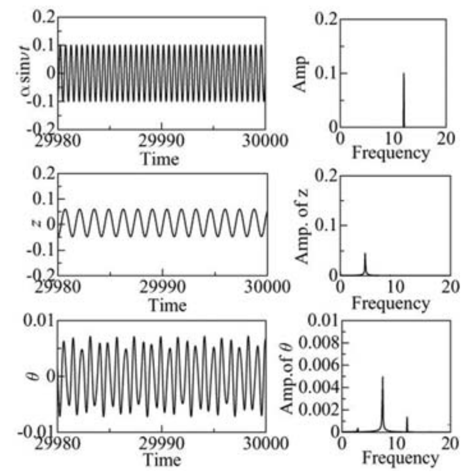

Fig.2 Time histories and their spectra of combination resonance (numerical, nondimensional)

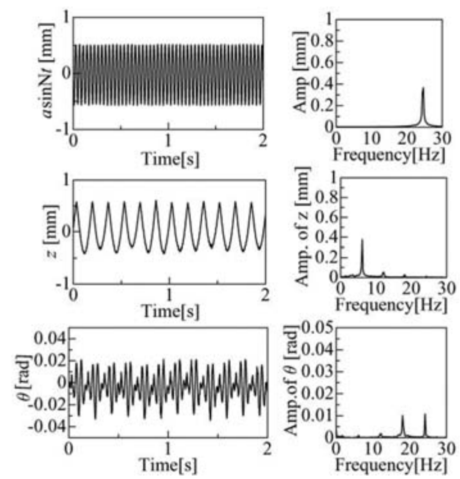

Fig.3 Time histories and their spectra of combination resonance (experimental)

EN-11

Dynamic shielded room for biomagnetism.

D. Costandache, *O. Baltag*
University of Medicine and Pharmacy “Gr.T.Popa”, Iasi, Romania

Abstract. The paper presents a shielded room made from nonferromagnetic materials used for biomagnetic studies and measurements in ambiental electromagnetic environment. The shielded room is placed in the centre of a triaxial Helmholtz coil system of big dimensions for dynamic control and compensation of the natural geomagnetic perturbations and the fields produced by human activity. The technical solutions and the performances of the installation are presented.

I. INTRODUCTION

The paper presents a complex installation formed by a shielded room made from nonferromagnetic materials placed in a triaxial Helmholtz system for compensation and dynamic control of the external magnetic field. This installation is used for basic studies and researches in biomagnetism and biomedical diagnosis.

The aluminum material selection has been done after measuring the shielding coefficients to audio range frequencies (20 Hz √ 20 KHz). The paper presents the method employed for shielding coefficient evaluation for different materials (Al, Coper, brass).

II. DESCRIPTION OF THE INSTALLATION

The room having the dimensions (3000 x 2000 x 2000)mm is made from aluminum sheets of 12 mm thickness. The room is mounted on a wood laminated structure in the centre of the triaxial Helmholtz system.

The triaxial Helmholtz system which allows the compensation on the three directions of the low frequency magnetic fields is realized from three pairs of large square Helmholtz coils, having the dimensions (4000 x 4000 x 4000)mm. The currents from the coils are controlled by a triaxial magnetometer. Each coil has two windings, one for manual compensation and the second for automatic control. The ratio of the two coils constants is 1/5.

The first coil allows the manual compensation of the continuous component of the magnetic field vector on the three directions (X, Y, Z).

The second coil allows the compensation of the alternative and slow variable components of the earth magnetic field using an automatic system controlled by a triaxial magnetometer. The magnetometer is working in a negative feedback system. The negative feedback loop is closed by the Helmholtz coils field where is placed the triaxial transducers block.

This structure presents the advantage of a flexibility and a high dynamic control of the magnetic field.

The manual control system consists from a current amplifier stage voltage controlled, using power operational amplifiers. A digital-analog converter gives the command voltage. The field programmed value is indicated (by means of an alphanumerical keyboard) on a digital display. The three channels for manual control are identically; the differences are the values of the coils constants, caused by different dimensions of the three coils.

The automatic control system is working in negative feedback loop on each channel. For each channel the feedback loop is closing in a chain made from: transducer – magnetometric channel – current source voltage controlled – Helmholtz coil – transducer. The three channels are independent calibrated. The response frequency of the channels is between (0 √ 400) Hz.

III. RESULTS AND PERFORMANCES

Experimentally was determined the aluminum shielding coefficients for alternating fields by using a simple installation. The installation consists from a magnetic field generator coil supplied by an audiofrequency generator and a search coil magnetometer. The measurements was performed for the frequency range (20 √ 8000) Hz.

The compensation range of the earth magnetic field is +/- 5.10-5 T (50.000 nT). The compensation level is almost 10-9 T (1 nT) residual field. The field is homogenous (inhomogeneity 10-4) in a volume having the dimensions (0,8 x 0,8 x 0,8) m.

IV. REFERENCES

[1] Kajiwara G., Harakawa K., Ogata H., High performance magnetically shielded room, IEEE Trans. Mag., vol. 32, pp.2582-2585, 1996

[2] Holmlund C., Keipi M., Meinander T., A.Penttinen, H.Seppa, Novel concepts in magnetic shielding, Proc. of 12th Int. Conf. on Biomagnetism Biomag 2000, Espoo/Helsinki, Finland, 2000

[3] Stroink G., Blackford B., Brown B., Horacek M., Aluminum shielded room for biomagnetic measurements, Rev. Sci. Instrum. Vol. 52(3), pp.463-468, 1981

[4] Platzek D., Nowak H., et all, Active shielding to reduce low frequency disturbances in direct current near biomagnetic measurements, Rev. Sci.Instrum., vol. 70 (5), pp.2465-2470, 1999

Fig.1. Shielded room

EN-12

Magnetic shielding design for magneto-electronic devices protection.

W. Wang, Z. Jiang
Electrical Engineering, University of Wisconsin - Milwaukee, Milwaukee, WI

With rapid progress in Magnetic Random Access Memory (MRAM) development, shielding for MRAM and other magneto-electronics devices becomes more important. Traditionally, magnetic shielding is done by cylindrical shells with length to diameter ratio greater than one [1]. Such shielding shapes are not compatible with the form factor of electronic chips, boards or systems. Novel magnetic shielding designs with low length to diameter ratio are needed. In this paper, we introduce a shielding strategy and demonstrate a case study to achieve shielding factor above 1000 with cylindrical shell length to diameter ratio below 0.3 and end-cap openings for signal and power I/O connections.

Although the active shielding is an efficient shielding approach, it demands an always-on power supply. This limitation partially off-sets the advantage of non-volatility in MRAM and other magneto-electronic device. Therefore, the passive magnetic shielding is preferred.

Traditionally, the challenge on passive magnetic field shielding is in the trade-off between shielding efficiency and shell volume/mass. For magneto-electronics shielding, there are three new challenges: (1) form factor. Since the magneto-electronic devices often co-exist with other electronic devices, the shielding shell should maintain a form factor that compatible with other components in the system, i.e. a cylindrical shell with length to diameter ratio much less than one. (2) Openings for signal and power I/O paths. 64 bits or 128bits signal buses are common in today's systems. Openings for such wide bus can significant degrade the shielding factors. (3) Signal path performance impact. System performances rely on the link speed among its components. For example, computer system performances heavily depend on the bus speed between CPU and DRAM. The shielding should not increase the critical signal bus lengths so that the signal link performance gets degraded.

Magnetic shielding for magneto-electronics can be applied in chip, board or system level. Shielding entire system leads to large volume and mass penalty. In contrast, the chip level shielding may impact the signal link performance between shielded magneto-electronic device and other electronic devices outside the shielding volume. Therefore, the board level shielding is the practical solution, since the critical on-board signal bus performance is not affected. And the volume/mass impact is acceptable.

For board shielding, the design goals are: (1) low cylinder length to diameter ratio; (2) multiple openings on end caps for signal and power I/O connections. The opening size should be large enough to handle wide bus bundles.

We propose a multi-layer shielding with mis-aligned openings on one side of the end caps. The I/O bus paths are similar to the flip chip packaging used in semiconductor IC chips. Fig. 1 shows a two-layer shell structures. The openings on the end caps are mis-aligned so that there is no direct path for external magnetic field penetrates into the protected volume. Each pair of openings on end-caps forms a channel for signal bus bundle. In most of electronics system, the time delay skew among all the bits within a bus group should be minimized. All those bits should be connected to outside in the same bundle to minimize link length skew.

The shielding effects of the proposed design are simulated numerically by using Maxwell 3D simulator. In the simulation, the inner cavity diameter is set at 100mm with depths of 10mm, i.e., length to diameter ratio of 0.1. The shell material is 0.5mm thick mu-metal. Both axial and radial gap are 10mm. On one side, the end-caps have 15mm diameter openings, while the other side uses closed end caps. The external magnetic field is set at 1 G. Since the axial shielding factors are much lower than radial shielding factors, we focus our efforts on axial shielding factors. Figure 2 shows axial shielding factor varies with the separation of the openings. Fig. 2 (a) shows angular dependency for two openings on the same circle with radius of 25mm. The axial shielding factor increased from 64 to above 1000 after 45 degrees, which is equal to center-to-center distance at 1.3x of the opening diameter. Fig. 2(b) shows the axial shielding factor dependency on the radial separation. The shielding factor reaches to 1000 after the separation of the 1.3x of opening diameter. Based above data, multiple pairs of openings can be simultaneously placed. Each pair provides a channel for one signal/power I/O bus bundle.

In summary, we proposed a novel shielding structure to protect the circuit board with the magneto-electronics devices. A numerical simulation based case study demonstrates the feasibility of the proposed shielding strategy.

[1] E. Paperno, et al, IEEE Trans. on Magnetics, Vol 40, No. 4 2170-2172

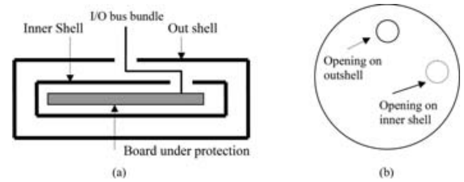

Fig. 1, Two-layer shell structure with mis-aligned openings (a) cross-section; (b) top view

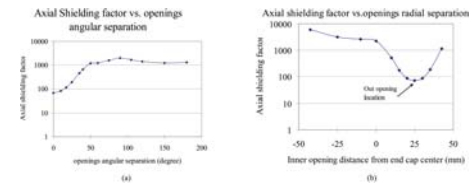

Figure 2, Axial shielding factor dependency on opening separations (a) angular separation; (b) radial separation.

Measurement and calculation of shielding performance of reinforced concrete structures.

M. Zhang, Z. Zhao, X. Cui
North China Electric Power University, Baoding, China

1. INTRODUCTION
Reinforced concrete constructions can be found everywhere. In substation, with the placement of protection devices into the switchyard, protection equipments may be destroyed seriously by the intense transient process for bad shielding performance of the reinforced concrete relay cell during the operation of switches. For example, as the power magnetic field more than 3uT is not allowed for CRT display, the shielding effect of reinforce concrete relay cell to magnetic field is important for the work of CRT display placed in relay cell. Therefore, it is necessary and significant to identify the shielding performance of reinforced concrete constructions. [1]
In this paper, a rigorous method with fewer unknown variables is proposed on the basis of method of moment and equivalent principle. And the shielding effectiveness of different concrete structures are measured and calculated.
2. DESCRIPTION OF THE APPROACH
Taking a general reinforced concrete building as an example, the considered space can be separated into three parts, namely the outside of the building, inside of the building and in the concrete. Surface cells with surface current are assumed on both the inner side and the outer side of the concrete. The outer field of the building is generated by the surface currents on the outer side of the building as well as the incident field. The field inside the building is generated by the surface currents on the inner side. While the field in the concrete itself comes from the surface currents on the inner side and the line currents distributed on the steel grid. Based on equivalent principle, the equations can be obtained on both sides of the concrete, from which the surface currents and the resulting electromagnetic fields can be obtained.
The equations can be solved by the Gauss elimination method to obtain the distribution of the electric and the magnetic currents on these surfaces. The electromagnetic fields inside and outside of the enclosure and the shielding effectiveness of the enclosure can be obtained as well.
3. MEASUREMENT AND CALCULATION OF SHIELDING EFFECTIVNESS
In order to obtain the shielding effectiveness of the reinforced concrete, several effect factors have been analyzed. Fig.1 and Fig.2 shows the electric and magnetic shielding effectiveness of concrete structure with metal grids, the steel conductor have diameter of 10mm and space of 200mm, the shielding performances of 0.2m from the center of 2m*2m single layer concrete and the conductivity of the concrete is 75.2ohm*m, the relative permittivity is 9.4, the thickness of the concrete is 0.2m.
It is obvious that at low frequency, the magnetic field shielding effectiveness is not obviously for the pure concrete. And for the reinforced concrete, at low frequency the shielding effectiveness is little different, but for the frequency more than 1MHz, the wire grid buried in the concrete shows its effect.
CONCLUSION
A method based on method of moments and equivalent principle suitable for estimation of the shielding effectiveness of reinforced concrete constructions is used. And the shielding effectiveness of different concrete structures are measured and analyzed.

[1] R. A. Dalke, C. L. Holloway, P. McKenna, M. Johansson, and A. S. Ali, “Effects of reinforced concrete structures on RF communications,” IEEE Trans. Electromagn. Compat., vol. 42, pp. 486–496, Nov. 2000.

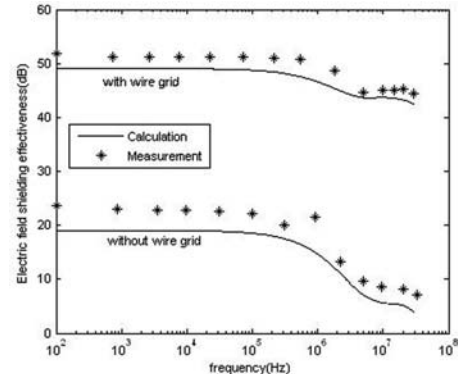

Fig.1 Electric field Shielding effectiveness of wire grid

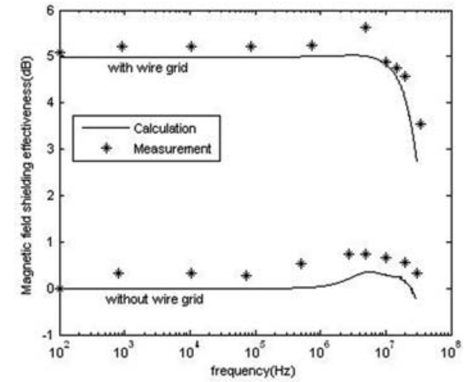

Fig.2 Magnetic field Shielding effectiveness of wire grid

EN-14

Reduction of magnetic shaking flux leakage from loosely coupled cylindrical magnetic shield shells having active compensation.

I. Sasada, R. Takahashi
Applied Science for Electronics and Materials, Kyushu University, Kasuga, Japan

We have proposed a new method of magnetic shielding by combining sets of a coil to carry compensation current and a backing up magnetic thin plate [1]. In this method, a compensation current generates repulsive forces acting on the environmental magnetic fields and a magnetic thin plate provides a good magnetic pathway to the compensating magnetic fluxes so that they exists only on one side of the thin plate. We have demonstrated that magnetic shielding factor as large as 3000 can be obtained with a pair of magnetic shells not connected with each other(see Fig. 1). By applying magnetic shaking technique [2] to the magnetic layers in the shell, the thickness of the layer can be made thinner due to a large enhancement of the magnetic permeability.

Unlike a full cylinder, a separate magnetic shell does not have a closed magnetic path for shaking magnetic fluxes, therefore the shell is prone to leak shaking magnetic fluxes. In this paper, an efficient method for reducing shaking leakage from magnetic shells are investigated.

Fig. 1 shows a cross section of a separate magnetic shield (left half) whose size is one-third of that of a magnetic shield we have planned to use for the MCG measurement. m1~m3 are magnetic layers consisting of 11 stacks of Metglas amorphous tapes. m2 and m3 are equipped with a toroidal shaking coil whose conductors are indicated a1, a2 and b1, b2. Spacing between m2 and m3 is 2 mm and that between m1 and m2 is 4 mm. The number of turns of the outer shaking coil (a2 and b2) are 18 and that of inner ones (a1 and b1) are 19. All the components within a shell were fabricated in a sigle rigid body as a composite with glass fiber prepreg and carbon fiber prepreg [3]. An idea to reduce the flux leakage from the shaking process is that m2 and m3 are subjected to the magnetic shaking at the same time but in an opposite direction. There are two ways of magnetic flux path in the lower shell with respect to the upper one; the one is to circulate over the corresponding magnetic layers and the other is heading on in gaps between extended flat parts. We will call the former circular symmetry and the latter mirror symmetry.

When the outer shaking current Is2=20 mA of 400 Hz and the inner shaking current Is1=0, the leakage of the shaking flux observed at x=0 and y=3 cm along the x-axis is huge (214 nT) as shown in Fig. 2. We are interested mostly in the x component of the leakage, because the shielding system will be rotated 90 degree angle and coaxial SQUID gradiometers in a Dewar will be inserted through the gap space along the y-axis down to the center to measure MCG, which is sensitive to the x component of the magnetic field. Of course, large y component is harmful because the base line (coaxial line) of the gradiometer is not always kept parallel to the x-axis. When Is1 is properly adjusted (Is1=11.8 mA for Is2=20 mA), the leakage can be reduced to 4.1 nT for the mirror symmetry combination (Fig. 3) and slightly smaller for the circular symmetry combination. It should be noted that unsuppressed component is mainly consisting of the third harmonics of 400 Hz shaking frequency which becomes clear when the shaking currents are increased. This may be because small portion of the shaking magnetic field magnetized m1 layer weakly and generated the third harmonic. We expect this can be cancelled by properly adding a small 1200 Hz current to Is2 or Is1.

Other interest phenomenon showing the important role of the magnetic shaking is shown in Fig. 4, where 10 uT of 10 Hz external magnetic field is applied along the y-axis and the magnetic field (1st~10th harmonics) is observed along the y-axis at the same point (x=0, y=3 cm). The figure shows the shielding system in Fig. 1 can attenuate a y-axis impressed magnetic field below two orders of magnitude smaller but limited by the odd harmonics emitted by shells when no magnetic shaking is applied. With the magnetic shaking, the odd harmonics are decreased to one seventh.

[1] I. Sasada, Y. Nakashima, MMM, FP-11 (2007) to be published.

[2]I. Sasad, T. Kimura, T. Takeda, M. Shimada, Journal of Appl. Phys. 99 (8): Art. No. 08P501, 2006

[3]I. Sasada, S. Kubo, K. Harada, Journal of Appl. Phys. Vol. 64, No. 10, pp.5696-5698, 1988

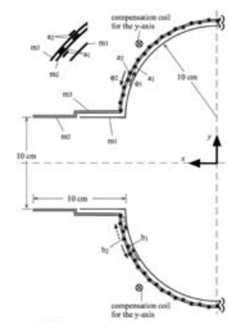
Fig. 1

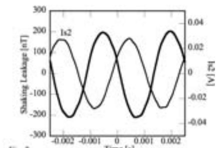
Fig. 2

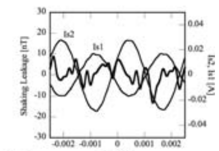
Fig. 3

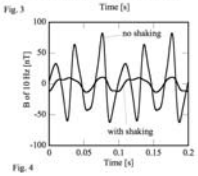
Fig. 4

EN-15

Analysis of perforated magnetic shields.

P. Sergeant[1], R. Sabariego[2], G. Crevecoeur[1], C. Geuzaine[2], L. Dupre[1]
1. Department of Electrical Energy, Systems and Automation, Ghent university, Gent, Belgium;
2. Department of Electrical Engineering and Computer Science, University of Liege, Liege, Belgium

This paper studies the effect on shielding performance of perforations in magnetic shields as a function of frequency, number of gaps, and dimensions of the gaps. The source is an axisymmetric induction heating device. The shield is an axisymmetric ring with 0.3 m radius and n perforations aligned in axial direction, repeated periodically along the circumference. The gap diameter is d. The considered geometry requires a 3D finite element model (FEM): a 2D approach such as in [1] is not possible. To optimize 3D shielding configurations without the computational burden of iteratively evaluating a 3D FEM, we use the aggressive space mapping (ASM) technique [2] that combines two models: a 3D time-harmonic finite element model where the shield is represented by a thin shell formulation [3], and a 2D axisymmetric FEM where the perforations are approximated by “axisymmetric air gaps” resulting in a segmented shield.

In Fig. 1, the two models are compared with each other and with measurements for an axisymmetric geometry (shield not perforated: 2D and 3D geometry are identical) at three frequencies: 100 Hz where the penetration depth is larger than the shield thickness, 10 kHz where the penetration depth is smaller than the thickness, and 1 kHz. The figure shows that both models correspond well with each other and with the measurements.

For several numbers of holes n with constant diameter d of 10 mm, Fig. 2 shows the shielding factor s(r) - defined as the induction in a point divided by the induction in the same point without shields - for a frequency of 100 Hz. If there are no perforations, the 2D and the 3D model yield similar results (3D model predicts a 2.5 percent lower shielding factor on average).

In case of perforations, the 2D model is not able to predict the shielding factor well: the predicted shielding efficiency is underestimated because the circumferential air gaps in the 2D model act as flux barriers that are not present in the 3D model. In order to be able to use the 2D model for perforated shields, the circumferential air gap should be smaller than d. Better correspondence between 2D and 3D model is achieved by introducing in the 2D model an equivalent air gap, obtained from reluctance considerations. Fig. 2 shows for 12 holes that the modified 2D model behaves similar to the 3D model.

A numerical optimization is carried out with the following objectives: good shielding factor and minimal shield volume. The parameters to optimize are n and d. The ASM technique optimizes the shield in a more accurate way than the modified 2D model. The difference with the ASM version explained in [2] is that the parameter extraction is not based on function values but on gradients. Although for constant n the optimum of the 2D FEM for d differs from the optimum of the 3D FEM, the ASM finds the optimal solution after 4 evaluations of the 3D and 55 evaluations of the 2D model, compared to 12 3D optimizations using a gradient algorithm (GA). As the evaluation of the 2D FEM is approximately 10 times faster than an evaluation of the 3D FEM, it is clear that space mapping is faster. It was observed that the lowest objective value can be obtained both for a few big holes and for many small holes, all having the same total surface of the holes.

[1] A. Hahn, A. Kost, L. Janicke, and K. Miethner, Fields and shielding by eddy currents in perforated boxes, International Journal of Applied Electromagnetics and Mechanics, Vol. 17, pp. 31-43, 2003.

[2] J.W. Bandler, Q.S.S. Cheng, S.A. Dakroury, A.S. Mohamed, M.H. Bakr, K. Madsen, and J. Sondergaard, Space mapping: The state of the art, IEEE Trans. Microwave Theory and Techniques, Vol. 52, No. 1, pp. 337-361, Jan. 2004.

[3] C. Geuzaine, P. Dular, and W. Legros, Dual formulations for the modeling of thin electromagnetic shells using edge elements, IEEE Trans. Magn., Vol. 36, No. 4, pp. 799-803, Jul. 2000.

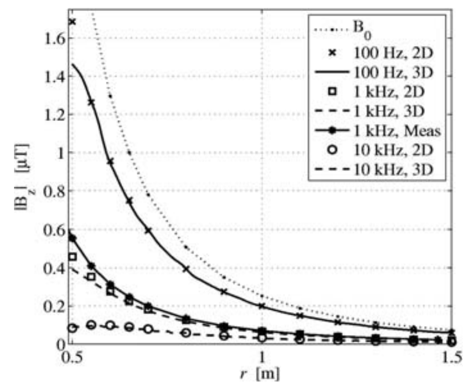

Induction norm in the z=0 plane as a function of the position r for f= 100 Hz - 1 kHz - 10 kHz, obtained by 2D FEM, by 3D FEM and by measurements for an unperforated shield (radius 0.3 m, height 0.19 m) or no shield (B0)

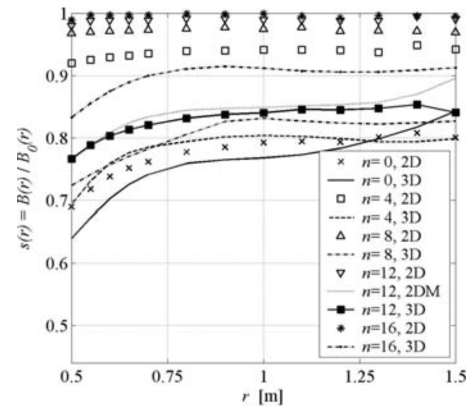

For 100 Hz, shielding factor in the z=0 plane for a shield (0.3 m radius, 0.19 m height) with several numbers of holes n with diameter 0.01 m as a function of the position r, obtained by the 2D FEM, by the modified 2D FEM with equivalent air gap (2DM) and by the 3D FEM

EN-16

Optimal Design and Analysis of Faraday Shield Used in High Frequency Coaxial Transformer.

X. Yang[1], *J. Lu*[2]

1. Province-Ministry Joint Key Laboratory of Electromagnetic Field and Electrical Apparatus Reliability, Hebei University of Technology, Tianjin, China; 2. School of Eng., Griffith University, Brisbane, QLD, Australia

Abstract— A numerical simulation and optimal design of a high frequency coaxial transformer (HFCT) employing a Faraday shield is presented. The magnetic flux and eddy current distributions for different winding configurations under both open circuit and short circuit conditions are discussed. The shield thickness should be less than two skin depths and the shield should be positioned approximately midway between the primary and secondary windings. The intra and inter capacitances of a HFCT with and without a shield were also numerically analyzed. The calculated coupling capacitance between the primary and secondary windings of the HFCT are in good agreement with the experimental results.

Index Terms—High Frequency Coaxial Transformer, Faraday Shield, Eddy current, Coupling capacitance

I. INTRODUCTION

Practical transformers have leakage inductances, intra-winding capacitances and an inter-winding capacitance between the primary and secondary windings. High frequency coupling noise between the primary and secondary windings can cause serious common mode noise problems. These parasitics can not be neglected if the operating frequencies are above 100 kHz. The problem of coupling noise is commonly addressed by introducing a Faraday shield between the primary and secondary windings. The purpose of this paper is to investigate the effects of a Faraday shield on the coupling capacitance, magnetic flux and eddy current distribution for a HFCT. The investigation considers the impact of different shield locations, shield thicknesses, and coil configurations on the total winding losses.

II. NUMERICAL ANALYSIS OF EDDY CURRENT LOSSES

Figure 1 shows the structure of the HFCT. The primary and secondary windings, and Faraday shield are threaded through four identical magnetic cores. Six turn coils are used for both the inner and outer windings with a 30 degree phase shaft between the inner and outer circumferential layers. Each coil is comprised of litz wire with 7 strands. The wires in each circumferential layer are placed in an equidistant fashion with respect to each other. Consequently, the current distribution in each winding exhibits symmetry and hence the total current in each winding is equivalent (optimal). Moreover, this configuration will minimize the temperature rise since the losses are the same and the distance between the lossy elements is maximized.

The Faraday shield is placed between the outer winding and inner winding. A FEM analysis was employed to calculate the magnetic field distribution. Power loss increases rapidly if the thickness of shield is larger than twice the thickness of the skin depth under both open circuit and short circuit conditions. A total power loss reduction, around 25% in the open circuit case, and 12% in the short circuit case were achieved using an optimized shield position (midway point between the primary and secondary layer).

Figure 2 (a) and (b) show the distributions of magnetic flux and current density in the HFCT with and without a Faraday shield under open circuit conditions with the outer winding representing the primary side. Comparing Fig. 2 (a) with (b), we can see that the power loss of the shield can be neglected and the magnetic flux distribution is not affected by the shield.

III. CAPACITANCE CALCULATION AND MEASUREMENT

A FEM electrostatic analysis and the theory of capacitances for multi-conductor systems are used to determine the inter and intra winding capacitances; Cps=19.96pF between the primary and secondary windings, Cp=7.67pF between primary winding and ground and Cs =3.55pF across the secondary winding. The following results are obtained with a grounded shield: Cps=0.08pF, while Cp=24.67pF and Cs=22.50pF. Measurements are in agreement with the calculations.

IV. CONCLUSION

The thickness of the Faraday shield should be less than twice the skin depth thickness, and its position should be approximately midway between the two windings but closer to the secondary winding in order to minimize the power loss. The optimized shield position leads to a reduction in the total power loss in the windings by approximately 25% for the open circuit case and 12% for the short circuit case. The outer winding should preferably be the primary winding due to the lower power loss. The inter-winding capacitance for a grounded optimized shield is reduced by a factor of 250.

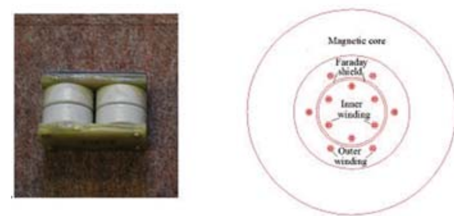

Fig. 1. Side views (left) and half of the cross-section (right) of the HFCT.

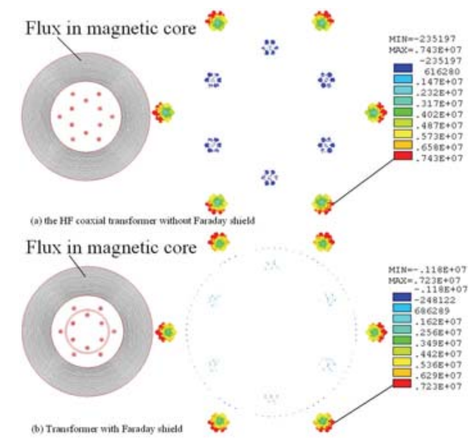

Fig. 2 Flux distribution (left) and current distribution (right) of the HF coaxial transformer without Faraday shield at an operating frequency of 300 kHz.

EN-17

Electromagnetic wave absorption properties of double layers absorbers made of hollow glass microspheres electroless plated with FeCoNiB and NiCoZn ferrites.

M. Han, F. Xiao, Y. Ou
State Key Laboratory of Electronic Thin Films and Integrated Devices, University of Electronic Science and Technology of China, Chengdu, China

With the advancement of electronic technologies, electromagnetic (EM) pollution has become a serious problem, and the demands to develop thinner, lighter, stronger EM wave absorbers with wider absorption bands are ever increasing[1, 2]. The commonly used absorber are the spinel ferrite and hexagonal ferrite, and some other absorbers, for instance, metal powders, microwires and nanotubes. However, both of them have a severe shortcoming: heavy weight. To overcome this problem, coating some low density materials with magnetic materials are suggested. In this contribution, light EM absorbers have been designed adopting a double-layers structure which are composed of a layer of $(Ni_{0.4}Co_{0.24}Zn_{0.36})Fe_2O_4$ ferrite and a layer of glass microspheres (low density) plated with FeCoNiB by an electroless chemical deposition technique.The NiCoZn ferrites were prepared by a traditional ceramic sintering route. XRD was employed to show that the FeCoSiB films coated on the hollow microspheres were in the amorphous state and the NiCoZn ferrites were in spinel structure. The microwave permittivity and permeability properties have been measured within the frequency range of 1 GHz – 18 GHz.

The uncoated the glass microspheres are shown in Fig. 1(a). The hollow structure of glass balls is also clearly indicated in Fig. 1(a). The coated glass microspheres are shown in Fig. 1(b). Magnetic hysteresis loop of coated glass microspheres is shown in Fig. 1(c), the coercivity of FeCoNiB is about 330 Oe. The low saturation magnetization (4.6 emu/g) is due to the hollow structure, where the magnetic layer only accounts a small fraction of total weight.

If the absorbers are attached on a conducting metal plate, then the EM wave absorbing performance of a double-layers absorber, which is generally evaluated by the reflection loss (RL) in dB, can be calculated based on the following equations [3, 4]:

$$Z_{in(2)}=[Z_2(Z_{in(1)}+Z_2\tanh(j(2\pi ft/c)(\mu_{2r}\varepsilon_{2r})^{1/2}))]/[Z_2+Z_{in(1)}\tanh(j(2\pi ft/c)(\mu_{2r}\varepsilon_{2r})^{1/2})] \text{ ---(1)}$$

$$Z_{in(1)}=(\mu_{1r}/\varepsilon_{1r})^{1/2}\tanh(j(2\pi ft/c)(\mu_{1r}\varepsilon_{1r})^{1/2}) \text{ --- (2)}$$

$$RL=20\log|(Z_{in(2)}-Z_0)/(Z_{in(2)}+Z_0)| \text{ ---(3)}$$

Where Z_0 is the impedance of free space,$Z_2 = (\mu_{2r}/\varepsilon_{2r})^{1/2}$, $Z_{in(1)}$ is the interface impedance between the bottom layer and the upper layer, $Z_{in(2)}$ is the interface impedance between the free space and the upper layer, t is the thickness of an absorber. If we suppose that an absorber is only made of glass microspheres/paraffin composite((weight ratio = 1: 2), and its thickness is 16 mm, then its EM wave absorption performance can be evaluated, as shown in Fig. 1(d). If the absorber is only made of NiCoZn ferrite/paraffin composite(weight ratio = 1: 2), its EM wave absorption performances are shown in Fig. 2(b) for two thicknesses (0.8 mm, 4.3 mm). Clearly, when only ferrites are used for absorbers, the absorption performance is bad. However, if we fabricate the absorbers with plated glass microspheres and NiCoZn ferrites by choosing a double-layers structure, the EM wave absorption properties can be enhanced significantly, as shown in Fig. 2(c) and (d). In Fig. 2(c), the t of hollow glass microspheres (bottom layer) and the ferrites (upper layer) are 2.2 mm and 4.3 mm respectively. In Fig. 2(d), the t of hollow glass microspheres (upper layer) and the ferrites (bottom layer) are 2.5 mm and 0.8 mm respectively. Especially, in Fig. 2(d), since the density of hollow glass microspheres are much lower than those of ferrites. Therefore, with the double-layer absorber structure, the total weight of absorbers can be greatly reduced, and this is very important for some application, such as aircraft.

[1] M. R. Meshram, N. K. Agrawal, B. Sinha, P. S. Misra, J. Magn. Magn. Mater. 271 (2004) 207.

[2] S. Sugimoto, S. Kondo, K. Okayama, D. Book, T. Kagotani, M. Homma, IEEE Trans. Magn. 35 (1999) 3154.

[3] J. Xie, M. Han, L. Chen, R. Kuang, L. Deng, J. Magn. Magn. Mater. 314 (2007) 37.

[4] Y. Naito, K. Suetake, IEEE Trans. Microwave Theory Tech. 19 (1971) 65.

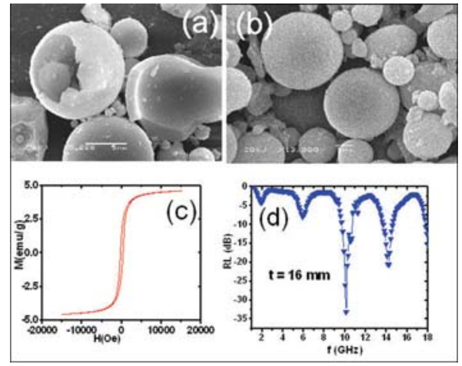

Fig. 1. (a) Uncoated hollow glass microspheres; (b) coated microsphere with FeCoSiB; (c) M-H loops of FeCoSiB plated; (d) reflection loss of single layer of plated glass microspheres-paraffin composites.

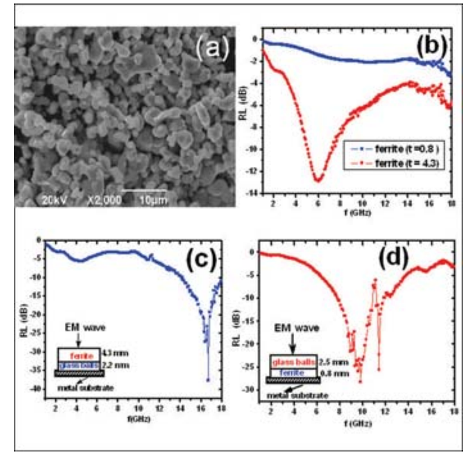

Fig. 2 (a) the morphology of NiCoZn ferrites; (b) the microwave absorption properties of single layer of NiCoZn ferrites; the microwave absorption properties of double-layers absorbers in (c) and (d).

EN-18

Open-type Magnetic Shield Structure and its Performance.

M. Fujikura[1], K. Segawa[1], K. Chikuma[1], K. Fujisaki[1], J. Mino[2], T. Morita[2], T. Saito[3], H. Hirano[3], T. Shinnoh[3]
1. Nippon Steel corporation, Chiba, Japan; 2. Nippon Steel Engineering Co., LTD., Tokyo, Japan; 3. Kajima Corporation, Tokyo, Japan

To obtain the degree of freedom in designing the magnetic shield room, we propose a new type of magnetic shielding structure named “open-type” [1]. Here, magnetic shielding performance of open-type is compared with that of conventional “closed-type”.
Example of proposed open-type shield structure is shown in Fig.1. The unit magnetic paths are placed with some openings and surround the needed spaces. The path consists of magnetic strips that are overlapping with their terminal edge in the direction of sheet thickness.
Top view of the magnetic path of open-type shield is illustrated in Fig.2 (A). The grain-oriented electrical steels (GO) were used to form the path. Thickness, width and length of GO are 0.35mm, 30mm and 300mm respectively. The rolling direction of GO is parallel to magnetic path directions. In case of closed-type shield, since the magnetic sheets are parallel to the wall, the equivalent magnetic path is considered to be Fig.2 (B). And flux leakage at the corner usually becomes problem in closed-type shield, we also consider the revised closed-type, which is shown as Fig.2 (C). Fig.3 shows the DC magnetization curve of the three types of magnetic path. The open-type magnetic path (A) has higher magnetic permeability than the closed-type (B), (C) have. It is considered that difference in the contact of the sheets in the paths affect the permeability. So, the Open-type shield is considered to have an ability of high-level shield performance.
How to suppress the flux leakage from the opening part is an important problem for the open-type shield. Since the width of magnetic material strip W and opening space between strips d are thought to affect the shield performance, the performance of the structure shown in Fig.1 was measured with changing W and d. The weight of GO materials is constant in this measurement. Using Hermhorz coil, which size is 2000mm square, forms the uniform field, frequency of 50Hz and peak of 100mT. The performance of the closed-type shield, which consists of 4 L-shape sheets of GO; 900mm width, 600mm length, bended in the center at the longitudinal direction, was also measured. Fig.4 shows the average leakage flux at the center part in the shield body as a function of opening size factor d/W. The leakage of the open-type shield decreases with decreasing d/W, and reaches 4mT at d/W of below 1. It is half of the case of closed-type that is 8mT. The open-type shield structures have good shield performance if the d/W is selected appropriately.

Acknowledgments
Kajima Corporation invented the Open-type magnetic shield structure. This work was carried out in the collaboration study between Kajima Corporation and Nippon Steel Corporation.

[1] T. Saito: JP 2002-164686A (2002)

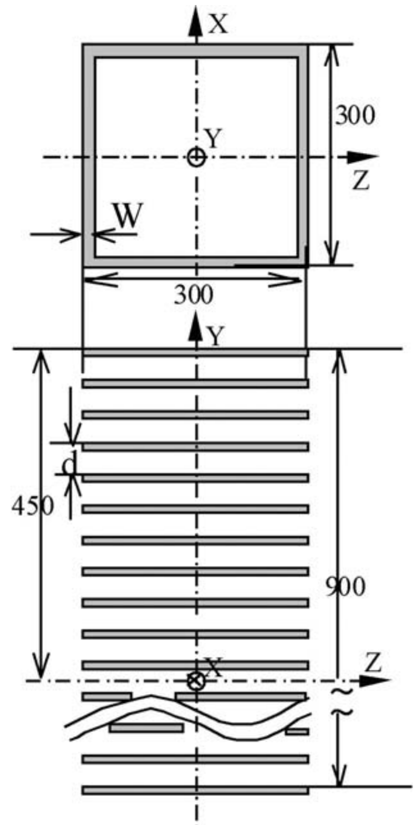

Fig.1 Open-type magnetic shield structure.

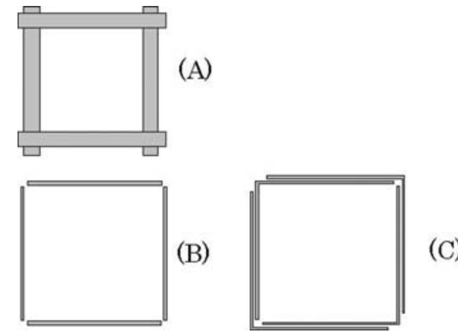

Fig.2 Top view of magnetic paths consist of 4 pieces of GO. (A) Open-type (proposed) (B) Closed-type (conventional) (C) Closed-type (revised)

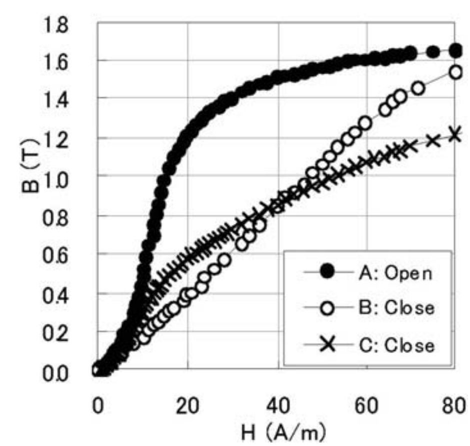

Fig.3 DC magnetization curves of magnetic paths for each shielding structures illustrated in Fig.2.

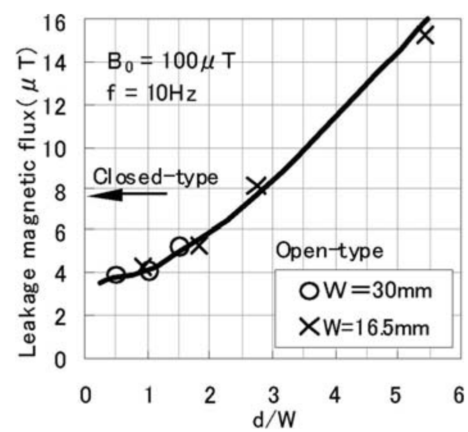

Fig.4 Effect of size factor d/W on the magnetic flux leakage in open-type shield.

EN-19

The Estimation on the shield capability of the Magnetic Shielding Room depending on the setting direction of GO based on the analysis with Homogenization Method for Thin Steel Plate.

Y. Tomizawa[1], *K. Fujisaki*[2,3], M. Fujikura[2], J. Mino[4], S. Tamaki[5], T. Morita[6]
1. Industrial Plant Engineering, Taiheikogyo Co.,Ltd, Toukai, Japan; 2. Technical Development Bureau, Nippon Steel Corp., Futtsu, Japan; 3. Graduate School of Environmental Studies, Tohoku University, Sendai, Japan; 4. Building Construction & Steel Structures, Nippon Steel Engineering Co.,Ltd, Chiyoda, Japan; 5. Nagoya Works, Nippon Steel Corp., Toukai, Japan; 6. NS Construction, Chiyoda, Japan

Introduction

In recent years, the studies to make good use of the electromagnetic steel are being developed.[1,2] And one of its utilization for the MAGNETIC SHIELD has just started, which can reduce the level of low frequency magnetic noise (leak magnetic flux) released from large power equipments, such as trains, power transmission wires (cables), transformer substations, etc. The above shield has to be installed to decrease the level of the magnetic noise in order to prevent the electronic devices and the precision instruments from various kinds of error caused by the magnetic noise. In particular, almost all the hospitals are required to install MRI in a magnetic shielding room because MRI, large power equipment, is usually set up near some precision instruments in such place.

It would be important to design shield structures, considering not only to apply GO (Grain Oriented steel sheet), which has superior magnetic characteristic, but also to make sure the setting direction of GO with the easily magnetized axis against the direction of the magnetic flux to be shielded, in order to improve the shield capability of the mentioned room.

It is suggested in this paper that the setting direction of GO affects the shield capability of a magnetic shielding room based on the estimation with the electromagnetic field analysis, using homogenization method for thin steel plate (so called Equivalent BH method).[3]

Construction of the magnetic shielding room with GO

The analysis model is shown in Fig.1 as a bird's-eye view. Assuming the actual location, MRI, regarded as a direct current coil (DC-coil), is placed close to D-wall, where the operation of MRI is done, and to F-wall, floor side. The magnetic shielding room is composed of the side-walls of GO, laid out like grids and of the top/bottom walls of laminated GO. As the all side-walls have the see-through structures in the mentioned room, which is invented by Kajima Corporation [4], it can reduce the mental pressure of the patients. In addition to it, this shielding room has such an advantage that there is no construction work to keep some gaps from the top/bottom walls to the ceilings and the floors because the top/bottom walls are completely flat.

In the case of the conventional design for shielding rooms, laminated GO is usually laid out regardless of the direction of the magnetic flux. This design, which lay out GO to cross the easily magnetized axis of GO each other like the top/bottom walls shown in Fig.1(a), aims at giving the equal shield capability to all walls of them.

However, it is proposed by the writers to lay out GO with easily magnetized axis, agreeing with the same direction of the released magnetic flux from MRI(DC-coil), in order to improve the shield capability of the room. Because MRI(DC-coil) always releases the magnetic flux with the fixed direction, which goes from MRI to D-wall at first, and next goes to A/C-walls and R/F-walls separately, and finally gets together to pass through B-wall. Then the indicated model shown in Fig.1(b) is proposed, which consists of GO with the easily magnetized axis laid out to agree with the same direction of the magnetic flux. And the shield capability of GO with the given model is estimated with Equivalent BH method.

Estimation result with Equivalent BH method

The distribution of the leak magnetic flux density at a height of DC-coil center in each wall is shown in Fig.2, using the electromagnetic field analysis with Equivalent BH method. According to the above result, the shield capability of the proposal model at A/C-walls is better than the conventional one although the shield capability of both models at B/D-walls is almost same.

It indicates that laying out GO with easily magnetized axis, agreeing with the same direction of the magnetic flux, improves the shield capability of such rooms as the shown proposal model.

When a magnetic shielding room is designed, it is definitely necessary to lay out GO based on the direction of easily magnetized axis of it and of the magnetic flux.

[1] K.Fujisaki, R.Hirayama, Y.Nemoto, "Electromagnetic Steel Solution in Electromagnetic Field", NIPPON STEEL TECHNICAL REPORT No.89, pp.80-84, (2004).

[2] T.Kubota, M.Fujikura, M.Mizokami,Y.Ushigami, "Electrical Steel Sheet for Eco-Design of Electrical Equipment", NIPPON STEEL TECHNICAL REPORT No.81, pp.53-57, (2000).

[3] K.Fujisaki, M.Fujikura, J.Mino, S.Satou, "3-dimensional Magnetic Field Analysis by Homogenization Method for Thin Steel Plate", Submitting to IEE Japan Transactions.

[4] T. Saito: JP2002-164686A(2002).

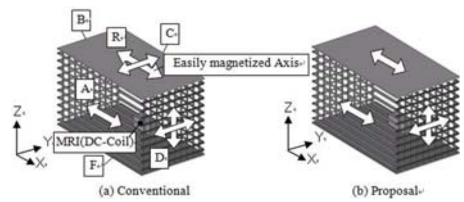

Fig.1 A bird's-eye view of analysis model.

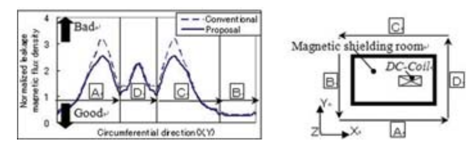

Fig.2 Normalized leak magnetic flux density of circumferential direction.

EN-20

Open-Type Magnetically Shielded Room Combined with Square Cylinders made of Magnetic and Conductive Materials for MRI.

K. Yamazaki[1], S. Hirosato[1], K. Kamata[2], K. Muramatsu[3], K. Kobayashi[4], A. Haga[5]
1. Takenaka Corp., Chiba, Japan; 2. Kagoshima National College of Technology, Kagoshima, Japan; 3. Saga University, Saga, Japan; 4. Iwate University, Iwate, Japan; 5. Tohoku-Gakuin University, Miyagi, Japan

Introduction

In order to reduce the leakage flux density to less than 0.5 mT outside the room and shield an electro-magnetic field at high-frequency for operating, an magnetic resonance imaging (MRI) scanner is usually installed in a magnetically shielded room (MSR) surrounded by a wall with magnetic and conductive layers. The small space enclosed by the wall causes patients a great deal of stress and discomfort because they are isolated from the operators and from the scenery outside. In order to improve amenity for patients in hospitals, open type MSRs for MRI, which use magnetic bars [1], canceling coils [2] instead of magnetic walls, and double-layered electro-magnetic shielded glasses instead of conductive walls, have been developed. However, these MSRs can't provide a sufficiently open feeling because of the lack of transparency and optical moiré pattern of the glass. Moreover, the electro-magnetic shielded glasses are expensive compared with magnetic and conductive walls. We have therefore developed a new open-type MSR using a combination of a square cylinder (147 x 147, t=1 mm) made of a magnetic material, silicon steel, placed inside a second square cylinder (150 x 150, t=3 mm) made of a conductive material, aluminum. The cylinders are piled up instead of a wall in order to provide open feeling. The conductive cylinder prevents the deterioration of magnetic property of magnetic cylinder due to stress. The cylinders piled up have also the effect of electro-magnetic shield by the electrical contact between square cylinders of aluminum. Therefore, the number of panes of shielded glass can be diminished and it improves the open feeling for the patient. In this paper, the optimal design of an open-type MSR for MRI combining square cylinders made of magnetic and conductive materials is discussed using 3-D magnetic field analysis and experimentally using a small model.

Method of Analysis and Measurement

First, from the standpoints of the leakage flux density (LFD) outside MSR, the optimal design of square cylinders made of magnetic materials is discussed using 3-D magnetic field analysis with a simple cubic MSR shown in Figure 1. LFDs along line O-P varying with the length and number of division of cylinders and width of the gap between cylinders were calculated. The relative permeability of silicon steel was assumed to be 3,000 and the current of the MRI magnet model is 87,500 AT. Next, the validity of the analysis and the practical realization of the designed MSR were investigated using a small experimental model shown in Figure 2. Sixty units composed of square cylinders of aluminum (t=3 mm) and silicon steel (t=1 mm) were accumulated on the opening of the model MSR. The relative permeability of the silicon steel of the cylinder and wall, and of the aluminum were assumed to be 1000 and 1, respectively. The current of each of the four circular coils as the MRI model is 1,485 AT. The contour of LFDs at a surface 100 mm away (A) from the opening obtained from calculation and experiment were compared and the effect of the division of cylinders was confirmed. Finally, the electro-magnetic shielding effect at frequencies from 60 to 180 MHz of models of some combinations of electro-magnetic shielded glass and square cylinders (300 mm, 450 mm of length) made of aluminum was measured using horizontal biconical antennas in an experimental electro-magnetic shielded room.

Results

Figures 2 and 3 show the LFD dependency on the length (l) of the cylinders and the width of gap. The optimal length is l= 300 mm which is around two times width, because the LFD for l=300 mm is smaller than those of l=50 and 100 mm, and almost the same as those of l=450 mm and 600 mm shown in Figure 2. The effect of the increase of gap between magnetic layers due to conductive layers on the LFD can be neglected because there is small difference between the LFD of gap=6 mm and 1 mm shown in Figure 3. Figure 5 shows the comparison of the distribution of LFDs obtained from calculation and from measurement at surface A using small model as shown in Figure 4. The figure shows that the tendency of the calculation is in good agreement with the measurement. In both measurement and calculation, the LFD of a cylinder divided into three parts by gaps of 30 mm is lower than that of a cylinder without gaps. This is because the flux reaching outer cylinder is reduced due to the gaps. On the other hand, the measured shielding effects of the combination of single electro-magnetic shielded glass and the square cylinder of aluminum, 300 mm of length, were higher than 100 dB at frequencies from 60 to 180 MHz, so that the MRIs could be operating (Figure is omitted). Consequently, as the optimal design of open-type MSR for MRI, we have developed the combination of single-layered electro-magnetic shielded glass together with a unit composed of cylinders, 150 mm x 150 mm and 300mm long, with aluminum (t=3 mm) outside and silicon plate (t=1 mm) divided into three parts inside.

[1] T. Saito, *Abstract of INTERMAG 2003 Conference*, CR-03 (2003).

[2] K. Yamazaki at al., *IEEE Tran. Magn.*, **43**, **6**, 2480 (2007).

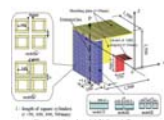

Fig. 1. Analyzed model (1/8 model)

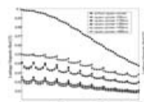

Fig. 2. Distribution of leakage flux density depending on the length of the square cylinder.

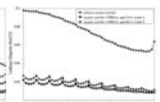

Fig. 3. Distribution of leakage flux density depending on the gap between square cylinders.

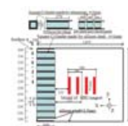

Fig. 4. Experimental small model of MSR and MRI magnet

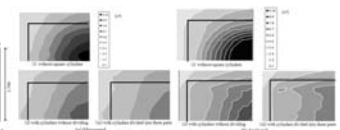

Fig. 5. Contour of leakage flux density of surface A in the experimental model.

EN-21

Shield Duct to Prevent Magnetic Field Leakage through Openings in Double-layered Magnetically Shielded Rooms.

K. Yamazaki[1], Y. Hatsukade[2], S. Tanaka[2], A. Haga[3]
1. Takenaka Corp., Chiba, Japan; 2. Toyohashi University of Technology, Toyohashi, Japan; 3. Tohoku-Gakuin University, Miyagi, Japan

Introduction

Magnetically-shielded rooms (MSR) made of multi-layered ferromagnetic materials such as μ-metal are used for electron beam lithography systems (EBLS) and biomagnetic measurements [1] [2]. However, a number of openings must be provided in the walls, ceiling and floor of such rooms for air conditioning and cables [3]. In the case of EBLS, especially, large sized openings (such as 500 mm x 500 mm^2) are required as the number of air changes increases depending on highly specific requirements for cleanliness, temperature and relative humidity. On the other hand, for biomagnetic measurements, large openings for windows and transparent doors are required to communicate with the outside and to provide comfortable atmosphere for subjects and patients. Usually, short shield ducts are attached around the openings to prevent leakage of magnetic flux through the openings [4]. This paper reports an optimal structure of short shield ducts to prevent the leakage of magnetic flux through the openings of a double-layered MSR, as investigated experimentally using a small model of an MSR and 3-D magnetic field analysis with the finite element method (FEM).

Model and Method of Measurement and Analysis

Figure 1 shows a one-tenth scale model (Magnetically Shielded Box: MSB) of a double-layered MSR with ducts connected to its inner and outer layers, investigated by experiment and analysis in this study. The thickness of the magnetic wall is 1 mm and the openings are 60 mm x 60 mm^2 on the inner layer and 70 mm x 70 mm^2 on the outer layer. Almost uniform magnetic noise, ΔB_o, of 8 μT at 0.1 Hz was applied to the MSB in the vertical direction to the opening by three-layered large sized coils. Leakage magnetic field ΔB_i ($\sqrt{\Delta Bx^2+\Delta By^2+\Delta Bz^2}$) at the point P, 60 mm (the same length as the width of the inner layer opening) from the opening in the MSB, was measured by a fluxgate magnetometer with short shield ducts (SSDs) which lengths were half, same, twice and three times as long as the width of the opening, attached to the inner and outer layer, respectively. Dividing ΔB_i by ΔB_o, the normalized leakage flux ratios (LFR=ΔB_i /ΔB_o) under numerous conditions, depending on the SSDs attached around the openings, were obtained. The optimal combinations of lengths of the attached SSDs with inner (L_{in}/D_{in}) and outer (L_{out}/D_{out}) openings were investigated. Next, the distributions of the magnetic fields inside the MSB were evaluated by 3-D FEM with the finite element method, which employed the magnetic vector potential when ΔB_o was 8 μT and the relative permeability of μ-metal was 12,000. LFRs at point P obtained by the FEM were compared with those from the experiment. The distributions of magnetic vectors inside and outside the opening were analyzed to clarify the optimal combination of ducts attached around the inner and outer opening.

Results

Figure 2 shows the measured relationships between L_{in}/D_{in}, L_{out}/D_{out} and LFR. The minimum and optimal combinations of L_{in}/D_{in} and L_{out}/D_{out} for LFR were 0.5 and 1.0. SSDs with inner and outer layers should not be overlapped, and the L_{out}/D_{out} should not be larger than 1. This tendency of the leakage flux ratios, LFRs shown in Figure 1 was almost in agreement with that obtained from 3-D FEM (figure omitted), verifying the validity of the analysis method. Figure 3 shows the analyzed distributions of magnetic flux inside and outside the opening. As shown in (b), the duct attached to the inner layer was saturated by magnetic flux from the duct with the outer layer at the overlapping space A, so that the duct at the inner layer could not absorb magnetic flux inside the duct to reduce leakage of the magnetic field through the opening. As shown in (c), extending the duct with an outer layer larger than twice L_{out}/D_{out} resulted in absorbing too much magnetic flux not only from inside, but also from the outside, so that magnetic flux inside the duct could not be reduced except near opening B. Near point C, magnetic flux was exhausted into inside from the duct attached to the outer layer. Therefore, an optimal combination of short shield ducts with inner and outer layers to prevent the leakage of magnetic flux through the openings of a double layered MSR is to not overlap ducts and to make the length of the duct attached to the outer layer no larger than the width of the opening (shown in (a)). Our manuscript discusses the optimal structure on a lattice made of magnetic materials installed at the opening.

[1] K. Yamazaki et al., *IEEE Tran. Magn.*, **36, 5**, 3649 (2000).

[2] J. Bork et.al., *Proc. of Biomag2000*, **919**, 1856 (2002).

[3] A. Mager, *Naturwissenshaften*, **69**, 383-388 (1982).

[4] M. Takahashi et al., *OYO BUTURI*, **52, 1**, 59 (1983) (in Japanese).

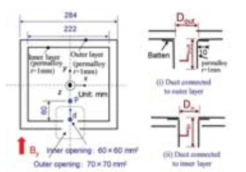

(a) Overview of magnetic shielded box. (b) Structure of short shield duct connected to the opening

Fig. 1 Magnetic shielded Box at one-tenth scale model of a double layered cubic magnetically shielded room.

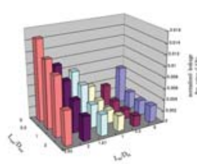

Fig. 2 Relationship between shielded duct, L_{in}/D_{in}, L_{out}/D_{out} and normalized leakage of magnetic field from the opening, LFR (measured).

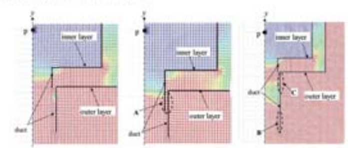

(a) L_{in}/D_{in}=0.5, L_{out}/D_{out} =1 (b) L_{in}/D_{in}=1, L_{out}/D_{out} =1 (c) L_{in}/D_{in}=0.5, L_{out}/D_{out} =2

Fig. 3 Analyzed distributions of magnetic flux inside and outside the opening .

Features of a Wall with Open-type Magnetic Shield.

T. Saito
Kajima Corporation, Tokyo, Japan

It has been commonly believed over 100 years that magnetic materials should be arranged without any space between them to achieve a sufficient magnetic shielding effect [1]. However, it was newly found that the aligned strips with gaps could achieve almost the same effect of magnetic shielding as conventional method which is complete plate without any gap [2]. Furthermore, sufficient magnetic shielding effect can be achieved with sizable gaps. Here this study reports the features of a wall with this "open-type" magnetic shield by some experiments about interval between strips, layers and rotation of strips.

1. Open-type magnetic shield

Fig. 1(a) illustrates the case in which the magnetic field/flux is generated by electric current and a plate like magnetic shielding material. To shield magnetic field for reducing the leakage to the front, we have generally put a plate like high permeability material, because magnetic flux go into it and make detour [3]. In contrast to this conventional method, open-type magnetic shielding method aligns strips like high permeability material with gaps as shown in Fig. 1(b). It can be air or vacuum in the gaps. The advantage that light and air can pass through this magnetic shielding wall will create wide range of applications.

2. Experimental System

Fig. 2 indicates the part of experimental system which is simply composed of two electric wires and magnetic strips. In fact, this part consecutively repeated to 15m in length. The two electric wires carry +50A and -50A direct currents. Magnetic shielding material was made of grain-oriented electrical steel sheet with 0.35mm in thickness. All strips for open-type magnetic shielding method are 900mm×20mm in size. The rolling direction of the electrical steel sheets/strips is vertical to the ground. The height of two wires and measuring points are same as those of the center of sheets/strips.

3. Features of wall with open-type magnetic shield

Fig. 3 shows the experimental result about the leakage of magnetic field when the gaps between strips are changed. It tells us the magnetic shielding efficiency with open type method of 25mm gap is not so worse in comparison with conventional method in the area more than 600 mm far from electric wire. Fig. 4 represents the effect of layers for each strip. It tells us that double layers for each strip with 50mm gap can achieve almost the same performance as single layer with 25mm gap. Fig. 5 indicates the effect of rotation for each stip. It tells us that almost same shielding performance can be achieved at 0 and 90 degree of rotation on the center axis of each strip.

[1] B. J. Patton: J.Geophys.Res., 67, 1117-1121(1962)

[2] T. Saito: JP 2002-164686A (2002)

[3] T. J. Sumner: J. Phys. D: Appl. Phys., 20, 1095–1101 (1987).

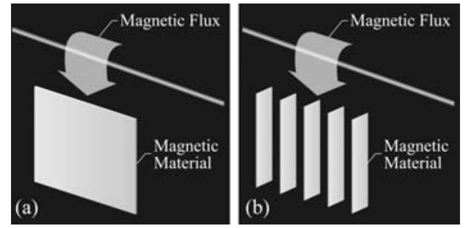

Fig. 1(a) Conventional magnetic shielding method Fig. 1(b) Open-type magnetic shielding method

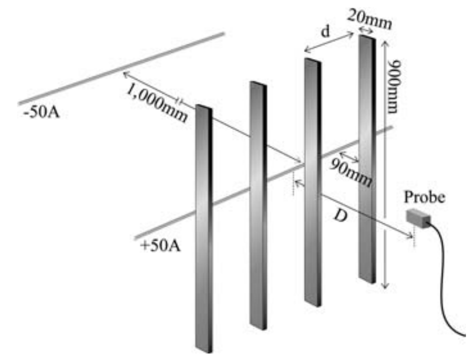

Fig.2 Experimental system

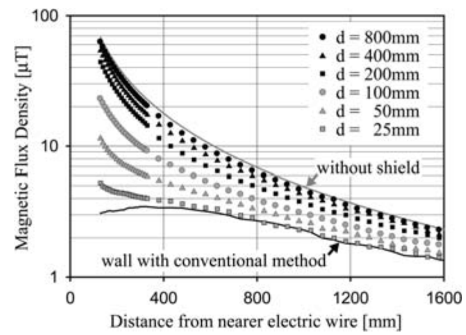

Fig.3 Experimental result about the leakage of magnetic field when the gaps between strips are changed

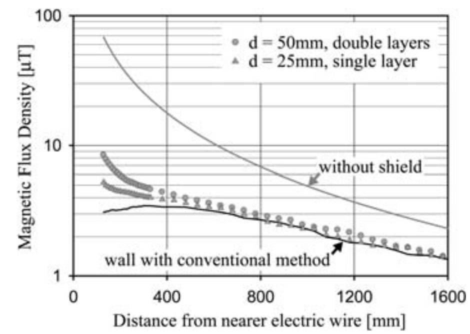

Fig.4 Experimental result about the effect of interval and layers for each strip

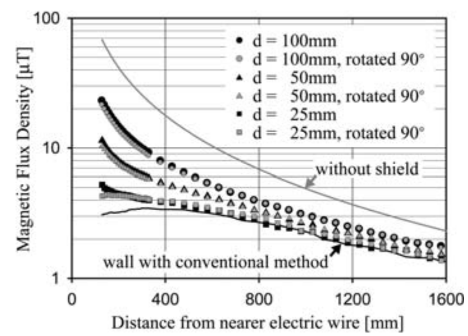

Fig.5 Experimental result about the effect of interval and rotation for each strip

Analysis of the shielding effectiveness of rectangular enclosure of metal structures with apertures.

M. Zhang[1], Z. Zhao[1], C. Gao[1], S. Wang[2]
1. North China Electric Power University, Baoding, China; 2. Northeast Electric Power Design Institute, Changchun, China

1.INTRODUCTION

The problem of electromagnetic field penetration into rectangular enclosures with apertures has received considerable attention in the power system because many relay cells in substations have been built in switchyards in recent years. Modern electronic circuits generally have weak signal levels and are sensitive to various kinds of electromagnetic disturbances. The shielding effectiveness of the relay cell should therefore be analyzed so that the electromagnetic field does not exceed acceptable levels [1].

The interaction between the inner and the outer surfaces of the enclosure which is not easily predictable is modeled by introducing magnetic currents on the apertures. In this paper, the cavity and the apertures are modeled by rectangular surface patches. The roof-top basic functions are used to expand the unknown electric and magnetic currents on the surfaces of the cavity and the apertures.

2. DESCRIPTION OF THE APPROACH

The model consists of a metallic box with a rectangular aperture excited by a source out of the enclosure. The wall of the enclosure is infinite thin screen.

By applying the equivalence principle, the aperture can be metallized. So the original problem can be divided into two simple independent problems. (1) the radiation of the source out of the enclosure; (2) the radiation of the source in the enclosure.

A set of equations can be obtained by means of the continuity of the tangential components of the electromagnetic field at the aperture. The pertinent boundary conditions at the surface of the enclosure can be described using the electric field.

3. VALIDATION

To verify the proposed approaches, electromagnetic shielding effectiveness at the center of a 55cm*55cm*60cm rectangular box with nine 8cm*8cm rectangular apertures located at the front size is measured, as in Fig. 1. The test is carried out in a compact anechoic chamber with three-meter method. The cavity is located on a desk 0.8m high.

The box is excited by a plane wave with normal incidence. Three different cases of the electric field shielding effectiveness at the center of the box are calculated using the above method and measured. In the first case, aperture 5 is open and the other eight apertures are closed. The results are shown in Fig. 2. In the second case, apertures 4, 5 and 6 are open and the other six apertures are closed. The results are shown in Fig. 3. In the last case, apertures 2, 4, 5, 6 and 8 are open and the other four apertures are closed. The results are shown in Fig. 4.

From the above result, we can see that the results calculated with the method presented in this paper are in agreement with the measurement results.

4. CONCLUSION

A rigorous method based on method of moments suitable for estimation of the shielding effectiveness of rectangular enclosures with apertures is presented. The comparison between the calculation results and the measurement results shows that the method is effective.

[1]G. Manara, M. Bandinelli, and A. Monorchio, “Electromagnetic penetration and coupling to wires through apertures of arbitrary shape,” IEEE Trans. On EMC, vol. 40, pp. 391-396, Nov.1998.

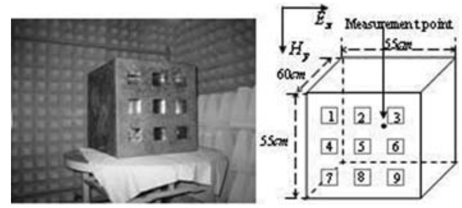

Fig.1 Model of the enclosure

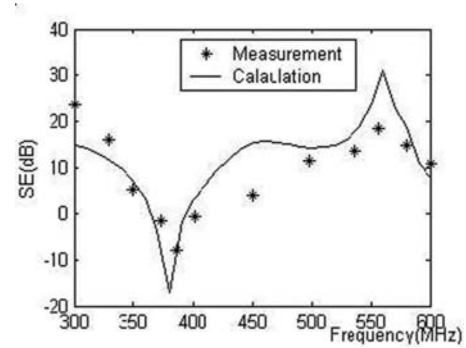

Fig.2. Shielding effectiveness with the aperture 5 opening

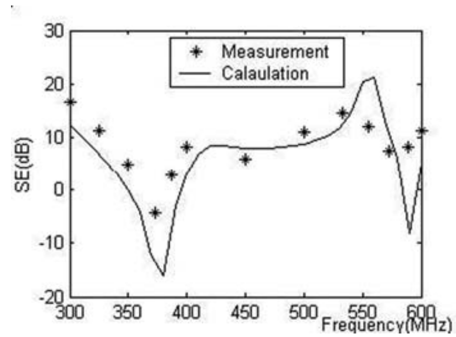

Fig.3. Shielding effectiveness with the aperture 4, 5, 6 opening

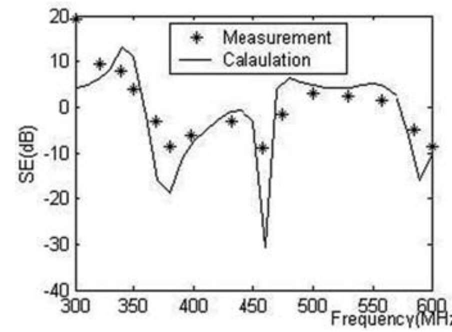

Fig.4. Shielding effectiveness with the aperture 2, 4,5,6,8 opening

Effect of La-substitution on magnetic and ferroelectric properties of $Bi_{(1-x)}La_xDy_{0.3}FeO_3$ system.

P. Kovur, S. P. Duttagupta, V. R. Palkar
Electrical Engineering, Indian Institute of Technology Bombay, Mumbai, India

Multiferroics are the materials having coexistence of magnetic and ferroelectric properties with coupling between two order parameters. These materials therefore find novel applications like multiple memories apart from MEMS sensors and actuators etc. However, there are very few materials which exhibit such properties at room temperature. The perovskite $BiFeO_3$(BFO)belongs to this class of multiferroic materials and has recently emerged as a promising magnetoelectric material. It exhibits antiferromagnetic behavior with a Neel temperature of 380°C and ferroelectric behavior with Tc≈810°C. We were successful in inducing ferromagnetism in this system without disturbing ferroelectric properties by doping with Dy at Bi site($Bi_{0.6}La_{0.1}Dy_{0.3}FeO_3$)[1]. La was used to stabilize the ferroelectric perovskite phase and to reduce leakage current[2]. Now it has been observed that in the presence of Dy, addition of La is not essential for the above purpose. Interestingly, the removal of La not only leads to orders of magnitude enhancement in magnetic properties but also improves the ferroelectric properties. In this paper, we are reporting the multiferroic properties of Dy modified BFO with and without La. Powder samples of $Bi_{0.6}La_{0.1}Dy_{0.3}FeO_3$(DL1)and $Bi_{0.7}Dy_{0.3}FeO_3$(DL0)were synthesized by using a newly developed wet chemicalroute.The reacted samples have been characterized by various techniques(X-ray powder diffraction,neutron diffraction,ferroelectric loop tracer and vibrating sample magnetometer). XRD patterns obtained for DL1 and DL0 samples are shown in Fig.1. *indicates the presence of $Bi_2Fe_4O_9$ and α-Bi_2O_3 as impurity phases. The impurity phases are neither magnetic nor ferroelectric at room temperature, so their presence could at the most reduce overall percentage of ferromagnetic and ferroelectric component from the system. From Fig.2,it is clearly evident that in the presence of Dy, La is not required to control the leakage current. In fact, both magnetic as well as ferroelectric properties improve to a large extent in the absence of La in the system (Fig.3 & Fig.4). The enhancement in properties could be explained on the basis of neutron diffraction results (Table1). Removal of La from the system is found to decrease the lattice cell volume, Fe-Fe and Bi-Fe bond distances also Fe-O-Fe bond angle. The decrease in bond distances and bond angle helps to enhance the magnetic properties as typically one finds in oxide systems with indirect interactions. The scaling up in lattice distortion and cell parameter c with removal of La leads improved ferroelectric properties as reported by Wang et al.[4].

[1]V.R.Palkar,et al.*JMR*,Vol.22, 2068(2007)

[2]D.Lee,et al.*Appl.Phys.Lett.*Vol.86,222903(2005)

[3]Liu X.F.,et al,*J.of Applied Physics*,Vol.99,023904(2006)

[4]Wang J.et al,*Science*,299,1719(2003)

lattice parameter	DL1	DL0
a(Å)	5.539	5.369
c(Å)	13.338	13.431
V(Å)	354.4	335.4
Fe-Fe(Å)	3.895	3.824
Bi-Fe(Å)	3.354	3.145
Fe-O-Fe(θ)	150.5	110

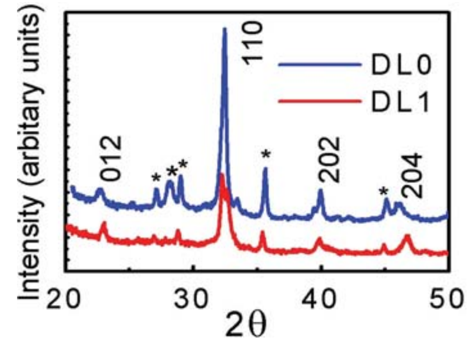

Fig.1 XRD of DL1 & DL0 samples

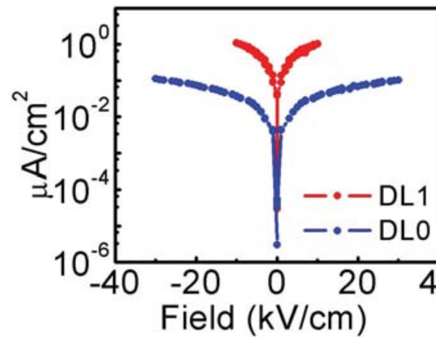

Fig.2 IV plot obtained for DL1 & DL0 samples

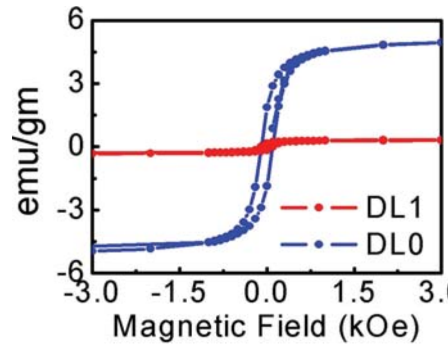

Fig.3 M-H loop for DL1 & DL0 samples

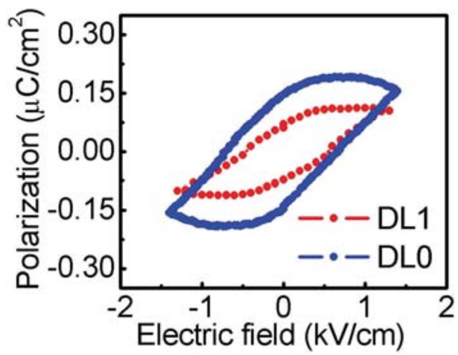

Fig.4 Ferroelectric loop for DL1 & DL0 samples

EO-02

Thermomagnetic characterization of the $CeNi_4Cr$ compound.

T. Tolinski[1], A. Kowalczyk[1], M. Reiffers[2], E. Gazo[2], M. Zapotokova[2], G. Chelkowska[3]
1. Institute of Molecular Physics, Polish Academy of Sciences, Poznan, Poland; 2. Institute of Experimental Physics, SAS, Kosice, Slovakia; 3. Institute of Physics, Silesian University, Katowice, Poland

Recently, Jain et al. [1] have studied the effect of partial substitution of Ni by Cr in $CeNi_5$ intermetallic compound. Their study of the pressure-composition isotherms for $CeNi_{5-x}Cr_x$ (x = 0, 1, 2) have been motivated by search for hydrogen storage materials. It was shown that all the compounds crystallized in the hexagonal $CaCu_5$ type of structure. Compounds of this structure have been in the focus of our interest in recent years [2,3], mainly from the point of view of the magnetic, transport, thermodynamic, structural and electronic properties. Therefore, in this paper we present these types of characterization for the $CeNi_4Cr$ representative. Figure 1 shows the result of the magnetic susceptibility measurements as a function of temperature. The reciprocal susceptibility did not show any distinct linear region, therefore we employed the modified Curie-Weiss law ($\chi_{dc}(T)=\chi_0+C/(T-\theta)$) to fit directly the $\chi_{dc}(T)$ dependence. The corresponding parameters' values are displayed in the figure. The striking results is the small value of the effective paramagnetic moment. Assuming that only Ce ions contribute to the moment one could expect the theoretical value of $2.54\mu_B$/f.u. This reduction can be caused by the mixed valence behavior of this compound, which is suggested also by the x-ray photoemission studies to be shown in the full paper. We will also discuss the magnetic susceptibility measured at low magnetic field, which seems to indicate an importance of the magnetism of chromium known from its antiferromagnetic nature. In Fig.2 the specific heat divided by temperature is plotted as a function of the temperature square for changing magnetic field strength. The extrapolation to T=0 provides directly the value of the electronic specific heat coefficient γ. It drops from 90 to 60$Jmol^{-1}K^{-2}$ for H increasing from 0 to 9T.

Acknowledgments: This work was supported by the funds for science in years 2007-2009 as a research project (T. Tolinski, A. Kowalczyk) and partly by the COST – ECOM P16, by Science and Technology Assistance Agency - APVT-51-031704, by VEGA 6165, by the contract CE of SAS. Liquid nitrogen was supply by US Stell Kosice.

[1] R.K. Jain, A. Jain et al., J. Alloys Compd. 430 (2007) 165.

[2] T. Tolinski, A. Kowalczyk et al., Phys. Rev. B 70 (2004) 064413.

[3] T. Tolinski, Modern Physics Letters B 21 (2007) 431.

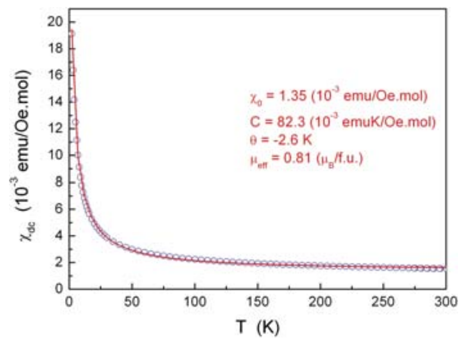

Magnetic susceptibility measurements as a function of temperature (circles) fitted with the modified Curie-Weiss law (line).

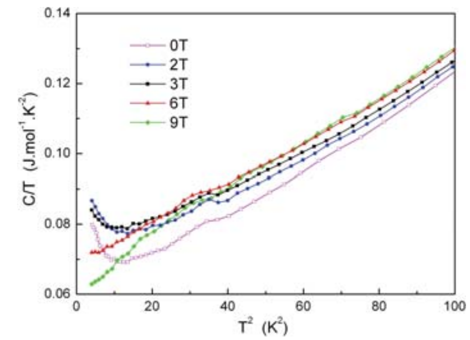

Specific heat C/T vs. T^2 for various values of the applied magnetic field at the low temperatures region.

EO-03

Two dimensional ferromagnetic clusters in Ho0.8La0.2Mn2O5.

H. Chou[1], C. Yu[1], C. Wang[2], C. Wu[2], W. Li[2]
1. Physics, National Sun Yat-sen Unversity, Kaohsiung, Taiwan; 2. Physics and Center for Neutron Beam Application, National Central University, Jhongli, Taiwan

I. INTRODUCTION

It has been known that a pure HoMn2O5 compound can only be formed in a pure oxygen environment with an oxygen pressure as high as three atmospheres. [1,2] The pure HoMn2O5 compound has an orthorhombic structure of space group Pabm [3] and undergoes an antiferromagnetic (AFM) transition at a Neel temperature (TN) ranging from 39 to 45K. In this study, we found that by doping 20% of La at the Ho site the pure Mn0.8La0.2Mn2O5 phase may be formed in one atmosphere. An unexpected ferromagnetic (FM) phase appears at 150K and changes back to AFM phase at lower temperature. This FM phase was examined by the superconducting quantum interference device (SQUID) and Neutron Dffractometer and is found to be a two dimensional ferromagnetic cluster.

II. EXPERIMENT

The precursors Ho1-xLaxMn2O5 were formed by a standard sol-gel method [1,2]. The sample was formed at 1000oC for 12 hours under one atmosphere of flowing Oxygen. The crystal structures of compounds were examined by standard X-ray diffractometery (XRD) from which the data were analyzed by a Generalized Structure Analysis System (GSAS) with Rietveld method. Their magnetic property was then measured using a SQUID magnetometer. Neutron diffraction was taken in NIST to explore the lattice and magnetic structure.

III. RESULTS AND DISCUSSION

The crystal structure of Ho1-xLaxMn2O5 compound was examined by a commercial 4-axis X-ray diffraction and a high resolution X-ray diffractometer in National Synchroton Radiation Research Center, Taiwan. It is found that Mn0.8La0.2Mn2O5 is a pure phase with no trace of an impurity phase up to the limitation of within reasonable accuracy of XRD. The AFM transition in Mn0.8La0.2Mn2O5 compound can be more clearly understood from the 1/M vs. temperature plot where the linear extrapolation of the high temperature paramagnetic part of the curves intersect with the temperature axis at a negative intercept. An unexpected FM transition appears at 150K, as shown in Figure 1. By measuring the ZFC and FC magnetization as a function of temperature and the hysteresis loops at various temperatures, the FM phase is indeed contributed to the formation of ferromagnetic clusters. The magnetic structure explored by Neutron diffraction at temperature lower than the Neel temperature reveals the compound is an incommensurate AFM phase. At the temperature where FM phase is initiated, the appearance of asymmetric broad neutron diffraction peaks, as shown in Fig. 2, indicates the formation of small portion of two-dimensional FM clusters in the paramagnetic matrix.

IV. CONCLUSIONS

A pure Mn0.8La0.2Mn2O5 phase can be stablized by doping 20% of La at Ho sites under one atmosphere of pure oxygen. A FM phase appears at 150K and can be attributed to the formation of two dimensional FM clusters

[1] J. A. Alonso, M. T. Casais, M. J. Martínez-Lope and I. Rasines, J. Solid State Chem. 129, 105 (1997)

[2] J. A. Alonso, M. T. Casais, M. J. Martínez-Lope, Martínez J. L. and M. T. Fernández-Díaz, J. Phys.: Condens. Matter 9, 8515 (1997)

[3] I. Kagomiya, K. Kohn, T. Uchiyama, Ferroelectrics 280, 131 (2002)

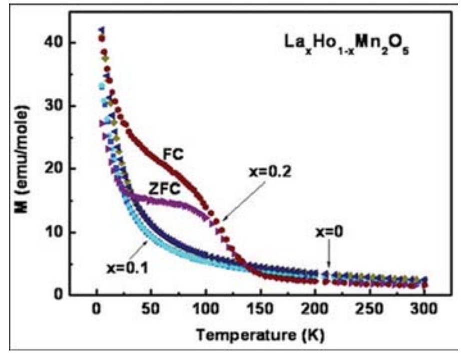

Fig. 1: The magnetization measurements as a function of temperature for Ho1-xLaxMn2O5 with x=0, 0.1 and 0.2.

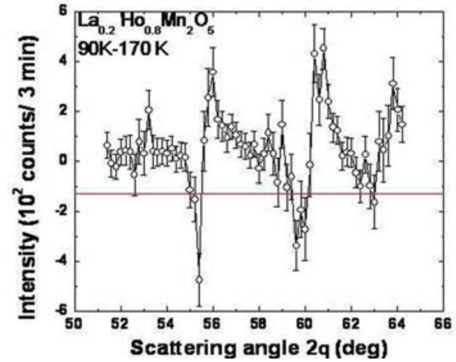

Fig. 2: The subtraction of 90K to 170K of Neutron diffraction pattern.

EO-04

The switching behavior of spin transition [Fe(PM-BiA)2(NSC)2] compound derived from pressure pulse type experiments.

R. Tanasa[1], A. Stancu[1], J. Linares[2], E. Codjovi[2], F. Varret[2], J. Letard[3]
1. Department of Physics, "Alexandru Ioan Cuza" University, Iasi, Romania; 2. Groupe d'Etude de la Matière Condensée (GEMaC) CNRS-UMR 8635, Université de Versailles, Versailles, France; 3. Groupe des Sciences Moléculaires, Institut de Chimie de la Matière Condensée de Bordeaux, UPR No. 9048 CNRS-Université Bordeaux I, Pessac, France

The field of molecular magnetism has known, in the last decade an important outburst, triggered by the need for new materials with multifunctional properties. Beside the molecular ferri- and ferro-magnetic compounds, the spin transition complexes based on the existence of two accessible states of different spin multiplicity rounds up the field. These complexes are inorganic solids characterized by two states: low spin (LS) and high spin (HS) with different magnetic properties (LS is diamagnetic while HS is paramagnetic), change of color, vibrational properties, molecular volume and dielectric constant. The crossover between these two states can be triggered by various external constrains like temperature, pressure, magnetic field or light intensity. Depending on the elastic interaction strength, the spin crossover between LS and HS can vary from gradual to a first order transition with hysteresis. In fact, this bistability is envisaged in potential applications like ultra high density and fast access storage data medium, sensors or displays.
Simultaneous with designing new materials showing enhanced properties at room temperature an equal effort is made in developing new characterization tools and understanding of switching behavior. As a static investigation tool, we have introduced the First order Reversal Curve (FORC) diagram method [1,2]. Another approach is to record the response of the system under fast perturbation, i.e. dynamical methods [3]. Till now, as fast perturbation was used a high magnetic field, pressure pulses [4] and laser pulses [5]. The fastest perturbation is obtained with the laser (nanoseconds), then magnetic field (0.1 seconds) and in the end pressure pulses (minutes). In fact, several years ago, a pressure pulse experiment was made in order to compare it with the magnetic field pulse, concluding that the pressure and magnetic field are inducing "mirror effect" [4].
In this paper, we present a series of systematical experiments to study the piezo switching of the [Fe(PM-BiA)2(NCS)2] complex. Compared with other types of perturbations, here we were able to shift the reference line from atmospheric pressure to 500 bars allowing a 400 bars negative and positive variation. In the first experiment, we have started from high spin saturation (high temperature phase), the temperature was decreased till the system is brought in the bistability zone. At a given temperature the pressure is increased with 400 bar and after that reduced back to its initial value (see Fig. 1). To get the full image of the switching in the bistability zone we were repeating the experiment for several temperatures. The results are presented in Fig. 2. In our second experiment, the pressure was first decreased and after that increased back to 500 bars (see Fig 3).
The response of the system to the pressure stimulus in the experiments indicated above can be understood easily recalling that the high pressure favors the LS states and the low pressure the HS states. Also, the major hysteresis loop limits the metastability region. The spin crossover system can be brought outside the major hysteresis loop, but when the perturbation is removed, the system drops to the closest stable state, which is on the major hysteresis loop.
In conclusion, we obtained the switching from the cooling branch of the thermal hysteresis loop to the heating branch of the same hysteresis and vice versa. Also, we have shown that in order to obtain a piezo-switch we have to correlate the pressure variation with the actual state of the system on the thermal hysteresis loop. In the full paper, we shall indicate and explain the differences between our results and the ones reported in the first experiment of this kind. Also, the link with the magnetic and laser pulses will be explored.
Acknowledgements: This work was partially supported by the European Network of Excellence MAGMANet (FP6-515767-2)

[1] R. Tanasa et al,. Phys. Rev. B, 71 (2005) 014431

[2] R. Tanasa et al., J. Appl. Phys. (2008) in press

[3] R. Tanasa et al., Chem. Phys. Lett. 443 (2007) 435

[4] A. Bousseksou et al.,C. R. Chimie, 6 (2003) 329

[5] E. Freysz et al. Chem. Phys. Lett. 394 (2004) 318

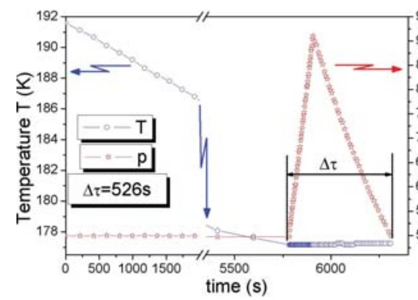

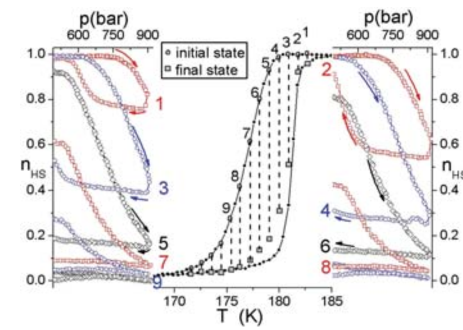

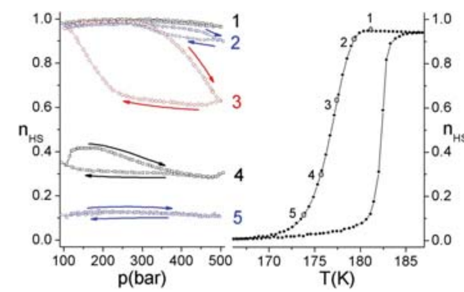

EO-05

Magnetic Properties of Zr_9Ni_{11} Intermetallic Compound.

V. Provenzano[1], R. D. Shull[1], R. M. Waterstrat[1], L. H. Bennett[1,2], E. Della Torre[1,2], H. Seyoum[3]
1. Magnetic Materials Group, NIST, Gaithersburg, MD; 2. Physics Department, George Washington University, Washington, DC; 3. Physics Department, University of the District of Columbia, Washington, DC

As part of a study of transition $metal_9$-transition $metal_{11}$ intermetallic compounds, we carried out some exploratory magnetic measurements on a number of these compounds. Unexpectedly, in one of these compounds (the Zr_9Ni_{11} compound), we observed an unusual magnetic behavior. The neutron diffraction results on the same Zr_9Ni_{11} compound provided valuable insight on two aspects of this unusual magnetic behavior: (i) spin-glass behavior that had not been previously seen in this 9-11 family of compounds, and (ii) oscillations in magnetization versus temperature curves. Here we report on the magnetic measurements that were carried out on the Zr_9Ni_{11} intermetallic compound. Though the main focus of the present study is on the magnetic property measurements, we shall also make brief reference to a parallel crystal structure study conducted on the same Zr_9Ni_{11} compound and whose results have been recently submitted for publication [1].
The samples used for both studies were prepared by arc melting the appropriate elements, using a water-cooled copper hearth, in an argon atmosphere. The purity of the starting constituents was 99.9 wt. % or better. After arc melting, the compound was homogenized in vacuum at 1030°C for one week and then water quenched. After the homogenizing treatment, in the temperature range from 2 K to 320 K, the magnetization of the Zr_9Ni_{11} compound was measured both as a function of temperature at constant field values and as a function field at constant temperatures, using a SQUID magnetometer. Figure 1(A) shows the temperature dependence of the zero field cooled magnetization (M_{ZFC}) and the field cooled Magnetization (M_{FC}) of the compound in a dc field of 100 Oe. The M_{ZFC} shows a peak centered at 36 K, whereas the M_{FC} shows an upturn at low temperatures. From 100 Oe to 400 Oe, the magnetization dependence with temperature of both M_{ZFC} and M_{FC} is similar to that at 100 Oe, except that the M_{ZFC} peak temperature (T_p) shifts to lower temperatures with increasing field. Above 400 Oe, there is no discernible difference between the M_{ZFC} and M_{FC} vs. T plots; both plots show the same trend and are essentially superimposed on each other. However, for the Zr_9Ni_{11} compound of particular interest are the characteristics of M_{ZFC} and M_{FC} vs. T plots for field values below 100 Oe down to 2 Oe. In this field range, T_p increases with increasing field. The peak temperature T_p of M_{ZFC} curves versus applied field are shown in Figure 1(B). The temperature dependence of the magnetization of the Zr_9Ni_{11} compound for field values of 100 Oe and above is typical of a spin glass. In fact, in the region between 100 Oe and 400 Oe, the decrease in T_p is proportional to H^b, where H is the applied field and b<1. The value of the exponent ("b") is found to be 0.61, which is close to the de Almeida-Thouless 2/3 power law that applies to spin glasses. However, the behavior of the magnetization below 100 Oe is not typical of a spin glass, in that T_p decreases with decreasing field [Fig. 1(B)].
The temperature dependence of the M_{ZFC} and M_{FC} vs. T plots at 400 Oe is shown in Figure 1(C). Consistent with a spin glass behavior is the shape of the M_{FC} vs. T plot, where the M_{FC} values deviate and reside above the corresponding M_{ZFC} values. Of particular interest is the presence of deviations with varying amplitudes (small peaks) in the M_{FC} vs. T plot at various temperatures, whereas, by contrast, the M_{ZFC} vs. T plot is smooth over the entire temperature range. These deviations are believed to arise from the Dzyaloshinskii-Moriya interactions occurring in the Zr_9Ni_{11} compound. In fact, it was the presence of these small peaks that helped explain the unusual variation in the neutron spectrum observed in the compound while collecting the spectral data. The crystal structure study conducted on the Zr_9Ni_{11} compound by TEM and neutron diffraction in the temperature range of 4 K to 1273 K revealed that the compound had a Zr_9Pt_{11}-type tetragonal structure plus columnar atomic chains of alternating Zr and Ni atoms lying along the c-axis. These spectral variations are consistent with deviations seen in the M_{FC} vs. T plot at 400 Oe. The small peaks seen in the M_{FC} vs. T plot at 400 Oe are believed to be the result of movements of the atoms along the chains over short distances [1].

[1] J.K. Stalick, L.A. Bedersky, and R.M. Waterstrat, "One-Dimensional Disorder in Zr_9M_{11} (M=Ni, Pd, Pt)", to be submitted for publication, Phys. Rev. B (2008).

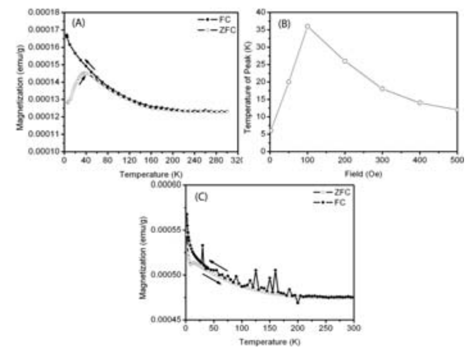

Figure 1 (A) M_{ZFC} (open symbols) vs. T and M_{FC} (closed symbols) vs. T plots at 100 Oe, (B) Peak temperature versus applied field, between zero Oe and 500 Oe, and (C) M_{ZFC} (open symbols) vs. T and M_{FC} (solid symbols) vs. T plots at 400 Oe.

EO-06

First-Order Reversal Curve Analysis of Spin-Transition Thermal Hysteresis Under Pressure in Terms of Physical-Parameter Distributions and Their Correlations.

A. Rotaru[1,2], J. Linares[1], E. Codjovi[1], F. Varret[1], A. Stancu[2]
1. Physique, GEMAC-Versailles University, Versailles, France; 2. Physique, Alexandru Ioan Cuza University, Iasi, Romania

The study of the elastic domain distributions as well as the parameters characterizing these distributions are of paramount importance in spin transition materials, as they are directly determining their general hysteretic properties. In order to evidence the elastic domain distribution the experimental First Order Reversal Curve (FORC) diagram method was proposed [1].
The FORC diagram method was proposed by Mayergoyz [2] for the identification of the Classical Preisach Model and its use was extended to virtually any hysteretic system, as an experimental characterization tool, by Pike [3]. The experimental FORC diagram method was initially mainly used in ferromagnetic materials but it proved its efficiency also for the characterization of ferroelectric materials [4,5] and thermal and light induced thermal hysteresis in spin transition materials [6,7].
Recently, it has been shown that First Order Reversal Curves (FORC) diagrams for the spin crossover compounds can be interpreted in terms of distributions of physical parameters such as the energy gap Δ between low spin (LS) and high spin (HS) states and the mean field interaction parameter J of Ising-like model [7].
In this contribution we present the pressure effect on these two distributions. We recorded the FORC curves of the spin transition solid [Fe0,6Zn0,4(btr)2(NCS)2]H2O at several pressures. The derived FORC distributions are shown in Figure 1 in the bias-coercivity c-b and in Δ-J axes. With respect to the previous work at ambient pressure [7] we observed an unexpected splitting of the distribution with a “quasi-reversible” component on most of the diagrams. This additional contribution might be due to kinetic effects with remain to be cleared up and mastered by further investigations. We have removed this extra-contribution for the plot in Δ-J axes and for the following.
Following [7] we analysed the joint probability distributions in terms of standard deviations σ and the dimensionless correlation parameter r defined as usually r=cov(b,c)/σ(b)σ(c). Detailed expressions can be found in [7]. As noticed by Tanasa et al. [7] the correlation factor can be associated with a rotation of the contour plots (ellipses in case of Gaussian distribution) by an angle α (defined modulo π/2) expressed through tanh(2α)=2σ(b)σ(c)/[σ^2(b)-σ^2(c)].
The statistical analysis data of the corrected distributions are listed in Table I.
These statistical data can be discussed as follows :
- pressure induces an overall increase in the equilibrium temperatures, expressed as db/dP~22KBar, in excellent agreement with previous investigations of the major loops and simple thermodynamic expectations [8].
- pressure also induces an overall increase in the interaction parameter values, which can be understood as the enhancement of elastic interactions by a stiffer lattice.
- the widths of the distributions are not significantly modified by pressure. This result support the assumptions made in [7] that these factors were due to crystal size effects and internal stresses which should not remain, irrespective of the external pressure.
- the correlation parameter also remains little affected by the external pressure. In [7] we assigned it to a distribution of the dilution parameter, which also cannot be affected by the effect of external pressure.

[1] C. Enachescu et al, Physica B, 343 (2004) 15.

[2] I. D. Mayergoyz, Mathematical models of hysteresis and their applications, Academic Press, 2003.

[3] C. R. Pike et al, J. Appl. Phys., 85 (1999) 6660.

[4] A. Stancu et al, Appl. Phys. Lett., 83 (2003) 3767.

[5] A. Stancu et al, Physica B, 372 (2006) 226.

[6] C. Enachescu et al, Phys.Rev.B, 72 (2005) 054413.

[7] R. Tanasa et al, Phys.Rev.B, 71 (2005) 014431.

[8] E. Codjovi et al, Comptes Rendus de l’Académie des Sciences Série II Fascicule C-Chimie, 4(3),(2001),81.

P(bar)	(K)	$\langle c \rangle$(K)	$\langle J \rangle$(K)	σ(J)(K)	$\langle \Delta \rangle$(K)	σ(Δ)(K)	r(J,Δ)	α(deg)
1	111.4	5.5	82.7	1.1	852.7	3.6	0.62	103
600	124.7	4.3	86.2	1.6	952.1	6.4	0.55	99
1200	137.2	3.0	87.9	1.5	1045.0	5.8	0.62	101
1600	146.0	2.7	90.4	1.2	1111.1	4.9	0.79	103

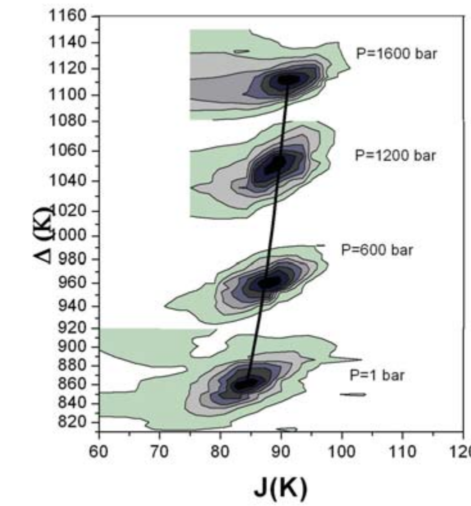

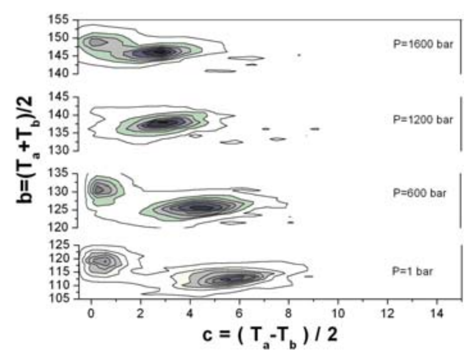

Thermodynamic and electronic properties of DyNi4Si compound.

M. Falkowski[1], A. Kowalczyk[1], M. Reiffers[2], T. Tolinski[1], E. Gazo[2], M. Zapotokova[2], G. Chelkowska[3]
1. Institute of Molecular Physics, Polish Academy of Sciences, Smoluchowskiego 17, Poznan, Poland; 2. Institute of Experimental Physics, Slovak Academy of Sciences, Watsonova 47, Kosice, Slovakia; 3. Institute of Physics, Silesian University, Uniwersytecka 4, Katowice, Poland

Intermetallic compounds formed between rare earth and transition metals have been intensively investigated both from the theoretical and experimental point of view. This is because they often present promising materials for practical applications, especially as powerful permanent magnets and hydrogen storage.

Heat capacity of the DyNi4Si compound has been studied in the temperature range 1.8-150 K in various applied magnetic fields. The specific heat was measured from pumped helium up to room temperature by employing the relaxation method, using the specific heat option of the Quantum Design PPMS system. The X-ray photoemission (XPS) spectra were obtained with monochromatized Al-Kα radiation with photon energy of 1487.6 eV using a PHI 5700/660 Physical Electronics Spectrometer. The energy spectra of the electrons were analysed by a hemispherical mirror analyzer with the energy resolution of about ~0.3 eV. The Fermi level, EF = 0, was referred to the gold 4f7/2 binding energy at 84 eV. All emission spectra were measured immediately after breaking the sample in a vacuum of 10-10 Torr.

DyNi4Si compound crystallize in the hexagonal CaCu5-type structure, space group P6/mmm. R atoms occupy the (1a) site, Ni(1) the 2c site and Ni(2) and Si are statistically distributed on the 3g positions. Our magnetic measurements indicate that DyNi4Si is ferromagnetic with the saturation moment of 7.9 μB/f.u. at 4.2 K (in H = 9T) and Curie temperature TC = 15.6 K [1].

Studying the specific heat is a powerful tool for obtaining information on magnetic properties and phase transitions. The total specific heat consists of electronic, phonon and magnetic contributions. The electronic specific heat coefficient γ was determined in the region, where the application of the Debye law C= γT+BT3 was physically acceptable providing γ = 72 mJ/mol -1K-2 (Fig.1). Zero field heat capacity of the DyNi4Si compound reveals a peak close to the magnetic ordering temperature, which eventually gets suppressed after application of the magnetic field (inset of Fig. 1).

The experimental photoemission spectrum (solid line) of the valence band region of DyNi4Si is shown in Fig. 2. The valence band spectrum at the Fermi level exhibits the domination of the Ni(3d) states below 3 eV. The multiplet structure of the Dy 4f state is visible in the energy range from 4 eV to 13 eV. The positions of the peaks are consistent with the metallic dysprosium (Fig. 2, dash line). The slight shift of peaks' positions towards the higher binding energy by about 0.3 eV in respect to the pure Dy is probably due to the different crystalline field for Dy in the DyNi4Si compound.

Acknowledgments
This work was supported by the funds for science in years 2007-2009 as a research project (A. Kowalczyk, M. Falkowski) and partly by the COST – ECOM P16, by Science and Technology Assistance Agency - APVT-51-031704, by VEGA 6165, by the contract CE of SAS. Liquid nitrogen was supply by US Stell Kosice.

[1]. M. Falkowski, B. Andrzejewski, A. Kowalczyk, Journal of Alloys and Compounds 442 (2007) 155.

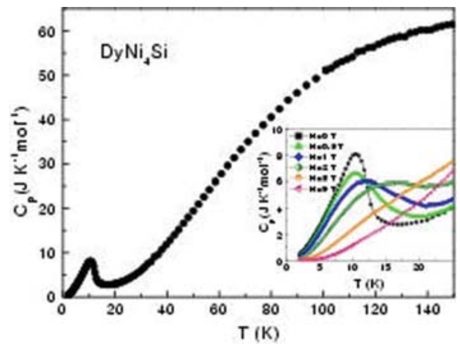

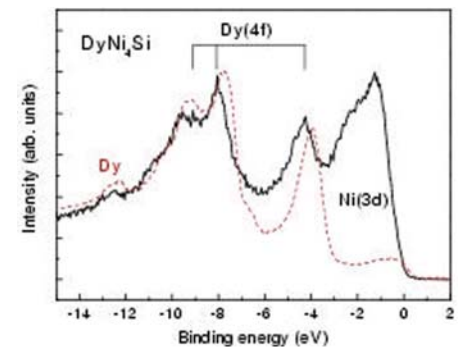

EO-08

Multiferroic, electronic and structural properties of Sr_2TiMnO_6 perovskite: experimental and ab-initio studies.

J. A. Rodriguez[1], D. A. Landinez-Tellez[1], C. Salazar-M[1], P. Pureur[2], F. E. Fajardo[1], J. Roa-Rojas[1]
1. Dept. of Physics, Universidad Nacional de Colombia, Bogotá, Colombia; 2. Institute of Physics, Universidade Federal do Rio Grande do Sul, Proto Alegre RS, Brazil

We present the synthesis and characterization of Sr_2TiMnO_6 (STMO), which is a new manganite-like material, that evidence dielectric and magnetic behaviors. Magnetic measurements show the ferromagnetic feature and polarization hysteresis curves reveal the ferroelectric character of STMO. Density Functional Theory (DFT) calculation, by means of wien2k software, reveals a half-metallic nature. Samples were synthesized by means the solid state reaction. The SrO, TiO_2 and MnO_2 (Aldrich 99.9%) powders, were stoichiometrically mixed according to the chemical formula. Mixture was ground to form a pellet and annealed, then regrinded, repelletized and sintered. X-Ray diffraction was performed with a PW1710 diffractometer. Zero Field Cooling (ZFC) and Field Cooling (FC) measurements of magnetization were carried out by using a MPMS Quantum Design SQUID and electric polarization curves by means a Radiant Ferroelectric Tester, which include a ±10 kV source. Rietveld refinement permitted to establish that the space group is I/4m and lattice parameters are a=5.4858 Å and c=7.7518 Å. From DFT, the results are a= 5.508(2) Å and c = 7.792(8) Å, which are more than 99% in agreement to our experimental results.
The magnetic properties have been investigated by measuring the DC magnetization in the temperature range 5 K to 300 K and at an applied magnetic field of 0.2 T. Temperature dependence of the DC magnetization as a function of temperature for STMO was measured by using the ZFC and FC recipes. We use the minimum observed in $d\chi/dT$ as a function of temperature to determine the critical temperature T_C = 44.8 K. It is very interesting the irreversibility observed in the ZFC and FC curves. This separation of ZFC and FC magnetization as a function of temperature is a characteristic of magnetic ordered frustrated systems. Hysteresis curve evidences a ferromagnetic behavior with finite magnetization saturation value (0.2 emu/cm^3, approximately). From the magnetization saturation and crystallographic parameter of cell it is possible to determine an effective magnetic moment 5.01 µB.
Measurements of polarization as a function of applied voltage were performed in order to establish the multiferroic behavior of STMO material. Figure 1 shows hysteretic loops of the material in a capacitor configuration, under several applied voltages, which reveal the characteristic ferroelectric response of STMO. Due the bulk characteristic of samples, in figure 1 we do not observe a well-saturated polarization up to the maximum applied voltage. On the other hand, the experiments show the possible occurrence of a non-conventional polarization effect, which is observed as an anomaly in the hysteretic behavior showed in figure 1. For hysteresis curves of polarization as a function of applied voltage a small asymmetry is systematically evidenced. Particularly, it is observed that the system is smoothly positively polarized.
Figure 2 shows the total and partial Density of States (DOS) due to the d-like atomic orbital of Mn atom. For the total magnetic moment, the most important orbitals are x^2-y^2 and xy+yz of Mn. The total calculated magnetic moment was 3.0 µB, which is an integer number of Bohr magneton that characterizes the half-metallic behavior. A detailed study of figure 2, shows that the material behaves as a half-metallic, because the total spin-up density of states across the Fermi Level is ~ 0.04 eV. The conductor nature of spin up channel is majority due the x^2-y^2 and xy+yz orbital of Mn. The conductor character of the spin up configuration and the theoretically determined magnetic moment of cell are in agreement with the ferromagnetic experimental response of material.

In conclusion, Sr_2TiMnO_6 presents a magnetic ordering transition with the presence of a typical irreversibility of ferromagnetic frustrated materials. The DOS shows that is a half-metallic. Experimental and theoretical magnetic moment is an integer value, which is else characteristic of half-metallic systems. Our results permit to infer that is possible produce multiferroic complex perovskites from the mixture of ferroelectric and ferromagnetic simple perovskites. On the other hand, our work suggests that several half-metallic perovskites could be evidence coupled magnetoelectric response.

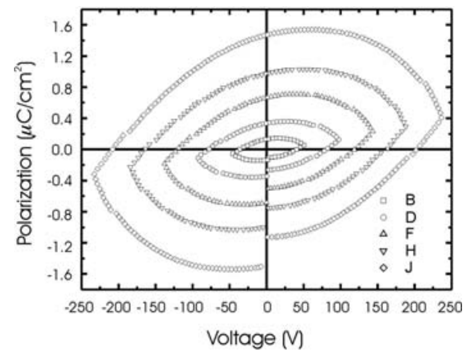

Figure 1. Hysteretic ferroelectric feature of polarization as a function of applied voltage for STMO.

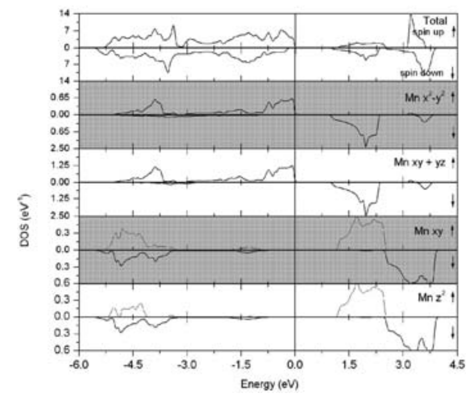

Figure 2. Total and partial density of states for Sr_2TiMnO_6.

EO-09

Physical Properties in Powder, Bulk and Thin Films of La2/3Ca1/3CrxMn(1-x)O3 with Low Doping.

D. L. Quintero, D. Girata
Physics Institute, Universidad de Antioquia, Medellin, Colombia

The manganites are of scientific and technological interest due to their physical properties and because for their applications in spin valves and systems based on the phase control. In this work we prepared La2/3Ca1/3CrxMn(1-x)O3 (LCMCrO) with x=0, 0.06, 0.07 and 0.08, in thin films by DC-magnetron Sputtering and in powder and pellets synthesized by solid state reaction, the characterization was made measuring magnetic, transport and structural properties. The characterization of the pellets and powder was performing as preliminary study in order to know the physical properties of the targets used for the thin films preparation. Since Rivadulla work we already know that the doping with Cr at low concentrations lead an increase in the magnetoresistance, MR, in a critical concentration of Cr 7% [1], that is way we decide to work around this concentration. In different works report that the only ion that replaces Mn is Cr3+, which is isoelectronic with Mn4+ [2-4], additional, due to the preparation technique the Cr can occupy any of the two places of the manganese ions, in a random way.

We found changes in the values of the MR, metal-insulator transition temperatures, TMI, Curie temperatures, TC, and magnetization, so the magnetic behavior is strongly dependent on the composition of the samples. For the XRD and EDX we found that all the samples are single phase and that the Cr is into the manganite structure, the powder samples are not homogeneous because the nature of the reaction while the thin films have uniform concentration and topology.

In figure 1 the results of resistance in function of the temperature confirm the metallic-insulator transition; witch is an expected result for lanthanum manganite with calcium at 33%. The Cr doping increase the resistance peak and reduce the TMI, this temperature is not so low for thin films. The magnetization reduces by the Cr doping but the magnetization value is not as low like other concentrations (Tc= 250K, 220K and 222K for Cr 0%, Cr6% and Cr 7%, for the samples in bulk at 2kOe), the TC also reduces but not significantly as TMI. There are a range of temperatures to which the sample is ferromagnetic but remains insulating, this region is getting bigger with the Cr concentration and we have not found evidence of this behavior in others reports. The figure 2 shows the MR in function of the magnetic field at TMI, we can noticed that for 7% of Cr the MR is higher than for others concentration, the MR value is appreciably high (more than 10%) for thin films; this result has not reported for other authors since until now we have not found works with manganite doped with Cr at low concentrations in thin films. For measurements of magnetic moment in function of the magnetic field for different temperatures, we had observed from the hysteresis loops that the coercitive field does not change significantly with the Cr addition.

In this work we discuss the Cr-Mn coupling and the influence of this coupling in the transport and magnetic properties of these doped manganites, we empathized in the evidence of the strongly correlated behavior of these materials and in the fact that all of the properties improve with the production of thin film rather that the powder and pellets material. The changes in the critical temperatures are not due to the variation of the fraction of the different valence Mn ions because we are doping with a very low levels of Cr. The increase of MR in the critical concentration could be explained by a FM coupling of the Mn and Cr ions, likewise as postulated exchange interaction between Mn ions.

[1] F. Rivadulla, M.A. López Quintela, L. E. Hueso, P. Sande, J.Rivas, R. D. Sánchez, Phy Rev B 62, 9 (2000).

[2] I.O Troyanchuk, M.V. Bushinsky, H. Szymczak,M. Baran, K. Bärner, J Mag Mag Mater 312, 470-475 (2007).

[3] O. Toulemonde, F. Studer, A. Barnabé, A. Maignan, C. Martin, B. Raveau, Eur Phys J B 4, 159-167 (1998)

[4] J. J. Tian, J. Fang, J. L. Cheng, W. F. Zhang, Phy Lett A 363,307-311 (2007).

[5] L. Sheng, D. Y. Xing, D. N. Sheng, C.S. Ting, Phy Rev Lett 79, 9 (1997).

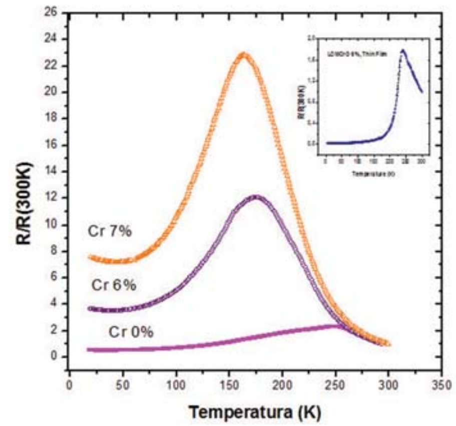

Normalized Resistance vs Temperature at zero field, the insert shows the resistance for LCMCrO 6‰ in thin film.

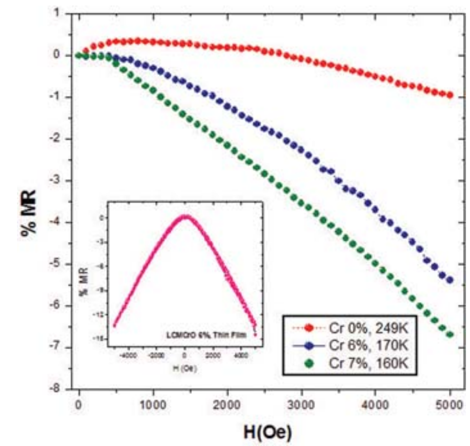

MR vs applied magnetic field at TMI, the insert shows the MR for the LCMCrO 6% in thin film.

EO-10

Magnetic relaxation behavior in $Nd_{0.5}Sr_{0.5}MnO_3$: observation of negative imaginary component of ac magnetic susceptibility.

A. N. Ulyanov[1], H. D. Quang[2], K. W. Lee[3], S. C. Yu[4], N. H. Sinh[5], Y. M. Kang[1], S. I. Yoo[1]
1. Department of Materials Science and Engineering, Seoul National University, Seoul 151-744, South Korea; 2. Solid State Physics Group, Department of Physics & Astronomy and SUPA Graduate School, University of Glasgow, G12 8QQ, United Kingdom; 3. Korea Research Institute of Standards and Science, Yusong, South Korea; 4. Department of Physics, Chungbuk National University, Cheongju 361-763, South Korea; 5. Cryogenics Laboratory, Department of Physics, College of Natural Science, Hanoi National University, 334 Nguyen Trai Road, Thanh Xuan, Hanoi, Viet Nam

Observation of colossal magnetoresistive (CMR) effect in thin films of mixed-valence Mn perovskite renewed interest for these materials studied since the 1950s [1]. Potential applications of noted materials require a serious study of their structure, transport and magnetic properties which are closely related. Last years much attention was also paid for the long time relaxation effects in perovskite manganites (e.g., see works [2-3] and references therein). We here present the first observation of short time magnetic relaxation in perovskite manganites.

$Nd_{0.5}Sr_{0.5}MnO_3$ samples were synthesized by the conventional solid state reaction and characterized by powder x-ray Cu Kα analysis. Magnetization measurements were performed with a SQUID magnetometer (Quantum Design MPMSXL) in the temperature region of 10-300 K. AC susceptibility measurements were carried out with AC7000 LakeShore susceptometer in temperature region of 77-300 K, frequency of 85 Hz and effective ac magnetic field of 10 Oe.

According to x-ray analysis results, samples were single phase and exhibited an orthorhombic cell in accordance with previous report [4]. The temperature dependence of magnetization for $Nd_{0.5}Sr_{0.5}MnO_3$ manganites is presented in Fig. 1. In accordance with the phase diagram [4], sample of this composition is antiferromagnetic insulator at low temperatures; at the temperature T_{CO}≈150 K the manganites undergoes a charge-ordering - charge-disordering phase transition and becomes ferromagnetic metal, and in the temperature interval of 180-270 K it undergoes a ferromagnetic paramagnetic (FM-PM) transition with Curie temperature T_C=270 K.

Figure 2 shows temperature dependence of real (χ'_{ac}) and imaginary (χ''_{ac}) components of ac susceptibility for $Nd_{0.5}Sr_{0.5}MnO_3$ sample. Large negative χ''_{ac} peak is observed in the FM-PM transition region and kink at χ'_{ac} is also observed at the noted temperature interval. No anomaly at *M-T* curve and its derivative are observed at the temperature region of 250-275 K where the imaginary part of ac susceptibility is negative. According to Palacio et al. [5], the negative χ''_{ac} can be observed if $\omega << \tau^{-1}$ (ω is a frequency of ac magnetic field, τ is the characteristic magnetization relaxation time). The negative χ''_{ac} was also observed in $Gd_5(Si_2Ge_2)$ alloy [6] and, following to Ref. [5], explained by domain wall anomalous relaxation motion under the alternating magnetic field. Other reasons for the negative imaginary component of ac susceptibility will be also discussed.

[1] G. H. Jonker and J. H. van Santen, Physica 16, 337 (1950).

[2] J. López, P.N. Lisboa-Filho, W.A.C. Passos, W.A. Ortiz, F.M. Araujo-Moreira, O.F. de Lima, D. Schaniel, K. Ghosh, Phys. Rev. B 63, 224422 (2001).

[3] A. Anane, J.-P. Renald, L. Reversat, C. Dupas, P. P. Veillet, M. Viret, L. Pinsard, and A. Revcolevschi, Phys. Rev. B 59, 77 (1999).

[4] H. Kuwahara, Y. Tomioka, A. Asamitsu, Y. Moritomo, and Y. Tokura, Science 270, 961 (1995.

[5] F. Palacio, F.J.Lazaro, and A.J. van Duyneveldt, Mol. Cryst. Liq. Cryst. 176, 289 (1989).

[6] E.M. Levin, V.K. Pecharsky, and K.A. Gscheidner, Jr., Phys. Rev. B 62, R14625 (2000).

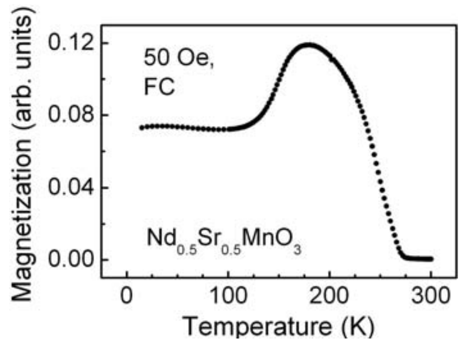

Fig. 1. Field cooled temperature dependence of magnetization obtained in field of 50 Oe for $Nd_{0.5}Sr_{0.5}MnO_3$ manganites.

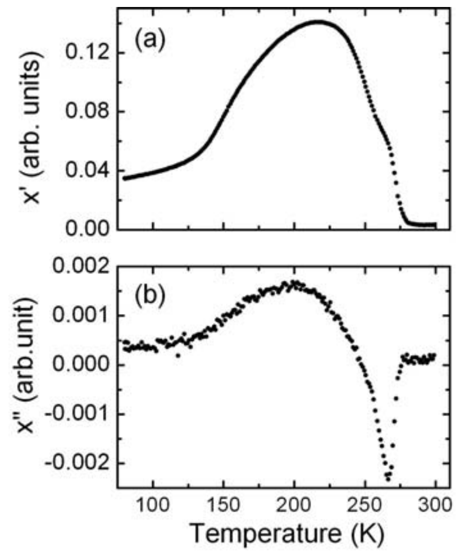

Fig. 2. Temperature dependencies of real (a) and imaginary (b) components of ac susceptibility for $Nd_{0.5}Sr_{0.5}MnO_3$ manganites.

EO-11

Synthesis and characterization of multiferroic polycrystalline transition metal doped $BiFeO_3$ thin films.

P. Kharel[1], S. Talebi[2,1], C. Sudakar[1], M. B. Sahana[1], *V. M. Naik*[2], R. Naik[1], G. Lawes[1]
1. Department of Physics and Astronomy, Wayne State University, Detroit, MI; 2. Department of Natural Sciences, University of Michigan-Dearborn, Dearborn, MI

Multiferroic materials, which exhibit simultaneous ferromagnetic and ferroelectric order, offer enormous potential for developing novel magnetoelectronic devices. $BiFeO_3$ is a widely studied multiferroic oxide because it develops both magnetic and ferroelectric order at high temperatures, making it attractive for devices. While $BiFeO_3$ orders antiferromagnetically at ~640 K, thin film samples have been shown to exhibit a sizeable ferromagnetic moment. There have been some studies on enhancing the multiferroic properties of $BiFeO_3$ films by adding transition metal dopants to the samples. Doping by Cr has been especially well studied, both theoretically and experimentally. However, there has been no systematic investigation to determine how different transition metal dopants affect the dielectric and magnetic properties of $BiFeO_3$ films. In the following, we discuss some of our results on $BiFeO_3$ samples doped with a range of transition metal ions (Cr, Co, Cu, Fe, Mn, V, Zn).

We have synthesized the thin film samples using metalorganic decomposition. Bismuth 2-ethylhexanoate, Iron (III) 2-ethylhexanoate, and transition metal organic precursor solutions were mixed in appropriate ratios and the mixtures were deposited onto silicon substrate, which was spun up to 5000 rpm for 15 s to ensure a uniform film. The organic residue was evaporated by heating at 550 °C for 90 seconds and the process was repeated to build up the final film thickness of ~1 μm. The samples were then annealed in nitrogen at temperatures between 500 and 600 °C for ~1 hour. X-Ray Diffraction patterns showed only the peaks expected for $BiFeO_3$, with the exception of the V and Co doped samples, which also showed secondary impurity phases. We confirmed that the dopant concentration was approximately 3 at% for all samples using EDAX.

We have measured the temperature dependent magnetization for both pure and doped samples using a Quantum Design MPMS SQUID magnetometer. Representative data are plotted in Fig. 1. The magnetic susceptibility for several of the transition metal doped films was enhanced relative to the undoped samples. The magnetization of the pure $BiFeO_3$ film was approximately 0.3 emu/cm^3 over the entire temperature range, with a small paramagnetic Curie tail at low temperatures. The transition metal doped samples exhibit increasing susceptibility with decreasing temperature and show much larger magnetizations, reaching 7.5 emu/cm^3 for the Cr doped sample. Additionally, certain samples showed splitting between the field cooled (FC) and zero-field cooled (ZFC) magnetization curves, which indicates the freezing of the net magnetic moment at low temperatures, possibly due to exchange bias coupling or superparamagnetic effects.

We have also investigated the dielectric response of these samples, in order to determine whether adding transition metal dopants could improve the ferroelectric properties by reducing the dielectric loss in the films. The temperature dependence of the dielectric loss is plotted in Fig. 2. The pure $BiFeO_3$ film (upper curve) shows a loss tangent (tan δ) ~1, indicative of a lossy dielectric material. On doping with transition metals, the dielectric properties of the samples improved substantially, with the dielectric loss being reduced by an order of magnitude for the Co, Cr, and Zn doped films.

In summary, we found that doping these polycrystalline $BiFeO_3$ films with transition metal ions substantially improved the dielectric characteristics of samples for almost all dopants, and improved the magnetic properties for several different transition metals. The Cr doped films showed the most significant improvements among all transition metal doped films.

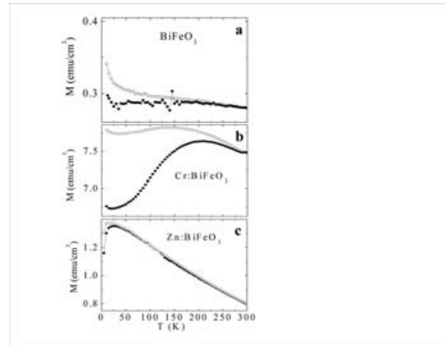

Fig.1. Magnetization of (a) pure $BiFeO_3$, (b) Cr doped $BiFeO_3$, and (c) Zn doped $BiFeO_3$. The open circles show the field cooled data, the filled circles show the zero field cooled data. All measurements were done with an applied field of 1 kOe.

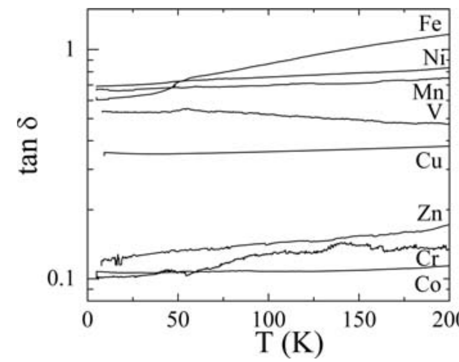

Fig. 2. Dielectric loss component as a function a temperature for different transition metal doped $BiFeO_3$ samples, as labeled. The curve labeled "Fe" represents pure $BiFeO_3$. Note the logarithmic scale.

EP-01

Influence of current induced magnetic inhomogeneities on spin wave propagation.

T. Neumann[1], A. A. Serga[1], M. P. Kostylev[2], B. Hillebrands[1]
1. Fachbereich Physik und Forschungsschwerpunkt MINAS, TU Kaiserslautern, Kaiserslautern, Germany; 2. School of Physics, University of Western Australia, Crawley, WA, Australia

We present the first comprehensive experimental study of the frequency dependent reflection and transmission of dipole-dominated backward volume magnetostatic spin waves (BVMSW) through the localized inhomogeneity created by a dc-current induced Oersted field. A resonant behaviour of the reflected and transmitted signal intensities was observed. The results build a foundation for the understanding of the spin-wave propagation in current induced periodic magnetic structures and are important for the design of dynamic magnonic crystals.

Dynamically controllable periodic magnetic structures, so called dynamic magnonic crystals, possess a large potential in the field of microwave signal processing on a nanosecond time scale. Such crystals can be realized with the help of dc-current carrying wires placed on the surface of magnetic films. By changing the dc-current the local bias magnetic field and thus the spin wave propagation is altered. Depending on the direction of the current w.r.t. the external magnetic field two principally different kinds of magnetic inhomogeneities occur: a magnetic hill (local increase of bias magnetic field) or a magntic valley (local decrease).

In order to determine the influence of dc-current induced magnetic inhomogeneities on the dynamics of spin waves we have studied the propagation of BVMSW pulses in a 5 μm thick yttrium iron garnet (YIG) film through a single inhomogeneity.

The measurements were preformed in the pulse regime in order to avoid overheating the sample as a result of the applied dc-current between -2 A and +2 A. The BVMSW pulses were excited by 280 ns long microwave pulses with a carrier frequency $\omega/2\pi$ between 7.01 GHz and 7.115 GHz in a bias magnetic field H=1800 Oe. The dc-current pulses were 180 ns long and thus only affected part of the corresponding BVMSW pulses. By comparing the unaffected part it was possible to verify that the experimental conditions remained the same. Figure 1 shows a sketch of the experimental setup. During the measurement the reflected and transmitted signal were detected simultaneously. The main results are displayed in Figure 2. The two upper panels contain the reflected intensities while the lower panels show the transmitted signal levels.

For a magnetic valley, which corresponds to the left panels in Figure 2, a barrier for the spin-wave propagation is created from which the spin wave pulses are reflected. The intensity of the reflected signal increases monotonically with increasing valley. This situation is associated to the so-called spin wave tunneling phenomenon [1].

In the case of a magnetic hill the behaviour proves to be more complex as resonances of the spin-wave intensity are observed. Minimal reflectivity is obtained when the dc-current is switched off and at a current of 1.02 A.

The reflection is maximal for currents of 0.52 A and 1.74 A. This behaviour was observed for all considered frequencies (and hence spin-wave wave vectors) with no significant wave vector dependence of the current values corresponding to the mentioned extrema. However, the maximally reflected intensity normalized w.r.t. the unperturbed level of the transmitted pulse with the same carrier frequency strongly depends on the wave vector. While close to the frequency of ferromagnetic resonance (FMR) the signal is almost completely reflected, the reflection is only partial for lower frequencies.

We interpret the existence of extrema in reflection as evidence of a resonant scattering [2].

By comparing the results obtained in reflection and transmission we can deduce that the spin wave energy is conserved and practically no energy is lost inside the barrier. Measurements at other bias magnetic fields from 800 Oe to 2200 Oe confirm the described observations.

In conclusion, we note that the spin wave propagation is significantly different for a magnetic hill and valley. In the first case the intensity depends non-monotonically on the current and is - for small current values - influenced strongly by current changes. Together with the described, strong resonance effects close to the FMR this must be kept in mind when designing dynamic magnonic crystals.

Support by the MATCOR Graduate Program and the Australian Research Council is acknowledged.

[1] S.O. Demokritov et al., Phys. Rev. Lett., vol. 93, 047201 (2004).

[2] M. Kostylev et al., Phys. Rev. B, vol. 76, 184429 (2007).

Figure 1

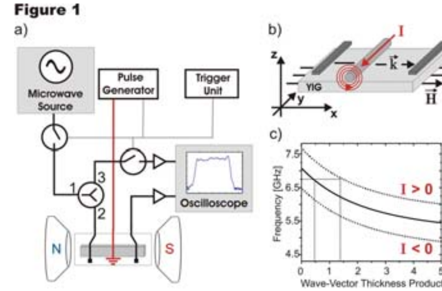

Experimental setup (a), section (b) and BVMSW dispersion relation (c)

Figure 2

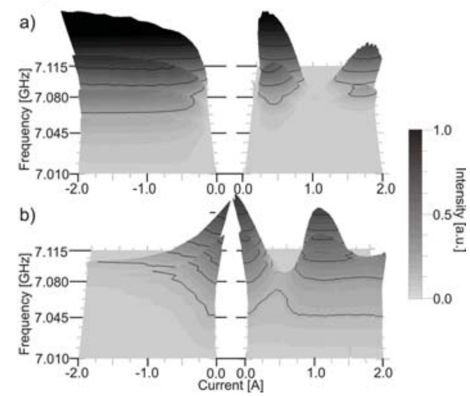

Relative intensities of reflected (a) and transmitted (b) BVMSW pulse

EP-02

A YIG/GGG/GaAs-Based Magnetically Tunable Wideband Microwave Band-Pass Filter Using Cascaded Band-Stop Filters*.

G. Qiu[1], B. T. Wang[2], *C. S. Tsai*[1,3]
1. Dept of Electrical Engineering and Computer Science, and Institute of Surface and Interface Science, University of California, Irvine, CA; 2. Wang, NMR Inc., Livermore, CA; 3. Institute of Electrooptics Engineering, National Taiwan University, Taipei, Taiwan

Electronically tunable microwave devices are essential in military and long-distance communications applications [1]. For example, tunable band-pass filters are used in the scanner receiver of electronic support measures systems. Yttrium iron garnet / gadolinium gallium garnet/gallium arsenide (YIG/GGG/GaAs)-based magnetically tunable band-stop filters with large bandwidth were realized recently [2].
In this paper, a microwave band-pass filter with large tuning ranges in center frequency and bandwidth using a pair of aforementioned band-stop filters in cascade is reported. Fig. 1 shows the basic band-stop filter utilized [2]. A YIG-GGG layer is laid upon the GaAs-based microstrip meander-line. An incoming microwave is coupled into the YIG/GGG layer and the maximum coupling and, thus, peak absorption of the microwave power occurs when its carrier frequency coincides with the ferromagnetic resonance (FMR) frequency of the YIG/GGG layer. A Y-direction bias magnetic field,H_{ext}, with non-uniform distribution along the X-axis is applied. The different bias magnetic fields at the four segments of the meander-line would result in a large widening of the resultant bandwidth in the stopband. Such band-stop filter has demonstrated a large tuning range in peak absorption frequency of 5.0 to 21.0 GHz and an absorption level of 35.5 dB together with a corresponding 3 dB bandwidth as large as 1.70 GHz[2]. Clearly, a band-pass filter with large tuning ranges in both the center frequency and the bandwidth can be realized using a pair of such basic band-stop filters in cascade in which different bias magnetic fields ($H_{02} > H_{01}$) are applied (Fig. 2).
In modeling and simulation, the band-pass filter was modeled as a series connection of the lumped-element equivalent circuit [3][4] for the two basic band-stop filters each with a four-segment meander-line. The combined equivalent circuit was then simulated using *Microwave Office* software. The simulated results on the transmission characteristics of the resulting band-pass filter are shown in solid line in Fig. 3.
The band-pass filter was constructed using a pair of wideband band-stop filters in cascade each with a YIG/GGG layer (YIG film 6.8 μm thick and 6.5×8.0mm^2 in the Y and X directions) laid upon a 4-segment microstrip meander-line. The microstrip meander-line with segment length of 5.7 mm was fabricated on a 350 μm thick GaAs substrate. The non-uniform bias magnetic field was facilitated by a pair of *NdFeB* permanent magnets [2]. The measured transmission characteristics of the band-pass filter (shown in circles in Fig. 3) at 2,750 Oe (H_{01}) and 4,150 Oe (H_{02}) shows a 3dB bandwidth of 1.73 GHz, out-of-band rejections of 33 dB, and an insertion loss of -4.25 dB. A good agreement between the measured and the simulated results in the tuning ranges of center frequency in the passband and the peak absorption frequency in the two guarding stopbands has been achieved. Note that the large difference between the simulated and the measured absorptions in the two stopbands was due to the limitation in the dynamic-range of the power sensor used. Finally, the insertion loss in the passband can be reduced using an optimized microstrip meander-line.
In conclusion, a wideband band-pass filter with tunable center frequency of 5.9 to 17.8 GHz and bandwidth of 1.27 to 2.08 GHz as well as large bandwidth in the two guarding stopbands has been realized using a pair of band-stop filters in cascade. By optimized design such magnetically-tunable microwave band-pass filters with even larger tuning ranges in both center frequency and bandwidth as well as smaller insertion losses can be realized.

*Supported by UC Discovery Program and Wang, NMR Inc. **[1]** See, for example,C.E.Patton, M.Z. Wu, K.R. Smith, and V.I.Vasyuchka, *Ferroelectrics*, 342, 101-106, 2006; V.G.Harris, Z. Chen, Y. Chen, S. Yoon, T.Sakai, A. Gieler, A.Yang, Y.He, K.S.Ziemer, N.X.Sun, and C.Vittoria, *Journal of Applied Physics*,99, 2006;B.K. Kuanr, D.L. Marvin, T.M. Christensen, R.E.Camley, and Z. Celinski,*Applied Physics Letters*,87, 2005. **[2]** G. Qiu, M. Kobayashi, B. T. Wang, and C.S. Tsai, *52nd Annual Conference on MMM*, Paper EH-03, Nov 5-9, TAMPA, FLORIDA, 2007;Also, to be published in special Issue, *Journal of Applied Physics*, May, 2008. **[3]** G. Bartolucci, R. Marcelli, *Journal of Applied Physics*,87, 6905-6907, 2000. **[4]** C.S.Tsai, G. Qiu, H. Gao, L. W. Yang, G. P. Li, S. A. Nikitov, and Y. Gulyaev, *IEEE Trans. on Magnetics*-41, 3568 – 3570, 2005.

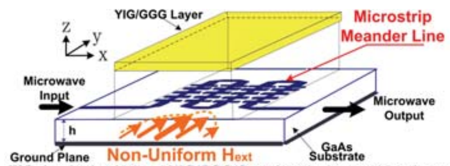

FIG. 1. A basic wideband YIG/GGG/GaAs-based microwave band-stop filter using microstrip meander-line and non-uniform bias magnetic field

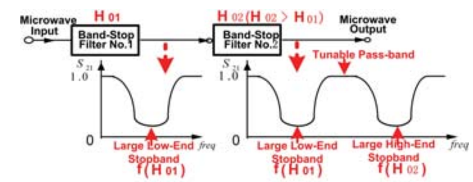

FIG. 2. Realization of a tunable band-pass filter using a pair of band-stop filters in cascade

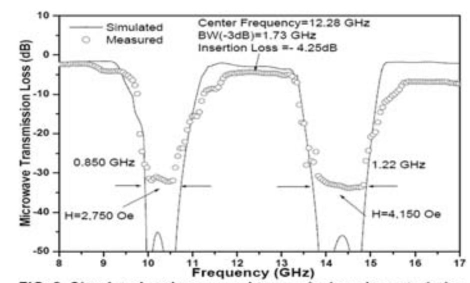

FIG. 3. Simulated and measured transmission characteristics of the tunable band-pass filter

EP-03

Bistable control of ferromagnetic resonance frequencies in ferromagnetic trilayered dots.

Y. Nozaki, K. Tateishi, S. Taharazako, S. Yoshimura, K. Matsuyama
Dept. of Electronics, Kyushu University, Fukuoka, Japan

In programmable microwave filters, it is essential to tune the frequency where the transmitted microwaves are strongly attenuated. In our previous study, we have numerically [1] and experimentally [2] examined that the ferromagnetic resonance (FMR) frequency f_{FMR} of NiFe/Cu/NiFe trilayered dot can be discontinuously changed by switching the relative orientation of magnetization from parallel (*P*) to antiparallel (*AP*). This is attributed to that the magnetostatic fringe-field exerted on each NiFe layer changes its polarity from negative to positive in relation to the magnetization direction. In this paper, to understand the influence of the fringe-field coupling on the FMR properties quantitatively, we have investigated the dependence of f_{FMR} on the aspect ratio of the dot. Figure 1 shows the scanning electron micrograph of the magnetic trilayered dots consisting of NiFe(18 nm)/Cu(9 nm)/NiFe(18 nm) fabricated on a microfabricated coplanar waveguide. The length *L* of the dot is varied from 0.5 to 2.5 μm, while the width *w* is always 0.3 μm. The variations of the FMR spectra of the dots during the magnetization reversal process was measured using a microwave probing system combined with a vector network analyzer. The external magnetic fields were applied at an angle θ_H to the long axis of the dot. Figure 2 shows the variation of f_{FMR} of the dot (*L*=2.5 μm) measured with sweeping the magnetic fields (θ_H=0) from 600 to -550 Oe. The f_{FMR} shows rapid increase at -92 and -397 Oe, where the magnetic configuration switches from *P* to *AP* and *AP* to *P*, respectively. In the case of *AP*, the increase of f_{FMR} with the magnetic field is smaller than that of the *P* configuration. This is attributable to the conflicted dependences of f_{FMR} on the magnetic field in top and bottom NiFe layers with *AP* configuration of magnetization [2]. Figure 3(a) shows the aspect ratio *L*/*w* dependence of f_{FMR}. The closed and open circles indicate the results for *P* and *AP*, respectively. In the case of *P*, the f_{FMR} decreases with decreasing the *L*/*w* because the shape anisotropy is suppressed. When *L*/*w* becomes smaller than 3.7, the metastable *P* configuration is no longer appeared at the remanent state by dominating the antiferromagnetic fringe-field coupling. It is interesting that the f_{FMR} of the dot with *AP* configuration shows little dependence on the aspect ratio. The decrease of *L*/*w* causes not only the suppression of the shape anisotropy but also the increase of the fringe field exerted on each NiFe layer. In the case of *AP*, the fringe field is positively applied to the magnetization in each NiFe layer so that the increase of the fringe field enhances the f_{FMR}. It is considered that the decrease of f_{FMR} owing to the suppression of shape anisotropy is compensated by the increase of the fringe field. Finally, we have tried to control the f_{FMR} at the remanent state by choosing the magnetized angle of the dot. Figure 3(b) shows the f_{FMR} at the remanent state as a function of θ_H. The strength of the magnetic field used to magnetize the dot is 1.4 kOe. It is obviously observed that the high-f_{FMR} state implying the *AP* configuration appears at θ_H in the range from 88 to 92 degrees, while the low-f_{FMR} state suggesting the *P* configuration is preferentially realized as $\theta_H < 88$ degrees. The opposed rotation of magnetization resulting the *AP* configuration at large θ_H is occurred to decrease the magnetostatic coupling energy of the dot. In the demagnetizing process along the in-plane hard axis of the dot, there is no energy barrier on the way to the *AP* configuration. As a consequence, the complete *AP* configuration can be realized even if the switching field of each magnetic layer is distributed in the multilayer. It is considered that this method is very useful to create the *AP* configuration especially for the multilayered dot with a large stacking number.

[1] M. Zhang et al., "Reconfigurable ferromagnetic resonance properties in nanostructured multilayers.", J. Appl. Phys. 99, 08G307 (2006).

[2] Y. Nozaki et al., "Influence of an interlayer magnetostatic coupling on ferromagnetic resonance frequencies of lithographically-patterned ferromagnetic bilayers", Paper ET-16, MMM 2007 (Tampa, FL), 8 Nov. 2007.

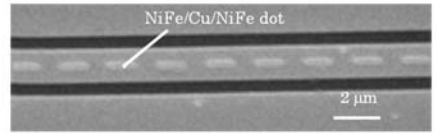

Fig. 1 Scanning electron micrograph of NiFe/Cu/NiFe dot array fabricated on a coplanar waveguide.

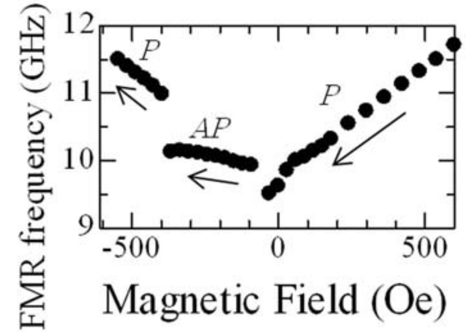

Fig. 2 Variation of f_{FMR} during the magnetization reversal process of the dot with *L*=2.5 μm.

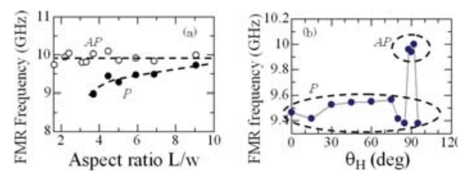

Fig. 3 Dependence of f_{FMR} at the remanent state on (a) *L*/*w* and (b) θ_H.

EP-04

An Electric Field Tunable Millimeter-Wave Ferrite-Piezoelectric Phase Shifter.

A. S. Tatarenko, *G. Srinivasan*
Physics, Oakland University, Rochester, MI

Abstract
A novel electric field tunable phase shifter with a barium ferrite-lead zirconate titanate (PZT) bilayer is designed and characterized. The 50-GHz phase shifter is based on ferromagnetic resonance (FMR) in barium ferrite. An electric field applied across PZT produces mechanical deformation that manifests as a shift in FMR, and therefore, a differential phase shift. Estimates of the phase shifts are in agreement with data.

Introduction
Ferrites are materials of choice for tunable microwave devices. The magnetic field (H) tuning of such devices could be achieved over a very wide frequency range, but is slow and requires high operating power. A similar, but rapid tunability and low-power requirements could be accomplished with ferroelectrics and electric fields (E). A combination of ferrite and ferroelectrics, therefore, could provide simultaneous E and H-tuning and the advantages of both methods [1].

This work is on an electric field controlled mm-wave barium hexaferrite-lead zirconate titanate (PZT) phase shifter operating close to FMR. In the presence of E, the piezoelectric deformation in PZT will result in an internal field $\delta H = - A E$ (A is the magneto-electric coupling coefficient) in the ferrite, leading to a frequency shift $\delta f = - 2.8$ GHz/kOe δH in FMR [2] and a differential phase shift $\delta\phi$. Here we discuss the performance characteristics of a 50 GHz barium ferrite-PZT phase shifter.

Experiment
First we measured the ME effect induced shift in FMR profiles. A bilayer of ferrite-PZT was prepared by bonding a single crystal ferrite slab to a PZT plate and it formed the short of a coaxial-to-wave guide adapter. Absorption vs f profiles were obtained for E and H perpendicular to the bilayer plane and parallel to the magnetic easy axis of the ferrite. Several peaks due to magnetostatic forward volume waves were observed and representative data in Fig.1 shows the E-induced frequency shift for the dominant mode. As E was increased from 0 to 8 kV/cm, a down-shift in frequency of 30 MHz was measured. The shift reversed sign with the reversal of direction of E.

The phase shifter studied consisted of a 3.5x1.6x0.1 mm$\underline{3}$ bilayer placed on the narrow side a rectangular waveguide. Phase vs. f characteristics as in Fig.2 were obtained as a function of H and for E=0 and 8 kV/cm. One observes a near-linear variation in the phase shift with E. Theoretical estimates of the phase shift are in good agreement with the data, as seen in Fig.2. The insertion loss was quite high, on the order of 15-20 dB.

The work was supported by grants from the Office of Naval Research and the Army Research Office.

1. "Ferrite-piezoelectric layered structures: Microwave magnetoelectric effects and electric field tunable devices," G. Srinivasan and Y. K. Fetisov, Ferroelectrics 342, 65 (2006).

2. "Microwave magnetoelectric effects in single crystal bilayers of yttrium iron garnet and lead magnesium niobate – lead titanate," S. Shastry and G. Srinivasan, M.I. Bichurin, V.M. Petrov, A.S. Tatarenko, Phys. Rev. B 70, 064416 (2004).

3. "A magnetoelectric microwave phase shifter," A. S. Tatarenko, G. Srinivasan and M. I. Bichurin, Appl. Phys. Lett. 88, 183507 (2006).

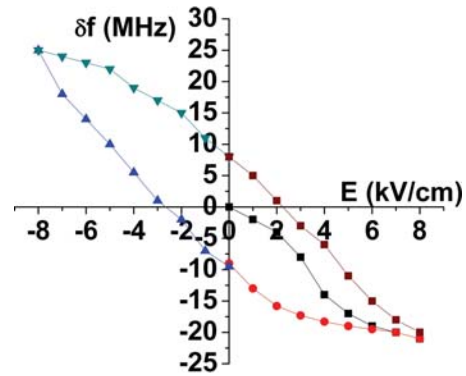

Fig.1: Electric field induced frequency shift of ferromagnetic resonance in a bilayer of single crystal barium ferrite and PZT for H=5968 Oe along c-axis.

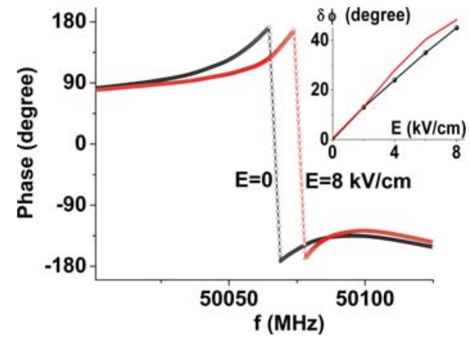

Fig. 2. Phase vs. frequency characteristics and differential phase shift vs. E for a bilayer of barium ferrite-PZT for H=5968 Oe along the c-axis.

EP-05

Design of Scandium and Indium doped hexaferrite microstripline phase shifters for X-band applications.

T. Sakai, *C. Chinnasamy*, V. Ilancheliyan, S. Yoon, C. Vittoria, V. G. Harris
Electrical&Computer Engineering, Northeastern university, Boston, MA

Tunable ferrite phase shifters are widely used as a basic component of microwave circuits in communication and radar systems. To meet the industry requirements in communication and radar systems, the new generation of ferrite phase shifters should be able to work at K-band and higher frequencies. However, at such high frequencies, ferrite phase shifters using spinel or garnet need high biasing field (5 kOe), applied over the length of the device, which is too excessive for practical devices. The solution to this problem in ferrite is to use self-biased hexaferrite, which is inherent of large anisotropy field with self biasing properties either in-plane or out-of-plane orientation. (Sc) and Indium (In) substituted hexaferrite materials are candidates for the ferrite substrate in the next generation of planar tunable ferrite phase shifters operating at millimeter-wavelength frequencies. We have synthesized, self-baised, designed, fabricated, measured, and modeled such a phase shifter operating at 10 GHz that utilizes a (Sc) and Indium (In) substituted hexaferrite crystals.
Scandium ($BaFe_{12-x}Sc_xO_{19}$, x= 0.5, 1) and Indium substituted ferrites ($BaFe_{12-y}In_yO_{19}$, y= 1, 2) have been prepared by using the modified coprecipitaion technique followed by sintering at moderate temperature. XRD patterns in Fig. 1 confirmed the formation of single phase Sc/In doped Ba-hexaferrite with the magnetoplumbite structure. Scanning electron micrograph (Fig. 2) of the $BaFe_{11}In_1O_{19}$ sample sintered at 1150 $^{\circ}$C shows the formation of larger grains, which are micrometer size and have better intergrain connectivity. After ball milling the samples were screen printed on alumina substrates and applied with high magnetic field (1.5 T) parallel to the surface of alumina substrates. All in-plane oriented thick films were annealed at certain temperatures and are measured with X-ray diffractometer, SEM (Scanning Electron Microscope), VSM (Vibrating Sample Magnetometer), and FMR (Ferromagnetic Resonance). The annealed in-plane oriented samples are substituted in a phase shifter design as shown in (Fig. 3). The design and modeling combined the conjugate method of microstripline on dielectric substrate and magnetostatic mode calculation in ferrites. This combination of a substantial phase shift and a relatively small external biasing field makes the Sc and In substituted hexaferrites as promising materials for low frequency (X-band) phase shifters. The results will be discussed in detail in the paper.

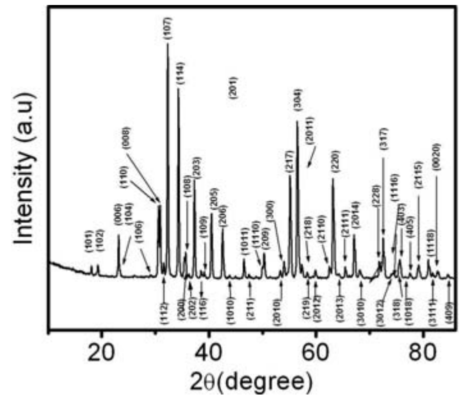

Fig.1 Fig. 1. X-ray diffraction pattern of the $BaFe_{11}Sc_1O_{19}$

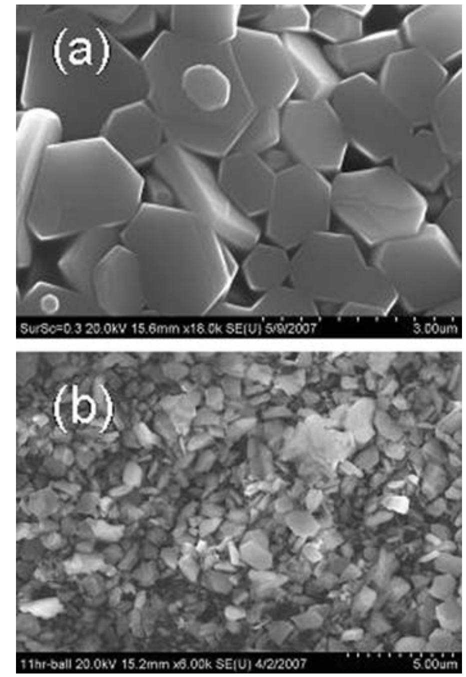

Fig. 2. Scanning electron micrographs of $BaFe_{11}Sc_1O_{19}$ (a) sintered at 1150 $^{\circ}$C for 2 h, and (b) after ball milling.

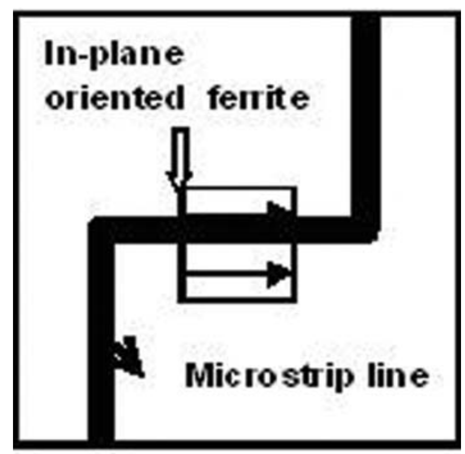

Fig. 3. Fabrication of microstrip line based phase shifter.

EP-06

Propagation characteristics of magnetostatic surface waves in a YIG-based one-dimensional magnonic crystal composed of rubber magnets.

K. Togo[1], K. Hatafuku[1], M. E. Dokukin[1], J. Kim[1], K. Shin[2], M. Inoue[1]
1. Toyohashi University of Technology, Toyohashi, Japan; 2. Kyungsung University, Pusan, South Korea

On the analogy of photonic crystals, where light traveling is modified via photonic bandgap and localization of waves originating in the spatial periodicity of propagation media, magnonic crystal is indeed an attractive medium for controlling the propagation of magnetostatic surface waves (MSSWs) [1]. In fact, Tkachenkoa et al. recently reported that the propagation and manipulation of spin waves in a magnonic crystal with an internally structured defect [2]. The propagation mechanism of MSSW is due to the dipole-dipole interaction of magnetization, and hence the magnetic periodicity such as a magnetic domain alignment inherently attributes to the interference effect of MSSW, leading to the bandgap nature in MSSW propagations. In this respect, we here demonstrate the propagation characteristics of MSSW in a YIG-based one-dimensional magnonic crystal whose magnetic periodicity was formed with rubber magnets.

The one-dimensional magnonic crystal and the measurement system of MSSW are illustrated in Fig. 1. A YIG film (14 µm thickness) grown epitaxially on a GGG substrate was used as a base propagation medium of MSSW, on which rubber magnets (0.5 mm width and 0.8 mm thickness) were placed at 0.5 mm spatial interval, so as to form the one-dimensional magnetic periodicity. For exciting and detecting MSSWs, a pair of Cu microstrip lines (150 µm width and 18 µm thickness) formed on a Teflon substrate by photolithography was used. An external magnetic field H_0 ranging from 100 Oe to 700 Oe was applied in plane perpendicular to the propagation direction of MSSWs. The propagation characteristics of MSSWs were examined with a network analyzer.

Figure 2 shows the transmission spectra of MSSWs observed in the magnonic crystal (solid curve) and the YIG film without the rubber magnets (broken curve). It is clearly seen at around 2 GHz that a stop band appeared for the case of magnonic crystal. The wavelength λ of MSSW is given by
$\lambda=4\pi d/\ln(\omega^2_M/(2\omega_H+\omega_M)^2-4\omega^2)$
with and, where γ is the gyromagnetic constant, H_0 is the external magnetic field, ω is the angular frequency of MSSW, while d and Ms are, respectively, the YIG film thickness and the saturation magnetization (1735 G). When $f = \omega/2\pi = 2$ GHz and $H_0 = 200$ Oe, λ is evaluated to be 1 mm, whose value quantitatively coincides with the periodicity of rubber magnets (0.5 mm interval), suggesting that the magnetic periodicity is effective for obtaining the artificial controllability of MSSWs. This is also confirmed by evaluating the center frequency of stop band as a function of the external magnetic field H_0. As shown in Fig. 3, by increasing the intensity of magnetic field, the stop band frequency increased monotonically, where good quantitative agreements among the experimental and theoretical values were obtained.

The work was supported in part by the Gran-in-Aid for Scientific Research (S), No. 17106004.

[1] Daniel D. Stancil, Theory of Mgnetostatic Waves, (Springer - Verlag, New York, 1993).

[2] V.S. Tkachenkoa, V.V. Kruglyakb and A.N. Kuchko : “Spin wave spectrum of a magnonic crystal with an internally structured defect”, Physica B 370 pp.73–77 (2005).

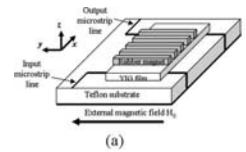

Fig. 1 Schematic drawings of the media and measurement system; (a) oblique view and (b) top view.

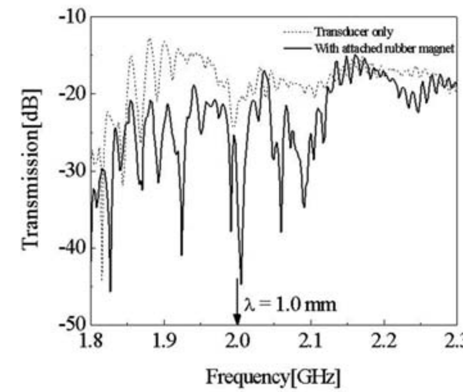

Fig. 2 Transmission frequency spectra of MSSWs in the magnonic crystal (solid curve) and the YIG substrate (broken curve) under the bias field of 200 Oe.

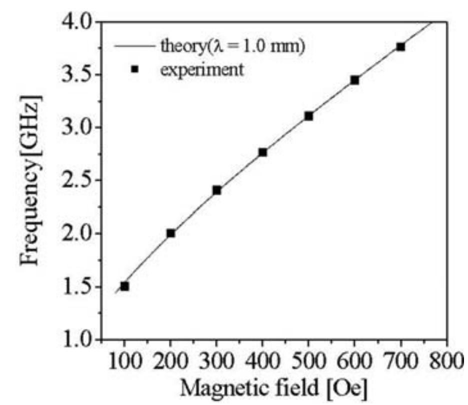

Fig. 3 Change in the stop band centre frequency as a function of the external magnetic field.

EP-07

A magnetosensitive microwave absorption characterization of terbium.

G. Alvarez[1], H. Montiel[2], R. Zamorano[3], R. Valenzuela[1]
1. Departamento de Materiales Metálicos y Cerámicos, Instituto de Investigaciones en Materiales de la Universidad Nacional Autónoma de México, Ciudad de México, Mexico; 2. Centro de Ciencias Aplicadas y Desarrollo Tecnológico de la Universidad Nacional Autónoma de México, Ciudad de México, Mexico; 3. Departamento de Ciencias de los Materiales, Instituto Politécnico Nacional, Ciudad de México, Mexico

We report on the effects of temperature and dc magnetic field on magnetosensitive microwave absorption measurements at 8.8-9.8 GHz (X-band), in powder samples of terbium. We have recently implemented two novel experiments to measure the magnetosensitive non-resonant microwave absorption [1-4], known as magnetically modulated microwave absorption spectroscopy (MAMMAS), and the low-field microwave absorption (LFA). In the MAMMAS measurement, the sample is subjected to a constant dc field, and its microwave absorption behavior is obtained as a function of temperature [1,3,4]. LFA measurement refers to the non-resonant microwave absorption around the zero DC field, in otherwise typical electron paramagnetic resonance setup [2,4-6].
Figure 1 shows that the MAMMAS signal increases as temperature decreases from 300 K to TN=227 K. In this temperature range the material is paramagnetic (PM)[7], and the paramagnetic microwave absorption increases [3,4] with the decrease in temperature. MAMMAS response reaches a maximum at TN, associated with the onset of an antiferromagnetic (AFM) helical ordering [8]. The absorption then decreases from TN and about TC= 220 K, a change in slope points to another microwave energy-absorbing process that changes the previous behavior; this feature is associated with a subsequent order-order transformation [8]. After that, the microwave absorption decreases with decreasing temperature until TF= 214 K is reached. Below TF, the microwave absorption slowly increases and we can attribute this behavior of the MAMMAS profile to the presence of a ferromagnetic (FM) structure, where the magnetic moments lie in the plane perpendicular to the hexagonal axis [8] of the crystalline lattice.
A frozen-strain model has been proposed [9] to take into account the influence of magneto-elastic interactions in the microwave absorption of Tb. This model predicts a non-resonant microwave absorption (LFA) at about 10 GHz and T= 230 K, which has not been observed [10,11]. In this work, however, we report the existence of such LFA signal at X-band, see inset in Fig. 1, in good agreement with the frozen-strain model. We discuss all the obtained results to give a new look, based on novel techniques, to an old problem.

[1].- G. Alvarez and R. Zamorano, J. Alloys Compd. 369 (2004) 231.

[2].- H. Montiel, G. Alvarez, I. Betancourt, R. Zamorano and R. Valenzuela, Appl. Phys. Lett. 86 (2005) 072503.

[3].- G. Alvarez, R. Zamorano, J. Heiras, M. Castellanos and R. Valenzuela, J. Magn. Magn. Mater. 316 (2007) e695.

[4].- G. Alvarez, R. Font, J. Portelles, R. Zamorano and R. Valenzuela, J. Phys. Chem. Solids 68 (2007) 1436.

[5].- F. J. Owens, J. Phys. Chem. Solids 58 (1997) 1311.

[6].- F. J. Owens, J. Phys. Chem. Solids 66 (2005) 793.

[7].- B.D. Cullity, Introduction to magnetic materials, ed. Addison-Wesley (Reading, MA, 1972).

[8].- W. C. Koehler, H. R. Child, E. O. Wolland and J. W. Cable, J. Appl. Phys. 34 (1963) 1335.

[9].- T. K. Wagner and J. L. Stanford, Phys Rev. 184 (1969) 505.

[10].- D. M. S Bagguley and J. Liesegang, Phys Letters 17 (1965) 96.

[11].- T. K. Wagner and J. L. Stanford, Phys Rev. B 1 (1970) 4488.

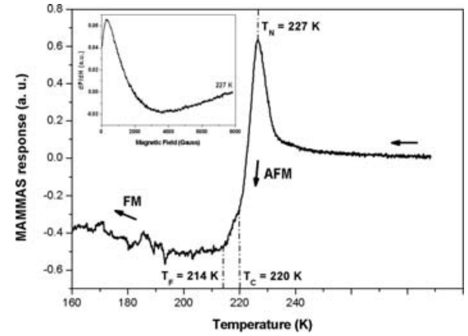

Fig. 1. MAMMAS spectrum of Tb powders for a decreasing temperature. The inset shows the LFA spectrum of Tb for 227 K.

EP-08

Magnetic tuning of surface acoustic wave devices within high frequency range.

C. Cavaco[1], L. A. Francis[2,1], L. Lagae[1], G. Borghs[1]
1. IMEC, Leuven, Belgium; 2. Université catholique de Louvain, Louvain-la-Neuve, Belgium

Surface Acoustic Wave (SAW) devices play a key role in wireless communication and sensor applications. SAW devices are e.g. commonly used in signal filtering for their small size, small power consumption and costs, although their frequent lack on tunability of acoustic wave velocity restricts their usefulness in crucial areas such as time delay and tuneable filter applications [1]. Several approaches have been used to address this problem [1-3], but until now tunable SAW devices working at frequencies above 1 GHz where never attained.
In this research a magnetic method was used to induce a variation in the acoustic velocity of SAW devices in a high frequency range. More specifically, we exploited the magnetoelectric effect defined as the induction of magnetization by an electric field or of electrical polarization by a magnetic field [4]. This effect usually originates in a magnetoelastic coupling, i.e., interaction between the magnetization and the strain of a magnetic material and has recently been applied to obtain electrical control over the system magnetic properties or vice-versa [5,6].
The used devices, as shown in Fig. 1, essentially comprise a $Co_{50}Fe_{50}$ magnetostrictive thin film sputtered in between two gold interdigital transducers (IDTs), i.e., in between two interpenetrating finger shaped electrodes over a piezoelectric substrate, $LiNbO_3$.
In this method surface acoustic waves are generated at the free surface of the piezoelectric substrate by applying a voltage to an input metal-film IDT which converts the voltage signal into mechanical waves, the second IDT works as an output transducer converting back the mechanical waves to an output voltage.
Since the thin $Co_{50}Fe_{50}$ film is magnetostrictive, its effective elastic modulus changes as the film is magnetized. Thus, a variation of the applied external magnetic field induces changes in the acoustic wave velocity, which can be measured through the phase shift created in the SAW delay line.
These phase shifts, as well the frequency spectrum, were measured using a HP 8753D Network analyzer (transmission parameter S_{21}). The induced phase shift across the device is converted to a variation on the acoustic velocity by:
$\Delta\nu = \Delta\theta\ \lambda\ \nu_0 / 360°\ L_{film}$;
where $\Delta\nu$ is the SAW velocity variation, $\Delta\theta$ is the phase variation induced by the magnetelastic coupling, λ is the SAW wavelength that corresponds to four times the width of one of the IDT fingers, L_{film} is the magnetostrictive thin film length and ν_0 is the substrate SAW velocity that is obtained through the relation $\nu = f \times \lambda$, where f is the center frequency of the SAW device.
The typical frequency response for a fabricated SAW device working at 1.49GHz and its phase and corresponding relative velocity changes in function of the applied external magnetic field are shown in Fig. 2.
The verified 0.11% variation of the SAW device acoustic velocity with an external magnetic field of 80mT, proves that it is possible to magnetically achieve a similar tunability to the one obtained through well know methods like voltage tuning methods. These voltage tuning methods work at lower frequencies (e.g. 660MHz [1]) or require extremely high voltages (e.g. 6kV [2]) to achieve a 0.62% or 0.1% variation of the SAW device acoustic velocity, respectively.
In conclusion, we have achieved a reproducible magneto-electric tunability over the acoustic velocity of a SAW device using the magnetostrictive and piezoelectric properties of $Co_{50}Fe_{50}$ thin films and $LiNbO_3$ substrates, respectively. The achieved tunability is similar to what was previously obtained through voltage induced methods but with higher operation frequencies for the magnetic method.

[1] J. Zhu et al., Appl. Phys. Lett. 89, 103513 (2006)

[2] A. J. Budreau et al., Proc. IEEE Ultrason. Symp. 1, 399 (1982).

[3] W. Robbins and A. Hietala, IEEE Transactions on Ultrasonics, Ferroelectrics and Frequency Control, vol. 35, No. 6, (1988).

[4] M. Fiebig, J. Phys. D 38, R123 (2005).

[5] V. M. Laletin et al., Appl. Phys. Lett. 87, 222507 (2005)

[6] H. Boukari et al., J. Appl. Phys. 101, 054903 (2007)

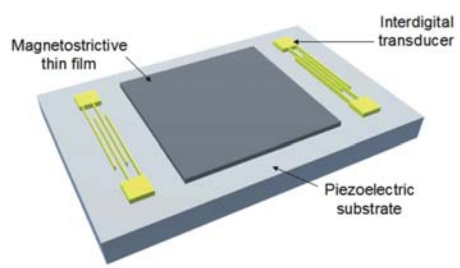

Fig. 1. Basic schematic of the used SAW devices.

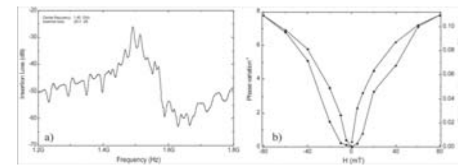

Fig. 2: a) Frequency response and b) Phase shift and relative velocity change in function of the applied external magnetic field of a fabricated 1.49 GHz band SAW device.

EP-09

Microwave Absorption Properties of The Hierarchically Branched Ni Nanowires Composites.

L. Qiao, J. Wang, X. Han, B. Gao, F. Wen, F. Li
Lanzhou University, Institute of Applied Magnetism, Key Laboratory for Magnetism and Magnetic Materials of Ministry of Education, LanZhou, China

The microwave absorption properties of the ferromagnetic metal-based materials draw much attention due to their advantages of higher saturation magnetization than ferrites[1][2][3].
In this work, the hierarchically branched Ni nanowires are fabricated by the electrodeposition within the branched nanoporous of anodic aluminum oxide (AAO) templates.
We fabricated the large area of branched nanoporous of AAO templates with 20×20 cm^2 by reducing the anodizing voltage multiple times in the anodization[4]. Initially, the anodizing voltage is 80 V, during the anodization, the anodizing voltage was reduced by a factor of 1/2 to form Y-branched pores. Ni was deposited in the pores by ac electrolysis in an electrolyte consisting of $NiSO_4$ (120g/L), boric acid (45g/L). Branched Ni nanowires were liberated from the AAO film by dissolving the alumina layer with 0.1 mol/L NaOH solution.
Fig. 1 shows the SEM micrographs of the hierarchically branched Ni nanowires, large-scale nanowires with 100 nm in diameter and 10-15μm in length were prepared. The diameter of each wire is below 1μm, which would decrease skin effect.
The composite samples were prepared by mixing the branched Ni nanowires with epoxy resin with 30% volume concentration of the particles. Fig.2 shows the frequency dependence of the relative complex permittivity of the sample. It can be found that the values of the real part of permittivity is about 9, and the imaginary part is about 0.5 over the 1-12 GHz
frequency range.
Fig. 3 shows the complex permeability of the composites. It is note worthy that the maximum value of the imaginary part of permeability appearing at 9 GHz implies that the natural resonance. According to the Kittel's equation, the natural resonance of nanowire is : $f_r = \gamma(H_a+4\pi M_s/2)$, where γ=2.8 GHz/kOe is the gyromagnetic ratio, the theoretical natural resonance frequency should be around 8.6 GHz. The skin-effect criterion is related to expression[5]:$\mu''(\mu')^{-2}f^{-1}=2\pi\mu_0 d^2\sigma/3$. Fig. 4 shows the value of $\mu''(\mu')^{-2}f^{-1}$ for the sample is markedly changed over 2-15 GHz, and the change extent is bigger than 0.03 ns. Therefore, it means that the magnetic loss in branched Ni nanowires is mainly caused by the natural resonance.
The reflection loss R (dB) of the branched Ni nanowires/epoxy resin composites were calculated, as shown in Fig. 5. It is shown that the maximum reflection loss reaches 13 dB at 8 GHz with 3 mm in thickness.

[1] C. Brosseau, and P. Talbot, J. Appl. Phys. 97, 104325 (2005).

[2] L. Z. Wu, J. Ding, H. B. Jiang, C. P. Neo, L. F. Chen, and C. K. Ong, J. Appl. Phys. 99, 083905 (2006).

[3] Jiu-rong Liu, Masahiro Itoh, Masao Terada, Takashi Horikawa, and Ken-ichi Machida, Appl. Phys. Lett. 91, 093101 (2007).

[4] Guowen Meng, Yung Joon Jung, Anyuan Cao, Robert Vajtai, and Pulickel M. Ajayan, Nature, 102, 7074 (2005)

[5]M. Z. Wu, Y. D. Zhang, S. Hui, T. D. Xiao, S. H. Ge, W. A. Hines, J. I. Budnick, and G. W. Taylor, Appl. Phys. Lett. 80, 4404 (2002).

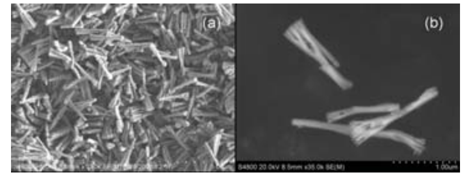

FIG. 1 (a) (b) SEM micrographs of the hierarchically branched Ni nanowires.

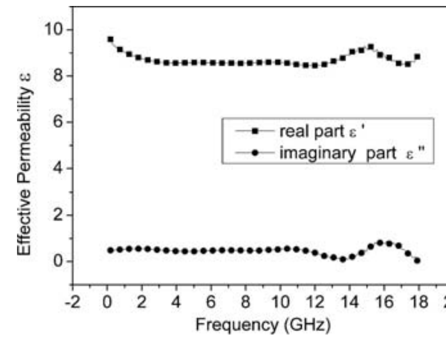

FIG. 2 Complex permittivity spectra for the branched Ni nanowires/epoxy resin composites.

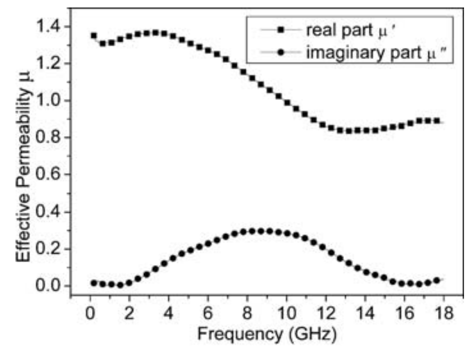

FIG. 3 Complex permeability spectra for the branched Ni nanowires/epoxy resin composites.

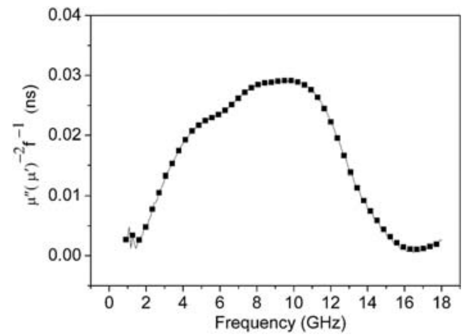

FIG. 4 values of μ″(μ′)-2f -1 for the branched Ni nanowires vs frequency.

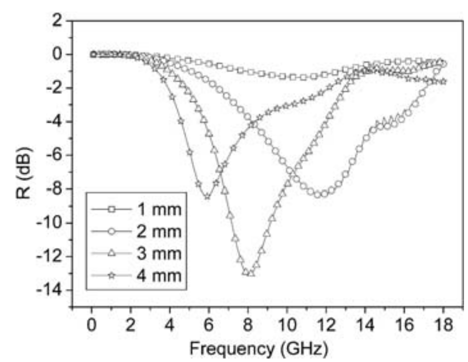

FIG. 5. The comparison of reflection loss calculated for the composites of the branched Ni nanowires - epoxy resin with thicknesses of 1–4 mm.

EQ-01

Magnetoresistance in Co/ZnO films.

X. Li[1,2], Z. Quan[2], *X. Xu*[2], H. Wu[2,1]
1. College of Chemistry and Chemical Engineering, Taiyuan University of Technology, Taiyuan, China; 2. School of Chemistry and Materials Science, Shanxi Normal University, Linfen, China

The discovery of giant magnetoresistance (GMR) in Fe/Cr multilayers[1] has attracted considerable scientific interest. Since then, many efforts have been devoted to studying the magnetization and magnetoresistance (MR) of multilayered systems. MR has also been observed in Fe/ZrO_2 discontinuous multilayers[2] and Co-ZnO inhomogeneous magnetic semiconductor films[3] *etc*. However, the mechanism of the presence of MR in transition metal doped semiconductor films is far from being fully understood.

In this work, a series of $[Co(0.6\ nm)/ZnO(x\ nm)]_{60}$ (x=0.3~3) multilayer films were prepared on glass substrates by magnetron sputtering at room temperature. After deposition, the samples were annealed under the pressure of 2×10^{-4} Pa at 400 °C for 120 min.

Fig. 1 shows the variation of MR ratio of $[Co(0.6\ nm)/ZnO(x\ nm)]_{60}$ films measured at room temperature with ZnO layer thickness. Here the MR ratio was calculated by $MR=[R(H)-R_0]/R_0\times100\%$, where R(H) and R_0 are the resistances with/without an applied magnetic field. When ZnO layer thickness is increased from 0.3 nm to 3 nm, MR ratios of the as-deposited Co/ZnO films are gradually decreased and MR ratios of the annealed films are increased. Fig. 2 shows the typical dependence of MR ratio on the magnetic field, which clearly reflects that MR ratios are strongly dependent on the ZnO layer thickness and the post-annealing process.

ZnO layer thickness also strongly affects R_0 values of Co/ZnO films (as seen in Fig. 3). With increasing ZnO layer thickness, R_0 values of both the as-deposited films and the annealed ones are increased, which is attributed to the increase of ZnO semiconductor fraction. The as-deposited films may behave the multilayers structure, whereas the post-annealing deteriorates the multilayers structure and leads to granular films. The granular structural $[Co(0.6\ nm)/ZnO(0.3\sim3\ nm)]_{60}$ films after annealing can be divided into three distinct structural regimes. (1) ZnO layer thickness≤0.7 nm: The large MR ratios of the as-deposited Co/ZnO films may come from the coupling between the magnetic Co layers mediated by the non-magnetic ZnO layers. Whereas, when the films were annealed at 400 °C for 120 min, Co grains could be grown and touched each other. This leads to the remarkable reduction of both R_0 and MR ratios. (2) ZnO layer thickness≥1 nm: The thicker ZnO layer in the as-deposited films makes the coupling between Co layers very weak, which causes MR ratios small. Co grains can be grown and dispersed in ZnO semiconductor host after annealing. Spin related tunnelling takes place between isolated Co grains under applying a magnetic field, this is the main reason for the increase of MR ratios in the annealed Co/ZnO films as compared with the as-deposited ones. (3) 0.7 nm≤ZnO layer thickness≤1 nm: This is the regime in which ZnO fraction is suitable to form labyrinth structure after annealing.

In summary, a series of $[Co(0.6\ nm)/ZnO(x\ nm)]_{60}$ multilayers were systematically investigated. We found a large MR ratio of 10.4% in as-deposited Co/ZnO films. MR ratios and R_0 are strongly dependent on the ZnO layer thickness and the post-annealing process.

The authors are grateful for the supports from NSFC (No. 10574085 and No. 60776008), NCET-07-0527 and YSF of Shanxi (No. 2007021022).

[1] M. N. Baibich, J. M. Broto, A. Fert, et al., Phys. Rev. Lett., 61 (1988) 2472.

[2] P. Auric, J. S. Micha, O. Proux, et al., J. Magn. Magn. Mater., 217 (2000) 175.

[3] S. S. Yan, C. Ren, X. Wang, et al., Appl. Phys. Lett., 84 (2004) 2376.

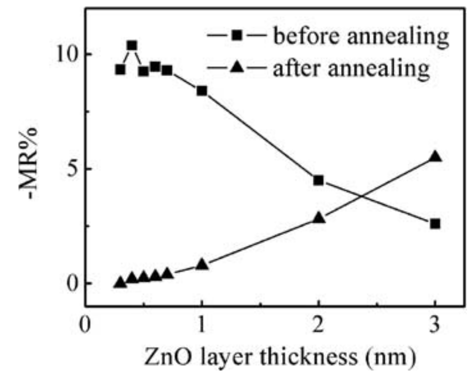

Fig. 1 The variation of MR ratios of $[Co(0.6\ nm)/ZnO(x\ nm)]_{60}$ (x=0.3~3) films with ZnO layer thickness

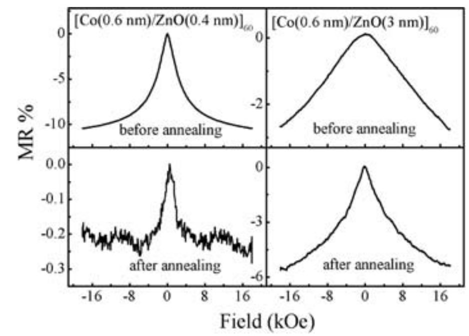

Fig. 2 The dependence of MR ratios of $[Co(0.6\ nm)/ZnO(0.4, 3\ nm)]_{60}$ films on the magnetic field

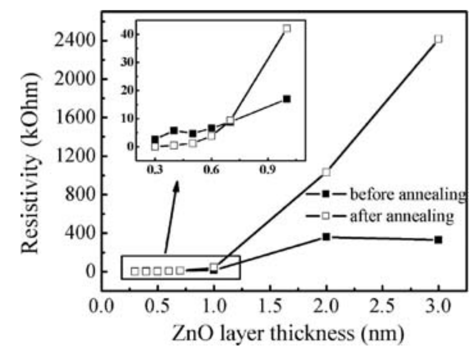

Fig. 3 R_0 values of $[Co(0.6\ nm)/ZnO(x\ nm)]_{60}$ (x=0.3~3) films as a function of ZnO layer thickness. The inset is the enlarged drawing of the rectangle.

EQ-02

Temperature dependent magneto-transport studies in ferromagnetic $Ge_{1-x}Mn_xTe$.

C. Sim[1,2], W. Chen[2], S. Lim[2], J. Bi[1], K. Teo[1], T. Liew[2], T. Chong[2]
1. Electrical & Computer Engineering, National University of Singapore, Singapore, Singapore;
2. Data Storage Institute, Singapore, Singapore

<p>**Introduction**

Advances in diluted magnetic semiconductors (DMS) has opened up new perspectives for realizing spintronics devices which combine microelectronics with spin-dependent effects that arise from the interaction between spin of the carrier and the magnetic properties of the material. The application of non-equilibrium growth methods such as molecular beam epitaxy (MBE) has been demonstrated to offer doping in excess of the thermodynamic solubility limit [1,2]. However for many semiconductor materials, the bulk solid solubility of magnetic or electronic dopants is not favorable for the coexistence of carriers and spins in high densities. In this aspect, IV-VI ferromagnetic $Ge_{1-x}Mn_xTe$ is an interesting material to study because it has been reported to have a high solubility limit of more than 95% Mn in GeTe and a highest Curie temperature of T_c = 140K [3]. So far, a comprehensive understanding of the magneto-transport behavior of this material has not yet been achieved. In this work, we conduct the temperature dependent magneto-transport studies on a $Ge_{1-x}Mn_xTe$ film with high Mn composition of x = 0.98 prepared on BaF_2 (111) substrate using a MnTe buffer layer by solid source MBE technique.
<\>>

Experimental Results

Figure 1 shows the M-H curves of the $Ge_{0.02}Mn_{0.98}Te$ film measured at 5 K with field applied in-plane (H ∥ plane) and perpendicular to plane (H ⊥ plane). We did not observe distinct magnetic anisotropy for different applied-field directions as the difference in coercivity is very small. The ratio of $M_r(\|)/M_r(\perp)$ increases from 1.44 at T = 5 K to 2.58 at T = 90K, where $M_r(\|)$ and $M_r(\perp)$ are the in-plane and perpendicular remanences, respectively. Our temperature dependence of coercive fields in the two cases is nearly the same. The result indicates that the magnetic moments are not all in-plane but part of them are out of plane. The existence of the out-plane magnetic moments could be due to surface roughness which may induce spin disordering in the film surface. As the temperature increases, the disordered spins are randomized, therefore the out-plane magnetic moments are attenuated at near the T_c. Magnetoresistance (MR) measurements were performed with (H ∥ plane) and (H ⊥ plane) from 20 to 120 K as shown in Fig. 2. A negative MR was observed for all temperature range for (H ∥ plane) [Fig. 2(a)]. Figure 2(b) shows the MR behavior of the (H ⊥ plane). The MR is entirely negative for T < 75 K. The disappearance of the negative MR above T > 95 K could be represented as a transition from ferromagnetism to paramagnetism at T_c = 95K which is consistent with our M-T curve results.

[1] H. Ohno et al., Appl. Phys. Lett. 69, 363 (1996).

[2] Munekata, H., H. Ohno, S. von Molnár, A. Segmüller, L. L. Chang and L. Esaki, Phys. Rev. Lett. 56, 777 (1989).

[3] Y. Fukuma, T. Murakami, H. Asada, and T. Koyanagy, Physica E (Amsterdam) 10, 273 (2001).

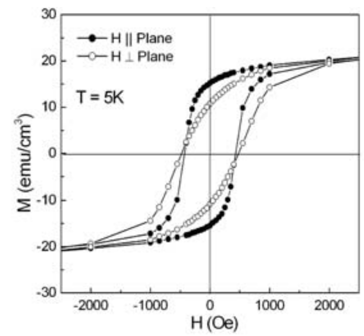

Figure 1: Temperature dependence of M-H curves of $Ge_{0.02}Mn_{0.98}Te$ with H ∥plane (solid circle) and H ⊥ plane (open circle).

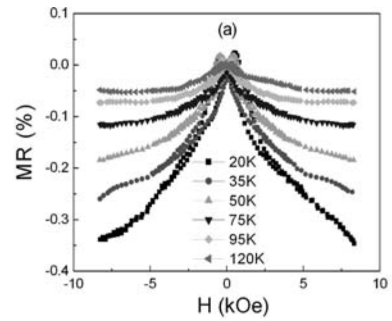

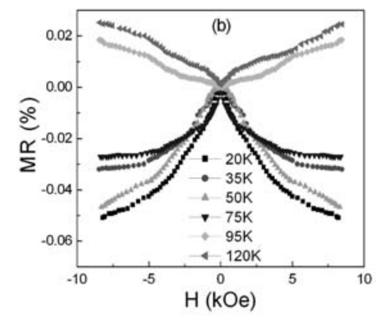

Figure 2: MR as a function of temperature for $Ge_{0.02}Mn_{0.98}Te$ with (a) H ∥plane and (b) H ⊥ plane.

EQ-03

Exponential decrease of neutral dangling bonds density in rare-earth doped amorphous Si films.

W. Iwamoto[1], *P. G. Pagliuso*[1], C. Rettori[1], A. R. Zanatta[2]
1. DEQ, IFGW - Unicamp, Campinas, Brazil; 2. Instituto de Física de São Carlos, USP, São Carlos, Brazil

Amorphous silicon films doped with rare-earth elements (*a*-Si:RE = Y, Gd, Er, and Lu) have been prepared by co-sputtering and studied by means of electron spin resonance (ESR). It was found that the rare-earth doping exponentialy depletes the neutral dangling bonds ^{0} density. The reduction of D^0 is significantly larger for the magnetic REs (Gd^{3+} and Er^{3+}) than for the non-magnetic ones(Y^{3+} and Lu^{3+}). These results are interpreted in terms of a RE volumetric effect and an exchange-like interaction, $\sim J_{RE\text{-}DB}\mathbf{S}_{RE}\mathbf{S}_{DB}$, between the spin of the magnetic REs and that of the D^0. All films were prepared in a high vacuum chamber (base pressure ~2.0×10^{-6} Torr), by radio frequency (13.56 MHz) sputtering a Si
(99.999% pure) target covered at random with small pieces of metallic RE (99.9% pure) elements. For the whole series of films the nominal RE concentration was estimated by the relative RE-to-Si target area (A_{RE}/A_{Si}). The ESR experiments were carried out at room-*T* in a *Bruker* X-band (9.47 GHz) spectrometer using a room-*T* TE_{102} cavity. The density of the dangling bonds species D^0 was determined from the ESR intensity as compared to a strong KCl-pitch standard sample. Room-*T* *Raman* scattering and X-ray diffraction measurements were performed in order to analyze the atomic structure of the *a*-Si:RE films.
Figure 1 shows the room-*T* D^0 ESR signal of *a*-Si and *a*-Si:RE films doped with magnetic (Gd^{3+} and Er^{3+}) and non-magnetic (Y^{3+}, and Lu^{3+}) RE elements. For these films RE ~ 0.2 at.%. The ESR signal of quartz substrate is shown for comparison. According to these data the RE-doping reduces the ESR signal intensity of the D^0 states and the reduction produced by Gd^{3+} and Er^{3+} is remarkably greater than that caused by Y^{3+} and Lu^{3+}. In this work it is shown that, as a function of the RE concentration, the D^0 density decreases exponentially.

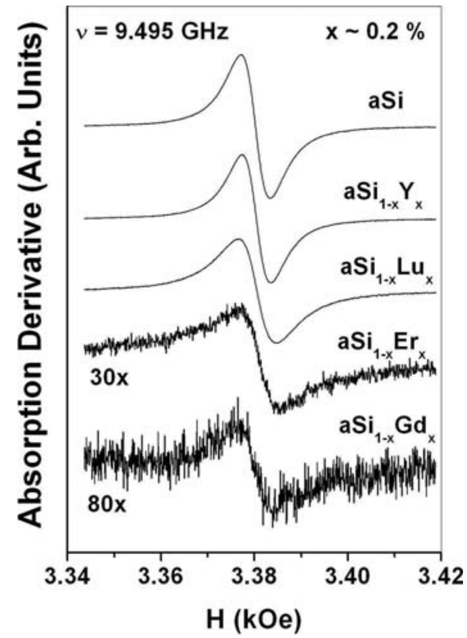

Figura 1. ESR spectra for RE-doped *a* - Si thin films.

EQ-04

Study on absence of room-temperature ferromagnetism in the Mn-AlN films with various Mn concentrations.

T. Sato[1], Y. Endo[2], Y. Kawamura[1], F. Kirino[3], R. Nakatani[1], M. Yamamoto[1]
1. Department of Materials Science and Engineering, Osaka University, Osaka, Japan; 2. Department of Electrical and Communication Engineering, Tohoku University, Sendai, Japan; 3. Conservation of Cultural Property, Tokyo National University of Fine Arts and Music, Tokyo, Japan

Introduction

Nitrides semiconductor doped with Mn, such as Mn-AlN and Mn-GaN, have been investigated as promising diluted magnetic semiconductors, because some groups have suggested that these materials show ferromagnetism at room temperature (RT) [1]. On the other hand, other groups have suggested that these materials do not exhibit ferromagnetism at RT [2, 3]. Thus, whether these materials exhibit ferromagnetism above RT remains to be elucidated. In this study, we investigated the magnetic behavior and structure of Mn-AlN ($Al_{1-x}Mn_xN$: $x = 0.05 – 0.24$) films fabricated by reactive DC magnetron sputtering, and report the absence of ferromagnetism at RT in these films. In addition, we discuss the origin of magnetic behavior in these films from the structural point of view.

Results and Discussion

Figure 1 shows the temperature dependence of DC susceptibility at a magnetic field of 10 kOe for 250-nm-thick $Al_{1-x}Mn_xN$ films with various Mn concentrations. For $x = 0.05$ and 0.10, each DC susceptibility markedly decreases with increasing temperature, which is considered to obey Curie-Weiss law. Neither remanent magnetization nor coercivity is observed at 10 and 300 K (It is not shown here.). These reveal that the magnetic behavior is paramagnetic in the temperature range of 10 – 300 K. For $x = 0.17$, the DC susceptibility increases up to 20 K and decreases above 20 K. At 10 K, both remanent magnetization and coercivity are observed as shown in inset of Fig. 1. These suggest that the magnetic behavior changes from ferromagnetic to paramagnetic near 20 K. Furthermore, for $x = 0.24$, the DC susceptibility increases up to 40 K and decreases above 40 K. However, the DC susceptibility is relatively low and the change in DC susceptibility with temperature is small. Neither remanent magnetization nor coercivity appears at 10 and 300 K (It is not shown here.). The magnetic behavior of the film with $x = 0.24$ cannot be determined using only the results from this study. Thus, these results demonstrated that these films have no room-temperature ferromagnetism and that the magnetic behavior depends on the Mn concentrations.

In order to clarify the origin of the magnetic behavior in the $Al_{1-x}Mn_xN$ films from the structural point of view, we observed grazing-incidence X-ray diffraction profiles and selected area diffraction (SAD) patterns of these films. Here, SAD patterns of 50-nm-thick $Al_{1-x}Mn_xN$ films with various Mn concentrations are shown in Fig. 2. For $x = 0.05$ and 0.10, only the diffraction rings derived from würtzite-type AlN are observed. These results suggest two possibilities as the origin of paramagnetic behavior; one is Mn ions incorporated into würtzite-type AlN and the other is Mn-rich particles with superparamagnetism [4] below the detection limit of TEM. For $x = 0.17$, not only the diffraction rings derived from würtzite-type AlN but also a diffraction ring is observed. This ring is considered to originate from a secondary phase such as Mn-N and Al-Mn. From this result, it is reveals that the change in the magnetic behavior with temperature is caused by the secondary phase. Furthermore, for $x = 0.24$, diffraction rings derived from ThH_2-type Mn_3N_2 as well as those derived from würtzite-type AlN are observed. These results suggest that the magnetic behavior is attributed to that of ThH_2-Mn_3N_2 which is antiferromagnetic below 925 K. Accordingly, it is considered that the change in magnetic behavior with x is caused by the change of film structure.

Summary

The magnetic behavior and structure of $Al_{1-x}Mn_xN$ ($x = 0.05 – 0.24$) films have been studied. It is found that all films with $x = 0.05 – 0.24$ have no room temperature ferromagnetism; a paramagnetic behavior for x below 0.10, a magnetic behavior with remanent magnetization only at 10 K and a paramagnetic behavior above 20 K for $x = 0.17$, and a magnetic behavior with a weak temperature dependence of DC susceptibility for $x = 0.24$. These magnetic behaviors are mainly considered to be due to the film structure.

[1] R. Frazier et al., J. Appl. Phys. 83 (2003) 1758.

[2] T. Kondo et al., J. Cryst. Growth 237-239 (2002) 1353.

[3] Y. Endo et al., IEEE Trans. Magn. 41 (2005) 2718.

[4] R. H. Kodama, J. Magn. Magn. Mat. 200 (1999) 359.

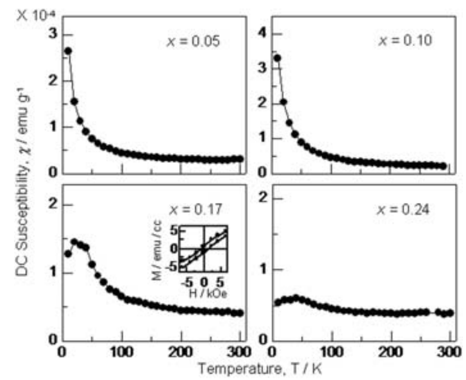

Temperature dependence of DC susceptibility for 250-nm-thick $Al_{1-x}Mn_xN$ films with various Mn concentrations.

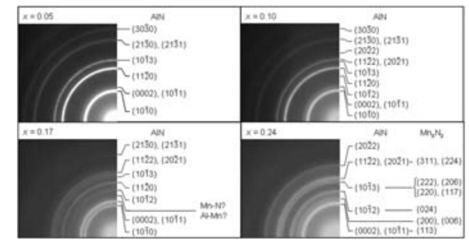

Selected-area diffraction patterns of 50-nm-thick $Al_{1-x}Mn_xN$ films with various Mn concentrations.

EQ-05

Growth parameter dependence of structural characterization of diluted magnetic semiconductor (Ga,Cr)As.

J. Lu, J. Bi, W. Wang, G. Gan, H. Meng, H. Zheng, J. Zhao
State Key Laboratory for Superlattices and Microstructures, Institute of Semiconductors, Chinese Academy of Sciences, Beijing, China

The earlier theoretical work predicted (Ga,Cr)As with higher Curie temperature (Tc) than that of (Ga,Mn)As [1]. However, recent theoretical progress indicates that it is difficult to increase Tc to room temperature even with Cr content x up to 0.15 [2]. Experimentally, (Ga,Cr)As epitaxial films grown on GaAs have been synthesized by several groups. Unlike the theoretical prediction, superparamagnetic behavior with short-range ferromagnetism for x = 0.1 and ferromagnetic behavior for x = 0.11 have been reported by different groups [3,4]. Recently, we obtained (Ga,Cr)As films with intrinsic ferromagnetic order by molecular-beam epitaxy (MBE) [5]. We found that the crystalline quality and magnetic property were very sensitive to the growth condition. In this digest, we report the influence of growth temperature (Ts), arsenic pressure and post-growth annealing on the structural and magnetic characterizations of (Ga,Cr)As films.
All the (Ga,Cr)As films were grown on epiready GaAs (001) substrates by low-temperature MBE. A 100 nm GaAs buffer layer was first grown at Ts = 560 oC, then three sets of (Ga,Cr)As films (set A, B and C) were grown. The detailed growth parameters are shown in Table I.
Clear streaky (1x1) RHEED patterns were observed during growth of (Ga,Cr)As films in set A except the film grown at 400 oC,which had a spotty pattern of the second phase, as shown in Fig. 1(a) and (b). Also, clear streaky (1x1) RHEED patterns were observed for the films in set B with Cr content x<0.1, but a spotty RHEED pattern without the second phase appeared when x = 0.1, as shown in Fig. 1(c) and (d). RHEED patterns of the films in set C were broken streaky, not shown here. From the changes in RHEED patterns, the tendency of Cr-As clustering is enhanced with increasing both Ts and x. The difference is that hexagonal Cr-As compounds are obviously formed at high Ts, but this second phase is not seen in samples with higher x grown at low Ts from RHEED patterns. This tendency is also verified by double-crystal x-ray diffraction (XRD) curves and atomic force microscopy (AFM) images. One can see from Fig. 2(a) that the peaks of (Ga,Cr)As films in set A shift from the left of the GaAs substrate peak to the right. The same phenomenon is also seen in set B. With increasing Cr content, the peak of (Ga,Cr)As film disappears as shown in Fig. 2(b). To understand the phenomenon of the peak shift, we also grew a (Ga,Cr)As film at 250 oC, and then followed by annealing at 650 oC. We found that the peak of (Ga,Cr)As film is also on the right of the substrate peak. Therefore, we may deduce that the peak shift might originate from the compressive strain caused by Cr-As clusters inhomogeneously embedded in the epilayer. The roughness also increases with increasing Ts and x obtained from AFM images, not shown here.
Magnetic circular dichroism (MCD) measurements proved that all the samples with the intrinsic ferromagnetism. However, compared with (Ga,Mn)As, Tc of (Ga,Cr)As is lower than 30 K, known from both MCD and SQUID measurements. For the samples grown above 250 oC in sets A and B, the ferromagnetic signal at room temperature may be associated with Cr-As clusters inside the (Ga,Cr)As matrix. Therefore, a lower Ts is expected for the homogeneous (Ga,Cr)As alloy. More homogeneous (Ga,Cr)As films (set C) have been synthesized at lower Ts.
In summary, we systematically investigated the growth parameter dependence of structure and magnetic properties of (Ga,Cr)As films. The optimized growth condition at lower growth temperature may be the key to get the homogeneous (Ga, Cr)As films with higher Tc.

[1] L. M. Sandratskii and P. Bruno, Phys. Rev. B 67, 214402 (2003).

[2] K. Sato et al., Recent private communication.

[3] A. Dakhama, B. Lakshmi, and D. Heiman, Phys. Rev. B 67, 115204 (2003).

[4] M. Yamada, K. Ono, et al., J. Appl. Phys. 91, 7908 (2002).

[5] H. D. Gan, H. Z. Zheng, J. F. Bi, Y. Ji, B. Q. Sun, G. R. Li, X. Z. Ruan, J. Lu, J. H. Zhao, cond. matt. 0711.0241.

Growth condition / Set	Cr content	As/Ga flux ratio	Growth temperature	Film thickness
A	0.04	36	250 to 400℃	100 nm
B	0.01 to 0.1	15	250℃	100 nm
C	0.04	5.5	150℃	70nm

Table I. The growth parameters of (Ga,Cr)As films.

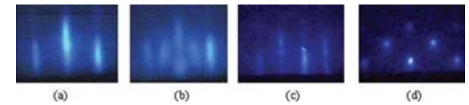

Fig.1 RHEED patterns taken after 100 nm (Ga,Cr)As films deposition, (a) and (b) correspond RHEED patterns of (Ga,Cr)As films grown at 250 oC and 400 oC in set A; (c) and (d) correspond RHEED patterns of (Ga,Cr)As films grown at 250 oC with the Cr concentration x = 0.01 (c) and x = 0.1 (d) in set B.

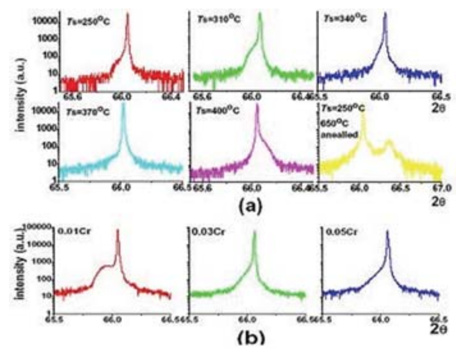

Fig.2 Double crystal XRD curves of (Ga,Cr)As films in set A (a) and set B (b).

EQ-06

Coexistence of ferromagnetism and paramagnetism in highly dilute $Ga_{1-x}Mn_xN$.

D. Sedmidubský[1], Z. Sofer[1], J. Hejtmánek[2], M. Maryško[2], K. Jurek[2]
1. Institute of Chemical Technology, Prague, Czech Republic; 2. Institute of Physics ASCR, v.v.i., Prague, Czech Republic

Gallium nitride doped by manganese belongs to a family of wide band gap dilute magnetic semiconductors which have been recently intensively studied as candidates for spintronic applications. The main potential of these materials is viewed in their ferromagnetic state persisting well above room temperature, which has been theoretically predicted and experimentally evidenced on thin films prepared by diverse techniques.

From the chemical point of view, Mn replaces Ga in wurtzite structure forming a substitutional solid solution. As predicted by our thermodynamic calculations, the Mn solubility in bulk $Ga_{1-x}Mn_xN$ is as low as a few per cent (2-3 at %) and decreases with increasing T and decreasing p_{N2}. This suggests that a number of results reported as yet has been obtained on samples whose composition (x>0.05) and synthesis condition (MBE and ion implantation in particular) were far from equilibrium. Hence the tendency of nanoscopic phase separation was high enough in such cases and might be one of the reasons for still significant discrepancies in magnetic and transport properties. In this respect, MO VPE is considered as a close to equilibrium method with a capability to provide high quality homogeneous thin films. However, only few reports [1-2] have appeared on MOVPE synthesis and characterization of $Ga_{1-x}Mn_xN$ so far.

In this paper we present a study of magnetic properties carried out on thin films deposited on sapphire substrates (0001 orientation) by MO VPE. The samples were prepared in a horizontal inductively heated reactor at T=1050°C from $Ga(CH_3)_3$, NH_3 and $Mn(MCp)_2$ precursors transported in N_2/H_2 carrier gas. The active $Ga_{1-x}Mn_xN$ layer was either deposited on a pure GaN buffer layer or directly on substrate. A typical thickness was 0.25 and 2.7 µm, respectively. The X-ray diffraction proved the wurtzite phase without any secondary phase related to Mn. The Mn concentration detected by electron microprobe and PIXE was well below the solubility limit, ranging from 0.2 to 0.7 at %, i.e. rather far from the value of 5% considered as optimal for ferromagnetism. The Hall measurements conducted at room temperature revealed n-type charge carriers reaching typical concentrations $1x10^{18}$ cm^{-3} and mobilities 230 $cm^2/(Vs)$. From the isothermal magnetization data recorded on SQUID magnetometer, three main components can be separated – a strong diamagnetic signal from the substrate (and undoped GaN) as well as two weak contributions from the $Ga_{1-x}Mn_xN$ film - a paramagnetic (PM) component characterized by Brillouin M(H) dependence at the lowest temperatures and a nearly temperature independent ferromagnetic (FM) component persisting above 300 K. The M(H) curves show clear hysteresis with coercivities less than 80 Oe and relative remanent magnetizations ≈ 0.1.

In order to analyze the magnetization data we assume that unlike GaMnAs, Mn occurs in trivalent state in GaMnN contributing by four spins to magnetic moment. This assumption is supported by electron spectroscopy and electronic structure calculations. According to our APW+lo calculations (Wien2k) performed within GGA+U (Mn-3d on-site repulsion U = 3 eV) for $Ga_{0.875}Mn_{0.125}N$, the partially filled majority spin states of Mn-t_{2g} character form an impurity band centered 1.3 eV above the valence band maximum (VBM), which evolves into deep acceptor levels in the localized regime. In contrary, the filled Mn-e_g states are dipped into VB and strongly hybridized with N-2p, whereas all minority Mn-3d states are empty and pinned to conduction band minimum (CBM). Although a slight spin polarization is observed at both CBM and VBM, the electron and holes induced by doping would not substantially contribute to total magnetic moment. Hence, we can directly recast the magnetic data to Mn concentration (expressed as x in $Ga_{1-x}Mn_xN$) provided a careful analysis of PM component is done.

The Brillouin fit applied on the M(H) curves after subtracting a constant FM part (and indeed a diamagnetic addenda) revealed characteristic temperature Θ_p around 0 K and concentrations of paramagnetic Mn x_{PM}=0.5-0.9x10^{-2}. By contrast, the FM part x_{FM} amounts only 0.02-0.2x10^{-2} i.e. 3.5-20% of the total Mn content. A reasonable agreement between magnetically and chemically determined Mn concentrations was found. Surprisingly, the highest FM/PM ratio was achieved for samples with lowest Mn concentration. This is difficult to explain in terms of percolation between bound magnetic polarons formed around donor impurities [3], unless a significant reduction of the polaron size with increasing x is considered. Despite this discrepancy, we can conclude that within the above mentioned model [3], the current concentrations of magnetic impurities (less than 1 at %) and possibly also the donor concentrations (2.5x10^{-3} at %) in the Ga1-xMnxN system under study fall below the percolation limit of metallic ferromagnetism. As a result, a mixed state of FM clusters dispersed in PM matrix is apparently established.

Acknowledgement. This work was supported by the Czech Science Foundation, grant GA104/06/0642 and the Ministry of Education of Czech Republic, project MSM6046137302.

[1] M.H. Kane et al., J. Cryst. Growth 287 (2006) 591.

[2] X.Yang et al., J. Cryst. Growth 305 (2007) 144.

[3] J. M. D. Coey et al., Nature Materials 4 (2005) 173.

Effect of strain relaxation on the anisotropic magnetoresistance of GaMnAs microbars.

E. De Ranieri[1], K. Olejník[2], K. Vyborn ý[2], A. C. Irvine[1], R. P. Campion[3], B. L. Gallagher[3], T. Jungwirth[2,3], H. Sirringhaus[1], J. Wunderlich[4,2]
1. Microelectronics Research Centre, University of Cambridge, Cambridge, United Kingdom; 2. Institute of Physics ASCR, Prague, Czech Republic; 3. School of Physics and Astronomy, University of Nottingham, Nottingham, United Kingdom; 4. Hitachi Cambridge Laboratory, Cambridge, United Kingdom

Introduction:

By patterning microstructures on a thin layer of GaMnAs, it is possible to partially relax the strain in this ferromagnetic film caused by the lattice mismatch with the underlying GaAs buffer layer. This technique can be used to modify the magnetic anisotropy and the transport properties of the GaMnAs structures[1,2,3]. We focus on the latter aspect by studying the influence of the patterning-induced strain relaxation on the anisotropic magnetoresistance (AMR) effect.

AMR is an effect emerging from the competition of the spin-orbit interaction and other symmetry-lowering terms (magnetization, anisotropic crystalline environment, strain) and it consists in the change in resistance of a ferromagnet depending on the orientation of the magnetization vector **M**.

For macroscopic Hall bars, the phenomenological description of the relative change in resistance dR_{xx} allows to identify non-crystalline and crystalline components[4,5] in the bulk AMR, represented by terms depending on the angle between **M** and the crystallographic axes and **M** and the current direction[5].

For a microscopic bar, an additional term accounts for the effect of the strain relaxation induced by lithographical patterning. The aim of the present study is to identify the contribution of the strain coefficient to the AMR as a function of temperature.

Materials and methods:

Four 1 µm-wide bars, aligned along the main crystallographic directions [100], [010], [110] and [1-10], are patterned in series with a 40 µm-wide bar along the [010] (see diagram in Fig.1a, with a picture of R2, R3 and R4) with two electron beam lithography steps: the mesa is defined by 500 nm trenches etched by reactive ion etching, then Cr/Au bond pads are evaporated.

The device was fabricated on a 25 nm GaMnAs layer, grown by low-temperature molecular beam epitaxy under compressive strain on a GaAs (001) substrate. The nominal Mn concentration is 5%. From SQUID magnetometry, the Curie temperature T_c of the as grown wafer is 60 K, at 5 K the easy axes are along the [100] directions while at T>25 K the [1-10] direction becomes the easy axes.

In transport measurements, the longitudinal resistance of the five bars is measured simultaneously with lock-in amplifiers while an external magnetic field of 4 T (much larger than the anisotropy field in order to saturate the sample) is applied in the plane of the sample, and the sample is rotated in the plane by 360°. Measurements are performed in a range of temperature from 4 to 70 K (the AMR effect is observable at 70 K because of the increase in T_c due to fabrication processes).

Results and discussion:

The polar plots in Fig.1b,c,d show dR_{xx} of the five studied bars as a function of the angle ϕ between the field and the [100] direction, at 4, 30 and 70 K respectively. The plots on the left show dR_{xx} for the microbars patterned along the [100] (green line) and [010] (dark-blue line) and the macrobar along the [010] (light-blue line) axes. The plots on the right show dR_{xx} for the microbars patterned along the [110] (black line) and the [1-10] (red line) axes.

By direct comparison of the light-blue and dark-blue lines in Fig.1b(left), a remarkable reduction of the signal is observed due to the patterning-induced strain relaxation in the microbar. This effect is comparable to the uniaxial contribution along the [010] axis, found by comparing the dark-blue and green lines. The unusually strong uniaxial component along the [010] direction may be the result of strain induced during the growth, which relaxes when the sample is patterned, giving rise to such a big effect. Also, dR_{xx} for the bars along the [110] direction is noticeably smaller than for those along the [100] direction, suggesting a relatively large contribution of the cubic term.

As the temperature increases, the magnitude of dR_{xx} decreases for all the studied bars as T approaches T_c. By looking at the evolution of the black and red lines in Fig.1b,c,d (right), it is clear that the relative strength of the uniaxial and cubic coefficients is changing.

Because of the limited number of data set with respect to the number of relevant phenomenological AMR coefficients we could not extract unambiguously the values for these coefficients. Further investigation of the effect of strain relaxation as a function of temperature will be carried out on samples with both macro- and microbars aligned along the main crystallographic directions and in samples with different film thickness and after annealing at 200°C to obtain better quantitative understanding of the effect of strain relaxation on the AMR.

[1] Wunderlich et al., Phys. Rev. B 76, 054424 (2007)
[2] Wenisch et al., Phys. Rev. Lett. 99, 077201 (2007)
[3] Hümpfner et al., Appl. Phys. Lett. 90, 102102 (2007)
[4] Doring, Ann. Phys. (Leipzig), 424, 259 (1938)
[5] Rushforth et al., Phys. Rev. Lett. 99, 147207 (2007)

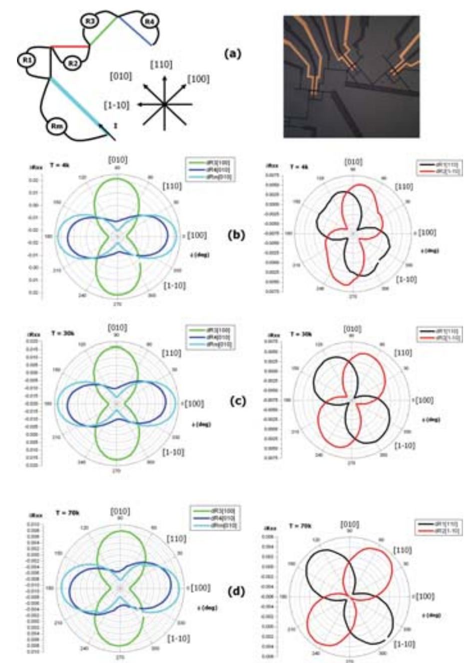

EQ-08

Preparation of $(Ge_{1-y}Pb_y)_{1-x}Mn_xTe$ thin films and their magnetic properties.

H. Asada[1], Y. Fukuma[2], D. Kitabori[1], A. Ohji[1], Y. Kamimoto[1], T. Koyanagi[1]
1. Department of Materials Science and Engineering, Yamaguchi University, Ube, Japan; 2. Yamaguchi Prefectural Industrial Technology Institute, Ube, Japan

1.Introduction

Carrier-induced ferromagnetism is a distinguish feature of Diluted Magnetic Semiconductors (DMSs), which enable to manipulate the magnetic order by external parameters such as irradiating light or applying electric field like FET. These experiments have been done in III-V DMSs such as $In_{1-x}Mn_xAs$ and $Ga_{1-x}Mn_xAs$.[1)-3)] The first experimental study of carrier-induced ferromagnetism was performed on $Pb_{1-x-y}Sn_yMn_xTe$.[4)], though the Cuire temperature T_C was of helium temperatures So far we have successfully grown IV-VI DMS $Ge_{1-x}Mn_xTe$ films up to Mn composition x=0.96 by using ionized cluster beam (ICB) technique.[5)] We have also demonstrated that the ferromagnetic properties of $Ge_{1-x}Mn_xTe$ such as the spontaneous magnetization and Cuire temperature can be controlled by the hole concentration, preparing the films with various carrier concentrations from 10^{19} to 10^{21} cm^{-3} by controlling Te composition.[6)] Another carrier control method is that Ge is substituted by Pb. Crystal structure of PbTe is a NaCl while bulk GeTe has rhombohedral distorted lattice. Therefore, $Ge_{1-x}Pb_xTe$ is interesting for ferroelectric phase transition.[7)] In $(Ge_{1-y}Pb_y)_{1-x}Mn_xTe$, ferroelectric transition temperature could be dependent on Pb and Mn composition. From a crystalline viewpoint for a spin-polarization source in IV-VI heterostructures, a NaCl type DMS is superior due to surface smoothness.

In this study, we have prepared various $(Ge_{1-y}Pb_y)_{1-x}Mn_xTe$ films by ICB methods and suggested that the carrier concentration can be controlled by Pb composition. Dependences of electrical and magnetic properties on Pb composition have been studied. Exchange integral J_{pd} between Mn ions and holes is discussed based on RKKY interaction. An increase of Mn composition in $(Ge_{1-y}Pb_y)_{1-x}Mn_xTe$has also been tried.

2.Experimental

$(Ge_{1-y}Pb_y)_{1-x}Mn_xTe$ were grown onto air-cleaved BaF_2 (111) substrates. Molecular GeTe, MnTe and PbTe were used as source materials. After thermal cleaning of a BaF_2 substrate (400 °C, 30 min.), $(Ge_{1-y}Pb_y)_{1-x}Mn_xTe$ layer was grown at 280°C. The chemical composition was checked by electron probe microanalysis.

3.Results and Discussion

Each crucible temperature was controlled to be Mn composition x≈0.1 due to the solubility limit of x=0.11 in bulk $Pb_{1-x}Mn_xTe$. The x-ray diffraction pattern of (111) plane was observed in the films with y=0 and y≧0.58 while the no other diffraction pattern of BaF_2 substrate was observed in the films with 0.04≦y≦0.52. The lattice constant linearly increased in proportion to y. Figure 1 shows the carrier concentration as a function of Pb composition in $(Ge_{1-y}Pb_y)_{1-x}Mn_xTe$ with Mn composition x≈0.1. Carrier concentration can be controlled from 10^{18} to 10^{21} cm^{-3} by Pb composition.

In order to investigate the electrical and magnetic properties, magnetotransport measurements were performed on hall bar pattern. Assuming that side jump scattering is dominant in the anomalous hall term, the magnetization M_{trans} is thus defined as $M_{trans} \propto (\rho_{hall}-R_0B)/\rho^2$, where R_0 is the ordinary hall coefficient, B is the magnetic induction, ρ_{hall} is the hall resistivity and ρ is the resistivity. The ordinary hall term R_0B is deduced from the hall measurement at room temperature. Figure 2 shows a typical M_{trans}-H curve at 9 K in $(Ge_{1-y}Pb_y)_{1-x}Mn_xTe$(y=0.39). The inset shows the magnetization curve at 5 K measured by SQUID. The curves clearly demonstrate ferromagnetism and the similar behavior observed in both results. T_C was estimated by Arrot-plots using M_{trans} measured at various temperatures. Dependence of T_C on Pb composition as shown in Fig.3. T_C drastically decreases with increasing Pb composition. Ferromagnetic behavior is not observed in magnetotransport measurement at 9 K for the films with y≥0.58. Bulk $Pb_{1-x}Mn_xTe$ is paramagetism while $Ge_{1-x}Mn_xTe$ is ferromagnetism. Therefore, exchange integral J_{pd} between Mn ions and holes in each sample has been calculated based on RKKY interaction. It was confirmed that the J_{pd} also decreased with increasing y, which made for the drastic decrease of T_C.

We have tried to increase the Mn composition in $(Ge_{1-y}Pb_y)_{1-x}Mn_xTe$ films with y≈0.47. Figure 4 shows T_c as a function of Mn composition. Carrier concentrations are $p=1.27\times10^{20}$ for x=0.08, $p=1.84\times10^{20}$ for x=0.15, $p=6.41\times10^{20}$ for x=0.22 and $p=2.71\times10^{21}$ cm^{-3} for x=0.29, respectively. As shown in the figure, T_C successfully increases till x=0.22.

1) H. Munekat et al., J. Appl. Phys. **81**, 4862(1997).

2) H. Ohno et al., Nature **408**, 944(2000).

3) Y. Ohno et al., Nature **402**, 790(1999).

4) T. Story et al., Phys. Rev. B **42**, 10477(1990).

5) Y. Fukuma et al., Physica E **10**, 273(2001).

6) Y. Fukuma et al., Appl. Phys Lett. **80**, 1013(2002).

7) S. Takaoka and K. Murase, Phys. Rev. B **20**, 2823(1979).

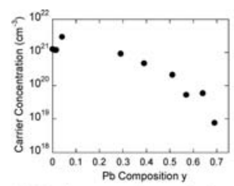

Fig.1 Carrier concentration as a function of Pb composition in $(Ge_{1-y}Pb_y)_{1-x}Mn_xTe$ with Mn composition x=0.1.

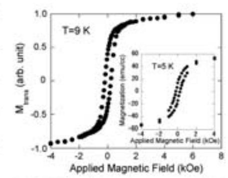

Fig.2 Typical M_{trans}-H curve at 9 K in $(Ge_{1-y}Pb_y)_{1-x}Mn_xTe$ (y=0.39). The inset shows the magnetization curve at 5 K measured by SQUID.

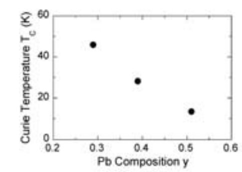

Fig.3 Dependence of Curie temperature on Pb composition in $(Ge_{1-y}Pb_y)_{1-x}Mn_xTe$ with Mn composition x=0.1.

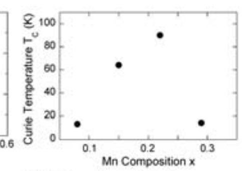

Fig.4 Dependence of Curie temperature on Mn composition in $(Ge_{1-y}Pb_y)_{1-x}Mn_xTe$ with Pb composition y=0.47.

EQ-09

Properties of ternary rare earth REXY compounds with 18 valence electrons.

F. Casper, C. Felser
Institute for inorganic and analytical chemistry, Mainz, Germany

Ternary rare earth compounds REXY, where RE is a lanthanide element, Y a transition element and Z is an sp element, offer a large variety of structure types. Our research focuses on compounds LiGaGe and MgAgAs (half-Heulser) structure which all have 18 valence electrons. The f-electrons are localized and therefor not count as valenze electrons. Magnetic and resistivity measurements were used to examine some of these compounds. Most of the compounds order antiferromagnetic at low temperatures. While compounds with LiGaGe structure are metallic, many of the compounds with MgAgAs structure are semiconducting. Additionally for some of these compounds a metal-insulator transition was found. The metal - insulator transition temperature depends strongly on the preparation conditions.

Some of these compounds show a negative giant magnetoresistance (GMR) above the magnetic ordering temperature in the paramagnetic temperature regime. Except for a weak deviation, this magnetoresistance scales roughly with the square of the magnetization in the paramagnetic state, and is related to the metal-insulator transition.

For inhomogenous compounds (REYZ with metallic impurities) a positive contribution to the magnetoresistance was found. The nonmagnetic inhomogeneous semiconducting LuNiBi compound shows a large postitve MR effect of 25% at room temperature (figure 1). The positive MR may be due to metallic bismuth impurities in the sample that cause an extraordinary magnetoresistance (EMR).

This work is supported by by DfG grant FE633/1-1 within SPP1166.

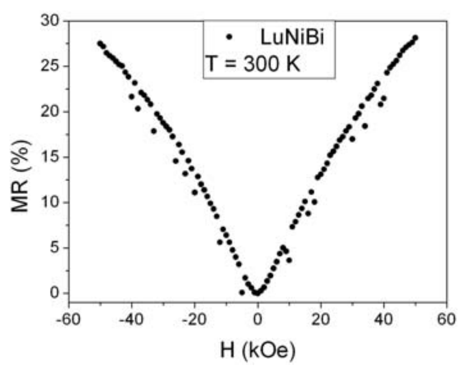

EQ-10

Effect of local magnetic field on the transport properties of GaMnAs.

J. Suh[1,2], J. Chang[1], E. Kim[2], M. Sapozhnikov[3], A. Fraerman[3]
1. Center for Spintronics Research, KIST, Seoul, South Korea; 2. Quantum-Function Spinics Lab. and Department of Physics, Hanyang University, Seoul, South Korea; 3. Institute for Physics of Microstructures RAS, Nizhny Novgorod, Russian Federation

II-IV DMS (diluted magnetic semiconductor) is reported to show an enormous Zeeman splitting and have the giant g-factor up to 500 [1] so that external magnetic field can significantly adjust the energy of the charge carriers. Assuming that the III-V DMS such as GaMnAs have the same level of large g-factor, the authors presumed that the localized inhomogeneous magnetic field essentially affects the transport properties of GaMnAs and even forms effective traps for spin polarized carriers. [2] Since giant g-factor was expected in GaMnAs, [3] it is very interesting to investigate the spin transport of DMS under the influence of such local field induced by an array of ferromagnetic nanodots. Controllable source of localized inhomogeneous field can be obtained with placing ferromagnetic nanodots on the top of GaMnAs microbridge. [4,5]

In this paper, we introduce novel device consisting of patterned Co nanodot on GaMnAs micronsized channel in order to explore a new functionality to control the transport properties of GaMnAs. 100 nm thick Ga1-xMnxAs layer (x = 0.05) was grown on a semi-insulating (001) GaAs substrate by molecular beam epitaxy (MBE, Riber) system. The standard UV photo lithography and Ar ion milling were used to fabricate 1 µm wide and 10 µm long GaMnAs microbridge parallel to [110] direction with four contact probes from the GaMnAs film. Van der Pauw and magnetoresistance (MR) measurements were carried out under applying magnetic field up to 1 kOe in the temperature range of 4.2 K.

Figure 1 presents the scanning electron microscopy (SEM) image of a fabricated device. The device is designed to measure resistance change of GaMnAs channel as a function of applied field with four probe measurement. Periodic single array of Co nanodots formed on the bridge is expected to produce local magnetic field. Long axis of elliptical Co dot is perpendicular to the bridge through which current flows. MFM observation clearly shows single domain is a stable state for Co dots.

Figure 2 shows MR of the pure GaMnAs bridge without a chain of Co nanodots measured at 4.2 K. It clearly shows the typical anisotropic MR (AMR) of GaMnAs which is similar to those reported elsewhere for GaMnAs thin films and yield information concerning the magnetic anisotropy.

Figure 3 presents both longitudinal and transverse MRs in the narrow field range of ± 600 Oe to search the effect of Co nanodots on the resistance. It is noted that additional steps marked by arrows were found in the longitudinal MR curves when applying longitudinal magnetic field. Such steps appeared only when magnetization of the sample was reversed. If we magnetize the sample in the same direction for a second time, no steps are observed as there is no magnetization reversal in the system.

This work is supported by KIST institutional program.

[1] M. Yamanouchi, D. Chiba, F. Matsukura, and H. Ohno, Nature 428 (2004) 539

[2] M. Berciu, and B. Janko, Phys. Rev. Lett. 90 (2003) 246804

[3] T. Dietl, M. Sawicki, M. Dahl, D. Heiman, E.D. Isaacs, M.J. Graf, S.I. Gubarev, and D.L. Alov, Phys. Rev. B. 43 (1991) 3154

[4] M.V. Sapozhnikov, A.A. Fraerman, S.N. Vdovichev, B.A. Gribkov, S.A. Gusev, A.Yu. Klimov, V.V. Rogov, Joonyeon Chang, Hyungjun Kim, Hyun Cheol Koo, Suk-Hee Han, and S.H. Chun, Appl. Phys. Lett. 91 (2007) 062513

[5] Jooyoung Suh, Joonyeon Chang, Eun Kyu Kim, M.V. Sapozhnikov, V.L. Mironov, and A.A. Fraerman, Phys. stat. sol. (a) (2007) in press

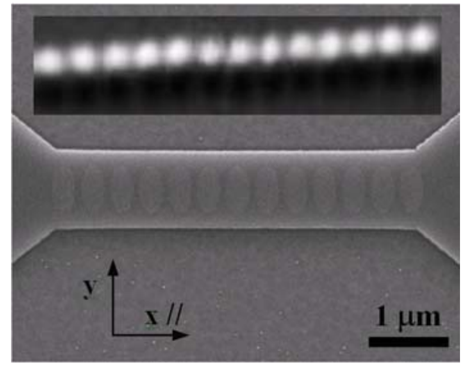

Fig. 1. SEM image of a fabricated device where a chain of elliptical Co nanodots was patterned on GaMnAs microbridge. Inset is the MFM image of Co nanodots on the microbridge.

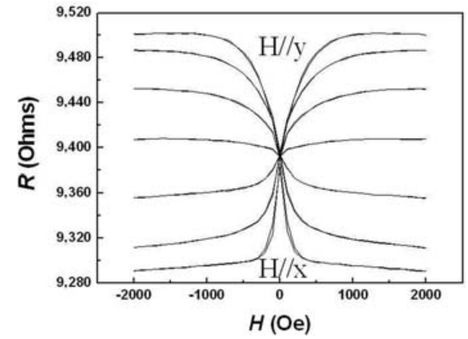

Fig. 2. Magnetoresistance (MR) of the pure GaMnAs microbridge under various in-plane magnetic field at 4.2 K.

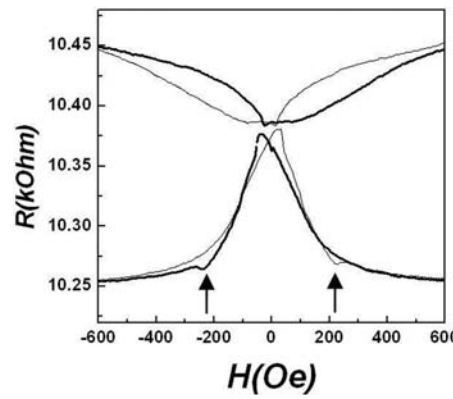

Fig. 3. Longitudinal (lower) and transverse (upper) MR of the GaMnAs microbridge with a chain of Co nanodots measured at 4.2 K.

ER-01

Structural and magnetic properties of Co-doped ZnO thin films.

M. Fonin[1], G. Mayer[1], S. Voss[1], E. Goering[2], U. Rüdiger[1], R. Schneider[3], D. Gerthsen[3]
1. Fachbereich Physik, Universität Konstanz, Konstanz, Germany; 2. Max Planck-Institut für Metallforschung, Stuttgart, Germany; 3. Laboratorium für Elektronenmikroskopie, Universität Karlsruhe, Karlsruhe, Germany

Ferromagnetic oxidic semiconductors combine electronic and magnetic properties and thus gained much interest in recent years. These materials are usually fabricated by doping a non-magnetic semiconductor with 3*d* metal ions. In a theoretical work, Dietl *et al.* [1] showed that a stable ferromagnetic phase with Curie temperatures above room temperature is possible in wide gap semiconductors such as ZnO. Experimentally ferromagnetism above room temperature has been observed in different diluted magnetic semiconductors (Co:TiO_2, Mn:TiO_2, Co:ZnO, Mn:ZnO, Mn:SnO_2, etc.) [2] during the last years. Nevertheless, the origin of this ferromagnetism is still under debate.

Co-doped ZnO has been prepared by rf magnetron sputtering from a composite ZnCo target (90:10 wt.%) with pure Ar on the one hand and a mixture of Ar and O_2 on the other hand as sputtering gases. Al_2O_3 and SiO_2/Si have been used as substrates. The Co contect was estimated by energy dispersive x-ray analysis (EDX) to be 3 at.% in the samples. X-ray diffraction (XRD) showed a *c*-axis oriented growth for both preparation conditions, which could also be confirmed by high resolution transmission electron microscopy (HRTEM). However, the latter showed the formation of Co-rich clusters in films on SiO_2/Si which were grown in a mixture of Ar and O_2 and post-annealed in pure O_2. The Co-rich clusters go together with Zn depletion, while oxygen is homogeneously distributed. The formation of a possible crystalline secondary phase such as CoO or Co_3O_4 has still to be examined. Films grown in pure Ar show a homogeneous Co distribution. For magnetic characterization, a superconducting quantum intereference device (SQUID) and x-ray magnetic circular dichroism (XMCD) were used. X-ray absorption spectroscopy (XAS) reveals that Co is incorporated as Co^{2+} into the ZnO host lattice and thus substitutes Zn at the lattice sites. In SQUID measurements, all films gave a paramagntic signal superimposed by a small ferromagnetic contribution. Figure 1 shows SQUID measurements of sample grown in pure Ar and post-annealed under vacuum at 750 °C. To obtain these results, a substraction of an as treated pure sapphire substrate was taken into account. However, the non linearity around $\mu_0H = 0$ T in the SQUID measurements may be not only due to the ferrmoagnetic contribution of ZnCoO but also due to the substrate. The Co-rich clusters do not enhance ferromagnetism, underlining the HRTEM results, that the clusters are not composed of pure Co. Figure 2 shows XMCD measurements at 15 K for different applied external fields. A clear XMCD signal can be seen at the Co L_3 edge (778.5 eV). In the inset of figure 2, the maximum XMCD signal is plotted versus the applied field. The dependence is clearly linear, as indicated by the fitted line. Thus XMCD measurements confirm the SQUID measurements, as they also show a linear dependence of the TEY-signal from the external applied magnetic field. XMCD measurements on Co-doped ZnO of other groups [3;4] also showed a pure paramagnetic contribution of Co to the magnetization of the sample, although they could see a large ferromagnetic component in SQUID measurements.

[1] T. Dietl *et al.*, Science **287**, 1019 (2000).

[2] J. M. D. Coey *et al.*, Nature Mater. **4**, 173 (2005).

[3] M Gacic *et al.*, Phys. Rev. B **75**, 205206 (2007).

[4] A. Barla *et al.*, Phys. Rev. B **76**, 125201 (2007).

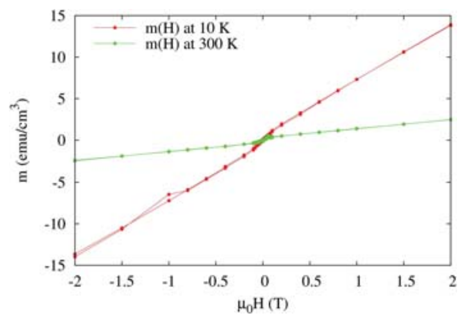

SQUID measurement of $Zn_{0.94}Co_{0.06}O$ at 10 K and 300 K, respectively after the substraction of an as treated (evaporation excluded) pure substrate.

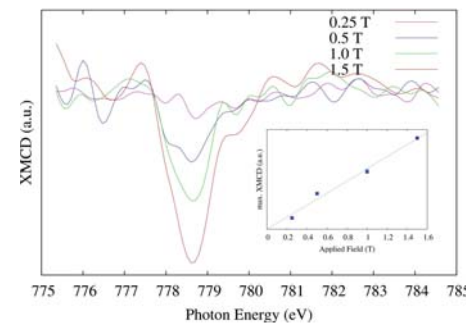

XMCD measurement of $Zn_{0.94}Co_{0.06}O$ for different applied external fields. A clear signal at the Co L_3 edge (778.5 eV) is visible. The inset shows the maximum XMCD signal as a function of the applied field. The dependence is linear as illustrated by the linear fit.

ER-02

Ferromagnetism observed in transition metal doped high K oxides.

Q. Wen, H. Zhang, Y. Song, Q. Yang, Y. Liu
State Key Laboratory of Electronic Films and Integrated Devices,, University of Electronic Science and Technology of China, Chengdu, China

Diluted magnetic oxides (DMO) with Curie temperature (Tc) above room temperature have attracted much attention. However, the presence and absence of ferromagnetism (FM) were alternatively reported for semiconducting oxides system by different research groups, which cast a shadow on the carrier-mediated ferromagnetic mechanism. Very recently, several researches reported large magnetic moment with high Tc in transition metal (TM) doped high-k oxides such as HfO2 [1] and CeO2 [2]. The FM in these insulating oxides challenges the carrier-induced FM mechanism and strongly support the F-center mediated exchange mechanism for diluted ferromagnetism. In the later mechanism, oxygen vacancy (Vo) traps an electron to constitutes an F center. The trapped electron occupies an orbital which overlaps the d shells of both TM neighbors, constituting a ferromagnetic polaron. The radius of the electron orbital is given as a0ε, where a0 is the Bohr radius andεis the dielectric constant.

For typical high-k oxides such as HfO2, La2O3 and CeO2, Vo is a typical defect [3,4] and the k constant is large. Therefore, it is anticipated that a RT FM can be generally obtained in TM doped high-k oxides. In present report, Co doped La2O3 and CeO2 samples were fabricated by the solid-state reaction method with a high sintering temperature of 1200 °C and 1400 °C in air, respectively. Complex magnetic behaviors were observed in both insulting oxides and their dependence on Co concentration is discussed.

X-ray diffraction spectroscopy of La2(1-x)Co2xO3-δ and Ce1-xCoxO2-δ with Co content from x = 0 to 0.08 were studied. It can be found that all samples have a single -phase structure, and none of the samples showed any evidence for impurity phases. A slight shift for most of the peaks can be seen with increasing Co ions concentration due to part of La or Ce atoms are substituted by Co atoms. XPS studies shows that the Co 2p3/2 and 2p1/2 core levels for Co-O bonding were at 780.38 eV and 796.92 eV, which, to an extent, eliminates the possibility of Co metal cluster.

The magnetization versus field curves (MH) for Co:La2O3 with different Co content were measured by vibrating sample magnetometer (VSM), as shown in figure.1. From the MH curves we found that: (i) undoped and very slightly Co doped (0.1%) samples show no FM signal but diamagnetic signal; (ii) well-defined hysteresis loops are observed in relatively heavily doped samples ($x \geq 0.5\%$); (iii) when x increase beyond 1%, the ferromagnetism become dominating and no diamagnetism was detected; (iv) a surprisingly soar of the FM signal was observed in the 2% Co doped La2O3 with a Ms of 0.05emu/g, and (v) when x > 2%, an inverse correlation between the magnetization and Co content was observed. A similar magnetic behavior was observed in Co doped CeO2. Undoped or slightly doped samples show no ferromagnetic signal, while relatively larger Co doping ($x \geq 1\%$) gives rise to distinct RT FM which steeply increases with x up to 2% and then drops with further increasing x. It is interestingly that the largest magnetization was also appeared at about 2% Co doped sample.

When x is very small, Co ions are far apart from each other and their spins are free, with no contribution to FM. As x increasing, magnetic polarons form since the concentration of both Co and Vo increase, and the F center mechanism become dominating. However, small Co content is not sufficient to produce a net magnetization in each magnetic polaron. Once x reaches to a critical value,i.e. 2%, a net moment on each polaron was developed, leading to the sudden soar of magnetic moment. When x increases beyond 2%, the decrease of Ms with Co is ascribed to the antiferromagnetic interactions between Co ions.

In conclusion, we reported that an Ms as large as 0.05emu/g and a Curie temperature above RT in Co doped La2O3 and CeO2, rendering them candidate DMOs for RT applications. Our results also confirm the oxygen-vacancy (F-Center) mediated FM mechanism for TM doped high-k oxides.

[1] M. Venkatesan, C. B. Fitzgerald, and J. M. D. Coey, Nature 430, 630 (2004)

[2] A. Tiwari, V. M. Bhosle, S. Ramachandran, et. al, Appl. Phys. Lett. 88, 142511 (2006)

[3] K. Xiong, P. W. Peacock, and J. Robertson, Mat. Res. Soc. Symp. Proc. 811, D641 (2004).

[4] A. Trovarelli ed., Catalysis by Ceria and Related Materials (Imperial College Press, London, 2002). pp.117

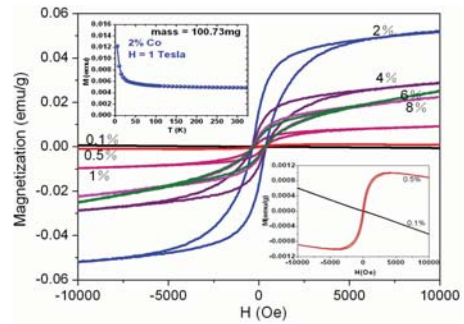

Fig.1 M-H curves for Co:La2O3 with different Co content measured at RT. Bottom-right inset: the enlarged M-H curve of 0.1% and 0.5% Co doped La2O3. Top-left inset: M-T curves of 2% Co doped La2O3 collected at 1 T.

ER-03

Evidence of oxygen vacancies enhancing the room temperature ferromagnetism in CeO_2 nanopowders.

M. Li, *S. Ge*, Y. Zuo, X. Zhou, L. Zhang, S. Yan
Lanzhou University, Lanzhou, China

Recently, ferromagnetism in nanoparticles of Al_2O_3, ZnO, SnO_2, CeO_2 has been observed by Sundaresan et al [1], and assumed to be the exchange interactions between unpaired electron spins arising from oxygen vacancies at the surfaces of the nanoparticles. In this study, we synthesized pure CeO_2 nanopowders by sol-gel method. Anneal studies were performed on samples to investigate the effect of oxygen vacancies. The products were characterized by X-ray diffraction (XRD), Raman spectroscopy and vibrating sample magnetometer (VSM).
Cerium nitrate and citric acid were dissolved in the mixture of distilled water and ethanol. Then the solution was stirred constantly at 65°C for 4 h during circumfluence and dried at 65°C in air to get the precursors. As-prepared smples were obtained by calcining the precursors at 320°C for 2 h in air. After the anneal in air or in the reducing forming gas, the hydrogenated, oxygenated and rehydrogenated samples were prepared respectively. In order to avoid the magnetic impurities, all the processes of experiment were carried out very carefully. Only the high pure reagent and gas source, and agate mortar were used, and all the tools used for handing the samples were non-magnetic and plastic based.
All of the samples' XRD patterns matched well with the fluorite structure of ceria, without any impurity phases. After the anneals, the crystalline quality is improved, and the particle size increases from about 10nm (by Scherrer formula) for as-prepared samples to about 14nm for rehydrogenated samples. Fig.1 shows the room temperature magnetic properties of the samples. Hysteretic behavior is observed and the loops have small coercivities in the range from 50 to 100Oe. The saturation magnetization Ms of the samples is weak, only 10^{-4}–10^{-3}emu/g, this order of magnitude is consistent with previous report [1]. Further more, the hydrogenated sample has much larger saturation magnetization than the as-prepared sample does. Fig.2 shows the Raman spectra performed at RT of as-prepared and hydrogenated samples. Two broad peaks can be observed near 442 and 590nm^{-1}, arising from the fluorite structure of ceria and the presence of O vancancies respectively [2]. The decrease of the intensity of 442cm^{-1} feature and the increase of 590cm^{-1} feature after the annealing in the reducing atmosphere indicate that there are more O vancancies in the hydrogenated CeO_2 nanopowders. Thus, with combination of the VSM and Raman data, it can be concluded that adding more oxygen vacancies can enhance the ferromagnetism of CeO_2 nanopowders. In addition, the saturation magnetization of rehydrogenated samples is smaller than hydrogenated ones', which can be understood in terms of the specific surface area of nanopowders decreases by crystal growth after the reanneals, if one considers that the ferromagnetism arises from the O vancancies at surface of nanopowders.
The above results show that the oxygen vacancies are essential to produce ferromagnetism in pure CeO_2 nanopowders. The force-field calculations suggest that the O vacancy is more stable at the surface than in the bulk [3], so the origin of ferromagnetism in pure CeO_2 nanopowders is close related to oxygen vacancies at the surfaces of CeO_2 nanopowders.

[1] A. Sundaresan, R. Bhargavi, N. Rangarajan, U. Siddesh and C. N. R. Rao, Phys. Rev. B 74, 161306(R) (2006).

[2] J.R. McBride, K.C. Hass, B.D. Poindexter, and W.H. Weber, J. Appl. Phys. 76, 2435 (1994).

[3] J.C. Conesa, Surf. Sci. 339 (1995).

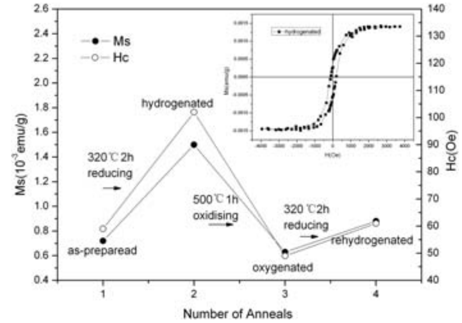

Fig.1 Variation of the saturation magnetization and coercivity with number of anneals. The inset shows Room-temperature M-H curves for hydrogenated samples.

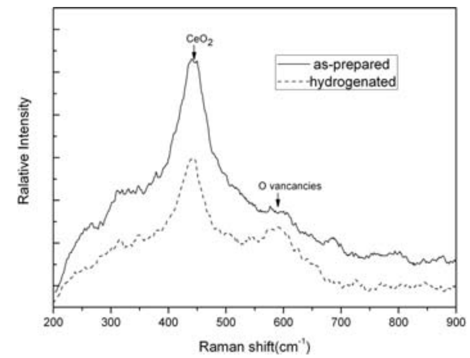

FIG.2 Raman spectra of as-prepared and hydrogenated samples.

ER-04

Zeeman splitting induced positive magnetoresistance in Co-doped ZnO and Co-doped Cu_2O ferromagnetic nanoparticles.

Y. Tian[1,2], J. Antony[1], R. Souza[1], D. Meyer[1], A. Sharma[1], *Y. Qiang*[1]
1. Department of Physics, University of Idaho, Moscow, ID; 2. School of Physics and Microelectronics, Shandong University, Jinan, China

Much interest has been put into developing new materials that utilize the spin of electrons, since the theoretical predictions of room temperature ferromagnetism in transition metal (TM) doped ZnO [1]. Although many efforts have been done on the magneto-transport of Co-doped ZnO, poor reproducibility and contradictory results make it still worth to be further studied. Recently, p-type TM doped Cu_2O joined the group of researched materials for its wide applications in optoelectronics and solar cells [2]. In this work, we compare and discuss giant positive magnetoresistance (PMR) obtained in Co-doped ZnO and small PMR of Co-doped Cu_2O nanoparticles.

Samples studied here are prepared by sputtering-gas-aggregation cluster source [3]. Electrical transport properties are measured using SQUID by four wire method with the applied magnetic field parallel to both the film plane and the current flow. MR is defined as

MR=100*($R_{(H)}$-$R_{(0)}$)/$R_{(0)}$, where $R_{(H)}$ and $R_{(0)}$ are the resistance with and without applied magnetic field, respectively.

Figure 1 shows the giant PMR in Co-doped ZnO nanoparticle films with different Co doping concentration. The PMR increases with increasing Co doping. It shows linear dependence on applied field in the low field limit and turns to saturate quickly in the high field limit. It is known that carriers in Co-doped ZnO are mainly produced by oxygen vacancies which lie close to the bottom of conduction band and act as a shallow donor level. Doping Co atoms can interact strongly with these weakly localized carriers due to s,p-d exchange interactions. Strong exchange interaction leads to large Zeeman splitting. When double occupation is allowed, two types (Type A and Type B) of sites contribute to the transport [4]. Type A has energy close to Fermi energy. Type B has one electron at a deep level, and the second electron also closes to Fermi energy. When magnetic field was applied, the suppression of spin dependent hopping between single occupied A and double occupied B sites, which leads to a large PMR with ln($R_{(H)}$/$R_{(0)}$) appearing a linear dependence on applied field H in the low field limit. At high field, transition between A and B sites cannot occur. Therefore, MR is independent of applied field and shows saturation behavior [5].

Figure 2 shows the PMR of 5% Co-doped Cu_2O nanoparticles. It can see that it shows similar behavior as the PMR found in Co-doped ZnO except for the much smaller MR amplitude. The most remarkable property for the Co-doped Cu_2O is that it has a vanishing density of states at Fermi level for both spin channels [5]. For spin up channel, E_F is no longer inside the conduction band, and for spin down channel EF is situated inside a crystal field gap, separating the occupied orbitals from the empty ones. As the electrical transport properties are mainly decided by the carriers near the Fermi level, the observed small PMR should be a result of this.

In conclusion, we report here a giant PMR in Co-doped ZnO nanoparticles is caused by giant Zeeman splitting effect and a small PMR in the Co-doped Cu_2O is related to the vanishing density of states at the Fermi level.

1. T. Dietl, H. Ohno, F. Matsukura, J. Cibert, and D. Ferrand, Science 287, 1019 (2000).

2. Jiji Antony, You Qiang, Muhammad Faheem, Daniel Meyer, David E. McCready, and Mark H. Engelhard, Appl. Phys. Lett. 90, 013106 (2007).

3. J. Antony, S. Pendyala, A. Sharma, X. B. Chen, J. Morrison, L. Bergman, and Y. Qiang, J. Appl. Phys. 97, 10D307 (2005).

4. K. A. Matveev, L. I. Glazman, Penny Clarke, D. Ephron, and M. R. Beasley, Phys. Rev. B 52, 5289 (1995).

5. Yuan-Hui Zhu, and Jian-Bai Xia, Phys. Rev. B 74, 245321 (2006).

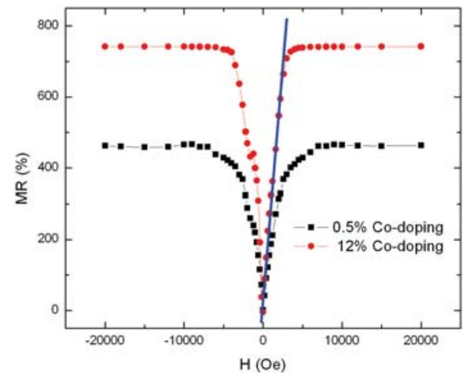

Figure 1 The field dependence of MR for 0.5% (black square) and 12% (red circle) Co-doped ZnO nanoclusters measured at 5K. The solid line is an eye guide.

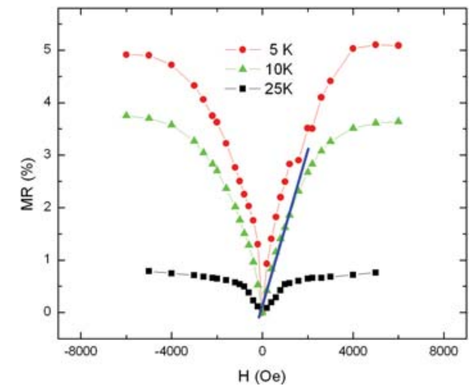

Figure 2 The field dependence of MR for 5% Co-doped Cu_2O measured at 5K (red circle), 10K (green triagonal) and 25K (black square), respectively.

ER-05

ZnO:Co films obtained by oxidation of ZnTe and Co diffusion.

I. Mínguez Bacho[1], O. de Melo[2,3], R. Sanz[1], A. Climent-Font[3,4], A. Jacas Rodriguez[1], M. Hernández-Vélez[1,3]

1. ICMM-CSIC, Madrid, Spain; 2. Facultad de Física, Universidad de La Habana, La Habana, Cuba; 3. Departamento de Física Aplicada, Universidad Autónoma de Madrid, Madrid, Spain; 4. Centro de Micro-Análisis de Materiales, Universidad Autónoma de Madrid, Madrid, Spain

ZnO is an interesting direct wide band gap (3.37eV) semiconductor with large exciton binding energy (60meV) whose properties make it very suitable material for optoelectronics applications, and potential ZnO-based devices. In addition, ZnO is a particularly promising candidate for applications in spintronics since it could exhibit ferromagnetic characteristics at room temperature when doped with selected transition elements to form novel materials [1].

Studies on Co-doped ZnO prepared by different methods have been reported along the last years [2-3]. In this work, ZnO:Co films have been obtained through a novel technique by high temperature annealing of ZnTe/Co/Si structures. Co films were first sputtered on Si substrates and then ZnTe thin films were grown by Isothermal Closed Space Sublimation (ICSS) technique [4] using Zn (99.99 %) and Te (99.999 %) as starting elemental sources. Finally, the multilayered samples were annealed at 823 K for 6 hours under Ar atmosphere. As a consequence of a non-negligible Oxygen content in the Ar flow and the high temperature kept during the annealing process, a thermally stimulated chemical reaction took place removing Te atoms from ZnTe films previously grown and then hexagonal ZnO crystalline phase was formed as it is confirmed by X-ray diffraction patterns showed in figure 1. From RBS studies it could be concluded that, no significant amount of Te remain in the annealed films and, on the other hand, Co atoms diffused almost homogeneously in such ZnO films.

Magnetic measurements have been performed by a SQUID magnetometer with a maximum applied field of 1.5T in the temperature range from 4 to 300 K. Figure 2a and 2b show the hysteresis loops at two selected temperatures, confirming the presence of ferromagnetic behavior even at the highest measurement temperature.

In conclusion, the ICSS technique combined with sputtering technique in such experimental conditions has been proved to be a reliable way to achieve Co doped ZnO thin films, whose ferromagnetic behavior has been confirmed at room temperature. Other studies to determine the formation of new very interesting diluted magnetic semiconductors by these procedures are in progress.

[1] T. Dietl, H. Ohno, F. Matsukura, J. Cibert, and D. Ferrand, Science 287, 1019 (2000)

[2] K. Rode, A. Anane, R. Mattana, J.P. Contour, O. Durand, and R. LeBourgeois, J.Appl. Phys. 93, 7676 (2003).

[3] H.S.Hsu, J.C.A.Huang, Y.H. Huang, Y.F.Liao, M.Z.Lin and C.H. Lee, Appl. Phys. Lett., 88, 242507 (2006).

[4] E. Larramendi, E. Purón, L. C. Hernández, M. Sánchez, S. De Roux, O. de Melo, G. Romero- Paredes, R. Peña- Sierra, M. Tamura, J. Crystal Growth 223, 447(2001).

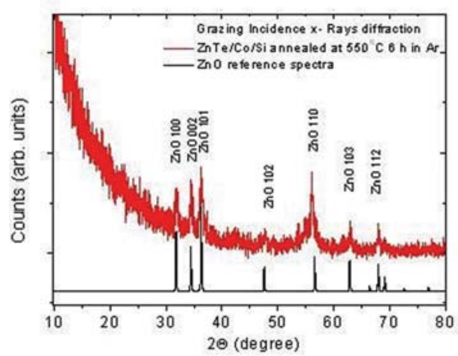

Figure 1.- Grazing incidence X- Ray diffraction pattern of an annealed structure. A simulated XRD pattern of ZnO is also included as a reference.

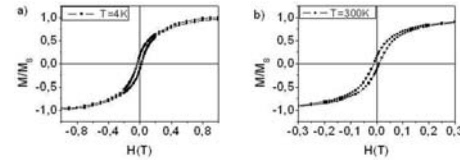

Figure 2.- Hysteresis loops showing ferromagnetic behavior at a) 4 K and b) 300K.

ER-06

Magnetic properties of TiO_2 /Co_3O_4 system.

A. Serrano[1], A. Quesada[1,4], I. Lorite[2], L. Pérez[1], J. Fernandez[2], J. Costa-Kramer[3], M. Martin-Gonzalez[3], S. Steplecaru[3], J. Llopis[1], M. Garcia[1]
1. Dpt Material Science, Universidad Complutense de Madrid, Madrid, Spain; 2. Dpt Electroceramics, Institute for Ceramic and glasses - CSIC, Madrid, Spain; 3. Institute of Microelectronics, CSIC, Madrid, Spain; 4. Institut for applied magnetism, Universidad Complutense de Madrid, Las Rozas, Spain

Carrier-induced ferromagnetism and dilute magnetic semiconductors (DMS) are of much interest from the industrial viewpoint, because of their potential applications as new functional materials, opening a way to introduce the spin degree of freedom into semiconductor devices. Current technologies require a continuous information exchange between semiconductors (controlling the logic) and the magnetic material that stores the information. High-speed semiconductor technologies are nowadays the base of a large amount of devices. The energy consumption and the high volatility of the information are disadvantages of these technologies. In magnetic materials the information storage relays on the magnetization orientation within the ferromagnetic material, being non-volatile devices. From the engineering point of view, materials combining both the semiconducting and the magnetic properties are of great interest. Co:TiO_2 has been one of the most studied DMS systems because of the interesting optical properties of TiO_2 (wide direct band-gap) [1] and one of the first systems showing room temperature ferromagnetism. [2]. However, many doubts arise about the real origin of the magnetism in this system, with some works claiming that the FM was due to secondary segregated phases.
Here we report on the properties of Ti-Co-O system prepared by milling and thermal annealing of TiO_2 and Co_3O_4.
TiO_2-Co_3O_4 samples with Co_3O_4 content of 0.05%, 0.1%, 0.2%, 0.5% were prepared by mechanical milling using agate balls. Samples were subsequently annealed in air for 24h at temperatures ranging between 500C and 900C. Samples were prepared using TiO_2 in both anatase and rutile phases.
Result shows that partial reaction between both phases leads to room temperature ferromagnetism (RT FM) . The magnetic properties strongly depend on the TiO_2 phase; RT FM is favoured using anatase TiO_2 (although the magnetic signal is very weak) while using rutile TiO_2 did not show magnetic properties different to those of Co_3O_4. Those results indicate that the RT FM is due to a partial reaction of the oxides and can not be ascribed simply to Co_3O_4 nor segregated metallic Co. However, none of the phases presents can explain the RT FM. Therefore, the results suggest the interface between the oxides as the responsible for the RT FM. The particular crystallographic ordering in this interfaces after partial reaction can lead to an structure for which exchange forces arise ferromagnetism as previously demonstrated for the Zn-O-Mn system.

[1] G. Lawes, A.S. Risbud, A. P. Ramírez, R. Seshadri, Phys. Rev. B 71, 045201(2005)

[2] Matsumoto, Science 291, 854 (2001)

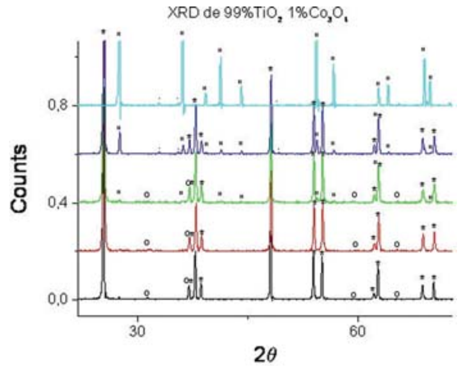

Figure1 .XRD measurements from the 99% TiO_2 (anatase)- 1%Co_3O_4 annealed at different temperatures. Circles, asterisks, semicolons and points correspond to Co_3O_4, TiO_2 (anatasa), TiO_2 (rutile) and $CoTiO_3$ respectively.

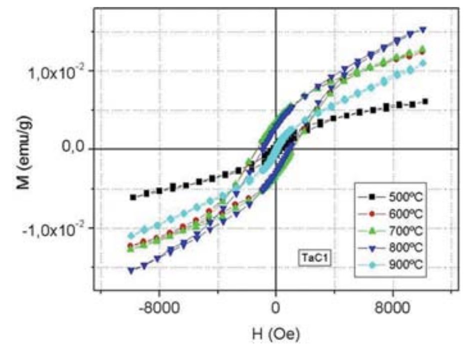

Figure 2. Magnetization curves at 300K for the 99% TiO_2 (anatase)- 1%Co_3O_4 annealed at different temperatures

ER-07

EXPERIMENTAL EVIDENCE OF DOUBLE-EXCHANGE CONTRIBUTION TO FERROMAGNETISM IN Mn-Zn-O: A XANES ANALYSIS.

A. Quesada[1,2], F. Rubio Marcos[4], M. García[2], J. Fernández[4], F. Wilhelm[3], A. Rogalev[3], J. Llopis[2], A. Hernando[1,2]
1. Institute of Applied Magnetism, Las Rozas, Madrid., Spain; 2. Departamento Física de Materiales, Facultad de Ciencias Físicas. Universidad Complutense de Madrid., Madrid, Spain; 3. ID12, European Synchrotron Radiation Facility., Grenoble, France; 4. Departamento de Cerámica, Instituto de Cerámica y Vidrio.CSIC., Cantoblanco, Spain

Following the first experimental observation of room temperature (RT) ferromagnetism (FM) in the Mn-Zn-O system in bulk samples1, Kundaliya et al.2 claimed that the FM found was not attributable to a DMS but to a secondary ZnxMn2-xO3-y phase. Moreover, Lawes et al.3 found no ferromagnetism down to 2 K in bulk samples prepared by chemical methods, and we attribute the FM observed to the double-exchange mechanism taking place between Mn3+ and Mn4+ ions4. In a attempt to achieve deeper understanding of the origin of FM in this system, this work focuses on the study of the influence of Mn oxidation states and the kinetics of Zn diffusion into MnO2 on the magnetic properties of Mn-Zn-O bulk samples.
2%MnO2-98%ZnO (named ZM samples) pellets were prepared following the method described by Sharma et al.1.
From the XANES spectra of the samples, it is possible to obtain a quantitative estimation of the Mn oxidation state, averaged for all the Mn atoms of the sample. In fact, the energy shifts on the absorption edge are directly related to the mean oxidation state of the absorbent atom5,6. The obtained mean oxidation state of Mn in each sample is shown in figure 1.
From the XANES spectra it is inferred that Mn4+ and Mn3+ coexist in the FM samples. Although this condition is necessary, it is not sufficient. The two oxidation states also coexist for non-FM compounds (ZM annealed at 800 C). The analysis of the oxidation state of Mn indicates that FM arises only when a small fraction of the Mn4+ atoms of MnO2 reduce to Mn3+, since the mean oxidation state of the FM compounds is approximately 3.9 and 3.8. We attribute the FM behaviour of this system to a double-exchange mechanism between Mn4+ and Mn3+ taking place at the Zn diffusion front in the surface of the MnO2 grains4. Zn stabilizes the two Mn oxidation states in its surrounding, presumably supplying the appropriate geometry for this mechanism to take place. At 500 C, two processes, both necessary for the appearance of FM in this system, are competing: the diffusion of Zn into MnO2, and the reduction of MnO2 to Mn2O3. The conditions for FM are thus very subtle: Zn atoms must diffuse superficially into MnO2 while a small amount of MnO2 has reduced to Mn2O3. There should be a determined value of the mean oxidation state of Mn and of the amount of Zn that has diffused onto MnO2 for which the FM reaches a maximum. From these conditions, further diffusion of Zn and/or a greater reduction of MnO2 yield the decay of FM, as the ZnMn2O4 paramagnetic spinel begins to appear, and the number of Mn4+ atoms becomes not sufficient. The Raman and XANES experiments indicate that changing the dynamics of the two competing processes, the reduction of MnO2 and the diffusion of Zn onto MnO2 grains, tunes the FM in the system.
In summary, we have experimentally shown that Mn4+ and Mn3+ coexist in bulk ferromagnetic Mn-Zn-O, confirming the hypothesis of double-exchange as the responsible for FM at RT. FM appears when only a small fraction of Mn4+ has reduced to Mn3+. Although the coexistence of the two oxidation states is a necessary condition for FM, the kinetics of the Zn diffusion into MnO2 also plays a crucial role in the magnetic properties of the system. The double-exchange mechanism between Mn ions is tuned by the competition between these two linked processes.

1.P. Sharma et al., Nat. Mater. 2, 673 (2003).

2.D. Kundaliya et al., Nat. Mater. 3, 709 (2004).

3.G. Lawes, A.S. Risbud, A.P. Ramírez, and R. Seshadri, Phys. Rev. B 71, 045201 (2005).

4.M.A. García et al., Phys. Rev. Lett. 94, 217206 (2005).

5.J. Wong, F.W. Lytle, R.P. Messmer, and D.H. Maylotte, Phys. Rev. B 30, 5596 (1984).

6.S.J.A. Figueroa et al., Catal. Today 107, 849 (2005).

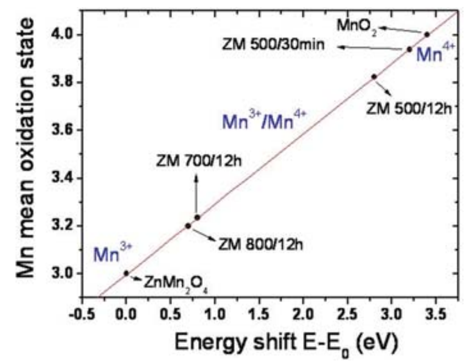

Figure 1. Oxidation state determination by the Mn K-edge energy shift of the samples.

ER-08

Ferromagnetism in bulk Co-Zn-O.

E. Enríquez[1], A. Quesada[1,2], F. Rubio-Marcos[3], L. Pérez[1], I. Lorite[3], M. García[1], M. Martín-González[4], J. Costa-Kramer[4], S. C. Steplecaru[4], J. Fernández[3], J. LLopis[1]
1. Dpt. Materials Science, Universidad Complutense de Madrid, Madrid, Spain; 2. Institute for applied Magnetism, Universidad Complutense de Madrid, Las Rozas, Spain; 3. Institute for Glass and Ceramics, CSIC, Madrid, Spain; 4. Institute for Microelectronic, CSIC, Madrid, Spain

The search for Diluted Magnetic Semiconductors (DMS) with Curie temperature above room temperature (RT) has recently attracted much attention. In particular, considerable work has been carried out using ZnO. However, the origin of ferromagnetism (FM) in these systems is still a matter of discussion. For the Co-Zn-O system, the situation is still more complicated as segregation of small metallic Co clusters can lead to RT FM1. Fitzgerald et al. claim also that the FM observed is mediated by carriers, thus intrinsic2. However, Lawes et al.3 prepared bulk samples confirming the substitution of the magnetic ions in the semiconductor matrix and found no magnetic ordering in this system down to 2K. In this work we will focus just on bulk samples prepared by the ceramic method.
$ZnO_{1-x}(Co_3O_4)_x$ samples with x=0.01, 0.05 and 0.25 (named ZC1 ZC5 and ZC25 respectively) were fabricated following the low temperature procedure of Sharma et al4. The magnetic characterization of the as cast starting powders revealed the typical diamagnetic behaviour for ZnO and a paramagnetic component over a small FM contribution for Co_3O_4 at RT. The small FM observed (0,001 emu/g(Co_3O_4Oe) was attributed to the presence of small metallic cobalt clusters in the samples.
The samples were then attrition milled in water medium. The structural characterization of the samples by means of X-ray diffraction (XRD) revealed only the presence of Co_3O_4 and ZnO, no secondary phases were found. The magnetization dependence with the applied magnetic field at RT showed a ferromagnetic component superposed to a paramagnetic behaviour for all the samples. After subtracting the paramagnetic contribution, the samples present the hysteresis loops shown in fig. 1.a.
The FM signal increases over an order of magnitude its value after the mixing procedure, the largest saturation magnetization corresponding to the ZC1 sample. The initial Co_3O_4 powder alone was also milled and in this case the milling process did not modify the magnetic properties of the sample (red curve). The increase of the FM signal after milling for samples containing ZnO indicates that some kind of interaction between ZnO and Co_3O_4 grains is taking place during the mixing process.
The samples were then in a third step exposed to thermal treatments in the 400 C to 1000 C range. The XRD revealed again only the presence of ZnO and Co_3O_4. The maxima corresponding to Co_3O_4 disappear at 800-900 C for all the samples, and only the maxima from ZnO remain. We suggest that a solid solution $Zn_{1-x}Co_xO$ with a wurtzite type structure is forming at these T explaining the fact that only peaks from the wurzite structure of ZnO are observed in the diffraction patterns. Annealing yields the decrease of FM for all the samples (see fig. 1.b.).
For Co_3O_4, the FM vanishes after annealing at 400 C, while it is still present for Zn containing samples after annealing up to 800 C. The different behaviour observed for the ZnO containing samples confirms that the FM signal observed in these samples is not related to any metallic Co cluster, which should disappear after annealing at about 400 C. It is worthy to note that for ZnO containing samples the FM signal is present up to 800 C, the same temperature at which Co_3O_4 is still present in the sample according to X-ray diffraction patterns. Thus, we can conclude that the wurtzite type solid solution formed in this reaction is not the responsible for the FM. The decrease of FM with the subsequent anneals suggests that the origin of these magnetic properties is not associated with carrier-mediated mechanisms in a DMS.
We propose that during alloying Co_3O_4 and ZnO electrostatically attract each other. The presence of ZnO at the Co_3O_4 surface promotes an electronic modification that leads to the reduction of the Co^{3+} atoms to Co^{2+} in the octahedral positions of Co_3O_4. This reduction changes the electronic configuration and atomic distances at the Co_3O_4 surface. The consequence of this modification is that superexchange interactions are substituted by exchange interactions between Co atoms at the surface, thus yielding RT FM.

1. J. H. Park, G. Kim, H. M. Jang, S. Ryu, Y. M. Kim, Co-metal clustering as the origin of ferromagnetism in Co-doped ZnO thin films, Appl. Phys. Lett. 84, 1338 (2004).

2. C.B. Fitzgerald, M. Venkatesan, J.G. Lunney, L.S. Dorneles and J.M.D. Coey, Cobalt-doped ZnO – a room temperature dilute magnetic semiconductor, Appl. Surf. Sci. 247, 493 (2005).

3. G. Lawes, A. S. Risbud, A. P. Ramírez, R. Seshadri, Absence of ferromagnetism in Co and Mn substituted polycrystalline ZnO Phys. Rev. B 71, 045201 (2005).

4. P. Sharma, A. Gupta, K.V. Rao, F.J. Owens, R. Sharma, R. Ahuja, J.M. Osorio Guillen, B. Johansson and G.A. Gehring, Ferromagnetism above room temperature in bulk and transparent thin films of Mn-doped ZnO, Nature Mater. 2, 673 (2003).

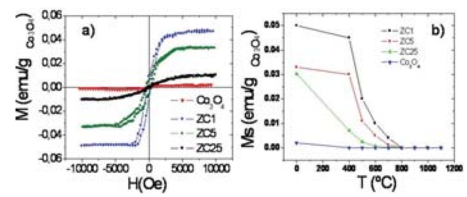

ER-09

Magnetism and Transport Properties of ZnO films doped with Co or Mn and Al.

G. Gehring, A. J. Behan, A. Mokhtari, H. J. Blythe, D. Score, J. R. Neal, M. Fox
Physics and Astronomy, University of Sheffield, Sheffield, United Kingdom

The subject of ZnO doped with magnetic ions continues to receive much attention [1-4]. It has been found that not all doped films exhibit ferromagnetism, and that the mobile carrier density, nc, can be very different in those compounds that do [5, 6]. It has been found that the addition of Zn interstitials, which affects both the number of neutral and ionised donors, leads to an increase in the ferromagnetism [7]. In fact, most of the work on doped ZnO has concentrated on the insulating phase, to such an extent that some authors now refer to ZnO as a dilute magnetic insulator (DMI) [5]. However, we have recently reported the observation of ferromagnetism in Al-doped films where nc is very high [6, 8], which highlights the importance of exploring the full range of carrier densities from the insulating to the metallic phases.

We discuss here how the electronic properties of these films, specifically carrier density and magneto-resistance are correlated with the magnetisation.

An Al ion doped into ZnO acts as a shallow donor so that it is expected to contribute one carrier per Al at room temperature. However the presence of the carriers due to Al provides screening for the other donor states in the sample so that they may also become ionised. Hence it is found that actually the carrier density rises by more than one carrier per Al ion[9,10]. In Figure 1 we show the carrier density as a function of the percentage of Al for Zn1-0.02-xAlxMn0.02O and Fig 2 shows an equivalent plot for Zn1-0.05-xAlxCo0.05O, the solid line indicates the carrier concentration expected if each Al ion contributed one carrier. All of these films were grown by PLD on sapphire substrates held at 450C at an oxygen pressure of 0.05mTorr. In the case of the Co and Mn doped films we have added a dotted line to indicate the density of magnetic ions and have also indicated the magnitude of the magnetisation as measured from a SQUID loop at room temperature.

It is clear that in all cases there are more carriers than can be accounted for by the Al ions. This effect is more pronounced for the samples that also contain Mn and Co indicating that these ions are also contributing to the carrier density. However the films with the largest magnetisations are those with the carrier density less than or comparable to half that of the magnetic ions as has been noted before [6,8].

The magneto-resistance, MR, of Co doped ZnO is shown in Figure 3. We note that comparable MR signals are seen for samples that are not ferromagnetic. These results are discussed and compared to earlier work [11]and also in terms of the importance of both the number of free carriers and types of defect responsible for the magnetism.

[1] P. Sharma et al., Nat. Mater. 2, 673 (2003)

[2] J.M.D. Coey et al, Nat. Mater. 4, 173 (2005)

[3] S.A. Chambers, Surface Science Reports 61, 345 (2006)

[4] J.M.D. Coey, Current opinion in Solid State and Mat. Sci. 10, 83 (2006)

[5] C Song et al Phys. Rev. B, 73, 024405 (2006)

[6] X.H. Xu et al, New J. Phys. 8, 135 (2006)

[7] K. K. Kittilstved et al, Phys. Rev. Lett. 97, 037203 (2006)

[8] AJ Behan et al Phys. Rev. Lett. in press

[9] XJ Liu et al J Phys Cond Matt 19, 296208 (2007)

[10] A Mokhtari et to be published

[11] Q. Xu et al, Phys. Rev. B 73, 205342 (2006) and Q. Xu et al, J. Appl. Phys. 101, 063918 (2007)

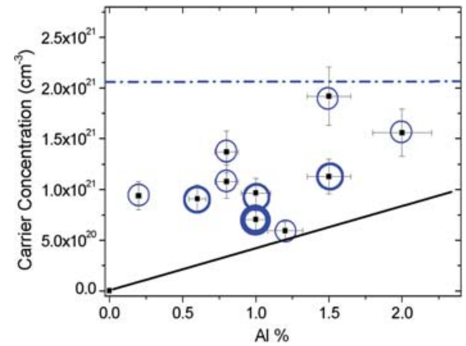

Fig.1 The carrier concetration as a function of Al concentration for ZnCoAlO the thickness of the circles indicate the magnitude of the magnetisation where the values range between 1.5 to 0.5 μb / Co.

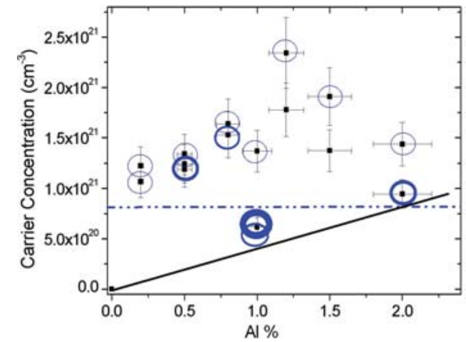

Fig.2 The carrier concetration as a function of Al concentration for ZnMnAlO the thickness of the circles indicate the magnitude of the magnetisation where the values range between 4+ to 0.5 μb / Mn.

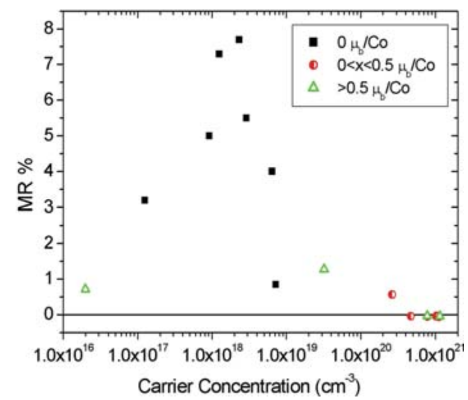

Fig. 3 The MR at 1T for the 5% Co doped samples. The samples with nc greater than 1021cm-3 contain Al.

ER-10

Ferromagnetism of manganese-doped indium tin oxide films deposited on flexible polymer substrates.

T. Nakamura, K. Tanabe, S. Isozaki, K. Tachibana
Department of Electronic Science and Engineering, Kyoto University, Kyoto, Japan

Diluted magnetic semiconductors (DMS) have attracted considerable attention because of their potential applications to spintronic devices. Low temperature deposition is required to grow magnetic films on polymer substrates for the development of flexible spintronic devices. There are several devices using transparent conducting films fabricated at low substrate temperatures in the market. Among the existing transparent conducting films, indium tin oxide (ITO) is widely used in flat panel displays, optoelectronics, solar cells, and so on. In this work, we fabricated Mn-doped ITO films on flexible polymer substrates, and investigated the magnetic, electrical, and optical properties of the films.

Mn-doped ITO films were grown on polyethylene naphthalate (PEN) substrates at room temperature using rf magnetron sputtering. For comparison, the films were deposited on glass substrates. The distance between the target and substrate was maintained at 50 mm. After the chamber was evacuated to a high vacuum of about 1×10^{-6} Torr, working gas of argon was introduced. Before the deposition, the target was pre-sputtered for 30 min to obtain a clean target surface. The process pressure was controlled at 7 mTorr during the sputter deposition. The rf power was 80 W.

Magnetic properties were characterized by a superconducting quantum interference device (SQUID) magnetometer. Magnetization versus applied magnetic field curves were measured at 77 and 300 K for the Mn-doped ITO film. The magnetic field was applied parallel to the film plane. A well-defined hysteresis loop with a coercive force of about 80 Oe was observed at 300 K, signifying room temperature ferromagnetism. The temperature dependence of the magnetization for the Mn-doped ITO film was measured from 5 to 400 K using SQUID. The magnetization data were taken in an applied field of 1000 Oe parallel to the film plane. The Curie temperature is estimated to be higher than 400 K.

Transport properties (resistivity, carrier density, and mobility) of the deposited films were measured by Hall effect measurements using van der Pauw geometry. The Mn-doped ITO films deposited at room temperature exhibited low electrical resistivity of the order of 10^{-3} Ωcm, although the resistivity of the films was increased by low temperature deposition.

Optical transmission spectra in the wavelength region of 300-800 nm were acquired using a UV-visible spectrophotometer. The transmittance exhibits interference in the visible range. The average transmittance of the Mn-doped ITO film ranges from 75 to 90%. The Mn-doped ITO film is optically highly transparent.

In summary, Mn-doped ITO films were deposited on flexible organic substrates as well as glass substrates by rf magnetron sputtering. The magnetization as a function of magnetic field exhibited hysteretic behavior at room temperature. According to the temperature dependence of the magnetization, the Curie temperature is higher than 400 K. The Mn-doped ITO film exhibited low electrical resistivity of the order of 10^{-3} Ωcm and high optical transmittance between 75 and 90% in the visible region. Mn-doped ITO films fabricated at low temperatures can be one of the most promising candidates of ferromagnetic transparent conductive materials for flexible spintronic devices.

Fabrication of shielded planar type single-pole head.

K. Ise, T. Kiya, K. Taguchi, K. Yamakawa
AIT, Akita Prefectural R&D Center, Akita, Japan

Introduction:

We have proposed a new single-pole head with planar structure [1] which is composed of a multi-charged-surface (MCS) main pole [2] to produce a strong head field and a wrap-around shield to realize a steep head field distribution for high density recording. This new head was fabricated using novel technique that is different from that for present recording heads. First recording test of the head was done. In this work, we report the detailed fabrication method and fundamental recording properties of the shielded planar head.

Head design and fabrication:

Fig.1 shows the schematic illustration of the proposed shielded planar head. The main pole consists of a truncated pyramid tip and a rectangular back pole. A shield yoke is equipped not only in down track direction but also in cross track direction.

In order to fabricate the head, following processes were used. A shape of the main pole tip was formed using a template of a quadrangular pyramid which was created by a chemical anisotropy etching of a Si (100) substrate. Next, magnetic material was embedded in the template. After formation of the main pole tip, a two-layered pancake-type coil was fabricated. After fabrication of a return yoke over the coil layer, the Si substrate was bonded to a dummy substrate by an anode bonding. Then, the Si substrate was removed by chemical etching to appear the pyramidal-shaped main pole tip. After that, the gap and the shield yoke layers were deposited on the etched surface. Finally, lapping process was performed to define the track width.

Fig.2 shows the plane view of the fabricated shielded planar head near the main pole. It was confirmed that the main pole and the wrap-around shield with a narrow gap were successfully formed. In this fabrication, Fe-Si-N film with Bs of 1.9 T was used for the main pole material. The nominal write track width was 1 μm. A number of the coil was six. DC resistance and inductance of the fabricated head were about 40 Ω and 1 nH, respectively.

Recording test:

In order to evaluate head performances, read-write tests were performed in sliding contact recording. A commercial TMR head and a Co-Cr system alloy medium with coercivity of 3.9 kOe were used for the evaluation of the fabricated head.

We successfully obtained read-back signals from the bits recorded by the fabricated head as shown in Fig.3. Although high recording performance was not yet obtained, it is suggested that the result has opened a path for new paradigm of recording head.

Acknowledgements:

This study was supported in part by Industrial Technology Research Grant Program in 2005 from New Energy and Industrial Technology Development Organization (NEDO) of Japan.

[1] K. Ise, S. Takahashi, K. Yamakawa, and N. Honda, IEEE Trans. on Magn., vol. 42, pp.2422-2424, Oct. 2006.

[2] S. Takahashi, K. Yamakawa, and K. Ouchi, J. Appl. Phys., vol.91, no.10, pp.6839-6841, 2002.

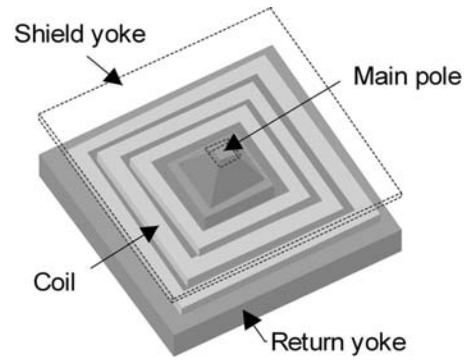

Fig.1 Schematic illustration of shielded planar head.

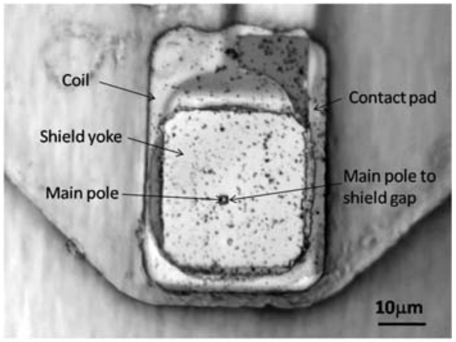

Fig.2 Photo of fabricated shielded planar head.

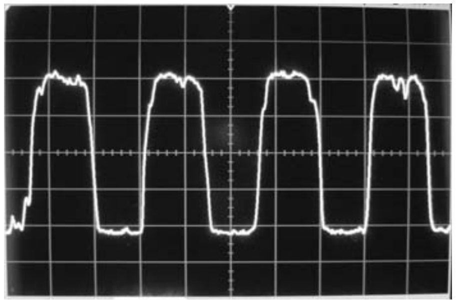

Fig.3 Read-back waveform of 40 kFCI. Fabricated shielded planar head and commercial TMR head were used for writing and reading, respectively.

ES-02

New Type Side Shield Head for Ultra High Density Recording.

Y. Kim, S. Kukhyun, K. Na
HDD Core Tech TF, SAIT(Samsung Advanced Institute of Technology), Yongin-Si, South Korea

I. INTRODUCTION

There is no revolutionary jump of areal density in magnetic recording especially in write head, we need to optimize writing head to increase track density[1][2]. By these reason we concentrate to increase track density by reducing leakage field to disturb the written data in side track. We propose new type side shield to satisfy these needs for write head, which we named shell shield.
This head can reduce side leakage without any degradation head field and field gradient at write gap.

II. ANALYSIS MODEL

A. Head Model

The head field and its gradient were calculated using the nonlinear finite element method (JMAG software)[3] with write head of 100 nm track width, 50 nm gap length, 200 nm yoke thickness, and 150 nm throat height. The number of elements is more than 38,000 and nodes are 67,000. The magnetic spacing was 20 nm. To find the optimization condition, shell thickness is changed from 50 to 170 nm and distance between pole tip and side shield is changed from 80 to 220 nm.

B. Track Width Simulation

To confirm the head performance, the write field was simulated with several coil currents 30, 50 and 70 mA and the media locations were 0, 50 and 250 nm from pole tip surface. The applied head field at each media position of recording disk was calculated to simulate minimum track width of each combination of head & media by using the calculation method explained in fig. 2 b).

C. Optimization

We used Minitab software to search optimized condition of shell shield and conventional wrap around shield head. We used central composite method in surface response method which is one typical method of DOE(design of experiment) [4]. We found three optimization points depends on the media nucleation field(Hn).

III. RESULTS AND DISCUSSION

Simulated head field distribution of conventional and shell side shield head were shown in Fig. 3 for comparison. In the figure, we can find out the head field is concentrated to the center of pole and the side leakage field is distributed to all area of shield.
To see the result we can imagine the shell side shield can concentrate field to the center of head pole and decrease side track erasure, so it would achieve high track density.
Fig. 4 shows the optimized results of conventional head and shell shield head. We can see the possible track width of conventional head is about 300 nm and shell shield head is about 250 nm. In addition to, the maximum field gradient of shell shield head is almost 120 Oe/nm, so the linear density of proposed head (about 110 Oe/nm) would be also higher than that of the conventional head.

IV. CONCLUSION

We suggest the shell side shield head for high density recording head and evaluate the performance by comparison between the optimized conditions of conventional wrap around side shield head and proposed shell side shield head.

[1] M. Mallary, A. Torabi, and M. Benakli, IEEE Trans. Magn., vol. 38, pp. 1719–1724, 2002.

[2] Kim, E.; Im, Y.H.; Yongsu Kim et al, IEEE Trans. Magn.,vol 37, pp. 1382-1385, 2001

[3] The Japan Research Institute, Ltd., http://www.jri.co.jp/proeng/jmag/e/ jmg/index.html

[4] Minitab Inc., http://www.minitab.com/resources/tutorials/Accessingthe Power/default.aspx

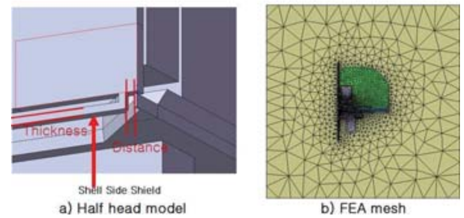

Head model a) half head shape of shell shield head to save computation power b) FEA mesh divided by JMAG software. We can see the small mesh around air-gap and main yoke

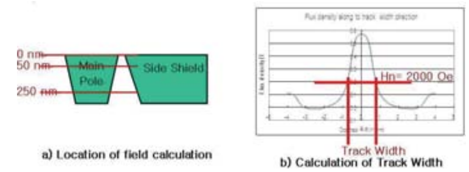

Calculation method of track width a) field calculation point to calculate ATE and maximum track pitch b) method for maximum track width calculation by comparing Hn with leakage flux

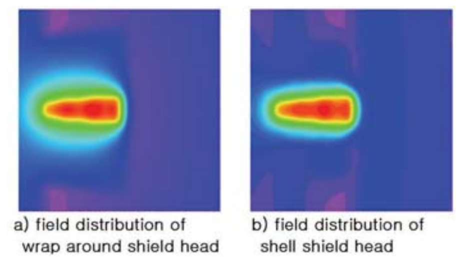

Calculated perpendicular head field distribution of wrap around head and shell shield head

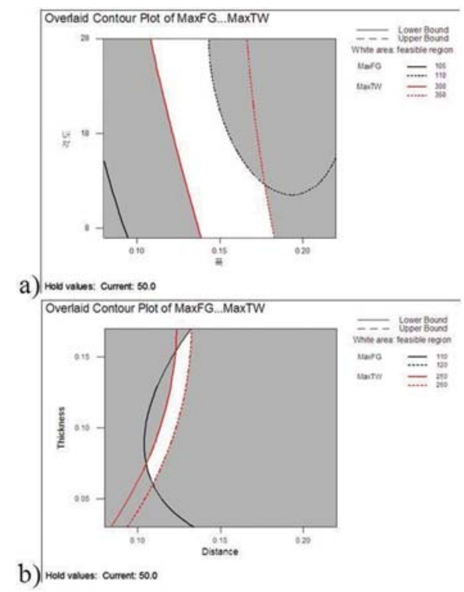

Optimization condition comparisons between conventional side shield head and shell side shield head. a) optimized condition of conventional side shield head and b) optimized condition of shell side shield head

ES-03

Optimal Side Shield Write Head Design for Ultra High Recording Density.

Y. Kim, S. Kukhyun, K. Shin
HDD Core Tech TF, SAIT(Samsung Advanced Institute of Technology), Yongin-Si, South Korea

I. INTRODUCTION

There is no revolutionary jump of areal density in magnetic recording especially in write head, we need to optimize write head to increase track density. We concentrate to increase track density by reducing leakage field to disturb the written data in side track[1][2], by optimizing side shield shape.

II. ANALYSIS MODEL

A. Head Model

The head field and its gradient were calculated using the nonlinear finite element method (JMAG software)[3]. The magnetic spacing was 20 nm. To find the optimization condition, the angle of side shield, which is shown in Fig. 1, is changed from 7 to 28 degree and distance between pole tip and side shield is changed from 80 nm to 220 nm.

B. Track Width Simulation

To confirm the head performance, the write field was simulated with several coil currents 30, 50 and 70 mA and the media locations were 0, 50 and 250 nm from pole tip surface. The applied head field at each media position of recording disk was calculated to simulate minimum track width of each combination of head & media by using the calculation method explained in fig. 2.

C. Optimization

We used Minitab software to search optimized condition of shell shield and conventional wrap around shield head. We used central composite method in surface response method which is one typical method of DOE(design of experiment) [4]. We found three optimization points depends on the media nucleation field(Hn).

III. RESULTS AND DISCUSSION

Simulated head field distribution of conventional wrap around side shield and separated side shield head were shown in Fig. 3 for comparison. In the figure, we can find out each head has different the maximum track width position, red arrow shows maximum track width position in Fig. 3, so the optimized condition is completely different.

Fig. 4 shows the optimization condition of wrap around head and separated side shield head. In the results, we can imagine the expected areal densities are almost same, track width is about 300 nm and field gradient is about 110 Oe/nm, but the optimized conditions are completely different. The condition in wrap around head is that angle is about 10 degree and distance is around 140 nm, and about 22 degree and around 150 nm in separated side shield head.

IV. CONCLUSION

We studied optimized conditions of side shield heads for high density recording and evaluate the performance by comparison between the optimized conditions of each heads, but two head types has almost same performance and in fabrication point of view, separated side shield is ease to manage because gap length is controlled easily by process time.

[1] M. Mallary, A. Torabi, and M. Benakli, IEEE Trans. Magn., vol. 38, pp. 1719–1724, 2002.

[2] Kim, E.; Im, Y.H.; Yongsu Kim et al, IEEE Trans. Magn.,vol 37, pp. 1382-1385, 2001

[3] The Japan Research Institute, Ltd., http://www.jri.co.jp/proeng/jmag/e/ jmg/index.html

[4] Minitab Inc., http://www.minitab.com/resources/tutorials/Accessingthe Power/default.aspx

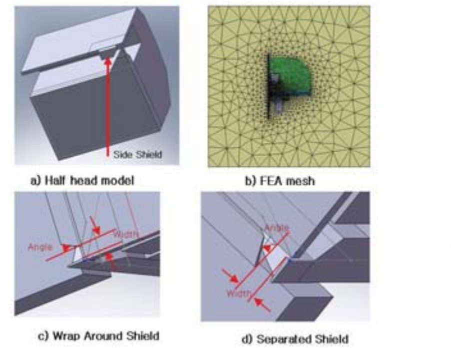

Head model a) half head shape to save computation power b) FEA mesh divided by JMAG software. We can see the small mesh around air-gap and main yoke c) Definitions of angle and width of wrap around shield head. d) Definitions of angle and width of separated shield head

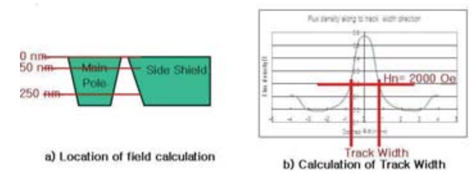

Calculation method of track width a) field calculation point to calculate ATE and maximum track pitch b) method for maximum track width calculation by comparing Hn with leakage flux

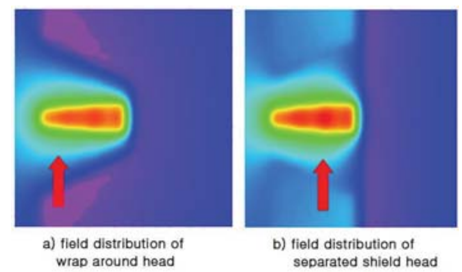

Calculated perpendicular head field distribution of wrap around head and separated side shield head

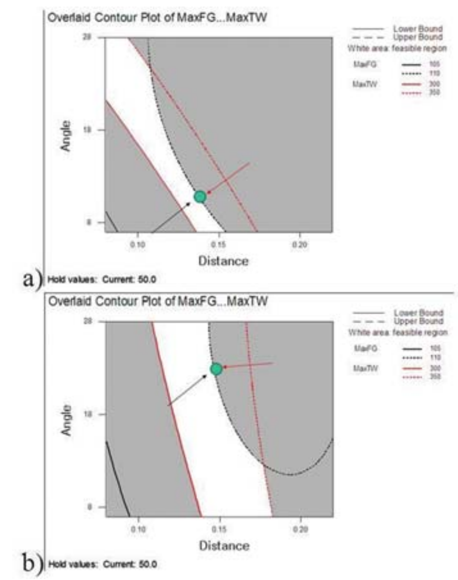

Optimization condition comparisons between wrap around head and separated side shield head. a) Optimized condition of wrap around side shield head and b) Optimized condition of separated side shield head

ES-04

Magnetic 1/f noise in MgO tunneling magnetoresistive sensors.

N. Smith, D. Mauri, J. A. Katine, Y. Hong
Hitachi Global Storage Technologies, San Jose, CA

The appearance of 1/f noise in the resistance across tunneling barriers, and tunneling magnetoresistive devices in particular, and is generally attributed to electrical, rather than magnetic origins, e.g., electron trapping sites inside the tunnel barrier [1]. This talk reports on the clear observance of a predominant magnetic component of 1/f noise in CoFeB/MgO/CoFe/CoFeB tunneling magnetoresistive sensors fabricated into small (~100 nm) test structures representative of TMR read sensors. The devices have tunnel barriers with typical RA product of ~2-3 ohm-um^2, and TMR ratios of ~80-100%.

Fig. 1 shows measured R-H loops for an 80nm circular (E-beam defined) device subject to two-axis orthogonal fields: a stationary H_long of 800 Oe is aligned collinearly (parallel or antiparallel) to the exchange pinning direction of the IrMn/CoFe/Ru/CoFeB pinned-layer (PL)/reference-layer (RL) synthetic antiferromagnet (SAF) A transverse field H_trans is then continuously swept to rotate the CoFe/CoFeB free-layer (FL). Fig. 2 shows measured rms low-frequency noise vs H_trans (during which the bias voltage is fixed at 140 mV) at selected frequencies of 0.3 MHz and 3 MHz. (Noise at zero bias voltage has been subtracted out.) A notable minimum in the low-f noise occurs when RL and FL magnetizations are aligned collinearly, either parallel (P) or antiparallel (AP). The absolute noise level is virtually the same for either P or AP states, but rises particularly fast for initial deviation from the AP state. This pattern is observed for both the 0.3 MHz and 3 MHz noise, the latter being essentially just smaller in amplitude by about sqrt(10) ~ 3, as would be expected for 1/f type noise. (The 1/f-like nature was also confirmed by spectral measurement over a frequency continuum.) Although the amplitude of the maximum noise level can vary from device to device, this basic pattern of field-dependent noise shown was observed in tens of devices . The overall noise amplitude scales fairly linearly with bias voltage <= 140 mV.

A field-independent minimum/collinear noise level was found to remain unchanged in "magnetically-poisoned" CoFeB/MgO/Ru/CoFe barriers which had the same RA but TMR < 1%. It represents an electronic 1/f noise intrinsic to this tunnel barrier. The field (and thus magnetic orientation) dependence of the excess 1/f noise (i.e., that above the minimum/collinear level) conclusively demonstrates its magnetic origin, and strongly suggests it arises from magnetization fluctuations of the relative angle θ between RL and FL magnetizations which naturally produce TMR resistance fluctuations which scale as $d\cos\theta/d\theta = \sin\theta$ and hence vanish for colinearity. Although the FL sees an 800 Oe H_long field in either case, the noticably larger levels of 1/f noise for the near-AP state, compared to the near-P state, suggest the origin of this noise is in RL fluctuations enhanced when H_long is antiparallel (hence destabilizing) with respect to the nominal RL magnetization orientation. This observation is consistent with alternative experimental conditions and device structures which will be described in the talk, including the lack of significant 1/f magnetic noise in the analogous tri-layer structure of CeFeB/MgO/CoFe without the IrMn pinning layer or the SAF PL/RL.

[1] E. R. Nowak, M. B. Weissman, and S. S. P. Parkin, Appl. Phys. Lett. vol. 74, pp. 600-603, 1999.

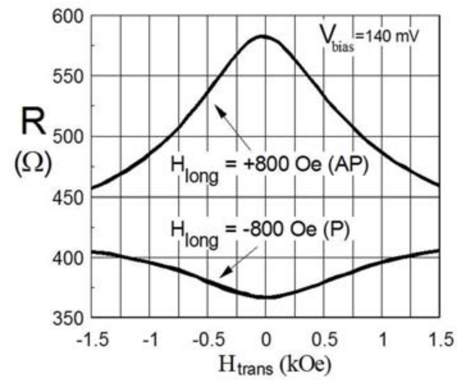

Fig. 1. Resistance vs H_trans, starting from P or AP states with fixed H_long = +800, or -800 Oe.

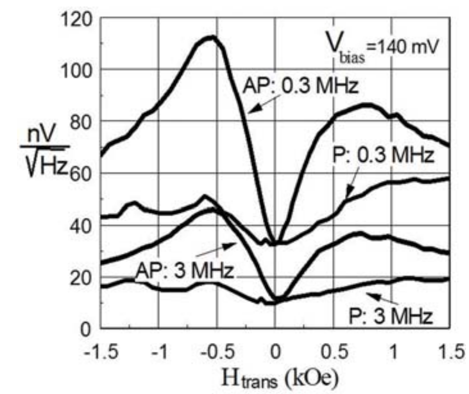

Fig. 2 Narrow band rms noise (30 kHz bandwidth) vs H_trans under identical conditions as in Fig. 1.

ES-05

Proposal of new method to fabricate nano-contacts in CoFe-NOL.

Y. Shiokawa, Y. Saki, S. Kawasaki, M. Doi, M. Sahashi
Electronic Engineering, Tohoku univ., Sendai, Japan

Domain wall MR with FeCo-AlO$_x$ NOL (nano-oxide-layer) spacer is much attracting attention as a future reader element for magnetic head because of its low resistance and high MR ratio [1]. The formation mechanism of CoFe-AlO$_x$ NOL has reported [2]. The ferromagnetic nano-contacts (NCs) were fabricated during *in-situ* annealing by the migration and cohesion of Al from CoFe-Al mixing layer in the vacuumed chamber with remained oxygen. Meanwhile, by *in-situ* annealing, Al diffused to the inside of CoFe layer at the same time (Fig.1). So, the concentration of Al on the surface of CoFe layer after annealing became poor due to these diffusion. Therefore, by the Natural-Oxidation (NO), CoFe in NCs were also oxidized with patterned Al. As result, the current intensity of conductive channels was weak in the current image of conductive-AFM.
In this study, we propose a new method to fabricate the NCs which is formed by the diffused Al, which was the problem in the past study, with partial reduction of oxygen in CoFe-NOL.
The ion beam sputtering method was used for the sample preparation. We fabricated the two kinds of the SV film. One was seed-layer/IrMn 7/$Co_{0.9}Fe_{0.1}$ 3 (pinned layer: PL)/Ru 0.85/$Co_{0.9}Fe_{0.1}$ 2.7 (reference layer: RL)/Cu 2 or Al 1.5/*in-situ* annealing (200°C, 30min)/$Co_{0.9}Fe_{0.1}$ 5 (free layer: FL)/Capping-layer (nm), the other was seed-layer/IrMn 7/$Co_{0.9}Fe_{0.1}$ 3/Ru 0.85/$Co_{0.9}Fe_{0.1}$ 2.7/NO (O2 pressure: 2.5×10-4 Torr, 39 min)/ $Co_{0.9}Fe_{0.1}$ 1/Cu 2 or Al 1.5/$Co_{0.9}Fe_{0.1}$ 5/Capping-layer (nm). An interlayer coupling field between a RL and a FL (H_{in}), and exchange bias field (H_{ex}) were measured for SV film systems with vibrating-sample magnetometer (VSM).
First, in order to confirm the diffusion of Al, we compared the SV composed Al spacer and GMR-SV composed Cu spacer without CoFe-NOL. By the change the spacer from Cu to Al, the magnetization of RL decreased by 14% and H_{in} increased from 0 Oe to 139 Oe. In addition, with *in-situ* annealing to Al, not only the magnetization of RL decreased by 73% but also H_{ex} decreased from 1872 Oe to 1087 Oe against GMR-SV. We thought these phenomena were caused by the diffusion of Al to the inside of RL and Ru in synthetic antiferromagnetic structure.
Figure.2 (a) and (b) show the M-H curve of the GMR-SV composed Cu spacer and the SV composed Al spacer with CoFe-NOL, respectively. In Fig.2 (a), the magnetization process of FL shows the H_{in} is about 7 Oe and the magnetization of FL increased by 18% corresponds to 0.9nm of CoFe. In consideration of the thickness of 0.9nm, this CoFe is thought CoFe of upper layer of CoFe-NOL. Thus, this result suggests that CoFe-NOL cuts the coupling between under RL and upper RL because CoFe is oxidized equally (Fig.3 (a)). In Fig.2 (b), by the change the spacer from Cu to Al, we didn't observe the cut between under RL and upper RL by CoFe-NOL, while observed the H_{in} of 160 Oe and the decrease of the magnetization of RL against GMR-SV with CoFe-NOL. These phenomena indicate that the followings: the diffused Al atoms arrive to the surface of CoFe-NOL, these metallic Al atoms rob oxygen in CoFe-NOL, and it makes the ferromagnetic NCs of Co or Fe in the insulator of (Co,Fe,Al)Ox (Fig.3). That is to say, the tri-layer of CoFe-NOL/CoFe/Al fabricates the NCs.We suggested the new method to fabricate the NCs, which was formed by the diffused Al into upper CoFe layer and induced partialdeoxidation of CoFe-NOL by the formation mechanism of AlO$_x$.

[1]H. Fuke, S. Hashimoto, M. Takagishi, H. Iwasaki, S. Kawasaki, K. Miyake, and M. Sahashi, IEEE Trans. Magn., 43, 2848 (2007)

[2]Y. Shiokawa, S. Kawasaki, T. Mano, R. Shiozaki, M. Doi, and M. Sahashi, 52nd annual conference on MMM, AU-09, Tampa, Florida, 2007

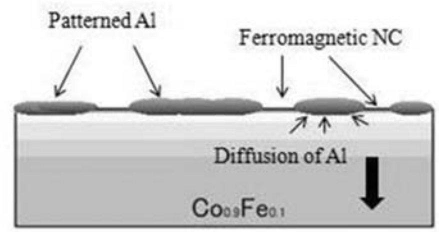

Formation mechanism of CoFe-AlO$_x$

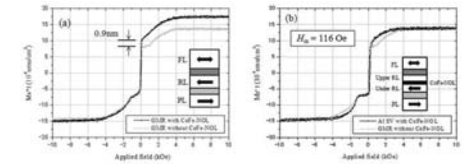

M-H curves. (a) GMR-SV composed Cu spacer with CoFe-NOL. (b) SV composed Al spacer with CoFe-NOL.

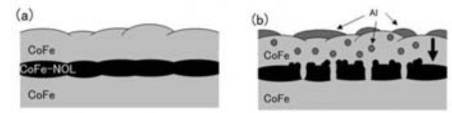

The model illustrations CoFe-NOL (a) before and (b) after the deposition of Al.

Effect of Spin Transfer Torque on 1/f Noise in TMR Heads.

J. Masuko, H. Akimoto, H. Kanai, Y. Uehara
Fujitsu Limited, Nagano, Japan

Introduction

It is suspected that magnetic noise is increased by narrowing the track width and by the spin transfer toque as a result of high current density in TMR heads. In particular, we are interested in the spin torque effect on magnetic noise in the frequency range below 1 [GHz] from a practical viewpoint. In the numerical [1] and experimental [2] studies of CPP-GMR, it is mentioned that 1/f noise is the result of chaotic magnetization precession induced by the spin transfer torque. And it is interesting to examine the magnetic normal modes [3] or the spatial distribution of resistance fluctuation in other words in this frequency range to understand the phenomena induced by the spin transfer torque.

Simulation Model

We investigated the spin torque effect on magnetic noise using macromagnetic simulation. The track width and the stripe height of the free layer are set to 69[nm] and 90[nm], respectively. Biasing field is applied to the free layer from PM. In addition, external field is applied perpendicular to the biasing field. A positive current is defined as the current from the reference layer to the free layer and a positive external field parallel to the magnetization of the reference layer. And the absolute value of external field is 300 [Oe].

Results and Discussion

Fig.1 is the current density dependency of the current – normalized magnetic noise spectrum and Fig.2 is the current density, direction of external field and spin polarization dependencies of integrated magnetic noise with the origin at zero sense current. 1/f noise appears only if the spin polarization P is not zero and the specific conditions between the polarity of current and field are satisfied.

Fig.3 is the spatial distributions of amplitude and phase of resistance fluctuation at 100 [MHz]; (i) P=0, current: positive, field: positive ((a), (e)), (ii) P=0.48, current: positive, field: positive ((b), (f)), (iii) P=0, current: positive, field: negative ((c), (g)) and (iv) P=0.48, current: positive, field: negative ((d), (h)). Comparing these conditions, 1/f noise only appears in (ii) and (ii) is different in the amplitude distribution and has a small spatial phase distribution. In addition, the maximum value of amplitude of (ii) is about two times larger than that of others. The magnetization of the free layer behaves as if it were at the resonant frequency without the external field as shown in Fig.3 (b) and (f). These results indicate that the spin torque effect has a superiority over the thermal fluctuation in a low frequency range and induces the coherent behavior of the magnetization.

Fig.4 is the frequency dependency of the spatial distributions of amplitude and phase in the same condition as (ii) of Fig.3. It is found that the spatial phase coherency is disordered at 1 [GHz] and the amplitude distribution comes to other conditions as shown in Fig.3 (a), (c) and (d). These results indicate that the thermal fluctuation has a superiority over the spin torque effect in a high frequency range and inhibits the coherent behavior of the magnetization.

[1] J. G. Zhu and X. Zhu, IEEE Trans. Magn., 40, 182 (2004).

[2] J. G. Zhu, N. Kim, Y. Zhou, Y. Zheng, J. Chang, K. Ju, X. Zhu, R. M. White, IEEE Trans. Magn., 40, 2323 (2004).

[3] R. D. McMichael and M. D. Stiles, J. Appl. Phys. **97**, 10J901 (2005).

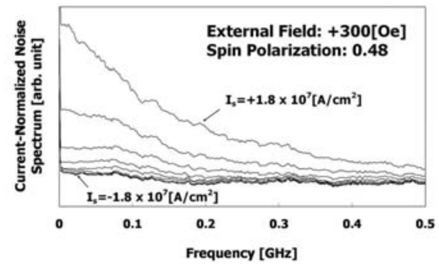

Fig.1: Current-normalized noise spectrum

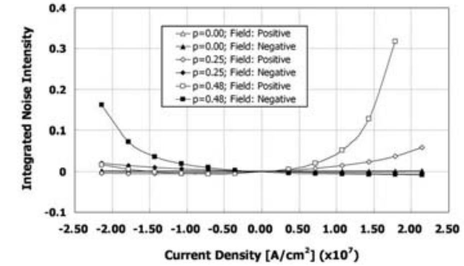

Fig.2: Integrated noise intensity

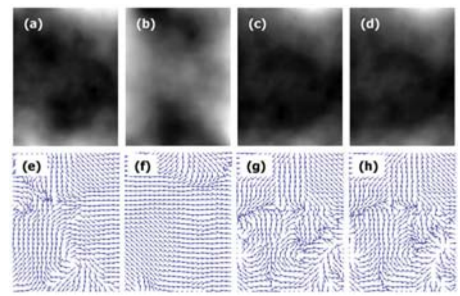

Fig.3: Field and spin polarization dependencies of resistance fluctuation Spatial distributions of amplitude (upper) and phase (lower) of resistance fluctuation. Large amplitude is represented by white and phase by the direction of arrow.

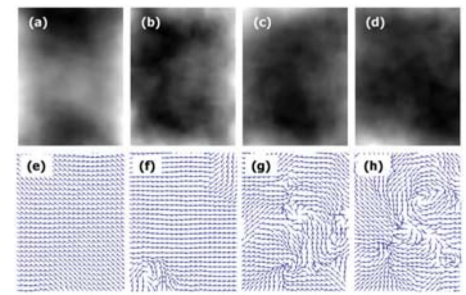

Fig.4: Frequency dependency of resistance fluctuation (a, e) 50 [MHz], (b, f) 200 [MHz], (c, g) 400 [MHz] and (d, h) 1 [GHz]

ES-07

The role of pre-oxidation on the interface structure of Co/MgO multilayers.

D. S. Eastwood[1], W. F. Egelhoff, Jr.[2], B. K. Tanner[1]
1. Physics, Durham University, Durham, United Kingdom; 2. National Institute of Standards and Technology, Gaithersburg, MD

Pre-oxidation of the bottom electrode of a magnetic tunnel junction (MTJ) in a low pressure of oxygen prior to depositing the oxide barrier layer has been shown to result in a major reduction in the coupling field between electrodes for both alumina and MgO based MTJ structures [1,2]. The coupling field, defined as the shift from zero of the center of the easy axis hysteresis loop, has been attributed to Néel orange-peel coupling associated with free poles induced across the MTJ barrier as a result of conformal roughness. Néel's model [3] predicts a variation of the coupling field which increases with roughness amplitude but decreases as the in-plane length scale of the roughness increases. The overall trend of Hf with barrier thickness is in good agreement with the variation found in Co/MgO/Co/IrMn MTJs [2]. Thus the implication is that the pre-oxidation suppresses the roughness amplitude, resulting in the drop in coupling field.

We have used grazing incidence specular and diffuse x-ray scattering to determine the layer and interface parameters of MTJs and Co/MgO multilayers grown on a 200Å NiFeCuMo seed layer deposited on thermally oxidised Si wafers. The films were deposited at room temperature, in a deposition chamber with base pressure of 7x10-8 Pa by dc-magnetron sputtering. To pre-oxidize samples, 10-3 Pa (≈10-5 Torr) O2 was admitted to the chamber and there was a 10 s delay prior to turning on the magnetron gun and depositing the MgO layer by reactive sputtering. For samples not pre-oxidized, Mg metal was deposited and subsequently oxidized by an oxygen plasma.

X-ray scattering in the standard reflectivity geometry was undertaken from Si/SiO2/20nm NiFeCuMo [20nm] {Co [10nm] / MgO [2nm] }5 / Co [2.5nm] / AlOx [1nm] multilayers at station I16 of the Diamond Synchrotron Light Source during its first period of user beam delivery. Data were fitted to a model structure using the Bede REFS code. Out-of-plane measurement of the diffuse scatter from the same samples was performed using the MAR two dimensional detector at the XMaS (BM28) beamline of the ESRF.

Unlike comparative data taken from annealed [4] or pre-oxidised AlOx based tunnel junction structures, no statistically significant change in either the overall interface width (from the specular scatter) or the topological roughness (from the diffuse scatter) was observed between the two types of specimen.
However, the diffuse scatter measured out of the plane of incidence was systematically different between samples.
Quantitative analysis of the intensity as a function of the wavevector component perpendicular to the plane of incidence revealed typical scaling law behaviour [5] at high wavevector. The correlation length, determined from the inflexion in the scattering distribution where fractal scaling behaviour ceases, was greater for pre-oxidised samples than for untreated samples. In other words, the pre-oxidation appears to result in suppression of the higher spatial frequency components of the roughness and a consequent reduction in coupling field. The results of the out-of-plane scatter suggest that the reduction in coupling in MgO based tunnel junction devices arises primarily from the change in the in-plane spatial frequency of the roughness, rather than a reduction in the out-of-plane roughness amplitude.

1. W. F. Egelhoff, Jr. et al, Appl Phys. Lett. 88 162508 (2006)

2. W. F. Egelhoff, Jr. et al, IEEE Trans Mag 42, 2664 (2006)

3. L. Néel, C. R. Acad. Sci. 255 1545 & 1676 (1962)

4. A.T.G.Pym et al, Appl. Phys. Lett. 88 162505 (2006)

5. T. Salditt et al, Phys. Rev. B 51 5617 (1995)

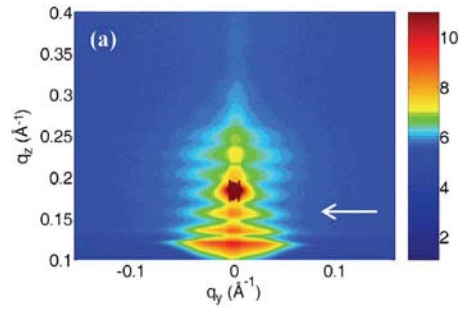

Fig 1(a): Diffuse x-ray scatter images from the structure after pre-oxidation

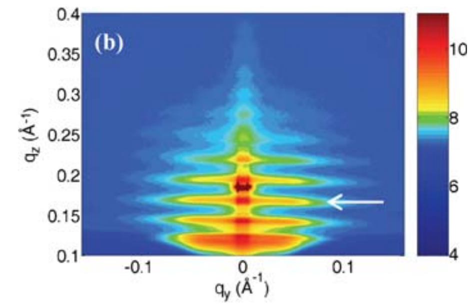

Fig 1(b): Diffuse x-ray scatter images from the structure without pre-oxidation

ES-08

Hard bias effect on magnetic noise in different types of tunnel magnetoresistive heads.

G. Han, B. Zong, P. Luo, Z. Guo
*Data Storage Institute, A*STAR, Singapore, Singapore*

Thermally excited magnetization fluctuation noise, often called as mag-noise, has become a major concern due to continued decrease in the dimensions of the read sensors to accommodate increasing storage density. High-frequency mag-noise, in addition to being practical concern, can be used as a nondestructive diagnostic tool for read head design. A characteristic feature of the mag-noise is that there exists a ferromagnetic resonance (FMR) at a frequency of several GHz. As the mag-noise magnitude in recording band is proportional to the peak value of the resonance[1], FMR measurements can serve as an alternative method to characterize the noise characteristics of sensors. The mag-noise is not only determined by the volume of the free layer, but also the sensor structure, in particular, the hard bias strength in terms of effective stiffness field. Hard bias effect on the mag-noise has been theoretically examined in our previous work [2]. However, no work is reported on the experimental study of the hard bias effect so far. To investigate the bias effect without involving in the variations of sensor major parameters (size, materials, variation of sensor structure, etc), we study the bias effect through artificially changing the hard bias direction with respect to the magnetization of the reference layer (RL).[|#[|#[|#
/11#|]/11#|]/11#|]The mag-noise is measured by a spectrum analyzer. The measurements are performed on TMR heads in finished slider form. Contact is made with the bonding pads of the head by means of a 50 ohm micro-probe. A magnetic field is applied perpendicular to the head's air bearing surface by an electromagnet. A 2 Tesla of magnetic field was applied to set the hard bias at any angle theta with respect to the RL magnetization direction.

Transfer curve was measured before noise measurement to understand sensor performances. For MgO-TMR head, no hysteretic loop is observed at various bias angles, while TiO-TMR head shows hysteretic jumps at near zero fields for theta=0^o. The transfer curve of AlO-TMR heads shows an open loop at high positive fields at small thetas. Examples of the noise spectra for these three types of TMR heads are shown in Fig.1(a,b,c). From these figures, one can see the different variations of the noise spectra for different TMR heads. However, this characteristic difference is not necessarily attributed to their different tunneling mechanisms, but rather the different structures and geometries. For MgO-TMR, one can see that for strong bias (theta=60^o - 90^o), the resonance peak is broad with a low magnitude. For low bias, the resonance shifts to low frequency with larger magnitude and narrower width. If one considers the resonance as two-peak structure, the variation in the main peak can be understood by the stiffness mechanism from the thermally activated fluctuations of the free layer. For the satellite peak at higher frequency, strong bias tends to enhance its amplitude without changing its position. This peak is believed to be from the composite RL and pinned layer. On the other hand, the main peak follows the stiffness-determined characteristics, i.e., the peak increases in magnitude and shifts to lower frequency as the hard bias becomes weak due to the peak frequency (fp) ~ sqrt(MsHstiff). For AlO-TMR heads, the resonance appears only at strong bias (theta=60^o – 90^o) at zero external field. The absence of the resonance at weak bias is due to the sensor saturating at antiparallel state, which is confirmed by the transfer curve measurements. At the weak bias, the FMR peaks can be seen at positive fields and its magnitude varies consistently with the change of the sensor sensitivity. For TiO-TMR heads, the noise characteristics can be understood with the combination of its transfer curves (Fig.1(d)). The dynamic region of the transfer curves shifts to negative and positive fields for theta=0^o and 15^o, respectively. As a result, the stiffness field decreases as theta decreases till theta=15^o, resulting in increasing resonance magnitude and lowering the resonance frequency. In comparison to theta=15^o, the stiffness field for theta=0^o increases in its value, but along an opposite direction. For theta=90^o, the situation seems different. First its transfer curve shifts up in comparison with theta=60^o or even 45^o, suggesting weaker biasing. The weaker bias for theta=90^o is in agreement with noise characteristics shown in Fig.1(a). Careful examination shows that this is from the misalignment of the bonded head from the field setting direction.

Field (H) dependence of the mag-noise show that there is a valley (or dip) in fp versus H curves for all measured heads. There is an offset in the dip position from the zero field. More detailed examination shows that the offset is determined by the hard bias direction and the internal field (e.g., interlayer coupling). More detailed discussion will be given in the presentation.

[1], K. B. Klaassen, X. Z. Xing, and J. V. Peppen; IEEE Trans. Magn. 41, no.7, 2307-2317, July, 2005

[2], Y. K. Zheng, G. C. Han and B. Liu, APMRC 2007

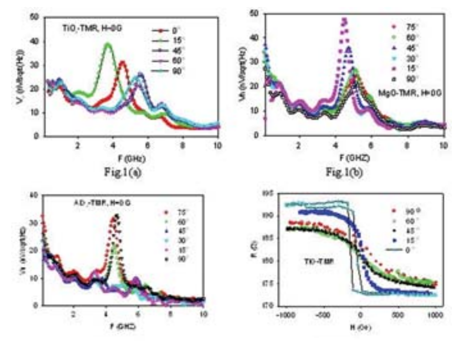

Fig.1(a) Fig.1(b) Fig.1(c) Fig.1(d)

ES-09

Effect of annealing and barrier thickness on MgO-based Co/Pt and Co/Pd multilayered perpendicular magnetic tunnel junctions.

L. Ye[1], C. Lee[1,2], J. Syu[1,3], Y. Wang[1], K. Lin[4], Y. Chang[4], T. Wu[1,2]
1. Taiwan SPIN Research Center, National Yunlin University of Science and Technology, Douliou, Taiwan; 2. Graduate School of materials science, National Yunlin University of Science and Technology, Douliou, Taiwan; 3. Graduate School of Optoelectronics, National Yunlin University of Science and Technology, Douliou, Taiwan; 4. Laser Application Technology Center, Industrial Technology Research Institute, Tainan, Taiwan

In this study, the effect of annealing conditions on the magnetic characteristics of multilayered perpendicular magnetic tunnel junctions (pMTJ) of the structures SiNx/Pt/$(Co/Pd)_{10}$/MgO/$(Co/Pt)_5$/Pt with various MgO barrier thicknesses are explored. It is reported [1] that inserting a 0.4 nm Mg layer can reduce the RA value while maintaining high magnetoresistance in very thin MgO barrier regions. Consequently, we also fabricated pMTJ of the structures SiNx/Pt/$(Co/Pd)_{10}$/Mg/MgO/$(Co/Pt)_5$ as a comparison. The magnetic properties were measured using an alternating gradient magnetometer (AGM). Current-inplane tunneling (CIPT) [2] was also conducted for the measurement of the magnetoresistance.
Figure 1 (a) shows the hysteresis loops of the free layers for (Co/Pd)/MgO/(Co/Pt) structures with various annealing temperatures from 25 to 250°C for one-half hour. Here the Co/Pd multilayer was used as the pinned layer and the Co/Pt multilayer acted as the free layer. Equivalent results for similar structures with insertion of Mg layer are shown in Fig. 1(b). From these figures we see that the coercivities increase as the annealing temperature increases for both pMTJ structures. This may arise from as improvement of the interface roughness during the annealing process. However, the squareness decreases with the increasing annealing temperature. Comparing Fig. 1(a) and Fig. 1(b), we see that insertion of an Mg layer makes the free layer coervivities even higher but adds long canted tails into the loops which, further deteriorate their squareness. Figure 2 displays the relationship between the MgO thickness and free layer coercivity under different annealing temperatures. It illustrates that the coervivities have a weak dependence on the MgO thickness, and annealing at 300°C causes an obvious increase in coervities compared with other temperatures.
Figure 3 shows the result of magnetoresistance measurement for the sample with MgO layer thickness 1.5 nm annealed at room temperature.
This work was supported by the Department of Industrial Technology, Ministry of Economic Affairs, Republic of China, under Contract No. 95-EC-17-A-01-S1-026, by the National Science Council of Taiwan, Republic of China, under Contract No. NSC 95-2112-M-224-003-MY3., and by the R.O.C. Ministry of Economic Affairs under Grant 6301XSW410.

[1] Koji Tsunekawa, David D. Djayaprawira, Motonobu Nagai, Hiroki Maehara, Shinji Yamagata, and Naoki Watanabe, "Giant tunneling magnetoresistance effect in low-resistance CoFeB/MgO(001)/CoFeB magnetic tunnel junctions for read-head applications", Appl. Phys. Lett. 87, 072503 (2005).

[2] D. C. Worledge and P. L. Trouilloud," Magnetoresistance measurement of unpatterned magnetic tunnel junction wafers by current-in-plane tunneling", Appl. Phys. Lett. 83, 84 (2003)

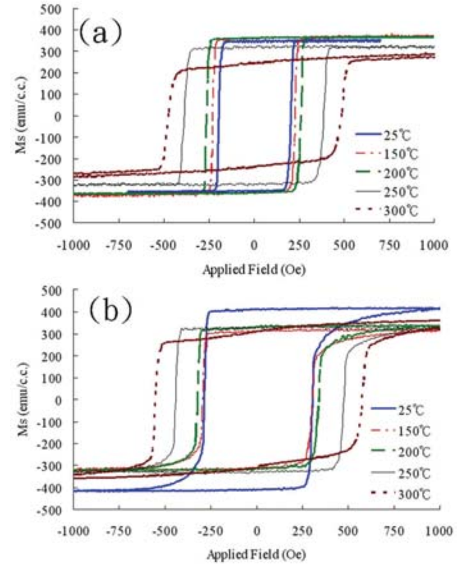

Fig. 1. Free layer hysteresis loops for the structure (a) $(Co/Pd)_{10}$/MgO/$(Co/Pt)_5$ and (b) $(Co/Pd)_{10}$/Mg/MgO/$(Co/Pt)_5$ under various annealing temperatures. The thickness of MgO layer is 1 nm.

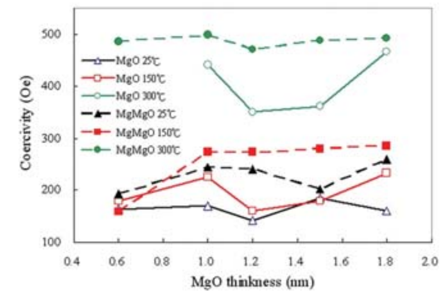

Fig. 2 The relationship between the coercivity and MgO layer thickness under various annealing conditions.

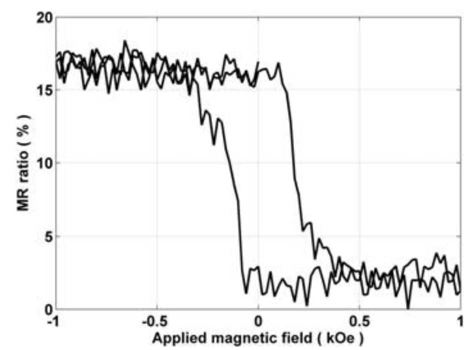

Fig.3 Magnetorsistance hysteresis measurements at room temperature using the current in-plane tunneling method for the structure $(Co/Pd)_{10}$/MgO(1.5nm)/$(Co/Pt)_5$

ES-10

Effects of Current-Confined-Path on the Spin-Torque Noise in CPP-GMR Heads with a Current-Screen Layer.

M. Shiimoto, H. Katada, K. Nakamoto, H. Hoshiya
Central research laboratory, Hitachi, Ltd., Odawara-shi, Kanagawa-ken, Japan

Introduction

Current-perpendicular-to-plane-giant-magneto-resistive (CPP-GMR) heads is one of the most promising candidate technologies to achieve high-areal-density recording. The CPP-GMR heads with a current-screen layer (nano-oxide layer having metallic nano-holes) has a high MR ratio because the sensing current is confined by the nano-holes [1]. Moreover, in the current-screen CPP-GMR heads, spin-torque noise [2] is not induced in well-biased heads [3], even though the sensing current is concentrated in metallic-conductive nano-holes. This suggests that the spin-torque noise behavior in screen CPP-GMR heads is different from that in all-metallic CPP-GMR heads. Furthermore, it was reported that critical current density is changed depending on the metallic-conductive area in tunneling magneto-resistive heads [4]. In this study, we investigated the effect of current-confined-path on spin-torque noise in CPP-GMR heads with a current-screen layer through the measurements and calculations.

Experiment and calculation

We measured broadband noise spectrum in two kinds of current-screen type CPP-GMR heads with resistance-area-product (RA) of 1.0 $\mu\Omega m^2$ and 0.25 $\mu\Omega m^2$, respectively. Note that the large RA indicates a small metallic-conductive area and vice versa. We prepared heads with the large asymmetry (>20%) and heads with the small asymmetry in order to analyze the spin-torque noise easily. The peak asymmetry is a good indictor of the relative angle of magnetization between the free layer and the reference layer. The operating voltage was set to 120 mV. We also calculated the head noise using micromagnetic simulation in which the sensing current only flows though the conductive area in the current screen layer.

Results and Discussion

Figure 1(i) shows the measured noise spectrum in the heads with 0% of the peak asymmetry. The RA of Heads A and B were 1.0 $\mu\Omega m^2$ and 0.25 $\mu\Omega m^2$, respectively. The head noise below 1 GHz in Heads A and B agreed with the sum of Johnson noise and mag-noise. Figure 1(ii) shows the measured noise spectrum in the heads with RA of 1.0 $\mu\Omega m^2$ (Head C) and 0.25 $\mu\Omega m^2$ (Head D). The peak asymmetry of both heads was more than 20%. The noise levels in Heads C and D were much larger than that of the well-biased heads shown in the figure 1(i). These large noise levels in these heads indicate that the spin-torque noise is induced. Comparing the noise profiles of Head C and D, shape of noise profile is significantly different. In the case of Head C, pronounced $1/f^n$ noise was observed below 1 GHz. On the other hand, in the case of Head D, the noise level in most of the bandwidth was increased and the noise profile was becoming chaotic. To understand this difference in profiles, we analyzed the spin-torque noise using simulation. Figure 1(iii) shows calculated noise spectrum in Heads C and D. The calculated noise profiles of both heads qualitatively agree with the experimental results shown in Figure 1(ii). The difference in noise profiles in heads C and D can be understood by considering the magnetic coupling in the free layer. The magnetization in the conductive areas fluctuates largely than that in the non-conductive area. Therefore, magnetic coupling between the large fluctuated magnetization in the conductive area and the stable magnetization in the non-conductive area induced $1/f^n$ noise.

The distribution of nano-metallic holes is important to enhance the magnetic coupling of the magnetizations. Figure 2 shows calculation model of two kinds of screen layer for Heads E and F. The calculation results for head noise in these heads are shown in table 1. The calculated noise in Head E was smaller than that in Head F, because the magnetizations in a nono-metallic hole for Head E have larger areas coupling with the stable magnetization than that for Head F. Therefore, controlling the distribution of metallic-nano-holes is important to suppress spin-torque noise in CPP-GMR heads with a current-screen layer.

[1] K. Hoshino, H. Hoshiya, and Y. Okada, IEEE Trans. Magn., vol. 43, 2196 (2007).

[2] N. Smith, J. A. Katine, J. R. Childress, M. J. Carey, IEEE Trans. Magn., 41 (2005) 2935.

[3] H. Katada, K. Nakamoto, H. Hoshiya, K. Hoshino, and N. Yoshida, IEEE Trans. Magn., 42 (2006) 2450.

[4] J. G. Zhu, J. Appl. Phys., 97, 10N703 (2005).

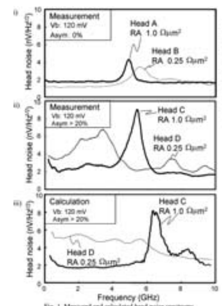

Fig. 1 Measured and calculated head noise spectrums.

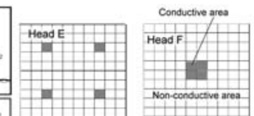

Fig. 2 Models of a current-screen layer of Heads E and F in micromagnetic simulation.

Table 1 Calculated head noise of Heads E and F.

	Head E	Head F
Vb (mV)	120	120
Asymmetry (%)	40	40
Head noise ($nV/Hz^{1/2}$)	2.6	4.8

Electrical 1/f noise in CPP-GMR with current-confined-pass nano-oxide layer.

M. Shimizu, M. Takagishi, M. Takashita, H. Iwasaki
Corporate Research & Development Center, Toshiba corporation, Kawasaki, Japan

Introduction

Large 1/f noise has been reported for TMR heads. It is assumed to be caused by charge trapping mechanism in the insulator barriers or near the FM-insulator interfaces [1]. On the other hand, single metal nano-hole also causes electrical 1/f noise, interpreted by defect motions [2]. CCP(current-confined-path)-CPP-GMR, which is one of promising candidates for future high-density recording heads, have Cu metal passes with a few nanometer in size, penetrated through an Al-O spacer layer [3]. Therefore, defects in or near the metal passes may cause 1/f noise, resulting in SNR degradation. However, there has been no report about 1/f noise for CCP-CPP-GMR. In this paper, we report 1/f noise characteristics for CCP-CPP-GMR with various RA (resistance area product) and discuss about 1/f noise level for small size element required for tera-bits high-density recording.

Experiments

Test chips were fabricated for CCP-CPP-GMR films with RA raging from 0.25 to 1.4 $\Omega\mu m^2$ and MR ratios up to 7.7% [3]. A 600 Oe field was applied to maintain a parallel magnetization configuration of pinned and free layers, so that the noise was measured as electrical origin. A spectrum analyzer was used to measure the noise power density up to 10 MHz. The noise magnitudes up to 7 Hz were also acquired applying a Fourier transform (FFT) on voltage series by using a voltmeter.

Results and Discussion

Fig.1 shows the noise power spectra from 50 kHz to 10 MHz at room temperature for all-metal and CCP-CPP-GMR with an RA of 0.45 $\Omega\mu m^2$. Both spectra are composed of a broadband 1/f component at low frequencies. All-metal CPP-GMR shows low 1/f noise, suppressed below background at f>200kHz, while CCP-CPP-GMR shows prominent 1/f noise even at f=3 MHz. It is found that CCP-CPP-GMR shows larger 1/f noise than all-metal CPP-GMR.

Fig.2 shows normalized noise parameter, $\alpha = fS_V A/V^2$, where A is the sample size, as a function of RA (A = 0.3×0.3 $\Omega\mu m^2$). High RA films show large α. However, α decreases with decreasing RA. The same level 1/f noise as all-metal films was obtained at an RA of less than 0.2 $\Omega\mu m^2$. This dependency implies that the increase in metal path number suppresses 1/f noise because high RA films have less metal paths. We also confirmed that smaller element size up to A = 0.14×0.14 $\Omega\mu m^2$, resulting in less metal pass numbers and an enhancement of 1/f noise, shows constant α independent of size. We estimated 1/f noise for small size elements by using the noise level shown in Fig.1. It is found that the 1/f noise of films with RA=0.2 $\Omega\mu m^2$ is in the order of 1 nV/rt.Hz at 10 MHz even for V=120mV and A= 0.02×0.02μm^2, corresponding to 1~2Tbit/inch^2. This estimation indicates that such 1/f noise is not a concern for CCP-CPP-GMR.

In conclusion, CCP-CPP-GMR has 1/f noise caused by current-confined-pass structure. This noise is suppressed by using lower RA films with many metal paths.

[1]L.Jiang, E.R.Nowak, P.E.Scott, and J.Johnson, Phys.Rev.B, 69, 054407 (2004)

[2]K.S.Ralls and R.A.Buhrman, Phys.Rev.B, 44, 5800 (1991)

[3]H.Fukuzawa, H.Yuasa, S.Hashimoto, K.Koi, H.Iwasaki, M.Takagishi, Y.Tanaka and M.Sahashi, IEEE Trans., Magn., 40, 2236 (2004)

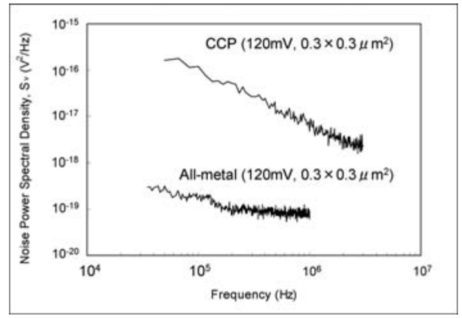

Fig.1 Power spectra of the voltage noise.

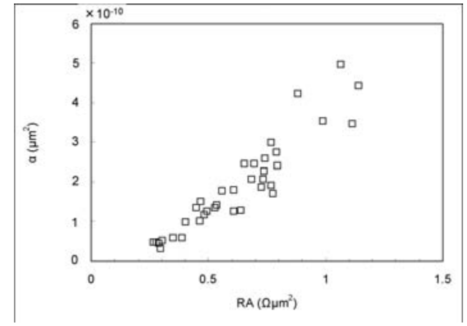

Fig.2 $\alpha = fS_V A/V^2$ vs RA for V=-80mV, A=0.3×0.3μm^2 and f=0.15 Hz.

ES-12

Dependence of Thermal Stability on Cap Layer and Top Lead for Current Screen CPP-GMR Sensor.

K. Hoshino, H. Hoshiya, Y. Sato

Storage Technology Research Center, Central Research Laboratory, Hitachi, Ltd., Odawara-shi, Japan

Introduction

Current-perpendicular-to-the-plane giant-magnetoresistance (CPP-GMR) film using a spin-valve (SV) structure is an attractive read sensor for high-density recording. However, it generally shows a small magnetoresistance (MR) ratio. To enhance the MR ratio, the concept of the confined current path was proposed [1] and some improvements in the MR ratio by inserting a current screen layer (nano-oxidized layer) into an SV were reported [2-4].

We also reported that a high MR ratio was obtained by inserting an oxidized CoFe layer into the SV structure as the current screen layer. It was found that the confined current path in the current screen layer reconstructed with increasing annealing temperature after deposition of CPP-GMR film [5]. Therefore, clarification of how to create the confined current path in the current screen layer was needed. In this study, to foster a better understanding of the formation of confined current path, we investigated the thermal stability of current screen CPP-GMR sensors with various cap layers and top leads after patterning CPP-GMR film.

Experiment

We fabricated three CPP-GMR sensors using various materials for the cap layers and top leads. CPP-GMR films had a synthetic-pinned bottom-type SV. An oxidized CoFe layer was used for the current screen layer, and it was inserted into the Cu intermediate layer. The thickness of the current screen layer before oxidation was around 1.5 nm. All films were annealed at 270°C for three hours after deposition, and we used a 100-nm thick Cu layer for the bottom lead. The size of the CPP-GMR sensors varied from 5.0 x 5.0 μm^2 to 0.3 x 0.3 μm^2. The MR curves were measured using the four-terminal method. The annealing temperature changed form 180 to 250°C over a three-hour period after patterning to evaluate thermal stability of a current screen CPP-GMR sensor.

Results and Discussion

Figure 1 shows the thermal stability of MR ratio for three types of CPP-GMR sensors with various cap layers and top leads. Type A had Cu (5 nm)/Ru (4 nm) cap layers and a Ta (2 nm)/Au (200 nm)/Ta (5 nm) top leads. The MR ratio drastically degraded above 200°C. The reduction can be explained by increasing of current path in the current screen layer because the resistance area product also decreased. Type B had Cu (2 nm)/Ta (7 nm)/Ru (2 nm) cap layers and a Ta/Au/Ta top leads. The MR ratio also degraded above 200°C. However, thermal stability improved by replacing the cap layers. For Type C, Ta (5 nm)/NiFe (15 nm) layers were inserted between the Cu/Ta/Ru cap layers and the Ta/Au/Ta top leads. The MR ratio was maintained up to 250°C.

Two possibilities were considered for the degradation of the MR ratio. The first possibility was due to the damage at the edge of the current screen layer. We observed that there was no dependence of the MR ratio on sensor size for types A and B. This indicated that damage at the edge of the current screen layer did not occur.

The second possibility was due to the structural change of the current screen layer. The reason for poor thermal stability may have been caused by stress induced from the cap layers and top leads. Thermal expansion coefficients of Cu and Au were larger than those of the Ru, Ta, and NiFe layers. For type A, thermal stress led to the structural change of the current screen layer. The current confined path enlarged, and the effect of the confined current path weakened. As a result, the MR ratio degraded. On the other hand, as the materials with low thermal expansion coefficients were used for type C, they suppressed thermal stress, and thus thermal stability was maintained as shown in Fig. 1. Therefore, the materials of cap layers and top leads are important for good thermal stability in CPP-GMR sensor.

Conclusion

The thermal stability of the CPP-GMR sensors depended on the materials of the cap layers and top leads. The MR ratio was maintained until 250°C for the CPP-GMR sensor with the Cu/Ta/Ru cap layers and the Ta/NiFe layer-insertion between the cap layers and top leads. The maintained MR ratio might be due to the suppression of thermal stress into the current screen layer during annealing.

[1] H. Fujiwara, T. Zhao, G. J. Mankey, K. Zhang, W. H. Butler, and S. Matsunuma, Trans. Magn. Soc. Japan, vol.3, No.3, pp. 95-102 (2003)

[2] A. Tanaka, Y. Seyama, A. Jogo, H. Oshima, R. Kondo, H. Kishi, C. Kamata, Y. Shimizu, S. Eguchi, and K. Satoh, IEEE Trans. Magn., vol.40, p. 203 (2004)

[3] H. Fukuzawa, H. Yuasa, S. Hashimoto, K. Koi, H. Iwasaki, M. Takagishi, Y. Tanaka, and M. Sahashi, IEEE Trans. Magn., vol.40, p. 2236 (2004)

[4] K. Nakamoto, H. Hoshiya, H. Katada, K. Hoshino, N. Yoshida, H. Takei, M. Shiimoto, M. Hatatani, and K. Watanabe, IEEE Trans. Magn., vol. 44, p. 95 (2008)

[5] K. Hoshino, H. Hoshiya, and Y. Okada, IEEE Trans. Magn., vol. 43, p. 2196 (2007)

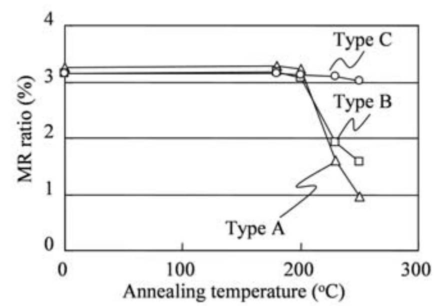

Fig. 1 Thermal stability of current screen CPP-GMR sensors with various structures

ET-01

Stoichiometry and sintering temperature influence on magnetostrictive properties of cobalt ferrites.

L. Boutiuc[1], O. Caltun[1], I. Dumitru[1], M. Feder[2], N. Lupu[3], H. Chiriac[3]
1. 'Alexandru Ioan Cuza" University, Iasi, Romania; 2. National Institute of Material Physics, Bucharest, Romania; 3. National Institute of R&D for Technical Physics, Iasi, Romania

In the last time the magnetostrictive materials started to be intensively studied due to the growing number of possible applications. Among these materials the cobalt ferrites could a promising materials because of the high values of magnetostriction coefficients [1].
In our study, two categories of samples, stoichiometric cobalt ferrite $CoFe_2O_4$ and cobalt ferrite with excess of iron $Co_{0.8}Fe_{2.2}O_4$, were prepared by conventional ceramic method. The samples were sintered for 5 hours in air at 1250°C, 1275°C, 1300°C and 1325°C followed by natural cooling. The structural characterization of the samples were performed by X ray diffraction analysis and scanning electron microscopy. The magnetic properties were measured using vibrating sample magnetometry and magnetostriction coefficients were measured using tensile strain gauge technique, at room temperature.
The X ray analysis shows that the studied samples are two-phase systems: spinel and hematite. The sample $CoFe_2O_4$ has a small concentration of hematite (97.80% spinel, 2.20% hematite) while $Co_{0.8}Fe_{2.2}O_4$ has higher concentration (75.60% spinel, 24.40% hematite). The lattice parameters of studied samples are not influenced by the sintering temperature and are: 8.3776 Å for $CoFe_2O_4$ and 8.3825 Å for $Co_{0.8}Fe_{2.2}O_4$.
The SEM micrographs of the samples,displays for the stoichiometric ferrites a microstructure with relatively uniform grains, with open porosity including big hematite particles. The iron rich cobalt ferrite display a microstructure with relatively fine grains and with a narrow dispersion of grains size but the big hematite grains are more frequent. For both categories of samples, the density increase with sintering temperature but the density of $Co_{0.8}Fe_{2.2}O_4$ sample are considerable lower than that of $CoFe_2O_4$ sample.
Magnetization and coercive fields of samples depend on sintering temperature. Iron-rich cobalt ferrite shows a higher specific magnetization comparatively with the stoichiometric cobalt ferrite justified by the iron cations excess. For $Co_{0.8}Fe_{2.2}O_4$, the increase of sintering temperature leads to a decrease of specific magnetization. The coercive fields of $Co_{0.8}Fe_{2.2}O_4$ samples are considerable higher than that of $CoFe_2O_4$ samples which can be explained by the higher content of hematite characterized by big grain size.
The magnetostriction coefficient was measured along and perpendicular to the apllied magnetic field direction. For both categories of samples, the magnetostriction coefficients decrease when the sintering temperature increase.
The measured magnetostriction coefficients along the magnetic field direction, have negative values and depend on the sintering temperature. $CoFe_2O_4$ sample has a higher value of magnetostriction comparing with $Co_{0.8}Fe_{2.2}O_4$ sample. The maximum of the magnetostriction coefficient is –196 ppm for $CoFe_2O_4$sintered at 1250°C and –132ppm for $Co_{0.8}Fe_{2.2}O_4$ sintered at 1250°C.
On the perpendicular to the apllied magnetic field direction the magnetostriction coefficients are positive and depend also on the sintering temperature. In this case, the maximum value of magnetostriction is 57ppm for $CoFe_2O_4$ sintered at 1250°C and 47ppm for $CoFe_2O_4$ sintered at 1250°C.
The study reveals that the sintering temperature and stoichiometry of the samples influence the magnetic properties and magnetostriction coefficients The excess of iron ions and the increase of sintering temperature reduce the magnetostriction coefficients.

Acknowledgement: The authors acknowledge the financial support offered by MATNANTECH Program under CEEX C73 S9 - MASTRICH.

[1] J. A. Paulsen, A. P. Ring, and C. C. H. Lo, J. E. Snyder and D. C. Jiles, J. Appl. Phys. 97 (2005) 044502

[2] Ovidiu Caltun, G.S.N. Rao, K.H. Rao, B. Parvatheeswara Rao, Ioan Dumitru, Chong-Oh Kim and CheolGi Kim, J. Magn. Magn. Mater, 316 (2007) e618-e620

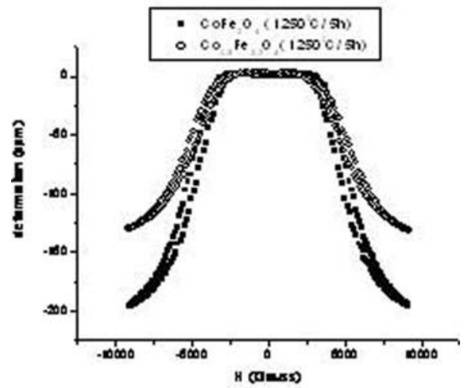

The field dependence of the magnetostriction coefficient parallel to the applied field direction

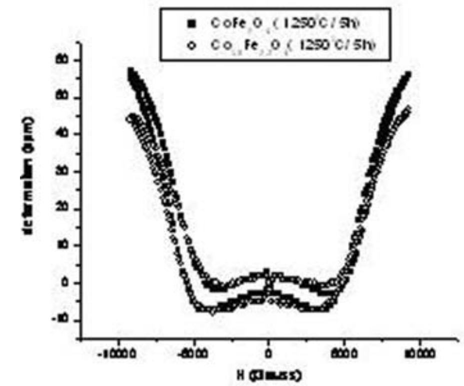

The field dependence of the magnetostriction coefficient perpendicular to the applied field direction

ET-02

Spontaneous magnetostriction of $R_2Fe_{13.6}Si_{3.4}$ (R = U, Lu).

A. V. Andreev[1], S. Dani š[2]
1. Institute of Physics, Prague, Czech Republic; 2. Charles University, Prague, Czech Republic

R_2Fe_{17} intermetallic compounds (R is a rare-earth metal) undergo a large spontaneous magnetostriction in the magnetically ordered state. This originates mainly from the Fe sublattice [1,2]. In combination with relatively low Curie temperatures T_C, this leads to Invar behavior in a wide temperature range. U does not form "2-17" binary compounds with 3d metals but the hexagonal Th_2Ni_{17}-type crystal structure can be stabilized by a small amount of a third element, e.g. Si [3]. In the Ref. [4], the magnetization of $U_2Fe_{13.6}Si_{3.4}$ was studied on single crystals together with $Lu_2Fe_{13.6}Si_{3.4}$ where Lu is non-magnetic analogue of U. The U contribution to the total magnetic moment estimated from the difference between the magnetic moments of $U_2Fe_{13.6}Si_{3.4}$ and $Lu_2Fe_{13.6}Si_{3.4}$ is almost negligible. Nevertheless, U influences strongly the magnetic properties. Based on comparison of magnetic anisotropy of $U_2Fe_{13.6}Si_{3.4}$ and $Lu_2Fe_{13.6}Si_{3.4}$ [4], as well as on Mössbauer spectroscopy results [5], the magnetic state of uranium was deduced with the U magnetic moment μ_U up to 2.6 μ_B ferromagnetically coupled with the Fe sublattice. In the present work, we studied the thermal-expansion anomalies accompanying the magnetic ordering in $U_2Fe_{13.6}Si_{3.4}$ and $Lu_2Fe_{13.6}Si_{3.4}$ in order to determine influence of the U sublattice on the spontaneous magnetostriction.

Single crystals of $U_2Fe_{13.6}Si_{3.4}$ and $Lu_2Fe_{13.6}Si_{3.4}$ were grown by the Czochralski method in a tri-arc furnace. A piece from each crystal was ground for X-ray powder-diffraction measurements, which were carried out on a Siemens D-500 diffractometer equipped with a helium-flow cryostat using filtered Co radiation. The diffraction patterns were taken in the temperature range 5-600 K.

The experimental temperature dependencies of the lattice parameters in the paramagnetic range were extrapolated to the magnetically ordered range using a value for the Debye temperature of 450 K, as determined from acoustic measurements on R_2Fe_{17} [2]. The relative differences between the experimental and the extrapolated values of the lattice parameters are the spontaneous linear magnetostrictive strains λ_a and λ_c. The spontaneous volume magnetostriction ω_s is equal to $2\lambda_a + \lambda_c$.

The thermal expansion of $U_2Fe_{13.6}Si_{3.4}$ and $Lu_2Fe_{13.6}Si_{3.4}$ is qualitatively similar. In both compounds, it is isotropic, the c/a ratio is nearly constant at low and room temperature. The spontaneous magnetostriction is also rather isotropic, λ_c exceeds λ_a only by 15% (Lu) or 30% (U), in difference with binary R_2Fe_{17} where the uniaxial component λ_c is very large, exceeds λ_a by factor of 4 and leads to a pronounced Invar effect along the c-axis [1,2]. In $U_2Fe_{13.6}Si_{3.4}$ and $Lu_2Fe_{13.6}Si_{3.4}$, λ_c is not high enough to overcome the phonon thermal-expansion contribution and to provide Invar-like behavior. This is also result of the relatively high Curie temperature T_C (larger by ~150-200 K than in binary R_2Fe_{17}).

Since both compounds have the easy-plane magnetic anisotropy, they should undergo an orthorhombic magnetostrictive distortion at the magnetic ordering. However, no distortion was observed which means that the anisotropic magnetostriction responsible for the distortion is below the experimental sensitivity $2*10^{-4}$, e.g. at least by one order of magnitude smaller than the exchange magnetostriction seen in the volume effect ~1%.

The observed similarity of spontaneous magnetostriction in $U_2Fe_{13.6}Si_{3.4}$ and $Lu_2Fe_{13.6}Si_{3.4}$ points to a dominant role of the Fe sublattice in formation of this property. Nevertheless, a certain quantitative difference allows us to distinguish the contributions originated from the Fe-Fe and U-Fe exchange interactions. The volume effect in the ground state of $U_2Fe_{13.6}Si_{3.4}$ is larger than in the Lu analogue, however, it becomes the same at elevated temperatures. In $Lu_2Fe_{13.6}Si_{3.4}$, it follows satisfactorily the square of the magnetic moment in a wide temperature range whereas in $U_2Fe_{13.6}Si_{3.4}$ it decreases evidently faster. Both features can be attributed to the contribution to the total volume effect ω_s from the U-Fe exchange interaction $\omega_{U\text{-}Fe}$ which is expected to decrease faster with increasing temperature than the main contribution from the Fe-Fe exchange interaction $\omega_{Fe\text{-}Fe}$.

Direct subtraction of $\omega_{Fe\text{-}Fe}$ from ω_s gives the lowest limit of $\omega_{U\text{-}Fe} = 2*10^{-3}$ in the ground state. However, this means $\omega_{U\text{-}Fe} = 0$ and, respectively, the non-magnetic state of U above 200 K whereas it is known from the measurements of magnetic anisotropy [4] and from the ^{57}Fe Mössbauer spectroscopy [5] that U is still magnetic at 300 K. The average Fe magnetic moment μ_{Fe} in the ground state of $Lu_2Fe_{13.6}Si_{3.4}$ and $U_2Fe_{13.6}Si_{3.4}$ is estimated to be 1.69 μ_B and 1.33 μ_B, respectively [5]. Assuming $w_{Fe\text{-}Fe}$ to be proportional to the square of the Fe magnetic moment, we can estimate $\omega_{Fe\text{-}Fe}$ in $U_2Fe_{13.6}Si_{3.4}$ as $6*10^{-3}$. Therefore, $\omega_{U\text{-}Fe} = \omega_s - \omega_{Fe\text{-}Fe} = 5*10^{-3}$ is surprisingly high, almost the same as $\omega_{Fe\text{-}Fe}$.

[1] D. Givord, R. Lemaire, IEEE Trans. Magn. MAG-10, (1974) 109.

[2] A.V. Andreev, In: Handbook of Magnetic Materials, v. 8, Ed. K.H.J. Buschow, (North-Holland, Amsterdam, 1995,) pp. 59-187 (and references therein).

[3] T. Berlureau, P. Gravereau, B. Chevalier, J. Etourneau, J. Solid State Chem. 104 (1993) 328.

[4] A.V. Andreev, Y. Homma, Y. Shiokawa, Physica B 319 (2002) 208.

[5] A.V. Andreev, D. Niznansky, Y. Homma, H. Onodera, Y. Shiokawa, Physica B 369 (2005) 100.

ET-03

Tuning the magneto-electric effect of multiferroic composites via crystallographic texture.

M. Vopsaroiu[1], M. Stewart[1], M. Cain[1], G. Srinivasan[2]
1. Functional Materials, National Physical Laboratory, Teddington, United Kingdom; 2. Physics Department, Oakland University, Rochester, MI

Multiferroics (MF) are an interesting class of materials, which can respond simultaneously to multiple stimuli (magnetic, electric, mechanical) by changing their physical properties. A very important feature of MF materials is the occurrence of the magneto-electric (ME) effect, which is defined as the coupling between the electric and magnetic fields. Normally this is defined by the linear ME coupling coefficient, α which can be induced either electrically ($\alpha_E = dM/dE$) or magnetically ($\alpha_H = dP/dH = \varepsilon_0\varepsilon_r \times dE/dH$). The effective ME coupling coefficient is essential for the functionality of the devices / sensors based on MF and its value can be altered by a number of factors such as material properties, microstructure, measurement geometry, temperature or mechanical stress conditions. In this paper we examine how the ME coupling is correlated to the intrinsic crystallographic texture of the magnetic phase of NiFeO / PbZrTiO bi-layer laminated MF (acronym NFO/PZT). Three different laminated bi-layers with a disk shape of about 8 mm diameter have been fabricated (figure 1). The samples have identical PZT layers, while the polycrystalline NFO layers have been fabricated with different microstructures. The code names of the samples are: NFO_111, NFO_110 and NFO_100, where the numbers denote the dominant crystallographic plane of the NFO of each sample. The PZT and NFO layers are 500 mm thick. They are glued together without perfect overlapping to allow the application of measurement wires to the PZT electrodes (figure 1). We measured the magnetically induced ME effect, which simply involves the determination of the induced open circuit voltage on the PZT electrodes under applied magnetic fields. This requires a combination of two collinearly applied magnetic fields: a DC bias field and a small amplitude AC magnetic field. The measurement geometry was transverse, i.e. electric polarization transverse to the applied magnetic fields (figure 1). Figure 2 shows the induced voltage versus DC bias field measured at constant amplitude and frequency of the applied AC magnetic field. The graphs show a typical non-linear behaviour for the laminated multiferroics with a peak in the induced voltage at the optimum DC bias field. The data indicates a clear difference between the position of the maximum ME effect of each sample. In order to maximize the linear ME effect, the samples must be biased at their optimum DC bias field. This is a critical parameter for the operation of multiferroic sensors and devices, as the requirement of high DC bias fields can limit their applicability. Figure 2 indicates that the bias field value can be easily tuned via the crystallographic properties of the magnetic phase. The NFO_111/PZT has an optimum DC bias of 465 Oe. We have achieved a reduction by almost a factor 3 for the NFO_110/PZT sample, which has a maximum ME effect at 160 Oe DC bias. This is due to the variation in the magnetostriction properties of different crystallographic phases of NFO. Using the optimum DC bias conditions, the linear ME effect can be measured by varying the amplitude of the applied AC field. Figure 3 shows the induced open circuit voltage as a function of the amplitude of the AC field at constant optimum bias. From the slope of the linear curves the magneto-electric coefficient can be derived as: $\alpha = (1/t)\times(dV/dH)$, where t is the thickness of the PZT layer. The values obtained for α are in units of (mV/Oe cm): 116 for NFO_111, 62 for NFO_110 and 19 for NFO_100.

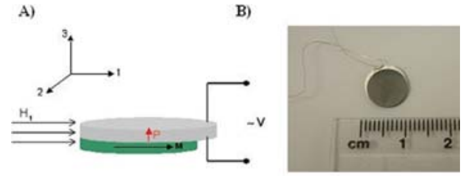

A) Diagram of a NFO/PZT bi-layer laminate showing the direction of the magnetization, electric polarization, the applied magnetic field and the measured voltage; B) Real image of a sample

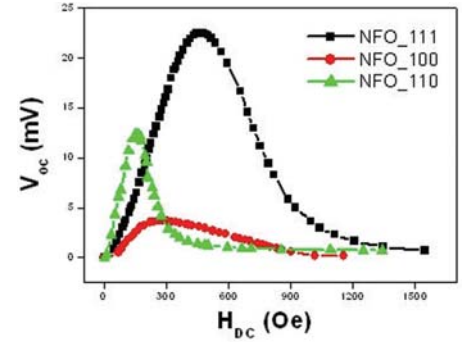

Open circuit voltage as a function of the DC applied magnetic field at constant AC field

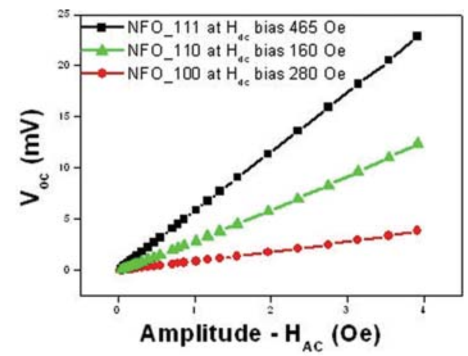

Open circuit voltage as a function of the amplitude of the applied AC field at constant DC bias

ET-04

Multiferroic properties of spin-spray deposited Ni0.23Co0.13Fe2.64O4 ferrite film on PZT substrate.

M. Liu, O. Obi, J. Lou, S. Stoute, Y. Chen, V. G. Harris, N. X. Sun
Electrical and Computer engineering, Northeastern University, Bosotn, MA

Multiferroic materials have drawn an increasing amount of interests due to their capability of efficient energy transfer between electric energy and magnetic energy and their potential applications in many multifunctional devices1. Such materials can display the magnetoelectric (ME) effect, a dielectric polarization variation as a response to an applied magnetic field, or an induced magnetization by an external electric field. Several synthesis methods have been developed for multiferroic composite materials, such as, pulsed laser deposition, physical vapor deposition, and sol-gel process.

Spin-spray process, which was invented in 1983, is developed to plate crystalline spinel ferrite film directly from aqueous solution2. Compared to conventional ferrite film preparation methods such as sputtering, MBE, PLD, etc., which require high temperatures (>600oC), spin-spray technique allows formation of crystalline ferrite film at low temperature of 60-100oC due to oxidation reaction and hydrolytic dissociation.

In this work, the synthesis of multiferroic materials prepared by spin-spraying Ni0.23Co0.13Fe2.64O4 (NCFO) ferrite on PZT substrate was reported. As shown in figure 1, uniform single phase ferrite NCFO film was coated on PZT substrate with excellent adhesion. Our adhesion tests results showed that these spin spray deposited ferrite films show strong adhesion which is crucial for achieving strong magnetoelectric coupling. The structure characterization were performed by XRD and AFM (Figure 2) which showed well defined single NCFO ferrite phase as well as PZT ferroelectric phase patterns without preferred orientation. The NCFO ferrite grain sizes are in the range of 150~350nm. Magnetic properties multiferroic materials were characterized by VSM as shown in Figure 3, which displayed a well defined full film hysteresis loop behaviors with a saturation magnetization of ~5000 G, an in-plane coercivity of 190Oe and out-of-plane coercivity of 260Oe. Magnetoelectric coupling was demonstrated by observing the shifts of the M-H curve by applying electric field on PZT substrate. As shown in Fig. 3(b), an applied E-field of 1 MV/m across the PZT substrate lead to an upward shift of the M-H loop at low applied magnetic fields.

Acknowledgements: This work is supported by NSF DMR-0603115 and by the ONR YIP Award N00014-07-1-0761 managed by Dr. Colin Wood.

1. W. Eerenstein, N. D. Mathur, J. F. Scott, Nature, 442, 759-765 (2006)
2. M. Abe, Electrochimica Acta, 45, 337-3343 (2000)

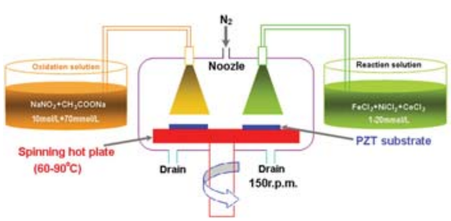

Fig. 1. Schematic of spin-spray process for multiferroic materials fabrication

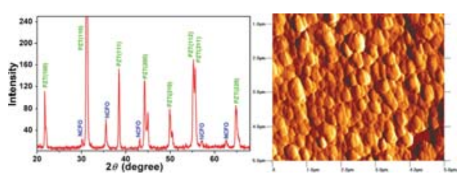

Fig. 2. X-ray diffraction patterns and AFM image of spin-sprayed NCFO ferrite film on PZT substrate.

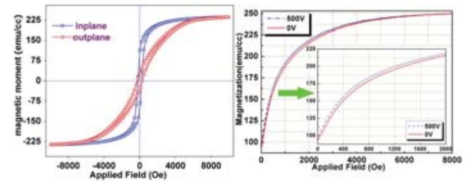

Fig. 3. Magnetic Hysteresis Loops of multiferroic material and its ME coupling demonstration by observing M-H curve shift when applying electric field.

ET-05

Stress and magneto-elastic properties control of amorphous Fe80B20 thin films during triode sputtering deposition.

I. Fernández-Martínez, J. L. Costa-Krämer, F. Briones
Inst. Microlectronica Madrid, CNM-CSIC, Tres CAntos, Spain

In-situ stress measurements during sputtering of amorphous Fe80B20 films are used to control their stress and magneto-elastic properties. Substrate curvature induced by the the deposited film is measured optically during growth and quantitatively related to deposition induced accumulated stress. The resulting magnetic properties are correlated with the measured stress for a wide range of sputtering pressures (2-25x10-3 mbar). A significant tensile stress develops at the film-substrate interface during the early growth stages (initial 2-3nm). At a critical thickness a transition is observed from tensile to compressive stress that is associated with amorphous islands coalescence. An increasing compressive stress follows which is related to the local distortion induced by ion peening effect. Monte Carlo simulations of the sputtering process describe quantitatively the experimental results as a function of Ar pressure and target bias voltage. A fine control of stresses, together with tunable anisotropy,high magnetostriction, excellent adhesion, and stability makes these films ideal for magnetostrictive-based NEMS actuators [1].
The substrate curvature evolution during deposition of Fe80B20 films under a range of Ar sputtering gas pressures for a constant target potential of -2 kV, is shown on Fig 1. Three regimes are clearly distinguished: I, II & III. The first one, I, a nearly instantaneous rise of an apparently compressive stress when target potential is switched on, is reversible and disappears when target potential is switched off. In the case of amorphous metallic films, surface diffusion is limited and no large adatom population is expected. The difference between the effective kinetic surface temperature and the bulk would give rise to a substrate bending equivalent to a surface stress of compressive character and sign. The amplitude of this effect, proportional to the instantaneous deposited power on the substrate, depends indeed strongly on the target bias potential, deposition rate and Ar gas pressure, but disappearing reversibly when growth is interrupted, it does not contribute to the total accumulated stress.
The stress accumulated during the initial few nanometers growth (regime II) is tensile, corresponding to the interface stress increase that accompanies the nucleation of islands strongly interacting with the glass substrate surface. This interface stress seems to be the dominant source of the large component of tensile stress measured, as it depends on the interaction between the growing film and the substrate.Confirming the above arguments, it has also been found experimentally that the stress sign and magnitude in regime II depends strongly on the type of substrate, changing as well if a buffer layer is present.
A critical thickness can be defined between this initial tensile (II) and the following compressive regime (III). This would be the thickness value at which the film becomes continuous and coalescence or building of a columnar structure takes over.
All the amorphous Fe20B20 films grown on the glass cantilevers exhibit a uniaxial anisotropy. The films were grown under a small external applied magnetic field that is used to confine the plasma and at 45 degrees incidence with respect to the cathode plane. For lower Ar pressures the induced magnetic uniaxial anisotropy points in the direction of the plasma confinement field. This uniaxial anisotropy results from local atomic-pair ordering in the amorphous matrix [2]. For Ar pressures above 8x10-3 mbar the stress induced anisotropy overcomes the effect of the field induced anisotropy. The total anisotropy direction starts deviating from the plasma confining field direction and turns perpendicular at about 14x10-3 mbar as shown in Fig. 2 at –2kV target potential.

[1] M R J Gibbs, E W Hill and P J Wright J. Phys. D: Appl. Phys. 37 (2004)

[2] J. C. Slonczewski, in Magnetic Annealing, edited by G. Rado and H. Suhl Academic, New York, Vol. I, 205 (1963)

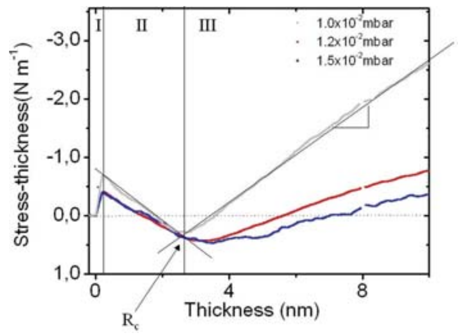

Substrate curvature evolution for three different pressures during the early stages of deposition. Three stress regimes are clearly distinguished. Regime I: initial instantaneous compression: thermal induced curvature. Regime II: Precoalescence tensile regime related with the interaction between the discontinuous film and substrate. Regime III: compressive stress due to ion peening.

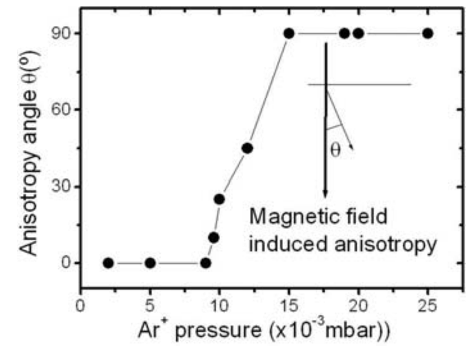

Uniaxial anisotropy angle direction as a function of Ar working pressure pressure for a fixed target potential of –2kV. The angle q is the angle with respect to the field direction during growth

ET-06

Poisson ratio of amorphous nanoporous alumina as determined from thermal expansion of Ni nanowires at low temperatures.

C. A. Ramos[1], E. Vassallo Brigneti[1], S. García[2], M. Vázquez[2]
1. Centro Atómico Bariloche and Insituto Balseiro, Comisión Nacional de Energía Atómica and Universidad Nacional de Cuyo, S. C. de Bariloche, Argentina; 2. Instituto de Ciencias de Materiales, CSIC, Madrid, Spain

We measured the thermal expansion (TE) of Ni nanowires (NW) embedded in amorphous nanoporous alumina (NPA). We observe an anomalous NW TE characterized by a TE coefficient alpha = -1.8 10-5/K as the sample (NW + NPA+ Al) is cooled down. From this anomalous NW TE we conclude the NPA is characterized by a Poisson coefficient nu = 0.42 indicating a significant departure from polycrystalline alumina (PCA). This result is consistent with the observed changes in the uniaxial anisotropy (UA): from easy axis at room temperature (T) towards easy plane at low T.

Recently there has been a growing interest in the study of magnetic NW grown on artificial templates [1]. While polycarbonate templates have been widely used to grow nanowires, amorphous NPA templates have the advantage of having a regular array with a very uniform alignment of the porous and a quite uniform pore-size distribution [2].

Our samples were grown by a two-step controlled anodization process using sulfuric (S1) and oxalic (S2) acid which yields a pore diameter typically of 20 (S1) and 35nm (S2) with interpore separation of 65nm (S1) and 105nm (S2). These templates were used to electro-deposit Ni nanowires (NW) in the NPA holes and thus create an ordered array of NW which can be used to study the magnetic anisotropy as a function of the topology [3, 4]

Previous studies on magnetic NW as a function of T [5-7] have shown an anomalous change of the magnetic anisotropy from easy axis at room T to a significantly different anisotropy at low T. These effects have been associated with magnetoelastic effects, though not always have they been measured by x-rays.

Also, recently there have been reports on the hardness of the NPA differing from that of polycrystalline alumina (PCA) [7] thus pointing to the fact that annealing is required for hardening these templates.

In this work we present thermal expansion measurements on S1 and S2 samples. The X-ray pattern shows the NW grow textured with the (110) plane along the wire direction. Thermal expansion measurements were performed using a Philips PW1700 apparatus with a low-temperature set up going down to 100K. The (311) reflection of Al was used as an internal reference for characterizing the room T scan which showed the Ni NW present an undistorted lattice parameter at this T.

When cooling down the Al peak follow very closely the expected thermal contraction of a bulk specimen [8]. The NW (220) peaks, however, expand as the sample is cooled. As the NW fill 10% of the NPA film [3] we may expect the NW to serve as a nanometric strain sensor, thus revealing the anomalous thermal expansion of the amorphous NPA as the sample is cooled down. As the NW can be considered a "perturbation" to the NPA we can derive some conclusion from the observed thermal expansion. If a uniform thin film is subject to strains in the plane the thermal expansion along the perpendicular direction is given by [9]

ezz = -nu (exx + eyy) /(1-nu) (1)

and exx = eyy. This in-plane strain should be originated in the differential thermal expansion between the Al substrate (1 mm) and the NPA (2-3 micons). The average thermal expansion coefficient of Al between 300K and 100K is about 18 10-6/K and that of PCA is tabulated as 6 10-6/K at room T. This leads to exx = 2.4 10-3 for the 300K-100K difference. The average ezz measured with in the NW is 3.6 10-3 (3.4 10-3 for S1 and 3.8 10-3 for S2) thus leading to an estimate of nu(NPA) = 0.42. A lower limit would be given by a zero thermal expansion of the NPA, thus leading to a larger strain and to nu(NPA) = 0.33. On the other extreme we may argue that the Ni NW only represents a lower limit to the ezz of the NPA, however, this would lead to an even larger value of nu(NPA), which should be limited by nu = 0.5. This shows the NPA differs significantly from the nu = 0.231 value of the PCA, and points to the fact that untreated NPA is more easily deformable than PCA.

Two contributions to the stresses acting on the NW are present: the one observed by measuring ezz, leading to sigma_zz = E ezz = (200GPa) 3.6 10-3 = 0.72 GPa and the in-plane one coming from the thermal expansion difference between the NPA and the Ni. As the NPA should "follow" the Al as long as is easily deformable we can estimate the in-plane strain on the Ni is directly caused by the difference between Al and Ni. This leads to sigma_xx = E exx = E (alpha(Al)- alpha(Ni)) Delta_T = E (-1.8 10-5 + 1.08 10-6)200 = 0.288GPa and similarly for sigma_yy. The three stresses contribute in the same direction to the magnetoelastic energy through the relation:

K = lambda_110 sigma (2)

where K is the magnetoelastic energy, sigma is obtained from the addition of the three independent contributions and taking lambda_110 = -30 10-6 [5] we obtain a UA contribution given by Delta_Ha = 1600Oe, very similar to the observed value [10].

[1] A. Fert and L. Piraux, J. Mag. Mag. Mater, 200 (1999) 338.

[2] M. Vázquez et al. Eur. J. of Phys B, 40 (2004) 489.

[3] C. A. Ramos, E. Vasallo, and M. Vázquez, Physica B, 354 (2004) 195.

[4] M. Vázquez et al., Trans. Mag. Soc. of Japan, 5 (2005) 157.

[5] S. Dubois, et al., Phys. Rev. B 61 (2000) 14315.

[5] A. Kumar, et al., Phys. Rev. B 73 (2006) 064421

[6] E. L. Sivla, et al., Physica B 384 (2006) 22.

[7] Z. Xia, et al. Rev. Adv. Mater. Sci. 6 (2004) 131

[8] F. C. Nix and D. MacNair, Phys. Rev. 60 (1941) 597.

[9] Theory of Elasticity, L. D. Landau, E. M. Lifshiftz, Pergamon Press, Second Edition (1970) Chap. II, page 53.

[10] E. Vassallo Brigneti et al. to be published.

Customizing the magnetic properties of magnetostrictive amorphous $(Fe_{80}Co_{20})_{80}B_{20}$ multilayers with orthogonal anisotropies by using different buffer layers to control the induced-deposition stress.

M. González-Guerrero[1], J. Prieto[2], P. Sánchez[1], C. Aroca[1]
1. Física Aplicada, ETSI Telecomunicación UPM, Madrid, Spain; 2. ISOM, Universidad Politécnica de Madrid, Madrid, Spain

The modulation of magnetic anisotropy in the thickness, by means of the deposition of multilayers with orthogonal anisotropies, has been previously proved to reduce the coercivity of magnetostrictive amorphous $(Fe_{80}Co_{20})_{80}B_{20}$ thin films, allowing a strict control of the magnetic anisotropy, the total magnetostriction not being affected [1]. The mechanical energy accumulated in every layer was thought to be the origin of that striking behavior. Here, we experimentally confirm that initial assumption, showing how buffer layers with different thermo-mechanical properties govern the total magneto-elastic energy of FeCoB multilayers, and provide the needed key to customize their magnetic properties.

FeCoB films, composed of five bilayers 26-9 nm thick with orthogonal anisotropies, were deposited on SiO_2 substrates buffered with different materials: Al, Cr, Cu and Mo. All the buffer layers are deposited with 50 W power and 5 mTorr Ar pressure, with a thickness around 100 μm. In Fig. 1(a) a schematic picture of the samples is shown.

The hysteresis loops of the samples show just one anisotropy axis, as in those shown in Fig 1(b), belonging to the sample with Mo buffer (this buffer layer was deposited with the sample continuously rotating during deposition).

Figure 2 shows the coercive (along the hard axis) and the anisotropy field of all the studied samples. Though all their hysteresis loops have the same shape, the magnetic anisotropy and the coercive field are quite different depending on the buffer material and the way it is deposited.

X ray diffractograms not shown in this digest suggest that the differences between depositing the buffer rotating or not rotating the sample lie in the promotion of nanocrystalline texture, that is transferred to a certain extent, to the FeCoB multilayers[2].

The behavior of the coercive field of the samples with different buffer layers points toward the influence of the thermal and mechanical properties of the buffer in the behavior of the magnetic layer, as expected, due to the well known influence of the substrate properties on the deposition conditions[3] and to the essential effect of the stress on the properties of FeCoB layers[4]. Buffer materials that bring together a high Young modulus, Y, high thermal conductivity, σ_t, and low coefficient of thermal expansion, CTE, do not allow the dissipation of the stress induced during deposition, producing a single domain-like behavior, with coercive field values higher along the easy axis and lower along the hard one, as well as smaller anisotropies.

In table I, the thermo-mechanical parameters of the buffer materials, and the coercive and anisotropy field values of the samples are displayed, showing the mentioned correlations.

[1] M. González-Guerreto et al., Appl. Phys. Lett., **90**, (2007), 162501.

[2] M. T. Umlor, Appl. Phys. Lett., **87**, (2005), 082505.

[3] J. A. Thornton, J. Vac. Sc. Technol. A, **4**, (1986), 3059.

[4] M. Kevin Minor et al., J. Appl. Phys., **91**, (2002), 8453.

Material	Y (GPa)	σ_t (W/K×m)	CTE×10^6 (K^{-1})	Y×σ_t/CTE (GPa×K/m)	H_C ^{HARD} (Oe)	H_C ^{EASY} (Oe)	H_K (Oe)
Al	70	235	23.1	712	4.6	2.5	33
SiO_2	72	1.4	0.5	201	3.8	3.8	33
Cu	130	400	16.5	3151	2.1	3.2	20.6
Cr	279	94	4.9	5352	1.8	4.6	12
Mo	329	139	4.8	9527	1.1	3	15.9

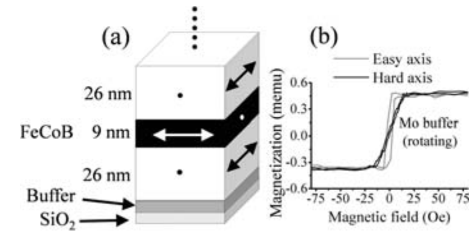

Fig. 1. (a) Schematic picture of the samples under study. The arrows indicate the direction of anisotropy induced in every layer. The FeCoB layers are super-scaled for clarity. (b) Hysteresis loops along the easy and hard axis of magnetization of the FeCoB multilayer deposited on the Mo-rotating buffer.

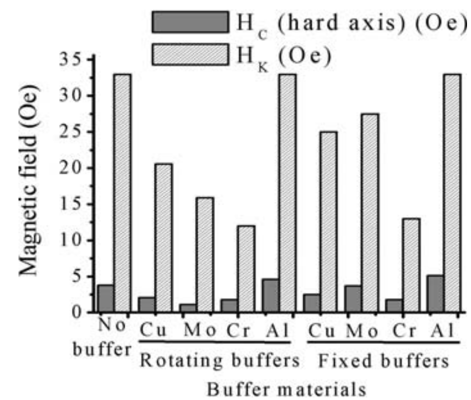

Fig. 2. Bar diagram showing the anisotropy and the coercive (along the hard axis) field of the same FeCoB multilayer deposited on a thermal oxide Si substrate with buffer layers of different materials, deposited well rotating the sample during the growing process, well keeping it fixed.

ET-08

Low Temperature Magnetoelastic Effects In Template Grown Ferromagnetic Nanowires.

J. De La Torre Medina, M. Darques, L. Piraux
Université Catholique de Louvain, Louvain-la-Neuve, Belgium

Arrays of electrodeposited Ni, permalloy Py (Ni80Fe20) and Co nanowires (NW) into polycarbonate (PC) membranes are studied by ferromagnetic resonance (FMR). Magnetoelastic (ME) effects are quantified by measuring transmission spectra by applying a DC field in the direction of the wires. In Ni NW, ME effects are evidenced at low temperature and are attributed to the thermal expansion coefficients mismatch between the NW and the PC membrane[1,2]. Figure 1, shows transmission spectra recorded at 33 GHz and at temperatures from 4.3 K to 300 K for Ni and Py NW arrays with pores diameter d=50 nm and membrane porosity P=2%. For the Ni sample, the resonance field shifts by a large value, indicating the presence of a strong ME effect as T decreases from 300 K down to 4.3 K. However, the resonance field shift δHr measured in the Ni sample is not only related to ME effects because the magnetocrystalline (MC) anisotropy is no longer negligible at low T[3]. This is, since electrodeposited Ni NW arrays are textured in the [110] direction (parallel to the wires)[2], variations of the MC anisotropy have to be considered together with ME effects at low T. Conversely, no ME effects are observed in Py NW into in the same membranes. The small δHr for the Py sample is related to variations of the saturation magnetization Ms with T. In the case of Co NW, the total anisotropy at 300 K results from the competition between magnetostatic (MS) and MC contributions. Control of the structure of Co by means of the electrolyte pH leads to three different regimes. At pH~2, the wires are polycrystalline, whereas at higher pH values the anisotropy is affected by the MC anisotropy which depends on the orientation of the hcp c-axis with respect to the wires[4]. At pH~4 the c-axis is perpendicular to the wires and the MC contribution reduces the MS anisotropy and at pH~6 the c-axis is parallel to the wires and the MC anisotropy ads to the MS one. At low temperature, ME effects appear in a similar way as in the case of Ni NW. Besides this, the non negligible hcp Co magnetostriction λ depends on the relative orientation between the magnetization M, the stress σ and the hcp c-axis[5]. In our NW λ is expected to be positive or negative if the c-axis is parallel or perpendicular to the wires. Further, the MC anisotropy of Co increases by a significant amount as the temperature is lowered[6], and a coupled MC-ME effect must be considered. In the FMR measurements, the DC field is parallel to σ and the c-axis can be perpendicular or parallel to the wires. In this configuration, from ref[5] we may expect that λ is negative or positive if the c-axis is perpendicular or parallel to wires. In addition, Co NW having like-fcc grains (pH~2) are expected to present both small variations of the MC anisotropy and negligible ME effects at low temperature because of the small polycrystalline grains and the MC constant at 300 K is of one order of magnitude smaller than for hcp Co. Figure 2 shows transmission spectra measured at 38 GHz and at 200 K (empty symbols) and at 300 K (filled symbols) for three samples, where the first one has like-fcc grains (pH~2), and the second (pH~4) and third (pH~6) ones have hcp grains. It is observed that the spectra of the second and third samples, shift toward higher and lower fields respectively (represented by the arrow in fig. 2). The difference in amplitude and direction of δHr shows the existence of two different mechanisms on the competition of the anisotropies involved at low temperature. Moreover, the spectra for the pH~2 sample shifts by a very small amount, which is of the order of the variation of the Ms with T. Finally, a more detailed analysis is in current progress in order to decouple the different anisotropy contributions at low T.

[1] J Meier, B Doudin, and J-Ph Anserment, J Appl Phys 79, 6010 (1996).

[2] S Dubois, J Colin, J L Duvail, and L Piraux, Phys Rev B 61, 14315 (2000).

[3] J J M Franse and G de Vries, Physica 39, 477 (1998).

[5] M Darques, A Encinas, P Bayle-Guillemaud, A Popa, and U Ebels, Appl Phys Lett 86, 072508 (2005).

[6] R M Bozorth, Phys Rev 96, 311 (1954).

[7] D M Paige, B Szpunar, and B K Tanner, J Magn Magn Mat 44, 239 (1984).

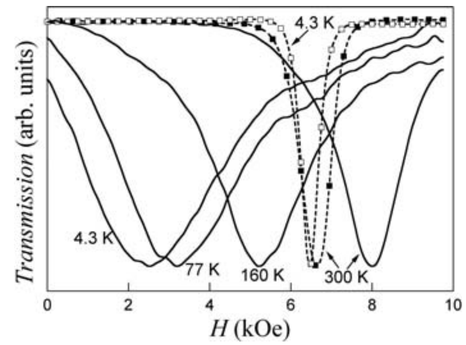

FIG 1. Transmission spectra recorded at 33 GHz as a function of temperature for Ni (continuous lines) and Py (broken lines with symbols) nanowires with d = 50 nm and P = 2%.

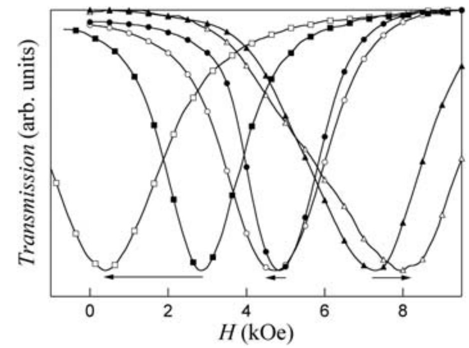

FIG 2. Transmission spectra recorded at 200 K (empty symbols) and at 300 K (filled symbols) for samples deposited at pH~2 (circles), at pH~4 (triangles) and at pH~6 (squares). The arrows indicate the resonance field shift direction.

Magnetostriction of Fe-Ti alloys.

C. Bormio-Nunes[1], A. B. Belarmino[1], C. T. Santos[1], V. C. Ugeda[1], L. Ghivelder[2], C. A. Baldan[1]
1. Escola de Engenharia de Materiais, Universidade de Sao Paulo, Lorena, Brazil; 2. Instituto de Física, UFRJ, Rio de Janeiro, Brazil

Hall [1] showed that small additions of transition metals (V, Cr, Mo) increase the λ_{100} magnetostriction of pure iron. Besides, very high magnetostriction values were found in FeGa alloys recently [2],about 90 ppm in polycrystalline materials [3] and λ_{100} = 400 ppm in single crystals [2]. Similar behavior is expected by adding Ti to Fe, because Ti has an atomic radius larger than Ga and could cause a significant dilatation on the Fe A2 structure. The A2 structure is the one that gives the highest magnetostriction (Fe-Ga) and is also present in the FeTi alloys (Ti~10at.% at 1290○C). Below 1290 ○C the α and the C14 phase coexist.
The $Fe_{100-x}Ti_x$ alloys (x = 10,15,20)were produced by arc melting. Samples were submited to heat treatments in the 1000≤T≤1250○C interval (5 h).
The microstructure characterization was done by scanning electron microscopy/backscattered electrons (SEM/BSE), energy dispersive spectroscopy (EDS) and X-ray powder diffraction. Magnetostriction measurements were made with a miniature capacitance dilatometer [4] and were carried out at temperatures close to 238 K for fields up to 1.5 T. The dc magnetization was measured using a PPMS-QD model 6000 for temperatures of 4.2,77 and 300K.
Tab.1 shows the samples characteristics. Tab.2 shows samples A-C saturation polarization (J_s) results. Sample A has the maximum J_s and sample B presents a higher J_s than sample C since A and B samples are richer in Fe. Sample C has higher Fe content in the α-phase than sample B, even though has the lowest J_s value. The C14 phase do not contribute to J_s because C14 is ferromagnetic only below 180 K [5] and the decrease of J_s due C14 is clearer at 300 K (B and C samples). In Fig.1, the microstructures of the samples show that C14 is present in samples B and C, but sample A is a single α phase sample. The matrix of samples B and C are C14 and α phases, respectively. Peaks of C14 phase are present in powder diffraction patterns of samples B and C (not shown). Fig. 2 shows longitudinal (λ_{long}) and transversal (λ_{trans}) magnetostriction at 238 K, plus $\omega=\lambda_{long}+2\lambda_{trans}$ (volume magnetostriction) and $\lambda_s=\lambda_{long}-\lambda_{trans}$ (saturation magnetostriction). The highest ω value was obtained for sample B decreasing for samples C and A respectively. This behavior is due to that the matrix in sample B is the C14 phase while in sample C is the α-phase.
Concluding, $Fe_{100-x}Ti_x$ Fe rich alloys contract in the presence of field and as the Ti content increases the contration decreases(in modulus) due the presence of C14 phase that do not contribute to the magnetostriction. The maximum λ_s value was -12 ppm (sample A), and this is very small compared to 90 ppm of Fe-Ga. Although Ti atom is larger than Ga, it causes a negative magnetostriction, the opposite effect of the Ga addition. Therefore, the lattice dilatation is not the source of the high magnetostriction in Fe-Ga alloys.
Acknowledgments to FAPESP under grants 04/09779-1 and 05/00148-1.

[1] R. C. Hall, J. Appl. Phys. 31 (1960) 1037.

[2] A.E. Clark et al, J. Appl. Phys 93 10, (2003) 8621-8623.

[3] C. Bormio-Nunes et al, J. Appl. Phys. 97 (2005) 033901.

[4] M. Rotter et al, Rev. Mod. Phys. 69 (1998) 2742.

[5] T.B. Massalski, Binary Alloy Phase Diagrams, 2nd ed., ASM, Metal Park, Ohio, USA, (1990), 1704.

SAMPLE	4.2 K	77 K	300 K
A	189	187	182
B	129	128	111
C	115	114	101

SAMPLE	COMPOSITION	HTT (○C)	EXPECTED PHASES	ATTAINED PHASES
A	Fe10Ti	1250	α,Fe-10Ti	α,Fe-9.2Ti
B	Fe15Ti	1200	α,Fe-10Ti + C14*	α,Fe-7.3 Ti + C14 (Fe71.8Ti28.2)
C	Fe20Ti	1000	α,Fe-5Ti + C14*	α,Fe-4.3 Ti + C14 (Fe70.9Ti29.1)

Tab.1 - FeTi samples composition, heat-treatment temperature (HTT), expected phases (based on the equilibrium phase diagram [5], actual phases and composition measured by EDS. *(Fe72.4Ti27.6)

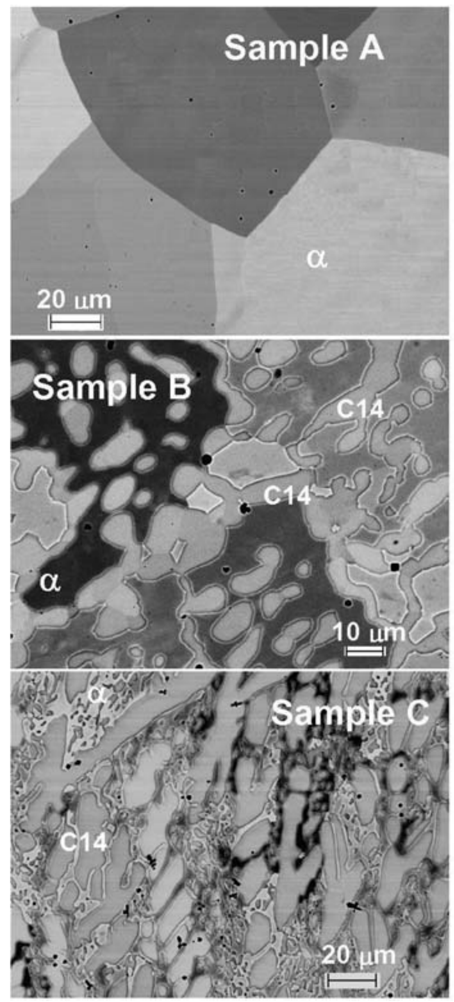

Fig. 1 - SEM images of the Fe-Ti samples A, B and C microstructures.

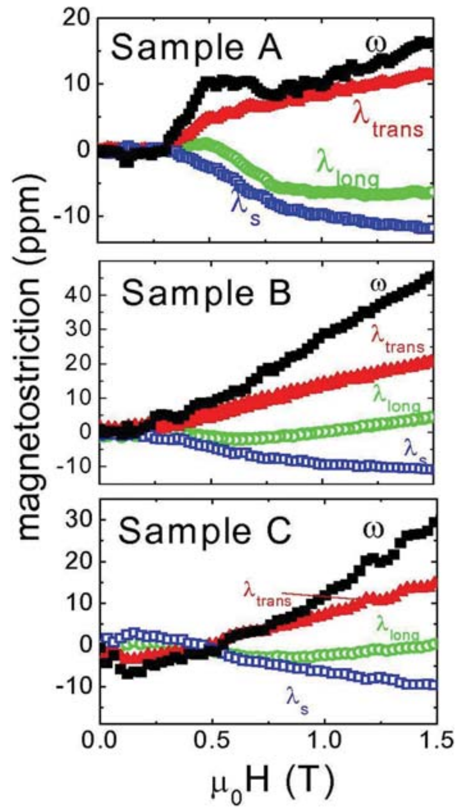

Fig. 2 - Magnetostriction vs field of samples A, B and C at 238 K

Picosecond magnetization dynamics of single-crystal Fe_3O_4 thin films.

C. Bunce[1], J. Wu[1], R. Chantrell[1], Y. Lu[2], Y. Xu[2]
1. Department of Physics, University of York, York, United Kingdom; 2. Electronics, University of York, York, United Kingdom

The time-resolved magnetization dynamics of epitaxial Fe_3O_4 ultra-thin films grown on a GaAs(100) substrate were investigated using a field pumped TRMOKE (time-resolved magneto-optical Kerr effect) experiment. The dynamic response of the magnetisation in the film to excitation by a 100 mT field pulse with a 90-10% rise time of 350 ps was recorded and compared to a single spin Landau-Lifshitz-Gilbert (LLG) simulation of the system. The comparison allowed the LLG damping factor and anisotropy constants of the system to be determined.
The 6 nm Fe_3O_4 thin film studied was created by oxidising an Fe film already deposited onto the GaAs substrate, the epitaxy of the film was checked using RHEED and the chemical composition was confirmed with XPS and XMCD as described by Lu et al [1]. The film has also been studied by Zhai et al [2] using FMR to determine its anisotropy which is a mix of a cubic anisotropy, an in-plane uniaxial term and an out-of-plane term where the relative contributions are functions of thickness.
The TRMOKE is based around a ½ turn 600 µm diameter micro-coil which generates an out-of-plane pulse field at the sample when a 7 kV electronic pulse generator discharges into it. An in-plane bias field larger than the coercivity is applied so the sample is initially in a single domain state as a result of which the pulsed field should induce a largely coherent damped precessional motion of the magnetisation vector. A 400 nm pulsed laser probe focussed onto the centre of the coil, measured the change in the out-of-plane component of the magnetisation vector. A stroboscopic arrangement between the pulsed laser and the electronic pulse generator allows time resolved measurements to be made with 25 ps resolution.
The equipment measures the variation of the out-of-plane component of magnetisation in the time domain as shown in figure 1. The LLB simulations take the constants which characterise the anisotropy system, the M_s and the damping factor as input parameters. The anisotropy system M_s can be determined for the sample by fitting the measurements in the frequency domain. The process is similar in principle to determining the parameters from FMR measurements, in this case the precessional frequency is determined from the measurements using an FFT and is fitted by FFT's of the LLG simulations. Figure 2 shows the frequency domain fitting for sample which determined the best fit anisotropy as a cubic term of -8×10^4, an in-plane uni-axial term of less than 1×10^4 and an out-of-plane uni-axial term of -1.6×10^6 ergs/cc. The cubic and out-of-plane terms compare well with those determined by Zhai et al [2] but the in-plane anisotropy appears to be absent from these measurements, this is assumed to be due to inter-sample variation.
Once the anisotropy parameters are known the measurements can be fitted more easily in the time-domain to find the best fit damping factor for each applied field. A selection of typical fits is shown in figure 1.
The damping factor does not show a significant systematic variation with applied field strength for either of two orthogonal in-plane directions. The value of the damping factor obtained from numerical LLG simulations is about 0.1, which is one order of magnitude higher than metallic thin films such as Fe, Co, Ni. While the mechanism of the large damping in Fe_3O_4 needs further investigation, our results suggest that Fe_3O_4 could operate at a significant higher working frequency than its metallic counterparts.

[1] Y.X. Lu et al. Phys. Rev. B 70 (2004) 233304
[2] Y. Zhai et al. J. Appl. Phys. 101 (2007) 09D126-1

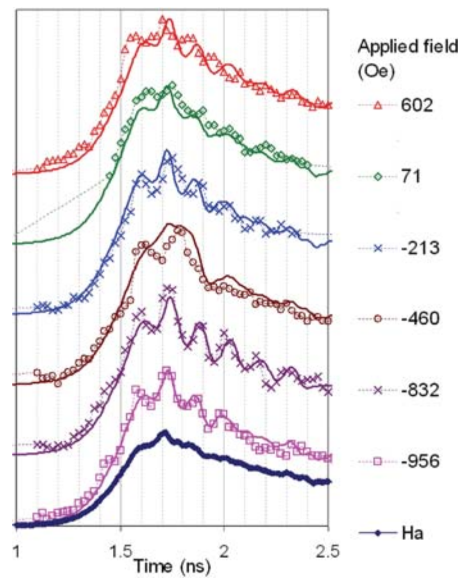

Figure 1: time domain TR-MOKE measurements for different applied in-plane bias fields, the connected points show the measurements and the smooth lines are the LLB fits

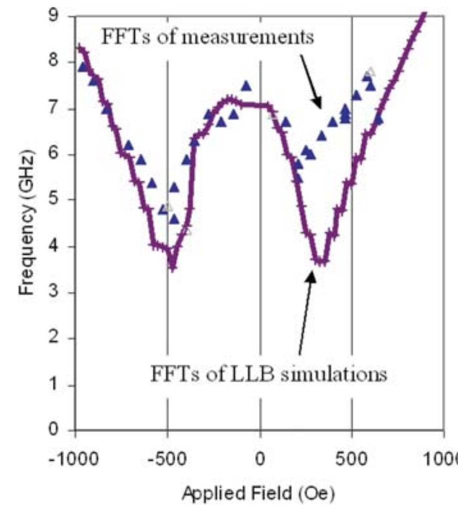

Figure 2: precessional frequency vs applied field, triangles mark the FFT of the time-domain data and the line is constructed from a series of LLG simulations

EU-03

Deconvolution of the ferromagnetic resonance absorption through the Verwey transition of magnetite.

H. Montiel[1], G. Alvarez[2], R. Valenzuela[2], R. Zamorano[3]
1. Tecnociencia, CCADET-UNAM, Mexico DF., Mexico; 2. Metalicos y Ceramicos, IIM-UNAM, Mexico D.F., Mexico; 3. Fisica, ESFM-IPN, Mexico D.F., Mexico

A ferromagnetic resonance (FMR) study was carried out on sintered polycrystalline samples of magnetite (Fe3O4), at a constant frequency of 9.4 GHz (X-Band) and dc magnetic fields (Hdc) in the 0–8000 G range. The temperature measurements were recorded in the 77-300 K range and was controlled by flowing cold N2 gas through a double walled quartz tube, placed at the center of the microwave cavity. An evolution of FMR lineshape was observed as a function of temperature, and which is related with the passage through the Verwey point (Tv~120 K) [1]. Deconvolution calculations were carried out on FMR spectra [2], and with it was possible to separate two contributions which can be associated with tetrahedral A and octahedral B sites of the crystal structure.
These contributions have different lineshapes: the one is a single broad symmetric Lorentzian line, in the entire temperature range, due to A-sublattice site, see Fig. 1; and the other one is of Dysonian-type (T>120 K), that is associated with B-sublattice site, as shown in Fig. 1. The Dysonian lineshape shows an asymmetric signal due to a conducting mechanism and it is described as a combination of absorption and dispersion components [3,4]. Above of 120 K, the Dysonian lineshape changed to Lorentzian lineshape in the B-sublattice site, due to a discontinuous drop in electrical conductivity upon cooling below Tv [1].
Additionally, the parameters FMR obtained of deconvolution fitting can be associated with change of the magnetic anisotropy, as a consequence of the charge localization below the Verwey transition; i.e. temperature dependence of the resonant field (Hres) and the peak-to-peak linewidth (DHLFA), can be related with an anisotropy decrease in the neighborhood of the Verwey transition, due to a charge rearrangement. These results suggest that the magnetization dynamics is influenced by the electronic nature of the metal-insulator transition mechanism and the structural transition at Verwey transition. Additionally, below the transition temperature, the anisotropy increases due to an additional contribution to magnetostriction that appears as a consequence of a distorted cubic phase [5].

[1] E. J. W. Verwey, Nature (London) 144 (1939) 327.

[2] H. Montiel, G. Alvarez, I. Betancourt, R. Zamorano and R. Valenzuela, Physica B 384 (2006) 297.

[3] G. Feher and A.F. Kip, Phys. Rev. 98 (1955) 337.

[4] F. J. Dyson, Phys. Rev. 98 (1955) 349.

[5] J.P. Wrigth, J.P. Attfield, P. Radaelli, Phys. Rev. B 66 (2002) 214422.

EU-04

Dynamic Magnetic Properties of $NiFe_2O_4$ Nanoparticles Embedded in SiO_2 Matrix.

S. Mitra[1], *K. Mandal*[1], E. Choi[2]
1. Materials Science, S. N. Bose National Centre for Basic Sciences, Kolkata, India; 2. National High Magnetic Field Laboratory, Tallahassee, FL

In recent years, ferrite nanoparticles have firmly been established as an important class of soft magnetic materials owing to its attractive magnetic properties at high frequencies, resistivity that is in the insulating range, and the high corrosion resistance [1]. Dynamic magnetic behaviors of sol-gel synthesized $NiFe_2O_4$-SiO_2 nanocomposite [2] system including temperature dependent relaxation phenomenon were examined and the results are reported in this article.

In X-ray diffraction (XRD) pattern (Fig.1) the peaks correspond to only the spinel phase of $NiFe_2O_4$ nanoparticles. The average crystallite size was determined from the peaks using Scherrer equation and it was found to be ~3.5 nm (sample SA), 5.6 nm (sample SB), 6.8 nm (sample SC) and 19 nm (sample SD). Particle sizes of the samples determined from transmission electron microscope (Fig.2) corresponds well with the particle sizes determined from XRD. The temperature dependence of the ac susceptibility measured in the frequency range of 10 Hz to 100 kHz shows a maximum in χ' which is interpreted as the blocking temperature T_B at that frequency (shown for representative samples SA in Fig.3). The position of the peak shifts towards higher temperatures as frequency increases. In absence of a magnetic field, at finite temperature, the ferromagnetic moments in a single domain particles fluctuate between their two energetically degenerate ground states on a time scale given by $\tau = \tau_0 \exp(KV/k_BT)$, where τ is the relaxation time and τ_0 is the inverse of attempt frequency estimated to be within 10^{-10}- 10^{-12} s for non-interacting single domain particles. At T_B, $\tau = \tau_{ex}$, the measurement time or the experimental time window of the instrument. For $T > T_B$, The particles rapidly achieve thermal equilibrium during the measurement time as $\tau < \tau_{ex}$ and the system shows superparamagnetism. On the other hand, at $T < T_B$, the particles are said to be blocked, i.e. their magnetic moments remain at a fixed direction during a single measurement as $\tau > \tau_{ex}$. Hence at $\tau = \tau_{ex}$, the ac susceptibility vs temperature data shows a peak. From Arrhenius law we get, $\ln\tau = \ln\tau_0 + KV/ k_BT$. It indicates linear dependence of $\ln\tau_{ex}$ on $1/T_B$ which was observed experimentally also (top right insets of Fig.3).

For magnetic relaxation study, samples are field cooled in presence of a field of 7T at different temperatures from 5K to 50K. After the removal of the field, magnetization evolves with time towards a demagnetized state. The M versus ln(t) curves (Fig.4) for representative samples SA measured at different temperatures shows a deviation from the linear behavior at the initial stage of measurement time. Hence a scaling hypothesis has been employed to analyse the experimental data.

[1] Hand Book of Nanophase Materials, edited by A. N. Goldstein (Marcel Dekker Inc., New York, 1997).

[2] S. Mitra, K. Mandal, P. A. Kumar, J. Mag. Mag. Mater, **306** (2006), 254.

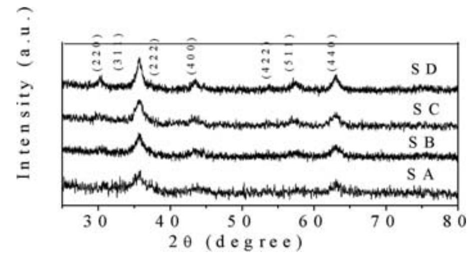

Fig.1: XRD pattern of Ni-ferrite nanoparticles (Samples SA, SB, SC and SD)

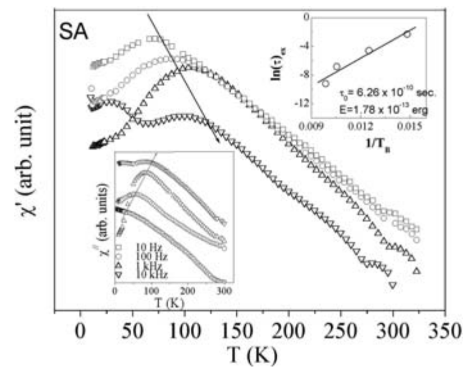

Fig.3: Real and imaginary (lower inset) part of ac susceptibility of sample SA.

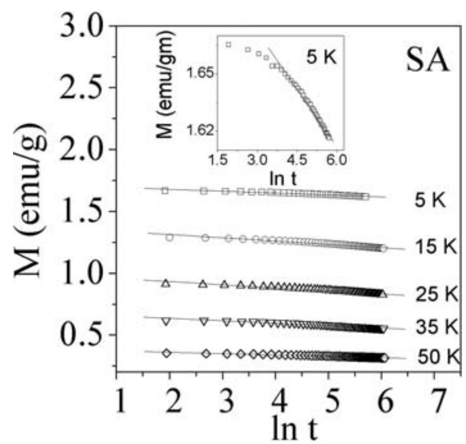

Fig.4: M vs ln (t) plot of sample SA.

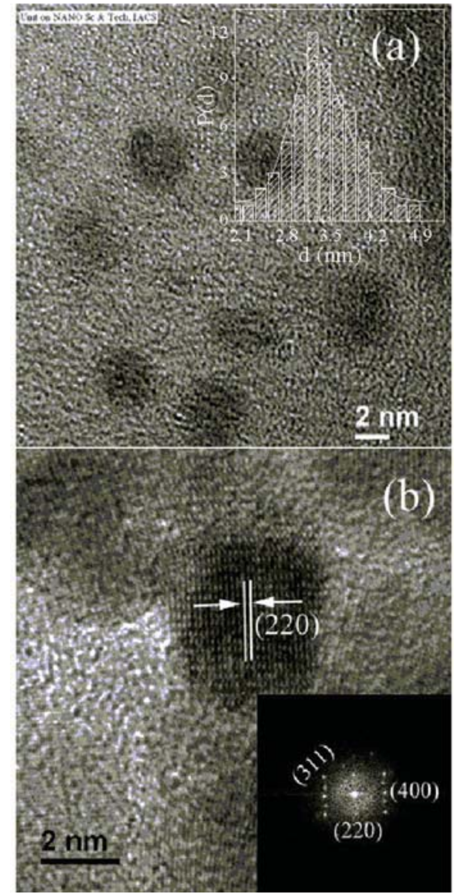

Fig.2: HRTEM micrograph of sample SA

EU-05

Analyzing the permeability and permittivity dispersion spectra of $(Ni_{0.4}Zn_{0.59}Co_{0.01})\,Fe_{1.98}O_4$ spinel ferrites with Fe deficiency.

M. Han, L. Deng
State Key Laboratory of Electronic Thin Films and Integrated Devices, University of Electronic Science and Technology of China, Chengdu, China

Spinel ferrites ($MeFe_2O_4$, Me = Ni, Co, Zn, Cu, Mg etc) are one of frequently used magnetic materials for radio frequency (RF) applications due to their high electrical resistivity, high permeability values and chemical stability, such as RF inductors[1], RF electromagnetic wave absorbers[2], RF noise suppressors[3], etc. For high frequency applications, the permeability dispersion behaviors are widely believed governed by the Snoek's law [4]. In order to further increase the resistivity of spinel ferrite, ferrites with Fe deficiency in compositions are often prepared so as to inhibit the electrons hopping between Fe^{2+} and Fe^{3+} in the octahedral sites of unit cells. In this paper, we have prepared the $(Ni_{0.4}Zn_{0.59}Co_{0.01})Fe_{1.98}O_4$ ferrites with Fe deficiency using a double sintering route. The starting oxides were ball milled for 1.5 h, then the milled powders were sintered at 980 ^{0}C for 2 h. The pre-sintered powder was then ball milled again for 3 h. The final sintering was carried out at 1230 ^{0}C for 2 h. The permeability and permittivity dispersion spectra were taken on HP4291B Impedance Analyzer within the frequency of 1MHz – 1 GHz. XRD investigation shows the final sintered sample having a typical spinel-like cubic structure.

It is widely accepted that there are two magnetizing mechanisms contributing to the permeability dispersion behaviors: domain wall movement (DW) and spin rotation [5]. Unfortunately, these two contributions are often mixed together in an obtained dispersion spectrum, which make analyzing their respective dispersion behaviors difficult. In this paper, we report an approach to separate the dispersion spectra into the DW components and spin rotation components. We find that good fittings with a nonlinear least square method can be obtained if we suppose the DW components with a resonance-type dispersion and the spin rotation components with a relaxation-type dispersion. In this way, the permeability dispersion behavior can be expressed as [6]:

$$\mu_r' = 1+ [\omega_d^2\chi_{d0}(\omega_d^2-\omega^2)]/[(\omega_d^2-\omega^2)^2+\omega^2\beta^2] + \chi_{s0}\omega_s^2[(\omega_s^2-\omega^2)+\omega^2\alpha^2]/\{[\omega_s^2-\omega^2(1+\alpha^2)]^2+4\omega^2\omega_s^2\alpha^2\} \quad (1)$$

$$\mu_r'' = \omega_d^2\chi_{d0}\omega\beta/[(\omega_d^2-\omega^2)^2+\omega^2\beta^2] + \chi_{s0}\omega_s\omega\alpha[\omega_s^2+\omega^2(1+\alpha^2)]/\{[\omega_s^2-\omega^2(1+\alpha^2)]^2+4\omega^2\omega_s^2\alpha^2\} \quad (2)$$

,where ω, χ_0,α, β denote the angular frequency, static permeability, damping constant of spin rotation, damping constant of domain wall movement respectively. The subscript d and s denote the domain wall component and spin rotation component. The fitting results are shown in Fig. 1(a) and (b). As shown, the spin rotation makes major contributions to the permeability dispersion, and the spin rotation resonance occurs at higher frequency. The fitting results for ω_d, ω_s, χ_{d0},χ_{s0},α and β are 6.6×10^7 Hz, 7.7×10^{11} Hz, 108, 304, 4476 and 6.1×10^7. The permittivity dispersion behavior is shown in Fig. 1(c). Rather than using the Debye's dielectric dispersion law with a single relaxation time, here we adopt the Cole-Cole dielectric dispersion law [7], which assumes that there should be a distribution of relaxation time for polarization processes due to the inhomogenous microstructures of materials. According to Cole-Cole law, the real part of permittivity can be expressed as: $\varepsilon'=\varepsilon_{r\infty}+(\varepsilon_{rs}-\varepsilon_{r\infty})\times[1+(\omega\tau)^{1-\gamma}\sin(\pi\gamma/2)]/[1+2(\omega\tau)^{1-\gamma}\sin(\pi\gamma/2)+(\omega\tau)^{2(1-\gamma)}]$, where ε_{rs},$\varepsilon_{r\infty}$,τ,$\gamma(0\leq\gamma\leq1)$ are the static permittivity, permittivity when frequency is infinity, the relaxation time, and the distribution of relaxation time, the corresponding fitting results are 24.8, 15.5, 4.99×10^{-8} s, 0.253 respectively. The RF electromagnetic wave absorbing performance generally evaluated by the reflection loss (RL) in dB can be calculated based on the equation [8]: $Z_{in} = Z_0(\mu_r/\varepsilon_r)^{1/2}\tanh\{j(2\pi ft/c)(\mu_r\varepsilon_r)^{1/2}\}$and $RL = 20\log|(Z_{in}-Z_0)/(Z_{in}+Z_0)|$. Supposing that single layer of our prepared NiZnCo ferrites are attached on a metal plate, the thickness of ferrites is 4.3 mm. The electromagnetic wave absorption performance has been evaluated and is shown in Fig. 1(d). Clearly, it has a good EM wave absorption (RL < -20 dB) within the frequency band of 164 MHz – 390 MHz.

[1] C. Yang, F. Liu, T. Ren, L. Liu, H. Feng, A. Z. Wang, H. Long, Sensors and Actuators A, 130–131 (2006) 365.

[2] R. Dosoudil, M. Usakova, J. Franek, J. Slama, V. Olah, J. Magn. Magn. Mater. 304 (2006) 755.

[3] K. H. Kim, M. Yamaguchi, N. Matsushita, M. Abe, J. Magn. Magn. Mater. 290–291 (2005) 1363.

[4] J. L. Snoek, Physica (Amsterdam) 14(1948)207.

[5] T. Nakamura, T. Tsutaoka, K. Hatakeyama, J. Magn. Magn. Mater. 138(1994) 319.

[6] Mangui Han, Difei Liang, Longjiang Deng, Appl. Phys. Lett. 90(2007) 192507.

[7] Hanru Li, Introduction to Physics of Dielectrics, 1st ed. (University of Science and Technology of Chengdu, Chengdu, 1990), 167.

[8] Y. Naito, K. Suetake, IEEE Trans. Microwave Theory Tech. 19 (1971) 65.

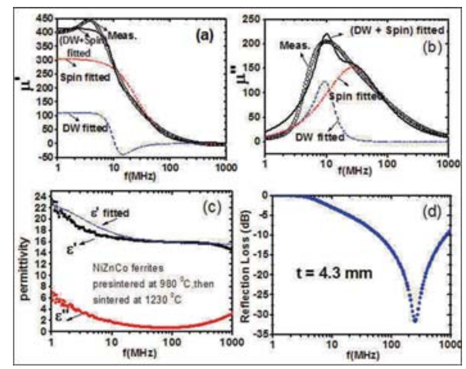

Fig. 1. (a), (b) The permeability dispersion spectra: (a) the real part; (b) the imaginary part; "DW" denotes domain wall movement; "Spin" denotes the spin rotation mechanism; (c) the permittivity dispersion spectra; (d) electromagnetic wave absorption properties;

EU-06

Magnetic and Microwave properties Sm-doped $SrFe_{12}O_{19}$ single crystals.

J. Jalli[1,2], Y. Hong[1,2], S. Gee[1,3], J. Lee[1,2], S. Bae[1,2], G. S. Abo[1,2], A. Lyle[1,2], H. Han[1,2], J. Kim[4], H. Lee[4], S. Lee[4]

1. Electrical and Computer Engineering, University of Alabama, Tuscaloosa, AL; 2. MINT Center, University of Alabama, Tuscaloosa, AL; 3. Seagate Technology, Bloomington, MN; 4. Pohang Superconductivity Center, Pohang University of Science and Technology, Pohang, South Korea

Introduction

Hexagonal strontium ferrite ($SrFe_{12}O_{19}$; SrM) has a magnetoplumbite structure with easy magnetocrystalline anisotropy along the c-axis of the hexagonal unit cell [1]. The large anisotropy field in these ferrites acts as a built-in magnetic field and permits the application of ferrimagnetic resonance (FMR) in millimeter wave devices [2]. Thus, microwave devices such as resonance isolators, circulators, tunable filters and oscillators can be operated in the millimeter-wave frequency range with moderate external magnetic bias fields. Substitution for Fe^{3+} and Ba^{2+} is an effective method for tailoring the magnetic properties of barium ferrite [3]. Although hexagonal ferrites have been extensively investigated in the past decades, the search for new cationic substitutions, especially the rare earth elements, has been a field of intense research and less reported to date. Rare-earth elements are very unique because of their characteristic structure of electronic shells; physical, mechanical and magnetic properties could be improved by doping these elements in the hexagonal crystal lattice of hexaferrites. In this work it was found that Sm-doped SrM single crystal possess 25 kOe of uniaxial anisotropy.

Experimental

Single crystals of samarium doped SrM (Sm-SrM), are grown in platinum crucible using a high temperature furnace. The primary mixture of $SrCO_3$:Fe_2O_3:Na_2CO_3 with small additions of Sm_2O_5 is used to grow single crystals. The reagents were blended and thoroughly ground together in a pestle for 1 hour. The finely blended powder is filled in a platinum crucible with approximately three-fourths of the volume. The platinum crucible is then placed in a top-lift enclosed furnace and fired at the temperature of 1450 °C for 12 hours to homogenize the melt. After completely homogenizing the melt for 12 hours, it is slowly cooled at the rate of 2.5 °C/hr to 1000 °C, and then cooled more rapidly in the furnace to room temperature. The, thus obtained, crystals were slowly separated by leaching in hot dilute nitric acid from the platinum crucibles.

Results and Discussion

The obtained crystals exhibited the typical hexagonal ferrite growth habit with a plate like geometry and are 4 to 6 mm in diameter and 2 to 3 mm in thickness, respectively. The hysteresis loop measured in the out-of-plane and in-plane directions of the Sm-SrM single crystal has a saturation magnetization of 69.8 emu/g and the uniaxial anisotropy of 25 kOe as shown in Fig. 1, respectively. It was observed that the magnetization is reduced to 69.8 emu/g from its bulk value of 74.3 emu/g but the anisotropy value is increased to 25 kOe from 18.7 kOe, respectively. The x-ray diffraction pattern confirmed that the structure is an extended single crystalline array of SrM with good c-axis crystallographic orientation. We also obtained the permeability spectra from the LLG equation assuming the damping constant (α) of 0.01 for single crystal BaM. The μ' in the out-of-plane direction was found to be 1.6 at 5 GHz and resonance frequency at 9.5 GHz respectively. Similarly, we obtained the μ' for the in-plane direction to be 1.1 at 60 GHz and thereafter the resonance occurs at 72 GHz as shown in Fig 2. To confirm the theoretical data with the experimental work we made circular disk samples by grinding the Sm-SrM single crystal coarse powder and measured the permeability spectra by the standard co-axial cable method and the data obtained is in good agreement with calculated μ' value. The detail microwave properties will be presented.

Conclusions

Samarium doped M-type strontium ferrite single crystals have been successfully grown from melts using a flux system of $SrCO_3$-Na_2CO_3. The large anisotropy, 25 kOe, of the Sm-SrM hexaferrites leads to high FMR frequency operation at relatively low external field compared with the traditional isotropic ferrites. The saturation magnetization and anisotropy field are greatly affected by the doping concentration of the element. Permeability measurements performed on a circular disk sample is in good agreement with the calculated value.

Acknowledgements

This work was supported by the Office of Naval Research under grant number N00014-06-1-0416.

[1] J. Smit and H.P.J. Wijn, Ferrites, Philips Techn. Library, Eindhoven (1959).

[2] Harvey S. Newman, Denis C.Web, Clifford M.Krowne, International conference on Millimeter and Submillimeter Waves and Applications III Proceedings of SPE. 181, 2842 (1996).

[3] D. B. Nicholson, Hewlett-Packard J. 41, 59 1990.

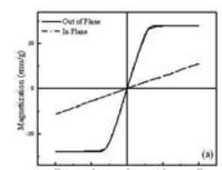

Fig. 1. Magnetic hysteresis loop of Sm-SrM single crystal.

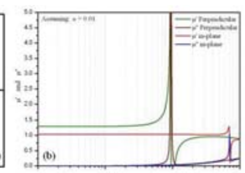

Fig. 2. Permeability spectra of the Sm-SrM single crystal.

EU-07

Relaxation Effect of $NiCr_{1.8}In_{0.1}Fe_{0.1}O_4$ with Magnetic Anisotropy.

S. Park, D. Choi, C. Kim
Department of Physics, Kookmin University, Seoul, South Korea

Introduction : Many researchers were conduct do researches on the chromite materials of spinel structure because of multiferroic effects.[1-3] The $NiCr_{1.9}Fe_{0.1}O_4$ is a ferrimagnet cubic normal spinel at room temperature, in which Ni^{2+} ions occupy the tetrahedral-sites and Cr^{3+} and Fe^{3+} ions occupy the octahedral-sites.[2] Also in the $NiCr_{1.9}Fe_{0.1}O_4$ is a cubic to tetragonal(c/a<1) transition for the Fe concentration x = 0.1 around 230 K.[4]
In this paper, we have studied the impact on magnetic properties of the $NiCr_{1.9}Fe_{0.1}O_4$ as a function of the nonmagnetic Indium(*In*) ion doping by using an x-ray diffraction and magnetization curve measurements and Mössbauer spectroscopy.
Experiments : Polycrystalline samples of the $NiCr_{1.9-x}In_xFe_{0.1}O_4$(x=0.0, 0.1) were prepared by annealing 24 hour in atmosphere at 1200 ^oC with a solid state reaction. The x-ray diffraction patterns of the samples at room temperature were obtained with Cu-$K\alpha$ radiation by an x-ray diffractometer (X'PERT). The temperature dependent moment curve was measured by a vibrating sample magnetometer(VSM). The hyperfine magnetic relaxation effects on magnetic anisotropy of samples were evaluated to analysis with temperature dependence of Mössbauer spectra. Mössbauer spectra were measured that a Mössbauer spectrometer of electromechanical type was used in the constant-acceleration mode with a ^{57}Co single-line source in a rhodium(*Rh*) matrix.
Results : The crystalline structure of $NiCr_{1.8}In_{0.1}Fe_{0.1}O_4$ sample at room temperature was determined to be a cubic spinel of *Fd-3m* with a lattice constant a_0 = 8.342 Å at 295 K by Rietveld refinement, while the Bragg R_B and R_F factors were 3.17 and 2.47 % (Figure 1). Figure 2 shows the temperature dependence of the zero field cooled(ZFC) and field coold(FC) magnetization curves for the $NiCr_{1.9-x}In_xFe_{0.1}O_4$(x=0.0, 0.1) under external field of 100 Oe. The magnetic Néel temperature(T_N) is determined by comparing the $d\sigma/dT$ curve of the ZFC measurements with the Mössbauer spectra analysis. As the $NiCr_{1.8}In_{0.1}Fe_{0.1}O_4$, the T_N is determined to be 130 K. Figure 3 shows Mössbauer spectra of $NiCr_{1.8}In_{0.1}Fe_{0.1}O_4$ at various temperature ranges. The Mössbauer spectra show two magnetic phases with the two different magnetic spin direction sites of the Cr^{3+} ion state.[1,5] Mössbauer absorption lines are sharp below 77 K and become broader with increasing temperature. The asymmetric intensities are different from those of the powder pattern 3:2:1. In order to explain the Mössbauer line broadering and 1,6 and 3,4 line-width difference due to the magnetic anisotropic relaxation effect, we use the Blume-Tjon[6] expression. It is noted that the relaxation effect increases rapidly as the temperature approaches the Néel temperature, 130 K.

[1] A. B. Sushkov, O. Tchernyshyov, W. ratcliff II, S. W. Cheong and H. D. Drew, Phys. Rev. Lett. **94**, 137202 (2005).

[2] S.-I. Park and C. S. Kim, J. Appl. Phys. **101**, 09N511 (2007).

[3] S. -W. Cheong, M. Mostovoy, Nature **6**, 13 (2007).

[4] R. J. Arnott, A. Wold and D. B. Rogers, J. Phys. Chem. Solids **25**, 161 (1964).

[5] K. Tomiyasu, I. Kagomiya, J. Phys. Soc. Japan, **73**, 2539 (2004).

[6] M. Blume, and J. A Tjon, Phys. Rev., **165**, 4469 (1968).

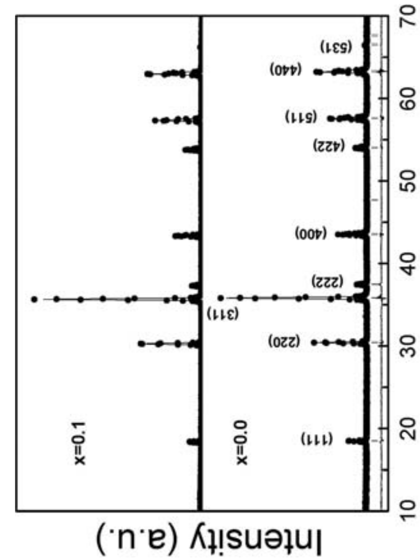

Fig. 1. The x-ray diffraction patterns of $NiCr_{1.9-x}In_xFe_{0.1}O_4$ at room temperature.

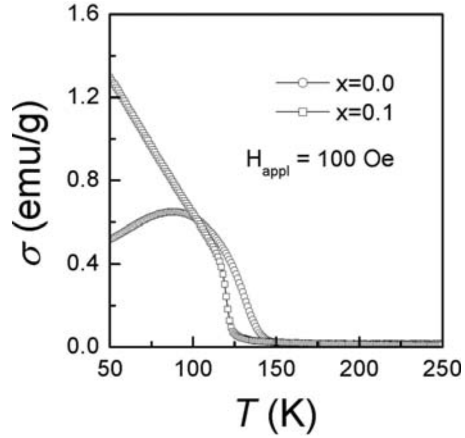

Fig. 2. The temperature dependence of zero field cooled curves $NiCr_{1.9-x}In_xFe_{0.1}O_4$.

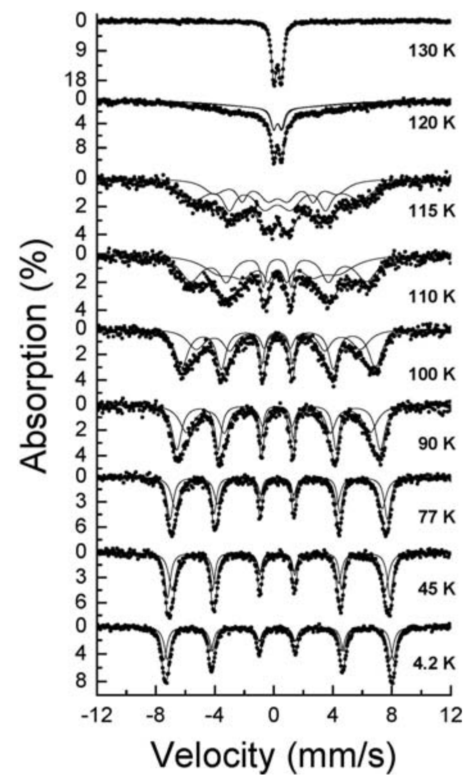

Fig. 3. The Mössbauer spectra of $NiCr_{1.9}In_{0.1}Fe_{0.1}O_4$ at various temperature ranges.

EU-08

Temperature dependence of magnetic losses in soft ferrites.

F. Fiorillo, C. Beatrice, L. Zhemchuzhna
Istituto Nazionale di Ricerca Metrologica INRIM, Torino, Italy

The magnetic properties of soft ferrites can be tailored to good extent by finely acting on their composition, so that anisotropy compensation may lead to the softest behavior upon the temperature range useful for specific applications [1]. Recognizing the effect of the magnetic anisotropy on the domain wall energy (i.e. coercivity) can provide partial explanation for the behavior of the quasi-static losses and their dependence on temperature. However, the contribution of the dynamic losses, predominant above a few hundred kHz, is poorly understood in the literature [2]. In this work we present significant results on the temperature dependence of loss and permeability in soft ferrites upon a wide range of frequencies (DC – 10 MHz). The frequency-temperature loss behavior of the material is explained and assessed through an approach founded on the statistical theory of magnetic losses [3], here applied to a physical system where eddy currents are not relevant. Fig. 1 shows representative energy loss vs. frequency behaviors at different temperatures in commercial Mn-Zn ferrite ring samples, designed to have good properties around 100 °C. Magnetic softening with increasing temperature applies at low and medium frequencies, while minor changes are observed beyond a few hundred kHz. We address these and other results by considering the separate contributions of domain wall (d.w.) displacements and moment rotations and clarifying the role of eddy currents. It is observed in all the investigated types of ferrites that strong decrease of ring thickness (e.g. from about 5 mm to 1 mm) does not lead to appreciable loss variation between DC and 10 MHz. Energy dissipation by the macroscopic eddy current paths can therefore be neglected. This result is substantiated by specific modelling of the electrical conduction versus frequency [4] and supplemented by the finding that the micro eddy currents circulating within the individual semiconducting ferrite grains are equally ineffective. The loss at any frequency, written as the sum of d.w. and rotational contributions $W = W_{dw} + W_{rot}$, can therefore be ascribed to spin damping mechanisms, usually accounted for through introduction of the phenomenological damping constant α_{LL}[5]. The d.w. term is $W_{dw} = W_h + W_{exc}$, the sum of hysteresis (DC) W_h and dynamic W_{exc} contributions. W_h is obtained by experiment, while W_{exc} can be formulated in terms of α_{LL} and the experimental parameter $k_{irr} = J_{irr}/J_p$, the fractional irreversible contribution to the peak polarization J_p. With known hysteresis loss value W_h, $W_{dw}(f)$ is calculated by reasonable guess of the α_{LL} value. The rotational term W_{rot}, largely prevailing in the MHz range, is associated with resonant absorption of energy. It is calculated by postulating a distribution function for the strength of the local effective anisotropy field H_k, the combination of the magnetocrystalline anisotropy fields and the internal demagnetizing fields. With small amplitude oscillations, the real χ'_{rot} and imaginary χ''_{rot} rotational susceptibility components are found as solutions of the Landau-Lifshitz-Gilbert equation for the damped precession of the magnetic moments. $W_{rot}(J_p,f)$ is calculated by taking the previous α_{LL} value and a Γ distribution for H_k, the average value $\langle H_k \rangle$being consistent with the upper part of the magnetization curve, and no additional arbitrary parameters. It is concluded, from theory and experiment (see Figs. 1 and 2), that the temperature induced variations of the magnetocrystalline anisotropy energy are chiefly reflected in the d.w. loss contribution W_{dw}, that is, in the low-medium frequency range properties. The rotational term W_{rot} is little affected by the value of $\langle H_k \rangle$and so is, consequently, the loss at high frequencies.

[1] J.J. Suh, B.M. Song, and Y.H. Han, IEEE Trans. Magn. 36 (2000) 3402.

[2] D. Stoppels, J. Magn. Magn. Mater., 160 (1996) 323.

[3] G. Bertotti, Hysteresis in magnetism (San Diego, Academic Press, 1998).

[4] O. Bottauscio, et al., J. Magn. Magn. Mater. 304 (2006) e746.

[5] H. Suhl, IEEE Trans. Magn. 34 (1998) 1834.

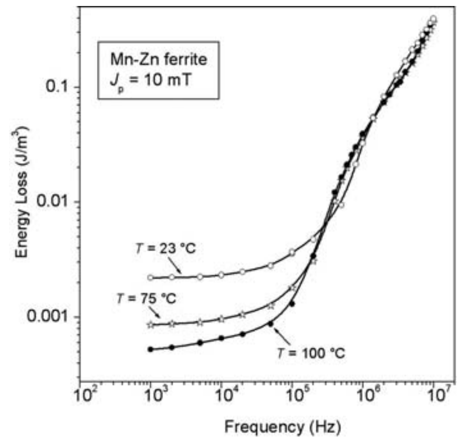

Fig. 1- Energy loss up to 10 MHz in a Mn-Zn ferrite ring sample at three different temperatures.

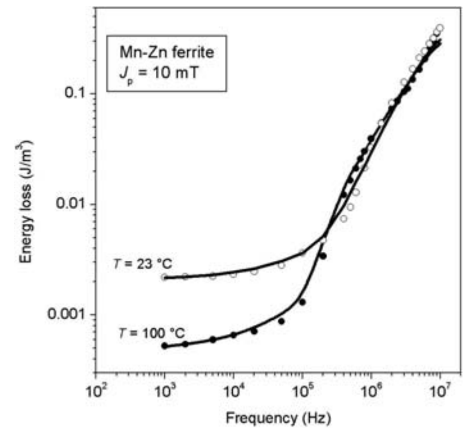

Fig. 2 - Energy loss vs. frequency (symbols) and its prediction (solid lines).

EU-09

Suppression of GHz noise emitted from a four-layered PWB with a ferrite-plated inner ground layer.

S. Yoshida[1], *K. Kondo*[1], T. Kubodera[2]

1. NEC TOKIN Corporation, Sendai Miyagi, Japan; 2. System Design Laboratory Co., Ltd., Ebina Kanagawa, Japan

Introduction

The most advanced digital electronic devices are equipped with multilayered printed wiring boards (PWBs), which are commonly composed of an inner ground and a power source layer and outer signal wiring layers. Recently, electromagnetic noise radiation from such PWBs has become a serious problem. Most of the noise radiation is attributed to high frequency currents up to several GHz excited in the inner ground and/or power source layer. In order to suppress such high frequency noise currents, however, it is not effective to mount the existing noise suppression parts such as impedance components or composite-type noise suppression sheets [1] on the outer signal wiring layers. We previously revealed that the Ni-Zn ferrite film kept high imaginary permeability even in the GHz range. The ferrite film of 3 μm thickness that was plated directly on a micro-strip line exhibited transmission attenuation power ratio (P_{loss} /P_{in}) exceeding 0.5 in the range of 2-8 GHz [2]. This means that the ferrite film sufficiently attenuated the GHz noise current. In the present study, we measured electromagnetic noise radiation from four-layered PWBs that incorporated ferrite films of 3 μm thickness plated directly on the inner ground or power source layers.

Experiments

Ferrite films $Ni_{0.2}Zn_{0.3}Fe_2O_4$ were deposited using spin-spray ferrite plating [2] directly on both sides of double-sided PWBs made of epoxy resin. Then the ferrite-plated PWBs were incorporated as the inner ground or the power layer into the following two different types of four-layerd PWBs (a) and (b). PWB (a), which was most commonly used structure, was composed of the outer signal layers and an inner ground and a power layer as illustrated in Fig.1. PWB (a) was composed of the outer signal layers, which contained the power supply lines as well, and two inner ground layers. On those PWBs, the following elements were mounted: a PLD (Programmable Logic Device) with a clock frequency of 75 MHz, four driver ICs (Integrated Circuits), resistors and capacitors. Electromagnetic noise radiation of 1-8 GHz were measured in an anechoic chamber for PWBs (a), (b) and those without ferrite films (PWBs (a') and (b')) when they were operated on the same condition.

Results and discussion

As shown in Fig.2, emission of radiated noise from the ferrite film-embedded PWB (a) was suppressed by 2 to 5 dB than that without the ferrite film (PWB(a')). This tendency became more prominent with increasing frequency. The similar noise suppression effect was also observed for the ferrite film-embedded PWB (b) by up to 4 dB. This suggests we can suppress noise radiation also in the case that the ground or the power plane are not placed symmetrically in the inner layers, meaning that there is a lot of flexibility in circuit designing of a power source layout. The noise suppression effect by the ferrite film observed for both PWBs (a) and (b) corresponded to the frequency dependence of P_{loss} /P_{in} due to magnetic loss characteristics in the film [2]. This confirmed that suppression of emission noise radiated from the four-layered PWB was attributed to the attenuation of GHz noise current in the ground and/or the power layer.

Conclusion

We successfully suppressed the electromagnetic noise in the GHz range radiated from multilayered PWBs by plating the ferrite films of 3 μm thickness directly on the inner ground and/or the power layer.

Acknowledgements

The authors would like to thank Mr. Yukihiko Kamata and Mr. Hiroshi Yoshida at Fenwal Controls of Japan, LTD. for their cooperation in fabricating PWBs and measureing the emmission noise.

[1] S. Yoshida, M. Sato, E. Sugawara and Y. Shimada, *J. Appl. Phys.* 85, 4636, 1999.

[2] K. Kondo, T. Chiba, H. Ono, S. Yoshida, Y. Shimada, N. Matsushita and M. Abe, *J. Appl. Phys.* 93, 7130, 2003.

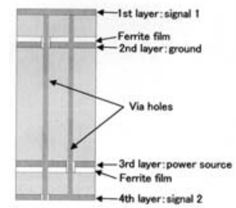

Fig.1 Cross section of four-layered PWB (a).

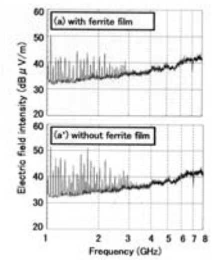

Fig.2 Noise radiation spectra of four-layered PWBs (a) and (a').

Fabrication of novel chip temperature sensing device using Mn substituted Li-Zn-Cu ferrite.

M. Naoe, M. Oishi, S. Okazaki, T. Sato, K. Yamasawa, Y. Miura
Spin Device Technology Center, Shinshu University, Nagano, Japan

Introduction

For local temperature sensing, the temperature telemeters by means of lumped elements using the conventional temperature sensitive ferrite were already reported [1]. However, it was difficult to integrate and miniaturize these lumped element temperature sensors, because of too low natural resonance frequency and resistivity of many conventional ferrites containing Fe^{2+} ion. This study describes a novel chip temperature sensing device using transmission-line technique with Mn substituted Li-Zn-Cu ferrite. The authors recently clarified remarkable temperature sensitivity of polycrystalline Mn substituted Li-Zn-Cu ferrites [2]. It was also found that such spinel ferrites have both large Snoek's product and high resistivity in previous study [3]. The transmission-line device using such ferrite substrate can be miniaturized by an increase of the operating frequency, and an integration of the lumped elements is attained simultaneously. Namely, our novel transmission-line device operates as an integrated *LC* resonance type temperature sensing device because such device has both temperature dependent distributed inductance and capacitance due to the ferrite substrate.

Device fabrication and experiments

Fig. 1 shows a schematic view of the fabricated chip temperature sensing device. Such device was attained by an introduction of spiral strip-line structure with Mn substituted Li-Zn-Cu ferrite substrate. 500 μm thick ferrite substrates were prepared by LTCC process. Spiral signal line and ground plane were formed by thin film process. An open-ended spiral line has total length of 130 mm, 3 μm thick, line/space of 50/50 μm, and spiral turns of 5. Its temperature dependence (T= –27 - 100°C) of frequency characteristics (f= 10 - 100 MHz) of input impedance was measured by using an impedance analyzer and a temperature controlled bath.

Results and discussion

Fig. 2 shows the frequency characteristics of input impedance of chip temperature sensing device in each ambient temperature. Frequency dependent input impedances exhibited double peaks in the range from 10 and 100 MHz. Since the chip device is an open-ended stub, it was considered that the minimal peaks around 30 - 40 MHz mean quarter wavelength $\lambda/4$ resonance and the maximal peaks around 40 - 65 MHz mean half wavelength $\lambda/2$ resonance, respectively. Both peaks decreased with an increase of temperature. A main cause is that complex permeability of ferrite substrate was increased by increasing temperature [2]. In order to consider a possibility of amplitude modulation type temperature sensing, the temperature dependence of input impedance in fixed excitation frequency was evaluated. Fig. 3 shows temperature dependent input impedance at 30.7, 41.5, and 65.4 MHz, respectively. With the temperature rise, the input impedance in fixed frequencies increased or decreased extremely like the PTC or the NTC thermistor because these dependencies were enhanced by $\lambda/4$ resonance or $\lambda/2$ resonance. For instance, input impedance at 41.5 MHz increased by 10.8 times in the range from –27 to 100°C. These results suggest a realization of the integrated chip temperature sensing device using temperature sensitive ferrite for high sensitive local temperature sensing.

[1] Y. H. Kim, S. Hashi, K. Ishiyama, K. I. Arai, M. Inoue, IEEE Trans. Magn., **36**, 3643 (2000).

[2] M. Naoe, T. Omura, T. Sato, K. Yamasawa, Y. Miura, Jpn. J. Appl. Phys., **47**, (to be published).

[3] T. Nakamura, T. Miyamoto, Y. Yamada, J. Magn. Magn. Mater., **256**, 340 (2003).

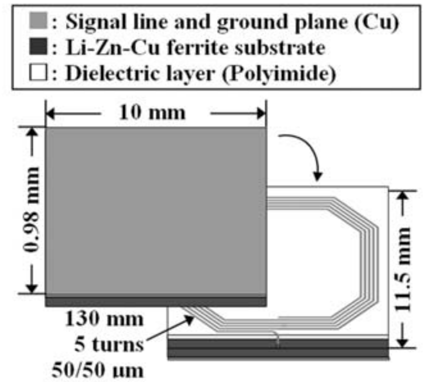

Fig. 1 Schematic view of chip temperature sensing device using spiral transmission-line technique and Li-Zn-Cu ferrite substrate.

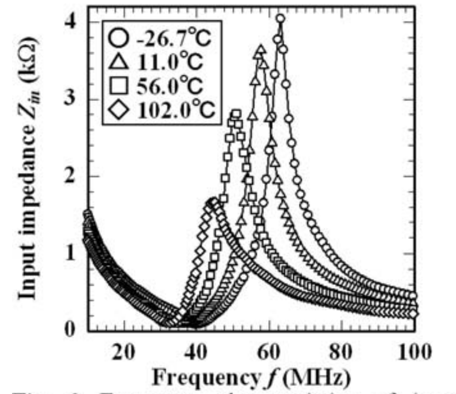

Fig. 2 Frequency characteristics of input impedance of chip temperature sensing device in each ambient temperature.

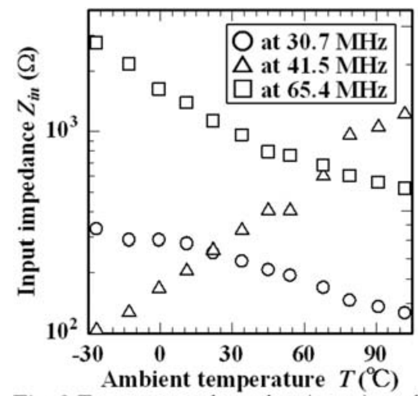

Fig. 3 Temperature dependent input impedance when the excitation frequency was fixed to 30.7, 41.5 and 65.4 MHz.

EU-11

Effect of Co-Z type ferrite on broadband antenna miniaturization.

J. Choi[1], K. Moon[1], J. Kim[1], I. Kim[2]
1. Metallurgy and materials engineering, Hanyang university, Ansan, South Korea; 2. Central R&D institute, Samsung eletro-mechanics Co. LTD., Suwon, South Korea

Introduction
Soft magnetic ferrites with a spinel structure have been extensively used in many surface mounting electronic devices because they show high permeability in radio frequency range, high electrical resistivity, good mechanical hardness and excellent chemical stability. Moreover, the production cost of these ferrites is very cheap compared with that of other magnetic materials. Unfortunately, these ferrites with a spinel structure cannot be used in devices operating in hyper frequency range (300-1000 MHz) [1.2], which is due to Snoek's limit. As such, Co2Z-type hexaferrites have been attracted much attention for microwave devices, especially a miniaturized antenna for digital broadcasting services such as digital video broadcasting-handheld (DVB-H) assigned from 170 MHz to 800 MHz.
In this experiment, the effects of the substitution of divalent ions (Zn at Co or Fe site and Fe at Co site) on the initial permeability of Co2Z-type ferrite were investigated. In addition, we analyzed the feasibility of miniaturized antennae using various Co2Z-type hexaferrites as a substrate.
Experimental Procedures
Co2Z-type hexaferrite with the nominal molecule composition of Ba3Co2Fe24O41 was fabricated by a solid state reaction method. BaCO3, Co3O4, α-Fe2O3 and ZnO powders, which were weighed according to the composition, were used as raw materials. These powders with de-ionized water were milled for 24 hr using zirconia balls. The ball-milled powder mixtures were dried at 100°C and then calcination was performed at 1200~1300°C in O2 atmosphere. The calcined powders were re-ground (2nd ball milling) for 30 hr. Before finishing the 2nd ball milling, polyvinyl alcohol (PVA) was added as a binder. These powders were granulated through a 0.12 mm sieve and then were pressed by 3 t/cm2 to form sheets, pellets (10mm) and toroidal shape samples (outer diameter:8mm, inner diameter:3mm). Finally, these samples were sintered in O2 atmosphere at 1200~1300°C
The crystal structure and phase identification of hexaferrites were analyzed by X-ray diffractometer (XRD, Rigaku D/MAX-2500) with Cu-Kα radiation. Morphologies and microstructures of the hexaferrites were observed by a scanning electron microscope (SEM, Jeol, 6330F). The density was measured by an Archimede's method. The magnetic properties were measured by a vibration sample magnetometer (Toei VSM-5) and an impedance network analyzer (HP 4291A). For the estimation of antenna characteristics, HFSS simulator (Ansoft, v. 9.2) has been used.
Results and Discussions
A tapered slot antenna with a size of 30 mm × 10 mm × 2.4 mm was fabricated as depicted in Fig. 1(a). Various synthesized Co2Z-type ferrites were used as the substrate of the antenna. The measured voltage standing wave ratio (VSWR) of the antenna with a Ba3Co2Fe24O41 ferrite (μ=6) substrate is presented in Fig. 1 (b). As shown in the figure, the band gap (VSWR<3) of this antenna is ~ 500 MHz but the maximum gain is obtained at 1.16 GHz. According to the specification of a Nokia 7700 sized terminal, it was reported that the realized gain of a DVB-H antenna was -10 to – 7 dBi in the frequency range of 470 - 702 MHz [3]. Thus this peak position is too high to apply to a broadband antenna such as DVB-H antenna.
In order to overcome the above problem, increasing permeability is known to be an effective method [4]. As shown in Fig. 2, the substitution of divalent ion (Zn, Fe) in Co2Z-type ferrite effectively increases the initial permeability. In particular, the initial permeability reaches 20 in Ba3Co2Fe23.7Zn0.3O41 ferrite. In a tapered slot antenna using this modified sheet, HFSS simulation results show that the peak position appears at 500 MHz with a bandwidth of 300 MHz. This indicates that modified Co2Z type ferrite can apply to a miniaturized broadband antenna.

[1] M. Yamaguchi, S. Arakawa, and K.I. Ari, IEEE Trans. Magn. 28 (1992), 3015.

[2] K. Kawabe, H. Koyama, and K. Shirae, IEEE Trans. Magn. 20 (1984), 1804.

[3] J. Holopainen, Antenna for handheld DVB-H terminal, master's thesis, Helsinki University of Technology, (2005)

[4] D.R. Jackson and N. G. Alexopoulos, IEEE Trans. Antennas Propagat. 39, 407 (1992).

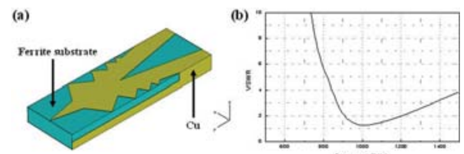

Figure. 1 (a) Design of tapered slot antenna and (b) VSWR changes as a function of frequency

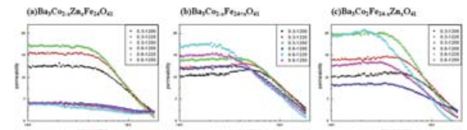

Figure. 2 Frequency dependence of initial permeability(x = 0.3, 0.6).

EV-01

Enhancement of magnetostriction in internally-biased Terfenol-D 2-2 composites.

L. Garcia-Gancedo[1], *S. C. Busbridge*[2], T. W. Button[1]
1. IRC in Materials Processing, School of Engineering, University of Birmingham, Birmingham, United Kingdom; 2. School of Environment and Technology, University of Brighton, Brighton, United Kingdom

Introduction:

Terfenol-D has excellent room temperature magnetomechanical properties, but its frequency range of applications is limited to a few kHz by eddy current effects [1]. Self-biased Terfenol-D 2-2 composites with laminations perpendicular to the [112] crystallographic direction and internal magnetic field along [112] improve the magnetomechanical performance of Terfenol-D by reducing the eddy current losses at high frequencies (via electrically insulated metallic layers) [2]. However the inclusion of non Terfenol-D layers within the composite is detrimental for its overall magnetostriction [3]. In this paper we investigate the effects on magnetostriction of the incorporation of different permanent magnetic materials layers within the composites.

Experimental results:

Seven composites formed by Terfenol-D, insulating material and permanent magnetic material were produced with different layer thicknesses of materials by alternatively bonding the layers of Terfenol-D and permanent magnet with the insulating material. Neodymium-Iron-Boron has been chosen as permanent magnetic layer due to its higher energy product, remanent magnetisation and coercive fields than all the other permanent magnets discovered so far. The internal magnetic field provided by the magnet layers ranges from 17 kA/m to 53 kA/m for the composites with lower and higher content of NdFeB respectively. Magnetostriction at the edges of the composites was measured using typical strain gauges techniques and was found to be between 600 and 800 ppm. The strain at the central region of the composites was measured using interference microscopy and was found to be up to 8% lower than at the edges.

Theoretical analysis:

Finite Element Analysis (FEA) of the magnetostriction of such composites has been carried out using the commercial package ABAQUS. Cubic elements of side length 40 µm were used for calculations, although it was found that the element size has little influence on the results as long as there are a sensible number of divisions. Comparison between experimental and theoretical results at the edge of three composites is shown in Figure 1, where it can be seen that the agreement between experiments and theory is better than 95%. The FEA has shown that the magnetostriction within the Terfenol-D layers effectively increased between 75 and 200 ppm (for the composites with lowest and highest internal fields, respectively) with respect to the bulk material, although the high elastic modulus of the $Nd_2Fe_{14}B$ and its nearly zero magnetostriction is detrimental for the overall strain of the composite. Therefore Alnico or Samarium-Cobalt could be better choices as permanent magnetic layers due to their elastic modulii are lower than that of $Nd_2Fe_{14}B$.

FEA and optimisation of strain has been carried out using different permanent magnetic materials. Table 1 shows the main magnetic and mechanical properties of the permanent magnetic materials used for the simulation. The internal field provided by the Alnico and Samarium-Cobalt is slightly lower than that provided by $Nd_2Fe_{14}B$, due to their poorer magnetic properties. A comparison of the strain at the edge of a composite with Terfenol-D, permanent magnetic layer and insulating layer thicknesses of 280 µm, 200 µm and 40 µm, respectively is shown in Figure 2. It can be seen that choosing Alnico as the permanent magnetic material layer produce the highest strains due its good magnetic properties and low elastic modulus and therefore improved magnetomechanical performance is also expected.

This work was supported in part by the European Union (Interreg IIIa, grant number 349)

[1] D. Kendall et al., J. Appl. Phys. (73), pp. 6174, 1993.

[2] L. G. Gancedo et al., IEEE Trans. Magn. (41), pp. 2781, 2005.

[3] L. Garcia-Gancedo et al., J. Mag. Magn. Mat.(310), pp. 2627, 2007

Material	Composition	Remanence, B_r (T)	Coercivity, H_C (kA/m)	Elastic Modulus (GPa)	Poisson's Ratio
Alnico	46% Fe, 24% Co, 14% Ni, 10% Al and 6% Cu	1.25	45	90	1
Samarium Cobalt	$SmCo_5$	0.90	875	110	0.5
	Sm_2Co_{17}	1.03	1160	150	0.8
Neodymium iron boron	$Nd_2Fe_{14}B$	1.29	955	200	0.24

Table 1. Main magnetic and mechanical properties of Alnico, Samarium Cobalt and Neodymium iron boron

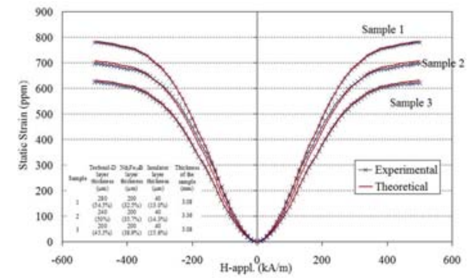

Figure 1. Comparison between experimental and simulated results for three composites with different layer thicknesses.

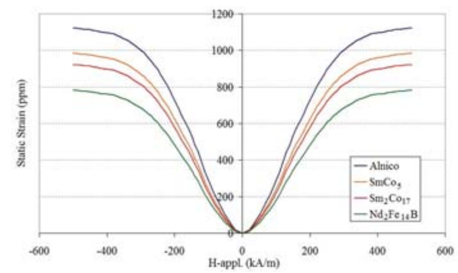

Figure 2. Simulated strain at the edge of a composite with Terfenol-D, permanent magnetic layer and insulating layer thicknesses of 280 µm, 200 µm and 40 µm respectively, where the permanent magnet is either Alnico, $SmCo_5$, Sm_2Co_{17} or $Nd_2Fe_{14}B$

EV-02

Magnetoelastic properties of Tb-Dy-Ho-Fe-Co alloys.

I. Tereshina[1], G. Burkhanov[1], O. Chistyakov[1], S. Nikitin[2], G. Politova[2]
1. Baikov Institute of Metallurgy and Material Science RAS, Moscow, Russian Federation; 2. Faculty of Physics, M.V. Lomonosov Moscow State University, Moscow, Russian Federation

The rare earth – iron intermetallics RFe_2 ($MgCu_2$–type Laves phase structure) are widely known as the most important class of magnetostrictive materials which show great potential for application in actuators and tranducers [1, 2]. In order to obtain benefits from the technical employment of magnetostrictive alloys, it is important to provide high values of magnetostriction λ at room temperature under an action of relatively small magnetic fields (in other words, alloys should have high values of magnetostrictive susceptibility $\Delta\lambda/\Delta H$).
The purpose of the present work was synthesis of novel magnetostrictive materials $Tb_xDy_yHo_zFe_2$ ($x + y + z = 1$) and $Tb_{0.23}Dy_{0.27}Ho_{0.5}Fe_{2-x}Co_x$ ($x = 0 - 2$) in high-pure state which posses high values of both: saturation magnetostriction and magnetostrictive susceptibility within the given interval of magnetic fields and temperatures. The complex investigation of the crystal structure, magnetic and magnetoelastic properties, determination of the main regularities of formation of high magnetostrictive characteristics depending on the composition, and also determination of the optimal compositions of the compounds were done.
First, regimes of purification of rare-earth (RE) metals using vacuum sublimation (for Dy and Ho) and distillation (for Tb) have been worked out; certification of the purified metals was performed using laser mass spectrometry. The synthesis of five samples of quasi-ternary $Tb_xDy_yHo_zFe_2$ system was performed using obtained high-purity rare-earth metals by arc melting in a helium atmosphere using a water-cooled copper bottom and non-consumable tungsten electrode. Prepared compounds were certified using metallographic and X-ray fluorescence analysis and X-ray diffraction. A combined analysis of magnetic properties by means of traditional magnetometric methods as well as ^{57}Fe Mössbauer spectroscopy was also performed. Magnetostriction was measured in magnetic fields up to 10 kOe and in 80 – 400 K temperature range by means of the strain-gauge method. Strain gauges were glued on their surface of the disk-shaped (d = 6 mm, h = 2 mm) samples. Magnetostriction measurements were performed in magnetic field applied along the axis of the gauge (longitudinal magnetostriction $\lambda_{\|}$).
Table 1 shows values of the saturation magnetostriction and magnetostrictive susceptibility of $Tb_xDy_yHo_zFe_2$ system at room temperature.
Detailed analysis of our results and available literature data [3, 4] showed that there are two pronounced maxima on the concentration dependencies of both saturation magnetostriction and magnetostrictive susceptibility in the range of concentrations of holmium: z = 0.25 - 0.3 and z = 0.5 - 0.6, respectively. Thus, the contribution to the magnetocrystalline anisotropy (MCA) energy from the rare-earth sublattice was minimized due to combination of rare-earth elements with different signs of MCA constants. A substitution of cobalt atoms for iron led to a decrease of the contribution to MCA from the 3d transition metal sublattice due to the fact that Fe and Co single-ion constants have different signs. Eleven samples of $Tb_{0.23}Dy_{0.27}Ho_{0.5}Fe_{2-x}Co_x$ (x = 0; 0.1; 0.2; 0.4; 0.6; 0.8; 1; 1.2; 1.4; 1.6; 2.) system were prepared and certified as showed before.
It was established that the unit cell volume and the value of longitudinal magnetostriction in $Tb_{0.23}Dy_{0.27}Ho_{0.5}Fe_{2-x}Co_x$ decrease monotonously with Co content increase. Concentration dependencies of Curie and spin-reorientation transition temperatures, saturation magnetization and the mean value of hyperfine field of Fe atoms demonstrate a non-monotonous behavior. It was found that $Tb_{0.23}Dy_{0.27}Ho_{0.5}Fe_{2-x}Co_x$ compounds with x = 1.3 have the maximum value of magnetostrictive susceptibility at room temperature, where the magnetic anisotropy is compensated in the rare-earth as well as in the 3d transition metals sublattice. Our investigations demonstrate the positive role of substitutions of Co for Fe in the improvement of magnetostriction properties in $RR'R''(Fe,Co)_2$

[1] A.E. Clark, in: E.P. Wohlfarth (Ed.), Ferromagnetic Materials, vol. 1, North-Holland, Amsterdam, 1980, 531 p.

[2] K.P. Belov, Magnetostriction Phenomena and and their Technical Application, Moscow, Nauka, 1987, 159 p. (in Russian).

[3] A.S. Ilyushin, Introduction to the Structure Physics if Rare Earth Intermetallic Compounds, Moscow, Publ. House MSU, 1991, 176 p. (in Russian).

[4] M. Wun-Fogle, J.B. Restorff, A.E. Clark, J.F. Lindberg, J. Appl. Phys., 83 (1998) 7279.

x	y	z	$\lambda_{\|}$, 10^{-6}	$\Delta\lambda_{\|}/\Delta H$, 10^{8} Oe^{-1}
0.3	0.7	0	850	27
0.37	0.5	0.13	750	33
0.4	0.43	0.17	740	35
0.32	0.4	0.28	700	35
0.23	0.27	0.5	620	38

EV-03

Modeling of bimorph type cantilever for actuators.

G. Yun[1,2], B. Narsu[1]

1. department of physics, inner mongolia university, Hohhot, China; 2. department of physics, inner mongolia normal university, Hohhot, China

A cantilever system fabricated by combining giant magnetostricitve films(GMFs) and nonmagnetic substrate (NMS) produces a class of multi-functional microelectromechanical system (MEMS) devices [1]. A series of works had devoted to model the behaviors of such a GMF-NMS system as sensors and actuators in the last decades [1-3]. But most of works have encountered some difficulties to predict and optimize the cantilever actuator [4, 5]. Recently, Honda et al. [6] prepared a versatile structure of Polyimide cantilever which TbFe film and SmFe film are coated on both surfaces of the substrate. This TbFe/Polyimide/SmFe can be applied as micromotors and micropumps. However, such development on the device fabrication requires the theoretical modeling to achieve more realistic and optimal configuration in the application.

The purpose of this work is to present a valid and efficient theory for the trilayer cantilever that consists of GMF1/NMS/GMF2, where GMF 1 and 2, respectively, with positive and negative magnetostriction constants. Especially, the difficult problems of cantilever modeling, mechanical features and optimal conditions of the trilayer cantilever for actuator application are mainly considered and resolved.

The results indicate, when the thickness of the GMF1 is kept constant, thicker substrate and GMF2 will result in larger force exerted outside (Figure 1a), namely the ability of taking load is swelled. At the same time, the free end exerted force will increase with the increasing stiffness of GMF2. And the exerted force of the trilayer cantilevers of GMF1/NMS/GMF2 is always greater than the bilayer ones of GMF1/GMF2 or GMF/NMS. But for the case where the total thickness of the trilayer cantilever is kept constant, the free end exerted force will experience a maximum as a function of the GMF2-to-GMF1 thickness ratio (Figure 1b). Furthermore, the maximum value of force exerted will reduce with the increasing substrate thickness and GMF2-to-GMF1 stiffness ratio, while the optimal thickness ratio corresponding to the maximum value of the exerted force is an increasing function of the stiffness ratio (Figure 2b and Figure 3).

Generally, in the case of fixed substrate thickness, in order to obtain larger exerted force of the trilayer cantilever, the substrate should be made of harder materials, and the films be thicker and softer. And while for the case of the total thickness is kept constant, however, the substrate should be made of thinner and softer materials, and the films be harder and the GMF-to-GMF thickness ratio should be designed at the optimal thickness ratio for the maximum exerted force.

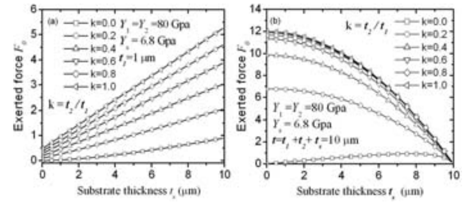

Figure 1: Influence of the sublayer thickness on the cantilever exerted force, Here Y, t and k respectively stand for elastic modulus, sublayer thickness and the thickness ratio. (a) substrate thickness fixed cantilever; (b) total thickness fixed cantilever.

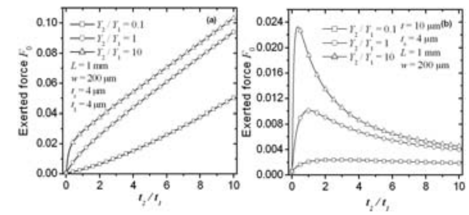

Figure 2: Influence of the sublayer elastic modulus (Y) on the cantilever exerted force. Here L and w respectively stand for length and width of the cantilever. (a) Substrate thickness fixed cantilever; (b) total thickness fixed cantilever.

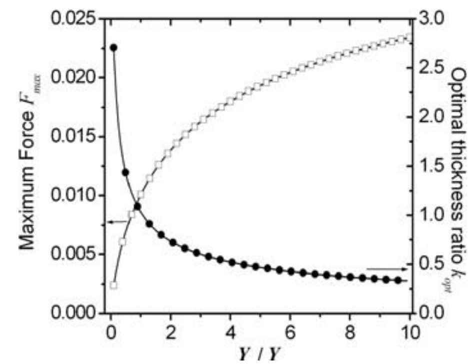

Figure3: Maximum force (left) and optimal thickness ratio (right) Vs. ratio of elastic modulus (Y2/Y1) for total thickness fixed cantilever.

[1] V. H. Guerrero and R. C. Wetherhold, J. Appl. Phys. 94 (2003), pp. 6659-6666; J. Magn. Magn. Mater. 271 (2004), pp.190-206.

[2] E. du. Tremolet de Lacheisserie and J. C. Peuzin, J. Magn. Magn. Mater. 136(1994), pp 189-196.

[3] R. Watts, M. R. Gibbs and J. Karl, Appl.Phys.Lett. 70 (1997), pp.2607-2609.

[4] V. Iannotti, G. Ausanio, C. Hison and L. Lanotte, J. Appl. Phys. 97 (2005), pp.104516-1-20.

[5] B.Narsu, Guohong Yun and Jianhong Rong, Sci. China: Ser E, 37 (2007), pp.914-922.

[6] T. Honda, K. I. Arai and M. Yamaguchi, J. Appl. Phys. 76 (1994), pp.6994-6999.

EV-04

Microstructure and magnetic properties of Fe-Ga composite.

K. Perduta[1], S. Busbridge[1], M. Nabialek[2]
1. School of Engineering, University of Brighton, Brighton, United Kingdom; 2. Institute of Physics, Czestochowa University of Technology, Czestochowa, Poland

Introduction

It has been recognized that substituting about 20 at.% of non-magnetic Ga for Fe in bcc solid solution results in a ten-fold increase of the magnetostrictive constant to 270 ppm in directionally solidified polycrystalline samples [1], and to 350 ppm in quenched single crystal [2]. The alloys of Fe and Ga may be useful in magnetostrictive actuators and sensors due to their large saturation magnetostriction at low saturation fields, high mechanical strength and good ductility [1, 3]. Eddy current losses are problematic at frequencies above 1 kHz. A solution to this problem is to embedded the magnetic particles in a non-conducting binder to create a composite. Epoxy-bonded Fe-Ga composites possess additional benefits of reduced eddy-current losses and low material cost.

In this work, we report the microstructure and magnetic characteristics of epoxy-bonded Fe-Ga particulate composite with different grain size.

Experiment, results and discussion

$Fe_{80}Ga_{20}$ alloy ingots each with a mass of ~15 g were prepared by arc-melting high purity elements. The bulk samples were initially crushed. Composite particles were obtained by blade-milling in an argon atmosphere and sieving to powders with three different size ranges: 20-50, 50-100 and 100-200 μm. The powders were then mixed with an epoxy binder and compressed under a pressure of 120 MPa along the shortest dimension to obtain rectangular samples of dimensions 7-10 mm x 10 mm x 40 mm. Compaction was carried out without an applied magnetic field. Volume fractions of Fe-Ga powder used was nominally 0.80.

Fe-Ga alloys exhibit a strong correlation between the structure and magnetoelastic properties and it is commonly believed that the formation of an ordered $D0_3$ phase, as the amount of Ga atoms approaches 25 at.%, has a detrimental effect on magnetostriction. X-ray diffraction does not show superlattice peaks, but only peaks originating from the disordered bcc structure. The absence of long range order in investigated samples is confirmed by Mössbauer studies.

The magnetic hysteresis loops for the bulk alloy, powders with different grains size and composites (Fig. 1) show little coercivity (H_c) and remanence, reflecting low anisotropy at room temperature. The tendency of the saturation magnetization to decrease with decreasing particle size (from M_s = 172 emu/g for the largest grain size to M_s=159 emu/g for the smallest ones) may be caused by the increasing surface area to volume ratio because the saturation magnetization at the surface is expected to be lower than that of the bulk alloy. M_s for the composites is less then for powders because the volume fraction of Fe-Ga is only 80 %. H_c shows the opposite behaviour with decreasing grain size and varies from 35.4 G for the largest grain size to 69.7 G for the grain size range from 20 to 50 μm. For bulk alloy H_c is an order of magnitude lower with a value of 3.4 G.

The highest saturation magnetostriction λ_s=360 ppm is obtained for composites whose grain size varies from 50 to 100 μm. The maximum value of λ_s for composites with the largest grains is slightly smaller (330 ppm). However, these samples show magnetostriction hysteresis, which is not observed in composites with the smallest grains (λ_s= 100 ppm) and for bulk alloy (λ_s= 70 ppm). We believe that the magnetostriction hysteresis may be associated with mechanical connection between the matrix and the Fe-Ga particles. In order to explain this effect we have observed the magnetostriction as a function of time from 80 s to 3000 s (Fig. 2). Longer measurement times should allow stresses in the epoxy-matrix to relax stresses so that changes occurring in the particles can be observed.

This work had been supported by the European Union (Interreg IIIa grant number 349).

[1] N. Srisukhumbowornchai, S. Guruswamy, J. Appl. Phys. **90** (2001) 5680

[2]. J. R. Cullen, A. E. Clark, M. Wun-fogle, J. B. Restor, and T. A. Lograsso, J. Magn. Magn. Mater. **226-230**, 948 (2001)

[3] A. E. Clark, K. B. Hathaway, M. Wun-Fogle, J. B. Restorff, T. A. Lograsso, V. M. Keppens, G. Petculescu and R. A. Taylor, J. Appl. Phys. **93**, 8621 (2003)

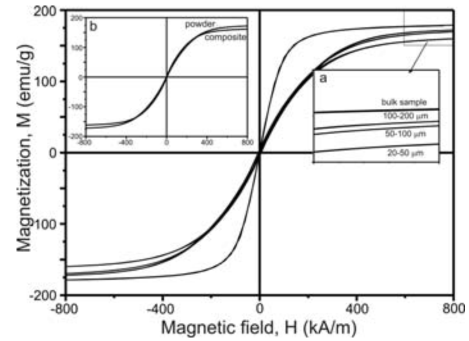

Fig.1. Hysteresis loops obtained for bulk sample and powders with three different size ranges: 20-50, 50-100 and 100-200 μm. In the insets there are: magnification of selected area (a) and hysteresis loops obtained for powder with grain size range 100-200 μm and composite made of them (b)

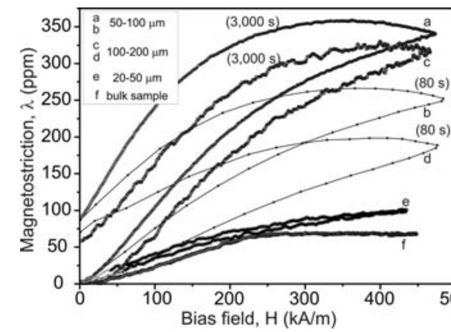

Fig.2. Magnetostriction curves for bulk sample and composites with three different size ranges: 20-50, 50-100 and 100-200 μm

EV-05

Giant Magnetostriction on the Metamagnetic Transition of the Ho_5Ge_4

A. M. Pereira[1], P. Algarabel[2], C. Sacristan[3], L. Morellon[2,3], C. Magen[4], M. R. Ibarra[2,3], J. B. Sousa[1], J. P. Araujo[1]

1. IFIMUP Faculdade de Ciências da Universidade do Porto, Porto, Portugal; 2. ICMA - Universidad de Zaragoza and Consejo Superior de Investigaciones Científicas, Zaragoza, Spain; 3. Instituto de Nanociencia de Aragón, Universidad de Zaragoza, Zaragoza, Spain; 4. Oak Ridge Natl Lab, High Temp Mat Lab, Oak Ridge, TN

Magnetostriction (MS) is defined as a deformation of a crystallographic mesh in magnetic materials when they acquire magnetization. The first magnetostrictive materials used as sensors or actuators were compounds with nickel, iron, and permalloy technologically applied on telephone receivers [1], hydrophones, and scanning sonars [2]. These materials exhibit bulk saturation strains up to 100 ppm.

Currently Terfenol-D is the material usually used for technological applications with many scholar papers and commercial patents. Examples of successful sensor designs include hearing aids, load cells, accelerometers, proximity sensors, torque sensors, magnetometers and many more [3-5].

More recently, the discovery on the $R_5(Si,Ge)_4$ system of a colossal MS [6] and other large magnetic effects, intensified the research on these family of compounds. This colossal MS (and other effects) is related with the martensitic-like transition which exhibits a colossal magnetic field-induced volume strain. Additionally, such strain can be induced thermally namely in the $Gd_5Si_2Ge_2$ and $Tb_5Si_2Ge_2$ compounds with an induced strain as high as ~10000 ppm along the crystallographic a axis of a single crystal [7,8]. These properties make them ideal candidates for replacement of materials currently used in actuators like Terfenol-D where linear strain is limited to ~2000 ppm and volume strain is close to zero.

Another type of MS was found in Gd_5Ge_4 compound which presents large MS at low temperatures when an external magnetic field or external pressure is applied, changing the system from AFM (antiferromagnetic) to FM (ferromagnetic), with a simultaneous change of structure from O(II)-Gd_5Ge_4 type to the O(I)-Gd_5Si_4 type. In the present work, we show that Ho5Ge4 compounds exhibit a similar behaviour as Gd5Ge4, at low temperatures. MS(H) and M(H) simultaneous measurements under dc magnetic field using the extensometers method (strain gauge technique) in a SQUID magnetometer (H_{max}=5T) were performed and extended to magnetic fields up to 27T (pulsed field).

The MS results are shown in Figs 1 a) and b), for the pulsed magnetic fields and DC magnetic field, respectively. For temperatures below T_{SR}~18K, the MS behaviour shows a critical increase at Hc ~ 2 T reaching strain saturation around MS=1700 ppm (at H=5T). The nature of this magnetostriction is related with a metamagnetic transition from a low magnetization state to a high magnetization state, also confirmed by our magnetization measurements.

Microscopically, this large spontaneous MS is probably related with the interactomic distance changes due to the formed covalent bond dimmers between Ge-Ge atoms (like in the Gd_5Ge_4), which increases the electronic charge corresponding to a direct change of the exchange interactions (RKKY), leading to the magnetic transition.

For temperatures above T_{SR} and below T_N~25K, the MS presents a smoother MS curve (without criticality) with a linear H dependence for high magnetic field and with higher MS values, developing a strong forced MS.

Above T_N, the MS behaviour starts to decrease, being negligible for T=40K until H=5T.

In the perpendicular configuration (applied magnetic field perpendicular to the longitudinal strain gauge filament) measurements (not shown) present a drastic decrease of MS saturation revealing large anisotropy effects in this compound. The volume change found was of $\Delta V/V$~ 600 ppm and λ_t=800 ppm for shape MS.

The simultaneous measurements of M(H) and MS(H) allow to infer about the correlation between both quantities. Our analysis of MS(H) and M(H) reveal quadratic dependence (MS(H) ~ CM^2) in the PM regime.

We will also discuss the absence of magnetic histeresis in both measurements, which is an important aspect for technological applications.

[1] F.V. Hunt, Electroacoustics: The Analysis of Transduction, and its Historical Background, (American Institute of Physics for the Acoustical Society of America, 1982).

[2] "The design and construction of MS transducers," Summary of Technical Report of Division 6, NDRC, Volume 13, 1946.

[3] "A Terfenol-D based magnetostrictive diode laser magnetometer," R. Weber and D. Jiles, U.S. Department of Commerce, grant ITA 87-02, 1992.

[4] T. Kobayosi, Repts of the Aeronautical Institute of Tokyo University, 52 1929.

[5] E. du Tremolet de Lacheisserie, MS Theory and applications of magnetoelasticity, (CRC Press, Inc., Boca Raton, 1993).

[6] Nersesse Nersessian, Siu Wing Or, Gregory P. Carman, Scott K. McCall, Wonyoung Choe, Harry B. Radousky, Mike W. McElfresh, Vitalij K. Pecharsky and Alexandra O. Pecharsky, Appl. Phys. Lett., (85) 4801-4803 2005

[7] C. Magen, L. Morellon, P. A. Algarabel, M. R. Ibarra, Z. Arnold, J. Kamarad, T. A. Lograsso,

D. L. Schlagel, V. K. Pecharsky, A. O. Tsokol, and K. A. Gschneidner, Jr., Phys. Rev. B, (72) 024416 2005

[8] V. O. Garlea, J. L. Zarestky, C. Y. Jones, L.-L. Lin, D. L. Schlagel, T. A. Lograsso, A. O. Tsokol, V. K. Pecharsky, K. A. Gschneidner, Jr., and C. Stassis Phys. Rev. B (72) 104431 2005.

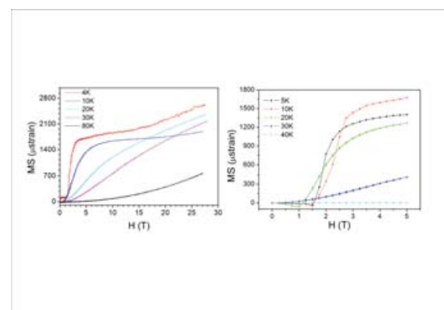

Fig.1 - Magnetostriction measurements: a) Pulsed magnetic field b) dc magnetic field.

EV-06

Voltage controlled magnetic properties of polycrystalline Terfenol-D film on PMN-PT single crystal substrate.

J. Kim, V. Ravindranath, S. Shin
Physics, KAIST, Daejeon, South Korea

To achieve ultra-high density integration in a magnetic random access memory (MRAM), suitable data recording and retrieval methods have to be determined. There were some studies for overcoming limitation of the conventional method of data recording using a magnetic field obtained from a current carrying conductor. Electric-write and magnetic-read memory device using magnetoelectric coupling between magnetic and electric properties have been proposed.[1] The a method of controlling the direction of magnetization easy axis using voltage has been reported in the Pd/Co1-xPdx/PZT/Pt/MgO heterostructures.[2] In the present work, we report a considerable change of magnetic anisotropy in Terfenol-D film on PMN-PT single crystal substrates for the study of voltage-control of magnetization easy axis.

Terfenol-D film was deposited on commercially available 300-um PMN-PT single crystal substrate with d33 value of 1500 pm/V by DC magnetron sputtering method. 10-nm thick polycrystalline terfenol-D film was grown at a sputtering power of 50 W, 5 mTorr Ar pressure at 300°C substrate temperature. After deposition, the film was annealed in a magnetic field applied in a direction perpendicular to the film plane for 20 min and cooled to room temperature. A Pt capping layer with a thickness of 3 nm was then deposited on Terfenol-D to prevent oxidation. Polar magneto-optical Kerr effect measurements were carried out with a 45°incident laser beam by using a photoelastic-modulator method. A voltage was applied using function generator and voltage amplifier across the PMN-PT substrate by Au electrode attached to the backside of substrate and the Pt capping layer. The Kerr ellipticity hysteresis loops of Terfenol-D film have been investigated in the presence of stress produced by the inverse piezoelectric effect of the PMN-PT substrate.

Fig. 1 presents the Kerr ellipticity hysteresis loops of the Terfenol-D/PMN-PT film. Each loop was measured at a given dc voltage shown in the inset of fig. 1. Fig. 2 shows variation of squareness and coercivity as function of applied voltage can be obtained from fig. 1. A change in coercivity from 240 Oe to 420 Oe and change in squareness from 0.45 to 0.9 have been observed. Both plotted graphs in fig. 2 show a similar butterfly loop. Considering the fact that the strain hysteresis curve of PMN-PT substrate shows well-known butterfly shape, the change of magnetic anisotropy of Terfenol-D film must be due to stress from PMN-PT substrate. The electric field induced stress changes in magnetoelastic energies given by . when voltage is increased from 0 V, PMN-PT substrate produce tensile stress. As a result, perpendicular mangetic anisotropy (PMA) of Terfenol-D film is decreased. On the other hand, when voltage is increased above electric coercivity field of PMN-PT (~90 V), PMA of Terfenol-D film is increased. It is clear that this large magnetoelectric effect in this system comes from the interplay between magnetostrictive property in Terfenol-D film and piezoelectric property of PMN-PT substrate.

[1] W. Eerenstein, N. D. Mathur1 and J. F. Scott, Nature 442, 759-765 (2006)

Fig. 1. Polar Kerr Ellipticity hysteresis loops at several electric field.[2] Jeong-Won Lee, Sang-Kook Kim and Sung-Chul Shin, Appl. Phys. Lett. 82 2458 (2003)

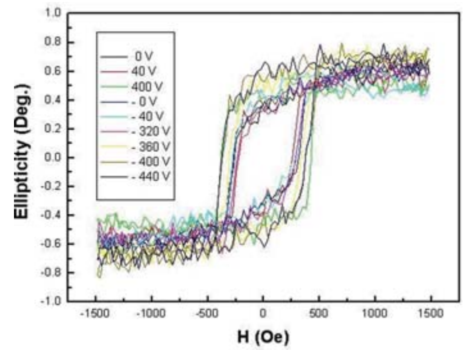

Fig. 1. Polar Kerr Ellipticity hysteresis loops at several electric field

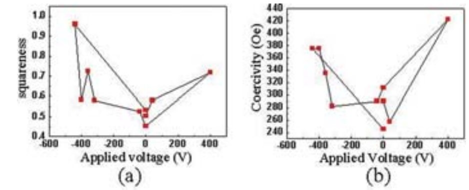

Fig. 2. (a) squareness (b) Coercivity of the polar Kerr Ellipticity hysteresis loop as function of applied voltage.

EV-07

Study of giant magnetostrictive acceleration sensors.

R. Yan[1], *Q. Yang*[1], W. Yang[1], S. Hou[1,2], F. Liu[1], W. Yan[1]
1. Hebei University of Technology, Tianjin, China; 2. Tianjin University of Commerce, Tianjin, China

I.INTRODUCTION

The rare-earth iron giant magnetostrictive material can be used to convert magnetic energy into mechanical energy and vice versa [1]. If an external force is applied onto magnetostrictive material, the magnetic status of the material will vary. This phenomenon is known as the inverse magnetostrictive effect or the Villari effect. This coupling between the magnetic and mechanical status of the material provides a capability of transduction, which can be utilized in a variety of ways [1-2]. According to the inverse magnetostrictive effect, a novel acceleration sensor can be developed using the giant magnetostrictive material. Compared with the other types of acceleration sensors, the giant magnetostrictive acceleration sensor has obvious advantages, such as high antiinterference resistance, withstanding heavy load, long service life, ability for working on adverse circumstances, and so on, which make them have more and more applications in the vibration detection field of aerospace industry, vehicle, chemical industry, civil engineering, and mechanical industry, etc [3]. In order to design and optimize giant magnetostrictive acceleration sensors effectively, it is necessary to found an accurate model, including the nonlinearities and the magneto-mechanical coupling. However, a little work on modeling of giant magnetostrictive acceleration sensor can be found. In this paper, a magneto-mechanical strong coupled model for input-output characteristics of magnetostrictive acceleration sensor has been founded.

II.A MAGNETO-MECHANICAL STRONGLY COUPLED MODEL FOR THE GIANT MAGNETOSTRICTIVE ACCELERATION SENSOR

Fig.1 shows a giant magnetostrictive acceleration sensor. When a force brought by acceleration exerts on the magnetostrictive rod, magnetic field in it will change. Magnetic flux density in the gap changes with the applied acceleration. Using a Gaussmeter, the magnetic flux density in the gap can be measured, then we can know the applied acceleration on the magnetostrictive sensor.

According the finite element method, it is necessary to give a functional of the sensor and then minimize it. The total energy of the sensor system includes elastic energy, work of external forces, magnetic field energy, potential energy of magnetic field boundary, mutual magnetoelastic energy and magnetocrystalline anisotropy energy. As for the Dirichlet condition, potential energy of magnetic field boundary is zero. If the giant magnetostrictive material is considered isotropic, the anisotropy energy is negligible.

The mechanical field boundary should be the contour of the magntostrictive sensor. In computing, neglecting the distortions of the rest parts of the sensor, the domain enclosed by the surface of the magntostrictive rod can be considered as the computed domain of the mechanical problem. In computation of the magnetic field, the magnetic vector potential is introduced.

Minimizing the functional of the sensor for each and every unconstrained vertex potential, we can obtain the magnetic vector potential and displacement vector. And then we can know the relation between magnetic flux density in the gap and applied acceleration on the sensor.

III.COMPUTED AND EXPERIMENTAL RESULTS

According to the magneto-mechanical strong coupled model for giant magnetostrictive sensors, the relation between magnetic flux density in the gap and applied acceleration on the sensor is calculated. In order to validate the presented model, it is necessary to measure the input-output relation of the sensor. The calculated and measured results are shown in Fig. 2. From Fig. 2, it can be seen that the calculated results is in agreement with experimental ones. Therefore the presented model in this paper is valid.

[1]D. C. Jiles, "Theory of the magnetomechanical effect," J. Phys. D: Appl. Phys., vol. 28, pp. 1537-1546, 1995.

[2]Toshiyuki Ueno, Jinhao Qiu, and Junji Tani, "Magnetic force control based on the inverse magnetostrictive effect," IEEE Trans. Magn., vol. 40, no.3, pp. 1601-1605, May 2004.

[3]Frederick T. Calkins, Alison B. Flatau and Marcelo J. Dapino, "Overview of magnetostrictive sensor technology," Collection of Technical Papers - AIAA/ASME/ASCE/AHS/ASC Structures, Structural Dynamics and Materials Conference, 1999, no. 4, pp. 2763-2772.

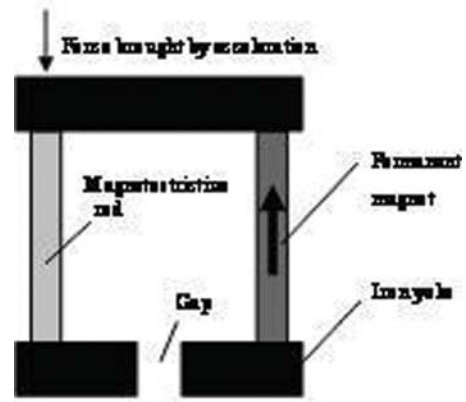

Fig. 1. Schematic diagram of the giant magnetostrictive acceleration sensor.

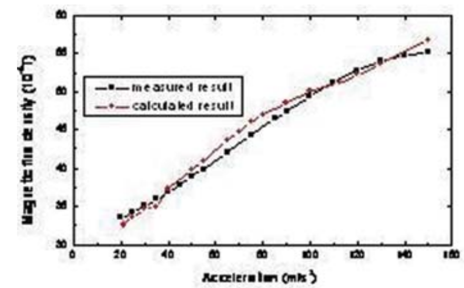

Fig. 2. The relation between magnetic flux density in the gap and applied acceleration on the sensor.

EV-08

Influence of the magnetic anisotropy on the magnetic entropy change of Ni2MnGa memory shape alloy.

J. C. Leitão[1], D. Rocco[1], J. Amaral[1], M. Reis[1], V. Amaral[1], N. Martins[2], P. Tavares[2]
1. Physics, Universidade de Aveiro, Aveiro, Portugal; 2. Chemistry, Universidade de Trás-os-Montes e Alto Douro, Vila Real, Portugal

Ni2MnGa Heusler alloy is studied for its particular magnetic properties and applications. We can cite the memory shape properties, a first order structural transition from martensitic to austenitic phase [1] and its magnetocaloric effect (MCE) [2]. Besides its magnetic entropy change (ΔS) due to the magnetic transition from ferromagnetic to paramagnetic state at the Curie Temperature Tc, its structural transition is also accompanied by an entropy change [3]. Taking into account this alloy's composition sensitivity, both transitions have been coupled into a single one, resulting in a giant magnetocaloric effect (GMCE) [4].
The MCE has both applied and academic interest. From the applied point of view, the magnetic refrigeration is highlighted; several study groups have joined efforts to discover a good material to be used in thermo-magnetic devices usable at room temperature, and the compound Ni2MnGa and its substitutes are promising. These materials have revealed interesting properties, good thermal conductivity, GMCE, low cost and more. Also, the ΔS, which is one of the physical quantities used to characterize the magnetocaloric potential, is a powerful tool to understand the physical mechanisms that rule the behavior of the material [4].
The studied Ni2MnGa alloy has a critical temperature Tc~375 K [5], and undergoes a structural transition between tetragonal martensitic and cubic austenitic phase at a temperature Tm~200 K. It has a saturation magnetization of 4,17 μB bellow Tm and 3,90 μB above [5]. The structural transition has a ΔS of 5 J/kg.K [5], the magnetic transition has -1.29 J/kg.K [7], and finally, the coupled transitions have 20 J/kg.K [6].
Thus, our objective is to study the high magnetic anisotropy of the two phases of this alloy through measurements of the magnetization and ΔS. These results are interesting for researchers dealing with memory shape alloys, no matter the application they are looking for.
Our initial results revealed a distinct magnetic behavior above and below Tm, revealed by the change of shape of the magnetization curves (figure 1). The visible crossing of the isothermal magnetization curves, around 1.5 T, reveals different magnetic anisotropies between the martensitic and austenitic phases. Above Tm the magnetization reveals a softer ferromagnetic behavior, while below Tm a decreasing of the magnetization is observed, indicating either an increase of the magnetic anisotropy or a change in the easy-direction of the magnetization.
From these magnetization isotherms we obtain, using the Maxwell Relations [7], the ΔS for several values of magnetic field, around the structural transition. The maximum value of ΔS increases up to 1.5 T, where the magnetization curves cross. This result is expected because the ΔS is a function of the area between magnetic isotherms. Further increase of the magnetic field change leads to a decrease of the maximum ΔS and only at ~8 T both areas (above and below the crossing of magnetization curves), are balanced, and, consequently, the ΔS is zero (see figure 2). We can clearly see the increase in the maximum peak value, reaching its maximum around 1.5 T, steadily decreasing from this value on. From this result we can conclude that the use of this alloy for magnetic cooling purposes around the structural transition is limited to the use of fields below 1.5 T, having its maximum entropy variation value of about 3.8 J/Kg.K; fields above this value will in fact reduce its magnetocaloric power.

Finally, we will also discuss the influence of the substitution of Galium by Bismth in the Ni2MnGa alloy, and analyse its influence on the magnetic anisotropy and magnetocaloric properties.

[1]Vasil'ev A., Bozhko A., Khovailo V., Dikshtein I., Shavron V., Buchelnikov V., Matsumoto M., Suzuki S., Takagi T. and Tani J. Phys. Rev. B 59 (1999) 1113.

[2]E. Brück, J. Phys. D: Appl. Phys. 38 (2005) R381–R391;

[3]V.A. Chernenko, S. Besseghini, Sens. Actuators A, (2007);

[4]M.S. Reis, V.S. Amaral, J.P. Araújo, P.B. Tavares, A.M. Gomes, I.S. Oliveira, Physical Review B 71 (2005) 144413;

[5]Leitão J. "Magnetocaloric effect of Ni2Mn(Ga,Bi) shape memory alloys" (Universidade de Aveiro, Aveiro, 2007);

[6]Khovailo V., Novosad V., Takagi T., Filippov D., Levitin R. and Vasil'ev A. Phys. Rev. B 70 (2004) 174413;

[7]Tishin A. and Spichkin Y. The Magnetocaloric Effect and its Applications;

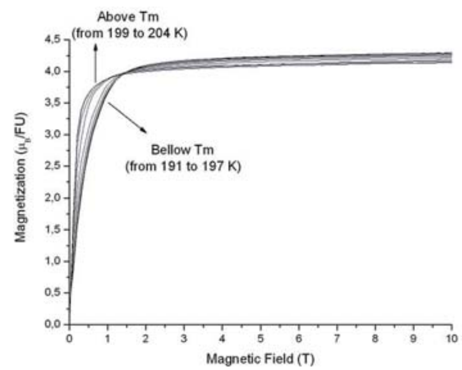

figure 1: Magnetization as a function of magnetic field for the Ni2MnGa memory shape alloy

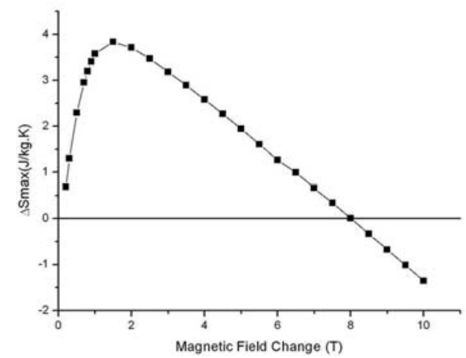

figure 2: maximum magnetic entropy change as a function of the applied magnetic field change

EV-09

Coincidence of magnetic and martensitic transition in NiMnGa thin films obtained by changing growth parameters.

F. Albertini[1], F. Casoli[1], S. Fabbrici[1], L. Righi[2], V. A. Chernenko[3], S. Besseghini[3], A. Gambardella[3]

1. IMEM-CNR, Parma, Italy; 2. Dipartimento Chimica GIAF, Università di Parma, Parma, Italy; 3. IENI – CNR, Lecco, Italy

NiMnGa alloys have attracted a great deal of interest for huge magnetic-field-induced strains and giant magnetocaloric effects [1]. Both effects are linked to the occurrence of a martentesitic transformation between a cubic and a lower-symmetry phase in the ferromagnetic state. The interplay between structural and magnetic degrees of freedom is furtherly enhanced when structural and Curie transition coincide: i.e. first order transition from lower-symmetry ferromagnet to cubic paramagnet. Such a condition has been obtained in bulk systems by means of suitable composition changes and exploited to improve the magnetocaloric and magnetomechanical performances [2,3]. Up to now a lot of work aimed at understanding the fundamental properties and at tailoring the giant effects has been done mainly on bulk material. The research on NiMnGa thin film represents a new field of interest thanks to important possible applications in the field of sensors, actuators, and refrigeration materials [4]. In this case the properties can be tailored by means of composition and growth parameters changes, substrate choice and orientation, growth and annealing temperatures, thickness, and nano- and micro-scale structure. Aim of the present paper is to study the effects of growth parameters on the main properties of NiMnGa thin films of different thickness in order to tailor magnetic and structural transitions and to make them coincide.

NiMnGa thin films of thickness ranging from 20 to 100 nm were deposited by r.f. sputtering on oxidized Si and MgO(100) substrates. The Ni2Mn1.2Ga0.8 target was obtained by induction melting; its composition and homogeneity were confirmed by means of Energy Dispersive X-ray (EDX) analysis. Film growth was performed at a substrate temperature of about 400° C and Ar pressure p=1.4X10-2 mbar, with different target voltage V from 700 to 1200 V, giving rise to growth rates ranging from 2.45 nm/min for V=700 V to 7.5 nm/min for V= 1200 V. Structural and morphological characterization were performed by means of X-Ray Diffraction, Scanning Electron and Atomic Force Microscopy. The magnetic properties were studied by Alternating Gradient Force Magnetometery. Thermomagnetic analysis (magnetic susceptibility vs. temperature) and resistivity measurements as a function of temperature were also performed in order to study magnetic and structural transitions.

The films were found to be polycrystalline with a granular morphology with mean grain size dependent on thickness and growth parameters. Magnetization mesurements confirm the ferromagnetic state of samples with saturation magnetization values at RT ranging from 350 to 400 emu/cm3, as expected for Mn-rich NiMnGa alloys. Selected results on transition temperatures are reported in Table I. It was found that Curie temperature (Tc) decreases by decreasing thickness and by increasing target voltage, independently of substrate.

An increase of Ni to Mn ratio by increasing target voltage has been evidenced by EDX analyses. The decrease of Tc by increasing Ni/Mn ratio is in qualitative agreement with the results reported on bulk Mn-rich systems [3]. A simultaneous increase of martensitic temperature has also been found. As an example in samples of thickness t=75 nm the martensite to austenite transformation (TAM) increases of 44°C by increasing target voltage from 900 to 1200V. Taking advantage of these results, the coincidence of magnetic and structural transition has been induced by modifying target voltage. In Figure 1 resistivity measurements versus temperature are reported for films of thickness t=75 nm grown at V=900 V and V=1200 V respectively. In the first curve (a) the martensitic transformation (step with thermal hysteresis) and Curie transition (kink) are well separated while in the second one (b) they merge (TMA =83.7 °C) and show a thermal hysteresis of 15 °C. A suitable way to decrease both transition temperature and thermal hysteresis is to increase the sample thickness (see curve c for 100 nm thick sample).

[1] A.Sozinov et al. Appl. Phys. Lett. 80 (2002) 1746 ; F.Hu et al. Appl. Phys. Lett. 76 (2000) 3460

[2] L.Pareti et al. Eur. Phys. J B 32 (2003) 303, A.A.Cherechukin et al. Phys. Lett. A 291 (2001) 175

[3] F. Albertini et al. J. Appl. Phys. 100 (2006) 023908

[4] V.A.Chernenko et al. Smart Mater. Struct. 14 (2005) S245, M.Khol et al. Mat. Sci. Eng. A 438 (2006) 940

Sample number	Thickness(nm)	Substrate	Target voltage (V)	TAM (°C)	TMA (°C)	Tc
1199	20	SiO2/Si	700	-	-	69.6
1200	40	SiO2/Si	700	-	-	82.3
1217	75	MgO	900	22.3	25.3	71.0
1218	75	MgO	1200	68.3	83.7	68.3-83.7
1228	100	MgO	1200	44.8	54.4	44.8-54.4

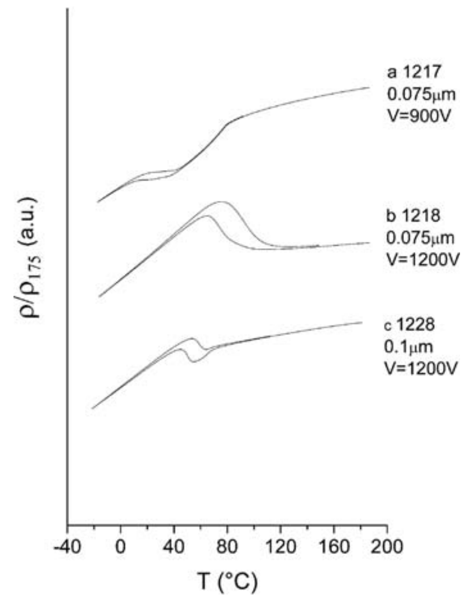

Figure 1 Normalized resistivity measurements as a function of temperature

EV-10

MFM domain imaging of textured Ni-Mn-Ga/substrate thin film composites.

R. Lopez Anton[1,2], V. Chernenko[3], J. Barandiaran[4], I. Orue[4], S. Besseghini[3], M. Ohtsuka[5], A. Gambardella[3]
1. ISIS, STFC Rutherford Appleton Laboratory, Didcot, United Kingdom; 2. ICMA, CSIC-Universidad de Zaragoza, Zaragoza, Spain; 3. CNR-IENI, Lecco, Italy; 4. Universidad del Pais Vasco, Bilbao, Spain; 5. IMRAM, Tohoku University, Sendai, Japan

Ni_2MnGa Heusler alloy and its off-stoichiometric derivatives exhibit a martensitic transformation resulting in a thermoelastic martensite with strong magnetocrystalline anisotropy. However, the relationship between the martensitic and magnetic structures on the micro(nano)scale is still a rather unexplored research area.
Thin films of Ni-Mn-Ga alloys are recently in the focus of interest. The thickness dependencies of the structural and magnetic properties of the martensitic Ni-Mn-Ga/substrate film composites have been studied [3-5]. These films are textured and exhibit plate-like twinning morphology with twin boundaries predominantly oriented parallel to the film plane, giving place to out-of-plane magnetization.
In this work, the influence of thickness and substrate nature on the occurrence of the perpendicular magnetic anisotropy and stripe domain pattern is analyzed.
The 10M-martensitic thin films with thicknesses of 0.1, 0.6 and 1μm were fabricated at T=50 C by r.f. magnetron sputtering of a $Ni_{49.5}Mn_{28}Ga_{22.5}$ (at.%) target on MgO(100). The texture characterization was made using X-ray beam-line at ANKA synchrotron source (FZK, Karlsruhe). In-plane and out-of-plane magnetization loops M(H) were studied by a SQUID magnetometer. In-plane minor M(H) loops were measured as a function of rotation angle by magneto-optical Kerr effect (MOKE). Magnetic force microscopy, MFM, and atomic force microscopy, AFM, measurements were performed with a Digital Instrument 3100 AFM probe microscope.
The X-rays measurements show drastic change from well-pronounced (220)-fiber texture of 1 and 0.6 μm films to a strong in-plane texture component for 0.1 μm film. The in-plane and out-of-plane M(H) hysteresis loops show coercivity values close to 105 Oe and 65-80 Oe, respectively. The initial out-of-plane magnetic susceptibility increases several times with decreasing film thickness while the anisotropy field is approximately constant, roughly corresponding to the value of (1-2)$\times 10^6$ erg/cm3 typical for the bulk. MOKE results show an interesting behavior not observed before for similar films: for 0.1 μm film, the in-plane magnetic susceptibility shows a dependence on the measuring direction not observed in the other samples.
The MFM image for 1 μm film (Fig.1) reveals a magnetic contrast produced by magnetic stripe domains forming a maze pattern (a similar result is also found for 0.6 μm film). The MFM observations for the 0.1 mm film show a patch-like pattern rather than stripes on the same length-scale. The magnetic domains in Fig.1 represent bright and dark regions associated with the magnetization being parallel or antiparallel to the out-of-plane direction. Neighboring domains are assumed to be separated by Bloch-like 180° domain walls. The averaged width of the magnetic domains, as measured from the MFM images, is shown in Fig.2 versus the square root of the film thickness. For comparison sake, this dependence is also shown for similar Ni-Mn-Ga alloys deposited on other substrates [3-5]. In the simplest case of stripe domains for thick enough ferromagnetic films, the classical theory yields an equilibrium domain width $\delta = (d\times \delta_{dw})^{1/2}$ [6], where d is the film thickness and $\delta_{dw}=a(E\times A)^{1/2}$ is the domain wall width. Here a is the interatomic distance, E is the exchange energy density, and A is an anisotropy constant. The varying slopes of the lines in Fig.2 are related to δ_{dw} which appears to be dependent on the substrate nature.
Crystallographic twins or possible associated 90° magnetic domains are not revealed in normal-to-plane observations in this work because of the aforementioned twin boundaries orientation. The strong in-plane texture component, observed in the 0.1 μm film on MgO(100) can cause the only exception from this regularity. The work is now under way to clarify this point.

[1] P. Mullner et all. J. Appl.Phys. Vol. 95, pp.1531-1536, 2004
[2] V.A.Chernenko et al. Sensors and Actuators A (2007), doi:10.1016/j.sna.2007.05.023
[3] V.A. Chernenko et al. J. Phys. Condens. Matter. Vol. 17, pp. 5215-5224,2005
[4] V.A. Chernenko et al. Acta Mater. Vol. 54, pp.5461-5467, 2006
[5] V.A. Chernenko et al. To be published in Mat. Sci. Forum, 2007
[6] E. Lifshitz. J. Physique. Vol. 8 (6),pp. 337-346,1944

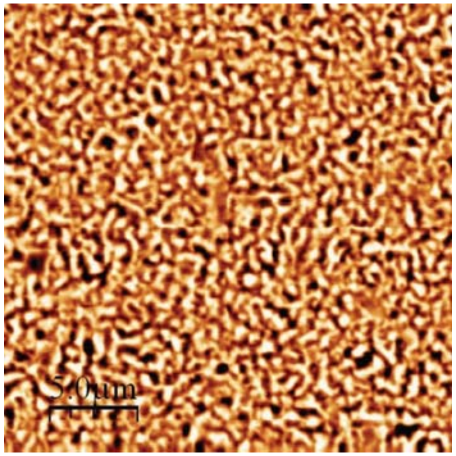

fig. 1

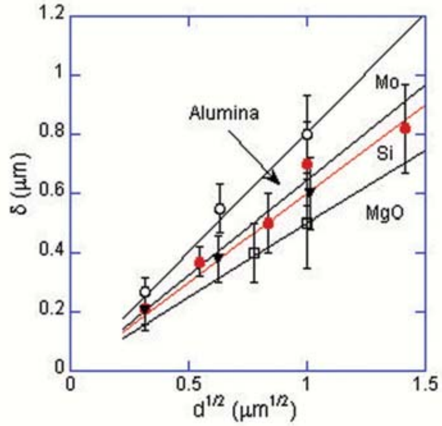

fig. 2

EW-01

Substrate dependent structure and magnetic properties in HoMnO3 films.

T. Han[1], J. Lin[2]
1. Department of Applied Physics, National University of Kaohsiung, Kaohsiung, Taiwan; 2. Center for Condensed Matter Sciences, National Taiwan University, Taipei, Taiwan

In the recent years, multiferroics open new avenues for the development of novel devices based on new functionalities such as control of the magnetic properties by means of electrical fields and vice versa [1]. HoMnO3 (HMO) is a multiferroic material with both ferroelectric and antiferromagnetic orderings. Large magnetodielectric effects were observed in polycrystalline HMO samples with orthorhombic (OT) structure [2]; however, experimental data on the single crystals or the films are very rare. In this work, we make efforts to synthesize and characterize HMO in the form of epitaxial films.

Single-phased hexagonal (HX) HMO target was first prepared with solid state reaction method. Then, HMO films were grown on (111)-yttrium stabilized zirconia (YSZ), LaAlO3 (110) and SrTiO3 (100) substrates at 850 oC by the method of pulsed laser deposition (PLD) with a 248 nm KrF excimer laser. The oxygen pressure during the growth is 50 mtorr, and the pulse frequency is 5Hz. After deposition, the films were in-situ annealed in an oxygen pressure of 100 mtorr for 10 min at the same temperature. The structural characteristics of the grown HMO films were examined by x-ray diffraction (XRD). The magnetic properties of the samples were measured by a superconducting quantum interference device magnetometer.

The XRD patterns of the HMO films deposited on (111)-YSZ substrate, strong (000l) peaks of HMO, and (111) peak of YSZ are identified, suggesting that the crystal structure of this HMO film is hexagonally grown with c-axis perpendicular to the surface of substrate. The crystal structures of HMO films are found to be either OT or HX. Various peaks for the HMO films on STO (100) representing different crystal orientations are observed. However, only strong (020) peak of HMO and (110) of LAO are observed in HMO/LAO film. These results indicate that the stability of film's structure is strongly dependent on the types of substrate. For HMO films, the (111)-YSZ produces a better HX structure and (110)-LAO yields a good OT structure.

Figure 1 and figure 2 display the magnetization (M) vs. temperature (T) for HMO/YSZ and HMO/LAO films with field parallel (in-plane) and perpendicular (out-of-plane) to the film surface, respectively. Solid symbols are the data with the zero field-cooled (ZFC) mode, while the open ones are for the field-cooled (FC) mode. In Fig. 1, both the in-plane and the out-of-plane M(T) curves of HMO/YSZ films display similar behavior with two transitions at ~ 80 K and 45 K, which correspond to the two different magnetic orderings of Mn3+ spins. The HMO/LAO film, on the other hand, shows an interesting anisotropy of M(T) as seen in Fig. 2. For in-plane measurement, ZFC-M(T) displays two cusps at ~ 42 K and 7 K, which correspond to the antiferromagntic orders of Mn3+ and Ho3+-ions, respectively. FC-M(T) shows a sudden rise at 45 K and it keeps increasing at 7 K, indicating the ordering temperature of Ho3+-ion is effectively suppressed under an applied field of 500 Oe parallel to ab-plane. For out-of-plane measurement, the ZFC- and FC-M (T) curves form a split-to-close loop for 10 K < T < 45 K, which is absent in the data of in-plane measurement. In conjunction with the neutron diffraction data of HMO [3], it is suggested that the observed close-loop in the out-of-plane M(T) data reveals the incommensurate to commensurate transition of Mn3+-structure.

In summary, the crystalline orientation of HMO films is strongly dependent on the substrate. It is found that the pure HX- and OT- HMO films can be grown on the YSZ(111) and LAO(110) substrates, respectively. Based on the results of M(T), it is observed that the magnetic behavior of the HX-HMO film is very different from that of the OT-HMO film. We except that this systematic study will serve as a guidance to make high quality HMO films with different structures. And, these films can be eventually utilized for the applications of multiferroic devices.

[1] W. Prellier et. al., J. Phys.: Condens. Matter 17, R803-R832 (2005). [2] B. Lorenz et al., Phys.Rev. B 70, 212412 (2004). [3] A. Munoz et al., Inorg. Chem. 2001, 40, 1020-1028 (2001).

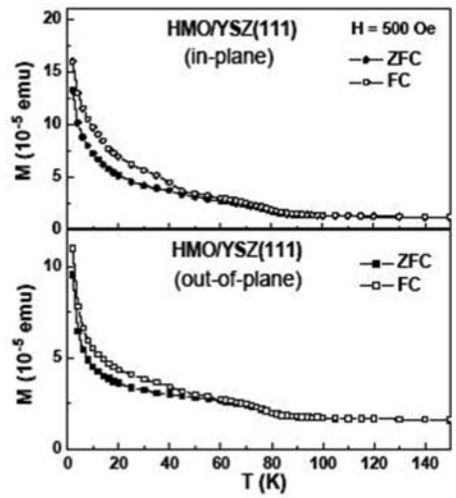

Fig. 1 Magnetization vs. temperature for HMO/YSZ (111) film.

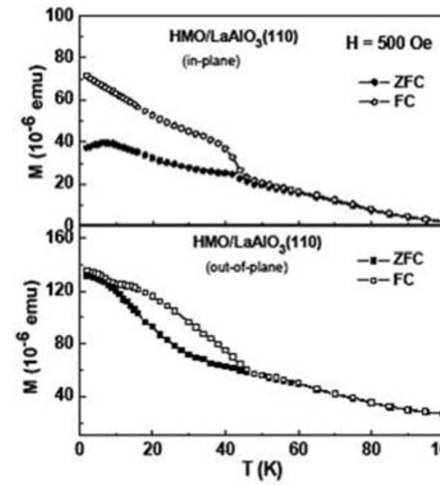

Fig. 2 Magnetization vs. temperature for OT-HMO/LAO film.

EW-02

Effect of iron-doping on the structural and magnetic properties of LuMnO3.

J. Lin[1], *T. Han*[2]
1. Center for Condensed Matter Sciences, National Taiwan University, Taipei, Taiwan; 2. Department of Applied Physics, National University of Kaohsiung, Kaohsiung, Taiwan

Hexagonal RMnO3 (R = rare earth element or Y) compounds present opportunities for the industrious applications due to their unique nature of multiferroism [1]. Namely, the ferromagnetism, ferroelectricity and ferroelasticity occur simultaneously in same material [2]. The characteristics of multiferroism includes a spontaneous magnetization which can be switched by an applied electric field, a spontaneous electrical polarization which can be reoriented by an applied magnetic field, and a strong coupling exists between these two properties. Most of hexagonal RMnO3 exhibit ferroelectric transitions at high temperatures (TC ~ 600 – 1000 K) and antiferromagnetic transitions at low temperatures (TN ~ 70 – 130 K). Additional phase transitions at temperature below 10 K are observed in some hexagonal RMnO3 with high magnetic moment of R3+, which is related to the R-R exchange correlations [3]. In this work, we prepare a series of LuFexMn1-xO3 (x = 0 ~ 0.5) samples by solid-state reaction method to study the effect of Fe-doping on their magnetic properties.

The polycrystalline samples of LuFexMn1-xO3 (x = 0 ~ 0.5) are prepared by the solid-state reaction method. Stoichiometric mixtures of high-purity (> 99.9 %) Lu2O3, MnO2, and Fe2O3 powders were ground and calcinated in air at 1100 oC for 13 hours. To ensure better homogeneity the mixed powders were ground again, compacted into small pellets and reheated in air at 1100 oC for 12 hours. The crystalline structure of the samples was examined by x-ray diffraction (XRD) measurement. The magnetic properties of the samples were measured by a physical property measurement system (PPMS).

Figure 1 shows the powder XRD patterns of the LuFexMn1-xO3 (x = 0 ~ 0.2) samples. All the observed peaks can be indexed on the basis of a hexagonal unit cell of space group P63cm. However, as Mn ions are partially substituted by Fe ions, the structure starts to change with increasing the Fe concentration x. Based on the x-ray analysis, the structures of these compounds change from the hexagonal (space group: P63cm) to the orthorhombic perovskite (space group: Pbnm). In the Fe-doped LuMnO3 samples, the lattice parameter a is slightly decreased but c is increased. The fact that a and c lattice parameters change systematically with increasing x indicates that the Fe-ions do replace the Mn ions.

The temperature-dependent magnetizations M(T) are measured in a magnetic field of H = 500 Oe under conditions of zero field-cooled (ZFC) and field-cooled (FC). The ZFC magnetization MZFC(T) and FC magnetization MFC(T) of the LuFexMn1-xO3 (x = 0 ~ 0.2) samples are displayed in Fig. 2, showing that the antiferromagnetic transition temperature (TN) shifts from 85 to 130 K with increasing the Fe-content. It is also found that the values of effective magnetic momentum increase as the iron content increases. According to the result of M-H curves at 10 K, the magnetic moment increases continuously from 0.009 to 0.017μB/f.u with increasing the Fe-content from 0 to 0.2. In case of a strong coupling between magnetic moment and electric polarization, the Fe-doped sample may have a stronger polarization/ferroelectric effect than that of pure LuMnO3 sample. However, further investigation on the properties of dielectric constant and polarization is essential for understanding the origin of the effect of Fe-doping on their magnetization.

In summary, a series of LuFexMn1-xO3 (x = 0 ~ 0.5) samples are synthesized and studied by the magnetization measurements. The XRD analysis shows that the structure of LuMnO3 change with increasing the Fe-content from the hexagonal to the orthorhombic perovskite. The magnetic characterization indicates that with an increase in the Fe-content, the antiferromagnetic transition temperature shift from 85 to 150 K. At the same time, the value of effective magnetic momentum increases from 0.009 to 0.017 μB/f.u as the Fe-content increases. In case of a strong coupling between magnetic moment and electric polarization, Fe-doped sample may have a higher polarization/ferroelectric effect than that of pure LuMnO3 sample, which should be a great advantage for its future applications.

[1] T. Kimura et al., Nature 426, 55 (2003). [2] W. Prellier et al., J. Phys.: Condens. Matter 17, R803(2005). [3] M. Fiebig et al., J. Appl. Phys. 93, 8194 (2003).

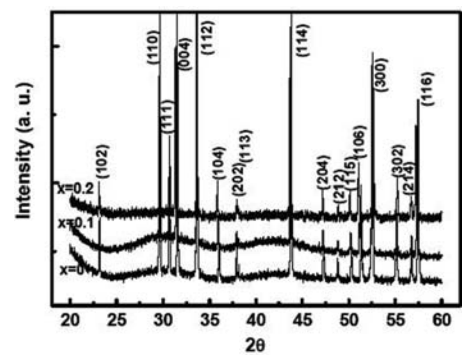

Fig.1 X-ray diffraction patterns of LuFexMn1-xO3 (x = 0 ~ 0.2) samples.

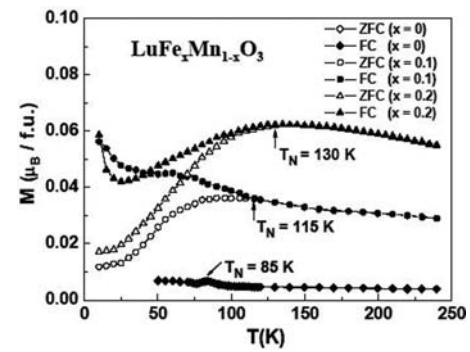

Fig. 2 Zero field-cooled (ZFC) and field-cooled (FC) magnetization vs. temperature for the LuFexMn1-xO3 compounds of x = 0 to 0.2.

EW-03

Magnetic hysteresis in $ErFeO_3$ near the 4.1 K ordering transition.

L. T. Tsymbal[1], Y. B. Bazaliy[2,3], G. N. Kakazei[3,4], F. J. Palomares[4], P. E. Wigen[5]
1. O. Galkin Donetsk Physics and Technology Institute, Donetsk, Ukraine; 2. University of South Carolina, Columbia, SC; 3. Institute of Magnetism, National Academy of Science, Kyiv, Ukraine; 4. Instituto de Ciencia de Materiales de Madrid, Madrid, Spain; 5. Ohio State University, Columbus, OH

The orthoferrite $ErFeO_3$ exhibits a number of interesting magnetic transitions [1]. Magnetism of the compound is due to both iron atoms and erbium atoms. The high temperature magnetic properties are characterized by the ordering of iron sublattice. At $T_N = 636$ K it orders into a non-collinear antiferromagnetic structure with the antiferromagnetic moment **G** along the crystallographic *a*-axis and a small ferromagnetic moment **M** along the *c*-axis. As the temperature is decreased, the spin-reorientation transition is reached where both vectors rotate by 90 degrees. The rotation transition happens continuously in the interval between $T_1 = 88$ K and $T_2 = 97$ K [1].
The spin-reorientation transition is already marked by the appreciable interaction between the iron and erbium magnetic subsystems. It was argued, that the very existence of this transition can be ascribed to Fe-Er interaction [2]. Recently some of us has shown that regardless of the transition mechanism the temperature dependence of rotation angle can be explained only if the magnetic moment of erbium is taken into account [3,4]. The magnetic moment of erbium becomes even larger as the temperature is further lowered. Eventually a compensation point $T_c = 46$ K is reached, where the iron and erbium magnetic moments are equal in magnitude and point in the opposite directions [5,6].
Finally, at very low temperature there is a transition with erbium ions playing the key role. At $T_{12} = 4.1$ K magnetic moments of erbium order into an antiferromagnetic structure [7] and vector **G** starts to rotate in the *(b,c)* plane [8-10]. The erbium ordering transition is characterized by the unusual anomalies [12-15].
In this work, we performed precise measurements of the magnetic hysteresis loops at a series of temperatures above T_{12} using the SQUID-magnetometer Quantum Design MPMS-5S and the Vibrating sample magnetometer OXFORD MagLab VSM. Single-crystal samples of $ErFeO_3$ were used in all measurements. Magnetic field was applied along the *a*-axis, i.e., along the direction of spontaneous ferromagnetic moment **M** || *a*. Representative results are shown in the Fig. 1. At relatively high temperatures square loops are found. As the temperature is lowered from about 30K towards T_{12} the coercive field decreases, and eventually the ``double-triangle'' loops emerge (see T = 9 K and T = 5 K loops in Fig. 1). We interpret the change of the loop shape as evidence of the emergence of a ferromagnetic domain structure at low magnetic fields. Hysteresis loops measured at constant temperatures explain the results found in temperatures sweeps at constant applied **H** || *a* (Fig. 2, left panel) in the situation when H is smaller than the loop width. Spontaneous magnetization obtained from hysteresis loops [3] is shown in Fig. 2, right panel.
In conclusion, we found that magnetic hysteresis loops in $ErFeO_3$ exhibit complicated shapes near the erbium ordering transition at $T_{12} = 4.1$ K. This work calls for theoretical understanding of the loop shapes (double-triangle loops) and especially of the relationship between the loop shapes and the proximity to the phase transition.

[1] K. P. Belov, A. K. Zvezdin, A. M. Kadomtseva, and R. Z. Levitin, ``Orientation Phase Transitions in Rare Earth Magnetic Materials'' (Nauka, Moscow, 1979) (in Russian).

[2] R. L. White, J. Appl. Phys. **40**, 1061 (1969).

[3] Ya. B. Bazaliy, L. T. Tsymbal, G. N. Kakazei, A. I. Izotov, and P. E. Wigen, Phys. Rev. B, **69**, 104429 (2004).

[4] Ya. B. Bazaliy, L. T. Tsymbal, G. N. Kakazei, and P. E. Wigen, J. Appl. Phys., **95**, 6622 (2004).

[5] V. N. Derkachenko, A. M. Kadomtseva, V. A. Timofeeva, and V. A. Khokhlov, JETP Lett., **20**, 236 (1974).

[6] L. T. Tsymbal, Ya. B. Bazaliy, V. N. Derkachenko, V. I. Kamenev, G. N. Kakazei, F. J. Palomares, and P. E. Wigen, J. Appl. Phys. **101**, 123919 (2007).

[7] W. G. Kochler, E. O. Wollan, and W. K. Wilkinson, Phys. Rev. **118**, 58 (1960).

[8] G. Gorodetsky, R. M. Hornreich, I. Yaeger, H. Pinto, G. Shachar, and H. Shaked, Phys. Rev. B, **8**, 3398 (1973).

[9] V. A. Klochan, N. M. Kovtun, and V. M. Khmara, **68**, 721 (1975).

[10] K. P. Belov, A. M. Kadomtseva, N. M. Kovtun, V. N. Derkachenko, V. N. Melov, and V. A. Khokhlov, Phys. Stat. Sol. (a) **36**, 415 (1976).

[11] A. M. Balbashov, N. K. Danshin, A. I. Izotov, M. A. Sdvizhkov, and L. T. Tsymbal, Solid State Physics (Leningrad) **31**, 279 (1989).

[12] I. M. Vitebskii, N. K. Danshin, A. I. Izotov, M. A. Sdvizhkov, and L. T. Tsymbal, JETP **98**, 334 (1990).

[13] V. D. Buchelnikov, N. K. Danshin, L. T. Tsymbal, and V. G. Shavrov, Physics Uspekhi **166**, 585 (1996).

[14] I. M. Vitebskii, N. K. Danshin, N. M. Kovtun, and M. A. Sdvizhkov, JETP **90**, 1118 (1986).

[15] I. M. Vitebskii, N. M. Kovtun, G. A. Troickii, and V. M. Khmara, Low Temp. Phys. **15**, 1066 (1989).

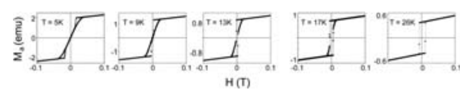

Magnetic hysteresis loops above the erbium orientation transition of $ErFeO_3$ at $T_{12} = 4.1$ K.

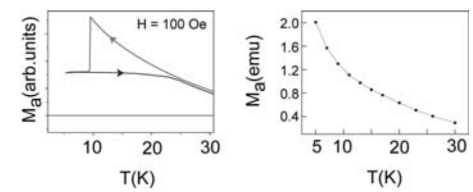

Spontaneous magnetization. Left: temperature hysteresis observed at constant external field, the arrows show the direction of temperature change. Right: magnetization calculated from the analysis of hysteresis loops [3].

EW-04

Mössbauer studies of ^{57}Fe-doped in $LiCoPO_4$ at low temperatures.

S. Moon, C. Kim
Department of Physics, Kookmin University, Seoul, South Korea

Introduction

Since the magnetoelectric (ME) effect was observed in Lithium-orthosphates, $LiMPO_4$ (M=Transition metal) have been extensively investigated for information storage and electronic, magnetic and optical switches [1-3]. Also, the high lithium- ionic conductivity has been studied already as a high potential cathode material by using in secondary Li-ion rechargeable battery [4]. Recently, the observation of ferrotoroidic (FTO) domains in $LiCoPO_4$ was reported by Bas. Van Aken et al [5]. They claimed that the ferrotoroidic system has asymmetric structure by migration of Co^{2+} ions in antiferromagnetic (AFM) structure with rotation of the spins. The studies of neutron scattering demonstrated the magnetic properties of $LiCoPO_4$ which was related between 2D and 3D magnetic systems [2, 5]. These structures exhibit a strong linear magnetoelectric (ME) effect. AFM ordering reduces the symmetry from mmm to mmm', and weak ferromagnetism along y axis reduces the symmetry from mmm' to 2'mm', therefore, finally, it has two AFM and two FTO domains in $LiCoPO_4$ [5].

From these complex magnetic structures, $LiCoPO_4$ show the various anomaly effects. Therefore, it is essential to determine the unusual magnetic properties of $LiCoPO_4$ in low temperatures for properly understand the mechanism. We present crystallographic and magnetic properties of $LiCo_{0.99}{}^{57}Fe_{0.01}PO_4$(LCFPO) using the Mössbauer spectroscopy and the x-ray diffraction (XRD)

Experiments

The polycrystalline sample of (LCFPO) was made by using a direct reaction. Lithium carbonate, ammonium dihydrogen phosphate, cobalt oxide, and iron metal (^{57}Fe) were mixed in stoichiometric ratios and sealed in evacuated quartz tubes. The temperature was slowly raised up to 700 ^{o}C over a period of 1 day. The crystal structure of the sample was examined by using an X- ray diffractometer with Cu- Kα radiation (λ=1.5406 Å) and was analyzed by using a Rietveld refinement. The Mössbauer spectra were recorded using a conventional spectrometer of the electromechanically type with a ^{57}Co source in a rhodium matrix.

Results and discussion

X-ray diffraction pattern for LCFPO showed a pure olivine single phase. The crystals structure was determined to be an orthorhombic with space group *P*nma. The determined lattice constants a_0, b_0, and,c_0 are 10.241Å, 5.924Å, and 4.698 Å, respectively.

The Mössbauer spectra of LCFPO at various temperatures ranging from 4.2 to 300 K are shown in Fig. 1. We have analyzed the Mössbauer spectra by using the full Hamiltonian. The Mössbauer spectrum shows a large asymmetric and distorted line broadening at 4.2 K. The magnetic hyperfine field (H_{hf}) and the quadrupole splitting (ΔE_Q) at 4.2 K were fitted and yielded the following results: H_{hf} = 127 kOe, θ = 16^o, ϕ = 0^o, η = 0.95, $\Delta E_Q = (1/2)e^2qQ[1+(1/3)\eta^2]^{1/2}$ = 0.36 mm/s, and R = 3.0. Here, η is the asymmetric parameter, and R is the ratio of the electric quadrupole interaction to the magnetic dipole interaction. It is noticeable that the magnitude of R is greater than 1 below T_N. This result indicates that the electric quadrupole interaction is larger than the magnetic dipole interaction in the below T_N region. Generally, the H_{hf} has a maximum value at 0 K and decreases with increasing temperature. In Fig. 2, we observe that the H_{hf} has a maximum at 9 K. The unusual reduction of H_{hf} below 9 K can be explained in terms of the temperature dependence of the cancellation effect between the orbital current field term and the Fermi contact term in H_{hf}. The magnitude quadrupole shift at below T_N was caused by large crystal field due to the asymmetric structure through the rotation of the spins. From the analysis of Mössbauer spectra, we suggest that the asymmetric structure of $LiCoPO_4$ is closely related to the elevation of ME effect.

[1] I. Kornev, Phys. Rev. B, 62, 12247 (2000).

[2] D. Vaknin, Phys. Rev. Lett., 92, 207201 (2004).

[3] M. Mostovoy, Phys. Rev. Lett., 96, 067601 (2006).

[4] S. B. Lang, IEEE. T. Dielect. El. In., 7, 466 (2000).

[5] B. B. V. Aken, Nature, 449, 702 (2007).

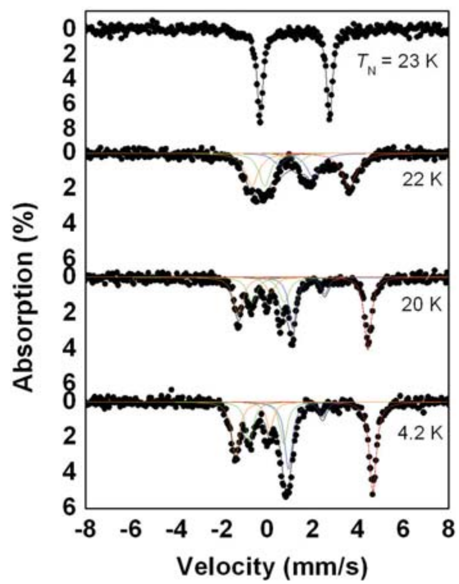

Fig. 1. Mössbauer spectra of $LiCo_{0.99}{}^{57}Fe_{0.01}PO_4$ at various temperatures.

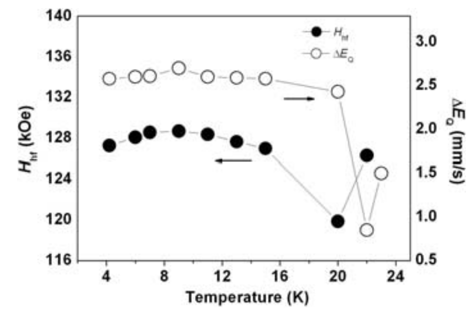

Fig. 2. The Temperature dependence of magnetichyperfine field (H_{hf}) and the electric quadrupole shift (ΔE_Q) at below T_N for $LiCo_{0.99}{}^{57}Fe_{0.01}PO_4$. ($T_N$ (23 K)).

EW-05

Effects of gallium distribution on terbium bismuth gallium iron garnet.

I. Park, C. Kim
Physics, Kookmin University, Seoul, South Korea

Introduction
Heavy rare earth (RE) iron garnet has canted magnetic structure which is described as a "double umbrella structure" at low temperature. The heavy RE ion spins form a double cone around the [111] axis, and these spin affect to the iron set of 16*a* site [1]. These materials related to the negative magnetization have been reported that the net magnetization has negative value at low temperature under field cooled condition for $Tb_2Bi_1Fe_5O_{12}$ [2], and $Ho(Fe_{0.6}Mn_{0.4})_{12}$ systems [3]. Terbium bismuth gallium iron garnet (TbBiGaIG) is the candidate material for Faraday rotator for wide band and temperature-stabilized optical isolators [4]. It is well known that heavy RE iron garnet shows compensation phenomenon. Compensation phenomenon attracted attention for new concepts of integrated optical isolators based on nonreciprocal optical mode interference [5]. In RE iron garnet system, both octahedral (16*a*) and tetrahedral (24*d*) sites are occupied by Fe^{3+} ions. When the gallium ion is substituted in garnet system, the cation distribution of gallium and iron ions between 16*a* and 24*d* sites depends on the temperature. The heat treatment is able to change the sign of the faraday effect by moving some of the Ga ions from 24*d* to 16*a* site [5-6].
In this work, we report on the structural and magnetic properties of $Tb_2Bi_1Ga_1Fe_4O_{12}$ powders, which prepared by sol-gel and vacuum annealing process. The distribution of gallium and iron in $Tb_2Bi_1Ga_1Fe_4O_{12}$ is explained by the analysis of the local structure of iron sublattices using Mössbauer spectroscopy.

Experiments
$Tb_2Bi_1Ga_1Fe_4O_{12}$ compounds were prepared by a sol-gel method. Terbium, bismuth, gallium, and iron nitrate were dissolved in 2-methoxyethanol (2-MOE) and acetic acid. The solution was refluxed at 80 °C for 24 h and dried at 120 °C for 48 h in oven. The obtained powder was sealed in evacuated quartz tubes. The annealing temperature was room temperature initially and was slowly raised to 1000 °C over a period of seven days.
The crystal structure of the sample was examined using an x-ray diffractometer with Cu-*K*α radiation and analyzed by Rietveld refinement. Mössbauer spectra were recorded using a constant acceleration Mössbauer spectrometer with a ^{57}Co source in Rh matrix.

Results and discussion
The x-ray diffraction pattern of the compounds shows a single phase crystal structure of space group (*Ia3d*) {Tb(24*c*); Bi(24*c*); Fe(16*a*); Ga(16*a*); Fe(24*d*); O(96*h*) (*u, v, w*)} with its lattice constant a_0 = 12.465 Å. The refined X-ray diffraction pattern of sample is shown in Fig. 1. In order to study the change of the detailed local structure, we have obtained Mössbauer spectrum. Mössbauer spectrum of $Tb_2Bi_1Ga_1Fe_4O_{12}$ at room temperature is shown in Fig. 2. The Mössbauer spectrum for the sample was composed of two six-line hyperfine patterns 24*d* (inner sextet) and 16*a* (outer sextet). The spectrum of $Tb_2Bi_1Ga_1Fe_4O_{12}$ at room temperature consists of 2 sets of 6 Lorentzians, which is the pattern of single-phase garnet. From the analyzed results of Mössbauer spectrum at room temperature, the absorption area ratios of Fe ions on 24*d* and 16*a* sites are 74.7 % and 25.3 % (approximately 3:1), respectively. In case of our previous results for $Tb_2Bi_1Fe_5O_{12}$, the absorption area ratios of Fe ions on 24*d* and 16*a* sites are 60.8 % and 39.2 % (approximately 3:2), respectively. This proportion is the conventional absorption area ratios of Fe ions of garnet. It can be analogized the Ga ion distribution by this result. It is noticeable that all of the nonmagnetic Ga atoms occupy the 16*a* site by vacuum annealing process. This is also in accord with the x-ray diffraction refinement results. We suggest that the control of site preference of Ga cation from 24*d* site to 16*a* site was accomplished by high temperature vacuum annealing process.

[1] F. Sayetat, J. Magn. Magn. Mater., 58, 334 (1986).

[2] I. J. Park, and C. S. Kim, J. Appl. Phys. 101, 09M512 (2007).

[3] J. B. Yang, W.B. Yelon, W. J. James, S. Cai, D. Eckert, A. Handstein, K. H. Müller, and Y. C. Yang, Phys. Rev. B, 65, 064444 (2002).

[4] Z. C. Xu, Appl. Phys. Lett. 89, 032501 (2006).

[5] L. Wilkens, D. Träger, H. Dötsch, A. M. Alexeev, A. F. Popkov, and V. I. Korneev, J. Appl. Phys. 93, 2839 (2003).

[6] R. Wolfe, J. Hegarty, J. F. Dillon, Jr, L. C. Luther, G. K. Celler, L. E. Trimble, IEEE Tran. Magn. MAG-21, 1647 (1985).

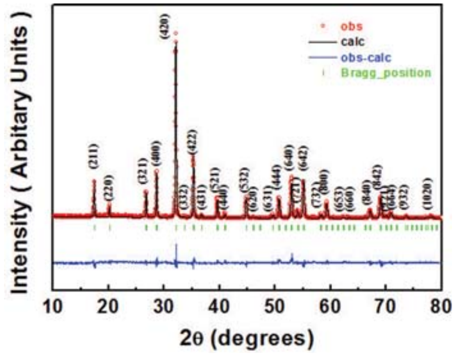

Fig. 1. Rietveld refinement of X-ray diffraction patterns for $Tb_2Bi_1Ga_1Fe_4O_{12}$.

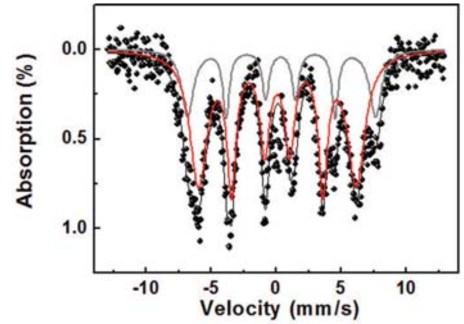

Fig. 2. Mossbauer spectrum of $Tb_2Bi_1Ga_1Fe_4O_{12}$ at room temperature.

EW-06

Physical properties of $Fe_{3-x}Mg_xO_4$ ferrite films on MgO(001) and $SrTiO_3$(001) grown by molecular beam epitaxy.

D. Lee[1], G. Chern[2]
1. Electrical Engineering Department, Da-Yeh University, Chang-Hua, Taiwan; 2. Physics, National Chung Cheng University, Chia-Yi, Taiwan

Ferrite has attracted much interest due to its broad magnetic properties and promising applications in microelectronic and microwave devices as well as sensitive sensors[1]. A lot of research has been focused on the magnetic properties of polycrystalline and single crystalline bulk materials or thin films. However, it is recognized that residual strain has played an important role in controlling the coercivity and other magnetic properties[2-3]. Therefore, synthesizing single crystalline ferrite thin films and establishing a comprehensive understanding on the strain effect become critical issues. In this paper, we fabricate a pure magnetite and a series of $Fe_{3-x}Mg_xO_4$films on MgO (001) and $SrTiO_3$(001), respectively. The thickness of $Fe_{3-x}Mg_xO_4$ thin films are around 1000 Å. MgO is utilized for the growth due to small lattice mismatch (~ -0.3%) and epitaxial films are expected. On the other hand, $SrTiO_3$(STO) substrate is intended to include in this study because of its relatively large lattice mismatch (~ 7.58%) and dissimilar oxygen sublattice to ferrites so a relaxed thin film may be obtained for comparison. X-ray diffraction (XRD) measured along z direction reveals that these films are indeed epitaxial and strained for films grown on MgO but it shows two-phases of crystalline orientation and thus relaxed for films grown on STO. Figure 1 shows the XRD results from the films grown on MgO(001). The major peaks at 94^0 are diffracted from MgO substrate and minor peaks (with mark) are from pure and mixed ferrite films with different Fe/Mg ratio, which indicate high crystalline quality of these ferrite films. However, the diffraction results from the films grown on STO show extra (l l l) series peaks indicating polycrystalline structure of these films. Relative to lattice matched substrate such as MgO(001), these films show extra (l l l) series peaks indicating the relaxed feature of these films.Magnetic hysteresis curves are measured for all films with the external field parallel to the plane. The saturation magnetization (Ms) for films grown on MgO reduces from 500 emu/cm^3 roughly linearly from x = 0 to x=1.5. However, Ms remains ~400 emu/cm^3 in the range of x=0.3 and 0.9 for the films grown on STO. The difference of Ms may be attributed by cation distribution. For the low Ms state found in film grown on MgO (strained case), Mg mostly replaced Fe from B site. However, for the high Ms state found in films grown on STO (relaxed case), Mg replaced both A and B sites. The mechanism for the high Ms may be related to the thin film layer-by-layer growth characteristic[4].

Resistance as a function of temperature (80 – 300 K) for all films is also carried out. Basically, the resistivity of the samples presents a typical Arrhenius temperature dependence with $\rho= \rho_0 \exp(Ep/k_BT)$ as shown in Fig. 2. The gap energies, which are estimated form the slopes of the straight lines gradually increase from 63 to 69 meV for the films with x=0.3 to x=1.2. However, the gap energy abruptly increases to 110 meV and tends to diverge as x >1.5, which may indicate a possible metal (semiconductor)-insulator transition. Both the magnetization saturation and the electrical transition at x=1.5 are related to the cation distribution in different crystalline sites. The cation distribution and the strain effect in these ferrite films will be discussed.

1.W. Huang, J. Zhu, H. Z. Zeng, X. H. Wei, Y. Zhang, and Y. R. Li, Appl. Phys. Lett. 89,262506 (2006).

2 A. Lisfi and C. M. Williams, J. Appl. Phys. 93, 8143 (2003).

3. J. H. Yin, J. Ding, and B. H. Liu, Appl. Phys. Lett. 88, 162502 (2006).

4. D.S. Lee et al., J. Appl. Phys.101, 09M523, (2007)

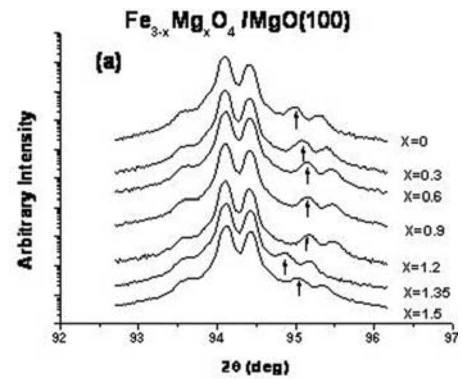

Fig.1 X-ray diffraction results from a series of Fe-Mg-O oxide films grown on MgO(001). The peaks at ~94 correspond to MgO(004) planes. A series of broad but well-defined peaks are observed between 94.5° and 95.5°, which are associated with Fe-Mg-O films.

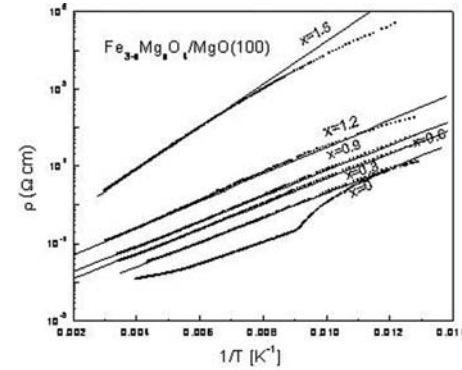

Fig.2 Representative curves of ρ vs 1/T for Fe3-xMgxO4 thin films on MgO substrate showing the linear region from which the activation energy and ρ0 values are obtained.

EW-07

Enhancement of magnetoelastic properties of highly magnetostrictive cobalt ferrite through control of sintering conditions.

I. Nlebedim, N. Ranvah, A. J. Moses, D. C. Jiles, P. I. Williams, Y. Melikhov, J. E. Snyder, F. Anayi
Wolfson Centre for Magnetics, Cardiff School of Engineering, Cardiff, United Kingdom

The use of magnetostrictive smart materials for development of sensors and actuators in a wide range of engineering applications has attracted remarkable research interest. This includes the need to develop low cost materials with improved mechanical, thermal and chemical properties of which ceramic oxides are good candidates. Among the ceramic oxides, Cobalt ferrite (Co-ferrite) and Co-ferrite based materials have been investigated as alternatives to the rare earth based magnetostrictive materials for sensor and actuator development [1,2].
Since magnetostrictive properties depend on the position and concentration of Co^{2+} ions, it follows that changes in the site occupancy will affect the magnetic and magnetostrictive properties of Co-ferrite. Studies have shown that magnetic and magnetostrictive properties can be optimized by both chemical substitutions [3,4,5] and heat treatment [6,7].
Most studies on the improvement of magnetostrictive properties of Co-ferrite have concentrated on samples prepared at a particular temperature in air. Since site occupancy of ions is crucial to improvement of magnetostrictive properties and can depend on sintering conditions, there is then a need for a systematic approach to understanding magnetostrictive behaviour as a result of heat treatment and sintering environment. This is particularly important due to the varying levels of magnetostriction obtained for Co-ferrite in different studies. Values ranging from 138ppm [8] to 225ppm [9] have been reported.
In this work, we present the results of a study on the effect of vacuum sintering, different sintering temperatures and holding times on the magnetic and magnetostrictive properties of Co-ferrite. Since oxygen partial pressure influences the compositional variation of Co-ferrite [6], the choice of vacuum condition is necessary to compare results with air sintered samples previously reported [8,9].
Co-ferrite powder was ball milled, pressed into buttons and sintered in vacuum at 10^{-5} Torr. Nine samples were studied, consisting of three samples sintered at each of three temperatures 800°C, 1000°C and 1200°C, and for different holding times of 6, 12 and 24 hrs. All samples were heated at a rate of 250°C/hr and cooled at the same rate in vacuum. The structures and microstructure of the sintered samples were characterized by x-ray diffractometry and scanning electron microscopy. Magnetic properties were studied with a superconducting quantum interference device (SQUID) up to a maximum applied field of 4000 kA/m. Room temperature magnetostriction was measured using strain gauges attached to the samples.
Coercive field (H_c) was found to decrease with sintering temperature and holding time as shown in Fig.1.
Using the Law of Approach to Saturation, we determined the variation of the first cubic anisotropy coefficient (K_1) with sintering temperature. The results show that K_1 is higher for smaller holding times at lower sintering temperatures. This indicates that vacuum sintering of Co-ferrite requires higher sintering temperature for lower anisotropy.
We observed that the highest magnetostriction (λ) was obtained for samples sintered at 800°C in vacuum. The results also show that the effect of change in sintering temperature is more pronounced than change in holding time. This is shown in Figs.2a and 2b for samples sintered for 24 hours at different temperatures, and for samples sintered at 800°C for different times.

From these results, it can be seen that λ is improved at lower vacuum sintering temperatures than at higher ones. This is likely due to the introduction of a detrimental second phase at higher temperatures as indicated by preliminary x-ray diffraction results. Additional results are needed for confirmation. Though higher λ is obtained for samples sintered in air [9], the value of λ obtained for vacuum sintering is comparable to other literature values obtained for air sintering [8]. Finally, comparing coercive fields for vacuum and air sintering, vacuum sintering seems to result in lower coercive field at lower temperature than air sintering [8].

1.R. W. McCallum et al., *Low Temp.Phys.* **27** (2001) 266.

2.L.H. Chen et al., *IEEE Trans.Magn.* **35** (1999) 3835.

3.Y. Melikhov, et al., *J. Appl. Phys.* **99** (2006) 08R102.

4.C.C.H. Lo, *IEEE Trans. Magn.* **43** (2007) 2367.

5.S.H. Song et al., *J. Appl. Phys.* **101** (2007) 09C517

6.G.D. Rieck and J.J.M. Thijssen, *Acta.Crystallogr B* **24** (1968) 982

7.G. Na et al., *J. Mat. Sci. Lett.* **12** (1993) 961

8.S.D. Bhame and P.A. Joy, *J. Phys.D: Appl.Phys.* **40** (2007) 3263

9.Chen Y. et al., *IEEE Trans. Magn.* **35** (1999) 3652

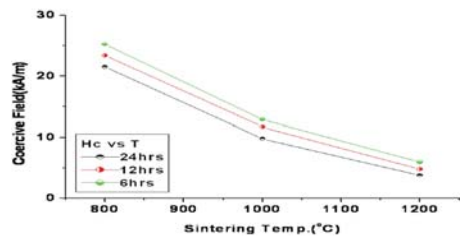

Fig.1 Variation of coercive field of cobalt ferrite samples with sintering temperature.

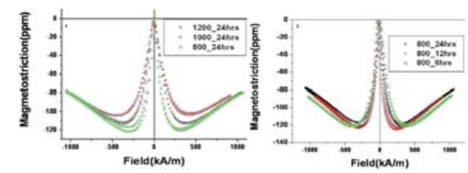

Fig.2 Magnetostriction of Co-ferrite sintered (a) for 24hrs at different temperatures (b) at 800°C for different times

EW-08

Comparative study of the microstructural and magnetic properties of cobalt ferrites synthesized by ceramic and oxidation wet methods.

M. Feder[2], L. Diamandescu[2], I. Bibicu[2], *O. F. Caltun*[1], I. Dumitru[1], L. Boutiuc Hrib[1], H. Chiriac[3], N. Lupu[3], M. Vilceanu[4], V. Vilceanu[4]
1. Physics, Al, I. Cuza University, Iasi, Romania; 2. National Institute of Materials Physics, Bucharest-Magurele, Romania; 3. National Institute of R&D for Technical Physics, Iasi, Romania; 4. AferoExim ltd., Buharest, Romania

The spinel powders with chemical compositions $CoFe_2O_4$ and $CoMn_{0.2}Fe_{1.8}O_4$ were synthesized by solid state ceramic and copecipitation and oxidation wet methods [1]. In the solid state ceramic method, the homogenized raw materials (α-Fe_2O_3, Co_3O_4 and $MnCO_3$) were calcined at 900oC ($CoFe_2O_4$) or 950oC ($CoMn_{0.2}Fe_{1.8}O_4$) for 5 hours, in air. The so calcined material was wet milled in ball mills for 16 hours. To obtain ferrites powders by the wet methods (coprecipitation and oxidation) the raw materials ($FeSO_4.7H_20$, $CoSO_4.7H_2O$, $MnSO_4.H_2O$ reagent grade) were dissolved in suitable proportions in water. The hydroxides were coprecipitated by adding a solution of 2N NaOH. The precipitates were then gradually oxidized by bubbling air at 80oC and pH>11, for 8 hours. These powders were washed, filtered and dried at 80oC. The fine-divided ferrite powders were pressed into disk and thoroidal shapes. The green density of all specimens was >55% of the theoretical one (dRX =5.30g/cm3). Successive sets of specimens were sintered in a box furnace in air, for 5 hours at temperatures in the range 1050o-1300oC.
The microstructure analysis on fractured surface of sintered samples was performed using surface electron microscope (SEM) and the magnetic properties were measured by means of a vibration sample magnetometer (VSM). The magnetostrictive properties were measured by strain gauge methods both in parallel and perpendicular to the applied magnetic field direction. Refinement the X-ray diffraction data show that the samples are mainly composed of spinel phase. Samples obtained by wet method are mono-phase system, while the other samples studied are two-phase system, as commonly obtained when solid state ceramic technique is used to get spinel ferrites [1]. The hematite content of the stoichiometric cobalt ferrite sample sintered by conventional ceramic method is bigger (13,10%) than the hematite content of the manganese substituted cobalt ferrite sample sintered by the conventional ceramic methods. Lattice parameters of studied samples are near to theoretical value for $CoFe_2O_4$ of 8.38Å [2]. The data obtained from MS lead to the conclusion that iron is present in the Fe^{3+} oxidation state, according to the isomer shift value. The SEM analysis confirmed the XRD data. In the micrographs of the sintered stoichiometric cobalt ferrite samples obtained by conventional ceramic method was observed large hematite particles having an average grain size of 13 microns distributed as islands between the spinel phase particles. The cobalt ferrite particles have, after the sintering process, a sub micron average grains size. In the micrographs of the manganese substituted cobalt ferrite, obtained by conventional ceramic method, the grain size distribution is more uniform and the hematite islands are rarely observed. In this case the average grain size is of few microns. The magnetostrictive properties shown in Figs. 1 depends on the microstructure of the samples. The samples sintered from conventional ceramic powders in the same condition as the sintered samples started from coprecipitated powders have very small specific magnetization values. The coercive field values for the samples sintered by the conventional ceramic method are bigger than the values of the coprecipitated samples. The specific magnetization threefold increased from 55 emu/g to 179 emu/g for the stoichiometric ferrite samples obtained from conventional and coprecipitated powders respectively. In the manganese substituted cobalt ferrite case the specific magnetization increased only twice, from 77emu/g to 168emu/g. The most important purpose of the manganese substitution of the iron cations is the decrease of the Curie temperature [3]. As results of the iron cations substitution the values of the maximum of the magnetostrictive coefficient decreased. For the samples obtained from conventional powders the decrease is more evident as in the case of the samples started from coprecipitated powders. Although of this decrease of the maximum value of the magnetostrictive coefficients, the ferrites sintered from coprecipitated powders are very good candidates for magnetostrictive sensors application due to the high specific magnetization and low coercive field values. The best candidates for magnetostrictive sensors are the manganese substituted cobalt ferrite samples also characterized by lower values of the Curie temperature.

Acknowledgements. These results were obtained in the MASTRICH project CEEX 73c/2006, financed by MATNANTECH Program of Romanian Ministry of Education and Research.

[1]. Alex.Goldman, Modern Ferrite Technology, 2nd Edition, Springer 2006, pp.151-166

[2]. J.Smit, H.P.J. Wijn, Ferrites, Philips Technical Library 1959, pp.144

[3] O.F Caltun., G.S.N. Rao, K.H. Rao, B. Parvatheeswara Rao, I. Dumitru, Chong-Oh Kim and CheolGi Kim, JMMM 316 e618-e620 (2007)

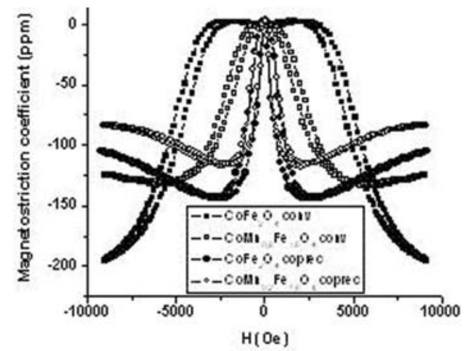

Fig.2 Magnetostrictive measurement results

EW-09

Nonequilibrium cation influence on the Néel temperature in ZnFe2O4.

I. Al-Omari[1], H. M. Widatallah[1], F. R. Sives[2], S. J. Stewart[1,2]
1. Physics, Sultan Qaboos University, Muscat, Oman; 2. IFLP-CONICET and Departamento de Física, Universidad Nacional de La Plata, La Plata, Argentina

The equilibrium cation distribution in ZnFe2O4 can be altered by employing nonequilibrium methods of synthesis and/or by reducing the ZnFe2O4 characteristic length down to nanometric ranges. As a consequence, the nonequilibrium distribution brings about changes in its long-range magnetic ordering that goes from antiferro, cluster-glass to ferrimagnetic state as the inversion, i.e. the fraction of tetrahedral A sites occupied by iron, increases [1,2]. The study of the magnetism of disordered ZnFe2O4 has been predominantly focused on its low temperature behavior and, to our knowledge, only one work has reported on its magnetization above ambient conditions [3]. A ferrimagnetic ordering has been reported to occur in disordered nanosized zinc ferrites below TN≈460-490 K. However, no studies have been performed in this system to determine how the ordering temperature TN depends on the inversion or particle sizes.
To this aim we present here results on the temperature dependence (above 295 K) of the magnetization of ZnFe2O4 nanoferrites having different degree of inversion (c from 0.05-0.5) and sizes (6-50 nm) (Fig. 1). The maximum temperature achieved (610 K) was selected as a compromise between avoiding to surpass the stability region of the disordered sate and being able to include a temperature region where the net magnetization were negligible. The sample shows a net magnetization in the 400 to 510 K range that mainly depends on the degree of inversion. Further, the reciprocal magnetization deviates from different temperature values of the linear behavior showed at high temperatures (inset Fig 1.). Our results show that, contrary to similar nanoferrite systems [4], a simple scaling law cannot be applied to explain the TN dependence with the grain sizes. This can be interpreted due to the lack of correlation between size and inversion that occurs in ZnFe2O4 [5] and the strong TN dependence on the JAB interaction strength [6]. These results will also be compared with theoretical predictions about TN found by assuming a random distribution of superexchange interactions.

[1] M. Hoffman et al. J. Mat. Scie. Lett. 39, 5057-5065 (2004)

[2] H. M. Widatallah et al., J. Magn. Magn. Mat., accepted

[3] J. H. Shim et al., Phys. Rev. B 73, 064404 (2006)

[4] C. N. Chinnasamy et al. J. Magn. Magn. Mat. 238, 281 (2002)

[5] S. J. Stewart et al. Phys. Rev. B 75, 073408 (2007)

[6] N. Ponpandian et al. Appl. Phys. Lett. 86, 192510 (2005)

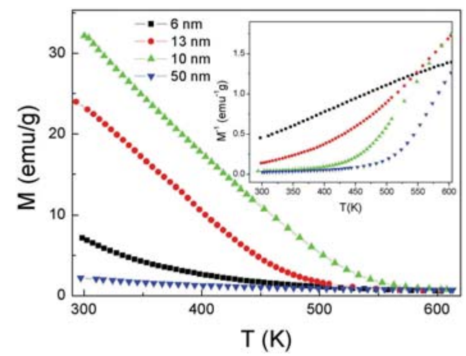

Figure 1: Temperature dependence of the magnetization on warming of nanocrystalline ZnFe2O4 obtained under a 10 kOe field. Inset: thermal dependence of the reciprocal magnetization (M-1 vs. T).

EW-10

Synthesis and magnetic properties of surface coated magnetite superparamagnetic nanoparticles.

K. Kim[1], M. Kim[2], Y. Choa[2], Y. Cha[1], T. Hwang[1], D. Kim[1]
1. Dept. of Physics, Yeungnam University, Gyeongsan, South Korea; 2. Dept. of Chemical Engineering, Hanyang University, Ansan, South Korea

Superparamagentic(SPM) iron oxide nanoparticles and their surface modification have been widely used experimentally numerous biomedical applications such as magnetic resonance imaging contrast enhancement, cell separation, tissue repair, detoxification, drug delivery and hyperthermia, etc.[1]. Therefore, we investigated the synthesis and magnetic properties of the magnetite nanoparticles and the surface coated nanoparticles, respectively. The magnetite nanoparticles were synthesized by the coprecipitation method. $FeCl_24H_2O$ and $FeCl_36H_2O$ (Fe^{3+} : Fe^{2+} = 1 : 2) were dissolved in deionized water under nitrogen with vigorous stirring at 80 ^oC and then the magnetite nanoparticles was obtained by adding NH_4OH was added to the solution. A 3-thioheneacetic acid (3TA) surface modification can introduce a dense and thin outer carboxylic acid group shell through a polymerization reaction. Therefore, the magnetite nanoparticles were encapsulated with 3TA. The 3TA was diluted to 2 mM by acetonitrile. A 1g amount of magnetite nanoparticles was added into the 10 ml of 3TA solution with stirring for 30 min. And $KMnO_4$ solution (2 mM) was dropped into it with stirring at 80 ^oC for 30 min. The solution was washed with ethanol for five times by magnetic separation.
Figure 1 (a) and (b) show the SEM images for morphology and the size distribution of the Fe_3O_4 nanoparticles and the surface modified with 3TA polymerization. The Fe_3O_4 and the 3TA coated Fe_3O_4 nanoparticles were spherically dispersed well. Figure 1 (c), (d) and (e) show the TEM, HRTEM images and the diffraction pattern of the magnetite nanoparticles. The average particle sizes are ~ 12 nm with fcc crystalline structure. In order to characterize the magnetic behaviors, the magnetic nanoparticles were measured by PPMS (Physical Property Measurement System) with the temperature range of 5 K to 300 K. The temperature dependence of the zero-field-cooled (ZFC) and field-cooled (FC) magnetizations of nanoparticles are shown in Fig. 2. The maximum in the ZFC curve defines the blocking temperature (T_B), where the thermal energy becomes comparable to the anisotropy energy barrier. T_B of uncoated and 3TA coated Fe_3O_4 exhibit ~ 245 K and ~ 220 K, respectively, which means the average particle size of 3TA coated Fe_3O_4 nanoparticles is a little bit smaller than those of uncoated Fe_3O_4[2]. The calculated average nanoparticle size of uncoated and 3TA coated Fe_3O_4 are obtained 10 nm and 8.9 nm, respectively, which can be predicted by Langevin function and ZFC curves[3]. As it is well known, above T_B, SPM particles become thermally unstable and the magnetizations exponentially decrease. Figure 3 (a) and (b) show the magnetization curves with the function of temperature for uncoated and 3TA coated Fe_3O_4 nanoparticles, respectively. The magnetization curves for uncoated and coated Fe_3O_4 show the typical SPM behavior above T_B. The values of magnetization (at 3 Tesla) of 3TA coated Fe_3O_4 nanoparticles are smaller than those of uncoated Fe_3O_4 as shown in Fig. 3 (c). It implies that Fe_3O_4 with coated 3TA are a little bit smaller than those of uncoated Fe_3O_4, which the reason would be resulted from the dead layer due to the interaction between core and shell interface. This result is consistent with that of ZFC magnetization results shown in Fig. 2 (a) and Stoner-Wohlfarth theory [4], which predicts an increase of the anisotropy energy barrier and, consequently, an increase of the T_B as the volume of the nanoparticles increase. Figure 3 (d) shows the coercivities which are decreased to nearly zero above TB. Below the T_B, the coecivity as a function of temperature follows well the linear relation [3]. As results, 3TA coated Fe_3O_4 nanoparticles were magnetically stable and dispersed well for biomedical applications.

[1] Ajay Kumar Gupta and Mona Gupta, Biomaterials, 26, 3995, (2005)

[2] Martinez B, Roig A, Obradors X, Molins E, Rouanet A and Monty C, J. Appl. Phys., 79, 2580 (1996)

[3] B. D. Cullity, Introduction to magnetic materials Addison-Wesley, 94 (1974)

[4] Sorensen C M 2002 Nanoscale Materials in Chemistry ed. (New York:Wiley), 169(2002)

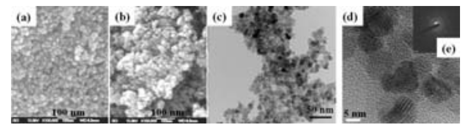

Fig. 1 SEM images of uncoated Fe_3O_4 (a), 3TA coated Fe_3O_4, TEM image (c), HRTEM image (d), and diffraction pattern (e) of the uncoated Fe_3O_4 nanoparticles.

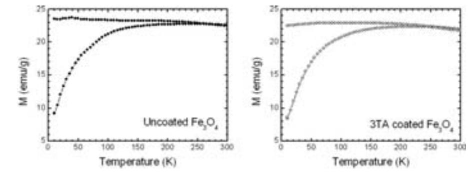

Fig. 2 Magnetization (M) versus temperature (T) measured in the ZFC and the FC modes at 300 Oe for the Fe_3O_4 and 3TA coated Fe_3O_4 nanoparticles (b), respectively.

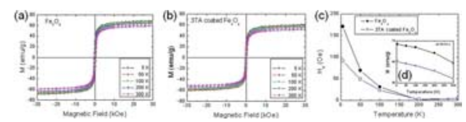

Fig. 3 The magnetization curves measured at 300 K to 5 K for uncoated Fe_3O_4 (a), 3TA coated Fe_3O_4 (b), the change of coercivities(c) and magnetizations(d) with a function of temperature for uncoated Fe_3O_4 and 3TA coated Fe_3O_4 nanoparticles, respectively.

EW-11

Magnetic properties of $Hf_{1-x}R_xFe_6Ge_6$ compounds.

J. Rubín[1], C. Piquer[1], N. Plugaru[1], J. Bartolomé[1], F. Grandjean[2]
1. Instituto de Ciencia de Materiales de Aragón, 50009 Zaragoza, Spain; 2. Dept. of Physics, Université de Liège, B-4000 Sart-Tilman, Belgium

The series RFe_6Ge_6 (R=rare earth) is a part of the family of AB_6X_6 compounds where A=Li, Mg, Sc, Nb, Y, Zr, Hf, B=Fe, Co, Ni, Mn, and X=Ge, Si [1]. The crystal structures are based on the SnCo-type (B35) hexagonal structure, which can be visualized as a sublattice of Co_6 hexagons (Kagomé planes) in a hexagonal sublattice of Sn atoms. The AB_6X_6 structures come out of the insertion of A atoms on the Sn-Sn axes (c-axis of B35). In the $HfFe_6Ge_6$-type, the substitution is complete on alternating FeGe units, with $a=a_h$, $c=2c_h$ (h standing for the CoSn(B35) unit cell), with a single Fe crystallographic site.
The RFe_6X_6 (X=Ge,Sn) compounds (R=Y, Gd-Lu) show unusual magnetic properties. In contrast to most rare-earth intermetallics, the Fe and the R sublattices are magnetically independent. While the Fe sublattice orders antiferromagnetically at about 485 K for the X=Ge and about 555 K for X=Sn, the R sublattice orders at much lower temperatures, from 3 K for $ErFe_6Ge_6$ and 45 K for $GdFe_6Sn_6$ [1]. The magnetic structure of the Fe sublattice consists of ferromagnetic hexagons with the magnetic moments along the c_h axis, which are antiferromagnetically coupled along this axis. The absence of coupling between both sublattices is due to a net cancellation of the R-Fe exchange at the rare-earth sites [3]. In some cases (R=Ti, Zr, Nb, Yb, Ho), the magnetic structure shows some magnetic moments deviated from the c_h axis at low temperature, as in the parent compounds FeGe. It has been claimed [4], that in compounds where there is no magnetic order of the R sublattice (the 3d, 4d, 5d metals and Yb), the values of the hyperfine field values classify in valence values of the R atoms, which has been attributed to hybridization of the Fe d states with the d valence states of the R metal. In fact, also the compounds where the R sublattice orders magnetically (Gd–Er) fall into the same valence dependence [2]. In the present work, we have followed the magnetic behaviour of the dilutions $Hf_{1-x}R_xFe_6Ge_6$ (R=Gd and Dy), where we have mixed trivalent and tetravalent atoms and the full rare-earth counterpart orders magnetically at low temperature.
Magnetization, ac magnetic susceptibility and ^{57}Fe Mössbauer spectroscopy experiments from 4.2 K to room temperature have been performed on $Hf_{1-x}Gd_xFe_6Ge_6$ (x=0, 0.4 and 1) and $Hf_{1-x}Dy_xFe_6Ge_6$ (x=0, 0.5 and 0.7). While the Gd sublattice of $GdFe_6Ge_6$ (x=1) orders magnetically at 29.3 K [2], a dilution of x=0.4 shows the same magnetic order at 10.5 K (Fig. 1). The Mössbauer spectra are shown in Fig. 2. The spectra of $HfFe_6Ge_6$ displays a sextet with asymmetric peaks below 50 K, which can be analysed as a fraction γ of Fe magnetic moments deviated from the c_h axis, as described in Ref. [5]. In contrast, $GdFe_6Ge_6$ shows a single sextet of symmetric peaks of small linewidths. The intermediate composition (x=0.4) also shows a sextet of symmetric peaks, but with linewidths of ≈0.4 mm/s at all temperatures. Similar spectra have been found in $Hf_{1-x}Dy_xF_6Ge_6$. The broadening of the diluted compounds can be produced by a disordered environment of the Fe sites as Gd/Dy substitute for Hf, which would mask a slight deviation of the magnetic moments, if there is any. The substitution of Hf by Dy or Gd decreases the hyperfine field values, B_{hf}, an effect which is slightly more pronounced in the case of Dy. The observed behaviour of B_{hf} in the $Hf_{1-x}R_xFe_6Ge_6$, R = Gd and Dy, series can be explained with a combination of two effects. On one hand, since Hf is tetravalent whereas Gd and Dy are trivalent, the progressive substitution of Hf by Gd or Dy leads to a depletion of the d valence band of the R sublattice. Consequently, the Fe magnetic moment and the hyperfine magnetic field decrease when x increases. On the other hand, due to the lanthanide contraction, the 5d(Dy) states are more localized than the 5d(Gd) states. As a result, the hybridization with the 3d Fe states is weaker in the Dy case, and the decrease of B_{hf} upon the Dy substitution is more pronounced.

[1] Venturini G, Welter R & Malaman B, J. Alloys Comp. 185, 99 (1992)

[2] Cadogan J M & Ryan D H, J. Alloys & Comp. 326, 166 (2001).

[3] Beckman O, Carrender K, Lundgren L & Richardson M, Phys. Scripta 6, 151 (1972).

[4] Mazet T, Isnard O & Malaman B, Solid State Comm. 114, 91 (2000).

[5] Mazet T & Malaman B, J. Phys.: Condens. Matter 12, 1085 (2000).

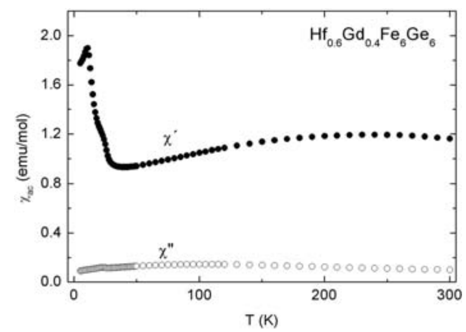

Temperature dependence of the real and imaginary magnetic susceptibility of $Hf_{0.6}Gd_{0.4}Fe_6Ge_6$.

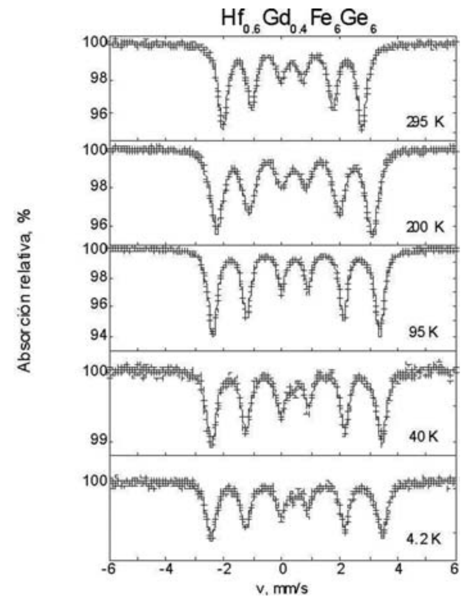

Mössbauer spectra of $Hf_{0.6}Gd_{0.4}Fe_6Ge_6$ at different temperatures.

EW-12

Mössbauer study of iron sulfide nano-compound.

S. Hyun, I. Shim, C. Kim
Physics, Kookmin University, SEOUL, South Korea

Introduction

The Fe–S system has been studied to investigate a complex phase diagram by many researchers [1]. The iron (II) sulfide (FeS) has been much interested for the phase stability and physical properties under high pressure and temperature [2,3]. Stoichiometric iron (II) monosulfide (FeS), troilite has a hexagonal close packed structure with antiferromagnetic ordering at room temperature. It undergoes α transition into the ideal (NiAs) hexagonal structure which includes the pyrrhotites ($Fe_{1-x}S$) between 120 ~ 140 °C [1,4]. Besides, pyrrhotites ($Fe_{1-x}S$) show ferrimagnetic behavior due to unbalanced ferromagnetic coupling. In this paper, we report the ferrimagnetic behavior of nanocompound iron(II) monosulfide (FeS) at room temperature.

Experiments

The iron sulfide, FeS, was fabricated using a polyol method. The sulfur solution was the first prepared with sulfur powder and oleylamine. Iron(III) acetylacetonate was mixed in oleylamine for 30 min. under vacuum, then heated up to 80 °C to clearly dissolve it and maintained for 30 min. under Ar atmosphere. It reheated up to 340 °C and injected rapidly the sulfur solution under Ar atmosphere. Then, it cooled down to room temperature.

The phase purity and crystallinity of synthesized sample were characterized by X-ray diffraction (XRD) measurements using Cu$K\alpha$ radiation (λ = 1.5406 Å). Mössbauer spectrometer of the electromechanical type with a 50 mCi ^{57}Co source in Rh matrix was used in the constant-acceleration mode. The Mössbauer parameters were obtained by a least-squares fitting program assuming Lorentzian line shapes. The magnetizations were measured by using a vibrating sample magnetometer (VSM).

Results and discussion

XRD was used to confirm the crystal structure and crystallographic parameters of FeS nanocompound, as shown in Fig. 1. An analysis of XRD patterns by Rietveld refinement method using FULLPROF program shows that the sample has a troilite hexagonal structure (space group *P-62C*) with a lattice constant a_0 = 5.985 ±0.001, b_0 = 5.985 ±0.001 and c_0 = 11.658 ±0.001 Å.

The hysteresis loop measured using VSM with maximum applied field 1 T at room temperature shows the ferrimagnetic behavior as shown in Fig. 2. The saturation magnetization (M_s) and the coercivity (H_c) values of the sample are found to be 1.8 emu/g and 251.1 Oe, respectively.

The Mössbauer spectra of FeS nanocompound were taken at various temperatures ranging from 4.2 to 295 K to understand localized nearest neighbor effects on effective field, as shown in Fig. 3. We notice that the Mössbauer absorption spectrum shows 2-sextets at room temperature, while it shows a clear 1-sextet at 4.2 K. We conclude that FeS nanocompound shows ferrimagnetic behavior at room temperature as pyrrhotites ($Fe_{1-x}S$) by analysis of Mössbauer spectrum. This is consistent with the result of hysteresis loop obtained by VSM measurement, too. The isomer shift value at room temperature is found to be (0.60 ~ 0.64) ± 0.01 mm/s, relative to the Fe metal, which are consistent with the Fe^{2+} valence state. The ferrous character of the Fe ions is also manifested by the magnitudes of the magnetic hyperfine fields: the magnetic hyperfine field of FeS nanocompound is approximately 327 ± 5 kOe at 4.2 K, which corresponds to ferrous ion.

[1] J. M. Soon, L. Y. Goh, K. P. Loh, Y. L. Foo, L. Ming, and J. Ding, Appl. Phys. Lett., 91, 084105 (2007).

[2] H. Ohfuji, N. Sata, H. Kobayashi, Y. Ohishi, K. Hirose, T. Irifune, Phys. Chem. Miner., 34, 335 (2007).

[3] L. Chen, M. Matsunami, T. Nanba, H. Kobayashi, Physica B, 378-380, 1116 (2006).

[4] J. E. Thomas, W. M. Skinner, and R. St. C. Smart, Geochim. Cosmochim. Ac., 67, 831 (2003).

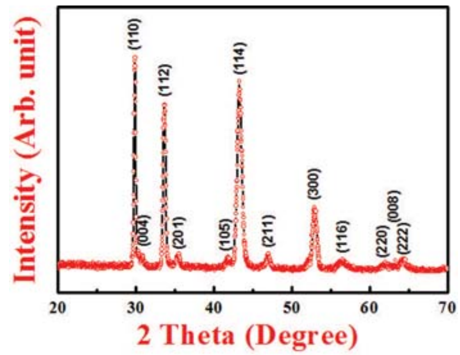

Fig. 1. X-ray diffraction pattern of FeS nanocompound prepared by polyol method.

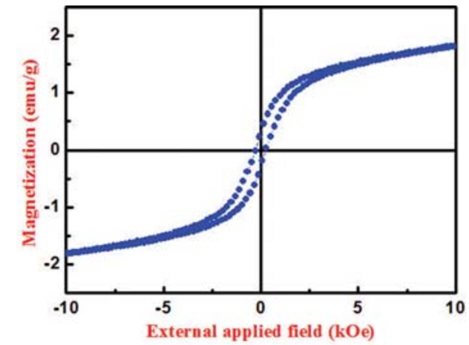

Fig. 2. Hysteresis loop of FeS nanocompound at room temperature.

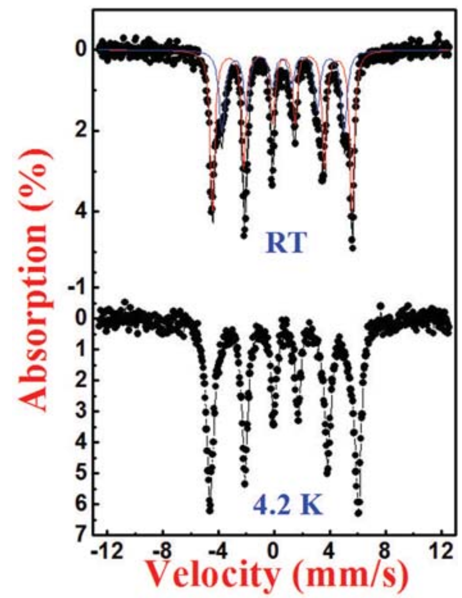

Fig. 3. Mössbauer spectra of FeS nanocompound at various temperatures.

EW-13

Preparation of Metal-Polymer composite films by metal- polymer co-electrodeposition method.

N. Fujita[1], M. Matsuba[1], Y. Toujou[1], T. Kazuya[1], N. Satoru[1], I. Masanobu[2], I. Mitsuteru[2]
1. Nara National College of Technology, Yamatokoriyama, Japan; 2. Toyohashi University of Technology, Toyohashi, Japan

Metal-oxide ferromagnetic granular films, such as Co-Al-O, Fe-Si-O, and Co–Sm-O, exhibit high electric resistance and high permeability at high frequencies; therefore, these films have the potential to be used for integrated thin-film inductive elements and electromagnetic shielding films. We reported that Co-Ce-O [1] and Fe-Ce-O [2] films were successfully deposited by the electrochemical method. In this study, ferromagnetic metal-insulated polymer composite films were synthesized from the reaction solution containing metal cation and water-soluble resin by a newly developed electrochemical method called the "metal-polymer co-electrodeposition method". Ferromagnetic metal cobalt (Co) is deposited by an ordinary metal reduction reaction. $Co^{2+} + 2e^- \rightarrow Co$. On the other hand, polymer resin is deposited combined with hydroxide ions near the cathode, which is generated by the electrolysis reaction of the water. $2H_2O + 2e^- \rightarrow H_2 + 2OH^-$. $(Resin)_3NH^+ + OH^- \rightarrow (Resin)_3N + H_2O$. Metal-polymer composite film was deposited galvanostatically at -1.3 mA/cm2 from the reaction solution containing 10 - 50 mM cobaltous acetate, 20 - 100 mM glycine, 2.5 ml/l water-soluble resin, adjusted pH 7.0 by DMAE and maintained at 333 K. It became clear that uniform stirring of the reaction solution was important to obtain an even film. The FT-IR spectrum (Fig. 1) of the deposited composite films matched that of the film deposited from the reaction solution containing only water-soluble resin. Electric resistance of the films deposited from Co concentration less than 30 mM showed over 30 MΩ. The deposited films showed the ferromagnetic hysteresis loop. Figure 2 shows the coercivity dependence on the Co concentration in the reaction solution. Coercivity decreased by increasing the Co concentration below 20 mM. On the other hand, coercivity increased by increasing the Co concentration above 30 mM. Figure 3 shows the X-ray diffraction pattern of the deposited films. Diffraction peaks attributed to hcp Co, and In2O3 (ITO substrate) were observed from the films deposited from the Co concentration above 35 mM. However, only In2O3 peaks were observed from the films deposited at a Co concentration less than 30 mM. These results suggest that the microstructure of the Co-polymer films changed at around Co concentration 30 mM. Figure 4 shows the XPS profile of Co 2p for the film prepared from the reaction solution containing Co concentration 30 mM. The Co 2p3/2 peaks that coincided with Co in metallic Co were observed. This result suggests that films containing ferromagnetic metal and polymer resin with high electric resistance were successfully prepared using the electrochemical method.

[1] N.Fujita,Y.Mori,R.Yagi,M.Izaki,M.Inoue, IEEE Trans. Mag., 38, p2619 (2002).

[2] N.Fujita, M. Izaki, M. Inoue, J.Mag. Mag. Mate, 300 p e350 (2006)

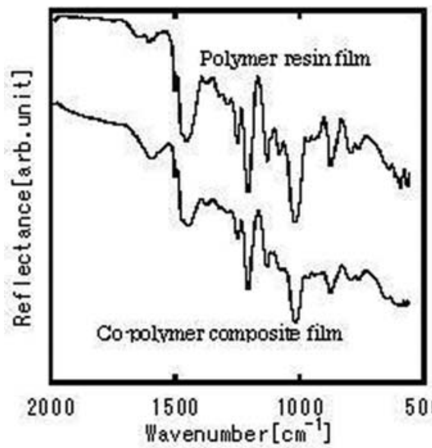

Fig. 1 FT-IR spectrum of Co- polymer composite film.

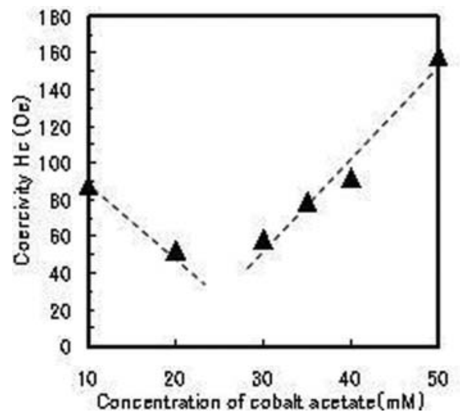

Fig.2 Dependence of the coercivity on the Co concentration in the reaction solution.

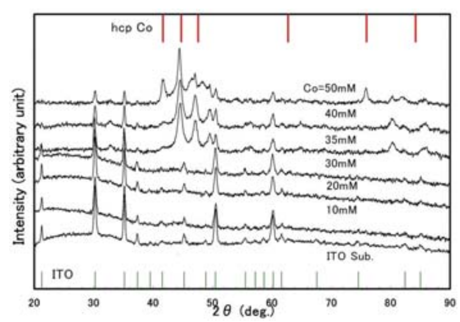

Fig.3 X-ray diffraction patterns of the Co-Polymer composite films.

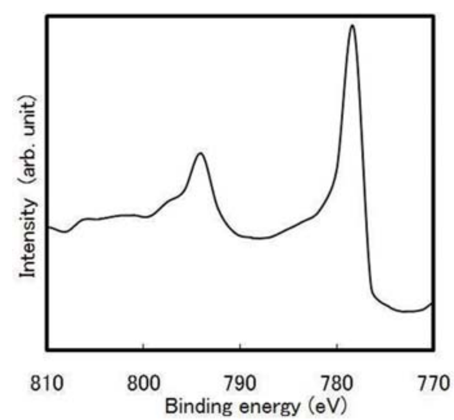

Fig. 4 Co 2p photoelectron spectra of the Co-polymer composite film.

EW-14

Nonlinear homogenisation technique for saturable soft magnetic composites.

O. Bottauscio[1], M. Codegone[3], V. Chiado' Piat[3], M. Chiampi[2], A. Manzin[1]
1. Electromagnetics, Istituto Nazionale di Ricerca Metrologica, Torino, Italy; 2. Dip. Ingegneria Elettrica, Politecnico di Torino, Torino, Italy; 3. Dip. Matematica, Politecnico di Torino, Torino, Italy

Soft magnetic composites are becoming competitive for applications in electrical machines and actuators, due to the improvement of their magnetic properties [1]. These materials are constituted of insulated iron powders, compacted through high compressive stress, leading to heterogeneous media having a granular nature. The presence of intergranular induced currents can affect the material behaviour and, particularly, the magnetic losses.
The analysis of devices including soft magnetic composites requires the knowledge of their effective electric and magnetic properties, which are influenced by the properties of the constituents, the interaction between them and the geometrical configuration. Well-known rules for determining the effective properties are the Maxwell–Garnett and the Bruggeman formula, valid under the assumptions of elliptical and spherical inclusions, and of linear magnetic properties [2]. Approaches based on energetic considerations have been also proposed and extended to nonlinear magnetic properties [3]. A more general framework consists in the application of the multiple scale expansion technique to the Maxwell equations, without limitation to inclusion shape and constituent properties.
A homogenisation technique based on the multiple scale expansion theory has been applied by the authors to heterogeneous linear materials [4]. Recent extension to nonlinear media have been proposed for magnetic flux driven problems, where the role of nonlinearity is included in the right-hand side of the differential problem equation and it is handled by a simple spatial average of the magnetic nonlinear characteristics of the constituents [5].
In this paper a novel formulation is proposed and applied to a current driven electromagnetic field problem, where the nonlinearity is included as an argument of the second-order differential operator. Thus the homogenisation process leads to the evaluation of effective nonlinear magnetic characteristics, which depend on the inclusion shape and dimension. The stochastic nature of the composite material is approximated by a fine periodic structure, identifying a basic elementary cell constituted of the inclusion and the surrounding non-magnetic layer. Nonlinear field problems are solved on the elementary cell, introducing the properties of the constituents, in order to determine a tensor of homogenized equivalent magnetic curves. The result of this procedure is the definition of an equivalent homogeneous material, having effective electrical conductivity and nonlinear magnetic curve, to be used in finite element field computations, with a significant reduction of the required computational burden.
In the results here reported, the ferromagnetic particle is assumed to have a cubic shape with side s_p equal to 0.05 mm or 0.2 mm (see Fig. 1). The particle is constituted of pure iron, with electrical conductivity equal to 10 MS/m and B-H curve reported in Fig. 2. The nonmagnetic layer around the particle has low conductivity (10 S/m) and variable thickness s_{layer} (from 0.2 µm to 1 µm), leading to interparticle conductivity of the order of the experienced values [1]. The homogenized electrical conductivity σ_e is plotted in Fig. 1 against the layer thickness, and the homogenized B-H curves are reported in Fig. 2 for different values of particle size and layer thickness.
In the full paper, the mathematical formulation will be described in details and applied to the analysis of the influence of the inclusion shape and dimension on the effective electrical conductivity and nonlinear properties of the soft magnetic composite.

[1] A. Jack, et al., "Soft magnetic composites for electrical machines – the state of the art (invited talk)", 18th Soft Magnetic Materials Conf., Cardiff (Galles), Sept. 2007.

[2] A. Sihvola, "Electromagnetic mixing formulas and applications", IEE Electromagn. Waves Series, vol. 47, pp. 63–68, 1999.

[3] H. Waki et al., "Analysis of Magnetic Shielding Effect of Layered Shields Based on Homogenization", IEEE Trans. Magn., vol. 42, pp. 847-850, 2006.

[4] O. Bottauscio et al., "Evaluation of effective electromagnetic properties in heterogeneous media", European Physical Journal - Applied Physics, vol. 39, pp. 113-118, 2007.

[5] O. Bottauscio et al. "Multiscale analysis of highly heterogeneous nonlinear media", presented at 52nd MMM Conf., Tampa, Florida, 2-5 Nov. 2007. To appear on J. Appl. Phys.

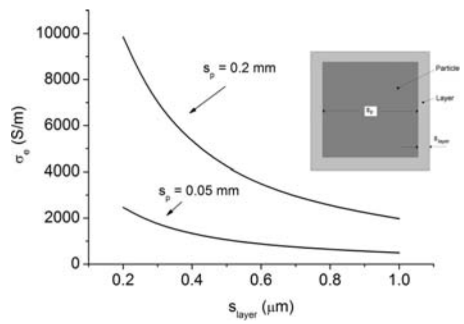

Fig. 1 Homogenized electrical conductivity for iron particle of dimension equal to 0.05 mm and 0.2 mm.

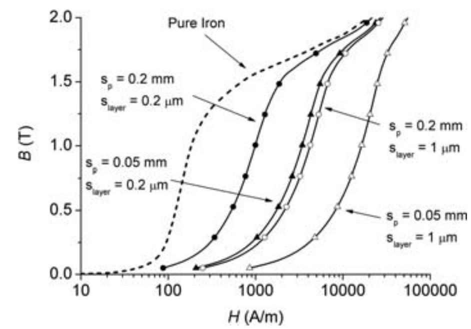

Fig. 2 Homogenized B-H curves for iron particle of dimension equal to 0.05 mm and 0.2 mm.

EW-15

Structural and magnetic properties of nanocrystalline strontium hexaferrite prepared by an ionic reaction technique.

J. Araujo[1], F. Cabral[1,4], *J. Soares*[2], M. Ginani[3], F. Machado[4], J. Cunha[5]
1. Departamento de Física Teórica e Experimental, Universidade Federal do Rio Grande do Norte, Natal, Brazil; 2. Departamento de Física, Universidade do Estado do Rio Grande do Norte, Mossoró, Brazil; 3. Departamento de Química, Universidade Federal do Rio Grande do Norte, Natal, Brazil; 4. Departamento de Física, Universidade Federal de Pernambuco, Recife, Brazil; 5. Instituto de Física, Universidade Federal do Rio Grande do Sul, Porto Alegre, Brazil

Hexaferrites have physical and chemical properties that make them very attractive for some technological applications. They have high saturation magnetization, high magnetic anisotropy and good chemical stability. Strontium hexaferrite $SrFe_{12}O_{19}$, in particular, exhibits high coercivity due to the existence of a large magnetocrystalline field in this material. The coercive field H_C does also depend on the microstructure of the material which, in turn, is influenced by the techniques used to prepare the sample. Therefore, a good control of the structural properties of the samples are necessary to optimize their magnetic properties. Furthermore, there are applications that require nanoparticles within the single magnetic domain regime and with a narrow particle size distribution. Strontium and barium hexaferrite, for instance, has been used in the preparation of permanent magnets and in plastic-ferrite materials, in magnetic recording media and in microwave devices [1,2]. The conventional solid state reaction route used to prepare powders of hexaferrite make use of heat treatments at temperatures above 1000 ^oC [3]. This technique yields particle size distributions that are coarser than those obtained using the ionic coordination reaction (ICR) technique, for instance.
In the present work, the formation of nanocrystalline strontium hexaferrites $SrFe_{12}O_{19}$ using a new route of an ICR technique was carefully investigated. In this processing, the biopolymer chitosan was used as a nanoreactor. Chitosan is an aminopolysaccharide extracted by a deacetylation procedure from chitin, the most abundant biopolymer in nature after cellulose. It is characterized by a high nitrogen content in the amino group which is mainly responsible for its ability to react with several types of metal ions through ionic coordination processes. The ICR technique is also attractive because of its low-cost, low-temperature synthesis, high homogeneity and a simple processing. The obtained precursor powders were calcined at temperatures in the range 600-900 ^oC. The amount of the hexaferrite phase present in each sample was determined using X-ray diffraction and from Mossbauer data. It was observed that the average particle size increases as the calcination temperature T_o is increased. In particular, the Rietveld refinement analysis yielded 41.6 nm for the sample calcined at 900 ^oC. This value is in good agreement with the one obtained from the SEM images.
The Mossbauer spectra were fitted to Lorentzian curves using a least-squares computer program. Five Lorentzian sextets corresponding to five non equivalent sites in the hexaferrite phase and one Lorentzian sextet corresponding to hematite were used to fit the samples calcined at 800 and at 900 ^oC. For the sample calcined at 600 ^oC, it was also necessary to add two Lorentzian sextets corresponding to the maghemite phase. For the sample calcined at 700 ^oC, it was only necessary to add one maghemite Loretzian sextet to fit the spectrum. The observed isomer shifts are in the range 0.10-0.28 mm/s relative to metallic iron indicating that the ionic state of iron ions on the five sites is ferric Fe^{3+}. In the M-type hexagonal structure of $SrFe_{12}O_{19}$ the Fe^{3+} ions occupy five different crystallographic sites: three are octahedral sites, one site is tetrahedral and one is trigonal bi-pyramidal. The point symmetry of these sites is consistent with an asymmetry parameter η=0, and an electric field gradient tensor with its principal axis parallel to the c-axis. The quadrupole splitting of the trigonal bi-pyramidal site was found to be substantially large because of its strongly distorted environment.
The hysteresis loop for the sample calcinated at 600 ^oC showed a behavior characteristic of a mixture of hard (Sr-hexaferrite) and soft (maghemite) magnetic materials. However, the magnetization measurements yielded squared hysteresis loops for the samples annealed at and above 700 ^oC. The overall results indicate that the particles in these samples are in the single domain regime. This is also supported by the theoretical models used to describe uniaxial single domain particle systems. For Sr-hexaferrite, the critical diameter D_{crit} of a spherical single domain particle is 940 nm. Moreover, the value for H_C at room temperature for a system of randomly distributed single domain $SrFe_{12}O_{19}$ particles under reverse magnetization is 6.70 kOe. This value is based on the coherent rotation Stoner-Wohlfarth model. As reported above, the values for the average particle size obtained for our samples are much less than the D_{crit} for an ensemble of $SrFe_{12}O_{19}$ particles. Besides, the theoretical value for H_c is close to the values obtained experimentally from our magnetization data (6.48 kOe). Furthermore, the ratio M_r/M_s (= 0.58) for the samples annealed at and above 700 ^oC does also agree with the theoretical ratio (=0.5) calculated for a system of randomly distributed single domain particle. These results are also in good agreement with the ones obtained from transverse susceptibility measurements. Thus, based on experimental results and on the framework of Stoner-Wohlfarth based models one can conclude that the magnetization reversal in these particles is mainly due to coherent rotation.
Acknowledgments: Work partially supported by CNPq, FINEP and FACEPE (Brazilian Agencies).

[1] J. F. Wang, C. B. Ponton, I. R. Harris, J. Magn. Magn. Mater. **234** (2001) 233.

[2] T. Fujiwara, IEEE Trans. Magn. **MAG-21** (1985) 1480.

[3] G. C. Bye and C. R. Howard, J. Appl. Chem. Biotechnol. **21** (1971) 319.

EX-01

Tunnel spin-polarization of low-work-function ferromagnets.

R. Patel, B. Min, S. Dash, M. de Jong, R. Jansen
MESA+ Institute for Nanotechnology, University of Twente, Enschede, Netherlands

The magnetic tunnel junction (MTJ) is a central element in many spintronic devices and applications. As such, it is crucial to be able to control the tunnel spin-polarization (TSP), while simultaneously achieving a proper resistance area (RA) product matched to a particular application. The requirement for low resistance MTJs pushes the tunnel barrier thickness to the limit where pinholes become an issue. Also, in spin tunnel junctions to semiconductors, for example for spin-injection and detection in spin-transistors, it is paramount to obtain contacts that have a high tunnel spin-polarization, as well as the proper resistance. In order for a spin-MOSFET to exhibit any sizeable magnetoresistance, the RA product of the magnetic source and drain contacts needs to be in a rather narrow window, and it was recently shown that Schottky barrier formation is a severe obstacle in achieving the proper RA product in contacts with conventional transition-metal ferromagnets [1,2]. To solve this issue, a novel approach to control the RA product of spin-tunnel junctions was recently developed [1], involving the introduction of an ultrathin (sub-nm) interlayer of a ferromagnetic material with a low-work-function at the tunnel interface of FM/Al2O3/Si spin tunnel contacts.
Here, we further examine the effect of such a low-work-function interlayer on the TSP using metal MTJs of the form Co/Al2O3/X/Ni80Fe20, where X is a material with low-work-function for which we have used Gd (3.1eV), Gd/Co bilayers, or Yb (2.6eV). These studies provide valuable insight into the effect of such an interlayer on the TSP, and simultaneously allows one to probe the interaction of the (spin of the) conduction electrons of rare-earth elements with transition-metal ferromagnets.
In figure 1 we see that the TSP for Al2O3/Gd/Ni80Fe20 interfaces decays with Gd thickness, but is always positive. The situation is different for the junctions with a Gd/Co bilayer of total thickness of 1 to 1.2 nm introduced between the Al2O3 and the Ni80Fe20. In that case, depending on the relative thickness of the Gd and Co in the bilayer, the TMR was found to be either positive (for large Co content) or inverted to a negative sign (at large Gd content, bottom right panel of figure 2). Since for Gd the 5d and 6s conduction electrons, rather than the localized 4f electrons, are expected to dominate the tunneling process, the difference reflects the nature of the coupling between the 5d/6s conduction electrons of Gd with Ni80Fe20 or Co, respectively. The negative TSP observed in figure 2 is consistent with an antiferromagnetic coupling of the Gd 5d and 6s electrons to Co. Figure 3 shows the TSP versus temperature for MTJs with an Al2O3/Yb(0.8nm)/Ni80Fe20 top electrode. The Yb was chosen because of its very low work-function, but also because it has a closed 4f shell with no magnetic moment. We find that the TMR decreases with insertion of the Yb interlayer, but more rapidly in comparison with a Gd interlayer. At 10K, the TMR is reduced to 15% for 0.8 nm of Yb, while for thicker Yb layers the TMR rapidly decays to zero.

[1] B.C. Min, K. Motohashi, J.C. Lodder and R. Jansen, Nature Materials 5, 817 (2006).

[2] R. Jansen and B.C. Min, Phys. Rev. Lett. 99, 246604 (2007).

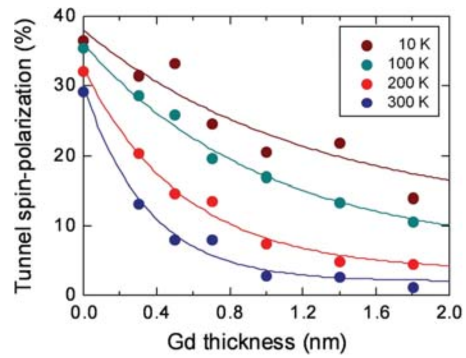

Fig 1. Tunnel spin-polarization versus Gd thickness for Co/Al2O3/Gd/Ni80Fe20 magnetic tunnel junctions, measured at T = 10, 100, 200, and 300K.

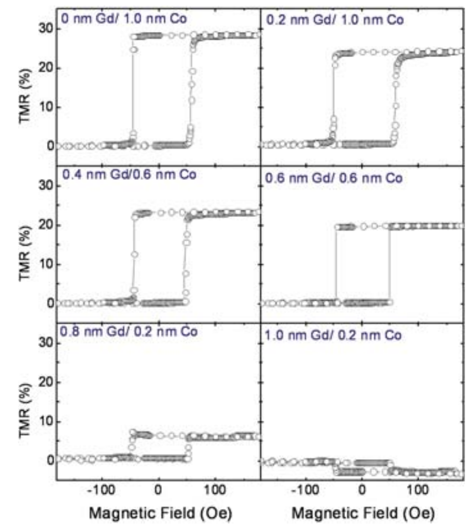

Fig. 2. Tunnel magnetoresistance curves for Co/Al2O3/Gd/Co/Ni80Fe20 tunnel junctions with the Gd and Co thickness as indicated (T=10K). The magnetization of the top electrode was pinned using a CoO exchange bias layer.

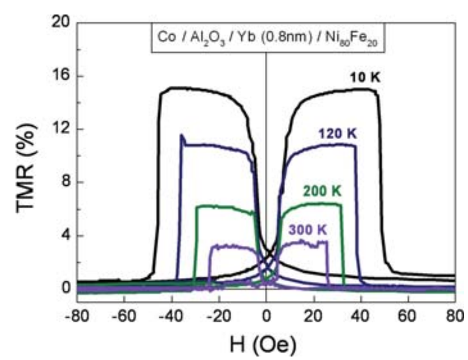

Fig. 3. Tunnel magnetoresistance curves for Co/Al2O3/Yb/Ni80Fe20 tunnel junctions with 0.8nm Yb, measured at different temperatures between 10 and 300K.

EX-02

Strain dependence of magnetoresistance in magnetostrictive magnetic tunnel junctions.

J. G. Deak
Advanced Technology, NVE Corporation, Eden Prairie, MN

The strain (ε) dependence of magnetoresistance (MR) was studied in various magnetic tunnel junctions (MTJ) utilizing magnetostrictive freelayer materials. The MTJs had similar bottom pinned layers and Al_2O_3 tunnel barriers. The freelayers differ in composition (CoFeB and Co70Fe30) and thickness (5 nm to 10 nm). The films were deposited on SiN coated Si wafers, which were flexed in order to induce ε, similar to a ε sensor. [1-3] R(H) was measured under tensile stress (σ) applied parallel to the easy-axis. MR was found to increase by a maximum of about 1% in the Co70Fe30 and 0.5% in the CoFeB devices as the ε exceeded 300 ppm. For all devices tested, resistance decreased in the parallel (Rp) and anti-parallel (Rap) orientations as tensile ε increased. This effect has not been explained. Various causes for the effect including improved domain alignment and thinning of the tunnel barrier under tensile ε due to Poisson's ratio (ν) were studied. Magnetic modeling shows domain reorientation does not produce the correct dependence of resistance on ε. Results suggest that the modification of the barrier thickness as σ is applied in the plane of the film must be taken into account.

Figure 1 shows representative R(H) loops for a CoFeB MTJ as a function of applied σ. Note that both Rp and Rap decrease and MR increases as σ is increased. Similar data was acquired on 60 devices, and measured average trends in MR, Rap, and Rp are given in Table 1.

Figure 2 shows a Stoner-Wohlfarth (SW) model including magnetostriction used in an attempt to explain the resistance and MR ε dependences. Similar plots were created for varying degrees of misalignment. Here, Rap decreases, Rp increases, and MR decreases as σ is increased. These trends in the magnetic simulation are a result of changing alignment in the layers as ε-anisotropy increases. They do not agree with measurement.

In an attempt to better predict the affect of ε on the magnetostrictive MTJs transport behavior, the change in the thickness of the tunnel barrier (d) under ε was taken into account, and included in a modified Simmon's model. [1,4] Figure 3 shows a plot of Rap, Rp, and MR showing that the correct trends are reproduced using this model.

Although the model could be improved, it does seem to reproduce the correct behavior. The ε-dependence of the elastic and inelastic tunneling conductivity should be taken into account in order to further linearize MTJ ε sensor response. [1] A better understanding of ε-dependence of MTJ transport characteristics might also be used to develop techniques for utilizing ε applied during the manufacturing process to improve MTJ performance.

[1] D. Wang, C. Nordman, Z. Qian, J. M. Daughton, and J. Myers, JAP 97#10, 10C906, (2005).

[2] H. Hauser, M. Ruhrig, and J. Wecker, JAP 95, 7528 (2002).

[3] M. Lohndorf, S. Dokupil, J. Wecker, M. Ruhrig, and E. Quendt, JMMM 272-276, 2023-2024 (2004).

[4] J. G. Simmons, JAP 34#6, 1793 (1963).

material	thick (nm)	avg Hc (Oe)	λ (ppm)	avg MR (%)	dRap/Rap/ε	dRp/Rp/ε	dMR/MR/ε
CoFeB	50	54.3	31.0	3.9	-119.9	-119.3	300.9
CoFeB	100	44.7	31.0	35.6	-51.8	-62.8	34.7
CoFe	50	172.6	85.8	42.4	-111.4	-180.4	246.6
CoFe	100	166.6	120.3	50.1	-120.7	-175.4	164.4

Measurement Summary A summary of the normalized dependence of Rap, Rp, and MR on ε.

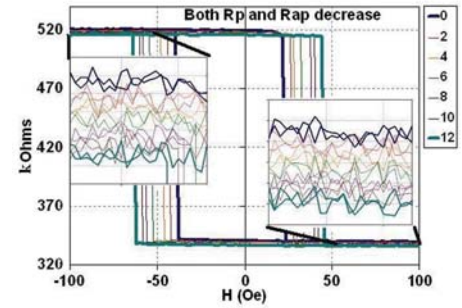

R(H) MEASURED for an MTJ with 5 nm thick CoFeB freelayer. The inset details the relative change in Rap, Rp, as ε is increased.

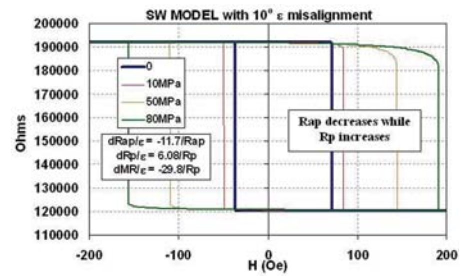

R(H) SIMULATED using SW model with $\lambda=10^{-5}$, M_s = 1600 emu/cc, P=0.5, and tensile stress applied at 10° to the easy-axis. A pinning field of 500 Oe is assumed. The inset shows normalized changes in Rap, Rp, and MR as ε is increased. Magnetic simulation alone cannot reproduce the measured behavior.

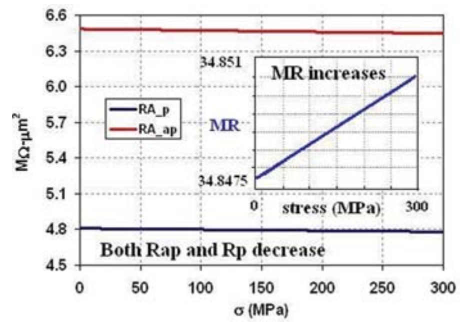

A plot of the calculated change in Rap, Rp, and MR for a MTJ using a Simmon's model modified to account for the strain's reduction of barrier thickness. The ν dependent change in the barrier thickness produces the correct trends in Rp and Rap. MR increases less strongly than measurement, but it is consistent with measurement.

EX-03

Broadband Ferromagnetic Resonance Linewidth Measurements of Magnetic Tunnel Junction Multilayers.

J. Sierra[1], F. Aliev[1], R. Heindl[2], S. Russek[2], W. Rippard[2]
1. Condensed Matter Physics, UAM, Madrid, Spain; 2. NIST, Boulder, CO

Magnetic tunnel junctions (MTJs) are being developed for a large range of applications including magnetic recording sensors, low-field magnetic sensors, magnetic random access memory, and high-frequency spintronics devices [1,2]. The quality of the MTJs depends sensitively on interfacial properties [3,4]. These properties include interfacial roughness, intermixing, oxygen content, which in turn depend on materials used in the stack, deposition conditions, and annealing conditions. Ferromagnetic resonance (FMR) has been shown to be an effective tool to get insight into both the magnetization dynamics and the quality of single ferromagnetic layers, multilayers and MTJs. Here we present broadband FMR measurements in MTJs over a frequency range of 0 to 20 GHz to characterize their dynamic properties.

Our MTJ were fabricated using Al2O3 tunnel barriers and CoFeB/NiFe free layers and underwent a sequence of anneals at various temperatures. We have used VNA-FMR technique to determine FMR resonance position and FMR linewidth [5]. We put MTJs covered with a thin layer of photoresistive material on top of a coplanar wave guide (CPW). In this way, FMR of the free layer of the MTJ has been excited in the presence of a permanent in-plane magnetic field (Hb) and by sweeping frequency of the excitation signal from the port 1 of the VNA, that creates the perpendicular RF component of the magnetic field (Hrf). The FMR signal was detected by measurements of the transmission to VNA port 2 through the CPW with the specimen on top. All experiments were done at room temperature.

It was found that the FMR linewidth of the free layer is considerably larger than that of an isolated free layer and that the linewidth increases in the regions of the free layer reversal and the fixed layer reversal. The increase in FMR linewidth was correlated with both the magnetization hysteresis curves in unpatterned films and low frequency noise in patterned devices. The large increase in free layer linewidth and its subsequent change upon annealing indicates that considerable disorder, originating in the exchange-biased fixed layer, is transferred to the free layer [6]. In addition, we have found that the regions of increased linewidth, as with the regions of increased 1/f noise, are history dependent, i.e. depend on the starting magnetic state of the MTJ. We show that the increase in FMR linewidth is a simple and effective method of monitoring the disordered magnetic structure, interfacial roughness, and the improvement during the annealing process. Hence, the study of FMR linewidth of the free layer of MTJs may be a useful diagnostic on the quality of the MTJs being developed for a variety of applications.

[1] A. A. Tulapurkar et al, Nature 438, 239 (2005).

[2] P. P.Freitas, R. Ferreira, S. Cardoso and F. Cardoso, J. Phys.: Condens. Matter. 19, 165221 (2007).

[3] J. S. Moodera, J. Nassar, and G. Mathon, Annu. Rev. Mater. Sci. 29, 381 (1999).

[4] E. Y. Tsymbal, O. N. Mryasov, and P. R. LeClair, J. Phys.: Condens. Matter 15, R109 (2003).

[5] Sangita S. Kalarickal et al, J. Appl. Phys. 99, 093909 (2006).

[6] Justin M. Shaw, Roy Geiss, and Stephen Russek, Appl. Phys. Lett. 89, 212503 (2006).

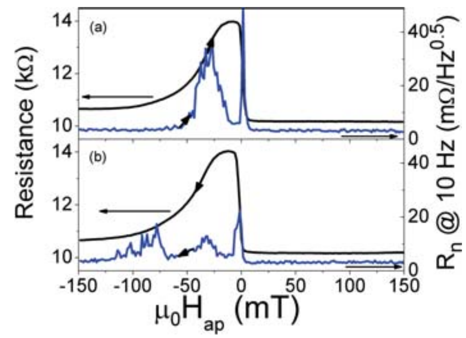

Fig. 1 Resistance of a symmetric MTJ bridge (a) from -150 to 150 mT (b) from 150 to -150 mT. Also plotted is the resistance noise measure at 10 Hz of the MTJ bridge for both positive and negative going branches.

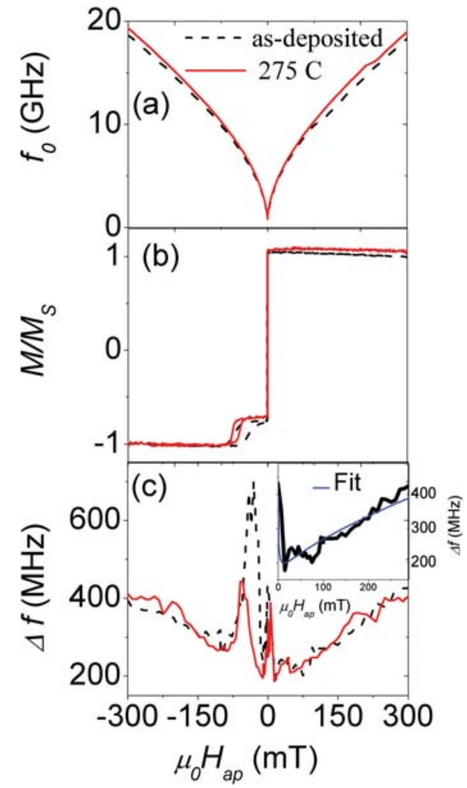

Fig. 2 FMR frequency (a), magnetization (b) and FMR linewidth (c) for the as deposited and 300 C annealed MTJs. The inset to (c) shows the fit to the linewidth data for the as deposited MTJ [4]

EX-04

Effect of interface roughness on magnetoresistance and magnetization switching in magnetic tunnel junction.

B. Chun[1], M. Coey[1], S. Lee[2], J. Hwang[2], J. Rhee[2], H. Yim[2], T. Kim[3], Y. Kim[4], Y. Kim[4]
1. School of Physics, Trinity College, Dublin, Ireland; 2. Department of Physics, Sookmyung Women's University, Seoul, South Korea; 3. Nanotechnology and Advanced Materials Engineering, Sejong University, Seoul, South Korea; 4. Department of Materials Science and Engineering, Korea University, Seoul, South Korea

Introduction:
A double barrier magnetic tunnel junction (DMTJ) has been introduced to suppress the bias voltage dependence of tunneling magnetoresistance (TMR) ratio. Because in the DMTJ, the voltage is divided between two tunnel barriers, and thus, the reduction of the TMR ratio at a given bias is smaller than that in the single barrier MTJ. In the DMTJ, however, top barrier flattening is one of the most important issue because the metallic polycrystalline free layer over the bottom tunnel barrier is difficult to grow uniformly, and consequently, the top barrier interface became rough [1]. To resolve this problem, we introduced an amorphous magnetic CoFeSiB to retard the columnar growth resulting in a wavy interface.
Experiment:
The DMTJ structure consisted of Ta 45/Ru 9.5/IrMn 10/CoFe 7/AlOx/free layer 7/AlOx/CoFe 7/IrMn 10/Ru 60 (nm). Various free layers such as CoFe 7, CoFeSiB 7, and CoFe 1.5/CoFeSiB 4/CoFe 1.5 were prepared by a six-target rf magnetron sputtering system under typical base pressure below 5 X 10–8 Torr. A magnetic field of 100 Oe was applied during deposition to induce the uniaxial magnetic anisotropy in ferromagnetic layer. Tunnel barriers were formed by oxidizing 1.0 nm thick Al layers under rf plasma environment in a load lock chamber. The 10 µm X 10 µm junctions were fabricated by a photolithographic patterning procedure and ion beam etching.
Results and Discussion:
In order to make a close examination of the morphology of the DMTJs, the samples were examined by high-resolution TEM (HRTEM) focusing on the tunnel barriers. Fig. 1 shows the HRTEM images of the DMTJs consisting of (a) CoFeSiB 7 (b) CoFe 1.5/CoFeSiB 4/CoFe 1.5, and (c) CoFe 7 (nm) free layer. The top tunnel barrier of Fig. 1 (a) and (b) were smoother than that of Fig. 1 (c). The absence of grain boundary in amorphous CoFeSiB layer appeared to retard the columnar growth that would otherwise resulted in wavy barrier interface, therefore in comparison with the CoFe-used one it offered smoother surface roughness.
The magneto-transport properties of DMTJs depending on the free layer structure are summarized in Table 1. The normalized TMR ratio at applied voltage of ±0.4 V and Vh (voltage where the TMR ratio becomes half of its nonbiased value) values in CoFeSiB 7 nm free layered DMTJ are larger than that of the other structure. By using the CoFeSiB layer, the asymmetry of the normalized TMR curves at ±0.4 V became smaller compared to the CoFe used one and in case of the full CoFeSiB free layer, the asymmetry was negligible. This result can be attributed to the fact that the top portion of the DMTJ structure, including the top barrier, was more uniform and less defective due to the amorphous layer.
When the CoFeSiB layer thickness increased, the interlayer coupling field (Hi) decreased. Because the Hi is relevant to the ferromagnetic interaction across the tunnel barrier, a junction with smoother barrier interfaces would offer a lower Hi.
The presence of the amorphous layer appears effective in terms of achieving flat and uniform top tunnel barrier. For reducing the Hi and suppressing the bias voltage dependence of the TMR ratio, the smooth free layer/tunnel barrier is indispensable.

[1] S. Colis, G. Gieres, L. Bär, and J. Wecker, Appl. Phys. Lett. 83, 5 (2003).

Free Layer Structure(nm)	TMR Ratio(%)	NTMR (-0.4V)	NTMR (0.4 V)	Vh (V)	Hi (Oe)
CoFeSiB 7	19	0.79	0.78	0.90	27
CoFe 1.5/CoFeSiB 4/CoFe 1.5	22	0.75	0.78	0.83	29
CoFe 7	27	0.51	0.74	0.69	35

The physical properties of DMTJs with various free layer structures Vh = half voltage, NTMR= normalized TMR ratio at given voltage

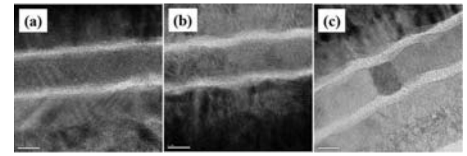

Fig. 1. HRTEM images of DMTJs consisting of a (a) CoFeSiB 7, (b) CoFe 1.5/CoFeSiB 4/CoFe 1.5, and (c) CoFe 7 (in nm) free layer, respectively. The white layers are indicate the top and bottom tunnel barriers.

EX-05

Appearance of a tunneling spectrum peak by electrical breakdown of tunneling junction.

K. Horikiri, K. Shiiki
Applied Physics and Physico-Informatics, Keio University, Yokohama, Japan

Recently, there has been considerable interest in using tunneling junctions in applications such as magnetic disk storage systems,[1] magnetoresistive random access memories,[2] Josephson junctions.[3] However, the very thin insulator of tunneling junctions suffers from electrical breakdown by voltage stress. Thus, reliability is an important issue for device applications. Although it is known that the tunnel resistance of a junction is reduced by an electrical breakdown,[4,5] the mechanism of electrical breakdown is not clear. Inelastic electron tunneling spectroscopy is a powerful tool for detecting very small changes in current-voltage (I-V) characteristics of devices.[6, 7] In this present study, the breakdown mechanism of tunneling junctions was investigated by obtaining tunneling spectra.

Tunneling junctions of Co (10 nm) /AlOx /Co (50 nm) and Al (100 nm) /AlOx /Al (100 nm) were fabricated on a glass substrate by ion-beam sputtering. The bottom electrode was deposited in the shape of a stripe using a metal mask. A 2.5-nm-thick Al layer was then deposited on the electrode. The insulator AlOx was formed by thermal oxidation in pure O2 at 200 °C for 24 h. The top electrode was deposited on the AlOx crossing for the bottom electrode. The I-V characteristics of the junction were measured by the four-probe method. When the applied voltage reached the critical voltage, the tunnel resistance of the junction decreased sharply and electrical breakdown occurred. d^2I/dV^2 spectrum of before and after breakdown junction was measured using a modulation method in liquid N2. [8]

Figure 1 (a) shows the d^2I/dV^2 spectrum of an as-made junction. A peak was observed near 0.03 V. No other peaks were observable up to 0.3 V. Figure 1 (b) shows the d^2I/dV^2 spectrum of a junction after breakdown. A peak appeared in the spectrum after electrical breakdown. This peak is very sharp and it appears to be made up of several combined peaks. After breakdown, all junctions exhibited a similar peak between 0.07 V and 0.09 V, irrespective of the way in which the voltage was varied. This peak was reproducible. Figure 2 shows d^2I/dV^2 spectra of an Al /AlOx /Al junction at 77 K after breakdown. Before breakdown, the only peak near 0.03 V was observed as same as a Co /AlOx /Co junction. After breakdown, a peak appeared near 0.07 V, as Fig.2 shows. It was confirmed that this peak appeared independent of the electrode and the Al oxide layer of the junction. This peak suggests that a level was created in AlOx by electrical breakdown. When the applied voltage was 0.09 V, an additional current starts to flow through the level. It is thought that this conduction channel is not a band but a level, since the peak is very sharp. It is generally thought that a pinhole is created in an insulator by inducing electrical breakdown in a tunneling junction, and that the current flows through the pinhole.[3, 4, 9] However, a pinhole current does not contribute a sharp peak to the d^2I/dV^2 spectrum. Thus, the results of our experiments suggest that a pinhole mechanism cannot explain electrical breakdown in this case.

[1] T. Miyazaki and N. Tezuka: J. Magn. Magn. Mater. 139, L231 (1995).

[2] J. S. Moodera, L. R. Kinder, T. M. Wong, and R. Meservey: Phys. Rev. Lett. 74, 3273 (1995).

[3] S. V. Lotkhov, E. M. Tolkacheva, D. V. Balashov, M. I. Khabipov, F.-I. Buchholz, and A. B. Zorin: Appl. Phys. Lett. 89, 132115 (2006).

[4] W. Oepts, H. J. Verhagen, D. B. de Mooij, V. Zieren, R. Coehoorn, and W. J. M. de Jonge: J. Magn. Magn. Mater. 198-199, 164 (1999).

[5] T. Morozumi, H. Kaiju, Y. Ohtaka and K. Shiiki: Jpn. J. Appl. Phys. 43, 197 (2004).

[6] R. C. Jacklevic and J. Lambe: Phys. Rev. Lett. 17, 1139 (1966).

[7] M. Bowen, A. Barthéléy, M. Bibes, E. Jacquet, J. –P. Contour, A. Fert, F. Ciccacci, L. Duò, and R. Bertacco: Phys. Rev. Lett. 95, 137203 (2005).

[8] A. B. Dargis: Rev. Sci. Instrum. 52, 46 (1981).

[9] R. Schad, D. Allen, G. Zangari, I. Zana, D.Yang, M. tundra and D. Wang: Appl. Phys. Lett. 76, 607 (2000).

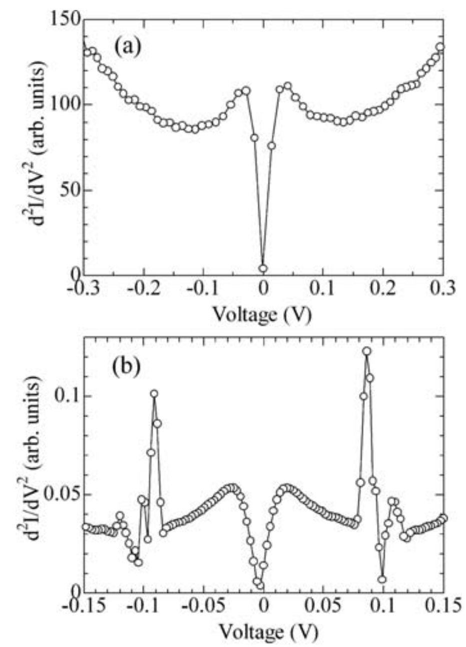

The d^2I/dV^2 spectrum of Co /AlOx /Co junction at 77 K. (a) As-made Co /AlOx /Co junction. (b) Co /AlOx /Co junction after breakdown.

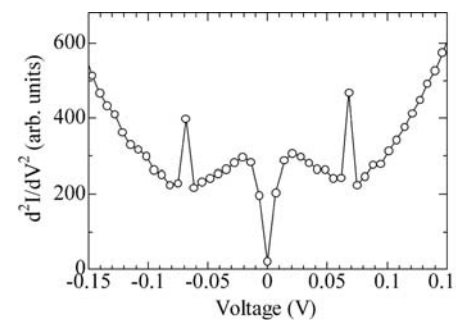

The d^2I/dV^2 spectrum of Al /AlOx /Al junction at 77 K, after breakdown.

EX-06

Magnetostriction and tunneling magnetoresistance of Co/AlOx/Co/IrMn junctions.

Y. Chen[1,2], S. Jen[1,2], Y. Yao[2,1]
1. Institute of Physics, Academia Sinica, Institute of Physics, Taipei, Taiwan; 2. Department of Materials Engineering, Department of Materials Engineering, Tatung University, Taipei, Taiwan

Yuan-Tsung Chen1, S. U. Jen1, and Y. D. Yao2
1Institute of Physics, Academia Sinica, Nankang, Taipei, Taiwan 11529 R.O.C.
2Department of Materials Engineering, Tatung University, Taipei, Taiwan 104 R.O.C.

Abstract
Mechanical and electrical properties of magnetic tunnel junction (MTJ) are interesting because the right combination of low magnetostriction (λs) and high tunneling magnetoresistance (TMR) of a certain type of MTJ can be applied in the read head sensor and magnetoresistance random access memories (MRAMs) fields [1]-[2]. However, those properties of the Co/AlOx/Co MTJ were less reported before. In this work, the top configuration Co/IrMn was inserted to study λs and TMR of the Co/AlOx/Co junction.
The cross-strip MTJs were fabricated following this sequences: Si(100)/Ta(30Å)/Co(75Å)/AlOx(δto)/Co(75Å)/IrMn(90Å)/Ta(100Å) deposited under an in-plane deposition field (h) = 500 Oe, where δto = 12, 17, 22, 26, and 30 Å is the thickness of the AlOx layer. TMR increases initially from 21% to 36% and then decreases to 24%, as to increases monotonically. This means the spin tunneling is weakened eventually, as to 26 Å. Moreover, λs of Co/AlOx/Co MTJs shows the concave-up feature [3]. We used the nanoprobe energy dispersive x-ray (EDX) equipped in high-resolution sectional transmission electron microscopy (HR X-TEM) to analyze Co, Al, O concentrations across each AlOx layer. The different concentration dependence along δto causes the λs feature. In addition, the microstructure of each Co/AlOx/Co MTJ observed with HR X-TEM (Fig. 1) shows that the interfaces between Co/AlOx and AlOx/Co are quite smooth. λs of Co/AlOx/Co MTJs is in general in the range from -23 ppm to -12 ppm. Finally, we find the optimal MTJ in this series has the following properties: TMR = 36% and λs = -15 ppm.
PACS. No: 75.47.-m; 85.75.-d; 75.30.Et
a)Corresponding author:
Yuan-Tsung Chen, tel: +886-227-880-058-2043,fax: +886-227-834-187,
e-mail: dream228@phys.sinica.edu.tw

[1] J. S. Moodera, L. R. Kinder, T. M. Wong, and R. Meservey, Phys. Rev. Lett. 74, 3273 (1995).

[2] S. S. P. Parkin, C. Kaiser, A. Panchula, P. M. Rice, B. Hughes, M. Samant, and S.-H. Yang, Nat. Mater. 3, 862 (2004).

[3] Y. T. Chen, S. U. Jen, Y. D. Yao, J. M. Wu, and A. C. Sun, Appl. Phys. Lett. 88, 222509 (2006).

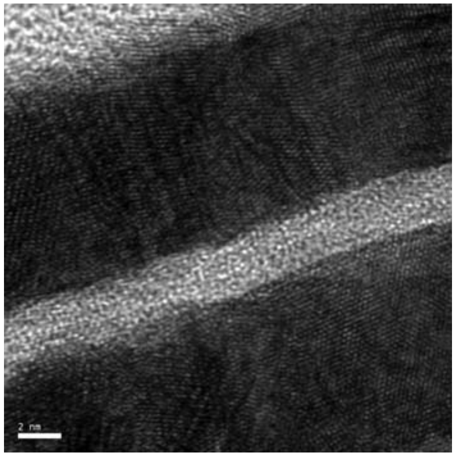

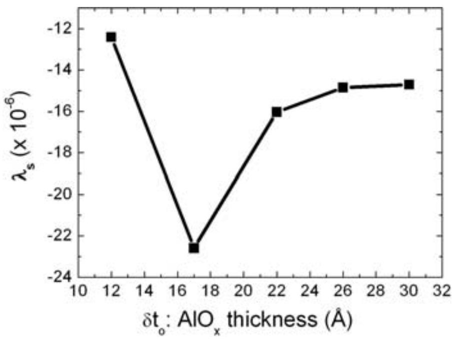

Magneto-transport in a single nano-object with a conductive AFM.

P. Zermatten, *G. Gaudin*, A. Schuhl
SPINTEC, CEA/CNRS, Grenoble, France

Transport measurement is one of the most efficient tools to get insight into the electronics properties of a sample: for example band structure properties in semiconductors or GMR effect in a magnetic stack. When the dimensions of the sample decrease to the nanometer scale, new physics could be involved like coherent electronic properties, enhanced tunnel magnetoresistance, spin transfer effect, …. In order to perform these measurements, the nano-object must be connected to two electrodes separated by an insulating layer embedding the object. The fabrication process involved is always complicated, expensive and time-consuming. It implies different and successive electronic lithography, etching and planarization steps. Moreover, when nanoparticles are obtained in a dense array, contacting a single particle is often impossible with such a fabrication technique. The particles are to close to each other compare to the size of the electrode so that the measurement is an average over different particles.

We developed a new technique based on the direct contact of a single nano-object by a conductive AFM tip. A commercial AFM has been modified: an external electronic set-up (stable current source and high resolution acquisition cards) is added as well as magnetic coils. A wide range of current from 10nA to 10mA can be applied with magnetic fields up to 1.5kOe and 400Oe respectively for out-of-plane and for in-plane direction. The noise in the detection is mainly due to the stability of the contact. Voltages as small as 10µV can be resolved. Two advantages can be outlined. Because the top electrode is directly the metallic tip, the fabrication process is much simpler and involves only one step of e-beam lithography followed by an ion beam etching step. We were able to contact nanopillars as small as 50nm diameter. Moreover, the spatial resolution is given by the tip apex which can be decreased down to some nanometers by FIB machining [1]. Contacting a single nanoparticle inside a dense array is then possible as the distance between the nanoparticles is larger than the tip apex.

First measurements have been performed on nanofabricated pillars. Full epitaxial Fe/MgO/Fe stacks [2] presenting high TMR values were patterned. We clearly evidenced the presence of surface states in the Fe density of state at the interface between the bottom Fe layer and the MgO layer. These interfacial states only appear for the minority electrons and they drastically modify the behavior of the TMR as a function of the applied bias voltage. They are responsible for example of the change of sign of the TMR for a certain bias voltage which could be very interesting for applications. Experiments were also performed on TMR stack with a very thin MgO layer in order to test the sensitivity of the technique. We were able to measure a small TMR signal 0.25% on these very low R.A. structures 0.3 Ohm*µm2.

One of our goals is to be able to directly contact nanoparticles obtained for exemple by a chemical way. The behavior of a single particle, not damaged by any fabrication step should give a great understanding on the magneto-transport properties at the nanometer scale. These particles can be very small, less than 10nm diameter, and packed in a dense array. Beside our results on nanofabricated Fe/MgO/Fe pillars we will present the different improvements of our technique to achieve such a goal: optimization of the stability of the AFM head and FIB-machining of the metallic tips to achieve the desired spatial resolution.

[1] H.Y. Ximen et al., Ultramicroscopy 42, 1526, (1992)

[2] C. Tiusan et al., J. Phys.: Condens. Matter 19, 165201, (2007)

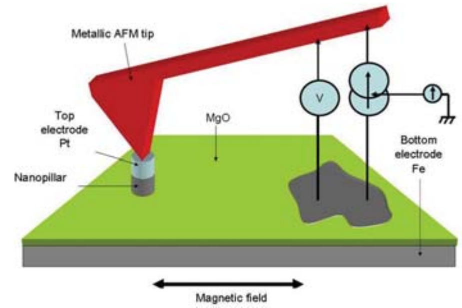

Fig. 1: Schematic of the experimental set-up

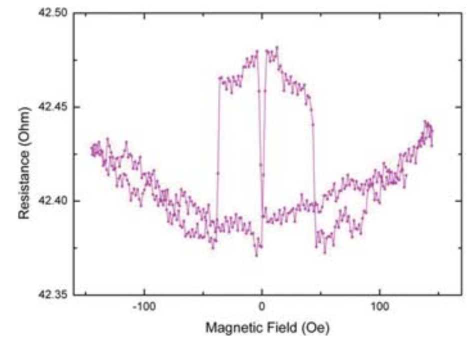

Fig. 2: TMR signal of a 100nm diameter pillar from a Fe/MgO/Fe with very thin MgO layer (0.3 Ohm.µm2)

EX-08

Huge electron mean free path in MgO - Detection of the valence band in buried Co2MnSi-MgO half-metallic ferromagnetic tunnel junctions by means of photo emission spectroscopy.

B. Balke[1], G. H. Fecher[1], A. Gloskowskii[1], S. Ouardi[1], C. Felser[1], M. Yamamoto[2]
1. University Mainz, Mainz, Germany; 2. Graduate School of Informatic Science and Technology, Hokkaido University, Sapporo, Japan

The X2YZ (X, Y = transition metal, Z = main group element) Heusler compounds have attracted scientific and technological interest for their potential use as materials for magneto-electronic devices. Reason is the exceptional electronic structure found in particular in the Co2YZ Heusler compounds (see [1, 2] and references there). Those compounds are predicted to be half-metallic ferromagnets.
One major research area, where Co2 based Heusler compounds are used, is on tunnelling magneto resistive(TMR) junctions. For materials with complete spin polarization, an infinite TMR ratio is expected.
From a TMR junction with both electrodes consisting of Co2MnSi films, Sakuraba et al measured a TMR ration of 570% at low and 67% at high temperature [3] compared to 159 % [4] for a Co2MnSi/AlOx/CoFe junction at 2 K and about 70% at 300 K. Overall, the drop of the ratio at room temperature suggests that still an improvement with respect to the temperature stability of the TMR is necessary.
This work reports on the detection of the valence band of buried half-metallic ferromagnets by means of hard X-ray photo emission spectroscopy (HAXPES). The measurements have been performed on "half" tunnel junctions that are thin films of Co2MnSi underneath MgO. Starting from the substrate, the structure of the samples is: MgO(buffer) - Co2MnSi - MgO(z) - AlOx(1-2 nm) with a thickness z of the upper MgO layer of 2 nm and 20 nm. The topmost AlOx layer is for protection of the MgO. Core level and valence band X-ray photo emission have been excited by hard X-rays of about 6 keV energy. Both, core level and valence band spectra have been used to estimate the mean free path of the electrons through the MgO layer to be 19 nm at kinetic energies of about 6 keV. In particular it is shown that the buried Co2MnSi films exhibit the same valence density of states like bulk samples that is typical for half-metallic ferromagnets.
However, for magnetic materials such as spintronics devices the measurement of the spin and charge is necessary for fully understanding of these materials.
Therefore it is necessary to develop spin polarized high resolution HAXPES.
With the spin dependent measurement one can investigate the spin diffusion length of the materials depending on the barrier and spacer layer material and thickness.
The observation if and how the spin polarisation of the bottom electrode is retained trough the MTJs and GMR devices will be possible with this technique.
In summary, this means that spin polarized high resolution HAXPES is a powerful and necessary tool to investigate different materials for tunneling barriers and spacer layers to optimize the structure, configuration and composition of the MTJs and the GMR devices to achieve sophisticated properties and results.

[1] C. Felser, G. H. Fecher, and B. Balke, Angew. Chem. Int. Ed. 46, 668 (2007).

[2] H. C. Kandpal, G. H. Fecher, and C. Felser, J. Phys. D: Appl. Phys. 40, 1507 (2007).

[3] Y. Sakuraba, M. Hattori, M. Oogane, Y. Ando, H. Kato, A. Sakuma, T. Miyazaki, and H. Kubota, Appl. Phys. Lett. 88, 192508 (2006).

[4] Y. Sakuraba, T. Miyakoshi, M. Oogane, Y. Ando, A. Sakuma, T. Miyazaki, and H. Kubota, Appl. Phys. Lett. 89, 052508 (2006).

EX-09

X-ray magnetic dichroism studies of half-metallic Heusler alloys and magnetic tunnel junctions.

N. D. Telling[1], P. S. Keatley[2], G. van der Laan[1,5], R. J. Hicken[2], E. Arenholz[3], Y. Sakuraba[4], M. Oogane[4], Y. Ando[4], T. Miyazaki[4]
1. Magnetic Spectroscopy Group, STFC Daresbury Laboratory, Warrington, United Kingdom; 2. School of Physics, University of Exeter, Exeter, United Kingdom; 3. Advanced Light Source, Lawrence Berkeley National Laboratory, Berkeley, CA; 4. Department of Applied Physics, Tohoku University, Aoba-yama 6-6-05, Japan; 5. Diamond Light Source Ltd, Harwell Science and Innovation Campus, Didcot, United Kingdom

The ability to achieve close to 100% spin-polarised materials is currently a major challenge in the area of 'spintronics' research. Such materials will have a huge impact on applications such as MRAM technology and sensors. Recently, large TMR values of 570% at low temperature have been obtained in structures incorporating Heusler alloy electrodes such as Co2MnSi [1]. These alloys have been predicted to possess a gap in the minority-spin density of states (DOS) at the Fermi level and thus be 100% spin-polarised, i.e. they are said to be 'half-metallic' ferromagnets.
The techniques of x-ray absorption spectroscopy (XAS), x-ray magnetic circular dichroism (XMCD), and x-ray magnetic linear dichroism (XMLD) provide an element-specific probe of electronic and magnetic interface states. Here we discuss the results of some recent experiments performed on Co2MnX/alumina structures (where X is Si, Al), at the Advanced Light Source, Lawrence Berkeley Laboratory. The gap in the minority-spin states leads to a local exclusion of the minority spin electrons around a given atom in half-metallic ferromagnets, i.e. the formation of an 'ideal' local moment system despite the delocalised electronic character of the material [2]. In recent work we provided the first experimental evidence of local moments on both Mn and Co atoms in Co2MnSi/alumina structures as distinct multiplet features in x-ray magnetic circular dichroism (XMCD) spectra [3].
In figures 1 and 2 are shown the XMCD spectra recorded around the Co and Mn L2,3 absorption edges for Co2MnSi (CMS) and Co2MnAl (CMA) films. From Fig.1 it can be seen that the multiplet features (indicated by arrows) are only observed in the CMS Co spectrum, whilst the CMA Co XMCD more closely resembles that from a Co/Al reference film. However the strongest multiplet feature found in the Mn XMCD spectrum from the CMS film was also observed in the CMA sample, although perhaps reduced in intensity (see Fig.2). Thus, if indeed these multiplet features are evidence of local moment formation then it appears that the Co moments are only localised in the CMS system, whilst the Mn moments are at least partially localised in both CMS and CMA films. Band structure calculations reveal that a minority-spin band gap only occurs for the Co LDOS in the CMS material, whereas both materials have a gap in the Mn LDOS [4,5]. This is entirely consistent with our XMCD results that indicate a more itinerant magnetic character of the Co atoms in the CMA sample, as can be seen by comparison of the XMCD from this sample with a standard metallic Co film.
In contrast to XMCD, the x-ray magnetic linear dichroism (XMLD) is weak in itinerant magnets (around 2% for Co), but many times larger when local moments exist [6,7]. Thus XMLD is an ideal probe of local moment formation in half-metallic ferromagnets. Our preliminary measurements of the XMLD in CMS films showed a substantial effect (~7%) at both the Co and Mn L2,3 absorption edges indicating the formation of local moments at both atomic sites. However the effect was substantially reduced at the Co L2,3 absorption edge for the CMA sample. This is consistent with the explanation given above for the more itinerant nature of Co in the CMA sample.

1. Y. Sakuraba, M. Hattori, M. Oogane, Y. Ando, H. Kato, A. Sakuma, T. Miyazaki and H. Kubota, Appl. Phys. Lett. 88, 192508 (2006)
2. J. Kübler et al, Phys. Rev. B 28, 1745 (1983)
3. N. D. Telling, P. S. Keatley, G. van der Laan, R. J. Hicken, E. Arenholz, Y. Sakuraba, M. Oogane, Y. Ando and T. Miyazaki, Phys. Rev. B 74, 224439 (2006)
4. M. Oogane et al, J. Phys. D: Appl. Phys. 39, 834 (2006)
5. I. Galanakis et al, Appl. Phys. Lett. 89, 042502 (2006)
6. A. A. Freeman et al, Phys. Rev. B 73, 233303 (2006)
7. E. Arenholz et al, Phys. Rev. B 74, 0944407 (2006).

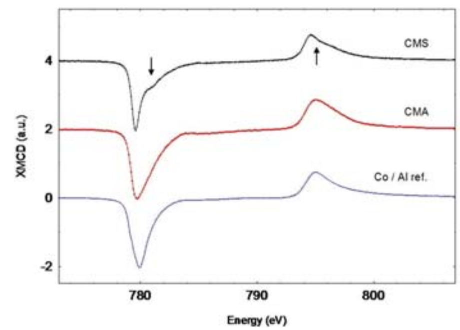

Figure 1: XMCD measured around the Co L2,3 absorption edges for the Co2MnSi film (CMS), the Co2MnAl film (CMA) and a reference Co/Al film.

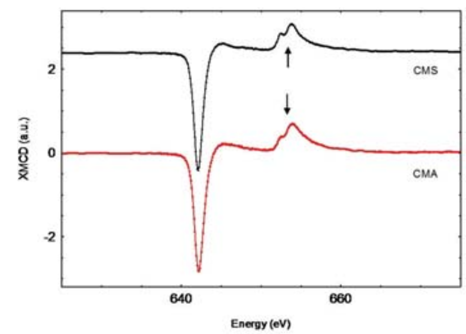

Figure 2: XMCD measured around the Mn L2,3 absorption edges for the Co2MnSi film (CMS) and Co2MnAl film (CMA).

EX-10

Fabrication of magnetic tunnel junctions with Co_2FeSi Heusler alloy and MgO crystalline barrier.

W. Lim, G. Choi, T. Lee
Department of Materials Science and Engineering, KAIST, Daejeon, South Korea

Recently half-metallic Heusler alloys have been studied to achieve higher TMR ratios. Among the predicted half metallic Heusler alloy, Co_2FeSi is an attractive material for spintronic devices due to high Curie temperature of 1100K, high spin polarization and no Mn containing composition[1]. Inomata[2] and Miyazaki[3] already reported 41% for Co_2FeSi/Al_2O_3/CoFe MTJs and 90% for CoFeB/MgO/Co_2FeSi at RT, respectively. In this study, we have obtained high TMR ratio up to 158.4% at RT in CoFeB/MgO/Co_2FeSi MTJs by coherent tunneling.

MTJs with the structure of Ta(5 nm)/Ru(90 nm)/Ta(5 nm)/CoFeB(3 nm)/MgO(2 nm)/Co_2FeSi(5 nm)/(top pinned layers) were deposited by a magnetron sputtering method in the UHV chamber of below 2×10^{-9} torr. Highly-oriented crystalline MgO(001) barrier was deposited by an rf method and examined by x-ray diffraction. Conventional photolithography and ion milling technique were used to fabricate the junctions of $10\times10\mu m^2$. All the samples were deposited at room temperature and annealed at T_{ann} (200~430°C) for 1 hour in the vacuum chamber of below 3×10^{-6} torr with a magnetic field of 1kOe.

Fig. 1(a) shows annealing temperature dependence of TMR ratio and RA product in CoFeB/MgO/Co_2FeSi MTJs. TMR ratio of CoFeB/MgO/Co_2FeSi MTJ increases gradually up to 350°C. Maximum TMR ratio is 158.4% at 350°C annealing and TMR ratio drops to 78% after 430°C annealing. RA products of the junctions were several $M\Omega\mu m^2$. To compare Co_2FeSi electrode with CoFeB electrode in MgO-based MTJs, we fabricate four types of MTJs with alternating stacking sequence of CoFeB and Co_2FeSi electrodes at both sides of MgO barriers. All the samples were annealed at 400°C after depositing at room temperature except the CoFeB/MgO/Co_2FeSi MTJ which showed the best results at 350°C annealing. As shown in Fig. 1(b), annealed CoFeB/MgO/CoFeB MTJ showed very high TMR ratio by coherent tunneling. However, TMR ratio and RA product decrease by using Co_2FeSi electrode even in one side. Furthermore bottom Co_2FeSi electrode shows lower TMR ratio and higher RA product than top Co_2FeSi electrode. This means bottom Co_2FeSi electrode makes some structural problems at both interfaces with the barrier. To analyze this structural difference in MTJs with Co_2FeSi electrodes, we use cross-sectional HRTEM images of annealed MTJs(Fig. 2). CoFeB/MgO/Co_2FeSi MTJ showed CoFeB[100](001)//MgO[110](001)//Co_2FeSi[100](001) epitaxial relationship between both electrodes and barrier and lattice misfit between both electrodes is about 3.5%. This epitaxial relationship made high TMR ratio by coherent tunneling. On the contrary, Co_2FeSi/MgO/Co_2FeSi MTJ showed large lattice misfit (about 6.7%) between both electrodes through Co_2FeSi[110](001)//MgO[100](001)//Co_2FeSi[110](001) epitaxial relationship. The reason of this large misfit may be caused by the fact that the growth of bottom Co_2FeSi electrode follows Cr-buffered MgO substrate but the growth of top Co_2FeSi electrode follows crystalline MgO barrier. This implies that epitaxial relationship between bottom Co_2FeSi electrodes and MgO barrier is locally broken and non-coherent tunneling through the MgO barrier degrades TMR ratios. This part will be discussed in more detail. Similarly very low TMR ratio of Co_2FeSi/MgO/CoFeB MTJ can be also caused by broken epitaxial relationship between bottom Co_2FeSi electrode and MgO barrier. Another reason for the lower TMR ratio for Co_2FeSi electrode may be high degree of antisite disorder in 350°C annealed state[4].

In this study, we have fabricated MTJs with Co_2FeSi Heusler alloy electrode and MgO barrier. Co_2FeSi is predicted to be a highly spin-polarized material, but has shown worse results than amorphous CoFeB electrode with crystalline MgO barrier. In addition, the growth of bottom Co_2FeSi electrode broke epitaxial relationship between electrodes and barrier. Further studies are required to reduce lattice misfit and improve TMR characteristics of Co_2FeSi/MgO/Co_2FeSi MTJs.

[1] S. Wurmehl, G. H. Fecher, H. C. Kandpal, V. Ksenofontov, C. Felser, H. –J. Lin, and J. Morais, Phys. Rev. B 72 (2005) 184434

[2] K. Inomata, S. Okamura, A. Miyazaki, M. Kikuchi, N. Tezuka, M. Wojcik and E. Jedryka, J. Phys. D: Appl. Phys. 39 (2006) 816

[3] T. Daibou, M. Shinano, M. Hattori, Y. Sakuraba, M. Oogane, Y. Ando, and T. Miyazaki, IEEE Trans. Magn. 42 (2006) 2655

[4] W. C. Lim and T. D. Lee: unpublished results

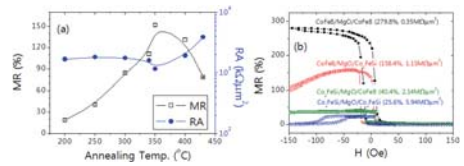

Figure 1 (a) Annealing temperature dependence of TMR ratio and RA product of CoFeB/MgO/Co_2FeSi MTJs (b) TMR curves of four types of MTJs with Co_2FeSi electrode and MgO barrier.

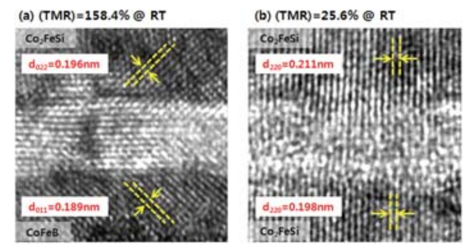

Figure 2 Cross-sectional TEM images of (a) CoFeB/MgO/Co_2FeSi and (b) Co_2FeSi/MgO/Co_2FeSi MTJs.

EX-11

(110) manganite electrodes for magnetic tunnel junctions.

I. C. Infante[1], F. Sánchez[1], J. Fontcuberta[1], S. Fusil[2], K. Bouzehouane[2], G. Herranz[2], A. Barthélémy[2]
1. Magnetic Materials and their Applications, Institut de Ciència de Materials de Barcelona, Bellaterra, Spain; 2. Unité Mixte de Physique CNRS/Thales, Orsay, France

Recent research in spintronics has been focused in the fabrication of magnetic tunnel junctions (MTJs) using highly spin-polarized conductive materials as the half-metallic manganites. For achieving this purpose, La-manganites (La1-xAxMnO3, being A an alkaline divalent earth), with the optimal composition at x =1/3, have been integrated into epitaxial heterostructures with (001) cubic orientation, typically grown on SrTiO3 (STO) substrates. However, it has been demonstrated that intrinsic problems as electronic phase separation and chemical segregation develop in (001) electrodes and (001) multilayers, depressing their magnetotransport properties [1]. The substrate-induced strain and the breakdown of the perovskite plane stacking and polarity discontinuity are claimed to cause these effects which are mostly located near the manganite-substrate interface [2]. Interestingly, heterostructure growth with orientation other than (001) one may suppress these problems and eventually improve device functionality, as both elastic properties and atomic termination (and thus charge) of the corresponding planes will be different. It has been shown that after capping La2/3Ca1/3MnO3 (LCMO) electrodes with STO insulating layers, the depletion of electronic and magnetic properties of (001)LCMO electrodes increases whereas those of (110)LCMO are less sensitive to the STO capping layer. Besides, the magnetic properties of the (110) LCMO are found to be similar to those before capping [3]. Thus, MTJs based on (110)LCMO manganites appear to be promising candidates for obtaining improved magnetotransport properties.
To enhance the functional properties of MTJs based on manganite electrodes, we have fabricated MTJs based on bilayer epitaxial heterostructures of (110) STO/LCMO grown on (110) STO substrates. The magnetization dependence of bare electrodes with (001) and (110) orientation (Figure 1a) show an increase of the Curie temperature and the overall magnetization in (110) ones. We have grown (110) STO/LCMO heterostructures and verified the tunneling transport across nanometric STO barriers using conducting atomic force microscopy (CAFM) [4], determining the tunneling barrier energy along [110] direction. Nanojunctions on the STO//LCMO/STO structure have been fabricated by a nanolithographic process [5] using a CAFM tip to drill nanoholes in a photoresist layer spinned onto the STO surface. Filling the holes with cobalt, the junction top ferromagnetic electrodes are defined, and after oxidizing a thin layer of Co into CoO (to control the Co magnetization via antiferromagnetic coupling between them), these CoO/Co electrodes were subsequently capped by sputtered Au layers for electric contacting. In Figure 1b we show the bias dependence of the tunneling current I (main panel) and conductance G (inset) across the Au/CoO/Co/STO/LCMO//STO(110) heterostructure measured at 4.2 K. The conductance of the junction changes depending on the relative orientation of each electrode: (i) with parallel (P) magnetized electrodes at 6 kOe, GP is low, and (ii) with anti-parallel (AP) magnetized electrodes at -1.2 kOe, GAP is high. Thus, a negative tunnel magnetoresistance [TMR = (GP-GAP)/GAP] is observed, which is expected on the basis of the positive and negative spin polarization of LCMO and Co electrodes, respectively [6]. The value of TMR (-11%) allows calculating the spin polarization of LCMO electrodes using Jullière model [7] and taking as the spin polarization of Co PCo=–37% [8]. Thus, PLCMO=+14%. This value is surprisingly lower than expected for half-metallic ferromagnets but it could be related to intrinsic problems such as symmetry matching between spin-dependent wave functions in Co electrodes and (110) STO barriers, although other non-intrinsic effects could also contribute. Further experiments are underway to measure other nanojunctions and obtain with better statistics the value of PLCMO.
We will report on the temperature, magnetic field and bias dependence results of these (110)LCMO based MTJs and discuss their perspectives for practical implementation in spintronic devices.

[1] M. Bibes et al. Phys. Rev. Lett. 87, 67210 (2001); M. Bibes et al., Phys. Rev. B 66, 134416 (2002)

[2] I. C. Infante et al., Phys. Rev. B 76, 224415 (2007)

[3] I. C. Infante et al. J. Appl. Phys., in press

[4] I. C. Infante et al., Appl. Phys. Lett. 89, 172506 (2006); I. C. Infante et al., J. Appl. Phys. 101, 093902 (2007)

[5] K. Bouzehouane et al., Nanoletters 3, 1599 (2003)

[6] J. M. De Teresa et al., Phys. Rev. Lett. 82, 4288 (1999)

[7] M. Jullière, Phys. Lett. 54A, 225 (1975)

[8] Co has negative spin polarization at the Fermi level, predicted by F. Batallan et al., Phys. Rev. B 11, 545 (1975); from Andreev reflection experiments [S. K. Upadhyay et al., Phys. Rev. Lett. 15, 3247 (1998)] PCo= 0.37

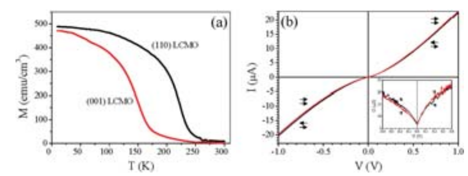

(a) Temperature dependence of the magnetization of 25 nm LCMO electrodes grown on (110) and (001) STO substrates. Measurements were obtained with a magnetic field of 5 kOe applied in-plane of the samples. (b) I(V) curves obtained at in-plane magnetic fiels of 6 kOe (parallel configuration) and -1.2 kOe (antiparallel configuration). Inset: Conductivity calculated from the I(V) curves. In both cases, parallel and antiparallel configurations are indicated by arrows.

EX-12

Magneto-transport characteristics of magnetic tunnel junction with a synthetic antiferro-magnetic amorphous CoFeSiB free-layer.

B. Chun[1], M. Coey[1], S. Lee[2], J. Hwang[2], J. Rhee[2], H. Yim[2], T. Kim[3], Y. Kim[4]
1. School of Physics, Trinity College, Dublin, Ireland; 2. Department of Physics, Sookmyung Women's University, Seoul, South Korea; 3. Nanotechnology and Advanced Materials Engineering, Sejong University, Seoul, South Korea; 4. Department of Materials Science and Engineering, Korea University, Seoul, South Korea

Introduction

To reduce the magnetization switching field (Hsw), in our previous study, we introduced a synthetic antiferromagnet (SAF) free-layered magnetic tunnel junction (MTJ) comprising amorphous ferro-magnetic Co70.5Fe4.5Si15B10 layers [1]. The amorphous CoFeSiB SAF free-layered MTJs showed both reduced TMR ratio and Hsw than those of the single free-layered MTJs. Despite the undesired low TMR ratio, the CoFeSiB SAF free-layered MTJs exhibited much lower Hsw values than that of the single free-layered MTJs. Therefore, in the present study, we attempted to develop a new SAF free-layered structure to improve the magneto-transport properties while maintaining the low Hsw by controlling the free-layer thicknesses.

Experiment

The MTJs consisting of Si/SiO2/Ta 45/Ru 9.5/IrMn 10/CoFe 7/AlOx 1.5/CoFeSiB 7-t (F1)/Ru 1.0/CoFeSiB t (F2)/Ru 60 (in nm) were prepared using a six-target dc magnetron sputtering system under the typical base pressure of less than 5X10–8 Torr. A photolithographic patterning procedure, including ion beam etching, was used to fabricate the 10 x 10 μm2 of MTJs.

Results and Discussion

Before we implement the CoFeSiB-used SAF layer into a full MTJ structure, we have characterized the magnetic hysteresis of various SAF structures including Ta 5/CoFeSiB (t1 = 3.5, 4.0, 4.5, 5.0)/Ru 1.0/CoFeSiB (7-t1)/Ta 5 (nm). As shown in Figure 1, a well-defined anisotropy and antipar-allel alignment is occurred during the magnetization reversal at (a) t1 = 3.5, (b) 4.0, and (c) 4.5 nm. However, the SAF characteristic was not observed at (d) t1 = 5.0 nm. Therefore, to observe the SAF characteristics in our system, the thickness difference between the lower and upper part of the lay-ers must have a critical range. And moreover, an increment in the Ms is observed by increasing the t1 thickness. For example, the sample (d) CoFeSiB 5.0/Ru 1.0/CoFeSiB 2.0 (nm) has a four times higher Ms value than that of the sample (a) CoFeSiB 3.5/Ru 1.0/CoFeSiB 3.5 (nm). Because in the SAF structure, magnetic flux forms closed loop and can reduce the magnetostatic energy in the free layer separated by nonmagnetic space layer. However due to poorly defined SAF characteristics in the (d) SAF structure, it has higher Ms value than that of the (a), (b), and (c) SAF structures.

To investigate the SAF effects on the magnetotransport properties, various SAF free-layered MTJs were fabricated on Si/SiO2 wafers including Ta 45/Ru 9.5/IrMn 10/CoFe 7/AlOx1.5/CoFeSiB 7-t (F1)/Ru 1.0/CoFeSiB t (F2)/Ru 60 (nm). As summarized in Table 1, the junction resistance (R), interlayer coupling field (Hi), TMR ratio, and Hsw all showed a dependence on F1 and F2 thick-ness. In the SAF-MTJ structure, when the amorphous F1 layer (a lower ferromagnetic layer in the SAF structure) was thinner than the amorphous F2 layer (an upper ferromagnetic layer), it is unable for the F1 layer to perfectly cover the tunnel barrier. As a result, more defective and rough points may exist at the tunnel barrier/free layer interface. The R and Hi are relevant to the tunnel barri-er/ferromagnetic free-layer interface conditions, the junction with rougher barrier interfaces induces a lower R and a higher Hi. Because in the rough junctions, the tunnelling current prefer-entially shunts through the electrically weakest points and the ferromagnetic interaction across the tunnel barrier becomes stronger, respectively. On the contrary, when the amorphous F1 layer becomes thick enough, the tunnel barrier can be perfectly covered, and, as result, the population of electrically weak points gets lowered. And moreover, by increasing the F1 layer thickness, the decrement of the surface roughness of the tunnel barrier/free-layer interface was observed. Because of this, when F1 layer became thick, it exhibited a higher R and a lower Hi values.

For the cell comprising (a) CoFeSiB 3.5/Ru 1.0/CoFeSiB 3.5 nm SAF free layer, the magnetization reversal was completed at the applied field of 3 Oe. For the (d) CoFeSiB 5.0/Ru 1.0/CoFeSiB 2.0 nm SAF free layered MTJ, however, it required 11 Oe of Hsw. We think that the reasons of exhibit-ing relatively lower Hsw were due to a lower magnetostatic energy in the free layer and well-defined SAF characteristics as previously shown in Fig. 1.

[1] J. Y. Hwang, J. R. Rhee, B. S. Chun, Y. K. Kim, and T. Kim, J. Appl. Phys. 99, 08T315 (2006).

Structure (nm)	R (ohm)	Hi (Oe)	TMR (%)	Hsw (Oe)
(a) 3.5/1.0/3.5	252	47	19	3
(b) 4.0/1.0/3.0	269	41	20	5
(c) 4.5/1.0/2.5	360	37	20	7
(d) 5.0/1.0/2.0	386	15	21	11

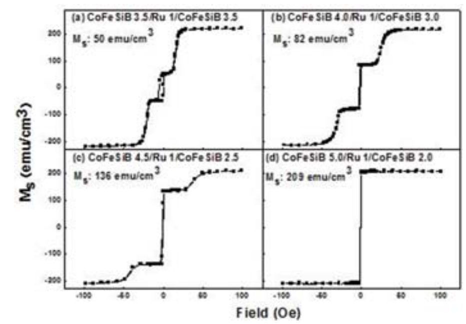

Fig. 1 Magnetization curves of the SAF free-layer structures consisting of Ta 5/CoFeSiB (t1=3.5, 4.0, 4.5, and 5.0)/Ru 1.0/CoFeSiB (7-t1)/Ta 5 (nm).

EX-13

Structure and magnetic properties of epitaxial full-Heusler alloy $Co_2FeAl_{0.5}Si_{0.5}$ films on MgO-buffered MgO (001) substrates and TMR using their electrodes.

H. Sukegawa[1,2], W. Wang[2], R. Shan[2], K. Inomata[2]
1. International Center for Young Scientists (ICYS), National Institute for Materials Science (NIMS), Tsukuba, Japan; 2. Magnetic Material Center, National Institute for Materials Science (NIMS), Tsukuba, Japan

Half-metals, which have 100% spin polarized conduction electron band, is an ideal material for spintronics devices, such as spin MOSFETs [1] and high density nonvolatile memory devices. Recently, Co-based full-Heusler alloys [2-3], whose structures are Co_2XY type $L2_1$, have attracted great attention as promising candidates of the half-metals since the fully spin-polarized band structures are predicted and they show high Curie temperatures above room temperature (RT). Very recently, a large tunnel magnetoresistance (TMR) ratio as high as 220% at RT (390% at 5 K) has been reported in a MgO(001)/Cr-buffer/$Co_2FeAl_{0.5}Si_{0.5}$ (CFAS)/MgO/CFAS magnetic tunnel junction (MTJ) [4]. However, Cr buffer impedes a highly $L2_1$-ordered structure due to the Cr interdiffusion by post-deposition annealing at a high temperature [5]. In this study we achieved a highly $L2_1$-ordered CFAS layer using an MgO buffer layer instead of a Cr buffer layer, and investigated structure and magnetic and TMR properties as a function of post-deposition annealing temperature. Multilayers were prepared on MgO(001) single crystal substrates using ultra-high vacuum magnetron sputtering system at RT. CFAS (30 nm) layer was deposited on MgO (20 nm) or Cr (40 nm) buffer layer. Post-annealing was carried out after the CFAS layer deposition. The multilayers were characterized by x-ray diffraction (XRD), vibrating sample magnetometer (VSM) and atomic force microscopy (AFM). MTJ structures of MgO buffer/CFAS/Mg/MgO/CFAS/CoFe/IrMn/Ru were deposited on MgO (001) substrates and patterned using electron-beam lithography and Ar ion-beam etching. TMR curves are measured by a 4-probe method.

Figure 1 shows the XRD pole figures of (111) superlattice line for a CFSA film on an MgO buffer layer for different post-annealing temperatures (T_a). The distinct peaks with 4-fold symmetry indicate the $L2_1$ structure of CFAS on the MgO buffer layer, of which intensity increases with increasing T_a. The (111) superlattice line was not observed for below T_a = 400°C, which indicates B2 structure of CFAS. Figure 2 shows saturation magnetization (M_s) and coercivity (H_c) for both MgO- and Cr-buffered CFAS (30 nm) films measured at RT as a function of T_a. The Cr-buffered film shows a rapid M_s drop and a H_c increase above 450°C, indicating the interdiffusion of Cr atoms into the CFAS layer significantly. This tendency is similar to the report demonstrated by Tezuka *et al.* [5]. Meanwhile, M_s starts to increases above 450°C without changing H_c for MgO-buffered film, suggesting $L2_1$ ordering without any interdiffusion. We plot T_a dependence of both *Ra* (average surface roughness) and *P-V* (peak-to-valley) values of MgO-buffered CFAS layer in Fig. 3. Even as-deposited sample shows very small *Ra* of 0.15 nm. The surface roughness is improved by the post-annealing process. A remarkable flat surface with both *Ra* of 0.1 nm and *P-V* of 1.0 nm was achieved by 500°C post-annealing as shown in the inset of Fig. 3. These facts indicate the use of the MgO-buffer for CFAS layer is a promising approach for achieving a higher TMR ratio. Detailed TMR properties will be presented and discussed.

The authors thank Prof. Tezuka for discussion. This study was supported by NEDO.

[1] S. Sugahara and M. Tanaka, Appl. Phys. Lett. **84**, 2307 (2004).

[2] Y. Sakuraba *et al.*, Appl. Phys. Lett. **88**, 022503 (2006).

[3] T. Ishikawa *et al.*, Appl. Phys. Lett. **89**, 192505 (2006).

[4] N. Tezuka *et al.*, Jpn. J. Appl. Phys. **46**, L454 (2007).

[5] N. Tezuka *et al.*, Appl. Phys. Lett. **89**, 112514 (2006).

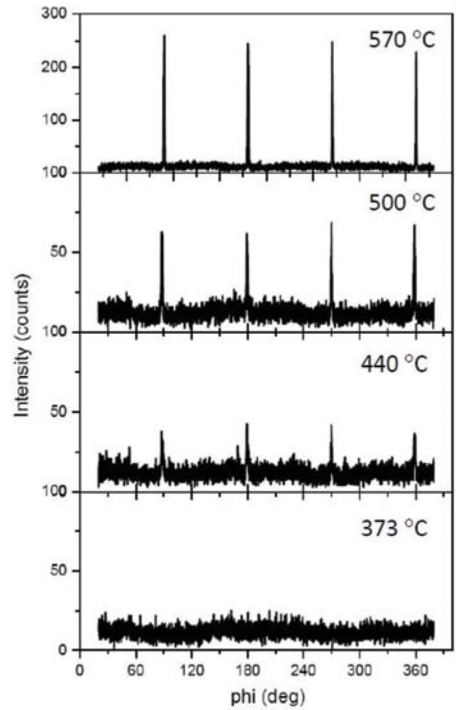

Fig. 1. XRD pole figures of (111) for $Co_2FeAl_{0.5}Si_{0.5}$ (CFAS) films after post-annealing.

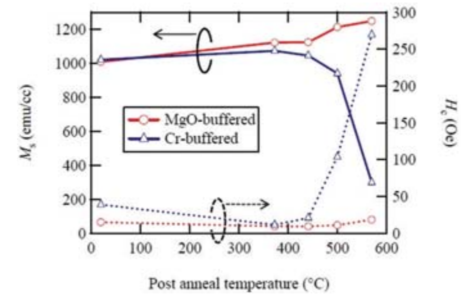

Fig. 2. Post-annealing temperature dependence of M_s (solid lines) and H_c (doted lines) for MgO- and Cr-buffered CFAS films.

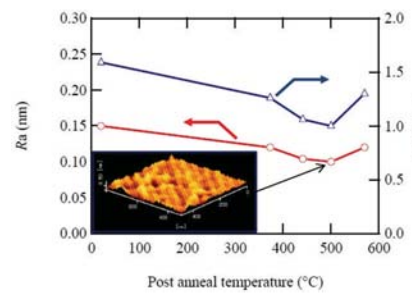

Fig. 3. Post-annealing temperature dependence of *Ra* and *P-V* of MgO-buffered CFAS films. Inset shows AFM image of MgO-buffered film post-annealed at 500°C.

Coherent effects for electronic equilibrium and transport in perfect magnetic junctions.

Y. G. Pogorelov[1], H. G. Silva[2,1]

1. IFIMUP/IN, Universidade do Porto, Porto, Portugal; 2. CEOT, Universidade do Algarve, Faro, Portugal

The analytical treatment of electron transport processes in spintronics layered nanostructures is commonly restricted to classical or semi-classical framework [1,2], where the equilibrium Fermi distribution $f(\varepsilon,T) = [e^{(\varepsilon - \mu)/T} + 1]^{-1}$ (with energy ε, chemical potential μ, and temperature T) is perturbed in each <it>i~~<\>>th layer by the trade-off between the external field *E* and the mean free path l_i, accordingly to the Boltzmann equation for diffusive transport regime. However, in highly perfect epitaxial junctions [3,4], an essentially ballistic regime is expected at distances closer than l_i from the junction. We show that in this condition a new specific perturbation of electronic distribution can appear, either in equilibrium and out of equilibrium, which can be important for the spintronics performance. A similar effect was already discussed for electrons near atomic point contacts [5]. To model the junction, we consider two ferromagnetic leads 1 and 2 with dispersion laws $\varepsilon_{i,\sigma}(k)$ ($i = 1,2$ and $\sigma = \pm$ for majority and minority carriers) linked by a thin non-magnetic barrier (Fig. 1). The steady state distributions far from the barrier, $f_{i,\sigma}^{\infty}(\mathbf{k})$, are defined by the respective $l_{i,\sigma}$, but close to the barrier they are defined by the transmission and reflection coefficients, $|T_{\sigma,\sigma'}(\mathbf{k})|^2$ and $|R_\sigma(\mathbf{k})|^2$ (at conserved energy and transversal momentum) as given in Eqs. (1). The second pair of equations relates to the current conservation in each (k,σ) channel. Eqs. (1) fully define the functions $f_{i,\sigma}(\mathbf{k})$ near the barrier, and the result essentially depends on the relative magnetic configuration (parallel, P, or antiparallel, AP) of the junction. For the P case (symmetric barrier with $|T(\mathbf{k})|^2 + |R(\mathbf{k})|^2 = 1$), one has trivially $f_{i,\sigma}(\mathbf{k}) = f_{i,\sigma}^{\infty}(\mathbf{k})$, but a non-trivial effect appears for the AP case, as can be already seen in the equilibrium state ($E = 0$, $f_{i,\sigma}(\mathbf{k}) = f_{i,\sigma}(-\mathbf{k})$). Then the explicit solution for simple parabolic dispersion $\varepsilon_{i,\sigma}(k) = \varepsilon_0 - \sigma\Delta - h^2k^2/2m$ and $T = 0$ (when $\mu = \varepsilon_F$) is: $f_{i,+}(k) = 1$, $f_{i,-}(k) = k/\sqrt{(k^2 - k_{\Delta}^2)} - k_{\Delta}^{-2}\ln[(k + \sqrt{(k^2 - k_{\Delta}^2)})/k_{\Delta}]/(k^2 - k_{\Delta}^2)$, for $k_\sigma < k < k_m$ and $k_\Delta = \sqrt{(4m\Delta)}/h < k_-$. Since $f_{i,-}(k) < 1$, there appears an additional deficit of minority spins, that is enhanced polarization and charge accumulation near the barrier, compared to the bulk leads. At finite field *E*, the conservation of equal spin currents requires a bigger shift of $f_{i,-}(\mathbf{k})$ than of $f_{i,+}(\mathbf{k})$, which should enhance the AP resistance and so the magnetoresistance of the device. The relaxation of accumulated charge and spin on scales $\sim l_-$ and $\sim l_{sf}$ from the barrier also contributes to this enhancement. A more involved analysis for the intermediate case between P and AP permits to estimate a similar effect for the spin torque performance of a perfect junction.~~

[1] R. E. Camley and J. Barnás, Phys. Rev. Lett. 63, 664 (1989).

[2] T. Valet and A. Fert, Phys. Rev. B48, 7099 (1993).

[3] S. Yuasa, et al., Science 297, 234 (2002).

[4] S. Yuasa, et al., J. Phys. D: Appl. Phys. 35, 2427 (2002).

[5] N. Agraït et al, Phys. Rep. 377, 81 (2003).

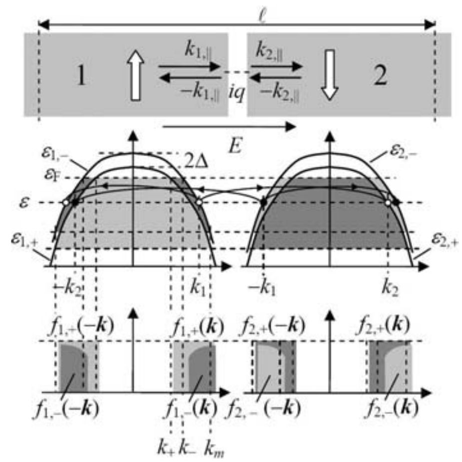

Fig. 1. Transmission and reflection processes at given energy ε and the resulting distributions of majority and minority spins on both sides of the barrier in the AP magnetic state. Light and dark shading indicates absolute spin orientations (up and down, respectively).

$$
\begin{aligned}
|T_{\sigma\sigma'}(\mathbf{k}_1)|^2 f_{1,\sigma}(\mathbf{k}_1) + |R_{\sigma'}(-\mathbf{k}_2)|^2 f_{2,\sigma'}(-\mathbf{k}_2) &= f_{2,\sigma'}(\mathbf{k}_2),\\
|T_{\sigma\sigma'}(-\mathbf{k}_2)|^2 f_{2,\sigma}(-\mathbf{k}_2) + |R_{\sigma'}(\mathbf{k}_1)|^2 f_{1,\sigma'}(\mathbf{k}_1) &= f_{1,\sigma'}(-\mathbf{k}_1)\\
f_{1,\sigma}(\mathbf{k}) - f_{1,\sigma}(-\mathbf{k}) &= f_{1,\sigma}^{(\infty)}(\mathbf{k}) - f_{1,\sigma}^{(\infty)}(-\mathbf{k}),\\
f_{2,\sigma}(\mathbf{k}) - f_{2,\sigma}(-\mathbf{k}) &= f_{2,\sigma}^{(\infty)}(\mathbf{k}) - f_{2,\sigma}^{(\infty)}(-\mathbf{k}).
\end{aligned}
\tag{1}
$$

EX-15

Spin Transport in a Double Magnetic Tunnel Junction Quantum Dot System with Non-collinear Magnetization.

M. Ma, M. Jalil
Department of Electrical and Computer Engineering, Information Storage Materials Laboratory, Singapore, Singapore

The spin polarized transport through a magnetic tunnel junction(MTJ) has attracted much research interest in recent years [1,2], due to its high tunneling magnetoresistance (TMR) for potential spin-based devices. In a MTJ system consisting of a quantum dot(QD) sandwiched between two ferromagnetic leads, i.e., an QD-MTJ system, the current through the system depends on the intrinsic polarization and the magnetization orientation of the two leads. If the QD is sufficiently small, its energy levels become quantized and discrete. Most previous models of discrete QD transport consider only a single energy level and neglect the substantial contribution due to hole transport in the QD [1].

In this paper, we propose a theoretical model to describe the spin transport in a noncollinear QD-MTJ system, with θ being the angle between the magnetizations of the leads. The model considers two discrete energy levels of the QD, i.e., the highest occupied(HO) energy level ε_h and lowest unoccupied(LU) energy level ε_e[2]. In our model, the QD can be occupied by at most two (excess) electrons or holes of opposite spins with intra-level Coulomb correlation energy of U_ξ (ξ= e/h for electrons/holes). The relaxation of an electron (hole) in the dot is denoted by Γ_ξ^σ, where $\sigma=\uparrow/\downarrow$ for up/down spin. A bias voltage V_b is applied between the two leads, i.e. the potential of left/right lead is $\mu_l=0$ and $\mu_r=-eV_b$, respectively. The QD energy levels are given by $\varepsilon_\xi=\varepsilon_{\xi 0}-0.5eV_b$, where $\varepsilon_{\xi 0}$ is the initial energy level at zero bias. The spin polarization of the lead is denoted by $p_\nu = (\gamma_\nu^\uparrow-\gamma_\nu^\downarrow)/(\gamma_\nu^\uparrow+\gamma_\nu^\downarrow)$, where ν=l,r signifies the lead, and γ_ν^σ is the line width function. The total current I and TMR at equilibrium were obtained by formulating the master equation. In the following calculations, we assume p_ν=p and $\Gamma_\xi^\sigma = \Gamma$.

We first investigate the I-V_b characteristic. As shown by Fig.1a, there are three distinct regions in the I-V_b characteristic, i.e., the low-bias Coulomb Blockade (CB) region with zero current, an intermediate single occupancy(SO) region, and a high bias double occupancy (DO) region. In the CB region, the sequential tunneling current is suppressed. In SO region, the QD could be occupied by only one electron or one hole. In DO region, the bias voltage is sufficiently large for the QD to be occupied by up to two electrons or two holes, which results in more tunneling channels, and hence an increase in the current.

Next we study the angular(θ) dependence of I-V_b characteristic (Fig.1a) and TMR (Fig.1b). We find that θ-dependence of current is much stronger in SO region compared to that in DO region. For instance, in SO region, the tunneling current is suppressed by 90% when θ changes from 0 to π/2; while in DO region, the corresponding reduction in tunneling current is only about 20%. Similarly, we found that θ-dependence of TMR is greater in SO region than that in DO region (Fig.1b). For example, when θ changes from 0 to π/2, the TMR in SO region increases from 0 to 0.84; while that in DO region reaches only 0.2. The smaller θ-dependence in DO region is due to the possibility of spin mixing in the tunneling current.

In Fig.2, we study the effect of spin flip in the dot on the tunneling current and TMR for both SO and DO regions. We found that a finite spin flip rate Γ enhances the current for θ≠0 case, leading to a suppression of the TMR for both SO and DO regions, with the suppression in the SO region being more pronounced. Thus, in general, the angular dependence of current and TMR is reduced by spin flip in the QD.

Finally, we study the dependence of the current and TMR on the intrinsic spin polarization p of the leads, as shown in Fig.3. We find that in contrast to the spin flip effect, an increase in the lead polarization enhances the angular dependence of current and TMR, especially in SO region. Additionally, we find that the TMR in both bias regions increases nonlinearly with p(Fig.3e), with the p dependence of TMR being greater as p increases (see Fig. 3f). Note that when the p value exceeds 0.775, the differential change in TMR with p for DO region exceeds that of the SO region. Thus, to achieve maximum sensitivity, the operating bias conditions should be set to the SO or DO regions, depending on whether the lead polarization p is smaller or larger than this critical value.

[1]. I.Weymann *et al*.,Phys.Rev.B 75,155308(2007).

[2]. M.J.Ma *et al*.,*Sequential tunnelling through a two-level quantum dot system coupled to magnetic leads*. Unpublished.

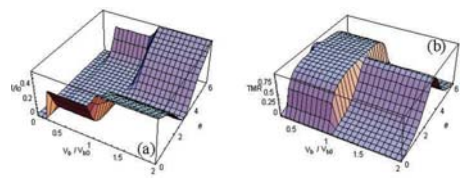

Fig.1 Bias voltage and angular dependence of (a) current and (b) TMR, where U=0.4meV, $\varepsilon_{e0}=-\varepsilon_{h0}$=0.1meV,p=0.99,Γ=0, V_{b0}=8mV, $I_0=6.4\times10^{-7}$A.

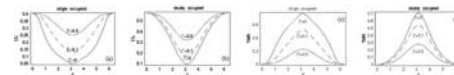

Fig.2 Angular dependence of current(a,b) and TMR(c,d) for various Γ values. $V_b=0.8V_{b0}$ in (a,c), $V_b=1.2V_{b0}$ in (b,d), p=0.9, other parameters are as same as in Fig.1.

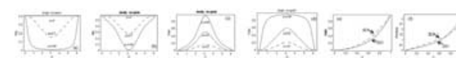

Fig.3 Angular dependence of current (a,b) and TMR (c,d) for various p values; and p dependence of TMR(e) and differential TMR(f). $V_b=0.8V_{b0}$ for SO, $V_b=1.2V_{b0}$ for DO, Γ=0, other parameter are as same as in Fig.1.

FA-01

Spin torque effects in magnetic nanostructures.

R. Buhrman
Cornell University, Ithaca, NY

The initial predictions and subsequent definitive demonstrations of the ability of a spin-polarized current that impinges onto a thin film nanomagnet to reversibly switch the orientation of the magnetic moment and/or to excite it into microwave precession by the torque exerted through the transfer of spin angular momentum from the incident conduction electrons have catalyzed what is now a quite broad and very active area of spin torque research. Since that initial work, there has been remarkable progress in advancing the fundamental understanding of this new spintronics phenomenon, and in successfully moving it towards technological implementations, particularly spin-torque MRAM and spin-torque microwave oscillator applications, that have the potential for broad impact. In this presentation I will discuss the basics of the spin torque effect and briefly survey the various approaches that can be employed to demonstrate and study it in both all-metallic, spin-valve-type nanostructures and magnetic multilayers, and in nanoscale magnetic tunnel junctions (MTJs). I will also briefly discuss some of many challenges that remain to be overcome before spin-torque based technologies can be successfully realized. After this survey of the basic phenomenon and some of its possible implementations, I will discuss some recent work that has sought to contribute to the rapidly advancing spin-torque research effort, by helping both to better understand quantitatively the details of the phenomenon and to understand and enhance the efficiency of the effect I will summarize results from studies of spin-transfer switching and microwave excitation in magnetic tunnel junctions (MTJs) which include the use of the spin transfer phenomenon to quantitatively determine, through spin-torque-excited ferromagnetic resonance (ST-FMR), both the bias dependent efficiency of the spin torque in high quality MTJs and the magnetic damping of individual free layer nanomagnets. I will conclude by briefly describing some recent work that has been examining spin torque effects in nanoscale structures with distinctly non-uniform magnetization, including the case where persistent dynamics of an individual magnetic vortex can be excited and detected. These studies are giving us some new information regarding magnetic dynamics in nanoscale structures. The results are also pointing to ways by which it may be possible to make better or more versatile spin-torque driven microwave oscillators, and, most significantly, to reduce the spin polarized current needed for the short-pulse switching of a thermally stable nanomagnet for MRAM applications.

FA-02

The development of magnetic tunnel junction memory: from first devices to Mbit MRAMs to emerging spin-torque transfer MRAMs.

W. J. Gallagher
IBM Watson Research Center, Yorktown Heights, NY

This talk will review the development of and outlook for magnetoresistive random access memory (MRAM). It will begin by explaining why the magnetic tunnel junction device in particular is an attractive device for high-speed memory [1]. The device and design choices that have been made for current Mbit-level MRAMs will then be described. While enormous advances have been made in magnetic tunnel junction materials for getting higher read signal, it has been developments to make writing more reliability that have been more important for the first MRAM products. Existing Mbit-level MRAMs all rely on x- and y- magnetic fields for bit selection within sub-arrays. This selection scheme necessarily involves the exposure of many half-selected bits on the x- and y-lines to half-select write fields. Furthermore, nearest neighbor bits feel the vector addition of stray write-fields plus the half-select fields. Particularly the latter combination (a nearest neighbor to the bit being written, which both feels a stray field and is subjected to a half-select field) leads to a non-negligible probability for bits to be accidentally written. A toggle writing scheme, which involves the rotation of magnetic storage layers rather than threshold switching, has been one successful approach to avoiding half-select upsets [2]. When combined with magnetic liners added to the x- and y-write wires to increase and concentrate the magnetic flux delivered to selected bits while lower that applied to neighboring bits, the probability of nearest-neighbor magnetic half-select write upset errors is reduced to a negligible level. This combination of approaches works well for eliminating unintended bit writing, and toggle MRAM products up to 4-Mbit [2] in capacity are in commercial production utilizing 180nm minimum feature sizes technology. Larger prototype toggle MRAM chip capacities, for example up to 16Mbit in 180nm technology, have also been demonstrated.
For scaling MRAMs to smaller feature-size technologies, bit thermal stability requirements lead to a need to increase write fields to a level that eventually becomes impractical. Fortunately in smaller devices, the direct injection of spins starts to become a more dominant effect for rotating magnetic moments. Thus spin-torque transfer devices [3] in their tunnel junction form [4] become an attractive alternative approach to MRAM. With these devices, write-selection id done through an access transistor in each cell, thus eliminating the magnetic half-select issue. The challenge remaining today is to lower the required write current so that smaller selection transistors can deliver sufficient current, thus enabling smaller cells. Producing spin torque transfer devicew with lowered required writing currents is the focus of considerable present research and development efforts.
In the final part of this presentation, the properties of existing and emerging MRAM approaches will be compared to those for other existing and other emerging nonvolatile memory technologies. For example phase change memory which offers potential for random access and multibit storage [5], seems a better approach for high density, but not necessarily so if high endurance or very high speed is also required. In those cases, MRAM would be preferred. Other situations in which one memory type or another would be a preferred solution will be described.

1. For a review of IBM MRAM developments see: W.J. Gallagher and S.S.P. Parkin, “Development of magnetic tunnel junction MRAM at IBM: From first junctions to a 16-Mbit demonstrator chip,” IBM Journal of Research and Development, 50, 5 (2006).

2. M. Durlam, et al. “A 0.18 um 4Mb Toggling MRAM,” IEDM Tech. Digest, pp. 34.6.1-3 (2003).

3. For a review of spin torque transfer physics and device development see: J.Z. Sun, “Spin angular momentum transfer in current-perpendicular nanomagnetic junctions, “ IBM Journal of Research and Development, 50, 81 (2006).

4. S. Assefa, et al., “Fabrication and characterization of MgO-based magnetic tunnel junctions for spin momentum transfer switching,” J. Appl. Phys. 102, 063901 (2007).

5. T. Nirschl, et al., “Write Strategies for 2 and 4-bit Multi-Level Phase-Change Memory,” 2007 IEEE International Electron Devices Meeting, paper 17.5.

FA-03

Spin torque devices for high density MRAM and nano-oscillators.

N. D. Rizzo, R. W. Dave, F. B. Mancoff, P. G. Mather, B. Butcher, S. Tehrani
Technology Solutions Organization, Freescale Semiconductor, Chandler, AZ

The spin torque effect enables new possibilities for magnetoelectronic devices such as a high density, low power spin torque memory (ST-MRAM) and spin torque nano-oscillators (STNOs).
The spin torque effect is dominant at bit sizes of 0.1μm or less, making it ideal for high density memory. However, maintaining a good bit shape at such dimensions is challenging using optical lithography. We fabricated MTJ nanopillars as small as 80nm with good pattern fidelity using optical lithography on 200mm diameter wafers. (Fig. 1.)
Since the programming current passes through the MTJ, a low resistance is needed to prevent dielectric breakdown. We fabricated low resistance area (RA) product MgO barriers using various oxidation techniques. (Fig. 2.) Natural oxidation is superior to radical oxidation for low RA barriers. For an optimized natural oxidation process, an MR% of over 100% was achieved at an RA as low as 5 $\Omega\mu m^2$ with a CFB free layer.
We patterned similar films into 0.1x0.2 μm bits and measured the quasistatic (0.1s pulse duration) spin-transfer switching currents (I_c) of several hundred bits across-wafer. (Fig. 3.) The average I_c for a 0.1x0.2 μm bit with CFB free layer was 0.6mA with a cross wafer relative standard deviation of 11%. To determine the high speed I_c, we measured I_c for different pulse duration and fit the standard formula for thermal activation to the data. (Fig. 4.) We found a high-speed switching current density of $J_{c0}\approx 6MA/cm^2$ along with a thermally-stable energy barrier $E_b\approx 50k_bT$. While the results are promising, we estimate that reducing J_{c0} by ≥2X while maintaining $E_b>40k_bT$ will be required to realize a practical ST-MRAM.
The spin torque effect can also cause free layer oscillations at GHz frequencies. An STNO is of applied interest because it has small size, high Q, and is tunable over a wide range. We fabricated giant magnetoresistance point contacts having diameters ranging from d<50nm to d≈300nm using either e-beam or optical lithography. The spin torque resonance was measured over a frequency range from <8GHz to >26GHz. The slope of the resonance frequency versus current decreased as d increased and was fit by a phenomenological spin-transfer model where the effective d extends ≈50nm past the contact edge into the surrounding magnetic film[1]. Also, phase locking between the resonances of two STNOs was demonstrated when the intercontact spacing between them ≤200nm.[2] Such phase locking offers a way of controlling arrays of STNOs and thereby increasing the output power to levels useful for applications.

[1]F. B. Mancoff, N. D. Rizzo, B. N. Engel, and S. Tehrani, Appl. Phys. Lett. **88**, 112507 (2006).

[2]F. B. Mancoff, N. D. Rizzo, B. N. Engel, and S. Tehrani, Nature (London) **437**, 393 (2005).

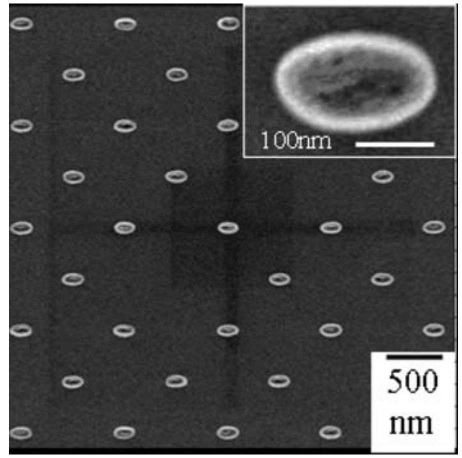

Fig. 1 SEM image of 0.1x0.2 μm bits patterned using optical lithography. Inset: Higher mag. image of 1 bit.

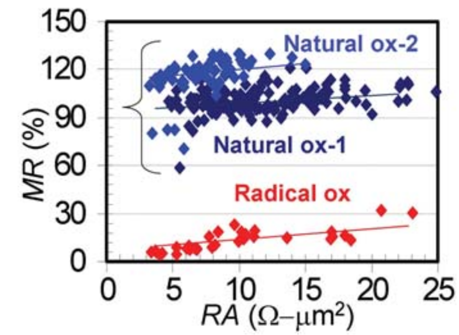

Fig 2. Continuous film MR% vs. RA for various oxidations of Mg with CFB free layer.

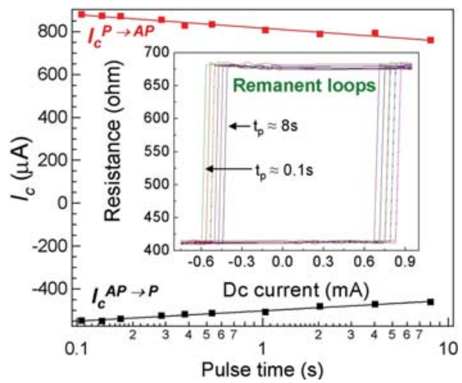

Fig.3. Switching current vs. pulse duration for a 0.1x0.2 μm bit. Lines are fits of thermal activation theory to data. Inset:R vs. I loops for different pulse duration t_p.

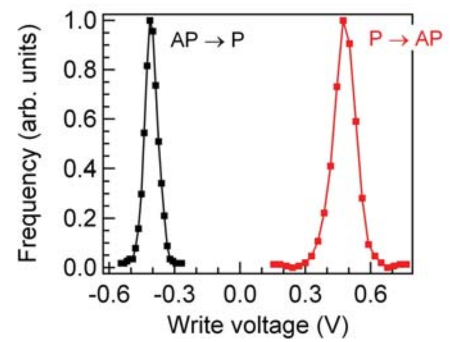

Fig. 4. Cross wafer switching distributions for 0.1x0.2 μm bits.

FA-04

Spin Torque Transfer Switching of Perpendicular Magnetoresistive elements for High Density MRAMs.

H. Yoda[1], T. Kishi[1], T. Kai[1], T. Nagase[1], M. Yoshikawa[1], M. Nakayama[1], E. Kitagawa[1], M. Amano[1], H. Aikawa[1], N. Shimomura[1], K. Nishiyama[1], T. Daibou[1], S. Takahashi[1], S. Ikegawa[1], K. Yakushiji[2], T. Nagahama[2], H. Kubota[2], A. Fukushima[2], S. Yuasa[2], Y. Nakatani[3], M. Oogane[4], Y. Ando[4], Y. Suzuki[5,2], K. Ando[2], T. Miyazaki[6]

1. Corporate R & D center, Toshiba, Kawasaki, Japan; 2. Nanoelectronics Research Institute, AIST, Tsukuba, Japan; 3. Computer Science, The University of Electro-Communications, Tokyo, Japan; 4. Applied Physics, Tohoku University, Sendai, Japan; 5. Materials Engineering Science, Osaka University, Osaka, Japan; 6. WPI Advanced Institute for Materials Research, Tohoku University, Sendai, Japan

I. Introduction

Most of spin torque works used MTJs with shape anisotropy[1],[2].However, the anisotropy fails to keep non-volatility st small size. A solution is to use perpendicular magnetization[3]. In this paper, the potentials are discussed.

II. Potential for small switching current,Ic

Analytic expressions of Ic are given in figure 2. The Ic for perpendicular is small by the second term in (i)-b. In perpendicular, both switching paths by spin torque and by thermal agitation are the same. In longitudinal, only spin torque makes the magnetization perpendicular and the Ic gets large.

III. Scalability of the non-volatility

Perpendicular materials with about 7nm diameter used in HDD have non-volatility. F=7nm gives the 8F^2 footprint of 0.00001um^2(figure 3)which corresponds to 50 Gbit.

IV. Scalability of the switching speed

The work memory switching time must be about 10 nsec.. The analytic expression is given in figure 2. It gives several nano-seconds for F=60nm.The Landau-Lifshitz-Gilbert simulation and the experiments also gave less than 10 nano-seconds(figure 3). The expression says the speed scales.

V. Scalability of the switching current

Table 1 summarizes demonstrations[2], [4], [5], [6], [7]. While perpendicular elements have larger coercivities, Ics don't differ much. Ic/Δ takes the small value for TbCoFe and CoFe super lattice. Further reduction in Ic can be made by smaller damping and higher spin polarization[7]. CMOS drivability gets worse at small size,but the switching current gets smaller(figure 5). The Ic scales.

VI. Conclusion

Pependicular MRAMs have good scalabilities.

This work is partly supported by NEDO.

[1] M. Hosomi et al., IEDM Tech. Dig., pp. 459-462, 2005.

[2] Y.Huai et al., Magn. Magn. Mater. 304, 88 2006

[3] H.Meng et al., ApplPhys. Lett.. 88, pp 172506, 2006

[4] S. Mangin et al., Nature Materials 5, p. 210, 2006.

[5] K. Yakushiji et al., Abstract of 52nd Annual Conference on Magnetism and Magnetic Materials, BB-01,p.78(2007)

[6] M. Nakayama et al., Abstract of 52nd Annual Conference on Magnetism and Magnetic Materials, BB-09,p.81(2007)

[7] T. Nagase et al.,American Physical Society March meeting 2008,New Orleans to be presented.

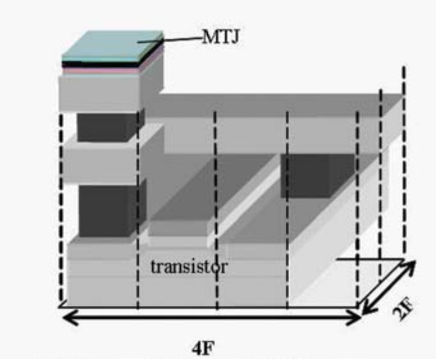

Fig.1 schematic drawing of spin torque transfer writing MRAM

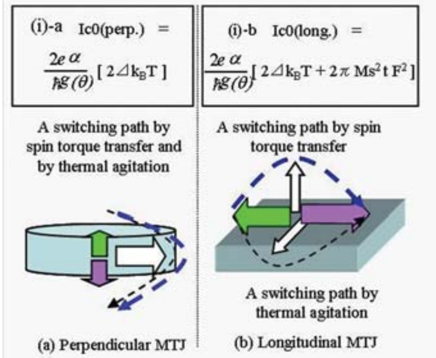

Fig.2 Comparison between perpendicular MRAM and longitudinal MRAM

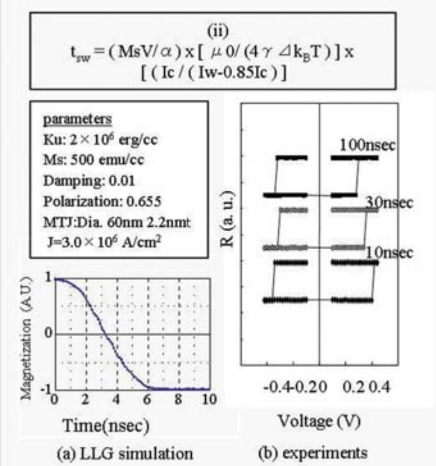

Fig.3 switching speed of perpendicular MTJ

Table.1 Review of spin torque transfer demonstrations

	perendicular					longitudinal
Material	TbFeCo	super lattice			FePt	CoFeB
		CoFe		Co/Ni		
Hc (Oe)	1200	800	1560	750	1840	43
Ms (emu/cc)	300	400	400	650	about 1000	800
Δ=Ku/kBT (Measured)	107	78	298	-	60	24*
Storage layer Volume (nm^3)	Dia.130x4t	Dia.90x4t	Dia.100x2.5t	50x100x2.9	Dia.100x1.36t	125x205x2.5
I(μA)	348	146	1059	850	1400	220
Current pulse	100nsec.	100nsec.	100nsec.	-	10usec	30nsec.
I/Δ	3.2	1.9	3.5	-	23	9.1
	MTJ	GMR	MTJ	GMR	GMR	MTJ

* Calculated by (MsHc)xV/2

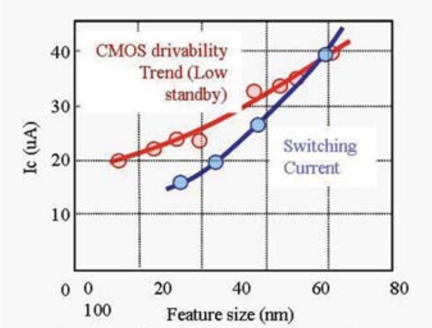

Fig. 4 Ic, critical switching current v.s. feature size for perpendicular MTJs

FB-01

Giant Spin Hall Effect in Perpendicularly Spin-Polarized FePt/Au Devices.

T. Seki[1], Y. Hasegawa[1], S. Mitani[1], K. Takanashi[1], S. Takahashi[1,2], S. Maekawa[1,2], H. Imamura[3,2], J. Nitta[4]
1. Institute for materials research, Tohoku Univ., Sendai, Japan; 2. CREST, Japan Science and Technology Agency, Tokyo, Japan; 3. National Institute of Advanced Industrial Science and Technology, Tsukuba, Japan; 4. Graduate School of Engineering, Tohoku University, Sendai, Japan

The generation and detection of spin currents are important issues for the further development of spin-electronics. Direct and inverse spin Hall effects (SHEs) in nonmagnetic semiconductors or metals, which convert charge current into pure spin current and vice versa, respectively, enable us to inject or detect spin current without ferromagnetic materials. Thus, it is expected that SHE provides a new functionality of materials for spin-electronic devices. The theoretical predictions of the SHE have stimulated scientific interests, and the optical detection of SHE was demonstrated in nonmagnetic semiconductors. Recently, the electrical detection of SHE was also reported in nonmagnetic metals such as Al [1] and Pt [2]. However, the complicated device structures or the sophisticated measurement techniques were required to detect SHE, and the small magnitudes of spin Hall signals limit the possibility of device applications of SHE.
Here, we present "giant SHE" at room temperature in perpendicularly spin-polarized FePt/Au devices [3]. We fabricated a multi-terminal device with a nano-sized Au Hall cross and a FePt perpendicular spin injector through the use of electron beam lithography and Ar ion etching. Perpendicularly magnetized FePt generates or detects the perpendicularly polarized spin current without external magnetic field, which allows us to simplify the device structure. Furthermore, the present multi-terminal device enables us to measure three kinds of Hall effects, that is, direct SHE, inverse SHE, and local Hall effect (LHE) using the same device.
We employed the non-local spin injection technique to detect the direct and inverse SHEs. In the case of the inverse SHE, the spin-polarized electric current is injected from FePt to Au, the spin current flows in Au due to the spin accumulation, and the non-local Hall voltage induced by SHE is detected by the Au Hall cross. For the direct SHE, on the other hand, the electric current flows in the Au cross, the spin current is generated by SHE, and the generated spin current is detected by the FePt spin injector. An important point is that the SHE is detected even at zero external magnetic field owing to the perpendicular magnetization of FePt.
Clear hysteretic transitions of the non-local Hall resistance were observed in both direct and inverse SHE geometries with sweeping the external magnetic field, and the shapes of the hysteresis loops were the same as that of the LHE. Since the LHE results from the anomalous Hall effect in FePt, the hysteresis loops observed in the SHE geometries reflect the magnetization reversal of FePt. In addition, the sign change of the spin accumulation in Au led to the polarity reversal of the hysteresis loops of the non-local Hall voltage, which is interpreted as the change of the direction of the spin current in the Au Hall cross. Those results clearly indicate that the non-local Hall resistance originates from the SHE in Au. With increasing the distance between the FePt spin injector and the Au Hall cross, the magnitude of the SHE exponentially decreased and the spin diffusion length in Au was obtained to be about 86 nm at room temperature.
From the resistance change of SHE, the spin Hall angle, which is the ratio of the spin Hall conductivity to the electric conductivity, was calculated to be 0.113. This large spin Hall angle in Au is interpreted by the skew scattering mechanism. The spin Hall angle showed the weak temperature dependence, which supports that the skew scattering contribution is dominant in the present Au. The maximum value of the resistance change in the multi-terminal devices is 2.7 mΩ at room temperature, which is significantly larger than those in previous reports [1,2]. We believe the large spin Hall signal opens a way of new writing and/or reading techniques for magnetic storage devices.
This work was partly supported by Industrial Technology Research Grant Program in 2005 from NEDO.

[1] S. Valenzuela et al., Nature 442, 176 (2006).

[2] T. Kimura et al., Phys. Rev. Lett. 98, 156601 (2007).

[3] T. Seki et al., Nature Materials (in press).

Electrical Generation, Modulation and Detection of Spin Currents in Silicon in a Lateral Transport Geometry.

B. Jonker, O. van 't Erve, G. Kioseoglou, A. Hanbicki, C. Awo-Affouda, M. Holub, C. Li, P. Thompson
Naval Research Laboratory, Washington, DC

The electron's spin angular momentum is one of several alternative state variables under consideration on the International Technology Roadmap for Semiconductors for processing information in the fundamentally new ways which will be required beyond end-of-roadmap CMOS technology (1). Electrical injection / transport of spin-polarized carriers is prerequisite for developing such an approach. While significant progress has been realized in GaAs (2), little has been made in Si, despite its overwhelming dominance of the semiconductor industry.

We report successful injection of spin-polarized electrons from an Fe /Al2O3 tunnel barrier contact into Si(001) n-i-p doped heterostructures (Figure 1), and spin transport across the Si/AlGaAs interface (3). The circular polarization of the electroluminescence (EL) due to radiative recombination in the Si tracks the Fe magnetization, confirming that the electrons originate from the Fe. The polarization reflects Fe majority spin, consistent with the common delta_1-symmetry of the Fe majority and Si(001) conduction band (CB). The electron spin polarization in the Si is ~30% at 5K, with significant polarization extending to at least 125K. In Si/AlGaAs/GaAs quantum well (QW) structures, the spin polarized electrons drift under applied field from the Si and recombine in the GaAs QW, where the polarized EL can be quantitatively analyzed, yielding an electron spin polarization of 10%. Spin transport occurs despite the poor crystalline quality of Si epilayers on GaAs, the 0.3 eV CB offset (Si band lower), and the fact that the sample surface was exposed to air before growth of the Si on the AlGaAs/GaAs and of the Al2O3 on the Si. Lateral transport structures and non-local detection techniques (Figure 2) are used to create a spin current which flows separately from the spin-polarized charge current (4). This spin diffusion current is sensitive to the relative orientation of the magnetization of the injecting and detecting contacts. Hanle effect measurements demonstrate that the spin current can be modulated by a perpendicular magnetic field, which causes the spin to precess and dephase in the transport channel. This effect is clearly manifested in the signal at the detector contact.

The realization of efficient electrical injection and detection using contacts compatible with "back-end" Si processing should greatly facilitate development of Si-based spintronics.

This work supported by the Office of Naval Research and core programs at NRL.

1. International Technology Roadmap for Semiconductors, 2005 Edition, http://www.itrs.net/reports.html. "Executive Summary" & "Emerging Research Devices."

2. for a recent review, see Jonker, B.T. & Flatte, M.E. in Nanomagnetism: Ultrathin Films, Multilayers and Nanostructures (in the series Contemporary Concepts of Condensed Matter Science, Elsevier, 2006), 227-272. ISBN 0-444-51680-8

3. B.T. Jonker et al, Nature Physics 3, 542 (August 2007)

4. O.M.J. van 't Erve et al, Appl. Phys. Lett. 91, 212109 (2007)

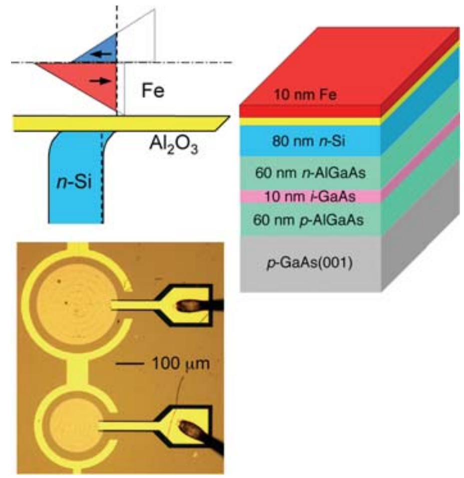

Figure 1. Schematic of sample structure and band diagram, and photograph of processed surface-emitting devices.

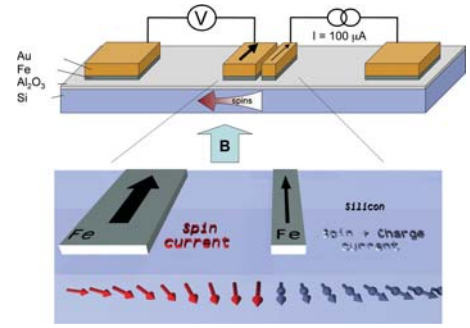

Figure 2. Lateral transport geometry used to generate, manipulate and detect pure spin currents in silicon.

FB-03

Electrical transport properties of MgO/ferromagnet contacts to p-Si for spin injection and detection.

T. Dimopoulos[1], T. Uhrmann[1], D. Schwarz[1], V. Lazarov[2], D. Kirk[2], A. Kohn[2], S. Weyers[3], U. Paschen[3], H. Brückl[1]

1. Nano-System-Technologies, Austrian Research Centers GmbH - ARC, Vienna, Austria; 2. Department of Materials, University of Oxford, Oxford, United Kingdom; 3. Microelectronic Circuits and Systems, Fraunhofer Institute, Duisburg, Germany

Ferromagnetic contacts to Si are recently studied for spin-polarized current injection and detection in hybrid devices [1],[2],[3],[4]. The inclusion of an insulator (I) as tunnel barrier between the ferromagnet (FM) and the semiconductor (SC) results to an interfacial resistance, necessary for a significant spin polarization of the injected current [5]. The resistance value should lie within a narrow window, its upper limit determined by a necessary discontinuity of the electrochemical potentials at the interface and its lower by the amount of spin-flip events in the SC [5]. The latter is sensitive to the doping type and density. Low-doped, n-Si should give rise to a larger spin-flip length [5], but on the other hand, due to the extended Schottky barrier, it results to a forbiddingly large contact resistance for spin injection [1]. The electron spin relaxation time in p-Si is expected to be smaller due to the additional electron-hole interaction [6]–nevertheless experimental evaluation is lacking.

In this digest we present the properties of FM contacts to p-Si, using MgO as tunnel barrier. We concentrate on the influence of the tunnel barrier thickness and wafer doping density on the contact resistance for spin injection and detection.

Micrometer and sub-micrometer size trenches were patterned by deep-UV lithography on p-doped Si wafers, with a doping density of $\rho=10^{15}$ to 10^{18} cm^{-3}, covered with a 42 nm-thick oxide layer. The trenches were subsequently opened down to the Si surface with a combination of reactive and HF wet chemical etching. MgO(x=0.5, 1, 1.5, 2.5 nm)/$Co_{70}Fe_{30}$(1 nm)/$Ni_{81}Fe_{19}$(4 nm)/Ta contacts were sputter-deposited on the freshly etched Si. Finally, Al top contacts were fabricated and temperature-dependent, DC current-voltage (I-V) characteristics were measured.

A cross section, transmission electron microscopy (TEM) image of the multilayer with x=2.5 nm is shown in Fig. 1. The MgO layer appears amorphous, and the FM bilayer polycrystalline. A SiO_x layer is formed between the MgO and Si with an estimated thickness below 1 nm.

Elements of 0.5 to 8 μm^2 were measured and the current was found to scale satisfactory with the area, suggesting a homogeneous current flow through the element. In Fig. 2(a) we show room temperature (RT) I-V curves, measured for 6 μm^2 contacts with different tunnel barrier thickness, on a wafer with $\rho=10^{17}$ cm^{-3}. Forward (negative) bias corresponds to the spin injection case, i.e. electron current flows from the FM to the SC, while the latter is in accumulation. Reverse bias corresponds to the detection case, i.e. electron current flows from the SC to the FM. The forward bias current density for x=0.5 nm is in some cases more than 2 decades higher than for x=2.5 nm. Even though considerable, the dependence of the current density on the barrier thickness is much weaker than the one observed in magnetic tunnel junctions. This is due to the existence of the Schottky barrier at the I/SC interface, contributing to the electrical transport characteristics.

In Fig. 2(b) we present RT I-V curves for elements with x=1.5 nm, for different wafer doping densities (normalized to the current value at –1.5 V). Interestingly, no rectification is observed for $\rho=10^{15}$ cm^{-3}, while it increases by more than a factor of 1000 for $\rho=10^{18}$ cm^{-3}. This increase of the rectification with increasing doping density is in sharp contrast to the case of identical contacts deposited on n-doped Si, in agreement with what is reported in the literature [1]. The observed behaviour can be explained by a suppression of the minority carrier (electron) current by electron-hole recombination in the bulk of the SC for larger doping densities. The reverse bias current (corresponding to detection) is greatly influenced, while the effect on the forward bias current is much less significant. The above argument is also supported by the enhanced temperature dependence of the I-V curves for higher doping.

In conclusion, we present the properties of FM contacts with MgO tunnel barrier on p-doped Si for spin injection and detection. The current is considerably increased with decreasing barrier thickness, while the rectification is minimal for low doping densities, in contrast to the case of n-doped wafers. This makes such contacts potentially interesting as injectors and detectors of spin polarized current in a two-terminal local measurement.

[1] B.C. Min et al., J. Appl. Phys. 99, 08S701 (2006)

[2] B.C. Min et al., Nature Materials 5, 817 (2006)

[3] K. Sugiura et al., Appl. Phys. Lett. 89, 072110 (2006)

[4] T. Uhrmann et al., accepted in J. Appl. Phys.

[5] A. Fert and H. Jaffrés, Phys. Rev. B 64, 184420 (2001)

[6] G. L. Bir et al., Sov. Phys. JETP 42, 705 (1976)

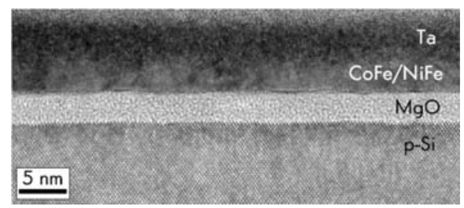

Figure 1: Cross section TEM image of the MgO/CoFe/NiFe contact.

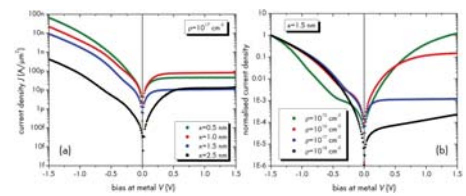

Figure 2: (a) I-V curves for $\rho=10^{17}$ cm^{-3} and different barrier thicknesses. (b) Normalized I-V curves for x=1.5 nm and different doping densities.

FB-04

Spin Coulomb Drag: a Limitation for Spintronics?

I. D'Amico[1], C. A. Ullrich[2]
1. Physics, University of York, York, United Kingdom; 2. Physics and Astronomy, University of Missouri-Columbia, Columbia, MO

An intense research effort is underway to improve our understanding of spin dynamics, especially related to nanocircuits and their components, with the aim of building novel (spin)electronics devices. In this context the theory of spin Coulomb drag (SCD) was recently developed[1]. It analyzes the role of Coulomb interactions between different spin populations in spin-polarized transport, showing that Coulomb interactions are an intrinsic decay mechanism for spin currents, a measure of which is given by the spin-transresistivity. As confirmed by experiments[2], SCD can be substantial in semiconductors, and it is bound to become one of the most serious issues in spin polarized transport, since, due to its intrinsic nature, it cannot be
avoided even in the purest material. More recently the
frequency dependence of SCD has been considered[3]: this is important for AC spintronics applications, optical spin-injection and spin-resolved optical experiments.
A critical issue for potential spintronics devices has been pointed out, namely the power loss in spin transport and dynamics due to SCD[3]. We have estimated that for three dimensional GaAs ac spintronic devices operating at terahertz frequencies, the power loss due to SCD can be of the order of several mW/cm^3. This can be a large fraction of the power loss due to the Drude resistivity, between 22% and 44% when considering densities between 10^{16} and 10^{18} cm^{-3} and mobilities of 10^4 cm^2/Vs. As the SCD becomes stronger in low dimensional structures, we expect the corresponding power loss to be even more relevant in such structures.
Another important aspect of SCD in the frequency domain is its effect on optical spin excitations[3]. A related issue is its interplay with the spin-orbit coupling[4]. Our calculations show that SCD may contributes substantially to the linewidth of spin optical excitations. Results for the intersubband spin plasmon in a parabolic quantum well are reported in Fig.1. In two dimensional structures spin-orbit coupling effects may also become important. In particular a threefold splitting of the intersubband spin plasmon mode has been predicted[5]. In Fig.2 we show that such a splitting would be very small in parabolic quantum wells. Let us compare the effects due to spin-orbit coupling and SCD by considering quantum wells corresponding to the maximum value of the SCD linewidth. We see then that the dispersion relation splitting due to the spin-orbit coupling becomes a negligible effect.
This suggests the possibility of a purely optical quantitative measurement of the SCD effect by means of inelastic light scattering. The proposed experiments would establish unequivocally the influence of and the limitations imposed by SCD on optical excitations.

[1]I. D'Amico and G. Vignale, Phys. Rev. B, 62, page 4853 (2000), I. D'Amico and G. Vignale, Phys. Rev. B 65, 085109 (2002),I. D'Amico and G. Vignale, Phys. Rev. B 68, 045307 (2003)

[2]C.P.Weber et al, Nature 437, 1330 (2005)

[3]I. D'Amico and C. A. Ullrich, Phys. Rev. B 74, R121303 (2006)

[4]I. D'Amico and C. A. Ullrich, work in progress

[5]C. A. Ullrich and M. E. Flatte', Phys. Rev. B 66,205305 (2002)

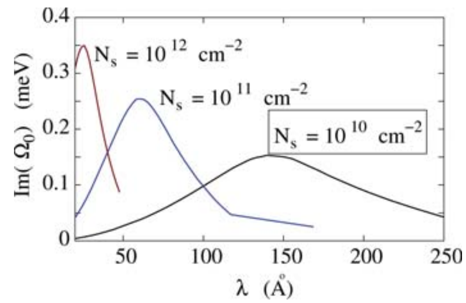

Fig.1: Linewidth of the intersubband spin plasmon due to SCD versus characteristic width of the parabolic quantum well calculated for different sheet densities, as marked. The figure shows results for q=0. Corrections due to a finite value of the in-plane wave vector q are negligible (not shown).

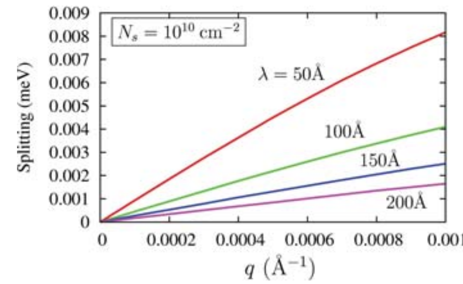

Fig.2: Maximum splitting of the intersubband spin plasmon due to spin-orbit coupling versus in-plane wave vector q for a parabolic quantum wells with sheet density N_s=10^{10} cm^{-2} and different characteristic widths (as marked). Notice that the peak value of the SCD linewidth for the same density (Fig.1) is almost two order of magnitude bigger than the corresponding spin-plasmon splitting.

FB-05

Organic spintronics: on the spin injection at the CuPc/GaAs interface.

M. Cinchetti[1], H. Ding[2], Y. Gao[2], J. Wüstenberg[1], M. Sánchez Albaneda[1], O. Andreyev[1], M. Bauer[1], M. Aeschlimann[1]
1. Department of Physics, University of Kaiserslautern, Kaiserslautern, Germany; 2. Department of Physics and Astronomy, University of Rochester, Rochester, NY

Organic semiconductors (OSC) have considerably attracted the interest of the scientific community due to the possibility of implementing very-low-cost and versatile electronic devices based on organic thin-film materials [1]. Recently, different pioneering experiments suggested that OSC represent as well a major opportunity for application in the growing field of spintronics [2,3]. In fact, OSC usually consist of elements with small atomic numbers, such as carbon and hydrogen, and thus intrinsically weak spin-orbit coupling is expected. This leads to long spin-polarization relaxation times that are particularly important for spintronics devices.
Spin injection from an active medium (AM) into OSC thin films is a fundamental prerequisite for the implementation of OSC-based spintronics devices. All experimental studies done so far to demonstrate the feasibility of spin injection into OSC are based on magnetoresistance or electroluminescence measurements, which result in a spin-dependent signal integrated over the whole spintronics device. According to the results presented in [4], great care has to be taken in the search of spin-injection in such experiments, since stray fields may mimic the spin effects. Spin- and time-resolved two-photon photoemission (2PPE) allows collecting direct experimental information about the efficiency of spin injection and the microscopic spin-flip mechanisms governing spin injection. Using this experimental technique we have studied a model system constituting the main ingredient of every OSC-based spintronics device, namely the heterojunction between an AM (in this case p-type GaAs) and copper phthalocyanine (CuPc).
In a first step, we have studied the formation of the CuPc/GaAs interface by means of ultraviolet photoemission spectroscopy (UPS). The energy band alignment of the interface as derived from the measurements is depicted in Figure 1. After having characterized the interface, we employed spin- and time-resolved 2PPE measurements, following the excitation scheme depicted in Figure 1: a circularly polarized pump pulse with photon energy of 1.56eV (denoted with R in the picture) creates spin polarized carriers in the GaAs substrate by optical orientation. Due to the large penetration depth of red light in GaAs these electrons are excited into the conduction band mainly outside the band bending area. Subsequently, some of these electrons will be accelerated towards the interface in the band bending potential and finally cross the CuPc/GaAs interface to end up in intermediate states above the LUMO of CuPc. Since the probing depth in the photoemission process is limited by the short inelastic mean free path of the photoelectrons, the probe pulse with photon energy of 3.12 eV (denoted with B) finally photoemits these electrons from the very surface region (and thus mainly out of CuPc) into a final state above the vacuum level. Figure 2 shows the efficiency of spin polarization injection for hot electrons with 1.4eV to 1.6eV energy above the Fermi level of the system, as a function of CuPc coverage. The efficiency is defined as the ratio between the spin polarization of the electrons originating from the bare GaAs substrate and of those which overcame the deposited CuPc film. The results show a highly efficient spin injection of hot electrons from GaAs into CuPc, with values even above 100% for CuPc coverages up to 10ML. This fact demonstrates beyond doubt that spin-injection takes place without any substantial spin-flip scattering at the interface.
In further measurements, we studied the temporal evolution of the spin polarization injected into the organic layer in the range from 10fs up to 1ps after injection from the GaAs substrate for different hot electron energies. The results indicate that the degree of spin polarization of electrons injected through the CuPc/GaAs interface into molecular orbitals just above the LUMO onset of CuPc is preserved longer than for electrons injected in energetically higher lying states. Thus, we can conclude that in order to achieve high efficiency in organic-based spintronics devices based on CuPc, injection of spin-polarized electrons energetically close to the LUMO onset of CuPc should be implemented by a careful choice of the bias potential.

[1] S.R. Forrest, Nature 428, 911 (2004);

[2] V. Dediu, et al., Solid State Commun. 122, 181 (2002);

[3] Z.H. Xiong, et al., Nature 427, 821 (2004);

[4] G. Salis, et al., Phys. Rev. B 70, 085203 (2004).

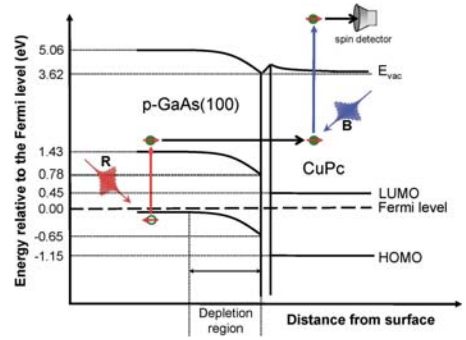

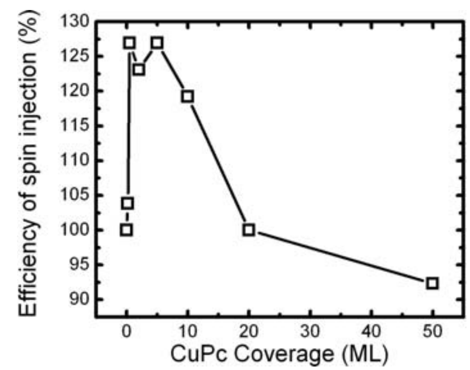

FB-06

Spin injection through MgO tunnel barrier in an InAs quantum well semiconductor.

S. H. Shim[1,2], Y. J. Park[1,3], J. Chang[1], Y. Lee[2], J. Moodera[3], S. Han[1]
1. Center for Spintronics Research, Korea Institute of Science and Technology, Seoul, South Korea; 2. National Research Laboratory for Nano Device Physics, Department of Physics, Korea University, Seoul, South Korea; 3. Francis Bitter Magnet Laboratory, Massachusetts Institute of Technology, Cambridge, MA

Spintronics is an emerging technology to overcome some of the physical limitations of conventional charge based electronics. Effective spin injection from ferromagnetic metal into semiconductors is prerequisite for the development of spin field effect transistor (spin-FET). Poor electrical spin injection is a major obstacle in the realization of spin-FET, which is attributed to the intrinsic conductance mismatch between metal and semiconductor. Tunnel contact is known to be a useful way to overcome the mismatch.[1] With the purpose, Schottky or Al_2O_3 tunnel contacts have been extensively studied to enhance spin injection, but the possible maximum spin polarization might be limited by the tunneling spin polarization from the ferromagnetic metal. An alternative approach to increasing spin polarization is to use a crystalline MgO(100) tunnel barrier. It was found that the majority electrons decay slowly and the minority electrons, on the other hand, decay rapidly in the MgO barrier.[2]
Here we present a manifest evidence of purely electrical detection of spin injection and accumulation in In-As quantum wells through MgO tunnel barrier. Spins injected from a Fe thin film accumulate and diffuse out in the InAs quantum well, with the spins being electrically detected by a neighboring Fe electrode. The injected spin polarization of the current crossing the Fe-InAs interface was increased, and the spin signal was much clearer than the previous experiment without MgO barrier.[3]
We have fabricated a mesoscopic lateral spin valve on InAs semiconductor. The device consists of two ferromagnetic Fe electrodes and an InAs high-electron-mobility transistor (InAs HEMT). A scanning electron microscope (SEM) image of a fabricated device is shown in Fig. 1(a). The essential parts of the device are 8.6-μm-wide InAs HEMT mesa and two ferromagnetic electrodes that work as the spin injector and detector. The ferromagnetic electrodes have different aspect ratio to give distinguishable magnetization-switching fields. A thickness of 30 nm was removed from the top surface by Ar-ion milling and then 2.2 nm MgO / 0.3 nm B/ 28 nm Fe film has been epitaxially grown by molecular beam epitaxy subsequently. Lastly, the film was capped by 12-nm-thick Au layer. Fig. 1(b) shows a schematic diagram of the cross section of InAs HEMT where the ferromagnetic electrode was deposited.
Spin injection can be detected electrically by measuring correlations of the magnetization of two ferromagnetic electrodes. Fig. 2 shows the nonlocal spin signal as a function of magnetic field applied along the easy axis of ferromagnetic patterns. For nonlocal measurement, the voltage is not measured directly where the charge current flows; instead, only the chemical potential that is sensitive to spin accumulation is measured using a ferromagnetic detector. The chemical potential in the parallel (antiparallel) magnetization makes an additive (subtractive) contribution to the nonlocal voltage.
Most of all, the regions where the magnetizations of ferromagnetic electrodes are parallel and antiparallel are evidently distinguished, since the resistance dips are much clearer and the plateaus are observed compared to the previous experiment without MgO tunnel layer.[3]
Purely electrical spin injection and detection in a semiconductor are important for constructing a spin-FET. Our layer structure is very similar to the previously reported structure except MgO layer.[3] Comparing to the previous experiment, we observed much clearer spin injection qualitatively and quantitatively. These experimental results will contribute significantly to the realization of a practical spin-FET. The introduction of MgO layer at the interface is proved to enhance spin injection from ferromagnetic metal to semiconductor as predicted by theoretical calculation.

[1] E. I. Rashba, Phys. Rev. B **62**, R16267 (2000).

[2] X. Jiang, R. Wang, R. M. Shelby, R.M. Macfarlane, S. R. Bank, J. S. Harris, and S. S. P. Parkin, Phys. Rev. Lett. **94**, 056601 (2005).

[3] Hyun Cheol Koo, Hyunjung Yi, Jae-Beom Ko, Joonyeon Chang, and Suk-Hee Han, Appl. Phys. Lett. **90**, 022101 (2007).

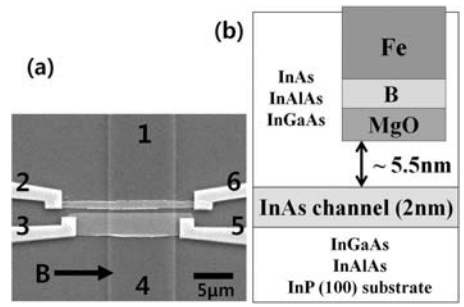

Fig 1. (a) SEM image of a lateral spin-valve device. An 8.6-μm-wide 2DEG channel, which is connected by terminals 1 and 4, is defined by dry etching. The external magnetic field, B, is applied along the easy axis of the ferromagnetic electrodes. (b) Schematic of the cross section where the ferromagnetic electrode was grown.

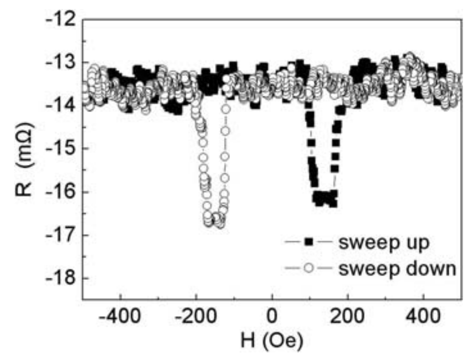

Fig 2. Nonlocal spin signal measured at 20 K. The nonlocal voltage is measured between terminals 7 and 9, while 1-mA-current flows from terminal 5 to 3.

FC-01

High sensitivity spin valve sensors with antiferromagnetically coupled flux guides.

I. G. Trindade[1,2], J. Oliveira[2], J. Teixeira[2], J. B. Sousa[1,2], P. P. Freitas[3], S. Cardoso[3], R. C. Chaves[3]
1. Physics, Faculdade de Ciências da Universidade do Porto, Porto, Portugal; 2. IFIMUP-IN, Porto, Portugal; 3. INESC-MN-IN, Lisboa, Portugal

Giant magnetoresistive sensors can have their field sensitivity enhanced by manyfold if located in the gap of two magnetically soft flux-guides [1]. These can detect magnetic fields in the picoTesla range [2-3] and nanosize magnetic beads, labeling biomolecules of medical interest[4].

A spin valve film, prepared by ion beam deposition, with the physical structure of Ta 2nm/$Ni_{80}Fe_{20}$ 2.5nm/$Co_{80}Fe_{20}$ 2.5nm/Cu 2nm/$Co_{80}Fe_{20}$ 2.5nm/$Mn_{77}Ir_{23}$ 6nm/Ta 2nm/$Ti_{10}W_{90}(N_2)$ is patterned into a long and narrow (3 microns wide) stripe. The sensor exhibits a Barkhausen-noise and hysteresis free response to uniform transverse (to the stripe lenght) applied magnetic fields, with a saturation field mainly limited by the free-layer demagnetizing field.
Thin films of an amorphous alloy of $Co_{88.4}(Zr_xNb_y)_{11.6}$ (CZN), with a thickness of 300 nm, were patterned by a lift-off process into long poles (80 microns wide, 104 microns long), and larger square yokes (150 microns by 150 microns) to form two identical flux guides, having their poles separated by 10 microns (gap width). A spin valve sensor centred in the gap of the flux guides exhibit a linear magnetoresistive response, characterized by a coercivity of 0.7 Oe, as shown in Fig. 1. In this device, a factor of 12 of field amplification is obtained and the sensor sensitivity is 50 mV/Oe.
Focused beam magneto-optic Kerr effect (MOKE) in the longitudinal geometry was used to measure hysteresis cycles of the yoke and pole regions of the CZN flux guides.
The MOKE curves show small hysteresis characterized by a coercivity of 0.7 Oe, similar to that typically obtained in the spin valve sensors coupled to the CZN flux guides.
Identical shape magnetic flux guides, integrating a multilayer film of ($Ni_{81}Fe_{19}$ 35nm/Ru .65nm)x10, having an antiferromagnetic coupling field of about 40 Oe, exhibit MOKE curves that overlap those of the CZN flux guides, in the range of ± 10 Oe, but with no detectable hysteresis (Fig. 2). This result indicates that the magnetization processes in the multilayer flux guides mainly occur by uniform rotation. Anisotropic magnetoresistance measurements in wide stripes of the multilayer films also indicate single-domain rotation processes.
Micromagnetic simulations indicate that spin valve sensors with 80% of the full linear signal in a field range of ±2 Oe can be attained by adding to the previously described flux guides of CZN, a thin antiferromagnetically (AFC) coupled bilayer of CoFeB but having longer poles.
Thin films of $Co_{70}Fe_{30})_{80}B_{20at\%}$ (CoFeB), prepared by ion beam deposition have as-deposited a spontaneous magnetic moment of 1200 emu/cm^3 and amorphous crystalline phase. Upon annealing at 320 ^oC, the films exhibit a crystalline phase.
A crystalline phase is also obtained by growing bilayers and multilayers of CoFeB 10nm/(Ru .9nm/CoFeB 10nm)xN on a buffer of Ta 2nm/Ru 1nm as indicated by XRD analysis. Furthermore, they exhibit an oscillatory antiferromagnetic coupling upon the Ru thickness with a maximum around t_{Ru}= 0.9 nm.
To integrate this higher magnetic moment trilayer film of CoFeB 10nm/Ru .9 nm/CoFeB 10nm, having an antiferromagnetic coupling field of 20 Oe, we use a self-alignment process, defining a gap with nearly the same width as the sensor.
The AFC trilayer, in turn, is magnetostatically coupled to recessed poles (gap width of 10 to 15 microns) of CZN.
The presence of that higher moment AFC trilayer in the previously described CZN flux guides effects the sensor response, reducing its coercive force from 0.7 Oe to less than 0.3 Oe while enhancing the sensitivity by a factor of 3.

[1] N. Kobayashi, S. Ohnuma, T. Masumoto and H. Fujimoi, Appl. Phys. 90, pp. 4159-4162 (2001)

[2] A. Guedes, J. M. Almeida, S. Cardoso, R. Ferreira and P. P. Freitas, IEEE Trans. Magn., 43, pp. 2376-2378 (2007)

[3] R. C. Chaves, P. P. Freitas, B. Ocker, W. Maass, Appl. Phys. Lett. 91, pp. 102504-1 (2007)

[4] G. Li, S. Sun, R. Wilson, R. White, N. Pourmand, S. Wang, Sens. Actuac. A, 126, pp. 98-106 (2006)

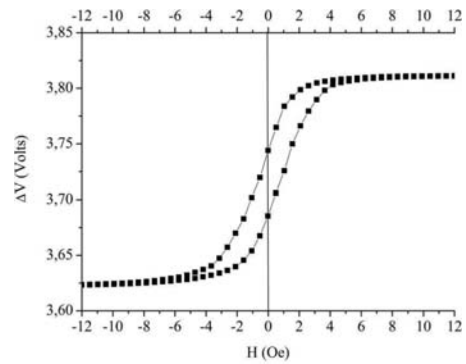

Fig. 1: Magnetoresistive response of spin valve sensor, having a stripe width of 3 microns and coupled to magnetic flux concentrators of a CZN thin film, having a thickness of 300 nm.

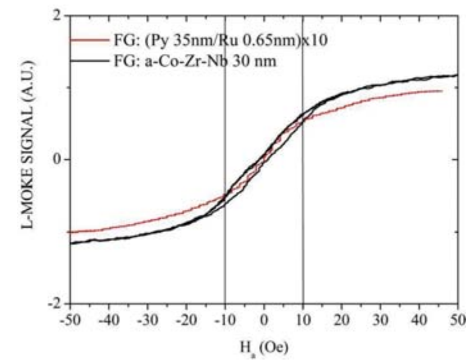

Fig. 2: Magneto-optic Kerr effect hysteresis cycles of fluxe guides, integrating either a multilayer film with an antiferromagnetic coupling field of 40 Oe, or a a-Co-Zr-Nb film with an induced uniaxial anisotropy field of 20 Oe. Flux guides have lateral dimensions; poles 104 microns long, 80 microns wide; yokes, 150 microns x 150 microns.

FC-02

Gate Controlled Magnetoresistance in a Balistic Nanodevice.

S. Kumar[1,2], S. Tan[1], *M. Jalil*[2]
1. SMI, Data Storage Institute, Singapore, Singapore; 2. ISML, ECE, National University of Singapore, Singapore, Singapore

Giant magnetoresistance (GMR) [1-3] refers to a large fractional change in resistance induced by an external magnetic field which changes the magnetization orientations of the two ferromagnetic (FM) layers separated by a non-magnetic (NM) spacer, from the parallel to the anti-parallel configuration. Magnetoresistance (MR) is a property of the multilayer device which depends on its material and geometry. Device MR cannot be modified once the device is fabricated.
Here, we propose a ferromagnetic (FM) transistor, in which the device MR can be modified by simply applying the gate voltage [4,5]. Our device is made of a high-electron-mobility-transistor (HEMT) structure with electrical gates fabricated on top of the electron conduction channel [Fig. 1]. The source and the drain of the device are made of FM materials. For magnetoresistive measurement, the source's magnetization is fixed in one direction, while the drain's magnetization is free to rotate. The electron conduction channel is shorter than the electron's mean free path in GaAs 2DEG, so as to ensure electron transport is ballistic in the 2DEG.
We studied the variation of MR and spin injection (SI) in the semiconductor by varying gate voltage under different conditions. The effects of following the device parameters were studied: 1) channel length, 2) 2DEG and FM material choice, and 3) multiple gates vs. single gate. We define MR as (G_p-G_ap)/(G_p+G_ap), where G_p and G_ap are conductance of parallel and antiparallel configurations, respectively. Conductance is obtained by assuming the continuity of electron wave function and electron flux through out the device. SI is defined as the ratio of majority and minority spin in parallel configuration.
Fig 1 and Fig 2 show the results for a single and a triple gate device, respectively. The results show an oscillating MR and SI trend with varying gate voltage. The oscillation frequency increases with the increase of the channel length. Therefore device with longer channel becomes more sensitive to the gate voltage. The effective mass of the 2DEG material too has an effect on MR oscillation similar to channel length, i.e. in this case, the frequency of oscillation increases with increasing effective mass. These show that the stability of the device can be improved by using smaller channel length as well as 2DEG material with smaller effective mass. The magnetic exchange energy, h_0 in the FM electrodes also affects the device performance. Higher h_0 results in a larger magnitude of MR and SI. However the frequency of the oscillation remains the same. Fig. 2 shows that the magnitude of MR and SI as well as the stability of the device can be improved drastically by using a triple gate device structure.
In conclusion we have designed a semiconductor based MR device that could perform the function of a metal spin valve, but with the advantage that its MR can be optimized (post-fabrication) and its stability enhanced by controlling the applied gate voltage.

[1] J. Yang, J. Wang, Z. M. Zheng, D. Y. Xing, and C. R. Chang, Phys. Rev. B 71, 214434 2005.

[2] S. G. Tan, M. B. A. Jalil, S. Bala Kumar, G. C. Han, and Y. K. Zheng, J. Appl. Phys. 100, 063703 2006.

[3] S. Bala Kumar, M. B. A. Jalil, and S. G. Tan, Phys. Rev. B 75, 155309 2007.

[4] H. Ohno, D. Chiba, F. Matsukura, T. Omiya, E. Abe, T. Dietl, Y. Ohno, and K. Ohtani, Nature London 408, 944 2000.

[5] M. Yamanouchi, D. Chiba, F. Matsukura, T. Dietl, and H. Ohno, Phys. Rev. Lett. 96, 096601 2006.

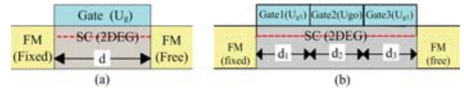

Fig 1. Device structure fro (a) single gate device, (b) triple gate device.

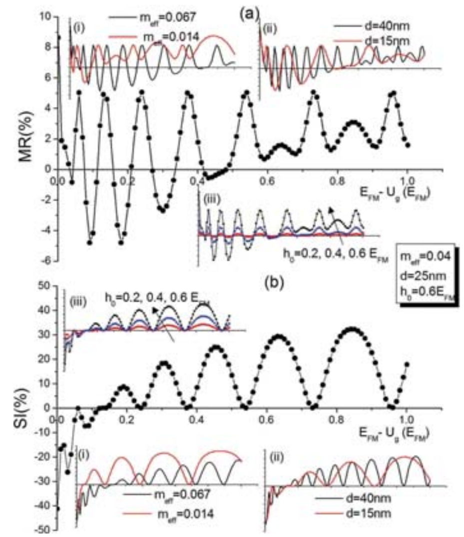

Fig 2. (a)MR and (b)SI variation for single gate device. (i), (ii),and (iii) shows the effects of 2DEG effective mass, channel length and magnetic exchange energy of the FM material. Unless otherwise indicated on the graph the material parameters are shown at the right of the graph.

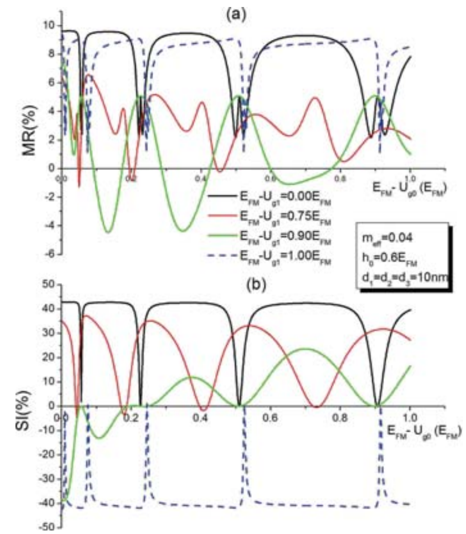

Fig 3. (a)MR and (b)SI variation for triple gate device. Unless otherwise indicated on the graph the material parameters are shown at the right of the graph.

FC-03

Magnetic-tunnel-junction-based programmable logic devices by spin transfer torque switching.

X. Yao, Y. Zhang, H. Meng, *J. Wang*
MINT Center & Electrical and Computer Engineering Department, Univ. Of Minnesota, Minneapolis,, MN

GMR and MTJ element based programmable logic devices[1-6] and a Full Adder[7] have been proposed for future reconfigurable and non-volatile computation devices and systems. A single-MTJ based full-function programmable logic device[5] has been experimentally demonstrated. Till now, all logic device designs use the magnetic field generated by a current line to switch the free layer magnetization. However, the fringe magnetic field from the current line can make the adjacent elements instable. Spin transfer torque (STT) or so-called current-induced magnetization switching (CIMS) has advantages in the device scaling compared to the field-switching mechanism. In this work, a single MTJ based logic device using STT switching mechanism is proposed and tested. Logic functions, such as AND, OR, NAND, NOR, and XOR, can be realized.
Fig.1(a) shows the device design for logic functions AND and OR. The MTJ element locates between the top and bottom electrodes. Each electrode has two inputs. For functions AND and OR, inputs A and B are used; and inputs C and D are grounded. Logic "1" (logic "0") is defined as positive (negative) current passing through the input terminals. The current density of each input is 67% (2/3) of the critical switching current density (Jc) of the MTJ. Nano-second current pulse can be used in the real application so that J=67%Jc is safe, which cannot switch the free layer by itself. For AND operation, the device is pre-set to parallel status. At this parallel state, the free layer can only be switched when both inputs are logic "1". When the inputs have mixed "1" and "0", there is no net current passing through MTJ. When both inputs are logic "0", the device prefers keeping parallel state. When operating OR function, the device is first set to high resistance state. For functions NAND and NOR, the inputs C and D are used and inputs A and B are grounded fig.1(b). logic "1" for the inputs is also defined as the positive current passing through the input terminals. The device is pre-set to antiparallel state and parallel state for function NAND and NOR, respectively.
XOR is one of the most important logic functions. Here we propose a design of a double-MTJ device to realize the XOR function. As shown in fig.1(c), the two free layers locate at the two sides of the fixed layer separated by the barriers. Because the critical switching current density of the free layer is proportional to its saturation magnetization(Ms)[8], free layer 1 which has smaller Ms has lower critical switching current density (Jc1) than that (Jc2) of free layer 2, which has larger Ms. The input current density, J, is in between of Jc1 and Jc2. This double-MTJ device has four resistance states, shown in the table of fig.1 (c). We define the highest resistance state (state d) is logic "1", and the other three low resistance states (state: a, b, c) are logic "0". For XOR function, the device is first set to antiparallel state (logic "1"). When both input A and B are "1" or "0", only one of the free layers switches. Therefore, the device shows low resistance state, "0". Otherwise, the device keeps logic "1".
To operate function AND, OR, NAND, NOR, the amplitude of each operating input is set to 67% (2/3) of the critical switching current density, which guarantees that single input current cannot switch the free layer by itself. Fig.2 (a) shows the experimental result of the current-induced switching in the MTJ device. The sample structure is: Si substrate/SiO2/bottom electrode/Ta3/CoFe2/FeSiO3/CoFe1/Al 0.65+oxidation/CoFe3/Ru0.8/CoFe3/IrMn15/Ta20/top electrode (Unit:nm). The device was patterned into 180 nm*250 nm ellipse shape by phase shift photo-lithography. The average critical switching current is 4.5*10^6 A/cm2. So, in our design, the current density for each input is 3*10^6A/cm2. When both operating inputs have the same direction, the total current density is 6*10^6 A/cm2, which has capability to switch the free layer magnetization. Fig.2(b) lists the actual input and output values for AND operation and their corresponding logic states.

[1]J. Shen, IEEE Trans. Magn.,33(1997) 4492

[2]W.C. Black, Jr. et al, J. Appl. Phys., 87(2000) 6674

[3]A. Ney, et al, Nature, 425(2003) 485

[4]R. Richter, et al, Appl. Phys. Lett., 80(2002) 1291

[5]J.G. Wang, et al, J. Appl. Phys., 97(2005) 10D509

[6]S. Lee, et al, IEEE Trans. Electron Dev., 54(2007) 2040

[7]H. Meng, et al, IEEE Elect. Dev. Lett. 26(2005) 360

[8]K. Yagami, et al, Appl. Phys. Lett., 85(2004) 5634

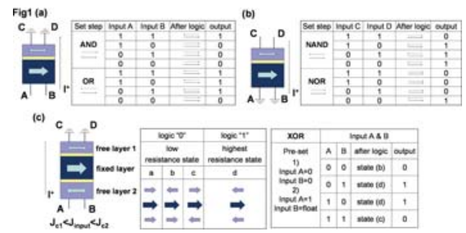

Fig.1 shows the schematic drawing of the device and the truth table for functions AND, OR (a) and NAND, NOR (b). XOR function can be realized by the device with two free layers, which is shown in (c).

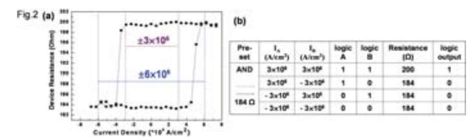

Fig.2 (a) The experiment result on current-induced magnetization switching of a single MTJ device. The dashed lines show the single input current density (3*10^6 A/cm2) and the total input current density (6*10^6 A/cm2). (b) The actual input and output values and the corresponding logic states for AND operation.

FC-04

Transport properties of fully epitaxial magnetic tunnel transistor with a MgO barrier.

T. Nagahama[1], H. Saito[1,2], S. Yuasa[1]
1. AIST, Tsukuba, Japan; 2. PRESTO, Japan Science and Technology Agency, Kawaguchi, Japan

Magnetic tunnel transistor (MTT) is a hot electron transistor consisting of semiconductor as collector, ferromagnetic layer as base, and ferromagnetic layer and tunnel barrier as emitter [1]. When the bias voltage (V_{eb}) is applied between emitter and base, the hot electrons traverse the base layer ballistically and pass over the Schottky barrier between the collector and the base layers, which is called collector current (I_c). The I_c heavily depends on the relative configuration of magnetizations of emitter and base. The change of collector current is called as "magnetocurrent effect (MC effect)"; MC ratio is defined as I_P-I_{AP}/I_{AP} .
In previous reported MTTs, the AlO_x has been used as a tunnel barrier. However, its amorphous structure gives rise to many scattering events during the tunneling, which prevents the transport of hot electrons for device operation. Consequently, the transfer ratio (TR ratio), which is the ratio between emitter and collector currents (I_c/I_e), and MC ratio become significantly small. On the other hands, in 2004, single-crystal MgO barrier was found for the magnetic tunnel junctions (MTJ), which has shown extremely high MR ratio coming from coherent-tunneling [2]. In the same way, employing MgO barrier is considered to improve the performance of MTT, e.g. MC ratio and TR ratio.
In order to realize high performance MTT, we prepared the MTT of GaAs(001)/Fe(20nm)/MgO(2.5nm)/Fe(5nm)/Co(10nm)/Au(20nm). After the growth of *n*-GaAs (n=1.8×10^{18} cm^{-3}), MgO tunnel junction was deposited in metal-MBE chamber at room temperature without breaking the vacuum. The films were fabricated into three terminal junctions with Schottky junction of 90×40μm^2 and MgO-tunnel junction of 10×10μm^2.
In figure 1, I_c and MC ratio are shown as a function of V_{eb}. Clear increase of both of I_c and MC are observed above threshold V_{eb} of 0.7 V. The maximum MC ratio is 208% at 40 K, which is 6 times larger than that for AlO-MTT of CoFe/AlO/Fe(001)(20nm)/ *n*-GaAs [3]. Regarding the TR ratio, I_c/I_e is 1.8×10^{-5} at V_{eb}=1.0 V. This is 2 orders larger than the value for the AlO-MTT. These results indicate that the MgO tunnel barrier is very favorable for MTT emitter.
In order to achieve MgO-MTT's potential, the scattering in the base layer should be suppressed. We have done two approach to solve this problems. The first is the reduction of the thickness of the base, and the second approach is a use of Ga-rich surface of GaAs collector. Ga-rich surface was obtained by annealing after GaAs growth at 800 K for 1 hour, and 2×6 reconstruction was observed by RHEED.
Table 1 shows typical values of MC ratio and TR ratio in the present MTTs at 40K. All the MTTs show MC ratios of larger than 200 %. MTT with 10 nm base made on Ga-rich surface shows the largest MC ratio of 288%, implying that the Ga rich surface and thin base layer are efficient for large magnetic signal. With respect to the TR ratio, it seems to be almost independent of the GaAs surface. The As atoms still exist at GaAs/Fe interface and diffuse into Fe(001) base layer. While it depends on the thickness of base layer. At V_{eb}=1.0 V, the TR ratio for MTT with 10 nm is twice of that for 20 nm base. In higher V_{eb}, TR ratio for 20 nm base-MTT has the maximum at 1.4 V, and decrease in V_{eb}>1.4 V. On the contrary, the 10 nm base-MTT keeps increasing of TR ratio beyond 2.0 V. As a result, MTT with 10nm base have much larger TR ratio maximum compared to 20 nm base. The different V_{eb} dependence of TR ratio is considered to relate to the band structure of Fe(001) layer and GaAs. More detail experiments and advanced theory are necessary to understand the V_{eb} dependence of I_c.

In summary, we study the magnetic tunnel transistor with single crystal MgO tunnel barrier. The MTT shows high-performance in magnetocurrent ratio and transfer ratio compared to MTT with AlO barrier. The transport characteristics are independence of GaAs surface and strongly depend on the thickness of base layer.

[1] R. Jansen, J. Phys. D: Appl. Phys. 36 (2003) R289.

[2] S. Yuasa et al., Nat. Mater. 3, (2004) 868: S. Parkin et al., Nat. Mater. 3, (2004) 862.

[3] M. Honda et al., Proc. of the Inter. Symp. on Mesoscopic Superconductivity and Spintronics (2003) 44.

	As-rich Fe(20nm)	As-rich Fe(10nm)	Ga-rich Fe(20nm)	Ga-rich Fe(10nm)
MC ratio (%)	203	233	250	288
TR_{1V} (×10^{-5})	1.8	3.0	1.8	3.5
TR_{max} (×10^{-5})	3.1 @1.4V	>15	4.5 @1.4V	>28

Table 1 Performance index for various MgO-MTTs. TR_{1V} and TR_{max} are the transfer ratio at V_{eb}=1V and the maximum value, respectively.

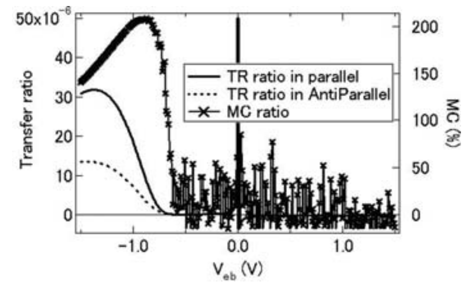

Fig.1 Transfer ratio and MC ratio for GaAs(001)/Fe(20nm)/MgO(2.5nm)/Fe(5nm)/Co(10nm)/Au(20nm) as a function of the voltage between emitter and base.

FC-05

A Planar Magnetic Content Addressable Memory Cell.

W. Wang, Z. Jiang
Electrical Engineering, University of Wisconsin - Milwaukee, Milwaukee, WI

Magnetic Content Addressable Memory (MCAM) simplifies CAM cell from ten CMOS transistors to one Magnetic Tunneling Junction (MTJ) by exploring both data storage and XOR logic function inside MTJ [1]. However, the original proposed MCAM cell structure contains a vertical ring, which poses challenges in both material and fabrication of the MCAM. In this paper, we propose a planar MCAM cell design where the top and bottom magnets are programmed by two different programming mechanisms so that the programming process of one magnet won't disturb the magnetic state of the other magnet in the same MTJ.

Fig. 1(a) is the cross-section view of the MTJ cell. The top magnet of MTJ is a SAF structure, which is programmed by cross-bar current lines in toggle mode. The bottom magnet is a simple magnet programmed by fringe magnetic field from the domain wall motion in a programming line underneath it. The magnetic domain wall inside the bottom programming line is driven by the spin polarized current.

Fig. 1(b) is the top view of the proposed cell. The bottom programming line has an obtuse angle in the middle and enlarged pieces at both ends. The obtuse angle is to produce a head-to-head domain wall after initialization process when a large external magnetic field is applied along the angle bisector. This domain wall will be driven bi-directionally by the spin polarized current during bottom magnet programming. The enlarged end pieces are designed to pin the domain wall motion. Although the current pulses generated by CMOS circuits are very well defined, the domain walls may still have significant drift after millions of repeated programming cycles. The domain wall motion stops when the spin polarized current density drops below a minimum threshold level [2]. The enlarged end pieces are designed to reduce the spin polarized current density below the threshold level, so that the domain wall is pinned at the junction of the thin and thick portions of the magnet.

In the proposed planar MCAM implementation, the top SAF magnet requires relatively low programming field, which is too weak to disturb the magnetization states in the bottom magnet. In contrast, the bottom programming line demands current density in the order of 10E8A/cm2. Such high current density will induce a strong magnetic field. Fortunately, the induced is perpendicular to the easy axis of the top SAF structure. The magnetization states inside the SAF structure is in scissor state [3] around the applied magnetic field. After the external field is removed, the SAF magnetization states return to their original states in parallel to its easy axis. Therefore, the magnetization states in the top SAF structure are not disturbed.

In order to demonstrate the feasibility of the proposed operation, we used LLG micro-magnetic simulator to investigate the programming margins for toggle mode SAF switching fields. Fig. 2 (left axis) shows the deviation of the final magnetization orientation from the expected direction. There is a clear jump between 80Oe (corresponding to 166 degree) and 100Oe (corresponding to 17 degree). Therefore, the switching field for the SAF structure is between 80Oe and 100Oe. Above mentioned final magnetization orientations deviate from the expected orientation (0 or 180 degree) due to some magnetization curling at the edges.

The programming field for SAF structure has an upper limit due to SAF saturation. Fig. 3 (right axis) shows the smallest angle between two magnetization orientations inside the SAF structure during toggle mode process. If we choose 10 degree as the minimum allowed angle for reliable operation, the upper limit of the SAF programming field is around 180Oe. Therefore, there is about 2× programming margin in SAF programming field.

In summary, we proposed a novel spin based planar CAM cell design. LLG simulation was performed to demonstrate the operation feasibility and the programming margin of 2× in the programming field.

1.W. Wang et al,IEEE Trans. on Magnetic, Vol. 43, No. 6, pp-2355-2357,

2.M. Klaui, et al, Phys Rev Let Vol. 94 page 106601

3.J. Zhu, IEEE Trans. On magnetics, Vol. 35, No. 2. pp 655-660

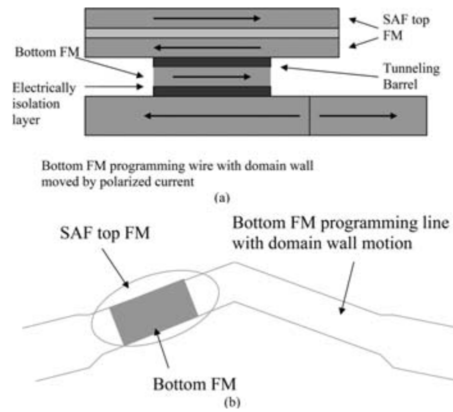

Figure 1, the proposed MCAM cell structure; (a) cross-section; (b) top view

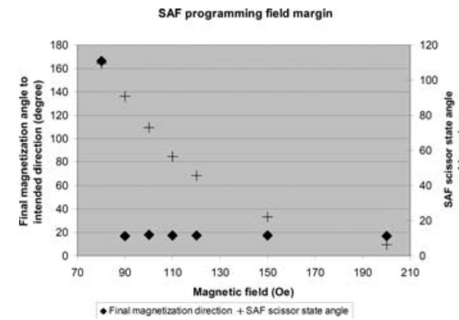

Figure 2, SAF programming field margin; left axis: final magnetization states deviation from the expected orientation (to determine the lower programming field limit); right axis: SAF scissor state angle (to determine the upper programming field limit)

FC-06

Investigation on Magneto-Optoelectronic properties in Metal/Organic Heterostructure Films.

N. Lee[1], T. Kim[1], J. Lee[2], H. Cho[3], C. Lee[3]

1. Department of Physics, Ewha Womans University, Seoul, South Korea; 2. Microgate, Inc., Anyang, South Korea; 3. School of Electrical Engineering & Computer Science, Seoul National University, Seoul, South Korea

Carrier injection, carrier separation at metal/organic (M/O) interfaces and carrier transport in the organic films are key processes in the organic semiconductor devices.[1,2] The understanding of the electrical properties at M/O interfaces is of great importance to improve device performance as well as to design novel organic devices.

In order to study the interfacial properties of M/O films, Cu-phthalocyanine(CuPC) films of a thickness ranging from 10 to 100 nm were deposited on nonmagnetic and magnetic layers such as Au, Al and permalloy(Py). Surface potential formed in the M/O films was measured by Kelvin probe method in vacuum.

Figure 1 shows that the variation of the surface potential could be related to not only the ionization potential of the organic film but also the apparent work function of the metal surface. For the CuPC on Py layer, as the thickness of the film increases, the surface potential was positively charged due to the displacement of holes from the Py surface to the CuPC film, whereas the negatively charged surface potential was observed for the CuPC on the Au and Al electrodes. This implies that the carrier injection (electrons or holes) at the M/O interface could strongly depend on the electronic structure of the interfacial region of the M/O bilayers. These results led us to investigate electromagnetic properties in M/O interfaces by using the electroluminescent (EL) and tunneling devices with different metallic electrodes.

EL devices with CuPC and Alq3 organic films were prepared beyond the Al and Py surfaces by the vacuum–deposition at a base pressure of 10^{-8} Torr. Figure 2 shows a schematic of the EL device structure.

In Figure 3, for the EL devices with the Py electrode, we observed a larger magneto-optical effect (~ 4.4%) at 300 K than that (~ 0%) of the EL devices with the Al. For both of EL devices with Al and Py, the magnetic field effect on the transport properties was not shown in the current range which is large enough for the electroluminescence. However, for the tunneling devices with Py electrode (Py/CuPC/Py), the magnetic field effect at room temperature was more pronounced in the low current range (a few nano-amperes range).

According to our x-ray results, the high resistance of the EL and tunneling devices with Al could result from the poor crystallinity of the CuPC film grown on the amorphous Al layer. The good crystal structure was observed in the CuPC film grown on the FCC(111) Py layer.

These results point out the importance of electromagnetic properties at the interfaces in the M/O heterostructure films for spintronics applications.

This work is supported by the Basic Research Program of the Korea Science & Engineering Foundation (R01-2006-000-11227-0) and the Korea Research Foundation Grant (KRF-2006-531-C00026).

Corresponding author : taehee@ewha.ac.kr

[1] K. Kao and W. Hwang, Electrical transport in solids with particular reference to organic semiconductors, Pergamon Press, New York, 1981.

[2] W. R. Salaneck, K. Seki, a. Kahn, J. J. Pireaux(Ed.), Conjugated polymer and molecular interfaces–Science and Technology for photonic and Optoelectronics Applications, Marcel Dekker, 2002.

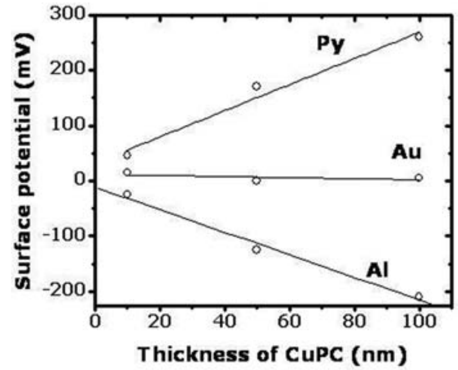

Fig. 1 Surface potential measured by Kalvin probe method as a function of the Cu-phthalocyanine(CuPC) film thickness. The CuPC films were deposited on the different metal films (Al, Au, Py) beyond Si substrate.

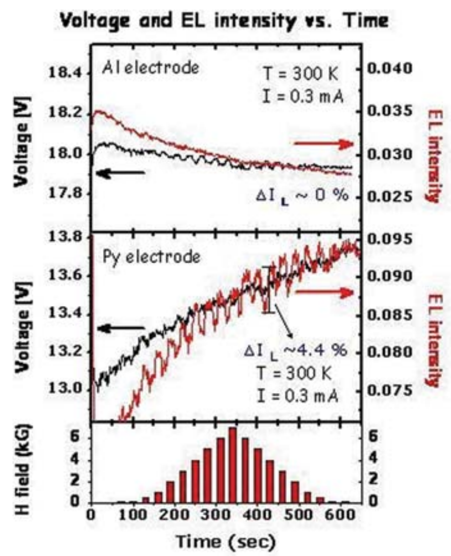

Fig. 3 Voltage and EL as a function of time: EL devices with Al (the top panel) and Py (the middle panel). The applied magnetic field as a function of time is shown in the bottom panel.

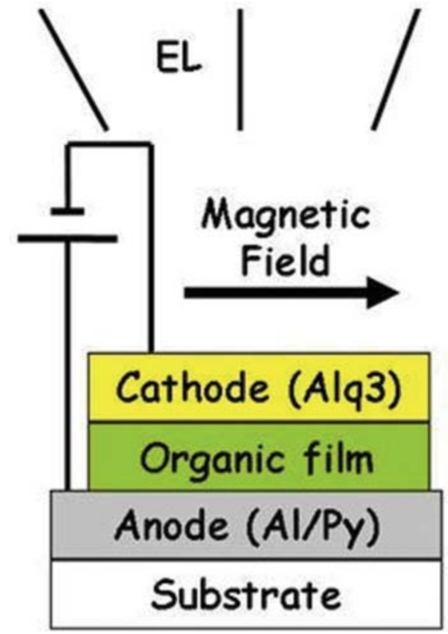

Fig. 2 Schematic of EL device structure. The Alq3 film was depositied as a Cathode.

FC-07

Electrical switching controlled by magnetic field.

J. Lee[1], S. Joo[1,4], T. Kim[1], *J. Hong*[1,4], K. Rhie[1,4], B. Lee[2], T. Kim[3], K. Shin[4]
1. Applied Physics, Korea University, Chochiwon, South Korea; 2. Physics, Inha University, Incheon, South Korea; 3. Physics, Pohang University of Science and Technology, Pohang, South Korea; 4. Korea Institute of Science and Technology, Seoul, South Korea

Magnetoresistance (MR) effects including giant MR, colossal MR etc. exhibit large changes in electrical resistance according to magnetic field, which has led to great interest of scientists due to improvements in the magnetic information storage, sensors and magnetoelectronics. Specially, in manganite system showing colossal MR effect the dramatic switching of resistive states can be achieved not only by a magnetic field, but also by an electric field [1]. This current switching of resistive state has received considerable attention because of their interesting physical phenomenon and potential applications as nonvolatile memories [2]. On the other hand, magnetoresistive switch effect with large MR had been reported in the Sb/MnSb nanoclusters/GaAs system [3] and Au/GaAs Schottky diode [4].

In this report, we have studied a switching of resistive states in a semiconductor npn junction structure based on Hg0.79Cd0.21Te. Our device shows more than three orders of MR change and threshold magnetic field can be tunable by a bias voltage on the device.

Figure 1 (b) magnetic field dependence of current measured at various bias voltages. It shows abrupt change of current at a threshold field whose value is determined by the bias voltage. Thus, the conducting state of our device is convertible from low resistive state to high one and this change is governed by magnetic field. All of the observed curves are successfully recovered when sweep direction of magnetic field is reversed. Current in this device can be increased more than 10X10(-6)A, but the amount of current is limited to 100nA in this data to protect the device from high-current damage. Switching effect may be caused by avalanche multiplication process in p-type region. This electrical switching device can be good candidate for a future reprogrammable electronic device.

1. A. Asamitsu, Y. Tomioka, H. Kuwahara and Y. Tokura, Nature, 388, 50, 1997

2. D. Hsu, J.G. Lin and W.F. Wu, Journal of Magnetism and Magnetic Materials 310, 978, 2007

3. Hiro Akinaga, Proceedings of the International Conference on MEMS, NANO and Smart Systems ICMENS'03, p. 134, 2003

4. Z.G. Sun, M. Mizuguchi, T. Manago and H. Akinaga, Appl. Phys. Lett, 85, 5643, 2004

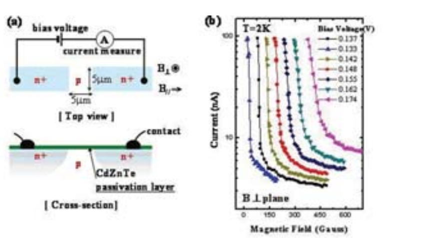

Figure 1. (a) Schematic of HgCdTe npn junction device. (b) current verse magnetic field for various bias voltage when magnetic field is applied to perpendicular to the sample plane.

FC-08

Micromagnetic Investigation of Interaction between Spin-Polarized Current and Spin-wave.

S. Seo, K. Lee
Korea University, Seoul, South Korea

I. Introducton

Excitation and propagation of spin-wave (SW) in a confined magnetic system have attracted a considerable interest because of its potential application for the logic device [1] as well as fundamental physics. Since the SW is a spin texture consisting of non-collinear magnetizations, it is possible to modulate the characteristics of SW by current injection. In order to study the interaction between a spin-polarized current and the SW in such a slowly varying magnetic environment, the adiabatic and non-adiabatic spin-transfer torque terms can be used. Here, we show the effect of spin-transfer torque on the characteristics of SW propagating along a wave guide.

II. Micromagnetic Simulation

We carry out micromagnetic simulations by solving the phenomenological Landau-Lifshitz-Gilbert (LLG) including the adiabatic and non-adiabatic spin torque terms;

$$\partial\mathbf{M}/\partial t = -\gamma(\mathbf{M}\times\mathbf{H}_{eff}) + \alpha/Ms\,(\mathbf{M}\times\partial\mathbf{M}/\partial t) - b_J/M_s^2\,(\mathbf{M}\times(\mathbf{M}\times\partial\mathbf{M}/\partial x)) - c_J/M_s(\mathbf{M}\times\partial\mathbf{M}/\partial x).$$

where $\mathbf{H}_{eff}$ is the effective field consisting of the anisotropy, exchange, magnetostatic, and external field (H_{ext}), M_s is 800 emu/cm^3, Gilbert damping constant $\alpha = 0.01$, the exchange constant $A = 1.3\times10^{-6}$ erg/cm, the anisotropy constant $K = 0$, and b_J ($= Pj_e\mu_B/eM_s$) and c_J ($= \beta\, b_J$) represent the magnitude of the adiabatic and non-adiabatic spin torque, respectively. The Permalloy nanostrip is selected as a wave guide. The geometry of the nanostrip is $2000 \times 120 \times 6$ (length (l) × width (w) × thickness (t)) nm^3 (Fig. 1.). To absorb reflected SWs from edges, an enhanced damping constant is adopted at both sides of the nanostrip (x = 0 ~ 50, 1950 ~ 2000nm). Upon applying AC bias field along the y-axis, i.e, $H_y = H_{ext}\sin(2\pi\omega_0 t)$ where $H_{ext} = 100$ Oe, and $\omega_0 = 2\sim20$ GHz, the magnetostatic surface wave is generated.

III. Results and Discussions

The dispersion relation of SW as a function of the current density (J_e) is shown in Fig. 2(a). As theoretically predicted [2, 3], the adiabatic spin torque provides the spin wave *Doppler* shift. However, the dispersion relation is obtained at relatively higher wave vectors (k_xs) than those predicted by theories. Interestingly, the splitting energy ($\Delta\varepsilon \propto \Delta k_x$ in Fig. 2(a)) show a different dependence on the ω_0 depending on the sign of current. The $\Delta\varepsilon_{(-J}e_{)}$ is proportional to the ω_0 whereas the $\Delta\varepsilon_{(+J}e_{)}$ is almost the same in the range of calculated frequency (ω_0). Note that the β term measures the relative magnitude of non-adiabatic spin torque with respect to the adiabatic one. The effect of the non-adiabatic spin torque on the SW mode is also studied. It is found that the β term does not affect the dispersion relation, but efficiently changes the amplitude of SW.

Fig 2. (b) shows the FFT power (P_{FFT}) over a temporal window for t = 30ns as a function of k_x. The P_{FFT} increases or decreases depending on the sign of J_e and the magnitude of β term. When $\beta < \alpha$, the P_{FFT} increases (decreases) when the J_e is positive (negative). It means that the amplitude of SW is enhanced or damped depending on the relative directions of SW propagation and electron flow. When $\beta = \alpha$, the P_{FFT} is the same regardless of J_e. When $\beta > \alpha$, the P_{FFT} increases (decreases) when the J_e is negative (positive). The enhancing or damping rate of SW increases with the J_e and β term.

IV. Conclusion

We perform micromagnetic investigation of interaction between spin-polarized current and spin-wave. It is confirmed that only the adiabatic spin torque contributes to the current-induced spin-wave *Doppler* shift. The non-adiabatic spin torque has a negligible effect on the dispersion relation, but significantly affects the amplitude of spin-wave.

[1] R. Hertel, W. Wulfhekel, and J. Kirschner, Phys. Rev. Lett. 93, 257202 (2004).

[2] Ya. B. Bazaliy et al, Phys. Rev. B 57, R3213 (1998).

[3] J. Fernandez-Possier et al, Phys. Rev. B 69, 174412 (2004).

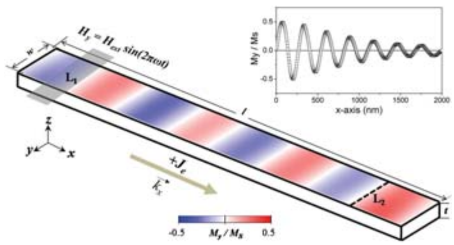

Fig. 1. Model geometry is depicted. The AC bias field is applied in the region of L_1. Inset shows M_y profiles along the x-axis.

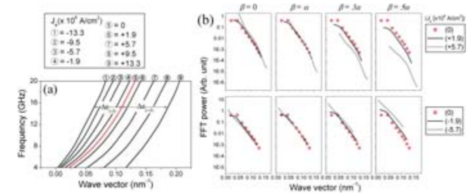

Fig. 2. (a) illustrate dispersion relation, k_x vs ω as a function of the applied current density. (b) the FFT power analyzing at the position of L_2 in fig 1, is shown as a function of wave vector for various β terms. $\Delta\varepsilon_{(+/-)J}$ is the splitting energy.

FD-01

Ferromagnetic oxides for spin filtering.

J. Fontcuberta[1], A. Barthelemy[2], M. Bibes[2], U. Lüders[1], M. Gajeck[2], K. Bouzehouane[2], J. F. Bobo[3], S. Fusil[2], E. Jacquet[2], J. P. Contour[2], A. Fert[2], F. Sánchez[1], X. Martí[1], F. Rigato[1], V. Laukhin[1], V. Skumryev[1], M. Varela[4]

1. ICMAB-CSIC, Bellaterra, Spain; 2. Unité Mixte de Physique CNRS-Thales,, Palaiseau, France; 3. Lab. de Nanomagnétisme pour l'Hyperfréquence CNRS-ONERA, Toulouse, France; 4. Dept. Física Aplicada i Òptica. U. Barcelona, Barcelona, Spain

Oxides are being intensively investigated as candidates for a new generation of electronic and magnetoelectronic devices. Of particular interest is the obtention of fully polarized spin sources as they could allow larger magnetoresistance values in magnetic tunnel junctions thus allowing further miniaturization of magnetic components. For this purpose, half-metallic ferromagnetic oxides have been intensively investigated in the last decades but so far, materials for room-temperature operation have not been obtained. However, during the last few years, spin filtering has emerged as a very powerful tool to obtain a large magnetoresistance in magnetic tunnel junctions, circumventing intrinsic materials limitations. Effective room-temperature spin filtering has been achieved with the so-called orbital symmetry filtering, as illustrated in magnetic tunnel junctions made using epitaxial MgO barriers, and record values of tunnel magnetoresistance have been obtained. A promising alternative to spin filtering is by using the so-called magnetic spin filtering as occurs in ferromagnetic tunnel barriers. Magnetic oxides are ideal candidates for this purpose and recent results suggest promising perspectives. We will review the status and perspectives of magnetic spin filtering. We will show that epitaxial engineering of oxides allows to design artificial sources of spin polarized electrons and we shall report on recent results suggesting that indeed these materials could offer for progress and opportunities for spintronics. Other alternatives for electric manipulation of magnetic elements will also be discussed.

Tunel Junction with multiferroic barriers

M. Gajek, M. Bibes, S. Fusil, K. Bouzehouane, J. Fontcuberta, A. Barthélémy and A. Fert Nature Materials, 6, 296 (2007)

Electric-field control of exchange bias in multiferroic epitaxial heterostructures

V. Laukhin, V. Skumryev, X. Martí, D. Hrabovsky, F. Sánchez, M.V. García-Cuenca, C. Ferrater, M. Varela, U. Lüders, J.F. Bobo, and J. Fontcuberta, Phys. Rev. Lett. 97, 227201 (2006)

NiFe2O4: A versatile spinel magterial brings new opportunities for Spintronics.

U. Lüders, A. Barthelemy, M. Bibes, K. Bouzehouane, S. Fusil, E. Jacquet, J.P. Contour, J.-F- Bobo, J. Fontcuberta and A. Fert., Adv. Mater. 18, 1733-1736 (2006)

FD-02

Giant planar Hall effect in epitaxial Fe_3O_4 thin films and its temperature dependence.

J. M. De Teresa[1], A. Fernandez-Pacheco[1,2], J. Orna[2], L. Morellon[1,2], P. Algarabel[1], J. A. Pardo[2,3], R. Ibarra[1,2]
1. Instituto de Ciencia de materiales de Aragon, CSIC-University of Zaragoza, Zaragoza, Spain; 2. Instituto de Nanociencia de Aragon, University of Zaragoza, Zaragoza, Spain; 3. Departamento de Ciencia y Tecnologia de Materiales y Fluidos, University of Zaragoza, Zaragoza, Spain

The planar Hall effect (PHE) is an interesting phenomenon in magnetic materials which allows the study of magnetization processes and has applications in sensitive low-field detection [1, 2]. This effect stems from the anisotropy of the resistivity tensor and, as a consequence, its magnitude is proportional to the anisotropic magnetoresistance (AMR) and to the absolute value of the resistivity [3]. Fe_3O_4 seems to be a promising material to produce giant PHE values due to its large resistivity compared to magnetic metals and its relatively large AMR values [4]. Previous studies on Fe_3O_4 thin films suggest potentiality for giant PHE at room temperature [5].
We have investigated the planar Hall effect in epitaxial Fe_3O_4 thin films with thickness ranging from 5 to 150 nm grown on MgO (001) substrates. Previous studies indicate the epitaxial growth and high crystalline quality of our Fe_3O_4 thin films and describe the optical lithography procedure [6]. In summary, the current flows through a micrometric electrode along the [100] direction and Hall contact pads are patterned in order to minimize offset voltages. The magnetic field is applied in the film plane forming a fixed angle (Θ) with the current direction. The maximum PHE is expected when the current and the magnetization are at Θ=45° (135°) degrees.
In figure 1 the result obtained at room temperature for the 40 nm film is shown. The absolute value of the PHE (ρ_{xy}) at maximum field is quite large (a few μΩcm) compared to the values observed in metallic magnetic thin films (typically 100 times smaller). We attribute this giant PHE effect to the high resistivity of the film together with a relatively large AMR value. This is corroborated by the set of measurements performed in all the films at room temperature and shown in figure 2. As the film thickness decreases, the longitudinal resistivity (ρ_{xx}) increases due to the influence of antiphase boundaries [7], which reflects in the enhancement of the PHE for the thinnest films. We have obtained a record value at room temperature of ρ_{xy}=60 μΩcm for the 5 nm film under 10 kOe. Our investigation as a function of temperature indicates a substantial enhancement of the absolute value of the PHE when crossing the Verwey transition (T_V≈120 K), which is a consequence of the increase of resistivity at T_V whilst keeping a significant AMR. As shown in figure 3, colossal values of PHE are observed below T_V, never attained before. A change in the sign of the PHE effect has been found in the film with thickness 20 nm at T≈150 K, which seems to be correlated with the change in the sign of the AMR previously observed [4]. Our results demonstrate the potentiality of the PHE in Fe_3O_4 thin films for studies of magnetization processes as well as for sensitive low-field detection in a wide range of temperature.

[1] H.X. Tang et al., Phys. Rev. Lett. 90 (2003)107201

[2] F. Montaigne et al., Sensors and Actuators 81 (2000) 324

[3] Campbell and Fert, Magnetic Materials 3 (1982) 747

[4] M. Ziese and H.J,. Blythe, J. Phys.: Condens. Matter 12 (2000) 13

[5] X. Jin et al., J. Appl. Phys. 99 (2006) 08C509; Y. Bason et al., J. Appl. Phys. 101 (2007) 09J507

[6] J.M. De Teresa et al., Microel. Eng. 84 (2007) 1660

[7] W. Eerestein et al., Phys. Rev. B 66, 201101(R) (2002)

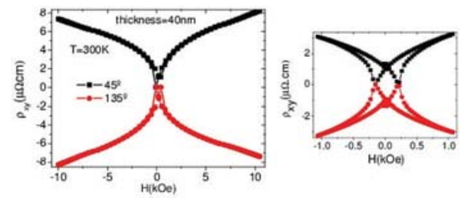

PHE at room temperature of the 40 nm Fe^3O^4 film and the zoom-in at low fields.

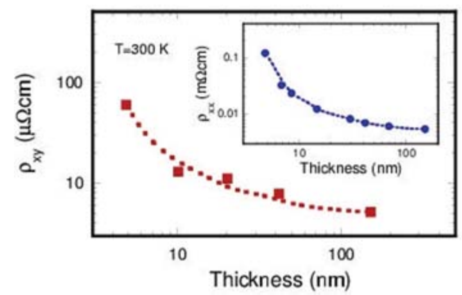

PHE and longitudinal resistivity versus film thickness at room temperature.

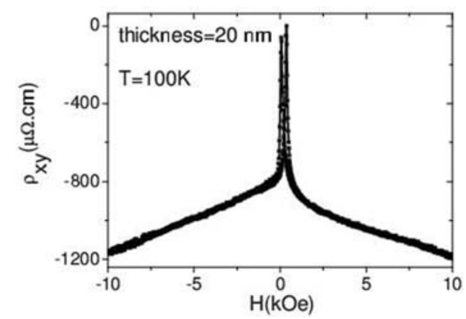

PHE at 100 K (below the Verwey transition) of the 20 nm Fe3O4 film.

FD-03

Time resolved precessional magnetization dynamics in Fe_3O_4 thin films measured by pulsed inductive microwave magnetometry.

S. Serrano-Guisan[1], C. Boothman[2], M. Abid[2], J. D. Coey[2], H. W. Schumacher[1]
1. Physikalisch-Technische Bundesanstalt, Braunschweig, Germany; 2. CRANN and School of Physics, Trinity College, Dublin, Ireland

The half metallic character of magnetite with a predicted 100% spin polarization and its high Curie temperature (≈850 °K) [1] makes it an attractive candidate for a variety of spintronics applications. Furthermore, magnetite nanoparticles are interesting for bio medical applications like hyperthermia cancer treatment [2]. In both fields the ultra fast precessional magnetization dynamics and especially the dissipation of magnetization precession due to Gilbert damping is of major importance. However, detailed studies are not available. Here we investigate time resolved precessional magnetization dynamics of sputter deposited Fe_3O_4 thin films using pulsed inductive microwave magnetometry (PIMM) [3]. The field dependence of the precession frequencies and the Gilbert damping parameter α is studied. We find a large Gilbert damping parameter which could be of advantage for magnetite based spin transfer torque applications.
The samples were prepared by DC magnetron sputtering on Si (111) substrates in a deposition system with a base pressure of 10^{-7} mbar. The deposition results in a strongly oriented f.c.c. thin film as observed by x-ray diffraction. The 50 nm thick magnetite film under investigation has a saturation magnetization of $\mu_B M_S \approx 0.5$ T with out-of-plane anisotropy. The temperature dependence of the magnetization shows a Verwey transition around 120 K (Figure 1) proving the correct stochiometry consistent with the inverse spinel lattice structrure.
For PIMM measurements the Fe_3O_4 films are placed onto a 50 Ω coplanar waveguide connected to a pulse generator and a sampling oscilloscope with 18 GHz bandwidth. Ultra short current pulses (rise time 50 ps, pulse width 100ps) from the pulse generator propagate in the coplanar waveguide and generate transverse magnetic field pulses ($H_p \approx 0.02$mT) at the magnetite thin film. The field pulses excite a precessional motion of the magnetization (M) which in turn induces a voltage signal into the waveguide that can be detected by the oscilloscope.
During PIMM experiments static in-plane fields up to 20 mT are applied in different in-plane field orientations. A time resolved trace of the magnetization dynamics is shown in Figure 2 (b). By fitting the time resolved data by an exponential damped sinusoid (b) or by fitting the Fourier transform of the precessional data by a Lorentzian (c) the field dependent precession frequency and Gilbert damping parameter α are obtained. As shown in Figure 3 the precession frequency increases with static fields as expected for ferromagnetic resonance. A Gilbert damping parameter of α = 0.13...0.08 is found. The value of α is thus about a factor of 10 higher than in high quality metallic thin films like permalloy. A decrease of α with increasing bias field is observed which could be due to a dispersion of anisotropy field [3,4].
The measured high Gilbert damping could be useful for spin transfer torque applications. Here a high damping [5] could allow an efficient spin angular momentum transfer from the magnetite to a neighbouring ferromagnetic free layer by a high density current. The high Gilbert damping together with the out-of-plane anisotropy could thus make such thin films an interesting candidate for perpendicular spin polarizers in spin transfer torque MRAM or spin transfer oscillators [6].
References:
[1] E. Snoeck et al., J. Appl. Phys 96, 3307 (2004)
[2] R. Hiergeist et al. J.Magn.Magn. Mat. 201, 420 (1999).
[3] T. J. Silva et al. J. Appl. Phys. 85, 7849 (1999)
[4] D. O. Smith, J. Appl. Phys. 29, 264 (1958)
[5] J. Hayakawa et al. 44, L 1267 (2005)
[6] D. Houssameddine et al. Nature Mater. 6, 447 (2007)

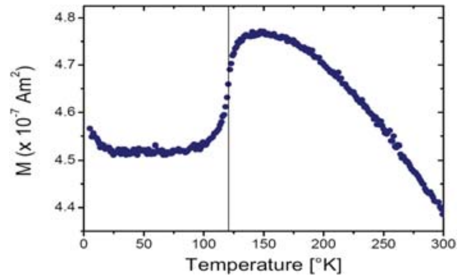

Fig. 1: Vervey transition of a 50nm Fe_3O_4 thin film: magnetization vs. temperature. The ordering transition is observed at T = 120°K

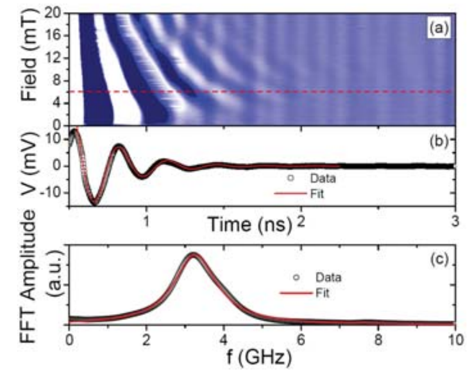

Fig. 2: Time resolved magnetization precession of a 50 nm Fe_3O_4thin film. (a) Static field dependence of precession. (b) precessional signal (dots) at 6 mT static field with damped sinusoidal fit (line). (c) Fourier transform of data at 6 mT with Lorentzian fit.

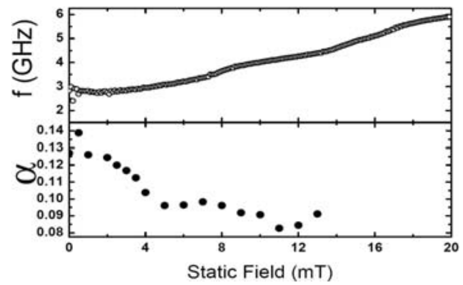

Fig. 3: Static field dependence of precession frequency and effective damping parameter.

FD-04

Angular dependence of the magnetoresistance measured across a single-grain boundary.

L. B. Steren, G. Alejandro, J. C. Rojas Sanchez, E. N. Monteblanco Vinces, H. Pastoriza
Physics, Centro Atomico Bariloche, S.C. Bariloche, Argentina

Bicrystalline substrates are appropiate devices to investigate the low field magnetoresistance (LFMR) of manganite compounds, by isolating an unique artificial grain boundary (AGB). During the last years a large experimental effort has been devoted to study the electronic and magnetic properties of these systems. The LFMR of ferromagnetic perovskites, its temperature and field dependence, and the non linear character of the I-V curves have been studied on (La, Ca)MnO_3, (La, Sr)MnO_3 and
Sr_2FeMoO_6 (1) bi-crystalline films by using different lithographed patterns of diverse size, shape and complexity.

In this work we present magnetoresistance measurements in Wheastone bridges of $La_{0.75}Sr_{0.25}MnO_3$ thin films crossing a single grain boundary. The films of 120 nm thickness, were deposited by dc-sputtering on 0.5x0.5cm bi-crystalline SrTiO3 substrates, at a temperature of 760°C. X-ray diffraction (XRD) patterns, obtained from a four-circle diffractometer, allows us to identify the orientation of the $La_{0.75}Sr_{0.25}MnO_3$ bi-crystal.
The Wheastone bridges were lithographed onto the $La_{0.75}Sr_{0.25}MnO_3$ films in order to measure the magneto-transport properties of the manganite compound. Two arms of the bridge crosses the AGB while the other two sense only single-crystalline regions. The magnetoresistance measurements were performed at 77K. The angular variation of the resistance has been measured by rotating the magnetic field in the plane of the films.
The angular dependence of the DC magnetization of the samples was measured in a vibrating sample magnetometer. The anisotropy of the manganite films, deduced from the magnetization data serves us to identify the crystal anisotropy contribution to the magnetoresistance from that of the AGB.
The magnetoresistance has been measured simultaneously in two arms of the Wheastone bridge. The SC that traverse the single-crystalline region and the GB, that crosses the artificial grain boundary. Typical curves measured for the GB arm are shown in Fig. 1. The high field component is associated to the colossal magnetoresistance effect observed in ferromagnetic manganites. The magnetoresistance is hysteretic at low field and it is strongly dependent on the field direction.
The low field magnetoresistance curves can be analysed in terms of two contributions. One of them, present also in the SC magnetoresistance curves, is anisotropic and clearly dependent of the crystalline symmetry of the crystal. This effect has been already reported in Ref. 2 for $La_{0.7}Ca_{0.3}MnO_3$ films. The other one, has a two-fold symmetry with the easy axis oriented along the AFG direction.
The distinction between the two low field components is difficult when the peak position of both effects are close, as shown in Fig. 1. In order to better examine the origin of both effects we perform a different experiment. We measured the angular dependence of the resistance of the SC and GB arms at different magnetic fields. We noticed that the intensity of both effects are strongly affected by the magnetic field. Above 5kOe, the magnetoresistance arising from the crystalline anisotropy of the samples has almost disappeared while the component associated to existence of the AGB is still present.

1 M. Paranhape, J. Mitra, A. Raychaudjuri, N. Tood, N.D. Mathur, M. Blamire, Phys. Rev. B. 68, 144409 (2003)

2 J.O'Donnell, J.M. Eckstein, M. Rzchowski, Appl. Phys. Lett. 76, 218 (2000)

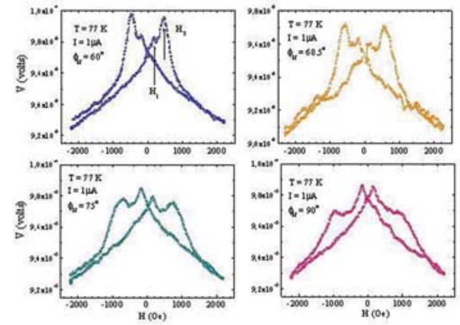

FD-05

Antiferromagnetic Heusler compounds with high spin-polarization.

G. Liu, X. Dai, G. Fecher, *C. Felser*
Institution for Inorganic and Analytical Chemistry,Johannes Gutenberg University of Mainz, Mainz, Germany

Half-metallic antiferromagnets are the ideal materials in spintronic devices since such a material would not give rise to great stray flux and thus would lead to smaller energy losses. In the last decades, only several materials have been theoretically predicted to be half-metallic antiferromagnets, including ternary Heusler MnCrSb,1 binary Heusler Mn3Ga2 and quaternary Heusler MnCoVAl and Mn1.5Co0.5VSi compounds3. Unfortunately, up to now, none of these alloys has been successfully synthesized in the desired structure. Therefore, many researchers turn to search for the half-metallic ferrimagnets with low magnetic moments. Some significant results have been achieved. However, in these half-metallic ferrimagnets, the magnetic moment are impossible to achieve the smaller value than 1 μB. In this work, we will turn to another route, that is, to develop antiferromagnets with high spin-polarization (but not 100% spin-polarization), which will be easy to design and fabrication, and can also do well work in realistic applications.

The Co2CrZ (Z=Al, Ga) compounds with L21 structure have been predicted to be half-metallic ferromagnets, but they have a magnetic moment of 3μB. In order to decrease the magnetization, we substitute a Cr atom for a Co atom in these compounds. So, a series of Cr2CoZ (Z=Al, Ga, In) compounds with CuHg2Ti-type structure were achieved. Based on this structure, their electronic structures with different lattice constants were calculated by the first-principle calculations as shown in Fig.1. The detailed parameters were listed in table I.

For Cr2CoAl alloys, one can see that its spin-polarization ratio at the Fermi level increases with the increasing lattice constant. The maximum of 42.3% occurs when the lattice constant is 5.82 Å. When the lattice constant is the optimized one of 5.74 Å, the Fermi level is at the edge of a pseudogap. So, we can understand the sharp increase of the spin-polarization ratio with the increasing lattice constant results from the upshift of Fermi level due to the extension of the lattice. For the Cr2CoGa compound, the optimized lattice constant is 5.75 Å where the maximum spin-polarization ratio of 45.07% was observed. The corresponding magnetic moment is about 0.3μB. The larger or the smaller lattice constant will lead to the destruction of antiferromagnetism which is nonsensical to our work. As to the Cr2CoIn compound, from the table I, it can be seen that the ratio of spin-polariztion is up to 70.1% at the lattice constant of 5.7 Å. The larger lattice constant will result in the disappearance of the antiferromagnetism. Although the optimized lattice of 5.99 Å is in the range where ferromagnetism occurs, we can expect to obtain the proper lattice constant by some methods such as the epitaxial technique which will not be difficult.

Furthermore, we must emphasize that these alloys are easy to crystallize in the CuHg2Ti-type structure and we have successfully synthesized them. In the absence of half-metallic antiferromagnets with 100% spin-polarization, these alloys will be a good candidate for the realistic application in spintronic devices.

In addition, based on the investigation of the Cr2CoZ system, we also found a rule to search for the new antiferromagnets with high spin polarization ratio: the CuHg2Ti-type Heusler alloys containing transition-metal atoms with less number of d electrons than eight is a rich field to develop such materials. The detailed discuss will be presented in the formal paper.

In summary, in this work we reported a new series of Heusler compounds:Cr2CoZ. These compounds crystallize in CuHg2Ti-type structure, and exhibit a high spin-polarization at the Fermi level and a magnetization close to zero,which make these compounds become a good candidate for spintronic devices. The electronic structures, magnetic structure, transport properties and the spin-polarization of these compounds will be detailedly investigated in experiments and theory, which will be shown in the formal paper.

1H. van Leuken and R. A. de Groot, Phys. Rev. Lett. 74, 1171 (1995).

2 S. Wurmehl, H. C. Kandpal, G. H. Fecher, and C. Felser, J. Phys.: Condens. Matter 18, 6171 (2006).

3 I. Galanakis, K. Ozdogan, E. Sasloglu, and B. Aktas, Phys. Rev. B 75, 092407 (2007).

Composition	a (Å)	P (%)	M(μB)
Cr2CoAl	5.65 5.74 5.82	9.87 18.9 42.3	0.009 0.068 0.052
Cr2CoGa	5.65 5.75 5.90	1.2 45.07 --	1.459 0.314 1.714
Cr2CoIn	5.7 5.85 5.99	70.1 -- --	0.175 1.373 2.306

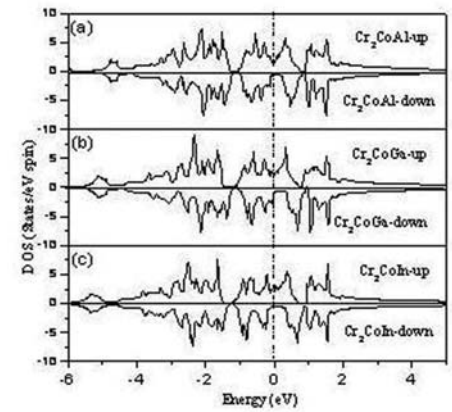

Fig. 1. The calculated spin-projected DOS plots for (a) Cr2CoAl at the lattice constant of 5.82 Å, (b) Cr2CoGa at the lattice constant of 5.75 Å and (c) Cr2CoIn at the lattice constant of 5.70 Å.

FD-06

Exchange constant and magnetic anisotropy in Co_2-based Heusler compounds.

J. Hamrle[1], O. Gaier[1], B. Hillebrands[1], M. Jourdan[2], H. Schneider[2], G. Jakob[2], T. Kubota[3], Y. Sakuraba[3], M. Oogane[3], Y. Ando[3], C. Felser[4]

1. Fachbereich Physik, Technische Universität Kaiserslautern, Kaiserslautern, Germany; 2. Institut für Physik, Johannes-Gutenberg-Universität, Mainz, Germany; 3. Department of Applied Physics, Graduate School of Engineering, Tohoku University, Sendai, Japan; 4. Institute of Inorganic and Analytical Chemistry, Johannes-Gutenberberg-Universität, Mainz, Germany

Co_2-based Heusler compounds are promising candidates for spintronics devices with the potential to provide 100% spin polarization. Here, we report on the determination of magnetic anisotropy, exchange interaction and magnetization reversal in Co_2FeSi, $Co_2Cr_{0.6}Fe_{0.4}Al$ (CCFA), Co_2MnSi and $Co_2MnAl_xSi_{1-x}$ Heusler compounds using Mageto-Optical Kerr Effect (MOKE) magnetometry and Brillouin ligh scattering (BLS) spectroscopy. The samples are studied as a function of composition, ordering and thickness [1-3].

Examples of BLS spectra of CCFA and Co_2FeSi are presented in Fig. 1a. CCFA, as well as all Heusler compounds studied here except Co_2FeSi, provide BLS spectra with several well-resolved BLS peaks, corresponding to different spin-waves modes. On the other hand, the BLS spectra of epitaxial L_21 ordered Co_2FeSi does not provide sharp peaks, as they are smeared out to a wide, single peak (Fig. 1a). It is a fingerprint of a random distribution of the internal field in Co_2FeSi, with a distribution width of about 4 kOe. We have attributed this random internal field to a presence of Dzaloshinskii-Moriya (DM) exchange which is described by a Hamiltonian $H=\mathbf{D}.(\mathbf{S}_1\times\mathbf{S}_2)$, different from ordinary Heisenberg exchange Hamiltonian $H=J\,\mathbf{S}_1.\mathbf{S}_2$. The presence of the random field distribution is also supported by constantness of the coercive field H_C as a function of the in-plane angle of the applied field, found in epitaxial Co_2FeSi films, smearing out the expected 4-fold anisotropy [3], which was found for example in CCFA films [1].

From the frequencies of the spin-waves modes we have determined the exchange constant A, the saturation magnetization M_S and the magnetocrystalline cubic volume anisotropy K_1 of the investigated Co_2-based Heusler compounds (Tab. 1) and compared them with phases of Co and Fe. The exchange constant A of the investigated Heusler compounds is about 0.4-0.6 μerg/cm, i.e. about 4-5 times smaller then A of Co and Fe. M_S of Heusler compounds ranges between 500-1000 emu/cm^3, whereas typical value of Co and Fe is 1400 emu/cm^3. Exchange stiffness D of Heusler compounds is about 2-3 times smaller than those of Fe and Co.

In Co_2MnSi films, we have studied the dependence of M_S, A and K_1 on the annealing temperature T_a, which provides different degrees of the L_21 order (i.e. B2 or L_21). The change of M_S and A with change of crystallographic order is less then 10% (see Tab. 1). On the other hand, K_1 drops by more then a factor of 10 during B2 to L_21 transition (Fig. 1b). Similar results are provided by the dependence of $Co_2MnAl_xSi_{1-x}$ on the nominal composition x (Fig. 2). Although M_S and A depend weekly on x (Fig. 2a,b), K_1 depends expressively on x (Fig. 2c).

The project was financially supported by the Research Unit 559 "New materials with high spin polarization" funded by the Deutsche Forschungsgemeinschaft, by the NEDO International Joint Research Grant Programm 2004/T093 and by the Stiftung Rheinland-Pfalz für Innovation.

[1] J. Hamrle, S. Blomeier, O. Gaier, B. Hillebrands, R. Schäfer, M. Jourdan, JAP **100**, 103904 (2006)

[2] O. Gaier, J. Hamrle, S. Hermsdörfer, B. Hillebrands, Y. Sakuraba, Y. Ando, submitted to JAP, arXiv:0708.3303

[3] J. Hamrle, S. Blomeier, O. Gaier, B. Hillebrands, H. Schneider, G. Jakob, K. Postava, C. Felser, J. Phys. D: Appl. Phys. **40**, 1563 (2007)

[4] B. Hillebrands, PRB **41**, 530 (1990)

[5] X. Liu, M.M. Steiner, R. Sooryakumar, G.A. Prinz, R.F. C. Farrow, G. Harp, PRB **53**, 12166 (1996)

	A [μerg/cm]	M_S [emu/cm^3]	$D=2A/M_S$ [nOe cm^2]	K_1 [kerg/cm^3]
CCFA(B2)	0.48±0.04	520±20	1.85	-20±10
Co_2MnSi (L_21)	0.60±0.05	1010	1.19	-70±5
Co_2MnSi (B2)	0.55±0.05	1100	1.00	-5±5
Co_2MnAl (B2)	0.45±0.05	780	1.15	-55±10
Fe(bcc) [3]	2.0	1430	2.80	480
Co(bcc) [4]	2.11	1140	3.70	0±10
Co(fcc) [4]	2.74	1410	3.89	-500±20
Co(hcp) [4]	2.85	1410	4.04	NA

Tab 1: Overview of determined values of exchange constant *A*, saturation magnetization M_S, exchange stiffness *D* and magnetocrystalline cubic volume anisotropy K_1 for the investigated Heusler compounds, compared with Fe and Co phases. All Heusler compounds presented here are grown as (100) oriented films. NA stands for 'not applicable'.

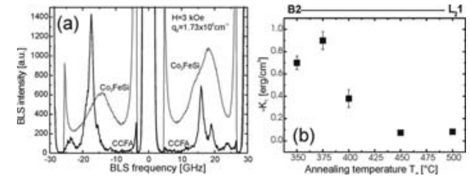

Fig 1: (a) BLS spectra of CCFA and Co_2FeSi. (b) Magnetocrystalline cubic volume anisotropy K_1 as a function of the annealing temperature of the Co_2MnSi(30nm)/Cr(40nm)/MgO(100) film.

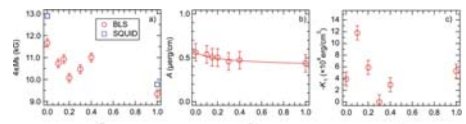

Fig 2: Dependence of (a) M_S, (b) *A* and (c) K_1 on the nominal composition *x* of $Co_2MnAl_xSi_{1-x}$(30nm)/Cr(40nm)/MgO(100) films. The changes in M_S and K_1 near x=0.2 correspond to observed structural changes (probably due to phase separation) for x>0.2.

FD-07

Spin transitions in $DyCoO_3$ investigated by measuring the electric quadrupole interactions.

F. H. Cavalcante, *A. W. Carbonari*, G. A. Cabrera-Pasca, J. Mestnik-Filho, R. N. Saxena
CRPq, IPEN, Sao Paulo, Brazil

Rare earth Cobaltites with perovskite structure $RCoO_3$, where R = rare-earth element, form a family of compounds in which magnetic transitions are associated to spin states of Co^{3+} ion. In the perovskite structure R^{3+} and Co^{3+} metal ion sites have twelve fold and six fold oxygen coordination, respectively. In this family, $LaCoO_3$ has been studied intensively due to two spin-state transitions of Co^{3+}. The first is associated with the transition from a nonmagnetic low spin state (LS) ($t_{2g}^6e_g^0$) to a paramagnetic intermediate spin state (IS)($t_{2g}^5e_g^1$) at around 50-100 K and the second transition (an insulator-metal character transition) from IS to high spin state HS ($t_{2g}^4e_g^2$) at 500-550 K. However, this interpretation has been criticized, first, because theoretical calculations indicate that IS state is energetically more favorable than HS state and second, a Jahn-Teller distortion is expected for a IS state as the degenerate orbital e_g^1 is partially occupied which is not compatible with the R-3c symmetry[1,2]. Differently from $LaCoO_3$, which presents a rhombohedral crystallographic structure and where the spin transitions are relatively easy to observe by magnetic measurements, the other compounds of the $RCoO_3$ family exhibit a orthorhombic structure, and Co spin transitions are difficult to determine by magnetic susceptibility measurements due to large magnetic moment of R ions. In particular, $DyCoO_3$ shows a large distortion of the CoO_6 octahedron and has been very little studied so far. A microscopic technique, in which local changes can be easily followed, is therefore very useful to investigate spin transitions in $RCoO_3$ family. Hyperfine interactions techniques offer a high sensitivity to local structure variations in the crystal lattice and, consequently, can be used to follow changes such as bond distances, symmetry, defect trapping etc. on a microscopic scale.

In the present work, the perturbed angular correlation (PAC) technique was used to measure the temperature dependence of quadrupole interaction (QI) in $DyCoO_3$ compound using $^{111}In \rightarrow ^{111}Cd$ and $^{181}Hf \rightarrow ^{181}Ta$ nuclear probes. These radioactive probes were introduced in the oxide lattice through a chemical process during the sample preparation. The PAC measurements with ^{111}Cd and ^{181}Ta probes were made in the temperature range of 10 K to 1200 K.
The temperature dependence of the quadrupole frequencies for ^{111}Cd at Co and Dy sites show unexpected behavior. Instead of decreasing with temperature as a result of thermal expansion of the lattice, the quadrupole frequencies (ν_Q) for ^{111}Cd at both Dy and Co sites show discontinuities at two different temperature regions: 200-350 K and 600-800 K. Above 800 K the quadrupole frequency increases with increasing temperature, as can be seen in figure 1. The second discontinuity in the temperature dependence of quadrupole frequency is clearly seen in the measurement taken with ^{181}Ta.
The asymmetry parameter measured with ^{111}Cd at Co sites shows high values in the temperature range of 100 K to 400 K, which indicates a strong distortion of the CoO_6 octahedron. However, above 400 K the asymmetry parameter decreases almost linearly with temperature. These results are discussed in terms of spin-state transitions and distortions in the crystal structure and compared to results previously published for PAC measurements in $LaCoO_3$[3], $GdCoO_3$[4] and $TbCoO_3$[4]. With these results it was possible to observe a systematic behavior of the temperatures assigned to the spin transitions as a function of the rare-earth ion radius.

1. M. A. Korotin, S. Yu. Ezhov, I. V. Solovyev, V. I. Anisimov, D. I. Khomskii and G. A. Sawatzky, Phys. Rev. B, 1996, 54, p. 5309.

2. T. Mizokawa and A. Fujimori, Phys. Rev. B, 1996, 54, p. 5368.

3. A. C. Junqueira, A. W. Carbonari, R. N. Saxena, J. Mestnik-Filho and R. Dogra, J. Phys:Condens. Matter, 2005, 17, p. 6989.

4. A. W. Carbonari, F. H. M. Cavalcante, R. F. L. Malavasi, G. A. Cabrera-Pasca, J. Mestnik-Filho, and R. N. Saxena, accepted for publication in J. Appl. Phys.

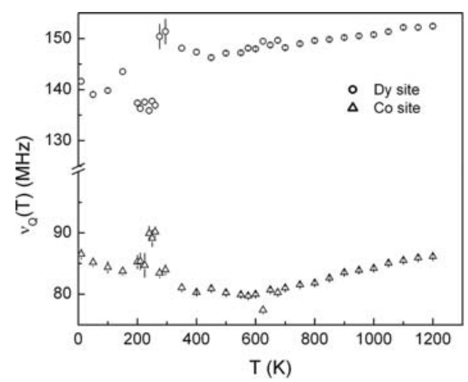

FE-01

Prototyping and Evaluation of Magnetic Communication Coils between Inside and Outside of Body for Controlling FES.

K. Kato[1], M. Goto[1], K. Sugano[1], M. Miyashita[1], F. Sato[1], H. Matsuki[1], Y. Handa[2], T. Sato[3]
1. Department of Electrical and Communication Engineering, Graduate School of Engineering, Tohoku University, Sendai, Japan; 2. Graduate School of Medicine, Tohoku University, Sendai, Japan; 3. NEC TOKIN Corp., Sendai, Japan

1. Introduction

FES is the therapy for rehabilitate lost movement function to apply electrical stimulation to paralyzed extremity. We adapt implanted direct feeding method for the FES (Fig. 1). One of the specific FES need is synchronizing all stimuli in order to rehabilitate function correctly. TDMA allows stimulus signals to multiplex, but a outer unit and inner units are separated in the way. So we must pick up the information from inner units to make reparation for receiving data and stimulate correctly. In addition, based on downsized inner units, it is not undesirable to make large coils of inner units. We realized two-way communication system by magnetic connection between voltage resonance and current resonance.

2. Principle of Communication Coils between Inside and Outside of Body

It is important to resonate current for transmit signal with coil. On the other hand, it is important to resonate voltage for receive signal with coil. In generally, the former is constructed by connect capacitance in series against coil and the latter is constructed by connect capacitance in parallel against coil. But it is difficult to transmit signal from voltage resonance system so that two-way communication is not realized in simply. So we show communication system we suggest in Fig. 2. Because there are power coils out of body, we decided that the part that a number of coils is fewer is outer unit. When communicate from inner to outer, magnetic flux generated by Lp interlinks Ls and transmit signal with current resonance. In the receive side, it is able to get high voltage in order to voltage resonance with Cpo and Lsp. At the same time, when communicate from outer to inner, Cso is enable to make current resonance state at lower frequency (foi) than the frequency from inner to outer (fio). Though the magnetic flux interlinks each inner coil, Ls side resonates at fio and different from foi so that inner unit is free of influence form Ls and Csi. Lp and Cpi make voltage resonance at foi and inner unit can get high voltage. In this way, we could realize communication antenna system between inside and outside of body.

3. Result

In FES, we can think magnetic connection between outer unit and inner units is very few. The values of each capacitance are shown in Table. 1. Based on the expressions, we experimented communication with this antenna. Input voltage is 10 Vp-p, fio is 2MHz and foi is 1.6MHz. The characteristic of the distance of coils and voltage is shown in Fig. 3. From this result we can recognize this system allows two-way communication.

A New Contactless Power-signal Transmission Device for Implanted Functional Electrical Stimulation (FES), IEEE Trans.Mag.40,4(2004)2964-2966, F.Sato, H.Matsuki et.al

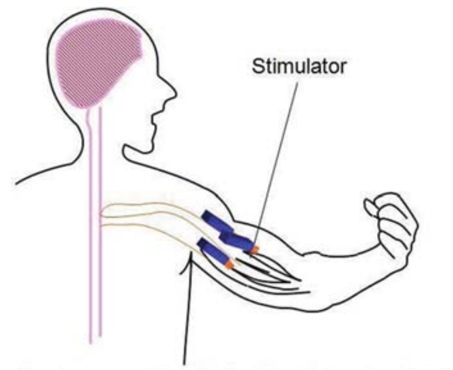

Fig. 1 Image of Implanted Direct Feeding FES

Table. 1 Expressions of Each Capacitance

$Cpo=\frac{1}{\omega_{io}^2 Lsp}$	$Cso=\frac{1}{Lsp}\left(\frac{1}{\omega_{oi}^2}-\frac{1}{\omega_{io}^2}\right)$
$Cpi=\frac{1}{\omega_{oi}^2}\frac{1-\omega_{oi}^2 CsiLs}{Lp(1-\omega_{oi}^2 CsiLs(1-k^2))}$	$Csi=\frac{1}{1-\omega_{io}^2 CsiLs(1-k^2)}$

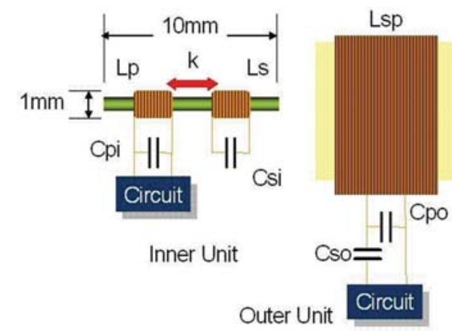

Fig. 2 Duplex Communication Coil System

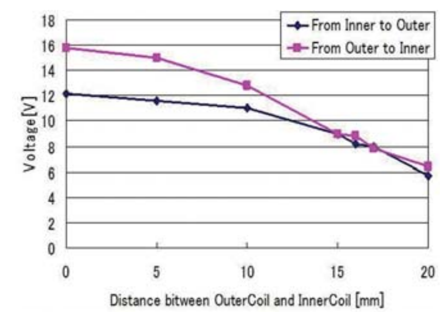

Fig. 3 Characteristics of the Distance of Coils and Voltage

FE-02

Bone Tissue Engineering using Magnetically Oriented Collagen.

T. Shinohara[1], T. Saito[2], D. Saito[1], A. Nakahira[3], M. Aoki[4], M. Kotani[2]
1. Research Institute for Advanced Technologies, Tokyo Denki University, Inzai-shi, Japan; 2. Graduate School of Engineering, Tokyo Deki University, Kanda, Japan; 3. Graduate School of Engineering, Osaka Prefecture University, Sakai, Japan; 4. Neomax, Hitachi Metals, Ltd, Oomachichou, Japan

Introduction
As the life span of human being is becoming increasing, people with bone problems is also increasing. Ceramics and metals are used as the biomaterial for repair and reconstruction of diseased or damaged bones [1]. However the mechanical and biocompatible characteristics of these materials are different to those of natural bones. Therefore, the development of biomaterials with characteristics similar to those of natural bones is expected.
As natural bones are consisted with collagen and hydroxyapatites, so that is an organic/ceramic hybrid composite material. In natural bones, the collagen is highly oriented in one direction, leading to the achievement of a mechanically strong material. To obtain structures similar to natural bones, it is necessary to orient collagen. Therefore, to develop artificial bone similar to natural bones, highly oriented collagen scaffolds for osteoblast cells are required, and the preferred orientation of collagen is a key technology. For this purpose, we developed magnetic circuit using permanent magnets, without using superconducting magnet, which showed magnetic field strength around 3 T, and collagen oriented clearly [2]. In this paper, fundamental bone formation by osteoblasts cultured on oriented collagen is reported.
Experiments
Collagen (type 1 from pig) provided by Nippon Ham was used as a starting material.
The collagen solution 0.5 wt% 2ml, 1.5 mol NaCl solution 0.2ml, and Dulbecco's Modified Eagle medium (α-MEM, Gibco provided), with 10% fetal bovine serum (FBS, BioWhttaker provided) were mixed, and cooled 0 Celcius degree, and then warmed to 22 Celcius degree then applied magnetic field 3 T by permanent magnet circuit for 24 hr, then warmed again to 37 Celcius degree, and kept for 1.5 hr, then the materials were observed by optical microscope.
Mouse osteoblast MC3T3-E1, provided by Riken cell bank, 1.6×106 cells/ml,0.5ml, were seeded on mixture of collagen, NaCl solution and MEM, then, warmed to 22 Celcius degree for 24 hours and then warmed to 37 Celcius degree and cultured in incubator with 5% CO2 for 50 days. The specimens were observed every 24 hr by optical microscope and SEM. The α-MEM solution changed every four days. After 50 days cultured, the specimens were observed by SEM, and then analyzed by EDS and X-ray diffraction.
Results and Discussions
The collagen oriented by permanent magnet circuit is shown in Fig 1. The orientation degree was more than 0.9. The shape of collagen fiber was straight, longer, and oriented clearly. The osteoblast cells seeded on collagen gel shrank with cultured days. The shrinkage of collagen-gel was formed by the mutual interaction of collagen and osteoblats, and related to the activity and mineralization of cells [3]. The surface area of collagen-gel dependence on culturing time was observed. The shrinkage of collagen-gel saturated 14days after cultured. From the results, it was considered that the mineralization process of osteoblasts began after collagen shrinkage completed.
The SEM photograph of osteoblasts cultured 42 days is shown in Fig 2. The small round bolls, diameter around couples of microns meter, covered over all of collagen fibers. These materials were analyzed by EDS. It clarified that was composed with Ca and P. The X-ray diffraction measurement result is shown in Fig 3. The material was identified to be hydroxyapatite which is main component of natural bones.

1) L. L. Hench, J. Am. Ceram. Soc., 81, 1705 (1998)

2) T. Shinohara, et al Phy. Stat. Solid (C) 4 No.12 4333 (2007)

3) T.Nishiyama, N.Tominaga, and T.hayashi, Ouyou Saibou Seibutugaku Kenkyuu 4 [1] 1 (1985)

Optical microscope photo of oriented collagen

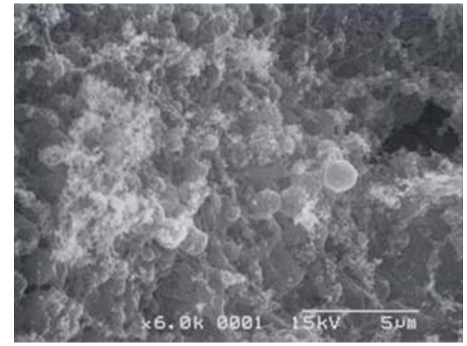

SEM photo of osteoblasts cultured for 42 days

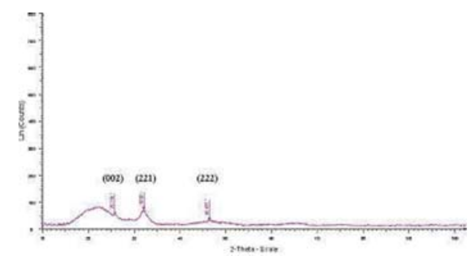

X-ray diffraction pattern of mineralized osteoblast

FE-03

Modification of motor evoked potentials caused by electrical peripheral nerve stimulation in transcranial magnetic stimulation.

O. Hiwaki[1], M. Odagaki[1], F. Hiroshi[1], A. Kodabashi[2], T. Fujimoto[2]
1. Graduate School of Information Sciences, Hiroshima City University, Hiroshima, Japan; 2. Fujimoto Hayasuzu Hospital, Miyakonojyo, Japan

1. Introduction
Transcranial magnetic stimulation (TMS) can evoke localized excitation of nerve cells in the motor cortex non-invasively. A cortical motoneuronal activation by TMS produces efferent signals going down through cortico-spinal tracts, thereby motor evoked potentials (MEPs) are observed at muscles which are innervated by the motor neurons. On the other hand, an electrical stimulus of peripheral nerves generates nerve potentials in sensory neurons going up to the primary somatosensory cortex. The potentials reached at the primary somatosensory cortex can be observed as electrical potentials or magnetic fields, which are named as somatosensory evoked potentials (SEPs) or somatosensory evoked fields (SEFs) respectively. It is supposed that the afferent sensory inputs into the sensorimotor cortex reached before TMS can influence the excitability of neurons in the motor cortex. The aim of the present study is to investigate whether the modification of the motor function is caused by the electrical peripheral nerve stimulus prior to the TMS. We analyzed MEPs evoked by the TMS following the electrical stimulus of the median nerve. SEFs were also measured in order to evaluate the afferent signals in the primary somatosensory cortex.
2. Materials and Methods
Four right-handed subjects (males aged 23-24 years) with no known neurological abnormalities participated in this study. Study procedures were approved by the ethics committee of Hiroshima City University. Informed consent was obtained from all subjects. The TMS stimulator was a Magstim Model 200 magnetic stimulator (Magstim, Whitland, UK) with a 70-mm figure-of-eight coil (2.2 T maximum output at the coil surface; monophasic pulse; duration, 1ms). The subjects lay supine on a medical chair and were instructed to maintain a slight contraction of the muscles of the right hand. The position of the coil on the left side of the subject's head was adjusted until visible contraction of the right hand muscle occurred. The coil was fixed at this site with a rigid multi-articular arm system. The median nerve at the right wrist was stimulated electrically prior to the TMS with interstimulus intervals (ISIs). The strength of the electrical stimulus was so adjusted that slight movement of the thumb was observed. ISIs were between 0 to 50 ms at 5 ms step. MEPs were measured at hand muscles: first dorsal interossei muscles (FDI), abductor pollicis brevis muscles (APB), abductor digiti minimi muscles (ADM), and forearm muscles: brachioradialis muscles (BR), extensor carpi radialis longus muscles (ECRL), flexor carpi ulnaris muscles (FCU) with Ag-AgCl electrodes on the bellies of these muscles. At each ISI, 10 successive trials were conducted, and the average of integral EMGs (iEMGs) in the period of 10 ms to 100 ms after the onset of TMS was calculated.
SEFs were measured in all subjects during right median nerve stimulation at the wrist by using a whole-head 160 channels axial SQUID gradiometer system (PQ1160C, Yokogawa Electronic, Tokyo, Japan). The passband of the bandpass filter was set at 1-500 Hz. Up to 400 responses were averaged. Single equivalent curent dipoles (ECDs) were estimated in local regions at 20 ms and 30 ms after the stimulus.
3. Results and Disscussion
The electrical stimulus of the median nerve was found to influence the iEMG of MEPs evoked by TMS. The MEPs of FDI was attenuated when ISI was 20 ms. This attenuation of MEPs was observed at ADM as well (Fig.1). Furthermore, the iEMGs of MEPs at FDI and ADM were enhanced when ISI was longer than 25 ms.
The ECDs of the SEFs measured with 160 channels SQUID at 20 ms and 30 ms after the peripheral nerve stimulus were located in the posterior wall of the central sulcus (area 3b in the primary somatosensory cortex). The direction of the ECD at 20 ms was the postero-anterior, whereas that of the ECD at 30 ms was the antero-posterior direction which was approximately opposite direction of ECD at 20ms.
These results indicated that the attenuation and enhancement of MEPs observed at ISI of 20 ms and beyond 25 ms respectively was probably caused by the excitation of the neurons in the area 3b. The direction of the estimated ECD at ISI of 30 ms was in opposite to that of 20 ms, though both the estimated ECDs were located in the area 3b in the primary somatosensory cortex. Therefore, it is likely that the area 3b of the primary somatosensory cortex is involved in the motor responses from peripheral inputs, and the direction of the electrical dipole in the area 3b is concerned with the modification of the motor function.

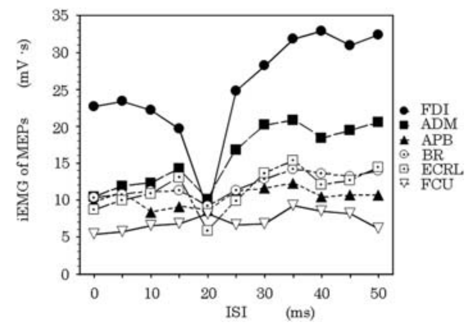

Fig. 1. Integral EMG of motor evoked potentials (MEPs) changing with interstimulus interval (ISI) between TMS and electrical stimulation of the median nerve at the wrist

FE-04

Detection of the terrestrial magnetism in migrating birds: Is it a question of vision?

S. Migalski[1,2], T. Meydan[2], J. T. Erichsen[1], V. P. Bingman[3]
1. Optometry and Vision Sciences, Cardiff University, Cardiff, United Kingdom; 2. Engineering, Cardiff University, Cardiff, United Kingdom; 3. Psychology, Bowling Green State University, Bowling Green, OH

The ability of birds to migrate over huge distances with outstanding accuracy is, in part, based on their capacity to use the earth's magnetic field for orientation. However, the "sensor" responsible for geomagnetic orientation is still unknown. It has been hypothesised [1, 2] that geomagnetic directional information is encoded by the birds' visual system. One explanation of the involvement of light as a possible transducer of magnetic field information is the "radical pair process theory" [2]. Photons of light striking the retina induce a chemical reaction within the photoreceptors. According to this theory, the yield of this reaction can be altered by the alignment of the ambient magnetic field with respect to the axis of the photoreceptive cell. Retinal activation is then processed further in the bird's brain, providing sufficient information to orient precisely. Support for the theory is given by studies showing that magnetic orientation in birds is disrupted by magnetic fields with resonance frequencies of 1.315 MHz [3] and 7 MHz [4]. Moreover, cryptochromes, which have been suggested as a possible centre of magnetic sensing in the eye, were found in the eye of migratory birds, and cryptochrome activity was increased during magnetic orientation [5].
It has been shown that migratory orientation in birds is preceded by head scanning, which is thought to calibrate the magnetic compass [6]. In this paper, head movements were studied to investigate homing pigeon behaviour with respect to different magnetic field conditions. An artificial magnetic field, equivalent to the earth's magnetic field, was generated with the help of a set of Helmholtz coils that are capable of producing static as well as sweeping magnetic fields, or the absence of any field. The constructed system is also equipped with a camera and, together with the equipment devoted to the generation of an artificial magnetic field, is fully automated by computer software. It is essential to ensure a high level of magnetic shielding when working with such low magnetic fields. Therefore, a specially designed shielding device, with a shielding factor of 850, was used. In this system, homing pigeons (*Columba livia*) were investigated using a novel approach: they were exposed to a sequence of several different magnetic field conditions, including a moving field, in the course of one experimental trial. Their behaviour was video recorded and analyzed to determine if their head movements were temporally correlated with changes in the field, indicating some kind of visual response to changes in the field.
Results showed that the birds tended to be especially active when experiencing a zero magnetic field, which presumably they had never experienced before. Particularly striking head movements and changes in postures were also observed during transitions to a sweeping field. Figure 1 depicts typical behavioural responses that occurred after a field transition to a sweeping field. In addition, increased eye movement during a sweeping field was noted. However, as eye movements can happen independently of the head movements, they are not recorded by our current software. Nevertheless, the eye movements may carry important information about the visuomotor origin of magnetic field detection in birds, and will be an important part of future analyses.
The data suggest that the different head movements and postures observed are indeed correlated to changes in the ambient magnetic field. Consequently, this finding, together with the indication that eye movements are involved in the response, implicates the homing pigeon's head as a location of the magnetic field sensor. However, further research is needed to determine whether changes in the artificially produced magnetic fields lead to statistically reliable changes in head movements, and whether these movements are visuomotor in nature.
Looking to the future, establishing a reliable behavioural assay for magnetic field responses in homing pigeons would serve as a basis for identifying the location and nature of the magnetic sensor, the neurobiological and psychophysical properties of magnetic field perception, as well as the behavioural responses related to such perception.

[1] Wiltschko, W. and R. Wiltschko, Naturwissenschaften 89: pp. 445-452, 2002

[2] Ritz, T., et al., Biophysical Journal 78: pp. 707-718, 2000

[3] Thalau, P., et al., Naturwissenschaften 92: pp. 86-90, 2004

[4] Ritz, T., et al., Nature 429: pp. 177-180, 2004

[5] Mouritsen, H., et al., Proceedings of the National Academy of Sciences of the USA 101: pp. 14294-14299, 2004

[6] Mouritsen, H., et al., Current Biology 14: pp. 1946-1949, 2004

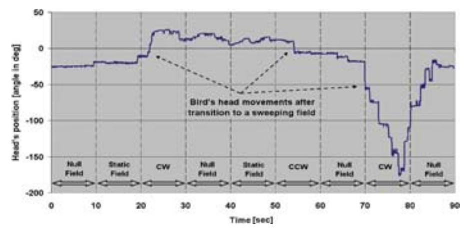

Figure 1. Analysis of the change in bird's head position with time, where a bird was exposed to different magnetic field conditions (CW field sweeping clockwise; CCW – field sweeping counterclockwise)

FE-05

Computation of Current Distribution in Rat Head by Transcranial Magnetic Stimulation and Electroconvulsive Therapy.

M. Lu[1], S. Ueno[2], T. Thorlin[3], P. Miranda[1], M. Persson[4]
1. Institute of Biophysics and Biomedical Engineering, Faculty of Sciences, University of Lisbon, Lisbon, Portugal; 2. Department of Applied Quantum Physics, Graduate School of Engineering, Kyushu University, Fukuoka, Japan; 3. Institute for Clinical Neuroscience, Sahlgrens University Hospital, Gothenburg, Sweden; 4. Department of Signals and Systems, Chalmers University of Technology, Gothenburg, Sweden

Introduction: Electroconvulsive therapy (ECT), in which electric current are applied to the brain through scalp electrodes, improves severe mental illnesses [1]. Transcranial magnetic stimulation (TMS) is another neurophysiology method to stimulate cerebral tissue non-invasively using eddy currents generated by impulses of magnetic field [2][3]. Both TMS and ECT have been employed for treatment of psychiatric disorders such as depression and Parkinson's disease etc. In addition to their widespread application in humans, TMS and ECT have been also applied to the animals experimentally. Zyss et al. presented the comparison of the effect of treatments of TMS and ECT in rats [4]. Ogiue-Ikeda et al. investigated the effect of TMS on long term potential in the rat hippocampus [5]. These experimental studies have well shown us the different effects of TMS and ECT in rat tissures. However, the current distributions in rat brain by TMS and ECT are still to be elucidated.
Models: In this paper we use a 3D rat model obtained from Brooks Air Force Laboratory, USA. For TMS case, a special figure-eight-shaped coil has been designed according to the rat dimensions and placed on the surface of the rat head as shown in Fig. 1. For ECT case, the ear clip electrodes are placed on the tip of rat ears. Current is injected into one ear and extracted from another ear. The electrical properties of rat tissues are modeled using the Four-Cole-Cole method.
Impedance Method: The rat model is composed of small cubic voxels and is represented as a 3D network of impedances. Kirchoff voltage law around each loop in this network generates a system of equations for the loop currents. These loop currents are driven either by Faraday induction for the TMS applicator or the injected current from the ECT electrodes. Details implementation of the impedance method can be found in literature [6].
Results: By employing the 3D impedance method, the current density distribution in the rat model are calculated for both TMS and ECT cases. Fig. 2 and Fig.3 show the current density distributions in rat head at slice layer of y= 44 mm by TMS and ECT, respectively. Form Figs. 2 and 3, we know the maximum value of current density in rat head are presented in CSF for TMS case and in muscle for ECT case. In rat brain, current density by TMS can be comparable to that by ECT. Detailed results will be presented in the extended paper.

1. R. Abrams, Electroconvulsive Therapy, 3rd ed.(Oxford University Press, New York, 1997)

2. A.T. Barker and R. Jalinous, Non-invasive magnetic stimulation of human motor cortex, Lancet, 1 (8437):1106-1107, 1985.

3. S. Ueno, T. Tashiro, and K. Harada, Localized stimulation of neural tissues in the brain by means of a paired configuration of time-varying magnetic fields, J. Appl. Phys., 64(10):5862-5864, 1988.

4. T. Zyss, Z. Gorka, M. Kowalska and J. Vetulani, Preliminary comparison of behavioral and biochemical effects of chronic transcranial magnetic stimulation and electroconvulsive shock in the rat, Biol. Psychiatry, 42:920-924, 1997.

5. M. Ogiue-Ikeda, S. kawato and S. Ueno, The effect of repetitive transcranial magnetic stimulation on long-term potentiation in rat hippocampus depends on stimulus intensity, Brain Research, 993:222-226, 2003.

6. N. Orcutt, and O.P. Gandhi, A 3-D impedance method to calculate power deposition in biological bodies subjected to time varying magnetic fields, IEEE Trans. Biomed. Eng., 35(8):577-583, 1988.

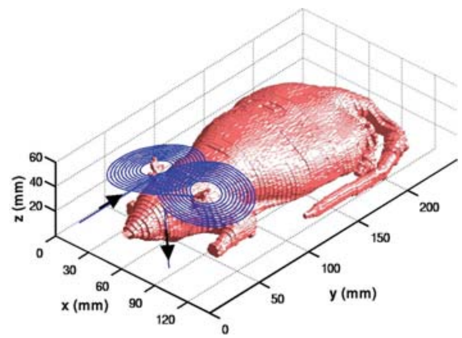

Fig. 1 Figure-eight-shaped coil placed on the rat head

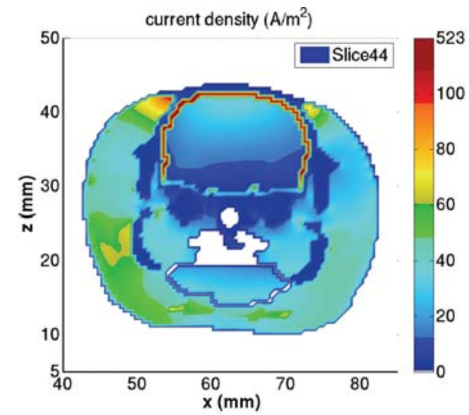

Fig. 2 TMS case: Current density distribution on the cross section at y=44 mm layer

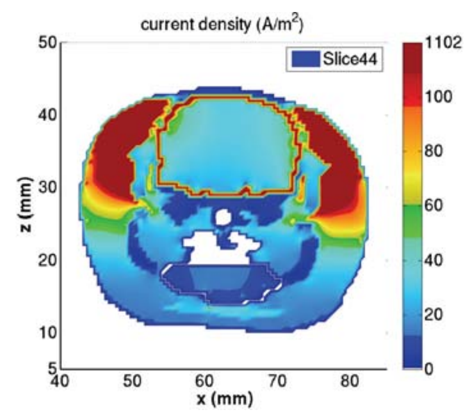

Fig. 3 ECT case: Current density distribution on the cross section at y=44 mm layer

FE-06

Spintronic biosensors based on Fe/MgO/Fe(001) tunnelling junctions.

R. Bertacco, S. Brivio, M. Cantoni, A. Cattoni, D. Petti
Center LNESS, Politecnico di Milano, Como, Italy

In the past few years we assisted to a continuously growing interest in magnetic field sensors for biological applications and, in particular, for biomolecular recognition. Examples of recognitions are DNA-DNA hybridization, antibody-antigen recognition and general ligand-receptor binding. [1] This reserach field is becoming more and more important for areas such healthcare, pharmaceutical industry, environmental analysis, and generally in biotechnological applications.
Generally the detection involves the use of a known biomolecule that probes a testing sample looking for a specific target analyte. Hence they are given the name of probe and target biomolecule, respectively. A common approach to detect biological molecules is to attach to the target molecule a label producing an externally observable signal. The label may be a radioisotope, enzyme, or a fluorescent molecule, as in the case of LIF techniques. Recently, magnetic beads have also been used as labels for biosensing, due to their advantages over other labels. The magnetic properties of the beads are stable over time, because the magnetism is not affected by reagent chemistry or subject to photo-bleaching (a problem with fluorescent labelling). There is also no significant magnetic background present in a biological sample and magnetic fields are not screened by aqueous reagents or biomaterials. In addition, magnetism may be used to remotely manipulate the magnetic particles. Finally, a number of very sensitive magnetic field detection devices have been developed during recent years, such as giant magnetoresistance (GMR) and spin-valve [2] magnetic sensors that enable the measurement of extremely weak magnetic fields, like those generated by a single magnetic microbead. Besides GMR sensors, measurements of single magnetic beads have been demonstrated using miniaturized silicon Hall sensors [3] and planar Hall effect sensors based on permalloy thin films [4]. More recently tunnelling magnetoresistance (TMR) sensors based on magnetic tunnelling junctions (MTJs) have been applied to biomolecular recognition due to their superior sensitivity and stability with temperature. A group from Brown University fabricated 2 micron x 6 micron MTJ sensors to detect single superparamagnetic M-280 Dynabeads.[5] Nevertheles MTJ based on MgO barriers display the highest values of magnetoresistance never measured at room temperature (410 %) [6] and show the promise of being spintronic transducers capable of detecting magnetic field in the pT range. This can enable detection of single 10 nm magnetic particles and, consequently, of single biomolecular reaction even for very small molecules. With these performances spintronic biochips show potential to become very powerful tools for molecular biology, and many groups are now working on spintronic biosensors emplying MgO based MTJs.
The spintronic group of Center LNESS has recently developed the capability of fabricating state of the art MTJ based on MgO barriers with TMR comparable with the highest values reported in literature. Fully epitaxial Fe/MgO/Fe(001) heterostructures are grown by MBE in UHV conditions and patterning is achieved by shadow masks (junction area of 200x200 microns) or optical lithography (down to the micron size). No exchange bias is required thanks to the action of properly designed magnetic anisotropies in the layers, while an in plane bias field of 18 Oe is needed in order to work in the linear region of the TMR. In these conditions a sensitivity of 3.5% / Oe (see Fig. 1) has been obtained on prototypical junctions with 200x200 microns area, which represents one of the best values reported up to now in literature.
The sensor surface is then passivated with a SiO2 capping layer and then probe molecules are immobilized via well defined protocols and conventional micro-spotting. Preliminary tests of DNA recognition, with the double magnetic and fluorescence label, are currently under development. In the paper we will present the first experiments of biomolecular recognition with great attention to the biological sensitivity of the biosensor.

[1] H. A. Ferreira et al., IEEE Transactions on Magnetics, 41, 4140 (2005)

[2] P.P. Freitas et al., Sens Actuat A Phys, 81(1-3), 2 (2000)

[3] P.A. Besse et al., Appl. Phys. Lett. 80(22), 4199 (2002)

[4] L. Ejsing et al., Appl. Phys. Lett. 84(23), 4729 (2004)

[5] W. Shen et al, Appl. Phys. Lett., 86, 253901 (2005)

[6] S. Yuasa et al., Appl. Phys. Lett. 89, 042505 (2006)

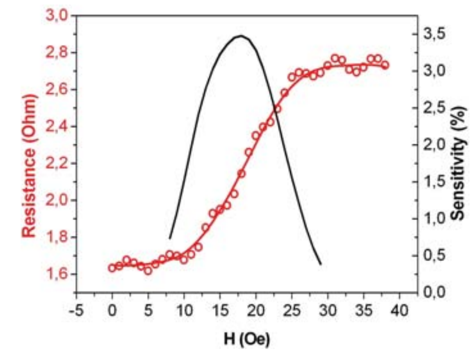

Fig. 1: Magnetoresistance (red empty dots) and sensitivity (continuous black line) of a 200x200 microns MTJ.

FE-07

MTJ based biosensor with top Au electrodes and functionalization layers.

F. A. Cardoso[1,2], S. Cardoso[1,2], V. C. Martins[1,3], P. P. Freitas[1,2]
1. INESC-MN, Lisboa, Portugal; 2. Instituto Superior Tecnico, Lisboa, Portugal; 3. Center for Biological and Chemical Engineering (CEBQ), Lisboa, Portugal

In the last few years, biochips based in magnetoresistive sensors have been used for biomolecular recognition assays [1-3]. In these assays biological probes are immobilized on the chip surface and complementary target biomolecules can be detected using a magnetic label. The detection of the magnetic label fringe fields is accomplished by a magnetoresistive sensor. An emerging interest in using magnetic tunnel junctions (MTJ) as magnetoresistive sensors is arising due to its higher magnetoresistance (up to 70% with AlOx barrier and 350% with MgO barrier) and its potential increase in sensitivity. However, due to its current-perpendicular-to-plane (CPP) configuration which increases the distance between the sensing layer and the particles, in similar sensor architectures, MTJs show lower particle sensitivity when compared to spin valves sensors (with current-in-plane configuration) [4].
In this work, a new architecture using MTJs with gold contacts and without passivation on top of it (as proposed in [5]) was fabricated. Since the passivation on top of the sensors was removed, the distance between the particles and the sensing layer is reduced to 1000 Å (thickness of the Au electrode) and a higher signal should be observed in the MTJ response. The inset of figure 1 shows a cross section of the chip. As observed, the biological probes will be immobilized on top of the gold contact.
MgO-barrier MTJs with linear response were successfully fabricated. The linear response was obtained by shape anisotropy (30x2 μm^2). As observed in figure 1, the MTJ shows a tunneling magnetoresistance (TMR) of 78%, a sensitivity of 1.89%/Oe and a resistance of 2000 kΩ. The signal-to-noise ratio (SNR) in function of the MTJ bias current was measured in order to determine the optimum working current (figure 2). The maximum SNR was attained for a current bias of 300 μA which will be used in the particles detection.
Figure 3 shows the MTJ voltage variation due to the presence of magnetic particles. The detection was made applying an external in-plane transverse 30 Oe + 15 0erms magnetic field. The signal was acquired using a lockin technique. A volume of 10μl of 250nm superparamagnetic particles (~10^11 particles/ml) was put over the chip and let to settle down during 10 minutes. A saturation signal of 860 μV was obtain. After washing, the signal came back to the baseline value meaning that all the particles were removed from the sensor (see fig. 3). It is important to note that these experiments with particles demonstrated that neither the Au contacts nor the MTJs were corroded by the liquid used in the experiments. Further experiments with different particles concentrations and with biological probes immobilized over the Au contact will be performed.

[1] “Detection of cystic fibrosis related DNA targets using AC field focusing of magnetic labels and spin-valve sensors”, H. A. Ferreira et al. (2005), IEEE Trans. Magn, vol. 41, no. 10, pp 4140-4142.

[2] “Detection of a micron-sized magnetic sphere using a ring-shaped anisotropic magnetoresistance-based sensor: a model for a magnetoresistance-based biosensor.”, Miller, M.M. et al. (2002), Appl. Phys. Lett. 81, 2211–2213

[3] “Design and performance of GMR sensors in the detection of magnetic microbeads in biosensors.”, Rife, J.C. et al. (2003), Sens. Actuat. 107, 209–218

[4] “Detection of 130 nm magnetic particles by a portable electronic platform using spin valve and magnetic tunnel junction sensors”, F. A. Cardoso et al. (2008), J. Appl. Phys., (in press).

[5] “Toward a magnetic microarray for sensitive diagnostics”, S. X. Wang, et al. (2005), J. Mag. Mag. Mat., 293, 731-736.

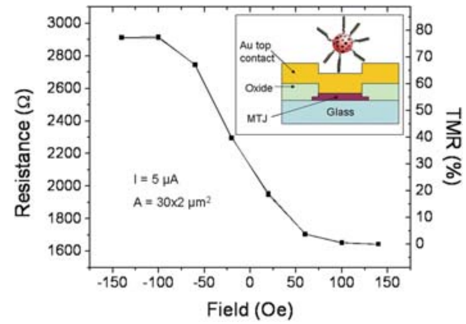

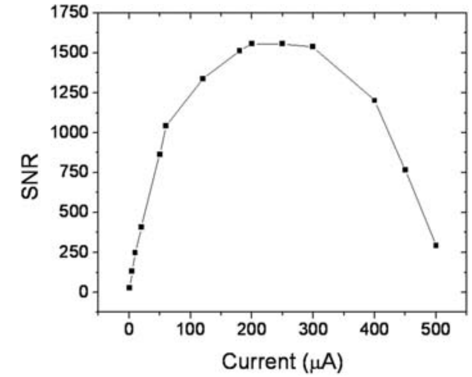

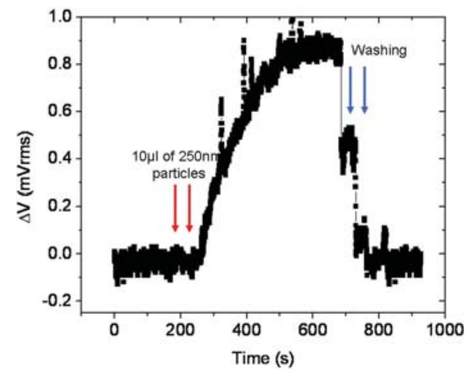

FE-08

Stem Cell Separator and Counter.

J. Loureiro[1,2], S. Cardoso[1,2], C. L. Silva[2,3], J. M. Cabral[2,3], P. P. Freitas[1,2]
1. INESC-Microsystems and Nanotechnologies, Lisbon, Portugal; 2. Instituto Superior Técnico (IST), Lisbon, Portugal; 3. CEBQ - IST, Lisbon, Portugal

Hematopoietic stem/progenitor cells (HSC) have vast potential for use in medical applications and the separation of these cells from blood has an important role in the stem cells research [1]. However, the most usual techniques, MACS and FACS, have some drawbacks like being cell-loosing or very time-consuming.
In this work a device based on magnetophoresis is being developed using microfluidics and in-situ magnetic fields, generated by current lines, in order to separate stem cells from blood in a more efficient and easy way [2],[3],[4],[5]. In the same device Spin Valve sensors are used to measure the efficiency of the separation (by counting the cells as they are separated).
The geometry of the separator makes it possible to change only the path of specific stem cells, that are magnetically labeled with 50nm magnetic beads functionalized with monoclonal antibodies, instead of separating all the magnetic elements in the fluid (which is vital to keep count of the stem cells).
The fluidic system consists in 2 micro-channels (150μm wide, 14μm thick and 40μm apart) joined over two gaps of 2.5mm and disposed in an "H"-type geometry (fig.1 and fig.2). The laminar flow is generated in the y-direction, from the inlet to the outlet. The fluidic system is bonded to the separator platform which consists in two successive lines (7μm wide and 500nm thick), deviated from the y-direction by an angle of 5 degrees, starting in one channel and ending in the other. At the end of each line there are three spin valves in both channels to count the cells that have been separated and those that might fail to be separated [6],[7].
To prove the concept and test the design, preliminary tests were made passing 2μm magnetic particles through the channels. These particles (χ=0.22 and $\rho=1.1\times10^{3}$ kg/m^3) feel a magnetic force of 9.5pN when passing over the current lines (due to a magnetic field of 6kA/m and a gradient of 2.2×10^6 kA/m when applying 100mA), which force them to be deviated in the x-direction. With velocities between 75-300μm/s, particles were observed to follow the line path, moving from the beginning of the line (in the first channel) until the end of it (in the second channel) (fig.3). When any particle fail to feel the first line (due to agglomeration for e.g.) it can be separated when passing over the next line. These measurements were made for a concentration of 1×10^5 particles/μl to make the optical inspection easier. The real experiment will be made with human hematopoietic stem/progenitor cells (CD34+ enriched cells), from umbilical cord blood samples.

[1] "Ex-vivo expansion of hematopoietic stem cells in bioreactors", Cabral, J.M. (2001) Biotechnology Letters 23, 741-751.

[2] "Flow through, Immunomagnetic Cell Separation", J.J.Chalmers, M.Zborowski, L.Sun and L.Moore, in Biotechnol. Prog. 1998, 14, 141-148

[3] "Separations based on magnetophoretic mobility", M. Zborowski, L.Moore, P.Stephen Williams and J.J.Chalmers, in Separation Science and Technology, vol.37, No.16, pp.3611-3633, 2002

[4] "Continuous sorting of magnetic cells via on-chip free-flow magnetophoresis", N.Pamme and C.Wilhelm, Lab-Chip, 2006, 6, 974-980

[5] "Analytical model for the magnetic field and force in a magnetophoretic microsystem", E.P.Furlani and Y.Sahoo, in J.Phys. D: Appl. Phys. 39 (2006) 1724-1732

[6] "Flow Velocity Measurement In Microchannels Using Magnetoresistive Chips", H.A. Ferreira, D. L. Graham, P. Parracho, V. Soares, and P.P.Freitas, IEEE Trans Magn., vol.40, pp. 2652-2654, July 2004.

[7] "Magnetoresistive sensors", P.P Freitas, R.Ferreira, S.Cardoso and F.Cardoso, in J.Phys.: Condens. Matter 19, N16 (23 April 2007), 165221 (21pp)

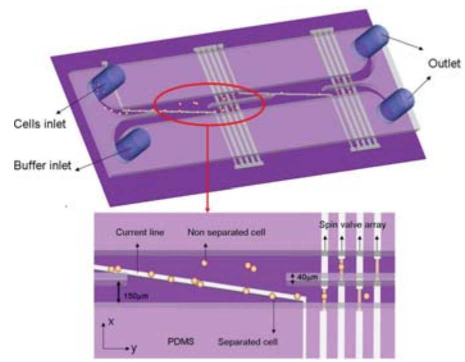

Figure 1: "H-type" fluidic platform, allowing stem cells to be separated from one channel to the other due to the magnetic field created by the oblique current lines. Each channel has spin valves at the end to count the cells

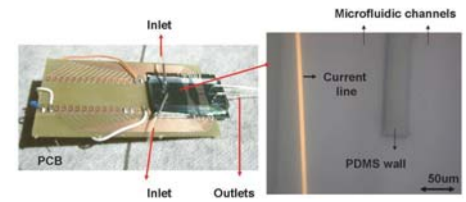

Figure 2: Real chip mounted on a PCB to allow electrical measurements (left); Microscope image of the microfluidic system showing the current line near the gap between both channels (right).

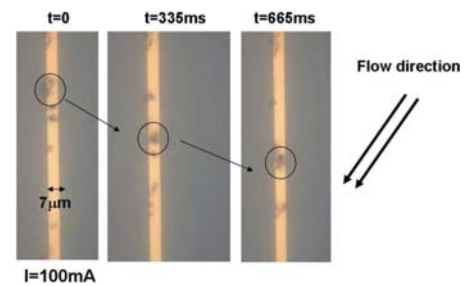

Figure 3: Time evolution of the 2μm particles position due to the fluid velocity and the magnetic field created by the current line (when applying 100mA) during the separation. These particles were moving over the line with a velocity around 75μm/s.

FF-01

Experimental realization of spin-wave logic gates.

A. A. Serga[1], T. Schneider[1], B. Leven[1], B. Hillebrands[1], M. P. Kostylev[2], R. L. Stamps[2]
1. Fachbereich Physik und Forschungsschwerpunkt MINAS, Technische Universität Kaiserslautern, Kaiserslautern, Germany; 2. School of Physics, University of Western Australia, Crawley, WA, Australia

We demonstrate the functionality of spin-wave logic gates and report on the first steps towards the implementation of all-spin-wave on-chip logic devices.
The proposed concept of a spin-wave (SW) logic gate is based on a Mach-Zehnder interferometer approach as it is shown in Fig.1-a. The gate mainly consists of a splitter that divides the power of the applied SW pulses into two channels (called the interferometer arms), two controllable phase shifters and switchers integrated into the arms, as well as a combiner where the signals modified in the arms interfere. Logical input signals are applied to the gates which vary either the phase or the amplitude of the spin waves in the interferometer arms. The logical output corresponds to the amplitude of the interference signal. By controlling the accumulated phase in one of the arms and keeping the phase at the output of the second arm constant one can implement a NOT gate [1]. The possibility to shift the phases in both arms by π allows the implementation of the XNOR operation [2]. With the additional ability to quickly manipulate the wave amplitudes using SW switches it is possible to create a NAND gate [2].
In our work the interferometer arms are realized as longitudinally magnetized SW waveguides made from a single-crystal yttrium-iron-garnet (YIG) film (Fig. 1-b). Travelling spin waves are excited and received by microstripe antennae. An additional microwave phase shifter is used for a preliminary adjustment of the SW phase difference Δϕ between the arms. The necessary phase or amplitude variations of the spin-wave pulses in the arms are produced due to dynamic inhomogeneities of the magnetizing field induced by dc current pulses through conductors placed near the film surface. We use the possibility to suppress the spin-wave transmission by applying a strongly localized Oersted field (stretched wires with currents I_1 and I_2 in Fig. 2-b) while the wave phase is controlled by the weakly localized Oersted field (the wire loops with currents I_3 and I_4 in Fig. 2-b). The functionality of the XNOR and NAND gate prototypes is demonstrated in Fig. 2-c, d. The structure is placed into a static magnetic field of 1885 Oe. SW packets are excited by microwave pulses of 20 ns duration with carrier frequency of 7.132 GHz.
In order to develop the on-chip SW logic gates a SW splitter and a combiner were fabricated by structuring the YIG film. The corresponding film structures have the shape of a fork and consist of two interferometer stripe-shaped arms (prongs of the fork) and a combiner/splitter part (handle).
Interference of SW pulses in the structures was visualized using time-, space- and phase-resolved Brillouin light scattering (BLS) spectroscopy. Figure 2 shows a representative example of a phase manipulation procedure in the SW combiner. As before the bias magnetic field of 1885 Oe is oriented along the arm length. The control current loop is placed in the middle of the lower arm.
The upper panels demonstrate snapshots of the pulses at different times when no current is applied to the loop. In-phase interference of the two lowest-order input SW width modes, which are characterized by a maximum of the SW intensity in the middle of the stripe width, results in the formation of a similar lowest-order mode in the output waveguide. The lower panels show snapshots of SW pulses, when the phases of the spin waves, which interfere in the combiner, differ by π due to the applied current pulse. In this case one sees two distinct maxima of SW intensity in the combiner. Such an intensity profile is characteristic for the second (anti-symmetric) width mode of a SW stripe waveguide.
Thus, depending on the applied current, the combiner output pulse is carried either by a symmetric or anti-symmetric width mode which can be attributed to a logical one or zero, respectively. The output signal can easily be read out by an optical BLS probe in the center of the output part of the waveguide or by using a microwave transducer to sum up the amplitude over the complete pulse (taking into account that the two maxima of the anti-symmetric mode are exactly out of phase). In the last case the logical one (symmetric mode) will lead to a high microwave output signal while the logical zero (anti-symmetric mode) will cause a near zero microwave signal.
This work has been supported by the Deutsche Forschungsgemeinschaft (Graduiertenkolleg 792), the Australian Research Council, and the European Community within the EU-project MAGLOG (FP6-510993).

1. M. P. Kostylev, A. A. Serga, T. Schneider, B. Leven, B. Hillebrands, Appl. Phys. Lett., vol. 87, 153501 (2005).

2. T. Schneider, A. A. Serga, B. Leven, B. Hillebrands, R. L. Stamps, and M. P. Kostylev, Appl. Phys. Lett., vol. 92 (in press).

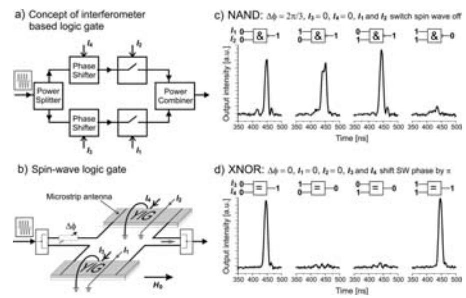

Design and functionality of SW logic gate prototypes.

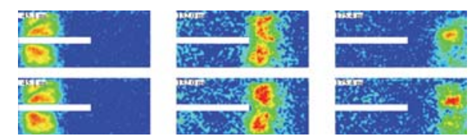

Intensities of SW pulses measured using BLS spectroscopy for different propagation times.

FF-02

Microwave signal processor based on spin waves in permalloy (Py) films.

G. A. Melkov[1], Y. V. Koblyanskiy[1], R. A. Slipec[1], A. V. Talalaevskij[1], *A. N. Slavin*[2]
1. Faculty of Radiophysics, Kiev National Taras Shevchenko University, Kiev, Ukraine; 2. Department of Physics, Oakland University, Rochester, MI

Most of the spin wave microwave devices existing today are based on the yttrium–iron garnet (YIG) films. Although YIG has a major advantage of a record-low ferromagnetic resonance (FMR) linewidth ($\Delta H \leq 0.5$ Oe), the practical applications of the YIG-based devices are limited due to relatively large magnitude of the bias magnetic field, low temperature stability, and relatively large size (several microns) of the elements of typical etch patterns in YIG. Most of these drawbacks can be eliminated by using metallic (e.g. permalloy (Py)) magnetic films. Unfortunately, the direct replacement of YIG by permalloy in standard passive spin wave delay lines [1] is not possible, because the spin wave propagation losses in permalloy (proportional to FMR linewidth $\Delta H \approx 25 \surd 50$ Oe) are almost 100 times larger than in YIG. Thus, the dipolar spin waves (or magnetostatic waves (MSW)) in permalloy have a very low mean free path (< 10 μm).

It is possible to overcome this difficulty by using the phenomenon of parametrically stimulated recovery of spin waves excited by the input microwave signal [2]. In this process the input antenna is, also, used for the reception of the output signal, and the delay time of the output signal is determined by the time when the pulse of external parametric pumping is supplied to the device.

The experimental investigations of the parametric interaction of the pumping pulse of the carrier frequency ω_p with the input microwave pulse of the carrier frequency $\omega_s = \omega_p/2$ in a permalloy (Py) film were performed on the experimental setup shown in Fig. 1. The Py film waveguide formed on the silica substrate had the dimensions 0.5 μm × 1.6 mm × 20 mm, and was placed in the opening inside the open dielectric resonator (ODR) made from a thermostable ceramics with dielectric constant $\varepsilon \approx 80$. The variable magnetic field of the ODR was parallel to the bias magnetic field $\boldsymbol{H}_0$, i.e. the case of parallel parametric pumping (see chapter 10 in [1]) was realized in our experiment. The wire antenna of the 50 μm diameter placed on the Py film was used for the excitation and reception of microwave spin waves. The spin waves excited by the input signal were propagating perpendicular to the direction of the bias magnetic field $\boldsymbol{H}_0$, and the velocities of the excited waves were in a wide range from $v \approx 0$, corresponding to slow and almost non-propagating volume MSW, to $v \sim 10^7$ cm/s, corresponding to the propagating surface MSW [2]. The slow spin waves, selectively amplified by pumping, practically did not move away from the antenna, and they formed the amplified output signal received at the antenna. We used the following parameters of pumping and signal pulses: $\omega_p/2\pi = 2\omega_s/2\pi = 9.4$ GHz, $\tau_p = 400$ ns, $\tau_s = 300 \surd 400$ ns, $P_p \leq 20$ dBW, $P_s = -27$ dBW.

When the pumping power was over 16 dBW, the delayed output signal of the duration of 100 ns, carrier frequency ω_s, and power $P_{out} \leq -50$ dBW was registered at the input antenna (see lower frame in Fig. 2). This signal was observed only if pumping was previously applied, and its delay time relative to the front of the input pulse was determined by the time at which the pumping pulse was supplied (T_p on Fig. 2).

Our experiments demonstrated that Py films can be used for the development of a microwave receiver which will allow us to perform controlled time delay with simultaneous time-compression of the input microwave pulses.

[1] A. G. Gurevich and G. A. Melkov, *Magnetization Oscillation and Waves* (CRC Press, N.Y., 1996).

[2] A. A. Serga *et al.*, Phys. Rev. Lett. **99**, 227202 (2007).

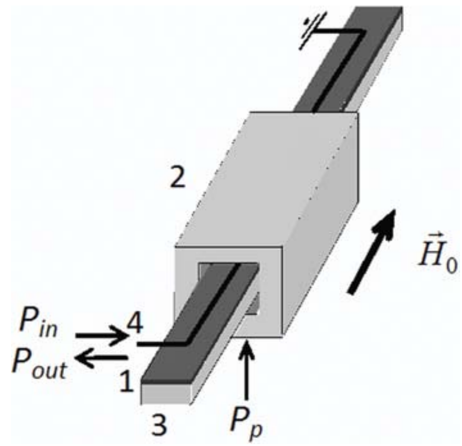

Microwave parametric signal processor based on a permalloy film: 1 – permalloy (Py) film, 2 – pumping dielectric resonator, 3 – substrate, 4 – wire antenna, P_p – power of pumping, P_{in} – power of the input signal, P_{out} – power of the output signal, H_0 – bias magnetic field.

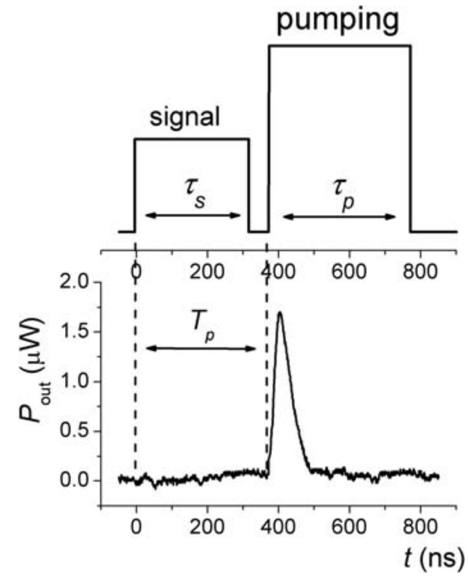

Lower frame: envelope of the output signal caused by parametrically-induced re-radiation from the Py film. Upper frame: relative temporal positions of the input signal pulse and pumping pulse.

FF-03

Design and optimization of one-dimensional YIG film based magnonic crystal.

A. Chumak[1,2], A. A. Serga[1], B. Hillebrands[1]
1. Fachbereich Physik und Forschungsschwerpunkt MINAS, Technische Universität Kaiserslautern, Kaiserslautern, Germany; 2. Department of Radiophysics, Taras Shevchenko National University of Kiev, Kiev, Ukraine

Artificial media with periodical variations of magnetic properties, so-called magnonic crystals are the magnetic analogue to photonic and sonic crystals which is suitable to work in the microwave frequency range. Spectra of spin-wave excitations in the magnonic crystals are significantly modified with respect to the uniform media and exhibit full band gaps, where spin waves are not allowed to propagate. Due to wide tunability of their characteristics magnonic crystals present excellent capability for the investigation of linear and nonlinear spin-wave dynamics. They are also promising for applications as microwave filters, switches, phase shifters, etc.
Here we present a one-dimensional magnonic crystal created by chemical etching of a surface of a single-crystal yttrium iron garnet (YIG) ferrite film. We have chosen this magnetic media because of its extremely small magnetic relaxation permitting a spin-wave path of a centimeter length. The periodic changes of the film thickness cause the variation of the spin-wave dispersion and crystal properties as well. It is obvious that stronger thickness changes result in more pronounced alteration of spin-wave propagation. However this dependence has not been covered in the literature yet. Thus we focused our efforts on experimental study of crystal characteristics as a function of the depth of the artificial periodic structure.
Photolithography and chemical etching with hot (115°C) O-Phosphoric acid were used for the YIG film structuring. The typical structure geometry is schematically shown in Fig.1. The crystal consists of 10 parallel grooves, which are perpendicularly oriented with respect to the spin wave propagation direction. The film thickness is 6 μm. The grooves width is 30 μm and the lattice constant Δ_c is 300 μm taking into account 270 μm distance between the grooves. In order to study the dependence of crystal characteristics on the groove depth the grooves were etched in 100 nm steps from 100 nm to 1.5 μm.
Two microstripe antennae placed (Fig. 1) 8 mm apart each other on each side of the magnonic crystal area were used to excite and receive the dipolar spin waves. A bias magnetic field of 1812 Oe was applied in the plane of the YIG film stripe, along its length and parallel to the direction of spin-wave propagation. Thus the geometry of backward volume magnetostatic wave (BVMSW) was realized. The measurements were performed in the frequency range 6800-7200 MHz. The typical experimental BVMSW transmission characteristic for the non-etched film is shown by the solid line in the Fig. 2. The spin-wave transmission through a magnonic crystal of depth of 300 nm is indicated by the dashed line. Spectrum rejection bands are clearly visible in this case. Their central frequencies were estimated using the simple condition $2\Delta_c = n\lambda$, where n is a number of the rejection band. The frequency values 7060 MHz, 7010 MHz, and 6960 MHz calculated for n = 1, 2 and 3 are in good agreements with experimental data.
The increasing of the groove depth up to 500 nm causes the pronounced widening and deepening of the rejection bands (dash-dotted line in Fig. 2). The further etching beyond 500 nm additionally decreases the transmission between the rejection bands. The structure of 1.5 μm depth does not allow any spin-wave transmission. This behavior can be explained by an increase of the interaction of a so-called "pure" magnonic crystal namely groove structure on the YIG film surface with the underlaying uniform magnetic film.

The experimental dependences of the SW rejection (in the rejection bands) and transmission (in the transmission bands) on the grooves depth are shown in Fig. 3. In addition the rejection to transmission ratio is presented. It is shown that the maximum ratio value is reached for a depth of 500 to 600 nm.
In conclusion, a one-dimensional linear magnonic crystal was designed and tested. The microwave transmission spectra were measured for different crystal geometrical parameters and, in particular, for different depth of the grooves. It was found that the rejection band width and deepness as well as the out-of-band transmission loss increase with increasing of the groove depth. The optimal groove depth has been determined.

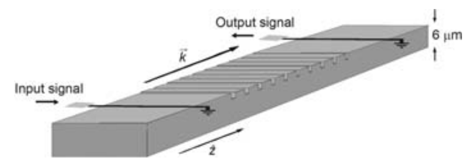

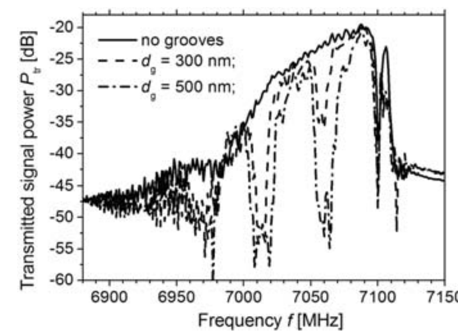

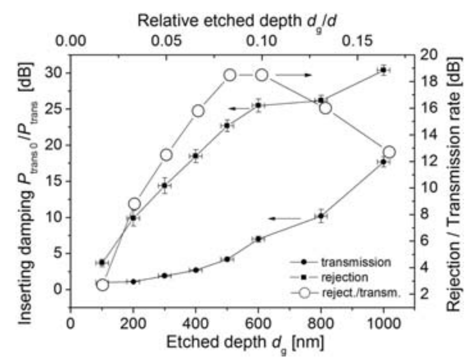

FF-04

Experimental Verification of Skin Effect Suppression in Multilayer Thin-Film Conductor Taking Advantage of Negative Permeability of Magnetic Film beyond FMR frequency.

S. Shiozawa[1], Y. Shimada[1], *M. Yamaguchi*[1], K. Kim[2], Y. Zhuang[3], M. Vroubel[3], B. Rejaei[3]
1. Electrical and Communication Engineering, Tohoku University, Sendai, Japan; 2. Physics, Yeungnam University, Gyeongsan, South Korea; 3. Electronic Components, Technology, and Materials, Delft University of Technology, Delft, Netherlands

Background: It has been a major concern of high frequency devices and circuits to suppress skin effect and the corresponding ac resistance increase in high-frequency-current carrying conductors for transmission lines, integrated inductors, antennas, etc, in order to realize high-Q and energy-saving systems. This paper demonstrates first experimental verification of skin effect suppression taking advantage of negative permeability of soft magnetic film obtained beyond FMR frequency range.

Idea: It is known that the skin effect is noticeable as the skin depth, δ, becomes thinner than the half thickness, t/2, of the conductor.

$\delta=(\rho/\pi f\mu_0\mu_r)^{-1/2}$ … (1)

where f is the frequency, ρ the resistivity, and μ_r is the relative permeability. Accordingly the ac resistance of a conductor with width w and length L is approximately expressed as;

$R_{ac}=\rho L /(2w\delta)$…(2).

Some of the authors theoretically claimed in [1] that the skin effect could be avoided in an alternate multilayered structure of metal/magnetic thin films shown in Fig. 1, provided that the magnetic layer has negative permeability and the volume average of relative permeability, μ_{rav}, becomes zero. The μ_{rav} is given by;

$\mu_{rav}= (1t_N + \mu_r t_F)/(t_N+t_F)$ …(3)

where t_N and t_F are the thickness of each metallic and ferromagnetic layer, respectively. It is possible to let $\mu=\mu_{rav}=0$ in eq. (1) if the magnetic material has negative permeability. Then the skin depth becomes infinitely deep. Such a condition should be realized by using a uniaxial magnetic film exhibiting negative permeability beyond the FMR frequency.

Experiments: The 0.3 μm-thick Al film and the 0.1 μm-thick zero-magnetostrictive NiFe film were sputter-deposited in turn to the total thickness of 6 μm on a Glass wafer. A 13 μm-thick Cu metal mask was used for ion milling process to complete the coplanar line as shown in Fig. 2. The signal line is 1000 μm long and 36 μm wide. The signal-to-ground gap is 11 μm. Because of the difficulty of the etching process, the characteristic impedance became 54.8 Ω, deviated a bit from the designed value of 50Ω. The bends on the ends of the line are to apply wafer probes from the top left and the bottom right directions to measure high frequency properties. For the NiFe layer, $4\pi M_s$= 10.0 kG, H_k=10 Oe (nominally, before microfabrication) and ρ=16.7 μΩcm. Easy axis direction is along the length direction of the coplanar line.Since the thickness of the metal and the magnetic films are t_N=0.3 μm and t_F=0.1 μm, respectively, the eq. (3) and the required condition of μ_{rav}=0 need the relative permeability to be μ_r=-3 for the NiFe film, which should be satisfied at (i)closely to the FMR frequency of 0.9 GHz, and (ii)6.0 GHz, as calculated from the L.L.G. equation using the materials' M_s, H_k, and the supposed damping constant of α=0.10. External large dc magnetic field, H_{ex}=0~5000 Oe, was applied to the easy axis direction to examine the ferromagnetic nature of the multilayer. This is also useful for the analysis since the effective anisotropy field becomes 10+H_{ex} Oe and accordingly the uncertainties in H_k and α will not matter seriously. Known π-type equivalent circuit analysis was used to extract the series resistance of the line.

Results and Discussion: Fig. 3 shows the frequency dependence of the measured resistance of the multilayer coplanar line. Without the external field, the resistance increases with frequency up to 3 GHz. This means the resistance does not become small at the FMR frequency of 0.9 GHz because of huge FMR losses. At higher frequency range, the resistance turns over to decrease from the top level of 3.2 Ω at 13 GHz to the bottom level of 1.9 Ω at 16.5 GHz. The existence of a frequency range where resistance monotonically decreases is the first experimental verification of the skin effect suppression. This never happens in the case of normal metal. The half-level frequency can be defined as the frequency where the resistance becomes the average of the top and the bottom levels. This parameter is used as a representative of the skin effect suppression hereafter. The half-level frequency is linearly to the applied external field and accordingly the FMR frequency, as summarized in Fig. 4. On the other hand, the half-level frequency can be obtained through eq. (1) and (2), after given the frequency profile of complex permeability from L.L.G equation. The calculated value rather agrees well under the strong external field where the uncertainties in H_k and α would not matter seriously. This is the verification of the skin effect suppression by negative permeability of magnetic material. It is quite interesting that the calculation predicts that the ac resistance can be smaller than that of all-metal conductor of the same thickness.

(1)Behzad Rejaei, and Marina Vroubel: "Suppression of skin effect in metal/ferromagnet superlattice conductors," JOURNAL OF APPLIED PHYSICS, **96**, (2004), 6863-6868.

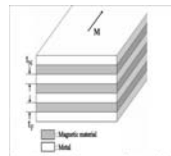

Fig. 1 Metal/ferromagnetic multilayer

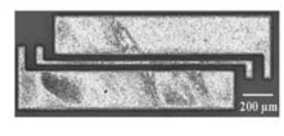

Fig. 2 Completed multilayer thin-film coplanar line

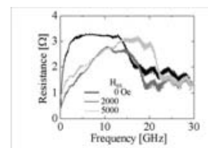

Fig. 3 Measured resistance of the multilayer thin-film coplanar line

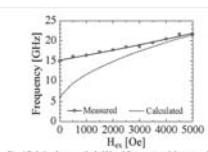

Fig. 4 Relation between the half-level frequency and the external field.

FF-05

Selective excitation and imaging of precessional modes in soft-magnetic squares.

A. Neudert[1], P. S. Keatley[1], V. V. Kruglyak[1], J. McCord[2], R. J. Hicken[1]
1. School of Physics, University of Exeter, Exeter, United Kingdom; 2. Institute for Metallic Materials, IFW Dresden, Dresden, Germany

The high frequency (hf) properties of soft magnetic thin film elements are essential to the operation of a variety of rf devices and magnetic field sensors [1]. The response of the magnetization to hf magnetic fields should normally be fast and homogeneous if optimum device performance is to be achieved. However patterning modifies the effective magnetic field within an element and determines the spectrum of dynamical modes that may be excited. This mode spectrum must therefore be characterized and fully understood if the hf magnetic response is to be controlled. We report on how time-resolved scanning Kerr microscopy has been used to understand the precessional mode spectrum of $Fe_{70}Co_8B_{12}Si_{10}$ square elements.
The film was magnetron sputtered onto a glass substrate and structured by ion beam etching. The sample consisted of squares of $Fe_{70}Co_8B_{12}Si_{10}$ of 40 µm width and thickness of 160 nm arranged into a square lattice with 10 µm edge-to-edge separation. Sample deposition was performed in a magnetic field so as to induce a uniaxial magnetic anisotropy parallel to one of the edges of the squares. Measurements of the hf dynamics were performed with a microscope (Fig. 1) that is able to measure all three components of the magnetization vector simultaneously. The magnetization was excited by the hf magnetic fields generated around the 80 µm center conductor of a coplanar waveguide fed with pulsed or sinusoidal current waveforms from a pulse or microwave generator. The pulse and microwave generators were phase locked to the laser so that stroboscopic imaging could be performed. The sample was placed face down on the waveguide with the laser spot focussed on the square element through the glass substrate. A polarizing beamsplitter and quadrant photodiodes were used to detect all three magnetization components simultaneously [2].
With a static magnetic field of 500 Oe applied parallel to the easy axis, pulsed field experiments revealed resonant modes with frequencies of 8.0 and 9.2 GHz. The spatial character of these modes was determined by applying a sinusoidal field with frequency equal to that of the desired mode and scanning the laser spot over the whole square. Images corresponding to different points in the cycle of oscillation are shown in Fig. 2. A time delay of 0 ps was assigned to the image showing maximum contrast at the center of the element. The mode at 8.0 GHz shows a phase difference between the excitation in the central part of the element and the dynamic magnetization closer to the vertical edges. This is reminiscent of the beating of a uniform mode with a backward volume type mode. The image of the 9.2 GHz mode shows a different pattern of contrast with a maximum in the center of the element and two regions closer to the horizontal edges where the dynamic magnetization is shifted in phase with respect to the center. The effective wave vector of this mode therefore lies perpendicular to the static magnetization, which is similar to the Damon Eshbach mode found in continuous films [3].
The finite effective wave vector gives rise to an associated frequency shift. The shift associated with the wave vector perpendicular to the magnetization is much larger than that due to the wave vector component parallel to the magnetization, which is not resolved within the experiment. The field dependence of the peaks was analyzed using the formula for the frequency of the Damon Eshbach mode,
$2\pi f=\gamma[H(H+M_s)+(2\pi M_s)^2(1-e^{(-2kd)})]^{1/2}$
with applied field H, saturation magnetization Ms, frequency f, gyromagnetic ratio γ, thickness d, and wave vector k depending on the mode number n as $k=n\pi/w$. The 8.0 GHz mode corresponds to the n=1 mode while the 9.2 GHz mode corresponds to the case n=3.
We will show how the resonant precessional modes of planar magnetic elements may be detected and then characterized. This information is important in understanding the response of the magnetization to magnetic fields of different temporal form.

[1]: Yamaguchi et al., JAP 85 (1999) p.7919
[2]: P.S. Keatley et al., JMMM 306 (2006) p.298
[3]: R.W. Damon and J.R. Eshbach, J. Phys. Chem. Solids, 19 (1961) p.308

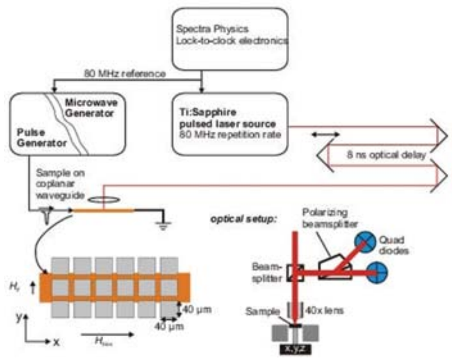

Fig.1: Sketch of the experimental setup

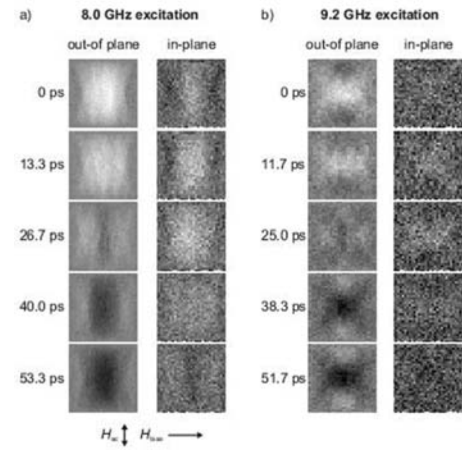

Fig.2: Images of the magnetization components of the 8.0 and 9.2 GHz modes at different points in the cycle of oscillation. The in-plane component perpendicular to the static field is shown.

FF-06

Electrically detected ferromagnetic resonance in electrodeposited spin valves under AC excitation.

N. Biziere, E. Murè, J. Ansermet
Institut de Physique des nanostructures, Ecole Polytechnique Federale de Lausanne, Lausanne, Switzerland

Abstract: We report on experimental evidence of DC voltage effects induced in a pseudo spin valve by an AC electrical excitation in the microwave range. Two Pseudo spin valve connecting in series were produced by electrodeposition in a polycarbonate membrane. We offer an original set up that allows broadband measurements of nanometric magnetic multilayers without using classical lithography techniques. Results are discussed in terms of AC spin torque and non linear mixing of magnetoresistance and electromagnetic excitations.

It has been demonstrated than a spin polarized current could influence the magnetic properties of magnetic multilayers. This effect known as the Spin Transfer Torque (STT) [1,2] opens new applications in domains of ultrafast switching or microwave generators [3,4] and has been studied mainly in the case of a DC injected current. However, the question of STT in the case of an AC current is to our knowledge rarely discussed, especially from the experimental point of view [5,6].

In this work we show that a pseudo spin valve submitted to a microwave electrical excitation of frequency ω generates a DC and a 2ω signals. The system studied is a nanowire composed of Co(30 nm)/Cu(5 nm)/Co(5 nm)/Cu(1 μm)/ Co(30 nm)/Cu(5 nm)/Co(10 nm) electrodeposited from a single cobalt/copper bath in a 6 μm thick polycarbonate membrane. On one side of the membrane a gold cap is sputtered on the whole surface allowing electrical contact to a pin placed in a SMA connector. Then the connector is closed by a cap in which a 25 μm diameter gold wire is weld to a screw. The latter permits to contact the other end of the gold wire to one (or few) magnetic nanowire. This simple technique offers a very attractive alternative to transmission waveguides since it avoids lithography process and many nanowires are accessible in one membrane.

The Giant Magneto Resistance (GMR) curve presented on figure1 shows the switching of each pseudo spin valve. The geometry insures CPP configuration and the external field is perpendicular to the current. When an AC current is injected in the nanowire we observe at the same time a variation of the DC and of the 2ω voltages (fig. 2) when ω reaches the FMR frequency. The very good sensitivity of electrical transport measurement offers the possibility to follow the evolution of the shape and frequency of the signals as function of the external field (fig. 3) and so the relative orientation of magnetic layers.

We will interpret these results from two different approaches. First we will consider the effect of AC STT predicted theoretically [7]. Second we will discuss the interplay between the magnetoresistance with the electromagnetic field created by the electric excitation [8,9]. Then we will show the similarity between both approaches.

1 J. Slonczewski, Journal of Magnetism and Magnetic Material, 159, 1996 L1.

2 L. Berger, Physical Review B 54, 9353, 1996.

3 J. A. Katine, F. J. Albert, and R. A. Buhrman, Physical Review Letters, 84, 3149, 2000

4 S. I. Kiselev et al, Nature, 425, 380, 2003.

5 J. C. Sankey et al., Physical Review Letters, 96, 227601, 2006.

6 A.A. Tulapurkar et al., Nature 438, 04207, 2005.

7 A. Kovalev et al., Physical Review B, 75, 014430, 2007.

8 N. Biziere et al, Journal Of Magnetism and Magnetic Materials 316, 340, 2007.

9 W.G. Egan and H.J. Juretschke, Journal of Applied Physics 34, 1477, 1963.

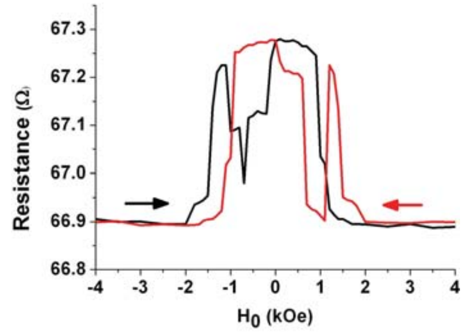

DC Resistance of the pseudo spin valve as function of the external field. Arrows represents the field sweep direction. The field is applied perpendicular to the nanowire axis.

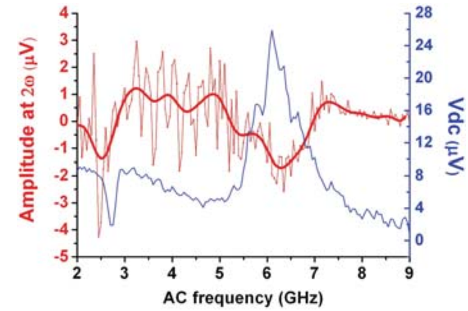

(blue line) DC voltage as function of the AC excitation frequency for zero applied field. (red line) Raw data of the 2ω signal as a function of the AC excitation and smoothed data (bold red line) as a guide for the eyes. We observe some features where a DC signal is detected.

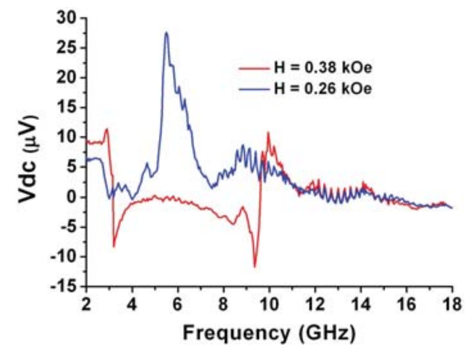

Evolution of the DC voltage as function of the AC excitation for an external field of 0.26 Koe (blue) and 0.38 kOe (red)

Ferromagnetic resonance modes below the critical thickness of stripe domain formation.

J. McCord[1], A. Gerber[2], E. Quandt[2]
1. Institute for Metallic Materials, IFW Dresden, Dresden, Germany; 2. Institute for Inorganic Functional Materials, CAU Kiel, Kiel, Germany

The understanding of high frequency precessional modes in low anisotropy soft magnetic thin films is of vital interest from a fundamental point of view for applications based on magneto-dynamics. In patterned samples low and high frequency modes, which result from magnetic vortices or domains, have been investigated in detail. Another class of soft magnetic materials, exhibiting multiple precessional modes are soft magnetic thin films with perpendicular magnetic anisotropy, possessing stripe domains.

The development of the high frequency precession modes in Permalloy $Ni_{81}Fe_{19}$ (NiFe) thin films with uniaxial in-plane and additional out-of-plane magnetic anisotropy component was investigated. As will be shown, signatures of out-of-plane anisotropy can be observed well below the critical thickness of stripe-domain formation.

NiFe films varying in thickness from 100 nm to 400 nm were deposited by rf sputtering in argon atmosphere onto oxidized silicon substrates. A magnetic field was applied to introduce an in-plane magnetic anisotropy. The static and dynamic film properties were investigated by regular quasi-static and pulsed microwave magnetometry.

Two exemplary hysteresis loops of the films are displayed in Fig. 1a. For small thicknesses regular square easy axis loops and above a critical thickness loop shapes typical for stripe domains are observed. From the dependence of the remanence ratio J_r/J_s as well as of the coercivity H_c the onset of occurrence of stripe domains at approx. t_{NiFe} = 250 nm can be deduced (Fig. 1b). The normalized permeability |µ| spectra is displayed in Fig. 2. A bias field of H_{ext} = 10 Oe is applied to eliminate additional effects from magnetic in-plane domains. For the thick films a bi-modal frequency response is found, which correlates with the films' internal out-of-plane domain structure. Yet, for t_{NiFe} < 250 nm, where no signatures of out-of-plane magnetization could be extracted from the static measurement, secondary precessional modes are excited. The dependence of f_{res} and the relative amplitude of the two dominating modes are displayed in Fig. 3. The dominating low frequency mode, which is related to the uniaxial anisotropy of the NiFe film, displays only a small change at the onset of stripe domain formation. The contribution of the high frequency mode, connected with the out-of-plane magnetization structure, continuously increases with increasing t_{NiFe}. No discontinuity, as for the static magnetic properties, is found in the modal spectra.

In summary, it is shown that different precessional modes of f_{res} can be activated by the existence of an even small magnetic out-of-plane anisotropy. An occurrence of static out-of-plane domains is not necessary for the bi-modal frequency response. Additional results from magnetic domain observations and a discussion of changes of overall high frequency permeability with stripe domain nucleation will be presented.

Funding by the Ministry of Education and Research (BMBF) through the project "MIMAK" is highly acknowledged.

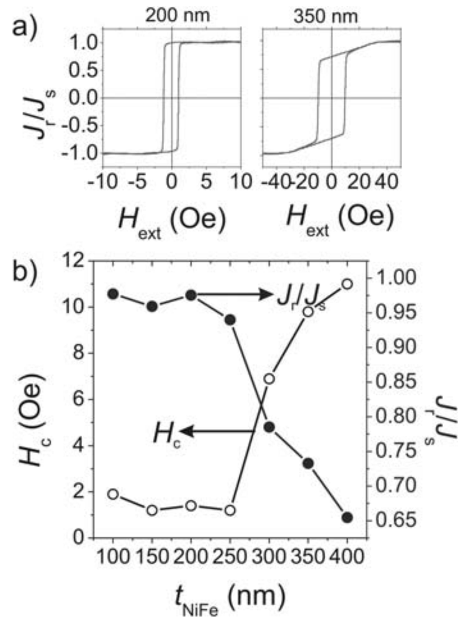

Fig. 1. (a) Easy axis hysteresis loops for NiFe films with different thicknesses (as indicated). (b) Remanence ratio J_r/J_s and easy axis coercivity H_c vs. NiFe thickness t_{NiFe}.

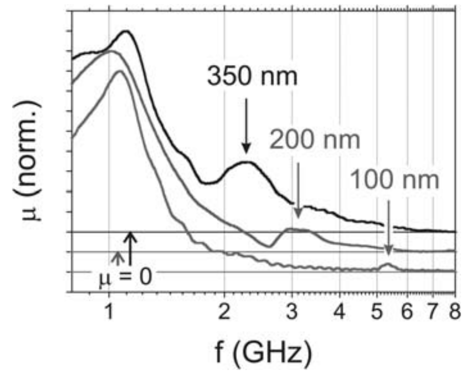

Fig. 2. (a) Normalized frequency spectra of amplitude of permeability µ for three different thicknesses t_{NiFe}.

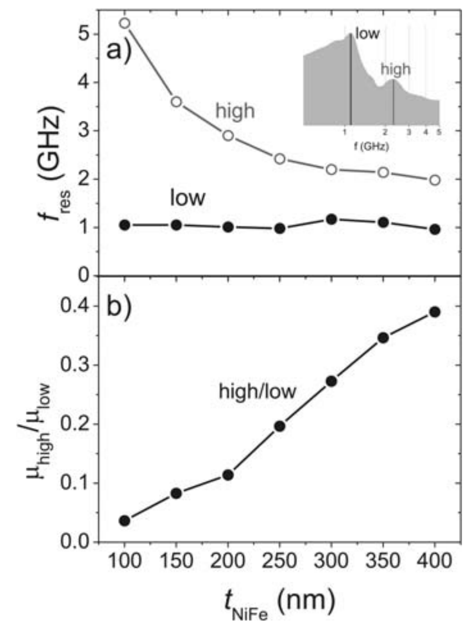

Fig. 3. (a) Precessional frequency f_{res} of the low and high frequency modes vs. t_{NiFe}. (c) Ratio μ_{high}/μ_{low} of the high frequency permeability mode relative to the low frequency mode.

FF-08

Ferromagnetic resonance study of Fe/FePt coupled films with perpendicular anisotropy.

D. Schmool[1], A. Apolinário[1], F. Casoli[2], F. Albertini[2]
1. Physics, Universidade do Porto, Porto, Portugal; 2. IMEM, CNR, Parma, Italy

Exchange spring magnets with perpendicular magnetic anisotropy represent new magnetic properties with respect to their constituent components. These systems typically consist of a hard magnetic layer and a soft magnetic layer which are strongly coupled. The modification of their bulk magnetic properties arises from this strong ferromagnetic exchange coupling, interfacial effects and competing magnetic anisotropies of the two magnetic layers.

We have studied the magnetic bilayer system which consists of an Fe (soft) film exchange coupled to an FePt (hard) layer which has an easy axis aligned along the direction perpendicular to the film plane. The entire structure has the form: MgO/FePt (10 nm)/Fe (2nm or 3.5nm)/ Ag (2nm), where the Ag overlayer acts as protection against oxidation. The epitaxial FePt layers were deposited on MgO (100) substrates using the RF sputtering technique at a substrate temperature of about 390 C. The epitaxy of this layer was studied using x-ray and electron diffraction techniques. Layer morphologies were further studied using atomic force microscopy (AFM), these studies reveal a granular morphology with grain sizes of the order of 40 – 50 nm.

We have made detailed angular measurements using the ferromagnetic resonance (FMR) at room temperature. This angular FMR study, which includes the orientations of in-plane and out-of-plane, was performed in order to study the magnetic anisotropies as well as the exchange coupling between the magnetic layers and interfacial effects. In particular, we have chosen to study two samples with 2 nm and 3.5 nm of Fe, which effectively constitute the rigid magnet (RM) and exchange spring (ES) regimes, respectively. The RM and ES regimes depend implicitly on the magnetic anositropies and properties of the two coupled layers [1].

In figure 1 (a) we show an example of an FMR spectrum for the RM (2 nm Fe) sample. Of the various resonances observed, only the three low field lines are due to the Fe layer. It will be noted that the FePt does not have any FMR signature in the field range studied due to it very high magnetocrystalline anisotropy. The other resonance features evident in the spectrum arise from the MgO substrate and show no significant angular variations. As such the only FMR signals observed in our samples will arise from the Fe layer. In figure 1 (b) we show the angular variation of the resonance field of the three Fe resonance lines. Of these, two resonances display a uniaxial anisotropy with the easy axes aligned along the direction perpendicular to the film plane and will be directly related to the exchange coupling with the hard (FePt) layer. The third resonance, while also manifesting a uniaxial anisotropy, displays an easy axis direction which is canted by about 50 degrees from the film normal. While the origin of this resonance is not entirely clear, we suspect it may arise from the interfacial region between the FePt and Fe layers. In figure 2 we show the corresponding FMR results for the ES (3.5 nm Fe) sample. It will be noted that in addition to the resonances observed in the RM sample, there are a further two resonance, whose angular dependences are illustrated in figure 2 (b). These also display a uniaxial like behaviour with easy axes close to the film normal. In all spectra lines were fit using a home made programme which allows multiple peak fitting of Lorentzian and Gaussian lines.

We develop a model of FMR based on the magnetic free energy of the coupled layers which is required to interpret the angular dependences of the resonance fields [1]. Existing models fall short of a full explanation of all the resonance lines and we are working to bridge this gap by considering the effects of boundary conditions and spin wave modes.

[1] G. Asti et al., Phys. Rev. B, 73, 094406 (2006)

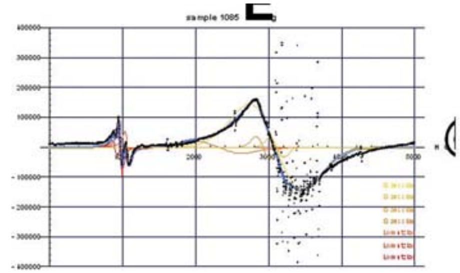

FMR spectrum of the RM sample, C, D and E indicate the three FMR resonances.

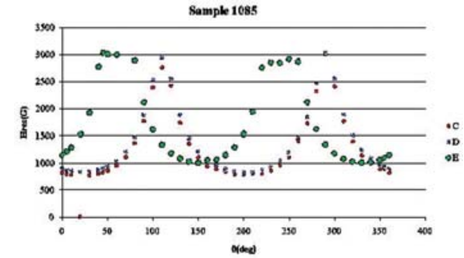

Angular dependences of the three FMR lines

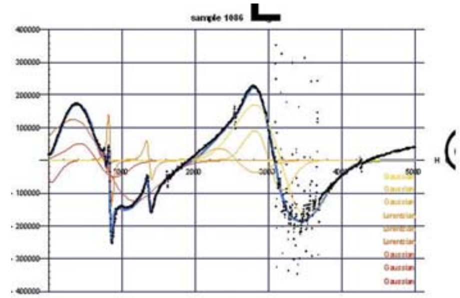

FMR spectrum of the ES sample

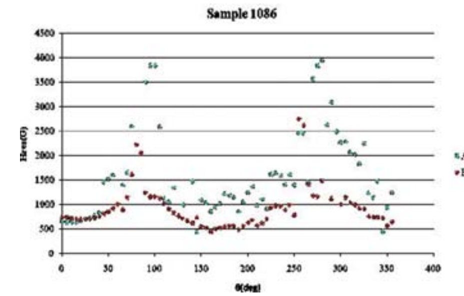

Angular dependences of the additional resonances (A and B)

FG-01

Inter-phase exchange coupling in $Sm(Co,Cu)_5$/α-Fe nanocomposite obtained by mechanical milling and annealing.

V. Pop[1,2], O. Isnard[2], D. Givord[2], I. Chicinas[3]

1. Faculty of Physics, Babes-Bolyai University, 400084 Cluj-Napoca, Romania, Cluj-Napoca, Romania; 2. Institut Néel, CNRS, associé à l'Université Joseph Fourier de Grenoble, BP166, 38042 Grenoble, Cedex 9, France, Grenoble, France; 3. Materials Sciences and Technology Dept., Technical University of Cluj-Napoca, 103-105 Muncii ave., 400641 Cluj-Napoca, Romania, Cluj-Napoca, Romania

Nanocomposites exchange-enhanced magnetic materials have a substantial potential for permanent magnets applications [1, 2]. It has been demonstrated [3-5] that the crystallite size of both phases, in particular, the soft one, is important in determining remanence enhancement and coercivity. Mechanical alloying/milling has been extensively applied to synthesize various metastable phases exhibiting exciting magnetic properties including spring magnets [6 -12]. The influence of the milling and annealing conditions on the magnetic inter-phase coupling of mechanically-milled rare-earth hard magnetic phase and α-Fe soft phase will be presented. Two hard magnetic phases were used: $SmCo_5$ and $SmCo_3Cu_2$. As soft magnetic phase was utilised α-Fe in 20 or 30 wt%. This study will be based on the hysteresis curves and dM/dH versus H curves.

The hard/soft magnetic nanocomposites were obtained by co-milling of the iron and hard magnetic phase powders in required proportion for different milling times. In order to investigate the influence of the annealing on the composite structure and microstructure, milled powder samples were annealed in evacuated silica tubes. More experimental details are described elsewhere [8-12].

The structure and the microstructure of samples were checked by X-ray diffraction and electron microscopy [8-12]. The as milled samples present very low coercivity and remanence. This behaviour could be connected with the damaged structure obtained after milling, as shown by X-ray diffraction. The coercivity and the remanence highly increase with the heat treatment compared to the as milled samples. The hysteresis curves are given in figure 1 for the samples milled for 8 hours and subsequently annealed. The coercivity and the remanence are increased by more than a factor of 10 and 4 respectively for samples milled up to 8 hours. For the long time milled samples the effect of the annealing is much more important on to structural refinement and magnetic properties. For optimal annealing conditions, the magnetization variation along the hysteresis cycle is smooth testifying for good exchange coupling between hard and soft magnetic phases. Optimum values were obtained for a heat treatment at temperatures between 550 °C and 600 °C for 1.5 h. It results that the annealing temperature is more important than the annealing time in the progressive improvement of the microstructure and optimisation of the inter-phase exchange coupling. Additionally to the hysteresis loops, the evolution of the coupling between the hard and the soft magnetic phases could be very well studied from the dM/dH versus H curves, figure 2. For example in this figure the increasing of the coercivity by appropriate annealing is well illustrated. For higher annealing temperature, as consequence of the recrystallization and increasing of the crystallite sizes, a decoupling between the hard and the soft magnetic phases could be evidenced by the presence of a characteristic peak at low field for uncoupled soft iron phase, figure 2. The drastic reduction of both the coercivity and the remanence of $SmCo_3Cu_2$/α-Fe composite can be mainly attributed to the deterioration of the microstructure of the $SmCo_3Cu_2$ hard phase during the milling.

1. R. Skomski, J. M. D. Coey, Phys. Rev. B 48, 15812 (1993)

2. T. Lieneweber, H. Kronmuller J. Magn. Magn. Mater. 176, 145 (1997)

3. E. F. Kneller and R. Hawig, IEEE Trans. Magn. 27, 3588 (1991).

4. T. Schrefl, J. Fidler, and H. Kronmüller, Phys. Rev. B 49, 6100 (1994).

5. W. F. Miao, J. Ding, P. G. McCormick, and R. Street, J. Appl. Phys. 79, 2079 (1996).

6. O. Gutfleisch, A. Bollero, A. Handstein, D. Hinz, A. Kirchner, A. Yan, K.H. Muller, L. Schultz, J. Magn. Magn. Mater. 242-245, 1277 (2002).

7. R. Grossinger and Reiko Sato,, J. Magn. Magn. Mater. 294, 91 (2005).

8. V. Pop, O. Isnard, I. Chicinas, D. Givord, J.M. Le Breton, J. Optoelectron. Adv. Mater., 8, 494 (2006)

9. V. Pop, O. Isnard, I. Chicinas, D. Givord, J. Magn. Magn. Mater. 310, 2489 (2007).

10. V. Pop, I. Chicinas, J. Optoelectron. Adv. Mater 9, 1478 (2007).

11. D.Givord, O. Isnard, V. Pop, I. Chicinas, J. Magn. Magn. Mater. 316, e503 (2007).

12. E. Dorolti, V. Pop, O. Isnard, D. Givord, I. Chicinas, J. Optoelectron. Adv. Mater. 9, 1474 (2007).

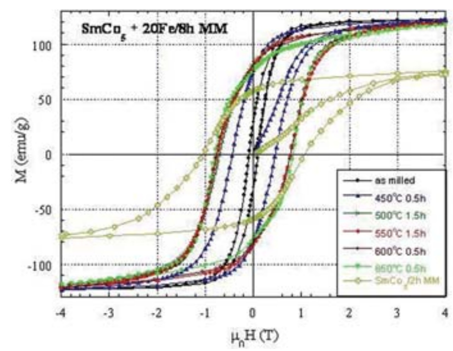

Figure 1. Hysteresis cycles for the $SmCo_5$ +20% Fe nanocomposites milled from 8 h and annealed compared to that of the SmCo5 hard phase milled for 2h.

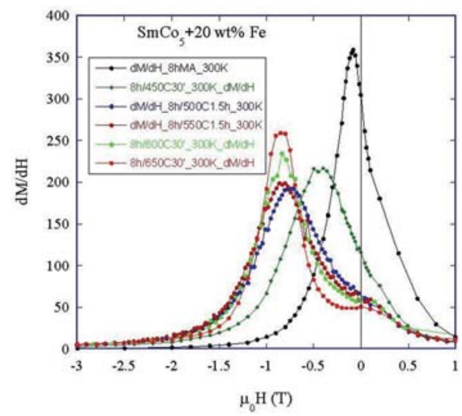

Figure 2. dM/dH versus H curves for the $SmCo_5$ +20% Fe nanocomposites milled from 8 h and annealed.

FG-02

Isotropic $Sm_x(Co,Fe,Mn)_{100-x}$ Magnets Via High-Energy Ball Milling.

A. Gabay[1], J. Liu[2], G. C. Hadjipanayis[1]
1. University of Delaware, Newark, DE; 2. Electron Energy Corporation, Landisville, PA

Mechanical alloying (or intensive milling) of Sm-Co-(Fe) alloys followed by devitrification annealing forms a uniform nanocrystalline structure leading to excellent isotropic hard magnetic properties [1-3]. The largest values of the maximum energy product $(BH)_{max}$ are typically observed in the $Sm_x(Co_{1-y}Fe_y)_{100-x}$ alloys with x = 12 - 13 and y = 0.2 - 0.3 [3-5]. This composition range corresponds to either the equilibrium mixture of 2:17 and 1:5 phases or the metastable "1:7" structure whose actual composition may vary from 1:5 to 2:17. The largest magnetization [and therefore the largest theoretical $(BH)_{max}$] should be expected, however, for the 2:17 phase and especially for exchange coupled nanocomposites of the hard 2:17 and soft Co-Fe phases. Unfortunately, the coercivity values exhibited even by the stoichiometric Sm_2Co_{17} and especially the $Sm_2(Co,Fe)_{17}$ alloys are relatively low. It has been shown a long time ago that the combined substitution of Fe and Mn for Co may increase considerably both the anisotropy field and saturation magnetization of the Sm_2Co_{17} phase [6]. An additional advantage of the Mn substitution, unlike the very popular Zr substitution, is that it does not shift the composition of the alloy towards the 1:5 stoichiometry (the Zr atoms occupy the Sm sites). In this work, we investigate this little explored substitution scheme in high-energy ball-milled (HEBM) alloys with a broad range of Sm concentrations (9 to 16.7 at.%). The combined Fe and Mn substitution for Co in the near-stoichiometric $Sm_{2.1}Co_{17}$ alloy markedly increases all the hard magnetic properties in the HEBM alloys annealed for 30 min at 600 - 800 °C (Fig. 1); in particular, the highest $(BH)_{max}$ increases from 11.6 to 16 MGOe. However, our attempts to introduce a soft magnetic phase by decreasing the Sm content below the 2:17 stoichiometry led to a decline of $(BH)_{max}$. Poor rectangularity of the hysteresis loops indicates an insufficient magnetic coupling within the composite magnet.

For Sm contents greater than that of the 2:17 phase, the results of the combined Mn and Fe substitution were always within the reach of the different substitution of Fe alone. For instance, very similar hard magnetic properties were obtained in the $Sm_{13}(Co_{0.7}Fe_{0.25}Mn_{0.05})_{87}$ and $Sm_{13}(Co_{0.8}Fe_{0.2})_{87}$ alloys. Like in the earlier studies [3], the latter composition exhibited the largest $(BH)_{max}$ of all (17 MGOe with the coercivity of 10.5 kOe). However, the $(BH)_{max}$ of this alloy rapidly deteriorates when annealed above 650 °C (Fig. 2), apparently because of a transformation of its single 1:7 structure into the equilibrium mixture of the 2:17 and 1:5 phases. This poor temperature stability may complicate fabrication of fully dense magnets via hot pressing. The $Sm_{11}(Co,Fe,Mn)_{89}$ alloy (open circles in Fig. 2) which is practically a stoichiometric 2:17 does not have this disadvantage: it exhibits a $(BH)_{max}$ of 15.5 - 16 MGOe when annealed at 700 - 750 °C. Thus, the (Fe,Mn)-substituted 2:17 alloys may present a particular interest for fabrication of isotropic hot-pressed magnets.

This work was supported by Air Force through STTR contract FA9550-07-C-0029.

[1] J. Wecker, M. Katter, L. Schultz, J. Appl. Phys. 69, 6058 (1991).

[2] J. Ding, P.G. McCormick, R. Street, J. Alloys Comp. 191, 197 (1993).

[3] J. Ding, P.G. McCormick, R. Street, J. Magn. Magn. Mater. 135, 200 (1994).

[4] Z.M. Chen, X. Meng-Burany, H. Okumura, G. C. Hadjipanayis, J. Appl. Phys. 87, 3409 (2000).

[5] J. Zhang, S.Y. Zhang, H.W. Zhang, B.G. Shen, B.H. Li, J. Appl. Phys. 89, 2857 (2001).

[6] R.S. Perkins, S. Strässler, A. Menth, AIP Conf. Proc. 29, 610 (1976).

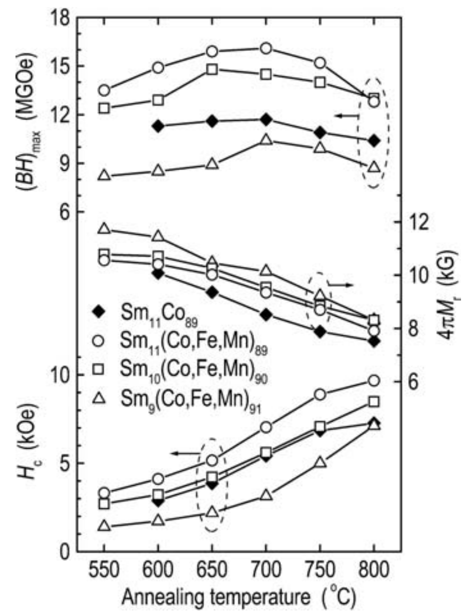

Fig. 1. Effect of annealing temperature on intrinsic coercivity, remanent magnetization and maximum energy product of high-energy milled and annealed $Sm_{11}Co_{89}$ and $Sm_x(Co_{0.85}Fe_{0.075}Mn_{0.075})_{100-x}$ alloys.

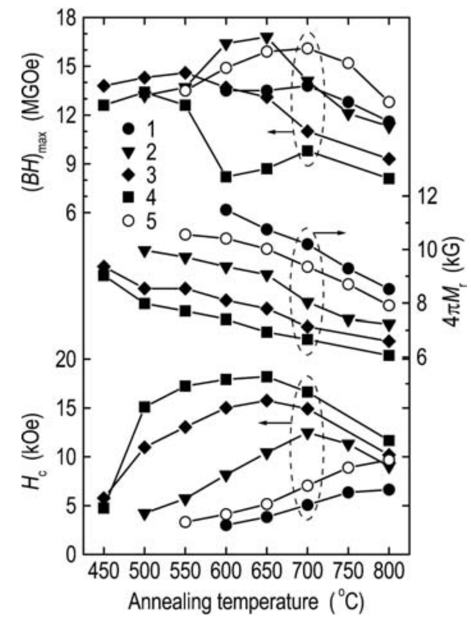

Fig. 2. Effect of annealing temperature on hard magnetic properties of high-energy milled and annealed alloys $Sm_x(Co_{0.8}Fe_{0.2})_{100-x}$ with x = 11 (1), 13 (2), 15 (3), 16.7 (4) and $Sm_{11}(Co_{0.85}Fe_{0.075}Mn_{0.075})_{89}$ (5).

FG-03

Effect of TiC and Cr additions on magnetic properties of nanocrystalline (Pr,Nd)FeB alloys.

V. C. de Franco[2], R. K. Murakami[3], H. R. Rechenberg[4], T. Yonamine[1], *F. P. Missell*[1,2], V. Villas-Boas[2]

1. Divisão de Metrologia de Materiais, INMETRO, Duque de Caxias, Brazil; 2. Centro de Ciências Exatas e Tecnologia, Universidade de Caxias do Sul, Caxias do Sul, Brazil; 3. Universidade do ABC, Santo André, Brazil; 4. Instituto de Fisica, Universidade de São Paulo, São Paulo, Brazil

Magnetic nanocomposites [1] consisting of a hard phase in a soft matrix, such as R2Fe14B/α-Fe, are promising materials for manufacturing resin bonded magnets. Obtaining the nanostructured magnetic material based on R-Fe-B depends strongly on processing and requires restraining grain growth in the material. Branagan and McCallum [2] found that Ti addition to Nd-Fe-B alloys leads to the suppression of α-Fe dendrites, while Chang et al. [3] have demonstrated that Ti suppresses the formation of the metastable cubic Pr2Fe23B3 phase in PrFeB alloys. The addition of C to the composition prevents the formation of detrimental TiB2 and also favors grain refinement [3, 4].
The hysteresis curves of some Pr9.5Fe84.5B6 + 3 at% TiC melt spun alloys obtained at different wheel speeds were discussed previously [5]. For material produced at a wheel speed of 25 m/s, and subject to no further annealing treatment, energy products of up to 14.4 MGOe were observed with a coercive field of 8.4 kOe. These values are up to 30% greater than those observed by Kramer et al. [6] for quenched and annealed Nd9.5Fe84.5B6 + 3 at% TiC. Coercive fields of nanocrystalline PrFeB alloys with Cr additions were also found to be considerably larger than in their Nd counterparts [7]. Recently, Ishii [8] et al. studied nanocrystalline NdFeBTiC materials with transition metal additions and reported very favorable results for Cr additions. For one alloy with composition Nd9.3Fe71.8B14.6C0.4Ti3Cr1 these workers reported a coercive field of 20 kOe. This work motivated us to investigate the effect of TiC and Cr additions on nanocrystalline PrFeB materials.
Alloys with composition (Pr9,5Fe84,5B6)97-x +3%TiC + Crx (x = 0, 0.25, 0.5, 0.75, and 1.0) were produced from 99% pure starting materials in an arc furnace and were melt-spun in a He atmosphere at wheel speeds of 20 - 25 m/s. Individual ribbon pieces were measured in a vibrating sample magnetometer at room temperature for each composition. They showed a certain variability in their magnetic properties, however, a hysteresis curve for a quenched but not-annealed ribbon with 1.0% Cr is shown in Figure 1. In this case Hc = 10.2 kOe, larger than the values observed previously in material without Cr addition [5], but far below the values reported in Ref. 8 for nanocrystalline materials of the type NdFeB + TiC + Cr. We found that very short anneals (3 min) were more effective than longer anneals (10 min) and an increase in annealing temperature resulted in a reduction in the coercive field (See Figure 2). All this points to grain growth as responsible for the worsening of the magnetic properties, in agreement with the observation in Ref. 5, that the best magnetic properties were obtained for as-quenched materials.
Although the PrFeB + TiC alloys were improved by Cr addition, our values of Hc are below those reported for NdFeB + TiC + Cr alloys. We are investigating Nd-containing alloys to acertain whether the Hc values of our alloys can be increased by this means. Our work also indicates that another possibility for increasing Hc might be increasing the quenching rate.

1. R. W. McCallum, A. M. Kadin, G. B. Clemente, and J. E. Keem, J. Appl. Phys. 61 (1987) 3577.

2. D. J. Branagan and R. W. McCallum, J. Alloys Compd. 230 (1995) 67.

3. H. W. Chang, C. H. Chiu, and W. C. Chang, Appl. Phys. Letters 82 (2003) 4513.

4. D. J. Branagan, M. J. Kramer, and R. W. McCallum, J. Alloys Compd. 244 (1996) 27.

5. R. K. Murakami, H. R. Rechenberg, V. Villas Boas, R. W. McCallum, J. Appl. Phys.99 (2006) 08B501.

6. M. J. Kramer, C. P. Li, K. W. Dennis, R. W. McCallum, C. H. Sellers, D. J. Branagan, L. H. Lewis, and J. Y. Wang, J. Appl. Phys. 83 (1998) 6631.

7. A. D. Barra-Barrera, R. K. Murakami, V. Villas-Boas, J. Magn. Magn. Mater. 226-230 (2001) 1455.

8. R. Ishii, T. Miyoshi, H. Kanekiyo, and S. Hirosawa, Intermag 2006 digest HF-03.

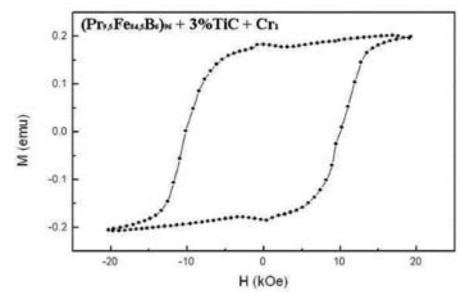

Figure 1 - Hysteresis curve of as-quenched ribbon.

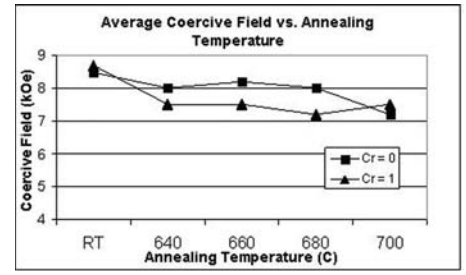

Figure 2 - Average coercive field vs. annealing temperature for Cr = 0 and Cr = 1

FG-04

Two Major Effects of Process Temperature on the Characteristic of Bulk Nanostructured Nd-Fe-B / Fe-Co Composite Magnets.

C. H. Chen[1], Y. Shen[2], M. Huang[3], A. K. Higgins[1]
1. University of Dayton Research Institute, Dayton, OH; 2. FutureTek Corp, Dayton, OH; 3. UES / Wright Patterson Air Force Base, Dayton, OH

Nanostructured magnets possessing exchange coupled magnetic hard and soft phases are predicted to produce an energy product (BH)max near 90 MGOe. Hot-deformation (HD) after hot-pressing (HP) can produce (BH)max of 48-55 MGOe for nanostructured bulk composites of Nd-Fe-B and coated soft-phase (<4%) [1]; but, it has not resulted in any higher (BH)max. One of the several obstacles to producing high performance magnets is the high process temperature, which significantly affects the characteristics of the magnets, especially those with a large volume of soft-phase.

As new technologies are needed for developing nanostructured magnets, it is necessary to understand the effects of process temperature on the characteristics of the magnets. We must determine if a useful coercivity can be retained when the grain growth can be suppressed for magnets with a large volume of soft-phase.

Two sets of specimens made of nano-grained Nd-Fe-B powder with and without Fe-Co phase were compacted in vacuum at 11 designated temperatures from 25 to 760°C as shown in Fig. 1. The Fe-Co (~4%) was electrically coated on the pre-crystallized Nd13.5Febal.Co6.7Ga0.5B6 powder. A large particle size (100-150μm) was selected for the hard phase to avoid the oxidation effect, and a small volume of soft-phase was used to avoid a thick coating layer. Each specimen weighed 5g and the pressing time was 2 min. The oxygen content of the magnets was carefully controlled at <0.18 wt%. Characterizations included hysteresigraph, TEM, and SEM.

Fig. 1 shows the Hci vs. process temperature for the specimens. Two major effects that significantly reduce Hci can be observed. One is the grain-growth effect at T > 620°C for the magnets with no soft-phase, and it is clearly seen at T > 660°C where the Hci decreases sharply. The peak Hci at 550~610°C indicates an occurrence of full crystallization. The 2nd major effect is the interdiffusion effect for the magnets with ~4% soft phase, which occurs at T >300°C. The Hci decreases monotonically from 17 kOe after HP at 300°C down to 3.7 kOe after HP at 760°C, evidencing the interdiffusion of the hard and the soft phases.

Table 1 lists the grain sizes and magnetic properties after processing at various temperatures. For magnets with 0% Fe-Co, HP at 580°C resulted in isotropic grain size of 40-80 nm and Hci of 20 kOe. HD at 760°C resulted in anisotropic grain sizes with 40-110 nm parallel to c-axis and 200-800 nm perpendicular to c-axis, and Hci = 14.1 kOe. For magnets with ~4% Fe-Co, the detrimental temperature effect on Hci is more severe due to the interdiffusion between the hard and soft phases. (BH)max values are also affected significantly by the two major effects.

Discussion:

Using current technologies, including coating, HP and HD, nanostructured magnets with ~ 1-3% soft-phase did show a small improvement in energy products (~5 to 8%) compared to the magnets without a soft-phase; but, the process has not resulted in (BH)max > 56 MGOe. A larger volume of soft-phase is required for higher magnetization, but the soft-phase has to possess an optimum separation between the hard-phase nano-grains for an effective exchange coupling and to produce a higher (BH)max, which can not be made using current technologies.

The grain-growth and the interdiffusion effects must be avoided in addition to dispersing the hard and the soft phases in nano-scale while controlling the oxygen content. Our experiments in the past years trying to make nanostructured magnets with coupled Nd-Fe-B and Fe-Co have provided evidence that three major challenges must be overcome before achieving significant progress:

1). Dispersing hard and soft phases in nano-scale while controlling oxygen as low as possible;

2). Effective compacting at T < 300°C to avoid interdiffusion and at T< 620°C to avoid excessive grain growth (This is the topic of this paper);

3). Effective aligning the nanostructured hard phase with the alignment as high as possible.

The US Air Force supported this research effort.

S. Liu, A. Higgins, E. Shin, S. Bauser, C. Chen, D. Lee, Y. Shen, Y. He, and M.Q. Huang, IEEE Trans. Magn. 42 (10) 2912 (2006)

Process	Temp.(C)	Grain Size (nm)		Hci (kOe)			(BH)max (MGOe)		
				x* = 0	x ~ 1%	x ~ 4%	x = 0	x ~ 1%	x ~ 4%
Cold-press	25	~<40		19.3		19.0	15.6		15.7
Hot-press (HP)	400	~<40		19.4		17.1	15.4		13.9
	580	~ 40-80		20.1	19.5	12.3	15.5	15.9	13.7
	760	~300-800		7.8		3.7	10.7		6.0
HD after HP @ 580°C	760	~40-110 (a)	~200-800(b)	14.1	12.5	3.6	48.2	51.3	31.3

Table 1. Grain size and weighted magnetic properties vs. process temperature for (Nd-Fe-B)/(Fe-Co) * x is the percentage of Fe-Co soft-phase; (a) // to c-axis, (b) Perpendicular to c-axis

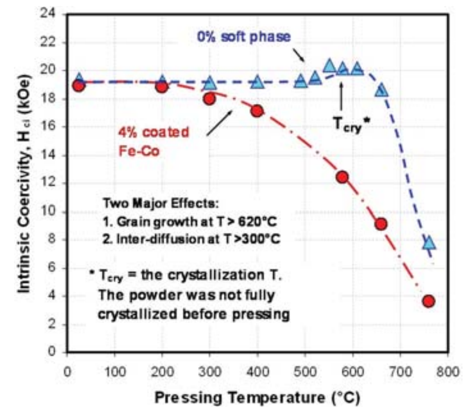

Fig 1. Hci vs pressing temperature for the magnets with and without soft phase

FG-05

$Nd_2Fe_{14}B$ based Magnetic Nanocomposites Synthesized by Electrodeposition, Microemulsion and Melt Spinning Techniques.

R. Ramanujan, Z. Liu, S. Viswanathan, P. K. Deheri, S. Shukla
School of Mater. Sci. Eng., Nanyang Tech. Univ., Singapore, Singapore

NdFeB based hard magnetic alloys are the most widely used permanent magnets for near room temperature applications. Nanocomposites of $Nd_2Fe_{14}B$/alpha-Fe are estimated to have a much higher maximum energy product $(BH)_{max}$ (up to 1 MJ/m^3) compared to single phase $Nd_2Fe_{14}B$ alloys [1]. However, this high energy product has not been experimentally demonstrated so far, apparently due to the difficulty in producing the uniform nanostructures required for efficient exchange coupling [2]. This implies that structures with nanosized grains must be obtained in hard magnetic nanocomposite materials in order to experimentally study the effect of exchange coupling on $(BH)_{max}$ [3,4]. Therefore, we have studied NdFeB nanostructured magnetic materials synthesized by techniques which can yield nanograins: electrodeposition, chemical synthesis and rapid quenching were utilized in these experiments.

NdFeB nanoparticles were galvanostatically deposited on copper substrates by pulse electrodeposition, thin films were prepared by systematically varying processing parameters such as composition, pH value, current density and duty cycle [5]. The as-prepared and vacuum annealed films were found to be aggregates of nanoparticles with size less than 10nm (Fig.1 inset). The XRD pattern of annealed thin films showed good crystallinity of the $Nd_2Fe_{14}B$ phase. The presence of Nd and Fe was confirmed through EDS analysis. The magnetic properties of the NdFeB thin film samples were measured by VSM, samples annealed at 580 °C for 10min exhibited coercivity HC and magnetization MS values of ~500 Oe and 0.270 emu/cm^2, respectively (Fig.1). Work is in progress to increase H_C by adjusting composition and optimizing the annealing process.

The microemulsion method was employed to synthesize nanocomposites of $Nd_2Fe_{14}B/\alpha$-Fe with controlled size and size distribution. A microemulsion of salt solution was added to a reducing agent NaBH4 solution with vigorous stirring. The black precipitate obtained was then washed with ethanol and methanol and capped with oleic acid. TEM studies show that the particles are reasonably monodisperse and the average size is approx. 10 nm (Fig.2a). Annealing in Ar at 650 °C for 30min resulted in $Nd_2Fe_{14}B$ and α-Fe phase formation, as seen in the XRD results (Fig.2b).

The rapid quenching melt spinning technique was utilized to synthesize NdFeB based nanocomposite alloys with Co, Dy, Sm and Ta alloying additions. For example, the effect of Ta doping on the magnetic properties of $Nd_9Fe_{86}B_5$ nanocomposites was investigated. 2% Ta doping enhanced HC despite a decrease in the remanence M_r (Fig.3a). The increased H_C is likely to be the result of a fine grain structure and precipitates which can act as pinning centers. The magnetic properties of melt spun $RE_2Fe_{14}B/Fe_{65}Co_{35}$ alloys were also investigated, since $Fe_{65}Co_{35}$ alloys have extremely high magnetization value [6]. The VSM results show that high M_S and M_r have been achieved (Fig.3b).

Our work on the synthesis of NdFeB based magnetic nanocomposites will be presented. Synthesis of exchange coupled hard magnetic nanocomposites has been achieved by electrodeposition, microemulsion and rapid quenching techniques, characterization and property evaluation have also been carried out.

[1] R. Skomski and J.M.D. Coey, Phys. Rev. B 48 (1993) 15812

[2] H.A. Davies and Z.W. Liu, J. Magn. Magn. Mater. 294 (2005) 213

[3] R.V. Ramanujan and Y. Zhang, Phys. Rev. B 74 (2006) 224408-1

[4] Z.W. Liu and H.A. Davies, J. Phys. D: Appl. Phys. 39 (2006) 2647

[5] M. Schwaltz, N.V. Myung and K. Nobe, J. Electrochem. Soc. 151(2004) C468

[6] R.M. Bozorth, Ferromagnetism, IEEE Press, New York, 1993, p. 195

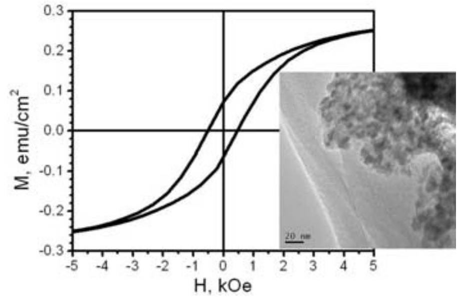

Fig.1 M-H loop of vacuum annealed NdFeB thin films (inset: TEM micrograph of as-prepared particles)

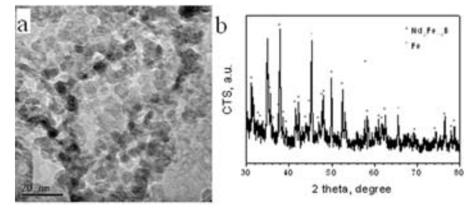

Fig.2 TEM micrograph of as prepared nanoparticles with ave. size of 10 nm (a) and XRD pattern of heat treated NdFeB/Fe nanocomposite (b).

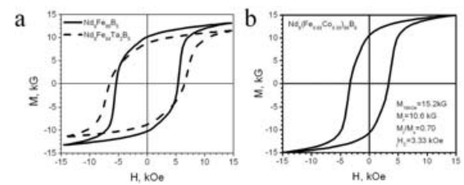

Fig.3 M-H loops for nanocomposite $Nd_9Fe_{86}B_5$ and $Nd_9Fe_{84}B_5Ta_2$ alloys (a) and $Nd_8(Fe_{0.65}Co_{0.35})_{86}B_6$ alloys (b).

FG-06

Improvement in Morphology and Magnetic Properties of Thick Nanocomposite Film-Magnets with Multi-Layered Structure.

H. Fukunaga[1], H. Nakayama[1], M. Nakano[1], M. Ishimaru[2], M. Itakura[2], F. Yamashita[3]
1. Department of Electrical Engineering and Electronics, Nagasaki University, Nagasaki, Japan; 2. Department of Applied Science for Electronics and Materials, Kyushu University, Kasuga, Japan; 3. Matsushita Electric Industrial Co., Ltd., Daito, Japan

Introduction

Recently, thick film-magnets are needed for applications to micromachines[1)]. Based on this requirement, we have proposed a pulsed laser deposition (PLD) method of preparing multi-layered nanocomposite film-magnets with the thickness of several tens of microns[2)].

In this contribution, we evaluated the morphology, magnetic properties, and microstructure of multi-layered Nd-Fe-B/Fe-B and Nd-Fe-B/α-Fe nanocomposite film-magnets with the thickness of several tens of microns. Furthermore, we found that their magnetic properties and morphology are improved by controlling their composition and by a newly developed PLD system with an auxiliary laser, respectively.

Experimental

The multi-layered films with the thickness of several tens of microns were deposited in vacuum for 1 hour by the PLD method proposed previously, which uses composite targets rotating at 7 rpm[2)]. The targets are composed of magnetically hard ($Nd_{2.6}Fe_{14}B$ or $Nd_{2.4}Fe_{14}B$-Nb) and soft (Fe_3B or α-Fe) segments, and enable us to deposit 14 layers/min. As the deposited films were amorphous, they were crystallized with an infrared furnace.

The roughness of the surface of deposited films was evaluated with a surface roughness meter by the line scan, 24 mm in length.

Results and Discussion

Typical hysteresis loop after crystallization is shown in Fig.1 (a) for a nanocomposite film-magnet deposited from $Nd_{2.6}Fe_{14B}/Fe_3B$ target. A $(BH)_{max}$ value over 60 kJ/m^3 was obtained. The nanostrucuture of this film was observed with TEM (Fig.1 (b)). It is clearly seen that thin layers with the thickness of several tens of nanometers are stacked periodically.

Improvements in magnetic properties were achieved by adding 0.5 at.% Nb (H_c=430 kA/m, M_r=0.83 T, and $(BH)_{max}$=85 kJ/m^3) and by using an α-Fe segment instead of an Fe_3B one (H_c =430 kA/m, M_r=1.0 T, and $(BH)_{max}$=90 kJ/m^3).

It was found by SEM observation that there exist many particles ranging from 1 to 20 μm on the surface of a deposited film. The analysis of composition with SEM-EDX (Energy Dispersive X-ray Spectrometer) clarified that each particle is composed of small droplets, grows on the surface, and is in the composite state. The smoothness of the films is deteriorated by the existence of particles, and the periodicity of the stacked layers would be disturbed in the particles. Therefore, we developed a new PLD system which has an auxiliary laser in addition to a main laser for ablating a target (Fig.2 (a)). The laser beam from the auxiliary laser hits droplets flying between the target and the substrate and ablates them. In addition, we found that the number of particles is decreased by inserting intervals during depositions.

Subsequently, we deposited multi-layered films by the newly developed method from a $Nd_{2.6}Fe_{14}B/Fe_3B$ target, and the height of particles on film surface was measured by the line scan, and is plotted in Fig.2 (b), together with the result for the multi-layered film deposited by the PLD systems reported previously. As seen clearly, the newly developed PLD method reduced the number of particles on the surface significantly, which suggests that the developed method is a promising one for improving the morphology of a thick multi-layered film.

1) M. Nakano et al., IEEE Trans. Magn. **23**, 2672 (2006).

2) H. Fukunaga et al., J. Alloys and Compounds, **408-412**, 1355 (2006).

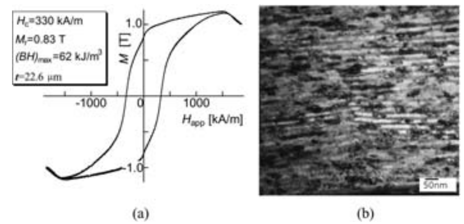

Fig.1 A typical hysteresis loop of a multi-layered NdFeB/FeB nanocomposite film-magnet (a) and its TEM image (b).

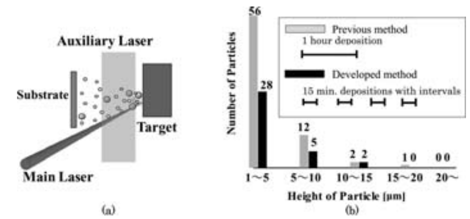

Fig.2 Schematic representation of the developed PLD system with auxiliary laser (a), and height of particles on the film surface deposited by the developed system, together with the result for the film deposited by the PLD method reported previously (b). In the developed method, the deposition for 15 min. was repeated 4 times (totally 1 hour) with intervals between depositions, although the deposition was carried out for 1 hour continuously in the previous method (the inset of Fig.(b)).

FG-07

Magnetic properties of Nd-Fe-B thin films with island structure prepared on Mo buffer layer.

T. Shima[1], H. Kato[1], T. Sato[2]
1. Faculty of Engineering, Tohoku Gakuin University, Tagajo, Japan; 2. Toyota Central R&D Labs., Nagakute, Japan

$Nd_2Fe_{14}B$ phase has a large magnetocrystalline anisotropy [1] and has been widely used as a permanent magnet with energy products ten times greater than ferrites. Recently, with increasing an awareness of environmental and energy issues, the market of hybrid vehicles has been explosively growing. In consequence, the interest in the development of a high performance permanent magnet is being attracted again. It is well known that coercivity *H*c of commercial Nd-Fe-B magnets is much smaller than that of the theoretical value [2]. Heavy rare earth elements such as Dy and Tb are inevitably added to enhance the *H*c of Nd-Fe-B sintered magnet. However, an urgent problem of scarce resources is forcing us to reduce the use of these elements. Furthermore, the mechanism of the magnetization process has not fully understood yet. In this study, in order to elucidate the coercivity mechanism, Nd-Fe-B thin films with island structure [3] were fabricated and their magnetization processes were investigated.
The (Cr/Mo/Nd-Fe-B/Cr) films were prepared on MgO (100) single crystal substrates using an UHV-compatible dc-sputtering apparatus. The base pressure is below 1×10^{-8} Pa). The nominal thickness *t* of the Nd-Fe-B layer was varied between 5 and 30 nm. The films were heated at 500 - 675 °C during the deposition of the Nd-Fe-B layer. The magnetic properties were measured by a superconducting quantum interference device (SQUID) magnetometer. The structure characterization was performed by an X-ray diffraction with Kα radiation. The film composition was determined by an electron probe micro-analysis (EPMA).
The $Nd_2Fe_{14}B$ phase was grown with the epitaxial relationship as $(001)_{MgO}$ // $(001)_{Mo}$ // $(001)_{Nd2Fe14B}$ for the films deposited in the temperature range from 540 to 625 °C. The island structure was formed for a sample with *t* = 5 nm, and its typical lateral size was 80 nm. The initial magnetization curves of the Nd-Fe-B films with different *t* are shown in Fig. 1. *t* was changed from 5, 8, 10 and 30 nm. The substrate temperature during deposition was fixed at 625 °C. It is clearly seen from this figure, the magnetization behavior was changed from single-domain (SD) particles to multiple-domain (MD) particles. The initial magnetization curve increases steeply for the MD particles (*t* = 30 nm), indicating that the magnetization process is dominated by domain wall displacement. On the other hand, the initial magnetization curve increases slowly with applied magnetic field for the SD particles (*t* = 5 nm). A mixture of different initial magnetization behaviors is observed in the films with *t* = 8 and 10 nm, indicating the co-existence of SD and MD particles. The maximum value of *H*c for a $Nd_2Fe_{14}B$ film was 18 kOe.
This work was partly supported by Toyota Motor Corporation. The magnetization measurement was performed at Magnetic Material Laboratory at IMR, Tohoku University. The structural characterization was performed at the Hi-tech Research Center of Tohoku Gakuin University.

[1] M. Sagawa, N. Togawa, H. Yamamoto, and Y. Matsuura, J. Appl. Phys., 55, 2083 (1984).

[2] S. Hirosawa, Y. Matsuura, H. Yamamoto, S. Fujimura, M. Sagawa, and H. Yamauchi, J. Appl. Phys., 59, 873 (1986).

[3] T. Shima, K. Takanashi, Y. K. Takahashi, and K. Hono, Appl. Phys. Lett., 81, 1050 (2002).

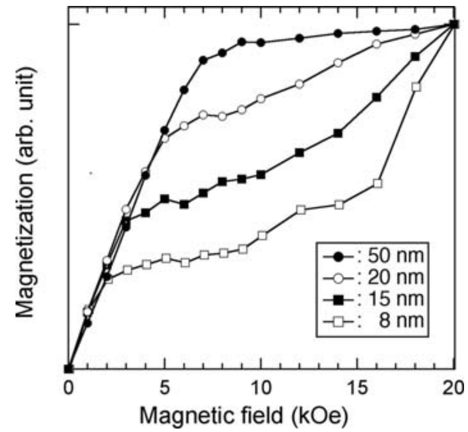

Fig. 1 Initial magnetization curves for Nd-Fe-B thin films with different film thickness. All films were prepared on Mo buffer layers. The nominal film thickness is 8 nm, 15 nm, 20 nm and 50 nm.

Highly Coercive Nanocrystalline Electro-Deposited CoPt Thin Films.

K. Zuzek Rozman[1], J. Kovac[2], P. J. McGuiness[1], S. Kobe[1]
1. Department for Nanostructured Materials, Jozef Stefan Institute, Ljubljana, Slovenia; 2. Department of Surface Engineering and Optoelectronics, Jozef Stefan Institute, Ljubljana, Slovenia

CoPt systems are very promising as magnetic storage media and for MEMS devices. They have a strong perpendicular magnetocrystalline anisotropy and they also exhibit excellent resistance to oxidation and corrosion.

Near-stoichiometric CoPt 50:50 thin films were prepared by electrodepositing from a single electrolyte. The electrolyte consisted of 2 mmol/l of Pt “p”-salt, 4 mmol/l of Co-sulphamate, 20 mmol/l of ammonium citrate and 0.2 mmol/l of glycine. The films of thickness up to 300 nm were deposited on glass/Cr/Au potentiostatically with the potential referenced to the potential of the Ag/AgCl electrode. The as-deposited films were annealed at temperatures up to 700°C for 60 min in forming gas (Ar+7%H_2) and examined with AFM, XRD, SQUID, SEM/EDXS and AES.

The surface of the as-deposited $Co_{45}Pt_{55}$ film was investigated with an AFM. The film shows a nanocrystalline structure with grain sizes ranging between 10 and 80 nm and a RMS roughness of 2.766 nm.

The XRD diagrams of the as-deposited and annealed $Co_{45}Pt_{55}$ presented in Figure 1 show the FCC CoPt phase with a predominant (111) texture, all additional peaks can be attributed to the substrate. After annealing at 500°C for 60 min no ordering into the $L1_0$ phase was observed. The ordering begins when the sample is annealed at 600°C for 60 min, with the appearance of the (001) and (110) reflections, which grow even larger when increasing the temperature to 700°C, where the (200) peak-splitting characteristic for the $L1_0$ ordering was also observed. In the XRD pattern of the sample annealed at 700°C an additional peak was observed at 2Θ=45.4°, which can be attributed to the Co_2Si phase. This implies interdiffusion between the CoPt film and the substrate. The magnetic properties of the annealed samples are displayed in Figure 2. A significant increase in the coercivity is observed with increasing annealing temperature, which is connected to the development of the $L1_0$ structure, reaching a value of $\mu_0 H_C$=1.2T, which is to the best of our knowledge the highest coercivity observed in electrodeposited CoPt films. On the other hand, the remanence decreases with the increasing annealing temperature because of the transformation of the highly symmetrical FCC phase into the $L1_0$ phase.

The in-depth composition across the film thickness and its dependence upon annealing according to the AES depth profiles is shown in Figure 3. The as-deposited film (Figure 3a) is Pt rich with a composition of $Co_{46}Pt_{54}$, which is not constant across the film thickness; there is an excess of Pt present at the surface in the middle and at the substrate-film boundary. Beneath the Co-Pt film the well-defined structure of the Au and Cr layers on the SiO_2 substrate is observed. After annealing at 700°C for 1 h in Ar+H_2 (Figure 3b), the film shows a more homogeneous composition. On the other hand, an interdiffusion of Co into the substrate was observed, which is in agreement with the XRD investigations that showed the formation of Co_2Si when annealed at 700°C. In the Co-Pt-Si system the interdiffusion of Co and Si is hard to avoid (Ref. 1). However, even though high coercivities can be achieved when choosing glass-based substrates, adding an appropriate diffusion barrier on the glass substrate would result in even better magnetic properties.

1. M. J. H. van Dal, A. A. Kodentsov and F. J. J. van Loo, Intermetallics 9 (2001) 451

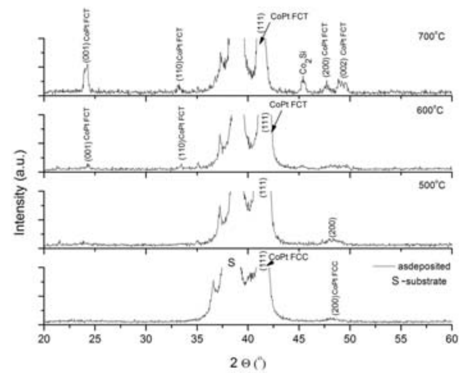

Figure 1. XRD patterns of CoPt films deposited on a glass/Cr/Au substrate and subsequently annealed in Ar+7% H_2 for 60 min

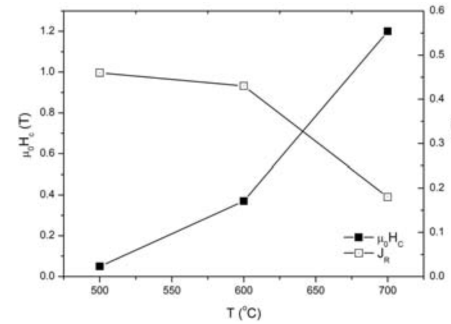

Figure 2. Coercivity ($\mu_0 H_C$) and remanence (J_R) of the CoPt films electrodeposited and annealed at different temperatures in Ar+7% H_2 for 60 min

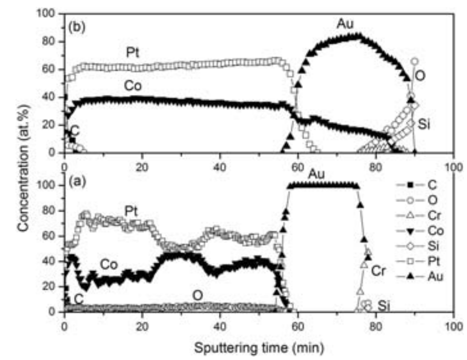

Figure 3. Compositional analysis by AES depth profiling for (a) an as-deposited CoPt film and (b) CoPt film annealed at 700°C in Ar+7% H_2 for 60 min.

FH-01

Magnetism and magnetocaloric effect in multiferroic $LuFe_2O_4$

J. Gass[1], N. Frey[1], M. Phan[1], *H. Srikanth*[1], M. Angst[2], B. Sales[2], D. Mandrus[2]

1. Department of Physics, University of South Florida, Tampa, FL; 2. Materials Science and Technology Division, Oak Ridge National Laboratory, Oak Ridge, TN

A systematic study of the DC, AC, RF susceptibility as well as the magnetocaloric effect (MCE) in $LuFe_2O_4$ single crystals is presented. The family of RFe_2O_4 (R = Y, Er, Yb, Tm, and Lu) compounds, which exhibit charge and magnetic order on a geometrically frustrated lattice, have received growing attention from the scientific community, owing to their extraordinarily interesting physical properties [1,2]. In particular in $LuFe_2O_4$, the observation of an electric polarization possibly originating from charge order [3] and the subsequent discovery of a giant room-temperature magnetocapacitance [4] has created a lot of attention [5]. Multiferroic properties along with the intrinsic geometric spin frustration in $LuFe_2O_4$ make it a very promising candidate material for magnetic refrigeration and other technologies. While recent magnetization and neutron results suggest a three-dimensional magnetic structure with additional transitions, understanding the unusual magnetic properties of $LuFe_2O_4$ still remains incomplete, partially due to the complex phase diagram [6,7]. The very complexity makes it attractive for magnetocaloric applications and we propose $LuFe_2O_4$ to be a good candidate material as it can show large magnetic field-induced magnetic entropy change over a wide temperature range due to the occurrence of multiple successive metamagnetic transitions.

Here, we present a systematic study of the magnetic properties and the first report of the magnetocaloric effect (MCE) in $LuFe_2O_4$. Correlation between the magnetism and MCE is established and the influence of the magnetic field on the metamagnetic transitions and MCE are analyzed and discussed. Our study underscores the important point that magnetic cooling power can be greatly enhanced in materials showing multiple successive magnetic phase transitions.

$LuFe_2O_4$ crystals were grown in an image furnace as described elsewhere [6,7]. DC and AC magnetization measurements were performed using a Physical Property Measurement System from Quantum Design in the temperature range of 5 – 300 K at applied fields up to 70kOe. The magnetic entropy change (ΔS_M) was numerically extracted using the Maxwell relation from a large family of M-H curves collected at different fixed temperatures.

Our magnetization reveal unusual magnetic behavior only in fields applied parallel to the c-axis of the crystal, in agreement with previous studies [1,6,7]. Zero-field-cooled (ZFC) magnetization curves at applied field ~100 Oe show the two transitions around 240K and 170K also indicated by neutron scattering [6]. Field-cooled (FC) magnetization curves at the same field exhibit three broad cusps, two of which coincide with the above transitions. The magnetic entropy changes $\Delta S_M(T)$ at these features were calculated from a family of M-H curves at fixed temperatures using the Maxwell relation: $\Delta S_M(T)= \int(\partial M/\partial T)_H dH$.

$\Delta S_M(T)$ curves show three peaks at temperatures which correspond to the cusps in the FC magnetization. As the magnetic field is increased, the positions of MCE peaks at ~170 and 240 K tend to remain unchanged, whereas the one at ~ 65 K significantly shifts to a lower value. Noticeably, the MCE peak temperature of ~65 K for ΔH = 3 kOe decreases to ~55 K which remains almost unchanged for $\Delta H \geq 42$ kOe. This is consistent with the observation that this low temperature metamagnetic transition in $LuFe_2O_4$ is kinetically arrested below ~55 K [7]. The magnitude of $\Delta S_M(T)$ at the peak temperatures varies differently as the applied magnetic field is increased. For $\Delta H \leq 21$ kOe, the magnitude of $\Delta S_M(T)$ is obviously larger for the case at ~55 K than for those at ~170 and 240 K, while the opposite trend is observed for $\Delta H > 21$ kOe. This suggests different mechanisms for AF-FM couplings/correlations for the metamagnetic transitions. An important conclusion is that enhanced spin entropy (at the kinetically arrested transition) yields large MCE at lower applied fields which is desirable for applications. From the practical magnetic cooling perspective, the application of magnetic field leads to a broadening of the metamagnetic transitions and hence a broadened $\Delta S_M(T)$ curve over very wide temperature range. As a result, the magnetic cooling power – which is proportional to the width of the $\Delta S_M(T)$ curve – is greatly enhanced. This opens up new opportunities for the developments of a new class of material with multiple successive metamagnetic transitions for magnetic refrigeration.

<p>

Work at USF supported by DOE through grant number DE-FG02-07ER46438. Research at ORNL sponsored by the Division of Materials Sciences and Engineering, Office of Basic Energy Sciences, U.S. Department of Energy

[1] J. Iida, Y. Nakagawa, N. Kimizuka, J. Phys. Soc. Jpn. 55, 1434 (1986).

[2] Y. Yamada et al., Phys. Rev. B 62, 12167 (2000).

[3] N. Ikeda et al., Nature 436, 1136 (2005). [4] M. A. Subramanian, T. He, J. Chen, N.S. Rogado, T.G. Calvarese, A.W. Sleight, Adv. Mater. 18, 1737 (2006).

[5] H.J. Xiang, M.-H. Whangbo, Phys. Rev. Lett. 98, 246403 (2007); Y. Zhang et al., ibid. 98, 247602 (2007); A. Nagano et al., ibid. 99, 217202 (2007).

[6] A. D. Christianson et al., arXiv:0711.3560v1

[7] M. Angst, W. Tian, R. Jin, B.C. Sales, D. Mandrus, unpublished.

FH-02

Design and processing of new ferrite materials from an atomistic perspective.

A. Yang[1], A. Geiler[1], X. Zuo[2], C. Vittoria[1], V. G. Harris[1]
1. Center for Microwave Magnetic Materials and Integrated Circuits, Electrical and Computer Engineering, Northeastern University, Boston, MA; 2. College of Information Technical Science, Nankai University, Tianjin, China

Ferrites of spinel and hexagonal crystal structure have been widely utilized in the design of various microwave and millimeter-wave components. These material structures consist of a closed packed oxygen framework in which magnetic and nonmagnetic cations reside at the interstitial sites. The electrical and magnetic properties of ferrite materials are largely determined by the distribution and valence of these cations. The ability to fine tune the cation distribution allows the material properties to be adjusted towards specific applications. The alternating target laser ablation deposition (ATLAD) technique was developed for just such a purpose. This technique allows the spinel[1,2,3] and hexagonal ferrite structures[4] to be deposited with control over the atomic scale distribution of cations by the controlled and sequential ablation of two or more targets. The ablation of the targets at carefully chosen intervals allows for the construction of unique ferrite structures. Previously, Zuo et al.[2] employed this technique to grow Mn-ferrite films having magnetic anisotropy fields as many as 100 times larger than conventionally grown films and, in some cases, aligned perpendicular to the film plane. The unique properties of these films correlated with a distinct inversion parameter (percentage of the divalent cations residing at octahedral sites in spinel ferrite) compared to the equilibrium value. Yang et al.[3] further demonstrated control of the distribution of Cu cations in spinel Cu-ferrite films and obtained a 65% enhancement in the saturation magnetization of the Cu ferrite films over the equilibrium value. Most recently, the application of the ALTAD technique was applied for the first time to the growth of hexagonal M-type barium ferrite ($BaFe_{12}O_{19}$).[4] In an extension of this work, Geiler et al. guided Mn substitutional cations to specific sublattices in the unit cell. By specific design the Mn resided preferentially on the octahedral sublattices in the spinel block within the hexagonal structure. Extended x-ray absorption fine structure analysis was utilized in all experiments to study the short range order of the atoms and the cation distribution. The ATLAD technique has been successfully employed to engineer the cation distribution in ferrite unit cells resulting in unique and useful microwave properties. First principle calculations were carried out and found to agree with the experimental results.

1 X. Zuo, et al., IEEE Trans. Magn., 40 (4), 2811 (2004).

2 X. Zuo, et al., Appl. Phys. Lett. 87, 152505 (2005).

3 A. Yang, et al., Appl. Phys. Lett., 86, 252510 (2005).

4 A. L. Geiler, et al., Appl. Phys. Lett., 91, 162510 (2007).

	Tetrahedral (A)	Octahedral (B)
Mn occupancy	43±5%	57±5%
Mn occupancy	80%	20%

	Mn @ A sites in spinel block	Mn @ B sites in spinel block	Mn @ A and B sites in spinel block	Mn @ bi-pyramidial sites	Mn @ 4f B sites	Mn 12k B sites
1-Mn	0	-1.6099	---	-1.2201	7.0475	6.5515
2-Mn	0	-0.52765	-0.34013	---	---	---

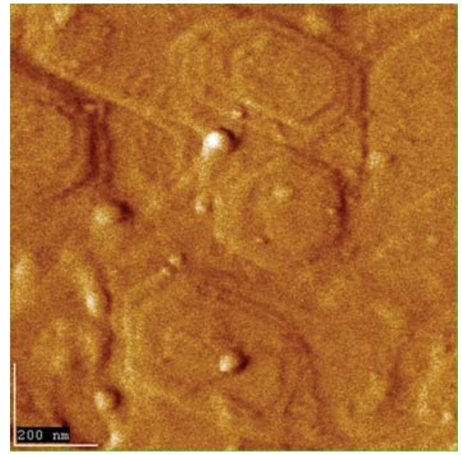

Fig. 1. Atomic force microscope image of ATLAD grown M-type barium hexagonal ferrite.

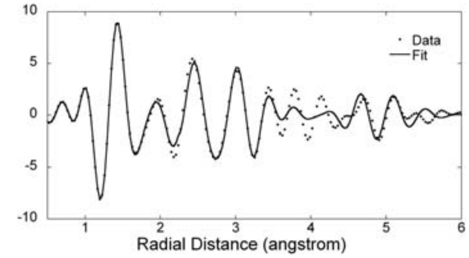

Fig. 2. Real part of the Fourier transform amplitude of extended x-ray absorption fine structure (EXAFS) data with the best fit from Mn K-edge absorption for a manganese substituted M-type barium hexagonal ferrite AT-LAD deposited thin films

FH-03

Texture analysis of ferrite materials by means of electron backscatter diffraction (EBSD).

A. D. Koblischka-Veneva[1], M. R. Koblischka[2], F. Muecklich[1]
1. Institute for Functional Materials, University of the Saarland, Saarbruecken, Germany; 2. Institute of Experimental Physics, Saarland University, Saarbrucken, Germany

The analysis of the achieved texture is of great importance for ferrite materials, either bulk or thin films. The commonly employed techniques like X-ray pole figures do, however, not reach the required resolution to resolve fine details within the grain structure. Therefore, a technique with a relatively high spatial resolution would be required. The recently developed electron backscatter diffraction (EBSD) technique, which works within a scanning electron microscope, enables a spatially resolved study of the crystallographic orientations by means of recording of Kikuchi patterns. To our knowledge, such an EBSD analysis was not yet performed in any oxidic magnetic material, and only very recently on magnetite thin films by us [1,2]. A good surface polishing/cleaning is essential for this analysis, as the method requires an undisturbed surface area for a high image quality (IQ). This information is recorded to each measured Kikuchi pattern, together with a parameter describing the quality of indexation. To each pattern, the three Eulerian angles determine the crystallographic orientation [3]. From this information, orientation maps and local pole figures can be constructed.

In this contribution, we present the results of EBSD scans on various ferrite materials, including bulk M-type hexaferrite $BaFe_{12}O_{19}$ (Ba-ferrite) and thin films of a spinel-type $(Ni,Zn)Fe_2O_4$ [(Ni,Zn)-ferrite] and thin films of $Ba_3Co_3Fe_{24}O_{41}$ (BCFO), which is a Z-type hexaferrite. Both types of thin films were grown by RF sputtering on Si substrates without an additional buffer layer.

The surface preparation process of the bulk ferrites is a delicate task, as for a high spatial resolution a mechanical polishing down to 40 nm colloidal silica is required, which is then followed by a thermal etching. For the thin films, no special polishing procedure is required.

Figure 2 presents a typical result obtained on a bulk ferrite sample. An IQ map and a inverse pole figure map in (0 0 1) direction is presented. Additionally, the detected grain boundaries are marked in black. The sample is polycrystalline and consists of several large grains. Two main growth directions of these large grains can be found. Here, it is remarkable that the growth of large ferrite grains is accompagnied by several small, randomly oriented grains filling the gaps between the large ones. Furthermore, several misoriented small subgrains are located within the large grains. Here, the spatially highly resolved EBSD mappings provide additional information as compared to the standard analysis techniques, which can contribute to an optimization of the growth process.

The EBSD-analyzed ferrite thin films are both also polycrystalline, and do not exhibit a preferred texture. The as-grown films only exhibit small grains with sizes ranging between 30 and 50 nm. An extended annealing time leads to a considerable grain growth, so that grains with sizes ranging between 100 nm and 1 μm could be obtained. Using EBSD with optimized parameter settings, step sizes within the scan grid down to 20 nm can be applied, so that grains of around 60 nm size (corresponding to three data points) can be properly identified.

This work is financially supported by DFG-project no. Mu959/19, which is gratefully acknowledged. We would like to thank D. Makovec (Ljubljana) for providing the Ba-ferrite samples.

[1] A. Koblischka-Veneva, M. R. Koblischka, F. Mücklich, S. Murphy, Y. Zhou, and I. V. Shvets, IEEE Trans. Magn. 42, 2873 (2006).

[2] A. Koblischka-Veneva, M. R. Koblischka, J. D. Wei, Y. Zhou, S. Murphy, F. Mücklich, U. Hartmann, and I. V. Shvets, J. Appl. Phys. 101, 09M507 (2007).

[3] K. Z. Baba-Kishi, J. Mater. Sci. 37, 1715 (2002).

[4] M. R. Koblischka, M. Kirsch, M. Brust, A. Koblischka-Veneva, and U. Hartmann, submitted to Phys. stat. solidi (a).

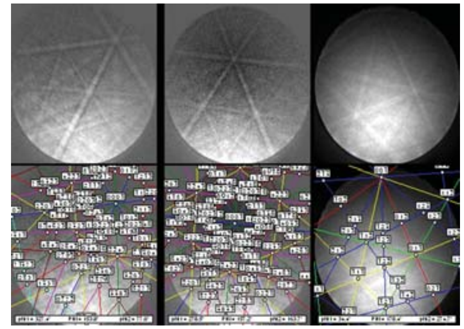

Fig.1 Kikuchi patterns and indexation for different ferrites; left and middle: $BaFe_{12}O_{19}$ in two different orientations, right: $(Ni,Zn)Fe_2O_4$.

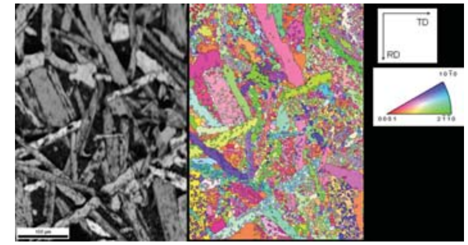

Fig.2 IQ-map and inverse pole figure map in (0 0 1) direction (i.e., perpendicular to the sample surface) of Ba-ferrite; the corresponding color code for the IPF map is given on the right side.

FH-04

Oxide electrode on LAO (110) substrate for studying low-symmetry perovskite oxides.

J. Kim[1], J. Kim[1], H. Na[1], B. Lee[1], I. Choi[1], C. Jung[1], S. Chae[2]
1. Dept. of Physics, Hankuk University of Foreign Studies, Yongin, South Korea; 2. School of Physics and Astronomy, Seoul National University, Seoul, South Korea

Perovskite oxides distorted from cubic structures have shown interesting properties. These include ferromagnetic insulator of YTiO3, Multiferroicity in BiMnO3 and BiFeO3.[1-3] The in-plane asymmetric atomic arrangements at the substrate surface of LAO(110) substrate allowed us to grow epitaxial thin films of YTiO3, which have an orthorhombic crystal structure with quite different a- and b-axes lattice constants.[1,4]
This time we tried to develope an oxide electrode on LAO (110) substrate for studying low-symmetry perovskite oxides. This oxide bottom electrode should have a metallic properties down to low temperature where interesting magnetic transition occours and should be grown coherently on top of LAO (110) substrate. While SrRuO3 is too big to be grown coherently and metallically on top of LAO(110) due to rather large mismatch, CaRuO3 (CRO) is a highly distorted perovskite oxide with smaller lattice constant.[4,5]
The CaRuO3 thin films were grown on the LaAlO3 (110) substrate using a pulsed laser deposition technique. A ceramic CaRuO3 target was ablated by using a KrF laser with a fluence of 2-3 J/cm^2 at 3-4 Hz. The base pressure of the vacuum chamber was 1×10^{-9} Torr. The oxygen partial pressure, P_{O2} was maintained at 60 mTorr. The temperature of substrate was varied from 640 °C to 800 °C and were cooled slowly to room temperature under a constant PO2. The high resolution x-ray diffractor meter (D8 discovery, Bruker) was used to characterize the crystallinity of CaRuO3 thin films. Figure 1 shows the x-ray diffraction θ-2θ scan pattern of CaRuO3 thin films grown at different growth temperature from 640 °C to 800 °C. The x-ray diffraction pattern shows only clear CaRuO3 single phase peaks with LaAlO3 substrate peaks. As the growth temperature increased, the intensity of CaRuO3 peaks was increased. The peak of CaRuO3 was also shifted which indicates that the volume of CaRuO3 is increased. [In this paper, we choose the pseudo-cubic unit cell notation for LAO and CRO]
Figure 2 shows the reciprocal space mapping of CaRuO3 thin films grown at different temperature, i. e., 740 °C and 800 °C. At 740 °C, the CaRuO3 thin films was grown coherently according to the LaAlO3 (110) substrate as shown in Figs. 2 (c) and (d). However, as the growth temperature increased up to 800 °C, the relaxation of peak was enhanced as shown in Figs 2(a) and (b). This indicates that the higher temperature for film growth might resulted in the volume expansion and lattice relaxation of inplane lattice constant of CaRuO3 thin film.
Figure 3 shows the temperature dependence of resistance of CaRuO3 thin films. As the temperature decreased, the resistance of CaRuO3 thin films was decreased which indicates the clear metallic properties of CaRuO3 thin films.[6] However, the resistance of CaRuO3 thin films shows different low temperature dependence and high temperature dependence. The linear $T^{0.5}$ dependence was observed above 50 K, whereas the linear $T^{1.5}$ dependence of resistance to below 50 K.

[1] S. C. Chae, Y. J. Chang, S. S. A. Seo and T. W. Noh, D.-W. Kim, and C. U. Jung, Appl. Phys. Lett. 89, 182512 (2006).

[2] J. Y. Son, Bog G. Kim, C. H. Kim, and J. H. Cho, Appl. Phys. Lett. 84, 4971 (2004).

[3] J. Wang, et al., Science 299, 1719 (2003).

[4] C. U. Jung, H. Yamada, M. Kawasaki, Y. Tokura, Appl. Phys. Lett. 84, 2590 (2004).

[5] G. Cao, S. McCall, M. Shepard, and J. E. Crow, Phys. Rev. B 56, 321 (1997), T. He and R. J. Cava, Phys. Rev. B 63, 172403 (2001).

[6]. S. Yamada, N. Fukuoka, T. Taniguchi, T. C. Ozawa, Y. Nagata, T. Uchida, and H. Samata, Thin Solid Films 478, 1 (2005).

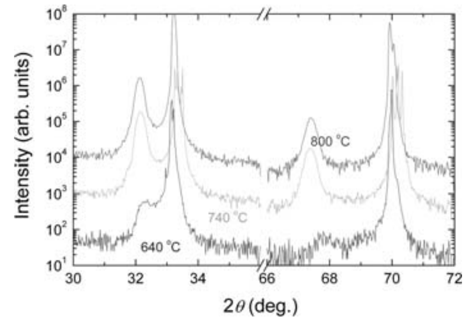

Fig. 1 X-ray diffraction patterns of CaRuO3 thin films grown at different temperatures on LaAlO3 (110) substrates.

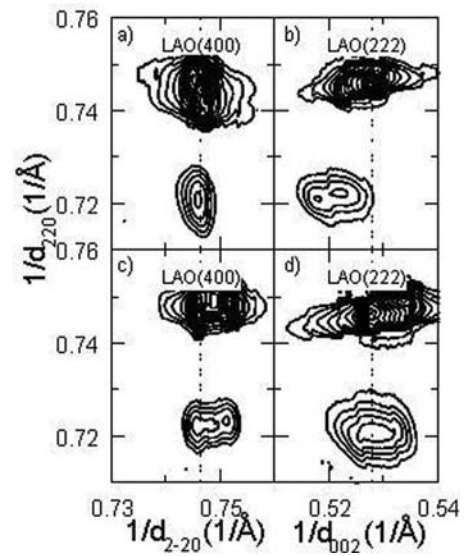

Fig. 2 X-ray reciprocal space mapping around the LaAlO3 (222) and LaAlO3 (400) peaks for CRO film grown at 800 oC (a), (b) and for CRO film grown at 740 oC (c), (d).

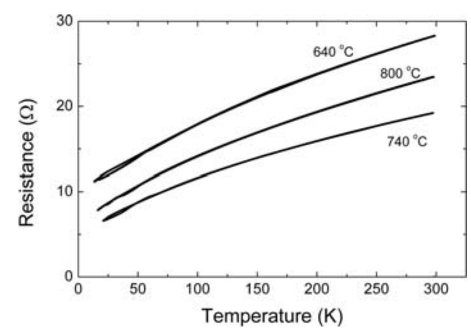

Fig. 3 Temperature dependence of resistance of CaRuO3 thin films.

FH-05

Mössbauer studies of the $Co_{1-x}Zn_xFe_2O_4$ Ferrite.

Y. Zhang[1], X. Yuan[1], Z. Ren[1], Z. Kou[1], X. Bai[2], *Y. Zhai*[1,2], Y. Xu[3], J. Du[2], H. Zhai[2]
1. Department of Physics, Southeast University, Nanjing, China; 2. National Laboratory of Solid Microstructures, Nanjing University, Nanjing, China; 3. Department of Electronics, University of York, York, United Kingdom

Many methods have been developed to prepare nanosized ferrite, the structure and physical properties of ferrite nanoparticles are related to the preparation method and synthesis conditions, such as pH value, temperature and concentration, etc. [1, 2, 3]. This paper reports a series of nanoparticles of Co1-xZnxFe2O4 (x =0, 0.20, 0.40, 0.50, 0.60 0.7and 0.80) ferrites prepared by chemical coprecipitation method under the temperature of 100 centigrade and pH of 11-12. The structure and magnetic properties of the powders were characterized by XRD, VSM, SQUID and Mössbauer measurements. The precipitated particles showed single-phase fcc spinel structure for all samples with different compositions of zinc. The average grain sizes and the lattice parameters of samples increase from 8.359Å to 8.399 Å and 9nm to 6nm respectively as increasing the Zn content, estimated from X-ray diffractions.
The Mössbauer spectra were taken at room temperature with a 57Co(Pd). They are composed of two sets of sextets and one set of doublet as Zn content x<0.7, corresponding to the part of the particles which is in ferrimagnetic ordered state with two components due to Fe3+ ions at octahedral/tetrahedral sublattice sites and part of particles with non magnetic order phase as shown in Fig.1. By fitting, various Mössbauer parameters were obtained. The hyperfine magnetic fields of the octahedral and tetrahedral sites are reduced from 460kOe to 168 kOe and 411 kOe to 0 with increasing the doped Zn contents from 0 to 0.6, suggesting a parallel changing tendency of magnetization measured by VSM. This indicates that Zn cation enters into the tetrahedral sites. The relative area of the subspectra of each Fe site changes strongly with the content of Zn. The areas covered by doublet increase as ranging from 10% to 58.5% with increasing the Zn concentration, and the spectra change to a single doublet as the Zn content x≥0.7, The doublet component may be originated from the part in superparamagnetic state.
Magnetization measurements were performed for each obtained sample with a VSM and a SQUID at the temperature of 300k and 5k respectively, which may give some evidence to support Mössbauer measurements. The value of the saturation magnetization and the coercivity are all decreasing with the doping Zn content increasing at 300k, and the relationship between saturation magnetization and the Zn concentration at 5k is similar to that at 300K. The Magnetic parameters of Co1-xZnxFe2O4 nanoparticles exhibited a strong dependence on composition and temperature. Hysteresis loops of two representative samples of Co0.6Zn0.4Fe2O4 and Co0.3Zn0.7Fe2O4 are shown in Fig. 2. For the sample of Co0.6Zn0.4Fe2O4, a well defined hystersis loop with Hc = 25 Oe was obtained at room temperature, while for sample of Co0.3Zn0.7Fe2O4, the coecivity Hc is nearly zero, which is nearly 3000 Oe at 5K. The magnetization also shows a large change at 300k and 5K. For two representative samples of Co0.6Zn0.4Fe2O4 and Co0.3Zn0.7Fe2O4, the magnetization increases from 52 emu/g to 92 emu/g and 32 emu/g to 87 emu/g with decreasing temperature from 300 K to 5 K. The temperature dependence of magnetization for various Zn content, measured by SQUID for both field-cooled (FC) and zero-field-cooled (ZFC) samples under a 100 Oe field, was also found the meeting point Tb of the FC and ZFC curves, to decrease as the doped Zn contents increasing. The details of data, analysis, and discussion will be given in full manuscript.

This work is supported by NSFC in project of 50472049, JSFC (Jiangsu) in project of BK2004070, National Laboratory of Solid State Microstructures, Nanjing University,Director by Senior member of IEEE Hongru, Zhai; nunber:SM08554958.

[1] F. Congiu, G. Concas, G. Ennas, A. Falqui, D. Fiorani, G. Marongiu, S. Marras, G. Spano, A.M. Alberto, M. Testa, J. Magn. Magn. Mater. 272–276 (2004) 1561.

[2] M. Rajendran, R.C. Pullar, A.K. Bhattacharya, D. Das, S.N.Chintalapudi, C.K. Majumdar, J. Magn. Magn. Mater. 232 (2001) 71.

[3] N. Hanh, O.K. Quy, N.P. Thuy, L.D. Tung, L. Spinu, Physica B: Condens. Matter 327 (2003) 382.

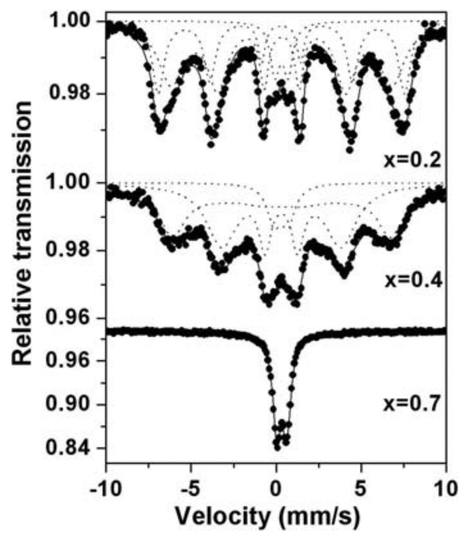

Fig. 1. Room temperature Mössbauer spectra of the $Co_{1-x}Zn_xFe_2O_4$ with Zn contents of 0.2, 0.4 and 0.7

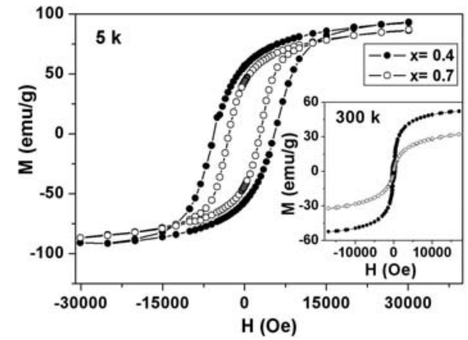

Fig. 2. Hysteresis loops of the $Co_{1-x}Zn_xFe_2O_4$ with x =0.4 and 0.7 measured at the temperature of 300 k and 5 k

FH-06

Synthesis of iron oxide nanoparticles of controlled size, shape and magnetic properties.

P. Guardia, A. Labarta, X. Batlle
Fundamental Physics, UB, Barcelona, Spain

Magnetic nanoparticles (MNP) are an ideal system to study finite-size and surface effects, all these yielding new interesting phenomena and enhanced properties with respect to their bulk counterpart [1]. Besides, the potential application of MNP for biomedical purposes relies on the synthesis of high quality materials, from both the crystalline and magnetic points of view. In this work, we report on the influence of a variety of parameters in the synthesis of iron oxide nanoparticles (magnetite/maghemite Fe3O4/Fe2O3) by the thermal decomposition of an organic iron precursor in an organic media [2]. It is well known that this method allows the preparation of highly crystalline MNP with excellent magnetic parameters [3,4]. We study the role of both the reductor and surfactant on the shape, size distribution and the magnetic properties. We aim at the synthesis of MNP with an average size of a few nanometers. A narrow size distribution of spherical particles with a high saturation magnetization of 80 emu/g at low temperature, is observed when using oleic acid as a surfactant. In contrast, decanoic acid yields a wider size distribution of cubic particles with a large saturation magnetization within 90-110 emu/g at low temperature. The use of a variety reductors also monitors the magnetic behaviour. In the case of hexadecanediol, nanoparticles have a uniform oxidation and a saturation magnetization similar to the bulk counterpart. In contrast, hidracine seems to promote a non-uniform oxidation that results in the appearance of exchange bias and in a smaller saturation magnetization of about 70 emu/g. The funding from the Spanish MEC (NAN2004-08805-CO4-02, NAN2004-08805-CO4-01, CONSOLIDER CSD2006-12 and MAT2006-03999), and from the Catalan DURSI (2005SGR00969) is acknowledged.

[1] X. Batlle and A. Labarta, J. Phys D: Appl. Phys 35 (2002) R15.

[2] P. Tartaj, et al, J. Phys D: Appl. Phys 36 (2003) R182

[3] S. Sun et al, J. Am. Chem. Soc. 126 (2004) 273.

[4] L. Zhen et al., Chem. Mater. 16 (2004) 8 1393

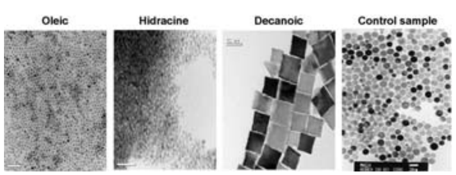

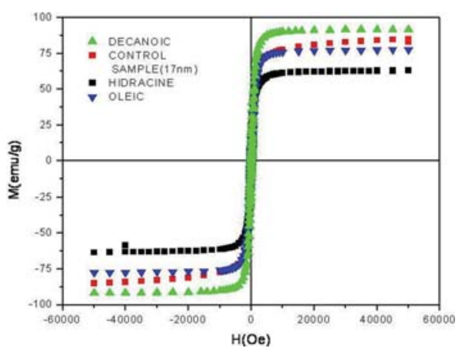

FH-07

The dispersion of $BaFe_{12}O_{19}$ particles in a liquid.

D. Lisjak[1], M. Drofenik[1,2]
1. Jozef Stefan Institute, Ljubljana, Slovenia; 2. Faculty of Chemistry and Chemical Engineering, University of Maribor, Maribor, Slovenia

$BaFe_{12}O_{19}$ (BaM) is a well-known material suitable for various applications, like hard magnets, magnetic recording, microwave and mm-wave devices and absorbers. Depending on the application BaM is used in the form of bulk, powder, films or composites. Composites are of special interest. The repeatability of the synthesis and the ultimate control of the composite's behaviour can only be achieved by a homogeneous incorporation of fully dispersed (= non-agglomerated) particles in the matrix. All particles tend to agglomerate due to Van der Waals attractive forces when they approach at distances of a few nanometres. However, attractive magnetic forces are much stronger and act at longer distances than Van der Waals forces. So the main problem in the synthesis of magnetic composites is to overcome the magnetic attraction between the particles and consequently, to prevent their agglomeration.
The existing solutions to the agglomeration problem have been addressed for soft magnetic particles, which can be synthesized directly in a carrier liquid or in a polymer matrix at low temperatures. The particles' surfaces are coated with a thin non-magnetic layer, which prevents any magnetic attraction between the particles. Such surface-modified particles can then be subsequently incorporated into various matrices. Most often superparamagnetic particles are used for the preparation of ferrofluids. In this case any magnetic attraction is absent in the absence of an external magnetic field and only the Van der Waals attraction has to be considered. Minimum temperatures of 500°C are required for the crystallization of BaM, and these temperatures are too high for any synthesis in liquids. On the other hand, hard magnetic particles of BaM become superparamagnetic at a diameter of around 3 nm, due to their large magnetocrystalline anisotropy. However, the synthesis of such small BaM particles is not trivial. The aim of this work was to study another possibility: the de-agglomeration of single-domain BaM particles in liquids.
Commercial BaM particles (Aldrich) with an approximate mean diameter of 100 nm and with an approximate mean thickness of 50 nm were chosen for this study. The particles exhibited a remanent magnetization of 17 A/m2kg, a coercivity of 306 kA/m and a magnetization of 31 A/m2kg at 1 T. The field of 1 T was not enough to saturate the particles. The contribution of the magnetic attraction between the BaM particles with respect to the Van der Waals attraction was estimated on the basis of known equations (refs. 1,2), and was several orders of magnitude larger than the Van der Waals attraction energy (Fig. 1). The magnetic attraction energy between such particles is lower than the thermal energy at separation distances larger than 10 nm. This means that such particles would be stable if they were covered with a nonmagnetic layer with a minimum thickness of 5 nm. The BaM dispersions were prepared using ultrasound or milling. Two surfactants, dodecylbenzenesulfonic acid (DBSa) and Sarkosyl "O" (SO), were examined for the electrosteric stabilization of the particles. The stability of the BaM particles in water was determined with sedimentation tests and with zeta-potential measurements. The zeta-potential measurements indicated that the surfaces of the particles were modified regardless of the conditions used. The sedimentation of particles treated with the DBSa started after 5 min, while the sedimentation of particles treated with SO started after just 1 min. The dispersions prepared with milling and with DBSa were significantly more stable than the others prepared with the ultrasound. The particles only settled under an external magnetic field.
The dispersed particles were further analyzed with thermogravimetry coupled with mass spectroscopy. The thickness of the DBSa layer was estimated to be thick enough (>5 nm) to prevent the particles' agglomeration. Nevertheless, only dispersions prepared with milling were really stable. This can be explained by the fact that the milling was more efficient in breaking the pre-existing agglomerates in the raw powder than was the ultrasound. As was observed with a transmission electron microscope, in the latter case, the DBSa did not only coat the dispersed particles, it also completely covered the smaller agglomerates in their entirety. Measurements of the magnetic and magnetorehological properties of the stable dispersion were also performed and will be presented.

1. S. Taketomi, R. D. Shull, J. Magn. Magn. Mat., **266**, (2003), 207;

2. P. C. Sholten, J. Magn. Magn. Mat., **39**, (1983), 99

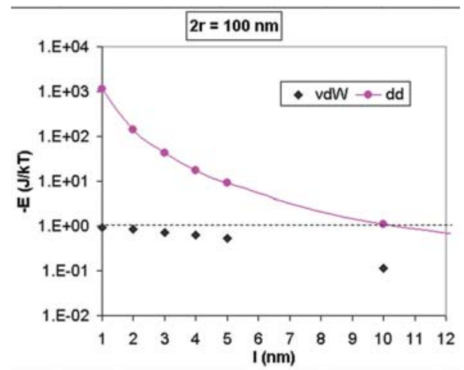

Figure 1: Van der Waals (vdW) and magnetic dipole-dipole interaction (dd) energy of the BaM with respect to the separation distance between the particles

FH-08

FREEZE Granulation:A novel technique for low-loss MnZn ferrites.

V. Tsakaloudi, G. Kogias, V. T. Zaspalis
Laboratory of Inorganic Materials, Centre for Research and Technology Hellas, Thermi-Thessaloniki, Greece

It is widely accepted that the magnetic quality of MnZn ferrites in terms of high initial permeability and low power losses lies on an optimized combination of chemical and morphological homogeneity of the sintered ferrite[1]. This study focuses on the evaluation of freeze granulation and subsequent freeze-drying,a novel technique applied on ferrite processing, on the quality of the compacted specimen and, consequently,on the magnetic quality of the final sintered MnZn ferrite.
The conventional spray-drying method, used in production-scale processing of MnZn ferrites,shows significant drawbacks,such as inflation defects visible as large voids in the interior of the granule.Moreover,the rapid water evaporation gives rise to the development of capillary stresses that may iniate undesirable diffusion phenomena that reduce the compositional and morphological homogeneity of the granule. Those imperfections may resist compaction and also be present in the compacted specimens[2].Freeze granulation on the other hand,is based on the spraying of the slurry droplets into liquid N_2 followed by subsequent freeze-drying.It is advantageous in terms of homogeneous granule density,absence of cavities in the granules,since due to elimination of the evaporation step it doesn't involve any capillary action and shrinkage of the droplet.The achieved homogeneity and density of the granule are retained after sublimation[3].
In this study, MnZn ferrite powders have been prepared by the conventional ceramic route as reported elsewhere[4].After mixing,prefiring and milling,binder is added to the slurry of the milled powder that is separated in two fractions.The first fraction is spray-dried,while the other is freeze-granulated and subsequently freeze-dried.The quality of granulates is compared through compaction testing,electron microscopy observation of granulates and compacted cylinders after BBO,pore surface area determination and power loss measurement of sintered toroids under equilibrium partial pressures of oxygen[5].
The observation of the microstructure of pre-sintered pressed cylinders so that the binder is burnt out,has shown that in the case of spray drying there is a strong "memory effect" that follows the compacted specimen during the sintering process.The granule structure can be recognized in the structure of the compacted specimen.This morphological inhomogeneity is now found to accompany the specimen during the sintering process,as the granule area can be clearly seen and even the intragranular void can be detected.It is,therefore,most possible that the temperature increase during sintering will lead to the entrapment of the voids and,finally,to the formation of isolated intragranular pores which will affect the sintered density and,consequently deteriorate the magnetic quality of the final MnZn ferrite.On the contrary,the cylinder prepared form granules after freeze-granulation is characterized by a totally homogeneous microstructure,where any voids or cavities of potential isolated pore formation are absent.
The Pore Size Distribution presented in Figure 1 of pre-sintereds pecimens compacted from the spray-dried and freeze-granulation processes confirms the above characteristics.In the case of the spray-drying process the total pore surface area remaining is much larger than in the case of freeze-granulation.The increased pore surface area will most probably lead to a decreased sintered density and lower magnetic quality of the final MnZn ferrite.The magnetic characterization of the sintered toroids at 100 kHz-200 mT indicated that freeze granulation leads to sintered toroids with lower power losses at lower densities,in comparison to the spray-dried granules,as presented in Figure 2.

The above results indicate that the novel technique of freeze granulation offers advantages in the MnZn ferrite manufacturing since it leads to better green compact microstructures and finally to better magnetic quality products.A draw-back of the process is the low bulk density of the granulated matter.This will have as unavoidable consequence a re-design of the pressing tools.

[1] A.Goldman, Handbook of Ferromagnetic Materials, Kluwer Publ., London 1999

[2] V.Zaspalis, V.Tsakaloudi, J. Am. Ceram.Soc. 87, 5 (2004) 824-829

[3]. B.Nyberg et al, Euro-Ceramics II, Vol.1, Deutsche Keramische Gesellschaft, 1993

[4]. V.Tsakaloudi, V.Zaspalis, J. Magn .Magn. Mater. 2, 3 (2007) 2540-2542

[5]. R.Morineau, M.Paulus, IEEE Trans. Magn. 5 (1975) 1312-1316

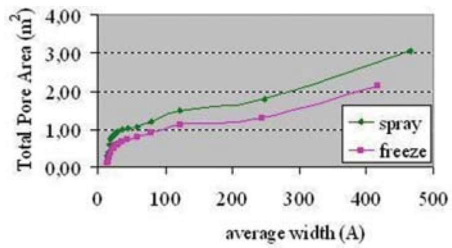

Pore size distribution in pre-sintered cylinders prepared from spray-dried and freeze-processed powders.

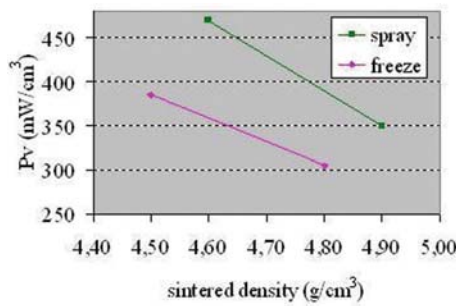

Power loss comparison at 100 kHz-200 mT-100<0>C between spray-dried and freeze-processed sintered toroids.

GA-01

Achieving tight physical and magnetic sigmas in bit patterned media recording disks.

D. Weller[1], A. Y. Dobin[1], D. Kuo[1], K. Y. Lee[1], J. Hwu[1], X. Yang[3], S. Xiao[3], G. Gauzner[1], M. Feldbaum[1], M. Ostrowski[2], G. Ju[3], H. J. Richter[1], B. Lu[1], B. Valcu[1], X. Zhu[3], R. van de Veerdonk[3]
1. Media R&D, Seagate Technology, Fremont, CA; 2. Recording Heads Operations, Seagate Technology LLC, Normandale, MN; 3. Research, Seagate Technology LLC, Pittsburgh, PA

Bit patterned media (BPM) is one option to extend areal density growth in magnetic recording to and beyond Terabit per square inch (Tbpsi) [1]. This technology relies on recording single bits on single magnetic islands (dots), which are pre-patterned on a rotating storage disk. There are many system challenges related to servo and bit formatting, in particular, avoiding write errors due to mis-synchronization of the write field relative to the bits. Entering into this problem are sigmas of size and placement and magnetic anisotropy of the dots. These need to be kept extremely tight to about 5% (1 sigma) as a percentage of size, spacing and Hk. Recording physics modeling indicates that densities approaching 10 Tbpsi are possible if this condition is met by combining BPM and domain wall assisted (exchange spring) media with trailing/side shield writers [2].

Electron Beam Writing (EBW), resist materials and developing strategies are in place to generate appropriate resolution with tight sigmas up to at least 2 Tbpsi [3]. More relevant rotating stage e-beam recordings for disks have been achieved up to about 450 Gbpsi. The developed resist pattern is transferred via reactive ion etching into a thin quartz substrate to form a template suitable for subsequent UV cure nano-imprint lithography (NIL). This intermediate NIL process is necessary to contain cost in a future manufacturing scenario. Different options exist to convert the imprinted resist pattern into magnetic islands: (1) etch pattern into disk substrate and coat over with magnetic film, (2) etch nanoholes in a dielectric down to a seed layer, e.g. Ru, and plate up magnetic material, e.g. Co3Pt or (3) carboxyl reactive ion etch or ion beam etch pattern into a full perpendicular film stack recording disk, based on CoX alloys or multilayers. Planarization of the surface to minimize any residual topography (roughness) is critical to achieve good flyability, especially when crossing from servo to data zones.

Fig 1 shows representative MOKE hysteresis curves of a continuous, non-granular CoX film before and after patterning at 250 Gdpsi. Dot size and placement sigmas of the patterned film is <5% (1 sigma). Analysis of the hysteresis curves using the Berger method [4] indicate switching field distributions (SFD) <5%. Complementary transverse susceptibility (TS) data indicate an intrinsic sigma_Hk of 4.5% [5] (Fig 2). Table 1 summarizes typical magnetic data from such patterned films and Fig 3 shows MFM images of an ac-demagnetized sample, indicating well resolved dots.

The main conclusion of the paper is that tight intrinsic magnetic sigmas of less than 5% are achievable in BPM at 250 Gdpsi. Maintaining these sigmas at Tbpsi and beyond and synchronizing the write timing to the patterned dots remain critical challenges going forward.

[1] H. J. Richter et al, APL 88, 222512 (2006); IEEE Trans Mag 42, 2255 (2006).

[2] A.Y. Dobin et al., Intermag 2008 (to be published).

[3] X. Yang et al., J. Vac. Sci. Tecnolog. B 25, 1071 (2007).

[3] A. Berger et al., IEEE Trans Mag. 41, 3178 (2005); J. Appl. Phys. 99, 08E705 (2006).

[4] G. Ju et al., J. Appl. Phys., 99, 083902 (2006); IEEE Trans. Mag. 43, 627 (2007).

Film	Thickness (nm)	Hc (Oe)	Hn(Oe)	Ho(Oe)	KuV/kT	SFD(%)	Sigma_Hk (%)
CoX	16	6340	5260	10280	320	4.9	4.5

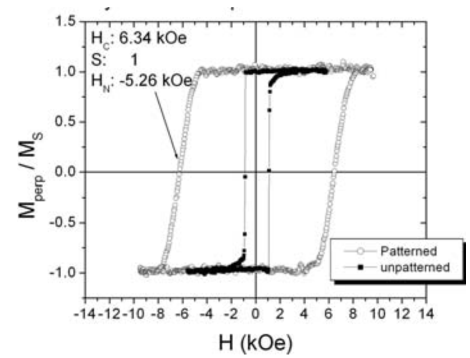

Fig 1: Perpendicular MOKE hysteresis curves of CoX before and after patterning at 250 Gdpsi.

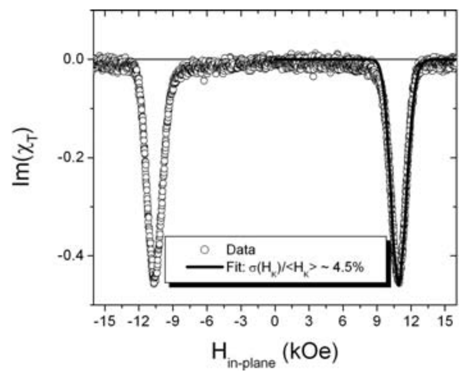

Fig 2: TS measurements of the patterned films in Fig. 1 indicating tight intrinsic sigma_HK=4.5%.

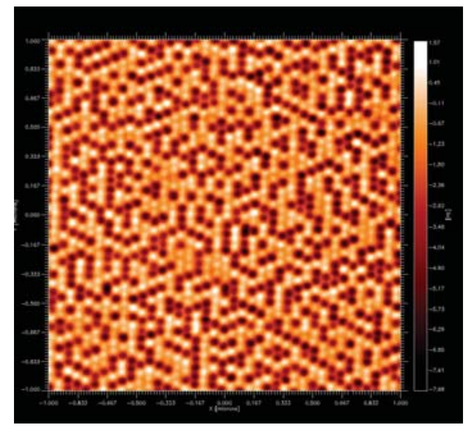

Fig 3: MFM image of an ac-demagnetized 250 Gdpsi patterned media sample.

GA-02

Modeling and Simulation of the Writing Process on Bit-Patterned Perpendicular Media.

H. Muraoka[1], S. J. Greaves[1], Y. Kanai[2]
1. RIEC, Tohoku University, Sendai, Japan; 2. Niigata Institute of Technology, Kashiwazaki, Japan

Bit-patterned perpendicular magnetic media are strong candidates for extending the thermal stability limit of current granular media [1]. However, since all of the bits are pre-fabricated, the physical structure is fundamentally different from conventional media and the write/read scheme must be totally re-established. Extraction of the necessary control parameters to maximize the recording density and to optimize performance is indispensable. The recording performance is known to be governed by various patterning fluctuations, such that the major media noise source is the dispersion of patterned dots [2]. The statistical characteristics of these fluctuations are therefore important. In this work, the influence of pattern fluctuations in experimental samples is discussed to determine the appropriate writing process, based on a recording model of bit-patterned media. Computer simulations were used to demonstrate the effectiveness of the model by maximizing the areal recording density through optimization of the media fabrication and recording conditions.

Unlike conventional, granular recording media, in which the micro-magnetic structure of the recording layer determines media noise, the noise in patterned media is dominated by fluctuations in the size and position of the patterned dots [3]. Measurements of these fluctuations were made for dot patterns fabricated by electron beam lithography. The statistical characteristics did not perfectly obey Gaussian distributions. The fluctuation of line edge roughness had dominant low frequency components for random distributions [4]. The measured line edge roughness was compared with several simulated random patterns created from Voronoi cells, and is shown in Fig 1. Auto-correlation of the location of neighboring patterns, indicated a positive, finite correlation. A random distribution was not observed in this sense.

Bit errors during writing (written-in errors) are fatal and dominant in bit-patterned media. The necessary condition to avoid these errors is that the difference in the write head field between any pair of neighboring dots exceeds the overall switching field distribution (SFD) of the dots. The difference in the write field is the product of the dot pitch and the head field gradient. The SFD has to take account of the magneto-static field from surrounding dots. This slope model requires that the entire SFD should be less than the product of the head field gradient and the dot pitch. For example, in the case of a dot pitch of 12.7 nm (2 Tbit/in^2 with an aspect ratio of 2), a head field gradient of 300 Oe/nm requires an overall SFD of 3810 Oe, which corresponds to a small standard deviation of 420 Oe to satisfy an error rate of 10^{-6} (4.5 σ).

Computer simulations of bit-patterned media were carried out. A shielded, single-pole writer with a tapered main pole was assumed and the head field distribution was calculated using a FEM model. Fig. 2 shows an example of successfully written bits at 2 Tbit/in^2. There are seven tracks shown, of which the center track was written with a …010101… pattern. The background dots were randomly pre-programmed to include magneto-static interference. The magnetic dot size was optimized before this writing test. Accurate write synchronization within approximately 2 nm was required in this case. Adjacent Track Erasure is another critical issue for error-free writing.

[1] R.L. White, R.M.H. New, R.F.W. Pease, IEEE Trans. Magn., 33, 990-995, 1997

[2] H.J. Richter, A.Y. Dobin, K.Z. Gao, R.J.M.v.d. Veerdonk, R.T. Lynch, J. Xue, D. Weller, P. Asselin, M.F. Erden, R.M. Brockie, IEEE Trans. Magn., 42, 2255-2260, 2006

[3] M. Albrecht, A. Moser, C.T. Rettner, S. Anders, T. Thomson, B.D. Terris, Appl. Phys. Lett, 80, 3409-3411, 2002

[4] M. Hashimoto, K. Miura, H. Muraoka, H. Aoi, R. Wood, M. Salo, Y. Ikeda, Digests of PMRC 2007, 16aA-01, 146, 2007

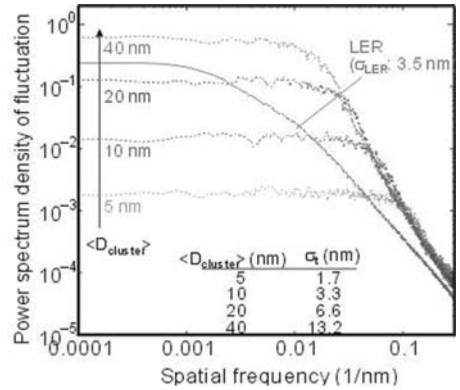

Fig.1 Measured power spectrum density of line edge roughness by electron beam lithography. The measurement, shown by the solid line, is compared with four simulations (dotted lines).

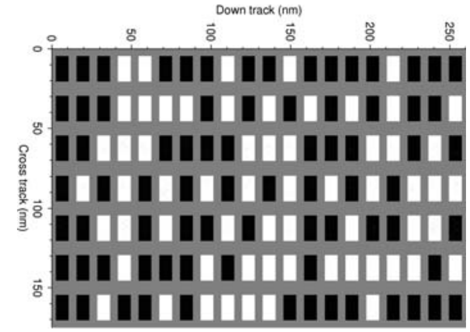

Fig. 2 A written track obtained from LLG simulations of 2 Tbit/in^2 bit patterned media at 300 K. The center track was written over random background dots. The writer had a 20 nm wide, 30 nm long main pole with a 235 Oe/nm gradient. The bit cell was 25 nm × 16 nm with a dot size of 16 nm × 8 nm.

GA-03

Nanoscale perpendicular magnetic island arrays fabricated by extreme ultraviolet interference lithography.

F. Luo, L. J. Heyderman, H. H. Solak
Laboratory for Micro- and Nanotechnology, Paul Scherrer Institut, Villigen, Switzerland

The increase of the recording density in hard disk drives has been achieved mainly by decreasing the size of the magnetic grains which record bits in the storage layer. However, the recorded data can be erased by thermal fluctuations of the magnetization when the grain volume is reduced so much that the magnetic energy per grain becomes comparable with the thermal energy. By patterning the magnetic recording media into isolated small elements, referred to as bit patterned media (BPM), the onset of this superparamagnetic effect can be delayed. In order to determine the viability of BPM for future magnetic recording, it is important to determine which factors (e.g. lithographic irregularities, distribution of intrinsic magnetic anisotropy, and magnetostatic interaction of the neighbouring islands) give the most important contributions to the switching field distribution (SFD).

In the current work, 50 nm-period arrays of magnetic islands with perpendicular anisotropy were fabricated by depositing Co/Pd multilayer films on substrates pre-patterned with SiOx pillars fabricated with extreme ultraviolet interference lithography (EUV-IL). This fabrication technique has the advantage that it not only provides high resolution, with periods own to a theoretical limit of 6.5 nm (half the EUV wavelength) and precise positioning of nanostructures, but also provides a high throughput (with parallel processing and exposure times in the 5-30 second range) and can expose large areas up to several mm's, depending on the structure size. The array of magnetic islands created on top of the SiOx pillars is magnetically decoupled from the magnetic material in the trenches between the pillars. This is facilitated by the negative sidewall profile of the pillars which prevents deposition of magnetic material on the pillar sidewalls.

The effect of the size distribution on the SFD was investigated on a 50 nm-period array. In order to unambiguously identify individual islands we chose three inhomogeneously exposed areas (comprising a total of 289 magnetic islands) at the edge of a SiOx pillar array. This allowed easy identification of each island so that it was possible to match each island switching field measured with magnetic force microscopy (MFM) with the island size measured with high resolution SEM. A map of switching fields for each individual island is shown in Fig. (a): the color corresponds to the switching field and the size is proportional to the magnetic island size measured from the SEM images. Fig. (b) and (c) show the distribution of switching fields and island diameter for all of the 289 islands measured together with Gaussian fits. The Gaussian fit of the size distribution yields σ = 1.2 nm (σ/<mean> = 5%), demonstrating the narrow size distribution obtained from EUV interference lithography. The mean switching field is 7200 Oe with σ = 830 Oe (σ/<mean> = 11.5%) which is comparable with previous results on samples produced by e-beam lithography [1]. Simulations of an SFD due solely to magnetostatic interactions show that these interactions are not responsible for the majority of the SFD. In addition, we do not observe a strong dependence of the switching field distribution on the island size. These results imply that it is rather a distribution of material properties, such as anisotropy, which is responsible for the SFD, in agreement with previous work [2].

In conclusion, we have fabricated perpendicular nanoscale magnetic island arrays on pre-patterned substrates with periods of 50 nm by EUV-IL. SEM and MFM measurements on the same islands allowed a direct comparison of the island sizes and switching fields. The results indicate that the SFD is dominated by a distribution of the material properties. Therefore it should be possible to decrease the SFD by improving the material homogeneity. Recent advances in EUV-IL have demonstrated that periods of 25 nm are achievable providing a competitive technology for fabrication of future data storage devices at 1 Tbit/in2.

[1] O. Hellwig, A. Berger, T. Thomson, E. Dobisz, Z. Z. Bandic, H. Yang, D. S. Kercher, and E. E. Fullerton, Appl. Phys. Lett. 90, 162516 (2007).

[2] T. Thomson, G. Hu, and B. D. Terris, Phys. Rev. Lett. 96, 257204 (2006).

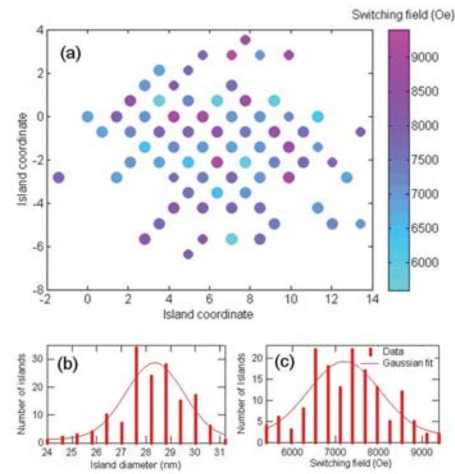

FIG. (a) Map of switching fields for each individual island: the color corresponds to the switching field and the size is proportional to the magnetic island size measured from an SEM image; (b) the distribution of island diameters (σ/<mean> = 5%) and (c) the distribution of remanent switching fields (σ/<mean> = 11.5%). The solid lines are Gaussian fits from which the array mean and sigma are determined.

Magnetic films on self-assembled nanoparticles: An approach for bit-patterned media.

M. Albrecht[1], C. Brombacher[1], H. Rohrmann[2], P. Kappenberger[4], O. Hellwig[3], A. Goncharov[5], T. Schrefl[5]

1. Institute of Physics, Chemnitz University of Technology, Chemnitz, Germany; 2. Data Storage, OC Oerlikon Balzers AG, Balzers, Liechtenstein; 3. San Jose Research Center, Hitachi Global Storage Technologies, San Jose, CA; 4. Nanoscale Materials Science, Empa, Duebendorf, Switzerland; 5. Department of Engineering Materials, University of Sheffield, Sheffield, United Kingdom

In modern magnetic recording materials the ‘superparamagnetic effect’ has become increasingly important as new magnetic hard disk drive products are designed for higher storage densities. In this regard, patterned media [1], where two-dimensional arrays of nanostructures with high magnetic anisotropy are used, is one of the concepts that might provide the required areal density in future magnetic recording devices.

In this presentation, I will introduce a novel magnetic gradient nanomaterial, which has been created by depositing Co/Pd multilayers onto two-dimensional arrays of self-assembled nanoparticles [2] as depicted in figure 1A. The so-formed nanostructures are monodisperse, magnetically exchange decoupled, single-domain, and exhibit a uniform magnetic anisotropy with an unexpected switching behavior induced by their spherical shape [3]. The Co layer thickness dependence and the bilayer dependence was studied for various particle sizes. Equivalent nanostructures can also be fabricated by Co/Pd film deposition into spherical indentations formed by spherical particle arrays [4] as shown in figure 2.

Recently, this approach was also extended to further thin film systems providing perpendicular magnetic anisotropy, i.e. FePt and CoPtCr-SiO2 alloys. For the latter, it is well known that the intergranular exchange can be controlled by the SiO2 content and by the sputter pressure during film deposition. It turned out that by tuning the growth conditions single domain nanocaps with enhanced magnetic coercivity fields can be achieved even for particle sizes down to 10 nm.

The authors greatfully acknowledge the financial support by the European Commission through the EU project ‘MAFIN’ (FP6-026513).

[1] T. Thomson, B.D. Terris, J. Phys. D 38, R199 (2005).

[2] M. Albrecht et al., Nat. Mater. 4, 203 (2005).

[3] T. Ulbrich et al., Phys. Rev. Lett. 96, 077202 (2006).

[4] D. Makarov et al., Appl. Phys. Lett. 90, 093117 (2007).

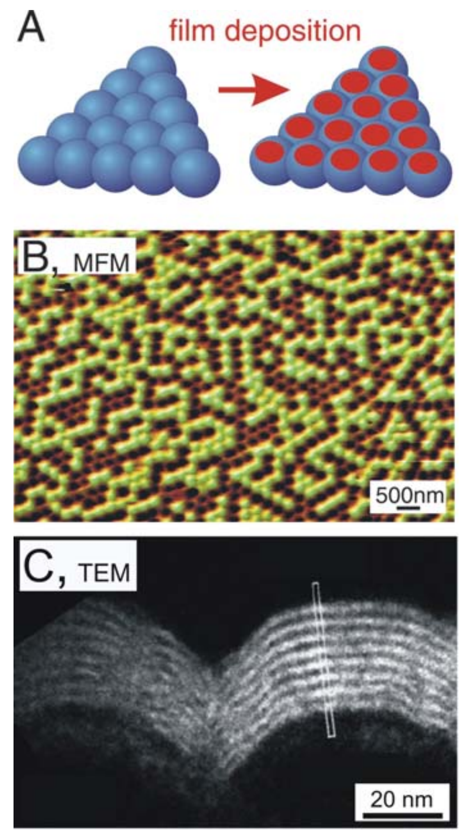

Figure 1: A, Schematic image showing the fabrication of cap structures onto a particle array. B, MFM image of an array of single-domain magnetic Co/Pd caps. C, TEM cross section image of 70 nm SiO2 particles capped with a Co/Pd multilayer film.

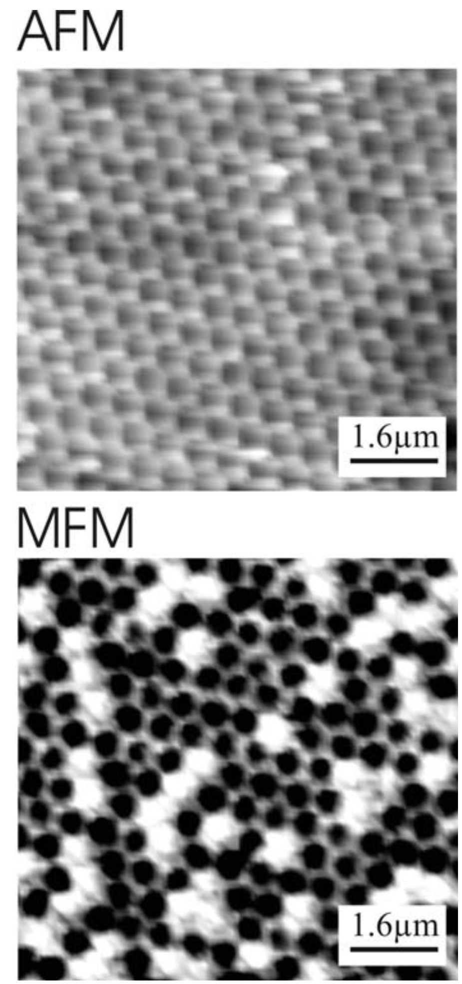

Figure 2: AFM and corresponding MFM image of the created mold after Co/Pd multilayer film deposition.

GA-05

Self-Assembly Pattern Multiplication for $1Tb/in^2$ Patterned Media Templates.

R. Ruiz[1], E. Dobisz[1], D. S. Kercher[1], T. Wu[1], T. R. Albrecht[1], H. Kang[2], P. F. Nealey[2]
1. San Jose Research Center, Hitachi Global Storage Technologies, San Jose, CA; 2. Department of Chemical and Biological Engineering, University of Wisconsin, Madison, WI

Patterned media for storage applications at densities beyond $1Tb/in^2$ requires fabrication of periodic patterns at 27nm full pitch and smaller. Templating patterns at these dimensions is particularly challenging when considering the stringent quality restrictions imposed by storage applications in terms of feature size distribution, line edge roughness, placement and long-range ordering. We present here a guided self-assembly approach that combines e-beam lithography with block copolymer self-assembly. E-beam lithography is used to pre-pattern a guiding substrate defining features with registration and long-range orientational and translational order. A block copolymer film is applied on top of the guiding pattern. The uniformity of the self-assembled features effectively corrects noise and non-uniformities introduced by the e-beam and the e-beam resist. We use image processing to quantify the pattern quality rectification achieved by the block copolymer.
We also use this guided self-assembly approach as a pattern density multiplier. The self-assembled pattern can be used to multiply the density of e-beam features by at least a factor of four. This density multiplication approach enables the possibility to pattern features at resolutions not accessible by state-of-the-art e-beam lithography but still taking full advantage of its registration and long-range ordering properties.

GA-06

Fabrication and Characterization of High-density Patterned Media.

N. Yasui[1,2], S. Ichihara[1], T. Nakamura[1], A. Imada[1], T. Saito[1], R. Horie[1], Y. Ohashi[1], T. Den[1], K. Miura[2], H. Muraoka[2]
1. Canon Research Center, Tokyo, Japan; 2. RIEC, Tohoku Univ., Sendai, Japan

An anodic alumina template, as being known to have perpendicular holes and highly ordered hole array, is particularly excellent for patterned media application.
We have adopted AlHf alloy for suppressing the surface roughness. Therefore, the anodic alumina film with high-density ordered holes of 1.86Tdots/in^2 (honeycomb) and 1.61Tdots/in^2 (square) corresponding with 20nm period was obtained as shown in Fig. 1.
We have developed a new anodizing process in order to fabricate pillar structure.[1] The media fabrication process is as follows: 1) The AlHf(35nm) / Nb(32.5nm) / Ti(2.5nm) / CoZrNb(150nm) / Ti(5nm) layered film was deposited on Si disk substrate (1 inch size) by a conventional sputtering technique. The film with shallow dimples of a square array was formed by FIB as shown in Fig. 2(a); 2) When AlHf(35nm) layer was anodized at 10.8V and 20 degree C in sulfuric acid solution of 1mol/L, the anodic alumina film was obtained as shown in a cross-sectional schematic drawing of Fig. 2(b) and a plane-view SEM image of Fig. 2(b'); 3) Then second anodizing process on the condition of 18V and 20 degree C in ammonium borate solution of 0.15mol/L was applied for the anodized film. As shown in a cross-sectional schematic drawing of Fig. 2(c) and a plane-view SEM image of Fig. 2(c'), Niobium-oxide growth was promoted from the bottom area of the holes, which was caused from anodization of the Nb(32.5nm) layer. The top surface of the pillars was polished for flatness; 4) Figure 3(d) and 3(d'), which are a cross-sectional schematic drawing and a plane-view SEM image, show the standing Niobium-oxide pillars formed by etching the alumina part of the film for 5 hours in 5weight% phosphoric acid solution at room temperature. We successfully obtained the pillar structure from the porous structure by a new anodizing process; 5) Magnetic recording layer, which consists of the hcp-Co$_{70}$Pt$_{30}$ / Ru / Pt / Ti layered structure, was deposited on the pillar structure. Finally, the magnetic patterned media, as shown in Fig. 3(A), were fabricated by coating of lubricant and DLC layers. Every niobium oxide pillars had same height with 25nm period. Coating process was effectively done without obvious sidewall coating as shown in a cross-sectional TEM image of Fig. 3(B).
Figure 4(a) and 4(b) show the read-back signal waveforms from the media with 65nm period (153Gdots/in^2) and 25nm period (1.03Tdots/in^2) measured by a spin-stand respectively.[2] Figure 4(c) shows the read-back signal waveforms from the media with 25nm period measured by a static-tester. These read-back signals were measured from different position. The signals from the media with 65nm period in the flying condition were resolved into a bit length of 1dot, 2dots and 3dots. Next, the read-back signals from the media with 25nm period in the flying condition were not resolved into a bit length of 1dot, but resolved into a bit length of 2dots and 3dots. Furthermore, the read-back signals from the media with 25nm period in the contact condition were resolved into a bit length of 1dot, 2dots and 3dots. Thus we proved that the media with 25nm period (1.03Tdots/in^2) had a potential of 1Tb/in^2 in the contact condition.

[1] N. Yasui, S. Ichihara, T. Nakamura, A. Imada, T. Saito, Y. Ohashi and T. Den, J. Magn. Soc. Jpn., (submitted)

[2] N. Yasui, S. Ichihara, T. Nakamura, A. Imada, T. Saito, Y. Ohashi, T. Den, K. Miura and H. Muraoka, J. Appl. Phys., (to be published)

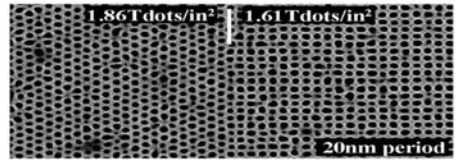

Fig. 1. Plane-view SEM image of anodic alumina template of 1.86 Tdots/in^2 (honeycomb) and 1.61 Tdots/in^2 (square).[1]

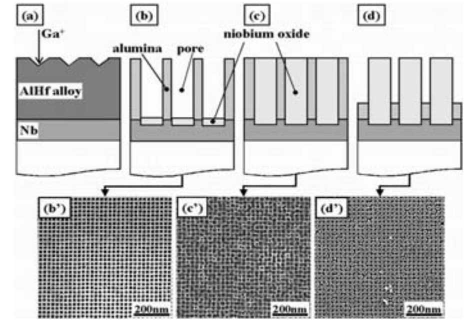

Fig. 2. Schematic drawings and SEM images of a new anodizing process flow.[1] (a) Dimple fabricated film. (b), (b')Conventional anodic alumina template. (c), (c') Niobium oxide growth. (d), (d') Niobium oxide pillar structure.

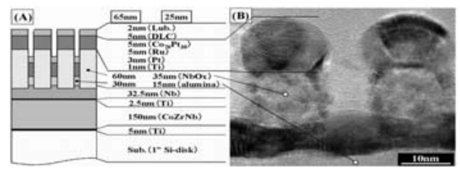

Fig. 3 (A) Layered structure of media with 65 nm and 25 nm periods. (B) TEM image of media with 25 nm period.[2]

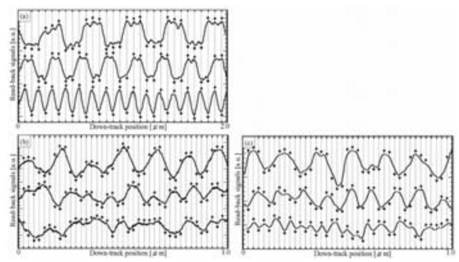

Fig. 4. Read-back signal waveforms of media with (a) 65nm and (b) 25nm periods in flying condition and media with (c) 25nm period in contact condition.[2]

GB-01

An investigation of noise increased in TMR readers during drive operation.

P. Wong
SAE Magnetics (HK) Ltd, Hong Kong, China

An investigation of noise increased in TMR readers during drive operation
Pak Kin Wong, Yi Mei Tam, Vincent M. F. Chiah and Tad Shimizu
SAE Magnetics (HK) Ltd.
Tunneling MR (TMR) reader head has been widely adopted in the production of hard disk drives with > 100 Gb/in2 recording density. With AlOx tunneling barrier, failure in drive reliability test due to barrier breakdown and pinhole development is rarely reported. Instead, the major failure mode in drive reliability test, with occurrence of 0~150dppm, is increase in noise after a few to hundreds of hours of drive operation. In this article, we report our investigations on the mechanism and possible triggers of such reader noise.

Figure 1 shows the typical instability observed after noise increased in drives. Firstly, we analyzed the failed readers for any distortion from the pre-set alignment of the magnetizations of the constituent layers of reader. High field QST technique is used, in which the reader response during field sweeping is captured. After each field sweeping, the reader noise is checked. We have observed that a small portion of the failure population have reader noise eliminated by sweeping field along the pre-set magnetization of the hard magnets (HM). The HFQST curves suggest a distortion of HM magnetization (Figure 2). The possible causes of HM distortion in drives will be discussed.
The noise in most of the failed readers cannot be eliminated by a sweeping field. We have applied field in HM direction of increasing magnitude to check at what magnitude the noise can be suppressed (Figure 3). We have found that the field required to suppress the noise falls between the field of reader shield saturation and HM saturation. After removing the field, the noise comes back. We conclude that the noise comes from the degradation of HM property, but in this case, it is not a non-permanent distortion in HM. To search for the reason of HM degradation, we put the failed heads at elevated temperature (140C) and observed a reduction in noise level, and in many cases, the noise is eliminated. Firstly, this indicates that the noise is not resulted from a degradation of HM remanence with thermal energy. Secondly, the recovery from noise hints a link between the noise and the mechanical stress which can possibly be relaxed or changed at elevated temperature. We have further investigated the effect of stress on the noisy heads. Mechanical deformations on the heads surface covering the whole reader is made by nano-indentation technique which a round-topped tip of 5um diameter. The deformation depth ranges from 3~6 nm, about 5% of the reader strip height (Figure 4). After such deformation, the noise level is significantly lowered and in most cases, the noise level comes down to be same as normal readers. Finally we conclude that the noise occurred in drive reliability test is likely caused by a modification of surface stress and morphology of the readers, instead of the intrinsic degradation of the HM. Further investigations imply that the stress related to noise occurrence is not intrinsic with the wafer geometries, but slider process related. Detailed results of the studies and a discussion on the possible mechanism of surface stress and morphology change in drive will be made in the article.

Figure 1. Unstable waveform after 339hours of drive operation.

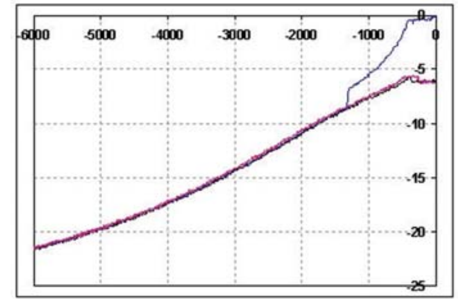

Figure 2. An example of HM distortion captured by high field QST. The field was swept along the direction of HM magnetization pre-set in production. The opening at zero field is closed with a field of 1300 Oe, which is the typical saturation field of HM in our shielded devices.

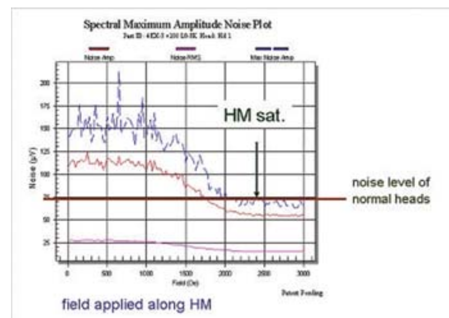

Figure 3. Noise is suppressed by applying a field along HM magnetization, with magnitude close to saturation field of HM.

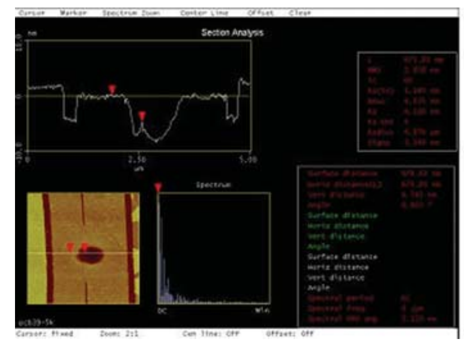

Figure 4. A shallow deformation around reader, 6nm in depth, made by a nano-indentor with tip diameter of 5um.

GB-02

Improvement of TMR effect of magnetic tunneling junctions with very thin MgO barrier sputtered by noble gas mixture at low RA product below 1.0 Ωμm^2

K. Noma[1], K. Komagaki[2], K. Sunaga[2], H. Kanai[2], Y. Uehara[2], T. Umehara[1]
1. Head Manufacturing, Fujitsu Ltd., Nagano, Japan; 2. Advanced Head Technology, Fujitsu Ltd., Nagano, Japan

1. Introduction

A Magnetic tunneling junction (MTJ) film with (001)-oriented MgO barrier layer is a hopeful material for a high-density read head because of its huge magnetoresistive ratio (MR-ratio) above 200%[1][2]. It is necessary to decrease RA product of the MTJ film to 1.0 Ωμm^2 for a development of the read heads of hard-disk drives with the areal recording density of 500 Gbits/in^2 because a junction size of 0.05 μm-square and a resistivity of the element below 400 Ω are required. However, MR-ratio of sputter-deposited MgO-based MTJ films rapidly dropped at RA below 1.5 Ωμm^2. The huge MR-ratio is caused by a coherent tunneling of electrons along [100] axis of the MgO crystallites[3] and imperfect crystallites at an initial layer of the MgO barrier seemed to increase an incoherent scattering and the decrease of MR-ratio at low RA. In this study, mixture of noble gases was used as a sputtering gas of the MgO barrier layer in the MTJ film for decreasing a density of vacancies caused by an impact with energetic particles on the surface or by a re-sputtering of oxygen atoms and their magnetoresistive characteristics were investigated.

2. Experiments

MTJ films were deposited on a silicon substrate at room temperature in an UHV sputtering apparatus. The structure of the MTJ films was underlayer/Ru/IrMn/CoFe/Ru/CoFeB/MgO/CoFeB/Ta/Ru. The MgO layer was sputtered with pure Ar, pure Ne or Ar-Ne mixed gas from a sintered MgO target and the other layers were sputtered with pure Ar gas. The deposited films were post-annealed with applying a DC magnetic field for ordering a uni-axial magnetic anisotropy in the pinned CoFe layer. MR characteristics were evaluated by a current-in-plane-tunneling (CIPT) measurement at room temperature[4].

3. Results and Discussion

At first, an MgO layer in MTJ films was sputtered with pure Ar or Ne gas at various pressure. Fig. 1 shows dependences of RA and MR-ratio on the pressure of Ar or Ne gas (p_{Ar} or p_{Ne}). The target value of RA was set at 1.8 Ωμm^2 by controlling the MgO layer thickness. The deposition rate of the MgO layer sputtered with Ne gas was three times larger than that with Ar gas at a same sputtering power. MR-ratio was the maximum at 0.06 Pa for the MTJ films sputtered with either Ar or Ne gas and that of the films sputtered with Ne gas was very lower than that with Ar gas. An excess incorporation of neon atoms into the MgO layer seemed to cause the lower MR-ratio.

At second, gas mixture of Ar and Ne gases was applied for sputtering of an MgO layer. The total pressure was fixed at 0.06 Pa and the partial Ne gas pressure, p_{Ne}, was varied from 0 to 0.06 Pa. The deposition rate of the MgO layer was increasing with an increase of p_{Ne} at same sputtering power. Fig. 2 shows dependences of RA on the thickness of MgO layer (t_{MgO}) sputtered at various p_{Ne}. RA at each t_{MgO} were mostly maximum at p_{Ne} of 0.01 Pa compared with those at p_{Ne} below 0.005 Pa, and those at p_{Ne} above 0.02 Pa. It suggests that the density of oxygen vacancies in the MgO layer was the minimum at p_{Ne} of 0.01 Pa and it increased at low p_{Ne} below 0.01 Pa. The decrease of RA at p_{Ne} above 0.02 Pa seemed due to the increase of the incorporation of neon atoms into the MgO layer. Fig. 3 shows dependences of RA and MR-ratio on p_{Ne} with the target value of RA of 1.0 Ωμm^2. MR-ratio of the films was higher at p_{Ne} of 0.01 to 0.03 Pa, compared with the films sputtered with pure Ar or Ne gas. These results suggest that the imperfection in the MgO crystallites due to the lack of oxygen or the incorporation of neon atoms are minimized at an optimum p_{Ne} of 0.01 Pa.

4. Conclusion

An improved MR-ratio of 90% is achieved at very low RA of 1.0 Ωμm^2 by applying Ar-Ne mixed gas as a sputtering gas of the MgO barrier layer. These films seem to be suitable for applying for a read head of a hard-disk drive with the areal density above 600 Gbits/in^2.

[1] S. Yuasa et al., Nat. Mater., vol. 3, 868(2004).

[2] K. Tsunekawa et al., Appl. Phys. Lett., vol.87(7) 2503(2006).

[3] W. H. Butler et al., Phys. Rev. B, vol.63(5) 054416(2001).

[4] D. C. Worledge and P. L. Trouilloud, Appl. Phys. Lett., vol.83(1) 84(2003).

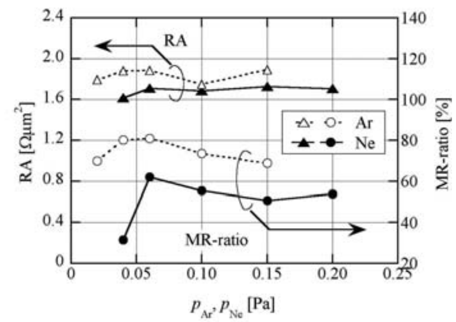

Fig. 1 p_{Ar} and p_{Ne} dependences of RA and normalized TMR ratio sputtered with pure Ar or Ne gas.

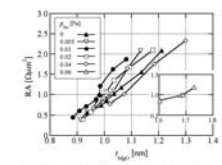

Fig. 2 RA versus t_{MgO} of MTJ films sputtered with Ar-Ne mixed gas at total pressure of 0.06 Pa.

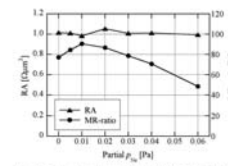

Fig. 3 Partial p_{Ne} dependences of RA and MR-ratio of MTJ films at RA around 1.0 Ωμm^2.

GB-03

Atomic layer deposition Al2O3 films for permanent magnet isolation in TMR read heads.

M. Kautzky, A. Demtchouk, Y. Chen, S. McKinlay, K. Brown, J. Xue
Advanced Transducer Development, Seagate Technology, Bloomington, MN

Conventional tunneling magnetoresistive (TMR) readers use bottom-type reader stacks stabilized with abutted permanent magnets isolated by thin dielectric layers. As recording areal densities push above 300 Gb/in2, physical reader widths of sub-100nm are required, driving demand for several design features: steep junctions to enable accurate read width targeting; controlled magnet vertical placement; and precise free layer-magnet separation. This places a large set of materials and process requirements on the dielectric isolation layer. Electrically, it must provide low leakage, high breakdown, and low stack edge damage. Geometrically, it must have high conformality on etched junctions, high within-wafer uniformity, and compatibility with self-aligned patterning schemes. Chemically, properties such as repeatable nucleation of high-coercivity, high Mrt permanent magnets, and long-term chemical and thermal stability are needed. In this paper we report the use of Al2O3 dielectric isolation layers fabricated using atomic layer deposition (ALD) to satisfy these requirements.

Thermal ALD processing consisting of alternate pulse/purge cycles of trimethylaluminum (TMA) and H2O was used for Al2O3 film deposition. Use of a self-aligned patterning scheme having resist on the wafer during deposition has led to development of a low-temperature deposition process. Resulting films show excellent thickness uniformity (<2% within-wafer), leakage current density (Jleak< 1x10-8A/cm2) and breakdown properties (Fbd > 9 MV/cm) (Fig 1.) TEMs of sub-100nm TMR readers fabricated using these processes show >95% conformality on junction sidewalls, indicating nonselective growth of ALD Al2O3 on the various stack and bottom shield surfaces (Fig 2). Permanent magnets with well-controlled junction grain structure and coercivities in excess of 2500 Oe have been deposited with existing processes. FEM modeling shows the effective stabilizing field from the magnets at the junction edge scales inversely with ALD layer thickness, in agreement with device-level free layer stability metrics showing improvements at lower ALD thicknesses (Fig 3). As the conformal ALD layer thickness is easily tuned, this technology provides flexibility in trading off reader amplitude and stability that should support scaling of the abutted TMR design out to 500 Gb/in2 and beyond.

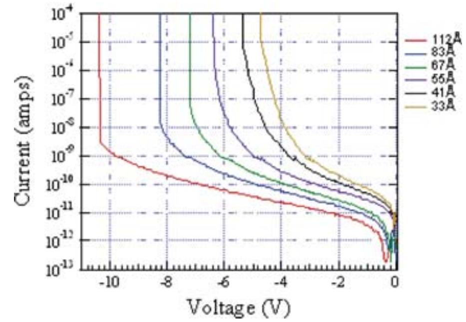

Fig. 1 I-V traces of low-temperature ALD Al2O3 sheet films as a function of thickness.

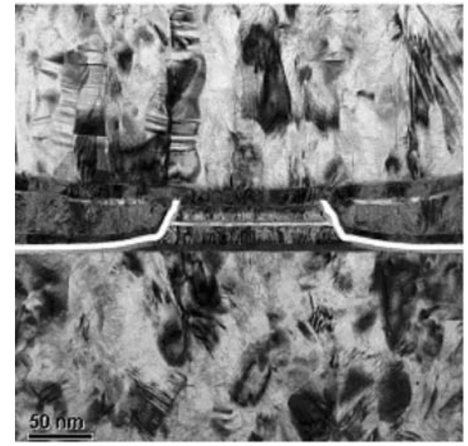

Fig. 2 TEM of TMR reader with ALD permanent magnet isolation layer.

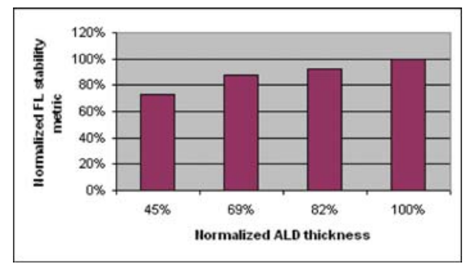

Fig. 3 Normalized improvement in device-level free layer stability metric with decreasing ALD isolation layer thickness.

GB-04

Analysis of the current-confined-paths in the film plane for CPP-GMR films.

H. Fukuzawa, M. Hara, H. Yuasa, Y. Fuji
Corporate R&D Center, Toshiba Corporation, Kawasaki, Japan

Introduction

Current-perpendicular-to-plane giant magnetoresistance (CPP-GMR) is attracting great attention for future high-density recording, because the lower resistance-area pruduct(RA) is advantageous for high data transfer rate. We have previously proposed current-confined-path (CCP) structures, using a nano-oxide layer (NOL) with small metal paths, in order to increase the MR ratio while maintaining small RA [1], and confirmed the MR enhancement [2]. However, CCP-NOL is a source of concern in terms of the variation of RA at an extremely small device size for higher density recording, because the CCPs are distributed in the film plane. Therefore, it is important to understand the status of distributuon of the CCPs in the film plane. Although there have been a few reports on the CCP nanostructure analysis by high-resolution transmission electron microscope (HRTEM) [3] or by three-dimensional atom probe (3DAP) [4, 5], the main factor to determine the variation of RA for future higher density recording is still unknown. In order to clarify this point, we have analyzed the distribution of the CCPs in the film plane by 3DAP.

Experiment and Result

The film structure of the CPP-GMR films with a CCP-NOL was substrate/Ta 5/Ru 2/PtMn 15 or IrMn 7/CoFe 3.4/Ru 0.9/(FeCo 1/Cu 0.25)*2/FeCo 1/CCP-NOL spacer 1.5/CoFe 1/NiFe 30 (unit: nm), where CCP-NOL of AlCu-NOL was formed by ion-assisted oxidation (IAO)[1]. The films were deposited onto high conductivity Sn-doped Si substrates necessary for obtaining the pulsed voltage required for field evaporation in the 3DAP. Figure 1 shows isoconcentration surface image at a level of 30 at. % Cu of the CCP-NOL from the top view. The CCP structure made by metallic Cu in the Al_2O_3 matrix is clearly detected in the 3DAP image; only Cu is shown in this image. The distances between Cu paths are about 10nm, coinciding with the grain size of underlayers of the CCP-NOL confirmed by HRTEM. In fact, the HRTEM result showed that the CCPs were not formed randomly on the grain of the underlayers, but in the center of the grain. It indicates that the decrease of the grain size of the underlayers can result in the increase of the number of the CCPs per unit area in the film plane, which improves the variation of RA even for a higher density recording head with smaller device size.

Figure 2 shows the the areal density of the CCP in the film plane extracted from the isoconcentration surface image by 3DAP as a function of RA, where RA was controlled by changing the formation process of the CCP-NOL. It should be noted that it is very difficult to derive the areal density of the CCP in the film plane because very thin CCP-NOL is formed in the middle of multilayer stack and it cannot be analyzed by conventional analysis methods such as HRTEM. As can be seen in the figure, the data shows the areal density of the CCP has very clear dependence on RA, and it increases with decreasing RA. Although this is intended to control RA, it is firstly confirmed by experimental data. It means that the RA was determined by the change of the areal density of the CCPs. A larger number of areal density of the CCP is naturally preferred for better distribution at a smaller device size. Therefore, the use of lower RA is very useful for a stable RA for higher-density recording, where the realization of lower RA for CPP-GMR films with a CCP-NOL is design matters.

In summary, nanostructure analysis showed that the grain size of the CCP-NOL underlayers and the design of an RA determin the distribution of the CCPs. The decrease of the grain size of the CCP-NOL underlayers and the use of small RA can extend the availability of the CCP-NOL for a high-density recording head.

[1] H. Fukuzawa et al., IEEE Trans. Magn. 40, 2236 (2004)

[2] H. Fukuzawa et al., Appl. Phys. Lett. 87, 082507 (2005)

[3] H. Fukuzawa et al., J. Appl. Phys. 97, 10C509 (2005)

[4] H. Fukuzawa et al., J. Phys. D: Applied Phys. 40, 1213 (2007)

[5] C. Y. You et al., Appl. Phys. Lett. 91, 011905 (2007)

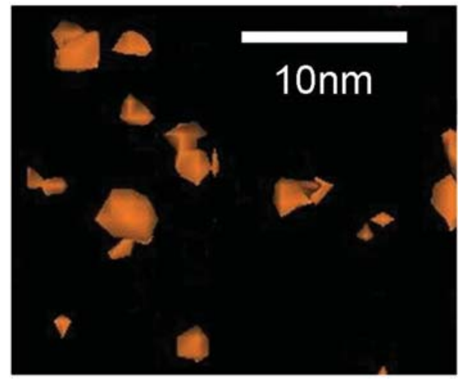

Fig. 1 Three-dimensional atom probe image of the CCP-NOL from the top view.

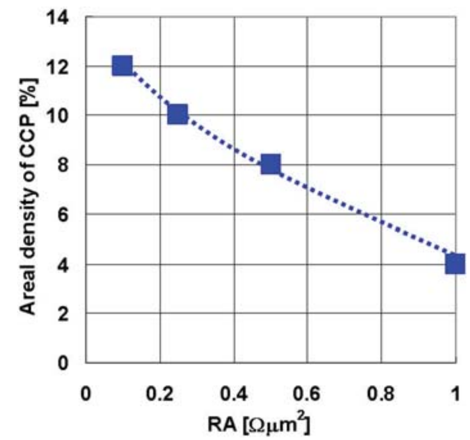

Fig. 2 Areal density of the CCP derived from 3DAP image as a function of RA. It increases with decreasing RA.

GB-05

Development of CPP-GMR Heads for High-Density Magnetic Recording.

J. R. Childress, M. J. Carey, S. Maat, N. Smith, X. Liu, H. Balamane, S. Chandrashekariaih, T. D. Boone, R. E. Fontana, P. Vanderheijden, Y. Hong, K. Carey, J. Tabib, J. Li, B. York, T. Lin, J. A. Katine, W. Jayasekara, N. Robertson, M. Alex, J. Moore, C. Tsang
Hitachi Global Storage Technologies, San Jose, CA

As commercial recording densities increase above 100 Gb/in2, current-perpendicular-to-the plane (CPP) sensors have replaced conventional current-in-plane GMR sensors due to advantages in term of fabrication, scaling, and sensor performance.[1] At today's lateral dimensions of ~100nm, tunneling magnetoresistance (TMR) CPP sensors are ideal due to their large MR(~20-100%). The resistance-area (RA) product of practical TMR sensors has been demonstrated as low as ~ 1 Ω-μm2 [2], so that reasonable impedances (a few hundred Ω) are achievable for sensors down to ~50 nm. Consequently, CPP-TMR sensors are the main sensor candidates for areal densities to 300 Gb/in2 and beyond.[3,4]
All-metal CPP-GMR sensors are an attractive alternative as the sensor dimensions are reduced below 50nm. With RA products in the range 0.03-0.10 Ω-μm2, CPP-GMR sensors deliver low impedance at the smallest conceivable dimensions, and therefore lower noise and higher bandwith performance.[5] Remaining challenges are low signal levels and current-induced noise and instability due to the spin-torque effect. Dual-spin-valve (dual-SV) sensors provide a significant increase in ΔR/R and cancellation of spin-torque due to the symmetric arrangement of the dual fixed reference layers. Their ultimate performance is however limited by a larger shield-to-shield spacing and a complex stack structure. On the other hand, alternative ferromagnetic alloys such as CoFeAl[6] and Heusler alloys[7] can result in sizeable ΔR/R even with less complex single-SV's. In this context we discuss progress achieved in developing CPP-GMR sensor for ultra-narrow magnetic recording head sensors with dimensions < 50nm.
Single- and dual-SV multilayers were deposited by sputtering. Antiparallel (AP)-coupled pinned layer structures consisted of a 7 nm-thick IrMn antiferromagnet, CoFe-based pinned layer (2-3 nm) and various reference magnetic layers (3-4 nm) based on either CoFe or magnetic Heusler alloys with higher electron spin scattering. Generally, the free layer had a magnetic thickness equivalent to 4-6 nm of Ni80Fe20 and was separated from the pinned layer structure by a Cu spacer layer. Compared to standard GMR and TMR sensors, the ΔR/R of CPP-GMR sensors benefits from thicker magnetic layers due to spin-diffusion length effects, but total thickness is limited by the desired shield-to-shield spacing (which determines the maximum linear density). Optimized film-level ΔR/R of ~ 10% have been obtained, even for relatively thin sensors with shield-to-shield spacings < 45nm. Read head sensors were defined by a combination of optical lithography and e-beam lithography to achieve physical widths between 30nm and 60nm, as shown in Fig.1. The final sensor height after mechanical lapping at the air-bearing surface was typically around 50 nm, resulting in sensor resistances of 30-60 Ω.
During magnetic recording readback tests, transfer curves of suspended read heads had a total ΔR/R similar to the wafer-level film values. Well-behaved microtrack profiles (Fig.2) were obtained for all sensor sizes. For the best performing heads, substantial operating bias voltages up to 50-100mV could be applied (corresponding to current densities ~ 1.5 x 10^8 A/cm2) before the onset of spin-torque induced instabilities, yielding signal amplitudes over 1mV (peak-to-peak) as well as head & electronics SNR around 30db. We demonstrate performance suitable for 400 Gb/in2 recording. The onset of spin-torque instabilities result in a sudden and dramatic increase in read error rate, fully reversible upon reducing the bias voltage below the threshold. We also observe the expected dependence of spin-torque on the sensor excitation level as the head-media spacing is reduced. Thus the reduction of spin-torque excitations, along with further increases in ΔR/R, are key to the application of CPP-GMR to recording heads at ever-increasing densities.

1. J.R. Childress and R.E. Fontana, C.R. Physique 6 997-1012 (2005).
2. Y. Nagamine et al., Appl. Phys. Lett. 89, 162507 (2006).
3. T. Kagami et al., IEEE Trans. Magn. 42, 93-96 (2006).
4. S. Mao et al., Digests of PMRC 2007, October 15-17 2007, Tokyo, paper 15pA-01 (2007).
5. M. Takagishi et al., IEEE Trans. Magn. 38, 2277 (2002).
6. K. Nagasaka et al., Jujitsu Sci. Tech. J., 42, 149-157 (2006).
7. J.R. Childress et al., IEEE Trans. Magn. 44, 90-94 (2008).

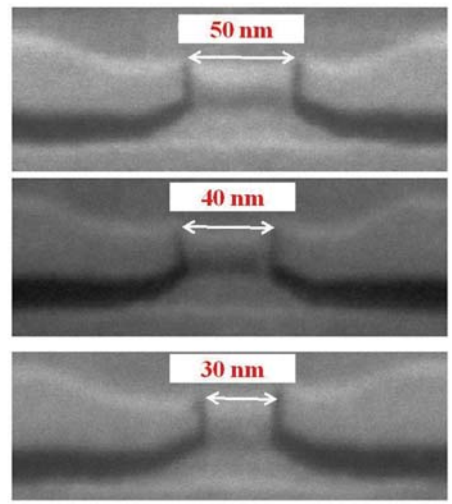

Fig.1: CPP-GMR sensors with width 50-30 nm, as viewed from disk surface.

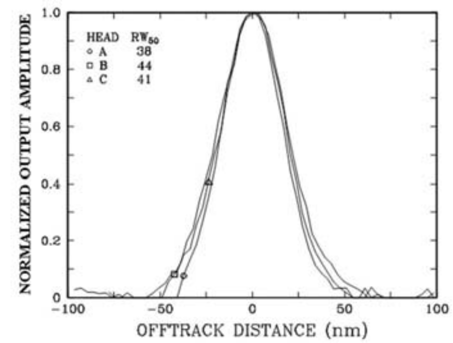

Fig.2: Microtrack profile of 30-nm wide CPP GMR heads.

GB-06

Current Confined Path (CCP) Giant Magneto Resistive (GMR) Sensors.

X. Peng, P. Kolbo, K. Nikolaev, S. Chen, Z. Wang, T. Boonstra, P. Anderson, S. Kalderon, P. Czoschke, A. Morrone, D. Dimtrov, S. Xue, Y. Chen
RHO, Seagate Technology, Bloomington, MN

Current-perpendicular-to the plane (CPP) giant magneto resistive (GMR) sensors with current-confined-path (CCP) layer inserted within the Cu spacer has been manufactured using ultrahigh vacuum PVD sputtering, photolithography, and ion milling processes. Compared with pure metallic CPP system, CCP insertion layer enables substantial increase of the sensor resistance and equivalent or better GMR ratio, and thus, a significant improvement of the Delta (RA). Such CPP-GMR sensors/heads with CCP layer have been tested under various biasing currents and it was found that the resistance of the sensors increases with increasing of biasing current and voltage, following typical metallic ohmic behavior. Also, CCP insertion enables higher bias voltage compared with the pure metallic sensors (without CCP insertion layer) and thus higher output voltage. This could be largely due to the vortex status cancels each other around the current confined paths (with is <6 nm) and enables better magnetic stability. Finally, the CPP-GMR heads with CCP layer were tested under high-density recording conditions using perpendicular magnetic recording heads media.
The Delta(RA) product of ~30 mΩμm2 has been achieved for these CCP devices. Spin stand testing demonstrated that these CCP heads recovered data with a BER of –4.3 at 1420 kbpi, indicating the potential capability for an areal density of > 500 Gb/in2. In the future, more focus will be on controlling of conducting channel size and distribution for even smaller sensors.

1 K. Nagashaka, Y. Seyama, R. Kondo, H. Oshima, Y. Shimizu and A. Tanaka. CPP operational mode of GMR heads, FUJISHU Sci. Technol. J. 37, 192(2001).

2 K. Nagashaka, A. Jogo, T. Ibusuki, H. Oshima, Y. Shimizu and T. Uzumaki. CPP-GMR Technology for future high-density magnetic recording, FUJISHU Sci. Technol. J. 42, 149(2006).

3 K. Nakamoto, H. Hochiya, H. Katada, k. Hoshino, N. Yoshida, H. Takei, M. Shiimoto, M. Hatatani, and K. Watanabe, Digest of TMRC-2007, A3, 2007 (to be published)

4 H. Yuasa M. Yoshikawa, Y. Kamiguchi, K. Koi, H. Iwasaki, M. Takagishi,

and M. Sahashi, J. Appl. Phys., 92, 2646(2002)

5 R. D. Slater J. A. Caballero, R. Loloee, and W. P. Pratt, Jr., J. Appl. Phys., 90, 5242(2001).

6 K. Nikolaev, P. Anderson, P. Kolbo, D. Dimitrov, S. Xue, X. Peng, T. Pokhil, H. Cho, and Y. Chen, J. Appl. Physics, 2008 (to be published).

7 N. Smith, J. Katine, J. Childress, and M. Carey, IEEE Trans. Magn., 41, 2935 (2005)

8 H. Fukuzawa, H. Yuasa, S. Hashimoto, K. Koi, H. Iwasaki, M. Takagishi, Y. Tanaka, and M. Sahashi, IEEE Trans. Magn., 40, 2236 (2004)

9 K. Hoshino and H. Hoshiya, IEEE Trans. Magn., 42, 2453 (2006)

10 A. Jogo, Y. Seyama, T. Ibusuki, K. Nagasaka, Y. Shimizu, T. Uzumaki and T. Tanaka, IEEE Trans. Magn., 42, 2456 (2006)

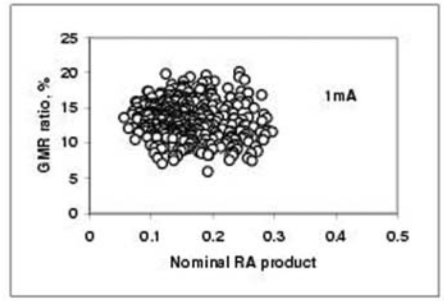

GMR as a function of RA for CCP sensors

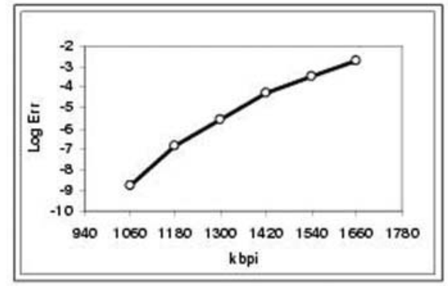

Bit error rate (BER) vs. linear density rolling off for CCP heads

GB-07

Current Density Limitation by Spin Transfer Torque for CPP-GMR Heads.

K. Yamada, M. Takagishi, M. Takashita, H. Iwasaki
Corporate R&D Center, Toshiba Corporation, Kawasaki, Japan

Introduction

It is well known that read heads using CPP-GMR with low RA and high dR/R are required for future tera-bits high-density recording [1]. However, spin transfer torque (STT) is one of important issues for low RA heads [2][3]. It is excess STT by high current density needed for high output that induces magnetic instability in the free layer [3][4]. Some papers suggest that non-uniform precession mode by magnon is suppressed on small element and that relaxation time is longer [5]. This would reduce critical current density limited by STT. In this paper, we study influence of element size on critical current density (Jc) of CPP-GMR with Current-Confined-Path (CCP) nano-oxide-layer spacer (NOL).

Experiment and Calculation model

We fabricated test chips with 66nm by 100nm in size, non-shield and longitudinal hard magnets. CCP-CPP-GMR films with $dR/R \approx 6\%$ and $RA \approx 0.3\Omega um^2$ were used [6]. The Onset of STT, critical current density Jc, was defined by measuring the one-side-field transfer curve saturation, resulting in 10% dR degradation, in the same way as we have reported for all-metal CPP-GMR [4].We also confirmed 1/f-like noise above Jc. Magnetization is simulated by micromagnetic model using modified Landau-Lifshitz-Gilbert equation with STT and thermal fluctuation effect with a damping parameter α of 0.02 [3]. Each magnetic layer is divided into 16x16 cells and no division in thickness. For example, cell size is 6nm by 6nm for 90nm square element. Longitudinal bias fields is applied to fit experiment. STT is transferred on boundary of cells in magnetic layers which are attached to metal path in spacer. Thermal fluctuation is considered by adding random field into the effective field. We used random distribution of 22 metal paths with a density of 2.8% in NOL.

Result and discussion

First, we estimated the spin polarity Po of CCP-CPP-GMR from measured transfer curves. Electron flows into the free layer on positive current. Fig. 1 shows experiment and calculation of dR vs current density. The measurement is well explained when Po is assumed to be 0.57 and 0.3 for positive and negative current. These Po values are reasonable to other report [2]. It is found that CCP-CPP-GMR shows almost the same Jc as that of metal-based CPP-GMR [4],.

Second, we made calculation for critical current density vs element size. Exchange bias from antiferromagnet is changed inverse proportionally to element size to keep a stable pinned layer. The same map of metal path is used by shrinking metal paths for smaller element. Aspect ratio of elemet is 1. Figure 2 shows Jc vs element size. Jc decreases linearly to size below 60nm, while it is the same above 60nm. This result requires higher MR than what we have reported [1]. Achieving higher Jc against STT, as well as developing higher MR, is needed especially for metal-based CPP-GMR with lower RA. Also Jc on T=4K of 35nm size is calculated. Jc is the same as that on 300K, and thermal fluctuation is not serious. To understand this dependency, power spectrum density (PSD) of GMR output is calculated for 90nm and 35nm element as shown on Figure 3. PSD of 35nm has sharper peaks, which indicates that effective damping is smaller than that of 90nm, and such a smaller damping corresponds to smaller Jc. Magnon scattering may play a role for this dependency [5].

[1] M. Takagishi, H. N. Fuke, S. Hashimoto, and H. Iwasaki, PMRC 2007, 15pC-07 (2007)

[2] J. C. Slonczewski, *J. Magn. Magn. Mater.*, **159**, L1 (1996),

[3] J.-G. Zhu, *IEEE Trnas. Magn.*, **40**, pp. 182 (2004)

[4] M. Takashita, M. Takagishi, and H. Iwasaki, Intermag 2006, ES-06 (2006)

[5] A. Y. Dobin, 52nd Magn. Magn. Mat. Conf., AD-04 (2007)

[6] H. Fukuzawa, H. Yuasa, S. Hashimoto, H. Iwasaki and Y. Tanaka, *Appl. Phys. Lett.*, **87**, pp. 082507 (2005)

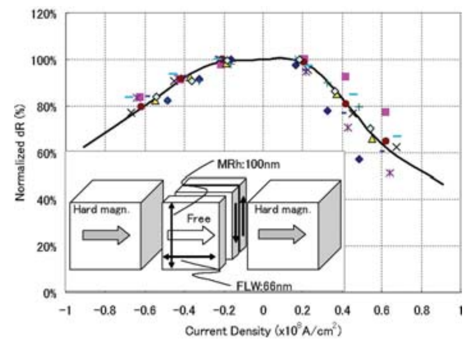

Fig. 1. dR on transfer curve vs current density. dR is normalized by that of enough small current. Dots are measurements and line is calculation.

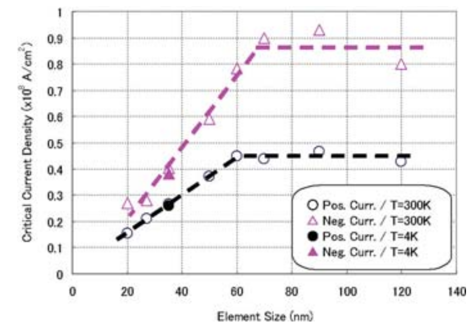

Fig. 2. Critical current density vs element size. Dashed lines are for eye guide.

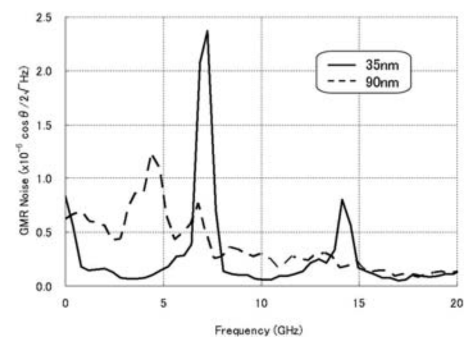

Fig. 3. Power spectrum density on critical current density.

GB-08

Suppression of spin-torque in current perpendicular to the plane spin-valves by addition of Dy caps.

S. Maat, M. J. Carey, N. Smith, J. R. Childress
Hitachi Global Storage Technologies, San Jose, CA

The magneto-transport and spin-torque of current-perpendicular to the plane giant magneto-resistive spin valves with and without Dy caps have been analyzed. Spin-valve giant-magnetoresistive sensors with current perpendicular to the plane (CPP-GMR) are of interest for future high-density magnetic recording applications due to their low resistance which is suitable for narrow trackwidth dimensions (<50nm). In the CPP geometry, the spin-torque effect[1-4] and the use of spin-polarized current to switch the magnetization of a magnetic layer is useful to realize novel devices such as spin-torque memory. However, for sensor applications, the spin-torque effect is a source of noise and undesirable excitations which limit the maximum output voltage and degrade the signal-to-noise ratio. Consequently it is desirable to find methods to cancel or damp spin-torque exitations in order to improve sensor performance.
Recently is has been reported how alloying of transition metal free layer with rare-earth elements increases the magnetic damping and reduces its susceptibility to spin-torque.[5] However alloying typically dilutes the magnetic moment. Here we show that the addition of a Dy cap on top of the free layer can also enhance the spin-torque critical current density threshold. The spin-valves under investigation were standard antiparallel-pinned spin-valves with structure IrMn(70Å)/CoFe(25Å)/Ru(7Å)/CoFe(25Å)/Cu(40Å)/CoFe(7Å)/NiFe(25Å)/Dy(t)/Ru. Films were patterned by e-beam lithography and ion milling to produce CPP test devices with diameters down to 50nm. The Dy cap addition (10-15Å thick) does not degrade the magnetic properties of the sensor free layer, although the magneto-resistance ratio is slightly reduced due to the additional series resistance from the Dy layer itself.. Figure 1 (a) and (b) show the resistance vs field loops for a 50 nm circular devices without and with a 15 Å Dy cap, respectively. While spin-torque induced instability was observed at 4×10^7 A/cm^2 in spin-valves without Dy, this instability was successfully suppressed by addition of a 15 Å Dy cap. Figure 2 shows the roll-off of the ΔRA upon applying a bias voltage. Positive polarity refers to current flowing from the free to the reference layer, negative current refers to current flowing from the reference to the free layer. The critical current density at which spin-torque is observed is increased at least twofold.

[1] J. C. Slonczewski, J. Magn. Magn. Mater. 159, L1 (1996).

[2] J. C. Slonczewski, J. Magn. Magn. Mater. 195, L261 (1999).

[3] J.A. Katine, F.J. Albert, and R.A. Buhrman, Appl. Phys. Lett. 76, 354 (2000).

[4] F.J. Albert, J.A. Katine, R.A. Buhrman, and D.C. Ralph, Appl. Phys. Lett. 77, 3809 (2000).

[5] S.G. Reidy, L. Cheng, and W.E. Bailey, Appl. Phys. Lett. 82, 1254 (2003).

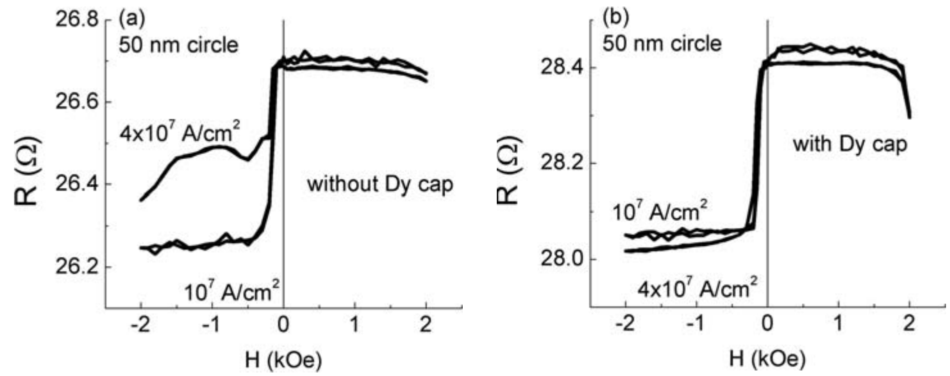

Resistance-field loops of 50 nm circular devices (a) without and (b) with a Dy cap.

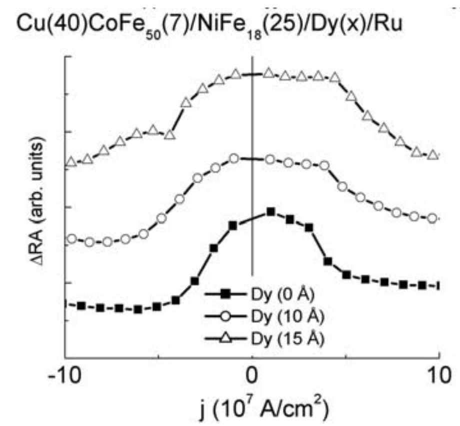

Magneto-resistance (ΔRA) of 50 nm circular devices without and with Dy cap as a function of bias voltage. The Dy cap increases the critical spin-torque current density. Positive polarity refers to current flowing from the free to the reference layer, negative current refers to current flowing from the reference to the free layer.

GB-09

Transport and magnetic properties of CPP-GMR sensor with CoMnSi Heusler alloy.

T. Mizuno, Y. Tsuchiya, T. Machita, S. Hara, D. Miyauchi, K. Shimazawa, K. Noguchi, K. Tagami
SQ Research Center, TDK CORPORATION, 543 Otai, Saku-shi, Japan

Introduction

CPP-GMR sensor is expected as a candidate for future generation read head because of its good scalability to small sensor size [1]. CPP-GMR sensor consisting of metallic materials such as CoFe, NiFe and Cu shows low resistance than MTJ's with TMR barrier, so this character will bring extendibility to super narrow track structures while keeping its high frequency response. However, its output voltage is still too small for application to hard disk head devices. The efficient injection of spin currents into spacer layer is needed for higher MR ratio. One candidate of high spin polarization materials is Heusler alloy and the recent progress of Co-based Heusler alloy has made it possible to obtain higher MR ratio than that of typical transition metals and alloys [2]. The objective of the present paper is to explore the possibility of CoMnSi (CMS) for enhancement of CPP-GMR ratio. Basic film level study was carried out and test junctions were made to investigate CPP-GMR ratio. We found that CMS was more effective to enhance CPP-GMR ratio than usual CoFe and NiFe alloys.

Experiment

CMS films were grown by magnetron sputtering on SiO2 substrate to evaluate its crystallization. After deposition, the CMS films were annealed up to 773K in vacuum. The annealing effect on the structural and magnetic properties were also investigated. The structure of CMS films was identified by x-ray diffraction (XRD). In order to investigate the effect of CMS on MR ratio, test junctions with an area of 0.2um-ϕ pillar were patterned for magneto-transport measurements in the current-perpendicular-to-plane (CPP) geometry by standard optical lithography. Spin-valve films with Cu spacer-layer which Pinned-layer and/or Free-layer were consisted of CMS alloy were made on the bottom electrode. Four-point probe R, DR/R measurements were taken by applying a constant current. The measurements were taken at room temperature using a 5mA sense current and a field range of 0.1[T].

Structural characterization

The composition of deposited CMS film was measured as Co:Mn:Si = 48:21:31 from X-ray fluorescence analysis. Figure.1 shows a θ–2θ XRD profile for a 70nm thick CMS film grown directly on a SiO2 substrate. The post annealing process was made for crystallization of CMS at 673K and 773K. Despite the absence of any seed layer, clear diffraction peaks were identified in the diffraction pattern. One can distinguish in the XRD pattern from (200) B2 ordered peak for 673K and 773K annealed sample. The sample annealed at 773K shows magnetization of 1.1[T] at room temperature while the samples of as-deposited and annealed at 673K did not show any magnetization.

Evaluation of CPP GMR ratio

Figure.2 shows CPP GMR ratio among these three types of CPP-GMR films.
Type-A: Both Pinned and Free-layer consists of CoFe alloys.
Type-B: Pinned-layer (CMS and CoFe alloy), Free-layer (CoFe and NiFe alloy).
Type-C: Both Pinned and Free-layer consists of CMS and CoFe alloys.
We have also checked the effect of composition of CMS on CPP GMR ratio for Type-C. Two samples which have different compositions were prepared as CMS-I (Co:Mn:Si = 48:21:31) and CMS-II (Co:Mn:Si = 46:25:29). As shown in figure.2 Type-C (CMS-I) shows relatively high CPP GMR ratio about 9.0% while the value of Type-A (CMS-I) was 3.6%. It suggests that Type-C (CMS-I) shows 2.5 times larger CPP GMR ratio than the value of Type-A which is same structure as traditional CPP-GMR film. Here we should notice that the MR ratio of Type-C (CMS-II) shows only 7.2 %. This smaller MR ratio is maybe due to the Co-poor or Si-rich composition of CMS-II.

Next the difference of free-layer between Type-B (CMS-I) and Type-C (CMS-I) was compared. The CPP GMR ratio of Type-B (CMS-I) shows half of Type-C (CMS-I). This suggests that Free-layer with CMS has great advantage of enhancement of CPP GMR ratio. However, there is still concern of CMS used in Free-layer from the point of magnetostriction. It was found that the magnetostriction of CMS is three to five times larger than that of CoFe alloys, and this will prevent CMS from practical use for sensor applications. In order to overcome this issue, we propose new Heusler-base material, which has almost the same magnetostriction as CoFe alloys while keeping its high MR ratio.

[1] M. Saito et al :Digest of the Intermag conference USA 2003, (2003) DD05.

[2] M. Saito et al :Digest of the Intermag conference Asia 2005, (2005) FB02.

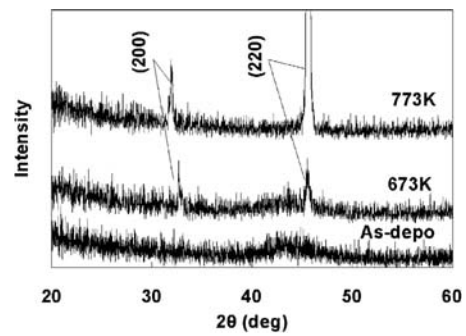

Figure.1 X-ray diffraction profiles for AlO2/CMS(70nm) on a Si substrate.

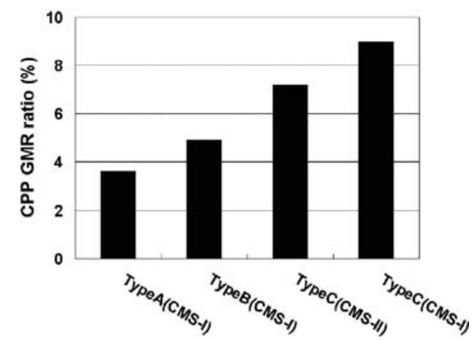

Figure.2 CPP GMR ratio among three types of films.

GB-10

Mesoscopic Extraordinary Magnetoresistance and the Effects of Impact Ionization and Velocity Saturation.

T. D. Boone, L. Folks, J. A. Katine, E. E. Marinero, N. Smith, B. A. Gurney
San Jose Research Center, Hitachi Global Storage Technologies, San Jose, CA

Magnetic field sensors utilizing the Extraordinary Magnetoresistance effect (EMR) have been proposed for implementation in future magnetic recording applications [1, 2]. These devices are hybrid distributed resistors comprised of a high mobility semiconductor in parallel and in contact with a low resistance metallic shunt. EMR devices are attractive possible future recording sensors because they contain no ferromagnetic materials and therefore have no magnetic noise, an increasingly significant source of noise in devices that use a ferromagnetic sense layer as they are made smaller.
Here we present characterization results from EMR devices with dimensions approaching that needed for magnetic recording head applications in the I-V-I-V configuration. This report includes results from a new device geometry that removes the semiconductor tabs below the mesa that form contacts to the EMR structure. Minimum feature sizes have been reduced to 50 nm and the magnetically sensitive surface area is designed to be 150 nm wide. The 2-DEGs used for these devices consisted of AlSb(2 nm)/InAs(12.5 nm)/AlSb(2 nm) quantum wells with room temperature mobility above 10,000 $cm^2/V \times s$. To achieve the signal levels required for magnetic recording, EMR devices must operate at relatively large current densities beyond $1x10^7$ A/cm^2. Previously, Brar et al. reported that high electron mobility transistors (HEMTs) with 10 micron channel widths made from type II heterostructures of AlSb/InAs/AlSb suffered from poor performance due to impact ionization within the channel at modest drain source voltages [3]. Therefore, we have investigated applied bias effects on the sensitivity of EMR devices and Hall crosses.
In previous investigations, mesoscopic EMR devices were created with abutted junctions formed by high angle deposition of metal directly on exposed edges of quantum wells. Those devices were characterized by sensing the voltage in an I-V-V-I four wire resistance measurement, and required unconventional fabrication techniques, such as edge cleaving and metal depositions through a shadow mask [1, 2]. In contrast, here we have demonstrated EMR devices with minimum feature sizes less than 100 nm using standard planar processing techniques. Rather than the I-V-V-I configuration, these devices were characterized in an I-V-I-V non-local resistance measurement [4]. It has been predicted numerically that the I-V-I-V configuration produces superior sensitivity to the I-V-V-I configuration [5,6].
Our devices have been characterized at room temperature in magnetic fields of +/- 5 kOe and applied currents up to 1 mA. We find that the sensitivity is linear with both applied magnetic field and applied bias up to current densities beyond 1×10^7 A/cm^2. Sensitivities of 6 μV/Oe were observed, which are comparable to GMR sensors of equivalent size excited by typical media fields of 200 Oe. To further understand transport in our EMR devices we fabricated Hall crosses with similar lateral dimensions, ranging from 100 nm to 1 um. Bias voltages up to 1V were applied resulting in current densities beyond $1x10^7$ A/cm^2. Average electron drift velocity and carrier concentrations were determined directly from the geometry, current and Hall voltage measurements. Consistent with impact ionization, carrier concentration within the channel increases monotonically as the applied voltage exceeds the band gap of 0.38 V. Additionally, the carrier velocity is observed to saturate between 3-7 $x10^7$ cm/sec, approaching the limit derived theoretically.[7]. Analysis of the scaling of transport with size, effects of 1/f noise and the implications for further miniaturization of Hall sensors and EMR devices will be discussed.

[1] S. Solin et al; Appl. Phys. Lett. 80, 4012 (2002).
[2] T. Zhou et al; Appl. Phys. Lett. 78, 667 (2001).
[3] Brar, B. Kroemer; H., Electron Device Letters 16, n 12. (1995).
[4] T. Boone et al; IEEE Trans. Mag, 12, (2006).
[5] J. Moussa et al; J. Appl. Phys. 94 (2003).
[6] M. Holz et al; Appl. Phys. Lett. 86 (2005).
[7] K. Brennan and K. Hess; Solid-State Electron., v27, (1984).

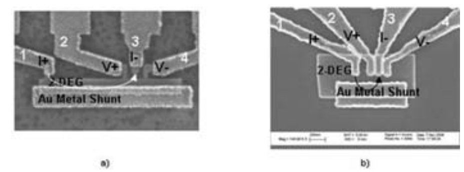

Fig. 1. SEM micrographs of EMR devices a) 50 nm tab minimum feature sizes and b) 50 nm "tabless" EMR structure.

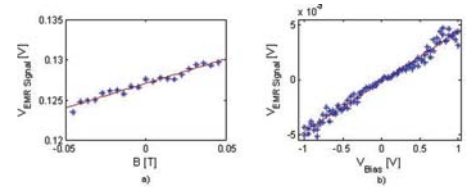

Fig. 2. Typical behavior for "tabless" EMR devices. a) EMR signal versus applied magnetic field and b) versus applied voltage bias.

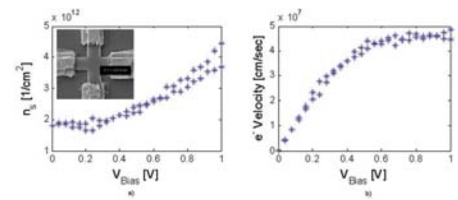

Fig. 3 a) Carrier concentration dependence on applied voltage for 300 nm Hall cross (inset). b) Drift velocity dependence on applied voltage. Note that beyond ~0.3 V the velocity begins to saturate.

GC-01

Ultrafast Magnetic Switching with Terahertz Fields.

H. Siegmann[1], S. J. Gamble[2,6], M. H. Burkhardt[2,6], A. Kashuba[3], R. Allenspach[4], S. S. Parkin[5], J. Stöhr[6]

1. PULSE Center Stanford University, Stanford, CA; 2. Dept. of Applied Physics, Stanford University, Stanford, CA; 3. Bogolyubov Institute for Theoretical Physics, Kiev, Ukraine; 4. IBM Research, Zurich Research Laboratory, 8803 Rueschlikon, Switzerland; 5. IBM Almaden Research, San Jose, CA; 6. Stanford Synchrotron Radiation Laboratory, Stanford, CA

The magnetization **M** may be switched to the opposite direction with a circularly polarized optical laser pulse [1]. We show that **M** can also be switched even multiple times with one half cycle pulse of terahertz(THZ) radiation. As THZ lasers become generally available[2], switching with THZ radiation is of general interest to observe and induce ultrafast changes of M. As a source of THZ radiation we use highly relativistic electron bunches containing $1.6\text{x}10^{10}$ electrons compressed to a temporal length of 0.140 ps (1 ps = 10^{-12}s). The electromagnetic fields of the bunch are best described by a cloud of virtual photons[3] flying in vacuo with the electrons at the speed of light. Fig.1 shows an example of a virtual photon spectrum, consisting of coherent THZ-photons and incoherent x-ray photons of low intensity. When the bunch enters a solid, it continues to fly with the speed of light while the virtual photons are slowed down and thus separate from the bunch leading to bremsstrahlung emitted in the forward direction and to coherent "transition radiation" emitted into the backward direction. However, the THZ photons penetrate into the solid up to the skin depth ≥50 nm. The sample is 10 nm thick and thus exposed to the THZ-fields. According to Fig.2 the coherent fields are gigantic with the compressed electron bunch. As the incoherent fields can be neglected with a thin sample the electron bunch interacts with the solid solely via the coherent THZ radiation. The switching pattern generated by one single compressed electron bunch is shown in Fig.3. The figure 8 shape of the pattern resembles the patterns seen before with uncompressed electron bunches of several ps duration [4]. Yet there are striking new features like the deviation from the circular shaped switching boundaries expected if the B-field acted alone. This distortion of the switching boundaries is due to a new type of magnetic anisotropy induced by the electric field E in the valence states. For symmetry reasons, any magnetic anisotropy induced by E must be $\propto E^2$,and therefore appears with compressed bunches only. The absence of beam damage with a bunch intensity of $4\text{x}10^{19}$ W/cm^2, evident in Fig.3 is a phantastic feat. It means that the metallic sample behaves like a ferromagnetic dielectric during the field pulse.

[1] C. D. Stanciu et al.,Phys.Rev.Lett.99, 047601 (2007)

[2] Benjamin S. Williams, nature photonics 1, 517 (2007)

[3] J.D. Jackson, **Classical Electrodynamics** (Wiley, New York, 1999)

[4] J. Stöhr and H.C. Siegmann, **Magnetism:** *From Fundamentals to Nanoscale Dynamics*,

Springer Series in Solid-State Sciences 152 (Springer, New York, 2006)

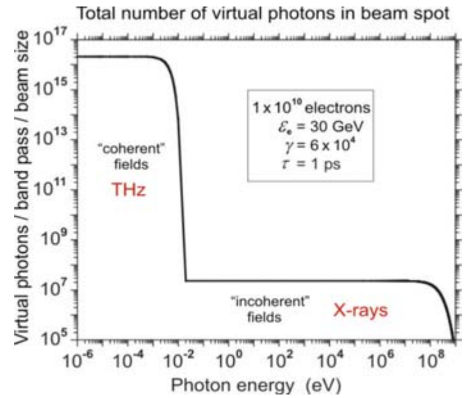

Fig.1:The virtual photon spectrum carried by a bunch of highly relativistic electrons. The bunch has a Gaussian shape in all 3 coordinates, the variance of the temporal bunch duration τ corresponds to a bunch length of cτ = 0.3 mm in the laboratory frame.

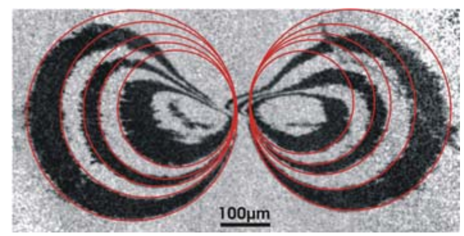

Fig.3 Magnetic pattern written by one bunch of electrons into a uniaxial CoFe-sample of 10 nm thickness. The magnetic pattern was recorded with spin-SEM. In the light grey regions, M points into the preset direction, while in the dark regions, M has switched into the opposite direction. The fitted circles are lines of constant torque assuming that only the B-field of the terahertz pulse is active. The deficit of torque in the upper part of the pattern reveals the opposing torque generated by the presence of the extreme electric field.

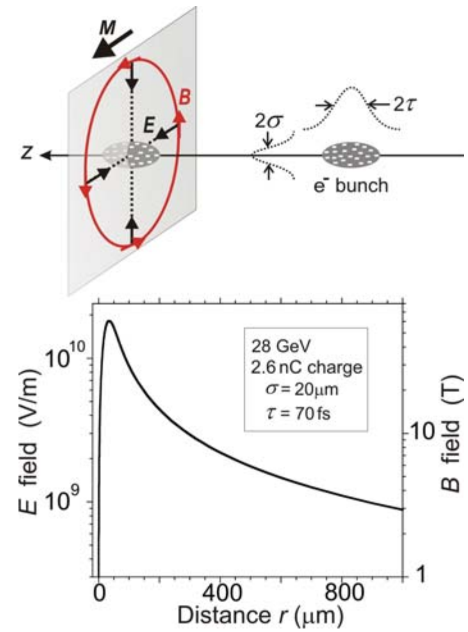

Fig. 2: Basic data of the present experiment. The electron bunch of energy 28 GeV per electron traverses a thin uniaxial ferromagnetic metal perpendicular to the surface, the magnetization M is uniform and initially set along the horizontal as shown. Bunch diameter σ and temporal length τ of the bunch are also given. The maximum value of the electric field E and the magnetic field B generated by the half cycle pulse of the coherent vitual photons is given as a function of distance from the bunch center.

GC-02

Terahertz Emission Spectroscopy as a Probe of Laser-Induced Ultrafast Demagnetization Dynamics.

E. Beaurepaire[1], J. Arabski[1], M. Vomir[1], J. Bigot[1], S. M. Harrel[2], J. M. Schleicher[2], C. A. Schmuttenmaer[2]
1. IPCMS-GEMME, CNRS, Strasbourg, France; 2. Dept. of Chemistry, Yale University, New Haven, CT

Laser-induced ultrafast magnetization dynamics have been the subject of a large amount of experimental studies since originally reported [1]. A recent time-resolved X-ray magnetic circular dichroism experiment confirmed the previous observation by magneto-optical measurements of a magnetization drop within a few hundreds of femtoseconds following the absorption of a femtosecond optical pulse, thus directly quantifying this effect [2]. The microscopic mechanisms of the ultrafast magnetization are still unclear and the dissipation of angular momentum is still debated. We have recently shown that the interaction of a thin ferromagnetic nickel film with femtosecond optical pulses leads to the emission of a short terahertz electromagnetic pulse that can be associated to the demagnetization [3]. However similar experiments by other workers lead to a different interpretation invoking surface magneto-optical non-linear response[4]. The aim of the present work is to present a detailed study of this phenomenon for Ni and Fe films varying the thickness and experimental geometry. From these results we show how surface and volume contributions to the demagnetization can be distinguished.
The experimental setup has been described elsewhere [3]. In brief, a regeneratively amplified Ti:Sapphire laser produces ~ 100 fs laser pulses centered at a wavelength of 800 nm with a repetition rate of 1 kHz. The beam is split into two parts, pump and readout, where the pump photoexcites the sample and the readout beam detects the emitted THz radiation in the far-field via free space electro-optic sampling in a 0.5 mm thick ZnTe(110) crystal. The detection system used is optimized to detect horizontally polarized THz radiation.
The ferromagnetic samples used are: (i) Al2O3 / Ni (x Å) thin films with a thickness x 50 Å < x < 500 Å deposited on glass substrates, obtained by sputter deposition on Ar etched glass substrates. In-plane uniaxial anisotropy in Ni films was achieved by deposition with an oblique incidence of ~45°. (ii) MgO (200 Å) / Fe (x Å) single crystal films deposited on MgO(001) under UHV in a MBE chamber. THz measurements are then performed after saturating the samples along the easy axis, providing 90% or higher remanence. The magnetization of the sample is modified via heating of the spins following the absorption of a 0.2 mJ pulse with spot size of ~ 5 mm (leading to ~ 1 mJ/cm2 fluence). The sample is placed between 5 and 15 mm away from the ZnTe detector, and thus the emission cannot be considered as emanating from a point dipole. Therefore, the THz waveforms E(t) might be distorted, but this can be accounted for when necessary.
Typical results representing the electric field emitted upon ultrafast demagnetization of Ni thin films are displayed in Figures 1-2. Four configurations have been used, depending on whether visible excitation and THz detection are on the same side (reflection geometry) or on opposite sides of the sample (transmission geometry), and whether the excitation comes from the glass side or the film side. The inset of Figure 1 displays the coordinate system used. As the sample is rotated around the z-axis, the amplitude of the y-polarized emission varies as the cosine of the angle between the magnetization axis and the x-axis. Thus, one concludes that the signals discussed here have a purely magnetic origin. There are two salient features in the waveforms of the electric field in the thicker Ni films (>200 Å). First, the waveform is nearly insensitive to whether the glass side or metal side of the sample has been excited, whereas the signal changes polarity when the sample is excited in transmission vs. reflection. We relate this feature to an interface non-linear effect, since the dissymmetry of the stack induces a change of the sign of the emitted electric field, assuming that Ni/glass and Ni/Al2O3 interfaces are characterized by different non-linear susceptibilities. A different behavior is found for thick Ni films and Fe films (disregarding thickness), where the shape of the emitted waveform is relatively independent of the excitation side (figures 1, 3). We interpret this effect as a signature of the demagnetization. We shall discuss the physical mechanism responsible of the waveform (magnetic dipole antenna [3] and current generation due to Lentz's law), and its connection with the time dependent demagnetization and re-magnetization of the sample.

[1] E. Beaurepaire, J.C. Merle, A. Daunois, J.-Y. Bigot, Phys. Rev. Lett. 76 (1996) 4250.

[2] C. Stamm, T. Kachel, N. Pontius, R. Mitzner, T. Quast, K. Holldack, S. Khan, C. Lupulescu, E.F. Aziz, M. Wietstruk, H.A. Dürr, W. Eberhardt, Nature Mater. 6, 740 (2007).

[3] E. Beaurepaire, G. Turner, S.Harrel, M. Beard, J.-Y. Bigot, and C. Schmuttenmaer

Appl. Phys. Lett. 84, 3464 (2004).

[4] D.J. Hilton et al. Opt. Lett. 19, 1804 (2005).

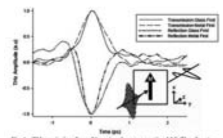

Fig 1. THz emission from 50nm in-plane magnetized Ni film. Inset: Experimental geometry.

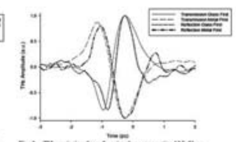

Fig. 2. THz emission from 5nm in-plane magnetized Ni film.

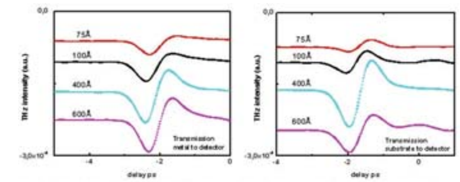

Figure 3. THz emission from MgO/Fe/MgO(001) films of various thickness and changing the orientation of the sample in front of the detector. The absolute value of the time origin is arbitrary.

GC-03

Atomistic and Multiscale calculations of picosecond magnetisation dynamics.

R. W. Chantrell[1], U. Nowak[1], O. Chubykalo-Fesenko[2], A. Rebei[3]
1. Physics, The University of York, York, United Kingdom; 2. ICMM, Madrid, Spain; 3. Seagate Research, Pittsburgh, PA

Since it was shown experimentally [1] that the magnetic state of a material can be changed on a picosecond timescale using pulsed lasers there has been an increasing experimental and theoretical interest in the phenomenon. Theoretically there is a need to go beyond the formalism of micromagnetics, especially since complete demagnetization is possible following a laser pulse and it is known that the standard formulation of micromagnetics is not capable of dealing with phase transitions. From a technological point of view an understanding of fast laser processes is made more pressing by the fact that ultra-high density information storage may require Heat Assisted Magnetic Recording (HAMR), which involves heating up to or beyond the Curie temperature. Micromagnetics is a continuum formalism using an approximation to the exchange which limits it to long wavelength magnetization fluctuations and consequently to temperatures well below the Curie temperature. To surmount this problem, atomistic models are currently under development and have already given important insight, for example into the properties of FePt [2]; an important candidate for ultra-high density recording media. The basis of atomistic models will be outlined. Essentially this consists of the use of a classical spin model based on the Heisenberg interaction. Dynamic properties are calculated using the Langevin dynamic approach (essentially the LLG equation augmented by a random field term representing thermal fluctuations) to describe the time evolution of the ensemble of coupled spins at non-zero temperature. The model enables representation of the temperature dependent static and dynamic magnetic properties and complete magnetic excitation spectrum. This is important because it allows the magnetic phase transition to occur at a realistic Curie temperature. We have recently developed [3] an atomistic model of the response of a material to a sub-picosecond laser pulse. The model assumes that the laser power gives rise to an elevated conduction electron temperature which couples to the spin system. In agreement with experiment the atomistic model is shown to exhibit a rapid reduction of the magnetisation, on the picosecond timescale, to an extent dependent on the strength of the coupling between the spins and the conduction electrons. The recovery of the magnetisation is a more complex phenomenon, taking place on a timescale determined by the extent to which the system is demagnetised. In the case of complete demagnetisation, recovery takes place randomly at many nucleation sites leading to severe frustration effects resulting in timescales on the order of nanoseconds for complete magnetisation recovery. The model has been used to simulate magnetisation reversal during the HAMR process, and simulations of the magnetisation reversal process will be presented. It is shown that a non-precessional reversal mechanism termed 'linear reversal' in which the magnetisation vanishes and recovers in the field direction is important for the HAMR process. We also consider the phenomenon of 'Opto-magnetism' which has recently been demonstrated experimentally [4,5]. Here the magnetic state is shown to be affected by the use of circularly polarised light in the absence of an externally applied field. Indeed in [5] complete reversal of the magnetisation is demonstrated on a sub-picosecond timescale. It is shown that in order to achieve reversal on this timescale the reversal process must be linear, since precessional timescales are too long. We discuss a recent model [6] of the physical interaction channel between the laser and spin system which requires the presence of RE spins. Calculations of the timescale for linear reversal as a function of the applied field and temperature will be presented. We also discuss the implications of the assumption of white noise in the Langevin Dynamic approach, which might be expected to break down at very short timescales. We present an approach introducing coloured noise in which the usual delta function correlations are replaced by correlated fluctions with a characteristic correlation time. The effect of correlations on the ultrafast demagnetisation process will be presented. Finally we consider the options for extending the atomistic calculations using a macrospin model based on the Landau-Lifshitz-Bloch equation, which has been shown [7] to encapsulate much of the important physics of the atomistic model.

[1] E. Beaurepaire, J.-C. Merle, A. Daunois, and J. Y. Bigot, Phys. Rev. Lett. 76, 4250 (1996).

[2] O.N Mryasov, U Nowak, K.Y Guslienko and R.W Chantrell, Europhys Lett., 69 805-811 (2005)

[3] N. Kazantseva, U. Nowak, R. W. Chantrell, J. Hohlfeld and A. Rebei

Europhys. Lett., 81, 27004 (2008)

[4] C. D. Stanciu, F. Hansteen, A.V. Kimel, A. Tsukamoto, A. Itoh, A. Kirilyuk, and Th. Rasing, Phys. Rev Lett 98, 207401 (2007)

[5] C. D. Stanciu, F. Hansteen, A.V. Kimel, A. Kirilyuk, A. Tsukamoto, A. Itoh, and Th. Rasing, Phys. Rev Lett., 99, 047601 (2007)

[6] A Rebei and J Hohlfeld, Phys. Lett. A (in press)

[7] O. Chubykalo-Fesenko, U. Nowak, R.W. Chantrell, D. Garanin, Phys Rev B 74, 094436 (2006)

GC-04

Femtosecond transfer of angular momentum in ferromagnets probed by X-ray spectroscopy.

H. A. Dürr
BESSY, Berlin, Germany

When energy is pumped into electronic excitations of a metal via absorbing a fs optical laser pulse it takes time to re-establish thermal equilibrium. This timescale is ultimately determined by energy transfer from the electronic system to the lattice. If for ferromagnetic metals laser excitation should also lead to an ultrafast quenching of the ferromagnetic order [1,2] angular momentum conservation dictates that an exchange of spin angular momentum with a reservoir such as the lattice has to occur [3-5]

There is considerable disagreement about the timescale for such spin-lattice relaxation. It was established early that spin-lattice relaxation should proceed on timescales 100 ps [1,3]. Such values are also obtained from the damping of magnetization precession [3]. There is growing evidence, although no direct obervation, that on the fs timescale the magnetic moment is affected by laser heating [2,3,5,6]. Even on the fs timescale total energy and angular momentum are conserved. It is debated whether the reduction of the magnetic moment, which corresponds mainly to spin angular momentum, occurs via spin-orbit coupling during coherent laser excitation [8] with an angular momentum transfer from the spins to the electron orbits or via a fs spin-lattice relaxation mechanism [7]. The latter mechanism can be viewed as an Einstein-de-Haas effect occuring on an ultrafast time scale and is schematically depicted in Fig. 1 (top).

Here we present the first time-resolved x-ray magnetic circular dichroism measurements using femtosecond pulses from a synchrotron-based slicing source [9]. An ultrafast laser pulse excited a Nickel film, and a succeeding x-ray pulse from the BESSY femtoslicing facility probed the Ni L_3-edge. By choosing either linear or circular x-ray polarization, the spectra represent snapshots of the magnetic state with an exposure time of about 100 fs [10,11]. Fig. 1 displays time resolved optical pump - x-ray probe measurements with the x-ray photon energy fixed at the Ni L_3 absorption maximum. At this photon energy and with an x-ray bandwidth of 3 eV the XMCD signal essentially corresponds to the integral over the L_3 absorption edge. It takes 120±70 fs to quench the ferromagnetic order as determined from fitting the data to a three-temperature model of energy transfer between electron, spin and lattice reservoirs (line in Fig. 1) [9]. XMCD measures a linear combination of spin, S, and orbital, L, angular momentum components along the magnetization direction as 2S+3L [9]. The temporal evolution of 2S+3L in Fig. 1 represents the first direct demonstration that spin angular momontum, S, is quenched and is transferred to the lattice on a 120 fs timescale and not to the orbita angular momentum, L. This show that electron orbits do not act as a reservoir for angular momentum and demonstrates the existence of a novel fs spin-lattice relaxation channel.

[1] A. Vaterlaus, et al., Phys. Rev. B 46, 5280 (1992).

[2] E. Beaurepaire, J.-C. Merle, A. Daunoise, J.-Y. Bigot, Phys. Rev. Lett. 76, 4250 (1996).

[3] B. Koopmans, et al., Phys. Rev. Lett. 95, 267207 (2005).

[4] W. Hübner, K.H. Bennemann, Phys. Rev. B 53, 3422 (1996).

[5] A. Scholl, L. Baumgarten, R. Jacquemin, W. Eberhardt, Phys. Rev. Lett. 79, 5146 (1997).

[6] H.-S. Rhie, H.A. Dürr, W. Eberhardt, Phys. Rev. Lett. 90, 247201 (2003).

[7] Koopmans, et al., Phys. Rev. Lett. 85, 844 (2000).

[8] G. P. Zhang, W. Hübner, Phys. Rev. Lett. 85, 3025 (2000).

[9] C. Stamm, et al., Nature Mat. 6, 740 (2007).

[10] K. Holldack, et al., Phys. Rev. ST Accel. Beams 8, 040704 (2005).

[11] K. Holldack, et al., Phys. Rev. Lett. 96, 054801 (2006).

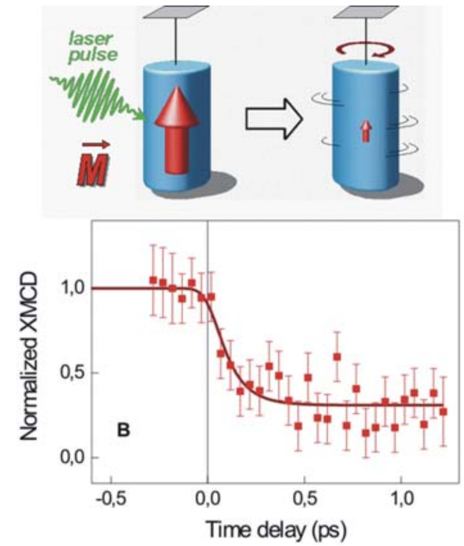

Fig.1 (Top) Schemativ ilustration of the laser induced ultrafast spin-lattice relaxation mechanism in analogy to the static Einstein-de-Haas experiment. (Bottom) Time-resolved XMCD signal with circularly polarized x-rays incident at 60″relative to the sample surface vs. pump-probe time delay (symbols) measured at the L_3 edge maximum. The photon energy resolution was 3 eV. Lines are fits of the three-temperature model to the data. The pump laser fluence was 8 J/cm^2. The XMCD data shown in this figure are normalized to the correponding data taken without laser pump pulses.

GC-05

Laser-induced reorientation of spins in Co/SmFeO3 heterostructures.

J. Loïc[1], F. Nolting[1], A. Kirilyuk[2], R. Pisarev[3], T. Rasing[2], A. Kimel[2]
1. SLS, Paul Scherrer Institut, Villigen-PSI, Switzerland; 2. IMM, Radboud University Nijmegen, Radboud, Netherlands; 3. Ioffe Physical Technical Institute, St. Petersburg, Russian Federation

The demand for the ever-increasing speed of information storage and manipulation has triggered an intense search for ways to control the magnetization of a medium by means other than magnetic fields. The control of magnetism by light is one of the promising approaches to this problem, because such methods may access timescales of a picosecond (10-12 sec) or less. In particular, it has been demonstrated recently that laser-excitation of a bulk antiferromagnet may result in sub-picosecond modification of magnetic anisotropy followed by 90-degree reorientation of antiferromagnetic spins within few picosecond [1].
Here we present experimental results on the laser control of spins in ferromagnet-antiferromagnet heterostructure Co/SmFeO3. For our study we have used bulk SmFeO3 (010) crystals that posses 90-degree in-plane spin reorientation, when heated from 445 K to 455 K. Co-layer (4 nm) has been deposited on the surface of the AFM and cupped by 2 nm Pt-layer.
We have investigated laser-induced and heat-induced magnetic changes in the Co/SmFeO3 heterostructure using a Photoemission Electron Microscope (PEEM) as well as employing X-ray Magnetic Circular (XMCD) and Linear Dichroism (XMLD). Strong temperature dependencies of the XMCD and XMLD signals at Co and Fe edges are observed and discussed. On figure 1 we observe a strong change with the temperature in the contrast of the Co XMCD at the L3 edge, indicating a 90° in-plane rotation of the Co magnetization.
We also induced a change of the SmFeO antiferromagnetic orientation by the mean of a laser by thermal activation. On figure 2.a is represented the Co XMCD image for a temperature of 425K and without laser. So we observed strong black and white domains. Figure 2.b shows the same image but with the laser hitting the sample. In the region where the laser heat the sample, we observed a change of both black and white domains which become gray. That mean we changed the orientation of the Co magnetization by 90 degrees and then the AFM direction of the SFO.

[1] A. V. Kimel, A. Kirilyuk, A. A. Tsvetkov, R. V. Pisarev and Th. Rasing, Nature 429, 850 (2004)

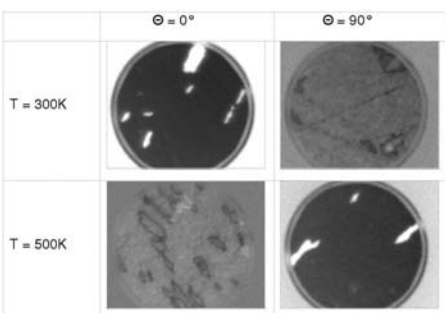

Co XMCD picture at the L3 edge (FOV = 50 μm) for an angle Θ of X-rays with respect to the sample of 0 and 90° and for temperatures of 300K and 500K showing an in-plane rotation of 90° of the Co magnetization.

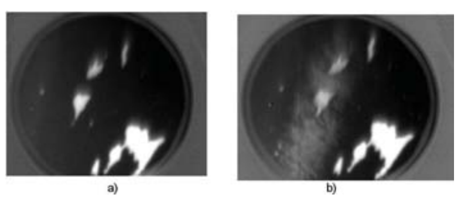

Co XMCD picture at the L3 edge (FOV = 50 μm) for an angle Θ of X-rays with respect to the sample of 0 and a temperature of 425 K : a) without laser and b) with laser.

GC-06

Heusler alloys: The role of band structure on the ultrafast demagnetization.

T. Roth[1], D. Steil[1], A. Conca[2], M. Jourdan[2], M. Aeschlimann[1], M. Cinchetti[1]
1. Physics, TU Kaiserslautern, Kaiserslautern, Germany; 2. Institute of Physics, University of Mainz, Mainz, Germany

As proposed in [1,2] the ultrafast demagnetization process is caused by an Elliot-Yafet type like spin flip scattering. In that case the lattice acts as an active sink to allow the conservation of the systems total angular momentum. This model was recently supported by an experimental analysis of a thin cobalt film on copper combining the complementary techniques of TR-MOKE with spin and time resolved two-photon photoemission (2PPE) [3]. There are other experiments that strongly favour an ultrafast electron lattice channel over an orbital to spin momentum transfer. Stamm *et al.* exploited the potential of an XMCD experiment with respect to its time resolved separation of spin S and orbital L momentum. Measurements on a thin nickel film showed that the process of demagnetization could only be explained to at maximum ten percent by a pure transfer of angular momentum within electronic system [4]. Therefore the main contribution should be carried by an electron lattice mediated spin flip.
In this contribution we report on the effect of the electronic band structure on spin dynamics. In a comparative study the 3d-ferromagnets Ni, Co and the Heusler alloy $Co_2Cr_{0.6}Fe_{0.4}Al$ (CCFA), both with strongly deviating bandstructures, were investigated by means of time resolved MOKE. In conjunction with the search for materials with high spin polarization, so called Heusler alloys form a class with intriguing physical properties. Heusler compounds possess a characteristic band structure exhibiting metallic behaviour for one spin direction and a band gap for the other. From the fs-magnetization point of view Heuslers serve therefore as a well suited test material in order to study the effects of a band gap on spin dynamics. A complete understanding of such processes would be extremely helpful for technical applications such as ultrafast magnetization-switching schemes for read-write processes.
In our study focus was put on the ultrafast magnetization dynamics following an optical excitation with a high intensive femtosecond laser pulse. A slightly pronounced difference in the first ultrafast demagnetization step is found for the CCFA. Additionally, the picosecond thermalization between the participating subsystems is drastically delayed in the case of the Heusler alloy. We ascribe this behavior to a blocked Elliot-Yafet like scattering due to the half metallicity of CCFA.
To investigate the magnetic response we use the MOKE in a pump probe set up. The pump pulse at a central wavelength of 800 nm and the weaker frequency doubled probe pulse both with a FWHM of 50 fs were generated by a Ti:Sapphire amplifier system with 1 kHz repetition rate.
The incident ultrashort optical pulse couples with its electric field component effectively to the electronic system. As a consequence the electronic system is driven far away from its equilibrium; a description by the Fermi-Dirac distribution is no longer valid. The induced imbalance in the electronic subsystem is essential to trigger spin dynamics. The relaxation of the created hot electron gas is the driving force in this case, leading to the observed ultrafast demagnetization. Subsequently, electron lattice or electron impurity scattering events set in. They are, with a certain probability, accompanied by a spin flip; the flip probability is assumed to be independent of the spin state. When increasing the pump fluence the total number of spin flip events and the rate of demagnetization will alter since the number of excited spin up and spin down electrons is not equal. In Fig. 1 the time resolved magneto optical Kerr rotation is recorded from the CCFA sample for a series of different pump fluences. Similar fluence dependent measurements were performed for nickel and cobalt (not shown here). To analyse the demagnetization step the data were fitted assuming an exponential decay of the following form: $\Delta M/M = A_0(\exp(-t/\tau_M) - 1) + 1$. From the fit the two parameters A_0 and τ_M were extracted. A_0 represents the maximal drop depth which increases with increasing pump fluence whereby τ_M denotes the decay time. The ratio A_0/τ_M is a measure of the number of flipped spins per time unit which is plotted against A_0 in Fig. 2. For the 3d-transistion metals the number of flipped spins increases with the parameter A_0 which is attributed to the more established imbalance between majority and minority spins after excitation. In contrast, the CCFA exhibits a rather constant behaviour meaning that the number of flipped spins is independent on the laser density, a signature of the band gap. The experimental data (squares in Fig. 2) is compared to a theoretical calculation (solid lines) connecting the Brillouin-function with the $F(T/T_C)$ function from Ref. [1]. Solely the macroscopic Gilbert damping α was optimized to attain best coincidence between theoretical model and experimental data. The apparent discrepancy will be discussed in terms of the high perturbation scheme.

[1] B. Koopmans *et al.*, PRL 95, 267207 (2005)

[2] B. Koopmans *et al.*, JMMM 286 (2005), S. 271-275

[3] M. Cinchetti *et al.*, PRL 97, 177201 (2006)

[4] C. Stamm *et al.* Nature Mater. 6, 740.743 (2007)

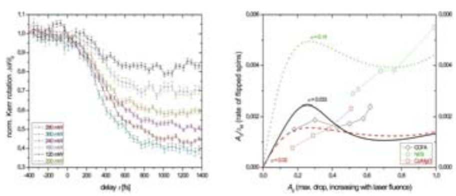

Fig. 1. Magnetic response of CCFA in the longitudinal Kerr configuration. Fig. 2. Analysis of the demagnetization step.

GC-07

Dynamics of the coercivity in (ultrafast) pump-probe experiments.

D. Steil, T. Roth, M. Cinchetti, M. Aeschlimann
FB Physik, AG Aeschlimann, TU Kaiserslautern, Kaiserslautern, Germany

In the last decade the field of ultrafast magnetization dynamic studies have attracted huge attention. It adresses fundamental open questions as well as possible applications including ultrafast magnetization switching [1]. Under irradiation of fs laser pulses ferromagnetic films show an ultrafast decrease of the magnetization signal within hundreds of femtoseconds. Time resolved experiments utilising the magnetooptical Kerr effect (TR-MOKE) have shown that the magnitude of demagnetization is dependent on the incident pump-pulse energy [2]. Demagnetization can be interpreted as a nonadiabatic energy, momentum and angular transfer process. Due to the different temperature dependencies of several anisotropy contributions the incident pump pulse triggers an ultrafast change in the overall anisotropy followed by a sudden alteration of the magnetization direction [4]. As a consequence the magnetization vector **M** performs an ultrafast reorientational motion. Knowledge about the behavior of the fs anisotropy is essential. Observing the evolution of the coercivity would surely help to clarify the phenomena of ultrafast demagnetization.
In this contribution we want to stress the fact that an optical pump-probe technique in the stroboscopic mode using many repeating cycles requires reversible processes and is, hence, in general not suitable to gain access to the time dependent behavior of the coercivity. Observed reductions of the coercivity with increasing pump power are due to laser induced static heating effect.
Hysteresis loops were recorded from an exipaxially grown 10 nm thick Co/Cu(001) thin film at the time delay of maximal demagnetization (approx. 500 fs). To judge the effect of different pump pulse powers on the width of the loops a plot of three different pump fluences is shown (Fig. 1a). The feature of interest is the decrease of coercivity with higher pump fluences. At a first glance one is surprised not to recognize any time dependent variation of the coercivity. There is no recovery of the coercivity to be found - even for time delays when the pump lags behind the probe.
By optically exciting a sample with an intense pump pulse a hierarchy of different heating phenomena take place: 1. Initial laser-heating. The incident laser pulse creates a hot electron system. Back relaxation is established by e-e scattering and interactions with the lattice (including E-Y spin flip processes). 2. After some picoseconds heat-diffusion becomes the dominant contribution. 3. Dependent on the thermal conductivity the substrate can act as a heat barrier and heat-accumulation occurs.
Let's now assume that there exists a time dependent coercivity $H_C = H_C(t)$. If we further assume that the change in H_C is caused by simple heating effects $H_C = H_C(t) = H_C(T)$, then the response should map the different temperature dependent steps.
The absence of any signature in the response of the coercivity (Fig. 1a) indicates that there is either no temperature dependence or technical restrictions inhibit such a measurement in a TR-MOKE experiment.
Fig. 1b shows the situation just before changing the orientation of magnetization of the sample in an external field. The first of N ($N \geq 100$)pump pulses for a fixed position on the hysteresis loop lowers the coercivity in such a way that the magnetization at (1b) 1.) $H = H_C - \Delta H_C (\Delta H_C < H_C)$ changes its orientation. In the time to the arrival of the second pump-pulse the coercivity will recover. However the recovery is not accompanied with a reorientation of the magnetization to its initial direction (1b) 2.) as the switching is an irreversible process.
The second pump pulse therefore meets the new magnetic state having no influence on the *measured* coercivity. Consequently, an effect triggered by the first pump-pulse will be detected as a time dependent signature merely by the neighboring probe pulse, because of the irreversibility of the process.
The measured change in coercitivity is just the optical equivalent of adiabatically heating the sample using a heat source.
To detect the evolution of the coercivity one must perform single-shot experiments. The condition to be fulfilled is that a single pump pulse significantly affects the coercivity. Surely this approach will suffer from a bad signal-to-noise ratio. Another way is to fast magnetic field sweeping (ms-time scale) to reset the whole system to its initial magnetic state. The application of short field pulses could present an experimental tool.
In conclusion we have shown that with present pump-probe setups it is not possible to measure time-dependent coercivity changes. Measured effects are mainly heating effects on long time scales.

[1] C. D. Stanciu et al, PRL 99, 047601

[2] M. Cinchetti et al, PRL 97, 177201

[3] E. Beaurepaire et al, PRB 58, 12134

[4] J-Y. Bigot et al, Chem. Phys. 318, 137-146

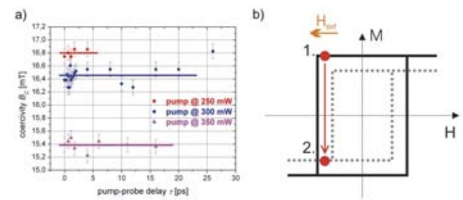

GC-08

LLB-Micromagnetic modelling of ultra-fast optical magnetisation dynamics.

U. Atxitia[1], O. Chubykalo-Fesenko[1], N. Kazantseva[2], D. Hinzke[2], U. Nowak[2], R. W. Chantrell[2]
1. POMT, ICMM-CSIC, Madrid, Spain; 2. Department of Physics, University of York, York, United Kingdom

Recent advances in ultra-fast pulsed laser experiments in magnetic media have opened new possibilities of controlling magnetisation dynamics at the femtosecond regime [1,2]. An essential part of these experiments is a heat pulse, produced by the laser, acting on the magnetic material. Although the underlying processes are complicated, magnetisation dynamics at high temperatures can reasonably be understood taking into account that during ultra-fast laser-induced processes, the electron temperature rapidly increases up to and above the Curie temperature T_c. Standard micromagnetic models, based on the Landau-Lifshitz-Gilbert (LLG) equation cannot account for effects taking place at high temperature. This is because of the assumption of a constant magnetisation length and the fact that high-frequency spin waves are not included into simulations.
In this work we present a new micromagnetic approach, based on the Landau-Lifshitz-Bloch (LLB) equation [3] and its Langevin dynamics [4]. This equation was derived by D. Garanin [3] for classical and quantum average spin polarisation. Its main features are the following (i) The magnetisation magnitude is not conserved. (ii) Two relaxation mechanisms: longitudinal and transverse are present. (iv) The damping parameters are temperature dependent. (v) It is based on the free energy rather than on the internal energy. (vi) At low temperatures it coincides with the standard LLG equation but it is valid up to and beyond the Curie temperature T_c. Previously, we have shown that this equation gives an excellent agreement with the atomistic models [5].
As an example of new LLB-based micromagnetics, we show its suitability to model high temperature dynamics below and above the Curie temperature. We assume laser pulses with Gaussian shape of 50 fs duration and different fluences. During the laser-induced demagnetisation we assume that the photon energy is transferred to electrons and phonons and the magnetisation is coupled to the electron temperature within the two-temperature model. For temperature dependence of the equilibrium magnetisation $m_e(T)$ we suppose the Curie-Weiss law and for anisotropy and exchange parameters - the scaling relations: $K(T)\propto m_e^3$ and $A(T)\propto m_e^2$.
First we model a demagnetisation process produced by a laser pulse with high fluence. Our model reproduces all essential features of the heat-assisted demagnetisation, Fig.1. We observe a very fast demagnetisation, occurring at femto-second scale, followed by a more slow (ps) recovery. The rate of the recovery is different depending on the minimum magnetisation value achieved during the demagnetisation. The observed slow recovery rate at high laser pulse fluence is due to the loss of correlations at high temperature since the micromagnetic exchange vanishes. These results are consistent with recent atomistic simulations [6].
In our second calculation, we reproduce the optical FMR experiments reported in Ref.[1]. We assume a thin film with in-plane anisotropy and a laser pulse which produces a maximum electron temperature T_e = 900 K. An external field of 0.35 T was applied perpendicular to the plane. During the laser pulse, the magnetisation value rapidly decreases. Consequently, the anisotropy value decreases, the system is no longer in equilibrium and a laser-induced precession appears as the magnetisation recovers. The results of our LLB simulation, Fig.2, are similar to the ones reported experimentally in Ref.[1].

[1] M. van Kampen et al Phys. Rev. Lett., vol. 88 (2002) p.227201.

[2] E. Beaurepaire et al Phys. Rev. Lett., vol. 76 (1996) p. 4250.

[3] D. A. Garanin, Phys. Rev. B vol.55 (1997) p.3050; Physica A, vol. 172 (1991) p.470.

[4] D. A. Garanin and O. Chubykalo-Fesenko, Phys. Rev. B vol. 70 (2004) p. 212409.

[5] O.Chubykalo-Fesenko, et al Phys. Rev. B, vol. 74 (2006) 094436

[6] N. Kazantseva et al., Europhys. Lett. 81 (2008) 27004.

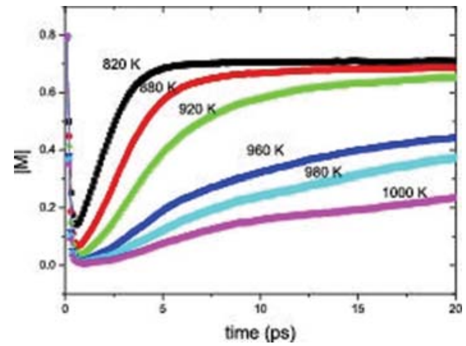

Fig. 1 Modelling of laser-induced magnetisation dynamics with LLB micromagnetics in a cube with 24 nm sides, discretized in cubes with 1.5 nm. Perpendicular anisotropy K(T=0)=5.3 10^4 erg/cm^3 and Ms(T=0) = 480 emu/cm^3 were supposed. The numbers indicate maximum electron temperatures obtained through the two-temperature model.

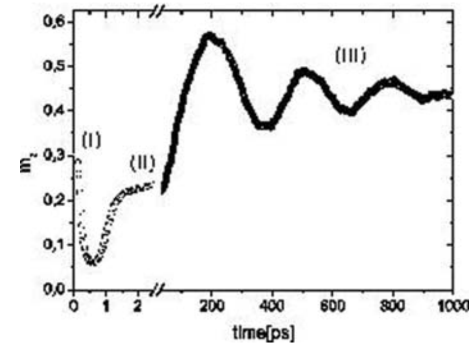

Fig. 2 Modelling of a fast demagnetisation dynamics (Ref. [1]) with low laser fluence in a thin film (48 x 48 x 6 nm) with in-plane anisotropy K(T=0) = 1.3 10^5 erg/cm^3 . Three regions: fs demagnetisation (I), ps recovery (II) and ns precession (III) are clearly distinguished

GD-01

Switching Characteristics and Bias Voltage Dependence of Spin Torque Switching in MgO based Magnetic Tunnel Junctions.

S. Oh[1], K. T. Nam[1], J. E. Lee[1], W. J. Kim[1], J. H. Jeoung[1], D. K. Kim[1], S. Y. Lee[1], K. Kim[2], U. Chung[1], J. T. Moon[1]

1. Memory Division, Semiconductor Business, Samsung Electronics Co., LTD., Yongin-City, Gyeonggi-Do, South Korea; 2. Semiconductor Device Lab, Samsung Advanced Institute of Technology, Yongin-City, South Korea

Spin-transfer torque MRAM (STT-MRAM) based on the current induced magnetization switching effect has been recently proposed and demonstrated by several research groups.The STT-MRAM has an advantage in scalability compared with conventional MRAM, because of its low operating current and the simple cell structure such as DRAM. However, there still exist some issues to achieve high density STT-MRAM: thermal instability, reliability of tunnel oxide, switching current, and switching current distribution. The switching current distribution of STT-MRAM can be triggered by the interlayer coupling, cell size dispersion and thermal excitation due to the joule heating effect. Fail bits are arising from the case the shift field (Hsh) by interlayer coupling is larger than the coercivity (Hc). Thus, minimization of the interlayer coupling is indispensable to achieve MTJ switching with stable memory states and the balanced switching current. The Hc distribution is very large, because of the local change of CoFeB composition during annealing process and shape dispersion by the MTJ fabrication. Thus, it is important to investigate the STT switching distribution due to this Hc distribution.

In the present work, we report the STT switching distribution of the MgO based MTJs where the interlayer coupling is minimized by optimizing patterning processes. The bias dependency of the STT switching measured at room temperature is also shown.

The stacking structure of MTJ for this work was PtMn/CoFe/Ru/CoFeB/MgO/CoFeB/Ta. All samples were annealed in vacuum for 30 min at 360°C under the magnetic field of 1 Tesla. In order to investigate STT, nano-sized MTJs were patterned by conventional lithography and etching process. Cell width and aspect ratio (AR) of MTJs were 70nm and 2, respectively. Especially, the thickness of MgO was carefully controlled below 1 nm to keep resistance area product (RA) about 25 ohm-um2. In this work, a positive bias voltage denotes that electron passes from the pinned layer to the free layer and the MTJ is switched from anti-parallel state (AP) to parallel state (P) in the positive magnetic field.

For MTJ switching with stable memory states, the interlayer coupling should be small compared with the Hc of MTJs. Generally, both CoFeB layers can be interacted by the direct magnetic coupling due to pinholes in the thin MgO layer. In addition, Neel coupling and stray field can arise from interface roughness and the dipoles of the pinned layer, respectively. Figure 1(a) exhibits the change of the Hsh by the interlayer coupling in various MgO thicknesses. In this case, the width of MTJ was 1um and the aspect ratio was 30 to estimate the pure Neel coupling. The continuous MgO film was formed by 5.8Å, where the Hsh was around -14Oe. When the MgO thickness was reduced below 5.8Å, the Hsh was abruptly increased by the direct magnetic coupling due to pinholes. Thus, the pure Neel coupling strength at MgO thickness for a stable STT switching is below -14Oe

To minimize the stray field, the MTJs were etched up to the free layer. As shown in figure 1(b), the bias voltage dependency of Hsh was scrutinized. The average Hsh at zero bias voltage was about -10Oe and this indicated that the etching process was stopped onto the MgO tunnel barrier. In this figure 2, it is shown that bias voltage dependency on the Hsh is due to the STT switching effect. Namely, when a positive magnetic field is applied, the positive bias voltage helps the AP to P switching and thus the negative Hsh increases.

Figure 2(a) shows the dependence of bias voltage on the Hc and Hsh at the samples with different Hc values. The Hc values were 120Oe and 40Oe, respectively. Figure 2(b) shows the R-V curves of these MTJs at 50ns pulse width. The switching voltages were almost the same as shown in this figure. Here, the Jc was about 4.5MA/cm2. This result shows the STT switching voltage is not sensitive about the Hc of MTJs. The Hc distribution is very large due to the local change of magnetic composition during annealing process and shape dispersion by the MTJ fabrication. In spite of this large Hc distribution, this shows that it is possible for STT switching to obtain low switching voltage distribution.

In addition to these results, the switching characteristics and a bias voltage dependence of STT switching in various annealing temperature will be presented in detail.

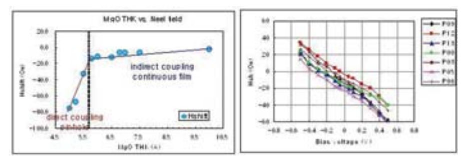

(a) The change of Hsh by interlayer coupling in various MgO thicknesses. In this case, the width of MTJ was 1um and the aspect ratio was 30. (b) Bias voltage dependence of Hsh with various MTJs.

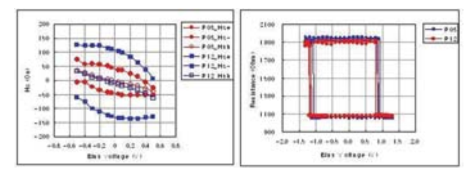

(a) The dependence of bias voltage on the Hc and Hsh at the MTJs with different Hc values. (b) The R-V curve at 50ns pulse width.

Impact of antiferromagnet-induced magnetization fluctuation control on switching current distribution reduction in MRAM.

Y. Katoh, H. Hada, N. Kasai
Device Platforms Research Laboratories, NEC Corporation, Kanagawa, Japan

Introduction
Magnetoresistive random access memory (MRAM) with magnetic tunnel junctions (MTJs) has attracted a great deal of attention due to its non-volatility and potential for high-speed operations. The write current for memory cell is designed based on both the average and distribution of MTJ switching current. We already clarified that the MTJ deformation causes 50% of the distribution, and have been analyzing the factor of other 50%. The importance of improving the distribution to reduce power consumption is high for all writing methods: a spin torque transfer[1], a 1-axis magnetic field[2], and a toggle operation[3]. In these MRAMs, an antiferromagnetic layer is commonly used to fix the magnetization direction of a pinned layer in an MTJ. In this work, we reveal that the antiferromagnetic layer is one of significant factors of switching current distribution. And we also show some efficient methods for distribution reduction about 20%.
Experiments and Results
To know all the factors of switching current distribution, we introduced the new assumption, “the magnetic domain structure of the pinned layer induces stray field.” A Landau-Lifshitz-Gilbert (LLG) simulation was performed in several cases with different domain structures and magnetization conditions. Fig. 1 shows the simulation results of the switching magnetic field (Hsw) distribution dependence on the MTJ size. It clarified that the domain structure exists and that its magnetic fluctuation causes the distribution in both cases of the single free layer and the toggle layer [4].
To determine the effect of pinned condition, we investigated Hsw distribution using some magnetic annealing treatment to control the magnetization condition of the pinned layer. The MTJ consisted of a free layer (NiFe), a tunneling layer (AlO), and a pinned layer (CoFe/Ru/CoFe/PtMn). The magnetic anneal temperature, time, and magnetic field were 275 degrees, 30 minutes, and 1.2 teslas toward the easy axis of the free layer, respectively. Fig. 2 shows the normalized variances of the switching magnetic field depending on the number of the annealing treatment. It improved at the second treatment more than it did at the first treatment. At the third time, the value did not improve any more. It is clarified that the magnetization condition of the pinned layer has much effect on the Hsw distribution, and it was considered to become stable after the second treatment.
To determine that the main factor is the CoFe pinned layer or the antiferromagnetic layer, we investigated the distributions with different pinned structures. They were (a) CoFe (1.2 nm)/Ru/CoFe (1.4 nm)/PtMn and (b)CoFe (1.2 nm)/Ru/CoFe (2.6 nm)/Ru/CoFe (1.4 nm)/PtMn as shown in Fig. 3. The free layer was a toggle type, and the MTJ shape was a 0.32 x 0.64 μm ellipse. Fig. 4 shows the normalized variances of the switching currents of these samples. It does not increase drastically with insertion of a thick CoFe layer. It indicates that the antiferromagnetic layer is the significant factor of distribution and that the effect of the material anisotropy is small.
To improve the Hsw distribution, we proposed two methods. Method1 is a pinned layer without an antiferromagnetic layer. It is (c)CoFe(1.2nm)/Ru/CoFe(2.6nm)/Ru/CoFe(1.4nm)/Ru as shown in Fig. 3. The magnetization is fixed with sufficient exchange coupling of magnetic layers. To control the magnetization direction by applying large magnetic field, it includes one thick magnetic layer. And it can compensate stray field from the edge among three magnetic layers. It was determined that 22% of the valiance improves with structure (c) as shown in Fig. 4.
Method2 is a new magnetic annealing procedure called swing anneal. It consists of an annealing treatment toward several degrees off from the easy axis and an additional treatment toward the easy axis. Because the torque depends on the direction difference between applied magnetic field and the magnetization in each domain, only the magnetization in the direction far from the easy axis could be modified in the swing anneal. Therefore, it was expected that antiferromagnet-induced fluctuation of magnetization in pinned layer decreased. It was determined that 17% of the valiance improves in the sample in Fig. 2 by the swing anneal.
The fabrication process was developed by the Toshiba-NEC MRAM development project.

[1] J. C. Slonczewski, J. Magn. Magn. Mater., vol. 159, pp. L1-L7, 1996.

[2] H. Honjo et al., 52nd Annual Conference on MMM Abstracts, p. 481, Nov. 2007.

[3] S. Tehrani et al., IEEE Proceedings, vol. 91, no. 5, pp. 703-714, May 2003.

[4] J. G. Deak, IEEE Trans. Magn., vol. 43, no. 6, pp. 2821-2833, June 2007.

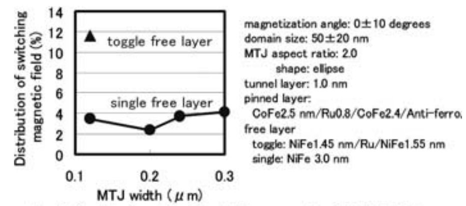

Fig. 1 Simulated results of switching magnetic field distribution

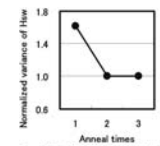

Fig. 2 Switching magnetic field distribution

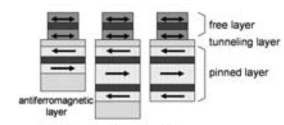

Fig.3 Pinned layer structure

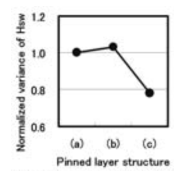

Fig. 4 Hsw variance dependence on pinned layer structure

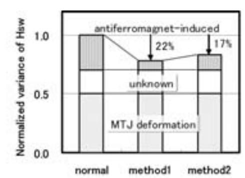

Fig. 5 Factor of switching magnetic field distribution

GD-03

Spin Torque Random Access Memory down to 22nm Technology.

X. Wang, Y. Chen, H. Li, D. Dimitrov, H. Liu
Seagate Technology, Bloomington, MN, MN

Magnetic Random Access Memory (MRAM) is one promising candidate for future nonvolatile and universal memory. MRAM writing based upon spin-polarized current induced magnetic tunneling junction (MTJ) switching has been proposed as SPRAM. In this paper, a combined magnetic dynamics and electric circuit model is developed to study physics and scalability of SPRAM. We use this model to explore one-transistor-one-MTJ SPRAM (Fig.1) design down to 22nm CMOS technology node. Constrains limiting SPRAM achievable capacities are analyzed; possible approaches to improve achievable capacities are discussed.

MTJ and CMOS are dynamically coupled in SPRAM writing operation. SPRAM switching behavior is highly dependent on the dynamics and histories of write current applied to MTJ, which shows as a time varying resistance in electric circuit and greatly affects the driving current provided by CMOS. We developed a dynamic MTJ switching model by combining micro-magnetic simulation of MTJ and SPICE simulation of CMOS circuit. Fig. 2 shows an example of the time varying MTJ resistance and CMOS driving current during MTJ switching. The fluctuations in resistance and current are signatures of MTJ magnetization oscillation during switching. The abrupt driving current changes correspond to MTJ resistance switched from one resistance state to the other resistance state. The asymmetry in low-to-high resistance switching behavior and high-to-low resistance switching behavior is due to CMOS forward and backward driving current strength difference. As discussed in [1], our dynamic MTJ-CMOS approach leads to much improved predictions at the required write current compared to the conventional static model without explicitly considering dynamic coupling between MTJ and CMOS.

Scaling down SPRAM requires shrinking both CMOS and MTJ dimensions. Although source-drain leakage from electron thermal diffusion and gate current leakage from quantum-mechanic tunneling put fundamental physics limit on CMOS size, it is believed that CMOS technology can achieve 22nm channel length with power-supply voltage around 1.0V [2]. Fig. 3 shows the current provided by CMOS as a function of MTJ resistance for 22nm channel length with different channel width. As CMOS scales down, decreased driving current requires decreasing MTJ writing current threshold. However the competition between the short time dynamic writability and the long time thermal stability is a well-known physics factor limiting magnetic device scaling down. In this paper, SPRAM design spaces at CMOS 22nm technology node are explored using our dynamic MTJ-CMOS model. Fig. 2 is one example of MTJ design achieving 34F2 capacity at CMOS 22nm technology node with channel width 100nm. However this design is far from achieving maximum potential capacity supported by CMOS 22nm technology node. In this paper, we will analyze tradeoffs between MTJ current threshold, MTJ thermal stability and CMOS driving strength. The analysis provides information on physics requirements and technology bottlenecks for MTJ to achieve maximum capacity supported by CMOS 22nm technology. Magnetic solutions for MTJ to fully achieve CMOS 22nm potential capacities are suggested.

1.Y. Chen, X. Wang, H. Li, H.Liu and D. Dimitar, Design Margin Exploration of Spin Torque Transfer RAM (SPRAM), to be published at 9th International Symposium on Quality Electronic Design, San Jose, March, 2008 .

2.ITRS (International Technology Roadmap for Semiconductors), http://www.itrs.net/

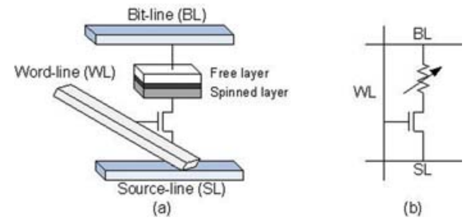

schematic picture and equivalent circuit of one-transistor-one-MTJ SPRAM

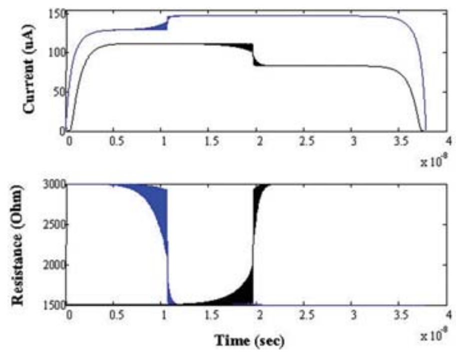

CMOS driving current and MTJ resistance as a function of time for switching from high resistance to low resistance (blue) and from low resistance to high resistance (black) at 22nm technology with 100nm channel width.

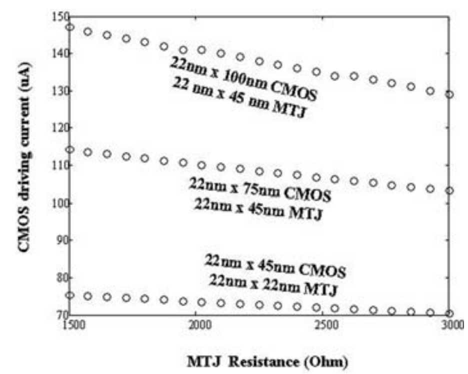

CMOS driving current vs MTJ resistance for 22nm channel length with different channel widths.

GD-04

Multilevel Magnetic Random Access Memory Based on Spin Transfer Torque Switching.

Y. Zhang, X. Yao, J. Wang
MINT Center & Electrical and Computer Engineering Department, University of Minnesota, Minneapolis, MN

Experimental demonstration of spin transfer torque (STT) switching [1], has attracted much attention due to its rich basic physics and potential industry applications, especially providing a promising writing scheme for ultra high density magnetic random access memory (MRAM). In recent years, studies focusing on lowering the critical switching current density and promoting the magnetoresistance (MR) signal have been reported intensively based on the STT induced magnetization switching. To further increase the storage density, the size of the cells needs be scaled down, for which perpendicular magnetized STT was demonstrated to maintain the thermal stability [2]. On the other hand, improving the storage capability of each memory cell can increase the recording density in theory. A multilevel MRAM, based on GMR spin-valve structure and external field induced magnetic switching, has been investigated by Jeong, et al [3], which faces the same challenges as the recent field-driven MRAM. In our work, novel design of multilevel STT MRAM based on MgO MTJ with perpendicular anisotropy is reported, which is also applicable to CPP-GMR or MTJ with in-plane anisotropy.

Fig.1(a) shows the proposed 2-bit 4-state STT MRAM cell. The full structure can be treated as two STT MTJs. The MTJ-1 consists of the fixed layer and freelayer1 with the resistance R1L and R1H when the two magnetic layers are parallel and antiparallel to each other and the critical switching current density is Jc1. With the higher critical switching current density, the freelayer1 will act as "fixed layer" for the freelayer2, and the Jc2 is the critical current density between the R2L and R2H for the MTJ-2. Here for both MTJs the current from top free layer to bottom pinned layer (electrons flow from bottom to top) is defined as the positive current. Based on the STT effect, the free layer can be written as "0" and "1" representing low resistance parallel state and high resistance antiparallel state respectively by a positive or negative current pulse. For an experimental demonstration in this two-level structure, the fixed layer consist a high perpendicular anisotropy FePt layer and a high spin polarization CoFeB layer which are also included in two composite magnetic free-layer, freelayer1(CoFeB/FePt/CoFeB) and freelayer2(CoFeB/FePt/FeSiO). In the composite freelayer, the CoFeB layer is also used as a soft layer to lower the switching current density and to enhance MR ratio due to CoFeB/MgO/CoFeB structure providing high TMR signal. In order to write two free-layers separately and make the free-layer1 work as the "fixed layer" of the MTJ2, the Jc1 should be larger than the Jc2 just as discussed above. In this case, a nano current channel (NCC) layer will be deposited in the freelayer2 to decrease the Jc2 distinctly [4].

A typical resistance vs current loop is shown in Fig1(b) to describe the writing and reading process of this multilevel MTJ-based memory cell. When a positive large pulse(Jc1) applied, both two free-layers will be parallel to the fixed layer. The resistance will be the sum of two lower states R1L+R2L labeled as "00". If a negative small pulse(Jc2) is followed, the MTJ1 won't be affected while the freelayer2 will be switched antiparallel to the freelayer1 and the resistance will be R1L+R2H labeled as "01". On the other hand, a negative large pulse will make the three magnetic layer antiparallel to each other with the highest resistance R1H+R2H(state "11") and a followed positive small pulse can reduce the resistance to R1H+R2L(state "10"). The four states can be sensed by a small current. For the high MR ratio of MTJ, the resistance change between "00" and "01" or between "11" and "10" will be clear. Thus the requirement of reading goes to R1H+R2L> R1L+R2H which means ΔR1>ΔR2 or MR1%*RlL>MR2%*R2L. The writing pulse sequence, the sensed resistance state and the logic state are listed as a form in Fig1(c). A reasonable experimental tolerance of the resistance level and switching current density can be expected because 1) the experiment data shows that the MgO MTJ has provided a large range of barrier resistance and MR ratio [5]; 2) we recently reported that the switching current density could be adjusted by a factor of 2 – 4 by using the composite free layer with perpendicular anisotropy [6].

1. J. A. Katine, F. J. Albert, R. A. Buhrman, E. B. Myers, and D. C. Ralph, Phys. Rev. Lett. 84, 3149 (2000).

2. H. Meng and J. P. wang, Appl. Phys. Lett. 88, 172506 (2006)

3. WC Jeong, BI Lee, SK Joo, J. Appl. Phys. 85, 4782 (1999).

4. H. Meng, and J.P. Wang, Appl. Phys. Lett. 89, 152509 (2006).

5. K. Tsunekawa, et al,, Appl. Phys. Lett. 87, 072503 (2005).

6. H. Meng and J. P. Wang, IEEE Trans. Magn. 43, 2833, (2007)

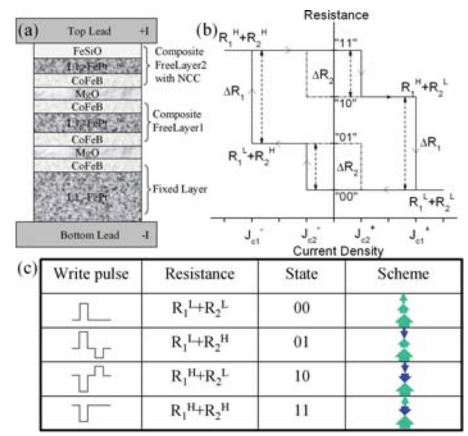

Fig.1 (a) the scheme of 2-bit STT MTJ cell (b) the schematic resistance vs current loop (c) the writing pulse sequence and the state of resistance and logic state

GD-05

Heat-assisted magnetization reversal using pulsed laser irradiation in patterned magnetic thin film with perpendicular anisotropy.

K. Waseda, R. Doi, B. Purnama, S. Yoshimura, Y. Nozaki, K. Matsuyama
Dept. of Electronics, Kyushu University, Fukuoka, Japan

Heat-assisted magnetization reversal is one of the promising candidates for the method to decrease the switching field efficiently without sacrificing the thermal stability of the bit information in magnetic random access memories (MRAMs). For the application to heat-assisted MRAMs, it is essential to establish the device configuration ensuring not only a high-speed heating and cooling of the memory cell but also the heating efficiency. In this paper, we have experimentally investigated both the heating efficiency and the cooling speed of the micron-scale TbFe thin film laterally connected with electrical lead patterns. Figures 1(a) and 1(b) shows the optical photograph and the schematic cross-section of the prepared device. The device consists of 100 nm-thick TbFe film with a lateral size of 50×50 μm^2 connected with electrical leads, 300nm-thick Cu loop conductor to produce the magnetic field perpendicular to the film plane, and 50 nm-thick Cr aperture. The patterned TbFe film was heated up using pulsed YAG laser irradiations through the Cr aperture. The pulse width and the wavelength of YAG are 1 ns and 532 nm, respectively. The amplitude of the laser irradiation was attenuated using optical filters with transmission coefficients T_{filter} in the range from 3 to 10 %. As shown in Fig. 1(c), a pulsed perpendicular magnetic field of 80 Oe (t_w=30, 50 and 100 ns) was applied with a delay of t_{delay} from the laser irradiation. The magnetization reversal of the TbFe film caused by the simultaneous applications of both the heating and the magnetic field was measured using the anomalous Hall effect. Figure 2 shows the temperature dependence of the normalized Hall voltage V_{AHE}. The V_{AHE}, which is proportional to the perpendicular component of magnetization in patterned TbFe film, is gradually decreased with increasing temperature and becomes zero at 383 K corresponding to the Curie temperature T_c. Figure 3(a) shows the ratio of magnetization reversal caused by applying both external magnetic fields and pulsed laser irradiations with various amplitudes. The increase of magnetization reversal is saturated as the T_{filter} becomes larger than 5 %. It is, therefore, expected that the patterned TbFe film is heated above the T_c as T_{filter}>5 %. Assuming an adiabatic process, the energy required for heating the patterned TbFe film with the volumetric heat capacity of 2.6×10^6 $Jm^{-3}K^{-1}$ from room temperature to the T_c is estimated as 7.2 nJ, which is 19 % of the measured irradiation energy of the pulsed laser with T_{filter}=5 %. Figure 3(b) shows the ratio of magnetization reversal caused by applying both pulsed magnetic field of 80 Oe and pulsed laser irradiations as a function of t_{delay} ranging from -100 to 100 ns. The data for t_{delay}>0 indicates the magnetization reversal in the cooling process after the laser irradiation. The time to cool the patterned TbFe film from the T_c to the critical temperature required for the magnetization reversal at 80 Oe is 17 ns. It is also found that the cooling time is almost independent of the width of the electrical leads connected to the patterned TbFe film. This suggests that the thermal diffusion is predominantly occurred through the top and bottom surface of the TbFe film. Therefore, faster cooling can be expected for a memory cell with a magnetic tunneling junction because metallic leads are connected to the top and bottom surface of the cell.

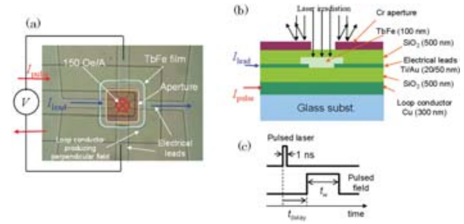

Fig. 1 (a) Optical photograph and (b) schematic cross-section of the device used for the experiments on heat-assisted magnetization reversal in patterned TbFe film. (c) Timing diagram of heat-assisted magnetization reversal experiment.

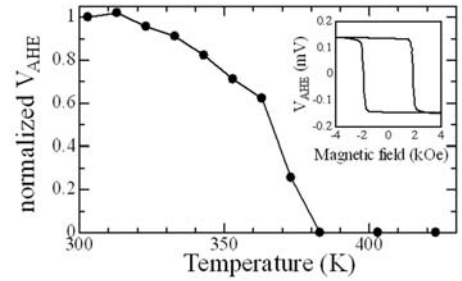

Fig. 2 Normalized Hall voltage V_{AHE} as a function of temperature. The inset shows V_{AHE} versus magnetic field curve at room temperature.

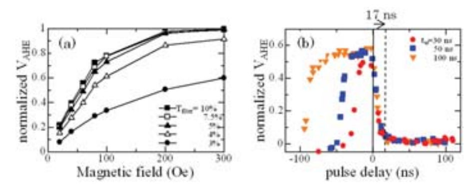

Fig. 3 (a) Variations in normalized V_{AHE} after applying external magnetic fields together with pulsed laser irradiations. (b) Pulsed-delay dependence of the variations in V_{AHE} induced by heat-assisted switching operation.

GD-06

Estimation of Thermal Stability Factor in Current-Induced Magnetization Switching.

H. Suh, K. Lee
Korea University, Seoul, South Korea

I. Introduction

The current-induced magnetization switching (CIMS) has been demonstrated in spin valve structures [1]. The CIMS provides various merits for the use in the magnetic random access memory (MRAM) such as better scalability and selectivity in comparison with the field-induced magnetization switching. For the application of CIMS in MRAM, the thermal stability factor, $\Delta=(H_kM_sV)/(2k_BT)$ should be larger than 60 where H_k is the in-plane anisotropy field, M_s is the saturation magnetization, $k_B$is the Boltzmann constant, T is the temperature, and V is the magnetic volume of cell. Because of its importance, experimental studies to estimate the thermal stability factor have been performed [2]. There are several methods to estimate the Δ in experiments of CIMS, but a reliable method has not been confirmed yet. In this work, we have tested three different methods to estimate the Δ and confirmed which one is the most efficient and reliable.

II. Three methods to estimate the thermal stability factor

Any method to estimate the Δ should adopt the Arrhenius-Néel equation, $\tau=\tau_0\exp(E_b^*/k_BT)$ where is the relaxation time, τ_0 is the reciprocal of the attempt frequency, E_b^* is the effective energy barrier [3]. In the presence of the spin-transfer torque, the energy barrier E_b^* can be described by $E_b^*=\Delta(1-J/J_{C0})$ where J is the current density, and J_{C0} is the threshold current density for the current-induced magnetic excitation [4]. In experiments, two unknown variables Δ and J_{C0} should be determined by fitting through a use of the modified Arrhenius-Néel equation. Three methods for fitting are as follows;

[Method 1] In method 1, the probability of not switching (P_{ns}) is measured as a function of the switching time (t) at a fixed current density. The eq. (1) is used to fit Δ and J_{C0}.

$\ln(P_{ns})=-t/\tau=-t/\tau_0\exp[-\Delta(1-J/J_{C0})]$. (1)

[Method 2] In method 2, the probability of not switching (Pns) is measured as a function of the current density (J) at a fixed current pulse (t). The eq. (1) is also used to fit Δ and J_{C0}.

[Method 3] In method 3, the average switching current density is measured as a function of the pulse-width τ_P. The eq. (2) is used to fit Δ and J_{C0}.

$J=J_{C0}[1-\{\ln(\tau_P/\tau_0)\}/\Delta]$.(2)

III. Model

We performed the macrospin simulation to test the three methods for estimating the thermal stability factor. The modified Landau-Lifshitz-Gilbert equation with including the spin torque term is used. The spin transfer torque is described by $\Gamma=(\gamma a_J/M_s)\mathbf{M}\times(\mathbf{M}\times\mathbf{M}p)$ where γ is the gyromagnetic ratio, **M** is the magnetization vector of free layer, **M**p is the unit vector of magnetization of pinned layer, a_J(=h_bar/2e(PJ/M_sd)), P is the spin-torque efficiency factor, d is the thickness of free layer. We assumed Ms=600emu/cm^3, P=0.7, and T=300K. The geometry of magnetic cell is 150×70×3 (length×width×thickness) nm^3 of which thermal stability factor is 54.4. For each case, more than 100 switching events were calculated.

IV. Results and Discussions

Figure 1(a) shows results obtained by the method 1 at $J=4.2\times10^6$ A/cm^2 and τ_0=1ns. In this method, we could not obtain the correct Δ and J_{C0}. It is because the variable, t is outside the exponential function whereas both unknown parameters are in the exponential function. Therefore any combination of Δ and J_{C0} can fit the simulation results.

In method 2 and 3, however, we could obtain a reasonable fitted value of Δ which nearly coincides with the correct one (=54.4) since the two unknown parameters, Δ and J_{C0} can be independently determined. Figure 1 (b) and (c) show results of method 2 and method 3 assuming τ_0=1ns, respectively. In method 2, the thermal stability factor (Δ) is determined by the slope of plot and is 50.5. We could also determine the J_{C0}(= 5.76×10^6 A/cm^2) by extrapolating J to the point of $-\ln\{-\ln(P_{ns})/(-\tau_0^{-1}t)\}=0$. In method 3, the thermal stability factor (Δ) is also determined by the slope of plot and is 51.8. We obtained J_{C0} of 5.72×10^6 A/cm^2 by extrapolating J to the point of $-\ln(\tau_P/\tau_0)=0$. Since the τ_0 is in principle another unknown parameter although it is conventionally assumed to be 1ns, a fitted value of Δ should be insensitive to the τ_0. Assuming τ_0=0.1ns, we obtained Δ =52.8 by method 2 and Δ =54.1 by method 3. It indicates both methods are reliable to estimate the thermal stability factor.

In conclusion, we have tested three different methods to estimate Δ and J_{C0} based on the modified Arrhenius-Néel equation. It was found that both of the method 2 and 3 are reliable.

[1] J. A. Katine, F. J. Albert, R. A. Buhrman, E. B. Myers, and D. C. Ralph, Phy. Rev. Lett. 84, 3152 (2000).

[2] J. Hayakawa et al., Jpn. J. Appl. Phys. 45, L1507 (2006); H. Takahashi et al., Materials Today Asia, K16, Beijing (2007).

[3] W. F. Brown, Phy. Rev. 130, 1677 (1963).

[4] Z. Li and S. Zang, Phy. Rev. B. 69, 134416 (2004).

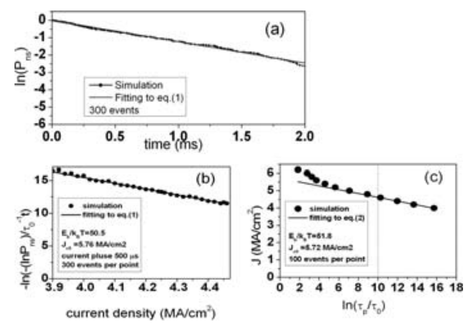

Fig. 1. (a) Method 1, $\ln(P_{ns})$ as a function of time, (b) Method 2, $-\ln(-\ln(P_{ns})/(-\tau_0^{-1}t))$ as a function of current density J, and (c) Method 3, current density J as a function of $\ln(\tau_P/\tau_0)$.

GD-07

Nano-ring MTJ and nano-ring MRAM.

X. Han, Z. Wen, H. Wei
State Key Lab of Magnetism, Institute of Physics, CAS, Beijing, China

Nano-ring-shaped magnetic tunnel junctions (NR-MTJ) were fabricated. The tunneling magnetoresistance (TMR) versus current (I) loops of the NR-MTJs for a spin-polarized current switching were measured and the TMR ratio of around 20%~50% with a Al-O barrier at room temperature were observed. The critical value of switching current for the free Co60Fe20B20 layer between parallel and anti-parallel magnetization states is smaller than 500 μA. The NR-MTJs arrays were also integrated above the transistors in CMOS circuit for 4x4 bit MRAM demo devices. After each positive and negative pulse writing current the high and low resistance of a NR-MTJ as a MRAM bit were read out using a low read current of between 10 and 20 μA which does not affect the magnetic state of the NR-MTJ. Such design could distinctly reduce MRAM energy consumption and memory cell size and increase the cell density compared with existing designs. It is suggested that the MRAM fabrication with the density and capacity higher than 6 Gbite/inch2 are possible based on 1 NR-MTJ + 1 transistor structure and current switching.

GD-08

Magnetic characterization of embedded MgO ferromagnetic contacts for spin injection in silicon.

T. Uhrmann[1], T. Dimopoulos[1], D. Schwarz[1], V. Lazarov[2], D. Kirk[2], A. Kohn[2], S. Weyers[3], U. Paschen[3], H. Brückl[1]

1. Nano-Systemtechnologies, Austrian Research Centers GmbH - ARC, Vienna, Austria; 2. Department of Materials, University of Oxford, Oxford, United Kingdom; 3. Fraunhofer Institute of Microelectronic Circuits and Systems, Duisburg, Germany

The control of the magnetic switching is a prerequisite for the successful implementation of a new data storage technology like magnetic random access memory (MRAM). An alternative MRAM design is based on the front-end implementation of the magnetic modules, employing spin-polarized current injection and detection through properly doped silicon. Each magnetic module consists of a tunneling barrier, a thin ferromagnet (FM) and a capping layer, embedded into a SiO_2 dielectric layer. The aim of this work is to study the magnetic properties of such magnetic modules.
The samples were fabricated on Si wafers with 42 nm thermally grown oxide. The oxide layer has been structured by deep-UV lithography in combination with CHF_3 reactive ion etching and buffered HF wet-chemical etching, in order to form eight different arrays of rectangular holes down to the silicon surface. The rectangular elements have widths of d= 300, 400, 450 and 500 nm and two different lengths l= 1500, 3000 nm. Directly after the HF wet etching, multilayers with the following compositions have been deposited, using RF (for the MgO film) and DC magnetron sputtering: MgO (x= 0, 0.5, 1.0, 1.5, 2.5nm)/ $Co_{70}Fe_{30}$(1nm)/ $Ni_{81}Fe_{19}$(4nm)/ Ta. The CoFe/NiFe bilayer has been chosen in order to combine the soft magnetic properties of NiFe with the high tunneling spin polarization of CoFe. The fabrication was completed by lift off processing to remove the resist and the multilayer from outside the holes. A RMS-roughness of 0.25 nm has been measured by atomic force microscopy (AFM). Additional structural investigations by transmission electron microscopy (TEM) for a MgO thickness of 2.5 nm have shown smooth interfaces with a low roughness. The FM bilayer is polycrystalline, while the MgO barrier appears to be amorphous. Due to processing, the rectangular edges are rounded, which should lead to a decreased switching field, compared to the ideal rectangular case.
The magnetic properties of the arrays were studied using Magneto-optical Kerr effect (MOKE) measurements. In Fig. 1 we present easy-axis MOKE loops (with the magnetic field aligned along the long axis of the elements), measured for the as-deposited multilayer with l= 3000nm and x= 2.5 nm. Such measurements have been done for every MgO barrier thickness and all fabricated array sizes. From the easy axis loops we extracted the switching field, H_S, and the switching field distribution, ΔH_S.
The magnetization switching is characterized by a high remanent moment that is desirable for a magnetic memory device. The hard axis loops (not shown here), on the contrary, show the typical rotation-like switching with very small hysteresis and remanence.
The dependence of H_S on the elements' width, d, is depicted in Fig. 2(a), where the switching field is decreasing over the width. Particularly important is the observed large magnetic selectivity, which in some cases surpasses 20 or 25 Oe.
As it can be seen in Fig. 2(b), $\Delta H_S/H_S$ is increasing with the width of the elements, and is generally larger for the length of 1500 nm, than for 3000 nm long elements.
The plot of the switching field as a function of the MgO thickness in Fig. 3 shows, that H_S has similar values for x= 0, 1.5 and 2.5 nm and reaches a maximum between x= 0.5 nm and 1.0 nm. This behaviour is most probably related to the early stages of the MgO layer growth. The barrier should be at the limit of film continuity at 1 nm, which induces interfacial roughness that may raise H_S.
In conclusion, the magnetic switching characteristics of embedded magnetic cells, for an alternative front-end MRAM design, have been evaluated by localized magneto-optical Kerr effect measurements. It is shown that the switching field and distribution depend strongly on the MgO tunneling barrier thickness and the element's width.

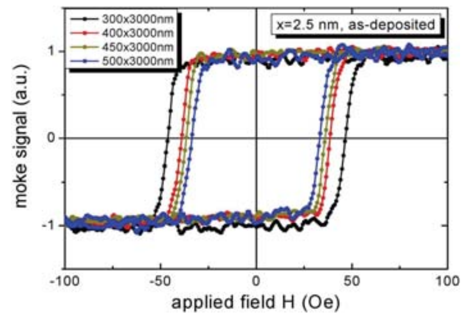

Easy axis magnetization loops for arrays of rectangular elements with varying width and 3000 nm length for a MgO thickness of x= 2.5 nm.

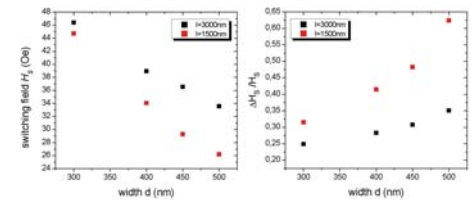

Dependence of the relative switching field (a) and the switching field distribution (b) on the elements' width for 2.5 nm MgO thickness.

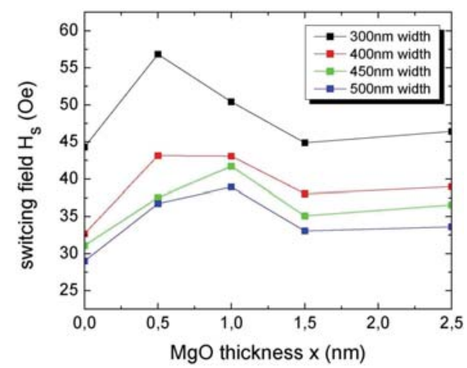

Dependence of the switching field H_s on the MgO thickness for l=3000nm.

GD-09

High thermal stability and low switching current in a perpendicular-CPP-GMR with an ultrathin epitaxial FePt free layer.

K. Yakushiji, S. Yuasa, A. Fukushima, H. Kubota, T. Nagahama, T. Katayama, K. Ando
National Institute of Advanced Industrial Science and Technology (AIST), Tsukuba, Japan

We have focused our study on spin-torque switching in a magnetoresistive memory cell with perpendicular magnetic anisotropy predicting high-density spin-torque switching type MRAM (so-called Spin-RAM). Large perpendicular anisotropy (K_u) and collinear demagnetizing filed to the perpendicular anisotropy field are expected to realize large thermal stability ($\Delta = K_u V / k_B T$) and small switching current density (J_c). Although basic properties in nanopillars with perpendicular anisotropy have been studied in recent years[1-3], there have been few systematic studies intensively on Spin-RAM application. In this study, we employed monatomic alternate layer deposition method to prepare high-quality ultrathin FePt switching layers. The deposition method is effective in preparing an ultrathin film (< 2nm) without deteriorating the film quality[4-6]. We investigated spin-transfer switching and thermal stability in epitaxial [Fe(1 monolayer(ML))/Pt(1 ML)]$_{12}$ / Au / [Fe(1 ML)/Pt(1 ML)]$_n$ CPP-GMR nanopillars.

A Film was prepared on an MgO(001) substrate by MBE method. Fe of 1 ML, a [Fe(1 ML)/Pt(1 ML)]$_n$ pinned layer with n = 12 (4.0 nm- thick), Fe of 2 ML, a 2.7 nm- thick Au spacer layer, Fe of 1ML, and a [Fe(1 ML)/Pt(1 ML)]$_n$ free layer were successively deposited on a Cr/Au buffer at 200 °C. The number of alternation period n for the free layer was varied at 3 (1.02nm), 4, 5 and 6 (2.04nm). Pillars were prepared in a circle shape with various diameters (d) from 100 nm to 170 nm.

Figure 1 (a) shows typical minor *R-H* loop at room temperature for a cell with the free layer thickness (t_{free}) of 1.02 nm (n = 3) and d = 130 nm. We obtain MR of 1.6 % and RA of 0.06 $\Omega\mu m^2$. The loop shifts about 1200 Oe because of the dipole interaction between the free and pinned layers. Fig. 1 (b) shows spin-torque switching property (*R-I* loop) measured at H = 1200 Oe with the current pulse duration of 100 ms. Sharp transitions of both AP to P and P to AP state were clearly observed. It was suggested that domain wall motion governed the magneto-switching because the coherent rotation should only take place for a pillar diameter below 50 nm. Average critical current density (J_{c0}) and Δ were estimated from current pulse duration (t) dependence of switching current (I_c), to be 1.2×10^7 A/cm^2 and 66, respectively. We consider that the high perpendicular anisotropy of FePt gave rise to practical Δ even in an ultrathin layer, and use of such an ultrathin free layer leads to small J_{c0} in spite of small MR and large damping property of FePt. Fig. 2 plots average critical current density (J_{c0_av}) versus average thermal stability (Δ_{av}) for cells with t_{free} = 1.02 nm (n = 3). Although a cell with in-plane anisotropy usually shows trade-off relationship between J_{c0_av} and Δ_{av}, J_{c0_av} shows little change against Δ_{av} in these perpendicular cells. Therefore, better performance was realized in cells with large pillar size: J_{c0_av} of 1.8×10^7 A/cm^2 and Δ_{av} of 97 were obtained in the cell with d = 165 nm.

This work was supported by New Energy and Industrial Technology Development Organization (NEDO).

[1] S. Mangin et al., Nat. Mater., 5, 210-215 (2006).

[2] H. Meng and J. P. Wang, Appl. Phys. Lett., 88, 172506 (2006).

[3] T. Seki et al., Appl. Phys. Lett., 88, 172504 (2006).

[4] S. Mitani et al., J. Magn. Magn. Mater., 148, 163-164 (1995).

[5] T. Shima et al., Appl. Phys. Lett., 80, 288-290 (2002).

[6] S. Imada et al., Appl. Phys. Lett., 90, 132507 (2007).

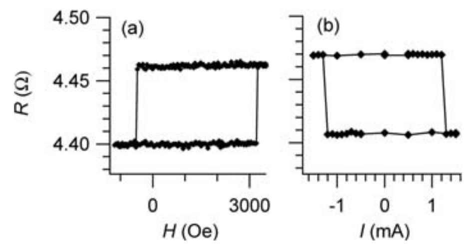

Fig. 1 Results of (a) MR measurement (*R-H*) for a cell with t_{free} = 1.02 nm and the pillar diameter of 150 nm, and (b) spin-transfer switching (*R-I*) at H = 1200 Oe with the current pulse duration of 100 ms.

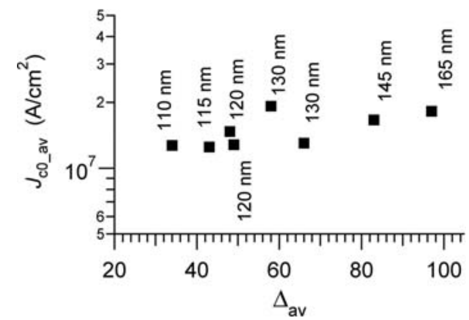

Fig. 2 Average critical current density (J_{c0_av}) versus average thermal stability (Δ_{av}) for cells with t_{free} = 1.02 nm (n = 3). Numerical values represent pillar diameter of cells.

GD-10

Stress assisted reversal of perpendicular magnetization of thin films with giant magnetostriction constant.

N. Saito, S. Nakagawa
Dept. of Physical Electronics, Tokyo Institute of Technology, Tokyo, Japan

I. INTRODUCTION

Perpendicular MRAM has been regarded as a next generation memory. However, high power consumption arising from writing process is one of the demerits for practical application. So we have proposed stress assisted magnetization reversal (SAMR) method[1]. The principle of SAMR is as follows. By applying a stress to magnetic thin films, magnetization turns from perpendicular to in-plane caused by an inverse magnetostrictive effect. Sequential application of a magnetic field and a release of the stress causes magnetization reversal at lower field than the original coercitivity. For example, by the use of SAMR, magnetization of DyFeCo thin films that have 4500 Oe of an original coercitivity is reversed at 100 Oe with applying 495 MPa stress[2]. However, 495 MPa is too high to induce such high internal stress to the film by piezoelectric effect for practical application. So we focused the Terfenol-D ($Tb_{0.27}Dy_{0.73}Fe_{1.9}$) that has giant magnetostrictive effect and aim to attain magnetization reversal at lower stress.

II. EXPERIMENTS

50 nm-thick Terfenol-D films were deposited at room temperature on disk-type cover glass substrates at Ar gas pressures of 0.08 Pa by facing targets sputtering system. Composite plates, consisted of $Tb_{0.27}Dy_{0.73}Fe_{1.9}$ alloy plate and Fe chips, were used as targets. Perpendicular magnetization was observed by using extraordinary Hall effect. A mechanical tensile stress was applied by distorting the center of the cover glass. Magnetostriction constant was measured by optical deflection technique. Atomic composition of the films was evaluated by inductively coupled plasma (ICP) spectroscopy analysis.

III. RESULTS AND DISCUSSIONS

Since the perpendicular M-H loop of Terfenol-D thin film revealed low squareness ratio and low coercivity of 50 Oe as shown in Fig.1(a), Fe composition in the film was slightly modified with keeping composition ratio between Tb and Dy. As a result, high squareness ratio and appropriate coercitivity in perpendicular direction were attained as shown in Fig.1(b). Since the saturation magnetization gradually disappeared at zero field about the film of Fe: 69.1 at.%, Fe 70.2 and 71.6 at.% films were chosen and studied about magnetization reversal characteristic. Fig.2 shows change of magnetostriction constant as a function of Fe compositions. Magnetostriction constant keeps high enough at a region of the composition ratio even away from Terfenol-D (Fe: 67.2 at.%).

Solid line and dashed line in Fig.3 indicate perpendicular M-H loops under various mechanical stresses. In addition, dots in Fig.3 (a) and (b) show results of SAMR of the films for Fe:70.2 and 71.6 at.%, respectively, by applying stresses of 165 and 330 MPa. Transverse and vertical axes of the dots show the applied fields during SAMR and residual magnetization after reversal, respectively. In the case of (a), magnetization turned to in-plane at 165 MPa stress. Inverse magnetostriction effect was confirmed at lower stress compared to that of DyFeCo thin films. SAMR measurement clarified that magnetization began to reverse at lower field. But magnetization was reversed completely at 700 Oe, that is, same field as no stress. In the case of (b), by contrast, magnetization turned to in-plane at 330 MPa. SAMR measurement told that magnetization was reversed at 300 Oe while the original coercitivity of this film is 600 Oe.

[1] M. Yamada, S. Nakagawa, IEEE Trans. Magn., vol. 43, no. 6, pp. 2346-2348, 2007

[2] N. Saito, M. Yamada, S. Nakagawa, "Improvement of stress-induced magnetization reversal process of DyFeCo thin films", J. Appl. Phys., to be published (2008)

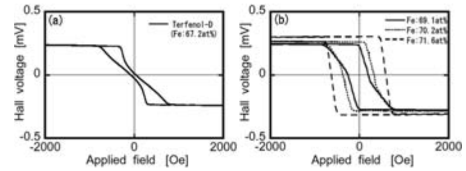

Fig1 Perpendicular M-H loops of (a) Terfenol-D and (b) the films with various Fe compositions.

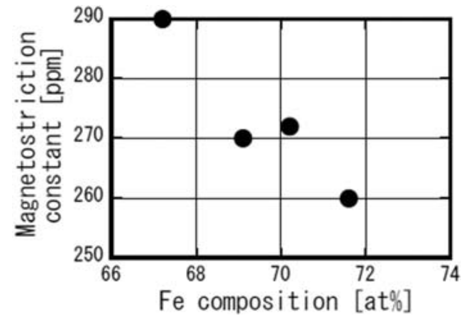

Fig.2 Change of magnetostriction constant as a function of Fe compositions.

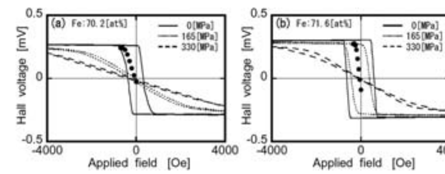

Fig.3 Perpendicular M-H loops under various mechanical stresses. Dots show results of SAMR by applying (a) 165 MPa and (b) 330 MPa stress. SAMR was performed after applying field from +10000 Oe to 0 Oe.

GD-11

A Novel Macro-Model for Spin-Transfer-Torque based Magnetic-Tunnel-Junction Elements.

S. Lee, H. Lee, S. Lee, H. Shin
Information Electronics Engineering, Ewha W. Univ., Seoul, South Korea

1. Introduction
Spin transfer torque (STT) switching in magnetic tunnel junction (MTJ) has important merits over the conventional field induced magnetic switching (FIMS) MRAM in avoiding half-select problem, and improving the scalability and selectivity [1]. Design of effective MRAM circuitry using STT-based MTJ elements requires an accurate circuit model which can exactly emulate the characteristics of MTJ in a circuit simulator such as HSPICE. In recently published works, there were attempts to model some characteristics of FIMS MTJs [2]. In this paper, we present a novel macro-model that fully emulates the important characteristics of STT-based MTJ.
2. A Novel Macro-Model for STT-based MTJ
In STT switching method, self-read disturbance becomes an issue because an STT MTJ uses the same current path for both reading and writing. Therefore, an accurate simulation model which can reproduce the characteristics of tunneling magneto resistance (TMR) is required [3]. The bias-dependent TMR effect has more influence on high resistance (RH) state and it also shows an asymmetric resistance versus current (R-I) characteristics [3]-[4]. Besides, TMR ratio and switching threshold of hysteresis shrink as the operating temperature increases [5].
Now we introduce a macro-model which can emulate all of the aforementioned characteristics shown in the R-I loop measured by Miura's group [6]. The equation for Miura's R-I loop fitted by Lorentz function is given as
y=y0+2*A*w/π*(4*(x-xc)^2+w^2) (1)
In equation (1), y0, A, w, and xc are incorporated as parameterized variables, and x is the amount of tunneling current across the MTJ. Two separate Lorentzian fittings for RH are achieved for positive current region (RH_P) and negative current region (RH_N) to reproduce the asymmetric characteristics.
As shown in Fig. 1, the macro-model includes nodes of BL1, BL0, and SL. RBIT is the bit-line metal resistance per cell and RL is the TMR value of STT MTJ at low resis-tance state. Gdelta is a voltage-controlled resistor and it represents the difference of resistance between RH and RL. Iwr or Isense flows through BL1~SL by writing (WR) or reading (RD) command signal, respectively. These currents are supplied externally. In writing operation, bi-directional current flows between BL1 and SL. Ewb detects both the direction and the amount of current flowing through RL. Ecomp1 realizes the hysteresis by comparing value of ne1 with temperature-dependent switching threshold. Ecomp2 and Esum realize asymmetric characteristic. Using (1), GHIGH_N and GHIGH_P emulate R-I loop for RH_N and RH_P regions, respectively. It also models the temperature dependence of TMR ratio. Gdelta gets a value among 0, function of ng1, and function of ng2 according to RL, RH_N, and RH_P states of MTJ, respectively
R-I loop for STT-based MTJ is simulated with HSPICE as shown in Fig. 2. As can be seen, the simulation results show excellent agreement with the measured data. Fig. 3 reveals the capability of macro-model to emulate the temperature dependence of the hysteresis characteristics, which shows the reduction of switching threshold and TMR ratio for high temperature.
3. Conclusions
STT-based MTJ has self-read disturbance problem. Therefore, development of an accurate circuit model which can emulate major characteristics of STT-based MTJ is very important to precisely control the amount of the current. This paper presents a novel HSPICE macro-model for STT-based MTJ element. The macro-model successfully reproduces the R-I loop with temperature-dependent hysteresis and asymmetric TMR effect of STT-based MTJ. This model allows easy integration of the MTJ memory cell with CMOS peripheral circuits in MRAM simulation using HSPICE simulator.

[1] Y. Huai et al., Jpn. J. Appl. Phys., vol. 45, p. 3835, 2006.

[2] S. Lee et al., Jpn. J. Appl. Phys., vol. 44, p. 2696, 2005.

[3] S. Yuasa et al., Nature materials, p. 868, Oct. 2004.

[4] M. Hosomi et al., Int. Elect. Dev. Meeting, p.459, Dec. 2005.

[5] S. Yuasa et al., Appl. Phys. Lett., vol. 89, p. 042505, 2006

[6] K. Miura et al., Symp. on VLSI Tech., p. 234, June 2007.

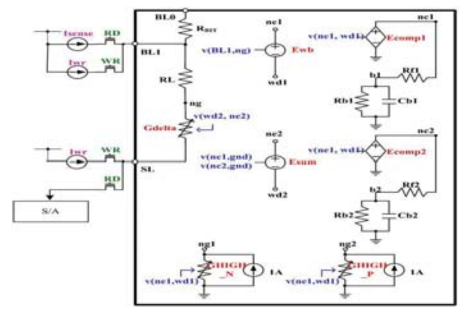

Fig. 1. Schematic of macro-model for STT-based MTJ element.

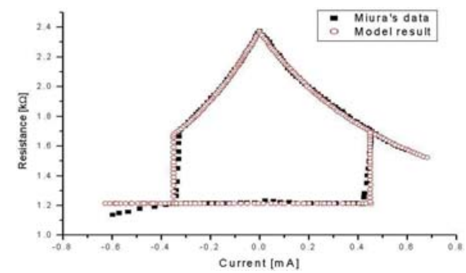

Fig. 2. Comparison of measured and simulated R-I loop.

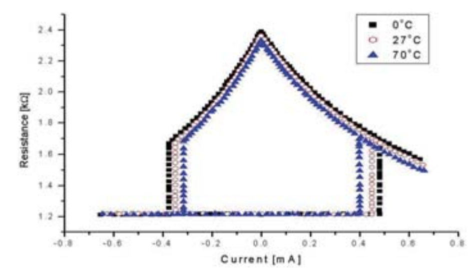

Fig. 3. HSPICE simulation results with various temperatures.

GD-12

Random number generation by current induced magnetization switching in a MgO magnetic tunnel junction.

A. Fukushima, K. Yakushiji, H. Kubota, S. Yuasa, K. Ando
NeRI, AIST, Tsukuba, Japan

Current induced magnetization switching (CIMS) at a current pulse longer than the attempt time (~ 1nsec), is the phenomenon which is well described by thermal activation model [1]. The switching probability increases monotonically nearby the threshold current where the switching probability is 0.5; the increasing ratio of the switching probability is roughly proportional to the inverse of the thermal stability parameter Δ ($\equiv$ KuV/kBT) [2]. The lower Δ makes easy to control the switching probability. Therefore, it is possible to use a magnetic tunnel junction (MTJ) as the "random number generator" by tuning the switching current of CIMS nearby the threshold current. We named the random number generation by CIMS as "spin dice" [3], which is expected to be genuine physical number generator.

On the other hand, in accordance with recent development of worldwide network society, high security communication becomes much important. High security communication demands a high-speed cyriptography which requiers a high-speed physical random number generator. Because the speed of CIMS is quite fast (~1 nsec), "spin dice" will be one of the most prominent candidates for such a high-speed cyriptography.

We generated the random numbers by the "spin dice", where we used a single MgO-MTJ. Usage of the MgO-MTJ with a large MR ratio has an advantage of a high output signal. The MgO-MTJ structure was buffer layer / antiferromagnetic layer / pinned layer (CoFeB 3 nm) / MgO 1 nm / free layer (CoFeB 2 nm) / cap layer. The size of the junction was 60 × 160 nm. The resistance in the parallel state was 180 Ω and the magnetoresistance ratio was 100 %. We chose the MTJ with Hshift ≈ 0, then generated the random number at Hexternal = 0 where the MTJ had 2 states.

The switching process for a random number generation is as follows. Firstly, the magnetization of the pinned layer and the free layer is aligned in anti-parallel state by the reset pulse. Then the magnetization of the free layer will be switched by the set pulse, which has opposite direction to the reset pulse. Binary random numbers are generated by applying repeatedly a sequence of the reset and set pulses, measuring the resistance after the set pulse, and attributing the value '1' to a switching event and '0' to a non-switching. In this experiment, the width of both reset and set pulse was 50 μsec, and the amplitude of the reset current was -1.8 mA.

The current dependence on the switching probability was measured from every 1000 switchings by changing the set current from 1.20mA to 1.40 mA. The threshold current was 1.31 mA. We evaluated that the intrinsic critical current Ic0 = 1.83mA, and Δ = 40 from the fitting the switching probability to the thermal activation model [1].

Next, we generated 10000 digits numbers by the set current of 1.31mA. In the generated numbers, occurrence of "1" was 4517 and that of "0" was 5483. We evaluated the randomness of the generated numbers by a run test and a poker test. The run test is to check the probability of the series events, such as "0", "00", "000", "0000" and versa, which will exponential decay as the number of series events increases. The poker test is to check the probability of the group events, such as "001", "010", "110", which will have the same probability.

Figure shows the results of the both tests. In the run test, the probability of the both "0" and "1" series events decreased exponentially as the number of series events increases. In the 3-bits poker test, the probability of the group events ("001", "010", "100") and ("110", "101", "011") showed good uniformity. These results indicate the random numbers generated by the "spin dice" has good randomness.

In summary, we demonstrated the random number generation by the "spin dice", which is the random number generator by CIMS, by using a MgO-MTJ with a large MR ratio. The randomness of the generated random numbers was evaluated by the run test and the poker test. The results agreed well with the estimated values from the probability of the single event.

Because CIMS is quite fast (~ 1 nsec) phenomenon and the switching results show good randomness, "spin dice" can be expected to be a next generation high-speed genuine physical random number generator.

This study was supported by New Energy and Industrial Technology Development Organization (NEDO).

[1] R. H. Koch et al., Phys. Rev. Lett. 92 (2004), 088302.

[2] M. Pakala et al., J. Appl. Phys. 98 (2005), 056107.

[3] A. Fukushima et al., 52nd MMM conference (2007), DE-11.

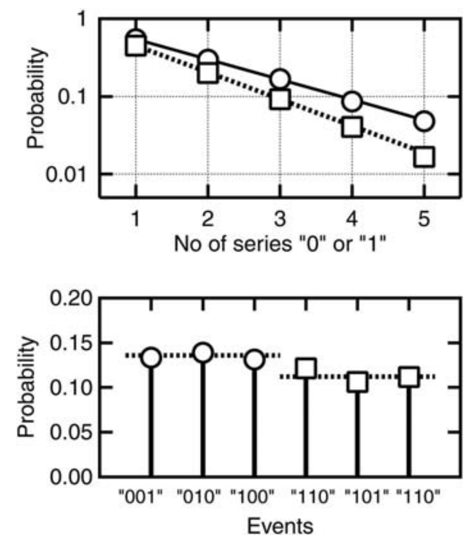

Upper: Probability of the series events of "0" (circle) or "1" (square); lines are the estimation from the switching probability of the single event. Lower: Probability of the two groups of the series events "001", "010", "001" (circles) and "110", "101", "001" (squares); dotted lines are the estimated value.

GE-01

Towards dense regular arrays of FePt nanomagnets by gas phase deposition onto bacterial S-layers within a horizontal magnetic field.

U. Queitsch[1], D. Pohl[1], A. Blüher[2], M. Mertig[2], L. Schultz[1], B. Rellinghaus[1]
1. Metastable and Nanostructured Materials, Leibniz Institute for Solid State and Materials Research Dresden, Dresden, Germany; 2. Max Bergmann Center of Biomaterials, Dresden University of Technology, Dresden, Germany

Regular arrays of ferromagnetic nanoparticles have a great potential for applications such as ultra-high density magnetic data storage media. $L1_0$-ordered FePt nanoparticles can be produced by gas phase preparation and subsequent in-flight annealing [1]. The random spatial distribution of the particles due to their statistical arrival necessitates the utilization of appropriate substrates to obtain regular particle arrangements. Recently, we have reported the successful application of bacterial surface layers (S layers) serving as templates for the regular arrangement of FePt nanoparticles from the gas phase [2]. In the present contribution, we report on experiments to create dense regular arrays of FePt nanoparticles. The influence of agglomeration at high particle densities is investigated and a route to reduce the degradation of regularity at high particle densities is introduced. The latter is achieved by the particle deposition in the presence of a magnetic field.
S layers are regular protein crystals with various symmetries and unit cell dimensions in the range from 3 to 30nm [3]. The used S layer is of the type Bacillus sphaericus NCTC 9602. It has a p4 symmetry and a lattice constant of 12.5 nm. S layer sheets are adsorbed on carbon coated copper grids and subsequently negatively stained with 2.5% uranylacetate. FePt nanoparticles are prepared via inert gas condensation. The density of the particles on the substrate is controlled by the deposition time. The deposited particles are characterized by transmission electron microscopy (TEM). The degree of regularity of the nanoparticle arrangement is determined by statistical evaluation of the particle positions. The particles are assigned three different sites of the protein lattice: A, B, and C denote sites corresponding to the minor four-fold symmetry axis, the minor two-fold symmetry axis, and the major four-fold symmetry axis of the S-layer lattice, respectively [2]. Particles which cannot be attributed to any of these sites remain undefined (fraction D). In order to make the result of the statistical evaluation more transparent to the reader, in all statistical plots the mere random occupation of sites is indicated by shaded grey columns.
Fig. 1 a) shows a typical TEM image of FePt nanoparticles deposited in a field of 1T applied parallel to the substrate on stained S layer sheets with a particle density of 30%. Fig. 1 b) shows the redistribution of the particle positions at increasing particle density. At ca. 3% particle density 52% of the particles adsorb at position A, 16% at B, 5% at C and 27% of the particles adsorb at undefined positions. Fourier analysis of the TEM images reveals a transfer of the symmetry and the lattices constant from the template to the particle arrangement due to the preferential adsorption at site A. With increasing particle density, the fraction of particles on site A is strongly decreased. Along with the decrease of the A site occupancy there is an increase of the fraction of undefined particles due to an increased degree of agglomeration at higher particle densities (Fig. 1 d)).
Fig. 1 c) shows the evolution of the particle arrangement with increasing density when the particles are deposited with a magnetic field of 1T applied in the plane of the substrate. At a particle density of 3%, the site occupancy is very similar to that observed for particles deposited without magnetic field (cf. Fig. 1b). The decrease of the occupancy of site A as observed when no magnetic field is applied and the increase of the undefined fraction with increasing particle density are strongly reduced in the presence of a field. At a particle density of 10%, still roughly 40% of the particles occupy site A. This value remains almost constant up to the highest investigated particle density of 37%. The effect of increasing the degree of order in the particle arrangement that goes along with the preferential occupation of A sites upon applying a magnetic field is due to the field induced dipolar particle-particle interaction which helps preventing the agglomeration (Fig.1 d)).

[1] Rellinghaus B, Mohn E, Schultz L, Gemming T, Acet M, Kowalik A, and Kock B F, 2006, IEEE Trans. Magn. 42 3048

[2] Queitsch U, Blueher A, Mohn E, Schaeffel F, Mertig M, Schultz L, and Rellinghaus B, 2007, Appl. Phys. Lett. 90 113114

[3] Sleytr U B, Messner P, Pum D, and Sara M, 1996 Crystalline bacterial surface proteins (Academic Press, San Diego

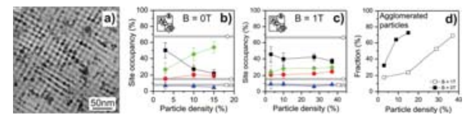

Fig. 1 (a) TEM images of FePt nanoparticles on stained S layers in a magnetic field of 1 T at a particle density of 30%. (b) Occupation of sites A - D as a function of the particle density. (c) Site occupancy upon deposition in an in-plane magnetic field. (d) Fraction of agglomerated particles as functions of the particle density after deposition with and without magnetic field.

GE-02

Magnetic anisotropy of a single Fe atom on Pt(111).

T. Schuh[1], T. Balashov[1], A. F. Takacs[1], W. Wulfhekel[1], A. Ernst[2], S. Ostanin[2], J. Henk[2], P. Bruno[2], T. Miyamachi[3], S. Suga[3]
1. Physikalisches Institut, Universität Karlsruhe, Karlsruhe, Germany; 2. Max-Planck Institut für Mikrostrukturphysik, Halle, Germany; 3. Graduate School of Engineering Science, Osaka University, Osaka, Japan

The storage of data in modern hard disks relies on the stability of the magnetization of magnetic bits. Reducing the size of the bits allows higher storage density. The smallest bit can be realized by a single atom and its stability by the magnetic anisotropy of the atom. We used a scanning tunneling microscope to image single Fe atoms on Pt(111) at 4 K. With inelastic tunneling spectroscopy the excitations of individual Fe atoms were measured. The excitations were detected in the second derivative of the tunneling current exhibiting a peak and a dip symmetric with respect to the Fermi energy. From the position of the extrema the excitation energy was determined. Assuming a spin of S = 1 for the Fe atom, the excitation energy is found to be identical to the uniaxial magnetic anisotropy. We determined the magnetic anisotropy to 5.7+-0.1 meV per atom in good agreement with XMCD measurements of single Co atoms on Pt(111) [1]. The experimental energy is compared with theoretical calculations of phonon energies and the magnetic anisotropy of single atoms in fcc and hcp adsorption sites.

[1] P. Gambardella et al., Science 300, 1130 (2003)

GE-03

High-moment synthetic magnetic nanoparticles for biomedical applications.

W. Hu[1], R. J. Wilson[1], C. M. Earhart[1], A. Koh[1,2], A. Z. Faranesh[3], R. Sinclair[1], S. Guccione[3], S. X. Wang[1,4]

1. Materials Science & Engineering, Stanford University, Stanford, CA; 2. Mechanical Engineering, Stanford University, Stanford, CA; 3. Radiology, Stanford University, Stanford, CA; 4. Electrical Engineering, Stanford University, Stanford, CA

Metallic nanoparticles (MNP) with large magnetization (such as Co, Fe and their alloys) have shown great potential in biomedical applications such as magnetic resonance imaging (MRI), biomagnetic sensing, and magnetic nanoparticle hyperthermia [1-3]. These metallic nanoparticles are commonly synthesized by chemical routes, which are powerful but the size of nanoparticles are often limited to below 20 nm. Beyond this size, it is difficult to attain monodispersity and the onset of ferromagnetism results in coercivity, remanent magnetization and consequently magnetically induced agglomeration. Furthermore, chemical stability of metallic magnetic nanoparticles in biological medium is usually reduced. In this work, we report a direct physical fabrication of aqueous stable disk-shaped synthetic magnetic nanoparticles (SMNP) with a diameter of ~100 nm and high moment ferromagnetic constituents. The particles exhibit a vortex state with nearly zero remanence, thus preventing agglomeration while retaining high magnetization at intermediate magnetic field. Our results indicate that SMNP are promising as multi-functional materials, e.g., as contrast agent for MRI and as heating element for cancer treatment.

SMNP composed of 24 nm $Co_{90}Fe_{10}$ (Ms=1600 emu/cm^3) sanwiched by thin layers of Ta (serve as protection layer) are fabricated using a "top-down" approach. First, nanotemplates are formed using the advanced patterning technique of nanoimprint lithography (NIL). These templates are then used as substrates for the deposition of magnetic films with precise thickness control. Finally, chemical solvents, etches and surfactants are used to release the nanoparticles and to stabilize them in solution. Fig. 1 shows monodisperse 120 nm diameter SMNP after release from the substrate.

The magnetic properties of SMNP are readily characterized by an alternating magnetometer (AGM). Hysteresis loops of vortex state are clearly observed. Based on the unique shape of the hysteresis loops, we proposed a method of applying these nanoparticles for hyperthermia. A DC bias magnetic field and an AC magnetic field are used to take advantage of hysteresis losses. Magnetic heating efficiency as a function of DC and AC field is estimated from the static minor hysteresis loop measurements and plotted in Fig. 2. A maximum of 560 W g^{-1} specific loss power (SLP) may be achieved for $fH = 4.1\times10^9$ A m^{-1}s^{-1}. MRI measurements of the transverse relaxation rate (R_2 and R_2*) show that these synthetic nanoparticles have MRI relaxation properties more desirable than commonly used iron oxides.

[1] X. X. Zhang, G. H. Wen, G. Xiao and S. Sun, *J. Magn. Magn. Mater.* **261**, 21 (2003)

[2] W. S. Seo, J. H. Lee, X. Sun, Y. Suzuki, D. Mann, Z. Liu, M. Terashima, P. C. Yang, M. V. Mcconnell, D. G. Nishimura and H. Dai, *Nature Mater*. **5**, 971 (2006)

[3] Y. H. Xu, J. Bai and J. P. Wang, *J. Magn. Magn. Mater*. **311**, 131 (2007)

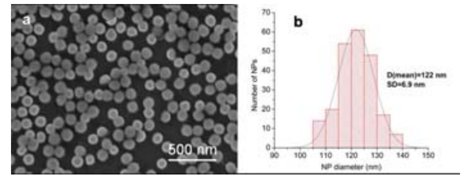

Figure 1. a, Scanning electron microscope (SEM) image of 120 nm diameter released synthetic magnetic nanoparticles. b, the corresponding particle size distribution.

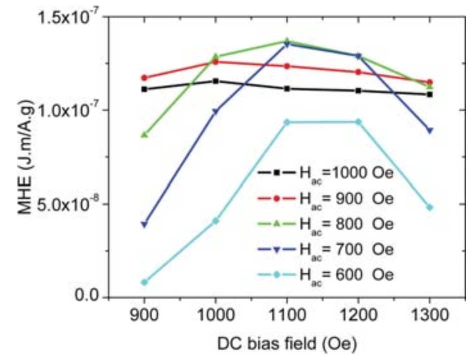

Figure 2. Magnetic heating efficiency (JmA^{-1}g^{-1}) as a function of DC bias field and AC field calculated from minor hysteresis loop measurements.

GE-04

Highly anisotropic FePt nanomagnets obtained via Fe ion implantation on Pt films.

R. A. Lukaszew[1,2], C. Clavero[1], J. R. Skuza[2]
1. Applied Science Dept., College of William and Mary, Williamsburg, VA; 2. Physics Department, College of William and Mary, Williamsburg, VA

For ensembles of magnetic nano-clusters to display intrinsic ferromagnetism, it is necessary that they possess either large magnetic anisotropy or that they are held at very low temperatures. This is because the ratio of anisotropy to thermal energies governs the orientational stability of the magnetic moment of the nano-clusters. This is particularly important for magnetic media where the nano-magnets must exhibit large magnetic anisotropy at room temperature and in addition perpendicular anisotropy for new perpendicular magneto-recording applications.
It has been known for quite some time that the L10 highly ordered FePt alloy exhibits the required large magnetic anisotropy and when prepared in thin film form, adequate deposition control can also ensure strong perpendicular magnetic anisotropy. But an important fabrication aspect for media applications is to achieve nano-magnets with this phase and perpendicular anisotropy.
Ion beam irradiations applied to FePt magnetic thin films have recently attracted strong interest to modify the magnetic properties in materials in useful ways for this application. Thus, control of the coercivity in Co/Pt multilayers using the irradiation of 30 keV He+ ions [1], and 130 keV He+ ions [2] has been reported. Ion beam projection onto Co/Pt multilayers using a stencil mask and fabrication of Co/Pt magnetic dots with diameters less than 100 nm [3] has also been demonstrated. Other researchers have implanted B+ ions onto as-deposited disordered FePt thin films and have studied the magnetic properties, surface roughness and crystalline structures before and after thermal annealing as a possible method to fabricate magnetic patterns with different coercivity without degrading the surface quality of the as-deposited films [4]. Many of these beam-induced patterning methods exhibit advantages for the fabrication of patterned media when compared with other conventional methods [5]. In our earlier work we have also demonstrated that rapid thermal annealing using synchrotron X-Ray radiation (XRTA) provides an adequate tool for modifying and probing structural modification of FePt thin films in real time. [6]
We have now investigated an alternative ion-beam approach by implanting Pt films with Fe+ ions followed by annealing treatments to ensure formation of the L1o phase and perpendicular magnetic anisotropy suitable for ultrahigh-density recording media. The Pt films were epitaxially deposited at room-temperature on (001) MgO substrates using DC magnetron sputtering. The ion-implantation was carried out at a heavy-ions accelerator. The microstructure, surface morphology and magnetic properties were characterized using XRD, AFM/MFM and polar Kerr magnetometry. In order to promote the formation of the L1o phase, the implanted samples were UHV annealed. Figure 1 shows the polar Kerr hysteresis loops measured on two different nano-composite ion-implanted samples. The left figure depicts hysteresis loops corresponding to one sample before and after in-situ annealing at 400C. We notice that the implanted sample exhibits paramagnetic behavior, typical of Fe nanoclusters embedded on the Pt matrix. After anneling the sample exhibits strong perpendicular magnetic anisotropy due to the onset of the L1o phase, as confirmed by XRD. The right curves correspond to various regions sampled by the light spot of the polar Kerr setup on a second sample implanted with a larger dose than the former and in-situ annealed at 400C. Both samples exhibit uncoupled magnetic nano-regions with strong perpendicular magnetic anisotropy due to formation of the L1o phase. Thus we have demonstrated that with our new experimental approach using ion-implantation and thermal treatments it is possible to tailor the magnetic anisotropy in useful ways for magneto-recording applications.

This work was possible with grants from NSF (DMR-0355171) the American Chemical Society Petroleum Research Fund (41319 - AC) and a Research Corporation Cottrell Scholar Award.

[1] C. Chappert, H. Bernas, J. Ferre, V. Kottler, J. –P. Jamet, Y. Devolder, F. Rousseaux, V. Mathet and H. Launois, Science 280 (1998), p. 1919.

[2] D. Revelsona, C. Chappert, H. Bernas, D. Halley, Y. Samson and A. Marty, J. Appl. Phys. 91 (2002), p. 8082.

[3] A. Detzel, R. Berger, H. Grimm, W.H. Bruenger, C. Dzionk, F. Letzkus, R. Springer, H. Loeschner, E. Platzgummer, G. Stengl, Z.Z. Brandic and B.D. Terris, IEEE Trans. Magn. 38 (2002), p. 1952.

[4]. T. Aoyama, I. Sato, H. Ito and S. Ishio, J. Magn. Magn. Mater. 287 (2005), p. 209.

[5] T. Aoyama, S. Okawa, K. Hattori, H. Hatate, Y. Wada, K. Uchiyama, T. Kagotani, H. Nishio and I. Sato, J. Magn. Magn. Mater. 235 (2001), p. 174.

[6]. J. R. Skuza, R. A. Lukaszew, E. M. Dufresne, D. A. Walko, C. Clavero, A. Cebollada, C. N. Cionca, and R. Clarke, Appl. Phys. Lett. 90, 251901 (2007)

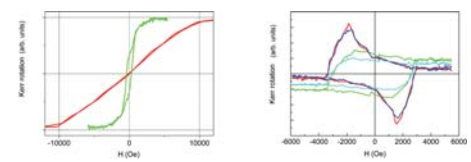

Figure 1. Polar Kerr Magnetometry performed on two FePt nano-composite samples with different ion-implantation dose. Left: the red loop corresponds to the first sample before annealing and the green loop corresponds to the sample after in-situ annealing at 400C. Right: the various hysteresis loops correspond to different regions illuminated by the laser spot on the second sample. We notice that this sample has various un-coupled nano-regions all with strong perpendicular magnetic anisotropy

GE-05

Surface relaxation and magnetism in mondisperse binary metal nanoparticles.

M. Farle
Physik, Universitaet Duisburg-Essen, Duisburg, Germany

Monodisperse magnetic nanoparticles (2 – 15 nm) of almost any type of material and composition can be synthesized by gasphase condensation [1] or organo¬metallic synthesis in well controlled sizes and different shapes (rods, tubes, spheres, cubes) [2,3]. These "building blocks" offer new exciting possibilities to create new artificial composite materials like ultra-hard (or soft) ferromagnets (or ferrimagnets), multifunctional hollow magnetic microspheres or luminescent magnetic particles. In biomedical technologies magnetic hybrid or functionalized particles find applications in site targeted therapy, diagnosis, cell separation and water purification. In this talk some of these possibilities will be briefly reviewed. While most of this work does not require a detailled under¬standing of the intrinsic magnetism of the nanoparticle, future nanotechnological devices based on a single nanoparticle require a knowledge of local crystal as well as electronic and magnetic structure and surface composition. Examples on how the interior and surface structure can be analysed with sub-Angstrom resolution [4,5] and with element specificity will be discussed. And finally, challenges for magnetic and electronic structure analysis [6] will be pointed out.

[1] O. Dmitrieva, et al. Phys. Rev. B 76 (2007) 064414

[2] O. Margeat, M. Tran, M. Spasova, M. Farle;

Phys. Rev. B 75 (2007) 134410

[3] C. Antoniak and M. Farle; Modern Physics Letters B 21 (2007) 1111-1131

[4] D. Sudfeld, et al; Mat. Res. Soc. Symp. Proc. 998E (2007) 0998-J01-06

[5] Rongming Wang, et al.; Phys. Rev. Lett. 100 (2008) 017205

[6] C. Antoniak, et al. ;Phys Rev. Lett. 97 (2006) 117201

GE-06

Synthesis and characterisation of polymer-coated Fe nanoparticles with high magnetisation.

J. Marin[2], *A. Garcia Prieto*[1], I. Orue[3], J. Vilas[2], M. Fdez-Gubieda[1], L. M. Leon[2]
1. Dpto Electricidad y Electronica, Universidad del Pais Vasco - UPV/EHU, Bilbao, Spain; 2. Dpto Química Macromolecular, Universidad del Pais Vasco - UPV/EHU, Bilbao, Spain; 3. SGIKER Medidas Magnéticas, Vicerrectorado de Investigación, Universidad del Pais Vasco - UPV/EHU, Bilbao, Spain

Magnetic nanoparticles have attracted great attention in the last years due to their interesting fundamental properties. Recently, the potential use in Biomedicine has increased the interest in these magnetic nanoparticles in the superparamagnetic region. This is because they can be used as magnetic carriers of drugs, antibodies or cells, they can be heated up by alternating magnetic fields and potentially kill the cancerous cells by hyperthermia or be used as contrast agents for MRI [1]. At present there is a big effort in synthesizing biocompatible magnetic nanoparticles with high susceptibility because this will improve the attraction and actuation of the particles by external magnetic fields.
With this aim we have synthesized Fe nanoparticles coated in a polymer. The role of the polymer coating is twofold: on one hand it prevents the Fe from oxidizing and leaching, and on the other hand it allows the functionalization of the particles. The Fe@polymer nanoparticles have been synthesized by a microemulsion method in two steps following a similar reaction route used by Zhou et al. [2].
The particles have been characterised by means of X-ray diffraction (XRD) and transmission electron microscopy (TEM). The magnetic properties have been studied by means of the 300 K hysteresis loop performed in a high-field vibrating sample magnetometer (VSM) and a zero-field cooling - field cooling (ZFC-FC) curve at 25 Oe in a SQUID magnetometer.
XRD (Figure 1) shows a clear Fe bcc phase and no presence of Fe oxides can be detected. The polymer coating is consequently properly preventing the oxidation of the Fe cores. From Rietveld fit of the data we get a lattice parameter of 2.866 Å, essentially the lattice parameter of bulk bcc Fe (2.87 Å), and a crystalline size of 35 nm. XRD can not resolve too small nanostructures and consequently this particle size can be considered an upper size limit. In fact TEM images show an important polydispersity, the smallest particles having a 7 nm core and 1.5 nm coating.
The polydispersity is confirmed in the magnetic measurements. In particular, the ZFC curve (Figure 2) displays a superparamagnetic behaviour with a blocking temperature of ~ 80 K. The peak is very broad, what means that there are multiple blocking temperatures due to multiple nanoparticle sizes. The 300 K hysteresis loop is shown in Figure 3. The saturation magnetisation is as high as 120 Am^2/kg. This value is in between that of the Fe oxide with highest saturation magnetisation (magnetite, 90 Am^2/kg) and bulk Fe (217.2 Am^2/kg) and to our knowledge it is among the highest found in the literature for Fe nanoparticles. Zooming into the low-field region shows that the loop is not fully superparamagnetic but has a coercivity of ~ 120 Oe and a remanence of ~ 19 Am^2/kg. This means that there is a non-negligible ferromagnetic phase possibly from monodomain particles that could explain the FC branch not collapsing with the ZFC one in Figure 2. Finally, the hysteresis loop shows a paramagnetic or antiferromagnetic contribution that could be due to the presence of an iron oxide. The latter hypothesis will be confirmed by Mössbauer experiments.
In conclusion, we have been able to synthesize high susceptibility Fe nanoparticles of sizes in between 7 and 35 nm coated by a polymer. The particles seem to have an oxide layer in between the core and the coating. Forthcoming Mössbauer experiments will prove the presence of Fe oxides.

[1] Q.A. Pankhurst, J. Connolly, S.K. Jones, J. Dobson, J. Appl. Phys. D **36** (2003) R167

[2] W.L. Zhou, E.E. Carpenter, J. Lin, A. Kumbhar, J. Sims and C.J. O'Connor, Eur. Phys. J. D **16** (2001) 289

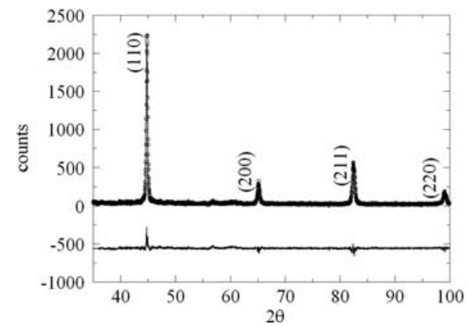

Figure 1: XRD spectrum (white circles) with the Rietveld fit. Reflections for Fe bcc are shown.

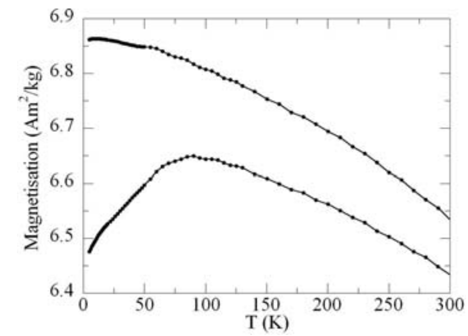

Figure 2: ZFC-FC measurement at 25 Oe.

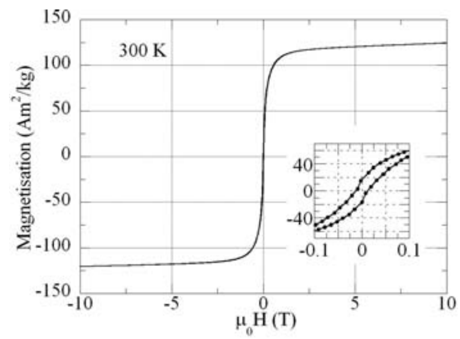

Figure 3: Hysteresis loop at 300 K. The inset shows the region at low fields to highlight the presence of coercivity and remanence.

GE-07

Bulk-like magnetic properties in Fe_3O_4 nanoparticles: surface anisotropy, orbital moment and crystal quality.

N. Pérez[1,2], P. Guardia[1,2], A. G. Roca[3], M. P. Morales[3], C. J. Serna[3], F. Bartolomé[4,5], L. M. García[4,5], J. Bartolomé[4,5], J. C. Cezar[6], A. Labarta[1,2], *X. Batlle*[1,2]
1. Física Fonamental, Universitat de Barcelona, Barcelona, Spain; 2. Institut de Nanociencia i Nanotecnologia IN2UB, Universitat de Barcelona, Barcelona, Spain; 3. ICMM, CSIC, Madrid, Spain; 4. ICMA, CSIC, Zaragoza, Spain; 5. Física de la Materia Condensada, Universidad de Zaragoza, Zaragoza, Spain; 6. ESRF, Grenoble, France

Magnetic nanoparticles (NP) [1] have attracted much research over the recent years due to their potential interests in a variety of biomedical applications [2]. Recently, we demonstrated [3] that magnetite Fe_3O_4 NP synthesized by the high-temperature decomposition of an organic Fe precursor in the presence of oleic acid molecules covalently bonded to the NP surface show unusually high saturation magnetization, M_S, values (80-85 emu/g), close to the expected for bulk Fe_3O_4 (92 emu/g). Furthermore, these M_S values are much larger than those in NP prepared by the usual co-precipitation method (55-60 emu/g), for which there is no chemical bond between the coating (dextrane, TMAOH, PVA, …) and the NP surface. In order to understand this behavior, we have studied the surface contribution to the magnetic anisotropy and the orbital contribution to the magnetic moment of Fe_3O_4 NP particles with mean diameter of a few nanometers, as a function of the coating (oleic acid versus PVA). Besides, high resolution transmission electron microscopy (HRTEM) has been used to evaluate the crystal quality of the NP. By means of ac susceptibility and time-dependent thermoremanence, we obtain a surface anisotropy contant $K_S = 3\times10^{-2}$ erg/cm^2 in oleic acid-coated NP, very similar to the values in literature for a variety of magnetite NP (K_S = (4-6)$\times10^{-2}$ erg/cm^2), suggesting that the occurrence of high M_S is not due to a decrease in the surface anisotropy. X-ray magnetic circular dichroism (XMCD) data confirm the dependence of the magnetic moment on the surface bond and suggests that the orbital contribution is smaller in covalently bonded NP, such that the latter approach a bulk-like behaviour. The occurrence of bulk M_S in Fe_3O_4 NP may thus be related to the crystal and magnetic state at the surface, as HRTEM suggests. This is of relevance in biomedical applications to reduce the strength of the magnetic field required to obtain a high magnetic response, while the issue of the orbital contribution in Fe_3O_4 is under hot debate nowadays. Work funded by Spanish NAN2004-08805-CO4-02, MAT2006-03999, NAN2004-08805-CO4-01, MAT2005-02454 and CONSOLIDER CSD2006-12, and Catalan 2005SGR0969.

[1] X. Batlle and A. Labarta, J. Phys D 35, R15, (2002).

[2] P. Tartaj et al., J. Phys D: Appl. Phys 36, R182 (2003).

[3] P. Guardia, B. Batlle-Brugal, A.G. Roca, O. Iglesias, M.P. Morales, C.J. Serna, A. Labarta, X. Batlle, J. Magn. Magn. Mat. 316, e756–e759 (2007).

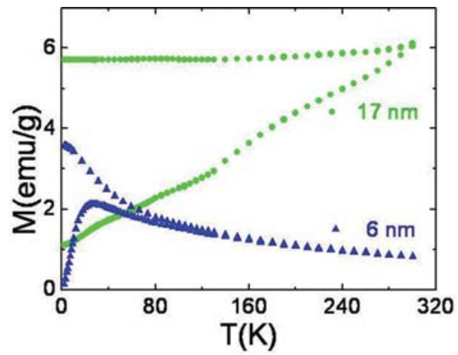

Zero-field-cooling and field-cooling curves for magnetite nanoparticles surfacted with oleic acid, as a function of particle size. The cooling field was 50 Oe.

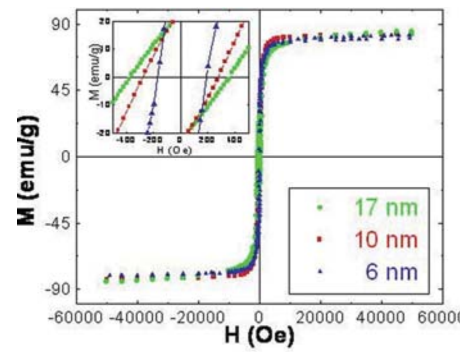

Hysteresis loops at T = 5 K for magnetite nanoparticles surfacted with oleic acid, as a function of the particle size. Inset: Low magnetic field region of the hysteresis loop.

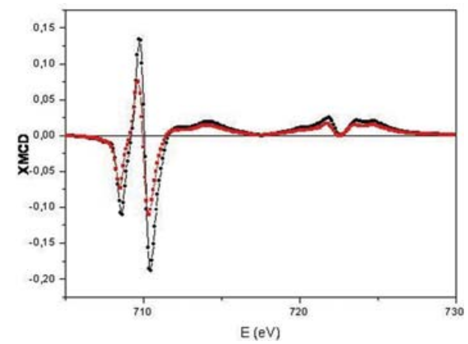

XMCD spectra at 5 K and 2 Tesla for 5 nm magnetite particles coated with oleic acid (solid black circles) and for 4 nm magnetite particles coated with PVA (solid red squares).

GE-08

On the spin reorientation of magnetic nano-dot arrays: Co/Au versus Co/Pt on SiGe.

A. Persson[1], L. Gridneva[1], M. A. Niño[2], J. Camarero[2], J. J. de Miguel[2], R. Miranda[2], C. Hofer[3], C. Teichert[3], T. Bobek[4], D. Arvanitis[1]
1. Physics Department, Uppsala University, Uppsala, Sweden; 2. Departamento de Física de la Materia Condensada, Universidad Autonoma de Madrid, Madrid, Spain; 3. Institut für Physik, Montanuniversität Leoben, Leoben, Austria; 4. Institute of Semiconductor Electronics, Aachen University, Aachen, Germany

High density magnetic nano-dot arrays can lead to novel magnetic storage media, in particular when the preferential direction of magnetisation can be changed from the commonly observed in-plane to out-of-plane. We present results on in-situ prepared Co/Au and Co/Pt based nano-dot arrays on selforganised SiGe, exhibiting magnetic remanence at room temperature. We present in-situ Co L-edge X-ray Magnetic Circular Dichroism (XMCD) spectroscopy measurements, in combination with spectro-microscopy results. Both measurements prove the occurrence of a perpendicular Co dot array magnetization and magnetic remanence. We characterize the spin reorientation of these dot arrays between the temperatures of 300 and 100K as a function of Co, Pt and Au cap thickness. We measure the Co dot orbital and spin moments both within the in- and out-of-plane magnetic phases. The local atomic structure of the Co atoms is characterized by means of Co K-edge Extended X-ray Absorption Fine Structure (EXAFS) measurements.
In order to produce the arrays of magnetic dots, a self-organized, Si(0.5)Ge(0.5) thin film grown by molecular beam epitaxy and capped with 3nm Si was used as a template. The surface consists of isotropically arranged, {113} faceted pyramids terminated by a (001) top surface, which was characterized by Atomic Force Microscopy (AFM). Due to the lateral size of the base length of about 200 nm the features are well suited for the detection of independent magnetic areas by X-ray Photoemission Electron Microscopy (XPEEM)-XMCD and the {113} facets, which are tilted 25.3° with respect to the surface, are advantageous to generate isolated nanomagnets, with no magnetic material in-between, by shadow deposition. /1,2,3/ (Au/Co/Au) and (Pt/Co/Pt) stacks were grown by electron beam evaporation, with the base pressure in the 10^(-10) Torr range; Au was deposited at room temperature under normal incidence to cover the substrate more efficiently, whereas Co was evaporated at grazing incidence (16 degrees), to selectively cover determined areas while avoiding others ("shadow effect") as previously described. /2,3/ Pt was deposited either at normal or grazing incidence. The XMCD spectroscopy measurements in X-ray absorption were performed at the bending magnet based beamline D1011 at MAX-lab. The XMCD data are compared to XPEEM-XMCD data taken under similar conditions at 300K at ELETTRA, as described earlier by Mulders et al. /1/.
The XPEEM-XMCD results indicate the existence of both in- and out-of-plane magnetisation, for Co/Au, Co/Pt, Au/Co/Au and Pt/Co/Pt dot arrays coupled in domains at room temperature, for a Co thickness of order 2-3 atomic Co layers, in contrast to what is found earlier for the corresponding thin films. The individual dots are found to carry a magnetic moment at 300K, as found earlier by directly depositing on the SiGe surface /1/. In all cases with a Au or Pt under-layer, we find a spontaneous macroscopic remanence both out-of-plane and in-plane. This finding is in contrast to what is found in the case of thin Co films, grown on Au. Even cooling the samples at 100K does not eliminate the in-plane component completely. The range of stability of the out-of-plane phase in the case of Au appears to be larger than in the case of Pt. For both systems the in- versus out-of-plane orbital moment anisotropy, is not always related with an out-of-plane magnetization and the occurrence of a spin reorientation. For Co/Au rather an overall increase of the orbital moment is found as one increases the amount of the capping Au layer in the range of a couple of monolayers. In particular, only a small variation of the Au cap thickness from 1.5 to 2.2 monolayers, leads to an abrupt increase of the orbital moment, indicating the strong correlation magnetism to structure for this system. For Pt/Co/Pt dots we find no such trend.
Hard x-ray near edge and EXAFS experiments were performed at beamline I811 of MAX-lab and at HASYLAB, beamline A1. EXAFS spectra were measured at room temperature over the Co K-edge in fluorescence yield mode. To maximize the signal-to-background ratio from the weak K-alpha fluorescence intensity from the dots long accumulation times were chosen. For the Au/Co/Au dots we find a strong reduction of the EXAFS amplitude for all neighbor shells versus a "standard" Co (hcp) foil. The best EXAFS fit indicates a loss of about 5 of the Co two nearest neighbor shell atoms. The EXAFS data indicate a non-pseudomorphic growth of Co on the Au underlayer. For the Pt/Co/Pt dots, the reduction of the two nearest neighbor shell atoms is found to be less severe than the one observed for Au.
Summarizing, we determine the thickness and temperature range of the spin reorientation transition for the Au/Co/Au and Pt/Co/Pt system for a regular array of nano-dots, and describe differences between the two systems. The spin reorientation can also occur with no orbital moment anisotropy, highlighting the sensitivity of the magneto-crystalline anisotropy upon small variations of the local structure.
The work has been supported by the EC (STRP NAMASOS NMP 505854), the Swedish Research Council, the Göran Gustafsson Foundation and the EC ARI Program.

1. A.M. Mulders, A. Fraile Rodríguez, D. Arvanitis et al. Phys Rev. B 71, 2144221 (2005)

2. C. Teichert, Appl. Phys. A 76, 653 (2003).

3. C. Teichert, J. Barthel, H.J. Oepen et al. Appl. Phys. Lett. 74, 588 (1999)

Perpendicular anisotropy in Co/Pt granular multilayers.

J. Bartolome[1], L. García Vinuesa[1], F. Bartolomé[1], J. Stankiewicz[1], F. Luis[1], F. Petroff[2], C. Deranlot[2], F. Wilhelm[3], A. Rogalev[3], P. Bencok[3], N. B. Brookes[3]
1. Instituto de Ciencia de Materiales de Aragón, CSIC/U. de Zaragoza, Zaragoza, Spain; 2. Unité Mixte de Physique, CNRS/Thales, Orsay (Paris), France; 3. ESRF, Grenoble, France

Granular Co thin film multilayer constitute a family of nanoparticle systems for understanding size effects in Magnetism. Co clusters of nearly spherical shape can be produced by sputtering of Co on amorphous alumina. Capping with a noble metal allows us to modify the matrix that surrounds the particle, thus modifying its magnetic properties. When capping with Cu or Au the particles behave as superparamagnetic with anisotropy constants that depend on the metal capping [1]. Instead, capping with Pt has a completely different effect. In this case Co particles are strongly coupled via the polarized Pt [2]. In this paper we show that the Co/Pt granular multilayers present strong perpendicu-lar anisotropy to the substrate plane.

The sample measured has been a trilayer of Al_2O_3/Co/Pt ; i.e. with just one Co granular layer. The nominal Co deposition was t_{Co} = 0.7 nm, which produces Co particles of 3 nm diameter. The capping Pt film has t_{Pt} = 1.5nm depth.

Indeed, magnetization measurements M(H) measured parallel and perpendicular to the substrate plane were performed at several temperatures. There is a characteristic step near H=0, showing that there are two subsystems, the high coercive one and a soft component. In the direction perpendicular the coercive field is H_C = 5 kOe at T = 5 K (Fig. 1), and decreases with temperature its disappearance at 200 K (Fig. 2), while in the direction parallel to the substrate plane there is no coercive field. This implies that the anisotropy is a collective property of the Co particles, and that spontaneously the selected anisotropy direction of the Co particles is perpendicular to the plane. This conclusion is of paramount importance for application as a large density memory device.

The anomalous Hall resistivity measurements performed on the same sample at 5 K in the perpendicular direction show as well strong anisotropic behavior, with a coercive field which coincides with the magnetization measurements.

To ascertain the origin of the perpendicular anisotropy we have performed XMCD spectroscopy of the L_2 and L_3 edges of Pt and Co.The polarization of the Pt by the magnetic Co is detected as a non-zero signal of the L_2 and L_3 Pt edges. In Fig. 3 the XAS and XMCD at the Co L_2 and L_3 edge spectra at several incidence angles are shown. The orbital to spin ratio m_L/m_S=0.10, is similar to that found for CoPt alloys [3], and is constant, independently of the incident angle. On the other hand, the intensity of the L_3 minimum is found to decrease clearly with increasing incident angle, which implies that the orbital moment in the perpendicular direction is larger than in the parallel one, thus proving the orbital origin of the induced anisotropy.

Acknowledgements. This work has been financed with the MAT05/1272 project.

[1] F. Luis, F. Bartolomé, F. Petroff, J. Bartolomé, L.M. García, C. Deranlot, H. Jaffres;M.J. Martínez, P. Bencok, F. Wilhelm, A. Rogalev and N.B. Brookes. Europhys. Lett. 76, 1 (2006)

[2] J. Bartolomé, L.M. García, F. Bartolomé, F. Luis, F. Petroff, C. Deranlot, F. Wilhelm, A. Rogalev. J. Magn. & Magn. Mat. 316, e9 (2007)

[3] W. Grange, M. Maret, J.P. Kappler, J. Vogel,A. Fontaine, F. Petroff and G. Krill. Phys. Rev. B. 58, 6298 (1998)

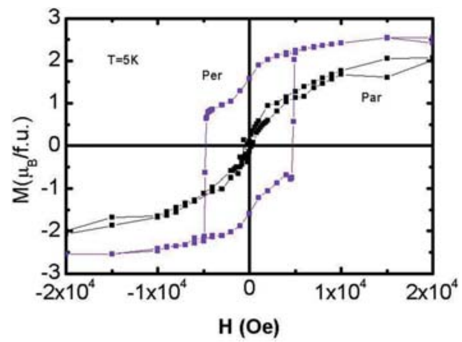

Figure 1. Hysteresis loops at T = 5 K for a trilayer of Al_2O_3/Co/Pt.

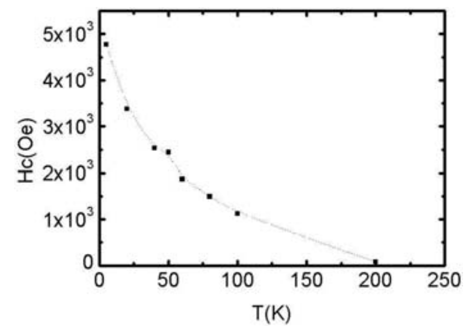

Figure 2. Dependence of the perpendicular coercive field with temperature.

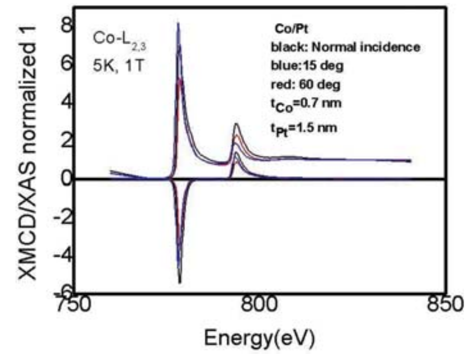

Figure 3. XMCD spectra at 5 K and 1 Tesla for a trilayer of Al_2O_3/Co/Pt, as a function of incident angle.

GE-10

Evidence of L10 chemical order in CoPt nanoclusters: direct observation and magnetic signature.

F. Tournus[1], A. Tamion[1], N. Blanc[1], A. Hannour[1], L. Bardotti[1], B. Prével[1], P. Ohresser[2], E. Bonet[3], T. Epicier[4], V. Dupuis[1]
1. LPMCN, Université de Lyon; Univ. Lyon 1; CNRS, Villeurbanne, France; 2. Synchrotron SOLEIL, Gif sur Yvette, France; 3. Institut Néel, CNRS/UJF, Grenoble, France; 4. MATEIS, CNRS; INSA Lyon; Université de Lyon, Villeurbanne, France

Magnetic particles have attracted much attention both for their fundamental interest and for their potential applications. In particular, small permanent magnets at the nano-scale would make possible ultra-high density magnetic storage devices. However, at such a size, the magnetization direction of a particle usually fluctuates at room temperature (superparamagnetism). In order to increase the magnetization thermal stability, great efforts have been directed towards an enhancement of the nanoparticles magnetic anisotropy energy (MAE). One of the preferred routes is to use magnetic alloys like FePt or CoPt: they can crystallize in the chemically ordered L10 phase, corresponding to a very high magnetocrystalline anisotropy for the bulk.
In this context, despite significant advances, it is still very difficult to produce well-defined CoPt nanoparticles in the L10 phase. Although this phase is the stable one at room temperature, an additional difficulty may come from the lowering of the order-disorder transition temperature (from the L10 phase to the chemically disordered A1 phase) due to the size reduction of the particles. Moreover, chemical ordering is in general obtained by annealing, which goes with problems of pollution or coalescence, difficult to avoid. As a consequence, in spite of a huge number of published results on these systems, there exists, to our knowledge, no convincing experimental study reporting a value of the intrinsic magnetic anisotropy for well-characterized L10 CoPt nanoparticles. Indeed, it is a tricky task to ensure that CoPt nanoparticles have a well-known magnetic size, are chemically ordered, are non-interacting, etc. to correctly deduce the intrinsic properties of well-defined nanoparticles from macroscopic magnetic measurements.
In this article, we report the synthesis and characterization of well-defined CoPt clusters, produced following a physical route, with a mean diameter of ~3 nm. We show that, despite a striking change of the Co magnetic moment, the magnetic anisotropy of chemically ordered nanoparticles increases in much lower proportions than what is observed for the bulk, with respect to the chemically disordered phase.
Samples made of diluted CoPt particles layers have been produced using the LECBD technique. As-prepared clusters are crystallized in the A1 phase and chemical ordering is achieved by annealing (2h at 650°C, under vacuum). We have been able to directly evidence the L10 chemical order (see Fig. 1) by high-resolution TEM (HRTEM), even for particles with a diameter down to 2 nm. Using amorphous carbon (aC) as capping layer, we have verified that annealing does not goes with cluster coalescence, so that the particle size distribution is preserved.
X-ray magnetic circular dichroism (XMCD) measurements on diluted thin films of CoPt clusters embedded in aC have been performed on both as-prepared and annealed samples, at the Co L2,3 edges. The x-ray absorption spectroscopy signal does not show any oxide contribution, and there is almost no difference in the edges profile between as-prepared and annealed CoPt particles. The mean orbital and spin magnetic moments per Co atom, mL and mS, have been determined using the sum-rules. We find that there is a striking enhancement of both mL and mS (and the mL/mS ratio too) upon annealing: mL changes from 0.12 to 0.18 mB/at.; and mS changes from 1.70 to 1.91 mB/at. According to TEM observations, this evolution is assigned to the L10 chemical ordering of the particles. Surprisingly, the values measured for chemically ordered particles are significantly higher than those reported for a presumably L10 thin film.
Magnetic measurements have been performed at various temperatures on the same samples, using a SQUID magnetometer. Hysteris loops have allowed us to check that the clusters magnetic size is the same as the geometric one and does not vary upon annealing; and that the particles are not interacting. Magnetic susceptibility measurements following the ZFC/FC procedure also indicate that chemical ordering goes with a significant increase of the CoPt clusters MAE, which is determined using a ZFC curves fit. We find a value of Keff = 0.19 MJ/m3, respectively 0.38 MJ/m3, for the as-prepared, respectively annealed, clusters. Although the MAE displays a 100% augmentation, it remains much lower than the one reported for the CoPt L10 bulk (~5 MJ/m3). A careful examination of the various physical explanations, taking into account the combined experimental results obtained by TEM, XMCD and SQUID, lead us to the conclusion that the reduced MAE of L10 CoPt clusters must be due to the small particle size. As a matter of fact, we may never be able to reach a magnetic anisotropy as high as the bulk one, for CoPt particles of a few nanometers diameter. This would constitute a serious setback for the expected technological applications...

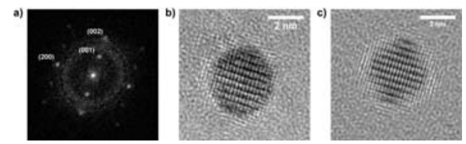

Fig. 1: a) Fourier transform corresponding to the HRTEM image of the annealed CoPt cluster shown in b). The (001) peak is the signature of L10 chemical order corresponding to the strong contrast modulation visible in b). c) HRTEM image simulation obtained with a perfectly L10 chemically ordered CoPt cluster, observed along the [010] direction, with a slight tilt.

GE-11

Magnetic Hardening of FePt Nanomagnets by Ultra Short Time In-Flight Annealing.

E. Mohn, *B. Rellinghaus*, L. Schultz
Institute for Metallic Materials, IFW Dresden, Dresden, Germany

The large magneto-crystalline anisotropy energy of $L1_0$ ordered tetragonal FePt has pushed the research on the preparation and characterization of FePt nanoparticles significantly during the last decade [1]. However, the necessity to subject those particles to (post-preparation) thermal annealing processes in order to initiate the otherwise kinetically hindered formation of the hard magnetic $L1_0$ phase constitutes a severe problem, since it often leads to inter-particle coalescence and sintering. Only few approaches were clearly proven to allow for the preparation of individual $L1_0$ ordered and thus magnetically hard FePt particles without sintering [2]. In our earlier experiments, the gas-phase preparation of FePt nanoparticles in combination with in-flight annealing was shown to allow for the formation of $L1_0$ ordered particles, however, with only a relatively small fraction of ordered particles and relatively poor coercive fields [3, 4].
In the present paper, we demonstrate that upon optimizing the particle trajectories within the optical annealing furnace, the fraction of $L1_0$ ordered particles can be significantly improved. The FePt nanoparticles are grown from a supersaturated metal vapour as provided by DC magnetron sputtering in an inert gas atmosphere and pass a light furnace in high vacuum prior to their deposition [4]. By laser positioning of the substrate it is assured that particles which reach the substrate have travelled within the narrow focal center of the light furnace which focuses the light of three halogen lamps onto a central tube of roughly 10 mm in diameter by means of elliptical mirrors. Owing to the construction of the light furnace any heating of the substrate is prevented as evidenced from monitoring the substrate temperature. Electrical powers of up to P = 4.5 kW can be supplied to the lamps of the furnace. Fig. 1 shows exemplarily the TEM image of FePt nanoparticles with a mean particle size of d_P = 7 nm that have been optically annealed with P = 3.5 kW. According to simulations of the (size dependent) interaction of the particles with the electro-magnetic field of the furnace this results in an annealing of the particles at roughly T_A = 900 °C for about t = 2 ms. As evidenced from HRTEM and electron diffraction studies and in agreement with the stability range of the $L1_0$ phase in a time-temperature-transformation diagram for the $L1_0$ ordering kinetics derived from DSC measurements of nanocrystalline FePt [5], likewise treated particles transform (partially) to the $L1_0$ phase. Statistical HRTEM investigations reveal that roughly 60% of the particles exhibit the $L1_0$ order and that larger particles order more easily than smaller ones. Fig. 3 shows the magnetization curve at T = 15 K for these optically annealed particles. Although the coercive field of $\mu_0 H_C$ = 0.65 T is relatively small, the open hysteresis curves indicates the presence of particles with much higher individual coercivities. Accordingly, the distribution of switching fields as derived from the field derivative of the isothermal remanent magnetization χ_{irr} = dMr/dH reveals that more than 50% of the particles' magnetization is switched only at fields above 1 T (cf. Fig. 4), and even at room temperature, roughly one fourth of the particles remain to have switching fields above 1 T.

[1] D. Weller et al., IEEE Trans. Mag. 36, 10 (2000).

[2] C.-B. Rong et al., Adv. Mater. 18, 2984 (2006). J.-M. Qui et al., Adv. Mater. 19, 1703 (2007).

[3] S. Stappert et al., J. Cryst. Growth 252, 440 (2003). B. Rellinghaus et al., J. Magn. Magn. Mater. 266, 142 (2003).

[4] B. Rellinghaus et al., IEEE Trans. Mag. 42, 3048 (2006).

[5] D.C. Berry and K. Barmak, J. Appl. Phys. 101, 014905 (2006).

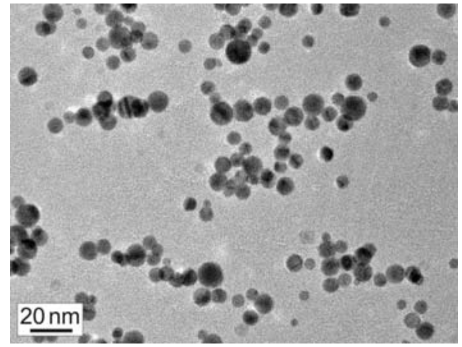

TEM image of FePt particles after in-flight optical annealing at P = 3.5 kW.

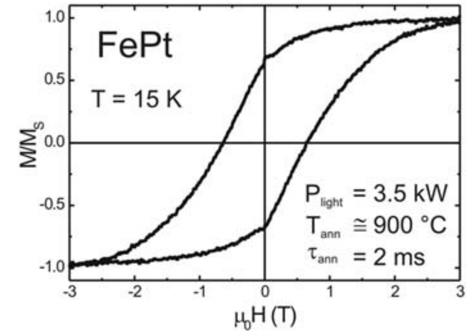

Magnetization curve at T =15 K for in-flight annealed FePt nanoparticles.

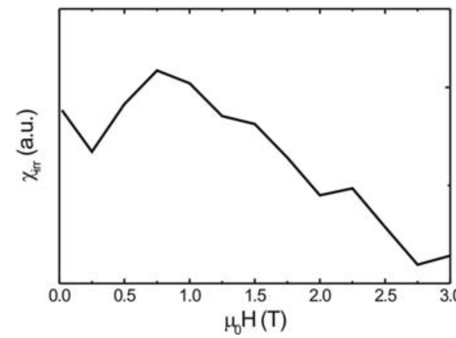

Switching field distribution of optically annealed FePt nanoparticles.

GF-01

Flying Characteristics on Discrete Track and Patterned Media With Thermal Protrusion Slider.

B. E. Knigge, Z. Z. Bandic, D. Kercher
San Jose Research Center, Hitachi Global Storage Technologies, San Jose, CA

Abstract—Future disk drives may have discretized bit patterns for increased thermal stability and higher areal density. This affects the surface topography resulting in different flying characteristics of currently used air bearing slider. The actual flying height drop vs. the pattern density and pattern depth has not been measured but simulated [1].
We have made flyable patterned media with angular sections having various topographies. This allowed the measurement of flying height modulation and clearance drop within one revolution in different sections of the disk.
Slider to disk clearance changes where measured using pulsed thermal protrusion.

I. INTRODUCTION/MOTIVATION

Patterned media and discrete track media flying characteristics have been recently simulated by Duwensee and Li [1]. Duwensee established an empirical relation between flying height as a function groove depth, groove width and groove pitch (Eq. 1). He found that homogenization methods applied to the generalized Reynolds equation are still an excellent approximation down to groove dimensions of a few nanometers, i.e. less than the mean free path of air.

dFH=d*(w/p) Eq. 1

Where FH= flying height, d= groove depth, w = groove width and p= groove pitch.

Discrete Track Media (DTM) and Patterned media fabrication methods have been discussed by Bandic [2] using direct e-beam writing, nanoimprinting, and reactive ion etching. We used direct e-beam writing and optical lithography methods to generate flyable media. Using optical lithography we generated holes at various widths, depths and pitch. This paper discuss the flying characteristics as measured by a laser Doppler vibrometer (LDV) and acoustic emission (AE) sensor when flying over patterned media sections. The FH drop is compared to simulation results.

II. EXPERIMENTAL SETUP

To measure slider to disk clearance we used pulsed thermal protrusion [3]. In order to perform localized clearance measurements a computer with simultaneous signal generation and data acquisition was programmed in Matlab and synchronized with spindle index.

III. RESULTS

In Figure 1 we show one of the patterned media layouts for flyability studies. We choose a large 180 deg patterned and flat section so that there is enough time for the air bearing to settle due to air bearing damping and enough time for the protrusion to fully develop.

Figure 2 shows the RMS of the acoustic emission signal with increased thermal actuation. Increased noise due to head disk contact is detected at ~45mW TFC power on the flat portion of the disk whereas the patterned portion of the disk shows contact at already at 20mW TFC power.

In Figure 3 we show the fly-height (FH), or clearance change, as a function of pattern density for 40nm deep holes and 17nm deep holes. The lowest density (least disk coverage) pattern had about 9% disk area covered by holes.

The linear fit (when including 0) shows a FH drop of about 0.4 and 0.17nm per % change in coverage, resulting at a 20nm FH drop at 50% pattern density for 40nm deep holes and 8.5nm FH drop for 17nm deep holes. Apparently, the slope is equal to the hole depth. One could translate equation 1 from DTM media to patterned bit media:

dFH=dhole*(Ahole/Aflat) Eq. 2

With Ahole=area of holes and Aflat=area of flat or islands and dhole=hole depth.

From Figure 3 we observe that equation 2 fits the data very well for 17nm deep holes but not as good for 40nm holes. From simulation results, nonlinearity is expected to occur for grooves deeper than ~30nm [1].

The air bearing pressure that builds up at the slider trailing pad carries most of the slider lift. By containing the pressure peak (such as it is done in holes) the FH drop is small compared to open (vented) grooves as on DTM media.

[1] Duwensee, M, Suzuki S, Lin J, Talke FE; MICROSYSTEM TECHNOLOGIES-MICRO-AND NANOSYSTEMS-INFORMATION STORAGE AND PROCESSING SYSTEMS 13 (8-10): 1023-1030 MAY 2007

[2] Z.Z. Bandic, E. Dobisz, T-W. Wu and T.R. Albrecht, Solid State Technology S7, S (2006).

[3] Knigge B, Suthar T, Baumgart P, IEEE TRANSACTIONS ON MAGNETICS 42 (10): 2510-2512 OCT 2006

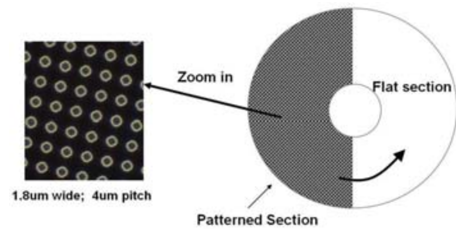

Figure 1: Patterned media layout for flyability study

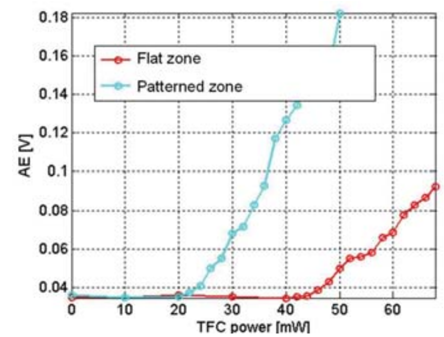

Figure 2: Touchdown Power on flat and patterned sections

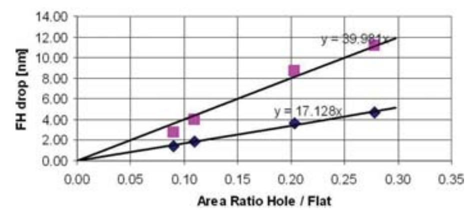

Figure 3: FH drop vs pattern density and hole depth

Nonuniform distribution of molecularly thin lubricant caused by inhomogeneous buried layers of discrete track media.

K. Fukuzawa[1,2], T. Muramatsu[1], H. Amakawa[1], S. Itoh[1], H. Zhang[1]
1. Micro/Nano Systems Engineering, Nagoya University, Nagoya, Japan; 2. PRESTO, JST, Kawaguchi, Japan

Introduction

Discrete track media (DTM) is expected to provide much higher recording density than conventional magnetic recording. On DTM, even if it is planarized, the layer under the carbon overcoat consists of quite different materials in the track and off-track regions (Fig. 1): magnetic metal and nonmetal material such as dielectric, respectively. Therefore, the intermolecular interactions between a lubricant molecule and the disk surface are different in these two regions. This could cause a nonuniform lubricant distribution, which would significantly affect the tribological performance of the head-disk interface (HDI) because the lubricant is a submonolayer-thick film. This paper presents a theory for the distribution of lubricant on a surface with inhomogeneous buried layers and, using it, predicts the distribution on DTM.

Estimation of thickness distribution on inhomogeneous buried layers

First, the estimation method was theoretically developed. In Fig. 1, at hydrodynamic equilibrium, the lubricants in the track and off-track regions have the equal disjoining pressures. This leads to different film thicknesses in the two regions because the regions consist of different materials and the disjoining pressures are not balanced if the lubricants in the two regions have the same thickness. Formulating the balance of the disjoining pressures by using the theory on intermolecular force [1], we obtained the thicknesses in the two regions. Next, the validity of the theoretical estimation was experimentally verified. A 2.3-nm-thick oxide layer on a silicon surface was locally fabricated by probe oxidation, and 10.3-nm-thick nonpolar lubricant (PFPE-Z03) was then applied onto it (Fig. 2). The intermolecular interaction in the oxide region is lower than that of the silicon region. AFM images show that the thickness in the oxide region decreased by 0.4 nm due to the decrease in the interaction. In addition, the lubricant thicknesses on the oxide regions were measured for combinations of oxide layers and lubricant films with various thicknesses of the order of 1 nm. Comparing the estimated thickness with the experimental ones, we found that the difference in the thickness was about 0.26 nm in the standard deviation. This indicates the validity of our estimation.

Thickness distribution of lubricant on DTM

Using the above theory, we estimated the lubricant thicknesses on DTM. Even if lubricant with an initial thickness of h0 is uniformly applied onto the disk, the lubricant moves from the off-track to track regions due to the pressure balance. Therefore, the lubricant is thicker in the track regions than the off-track region at equilibrium, as shown in Fig. 3. This shows that the difference in thickness is smaller when the carbon thickness hc is rather large. This is because the thick carbon shields the intermolecular interaction from the underlying layer. On the other hand, the difference is larger when hc is small. Reducing the magnetic spacing requires a thinner carbon overcoat. Thus, the nonuniform distribution will be an important issue in designing HDIs of DTM.

Summary

A method of estimating the thickness distribution on a surface with inhomogeneous buried layers was presented. It revealed that the lubricant distributes nonuniformly on DTM.

[1] J. N. Israelachvili, Intermolecular and Surface Forces, Academic Press (1992).

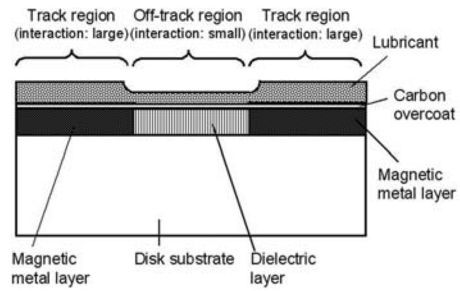

Fig. 1. Schematic DTM disk.

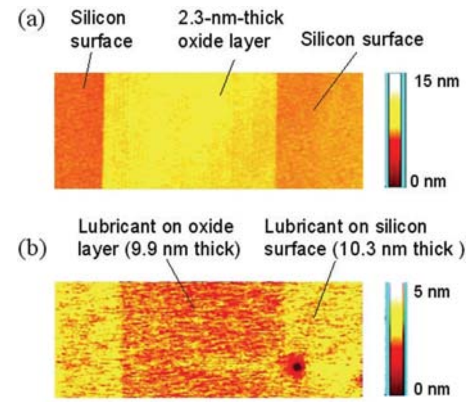

Fig. 2. AFM images of (a) oxide layer and (b) lubricant film on it. The width of the images is 6.3 μm. The lubricant thickness on the oxide layer is 0.4 nm less than on the silicon surface.

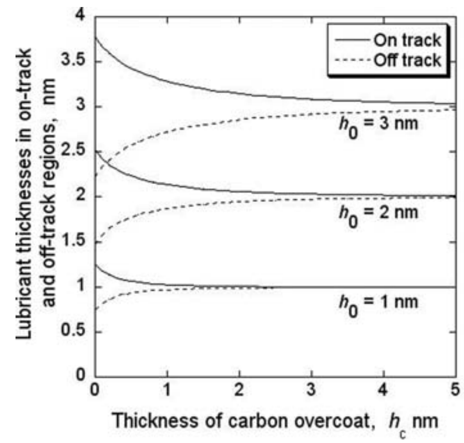

Fig. 3. Estimated lubricant thickness for a DTM.

GF-03

Parametric Study of Contact Performance for Discrete Track Recording Media Using Finite Element Analysis.

C. Yeo, *A. A. Polycarpou*
Mechanical Science and Engineering, Univ. of Illinois at Urbana-Champaign, Urbana, IL

ABSTRACT
As the pattern size of discrete track recording media is required to be smaller for achieving higher recording densities (Tb/in^2 and beyond), geometrical parameters such as land width, ratio of land width to track pitch, and groove depth become very important in improving head-disk-interface reliability. Computational simulations using finite element analysis have been performed on representative patterned surfaces to investigate the contact behavior of the discrete patterns. To recommend design trends for the geometrical parameters for improved contact performance, design-of-experiment analysis has been performed and a prediction model of critical contact force is proposed as a function of the relevant geometrical parameters.

INTRODUCTION
Pattern media have been widely investigated in the hard disk drive (HDD) industry to achieve higher recording densities. Discrete track recording (DTR) media is manufacturable with lower fabrication cost and higher accuracy, which enables DTR media to be more attractive for mass-production, compared to bit pattern media [1]. For these reasons, research on DTR media in relation to magnetic performance, fabrication techniques, and head slider flyability has been conducted [2-3]. However, there have only been few works on the head-disk-interface (HDI) contact mechanics of DTR media. In this paper, computational contact simulations using finite element analysis (FEA) have been performed on DTR media. Based on specified pattern dimensions such as land with (w), groove depth (d), and the ratio of land width to track pitch (w/p), the elastic and plastic contact performance of DTR media has been investigated. Through design-of-experiment (DOE) analysis, dimensional design directions of DTR media are proposed to achieve recording densities of 1 Tb/in^2 and beyond.

SIMULATIONS
Two-dimensional plane strain elements were used to model the DTR media in the FEA simulations. The nominal contact width of the rigid plane was chosen to be 3.12 microns moving downward (loading) and upward (unloading), while the deformable patterned media body was stationary. The finite element mesh of DTR media consists of 36,046 – 228,104 nodes and 34,688 – 228,195 elements depending upon the specific pattern dimensions examined. The radius of the pattern top curvature was 134 nm for small land width (w = 40 nm) patterns and 834 nm for large land width (w = 100 nm) patterns. The material type was isotropic and elastic-perfect plastic, and the friction coefficient was 0.2. The DTR media consisted of two layers. A 2.5 nm thick carbon overcoat (COC) was applied onto the pattern top made of "bulk" magnetic material.

RESULTS AND DISCUSSION
Based on the FEA simulation results, it was found that the outer located patterns exhibit higher contact stresses and deformations, and thus the material yield initiates on the outermost pattern as shown in Fig. 1. The material behavior during contact caused the outer patterns to have lower normal (downward direction) surface displacements but higher tangential movement to the contact center, which resulted in severe contacts. Once after the material yield initiated on the outermost patters, the contact stiffness values of DTR media showed decreasing trend due to the growing plastic region on the patterns. To establish design guidelines, 2^3-factorial DOE was performed using the aforementioned FEA contact simulations, thus investigating the effects of the three geometrical factors on the DTR contact performance. The analysis of the main effects showed that the larger the land width, the larger the ratio of land width to pitch, and the smaller groove depth, they all improve the contact performance. However, based on the model analysis of the critical contact force in relation to the three geometrical factors, it was found that under some restrictions of one geometrical factor, the design directions of the two geometrical factors were not the same as those from the main effects analysis, but they were dependent on the given restrictions. Therefore, for optimum contact performance of DTR media, the three geometrical factors should be carefully determined based on the restrictions given by requiring recording density or nanofabrication methodologies.

1) Terris, B. D., Folks, L., Weller, D., Baglin, J. E. E., Kellock, A. J., Rothuizen, H., Vettiger, P., "Ion-beam Patterning of Magnetic Films using Stencil Masks," Appl. Phys. Lett. 75(3), 403-405 (1999).

2) Wachenschwanz, D., Jiang, W., Roddick, E., Homola, A., Dorsey, P., Harper, B., Treves, D., Bajorek, C., "Design of a Manufacturable Discrete Track Recording Medium," IEEE Trans. Magn. 41(2), 670-675 (2005).

3) Duwensee, M., Suzuki, S., Lin, J., Wachenschwanz, D., Talke, F. E., "Simulation of the Head Disk Interface for Discrete Track Media," Microsyst. Technol. 13, 1023-1030 (2007).

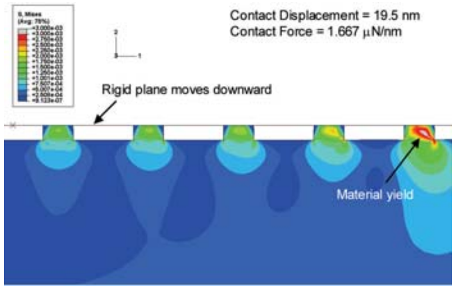

Fig. 1. Contact stress distribution of individual patterns (right half of the patterns).

GF-04

Numerical and Experimental Investigation of “Flyability” of Sliders on Discrete Track Recording Media.

Y. Yoon[1], M. Duwensee[2], J. Lin[3], S. Suzuki[3], F. E. Talke[1]
1. Mechanical Engineering, University of California, San Diego, La Jolla, CA; 2. Hitachi Global Storage Technologies, San Jose, CA; 3. Western Digital Corporation, San Jose, CA

Introduction

To achieve storage densities near 1Tbit/inch2, discrete track recording (DTR) media are being investigated presently. DTR media reduce magnetic “cross-talk” in the radial direction by physically separating adjacent recording tracks from each other [1]. Fig.1 shows a scanning electron microscope (SEM) image of typical discrete track recording media.

The flying behaviour of a slider over discrete track media is affected by the presence of the grooves on the disk. In particular, the steady state flying height of a slider flying over discrete track media is lower than that of a slider over smooth media. Numerical investigations by Duwensee et al. [1, 2] have shown that the “flying height loss” Δh of a slider over discrete track media can be determined by $\Delta h = d \times w/p$, where d is the groove depth, w is the groove width, and p is the track pitch.

In this study, an experimental investigation of the flying characteristics of magnetic recording sliders over discrete track media is performed. In addition, experimental measurements of “flyability” of two types of recording sliders are compared with numerical predictions.

Experimental setup and results

The flying characteristics of magnetic recording sliders over DTR media was investigated using acoustic emission (AE) sensors and laser Doppler vibrometer (LDV) instrumentation. Fig. 2 shows the schematic of the experimental setup. Fig. 3 and Table 1 illustrate the DTR media parameters used. To investigate the flying characteristics of magnetic recording sliders over DTR media, two pico sliders were used as showed in Fig. 4. Slider “A” is designed to fly at 11 nm over “smooth” media, while slider “B” flies at 20 nm.

Fig. 5 shows the standard deviation of flying height for sliders “A” and “B” as a function of groove depth. For slider “A”, designed to fly at 11 nm over smooth media, a small standard deviation of flying height is observed for a groove depth of 20 nm, indicating that the slider flies stable on this media. However, for a groove depth of 30 nm and 40 nm, large flying height fluctuations are observed, showing that the slider does not fly stable for those conditions. For slider “B”, designed to fly at 20 nm over smooth media, stable flying behavior is observed for a groove depths of 20 nm and 30 nm, respectively. However, for a groove depth of 40 nm, a large standard deviation of flying height is observed, indicating the slider is not flying stable.

Numerical model and results

To correlate the experimental results with numerical predictions, we have simulated the flying characteristics of the two sliders over DTR media using the “CMRR” finite element air bearing simulator [3]. Figure 6 shows the numerical predictions for the steady state flying height of sliders “A” and “B” for the three different DTR media used. We observe that slider “A” is predicted to fly at a flying height of 5 nm on DTR media with a groove depth of 20 nm. However, the predicted flying height is near zero for a groove depth of 30 nm and 40 nm, i.e., slider “A” cannot be expected to fly stable on DTR media with a groove depth of 30 nm or 40 nm. The above predictions are in excellent qualitative agreement with the experimental measurements of Fig. 5 which show that slider “A” flies stable on DTR media with a grove depth of 20 nm but does not fly stable on DTR media with a groove depth of 30 or 40 nm, respectively. For slider “B”, the numerical predictions show that this slider flies on DTR media with a groove depth of 20 nm and 30 nm, respectively, while it cannot fly on DTR media with a groove depth of 40 nm. This result is likewise in excellent qualitative agreement with the results of Fig. 5, i.e., slider “B” flies stable on DTR media with 20 or 30 nm groove depth, respectively, but does not fly stable on DTR media with 40 nm groove depth.

From the above numerical and experimental results we conclude that very good qualitative agreement exists for the numerically predicted and experimentally measured flying characteristics of magnetic recording sliders on DTR media. Additional experiments should be performed using DTR media with different groove characteristics to “fine-tune” the comparison between experimental and numerical results.

[1] Duwensee, M., Suzuki, S.,Lin, J.,Wachenschwanz, D.,and Talke, F. E., “Air Bearing Simulation of Discrete Track Recording Media”, IEEE Trans. Mag., 42(10):24892491, 2006.

[2] Duwensee, M.,Suzuki, S.,Lin, J.,Wachenschwanz, D.,and Talke, F. E., “Simulation of the Head Disk Interface for Discrete Track Media”, Microsystem Technologies, Published Online, 2006.

[3] Wahl, M.H., “Numerical and Experimental Investigation of the Head/Disk Interface”, PhD Thesis, University of California, San Diego, 1994

Groove depth (d)	20 nm	30 nm	40 nm
Groove width (w)	70 nm	90 nm	110 nm
Track pitch (p)	210 nm	200 nm	200 nm
w/p	0.3	0.45	0.55

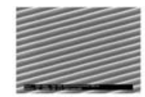

Fig 1: Scanning electron microscope image of discrete track recording media

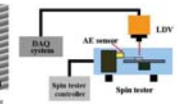

Fig. 2: Schematic of experimental setup

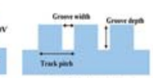

Fig. 3: DTR parameters

Fig. 4: Air bearing designs:
a) Slider A b) Slider B

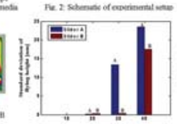

Fig 5: Standard deviation of flying height vs. groove depth

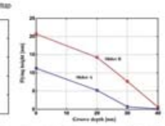

Fig. 6: Numerical predictions of flying height vs. groove depth

Dynamic analysis schemes for flying head sliders over discrete track media.

S. Fukui, T. Kanamaru, H. Matsuoka
Dept. of Applied Mathematics and Physics, Tottori University, Tottori City, Japan

Introduction

Recently the spacing between the slider and the disk has been reduced to 10 nm or less and the recording media with grooves such as the discrete track media (DTM) is estimated one of the most promising media for achieving ultrahigh track density. Analyses of the static and dynamic characteristics of flying head sliders over DTM by the molecular gas-film lubrication (MGL) equation [1] become increasingly important. To obtain the dynamic characteristics of the air bearing, the perturbation method in frequency domain had been established [2].

In this paper, the highly accurate and numerically stable cubic interpolated propagation (CIP) method in time domain [3,4] was newly applied to fundamental MGL problem and slider dynamics. Moreover, the perturbation method in frequency domain was also applied to obtain air bearing stiffness and damping coefficient of the air bearing over DTM.

Dynamic air film pressures caused by a running single projection

Figure 1 shows the projection position on the running disk under the fixed slider and corresponding pressure distributions calculated by the CIP method. Negative pressure regime follows at approximately half the speed of the single projection, which agrees well with the theoretical result.

Static and dynamic pressures by the DTM (Fig. 2)

Figure 3 shows an example of the static pressure distributions with/without groove (groove depth=10nm) for plane inclined slider with the minimum spacing of 10 nm. Figure 4 shows the corresponding dynamic pressure distributions in phase (stiffness) caused by 10 kHz translational excitation calculated by the perturbation method. It is found that DTM groove decreases both the static pressure and air film stiffness.

Conclusion

The numerical schemes to obtain the static and dynamic pressures and slider dynamics caused by DTM are established by the use of the CIP method in time domain and the perturbation method in frequency domain.

[1] S. Fukui and R. Kaneko, Handbook of Micro/Nanotribology, CRC Press (1995) 559-603

[2] S. Fukui and R. Kaneko, JSME Int. J. Ser III, 33 (1990) 76-81

[3] H. Takewaki and T. Yabe, J. Comput Phys, 70 (1987) 355-372

[4] S. Fukui, H. Matsui, K. Yamane and H. Matsuoka, Microsyst Technol 11 (2005) 812-818

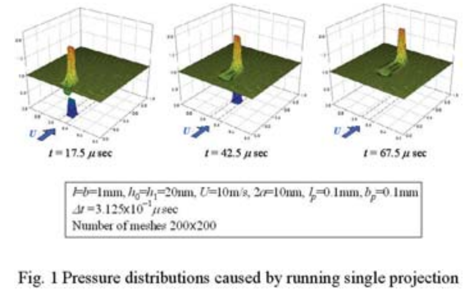

Fig. 1 Pressure distributions caused by running single projection

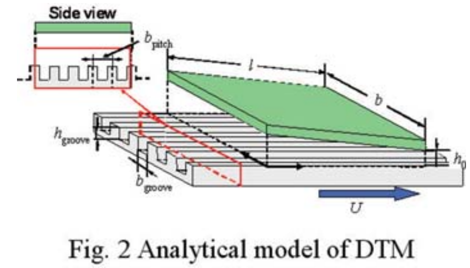

Fig. 2 Analytical model of DTM

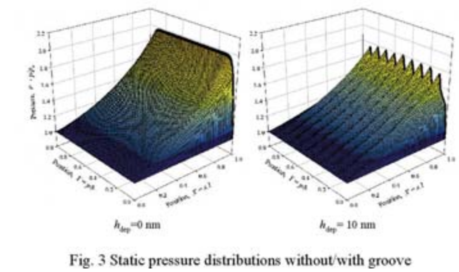

Fig. 3 Static pressure distributions without/with groove

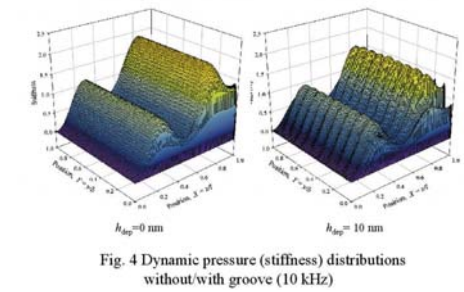

Fig. 4 Dynamic pressure (stiffness) distributions without/with groove (10 kHz)

GF-06

Effect of van der Waals Force on Ultimate Head-to-Disk Interface.

K. Ono
Storage Technology Research Center, Hitachi Central Research Laboratory, Fijisawa-shi, Japan

1.Introduction
To achieve a stable and reliable head-to-disk interface in the near-contact recording regime, a sphere-to-flat interface is indispensable for reducing the adhesion and friction forces and the contact pressure [1]. Such an interface seems to be realized by using thermal protrusion resulting from thermal flying height control. The areal density of 2 Tb/in^2 requires a mechanical spacing of 2–2.5 nm and a clearance of less than 0.5 nm, meaning that the slider will frequently come into contact with the disk. When the separation between head and disk decreases to less than 1 nm, van der Waals (vdW) force begins to play an important role in addition to the lubricant meniscus force. This paper describes an analytical study of the touchdown of a spherical pad slider to a disk due to elastic deformation when the two surfaces are attracted to each other by vdW force under static air-bearing pressure.
2.Analytical Model and Method
The thermally protruded surface of the center pad is modeled as a spherical pad with radius of curvature R, height δ, and base radius a (see Fig.1). If R is 10–30 mm, the maximum possible meniscus force, $4\pi R\gamma$, is 3–9 mN. Since the air-bearing lift force (>20 mN) overcomes the meniscus adhesion force, the slider can stably fly over the disk surface. Therefore, an additional attractive force between the two surfaces is caused by van der Waals force when the pad contacts the disk. Thus, only the vdW force and static air-bearing pressure, P_{ab}, on the center pad was considered. The minimum gap at the tip of the pad is denoted by d. For analytical simplicity, the center pad is assumed to be circular with radius b, and P_{ab} is applied within this area. Elastic deformation of the mating surfaces is calculated numerically based on boundary finite element method. The vdW pressure is given by $A/(6\pi h^3)$ (A: Hamaker constant, $h(r)$: local spacing). Hertz pressure is applied to the contact area. For various values of initial separation d_0 from un-deformed disk surface, the convergent solutions for disk deformation, attractive pressure, final separation d, etc. were iteratively calculated. Parametric analysis of the effects of R, P_{ab}, and roughness height σ on attractive force F_a, disk deformation, and attractive pressure was conducted for $\delta = 10$ nm, $b = 30$ μm, $A = 10^{-19}$ J, and $\gamma = 22$ mN/m.
3. Analytical Results and Discussion
Figure 2 (a) and (b) show attractive force F_a versus final separation d and disk deformation versus radial position for $P_{ab} = 3$ MPa and $R = 20$ mm, taking σ as a parameter. In the calculation, d_0 was changed from 0.7 nm to –0.5 nm by 0.1 nm. Meniscus force $F_m = 4\pi R\gamma$ and vdW force $F_v = AR/(6d^2)$ for a rigid sphere-to-flat interface are also plotted in Fig. 2(a) for comparison. In a rigid-surface interface, $F_m > F_v$ when $d > 0.25$ nm. The disk height beneath the spherical pad was less than –1 nm, and the adhesion force F_a was –8 mN before touchdown due to the 3-MPa air-bearing pressure. When d decreases from 1.1 nm, it jumps to σ and F_a changes abruptly to a higher value since the disk surface adheres to the spherical pad surface because of elastic deformation. This critical separation corresponds to the touchdown height. After the disk touches down on the pad, the attractive pressure is determined by the roughness height σ, whereas F_a is affected by σ and R. F_a increases further with a decrease in d_0 because of the increase in adhering area. Note that F_a immediately after touchdown is less than F_m at $\sigma = 0.55$ nm, whereas F_a is nearly equal to F_m at $\sigma = 0.50$ nm and substantially larger than F_m at $\sigma = 0.45$ nm. Assuming that F_a should be less than F_m for wear durability, σ must be more than 0.50 nm. The similar calculated results for $R = 10$ and 30 mm are shown in Fig.3.It is found that the allowable minimum roughness height satisfying $F_a < F_m$ at touchdown was 0.55, 0.50, and 0.45 nm for $R = 30$, 20, and 10 mm, respectively.The effects of other parameters on the head-to-disk interface will be discussed in the presentation and full paper.
4. Conclusion
The minimum possible touchdown height for non-contact recording is ~1 nm and the allowable minimum glide height is 0.5 nm if the pad radius is 20 mm. They can be reduced by reducing the pad radius of curvature.

[1] K. Ono, "Dynamic Instability of Flying Head Slider and Stabilizing Design for Near-Contact Magnetic Recording," Presented at PMRC 2007, Submitted to J. Magnetism and Magnetic Materials.

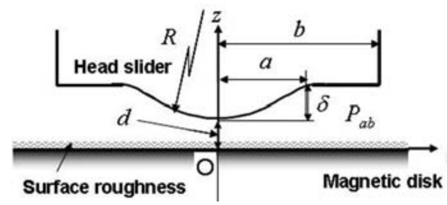

Fig. 1 Analytical model of head-disk interface

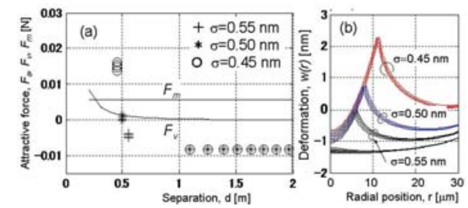

Fig. 2 (a) Adhesion force vs. separation and (b) deformation vs. radial position with *R* = 20 mm.

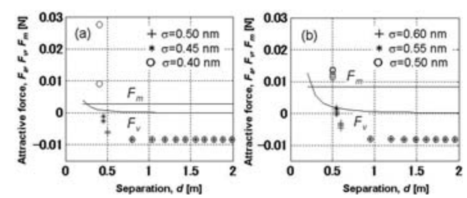

Fig. 3 Adhesion force vs. separation for (a) *R*=10 mm (a) and (b) *R*=30 mm.

GF-07

STUDY ON CONTACT OF THERMAL ACTUATED SLIDER AND DISK.

M. Zhang[1], B. Liu[1,2], S. Hu[1]
1. Spintronics, Media and Interface Division, Data Storage Institute, Singapore, Singapore; 2. Nanyang Technological University, Singapore, Singapore

Thermal actuated sliders provide better reading/writing properties and HDI stability in HDD. With the increase of recording density, the flying height of slider should be reduced gradually, which increases the possibility of contact between slider and disk. On the other hand, the contact recording technology is being explored in order to realize the maximum reduce of magnetic spacing for extremely high-density magnetic recording. In this paper, the contact between thermal actuated slider with disk was studied experimentally.
The contact was tested on a spinstand integrated with a Laser Doppler Vibrometer (LDV) and an Acoustic Emission (AE) sensor, as shown in Fig. 1.
When a thermal actuated slider contacted with disk, it was found single mode frequency (corresponding to air bearing resonance frequency of pitch mode) dominated the vibration, as shown in Fig. 2. It also was observed the lubricant redistribution after short time contact, the lubricant modulation frequency corresponds to slider resonance frequency, as shown in Fig. 3.
The testing results with different driving voltage showed: when the voltage was less 3V, no contact happened; the both LDV and AE signals showed the contact happened around 4V; when the driving voltage further increaseed from 4V to 8V, the strongest signal did not happen at the maximum driving voltage and corresponded to the voltage (~4V) at which contact just happens, as show in Fig.4. These results showed contact signal was strongest when the slider changed from flying to contact or from contact to flying. When the frequency of driving voltage increaseed from 20Hz to 80Hz, the above phenomena was same, only the amplitude of contact signal decreased with increase of the driving frequency as shown in Fig. 5.
The comparison of contact between the thermal actuated slider and disks with and without mobile lubricant showed the thermal actuated slider contacted the mobile lube disk with lower voltage than that of bonded lube disk; and the AE signal for the contact of the thermal actuated slider with bonded lube disk was higher than that with the free lube disk with same (large) driving voltage, as shown in Fig. 6.
The comparison of AE, LDV and reader signal showed the reader signal was very sensitive for the contact monitoring. When a slight contact happened between slider and disk, AE signal had little difference with/without contact, LDV signal obviously has three peaks (correspond to slider's resonance frequency) after contact happened and reader signal strength increases at all frequency (0-2MHz) besides a few peaks after contact happened, as showed in Fig. 7.

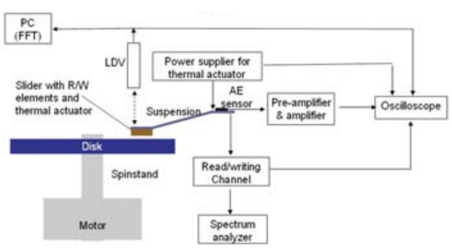

Fig.1 Experimental Setup

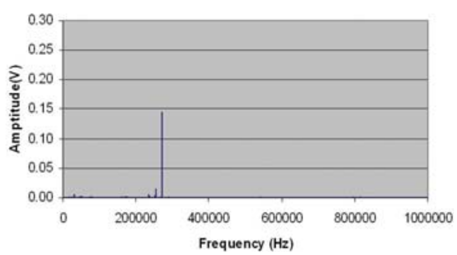

Fig.2 Vibration spectrum for a constant voltage

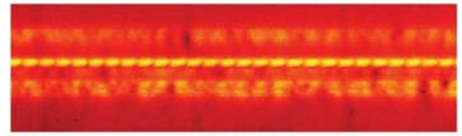

Fig. 3 OSA image of lubricant on disk

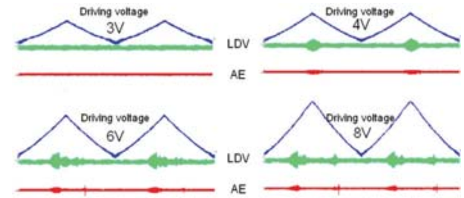

Fig.4 Vibration for different driving voltage

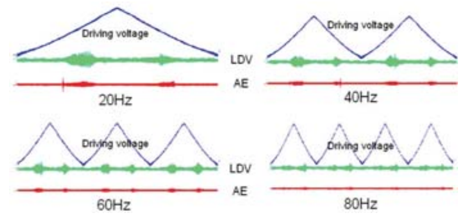

Fig.5 Vibration for different driving frequency

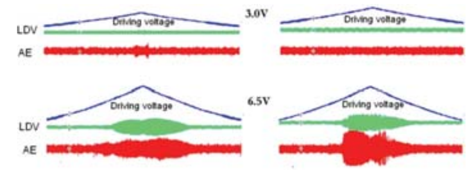

Fig.6 Vibration for different disks

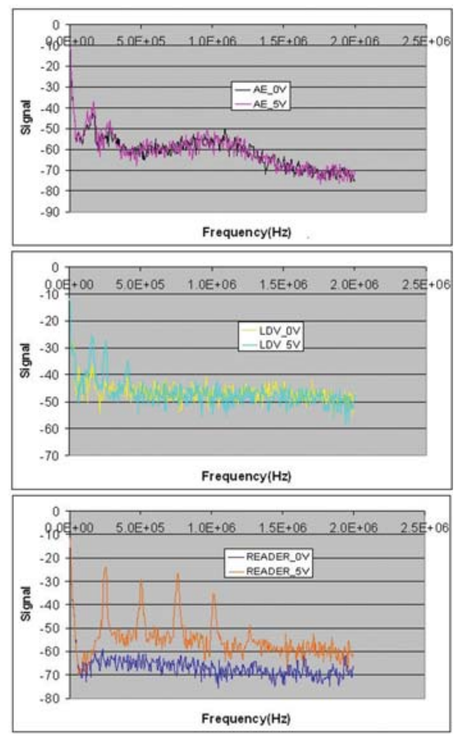

Fig.7 Comparison of LDV, AE and reader signals spectrum for a slight contact

Numerical and Experimental Analyses of Nanometer-scale Flying Height Control of Magnetic Head with Heating Element.

J. Juang[1], T. Nakamura[3], B. Knigge[1], Y. Luo[2], W. Hsiao[2], K. Kuroki[3], F. Huang[1], P. Baumgart[1]
1. San Jose Research Center, Hitachi GST, San Jose, CA; 2. Hitachi GST, San Jose, CA; 3. Hitachi GST, Fujisawa-shi, Kanagawa-ken, Japan

Flying height (FH) control using thermal actuation has been introduced recently in HDD products as a new technique for compensating static FH variations of magnetic heads and reducing the risk of harmful head-disk contact. The cycle time of wafer and slider fabrication is long and some key parameters are not easily measurable, such as minimum and writer FH, and in-situ slider protrusion profiles. Therefore, it is of great importance to develop a model that can predict the actuation performance of different designs more accurately and reduce the product development time. For a flying slider, the performance of thermal actuation is determined not only by the head/heater structure and materials, but also by the ABS-dependent thermal boundary condition, forming a complex nonlinear thermal-structural coupled-field problem. The write pole-tip and read sensor protrude differently under different ambient temperatures, heater, and write settings. This paper describes a comprehensive model and validates it by measurements under various conditions.

Simulation and Measurements

In the first step we create a 3-D finite element model of the entire slider with detailed head/heater structure, and then conduct electrical-thermal-structural analysis using velocity slip and temperature jump boundary conditions to formulate the heat transfer across the head-disk interface when the slider flies on a spinning disk (Fig. 1). An iteration procedure, proposed earlier, is used to obtain the equilibrium solution. The slider and disk deformation due to air-bearing pressure is included since the pressure increases significantly when the FH is reduced to sub-5nm regime. Another critical parameter, pole-tip recession (PTR), created by lapping and etching processes, is also included in the model. Comparisons between simulation and measurements were made in both nonflying and flying conditions. In the nonflying condition, the slider is attached to an aluminum plate, and the protrusion profile is obtained by the difference of two images taken by Wyko (interferometer) tool when the heat source is turned on and off. The simulation shows excellent agreement with the measurement for the whole bulge profiles at all three conditions as shown in Fig.2. To measure the FH and clearance change profiles of the head element area in the flying condition, we have developed a new measurement method based on principle of conventional flying height tester (FHT). The FH is typically measured by detecting the interference light intensity, which may be expressed by refractive index (n, k), wavelength and FH. The element area consists of various materials with different optical properties. However, for a low flying slider the FH is proportional to the intensity in spite of the mixture of various materials. The FH profile including the element area can then be measured by using a microscopic light spot. Figure 3 shows a comparison of clearance change between simulation and FHT with a heater power of 65mW. It is seen that the model prediction agrees reasonably well with the FHT over the entire shape of the bulge. The clearance drop of the reader predicted by the model is ~0.5nm more than the average value of measured data, which has a standard deviation of ~0.56nm. The effect of slider and disk deformation on the FH due to the air-bearing pressure is shown in Fig. 4. The minimum FH of the case with rigid disk and slider is ~0.5nm lower than that of the more realistic one, and the effect of the slider is more noticeable than that of the disk, even though the disk may deform up to about 2nm. However, only a portion of the disk and slider compression contributes to the FH increase because of the self-compensation of an air-bearing.

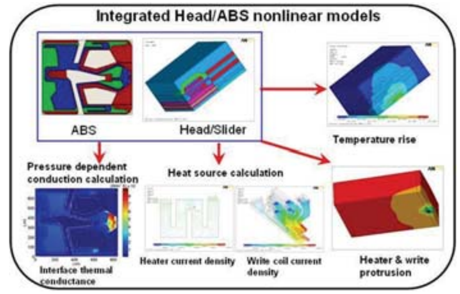

Fig. 1 Integrated head and ABS nonlinear model.

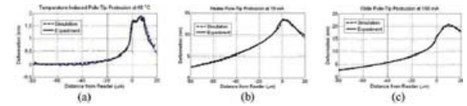

Fig. 2 Comparison of nonflying protrusion profiles along centerline of slider length under three conditions: a) higher ambient temperature, b) current through heater, c) current through write coil.

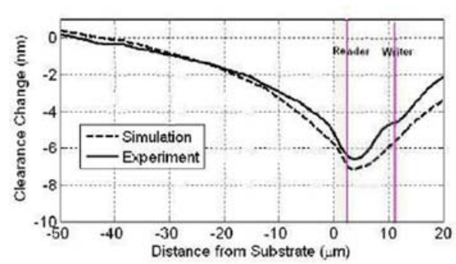

Fig. 3 Comparison of clearance change between simulation and optical measurement under flying condition (heater power: 65mW).

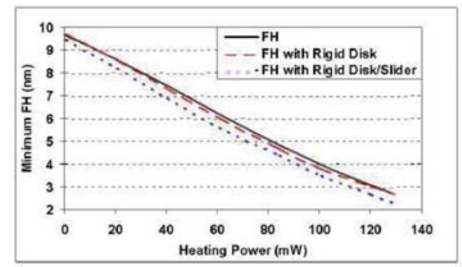

Fig. 4 Effect of slider and disk deformation due to air-bearing pressure.

GF-09

Dynamics of Fly-Contact Head-Disk Interface.

S. Yu, B. Liu, W. Hua, W. Zhou, C. Wong
Data Storage Institute, Singapore, Singapore

Introduction
Reducing the mechanical spacing between the head and the disk in hard disk drives is critical for achieving ultra-high recording densities. Realizing the flying interface with less than 2 nm clearance will be a significant challenge due to the instability induced by the adhesion forces between the slider and the disk. Therefore, a breakthrough is necessary to further reduce the mechanical spacing.
In-contact recording scheme, as proposed by many researchers, is a possible choice. However, the conventional ABS designs for in-contact recording, such as the tripad contact slider [1], have some drawbacks. For example, the contact force between the slider and disk is high, which may cause the serious wear and slider vibrations in fly-height (FH) and off-track directions.
To overcome the above-mentioned drawbacks, a new head-disk interface (HDI) scheme, i.e. fly-contact interface, is proposed by combining the major advantages of the fly and the in-contact recording schemes [2]. It allows the most of slider's air-bearing surface (ABS) to fly while having the tiny read/write head area in contact with the lubricant on disk the surface. The thermal nano-actuator technology can help to realize fly-contact scheme with the contact-on-demand mechanism. There are two main challenges for making a stable and reliable fly-contact interface. One is the sliders' bounce and the other is the wear between the slider and the disk. A key factor for minimizing the bounce and wear is to control and minimize the normal contact force and adhesion force exerted between the slider and the disk.
In this study, a series of simulations were carried out to investigate the contributions of contact force and adhesion force on the stability and reliability of the fly-contact HDI, and how to achieve a low contact force and a small flying-height variation.
Simulation on dynamics of fly-contact head-disk interface
In this study, the effects of different surface profiles of the contact pad on performance of fly-contact interface were investigated. A femto slider with a sphere-topped cylinder pad at the trailing center is used in this study, as shown in Fig. 1. The radius of the cylinder is 25 μm. The crown height varies from 1 nm to 20 nm, while the total height of the sphere-topped cylinder pad keeps constant. So the sphere-topped cylinder pad has the same height but different curvature radius. The slider flies over a disk with surface waviness. The DSI's self- developed air bearing simulation program, ABSolution, is used to simulate the dynamics of the head disk interface.
Fig. 2 shows the FH and FH variation of slider when the crown height h varies from 1 nm to 20 nm. It can be seen that the slider will keep contacting with disk when h is smaller than 6nm, but will bounce when h is between 6 nm and 17 nm. When h is larger than 17 nm, the slider will keep flying status. From Fig. 3, it can be seen that the best choice of the sphere height is around 5 nm, as it can achieve both the low FH variations and the low contact force. In addition, it can be seen that the FH modulation due to the disk waviness in the fly-contact interface is much smaller than the one in the flying interface.
Conclusion

ABS design for fly-contact HDI needs to consider the balance of minimizing both the FH variation (bounce) and contact force (wear). The best choice of the ABS design is that the slider keeps a slight contact with disk without any bounce, because such design can achieve both the low FH variations and the low wear. In addition, the fly contact interface has much better capability in following disk waviness than the flying interface does.

[1] A. Sato, K. Ajiki, M. Yanagisawa and Y. Tsukamoto, "Head-disk interface design for in-contact recording using wet systems", IEEE Trans. Magnetics, Vol. 33, No. 5, pp. 3301-3304, 1997.

[2] B. Liu, M. S. Zhang, S. K. Yu, W. Hua, C. H. Wong, W. D. Zhou, Y. J. Man and Y. S. Ma, "Towards Fly and Lubricant Contact Recording", Proceedings of the PMRC 2007, Tokyo Japan, Oct 15-17, 2007.

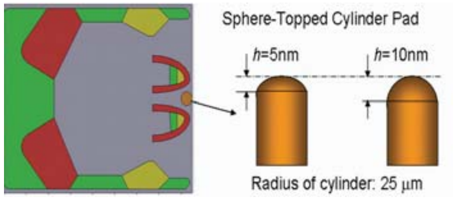

Fig. 1 ABS design with a sphere-topped cylinder pad

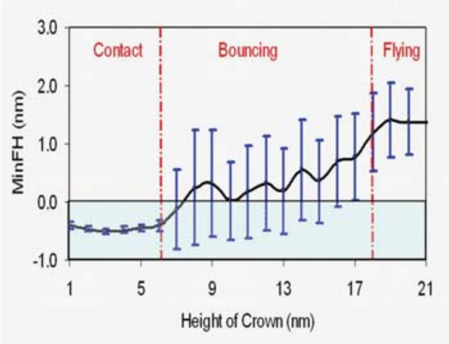

Fig. 2 FH and FH variation of the slider

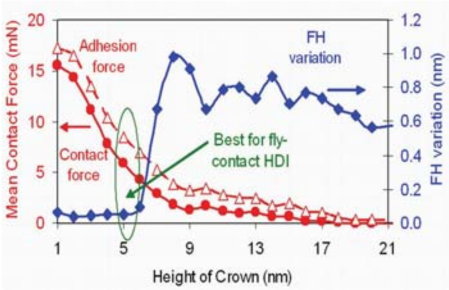

Fig. 3 Dynamic performance of fly-contact HDI

GF-10

Slider Optical Constant Distribution, n and k Correlation, and FH Measurement Accuracy.

Z. Yuan[1], C. Ong[1], B. Liu[1], J. Liu[2], S. Yoshida[2]
1. DSI, Singapore, Singapore; 2. Hitachi Asia, SG, Singapore

As the linear density increases continuously, the head medium spacing decreases down to nm level. The absolute flying height (FH) value is very important to evaluate the stability and reliability of HDI. The white light interferometry method has been used to measure FH for many years. Due to the strong negative pressure in modern slider design, the unload calibration process becomes unstable and has a big concern on the testing repeatability. To improve it, the latest version FH tester adopts the laser phase detection method and can achieve on-flying calibration. It significantly improves the repeatability of FH testing on the same spot. But the accuracy of FH measurement still largely depends on the dispersion range of optical constant.
The slider wafer material is the composition of TiC and Alumina. The optical constant (n+ik) of two materials has a big difference, which is 3.5+2.5i for TiC and 1.7+0i for Alumina. The effective n and k values largely depend on the area composition ratio of two materials. With 60X25 mircon spot size of Ellipsometer mapping over slider ABS, more than 1 thousand points were captured and the point by point plot of n and k is shown in Fig. 1. Both n and k values scatter in a certain range due to the change of the composition ratio of two materials at each individual spot. When the n value of each point is plotted versus the k value at the same point as shown in Fig. 2, it shows there is a quasi-linear relationship between n and k.
The current commercial FH tester only takes a pair of the averaged n and k values for FH calculation. If it's assumed that the FH of all the testing spots is at 5 nm, the calculated testing FH by the input of averaged n and k is plotted in Fig. 3. At 650 nm wavelength, the white light interferometry method produces more FH testing errors than the laser phase detection method for this type of slider.
In Fig. 4, the dispersion range of both n and k measured in Fig.1 is used, but the n and k value can be combined freely, then the mesh of testing FH versus n and k is plotted (only k axis is shown) in the same way of Fig. 3. The line 1 in Fig.4 is the measured n and k correlation. The n and k correlation varies when there is a change on slider roughness, overcoat thickness, and the optical constant of overcoat. If the n and k correlation takes line 2 in Fig. 4, the laser phase detection method can generate +/- 3 nm FH testing error.
In this work, a model to calculate the n&k dispersion versus the composition ratio of TiC and Alumina, slider roughness, and Si/DLC overcoat thickness was developed. The slider samples with different roughness and overcoat thickness were prepared and measured to verify the model. From both theoretic and experiment study, the laser phase detection method has smaller FH error at current roughness and overcoat thickness. As the overcoat thickness decreases, the FH error of phase detection method tends to increase. The accuracy of both optical methods largely depends on slider fabrication process defined n&k correlation rather than the absolute value of n&k dispersion.

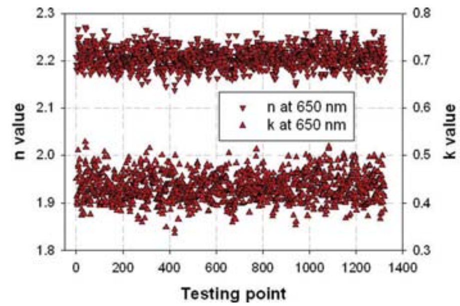

Figure 1 n and k scanning over the ABS of slider by Ellipsometer

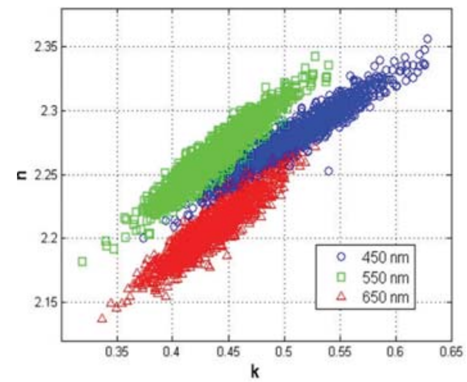

Figure 2 Correlation of n and k

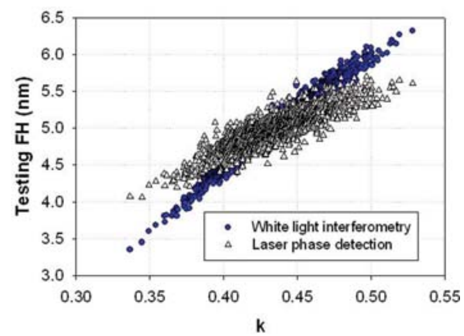

Figure 3 Testing FH by the averaged n and k

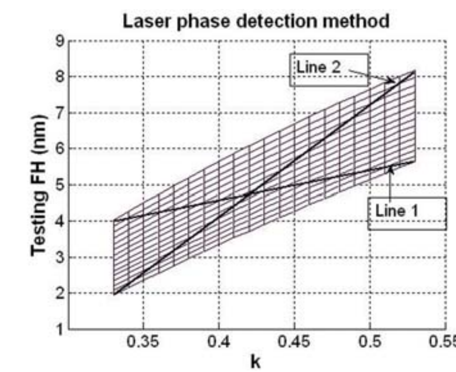

Figure 4 FH error by phase detection method.

GF-11

A Method for Identification of Pitch and Roll Stiffness of Head-Gimbal Assembly at Flying State.

Q. Zeng, Y. Fu, C. Yang, B. Aujla, E. Cha
SAE Magnetics, Milpitas, CA

Introduction: In a hard disk drive, the slider flies on the rotating disk with about a 10 nm gap between the slider and the disk by balancing between the air pressure on the bearing surface and gramload (GL) and static torques (PST, torque in pitch direction, and RST, torque in the roll direction) from the suspension. The torques come from the pitch/roll static attitudes, PSA/RSA, and the X/Y offsets between the slider and the dimple. PST from PSA can be calculated as a product of PSA and the pitch stiffness, Kp, of the gimbal structure. Similarly, RST is the product of RSA and Kr. A large Kp and/or Kr results in a large flying height (FH) distribution, which hurts drive yield and/or reliability, so Kp/Kr are key parameters. One question is how to measure them. In fact, there are many ways to measure the gimbal stiffness, and each of them has pros and cons. The main requirements of Kp/Kr measurement are: 1) Same boundary condition as inside drives, such as mounting at the baseplate; 2) Under the gramload; 3) At the designed Z-height (ZH) to assure the gimbal legs have the correct profile; 4) Non-destructive; 5) Accurate, quick, easy and cheap. Few methods can meet all those requirements. Here, we propose a method to identify the Kp/Kr under the flying condition that meets almost all of those requirements. The basic procedure is that we use the slider flying attitudes measured by an optical FH tester to back calculate the Kp and Kr values with an air bearing simulation code. The key idea is using multiple states (such as two different ZH) to cancel effects of unknown parameters and model offset to obtain accurate results.

Measurement procedure: The procedure of Kp identification: 1) Measure the slider flying attitudes (pitch angle) at different ZH. A ZH change will change GL and PSA, but keep other parameters unchanged. 2) Measure or calculate the suspension dGL (gramload change due to ZH change) and dPSA (PSA change due to ZH change); 3) Using an air bearing code to find PST value to match the measured pitch angle for the different ZH; 4) Then we can calculate the pitch stiffness:

$Kp_{ij}=(PST_i-PST_j)/[(ZH_i-ZH_j)*dPSA]$, (i is ZH index)

n ZHs give n*(n-1)/2 of Kp values. Then, we can average these values to obtain the final result, and also can check its non-linearity. Using the two ZH data can eliminate effects of many unknown factors. Kr identification is similar. Instead of changing ZH, we use additional fixtures with different RSA biases for the FH test.

Case studies and results: Kp identification of HGA1 is shown in Fig. 1. First, dGL and dPSA were measured, and shown in the figure. Assuming gramload and PSA meet the designed values, 2.5 gram and 1.50 deg respectively; we can calculate the GL and PSA values at each ZH with dGL and dPSA. Then, FH at five ZH of ten samples were measured, and the averaged measured pitch angles were shown in column 4 of the figure. Third, back calculations of PST to match measured pitch angles were done at each ZH with the correspondent GL. The calculated PST was shown in column 5. Finally, we can calculate the Kp with each combination of two different ZHs. Averaging all Kp values gives the final result, which is about 0.73 uN*m/deg. Averaging three Kp values with negative ZH change gives the 0.85 Kp, and the 0.61 Kp by averaging three Kp values with positive ZH changes. These two Kp values are quite different. This could be due to a non-linearity. At each ZH, a Kp value can be calculated by PSTi/PSAi. They are shown in Column 6, and it looks "unreasonable". However, if we assume mean PSA is 1.85 degree instead of 1.50 degree, values in Column 6 are much "reasonable", as shown in Fig. 2. The true PSA is unknown. Fortunately, both PSA values give the same Kp value (0.73) with the proposed method, so the method is robust.

Figure 3 shows the comparison between the measurement and FE model. The small difference between them was expected, and it could be due to GL effects. Figure 4 shows differences between measurement and model, and between different measurement methods. The differences are quite large, and they are also HGA design dependent. Looks like it is difficult to model and measure the Kp value correctly, so we should pay more attention to it. The proposed methods have been applied in many cases. It was found that quite consistent results can be obtained with the method, and it is good for flying height targeting.

HGA1	dGL (gram/um)	dPSA (deg/um)	FH Test data	Air Bearing Simulation	HGA Kp					
	0.00236	0.00882			"Single" ZH	Relative to one ZH				
Z-height change (um)	GL (gram)	PSA (degree)	Measured pitch angle (urad)	PST to match measured pitch (uNm)	PSTi/PSAi	Relative to ZH1	Relative to ZH2	Relative to ZH3	Relative to ZH4	Average
-101.6	2.86	0.60	95.54	0.726	1.201					0.85
-50.8	2.62	1.05	103.85	1.144	1.087	0.934				
0	**2.50**	**1.50**	112.15	1.484	0.989	0.847	0.759			**0.73**
50.8	2.62	1.95	120.77	1.769	0.908	0.776	0.697	0.635		
101.6	2.74	2.40	130.40	2.036	0.849	0.731	0.663	0.615	0.594	0.61

Figure 1 Kp identification of HGA 1 with the mean PSA

-101.6	2.86	0.95	95.54	0.726	0.760					0.85
-50.8	2.62	1.40	103.85	1.144	0.816	0.934				
0	**2.50**	**1.85**	112.15	1.484	0.802	0.847	0.759			**0.73**
50.8	2.62	2.30	120.77	1.769	0.770	0.776	0.697	0.635		
101.6	2.74	2.75	130.40	2.036	0.741	0.731	0.663	0.615	0.594	0.61

Figure 2 Kp identification of HGA 1 with the "guessed" PSA

HGA design	Measured		FE model		Difference	
	Kp	Kr	Kp	Kr	Kp	Kr
1	0.73	0.91	0.61	0.75	0.12	0.16
2	0.94	0.77	0.77	0.60	0.17	0.17

Figure 3 Comparison: Measurement with proposed method (ZH-FH) vs. FE model

HGA design	Model		Measurement			
	Vendor	SAE	Vendor	SAE dynamic 1	SAE dynamic 2	ZH-FH
3	0.71	0.64	0.46	0.67	0.52	0.59
4	0.77	0.87	0.74	0.71	0.75	1.03

Figure 4 Modeling and Measurement of Kp

GG-01

2D finite element simulations for bulk steel hysteresis curve derivations.

P. Meilland[1], S. He[2], S. Depeyre[2], M. Bernadou[2], J. Cagnol[2]
1. ArcelorMittal Maizières Research, Maizières-lès-Metz, France; 2. Pôle Universitaire Léonard de Vinci, Paris-La Défense, France

Context
Understanding the relation between microstructure and magnetism is a key element to steel manufacturers such as Arcelor Mittal, as they open the way to exhaustive characterization of the properties consistency. Despite numerous preceding efforts [1-7], only parametric models have operated for bulk magnetic behavior. Finite element simulations are on their side limited to typically the size of recording heads [8-11].
Simulations
With a specific self adapting mesh refinement strategy, 2D finite element simulations were run on 72 * 45 µm structures. In figure 1, the frame around the sample simulates the magnetic yoke used in experimental determination of hysteresis loops.
A simulation step consists in starting from an initial condition with an applied external field Hext, and finding the magnetic microstructure which minimizes an energy function adapted from iron's constants. With initial saturation-like conditions, iterating the steps by gradually decreasing Hext allows deriving the hysteresis cycle :this requires to plot the avrage magnetisation M vs Hext.
Such simulations were applied to 3 cases to derive hysteresis cycles displayed in fig. 2 : a single crystal, with easy magnetization parallel to the edges of the material ; an 80 grain polycrystal, with and without inclusions. In each case, the simulations outlined 2 major phases as the applied external field Hext decreases:
First the material, which is initially close to saturation, goes through the creation of large domains with continuous 180° walls across the whole sample's length.
Second, the 180° walls move, thus changing the volume of the large domains.
Discussion and conclusion
As its initial conditions correspond to a deep magnetic energy well, the large domain creation phase for the single crystal requires a higher decrease of Hext than the 80 grain polycrystal. However, when the large transgranular 180° domains walls are created, both structures feature similar magnetization rates, i.e. the slopes of the curves are equivalent.
For the microstructure with non magnetic inclusions, a higher decrease of the external field seems required for the creation of the transgranular 180° walls. However, when these are created, the magnetization rate is similar to the case without inclusions. This could suggest the simulation conditions don't report pinning of the domain walls by the inclusions. This may be a limitation of the 2D approach, which does not reflect the true nature of domain walls. To overcome this issue, 3D simulations at similar scale are required.
Acknowledgments
This work received financial support from the European Commission under contract RFSR-CT-2004-024 . The authors also thank Prs Fiorillo, Bertotti and their team from INRIM for their help.

1. Kersten M., Grundlagen Theorie der Ferromagnetischer Hysterese und der Koerzivkraft (Hirzel, 1943).

2. Becker R., Döring W., Ferromagnetismus (Springer-Verlag, Berlin, 1939).

3. Néel L., Bases d'une nouvelle théorie générale du champ coercitif, Ann. Univ. Grenoble, Sect. Sc. Math. et Phys., 1949, Vol. 22, pp 299-343.

4. Preisach F., Z. Phys., Vol. 94, P. 277, 1935.

5. Mayergoyz, I.D., Mathematical models of hysteresis loops, IEEE Trans. Mag., vol. 22 (5), pp 603-608, 1986.

6. Bertotti G., Generalized Preisach model for the description of hysteresis and eddy-current effects in metallic ferromagnetic materials, J. Appl. Phys. 69 (8), pp 4608-4610, 1991.

7. Jiles D.C., Atherton D.L., Theory of ferromagnetic hysteresis, J. Magnetism and Magnetic Materials, 61 (1986) pp 48-60.

8. Rave W., Hubert A., Magnetic ground state of a thin-film element, IEEE Trans. Mag., vol. 36 (6), pp. 3886 –3899, 2000.

9. Rave W., Ramstöck K., Micromagnetic calculation of the grain size dependence of remanence and coercivity in nanocrystalline permanent magnets, J. Magnetism and Magnetic Materials, 171 (1997) pp 69-82.

10. Fidler J., Schrefl T., Micromagnetic modelling – the current state of the art, Journ. Phys.D, Appl. Phys. 33, (15), R135-156, 2000.

11. Meilland P., Bernadou M., Depeyre S., He S., Prediction of magnetic microstructure in iron with new finite-element model, ReV. Progr. Quant. Nondest. Evaluation, Vol 21, p. 1607-1612, 2001.

12. Carey R. and Isaac E. D., "Magnetic domains and techniques for their observation", Academic Press, Londres (1966).

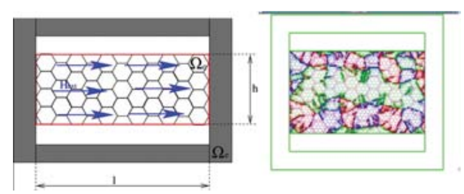

Figure 1: (left) Model microstructure; (right) Example of domain organisation derived from energy minimization, displaying large transgranular 180° domain walls [12].

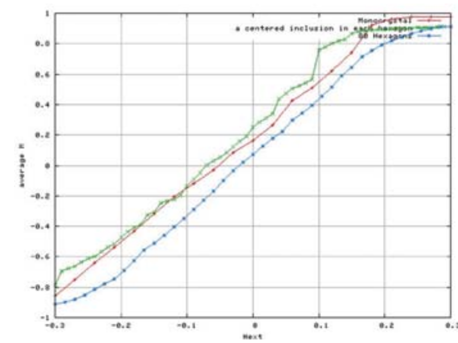

Figure 2: Hysteresis curves for the 3 simulation cases. Hext and M are in arbitrary units. (red): single crystal; (blue): polycrystal; (green): polycrystal with 1 inclusion per grain.

Rotational saturation properties of isotropic vector hysteresis models using vectorized stop and play hysterons.

T. Matsuo
Electrical Engineering, Kyoto University, Kyoto, Japan

1. Introduction

Stop and play models are efficient and precise hysteresis models. There are two types of their vector versions: one is represented by the superposition of scalar models along the azimuthal direction [1], [2] whereas the other is given by the geometrical vectorization of stop and play hysterons [2]-[5]. The latter is more efficient than the former that requires integration along the azimuthal direction. This article discusses rotational hysteretic properties of latter vector models under saturated condition. A modification to improve their rotational properties is proposed.

2. Vector stop model

A vectorized stop hysteron $\mathbf{s}_\eta$ is given as

$\mathbf{s}_\eta(\mathbf{B}) = \eta(\mathbf{B}-\mathbf{B}^0+\mathbf{s}_\eta^{\,0}) / \max(\eta,|\mathbf{B}-\mathbf{B}^0+\mathbf{s}_\eta^{\,0}|)$ (1)

where η is a hysteron radius and $\mathbf{B}^0$ and $\mathbf{s}_\eta^{\,0}$ are the vectors $\mathbf{B}$ and $\mathbf{s}_\eta$ at the previous time-point. For a rotational input of $\mathbf{B}$, $\mathbf{s}_\eta$ becomes perpendicular to $\mathbf{p}_\eta = \mathbf{B} - \mathbf{s}_\eta$ at steady state as is shown in Fig. 1(a) when $|\mathbf{B}| > \eta$.

Vector hysteresis model using (1) is given as

$\mathbf{H} = \int_0^{B_S} \mathbf{g}(\eta, \mathbf{s}_\eta(\mathbf{B}))\, d\eta$ (2)

where $\mathbf{g}(\eta, \mathbf{s})$ is a shape function vector that is parallel to $\mathbf{s}$, B_S is the saturation magnetic flux density. This vector model exhibits hysteretic property even when $|\mathbf{B}| > B_S$. To suppress the hysteretic property for $|\mathbf{B}| > B_S$, $\mathbf{s}_\eta$ is redefined as

$\mathbf{s}_\eta(\mathbf{B}) = \eta(\mathbf{B}-\mathbf{B}^{0*}+\mathbf{s}_\eta^{\,0}) / \max(\eta,|\mathbf{B}-\mathbf{B}^{0*}+\mathbf{s}_\eta^{\,0}|)$ (3)

$\mathbf{B}^{0*} = B_S\mathbf{B}^0 / \max(B_S,|\mathbf{B}^0|)$. (4)

This is a natural extension of the scalar version discussed in [6]. For a rotational input of $\mathbf{B}$, $\mathbf{s}_\eta$ given by (3) and (4) becomes parallel to $\mathbf{B}$ at steady state as is shown in Fig. 1(c) when $|\mathbf{B}| > B_S$.

Another way to prohibit the hysteretic property after the saturation is given by

$\mathbf{s}_\eta(\mathbf{B}) = \eta(\mathbf{B}-\mathbf{p}_\eta^{\,0*}) / \max(\eta,|\mathbf{B}-\mathbf{p}_\eta^{\,0*}|)$ (5)

$\mathbf{p}_\eta^{\,0*} = (B_S-\eta)\, \mathbf{p}_\eta^{\,0} / \max(B_S-\eta,|\mathbf{p}_\eta^{\,0}|)$, $\mathbf{p}_\eta^{\,0} = \mathbf{B}^0-\mathbf{s}_\eta^{\,0}$. (6)

The stop hysteron (5) is equivalent to (3) for the alternating input. The response of (5) differs from those of (1) and (3) for a rotational input of $\mathbf{B}$ when $B_T < |\mathbf{B}| < B_S$, where $B_T = \{(B_S-\eta)^2+\eta^2\}^{1/2}$. $|\mathbf{B}-\mathbf{s}_\eta|$ becomes $B_S-\eta$ at steady state as is shown in Fig. 1(b) when $B_T < |\mathbf{B}| < B_S$.

Vector relations for rotational inputs of $\mathbf{B}$ are summarized in Table 1, where three types of stop hysterons are compared; [i] original type using (1), [ii] the modified type using (3) and (4), and [iii] the modified type using (5) and (6). The angle between $\mathbf{B}$ and $\mathbf{s}_\eta$ discontinuously changes from $\cos^{-1}(\eta/|\mathbf{B}|)$ (Fig. 1(a)) to 0 (Fig. 1(c)) at $|\mathbf{B}| = B_S$ when the stop hysteron [ii] is used. The stop hysteron [iii] achieves a continuous angle change, which naturally corresponds to the fact that $\mathbf{B}$ becomes parallel to $\mathbf{H}$ for a large rotational magnetic field.

A rotational property of non-oriented silicon steel sheet (JIS: 50A1300) is represented by three vector stop models using stop hysterons [i], [ii], and [iii]. Because of the lack of measured data for large B, B_S is artificially set to 1.9 T for the vector stop models. Fig. 2 (a) shows the simulated and measured rotational hysteresis losses. The model [i] gives monotone increasing in the rotational loss. The model [ii] results in a sharp decrease in the rotational loss at B_S. The model [iii] achieves an acceptably natural loss property. The discrepancy from the measured loss can be reduced by using a weighting function proposed in [2]. The rotational loss given by both models [ii] and [iii] becomes 0 when $|\mathbf{B}| > B_S$ because $\mathbf{s}_\eta$ becomes parallel to $\mathbf{B}$. B_S used in the simulation is, however, too small for the rotational loss to become 0.

3. Vector play model

A vectorized play hysteron $\mathbf{p}_\eta$ is given as

$\mathbf{p}_\eta(\mathbf{B}) = \mathbf{B}-\mathbf{s}_\eta(\mathbf{B}) = \mathbf{B} - \eta(\mathbf{B}-\mathbf{p}_\eta^{\,0}) / \max(\eta,|\mathbf{B}-\mathbf{p}_\eta^{\,0}|)$ (7)

where $\mathbf{p}_\eta^{\,0}$ is the vector $\mathbf{p}_\eta$ at the previous time-point. Vector hysteresis model using (7) is given in a similar way to (2). Similarly to the stop model, $\mathbf{p}_\eta^{\,0}$ can be replaced by $\mathbf{p}_\eta^{\,0*}$ given as (6). Fig. 2(b) shows the rotational hysteresis losses simulated by two vector play models; [i] original model using (7) and [ii] the modified model using $\mathbf{p}_\eta^{\,0*}$ instead of $\mathbf{p}_\eta^{\,0}$. The model [i] yields a constant rotational loss for $|\mathbf{B}| > B_S$ (=1.9T). The model [ii] gives an acceptably natural loss property. The discrepancy from the measured loss can be reduced by using a weighting function proposed in [2].

[1] T. Matsuo, M. Shimasaki, IEEE Trans. Magn., vol. 43, pp. 1389-1392, 2007.

[2] T. Matsuo, M. Shimasaki, IEEE Trans. Magn. (to be published).

[3] A. Bergqvist, Physica B, vol. 233, pp. 342-347, 1997.

[4] C. Serpico, M. d'Aquino, C. Visone, D. Davino, Physica B, vol. 343, pp. 117-120, 2004.

[5] J.V. Leite, N. Sadowski, P. Kuo-Peng, J.P.A. Bastos, IEEE Trans. Magn., vol. 41, pp. 1500-1503, 2005.

[6] T. Matsuo, Y. Terada, M. Shimasaki, IEEE Trans. Magn., vol. 40, pp. 1776-1783, 2004.

type	Eqs.	$\eta < \lvert\mathbf{B}\rvert < B_T$	$B_T < \lvert\mathbf{B}\rvert < B_S$	$B_S < \lvert\mathbf{B}\rvert$
[i]	(1)	Fig. 1(a)	Fig. 1(a)	Fig. 1(a)
[ii]	(3), (4)	Fig. 1(a)	Fig. 1(a)	Fig. 1(c)
[iii]	(5), (6)	Fig. 1(a)	Fig. 1(b)	Fig. 1(c)

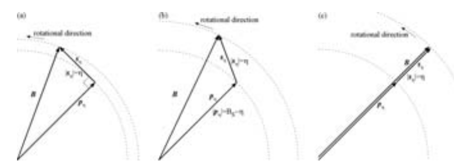

Fig. 1 Vector relations for rotational inputs of B.

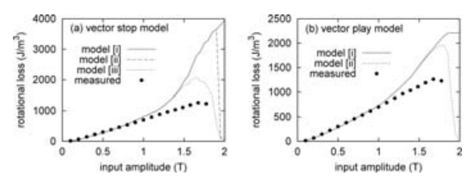

Fig. 2 Rotational hysteresis losses given by vector stop and play models.

GG-03

Viscous behavior of ferromagnets in the voltage and current driven regimes.

S. E. Zirka[1], Y. I. Moroz[1], P. Marketos[2], *A. J. Moses*[2], D. C. Jiles[2]
1. Department of Applied Physics and Technology, Dnepropetrovsk National University, Dnepropetrovsk, Ukraine; 2. School of Engineering, Cardiff University, Cardiff, United Kingdom

The time delay of the magnetization M (magnetic induction B) behind the applied field H is observed over the whole time range. It is a common concept that in a short time domain the time lag is caused by diffusion aftereffect whereas over longer times temperature dependent magnetic viscosity takes place [1]. Each of these phenomena is characterized by a set of time constants which may overlap. For this reason, different types of the relaxation mechanisms are often described by the same expressions and studied by similar experiments.
It should be noted that the viscous behavior of the magnetic medium manifests itself under any excitation conditions, including the current-driven regime used in the viscosity experiments [2] and voltage-driven magnetization typical for testing soft magnetic materials. For example, the losses and B-H loops given by steel manufacturers are measured in regimes when the derivative dB/dt is a controlled sinusoidal variable. Since in the conducting media this derivative determines the macroscopic eddy currents, the presence of the magnetic viscosity leads to changes in the hysteresis loop, which cannot be explained by these "classical" eddy currents. So the additional widening of the dynamic hysteresis loop and corresponding excess loss can be viewed as the consequence of the magnetic viscosity [1]. The purpose of the paper is to link the current- and voltage-driven regimes in electrically conducting media from the magnetic viscosity viewpoint. We also draw attention to the fact that different magnetic materials have similar viscous behavior which is observed over time domains ranging from fractions of microseconds to tens of seconds.
The viscous behavior of soft material in the microsecond range is illustrated by the magnetization processes in amorphous material under a constant magnetization voltage (dB/dt=const) [3]. Dynamic magnetization curves measured on metallic glass ribbon are shown by the solid lines in Fig. 1. They correspond to a B swing from negative remanence to positive saturation.
As can be seen in Fig. 1, the higher the dB/dt the greater is the shift of the dynamic curve to the right. It was found expedient to reproduce experimental curves in Fig. 1 by means of the Thin Sheet Model (TSM) [4].
It is remarkable that the excess field term in the TSM is valid for a wide majority of soft materials and is also observed at much lower dB/dt than those shown in Fig. 1. An example is grain-oriented (GO) electrical steel, for which the TSM works quite accurately even at lowest measurable frequencies.
The calculated loops in Fig. 2(a) have been obtained through the TSM whose parameters have been chosen so as to reach the best coincidence of the calculated and modeled loops under sinusoidal induction (f=100 Hz, Bm=1.7 T). The same excellent coincidence of the TSM-modeled and experimental dynamic loops has been obtained for thin non-oriented steels [4] and in our preliminary studies of the soft magnetic powder composites [5].
The transients calculated using the TSM for sinusoidal field with amplitude close to the coercive force of the GO steel above are shown by dashed lines in Fig. 2(b). Similar to that found from the measured loops, a decrease of the calculated total loss with increasing magnetizing frequency is observed in the current-driven regime with a fixed peak magnetic field (it can be seen in Fig. 2(b) that the area of the loop at 500 Hz is substantially less than that at 5 Hz). This is explained by the fact that at shorter period, the induction has no time to rise due to the eddy currents and magnetic viscosity. This leads to decreasing hysteresis loss which is the prevailing loss factor in the regime considered.
Among other problems, the TSM technique allows one to reproduce the constant field regime commonly used in studying magnetic viscosity. In the full paper we compare their representation by the TSM and by the well-known exponential and logarithmic laws [2]. In contrast to the vague frequency properties of the equations in [2], the viscous-type TSM is characterized by definite frequency dependence of the energy loss per cycle that makes it suitable for many technological applications.

ACKNOWLEDGMENT
The work was supported by EPSRC Grant EP/C518616/1.

[1] G. Bertotti, Hysteresis in magnetism: Academic Press, San Diego, 1998.

[2] R. Street and J.C. Woolley, "A study of magnetic viscosity," Proc. Phys. Soc., London, Sect. vol. A 62, pp. 562-572, 1949.

[3] C.H. Smith, D. Nathasingh, and H.H. Liebermann, "Thickness dependence of magnetic losses in amorphous FeBSiC ribbon under step dB/dt magnetization," IEEE Trans. Magn., vol. 20, no. 5, pp. 1320-1322, 1984.

[4] S.E. Zirka, Y.I. Moroz, P. Marketos, A.J. Moses, and D.C. Jiles, "Measurement and modeling of B-H loops and losses of high silicon non-oriented steels," IEEE Trans. Magn., vol. 42, no. 10, pp. 3177-3179, 2006.

[5] P. Marketos, J. Hall and S.E. Zirka, "Power loss measurement and prediction of soft magnetic powder composites magnetized under non-sinusoidal excitation," Submitted to Intermag-2008

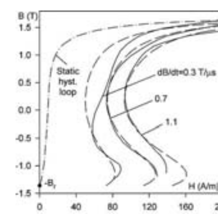

Fig. 1. Experimental (solid lines) and modeled (dashed lines) dynamic curves of an amorphous material at constant dB/dt

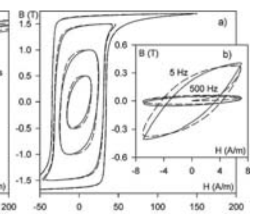

Fig. 2. Measured (solid lines) and calculated (dashed lines) loops of GO steel: a) voltage-driven regime; b) current-driven regime

GG-04

Size effects influence on hysteresis and relaxation for a Random Anizotropy Ising System.

C. Enachescu, A. Stancu
Department of Physics, Alexandru Ioan Cuza University, Iasi, Romania

The problem of the correlation between the particle size and the kinetic behavior in magnetic media is of increasing importance due to the technological use of nanoparticulate media in various applications [1]. Ising type models proved to be an efficient tool to describe the effect of surface magnetic moments and the rate dependent properties of these systems. They have been used previously mainly to characterize thermal effects [2] and recently to calculate First-order reversal curves (FORC) distributions for nanoparticulate media [3]. In this paper we propose to analyze the size influence on the hysteresis properties, relaxation curves and other kinetic effects using a Random Anisotropy Ising Model (RAIM).

We consider that in the RAIM every molecule has a spin s=±1 and an anisotropy field H_k, Gaussian distributed. The energy barriers have the expressions

$E_b=\mu H_k/2(1\pm H/H_k)^2$ for s=±1 and H>/<±H_k.Otherwise they are 0.

We refer here to spherical shape systems, with diameter varying from 7 molecules(total 123 molecules, 73.1% on surface) to 31 molecules (total 14127 molecules, 15.9% on surface). The anisotropy field is oriented on the z axis direction. To compute local interaction field for a molecule, we consider its interactions with all the other molecules in the system. The interactions are positive and decrease proportionally with the cube of the distance between molecules. At every step, we compute the energy barriers and then decide,using Monte Carlo Metropolis method, if the moment will commute.

Our investigation has been carried on two directions: first we computed hysteresis cycles for different systems and field scanning rates and secondly we calculated relaxation curves at different fields and for different system sizes.

The results presented in figs. 1-2 show that: (i) clusters of positive and negative magnetized molecules are formed; they are dependent on interaction strength (ii) the coercivity diminishes for a decreasing size of the system and for longer waiting times. A stabilization is observed for a sphere diameter of 31 molecules, that correspond to a percentage of 15,9% molecules on surface, close to the observed ones [1].

In fig. 3 up we present relaxation curves for different particle sizes, in constant external field. We noticed that, for increasing sphere diameter, the relaxation time is increasing. More, even if the hysteresis cycles for spheres with diameter of 27 and 31 molecules are quite similar, the relaxation time for the second system is about 3 times higher.In fig. 3 down, we represent on a logarithmic scale the relaxation time (the moment when the system passes through 0 is considered) in function of the system size for different external fields. One may notice that, for small sphere size, there is almost an exponential dependence between diameter and relaxation times, but as the system size grows the relaxation time increases dramatically.

In conclusion we notice that the RAIM model proved to be tractable to describe the behavior of isolated single-particle and can provide useful information. In the full paper we also discuss the correlations evolution during magnetization process and the influence of the system compactness on hysteresis and relaxation.

Acknowledgement:Work was supported by the Romanian CEEX under the contract ESMMN.

[1] D. Garanin, H. Kachkachi, Phys. Rev. Lett., vol. 90, art. 065504, 2003

[2] D. P. Landau, Phys. Rev. B, vol. 13, p. 2997, 1976

[3] C. Enachescu, A. Stancu, IEEE Trans. Magn,, vol. 42, p. 3156, 2006

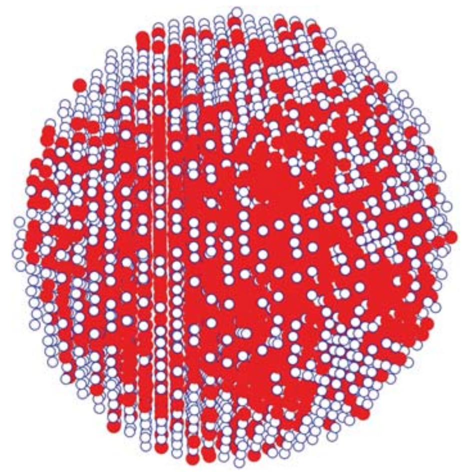

A spherical particle during magnetization processes. Clusters of molecules in the same state can be noticed.

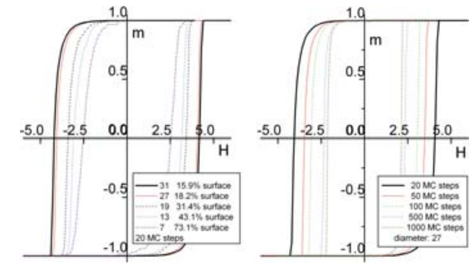

Dependence of hysteresis cycles of a RAIM spherical monoparticle on its diameter(left) and on the number of Monte Carlo steps (right)

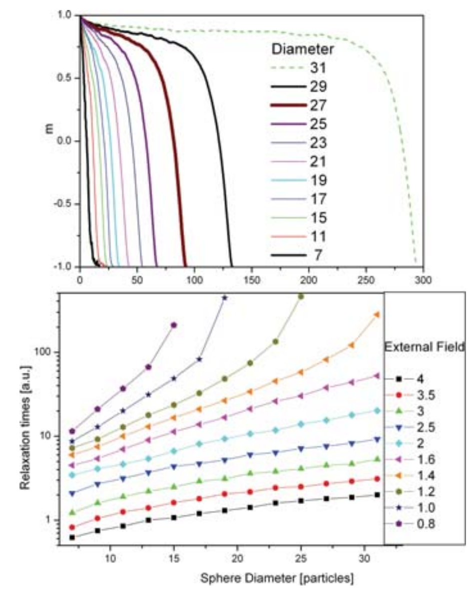

Relaxation curves for RAIM spherical monoparticles(up). Relaxation times as a function of the sphere diameter and external field (down).

Correction of permeability of a soft ferromagnet measured by using vibrating sample magnetometer.

M. Chan, C. Ong, Y. Wong
Department of Applied Physics and Materials Research Center, The Hong Kong Polytechinc University, Hong Kong, China

Vibrating sample magnetometer (VSM) is a high-sensitivity system for probing the magnetic properties of a small specimen. The magnetic induction B_{int} and magnetic field H_{int} inside a specimen in an applied magnetic field H_{app} are related with:

$B_{int} = \mu_0 \mu_r H_{int} = \mu_0 (H_{int} + M)$ (1)

where μ_r, μ_0 and M are the relative permeability, permeability of vacuum and magnetization. Determination of μ_r is particularly important for practical use. B_{int} and H_{app} are detected with a pick-up coil and a sensor outside the specimen, but H_{int} is not directly measurable. For a magnetic sample, a demagnetization field $H_d = DM$ exists inside the specimen with D being the demagnetization factor. H_d weakens the magnetic field inside the specimen to $H_{app} – DM$. An apparent relationship defining the measured permeability μ_m is expressed as:

$B_{int} = \mu_0 \mu_m H_{app}$ (2)

Combining (1) and (2), one obtains [1]:

$\mu_m / \mu_r = 1/(1+D\mu_r)$ (3)

When $\mu_r >> 1$ and D has a moderate value, the measured μ_m value is much smaller than the true value μ_r. One method to make correction is to calculate D values for various sample shapes, and the apply Eq. (3) to calculate μ_r from the measured μ_m [2]. However, this method may generate great error. Hence, we propose the following method, with the aid of finite element analysis (FEA), to give an estimate of μ_r based on VSM measurements. The method is applied to permalloy to check the validity.

1. A commercial FEA package is used to set up a model (Fig. 1) containing a block-shaped specimen in a magnetic field. The width x and thickness y of the block are equal and perpendicular to the applied field. Its length z is parallel to the field.
2. μ_r is set at $\mu_{r,1}$=10, $\mu_{r,2}$ = 500 and $\mu_{r,3}$ = 3000 respectively. For each $\mu_{r,i}$ (i = 1, 2, 3), the ratio z/x is varied over a range from 1 to 1000 (labeled by an index j). For each combination, a magnetic field H_{app} is applied (outside the specimen) to build up a magnetic induction field inside the specimen. The average magnitude of the induction field $< B_{int} >_{i,j}$ is derived. A representative permeability, denoted as $\mu_{m\ i,j}^*$, is defined with the formula:
$< B_{int} >_{i,j} = \mu_0 \mu_{m\ i,j}^* H_{app}$ (4)
3. For each of the three $\mu_{r,i}$ (i = 1, 2, 3), the calculated values $\mu_{m\ i,j}^*$ are plotted in Fig. 2 against z/x, and are fitted to a function $\mu_{m\ i,j}^* = A_{2,i} + (A_{1,i} - A_{2,i}) / (1 + ((z/x)/r_0)^{P_i})$. The fitting parameters for each $\mu_{r,i}$ (i = 1, 2, 3) are shown in Table 1.
4. VSM measurements are performed to get B_{int} - H_{app} loops for several block-shaped samples specified with various z/x ratios between 1 and 1000 (labeled by k). For each sample, the slope of the curve at $B_{int} \approx 0$ is derived and plotted in Fig. 2, which gives an experimental permeability $\mu_{exp\ k}^*$. The best fit to the data of $\mu_{exp\ k}^*$ is obtained with a set of fitting parameters A_1^*, A_2^*, r_o^* and P^*. Each parameter is combined with those of the same kind listed in Table 1 to create an estimate of μ_r by applying interpolation technique, which is denoted as $\mu_{r\ q}^*$ (q = 1,…,4). A final estimated value of μ_r is set as $<\mu_r^*> = \Sigma^4_{q-1}\mu_{r\ q}^* / 4$.

The applicability of the method to permalloy is checked and discussed. The method is further extended to cover the other sample shapes, such as hollow cylinder.

[1] J.R. Reitz and F.J. Milford, in "Foundation of Electromagnetic Theory", Addison-Wesley Publishing Company, London, 1967, p.213.

[2] A. Aharoni, "Demagnetization factors for rectangular ferromagnetic prisms", J. Appl. Phys. 83, 3432 (1998).

$\mu_{r,i}$	$\mu_{r,1}$ = 10	$\mu_{r,2}$ = 500	$\mu_{r,3}$ = 3000
$A_{1,i}$	1.87 ± 0.09	2.34 ± 0.32	2.41 ± 0.27
$A_{2,i}$	9.57 ± 0.24	510 ± 18.6	3226 ± 137
$r_{o,i}$	8.34 ± 0.41	45.2 ± 3.65	149 ± 9.8
P_i	3.56 ± 0.39	1.51 ± 0.06	1.53 ± 0.03

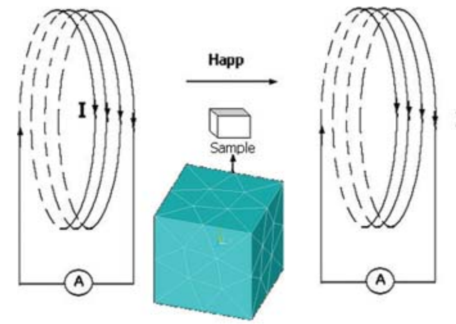

Fig. 1 Schematic diagram showing a model for FEA analysis.

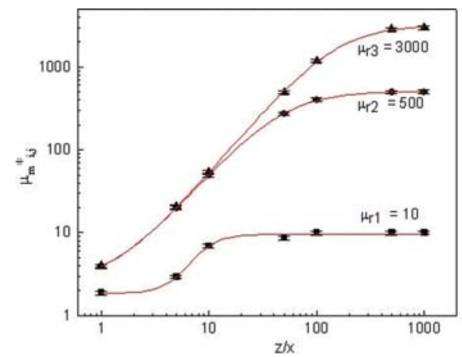

Fig. 2 Plots of $\mu_{m\ i,j}^*$ (i = 1, 2, 3) against z/x ratio for various μ_r values.

GG-06

The temperature dependence of magnetostatic interactions in nanowires systems.

A. Diaconu, I. Dumitru, A. Stancu
Department of Solid State and Theoretical Physics, "Alexandru Ioan Cuza" University, Iasi, Romania

Magnetic nanowires have potential applications in many areas of advanced nanotechnology, including patterned magnetic media, nanosensors magnetic devices and materials for microwave applications [1]. Using the electrodeposition technique the Fe, Co and Ni wires with diameters ranging from 4 to 200 nm, and lengths of up to few microns can be produced easily.
Starting from the magnetic properties of the individual wires, the paper evaluates the temperature effects on the magnetostatic interaction field between wires and on the magnetic properties of wires ensemble. The systems used in our simulations are Co nanowires arrays with different geometries: square and hexagonal lattice.
The hysteresis loop of the nanowires system was calculated using an Ising type model, in which the wires magnetization vector has two preferred directions along nanowires axis. The nanowires, considered as single domain, exhibit a magnetic anisotropy with an easy magnetization along the axis of the wire. The values of the uniaxial anisotropy field are normally distributed. Each wire is divided into a number of magnetic dipoles witch have the magnetizations parallel with the wires magnetization direction. The magnetostatic interactions are calculated along the symmetry axis of each wire as a sum of the fields creates by all the magnetic dipoles. The value interaction field depends on the wire magnetizations and, consequently, on the magnetization of the system. The demagnetizing field along wires axis, for different wires length and diameters, was evaluated using a procedure based on the equivalent magnetic charges on the wires ends [2]. A standard Metropolis-Monte-Carlo numerical procedure was used to evaluate which wire is reversing the magnetic moment.
Each nanowire the 2D array has a normalized magnetic moment which can takes the values as function of moment orientation: up (+1) or down (-1). Considering the nanowire arrays as an assemble of uniaxial single domain particles and the angle between this direction and applied field is zero, the height of the energy barriers corresponding to the magnetic moment vector rotation from in to out of the static field direction is given by the classical Stoner-Wohlfarth expression: $\Delta E_{\pm}=KV/k_bT[1\pm H/Hk]^2$ where Hk is the uniaxial anisotropy field, K is the anisotropy constant, V is the wire volume and H is the effective field acting on a wire, k_b is the Boltzmann constant and T is the system temperature. The magnetic dipole switches from up to down state with the probability given by $p=\exp[-\Delta E_{\pm}/k_bT]$, where $\Delta E_{\pm}$ are the heights of the energy barriers defined before. The net magnetization of the system is the sum of the magnetization of constituent wires.
In simulation we considered a sufficient number of wires for a given wire network in order as the magnetic interaction field to be independent of the number of wires.
It was drawn the hysteresis loops for a set of geometric parameters: diameter and length of wires and lattice constant for two temperatures 5K and 200K (Fig.1). As it is expected, the interactions have an essential role in defining the shape of the hysteresis loop of the nanowire system.
The magnetostatic interactions between wires as function of the array lattice constant were analyzed using the FORC (First Order Reversal Curve) diagram [3,4]. For each considered case the determined FORC diagrams (ex: Fig 2) are function of the geometric wires parameters like wires diameters and lengths was drawn. The distribution of the interaction field was also determined as function of temperature and geometric parameters.

Acknowledgement: The authors acknowledge the financial support offered by Romanian CERES Program under P-CD 5575 - SMMA.

[1] L. Clime, F. Beron, P. Ciureanu, M. Ciureanu, R.W. Cochrane, A. Yelon, J. Magn. Magn. Mat. 299 (2006) 487.

[2] I. Dumitru, L. Spinu, F. Li, J.B. Wiley, D. Cimpoesu, A. Stancu, IEEE Trans. Magn. 42, (2006) 3225.

[3] I. D. Mayergoyz, Mathematical models of hysteresis and their applications, Academic Press, 2003.

[4] C. R. Pike, A. P. Roberts and K. L. Verosub, J. Appl. Phys., 85 (1999) 6660.

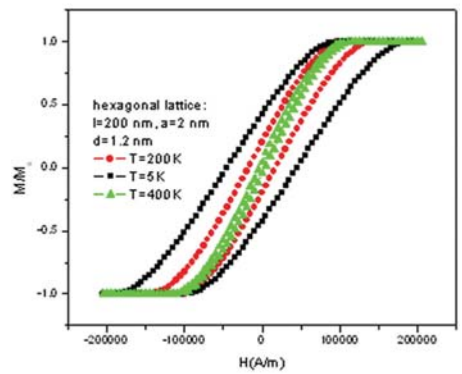

Fig. 1 The hysteresis loops for an array with hexagonal lattice and wires parameters: length l=200 nm, diameter d=1.2 nm, distance between wires a = 2 nm

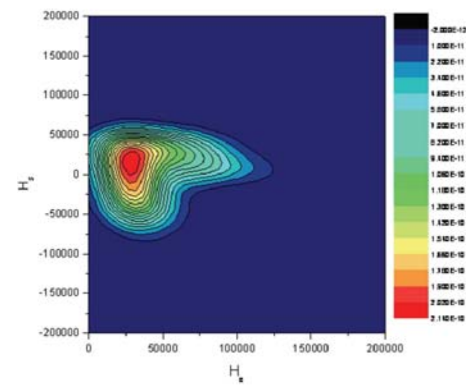

Fig. 2 The FORC diagram at 5K for an array with hexagonal lattice and wires parameters: length l=200 nm, diameter d=1.2 nm, distance between wires a = 2 nm

GG-07

A magnetostriction model with stress dependence for real-time control applications.

D. Davino[1], A. Giustiniani[2], C. Visone[1]
1. Engineering Department, University of Sannio, Benevento, Italy; 2. DIIIE, University of Salerno, Salerno, Italy

This paper proposes a magnetostriction model with a dependence on the applied stress, aimed to real-time control system applications.
Devices employing magnetostrictive materials suffer an hysteretic behavior, as all ferromagnetic materials based devices do [1]. As a consequence, one should expect a decrease of the control system performances when making use of them. With the aim to overcome such a drawback, several solutions have been proposed to compensate hysteresis in a feedback control system, [2],[3]. Unfortunately, the magnetostrictive behavior depends on the stress experienced by the active material [1]. In real *dynamic* conditions the device could experience time-varying forces that can significantly change the actuator behavior. Therefore, the models would require a generalization to take into account the effects of variable stress. In past years, some papers have been proposed to model magnetic and magnetostrictive materials under variable stress [4, 5], but they hardly arrived at an easy identification procedure and implementation of the algorithm.
In this paper we propose a phenomenological magnetostrictive model defined by the following:
$s(t) = G\{f[i(t), T(t)-T0]\}$,
where $s(t)$ is the displacement, $G\{.\}$ is a classical Preisach Model [1], $i(t)$ is the input current and $T(t)$ is the applied load. The function f defines an *effective current* for the operator $G\{.\}$ [6] while $T0$ represents a compressive prestress applied to the active material that can be used as *working point* for the effective current.
Concerning the application of the model, the operator $G\{.\}$ and its inverse $G-1\{.\}$ (which exists under some hypothesis [7]) can be easily identified by applying the constant prestress $T0$, because the condition $f[i(t), 0]=i(t)$ applies. Then, a standard procedure for the identification of the Preisach model can be used, as the classical one found in [5] or the neuro-fuzzy based one proposed by the authors in [3].
The effective current function is formally defined by the equation $f[i, T-T0] = G-1\{s\}$ but, since the inverse operator $G-1\{.\}$ depends on the current past history, a working hypothesis must be done: the reconstruction of the function is performed by taking the current values i at constant loads T over an assigned hysteresis branch, as the upper curve of the limit cycle.
This model has been applied to the magnetostrictive measurements of a real actuator loaded by a compression-tests machine. In fig.1 are shown some measured cycles with respect to the positive input current. The operator $G\{.\}$ has been identified at 200N load and then the *effective current f* has been reconstructed at several constant loads, as shown in fig.2.
Finally, fig.3 presents the time signals of the measured displacements at 80 and 140N compared to the direct model $s(t) = G\{f[i(t), T(t)-T0]\}$ and to a classical Preisach model without stress correction ($s(t) = G\{i(t)]\}$). The error reduction is quite evident for a 140N load and is is still acceptable when a 80N load is applied.

[1] G. Engdahl (ed.), *Handbook of Giant Magnetostrictive Materials*, Academic Press, 2000.

[2] S. Mittal, C.H. Menq, IEEE/ASME Trans on Mechat., 5(4) (2000) 394-409.

[3] C. Natale et al,Physica B 306(1-4) (2001) 161–165.

[4] A.A. Adly et al, J. Appl. Phys. 69 (8) (1991) 5777-5779.

[5] A. Bergqvist, G. Engdahl, IEEE Trans on Magn., 27(6) (1991) 4796–4798.

[6] I.D. Mayergoyz, *Mathematical Models of Hysteresis*, Springer, 1991.

[7] M. Brokate, IEEE Trans on Magn., 25(4) (1989) 2922–2924.

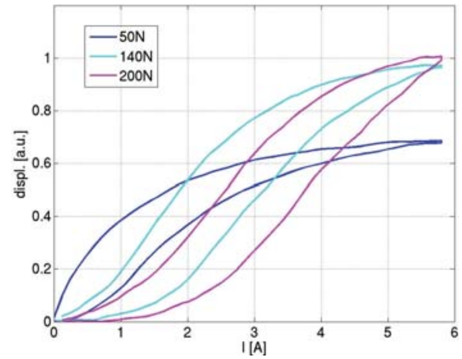

Measured magnetostrictive cycles at different compressive loads.

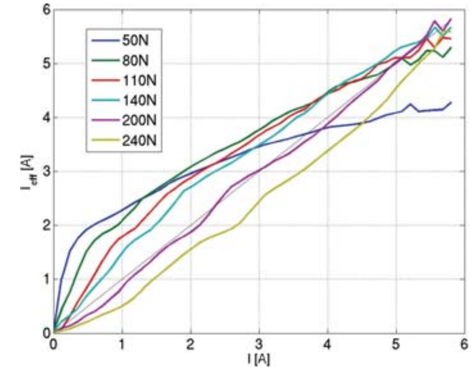

The constant load curves of the effective current function.

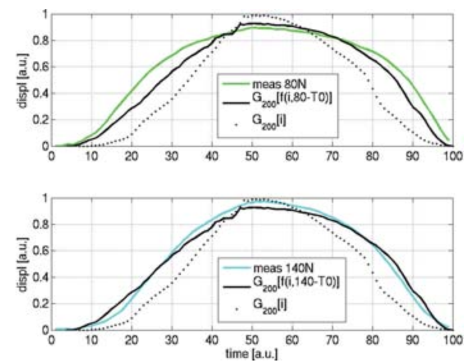

A comparison of the proposed model with measurements at different loads.

GG-08

An Improved Engineering Model of Vector Magnetic Properties of Grain-oriented Electrical Steels.

Y. Zhang[1], Y. Eum[2], *C. Koh*[2], D. Xie[1]
1. School of Electrical Engineering, Shenyang University of Technology, Shenyang, Liaoning 110023, China; 2. School of Electrical & Computer Engineering, Chungbuk National University, Cheongju,Chungbuk 361- 763, South Korea

Grain-oriented electrical steels are widely used as industrial materials in transformers. It is necessary to develop the effective expression of the vector magnetic properties in order to analyze field performance and loss characteristics of three phase transformers accurately. The objective of this paper is to give an improved expression of the vector magnetic hysteresis model based on Fourier series expansions of measured **B** and **H** waveforms in the viewpoint of engineering application. The accuracy of the improved model is checked by comparing with experimental data, and the effectiveness of the suggested modeling algorithm, when combined with finite element analysis, is verified with the single-phase transformer core model.

An expression of 2D vector magnetic property of grain-oriented silicon steels proposed in [1] can be defined as follows:

$H_k=\nu_{kr}B_k+\nu_{ki}\partial B_k/\partial\tau$ (k=x,y) (1)

where the magnetic reluctivity coefficients ν_{kr} and ν_{ki} can be expressed by means of Fourier series expansion of the measured magnetic field intensity waveforms.

In this paper, it is revealed that the hysteresis model considering only the first and third harmonics is not accurate enough to describe the vector magnetic property, especially when the material is highly saturated. On the other hand, with the increasing of the number of harmonic terms under consideration, the expressions of ν_{kr} and ν_{ki} in (1) become more complicated with the quartic function of $(B_k,\partial B_k/\partial\tau)$, which will result in the divergence of finite element analysis when combined with the vector magnetic property. The accuracy of the model and the computational cost when combined with finite element analysis, therefore, conflict with each other. In this paper, a new expression of ν_{kr} and ν_{ki} satisfying above two requirements is proposed as follows:

$\nu_{kr}=C^{kr}_0+C^{kr}_1\cos^2\tau+C^{kr}_2\cos^4\tau+C^{kr}_3\sin^2\tau+C^{kr}_4\sin^4\tau$ (2-a)

$\nu_{ki}=C^{ki}_0+C^{ki}_1\cos^2\tau+C^{ki}_2\cos^4\tau+C^{ki}_3\sin^2\tau+C^{ki}_4\sin^4\tau$ (k=x,y) (2-b)

where τ is in a range from 0 to 2π, and the parameters *C* can be obtained from the measured H-waveforms under different B-waveform conditions.

The proposed expression of vector magnetic property is verified with experimental data. In this paper, the B-spline interpolation algorithm is utilized to smooth the measured data. Fig.1 shows B-splined surfaces of magnetic reluctivity ν_{xr} and ν_{yi}, under the sinusoidal magnetic flux density of B_{max}=0.9T, as a function of τ and the inclination angle θ of the applied magnetic flux density. Fig.2 shows the comparison of H-waveforms between the results computed from (1) and (2) and measured data. It is shown that the measurement data and computed results are in good agreement.

Finally, the suggested algorithm is applied to the finite element analysis for a single-phase transformer core model, of which the width and height are 400mm and 180mm, respectively, with a rectangular hole of 220mm×40mm. In this paper, the hybrid finite element and material modeling equations are derived in detail and the convergency of the nonlinear analysis is discussed. Fig.3 shows the flux distribution when the average magnetic flux density is B_{avg}=0.5T. The calculation results show that, compared with conventional magnetic property modeling algorithm, the suggested algorithm gives more effective and reliable field performance analysis of electromagnetic devices.

[1] M. Enokizono, H. Shimoji and T. Horibe, “Loss evaluation of induction motor by using magnetic hysteresis E&S model,” IEEE Trans. on Magn., vol. 38, no. 9, pp. 2379-2381, Sept. 2002.

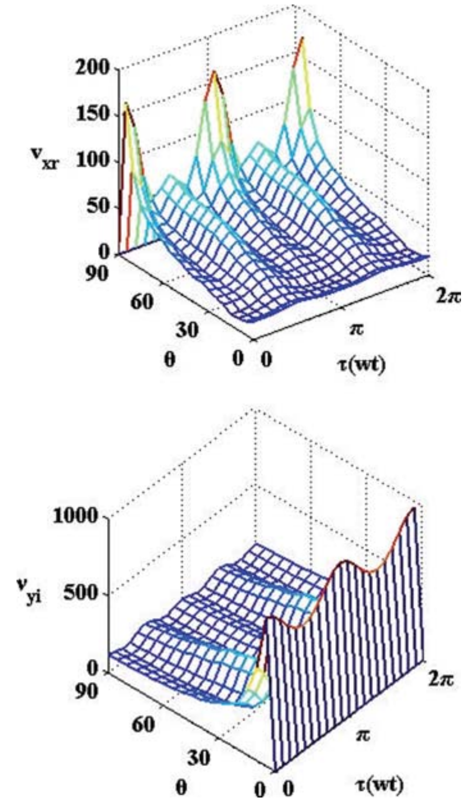

Fig. 1. B-splined ν_{xr} and ν_{yi} from measured data when B_{max}=0.9T.

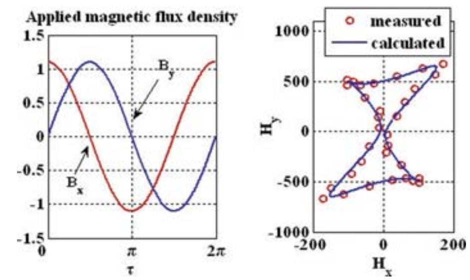

Fig. 2. Comparison of H-waveforms between computed and measured results.

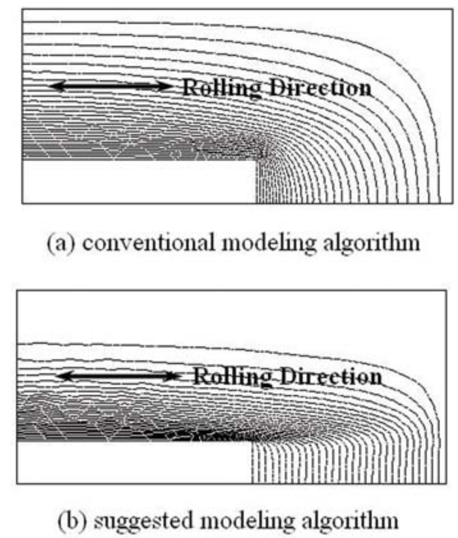

Fig. 3. Flux distribution of single-phase transformer core model when B_{avg}=0.5T.

GG-09

Magnetic behaviour of assemblies of nanoparticles with core/shell morphology:Interparticle interaction effects.

M. Vasilakaki[1], K. N. Trohidou[1], J. A. Blackman[2]
1. Institute of Materials Science,NCSR "Demokritos", Athens, Greece; 2. Departmen of Physics, Reading University, Reading, United Kingdom

We have studied the hysteresis behaviour of assemblies of composite magnetic nanoparticles with ferromagnetic (FM) core and antiferromagnetic (AFM) shell morphology, using the Monte Carlo simulation technique. The system has been modelled by considering random assemblies and ordered arrays of nanoparticles on a hexagonal lattice. We consider both dipolar and exchange interparticle interactions between the nanoparticles. The core/shell interface leads to an exchange bias effect and the high-density of the assembly produces strong interparticle interactions[1,2]. We have introduced a model that takes into account explicitly the dynamics of the FM/AFM interface region. In this model, each composite nanoparticle consists of four different regions: the FM core, the FM interface, the AFM interface and the shell.
In the present work we study the magnetic behavior of an assembly of composite nanoparticles that results from the interplay between the intrinsic properties (single particle anisotropy and the exchange coupling between the atomic spins of each nanoparticle) and the extrinsic properties (dipolar and the exchange interparticle interactions). Our results demonstrate the dependence of the exchange bias and the coercive field on the dipolar strength($g=\mu^2/d^3$).
In figure 1 we present results for the coercive (H_c) and exchange bias field (H_E) as a function of interparticle spacing (d_0) for the ordered arrays of nanoparticles with core radius R_C=5a and shell thickness t_{sh}=4a, both the core and the shell thicknesses are expressed in lattice spacings a. The results are presented for magnetically hard (α=6.5, upper part) and magnetically soft (α=1, lower part) materials, where the dimensionless parameter α is defined as the ratio of the magnetization density squared over the core anisotropy strength, $\alpha=\mu^2/K_c$. In both cases we observe a decrease of the coercive field with increasing the nanoparticle density, which we attribute to the broadening of the energy barrier distribution and the appearance of low-energy barriers in the system. The reduction of H_c is more pronounced in strongly dipolar materials and large nanoparticles. On the other hand the exchange bias shows a weak increase with increasing nanoparticle density. We attribute this behaviour to the distinct role of dipolar interparticle interactions during the magnetization reversal process in the left and right branch of the hysteresis loop, which are characterized by different energy barriers due to the unidirectional interface anisotropy. The same behaviour is also observed in randomly placed assemblies of nanoparticles as it is presented in figure 2, where we have plotted the H_c and H_E as a function of particle density for an assembly of randomly placed nanoparticles of core radius R_c=5a and shell thickness t_{sh}=4a. The decrease of H_E in this case is in agreement with the behavior observed on Co/Mn samples [3].

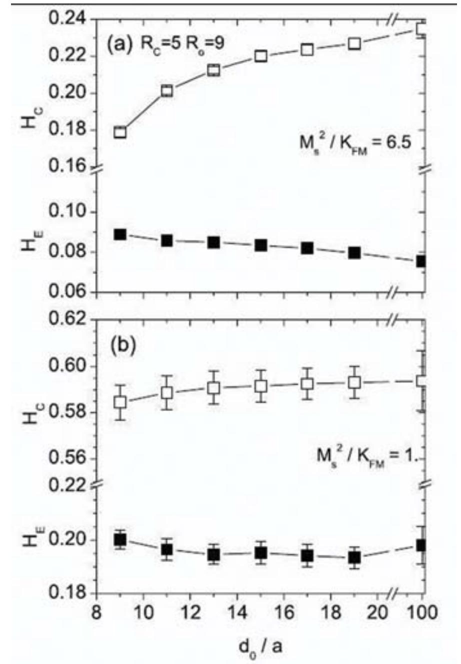

Fig 1 Coercive (H_c) and exchange bias field (H_E) versus interparticle spacing (d_0) for ordered arrays of nanoparticles with core radius R_c=5a and shell thickness t_{sh}=4a. The upper part of the figure gives the results for strongly dipolar materials (α=6.5) and the lower for weakly dipolar materials(α=1) at temperature T=0.1

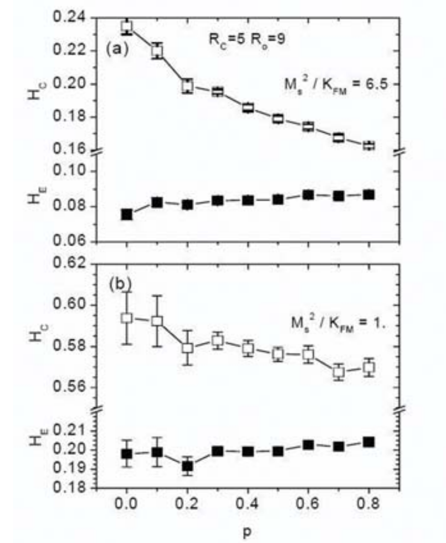

Fig 2 Variation of coercivity (H_c) and exchange bias field (H_E) with particle density for a thin film containing randomly placed nanoparticles. Film thickness is six monolayers (6 ML) and contains nanoparticles with core radius R_C=5a and external radius R_o=9a. (a) strongly dipolar (α =6.5) and (b) weakly dipolar (α=1.0) material. Low temperature is assumed (T=0.1)

[1]E. Eftaxias and K.N. Trohidou, Phys.Rev.B 71(2005)4406 [2]Kechrakos D., Trohidou K. N., Vasilakaki M., J.Magn.Magn.Mater. 316(2007)e291–e294

[3]Neus Domingo, Alberto M. Testa, Dino Fiorani, Chris Binns, Stephen Baker, Javier Tejada, J.Magn.Magn.Mater.316(2007)e155

Compensation of Hysteresis and Time- dependent Error for Magnetostrictive Actuators.

H. Choi, Y. Park
Mechatronics Engineering, Chungnam National University, Daejeon, South Korea

Smart actuators, such as piezoelectric and magnetostrictive actuators are widely accepted for fine positioning control. They, however, inherently possess hysteresis, which hinders the wide applications of them [1]. In addition, magnetostrictive actuator exhibits hysteretic nonlinearity and time-dependent error. This paper proposes two stage compensation scheme to control the magnetostrictive actuator precisely: First, hysteresis compensation, and second, time-dependent error compensation.

Fig. 1 (a) is hysteresis data according to time. Fig. 1 (b) is an enlarged view of a certain time range. It is clear that the shapes of wave are distorted.

The Preisach model is modified and used to compensate hysteresis [2].

Fig. 2 (a) is hysteresis-compensated data according to time. Fig. 2 (b) is an enlarged view of a certain time range. It is obvious that the shapes of wave are corrected. Nevertheless, the data in Fig. 2 (a) reveals some errors according to time. It is called time-dependent error and needs to be compensated.

Fig. 3 shows the time-dependent error data obtained from Fig. 2 (a). The error can be approximated by using the following equations.

$E = at+b$ (t≦150)

$E = c\times e^{(-t/d)}-k/t$ (t>150)

Using a regression, the coefficients in the equations can be obtained, i.e., a=-0.012, b=4.5, c=5, d=500, k=150. Fig 3 (b) is comparisons between error data & approximation data.

Fig. 4 shows simulation result with the compensation of hysteresis and time-dependent error. Maximum error without compensation of time-depent error equation is 4.5µm, but Maximum error with combined compensation is 0.4µm. It can be concluded that compensation of both hysteresis and time-dependent error is needed for precise control of magnetostrictive actuator.

[1] Y.W. Park, Y.T. Seoka, H.J. Park, J.Y. Chung "Hysteresis modeling based on saturation operator without constraints", Journal of Magnetism and Magnetic Materials 310 (2007) 2647–2649

[3] Kyung-Bin Im, "Hysteresis Compensation and Control of Magnetostrictive Actuator Using Modified Preisach Model", Master's thesis at Chungnam National University in Korea, 2007.

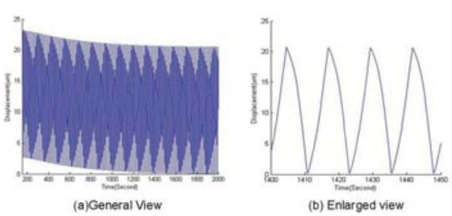

Fig. 1 Hysteresis data according to time

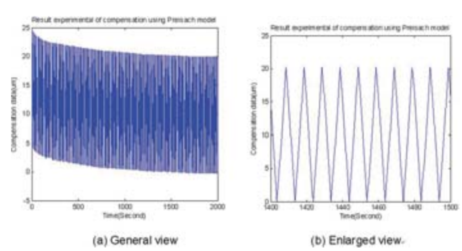

Fig. 2 Compensated Curve of Hysteresis

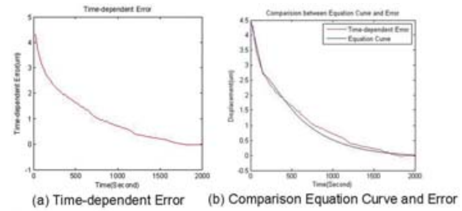

Fig. 3 (a) Time-dependent Error (b) Comparison Equation Curve and Error

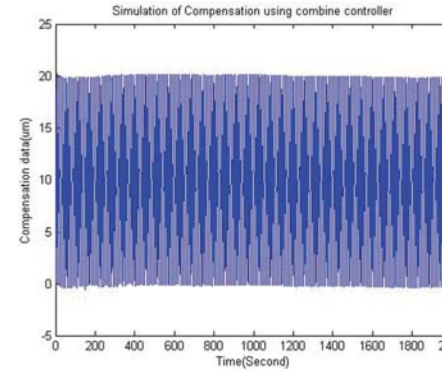

Fig. 4 Simulation of Compensation using combination controller

GG-11

Rotational hysteresis first-order reversal curves diagrams as test problem for vectorial hysteresis models.

L. Stoleriu[1], P. Postolache[1], P. Andrei[2], A. Stancu[1]
1. Department of Physics, Alexandru Ioan Cuza University, Iasi, Romania; 2. Department of Electrical and Computer Engineering, Florida State University and Florida A&M University, Tallahassee, FL

In recent years, one can observe a strong interest in the development of more efficient vector hysteresis models which can describe correctly the magnetization processes in ferromagnetic materials taking into account the vector nature of both applied field and magnetic moment. The intense studies concentrated on scalar hysteresis models have provided a number of models with reliable identification techniques which can explain a wide range of typical scalar measurements specific to most of the magnetometers commonly available in the laboratories. The scalar Preisach-type models complemented with the identification based on a set of First-order reversal curves (FORC) is a typical example of a scalar hysteresis model [1] which can provide accurate results in a large variety of cases.
However, the development of vector models was not as successful, due to the difficult implementation of the variants proposed by different authors (e.g. [2], [3]), and to the lack of clear and tractable identification techniques.
In a previous paper [4] we have presented a complete implementation of a vector Preisach-Mayergoyz model with an identification algorithm based on a set of scalar FORCs, measured systematically for different angles between the global easy axis of the magnetic system and the applied field direction. We also developed a new vectorial model with a remarkable numerical efficiency related to the fact that can be easily implemented on parallel computer environments [5]. Essentially, this model, referred to as the Preisach-LLG model, uses the concept of vectorial pseudoparticle for which the equilibrium state in a given applied field is calculated with the well known Landau-Lifshitz-Gilbert algorithm. A statistically stable vectorial distribution of interaction fields is taken into account which makes possible the de-coupling of the differential equations describing the magnetic behavior of each pseudo-particle.
In this paper we are evaluating the possibility to use a set of FORCs measured on the rotational hysteresis as a testing method for the vector hysteresis models performances. The rotational hysteresis loop can be experimentally obtained in the following sequence of fields. First, one saturates the sample on one direction, and then the field is decreased to a certain value. The field is maintained at a constant value and it is rotated 360°. For a number of values of the rotation angle the projection of the total magnetic moment on the field direction is measured. When the field is rotated back 360° towards the initial direction the magnetic moment is not following the same path and a hysteresis loop is obtained. The surface of this hysteresis loop can be covered systematically with first-order reversal curves, in a similar manner as it is done for any typical ferromagnetic hysteresis loop. From these FORC-type data, using the second order mixed derivative [6] one can obtain a FORC distribution which is representative for the sample and which is sensitive to various physical characteristic parameters and which is describing the vectorial switching properties of the material.
Fig. 1 presents the rotational hysteresis curve obtained on a commercial magnetic tape sample as well as the first-order reversal curves - with θ_r one denotes the values of the angle for which the reversal of the rotation direction takes place. The FORC diagram presented on the right hand side is the color map representation of the above mentioned FORC distribution. Fig. 2 shows the results of the simulation of the experimental procedure with Preisach-LLG model.

In the full paper we shall discuss the ability of the vectorial models to describe various rotational FORC diagrams. The models with the optimum set of parameters obtained from the identification procedure will be tested on the rotational hysteresis FORC diagram and the differences will be discussed.
A micromagnetic model will give the dependence of the rotational FORC diagram on the dispersion of the anisotropy field, easy axis orientation and inter-particle interaction distributions.
Acknowledgments: This work was supported by the Romanian AMCSIT-CEEX 324/2006 (MATHYS) Grant.

[1] I. D. Mayergoyz, Mathematical models of hysteresis and their applications, 1st ed. (Elsevier, Amsterdam ; Boston, 2003).

[2] I. D. Mayergoyz and G. Friedman, Journal of Applied Physics 61, 4022-4024 (1987).

[3] E. Della Torre and G. Kadar, Journal of Applied Physics 63, 3004-3006 (1988).

[4] L. Stoleriu, P. Andrei, A. Stancu, 52-nd MMM Conference paper AP-06, Journal of Applied Physics (in press).

[5] A. Stancu, L. Stoleriu, and P. Andrei, Journal of Magnetism and Magnetic Materials 316, E309-E312 (2007).

[6] A. Stancu, C. Pike, L. Stoleriu, P. Postolache, and D. Cimpoesu, Journal Of Applied Physics 93, 6620-6622 (2003).

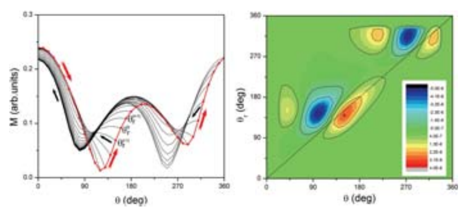

Experimental rotational hysteresis FORC and the resulting FORC diagram

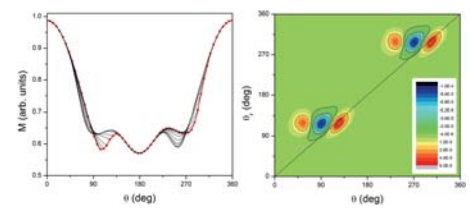

Simulated rotational hysteresis FORC and the resulting FORC diagram

GG-12

Identification of the parameters of reduced vector Preisach model by neural networks.

M. Trapanese
Dipartimento di Ingegneria Elettrica, Elettronica e delle Telecomunicazioni, University of Palermo, Palermo, Italy

All Preisach models describe hysteresis loop by a superposition of the magnetization values of Preisach particles, the hysterons, which are mathematical functions that can have two values. The switching from one value to the other is triggered when the external field reaches specific values. In its classical formulation [1]. Preisach model does not take into account the intrinsic vectorial nature of magnetizaion of any material. However, several Vector Preisach Models (VPM) have been proposed: one approach considers the superposition of an infinite number of scalar models pointing along all possible directions [2]; another one is based on the energy minimization of uniformly magnetized particles placed on a vectorial field [3]. In this paper the Reduced Vector Preisach Models (RVPM) is considered [4]. All Preisach Models are identified through the careful choice of their parameters. In the case of RVPM seven parameters must be identified for each axis: the saturation magnetization; the squareness; the average critical field; the zero field susceptibility; the standard deviation of the interaction field; the standard deviation of the critical field; and the moving parameter.
Several procedures have been developed in order to identify Preisach parameters; some of them implies the solution of set of differential equations and the experimental knowledge of several parameters, while others use artificial intelligence techniques. Almost all of these papers refer to CPM, which is a scalar model, but some authors have also examined the problem of the identification in the vector Preisach model. However, the use of neural networks to the identification problem for RVPM has not been very extensively examined.
This paper presents a methodology for identifying RVPM parameters by using neural networks. The neural network used is a multiplayer perceptron trained with the Levenberg-Marquadt training algorithm. The network is trained by some hysteresis data, which are generated by using Reduced Vector Preisach Model with pre-assigned parameters.
The trained network is able to yeld the parameters that must be used in order to reproduce, by using RVPM, the hysteresis loop that has been submitted.
The identification procedure can be divided into two steps: A) network training; B) output of the results.
The neural network, that has been chosen, is a three layer neural network: in the proposed approach, the first layer consists of linear neurons, the second layer of neurons with hyperbolic tangent sigmoid function, and the output layer of linear neurons. The input is made up of a vector describing a hysteresis curve. The first layer makes a linear reduction from the high dimension input space to a slightly lower dimension space. The output of the first layer is therefore the feature vector that sums up the most relevant characteristics of the input space and is strictly connected to the relevant properties of the hysteresis loop: remanence, coercive field, and slopes in correspondence of some points of the loop. The output layer is made up of neurons that are the free parameters of the RVPM that permits to reproduce the hysteresis curve that best matches the inputs.
The Levenberg-Marquadt algorithm has been used for the training phase.
In order to verify the ability of the trained neural network to obtain the right parameters of the submitted curves three tests were performed: in the first one the same vectors used for the training were submitted to the network, in the second one vectors that did not belong to the training set were submitted to the network, and in the third one an experimental hysteresis curve obtained in non static condition was used. In all cases, the abscissa field is equal to the ones used in the training phase. In the first test set the error made by the network in this case was always lower than 0.1% for all the parameters for every vector.
The second test set consisted of several vectors obtained by using RVPM with parameters not used in the training phase whose values were inside the intervals of the training parameters. RVPM was able to reconstruct the submitted curves. The errors on parameters are reported in table 1.
Finally, in the third experiment the network showed the ability to reconstruct an experimental curve.

[1] F. Preisach, Zeitschrift fuer Physik, B 94, 277 (1935).

[2] E.C. Stoner and E.P. Wohlfarth, Philos.Trans.R.Soc. London A, Math. Phys. Sci., vol. 240, pp. 599-642 (1948).

[3] I.D. Mayergoyz, Mathematical Models of Hysteresis, (New York, Springere-Verlag, 1991).

[4] E. Della Torre and U. Patel, Proc. Cefc. Conf., Perugia, Italy, June 2003.

Saturation Magnetization	Squareness	Critical field	Zero field suscettibility	Standard deviation interacion field	Standard deviation critical field	Moving parameter
1.2%	12%	7%	3%	15%	12%	4%

GH-01

Analysis of Permanent Magnet Demagnetization Accounting for Minor BH-curves.

Y. Zhilichev
Magnequench International, Inc, Durham, NC

When sizing permanent magnets in electric motors, generators and magnetically biased inductors they are designed to withstand the demagnetization fields. It is well known that an operating point of the magnet (or its portion) may slip below the knee of a demagnetization curve at high temperatures and under heavy overloads. Then the magnet operates on a recoil line that is different from the major bh-curve. The paper describes a calculation algorithm that allows us to account for the minor bh-curves when optimizing the magnet thickness. The model incorporates a series of recoil lines in the second and third quadrants. For each temperature, a major and few minor bh-curves are required [1]. A set of recoil lines are generated for each minor bh-curves (Fig.1). The slope of the recoil line is equal to that one of the linear part of bh-curve while the offset depends on the load line of the magnet operating point. In an FEA model, the magnet is presented by a set of operating points, and therefore each element of the mesh runs on its own bh-curve that could be different from the major one. This is typical for the multipole magnetization where the transition zone between the poles is difficult to saturate. The demagnetization analysis embraces few separate calculation steps. First the magnetization process is simulated [1]. As a result the magnet is represented by a table of magnetization components in each node of the mesh. The magnet table is imported from the magnetization model into the application FEA model and corrected to account for an operating temperature [2]. Then the magnet is simulated at the elevated temperature in presence of the demagnetization field energized by currents in the application. Each node of the mesh in the magnet area where the magnetic field is opposite to the magnetization is analyzed. If its operating point slips below the knee of demagnetization a corresponding recoil line is used to replace the bh-curve for this particular node. As a result a new magnetization table for the magnet is generated. Then it is used to analyze the performance of the application like torque, back-emf, etc. As an example, an 8-pole permanent magnet fan motor is considered (Fig.2a). Fig. 2b shows a magnet pole of a 1 mm thick injection molded NdFeB magnet ring after it was magnetized and imported into the motor model [2]. The distribution of magnetization changes after the magnet is subjected to the demagnetization field at 100-degree C. Fig. 3 shows the magnetization distribution across the pole in percentage of saturation before and after the magnet is subjected to the peak demagnetization field. The demagnetization effect was calculated based on the recoil line model for the fixed position of the magnet poles relative to the demagnetization field. The angle between the poles and demagnetization field may change in the motor (for example, for a trapezoidal current waveform, six-step drive, etc.) Therefore the last calculation step should be repeated for all possible angles between the poles and field to account for the total flux loss. This analysis helps to assess if the magnet withstands the demagnetization for the particular combination of the current and temperature. In summary, the algorithm developed accurately predicts the flux loss due to the thermal and demagnetization effects. It allows us to optimize the magnet size or/and to set the constraints for the maximum temperature and current.

[1] Y. Zhilichev, P. Campbell and D. Miller, In-situ Magnetization of Isotropic Permanent Magnets, IEEE Trans on Magnetics, Vol. 38, No 5, 2002

[2] OPERA-3D, User guide. Vector Fields Ltd., Oxford, UK, 2000

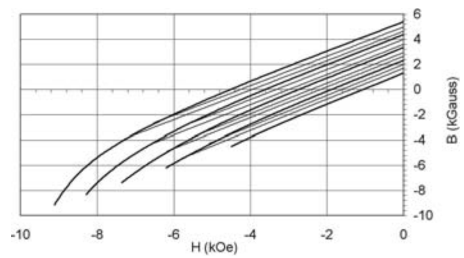

Fig. 1. Major and minor bh-curves with the corresponding sets of recoil lines.

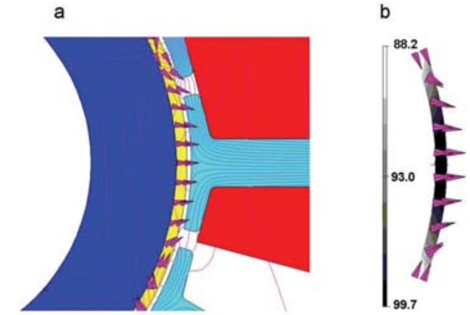

Fig. 2. Field plot in (a) the motor cross-section and (b) magnet pole. The pole is nearly saturated (99.7%) in the middle and partially magnetized (88.2%) in the transition zone.

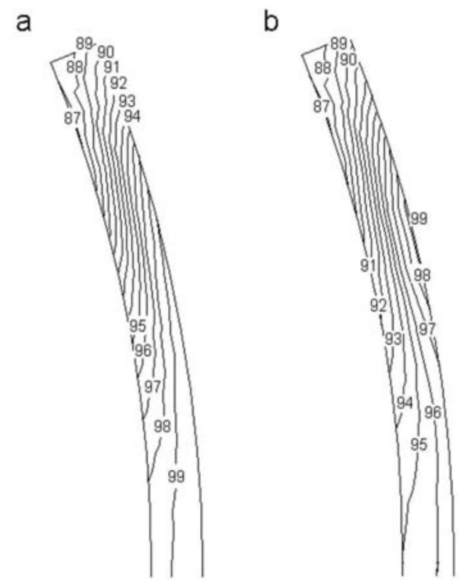

Fig. 3. Magnet pole (a) before and (b) after exposing to the demagnetization field. The lines show % of saturation.

GH-02

A Hybrid Dual-Memory Motor.

C. K.t.[1], G. Yu[1,2], J. Jianzhong[2]
1. Electrical and Electronic Engineering, the University of Hong Kong, Hongkong, China; 2. Automation, Shanghai University, Shanghai, China

I.INTRODUCTION

Because of inherently high efficiency and high power density, permanent magnet (PM) brushless motors have been widely accepted. However, they suffer from a key problem that the air-gap flux can hardly be controlled. The concept of hybrid field excitation (PM and field winding) has been proposed in which the field current is adjusted to control the air-gap flux [1]. Nevertheless, since the field winding needs continuous excitation, it degrades the efficiency. Recently, the class of memory motors has been proposed, which utilizes the property of low coercivity of the AlNiCo PM material in such a way that the magnetization of PMs can be tuned by applying temporary current pulses[2]. However, the AlNiCo PMs are prone to accidental demagnetization by armature reaction, and the process of magnetization involves complex control of armature currents. Also, its PM rotor is not mechanically robust enough to withstand high-speed operation [3].

The purpose of this paper is to incorporate both the hybrid field excitation and the dual-magnet arrangement into the memory motor so that the resulting hybrid dual-memory motor can offer the advantages of online PM and flexible air-gap flux adjustment, while eliminating the problems of accidental PM demagnetization, control complexity and mechanical integrity.

II.PROPOSED MACHINE

The proposed motor configuration is shown in Fig.1(a). Firstly, it adopts a DC winding to directly perform online magnetization or demagnetization, hence avoiding complicated vector control of armature currents and insignificant copper loss. Secondly, the use of dual-magnet arrangement, namely the NdFeB provides the main flux and the AlNiCo provides flux regulation, can effectively perform flux control. Thirdly, it adopts the double-layer stator outer-rotor topology which facilitates the integration of windings and PMs as well as direct-drive operation. Also, the double-layer stator can offer immunity of PMs from demagnetization by armature reaction. Finally, the use of solid-rotor design can provide high mechanical integrity to withstand high-speed operation.

Fig. 2(b). shows the equivalent magnetic circuits where F_{DC+} and F_{DC-} are the temporary MMF excited by the DC winding for magnetization and demagnetization, F_{PA} and F_{PN} PN are the MMFs of AlNiCo and NdFeB PMs. Hence, the control range of air-gap flux ($\Phi_{\delta min}$, $\Phi_{\delta max}$) can be analytically derived, which is very essential for initialization of motor dimensions and parameters.

III.RESULTS

By using finite element analysis, the magnetic field distributions under outward-magnetized (OM), non-magnetized (NM) and inward-magnetized (IM) AlNiCo PMs are shown in Fig. 2(a)-(c). The corresponding air-gap flux density distributions and the resulting no-load EMF are shown in Fig. 3, verifying that it offers effective flux and hence EMF control. Also, Fig. 2(d) shows the field distribution solely due to the rated armature reaction. It verifies that the PMs are immune from accidental demagnetization. By adopting the OM AlNiCo PMs to achieve flux strengthening, the start-up transient response can be significantly improved as depicted in Fig. 4. In contrast, by adopting the IM AlNiCo PMs to achieve flux weakening, the constant-power operating range can be extended to over 3 times the base speed as depicted in Fig. 5.

[1]K.T. Chau, Y.B. Li, J.Z. Jiang and S. Niu, "Design and control of a PM brushless hybrid generator for wind power application," IEEE Transactions on Magnetics, Vol. 42, No. 10, 2006, pp. 3497-3499.

[2]V. Ostovic, "Memory motor – A new class of controllable flux PM machines for a true wide speed operation," IEEE Industry Applications Magazine, Vol. 9, 2003, pp. 52-61.

[3]C. Yu, K.T. Chau, X. Liu and J.Z. Jiang, "A flux-mnemonic permanent magnet brushless motor for electric vehicles," Magnetism and Magnetic Materials Annual Conference, 2007, Paper No. ES-10.

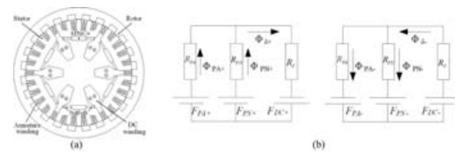

Fig. 1. (a) Machine configuration. (b) Equivalent magnetic circuits.

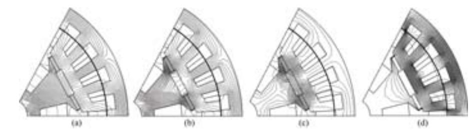

Fig. 2. Magnetic field distributions. (a) OM AlNiCo. (b) NM AlNiCo. (c) IM AlNiCo. (d) Armature reaction.

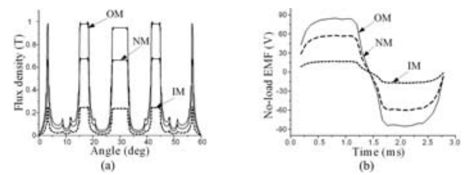

Fig. 3. Air-gap flux density distributios and no-load EMF waveforms under outward-magnetized AlNiCo, non-magnetized AlNiCo and inward-magnetized AlNiCo.

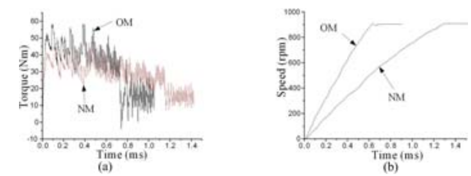

Fig. 4. Startup transient responses under outward-magnetized AlNiCo and non-magnetized AlNiCo.

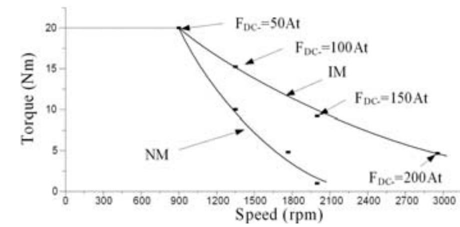

Fig. 5. Torque-speed capabilities under non-magnetized AlNiCo and progressively inward-magnetized AlNiCo.

GH-03

Study on Detachment of a Permanent Magnet-Wheel for a Wall-Climbing Mobile Robot using Magnetic Inducement.

H. Yi[1], J. Kim[1], S. Han[2]
1. Mechanical Engineering, Yeungnam University, Gyeongsan, South Korea; 2. Automobile engineering, Yeungnam College of Science & Technology, Daegu, South Korea

Robots are needed to automate works on a vertical plane of a large structure such as a ship and several devices such as suction cups [1][2]and magnetic disk [3]to make possible the robot to be attached to vertical plane have been developed in past years. Here, we propose a new design of the permanent magnet wheel for mobile robots to improve the adhesive force and facilitate the detachment of the wheel. Fig 1 shows the structure of permanent magnet wheel and operating principle for detaching using inducing pin. If the inducing pin is inserted, the part of magnetic flux from permanent magnet is induced to flow through the pins, which results in weakening of attaching force as shown Fig. 1 (a). To characterize the performance, the sample model of permanent magnet wheel and experiment apparatus are constructed as illustrated in Fig. 2 and Fig. 3 respectively. Specification of permanent magnet wheels are shown in table 1. In the design of magnetic wheel, the shape of wheel and the arrangement of magnets are mainly important. Therefore, we examine magnetic attaching force according to the number and the arrangement of magnets. The experimental apparatus is consisted of a computer to acquire data and control a motor, an oscilloscope to analyze values of attaching force, a gauss meter to measure attaching force and a load cell (50kgf). Using load cell, the attaching forces were measured according to the type of wheels. The table 2 shows the experiment results according to type of wheels without and with indution pins. Induction pins redude the attaching forces by at least 70 percent which results in easy detachment of permanent magnet wheel.

[1]Wang yan, Liu Shuliang, 1999, "Develop -ment & Application of Wall-Climbing Robots" Proceedings of the 1999 IEEE Interna¬tional Conference on Robotics & automa¬tion Detroit Michigan, May, pp.1207-1212.

[2]A.NISHI, 1996, "Development of wall- climb¬ing Robots" Computers Elect. Engng, Vol 22. No 2 pp123-149.

[3]S.Hirose and H.Tsutsumitake, 1992, "Disk Rover : A wall-climbing Robot using Perma¬nent Magnet Disks." Proceedings of the 1992 IEEE/RSJ International Conference on Intelli¬gent Robots and System, July 7-10, pp.2074 -2079.

Type of Wheel	Wheel (1)	Wheel (2)	Wheel (3)
Size of magnet (mm)	Φ 10 (4EA)	Φ 20 (1EA)	Φ 20 (3EA)
Size of wheel (mm)	D40*10 (2EA)	D40*10 (2EA)	D50*10 (2EA)
Thickness of magnet	5 mm	10 mm	10 mm
Thickness of wheel	25 mm	30 mm	30 mm
Φ (mm) & count of axis	Φ9 & 4EA	Φ9 & 4EA	Φ11 & 4EA

Type of wheel	Force w/o pins	Force w/pins	Ratio
Wheel (1)	7.35 kgf	1.3 kgf	17.7 %
Wheel (2)	7.71 kgf	1.3 kgf	16.8 %
Wheel (3)	28.8 kgf	10.5 kgf	36.4 %

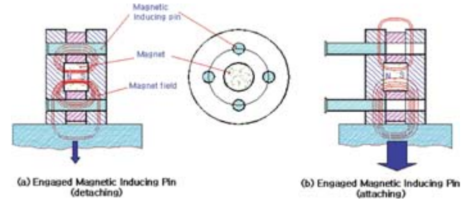

Fig 1. Schematic diagram of permanent magnet wheel (a) detaching (b) attaching

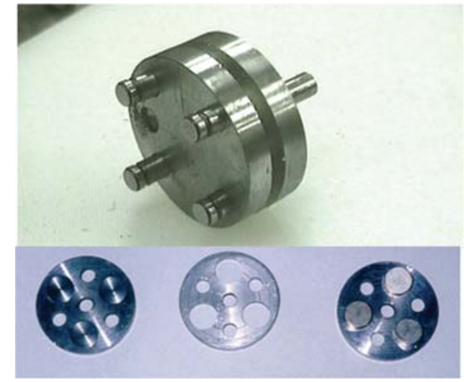

Fig 2. Permanent magnet wheels

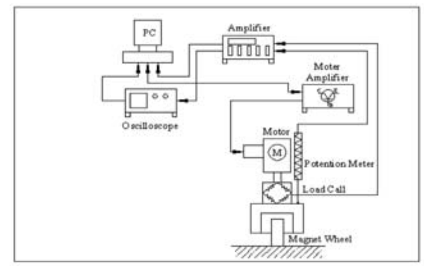

Fig 3. Diagram of experiment setup

GH-04

Ironless and leakage free voice-coil motor made of bounded magnets.

G. Lemarquand[1], *M. Remy*[2], B. Castagnede[1], G. Guyader[2]
1. LAUM, Universite du Maine, Le Mans, France; 2. Renault, Guyancourt, France

Voice-coil motors, such as those used in traditional electrodynamic loudspeakers, present a number of well-known drawbacks [1]. First, a significant part of the magnetic field created by the motor does not contribute towards making the membrane move. Second, the presence of iron in such motors leads to several kinds of non-linearities. These include Eddy currents, the magnetic saturation of the iron and the variation of the coil inductance with its position causing a reluctant effect. It is desirable for the force applied on the moving part to be an image of the driving current. However, if the inductance of the coil varies, a reluctant force occurs and interferes with the Laplace force. This can be compared to the cogging torque in brushless motors, arising from a reluctant effect, which prevents a smooth rotation of the motor and results in undesirable vibration and noise [2].
By suppressing the iron in the voice-coil motor, the inductance of the coil no longer depends on its position, resulting in the vanishing of the reluctant force and the other non-linearities due to iron listed previously. In addition, the inductance is diminished and consequently, so is the electrical impedance. Several structures of ironless voice-coil motors have already been proposed [3]. Another specification of the intended motor is for it to be leakage free (Fig. 1.a).
However, structures that involve sintered magnets can be difficult to assemble. By using bounded magnets this problem can be solved and furthermore, better cross section shapes and optimized magnetization of the structure can be realized, even though the magnetizer is harder to realize. With such magnets the magnetization is usually two-thirds lower than for sintered magnets. The aim of the work conducted is to design and study the magnetic performances of a loudspeaker motor having a magnet with an ellipsoidal cross section as shown in Fig. 1.b. Fig. 2 shows how this kind of magnet could be integrated into the loudspeaker. A double coil winding can be used with such a structure.
The ellipsoidal motor is discretized in order to enable analytical calculations of the magnetic field to be performed using the Coulomb's model of permanent magnets [4]. This discretization, using seven magnets of equal angular section for example, is shown in Fig. 3. For each magnet the magnetization is uniform and considered to be always parallel to the outer edge of the ellipsoid in order to avoid magnetic flux leakages. The surface charge density of each triangular magnet is then calculated.
A comparison of the magnetic performances of the two structures illustrated in Fig. 1 is then presented. The calculations are performed for two structures having the same cross section area. Results show that the ellipsoidal shape gives better results than the rectangular one. The value of B_{radial} is bigger across the entire coil displacement and its symmetry around the rest position of the coil is much better.
The magnetic field is then calculated for different values of the ratio between the lengths of the semimajor axis a and the minor axis h of the ellipsoidal magnet. Results show that B_{radial} gets bigger when the ratio augments. However, over a certain value of this ratio the increase in induction intensity is negligible compared to the rise of volume.

[1] M.R. Gander, "Moving-coil loudspeaker topology as an indicator of linear excursion capability", JAES, vol. 29(1), 1981.

[2] K. Atallah and D. Howe, "The Application of Halbach Cylinders to Brushless AC Servo Motors", Trans. Mag., vol. 34(4), 1998.

[3] G. Lemarquand, "Ironless Loudspeakers", Trans. Mag., vol. 43(8), 2007.

[4] H. Rakotoarison et al., "Using Coulombian Approach for Modeling Scalar Potential and Magnetic Field of a Permanent Magnet With Radial Polarization", Trans. Mag., vol. 43(4), 2007.

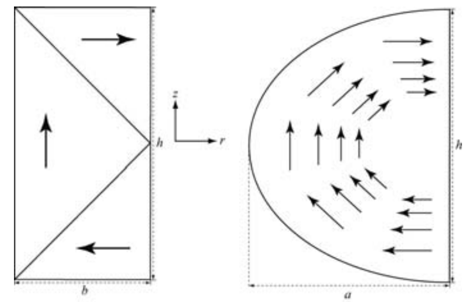

(1.a) (1.b)

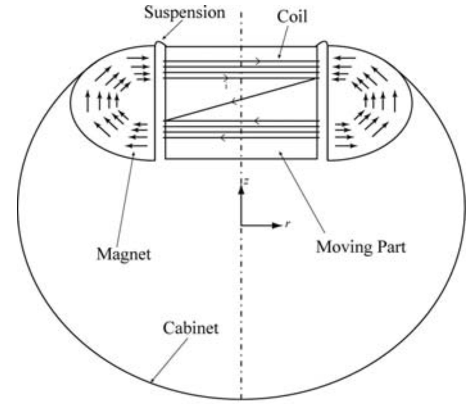

(2)

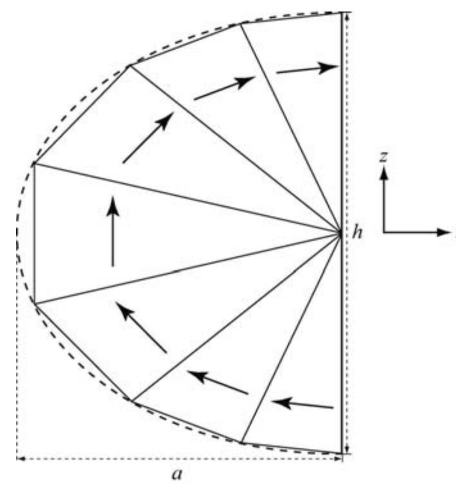

(3)

GH-05

Generic Algorithm-Based Optimal Design of New Electromagnetic Engine Valve Actuator for Reduction of Transition Time.

J. Kim[1], K. Han[2], J. Chang[3]

1. Mechanical Engineering, Yeungnam University, Gyeongsan, South Korea; 2. Electrical Engineering, Florida Institute of Technology, Melbourne, FL; 3. Transverse Flux Machines Research Group, Korea Electrotechnology Research Institute, Changwon, South Korea

Electromagnetic engine valve actuator using permanent magnet as shown Fig. 1(a) is a new concept to overcome the inherent drawbacks of conventional solenoid-driven electromagnetic engine valve actuator such as high power consumption [1]. We presents generic algorithm and finite element analysis- based optimal design of new electromagnetic engine valve actuator in a limited space of the entire construction by multidisciplinary simulation using MATLAB and MAXWELL. This aim is maximizing the frequency of vibration in order to reduce the transition time of engine valve. The transition time is defined as the duration for the valve to move from closed position to opened position or from opened position to closed position and as the transition time is smaller, the engine valve actuator can accomplish higher maximum engine speed. The transition time of existing design is 3.9 milliseconds which achieve about 5,000 rpm of maximalum engine speed. The transition time of actuator valve is shortened by the increment of the frequency of vibration because the actuator is mainly operated by mass-spring oscillation.

Accordingly, the objective function in this opimization design is to maximize wn=(k/m)^1/2. Here, k is the equivalent spring stiffness, and m is the moving mass. The available maximal stiffness of spring is proportional to the magnitude of magnetic latching force because the magnetic force by permanent magnet is designed 100 N larger at lower and upper end of stroke than spring force for latching purpose considering gas disturbance force and the moving mass includes the mass of armature and engine valve those are one rigid body. The design variables are showns in Fig. 1(b). and Several constraints to achieve a realistic design are required. When optimizing proposed structure, it is possible to synthesize designs based on some physics-based trial-and-error or the more traditional and familiar techniques such as conjugate-gradient and the quasi-Newton methods. However, neither way generally leads to optimal solution especially in the multi-parameter optimization problems. Unlike those local optimization techniques, GAs are neither highly dependent on the initial conditions nor constraints on the solution domain. For this reason, a GA, global search technique, is employed in this study [2]. Table 1 shows the optimized dimension of actuator. The size of armature is decreased which results in reduction of moving mass while width of teeth and core are increased. To demonstrate the enhancement of dynamic performance due to the optimization, dynamic finite-element analysis (FEA) was executed using the nonlinear FE analysis solver MAXWELL. The table 2 shows the comparison of characteristics of existing design and optimal design. The magnetic latching force at end position of stroke falls from 1525 N to 1262 N which reduces the obtainable maximal stiffness of spring by 18.4 % from 358 kN/m to 292 kN/m and at the same time, the moving mass including armature and engine valve falls by 52.1 % from 284 gram to 136 gram. Accordingly, the natural frequency is improved by 30 % and the transition time is shortened from 3.9 milliseconds to 3.56 milliseconds by 8.7 %.

[1]. J. Kim and D. K. Lieu (2005) Designs for New, Quick-Response, Latching Electromagnetic Valve, Proceeding of International Electric Machines and Drives Conference 2005, 1773~1779

[2]J. M. Johnson and Y. Rahmat-Samii (1997) Genetic Algorithms in Engineering Electromagnetics, IEEE Antennas Propag. Mag., vol. 39, no. 4, 7-21

Symbol	Existing dimension	Optimal dimension	Symbol	Existing dimension	Optimal dimension
Lac	38.1	38.1	Ha	19.03	12
Wac	120.65	120.65	Wt	34.29	27.325
Hac	93.34	95	Ht	19.05	19
Wco	31.75	31.75	Wc	19.05	28
Wm	44.45	44.45	Hc	27.05	20
Hm	4.7625	4.7625	Hbi_1	19.05	28.75
Wa	44.45	30.216	Hbi_2	4.7625	3.5

characteristics	existing design	optimal design
magnetic latching force	1525 (N)	1262 (N)
available spring stiffness	358 (kN/m)	292 (kN/m)
moving mass	0.284 (kg)	0.136 (kg)
natural frequency	1123	1465
transition time	3.9 (msec)	3.56 (msec)

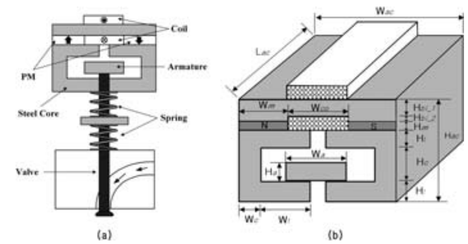

Fig.1 New engine valve actuator (a) schematic diagram (b) optimization design variables

GH-06

Self-Assembly of Millimeter-Scale Components using Integrated Micromagnets.

S. B. Shetye, D. P. Arnold
Interdisciplinary Microsystems Group, University of Florida, Gainesville, FL

INTRODUCTION

Assembly of large number of small components is essential for mass-production of integrated, microelectronic devices. Self-assembly—where the parts are designed to autonomously assemble in a predetermined fashion—offers the potential for higher throughput and the ability to more effectively handle smaller parts (sub millimeter) compared to manual or robotic methods [1]. Existing self-assembly approaches use gravity, capillary, electrostatic and magnetic forces [2].

Unlike prior approaches, which used external magnetic fields to manipulate the components, this article demonstrates self-assembly using the intermagnetic forces between hard micromagnets embedded on the individual parts. To demonstrate this concept, 1 mm x 1 mm x 500 µm silicon blocks are self-assembled onto a planar template substrate in a simple array pattern.

Magnetic assembly occurs when the magnets on two respective parts align such that the intermagnetic force exceeds the mixing force. Using a shaker assembly, an array of components is shown to assemble in dry environment in about 10 seconds with a yield of approximately 96 %.

COMPONENT FABRICATION

Wafer-level microfabrication on 500 µm thick, 100 mm diameter silicon wafers is used to fabricate individual micromagnets varying from 25 % to 75 % of the chip surface area. Fig. 1. shows the fabrication process. Small cavities etched in the silicon surface are filled with SmCo magnetic powder to create embedded micromagnets [3]. The wafer is then diced to create the individual 1 mm x 1 mm block components. Substrates with arrays of "receptor sites" are made by gluing discrete components to plastic sheets in arrays of 4 x 3 and 3 x 3.

EXPERIMENT

Because of the inverted assembly setup, the minimum force required for self-assembly is assumed to be the weight force of the component (~12 µN). The estimated force using both analytical [4] and FEM methods for the 850 µm x 850 µm x 60 µm and 500 µm x 500 µm x 60 µm magnets is about 200 µN and 123 µN, respectively, which are both much higher than the weight force of the component.

The experimental setup shown in Fig. 2 is similar to the one presented in [5]. A small glass container with parts (≈ 5 times as the number of receptor sites) is placed on an electromechanical shaker. The substrate with its face down, is lowered into the glass container using a 3-D micropositioner and positioned at a height of about 9-9.5 mm above the parts. The shaker displacement at 3 Hz and 2 V is 1.8 mm p-p causing the parts to bounce up and down and self assemble onto the substrate. Fig. 3. shows the progression of magnetic self-assembly for t = 0, 5, and 10 s. Table 1 summarizes the results. The longer assembly time for the 3 x 3 substrate and lower yield is attributed to the denser packing of receptor sites, which causes any misaligned parts to deter the assembly of its adjacent parts until being knocked out of place.

CONCLUSION

The concept of magnetic self-assembly and successful experimental assembly of parts to substrate is demonstrated at the millimeter scale. The estimated force between the embedded micromagnets is much higher compared to the component weight force, thus driving the self-assembly mechanism.

ACKNOWLEDGEMENTS
Financial support for this project is provided by NSF grant DMI-0556056.

[1] C. J. Morris, et al., IEEE transactions on Advanced Packaging, 2005, vol. 28, no. 4, pp. 600- 611.
[2] S. B. Shetye, et al., IEEE Trans. Magn., Vol. 43, No. 6, pp. 2713-2715, June 2007.
[3] B. Bowers, et al., Proc. Transducers 07, vol.2, pp. 1581-1584.
[4] J. S. Agashe, et al., Intermag 2006, pp. 320.
[5] S.H. Liang, et al., 18th IEEE Conference on MEMS, pp. 592- 595.

No. of receptor sites (magnet area)	Spacing between receptor sites	Assembly time (100%)	Yield % (10 s)
12 (75 %)	2 mm	10 s	96
9 (75 %)	0.5 mm	18 s	90
12 (25 %)	2 mm	12 s	91

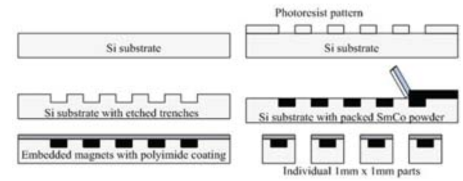

Fig. 1. Fabrication process flow for embedded magnets

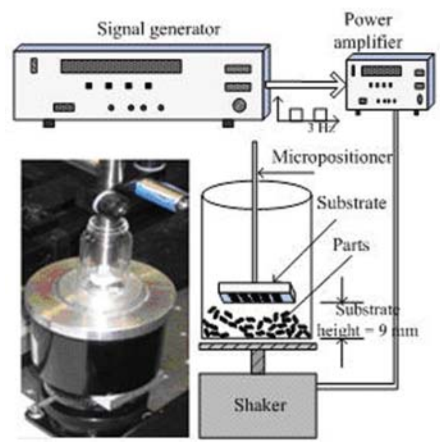

Fig. 2. Experimental setup for magnetic self-assembly

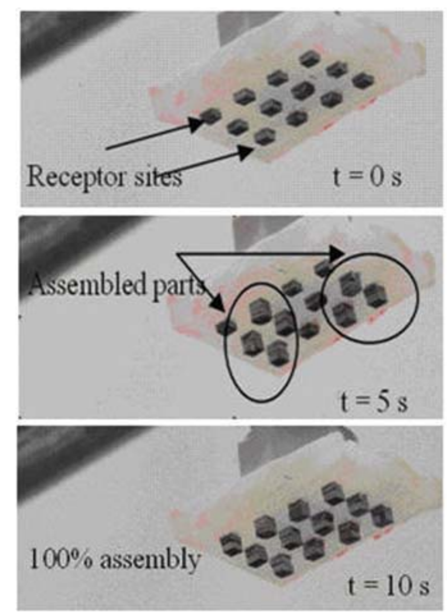

Fig. 3. Magnetic self-assembly demonstration

Minimization of Cogging Torque in an IPM Machine.

C. Hwang[1], P. Li[1], C. Liu[2]
1. EE, Feng Chia University, Seatwen, Taichung, Taiwan; 2. EE, National Sun Yat-sen University, Kaohsiung, Taiwan

I. Introduction

High-speed interior permanent magnet (IPM) synchronous motors always use 2-pole rotor. However, machines equipped with two magnet poles exhibit a high level of cogging torque.

In this paper, the optimal pole-arc to pole-pitch ratio for minimum cogging torque in IPM machine is used as initial values of the design variables, then the Taguchi method is used for the determination of the initial optimal values[2], and Rosenbrock's method is applied to determine the near optimal settings of the design parameters [3].

II. Model of IPM Motor

Fig. 1 shows a three-phase, 2-pole/6-slot IPM motor. The initial design parameters are stator outside diameter = 90 mm, inner diameter = 53 mm, stack length = 65 mm, and rotor outside diameter = 52 mm. The core is made of nonoriented silicon steel, and two sintered NdFeB magnets with a remanence of 1.2 T and a relative recoil permeability of 1.05 are inserted in the rotor. The magnet thickness is 3 mm with an angular pole-arc of 150 electrical degrees. The rotating speed is 12000 rpm.

III. Design of Experiment

There are four factors, M, D, B, and G, corresponding four design variables are chosen as shown in Fig. 1, and each at three levels. Where M is the thickness of magnet in mm (2.5, 3.0, 3.5), D is the pole-arc of magnet pole in electrical degree (145, 150, 155), B is the width between magnet and air gap in mm (3.5, 4.0, 4.5), and G is the air gap length in mm (0.5, 0.5, 0.5). A standard Taguchi's orthogonal array L-9 used for the matrix numerical experiments is shown in Table I. The peak-to-peak values of cogging torque Tcmax are calculated for each experiment using finite element analysis as also shown in Table I.

IV. Analyze the Results

After conducting the matrix experiments and obtaining all the experimental data, analysis of means and analysis of variance are carried out for estimating the effect of design parameters and for determining the relative importance of each design parameter. Fig. 2 illustrates the main factor effects on cogging torque. It reveals that the factor-level combination (M1, D1, B3) contributes to minimization of the cogging torque.

Finally, Rosenbrock's method is applied to find the optimal values of the design variables. They are M = 2.45 mm, D = 144.2 electrical degrees, and B = 4.31 mm. The results are found using the FEM analyses. The value of cogging is 0.35 Nm. Fig. 3 compares the result of cogging torque.

Acknowledge

This work was supported by the National Science Council of Taiwan through grant number NSC 96-2221-E-035-105

[1] K. Miyashita, S. Yamashita, S. Tanabe, T. Shimozu and H. Sento, "Development of a high Speed 2-pole Permanent Magnet Synchronous Motor," IEEE Trans. on Power Apparatus and Systems, vol. PAS-99, no. 6, pp. 2175-2181, Nov/Dec 1980.

[2] S. X. Chen, T. S. Low, and B. Bruhl, "The Robust Design Approach for Reducing Cogging Torque in Permanent Magnet Motors," IEEE Trans. on Magnetics, vol. 34, no. 4 pp. 2135-2137, July 1998.

[3] N. Takahashi, Optimal Design Using Finite Element Method for Magnetic Field Analysis, Morikita Publishing Company, Tokyo, 2001.

Experiment	M	D(deg)	B(mm)	G(mm)	Tcmax
1	2(M1)	145(D1)	3.5(B1)	0.5	0.6250
2	2(M1)	150(D2)	4(B2)	0.5	0.8200
3	2(M1)	155(D3)	4.5(B3)	0.5	0.9320
4	2.5(M2)	145(D1)	4(B2)	0.5	0.5970
5	2.5(M2)	150(D2)	4.5(B3)	0.5	0.6940
6	2.5(M2)	155(D3)	3.5(B1)	0.5	1.5600
7	3(M3)	145(D1)	4.5(B3)	0.5	0.5020
8	3(M3)	150(D2)	3.5(B1)	0.5	1.2070
9	3(M3)	155(D3)	4(B2)	0.5	1.5160

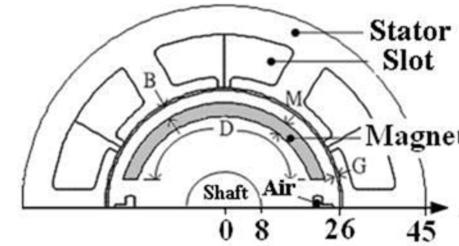

Fig. 1. Model of IPM motor.

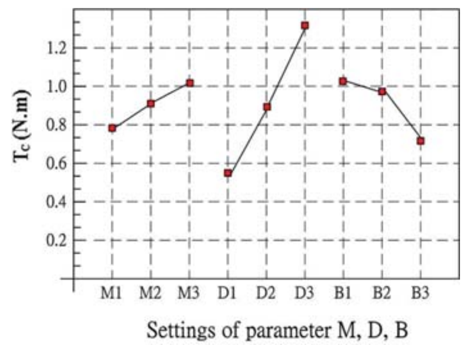

Fig. 2. Main factor effects on cogging torque.

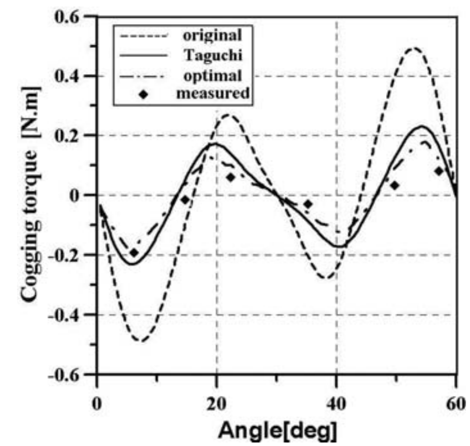

Fig. 3. Comparison of cogging torques.

Static Eccentricity Fault Diagnosis in Permanent Magnet Synchronous Motor using Time Stepping Finite Element Method.

B. Ebrahimi, J. Faiz, A. Zargham Nejhad
Department of Electrical and Computer Engineering, University of Tehran, University of Tehran, Tehran, Iran

This paper introduces a new index for noninvasive diagnosis of the static eccentricity (SE) in Permanent magnet synchronous motors. Use of this index makes it possible to precisely determine the eccentricity degree. The index is the amplitude of the harmonic components with a particular frequency pattern. The occurrence and increase of the fault causes a rise in amplitude of the harmonic components which can be used to diagnose the fault and determine its degree. A permanent magnet synchronous motor (PMSM) under static fault is modeled using time stepping finite element method. This modeling includes all geometrical and physical characteristics of the machine components, non-uniform permeance of the air gap and nonlinear characteristics of the PM material. Referring Fig1, the core of the fault diagnosis technique is TSFE method which is used to process the proposed signals. The transient equations of the external circuit showing electrical sources and circuit elements are combined with the field equations in FEM and mechanical equations due to rotor rotation, and stator phase current is estimated as unknown variable. Since the air gap magnetic field of the faulty motor is asymmetrical, current, torque and speed of the motor are also asymmetrical. These asymmetries produce many harmonics in the field, current and torque of the motor. The frequency pattern injected to the stator current can be the criterion function for non-invasive fault diagnosis. Fig2a and Fig2b show the frequency spectrum of the stator current for a healthy PMSM and the PMSM with 10%SE respectively. Comparison of these figures indicates that 10% SE results in harmonic components with considerable amplitudes in the stator current with frequencies 37.5Hz, 62.5Hz and etc. The amplitude of harmonics 37.5Hz increase from -88dB in the healthy motor to -65dB in the faulty motor. This increase is from -101dB to -68dB for harmonic 62.5Hz. This considerable increase of the harmonic components is a suitable index for SE fault diagnosis. Fig2c indicates that amplitudes of harmonics 37.5Hz and 62.5Hz are again increased. Comparison of Fig2b and2c shows that 10% increase of the SE degree results in the increase of the harmonic component amplitude of 37.5Hz to -58dB and 62.5Hz to -61dB. Higher SE degree, 30%, shows that the trend of increase in harmonics 37.5Hz and 62.5Hz continue so that the amplitude of harmonic 37.5Hz reaches -54dB and 62.5Hz reaches -58dB. Amplitudes of harmonics 37.5Hz and 62.5Hz are a suitable index for fault diagnosis and determination of eccentricity degree. The frequency pattern of $(1\pm(2k-1)/P)fs$ is suggested for SE fault diagnosis, where fs is the supply frequency, P is the number of poles and k is an integer. Harmonic frequencies 37.5Hz and 62.5Hz are computed from this pattern by substituting fs=50,P=4 and k=1,2,…. Table I summarizes the amplitudes of harmonic components $(1\pm(2k-1)/P)fs$ for k=1,…,7. Referring to Fig 2, shows that SE increases the harmonic components of the stator current which causes oscillating torque. By increasing the SE degree, amplitudes of the harmonics in the stator current rise and more ripples are observed on the developed torque. For this reason the analysis of the torque spectrum of the healthy motor and a motor with 10%-30% SE are shown in TableII, respectively. TableII shows the rise of harmonic components $(1\pm(2k-1)/P)fs$ in the torque of the faulty motor.

Percentage of eccentricity	(1-3/P)fs	(1-1/P)fs	(1+1/P)fs	(1+3/P)fs	(1+5/P)fs	(1+7/P)fs
0	-96	-88	-101	-92	-90	-95
10	-63	-64	-68	-70	-69	-63
20	-57	-58	-61	-65	-63	-57
30	-53	-54	-58	-62	-59	-53

Percentage of eccentricity	(1-3/P)fs	(1-1/P)fs	(1+1/P)fs	(1+3/P)fs	(1+5/P)fs	(1+7/P)fs
0	-83	-55	-60	-73	-76	-52
10	-44	-37	-33	-48	-57	-44
20	-43	-34	-30	-46	-48	-40
30	-41	-30	-28	-45	-42	-37

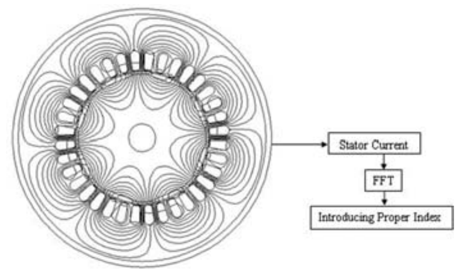

Fig. 1. Static eccentricity fault diagnosis algorithm for PMSM

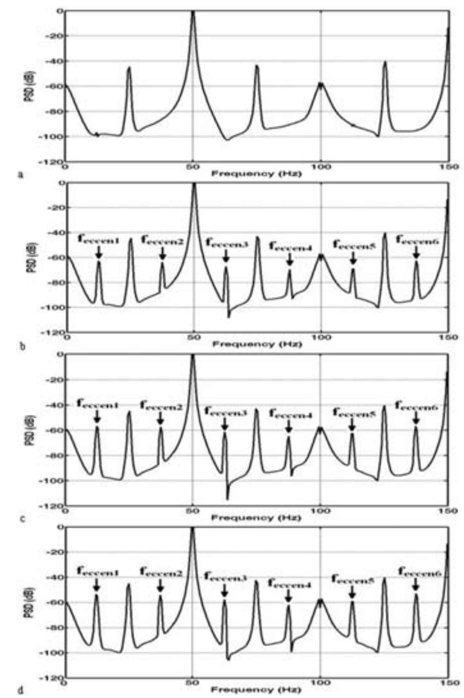

Fig. 2. Normalized plots of the line current spectra of a PMSM (a) healthy, (b) 10%, (b) 20% and (c) 30% static eccentricity

GH-09

Six-degree-of-freedom motion analysis of a planar actuator with a magnetically levitated mover by six-phase current controls.

Y. Ueda, H. Ohsaki
Department of Advanced Energy, The University of Tokyo, Kashiwa, Japan

Introduction:
There are a large number of electronic devices employing numerous actuators. So, it has been required to improve their performance such as high-speed, high-precision, drive with multi-degrees of freedom, smaller and lighter structure, and so on. Direct drive with multi-degrees of freedom is an emerging technology that has been studies actively [1]. Planar actuators can be directly driven in the translational directions on a plane. Conventional planar actuators have a large number of armature coils [2] [3]. These actuators require large-scale power supplies, though, so they are not suitable for small actuators.
The purpose of this study is to design an actuator with a small mover capable of large planar motion and positioning with six degrees of freedom by six-phase current controls. So far, the large rotational and translational motions on a plane could be independently controlled [4]. This paper proposes a new control method of positioning on the plane with the mover levitated magnetically. The six-degree-of-freedom motions obtained by numerical analysis are also presented.
Stability of the magnetic levitation:
The fundamental structure of our proposed planar actuator is shown in Fig. 1. The mover consists of a two-dimensional Halbach magnet array. The stator has three sets of air-core two-phase armature conductors, which are arranged on a triple-layered printed circuit board. Therefore, this planar actuator would be suitable as a small actuator.
This planar actuator can be driven with the same principle as linear synchronous motors when two-phase currents are supplied to the two-phase armature conductors. Therefore, the electromagnetic force has sinusoidal dependence on the phase difference θ_d between magnetic fields generated by the armature currents and the Halbach array. The six-degree-of-freedom force can be calculated from Lorentz force. Numerical analysis of the static force characteristics for only the armature currents for x-drive was carried out. In this paper, the orientation of the mover was defined from the angles α, β and γ as counterclockwise rotations about the z-, y- and x-axes, respectively. The dimension and mass of the mover are 11 mm x 11 mm x 2 mm and 1.8 g, respectively.
Fig. 2 shows the analysis result of the translational force F_x, F_z and the torque T_y for $\alpha = \beta = \gamma = 0$ deg. The translational force F_x and suspension force F_z can be generated independently by controlling the amplitude and the phase of the two-phase currents. The positive F_z is generated when θ_d is in the range between 90 and 270 deg. Fig. 3 shows the analysis result of T_y vs. β characteristics for $\alpha = \gamma = 0$ deg and θ_d in the range between 90 and 270 deg. When β become larger T_y become smaller, and, so β motion is stable in this range. Slight β motion hardly influences F_x, F_z, T_x and T_z. Fig. 4 shows the analysis result of T_x, T_z vs. γ characteristics for $\alpha = \beta = 0$ deg and $\theta_d = 135$ deg. When γ become larger T_x become smaller, and, so γ motion is also stable. Slight γ motion hardly influences F_x, F_z and T_y. However, T_z is also generated. Therefore, it is required to suppress α motion to maintain the stability of the mover motion. Fig. 5 shows the analysis result of F_z and T_z vs. α characteristics for $\beta = \gamma = 0$ deg and $\theta_d = 135$ deg. When α become larger T_z become larger, and, so α motion is unstable. Fig. 5 also indicates that T_z is generated and F_z is not generated when α is equal to 25 deg. If the armature conductors for the yaw drive are tilted around z-axis by 25 deg from those for x-drive, T_z can be controlled, and, so α motion can be stabilized.
Conclusions:
This paper proposes a new control method of positioning on the plane and stably magnetic suspension of the mover based on numerical analysis result of the force characteristics. This control method enables to generate suspension force and three-degree-of-freedom force on a plane independently with stable torque for β and γ by six-phase current controls. Numerical analysis of six-degree-of-freedom motions of the mover has been conducted.

[1] Investigating R&D Committee on Multi-dimensional Drive System, IEEJ Tech. Rep., no. 1081, Jul. 2005.

[2] W. J. Kim et al., Precision Eng., vol. 22, no. 2, Apr. 1998, pp. 66-77.

[3] J. W. Jansen et al., IEEE Trans. Magn., vol. 43, no. 1, Jan. 2007, pp. 15-25.

[4] Y. Ueda et al., Proc. of Int. Conf. on Electrical Machines and Systems (ICEMS 2006), DS1E2-06, Nov. 2006.

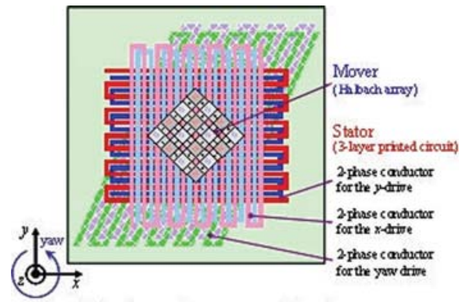

Fig. 1 Fundamental structure of the planar actuator

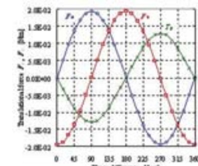
Fig. 2 Analysis result of F_x, F_z, T_y for $\alpha = \beta = \gamma = 0$ deg

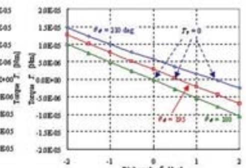
Fig. 3 Analysis result of T_y for $\alpha = \gamma = 0$ deg

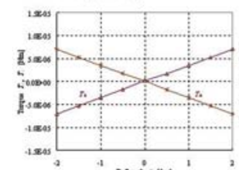
Fig. 4 Analysis result of T_x, T_z for $\alpha = \beta = 0$ deg

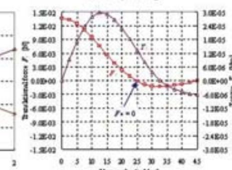
Fig. 5 Analysis result of F_z, T_z for $\beta = \gamma = 0$ deg

GH-10

Optimal Halbach Permanent Magnet Shapes for Slotless Tubular Actuators.

J. J. Paulides, K. J. Meessen, B. L. Gysen, E. A. Lomonova
Technical university Eindhoven, Eindhoven, Netherlands

This paper describes the merits of various halbach permanent magnet (PM) arrays applied to tubular PM actuators. These actuators are increasingly used due to their high efficiency, high power/force density, and excellent servo characteristics [1]. In this respect, it has been shown that the topology of the slotless tubular PM actuators using quasi-Halbach magnetization patterns have a number of attractive characteristics, such as a sinusoidal back-electromotive force waveform, which coincides with a very low electromagnetic force ripple, and the possibility of being optimized to achieve almost zero cogging force [2]. A further advantage is that quasi-Halbach magnetized magnets are virtually "self-shielding", and therefore, the magnetic flux which passes through the translator back-iron is relatively weak. Hence, a nonmagnetic translator back-iron is considered. In most publications a square quasi-Halbach array is used, where this paper will describe the semi-analytically means to enhance the air-gap field by varying the permanent magnet shapes, as illustrated in Fig. 1, of the PMs in the Halbach array.
The semi-analytical method in this paper only examines the airgap field due to the PMs, where a linear demagnetization characteristic, fully magnetized PMs in the direction of magnetization, infinite iron permeability and motor axial length are assumed. As shown in Fig. 1, three regions are considered: the first includes the PMs, the second includes the airgap, and the third the slotless winding region. However, in slotless tubular actuators, both the windings and the airgap have a permeability equal to unity and, hence, the problem can be reduced to two regions, namely the permanent magnet region (Rr to Rm) and a source free region (Rm to Rs). The results are determined using the semi-analytical calculation approach [2] based on the magnetic vector potential, which provides for a very good agreement with the finite element analysis, as shown in Fig. 2. This analysis is also used to determine the optimal magnet to air ratio and magnet ratio ($\tau mr/\tau p$) for various radii and magnet versus source free lengths. However, this analysis is difficult to implement when changing the magnet to a trapezoidal shape, therefore, an alternative semi-analytical method is used [3]. This approach provides the means to calculate the field of the individual magnets and by summation the total field can be determined, further the stator back-iron (infinite permeability) is included by the method of imaging [4]. The results of this analysis are shown in Fig. 3, where the influence of the angle αm is shown on the optimal value of the airgap flux density. This figure clearly shows that the maximum airgap flux density and rms airgap field can be increased by 10% and 1.5%, respectively, while implementing trapezoidal instead of rectangular shaped magnets. However, probably more importantly, the shape of the Halbach trapezoidal permanent magnets can be used to adjust the shape of the airgap field, and hence, the harmonic content of the back-emf waveform can be minimized. The trapezoidal magnet shape, therefore, directly influences the force (density and ripple) and the acceleration of the tubular PM actuator. The full paper will present these results in various tables that can be used to select the appropriate angle for the trapezoidal magnet to minimize the airgap field harmonic content and maximize the RMS value for brushless AC excitation and to maximize the airgap field in the central 120° current conducting region for brushless DC excitation.

[1] J. F. Eastham, "Novel synchronous machines: Linear and disc," Proc. Inst. Elect. Eng., vol. B-137, pp. 49-58, 1990.

[2] J. Wang, D. Howe, and G. W. Jewell, "Fringing in tubular permanent magnet machines: Part I -Magnetic field distribution, flux-linkage, and thrust force," IEEE Trans. Magn., vol. 39, no. 6, pp. 3507–3516, Nov. 2003.

[3] M. G. Lee and D. G. Gweon, "Optimal design of a double-sided linear motor with a multi-segmented trapezoidal magnet array for a high precision positioning system," Journal of Magnetism and Magnetic Materials, vol. 281, Issue 2-3, pp. 336-346, June 2004.

[4] K. J. Binns, P. J. Lawrenson, and C. W. Towbridge, The analytical and numerical solutions of electrical and magnetic fields. Chichester, England: John Wiley & Sons, 1994.

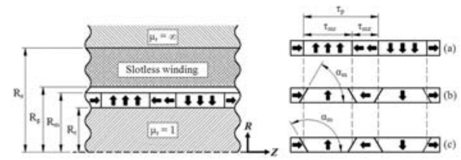

Cross-section of slotless tubular PM actuator

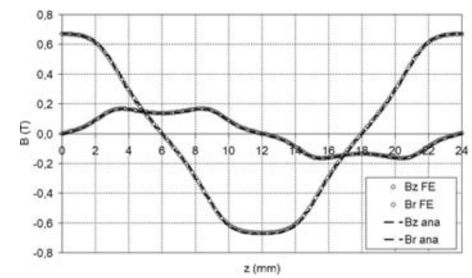

Flux density in the middle of the source free region

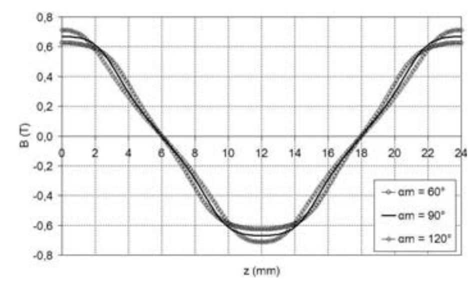

Flux density for the trapezoidal magnets

Development of Inverse Magnetostrictive Actuator.

H. Park, Y. Park, H. Choi
Mechatronics Engineering, Chungnam National University, Daejeon, South Korea

An electromagnetic actuator with coil such as magnetostrictive actuator converts electrical energy to mechanical energy, and to control magnetic forces. It, however, has some problems such as heat generation and bulky size. To overcome such problems, Ueno et al. proposed an electromagnetic actuator without coil. They harnessed inverse magnetostrictive effect of a magnetostrictive material (MM), as shown in Fig. 1 (a), and treated MM as a variable resistance [1]. This paper proposes an electromagnetic actuator with inverse magnetostrictive effect, as shown in Fig. 1 (b), and treats MM as flux source.

Fig. 2 (a) is a schematic view of the actuator, Fig. 2 (b) a photograph of the actuator. Spring model is used to model displacements and forces of MM and piezo, as shown in Fig. 3. It is assumed that the cover and bobbin in Fig. 2 (b) are rigid enough. Piezo is expanded along the –y direction and generates a force (F_p) when a voltage is applied to it, while MM tends to expand along the y direction and generates a force (F_{G0}) due to PM. Total force at (F) is the difference between F_p and F_{G0} applied to MM. Thus, changed displacement applied force onto MM are expressed as,

$x=F/(k1+k2)$, $F_G=-k2F/(k1+k2)$ (where, $x_p=-x_G=x$) (1)

Magnetic flux density of MM consists of two components; One is magnetic flux density by external force, and the other by permanent magnet. Therefore, magnetic flux in MM is expressed as,

$\Phi_G=\int B_G dA=\Phi_\sigma+\Phi_H$(2)

Fig. 4 shows magnetic equivalent circuit of the proposed actuator. Direction of magnetic flux (Φ_σ) by external force is opposite direction of flux (Φ_H) by PM. Total magnetic flux in magnetic equivalent circuit is expressed as the sum of flux (Φ_{PM}) by PM, flux of MM (Φ_σ) by external forces and flux leakage (Φ_l).

$\Phi_{TOT}=\Phi_{PM}+\Phi_\sigma+\Phi_l$(3)

Assuming that flux leakage is very small than flux by PM and flux of MM by external force, magnetic force at airgap by external forces can be obtained.

$F_\sigma=2\Phi_{PM}\Phi_\sigma+\Phi_\sigma^2/2A_{ag}u_0$(where, $\Phi_{PM},\Phi_\sigma>>\Phi_l$) (4)

This equation is used to predict the magnetic force at airgap. The predicted force is compared with the measured force (Fig. 5).

The applied voltages from a PI piezo amp are between 0 and 500 volts. The magnetic force at airgap is measured by using a PCB force sensor. When the input voltage is 500V, the different between predicted and measured forces is about 0.7N. Cause of those errors is analogized loss of magnetic flux in magnetic circuit that is leakage in flux path.

[1] Toshiuki Ueno, Jinhao Qiu, and Junuj Tani, "Magnetic Force Control with Composite of Giant Magnetostrictive and Piezoelectric Materials", IEEE Transactions on Magnetics, Vol. 39, No. 6, November, 2003

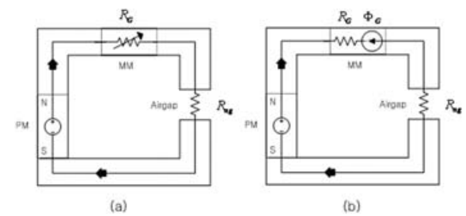

Fig.1 Comparison between existing analysis and proposed analysis of MM

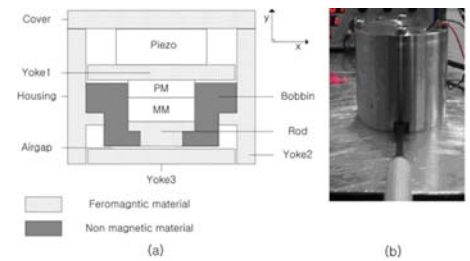

Fig. 2 Schematic view (A) and photograph (B) of the actuator

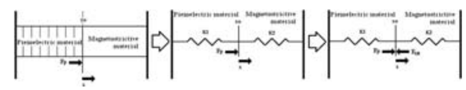

Fig. 3 spring model of smart materials

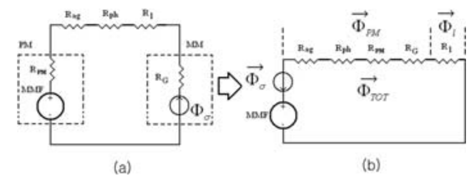

Fig. 4 Magnetic equivalent circuit (a) and digest (b) of proposed actuator

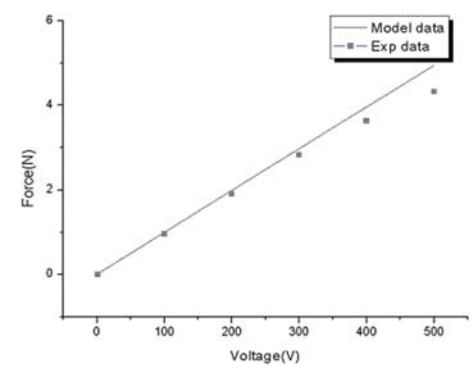

Fig. 5 Comparison between proposed model and experiments data of magnetic force

GL-01

Interface effects in the magnetic properties of $La_{0.7}Sr_{0.3}MnO_3/SrTiO_3$ heterostructures.

F. Y. Bruno[1], J. Garcia-Barriocanal[1], A. Rivera[1], Z. Sefrioui[1], C. Leon[1], J. Santamaria[1], N. M. Nemes[2], M. Garcia-Hernandez[2], M. Varela[3], S. J. Pennycook[3]
1. GFMC. Dpto. Fisica Aplicada III., Universidad Complutense de Madrid, Madrid, Spain; 2. Instituto de Ciencia de Materiales de Madrid, Consejo Superior de Investigaciones Cientificas, Cantoblanco, Spain; 3. Condensed Matter Science Division, Oak Ridge National Laboratory, Oak Ridge, TN

Recentlty, large tunneling magnetoresistance (TMR) was observed at 4 K in magnetic tunnel junctions (MTJs) based on $La_{0.7}Sr_{0.3}MnO_3$ (LSMO) electrodes separated by a thin $SrTiO_3$ (STO) barrier [1]. However, the reported TMR for these MTJs shows a rapid decrease with increasing temperature and vanishes around 200K, well below the Curie temperature (Tc) of the bulk electrodes. It has been suggested [2, 3] that this strong degradation of TMR with temperature might result from modified magnetic properties at the LSMO/STO interface. In this work we report on the growth of LSMO/STO superlattices with fixed LSMO thickness (6 unit cells (u.c.)) and changing the STO thickness from 1 to 24 u.c., to investigate the influence of STO in the magnetic properties of the LSMO layer.

Superlattices were grown on (100) oriented STO substrates using a high-pressure (2.9 mbar) pure oxygen sputtering system at a substrate temperature of 900 °C. This provides a thermalized and ordered growth at a slow rate (0.02 nm/s) which allows an accurate control of the layer thickness.[4]Figure 1 shows XRD spectra around the superlattice (001) Bragg peak for the $[\mathrm{LSMO\ 6\ u.c.\ /\ STO\ n\ u.c.}]_8$ superlattices. The multiple satellite peaks observed around the Bragg peak indicate the coherent heteroepitaxial growth of LSMO and STO layers with sharp interfaces. Magnetic properties were measured in a vibrating sample magnetometer with the field applied along the film plane. Hysteresis loops were measured at 10K (figure 2(a)) showing a ferromagnetic behavior for all samples. The saturation magnetization (M_S) at 10K is shown in the inset of figure 2(a). Saturation magnetization values M_S of 3.8 μ_B/at_{Mn} are obtained for the superlattices with STO thickness (d_{STO}) of 1 u.c. and 2 u.c., close to the bulk LSMO value, while M_S shows a sharp decrease for larger d_{STO} towards a value of about $M_S = 2.6\ \mu_B/at_{Mn}$. Figure 2(b) shows temperature dependent magnetization for the same superlattices. Samples were field cooled and measured warming up in 100 Oe. The Curie temperature (taken as a linear extrapolation of the maximum slope in magnetization curves to zero magnetization) is shown in the inset of figure 2(b). Interestingly T_C is found to be about 200 K and independent of STO thickness for d_{STO} larger than 10 u.c., while a clear rise in T_C is observed as STO thickness decreases towards 1 u.c.. The same trend is followed by T_P, the temperature at which a maximum occurs in resistance versus temperature measurements (see inset of figure 2(b)). This result might explain the observed vanishing of TMR in LSMO/STO/LSMO MTJs [1] above 200 K, since our data points to the degradation of the magnetic properties of LSMO close to the interface with STO. In fact, superlattices with thicker LSMO layers show higher T_C and T_P values (not shown), which suggests that the interface itself is responsible for the degraded magnetic properties observed when the LSMO layer is thin enough. Atomic resolution STEM and EELS measurements are currently under way to determine if the Mn oxidation state in the LSMO layer is modified close to the interface.

[1] M. Bowen, M. Bibes, A. Barthelemy, J.-P. Contour, A. Anane, Y. Lemaitre, and A. Fert, Appl. Phys. Lett. 82, 233 (2003).

[2] V. Garcia, M. Bibes, A. Barthélémy, M. Bowen, E. Jacquet, J.-P. Contour, and A. Fert, Phys. Rev. B. 69, 052403 (2004).

[3] Y. Ishii, H. Yamada, H. Sato, Y. Ogawa, M. Kawasaki, Y. Tokura, and H. Akoh, Appl. Phys. Lett. 89, 042509 (2006).

[4] Z. Sefrioui, V. Cros, A. Barthélémy, V. Peña, C. León, J. Santamaria, M. Varela, y S. J. Pennycook, Appl. Phys. Lett, 88, 022512 (2006).

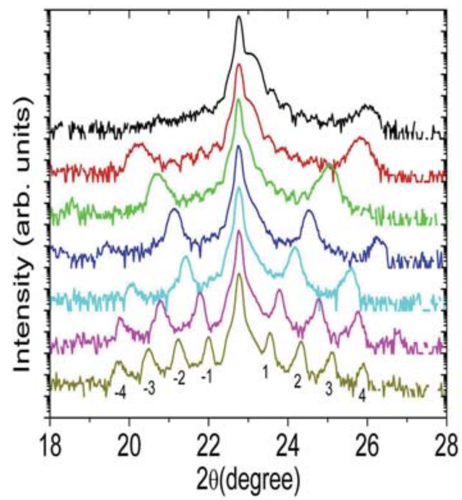

θ - 2θ X-Ray diffraction scan around (001) Bragg reflection of $[La_{0.7}Sr_{0.3}MnO_3/SrTiO_3]_8$ superlattices. Satellite peaks order is shown. The LSMO layer thickness is 6 unit cells, the STO layer thickness is from top to bottom: 1, 2, 5, 7, 12, 18, 24 unit cells.

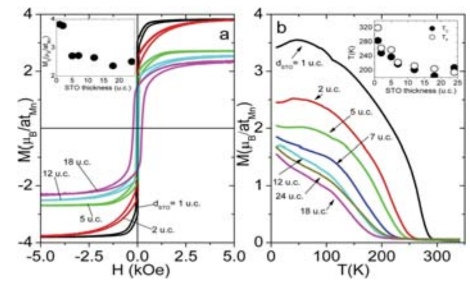

(a) Magnetization as a function of magnetic field applied in the film plane. The temperature was fixed at 10K. Inset: saturation magnetization (M_S) at a temperature of 10K. (b) Temperature dependence of magnetization. Inset: variation of Curie temperature (T_C) and temperature of the maximum in resistance versus temperature measurements (T_P).Samples are $[La_{0.7}Sr_{0.3}MnO_3/SrTiO_3]_8$superlattices with LSMO layer thickness 6 unit cells and STO layer thickness d_{STO}.

GL-02

Control of the degree of out-of-plane anisotropy of CoFe/Tb multilayer by applying an external in-plane field during film deposition.

K. Lee, Y. Jang, J. Kim, S. Lee, B. Cho
School of Photonics, MSE, GIST, Gwangju, South Korea

In the most applications of a magnetic spin valve sensor, the magnetization of a soft sensing layer is oriented perpendicular to that of a hard magnetic layer. In order to obtain the cross configuration, several methods have been investigated, such as using the external bias field, shape anisotropy, and step edge anisotropy [1-4]. However, these methods have some drawbacks, such as complicated sensor design and lithographic process. Recently, a new type of spin valve, which has a structure with alternating out-of-plane and in-plane magnetization configuration, has been suggested [5-7]. Multilayer of transition metal (TM)/rare-earth metal (RE), such as CoFe/Tb and Fe/Tb, was used to form an out-of-plane anisotropy. The sensitivity and the in-plane field range of sensing is strongly dependent of the thickness of the RE layer. Thus, it would be important to investigate the properties of the out-of-plane anisotropy in the multilayer of TM/RE to optimize the sensitivity and the in-plane field range of sensing. In this work, we studied the out-of-plane anisotropy of $Co_{50}Fe_{50}$/Tb multilayer film by changing the thickness of Tb layer and applying an external in-plane field of 200 Oe during the position of layers. A double bilayer of $[Co_{50}Fe_{50}(2\ nm)/Tb(t_{Tb})]_2$ was deposited by magnetron sputtering at a base pressure of 5×10^{-8} Torr. Figures 1(a) and (b) show isothermal magnetization at room temperature of $[Co_{50}Fe_{50}(2\ nm)/Tb(t_{Tb})]_2$ with t_{Tb} = 1 nm and 3 nm, respectively. The multilayers were fabricated without applying an in-plane external field. As expected, the multilayer with t_{Tb} = 1 nm shows a strong out-of-plane anisotropy, as shown in Fig. 1(a). Meanwhile, the sample with t_{Tb} = 3 nm exhibits a similar hysteresis behavior regardless of the field orientation, as shown in Fig. 1(b). In general, the out-of-plane anisotropy in a multilayer is believed to be induced by a mixed interface and maintained by the exchange interaction between the adjacent transition-metal layers [8]. Thus, it is likely that, as the t_{Tb} increases over the critical thickness, the net magnetic moment of multilayer becomes to be tilted to in-plane direction, because the unmixed Tb moments in the layer leads to parallel alignment of the out-of-plane moment at the interface [8-9]. Figure 2(a) and (b) shows isothermal magnetization at room temperature of $[Co_{50}Fe_{50}(2\ nm)/Tb(t_{Tb})]_2$ with t_{Tb} = 1 nm and 3 nm, respectively, which was fabricated with applying an in-plane external field of 200 Oe during deposition of layers. In contrast to the case in Fig. 1(a), the sample with t_{Tb} = 1 nm, fabricated with the in-plane external field, shows a strong in-plane anisotropy, as shown in Fig. 2(a). This indicates that the formation of the out-of-plane anisotropy at the mixed interface of TM/RE bilayer is affected critically by the small external field, applied during the deposition. The multilayer with t_{Tb} = 3 nm shows no preference in the in-plane and out-of-plane anisotropies, as shown in Fig. 2(b). Although the hysteresis behavior in Fig. 2(b) is quite similar to the case in Fig. 1(b), it can not be accounted in terms of the unmixed Tb moments scenario. At present, we do not understand the origin of the spin orientation of the multilayer with t_{Tb} = 3 nm, fabricated with the applied field. However, it would be worthwhile to notice that the degree of the out-of-plane anisotropy can be controlled by changing the thickness of RE metal layer and applying an in-plane external field during deposition. Based on our preliminary data as in Figs. 1 and 2, we found that the out-of-plane anisotropy in the multilayer of $[Co_{50}Fe_{50}(2\ nm)/Tb(t_{Tb})]_2$, which was believed to be induced by the mixed interface, can be affected critically by the small applied filed during deposition. Because the degree of out-of-plane anisotropy was found to be changed by adjusting the thickness of RE layer and the applied field, it will be discussed in detail how the thickness and field parameters affect the spin orientation in the TM/RE multilayer.

[1] M. Tondra, J. M. Daughton, D. Wang, R. S. Beech, A. Fink, and J. A.Taylor, J. Appl. Phys. 83, 6688 (1998)

[2]X. Liu, C. Ren, and G. Xiao, J. Appl. Phys. 92, 4722 (2002)

[3]Y. Lu, R. A. Altman, A. Marley, S. A. Rishton, P. L. Trouilloud, G. Xiao,W. J. Gallaghar, and S. S. P. Parkin, Appl. Phys. Lett. 70, 2610 (1997)

[4]D. Lacour, H. Jaffrès, F. Nguyen Van Dau, F. Petroff, A. Vaurès, and J.Humbert, J. Appl. Phys. 91, 4655 (2002)

[5] Sebastiaan van Dijken and J. M. D. Coey, Appl. Phys. Lett. 87, 022504 (2005)

[6] B. Szymanski, F. Stobiecki, M. Urbaniak, J. Alloys and Compounds 423, 236 (2006)

[7] F. Stobiecki, B. Szymanski, T. Lucinski, J. Dubowik, M. Urbaniak, M. Schmidt and K. Röll, J. Mag. Mag. Mat. 272-276, e1751 (2004)

[8] A. E. Freitag and A. R. Chowdhury, J. Appl. Phys. 85, 4696 (1999)

[9] Andrea E. Freitag and Ataur R. Chowdhury, J. Appl. Phys. 82, 5039 (1997)

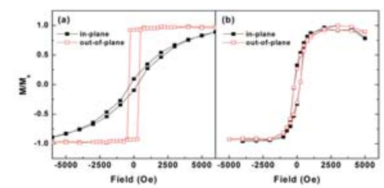

FIG. 1. In-plane and out-of-plane hysteresis loops at room temperature for the multilayer of $[Co_{50}Fe_{50}(2\ nm)/Tb(t_{Tb})]_2$ with (a) t_{Tb} = 1 nm and (b) 3 nm, deposited without applying an external in-plane field.

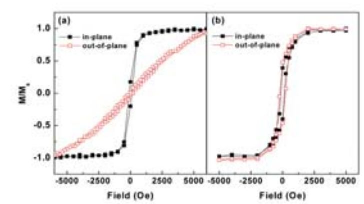

FIG. 2. In-plane and out-of-plane hysteresis loops at room temperature for the multilayer of $[Co_{50}Fe_{50}(2\ nm)/Tb(t_{Tb})]_2$ with (a) t_{Tb} = 1 nm and (b) 3 nm, deposited with applying an in-plane external field of 200 Oe.

GL-03

Effect of the Cr insertion layer on synthetic antiferromagnetic coupling in magnetic tunnel junctions.

K. Kim[1], W. Kim[2], S. Oh[2], D. Kim[2], I. Hwang[1], K. Kim[1], S. Seo[1], J. Jeong[2], K. Nam[2], J. Lee[2]
1. Semiconductor Devices Lab, Samsung Advanced Institute of Technology (SAIT), Yongin-Si, South Korea; 2. Process Development Team, Samsung Electronics Co., Ltd, Yongin-Si, South Korea

Synthetic antiferromagnetic (SAF) layers have been generally applied to the spintronics devices using a structure of spin valves or magnetic tunnel junctions, such as HDD read sensor, and magnetic random access memory (MRAM). Magnetic tunnel junctions (MTJ) with SAF layer consist of seed layer/PtMn/PL1/NM/PL2/MgO/FL/capping layer, where FL is the ferromagnetic free layer, PL1 and PL2 are the two ferromagnetic pinned layers antiferromagnetically coupled through a non-magnetic (NM) layer due to the RKKY interlayer exchange coupling. Because the SAF structure[1,2] has an antiparallel alignment of the magnetization of PL1 and PL2, it has an advantage of a reduction in the magnetostatic coupling between the pinned layer and the free layer. Moreover, the SAF structure has an another advantage for the SAF free layer, because it can achieve a low net magnetization for the low switching field and shows a higher thermal stability than a single FL. These characteristics are more important as the size of magnetic device is reduced to the nano-scale regime.

Since the large tunneling magnetoresistance ratio (TMR) was reported in the MgO-MTJ with amorphous ferromagnetic materials, such as CoFeB [3], the amorphous ferromagnetic materials have been substituted for the crystalline ferromagnetic materials, such as CoFe, NiFe, because the amorphous electrodes are critical to develop the highly textured MgO tunnel barrier., However, SAF structure using the amorphous materials shows much weaker interlayer exchange coupling strength when compared to the SAF structure using the crystalline phase. Therefore, it is necessary to develop the method for the enhanced exchange coupling strength in the SAF structure using the amorphous materials.

In this study, we have investigated the effect of Cr insertion on the exchange coupling strength in SAF structure. The stacking structure of MTJ was seed layer/PtMn/CoFe/(Cr)-Ru-(Cr)/CoFeB/MgO/CoFeB/Ta. Some samples were annealed in a vacuum for 2hr in the range up to 400'C under the magnetic field of > 0.5 Tesla. The magnetic and structural properties were characterized by a vibrating sample magnetometer (VSM), and high resolution transmission electron microscopy (TEM), respectively. The MTJs were patterned into 0.3 x 0.8 um2 cell sizes for the measurement of electrical properties, such as TMR, RA.

Figure 1 shows the magnetization curves of as-prepared MTJs with the different condition of Cr insertion layers. The magnetic properties of SAF layer depend on the insertion position and the thickness of Cr layer. When the Cr layer is located between the top interface of Ru and amorphous CoFeB, the exchange coupling strength are reduced, however, at the bottom interface of Ru and crystalline CoFe, the exchange coupling strength are enhanced. The saturation field (Hsat) of reference MTJ with Ru 9A shows ~1900 Oe, but that of MTJ with Cr(2A,bottom))/Ru(7A) shows the enhanced value of ~2300 Oe. The saturation field (Hsat) values are shown in Figure 2. This trend is not changed after magnetic vacuum annealing process at the relatively low temperature, but the different trend is observed after the high temperature annealing. The effects of the inserted Cr layer are investigated based on the structural analysis using HR-TEM, and the TMR properties.

1) S.S.P. Parkin, et al. Phys.Rev. Lett. 64, 2304 (1990)

2) S.S.P. Parkin, Phys.Rev. Lett. 67, 3598 (1991)

3) D. Djayaprawira, et al. Appl. Phys. Lett. 86, 92502 (2005)

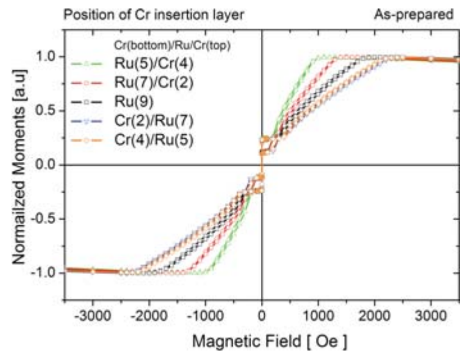

Figure 1. The magnetization curves of as-prepared MTJs with the different condition of Cr insertion layers

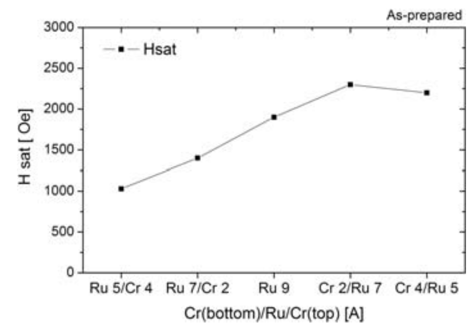

Figure 2. The plot of the saturation field (Hsat) of as-prepared MTJs with the different condition of Cr insertion layers.

GL-04

Preparation and magnetic characterization of Fe/MgO layered granular thin films.

A. García-García[1], J. A. Pardo[2,3], *P. A. Algarabel*[1], C. Magén[4], P. Štrichovanec[2], L. Morellón[1,2], J. M. De Teresa[1], A. Vovk[2], M. R. Ibarra[1,2]
1. Instituto de Ciencia de Materiales de Aragón, Universidad de Zaragoza-CSIC, Zaragoza, Spain; 2. Instituto de Nanociencia de Aragón, Universidad de Zaragoza, Zaragoza, Spain; 3. Departamento de Ciencia y Tecnología de Materiales y Fluidos, Universidad de Zaragoza, Zaragoza, Spain; 4. Centre d'Elaboration de Matériaux et d'Etudes Structurales, CNRS, Toulouse, France

Granular thin films, in which magnetic single-domain nanoparticles ("superspins") are dispersed in a non-magnetic matrix, are a very active current research topic, because their magnetic and magnetotransport properties suggest various technological applications. They are represented, e.g., by discontinuous metal insulator multilayers (DMIMs) that resemble frozen ferrofluids to a large extent. DMIMs consist of metallic layers with different degrees of discontinuity intercalated between insulating spacer layers. When the metallic layer consists of closely spaced ferromagnetic granules, different types of collective behaviour appear due to magnetic interparticle interactions (of dipolar or tunnelling exchange origin): superparamagnetism (SPM), superspinglass (SSG) or superferromagnetism (SFM) [1,2]. DMIMs have the advantage that their magnetic behaviour can be controlled by modifying the nominal thickness of the deposited ferromagnetic metal [3].
Recently, we have prepared DMIMs of the system $[Fe(t)/MgO(3\ nm)]_N$, with the nominal thickness (t) of the iron layer ranging from 0.4 nm to 1.5 nm, and the number of bilayers (N) chosen to keep the total amount of iron constant between the samples. The layered granular thin films have been grown by sequential pulsed laser deposition with a KrF laser from the corresponding targets. An ultra-high vacuum atmosphere (10^{-9} Torr) and laser fluence on the target around 8 J/cm^2 has been used to deposit the multilayers at room temperature on Corning glass substrates.
Structural and magnetic characterization of the samples has been performed by X-ray reflectivity (XRR), high resolution transmission electron microscopy (HRTEM) and magnetization measurements using a SQUID magnetometer. From XRR the layers thickness and interphases roughness have been obtained by fitting of the experimental results using the LEPTOS software (BRUKER AXS).
The HRTEM observations have been performed using a TECNAI F20 microscope. As an example we show in Figure 1 a cross-section view of the sample with iron nominal thickness t=0.81 nm. The multilayer structure is clearly shown, and polycrystalline growth of Fe and MgO is observed. The size distribution and dispersion of the metallic clusters were studied by HRTEM plan-view on single Fe/MgO bilayers deposited on carbon grids with the same Fe-to-MgO ratios as in the multilayers (see Figure 2).
The magnetization measurements have allowed us to perform a preliminary characterization of the different magnetic states present in the samples. For $t \geq 0.9$ nm the DMIMs present a ferromagnetic behaviour with remnant magnetization and a low coercive field (≈ 12 Oe). These results indicate a physical percolation of the Fe grains producing a continuous ferromagnetic iron layer. The zero-field cooling (ZFC) and field cooling (FC) curves clearly show irreversible behaviour at low temperatures (see Figure 3). The blocking temperatures (T_B), obtained from the splitting between the ZFC and FC data, decrease with t, indicating a decrease of the mean particle volume. The fit of ZFC/FC curves using Curie-Weiss law allows to estimate the average granules size for the films with t < 0.7 nm. The results of the estimations correlates with the data obtained from direct HRTEM investigations.

[1] Xi Chen et al., Phys. Rev. B **72**, 214436 (2005)
[2] S. Bedanta et al., Phys. Rev. Lett. **98**, 176601 (2007)
[3] W. Kleemann et al., Phys. Rev. B **63**, 134423 (2001)

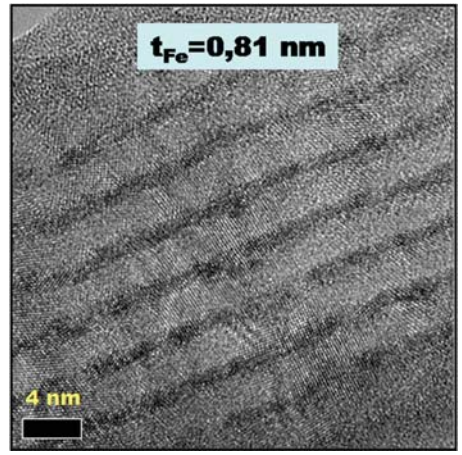

Figure 1. Cross section of the Fe/MgO multilayer with t=0.81 nm.

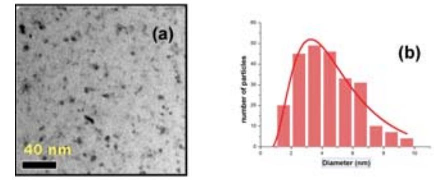

Figure 2. (a) Plan view and (b) grain size distribution (showing the best log-normal fit) of the Fe/MgO bilayer with t=0.81 nm.

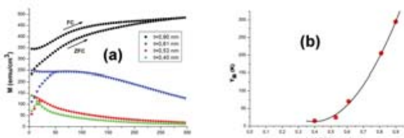

Figure 3. (a) Temperature dependence of the FC and ZFC curves for some selected samples with the nominal Fe thickness t indicated. (b) Behaviour of the blocking temperature (T_B) with t (the line is a visual guide).

GL-05

FMR Investigation of $(Ga_{1-x},Mn_x)As$ Tri-layers.

M. Cubukcu[1], K. Khazen[1], H. von Bardeleben[1], J. Cantin[1], M. Elsen[2], H. Jaffrès[2], J. George[2], L. Thevenard[3], A. Lemaître[3]
1. Institut des Nanosciences de Paris (INSP), Université Paris 6, UMR 75-88 au CNRS, Paris, France; 2. Unité Mixte de Physique CNRS-Thales, associée à l'Université Paris XI, Palaiseau, France; 3. Laboratoire de Photonique et Nanostructures, Marcoussis, France

Ferromagnetic(FM) semiconductors $(Ga_{1-x},Mn_x)As$ based magnetic tunnel junction, which consists of tri-layers with two ferromagnetic $(Ga_{1-x},Mn_x)As$ layers separated by a non magnetic (Ga,As) layer, are interesting objects for future spintronics application. In the as-prepared state $(Ga_{1-x},Mn_x)As$ thin films have rather low critical temperatures and a magnetization much lower than 5µB/Mn ion. A decisive step for the optimization of the magnetic properties is a thermal annealing in the 250°C temperature range. The efficiency of such annealing depends also on the surface conditions which in the case of multilayer structures are imposed at least for the lower layer by the structure itself. But the top layer might equally be affected differently due to the particular properties of the barrier layer[1-2]. We have investigated by ferromagnetic resonance(FMR) spectroscopy the affect of annealing on such tri-layers. A further interesting subject is interlayer exchange coupling(IEC) which might be expected to become important for ultra-thin barrier layers. We have studied tri-layers with two different barrier layer thicknesses to address this subject.
The tri-layers were grown by low temperature MBE at 250°C and had the following structure: a $(Ga_{1-0.05},Mn_{0.05})As$ 100nm bottom layer and a 30nm $(Ga_{1-0.05},Mn_{0.05})As$ top layer separated by a Be doped (In,Ga)As barrier layer of 4nm or 6nm thickness. The tri-layers were studied in the as-grown state and after a low temperature(250°C /1h) standard thermal annealing which has been found to be optimal for the annealing of $(Ga_{1-x},Mn_x)As$ single layers. These tri-layers had been previously studied by tunneling magnetoresistance(TMR) measurements. The FMR measurements were performed at 9GHz in the 4K to 150K temperature range. The spectra were taken for both the in-plane and out of plane orientations of the applied magnetic field and the FMR parameters were obtained from a classical Smit-Beljers analysis. The FMR investigations of the tri-layers allow a more detailed analysis of these layers as compared to SQUID measurements give access to the four magnetocristalline anisotropy constants(K_i) and the critical temperature(Tc).
I. As-grown tri-layers: We observe for both types of layers two distinct FMR spectra which from their respective intensities can be associated with the uniform mode spectra of the lower and upper layers.The observation of two distinct FMR spectra demonstrates that in spite of identical growth parameters the magnetic properties of the two layers are not identical which we attribute to the different strains in the layers. They show further that IEC is not important under these conditions. The saturation magnetizations were 27 emu/cm^3 and 29 emu/cm^3 for bottom and top layers respectively. The critical temperatures of the two layers were 70K and 95K respectively. The analysis of the angular variations of the FMR spectra allows us to determine the magnetocristalline anisotropy constants and their variation with temperature for the two layers.
II. Annealed tri-layers: The properties of both layers were modified by the annealing treatment. The measurement of the respective Tc of the layers, both by FMR and SQUID, reveals an enhancement only for the top layers(Tc=135K). The FMR intensity and the SQUID measurements show that the magnetization is increased by the factor 1.15 for the top and by a factor 1.05 for the bottom layers. Fig.1 shows the dominant anisotropy constants of the layers for the sample with 4nm thick intermediate layer. These values are obtained from angular dependence of the resonance spectra for different applied field orientations. Here again the modification is for both top and bottom layers but more important for the top layer. These values are compared with the $(Ga_{1-x},Mn_x)As$ reference mono-layer[3] and some metallic systems in order to better understand the causes for the magnetic properties modifications. The hole concentration[p] and strains(Δa/a) in the layers are estimated using the anisotropy constants and the mean field model predictions. The results show that despite the small difference of strains in the bottom layer before and after annealing the hole concentration is the same. But [p] and Δa/a are significantly modified for the top layers. These results are consistent with the previous studies on the annealing effect on multi-layers.
Contrary to the conclusions drawn from the TMR results we find no evidence for interlayer exchange coupling in the FMR measurements.

[1] D.Chiba et al. Appl.Phys. Lett, 82, 3020(2003) [2] Y.Sato et al. Journal of superconductivity: incorporating Novel Magnetism, 18, p.345,(2005) [3] Kh.Khazen et al. "FMR investigation of (Ga,Mn)As thin films with constant Mn and variable free hole concentrations", submitted to Phys. Rev. B,(2007)

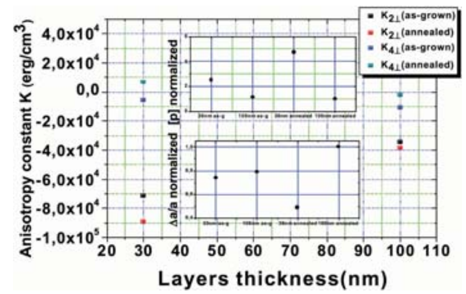

Anisotropy constant dependence on the layers thickness $(Ga_{1-x},Mn_x)As$ at 4K for as-grown and annealed samples with 4nm thick intermediate layer. Insert: relative hole concentration and lattice parameter variation for different layers as-grown and annealed.

GL-06

Interplay between magnetic anisotropy and interlayer exchange coupling in amorphous CoSi / Si multilayers.

L. M. Álvarez-Prado, C. Quirós, L. Zárate, J. I. Martín, J. M. Alameda
Departamento de Física, Universidad de Oviedo, Oviedo, Spain

Interlayer Exchange Coupling (IEC) of magnetic layers across semiconducting spacers with thickness in the nanometer range is an interesting subject since it strongly modifies the magnetization reversal processes of multilayered films but its origin still remains unclear. Recent studies have focused on the Co-Si system, reporting unequivocal indications of the presence of weak antiferromagnetic (AF) coupling for the case of amorphous CoSi magnetic alloys separated by Si spacers [1-2]. Such a weak coupling leads to one of the most peculiar properties of this Co-Si system: the fact that coupling fields (~ Oe) are significantly smaller than anisotropy fields (tipically 10-30 Oe), reversing the typical balance observed in other AF multilayers. As a consequence of this particular energetic balance, the study of the interplay between magnetic anisotropy and interlayer coupling for the Co-Si system is specially interesting.
Three samples have been prepared in order to gain insight on this interplay. First one is a single magnetic film (with Si capping and buffer) having the following structure: (3 nm Si / 5 nm Co73Si27 / 3 nm Si / Si (111) substrate). The two other samples are multilayers of two magnetic periods separated by a semiconducting Si spacer (again with Si capping and buffer): (3 nm Si / 5 nm Co73Si27 / 3 nm Si / 5 nm Co73Si27 / 3 nm Si / Si (111) substrate). Although the two multilayers have the same nominal structure, in one case the magnetic easy axis of both magnetic layers is parallel, but in the second multilayer the in-plane magnetic easy axes of the top and bottom magnetic layers are perpendicular.
First thing to point out is that the single magnetic film shows the typical behaviour of samples with in-plane uniaxial anisotropy. This is shown in fig. 1, where magneto-optical transverse Kerr effect loops have been measured by applying the magnetic field at different angles respect to the sample easy axis. In fact, 90 deg. corresponds to a magnetic hard axis with an anisotropy field of about 10 Oe, whereas at 0 deg. the loop is perfectly squared with a coercive field of 0.4 Oe. The origin of this uniaxial anisotropy is related to the growth geometry [1], since oblique incidence (around 30 deg. off substrate normal) has been used to sputter the Si target.
The loops for the sample consisting of two magnetic periods with parallel anisotropies are shown in fig. 2(a). In this case, no significant changes are observed concerning the hard axis. However, for the easy axis, and also for the intermediate angles, the shape of the loops is drastically modified with respect to the one period case. Now a clear plateau is observed at around zero magnetic field, indicating the stabilization of the AF alignement. The switching fields are in the 2-3 Oe range, confirming the weak nature of the coupling.
Finally, a third sample has been prepared, but now with crossed individual in-plane uniaxial magnetic anisotropies, by making a 90 deg. rotation around substrate normal inmediately before the growth of the top magnetic layer [3-4]. In this case, as it can be seen in fig. 2(b), the reversal process is strongly modified as compared to the other multilayer (see fig. 2(a)) since only when the magnetic field is applied along the – 45 deg. direction, that is, one of the bisecting directions between the easy axis of both layers, the AF alignement is stabilized. This procedure shows an easy way to modify the magnetization reversal process and the angular range where the AF alignement is stabilized. It is also worth mentioning that this trend has been obtained by micromagnetic simulations.

Work supported by the Spanish CICYT under grant FIS2005-07392 and NAN2004-09087. C. Q. acknowledges support from the Spanish Government and the European Social Fund through the "Ramón y Cajal" program.

[1] C. Quirós et al., Phys. Rev. B 71, 024423 (2005).

[2] L. Zárate et al., Phys. Rev. B 74, 14414 (2006).

[3] S. M. Valvidares et al., Phys. Rev. B 64, 134423 (2001).

[4] L. M. Álvarez-Prado et al., Phys. Rev. B 76, 214419 (2007).

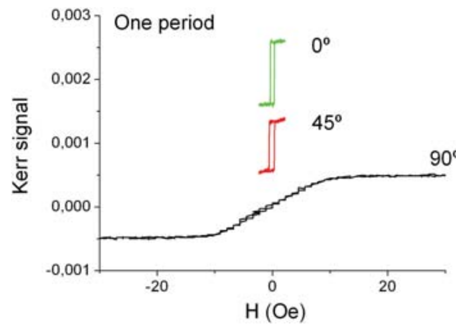

Figure 1. Magneto-optical transverse Kerr effect loops measured in a sample having one magnetic layer of 5 nm Co73Si27. The angle indicates the direction of the magnetic field respect to the easy axis. The loops have been vertically shifted for clarity.

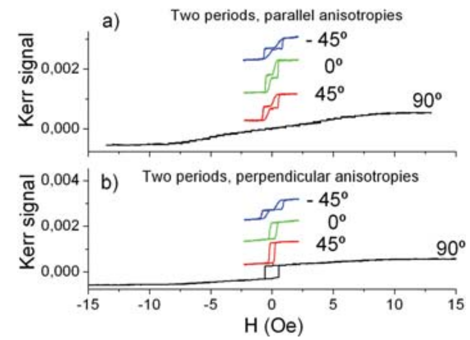

Figure 2. (a) Magneto-optical transverse Kerr effect loops measured in a sample made of two magnetic periods having parallel uniaxial anisotropies. The angle indicates the direction of the magnetic field respect to the easy axis. (b) Same than (a) but for sample having in-plane perpendicular uniaxial anisotropies.

GL-07

Creation of out–of–plane magnetization ordering by increasing multilayer number N in $[Co/Au]_N$ multilayers.

M. Tekielak[1,2], P. Mazalski[1], A. Maziewski[1,3], R. Schäfer[2], J. McCord[2], B. Szymanski[4], M. Urbaniak[4], F. Stobiecki[4]
1. Department of Physics, Univeristy of Bialystok, Bialystok, Poland; 2. Leibniz-Institut für Festkörper- und Werkstoffforschung Dresden e.V, Dresden, Germany; 3. Laboratoire de Physique des Solides, Université Paris-Sud, Orsay, France; 4. Institute of Molecular Physics, Polish Academy of Sciences, Poznan, Poland

The properties of magnetic multilayers can be easily manipulated by varying the thickness of the magnetic and/or nonmagnetic layers as well as the number of layers [1–3]. Increasing the thickness d of a single magnetic layer, a spin reorientation transition (SRT) from out-of-plane to in-plane magnetization occurs above a critical thickness $d \rangle d_{SRT}$ [4]. An interesting study of magnetic ordering, using Mössbauer spectroscopy and magnetic force microscopy (MFM), has been performed in [5] on Co/Au multilayers with different bilayer repetition number N. With increasing N an increase of the mean out-of-plane component of magnetization was observed.
In this paper the influence of the Co layer thickness as well as the number of repetitions N on the magnetic properties of $[Co/Au]_N$ multilayers was investigated systematically. The studies were focused on the key characteristics of magnetic hysteresis loops and domain structure parameters using both, MFM and magneto–optical Kerr microscopy.
The multilayers $[Co(d)/Au(3\ nm)]_N$ with d = 1, 2, 3 nm and N = 1–12 were prepared by dc magnetron sputtering in UHV conditions on oxidized silicon substrates. The SRT was found to occur at a thickness d_{SRT} of about 1.4 nm.
The magnetic properties were analyzed at room temperature by employing different complementary magnetic characterization techniques. The magnetization reversal processes were studied using a magneto-optical Kerr effect (MOKE) based magnetometer and/or vibrating sample magnetometry (VSM) as a function of magnetic field applied either parallel $H_{\|}$ or perpendicularly $H_{\perp}$ to the sample surface. The visualization of the magnetic domain structure was performed by wide–field Kerr microscopy in the polar and longitudinal modes with out–of–plane and in–plane magnetization sensitivity, respectively. Atomic and magnetic force microscopy (AFM/MFM) were used for surface structure analysis and magnetic domain structure imaging beyond the optical resolution. Either $H_{\|}$ or $H_{\perp}$ applied field induced changes of domain structures were studied.
The repetition number N and cobalt thickness d strongly influence both, the domain structure and the magnetization processes. For d = 1 nm and N = 1, below the SRT, a domain structure with magnetization perpendicular to the sample plane and a rectangular hysteresis loop are observed. With increasing N, we observed: (i) a decrease of the domain period; (ii) an increase of the saturation field H_S; (iii) an increase of the nucleation field H_N; starting from negative values (for small N with square hysteresis loops) up to positive with amplitude for larger N close to H_S.
The evolution of domain structure together with corresponding hysteresis loops as a function of N (for d = 2 nm) are illustrated in Figure 1. For $N \leq 6$ domains with in–plane magnetization are observed. A crossover from in–plane to out–of–plane magnetization ordering was observed for N between 6 and 12. The magnetostatic forces induce a domains ordering transition to a band domain structure with perpendicularly aligned magnetization and submicrometer size. Submicrometer domain periods were measured for all samples with N = 12 and different d.
The evolution of the magnetization curves with $H_{\perp}$ and increasing repetition number is illustrated in Fig.1D – F. The following changes are observed with increasing N: (i) a decrease of the saturation field H_S; (ii) an increase of the domain structure nucleation field H_N; (iii) an increase of the saturation Kerr rotation.
In conclusion, an influence of the magnetostatic interaction on the magnetization behavior was observed in $[Co/Au]_N$ multilayers. By increasing the repetition number beyond N = 12 an out–of–plane magnetization ordering is created. The fundamental differences in magnetization behavior with different Co thicknesses will be discussed in detail. Similar effects related with a spin–reorientation phase transition were studied experimentally [6] and by means of micromagnetic simulations [7] for larger cobalt layer thickness.
This work was supported by the Marie Curie Fellowships for "Transfer of Knowledge" ('NANOMAG–LAB" N 2004–003177).

[1] J.R. Barnes, S.J. O'shea, M.E. Wellad, J.Y. Kim, J.E. Evetts, R.E. Somekh, J. Appl. Phys. 76, 2974 (1994).

[2] O. Donzelli, D. Palmeri, L. Musa, F. Casoli, F. Albertini, L. Pareti, G. Turilli, J. Appl. Phys. 93, 9908 (2003).

[3] L. Belliard, J. Miltat, V. Kottler, V. Mathet, C. Chappert, T. Valet, J. Appl. Phys. 81, 8 (1997).

[4] M. Kisielewski, A. Maziewski, M. Tekielak, A. Wawro, L. T. Baczewski, Phys. Rev. Lett. 89, 8 (2002).

[5] S. Hamada, H. Hosoito, T. Ono, T. Shinjo, JMMM 198, 496 (1999).

[6] M. Hehn, S. Padovani, K. Ounadjela, J. P. Bucher, Phys. Rev. B 54, 5 (1996).

[7] M. Kisielewski, A. Maziewski, V. Zablotskii, JMMM 316, 277 (2007).

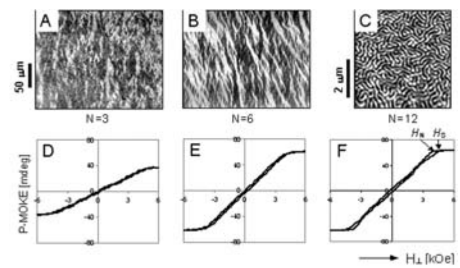

Fig.1. Domain patterns (A - C) and corresponding magnetooptic hysteresis loops (D - F) measured for $Si/[Au(2nm)/Si(1nm)]_{10}/[(Co(2nm)/Au(3nm)]_N$ samples with different *N*. The images size are: (A, B) 200 µm x 150 µm, (C) 5 µm x 5 µm. Images (A, B) and (C) were obtained by longitudinal Kerr effect based microscopy and MFM, respectively.

GL-08

Magnetostatic waves in the magnetic/nonmagnetic periodic structures.

M. Krawczyk
Faculty of Physics, Adam Mickiewicz University, Poznan, Poland

We propose a new method for solving Walker equation [1]for the magnetostatic potential, ψ (Eq. (1)). From this equation with spatially depended permeability tensor, μ we can calculated dispersion relation of magnetostatic waves (MW) propagating in magnonic crystals (MC), i.e. structures composed of periodically distributed different magnetic or magnetic and nonmagnetic components. This equation is solved by the plane wave method adopted from photonic crystal band structure calculations: we use Bloch theorem and Fourier series to transform the Walker equation to the reciprocal space; the final infinite set of equations are transformed into eigenvalue problem Eq. (2) for the MW frequency (ω) and than solved numerically. We show possibility of applying this method for determining MW spectra in one dimensional (1D) and also in two dimensional (2D) magnonic crystals by checking convergence with increasing number of plane waves used in Fourier expansions, for different configurations: e.g. superlattices or dipolar systems composed of magnetic dots (or antidots) periodically distributed in a nonmagnetic (or magnetic) medium. The presented results of numerical calculations refer mainly to the superlattices composed of ferromagnetic materials separated by a nonmagnetic interlayer. The results include the effect of material and structural parameters on the MW
spectrum of the considered structures for different directions of MW propagation. The forming of the magnonic bands for the cases of the backward (Fig. 1), forward and surface (Fig. 2) MWs (well known from the ferromagnetic thin films [2]) in magnonic crystals are presented, their dependencies on direction of the wave vector are exploited, as well. We interpret the resulting spectra within the magnonic model with the help of the calculated magnetic field distributions (Fig. 3 and 4). The calculation results allow to better understanding of features of MW propagating in 1D and 2D magnonic crystals, which could be useful in designed a magnetostatic wave-based and a spin-wave logic devices [3,4].

[1] L. R. Walker, Phys. Rev. **105**, 390 (1957).

[2] R. W. Damon and J. R. Eshbach, J. Phys. Chem. Solids

19, 308 (1961);

A. G. Gurevich and G. A. Melkov, *Magnetization Oscillations and Waves*, (CRC Press, NY, 1996).

[3] P.K. Amiri and B. Rejaei, J. Appl. Phys. **100**, 103909 (2006).

[4] A. Khitun et al., Nanotechnology **18**, 465202 (2007).

$$\nabla \cdot (\hat{\mu}(\vec{x})\nabla\psi(\vec{x})) = 0,$$

Eq. (1). The Walkar equation.

$$\begin{pmatrix} 0 & I \\ \hat{A} & \hat{B} \end{pmatrix} \begin{bmatrix} \psi \\ i\omega\vec{\psi} \end{bmatrix} = i\omega \begin{bmatrix} \psi \\ i\omega\vec{\psi} \end{bmatrix},$$

Eq. (3). Eigenvalue problem used in calculations. Submatrices A, B and a vector ψ are indexed by the reciprocal lattice vectors.

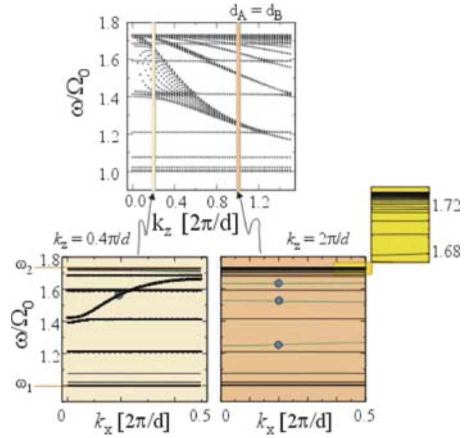

Fig. 1. The band structure of the backward MW versus wave vector parallel to the external magnetic field: k_z (top). Backward MW dispersion relations in the first Brillouin zone for two values of k_z (bottom).

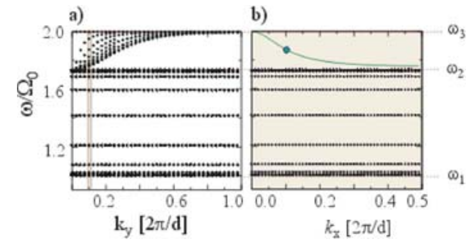

Fig. 2. a) Magnetostatic band structure of the surface MW versus wave vector perpendicular to the magnetic field k_y. b) Dispersion of magnetostatic waves versus k_x in the first Brillouin zone for $k_y = 0.2$.

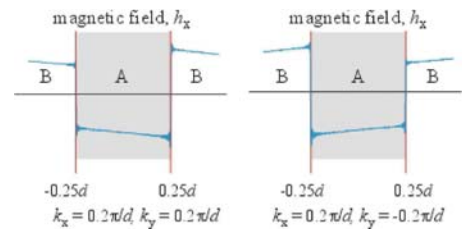

Fig. 3. Dynamic magnetic field h_x across a unit cell of the superlattice for the 'surface' magnetostatic wave marked by the circle on the Fig. 2b, for two wave vectors k_y with opposite sign.

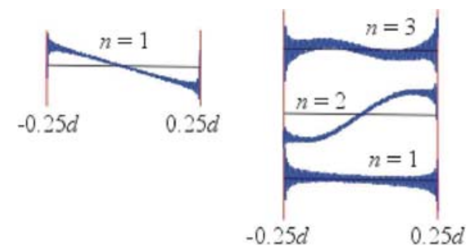

Fig. 4. Dynamic magnetic field inside a ferromagnetic layers for the backward MWs marked by circles on Fig. 1.

GL-09

Investigations on magnetic properties of NiFe film doped with Gd by ferromagnetic resonance.

Y. Fu[1], L. Sun[1,3], J. Wang[1], Z. Kou[1], *Y. Zhai*[1,2], X. Bai[2], J. Wu[3], Y. Xu[4], J. Du[2], H. Lu[2], H. Zhai[2]
1. Department of Physics, Southeast University, Nanjing, China; 2. National Laboratory of Solid Microstructures, Nanjing University, Nanjing, China; 3. Department of Physics, University of York, York, United Kingdom; 4. Department of Electronics, University of York, York, United Kingdom

The effect of small doping of Rare Earth element on the structure and magnetic properties of thin films of transition metal alloys is an interesting topic though Re-TM alloys have been well studied as permanent magnet and magnetooptical recording media. This paper reports the study on the magnetic anisotropy and magnetization dynamic damping of thin films of NiFe alloy doped with different content of Gd by Ferromagnetic Resonance (FMR). The FeNi-Gd films with buffer and capping layers of 5 nm thick Ta were deposited on silicon substrates by magnetron sputtering with base pressure of 1.0×10^{-5} Pa. The thickness of the films was kept at 30 nm. The Gd content was adjusted by varying the number of Gd chips on NiFe target and checked by SEM and X-ray diffraction. The content of Gd in the NiFe-Gd films was 0, 2.9%, 5.7% and 9.3%, while the proportion of Ni and Fe was kept at 83:17. FMR were performed ex situ with a Brucker ESR Equipment of model ER-200D-SRC at microwave frequency of 9.78GHz. The dependences of resonance field and linewidth on various orientations of the magnetic field were obtained.

The film of NiFe-2.9%Gd was identified as in cryctalline structure with lattice constant slightly larger than the pure NiFe film, indicating some Gd atoms are dissolved in the NiFe lattice. A small amorphous halo in XRD pattern shows that a small amout of amorphous phase appears. Two other films with higher Gd content are identified as in amorphous state. The open circles in Fig. 1(a) to (d) display the experimental angular dependence of FMR field on out-of-plane orientation θ_H. It shows that as the content of Gd increases, the resonance field decreases strongly from 12220 Oe to 6960 Oe when the field is along the film normal, and the trend of the decrease of resonance filed with θH tends to be more flat, indicating that the effective magnetization in the NiFe-Gd films drops or perpendicular anisotropy enhances with increasing Gd content.

The open circles in Fig. 2 display the experimental angular dependence of FMR linewidth on field orientation. It shows that the linewith increases rapidly when the field orientation leaves from the film normal and reaches a maximum when the field rotates to near 10-20 degree, then the linewidth decreases slowly. The maximum of linewidth of each film changes from 330Oe to 110Oe, as the content of Gd increases.

Theoretical fitting of the angular dependences of FMR field and linewidth by Landau-Lifshitz-Gilbert equation agrees well with the experiments as shown by the solid lines in Fig. 1 and Fig. 2. Various parameters were obtained by the theoretical fitting of resonance field and FMR linewidth. The results show that the gyromagnetic ratio, as well as Lande g factor, rise as the content of Gd increases, with $\gamma=1.84\times10^7$ $(\mathrm{Oe}\times\mathrm{s})^{-1}$ at 0% and$\gamma=1.94\times10^7$ $(\mathrm{Oe}\times\mathrm{s})^{-1}$ at 9.3%. The obtained perpendicular anisotropy constant increases strongly with Gd content. Gilbert damping factor determined by the theoretical fitting of resonance linewidth, also indicates an increase with Gd content, from $G=1.07\times10^8$ s^{-1} at 0% to 1.59×10^8 s^{-1} at 9.3%, suggesting a parallel changing tendency of effective magnetization and magnetic damping. Details will be described in the full text.

This work is supported by NSFC in project of 50472049, JSFC (Jiangsu) in project of BK2004070, National Laboratory of Solid State Microstructures, Nanjing University.

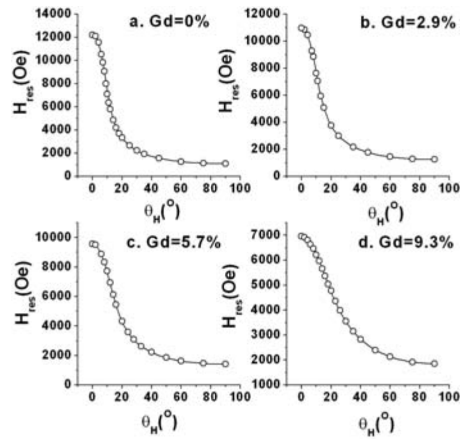

Fig. 1. Angular dependence of FMR field on out- of-plane orientation θ_H with increasing Gd content.

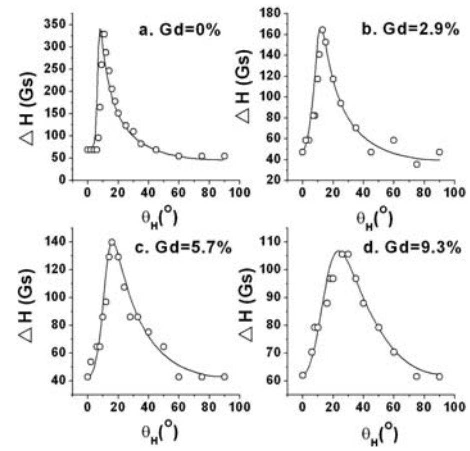

Fig. 2. Angular dependence of FMR linewidth on out- of-plane orientation θ_H with increasing Gd content.

GL-10

Hard Magnetic Nanocomposite [NdFeBNbCu/FeBSi]xn Multilayer Films with Low Crystallization Temperature.

H. Chiriac, M. Grigoras, N. Lupu, M. Urse
National Institute of Research & Development for Technical Physics, Iasi, Romania

INTRODUCTION

Nanocomposite magnets consisting of a fine mixture of magnetically hard and soft phases are attractive materials for permanent magnet development [1,2]. For hard magnetic thin films a lower crystallization temperature is desired for the reduction of the grain size and applications connected with Si technology. In this paper the influence of the thickness ratio of the layers and annealing conditions on the magnetic properties of Ta/[NdFeBNbCu/FeBSi]xn/Ta films is reported. The aim of this study is the achievement of the hard magnetic thin films with low crystallization temperature and a homogenous distribution of the soft and hard magnetic phases.

EXPERIMENTAL DETAILS

Sandwich magnetic films have been prepared in vacuum by successive depositions using the r.f sputtering technique. Ta films with the thickness of 20 nm were used as buffer and capping layers. The structure of the samples was investigated by X-ray diffraction (XRD) technique. The magnetic characteristics were determined by a VSM. The samples have been annealed for 20 min (optimum annealing time) at temperatures between 630oC and 700oC. In order to improve the specific magnetic properties, the samples were treated at 630oC and then cooled in a magnetic field of 8 kG applied in the film plane.

RESULTS AND DISCUSSION

The magnetic properties have been determined for films of various thickness of NdFeBNbCu layers varying from 30 to 180 nm and of the FeBSi layers from 2.5 to 20 nm. The best results were obtained for two samples with ratios of the thickness NdFeBNbCu/FeBSi layers of 90/5 and 180/15. The annealing temperature dependence of coercivity Hc and Mr/Ms ratio of [NdFeBNbCu(x)/FeBSiy)]xn films (with x = 90 nm and 180 nm and y = 5 and 15 nm) are showed in Fig. 1. The best hard magnetic characteristics were obtained for [NdFeBNbCu(180)/FeBSi(15)]x3 films annealed at 680oC and reasonable values were also obtained for [NdFeBNbCu(90)/FeBSi(5)]x6 films annealed at 630oC. For the [NdFeBNbCu(90)/FeBSi(5)]xn films, a reduction of 50oC in the annealing temperature and an increase of the hard/soft phases ratio from 12 at 18, lead to an enhancement of remanence Mr and relatively good values for Hc of 17,1 kG.

The XRD patterns for [NdFeBNbCu(x)/FeBSi(y)]xn films (x = 90 nm and 180 nm; y = 5 and 15 nm) annealed at 630oC and 680oC, respectively, present the same type of phases, but their volume is lower for [NdFeBNbCu(90)/FeBSi (5)]x6 film. For the [NdFeBNbCu(90)/FeBSi(5)]x6 film annealed at 630oC for 20 min., the average crystalline size of Nd2Fe14B phase is of about 22 nm while for [NdFeBNbCu(180)/FeBSi(15)]x3 film annealed at 680oC for 20 min. is about 31 nm. The average crystalline size of the soft magnetic phases is between 8 and 10 nm. The smaller thickness of hard and soft layers (90/5)leads to an enhancement of the diffusion process during the crystallization treatment at 630oC.

For samples annealed at 680oC only a positive dM was measured indicating the existence of the exchange coupling between the soft and hard grains. For sample annealed at 630oC an initially negative dM for a magnetic field between 0 and 14.8 kG was measured indicating the existence of magnetostatic interactions between soft and hard grains and then a positive dM was observed. Fig. 2 shows the hysteresis loops of [NdFeBNbCu(90)/FeBSi(5)]x6 film annealed at 630oC (a), and then cooled in magnetic field of 8 kG (b). The cooling in magnetic field leads to a noticeable enhancement of the Ms of about 12 emu/g and Hc of about 1.37 kG. The kink of the hysteresis loop from II quadrant disappeared and a better squareness was observed.

Although the [NdFeBNbCu(180)/FeBSi(15)]x3 film annealed at 680oC has the best magnetic properties, the [NdFeBNbCu(90)/FeBSi(5)]x3 film annealed at 630oC and then cooled in field can be a good hard magnetic material for applications connected with Si technology as micromagnets for MEMS.

[1] K.H.Chen and Z.Q.Jin, J. Appl. Phys., vol.96, no.2 (2004).

[2] M. Uehara, N.Gennai, M.Fujiwara, T.Tanaka, IEEE Trans. Magn. vol.41, no.10 (2005).

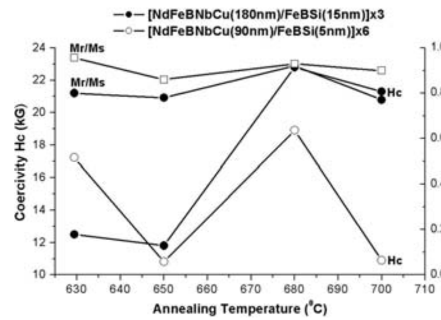

Fig.1. The annealing temperature dependence of coercivity Hc and Mr/Ms ratio of [NdFeBNbCu(x)/FeBSi(y)]xn films

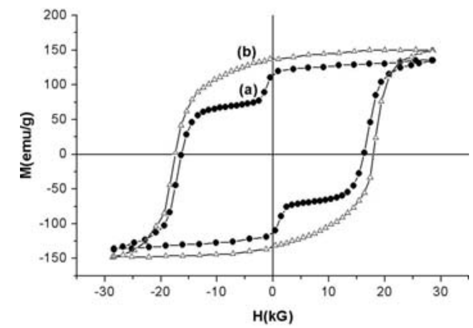

Fig.2. Hysteresis loops for film annealed at 630oC (a), and then cooled in magnetic field of 8 kG (b)

GL-11

Magneto-optical circular dichroism properties of fept layers with perpendicular anisotropy.

C. de Julian Fernandez[1], R. Novak[2], F. Albertini[3], F. Casoli[3], S. Fabbrici[3], A. Caneschi[1]
1. Chemistry, INSTM- University of Florence, Sesto Fiorentino (FI), Italy; 2. Physics, INSTM-University of Florence, Sesto Fiorentino (FI), Italy; 3. Magnetic Materials, IMEM - CNR, Parma, Italy

Magneto-optical techniques allow the investigation of the reversal process in magnetic surfaces and granular systems and of their electronic structure. In the case of magnetic metals and their surfaces the use of VIS or nIR lights allow to explore the interband and intrabands transitions that involves the 3d band. Due to the magneto-optical effect is related with the spin-orbit coupling, this technique is quite sensible to structural and chemical orders which determine also the magnetic anisotropy [1]. In this work we investigate the magneto-optical properties at different wavelengths of nanometric films based in epitaxial FePt and Fe-FePt bilayer that exhibit perpendicular anisotropy. Magnetic circular dichroism technique (MCD) is used because it allows to investigate the magneto-optical properties and the reversal process of the entire layers.
FePt films of 10 nm were deposited by RF sputtering directly on a MgO (100) single-crystal in order to obtain the epitaxial growth. The growth was performed at substrate temperatures in the range 415°C and 430 °C. The films were obtained by alternating the deposition of very thin Fe and Pt layers with nominal thickness of about 0.2 nm. The chosen ratio between the individual thickness corresponds to a nominal atomic composition of Fe53Pt47. The ordered L10 phase growths epitaxially [2] with the c-axis perpendicular to the substrate. Lower chemical order was observed in the film annealed at 430° C. On this film a second layer of 5 nm of Fe was deposited which constitutes the bilayer Fe-FePt.
The MCD hysteresis loops at 1.7 K were recorded using different continuous lasers covering the VIS-nIR spectrum range (476 nm - 904 nm). Details of the experimental set-up are described in [3]. The MCD hysteresis loop of the FePt film annealed at 415° C and measured with a wavelength 476.5 nm is represented in the figure 1. A square hysteresis loop is observed with a negative saturation MCD (-5.3 mrad) for positive magnetic fields. The large squareness ratio, near 1, and the large coercive field of 2.9 T confirm the high quality of the ordered c-axis epitaxial film and the orientation of the easy axis in this direction. The shape of MCD hysteresis loop measured using 632.8 nm is very similar to the measured with 476.5 nm, but the saturation MCD is positive and approximately 5 times smaller (+1.18 mrad).
In the figure 2 the MCD hysteresis of the Fe-FePt film measured with 514.5 nm, 632.8 nm and 904.0 nm are represented. The hysteresis loop measured with the blue beam exhibits positive MCD in the saturation while with the red and n-IR beams that values are negative. Moreover the absolute saturation MCD increases with the increase of the wavelength being 13.9 mrad, -20,6 mrad and –23,4 mrad for the beams with wavelength 514.5 nm, 632.8 nm and 904.0 nm, respectively. The obtained hysteresis indicate the presence of two critical field, HC1 ≈1.3 T and HC2 ≈ 0.64 T being the coercive field 0.13 T. The reversal process does not indicate a full exchange coupling between the hard and soft layers. In fact micromagnetic calculations [4] indicate that 5 nm Fe layer is a thickness for which decoupling could be possible. Finally the shape of the hysteresis loop measured with 514,5 nm is slightly different of the loops measured with largest wavelengths, which are equal. The MCD values measured with 514,5 nm in the magnetic field range between HC1 and HC2 are smaller than the measured with larger wavelength. This suggests that modification of the MO signal due to the change of the wavelength is not similar in the Fe and FePt layers.

Comparing the results, quantitatively the Fe-FePt film shows largest MCD signal than the FePt film. This difference can be due to larger Fe contain but it is not enough for explain the differences. Moreover in the Fe-FePt film the MCD changes from positive to negative values for largest wavelengths and the absolute MCD increases. The opposite behaviours are observed in the FePt film. Spectroscopic measurements are in progress to clarify these results.

[1] A. Cebollada et al. Phys. Rev. B 50 (1994) 3419; H. Ebert,G.Y. Guo, G. Schütz IEEE Trans. Magn. 31 (1995) 3301.

[2] F. Casoli, et al. IEEE Trans. Magn. 41 (2005) 3223.

[3] L. Cavigli et al. J. Magn. Magn. Mater. 316 (2007) 798.

[4] G. Asti et al. Phys. Rev. B 73 (2006) 094406

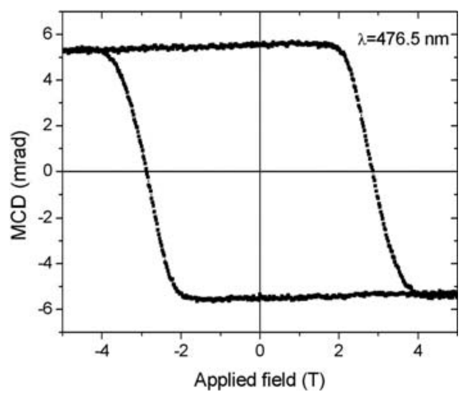

MCD hysteresis loop of the FePt film measured at 476,5 nm

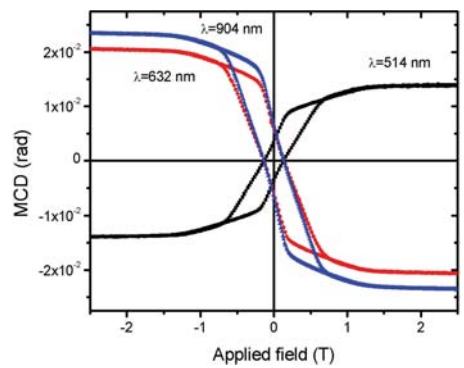

MCD hysteresis loops of the Fe-FePt bilayer at different wavelegths

GL-12

Structural and Magnetic Properties of Fe/Polyimide Multilayer Thin Film.

J. Kim, S. Kim, N. Oh, H. An, J. Kim, D. Jeong, C. Kim, C. Yoon
Materials Science and Engineering, Hanyang University, Seoul, South Korea

Multilayer films consisting of alternating magnetic and nonmagnetic layers have attracted much attention since the discovery of giant magnetoresistance (GMR) effect. When these magnetic layers become thinner, the volumetric magnetic energy becomes small enough to cause for the superparamagnetic behavior to appear in the multilayer. In general, superparamagnetism is indicated by a hysteresis loop with reduced low-field susceptibility and virtually zero coercivity due to volumetric reduction of the magnetic layers [1]. In present study, we demonstrate that continuous 4-nm-thick Fe multilayer embedded within a flexible polymer matrix can exhibit superparamagnetic behavior at room temperature for possible use as a magnetic pump membrane.
The Fe/Polyimide (PI) multilayer thin films were produced by alternating the spin-coating of polyimide (PI) precursor (p-phenylene biphenyltetracarboximide type polyamic acid) and the deposition of Fe film by direct-current magnetron sputtering. The Fe/PI multilayer was heat-treated at 400°C for 1 hour in vacuum (~10-3 Pa) to obtain fully cured PI film. The final PI thickness was controlled by changing the concentration of the precursor solution. The Fe and PI post-annealed thickness were verified using transmission electron microscopy (TEM) and the magnetic properties were investigated by using a vibrating sample magnetometer (VSM).
Figure 1shows magnetic hysteresis loops obtained from samples contianig three layers of Fe films with different thicknesses. As the thicknes of the Fe film decreased, the saturation magnetization decreased nearly proportioally. At 4 nm,the magnetization no longer saturated, reaching a superparamagnetic state. Since small magnetic nanoclusters in an insulating matix are expected to be superparamagnetic [2], it is unusual that a continuous Fe film should exhibit superparamagnetism. We believe that the superparamagnetic state originated from loss of magnetic moments at the PI/Fe interfaces. Because polyamic acid reacts with the Fe film during imidization, a fraction of the Fe film near the interfaces oxidized to reduce the magnietc moment of Fe [3]. In fact, when the thickness of the Fe film decreased below 4 nm, the continuous film was replaced by development of the nano-sized Fe2O3 particles.
Figure 2 (a) and (b) show cross-sectional TEM images of the Fe/PI multilayer continaing 10 and 20 Fe layers. The images clearly demonstrate well-defined multilayer structure with regularly spaced 4-nm-thick Fe films. The PI thickness between two adjacent Fe films was 7 nm. The hysteresis loops measured from the two film stackes indicated superparamagnetic state with susceptibility of 3.0 x 10-3 (unit) for the 10 Fe layers and 1.2 x 10-2 for the 20 Fe layers. The magnetization of the 20 Fe layers was nearly twice that of the 10 Fe layers. The magnetic measurement data suggests that the magnetic properties of the Fe/PI membrane can be altered as needed by changing the number of the Fe films inserted within the PI matrix.
Shown in Fig 3 is the magnetic membrane fabricated by dissolving the Si substrate by the back of the film stack. In order to provide the stiffness and the mechanical stability to the magnetic membrane, the top of film Fe/PI multilayer was coated with ~1 µm PI film.
We demonstrated that a superparamagnetic multilayer can be fabricated by inserting regularly spaced continuous Fe films into a PI thin film. Such magnetic polymer membrane can potentially utilized in remotely activated magnetic pump operating at micrometer scale.

[1] X. -T. Tang, G. -C. Wang, and M. Shima, J. Appl. Phys. 99, 123910 (2006)

[2] I. L. Soroka, V. Stanciu, J. Lu, P. Nordblad, and B. Hjörvarsson, J. Phys. Condens. Matter 17, 5027 (2005)

[3] S. K. Lim, C. S. Yoon, C. K. Kim, and Y. H. Kim, J. Phys. Chem. B 108 18179 (2004)

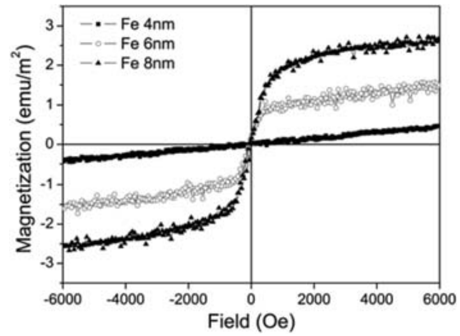

Figure 1. Magnetic hysteresis loops obtained from samples contianig three layers of Fe films with different thicknesses

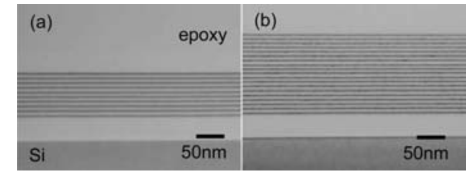

Figure 2. Cross-sectional TEM images of the Fe/PI multilayer continaing (a) 10 and (b) 20 Fe layers

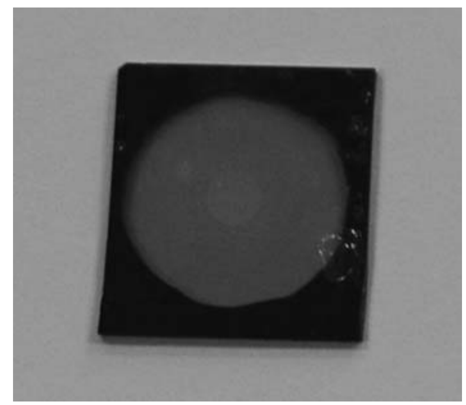

Figure 3. The magnetic membrane fabricated by dissolving the Si substrate by the back of the film stack

GL-13

The magnetic anisotropies of FeCo and FeCoGd films.

L. Sun[1,2], J. Wang[1], Y. Fu[1], Z. Kou[1], *Y. Zhai*[1,4], X. Bai[4], J. Wu[3], Y. Xu[2], J. Du[4], H. Lu[4], H. Zhai[4]
1. Department of Physics, Southeast University, Nanjing, China; 2. Department of Physics, University of York, York, United Kingdom; 3. Department of Electronics, University of York, York, United Kingdom; 4. National Laboratory of Solid Microstructures, Nanjing University, Nanjing, China

The effect of small doping of Rare Earth element on the structure and magnetic properties of thin films of transition metal alloys is an interesting topic though Re-TM alloys have been well studied as permanent magnet and magnetooptical recording media. The magnetic anisotropy of FeCo and FeCo-Gd films were investigated by using Ferromagnetic Resonance (FMR). The FeCo and FeCo-Gd films were deposited on silicon substrates by magnetron sputtering with base pressure of 1.0×10^{-5} Pa. FeCo layers were grown on the Si substrates at a rate of approximately 0.23 nm per second and the sputtering speed for FeCo-Gd layers was 0.07nm/sec. Both the buffer and capping layers were 5 nm thick Ta. The Gd content was adjusted by number of Gd chips on FeCo target then checked by SEM. The thicknesses of $Fe_{50}Co_{50}$ films were determined as 4nm, 20nm, 30nm and 100nm respectively with the same composition, while the thickness of FeCo-Gd was kept as 30 nm with changing content of Gd as 5%, 10%, 12% and 15%. X-ray diffraction shows a well-defined crystalline (110) peak for FeCo layers, while for FeCo-12% and 15%Gd films no X ray diffraction peak appears except a broad halo, implying amorphous state. However for Gd content smaller than 12%, there are both a FeCo crystalline peaks and a small amorphous phase halo in X ray diffraction pattern, indicating the coexistence of crystalline FeCo and amorphous FeCo-Ga phases.

FMR were performed ex situ with a Brucker ESR Equipment of model ER-200D-SRC at microwave frequency of 9.78GHz. It is interesting that for FeCo film and FeCo-Ga with lower content of Gd only a half of the resonance peak near zero field was observed for all the out-of-plane FMR spectra with field scanning up to 14000 Oe, but the peak moved with field orientation as shown in Fig. 1. When the content of Ga increases to 12%, the whole resonance peak appeared as shown in Fig. 2. It is assumed that for FeCo films its high values of perpendicular anisotropy and Ms lead to the near zero field resonance peak. By assuming the near zero field resonance as natural resonance due to high anisotropy in FeCo film the perpendicular anisotropy constant K was roughly estimated by the expression

$\omega=\gamma H_K=2\gamma K/M_s$

By using the bulk values of saturation magnetization Ms[1] and gyromagnetic ratio[2] of $Fe_{50}Co_{50}$, the value of K was determined as 3.2×10^{6}erg/cm^3, which is really a reasonably large value. Then the theoretical FMR resonance field could be calculated by Landau-Lifshitz equation. We found the experimental angular dependence of resonance field can be reproduced very well theoretically.

Based on Landau-Lifshitz equation, the theoretical fitting of the angular dependences of FMR field of FeCoGd films with content of 12% and 15% were also made and various parameters were obtained. It is found that the saturation magnetization decreases with increasing content of Gd from 1400Gs at 12% of Gd to 1100Gs at 15% of Gd and the gyromagnetic ratio, as well as Lande g factor, rises as the content of Gd increases, with g=2.16 at 12% and g=2.27 at 15%. The obtained perpendicular anisotropy constant increases strongly with Gd content. The theoretical calculation and analysis will be discussed in the full text.

This work is supported by NSFC in project of 50472049, JSFC (Jiangsu) in project of BK2004070, National Laboratory of Solid State Microstructures, Nanjing University.

[1] HR.Zhai, “Magnetism in metals”, in “Physics in metals” (Chinese), edited by Duan Feng, Science Press, 454(1998)

[2] G..G..SCOTT and H.W.STURNER, Physics Review,184(2), 490(1969)

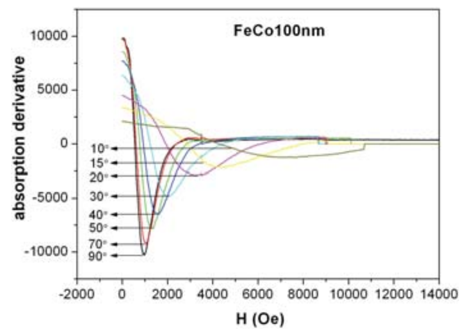

Fig. 1. FMR spectrum of FeCo film with the thickness of 100 nm. 0°states for the spectrum when H is along the film normal.

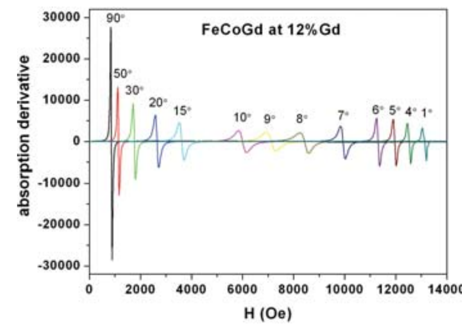

Fig. 2. FMR spectrum of FeCoGd film with thickness of 30 nm and 12% of Gd.

GM-01

The energy loss by drag force of superconductor flywheel energy storage system with permanent magnet rotor.

J. Lee, Y. Han, S. Jung, T. Sung, B. Park
Korea Electric Power Research Institute, Daejeon, South Korea

The energy loss is one of the most important problems for the practical use of Superconductor Flywheel Energy Storage system (SFES). The energy loss of the SFES is mainly generated by drag force in the part of magnetic field such as Superconductor Magnetic Bearing (SMB) and PM type Motor/Generator (PMSM/G)[1]. The energy loss by drag force in PMSM/G is much larger than that by drag force of superconductor bearing. In this paper, we assessed the characteristics of the energy loss by drag force generated in SFES and especially the energy loss by drag force according to a change of stator core size of PMSM/G. To do this, the vertical axial type superconductor flywheel energy storage system with journal type superconductor bearing like Fig. 1 (a) is manufactured. To quantitatively assess the energy loss by drag force in the stator core with permanent magnet rotor, after measuring the energy losses by drag force in superconductor bearing and the degree of a vacuum, the energy loss by drag force in the stator core with permanent magnet rotor empirically is measured. Fig. 2(a) shows installation method of the stator core and the PM rotor in flywheel to assess energy loss by drag force according to various stator core sizes. Fig. 2(b) shows PMSM/G model composed of the stator core with the laminated Si-steel and permanent magnet rotor with the diametrically magnetization in lower part of flywheel axis. Like Fig 2(b), when the inner radius Ri and outer radius Ro of stator core, we measured the rotational speed reduction and calculate the energy losses by drag force. where used cores for the test are Ri =30[mm], Ro=42[mm] core(Type A), Ri=30[mm], Ro=52[mm] core(Type B), Ri=40[mm], Ro=48[mm] core(Type C), Ri=40[mm], Ro=52[mm] core(Type D), and Ri=40[mm], Ro=62[mm]core(Type E).
Table 1 shows the hysterisis loss coefficient and the eddy current loss coefficient given by Fig. 3 for each core. From the results of Fig. 3, when inner radius is fixed and outer radius of stator core is increased, energy loss of the SFES is decreased. But from the results of Fig. 4 when inner radius of the core is varied, degree of energy loss in the high speed area and the low speed area is different due to difference of eddy current and hysterisis coefficient. Therefore small inner radius type core is advantageous in flywheel system for high speed rotation and large inner radius type core is advantageous in flywheel system for low speed rotation. From the results, through only change of stator core size, the energy loss by drag force can be reduced. It is confirmed that the energy loss by drag force can be reduced by means of suitable core design according to rotational speed of the SFES, and it will be very useful to design the low loss PM type motor/generator for the SFES.

[1] K. Demachi and K. Masunaga, Pysica C 412-414 (2004) 789-794

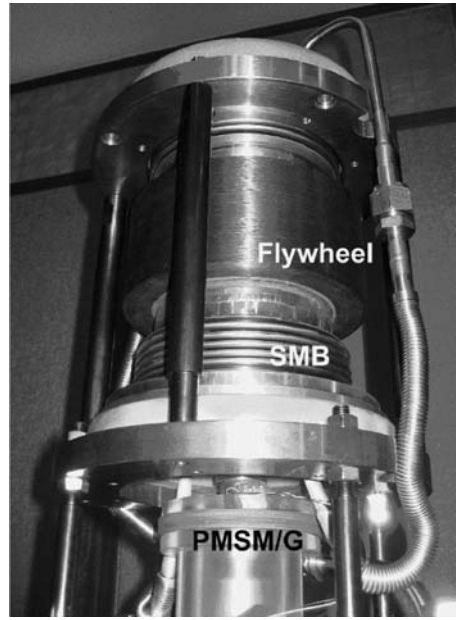

Fig. 1 Photograph of SFES prototype

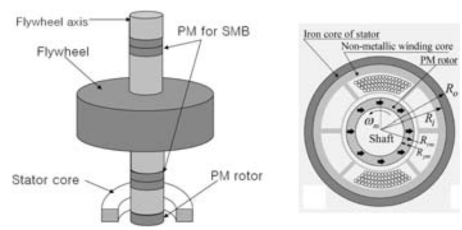

Fig. 2 (a) Wheel structure (b) Rotor and stator

Variable	Eddy current loss coefficient	Hysterisis loss coefficient
Type A	1.556E-8	7.732E-5
Type B	1.526E-8	6.646E-5
Type C	1.930E-8	7.847E-5
Type D	1.883E-8	7.013E-5
Type E	1.724E-8	6.850E-5

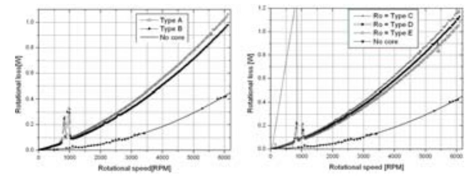

Fig. 3 Energy loss by drag force in (a) type A and B core (b) type D, C, and E core

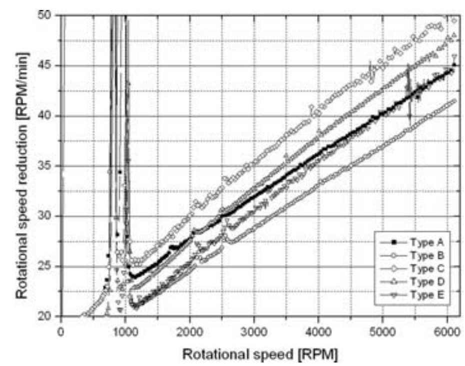

Fig. 4 Rotational speed reduction according to core type

GM-02

Analysis of eddy-current loss in a double-stator cup-rotor PM machine.

S. Niu[1], K. Chau[1], J. Jiang[2]
1. Depart. of Electrical and Electronic Engineering, The University of Hong Kong, Hong Kong, China; 2. School of Electromechanical Engineering and Automation, Shanghai University, Shanghai, China

I. INTRODUCTION

Due to its high power density and high efficiency, the double-stator cup-rotor PM machine has been identified as one of the most promising candidates to work as the integrated-starter-generator (ISG) for hybrid electric vehicles. However, because of its special structure, this machine generally suffers from difficulty in electromagnetic field analysis. Recently, the CFT-TS-FEM has been developed to analyze the dynamic characteristics of PMBDC machines [1]. Increasingly, a grid model of PMs has been incorporated into the CFT-TS-FEM to analyze the eddy-current loss in PMs of electric motors [2].

The purpose of this paper is to propose and analyze a new double-stator cup-rotor PM machine. In particular, the CFT-GM-TS-FEM will be newly developed to analyze the eddy-current loss of a 3-phase 24-slot 22-pole double-stator cup-rotor PM motor.

II. MACHINE STRUCTURE

Fig. 1(a) shows the structure of the proposed double-stator cup-rotor PM machine in which there are two concentric stators and one cup-shaped rotor. Firstly, the cup-shaped rotor can effectively shorten the magnetic circuit length, hence improving the torque density. Secondly, a fractional-slot winding, namely the slot-pitch is 11/12 of the pole-pitch, is adopted which can minimize the cogging torque. Finally, in order to analyze the eddy-current loss with different winding distributions, the single-layer winding and the double-layer winding are separately assessed as shown in Fig. 1(b) and Fig.1(c).

III. ANALYSIS APPROACH

The CFT-GM-TS-FEM is developed. In the rotor domain, the key is to model the PMs and rotor iron core by a grid having N bars along the circumferential direction and M slices along the axial direction. The grid model is shown in Fig. 2. It can be seen that the eddy-current flow can form a complete loop which enhances the accuracy to calculate the eddy-current loss. Thus, the current density in the PM is calculated and the corresponding eddy-current loss is obtained.

IV. RESULTS

Fig. 3 shows the eddy-current losses in the PMs and the rotor iron core with the single-layer winding. The corresponding eddy-current losses with double-layer winding can be obtained similarly. It can be seen that the eddy-current loss in the PMs increases greatly within the commutation time. It is due to the fact that during the commutation of phase currents, there is a drastic change in the armature field and also the magnetic field in PMs, hence greatly increasing the eddy-current loss. Also, it can be found that the eddy-current loss with the double-layer winding is much less than that with the single-layer winding. The reason is that the single-layer winding has more concentrated winding distributions, which causes greater local armature reaction and hence higher eddy-current loss. However, due to the fact that the single-layer winding has higher self-inductance and lower mutual inductance than the double-layer winding, it offers improved controllability for ISG application. Thus, the single-layer winding is used for experimentation.

Fig. 4 shows the simulated phase current waveforms (with and without considering the eddy-current loss) and the measured one when the machine operates at the rated conditions. It can be seen that the simulated waveform, that has considered the eddy-current loss, can closely match with the measured one. Table I shows the comparison between the calculated and measured efficiencies in the proposed machine with the single-layer winding. It verifies that the calculated efficiency, that has considered the eddy-current loss, closely agrees with the measured one.

[1]Y. Wang, K.T. Chau, C.C. Chan and J.Z. Jiang, “Transient analysis of a new outer-rotor permanent-magnet brushless DC drive using circuit-field-torque time-stepping finite element method,” IEEE Trans. on Mag., vol. 38, no. 2, pp. 1297-1300, 2002.

[2]W.N. Fu and Z.J. Liu, “Estimation of eddy-current loss in permanent magnets of electric motors using network-field coupled multislice time-stepping finite-element method,” IEEE Trans. on Mag., vol. 38, no. 2, pp. 1225-1228, 2002.

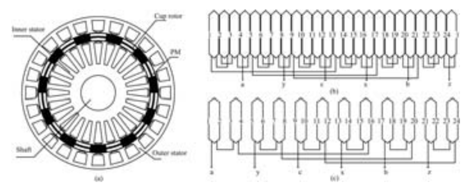

Fig. 1. Proposed machine. (a) Machine configuration. (b) Double-layer winding. (c) Single-layer winding.

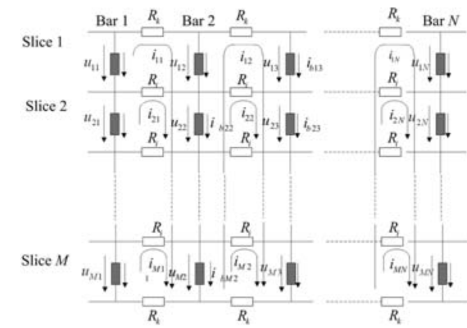

Fig. 2. Grid model of PMs and rotor iron core.

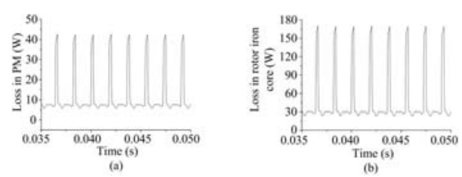

Fig. 3. Waveforms with single-layer winding. (a) Eddy-current loss in PMs. (b) Eddy-current loss in rotor iron core.

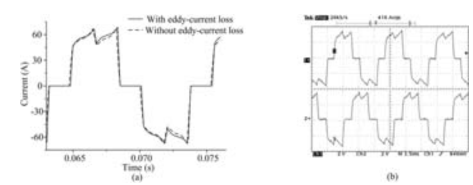

Fig. 4. Phase current waveforms with single-layer winding. (a) Calculated. (b) Measured (40A/div).

TABLE I
COMPARISON OF CALCULATED AND MEASURED EFFICIENCIES

	Calculated		Measured
Output power	2500W	2500W	2500W
Stator iron core loss	160W	160W	NA
Windage loss and stray loss	30W	30W	
Stator copper loss	100W	100W	
Eddy-current loss in PMs	15W	0W	
Eddy-current loss in rotor iron core	60W	0W	
Input power	2865W	2790W	2900W
Efficiency	87.3%	89.6%	86.2%

GM-03

Comparison of stator-permanent-magnet brushless machines.

C. Liu, K. Chau
Dept. of Electrical and Electronic Engineering, The University of Hong Kong, Hong Kong, China

I. INTRODUCTION

Due to high efficiency and high power density, permanent-magnet (PM) brushless machines have been widely used. The corresponding stator-PM versions, including the doubly-salient PM (DSPM) and PM hybrid brushless (PMHB), take the definite advantage of high mechanical integrity. Their outer-rotor topologies are particularly attractive, since they enable direct driving for electric vehicles [1] and wind power generation [2]. However, a quantitative comparison of these two emerging machines is absent in literature.

The purpose of this paper is to quantitatively compare the outer-rotor DSPM and PMHB machines based on the same peripheral dimensions. Moreover, their cost analysis will be revealed.

II. FEATURES

Fig.1 shows the topologies of the proposed machines. The DSPM is simply excited by PMs, whereas the PMHB is hybrid-excited by both PMs and DC field windings. So, the PMHB can provide flexible air-gap flux control. Also, it utilizes an additional air bridge in shunt with each PM to amplify the flux weakening ability. For comparison, both machines adopt the 36/24-pole fractional-slot winding structure.

III. COMPARISONS

Based on the same peripheral dimensions, the outer-rotor DSPM and PMHB machines are designed. Their key design data are summarized in Table I. Since the DSPM can accommodate more PMs than the PMHB, its power density is higher. However, this merit in power density is offset by the high cost of PMs. From Table II, it can be seen that the total material cost of the PMHB is only 57.2% of the DSPM. Actually, the corresponding costs per unit torque and unit power are less than that of the DSPM. Therefore, the PMHB is more cost-effective to produce the desired torque and power.

Fig.2 shows the magnetic field distributions of the two machines. It can be seen that the PMHB has a good ability of flux control. Also, Fig.3 shows their air-gap flux density. It can be found that the PMHB have a very wide range of flux regulation (up to 9 times). Due to the use more PMs, the DSPM can produce higher torque. Nevertheless, as shown in Fig.4(a), the PMHB can utilize flux strengthening to increase the torque up to 85.7% of the DSPM even though its PM volume is only 19.2% of the DSPM. Also, as shown in Fig.4(b), the PMHB can significantly extend the operating range up to 4000 rpm, and provide flux weakening at high speeds to achieve higher efficiency than the DSPM.

Fig.5 shows the no-load EMFs of these machines at different speeds. Because of uncontrollable flux, the DSPM generates the EMFs which are speed dependent. With flux control, the PMHB can uniquely achieve a constant EMF, namely flux strengthening at 300 rpm and flux weakening at 2700 rpm. This property is particularly useful for wind power generation. On the other hand, Fig.6 shows the transient starting torques (normalized by the rated values) for a load of 40 Nm when the armature current is limited to 2 times the rated value. It can be seen that the PMHB can produce a very high starting torque with flux strengthening. The corresponding normalized value is even higher than that of the DSPM. This property is particularly useful for cranking hybrid electric vehicles.

[1]M. Cheng, K.T. Chau and C.C. Chan, "Design and analysis of a new doubly salient permanent magnet motor", IEEE Trans. Magnetics, Vol. 37, No. 4, 2001, pp. 3012-3020.

[2]K.T. Chau, Y.B. Li, J.Z. Jiang and S. Niu, "Design and control of a PM brushless hybrid generator for wind power application," IEEE Trans. Magnetics, Vol. 42, No. 10, 2006, pp. 3497-3499.

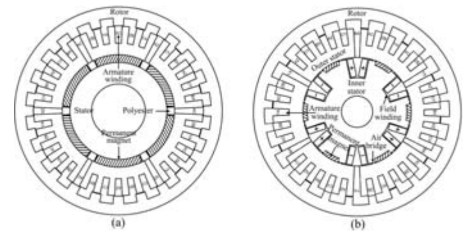

Fig. 1. Machine topologies. (a) DSPM. (b) PMHB.

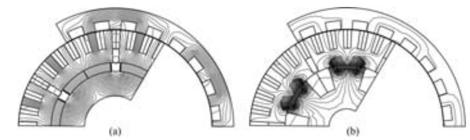

Fig. 2. Magnetic field distributions. (a) DSPM. (b) PMHB at −350 A-turn.

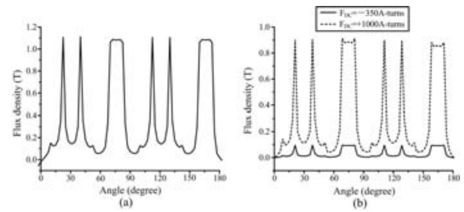

Fig. 3. Air-gap flux density distributions. (a) DSPM. (b) PMHB.

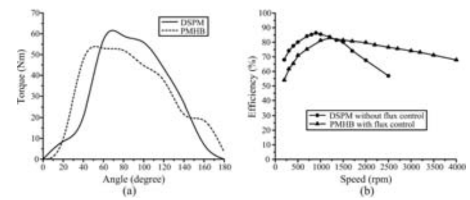

Fig. 4. Steady-state characteristics. (a) Torque versus angle. (b) Efficiency versus speed.

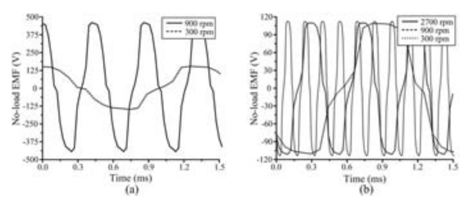

Fig. 5. No-load EMF waveforms at various speeds. (a) DSPM. (b) PMHB

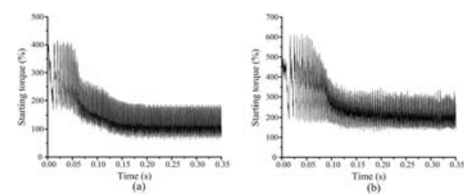

Fig. 6. Normalized transient torques at start-up. (a) DSPM. (b) PMHB.

TABLE I KEY DATA OF DSPM AND PMHB MACHINES

	DSPM machine	PMHB machine
Number of phases	3	
Armature current density	5 A/mm^2	
Rotor outside diameter	270.0 mm	
Rotor inside diameter	221.2 mm	
Stator outside diameter	220.0 mm	
Air-gap length	0.6 mm	
Stack length	80.0 mm	
PM material	38SH Nd-Fe-B	
Rated power	3.2 kW	2 kW
Shaft diameter	70 mm	40 mm
Rated torque	34 Nm	20 Nm
Rated voltage	380 V	220 V
Speed	900 rpm	0-4000 rpm
Power density	122 W/kg	73 W/kg
PM volume	284.8 cm^3	54.7 cm^3
DC winding volume	-	230.2 cm^3

TABLE II COSTS OF DSPM AND PMHB MACHINES

	DSPM machine	PMHB machine
PM cost	116.3 USD	22.3 USD
DC winding cost	-	20.0 USD
Armature winding cost	27.8 USD	27.8 USD
Iron cost	25.8 USD	27.1 USD
Total material cost	169.9 USD	97.2 USD
Cost per unit torque	5.0 USD/Nm	4.9 USD/Nm
Cost per unit power	53.1 USD/kW	48.6 USD/kW

GM-04

Segmentation of magnets to reduce losses in permanent magnet synchronous machines.

P. Sergeant, A. Van den Bossche
Department of Electrical Energy, Systems and Automation, Ghent university, Gent, Belgium

The currents in the magnets on the rotor surface of permanent magnet synchronous machines (PMSM) are generated by on the one hand higher order stator space harmonics introduced by the stator slots (studied in [1] and [2]), and by on the other hand high frequency components in the supply voltages in case of supply with pulse width modulation (PWM), studied in this paper. The aim is to focuss on the effect of axial and circumferential segmentation of the magnets on the losses in the magnets and the (massive) rotor yoke. The losses should be minimal because a too high temperature in the NdFeB magnets deteriorates their magnetic properties.
For a PMSM with known geometry, a study of losses in the magnets requires the exact knowledge of the magnet conductivity. To determine the conductivity accurately, firstly one magnet - identical to the magnets in the PMSM - was tested separately outside the PMSM. Secondly, the obtained conductivity was used in a time-harmonic numerical model to study the losses inside the PMSM for sinusoidal waveforms. In a last part, the losses for square waveforms are approximated by a superposition of losses for sinusoidal waveforms.
By the identification of the magnet conductivity outside the PMSM, disturbing factors such as large eddy currents in the rotor yoke and uncertainty on the air gap are eliminated. The circuit consists of the magnet on a top of a finger shaped yoke in laminated grain oriented magnetic material with an excitation and a measurement winding. A 3D time-harmonic finite element model (FEM) was made of the setup. The determination of the conductivity is an inverse problem that can be solved from the measured losses against frequency and the 3D numerical model. For sinusoidal flux with constant amplitude, Fig. 1 shows that for a magnet conductivity of 0.6 MS/m, the measurements and simulations correspond well.
With this conductivity, the second part of the research - the study of losses in the (segmented) magnets inside the machine - can be carried out. To avoid a computationally demanding 3D time-harmonic model of the entire PMSM, a 2D and a 3D numerical model are combined like in [2]: the field pattern in the air gap is found from a 2D FEM of the entire PMSM. This pattern is used as a source term in a 3D FEM of the magnet and rotor iron only. At the high frequencies of PWM however, the eddy currents are too large to neglect their influence on the imposed induction like in [2]. Therefore, the 2D model is a time harmonic simulation (not static as in [2]) that has also the correct conductivity for rotor yoke and magnet.
The losses are shown in Fig. 2 for 10 kHz sinusoidal frequency. The measured loss in case of unsegmented magnets (1622 mW) is close to the simulated one (1735 mW) in the figure. Correspondence was observed for frequencies in the range 100 Hz to 50 kHz. Creating axial and circumferential segmentation in the magnets causes a large reduction of losses in the magnet, especially when the segments are in circumferential direction (Fig. 2). The losses in the massive rotor yoke are small compared to the losses in the magnet. With increasing amplitude of the input voltage, the losses increase quadratically with the voltage as expected for eddy current losses.
In a third step, losses in the PMSM have been measured for square waves. The correspondence with superposition of losses in the sinusoidal case - only valid in case of linear system - is acceptable: at 10 kHz for example, the losses for a square wave of 10 V rms are 1.825 W while the losses for the superposition of relevant sinusoidal waveforms up to 90 kHz are 1.801 W. The full paper will present a more detailed study of losses for square waveforms, also for different rotor angles of the PMSM.

[1] M. Nakano, H. Kometani, and M. Kawamura, A study on eddy current losses in rotors of surface permanent magnet synchronous machines, IEEE Trans. Magn., Vol. 42, No. 2, pp. 429-435, March 2006.

[2] J. Ede, K. Atallah, G. Jewell, J. Wang and D. Howe, Effect of axial segmentation of permanent magnets on rotor loss in modular permanent magnet brushless machines, IEEE Trans. Industry Applications, Vol. 43, No. 5, pp. 1207-1213, Sep. 2007.

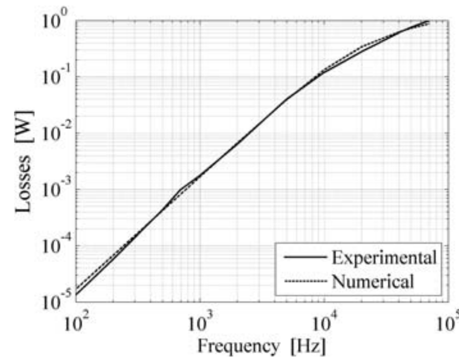

Measured and simulated eddy current loss of the magnet tested under constant flux amplitude in a magnetic circuit outside the motor correspond well for a magnet conductivity of 0.60 MS/m.

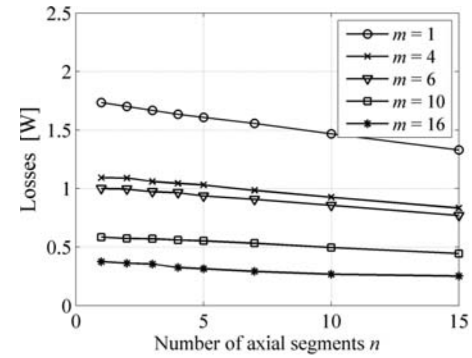

The eddy current loss in the magnets decreases strongly for increasing number of circumferential magnet segments m and decreases weakly for increasing number of axial magnet segments n

GM-05

Cogging Torque Reduction in Brushless DC Motors Due to the Magnetization Distribution in Permanent Magnets.

T. Ishikawa[1], K. Yonetake[1], M. Matsunami[1], M. Tsuchiya[2]
1. Electronic Engineering, Gunma University, Kiryu, Japan; 2. Tokyo Parts Industrial Co.,LTD., Isesaki, Japan

1. INTRODUCTION: Brushless DC motors with permanent magnet are widely used in industrial applications and computer peripheral devices. They become smaller and higher power by use of high-grade magnet. As a result, the torque ripple is increased. This ripple can lead to mechanical vibration, acoustic noise and problems in drive systems. Therefore, it is necessary to reduce the torque ripple. The torque ripple contains both cogging torque and commutation torque components, and the cogging torque is the primary ripple component of the brushless DC motors. In the literature, several methods have been proposed to reduce the cogging torque such as changing stator teeth shape, changing magnets shape, shifting magnets and skewing [1]-[4]. Another method of reducing cogging torque has been studied by changing the magnetization distribution in the permanent magnets [5]-[8]. In [8], we have shown that the cogging torque changes large, small and then large again, when the magnetized region of permanent magnets becomes large. In the analysis, the magnetization distribution has been assumed as a linear function. However, the calculated value of cogging torque does not quantitatively agree with the experimental ones. This paper assumes the magnetization distribution as a sigmoid function, whose shape changes smooth. First, this paper experimentally investigates the cogging torque by changing the excitation voltage of magnetizer. Next, this paper analyzes the cogging torque and magnetic flux density by assuming the magnetization distribution in the magnet as the sigmoid function and compares with the measured ones of the experimental motor.

2. COGGING TORQUE FOR THE EXCITATION VOLTAGE OF MAGNETIZER: Fig. 1 shows the cross section of the exterior-rotor type brushless DC motor with 12 poles and 9 teeth. The Nd-Fe-B permanent magnets are radially magnetized. Fig. 2 shows the measured cogging torque characteristics of the motor when it uses the permanent magnets magnetized with the excitation voltage of 800V, 1000V and 1200V, respectively. The cogging torque magnetized with the excitation voltage of 1000V is small in comparison with those of 800V and 1200V. Therefore, it is found that there is the optimum level of the excitation voltage to reduce the cogging torque. The optimum voltage is about 1000V for the experimental motor.

3. ANALYSIS OF COGGING TORQUE CHARACTERISTICS: The magnet is divided into 30 segments, and the residual magnetization ratio in each segment is assumed by (1). In the equation, a1, a2 and a3 are the maximum value, shift and inclination of the sigmoid function, respectively. The simulation is performed by setting the arbitrary values of three parameters of sigmoid function and by calculating with 2-D nonlinear FEM. Figs. 3 and 4 show the components of flux density and cogging torque. When the parameter a1=1.3, a3=0.255 and a2 changes from 0.55 to 0.67, the calculated flux density and cogging torque have good agreement with the experimental ones for the excitation voltage of 800 through 1200V. When the parameter a2 becomes large, the magnetized region becomes large. This corresponds to the high excitation voltage.

4. CONCLUSIONS: It is shown experimentally that the cogging torque can be very small by choosing the excitation voltage of magnetizer to be the optimum level. This paper has proposed that the magnetization distribution is expressed by the sigmoid function, when the excitation voltage of magnetizer is changed. It is possible to explain the cogging torque characteristics quantitatively by changing the parameter of sigmoid function according to the excitation voltage.

[1] T Li et al. IEEE Trans on Mag, vol. 24, pp. 2901-2903, 1988

[2] T. Ishikawa et al. IEEE Trans on Mag, vol. 29, no. 2, pp 2028-2031, 1993

[3] Z. Q. Zhu et al. IEEE Trans on Mag, vol. 28, pp. 1371-1374, 1992

[4] L. Dosiek et al. IEEE Trans on IA vol. 43, no. 6, pp.1565-1571, 2007

[5] J. Hur et al. IEEE Trans on Mag, vol.34, no.5, pp.3532-3535, 1998

[6] S. C. Park et al. IEEE Trans on Mag, vol.36 no.4 pp.1898-1901, 2000

[7] C. S. Koh et al. IEEE Trans on Mag, vol.38, no.2 pp.1217-1220, 2002

[8] K. Yonetake et al. IEE Japan, RM-07-59, 2007

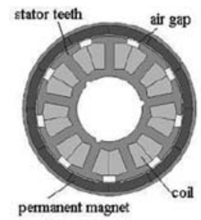

Fig. 1

$$f=\frac{a1}{1+e^{-\frac{|x|-a2}{a3}}}\quad (\text{if } f\le 1),\ f=1\quad (\text{if } f>1)\qquad (1)$$

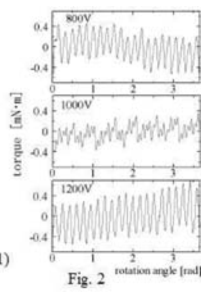

Fig. 2

Fig.1: Cross section of the experimental motor Fig.2: Cogging torque for different excitation voltages of magnetizer Equation (1)

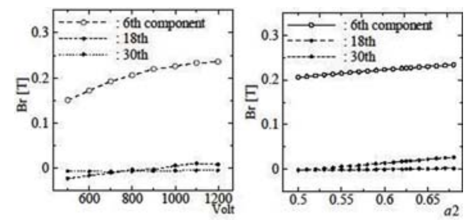

Fig.3: Flux density characteristics, left: measured, right: calculated

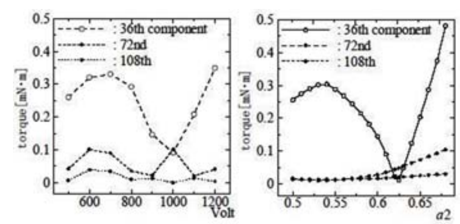

Fig.4: Cogging torque characteristics, left: measured, right: calculated

GM-06

Negative Stiffness of Toroidally-Wound BLDC Machine.

M. Noh, H. Lee
Mechatronics Engineering, Chungnam National University, Daejeon, South Korea

Toroidally-wound brushless direct-current (BLDC) machines are compact, highly efficient, and can work across a large magnetic gap [1,2]. For these reasons, they have been used in flywheel energy storage systems and left ventricular assist devices [3]. The common feature of these systems is a spinning rotor supported by a set of (either mechanical or magnetic) bearings. From the viewpoint of dynamics and control, it is desirable to increase the first critical speed of the rotor. The first critical speed of the rotor is determined by the radial stiffnesses of the bearings and the rotor mass. The motor also affects the first critical speed if the rotor is displaced from the rotating center, because the rotor magnet tends to stick to the stator iron. This radial instability can be expressed as a negative stiffness.

In this paper, we analytically derive the flux density distribution in a toroidally-wound BLDC machine. Using this flux distribution, we can obtain an analytic expression for the negative stiffness of the motor after assuming that the radial displacement of the rotor perturbs the flux density distribution linearly.

For a two-pole, radial gap, toroidally-wound machine as shown in Fig. 1, the flux density distribution in the air gap can be obtained by solving the potential equation $\nabla^2\psi=\nabla M$, where ψ is defined as $H=-\nabla\psi$ and M the magnetization vector. Since the machine has two poles, the magnetization vector can be written as $M=H_c \cos\theta$. Applying appropriate boundary conditions, the above potential equation can be solved analytically. This analytic solution is verified against a finite element analysis.

Once the flux density distribution is obtained, we can introduce a small perturbation due to the radial displacement (see Fig. 2). The perturbed flux density distribution can be integrated along the rotor surface to calculate the force due to the radial displacement. If we differentiate this force with respect to the displacement, we can calculate the negative stiffness of the machine. Finite element analyses show the validity of the negative stiffness model.

[1] L.W. Langley and R.L. Fisher, Toroidally Wound Brushless DC Motor, US Patent 4,547,713, 1985.

[2] F. Caricchi, F. Crescimbini, O. Honorati, “Low-cost compat permanent magnet machine for adjustable-speed pump application,” IEEE Trans. Ind. App. vol.34, pp.109-116, 1998.

[3] M.D. Noh, et. al., “Magnetic levitation for the PediaFlow(tm) ventricular assist device,” Proc. Advanced Intelligent Mechatronics, 2005.

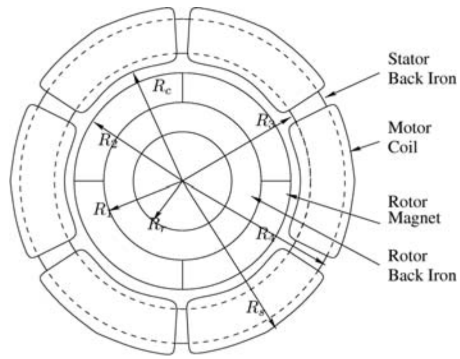

Schematic diagram of two-pole three-phase toroidally-wound BLDC machine

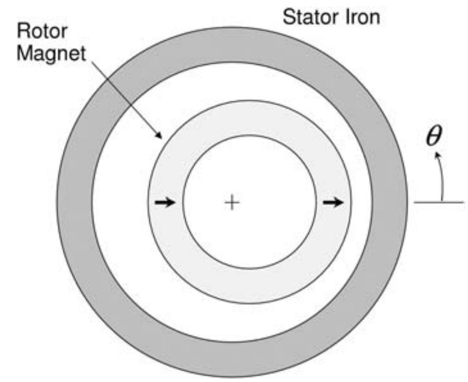

Displaced rotor magnet with respect to the stator iron

GM-07

A STUDY ON THE DESIGN OF AN INSET PERMANENT MAGNET TYPE FLUX-REVERSAL MACHINE.

T. Kim
Electrical Engineering, Gyeongsang National University, Jinju, South Korea

I. Introduction

Flux-reversal machine (FRM) is a doubly salient machine with permanent magnets on the stator. The permanent magnet flux linkage in the stator phase concentrated coils reverses polarity with the rotor traveling [1]. Its simple structure makes it cost effective and suitable for mass production. It has a low self and mutual inductances, hence a low electrical time constant and high fault tolerance. However, there is notable permanent magnet flux leakage (fringing) and cogging torque caused by its structure. This flux leakage deteriorates the power density and torque ability of the FRM. The cogging torque also produces a pulsating torque ripple resulting in vibration and acoustic noise that is detrimental to the machine performance. In this paper, the new inset permanent magnet type FRM to improve the performance of the FRM is proposed both theoretically and experimentally. To analyze the characteristics of the proposed FRM, a two-dimensional finite-element method (2D FEM) is used. From the analysis and experimental results, it is shown that the proposed FRM has an improved performance.

II. The proposed FRM

Fig. 1 compares the proposed inset magnet type FRM with the conventional one. This new FRM has the permanent magnets parallel to the stator magnet flux lines and thus is much more difficult to demagnetize. To prove the performance improvement of the proposed FRM, these FRMs were designed to have the same specifications (such as stator and rotor outdiameter, stack width, and winding turns) except the amount of the permanent magnet used.

III. Results and Discussion

The torque and back electromotive force (BEMF) constant of the FRM are the same. So we can know the torque ability from the BEMF waveform. Fig. 2 compares the BEMF of the conventional and that of the proposed FRM at 1500 rpm. There is no difference in the generated BEMF although the amount of the permanent magnet used in the proposed FRM is the half compared to the conventional one. This is because the flux leakage in the air-gap is reduced and the magnetic circuit becomes effective. Fig 3 and 4 show the cogging torque and iron loss, respectively. It is shown that the proposed FRM also has small cogging torque and iron loss. This is due to the small variation of the air-gap flux density in the proposed FRM. From these analysis results, we can know that the proposed inset type FRM is much more effective to improve performance such as power density, torque ability, and cogging torque. Also it is very useful for material (permanent magnet) cost reduction.

[1] R. P. Deodhar, S. Anderson, I. Boldea, and T. J. E. Miller, "The flux-reversal machine: A new brushless doubly-salient permanent magnet machine," IEEE Trans. Ind. Applica., vol. 33, no. 4, pp. 925-934, July/August 1997.

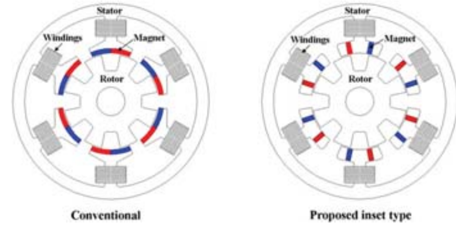

Fig. 1 The proposed inset magnet type FRM

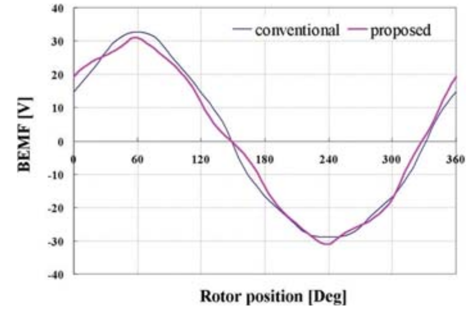

Fig. 2 Comparison of the generated EMF

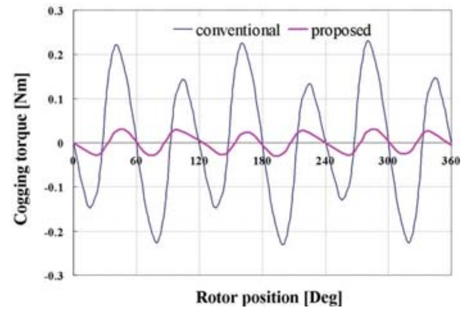

Fig. 3 Comparison of cogging torque

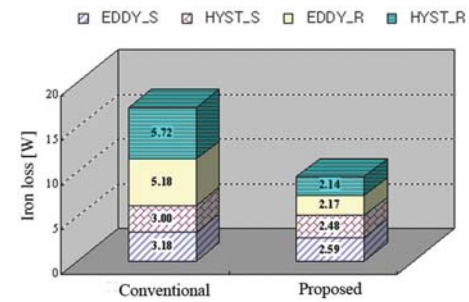

Fig. 4 Comparison of iron loss

GM-08

A Comprehensive Comparsion of Flux-Switching and Flux-Reversal Brushless PM Machines.

H. Wei, C. Ming, Z. Wenxiang, Z. Jianzhong, J. Hongyun
School of Electrical Engineering, Southeast University, Nanjing, China

PURPOSE:
The brushless PM machines having magnets in rotor, either being surface-mounted or interior, have been widely studied and used, which are classified as rotor-PM machines. However, the location of the magnets and the poor thermal dissipation compromise the performance and applications of the rotor-PM machines. Fortunately, a new type brushless PM machines, which can be classified as stator-PM machines, are emerged, including the doubly-salient permanent magnet (DSPM) machine [1], the flux-reversal permanent magnet (FRPM) machine [2], and the flux-switching permanent magnet (FSPM) machine [3]. All of the stator-PM machines have the commonness in the followings: (i) The magnets are located in the stator instead of rotor; (ii) The rotors are composed of the laminations with saliency, similar to that of the switched-reluctance machines; (iii) The concentrated windings are employed to reduce the end-windings; (iv) The electromagnetic torque is dominated by the interactions between the magnets field and armature currents, i.e., the PM torque, and the reluctance torque can be negligible. Although the stator-PM machines are proposed as competitive candidates to replace the rotor-PM counterparts, the performance evaluation between the three stator-PM machines is only restricted on FSPM machine and DSPM machine [4]. Therefore, in this paper the electromagnetic performance of a FSPM and FRPM motors are compared and evaluated.
METHOD:
Both the FSPM and the FRPM motors chosen to be investigated have the same stator teeth number, rotor poles number, stator outer diameters, stack lengths, and rotor inner diameters. The common specifications are listed in Table 1. Based on the FE analysis, the static characteristics of the two motors with the same volumes are compared and evaluated, including the magnetic field distribution, airgap flux density waveform, phase PM flux-linkage, phase back-EMF, inductances, cogging torque, and electromagnetic torque, etc. In addition, due to the different locations and volumes of the permanent magnets, the corresponding ratios of the torque vs. magnets consumption, torque vs. mass, etc, are also taken into account.
RESULTS:
Fig. 1 shows the topologies of the DSPM and SPM motors and the field distributions at no-load. According to the predicted and the experimental results, it is found that the two motors have some important commonness, which are different from those of DSPM motor: (i) The coil PM flux-linkage of the both motors are bipolar; (ii) The flux-linkage and back-EMF harmonics in coils composing one phase windings can be canceled, resulting in the phase back-EMF waveforms are essentially sinusoidal for both motors as shown in Fig. 2, although the concentrated windings are employed; (iii) The back-EMF per turn of the FSPM motor is significantly larger than that of the FRPM counterpart, which indicates the torque capability of the FSPM motor is prior to that of the FRPM motor. Hence, the FRPM is specifically designed to have the same peak value of phase back-EMF as that of FSPM motor with more copper as shown in Fig. 3. In the full-paper, a detailed comparison between the two motors will be presented and evaluated.

[1]Y. Liao, F. Liang and T. A. Lipo, A novel permanent magnet machine with doubly salient structure, IEEE Trans. Ind. Appl., vol. 31, no. 5, pp. 1069-1078, 1995.

[2]R. P. Deodhar, S. Andersson, I. Boldea and T. J. E. Miller, The flux-reversal machine: a new blushless doubly-salient permanent-magnet machine, IEEE Trans. Ind. Appl., vol. 33, No. 4, pp. 925-934, 1997.

[3]E. Hoang, A. H. Ben-Ahmed, J. Lucidarme, Switching flux permanent magnet polyphased synchronous machines, in Proc. 7th Euro. Conf. Power Electronic and Applications, vol. 3, 1997, pp. 903-908.

[4]Hua W., Zhu Z. Q., Cheng M., Pang Y., Howe D., Comparison of flux-switching and doubly salient permanent magnet brushless machines, in Proc. 8th International Conference on Electrical Machines and Systems, Vol. I, 2005, pp. 165-170

TABLE I Design Specifications of FSPM and FRPM Motors

Common Items	Specifications
Phase number, m	3
Stator outer diameter, D_{so} (mm)	128
Airgap length, g (mm)	0.35
Stack length (mm), l_a	75
Stator slot number, P_s	12
Rotor pole number, P_r	10
Rotor inner diameter, D_{ri} (mm)	22
Magnet thickness, h_{pm} (mm)	4.61
Motor volume, V_{motor} (mm^3)	965079

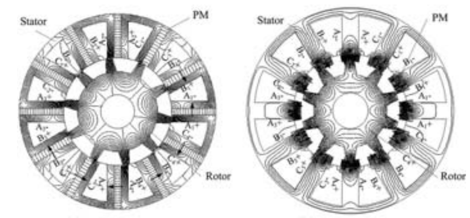

(a) FSPM motor (b) FRPM motor
Fig. 1. Topologies and Open-circuit field distributions.

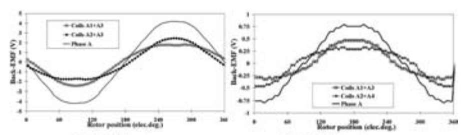
(a) FSPM motor (b) FRPM motor
Fig. 2. Coils and phase back-EMF per turn.

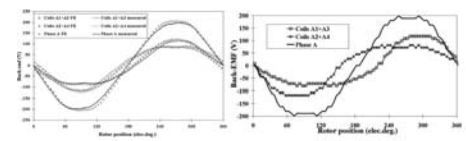
(a) FSPM motor (measured,70 turns/coil) (b) FRPM motor (pedicted, 250turns/coil)
Fig. 3. Coil and phase back-EMF.

GM-09

Optimization and electromagnetic analysis of stator interior permanent magnet machine with minimum cogging torque.

J. Zhang, *M. Cheng*, W. Zhao
school of electrical engineering, Southeast University, Nanjing, China

Introduction: The doubly salient permanent magnet (DSPM) machine, which incorporates the switched reluctance machine with permanent magnet (PM), has been advent since 1990's. As there is no winding, no brush and no PM on the rotor, the DSPM machine offers the advantages of high power density and high reliability [1]. In [2], a double salient flux-switching permanent magnet (FSPM) machine with bipolar flux variation is proposed, which may improve the power density dramatically. However, the FSPM machine suffers from large cogging torque and high PM material consumption. Then it is unsuitable for the FSPM machine to apply in large power capability, such as modern wind turbines. In [3], a new stator interior permanent magnet (SIPM) machine, which may be understood as an improved FSPM machine, is proposed. The SIPM machine has reduced cogging torque while the power density is still keeping higher as the FSPM machine. The purpose of this paper is to carry out the optimization of the SIPM machine for minimizing the cogging torque and analysis the electromagnetic performance.

Method: In this paper a new SIPM machine is proposed as shown in Fig. 1(a). It is shown that the SIPM machine has the same salient-rotor as switched reluctance machine. The stator, if neglecting the PM which is inserted into the stator tooth, is nearly same as the brushless DC machine. The retained iron bridge keeps the stator in a whole and improves the stiffness of the machine. The extended tooth pole shoe not only decreases the airgap flux density, but also reduces the PM material cost, since the higher airgap flux density may cause large flux leakage and saturation in iron core. The SIPM machine may be optimized by selecting proper variable parameters, namely PM thickness, PM length, stator tooth width and slot opening. Before the optimization begins, the original design of the SIPM machine may be seen same as the FSPM machine since there has close ties between two machines. During the optimization, the variable parameters are designed to keep the output power same as the original design. The finite element analysis (FEA) is then used to analysis the electromagnetic performance of the machine under certain parameters.

Results: Fig. 1(b)shows the magnetic field distributions of the SIPM machine. Fig. 2(a) shows the cogging torque ripples of the SIPM machine according to the variation of the PM thickness. It is shown that the thinner PM thickness is more favor for minimizing cogging torque. Fig. 2(b) shows the cogging torque ripples according to the variation of the stator slot opening. It is shown that there has an optimal slot opening where the minimized cogging torque is achieved. A prototype machine is designed, built and tested. The comparison of cogging torque is shown in Fig. 3. It can be seen that the experimental results agree with the predicted ones very well, therefore have verified the correctness of the theoretical analysis.

[1] Y. Liao, F. Liang, and T.A. Lipo, "A novel permanent-magnet motor with doubly salient structure," IEEE Trans. on Ind. Appl.,31,5,pp.1069-1078,1995.

[2] Z. Q. Zhu, Y. Pang, D. Howe, S. Iwasaki, R. Deodhar, and A. Pride, "Analysis of electromagnetic performance of flux-switching permanent-magnet machines by nonlinear adaptive lumped parameter magnetic circuit model," IEEE Trans. on Mag.,41,11,pp.4277-4287,2005.

[3] J. Zhang, Z. Chen, M. Cheng, "Design and comparison of a novel stator interior permanent magnet generator for direct-drive wind turbines", IET Renew. Power Gener.,1,4, pp.203-210,2007.

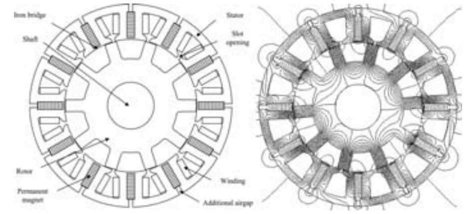

Fig. 1 Cross section and magnetic field distributions of a 12/10-pole SIPM machine

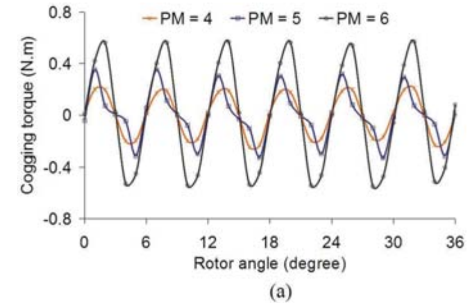

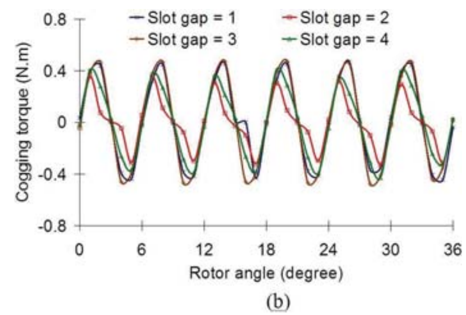

Fig. 2 Cogging torque ripples. (a) Slot gap = 2 mm; (b) PM thickness = 5 mm

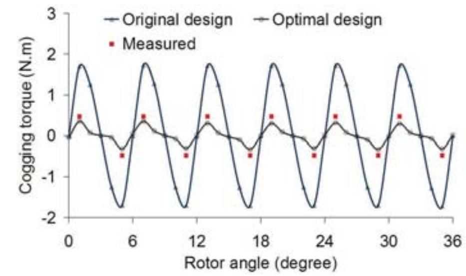

Fig. 3 Comparison of cogging torque

GM-10

Design and analysis of line-starting three- and single-phase interior permanent magnet synchronous motors; direct comparison to induction motor characteristics.

T. Mar či č[1], B. Štumberger[2,1], G. Štumberger[2,1], M. Hadziselimovi ć[2,1], P. Virti č[1], D. Dolinar[2,1]
1. TECES, Research and Development Centre for Electrical Machines, Maribor, Slovenia; 2. University of Maribor, Faculty of Electrical Engineering and Computer Science, Maribor, Slovenia

Introduction

The line-start interior permanent magnet synchronous motor (LSIPMSM) presents an interesting and energy-high-efficient alternative for induction motors (IMs) widely used in low-cost electric drives, where the usage of a voltage-source inverter is too expensive. The LSIPMSM unites the advantages of the IM (robust construction and line-starting capability) and the usual interior permanent magnet synchronous motor (high values of torque per unit current density, power factor and efficiency; especially when compared to IMs with small rated power). The LSIPMSM has permanent magnets buried bellow the squirrel-cage, thus it operates in steady-state as a usual synchronous motor, where the rotor speed is mainly voltage source frequency dependant; the squirrel-cage is used for line-starting and damping of dynamic oscillations at fast load changes.
However, the design of LSIPMSMs is somehow troublesome, because of various performance degrading effects when the motor is line-started (permanent magnet breaking torque [1,2], breaking reluctance torque, asynchronous and synchronous parasitic torques). A wider usage of LSIPMSMs therefore demands an accurate and experimentally verified design procedure, because the motor designer has to find many compromises in the design process. If a LSIPMSM should replace an existing IM, then the LSIPMSM has to be able to line-start and synchronize under load. Furthermore, the LSIPMSM has to have a higher or at least an equal torque per unit stator current density value and a higher efficiency value in its steady-state synchronous operational region.

Three- and single-phase LSIPMSM design procedure

The formalized three- and single-phase LSIPMSM design procedure is the main focus of the proposed paper. The proposed procedure was experimentally validated by conducting measurements on prototypes. The three- and single-phase LSIPMSMs and IMs had equal: stator lamination geometry, stator winding design, skewing factor, squirrel-cage design and equal materials, respectively; which enabled the direct comparison of LSIPMSM and IM performance characteristics. As far as the authors of this paper are aware, such a design procedure supported by measurements of three- and single-phase LSIPMSMs and IMs with equal squirrel-cage design, has not been reported yet.
The design procedure includes the usage of the finite element method (FEM) for an accurate energy balance determination in different steady-state operating points of LSIPMSMs, where the LSIPMSM problem is considered as 2D. 3D effects are included in form of concentrated parameters. Lumped parameter models are employed in analysis of dynamic states of LSIPMSMs, where the electrical and also the mechanical subsystem are considered. The proposed LSIPMSM design procedure represents a compromise between the solution accuracy and the time which is needed to obtain the solution. Several details of the proposed procedure are to some extent similar to the individual methods used in [1-4].
The full paper will present all details of the LSIPMSM design procedure and also the used experimental methods for determination of parameters and characteristics of three- and single-phase capacitor-run and capacitor-start LSIPMSMs. Furthermore, the predicted calculation results in steady and dynamic states are going to be compared to measurement results.

Some measurement results

The aforementioned LSIPMSM design procedure was validated by experimental results. Also it was experimentally confirmed that and all the tested LSIPMSMs had sufficient line-starting capability. The measured characteristics of three-phase and single-phase capacitor-start LSIPMSMs and IMs efficiency (EFF), power factor (PF) and their product (EFF*PF) in steady-state are shown in Fig. 1a and Fig. 1b, respectively. The three-phase IM was rated for 1,1 kW and the single-phase capacitor-start IM was rated for 0,55 kW; both at 1400 rpm and 50 Hz supply. Figs. 1a and 1b evidently show that the LSIPMSM's efficiency and power factor are superior when they are compared to the IM's efficiency and power factor values. In thermal equilibrium the three-phase LSIPMSM's winding overtemperature was around 35°C lower than the IM's; the single-phase capacitor-start LSIPMSM's winding overtemperature was around 28°C lower than the IM's. A detailed analysis will be provided in the full paper.

[1] K. Kurihara, and M. A. Rahman, "High-Efficiency Line-Start Interior Permanent-Magnet Synchronous Motors," IEEE Trans. Industry Applications, vol. 40, pp. 789-796, May/June 2004.

[2] M. Popescu, T. J. E. Miller, M. I. McGilp, G. Strappazzon, N. Trivillin, and R. Santarossa, "Line-Start Permanent-Magnet Motor: Single-Phase Starting Performance Analysis," IEEE Trans. Industry Applications, vol. 39, pp. 1021-1030, July/August, 2003.

[3] M. A. Jabbar, Z. Liu, and J. Dong, "Time-Stepping Finite-Element Analysis for the Dynamic Performance of a Permanent Magnet Synchronous Motor," IEEE Trans. Magnetics, vol. 39, pp. 2621-2623, Sep. 2003.

[4] M. A. Rahman, and P. Zhou, "Analysis of Brushless Permanent Magnet Synchronous Motors," IEEE Trans. Industrial Electronics, vol. 43, pp. 256–267, Apr. 1996.

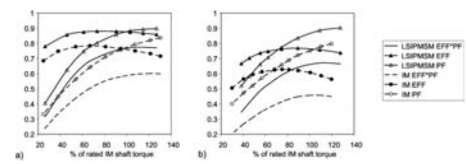

Fig. 1. Measured efficiency and power factor characteristics of a) the three-phase and b) the single-phase capacitor-start LSIPMSMs and IMs.

GM-11

Design and analysis of large capacity line-start permanent magnet synchronous motors.

Q. Lu, Y. Ye
college of electrical engineering, Hangzhou, China

Introduction

The iron and steel industry needs a lot of large-capacity motors to drive fans and pumps, so that the efficiency of motors is important to save energy. Now high efficiency induction motors are popular. Due to their efficiency and power factor are improved to their limitation by optimization, the higher efficiency line-start permanent magnet synchronous motors(LPMSM) will replace them. LPMSM starts up by induction torque and runs by synchronous torque, which has advantages of both induction motor and permanent motor.

Design and analysis of LPMSM

Since the permanent magnet produces reverse torque during staring, the LPMSM's starting capacity with load is lower than that of induction motor. The staring torque has two minimum values, one at low speed and the other at a little higher than half of synchronous speed. If the minimum staring torque is lower than load torque, the LPMSM can't start successfully. Therefore, the most important is to obtain its' dynamic starting torque when designing LPMSM. In order to lower the manufacture cost, the LPMSM keeps the structure of induction motor as possible, but its stator is skewed by one rotor slot pitch to reduce the cogging harmonic.

Fig.1 shows the 2D dynamic FEM model of the designed 4-poles, 250kW LPMSM. Since the 2D dynamic FEM model can only consider the effective length of lamination, the windings end should be calculated by analytical method. To stator windings, the resistance and leakage inductance per phase are obtained and then added to every phase windings. To rotor squirrel-cage bars, the resistance and leakage inductance of end ring are calculated and then they are inserted to rotor windings. In this dynamic FEM model, the mesh of rotor bars need be small enough to consider skin effect. The air gap length is divided into four equal parts, which two parts near stator is motionless and the others belong to moving parts. Fig.2a), b), c) shows magnetic field at no load, no-load air gap flux density, back-EMF respectively.

When the LPMSM is used to drive fans, the initial load is assumed 30% of rating load and then increases along with the speed square. After applied this load, the dynamic staring process is obtained by FEM method, the results are shown in Fig.3. After the oscillation at low speed due to permanent magnet, the motor increases to synchronous speed 1500r/min. The starting time is longer than that of induction motor. The starting current and electromagnetic torque are much bigger than rating values. Fig.3 b) shows half of the rating current because the model is half of this motor. The calculation value of whole motor is 424.3A, which is smaller than that of induction motor, 437.5A. The simulated efficiency, power factor are 0.96, 0.932, which is higher than that of induction motor.

By the model, the effect of permanent magnet is investigated, including the position and size. The air gap flux density becomes higher when permanent magnet is closer to rotor bars. The factual distance between permanent magnet and rotor bars is limited by flux density. The height of permanent magnet also affects the air gap flux density, but it has the optimal value. The results will be described in full paper.

Prototype and conclusion

A prototype is making in factory now. By experiment of induction motor, the 2D dynamic FEM model is proved correct. Therefore the results of LPMSM are believable. Since LPMSMs have higher efficiency and power factor than induction motors, the energy will be saved by adopting them in industry.

[1] R.Y. Tang, Modern Permanent Magnet machines- theory and design (In Chinese), China machine press, 2006

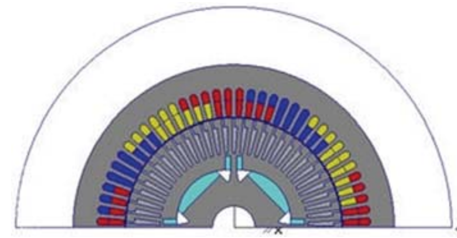

Fig. 1 FEM model of LPMSM

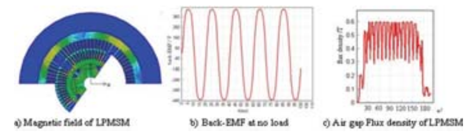

Fig.2 The magnetic field, back-EMF, air gap flux density of LPMSM

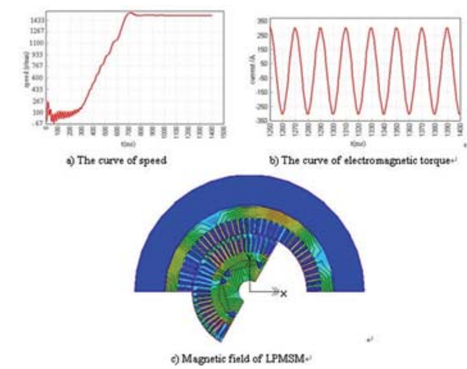

Fig.3 The LPMSM with load

GM-12

An Application of the Latin Hypercube Sampling Strategy for Optimal Design of Large Scale Permanent magnet pole using Adaptive Response Surface Method.

P. Shin[1], *S. Woo*[1], Y. Zhang[2], C. Koh[2]
1. Electrical Engineeirng, Hongik University, Chungnam, South Korea; 2. Electrical and Computer Engineering, Chungbuk National University, Chungbuk, South Korea

1. Optimization Algorithm and Strategy

An efficient hybrid optimization algorithm is applied to a large scale permanent magnet of BLDC motor(6MW) which is used for the propulsion system of electric trains or vessels. The proposed hybrid optimization algorithm consists of an optimal Latin Hypercube Sampling(LHS) strategy based on multi-objective Pareto optimization and an adaptive response surface method(RSM) with (1+λ) evolution strategy[1,2]. The optimal LHS strategy is to insert the sampling points adaptively in successive "zoom-out" design space and to improve the quality of distribution of sampling data[2]. The algorithm has 4 steps: 1) to generate the initial sampling points using LHS, 2) to construct the response surface and to find a pseudo-optimal point using (1+λ) evolution strategy, 3) to check the convergence, 4) to generate additional sampling data within the reduced design space at the neighborhood of the pseudo-optimal point. Once the pseudo-optimal point is found, it is used as a central point for the definition of "zoom-out" design space, in which the additional sampling points are inserted by means of LHS algorithm. Then, the response surface is constructed again and the procedure repeats until the true global optimal point is found. The response surface method also uses the multiquadric radial basis function to interpolate the objective function in design parameter space[3,4].

2. Numerical Example and Results

In order to verify the developed algorithm, a 6 MW BLDC motor is simulated with 4 design parameters(arc length and 3 variables for magnet) and 4 constraints for minimizing of the cogging torque. The rotor has 32 magnet poles, whose cross-section is 60mm x 260mm, and the stator has 196 slots. The optimization procedure has two stages; the fist is to optimize the arc length of the PM and the second is to optimize the magnet pole shape by using the proposed hybrid algorithm.
In the first stage, as shown in Fig. 1(a), the angle P_A is taken as a design variable with a constraint to make sure of the minimum volume of the PM.
The objective function, F_{1st} is
minimize $F_{1st}=\Sigma\{(W_i-W_0)/W_0\}^2$,subject to $0.4\leq P_A\leq 10.0$ deg. (1)
where W_i and W_0 are the stored magnetic energy in the motor at *i*-th computing position and the average magnetic energy, respectively. As result of the 1st stage, the arc length of the magnet is optimized to 2.67 degrees as shown in Fig.1(b).
In the second stage, the pole shape of PM is optimized under the constraints of the optimum arc length. The PM pole shape is parameterized with 3 design parameters (h_1, h_2, h_3) as shown in Fig. 2(b). The design target is defined as:
minimize $F_{obj}=\Sigma(W_i-W_0)$, subject to $0\leq h_1\leq 2$, $0\leq h_2\leq 5$, $0\leq h_3\leq 10$ [mm] (2)
The design sensitivity is also computed by using the results of FE analysis to get a more elaborate response surface with less sampling points. In the 1st iteration of the optimization procedure, a response surface is constructed by using 125 sampling data points generated by LHS experiment and the first pseudo-optimal point is obtained at (h_1, h_2, h_3)= (0.0, 3.8, 5.5). In the second iteration, 44 additional sampling points are inserted at the neighborhood of the first pseudo-optimal point in the reduced design space by a factor of 0.85. At the 3rd iteration with 48 additional sampling points, the final optimal point (0.6, 2.1, 6.2) is obtained. The optimized cogging torque is tremendously reduced to 390(Nm) from 2,158 (Nm)of the initial model. Fig. 2(a) shows the sampling points and corresponding response surface, and Fig. 2(b) shows the optimized shape of PM with the final design values and the initial shape. It seems that 3 iterations are good enough to obtain the optimal design parameters in the proposed hybrid optimization strategy.
Consequently, the proposed hybrid optimization algorithm has novel advantages in its good convergence and low computing cost compared with other methods.

ACKNOWLEDGEMENT

This study was supported by research grant from the Underwater Vehicle Research Center of Agency for Defense Development, Korea, 2007.

[1]P. Alotto, and M.A. Nervi,"An efficient hybrid algorithm for the optimization of problems with several local minima," Int. J. Numer. Meth. Engng, Vol.50, pp. 847-868, 2001

[2]Yanli Zhang, H.S. Yoon and C.S.Koh, "Study on a Robust Optimization Algorithm Using Latin Hypercube Sampling Experiment and Multiquadric Radial Basis Function," Proceeding of KIEE EMECS Annual Spring Confernce, pp.162-164, April 2007

[3]S. Rippa, "An algorithm for selecting a good value for the parameter c in radial basis function interpolation," Advances in Computational Mathematics, vol. 11, pp.193-210, 1999

[4]P.S. Shin, and et.al., "Shape Optimization of a Large-Scale BLDC Motor Using an Adaptive RSM Utilizing Design Sensitivity Analysis," IEEE Trans. on Magnetics, vol. 43, no. 4, pp.1653-1656, April 2007

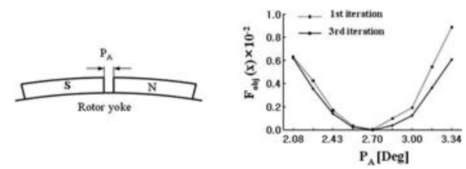

(a) Arc length optimization model of PM poles (b) Results of arc length optimization(2.67 deg.) FIGURE 1. Arc length model of PM poles and optimization results.

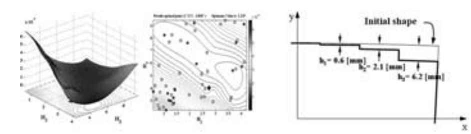

(a) Response surface with sampling points. (b) Optimized shape of the permanent magnet FIGURE 2. Optimization results of the third iteration

GN-01

Development of an axial-flux brushless motor for low-profile fan applications.

L. Hsu[1], C. Huang[1], M. Tsai[1], G. Yan[2]
1. Electric Motor Technology Research Center,National Cheng Kung University, Tainan, Taiwan;
2. Metal Industries Research & Development Centre, Kaohsiung, Taiwan

With the rapid development of electronics, numerous noteworthy designs of cooling components have been also proposed to protect systems from overheating. High performance cooling products such as heat pipes, heat sink modules are being constantly developed, but fans remain one of the most economical ways to remove heat. In the past, fans could be satisfied by conventional radial-flux brushless motors. However, as the drive specifications have become more demanding, it has been difficult to design a radial-flux motor that can achieve the required decrease in thickness. Hence, the axial-flux motor became a more attractive choice due to its low profile [1] [2]. In this paper, a slim axial-flux brushless motor is developed for low-profile fan application, as shown in Fig.1. The structural motor design has to eliminate any surplus space, which a three-phase printed circuit broad (PCB) winding is utilized.

Prior to prototype development, a full assessment of the electromagnetic design to calculate the geometrical parameters is essential. Without considering the impellers, the present study is primarily concerned with the design of the fan motor for which to achieve desired performance subject to constraints, such as limited space, flux saturation, and driving voltage. In the design process, the thickness of the motor is assumed to be smaller than 2.5 mm and possess an exterior diameter of less than 1.2 mm, for compact size purposes. The motor constant, which describes how efficiently a motor produces torque, is taken as the objective function. The genetic algorithm is used to find the suitable variables based on the objective function where the constraints and independent variables are given analytically with an equivalent magnetic circuit. Finite element analysis (FEA) is then applied to validate the analytical calculations. In order to confirm the design results, the slim axial-flux motor and low-profile fan were constructed as shown in Fig.2. The fan motor utilizes a three-layer PCB winding which is 0.6 mm in height. Each layer has six concentric coils. The number of turns per coil is determined by 21 turns. A sintered NdFeB magnet is applied to provide sufficient flux energy, and a commercially available drive IC has been adapted to make the motor rotate successfully. Figure 3(a) shows the back-EMF waveform which was measured at a speed of 1000 Hz. The peak value was 0.63 V which meant that the back-EMF constant was 0.39.This paper applies the mathematic motor model to estimate the characteristics of the fan motor. Substituting the winding resistance and back-EMF constant into the motor model, reasonable performances of the proposed motor could be found. Figure 3(b) shows the estimated relationships between torque and speed when the input voltages were 5 and 3.3 Volts. More Characteristics of the fan motor are also presented in Fig.4. In conclusion, the simulated and measured results suggest that the developed fan motor may be a promising component in cooling applications.

[1]J. F. Gieras, R. J. Wang, and M. J. Kamper, Axial Flux Permanent Magnet Brushless Machines, Kluwer, 2004.

[2]M. C. Tsai and L. Y. Hsu, "Design of a Miniature Axial-Flux Spindle Motor With Rhomboidal PCB Winding," IEEE Trans. Magnetics, vol. 42, no. 10, pp. 3488-3490, Oct. 2006.

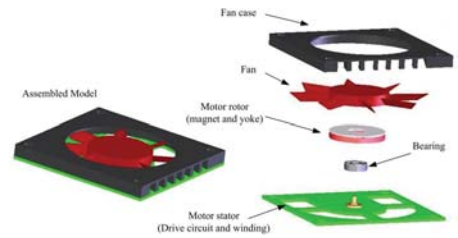

Fig. 1. Proposed axial-flux brushless motor for fan products

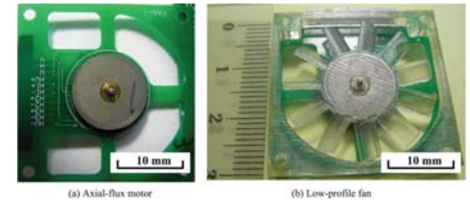

Fig. 2. Photographs of the motor and fan

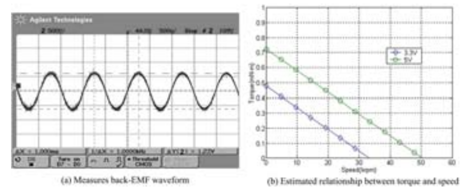

Fig.3 Characteristics of the developed fan motor

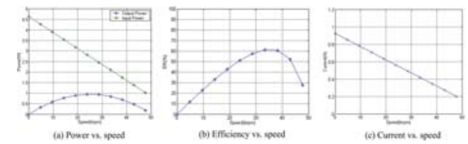

Fig.4 Characteristics of the fan motor as the input voltage is 5V.

GN-02

Sliding Mode Control for Optical Image Stabilization Actuators.

H. Yu[1,2], T. Liu[1], C. Chiang[1]
1. Department of Mechanical Engineering, National Chiao Tung University, Hsinchu, Taiwan; 2. Electronics and Opto-electronics Research Laboratories, Industrial Technology Research Institute, Hsinchu, Taiwan

When photographers take pictures in dark, the burred images will easily cause from hand jitter especially in longer exposure time. Thus, optical image stabilization actuators (OISAs) become the most popular mechanically compensative approach to improve the image quality of cameras, recently. The representative methods for OISA have lens shifting [1] [2], and image sensors shifting [3] [4]. However, lens shifting method is not appropriate for structural miniaturization and slimming in mobile phone cameras (MPCs) with mega-pixel resolution because a compensative lens which causes non-linearity is adopted to compensate the optical axis. Relatively, image sensor shifting method is more suitable than the lens shifting method; hence the OISA design method in this work is proposed by shifting image sensor. Several literatures concerning OISA are emphasized mainly OISA design methods [3] [4], and they are devoted to minimize structural dimensions and maximize electromagnetic force with low power consumption. Although proportional-integral-derivative controllers and digital lag-lead compensators have been proposed to position dual axes in OISA system, but they lack robustness to compensate non-uniform friction, uncertainty, and external disturbance. Therefore, this work aims at the sliding mode control (SMC) using pole placement to achieve fast time response and accurate position despite vibration from hand jitter and friction in the OISA system [5]. In order to suppress image caused by hand jitter, the mechanical structure of the OISA has been designed as shown in Fig. 1. The mechanism of the OISA system is mainly composed of a movable platform and a stationary base. The movable platform for carrying image sensor equipped with an upper cover, a printed circuit board (PCB) with coils, a thrust ball bearing, and a lower base. The movable platform is actuated on two-dimensional plane while driving current is applied to the coils which layout on the PCB. Four permanent magnets are symmetrically assembled on a stationary base to create a strong magnetic field for actuating the image sensor on the movable platform. Moreover, two gyro sensors of yawing and pitching mounted on the OISA system sense the vibration, and two Hall effect sensors of both horizontal and vertical directions fixed on the PCB can be adopted to track the position of the movable platform by measuring the magnetic fields of the permanent magnets, and then inform the current position of the image sensor to computer exactly. All elements are tightly integrated in a small package, and work together to precisely control the position of the image sensor on the movable platform. Once the optical axis of a MPC is off center by vibration, OISA adjusts the center of image sensor to the optical axis. The computer processes the signals which acquire from the gyro and hall sensors via signal acquired cards, and SMC algorithm has been developed to position accurately. Accordingly, sliding functions of dual axes are arranged in terms of errors and are based on the pole placement technique by choosing the desired eigenvalues to obtain sliding margins. Additionally, the sliding surface can be reached in finite time for matching uncertainty and disturbance; hence the simulated block diagram by using SIMULINK is shown in Fig. 2(a). As a consequence, the SMC algorithm works well despite uncertainty and disturbance, and the resulting time responses of simulation and experiment are shown in Fig. 2(b). The setting time is 0.2sec when the movable platform of the OISA moves at 0.5mm stroke.

[1] K. Sato, S. Ishizuka, A. Nikami, and M. Sato, "Control technique for optical image stabilizer system," IEEE Transactions on Consumer Electronics, vol. 39, no. 3, pp. 461-466, Aug. 1993.

[2] D. H. Yeom, N. J. Park, and S. Y. Jung, "Digital controller of novel voice coil motor actuator for optical image stabilizer," in 2007 Proc. International Conference on Control, Automation and Systems, pp. 17–20.

[3] C. W. Chiu, P. C. P. Chao, and D. Y. Wu "Optimal design of magnetically actuated optical image stabilizer mechanism for cameras in mobile phones via genetic algorithm," IEEE Transactions on Magnetics, vol. 43, no. 6, pp. 2582–2584, June 2007.

[4] H. C. Yu and T. S. Liu, "Design of a slim optical image stabilization actuator for mobile phone cameras," Physica Status Solidi (c), vol. 4, no. 12, pp. 4647–4650, Nov. 2007.

[5] V. I. Utkin, Sliding Modes in Control Optimization, New York: Springer-Verlag 1992.

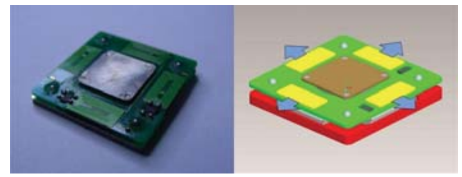

Fig. 1. Optical image stabilization actuator.

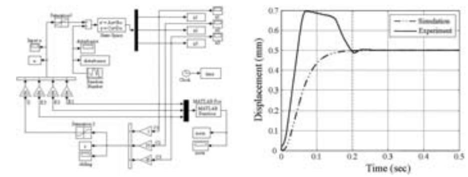

Fig. 2. (a) System block diagram of SMC; (b) Time responses of simulation and experiment.

GN-03

Characteristic Comparison between the Spiral and Lamination Stator in Axail Field Slotless Machines.

S. Lee[1], J. Hong[1], T. Lee[2], J. Park[2]
1. Automotive Engineering, Hanyang university, Seoul, South Korea; 2. Mechanical Engineering, Hanyang university, Seoul, South Korea

Axial flux type machines are used for VCR, CD player, and the spindle motor applications due to the small size and rugged construction features [1]. Therefore, many papers dealt with the characteristic comparison regarding several axial flux type machines compared with radial gap permanent magnet (PM) machines [2], [3]. However, the study on the electromagnetic, mechanical, and manufacturing characteristics according to the change of the stator structures is not performed.

For easy manufacture, the lamination stator is more useful than the spiral stator but the lamination stator in axial flux type machines increases the eddy current loss. On the other hand, the spiral stator increases the magnetic resistance under the same stator volume compared with the lamination stator because the compress condition between layers in radial direction is not precise by the complexity of manufacture. Therefore, the required current quantity and the machine efficiency are determined by the relationships between the eddy current loss and the back electromotive force (back-EMF) according to the use of the spiral or the lamination stator.

In order to reduce the noise generated from the vibration, the structural resonances move to higher frequencies by increasing the stiffness. Although the weight, the volume, and the whole shape of the spiral and the lamination stator are nearly same, the resonant frequencies of each stator are different due to the difference of the stiffness by structure features.

In this paper, the characteristic comparison, which consists of back-EMF, copper and core loss, current shape, resonant frequency, SPL, and manufacturing cost etc., is experimentally shown between the spiral and the lamination stator in an axial field slotless machine. Therefore, this research is usefully applied to the study on the initial design stage of axial flux type machines.

Fig. 1(a) shows the configuration of the rotor in an axial field slotless single air-gap machine which has 12 poles and 9 slots and mechanical air-gap between PM and coil is 1.5 mm. It is operated by sine-wave method and its nominal operating speed is 100 ~ 2000 rpm and rated torque is 3.0 Nm at the 500 rpm. Fig. 1(b) expresses the spiral and the lamination stator which are made of the same silicon steel. The stack length in axial direction is 2.5 mm and the width of stator in radial direction is 12.75 mm. When the thickness of one layer 0.5 mm, the lamination stator is stacked by 5 layers in axial direction and the spiral stator consists of 51 layers in radial direction.

In order to measure the back-EMF and core loss, Fig. 2(a) shows the experimental configuration. The axial machine is revolved by the dc machine. When dc machine rotates alone and with the axial machine at the same speed, the difference of input power of dc machine is occurred by the core loss. Fig. 2(b) shows the configuratin of noise experiment in the anechoic room. The background noise is 21 dBA and measured 0.5 m away from the axial machine by microphones. As a load of the axial machine, a fan is coupled with the axial machine.

As the electromagnetic characteristics, Fig. 3(a) and (b) show the back-EMF and core loss according to the change of operating speed under the no-load condition. Although the mechanical width of two stators is the same, the spiral stator has the magnetic air-gap between layers due to the complexity of manufacture. Therefore, back-EMF constant of the axial machine using the spiral stator is entirely 10% lower than the lamination stator. However, the perpendicular surface for alternating magnetic field and the magnetic path of eddy current in lamination stator are bigger than the spiral stator. Especially, the core loss of the lamination stator is increased by a function of the square against operating frequency but that of the spiral stator is entirely proportional to the operating frequency.

As the mechanical characteristics, resonant frequencies of the lamination stator move to almost 10% higher than the those of the spiral stator because the stiffness of the axial machine by changing from the spiral stator to the lamination stator is enhanced. The more detailed results and discussion will be given in the full paper.

[1]Ying-Chi Chuo, et al, "Development of a Miniature Axial-Field Spindle motor," IEEE Trans. on Magn., vol. 41, no. 2, pp. 984-976, Feb. 2005.

[2]I Kartik Sitapati, et al, "Performance Comparisons of Radial and Axial Field, permanent -Magnet, Brushless Machines," IEEE Trans. Ind. Appicant., vol. 37, no. 5, pp. 1219-1226, Sept./Oct. 2001.

[3]E. P. Furlani, "Field Analysis and Optimization of NdFeB Axial Field Permanent Magnet Motors," IEEE Trans. on Magn., vol. 33, no. 5, pp. 3883-3885, Sept. 1997.

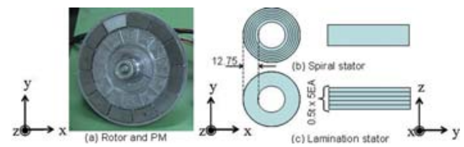

Fig.1. The configuration of axial flux machine

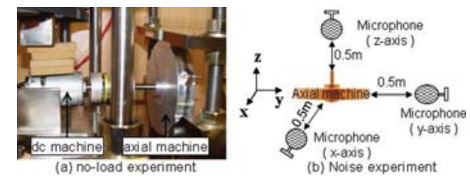

Fig. 2. The configuration of experiment

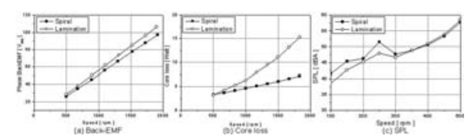

Fig.3. The characteristic comparison

GN-04

Investigation and comparison of inductance calculation methods in interior permanent magnet synchronous motors.

T. Sun, S. Kwon, J. Lee, J. Hong
Department of Mechanical Engineering, Hanyang University, Seoul, South Korea

I. Introduction

The dominant influences in the correct prediction of the steady-state characteristics and precise vector control for the interior PM synchronous motors (IPMSM) are the d- and q-axis armature inductances [1]. Due to the nonlinear electromagnetic characteristics including the saturation and cross-coupling effect in the rotor of IPMSM [3], the d- and q-axis armature inductances of IPMSM become much difficult to be calculated accurately.

In spite of the fact that the corresponding evaluation methods have been discussed for last two decades, there is still no standard for calculation processes of the inductances of IPMSM. Although some papers [4] claimed that the accurate results were calculated by analytical methods, the finite element analysis (FEA) still is the most trustable method. Among the proposed FEA methods, three can be classified. They are frozen permeabilities method, vector control method, and differential flux-linkage method, respectively. First, the principle and calculation process of each method will be investigated briefly in this paper. The solving method of FEA, computation time and complexity can be compared. After considering the end winding leakage inductance, the calculated results of all three methods then will be compared with experiment results and analyzed. In this paper, the preferred AC standstill method will be applied to reveal the accuracy of each calculation method. The final conclusions of this paper will be helpful to choose proper method to evaluate d- and q-axis inductances of IPMSM.

II. Investigation of Evaluation Methods

A. frozen permeabilities method

[1] proposed a method to calculate the pure flux linkages due to the exciting current by removing the magnetomotive force of PM. Considering the different operating points, the total permeabilities are changed with different current values. Thus, the magnetic flux distribution produced by armature current can be calculated in linear analysis. Depending on the relationship between the co-energy and current, the inductances can be calculated [1]. The absence of the flux linkages of PM, however, reduces the saturation and hence generates calculation error.

B. vector control method

Based on the d- and q-axis steady-state equation of IPMSM, the vector control method was proposed in [2]. It can be seen that the d- and q-axis inductances can be calculated directly depending on the relationship of vectors. The drawback of this method is the constant flux linkage of PM, which should have varied with operating point.

C. differential flux-linkage method

In this method, the flux linkages of PM in two nearby operating points are regarded approximately as the same. Thus, the inductance can be calculated as the ratio of differences in flux linkages to currents of these two operating points [3]. This method is limited by the hard determined current variation steps. In practice, it is also difficult to realize the precise current controller.

III. Comparison of Results and Discussion

The photo and cross-section of the analyzed IPMSM in this paper are shown in Fig. 1. The adopted experiment scheme, AC standstill method, is shown in Fig. 2. Fig. 3 show the calculated d- and q-axis inductances by the vector control method. The sensitivity of inductances requires critical simulation conditions including temperature, current vector angle and current amplitude. The other simulation and experiment results will be published in the extended paper. Except the accuracy, more details will be compared and discussed.

[1] J. Y. Lee, etc., "Determination of parameters considering magnetic nonlinearity in an interior permanent magnet synchronous motor," IEEE Trans. Magn., Vol. 42, No. 4, Apr. 2006.

[2] G. H. Kang, etc., "Improved parameter modeling of interior permanent magnet synchronous motor based on finite element analysis," IEEE Trans. Magn., Vol. 36, No. 4, Jul. 2000.

[3] K. M. Rahman, and S. Hiti, "Identification of machine parameters of a synchronous motor," IEEE Trans. Ind. Appl., Vol. 41, No. 2, Mar./Apr. 2005.

[4] E. C. Lovelace, etc., "Design and experimental verification of a direct-drive interior PM synchronous machine using a saturable lumped-parameter model," Ind. Appl. Conf., Vol. 4, pp. 2486-2492, Oct. 2002.

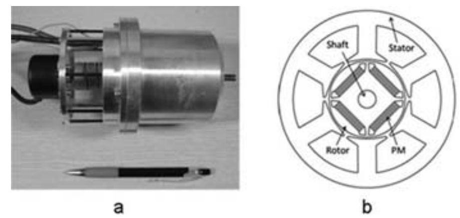

Fig.1 (a) photo of analyzed IPMSM; (b) cross-section of the analyzed IPMSM.

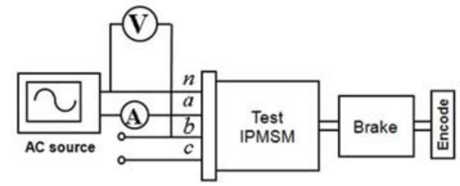

Fig.2 Experiment scheme: AC standstill method

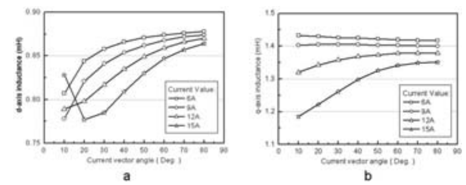

Fig.3 The calculated inductances in vector control method (60°C): (a)d-axis inductance; (b)q-axis inductance

GN-05

Two-DOF micro magnetostrictive bending actuator for wobbling motion.

T. Ueno[1], C. Saito[2], N. Imaizumi[2], T. Higuchi[1]
1. University of Tokyo, Tokyo, Japan; 2. Namiki Precision Jewel Co., LTD, Tokyo, Japan

A 2-DOF micro-magnetostrictive bending actuator using an iron-gallium alloy (Galfenol) was investigated. Galfenol is an iron-based magnetostrictive material with magnetostrictions greater than 200 ppm, a high relative permeability $\mu r > 70$ and a Young's modulus of ~70 GPa. This material is machinable by conventional cutting techniques, and can operate under tensile, bending, and impact loads without degradation in performance. A micro actuator using Galfenol, therefore, has advantages over a PZT type actuator in design simplicity, low drive voltage requirements, high robustness, and a wide temperature operating range. Here we propose 2-DOF micro magnetostrictive bending actuator as shown in Fig. 1. The actuator consists of two orthogonal bimorphs of Galfenol and Ni and winding coils. The actuator is basically a rod of Galfenol of 1 mm square and 13.5 mm length (magnetically easy axis in longitudinal direction). The two ditches of 0.375 mm depth on which Ni plates of same thickness bonded are made by ultra-high precision cutting technique. The bimorphs yield bending deformation with current flow (magnetic field is applied) because the elongations (magnetostrictions) of Galfenol (positive 200 ppm) and Ni (-40 ppm) are constrained by the bonding surface. The actuator is aimed to provide two orthogonal bending deformations which can be used as positioning (the tip is controlled in XY plane), or wobbling motion for micro motor, or drilling device. The static and dynamic displacements of the tip (X and Y) in the case of one side fixed (cantilever, see Fig.1) were measured by fiber optical sensors. The result of Fig.2 contains two cases when the currents flow to X or Y coil. Even the current flows in one coil, two bending deformations simultaneously occur because the magnetic field is applied to both bimorphs. Basically, the displacement (e.g. X) with the current induced to coil (X) with correspondent position is larger than another (Y), because of higher magnetic field. Clear butterfly curves were observed with the maximum of 6 μm (X) and 17 μm (Y). The displacement of Y is larger than X because the bimorph of Y is located near the fixture. Figure 3 shows frequency responses of the displacement against current. The resonances of two first bending modes are relatively close 2.61 and 2.86 kHz. This result indicates that wobbling motion (round trajectory of the tip) with magnified displacement could be obtained at frequency range between two resonances. The configuration and magnetic circuit (open loop) here is primitive to see bending behavior, which will be improved for practically applications.

A. E. Clark, M. Wun-Fogle, J. B. Restorff, "Magnetostrictive Properties of Body-Centered Cubic Fe-Ga and Fe-Ga-Al Alloy," IEEE, Trans. Mag., 37 (2000), 3238-3240.

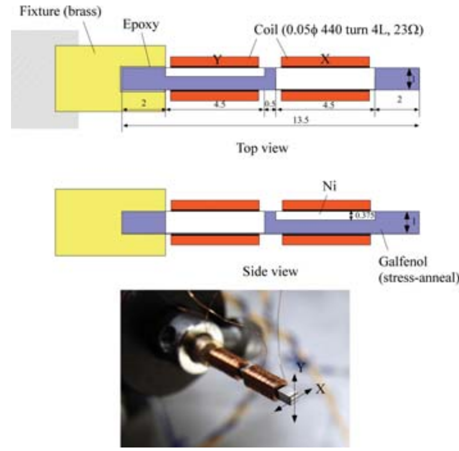

Configuration of actuator

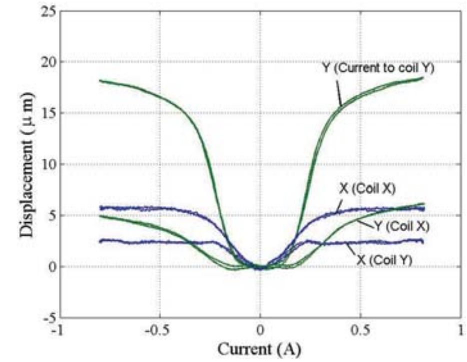

Static displacement (XY)

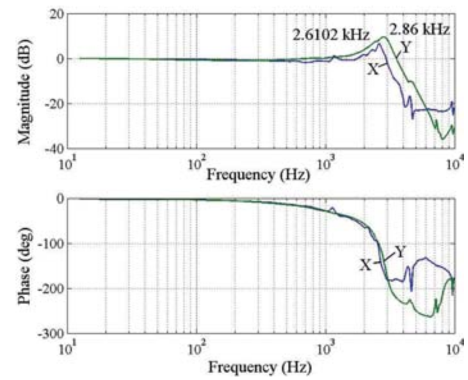

Frequency response displacement to current

GN-06

Thrust calculations and measurements of cylindrical linear oscillatory actuator with halbach array moving magnet using transfer relations theorem.

S. Jang[1], *H. Kim*[1], J. Choi[1], S. Lee[2]
1. Chungnam National University, Daejeon, South Korea; 2. Korea Institute of Industrial Technology, Kwangju, South Korea

Introduction

It is well known that the accurate calculation of the field distribution is essential for the design of the linear electromagnetic machines (LEMs). With the availability of powerful software tools, numerical analysis of the field distribution has become common practice. However, while numerical techniques, such as finite element (FE) analysis, provide an accurate means of determining the field distribution, with due account of saturation etc., they remain time-consuming in case of being employed for investigating the influence of the design parameters on the machine behavior. Contrary to this, analytical techniques do not provide accurate field solutions considering saturation due to analytical burden and several assumptions. However, the machine performances according to design parameters can be predicted rapidly by using analytical field solutions, which are favorable in terms of initial design of the machines.

Many analytical techniques have been investigated to predict field distribution in the LEMs. D.L. Trumper [1] dealt with the design and analysis of flat linear machines using the TRT invented by the Melcher. Their derivation procedures can be easily adapted to the cylindrical LOA shown in Fig. 1, which has Halbach magnet array as a mover and single-phase slotless windings as a stator.

Therefore, using transfer relations derived in terms of a magnetic vector potential and a two-dimensional cylindrical coordinate system, this paper derives the analytical field and thrust solutions of the cylindrical LOA. Analytical results compare well with corresponding non-linear FE analysis. In particular, back-emf and thrust measurements are given to confirm the analysis.

The simplified analytical model of cylindrical LOA

Fig.2 shows the analytical model simplified by the symmetry of the cylindrical LOA shown in Fig.1 The PM regions carry a primed coordinate frame which is displaced from the base coordinate frame by a vector $-z_0$iz. The magnet array is represented by an infinite Fourier series in radial (M_{rn}) and axial (M_{zn}) magnetization components. A similar Fourier representation is also applied to J.

Transfer relations formula

The transfer relations which relate the fields evaluated at the surfaces identified in the model of Fig. 2 are developed in [2] as followings;

$$\begin{bmatrix} B_{zn}^{f} \\ B_{zn}^{g} \end{bmatrix} = -k_n^2 \begin{bmatrix} F_0(\delta,\gamma) & G_0(\gamma,\delta) \\ G_0(\delta,\gamma) & F_0(\gamma,\delta) \end{bmatrix} \begin{bmatrix} A_{\theta n}^{f} \\ A_{\theta n}^{g} \end{bmatrix} - j\mu_0 k_n M_{rn} \begin{bmatrix} F_0(\delta,\gamma)+G_0(\gamma,\delta) \\ G_0(\delta,\gamma)+F_0(\gamma,\delta) \end{bmatrix} \quad (1)$$

$$\begin{bmatrix} B_{zn}^{d} \\ B_{zn}^{e} \end{bmatrix} = -k_n^2 \begin{bmatrix} F_0(\gamma,\vartheta) & G_0(\vartheta,\gamma) \\ G_0(\gamma,\vartheta) & F_0(\vartheta,\gamma) \end{bmatrix} \begin{bmatrix} A_{\theta n}^{d} \\ A_{\theta n}^{e} \end{bmatrix} \quad (2)$$

$$\begin{bmatrix} B_{zn}^{b} \\ B_{zn}^{c} \end{bmatrix} = -k_n^2 \begin{bmatrix} F_0(\vartheta,\beta) & G_0(\beta,\vartheta) \\ G_0(\vartheta,\beta) & F_0(\beta,\vartheta) \end{bmatrix} \begin{bmatrix} A_{\theta n}^{b} \\ A_{\theta n}^{c} \end{bmatrix} + \mu_0 J_n \begin{bmatrix} F_0(\vartheta,\beta)+G_0(\beta,\vartheta) \\ G_0(\vartheta,\beta)+F_0(\beta,\vartheta) \end{bmatrix} \quad (3)$$

$$F_0(x,y) = -\frac{I_1(k_n x)K_0(k_n y)+K_1(k_n x)I_0(k_n y)}{k_n\{I_1(k_n y)K_1(k_n x)-K_1(k_n y)I_1(k_n x)\}} \quad (4)$$

$$G_0(x,y) = -1/\left[k_n^2 x\{I_1(k_n y)K_1(k_n x)-K_1(k_n y)I_1(k_n x)\}\right] \quad (5)$$

$F_0(x,y)$ and $G_0(x,y)$ are the geometric parameters and here I_1 and K_1 are modified Bessel functions of the first and second kind, of order one and I_0 and K_0 are also modified Bessel functions of the first and second kind, of order zero.

Results and discussion

Fig.3 shows the comparison of predictions with non-linear FEA for flux density due to PMs and stator currents. As shown in Fig.4 (a), the back-emf is measured by driving actuator as a generator at a given speed that depends on the speed of the other actuator driven as a motor. Fig.4 (b) shows the comparison of predictions with non-linear FE calculations and measured results for the thrust according to load current and back-emf according to mover speed.

In good agreement with the predicted values from the analyses, the measured results confirm the validity of the TRT analysis. The more detailed results, discussion and mathematical expressions will be given in final paper.

[1] David L. Trumper, Won-jong Kim, and Mark E. Williams, IEEE,Trans. IAS, vol.32, pp.371-379, 1996.

[2] J. R. Melcher, Continuum Electromechanics. Cambridge, MA: MIT Press, 1981.

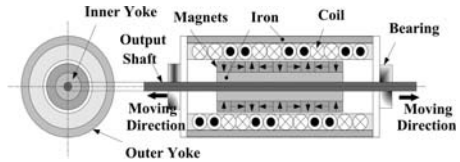

Fig. 1. The structure of the cylindrical LOA.

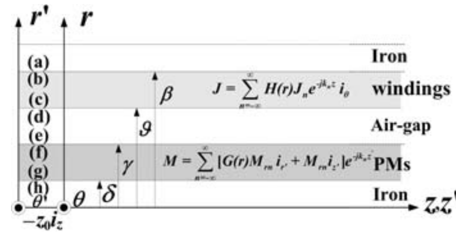

Fig. 2. The simplified analytical model.

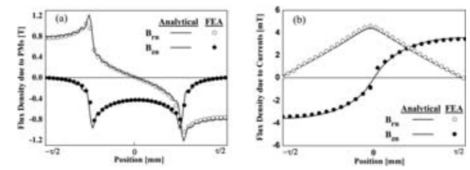

Fig.3. Comparison of predictions with non-linear FEA: (a) flux density due to PMs at the boundary surface (e), (b)flux density due to stator currents at the boundary surface (e).

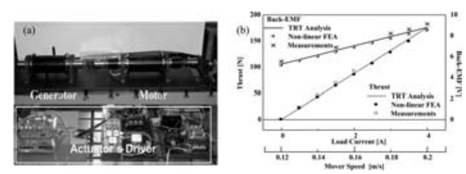

Fig.4. Testing apparatus for (a) back-emf measurements and (b) Comparison of predictions with non-linear FE calculations and measured results for thrust according to load current and back-emf according to mover speed.

CHARACTERISTIC ANALYSIS OF A FLUX-REVERSAL MOTOR WITH FOUR-SWITCH CONVERTER.

H. Kang[2], *T. Kim*[1], B. Lee[2]
1. Electrical Engineering, Gyeongsang National University, Jinju, South Korea; 2. Sungkyunkwan University, Suwon, South Korea

I. Introduction

Flux-reversal machine (FRM) is a new brushless doubly salient machine with permanent magnets on the stator. The permanent magnet flux linkage in the stator phase concentrated coils reverses polarity with the rotor traveling [1]. Its operation is similar to that of the brushless DC motor, so it can be driven by alternating pulses of rectangular currents of 120 degree base and with a 120 degree shift between three phases of the stator. The pulse width modulation (PWM) pattern is also used in six-switch converter to control the speed of the motor. However, in recent years, many different converter topologies have been developed and various PWM control strategies have been proposed to reduce the converter construction cost by using minimum number of switches. One of them is four-switch converter topology with a novel PWM control technique based on the current controlled PWM method [2]. In this paper, we introduce the performance of the FRM under the four-switch converter compared to the six-switch converter. To analyze various characteristics, two-dimensional time-stepped voltage source finite element method (2D FEM) is used.

II. Six-switch and Four-switch Converter

Fig. 1 shows the six-switch and four-switch converter topology for three-phase FRM. The four-switch converter has two switch legs (four switches). And one phase of the motor is always connected to the midpoint of the dc-link capacitors.

III. Analysis Results and Discussion

Fig. 2 compares the calculated phase current in each converter. The current regulation is performed by using hysteresis current control. The purpose of regulation is to shape quasisquare waveform with acceptable switching band. In the case of the four-switch converter, in order to compensate the back-EMF current of phase C, phase A and phase B currents should be sensed and controlled independently and the switching signals of S1 (S3) and S4 (S2) should be created independently. So the switching ripple band is larger than that of the six-switch converter. Fig. 3 shows the torque ripple waveform. The four-switch converter has higher torque ripple and lower average torque at the same input voltage. This is due to the switching ripple band. Fig. 4 shows the iron loss characteristic. The hysteresis loss in the stator and the rotor is similar in both converters. In the stator, however, the eddy current loss of the four-switch converter is much larger than that of the six-switch converter. This can be explained from the fact that the magnetic flux changes quickly under the four-switch converter. Therefore, to improve the performance of the FRM with four-switch converter, more compensated PWM control strategy should be developed. The experimental results will be also shown to confirm the validity of the analysis results in the full paper.

[1] R. P. Deodhar, S. Anderson, I. Boldea, and T. J. E. Miller, "The flux-reversal machine: A new brushless doubly-salient permanent magnet machine," IEEE Trans. Ind. Applica., vol. 33, no. 4, pp. 925-934, July/August 1997.

[2] B. K. Lee, T. H. Kim, and M. Ehsani, "On the Feasibility of Four-Switch Three-Phase BLDC Motor Drives for Low Cost Commercial Applications: Topology and Control," IEEE Transaction on Power Electronics, vol. 18, no. 1, pp. 164-172, January 2003.

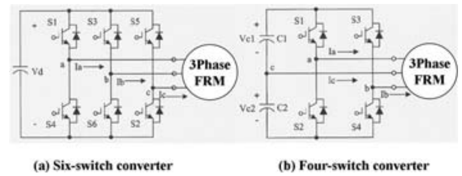

Fig. 1 Six-switch and Four-switch converter topology for three-phase FRM

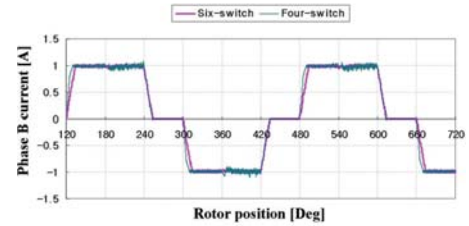

Fig. 2 Comparison of phase current

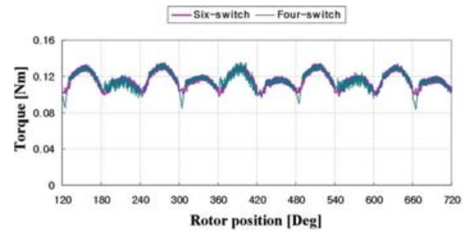

Fig. 3 Comparison of torque ripple

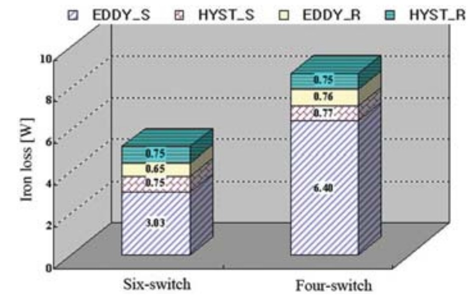

Fig. 4 Comparison of iron loss

GN-08

Iron Loss Calculation in an Amorphous Transformer Using Coupled Preisach Modeling & Finite Element Method.

Y. Cho, S. Mun
Electrical Engineering, Hanbat National University, Daejeon, South Korea

The analysis of the thin lamination model of the amorphous transformer by Finite Element Method (FEM) requires the many region division and much calculating time, and it has difficulty in calculating for modern computer. This paper deals with the iron loss calculation of an amorphous transformer using a coupled Preisach modeling & FEM. For the analysis by FEM of the amorphous transformer, of which the lamination is very narrow, many element (i.e. division region) and computation time are required. In order to solve these problems, the lamination model of the amorphous transformer is transformed into an equivalent anisotropy model with permeability.
The simple lamination model and equivalent anisotropy block model are shown in Fig.1.
By using the packing factor p,
$\mu rx \approx 1/1\text{-}p$, $\mu ry \approx p\mu r$, $p=wi/wi+wa$
Where, wi and wa denote the iron and insulation width, respectively.
The amorphous transformer permeabili μr has been calculated using Preisach modeling[1]-[4], and the packing factor p is 0.85.

[1] J. H. Lee, D. S. Hyun, " Hysteresis Analysis for the Permanent Magnet Assisted Synchronous Reluctance Motor by Coupled FEM & Preisach Modelling", IEEE Trans. on Magn., Vol. 35, No. 3, pp1203-1206, May, 1999.

[2] J. H. Lee, J. C. Kim, D. S. Hyun, "Hysteresis Modeling of Synchronous Reluctance Motor considering PWM Input Voltage", Journal of Physica B, Vol. 275, pp238-247, January, 2000.

[3] I. D. Mayeroyz, "Mathematical Models of Hysteresis," IEEE Trans. In Magnetics, Vol. MAG-22, No.5, pp.603-608 Sept. 1986

[4] A. Ivanyi, Hysteresis Models in Electromagnetic Computation, AKADEMIAI KIADO, BUDAPEST

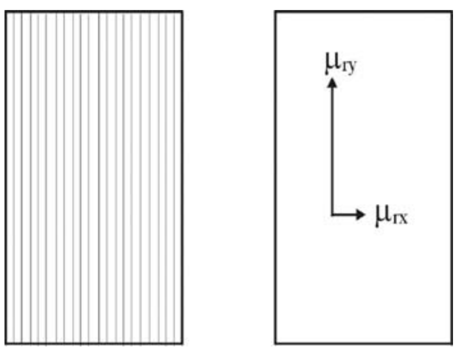

Fig.1 lamination model and equivalent anisotropy block model References

GN-09

Reduction of Lateral Force using V-skew in Permanent Magnet Linear Synchronous Motor.

D. Lee, K. Jang, G. Kim
Electrical Engineering, Changwon National University, Changwon, South Korea

Permanent Magnet Linear Synchronous Motor(PMLSM) has high efficiency, high energy density and high control ability. But, detent force is always produced by the structure of slot teeth and end effect. As detent force is acted as noise and vibration of the apparatuses, it is decreased the control ability because it acts as thrust ripple. Therefore, the detent force reduction techniques is essentially demanded in PMLSM[1].

Generally, skewing PM is widely used as the method of detent force reduction. But, if it is skewed PM, the force is generated as two components: one is a thrust in moving direction; the other is a lateral force in perpendicular direction of moving direction. The lateral force develops additional mechanical loss as breaking force and it has bad influence on the characteristics of PMLSM. But, these calculation cannot be solved by 2-dimensional Finite Element Analysis(FEA).

In this paper, the V-skew PM arranges of PMLSM to eliminate lateral force are proposed and 3-dimensional FEA is applied to analyze the PMLSM. The results are compared with experimental values to verify the proposed method.

Fig. 1 shows the PM arrangement on the stator. No-skew model, a general skew model and the V-skew model which is proposed in this paper is shown. The structure of stator and mover except the PM arrangement are same.

Fig. 2 shows measurement equipments of the PMLSM. Detent force is measured by using the load cell (model: CAS, SB-20L), the encoder, and the indicator as shown in Fig. 2 (b). The mover is fixed to the load cell. And the detent force is displayed on the indicator. The displacement of mover is measured by using the encoder and its magnitude is 1mm.

Table 1 shows detent force, thrust and distortion factor of thrust according to the PM arrangement. The thrust distortion factor of general skew and V-skew model decreased remarkably than No-skew model because the 5th and 6th harmonics components of thrust are decreased greatly. In the thrust of table 2, the analysis value of thrust is 900.12[N]and experimental one is 869.2[N] at rated current in the case of the general skew model. That is, the difference of two values is 30.92[N]. This difference is due to friction force by lateral force. However, in the case of the no-skew and V-skew model, the analysis values are agreed well with experimental values because the lateral force is not produced.

Fig. 3 displays the peak-values of thrust versus armature current variation. To ignore the effect of the detent force, the peak to peak values are compared. The thrust of general skew model is decreased more than those of the other models according to the increase of current as shown in Fig. 3.

The measurement of lateral force by using load cell is difficult because of mechanical structure. So, the lateral force is analyzed by 3D FEA. Fig. 4 shows the lateral force according to the PM arrangement. The peak-value of lateral force of general skew model is 31.95 [N]. The other side, the lateral force of No-skew and V-skew model becomes 0[N] because they have symmetry structure about Z-axis direction. Theoretically, the lateral force of No-skew and V-skew model must amount to "0"[N], but they have some values because the FEA has computation error.

Conclusively, in the case of the V-skew model, the detent force and distortion factor of thrust are smaller than No-skew model. Also, the lateral force is almost zero.

[1]Ki-Chae Lim, Joon-Keun Woo, Gyu-Hong Kang, Jung-Pyo Hong, Gyu-Tak Kim,, "Detent Force Minimization Techniques in Permanent Magnet Linear Synchronous Motor", IEEE Trans. on Magnetics, Vol. 38, No. 2, pp. 1157-160, 2002

TABLE 1. THE SPECIFICATIONS OF ANALYSIS MODEL

	Items	Symbols	Values (unit)
Stator (PM)	Number of poles		8
	Residual induction	B_r	1.32 (T)
	Height of PM	h_{PM}	9.0 (mm)
	Length of PM(No-skew)	l_{PM}	93 (mm)
	Length of PM(Skew)	l_{PM}	99 (mm)
	Length of PM(V-skew)	l_{PM}	99 (mm)
	Width of PM	w_{PM}	26.5 (mm)
	Pole pitch	τ	30(mm)
	Skew Length		10(mm)
Mover (Primary)	Turns		304
	Height of teeth	h_t	16.95 (mm)
	Width of teeth	w_t	14 (mm)
	Slot pitch	τ_s	40 (mm)
	Rated current	I	6.53 (A)
	Mechanical air-gap	l_g	1.4 (mm)

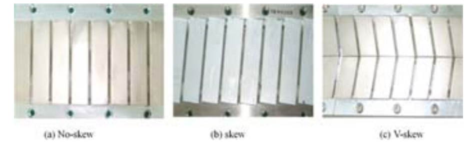

Fig. 1 The PM arrangement

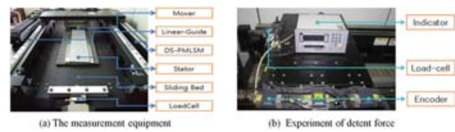

Fig. 2 Measurement equipments

TABLE 2. DETENT FORCE, THRUST & DISTORTION RATIO

Model	Detent force	Detent force (experiment)	Thrust	Thrust (experiment)	Distortion ratio
No-skew	68.3[N]	53.3[N]	903.03[N]	907.97[N]	4.67[%]
Skew	23.3[N]	19.2[N]	900.12[N]	869.2[N]	2.42[%]
V-skew	25.3[N]	26.4[N]	903.89[N]	904.9[N]	2.45[%]

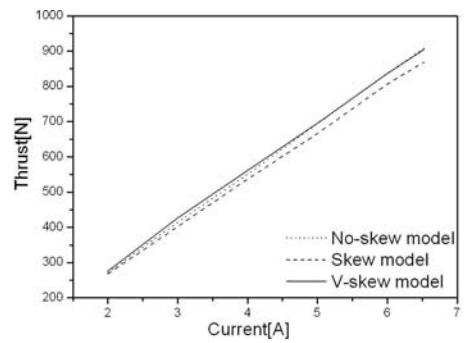

Fig. 3 Thrust according to current

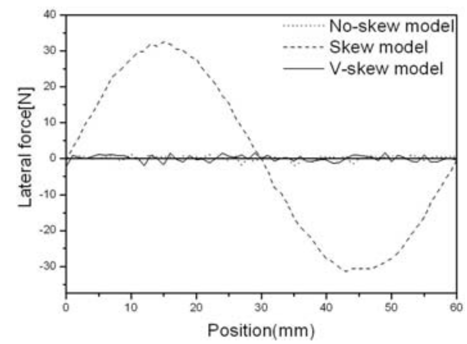

Fig. 4 Lateral force

GN-10

Axial-gap type permanent magnet motor modeling for transient analysis.

S. Won, J. Choi, J. Lee
Electrical Eng., Hanyang University, Seoul, South Korea

1.Introduction
Nowadays the portable devices are getting popular and accordingly needs for the axial-gap motors for portable devices are getting increase[1].
However, the analysis methods for the axial-gap type motors are not simple. Unlike the radial-gap type motors which can be easily transformed to 2-dimensional analysis model, the axial-tap type motors have many restrictions in transforming to 2-dimentional analysis model. Moreover, the 3-dimentional analysis of the motors takes quite a long time even though very fast microprocessors are used. There has been several attempts to solve this problem, some researchers have proposed new methods for analyzing axial-gap type motors or flat type vibration motors[2][3].
The authors propose novel modeling method for the axial-gap type permanent magnet motors which uses one coil mesh and one magnetic field distribution map. The magnetic field distribution map is acquired from static 3-dimentional finite element analysis.
This method is very powerful because the 3-dimentional transient analysis of the axial-gap type motor which is a laborious and time-taking job can be finished in minutes using this method.
2.Method description
As shown in fig. 1, most of axial-gap type permanent magnet motors have no magnetic core in the winding coils in order to remove the axial unbalance force caused by magnetic fluxes between permanent magnet and magnetic core. The motor torque mostly depends on the Lorentz force which is product of the magnetic flux density and winding current. Thus, if the tetrahedral mesh of the winding coil is used for the Lorentz force calculation, the force density at the particular point of the coil can be easily obtained by the coil mesh element of the point and the winding current. By summing all the product of the force values and the radius of the point, the axial-gap type motor torque and the back-emf can be calculated quickly.
After that, using this torque and back-emf values, the transient analysis of the motor can be performed combined with the external electric circuit. This process is very faster than the finite element analysis; the total time of the transient analysis is tremendously short.
3.2phase vibration motor
To verify this method, the authors performed the simulation with the 2 phase vibration motor which is widely used in the cellular phone nowadays. This motor produces the vibration by rotating the eccentric rotor which containing the coils. Fig.2 shows the vibration motor exploded structure. This motor has 4poles and 2 coils but because the coil is doubly winded, the motor actually has 4phase characteristics.
The vibration motor has some current noises due to the commutator and brushes while phase is shifting. This current noise is very important because this is related to the life time of the motor. In the simulation, the authors made up the electric circuit which functions the commutator and brush, as a result, the calculated back-emf and current noise values were obtained. Fig. 3 shows the result. The extended paper will contain the comparison with the measured values.
4.Conclusion
The axial gap-type permanent magnet motors are very important devices in modern industry. The thinner the electric devices are, the more axial gap-type motors are needed. So, it is impossible to predict the performance of the axial-gap type permanent magnet motors. This paper is very useful to the researchers who search the method to analyze the axial-gap type motors.

[1]J.F Gieras, R. Wang, M.J Kamper, “Axial flux permanent magnet brushless machines”, Kluwer Academic Publishers, 2004.

[2]E.P. Furlani, “A method for prediction the field in permanent-magnet axial-field motors”, IEEE Trans. Magn., vol. 28, pp. 2061-2066, Sept. 1992.

[3]S.H.Won, J.Lee, “Analysis of Flat-type vibration motor for mobile phone”, IEEE Trans. Magn, vol. 41, pp.4018-4020, Oct. 2005.

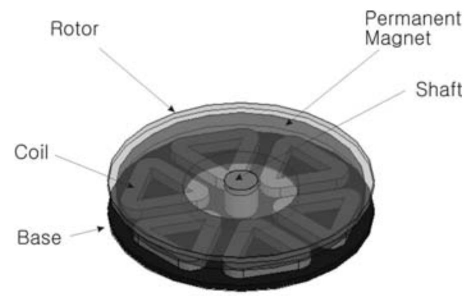

Axial-gap permanent magnet motor structure

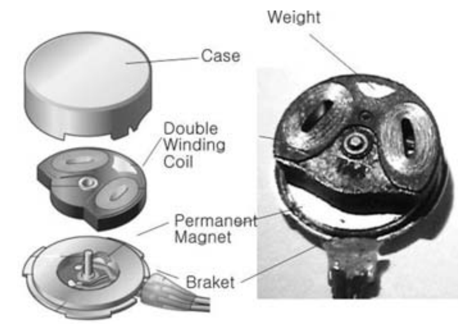

Phase vibration motor

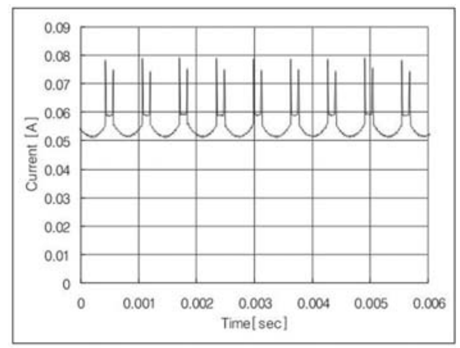

Simulated current waveform of 2 phase vibration motor

Analysis of Total Harmonic Distortion in microspeaker considering electromagnetic mechanical acoustic coupling effect.

J. Kwon[1], S. Hwang[1], G. Hwang[2]
1. Mechanical Engineering, Pusan National University, Busan, South Korea; 2. Computer Engineering, Youngsan University, Yangsan-city, South Korea

With the increase of the interest in sound quality, the approach of Total harmonic distortion (THD) analysis is becoming more important in microspeaker. Harmonic distortion is occurred by uneven magnetic field and nonlinear diaphragm response. For previous research, uneven magnetic field is analyzed along the voice coil position and then magnetic distortion is found by using spectra of flux linkage [1]. However, magnetic distortion affect mechanical response and then mechanical response change the magnetic distortion. Thus, to find exact solution, it should be considered coupling effects of magnetic distribution and mechanical displacement. In this paper, harmonic distortion is analyzed by considering magnetic and mechanical coupling effects.
In General, the structure of microspeakers is similar to that of loud speakers in view point of electromagnetic and mechanical system. When electric current flows in the voice coil, electromagnetic force is generated by Fleming's left hand rule. The magnetic force excite voice coil on diaphragm and then vibrate diaphragm. Finally sound is made by vibrating.Voice coil current can be also determined by solving voltage equation of the equivalent circuit. The voice coil motion generates the back electro motive force (EMF). Because inductance and back EMF are very small, they are able to be neglected. Thus, in this paper, it is assumed that input current is perfect sinusoidal signal. Fig. 1 shows the means of the flux density along the voice coil position. In this figure, because the magnetic field generated by voice coil current is very small, it is neglected. It is assumed that the magnitude of the response displacement is linear to magnitude of exciting force. The phase of displacement is not concerned in exciting force. The initial exciting forces are obtained by inputting response displacement of 0.1N forces.
The spectra analysis of exiting force is performed by Fourier transform. The converged solution is found by iteration. Fig. 2 shows the converged solutions of displacement and magnetic force at 300Hz.
The spectra of the force at 300Hz are presented at fig. 3. THD is the proportion of sound pressure level (SPL) at higher order frequencies to SPL at fundamental frequency. Fig 4 shows simulated and experimental THD along the frequency variable. THD at lower frequencies than resonance is high, because higher order frequencies include resonance frequency. At higher frequency band, THD is low due to small displacement. For high sound quality, THD is important design factor. To make low THD in microspeaker, it is able to predict by analysis approach. In this paper, harmonic distortion is analyzed by considering magnetic and mechanical coupling effects. Simulated results of THD are compared with experimental data. Results show that THD in lower frequency range is higher due to high displace on voice coil and high mechanical response of high order frequency.

[1] S. M. Hwang, K. S. Hong, H. J. Lee, J. H. Kim, and S.K. Jeung, "Reduction of harmonic distortion in dual magnet type microspeaker", IEEE Transactions on Magnetics, 40(4):2004-2006, 2004

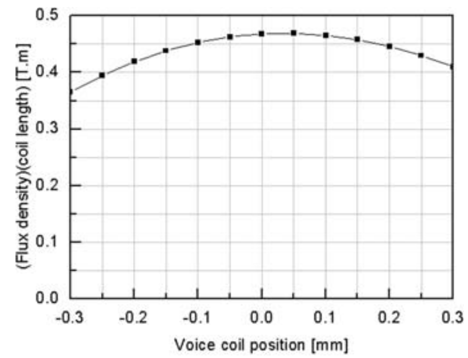

Flux density on voice coil along the coil position

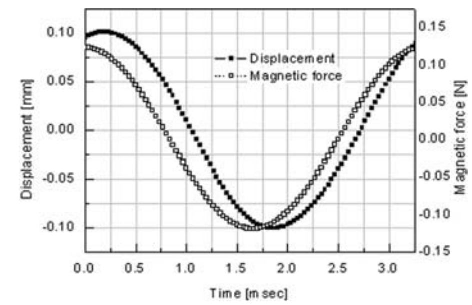

Magnetic force and displacement at 300 Hz

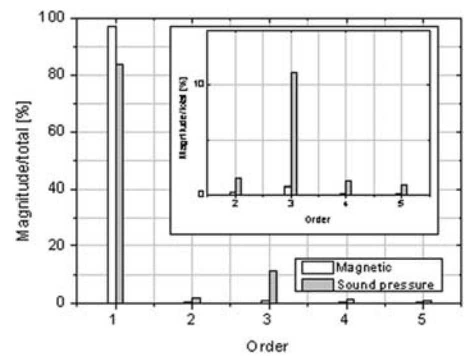

Frequency spectra of magnetic force and sound pressure at 300Hz

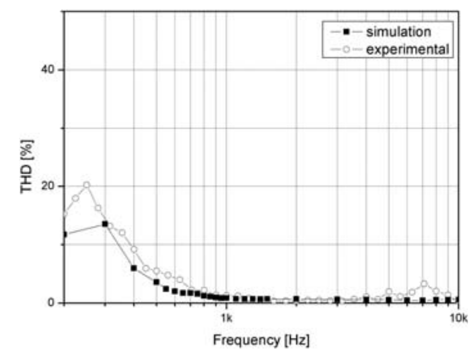

THD comparison between simulated and experimental results

GO-01

Wide dynamic range digital FLL system using high-T_c SQUID for biomagnetic measurements.

D. Oyama[1,2], K. Kobayashi[1], M. Yoshizawa[1], Y. Uchikawa[3]
1. Graduate School of Engineering, Iwate University, Morioka, Iwate, Japan; 2. Japan Society for the Promotion of Science Research Fellow, Tokyo, Japan; 3. Department of Electronics and Computer Engineering, School of Science and Engineering, Tokyo Denki University, Hatoyama, Saitama, Japan

Introduction

For a next stage of biomagnetic measurements, easy handling of devices is required. Especially, operations by hand, without liquid helium and outside a magnetically shielded room (MSR) are eagerly desired. Mobile high-T_c SQUID system is one of the methods to realize it.
Wide dynamic range is needed for mobile SQUID system because of its weakness against magnetic noise. In recent years, wide dynamic range systems have been demonstrated by several groups using background magnetic field compensation scheme [1, 2]. These systems are too complex for multi-channel biomagnetic measurement. On the other hand, we had developed a digital flux-locked loop (digital FLL) system that only reads magnetic field with wide dynamic range for low-T_c SQUID [3]. However, careful designing is needed for high-T_c SQUIDs which have smaller output voltage and worse noise performance than low-T_c SQUIDs.
We have obtained optimum parameters experimentally and operated a high-T_c SQUID using a digital FLL system as a first step to develop the mobile SQUID system. A large dynamic range is achieved and magnetocardiogram (MCG) signal is successfully detected using this system.

Digital FLL system with high-T_c SQUID

We made a prototype system for confirming its wide dynamic range and high resolution. It was composed by a small cryostat, a high-T_c SQUID, a digital FLL electronics and a computer.
A vacuum bottle was used as the cryostat for mobile SQUID system. It could be had by hand and its capacity of liquid nitrogen was about 0.5 L.
The affective magnetometer area of the SQUID was 0.54 mm^2, and sensitivity B/Φ was 3.84 nT/Φ_0. The maximum voltage modulation was 7.0 µV.
Our digital FLL system includes a double-counter method which achieves wide dynamic range by flux-quanta counting using a one-chip microcontroller and a computer. The digital FLL electronics was composed by a generally used 8 bit one-chip microcontroller, a 12 bit A/D converter, a 16 bit D/A converter, and inexpensive devices easily obtained. A time delay of the digital feedback loop was 8.4 µs.
On this electronics, output amplification of the D/A converter was set at 16 bit / 1.4 Φ_0. Input amplifiers which amplify the output voltage of SQUID and connected to the A/D converter determine the dynamic range and slew rate of the system.
Its maximum slew rate was calculated as 5.5 kΦ_0 in the case of theoretically optimum value of input amplifiers. It was 119 dB for 5 V / 12 bit A/D converter and the SQUID's maximum voltage modulation. However, too large amplification increases a noise level of the system. It must be tuned to experimentally optimum condition to have both wide dynamic range and low noise level.
Fig.1 shows performances of the system. Fig.1(a) shows noise spectra at the cases of amplifications of 119 dB, 109 dB and 100 dB. They were measured in an MSR. Fig.1(b) was active areas of each the amplification. They mean the system can measure magnetic signal just in these areas respectively. The lines of 109 dB and 100 dB were measured, but 119 dB was calculated. With 119 dB amplifiers, digital FLL system could not step the Φ_0 accurately, because of its wrong noise performance. The 109 dB line and the 100 dB line showed similar noise performance, but 109 dB amplifiers brought the system wider dynamic range. We chose 109 dB amplifiers for the prototype system.

MCG measurement

To demonstrate a large dynamic range and a high resolution of this system, we measured MCG waveform in the case of existing large magnetic noises. The demonstration was carried out in an MSR, and applied about 30 nT$_{pp}$ at 0.5 Hz and 5 nT$_{pp}$ at 50 Hz magnetic sinusoidal waves as dummy noises of background magnetic field. Fig.2(a) shows a measured waveform before digital filtering. Fig.2(b) shows a waveform that is band-pass-filterd (5Hz to 40Hz) and averaged 195 times. We can see QRS complex of MCG cleary. These figures are proof that the system was cleary mesured about 60 pT MCG waveform in a large magnetic noise condition.

Discussion and conclusion

We developed a prototype of wide dynamic range high-T_c SQUID system for biomagnetic measurements. It achieved a wide dynamic range that can detect MCG waveform in the case of existing large noises. Althogh high-T_c SQUIDs generally have smaller output voltage than low-T_c SQUIDs, dynamic range can be increased by optimum system designing.
However, practical biomagnetic measurements need much higher noise performance. This system is well suitable for multi-channel system, so that noise performance will be improved by statistical signal processings.

[1] D. Drung, *et al*., *Supercond. Sci. Technol*. **16**, 1320 (2003).

[2] D. F. He, *et al*., *Physica B*, **329-333**, 1489 (2003).

[3] D. Oyama, *et al*., *IEEE Trans. Mag.*, **42**, 10, 3539 (2006).

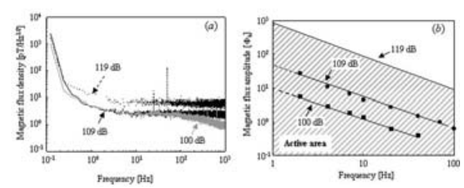

Fig.1 Performance of the digital FLL system with a high-T_c SQUID. (a) is noise spectra and (b) is active areas at the cases of each amplifications.

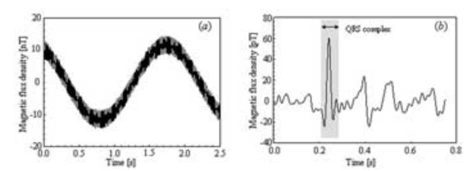

Fig.2 Demonstration of MCG measurement. (a) is raw waveform and (b) is obtained by band-pass-filter and averaging.

GO-02

Double relaxation oscillation SQUID mounted on Pulse Tube cryocooler.

M. J. Eshraghi, I. Sasada
Applied science for electronics and materials, Kyushu University, Kasuga, Japan

Superconducting quantum interference devices have been applied to diagnose heart diseases and brain functions as detecting MCG and MEG fields [1,2]. Instead of using liquid helium to keep low temperature for operating the SQUID system, a refrigerator such pulse tube cryocooler may be used.
In the pulse tube cryocooler, helium gas flows in and out of the compressor and the valve motor via a high pressure and a low pressure hose [3]. And the valve motor receives the power from the inverter via the power lines. The valve motor is controlled by a three-phase inverter to rotate in 0.9 Hz. The inverter acts with 10 kHz switching frequency and its harmonics surprisingly reaches up to around 20 MHz. The conducted switching noise current causes a critical interference with the operation of the SQUID sensor which is installed in 4 K stage of the pulse tube cryocooler.
Large part of the unbalanced noise current flows in the neutral line, however, a part of the current leaks out into the flexible hoses. Fig. 1 shows the current noise shapes of the power lines and the flexible hoses around the moment of the switching timing of the inverter.
By decreasing the impedance of the neutral line, it should be possible to force the some part of the unbalanced current to flow into the neutral line and to reduce the amount of the conducted noise current to the PT-Dewar.
After covering the three phase lines and the neutral line with a copper mesh cover and connecting both ends of the copper mesh cover to the neutral points at both ends, the conducted noise currents are measured in the high and low pressure flexible hoses and the power lines (Fig. 2). It is proved that there is approximately six times reduction in the conducted noise from the compressor and the inverter to the valve motor.
Finally, the SQUID operates normally as drawing an ideal demonstration, as shown in Fig. 3. The magnetic noise of 1.8Hz ;which is the frequency of Helium gas excursions; has been measured by Double Relaxation Oscillation SQUID mounted on the cold head of the Pulse Tube. The amplitude of this noise is around 1 nT. We are performing some experiment on the temperature variation of the heat regenerative material during the cycle of the pulse tube to prove that this noise come from the magnetic phase transition of the regenerative material due to the temperature fluctuation caused by passing cold helium gas[5]. At this level we used copper stage for mounting SQUID on the cold head of Pulse tube. The copper itself generates random magnetic noise because of self generated current inside the bulk; these currents will be increased by reducing the temperature [4]. So we are changing the copper stage by CFRP one to reduce the noise floor below the -80db to be appropriate for measuring heart magnetic field (fig 4.).

(1) H. Nowak, Magnetism in Medicine, W. Andre and H. Nowak, Eds. Berlin : Wiley-VCH, pp.88-135 (1998)

(2) Jin-Mok Kim, Yong-Ho Lee, Kiwoong Kim, Hyukchan Kwon, Yong-Ki Park, and Ichiro Sasada, IEEE Trans. Appl. Supercond., Vol.15, No.2, pp.644-647 (2005)

(3) R. N. Richardson and B. E. Evans, Int J. Refrig., Vol.20, No.5, pp.367-373 (1997)

(4) T. Varpula and T. Poutanen, J. Appl. Phys.,1984,VOL 55, 4015-4021

(5) Fujimoto S.; Kazami K.; Takada Y.; Yoshida T.; Cryogenics, Volume 35, Number 2, 1995, pp. 143-148(6)

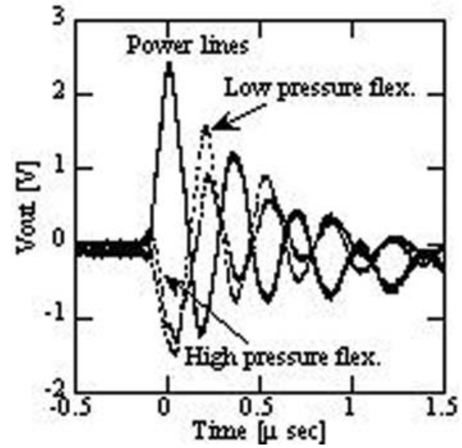

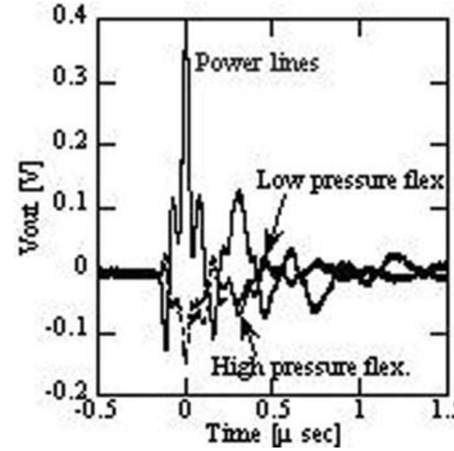

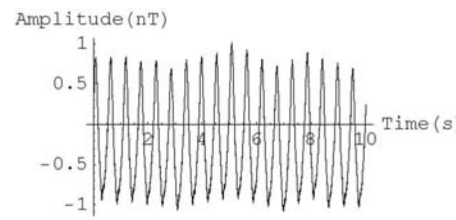

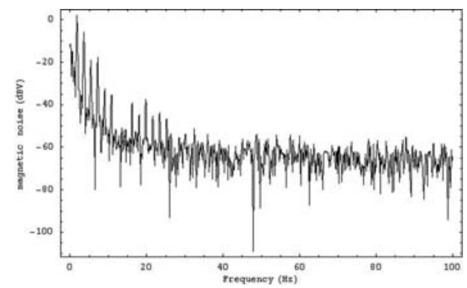

GO-03

Quantitative magnetic immunoassays with a SQUID by means of mutual inductance calculations.

A. Bruno, H. R. Carvalho, S. R. Louro, C. Paulo
Physics, Pontifical Catholic University of Rio de Janeiro, Rio de Janeiro, Brazil

Magnetic particles have been found useful in many bioscience applications including immunoassays, cell separation, DNA and RNA purification. The basic principle consists of providing the external surface of the particle with ligands having affinity to the target molecules. Once the particles are mixed with a sample containing the target molecules, they bind to the magnetic particles. After that, the magnetic complex can be easily separated using a magnetic separator, and the magnetic field generated by the particles can be measured.
Recently, SQUID systems have been proposed to perform magnetic immunoassays. They are based in the magnetic flux obtained by remanence [1], relaxation [2], and susceptibility measurements [3]. Usually the immunoassay quantitative result is reached by obtaining the mass of particles through an experimental calibration curve, which relates the measured magnetic flux to the estimated mass of particles. The mass of particles indicates the number of target molecules present in the sample.
In this paper we propose to quantify the immunoassays by estimating the specific magnetization of the samples, after calculating their remanent magnetic moments by means of mutual inductance calculations between them and a SQUID. Most of SQUID commercial magnetometers estimate the magnetic moment of a sample by modeling it as a magnetic dipole. The magnetic moment is then obtained by performing a curve fitting procedure to the signal obtained as the sample is displaced through the magnetometer coil. However, as pointed out in a recent publication [4], if the sample is large when compared to the magnetometer coil, the magnetic dipole model is no longer valid and the magnetic moment is underestimated.
We recently developed a SQUID magnetometer for magnetic immunoassays which allows fast measurements of the remanent magnetization of a sample [5]. We used a bare two-hole SQUID sensor and the measurement is carried out by displacing the sample through one of the SQUID holes inside the liquid helium bath. Since the sample has about the same size of the SQUID hole, we cannot use the magnetic dipole approximation, in order to calculate its magnetic moment. Instead, we used the standard tables and formulas prepared by Grover [6] for mutual inductance calculations between two coaxial cylindrical current sheets to estimate successfully the magnetic moment of our samples.
Commercial silica coated magnetic particles were used in the experiments [7]. They are routinely used to bind nucleic acids, and also viruses, bacteria, etc. According to the manufacturer, the content of magnetite of each particle is about 80% in weight. We measured their size distribution using a laser particle size analyzer which shows a normal-like distribution and a median particle size of 0.90 µm. Using magnetite and silica densities the median size of magnetite within the particle was estimated in 0.77 µm. Magnetite particles in this size range are classified as pseudo single domain particles. The magnetic properties of those particles at low temperatures have been studied extensively [8]. Their reduced remanence (remanent magnetization / saturation magnetization) is expected to vary from 0.39 to 0.33 when their median sizes vary from 0.22 µm to 3.0 µm respectively. Using a typical reduced remanence particle size dependence [9] we estimated ours in 0.35. In order to avoid precipitation and aggregation, a viscous media consisting of polyethylene glycol was used to disperse the magnetic particles. As sample holders, we used glass microtubes. About 10 µl of the particle suspensions were transferred to the microtubes, leading to a cylindrical sample with 1.3 mm diameter about 7 mm long.
The magnetite mass present in the sample was obtained by: $m = \mu / (0.35 \times 98)$, where μ is the measured remanent magnetic moment in Am^2 and 98 Am^2/kg is the specific saturation magnetization of magnetite at 4.2 K. Fig. 1 shows the flux obtained as the microtube is displaced relative to the SQUID (symbols) and the fit by mutual inductance calculations (solid line) from where the magnetic moments are obtained. The legend shows the masses obtained with the above relation.

[1] R. Kotitz, H. Matz, L. Trahms,H. Koch,W. Weitschies, T. Rheinlander, W. Semmler and T. Bunte, 1997 IEEE Trans. Appl. Supercon. 7 3678

[2] Y. R. Chemla, H. L. Grossman, Y. Poon, R. McDermott, R. Stevens, M. D. Alper and J. Clarke, Proc. Nat. Acad. Sci. USA, 2000 97 14268

[3] K. Enpuku, D. Kuroda, T. Q. Yang and K. Yoshinaga 2003 IEEE Trans. Appl. Supercon. 13 371

[4] D. Hautot, Q. A. Pankhurst and J. Dobson, 2005 Rev. Sci. Instrum. 76 045101

[5] H. R. Carvalho, A. C. Bruno, S. R. Louro and P. Costa Ribeiro, 2007 IEEE Trans. Appl. Supercon. 17 820

[6] Grover F W, Inductance Calculations. New York: Dover 2004, ch. 15

[7] MagPrep, Merck KGaA, Frankfurter Str. 250, D-64293 Darmstadt, Germany

[8] O. Ozdemir. D. J. Dunlop and B. M. Moskowitz, 2002 Earth Planet. Sci. Lett. 194, 343.

[9] D. J. Dunlop and O Ozdemir, 2001 Rock Magnetism. (Cambridge: Cambridge University Press) ch. 12

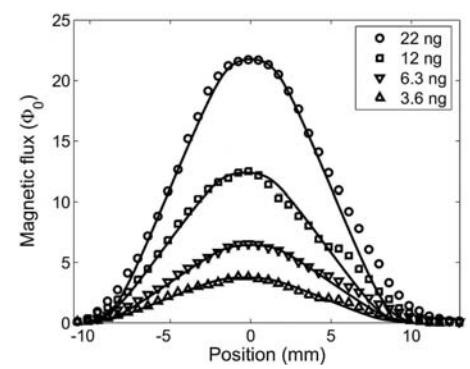

GO-04

Detection of MCG signal by using MgB_2 SQUID on pulse-tube cooler.

D. Oyama[1,2], Y. Harada[3], Y. Fujine[1], K. Kobayashi[1], Y. Uchikawa[4], M. Yoshizawa[1]
1. Graduate School of Engineering, Iwate University, Morioka, Iwate, Japan; 2. Japan Society for the Promotion of Science Research Fellow, Tokyo, Japan; 3. Japan Science and Technology Agency Innovation Satellite Iwate, Morioka, Iwate, Japan; 4. Department of Electronics and Computer Engineering, School of Science and Engineering, Tokyo Denki University, Hatoyama, Saitama, Japan

Introduction

Superconducting quantum interference devices (SQUIDs) are widely used for biomagnetic measurement, such as magnetocardiogram (MCG) and magnetoencephalogram (MEG). In many cases, biomagnetic measurement systems use low-T_c SQUIDs and need liquid helium to cool them. However, the expensive price of liquid helium and its difficulty in handling hinder the usage of SQUIDs in area of biomagnetic measurement. On the hand, high-T_c SQUIDs made by oxide superconductors are easily cooled by cheaper liquid nitrogen. Although the high-T_c SQUID has such an advantage, it has problems when it is used in biomagnetic measurements, because they are lower sensitive, more difficult to product and more fragile than low-T_c SQUIDs. To solve these problems, we are developing MgB_2 SQUIDs [1] by using high quality as-grown films [2]. The T_c of our films produced by a molecular beam epitaxy (MBE) is 37 K. This temperature is adequate to be cooled by pulse-tube cooler, which requires no liquid cryogen and has advantages in low magnetic noises from mechanical vibration compared to other types of coolers [3]. We have developed the MgB_2 SQUID system cooled by a pulse-tube cooler. MCG signal is successfully detected using this system.

MgB_2 SQUID system cooled by cryocooler

Fig.1 shows the block diagram of the MgB_2 SQUID system cooled by a pulse-tube cooler. A commercially available pulse-tube cooler was used. The cold head of the cryocooler is connected to the compressor via a valve unit. Because the valve unit produces magnetic noises, the cold head and the refrigerator part is installed in a magnetically shielded room, and the valve unit is set outside of it. They are connected by using a long copper tube.

An MgB_2 SQUID and a pickup coil are installed inside the cold cylinder connected to the refrigerator. The pickup coil is made of Cu as thin film on a glass-epoxy substrate, although a pickup coil is usually made of superconducting material to detect low frequency magnetic field. Because this plate can be cooled at the same temperature as the cold cylinder, resistance may be decreased enough to measure biomagnetic signal. The pickup coil has a 10 turns square eddy loop that is in 30 x 30 mm^2 area to detect magnetic field, and a single turn input coil to apply the magnetic signal to SQUID. The MgB_2 SQUID chip is put right above the input coil. Therefore magnetic field and coldness are transmitted from the pickup coil plate to the MgB_2 SQUID.

This refrigerator can reach about 5 K without any loading. Temperature of the sample stage is controlled by a heater.

DC coupling between SQUID chip and preamplifier is used and a flux-locked loop (FLL) circuit works in direct readout mode. To operate the SQUID, some parameters are digitally controlled by a computer through the digital FLL electronics.

Results

The lowest temperature of this system was 5.6 K. Characteristic evaluations of the MgB_2 SQUID were carried out at 28.6 K. The bias current was 370 μA, the maximum voltage modulation was 10.2 μV. A sensitivity B/Φ was about 19.3 nT/Φ_0 at 2 Hz. The cutoff frequency of the pickup coil was 0.5Hz.

Fig.2 shows a magnetic noise spectrum of the system measured in a magnetically shielded room. The white flux noise was about 9.5 pT/$Hz^{1/2}$. The largest peak is power line noise at 50 Hz. Other peaks were observed at 1.2 Hz and its harmonics. The origin of these noises is enigma.

Fig.3 shows an MCG waveform measured by this system. This waveform was obtained by applying a software band-pass filter (2 to 40 Hz) and 560 times averaging. QRS compelx is shown clearly, and this figure proves that the system can detect MCG waveform.

Conclusion

MgB_2 SQUID system cooled by a pulse-tube cooler is proposed. It is composed with a Cu pickup coil and careful design for noises. MCG waveform was measured by this system at 28.6 K.

[1] R.S.Gonnelli, *et al.*, *Physica C*, **435**, 59 (2006).

[2] Y. Harada *et al.*, *Physica C*, **412-414**, 1383 (2004).

[3] D.F.He, *et al.*, *Physica C*, **392-396**, 1416 (2003).

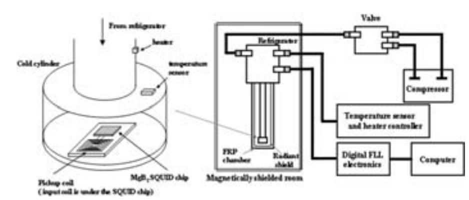

Fig.1 Block diagram of the MgB_2 SQUID system cooled by pulse-tube cooler.

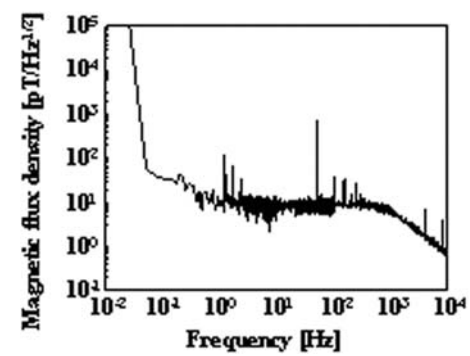

Fig.2 Flux noise spectrum of the system.

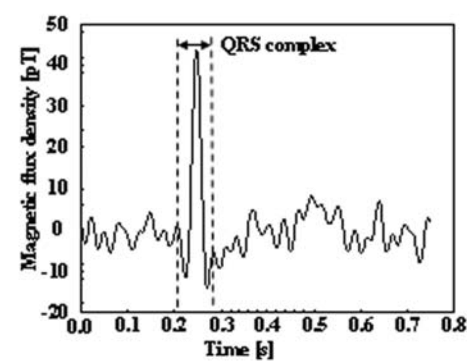

Fig.3 MCG waveform measured by the MgB_2 SQUID system cooled by pulse-tube cooler.

GO-05

Biomagnetic Signal Detection Using Very High Sensitive MI Sensor for Medical Applications.

T. Uchiyama[1], S. Tajima[1], S. Shibata[1], L. Ji[1], K. Bushida[2]
1. Electrical Engineering, Nagoya University, Nagoya, Japan; 2. UNITIKA LTD, Tokyo, Japan

Introduction

Superconducting quantum interference device (SQUID) magnetometers have ultra high sensitivity, which is useful for detection of biomagnetic signal. For example, magnetocardiography (MCG) is a noninvasive technology that measures the magnetic field of the heart by SQUID. It was developed for the general purpose as a noninvasive, non-contact diagnostic tool of obstructive coronary artery disease (CAD), and especially of cardiac ischemia. The SQUID has been also used to measure and localize seizure activity in the human brain. In usual cases, SQUID magnetometer needs both magnetic shield equipment and a refrigerator.

Recently, micro magnetic sensors due to Magneto-Impedance (MI) effect have been developed by Mohri et.al. MI sensor has future such as high sensitivity, high stability, high spatial resolution, small size, lightweight and low power consumption. The integrated MI sensors being used commercially in the mobile phone today. The optimal sensitivity of the MI sensor of around 100pT has been reported (1). The development of very high sensitive MI sensor system is expected to detect biomagnetic signal for the purpose of both convenient and accurate health care medicine. In this paper, we demonstrate the performing of biomagnetic recording by use of MI sensor.

Result and Conclusion

In order to investigate sensitivity of 1 cm long amorphous wire MI sensor with 600 turns of pick-up coil, we have measured the spectrum of output noise. The rms noise of the MI sensor is estimated to be 3pT/Hz$^{1/2}$ at 1Hz, while high-resolution imaging SQUID microscope has rms noise of 0.1p T/ Hz$^{1/2}$ at 1Hz(2).

The cardiogram signal is clearly detected by MI sensor when the sensor head is very close to chest surface. The wave form of the cardiogram, which was measured under the no shield environment, is shown in Fig.1(a) and Fig.1(b).The futures of QRS and T waves correspond with electrocardiogram. The maximum field strength of several nT is almost 50 times larger than the magneto-cardiogram measurement by SQUID system having Sensor-to-Chest spacing of around 50 mm. The maximum magnetic field strength of magneto-cardiogram increases with decreasing Sensor-to-Chest spacing. The maximum field strength of several nT was measured for a rabbit heart using SQUID microscopy brought the sensor within less than 100 μm of epicardium(2)

It is interesting to measure biomagnetic field around the blood vessel, because fMRI blood oxygen level-dependent (BOLD) signals are utilized for neuroscience to study brain activity. BOLD fMRI does not measure neuronal activity directly but depends on cerebral blood flow, cerebral blood volume, and cerebral metabolic rate of oxygen consumption.

The wave forms of the magnetic field at the hand surface around the vein measured by MI sensor are shown in Fig.2. The main frequency components of the waves are heart beat frequency component and respiration frequency component. Compared with the magnetic field measured before lunch and it measured after lunch, the amplitude of respiration frequency component evidently increased after lunch. It seems that the biomagnetic field around the vein is related with both blood flow and metabolism.

In conclusion, very high sensitive MI sensor has feasibility of biomagnetic signal detection and it will be available to check heart disease or to study blood-flow related phenomena in metabolism.

(1)”Amorphous Wire CMOSIC Based Magneto Impedance Sensors, Topics, and Future”, K. Mohri, and Y. Honkura, SENSER LETTERS, Vol, 5, 267-270, (2007)

(2)”High resolution imaging of cardiac baiomagnetid fields using a low-transition-tempereture superconducting quantum interference device microscope”, L.E. Fong, J. R. Holzer, K. McBride, E. A. Lima, F. Boudenbaucher, M.Randparvar, APPLIED PHYSICS LETTERS, Vol. 84, No. 16, pp. 3190-3192,(2004)

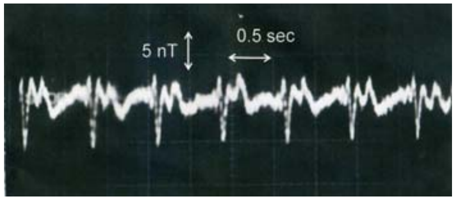

Fig.1(a) Series of cardiogram signal measured by MI sensor.

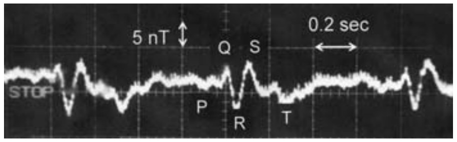

Fig.1(b) Detailed future of cardiogram signal measured by MI sensor.

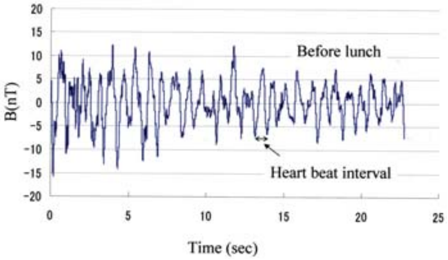

Fig.2(a)Magnetic field variation at the hand surface around the vein measured before lunch.

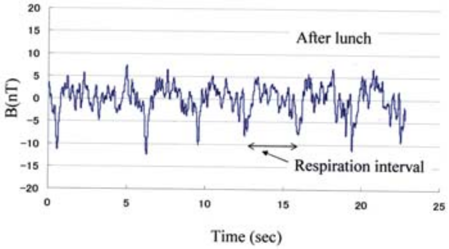

Fig.2(b) Magnetic field variation at the hand surface around the vein measured an hour after lunch.

GO-06

Giant magnetoimpedance of electrochemically surface modified Co-based amorphous ribbons.

V. Fal Miyar[1], M. Cerdeira[1], J. A. García[1], A. P. Potatov[2], A. R. Pierna[3], F. F. Marzo[3], J. M. Barandiarán[4], G. V. Kurlyandskaya[4]
1. Department of Physics, University of Oviedo, Oviedo, Spain; 2. Institute of Metal Physics, Ekaterinburg, Russian Federation; 3. Dpto. de Ingeniería Química y Medio Ambiente, Universidad del País Vasco, San Sebastián, Spain; 4. Department of Electricity and Electronics, Basque Country University, Bilbao, Spain

Areas of technological applications of magnetic materials have been significantly extended with the development of magnetic biosensors [1]. In the majority of biosensors with a magnetic sensitive element, the working principle is based on the detection of stray fields of magnetizable nanoparticles; these are employed as biomarkers [1-3]. The magnetoimpedance effect (MI) [4] was proposed both for magnetic label and label free detection of biological substances [3, 5-6]. Some of the MI prototypes were designed using Co-based amorphous ribbons without protective covering, the most economic design for disposable single stripe usage. Therefore it was necessary to study MI and corrosion stability of such materials in biofluids. Although some corrosion studies were done using traditional electrochemical methods [7] there was no work done on comparative analysis of the magnetic properties, MI and corrosion stability of the ribbons of the same composition. In this work magnetization curves and MI effect in $Fe_{2.5}Co_{64.5}Cr_3Si_{15}B_{15}$ amorphous ribbons in as-quenched state and after electrochemical surface modification in different regimes were comparatively analyzed.

$Fe_{2.5}Co_{64.5}Cr_3Si_{15}B_{15}$ amorphous ribbons were prepared by melt spinning technique. Their amorphous states were checked by X-Ray diffraction (Fig. 1). Samples of 100 x 1 x 0.025 (mm^3) were used for magnetic and MI measurements before and after electrochemical surface modification in a conventional three-electrode glass cell. A phosphate buffered saline (PBS) solution has been used as an electrolyte being 0.138M of NaCl, 0.0027M of KCl for 0.1M of PBS. The pH value of this solution was 7.3 and the temperature was maintained at 37°C during the treatment in order to simulate the human body living conditions. The working electrodes were polarized from the corrosion potential (250 mV) at a scan rate of 0.5 mVs^{-1} in the anodic direction up to the values of 0.4, 0.5, 0.6 and 1 V. The surface morphology of all samples was studied by optical and scanning electron microscopy. The longitudinal hysteresis loops were measured before and after treatments using the conventional inductive method at a frequency of 20 mHz (Inset Fig 1. a). The electrochemical treatments do not change the very small coercivity of the ribbons but they cause certain changes in the magnetization processes. It is clear the different intervals: above 0.6 Oe (saturation field) and below ±0.1 Oe (high permeability interval) for 1V treated sample.

The MI was measured by a standard four point technique [5]. Driving current flow (amplitudes of 0.2 to 10 MHz) and external magnetic field application directions were parallel to the ribbon axis. The impedance changes for each field value were calculated using the Ohm's law at a constant value of the selected driving current intensity of 5-60 mA (I_{rms}). The MI measurements were carried out in decreasing (down branch) and increasing (up branch) fields, starting at the maximum positive field. The MI ratio, $\Delta Z/Z$ was defined as follows: $\Delta Z/Z = 100*(Z(H) - Z(H_{max}))/ Z(H_{max}))$, where Z is the impedance modulus and $H_{max}=\pm 73$ Oe is the maximum external magnetic field, at which the sample is magnetically saturated.

Selected results of the MI studies are shown in Fig. 1b-c. It is seen that MI responses for selected driving current and frequency depend on the value of the maximum voltage corresponding to the electrochemical treatment. The tendency for low field interval of ± 5 Oe is the higher the maximum voltage the higher the $\Delta Z/Z$ value. Even more clear difference in MI behavior for the ribbons after surface modification in different regimes was observed for dependence of the maximum of the $\Delta Z/Z$ ratio on driving current intensity: the higher the maximum voltage the higher the $\Delta Z/Z$ value. The MI behavior is explained on the basis of a simple model taking into account the classic skin penetration depth, the possible contribution surface anisotropy and the roughness changes.

[1]D.R. Baselt, G.U. Lee, M. Natesan, S.W. Metzger, P.E. Sheehan and R. J. Colton, Biosens. Bioelectron., vol. 13, pp. 731-739, 1998.

[2]M.M. Miller, G.A. Prinz, S.-F. Cheng and S. Bounnak, Appl. Phys. Lett, vol. 81, pp. 2211-2213, 2002.

[3]G.V. Kurlyandskaya, M.L. Sánchez, B. Hernando, V.M. Prida, P. Gorria and M. Tejedor, Appl. Phys. Lett. vol.82, no 18, pp. 3053- 3055, 2003.

[4]R. S. Beach and A. E. Berkowitz, Appl. Phys. Lett., vol. 64, no. 26, pp. 3652-3654, 1994.

[5]G. Kurlyandskaya and V. Fal Miyar, Biosens. Bioelectron., vol. 22, pp. 2341- 2345, 2007.

[6]G. V. Kurlyandskaya, V. Fal Miyar, A. Saad, E. Asua, and J. Rodriguez, J. Appl. Phys. vol. 101, pp. 054505 1-9, 2007.

[7]F. F. Marzo, A. R. Pierna, J. Barranco, G. Vara, A. Lorenzo, A. Perez and J.A. García, Port. Electrochim. Acta., vol 25, pp. 131-137, 2007.

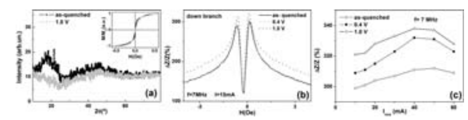

Figure 1. X-Ray diffraction and hysteresis loops (inset) of Co-based ribbons in as-quenched state and after electrochemical surface modification with the maximum voltage of 1 V (a); MI responses of Co-based amorphous ribbons in selected states (b); dependence of the maximum of the MI ratio on driving current intensity Co-based for amorphous ribbons after selected electro-chemical treatments.

GO-07

Spatially arterial pulse diagnostic apparatus using array Hall devices.

S. Lee[1], G. Kim[2], M. Ahn[3], Y. Park[3], D. Hwang[1], J. Rhee[4], H. Yoon[5]
1. Oriental Biomedical Engineering, Sangji University, Wonju, South Korea; 2. Oriental Medicine Science, Sangji University, Wonju, South Korea; 3. Oriental-western Biomedical Engineering, Sangji University, Wonju, South Korea; 4. Physics, Sookmyung Women's University, Seoul, South Korea; 5. Biomedical Engineering, Yonsei University, Wonju, South Korea

The commercial and medical pulse diagnostic apparatus (PDA) includes a pressure sensing sensor including a silicon layer, which is adhered closely to the upper skin at the radial artery and close up the air layer tight to sense the pressure change of the air layer, which depends on the vibration of a pulse wave[1].

This research shows the process of achieve- ment and analysis of 3-dimensional spatial pulse wave archived by a spatially arterial pulse diagnostic apparatus (SAPDA), wherein a pulse sensing part array consists of multiple Hall device and is located over a skin contacting part which consists of a magnetic material[2].

To achieve the objectives of the SAPDA, the detecting senor is characterized by comprising a skin to examine the pulse. This system is composed of pulse sensing part, skin contacting part and spatial part. A pulse sensing part, located some distance over the skin contacting part and formed as an array type with at least one Hall device, and other part, a spatial part is located between the skin contacting part and the pulse sensing part, as shown in Fig. 1

Fig. 1 shows the schematic of a cross section of one embodiment of SAPDA sensing part with array Hall devices and 3-dimensional image treatment system. The sensing part of SAPDA is composed of 15 arrays of the A3516 model Hall sensor and the cylindrical type permanent magnets having a size of 1.5 mm dia.×1 mm thick. The flexible spacer between the sensors and the magnets can control the applied pressure of the arterial tube as the doctors' three fingers press the arterial tube. So to realize the ideal pulse diagnosis system it is necessary for the system to have a device to apply certain pressure on the sensors, and both the pressure applied by the device and the pressure obtained from the artery should be recorded. The distance between the elements of an array is about 2 mm, and all the cylindrical magnets have an intensity of 100 Oe.

On the other hand, by varying the contact pressure height of a permanent magnet on the skin, a new method of characterizing the spatial pulse wave based on the degree of floating, the width, and the depth was introduced. These, unlike the traditional pulse diagnosis, do not involve the analysis of diastolic blood pressure and pulse wave velocity.

We measured signals at the "Chon". "Gwan". and "Chuck" region, as shown in Fig. 2(a) using the testing product of SAPDA system, passed signals through the voltage detecting hard ware system as shown in Fig 1(b). made a differential input, an automatic zero set, a noise filtering, a high power gain and output attenuation, output them with 12 bit resolution at 30 FPS (frame/s), RS232C, simulated the result with a predetermined computer processing, and obtained three dimensional image of Fig. 2(b). By the computer processed 3-dimensional image of signals detected by SAPDA, wherein is marked one point pulse to analyze the temporal pulse wave, we can select it. Fig. 2(c) show an example of measuring time (second) versus temporally typical signal of one point pulse obtained from the analysis for an arbitrary 3-dimensional pulse image of one position of small size permanent magnet.

So far, the preferable embodiments of the SAPDA have been described herein, but it will be evident that the SAPDA cannot be defined only by the described embodiments herein, and it will be understood that the SAPDA herein described are generally applicable and executed as various modified embodiments by those skilled in the art, For example. materials and numerical values for a skin contacting part, a pulse sensing part and a spatial part can be various within the technical thought of the SAPDA. Also, Fig. 2(c) shows the signal of one point obtained by the analysis of composition of color 3-dimensional images of testing product of SAPDA. The spatial change of the pulse height in arterial pulse incurred one permanent magnet within 1 mm. We confirmed that one example of measuring pulse signal was reproducible and provided many information for oriental medical diagnosis. To resolve the subtle and subconscious arterial pulse, a more controlled study should be conducted and the real spatial data obtained through future research and development.

This work was supported by the Korea Foundation for International Cooperation of Science & Technology(KICOS)in 2007.

[1] K. W. Mun and k. S. Soh, J. Kor. Phys. Soc. 40, 289(2002).

[2] S. W. Kim, Y. G. Choi, H. S. Lee, D. H. Park, D. G. Hwang, S. S. Lee, G. W. Kim, S. G. Lee, and S. J. Lee, J. Appl. Phys. 99, R908(2006).

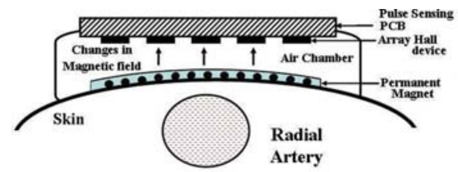

Fig. 1. Schematic of a cross section of one embodiment of SAPDA sensing part.

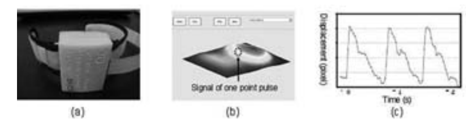

Fig. 2. (a) One photo of the real testing product of SAPDA, (b) the computer processed 3-dimensional image of signals detected by SAPDA, wherein is marked one point pulse to obtain the temporal pulse wave. (c) Example of measuring time (second) versus temporally typical signal of one point pulse obtained from the analysis for an arbitrary 3-dimensional pulse image of one position of small size permanent magnet.

GO-08

Various Types of Hall Sensors for Single Particle Detection.

O. Kazakova[1], J. Gallop[1], D. Cox[1,2], A. Cuenat[1], L. Brown[1], K. Suzuki[3], L. Bernau[4], I. Utke[4]
1. NPL, Teddington, United Kingdom; 2. Surrey University, Guilford, United Kingdom; 3. NTT Basic Research Laboratories, Kanagawa, Japan; 4. EMPA, Thun, Switzerland

We present our first results in realizing a measurement system based on two different types of Hall sensors, made of a conventional 2DEG InAs/GaSb-based heterostructure and a novel metallo-organic Co-C composite. While in the 2DEG system the ordinary Hall effect is due to the Lorentz force acting on charge carriers in a semiconductor, the latter system additionally demonstrates a strong extraordinary Hall effect originating in spin-orbit interactions in a ferromagnetic material [1]. The work aims to optimize fabrication and measurement performance of both types of sensor. The quantum well AlGaAs/InAs (12 nm)/GaSb (18 nm)/AlGaAs heterostructure was grown by molecular beam epitaxy on an undoped InAs (001) substrate [2]. Arrays of large Hall crosses (100x20 μm^2) connected in parallel were fabricated by optical lithography and reactive etching (Fig. 1a). The good ohmic contacts were achieved using germanium layer on the electrical pads.
The metallo-organic Co-C Hall crosses were fabricated by direct writing in a FIB system. The Co–C deposit is obtained by decomposing of dicobalt octacarbonyl [$Co_2(CO)_8$] with an electron beam [2]. Using this technique we were able to fabricated Hall sensors with the cross area down to (300 nm)^2 (Fig. 1b).
The best-achieved resistance is 2 kΩ and 2.8 kΩ for Co-C and 2DEG complete devices, respectively. The Hall voltage was measured as a function of the magnetic field applied perpendicular to the sample plane (Fig. 2). All devices demonstrate a significant offset voltage, which is predominantly proportional to device bias current indicating non-orthogonality between voltage taps and the current flow. Very small offsets (a few μV) arise even at $I_H = 0$, presumably due to thermoelectric effects. Hall voltage is linearly dependent on I_H proving a good ohmic contact between the metal electrodes and the Hall cross material. For the Co-C device, the Hall voltage saturates at B ≈ 1 T. However, no sign of saturation have been observed in 2DEG devices up to B = 2 T. The present sensitivity S_B in the linear region is about 0.014 V/AT and 34.2 V/AT for Co-C and 2DEG crosses, respectively. This corresponds to Hall coefficients R_H(Co-C) ≈ 4x10^{-9} Ωm/T and R_H(2DEG) ≈ 4x10^{-7} Ωm/T, thus being two order of magnitude better in the 2DEG heterostructures. The presence of hysteresis in the V_H–B curve indicates significant remanent magnetization in the Co-C deposit. The relatively low Hall coefficient and the remanent magnetization are potential drawbacks for a noninvasive biosensor. Thus, further optimization of material properties is required for successful design of a metallo-organic Co-C Hall sensor.
Further we investigated the room-temperature noise in InAs/GaSb Hall sensors in the frequency range 1 Hz – 13.0 kHz. For all bias currents the 2DEG devices exhibit a *1/f* like spectrum at low frequencies and a white noise region at higher frequencies. We calculate that for $I_H = 0$ the average spectral density of the voltage noise is S_V = 1.3x10^{-8} V/√Hz at *f* = 4 - 8 kHz, which is only twice larger than the expected Nyquist noise at room temperature. Both the observed *1/f* and white noise values increase with the bias current, although the latter has a less strong current dependence. *1/f* voltage noise shows a clear linear dependence on bias current at *f* ≈ 100 Hz. Similar behaviour in 2DEG systems was previously attributed to bulk mobility fluctuations within the channel, arising from scattering of 2D phonons. Chen et al. [3] find that the *1/f* component of the noise spectrum is strongly temperature dependent and also can be affected by illumination of the 2DEG. At higher frequencies (>2 kHz) the noise increases much slower with current providing the best operating regime for such a sensor if it can be used with a lock-in technique involving kHz modulation.
In the white noise region for the measured S_V value and I_H = 0.5 mA, the minimum detectable magnetic field change in a 1 Hz bandwidth equals ΔB = 2.4x10^{-6} T.
Our results show that the InAs/GaSb Hall devices are capable of detecting a single magnetic bead of diameter down to 200-400 nm. Although the Co-C devices are as yet not as sensitive, the ease with which a simple nanoscale Hall cross may be fabricated from this material suggests that further investigation is worthwhile.

1. G. Boero, et al., Appl. Phys. Lett. **86**, 042503 (2005).

2. K. Suzuki, et al., Phys. Rev. Lett. **98**, 136802 (2007).

3. X. Y. Chen, et al., Phys. Rev. B **55**, 5290 (1997).

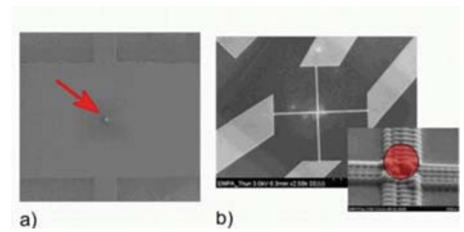

SEM images of InAs/GaSb (a) and Co-C (b) Hall sensors. A single magnetic bead is attached to the InAs/GaSb device. The cross area is 20x100 μm^2 (a) and 400x400 nm^2 (b).

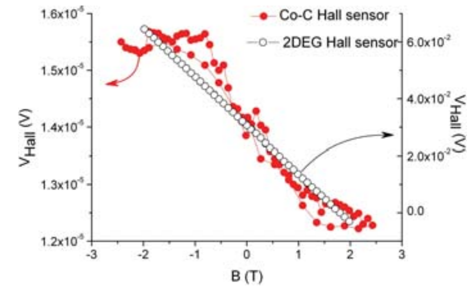

Hall voltage vs applied magnetic field in Co-C and InAs/GaSb Hall sensors.

GO-09

Microwaves Doppler transducer for noninvasive monitorisation of the cardiorespiratory activity.

O. I. Baltag[2], M. P. Costin[1,2]
1. Computer Science Institute, Romanian Academy, Iasi, Romania; 2. Faculty of Biomedical Engineering, "Gr.T.Popa"University of Medicine and Pharmacy, IASI, Romania

Abstract —The paper present a devices for detecting the cardiorespiratory activity by means of a microwaves Doppler detector of motion, which should permit the detection without an intimate contact with the patient.
Keywords — microwave, Doppler frequency, noninvasive monitoring, cardiorespiratory activity,

I. INTRODUCTION

The cardiorespiratory activity is an important parameter for the observation of the human body activity [1]. The absence of breathing, apnea, represent the obstruction of the air flow which passes through the nose or through the oral cavity to pass to the lung, for an interval longer than 20 seconds. It is difficult to forecast the absence of the breathing which can be deathly in a few minutes. . Few clinical aspects are relevant for cardiorespiratory monitoring.
- after anesthesia, both the respiratory centre and the respiratory muscles can be affected, leading to a rise in the CO2 concentration and a drop in the O2 concentration;
- another clinical situation that affect respiratory activity is the sedation of the patients during the examinations such us magnetic resonance imaging.

II. EXPERIMENTAL SETUP

The microwave transducer makes use of the Doppler effect in the microwave range in order to detect the complex motion of the thorax anatomic structures as the result of the cardiorespiration activity [2]. The main element of the installation consists of the Doppler transducer made of a microwaves devices realized in stripline technology.
The utilization of high frequency electromagnetic waves implies certain difficulties connected to the electromagnetic waves propagation through the biological structures, to the complex phenomena of reflection, refraction, absorption, diffusion and interference that can occur on the skin, in depth of certain tissues, a different electromagnetic field absorption (at the input and output) of the wave by the human body. In order to ensure a minimum level even below the one permitted by standards for the electromagnetic field intensity, one has to use generators of small power, of the order of a some of milliwats. We preferred to use a frequency of some GHz, given the fact that the phenomena specific to the microwaves propagation are more obvious at this frequencies; yet, another reason is determined by the simplicity of the Doppler transducer at these frequencies. At this frequencies the skin depth in muscles, lung and blood is of a few millimeters, reaching 2-9 mm in fat. One can notice a good correlation between the complex Doppler signal and the signal due to the respiratory activity. The signal given by the manometer follows the respiratory activity, its maximum values corresponding to the thorax outward motion by air inspiration and its minimum values corresponding to the reverse thorax motion.

III. RESULTS

The records from Fig. 1, were made in the apnea condition after inspiration. The diagrams present the signals picked-up by the photopletismograph as a reference signal, and the Doppler signals corresponding to the zone against the thorax. In most of the diagrams, one can remark a time alteration of the amplitude of the signal pick-up by the photopletismograph; this is the result of the apnea state installed at the beginning of every measurement. From the A, B… L, diagrams one can remark variable amplitude of the Doppler signal depending on the transducer's position as related to the thorax.
As it might be observed, the highest signal amplitude is in the zones E, F, H zones meaning the region were the heart is placed, due to the heart's contraction motions and to the larger blood volume pumped through the organism by means of the aortic artery. At the same time increased signal values are recorded in the K zone corresponding to the direction of the descending thoracic abdominal aorta.
(Fig. 1. Cardiac activity map of the Doppler signal)
The experimental results confirm the possibility to use a microwave Doppler detector of motion for detection, recording and explaining the signals produced by the cardio-respiratory activity. The method permits to detect the apnea and sleep apnea, the breathing frequency, as well as the heart activity. The radiant energy is much below the admitted limits; the energy density at the horn antenna output is 3 mW. One can also remark a good correlation between the complex Doppler signal and the ECG signal, the breathing and the pulse photoelectric transducer.

[1] E. Folke, et all, "Critical revue of noninvasive respiratory monitoring in medical care" Medical 7 Biological Eng & Comp. vol. 41, pp.377-383, 2003.

[2] [2] R. Tipa, O. Baltag, Rom., Microwaves Doppler transducer for contactless cardiorespiratory monitoring, Journ. Phys., vol. 53, No. 1-2, pp.315-320, 2008.

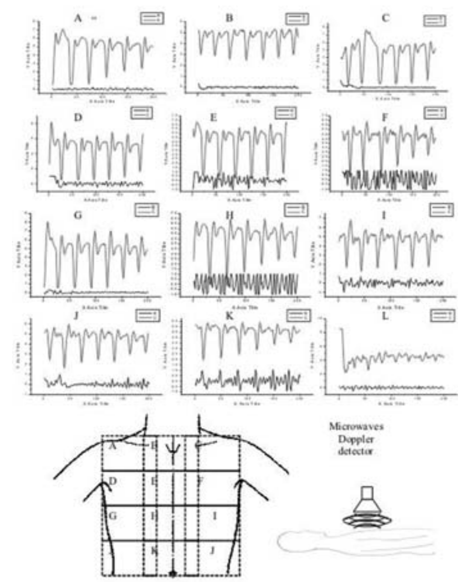

GO-10

Investigating the cortical connectivity in the brain by combined TMS and EEG.

K. Iramina[1,2], T. Arimatsu[1], H. Sato[1], A. Hyodo[2], T. Hayami[3], S. Ueno[4]
1. Department of Intelligent Systems, Kyushu University, Fukuoka, Japan; 2. Graduate School of Systems Life Sciences, Kyushu University, Fukuoka, Japan; 3. Digital Medicine Initiative, Kyushu University, Fukuoka, Japan; 4. Department of Applied Quantum Physics, Kyushu University, Fukuoka, Japan

Cortical reactivity and the functional connectivity in the brain are able to be investigated by the combined measurement of EEG and transcranial magnetic stimulation (TMS). When the TMS was applied to the motor area, the posterior parietal cortex(PPC) and the cerebellum, this study focused on the differences in the cortical reactivity of these areas. It is difficult to measure evoked EEG by magnetic stimulation because of the large artifact induced by magnetic pulse. We used an EEG measurement system to eliminate the electromagnetic interaction emitted from TMS. A temporary intercepting the input of the amplifier was equipped in the preamplifier of EEG which was controlled by the trigger signal from the magnetic stimulation device. Applying such improved EEG, it proved that artifact can be removed. However, large residual artifact got mixed in electrodes near the stimulus point of TMS. To remove this artifact, independent component analysis was applied to the measurement signals and only the artifact component was removed from the EEG signals. In addition by using ICA, we could reduce the artifact from the EEG signal. EEG signals on the all electrodes over the head within 10 ms after TMS stimulation were able to be obtained.
We investigated the differences in the cortical reactivity of the motor area, the posterior parietal cortex and the cerebellum when the TMS was applied to each area. 60 channels EEG over the whole head are measured, and the EEG topography on the surface of the head and current distribution on the cortex were calculated. EEG data were filtered from 0.1 Hz to 350 Hz, and the data were averaged with the trigger at TMS onset. Stimulus intensity of TMS was determined based on the threshold intensity of the muscle movement when the motor area was stimulated. The stimulus intensity was 80 % of the motor threshold. A figure-of-eight 70 mm coil was used (inner diameter: 53mm, outer diameter: 73 mm) and was kept tangentially over the scalp. The magnetic flux density at the center of each coil was around 1T. Direction of the induced current of TMS was from posterior to the anterior of the head.
Fig.1 shows the EEG waveforms superimposed of 60 channels data when the motor area, the right PPC and the cerebellum were stimulated respectively. It was possible to measure the evoked EEG after the stimulation 10 ms. Fig. 2 shows the current distribution map on surface of brain when the motor area, the right PPC and the cerebellum were stimulated respectively. Based on the EEG topography, when motor area was stimulated, we could observe that the evoked potential transmitted from the stimulated hemisphere to its contralateral hemisphere. However, such spreading was not clearly observed when posterior parietal cortex and cerebellum were stimulated. Distinct differences in cortical reactivity of motor, posterior parietal cortex and cerebellum to magnetic stimulation were observed. When motor area was stimulated by TMS, it was observed that the spreading of the evoked electrical activity to the contralateral hemisphere in about 20 ms. However, when the posterior parietal cortex was stimulated, transmitting to the contralateral hemisphere was not observed. When the cerebellum was stimulated, evoked electrical activity propagates to the anterior in the ipsilateral hemisphere and the contralateral motor area. These results suggest that the motor area has strongly interhemispheric connection and the posterior parietal cortex has no interhemispheric connection. For the cerebellum, cerebellum-cerebrum connection, intrahemispheric and interhemispheric connections has observed by TMS and EEG measurement.

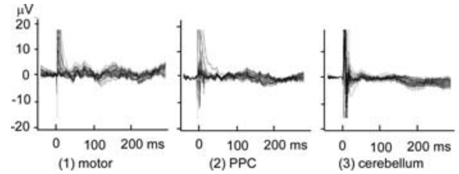

Fig.1 EEG waveforms superimposed of 60 channels data. (a) motor area stimuration (b) right PPC stimulation (c) the cerebellum stimulation

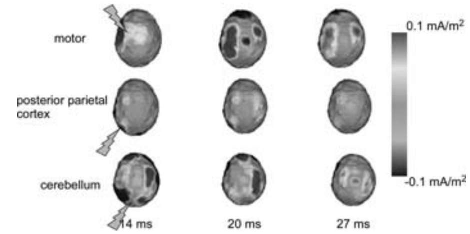

Fig.2 Current distribution map on surface of brain

GO-11

Fabrication of new magnetic micro-machines for low-invasive surgery.

C. Troisi[1], M. Knaflitz[1], E. Olivetti[2], L. Martino[2], *G. Durin*[2]
1. Dep. of Electronics, Politecnico di Torino, Torino, Italy; 2. Istituto Nazionale di Ricerca Metrologica, Torino, Italy

Magnetic micro-machines (MMM) have been proposed as effective tools for low-invasive medical applications, as they can be easily driven by an external rotating magnetic field, without cables or on board power supply. These machines are small objects (4-10 mm), generally built with two main components: a central magnetic part, properly magnetized, and a screw shaped structure. These elements are functional to the MMM's displacement, as the rotation is obtained by fixing the magnetization perpendicularly to the body's axis, and by applying an external rotating field which induces a synchronous rotation. The rotation is then converted into an axial motion through the screw shaped geometry. The frequency, the magnitude, and rotation plane of the external field are used to control speed and direction of the MMM, allowing to drive them along complex paths [1]. For these properties, MMM have been show to be use effectively in low-invasive medical applications, like hyperthermia, drugs delivery, tumor cells mechanical destruction [2,3].

Due to the small dimension required, manufacturing of MMM can be really complex and expensive, often involving sputtering or precise etching processes. Moreover, magnetic part and spiral structure are often different pieces glued together limiting the volume available for magnetic moment generation. In this paper, we propose an innovative and low cost MMM manufacturing process, based on moulding of a Sm-Co powder and acrylic (or polyurethanic) resin composite gel cast in silicon moulds. Those moulds can be prepared using a metallic master such as a standard screw or any proper designed element. Elastic moulds composed of a single block allow an easy extraction and are preferable over rigid moulds, composed of two separated halves.

During the polymerization of the resin, an uniform external magnetic field is kept perpendicularly to the body's axis, aligning the Sm-Co particles along the desired direction and increasing the total magnetization as well. This magnetic field of about 0.8 T is generated by two NdFeB magnets located at two sides of the mould.

Fig. 1 shows our first prototype of a spiral-type MMM of 10.7 mm length and 2.0-mm diameter, manufactured according to the described moulding process, using a standard screw as a metallic master. As shown in the table, the percentage of the magnetic power is still pretty low, giving a magnetic moment of 1.528 emu, corresponding to a total magnetization of the order of 63 mT. Further solutions to improve the compactness of the powder and to make use of a designed screw with different threads are under development.

To explore the magnetic properties and characteristics of the motion of this MMM, we have made a series of experiments under different amplitude and frequency of an external rotating magnetic field, and under different oils of known cinematic viscosity. As reported by other authors, the MMM velocity is roughly linear on the field frequency, getting the largest value of about 9 mm/min for a field of 3.88 kA/m at 0.56 Hz in a low viscosity oil, as shown in fig. 2. Other oils with lower cinematic viscosity are plotted as well, showing as the velocity gets progressively reduced, as expected. The viscosity also controls the maximum rotational frequency (step-out frequency) over which the machine cannot longer synchronize with the external field.

Moment and velocity for this MM are still to be optimized, expecially when compared to the data published of literature. For instance in [2], v/f is of the order of 0.64 mm, while we get a smaller value of about 0.27 mm. But this is not surprising expecially because our MMM has not a optimized angle of the thread (which should be about 45° instead of our 13° as shown in fig. 1). We are currently working on optimization of the MMM preparation using non-standard masters, and with different powders and resins, to get better performances. This will enable us to get working MMM with a reasonable cost and easiness of preparation.

[1] K. Ishiyama, M. Sendoh, A. Yamazaki and K. I. Arai., Sensors and Actuators A. 91,141 (2001)

[2] K. Ishiyama, M. Sendoh, and K. I. Arai., J. Magn. Magn. Mater., 242-245, 41 (2002)

[3] M. Sendoh, A. Yamazaki, A. Chiba, M Soma, K. Ishiyama, and K. I. Arai. Proceedings of the 2004 International Symposium on Micro-Nanomechatronics and Human Science, 319 (2004)

MMM Volume	MMM Mass	MMM Density	Resin Density	Powder Density	Powder Mass	Magnetic Moment
31,6 mm^3	0,064 g	2,025 g/cm^3	1,12 g/cm^3	8,35 g/cm^3	0,008 g	1,528 emu

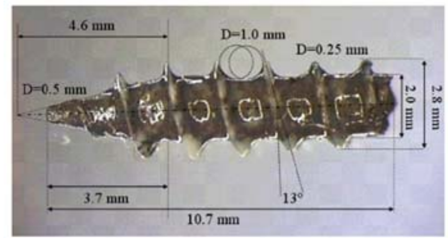

Photograph of the fabricated magnetic micromachine and his features.

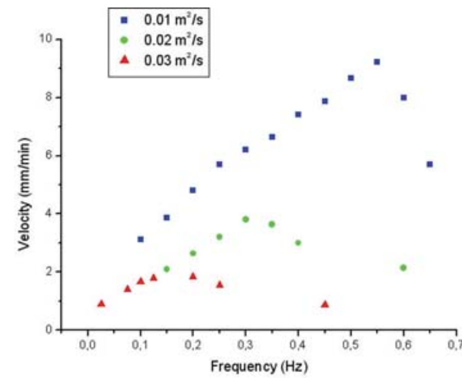

Relationship between frequency of the rotational magnetic field and swimming velocity.

Magnetic Tracking of Eye Motion in Small, Fast-Moving Animals.

A. Plotkin[1], E. Paperno[1], G. Vasserman[2], R. Segev[2]
1. Electrical and Computer Engineering, Ben-Gurion University of the Negev, Beer-Sheva, Israel; 2. Life Sciences, Ben-Gurion University of the Negev, Beer-Sheva, Israel

Modern magnetic tracking systems are successfully used for increasingly sophisticated applications in the fields of biomedicine, neuroscience, bionics, etc. Such systems are especially effective for eye tracking in humans and animals. No other technology, including video tracking, provides the speed and resolution required for eye movements measurements.

Conventional magnetic eye tracking systems employ a cubic transmitting frame to monitor a scleral search coil. A principal drawback of this technique is the inability to monitor the scleral search coil location. Another drawback is that the scleral search coil is unable to monitor the torsional eye movements. Finally, in many applications, the large, bulky cubic transmitting frame is inconvenient to use.

In this work we suggest a new approach and system to overcome the above drawbacks. We replace the cubic transmitting frame with an array of eight transmitting coils (see Fig. 1). The transmitting coils are arranged in a special pattern that allows unambiguous tracking of both the location and orientation of a single search coil [1].

We also replace the conventional scleral search coil with a tiny solenoid that is attached to the eye aside from its optical axis (see Fig. 1). Such a coil can accommodate a much larger number of layers, which allows us to increase the signal-to-noise ratio and the tracking resolution.

To test the efficiency of the new approach we measured the eye movements of the archer fish [2]. This fish has the capability to shoot down insects above water by spitting a jet of water from its mouth. The archer fish has an expert visual system that is expected to provide insights into the brain visual processing. We challenge our new system with an application where both the eyes and the head of an archer fish (see Fig. 2) should be monitored while the fish is shooting. Our experiments with a 60x60 cm transmitting array and a 2-mm diameter, 2-mm length search coil have shown the ability of the new system to monitor the fastest movements of the fish eyes (see Fig. 3). We have obtained the tracking resolution of 3 millidegree and 8.3 micrometer rms for a 200-Hz bandwidth at a 25-cm distance from the transmitting array center. The tracking resolution decreases down to 30 millidegree and 83 micrometer rms for a 40-cm distance.

The above results demonstrate very high system efficiency in tracking both the location and orientation. The new transmitting array and the new search coil are convenient in use and can successfully be applied to many other applications with behaving animals.

[1] A. Plotkin and E. Paperno, “3D Magnetic tracking of a single subminiature coil with a large 2D-Array of uniaxial transmitters,” IEEE Trans. Magn., vol. 39, pp. 2295-3297, 2003.

[2] R. Segev, E. Schneidman, J. Goodhouse, and M. J. Berry, II, “Role of eye movements in the retinal code for a size discrimination task,” J. Neurophysiol, vol. 98, pp. 1380-1391, 2007.

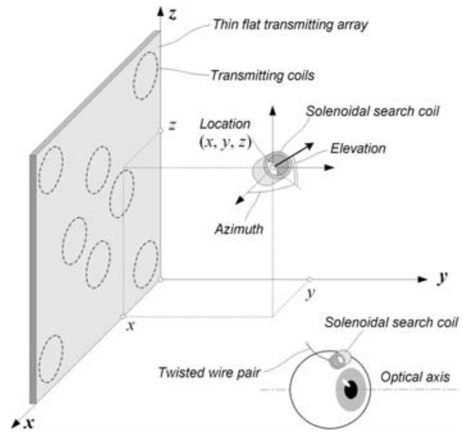

Fig. 1. Tracking system configuration.

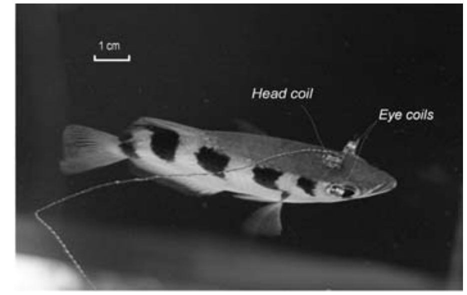

Fig. 2. Archer fish with a sensing coil on the head and on each eye.

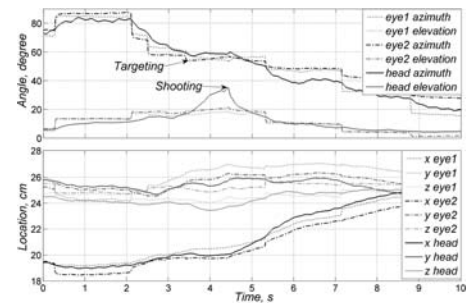

Fig. 3. An example of the experimental data.

GO-13

Minimization of Computational Errors in Diffusion Simulation of Nuclear Magnetization.

T. Imae[1,2], H. Shinohara[2], M. Sekino[3], H. Ohsaki[3], S. Ueno[4], K. Mima[1], K. Ootomo[1]
1. Department of Radiology, University of Tokyo Hospital, Tokyo, Japan; 2. Graduate School of Human Health Science, Tokyo Metropolitan University, Tokyo, Japan; 3. Graduate School of Frontier Sciences, University of Tokyo, Chiba, Japan; 4. Graduate School of Engineering, Kyushu University, Fukuoka, Japan

Introduction

Diffusion-weighted imaging (DWI) using magnetic resonance imaging (MRI) reflects the diffusion of water molecules in a sample. The diffusion of water molecules in biological tissues is restricted by cell membranes and other microscopic structures. If we can theoretically predict signals of diffusion MRI for samples having various microscopic structures, we can estimate the unknown diffusion parameters, such as shape and permeability through a comparison of theoretically predicted signals and experimental results[1)]. Therefore, establishment of a method to predict the signals of DWI is important. The finite-difference method is a general numerical method for solving partial differential equations in discrete space and time[2)], and is applicable to the diffusion equation of nuclear magnetization, but this method has computational errors due to discretization. The lengths of the spatial step Δx and time step Δt are representative conditions for calculation, and the computational errors depend on these lengths. However, the relationship between computational errors and the lengths of the spatial step Δx and time step Δt involved is not clear. The purpose of this study is to obtain the lengths of the time step and spatial step which minimize the computational errors in a finite-difference diffusion simulation. We evaluated the difference between the signals of the numerical solution and explicit solution of the diffusion equation of nuclear magnetization under the same conditions. We found combinations of the time step and spatial step which minimize this difference.

Methods

The dynamics of macroscopic magnetization in a one-dimensional diffusion of molecules was derived from the following Bloch-Torrey equation[3)]:

$$\partial(CM)/\partial t=D\partial^2(CM)/\partial x^2+i\gamma GxCM \qquad (1),$$

where C is the number of water molecules per unit volume, M is the magnetization vectors per molecule, D is the diffusion coefficient, γ is the gyromagnetic ratio and G is the intensity of the motion-probing gradient (MPG). This equation was transformed into the finite-difference equation in discrete space and time as the numerical solution of the diffusion equation. The explicit solution of the diffusion equation was obtained using the Fourier transformation and Lagrange's partial differential equations. The observed signals are the spatial integration of magnetization in MRI. For a comparison of the numerical solution and the explicit solution, we defined the initial magnetization for the explicit solution using the rectangular function having width Δx, magnitude A, and position k_0. The signals of numerical solution S_d and explicit solution S_e were derived under the same initial conditions after a time step Δt. We defined the computational error as the difference between the signals of the numerical solution and the explicit solution:

$$E=(S_d-S_e)^2 \qquad (2).$$

Results and Discussion

The Fig. shows the relationship between the optimum lengths of the time step and the resulting spatial step for the following parameters: A=1, k_0=5, D=1.95×10^{-6} [mm^2/ms] and G=10×10^{-3} [mT/ms]. Optimum Δx increased as optimum Δt increased. The Fig. revealed that the lengths of the time step and spatial step which minimize computational errors depended on the value of k_0 (the distance from the origin divided by the interval between the spatial grid points). In an actual model which had a certain range, each grid point has a different combination of optimum lengths of the time step and the spatial step. However, we have to determine one combination of lengths of the time step and spatial step for the whole model. A method to determine that combination is to substitute the number of grid points divided by 2 into k_0. This definition of k_0 provides a practical way for optimizing the whole model and this method is efficient in bringing about a decrease of computational errors in the models.

Conclusion

A decrease in the lengths of the spatial step and time step results in an improvement of computational errors, albeit with an increase in the time for computation. Practically, we can define the time for calculations and computational errors, and we can choose the optimum combination of the lengths of the spatial step and time step based on this study.

1) C. A. Clark and D. Le Bihan, Magn. Reson. Med. 44, 852 (2000).

2) C. L. Chin, F. W. Wehrli, S. N. Hwang, M. Takahashi, and D. B. Hackney, Magn. Reson. Med. 47, 455 (2002).

3) H. C. Torrey, Phys. Rev., 104, 563 (1956).

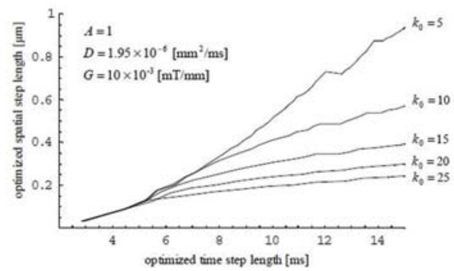

Fig. Relationship between the optimum lengths of the time step and the resulting spatial step. Optimum Δx increased as optimum Δt increased.

GO-14

Discriminative detection of extracellular and intracellular sodiums in nerve fibers by magnetic resonance spectroscopy.

S. Yamaguchi-Sekino[1], H. Tatsuoka[2], M. Sekino[3], H. Ohsaki[3], Y. Abe[1], S. Ueno[4]
1. Department of Biomedical Engineering, Graduate School of Medicine, The University of Tokyo, Tokyo, Japan; 2. Research Center for Frontier Medical Engineering, Chiba University, Chiba, Japan; 3. Department of Advanced Energy, Graduate School of Frontier Sciences, The University of Tokyo, Chiba, Japan; 4. 4Department of Applied Quantum Physics, Graduate School of Engineering, The Kyusyu University, Fukuoka, Japan

Introduction

The electrical activity in neurons, known as an action potential, is the direct consequence of changes in the concentration of extracellular Na (Na_e) / intracellular Na (Na_i) ions. Influx of extracellular Na_e into the cell fluid causes electric potential difference, resulting in the generation of action potential. Since Na_e / Na_i changes reflect the nerve excitation, development of Na_e / Na_i imaging potentially becomes a direct imaging method for nerve excitation. However, the detection method for Na_e / Na_i changes has not been developed sufficiently.

In the present study, measurement of Na_e / Na_i in the bullfrog sciatic nerves was performed by ^{23}Na-MRS (magnetic resonance spectroscopy) using ^{23}Na frequency shift reagent Na_4HTmDOTP.

Materials and Methods

<^{23}Na chemical shift reagent >

^{23}Na chemical shift reagent Na_4HTmDOTP was purchased from Macrocyclics (Dallas, USA). TmDOTP is membrane impermeable and induce frequency shifts in the extracellular cation resonances sufficient to clearly resolve them from the intracellular cation resonances [1].

<^{23}Na-MRS of sciatic nerve>

Magnetic resonance spectroscopy (MRS) is used for noninvasively investigating metabolism and the concentration of biomolecules in biological tissues. Bullfrogs were anesthetized with eugenol and sciatic nerve was isolated surgically. The nerves were maintained in Ringer solution until the further use. Action potentials of the sciatic nerve were measured by a pair of platinum electrodes attached to the nerve bundle. The separation between the recording electrodes was 5 mm. The distance between the stimulating electrodes and the recording electrodes was approximately 40 mm.

Before acquisition of ^{23}Na-MRS, nerves were submerged into the Ringer solution containing 5.0 mM TmDOTP for 5 minutes. MRS was performed on a Varian 4.7-T magnetic resonance spectrometer. The free induction decay (FID) signals were recorded from nerves. To obtain the shift of Na_e / Na_i resonance, ^{23}Na spectra were acquired from the whole sample with TR 200 ms and 1024 averages. The spectra were obtained by a weighted Fourier transformation of the FID signals (line broadening factor = 16).

Results and Discussion

To determine the effective concentration of TmDOTP, frequency shifts in saline containing various TmDOTP conc. were performed. Fig. 1A shows the frequency shifts of ^{23}Na-MR spectra in saline containing 0.01 – 0.08 M TmDOTP. TmDOTP showed concentration-dependent frequency sift within 20 - 60 ppm (4000 - 12000 Hz). Based on this result, TmDOTP conc. was determined as 5 mM.

Since TmDOTP binds to Ca^{2+} and possibly affects nerve excitation [1], the action potential of TmDOTP solution-immerged nerve was examined. Fig. 1B shows the action potential of the nerve before acquisition of ^{23}Na-MRS. We found a single peak in the recorded action potentials generated from Aα fibers (fast-conductiong, responsible for motor function). TmDOTP had no effects on the generation of action potential.

Fig. 2 shows ^{23}Na-MR spectra in Ringer solution-immerged nerve and TmDOTP solution-immerged nerve. Na_e and Na_i signals were detected clearly in the spectra of TmDOTP solution-immerged nerve while single peak was detected in Ringer solution-immerged nerve.

Conclusion

The present study demonstrated the measurement of Na_e / Na_i in sciatic nerves by ^{23}Na-MRS using ^{23}Na frequency shift agent Na4HTmDOTP. Na_e and Na_i signals were detected clearly in the spectra of TmDOTP solution-immerged nerve. These results suggests the potential application of Na_e / Na_i imaging for direct imaging of nerve excitation.

[1] C. Weidensteiner et al., Magnetic Resonance in Medicine, vol. 48., pp. 89 –96 (2002)

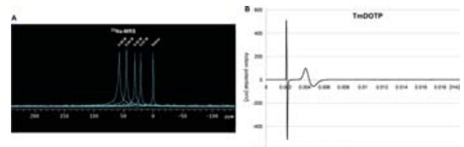

Fig. 1 A: ^{23}Na-MR spectra in saline containing 0.01, 0.02, 0.04 and 0.08 M TmDOTP. The TmDOTP caused concentration-dependent frequency sift in the spectra. 1 ppm = 200 Hz B: Action potentials of the nerve before acquisition of ^{23}Na-MRS. TmDOTP had no effects on the generation of action potential.

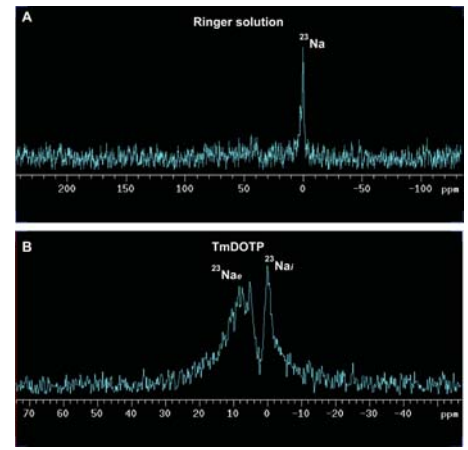

Fig. 2 A: ^{23}Na-MR spectra in Ringer solution-immerged nerve. A single peak was detected in the spectra. B: ^{23}Na-MR spectra in TmDPTP solution-immerged nerve. Na_e and Na_i signals were detected clearly in the spectra.

GO-15

Detection of single Magnetic bead using Spin Valve Structure for an Array of PHR Sensor.

S. Oh, H. Tran Quang, K. Kim, C. Kim
Chung nam univ., Daejeon, South Korea

Abstract
Commercially available magnetic bead is commonly used in biological applications. We have observed signal in single magnetic bead (M-280 Streptavidin) by Planar Hall Resistance (PHR) sensor.
PHR has been measured in spin valve structure NiFe/Cu/NiFe/IrMn as a function of magnetization measured by vibrating sample magnetometry (VSM) and the PHR sensor signals are measured by four probe method. PHR sensor fabricated by lithography method with patterned size of 3 x 3 μm2. Using this sensor, we detected the single magnetic bead.

Introduction

Recently, there is tremendous improvement into a Lab on a Chip or Micro Total Analysis Systems (μ_TAS) that has received to be growing attention by researchers [1-2]. The sensitivity of the nano scale sensors are much higher than the sensitivity of the micro scale sensors but decreasing the size of the sensor needs much time to detect the bio molecule [3] In this paper, we explain the movement and detection of micrometer sized magnetic bead. The first work based on this approach, the bead array counter (BARC) bio sensor and used 2.8 μm magnetic labels (Dynabead M-280) which are applicable for biowarfare agents [4].

Experimental Methods

Spin valve structure (NiFe/Cu/NiFe/IrMn) were fabricated by DC magnetron sputtering under working pressure of 3 mTorr and the base pressure of 3 x 10 -8 Torr on SiO2 wafer at room temperature. During sputtering process a uniform magnetic field of 300 Oe is applied in the film plane used to induce a uniaxial magnetic anisotropy. Samples with size of 3x3 μm2 for PHR measurements were prepared by lithography and lift-off etch method for the junction and electrodes. We used lift-off etch method in order to get more clean surface instead of dry etch method. To make passivation layer Si3N4 (200 nm)/ SiO2 (20 nm) /Au (20 nm), we used the RF magnetron sputtering with working pressure 2 mTorr. The signal of the single magnetic bead was done by using the four probe method.

Results and Discussion

Fig.1 shows the spin valve structure of Ta (5 nm)/ NiFe (3 nm)/Cu (1 nm)/NiFe (4 nm)/IrMn (20 nm)/Ta (5 nm). The as-sintered pinned Permalloy layer displayed an exchange bias of 639 Oe which is very high.

Fig.2 shows the SEM image of the junction with one single magnetic bead with size 2.8 μm and the clear image of the junction is shown on one side of the image.

For the pattern size of 3x3 μm2, the sensor signal is shown in Fig.3 where the PHR voltage versus time was plotted. During the measurement, we applied a magnetic field of 20 Oe. The PHR Voltage changed very slowly up to150 μV but after that there is a sudden change in the signal of 200 μV during bead drop which was clearly shown in the fig.3.

Conclusion

The present work deals with movement and detection of micrometer sized magnetic beads and we have successfully demonstrated the detection of 2.8 μm single magnetic bead. Earlier, we reported our work in which we fabricated the sensors with different junction size and different magnetic bead sizes.

[1] Shuichi shoji, Electronics and communications in japan, part 2, Vol.82, No.2, 1999.

[2] Joseph Wang, Nucleic acids research, 2000, Vol.28, No.16, 3011-3016

[3] Paul E.Sheenhan et al., Nanoletters, Vol.5, No.4, 803-807 (2005)

[4] David R.Baselet et al., Biosensors and electronics 13 (1998) 731-739.

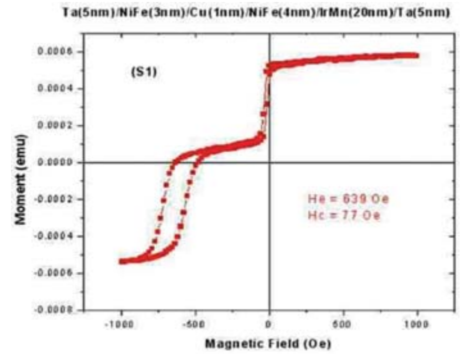

Fig.1. Hysteresis loops of NiFe/Cu/NiFe/IrMn spin-valve structures

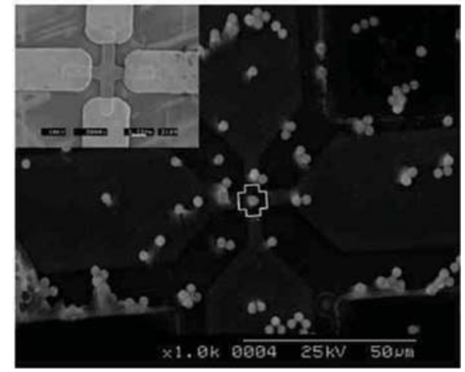

Fig.2. SEM image of the fabricated 3×3 um2 PHR junction

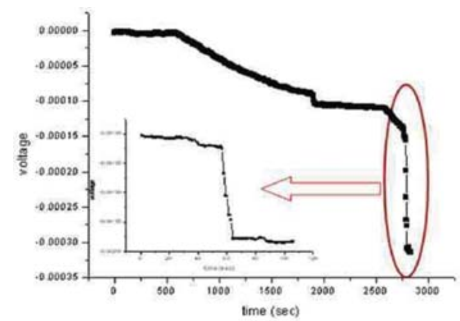

Fig.3. Real-time profile for single magnetic bead on PHR sensor

GP-01

Extraction of design parameters of linear switched reluctance motor based on force calculation.

S. Jang[1], *J. Park*[1], J. Choi[1], H. Sung[2]
1. Electrical Engineering, Chungnam National University, Daejeon, South Korea; 2. Korea Institute of Machinery & Materials, Daejeon, South Korea

Introduction

The Switched Reluctance Motor (SRM) is an electric machine that consists of a simple structure with a winding only on the stator and not on the rotor. The costs are lower than other motors due to its simple construction. It is easy to implement a high speed drive system and both the torque and efficiency of the unit volume are highly superior to all others [1]. However, the SRM has disadvantages that torque ripple and vibration/noise are big. Especially, torque ripple happens by structure of SRM, so it can confirm general characteristic of SRM through analysis considering teeth/slot structure [2]. The Linear Switched Reluctance Motor (LSRM) has the advantage of SRM stated above and structure. However, contrary to the structure of conventional SRM, the LSRM presented in this paper has structure moving stator and a long air-gap. Hence, magnetic force characteristics are analyzed to air-gap distance.

This paper deals with extraction of design parameters of LSRM based on force calculation using space harmonic analysis, 2D/3D FEM and experimental measurement. First, analytical solutions for flux density due to mover winding currents are derived in terms of magnetic vector potential and a 2D rectangular coordinate system, for the case when the mover is located at aligned and unaligned position. The analytical results are compared with those obtained from a 2D finite element method (FEM). Second, using Fourier series expansion, this paper predicts the force profile of LSRM analytically. And then, accurate results such as force measurement and 2D FEM are given to confirm the analysis. Finally, we extract design parameters such as overhang, teeth width of mover and stator based on force calculation using 3D FEM.

Analysis model of the LSRM and assumption

Fig. 1 shows the analytical model of LSRM which consists of 6-pole/concentrated winding type mover, 4-pole stator corresponding with 6-pole mover. The symbols of LSRM are as followings: “A” is positive phase and “a” is negative phase. The teeth and slot width, teeth and back-iron height and stack length of mover are *wmp, wms, hmp, hmy* and *stm* respectively. Those of stator are *wsp, wss, hsp, hsy* and *sts* respectively. The air-gap length of LSRM is *g*.

Results and discussion

R. Krishnan [2] presented analytical formulas for force at aligned and unaligned position using the normal flux density. This paper calculates continuous force of LSRM according to mover position using analytical formulas for force presented in [2] and Fourier series expansion. Fig. 2(a) and 2(b) show the analytical results of normal and propulsion force according to mover position. The analytical results are compared with those obtained from 2D FEM. In our manuscript, we will present design parameters such as overhang, teeth width of mover and stator based on force calculation using 3D FEM.

[1] Youn-Hyun Kim, “Characteristic analysis and design of a single phase switched reluctance motor for high speed application,” KIEE International Trans. EMECS, vol. 4-B, no. 3, 2004, pp.114-121.

[2] R. Krishnan, Switched reluctance motor drives, CRC press, 2001.

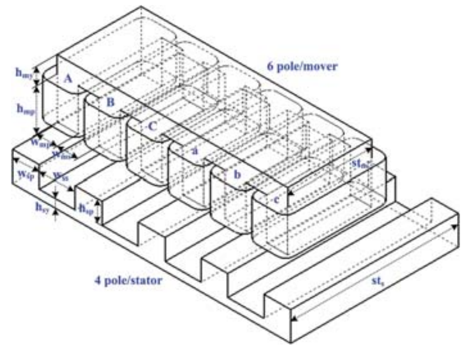

Fig. 1. Analytical model of LSRM.

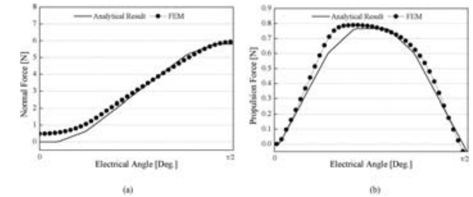

Fig. 2. Force calculation of LSRM.

GP-02

Dynamic Analysis of Rotor Eccentricity in Switched Reluctance Motor with Parallel Winding.

L. Jian
Electrical Engineering, Dong-A University, Busan, South Korea

Abstract. This paper investigated the rotor eccentricity effects of switched reluctance motor and the reduction of these effects by different winding methods. The motor was simulated by using 2D transient magnetic FE analysis coupled with external circuits. The main exciting force of the vibration is the electromagnetic force in the stator that is calculated using Maxwell stress method. Serial connection and various parallel connections of windings were modeled in the external circuit. The influence of winding method counteracting unbalance forces on the rotor vibration behavior is investigated in this paper. Dynamic FEM simulation is utilized to study the current distribution in the paralleled paths under rotor eccentricity.
Keywords: rotor eccentricity, switched reluctance motor, unbalanced magnetic pull, parallel paths.
In order to maximize the power density of the motor at a fixed inverter volt-ampere rating, the SRM must be designed with a sufficiently narrow air gap that at the aligned position the machine saturates at a current much less than its peak operating current [1]. The air gap of SR motors in fractional horsepower applications is usually 0.2mm-0.4mm which is much smaller than PM motors and induction motors. Also so it is more sensitive to rotor eccentricity. It is therefore essential to keep the rotor eccentricity to a minimum by using strict control of manufacturing and assembling procedures. However, for economic reasons, and especially for mass produced machines, it is not always possible to do so. The use of parallel paths in stator windings offers another way to reduce the noise introduced by rotor eccentricity.
The basic reason for using parallel paths can be explained Figure 1. (a), which shows the schematic diagram of a 12/8 SRM stator winding arrangements having concentric-type pole windings. Let us assume that the rotor is shifted downwards. The magnetic flux per pole produced by pole winding A1 with same current is less than that by winding A3 since the flux due to A1 has to pass through a larger air gap. In other words, the inductance of winding A1 is less than that of winding A3. If the windings in each phase are connected in series, e.g. A1, A2, A3 and A4 are in series and carry the same current, then the magnetic flux produced by A1 would be less than that produced by A3. The unbalance of the magnetic fluxes introduced an unbalanced magnetic pull and low pole-air force waves to cause noise and vibration. If, however, windings A1, A2, A3 and A4 are connected in parallel, as shown in Fig.2 (c)-3, the current flowing in A1 would be larger than that in A3 since the inductance voltage drop per unit current in A1 is small than that in A3. The large current in A3 will offset, to a certain extent, the unbalance in magnetic flux distribution, and hence will reduce the unbalanced magnetic pull and noise emission.
The influence of winding method counteracting unbalance forces on the rotor vibration behavior is investigated in this paper. Dynamic FEM simulation is utilized to study the current distribution in the paralleled paths under rotor eccentricity. As shown in Fig.2 (c)-3, the coil of opposite stator poles is paralleled. The inductances of paralleled paths are different due to the non-uniform air gap. The normal force on the stator poles are unequal and have the tendency to draft rotor back to its center.
More detailed explanation and results will be given in the full paper.

[1]R. Krishnan, Switched Reluctance Motor Drives: Modeling, Simulation, Analysis, Design, and Applications. Boca Raton, CRC: 2001, pp. 79–120.
[2]Sheth, N.K.; Rajagopal, K.R, "Effects of nonuniform airgap on the torque characteristics of a switched reluctance motor", Magnetics, IEEE Transactions on Volume 40, Issue 4, Part 2, July 2004 Page(s):2032 - 2034

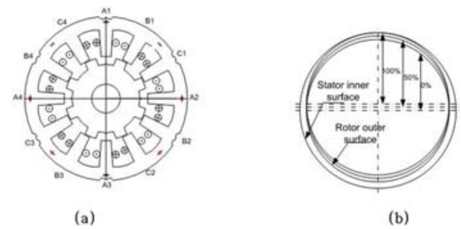

Figure 1 (a) Cross section and winding distribution of 12/8 switched reluctance motor. (b) Airgap nonuniformity caused by rotor eccentricity.

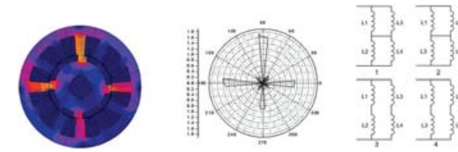

Figure 2. (a) (b) Unbalanced flux density distribution with serial connection; (c) Different parallel winding method.

GP-03

Comparison of 12/8 and 6/4 Switched Reluctance Motor: Noise and Vibration Aspects.

L. Jian
Electrical Engineering, Dong-A University, Busan, South Korea

The wide application of switched reluctance motors (SRM) is limited by their higher vibration and acoustic noise. It has been shown that the dominate source of the vibration and acoustic arises from the radial force acting on stator. The 12/8 SR motor have 2 times of poles as the 6/4 SR motor, thus with the same output torque the magnetic force should be half as the later one. It's widely believed in industry that the 12/8 SR motor is more quietly than 6/4 one. Two prototypes (in Fig.1) were developed during the past two years. The From load test, the spectrum of vibration was measured for these two prototypes. Note these two prototypes have the same stack length and outside diameter and test was undertaken at same conduction.
The radial force acting on one stator pole is abstracted from the FEA results and displays in Fig. 2. The force is a function of time and gets its peak value at commutation. The frequency of radial force in 12/8 is two times as that in 6/4 since there are eight rotor poles pass over the excited stator phase in one rotation in 12/8 prototype while there are only four poles in 6/4 prototype. The vibration doesn't reduce so much as radial force when we compare Fig. 2 and Fig. 3.
The vibration and magnetic excitation seems to have a complicated relationship which depends on the impedance of stator and housing [1]. An accurate determination of resonant frequencies and mode shapes of the SRM stator is therefore essential for low acoustic noise design. Based on the structural finite element method and elasticity theory, 3D vibration modes and resonant frequencies of prototypes were calculated[2].
The meshing of stator core without and with housing was shown in Fig. 4 which contains 25088 and 147209 elements respectively, thus the calculation time of the second model would take much longer time. The 8th and 11th mode shape and frequency were shown if Fig. 5.
More detailed explanation and results will be given in the full paper.

[1] R. S. Colby, F.M.Mottier, and T.J.E. Miller, "Vibration Modes and Acoustic Noise in a Four-Phase Switched Reluctance Motor", IEEE Transactions on Industry Applications, Vol. 32, NO. 6. Nov./Dec. 1996.

[2] Wei Cai, Zhangjun Tang and Avoki M.Omekanda, "Low-vibration design of switched reluctance motors for automotive applications using modal analysis", IEEE Trans. on Indus Applications, Vol, 39, NO.4, Jul./Aug. 2003.

Fig.1 Prototypes of 6/4 and 12/8 SR motors

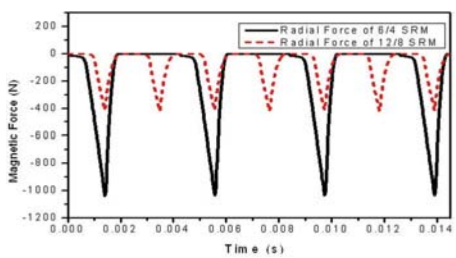

Fig. 2 Radial forces acting on one stator pole of 12/8 prototype and 6/4 prototype.

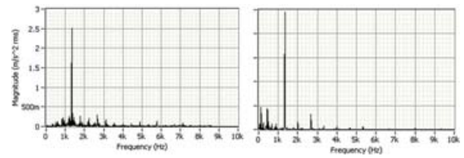

Fig 3. Spectrum of vibration measured from load test under same condition.Left: 12/8, right: 6/4.

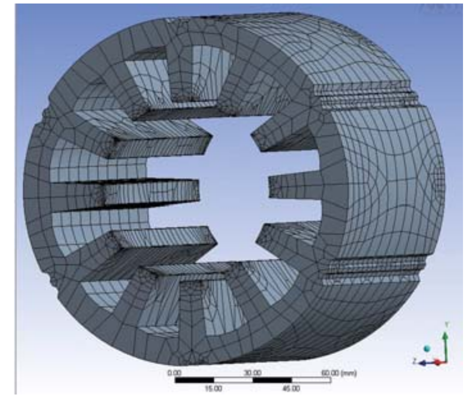

Fig.4 Meshing of stator core with housing. (Node:390222 Element:147209)

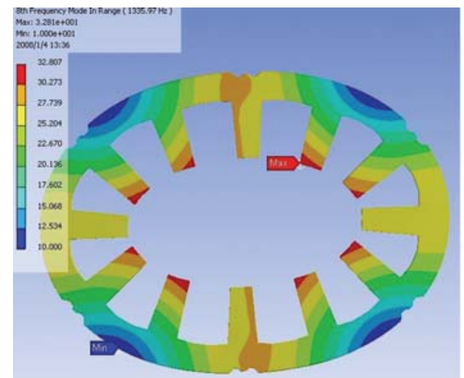

Fig. 5 8th frequency mode in range 1336 Hz

GP-04

Comparison of iron losses in switched reluctance motor with different winding arrangements and switching sequences.

T. Sun, J. Hong
Department of Mechanical Engineering, Hanyang University, Seoul, South Korea

I. Introduction

Some drawbacks including low electrical utilization, acoustic noise and special drive much limit the performance and application of switched reluctance motors (SRM). In order to improve these, several different stator winding arrangements and switching sequences have been proposed [1]-[3]. Although all these methods claimed that the advantages in dynamic performance were achieved, none of them demonstrated the steady-state characteristics, especially in the aspect of losses and efficiency. Unlike the PM synchronous motors, the SRM has great changes in the flux density of the rotor. Hence, the iron losses become much significant. As well known, the iron losses consist of hysteresis loss and eddy-current loss [4]. The hysteresis loss is proportional to the frequency and amplitude of flux density, while the eddy-current loss is proportional to the square of the both. The different winding arrangements and switching sequences directly cause the different frequency and amplitude of flux density, although the dimensions of motor bodies are completely same.

This paper will compare the iron losses of SRMs with different winding arrangements and switching sequences. The non-sinusoidal driving current makes the conventional iron-loss calculation method unavailable. This paper will adopt the method which was introduced and verified in [4] to solve this problem. By using of the Fourier transform and experimental iron-loss curves, this method can evaluate iron losses with any shape and period of flux density. Finally, the iron losses in the stator and rotor, and the ratio of the total iron losses to the input power will be compared. These results can give more reference for the SRM design and the selection of drive method.

II. Analyzed SRM Models

The fundamental structure of the analyzed model is a 6/4 V-type SRM. The concentrated winding, distributed winding and tororidal winding are combined with this structure, respectively. The winding arrangements and corresponding switching sequences are shown in Fig. 1.

III. Iron-loss Calculation Method

A. finite element analysis

The finite element analysis (FEA) is used to solve the magneto static analysis. The ideal square shape currents with the same amplitude are used to excite the four models. The calculated flux density of each element then is decomposed into the normal- and tangential-direction variations.

B. harmonic analysis

After obtain the flux densities of each element, the frequency and amplitude of each harmonic component are analyzed by using Fourier transform.

C. interpolation in experimental data curve

A group of iron-loss data which is tested by Epstein is shown in Fig. 2. The total loss including hysteresis loss and eddy current loss of each element can be obtained by interpolating these data curves with the frequencies and amplitudes calculated in the last step. Finally, summing the results calculated in each element, the losses of any desired region can be evaluated.

IV. Comparison of Results and Discussion

Fig. 3 shows the final comparison results on the total iron losses and the ratio of iron losses to the input power. The results are unified by those of the model with concentrated winding. It can be seen that the model with distributed winding has the lowest iron losses. The bipolar conduction improves the iron losses significantly.

[1]B. C. Mecrow, “New winding configurations for doubly salient reluctance machines,” IEEE Trans. Ind. Appl., Vol. 32, No. 6, Nov/Dec. 1996.

[2]J. W. Moon, etc., “Drive characteristics of full-pitched winding SRM using mutual inductance,” KIEE Trans., Vol. 47, No. 9, Sep.1998.

[3]J. Y. Lee, etc., “Dynamic analysis of toroidal winding switched reluctance motor driven by 6-switch converter,” IEEE Trans. Magn., Vol. 42. Issue. 4, pp. 1275-1278, Apr. 2006.

[4]J. J. Lee, etc., “Loss Distribution of Three-Phase Induction Motor Fed by Pulsewidth-Modulated Inverter,” IEEE Trans. Magn., Vol. 40. No. 20, Mar. 2004

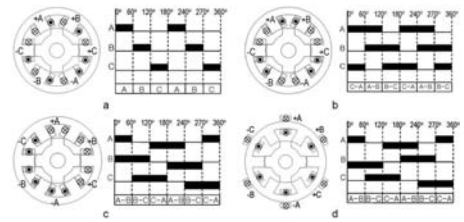

Fig.1 Analyzed model: (a) concentrated winding with unipolar conduction; (b) concentrated winding with bipolar conduction; (c) distributed winding with bipolar conduction; (d) toroidal winding with bipolar conduction.

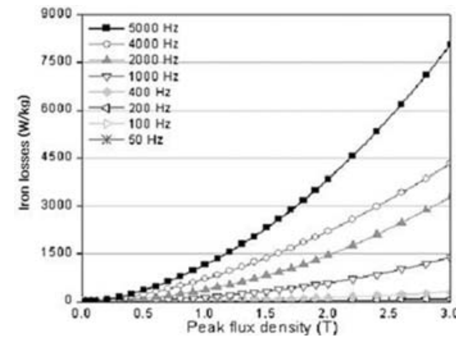

Fig.2 The iron-loss data curves tested by Epstein

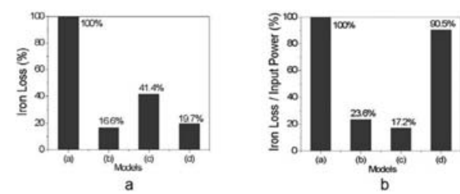

Fig.3 Analysis results: (a) comparison of iron losses; (b) comparison of the ratio of iron losses to the input power

Optimum Design Criteria for Maximum Torque Density and Minimum Torque Ripple of Synchronous Reluctance Motor according to the Rated Wattage using Response Surface Methodology.

Y. Choi, S. Mun
Electrical Eng., Hanbat National University, Deajeon, South Korea

Introduction

Issues such as efficiency and torque/ampere are important in evaluating the performance of a SynRM. Such characteristics depend upon the rotor shape of the machine related to the ratio Kw of total flux barrier width to total iron sheet width and, therefore, require a numerical evaluation and design. However, it is not a fixed value that is applied to all shapes with regard to a variation of rotor in a SynRM. So, Reference [1] proposed that a design solution is found through the comparison of inductance difference and ratio according to the rotor shape variations under each rated wattage. However, Reference [1] have been performed the situations that each flux barrier width are same those for each ratio Kw, respectively, and torque ripple are not considered.

If each flux barrier is same width, it is impossible to gain a torque ripple reduction across the wide current range as well as obtain the good performance. Also, if various flux barrier width of rotor is existed in some ratio Kw, it is expected to gain another characteristics with regard to difference and ratio of inductance and torque ripples.

The RSM has been achieved to use the experimental design method in combination with Finite Element Method and well adapted to make analytical model for a complex problem considering a lot of interaction of design variables [2]-[4].

The focus of this paper is found firstly a design solution through the comparison of inductance difference and ratio and torque ripple according to rotor shape variations under each rated wattage and, Secondly, a mixed resolution rotatable central composite design (CCD) is introduced and analysis of variance (ANOVA) is conducted to determine the significance of the fitted regression model.

Design model and Procedure

The process of optimization design is shown in Fig.1.

The shape coordinates of the rotor have been drawn as a condition of ratio Kw. In Fig. 1, design variables of flux barrier width are determined to improve torque performance of a SynRM. And then, analysis data is obtained through finite element method based on central composite design mostly used in RSM, and optimum point is determined through analysis of the data. Finally, it can be obtained the maximum torque density & minimum torque ripple of Synchronous Reluctance Motor (SynRM) according to the rated wattage.

Fig. 2 shows the point variables and variation direction example for the shape change according to flux barrier width in 3 number of flux barrier. Each pair (W1, W8), (W2, W7), (W3, W6)… move symmetrically on the basis of q-axis. And points of P1-P8 move as a condition that flux barrier widths are varied [5].

Fig. 3 shows flux plots of a optimum design example for 3HP.

More detailed results and discussion will be given in final paper. And the mathematical expressions for response surface methodology will be also given in extended version.

[1]S. B. Kwon, S. J. Park, J. H. Lee, "Optimum Design Criteria Based on the Rated Watt of a Synchronous Reluctance Motor Using a Coupled FEM and SUMT", IEEE Transactions on Magnetics, Vol.41, No.10, pp 3970~3972, Oct. 2005.

[2]F.Gillon and P. Brochet, "Shape optimization of a permanent magnet motor using the experimental design method," IEEE Trans. Magn, Vol.35, no. 3, pp. 1278-1281, 1999

[3]A. I. Khuri and J. A. Cornell, Response Surface: Designs and Analysis. New York, NY: Marcel Dekker, Inc., 1996

[4]C. M. Borror, Response Surface Methods for Experiments Involving Noise Variables. New York, NY: UMI, 1998

[5]J. M. Park, S. I. Kim, J. P. Hong, J. H. Lee, "Rotor design on Torque Ripple Reduction for a synchronous reluctance motor with concentrated winding using response surface methodology", IEEE Transactions on Magnetics, vol. 42, No.10, pp.3479-3481, Oct. 2006.

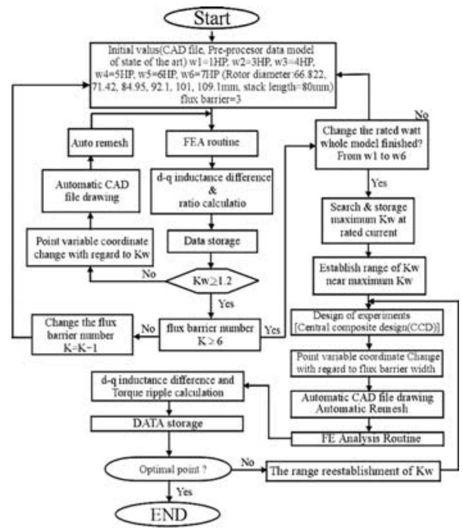

Fig. 1 The flow chart of design procedure

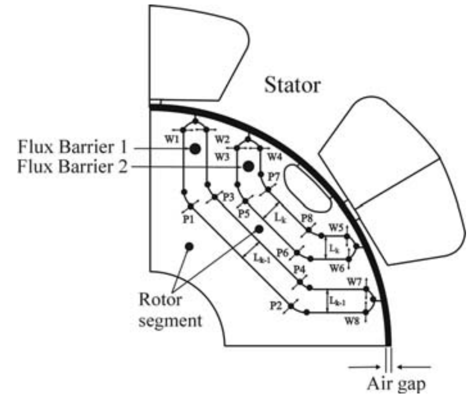

Fig. 2 The variation direction of the flux barrier width

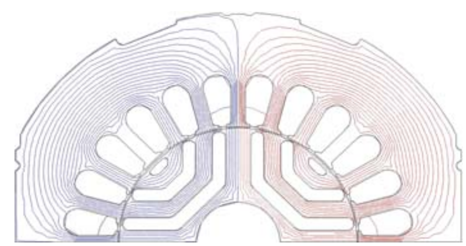

Fig.3 Flux plots of a optimum design example for 3HP

GP-06

The Evaluation of On-line Observer System of Synchronous Reluctance Motor Using a Coupled FEM & Preisach Model.

H. Lim[1], J. Lee[1], M. Lee[1], D. Lee[2]

1. Electrical Engineering, Hanbat National University, Daejeon, South Korea; 2. Electrical Engineering, Hanyang University, Seoul, South Korea

Introduction

The influence of the saturation cannot be neglected since the high-speed operation and precision sensorless vector control of Synchronous Reluctance Motor (SynRM) are required. The q-axis usually shows minimal saturation in high saliency ratio, but the high performance of d-axis usually shows significant saturation when the machine is being operated at rated operations.

In the case of d-axis excitation, the saturation is the combined effect of saturation in the stator yoke, stator teeth, and rotor rib, and can reduce the Ld inductance, which has an effect on the torque density, power factor and efficiency of SynRM, by as much as 50%.

Therefore it is difficult to expect a good control response performance from SynRM without considering the above defects.

Fortunately, the advantages of finite element method (FEM) unlike voltage equation modeling are primarily their ability to model the complicated internal structure within a SynRM and ability to model magnetic saturation to high degree of accuracy.

In high speed applications, iron loss can become the major cause of power dissipation. Therefore, whereas in other kinds of machines a rough estimation of iron loss can be accepted, their importance in SynRM justifies a greater effort in calculating them more precisely. Preisach's model, which allows accurate prediction of iron losses, is adopted in the procedure to provide a nonlinear solution [1]-[3].

In this paper, a coupled finite element analysis and Preisach's modeling for SynRM are presented and is the sensorless vector control parameters estimation is performed under the effect of saturation and iron loss.

For considering the dynamic characteristics, moving mesh technique is used and vector control algorithm is combined with an analysis tool. Extensive experimental works have been conducted to verify the accuracy of the analysis.

Analysis Model

A direct convergence method, which is not diverged at any initial value and has the advantage to converge quicker than Newton-Raphson method, iterates the procedure to provide a nonlinear field solution. Indirect field-oriented control algorithm is applied to the proposed analysis model for the example of dynamic characteristics. This technique is illustrated in Fig. 1.

To verify the validity of the proposed method, the TMS320C31 DSP control unit and Power Circuits are equipped as shown in Fig. 2.

Analysis Result And Discussion

Fig. 3(a), (b) 3 phase current characteristics of each analysis in single B-H and proposed method, respectively.

It is observed that whereas current responses in the single B-H analysis of Fig. 3(a) is nearly match to sinusoidal ones, another (b) highly distorted as hysteresis phenomena is existed as shown in Fig. 3.

Fig 4(a), (b) show the i, λ phase relationships in single B-H and proposed method, respectively. The i-λloci, which is total hysteresis loss of a SynRM, can be investigated on the basis of proposed analysis method.

More detailed results and discussion will be given in final paper.

[1] J. H. Lee, J. C. Kim, D. S. Hyun, "Dynamic Characteristic Analysis of Synchronous Reluctance Motor Considering Saturation and Iron Loss by FEM", IEEE Transaction on Magnetics, Vol. 34, No. 5, pp. 2629-2632, Sep. 1998.

[2] J. H. Lee, D. S. Hyun, "Hysteresis Characteristics Computation on PWM Fed Synchronous Reluctance Motor Using Coupled FEM & Preisach Modeling", IEEE Transaction on Magnetics, Vol. 36, No. 7, pp 1209-1213, July 2000.

[3] J. H. Lee, J. C. Kim, I. S. Jung, D. S. Hyun, "Vector Control Scheme of Synchronous Reluctance Motor Considering Iron Core Loss", IEEE Trans. on Magn., Vol. 34, No. 5, pp 3522-3525, September, 1998.

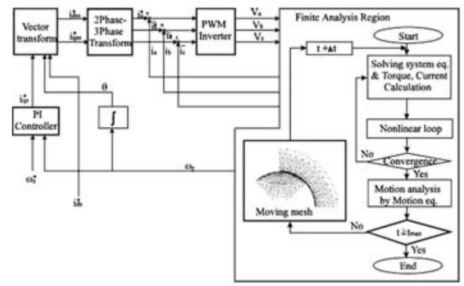

Fig. 1. Scheme of simulation

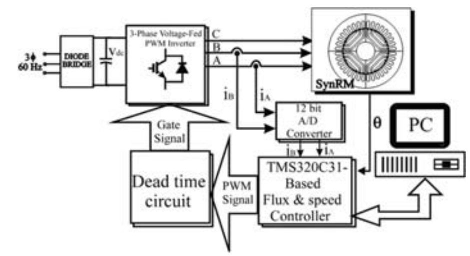

Fig. 2. Experimental system configuration

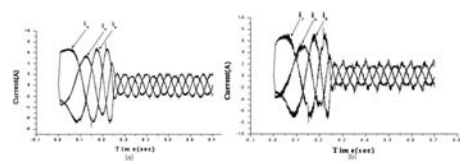

(a) Single B-H curve (b) Coupled Preisach & FEM Fig. 3. 3 Phase current characteristics.

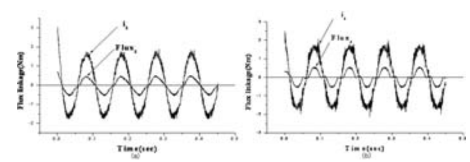

(a) Single B-H curve (b) Coupled Preisach & FEM Fig. 4. i, λphase relationships

GP-07

Design and Characteristic Analysis of Synchronous Reluctance Motors with Axial Lamination Rotor.

S. Hahn[1], J. Hong[1], J. Kim[1], D. Koo[2]
1. Department of Electrical Engineering, Dong-A University, Busan, South Korea; 2. Mechatronics Research Group, Korea Electrotechnology Research Institute, Changwon, South Korea

INTRODUCTION
This paper deals with a design and characteristic analysis of Synchronous Reluctance Motors(SynRM) using an equivalent magnetic circuit modeling. SynRM is classified into several types according to a rotor's shape such as segment-type, flux-barrier type, and axial lamination type. In this paper, a rotor's shape of an axial lamination is considered to design and characteristic analysis of SynRM using an equivalent magnetic circuit modeling.
Voltage, torque and power factors of SynRM model are defined by mathematical theories for explaining an operating principle. Inductances of d-q axis are related to determine a specification of design parameters and are determined by voltage-torque equations. These are important electric parameters to design of a rotor's shape using an equivalent magnetic circuit modeling.
In this paper, SynRM model with an axial lamination rotor is modeled using an equivalent magnetic circuit method. And this method determines design parameters such like current and inductances to satisfy a specification of SynRM model. This model is designed using an equivalent magnetic circuit modeling to consider zig-zag magnetic flux and analyzed by finite element method. The results such as current and torque variation using E.M.C.M are compared with ones by F.E.M. Moreover steady torque of SynRM model compared with the experimental ones.
THEORETICAL CONSIDERATIONS
Voltage equations of SynRM are similar to a general induction motor, but these exclude a term related to a rotor. Eq(1) and Eq(2) are d-q axis voltage and current equations of SynRM with an axial lamination rotor.
$V_q=V\sqrt{2}\cos\delta=R_sI_q+j\omega L_dI_d$, $V_d=V\sqrt{2}\sin\delta=R_sI_d-j\omega L_qI_q$ (1)
$I_q=V\sqrt{2}(R_s\cos\delta-\omega L_d\sin\delta)/(R_s^2+\omega^2L_dL_q)$, $I_d=V\sqrt{2}(R_s\sin\delta-\omega L_q\cos\delta)/(R_s^2+\omega^2L_dL_q)$ (2)
PROTOTYPE MODEL
Fig. 1 shows prototype model manufactured by an equivalent magnetic circuit modeling. As seen in Fig. 1, the rotor of SynRM model consists of magnetic and non-magnetic steel layers laminated alternately. The center of the rotor consist of non-magnetic steel is filled out a plastic material.

RESULTS OF ANALYSIS AND TEST
1. Results from F.E.A
Current and torque variation by FEA is shown in Fig. 2. As seen in Fig. 2, the results of current and torque variation show good agreement with other values according to estimating methods.

2. Results from test
2.1. Alternating current test
Saturated inductances of SynRM model are measured by an alternating current standstill test. Fig. 3(a) shows electric circuit for a measurement according to d-q axis alignment of a rotor. Fig. 3(b) is inductance curves obtained from the measurement to increase the frequency from 50Hz to 500Hz.
2.2. Measurement of steady torque.
Instrument setup for measuring a steady torque consists of a handle gear, torque sensor and SynRM is shown in Fig. 4. To flow DC current of SynRM model, steady torque is measured at respective positions for a rotation.
Fig. 5 shows steady torque curves of analyzed and measurement results.
CONCLUSION
This paper presents design and characteristic analysis of synchronous reluctance motor using an equivalent magnetic circuit modeling to consider zig-zag magnetic flux. The results such as current and torque variation using E.M.C.M are compared with ones by F.E.M. And steady torque of SynRM model compared with the experimental ones.

[1] I. Boldea, "Reluctance Synchronous Machines and Drives", CLARENDON PRESS OXFORD, 1996.

[2] T. Matsuo and T. A. Lipo, "Rotor Design Optimization of Synchronous Reluctance Motor Design", IEEE Trans. on Energy Conversion, Vol. 9, No. 2, pp. 359~365, June, 1994.

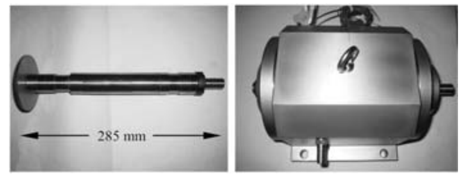

Fig. 1. Prototype model of SynRM (a) Rotor (b) Outside

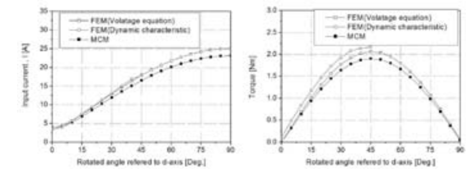

Fig. 2. Input current and torque according to analysis methods (a) Input current (b) Torque

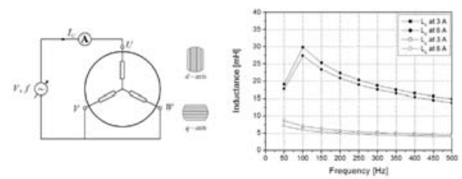

Fig. 3. Alternating current standstill test (a) Electric circuit (b) Inductance

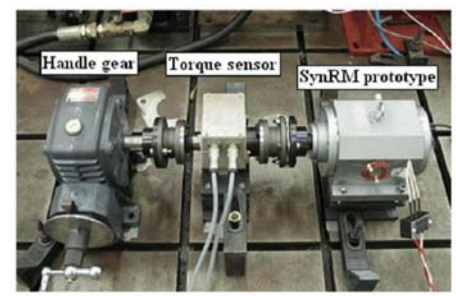

Fig. 4. Instrument setup for measurement of steady torque

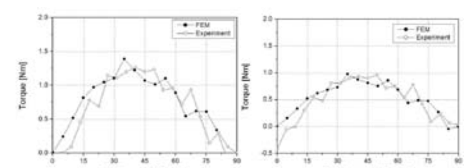

Fig. 5. Steady torque of SynRM model (a) Input : 4[A] (b) Input : 6[A]

GP-08

Design Solutions To Minimize Iron Core Loss In Synchronous Reluctance Motors Using Preisach Model & Finite Elements Method(FEM).

H. Lim[1], J. Lee[1], M. Lee[1], D. Lee[2]
1. Hanbat National University, Daejeon, South Korea; 2. Electrical Engineering, Hanyang University, Seoul, South Korea

This paper deals with an automatic design procedure for the minimization of iron core loss in a synchronous reluctance motor (SynRM). The focus of this paper is the design relative to hysteresis loss on the basis of rotor shape of a SynRM in the same torque density. The coupled Finite Elements Analysis (FEA) & Preisach model have been used to evaluate the iron core loss with the rotor shape. The proposed procedure allows to define the rotor geometric dimensions starting from an existing motor or a preliminary design. The iron loss has been reduced with a rotor design variation.

[1] J. H. Lee, J. C. Kim, and D. S. Hyun, "Dynamic characteristic analysis of synchronous reluctance motor considering saturation and iron loss by FEM," IEEE Trans. Magn., vol. 34, pp. 2629–2632, Sept. 1998.

[2] J. H. Lee and D. S. Hyun, "Hysteresis analysis for the permanent magnet assisted synchronous reluctance motor by coupled FEM & Preisach modeling," IEEE Trans. Magn., vol. 35, pp. 1203–1206, May

1999.

[3] J. H. Lee, J. C. Kim, I. S. Jung, and D. S. Hyun, "Vector control scheme of synchronous reluctance motor considering iron core loss," IEEE Trans. Magn., vol. 34, pp. 3522–3525, Sept. 1998.

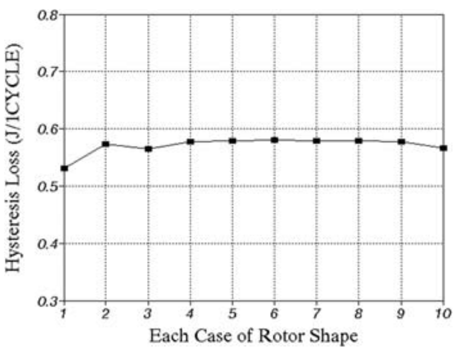

Fig.1 Total hysteresis loss of each rotor shape

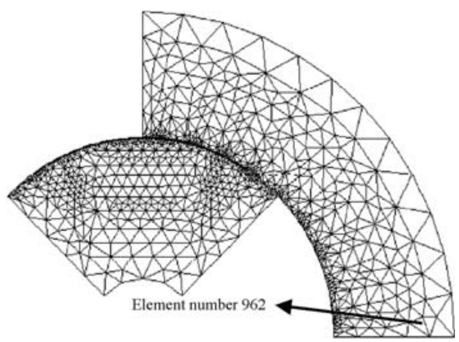

Fig.2 Mesh shape and element number 962

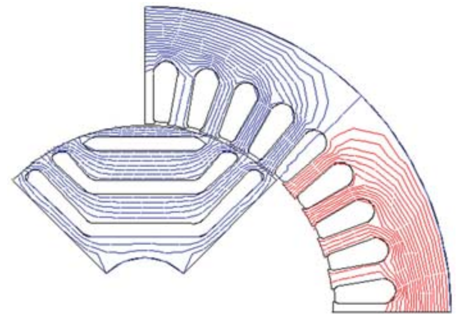

Fig. 3 Flux plot and rotor shape of case1

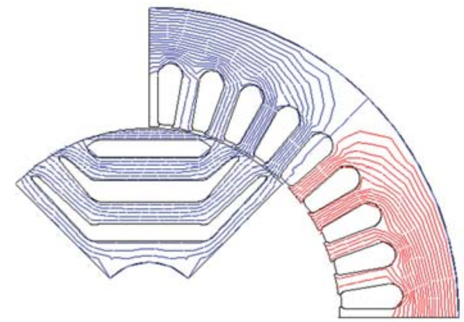

Fig. 4 Flux plot and rotor shape of case6

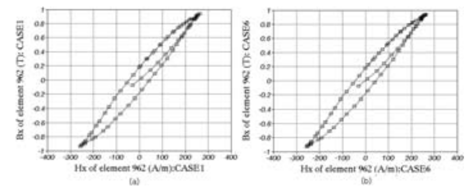

FIG. 5 B-H LOOP OF ELEMENT 962 IN CASE1 (a) AND CASE6 (b)

GP-09

Optimum Design of Synchronous Reluctance Motors Based on Torque/Volume Using Finite Element Method & Sequential Unconstrained Minimization Technique.

S. Mun, Y. Cho
Electrical Engineering, Hanbat National University, Daejeon, South Korea

Synchronous reluctance motor (SynRM) present many advantages if compared to induction motors that concern the simple, rugged rotor design, no rotor cage and consequently no copper losses and no rotor parameters to be identified. Issues such as efficiency and torque/ampere are important in evaluating the performance of a SynRM[1].

Such characteristics depend upon the rotor shape of the machine related to the ratio Kw of total flux barrier width to total iron sheet width and, therefore, require a numerical evaluation and design. If Kw = about 0.5, it is possible to gain a high inductance difference Ld-Lq across a wide current range as well as obtain the maximum output torque[2],[3].

And a paper which is discussed the influence of the ratio Kw of total flux barrier width to total iron sheet width on a SynRM have been presented [4]. However, Reference [2] investigated the axially laminated type and reference [3] discussed the 6 flux barrier type respectively, and output powers are different. Reference [4] proposed the design of the 340W home appliance SynRM then, Kw is 1.

Therefore, it is not a fixed value that is applied to all shapes with regard to a variation of rotor in a SynRM.

So, Reference [5] proposed that a design solution is found through the comparison of inductance difference and ratio according to the rotor shape variations under each rated wattage.

And Starting from an existing design, the best design solution is selected, and we could be seen that the flux barrier number, Kw can be a fixed value related to the rotor diameter (3HP, 3.5HP, 4.5HP, 5.5HP, 6HP, 7HP, 8HP, each stack length are different.).

In this paper the ratio Kw of total flux barrier width to total iron sheet width and flux barrier numbers and additional rotor diameters of a SynRM is defined as design parameter.

Results and Discussion

Fig. 3 shows an example of zandel functions and design solution of 1HP machines(rotor diameter: 66.822mm).

And Fig. 4 shows the rotor optimum design function characteristics according to increasing rotor diameter at each rated current. One should notice that the design solutions should be related to the rotor diameter and it will be the important data in motor design of similar specifications.

The more detailed optimum design procedure and discusses will be represented in next extended version.

More detailed optimization process, results and discussion will be given in final paper. And the mathematical expressions for Sequential Unconstrained Minimization Technique will be also given in extended version.

[1]J. H. Lee, "Efficiency Evaluations of Synchronous Reluctance Motor Using Coupled FEM and Preisach Modeling", IEEE Transaction on Magnetics, Vol. 39, No. 5, pp 3271-3274, September, 2003.

[2]Takayoshi Matsuo, Thomas A.Lipo, "Rotor Design Optimization of Synchronous Reluctance Machine", IEEE Transaction on Energy Conversion, Vol.9, No.2, pp.359-365, June 1994

[3]Hiroyuki Kiriyama, Shinichiro Kawano, Yukio Honda, Toshiro Higaki, "High Performance Synchronous Reluctance Motor with Multi-flux Barrier for the Appliance Industry", IEEE Industry Application Vol. 1. pp. 111-117, 1998.

[4]Jung Ho Lee, "Design and Efficiency Characteristic Test of 340W Home Appliance Synchronous Reluctance Motor", Transaction of KIEE, Vol.52B. No.2, Feb., 2003.

[5]S. B. Kwon, S. J. Park, J. H. Lee, "Optimum Design Criteria Based on the Rated Watt of a Synchronous Reluctance Motor Using a Coupled FEM and SUMT", IEEE Transactions on Magnetics, Vol.41, No.10, pp 3970~3972, Oct. 2005.

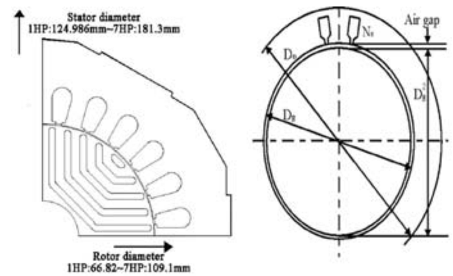

Fig. 1 Initial rotor and stator design

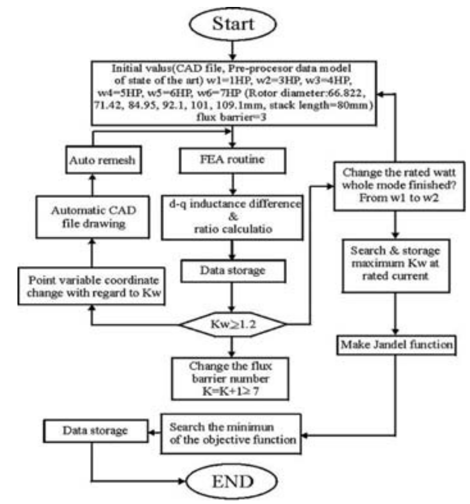

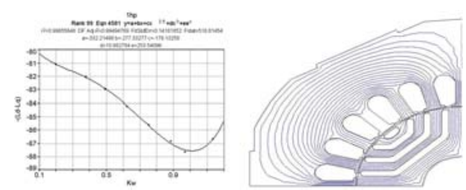

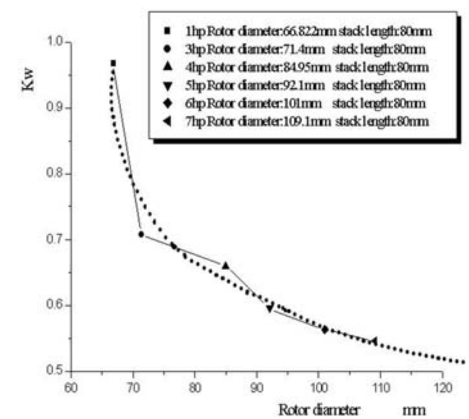

GP-10

Reduced windage loss rotor of SRM using magnetic saturation for high speed application.

S. Won, J. Lee
Electrical Eng., Hanyang University, Seoul, South Korea

1.Introduction

The increasing popularity of the switched reluctance motor is mainly due to the simple rotor structure and the fact that its speed-torque characteristics can be tailored to suit the desired application. Especially, for high speed applications like vacuum cleaners, the motor speed is up to 40000 rpm, where the windage losses by rotor shapes are considerably higher than for an equivalent cylindrical rotor of the same diameter [1].

This paper presents a novel switched reluctance motor rotor shape which has ribs between the rotor salient poles on the rotor outer surface. Fig. 1 shows the conventional switched reluctance motor and the proposed rotor shape which is an aerodynamically cylindrical rotor but magnetically same as a conventional rotor.

2.Parametric Simulation

Because the proposed rotor has ribs between the salient poles of the rotor, these ribs must be saturated while the stator poles overlap the ribs, for the rotor gets reluctance torques. Thus, the proposed rotor can not produce sufficient torque until the ribs are saturated and the resultant torque of proposed rotor is slightly less than the conventional rotor. But because the windage loss at high speed is overwhelming this torque discrepancy, the total power need to rotate the shaft is much less than conventional switched reluctance motor. Fig. 2 shows the flux density distribution of the proposed rotor ribs that is saturated.

Because the instantaneous torque of the SRM is proportional to the variation of inductance, we need to know the inductance variations according to angles and current values. The parametric finite element analyses are performed to get these inductance variations. Fig. 3 show inductance profile maps of the conventional rotor and the proposed rotor. Compared to the conventional rotor, the proposed rotor has high inductance values and relatively not so steep inductance variation slope according to angle at low current(below 2~3 A) because the ribs are not saturated while current values are low. Eventually, the motor torque is not enough while current values are below 2~3 A, but above 3A, the motor can produce sufficient torque.

3.Motor performance calculation

To predict the dynamic performance of SRM, it is needed to solve differential equations for the appropriate switched conditions including the mechanical equations. In order to know the load torque which includes windage loss, several experiments were performed. Using this inductance profile and load torque curve, the authors can perform the dynamic characteristics analysis without performing a transient finite element analysis which is burden job in simulation time aspect.

The simulation is performed at speed of 35000rpm, where the motor has quite large windage loss. From the results of this simulation, we can find out that the proposed rotor shape is very useful at high speed. The extended paper will contain detailed comparison graph.

4.Conclusion

The proposed rotor has higher efficiency at high speed. The novel rotor shape does not compromise simple rotor structure of conventional switched reluctance motor and has higher efficiency at high speed by reducing the windage loss. The new rotor shape can be produced from the existing facilities. The rib structure which makes the proposed rotor reduce windage losses can be easily obtained without an additional manufacturing process. This study will be very useful not only for researchers who study on electric machines, but also for engineers who have been engaged in manufacturing field for electrical home appliance machines.

[1]S.D.Calverley, G.W.Jewell and R.J.Saunders, "Aerodynamic losses in switched reluctance machines", IEE Proc.-Electr. Power Appl., Vol. 147, No. 6, Nov, 2000, pp.443-448.

[2]K.N.Srinivas, R.Arumugam, "Dynamic Characterization of Switched Reluctance Motor By Computer-Aided Design and Electromagnetic Transient Simulation", Magnetics, IEEE Transactions on, Volume: 39, No.3, May 2003, pp.1806-1812.

Manufactured SRM : the assembled motor(up left), the stator(up right), the proposed rotor(down left), the conventional rotor(down right)

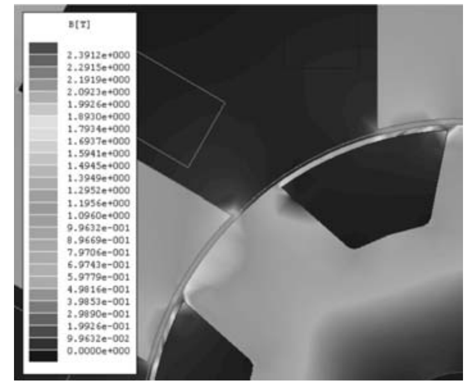

Saturation in ribs

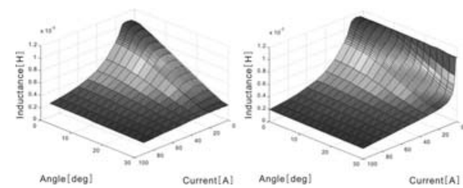

Comparison of inductance map

GP-11

Calculation of force characteristics of an electromechanical system using co-energy.

M. Hadziselimovic[1,2], P. Virtic[1], G. Stumberger[1,2], T. Marcic[1], B. Stumberger[1,2]
1. University of Maribor, FE&CS, Maribor, Slovenia; 2. TECES, Maribor, Slovenia

Introduction

The paper proposes a new method for determining force characteristics of an electromechanical system by using co-energy considering only the main flux linkage. An electromagnetic brake (EMB) was used as the tested electromechanical system. The co-energy is calculated by integrating the flux linkages in terms of exciting currents. The flux linkage depends on the exciting current and on the variable air-gap thickness. The characteristics of flux linkages can be determined numerically using finite element method (FEM). Using flux linkage characteristics the current and air-gap thickness dependant co-energy characteristics can be determined in the entire range of operation. Considering the co-energy variation caused by the air-gap thickness variation, the attractive force characteristics can be obtained.

Numerous papers have been published dealing with the determination of magnetically nonlinear characteristics of flux linkages in different electromagnetic devices [4-5]. Paper [6] deals with determining force characteristics using co-energy caused by the total flux linkage ψ of the actuator. The co-energy determined in this way contains also the leakage flux which does not close trough the armature and can therefore not contribute to force generation.

The procedure for determining force characteristics of an EMB using co-energy considering only the main flux of an EMB has not been described yet.

The results presented in this paper are used as a part of the EMB magnetically nonlinear dynamic model which is used for prediction of reaction times.

Electromagnetic brakes

Electromagnetic brakes (EMBs) are often used for breaking (or locking) rotors of electrical machines. The EMB consists of a magnetically nonlinear yoke and armature, winding, rotating disk, friction brake pad and steel springs (Fig. 1). The current carrying winding excites the magnetic circuit of the EMB with the total flux linkage ψ. The main part of aforementioned flux, the main flux linkage ψ_m, couples the electrical and the mechanical subsystem of the EMB and passes through the air-gap, yoke and armature. The attractive force between the yoke and the armature depends exclusively on the main flux linkage ψ_m. The difference between the total flux linkage ψ and the main flux linkage ψ_m is the leakage flux linkage ψ_σ, which does not pass through the air-gap.

Comparison of results obtained by FEM and measurements

The comparison of results obtained by FEM and measurements is presented in Fig. 2. It shows that electromagnetic forces calculated with the total flux linkages (F) exhibit the largest discrepancies from measurements. The electromagnetic force characteristics calculated via co-energy determined with the main flux linkages (F_m) and by Maxwell stress tensor method using FEM (F_{Maxw}) are closer to the measured (F_{meas}) electromagnetic forces.

The comparison of results obtained by FEM and measurements for whole operating range (different air-gap and current excitations) will be presented in full version of this paper.

Conclusion

The paper will show that the electromagnetic forces have to be calculated considering the main flux (linkage) when using co-energy, because only the main flux linkage couples the electrical and mechanical subsystems. The leakage flux linkage is not negligible and has to be taken into account. The consideration of leakage flux linkage is important for predicting the dynamic response characteristics using dynamical model of the EMB.

The results presented agree very well, which confirms the quality of the proposed method. As far as the authors of this paper are aware, this is the first work that describes the determination of current and air-gap thickness dependant force characteristics using co-energy.

[1] P. C. Krause, "Analysis of Electric Machinery," New York, 1995.

[2] I. Zagradisnik, and B. Slemnik, "Elektrical rotational machines," Maribor, 2005.

[3] D. Cundev, "Computation of electromechanical characteristic of sailent poles synchronous motor with damper based on FEM," Journal Mat. Protec., vol. 161, pp. 241-246, 2005.

[4] G. Stumberger, "Evaluation of Experimental Methods for Determining the Magnetically Nonlinear Characteristics of Electromagnetic DevicesIdentification of linear synchronous reluctance motor parameters," IEEE Transact. on Magnetics, vol. 41, no. 10, pp. 4030–4032, Oct. 2005.

[5] M. Hadziselimovic, "Magnetically nonlinear dynamic model of synchronous motor with permanent magnets," Journal Magn. Mat., vol. 316, pp. e257-e260, 2007.

[6] R. Golle, "A finite element method based dynamic analysis of a long-stroke linear actuator," Journal Mag. Mat., vol. 196-197, pp. 943-945, 1999.

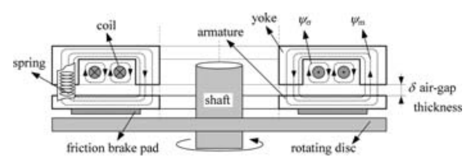

Cross-section of an EMB

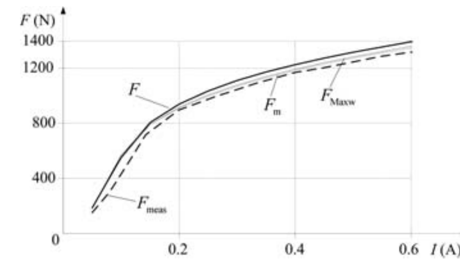

Comparison of electromagnetic forces for rated air gap thickness

GR-01

Exchange bias in surface-crystalline FeNbB ribbons.

L. Kraus[1], O. Zivotsk ý[2], K. Postava[2], P. Švec[3], D. Jani čkovi č[3]
1. Institute of Physics v.v.i., Academy of Sciences of the Czech Republic, Prague, Czech Republic; 2. Department of Physics, Technical University of Ostrava, Ostrava, Czech Republic; 3. Institute of Physics, Slovak Academy of Sciences, Bratislava, Slovakia

Exchange bias in magnetic multilayers is of great importance for practical applications. The characteristic feature of exchange bias is the shift of the hysteresis loop from its normal position at H = 0 to the value $H_b \neq 0$, called the bias field. Similar behavior has been observed in surface crystallized Co-based amorphous ribbons [1,2]. Recently a surface crystallinity was found in as-quenched FeNbB ribbons [3]. The investigation of exchange bias in these materials is reported here. $Fe_{80.5}Nb_{6.9}B_{12.6}$ ribbons, 28 μm thick and 10 mm wide, were prepared by the flow-casting method. The as-quenched ribbons exhibit partial crystallinity on both surfaces while the bulk of ribbon is amorphous. The X-ray diffractions taken from both sides of ribbon (Fig.1) indicate the presence of α-Fe. The coexistence of amorphous phase and crystalline α-Fe on the ribbon surfaces has also been confirmed by the conversion electron Mössbauer spectroscopy (CEMS) and magneto-optical Kerr effect (MOKE) [3]. The crystalline phase can be removed by a short etching of ribbon in a diluted nitric acid. The properties of the two surfaces are different. A high texture of the crystallites and their concentration in a very thin layer (about 2 nm thick) is typical for the wheel side. On the shiny side the crystallites are more or less randomly oriented and they extend deeper into the ribbon interior. The effective thickness of the surface layer on the shiny side is more than 30 nm. The coercive forces of the surface layers, measured by MOKE, are 0.8 kA/m and 3.2 kA/m for the wheel and shiny side, respectively [3].
The bulk magnetic properties of the ribbon are investigated by a DC hysteresis-loop tracer. The unstrained ribbon shows the hysteresis loop with low coercivity ($H_c \approx 3.5$ A/m), low remanence ($J_r/J_s \approx 0.04$) and saturation field about 600 A/m, which is typical for amorphous magnetostrictive alloys with random internal stresses. When tensile stress is applied to the ribbon the remanence steeply increases because of positive magnetostriction. The shape and position of low-field hysteresis loop now depends on the magnetic history of sample. Three hysteresis loops, measured with applied stress of 600 MPa, are shown in Fig.2. After demagnetization of sample, by decreasing alternating magnetic field, the usual symmetric hysteresis loop is observed (full line). If, however, the sample is saturated in a strong magnetic field H_{pre}, before the measurement, the low-field hysteresis loop substantially changes. It can be decomposed into two parts: (a) a small symmetric loop, which is responsible for about 10% of the magnetization reversal, (b) a larger loop with smaller H_c and the center shifted in the direction of the premagnetizing field. The small, symmetric, loop can be attributed to that part of ribbon, which is not affected by the hard magnetic surface layers. On the other hand, the behavior of larger loop can be explained by an exchange coupling between the Fe grains and the bulk amorphous phase.
For applied tensile stress σ, between 100 and 600 MPa, both the bias field H_b and the coercive force H_c linearly increase with σ. It may be explained by an increase of remanent magnetization of hard magnetic layers due to the stress induced magnetic anisotropy. Such behavior, however, seems to be in contradiction with the expected properties of polycrystalline iron, which should behave (in average) as a medium with negative magnetostriction. Experience, however, shows that exceptions from this rule are possible (e.g. [4]).
Similar behavior as in the ribbon under tensile stress can be observed when the ribbon is wound into a toroid. In this case, however, the outer half of ribbon is extended while the inner one is compressed. Thus practically only the outer half of ribbon contributes to the low-field hysteresis loops. It is observed, as expected, that the bias field is proportional to the curvature of toroid. Differences are, however, observed if the toroid is wound with the shiny side out or in. For the ribbon wound with the wheel side out the bias field is about four times smaller than for the toroid with the shiny side out. This indicates that mainly the harder surface layer on the shiny side ($H_c \approx 3.2$ kA/m) is responsible for the exchange bias.

[1] K.H. Shin, C.D. Graham Jr., Y. P. Zhou, IEEE Trans. Magn. 28 (1992) 2772.

[2] C. G. Kim, K. J. Jang, H. C. Kim, S. S. Yoon, J. Appl. Phys. 85 (1999) 5447.

[3] O. Zivotsk ý et al., J. Magn.Magn. Mater., to be published.

[4] D.C. Jiles, D.L. Atherton, J. Phys. D: Appl. Phys., 17 (1984) 1265.

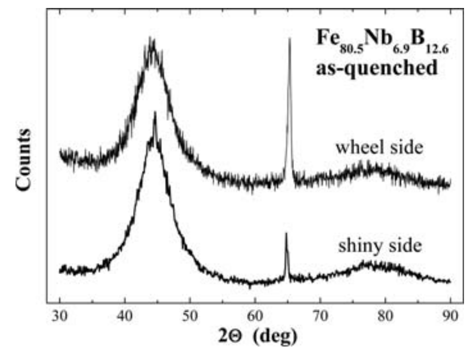

Fig.1

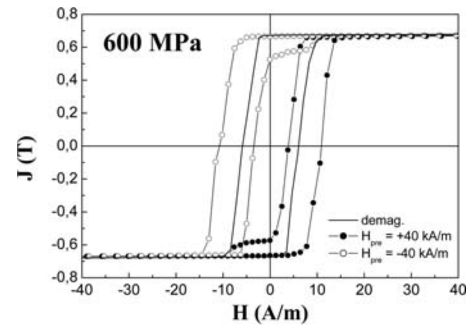

Fig.2

GR-02

Surface magnetic properties and depth sensitivity of as-quenched FeNbB ribbons.

O. Zivotsky[1], K. Postava[1], L. Kraus[2], K. Hrabovska[1], J. Pistora[1]
1. Department of Physics, VSB-Technical University of Ostrava, Ostrava, Czech Republic; 2. Institute of Physics, Academy of Sciences of the Czech. Rep., Prague, Czech Republic

In this paper the surface magnetic properties of as-quenched (AQ) $Fe_{80.5}Nb_{6.9}B_{12.6}$ ribbons are investigated using longitudinal magneto-optical Kerr effect (MOKE). These materials belong to the NANOPERM-type magnetic alloys, which are often applied in the area of nanocrystalline soft magnetic materials and magnetic sensors. It was shown [1] that preparation process of these materials causes the origin of very thin crystalline layer on the surface and its depth can be increased by postpreparation heat treatment (annealing). Hence there is a need to study the magnetic properties and the depth profile in the near-surface region of the alloys.
10 mm wide and 28 μm thick ribbons were prepared by conventional planar flow casting method and additionally spark-cut to the 9 mm discs to eliminate the in-plane shape anisotropy. MOKE methods are very sensitive to the ultra thin films and surfaces and enabled us to obtain the magnetic information from the ribbon surface depth up to 30 nm. MOKE experimental setup based on differential intensity method is used to obtain the magneto-optical (MO) angles of Kerr rotation $\theta_{Ks,p}$ and ellipticity $\varepsilon_{Ks,p}$ for s- and p-polarized light at different incident angles. The longitudinal hysteresis loops detecting the magnetization component in the sample plane and in the plane of incidence are obtained. We did not observe any polar (out of plane) component of magnetization.
Figures 1a, b and 1c, d show the magneto-optical Kerr angles of θ_{Ks} and ε_{Ks} from wheel and shiny ribbon side at the incident angle of 80°. External magnetic field H is applied along the original ribbon axis. Shape differences in the case of wheel and shiny loops from Fig. 1 confirm different magnetic properties at both ribbon sides with the coercive fields of 10 Oe (wheel side) and 40 Oe (shiny side).

A. Wheel ribbon side

Magneto-optical angles measured on wheel side show different shapes of loops not only in the case of s-polarized light (Figs. 1a, b), but also for p-polarized light (not shown here). From this fact one can imply that the near-surface region on the wheel side is inhomogeneous and MOKE detects the contributions of two phases, crystalline and amorphous ones. Partial surface nanocrystallization with strong texture was confirmed also by the conversion electron Mössbauer spectroscopy (CEMS) and X-ray diffraction (XRD) measurements, which determine 14% of crystalline phase in the near surface region of thickness of about 200-300 nm (CEMS sensitivity).
Existence of crystalline phase in thin surface layer was checked in two ways: i) electrochemical surface polishing ii) etching of surface in diluted HNO_3. After short polishing and etching, the surface crystalline layer was removed, because measured MOKE angles have the same shape for both polarizations and coercive field decreased to 3 Oe (see subplots e, f of Fig. 1). Optical and magneto-optical parameters of remaining amorphous phase can be established by comparing the measured data in the range of incident angles from 20° to 80° with the theoretical model based on the light propagation in layered anisotropic media. Refractive index n_a and Voight constant Q_a of amorphous phase were calculated as: $n_a = 3.02 - i4.18$; $Q_a = 0.0156 + i0.0025$.
Knowing the MO parameters of amorphous phase we can now analyze MOKE of the as-quenched non-polished and non-etched ribbon. We assume that the near-surface region of AQ sample consists of an upper hard crystalline layer and the soft amorphous bulk with the parameters established in the previous step. To complete the ribbon depth profile from the wheel side we fitted all measured data with the two-layer model and found the parameters of the crystalline phase $n_c = 2.92 - i3.07$; $Q_c = 0.0256 + i0.0024$ with the thickness $d_c = 2$ nm. The refractive index n_c is very close to the pure iron ($n_{Fe} = 2.90 - i3.07$), which confirms the CEMS and XRD results.

B. Shiny ribbon side

We can see that θ_{Ks} and ε_{Ks} hysteresis loops (subplots 1c, d) obtained from shiny side have the same shapes. In contrast to the wheel side this behaviour can be explained by a single-layer model with an effective optical medium composed of crystalline and amorphous phases of the thickness, which is larger than the penetration depth of light. Higher value of coercive field indicates that the surface crystalline layer is harder than that on the wheel side. Moreover, the existence of crystalline layer from shiny side was confirmed also by CEMS. Calculated effective optical and magneto-optical parameters ($n_S = 2.87 - i3.46$; $Q_S = 0.0196 + i0.0044$) of detected layer can be also compared to pure iron.

[1] O. Zivotsky et al., J. Magn. Magn. Mater. (2007) in press.

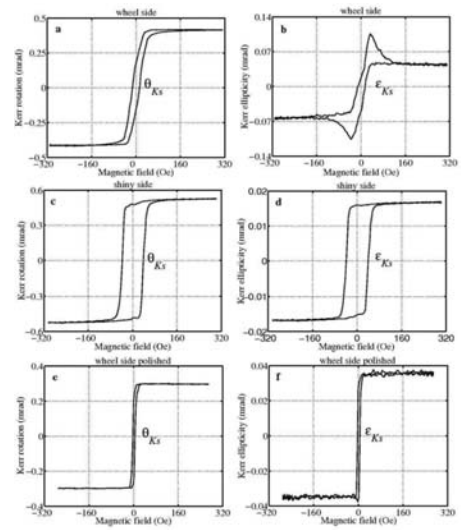

Magneto-optical hysteresis loops obtained from wheel (subplots a, b) and shiny (subplots c, d) side of as-quenched FeNbB ribbon. After short polishing (subplots e, f), the surface crystalline phase from wheel side is removed.

GR-03

Some Magnetic Properties of Bulk Amorphous Fe-Co-Zr-Hf-Ti-W-B-(Y) Alloys.

M. Hasiak[1], K. Sobczyk[2], J. Zbroszczyk[2], W. Ciurzynska[2], J. Olszewski[2], M. Nabialek[2], J. Kaleta[1], J. Swierczek[2], A. Lukiewska[2]
1. Institute of Materials Science and Applied Mechanics, Wroclaw University of Technology, Wroclaw, Poland; 2. Institute of Physics, Czestochowa University of Technology, Czestochowa, Poland

Bulk amorphous alloys are multicomponent systems and may be prepared at the quenching rate 1-10^2 K/s. The relatively low quenching rate enables to obtain them in the form of rods and tubes by solidification of molten material in a copper mould or thick ribbons using a melt spinning method. These alloys are a new group of materials and exhibit many interesting properties.
In this paper we present the results of microstructure, and low and high magnetic field properties studies of the bulk amorphous $(Fe_{0.61}Co_{0.10}Zr_{0.025}Hf_{0.025}Ti_{0.02}W_{0.02}B_{0.20})_{100-x}Y_x$ (x = 0 or 2) alloys in the as-quenched state and after annealing below the crystallization temperature. Ingots were prepared from high purity components by arc melting in argon atmosphere. Amorphous samples in the form of rods 2 cm long and 1 or 2 mm in diameter were obtained by a suction casting method. The amorphicity of the samples in the form of rods and after powdering was checked by X-ray diffractometry. The microstructure of the samples was studied by Mössbauer spectroscopy. The Curie and crystallization temperatures were determined by means of a force magnetometer. Low field magnetic properties, i.e. initial magnetic susceptibility (χ_0), its disaccommodation ($\Delta(1/\chi) = 1/\chi_2 - 1/\chi_1$, where χ_1 and χ_2 are the susceptibilities measured at t_1 = 2 s and t_2 = 120 s after demagnetization of the sample, respectively), maximum susceptibility (χ_m) and core losses (P), were measured by a completely automated set-up. Using a vibrating sample magnetometer (VSM Lake shore type) the approach to the ferromagnetic saturation was also studied. All investigations were carried out for the samples in the as-quenched state and after annealing at 720 K for 15 min.
All samples in the as-quenched state were fully amorphous. In the X-ray diffraction patterns one could see only a broad maximum which is characteristic of an amorphous state.
The as-quenched alloys show relatively high initial magnetic susceptibility. Moreover, these alloys show good thermal stability of the initial magnetic susceptibility (Fig. 1, curves a and b). In the temperature range from 130 K to 475 K only a slight increase of χ_0 is observed. At higher temperature (near the Curie temperature) the initial magnetic susceptibility rapidly drops. From this figure it is also seen that the addition of 2 at.% of yttrium to the $Fe_{61}Co_{10}Zr_{2.5}Hf_{2.5}Ti_2W_2B_{20}$ master alloy causes only a slight decrease of χ_0 and Curie temperature. It is worth noticing that this addition causes about four-folded decrease of the maximum of magnetic susceptibility disaccommodation (Fig. 1, curves c and d) which is very important feature from application point of view.
Assuming a gaussian distribution of relaxation times the isochronal disaccommodation curves $\Delta(1/\chi) = f(T)$ were decomposed into three elementary processes and their mean activation energies were found. From results obtained we can state that the observed phenomenon is connected with ordering of atomic pairs near the free volumes, which play the similar role as point defects in crystalline materials. After the annealing of the samples at 720 K for 15 min the intensity of disaccommodation distinctly decreases which is connected with the annealing out of some free volumes. It is worth adding that disaccommodation intensity in the bulk amorphous alloys is lower than in classical amorphous ribbons due to lower quenching rate. It is connected with the increase of the atom packing density because of irreversible relaxation processes occurring during the sample preparation.

The studied alloys are the soft ferromagnets and the core losses measured for them are of the same order as observed in the classical silicon – iron alloys. Magnetic softness of these alloys was also manifested during investigations of the approach to the ferromagnetic saturation. The saturation magnetic polarization is equal to 1.08 T and 1.04 T for the alloy without yttrium and containing 2 at.% of Y, respectively. From the analysis of the magnetization curves in high magnetic fields we have evaluated the width of quasi-dislocation dipoles present in the samples which is equal to 3.16 nm and 2.95 nm for the $Fe_{61}Co_{10}Zr_{2.5}Hf_{2.5}Ti_2W_2B_{20}$ and $(Fe_{0.61}Co_{0.10}Zr_{0.025}Hf_{0.025}Ti_{0.02}W_{0.02}B_{0.20})_{98}Y_2$ bulk amorphous alloys in the as-quenched state, respectively. Reassuming, the addition of 2 at.% of yttrium to the $Fe_{61}Co_{10}Zr_{2.5}Hf_{2.5}Ti_2W_2B_{20}$ alloy causes the distinct decrease of disaccommodation intensity without drastic drop of initial susceptibility and the saturation magnetic polarization.

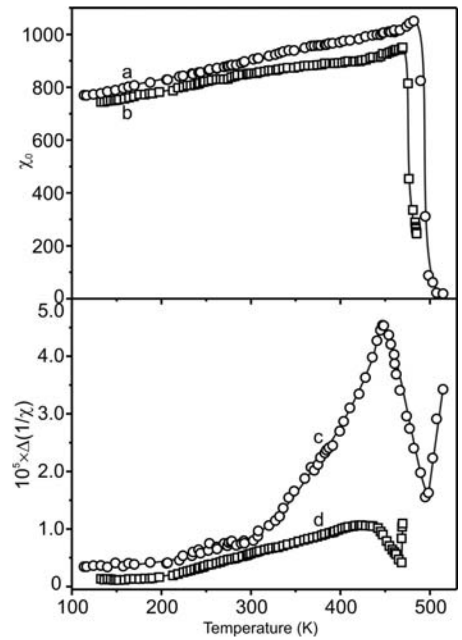

Initial magnetic susceptibility (a, b) and isochronal disaccommodation curves (c, d) of the $(Fe_{0.61}Co_{0.10}Zr_{0.025}Hf_{0.025}Ti_{0.02}W_{0.02}B_{0.20})_{100-x}Y_x$ in the as-received state: x = 0 (a, c), x = 2 (b, d).

GR-04

Magnetic properties of as - quenched Fe87-xZr3.5Nb3.5B6Cux nanocrystalline ribbons.

J. Hu[1], B. Li[2], H. Qin[1], R. Zhang[1], M. Jiang[1]
1. Department of Physics, Shandong University, Jinan, China; 2. Central Iron & Steel Research Institute, Beijing, China

Soft magnetic Fe-M-B (M=Zr, Nb and Hf) nanocrystalline ribbons are of potential applications in many fields. Nanocrystalline Fe-M-B ribbons were usually fabricated by crystallization of amorphous ribbons through annealing processes. The good soft magnetic properties of those annealed ribbons mainly originate from the microstructure consisting α-Fe nanograins with sizes of 8-20 nm. Recently, we reported that nanocrystalline ribbons Fe-Cu-Nb-Si-B and Fe-Zr-B-Cu with high Cu contents with good soft magnetic properties can be fabricated by melt-spinning technique without additional annealing [1]. In the present work, we prepared as quenched ribbons Fe87-xZr3.5Nb3.5B6Cux with wheel speed V=35 m/s. Nanostructure was obtained in Fe87-xZr3.5Nb3.5B6Cux as quenched ribbons. The permeability and giant magnetoimpedance were investigated.

As quenched ribbons with low Cu content are mainly amorphous. With addition of Cu content, nanostructure α-Fe appears. An appropriate addition of Cu enhances the nucleation of α-Fe in as quenched ribbons (see Fig.1). Cu clusters induces significant fluctuation in Fe concentration, causing high density of nucleation sites for primary crystallization. Based on Scherrer's equation, the grain size D of α-Fe for as quenched ribbon x=3 was estimated as 13 nm. It seems that the amount of amorphous may enhance again with addition of high Cu content (x>=3.5), which may be due to the reduction of effective number density of Cu enriched cluster accompanying the coarsening of the Cu cluster. The Cu content dependence of permeability μ' was shown in Fig.2. The μ' value with amorphous x=0 is only 2100. With increasing Cu content, the μ' increases, experiences a maximum of about 24090 at x=3, and finally drops. We also investigated the GMI effect of as quenched Fe87-xZr3.5Nb3.5B6Cux ribbons (Fig.3 and 4). The strongest magnetoimpedance $\Delta Z/Z0$ among x=0-5 also occurs at x=3, consistent with permeability dependence. The value $\Delta Z/Z0$ (under H=90 Oe) at x=3 is 37.55 %. The drop of magnetoimpedance and permeability at high Cu content (x>=3.5) may be correlated with the reduction of effective number density of Cu clusters.

[1] J. Hu, B. Li, H. Qin, M.H. Jiang, IEEE Trans. Magn. 41, 3268 (2005)

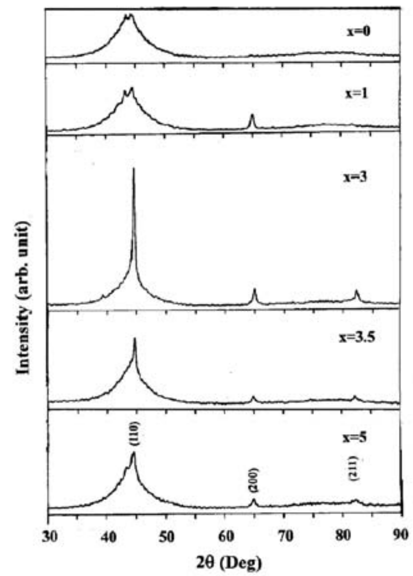

Fig.1 X- ray diffraction patterns for as-quenched Fe87-xZr3.5Nb3.5B6Cux ribbons

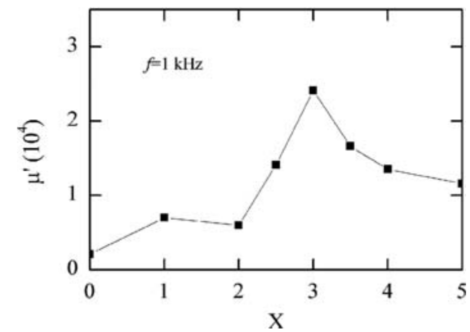

Fig.2 The Cu content dependence of real permeability for as quenched ribbons Fe87-xZr3.5Nb3.5B6Cux

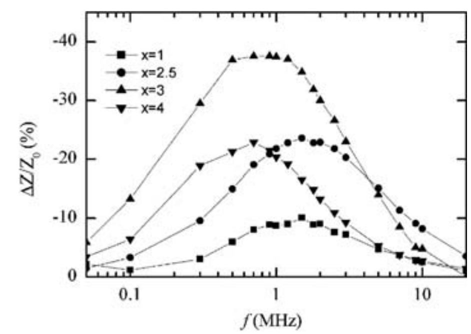

Fig.3 The frequency dependence of magnetoimpedance $\Delta Z/Z0$ under H=90 Oe for as quenched Fe87-xZr3.5Nb3.5B6Cux

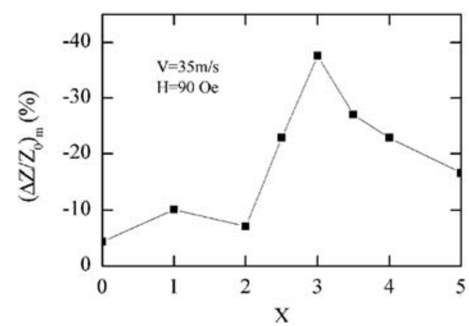

Fig.4 The Cu content dependence of magnetoimpedance $(\Delta Z/Z0)m$ under H=90 Oe for as quenched Fe87-xZr3.5Nb3.5B6Cux

GR-05

Dynamics of the magnetic susceptibility of milled FexAl100-x (x = 70,71) alloys.

D. Alba Venero[2], R. Rodríguez García[2], *L. Fernández Barquín*[2], E. Apiñaniz[1], J. J. Garitaonandia[1], F. Plazaola[1]

1. University of the Basque Country, Bilbao, Spain; 2. Universidad de Cantabria, CITIMAC, Santander, Spain

The presence of magnetic inhomogeneitities is a leitmotiv in systems with magneto- and/or bio-electronic applications, the latter pursued over these days [1, 2]. One of such curious systems is that constituted by Fe-Al alloys [3, 4]. In the rich Fe-side, there is an intriguing change of lattice around Fe75Al25, from a B2 to a DO3 structure. Recent reports reveal that disordered Fe70Al30 alloys become structurally modified in two steps (above RT); these structural variations result in changes of the magnetization [5]. This points out that the alloying of Fe and Al is extremely influenced by tiny changes in the structure, resulting in crucial implications in the magnetic behavior, as confirmed theoretically [6]. In the surroundings of the Fe70Al30, ferromagnetism, which evolves to a spin glass (SG) state, is present. To understand such phenomenologies, the presence of magnetic clusters should be taken into account. In this sense, SANS measurements showed their presence, which was also studied in through the modification of the spin excitations [7]. Ferromagnetic resonance in four alloys of Fe-Al showed significant variations of the resonant field. The interpretation was based in the presence of magnetic clusters [8].

In this paper, we have selected Fe70Al30 and Fe71Al29 and analyzed the SG transitions. The alloys were prepared by induction and were object of a powdering process by mechanical milling and subsequently annealed. To analyze the dynamic response of the magnetic clusters, the AC-susceptibility was measured. The applied oscillating field h = 0.1 Oe and seven frequency ($100 \leq \nu \leq$ 7kHz) values were selected. The Figure shows the thermal variation of the real $\chi'(\nu, T)$ and complex $\chi''(\nu, T)$ components in Fe71. The real component presents a slow decrease with decreasing temperature until approximately 100 K are reached, with a sudden drop of the value. This variation is similar to that obtained in zero-field-cooled magnetization. The behaviour for Fe71 resembles that of a reentrant spin glass. The complex component displays a peak around 60 K. For the Fe70 the behaviour is similar but reveals two transitions.

In addition, there is a shift to higher transition temperatures whenever the frequency is increased. The analysis of the results will be developed in three different steps, as reported in heterogeneous amorphous (FeZrB) or crystalline (CeNiCu) metallic alloys. We will initially apply the process for the lowest transition, which marks a drastic reduction [9]. The first step is to quantify the frequency-shift (δ); $\delta = 0.078(5)$ in Fe70 and $\delta = 0.066(9)$. These values are comparable to reentrant FeZrB glasses [9]. In a second step, it is necessary to extract the zv dynamic exponent. Our fits result in zv = 7.2(1) in Fe70 and 9.8(1) for Fe71. These lie inside the fragile regime giving an indication of a SG transition. The β-coefficients of the transition are $\beta = 1.0(1)$ (Fe70) and 1.1(1) (Fe71), which are larger than expected. A discussion of their physical meaning in connection with the clustered magnetic environment will be presented.

[1] R. C. O Handley, Modern Magnetic Materials (John Wiley, NYC, 2000).

[2] L. Fernández Barquín and R. García Calderón, J. Phys.: Conf. Ser. 17, 87 (2005).

[3] J. W. Cable, L .David and R. Parra, Phys. Rev. B16, 1132 (1977).

[4] Z. H. Liu, G. D. Liu, M. Zhang, G. H. Wu, F. B. Meng, H. Y. Liu, L. Q. Yan, J. P. Qu, and Y. X. Li, Appl. Phys. Lett. 85, 1751 (2004); K. Szymánski, D. Satula, L. Dobrzynski, E. Voronina, E. P. Yelsukov, and T. Miyanaga, Phys. Rev. B 72, 104409 (2005); D. Kaptás, E. Svab, Z. Somogyvári, G. André, L. F. Kiss, J. Balogh, L. Bujdosó, T. Kemény, and I. Vincze, Phys. Rev. B 73, 12401 (2006).

[5] D. Martínez Rodríguez, E. Apiñaniz, F. Plazaola, J. S .Garitaonandia, J. A. Jiménez, D. S. Schmool, and G. J. Cuello, Phys. Rev. B 71, 212408 (2005).

[6] E. Apiñaniz, F. Plazaola, and J. S. Garitaonandia, Eur. Phys. J. B 31, 167 (2003); A. V. Smirnov, W. A. Shelton, D. D. Johnson, Phys. Rev. B 71, 64408 (2005).

[7] K. Motoya, S. M. Shapiro, Y. Muraoka, Phys. Rev. B 28, 6183 (1983); W. Bao, S. Raymond, S. M. Shapiro, K. Motoya, B. Fak, and R. W. Erwin, Phys. Rev. Lett. 82, 4711 (1999).

[8] D. Martín Rodríguez, D. S. Schmool, J. S. Garitaonandia, and F. Plazaola, J. Magn. Magn. Mat. 316, e484 (2007).

[9] L. Fernández Barquín, J. Gómez Sal, P. Gorria, J. S. Garitaonandia, and J. M. Barandiarán, Eur. Phys. J. B 35, 3 (2003); N. Marcano, J. C. Gómez Sal, J. I. Espeso, L. Fernández Barquín, and C. Paulsen, Phys. Rev. B 76, 224419 (2007).

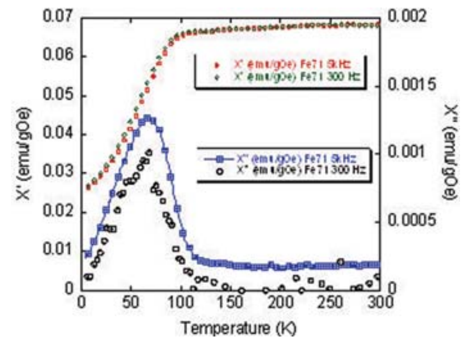

Figure. Thermal variation of the AC-susceptibility of Fe71Al29.

GR-06

EXAFS studies and magnetic behavior of FeCuZr Ball-milled alloys.

A. Martinez[1], J. J. Romero[1], G. Castro[2], A. Yang[3], V. G. Harris[3], J. C. Woicik[4], A. Hernando[1], P. Crespo[1]
1. Intituto de Magnetismo Aplicado, Las Rozas, Spain; 2. Sp-line European Synchrotron Radiation Facility, ESRF, Grenoble, France; 3. Northeastern University, Boston, MA; 4. National Institute of Science and Technology, Gaithersburg, MD

Metastable alloys of nominal composition (Fe0.5Cu0.5)100-xZrx (x=0-20 at%)have been synthesized by high energy ball milling (HEBM) in a planetary mill with hardened steel vials. To avoid oxidation of the powder upon the milling process the vials were sealed under nitrogeno atmosphere prior to the milling. The starting materials were Fe, Cu and Zr in powder form, with a purity of 99.9 %. The final milling time was 120 h. The final composition of the powder was determined by using scanning electron microscopy (SEM) equipped with an energy dispersive x-ray analysis (EDX). A maximum value of 2 at.% of additional Fe has been determined through this analysis, although no traces of Ni or Cr coming from the milling media have been detected.
In spite of the high and positive enthalpy of mixing between Fe and Cu for equiatomic composition, nanocrystalline (with a face cubic centered structure) or amorphous alloys have been obtained depending on the Zr content.
The alloy formation is confirmed by Mössbauer spectroscopy and by means of X-Ray Absorption Fine Spectra (XAFS). The later is a powerful technique for studying nearest neighbour distances in these type of alloys for the different elements, since the energy of the radiation can be tuned for studying a particular element [1]. XAFS studies point out a drastic decrease of peak intensity as well as in the nearest neighbour distances for Zr contents above 13 at% that indicates a transition to an amorphous structure. Magnetic measurements show that both, the Fe magnetic moment and the ordering temperature of the alloys drop substantially when compared with equiatomic FeCu solid solutions [2]. The Curie temperature for equiatomic Fe0.5Cu0.5 is around 500K, while for (Fe0.5Cu0.5)100-xZrx alloys, values below 285K are obtained. The later values are similar to that observed in Ferich Zr alloys, in spite of the much higher Fe content. The origin of the complex magnetic properties of iron rich metallic glasses containing low concentrations of early transition metals (Zr,Sc,Hf,Y) have attracted considerable interest during more than two decades, giving rise to several controversial microscopic interpretations [3,4].
In addition, (Fe0.5Cu0.5)100-xZrx alloys exhibit an anomalous temperature dependence of the thermoremanence, as an example figure 1 illustrates this behavior for an alloy with x=13 at.%. Thermorremanence (TRM) measurements are performed by cooling the sample under the presence of an applied magnetic field down to 5K. Then, the field is removed and the remanent magnetization is measured while heating up the sample. TRM decreases with increasing temperature until it reaches a minimum value for temperatures close to Curie temperature (Tc), as expected. However, further increase in temperature promotes a spontaneous increase of the magnetization that is observed up to 350K, which is maximum temperature that can be reached in our system. This behaviour is reversible, meaning that no irreversible structural changes take place in the alloys. More likely, this anomaly seems to be related with changes in the interatomic distances with temperature, as occurs in invar alloys [5].
Preliminary XAFS measurements of the nearest neighbour distances have been performed at different temperatures. Figure 1 compares the evolution of the nearest-neighbour (Dnn) distances of iron atoms with that of the TRM measured after cooling the sample under an applied magnetic field of 10000 Oe. It should be remarked that the Dnn distances are nearly temperature invariant for temperatures below Tc, as corresponding to the proposed invar effect. On the other hand, at temperatures over Tc the normal thermal expansion is evident. This thermal expansion is accompanied by an increase of the magnetic signal on the TRM. The increase of first near-neighbours distances with temperature produced by thermal expansion, can yield to and enhancement of the density of the states at Fermi level that could promote, at least locally, the ordering of the magnetic moments above Tc [2]

[1] V.G. Harris et al, Phys. Rev. B 54 (10), 6929 (1996)

[2] P. Crespo et al., Phys. Rev. B 48 (10): 7134 (1993)

[3] P. Crespo et al. Phys. Rev. B 61, 14346-14349 (2000)

[4] A. Hernando et al. PRB, 61, 3219 (2000)

[5] D. H. Ryan et al. PRB 35 (16), 8630 (1987)

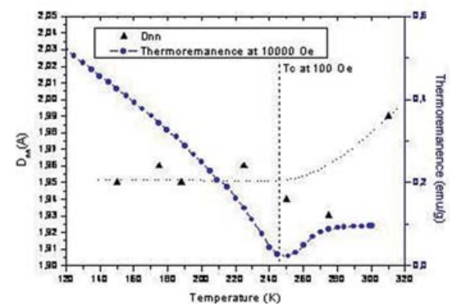

GR-07

Mossbauer and structural studies of the system FeAlNb prepared by mechanical alloying.

L. E. Zamora[1,3], G. A. Perez Alcazar[1,3], J. M. Greneche[2], J. M. Gonzalez[3]
1. Fïsica, Universidad del Valle, Cali, Colombia; 2. Laboratoire de Etat Condense, Université du Maine, 72085, Cedex 9, Le Mans, France; 3. Unidad Asociada, ICMM-IMA, Apdo. 155, 28230 Las Rozas, Madrid, Spain

The alloys of the system (Fe60Al40)100-xNbx (x=0, 5, 10, 15 and 20) were synthesized from elemental powders in a planetary high-energy ball mill during 12, 24 and 36 hours. X-ray diffraction (XRD), magnetic measurements and Mössbauer spectrometry were used to study the structural, magnetic and hyperfine properties of the system. We studied the influence of Nb content and of different milling times on the structural and magnetic properties. When Nb content increases it appear two phases the hcp (Fe,Al)2Nb and bcc (Fe,Al) and when the milling time increases the peaks due to the Nb phase disappear while those attributed to the bcc Fe-Al phase are broadened given evidence for the highly disordered structure of the powders.

Results and discussion

Mechanical alloying was carried out in a planetary high-energy ball mill (Fritsch Pulverisette 7) starting from pure element powders (>99.8%). The nominal composition of the alloyed powders were (Fe60Al40)100-xNbx (x=0, 5, 10, 15 and 20) and all samples were milled under the same milling conditions with a powder mass to ball mass ratio fixed at 1:15 and for 12, 24 and 36 h. The structure of the samples, their lattice parameters and the grain sizes were determined by the Rietveld refinement of the X-ray diffraction (XRD) patterns using the MAUD program. Transmission Mössbauer spectra (MS) were collected by using a conventional spectrometer working at different temperatures and using a 925 MBq source of 57Co in Rh matrix. The MS were fitted by using the MOSFIT program.

The formation of the nanocrystalline structure during MA was followed by X-ray diffraction and the obtained crystallite sizes were less than 30 nm for all samples. Figure 1 shows the XRD patterns of the system (Fe60Al40)100-xNbx (x=0, 5, 10, 15 and 20) for 12 hours of milling. After x=10 they were refined by means of 2 components ascribed to a bcc (Fe,Al) phase and a hexagonal (Fe,Al)2Nb phase while those of samples with x=0 and 5 only with the bcc (Fe,Al) phase. The obtained lattice parameters of the bcc Fe-Al phase increase from 0.2912 nm for x=0 up to 0.2986 nm for x=20. For x=10 the hcp (Fe, Al)2Nb the lattice parameters are a=0.4894 nm and c=0.7893 nm and for x=20 they are a=0.4876 nm and c=0.7906 nm.

Figure 2 shows the room temperature (RT) Mössbauer spectra (MS) of the system (Fe60Al40)100-xNbx (x=0, 5, 10, 15 and 20) for 12 hours of milling. The spectra for x=0 and x=5 were fitting using a magnetic distribution and a singlet, showing the existence of magnetic and paramagnetic sites and the ferromagnetic character of these sample at RT. After x=10 the samples present broad asymmetrical quadrupolar doublets, which allow to conclude that these samples are paramagnetic at RT.

As the milling time increases, for x=0 and 5 only bcc (Fe,Al) phase was found and after x=10 the peaks due to the Nb phase disappear while those attributed to the bcc Fe-Al phase are broadened and their intensities increase given evidence of the highly disordered structure of the powders.

For x=20 they show a larger degree of disorder which occurs faster due the larger Nb content. From the refinement which has been performed in the same conditions as above, one observes an extremely large lattice parameter (near 3.47 nm) and a very small grain size (2 nm). Such a rough description allows concluding a priori that the 36 milled powders also results from a random packing of FeAl cubic clusters.

The XRD patterns of the x=20 samples milled during 12, 24 y 36 hours(a) are very similar to the last showed in Fig. 1, showing their disordered character. RT MS of these samples, consist of asymmetrical quadrupolar doublets with broadened lines. Its asymetry changes sign going from the 12 to the 36 hours sample. The best fits of the spectra were conducted by means of only QD, allowing to conclude that all samples are P at RT. Differently for the compositions x=0 and x=5, when the milling time increase the magnetic behaviour increase.

Increasing both, milling time and Nb content, give rise to an increasing degree of disorder with a tendency to amorphization, with crystallite size changing from 13 to 1 nm. Mössbauer measurements permitted us to prove that for samples with x=0 and x=5 at RT a change from F to P phase is present and for x = 10 or more they are P, and in this case the F phase disappears as a consequence of the bigger content of Nb.

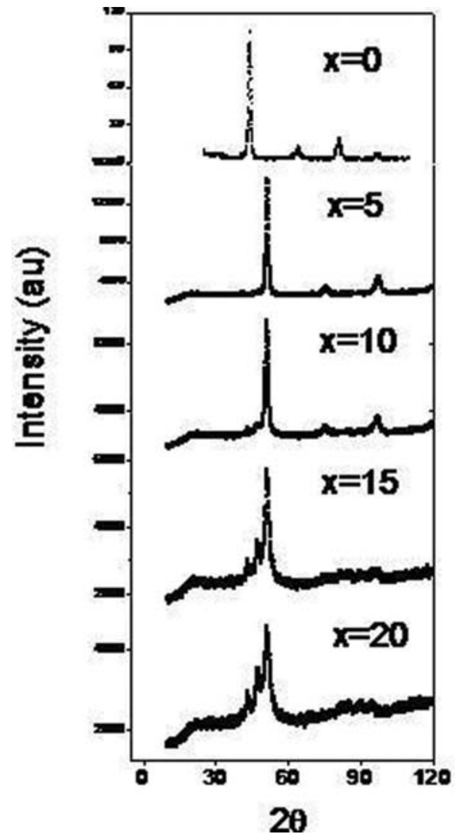

XRD paterns for the samples milled during 12 h.

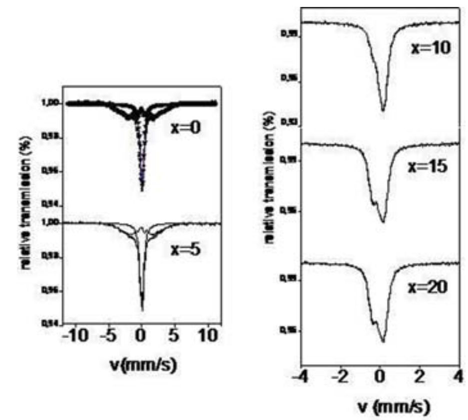

Mössbauer spectra of the different samples milled during 12 h.

GR-08

Magnetic and structural characterization of mechanically alloyed Fe50Co50 samples.

G. A. Pérez Alcázar[1], L. E. Zamora Alfonso[1], J. F. Marco[2], J. J. Romero[3], J. M. Gonzalez[4], F. J. Palomares[5]

1. Physics, Universidad del Valle, Cali, Colombia; 2. Instituto de Física-Química Rocasolano, CSIC, C/Serano, 119. 28006, Madrid, Spain; 3. Instituto de Magnetismo Aplicado, UC, P.O. Box 155, 28360, Las Rozas, Madrid, Spain; 4. Unidad Asociada, ICMM-IMA, P.Box 155, 28360, Las Rozas, Madrid, Spain; 5. Instituto de Ciencia de Materiales de Madrid, CSIC, C/Sor Juana Inés de la Cruz, 28049, Cantoblanco, Madrid, Spain

Samples of Fe50Co50 produced by mechanical alloying (MA) during 0.5, 2, 4, 8, 12, 24 and 48 h were characterized by x-rays diffraction (XRD), Mössbauer spectrometry (MS) and x-ray photoelectron spectroscopy (XPS). The XRD results showed that up to 8 h the α-Fe and Co-HCP phases coexist and that for 12 h and higher milling times only the peaks of a BCC phase were detected. The Mössbauer spectra at room temperature (RT) of the samples between 0.5 and 4 h showed only a sextet which nearly corresponds to that of the α-Fe, and those after 4 h two sextets, which correspond to sites of α-Fe and of Fe surrounded by Co atoms. The fit of the spectra with a hyperfine field distribution confirms the previous interpretation. The mean hyperfine field was 33T for samples milled between 0.5 and 4 h, then continuously increases up to 35.1 T for 12 h and then change up to 35.2 for 24 and 48 h. The XPS measurements shown the presence of a superficial shell formed by carbides and oxides of Fe and Co and that for 12 h metallic Fe and Co are yet present. Then the BCC FeCo disordered alloy is completely formed after 12 h.

Experimental procedure and results

Fe and Co powders with purity bigger than 99.9% were mixture at the equiatomic Fe50Co50 composition and MA during 0.5, 2, 4, 8, 12, 24 and 48 h, using a ball mass to powder mass ratio of 15:1. The prepared samples were characterized by XRD, MS and XPS at room temperature (RT). The XRD patterns were refined by the Rietveld method using the GSAS program and the Mössbauer spectra were fitted by using the MOSFIT program. The calibration samples were Si and α-Fe for XRD and MS, respectively.

The XRD patterns obtained for samples with 0.5 to 8 h show the sequence peaks of the HCP Co and those of the BCC Fe, and only the peaks of a BCC phase for samples with 12 h and more. The obtained lattice parameters of the HCP phase were a=0.251 and c=0.411 nm independent of the milling time, and that of the BCC phase is nearly 0.2867 nm between 0.5 and 4 h, and then gradually decreases up to 0.2856 nm for 48 h. This decrease is due to the continuous substitution of Fe by Co atoms in the BCC lattice of Fe.

The obtained mean grain size of the BCC phase decreases from 50 nm for 0.5 h to 12 nm for 8 h and then remains nearly constant. They present a spherical shape. The grains of the HCP phase change from a prolate (with dimensions of 30x7nm) to an oblate shape (with dimensions 2x20nm) when the milling time increase passing by a spherical shape at 4 h (with 20 nm).

Figure 1 shows the Mössbauer spectra at RT of the prepared samples. The fit was with one sextet for samples milled from 0.5 up to 4 h, and two sextets for the other samples. For the samples with 24 and 48 h it was necessary to add a broad doublet in order to obtain the best fit, whose Mössbauer parameters were $\delta \sim 0.54$ mm/s and $\Delta Q \sim 1.54$ mm/s. It was not possible to associate these parameters to an knowledge phase. The spectral area of this doublet is less than 4 % and due this it was not detected by XRD. The Mössbauer parameters of the sextet used to fit the spectra of samples with 0.5, 2 and 4 h nearly correspond to that of pure Fe.

One of the two sextets obtained from the fitting of samples with 8 h ore more nearly corresponds to that of the pure Fe and the other (a broader one) presents a hyperfine magnetic field of about 36 T. After 4 h of milling the spectral area of Fe decreases and that of the BCC FeCo phase increases. These results are in accordance with those obtained by XRD and can be interpreted in the following way: between 0.5 up to 4 h of milling the grain size of the α-Fe and Co present changes but it was not detected diffusion each other. For bigger milling times Co begins to diffuse inside the BCC Fe lattice and two types of Fe sites can be detected, one similar to that of pure Fe with $B \sim 33$ T and other with Co substituting Fe with $B \sim 36$ T. This substitution continues and the number of pure Fe sites decreases and that of Fe with Co increases.

A second fit of the spectra where made with a hyperfine field distribution showing a narrow peak around 33 T for the samples with 0.5, 2 and 4 h, and two peaks around 33 T and 36 T, respectively, for the samples with 8 h ore more. The peak around 33 T decreases with the milling time and that at 36 T increases. The mean hyperfine field increases from 33 to 35.1 T when the milling time increases up to 12 h, and then increase up to 35.2 T for 24 and 48 h. Our study did not detect Fe sites with $B < 33$ T which can be attributed to Fe atoms diffused into the Co matrix.

Finally, the XPS studies conducted on as-prepared samples with 12 and 24 h showed that they present a shell composed by Fe and Co carbides and oxides. When these samples were cleaned by bombarding with Ar, metallic and alloyed Fe and Co peaks were detected in the 12 h sample whereas only alloyed Fe and Co peaks were detected in the 24 h samples. These results permit to conclude that the disordered Fe50Co50 alloy is formed between 12 and 24 h.

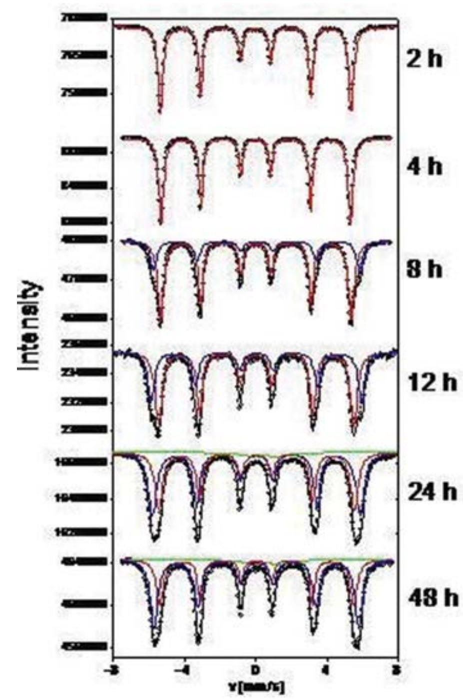

Fig. 1. Mössbauer spectra of the different samples.

GR-09

Residual strain induced in a crystal lattice upon annealing under stretching load in soft-magnetic Fe-based nanocrystalline alloys.

N. V. Ershov[1], Y. P. Chernenkov[2], V. I. Fedorov[2], V. A. Lukshina[1], A. P. Potapov[1]
1. Institute of Metal Physics, Ural Division, Russian Academy of Sciences, Yekaterinburg, Russian Federation; 2. St.-Petersburg Institute of Nuclear Physics, Russian Academy of Sciences, Gatchina, Russian Federation

Soft-magnetic Fe-based alloys have an essential and usefull property: upon annealing in a magnetic field or under stretch loading in these alloys a magnetic anisotropy is easily induced. An investigation of the nature of magnetic anisotropy in crystalline Fe-rich α-FeSi alloys have revealed an ordered arrangement of the Si atoms preferentially oriented in the direction parallel to the axis of the magnetic anisotropy induced during field or stress annealing [1,2]. The effect of annealing under stretch loading on the anisotropy of magnetic properties of a nanocrystalline alloy of Fe–Si–B–Nb–Cu system (finemet) for the first time was studied in [3] and it was shown that an anisotropy of easy plane type perpendicular to the stretching axis is formed. This is why we undertook the present investigation of the structure of these alloys in order to reveal its fine details that could provide a reason for the appearance of a transverse magnetic anisotropy after annealing under load.
Three series of samples of the alloy $Fe_{87-X}Si_XB_9Nb_3Cu_1$ were investigated where silicium is introduced at the expense of ferrum, in concentrations from 0 to 13.5 at.% (X = 0 - 13.5). A first series was prepared in the form of thin tapes via high-rate quenching from the melt on the rotating copper disk. To obtain a second series of samples, the initial tapes were annealed at the temperature of nanocrystallization (520°C, 120 minutes). Samples of a third series were also obtained from the initial tapes with the help of a thermomechanical treatment that consisted in their annealing and subsequent cooling under stretch loading (520°C, 120 min; a load of 440 MPa).
X-ray diffraction measurements were performed in the transmission geometry with the use of a monochromatized radiation K_α Mo and the laboratory diffractometer equipped with a four-circle goniometer. The Bragg and superstructure reflections were registered in conditions when the scattering vector lied in the plane of samples. From the position of these reflections the corresponding spacings between the planes in the FeSi phases were estimated via measurements along and transverse to the tape axis, parallel and perpendicular to the tensile stress direction (TSD). For the first time such an investigation of the samples of finemet with the silicium content X = 15.5 subjected to annealing under a load of different value were performed by Ohnuma et al [4]. However, in [4] the position of only one reflection was under study, which did not completely clarify the character of lattice residual deformations.
In the initial state, i.e., immediately after quenching, all the alloys are in condition of ultrafine grain (an average grain size is approximately of 2 nm in diameter). Their structure is independent of a direction and the silicium content. After an annealing that provides for nanocrystallization, a distribution of interplanar spacings remains isotropic but with a large size of crystallites – up to 10–12 nm. The lattice parameter with increasing X decreases somewhat rapidly than that typical of bulk samples of FeSi alloy. At a silicium content of 13.5%, the superstructure peaks (111) and (200) from the Fe_3Si phase were registered as most intense.
After annealing under stretching load, the interplanar spacings in TSD increase. But the lattice of nanocrystals is deformed not isotropically. It turns out that the value of a change in the spacing Δd_{hkl} between the planes (hkl) depends on the angle between the direction of the wave vector [hkl], when it is parallel to TSD, and the nearest axis <111>. The greater this angle, the larger the deformation. For the direction [111], Δd_{111} has a minimum value; in the direction of easy magnetization [100], Δd_{100} is maximum. This is why the lattice deformation is of tetragonal character when an increase in the interplanar spacing in the direction of the <100> axis the nearest to TDS is the largest. At X = 13.5, more than half the volume of the FeSi phase is occupied by the phase Fe_3Si, whose crystal lattice after annealing under stretch loading has the same character of deformation.
After cooling, a deformed structure of nanocrystals, which has formed upon annealing under stretch loading, remains unaltered due to high strength characteristics of the amorphous matrix. Since the nanocrystals with a constituent composition close to stoicheometry (Fe_3Si) have a negative value of magnetostriction, then at tetragonal deformation – as a result of stretch loading along the axis [100] which makes a minimum angle with TSD, – a magnetization is induced in the plane normal to the axis of loading, namely, along one of the easy axes [010] or [001]. Since the number of crystallites is very high and their distribution reveals no effect of texture, then a great deal of the crystallites stretched along the tape contribute to a transverse distribution of magnetization and bring about the appearance of the magnetic anisotropy of easy plane type which is transverse to TSD.
The work was supported by the Russian Foundation for Basic Research, project no.06-02-17082.

[1] Yu.P. Chernenkov, V.I. Fedorov, V.A. Lukshina, B.K. Sokolov, N.V. Ershov. Phys. Met. Met. 92, 193-198 (2001)

[2] Yu.P. Chernenkov, N.V. Ershov, V.A. Lukshina, V.I. Fedorov, B.K. Sokolov. Physica B. 396, 220-230 (2007)

[3] A.A. Glazer, N.M. Kleinerman, V.A. Lukshina, A.P. Potapov, V.V. Serikov. Fiz. Met. Met. 12, 56-61 (1991) (in Russian)

[4] M. Ohnuma, K. Hono, T. Yanai, M. Nakano, H. Fukunaga, Y. Yoshizawa. Appl. Phys. Lett. 86, 152513-(1-3) (2005)

GR-10

Magnetic properties and reaction kinetics of synthesized Fe-Ni-Co alloy during H2 reduction of Ni0.5Co0.5Fe2O4.

M. Bahgat, *M. Paek*, J. Pak
Metallurgical and material engineering, Hanyang university, Ansan, South Korea

There is considerable technological and theoretical interest in magnetic nanoparticles due to the characterized enhancement in its magnetic recording density, recording speed, the noise suppression, and the material lifetime with the decrease in magnetic particle size 1,2). Fe–Co–Ni alloys have been demonstrated to have a low coercivity and high-saturation magnetization 3, 4). In the present work, double sintering ceramic technique was applied for the synthesis of Ni0.5Co0.5Fe2O4 at 1100 and 1200 oC. The reduction kinetics and magnetic properties of the synthesized Fe-Ni-Co alloy nanoparticles was thoroughly investigated.
Ni0.5Co0.5Fe2O4 compacts were reduced at 800, 900, 1000 and 1100 °C in constant flowing hydrogen gas atmosphere (100% H2). The course of reduction was followed up thermogravimetrically. The synthesized nickel cobalt ferrite powder and the reduced products were characterized by XRD, porosity measurements, FE-SEM, optical microscope and VSM.
Ni0.5Co0.5Fe2O4 was synthesized successfully with average crystallite size about 52.1 nm.
The pore size measurements show that the synthesized ferrite compacts at 1100 oC have higher total porosity (44.04%) relative to that at 1200 oC (30.98%). The SEM micrograph of the synthesized ferrite powder at 1100 oC is shown in Fig. 2. Dense grains of Ni0.5Co0.5Fe2O4 are formed in a very well regular crystalline shape with presence of large number of micro-pores.
It can be seen that for each reduction curves, the rate of reduction was highest at early stage and gradually decreased with time till the end of experiment. The reduction rate increased as the reduction temperature increased either in the initial or final reaction stages.
Complete reduction was achieved with synthesis of Fe-Ni-Co alloy of average crystallite size about 18-20 nm. To illustrate the rate controlling mechanism the apparent activation energy (Ea) of reduction was calculated and it was found that the initial reduction stages are controlled by the combined gas diffusion and interfacial chemical reaction mechanisms with more contribution for the gas diffusion mechanism while the final reduction stages are controlled by the interfacial chemical reaction mechanism.
The magnetic measurements indicated a significant decrease in coercivity (Hc) with increasing the reduction temperature while reversely the saturation magnetization (Bs) shows sharp increase with increasing reduction temperature as shown in Fig. 2. Namely the Hc values decreased from 328.2, 95 to 52.5 Oe while the Ms values increased from 54.8, 241.7 to 277.2 emu/g for fired, 900 and 1100 oC reduced samples respectively.
The significant decrease in coercivity (Hc) is correlated to grain growth and sintering effect with increasing the reduction temperature that leads to a great continuity of grain domains. However the sharp increases in saturation magnetization (Ms) are explained by the formation of metallic alloying elements Fe, Ni, Co as products of reduction process whereas Fe–Co–Ni alloys have been demonstrated to have a low coercivity and high-saturation magnetization 3,4). So the micro-structural development of the synthesized Fe/Ni/Co alloy with the increase of reduction temperature could be responsible for the promotion in its magnetic behavior.

1) D.L. Lesile-Pelecky, R.D. Rieke, Chem. Mater. 8 (8) (1996) 1770.

2) H. Gleiter, Nanostruct. Mater. 6 (1995) 3.

3) T. Osaka, M. Takai, K. Hayashi, K. Ohashi, M. Saito, and K. Yamada, Nature, vol. 392, pp. 796–798, 1998.

4) X. Liu, P. Evans, and G. Zangari, IEEE Trans. Magn., vol. 36, pp. 3479–3481, Sept. 2000.

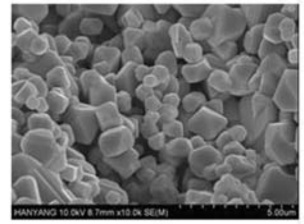

Fig. 1: SEM micrograph of fired $Ni_{0.5}Co_{0.5}Fe_2O_4$ compacts at 1100 °C

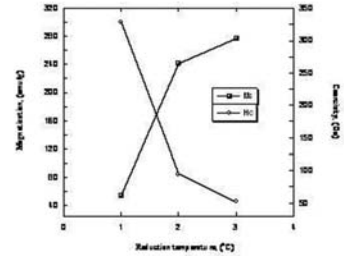

Fig. 2: The measured coercivity (Hc) and magnetic saturation (Ms) values of fired $Ni_{0.5}Co_{0.5}Fe_2O_{4\,(1)}$ and after reduction at $900_{(2)}$ and 1100 $°C_{(3)}$.

Magnetocaloric effect in the FeCrCuNbSiB amorphous materials.

A. Kolano-Burian[1], M. Kowalczyk[2], R. Kolano[1], R. Szymczak[3], H. Szymczak[3], T. Kulik[2], J. Szynowski[1]
1. Institute of Non-Ferrous Metals, Gliwice, Poland; 2. Faculty of Materials Science and Engineering, Warsaw University of Technology, Warsaw, Poland; 3. Institute of Physics, Polish Academy of Sciences, Warsaw, Poland

Considerable advances have been made recently in developing new types of magnetic materials exhibiting large magnetic entropy change, which can be used in magnetic refrigeration near room temperature [1-3]. The aim of this work was to analyse magnetic properties of the FeCuNbSiB amorphous alloys modified with Cr from a point of view of their potential application for magnetic refrigeration at a room temperature.

The amorphous soft magnetic ribbons from the $Fe_{78-x}Cr_xCu_1Nb_5Si_4B_{12}$ alloy (x = 0, 5 and 8) were fabricated by melt-spinning technique. The SQUID magnetometer was used to measure magnetisation of all studied samples at different temperatures. Fig. 1 shows M(T)dependence for the $Fe_{70}Cr_8Cu_1Nb_5Si_4B_{12}$ sample measured at different applied magnetic fields up to 50 kOe. From the M(T)dependence, measured at 2 kOe, the T_c was determined by differentiation ($\delta M/\delta T$). It was found that with the increase of Cr content in the alloy, the T_c considerably decreases reaching the values of 170°C, 90°C and 20°C for the alloys containing 0, 5 and 8 at. % Cr, respectively.

The ferromagnetic-to-paramagnetic transition in these alloys is not as sharp as in perovskite type materials, which are considered as suitable for application in magnetic refrigerators. However, in the alloy containing 8 at. % Cr this transition occurs close to the room temperature, which is illustrated in Fig. 2 showing B(H) curves for the $Fe_{70}Cr_8Cu_1Nb_5Si_4B_{12}$ alloy measured within a temperature range from 200 to 400 K using VSM. For the comparison, Fig. 3 shows B(H) curves for the $Fe_{78-x}Cr_xCu_1Nb_5Si_4B_{12}$ alloys containing 5 and 8 at. % Cr measured at the temperature of 300K.

Under this work, calculations of the magnetic entropy changes (ΔS_H) resulting from spin ordering were made for all alloys examined. For the isothermal processes, the ΔS_H of the magnetic system due to the application of a magnetic field H is [4]:

$$\Delta S_H(T,H)=\int_0^H(\partial M/\partial T)_H dH$$

Fig. 4 shows temperature dependence of the magnetic entropy changes at different applied magnetic fields for the $Fe_{70}Cr_8Cu_1Nb_5Si_4B_{12}$ alloy.

It has been concluded under this work that an increase in Cr content in the $Fe_{78-x}Cr_xCu_1Nb_5Si_4B_{12}$alloy from 5 at. % to 8 at. % Cr results in a decrease in magnetic entropy changes at the magnetic field of 20 kOe from 2.5 $Jkg^{-1}K^{-1}$ to 1 $Jkg^{-1}K^{-1}$, respectively.

[1] V.K. Pecharsky, K. A. Gschneidner Jr., International Journal of Refrigeration 29 (2006) 1239

[2] E. Brück, O. Tegus, D.T.C. Thanh, K.H.J. Buschow, JMMM 310 (2007) 2793

[3] C. Gomez-Polo, L.M. Socolovsky, J.C. Denardin, M. Knobel, J.I. Perez-Landazabal, V. Recarte, JMMM 316 (2007) e876

[4] K.A Gschneider Jr., V.K. Pecharsky and A.O. Tsokol, Rep. Prog. Phys. 68 (2005) 1479

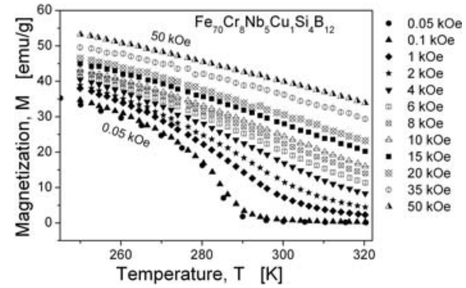

Fig. 1 Temperature dependence of magnetization for the $Fe_{70}Cr_8Cu_1Nb_5Si_4B_{12}$ alloy at different values of the applied magnetic field

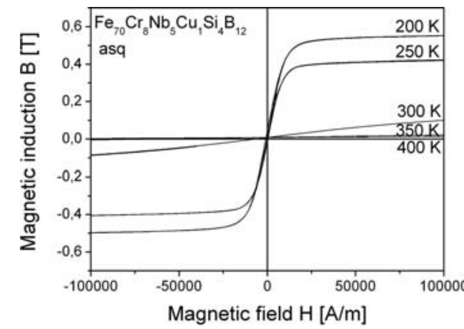

Fig. 2 Magnetisation curves measured for the $Fe_{70}Cr_8Cu_1Nb_5Si_4B_{12}$ alloy in the as-quenched state within a temperature range from 200 to 400 K

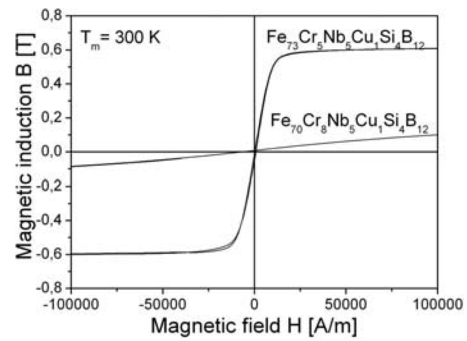

Fig. 3 Comparison of magnetisation curves for the $Fe_{78-x}Cr_xCu_1Nb_5Si_4B_{12}$ alloys containing 5 and 8 at. % Cr measured at the temperature of 300K

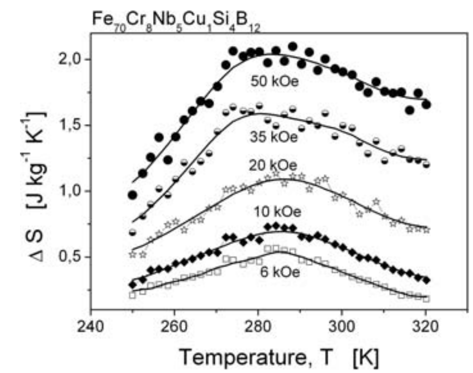

Fig. 4 Temperature dependence of the magnetic entropy changes at different values of the magnetic field applied

Thermal and magnetic field-induced martensite-austenite transformation in melt spun Mn50Ni40In10 ribbons.

J. L. Sanchez Llamazares[1], B. Hernando[1], J. D. Santos[1], M. J. Pérez[1], C. García[2], J. González[2], R. Varga[3]
1. Departamento de Fisica, Universidad de Oviedo, Oviedo, Spain; 2. Departamento de Física de Materiales, Universidad del País Vasco, San Sebastián, Spain; 3. Institute of Physics, UPJS, Kosice, Slovakia

Recently, it has been shown that melt spun ribbons of the alloy Mn50Ni40In10, show martensite-austenite transformation with both phases exhibiting ferromagnetic ordering [1]. Its valence electronic concentration per atom, e/a, is 7.801, and martensite shows a lower saturation magnetization than austenite. The alloy is therefore of significant prospective importance for applications in both, magnetically driven actuators due to magnetic shape memory effect, and as working substance in magnetic refrigeration technology. In the present contribution, we report results of dc magnetization measurements as a function of temperature under different applied magnetic fields and M(H) curves at selected temperatures, in order to reveal the distinctive features of the thermal and field-induced martensite-austenite transition in this alloy. A complementary characterization of its chemical composition, structure of the phases formed and sample microstructure was carried out by means of energy dispersive X-ray microanalysis (EDS), scanning electron microscopy (SEM), and X-ray diffraction (XRD) at different temperatures. After a carefully study by EDS microanalysis on the cross section and both ribbon surfaces we concluded that chemical elements are homogeneously distributed in the alloy that shows the average composition Mn49.5Ni40.4In10.1. Zero-field cooling (ZFC), field cooling (FC), and field heating (FH) thermomagnetic curves recorded at 50 kOe are shown in Figure 1. The curves revealed the occurrence of a large thermal hysteresis of the structural martensitic transformation of 38 K, as well as a splitting between ZFC, and FC or FH curves in the martensitic region. The latter is attributed to a field-induced partial freezing of austenite phase into martensite upon cooling. The characteristic temperatures of the respective martensite-austenite phase transformation were MS = 213 K, Mf = 173 K, AS = 222 K, and Af = 243 K. Low- and high-field heating and cooling dM/dT(T) curves showed that the phase transition occurs in a broad temperature interval. XRD diffractograms recorded at temperatures below and above the transformation confirmed the single phase character of ribbons. Austenite phase crystallizes in a bcc L21–type crystal structure (Curie point of 311 K), transforming into a modulated fourteen -layered (14M) monoclinic martensite. The effect of magnetic field on reverse transformation was studied by measuring magnetization isotherms, under increasing and decreasing the field, in the transformation temperature range. The results are shown in Figure 2. M(H,T) curves have the signature of metamagnetism owing to the effect of the magnetic field on the transformation. From relatively low magnetic field values a progressive magnetic field induced transformation from martensite to austenite is observed. Consequently, a large hysteresis between field-up and field-down curves is observed. As temperature approaches to pure austenitic or martensitic phase existence regions, these effects vanish. A field over 50 kOe is required for a complete reverse transformation.

[1] J.L. Sánchez Llamazares, T. Sanchez, J.D. Santos, M.J. Perez, M.L. Sanchez, B. Hernando, Ll. Escoda, J.J. Suñol, R. Varga, Appl. Phys. Lett. 92 (2008) in press.

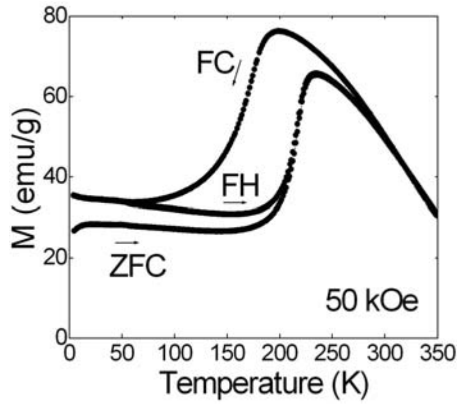

Fig. 1 Zero field cooled (ZFC), field cooled (FC), and field heated (FH) thermomagnetic curves recorded at 50 kOe for as-spun Mn50Ni40In10 ribbons.

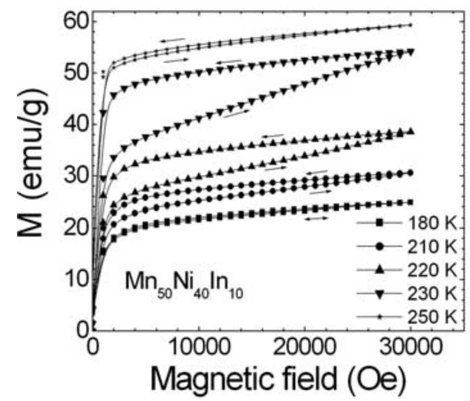

Fig. 2 Magnetization isotherms M(H,T) for Mn50Ni40In10 ribbons measured in the temperature interval where the reverse martensitic transformation occurs. Arrows indicate whether the curve corresponds to increasing or decreasing of the magnetic field.

GR-13

Influence of the Fe/B ratio on the magnetocaloric response of $Fe_{92-x}Cr_8B_x$ (x=12, 15) amorphous alloys.

V. Franco[1], A. Conde[1], L. F. Kiss[2]
1. Department of Condensed Matter Physics, Sevilla University, Sevilla, Spain; 2. Research Institute for Solid State Physics and Optics, Hungarian Academy of Sciences, Budapest, Hungary

Research on the magnetocaloric properties of materials has been revitalized since the feasibility of developing near room temperature magnetic refrigerators was demonstrated and the coetaneous discovery of the giant magnetocaloric effect (GMCE) in the last decade of the previous century. In an era of increasing energy costs and of concerns about the actual influence of human activity on the environment, magnetic refrigerators constitute a promising technology, as they are energetically more efficient than those based on conventional gas compression-expansion, and are more environment-friendly, as neither ozone-depleting nor global-warming volatile refrigerants are required. However, due to the thermal and magnetic hysteresis and reduced frequency response of GMCE materials, with a coupled magneto-structural phase transition, current refrigerator prototypes mainly use materials with a second order magnetic phase transition. Among them, there is an increasing interest in amorphous alloys, as their reduced magnetic hysteresis (virtually negligible), the high electrical resistivity (which would decrease eddy current losses), tunable Curie temperature and, in the case of bulk amorphous alloys, outstanding mechanical properties are beneficial characteristics for a successful application of the material.
However, tuning the temperature at which the peak magnetic entropy change takes place, to make it closer to room temperature, usually comes along with a reduction in the magnetocaloric response of the alloy. Recently, it has been shown that the change of the Fe/B ratio in a Nanoperm type alloy allowed to displace the optimal working temperature of the material without altering the magnitude of the peak entropy change. The aim of this work is to analyze if this compositional effect can be extended to other series of alloys. For that purpose, $Fe_{92-x}Cr_8B_x$ (x=12, 15) amorphous alloys have been studied. It will be shown that reducing the B content of the alloy produces a decrease in the Curie temperature of the sample (and therefore, of the temperature of the peak), but at the expense of a reduction in its magnitude (for a maximum applied field of 50 kOe, the peak entropy change is 2.6 J kg^{-1} K^{-1} and 3.0 J kg^{-1} K^{-1} for the alloys with 12 and 15 at. % B, respectively). The field dependence of the magnetocaloric response of these alloys will be studied on the basis of the recently proposed universal curve for the magnetic entropy change in materials with a second order magnetic phase transition.

GR-14

XMCD-PEEM imaging of the micromagnetic structure of Co_2FeSi Heusler compound.

A. Gloskovskii[1], C. Blum[1], J. Barth[1], G. Fecher[1], P. Nagel[2], S. Schuppler[2], G. Schönhense[3], C. Felser[1]

1. Institut für Anorganische Chemie und Analytische Chemie, Johannes Gutenberg - Universität, Mainz, Germany; 2. Forschungszentrum Karlsruhe, Institut für Festkörperphysik, Karlsruhe, Germany; 3. Institut für Physik, Johannes Gutenberg - Universität, Mainz, Germany

The Heusler compound Co_2FeSi is a promising material for magnetoelectronic devices. With a Curie temperature of 1100 K, a saturation magnetisation of 6 Bohr magnetons and a high spin polarisation at the Fermi edge it fulfills the essential requirements for magnetic sensors or spin valves [1]. An essential feature for such devices is the micro-magnetic domain structure. X-ray magnetic circular dichroism-photoemission electron microscopy has been used for a direct observation of the domain structure of single- and polycrystalline samples.

Polycrystalline Co_2FeSi samples were etched with a solution of 0,2 mol/L in 9,25% HCl and cut along the crystallites. The crystallites are about 1 mm thick and extend along the sample surface. The samples were mechanically polished before the measurements. The (110) surface of as-grown single crystal was polished with an orientation better than 0.1^o (MATECK). The freshly built-in single crystal exhibited oxidation of the surface. The magnetic contrast was strongly suppressed by the magnetically dead oxide layers. In a first step, the single crystal was cleaned by ion-bombardement (Ar^+, 500 eV) for 120 min to remove organic impurities that remained from the cleaning process after polishing. This sample is termed "mildly sputtered". Afterwards, it was sputtered with increased energy (1 keV). For healing and to allow for reordering of the surface, a heating at 620 K for 10 min followed the sputtering. The sputtering-heating cycle was repeated 3 times. This sample is termed "massively sputtered". Before the third measurement the sample was polished again using the same method as for the polycrystalline sample. Immediately after polishing process the "re-polished" sample was transferred into the vacuum to prevent oxidation of the surface. The experiments were done at WERA beamline of ANKA (Karlsruhe) and UE56-SGM beamline of BESSY (Berlin). All measurements reported below were performed for non-magnetised samples.

In full-field imaging photoemission electron microscopy (PEEM) combined with XMCD (X-ray magnetic circular dichroism) the magnetic contrast is very high and provides element selectivity. All XMCD-PEEM images were recorded at Fe L_3 edge.

The micromagnetic structure of two crystallites in the polycrystalline sample is shown in Fig. 1a. The crystallite at the bottom exhibits the ripple structure characteristic to polycrystalline samples studied earlier by us [2]. The upper crystallite consists of larger magnetic domains. The "mildly sputtered" sample shows the weak magnetic contrast and randomly distributed small magnetic domains (not shown). Large magnetic domains with sizes up to 100 µm appear after 3 sputtering-annealing cycles (Fig. 1b). It cannot be excluded that the crystal stoichiometry at the surface may have been altered by selective sputtering (in our case of silicon). In this case, a strong magnetic coupling of the underlying stoichiometric Co_2FeSi with the thin "Si-poor" surface layer may be responsible for the observed magnetic contrast. An attempt to recover the initial stoichiometry of the crystal surface by polishing led to the much weaker magnetic contrast shown in Fig. 1c. The size of magnetic domains domains was reduced to less than 10 µm.

Important information about the magnetic structure and chemical composition can be extracted from laterally resolved X-ray absorption spectroscopy. Local absorption spectra from the surface of the Co_2FeSi single crystal prepared in three different ways were taken at the Co L-edges (not shown here). The shoulder that appears at about 4 eV above the Co L_3 absorption edge is an indication of the Heusler type $L2_1$ structure. It is present for the "mildly sputtered" sample but vanishes in the "massively sputtered" single crystal. The $L2_1$ structure of the sample surface was partially recovered by re-polishing the single crystal.

To conclude, we have prepared the surface of Co_2FeSi by different methods and studied its micromagnetic structure by means of XMCD-PEEM. Magnetic domain patterns and magnetic contrast are strongly influenced by how the surfaces are prepared.

The authors acknowledge financial support by the Deutsche Forschungs Gemeinschaft (project TP7 in research unit FG 559) and as well as by BESSY (BMBF 05 ES3XBA/5).

[1] C. Felser, G.H. Fecher, B. Balke. Angew. Chemie (Int. Ed.) 46 (2007) 668.

[2] C. Felser, B. Heitkamp, F. Kronast, D. Schmitz, S. Cramm, H. A. Dürr, H.-J. Elmers, G. H. Fecher, S. Wurmehl, T. Block, D. Valdaitsev, S. A. Nepijko, A. Gloskovskii, G. Jakob, G. Schönhense, and W. Eberhardt. J. Phys.: Condens. Matter, 15 (2003) 7019.

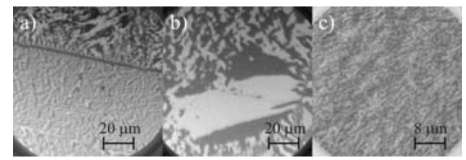

Figure 1. XMCD-PEEM image of (a) polycrystalline Co_2FeSi. The Co-enriched boundary between the crystallites is visualised as a black stripe; (b) massively sputtered Co_2FeSi single crystal. The magnetic domains show the out-of-plane orientation. The surface of the single crystal could have a lack of Si after sputtering; (c) re-polished Co_2FeSi single crystal. The magnetic contrast is considerably depleted in comparison to the "mildly" and "massively sputtered" surfaces. A micro-magnetic structure at the surface in a-c was taken at the Fe L_3 edge.

GR-15

Transport and Magnetism in $Nd_5Si_{1.45}Ge_{2.55}$

A. M. Pereira[1], C. Magen[4], P. Algarabel[2], L. Morellon[2,3], M. E. Braga[1], F. Carpinteiro[1], M. R. Ibarra[2,3], J. Ventura[1], J. B. Sousa[1], J. P. Araujo[1]
1. IFIMUP Faculdade de Ciências da Universidade do Porto, Porto, Portugal; 2. ICMA - Universidad de Zaragoza and Consejo Superior de Investigaciones Científicas, Zaragoza, Spain; 3. Instituto de Nanociencia de Aragón, Universidad de Zaragoza, Zaragoza, Spain; 4. Oak Ridge Natl Lab, High Temp Mat Lab, Oak Ridge, TN

Recent scientific and engineering efforts are directed towards thermomagnetic cooling, since it is considered environmental friendly as it eliminates the use of the traditional chlorofluorocarbons (CFCs). Conventional vapour-cycle refrigeration achieves cooling efficiencies approaching 40% of the theoretical Carnot limit. The thermomagnetic cooling (magnetorefrigeration) achieves a cooling efficiency of 60%.
The research on magnetic materials for refrigeration is increasing, with $Gd_5Si_2Ge_2$ compound being one of the best candidates for this technological application due to the giant MCE observed near room temperature (RT) [1, 2]. Since this interesting discovery, the 5:4 rare-earth compounds $[R_5(Si_xGe_{1-x})_4$ with R=rare-earth] are being object of extensive studies, not only due to the MCE that some of these compounds present, but also to their peculiar physical and chemical properties, namely strong magnetoelastic effects [3], giant magnetoresistance [4], exotic transport phenomena [5] and more recently a new magnetic regime in the PM phase attributed to a Griffiths-like phase [6]. These unexpected and unusual properties occur due to the strong interplay between the structure and magnetic properties characteristic of this family of compounds [7]. The compound here studied is the $Nd_5Si_{1.45}Ge_{2.55}$ that crystallizes on a Monoclinic (M) structural phase (P1121/a) stable down to 4 K [8, 9] and presents a purely magnetic transition (PM-FM) at T_C~57 K. We study in detail the transport and magnetic properties of this light rare-earth compound as a function of temperature, in the range 10-300 K, namely the electrical resistance R(T), thermopower S(T) and magnetization M(T). From R(T) (see Fig.1) and its temperature derivative (obtained numerically), we observe a change on the R(T) behavior around T_C ~ 56 K due to a magnetic transition without any thermal hysteresis, establishing the second order nature of the transition. On cooling, a spin reorientation transition is observed at T*~37 K with the appearance of an additional T^2 term. Above T_C, an almost linear thermal dependence is observed on R(T) due to the electron-phonon interaction characteristic of metallic systems in the PM state. The S(T) results (see Fig.2), are in full agreement with the R(T) ones. Our magnetization data confirm previous results [9] with a second order ferromagnetic transition at T_C=57K and absence of any structural transition. In the reciprocal susceptibility an anomalous behavior is observed at T**~115 K, attributed to a small amount of a 5:3 secondary phase [10].

[1] K.A. Gschneidner, V.K. Pecharsky and A.O. Tsokol, Rep. on Prog. in Phys. I 68 (2005) 1479.

[2] V.K. Pecharsky and K.A. Gschneider Jr., Phys. Rev. Lett. 78 (1997) 4494.

[3] L. Morellon, J. Blasco, P.A. Algarabel and M.R. Ibarra Phys. Rev. B 62 (2000) 1022.

[4] L.Morellon, J. Sankiewicz, B. Garcia-Landa, P.A. Algarabel and M.R. Ibarra, Appl. Phys. Lett. 73 (1998) 3462.

[5] J.B. Sousa, A.M. Pereira, F.C. Correia, J.M.Teixeira, J. P. Araujo, R.P. Pinto, M.E. Braga, L. Morellon, P.A. Algarabel, C. Magen and M.R. Ibarra, J. Phys.: Condens. Matter 17 (2005) 24612476.

[6] C. Magen, P.A. Algarabel, L. Morellon, J.P. Araujo, C. Ritter, M.R. Ibarra, A.M. Pereira and J.B. Sousa, Phys. Rev. Lett. 96 (2006) 167201.

[7] V.K. Pecharsky and K.A. Gschneidner Jr., Adv. Mater. 13 (2001) 683.

[8] Ch.F. Yang, G.H. Rao, G.Y. Liu, Z.W. Ouyang, W.F. Liu, X.M. Feng, W.G. Chu and J.K. Liang, J. Alloys and Compounds 346 (2002) 190.

[9] C. Magen, C. Ritter, L. Morellon, P.A. Algarabel and M.R. Ibarra, J. Phys.: Condens. Matter 16 (2004) 7427.

[10] P. Boulet, F. Weitzer, K. Hiebl and H. Nol, J. Alloys and Compounds 315 (2001) 66.

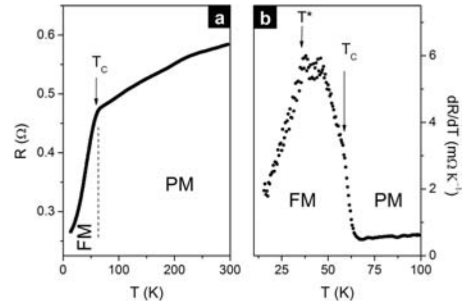

Fig. 1: (a) Temperature dependence of the electrical resistance R(T) of $Nd_5Si_{1.45}Ge_{2.55}$ between 10 and 300K; (b) temperature derivative of the electrical resistance (dR/dT) as function of temperature.

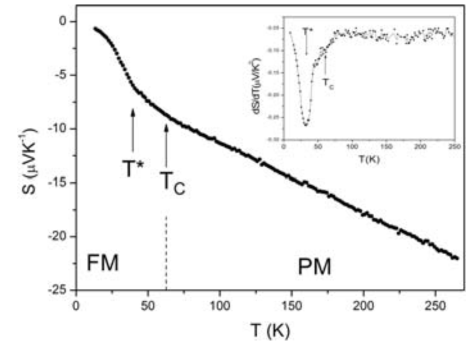

Fig. 2: Temperature dependence of thermopower in the range 10-300K. Inset: Temperature derivative of thermopower as a function of temperature (dS/dT).

GR-16

Magnetism and phase transformation in Fe / Fe oxide milled nanopowders.

O. Crisan[1], R. Nicula[2], I. Skorvanek[3]
1. National Institute for Materials Physics, Bucharest-Magurele, Romania; 2. Institute of Physics, Rostock University, Rostock, Germany; 3. Institute of Experimental Physics, Slovak Academy of Sciences, Kosice, Slovakia

The exchange bias effect has been shown to occur in granular ball-milled Fe / Fe oxide nanopowders. On the other hand, ball milling of mixtures of Fe and magnetite was shown to result in formation of wüstite (FeO) via a chemical reduction reaction occurring during the ball milling. The evolution of phase composition in such mixtures has a strong influence on the magnetic properties and the exchange bias effect, in particular.
We report in the present paper the structural and magnetic properties of mixed Fe / Fe3O4 nanopowders obtained by ball milling and submitted to annealing treatments.
The nanopowder system made of Fe / Fe3O4 with a 2:8 wt.% ratio has been milled for 50 h in a Retzsch PM 400 planetary ball mill. The sun wheel frequency was 200 rpm and sun wheel / vial frequency ratio was 1.5. We used 8 tungsten carbide balls with 20 mm diameter. The powder and balls were sealed in hexane to avoid oxidation. The temperature-dependent in-situ X-ray diffraction of the synchrotron radiation was done in energy-dispersive mode at DESY-Hasylab, Hamburg at Max 80 F2.1 beamline with $\lambda = 1.2$ Å. The magnetic measurements have been performed with a vibrating sample magnetometer (VSM) in a temperature range between 4.2 K and 300 K. The hysteresis loops were recorded as follows: (i) cooling to 4.2 K without the presence of external field and first loop (ZFC at 4.2 K) was measured; (ii) heated up and recording the loop at 280 K; (iii) again, cooling to 4.2 K in 5 T applied field (FC) and the loop was measured.
The XRD spectra of the as-milled sample taken at 25°C, 250°C and 400°C are presented in Fig. 1. The XRD spectrum at 25°C shows broad lines, typical for topologically disordered, nanostructured materials, as obtained after ball milling. The main Bragg reflections of the body-centered-cubic α-Fe, cubic FeO (S.G. Fm3m) and cubic Fe3O4 (S.G. Fd3m) are indexed in the spectrum. The occurrence of the wüstite is due to an incomplete reduction reaction Fe + Fe3O4 = 4 FeO, activated by the high deformation energies developed during the milling. The reaction is incomplete because the Bragg reflections of initial Fe and Fe3O4 powders are also present in the sample. With increasing the temperature, as expected, the Bragg reflections are narrower due to the increase of the grain size. For the sample annealed at 200°C we observe the gradual decrease of the relative intensity of the main Bragg peaks of the wüstite. Meanwhile the α-Fe and Fe3O4 Bragg reflections increase compared to the 25°C spectrum.
At 450°C, sharp and intense Bragg lines are observed for the α-Fe and Fe3O4 phases at the expenses of FeO whose relative intensity reaches only about 7% of Fe3O4 phase. The strong reduction of the FeO content proves that the redox reaction that produced the wüstite is reversible and with increasing the annealing temperature up to 450°C, iron and magnetite become the predominant phases.
Hysteresis loop FC@5T at 4.2 K for the as-milled sample (Figure 2) exhibits a shift of the coercive field towards negative values, compared to the loops ZFC at 4.2 K and at 280 K. Coercivity increases from 41 mT at 280 K to 80 mT at 4.2 K and reaches 138 mT for the FC@5T loop. The exchange bias field calculated in the as-milled state is about 45 mT. The hysteresis loops FC@5T at 4.2 K for the samples annealed at 250°C and 400°C present a less pronounced shift toward towards negative values. The exchange bias field decreases with increasing the annealing temperature (inset of Fig. 2) down to 8 mT for the sample annealed at 450°C. Since the wüstite content decreases also with increasing the annealing temperature, it seems that the exchange bias field observed in the Fe / Fe3O4 mixed nanopowders is mainly due to the high fraction of FeO formed during milling. Also, the high degree of disorder and important number of FM / AFM and FM /FI interfacial regions may account for the observed exchange bias in the ball milled mixed Fe / Fe oxide nanopowders.

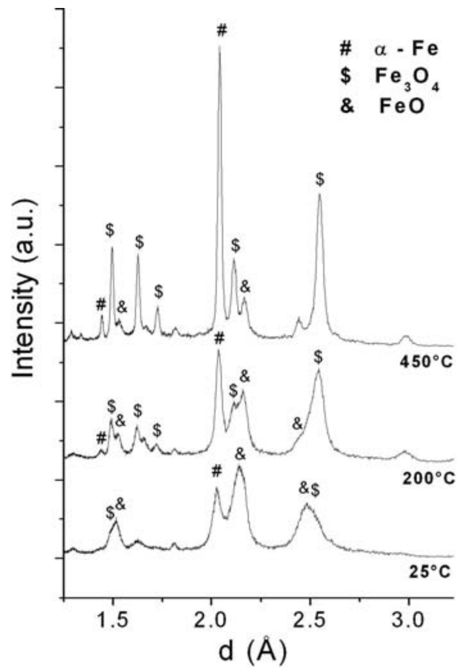

Fig. 1 X-ray diffraction spectra taken at 25°C, 200°C and 450°C for the Fe / Fe3O4 as-milled sample. The spectra are given in units of reticular distance d.

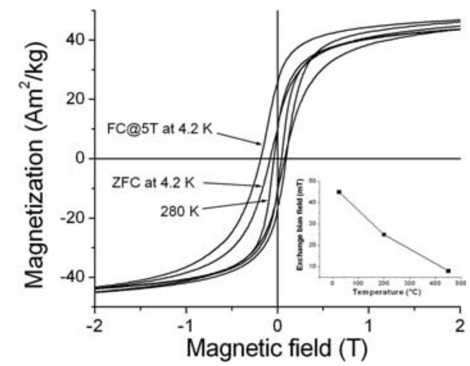

Fig. 2 Hysteresis loops of the as-milled sample: ZFC at 4.2 K, at 280 K and FC@5T at 4.2 K, magnified in the low field part. Inset: the exchange bias fields vs. annealing temperature.

Magnetic properties of high Bs Fe-based amorphous powders produced by Spinning Water Atomization Process (SWAP).

I. Otsuka[1], K. Wada[1], Y. Maeta[1], T. Kadomura[1], M. Yagi[2]
1. EPSON ATMIX CORPORATION, Hachinohe-shi, Aomori-ken, Japan; 2. Sojo University, Kumamoto, Japan

The authors have successfully developed Fe-based amorphous powders by our original atomization process “Spinning Water Atomization Process (SWAP)” [1]. Today, the very low loss consolidated cores made of Fe76 system amorphous powders with good magnetic-softness are widely used for switching power sources of electronic equipment. For further development, in order to deal with the recent progress of miniaturization and high output current of power supplies, amorphous powder cores with high magnetic induction Bs are essential.

In the present work, high Bs Fe-based amorphous powders were produced by a newly improved SWAP having extremely high-cooling rate over 10^6 K/s [2].

The composition of alloy powders were $Fe_x(Si_{0.7}B_{0.3})_{98-x}C_2$ {x = 78,79,80,81,83,84 at%}. The particle sizes of powder used for magnetic property measurements were below 150 micrometers in diameter. Annealing of the powders was carried out at 578-728K for 3.6Ks in a nitrogen atmosphere. Examination of structure and morphology were carried out by using X-ray diffractometry (XRD) and scanning electron microscopy (SEM), respectively. The specific gravity of powder was measured by gas pycnometer. The magnetic properties were measured by vibrating sample magnetometer (VSM) with maximum applied field of 20 kOe.

The morphology of powder observed by SEM is shown in Fig.1. Smaller particles were spherical, and lager particles were rather flat with round edges. Fig.2 shows the result of XRD of Fe-Si-B-C alloy powders. In the powder particle size -150 micrometers, the broad peak providing to be in the amorphous state was retained for up to the $Fe_{83}(Si_{0.7}B_{0.3})_{15}C_2$ powder, where as a peak was slightly observed for the $Fe_{84}(Si_{0.7}B_{0.3})_{14}C_2$ powder. Fig.3 shows the saturation flux density (Bs) and coercive force (Hc) of the powders. The saturation flux density Bs of powders increased with increasing iron content. The Bs value for the $Fe_{83}(Si_{0.7}B_{0.3})_{15}C_2$ powder was 1.64 T, which was 31% higher than that of our previously developed Fe76 system amorphous powder [3], and comparable to a newly developed high Bs Fe-based amorphous ribbon [4]. On the other hand, although the coercive force was also increased with increasing iron content, a fairly low level of about 0.50 – 0.90 Oe was kept for up to the Fe83 system powder. The considerable increase of coercive force for the Fe84 system was thought to be closely related to the crystallization, as shown in Fig. 2.

The high Bs amorphous powders obtained in this study are expected to be markedly available for downsizing of magnetic cores.

[1] M. Yagi, H. Nakanishi, I. Otsuka, H. Yamamoto, H. Satake and A. Shintani, J. Magn. Soc. Jpn., 26, 513-517 (2002).

[2] I. Otsuka, K. Wada, Y. Maeta, A. Watanabe, H. Izaki and M. Yagi, Abstract of 10th joint M.M.M/INTERMAG, 390, FQ-06 (2007)

[3] I. Endo, I. Otsuka, R. Okuno, A. Shintani, M. Yoshino and M. Yagi, IEEE Trans. Magn., 35, 3385 (1999)

[4] Y. Ogawa, M. Naoe, Y. Yoshizawa, R. Hasegawa, Journal of M.M.M., 304, 675-677 (2006)

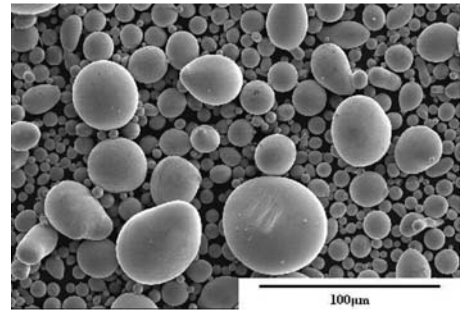

Fig.1 Morphology of the powder (-150µm) produced by SWAP.

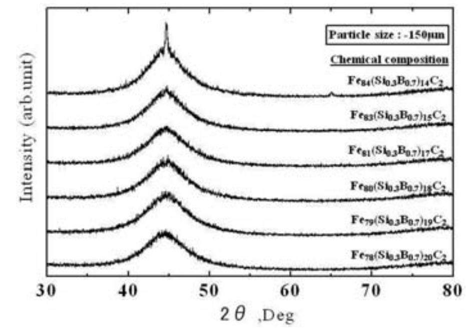

Fig.2 X-ray diffraction patterns of Fe-based alloy powders.

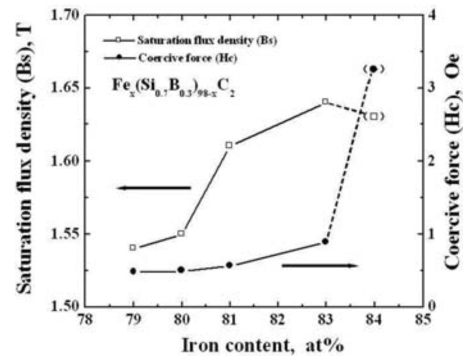

Fig.3 Saturation flux density Bs and coercive force Hc.

Study on the microstructure and soft magnetic properties of Ni-Fe particles synthesized by a conventional and a microwave-assisted polyol method.

Y. Shimada[1], Y. Endo[1], S. Okamoto[2], M. Yamaguchi[1], O. Kitakami[2]
1. Dept. of Electrical and Communication Engineering, Tohoku University, Sendai, Japan; 2. IMRAM, Tohoku Univ., Sendai, Japan

Particulate materials with high permeability are currently of practical use at high frequencies because they have high resistivity which suppresses eddy current loss. Recently we reported composites(1) which include 70nm Permalloy particles and 1 micron Fe particles exhibiting enhanced permeability for a certain volume ratio maintaining the high resistivity feature. For further improvement a method to synthesize submicron particles with a good soft magnetic property at a higher production rate must be developed. From this standpoint we performed an investigation of Permalloy nanoparticles synthesized by a conventional polyol method(CPM) in comparison with a microwave-assisted polyol method(MWPM) which was reported to accelerate a chemical reaction. The particle morphology, crystal structure, magnetization characteristics, high frequency permeability and variation by heat treatment are studied. The chemical process for synthesizing nanoparticles is similar to that reported by Viau et.al.(2). Chlorides of Ni and Fe were dissolved into ethylene glycol with Ni/Fe ratio 50/50 and concentration of 0.2M per litter. The solvent was kept at 155 degrees for 15min. either by a heater or in a microwave reactor and cooled to RT. Particle size was controlled by adding an appropriate amount of K2PtCl4 solution. Annealing was made at 250 and 350 degrees for 1 hour in Ar+H2 atmosphere. Firstly it was confirmed that XRD peaks for all particle sizes can be identified as those from Ni80Fe20 alloy except for small-angle broad peaks which indicate inorganic residuals and another small-angle weak peak suggesting iron oxide that is often found for MWPM. It should be stressed that composition close to Ni80Fe20, saturation magnetization of about 80emu/g and coercivity of about 40 Oe are obtained for all samples regardless of particle size variation from 70 to 500nm. An example is shown in Figure 1. From the width of (111) peaks the crystal size in the particles is estimated to be 4-6 nm and again changes little regardless of large variation of the particle size. As was discussed in Ref.2, this suggests that the particles are assembly of nanocrystals of Ni80Fe20. These nanocrystals are responsible for the basic properties described above. As seen in Figure 2 the nanocrystals by MWPM grow faster than CPM by heat treatment up to 350 degrees, while the lattice spacing of (111) exhibits no significant change. The saturation magnetization increases up to 90-95emu/g which is close to the bulk value. Coercivity tends to decrease faster for MWPM than for CPM. For example, coercivity for the samples in Figure 2 decreases to 18 Oe for MWPM and to 30 Oe for PCM after heat treatment at 350 degrees. From SEM images it was found that the morphology of particles by CPM changes little by heat treatment while aggregation of the particles occurs for MWPM as seen in Figure 3.

In conclusion the magnetic properties of Ni80Fe20 particles by the polyol method are determined by nanocrystals in the particles and their magnetic properties vary little against large size difference. The nanocrystals tend to grow and improve their magnetic softness by heat treatment, but particle aggregation hinders higher temperature heat treatment. The MWPM has a higher potential to provide a high speed process for magnetically soft particles. Nanoparticle annealing in NaCl(3) which is effective to suppress particle aggregation is in preparation to establish a method to produce magnetically soft submicron particles.

(1) Y.Shimada, M.Yamaguchi, G.W.Qin, S.Okamoto and O.Kitakami, J.Appl.Phys., 101, 09M505 (2007).(2)G.Viau,F.Fievet-Vincent,F.Fievet, Solid State Ionics,84,259(1996)

(3)K.Elkins et.al., J.Phys.D,Appl.Phys.,38,2306(2005)

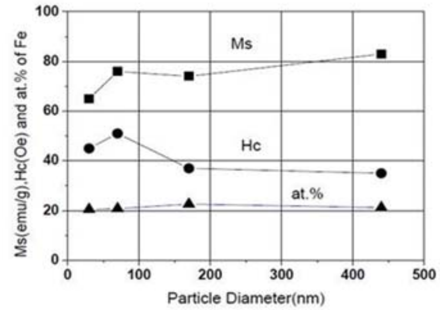

Figure 1. Dependence of composition, saturation magnetization and Hc on the particle size. The particles were systhesized by the conventional polyol method.

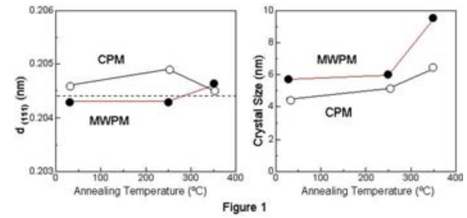

Figure 2. Variation of (111) lattice spacing and nanocrystal size by heat treatment.

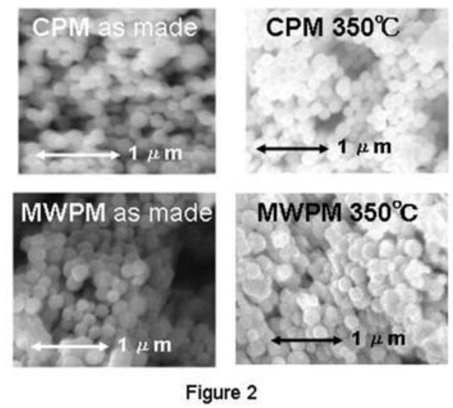

Figure 3. SEM images of as-made and after heat treatment at 350degrees.

GR-19

Synthesis, Phase Transfer and Magnetic Properties of Monodisperse Magnetite Nanocubes.

H. Yang[1], D. Hasegawa[2], M. Takahashi[1], T. Ogawa[2,3]
1. Niche, Tohoku University, Sendai, Japan; 2. Dep. of Electronics Engineering, Tohoku University, Sendai, Japan; 3. Cress, Tohoku University, Sendai, Japan

Magnetite (Fe3O4) is not only a common magnetic material but also an important class of half-metallic materials. The synthesis of Fe3O4 nanoparticles has long been of keen interest in magnetic data storage, biological application, and ferrofluids. [1, 2] Different shapes of particles can introduce electronic, optical, and magnetic properties that are different from those of their spherical counterparts. Hence, the effective control of the shape of magnetic nanoparticles is an emerging research topic.
In this work, we present a one-pot synthesis of monodisperse Fe3O4 nanocubes with controllable size from 6.0 to 30.0 nm. Using α-cyclodextrin (CD), Fe3O4 nanocubes were successfully "pulled" into water from hexane. The magnetic properties of Fe3O4 nanocubes with different size have been investigated.
Fe3O4 nanocubes were synthesized by a modified polyol process in organic phase. Fe(acac)3 and 1,2-hexadecandiol were dissolved in benzyl ether with oleic acid and oleyl amine and then refluxed. The phase transfer was conducted by vigorously stirring the mixtures of hexane suspensions of Fe3O4 nanocubes and equal volume of α-CD aqueous solution.TEM was employed to determine the morphology and size of Fe3O4 nanocubes. Magnetic measurements were conducted using a SQUID with fields up to 5 T and temperatures from 5 to 300 K.
Our approach enables the control of the reactivity of the carboxylic group of oleic acid and as a result the nucleation and growth dynamics of the particles. By careful adjustment of the stabilizer molar amount as well as the other reaction parameters we have obtained the size-controlled monodisperse magnetite nanocubes in one-pot without a laborious multistep seed-mediated growth. Fig.1 shows the TEM images of monodisperse Fe3O4 nanocubes with different sizes from 6.5 nm to 30.0 nm. With a size less than 15.0 nm, the nanocubes usually have a very narrow size distribution of less than 7% and the aspect ratios close to one. However, with a size more than 25 nm, the size distribution increases greatly and the aspect ratios located between 1 and 1.5.
By the formation of surfactant bilayers with charged hydrophilic ions of α-CD, Fe3O4 nanocubes can irreversibly transfer from hexane into water (as shown in Fig.2). The α-CD stabilized nanocubes can be stable for long periods of time in aqueous phase under ambient atmospheric conditions.
The hysteresis loops of the Fe3O4 nanocubess with different sizes at 300 and 5 K are shown in Fig. 3. The saturation magnetization (Ms) at 300K of Fe3O4 nanocubes with a size of 6.5, 15.0, and 30.0 nm were 39.5, 80.5, and 83.0 emu/g, respectively. The Fe3O4 nanocubes with a size less than 25.0 nm size possess typical superparamagnetic features at room temperature. However, the 30.0 nm Fe3O4 nanocubes shows a ferromagnetic behavior with a high Ms close to that of the commercial magnetite powder. The field-dependent magnetizations at 5 K are presented in Fig. 3b. The Fe3O4 nanocubes with three different sizes show a size-dependent ferromagnetic behavior at 5K. The HC, increased from 190 Oe for 6.5 nm, to 500 Oe for 15.0nm and 790 Oe for 30.0 nm Fe3O4 nanocubes. The coercivity of magnetic nanocubes is surely related to the magnetic anisotropy. The volume of nanocubes is the dominant factor in the magnetic anisotropy of Fe3O4 nanocubes. As a result, the coercivity of Fe3O4 nanocubes is clearly increased with increasing nanocubes size. In addition, the high coercivity of 30.0 nm Fe3O4 nanocubes maybe also result from the shape anisotropy contribution since they have an aspect ratios of more than 1.

[1] S. Soeya, J. Hayakawa, H. Takahashi, et.al. Appl. Phys. Lett. 80, 823 (2002).
[2] S. Sun, H. Zeng, J. Am. Chem. Soc. 124, 8204 (2002)

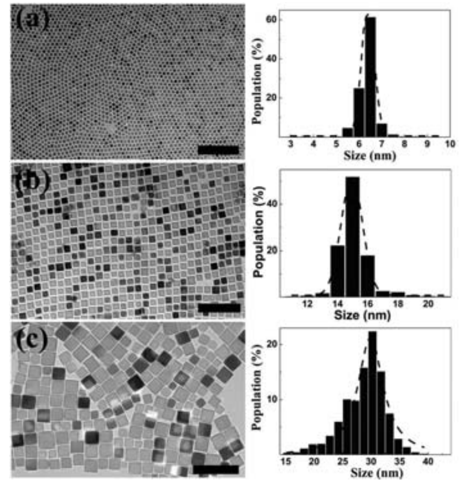

Fig. 1 TEM images of Fe3O4 nanocubes with different size (a) 6.5 nm, (b) 15.0 nm, and (c) 30.0 nm and the corresponding size distribution histograms (d), (e) and (f).

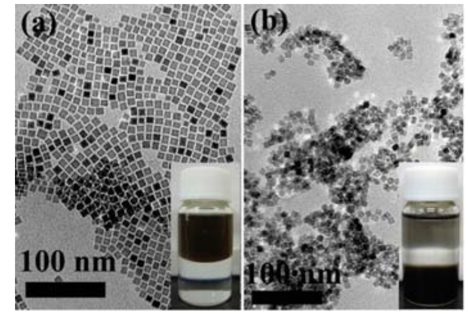

Fig. 2 TEM images and photographs (insert) of Fe3O4 nanocubes (a) before and (b) after phase transfer.

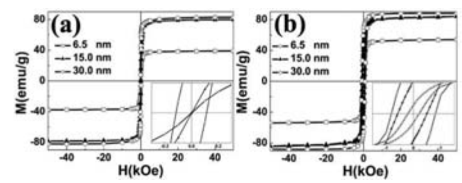

Fig. 3 Hysteresis loops at 300 K (a) and at 5K (b) for Fe3O4 nanocubes with different size of 6.5 nm, 15.0 nm, and 30.0 nm.

GR-20

Size controlled Fe nanoparticles through polyol process and their magnetic properties.

R. J. Joseyphus[1,2], K. Shinoda[2], D. Kodama[2], B. Jeyadevan[2]
1. Department of Physics, National Institute of Technology, Tiruchirappalli, India; 2. Graduate School of Environmental Studies, Tohoku University, Sendai, Japan

Materials with higher saturation magnetization are required for biomedical applications such as hyperthermia and drug delivery [1,2]. Although Fe3O4 is commonly used for such applications due to its biocompatibility, the saturation magnetization of the nanoparticles is only around 60 emu/g. In order to overcome the drawbacks associated with low saturation magnetization and biocompatibility core-shell nanoparticles with a highly magnetic core such as Fe and biocompatible shell such as Fe3O4 is an alternative solution. To prolong the duration of the nanoparticles in the circulatory system, the particles are coated with a polymer such as polyethylene glycol. Materials synthesized through chemical methods have the advantage that they could be easily surface modified for biological applications. The synthesis of pure Fe through chemical methods has been so far impossible to achieve due to the highly oxidizing nature of Fe. However we have successfully demonstrated the synthesis of highly magnetic submicron sized Fe through reduction in polyols [3]. Also the synthesis of highly magnetic Fe based alloy such as FeCo by polyol process has been already achieved [4]. In this paper we present our results on the synthesis of size controlled Fe nanoparticles through polyol process and their magnetic properties.

The precursors used in the synthesis of Fe by using polyol process are FeCl2.4H2O and NaOH. In a typical reaction, the precursors were introduced in ethylene glycol with an [OH-]/Fe molar ratio as high as 40 to enable reduction. The reaction temperature and duration were 170 oC and 2 min, respectively. H2PtCl6 is used as the Pt precursor. The Fe particles thus synthesized were washed with alcohol and characterized using X-ray diffraction, electron microscopy and magnetic measurements.

The Fe particles synthesized using 0.1 M of FeCl2.4H2O in ethylene glycol are found to exhibit cubic morphology with an average size around 150 nm. Size reduction of the Fe particles was achieved by introducing very low molar concentration of Pt as a nucleating agent. Figure 1 shows the variation in the particle size and saturation magnetization with increasing Pt concentration. It is observed from the figure that with increasing Pt concentration the average particle size decreases and becomes around 15 nm with the Pt concentration of 2x10-7 M. The saturation magnetization (Ms) which is 210 emu/g (bulk 218 emu/g) for the 150 nm particles also decreases and becomes 80 emu/g for the 15 nm particles which is commonly observed due to oxidation of Fe nanoparticles [5]. The particles showed cubic morphology which is retained with sizes upto 80 nm and it becomes spherical and agglomerated with further size reduction. The cubic shape of the Fe particles suggest the crystal structure (bcc for Fe) dependent shape under thermodynamic conditions [6] upto submicron regime and the equilibrium condition is lost when the size is reduced in the nanoscale using nucleating agents. Also with increase in Pt concentration to 0.05 M, Fe50Pt50 nanoparticles in the size range 2-4 nm could be obtained [7].

The stability of the Fe particles were checked by annealing the Fe powders in air by wrapping in an Al foil. The XRD pattern (not shown) showed that the particles are fairly stable on annealing even at 500 oC for 30 min (Ms=190 emu/g) and prolonged annealing for 15 h is required for the disappearance of the peak corresponding to Fe. It is also observed that the asprepared particles had a thin layer of around 3 nm thick oxide shell, whose thickness increased with annealing. The thin oxide shell may be responsible for preventing rapid oxidation of the cubic asprepared particles and showed higher saturation magnetization of 210 emu/g whereas the commercial powders showed a saturation magnetization of only 190 emu/g. The control of oxide shell thickness could be of much use in utilizing these Fe particles for biomedical applications.

[1] Q. A. Pankhurst, J. Connolly, S. K. Jones and J. Dobson, J. Phys. D: Appl. Phys. 36 (2003) R167-R181.

[2] R. E. Rosensweig, J. Magn. Magn. Mater. 252 (2002) 370-374.

[3] R. J. Joseyphus, D. Kodama, T. Matsumoto, Y. Sato, B. Jeyadevan and K. Tohji, J. Magn. Magn. Mater. 310 (2007) 2393-2395.

[4] D. Kodama, K. Shinoda, K. Sato, Y. Konno, R. J. Joseyphus, K. Motomiya, H. Takahashi, T. Matsumoto, Y. Sato, K. Tohji and B. Jeyadevan, Adv. Mater. 18 (2006) 3154-3159.

[5] C. H. Griffiths, M. P. O'Horo and T. W. Smith, J. Appl. Phys. 50 (1979) 7108.

[6] F. Dumestre, B. Chaudret, C. Amiens, P. Renaud and P. Fejes, Science 303 (2004) 821-823.

[7] R. J. Joseyphus, K. Shinoda, Y. Sato, K. Tohji and B. Jeyadevan, J. Mater. Sci (In Press).

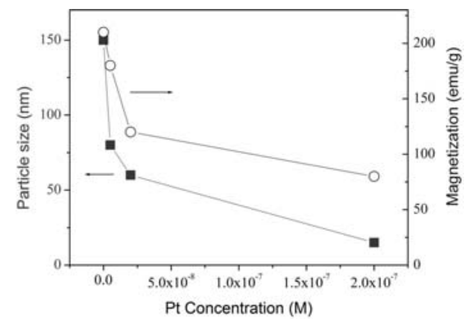

The variation of particle size and saturation magnetization of Fe with Pt concentration.

Magnetic behaviour of $Gd_4(Co_{1-x}Cu_x)_3$ compounds.

T. M. Seixas[1,2], M. A. Salgueiro da Silva[2], J. M. Machado da Silva[1,2], H. F. Braun[3], G. Eska[3]
1. Instituto de Física dos Materiais da Universidade do Porto (IFIMUP), Porto, Portugal; 2. Departamento de Física da Universidade do Porto, Rua do Campo Alegre, 687, 4169-007, Porto, Portugal; 3. Physikalisches Institut, Universitaet Bayreuth, D – 95440, Bayreuth, Germany

In order to study the effects caused by substituting Co for Cu on the magnetic properties of $Gd_4(Co_{1-x}Cu_x)_3$ compounds with $x = 0.05$, 0.1, 0.2, 0.3, SQUID magnetisation measurements were performed on polycrystalline samples in the temperature range 5 K – 300 K using applied magnetic fields from 0 to 5 T. Details of samples preparation and characterisation methodology are described elsewhere [1].

As shown in Fig. 1, the curves of the spontaneous magnetic moment ($M_S(T)$) corresponding to $x =$ 0.05, 0.1 exhibit essentially the same behaviour as that previously reported for ferrimagnetic Gd4Co3 [2], despite minor differences in their Curie temperatures and saturation moments ($M_S(0)$). For $x = 0.2$, however, a succession of two zero-field magnetic phases is apparent below the Curie point at $T_{C1} \equiv T_C \approx 211.3$ K: an intermediate phase, hereafter denoted FERRI I, extending from T_{C1} down to a second critical temperature T_{C2} not exceeding 170 K, with a spontaneous magnetization clearly lower than the spontaneous magnetization of compounds with $x < 0.2$ in the same temperature range; a low temperature phase, hereafter denoted FERRI, which orders below T_{C2} and shows a $M_S(T)$ curve similar to that of the compounds with $x < 0.2$ below their respective Curie temperatures. For $x = 0.3$, a single magnetic phase (FERRI) is again present with a lower Curie temperature.

The Arrot plots of the $Gd_4Co_{2.4}Cu_{0.6}$ compound at temperatures within the region of the FERRI I phase reveal the existence of two magnetic moment states (M_S, spontaneous; M_{HF}, high field) and a field-induced transition between them. At 175.0 K, the ratio of the values of the two magnetic moments is $M_S/M_{HF} \approx 0.68$. The existence of a high field metamagnetic process suggests that, within the FERRI I phase, due to a competition between anisotropy and exchange interactions, either a fraction of the Gd^{3+} magnetic moments or just a component (e. g. the basal component) of each Gd^{3+} magnetic moment is disordered. This conclusion is consistent with the low field isofield magnetisation curves.

A magnetic phase diagram based on isothermal and low field isofield magnetic measurements is shown in Fig. 2. It exhibits a particularly interesting magnetic diversity, including c-axis, canted and partially disordered ferrimagnetism.

As seen in Fig. 3, the saturation magnetic moment of Co atoms decreases exponentially with increasing Cu content. Such behaviour of $M_{Co}(x)$ may originate from the combined effect of the 3d band filling by 4s electrons from Cu atoms and a strong dependence of Co moment on the number of local Co neighbouring atoms.

[1] T. M. Seixas et al, accepted for publication in J. Appl. Phys.

[2] T. M. Seixas et al, Physica B 353 (2004) 34-40.

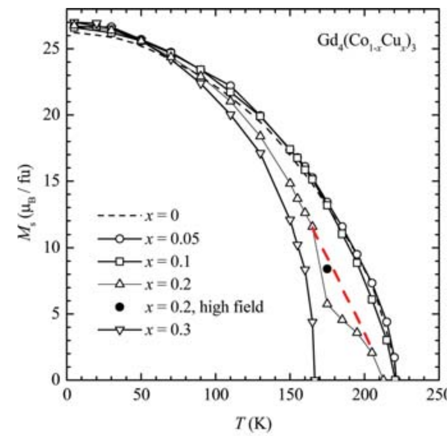

Fig. 1 Spontaneous magnetisation of $Gd_4(Co_{1-x}Cux)_3$ compounds. For $x = 0.2$, an additional point corresponding to the high field moment state is shown, together with the hypothetical temperature variation of such high field magnetisation (dashed line).

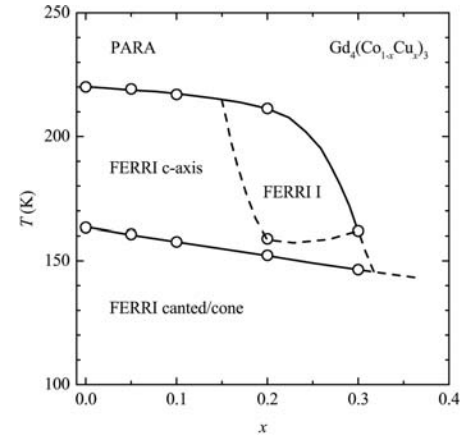

Fig. 2 Magnetic phase diagram of $Gd_4(Co_{1-x}Cu_x)_3$ compounds.

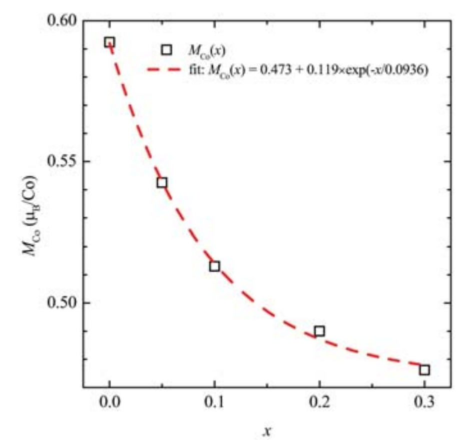

Fig. 3 Saturation magnetic moment of Co in $Gd_4(Co_{1-x}Cu_x)_3$ compounds.

GR-22

Exact Calculation of The Magnetostatic Interaction in Arrays of Nanowires.

J. Velázquez
CAI Difracción Rayos X, Universidad Complutense de Madrid, Madrid, Spain

The magnetostatic interaction between nanowires is a subject of both theoretical and technological interest because of its effect on the magnetic properties of arrays of nanowires [1] and the possibility of magnetic recording for perpendicular magnetic storage media [2]. Although the magnetostatic interaction between magnetic wires is often treated as dipolar in a first approximation [3], it shows a strong non-dipolar character enhanced by the short distances between nanowires in an array [4].
The magnetostatic interaction between nanowires is due to the coupling between the field created by each nanonowire due to its magnetization and the magnetization of the neighboring nanowires. The aim of this work is to develop an exact calculation of the magnetic field created by an uniformly magnetized wire.
By considering a system of reference with origin in the centre of the wire and the z-axis parallel to its axis, and taking into account the expression of the inverse of the distance (from an element of surface of the wire to any point of the space) in a series of products of Bessel's functions, the expression of the magnetic potential, V_m, is:
$V_m = (MR/2)\int(d\lambda/\lambda)Jo(\lambda r)J1(\lambda R)\ [\exp(-\lambda|z-(L/2)|)-\exp(-\lambda|z+(L/2)|)]$
varying λ between 0 and ∞ and being M, L, and R the magnetization, length and radius of the wire, respectively. Jo and J1 are Bessel's functions and r is the radial distance to the axis of the wire. Note that the potential depends on r and z. From V_m and using partial derivatives, the radial, H_R, and axial, H_Z, components of the field created by an uniformly magnetized wire can be obtained: $H_R(r,z)=-\partial Vm(r,z)/\partial r$, $H_Z((r,z)=-\partial Vm(r,z)/\partial z$. These fields are expressed in integrals of products of Bessel's functions, and asymptotic expressions can be obtained for (R/L)<<1 then coinciding with the dipolar case (radial dependence with r-3).
The attached Figure shows the dependence of H_Z and H_R with the distance from the axis of nanowire, x, where x=(r/R),with R = 15 nm, L = 4 µm (L/R= 267), $\mu_o M$ = 1 T, for the axial coordinate z*= 1.05, being z*=z/(L/2), that is just above the end of the wire.
As can be seen, the axial field H_Z decreases with distance from the axis of the wire, while H_R shows a maximum. This maximum depends on the relation (L/R) so that the smaller it is the maximum moves towards smaller values of x and higher values of field. (see inset in the Figure). Moreover, the distance xo such that H_Z (xo,z*) =H_R (xo,z*) only depends on L and z* (in fact, the dependence is linear) and is independent of M and R. As for x> xo is H_R (x, z)> H_Z (x, z), the process of magnetization in a nanowire is influenced by this interactive field perpendicular to the axis of the nanowire. The design of arrays of nanowires, with given distances between nanowires (and where each nanowire interact with all its neighbors), should take into consideration this fact: axial coupling for short distances and radial coupling for something greater distances, depending the limit distance on the length of the nanowire (xo increases linearly with L) and the axial coordinate z (xo decreases linearly with z*).
Acknowledgments
The author wishes to thank Prof. Manuel Vázquez for helpful discussions

[1] C. A. Ross, M. Hwang, M. Shima, J. Y. Cheng, M. Farhoud, T. A. Savas, Henry I. Smith, W. Schwarzacher, F M. Ross, M. Redjdal, and F. B. Humphrey, Phys. Rev. B., vol. 65, pp. 144417-8, 2002

[2] K. Nielsch,, R.B. Wehrspohn, J. Barthel, J. Kirschner, S.F. Fischer, H. Kronmüller, T. Schweinböck, D. Weiss, U. Gösele, J. Magn. Magn. Mat., 249,pp. 234–240, 2002

[3] L.C. Sampaio, E.H.C.P. Sinnecker, G.R.C. Cernicchiaro, M. Knobel, M.Vázquez, and

J. Velázquez, Phys. Rev. B, vol. 61 (13), p. 8976-8983, 2000; C.A. Ramos, E. Vasallo Brigneti, M. Vázquez,, Physica B, vol. 354 195–197, 2004

[4] J. Velázquez, K. Pirota, and M. Vázquez, IEEE Transactions on Magnetics, 39 (5), pp. 3049-3051, 2003.

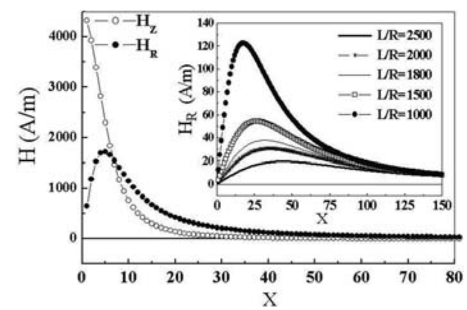

Dependence of H_Z and H_Z with the distance to the axis of the wire

Performance Analysis of Flyback Converter Based on Time-stepping FEA Incorporating Magnetic Hysteresis Effect.

J. Chen[1], *Y. Guo*[2], J. Zhu[2], Z. Lin[2]
1. College of Electromechanical Engineering, Donghua University, Shanghai, China; 2. Faculty of Engineering, University of Technology Sydney, Sydney, NSW, Australia

1. Introduction

This paper presents a general method for flyback converter transient performance analysis based on the time-stepping finite element analysis (FEA) of electromagnetic field considering magnetic hysteresis effects. The soft magnetic core hysteresis is modeled by an improved scalar Preisach model [1], and is integrated in the FEA model. A new coupling method based on the system state observer, which takes advantage of both the direct and indirect methods, is introduced. The system model is implemented in Matlab/Simulink. The developed model demonstrates a good example how the FEA can be conveniently coupled with electrical and electronic circuit analysis to provide high accuracy. As an example, an existing flyback dc/dc converter is simulated. The effects of magnetic hysteresis on the converter performance are clearly shown by the simulation results with and without incorporating the Preisach model of magnetic hysteresis.

2. Coupling of FEA with Hysteresis Model and Feeding Circuit

Fig.1 shows the flyback converter circuits corresponding to three different operational modes. The FEA region is marked by the dotted line, which couples the feeding and output circuits. In the improved Preisach model, the magnetization M corresponding to magnetic field strength H can be derived as in Fig.2. The most significant advantage of the improved model is that its implementation only needs the limiting B-H loop, which is usually available from manufacturer.

Solving the governing equation (Fig.3) with the relative permeability determined by the Preisach model and the applied current density steps in time, we can obtain the magnetic field distribution in the transformer in each time step. The differential inductance of the primary winding of the transformer can then be calculated, where k refers to the k-th time step.

Fig.4 gives the state-space variable equations of feeding circuit in different operational modes and uniform format. Description of the equations, as well as the coupling method based on system observer, will be detailed in the full paper.

3. Simulation

An existing flyback dc-dc converter is simulated. The specifications include: input voltage of 370 Vdc; output voltage/current of 5V/3.6A; 67 kHz; duty ratio of 0.33; winding turns of 96/8; TDK PC40-EE25 ferrite for transformer core [2].

The developed model is implemented in Simulink and comprehensive performances of the converter are simulated. As an example, Fig.5 shows the primary winding current, where the red (inner) line is obtained by including hysteresis and the blue (outer) line is obtained by considering the initial B-H curve only. The effect of magnetic hysteresis on the converter performance is clearly shown.

Complete simulation and experimental results will be presented in the final paper.

[1] SYR Hui, IEEE Trans Power Electro, 11(2), 251 (1996)

[2] JX Chen, IEEE IAS Annual Conf, 2295 (2007)

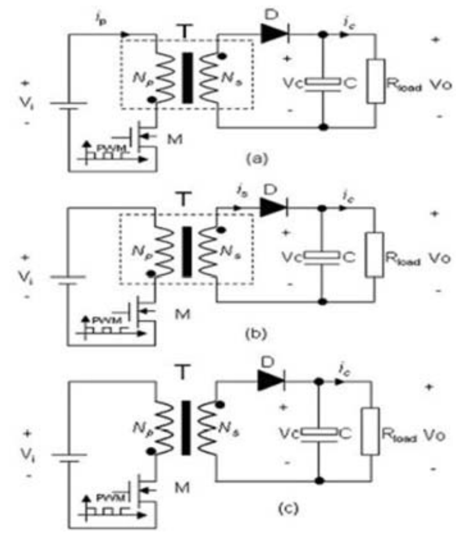

Fig.1 Flyback converter in continuous and discontinuous current modes

$$M(H) = T(H, -H)$$
(initial curve)
$$M(H) = M(H^k) - 2T(H^k, H)$$
(downward trajectory)
$$M(H) = M(H^k) + 2T(H, H^k)$$
(upward trajectory)
$$T(\alpha,\beta) = \frac{M_u(\alpha) - M_d(\beta)}{2} + F(\alpha)F(-\beta),$$
$$F(a) = \begin{cases} [M_d(a) - M_u(a)]/\sqrt{4M_d(a)} & ;(a \ge 0) \\ \sqrt{M_d(-a)} & ;(a < 0) \end{cases}$$

Fig.2 Hysteresis modeling

$$\nabla \times \left(\frac{1}{\mu_r} \nabla \times \mathbf{A} \right) = \mu_0 \mathbf{J}_s$$
$$\begin{cases} L_p = L(i^k) = \dfrac{d\psi^k}{di^k} = \dfrac{\psi^k - \psi^{k-1}}{i^k - i^{k-1}} \\ \psi^k = 2W_k / i^k \end{cases}$$

Fig.3 Governing equation and differential inductance

Mode 1
$$\begin{cases} L_p \dfrac{di_p}{dt} + R_p i_p = V_i \\ (R_c + R_{load}) C \dfrac{dV_c}{dt} + V_c = 0 \end{cases}$$

Mode 2: ip=0
$$\begin{cases} L_s \dfrac{di_s}{dt} = R_s i_s + R_c C \dfrac{dV_c}{dt} + V_c \\ R_{load} i_s = (R_c + R_{load}) C \dfrac{dV_c}{dt} + V_c \end{cases}$$

Mode 3: ip=is=0
$$(R_c + R_{load}) C \frac{dV_c}{dt} + V_c = 0$$

Output equation
$$V_o = (i_s - C \frac{dV_c}{dt}) R_{load}$$

Uniform format
$$\begin{cases} s(t) = f(X, I_{pm}, Y_{rated}, s_{pwm}, t) \\ X'(t) = A(s)X(t) + B(s)U(t) \\ Y(t) = CX(t) \end{cases}$$

Fig.4 State-space variable equations

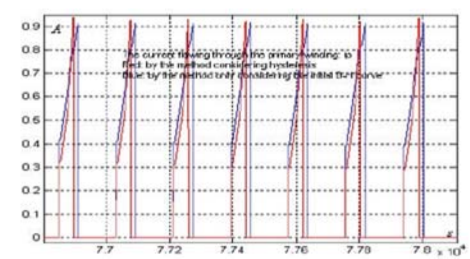

Fig.5 Primary winding current

GS-02

Chaoization of Permanent Magnet Synchronous Motors Using Stator Flux Regulation.

Z. Wang, K. Chau
Department of Electrical and Electronic Engineering, The University of Hong Kong, Hong Kong, China

I. INTRODUCTION

Because of the random-like but bounded nature, chaos has been positively utilized in many industrial applications [1]. Rather than using mechanical means to generate chaotic motion for some niche applications such as mixing and compaction, electrical chaoization of motors takes the definite advantages of lightweight and compact size. In [2], a design-oriented approach was developed to chaoize a doubly salient permanent magnet motor for soil compaction. Although it can spontaneously produce chaotic motion once power on, this design-oriented approach is inflexible since the motion boundary can not be tuned once the motor is designed. In [3], a time-delay feedback control approach was developed to chaoize a DC motor for liquid mixing. Although the motion boundary can be controlled by tuning the feedback control parameters, the corresponding torque response is sluggish. Also, the use of DC motors for industrial application is inefficient and needs regular maintenance.

The purpose of this paper is to propose and implement a new stator flux regulation based direct torque control approach to chaoize the permanent magnet synchronous motor (PMSM). Thus, it can produce electrically chaotic motion, while offering the advantages of controllable chaotic boundary, fast torque response, inherently high efficiency and maintenance-free operation.

II. CONTROL SCHEME

For a PMSM with no saliency, the electromagnetic torque T can be expressed as $(3/2)(n_p/L_s)|\psi_s||\psi_f|\sin\delta$ where n_p is the number of pole pairs, L_s is the stator inductance, ψ_s is the stator flux, ψ_f is the rotor flux, and δ is the angle between ψ_s and ψ_f. Consequently, T can be directly controlled by regulating the ψ_s. Fig. 1(a) shows this direct torque control block diagram. The reference torque T^* is generated by a sliding mode speed controller, which is robust to load changes and system disturbances. By defining the sliding surface S as $\omega\text{-}\omega^*+c\int(\omega\text{-}\omega^*)d\tau$, it can be derived that $T^*\text{=-}J g\,\mathrm{sgn}(S)+B\omega$ where J is the rotor inertia, B is the viscous damping, c is a positive control parameter, and g should be large enough to satisfy $g>|c(\omega\text{-}\omega^*)|$. Then, Fig. 1(b) shows the selection of switching status for stator flux regulation. It is determined by the section where ψ_s locates, and the outputs of two hysteresis loops for torque and flux. By properly choosing the control parameters for stator flux regulation such as the hysteretic limitation of flux $\Delta\psi$, the chaotic motion with controllable boundary can be realized.

III. SIMULATION AND EXPERIMENTAL RESULTS

The key motor parameters for the proposed chaoization are listed in Table 1. Firstly, by setting $\Delta\psi$ as 0Wb, the stator flux trajectory and rotor speed waveform are simulated as shown in Fig. 2. It illustrates that chaotic motion can be successfully generated, exhibiting random-like but bounded nature. Then, by changing $\Delta\psi$ to 0.01Wb, the corresponding simulated trajectory and waveform are shown in Fig. 3. It confirms that the boundary of chaotic motion can be successfully regulated, which is an important feature that cannot be achieved by design-oriented chaoization.

In order to verify the proposed chaoization, the whole system is prototyped. Figs. 4 and 5 show the measured stator flux trajectories and rotor speed waveforms when $\Delta\psi$=0Wb and $\Delta\psi$=0.01Wb, respectively. They well agree with the simulated trajectories and waveforms. It should be noted that the corresponding chaotic patterns do not match in general, which is actually the random-like nature of chaos. Nevertheless, the corresponding boundaries do closely match.

[1] Z. Wang, K. T. Chau and C. Liu, "Improvement of electromagnetic compatibility of motor drives using chaotic PWM," IEEE Trans. Magn., vol. 43, no. 6, pp. 2612-2614, 2007.

[2] K. T. Chau and Z. Wang, "Design of permanent magnets to chaoize doubly salient permanent magnet motors for electric compaction," J. Appl. Phys., vol. 99, pp. 08R306:1-3, 2006.

[3] S. Ye and K. T. Chau, "Chaoization of DC motors for industrial mixing," IEEE Trans. Ind. Electron., vol. 54, no. 4, pp. 2024-2032, 2007.

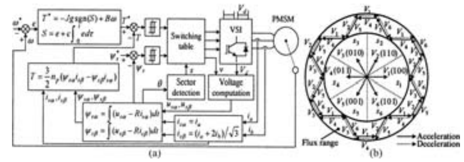

Fig. 1. Direct torque control based on stator flux regulation: (a) Block diagram; (b) Selection of switching status.

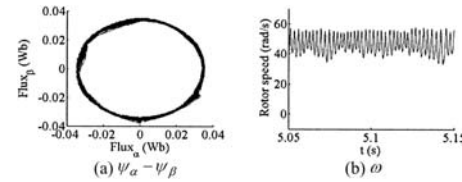

Fig. 2. Simulated results with $\Delta\psi$=0Wb.

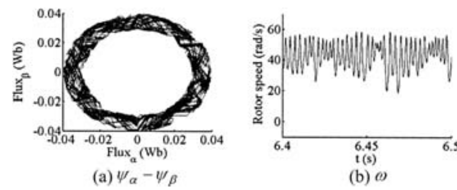

Fig. 3. Simulated results with $\Delta\psi$=0.01Wb.

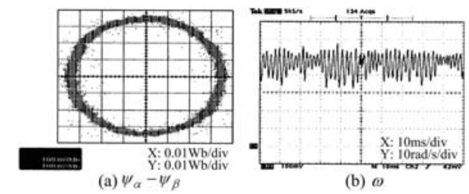

Fig. 4. Measured results with $\Delta\psi$=0Wb.

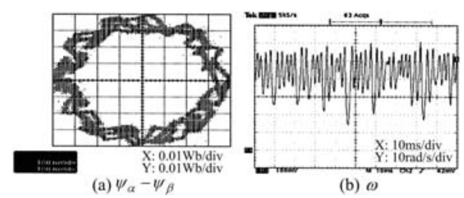

Fig. 5. Measured results with $\Delta\psi$=0.01Wb.

TABLE 1. Motor parameters

Number of pole pairs	4
PM flux	0.0344 Wb
Stator resistance	4.3 Ω
Stator inductance	6.0 mH
Rotor inertia	7×10^{-6} Nm/(rad/s^2)
Viscous damping	6.88×10^{-6} Nm/(rad/s)

GS-03

Fundamental Resarch about Parameter Design of Contactless Power Station for Moving Electric Loads.

N. Nakajima, Y. Kakubari, F. Sato, H. Matsuki
Tohoku University, Sendai, Japan

1. Background
Contactless Power Station (CLPS) is a power transmission device. When a moving electric load is supplied power, many problems will occur in the case that its terminal contacts like a pantograph of a train. For example, electrification, generation of dust by the wear of the terminal. To solve these problems, we think contactless power supply by electromagnetic induction is effective.
2. Principle
In this research, CLPS is a power transmission system using a transformer which is constructed by two flat coils facing to each other. Fig.1 is Equivalent circuit schematic of this transmission system. Now, we analyze appropriate parameter which stabilizes output voltage.
In Fig.1, the ratio of output voltage and input voltage are expressed like formula (1).
Formula (1) HERE
Output voltage depends on load resistance,
so output voltage decreases as load resistance decreases. Internal impedance and output open voltage of this equivalent circuit are expressed like formula (2) and formula (3).
Formula (2) HERE
Formula (3) HERE
Internal impedance causes output voltage fluctuation by load disturbance, so we needed to device internal impedance minimization method to restrain output voltage fluctuation. From formula (2), the condition that internal impedance becomes zero is expressed like formula (4), and formula (5) expresses output voltage in this time.
Formula (4) HERE
Formula (5) HERE
Formula (5) indicates that output voltage is not depends on the load reactance. So we are able to avoid the effect of impedance which decreases voltage when we set the value of primary capacitor as it fills the formula (4).
Additionally, the capacitance of secondary capacitor is configured from the viewpoint that the transmission efficiency becomes maximum value. From the formula of the transmission efficiency of this system (Fig.1), the capacitance of secondary capacitor which makes transmission efficiency maximum is formula (6) (r1 and r2 is the resistance of the primary and secondary coil).
Formula (6) HERE
When we make coils, we often use strand wires in parallel to make a coil that has the inductance and the size we want. This time, difference of current is often generated by difference of inductance which is generated between each strand wire. As a method to control this difference of current, we can use the method that we divide the resonant capacitors into number of strand wires and connect the capacitors and the strand wires (Fig.2 and Fig3). Formula (7) is current ratio of two strand wires when a capacitor is divided. Formula (8) is the one when a capacitor is not divided.
Formula (7) HERE
Formula (8) HERE
Fig.4 is characteristic of current ratio vs. inductance ratio of each strand wire. According to Fig.4, the current ratio with non divided capacitor fluctuates widely. One the other hand, the current ratio with divided capacitors hardly fluctuates.

3. Consideration
We transmitted power with the scale model which we made experimentally on condition of output voltage stabilization. As a result, we succeeded in restraining voltage decrease in Fig.5. And Fig.6 shows load characteristic of efficiency. From the result, the precepts of stable contactless electricity supply for moving electric loads that have large fluctuation of load resistance are expected. In the future, we will put more proper setting for moving electric loads in perspective of coil geometry.

$$\frac{V_{out}}{V_{in}} = \frac{\omega^2 C_{1s} k \sqrt{L_1 L_2}}{AR + j\omega L_2 \left\{\omega^2 C_{1s} L_1 \left(1-k^2\right) - 1\right\}} \quad \ldots(1)$$

$$A = -\omega^4 C_{1s} L_1 C_2 L_2 (1-k^2) + \omega^2 (C_{1s} L_1 + C_2 L_2) - 1$$

$$Z_0 = \frac{j\omega L_2 \{1-\omega^2 L_1 C_{1s}(1-k^2)\}}{1-\omega^2(L_1 C_{1s} + L_2 C_2) + \omega^4 L_1 C_{1s} L_2 C_2 (1-k^2)} \quad \ldots(2)$$

$$\frac{V_{out(open)}}{V_{in}} = \frac{\omega^2 k C_{1s} \sqrt{L_1 L_2}}{-\omega^4 C_{1s} L_1 C_2 L_2 (1-k^2) + \omega^2 (C_{1s} L_1 + C_2 L_2) - 1} \quad \ldots(3)$$

$$C_{1s} = \frac{1}{\omega^2 L_1 (1-k^2)} \quad \ldots(4)$$

$$\left.\frac{V_{out}}{V_{in}}\right|_{Z_0=0} = \frac{1}{k}\sqrt{\frac{L_2}{L_1}} \quad \ldots(5)$$

$$C_2 = \frac{(R+r_1)\sqrt{r_1}}{\omega^2 R \sqrt{L_2 (r_1 L_2 + k^2 r_2 L_1)}} \quad \ldots(6)$$

$$\frac{I_2}{I_1} = \frac{M-L_1}{M-L_2} \quad \ldots(7)$$

$$\frac{I_2}{I_1} = \frac{2+\omega^2 C_{1s}(M-L_1)}{2+\omega^2 C_{1s}(M-L_2)} \quad \ldots(8)$$

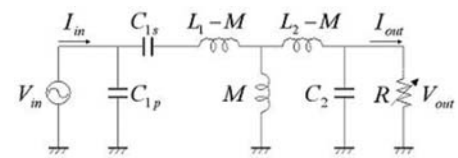

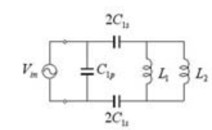

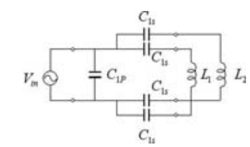

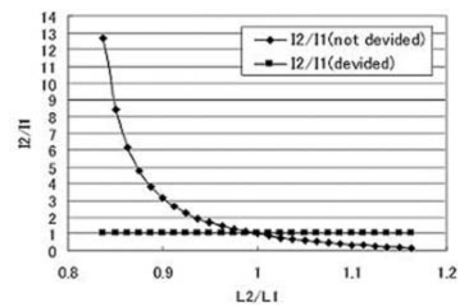

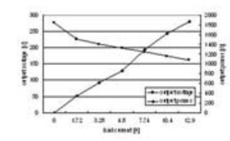

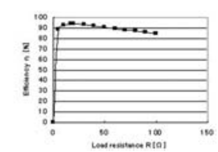

Experimental Verification and Performance Analysis of Permanent Magnet Wind Turbine Generators considering Magnetic Losses using D-Q Axis Model.

S. Jang[1], *J. Choi*[1], K. Ko[1], B. Kim[2]
1. Chungnam National University, Dae-jeon, South Korea; 2. Korea Electric Power Research Institute, Daejeon, South Korea

Introduction

Owing to concern over the environment, there is currently a significant amount of interest in renewable sources of electrical power generation of which one of the most promising is wind power [1]. Generators for this application are widely classified into two types: one is gearbox-coupled generator such as an induction generator (IG), the other is gearless direct-coupled generator such as a permanent magnet synchronous generator (PMSG). Compared with the IG, the direct-drive wind PMSG have many advantages, such as a much reduced size of the overall system, a rather low installation and maintenance cost, etc [2]. Therefore, particular attention has been paid to study on the direct-drive wind PMSG such as design and performance analysis.

In order to implement the performance analysis of the PMSG, a variety of techniques such as finite element (FE) method, equivalent circuit method (ECM), method using d-q axis model can been employed. In particular, d-q axis model not only provides rapid and quite accurate performance analysis of the PMSG in itself but also can be easily coupled with dynamic model of the wind turbine and power conversion devices for dynamic analysis of wind power systems.

Therefore, this paper deals with experimental verification and performance analysis of PM wind turbine generator considering losses using D-Q axis model. First, voltage and output equations of the PMSG are derived from D-Q axis model. And then, mathematical expressions for losses such as core and copper losses are also made. Using these equations and MATLAB/SIMULINK, a simulation block diagram shown in Fig. 1 is obtained. Finally, the performance of the PMSG such as output power, efficiency and losses under various speed and load conditions are predicted. In particular, measurements and FE results for its performance are given to confirm the analysis.

Results and Discussion

Figure 2(a) shows a rotor and a stator of the PM wind turbine generator used in performance analysis. As shown in Fig. 2 (b), since predicted results for core loss are shown in good agreement with data provided by manufacturer, it can be judged that the values for derived coefficients (kh, ke and ka) in core loss equation of Fig. 2(b) are reasonable. The values and derivation procedures of coefficients will be given fully in final paper. Fig. 3 shows the performance analysis results of the PM wind turbine generator under various load and speed conditions. The results predicted by D-Q model are shown in good agreement with FE results and measurements. It can be seen that iron losses are not affected by the variation of the load, while they are varied by the rotational speed. It can also be seen that as the load and the rotational speed are increased, the output power decreases and increases, respectively. From the fact that the efficiency is much more affected by the variation of the load than speed, it can be predicted that the main loss of the PM wind turbine generator is the copper loss. Nevertheless, since the generator is a totally enclosed non-ventilated machine and is located on a tower out of doors in hot environments due to solar absorption, calculation of the iron loss has important meanings in terms of thermal sources. More detailed results, discussion and mathematical expressions will be given in final paper.

[1]A. J. G. Westlakes, J. R. Bumby and E. Spooner, IEE Proc,-Ekectr. Power Appl, vol. 143, no. 3, pp.269-280, 1996.

[2]W. Wu, V. S. Ramsden, T. Crawford, and G. Hill, IEEE Ind. Appl. Conf. vol. 1, pp.147-154, 2000

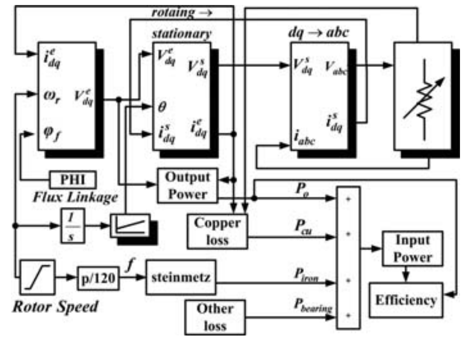

Fig. 1. Simulation block diagram for the performance analysis of the wind turbine PMSG.

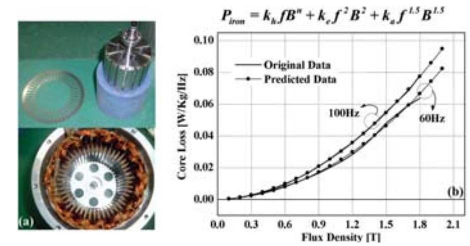

Fig. 2. (a) Manufactured stator and rotor of the wind turbine PMSG and (b) comparison of predictions with data provided by manufacturer for core loss.

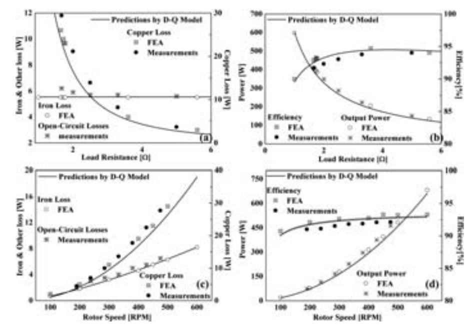

Fig. 3. Performance analysis: under various load and fixed speed conditions [(a) losses, (b) power and efficiency] and under various speed and fixed load conditions [(c) losses, (d) power and efficiency].

GS-05

Design, Fabrication and Experimental Validation of a Miniaturized Generator with Planar Coils via Genetic Algorithm.

P. Chao[1], J. Shen[2], E. Chiu[1], J. Huang[2]
1. Electrical and Control Engineering, National Chiao Tung University, Hsinchu, Taiwan; 2. Mechanical Engineering, Chung Yuan Christian Univ., Chung Li, Taiwan

This study presents an optimal design process of a miniaturized generator in size of 5x5x2mm3 using the method of Genetic Algorithm (GA) [1]. The associated experiments are also conducted to validate its performance. This generator is capable of serving as a transducer in a self-power system to scavenge energy from translational or rotational vibrations [2-10]. The obtained power could be applied to a rotor balancing ring [11], as schematically illustrated by Fig. 1, or to the pervasive networks of wireless sensor and communication nodes [12-13]. The designed generator (Fig. 2(a)) consists of patterned planar copper coils (Fig. 2(b)) and a multipolar hard magnet made of NdFeB (Fig. 2(c)), where the patterned coils are fabricated using the method of filament winding and the NdFeB magnet is magnetized to induce 1.1 Telsa around each pole. To perform modeling, a periodic magnetic model along the circumferential path of the magnet is first assumed with help from measured peak magnetic flux densities. This is followed by the application of Faraday's law, as illustrated by Fig. 3, to predict generated electromotive forces (emf's) in terms of the relative rotational speed between the magnet and coils. The predicted emfs are further validated by finite element analysis and experimental data, as shown in Fig. 4(a). It is also found that the generated current would be saturated to some limitation while the relative speed increased to a certain level, as shown in Fig. 4(b). Finally, the Genetic Algorithm is successfully applied to optimize the miniaturized generator, with varied geometric sizes, configuration and loop number of planar as design parameters.

[1] M. Mitchell, An Introduction to Genetic Algorithms. The MIT Press, 1998.

[2] S. Roundy, P. K. Wright, K. S. Pister, "Micro-electrostatic vibration-to-electricity converters", in Proceedings of the 2000 ASME International Mechanical Engineering Congress and Exposition, New Orleans, LA, USA, 2002.

[3] P. Glynne-Jones and N.M. White,"Self-powered systems: a review of energy sources", Journal of sensor review, vol. 21, No. 2, 2001, pp. 91-97.

[4] M. El-hami et al., "Design and Fabrication of a New Vibration-Based Electromechanical Power Generator," Sensors and Actuators A: Physical, vol. 92, nos. 1–3, 2001, pp. 335–342.

[5] M. Miyazaki et al., "Electric-Energy Generation Using Variable-Capacitive Resonator for Power-Free LSI," Proc. Int'l Symp. Low Power Electronics and Design (ISLPED), ACM Press, 2003, pp. 193–198.

[6] W.H. Ko, Piezoelectric Energy Converter for Electronic Implants, US Patent 3,456,134, US Patent and Trademark Office, 2004.

[7] P. Glynne-Jones et al., "Towards a Piezoelectric Vibration Powered Microgenerator," IEE Science, Measurement, and Tech., vol. 148, no. 2, Mar. 2001, pp. 68–72.

[8] G.K. Ottman, H.F. Hofmann, and G.A. Lesieutre, "Optimized Piezoelectric Energy Harvesting Circuit Using Step-Down Converter in Discontinuous Conduction Mode," IEEE Trans. Power Electrics, vol. 18, no. 2, 2003, pp. 696–703.

[9] S. Roundy, "Toward Self-Tuning Adaptive Vibration Based Micro-Generators," Proc. SPIE Int'l Symp. Smart Materials, Nanoand Micro-Smart Systems, SPIE Press, 2004, pp. 373–384.

[10] G.A. Lesieutre and C.L. Davis, "Can a Coupling Coefficient of a Piezoelectric Device Be Higher Than Those of Its Active Material?" J. Intelligent Material Systems and Structures, vol. 8, no. 10, Oct. 1997, pp. 859–867.

[11] C. W. Chiu and P. C.-P. Chao, "Design of filament winding planar coils for a generator," Technical Report to Industrial Technology Research Institute (ITRI) of Taiwan, Dec, 2003.

[12] B. Otis and J. Rabaey, "A 300_W 1.9GHz Oscillator Utilizing Micro-Machined Resonators," IEEE J. Solid State Circuits, vol. 38, no. 7, July 2003, pp. 1271–1274.

[13] S. Roundy, P.K. Wright, and J. Rabaey, Energy Scavenging for Wireless Sensor Networks with Special Focus on Vibrations, Kluwer Academic Press, 2003.

Fig. 1. Schematic illustration of a self-powered balancing ring in a rotor system.

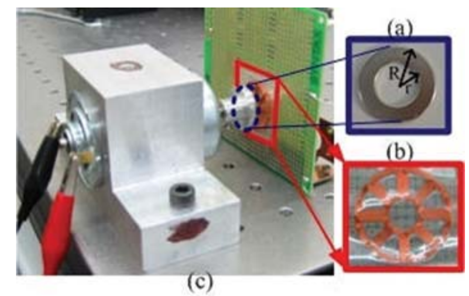

Fig. 2. (a) The hard NdFeB magnet; (b) The fabricated patterned coils; (c) The miniaturized generator system.

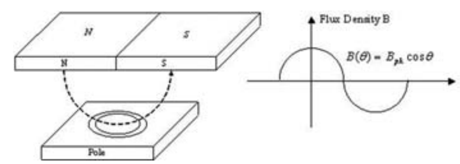

Fig. 3. Application of Faraday's law between a magnet pole and copper coil.

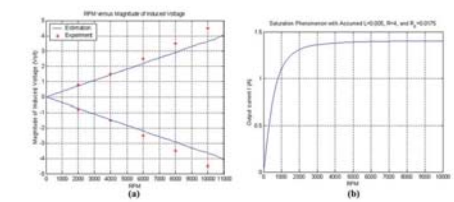

Fig. 4. (a) The comparison between the predicted and experimental emf's; (b)The generated current that is saturated at high speeds.

GS-06

Electromagnetic Analysis and Parameter Estimation of Permanent Magnet Wind Turbine Generators Considering Skew Effects.

S. Jang, *J. Choi*, K. Ko
Chungnam National University, Dae-jeon, South Korea

Introduction

Stimulated by the demand from the wind energy industry and with the advent of rare earth magnetic materials which combine high remanence and coercive force, particular attention has been paid to the development of various types of permanent magnet (PM) generators for low speed, direct-coupled wind turbine application [1]. Generally, since the wind power systems are very expensive and require high reliability, their performance must be verified by dynamic simulations performed under various conditions. In order to facilitate the accurate dynamic simulations of wind power systems, the parameter estimation of the machines is essential.

Therefore, this paper deals with electromagnetic analysis and parameter estimation of the PM wind turbine generators considering skew effects. First, this paper predicts the open-circuit and the armature reaction field distributions using analytical solutions derived in terms of the magnetic vector potential and a two dimensional (2-d) polar coordinate system. On the basis of the field solutions, parameters such as back-emf constant and inductance are estimated, and the influence of stator skew on the cogging torque and back-emf wave form is also investigated. The analytical results are validated extensively by non-linear finite element (FE) analyses. In particular, test results such as back-emf, inductance and cogging torque measurements are given to confirm the analyses. Finally, using estimated parameters and equivalent circuit method(ECM), the variation of generating characteristics such as output power, terminal voltage and load current according to load are investigated and validated by FE calculations and measurements.

Structures and Experimental Sets of PM generator

Figure 1 (a) shows the schematic and the picture of the actual manufactured PM generators, which consists of a 16-pole rotor with parallel magnetized NdFeB magnets and a slotted stator with 3-phase windings. Figure 1 (b) shows the testing apparatus for the measurement of generating characteristics. As shown in Fig. 1(b), the testing apparatus consists of the PM generator, an induction motor, V/F inverter for drive of the induction motor, a 3-phase resistance load and a power analyzer for the measurement of the generating characteristics.

Results and Discussion

Figure 2(a) shows the comparison of predictions with FE calculations for magnetic fields due to PMs and stator currents considering slotting effect. Figure 2(b) also shows the comparison of predictions with FE calculations and measurements for the cogging torque according to stator skew. The analytical results are shown in good agreement with FE results and measurements. It can also be seen that the cogging torque is dramatically reduced by stator skew. Figure 3 shows the predictions, FE calculations and measurements for the line-line back-emf according to stator skew. It can be observed that stator skew make the line-line back-emf have more sinusoidal waveform and smaller root mean square (RMS) value. As shown in Fig. 4, since the generating characteristics of the PM generator with skew predicted by the ECM are shown in good agreement with those obtained from non-linear FE calculation and experiment, it can be judged that the validation for the electromagnetic analysis and parameter estimation of the PM generator presented in this paper is confirmed. The more detailed results, discussion and mathematical expressions will be given in final full paper.

[1] Chen J.Y., Nayar C.V. and Baker, D., International Conference on Power Electronic Drives and Energy Systems for Industrial Growth, vol. 1, pp.353-358, Dec. 1998.

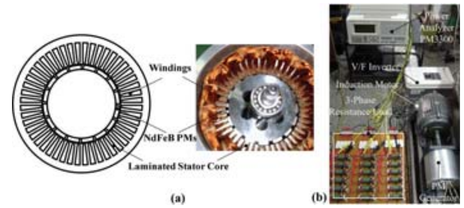

Fig. 1. PM generator for wind power applications: (a) schematic and picture of the actual fixture model and (b) testing apparatus.

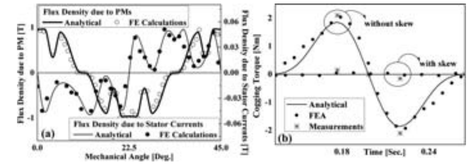

Fig. 2. Comparison of predictions with (a) FE calculations for the magnetic fields and (b) measurements and FE calculations for the cogging torque according to stator skew.

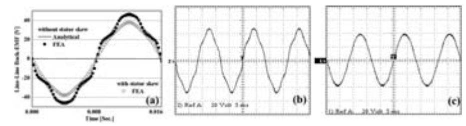

Fig. 3. Line-line back-emf: (a) Comparison of predictions with FE calculations, (b) measurements for the case when stator is not skewed and (c) measurements for the case when stator is skewed.

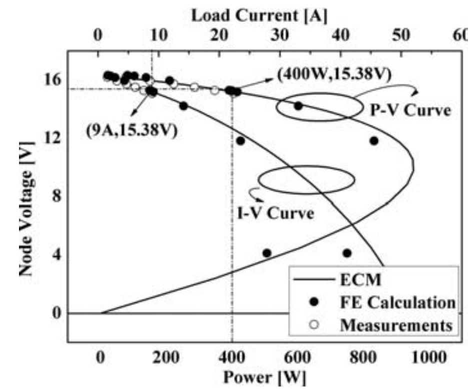

Fig. 4. Predicted, FE and measured results for generating characteristics of the PM generator with skew under various load conditions.

GS-07

Operating time estimation in acceleration and deceleration mode of high power FESS using electromagnetic field analysis of PM synchronous motor/generator.

D. You[1], S. Jang[1], J. Lee[2], T. Sung[2]
1. chungnam national univ., daejeon, South Korea; 2. Korea Electric Power Research Institute, Daejeon, South Korea

Introduction

A high power flywheel Energy Storage System (FESS) has focused largely on developing the distributed power source in summer or midnight and power utility load-leveling systems that are competitive with traditional electrochemical battery installations [1]. The flywheel rotor is rotated by an electric machine operated as a motor at ordinary times, whilst in case of a breakdown of electric current, that rotated by its inertia makes the electric machine operate as a generator. In general, since the faster rotational speed of the flywheel rotor in motoring mode is, the larger its motion energy due to inertia in generating mode is, high speed machines as motor-generator mounted on flywheel rotor are mainly used in the flywheel energy storage systems (FESS). Here, the important factor is to be continuously offering the electrical energy from mechanical rotation energy of flywheel rotor for a long time. Thus, high speed machine for the high power FESS must be designed considering high power requirement for rotating the large and heavy flywheel in high speed and rotational loss reduction for supplying the electric energy for hours. the rotational loss is defined as mechanical loss by mechanical friction including windage loss and iron loss by magnetic field parts including eddy current loss when flywheel is rotated. Therfore, the aim in our works is to offer operating time estimation in acceleration and deceleration mode of the high power FESS from calculation of required power and core loss using electromagnetic field analysis of the applied high speed machine.

In this paper, permanent magnet synchronous motor (PMSM) is designed by analytical method of electromagnetic field to satisfy the required power in motoring and generating mode. This design model consists of the surface-mounted PM rotor with diametrical magnetization and slotless iron-cored stator as shown in Fig. 1. And, its performance is evaluated in generating mode with various resistance load and idling mode without generating load considering the required electric power and core loss. In order to facilitate design, analysis and accurate dynamic range of high speed PM machines, a variety of techniques can be employed to predict the magnetic field distribution. Numerical techniques, such as finite element (FE) analysis, provide an accurate means of determining the field distribution, with due account of saturation etc., while they remain time-consuming and do not provide as much insight as analytical solutions into the influence of the design parameters on the machine behavior [2]. Therefore, this paper places the focus on characteristics for the generation of electricity of high speed machine and derives analytical solutions for open-circuit field, armature reaction field and back-emf in terms of magnetic vector potential and a two dimensional (2-D) polar coordinate system as shown in Fig. 2.

In verification for analysis and design, a 5kWh-class FESS with the whole flywheel rotor weights 215kg, the Active Magnetic Bearing (AMB) for elimination of mechanical friction and Floating Magnetic Bearing (FMB) for stable levitation of flywheel is manufactured as shown in Fig. 3(a). And, the designed 15kW-class PM Synchronous Motor/Generator (PMSM/G) is used for high power energy storage in dynamic range of flywheel speed 12000~18000rpm. These all parts are installed in vacuum chamber. As the experimental result for storage energy evaluation of the presented high power FESS, Fig. 3(b) shows the phase Back-emf of PMSM/G at a flywheel speed 3600rpm and Fig.3 (c) shows the flywheel speed for operating time determination according to driving mode of the PMSM/G. The more detailed results and discussion will be given in final paper. The mathematical expressions related to analytical results will also be given fully in final paper.

References

[1] Mark Matthew Flynn, PhD. dissertation, Univ. of Texas at Austin, USA, 2003.

[2] J. Wang, G. W. Jewell and D. Howe, IEEE Trans. Magn., vol. 35, no. 3, pp.1986-2000, 1999.

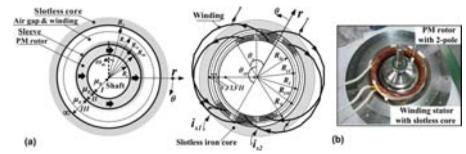

Fig.1. 15kW-class PMSM/G: (a)magnetic field analysis model of PM rotor and winding stator (b)a manufactured PMSM/G

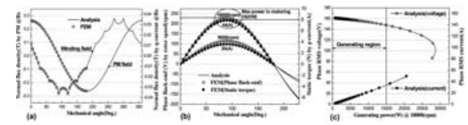

Fig.2. Analysis results of PMSM/G: (a)normal flux density in magnetic field (b)phase Back-emf and torque in motoring (c)electrical power output in generating

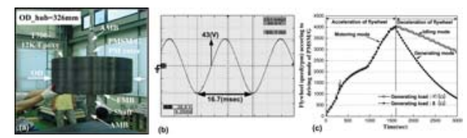

Fig.3. Experimental results of FESS:(a)phothograph of flywheel rotor (b)phase Back-emf of PMSM/G@flywheel speed 3600(rpm) (c)flywheel speed according to driving mode of PMSM/G

GS-08

Magnetic Switch Topologies.

W. Johnson
Electrical and Computer Engineering, University of Kentucky, Lexington, Ky, KY

Paper Overview:
After a brief history of control technology a discussion of several magnetic switching design styles is given. The magnetic switching styles are compared to solid-state switches using solid-state terminology and magnetic theory to detail the physical differences between the two.
Perspective:
Solid-state switches have vastly improved switching capabilities over magnetics switches but only within a limited range. Due to material advances saturation can be reached very quickly allowing for good state transitions. This is especially significant in high voltage and high current applications where the magnetic core allows for true decoupling of the source and control thus showing the magnetic technology's primary benefit of inherent isolation.
Topologies of Magnetic Switches:
As with solid-state devices, two fundamental types of magnetic switches can be created, normally-Off (inherently Off or n-type) and normally-On (inherently On or p-type). Both types of switches from a magnetic perspective are created using a core that can quickly reach magnetic saturation, equivalent to the solid-state ohmic region.
In Figure 1 an anhysteretic B-H curve, shows the areas of operation for amplification and switching of a magnetic device. Notice that the B-H curve saturates in two quadrants and thus has bi-directional capabilities, something that solid-state devices are unable to do. However, the magnetic device has difficulty when used in typical DC applications and is thus excluded from many applications. (Further discussion of the differences between the solid-state switching curves and the B-H switching curves will be presented.)
Inherently Off (n-Type) Magnetic Switch:
Most magnetic amplifiers and switches are designed using the n-type topology due to its inherent safety and similarity to the transformer. (Literature on the n-type topology is abundant and references will be given.) This magnetic switch style is generally designed using an area-product methodology, similar to transformer designs, as the magnetic core during turn-Off must quickly drop out of saturation while absorbing worst case field energy. The switching time to turn-Off (tOff) is governed by the turns count and the core area (Ac) where a larger Ac reduces the turn-Off time as shown in Figure 2. (The area-product design method and equations of the n-type switch will be given. Emphasis will be placed to the physical interpretation of the method.)
Inherently On (p-Type) Magnetic Switch:
In contrast to the n-type switch, the p-type magnetic switch obtains better turn-On (tOn) switching performance with a smaller Ac. A control coil is regulated to insure that the magnetic field of the core is zero (or of opposite polarity to the primary coil) during an 'Off' sequence. This switch style is not governed by the traditional area-product method of design as a smaller Ac improves performance. This is because the core is no longer designed to absorb field energy thus the traditional area-product rule no longer applies. (Further physical interpretation for not using the traditional area-product design method will be given.)
The p-type magnetic switch must now be designed around 'switching' losses that are governed by its B*H product and not its I*V product as with traditional area-product designs. (A full p-type design discussion will be given in the paper.)
Switch Extremes:
Magnetic switch designs (n-type or p-type) vary due to their inherent (On or Off) state which occurs when control coil current is removed. Physically, the difference can be resolved to the relative size of Ac and the two methods of design, B*H vs I*V.
While the control methods of the two switches are exactly opposite, as shown in Figure 3, and their design methods appear different, this paper will give a proof that the two switches and design types are in fact a single switch where Ac has been taken to an extreme. This paper will conclude with a simple design and experimental results for verification of the given design procedures.

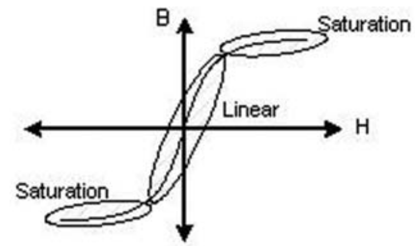

Figure1: Typical Magnetic Anhysteretic Switch Curves

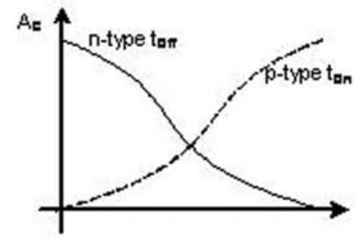

Figure 2: Typical Timing Curves for n-Type and p-Type Magnetic Switches

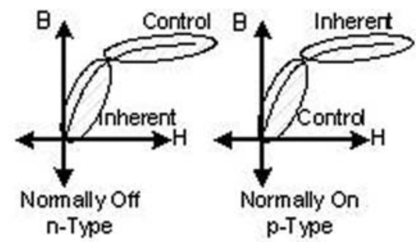

Figure 3: Operating Point vs n-type and p-type Magnetic Switches

GT-01

Influence of Notch Shape and Size on Current-Driven Domain Wall Motions in a Magnetic Nanowire.

H. Murakami[1], *T. Komine*[1], T. Nagayama[1], R. Sugita[1], Y. Hasegawa[2]
1. Department of Media and Telecommunications Engineering, Ibaraki University, Hitachi, Japan; 2. Saitama University, Saitama, Japan

1. Introduction
Spin-current-induced domain wall motion in a nanowire has attracted much attention [1], and new memory and logic devices with current-induced wall motion are suggested by some authors [2]. In order to control domain wall motion in memory devices with large capacity, a magnetic wall pinning such as a notch is necessary [3]. However, influence of notch shape and size on wall pinning in current-induced wall motion has not been discussed yet. In this study, influence of notch shape and size on current-induced wall motion has been investigated in the micromagnetic framework.
2. Calculation model
Fig. 1 shows the calculation model of nanowire with a rectangle and a triangle notch. The nanowire length of 200 nm was assumed and the infinite boundary condition was imposed at the nanowire edges along the longitudinal direction. The magnetic nanowire has a saturation magnetization of 800 emu/cm^3, exchange stiffness constant of 1.0×10^{-6} erg/cm, Gilbert damping constant of 0.02, and non-adiabatic damping constant of 0.02.
The notch shape was assumed to be rectangle or triangle. The dimensions of notches are shown in Table 1. In order to investigate the domain wall motion, the Landau-Lifshitz-Gilbert equation with spin torque terms was solved by simultaneously calculating current distribution in a nanowire. The critical current density and critical magnetic field were calculated by varying an induced current and an applied field. The influence of notch shape and size on domain wall motion was discussed.
3. Results and discussion
Fig. 2(a) shows the phase diagram in a current density and an applied field for domain wall motion in a nanowire with a rectangle notch. The current density is defined as a maximum current density around a notch. In Fig. 2, the critical current density monotonically decreases as the applied field increases. The effect of wall trap on domain wall motion increases as the notch size becomes larger. Fig. 2(b) also shows the phase diagram for triangle notch. In triangle #1, the phase diagram is similar to that in rectangle cases. On the other hand, in other triangle (#2-4) the critical current is almost constant up to a certain applied field. Thus, the triangle notch is more effective than rectangle notch for wall pinning. Fig. 4 shows the wall motion modes in triangle #4. There were four wall motion modes in this case: (i) the domain wall oscillates around the notch by maintaining transverse wall, and stops. (ii) the domain wall moves beyond the threshold of applied field by maintaining transverse wall. (iii) the domain wall moves and alternatively changes from transverse wall into anti-vortex wall. (iv) the domain wall breaks down into multi-domain.
4. Summary
In this study, influence of triangle and rectangle notches with various sizes on current-induced domain wall motion has been investigated by utilizing micromagnetic simulation. Each notch plays a role of wall trap, and the effect of wall trap increases as the notch size increases. The phase diagram in a critical current density and a critical field for notch shape is clarified. There are four modes in domain wall motion by various current densities and magnetic fields.
Acknowledgment
This research was supported in part by a '07 Grant-in-Aid for the Encouragement of Young Scientists from the Japan Society for the Promotion of Science.

[1] Z. Li, J. He, and S. Zhang, J. Appl. Phys. 99, 08Q702 (2006).
[2] S. S. P. Parkin, U.S. Patent No. 6834005 (2004)
[3] J. He, Z. Li, and S. Zhang, J. Appl. Phys. 98, 016108 (2005).

Type	Rectangle				Triangle			
#	1	2	3	4	1	2	3	4
d [nm]	4	8	12	16	8	12	16	20
s [nm]	4	4	4	4	12	20	28	36

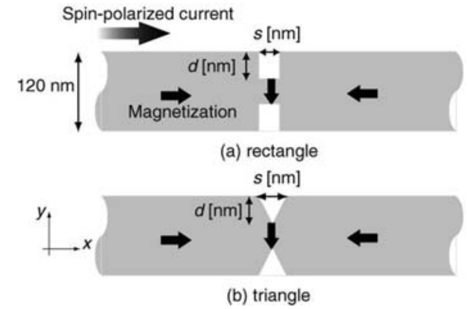

Fig.1 Simulation models for (a) rectangle notch and (b) triangle notch.

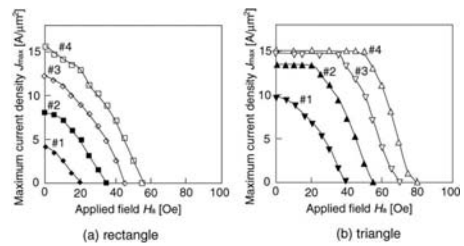

Fig.2 Phase diagrams for wall motions in nanowire with (a) rectangle notch and (b) triangle notch.

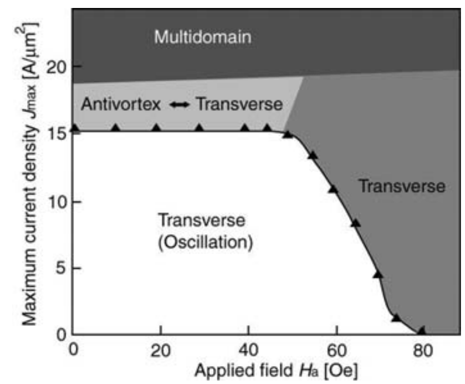

Fig.3 Phase diagram for domain wall motions in nanowire with triangle notch #4.

GT-02

Multi-level transitions of closely-arranged spin valve pillars by spin transfer switching.

N. Funabashi, K. Machida, K. Aoshima, Y. Miyamoto, N. Kawamura, K. Kuga, N. Shimidzu
NHK Science & Technical Research Laboratories, Tokyo, Japan

Introduction

The spin transfer switching (STS) technique has progressed remarkably since its theoretical prediction.[1] Especially, it is expected to use STS for the writing process of high-density random access memory. We have proposed new magneto-optical spatial light modulator (MO-SLM) driven by STS for high resolution and high speed applications such as holographic memories and 3-D TV systems. MO-SLM is the known device that controls light modulation by optical polarization rotating with the magnetization direction of the pixels.[2] We have succeeded to observe the fundamental STS properties by magneto-optical Kerr effect using visible light.[3] In order to achieve gradational light modulation, we have considered that division of a pixel to some small segments and control of multi-level magnetization states by STS. In this study, we fabricated two closely-arranged spin valve (SV) pillars sharing a pair of top and bottom copper electrodes and tried to control of multi-level transitions by STS.

Experimental method

Fig. 1 shows a schematic configuration of our fabricated device. The structure of paired SV pillars consists of Cu bottom electrode layer, synthetic pinned layer of [Ru(5)/Cu(20)/$Ir_{22}Mn_{78}$(10)/$Co_{75}Fe_{25}$(5)/Ru(0.75)/$Co_{75}Fe_{25}$(5.5)], Cu spacer of [Cu(6)], free layer with capping of [$Co_{40}Fe_{40}B_{20}$(3)/Cu(5)/Ru(5)], and Cu top electrode layer, where the numbers in parentheses are thicknesses in nanometers, deposited by ion beam sputtering. The bottom and top electrodes are shared by the paired pillars. The each size of pillars is set at 300 nm × 100 nm as shown in Fig. 1, using electron beam lithography and liftoff processes. The distance d between two pillars was varied up to 1 μm. In this study, the single pillar (Sample A), the closely arranged pillars with d of 1 μm (Sample B) and 300 nm (Sample C) are discussed in detail.

Results and discussion

The MR ratio of Sample A was about 0.7 % and the critical current density J_{c0}, calculated from the pulsed current in the range from 10 μs to 10 ms, was about 5×10^7 A/cm^2. The MR loops of Samples A, B, and C showed same shape, however, the loops of B and C possessed slight steps at the half-maximum of MR ratios. The STS characteristics from anti-parallel (AP) state to parallel (P) state and histograms of J_cs were shown in Fig. 2, where the STS characteristics were measured by applying a pulsed current with the duration of 500 μs without magnetic field. Samples B and C showed two-step transitions at J_{c1} (the first step) and J_{c2} (the second step). In the case of sample B, since J_{c1} was approximately equal to J_{c2}, both J_{c1} and J_{c2} were handled as J_c. The average values of J_c for samples A and B were -3.9×10^7 A/cm^2 and -3.7×10^7 A/cm^2, and the variances σ^2 of J_c for samples A and B were estimated almost same values of 4.9×10^5 A/cm^2 and 5.1×10^5 A/cm^2, respectively. The sample with d of 1 μm did not affect on the STS characteristics. On the other hand, the average values of J_{c1} and J_{c2} for Sample C were -3.6×10^7 A/cm^2 and -4.5×10^7 A/cm^2, and the J_{c1} and J_{c2} are clearly distinguishable. We succeeded to control the multi-level transitions in spin transfer switching of pillars with d of 300 nm. At the intermediate step, the magnetization directions of each pillar were considered that one was P-state and the other was AP-state, because the dV/dI at this step was a half value of $\Delta dV/dI$. The origin of the steady intermediate state and the smaller J_{c1} seemed to be the magnetic interaction and the peculiar switching mode of STS because the plateau width of the STS characteristics in Samples B and C showed the correlation with d.[4] The σ^2 of J_{c1} and J_{c2} for sample C were 3.9×10^5 A/cm^2 and 1.1×10^6 A/cm^2, respectively. The σ^2 of J_{c1} was smaller than σ^2 of J_c and the σ^2 of J_{c2} was larger than σ^2 of J_c. This result supports those assumptions.

Conclusion

Two closely-arranged SV pillars were fabricated and the STS characteristics were investigated. We succeeded to control of multi-level transitions using STS by changing the distance d between SV pillars. The origin of the steady intermediate state seemed to be the static magnetic interaction and the peculiar switching mode of STS.

1 J. C. Slonczewski, J. Magn. Magn. Mater. 159, L1 (1996).

2 J. H. Park, K. Nishimura, D. H. Lee, J. K. Cho, and M. Inoue, J. Appl. Phys. 91, 7014 (2002).

3 K. Aoshima, N. Funabashi, K. Machida, Y. Miyamoto, N. Kawamura, K. Kuga, N. Shimidzu, T. Kimura,Y. Otani, and F. Sato, Appl. Phys. Lett. 91, 052507 (2007).

4 K. Machida, N. Funabashi, K. Aoshima, Y. Miyamoto, N. Kawamura, K. Kuga, and N. Shimidzu, J. Appl. Phys. In press (2008).

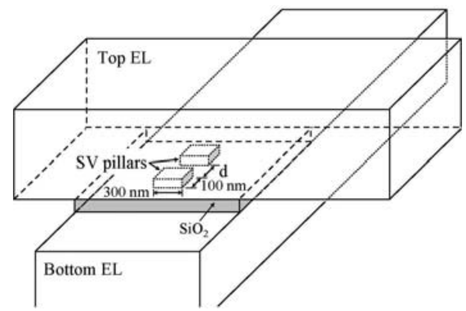

Fig.1 Schematic configration of closely arranged SV pillars.

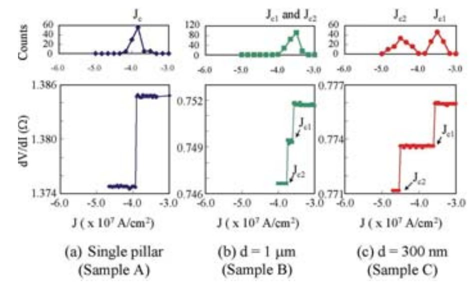

Fig.2 STS characteristics and histograms of J_cs

GT-03

Dependence of current induced switching properties on MgO formation method.

J. Langer[1], J. Wrona[1], B. Ocker[1], W. Maass[1], A. Thomas[2], K. Rott[2], M. Schaefers[2], G. Reiss[2]
1. Singulus Nano Deposition Technologies GmbH, Kahl am Main, Germany; 2. Department of Physics, Bielefeld University, Bielefeld, Germany

To compete as non-volatile memory, MRAM elements based on TMR barriers have to keep path with the scaling down nodes in the semi conductor industry. Classical elements using magnetic field induced switching are limited, mainly since the creation of the external field requires too much current. A new switching regime avoiding an external magnetic field by using the current driven through the tunnel element may be one promising path to overcome this constrains. The current density necessary to switch the element is there nearly independent from the size of the elements. Current densities in the range of 1×10^6A/cm^2 have been actually demonstrated. For competitive storage cells it needs to be reduced further by almost one order of magnitude.
The crucial point is the formation of the MgO tunnel barrier. It is shown, that a switching of the tunnel element can be realized utilizing different production methods for the MgO. Either a sputtering from an MgO-target or sputtering metallic Mg with a subsequent oxidation step can be applied. We will present a direct comparison of three methods: By using the Singulus TIMARIS platform we are able to deposit identical layer stacks for bottom and top electrode and either use a rf-process or metallic deposition with a subsequent oxidation step (natural or remote plasma with low energy ions). Beside the switching behaviour we will also discuss issues important for large scale deposition of the different process.
First results utilizing sputtering from metallic Mg showed, that the TMR- and RA-values are only weakly depending on the Mg thickness and on the oxidation conditions. Subsequently we can achieve an easily controllable RA and MR uniformity. In addition to the good uniformity control, the RA can be adjusted in the 10Ωμm^2 range, which is important for current induced switching. The mechanism of different barrier formation compared to the rf-sputter process will be discussed.

GT-04

Dynamics of current-induced magnetic switching of a single-molecule magnet.

M. Misiorny[1], J. Barnas[1,2]
1. Department of Physics, Adam Mickiewicz University, Poznan, Poland; 2. Institute of Molecular Physics, Polish Academy of Science, Poznan, Poland

Single-molecule magnets (SMMs) draw attention as potential candidates for applications in spintronics devices and information storage technology. Consequently, the key question arises how to effectively manipulate the SMM to write a bit of information on it. It has been shown that the current-induced magnetic switching (CIMS) [1,2,3] is a good alternative to the application of an external magnetic field.
There are, however, several challenging aspects of the current-induced manipulation of SMM's spin. First, one can hardly control the relative orientation of the molecule's easy axis and leads' magnetizations [4,5]. Second, intrinsic spin-relaxation time of the molecule significantly influences the switching parameters. The main objective of the following work is an analysis of how such intrinsic spin-relaxation affects the dynamics of the SMM's spin reversal induced by spin-polarized current.
When the energy ε of the lowest unoccupied orbital (LUMO) level of the molecule is sufficiently low, electronic transport between the leads takes place owing to tunneling between the electrodes and the LUMO level. The CIMS can then occur when the LUMO level is exchange coupled to the SMM's spin. When the energy ε is large enough, electron tunneling to the molecule is energetically forbidden at bias voltages of interest. However, current still can flow due to higher order processes, e.g. cotunneling ones, and CIMS of the molecule's spin is still possible [1] when the electrons virtually entering the molecule couple to the molecule's spin via the exchange interaction.
Switching of the SMM's spin takes place consecutively via the magnetic states of the molecule. These states are described by the eigenvalue m of the z-component of the total spin. Two main sources of SMM's spin relaxation processes are the coupling of the molecule to the ferromagnetic leads [1,2,3] and intrinsic spin-relaxation due to interaction with the environment. The latter ones are included into considerations as the relaxation time τ_R in addition to the current-induced transitions between the molecular spin states. The probabilities of finding the molecule in all possible molecular spin states are then determined from the relevant master equations. The molecule is initially saturated in the state m=-10, and then a constant voltage is applied.
In Fig.1(a) we show evolution of the z-component of the molecule's spin in the case of parallel magnetic configuration and high LUMO level (current flows then due to higher order processes). The results clearly show that the molecule's spin becomes switched when the voltage exceeds some critical value, Fig.2. The current-induced spin-flip processes become activated when eV is of order of the anisotropy energy gap. The intrinsic spin-flip relaxation processes, however, tend to restore the initial state. Therefore, the lowest threshold voltage occurs in the absence of intrinsic spin relaxation. The switching takes also place in the presence of intrinsic spin relaxation processes, although the threshold voltage becomes slightly increased. Apart from this, the switching time also increases with increasing τ_R^{-1}, Fig.1(a). Similar behavior also occurs in the case when magnetic moments of the leads are antiparallel.
Assume that the positive bias corresponds to electrons flowing from left to right (e>0). Spin-up electrons leaving the left electrode, Fig.1(b), can change its spin orientation when interacting via exchange coupling with the molecule's spin, and this way can increase the spin number m of the molecule's spin. Intrinsic relaxation processes tend to restore the initial state. When the current exceeds some critical value, the competition between intrinsic spin relaxation (lowering the quantum number m) and current-induced processes (increasing the number m) leads to spin reversal of the molecule. This takes place in both, parallel and antiparallel magnetic configurations. For reversed bias polarization only switching from the state m=10 to the state m=-10 is possible.

[1] M. Misiorny, J. Barnas, Phys. Rev. B 75, 134425 (2007).

[2] C. Timm, F. Elste, Phys. Rev. B 73, 235304 (2006).

[3] M. Misiorny, J. Barnas, Phys. Rev. B 76, 54448 (2007).

[4] C. Timm, Phys. Rev. B 76, 14421 (2007).

[5] M. Misiorny, J. Barnas, Solid State Sciences (in press).

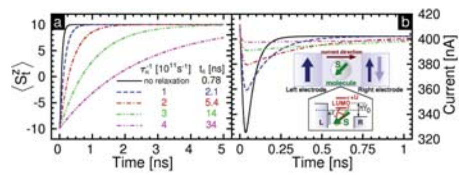

The effect of intrinsic relaxation processes on the magnetic switching of the molecule Mn_{12} in the limit of high LUMO level for parallel magnetic configuration. The polarization parameters of the electrodes are: P_L=1 and P_R=0.5. Moreover, V=1.5 mV, J=100 meV and T=0.01 K.

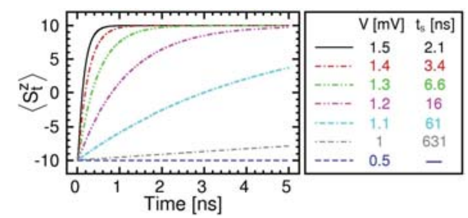

The dynamics of the switching process for different values of the bias voltage V in the presence of intrinsic spin-relaxation (τ_R^{-1}=10^{11} s^{-1}).

GT-05

Spin mechatronics to facilitate spin transfer switching in magnetic tunnel junction.

S. Kumar[1,2], *N. Chen*[1], S. Tan[1], M. Jalil[2]
1. SMI, Data Storage Institute, Singapore, Singapore; 2. ISML, ECE, National University of Singapore, singapore, Singapore

Recent studies have shown that spin-current can be generated via spin orbit interaction [1] as a result of nano-mechanical torsion in some material system. In this article we will focus on the inverse effect whereby the spin current passing through the material system causes mechanical motion on the nanometre scale [2]. We propose to utilize this effect to exert a spin-current-induced strain on the free layer of a magnetic tunnel junction such that its anisotropy constant reduces, thereby lowering the field or the spin current density required to switch the magnetization of the free layer [3]. As is well known, the grave challenge faced by spin current switching is the high critical current density. This problem can be solved by using free layer material of low anisotropy constant, but this causes magnetization stability problem and magnetic noise. Our device allows the anisotropy constant to be modified in a time-select manner, enabling low current switching to be achieved at no expense of device stability.

The schematic design of our device is shown in Fig 1. During the writing process, control spin current is injected upwards in the SC layer and this induces mechanical torque about the vertical axis (x). The SC rotates about x, with respect to the lead, forcing a insulating "flag" structure to displace along the z-axis, which thus causes strain onto the memory multilayer whose plane is placed perpendicular to z-aixs. The strain in the multilayer alters the anisotropy constant [4], thus lowering the switching field of the multilayer.

The underlying theory of this entire spin mechatronic process is related to the spin orbit interaction Hamiltonian of the semiconductor [5]:

$H\_SOI=\alpha[\sigma_x (u_{zx} k_z -u_{xy} k_y)+ \sigma_y (u_{xy} k_x -u_{yz} k_z)+ \sigma_z (u_{yz} k_y -u_{zx} k_x)]+ \beta[\sigma_x k_x (u_{yy} -u_{zz})+ \sigma_y k_y (u_{zz} -u_{xx})+ \sigma_z k_z (u_{xx} -u_{yy})]$

where α and β are spin orbit constants, k's denote electron momentum, σ's are the Pauli matrices and u's are the strain parameters.

The physical displacement that causes strain is expressed as: $d=L\gamma PJA/4Ke$ where L, K, γ, A=ab are device geometry dependent parameters, J refer to the current density. From the value of d, the additional strain induced in the free layer and thus the change in effective magnetic anisotropy, K_eff is computed.

Our results are displayed in Fig 2, which show a considerably large change of K_eff with the variation of the electron spin polarization. One of the important finding crucial for the working of this device is that as the spin polarization (P) of the current increases, K_eff may decrease or increase with increasing P depending on the region of spin polarization. At low P, K_eff actually declines to its minimum first with the increase of P, before increasing linearly at the higher P values. The P value where K_eff is minimum depends on the thickness of the free layer (t). For larger t, higher P would be needed to achieve the minimum K_eff. These results show that using spin polarization to modulate K_eff might be a practical approach in view of the high sensitivity of K_eff to the change of P. Furthermore, this method has advantage that the entire spin mechatronic process is carried out at fixed control current and voltage, which can be set to low values way below the switching current density. This suggest that even non-insulating flag structure could be used in this device and the control spin current plays the role of exerting strain through the flag as well as switching the magnetization.

In summary, we have designed a memory device that utilize the spin mechatronic process to lower the storage layer's anisotropy constant in a time-select manner, enabling spin transfer switching to be achieved at low current density.

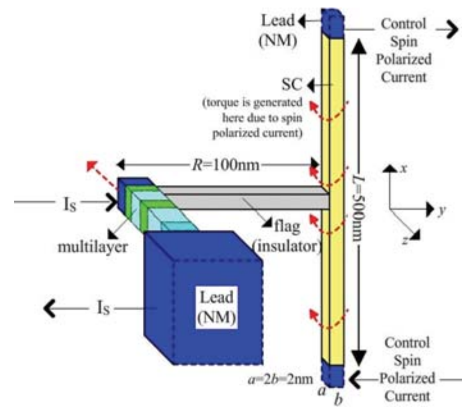

Figure 1: Device structure and design. Dotted arrow indicates the mechanical force. Figure is not drawn according to scale.

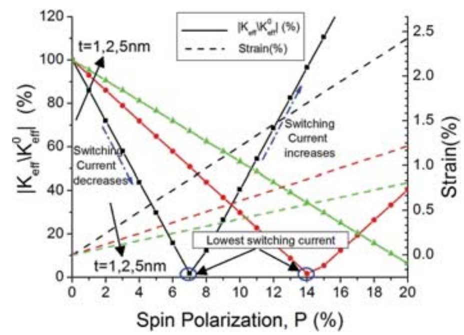

Figure 2: Shows the variation of K_eff and strain with spin polarization.

GT-06

Spin transfer in Co/Cu/Co nanocontacts.

M. N. Baibich, M. P. de Lucena, D. L. Baptista, R. B. da Silva, J. E. Schmidt, L. G. Pereira
Instituto de Física UFRGS, Porto Alegre, Brazil

We present preliminary results on spin transfer in arrays of nanocontacts built on Co/Cu/Co sandwiches. The nanocontacts were obtained by punching holes on a PMMA resin film with an AFM tip, forming 5x5 arrays. We have observed characteristic jumps of nearly 1%

The discovery that a spin-polarized current can exert torque on a ferromagnet through transfer of spin angular momentum offers a new method to manipulate a magnetization without applying any external magnetic field. The concept of magnetization reversal by spin transfer from a spin-polarized current was introduced by Slonczewsky [1] and Berger [2]. Later experiments on nanopillar-shaped spin-valve structures [3-6] nanowires [7] and nanocontacts [8] have confirmed this effect. The magnetization reversal by spin injection should be of great interest for application in non-volatile magnetic memories, programmable fast magnetic logic, and in high frequency devices for telecommunications. In this work we present a study of current-driven effects in nanocontact-shaped samples using their magnetoresistance properties.

In order to study the spin-transfer effect, we grew a Co/Cu/Co magnetic sandwich by sputtering, deposited on a silicon (1,1,1) substrate covered by 800 nm of copper, which serves as the bottom electrode. The structure of the film can be represented by Co(30nm)/Cu(8nm)/Co(3nm). After deposition the samples were covered by a thick layer of a solution of 2% PMMA (of 950k a.m.u.) in Anisole by spin coating at 4500 rpm for 45 seconds. The average thickness was estimated to be 50 nm. Right after this, the resin was patterned by lithography using the tip of an AFM system (figure 1), producing a 5x5 holes matrix with average spacing around 250 µm and opening about 40nm.

We deposited 50 nm of gold over this structure, forming the top electrode.

All measurements were made at room temperature with the current perpendicular to the plane and the magnetic field in the plane. We took as convention that negative current corresponds to electron flow from the thinner to the thicker ferromagnetic layer.

The resistance of the system was measured initially at 1200 Ω for currents in the 10 nA range, and no spin transfer was observed. By sweeping the current up to 100 µA, the resistance dropped significantly. Measuring once again in low currents we have observed the typical plots of figure 2, where the top panel corresponds to 25 Oe, and the bottom one to 45 Oe. We believe this drop in the overall resistance by going to high currents is related to the rearrangement of the current paths within the sample. Only a few of the 5x5 contacts is really connected to the Co/Cu/Co at first. After a few measurements, these are "burnt" and the resistance increases. When the current is swept to very high values, we break the insulator and establish new current paths (new nanocontacts).

As can be seen in figure 2, spin transfer is clear from the discrete jumps in resistance (about 1 %); changing the external field displaces the current needed to have moment switching.

In conclusion, we have prepared arrays of nanocontacts on Co/Cu/Co that present spin-induced moment switching with jumps in the resistance that can reach 1 %. The actual paths for conduction are not known, for the final result comes through breaking the insulating layer to establish conduction.

This work was partially supported by CAPES and FAPERGS, Brazil

[1] J. Slonczewski, J. Magn. Magn. Mater. 159(1996)1.
[2] L. Berger, Phys. Rev. B 54 (1996) 9353.
[3] J.A. Katine et al., Phys. Rev. Lett. 84 (2000) 3149; F. J. Albert et al., Appl. Phys. Lett. 77 (2000) 3809.
[4] J.Z. Sun et al., Appl. Phys. Lett. 81 (2002) 2202.
[5] J. Grollier et al., Appl. Phys. Lett. 77 (2001) 3663.
[6] U. Urazdhin et al., cond-mat/0303149.
[7] J.E. Wegrove et al., Europhys. Lett. 45 (1999) 626.
[8] M. Tsoi et al., Phys. Rev. Lett. 80 (1998) 4281.

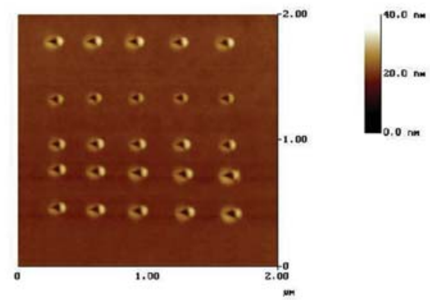

Figure 1. AFM image of the perforated PMMA layer, showing the 5x5 matrix.

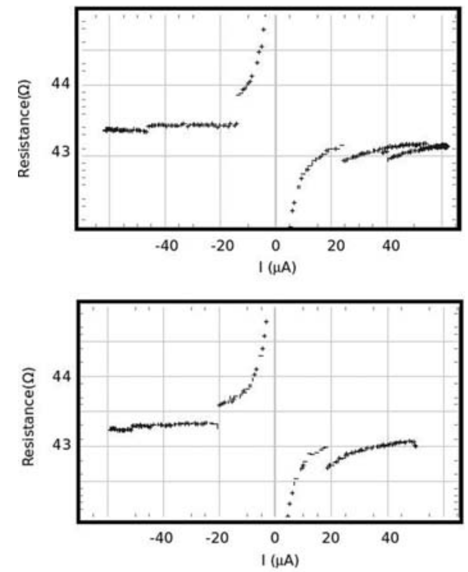

Figure 2. R vs. I plots at 25 Oe (top), and 45 Oe (bottom)

GT-07

On the relation of the inelastic spin torque and the spin polarization.

W. Wulfhekel[1], A. F. Takacs[1], T. Balashov[1], M. Däne[2], A. Ernst[2], P. Bruno[2]
1. Physikalisches Institut, Universität Karlsruhe, Karlsruhe, Germany; 2. Max-Planck Institut für Mikrostrukturphysik, Halle, Germany

The spin torque effect, in which the spins of the electrons in an electric current exert a torque on the magnetization of a magnetic electrode, is an effect of high fundamental interest [1] and large potential in applications [2]. In the standard description of this effect in all metal junctions derived by Slonczewski, the torque is created by elastic electron scattering [1]. With the observation of the spin torque effect in magnetic tunnel junctions [3], the additional parameter of bias voltage across the junction was introduced and inelastic contributions of the spin torque effect are currently discussed.

These inelastic contributions to the torque might be of utmost importance in spin torque effect. In case a magnetic electrode is intended to be switched between different metastable magnetic states, an energetic barrier has to be overcome and energy has to be pumped into the magnetic electrode. The switching process itself has been found to be related to a precession of the magnetization [4], which is the lowest magnetic excitation of the electrode, the coherent rotation or the momentum q=0 magnon. While this low excitation mode does not involve an increase of exchange energy, it has a finite energy due to shape or magnetocrystalline anisotropy of the magnetic electrode. In case the bias of the junction is larger than this energy, even higher magnon modes with non uniform precession, i.e. magnons with q>0, may contribute to the spin torque effect. So far, these excitations have not been intensively studied experimentally and it is unclear, how much they contribute to the size of the spin torque effect. In this contribution, we present the magnon creation by inelastic scattering of electrons and holes, relate the inelastic scattering probability to the spin polarization of the tunneling current and discuss the importance of this inelastic mechanism for the spin torque effect.

[1] J.C. Slonczewski, Phys. Rev. B 39, 6995 (1989).

[2] E.B. Myers et al., Science 285, 867 (1999).

[3] G.D. Fuchs et al., Appl. Phys. Lett. 85, 1205 (2004).

[4] M. Tsoi et al., Nature 406, 46 (2000).

GT-08

Microscopic theory of spin transfer torque based on the spin spiral texture.

Y. Le Maho[1], F. Piechon[2]
1. Institut d'Electronique Fondamentale, CNRS / Univ. Paris Sud, Orsay, France; 2. Laboratoire de Physique des Solides, CNRS / Univ. Paris Sud, Orsay, France

As spin transfer torque looks very promising regarding the control of domain wall dynamics in nanoscale ferromagnets, the recent observation of current induced domain wall propagation has drawn much attention. The required critical current density for spin transfer torque to depin ferromagnetic domain walls 10^{11}[A/m^2] is still much too high regarding applications and better understanding of the mechanism is needed in order to reduce the critical current as much as possible. Two parameters u and β are commonly used to describe spin transfer torque [1]. Several authors have calculated u and β within the *sd* model ranging from quantum Kubo formalism [1] or Keldysh formalism [4] to classical Boltzmann theory [2] and even drift diffusion [3]. Most of these theories focused only on linear deviations around the uniform magnetization profile. They do not apply when domain wall width is of the same order of magnitude as the Larmor precession length λ_L, as it is the case for films with perpendicular magnetic anisotropy.
We extend the latter classical theory of spin transfer torque by looking at the quantum Boltzmann transport equations for the Wigner distribution function in the spin spiral magnetization texture $m(r)=\cos(x/\lambda)\,\mathbf{y}+\sin(x/\lambda)\,\mathbf{z}$, where λ is the spin spiral period. Within this theoretical approach a full derivation of collision integrals is given, which provides means to study the microscopic processes more carefully and to account for non trivial spin accumulation beyond the classical local limit in the diffusive regime.
Our approach may be converted within a gauge transformation into a problem where the exchange field seen by an electron crossing the spin spiral contains a uniform component, which depends on the local magnetization of the *d* electrons, and a velocity dependent magnetic field. The latter field is proportional to the ratio λ_L/λ between the larmor precession length λ_L and the spin spiral period λ. The use of this local frame is very convenient for our purpose because the exchange field is then translationnally invariant. If λ_L is of the order of magnitude of λ, the velocity dependent magnetic field becomes of the order of the constant field and so conduction electron spins are no longer roughly aligned with respect to the local magnetization of *d* electrons. As a consequence conduction electron spin density is non local and there is a non trivial spin accumulation. Because of this non local feature, a traveling electron will not only be sensitive to the first order spatial gradients of the magnetization $\partial_x m$ as in the classical limit, but also to the higher order ones $\partial^2{}_x m$, $\partial^3{}_x m$... However since the spiral higher order derivatives $\partial^p{}_x m$ readily rewrite in terms of the magnetization and its first order derivative, we are able to represent the non local conduction electron spin density in terms of solely $m(r)$, $\partial_x m(r)$ and $m\times\partial_x m(r)$ and consequently to introduce an effective u_{eff} and an effective β_{eff} which naturally extend the usual spin transfer torque parameters u and β.
The Wigner distribution function is first solved by considering 1) scattering by quenched disorder and 2) the first Born approximation for the collision integral in the local frame. Term u is seen to depend only on the diagonal components of the distribution function in the local frame, corresponding to spin $\uparrow$ and spin $\downarrow$ channels. In contrast, term β depends only on the off-diagonal component of the distribution function and vanishes in the absence of spin flip processes, in agreement with recent theoretical works. Without a spin relaxation process it is seen that each conduction electron carries a finite contribution to β, however summation over all the conduction electrons make β vanish [2]. We show that these features still hold for dynamic spin flip scattering due to spin waves, which is in fact much more important than scattering by spin disorder at room temperature. We show that scattering rates as well as scattering in depend strongly on the ratio $\eta=\lambda_L/\lambda$. As a result u and β are much modified when η varies from zero (adiabatic limit) to some small finite integers.
One of the author acknowledges important discussions with D. Ravelosona, A. Thiaville and also support by C. Chappert.

[1] G. Tatara and H. Kohno, Phys. Rev. Lett. 92, 086601 (2004).

[2] F. Piechon and A. Thiaville, Phys. Rev. B. 75, 174414 (2007).

[3] S. Zhang and Z. Li, Phys. Rev. Lett. 92, 207203 (2004).

[4] Y. Tserkovnyak, H.J. Skadsem, A. Brataas, and G.E.W. Bauer, Phys. Rev. B. 74, 144405 (2006); H.J. Skadsem, Y. Tserkovnyak, A. Brataas, and G.E.W. Bauer, Phys. Rev. B. 75, 094416 (2007).

[5] H. Kohno, G. Tatara, and J. Shibata, Phys. Rev. Lett. 96, 189702 (2006); R.A. Duine, A.S. Nuinez, J. Sinova, and A.H. MacDonald, Phys. Rev. B. 75, 214420 (2007).

Current-induced domain wall motion in permalloy nanowires.

W. Zhang[1], P. Wong[1], Y. Xu[1], X. Zou[2], J. Wu[2]
1. Spintronics and Nanodevice Laboratory, Department of Electronics, University of York, York, United Kingdom; 2. Department of Physics, University of York, York, United Kingdom

It has attracted great interest recently to use polarised current induced magnetic switching in future spintronic devices such as random access memory (MRAM) and magnetic logic gates. In one of our previous studies[1], we have observed directly the magneto-resistance of domain wall from I-V measurements at zero external magnetic fields using current induced unpinning of a domain wall. In this report, we have further carried out a detailed study of the magnetic reversal and transport in the nanowires and found two different spin configurations at the nanocontacts.

Single-shot focused MOKE measurements with the laser spot close to the nanocontacts have been carried out to study the magnetic reversal in a longitudinal configuration with the magnetic field applied along the wire. As shown in Figure 1 by the MOKE loops from a $Ni_{80}Fe_{20}$ wire with a narrow contact of 200 nm, there are two different coercivities, one is around 63 Oe (Fig.1a) and the other one around 30 Oe (Fig.1b). This indicates that at zero applied magnetic field after reversal from saturation, there are two kinds of magnetization states near the nanocontact, one is parallel without a domain wall (Fig.1a), and the other one is anti-parallel with a domain wall at the nanocontact (Fig.1b).

I-V measurement was performed at zero applied magnetic field after reversal from saturation. It is found, as shown in Fig.2a, that the dc current induces a drop of the resistance, similar to our previous results[1] and the extra electrical resistance has been proved to be caused by a domain wall scattering in nanowires [2]. The current density at the nanocontact, required to change the resistance is of the order 10^7 A/cm^2 for the wire. This is related to the antiparallel configuration with a domain wall at the nanocontact as shown in Fig.1b.

In contrast with that in Fig.2a, there is a sharp increase of the resistance with the increasing current as shown in Fig.2b. This case is related to the parallel configuration as shown in Fig.1a. This further confirms that there are two kinds of magnetization configurations at zero magnetic field after reversal from the saturation also suggested from the MOKE Figure 1; one is with a domain wall at the nanocontact and the other without domain wall. In anti-parallel configuration in Fig.2a, the spin polarised current reversed the spin near the nanocontact from the right to the left and then pushed the domain wall away from the contact leading to a resistance drop, and in parallel configuration in Fig.2b, the injection of a domain wall into the nanocontact leading to an increase of the resistance and the formation of a domain wall at the contact.

[1] S. Lepadatu, and Y. B. Xu, Phys. Rev. Lett. 92 (12), 127201-1 (2004).

[2] U. Ebels, *et al.*, Phys. Rev. Lett. 84, 983 (2000); S. Khizroev, *et al.*, Appl. Phys. Lett. 86, 042502 (2005).

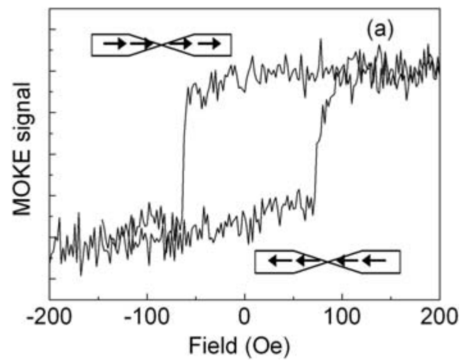

Fig.1a: Hysteresis loop of $Ni_{80}Fe_{20}$ wire with 200 nm wide nanocontact where the coercivity is around 63 Oe.

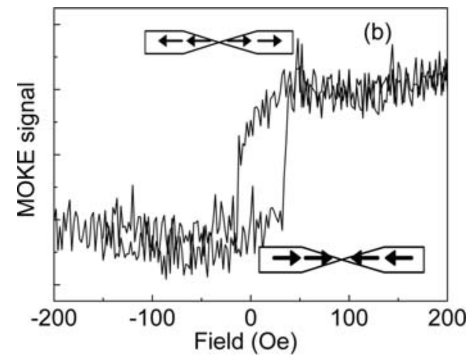

Fig.1b: Hysteresis loop of $Ni_{80}Fe_{20}$ wire with 200 nm wide nanocontact where the coercivity is around 30 Oe.

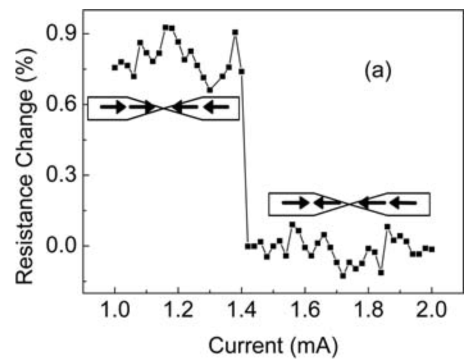

Fig.2a: Resistance vs. applied current plot for $Ni_{80}Fe_{20}$ wire with 200 nm wide nanocontact (resistance drop).

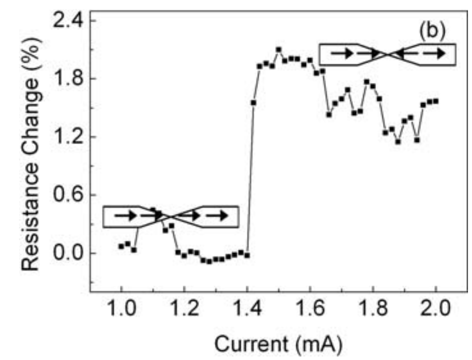

Fig.2b: Resistance vs. applied current plot for $Ni_{80}Fe_{20}$ wire with 200 nm wide nanocontact (resistance increase).

GT-10

Spin transfer switching in magnetic tunnel junction using a composite free layer.

W. Chen, D. Wang, C. Yen, Y. Lee, S. Yang, C. Shen, C. Tsai, C. Hung, K. Shen, M. Kao
Electronics and Optoelectronics Research Lab. (EOL), Industrial Technology Research Institute (ITRI), Hsinchu, Taiwan

Spin-transfer-driven magnetization switching has drawn considerable attention to potential applications of high density magnetic random access memory (MRAM). Such attention is aroused due to its simplified design and less cross talk [1]. Spin-transfer switching is performed through s-d interaction by injecting spin-polarized currents into magnetic cells. One of the most challenging targets of the spin torque switching architecture is to reduce the critical current of magnetization reversal and meanwhile keep the thermal stability at a reasonable level. In general, the reduction of the critical current requires that the magnetization of the free layer is lowered and the damping constant of it is reduced. In this report, spin transfer switching in the magnetic tunnel junction (MTJ) using the CoFeB/insert/NiFe composite free layer (CFL) is demonstrated to show a relatively low switching current density.

Two sets of MTJ structures are deposited on thermally oxidized Si substrates at room temperature using magnetron sputtering system. The first set of has a MTJ with a single free layer: Ta/PtMn/SAF pinned/AlOx/CoFeB (2 nm)/Ta capping layer. The second set has a CFL structure: Ta/PtMn/SAF pinned/AlOx/CFL/Ta capping layer, where CFL is CoFeB (x nm)/insert spacer (y nm)/NiFe (z nm). The insert spacers used in CFL are Ru, Ta and Cu, and the thickness (y) varies from 0.3 nm to 2.2 nm. After the film deposition, the samples are vacuum-annealed ex-situ in a field of 1 Tesla along the direction of the deposition field. The MTJs were fabricated by the e-beam writer and the reactive ion etching system. The MTJs are ellipses with a short axis of 150 nm and a long axis of 300 nm, and the resistance-area product (RA) ranges from 20 to 30 ohm-um^2.

For the comparison with the MTJ using a single free layer, the critical current density (Jc0) is significantly reduced in MTJ using a composite free layer. Jc0 for optimum CoFeB/Ru/NiFe CFL and CoFeB/Ta/NiFe CFL is determined by extrapolation to be 7 MA/cm^2 and 2 MA/cm^2 respectively, as shown in figure 1. Thus MTJ with optimum CFL has a much lower critical current density (Jc0) than that using a single free layer. These results suggest that the precession of magnetic moment in the NiFe of CFL may assist the precession of magnetic moment in the CoFeB of CFL and make CFL switchable at a much lower current density. In a word, this kind of free layer structure has the potential to make low switching current density and high thermal stability coexist.

[1]Z. Diao, Z. Li, S. Wang, A. Panchula, E. Chen, L.-C. Wang, Y. Huai "Spin-transfer torque switching in magnetic tunnel junctions and spin-transfer torque random access memory" J. Phys. Condens. Matter. vol.19, 165290, 2007.

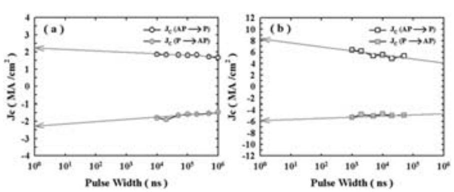

Figure 1 Relationships between the critical current density (Jc) and the log scale current pulse width for the (a) CoFeB/Ta/NiFe CFL and (b) CoFeB/Ru/NiFe CFL

GT-11

Current-induced Domain Wall Motion in L- and C-shaped Permalloy Nanowires.

J. Yoon[1,4], J. Lee[2,3], C. You[4], S. Choe[3], K. Shin[2], M. Jung[1]
1. Quantum Material Research Team, Korea Basic Science Institute, Daejeon, South Korea; 2. Center for Spintronics Research, Korea Institute of Science and Technology, Seoul, South Korea; 3. physics, Seoul National University, Seoul, South Korea; 4. physics, Inha University, Incheon, South Korea

In a magnetic nanowire, a single domain wall (DW) can be generated in the interface separating two magnetic domains whose magnetization directions are opposite. The DW can be moved by applying current as a result of spin-transfer-torque effect. The dynamics of DW motion in magnetic nanowire opened the door to new practical applications such as novel magnetic shift register memory [1] and logic devices [2]. Many kinds of experimental and theoretical studies on the current-driven DW motion have been reported so far [3-5]. However, the current-driven dynamics of DWs is not well understood. We investigated the current-driven DW motion for L- and C- shaped Permalloy nanowires by magnetic force microscopy (MFM).
We selected L- and C-shaped nanowires of Py ($Ni_{81}Fe_{19}$), because these shapes are easy to generate a DW at the wanted place with external magnetic field. Two Py nanowires with different shapes were fabricated on a SiO_x/Si substrate by means of magnetron sputtering. The nanowires were patterned with standard electron-beam lithography and lift-off method. The samples are the 600-nm wide L-shaped and the 300-nm wide C-shaped nanowires with the same thickness of 20-nm, respectively. The width was determined with a scanning electron microscope (SEM) and the thickness was determined with an atomic force microscope (AFM). To visualize the current-induced DW motion, the MFM (SPI4000/SPA-300HV, SII NanoTechnology) was used. In order to minimize the influence of the stray field from the magnetic probe on the DW, a low-moment probe (SI-MF40L) coated with CoCr was used for MFM images.
In order to generate a DW at specific place, we employed the L- and C-shaped nanowires. A saturation magnetic field (200 Oe) was applied to -y(+y) direction for L-shaped (C-shaped) nanowire. After the whole nanowire formed a single domain, the external magnetic was reduced to zero. Due to the shape anisotropies of L- and C-shaped of the nanowires, the head-to-head DW is generated at the bending corner. For the given wire geometry, vortex DW is more stable than the transverse Néel wall. The detail head-to-head vortex DW is imaged as a dark contrast in Fig. 1 (a). After 500-ns duration pulse was applied to the L-shaped nanowire, we took MFM images as shown in Fig. 1 (b). It is clearly shown that the DW moved 1.2-µm as a result of the pulse-current-induced DW motion. From these experiments we found the critical current density (J_C) of L-shaped nanowire is 5.0×10^{11} A/m^2, and the DW velocity (v) in L-shaped nanowire is 2.4 m/s. For the C-shaped nanowire, we performed the similar experiments to the L-shaped case. Successive MFM images were taken after each 1-µs pulse (Fig. 2 a-c) and (Fig. 2 d-f) for each polarity of the current. We found $J_C = 5.4 \times 10^{11}$ A/m^2 and $v = 2.0$ m/s for the C-shaped nanowire. It should be also noted that the J_C and v values are in agreement with those reported [5]. The J_C and v values are similar for both nanowires, while their curvatures and widths are quite different. The curvatures of the L- and C-shaped nanowires are 1.5-µm and 8-µm, respectively. We can conjecture the pinning potential from the curved geometry is weaker than one of the nanowire imperfections.
In conclusion, we designed L- and C-shaped nanowires in order to confine a DW at specific place. A head-to-head vortex DWs were placed at the bending corner at both geometries. Successive current-driven DW motions were imaged by MFM. We found similar critical current densities and DW velocities for the L- and C-shaped Py nanowires in spite of their different curvatures and wire widths. We conjectured that the pinning effect of the curvature is smaller than one of the imperfections of nanowire.

[1] S. S. P. Parkin, U.S. Patent No. 6834005 December 21 (2004).

[2] D. A. Allwood, G. Xiong, C. C. Faulkner, D. Atkinson, D. Petit, and R. P. Cowburn, Science 309, 1688 (2005).

[3] M. Tsoi, R. E. Fontana, and S. S. P. Parkin, Appl. Phys. Lett. 83, 2617 (2003).

[4] Yamaguchi, T. Ono, S. Nasu, K. Miyake, K. Mibu, and T. Shinjo, Phys. Rev. Lett. 92, 077205 (2004).

[5] M. Hayashi, L. Thomas, C. Rettner, R. Moriya, Y. B. Bazaliy, S. S. P. Parkin, Phys. Rev. Lett. 98, 037204 (2007).

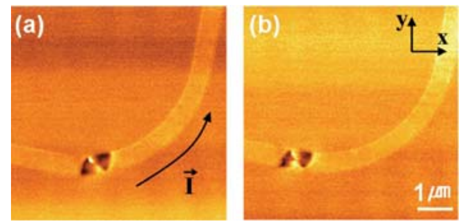

Fig. 1 Magnetic images of current-induced domain wall motion in L-shaped Py nanowire.

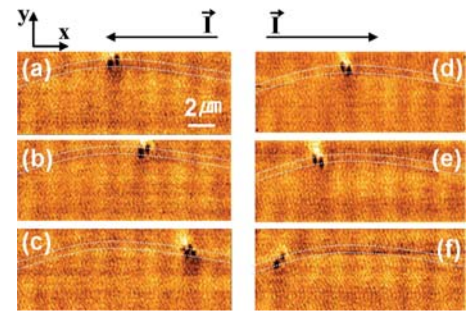

Fig. 2 Magnetic images of current-induced domain wall motion in C-shaped Py nanowire.

GT-12

Experimental study of thermally activated magnetization reversal with a spin-transfer torque in a nanowire.

K. Seon Ock[1], W. Kim[1], T. Lee[1], K. Kim[2], S. Choe[2], Y. Jang[3], S. Yoon[3], B. Cho[3]
1. Department of Materials Science and Engineering, Korea Advanced Institute of Science and Technology, Daejeon, South Korea; 2. Department of Physics and Astonomy, Seoul National Univesity, Seoul, South Korea; 3. Department of Materials Science and Engineering, Gwangju Institute of Science and Technology, Gwangju, South Korea

1. Introduction

Intensive theoretical and experimental studies for a spin-transfer torque (STT) have been recently conducted in view of its application as well as fundamental of physics. Recently it had also presented that the thermally activated magnetization reversal with a STT should introduce a new effective temperature or effective energy barrier.[1][2] In this work, we obtained the thermal effect of STT in a nanowire structure with perpendicular magnetic anisotropy (PMA).

2. Experiments

A 500 nm width nanowire pattern was prepared on a thermally oxidized Si-wafer by E-beam lithography. In the nanowire pattern magnetic film of Ta(1 nm)/Co-Re-Pt(8 nm)/Ta(0.5 nm) structure with PMA was deposited using a DC magnetron sputter system, followed by removal of ER through lift-off process. On the top of the nanowire we deposited Ta(5 nm)/Au(100 nm) as electrodes as shown in Fig1. The magnetic properties was measured using a VSM for unpatterned films and MOKE for patterned nanowires. The thermally activated magnetization reversal process was measured by a nanosecond magneto-optical magnetization microscopy (NS-MOMM) system. By the NS-MOMM system, first we made an reversed domain on the nanowire by thermal assisted field writing and selected a strongly pinned position using magnetic field. Then we measured the depinning time for the domain propagation with varied current density in the presence of magnetic field.

3. Results and discussion

Magnetic property of continuous film of substrate/Ta(1 nm)/Co-Re-Pt(8 nm) showed M_s of 450 emu/cm^3 and perpendicular anisotropy of 2.2×10^6 erg/cm^3 As shown in Fig2, magnetic properties of the continuous film and nanowire did not change much although there is some change in loop shape due to rough nanowire edge effect. By using the very thin seedlayer structure, we tried to minimize the shunt current and maximize the STT effect on the nanowire. Reversal behavior of the nanowire showed mixed mode of reverse domain nucleation and domain wall motion although wall motion was slightly dominant.

Below the magnetization reversal field (coercive field; 580 Oe [Fig2(b)]) of the nanowire, we injected the 5 μs current pulse from 2.0×10^7 A/cm^2 to 3.5×10^7 A/cm^2 for the thermally activated magnetization reversal. As shown in Fig3, the depinning occurs faster with increasing the current density. In addition, the increase of applied field H leads to the reduction of the slope of critical current density for depinning vs. depinning time. This result indicates that the measured depinning time, τ have the exponentially linear relation with current density, J, which means it follows Arrhenius' law as shown below.

$$\tau=\tau_0\exp(E_b(H,J)/k_BT)$$

,where τ_0^{-1} is an attempt frequency, E_b is the energy barrier as a function of J and applied field H, k_B is the Boltzmann constant, and T is temperature. This experimental results are consistent with the numerical analysis (the generalized Néel-Brown formula) of Z. Li and S. Zhang, which describes the effect of the spin torque by the modification of the energy barrier.[1]

4. Summary

We made a nanowire adequate for measuring the STT effect by using just 1 nm seedlayer structure films with PMA. In this nanowire the thermally activated magnetization reversal was investigated by injecting current for the thermal effect of the STT. The exponentially linear relations between τ and current density at a constant applied field are obtained and this is in accordance with the generalized Néel-Brown formula.

5. Reference

[1] Z. Li and S. Zhang, Physical Review B, 69, 134416 (2004)

[2] M. A. Zimmler et al., Physical Review B, 70, 184438 (2004)

[3] Y. Takeda et al., Journal of Magnetism and Magnetic Materials, 152, 243 (1996)

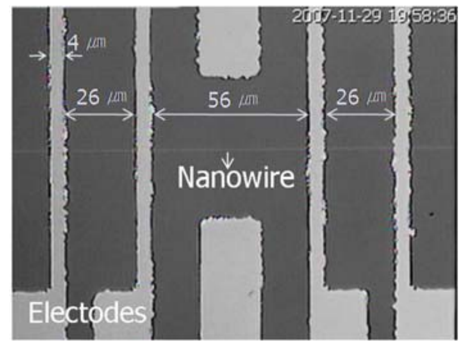

Fig1. A nanowire pattern with electrodes

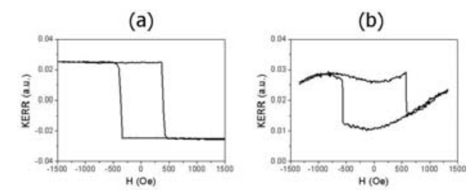

Fig2. Hysteresis loop of (a) a continuous film (b) a nanowire

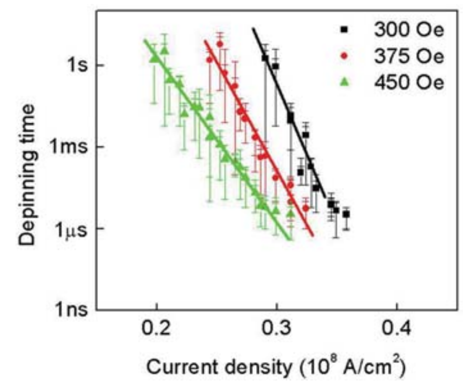

Fig3. Current density (J) vs. depinning time (τ) with various applied magnetic field (H)

GT-13

Spin-Transfer Switching in Elliptical Spin Valves in Subnanosecond Regime.

R. Heindl[1], T. Silva[1], W. Rippard[1], S. Russek[1], J. Katine[2]
1. Electromagnetics Division - Magnetics Group, National Institute of Standards and Technology (NIST), Boulder, CO; 2. Hitachi San Jose Research Center, San Jose, CA

In this paper, we present experimental measurements of spin-transfer-induced magnetization reversal in current-perpendicular-to-plane GMR spin valves using very short current pulses (0.1 to 3 ns). For the current densities of $1 < J/Jc0 < 5$, the magnetic reversal is presumably deterministic in nature, and we expect that thermal fluctuations influence the switching process only in virtue of the distribution of initial magnetization states when the current pulse is applied. The experimental data is compared with Landau-Lifshitz-Gilbert macrospin and micromagnetic simulations (OOMMF) that both include the spin-torque effect.
In the region where $J < Jc0$ the switching probability P(tp) can be explained by the Arrhenius-Neel-Brown thermally activated magnetization reversal for which $P(tp) \sim \exp(-tp/\tau)$, where tp is the pulse time and τ is the modified relaxation time in the presence of spin-torque. Most of the work on spin transfer switching probability has been done in this region, where switching times vary from couple of tens of nanoseconds to microseconds. In order to successfully switch the magnetization in subnanosecond time, larger pulse currents have to be applied with $J > Jc0$.
Our experimental data (Fig. 1) of P(tp) are compared to macrospin ($T > 0$) and micromagnetic ($T = 0$) simulations of devices with similar dimensions. For both simulations, following parameters were used: Ms = 800 kA/m, alpha = 0.012, P = 0.4.
The room temperature macrospin simulations show much sharper temporal switching distributions than the experimental data (Fig. 2a). For example, the data in Fig. 1 for 104 x 40 x 3 nm device at J/Jc0=2.5 shows that the pulse time difference between 5% and 95% switching probability is approximately 500 ps, while the simulated data in Fig. 2a shows that for the similar pulse duration, the pulse time difference for switching probabilities between 5% and 95% is only 200 ps.
The macrospin simulations do not show any dependence of Jc0 on the device size. However, micromagnetic simulations that account for inhomogeneity of the induced dynamics predict that Jc0 increases with the device size decrease, and that it is also highly sensitive to the device symmetry. Our data indicates that Jc0 is not the same for different device sizes, although extrapolation of Jc0 from room temperature measurements is very sensitive to the fitting and extrapolation parameters. The micromagnetic simulations for a 104 x 40 x 3 nm device (Fig. 2b) indicate that switching in such devices is actually much more complicated than macrospin simulations presume, characterized by growing c-state oscillations localized at the opposite ends of the device, followed by highly turbulent incoherent dynamics that precede switching. For the example presented in Fig. 2 in the case of 1 mA current (J = 2Jc0), the regular c-state oscillations build steadily for the first 2.5 ns, then the dynamics become turbulent for the remaining 0.43 ns. All simulations indicate that the c-state oscillates up to very large amplitudes until the symmetry of the excitation breaks down, followed by incoherent dynamics that evolve until switching occurs. Sometimes vortices (and anti-vortices) are generated that propagate randomly through the device. We conclude that the complexity of the dynamics predicted by micromagnetics is in part responsible for the larger measured temporal switching distribution than what is calculated from the macrospin model.

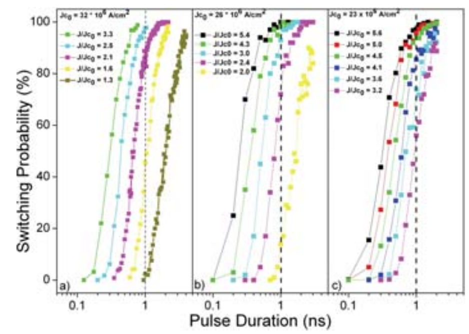

Fig 1: Switching probability distribution as a function of pulse duration for various pulse amplitudes. a) 104×40 nm2 b) 125×50 nm2 and c) 177×60 nm2 ellipses.

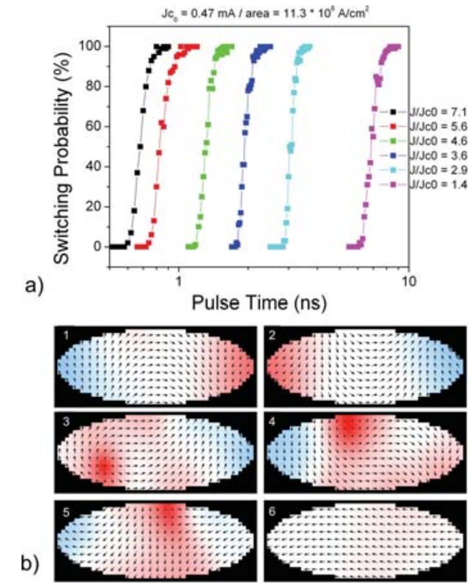

Fig 2a: Macrospin simulation of switching probability vs. pulse duration and different current amplitudes. Device dimensions are 104nmx40nmx3nm. Each point is an average of 100 trials. Fig 2b: OOMMF simulation of a 104nmx40nmx3nm ellipse at 1 mA current. Switching time was 2.93 ns. Oersted field are included in calculation. The colors in the snapshots indicate the amplitude of the z-component of the magnetization. Red is "up", and blue is "down." 1. Regular dynamics. End mode oscillations. 2. Regular dynamics. End mode oscillations, cont. Note: End modes are 180deg out of phase. 3. Turbulent dynamics. Vortex formation. 4. Turbulent dynamics. Vortex propagates along left edge from lower left to upper middle. 5. Turbulent dynamics. Switching. 6. Fully switched state.

GT-14

Shape dependence of current-induced magnetization switching.

C. Tsai, Y. Lee, D. Wang, W. Chen, C. Yen, C. Shen, S. Yang, C. Hung, K. Shen, M. Kao
Electronics and Optoelectronics Research Laboratories, Industrial Technology Research Institute, Hsinchu, Taiwan

In 1996, Slonczewski [1] and Berger predicted that the current flowing through magnetic multilayer could induce magnetization switching. Recently the spin-transfer torque effect has been considered the next generation technology of magnetic random access memory. However, the shape dependence of the magnetization dynamics has been rarely discussed precisely while operating the magnetic tunnel junction (MTJ) cells. To estimate the spin-transfer dynamics with shape dependence, the spin transfer torque term predicted by Slonczewski is introduced into the Landau-Lifshitz-Gilbert equation thus it can be written as shown in Eq.(1). We assume the unit vector **m** and **x** are denoted along the magnetic momentum of pinned layer and free layer respectively and the current flows perpendicularly to the plane of the MTJ cell. The effective anisotropy field $\mathbf{H}_{ani}$ includes the intrinsic anisotropy field $\mathbf{H}_{in}$ and shape anisotropy field $\mathbf{H}_d$.$\mathbf{H}_{app}$ is the applied field,P is the spin polarization coefficient and J is the current density. In our case, the shape anisotropy field is fully introduced in the LLG equation to get the whole picture about the shape dependence of switching properties(Eq. (2))Where Nx, Ny, and Nz are demagnetization factor along x, y, z directions and the easy axis of the MTJ cell is assumed in the x direction.

The analytical approach based on the equations similar to Eq.(1) has been already demonstrated by some studies. However, our presented calculation is more general and holds for different shapes of MTJ cells. The shape-dependent switching behaviors caused by instability condition of magnetic momentum leads to the critical current density as shown in Eq.(3). Moreover, it is important to be noted that the shape anisotropy term is accompanied with a correction factor (1-3Nx) instead of the pure out-of-plane anisotropy 2πMs along the z axis. Thus the shape dependence of the magnetization switching can be explicitly described by the correction term. Fig.1 shows the calculated results of the critical current density while increasing the aspect ratio of the MTJ cells.

Besides, the shape anisotropy makes a significant contribution to the energy barrier of the MTJ cells. Fig.2 shows the incr命nment ratio compared with the critical current density and the energy barrier. When the aspect ratio is up to 2.0, it should be noted that the energy barrier is greatly enhanced up to 240% while the increment of critical current density is just 4%. Therefore, it implies us the higher aspect ratio MTJ cell provides higher thermal stability but nearly the same critical current density.

A series of samples by using identical MTJ structure but different aspect ratio (1.2, 1.8, 2.1 respectively) have been demonstrated in Fig.3. It shows the experimental results of the switching phase diagram with the critical current density operated at different pulse width. The inverse of the slope stands for the thermal stability of the MTJ cells. It can be observed that the MTJ cells with larger aspect ratio provides higher thermal stability but almost the same current density. Thus, the experimental results show the great consistency with theoretical prediction that a well-designed aspect ratio MTJ cell would provide high thermal stability and proper critical current density.

[1]Slonczewski, J. C. (1996). J. Magn. Magn. Mater. 159, L1-L7

$$\frac{d\hat{m}}{dt} = -\gamma_0 \hat{m}\times(\vec{H}_{app}+\vec{H}_{ani}) + \alpha\hat{m}\times\frac{d\hat{m}}{dt} - P\frac{h}{2e}J\hat{m}\times(\hat{m}\times\hat{x})$$

$$\vec{H}_{ani} = \vec{H}_{in} + \vec{H}_d$$

Eq. (1)

$$\overrightarrow{H_d} = 4\pi M_s(N_x\widehat{m_x} + N_y\widehat{m_y} + N_z\widehat{m_z})$$

Eq. (2)

$$J_{c0} = \frac{2e\alpha}{p\hbar} t_F M_s (H_{appl} + H_{an} + 2\pi M_s(1-3N_x))$$

Eq. (3)

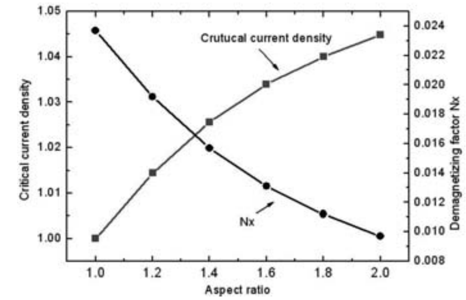

Fig.1. Jc and easy-axis demagnetizaion factor Nx versus aspect ratio of MTJ cells

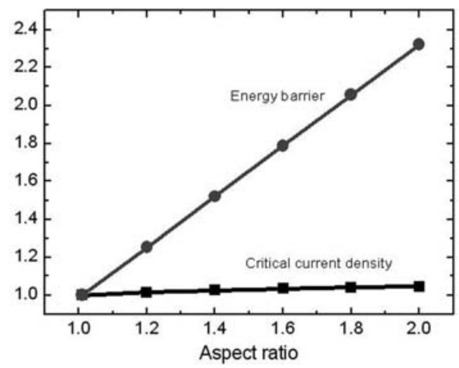

Fig. 2. Comparison between the Jc and the energy barrier with the aspect ratio form 1.0 to 2.0

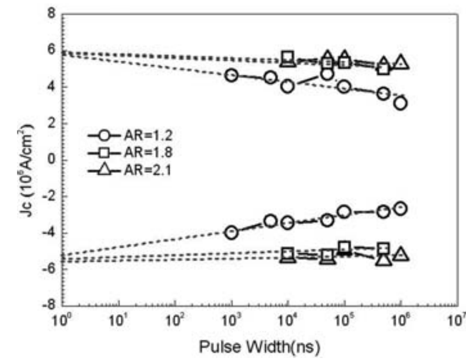

Fig. 3. Experimental results of the Jc versus writing pulse width

GT-15

Static and Dynamic Depinning Current Density in Current-Induced Domain Wall Motion.

S. Seo[1], H. Lee[2], W. Kim[3], T. Lee[3], S. Choe[4], D. Kim[5], K. Lee[1]
1. Korea University, Seoul, South Korea; 2. POSTECH, Pohang, South Korea; 3. KAIST, Daejon, South Korea; 4. Seoul National University, Seoul, South Korea; 5. Chungbuk National University, Cheongju, South Korea

I. Introduction
The current-induced domain wall motion (CIDWM) has attracted a considerable interest because of its fundamental physics and potential application for new spintronic devices [1, 2]. The adiabatic and non-adiabatic spin torque terms have been proposed to describe CIDWM. Despite lots of studies, there is a controversy over the so-called β term measuring the relative magnitude of the non-adiabatic torque with respect to the adiabatic one [3]. From the viewpoint of application, equi-spaced mechanical notches can be used to control the position of DW in a nanostrip. Therefore, it is important to investigate the depinning current density (J_C) of DW from a notch. In this work, we investigate J_C and its dependence on β by means of micromagnetic modeling. Two kinds of J_C's are studied. The *static* J_C ($=J_{St}$) is a threshold to depin a DW initially placed within a notch. The *dynamic* J_C ($=J_{Dy}$) corresponds to the case that a DW is initially placed outside a notch. The J_{Dy} is determined by how large current density can let the DW pass through the notch. Note that the velocity of DW (ν_{DW}) reflects the momentum of DW and is closely related to the tilting angle of DW. In the *static* case, the initial ν_{DW}^0 is determined by the adiabatic spin torque. In the *dynamics* case, however, the ν_{DW} at the position of notch is smaller or larger than ν_{DW}^0 depending on β since the tilting angle of DW is significantly affected by β. In this work, we show that by comparing the J_{St} and J_{Dy}, it is possible to get a clue for resolving the controversy over the β term.
II. Micromagnetic Simulation
We use the modified Landau-Lifshitz-Gilbert equation with including the spin torque terms;
$\partial M/\partial t = -\gamma(M\times H_{eff}) + \alpha/Ms(M\times\partial M/\partial t) - b_J/Ms^2(M\times(M\times\nabla M)) - c_J/Ms\,(M\times\nabla M)$
where H_{eff} is the effective field consisting of the anisotropy, exchange, magnetostatic, and current-induced Oersted fields. The model parameter is selected for the Permalloy. The b_J ($= Pj_e\mu_B/eMs$) and c_J ($= \beta\, b_J$) present the magnitude of the adiabatic and non-adiabatic spin torque, respectively. Inhomogeneous current distribution due to a notch is calculated by solving the Laplace's equation. The model system is shown in Fig. 1(a). The dimension of nanostrip is $1000\times75\times10$ (length (l) $\times$ width (w) $\times$ thickness (t)) nm^3 divided into $2.5\times2.5\times10$ nm^3 cells. The shape of a notch is a triangle. The width of nanostrip at the center of notch is 50 nm. In case of the J_{Dy}, the distance between initial DW position and notch is assumed as 250 nm. Two types of DWs, clockwise transverse wall (CW-TW) and anti-clockwise TW (ACW-TW) are considered.
III. Results and Discussions
Fig. 1. (b) and (c) show J_C as a function of the non-adiabatic contribution (β/α) for ACW-TW and CW-TW, respectively. In both types of DWs, J_C decreases with increasing β/α. When β<α, J_{Dy} is slightly larger than J_{St}. In this case, ν_{DW} is smaller than ν_{DW}^0 because the tilting angle of DW measured from the nanostrip plane is negative. When β=α, the J_{Dy} and J_{St} are identical since the tilting angle is zero. When β>α, the DW gains an additional kinetic energy due to a positive tilting in the *dynamic* case and therefore the J_{Dy} is smaller than the J_{St}.
Reminding the present debate over the magnitude of β term, our result indicates that it is possible to determine the non-adiabatic contribution, at least if β>α, β=α or β<α, by comparing J_{Dy} and J_{St}. When β>2α (4α), J_{St} of ACW-TW (CW-TW) is larger than J_{Dy} by factor of 1.5 (Inset of Fig. 1 (b) and (c)). In this range of β, thus, it is difficult to stop a DW at the next notch, which can be a serious problem for the application of CIDWM in the mass storage device. Moreover, J_{St} of ACW-TW are different for different sign of current. The $(+)J_{St}$ is larger (smaller) than the $(-)J_{St}$ with β>α (β<α). This asymmetric behavior is caused by the different shape of potential well at the notch. As shown in Fig. 1(d), the CW-TW experiences a single energy minimum at the center of notch whereas the ACW-TW does double minima. In our system, when the sign of current is minus, the ACW-TW experiences the minor energy barrier located at the center of notch. Thus, *static* depinning process with (–)J is similar to the *dynamic* one.
IV. Conclusion
The J_C depends on the chirality and the initial position of DW, i.e. *static* and *dynamic* depinning. By comparing J_{Dy} and J_{St}, it is possible to get a clue about the non-adiabatic contribution.

[1] S. S. P. Parkin, U.S. Patent No. 6,834,005 (2004).

[2] D. A. Allwood et al, Science 309, 1688 (2005).

[3] G. Tatara and H. Kohno, Phys. Rev. Lett. 92, 086601 (2004); S. E. Barnes et al, Phys. Rev. Lett. 95, 107204 (2005); Y. Tserkovnyak et al, Phys. Rev. B 74, 144405 (2006).

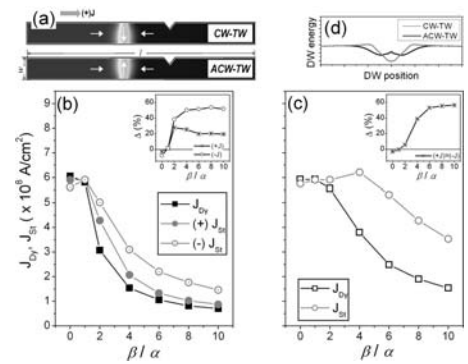

Fig. 1. (a) depicts geometry of the nanostrip. The critical depinning current density as a function of the β term for (b) ACW-TW, and (c) CW-TW. Inset of (b) and (c) show Δ(%) (= (J_{St} - J_{Dy}) / J_{St} × 100). (d) shows DW energy landscape as a function of DW position.

GT-16

Current-assisted variation of magnetization reversal process in tri-layer-ring spin valve.

D. Chen[1], C. Yu[2], Y. Yao[1,3]

1. Department of Material Science and Engineering, National Chiao Tung University, Hsinchu, Taiwan; 2. Institute of Physics, Academia Sinica, Taipei, Taiwan; 3. The Department of Materials Engineering, Tatung University, Taipei, Taiwan

A tri-layer spin valve in ring shape has been fabricated by e-beam lithography and lift-off technique. The structure is Py(20nm)/Cu(10nm)/Py(10nm) from bottom to up with 1.2 µm in outer diameter, and 0.4 µm in width. Copper electric contacts are used to connect the spin valve device and pad leads. Magnetoresistance (MR) curves were obtained by current-in-plan (CIP) and two-terminal measurements (Fig.1) at room temperature. Single layers of Py ring (20nm and 10nm in thickness) were also fabricated and measured to compare with the tri-layer structure. The result of OOMMF simulation for 10nm single layer of Py ring shows no vortex state in the magnetization reversal process, that is, only one-step switch (onion to reverse onion) exists in reversal process. For 20nm Py ring, however, two-step switch (onion-to-vortex and vortex-to-reverse-onion) was observed. The experimentally obtained MR curves (Fig.2 & 3) for both single Py ring layers confirm the same results with simulation. The MR signal of tri-layer spin valve for 10 µA current (Fig.4) shows an obvious spin valve signal combined with anisotropic magnetoresistance (AMR) effect. With field relaxed and increasing toward negative direction till around -45 Oe (configuration 1), the 10nm Py ring switches to reverse onion state, whereas the 20 nm one remain onion state. This causes MR at the highest state due to AMR effect and antiparallel configuration between the two Py ring layers. At configuration 2, the 20nm Py ring is in the vortex state with the 10nm one remaining at reverse onion state. Therefore, about half of the moments are in the parallel state, hence the MR is lower than that in configuration 1. After field exceed -185 Oe (configuration 3), both Py layers are in reverse onion state. The MR is in the lowest level not only due to the parallel configuration but also AMR effect. The current dependent MR behavior has been observed by increasing the measuring current to 1 mA. With current magnitude higher than 700µA, the obvious change in MR curves was observed. Fig.5 shows MR curve at 1 mA. The main difference from that at 10 µA (Fig. 3) is in the configuration 2, that is roughly -45 ~ -70 Oe. In this region (for 1mA current), the MR abruptly decrease and increase back to the level in configuration 3. Joule heat generated by current could be more proper to account for this phenomenon. The current density estimated (about 3 x 10^-6 A/cm2) here is far lower than the order of spin transfer torque (STT). Hence, for 20 nm Py ring layer, thermal activation induced by joule heating could cause multi-domain magnetization during the transition from onion state to vortex state. This causes most of moments not in well order arrangement, thus decrease the antiparallel effect between the two Py ring layers.

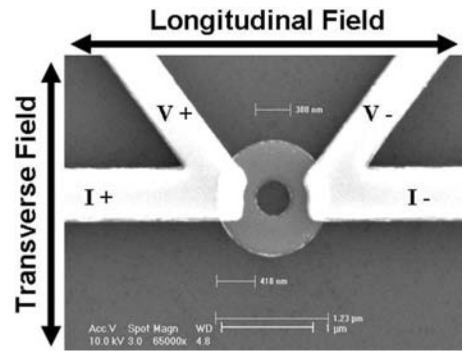

Fig.1

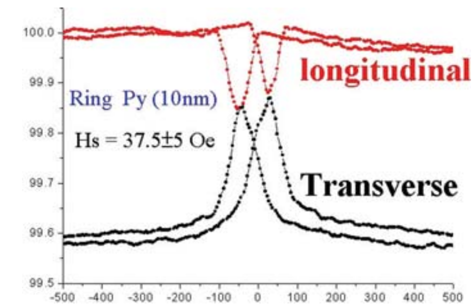

Fig.2

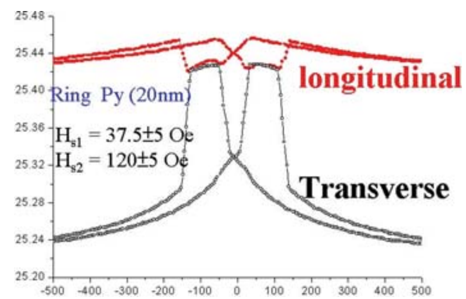

Fig.3

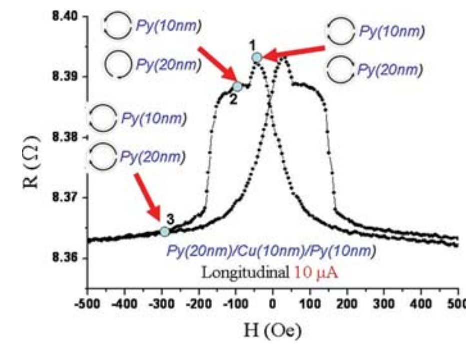

Fig.4

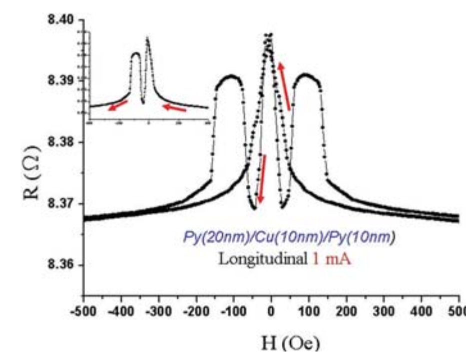

Fig.5

GT-17

Domain wall dynamics in the microwave frequency range probed by Spin diode effect.

S. Laribi[1,2], *A. Anane*[1], J. Grollier[1], V. Cros[1], K. Bouzehouane[1], G. Faini[3], A. Fert[1]
1. Unité Mixte de Physique CNRS/Thales and Université Paris Sud 11, Route départementale 128, 91767, Palaiseau, France; 2. ST Microelectronics, 850 Rue Jean Monnet, 38926, Crolles, France; 3. Phynano team, Laboratoire de Photonique et Nanostructures, LPN-CNRS, Route de Nozay, 91460, Marcoussis, France

The recent developments in current induced magnetization switching in nanopillars structures have onset a renewal in the field of current induced domain wall motion. The first theoretical ideas on the mechanism of spin-transfer torque from the conduction electron to the inhomogeneous magnetization configuration of a domain wall date to L. Berger [1]. But it is only recently that the improvement of the fabrication techniques and specially the design of adequate pining sites have permitted to make significant progress from the experimental point of view [2-5].
To detect electrically the motion of a domain wall there are basically two strategies. The first one is to rely on the anisotropic magnetoresitance (AMR). This is the main technique used when the nanowires are composed of a single ferromagnetic material (very often NiFe). The other possibility is to use the giant magnetoresistance effect (GMR). Here the nanostripe is a GMR stack with a pinned and a free layer. In this case, the measured resistance is proportional to the domain wall position. We have fabricated stripes with various geometries with Co/Cu/NiFe structure; the domain wall is nucleated in the NiFe layer.
In the present study, we have used two different geometries: regular wires and a more complex “diode” geometry (see Fig. 1). Magnetic force microscopy (MFM) imaging has been used to verify that the domain wall is indeed pinned in the trap as shown on Fig 1.
By setting the right experimental conditions (field and dc current), we have observed two level resistance fluctuations. The statistical analysis of the dwell times has allowed us to estimate the energy depth of the pinning trap. This energy is highly dependent on the position in the (field, current) parameter space. The fact that we observed the two level fluctuations means only that the dynamic of the domain wall fluctuation occurs in the right time window (10-4 Hz to 100 Hz) to allow use of DC measurements techniques. It is therefore probable that outside this window the fluctuation are still there. This conclusion is supported by the dV/dI measurements at few kHz [6]: peaks are observed on the current dependence of the differential resistance.
In nanopillar geometry, the discovery of universal resistance fluctuations has paved the way to the microwave coherent emission. Having this in mind we have studied the microwave frequency response of a domain wall. We chose to make measurements where we inject ac power into the sample and we detect the dc voltage, this is the so called “spin torque diode effect”[7]. We have successfully observed the rectification effect (Fig. 2), with characteristic frequencies lying from 1.5 to 3.5 GHz. Furthermore they are tunable with modification of the external applied magnetic field. Those experiments are a first step toward understanding the magnetic domain wall behaviour in the microwave frequency range.

[1] L. Berger, J. Phys. Chem. Solids 35, 947 (1974); J. Appl. Phys. 49, 2156 5(1978)

[2] J. Grollier et al., Appl. Phys. Lett. 83, 509 (2003)

[3] E. Saitoh et al., Nature (London) 432, 203 (2004)

[4] L. Thomas, M. Hayashi, X. Jiang, R. Moriya, C. Rettner, and S. S. P. Parkin, Nature (London) 443, 197 (2006)

[5] D. Bedau, M. Kläui, S. Krzyk, U. Rüdiger, G. Faini and L. Vila Phys. Rev. Lett. 99, 146601 (2007)

[6] S. Laribi et al. Appl. Phys. Lett. 90, 232505 (2007)

[7] A. A. Tulapurkar, et al., Nature, 438, 339 (2005)

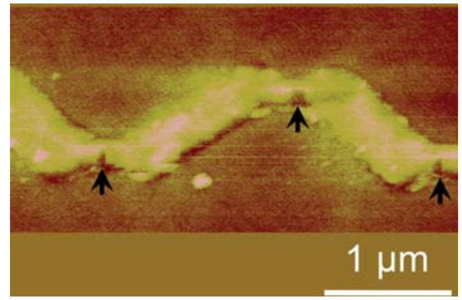

MFM image of a “diode” geometry stripe. The arrows point to the pinned domain walls

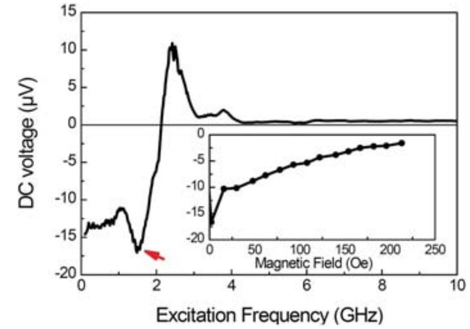

DC voltage as a function of the excitation frequency with a constant power of -15 dBm. In inset is plotted the amplitude variation of the peak labelled with the arrow with magnetic field.

GT-18

Current induced domain wall motion with step structure.

H. Ashida, T. Ochiai, Y. Shimizu, A. Tanaka
Fujitsu Limited., Atsugi, 243-0197, Japan

1. Introduction

Since the **c**urrent **i**nduced magnetic **d**omain **w**all **m**otion (CIDWM) was theoretically predicted,[1-3] the spintronics devices using CIDWM have been extensively studied. Domain wall (DW)-based shift register memory proposed by Parkin[4] is expected to be the high integration memory (>1Gbit), because the data of the numerous bits can be stored in a narrow wire. The basic CIDWM phenomena can occur in a submicron-size ferromagnetic wire, and DW motion has been confirmed with the current density of 10^{11} - 10^{12}A/m^2. On the other hand, the stable control of the DW motion is important for the memory application. DW pinning by two-dimensional shapes such as the neck, and the zigzag structures has been reported to trap the DW.[5-8] In this paper, we report on the pinning effect in three-dimensional step structure in order to achieve DW displacement control.

2. Experiment

The sequence of fabrication is shown in Fig.1. The steps (depth:Ds = 20 - 60 nm) were fabricated on a silicon substrate by RIE (Reactive Ion Etching). After NiFe (40 nm) deposition, the wire was patterned with the width of 400 – 500 nm using the conventional lithography and the ion milling. Finally, the electrode pads were made by the lift-off technique. Fig.3 shows an AFM image of the sample. We evaluated the depinning magnetic field (H_{dpin}). Further more, the critical current density (J_{th}) of CIDWM was investigated from the displacement of the DW measured using MFM without an external assist magnetic field.

3. Results and Discussion

The DW was introduced by the external magnetic field and was easily trapped at the step edge. The H_{dpin} as a function of Ds is shown in Fig.2. H_{dpin} increases with increasing Ds. Therefore, DW pinning is able to be controlled by Ds. Fig.4 shows a result of CIDWM phenomena. Fig.4(a) is the AFM image, and Fig.4(b) is the MFM image before applying current pulses. In Fig.4(c) - (e), the DW was moved and trapped by the step edges by applying the pulse of $|J_{th}| \fallingdotseq 3.0\times10^{11}$A/m^2 (Pulse = 0.5µs). It is probably because that the pinning potential of the step edges is larger than that of the straight line part.

Togawa *et al.* suggested that the Joule heating assists the DW motion because the DW motion occurred when the wire resistance was increased to more than 1.5 times of the initial value.[7] In our experiment, there was a similar resistance increase. Therefore, we consider that the DW displacement of this result was induced by the spin torque effect and the Joule heating assist. To conclude, we investigated the CIDWM in the step structure. It was found that the step edge can block the DW motion and trap the DW effectively. Our experiments demonstrate the feasibility of controllable displacement of the DW in a magnetic wire using the step structure.

4. Acknowledgement

We would like to thank Prof. Teruo Ono for valuable discussion. The present work was partly supported by NEDO Spintronics nonvolatile devices project.

[1]L.Berger: J.Appl.Phys. 55(1984)1954

[2]J.C. Slonczewski: J.Magn.Magn.159(1996)L1

[3]G.Tatara,et.al: Phys.Rev.Lett.92(2004)086601

[4]S.S.P.Parkin, US Patent,21 December, No.6834005

[5]Y.Yamaguchi,et.al: Phys.Rev.Lett. 92(2004)077205

[6]M.Klaui,et.al: Phys.Rev.Lett. 95(2005)026601

[7]Y.Togawa,et.al: Jpn.J.Apl.Phys.Vol.45-27(2006)L683

[8]M.Hayashi,et.al: Phys.Rev.Lett. 96(2006)197207

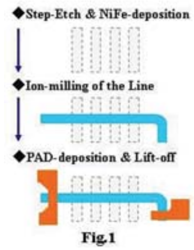

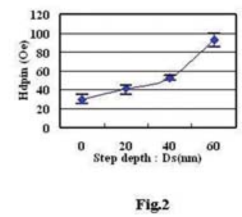

Fig.1 The sample fabrication sequence.
Fig.2 The dependence of H_{dpin} and Ds.

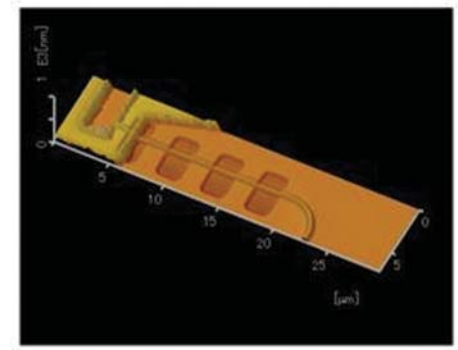

Fig.3 AFM image of the NiFe sample with thickness 40 nm, width : w = 452 nm, step depth : Ds = 40 nm. The electrode pad is Ti5/Au85 nm.

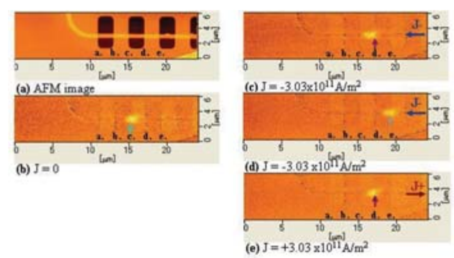

Fig.4 AFM (a) and MFM images (b) - (e) of the 40 nm-thick NiFe wire (Ds = 40 nm).

Magnetocaloric Effect in Ni-Mn-Ga Alloys.

K. Mandal[1], D. Pal[1], O. Gutfleisch[2], J. Lyubina[2], N. Scheerbaum[2]
1. Materials Science, S. N. Bose National Centre for Basic Sciences, Kolkata, India; 2. Institut für Metallische Werkstoffe, Leibniz Institute für Festkörper- und Werkstoffforschung Dresden (IFW Dresden), Dresden, Germany

During last few years, magnetic refrigeration has attracted significant attention as it is found to be more energy efficient and environment friendly compared to the conventional gas refrigeration [1, 2]. Recently, large MCE in non-rare-earth based Ni-Mn-Ga Heusler alloys, well known for their magnetic shape-memory effect, has also been reported [3].
Both stoichiometric and off-stoichiometric compounds with composition close to Ni_2MnGa show a cubic $L2_1$ austenite phase at higher temperature. Upon cooling the alloy, it undergoes a martensitic transformation to martensite phase. On changing the temperature a first-order structural transition takes place between these two phases at martensitic transition temperature causing an abrupt change of magnetization. It was found that martensitic transformation and Curie temperature are strongly influenced by the alloy compositions and a large change in entropy and hence MCE was observed when the structural transition coincides with the magnetic transition at Curie temperature. In the present work, $Ni_{2+x}Mn_{1-x}Ga$ (x=0.16, 0.18, 0.20, 0.22, 0.24, 0.26) alloys were prepared and studied to understand the effect of substituting Mn with Ni on the structural and magnetic transition.

The thermal behaviour of six samples studied by DSC measurements has been plotted in Fig.1. Martensite-austenite transformation temperatures increase significantly when the nickel content is increased from x=0.16 to 0.26. Figure2 shows the XRD pattern at room temperature of (a) $Ni_{2.18}Mn_{0.82}Ga$ and (b) $Ni_{2.26}Mn_{0.74}Ga$ samples with martensitic transition temperatures respectively below and above room temperature. The first sample shows a cubic $L2_1$ structures at room temperature whereas the second one shows non-modulated (NM) martensite phase at room temperature.

Magnetic properties of the samples have been studied in details. MCE has been determined for all the samples around their T_c and T_m by calculating the change in magnetic entropy due to a magnetic field change of 0-5 T using the Maxwell's thermodynamic relations.
Among the above samples, $Ni_{2.22}Mn_{0.78}Ga$ composition in which T_c and T_m are very close to each other shows maximum change in $|\Delta S|$. Large change in magnetization with temperature along with significant hysteresis effect is observed within 290 K and 292 K. To study this part more carefully, M vs H data were taken within 287 K and 292 K at 0.5 K intervals. Maximum values of $|\Delta S|$ are found to be 28 J/Kg.K at 289.5 K with ΔT=3 K and 96 J/Kg.K at 290.75 K with ΔT=0.5 K as shown in Fig.3. The effect of hydrostatic pressure on magnetic and MCE properties has also been studied. A pressure of 8 kbar shifts the martensitic transition temperatures as well as the T_c of the samples towards higher temperature. The $|\Delta S|$ in presence of 8 kbar pressure is approximately 28.5 J/Kg.K at 297.5 K with ΔT=3 K and 86 J/Kg.K at 297.0 K with ΔT=0.5 K as shown in Fig.3 also. The large magnetic hysteresis observed in the M vs H curves at ambient pressure almost vanishes due to the application of 8 kbar pressure.

[1] V.K. Pecharsky and K. A. Gschneidner, Phys. Rev. Lett. **78**, 4494 (1997).

[2] K. Mandal, D. Pal, O. Gutfleisch, P. Kerschl and K.–H. Müller, J. Appl. Phys. **102**, 053906 (2007).

[3] M. Pasquale, C. P. Sasso, L. H. Lewis, L. Giudici, T. Lograsso and D. Schlagel, Phys. Rev. B **72**, 094435 (2005).

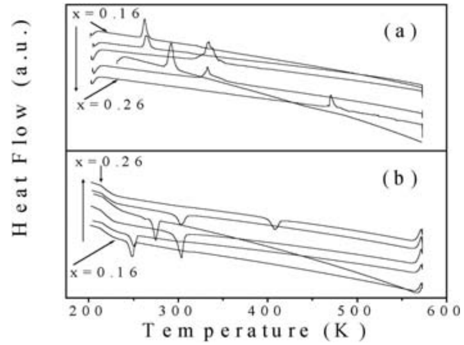

Fig. 1: (a) Heating and (b) cooling cycle of differential scanning calorimetry study of $Ni_{2+x}Mn_{1-x}Ga$ (x=0.16, 0.18, 0.20, 0.22, 0.24, 0.26) alloys.

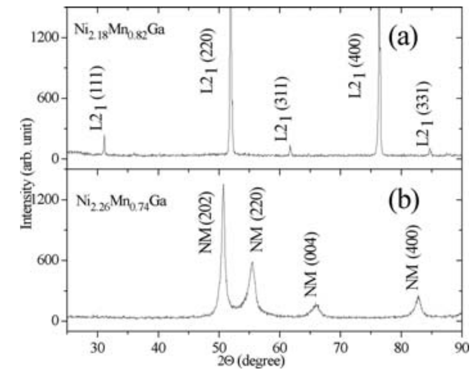

Fig. 2: X-ray diffraction pattern of $Ni_{2+x}Mn_{1-x}Ga$ (x=0.18, 0.26) alloys at room temperature using Co-target.

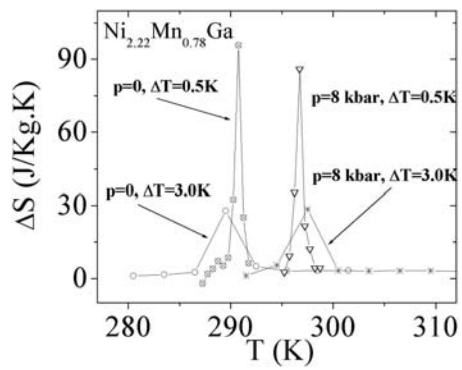

Fig. 3: Temperature dependence of isothermal entropy change $|\Delta S|$ of $Ni_{2.22}Mn_{0.78}Ga$ alloy in absence and in presence of 8 kbar pressure.

GU-02

Magnetic properties and magnetocaloric effect in $Tb_8Co_{16-X}A_X$ compounds where A=Al or Cu and x ≤ 4.

R. Tetean, E. Burzo, I. G. Deac
Physics, Babes-Bolyai University, Cluj Napoca, Romania

Magnetic materials showing a large magnetocaloric effect (MCE) have attracted considerable attention for their potential application in magnetic refrigeration technology. The RCo_2 intermetallic compounds (R= rare earth metal) were intensively studied due to the metamagnetic transition of cobalt. When R is nonmagnetic there are necessary high fields (> 70 T in YCo_2) in order to induce magnetic moments on cobalt atoms. If R is magnetic, the internal field is high enough to polarize the cobalt sublattice. Due to the high value of the R magnetic moment large entropy changes at the transition temperature were reported [1,2].

The $Tb_8Co_{16-X}A_X$ where A=Al or Cu and x ≤4 compounds were prepared by arc melting the constituent elements in a purified argon atmosphere. The samples were heat treated in vacuum, at 1000°C, for 5 days. The X-ray analysis shows the presence of one phase only, for x ≤ 4, of C15 type. The magnetic measurements were performed in the temperature range 4.2-900 K and external fields up to 9T The entropy changes were determined from magnetization isotherms. The saturation magnetizations, at 4.2 K, increase as cobalt is replaced by Cu or Al. The above behavior is in agreement with the presence of a ferrimagnetic type ordering, the cobalt and terbium magnetic moments being antiparallely oriented. The cobalt moments are little dependent on A content having values in the range 1.15 μ_B/atom. The above value is in agreement with that obtained from band structure calculations. As example in $TbCo_2$ a value of M_{Co}=1.12 μ_B was obtained. The exchange interactions between Tb and Co are of 4f-5d-3d type. The Tb 5d band polarizations are parallely oriented to 4f moments and decrease starting from 0.47 μ_B (x=0) when increasing the content of nonmagnetic elements. The Curie temperatures increase slowly and then decrease when A content increase.

The temperature dependences of reciprocal susceptibilities follow a hyperbolic law of Néel- type, characteristic for ferrimagnetic ordering. According to addition law of susceptibilities and supposing that the Curie constant of terbium is the same as that of Tb^{3+} ion, we have determined the contributions of Co, to the Curie constants and the effective cobalt moments, M_{eff}(Co), respectively. The M_{eff}(Co) values are only slightly composition dependent being 2.81±0.09 μ_B/atom. The ratio $r=S_P/S_0$ between the number of spins obtained from effective iron moments, S_P, and saturation moments, S_0, is quite constant having values around 1.73 for A=Al and 1.76 for A=Cu. In the local moment limit we have r=1.0. The r values suggest that cobalt have rather high degree of itinerancy.

The above behaviour can be analyzed in the spin fluctuation model. When the amplitude of local spin fluctuations (LSF) is large and fixed, there is a local moment limit, where only the transverse components of LSF are important. As the amplitude of LSF is small, there is the weakly ferromagnet limit, where the longitudinal components of LSF or temperature variation of amplitude of LSF play an important role. From the r values in $Tb_8Co_{16-X}A_X$ system we conclude that there are significant contributions from longitudinal components of LSF which increase when A content is greater, although the transverse components dominate.

The temperature dependence of magnetic entropy change in 7T and 9T external applied fields for the compounds with x = 1, 2, 3 and A=Al are plotted in Fig.1. The entropy change values show maxima around the Curie temperatures and are rather high for compounds showing a second order phase transition. As example in $TbCo_{13}Cu_3$ a value of 7.3 J/kgK was determined while in case of $TbCo_{13}Al_3$ the value was 6.7 J/kgK. Around 63 % of the heat is absorbed in a temperature range ±12 K, centered at the Curie point.

The origin of the large magnetic entropy change in these compounds could be attributed to the considerable variation of the magnetization near the transition temperature.

[1] A.M. Tishin and Y.I. Spichkin, The Magnetocaloric effect and its Applications, 1st ed., Institute of Physics, New York (2003). [2] Ekkes Bruck in Handbook of Magnetic Materials, edited by K.H.J. Buschow, Elsevier Science, New York, Vol. 17, 235-292 (2008)

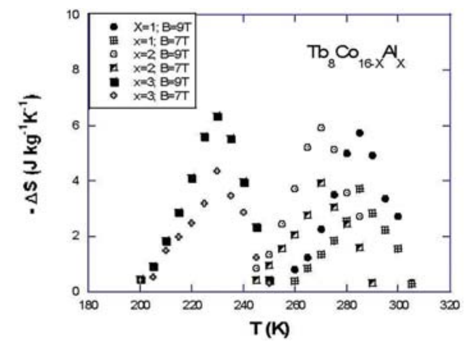

Fig.1. Magnetic entropy change of the compounds with x=1, 2, respectively 3 as function of temperature in 7 and 9T.

GU-03

Synthesis and evaluation of magnetocaloric effect of rare earth nitrides.

Y. Hirayama[1], S. Nishio[1], T. Kusunose[2], T. Nakagawa[3], T. A. Yamamoto[1]
1. Graduate School of Engineering, Osaka University, Osaka, Japan; 2. Institute of Scientific and Industrial Research, Osaka University, Osaka, Japan; 3. Graduate School of Science and Engineering, Tokyo Institute of Technology, Tokyo, Japan

In the hydrogen society coming in near-future, it must be important to transport and storage hydrogen with the high energy density as possible. The highest hydrogen densities with respect both to mass and volume are given by the liquid hydrogen. To liquefy hydrogen, we have to cool it down to 20K. In general, the efficiency of the conventional cooling system working with a gaseous refrigerant decreases with temperature, so that much energy is required to liquefy hydrogen. On the other hand, the magnetic cooling method may provide a higher efficiency even at these low temperatures because it is based on the magnetocaloric effect which associates intrinsically small irreversibility. From a ferromagnet, a magnetic entropy change ΔS is extracted by swinging external applied field, and it is maximized in the vicinity of its Curie temperature. hus obtained ΔS is converted directly into heat, $Q=T\Delta S$. Its application to the hydrogen liquefaction system was indeed proposed [1]. To realize the magnetic cooling and liquefaction of hydrogen, it is necessary to find the suitable magnetic refrigerant material. We have pointed out mononitrides of rare earth elements, Gd, Tb, Dy, Ho, Er, are promising candidate materials because of its remarkable characteristics; (1) their packing densities of rare earth atoms are significantly higher than those of metallic phases of the hcp structure, (2) they are ferromagnetism and their Curie's temperatures lie in a region, 6 to 70 K. In these nitrides, magnetic moments undergoing the ferro–paramagnetic transition at relevant temperatures are closed packed.

We synthesized binary rare earth nitrides ($Gd_{0.5}Tb_{0.5}N$, $Tb_{0.5}Dy_{0.5}N$ and $Dy_{0.5}Ho_{0.5}N$) by two methods, carbothermic reduction (CTR) and hot isostatic pressing (HIP). To examine the phase occurring in the product, their XRD patterns were measured. To evaluate the MCE i.e. ΔS, we took two routes; one is measurements of specific heats as functions of temperature, T=3–80 K, under magnetic field, H =5 T or zero field, $C_H(T)$ and $C_0(T)$.The $\Delta S(T)$ induced by isothermal demagnetization from H to 0 is given by equations $\Delta S(T)=S_0(T)-S_H(T)=\int_0^T C_0(T)/T dT-\int_0^T C_H(T)/T dT$, where S_H and S_0 are absolute entropies under magnetic field H and zero field, respectively. In executing these integrals, the specific heat below 3 K was assumed to obey the Debye's theory, proportionating to T^3. The samples obtained by the CTR were too brittle and porous to measure the specific heat. Another route is measurements of magnetization as function of temperature and applied field, $M(T,H)$, T=3–100 K, H=0–5 T. From the data sets, $\Delta S(T)=\int_H^0 (\partial M/\partial T)_H dH$. Note that the latter equation is driven by using the Maxwell's relation, $(\partial M/\partial T)_H=(\partial S/\partial H)_T$.

The lattice parameters determined by the XRD patterns of the samples prepared by the two methods are plotted in Fig. 1 against average radius of trivalent ions of the constituent elements together with previously reported data [2-4]. They fall onto a straight line, indicating that they belong to a class of material. Fig. 2 shows $S(T)$ curves calculated from $C_H(T)$ and $C_0(T)$ measured at 5T and 0T of $Dy_{0.5}Ho_{0.5}N$ synthesized by the HIP method, and ΔS and ΔT calculated from these curves, where ΔT is the adiabatic temperature change.The same data processing procedures were done for other samples synthesized by the HIP method. Their $S(T)$ curves have peaks at temperatures varying in a range of 6K-70K continuously depending on the constituent elements and the composition. The obtained $\Delta S(T)$ curves reasonably agreed with each other regardless of synthesis methods, HIP or CTR, and of evaluation method, magnetization or specific heat. Fig. 2 indicates that magnetic refrigerants of $Dy_{0.5}Ho_{0.5}N$ would adiabatically cool itself down by five degree at least from a temperature in a region of 20–40 K. We are going to show results indicating that the rare earth nitrides are promising magnetic refrigerant materials for hydrogen liquefying system working below liquid nitrogen temperature.

[1] V.K. Pecharsky, K.A. Gshneidner Jr, J. Magn. Magn. Mater. 200 (1999) 44.

[2] T. Nakagawa, K. Sako, T. Arakawa, T.A. Yamamoto, J. Alloys Compd. 364(1–2) (2004) 53–58.

[3] T.A. Yamamoto, T. Nakagawa, K. Sako, T. Arakawa, J. Alloys Compd. 376 (2004) 17–22.

[4] T. Nakagawa, T. Arakawa, K. Sako, N. Tomioka, T.A. Yamamoto, K. Kamiya, T. Numazawa, J. Alloys Compd.408–412 (2006) 191–195.

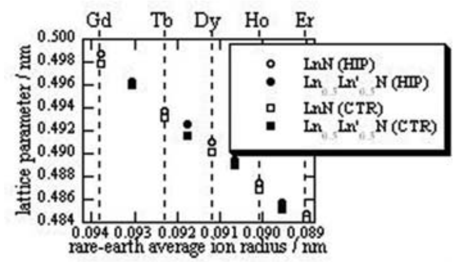

Lattice parameters determined from XRD pattern plotted against average radius of trivalent rare-earth ions.

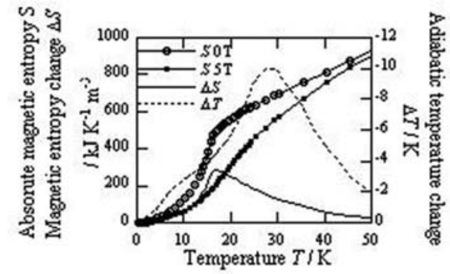

Entropy S measured under field of 0 T and 5 T of $Dy_{0.5}Ho_{0.5}N$ which were calculated from heat capacity measurements. There as well shown ΔS and ΔT graphically obtained from these curves.

GU-04

Anisotropy of magnetocaloric effect in R2Fe17 single crystals with heavy RE metals and Y.

K. P. Skokov[1], Y. G. Pastushenkov[1], Y. S. Koshkid'ko[1], T. I. Ivanova[2], S. A. Nikitin[2]
1. Department of Physics, Tver State University, Tver, Russian Federation; 2. Department of Physics, Moscow State University, Moscow, Russian Federation

The first studies of the magnetocaloric effect (MCE) anisotropy were carried out rather long ago [1]; however, until recently, they were quite scarce [2-3]. The MCE anisotropy can be measured directly as the adiabatic temperature change ΔT or indirectly from magnetization and heat capacity [4]. The majority of studies use indirect measurements to measure the MCE. Also, the studies in this field mostly use polycrystaline samples. The present study shows the advantages of direct measurements of the MCE anisotropy in R2Fe17 single crystals and discusses some problems arising when polycrystalline samples are used. This study shows that the direct measurement of ΔT(H) in single crystals along different crystallographic directions makes it possible to get accurate data on MCE anisotropy. These data are important for developing new types of magnetic refrigerators. Fig.1 shows the temperature dependencies of MCE in Y2Fe17 single crystals (Fig.1a), Dy2Fe17 single crystals (Fig.1b), Er2Fe17 single crystals (Fig.1c), and Ho2Fe17 single crystals (Fig.1d), measured along the c-axis (a hard magnetization direction (circle)) and the a-axis (an easy magnetization direction (triangle)) for this group of compounds.

As we can see from this figure, for theY2Fe17 compound, the temperature dependencies of MCE measured along different crystallographic directions differ near Curie temperature by 10%. This is caused by the fact that magnetic anisotropy of the compound in the Curie temperature region has a nonzero value. Consequently, when the MCE is measured on polycrystalline samples, the ΔT value is lower due to the random grain orientation.

For the compounds with magnetic RE metals, such as Dy, Ho, or Er, the difference in MCE values observed during the magnetization of a magnetic material along different crystallographic axes can reach 40-50% (Fig.1b-1d), which is considerably lower than the experimentally measured ΔT values on polycrystalline samples. In addition, as Fig. 1c-1d shows, the MCE measured along different crystallographic directions in the Curie temperature region has a different sign, which makes it impossible to determine the accurate values of this effect in polycrystalline samples. It should be noted that the MCE values for the compounds with Dy, Ho, and Er are almost the same as the values for the compounds with nonmagnetic Y. This is explained by the fact that, for this group of compounds, the main contribution to the MCE is made by the Fe sublattice.

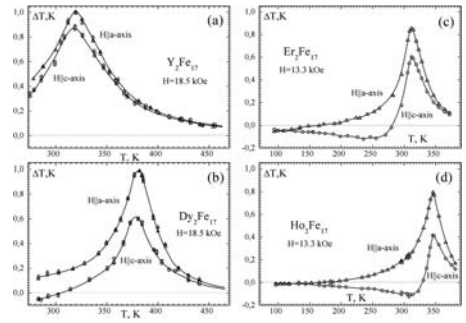

Fig.1. Temperature dependencies of MCE, measured along a- and c-axes in R2Fe17 single crystals.

1. Akulov N.S., Kirensky L.W., J. Phys.USSR (1940) V.3. P.31-34.

2. Belov K.P., Talalaeva E.V., Chernikova L.A., Ivanova T.I. et al., Sov. Phys. JETP (1977) V.45, 307-310.

3. Nikitin S.A., Andreenko A.S., Zvesdin A.K., Popkov A.F., RAN Isvestija, Metalls (1980) V.44, P.1343-1347.

4. Pecharsky V.K., Gschneider K.A., I. Appl. Phys. (1999) V.1. 565-575.

GU-05

Magnetocaloric effect in Gd4(Bi_xSb_{1-x})$_3$ alloys.

N. A. de Oliveira, M. B. Gomes
Instituto de Física, Universidade do Estado do Rio de Janeiro, Rio de Janeiro, Brazil

The magnetocaloric effect, which is basically the temperature change of a magnetic material upon magnetic field variation, was first discovered by Warburg[1] in the later years of the 19^{th} century. The early application of this effect was made to reduce the temperature of magnetic salts to very low values[2]. However, the most important application of the magnetocaloric effect happened in 1976 when Brown[3] developed a prototype of a magnetic refrigerator using gadolinium as magnetic refrigerant. Since the Brown's work, many efforts have been done in order to bring magnetic refrigeration to our daily life. In 1997 Percharsky and Gschneidner[4] reported on large values of the magnetocaloric potential ΔS in the compound $Gd_5Si_2Ge_2$. After this discovery, a great deal of experimental and theoretical works has been developed in order to find new magnetic materials suitable for application in magnetic refrigeration. In order to be used as magnetic refrigerant in magnetic refrigerators, the magnetic material should exhibit large values of the magnetocaloric potentials ΔS and ΔT_{ad} in the temperature range of the operation of the refrigerator. Applied pressure and doping with suitable impurities are important physical mechanisms to enhance the magnitude of the magnetocaloric potentials and trigger their position to desirable temperature range. For instance, it has been shown that the magnetocaloric potentials in the compound $Gd_5Si_2Ge_2$ extremely depends on the Ge concentration. Besides, it has also been shown that when transition elements such as Fe and Ni are introduced in the compound $Gd_5Si_2Ge_2$ the magnetic ordering temperature is shifted towards room temperature and the magnetocaloric potential ΔS is somewhat reduced. Despite of much experimental works in this line of research, there are only a few theoretical papers dealing with the effects of applied pressure and doping on the magnetocaloric properties of metallic compounds. A complete discussion about this subject is very important not only to understand the physical mechanisms behind the magnetocaloric effect but also to help in the search of new magnetic materials suitable for application in magnetic refrigeration.

In this work, we theoretically discuss the magnetocaloric effect in the doped compound Gd4(Bi_xSb_{1-x})$_3$. It should be noted that in this doped compound the impurities enters substitutionally in the sites occupied by non rare earth ions. Although Bi and Sb are non magnetic ions, they play an important role in the magnetic properties of the doped compound Gd4(Bi_xSb_{1-x})$_3$. That is because, the exchange interaction between Gd ions in this doped compound depends on the impurity concentration. In order to describe the magnetocaloric effect in this doped compound, we use a model Hamiltonian of interacting 4f-spins with an interaction with the applied magnetic field. Since there is no evidence of first order phase transition in this compound, the magnetoelastic interaction can be neglected. The crystalline electrical field is not important either, because Gd ions has no orbital angular momentum. The chemical disorder in the electron gas in the compound Gd4(Bi_xSb_{1-x})$_3$, which modifies the conduction electron energy band and consequently affect the indirect 4f-4f spin interaction, is treated in the non-diagonal Coherent Potential Approximation (CPA). The 4f-4f spin interaction is treated in the conventional mean field theory. The total entropy is considered as the sum of the contribution from the magnetic ions, the conduction electrons and the crystalline lattice. The magnetic part of the entropy is obtained after the self-consistently solution of the magnetic state equation. The crystalline lattice entropy is taken into account in the Debye approximation. The contribution from the conduction electrons to the total entropy is taken as γT where γ is the Sommerfeld coefficient.

For a fixed set of model parameters, we calculate the magnetic, the thermodynamic and the magnetocaloric properties in the doped compound Gd4(Bi_xSb_{1-x})$_3$ as a function of Bi concentration. Our theoretical calculations show that as the Bi concentration is increased, the conduction electron bandwidth and the exchange interaction parameter increase. As a result the Curie temperature in the doped compound Gd4(Bi_xSb_{1-x})$_3$ increases with increasing Bi concentration. As far as the magnetocaloric is concerned, our calculations show that the magnitude of the magnetocaloric potential ΔS smoothly decreases and the magnetocaloric potential ΔT_{ad} remain almost the same as the Bi concentration increases. These conclusions are in good agreement with the available experimental data[5]. We also calculate the effect an applied pressure on the magnetocaloric properties of this doped compound. In this case experimental data are necessary to compare with our theoretical calculations. The present model can be straightforwardly extended to systematically calculate the effect of applied pressures and impurities on the magnetocaloric properties of many rare earth based compounds.
We acknowledge partial financial support from the Brazilian agencies CNPq and FAPERJ.

[1] E. Warburg, Ann. Phys., 13 (1881) 141.

[2] P. Debye, Ann. Phys., 81 (1926) 1154.

[3] G. V. Brown, J. Appl. Phys., 47 (1976) 3673.

[4] V. K. Pecharsky and K. A. Gschneidner Jr, Phys. Rev. Lett. 78 (1997) 4494.

[5] X. J. Niu, K.A. Gschneidner Jr., A. O. Pecharsky, V. K. Pecharsky, J. Mag. Mag. Mat. 234 (2001) 193206

GU-06

Magnetocaloric effect in $La(Fe_xSi_{1-x})_{13}$ under applied pressure.

N. A. de Oliveira[1], L. G. de Medeiros Jr[1], A. Troper[1,2]
1. Instituto de Física, Universidade do Estado do Rio de Janeiro, Rio de Janeiro, Brazil; 2. Centro Brasileiro de Pesquisas Físicas, Rio de Janeiro, Brazil

The magnetocaloric effect[1] has been intensively studied in the literature in the last years. Since the discovery of the giant magnetocaloric effect in $Gd_5Si_2Ge_2$ experimentalists and theoreticians have been searching for new magnetic materials with large values of the magnetocaloric potentials ΔS and ΔT_{ad}. Experimental data [2] show that the isothermal entropy changes ΔS in the compounds $La(Fe_xSi_{1-x})_{13}$ (x=0.88, 0.89 and 0.90) exhibit large values around the phase transition which is of first order. Moreover, experimental data [2] also show that the peaks of the isothermal entropy changes in this series of compounds doped with hydrogen are pushed towards higher temperatures. However, the magnitudes of the magnetocaloric potential ΔS are almost the same. On the other hand, it has been experimentally [3] shown that an applied pressure as large as 8 kbar changes significantly the magnetic ordering temperature in the doped compound $La(Fe_{0.89}Si_{0.11})_{13}$ and yields large values of the magnetocaloric potential ΔS. These experimental evidences indicate that the series of compounds $La(Fe_xSi_{1-x})_{13}$ has an enormous potential to be used as magnetic refrigerants in magnetic refrigerators in a wide range of temperatures. The theoretical description of the magnetocaloric effect in the compounds $La(Fe_xSi_{1-x})_{13}$ is very important not only to explain the available experimental data, but also to understand the underlying physics behind the magnetocaloric effect in these compounds.

In order to calculate the magnetocaloric effect in the compounds $La(Fe_xSi_{1-x})_{13}$, we use a microscopical model in the framework of the band theory of magnetism. We use a Hubbard like model Hamiltonian and treat the electron-electron interaction in the mean field approximation.The effect of an external pressure was taken into account through the renormalization of the electron dispersion relation. The magnetoelastic coupling interaction, which governs the nature of the phase transition, was also phenomenologically included in the model through the renormalization of the 3d-electron band width.The crystalline lattice entropy was considered in the Debye approximation. We apply the model to calculate the magnetocaloric effect in the doped compound $La(Fe_{0.89}Si_{0.11})_{13}$ at ambient pressure and under applied pressure. Our theoretical calculations show that the isothermal entropy change upon magnetic field variation from 0 to 5 T is in a very good agreement with the available experimental data at ambient pressure and low applied pressure[3] (see figure). We also calculate the magnetocaloric effect when both the magnetic field and pressure are changed. Our calculations predict that both the isothermal entropy change and the adiabatic temperature change upon magnetic field variation from 0 to 5 T and a linear pressure variation from 4.5 kbar to 0 reach large values in a wider range of temperatures. This kind of behavior of the magnetocaloric potentials are due to the competition between the magnetic field and pressure in the establishment of the magnetic order. This result points out that this procedure of changing both the magnetic field and pressure can be very useful to improve the performance of magnetic refrigerators working in Ericsson cycle. We also calculate the barocaloric effect in $La(Fe_{0.89}Si_{0.11})_{13}$ at constant magnetic field, i.e., the magnetic field is kept constant while the applied pressure is changed. Our theoretical calculations show that the barocaloric potentials $[\Delta S]_B$ and $[\Delta T_{ad}]_B$ upon pressure variation from 4.5 kbar to 0 reach sizeable values in a wider range of temperatures as compared with the magnetocaloric counterparts, calculated at fixed applied pressure of 4.5 kbar. These theoretical results, which need experimental data to be confirmed, show that the barocaloric effect and the magnetocaloric effect under variation of pressure and magnetic field can be an important tool to develop magnetic refrigerators.

We acknowledge partial financial support from the Brazilian agencies CNPq and FAPERJ.

[1] K. A. Gschneidner Jr, V. K. Pecharsky and A. O. Tsokol. Rep. Prog. Phys. 68, 1479 (2005.

[2] A. Fujita, S. Fujieda, Y. Hasegawa and K. Fukamichi, Phys. Rev. B 67, 104416 (2003).

[3] Young Sun,Z. Arnold and J. Kamarad, Guang-Jun Wang, Bao-Gen Shen, and Zhao-Hua Cheng, Appl. Phys. Lett. 89, 172513 (2006).

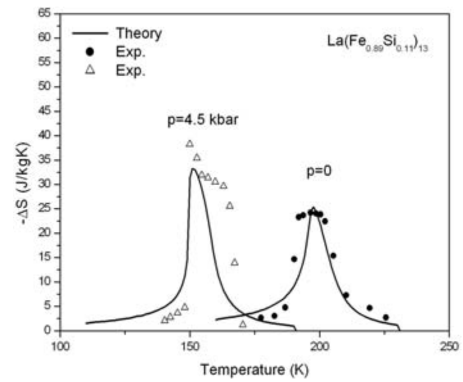

Isothermal entropy change in $La(Fe_{0.89}Si_{0.11})_{13}$ upon magnetic field variation from 0 to 5 T at ambient pressure and under applied pressure of 4.5 kbar. Solid lines are theoretical calculations and symbols are experimental data[3]

GU-07

Magnetocaloric Effect of the PrNi5-xCox Hard Magnets.

D. L. Rocco[1], R. P. Fernandes[2], M. S. Reis[1], J. S. Amaral[1], V. S. Amaral[1], J. P. Araújo[3], P. B. Tavares[4], A. A. Coelho[5]

1. Departamento de Física e CICECO, Universidade de Aveiro, Aveiro, Portugal; 2. Technische Universität Hamburg-Harburg, Institut für Keramische Hochleistungswerkstoffe, Hamburg, Germany; 3. IFIMUP, Departamento de Física, Universidade do Porto, Porto, Portugal; 4. Departamento de Química and CQ-VR, Universidade de Trás-os-Montes e Alto Douro, Vila Real, Portugal; 5. Departamento de Física Gleb Wataguin, Universidade Estadual de Campinas – UNICAMP, Campinas, Brazil

The PrNi5-xCox hard magnets compounds are derived from quite different materials (from the magnetic point of view): PrCo5 e PrNi5. While PrCo5 shows a high ordering temperature (TC), higher than Nd-Fe-B magnets [1], PrNi5 compound is paramagnetic due to the high crystal field [2]. However, the gradual substitution of Co by Ni leads to the competition between the magnetocrystalline anisotropy of both 4f (Pr) and 3d (Co) sublattices causing therefore a spin reorientation and decreasing of the magnetic ordering temperature. This feature is quite interesting due to the possibility to adjust the TC around room temperature, which allows these compounds to be used as refrigerant material in the magnetic refrigerator operating at room temperature. The magnetic refrigeration (MR) is a new technology and is considered as a promising alternative to replace the well-established compression-evaporation cycle [3]. The physical phenomenon associated to magnetic refrigeration is the magnetocaloric effect (MCE), which corresponds to the temperature increase of a magnetic material when there is an alignment of its magnetic moments with an external magnetic field, under adiabatic conditions [4].

In order to control the critical temperature around the room temperature and then analyze their potential for application on MR, we prepared a set of the samples of PrNi5-xCox (x = 2.07, 2.15, 2.25 and 2.40) by arc melting. Ingots were melted and then annealed in an evacuated quartz tube at 1020 K for seven days. X-ray diffraction shows a hexagonal CaCu5 (P6/mmm) type structure. EDS analyze shows that the annealed samples are single phase. We also performed magnetic characterization, and figure 1 shows the temperature dependence of magnetization for all studied compounds. We can note that those measurements have, at low temperatures, a peak at TSR ~ 143 K, which is associated to spin reorientation (SR) process [5,6]. In fact, the spin reorientation transition starts, increasing temperature, when the magnetic moment leaves the ab-plane at TSR1 and assumes a cone-type magnetic structure. Further increasing of the temperature, at the TSR2, leaves the magnetic moment from the previous position to then point along the c-axis [7]. We still can see in figure 1 at higher temperatures the magnetic transition from the paramagnetic disorder phase to the ferromagnetic order regime. It is important to emphasize that we found the critical temperature around room temperature for x~2.20. The inset of figure 1 shows the TC and SR transition as function of Co content x. In spite of the apparent linear behavior of Tc(x) –inset of figure 1-, we could show in [8] that the behavior is not linear, but there is a logarithmic dependence that is associated to a percolation process. However, the SR transition is constant as x.

From the M vs H curves near TC, and using the appropriate numerical approximation [9], it was possible to determine the magnetic entropy change (ΔS) or, equivalently, the MCE under an external applied field of 1 T. Figure 2 presents these results for the x= 2.07 and 2.40 compounds. Samples with lower values of Co content (x<2.15) presents an overlap of the ΔS curves associated to the SR and para-ferro transition; and therefore provides a quite large full width at half maximum (δTFWHM) of the ΔS. For instance, δTFWHM=160 K for x = 2.15, which corresponds to 8 times higher than the value of the pure Gd. Thus, this series has an appreciable relative cooling power (RCP), which therefore is useful to be used in magnetic refrigerator operating in a large range of temperature, from room temperature down to 150 K.

[1] E. M. T. Velu et al. IEEE Transactions on Magnetics, 25, 3779-3781 (1989

[2] P. J. von Ranke, et al. Phys. Rev. B, 58, 14436 (1998).[3] E. Bruck, et al. J. Magn. Magn. Mater., 310, 2793-2799 (2007).

[4] A. M. Tishin, et al. Institute of Physics Publishing, Bristol (2003).

[5] A. V. Andreyev, et al. Phys. Met. Metall.Vol. 60, n 4, 96-101 (1985).

[6] H. Gamari-Seale et al. Magn. Magn. Mater. 150, 63 (1995).

[7] M. R. Ibara et al. Phys. Rev. B 44, 9368 (1991).

[8] D. L. Rocco et al (to be published).

[9] V. K. Pecharsky et al. J. App. Phys. 86, 565-575 (1999).

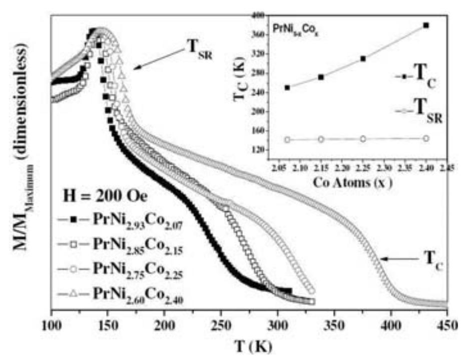

Figure 1 - Temperature dependence of the magnetization for PrNi5-xCox. Inset shows the Curie temperature and spin reorientation transition as function of Co amount (x).

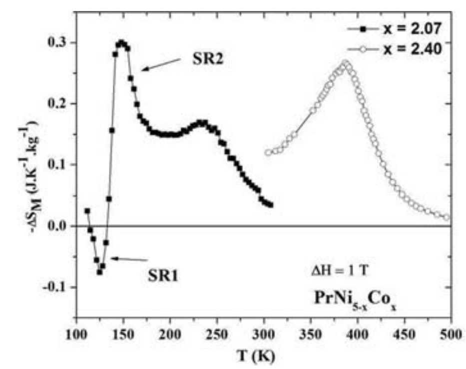

Figure 2 - Magnetic entropy change curves of the some PrNi5-xCox compound.

GV-01

Laser induced magnetisation switching in films with perpendicular anisotropy: a comparison between measurements and an LLB macro-spin model.

C. Bunce[1], *J. Wu*[1], G. Ju[2], B. Lu[2], D. Hinzke[1], N. Kazantseva[1], R. Chantrell[1], U. Nowak[1]
1. Department of Physics, University of York, York, United Kingdom; 2. Seagate Research, 1251 Waterfront Place, Pittsburgh, PA

This paper presents time-domain measurements of the magnetisation reversal process induced by an ultra-fast laser pulse in a perpendicular anisotropy CoPt thin film experiencing a constant reversing field less than its coercivity. It also presents the comparison of the experimental data with that from micromagnetic simulations based on the Landau-Lifshitz-Bloch (LLB) [1,2,3] equation.
The sample presented here is a CoPt multilayer thin film sputtered on a 2 ½ glass inch platter with perpendicular anisotropy. It had a square hysteresis loop (squareness = 1) with a coercivity (Hc) of 0.8 T and a magnetic moment Ms of 320 emu/cc at room temperature. The dynamic coercivity measurements allow the anisotropy and anisotropy constant and associated grain size to be estimated as 4×10^6 ergs/cc and 10 nm.
The all optical pump-probe stroboscopic time resolved MOKE experiment measures the evolution of the perpendicular component of magnetisation over 1 nsec after an intense 150 fs 'pump' laser pulse arrives at the sample causing transient heating. The experiment was arranged in a way such that the sample was initially saturated in one direction and then placed in a reversing field with a strength (0.52 T), much lower than its DC coercivity, whilst the measurement was conducted. It was observed that for pump pulses with a fluence higher than about 0.14 mJ/cm^2, ultrafast demagnetisation of the sample occured within 500 fs followed by a partial recovery along the original magnetisation orientation in spite of the applied field direction during the the first 50 ps. After this the magnetisation gradually started switching into the direction of the applied field. This final process is occurring at a similar rate to the temperature changes (ns). It is interesting to note a partial recovery along the original magnetisation orientation. We believe that this reflects the two different characteristic times for longitudinal relaxation and super-paramagnetic relaxation.
For comparison with the experimental data, we numerically solved the LLB equation [3] for a granular film with a weak exchange coupling between the grains using material parameters measured from our experiments as well as from atomistic calculations. The latter are the input parameters for the LLB equation such as the temperature dependent perpendicular and parallel susceptibility as well as the equilibrium magnetisation. The values for the exchange stiffness are gained from [4,5]. The temperature profile used is derived from fitting the two-temperature model to the experimental reflectivity data measured.
Figure 1 shows the experimental measurement and the calculated z-component of the magnetisation versus time, for two different laser powers – one high enough to cause reversal and one not. The key parameters used for the simulations were Ms = 520 emu/cc, a uni-axial anisotropy Ku = 1×10^6 erg/cc, a cell size of 9.5 nm, no inter-grain exchange coupling, $\alpha_T = 0.133$. The peak electron temperatures used were 600K and 900K corresponding to the low and high pump-powers used in the experiment respectively. The laser pulse causes a rapid demagnetisation followed by a recovery with a characteristic time depending on the degree of demagnetisation [6]. The second important energy transfer process is from the conduction electrons to phonons which result in a heating of the lattice on a time-scale of 5 ps. Thereafter, in the experiments, we note a gradual reversal of the magnetisation over the nano-second timescale – for the higher power case. This behaviour is qualitatively reproduced by the LLB model calculations supporting our interpretation of the measurements, namely that the reversal is a super-paramagnetic one, and suggesting LLB equation based models as a powerful approach to understand pulsed laser processes.

[1] D. A. Garanin, Phys. Rev B 55, 3050 (1997)
[2] O. Chubykalo-Fesenko, U. Nowak, R. W. Chantrell, and D. A. Garanin, Phys. Rev. B 74, 094436 (2006)
[3] U. Atxitia, O. Chubykalo-Fesenko, N. Kazantseva, D. Hinzke, U. Nowak and R.W. Chantrell, Appl. Phys. Lett. 91, 232507 (2007)
[4] D. Hinzke, U. Nowak, O. N. Mryasov, and R. W. Chantrell, Appl. Phys. Lett. 90, 082507 (2007)
[5] D. Hinzke, N.Kazantseva, U. Nowak, O. N. Mryasov, P.Asselin, and R. W.Chantrell submitted for publication in Phys. Rev. B
[6] N. Kazantseva, U. Nowak, R. W. Chantrell, J. Hohlfeld, and A. Rebei, Europhys. Lett. 81, 27004 (2008)

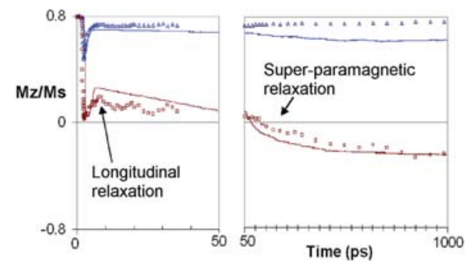

Figure 1: comparison between the measured data and the LLB simulations for the cases of low and high pump powers

Spin dynamics in patterned nanoscale Fe dot arrays.

J. Wu[1], S. Lepadatu[1], C. Bunce[1], X. Zou[1], D. Niu[2], Y. B. Xu[2], R. Chantrell[1], G. P. Ju[3]
1. Physics, University of York, York, United Kingdom; 2. Electronics, University of York, York, United Kingdom; 3. Seagate Research, Pittsburgh, PA

The ultrafast spin dynamics in patterned magnetic structures is one of the most important issues for the applications including high density magnetic recording and spintronics. In this presentation, we report time-resolved MOKE measurements of single crystal Fe film patterned into dot arrays with feature sizes down to 50nm. The effect of the enhanced shape anisotropy and modified magnetocrystalline anisotropy on the magnetization recovery process has been observed following femtosecond optical excitation in these nanometer scale structures.

The samples were grown by molecular beam epitaxy, and then patterned with focused ion beam milling into square dot arrays with size varying from 500nm to 50nm. Spin dynamics responses of the Fe dot arrays have been measured with pump-probe technique using a femtosecond laser. The results from a 50 nm dot array with the magnetic field applied in the sample plane and along the easy magnetic axis of the Fe film are shown in figure 1. Here the pump fluence is kept fixed at $28mJ/cm^2$ and the magnetic field strength is varied from 735Oe up to 1.84kOe for the different measurements. After femtosecond optical excitation an ultrafast demagnetization process is observed in the first 400fs. Following this, the magnetization begins to recover monotonically and after about 50ps a damped precessional response is observed before the magnetization fully recovers to the initial state. The frequency of the precession increases with the increase of bias field strength while the damping of the precession decreases with the increase of bias field strength. The measured frequency as a function of bias field has been fitted the Kittel formula $f=(\gamma/2\pi)[H(H+4\pi M_{eff})]^{1/2}$, where γ=221000 is the gyromagnetic constant, H is the applied bias field and M_{eff} is the effective magnetization [1]. Because of the reduced uniaxial anisotropy as indicated by the Focus MOKE results, its contribution to the precession frequency is neglected. The best fitting is obtained for a value of M_{eff} =800emu/cm^3 which is smaller than the actual M_s=1700emu/cm^3. It has been previously found by Xu et al [2] that there is a large interface induced perpendicular anisotropy K=10^{7}emu/cm^3. Considering the influence of the interface perpendicular anisotropy, $M_{eff}=M_s-(K/2\pi M_s)$ is around 760emu/cm^3 which is in good agreement with the reduced effective magnetization.

We have also measured the continuous Fe thin film without patterning and no precession process was observed. The results suggested that the magnetization recovery process in the patterned dot arrays is related to the modified magnetic anisotropies. We have further carried out MOKE measurements to determine anisotropies as shown in figure 2. The continuous Fe film shows a strong uniaxial anisotropy of around 1000Oe, but this uniaxial anisotropy has been greatly reduced in the patterned dot arrays. The modified magnetic anisotropy of the Fe dot array is expected to be a combination of shape anisotropy and possible change in intrinsic anisotropy due to the patterning.

In summary, we have demonstrated that the modified magnetic anisotropy of nanopatterned structures plays an important role in determining the magnetization relaxation dynamics following femtosecond optical excitation, which should be significant for understanding and controlling the fast switching in patterned magnetic recording media and spintronics devices.

[1] J. Wu, D. S. Schmool, N. D. Hughes, J. R. Moore, and R. J. Hicken, J. Appl. Phys. 91, 278 (2002).

[2] Y. B. Xu et al., J. Appl. Phys. 89, 7156 (2001);

Y. Zhai et al., ibid. 93, 7622 (2003).

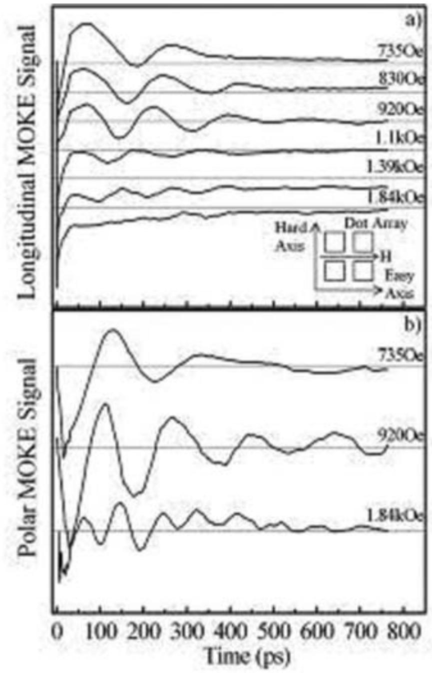

Figure 1 (a) Longitudinal b) Polar TRMOKE responses of the Fe dot array with magnetic field applied along the easy magnetic axis

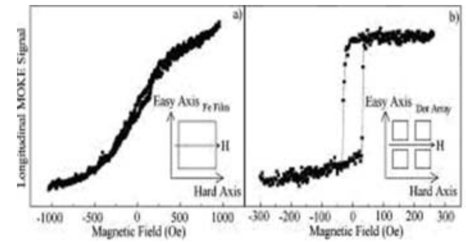

Fig 2 Longitudinal MOKE loops of (a) the FE film(b) the Fe dot array, measured with the fieldapplied along the hard axis of the Fe film.

GV-03

FMR study of self-organized plane arrays of metallic magnetic elements.

M. Kostylev[1], R. Magaraggia[1], F. Y. Ogrin[2], V. Mescheryakov[3,4], N. Ross[1], R. L. Stamps[1]
1. School of Physics, University of Western Australia, Crawley, WA, Australia; 2. School of Physics, University of Exeter, Exeter, United Kingdom; 3. Moscow Institute of Radioelectronics and Automation, Moscow, Russian Federation; 4. Instutute of Crystallography of Russian Academy of Science, Moscow, Russian Federation

In the recent years much attention has been given to the study magnetic properties of periodically patterned metallic magnetic films. This area is important since magnetic periodical structures can be used for magnetic memory [1], magnetic logic [2], and microwave signal processing [3] applications.

Structuring centimetre-sized areas of films into dots or rings with diameters 100-400 nanometres using traditional lithography tools requires high precision instruments and is very time consuming. However there is another way to achieve the same goal in a more cost-efficient way. This is using a "natural lithography" based on a self-organization of polystyrene nanospheres on a hydrophilic surface into a highly in-plane periodic monolayer array. Such a structure formed on a surface of a multilayer stack containing magnetic metallic layers may serve as a lithographic mask for fabrication of a periodic array of magnetic dots [4]. Fig. 1 shows an AFM image of an exemplary array of nanodiscs fabricated using this technology. Such a perfect periodicity is observed over an area more than 1 cm in diameter.

Dynamic collective behaviour of the self-organized arrays was characterized by conventional and coplanar-waveguide [5] ferromagnetic resonance (FMR). A sample with the dot thickness of 30 nm, the mean dot diameter of 300 nm and the mean dot separation of 300 nm was studied. Fig. 2 shows results of measurements of in-plane and out-of-plane conventional FMR spectra for the sample. The out-of plane trace shows several peaks which may be attributed to different radial standing spin waves on the dots. The presence of several peaks shows that this fabrication technique is able to produce samples with small dispersion of geometrical and magnetic parameters. However the parameter dispersion is not entirely negligible, since one sees than the resonance line is about 10 times as large as expected for an unstructured Permalloy film. We explain this by a small difference in "magnetic" diameters and shapes of individual elements resulting in a small variation of resonance fields from dot to dot.

The frequency difference between the main in-plane and the main out-of-plane resonance is about 3.8 GHz. This value is much smaller than the usual one for unpatterned Permalloy films. This shows that the static internal magnetic field and the static magnetization in the dots are considerably inhomogeneous. Furthermore, considerable effective dipole pinning of dynamic magnetization at the edges of the dots is present [6]. The work is now underway to extract the mean "magnetic" diameter of dots from these measurements.

Fig. 3 shows the results of the measurements using the coplanar-waveguide FMR technique. The measurements were done in a range of frequencies and in-plane magnetic fields. Using this technique we were able to trace the ferromagnetic resonance response of the array in the range of frequencies 4-15 GHz. Note that this is not an easy task for this technique, since the amount of magnetic material contained in the sample is very small, and the measurements are done at the response levels close to the setup sensitivity threshold. The experimental point obtained by the conventional FMR technique is also shown in the figure. One sees a very good agreement of results of both measurements.

Support by the Australian Research Council is gratefully acknowledged.

[1] S.A.Wolf et. al., Science 294, 1488 (2001).

[2] A.Imre et al., Science, 311, 205 (2006).

[3] J.Baker-Davis et al., IEEE Trans. On Mag., 42, 3344-3346 (2006).

[4] S. M. Weekes, F.Y. Ogrin, et al., Langmuir, 20, 11208 (2004).

[5] D.C.Crew et al., J. Appl. Phys. 97, 10A707 (2005);

[6] K.Yu. Guslienko et al., Phys. Rev. B, 66, 132402 (2002).

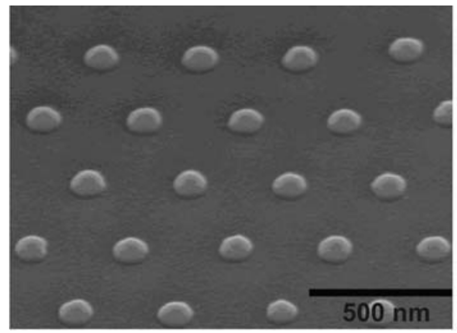

Fig. 1

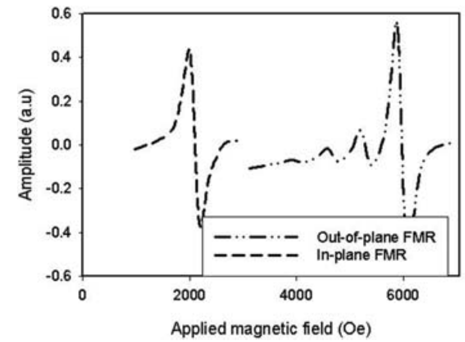

Fig. 2

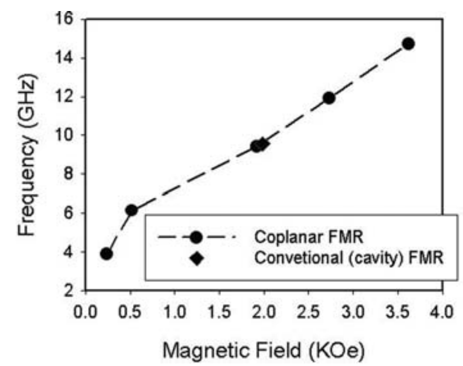

Fig. 3

GV-04

Complex broadband magnetic response of periodic arrays of FeNi dots and of Fe/Cr multilayers studied by using FMR-VNA technique.

J. Sierra[1], *A. Awad*[1], V. Pryadun[1], F. Aliev[1], G. Kakazei[2]
1. Departamento de Fisica de la Materia Condensada, Universidad Autonoma de Madrid, Spain, Madrid, Spain; 2. Institute of Magnetism NASU, Kiev, Ukraine

Recently dynamic properties of magnetic nanostructures such as thin films, multilayers and laterally patterned media attracted much attention both from fundamental and applications points of view. Spatial regularity of the arrays of magnetic dots as well as epitaxial growth of magnetic multilayers permits observation of well defined modes of collective excitations. For magnetic dots with sufficiently large diameters a vortex state is expected to give rise to variety of radial and azimuthal modes [1-3]. Magnetic field dependence of resonant frequencies of these modes remain poorly understood. As to the magnetic multilayers, the optic and acoustic modes excited in these magnetic nanostructures have been mainly investigated for fixed frequencies above 9.7GHz with samples inside RF cavities. Magnetic field dependence of the dynamic response in these nanostructures remains practically unexplored for the frequency range below 9 GHz.
Two-port vector network analyzer (VNA) technique up to 8.5 GHz in transmission mode was used to measure the complex dynamic response of the samples placed on the top of a coplanar wave guide (CPW). A microwave signal was supplied from the VNA port 1 and the transmitted signal crossing the CPW was detected by port 2. Magnetic susceptibility was evaluated by using information from scattering matrix parameters S21 and S11 [4]. This technique was applied to measure in-plane dynamic response in Fe/Cr multilayers and in the periodic arrays of FeNi circular magnetic dots.
For the arrays of FeNi dots with diameter of 1μm, aspect ratio L/R=0.1 and with centre to centre distance varying between 1.2 to 2.5 μm both VSM and MOKE measurements show a typical magnetization curve for the vortex ground state with a nucleation field of ~(200-300 Oe) and annihilation field of ~(400-600 Oe). In the previous ferromagnetic resonance (FMR) studies the in-plane resonance peak has a resonance field Hr of 1100 Oe and resonance linewidth ΔH of 26 Oe [2]. In the present VNA study resonance peak occurs in the fields above 300 Oe, i.e. above nucleation field. The FMR peak in the whole frequency range (5–13 GHz) was perfectly described by Kittel formula that takes into account the demagnetizing factor of individual magnetic dot.
Room temperature FMR studies of the array of FeNi dots also found that the main FMR linewidth (close to vortex annihilation/creation region) may be dependent on the magnetic history and that FMR linewidth broadens close to the vortex nucleation field (Fig.1). For the magnetic fields below 300 Oe, where magnetic vortex state forms, we have observed the field dependence of the at least two different radial/azimuthal modes (fr>6GHz) to show minima close to the zero magnetic field.
Dynamic response in the antiferromagnetically coupled [Fe/Cr]n multilayers (n=10,20,40), which was investigated as a function of magnetic field (up to 60 kOe) and in a wide temperatures range (between 300K and 2K), mainly reveal acoustic resonances. Magnetic field dependences of this resonance for different orientations of magnetic field in respect to crystalline axes (easy vs. hard) allow to resolve field induced orientation transition bellow 400 Oe between these axes when magnetic field is directed along hard direction (Fig.2). The high field dynamic response reveals presence of multiple resonant modes at frequencies below GHz. These modes are visible only at low enough temperatures (below 100K) and at magnetic fields close to the saturation field (of about 10 kOe). We tentatively relate these features to merging of optic and acoustic modes predicted to exist close to complete the alignment of initially antiparallel ferromagnetic layers in the Fe/Cr superlattice [5].

[1] V. Novosad et. al. Phys. Rev. B72, 024455 (2005).

[2] G.N. Kakazei et. al. Phys Rev. B74, 060406R (2004).

[3] L. Giovannini, et al., J. Phys. Cond. Matter 19, 225008 (2007).

[4] Sangita S. Kalarickal et al, J. Appl. Phys. 99, 093909 (2006).

[5] P.E. Wigen and Z. Zhang, Brazilian Journal of Physics, 22, 267 (1992).

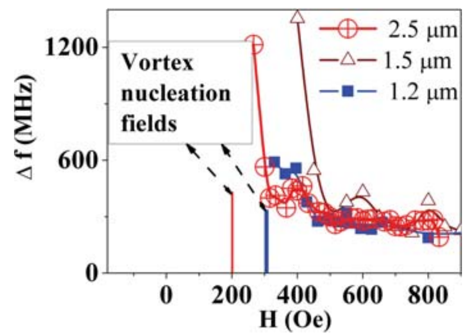

Fig. 1 FMR linewidth dependence on the applied magnetic field decreasing to zero from saturation field for three Py dots arrays studied. It is seen that the FMR linewidth starts to broaden close to the vortex nucleation field.

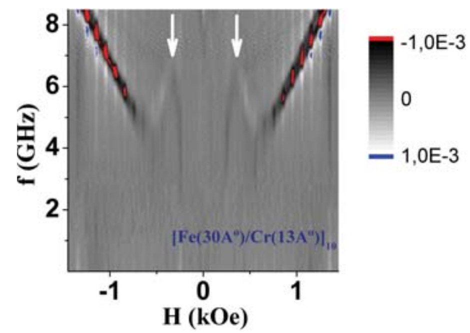

Fig. 2 Resonance frequency as a function of magnetic field oriented along hard axis of [Fe/Cr]10 multilayer and measured at 300K. The RF excitation is perpendicular to the DC field. Arrows indicate hard-easy axis orientation transition.

GV-05

Linear and Nonlinear Dynamics of the Gyrotropic Motion of a Magnetic Vortex in Ferromagnetic Nanodots.

K. Lee, S. Kim
Research Center for Spin Dynamics and Spin-Wave Devices & Nanospintronics Laboratory, Seoul National University, Seoul, South Korea

A magnetic vortex (MV) in confined magnetic elements continues to grow in considerable interest in the research area of nanomagnetism and spin dynamics because of its peculiar static and dynamic properties [1-3], and practical application to information storage devices [4]. Recently, the non-trivial dynamic phenomena, including resonant excitations [1] and dynamic reversal of vortex core (VC) [2], driven by small amplitude oscillating magnetic fields or ac currents, have attracted much attentions because these properties are crucial to realize magnetic memory devices or resonators based on MVs. Quite interestingly, it was also found that the underlying physics of the VC reversal is related closely to the gyrotropic motion. It is thus essential to understand complex VC gyrotropic motions including initial transient motion and steady-state orbital motions driven by single harmonic oscillating magnetic fields or currents.

In the present work, we conducted micromagnetic numerical [4, 6] and analytical calculations [5] of MV motions under time-variable in-plane magnetic fields, $\mathbf{H}(t)=A\sin(2\pi\nu t)\mathbf{y}$ with different frequency ν and amplitude A for the model system of a Permalloy (Py) circular dot of $2R$ = 300 nm diameter and L = 10 nm thickness. Figure 1 (a) shows the simulation results of initial transient and steady-state motions for the given ν and A values. From the frequency spectra of these motions [the third column in Fig. 1], it is found that there are clear two peaks: one is a sharp large peak at ν, and the other is a relatively wide small peak at the eigenfrequency, ν_0 = 330 MHz, characterized by the given material and geometry parameters. The former and latter correspond to the stable and transient motions of the VC, respectively. The transient VC motion is not chaotic but is associated with the eigenmode of the gyrotropic motion in the given material and geometry.

In order to compare those simulation results with the analytical calculations based on Thiele's equation of motion with a "side-charge-free" model [3], the VC orbital trajectories and their frequency spectra are numerically calculated using Thiele's equation, as seen in Fig. 1(b), including the potential energy profile, $W(\mathbf{X})= W(0)+ \kappa\mathbf{X}^2/2$, where $\mathbf{X}$ is the VC position, and κ is the stiffness coefficient (a function of R, L [3]). These comparisons (orbital trajectories and frequency spectra) show excellent agreements in not only the steady-state but initial transient motions between the micromagnetic simulations and the numerical solutions.

In the case of relatively large amplitude applying fields, nonlinear motions of the VC are dominating as seen by the frequency spectra in Fig. 1(c). The relatively broad peak corresponding to the initial transient motions is shifted far away from ν_0 = 330 MHz (for the linear case) with increasing amplitude of the oscillating field. Such nonlinearity of large-amplitude VC gyrotropic motion can be verified by taking into account some higher-order terms in $W(\mathbf{X})$, which is demonstrated by the numerical calculations of Thiele's equation with a forth-order potential energy term ($\beta\mathbf{X}^4/4$) in $W(\mathbf{X})$. For a specific value of β/κ = 4.5 x 10^{13} m^{-2}, the orbital trajectories and the frequency spectra agree quite well with the simulation results [compare Figs. 1(d) and (e)].

This work not only offers a theoretical way to understand complex responses of the gryomotions of a VC to an external driving force in the linear and nonlinear regimes, but also opens up a new opportunity to explore the nonlinear regime of vortex dynamics with the help of the generalized Thiele's analytical equation of motion.

We thank K. Guslienko for discussions. This work was supported by Creative Research Initiatives (Research Center for Spin Dynamics & Spin-Wave Devices) of MOST/KOSEF

We thank K. Guslienko for discussions. This work was supported by Creative Research Initiatives (Research Center for Spin Dynamics & Spin-Wave Devices) of MOST/KOSEF.

[1] S. Kasai et al., Phys. Rev. Lett. 97, 107204 (2006).

[2] S. Choi et al., Phys. Rev. Lett. 98, 087205.(2007); B. Van Waeyenberge et al., Nature 444, 461 (2006); K. Yamada et al., Nature Mater. 6. 296 (2007).

[3] K. Y. Guslienko et al., J. Appl. Phys. 91, 8037 (2002).

[4] K.-S Lee et al., Phys. Rev. B 76 174410 (2007); S.-K. Kim et al., Appl. Phys. Lett 91, 082506 (2007).

[5] K.-S. Lee and S.-K. Kim, Appl. Phys. Lett 91, 132511(2007).

[6] See http://math.nist.gov/oommf.

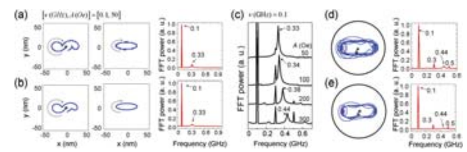

FIG. 1. Orbital trajectories of VC motions and their FFT powers under an in-plane oscillating field: (a) micromagnetic simulation and (b) numerical solution of Thiele's equation. (c) Variations of the FFT powers with the amplitude of the oscillating field (micromagnetic simulations). (d) and (e) show orbital trajectories of VC motions and their FFT powers: (d) micromagnetic simulation and (e) numerical solution of Thiele's equation with a given value of β/κ = 4.5 x 10^{13} m^{-2}.

GV-06

Nonlinear phenomena in magnetic nanoparticle systems at microwave frequencies.

M. Pardavi-Horvath[1], G. S. Makeeva[2], O. A. Golovanov[3]
1. SEAS, The George Washington University, Washington, DC; 2. Penza State University, Penza, Russian Federation; 3. Penza Military Institute of Artillery, Penza-5, Russian Federation

Magnetic nanocomposites of nanometer size magnetic particles embedded in a non-magnetic, insulating matrix provide a novel solution for low loss microwave materials up to mm wave frequencies. The electromagnetic properties of magnetic materials change drastically upon reducing the dimensions into the nano-range, including the early onset of nonlinear effects, important for high power applications and non-linear signal processing. To investigate this effect, the nonlinear interactions of electromagnetic waves (EMW) in magnetic nanoparticle materials at microwaves were numerically simulated using rigorous mathematical models to solve the 3D nonlinear diffraction boundary problem. The solution is based on the full Maxwell`s equations with electrodynamic boundary conditions, complemented by the Landau-Lifshitz equation of motion of the magnetization vector, including the exchange term.

A monochromatic plane EMW (TEM mode, magnitude $C^{+}_{1(1)}(\omega)$, frequency ω) is incident on the input cross-section S1 of the array of ferrite spheres (Fig.1). A bias magnetic field H_0 is applied normal to the direction of the propagating plane EMW. The modulus of scattering parameters of the multimode, multi-channel S matrix was calculated by the numerical method of autonomous blocks with virtual Floquet channels. The results of computing of the transmission coefficients $|S_{12}|$ on an array of 250 nm spheres, depending on the normalized frequency ω/γ (γ gyromagnetic ratio), for various separation of the spheres are shown in Fig.2. The minima (1-3) in $|S_{12}|$ correspond to the eigenfrequencies ω_p of characteristic magnetostatic oscillations of the ferrite spheres. The central line is the homogeneous magnetization precession' low-order mode, others are the inhomogeneous magnetization precession modes in ferrite spheres. The increase of the interaction effects upon decreasing separation is clearly visible.

The instability regions of parametric generation in the nonlinear ferrite sphere array, depending on the magnitude $C^{+}_{1(1)}(\omega_H)$of the pumping wave ω_H, are simulated using our computational algorithm for the numerical analysis of the bifurcation points of the nonlinear Maxwell's operator. The threshold magnitudes of the pumping EMW, $C^{+}_{1(1)}(\omega_H)$are determined by computing the bifurcation points. The curves shown in Fig.3. divide the instability regime for the parametric generation from the stable regime of regenerative parametric amplification at f_0= 9.330 GHz for the three separations shown of Fig.2. With decreasing separation, i.e. increasing interaction between the spherical elements of the array, the instabilities occur at lower power, demonstrating the power sensitivity of small particle systems.

Using this approach it is possible to investigate the nonlinear effects (nonlinear diffraction, frequency multiplication, Suhl instabilities, self-excited oscillations, chaos, parametric amplification and parametric excitation of dipolar magnetostatic waves, dipole-exchange spin-waves) in three-dimensional systems of magnetic nanoelements microwave and magnetophotonic applications, sensor arrays, Tbyte information storage, taking into account the topology of nanoarrays and constrained geometries.

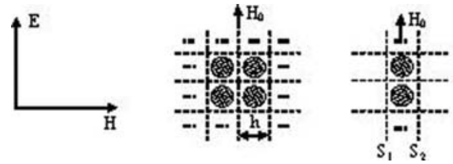

Geometry of the system

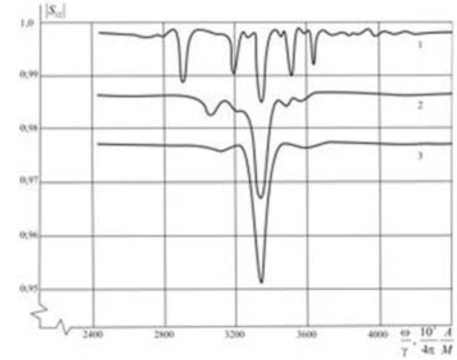

Diffraction of TEM- waves on a 250 nm radius ferrite nanosphere array for various separation h of spheres: 1 – h=3000 nm; 2 – 750 nm ; 3 – 600 nm. Bias field H_0 =ω/γ, M_0 =0.026 T; $|S_{12}|$ - modulus of transmission coefficient; γ - gyromagnetic ratio; $C^{+}_{1(1)}(\omega)$ = 0.01 A/m - magnitude of the incident wave.

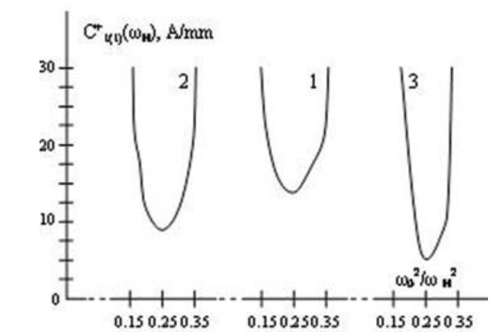

Threshold of parametric instability for various separation, h, of spheres, as in Fig.2.: 1 – h=3000 nm; 2 – 750 nm ; 3 – 600 nm; the frequency of the signal wave f_0 =9.330GHz; ω_0=2π f_0, ω_H - frequency of the pumping wave; $C^{+}_{1(1)}(\omega)$ - magnitude of the incident pumping wave.

GV-07

Parametric spin wave excitation and cascaded processes in thin films.

K. Livesey, M. Kostylev, R. Stamps
School of Physics, University of Western Australia, Crawley, WA, Australia

When there are weak nonlinearities in a system, parametric excitation can occur whereby energy is resonantly transferred from one excitation mode to another. An example of this is seen in magnetic systems where the uniform spin wave (k=0) decays into travelling spin waves above a critical amplitude or angle of precession.

This has long been known to occur in high power ferromagnetic resonance (FMR) experiments but recently there has been evidence of nonlinear processes occurring during large-angle magnetic switching of thin films [1]. These nonlinearities are therefore important in understanding the writing of magnetic information. However, the thresholds observed during switching are apparently much larger than those measured in FMR. The question then is: is parametric excitation really occurring during switching?

We use a classical perturbative approach [2] to write the magnetic Hamiltonian of a finite thickness film. We include contributions from exchange, uniaxial anisotropy, Zeeman and dipolar energies. The Hamiltonian goes through a succession of transformations (Holstein Primakoff, Bogolyubov and quasi-linear transformations) in order to be split into a linear part and a nonlinear part consisting of terms due to three-wave interactions, four-wave interactions, etc. We then solve Hamiltonian equations of motion to determine analytic thresholds when both three- and four-wave interactions are resonant during switching. These thresholds are given both in terms of precession amplitude and in terms of the average angle of precession [3].

We find that the threshold is the same as in FMR and is in fact exceeded during switching. However, as switching occurs on very short time-scales - on the order of a few nanoseconds - there may not be enough time to excite spin waves to an amplitude sufficient for detection in experiment. This is illustrated in Fig.1. The minimum precession angle required to excite a detectable number of waves in a given time (solid line) and the parametric threshold angle (dashed line) are plotted for a 10nm Permalloy film. These two curves converge as time goes towards infinity. The apparent experimental discrepancies between FMR and switching are thus due to the different time-scales of the experiments.

Lastly, we have examined the effect of finite thickness on the threshold using Permalloy material parameters. Even for nm-thick films, finite thickness effects are considerable and a 2D model is inappropriate. The comparison between our 3D model and the 2D model is given in Fig.2. The confined direction allows for so-called “cascaded” spin wave processes [2] to occur. These cascaded processes correspond to four-wave interactions consisting of two three-wave interactions (hence second order in perturbation theory) and two possibilities are illustrated in Fig.3. When the first exchange branch is exactly double the FMR frequency of the film, process (b) in Fig.3 is on resonance, which leads to a minimum in threshold. By varying the film thickness for a fixed field this can be made to occur, for example, with applied fields around 20 Oe the threshold is at a minimum for film thickness of 70nm (see Fig.2).

Support by the Hackett Student Fund (UWA), the Australian Research Council and Seagate is acknowledged.

[1] T.J. Silva, P. Kabos and M.R. Pufall, Appl. Phys. Lett. **81**, 2205 (2002).

[2] V.S. L’vov, Wave Turbulence Under Parametric Excitation (Springer-Verlag, Berlin, 1994).

[3] K.L. Livesey, M.P. Kostylev and R.L. Stamps, Phys. Rev. B **75**, 174427 (2007).

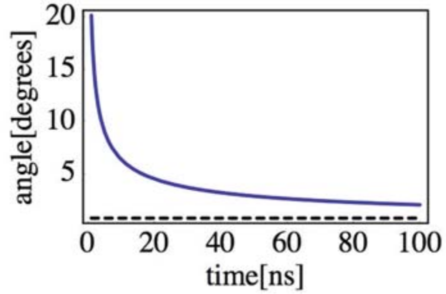

Figure 1. The average angle of precession needed to measure the effect of parametrically excited waves (solid line) in a given duration of precession. As time goes towards infinity, this angle approaches the threshold angle which is given by the dashed line.

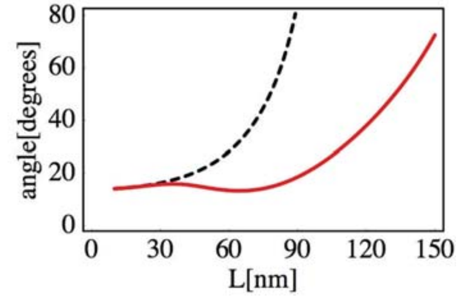

Figure 2. The threshold angle to measure parametric excitation as a function of film thickness. The solid line shows the result of our 3D model and the dashed line shows the result for a 2D model with no thickness variation allowed. Material parameters are those for a Py film with bias field 20 Oe and pulsed field 10 Oe, and the precession is taken to last for 2ns.

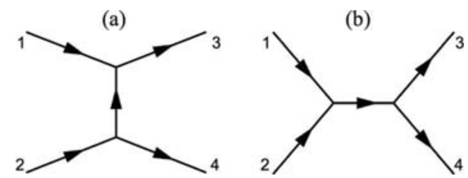

Figure 3. Two examples of cascaded processes.

GV-08

Micromagnetic modeling of the magnetization dynamics in a circularly exchange biased tunnel junction.

O. G. Heinonen[1], D. K. Schreiber[2], A. K. Petford-Long[3]
1. Seagate Technology, Bloomington, MN; 2. Materials Science and Engineering, Northwestern University, Evanston, IL; 3. Materials Science Division, Argonne National Laboratory, Argonne, IL

The magnetic vortex structure is typically the stable magnetic configuration in micron-sized ferromagnetic (FM) Permalloy (Py) disks with a thickness of tens of nanometers. The vortex affects both the quasi-static and the dynamic response of the magnetization to a magnetic field pulse. Recently, the magnetization dynamics of both single-layer and exchange-biased bilayer vortex structures excited by a magnetic field pulse has been investigated experimentally and through simulation [1, 2], as has the quasi-static response of an FM/I/FM trilayer (I=spacer) [3]. However, for the trilayers there has been no discussion of the exchange and magnetostatic interactions between the two FM layers across the spacer, which should affect the magnetization dynamics of the system. Simulations of the dynamic response of a circular AF/FM/I/FM tunnel junction structure (AF=antiferromagnetic layer) have been carried out using the Landau-Lifshiftz-Gilbert (LLG) equations of motion. The magnetization in the FM layers was set in a vortex configuration, and the simulation parameters were selected to simulate an IrMn AF layer and two Py FM layers, separated by a thin MgO layer of different thicknesses. The AF-exchange bias and the magnetization in the adjacent pinned FM layer have parallel chirality. The sign and strength of the interlayer exchange coupling between the pinned and free FM layers were varied and ground states with vortices in the FM layers that are either of the same or opposite chirality were chosen, resulting in four unique configurations (Figure 1).

A magnetic field pulse normal to the plane gave rise to strongly coupled circularly-symmetric eigenmodes with one radial node (the so-called (1,0) mode) in the pinned and free layers, for both positive and negative interlayer exchange coupling. A simple analytical model was used to further study these circularly symmetric eigenmodes. The radial part of the (1,0) mode was taken to be $J_1(k_R r)$, where $x = k_1 R$ is the first zero of $J_1(x)$, and it was assumed that the out-of-plane component of the magnetostatic field, resulting from the magnetization dynamics in one layer, was zero in the other layer, while the in-plane magnetostatic field was the same in both layers. Coupling between the layers due to the out-of-plane magnetization at the vortex cores was ignored.

The resulting coupled modes had two branches, a center-of-mass (CM) mode (magnetization in the two layers moves in phase), and a difference (DM) mode (magnetization in the two layers moves out of phase). As the main restoring force is given by the magnetostatic field, the CM modes have higher frequencies than the DM modes.

The linearized equations of motion were solved for the four local equilibrium configurations, shown in Figure 1, and the results are plotted in Figure 2. The lower branch for AF interlayer exchange and opposite chirality vanished with vanishing exchange bias. However, the lower branch for same chirality and AF interlayer exchange softens with decreasing exchange bias and vanishes at finite exchange bias. This correspond to a static displacement of the vortex magnetization structures in the two layers, which, for low enough exchange bias, becomes a minimum energy-configuration as the reduction in interlayer exchange energy can balance the increase in magnetostatic energy as the vortices magnetizations are displaced.

This manuscript was created by UChicago Argonne, LLC, Operator of Argonne National Laboratory ("Argonne"). Argonne, a U.S. Department of Energy Office of Science Laboratory, is operated under Contract No. DE-AC02-06CH11357.

[1] M. Buess, et al., Physical Review B, 2005. 71(10): 104415.

[2] O.G. Heinonen, D.K. Schreiber, and A.K. Petford-Long, Physical Review B, 2007. 76(14): 144407.

[3] K.S. Buchanan, et al., Physical Review B, 2005. 72(13): 134415.

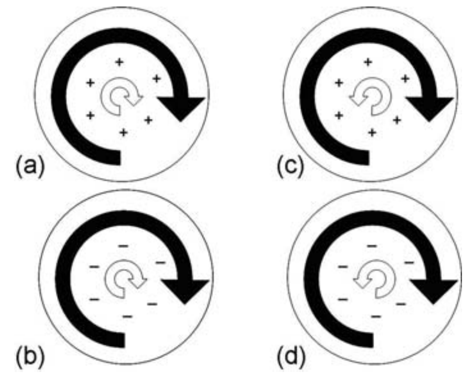

Figure 1: Schematics of the magnetization structure. The filled arrow indicates the chirality of the pinned layer and the empty arrow the chirality of the free layer. The exchange interaction between the layers is '+' for FM and '–' for AF exchange. In all cases the interlayer exchange coupling strength was 40 Oe.

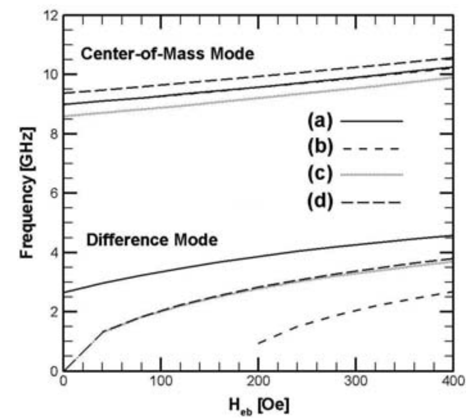

Figure 2: Plot of the coupled (1,0) mode frequency versus AF exchange bias strength for the CM modes (upper branch) and DM modes (lower branch) for the magnetization structures shown in Figure 1. CM modes (a) and (b) are degenerate, as are DM modes (c) and (d).

GV-10

Size dependence of the magnetic switching of Co-nanoislands studied by spin-polarized scanning tunneling spectroscopy.

D. Sander, S. Wedekind, G. Rodary, K. Jürgen
Max Planck Institute, Halle, Germany

The magnetic properties of nanometer size Co islands on Cu(111) are studied by spin-polarized scanning tunneling microscopy and spectroscopy (spin-STM, spin-STS). Co islands are prepared by deposition of sub-monolayer quantities of Co at 300 K onto a clean Cu(111) surface. STM reveals the growth of double-layer high Co islands, which exhibit often an equilateral triangular shape with base lengths between 3 nm and 45 nm. Spin-dependent STM measurements are performed with a Cr-covered W-tip, where 100 layers of Cr are deposited at room temperature onto a chemically etched and subsequently flashed (2100 C) W-tip. We obtain spectroscopic data of the differential conductance dI/dV, by applying a small AC modulation voltage (10 mV, 4 kHz) to the gap voltage V, and we monitor the resulting modulation of the tunnel current I by phase sensitive detection with a lock-in amplifier.

The spin-dependent measurements are performed at the center of the Co islands at 8 K and in a magnetic field of up to 6 T, which is oriented normal to the sample surface. It has been reported before that the magnetic field dependence of the differential conductance of the tunnel current measured on a Co island can be ascribed to a field-driven change of the Co magnetization direction along the sample normal, in response to the external field [1]. Thus, a switching of the magnetization direction of a Co island can be identified from a characteristic change of the differential conductance signal. In an extension of the previous study [1] we investigate here the size dependence of the magnetic switching of individual Co islands comprised of several hundred up to several thousands atoms.

Our measurements of the differential conductance during a magnetic field scan show a sharp drop of the differential conductance at field values which depend on the Co island size. We ascribe this drop to the magnetic switching of the Co islands, where we find switching fields between 0.6 T for islands containing 1300 atoms (base length 12 nm), and 2.2 T for larger islands with 8500 atoms (base length 31 nm). For even larger islands of 17000 atoms (base length 41 nm) a reduced switching field of 1.95 T is observed. For smaller islands with 1100 atoms or less, we find, starting from zero external field, a smooth drop of the differential conductance in proportion to the magnetic field, and no abrupt switching is observed. The drop of the differential conductance with respect to field saturates around 1.5 T for islands with 450 atoms (base length 7 nm). At this field the drop of the differential conductance equals within error margins of +/- 10 % the drop of the differential conductance observed for the magnetic switching of larger islands.

Our results suggest that double-layer Co islands on Cu(111) exhibit a size-dependent transition from superparamagnetic to single-domain ferromagnetic behavior with increasing island size. We have not observed magnetic domains within the Co islands under investigation. Therefore we may tentatively analyze the maximum coercive field according to the Stoner-Wohlfarth model of magnetization reversal by coherent rotation [2]. This approach gives K = 0.5 Ms Hc = 1.6 MJ / m3, with the switching field Hc = 2.2 T and the saturation magnetization of Co of Ms = 1.447 MA / m. This value of K = 1.6 MJ / m3 is a factor of three larger than the value of bulk hcp-Co [3]. Such an increase of the magnetic anisotropy is often observed on the nanoscale, and it points towards potential contributions of strain, strain relaxation, and interfaces to the magnetic anisotropy [3]. The decrease of the switching field from 2.2 T (8500 atoms) to 1.95 T (17000 atoms) with increasing island size is ascribed to a possible multi-domain and/or incoherent magnetization state, which is expected to induce a lower switching field [4].

[1] O. Pietzsch, A. Kubetzka, M. Bode, R. Wiesendanger, Phys. Rev. Lett. 92 (2004) 057202.

[2] E. Kneller, Ferromagnetismus, Springer, Berlin 1962.

[3] D. Sander, J. Phys.: Condens. Matter 16 (2004) R603.

[4] S. Rohart, V. Repain, A. Thiaville, S. Rousset, Phys. Rev. B 76 (2007) 104401.

GW-01

Chemical order and size effects on the magnetic anisotropy of FePt and CoPt nanoparticles.

F. Tournus[1], S. Rohart[1,2], V. Dupuis[1]
1. LPMCN, Université de Lyon; Univ. Lyon 1; CNRS, Villeurbanne, France; 2. LPS, Université Paris Sud; CNRS, Orsay, France

The effect of the L10 ordering in FePt and CoPt on the magnetic anisotropy in bulk crystals or thin films has been widely studied on both experimental and theoretical points of view. In the case of nanostructures, although many experimental studies have been performed, the impact of the dimension reduction on the magnetic anisotropy energy (MAE) has not been clearly evidenced. As the surface modifies the local chemical environment, it can have a large impact on the MAE. As it will be shown in this paper, contrary to the results on pure Fe and Co clusters it induces a lowering of the MAE for L10 ordered clusters. In this paper, we extend the phenomenological anisotropy model of Néel to describe the effect of chemical ordering in FePt and CoPt clusters. Taking advantage of its simplicity, which allows us to perform an extensive study of FePt and CoPt clusters, we use this phenomenological model to investigate the MAE of clusters. Taking into account finite size effects by mean of a statistical analysis on a large number of nanostructures, we demonstrate the impact of L10 chemical ordering on the MAE and show how the surface and the finite size modify the results as compared to the bulk.
The magnetocrystalline anisotropy (MCA) is directly linked to the local environment around magnetic atoms. For a whole structure, it is the signature of the system symmetries. It can be described using a phenomenological pair model, first introduced by Louis Néel. In its original form, for a single element crystal, the MCA energy is written as a pair interaction over the first neighbors. Considering a given structure of volume V, the total MCA energy is evaluated by performing a sum over all the nearest neighbors pairs, assuming that the magnetization is homogeneous over the whole structure (macrospin approximation). This leads to a quadratic form, that can be diagonalized into an orthonormal
basis set (biaxial second order magnetic anisotropy), allowing us to determine the easy magnetization direction and the anisotropy constant K1 corresponding to the magnetization switching from one minimum to the other one (K1*V is the enery barrier).
This crude model, which is suitable for systems where symmetry is locally broken (surfaces), can be extended to the case of an alloy, by introducing a different Néel anisotropy parameter for each type of neighbors pairs. Then, in the bulk case, using statistical considerations we can find an analytical expression of the MAE variation with the long-range order (LRO) parameter S corresponding to the L10 chemical order. The model appears to be in satisfactory agreement with experiments and with first-principle calculations.
In the case of a finite size system, we need to perform a statistical analysis to determine the relation between the LRO parameter S and the anisotropy constant K1. We have used this Néel anisotropy model to investigate the consequence of the size reduction in FePt and CoPt nanoparticles, with respect to their chemical order, focusing our study on nearly spherical clusters, with a perfect truncated octahedron shape. We have found a significant deviation from the bulk behavior (see Fig. 1). Moreover, our calculations have revealed that, while the anisotropy constant K1 is enhanced in the case of small chemically disordered particles, it decreases in the case of perfectly L10 ordered particles when going to small sizes (see Fig. 2).

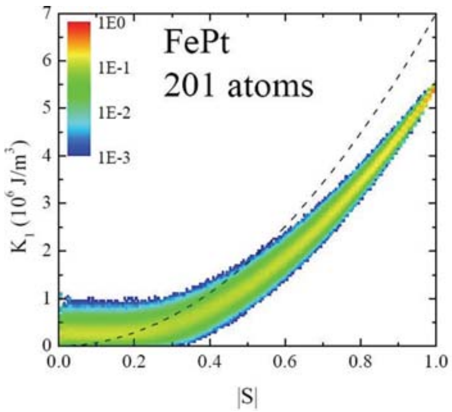

Fig. 1: Variation of the anisotropy constant K1 versus |S| for a 201 atoms FePt cluster. The color scale represents in the (|S|,K1) plane, the density of probability for a cluster with chemical LRO parameter |S| to have a MCA K1 (the corresponding color bar is shown in inset). The dashed line corresponds to the bulk behavior.

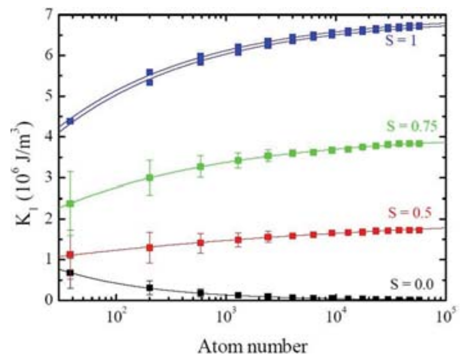

Fig. 2: Variation of the mean anisotropy constant K1 versus the number of atoms in the cluster for FePt clusters of different |S| parameters. The dots correspond to the calculated K1, the error bar representing the dispersion of the K1 distributions. The lines are obtained by fitting the calculated values with a power law.

GW-02

A study of the optimum dose of ferromagnetic nanoparticles suitable for cancer therapy using magnetic fluid hyperthermia.

M. Pavel[1,2], G. Gradinariu[1,2], A. Stancu[1]
1. Department of Solid State and Theoretical Physics, "Alexandru Ioan Cuza" University, Faculty of Physics, Iasi, Romania; 2. Department of Oncology, University of Medicine and Pharmacy "Gr. T. Popa", Iasi, Romania

Magnetic fluid hyperthermia (MFH) is a modern topic of interdisciplinary research of applied physics (in particular magnetism) and biomedicine. Presently, a successful realization of this promising therapy is hampered by some unsolved problems. One of these problems is the choice of the correct particle concentration in order to achieve a defined temperature increase in the tumor tissue. A computer-based model was created using COMSOL:Multiphysics in order to simulate the heat dissipation within the tissue for typical configurations of the tumor position in relation to neighboring blood vessels as well as particle distribution within the tumor. The temperature achieved on the tumor border was investigated taking into account physiological parameters of different types of tissue. Using the correct nanoparticle dosage and considering their specific loss power, it is possible to estimate the efficiency of this therapeutic method. If the tumor shape and position are known by suitable medical imaging techniques (e.g. MRI, CT), simulations like this one could provide data in order to achieve the optimum dose and particle distribution in the tumor. Using biocompatible strengths and frequency values for the alternating magnetic field, we studied the reactions of different types of cancerous tissues when MFH therapy is used. We designed distinct simulations of a spherical tumor located in a cubical region of volume 1 cm3 from the tissue we intended to analyze.
A systematical variation of the parameters involved (e.g. tissue density, tumor/tissue perfusion rate, tumor diameter, particle concentration and physical properties, field amplitude and frequency) was performed in order to understand the effect of these parameters on the outcome of hyperthermia treatment. We focused on studying the variation of particle concentration in order to achieve an optimal therapeutically temperature at tumor border. Moreover we were interested in comparing the intra-tumoral temperature distribution for a single and respectively multiple point injection for several ferromagnetic materials. In all the simulations, we were interested in obtaining a temperature higher than 42.5°C, the minimum temperature that increases the susceptibility for apoptosis in cancerous cells.Further on some of the results from the simulations will be presented.
In the first simulation two small blood vessels are located at approximately 2.5mm and 4mm away from the tumor region. For different concentrations of ferromagnetic nanoparticles ranging between 6 and 10mg/cm3 homogeneously distributed in different cancerous tissues (brain, skin, liver, breast, rectum, lung), with a diameter of 2.7-3 mm, for a frequency of 260kHz and a field amplitude of 7kA/m (LP=4.15*109W/m3), a border temperature ranging between 44-46°C was obtained (Figure 1). Moreover, for larger tumors (diameter of 3.5-4mm), in the conditions of lower nanoparticle concentrations – 4-5mg/cm3 and using the same values for H, f and particle size, the temperature was 42.5-43.5°C at the border between tumor and healthy tissue.
Furthermore, we attempted to estimate a spatial temperature distribution in a liver tumor, using magnetite and maghemite nanoparticles comparatively. We opted for less homogeneity assuming that particles are injected in equal quantities in multiple regions (3-9) within the tumor. Although maghemite nanoparticles may be used at a lower concentration (3–4 mg/cm3) compared to magnetite, we observed that they tend to generate either to much or insufficient heat when we varied their radius within the limits of 21 and 23nm.
For the next simulations we assumed the presence of a single blood vessel with a diameter of 0.1 mm, positioned at 3.5-4 mm from the tumor. For liver tissue, we used constant field amplitude of 7.5kA/m, and we varied the frequency, the concentration of nanoparticles and their distribution. We then considered a tumor volume of 18mm3 (aprox.3mm*3mm*2mm), for a frequency of 250kHz and for concentrations ranging between 10mg/cm3 and 5mg/cm3 (the first being the upper biocompatible limit) the temperature around the tumor ranged from 46.19°C to 41.7°C thus providing us with a possible dose and type of particle distribution that could be used to treat small liver tumors.
In conclusion, our results show that, using these models, we can successfully estimate the impact of the particle dose on the efficiency of hyperthermia therapy taking also into account the local features (e.g. tumor density, type and perfusion rate) and external factors (e.g. field amplitude and frequency) involved. It could be thus a good method to evaluate the prospects of the therapy for a given patient who has a well described condition and also to establish an optimum starting dose for MFH therapy in such a case.

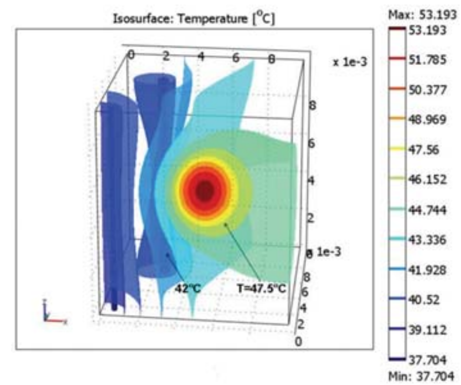

Spatial temperature distribution in a skin tumor tissue for H=7kA/m and f=260kHz and particle concentration of 10 mg/cm3 (particle diameter = 18 nm), where T is the tumor border temperature.

GW-03

Influence of dipole interaction and thermal effect on static magnetization process of magnetic nanoparticle assembly.

D. Hasegawa[1], T. Ogawa[2], M. Takahashi[3]

1. Electronic Engineering, Tohoku University, Sendai, Japan; 2. CRESS, Tohoku University, Sendai, Japan; 3. NICHe, Tohoku University, Sendai, Japan

Introduction

Many works on the synthesis and the magnetization process of magnetic nanoparticles have been investigated. In the case of the magnetic material with small magnetic anisotropy such as Iron, its nanoparticles which are magnetically isolated show superparamagnetic behavior, and their static magnetization process can be explained by the Langevin function. However, the magnetization process actually changes from simple superparamagnetic behavior with increasing volume fraction and decreasing temperature due to influence of the magnetic dipole interaction [1, 2]. Especially, the nanoparticles show super spin-glass behavior under the strong dipole interaction and/or low temperature [1, 2]. Therefore, in this study, we evaluated the influence of the dipole interaction and temperature effect on the static magnetization process quantitatively by the Monte Carlo simulation.

Model and parameter

Magnetic single domain nanoparticles that were arraying on the lattice points of 16×16×16 unit cells of face center cubic structure were assumed as a geometric model. The directions of each magnetic moment were determined from thermal energy and total magnetic potential considering with the Zeeman energy and the dipole energy. Here, the dipole field was determined under the periodic boundary condition. Saturation magnetization (M_s) was assumed 1700 emu/cm^3. Temperature (T), particle diameter (D_p), and volume fraction (v_f) were variable. The temperature dependence of M_s is not considered.

Result and discussion

Fig. 1 shows the temperature dependence of the static initial susceptibility (χ_{par}) for 3 and 9nm nanoparticles with various volume fractions. Here, χ_{par} for none interaction case which is calculated from the Lagevin function ($\chi_{par} = \chi_{Langevin} = VM_s^2 / 3k_BT$; V is the volume of a particle) is shown by a dotted line. For D_p = 3nm, χ_{par} with v_f = 0.0001 decreases monotonously with increasing T. This dependence coincides with that for none interaction case in the range from 10 to 900 K. For the nanoparticles with v_f = 0.001, χ_{par} also decreases monotonously with increasing T. However, χ_{par} is smaller compared with that for none interaction case at 10 K, and approaches $\chi_{Langevin}$ with increasing T, which results in agreement with $\chi_{Langevin}$ at about 50 K. Increasing v_f, χ_{par} at 10 K decreases, and the temperature to which χ_{par} and $\chi_{Langevin}$ are corresponding with each other increases. Moreover, χ_{par} with v_f = 0.1 and 0.5 shows independent behavior of T in the low temperature range. This indicates that nanoparticles cannot show magnetically isolated superparamagnetic behavior due to strong dipole interaction. In addition, for D_p = 9nm, χ_{par} with v_f = 0.1 and 0.5 also shows independent of T the range from 10 to 900 K.

Fig.2 shows the normalized susceptibility ($\chi_{par} / \chi_{Langevin}$) against the energy ratio of dipole interaction and thermal effect ($E_{dipole} / E_{thermal}$) for 3 and 9nm with various v_f and T. Here, E_{dipole} and $E_{thermal}$ were defined as follows,

$E_{dipole} = 2\Pi M_s^2 V v_f$,

$E_{thermal} = k_B T$ (k_B is the Boltzmann constant).

The normalized susceptibility is uniquely scaled using the energy ratio though V, D_p, and T have changed. For $E_{dipole} / E_{thermal} < 0.01$, the normalized susceptibility is almost 1.0, suggesting that the influence of the dipole interaction can be negligibly small and nanoparticle assembly shows simple superparamagnetic behavior, which can be explained by the Langevin function. On the other hand, for $E_{dipole} / E_{thermal} > 5.0$, normalized susceptibility logarithmical decreases with -1.0 of slope. This indicates that χ_{par} is determined from only the volume fraction of nanoparticles as follow, $\chi_{par} = 1/(6\Pi v_f)$.

For $0.01 < E_{dipole} / E_{thermal} < 5.0$, nanoparticle assembly shows superparamagnetic behavior, however its static magnetization process can not be simply explained by the Langevin function due to the influence of the dipole interaction.

[1]Roy W. Chantrell, M. El-Hilo, and Keven O'Grady, IEEE Trans.Magn., 27, 3570 (1991).

[2]Weili Luo, Sidney R. Nagel, T. F. Rosenbaum, and R. E. Rosensweig, Phys. Rev. Lett., 67, 2721 (1991).

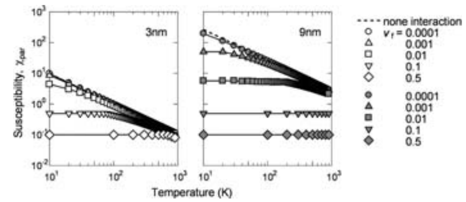

Fig. 1 Temperature dependence of simulated static susceptibility (χ_{par}) for 3 and 9 nm nanoparticles with various volume fractions (v_f).

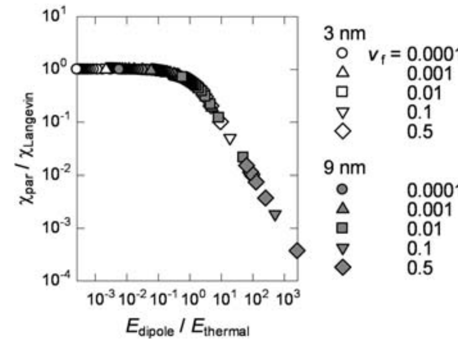

Fig. 2 Simulated susceptibility (χ_{par}) normalized by calculated susceptibility ($\chi_{Langevin}$) from the Langevin function against the ratio between dipole and thermal energy ($E_{dipole} / E_{thermal}$) for 3 and 9 nm nanoparticles with various volume fractions (v_f).

GW-04

Numerical Modeling and Characterization of Micromachined Flexible Magnetostrictive Thin Film Actuator.

H. Lee, C. Cho
Mechanical Engineering, Inha University, Incheon, South Korea

Many research groups had a great deal of interest in the theoretical and numerical design and fabrication of thin film structures using magnetic materials.[1-3] Most of the magnetostrictive thin film actuators are designed in the Si substrate for the use of the micromachining process.[4-6] The development of micro-actuators based on magnetoelastic response requires high magnetostriction performance of the thin films with flexible substrates. Si substrate has highly brittle property, so it can not only be used in impact or bent environment but also high deflection. But flexible polyimide substrate can be an effective material for sensor and actuator applications in the hasher environment and higher magnetostriction with lower cost than Si substrate. For that reason, some researchers used the commercial polyimide film, but commercial polyimide film is not easy to get micromachining process for complex substrate shapes and various thicknesses. So, alternative flexible substrate should be adopted. And some studies show numerical models for magnetostriction, but there is limitations for large deformation as a actuator. So, in this study, a finite element model with in-plane and out-of-plane displacement for large deformation of the magnetostrictive thin film actuator is developed, and NiFe magnetostrictive thin film structures are designed with the micromachined flexible substrate using SU8-2025 and SU8-2075 (Shell Chemical Corp.). For the numerical analysis of large deformation of the magnetostrictive thin film structure, a plate element shown in Fig.1 is proposed. The element stiffness matrix and force matrix are calculated, and numerical analysis is performed from the plate model. A Magnetostrictive thin film actuator is also designed. Fig.2 shows schematic design and its principle of operation. It is fabricated from the first step of the micromachining of substrate with the suggested design using SU-8. After that, NiFe thin film is deposited using sputter and electroplating process, and thicknesses of deposited NiFe films are 2, 5 and 10um. The deposited film thicknesses are measured by X-ray diffraction (XRD). Fig.3 shows the fabricated actuator. After the fabrication, magnetic moment of the film is measured to characterize the magnetic properties of the NiFe film with the SU-8 substrate using VSM (Vibrating Sample Magnetometer) and deflections of the actuator under the external magnetic field due to the magnetostriction is measured using capacitance method to characterize the magnetomechanical characteristics. And also the numerical results of magnetostriction analysis from the developed finite element model are compared with experimental results in Fig.4. Maximum net deflection is about 147μm under 0.5T for micro-device application.

1.M E H Benbouzid, G Reyne and G Meunier, IEEE Trans. Magn.29(6) (1993) 2467.

2. R Watts, M R J Gibbs, W J Karl and H Szymczak, Appl. Phys. Lett, 70(19) 1997 2607.

3. M Besbes, Z Ren, A Razek, IEEE Trans. Magn. 32(3) 1996 1058.

4. M R J Gibbs, E W Hill and P J Wright, J. Phys. D: Appl. Phys. 37 (2004) R237.

5. H Janocha, Sens. Actuator A-Phys. 91 (2001) 126.

6. C Body, G Reyne and G Munier, IEEE Trans. Magn. 33 (2) (1997) 2163.

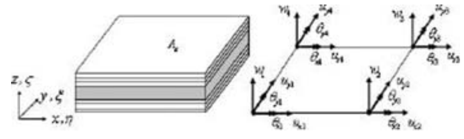

Fig.1 A plate model for large deformation FE analysis.

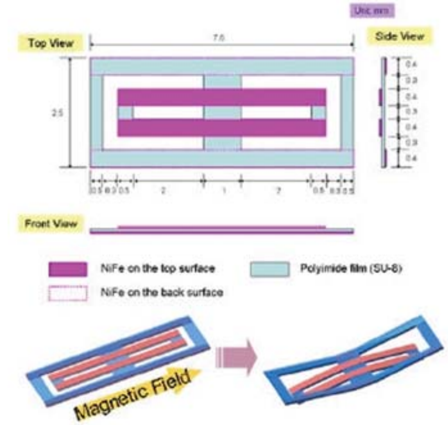

Fig.2 The schematic design and the principle of operation.

Fig.3 Fabricated magnetostrictive actuator.

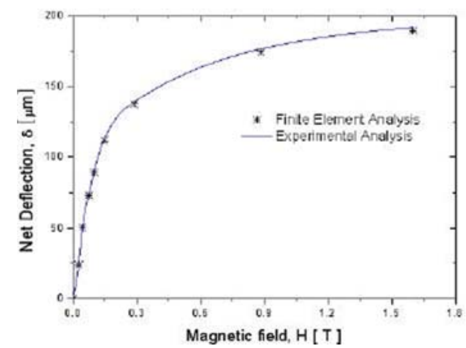

Fig. 4 Comparison of net deflection results between FE analysis and experimental analysis.

GW-05

Semi-analytical calculation of the armature reaction in a slotted tubular permanent magnet actuator with distributed windings.

B. Gysen, J. Paulides, E. Lomonova, A. Vandenput
Electrical Engineering, Eindhoven University of Technology, Eindhoven, Netherlands

Tubular actuators are increasingly employed in the industry due to their high force density, excellent servo characteristics, virtually zero attraction force and the absence of end windings. In order to obtain an optimal design subject to various specifications, accurate modeling of the behavior of the actuator is inevitable. Various techniques exist for modeling the magnetic behavior of the tubular actuator, including the magnetic equivalent circuit (MEC) [1], the Schwarz-Christoffel (SC) mapping technique [2], the finite element method (FEM) [3] and the semi-analytical approach [4]. The latter one is the most preferred for optimization, due to the high accuracy and fast computational time.

Extensive analysis of the magnetic field distribution in the air gap of a tubular permanent magnet actuator is found in the literature [4], however they all consider a slotless machine. This paper considers the field calculation due to the stator windings of a slotted tubular PM actuator. For simplicity, the end effects are excluded and an infinite length of stator and translator is considered. Since only the field due to the stator windings is considered, the magnets are regarded as an air region since their relative permeability is close to unity. The periodicity of the stator is used and therefore, the field solution can be written as a Fourier series with period $2\tau_{wp}$, with τ_{wp} the winding pitch. If a multi phase system is considered, superposition will be used in order to obtain the total field solution. A cross section of one period for a three phase system is given in Figure 1. During the calculation of the field solution of one phase, the influence of the slotting effect of the other phases is excluded, therefore the slot openings are considered as full iron as indicated in Figure 1. The iron is assumed infinitely permeable and since the magnets are considered as an air region, only two regions need to be distinguished, the air gap and the slot with current density, region I and II, respectively.

The current density of each phase can be described as a Fourier series with a fundamental period of $2\tau_{wp}$. The Maxwell equations can be described in terms of the magnetic vector potential, and therefore the field equations result in a Laplace equation for region I and a Poisson equation for region II. These equations are solved subject to the Dirichlet boundary conditions. In the final paper the extensive analysis will be given in terms of the geometric parameters and material properties. The solution is verified with a finite element calculation for linear iron where the current density in the coils is 5 A/mm^2 for the parameters given in Table 1.

The solution in Figure 2 is calculated at the center radius of region I. Excellent agreement with the FE solution within 2 % is obtained. In the final paper, figures of the total field solution due to all the phases will be given for both regions.

[1] J.L.G. Janssen, J.J.H. Paulides, E.A. Lomonova, A.J.A. Vandenput, "Analysis of a variable reluctance permanent magnet actuator," Industry Applications Conference, 42nd IAS Annual Meeting, pp. 502-509, 23-27 Sept. 2007.

[2] B.L.J. Gysen, J.J.H. Paulides, E.A. Lomonova, A.J.A. Vandenput, "Analytical and numerical techniques for solving Laplace and Poisson equations in a tubular permanent magnet actuator: Part II. Schwarz-Christoffel mapping," IEEE Transactions on magnetics, to be published.

[3] J.L.G. Janssen, J.J.H. Paulides, E.A. Lomonova, A.J.A. Vandenput, "Cogging force reduction in tubular permanent magnet actuators," Electrical Machines and Drives Conference, vol. 1,pp. 266-271, 3-5 May 2007.

[4] J. Wang, G. Jewell, D. Howe, "Design optimization and comparison of tubular permanent magnet machine topologies," IEE Proc.-Electr. Power Appl., vol. 148, pp. 456-464, Sept. 2001.

Parameter	Value
R_r	5 mm
R_i	11 mm
R_c	25 mm
τ_{wp}	40 mm
b	4 mm
J_A	5 A/mm^2

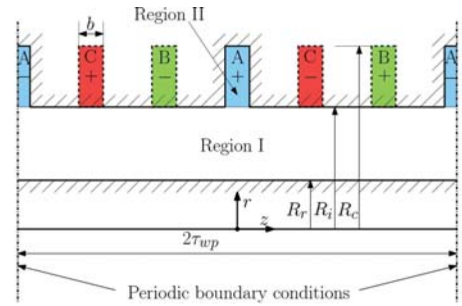

Figure 1. Cross section of one period for calculation of the armature reaction.

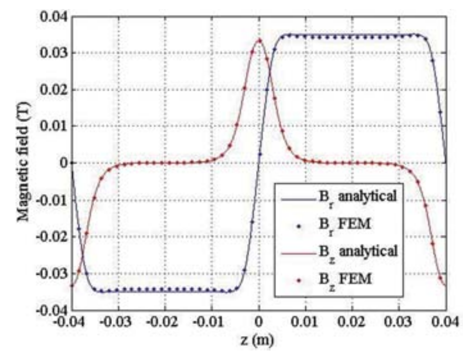

Figure 2. Magnetic field solution in region I

GW-06

Sequential optimization method for the design of electromagnetic devices.

G. Lei[1], *Y. Guo*[2], J. Lavers[3]
1. College of Electrical and Electronic Engineering, Huazhong University of Science and Technology, Wuhan, China; 2. Faculty of Engineering, University of Technology, Sydney, NSW, Australia; 3. Department of Electrical and Computer Engineering, University of Toronto, Toronto, ON, Canada

Abstract —Sequential least square method and sequential linear Bayesian method are presented for the design of electromagnetic devices. In our implementation, optimization design is composed of coarse optimization process (COP) and fine optimization process (FOP). The main purpose of the former is to reduce the design space, while the latter is to update the optimal results. To illustrate the efficiency of the new methods, the TEAM Workshop problem 22 is investigated.

I. INTRODUCTION

Many electromagnetic optimization problems are solved by means of highly accurate models coupled with direct optimization algorithms, such as genetic algorithm, clonal selection algorithm and differential evolution algorithm (DEA) [1], [2]. However, these approaches are computationally expensive. As an alternative, many approximate models, such as response surface model, radial basis functions model and Kriging model are also widely used, which are proved fast, but not very accurate [3]. In traditional optimization methods, models and algorithms are almost discussed separately. But in deed, optimization is a simultaneous updating process about them. In this paper, we try to discuss both of them with sequential optimization method (SOM).

II. SOM

Given a set of n sample points x[n] and responses y[n], now, for an input x, the response value can be expressed as a realization of a low-order polynomial regression model and a random function. Quadratic polynomials are used in our implementation. Then we have a matrix notation of the approximate model as $y[n]=H\beta+w$, where β is a vector of regression parameters to be estimated, H is a known observation matrix of x[n], and w is a noise vector with zero mean and covariance. Generally, βs are estimated by least square estimator (LSE) and linear Bayesian estimator (LBE). However, matrix inversions are required in LSM and LBE, and when the dimension of response vector is large or the step size is small, many difficult problems are what we must face. So we present two improved sequential estimation methods(SEM), which are termed sequential LSE (SLSE) and sequential LBE (SLBE) [4]. It is of great interest that, except for the initialization procedure, no matrix inversions are required in SEM. Fig.1 is the flowchart of SOM.

III. EXPERIMENTS AND RESULTS

The TEAM Workshop problem 22 (SMES) is a well known benchmark problem for optimization methods [1]. SMES is a superconducting magnetic energy storage device that consists of two solenoids. The dimensions of the inner solenoid stay fixed, while the dimensions of the outer solenoid (R2,h2/2,d2) should be optimized to reduce stray fields while keeping the stored energy close to 180 MJ. Table I shows the optimization results given by our proposed methods. Three main conclusions can be drawn from the Table. Here SLSM means LSE used in COP and SLSE used in FOP, and the similar meaning to SLBM.

1) For the direct optimization method, the optimal design parameters given by DEA are [3.11 0.302 0.301]. The mean stray field Bstray is 0.94 mT, energy E is 179.86 MJ, and 1910 finite element sample points (FESPs) are needed.

2) For the optimization with SLSM, 249 FESPs are needed to get the optimal results, which are [3.10 0.232 0.394]. Bstray is also 0.94 mT, E is 179.94MJ, and the error is 0.03%, which is smaller than that given by DEA.

3) For the optimization with SLBM, only 198 FESPs, about 1/10 that by DEA, are needed to get the optimal results. The optimal results are [3.08 0.260 0.364], E is 179.93MJ; the error is 0.04%. Bstray is 0.91 mT, which is better than that by DEA and by SLSM. Obviously, SLBM is the best one of the three methods.

IV. CONCLUSION

SOM presents a new way for the effective analysis procedure of electromagnetic optimization problems. Compared with the methods using direct optimization algorithms, SLSM and SLBE only need a small sample data, and the overall computational effort needed is much less than that by direct optimization method.

[1] F. Campelo, F. G. Guimaraes, H. Igarashi and J. A. Ramirez, "A clonal selection algorithm for optimization in electromagnetics", IEEE Trans. Magn., 41(5): 1736-1739, 2005.

[2] R. Storn and K. Price, "Differential evolution—A simple and efficient heuristic for global optimization over continuous spaces", Journal of Global Optimization 11: 341–59, 1997.

[3] L. D. Wang and D. A Lowther, "Selection of approximation models for electromagnetic device optimization", IEEE Trans. Magn., 42(2):1227-1230, 2006.

[4] S. M. Kay, Fundamentals of Statistical Signal Processing: Estimation Theory, Prentice-Hall USA, 1993.

Var. Unit	R2 [m]	h2/2 [m]	d2 [m]	Bstray [mT]	Bmax [T]	E [MJ]	FESPs
DEA	3.11	0.302	0.301	0.94	4.34	179.13	1910
SLSM	3.10	0.232	0.394	0.94	4.65	179.94	249
SLBM	3.08	0.260	0.364	0.91	4.67	179.93	198

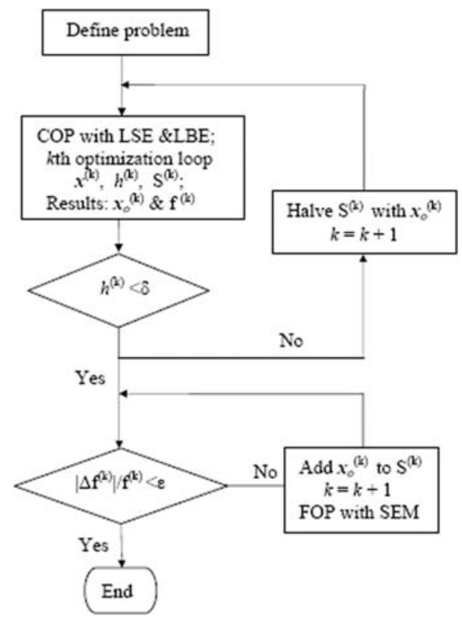

GW-07

A new field-circuit coupled method for the computation of additional losses in transformer.

G. Jian[1], *L. Heyun*[1], H. Siulau[2]
1. School of Electrical Engineering, Southeast University, Nanjing, China; 2. Department of Electrical Engineering, Hong Kong Polytechnic University, Hong Kong, China

Apart from the standard copper and iron losses described in common textbooks, there are significant stray loss and winding eddy current loss in oil-type power transformers. The major challenge for modern transformer designers is to develop the necessary tools to precisely simulate the machine performance so as to realize optimum transformer performance at low cost in real practice [1]. Traditionally, finite element methods (FEM) are often used to calculate eddy current losses in transformers, in which the ampere-turns (ATs) in the primary and secondary windings are assumed to be equal. However, the primary windings ATs are balanced not only by those in the secondary windings, as the eddy current in the structure and the self-leakage magnetic field need to be balanced by the primary ATs as well.

A novel field-circuit coupled method for calculating the additional losses of transformer is presented to overcome the shortcoming of common FEM in this paper. For a three-dimensional eddy current field, the ***A-V-A*** formulations with the coulomb gauge can be derived whilst every phase winding is treated as an independent circuit [2]. By combing the ***A-V-A*** formulations and the winding circuit equations, a global system of equation for the field-circuit coupled solution can be obtained, in which the eddy current field and the circuit equations are solved simultaneously. Induced currents in the secondary windings and the additional losses of transformer are calculated.

To validate the proposed method, an 800kVA, 3-phase oil-type transformer is selected as the test sample and a quarter model of which is shown in Fig.1. The induced currents in the secondary windings are shown in Table I. It can be seen that the current ratio I_2/I_1 in all the three phases are smaller than N_1/N_2. This means that the unbalance ATs between the primary and secondary windings are balanced by the sum of the eddy current in the structures and the self-leakage magnetic field of the primary windings.

Fig.2 shows the distributions of the structures losses. Table II gives the eddy current losses in the structures and the total copper losses. It can be seen that the calculated result of the field-circuit coupled method is in good agreement with the measured data. Compared with common FEM, the proposed method is more accurate in finding the additional losses of power transformers.

In summary, this paper presents a new field-circuit coupled calculation method for the computation of the additional losses in a transformer. As will be elaborated in the full paper, the computed results show that i) the current ratio $I_2/I_1 < N_1/N_2$ in all the three phases. This is because the unbalance ATs between the primary and secondary windings are balanced both by the eddy current in the structures and the self-leakage magnetic field of the primary windings; and ii) when compared with conventional FEM, the proposed field-circuit coupled method is more accurate for computing the additional losses in a oil-type power transformer.

[1] S V Kulkarni, S A Khaparde. "Stray loss evaluation in power transformers - A Review". Power Engineering Society Winter Meeting, 2000, vol.3, pp.2269-2274.

[2] R. Y. Tang, S. H. Wang. "Transient simulation of power transformers using 3D finite element model coupled to electric circuit equations". IEEE transactions on magnetics, vol.36, no.4, pp. 321-326, 2000.

N_1/N_2	I_a/I_A	I_b/I_B	I_c/I_C
450/18	1101.84 / 46.19	1127.19 / 46.19	1114.46 / 46.19

Structures	Loss(W)		
Method	Field-circuit coupled	FEM	Measured
Tank	355	29	
Core	197	90	
Winding	272	281	
Clamp	176	6	
I^2R	6320	6527	
Total	7320	6933	7600

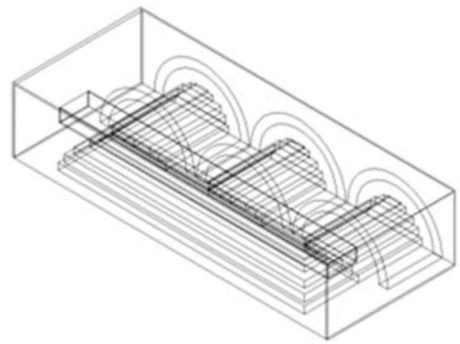

Fig.1. The ¼ model of the transformer.

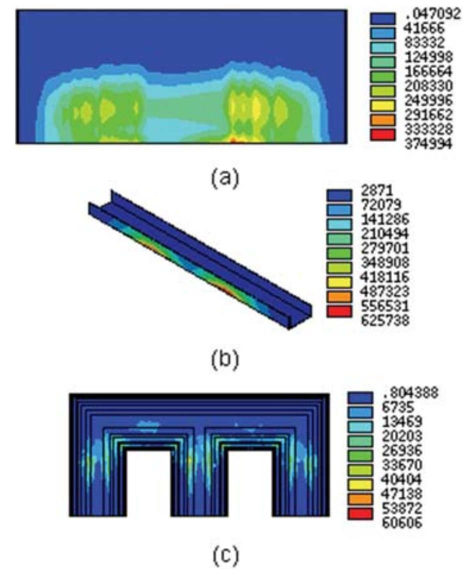

Fig.2. The distributions of eddy current losses (W/m^3). (a) tank loss (b) clamp loss (c) core edge loss.

GW-08

Accurate eddy current losses computation for ferromagnetic cores working in strongly distorted regimes.

L. Mandache[1], D. Topan[1], K. Al-Haddad[2]
1. Electrical Engineering, University of Craiova, Craiova, Romania; 2. Genie Electrique, Ecole de Technologie Superieure, Montreal, QC, Canada

Abstract:
The paper is based on an advanced time-domain modeling technique of eddy currents and their power losses in ferromagnetic cores for transformers, inductors and other electric machines, working in strongly distorted regimes, including switching regimes, as in power electronics.
The model takes its mathematical root from the Maxwell's theory, and does not deal with analytic approximation. The entry data are the first-magnetization curve given by the manufacturer data sheet, the specific power losses (given for a reference flux density and a reference frequency), as well as the geometric dimensions of each ferromagnetic piece. Any soft ferromagnetic materials, like ferrite, silicon steel sheet core or multilayered ferromagnetic amorphous alloy film can be modeled using this principle, according the given examples.
The model is suitable to be included in a time-domain circuit simulator, like SPICE, in order to simulate the whole circuit that includes the magnetic device (ferromagnetic core and their windings). The simulation results give us the time-domain flux distribution in the magnetic core, the eddy current losses on each piece, as well as any working parameter of the circuit which includes the magnetic device.
As a simple example, a common case of a single phase inductor is shown: experimental results are compared with the corresponding simulation, obtaining the expected similarity.
Totally feasible and linked to the practice of common modern applications, our method has the capability to become a valuable tool for applicative research and design activity.

Generalities:
Many actual industry applications are tightly linked to power converters, distinguished by strongly distorting working regimes. The presence of ferromagnetic cores makes the optimal design a very difficult task. The core may work on minor hysteresis loops, having or not a bias component that strongly modifies the dynamic permeability. In addition, the medium frequency magnetic field provokes important eddy currents which bring power losses and distort the B-H loop of the magnetic core. These losses are dominant in the core heating process.
Unfortunately, the designer has often the tendency to improve the magnetic core size in order to reduce the maximum flux density and consequently to keep the core losses on low values. Contrarily, a rigorous design requires a smallest weight and size, as guaranty of a lowest manufacturer price. One must find an optimal compromise between total losses and the device size: maximum power losses in a smallest size for a given insulation class and cooling conditions.
Our paper is focused on a totally feasible method for the time-domain modeling of soft ferromagnetic materials on behalf of the dominant effect of eddy currents. The model remains unchanged from low to medium frequencies, in the domain of Maxell's theory restrictions. The model can be easily included in a time-domain circuit simulator, like SPICE, being suitable to simulate any device with ferromagnetic core, working in harmonic or distorting regime as in power electronics.
The main principle is the well-known modeling of a magnetic circuit through an electric circuit, based on the formal similarity between the magnetic field and electric field lows.
The given magnetic circuit is treated as an assembly of many ferromagnetic pieces and air-gaps. Each ferromagnetic piece is chosen considering the simplifying assumption of a uniform magnetic flux density through its cross section.
In order to develop a useful implementation of the model, we performed a SPICE subcircuit which can be included in any time-domain circuit simulation (see the figure). The complete netlist of the subcircuit will be included in the full paper.
Conclusions:
Our method is remarkable through its degree of generality, simplicity and feasibility. It allows performing a high precision time-domain analysis of circuits with nonlinear magnetic devices. It is an excellent tool that helps to solve firmly the specific problems of magnetic devices through an efficient way, without groping and forced approximation. The method is explained by the Maxwell-Hertz theory.

Selection:

1) T. Fujiwara, R. Tahara, Eddy current modeling of silicon steel for use on SPICE, IEEE Transactions on Magnetics, Volume 31, Issue 6, Part 2, Nov. 1995, pp. 4059 – 4061.

2) H. Chemkha, F. Rioux-Damidau, A fast and accurate model for eddy current computation in thin conducting shells, IEEE Transactions on Magnetics, Volume 33, Issue 2, Part 2, March 1997, pp.1342 - 1345

3) L.R. Dupre, O. Bottauscio, M. Chiampi, F. Fiorillo, M. Lo Bue, J. Melkebeek, M. Repetto, M. Von Rauch, Dynamic Preisach Modelling of Ferromagnetic Laminations under Distorted Flux Excitations, IEEE Transactions on Magnetics, Vol. 34, no. 4, Part 1, July 1998, pp 1231 – 1233.

4) F. Fiorillo, L. R. Dupré, Comprehensive Model of Magnetization Curve, Hysteresis Loops, and Losses in Any Direction in Grain-Oriented Fe-Si, IEEE Transactions on Magnetics, Vol. 38, no. 3, May 2002, pp. 1467 – 1476.

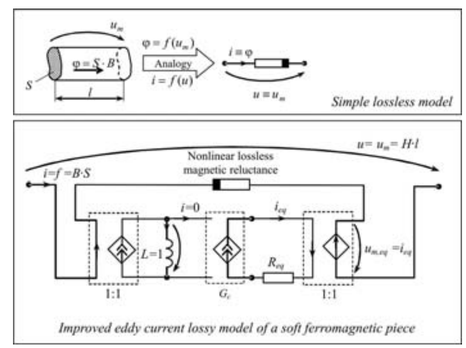

GW-09

Modeling of effect of plastic deformation on Barkhausen noise and magnetoacoustic emission in iron with 2% silicon.

M. J. Sablik[1], B. Augustyniak[2], F. J. Landgraf[3]
1. Mechanical and Materials Engineering Div., Bldg. 139,, Southwest Res. Inst., San Antonio, TX; 2. Physics, Gdansk Institute of Technology, Gdansk, Poland; 3. Metallurgical Engineering, University of Sao Paulo, Sao Paulo, Brazil

Before one models the effect of plastic deformation on magnetoacoustic emission (MAE), one must first treat non-180 degree domain wall motion. In this paper, we take the ABBM model [1] and modify it to treat non-180 degree wall motion. We then insert a modified stress-dependent Jiles-Atherton model, which treats plastic deformation[2], into the modified ABBM model to treat the field and stress dependence of magnetic Barkhausen noise (HBN) and of MAE.

Sablik [3] derives the following expression for the Barkhausen noise power using ABBM [1] and a constant rate of field increase, h :

$Ib=(Ac/Ag)S \{Mc(H)/[S (Mc(H)/Ps) + \rho/(S)(G)(h)]\}$,

where $Ag=(G/\rho)^{**}2$ and $Mc(H)=(\mu i/\mu 0)(\mu i-\mu 0)$. S is the average surface area of a moving 180 degree wall, ρ is electrical resistivity, G=0.1356, μi represents the irreversible permeability as a function of field H, $\mu 0$ is permeability of free space, Ps is the correlation length of coercive field correlations, and Ad is a parameter describing average spatial fluctuations of domain wall coercive field interactions. Here, $\mu i= \mu 0 [1 + dMi/dH]$, where Mi is the irreversible part of the magnetization, which is computed self-consistently [4] from an equation for dMi/dH.

Under plastic deformation, the number of Barkhausen emission centers increases with increased dislocation density Zd. We treat this change as proportional to the square root of the relative dislocation density increase, just as coercivity changes in the same way, so that:

$Ad = Ad0 (Zd / Zd0)^{**}1/2$,

where the zero subscript refers to conditions prior to plastic deformation. In Fig. 1a, modeling results are compared with experimental data. The results are for the Barkhausen power integrated over all H in iron with 2%Si. Given the error bars (not shown) in the experimental data, the fit is reasonable.

MAE is due to motion of non-180 degree domain walls, whereas magnetic Barkhausen noise is due to motion of 180 degree walls. Extending the ABBM model to non-180 degree walls means one must now include a contribution given by

$dMe/dt = \chi(H)([1.5\ \sigma/\mu 0]\ [d2\lambda/dMdt]\}$

$= \chi(H)([1.5\ \sigma/\mu 0]\ [d2\lambda/dMdH])\ h$,

where σ is an average residual stress contributing to the effective field owing to the deformation, $\chi(H)$ is the susceptibility dM/dH, M(H) is the total magnetization and λ is the magnetostriction. λ and χ are computed as in [4], but treating plastic deformation as in [2]. On using the ABBM formalism, one obtains:

$Im=[(Ac/Ag)/Sn]\{Mc(H)F(M)/[(F(M)Mc(H))Sn/Ps+\rho/(Sn\ G\ h)]\}$,

where $F(M) = (1.5\ \sigma/\mu 0)\ (d2\lambda/dMdH)$. We use the total μ here instead of μi in the expression for Mc(H) because MAE, involving elastic waves, is a more macroscopic phenomenon. The surface area Sn of the non-180 degree domain walls should be smaller than that of the 180 degree domain walls. We denote the MAE formalism up to now as Model 1. In this model, we use our previously stated result for Ad. However, Model 1 does not produce a good enough fit to the experimental data, as we shall see.

In Model 2, to get a better fit, we note that the number of 90 degree walls stops increasing once dislocation tangles set in. Correspondingly, we write:

$Ad = Ad0 (Zd/Zd0)^{**}1/2$ if $e < ec$,

$Ad = Ad0 (Zdc/Zd0)^{**}1/2$ if $e=ec$ or $e>ec$,

where ec is the deformation where dislocation tangles start and Zdc is the corresponding dislocation density.

In Fig. 1b, modeling results for MAE are compared with experimental results. Results for both Model 1 and Model 2 are shown. Model 2 gives a much better fit.

We will present additional modeling, accounting for effects of changes in residual stress with increasing deformation. We expect to show that the decrease in the experimental MAE result beyond ec is due to changes in the average residual stress as deformation e increases. This should be consistent with the result of Kleber [5], who shows in different materials an increase or decrease in MAE depending on whether the dominant effect is change in dislocation density or change in average residual stress.

[1] B.Alessandro, C.Beatrice, G.Bertotti, and A.Montorsi, J.Appl.Phys., vol. 68, pp. 2901-2915, 1990.

[2] M.J. Sablik, T. Yonamine, F. J. G. Landgraf, IEEE Trans. Magn., vol.40, pp.3219-3228, 2004.

[3] M.J.Sablik, J.Appl.Phys., vol.74, pp.5898-5900, 1993.

[4] M.J.Sablik and D.C. Jiles, IEEE Trans. Magn., vol.29,

pp. 2113-2120, 1993.

[5] X.Kleber and A.Vincent, NDT&E Internatl., vol.37, pp.439-445, 2004.

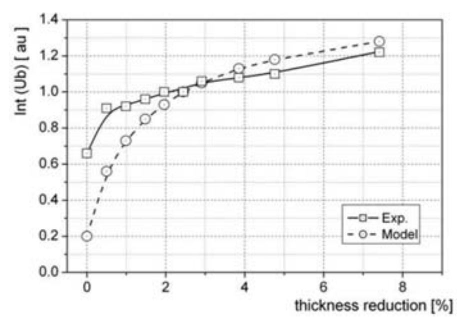

Fig1a - Integrated HBN signal vs deformation

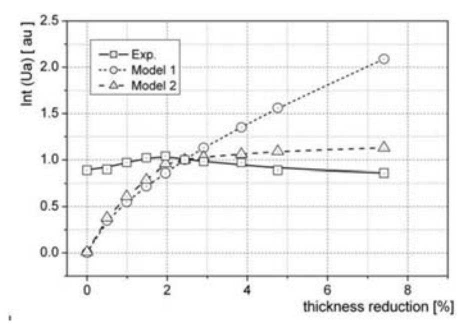

Fig2b Integrated MAE signal vs. deformation

GW-10

Fluxmetric and Magnetometric Demagnetizing Factors in Cylindrical and Rectangular Geometries.

A. Vashghani Farahani, A. Konrad
Electrical and computer engineering, University of Toronto, Toronto, ON, Canada

Introduction and background

<p>In magnetic measurements, instead of precise distributions of the internal magnetic field $\mathbf{H}_i$ and the magnetization $\mathbf{M}$, one is interested in the average response of the magnetic material to the applied field $\mathbf{H}_a$. When $\mathbf{H}_a$ is along one of the symmetry axes, the average demagnetizing field $\mathbf{H}_d^{ave}$ and the average magnetization $\mathbf{M}^{ave}$ along that axis are related by the fluxmetric N_f and magnetometric N_m demagnetizing factors, $\mathbf{H}_d^{ave} = -N_{f,m}\,\mathbf{M}^{ave}$. To calculate N_f, the fields are averaged over the mid-plane cross section normal to $\mathbf{H}_a$, while to calculate N_m the fields are averaged over the whole volume of the magnetic body. The importance of rectangular and cylindrical geometries has motivated many researchers to work on accurate values of $N_{f,m}$ in these geometries. Analytic results have been found in a few special cases, but generally numerical methods are required. The most recent works on this subject appear in a series of papers[1-4] by Chen et al. These authors have developed results for the demagnetizing factors $N_{f,m}$ as a function of susceptibility χ and aspect ratio γ for both geometries, in tabular and graphical formats. Since they have assumed χ is constant and because the magnetic flux density $\mathbf{B}$ is solenoidal, volume density of magnetic poles ρ_v is zero. Therefore the problem is reduced to finding the surface magnetic pole densities σ . The surface of the magnetic material is divided into elements and on each element σ is considered to be constant. Magnetostatic interactions of these elements leads to a set of algebric equations that can be solved to obtain σ, which can be used to find $N_{f,m}$. Two different approaches to find N_f and N_m are used. In one of them $\mathbf{M}$ and in the other one the demagnetizing field $\mathbf{H}_d$ is averaged. Whenever the results are not the same, an interpolation/extrapolation technique is introduced to obtain the correct value for $N_{f,m}$. In rectangular geometries a limiting process is used to obtain $N_{f,m}$ as the number of elements N_p increases.

A different approach

This digest introduces a different approach to obtain $N_{f,m}$. The formalism considers $\chi=\chi(\mathbf{r})$ [5]. This is especially important for ferromagnetic materials where the relation between $\mathbf{M}$ and $\mathbf{H}_i$ is not linear. It is based on an iterative method that solves for the field distributions $\mathbf{H}_i$ and $\mathbf{M}$ in the magnetic material directly [6]. While in the approaches for the surface pole distribution the total number of elements is on the order of hundreds, in this approach it is on the order of 10000. Moreover, once the structure matrix (which summarizes the magnetostatic interactions between elements) for the geometry under consideration is calculated, the demagnetizing factors $N_{f,m}$ for different χ and $\mathbf{H}_a$ can easily be obtained. Once the structure matrices for larger geometries are found, one can find the structure matrices for smaller inscribed geometries without further computation time. Another benefit of this approach is that the final results for $\mathbf{H}_i$ and $\mathbf{M}$ are supported by a uniqueness theorem [5]. Therefore it is possible to use the resulting $N_{f,m}$ with theoretical confidence.

Results

One can use the solutions $\mathbf{M}$, $\mathbf{H}_d$, and $\mathbf{H}_i=\mathbf{H}_a+\mathbf{H}_d$ to obtain necessary field averages on the whole magnetic body or over the mid-plane cross section. Two different equations are used to obtain $N_{f,m}$. These are the defining equation $\mathbf{H}_d^{ave} = -N_{f,m}\,\mathbf{M}^{ave}$ and $N_{f,m} = \mathbf{H}_a/\mathbf{M}^{ave} - 1/\chi$. To obtain this equation, $\mathbf{M}=\chi\mathbf{H}_i$ is used. In the following figures, subscripts 1 and 2 refer to these equations respectively. As the number of iterations n increases, the constitutive equation $\mathbf{M}=\chi\mathbf{H}_i$ is approached. Therefore the solutions $N_{f,m:2}$ converge to $N_{f,m:1}$. Results for appropriate energy integral is calculated at the end of each iteration. This energy is minimized by the final unique distribution solution [5].

[1] E. Pardo, D.-X. Chen, and A. Sanchez IEEE Trans. Magn., 40, No.3, 1491 (2004)

[2] D.-X. Chen, E. Pardo, and A. Sanchez IEEE Trans. Magn., 41, No.6, 2077 (2005)

[3] D.-X. Chen, J. A. Brug, and R. B. Goldfarb, IEEE Trans. Magn., 27, No.4, 3601 (1991)

[4] D.-X. Chen, E. Pardo, and A. Sanchez, J. Magn. Magnetic Materials, 306, 135 (2006)

[5] A. V. Farahani, A. Konrad, IEEE Trans. Magn., 43, No.4, 1517 (2007)

[6] A. V. Farahani, A. Konrad, IEEE Trans. Magn., 41, No.10, (2005)

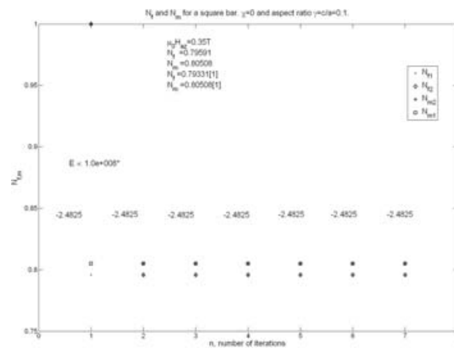

χ=0 means a uniform M. Therefore $N_{f,m:1}$ and $N_{f,m:2}$ converge very fast. Dimensions are 2a×2b×2c. $\mathbf{H}_a$ is along z.

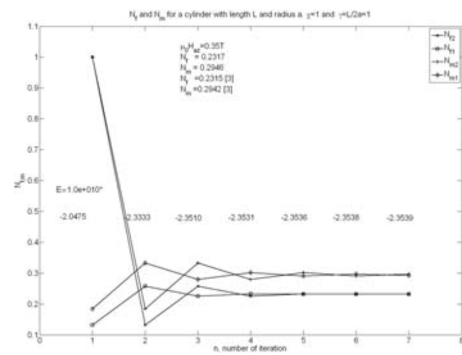

Height of cylinder is L and its radius is a. $\mathbf{H}_a$ is in axial direction. Convergence of $N_{f,m:1}$ and $N_{f,m:2}$ for χ =1 is slower.

GW-11

Transmutation of momentum into position in magnetic vortices.

S. Komineas[1], N. Papanicolaou[2]
1. Max-Planck Institute, Dresden, Germany; 2. Department of Physics, University of Crete, Heraklion, Greece

Introduction:
Magnetic vortices are magnetization configurations with a nontrivial topological structure and are thus characterized by a topological invariant. An antivortex is a configuration where the magnetisation vector winds around the center in a sense opposite to that of a vortex and has been observed in a specially designed magnetic element. It is also possible to construct nontrivial magnetic configurations in the form of vortex-antivortex (VA) pairs. They play a central role in dynamical processes that lead to vortex polarity switching in ferromagnetic elements reported in recent experiments [1,2,3]. In the case of like vortex polarities, a VA pair undergoes Kelvin motion in a direction perpendicular to the line connecting the vortex and the antivortex [4], with velocity that is inversely proportional to the distance between the two vortex centers. In the case of opposite polarities, a VA pair undergoes rotational motion around a fixed guiding center [5]. As it turns out, the three-vortex process that leads to vortex-polarity switching involves both types of VA pairs and may be thought of as a composition of Kelvin and rotational motion. We will present a study for a three-vortex process in which a Kelvin pair collides against a single vortex initially at rest [6].

Vortex pair scattering:
We assume that a single vortex C is initially at rest at the origin. We further assume that a Kelvin pair consisting of a vortex (A) and a antivortex (B) is somehow created in the neighborhood of the original vortex. The AB pair will undergo Kelvin motion, we assume the case that this will be along the y axis, and eventually collide with the single vortex C. The process was simulated using the Landau-Lifshitz (LL) equation. During collision, antivortex B rotates around vortex C before rejoining its original partner A to form a new VA pair that scatters off at an angle in the third quadrant. The target vortex C is shifted to a new position in the fourth quadrant thanks to transmutation of VA pair momentum into vortex position. The scattering is slightly inelastic in the sense that the outgoing AB pair moves out with greater velocity (v=0.15).

The unexpected result in this numerical simulation is that the VA pair AB is scattered at an angle to the y axis which is the initial axis of propagation. In a naive approach to the problem one would think that the VA pair scattering and the corresponding change in its linear momentum does not seem to be accompanied by a corresponding change in momentum of any other object taking part in the process. This would appear to contradict the conservation of linear momentum in this conservative system.

Such a peculiar behavior can be explained (qualitatively and quantitatively) by the unusual nature of the linear momentum. The two components of linear momentum (impulse) P can be written as moments of the topological vorticity γ [7]. The latter is a key quantity which gives the skyrmion number N (multiplied by 4π) when integrated in space. It should be noted that P is actually a measure of position for an isolated vortex, it has really the meaning of linear momentum for a Kelvin VA pair. The numerical simulation of Fig. 1 shows that the linear momentum (impulse) of a VA pair is transferred to vortex impulse which is tantamount to a translation in the vortex position. A genuine transmutation of momentum into position takes place during the three-vortex collision. Therefore, the definition of the impulse given is not only consistent with the symplectic structure of the Landau-Lifshitz equation [7] but it is indeed physically relevant.

Switching of vortex polarity:
The preceding numerical experiment was repeated for a Kelvin pair with relatively large velocity v=0.5. While the initial stages of the process are similar to those encountered in the case of slow Kelvin motion, as soon as antivortex B begins to rotate around the target vortex C they collide and undergo a spectacular annihilation leaving behind the vortex A which may be thought of as the target vortex C with polarity flipped (vortex core switching).

[1] A. Neudert et al, J. Appl. Phys. 97, 10E701 (2005).

[2] B.V. Waeyenberge et al., Nature(London) 444, 461 (2006).

[3] K. Yamada et al., Nature Materials 6, 269 (2007).

[4] N. Papanicolaou and P.N. Spathis, Nonlinearity 12, 285 (1999).

[5] S. Komineas, Phys. Rev. Lett. 99, 117202 (2007).

[6] S. Komineas and N. Papanicolaou, arXiv:0712.3684v1.

[7] N. Papanicolaou and T.N. Tomaras, Nucl. Phys. B 360, 425 (1991).

GW-12

Reduction Design of Eddy Current Loss in Permanent Magnet.

J. Jung, S. Lee, J. Hong
Department of Mechanical Engineering, Hanyang University, Seoul, South Korea

1. Introduction

Interior permanent magnet synchronous motor (IPMSM) is used for traction motor and compressors because it can use both magnetic and reluctance torque and it is suitable for flux weakening control which realizes high power and wide speed range. In addition, by using the Nd-Fe-B permanent magnet (PM) in IPMSM, the maximization of the torque per unit rotor volume (TRV) and the minimization of the total size are possible.

The factors which affect the demagnetization in PM are divided into thermal, permeance coefficient and variation of external magneto motive force (MMF). Especially, demagnetization by the thermal effect is dominant because the rotor of traction motor is directly connected with the engine shaft. The eddy current loss in PM causes of the increase in temperature in PM and the high temperature decreases the performance of the PM [1]. Therefore, the eddy current loss in PM is important design factor in the design of IPMSM. In order to exactly calculate the eddy current loss in PM, transient analysis with 3-dimensional finite element method (3D FEM) is necessary. However, it requires huge computation time.

Since the flux variation usually affects the eddy current loss in PM [2], the flux variation should be minimized. Therefore, the variation of flux quantity per pole according to the change of the rotor position through 2D FEM is used and it is designated by the objective function in response surface methodology (RSM). In order to verify the validity of suggested method, optimized model is analyzed by transient analysis with 3D FEM.

2. Analysis model

The prototype is applied to the traction motor. The configuration of prototype is shown in Fig. 1. The PM of prototype is made of Nd-Fe-B magnet. Its nominal operating temperature is about 120 ~ 150deg.

3. Reduction method of eddy current loss in PM

Eddy current loss is proportional to the square of frequency and peak-peak quantity of flux variation [2]. The frequency of the flux variation per pole is determined by the combination of pole and slot number. However, peak-peak value of flux variation can be minimized by the change of geometry of the motor. Therefore, the peak-peak quantity of flux variation per pole is selected as the objective function in this paper. Fig. 2 shows comparison of the flux variation per pole in the flux weakening condition. The flux variation per pole is calculated by the difference between vector potential A1 and A2 as shown in Fig.1.

The value of the objective function is optimized by the magneto static analysis with 2D FEM. In the optimized model, the square of peak-peak quantity for the flux variation per pole is decreased about 40% compared with prototype as shown in Fig.2. Therefore it can be expected that eddy current loss of optimized model is decreased 40%.

4. Result and Discussion

In order to verify the suggested design method, transient analysis with 3D FEM is performed. Fig. 3 shows the configuration of the optimized model and the distribution of eddy current, respectively. The variation of eddy current loss in PM is expressed in Fig. 4. The reduction ratio of eddy current loss by 2D FEM and 3D FEM is about 40% and 50%, respectivly. However, the tendency of the change of eddy current loss can be resonably found using the suggested method in this paper.

[1] Gyu-Hong Kang, et al.,"Analysis of irreversible magnet demagnetization in line-start motors based of the finite element method," IEEE Trans. Magn., vol.39, no. 4, pp.1488-1491, May. 2003.

[2] H. Polinder and M. J. Hoeijmakers, "Eddy-current loss in the segmented surface-mounted magnet of a PM machine," Electric Power Application, IEE Proceedings, vol.146, issue 3, May. 1999.

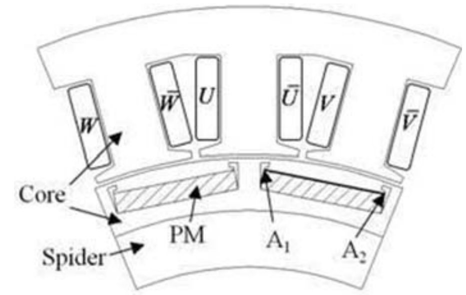

Fig.1. Configuration of prototype

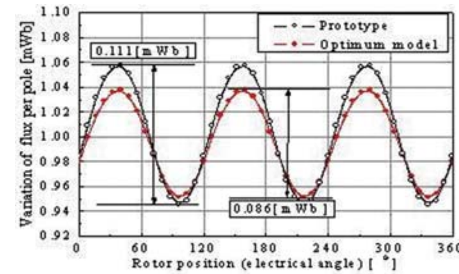

Fig.2. Comparison of the variation of flux per pole

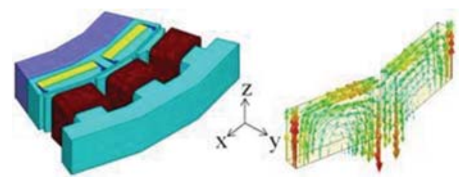

Fig.3. 3D model for analysis and eddy current distribution

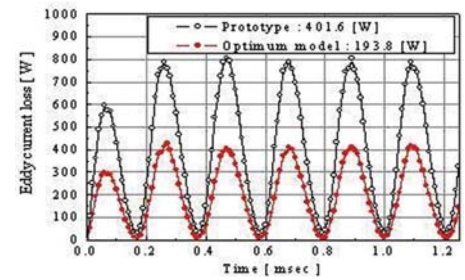

Fig.4. Eddy current loss in PM calculated by transient analysis with 3D FEM

GX-01

Magnon thermalization and formation of coherent Bose-Einstein condensate.

S. O. Demokritov[1], V. E. Demidov[1], O. Dzyapko[1], G. A. Melkov[2], A. N. Slavin[3]
1. Institute for Applied Physics, University of Muenster, Muenster, Germany; 2. Department of Radiophysics, National Taras Schevchenko University of Kiev, Kiev, Ukraine; 3. Department of Physics, Oakland University, Rochester, MI

Bose-Einstein condensation (BEC) it is one of the few quantum phenomena that manifest themselves on the macroscopic scale. In particular, Bose-Einstein condensation in quasi-equilibrium ensembles of quasiparticles injected into solids using different types of pumping has recently attracted enormous attention (see, e.g., [1,2]). One of the main advantages of quasiparticles is their small mass and the possibility to pump a large number of quasiparticles, which both result in Bose-Einstein transition at relatively high temperatures. Recent observations have shown [3], that a magnon BEC can even be achieved at room temperature.
In this work we study in detail the processes in the magnon gas leading to the overpopulation of the lowest energy level of the system and prove the spontaneous coherency of the overpopulated state. The samples were cut from yttrium-iron garnet (YIG) film in the form of stripes with lateral dimensions of 1.5 mm by 30 mm. The stripes were placed into a uniform static magnetic field of H=700-2000 Oe. The injection of magnons was performed by means of parallel parametric pumping with a frequency of 8.1 GHz. Thus, primary magnons at a frequency f_p =4.05 GHz were created. The pumping field was created using a wire resonator with the diameter of 25 μm attached to the surface of the sample. The detection of magnons and their distribution over frequencies (energies) was performed by means of a time-resolved Brillouin light scattering technique [3].
For small powers below the threshold of formation of BEC, using continuous pumping we were able to study in detail the temporal characteristics of the process of redistribution of the primary magnons over the spectrum and determine the thermalization time as a function of the pumping power (see Fig. 1). We show that the redistribution of primary magnons occurs in a series of multiple scattering events [4]. The thermalization of the magnon gas to a quasi-equilibrium state is only possible for pumping powers above a certain value P_th. Above this threshold the thermalization time quickly decreases to 50 ns.
The spontaneous coherency of the created state has been studied using short-pulse magnon injection with the duration of 30 ns, which is smaller than the found thermalization time. The observed relaxation process is illustrated in Fig. 2, where the BLS intensity is shown as a function of the delay time with respect to the start of the pumping pulse and the magnon frequency. It is seen in the figure that, as in the case of continuous pumping, the short-pulse injection of magnons at a frequency f_p is followed by their accumulation at the frequency of the lowest magnon state f_min.
The studies of the decay rate for BLS intensity at f_min have revealed its dependence on the pumping power, showing a stepwise doubling of the decay with pumping power increasing from 2.5 to 4 W (see Fig. 3). This doubling was associated with different sensitivity of the BLS technique with respect to coherent and incoherent magnons. Since for incoherent magnons the BLS intensity is proportional to their number, and for coherent magnons it is proportional to this number squared, the doubling of the decay rate indicates an emergence of coherence in the magnon gas.
In this way our experimental data clearly show that the magnons accumulated at the lowest energy level are coherent at high enough pumping powers and this coherence emerges spontaneously if the density of magnons exceeds a certain critical value. This finding gives the direct experimental evidence of the BEC transition in a magnon gas at room temperature.

This work was supported in part by the Deutsche Forschungsgemeinschaft, US Army Research Office (MURI Grant No.W911NF-04-1-0247), and by the Science & Technology Center of Ukraine.

[1] Ch. Rüegg et al., Nature 423, 62 (2003).

[2] R. Balili, V. Hartwell, D. Snoke, L. Pfeiffer, and K. West, Science 316, 1007 (2007).

[3] S.O. Demokritov et al., Nature 443, 430 (2006).

[4] V. E. Demidov, O. Dzyapko, S.O. Demokritov, G.A. Melkov, and A.N. Slavin, Phys. Rev. Lett. 99, 037205 (2007).

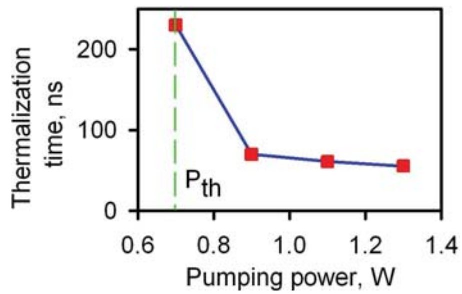

Fig. 1

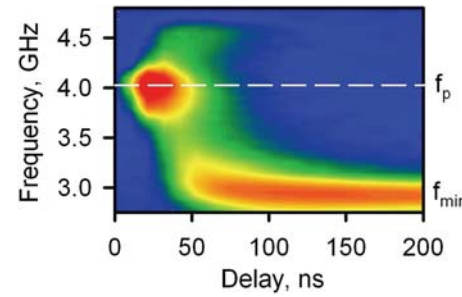

Fig. 2

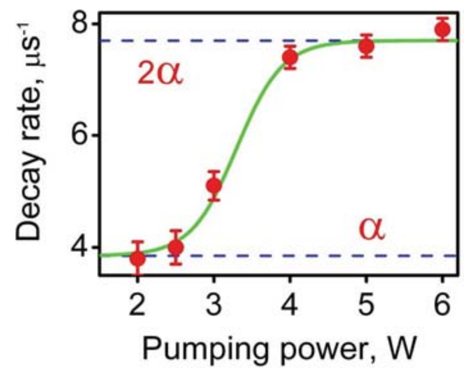

Fig. 3

GX-02

Critical Temperature for Thermal Runaway in a Magnetic Material.

F. Farahmand, *F. P. Dawson*, J. Lavers
ECE, The University of Toronto, Toronto, ON, Canada

Introduction

Magnetic devices are usually operated at elevated temperatures. However, the design must ensure that the core temperature does not exceed a critical value otherwise thermal runway will occur. Thermal runaway implies that there is no steady-state balance between the generation of heat due to magnetic core losses and the removal of heat by radiation and convection. Estimates of the core temperature rise assuming a free convection environment and a core loss that is independent of temperature have been reported [1]. The core temperature rise that incorporates the core loss temperature dependence below the critical temperature has also been reported [2]. However, no attempt has yet been made in determining the critical temperature. This paper provides an analytical approach for calculating the critical core temperature. The core loss, as provided by manufacturers, is expressed as a quadratic function of temperature. The impact of the ambient temperature and winding losses on the critical core temperature is also included in the analysis.

Computing critical temperature

At the steady state temperature, losses generated in a magnetic component are balanced by heat which is dissipated from the component. The generation of loss can be defined as a function of temperature as follows:

$$Qgen = Qcu + Qcore = Qcu + Cq\times(Ct1\times Tcore^2 - Ct1\times Tcore + Ct0) \quad (1)$$

Similarly, the dissipation of loss by convection is given by:

$$Qdis = h\times Acnv\times(Ts - Tamb) \quad (2)$$

In (1) and (2), Qgen, Qdis, Qcu and Qcore are the generated loss, the dissipated loss, the winding loss and the core loss respectively; Tcore is the mean temperature in the core; Ts is the mean temperature on the surface; Tamb is the ambient temperature; h is the effective convection coefficient; Acnv is the convective area; Cq is a factor which depends on the frequency, flux density and the volume of the core and Ct0, Ct1 and Ct2 are constants for a given magnetic material.

The largest impact of the loss – temperature dependence in the core can be obtained assuming that Qcu = 0 and Tcore = Ts. Using these assumptions, Figure 1 shows the graphs of normalized Qgen (blue line) and Qdis. The following modes of operation are distinguished in Figure 1: (i) normal operation for which Qdis intercepts Qgen (green line); (ii) runaway for which Qdis does not intersect Qgen (cyan line) and (iii) the critical operation for which Qdis is tangent to Qgen (red line). The temperature obtained from the latter mode of operation is the critical temperature above which thermal runaway occurs.

These modes of operation are discussed in the full paper. The full paper also discusses the impact of the ambient temperature and winding losses on the critical temperature. A rise in the ambient temperature increases the critical temperature. However, the temperature rise of the core at the critical temperature is reduced. A winding loss of Qcu displaces the loss – temperature curve to the right by a value equal to Qcu/Cq. This results in an increase in the critical temperature.

[1] F. Farahmand, F. P. Dawson and J. D. Lavers, "Temperature rise and free convection heat transfer coefficient for 2-D pot-core inductors and transformers," Industry Applications Conference, 2005. Fourtieth IAS Annual Meeting, vol. 4, 2-6 Oct. 2005 pp. 2622-2629

[2] F. Farahmand, J. D. Lavers and F. P. Dawson, "Impact of Nearby Adiabatic and Isothermal Barriers on the Thermal Characteristics of a Vertically Oriented Pot-Core Magnetic Component," Magnetics, IEEE Transactions on, vol. 43, no. 4, April 2007 pp. 1429-1432

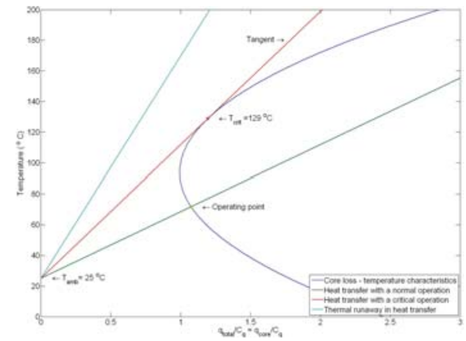

Figure 1. Different types of operation for a 3C90 ferrite: Ct2=0.000165, Ct1= 0.031 and Ct0=2.45

GX-03

Effects of double-axis electromagnetic stirring in continuous casting.

R. Otake[1], T. Yamada[2], R. Hirayama[3], K. Fujisaki[1,3], S. Shimasaki[1], S. Taniguchi[1]

1. Graduate school of TOHOKU university, Sendai, Japan; 2. Nittetsu Plant Designing Corp., Futtsu, Japan; 3. Nippon Steel Corp., Futtsu, Japan

Introduction

In continuous casting process of steel billet, in-Mold ElectroMagnetic Stirring (M-EMS) is often used for making high quality steel. M-EMS is effective to prevent entrapment of nonmetallic inclusions to solidified shell and to increase fine equiaxed structure. However deformation of free surface caused by M-MES promotes engulfment of mold powder to the molten steel and gives bad effects to quality of steel. To resolve this issue, application of Double-Axis ElectroMagnetic Stirring (DAEMS) in continuous casting is investigated. DAEMS is composed of a rotational and a vertical EMS [1]. Vertical EMS suppresses the deformation of the free surface caused by rotational EMS and DAEMS can generate strong electromagnetic force without free surface deformation. Therefore intensity balance between rotational EMS and vertical EMS is important. In this study, basic characteristic of DAEMS is investigated with varying the vertical EMS force intensity and with keeping rotational EMS force constant by means of unsteady three-dimensional magnetohydrodynamic calculation [2] of continuous casting model using molten gallium.

Evaluation by means of numerical analysis

Continuous casting model of round steel billet using molten gallium is designed by using *Re* and *Fr* approximation. In this study, round shape model is transformed to square model (Fig. 1) with equivalent area in order to simplify the problem. To investigate the influence of vertical stirring intensity, the current applied to vertical EMS is varied from 0 to 4606$A^{rms}T$ with keeping rotational stirring constant.

In continuous casting process, the free surface stability is important to prevent the engulfment of mold powder to the molten steel. To evaluate the free surface stability, the averaged standard deviation of the free surface height σ is defined as equation (1). σ is considered to be an index of instability of free surface and large σ means that the free surface becomes instable.

$$\sigma = \Sigma\,(\sigma_i S_i / S) \qquad (1)$$

Where, σ_i and S_i are the standard deviation of free surface height and cross sectional area of each cell respectively. *S* is cross sectional area of billet. From Fig.2, it is found that there is an optimum vertical stirring intensity from the view of meniscus stability. It is considered that there are three phenomena (Fig.3) depending on the vertical stirring intensity. Upward spiral flow caused by rotational-EMS generates instability of the free surface at *A* in Fig.2 [3]. Moderate vertical stirring force cancels this spiral flow and stabilizes the free surface at *B* in Fig.2. On the other hand, an excessive vertical stirring generates reversal flow under the free surface and causes instability of free surface at *C* in Fig.2.

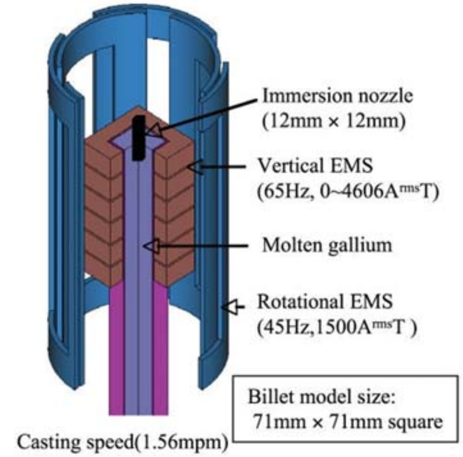

Fig. 1: Schematic of numerical model.

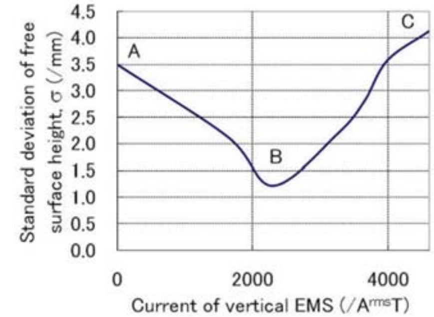

Fig. 2: Free surface stability.

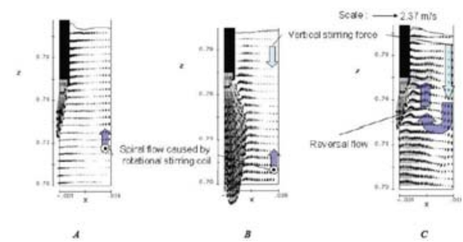

Fig. 3: Velocity vector on vertical cross section of the model at *A*, *B* and *C* in Fig. 2.

[1] S. Taniguchi, K. Ueno, S. Shimasaki, M. Okubo, T. Ando, and K. Kasahara, "Electromagnetic Stirring of Liquid Metal by Simultaneous Imposition of Rotating and Traveling Magnetic Fields", Tetsu-to-Hagané, (Japanese) 92(2006), 8-15.

[2] K. Fujisaki, T. Ueyama, "Magnetohydrodynamic calculation for free surfaces", J. Appl. Phys., 83(1998), 6356-6358.

[3] K. Fujisaki and Takahiro Yamada, "MHD calculation for free surface velocity", J. Appl. Phys., vol.89 (2000), 6734-6736.

GX-04

Diamagnetic levitation of solids at micro scale.

C. Pigot, G. Poulin, R. Gilbert
Magnetic Microsystems, G2ELab, Grenoble, France

Friction is one of the major limitations of micro- and nano-systems. An original solution based on diamagnetic levitation is proposed. Diamagnetic media are repulsed by strong magnetic fields. Static levitation at microscale can be obtained at room temperature, with no supplied energy, no feedback loop nor superconductors. Successful levitation of bismuth, silicon and copper on integrated micro-magnets, was demonstrated both theoretically and experimentally.
As a simple solution is aimed, permanent magnets are used to achieve levitation. They provide ever lasting permanent magnetic fields with no supply. Tough, diamagnetic forces are very weak. For instance, at millimetre scale, only a few grams of the best diamagnetic material can be made levitated and only with the strongest available magnets. Therefore this kind of levitation is seldom used. Diamagnetic volume forces are in proportion to the susceptibility of the materials, the magnetic field and its gradients. A way to increase these forces is to increase the gradients by reducing the size of the whole system, that is to say the size of the particle and the magnets. Effectively, as the size of a magnet is reduced, the field map is homothetically reduced. The value and the direction of the radiated field remain the same, but the gradient increase in proportion to the scale reduction. To sum up, the volume diamagnetic forces increase in proportion to the scale reduction. Since the density is constant at any scale, the diamagnetic forces are in the same order of magnitude than weight when the size of the system is some tens of micrometers.
First, the behaviour of a spherical particle of bismuth in air is considered. This particle has a diameter of 10 µm and a magnetic susceptibility of 160.10^{-6}. The magnets are infinitely long rails separated by a 45 µm gap. These NeFeB magnets are 50 µm large and 30 µm thick and present a measured remanence of 1.4 T. Fig 1 shows the total energy, sum of the gravitational and magnetic energies, in a plan perpendicular to the long dimension of the magnets. The total energy is minimum when the particle some 10µm above the surface of the magnets, in the middle of the gap, this position being a stable position.
The studied structure was then realised through adapted micro-system processes. A silicon wafer is etched with deep RIE. The magnetic layer is then high rate sputtered above the whole wafer and follows the pattern of the underlying wafer. Particles of bismuth are then spread over the magnetic arrays and observed with an optical microscope. Images such as Fig. 2 are obtained. All the bismuth particles are subject to the influence of the magnets. As shown Fig.1, the energy of the diamagnetic particles is maximum near the edges of the magnets and quickly decreases with the distance. The diamagnetic particles that are above the gap do levitate. Despite the use of non-spherical particles in real experiments, theory is fully validated. The levitating particles can also levitate on a long distance, up to 1 mm, in a direction parallel to the magnet, strongly guided by the rails. The particles that are above the magnets stick on the magnet, but are aligned along the medium axis of the rails.
Further tests were performed with other materials such as silicon and copper. As their susceptibility is lower, they need either to be levitated in paramagnetic water or tested at smaller dimensions. In paramagnetic liquid, as tested, the particles are submitted to two added forces: the Archimede force and the magneto-archimede force. Archimede force results from the difference of density between the particles and the surrounding media. Magneto-Archimede force is due to their difference of susceptibility. The paramagnetic media is attracted by the magnets. It then applies a 'magnetic' Archimede force that repeals the particle with lower susceptibility from the magnetic sources. This allows the 'levitation' in liquid, that we may call 'confinement' of dense material (copper) or weak diamagnetic material (silicon), as shown Fig 3.
Diamagnetic levitation of solid is actually demonstrated at micrometric scale with thick integrated magnets. Scale reduction laws allow the levitation of material in air. Material with low susceptibility (silicon) and high density (copper) can be confined in paramagnetic milieu. This opens a wide range of applications in sensors, actuators or material micro-handling.

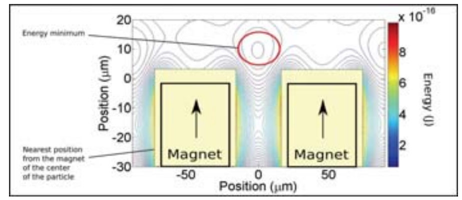

Fig 1: Total energy isovalues of a bismuth particule above micromagnets

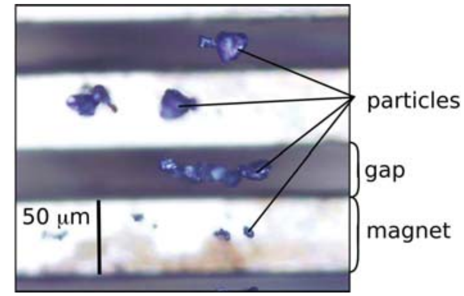

Fig 2: levitation of Bismuth particles in air

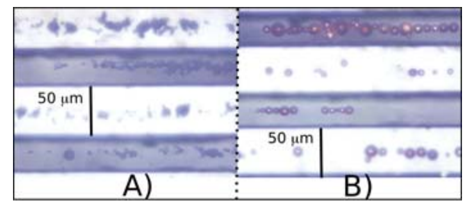

Fig 3: levitation in paramagnetic water of A) Silicon, black particles B) Copper, orange particles

GX-05

Construction of Quasi-Cyclic LDPC Codes and the Performance over Magnetic Recording Channels.

X. Liu[1], H. Cheng[1], Z. Wang[2]
1. Dept. of Electronics & Comm. Engr., Sun Yat-Sen University, Guangzhou, China; 2. School of Electrical Engineering and Computer Science, Oregon State University, Corvallis, OR

Abstract: A novel algorithm for constructing Quasi-Cyclic low density parity check (QC-LDPC) codes is proposed. The experiment results show that the proposed QC-LDPC codes are superior in error-correction performance to other codes applied to the AWGN and magnetic recording channels.

1 Introduction

Low-density parity check (LDPC) codes, originally proposed by Gallager in 1962, were rediscovered by Mackay and Neal in 1996. Similar to Turbo codes, LDPC codes are also a class of Shannon limit approaching codes when decoding with the soft-decision belief propagation algorithms such as sum-product algorithm. The Quasi-Cyclic LDPC code is a class of code which can reduce the complexity of encoding and decoding, and lower the requirements of memory. These codes can be encoded with simple shift registers and decoded in parallel. At present, most QC LDPC codes are constructed based on geometry and algebra theories. However, the codeword length and code rate defined by the parity-check matrices constructed with these theories and the corresponding design rules are restricted by the parity-check matrix, can not be pre-defined and chosen. So the code parameters can not be chosen flexibly. Considering such factors as the error-correction performance, complexity of encoding and decoding, implementation with hardware and parameters choice, a novel algorithm for constructing QC-LDPC codes of flexible code length and code rate is proposed.

2 Construction of QC-LDPC Codes

Parity-check matrix of QC-LDPC codes can constructed as follows. Firstly, two matrices are set as follows:

,,

where, . If a parity-check matrix of dimension is required constructing with the circulant sub-matrices of dimension, the parameters c and t can be computed according to the expressions $c = m/L$ and $t=n/L$. Then, the mother matrix of dimension can be put in shape based on the PEG algorithm. The matrix (and the parity-check matrix H) that is constructed in this way has a large girth.

As for the shift-times matrix P, it can be expressed by

,

where, aij is known and defined in matrix, pij is the element defined in matrix, i is the row index in the matrix M, and z is defined as the sequence number, beginning with 0, of occurrences of the element '1' at each row of matrix where aij =1. For example, z is equal to 0 at the first occurrence of '1' at each row, to 1 at the second occurrence of '1' at each row, and so on. So, z is equal to k-1 if the element '1' occurs at the k-th occurrence at each row.

Assume that a parity-check matrix is to be constructed on condition of the codeword length n=48, parity-check bits length m=32 and sub-matrix dimension L=8. With the above parameters, the matrix can be constructed with dimension computed as and $t=n/L=6$.

After the matrices and are obtained, the parity-check matrix can be constructed through replacing each element '0' in matrix with a full-zero matrix of dimension $L\times L=8\times 8$ and each element '1' in matrix with a circulant permutation matrix of dimension $L\times L=8\times 8$ according to the rules predefined. The so constructed parity-check matrix, H, has the property of 'Quasi-Cyclic' and flexible matrix-parameters because different QC parity-check matrices can be constructed by modifying the codeword length n, the parity-check bits length m and the sub-matrix dimension .

3 Simulation Results

In our simulation, three groups of codes with different codeword lengths are constructed, the parameters (n, m) of which are (1008, 504), (504, 252), and (256, 128), respectively. Simulations are carried out with the BPSK modulation over the Gaussian noise AWGN channels and the magnetic recording channels. The comparison of the BER/FER performance between the QC-LDPC codes based on the proposed algorithm and the random LDPC codes generated by the original PEG algorithm is shown in Figs. 1-4, where different code word parameters are employed and the AWGN channels are employed (the results over the magnetic channels are ignored due to the limited 2 pages).

Fig. 1 BER/FER performance of code Fig. 2 BER/FER performance of code

Fig. 3 Performance of (1008, 504) code   Fig. 4 Performance of (1008, 504) code at different iterations

4 Conclusion

This paper proposes a novel construction method of QC-LDPC codes based on the PEG algorithm. Simulation shows that the proposed codes have almost the same performance as the codes constructed with the random PEG algorithm. The proposed codes are easy to be implemented with hardware because of the quasi-cyclic structure of the codes. In addition, the parameters of the codes are flexible to be adjusted and the codes are applicable to applications compared to the codes generated by other methods of geometry and algebra.

A Novel Electromagnetic Device for Latching Valve in Automotive Engine.

J. Kim[1], J. Chang[2]
1. Mechanical Engineering, Yeungnam University, Gyeongsan, South Korea; 2. Transverse Flux Machines Research Group, Korea Electrotechnology Research Institute, Changwon, South Korea

One of the most promising way to improve fuel economy, reduce CO2 emissions and increase torque output in internal combustion engine is to achieve variable valve timing (VVT)[1][2]. Here, we propose a novel electromagnetic valve drive system to achieve VVT, and discuss the design, finite element analysis and construction of the experimental apparatus. New engine valve system is composed of cam, springs (cam spring, disable spring and valve spring), spring latches, ring holders for springs, and engine valve. Fig. 1 shows the schematic diagram of actuator. The engine valve is operated by the rotation of cam, spring force and timed control of latches. First, the cam lobe compresses the cam spring. The cam spring stretches the disable spring and the disable spring compresses the valve spring and opens the valve. Timed release of ring controls energy delivered to the latch of valve spring and partially compresses the cam spring but, it does not has force to lock the disable latch. The valve spring opens and stretches the disable spring which then compresses the cam spring and latches the disable spring. The other lobe decelerates the cam spring and returns energy to camshaft. Variable valve timing can be accomplished by timed control of electromagnetic latches. Fig. 2 shows the schematic diagram of electromagnetic latch system. It consists of steel-made arms, compression spring, pivot and solenoid which is composed of coil and steel-made core. If coil is not energized, the disk on the valve stem can move up and down because the latch of arm is opened by spring force. If the current is applied to coil, the solenoid attracts the arm and the arm latches the disk. To prove the concept of the proposed electromagnetic engine valve system, an experimental apparatus was designed and constructed which are shown in Fig. 3 and the characteristics are measured. In addtion, 2-D symmetric static finite elecment analysis (FEA) are performed. One of result of experments and FEA, the attractive latching force is shown in fig. 4.

[1] P. Barkan, and T. Dresner, 1989, "A Review of Variable Valve Timing Benefits and Modes of Operation," SAE Technical Paper Series, Paper 891676.

[2] M. Pischinger, W. Salber, F. Staay, H. Baumgarten, and H. Kemper, 2000, "Benefits of the Electromechanical Valve Train in Vehicle Operation," SAE Technical Paper Series, Paper 2000-01-1223

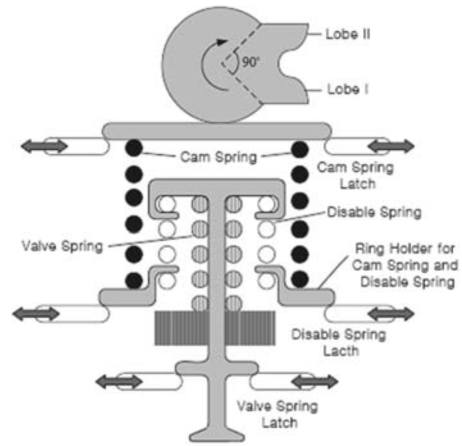

Fig 1. Schematic diagram of new proposed engine valve actuator

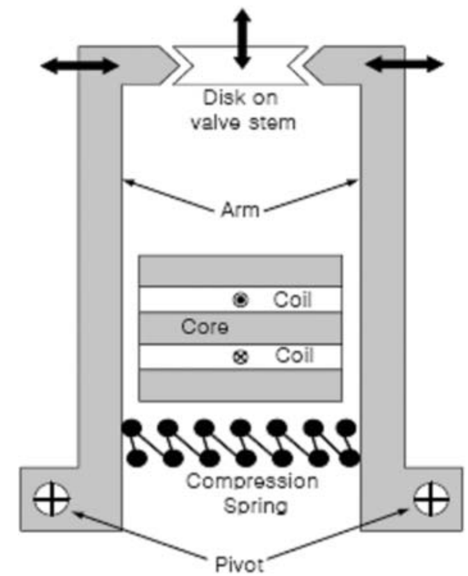

Fig. 2 Schematic diagram of latch system

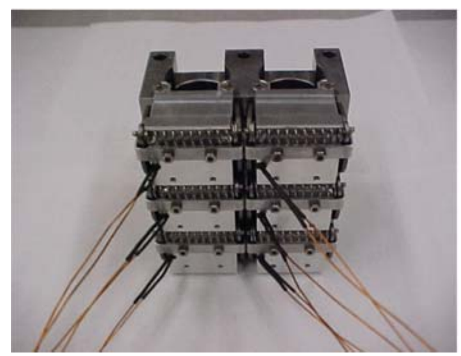

Fig. 3 Picture of constructed apparatus

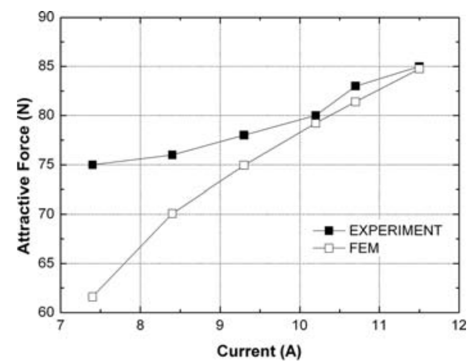

Fig. 4 Attractive latching force

GX-07

Air gag's influence on the performance of the transformer of an electromagnetic pump.

D. Morinigo[2,1], M. A. Rodríguez[1,2], A. Rivas[1], J. Martin[1]
1. Light Alloys, CIDAUT Foundation, Valladolid, Spain; 2. Electrical Engineering, University of Valladolid, Valladolid, Spain

INTRODUCTION: An electromagnetic pump (EP) is a MHD device to drive molten metals by means of electromagnetic fields and without mechanical parts in contact with them [1]. The studied EP (Fig1) is made up of two elements series-connected: a transformer and a C-shaped electromagnet. The secondary of the transformer is a channel, containing a molten metal encased in electrically nonconducting ceramic walls(not shown in Fig1). When the primary coil is fed with a 1-phase AC voltage, an electric current density J is induced in the molten metal(Fig1b). The electromagnet produces a B field in a specific section of the channel (slot) and perpendicular to the induced J(Fig1c). The cross product of the J and B fields in the molten metal produces a 3D field of electromagnetic volumetric forces, distributed along the channel, which provides the pumping action on the molten metal. The total pressure developed by the EP is assumed to be proportional to the electrical current consumed by the EP to the second power. The control system that runs this EP was designed considering this relationship. This pump is used in a metallurgical process to produce automotive aluminium components [2]. Due to the difficulty in the assembly of the EP, the core of the transformer is divided into two parts, between which an airgap exits (Figure 2). The top U-shaped part rests on the bottom I-shaped part. The vibrational magnetic force that appears between this two sections when the primary coil is fed with an AC voltage is the cause of variations in the gap's length. The aim of this paper is to show the results of an experimental work carried out to demonstrate and study the influence of the length of the gap on the performance of the EP, which had been previously observed in real conditions in a foundry plant. As the airgap length increases, the magnetizing current also increases, and the pumping effect no longer is proportional to the consumed current to the second power, besides other negative effects.

EXPERIMENTAL TESTS AND RESULTS: To evaluate the effect of the gap's length, a number of traditional transformer no-load tests were performed at different lengths of the gap: Regular gap(RG), RG+0.2mm, RG+0.4mm, RG+0.6mm. By RG means the gap that exists when the top U-part rests on the bottom I-part. In all experimental tests, the electrical current and the voltage were registered using a PC-based DAQ. These two sets of data allowed us to calculate the parameters of the electric equivalent circuit of the transformer: Magnetizing reactance(Xμ) and Resistance equivalent to iron losses. Results are shown in Fig3. In Fig3a, the supply voltage of the no-load test is represented vs the consumed current for different lengths of the non-electromagnetic gap. This curve resembles a saturation curve because supply voltage is proportional to magnetic flux and current is proportional to magnetic field intensity. It is easy to conclude that, in order to keep the magnetic flux level in the core, a higher current is needed as gap length increases. The higher the gap is, the higher the current consumed by the transformer is. Saturation of the core is reached sooner for smaller lengths of the gap. When the gap is high, its magnetic reluctance is bigger than core's reluctance. This causes the saturation curve to lean to the right. In Fig3b it is represented the calculated Xμ vs supply voltage for different gap lengths. From Fig3 it can be observed that Xμ depends heavily on the gap length for low voltages and is bigger also for low voltages, and the value of Xμ drops dramatically as supply voltage increases, or a saturation level is reached. Fig3 shows the great influence of the gap on the performance of the transformer of the pump. All observed effects on the operation of the pump, by lab experimentation and real operation in a foundry plant, are negative. The gap means, above all, higher magnetizing current to keep the necessary magnetic flux level in the transformer core. This high magnetizing current does not contribute to the creation of the output pressure on the molten metal and helps to saturate the core. Another side effect is the increment of the consumed power to produce the same output pressure and flow rate and therefore reducing the efficiency of the pump.

[1]D. Moriñigo et al. Experimental and computational investigation of an electromagnetic pump used for manufacturing aluminium parts. Magnetohydrodynamics, v.43 (2007), 1, pp 119-134

[2] R. Cuesta, J.A. Maroto, J. Martín. Science and Engineering for the production of aluminium cast components. Aluminium Process and Product Technology, Vol. IV (2007), 2, pp 50-53

Figure 1: (a) Assembly of the electromagnetic pump with all ceramic shapes deleted, (b) Current induced in the molten aluminium by the transformer (c) Cross product of the electric current and magnetic flux density.

Figure 2. Picture of the disassembled transformer: coil and U and I parts manufactured with laminated silicon steel plates.

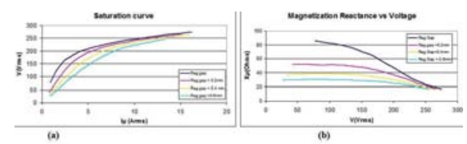

Figure 3: Saturation curve and magnetization reactance vs supply voltage for different lengths of the gap

GX-08

A New Calibration Procedure for Magnetic Tracking Systems.

A. Plotkin[1], V. Kucher[1], Y. Horen[2], E. Paperno[1]
1. Electrical and Computer Engineering, Ben-Gurion University of the Negev, Beer-Sheva, Israel; 2. Electrical and Electronic Engineering, Shamoon College of Engineering, Beer-Sheva, Israel

The maximum possible accuracy of a magnetic tracking system (see Fig. 1) cannot be achieved without an efficient calibration procedure. However, it is a nontrivial task due to a large number of system parameters that has to be calibrated. These parameters include the magnetic positions of the transmitting coils, their magnetic moments, the magnetic position of the sensor, its sensitivity, and the gain of the sensor output amplifier.

According to the conventional approach [1], all the above parameters are calibrated individually [1]. This is not efficient because a large number of individual calibrations require many calibration setups. Individual independent calibrations also cause the accumulation of errors. Another principal disadvantage of the conventional approach is in its inapplicability to the assembled system. Thus, it does not consider the assembling tolerances.

In this work, we suggest a new approach that allows us to calibrate the entire system in a single setting. We calibrate all the parameters simultaneously by solving a system of equations. The constants in these equations are the parameters that define the origin, orientation, and scale of the reference coordinate frame and the sensor output acquired at different sensor positions. The unknowns are all the other systems parameters.

To define the origin and orientation of the reference frame (see Fig. 1), we first relate it to a mechanical object, for example to the housing of the transmitting array. We then use special mechanical supports to align the sensor with the edges of the transmitter housing.

To define the scale of the coordinate frame, we measure the distance between two arbitrary sensor locations with a precise tool (a caliper). This is the only external measuring tool that is involved in the entire calibration procedure.

To complete the calibration procedure, we place the sensor in a number of arbitrary positions to provide the uniqueness of the solution of the above system of equations.

To illustrate the efficiency of the suggested approach, we applied the calibration procedure to a magnetic tracking system employing 64 transmitting coils [2]. We first accurately defined a linear sensor trajectory (see the dashed line in Fig. 2) by moving it with the help of a specially designed mechanical slider. We then compared the sensor trajectories measured by the tracking system before (the grey circles in Fig. 2) and after applying the calibration (the black circles in Fig. 2).

We relate the large tracking errors in the first case to the difference between the magnetic and geometric positions of the transmitting coils (see Fig. 1) and the difference between the theoretical and true magnetic moments. These differences are caused by the non-ideality of the transmitting coils winding.

The suggested approach is generic and can be applied to many different types of tracking systems. It minimizes the number of calibration setups, simplifies the calibration procedure, and increases its accuracy. It is applied to the assembled system and does consider the assembling tolerances. All the system parameters can be calibrated not only be the system manufactures but also by the users.

[1] C. Hu, M. Q.-H. Meng, and M. Mandal, "The calibration of 3-axis magnetic sensor array system for tracking wireless capsule endoscope," Proceedings of the IEEE/RSJ International Conference on Intelligent Robots and Systems, pp. 162-167, Oct. 2006.

[2] A. Plotkin and E. Paperno, "3D Magnetic tracking of a single subminiature coil with a large 2D-Array of uniaxial transmitters," IEEE Trans. Magn., vol. 39, pp. 2295-3297, 2003.

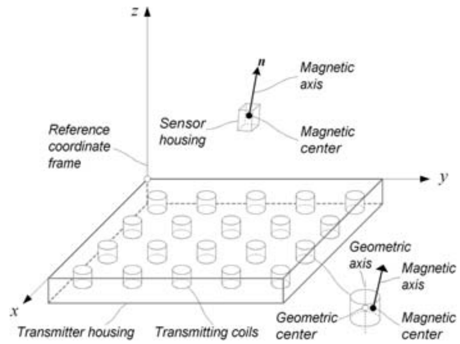

Fig. 1. A magnetic tracking system. The magnetic positions of the sensor and transmitting coils include the locations of their magnetic centers and the orientations of their magnetic axes.

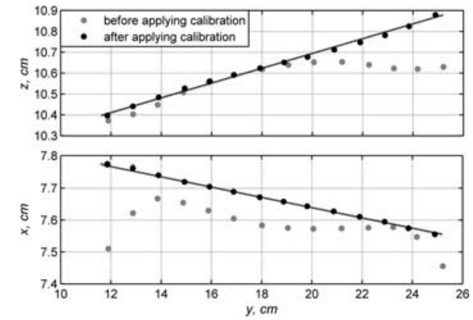

Fig. 2. Calibration efficiency. The sensor motion along a straight line was found before (the grey circles) and after (the black circles) applying the calibration.

GX-09

Microstructural changes in Fe-doped $Gd_5Si_2Ge_2$

B. Podmiljsak[1], I. Skulj[2], B. Markoli[3], P. McGuiness[1], S. Kobe[1]
1. Jozef Stefan Institute, Ljubljana, Slovenia; 2. Institute of Metals and Technology, Ljubljana, Slovenia; 3. University of Ljubljana, Ljubljana, Slovenia

$Gd_5Si_2Ge_2$-based alloys can exhibit a giant magnetocaloric effect (MCE); this gives them the potential for use in cooling and refrigeration technologies. The temperature at which the magnetocaloric effect is observed can be easily adjusted between ~190 and 300 K by varying the chemical composition [1].

It is generally accepted that the giant magnetocaloric effect in $Gd_5Si_2Ge_2$-type alloys involves a magnetic-field-induced crystallographic structural change from the high-temperature monoclinic paramagnetic phase to the low-temperature orthorhombic ferromagnetic phase [2]. The problem here is the large hysteretic losses that occur in the same temperature range as the GMCE [3]. Provenzano et al [4] reported that a small amount of iron (substituting for 5 per cent of the germanium) reduced the hysteretic losses by more than 90 per cent. It also shifted the magnetic entropy peak from 275 K to 305 K and broadened its width.

In this investigation we have looked at the effect on the microstructure of $Gd_5Si_2Ge_2$ resulting from a substitution of Si by Fe, according to the formula $Gd_5Si_{(2-x)}Fe_xGe_2$, with x = 0, 0.125, 0.25, 0.5, 0.75 and 1.

The electron microscopy secondary-electron images (Figure 1) show that the surface changed from one exhibiting regular pentagons and hexagons, reminiscent of a buckyball (x = 0), to a surface with a sinew effect, rather like columnar grains running at angles to each other (x = 0.5), to a smooth upper surface, much more characteristic of an intermetallic arc-melted button (x = 1). The formations – the buckyballs and the sinews – are clearly related to the cooling rate, which is very fast in such a system, but the very small amounts of iron are clearly the decisive factor.

Optical micrographs show that all the samples are composed of multi-phase structures. The composition with no iron consists of the $Gd_5(Si,Ge)_4$ matrix phase and a grain-boundary phase. A new matrix phase appears with the addition of iron. The composition of this new matrix phase suggests that it is a $Gd_5(Si,Ge)_3$-type phase. With increasing amounts of added iron the amount of original matrix phase is seen to decrease until it disappears completely in the sample with x = 1, the point where half of the silicon is replaced by iron. Three different grain-boundary phases were identified. The grain-boundary phase found in sample x = 0 is not significantly different from that of the matrix phase, and this phase is only present in this sample. With the addition of iron a second grain-boundary phase appears. The composition of this phase does not vary with increasing amounts of added Fe, and the ratio for Gd:Si:Fe is approximately 1:1:1. A third grain-boundary phase starts forming in the structure of the samples when x becomes larger than 0.5.

The magnetic measurements (Figure 2) show that with the increasing amount of iron we have a continuous decrease of the magnetic transition temperature, with the Tc falling from 300 K for x = 0 to below 100 K for the x = 1 sample. The maximum values of ΔS follow the Curie temperatures and tend to decrease in line with the amount of iron. Sample x = 0.125 has the maximum ΔS value, equal to almost 10 J/kgK for a field change of 1.5 Tesla.

From our results we are able to conclude that $Gd_5Si_{(2-x)}Fe_xGe_2$ alloys where x varies between 0 and 1 show very significant differences in terms of both their macrostructures and microstructures. The original matrix phase with the $Gd_5(Si,Ge)_4$ composition when x = 0 becomes a new matrix phase with the $Gd_5(Si,Ge)_3$ composition when x = 1. However, the iron contributes mainly to the grain-boundary phases that are formed.

[1] A.O. Pecharsky, K.A. Gschneider Jr., V.K. Pecharsky: JMMM Vol. 267 (2003), p. 60.

[2] W. Choe, et al., Phys. Rev. Lett. 84 (2000), p. 4617.

[3] E. M. Levin, V. K. Pecharsky, K. A. Gschneidner Jr., Phys. Rev. B 62 (2000), R14625–R14628.

[4] V Provenzano, A J Shapiro, R D Shull, Nature 429 (2004), p. 853-857

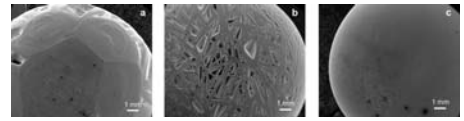

Figure 1: SEI taken of arc-melted buttons with x = 0 (a), x = 0.25 (b) and x = 1 (c) compositions.

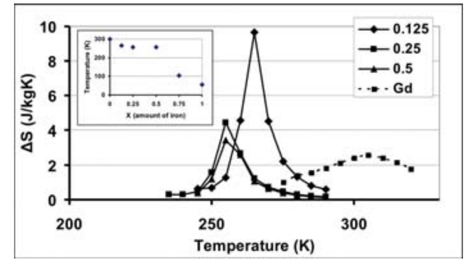

Figure 2: Calculated magnetic measurements for a field change of 1.5 Tesla. The inset shows the Curie temperature dependence versus the amount of iron

GX-10

Stress-strain relationship of magnetorheological fluids under tension mode.

S. A. Mazlan, N. B. Ekreem, A. G. Olabi
School of Mechanical and Manufacturing Engineering, Dublin City University, Dublin, Ireland

A magnetorheological (MR) fluid comprising micron-sized particles and a carrier liquid which has a unique ability to transform from liquid to solid, reversible and controllable, as a function of magnetic field strength. Tension in a squeeze mode is as an operational mode where two flat parallel surfaces, stand opposite each other, are pulled against each other by an external force, acting at the path of the magnetic flux lines. In the absence of the magnetic field, the particles initially in the space between two walls are unrestrained to move and are dispersed throughout the carrier medium. In the presence of the magnetic field, the particles are organized along the direction of the applied magnetic field; constructed into a uniform polarity and connected to the walls [1].
A tension apparatus was based on the same basic concept to that used for investigating MR fluid under compression mode done by us in the previous study [2]. The tension experiments were performed to determine the stress-strain curve behaviour of MR fluids under different initial gap sizes and tensile speeds. MRF-241ES (water-based MR fluid) and MRF-122-2ED (hydrocarbon-based MR fluid) were used in this investigation, supplied by Lord Corporation. The gap size was set initially to 1.0 mm, and 1.6 Amps of applied current value was maintained throughout the experiment. This was followed by pulling up the upper cylinder at various constant speeds of 0.5, 1.0, 1.5 and 2.0 mm/min, and simultaneously the load and displacement were recorded. The same sequence of the procedure was carried out in the second and third experiments, except that the initial gap size was set to 2.0 mm.
Stress-strain relationship of MR fluids under different initial gap sizes is depicted in Fig. 1. As can be seen, at 2.0 mm of the initial gap size, the values of the tensile stress are constantly smaller the values of tensile stress at 1.0 mm of initial gap size. Furthermore, MRF-241ES has showed a higher tensile stress as compared to MRF-122-2ED at the same initial gap size.
In another observation, the values of the tensile stress almost the same at different tensile speeds at constant applied current (1.6 mm/min) and initial gap sizes (1.0 and 2.0 mm). The stress-strain curves were observed to be well overlapped on each other as shown in Fig. 2.
The tension process of MR fluids showed similar trends notwithstanding that the initial gap size was varied from 1.0 to 2.0 mm and the tensile speeds ranged between 0.5 to 2.0 mm/min, depending on the type of carrier fluid. The stress-strain relationship during tension process can be divided into type 1 and 2. At a constant current, tensile behaviour of MRF-241ES showed different trends with the tensile behaviour of MRF-122-2ED for both initial gap sizes. Tian et al. found that the tensile behaviour of Electrorheological (ER) fluid depends on the strength of the external field [3]. The same tensile behaviour of MRF-241ES (type 1) and MRF-122-2ED (type 2) have been observed with the tensile behaviour of ER fluid at 0.6 kV and 0.4 kV of electric field, respectively. However, the values of tensile stress of MR fluids are higher than the tensile stress obtained in ER fluid.
This study showed that tensile behaviour is greatly affected by the type of carrier fluid which is highly dependent on its magnetic properties. Similar trends have been observed at different initial gap sizes. Higher values of tensile stress of MR fluid can be obtained at a lower initial gap size. Experimental results also revealed that the behaviour of MR fluids is not influenced by tensile speed.

[1] T. Shiraishi, S. Morishita and H. P. Gavin, J. Appl. Mech.-T ASME, 71, 201 (2004).

[2] S. A. Mazlan, N. B. Ekreem and A. G. Olabi, Smart Mat. Struct., 16, 1678 (2007).

[3] Y. Tian et al., J. Appl. Phys., 94, 6939 (2003).

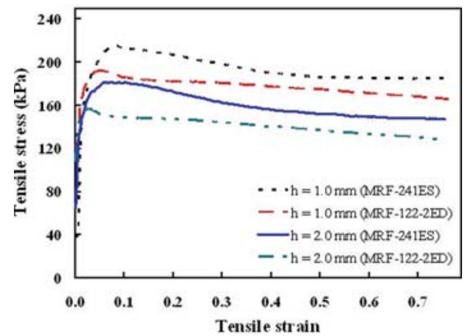

FIG. 1. Stress-strain relationship of MR fluids at constant current of 1.6 Amps and tensile speed of 1.5 mm/min.

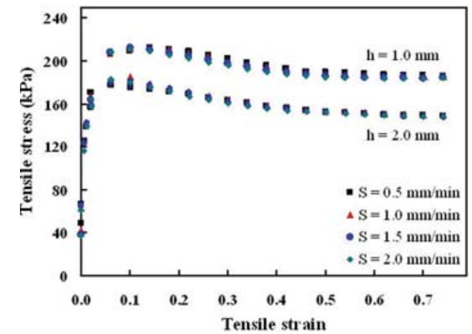

(a)

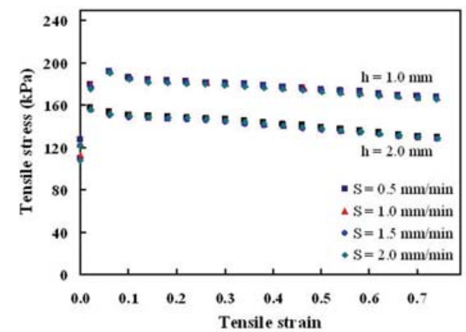

(b) FIG. 2. The effect of stress-strain relationship under different tensile speeds of (a) MRF-241ES and (b) MRF-122-2ED.

GX-11

Novel magnetic composite particles of carbonyl iron embedded in polystyrene and their magnetorheological characteristics.

F. Fang, *H. Choi*
Department of Polymer Science and Engineering, Inha University, Incheon, South Korea

Introduction
Magnetorheological (MR) fluids, named as fantastic and intelligent fluids, are capable of being solidified with an aid of an external magnetic field and re-liquefied by removing the magnetic field. This abrupt state-changing process which causes distinctive rheological properties has great potential in designing diverse high performance engineering products including active damper, torque transducer and MR polishing equipment [1-2]. Generally, high yield stress and low apparent viscosity without magnetic field as well as good stability and durability have become very crucial factors for the MR fluid application. Among various magnetic materials (magnetite, maghemite, carbonyl iron etc), carbonyl iron (CI) particles have been adopted as a superior candidate for MR fluids due to their high saturation magnetization as well as appropriate particle size [3-4]. However, the large density mismatch between CI particles and medium oil leads to serious sedimentation drawback. Therefore, many strategies have been explored to solve this problem [5-7]. In this study, we fabricated novel magnetic CI/polystyrene (CI/PS) composite via facile solvent casting method. The CI particles were found to be embedded within PS matrix, by which way prevent them contacting each other directly, consequently improving stability of the CI suspension.
Experimental
A facile solvent casting method was employed to prepare the CI/PS composite particles with spherical shape. Commercially purchased PS was dissolved in chloroform by sonication for about 3h at first. CI particles (particle size of 4.5~5.2 micron in diameter and 7.86 g/cm3 of density) were transferred into the above-prepared PS/chloroform solution and then quickly added into a water phase containing poly(vinyl alcohol) (PVA) and sodium dodecylsulphate (SDS) as a stabilizer and an emulsifier, respectively. The whole dispersion was energetically stirred at 500rpm for 12h. The obtained composite particles were washed with deionized water, dried at 60 degree C for 24h and finally dispersed in lubricant oil (Yubase 8 oil, SK Corp., Korea) to prepare MR fluid.
Information on morphology, density, composition and magnetic property was investigated via SEM, pycnometer, TGA and VSM, respectively. MR characterizations were performed at 20°C via a rotational rheometer (Physica MCR 300, Stuttgart, Germany) equipped with a MR device (MRD 180).
Results and Discussion
Figure 1 shows characteristic morphologies of the fabricated CI/PS composite particles. It is apparent that many CI particles are separately embedded in spherical PS matrix. Besides this, we can also assume that there must be several CI particles within the inner of PS spheres. Average size of the CI/PS composite particles was about 50µm which is much larger than individual CI particles.
MR characteristics of the CI/PS based suspension were examined via rotational and oscillation test modes. Figure 2 describes shear stress curves as a function of shear rate with and without a magnetic field. Dynamic yield stress was found to be enhanced by increasing magnetic field strength. Although the CI/PS particle based MR fluid exhibited relative lower stress value than that of pure CI suspension due to the introduction of non-magnetic PS matrix, it still represents an ordinary plateau region for the whole range of applied shear rate when the magnetic field was applied [6-7]. Without magnetic field, the MR fluid showed a Newtonian fluid behavior. In addition, the oscillation test was made to investigate the viscoelastic performances of the CI/PS suspension under a small deformation.
Finally dispersion stability of the MR fluid was found to be sustained, which may be attributed to the little difference in density between the continuous phase (density: 0.96 g/cm3) and the CI/PS particles (density: 2.5 g/cm3) detected by a pycnometer.

[1] H. R. Brand, H. Pleiner, Phys. Rev. Lett. 86, 1385 (2001)

[2] I. Bica, J. Ind. Eng. Chem. 12, 501 (2006)

[3] G. Bossis, P. Khuzir, S. Lacis, O. Volkova, J. Magn. Magn. Mater. 258-259, 456 (2003).

[4] S. T. Lim, M. S. Cho, I. B. Jang, H. J. Choi, M. S. Jhon, IEEE Trans. Magn. 40, 3033 (2004)

[5] M. S. Cho, S. T. Lim, I. B. Jang, H. J. Choi, M. S. Jhon, IEEE Trans. Magn. 40, 3036 (2004)

[6] S. T. Lim, H. J. Choi, M. S. Jhon, IEEE Trans. Magn. 41, 3745 (2005)

[7] F. F. Fang, I. B. Jang, H. J. Choi, Diamond Relat. Mater. 16, 1167 (2007)

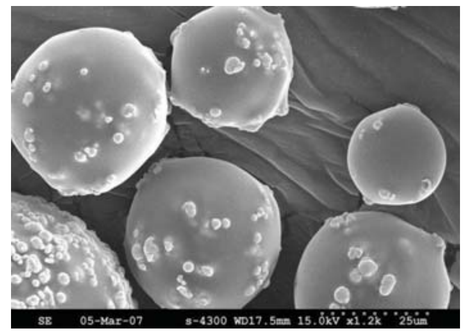

Fig. 1 SEM images of CI/PS composite particles

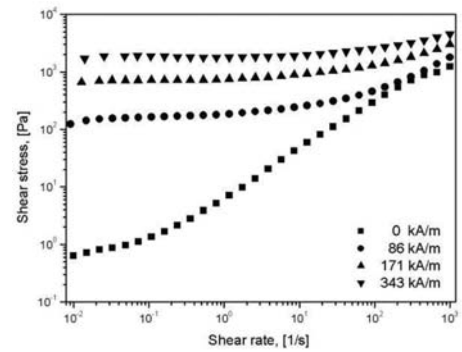

Fig. 2 Flow curves for CI/PS composite particles based MR fluids

GX-12

Barkhausen noise statistical properties in ferromagnetic thin films: dimensionality and range of the relevant interactions.

F. Bohn[1], M. A. Corrêa[2,1], A. Viegas[3], L. F. Schelp[1], R. L. Sommer[4]
1. Departamento de Física, Universidade Federal de Santa Maria, Santa Maria, Brazil; 2. Campus Caçapava do Sul, Universidade Federal do Pampa, Caçapava do Sul, Brazil; 3. Departamento de Física, Universidade Federal de Santa Catarina, Florianópolis, Brazil; 4. Centro Brasileiro de Pesquisas Físicas, Rio de Janeiro, Brazil

Barkhausen noise (BN) corresponds to the voltage pulses induced in a sensing coil wound around a ferromagnetic material when it is submitted to a variable magnetic field. BN is a measure of the complex microscopic magnetization process and, for this reason, it is used to characterize soft magnetic materials. Most of the studies were aimed to explain the statistical properties of BN such as the power law distributions of Barkhausen jump sizes and durations which present exponents, τ and α, respectively. These power laws are understood as the fingerprint of a critical behavior of the magnetization process. Statistical properties suggest a behavior independent of microscopic and macroscopic details, where just few general properties as the system as the dimensionality and range of the relevant interactions are needed to define the dynamical behavior of these systems. For bulk materials, Durin et. al.[1] suggested that the jump sizes distributions exponents can be grouped in two universality classes: τ=1.50±0.05 and τ=1.27±0.03. The first class includes the polycrystalline and partially crystallized amorphous alloys and it is associated to a dynamics governed by long-range interactions. The second one includes the amorphous alloys under stress and it is related to short-range interactions. The exponents for the jump durations distributions are α=2.0±0.2 and α=1.5±0.1, respectively, a behavior owed to the same short-long range character for the interactions governing domain walls (DWs) dynamics. For two-dimensional systems, d=2, the results are less clear due to experimental and theoretical difficulties. Theoretical models and simulations indicate that two and three-dimensional systems present distinctive exponents. Vásquez et. al.[2] approached the long-range interaction problem and predicted τ=1.33 and α=1.5, d=2, and τ=1.5 and α=2, d=3. Moreover, Queiroz[3] studied the short-range single-interface model, neglecting long-range dipolar interaction, and predicted τ=1.06, d=2, and τ=1.275, d=3. On the experimental side, in the case of thin films, the study of the BN statistical properties is rather complicated because of the typical low signal levels. Although the exponents obtained for films are smaller than that obtained for bulk samples, even considering the thinner films reported to date, a true dimensional transition has not been observed.

In this work, we investigate the BN statistical properties in amorphous and polycrystalline ferromagnetic thin films, thickness range 10-1000 nm, in order to understand the effects of the interplay between the system dimensionality and the range of the relevant interactions governing the DWs and magnetization dynamics. The exponents obtained from the experimental distributions of jump sizes and durations, are compared with the ones predicted by the two and three-dimensional theoretical models. Selected results are shown in the figures below that display the general behavior of the experimental τ and α exponents as a function of thickness for amorphous $Co_{77}Fe_{23}$ and polycrystalline $Ni_{81}Fe_{19}$ films. The dashed lines indicate τ and α, related to the two universality classes[1] and the solid ones are the limits of the error bars. The key to understand the noise statistical properties in ferromagnetic thin films resides basically in the combination of the effects of system dimensionality and range of relevant interactions. For films thicker 50 nm, the exponents are very similar to the values observed for several bulk soft magnetic (split in two universality classes mentioned above). Irrespective to the thickness and intense modifications of the magnetic behavior, observed in magnetization curves, for amorphous τ~1.3 and α~1.5, while for polycrystalline thin films τ~1.48 and α~2, which are in accordance with the predictions of ref.1, a clear indication that the films in this range of thickness present a typical three-dimensional magnetic behavior. The most striking feature is observed for films thinner than 50 nm, where the exponents decrease to τ~1.07 and α~1.05, for amorphous, and τ~1.35 and α~1.5 for polycrystalline films, values in a very good agreement with theoretical predictions for systems with two-dimensional magnetic behavior. We interpret the crossover of the experimental exponents as a clear indication of a dimensional transition of the magnetic behavior from a three to a two-dimensional magnetic character. We believe that this dimensional transition, around 50 nm, is mainly associated with the transformation of DWs from Bloch to Néel structures as the thickness is reduced. Thus, our results provide experimental evidences for the validity of the cited proposed models and indicate that the DWs dynamics and noise statistical properties are strongly affected by the system dimensionality and range of the relevant interactions.

[1] G. Durin et. al., Phys. Rev. Lett. **84**, 4705 (2000).

[2] A. Vásquez et. al., Phys. Rev. Lett. **84**, 1316 (2000).

[3] S. L. A. Queiroz, Phys. Rev. E **69**, 026126 (2004).

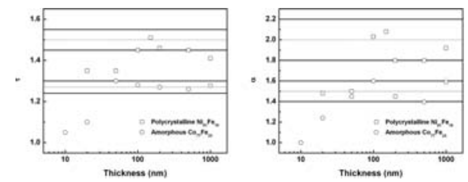

GY-01

Coloring media by using nanopipette to store more data.

M. Rashidi, F. Wang
Centre for Grid Computing, Cambridge-Cranfield HPCF, Cranfield, United Kingdom

1. Principle

Storage capacity can be increased greatly if one stored data is stored in 3D, i.e. by using the color of the media to store more information. As shown in Fig.1, eight colors are recognizable by overlapping dots to additively form a color from the three primary colors as well as the black color. For any specific color recognized by the “scanner”, the presence/absence of each primary color can be uniquely determined.

If every pixel represents a 3-bit color then each “super bit” could represent 23 = 8 values. In the simplest scenario, a dot equaling 3 bits provides tripled capacity, compared with the 2D base case. This way of encoding information could be used to store much more information on CD-Audio, CD-ROM, DVD-Video and DVD-ROM media, which are volume produced through the injection molding process and may be become fashionable again in the future, using nano-scale technology. The world’s smallest pipette is capable of dispensing droplets with a volume of a billionth of a trillionth of a litre [1]. This pipette and its related devices can be used to inject “ink” to color the media. The controlled delivery and manipulation of well-defined fluid volumes would be the key process in the above colorful storage system. Magnetic color particles αγ-Fe2O3, whose diameter is about 20 nm [2], have been chosen as the coloring agent since they are stable against heat and light and do not fade or discolor for a long period of time. Because of the fineness of the magnetic particles, their transparency is good and the color emitted is clear and easily identifiable.

A focused laser beam is used in either writing or reading. To reliably and accurately scan one of multiple colors, one would need the “writer” and the “reader” set to use exactly the same color wavelength ranges. The bits are read by illuminating the disk with an optical stylus. Colors are identified by variations in the reflected light.

2. Experimental Demonstration

A prototype is being constructed at our lab (Fig.2). The binary digits are encoded to colors, with a minimum pixel size of 5.3 μm (accordingly a 512×512 pixel array and a die size of 2.7×2.7 mm2) [3]. Such a pixel size is desirable to ensure sufficient dynamic range and signal-to-noise ratio taking into account the imaging optics parameters, the processor parameters and the sensor die size, etc.

The scanned image is of 256 color BMP format (Fig.3), where each pixel is represented by eight bits. This format can be stored uncompressed with 54 byte header followed by a 1024 byte palette table, in which 4 bytes define each color, one for red, one for green, one for blue and one reserved. The actual image pixel information starts after this from lower left hand corner. The header and palette are used to breakdown the image file and the image is then analyzed to decode the original information by a reverse mapping mechanism [3].

[1] P W Sutter and E A Sutter, “Dispensing and surface-induced crystallization of zeptolitre liquid metal-alloy drops”, Nature Materials, 15 April, 2007

[2] Magnetic color toner for electro photographic copying machine, United States Patent 4758490

[3] Thing Chen, et al, “How Small Should Pixel Size Be”, Information System Laboratory, Stanford University, 2007

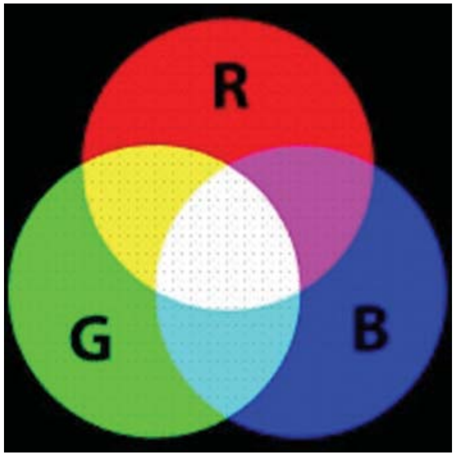

Fig.1 The RGB color model: red, green, and blue are combined in various ways to reproduce other colors.

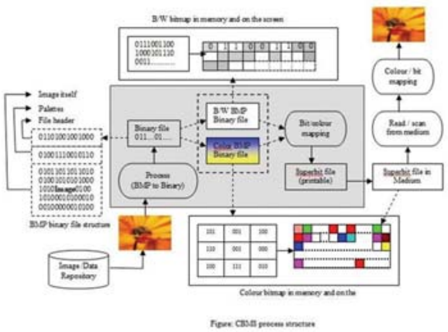

Fig.2

Fig.3

GY-02

AFM friction investigation with temperature.

D. Kim
Samsung Information Systems America, Inc, San Jose, CA

ABSTRACT The adhesion/friction properties of magnetic media play a critical role in HDI dynamics in the pursuit of recording density of 1TB and beyond. In this study, AFM friction was investigated on different media lubricant system and found strong correlation both to strain gauge signal in component level and media surface energy which resulted in modification to classical friction theory suggested by Colomb.
EXPERIMENTAL The commercially available DI 3100 AFM instrument equipped with in-house Peltier plate was employed for measurement of friction force at the tip surface in various temperature. In the “friction” mode, the sample is scanned back and forth in a direction orthogonal to the long axis of the cantilever beam and the laser beam is reflected out of the plane by the degree of twisting which is related to the magnitude of friction force. Subsequently, total surface energy was analyzed by the contact angle method. Finally, VENA CSS system was used to explore the correlation between friction signal by AFM and strain gauge output by Vena System.
RESULTS AND DISCUSSIONS Different types of magnetic media were investigated to study the frictional behavior at various environmental condition and correlation was found with strain gauge signal during CSS take-off/touch-down cycles. Figure 1 illustrates typical example of friction signal at amb/high temperatures. As shown in Fig 1, pronounced shift in friction was observed with respect to temperature and hysterisis seems to be negligible after switching back to ambient condition. The transition in friction is attributed to lube mobility and surface energy with temperature as reported in various technical papers [1-5]. One intriguing feature of commercially available AFM tip is physical limitation of thermal conductivity even with the help of conductive metal coating. As an alternative solution, helium gas was supplied inside the enclosure of the AFM apparatus to minimize the effect on fluctuation of the resonant peak from thermal AFM tip which is manifested in Figure 2. Several high friction media was built into drive. The modulation at suspension sway mode due to excess friction and oscillation in fly height was discovered resulting in weak writes. In some extreme case, modulation at ABS frequency occurred. All these phenomena result in increased slider instability /head degradation/scratch attributed from lube bridge/excessive lubricant thickness. Finally, the empirical relationship between friction force at zero external load and surface energy was modeled as, where L is the applied load, u is the friction coefficient and A is the effective area with the help of experimental results in Fig 3. As a first order, the adhesive and rachet mechanism accounts for friction force in the presence of asperities. Nevertheless, all the media used for this study had a similar roughness and thus microscopic adhesive force should be a vital factor accounting for transitions in friction force in different environmental condition.
CONCLUSIONS:
The nanoscale AFM friction study enables us to characterize tribological properties of various hard disk lubricant system in a more efficient manner without having to conduct time-consuming component level CSS as was done conventionally. Friction force was found to be linearly related to the surface energy and friction force went to zero when the surface energy approached finite bulk film energy and these results suggested modification to the classical adhesion theory is necessary for molecularly-thin boundary lubricants.

[1] T. E. Karis and M. S. Jhon, “The relationship between PFPE molecular rheology and tribology,” Tribol. Lett., vol. 5, pp. 283–286, 2004.

[2] R. J. Waltman, “Autophobic dewetting of z-tetraol perfluoropolyether lubricant films on the amorphous nitrogenated carbon surface,” Langmuir, vol. 20, pp. 3166–3172, 2004.

[3] G. W. Tyndall, P. B. Leezenberg, R. J. Waltman, and J. Castenada, “Interfacial interactions of perfluoropolyether lubricants with magnetic recording media,” Tribol. Lett., vol. 4, pp. 103–108, 1998.

[4] G. W. Tyndall, R. J.Waltman, and D. J. Pocker, “Concerning the interactions between zdol perfluoropolyether lubricant and an amorphousnitrogenated carbon surface,” Langmuir, vol. 14, pp. 7527–7536, 1998.

[5] Z. Zhao and B. Bhushan, “Tribological performance of PFPE and X-1P lubricants at head-disk interface. Part I. Experimental results,” Tribol. Lett., vol. 6, pp. 129–139, 1999.

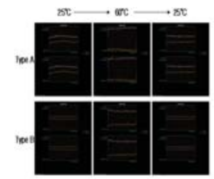

Figure 1. Friction force change with temperature

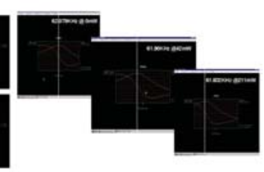

Figure 2. Thermal effect of cantilever tip.

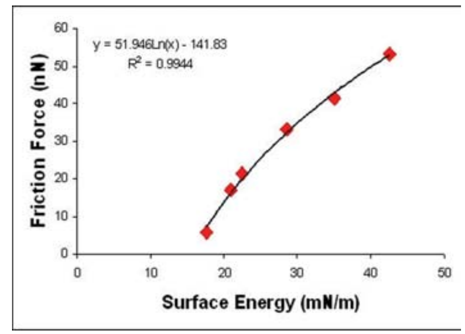

GY-03

Arsenic Removal from Water by Magnetic Separation: A Review and a Case Study Using Magnetic Aggregates and Magnetic Stabilized Bed.

A. M. Estevez[1], *P. A. Augusto*[2,1], J. M. Rodriguez[1], A. Alvaro[1]
1. Department of Chemical Engineering, University of Salamanca, Salamanca, Spain; 2. DEQ, Faculdade de Engenharia da Universidade do Porto, Porto, Portugal

Abstract
In this paper we present a short overview of the attempts performed so far to apply magnetic separation in order to achieve the removal or reduction of arsenic content in water; we also compare them with traditional methods.
We present the magnetic separation process we are using in order to remove arsenic. Finally we present some of the preliminary adsorption results.

Arsenic Toxicity
Water, when containing arsenic in amounts above the limits defined by law (10 µg/l) [1], represents an hazard for public health, specially if in taken continuously [2,3].
Arsenic is found commonly in water under an inorganic form, mainly as arseniate (As V) in superficial waters and as arsenite (As III) in underground waters. As(III), for ordinary biological systems, is more toxic than As (V) [4,5].

Arsenic Removal: Traditional Processes
Several processes to achieve the elimination of arsenic from water, were developed and applied, being the main ones based on precipitation-coagulation techniques, separation by membranes, ion-exchange processes, and adsorption [1,2]. They are usually expensive, not adequate to be applied in small water facilities, an require a previous oxidation of As(III) to As(V) in order to be more efficient, or they are sensitive to the presence of other substances in water.

Arsenic Removal: Magnetic Separation
The idea to use ferromagnetic iron oxides as adsorbent media for arsenic removal has been suggested. However, its application faces some difficult practical challenges. [6, 7, 8]. The only attempts to use the magnetic properties of this type of adsorbent media are: the removal of arsenic from geothermal water by HGMS [9], and a low-field magnetic separation of monodisperse Fe_3O_4 nanocrystals [10]. The first case, constitutes an expensive method, requires some pre-treatment stages, and the final removal efficiencies are between 40-80 %. The second case reduces the mass of waste associated with arsenic removal from water; however it is a laboratorial-scale device and constitutes a not very-well developed technique.

Case Study: Magnetic Stabilized Bed
Bearing in mind high adsorption capacity of the hydrated iron oxide FeOOH, we are performing, in the present study, the conjugation of the magnetic stabilized bed technique [11,12,13,14] with adsorption of arsenic by ferromagnetic iron oxides, by applying some magnetic aggregate structures [15,16].
We are using the Magnetic Stabilized Bed (MSB) system depicted in Figure 1.
Its working principles will be detailed in the conference and in the subsequent paper.

Preliminary experiments
Preliminary experiments were performed regarding arsenic elimination by promoting in a first stage its adsorption in the previously prepared adsorbents: hydrated iron oxide, magnetite and magnetic aggregates of iron and silicon with different ratios Fe/Si. Arsenic content determination, before and after the adsorption stage was performed by the semi-quantitative Quantofix® test.

Experimental results and discussion
Arsenic adsorption results are presented in Figures 2, where a high adsorption, very close to 100%, is observed. In general terms, we may conclude that iron is the main responsible for adsorption, while Si is the main responsible for mechanical consistence of the aggregate.
In Figure 3 is depicted the adsorption kinetics of arsenic. We may conclude from the figure that adsorption of As by our magnetic adsorbents is a fast process.

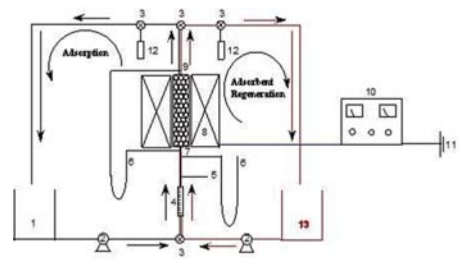

Figure 1 – Experimental set-up: 1.- Deposit (arsenic contaminated water); 2.- Pumps; 3.- Valves; 4.- Rotameter; 5.- Thermometer; 6.- Manometer; 7.- Distributor; 8.- Solenoid genenrating the magnetic field; 9.- Magnetic stabilized bed (MSB) of adsorbent particles. 10.- Continuous electrical current generator; 11.- Electrical current network; 12.- Sample exit; 13.- Deposit (regenerator fluid).

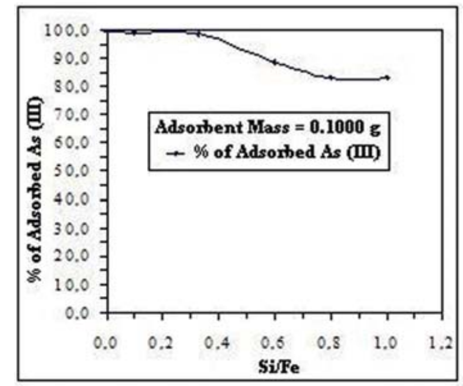

Figure 2 – Arsenic adsorption as a function of the Si/Fe ratio of the aggregates prepared.

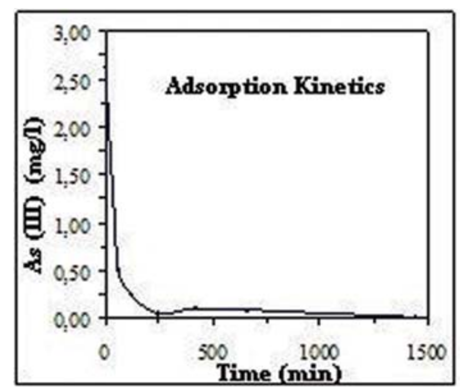

Figure 3 – Arsenic content of water versus time during the adsorption experiments.

Investigation of Nanoparticle Clusterization in Magnetic Fluids Driven by Surface-Coating Desorption.

F. M. Oliveira, P. C. Morais, K. S. Neto, A. P. Canizares, L. C. Figueiredo
Instituto de Física, Universidade de Brasília, Brasília, Brazil

A key aspect related to magnetic fluid (MF) samples with important consequences to most of the applications is the clusterization process which tight single nanoparticle units together in a more complex agglomerate (Klokkenburg et al). Clusterization in MF samples can be induced for instance by application of an external magnetic field, by either changing the sample's temperature or nanoparticle's concentration or by changing the characteristics of the molecular surface layer that ultimately helps stabilizing the magnetic colloid. Static magnetic birefringence (SMB) measurements provide important, though indirect, information regarding the clusterization process in MFs, such as average size and size dispersion of the built-in cluster (Skeff Neto et al.). Therefore, SMB measurements provide an indirect way to track the aging of MF samples by looking at the field dependence of the sample's SMB signal (Skeff Neto et al). In the present study we report on the investigation of the aging of biocompatible MF samples consisting of maghemite nanoparticle, surface-coated with dimercaptosuccinic acid (DMSA), suspended in physiological solution. Magnetic fluids containing different nanoparticle sizes and different surface grafting were used as the stock samples. Samples were labeled DMSA1 and DMSA2, with average core-diameters of 7.9 nm and 7.2 nm, respectively. The sample DMSA1 presents lower surface grafting coefficient in comparison to sample DMSA2. Stock samples were diluted in pure water while the SMB data were collected at day zero, day two, and day five after dilution.

Figure 1 shows the SMB data obtained from sample DMSA1 after dilution, at day-0. Open symbols in Fig. 1 represent the normalized SMB data of sample DMSA1 at 1:2 dilution (circles) and at 1:6 dilution (squares). Figures 2 and 3 represent, respectively, the time evolution (day-0 and day-5) of the SMB data obtained from samples DMSA1 and DMSA2 after 1:4 dilution. The solid lines in Figs. 1-3 represent the best curve fitting of the experimental data (symbols) according to the model discussed by Skeff Neto et al.. Symbols in the inserts of Figs. 1-3 result from the curve fitting of the SMB signal.

The analysis of the SMB data shown in Fig. 1 indicates reduction on the average chain-length and chain-length dispersion as the stock sample is diluted down to 1:2 and further reduction for the 1:6 dilution. Nevertheless, the analyses of the SMB data shown in Figs. 2 and 3 indicate little changes on both the average chain-length and chain-length dispersion as the diluted samples are left to aging from day-0 towards day-5. These findings lead us to conclude that changes on the average chain-length and chain-length dispersion after dilution are more likely-driven by the onset osmotic gradient between the nanoparticle surface and the bulk solution. Further, changes on the average chain-length and chain-length dispersion are dominated by a fast process, more likely-related to desorption of molecular species from the nanoparticle surface (Oliveira et al.).

Klokkenburg M., Erné B. H., Meeldijk J. D., Wiedenmann A., Petukhov A. V., Dullens R. P. A., Philipse A. P.: Phys. Rev. Lett. Vol. 97, 2006, 185702.

Oliveira F. M. L., Avelino S. R., Gravina P. P., Skeff Neto K., Morais P. C.: J. Non Crystal. Sol. Vol. 352, 2006, pp. 3689-3691.

Skeff Neto K., Bakuzis A. F., Morais P. C., Pereira A. R., Azevedo R. B., Lacava L. M., Lacava Z. G. M.: J. Appl. Phys. Vol. 89 (6), 2001a, pp. 3362-3369.

Skeff Neto K., Bakuzis A. F., Pereira A. R., Morais P. C.: J. Magn. Magn. Mater. Vol. 226-230, 2001b, pp. 1893-1895.

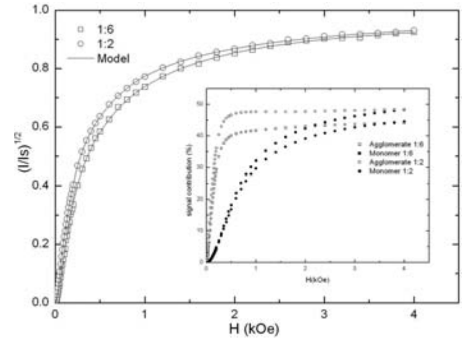

Fig 1. SMB signal of sample DMSA1 at different dilutions. The insert shows the evaluated contribution of monomers and agglomerates.

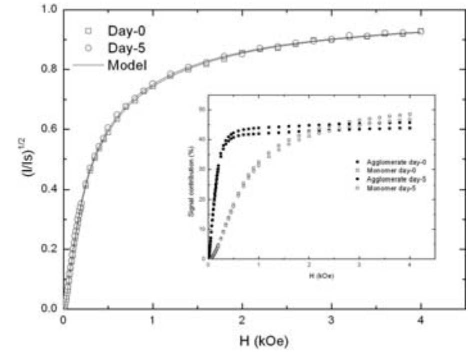

Fig 2. SMB signal of sample DMSA1, submitted to the 1:4 dilution, as a function of time. The insert shows the evaluated contribution of monomers and agglomerates.

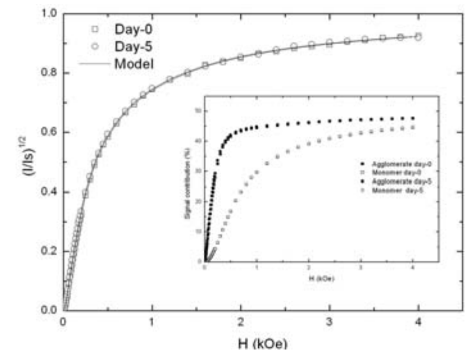

Fig 3. SMB signal of sample DMSA2, submitted to the 1:4 dilution, as a function of time. The insert shows the evaluated contribution of monomers and agglomerates.

GY-05

Detection of Low-Concentration Magnetic Fluid inside Body by Needle-Type GMR Sensor.

S. Yamada, C. P. Gooneratne, M. Iwahara, M. Kakikawa
Institute of Nature and Environmental Technology, Faculty of Engineering, Kanazawa University, Kanazawa, Japan

Introduction

Magnetic nanoparticles are injected inside the body to deliver medicines or to act as self heating agents to kill cancerous tumors. Recent cancer treatment research has focused on the effectiveness of killing localized or deeply seated cancer tumors. However, effective and minimally low-invasive detection of magnetic fluid inside the body is necessary to confirm the presence and location as well as for possible estimation of content density.

Detection Theory and Proposed GMR Sensor

The theoretical aspect of detection inside the body is based on the difference between magnetic flux densities (B_1 and B_0) inside and outside a cavity with permeability greater than 1, under uniform magnetic fields as shown in Fig. 1. A uniquely designed, minimally invasive giant magnetoresistance (GMR) needle sensor is fabricated as shown in Fig. 2, for inserting into the body for detecting low concentration magnetic fluid (weight density, D_w of less than 1 %). A sensing area of 75 µm × 40 µm is present at the tip of the needle. The bridge structure of the GMR sensor is able to detect a magnetic fluid filled area in the body (B_1) as opposed to an area without (B_0) simultaneously. When the ratio of the height to diameter, m, and the corresponding demagnetizing factor, N, of a given cavity remains constant, the relationship between the change in magnetic flux density inside and outside a cavity and the weight density of the magnetic fluid, D_w is given as [1],

$(B_1\text{-}B_0)/B_0 = 4(1\text{-}N)D_w/h_s\gamma_f, \rightarrow (1)$

where h_s and γ_f are the space factor(0.523) of spherical magnetite and the specific gravity(4.58). It is also worth to note that physical dimensions of cancerous tumors are difficult to predict and more so the fluid spreads inside the tissue and decreases the density, so it is of interest to investigate the possibility of detection of low concentration magnetic fluid inside cavities with various shapes and sizes.

Experimental Method and Analysis

Initial experiments were done by measuring the applied flux density (B_0 = 100 µT) and magnetic flux density inside magnetic fluid filled embedded cylindrical cavities of m = 0.625, and magnetic fluid weight density was estimated as shown in Fig. 3. Next, experiments to detect magnetic fluid inside a body were performed by injecting magnetic fluid of varying density into cylindrical pieces of agar (m = 1) and placing them in a potato starch medium. The needle-type GMR sensor was inserted at 10 mm intervals and hence, to the middle of agar pieces and the results are shown in Fig. 4 for a weight density percentage of 0.574 %. The change in signal corresponds to the difference between the signal obtained inside the magnetic fluid and in potato starch (reference medium). It can be seen from the results that the GMR needle sensor can detect the magnetic fluid inside cylindrical agar pieces with diameters ranging from 7 to 19 mm. Since m and hence N is the same, the signal do not vary so much between the samples.

Conclusion

Most applications such as hyperthermia therapy in cancer treatment can be performed with minimal error if detection and estimation of weight density of magnetic fluid inside the body are possible. The experiments performed in this paper shows that the fabricated novel needle-type probe has a good potential to be used for such purposes.

[1] S.Yamada, et al., "Detection of Magnetic Fluid Volume Density with SV-GMR Sensor," J. Magn. Soc. Jpn., 31, p.44-47 (2007).

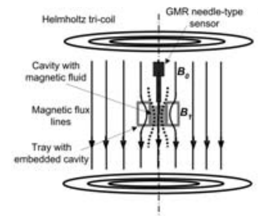

Fig. 1. Magnetic flux distribution inside and outside cavity filled by magnetic fluid.

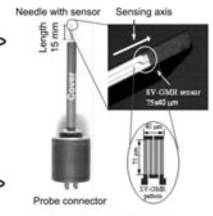

Fig. 2. Fabricated GMR needle sensor

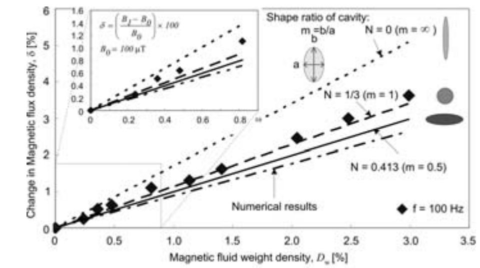

Fig. 3. Estimation of low concentration magnetic fluid weight density

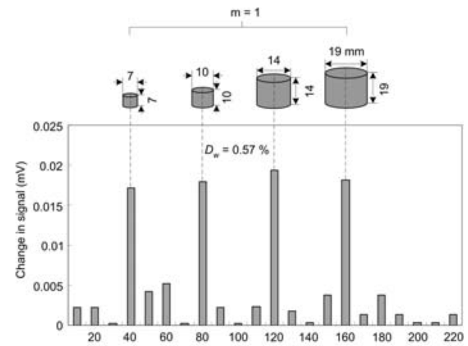

Fig. 4. Detection of magnetic fluid inside agar

GY-06

Suppression of electromyogram of hand muscle elicited by transcranial magnetic stimulation over the primary motor cortex.

M. Odagaki, S. Ohishi, H. Fukuda, O. Hiwaki
Graduate School of Information Sciences, Hiroshima City University, Hiroshima, Japan

1. Introduction

Transcranial magnetic stimulation (TMS) is a non-invasive technique for exploring all aspects of brain function in clinical use. Cortical motor neuronal activation by TMS produces efferent signals that pass through the cortico-spinal tracts. As a result, motor evoked potentials (MEPs) are observed at muscles innervated over the motor neurons.

Voluntary finger movements are performed by cooperative interaction of several muscle groups. TMS can evoke the excitation of particular peripheral muscles, and muscle contraction is observed. A large difference in behavior between voluntary movement and involuntary movement produced by TMS is likely to be observed.

In the present digest, both electromyograms (EMGs) and tracks of finger movement were measured during a finger tapping task, and the effect of TMS over the primary motor cortex on voluntary finger movements was examined.

2. Method

The experimental system consists of a magnetic stimulator, an EMG measurement device, and a three-dimensional tracking system.In order to observe the muscle contraction, measurement electrodes for EMGs were placed on the abductor pollicis brevis (APB) and first dorsal interosseous (FDI) muscles of the right hand. When the subject raises his/her thumb, this movement is detected by an LED sensor. The measurement of EMGs and the tracking system are then started simultaneously upon being triggered with by the LED sensor output signal.

A diagram of the time series of this experiment is shown in Figure 1. The subject performed a single thumb-tap synchronized to the sound of a metronome with an interval of 4.8 s. A magnetic coil for TMS is located over the left motor cortex, and stimulations were carried out at stimulation timings of 0, 10, 100, and 350 ms for each task. The stimulation timing was obtained from the time at which the thumb is raised. The number of stimulations was ten for each task. A TMS pulse with an intensity of 70% was applied over the left M1 area by changing the stimulation timing.

3. Results and discussion

Figure 2 shows the measurement result of the relationship between the finger tapping time and the TMS timing. As shown in the figure, the tapping time was significantly increased at stimulation timings of 0 and 10 ms. The measurement results of EMGs obtained from APB at the stimulation timing of 10 ms are shown in Figure 3. As shown in this figure, MEPs were evoked at a latency of 20 ms, and suppression of the voluntary EMGs was observed approximately 100 ms after MEPs disappeared.

The overlapped displacement waveforms with no-TMS and TMS with a delay of 10 ms are shown in Figure 4. Decreasing displacement indicates that the finger is moving upward. A loss of strength appears to have occurred during finger tapping. Furthermore there is a significant difference in positive slope between both displacement waveforms. These evidences indicates that both brain cells and muscles exceeded their respective thresholds at different times. It is thought that voluntary EMGs were inhibited for 100 ms while both tissues went into a refractory period.

4. Conclusion

The suppression of voluntary EMG was confirmed when TMS was applied at timings of 0 and 10 ms, indicating that tissue excitation elicited by TMS causes a loss of control of the peripheral muscle during voluntary movement.

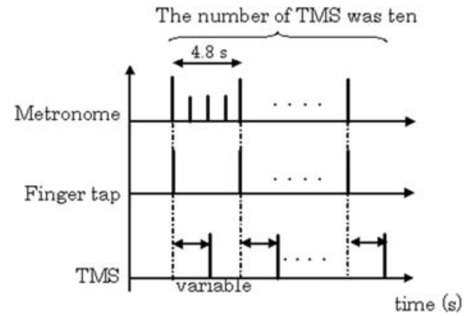

Figure 1 Time series of the experiment

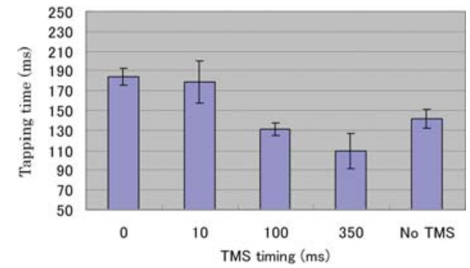

Figure 2 Average tapping time

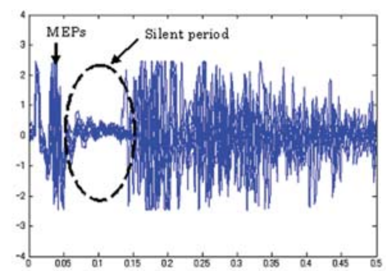

Figure 3 Overlapped EMGs obtained from APB

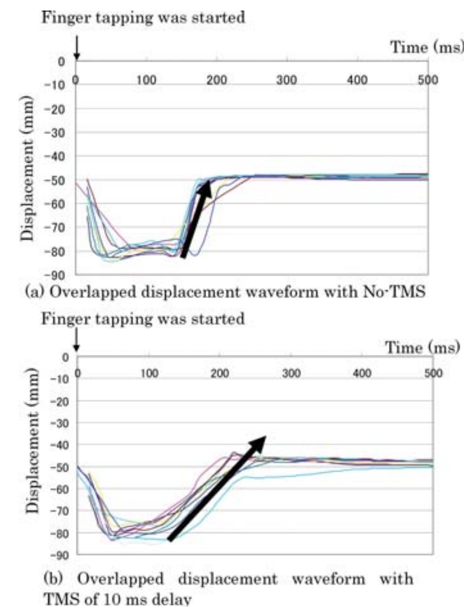

(a) Overlapped displacement waveform with No-TMS

(b) Overlapped displacement waveform with TMS of 10 ms delay

Figure 4 Displacement waveforms

GY-07

Formation of beta-Sheet Rich Fibrils in Cortex Cells from Mice Fetuses Cultured with Ferritin and Exposed to Radio Frequency Magnetic Fields.

O. Cespedes, O. Inomoto, S. Kai, S. Ueno
Applied Quantum Physics Department, Kyushu University, Fukuoka, Japan

Summary:
In our work we have studied the effects of radio-frequency (RF) magnetic fields in brain cells cultured with iron-saturated cage proteins (ferritins). We have observed that the cultures show signs of protein aggregation, with microscopic fibrils rich in b-sheet structure visible under optical microscope. This may have dire consequences for neurodegenerative disorders and their relation with RF magnetic fields exposure.

Introduction:
Many forms of dementia, including Alzheimer's and Parkinson's, are related to the aggregation of misfolded proteins into insoluble fibrils with a b-sheet rich secondary structure where the free radicals play an important role acting as catalyst in the process. Iron is involved in the formation of oxygen-free radicals, and iron accumulation has been found within brain regions displaying vulnerability to neurodegeneration [1].
Between 15-25 % of the iron in the body is stored inside ferritins [2], an iron cage protein that has been associated to neurodegenerative diseases with evidence of having been produced locally by the glial cells. These proteins are composed of a peptidic cage of 12 nm in diameter and 440 kDa inside which there are stored up to 4500 iron ions in the form of a ferrihydrate nanoparticle.
Results and Discussion:
We observe a reduction in the optical absorbance of solutions of ferritins exposed to RF fields. The maximum change occurs at energies corresponding to half the ferrihydrate energy gap, indicating changes in the nanoparticle's surface structure, i.e. a possible decrease of the number of iron ions (Figure 1). The mechanism for this interaction would be in the changes in the internal energy of the nanoparticle when exposed to alternating magnetic fields.
We studied then the consequences of this effect in brain cell cultures extracted from the cortex of mice fetus (DDY strain) kept at standard conditions of 10 % serum in DMEM medium at a temperature of 37 C and 5 % CO2. We divided the samples in four groups:
1.- Samples cultured with 1 microM of iron saturated ferritin and exposed to magnetic fields of 1 MHz and 25 microT for 1 hour a day during 4 days. The cells were kept at 37 C with no gas exchange (5% CO2).
2.- Samples cultured with 1 microM of iron saturated ferritin and undergoing the same conditions for one hour a day but not exposed to magnetic fields.
3.- Samples cultured with ferritin and exposed to magnetic fields for only 15 minutes a day (with the remaining 45 minutes at the same conditions of the sham and 1-hour exposed samples).
4.- Samples exposed to magnetic fields of 1 MHz and 25 microT for 1 hour a day but with no added ferritins.
The first group showed the formation of b-sheet rich fibrils about 10 microm in length and < 1 microm in width accompanied of a swelling of the microglial cells. The cells from this group died after the fourth day of exposure to the magnetic field, whereas the other samples remained alive for 6 (# 2 and 3) and 10 days (# 4), with no fibril formation (figure 2).
We can therefore conclude that radio frequency magnetic fields in the 10 microT and 1 MHz range may have the potential to significantly alter the concentration of Fe2+ ions in areas with high concentration of iron rich ferritins, which might have dire consequences for oxidative stress and protein aggregation.
Acknoledgments: This study is supported in part by the grants (S)17100006 and 19.07371 from the Japan Society for the Promotion of Science (JSPS).

[1] Silvia Mandel, Tamar Amit, Orit Bar-Am and Moussa B.H. Youdim, Prog. Neurobio. 82, 348 (2007).

[2] Pauline M. Harrison and Paolo Aorisio, Biochim. Biophys. Acta 1275, 161 (1996).

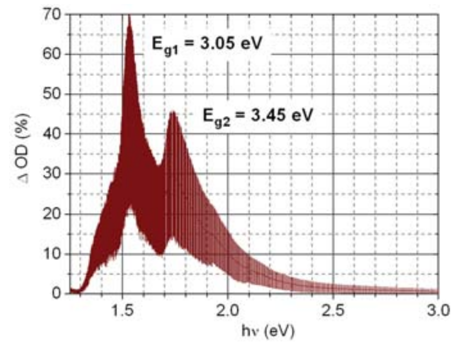

Figure 1: Distribution in the percentage of reduction in the optical density (log. of the absorbance) of ferritin solutions after they have been exposed to a magnetic field of 20 microT and 1 MHz for eight hours. The two peaks correspond to the half transitional energies for the ferrihydrate nanoparticle (signal near the energy gap is saturated).

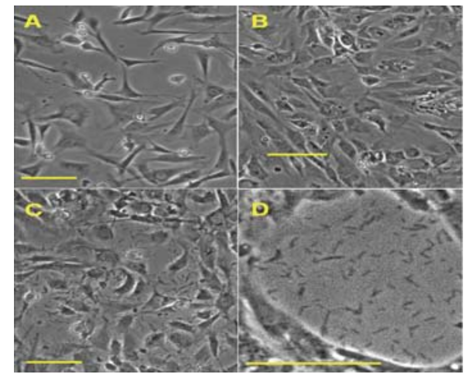

Figure 2: Optical microscope images of cultures of cells from the cortex of mice fetus' brains. A) Brain cells cultured with 1microM iron-saturated ferritin but not exposed to magnetic fields (sham). B) Brain cells exposed to RF magnetic fields (20 microT, 1MHz) for 1 hour a day during 4 days. C) Brain cells cultured with 1 microM iron-saturated ferritin and exposed to RF magnetic fields (20 microT, 1MHz) Note the small fibrils at the inter-cell spaces. D) Detail of the fibrils. Scale bars are 50 microm.

GY-08

Effects of Radio Frequency Magnetic Fields on the Iron Release from Cage Proteins via 6-Hydroxydopamine.

O. Cespedes, S. Ueno
Applied Quantum Physics Department, Kyushu University, Fukuoka, Japan

Introduction:
In this study we show how radio frequency magnetic fields of 200 kHz to 3 MHz and amplitudes from 10 to 100 microT alter the 6-hydroxidopamine entry time and reduction rates of iron ions from iron cage proteins (ferritins). We propose a mechanism for this effect based on changes in the internal energy of the inner ferrihydrate nanoparticle, which is verified by iron-release spectroscopy experiments.
Materials and Proposed Mechanism:
Ferritin [1] is a ubiquitous protein which role is to capture and store the harmful Fe2+ ions in the body. It is formed by a roughly spherical peptidic cage of 440 kDa in mass and 12 nm in diameter (apoferritin) and an inner ferrihydrate nanoparticle containing the stored iron. To be released, the iron has first to be reduced from Fe3+ to Fe2+. One of the molecules with this role is 6-hydroxydopamine, which goes into the ferritin cage and produces deprotonated quinone, H2O molecules and Fe2+ ions. This reaction is related to Parkinson's disease via the catalyst role played by the Fe2+ ions in the oxidative stress. Iron release from the ferritin can be monitored by the addition of ferrozine, an iron chelator that acts as colorimetric probe.
We propose a mechanism for the interaction with RF magnetic fields as follows: when an alternating magnetic field of high enough frequency is applied, the magnetization of the nanoparticle (magnetic moment of about 0.1 Bohr magneton per iron atom) will lag the applied field, resulting in an increase of its internal energy. The nanoparticle may relax via either Néel or Brownian processes. The former will result in the irradiation of phonons from the nanoparticle (the magnetization rotates within the crystal).In a Brownian process, the nanoparticle will try to mechanically rotate and align itself with the magnetic field, colliding with the surrounding water molecules and the proteic cage that encloses it.
Results and Discussion:
In our experiments we have worked with iron-saturated ferritins with nanoparticle diameters of 8 nm (about 4500 Fe ions). We observe that proteins exposed to the RF magnetic fields have a higher rate of iron release during the first 1-3 hours at neutral pH with differences of almost 50 % at long exposure times (Figure 1a). However, as the molecule reaches its release saturation level or as the pH is lowered, the iron released from proteins exposed to magnetic fields is drastically decreased in comparison to control samples. At a constant frequency-magnetic field (f x B) product, the biggest effect is obtained at frequencies of 1 MHz, suggesting a relaxation time of order 1 microsecond (Figure 1b).
The flow of iron ions released from control ferritin samples at low pHs is enough to block the hydrophilic terminals, and the molecules coagulate and precipitate. In contrast, in the case of ferritin molecules exposed to magnetic fields for several hours, the iron released by the 6-hydroxydopamine is almost quenched and the precipitation occurs more slowly or not at all (Figure 2).
Our study has given evidence that RF magnetic fields have the possibility to alter the iron release dynamics from iron cage proteins, with important changes in protein functioning and solubility. The good functioning of these proteins is essential to avoid oxidative stress and therefore this effect could have important physiological consequences.

Acknoledgments: This study is supported in part by the grants (S)17100006 and 19.07371 from the Japan Society for the Promotion of Science (JSPS).

[1] Pauline M. Harrison and Paolo Aorisio, Biochim. Biophys. Acta 1275, 161 (1996).

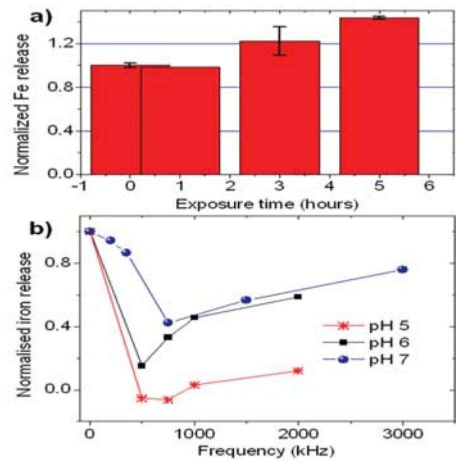

Figure 1: a) Normalized iron release from a solution of 1microM ferritin in function of the exposure time to a magnetic field of 20 microT and 1MHz after 1 hour of adding 200 microM of 6-Hydroxydopamine and 100 microM of ferrozine. b) Saturation level of iron release in function of the frequency of the applied magnetic field and total solution pH.

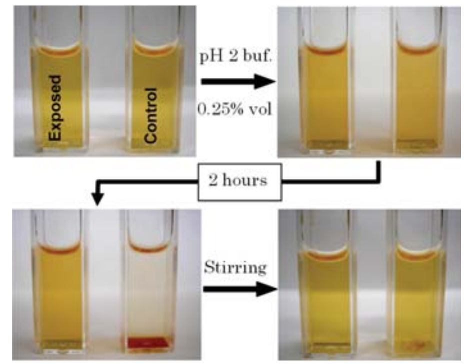

Figure 2: Precipitation of ferritins. After adding a low pH buffer to a solution of 200 microM 6-Hydroxidopamine, 100 microM ferrozine and 1 microM ferritin, the rapid iron release in control samples blocks of the ferritin hydrophilic terminals, leading to coagulation and precipitation. Samples exposed to RF magnetic fields have a much smaller and slower iron release, keeping free the hydrophilic terminals and avoiding aggregation.

GY-09

Short and long duration of rTMS effects on perceptual reversals.

S. Ge[1], T. Hayami[2], A. Hyodo[3], S. Ueno[4], *K. Iramina*[1,3]
1. Department of Intelligent Systems, Kyushu University, Fukuoka, Japan; 2. Digital Medicine Initiative, Kyushu University, Fukuoka, Japan; 3. Graduate School of Systems Life Sciences, Kyushu University, Fukuoka, Japan; 4. Department of Applied Quantum Physics, Kyushu University, Fukuoka, Japan

In this study, we focused on the effect of repetitive transcranial magnetic stimulation (rTMS) on neuronal excitability. The rTMS is a non-invasive and painless method of modifying the excitability of the cerebral cortex, which allows repetitive pulses of electricity passed through a coil placed on the scalp. A magnetic field is generated around the coil. This field penetrates the skull and depolarizes underlying neuronal tissues. This causes the activation or inhibition of neuronal tissues to be changed.
Ambiguous figures are visual stimuli which are interpreted in multiple ways by the human visual system. For a given ambiguous figure, the perception will switch spontaneously between several possible interpretations even while the figure stays unchanged. This process is called perceptual reversals. Some studies about perceptual reversals of ambiguous figures indicated that the parietal area in the brain, especially, the superior parietal lobule (SPL) is involved in perceptual reversals [1] [2]. However, whether the activation in the superior parietal lobule inevitably causes the perceptual reversals or how it effects the perceptual reversals is unclear by using fMRI, EEG, MEG et al. In the present study, we explored the rTMS effect over the right SPL in the perceptual reversals of ambiguous figures.
The spinning wheel illusion was used as the ambiguous figure's stimulation in this study. The perception of a spinning wheel is moving in either clockwise or counterclockwise, with switches between these two percepts occurring spontaneously. Subjects were required to respond as quickly and accurately as possible by clicking a mouse button to indicate the perceptual reversals in the direction of rotation. The time interval between two successive perceptual reversals was recorded as the inter-reversal time (IRT) after rTMS. A figure-of-eight 70 mm coil was used as the TMS. Stimulus strength was set at 90% of the subjects' individual resting motor threshold. In this study, rTMS trains were applied over the right SPL or the right posterior temporal lobe (PTL). As a control stimulation, no rTMS trains were applied over the subject's skull. Furthermore, in order to investigate the rTMS effect with different stimulus duration, two kinds of experiments, i.e., short-duration experiment and long-duration experiment were performed. In the short-duration experiment, a 60-pulse train of 1Hz rTMS was applied. While in the long-duration experiment, a 240-pulse train of 1Hz rTMS was applied.
In a dynamic aspect of perceptual rivalry, a well-known empirical proposition, which called Levelt's proposition [3], says that the intervals of perceptual alternation follow a gamma distribution in both binocular rivalry and ambiguous figure perception. Hence, we considered that the IRT were followed a gamma distribution in the present study. For each subject, the frequency distribution of IRT was calculated. We then used the gamma distribution to fit the IRT data and calculated the parameter α,β and of gamma distribution. After that, the average of frequency distribution of IRT can be calculated (average=α*β, hereinafter abbreviated as AIRT). The AIRT of each subject were calculated.
Based on the short-duration experimental results, it was found that compared to the PTL stimulation and no-TMS, rTMS applied over the right SPL leads to a significant facilitatory effect on perceptual reversals. On the other hand, there was no significant difference between the PTL stimulation and no-TMS. In contrast, in the long-duration experiment, it was found that compared to the PTL stimulation and no-TMS, rTMS applied over the right SPL leads to a significant suppression effect on perceptual reversals. On the other hand, there was no significant difference between the PTL stimulation and no-TMS. Therefore, we considered that the difference of rTMS-evoked cortical activation should be the main reason to cause difference in IRT. Thus we concluded that the right SPL maybe plays a critical role in perceptual reversals of ambiguous figures. Under the circumstance of the present study, a 1 Hz 60-pulse rTMS probably causes facilitatory effect on perceptual reversals, while a 1 Hz 240-pulse probably causes suppression effect on perceptual reversals.

[1] E.D. Lumer, K.J. Friston, G. Rees, Neural correlates of pereptual rivalry in the human brain, Science, 280, pp.1930-1933, 1998.

[2] P. Sterzer, M.O. Russ, C. Preibisch, A. Keinschmidt, Neural correlates of spontaneous direction reversals in ambiguous apparent visual motion, Neuroimage, 15, 4, pp.908-916, 2002.

[3] W.J.M. Levelt, Note on the distribution of dominance time in binocular rivalry, British Journal of Psychology, 58, pp.143-145, 1967.

HA-01

Prospects for Spin Memory Devices and Their Element Technologies in the Next 10 Years.

S. Nakamura
Corporate R&D Center, Toshiba Corporation, Kawasaki, Japan

The discovery of GMR in magnetic multilayers by Fert and Grünberg [1] led to the appearance of TMR, the ratio of which is currently about 500 % at room temperature. These MRs are due to the spin-dependent transport of two spin currents of up and down. In such systems, when the current crosses a magnetic layer, the layer receives angular momentum from the spin current. The spin-transfer torque, predicted by Slonczewski and Berger [2], has attracted much attention, since it generates a variety of magnetic dynamics including spin wave excitation, switching, and precessional motion.
The first spintronic device that has been realized is the GMR head, the commercialization of which started in 1998. With a view to achieving the next big market, the development of MRAMs that utilize the TMR and memory function of the magnet has been advancing rapidly. The MRAM using magnetic field for writing was commercialized two years ago. And currently, the competitive developments for practical use are shifting to those employing spin-transfer torques for writing. The latter MRAM will be put practical use within several years [3].
In this talk, at first, we will focus on the spin-memory devices that are expected to be available 10 years from now. The advantages and disadvantages of the spin-memory devices, among the competitive memories and emerging non-volatile memories, indicate the likely direction of development of the devices. Then, we will discuss element technologies needed for the evolution. One of the technologies is the spin-current modeling technique. It is already possible to calculate the spin-transfer torque in non-collinear multilayers with complex structures including Syn. AF, the results of which agree with the experiments [4]. Such spin current simulations would not only facilitate understanding of the underlying physics, but also help memory designers unfamiliar with spin-electronics to design devices with new functions.

[1] M. N. Baibich et al., Phys. Rev. Lett., 61, 2472 (1988) ; G. Binasch et al., Phys. Rev. B 39, 4828 (1989).

[2] J. C. Slonczewski, J. Magn. Magn. Mater., 159, L1(1996); L. Berger. Phys. Rev. B54, 9353(1996).

[3] For current status of MRAM development, please refer to the symposium on Spin Torque Transfer Research at Intermag2008.

[4] H. Morise and S. Nakamura, submitted to Intermag2008.

HA-02

Spintronics devices based on the Tunneling Anisotropic Magnetoresistance and the Coulomb Blockade Anisotropic Magnetoresistance effect.

J. Wunderlich[1,2], B. Park[1], A. C. Irvine[3], A. Shick[2], R. P. Campion[4], V. Novak[2], D. A. Williams[1], B. L. Gallagher[4], T. Jungwirth[2,4]

1. Hitachi Europe Ltd., Hitachi Cambridge Laboratory, Cambridge, United Kingdom; 2. Institute of Physics ASCR, Prague, Czech Republic; 3. Microelectronics Research Centre, University of Cambridge, Cambridge, United Kingdom; 4. School of Physics and Astronomy, University of Nottingham, Nottingham, United Kingdom

The history of spintronic devices, used already in hard drive read heads or magnetic random access memories, is reminiscent of that of the conventional microelectronics. It started about 15 years ago with a simple "spintronic wire" – an Anisotropic Magnetoresistance (AMR) sensor, followed by more elaborate diode-like spin-valve elements based on the Giant magnetoresistance (GMR) [1] or the Tunneling magnetoresistance (TMR) effects [2,3].

GMR and TMR also opened new paths to design magnetic random access memories (MRAM), where information is stored as the orientation of the magnetization of a small patterned structure, and read by a resistance measurement.

The transport characteristics of conventional GMR or TMR devices are controlled by external magnetic fields to fix the orientation of the magnetization. However, magnetic field control is not an efficient and scalable writing technique.

Building further on the analogy with conventional electronics, and with the field effect transistors in particular, adding a control by external electric fields [4] appears as a natural route to a new generation of nano-scaled spintronic elements.

In this talk we discuss two novel spintronics effects, the Tunneling anisotropic magnetoresistance (TAMR) [5] and the Coulomb blockade anisotropic magnetoresistance (CBAMR) [6]. The CBAMR effect reflects the magnetization orientation dependence of single-electron transport in a ferromagnetic SET. CBAMR devices are hybrid single-electron/spintronic elements delivering tuneable high magneto-sensitivity combined with non-volatile memory effect. This combined transistor and non-volatile memory functionality is inherent to the CBAMR effect and new logic-functionalities in CBAMR based devices may be envisaged.

The TAMR results from the magnetization orientation dependent density of states (DOS) at the tunneling barrier. After its discovery in diluted magnetic semiconductors, subsequent theoretical work predicted [7] that the TAMR is generic in ferromagnets with SO-coupling, including the high Curie temperature transition metal systems. Experimental demonstration of the TAMR in tunnel junctions with ferromagnetic metal electrodes has recently been reported in an epitaxial Fe/GaAs/Au [8] stack and in high magnetic field saturated conventional TMR devices with CoFe ferromagnetic electrodes [9]. The observed TAMR in these structures was relatively small, < 0.5%, consistent with the weak SO-coupling in the ferromagnetic electrodes.

We present a study of vertical tunnel devices in which the ferromagnetic electrode comprises alternating Co and Pt films [10]. Large and tuneable magnetic anisotropies are generated at the interfaces by combined effects of induced moments and strong SO-coupling in such ferromagnetic/heavy element transition metal multilayers. We show that placing these interfaces adjacent to the tunnel barrier opens a viable route to highly sensitive metal TAMR structures. In stacks with the ferromagnetic electrode terminated by a Co film the TAMR magnitude saturates at 0.15% beyond which it shows only weak dependence on the magnetic field strength, bias voltage, and temperature. For ferromagnetic electrodes terminated by two monolayers of Pt we observe order(s) of magnitude enhancement of the TAMR and a strong dependence on field, temperature and bias.

A discussion of the usability of TAMR and CBAMR for magnetic field sensors in ultra-high density hard disk drive will finalize the talk.

[1] M. N. Baibich,et al., Phys. Rev. Lett. 61, 2472 (1988).

[2] M. Jullière, Phys. Lett. A54 225 (1975).

[3] J. Moodera et al, Phys. Rev. Lett. 74, 3273 (1995).

[4] S. Datta and B. Das, Appl. Phys. Lett. 56, 665 (1990).

[5] C. Gould et al., Phys. Rev. Lett. 93, 117203 (2004).

[6] J. Wunderlich, et al., Phys. Rev. Lett. 97, 077201 (2006).

[7] A. B. Shick, et al., Rev. B 73, 024418 (2006).

[8] J. Moser et al., Phys. Rev. Lett. 99, 056601 (2007).

[9] Li Gao, et al., Phys. Rev. Lett. 99, 226602 (2007)].

[10] B.-G. Park., et al., Phys. Rev. Lett. (2008)].

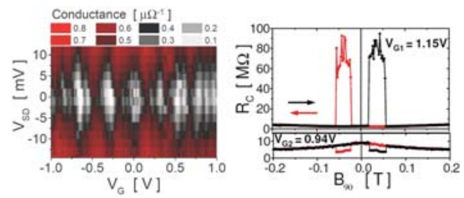

Left panel: CB conduction diamonds in the VG-VSD plot, (VSD, VG is the source-drain, gate voltage, respectively). Right panel: Vg dependent MR. The high electro- and magneto-sensitivity and hysteretic behaviour of the device are apparent: the resistance decreases by ~100% at 20mT for VG =0.94 V while it increases by more than 1000% for VG=1.15 V.

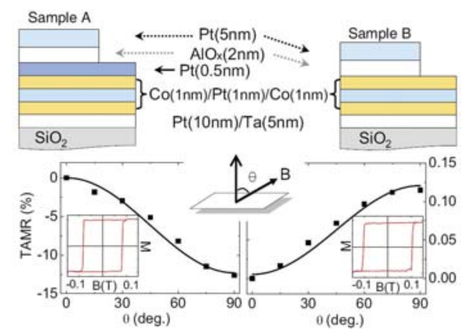

Upper panels: schematic layer structures of a TAMR device terminating with a Pt (left) and Co (right) Lower panels: TAMR traces defined as (R(theta) – R(0))/R(0) at -5 mV bias and 4 K. Insets: SQUID magnetization measurements in out-of-plane magnetic fields.

HA-03

Engineering magnetic nanostructures into complex devices for spin electronics.

C. Chappert
1. IEF, CNRS - UMR 8622, Orsay, France; 2. IEF, Université Paris Sud, Orsay, France

Since the first spin valve read head(IBM, 1997), the applications of spin electronics have undergone an outstanding acceleration towards nano-integration of magnetic devices into solid state electronics. Among best examples are the Spin-RAM demos recently proposed by Sony [1] or Hitachi [2], providing dense magnetic non volatile memories using spin angular momentum transfer switching. This move was made possible by a chain of scientific breakthroughs that illustrate how Nanosciences can impact electronics. For instance, giant magnetoresistance of multilayers arising when individual film thickness is of order of the mean-free path, the magnetic tunnel junction (MTJ) where the barrier thickness is below decay length of tunnelling wave functions, the perpendicular magnetic anisotropy in multilayers originating from interface effects, on more recently the spin angular momentum transfer torque, a quantum effect due to exchange interaction of electron spin with magnetization. One parameter should be important for future development: the fact that the intrinsic speed of magnetization dynamics lies in the GHz range and above, i.e. the range of CPU speed in CMOS electronics, and that of wireless communications. So intense research effort is currently devoted to improve the performance of today's devices, and fully understand and control the effect they use, for instance through new materials such as oxides or diluted magnetic semiconductors.

But today's spin electronics devices, although already quite efficient, retain at minimal functional complexity: basically, they are just variable resistances indexed on a magnetization direction, and their use is so far limited to sensor or memory use. Even though materials already exist with high enough magnetic anisotropy to fabricate thermally stable magnetic particles of size down to a few nm [3], the solid state implementation of such magnetoresistive "switches" will find scalability limits together with those currently predicted for CMOS.

So research should also start to focus on the challenges beyond the magnetic switch model. I can see several steps, which are summarized in Figure 1:

1- move beyond the sole memory application, by moving to magnetic logic devices.

In a first step, this will introduce MTJs inside CMOS, and this is already in progress [4]. A different approach tries to couple "analog logic" using interaction between magnetic nano-objects (particles, domain walls, vortices…) to "digital logic" (either purely CMOS or mixing also magnetic elements), in order to improve energy cost, speed, wafer area, etc… [5, 6].

On the longer term, going "Beyond CMOS" requires a more drastic integration of elaborate logic functions inside every single device. This requires development of multi-terminal spin electronics devices (by contrast to MTJ which is a 2-terminal device), where the magnetic function could also be used to operate re-programming of the logic function with voltage based logic inputs. This may require introduction of molecules, bottom up approaches, etc…

2- move towards a "carriers free" spin electronics

The move towards very complex "Beyond CMOS" spin electronics devices will also require new ways of controlling the magnetization. The trend should be to assist or replace today's action through electric currents (used to create magnetic fields or spin transfer torque) by electric field control, which is expected to dissipate less energy, and also may allow more local and individual control of separate magnetic parts in a multiterminal logic component. First reports of electric field control use direct influence on band structure [7, 8] or coupling of piezoelectric and magnetoelastic materials [9], the latter being actually be intrinsic into multiferroic materials [10].

The "holy grail" of spin electronics however remains a spin logic of spin current with zero charge current. Some preliminary results or propositions are already coming out with evidence of spin current induced switching of nanoparticles [11].

[1] Hosomi, M. et al., Electron Devices Meeting, 2005. IEDM Technical Digest. IEEE International, 2005

[2] Kawahara, T. et al., International Solid-State Circuts Conference ISSCC, Technical Digest, 2007

[3] Weller, D. et al., IEEE Transactions on Magnetics 36, 10 (2000)

[4] Zhao, W. et al., 8th International Conference on Solid-State and Integrated Circuit Technology ICSICT 2006, Technical digest (2006)

[5] Allwood, D. A. et al. Science 309, 1688 (2005)

[6] Imre, A. et al. Science 311, 205 (2006)

[7] Chiba, D. et al., Appl. Phys. Lett. 89 (16), 162505 (2006)

[8] Weisheit, M. et al., Science 315 (5810), 349 (2007).

[9] M. Yamada and S. Nakagawa, IEEE Trans. Magn.43, 2346 (2007)

[10] Ramesh, R. and Spaldin, N., Nat Mater 6 (1), 21 (2007)

[11] Kimura, T.et al., Physical Review Letters 96 (3), 037201 (2006)

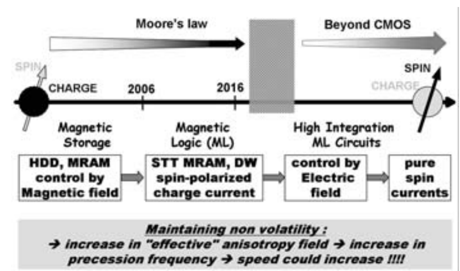

Figure 1: Tentative summary of roadmap for spin electronic devices, with reference to Moore's law.

HA-04

Manipulating single spins and coherence for semiconductor spintronics.

D. D. Awschalom
Center for Spintronics and Quantum Computation, University of California, Santa Barbara, CA

Potential applications of solid state spintronics and quantum information processing may require coherently controlling and reading single electron spins at gigahertz frequencies, as well as enabling engineering pathways for integrated communication [1]. Here we present recent developments within two experimental efforts aimed at manipulating individual spin coherence in semiconductors. The non-destructive detection of a single electron spin in a quantum dot (QD) is demonstrated using a time-averaged magneto-optical Kerr rotation (KR) measurement [2]. This technique provides a means to directly probe the spin off-resonance, thus minimally disturbing the system. The ability to sequentially initialize, manipulate, and read out the state of a qubit, such as an electron spin in a quantum dot, is necessary for future quantum information processing. To this end, we have extended the single dot KR technique into the time domain with pulsed pump and probe lasers, allowing for observation of the coherent evolution of an electron spin state [3]. The dot is embedded in a diode structure to allow controllable gating/charging and optical readout of the state. Measurements of single spin precession in an applied magnetic field allow a direct determination of the electron g-factor and transverse spin lifetime. These observations reveal information about the relevant spin decoherence mechanisms, while also providing a sensitive probe of the local nuclear spin environment. Recently, we have developed a scheme for high speed all-optical manipulation of the spin state that enables multiple operations within the coherence time [4]. The results represent progress toward the control and coupling of single spins and photons for quantum information processing [5] as well as quantum non-demolition measurements of a single spin.
Diamond is a material of extremes: it is the hardest naturally occurring material, it is the best thermal conductor on the planet, it has a very high semiconductor bandgap, and it is transparent over a wide range of optical frequencies. Furthermore, diamond-based materials have recently emerged as a unique electronics platform for quantum science and engineering [6]. The Nitrogen-Vacancy (N-V) color center in diamond is well suited for studying electronic and nuclear spin phenomena, since its spin state can be both initialized and read out optically at room temperature. We report on experimental progress towards coherent control and coupling of single spins in diamond. Using magneto-photoluminescence imaging and electron spin resonance measurements, we have directly imaged single electron spins and manipulated them at GHz frequencies [7], observed their coherent coupling to single nearby dopant spins (N) including controlled polarization and readout [8], and performed coherent control (Rabi oscillations) and spin echo lifetime measurements [9]. Finally, photonic bandgap structures from diamond films with Q-factors approaching 1000 suggest potential pathways for spin-based photonics in this system. These results pave the way towards room-temperature coherent control of coupled spin states in diamond and new quantum technologies.

1. David D. Awschalom and Michael Flatté, Nature Physics 3, 153 (2007).

2. J. Berezovsky, M. H. Mikkelsen, O. Gywat, N. G. Stoltz, L. A. Coldren, D. D. Awschalom, Science 314, 1916 (2006).

3. M. H. Mikkelsen, J. Berezovsky, N. G. Stoltz, L. A. Coldren, D. D. Awschalom, Nature Physics 3, 770 (2007).

4. J. Berezovsky, M. H. Mikkelsen, N. G. Stoltz, L. A. Coldren, D. D. Awschalom, submitted (2007).

5. S. Ghosh, W.H. Wang, F. M. Mendoza, R. C. Myers, X. Li, N. Samarth, A. C. Gossard, D. D. Awschalom, Nature Materials, 5, 267 (2006).

6. D.D. Awschalom, R.J. Epstein, and R. Hanson, Scientific American 297, 84 (2007).

7. R. J. Epstein, F. M. Mendoza, Y. K. Kato, D. D. Awschalom, Nature Physics 1, 94 (2005).

8. R. Hanson, F. M. Mendoza, R. J. Epstein, D. D. Awschalom, Phys. Rev. Lett. 97, 087601 (2006).

9. R. Hanson, O. Gywat, D. D. Awschalom, Phys. Rev. B 74, 161203(R) (2006).

HA-05

The road to silicon spintronics.

R. Jansen
MESA+ Institute for Nanotechnology, University of Twente, Enschede, Netherlands

Semiconductor electronics has been the cornerstone of information technology for many decades. It is based on the manipulation, control and storage of electrical charge in circuits used for logic and memory applications, with the transistor as the central element. Semiconductor materials prevail because they allow power amplification, with silicon being by far the dominant material. However, as concerns are raised about the further advancements of semiconductor devices in future chip generations, alternative technologies are actively being explored. The field of spintronics aims to improve the performance and enhance the functionality of electronic circuits and systems by making use of the spin of electrons. While significant progress has been made in recent years in combining spin with III-V (GaAs) based semiconductor materials, silicon-based spintronics is still at its infancy.

While it is clear that implementing spin-functionality into silicon is potentially highly rewarding, it has turned out to be a major challenge. Amongst the key advances to be made are to develop robust and efficient ways to inject electron spins into Si, and to develop suitable (optical, electrical) methods to detect and manipulate the spin-polarization in the Si. However, perhaps the most challenging aspect is to design fully electrical silicon based spin-devices with useful functionality and large spin-signals in a simple and preferably two-terminal geometry. With respect to the latter, efforts have so far focused on devices such as the spin-MOSFET, a transistor with a Si channel and a ferromagnetic (FM) source and drain. It is now clear that this demands careful consideration of the requirements for the FM injector and detector contacts [1,2,3], going beyond the obvious need for a high spin polarization of the contacts. For example, it is found that Schottky barrier formation on Si can be detrimental to the magnetoresistance of such a device [3]. This is partly because of the resulting large resistance area (RA) product of the contacts and partly because of the potential energy landscape, which affects spin flow across the interface [4].

As a solution, novel approaches are developed [3] to control the Schottky barrier height and resistance-area (RA) product of spin tunnel contacts to Si, e.g. using low work function materials. These include ferromagnets as well as non-magnetic materials, inserted as ultrathin (sub-nm) interfacial layers into FM/Al2O3/Si spin-tunnel contacts on either side of the tunnel barrier. In this way, the RA product of FM/Al2O3/Si contacts can be tuned over 8 orders of magnitude (see fig. 1). Equally important, complementary tunnel magnetoresistance data (fig. 2) show that a reasonable tunnel spin-polarization is simultaneously maintained. Interestingly, the Schottky barrier can even be inverted, in which case an interfacial accumulation layer (i.e. a 2-dimensional electron gas) can be established, creating new device options. Such engineered spin-tunnel contacts with low work function materials therefore not only qualify as conductivity-matched source and drain electrodes for spin-transistors, but also open up new avenues to design spin devices based on Si quantum structures for application in silicon spintronics.

[1] A. Fert and H. Jaffrès, Phys. Rev. B 64, 184420 (2001).

[2] A. Fert, J.-M. George, H. Jaffrès and R. Mattana, IEEE Trans. Elec. Dev. 54, 921 (2007).

[3] B.C. Min, K. Motohashi, J.C. Lodder and R. Jansen, Nature Materials 5, 817 (2006).

[4] R. Jansen and B.C. Min, Phys. Rev. Lett. 99, 246604 (2007).

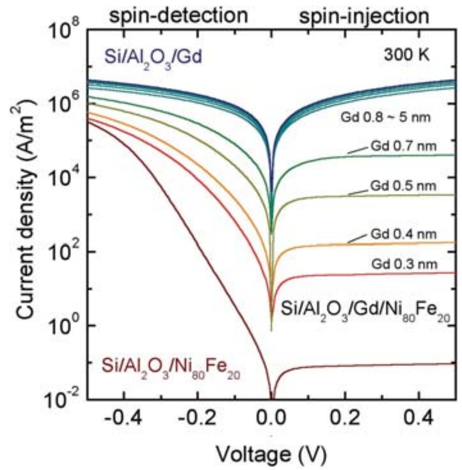

Fig. 1. Electrical I-V characteristics of silicon/Al2O3/Gd/Ni80Fe20 spin-tunnel contacts for different thickness of the low-work function Gd interlayer, as indicated. The Schottky diode behavior gradually disappears with increasing Gd thickness, and is fully suppressed for 0.8 nm of Gd, with a corresponding reduction of the RA product of the contacts by 8 orders of magnitude [3].

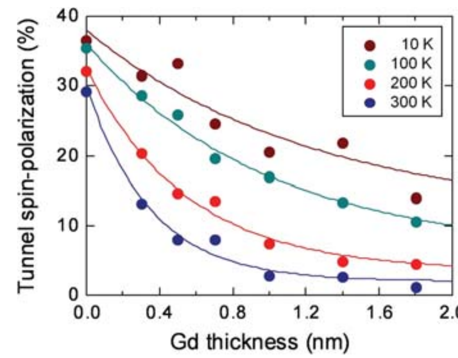

Fig. 2. Tunnel spin-polarization versus Gd thickness for Co/Al2O3/Gd/Ni80Fe20 magnetic tunnel junctions, measured at T = 10, 100, 200, and 300K [3].

HA-06

Spin Manipulation in Semiconductors and Metals.

H. Ohno
1. Laboratory for Nanoelectronics and Spintronics, Research Institute of Electrical Communication, Tohoku University, Sendai, Japan; 2. ERATO, JST, Sendai, Japan

Electrical manipulation of spins in semiconductors and metals is now an established branch of spintronics, through which we can learn about the origin of magnetism, electrically reverse the magnetization direction and generate microwave power. Here, I choose two topics that delineate the importance of such manipulation of spins in condensed matter. One is the domain wall manipulation by spin-polarized current in a ferromagnetic structure, which reveals rich physics involved in spin-transfer torque driven domain wall motion [1]. The other is the current-induced magnetization switching in magnetic tunnel junctions having a synthetic ferrimagnetic free layer [2]. The latter is one of the possibilities to satisfy both thermal stability and low threshold current density in current-induced switching. Finally, I will discuss about the future directions made possible by these developments.

This work was supported in part by the “Research and Development for Next-Generation Information Technology” program from the Ministry of Education, Culture, Sports, Science and Technology of Japan.

[1] M. Yamanouchi, J. Ieda, F. Matsukura, S. E. Barnes, S. Maekawa, and H. Ohno, Science, 317, 1726, 2007.

[2] J. Hayakawa, S. Ikeda, Y. M. Lee, R. Sasaki, T. Meguro, F. Matsukura, H. Takahashi, and H. Ohno, Jpn. J. Appl. Phys., 45, L1057, 2006.

HB-01

Micromagnetic Model Analysis of a Single-Pole-Type Head for 1 – 2 Tbit/in^2

Y. Kanai[1], K. Hirasawa[1], T. Tsukamoto[1], K. Yoshida[2], S. Greaves[3], H. Muraoka[3]

1. Niigata Institute of Technology, Kashiwazaki, Japan; 2. Kogakuin University, Tokyo, Japan; 3. Tohoku University, Sendai, Japan

<u>Introduction</u>

The single-pole-type (SPT) head is one of the most important components needed to achieve a high areal density in perpendicular magnetic recording system. The switching speed of the SPT head, as well as the write field amplitude, is critical for recording at high data rates, especially when writing on a bit-patterned medium (BPM) [1]. In this paper, SPT heads, having an air bearing surface (ABS) area of 25 nm × 25 nm, were investigated using a Landau-Lifshitz-Gilbert (LLG) micromagnetic analysis. The recording performance, which includes field strength, adjacent track erasure field, switching speed, was discussed for 1 – 2 Tbit/in^2.

<u>SPT head model</u>

We consider the SPT head model whose main pole tip was tapered both in down-track and cross-track directions, for which the width of the main pole at ABS was 25 nm and its length was 25 nm. The side and trailing shields were located 20 nm and 30 nm from the main pole, respectively. The ABS – soft underlayer (SUL) spacing was 25.5 nm. The entire recording system, comprising the SPT head and the double-layered medium, was treated micromagnetically using the finite-difference method with cubic cells of 5 nm, giving a total cell count exceeding ten million. The material characteristics: saturation magnetization M_s, anisotropy energy K_u, and exchange constant A, are; 1910 emn/cm^3, 3×10^4 erg/cm^3, and 1×10^{-6} erg/cm for the head; 955 emn/cm^3, 3×10^4 erg/cm^3, and 1×10^{-6} erg/cm for the soft underlayer. A Gilbert damping factor of 0.2 was used. The recording layer was assumed to be air and the recording field distributions were observed in a plane 16.5 nm from the ABS.

<u>Results and discussion</u>

In Fig. 1, the temporal head field variation is shown for the ultra-fast current rise time of 1 ps (Current-A), together with the response to current rise times of 0.2 ns (Current-B) and 0.4 ns (Current-C), where the current rise time is defined as the time for the current to switch from the negative peak (-100%) to the positive peak (+100%). The delay before the head field begins to switch (i.e. the head field is between -100% and -90% of its maximum value), called the non-response period hereafter, and the head field rise times (the time for the head field to change from -90% to +90% of its maximum value) are shown in Fig. 2 for various driving currents. It was found that the non-response period could be shortened by reducing the current rise time, however, the head field rise time never became small. In addition, we assumed another two types of driving current; Current-D: rise time of 0.4 ns with 100% overshoot; Current-E: rise time of 0.2 ns with 100% overshoot, showing that only fast switching current with overshoot (Current-E) was effective.

For the head structure, the head field rise time was 0.28 ns for unshielded head, it was also 0.28 ns for the un-tapered, unshielded head with an ABS of 100 nm × 180 nm. From these results, it can be said that the head field response would never be worse if the ABS area were reduced.

With regard to the write synchronization, increasing the write head rise time was confirmed to have an unfavorable effect on the write margin in which bits can be correctly written, and the write margin narrowed rapidly for rise times of more than 0.70 ns (-90% to +90%) [2]. This timing window is quite narrow compared to the calculated head field rise times and the non-response periods.

Finally, micromagnetic simulation of media magnetization indicated that the written tracks were very poor for unshieded head because of the low head field gradient, meaning side and trailing shields are indispensable even for BPM. For continuous media, 650 Gb/in^2 (70 nm track pitch x 1800 kfci) was obtained, however, media anisotropy energy of 3.6 erg/cm^3 was too low for long-term thermal stability. When BPM having long-term thermal stability was assumed, the obtained smallest bit cell without adjacent track erasure (ATE) was 30 nm x 15 nm, giving an areal density of 1.43 Tbit/in^2.

[1] Y. Kanai, K. Hirasawa, T. Tsukamoto, K. Yoshida, S. Greaves, and H. Muraoka, "Micromagnetic recording field analysis of a fast-switching single-pole-type head using a PC cluster system," PMRC2007, 16aB-04, Tokyo, Japan, Oct. 2007.

[2] N. Degawa, S. Greaves, H. Muraoka, and Y. Kanai, "Optimisation of bit Patterned media for 1 Tb/in^2," PMRC2007, 16pE-04, Tokyo, Japan, Oct. 2007.

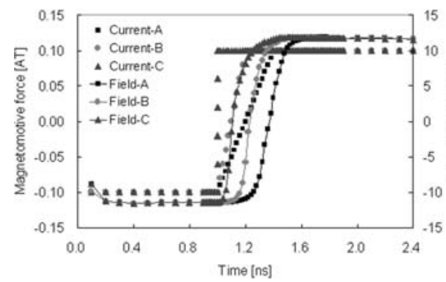

Fig. 1: The temporal head field variations for various driving currents.

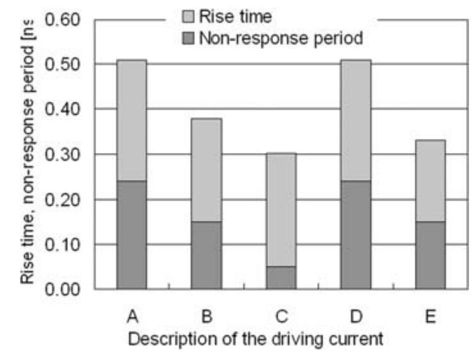

Fig. 2: The head field rise time (- 90 % to + 90 %) and non-response period: the delays before the head field begins to switch (-100 % to – 90 %).

HB-02

1 Turn Solenoid PMR Writer Design for High Frequency Writing.

E. Kim, K. Sunwoo
HDD Core Tech TF, Samsung Advenced Institute of Technology, Yongin, South Korea

Recently HDD adapted PMR mechanism and keep increasing the areal density. Further increase of recording density, especially the linear density requires high frequency data writing. But, current PMR write head shows switching delays at high frequency and the head field rising time becomes a critical factor in recording performances for current high frequency data rate[1]. Head inductance and eddy current loss are main reasons for this head response delay and these can be reduced by increasing the resistivity of pole materials or decreasing the yoke length[2]. But changing the resistivity also changes other magnetic properties of pole material, such as saturation magnetization and coercivity. So, the more effective way to reduce the head inductance and eddy current effect is to decrease the yoke length of head. We suggested the 1 turn solenoid coil PMR head structure with very short yoke length which is less than 2.0 um to improve the high frequency performances of head as shown in Fig 1. Because of this short yoke length, we can delete the sub yoke layer and this simple structure can reduce the number of masks and processes also. But, the static head field strength and field gradients are smaller than currents PMR write head of 10um yoke length with 3 coil turns because of reduced number of coil turns. So we do FEM simulation for our 1 turn solenoid head modeling with different main pole and return pole shape and thickness to improve write field strength and field gradients. Because of etching process, return yoke tip has wedged-type shape at gap area and we considered this real shape as shown in Fig 2. Increasing main pole thickness could increase the head field, but it also increases the skew effect and degrades the writing performance. So we kept the pole thickness at ABS constant and only increased at the region under coil as shown in Fig 3. The simulated perpendicular head field along down track direction. It shows that our optimized head design shows more than 20% increase of head field compared with original 1 turn solenoid coil head design and shows comparable static writability with current 3 turn solenoid coil head. We find that there are some critical current where the field strength become sensitive to main pole thickness, i.e. write head field strength doesn't changed with head design at 30mA current density, but it increased with increasing pole thickness over 40mA current density. Also simulated results show that our short yoke length head has more than 50% faster head field rising time than current PMR head as shown in Fig.5.
We suggested short yoke length 1 turn solenoid coil PMR head and simulation results show that our optimized head has comparable static performance with conventional head and better writability for high frequency. Also our simplified structure can reduce the making process.

[1] Kimio Nakamura et.al, IEEE Magnetics, vol.35, No.5, 2529 (1999)

[2] Y. Nonaka et. al, IEEE Magnetics,vol.36,No.5,2514(2000)

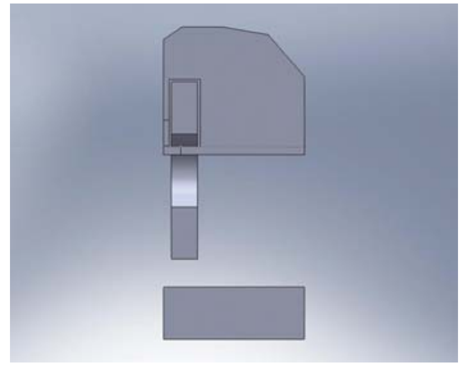

Schemetic diagram of 1 turn solenoid coil short yoke length head

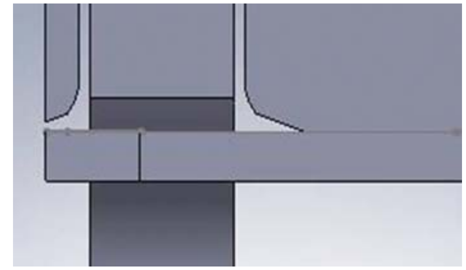

modeled wedged return yoke tip head shape.

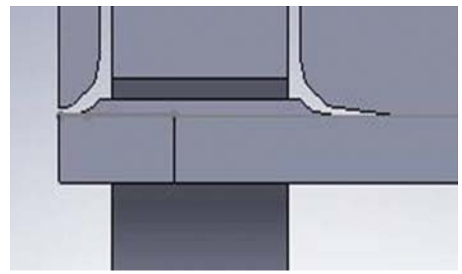

Modeled increase pole thickness under coil area and wedged pole and return yoke tip head shape

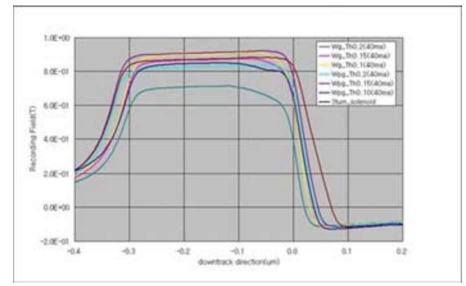

Simulated perpendicular head field along down track directino with different head shape

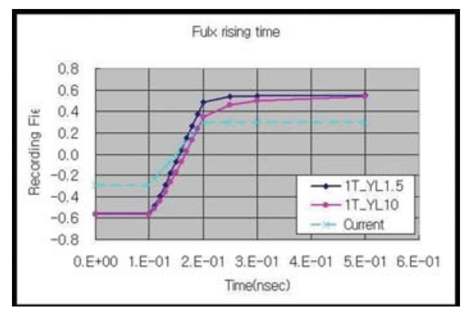

Simulated head field rising time with different yoke legnth

HB-03

Advanced heads for areal desnity at 500Gb/in2 and towards 1Tb/in2.

M. Ho, S. Mao, S. Li, L. Zhong, E. Champion, S. Song, J. Wang, T. Pan, K. Stoev, C. Macchioni, Y. Chen, L. Wang, Q. Leng, M. Pakala, Y. Li, U. Tran, M. Chapline, W. Yu, L. Hong, D. Li, Y. Shen
Western Digital Corp, Fremont, CA

As areal densities of commercial magnetic recording progress beyond 300Gb/in2[1], the advantages of combining high sensitivity TuMR read head[2] and high writability PMR write head[3] becomes increasingly significant. In this regard, these two head technology breakthroughs are the key enablers to keep the current annual compound growth rate of areal density at 40% in the HDD industry.
Regarding to readers, the achievements of high dR/R(80-200%) and low RA(1-3 ohm*um2) has made TuMR the choice of read head material for high areal density recording applications at 1Tb/in2[4]. Furthermore, the CPP configuration of TuMR reader exhibit two additional advantages over conventional CIP reader configuration. The first is better linear resolution from read gaps that could be made as thin as the sensor stack. The second is reduced side-reading from more planar top shield geometry due to the absence of conductor leads at track-edges.
Regarding to writers, the combination of the perpendicular writer and the soft-underlayer provides much larger writability, sharper field gradient and lesser side-reading over conventional longitudinal writing. The drastic improvement of both writability and field gradient allows us to develop a higher coercivity disk; therefore it opens up the possibility for more aggressive magnetic grain size reduction in order to achieve higher areal density and lower disk noise without sacrificing thermal stability.
In this work, we first discuss the challenges of integrating high sensitivity TuMR reader and perpendicular writer. We explore its potentials and push the design limitations on continuous media. Then we will present the design and magnetic recording performance of integrated recording heads at high areal densities.
The read sensor comprised a bottom TuMR film with a synthetic reference layer and a synthetic free layer yielding a dR/R up to 160% and a low RA down to 1.5ohm*um2. Track widths as narrow as 40nm were defined using optical lithography(Fig. 1). Magnetic stabilization was achieved by an insulated abutted-junction with CoPt-alloy hard magnets adjacent to the sensor track-edges. A narrow read gap of around 32 nm was achieved. After wafer fabrication, the read heads were lapped to stripe heights of 60-100 nm.
To achieve high areal density, various writer designs have been explored. We found that the trailing shield design provides high write field and field gradient. It also imposes less process requirement. The fabrication process and sigma control is one generation down when compared to other exotic writer schemes. The achievable higher write field and field gradient was further utilized to improve head&media matching, namely reduction of magnetic grain size in disks. Write gaps as small as 20nm and physical pole widths as small as 65nm were fabricated. After lapping, the write heads have nose lengths of 40 – 120 nm.
Parametric recording study of these TuMR perpendicular heads was performed on low noise perpendicular media with an areal moment of 0.6-0.7 memu/cm2. Results indeed showed the write heads have strong write field yielding 35 to 45 dB reverse overwrite at narrow magnetic write widths of 85 – 115 nm. In addition, the read heads also showed large signal amplitude exhibiting high non-disk signal-to-noise ratios of around 24-28 dB over a wide bandwidth of 280MHz. Regarding to track resolution, microtrack profile showed magnetic read widths as narrow as 40 nm were achieved. Regarding to linear resolution, T50 widths as low as 18 nm were achieved due to the narrow read gap as well as the sharp write field gradient. Moreover, our integrated heads showed on track error rate of 10-5 at a linear density 1420 kbpi (Fig. 2). In conclusion, all the above results indeed indicated that our recording heads have the capability to achieve areal densities above 500Gb/in2.

References:

[1] S. Mao et al, "Commercial TMR heads for hard disk drives: Characterization and extendibility at 300 Gbit/in2", IEEE Tran. Magn., 42, 97-102, (2006).

[2] M. Ho et al, "TMR read heads for areal density perpendicular recording", TMRC 2006.

[3] M. Mallary et al, "One Terabit per square inch perpendicular recording conceptual design", IEEE Tran. Magn., 38, 1719-1724, (2002).

[4] S. Mao et al, "Design and Challenges for 1Tbit/in2 Reader", PMRC 2007 (2007).

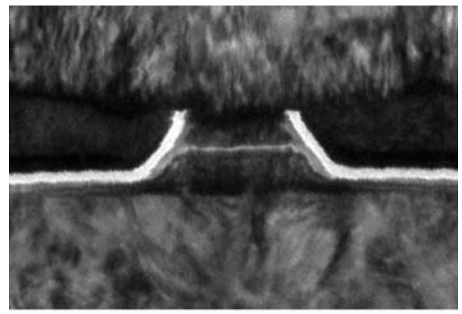

Figure 1. ABS view of TuMR read head showing a track width of 40nm and a read gap of 32nm

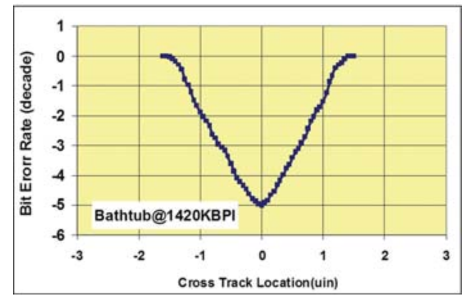

Figure 2. Bathtub curve showing an on-track error rate below 10-5 at linear denisty of 1420kbpi

HB-04

Writing performance of a planar single-pole head with a main pole fabricated by ion beam milling.

Y. Ohsawa[1,2], K. Yamakawa[2], H. Muraoka[2]
1. CR&D center, Toshiba Corp., Kawasaki, Japan; 2. RIEC, Tohoku Univ., Sendai, Japan

Introduction
Continuing growth of recording density will require using media with increasing anisotropy energy to maintain thermal stability of recorded signals. To meet this requirement, the write heads have to produce a large field in spite of extremely narrow track width of the main pole (MP). Since saturation magnetization of the main-pole material has reached to the practical maximum of 2.45T, design of pole tip structure to increase head field becomes more important. The tapered structure of the main pole was shown to exhibit higher head field than a conventional pole structure [1]. We proposed the shielded planar single-pole-head [2] where the multi-charged-surface MP [3] combined with a shield was employed. From the recording simulation this head revealed to have a potential for achieving recording densities of more than 1 Tbit/in2 [4], and a moderate taper angle between 35 and 55 degrees seems to be practical in terms of avoiding adjacent track erasure [5]. However the main pole fabrication process using plating in the etch-pit on the Silicon template is complex and challenging that ordinary process, e.g., ion beam milling is preferable for fabrication, which has being few reports. In this work, a sufficient head field of 15 kOe and a very steep field gradient of 500 Oe/nm are demonstrated with a 20nm-trackwidth MP.
Main pole taper profile
A trace image of a main pole that fabricated by ion-beam etching taken from the cross-sectional transmitting electron microscopy (TEM) is shown in Fig. 1. The trace is a typical one by the ion milling among many profiles of the main pole tip that can be obtained with variation of mask and beam conditions. This typical profile can be characterized as a two-step-tapered structure in which outer portion (far from mask edge) of the etched area shows gradual taper profile.
Writing Performance
Perpendicular field as a function of down track position estimated from a 20nm-trackwidth MP profiles by the ion milling (refer to Fig. 1) and template [2] process is shown in Fig. 2. The inset shows the MP and shield structure. The MP is composed of a two-step-tapered structure with the inner (shown as angle ‘A’) and the outer (shown as angle ‘B’) tapers. The MP fabricated by ion milling or by template process is designed to have the inner (A) /outer (B) taper angles of 55 / 15 or 55 / 0 degrees, respectively. Regardless with the angle combination, maximum value of a set of the field strength and the gradient of about 15 kOe and 500 Oe/nm, respectively, which are capable for Tbpsi recording with a bit patterned media (BPM) [4] was obtained. Furthermore, tail part of the profile along the cross-track direction was suppressed considerably with outer taper angle (B) of 15 degree compared with that of 0 degree. The main reason of the suppression is due to the MP configuration with gradual outer taper which is character of ion milling process. This leads to have wider margin for MP and shield design in a planar head.
Conclusions
Writing potential of a shielded planar head with an ion milling processed MP was estimated. Magnetic field simulation revealed that the ion milling processed MP has enough writing potential in both field strength (15kOe) and field gradient (500 Oe/nm) for the Tbpsi recording. Furthermore, better characteristic in side writing performance compared with that of template method is clarified. The shielded planar head with the ion milling processed MP is one of the strong candidates as a writer in the Tbpsi recording age. This work was supported in part by Research and Development for Next-Generation Information Technology of MEXT.

1) M. Mochizuki, Y. Nishida, Y. Kawato, T. Okada, T. Kawabe, and H. Takano, “Study on the write-field profile and intensity of narrow-track-width SPT head,” J. Magn. Magn. Mat., 235, 191-195, (2001).

2) K. Ise, S. Takahashi, K. Yamakawa, and N. Honda, “New Shielded Single-Pole Head with Planar Structure,” IEEE Trans. Magn., 42, 2422-2424, (2006).

3) S. Takahashi, K. Yamakawa, and K. Ouchi, “Single-pole type head with multicharged surfaces for ultrahigh density recording,” J. Appl. Phys., 91, 6839-6841, (2002).

4) N. Honda, K. Yamakawa, and K. Ouchi, “Recording Simulation of Patterned Media Toward 2 Tb/in2,” IEEE Trans. Magn., 43, 2142-2144, (2007).

5) K. Yamakawa, K. Ise, S. Takahashi, N. Honda, and K. Ouchi, “Shielded Planar Write Head,” Digest of PMRC 2007, 15pA-03, 20-21, (2007)

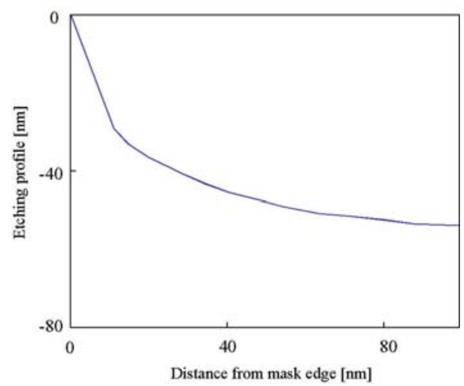

Main pole taper profile fabricated by ion milling process

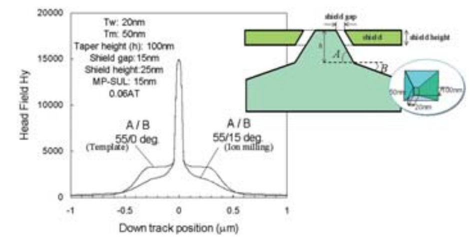

Perpendicular field strength as a function of the down track position.

HB-05

Thin film processing realities for Tbit/in^2 recording.

R. Fontana[1], N. Robertson[1], S. Hetzler[2]
1. Hitachi GST, San Jose, CA; 2. IBM Research Division, San Jose, CA

Magnetic recording has maintained a cost/bit advantage over solid state storage by using a single transducer to assemble bits with sub-lithographic dimensions on an unpatterned substrate. In particular, the bit cell length is a sub lithographic dimension determined by the distance the disk rotates during the time interval between current pulses applied to the write yoke. This paper explores the ability of magnetic recording to maintain this advantage by examining the process challenges associated with the fabrication of head structures at 1 Tbit/in^2 . Today, magnetic disc products have areal densities of 200 Gbit/in^2, a bit cell size of 150 nm x 20 nm formed with a minimum feature, F =75 nm, for the MR sensor. This feature is 35% larger than the present IC critical feature, F = 55 nm, for NAND equal line and space dimensions. Using the NAND minimum feature, today's recording bit has a cell size of 2.70F x 0.36F and an area of 0.98F^2. In comparison, the competing NAND cell, two bits per cell, has an area of 3F^2.

Assuming annual areal density growth rates of 40%, in 2012 the manufacture of 1 Tbit/in^2 recording heads will require processing of structures with minimum features in the 25 nm range. Table I lists the design points of three 1 Tbit/in^2 head proposals by Wood [1], Mallory [2], and Kryder [3] where the physical sensor and pole tip widths are estimated using processing assumptions from Fontana and Hetzler [4]. Figure 1 shows the geometries of a perpendicular head structure appropriate for Table I. Figure 2 shows the most recent semiconductor ITRS lithography projections [5]. In 2012 these data project the 3σ control of critical dimensions (12% of DRAM half pitch) as 3.8 nm, the 3σ control of overlay (20% of DRAM half pitch) as 7 nm, and the minimum dimension for fabricating isolated MR sensors (microprocessor MP gate resist) as 24 nm. These values suggest that in the 2012 time frame 24 nm MR sensor widths can be fabricated. However, achieving flare lengths of 20 nm is questionable since the flare length is determined by at least five process actions: overlay of the MR sensor to a reference point (3σol), overlay of the flare to the same reference point (3σol), dimension control of the back edge of the sensor (0.5 x 3σcd), dimension control of the x and y dimensions of the flare structure (3σcd), and the lapping tolerance for the final sensor height (3σcd). For this paper, the 3σ lapping tolerance is assumed equivalent to the dimension control of the sensor width, i.e. 12%, so that the variation of the area of the sensor is less than 25%. These tolerances produce a flare height variation of +/- 12 nm or +/- 60% for a 20 nm target.

Several implications result for 1 Tbit/in^2 head design points. Critical head dimensions will require smaller features than NAND flash. Control of yoke length will be limited by overlay. Most critically, 1 Tbit/in^2 head structures will require state of the art lithography equipment rather than tooling that lags the ITRS roadmap by 2-3 years as is the case today. In addition to these issues, the process implications of moving minimum feature processing from the head to the disk will also be discussed in the paper.

1.Wood et. al. Recording Technologies for Terabit per Square Inch Systems, IEEE Transactions on Magnetics, Vol. 38, No. 4, July, 2002, pp 1711-1718

2.Mallory et. al. One Terabit per Square Inch Perpendicular Recording Conceptual Design. IEEE Transactions on Magnetics, Vol. 38, No. 4, July, 2002, pp 1719-1724

3.Kryder et. a1. High density perpendicular recording – advances, issues, and extensibility, Journal of Magnetism and Magnetic Materials, 287, 2005, pp. 449-458

4.R. Fontana, S. Hetzler, "Magnetic memory devices: minimum feature and memory hierarchy discussion", Journal of Appl. Physics, Vol. 99, No. 8, Part III, pp. 08N901-1 – 08N901-6, April 2006

5.2007 ITRS Lithographic Projections, www.itrs.org.

Parameter	Wood	Mallory	Kryder
Density (Gbit/in^2)	1000	1000	1000
BAR (Bit Aspect Ratio)	3.43	6.92	5.76
KTPI (K Tracks /Inch)	540	380	417
KBPI (K Bits / Inch)	1850	2630	2400
MR Physical width (nm)	24	33	31
Yoke Physical width (nm)	39	53	50
Yoke Flare Length (nm)	20	20	20
Track Pitch (nm)	47	67	62
Bit Pitch (nm)	14	10	11
Read Gap (nm)	28	20	22

Table I. 1 Tbit/in^2 Design Points

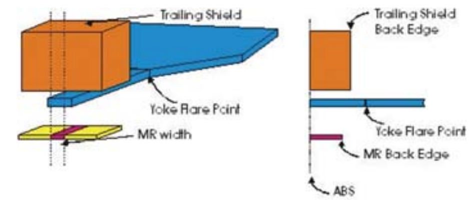

Figure 1. Generic Perpendicular Head Geometry

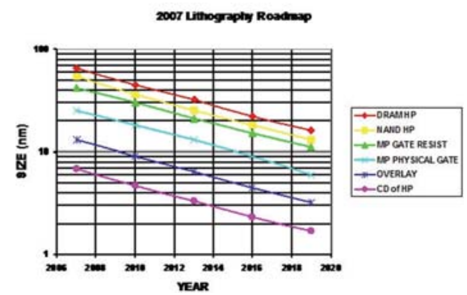

Fig 2. ITRS Lithography Projections

HB-06

Exchange Coupling in Synthetic Antiferromagnetic Multilayers for Write Head.

Y. Xu[1], H. Jiang[2], K. Sin[2], Y. Chen[2], J. Wang[1]
1. Dept. of Electrical and Computer Engineering, University of Minnesota, Minneapolis, MN; 2. Western Digital Corporation, Fremont, CA

I. INTRODUCTION
Since the discovery of long range oscillatory indirect magnetic exchanging coupling in ferromagnetic/non-magnetic/ferromagnetic (FM) sandwich structures [1], many important aspects have been understood and applications have been realized. The examples include early giant magnetoresistance (GMR) sensors [2] and synthetic antiferromagnetic (SAF) multilayers [3] as soft underlayer (SUL) in perpendicular recording. The exchange coupling between the FM layers depends on the thickness of the non-magnetic layer and is very sensitive to the structure defects and interface quality. This effect offers us an extra path to control the effective anisotropy of the layers as well as the magnetic configuration and switching sequence of the whole structure.
Soft magnetic films in write head are required to have well-defined in-plane anisotropy with proper magnitude to enable the usage of them in in-plane hard axis direction, in addition to the requirements of high saturation magnetization (Ms), low remanent magnetization (Mr) and low coercivity field (Hc). In this report, we demonstrate that the SAF multilayers with three layers of FM layers and two non-magnetic layers provides the control of effective anisotropy and switching sequence of each layer through the exchange coupling, which shows discrete steps of magnetization in the easy axis (E.A.) hysteresis loop. It is now possible to use the SAF multilayers in their E.A. direction and have a step function-like operation in write head. Bilinear and biquadratic exchange coupling constants [4, 5] were extracted from the measurements and compared..
II. EXPERIMENT
The SAF multilayers were deposited by sputtering. The film structure is shown in Fig. 1, which consist three ferromagnetic layers (M1, M2, and M3) separated by two Ru layers. The ferromagnetic material is FeCoN. M2 is twice as thick as M1 and M3. Two different underlayers (UL1 and UL2) were used to induce different interface roughness in the structure. Magnetic properties were measured by vibrating sample magnetometer (VSM).
III. RESULTS AND DISCUSSION
The hysteresis loops of SAF multilayers are shown in Fig. 2, A, B and E. Calculation of hysteresis loops assumed coherent rotation in three coupled single magnetic single domain thin films and were obtained by minimizing the energy per unit area (Fig. 3),where d_1, d_2 and d_3 are thickness of each FeCoN layer, θ1, θ2, and θ3 are angles between magnetization of FeCoN and its E.A., ϕ is the angle between the applied field and E.A. (Fig. 1B), J_{12} and J_{23} are the bilinear exchange coupling constants between M1 and M2, and M2 and M3, respectively. Jq_{12} and Jq_{23} are the biquadratic exchange coupling constants of these layers. The E.A. of the three FM layers were assumed to be aligned. By fitting the measured hysteresis, J and Jq were extracted and listed in Table 1. The different interface roughness induced by different ULs affects the both bilinear and biquadratic exchange coupling, though the bilinear exchange couplings are impacted more severely. Larger roughness at the interface corresponds to decreased exchange coupling.

1) Phys. Rev. Lett. 64, 2304 (1990).
2) Phys. Rev. Lett. 61, 2472 (1988).
3) Phys. Rev. Lett. 57, 2442 (1986).
4) IEEE Trans. Magn. 41, 3151 (2005).
5) Phys. Rev. B 58, 101 (1998).

	J12 (erg/cm2)	J23 (erg/cm2)	Jq12 (erg/cm2)	Jq23 (erg/cm2)
UL1	1.18	0.55	0.43	0.19
UL2	0.55	0.05	0.35	0.35

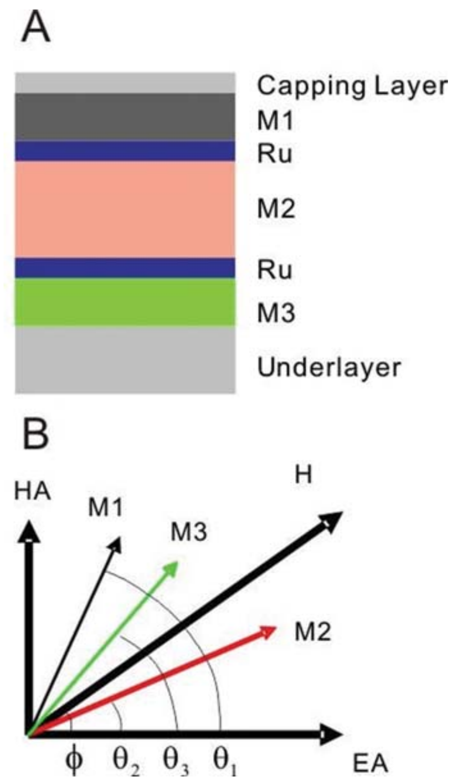

Fig. 1 (A) The layer structures the synthetic antiferromagnetic multilayers. M1, M2, and M3 stand for ferromagnetic layer 1, 2, and 3, respectively. (B) The schematic diagram of the angles between applied field, moment of each ferromagnetic layers and the easy axis.

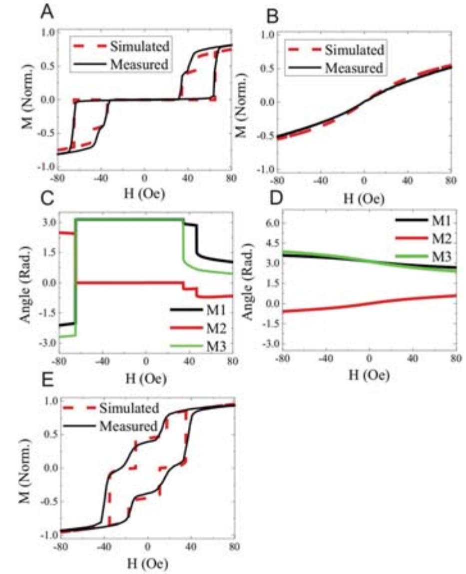

Fig. 2 (A) and (B) Measured and calculated easy axis and hard axis hysteresis loops of sample with UL1. (C) and (D) Calculated angles between each ferromagnetic layer and easy axis of the films vs. applied field. H is along EA in (C) and HA in (D). (E) Measured and calculated EA hysteresis loops of sample with UL2.

$$E = K(d_1 \sin^2\theta_1 + d_2 \sin^2\theta_2 + d_3 \sin^2\theta_3) - MH(d_1 \cos(\theta_1 - \phi) + d_2 \cos(\theta_2 - \phi) + d_3 \cos(\theta_3 - \phi)) + J_{12} \cos(\theta_1 - \theta_2) + J_{23} \cos(\theta_2 - \theta_3) + Jq_{12} \cos^2(\theta_1 - \theta_2) + Jq_{23} \cos^2(\theta_2 - \theta_3)$$

Fig. 3

HB-07

Laminated high moment FeCo films for perpendicular magnetic recording.

B. Ocker, K. Schuller, J. Wrona, J. Langer, W. Maass
Singulus Nano Deposition Technologies GmbH, Kahl am Main, Germany

Since several years high moment FeCo compositions are of great interest for writing head applications in the magnetic recording industry. With the implementation of the perpendicular magnetic recording new challenges at the material properties came up. Sputter deposited high B_s materials offer more flexibility in optimizing magnetic film properties in order to achieve desired writer performance [1], [2]. Laminations of these films offers an additional wide range for optimization [3]. We investigated single $Fe_{70}Co_{30}$ films and laminated films with magnetic and nonmagnetic spacers. The magnetic alignment of these films is strongly influenced by the direction of the material flow during the deposition process. The linear dynamic DC magnetron sputter process provides films with a very good uniformity of the magnetic properties across the wafer and in particular a nearly perfect anisotropy with an excellent alignment of the easy axis. The remanence in the hard axis direction is lower than 4% for the single films and has been improved by the laminations to better than 1 %. The magnetic moment of the single $Fe_{70}Co_{30}$ films were > 2.4 T.

[1] H. Jiang, K.Sin, Y. Chen, “High Moment Soft FeCoN/NiFe Laminated Thin Films”, IEEE Trans. Magn., vol. 41, no 10, pp. 2896-2898, Oct. 2005

[2] Y. Chen, K. Sin, H. Jiang, Y. Tang, K. Sasaki, A. Torabi, L. Wang, M. Park, D. Bai, Y. Shen, P. Luo, F. Liu, K. Stoev, W. Lin, and J. Zhu, “High Moment Materials and Fabrication Processes for Shielded Perpendicular Write Head Beyond 200 Gb/in^2”, IEEE Trans. Magn., vol. 43, no 2, pp. 609-614, Feb. 2007

[3] Y. Okada, H. Hoshiya, T. Okada, and M. Fuyama, “Magnetic properties of FeCo multilayered films for single pole heads”, IEEE Trans. Magn., pt. 2, vol. 40, no. 4, pp. 2368-2370, Jul. 2004

HB-08

Comparison of Electrical and Magnetic Flux Rise Times in Tape Heads Using Impedance Measurements and High Speed Kerr Magnetometry.

A. Kaya[1,3], *J. A. Bain*[1], J. P. Nibarger[2], K. D. McKinstry[2]
1. Carnegie Mellon University, Pittsburgh, PA; 2. Sun Microsystems, Louisville, CO; 3. Hitachi Global Storage, San Jose, CA

Increasing frequency requirements in modern tape heads requires detailed knowledge of the relationship between input current and flux rise time. To further this understanding we have performed high frequency impedance measurements, time domain reflectometry, and high speed Kerr magnetometry of the pole tips of a commercial tape head. The results of these studies are combined with a complete electrical model of the head which reproduces all of the observed measurements in the low drive current regime.
Head measurements were performed at the chip level in order to minimize interconnect effects. Head inductance, at drive levels below saturation, was measured to be 50 nH, in series with 18 Ohms of resistance and in parallel with 1.3 pF of capacitance. The flux rise time at the pole tips as a function of drive current is shown in Figure 1. It should be noted that when the head is driven into saturation clipping effects create substantial improvements in rise time, decreasing the 10-90% rise time to 1.05 ns, as has been shown previously in disk heads.
A simulation of the current in the head is shown in Figure 2. The model results indicate that the current rise time of the inductor is 2.1 ns when driven with a 50 Ohm transmission line, in agreement with the observed flux rise time at the pole tips at low drive current. This agreement between flux rise time and calculated current rise time indicates that little phase lag occurs between current and flux in the pole tips at these frequencies (> 500 MHz).
An important consequence of these observations is that eddy currents are much less active in the pole materials than would be suggested by their sheet film properties. The pole material in these heads has a thickness of 4 microns, a sheet film relative permeability of 800, and an electrical resistivity of 100 micro-Ohm-cm. These numbers suggest eddy currents should create significant phase lag between flux and current at 80 MHz (i.e. skin depth = thickness/2). The lack of phase lag between magnetic response and current for a 2 ns rise time indicates that the skin depth must be greater than 2 microns at a frequency of 500 MHz.
This increase in eddy current frequency can only be explained by a decrease in relative permeability of the head poles to approximately 100. Internal demagnetizing fields within the heads cause this permeability reduction and permit the higher frequency performance. This work therefore indicates that for quantitative design of heads for high frequency, pole geometry is critical for determining frequency response of the complete head, and a significant increase in head frequency response can be possible if demagnetizing fields are present.

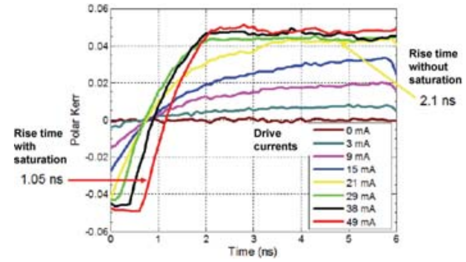

Figure 1: Measured flux rise time as determined by high speed kerr microscopy at the pole tips of the head under various levels of drive current.

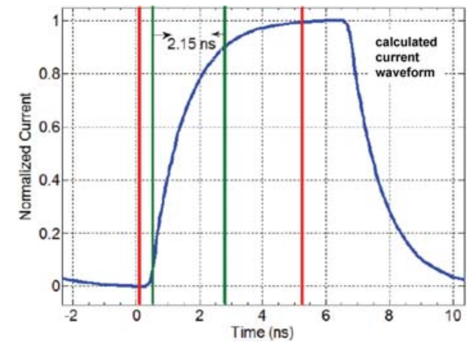

Figure 2: Calculated current rise time on the coil of the head, when a perfect voltage step is delivered to the head by a 50 Ohm transmission line.

HB-09

Crosstalk between write transducers.

P. Herget, *R. G. Biskeborn*
IBM Corporation, San Jose, CA

A trend for improving performance in tape recording systems has been the miniaturization of head magnetic transducers and arrays. Smaller transducers enable packing more into a given span in the head, and this in turn enables higher data rate. A smaller span enables higher areal densities by reducing sensitivity to miss-tracking caused by changes in tape dimensions. However, it is well known that writers brought very close together can interact with one another [1]. When this happens, current in one writer alters the signals written to tape by the nearest neighbors. This paper discusses this phenomenon using modern recording heads.
<P>
Experiments were conducted on heads built using HDD wafer processing. Accordingly, the write transducers studied have high moment iron alloy cores and conventional pancake coils, and the separation between the writers was limited by the coil dimensions. In the tests, an isolated pulse waveform is applied to one transducer, while DC current is applied to its adjacent neighbors. The signals recorded on both sets of written tracks are read back. A weak remnant of the isolated pulse pattern is observed in the DC written tracks over a narrow range of DC current. Coupling in the writer leads was ruled out, as observations with widely spaced heads having identical cabling showed no such signals. On the AC driven tracks, the recorded isolated pulses have a normal shape, but close inspection shows that their timing is slightly off.
<P>
In the absence of DC current, the distance between adjacent positive and negative peaks is precisely half the period. When DC current is applied to the nearest adjacent writers, the positive and negative peaks shift in opposite directions. The positive and negative peaks are found to shift by the same amount. This is shown schematically in Fig. 1.
<P>
The measured dependence of the single pulse transition shift on DC current is shown in Fig. 2. The data include shifts that are longer than the rise time for current in a modern head (1-2 nanoseconds). This suggests that the field created by the DC currents in the neighbors modulates the center transducer 'write bubble' field [2], thus producing a physical shift in the transition locations on tape. The shift directions depend on the relative current polarities, while their magnitude is a measure of the coupling strength. When the applied DC currents in the two neighbors are in opposite directions, the shift vanishes.
<P>
The optimal operating current for the head and tape combination used for these data is approximately 20 milliamperes, which is typical for present day tape recording devices. At the experimental tape speed of 3 meters/s, the transition displacement on tape is approximately 6 nanometers. This is related to transducer design specifics, as well as to writer-to-writer spacing in the head. As that spacing is increased, the magnetic flux coupling between writers and the transition shift diminishes. No effect is observed for heads built on the industry standard pitch of 166.5 micrometers.

[1] K. Tanaka, *IEEE Trans. Mag.*, v. MAG-20, n. 1, p 160, 1984

[2] J. C. Mallinson, *The Foundations of Magnetic Recording*, Second Edition, Academic Press, Inc., pp. 49-52, 1987

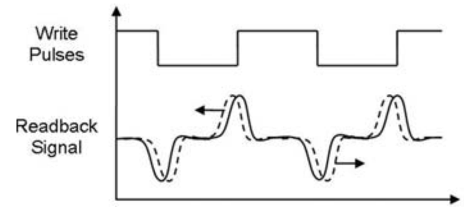

Figure 1: Transition shifts due to DC current in neighboring tracks.

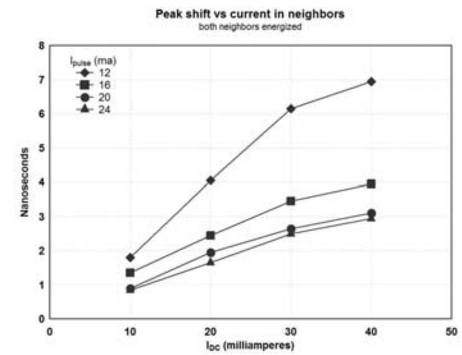

Figure 2: Transition shift as a function of DC current.

HC-01

Dynamic interaction between vortices, antivortices and holes in domain walls investigated by means of time resolved Photoemission Electron Microscopy (PEEM).

K. Kuepper[1], S. Wintz[1], M. Buess[2], J. Raabe[2], C. Quitmann[2], J. Fassbender[1]
1. Ion Beam Physics and Materials Research, FZ Dresden-Rossendorf e. V., Dresden, Germany;
2. Swiss Light Source, Paul Scherrer Institut, Villigen, Switzerland

In this work we study the interaction of vortex cores with either holes in domain walls of Landau structures or other vortices and antivortices, which are also interconnected through the adjacent domain walls of a single cross-tie structure.
During the last few years the investigation of magnetic vortices and their dynamic properties has attracted great attention due to the fundamental interest in the physics of solitons and since they might be used as non volatile memory devices in future applications, e. g. [1,2]. One striking feature of magnetic vortices is that the cores are attracted and can be trapped by artificial defects. If more than one of such defects are created a switching between different vortex core trapped states, which might serve as discrete levels in a multivalent memory device, can be achieved. We report the imaging of the magnetic excitation spectrum in presence of holes, fabricated by focused ion beam milling, in the magnetic domains and domain walls of Landau structures by means of x-ray magnetic circular dichroism photoemission electron microscopy (XMCD-PEEM). The vortex core in the center of the structure is not modified by ions, here we investigate the interaction of unmodified vortex cores with holes far away (> 1 Mikrometer) in the domain walls and the domains of Landau structures. Due to the very high lateral and temporal resolution the magnetization dynamics and the corresponding Eigen modes (Fig. 1), which are characteristic for the vortex-hole interaction, are investigated in detail [3]. Analyzing the vortex movement unravels an acceleration of the vortex gyrotropic mode if holes are present in the middle of domain walls. The presence of holes in the middle of domains has no significant influence on the vortex speed. The experimental results are compared to micromagnetic simulations.
Another fascinating property of micromagnetism comes from the possibility to control the domain and vortex configuration through the sample shape and size. For instance, in a rectangular platelet a configuration containing a stable combination of two vortices and an antivortex can be created. Such a single cross-tie wall can be understood as being a coupled micromagnetic system with three static solitons. Here we report on its magnetization dynamics including the vortex-antivortex interactions [4]. The spectrum of eigenmodes is investigated as well as the effect of different vortex core orientations. These are important for the magnetization dynamics because they determine the sense of rotation for the gyrotropic motion. Since three cores are present in total 2^3 = 8 configurations are possible. In Fig. 2 a) micromagnetic simulations of the vortex (left, right) and antivortex displacements upon field pulse excitation are shown for the first 16 ns. It is clearly observed that different types of configurations lead to completely different dynamic behaviors. The origin is the dynamic coupling of the cores which is mediated by the exchange coupling through the adjacent domain walls. This coupling is significant and introduces unexpected effects, such as the quenching of gyrotropic motion for the antivortex in certain core configurations. Another consequence is the absence of simple eigen modes describing the vortex gyration. The experimental investigation of the vortex core dynamics allows to determine the actual core configuration although the lateral core size is below the spatial resolution of the photoemission microscope. This is done by comparing the experimentally determined core displacements with the micromagnetically simulated ones as shown in Fig. 2 b).

References:

[1] S. B. Choe et al., Science 304, 420 (2004), J. Raabe et al., Phys. Rev. Lett. 94, 217204 (2005).

[2] B. van Waeyenberge et al., Nature 444, 461 (2006)

[3] K. Kuepper et al., manuscript in preparation.

[4] K. Kuepper et al., Phys. Rev. Lett. 99, 167202 (2007)

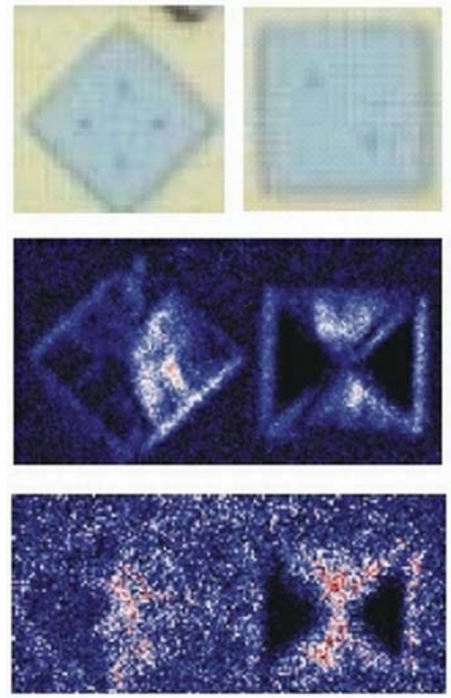

Fig. 1: Upper panel: Light microscopic image of two samples comprising holes in the domain walls. Lower panels: Fourier images, extracted from the corresponding time resolved PEEM series at 0.7 GHz and 2.2 GHz, respectively.

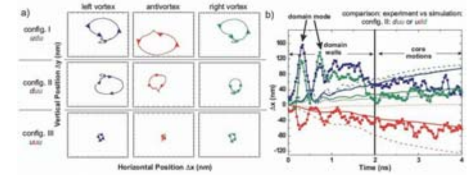

Fig. 2: a) Simulated vortex/antivortex trajectories of the three possible vortex/anti-vortex core configurations. b) Comparison with the horizontal component of the experimental data.

HC-02

Current-induced resonant motion of the magnetic vortex core in a ferromagnetic circular disk.

S. Kasai[1], F. Peter[2], M. Im[2], K. Yamada[1], Y. Nakatani[3], K. Kobayashi[1], H. Kohno[4], T. Ono[1]
1. Institute for Chemical Research, Kyoto University, Uji, Japan; 2. Center for X-Ray Optics, Lauence Berkeley National Lab, Berkeley, CA; 3. Department of Computer Science, University of Electro-communications, Chofu, Japan; 4. Graduate School of Engineering Science, Osaka University, Toyonaka, Japan

The concept of controlling magnetization on the nanoscale ferromagnetic structures by spin-polarized currents has constructed a new category in the field of the spin-tronics. The current-driven magnetic domain wall (DW) motion [1-4] in ferromagnetic nano-wires has been considered as one of the most promising candidates for realizing new spin-tronics devices, such as the magnetic race-track memory [5]. The underlying physics of the current-driven DW motion is the so-called spin transfer torque, described as an interaction between spin-polarized conduction electrons and local magnetic moments. However, the current-driven DW motion is affected by many manifold contributions such as increase of the joule heating, effect of edge roughness, deformation of domain wall structures, non-adiabatic current effect, and stochastic character. Fundamental understandings about the spin transfer effect on the magnetic domain structures are still required.
The current-induced resonant excitation of the magnetic vortex [6,7] is a promising path to study the spin-transfer torque[8-9]. The magnetic vortex core confined in a ferromagnetic circular disk has a characteristic excitation called translational mode that corresponds to the circular motion of the vortex core. The motion can be resonantly excited around the dot center using an ac current, and the radius of this circular motion is proportional to the excitation current density. The advantage of this system is free from the manifold contributions described above. Thus, exploring the magnetic vortex dynamics upon excitation by spin-polarized currents is a promising path to understand in general the impact of current effects on the dynamics of non-collinear spin structures on the nanoscale including the current-driven DW motion.
In this presentation, we will talk about the time-resolved soft X-ray microscopy with < 70 ps time resolution [10] used to image the dynamics of the magnetic vortex translational motion excited by an ac current. The sample was prepared on the 200 nm thick Si3N4 membrane substrate. The diameter and thickness of the permalloy disk were 1.5 μm and 40 nm, respectively. To achieve the time-resolved measurement by the pump-probe method, the phase of the excitation current should be synclonized with timing of the X-Ray pulse. Thereby, a pulse modulated ac voltage of 100 ns in duration was applied to excite the motion of the magnetic vortex core. Excitation frequencies were varied from 150 MHz to 250 MHz.
The motion of the vortex core was found for the excitation frequency (f) of 210 MHz $<f<$ 230 MHz which is close to the resonant frequency (218 MHz) estimated from the Landau-Lifschitz-Gilbert equation. This is direct evidence of the current-induced magnetic vortex translational motion. Detailed analysis with the micromagnetic simulation enables us to estimate the spin polarization of the conduction electron to be ~0.6.

[1] A. Yamaguchi, T. Ono, S. Nasu, K. Miyake, K. Mibu, and T. Shinjo, Phys. Rev. Lett. 92, 077205 (2004).

[2] N. Vernier, D. Allwood, D. Atkinson, M. Cooke and R. Cowburn, Europhys. Lett. 65, 526 (2004).

[3] M. Yamanouchi, D. Chiba, F. Matsukura, and H. Ohno, Nature (London) 428, 539 (2004).

[4] M. Hayashi *et al*., Phys. Rev. Lett. 96, 197207 (2006).

[5] S. S. P. Parkin, US Patent 309,6,834,005 (2004).

[6] T. Shinjo, T. Okuno, R. Hassdorf, K. Shigeto, and T. Ono, Science 289, 930 (2000).

[7] A. Wachowiak, J. Wiebe, M. Bode, O. Pietzsch, M. Morgenstern, R. Wiesendanger, Science 298, 577 (2002).

[8] S. Kasai, Y. Nakatani, K.. Kobayashi, H. Kohno, and T. Ono, Phys. Rev. Lett., 97,107204 (2006), J. Mag. Mag. Mater. 310 2351 (2007).

[9] K. Yamada, S. Kasai, Y. Nakatani, K. Kobayashi, H. Kohno and T. Ono, Nature Mater. 6 269 (2007).

[10] P. Fischer, D.-H. Kim, B.L. Mesler, W. Chao, E.H. Anderson, JMMM 310(2) pt 3 2689 (2007).

HC-03

Elementary Eigenmodes of Magnetic Vortex Gyrotropic Motions in Magnetic Nanoelements.

K. Lee, S. Kim, D. Jung, Y. Yu, Y. Choi
Research Center for Spin Dynamics and Spin-Wave Devices & Nanospintronics Laboratory, Seoul National University, Seoul, South Korea

From both fundamental and technological points of view, a magnetic vortex (MV), which consist of in-plane curling magnetizations (**M**s) and out-of-plane **M**s at the center region (called the vortex core) in soft magnetic nanodots, has attracted much attention because of its nontrivial static and dynamic properties [1-3]. The nanometer-sized vortex core (VC) has the bistate **M** orientations, either up or down. Owing to the bistate VC orientations with high thermal stability, the MVs can be used as information carrier for future information-storage devices such as vortex-based random access memory, so called VRAM [4]. For the sake of utilizing the vortex state as a memory unit, it is necessary to find the reliable low-power control of VC orientation switching. Recently, ultrafast VC switching by applying very small amplitude of linearly oscillating magnetic field pulse or spin-polarized current along a certain axis in the film plane, has been verified experimentally [1]. Such reliable low-power switching of VC is an important step for realizing VRAM. Using this linearly oscillating magnetic field or current, however, we can not switch VC to a desired orientation because the linearly oscillating magnetic field reverses both upward and downward VC orientations. Now, we solve this problem by using an asymmetric resonant character of vortex gyrotropic motion in response to circular rotating magnetic field or current [4]. In this presentation, we report the elementary circular eigenmodes of vortex gyrotropic motion and their asymmetric resonant character and how we can apply such resonant character to control the VC reversal.

Based on Thiele's equation of vortex motion [5], we derived a dynamic susceptibility tensor of the VC motion [6], which is a useful to represent quantitatively the vortex response to any polarized oscillating field. Through the diagonalization of this tensor, we obtained the clockwise (CW) and counter-clockwise (CCW) rotating circular eigenvector basis of the VC motion in response to the CW and CCW rotating fields ($\mathbf{H}_{CW}$ ($\omega_{\mathbf{H}}$)and $\mathbf{H}_{CCW}$ ($\omega_{\mathbf{H}}$)) or currents ($\mathbf{I}_{CW}$ ($\omega_{\mathbf{I}}$)and $\mathbf{I}_{CCW}$ ($\omega_{\mathbf{I}}$)). As a result, we found that the CW and CCW eigenmodes of the gyrotropic motion and each circular eigenmotion can be expressed analytically by $\mathbf{X}_{CCW}=\chi_{CCW}\mathbf{H}_{CCW}$ and $\mathbf{X}_{CW}=\chi_{CW}\mathbf{H}_{CW}$.. From both analytical equations, we can numiercally calculate the amplification and phase delay of the eigenmotion in response to $\mathbf{H}_{CCW}$ and $\mathbf{H}_{CW}$ as shown in Fig. 1(a). These analytical calculations (solid line) are in good agreement with the micromagnetic simulation results (symbols). Depending on the VC polarization, p, only one of either the CCW or CW eigenmode shows the resonance effect, the other one showing non-resonance (sharp peak line vs straight line).

Due to the distinctly different asymmetric resonance effect near the resonance frequency, ω_D, the $\mathbf{H}_{CCW}$ and $\mathbf{H}_{CW}$ can be used to selectively excite the large gyrotropic motion of either CCW or CW rotation for a given VC orientation. Since the velocity of the VC motion is proportional to the amplitude of the gyrotropic motion for a given frequency and the VC orientation switches when the velocity of the VC motion reaches its critical value, v_{cr} ~ 350 20 m/sec [3], we can switch the VC orientation selectively using $\mathbf{H}_{CCW}$ and $\mathbf{H}_{CW}$, i.e., the $\mathbf{H}_{CCW}$ can selectively switch only the up-core, but the $\mathbf{H}_{CW}$ can switch only the down-core. To verify these, we conducted micromagnetic simulations on a Permalloy (Py) nanodisk of $2R = 600$ nm diameter and $L = 20$ nm thickness with the up-core orientation. As shown in Fig. 1(b), the amplitude of the orbital motions for the CCW motion by $\mathbf{H}_{CCW}$ is extremely large compared with those for the CW motion by $\mathbf{H}_{CW}$ and the upward VC orientation is switched to the downward VC orientation by $\mathbf{H}_{CCW}$ but not by $\mathbf{H}_{CW}$. These asymmetric resonance effect and selective VC switching are also observed when we apply circular rotating currents, $\mathbf{I}_{CCW}$ and $\mathbf{I}_{CW}$ [See Fig. 1(c)].

This work offers a principal further step toward practical applications of vortex states for ultrafast information-storage, -recording and -readout in vortex-based random access memory (VRAM).

[1] B. Van Waeyenberge et al., Nature 444, 461 (2006); K. Yamada et al., Nature Mater. 6. 296 (2007).

[2] S. Choi et al., Phys. Rev. Lett. 98, 087205.(2007); K.-S Lee et al., Phys. Rev. B 76 174410 (2007).

[3] S.-K. Kim et al., Appl. Phys. Lett. 91, 082506 (2007); K. Y. Guslienko et al., Phys. Rev. Lett. (in press) e-print arXiv:cond-mat/0708.1359.

[4] S.-K. Kim et al., Appl. Phys. Lett. (in press).

[5] K. Y. Guslienko et al., J. Appl. Phys. 91, 8037 (2002); K.-S. Lee and S.-K. Kim, Appl. Phys. Lett 91, 132511(2007)

[6] K.-S. Lee et al., e-print arXiv:cond-mat/0712.0758.

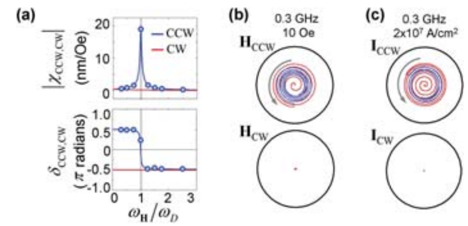

FIG. 1. (a) Numerical calculation of the analytical equations (solid lines) of $|\chi_{CCW,CW}|$ and phase delay δ as well as their simulations (symbols) results for the CCW (blue) and CW (red) eigenmodes. VC trajectories of the gyrotropic motions of a VC driven by $\mathbf{H}_{CCW}$ and $\mathbf{H}_{CW}$ in (b) as well as by$\mathbf{I}_{CCW}$ and $\mathbf{I}_{CW}$ in (c). The red and blue colors of the trajectories indicate the motion of the initial VC with the upward orientation and with reversed orientation after the VC switching, respectively.

HC-04

Unidirectional switching of the vortex core polarization by excitation with rotating magnetic fields.

H. Stoll[1], B. Van Waeyenberge[1,2], K. Chou[1], M. Curcic[1], M. Weigand[1], V. Sackmann[1], A. Puzic[1], A. Vansteenkiste[2], T. Tyliszczak[3], G. Woltersdorf[4], C. H. Back[4], G. Schuetz[1]
1. Max Planck Institute for Metals Research, Stuttgart, Germany; 2. Department of Subatomic and Radiation Physics, Ghent University, Gent, Belgium; 3. Advanced Light Source, LBNL, Berkeley, CA; 4. Department of Physics, University of Regensburg, Regensburg, Germany

We report on experimental observations of selective switching of the vortex core polarisation in sub-micron sized ferromagnetic Landau structures by applying rotating magnetic fields. The vortex core can be switched in a unidirectional way either to it 'up' or 'down' position depending on the sense of rotation (CW or CCW) of the external field.
The magnetic vortex [1] is a well known configuration of a ground state in geometrically confined ferromagnetic elements. It consists of an in-plane curling magnetization which in the centre, in order to avoid a singularity, turns out-of-plane and forms the vortex core. This vortex core has a radius of about 10-20 nanometres [2] and plays a key role in the magnetization dynamics [3,4]. As the out-of-plane magnetisation of the vortex core polarization (p) can point in two directions, either 'up' or 'down' (p= 1 or -1), it could be regarded as memory element. The high stability of the vortex structure and its very low stray fields would offer distinct advantages for applications requiring high density integration. Switching of the vortex core can be achieved, for instance, by applying a magnetic field perpendicular to the sample plane. However, field strengths of about 0.5 T are reported to be necessary [5,6] to crash the vortex core in this way and to rebuild it on the opposite side. Such high fields are intricate to realize on the small length scales necessary in practical devices for data storage.
Recently we discovered a new way to switch the vortex core polarization [7]. It was shown experimentally by X-ray microscopy that short, low-amplitude bursts of an alternating linear magnetic field reverse the vortex core. Burst with lengths down to a single period (4 ns) and amplitudes down to 1.5 mT [7] could toggle the polarization state of the vortex core. Based on micromagnetic simulations we also suggested that this dynamic vortex core reversal is mediated by the creation and annihilation of vortex-antivortex (VA) pairs [7]. This VA mediated switching scheme is now generally accepted for dynamic vortex core switching not only with excitation by magnetic field pulses but also by spin torque.
So far experiments and most simulations were performed with linear field pulses or bursts which toggle the vortex core from 'up' to 'down' and vice versa. For data storage application an unequivocal switching direction would be highly desirable. This could be achieved by circular rotating excitation fields [8-9].
Experiments have been performed by scanning transmission X-ray microscopy (STXM) at the Advanced Light Source (ALS, beamline 11.0.2) at Berkeley, CA, on square shaped, 500 nm large and 50 nm thin Permalloy elements. In-plane rotating magnetic fields were produced by cross-shaped striplines below the samples. The CW or CCW rotating fields were generated by ac currents in horizontal and vertical direction with the same frequency but a +90° or -90° phase difference respectively.
We observed that we could only excite the vortex core movement with the correct sense of rotation (CW or CCW) of the external rotating field depending on the vortex core polarisation [10]. When the amplitude of the rotating field was increased above a distinct threshold the gyrotropic vortex motion stopped, indicating that the vortex core polarization has been switched. For re-switching an external field with the opposite sense of rotation had to be applied. All these results are consistent with micromagnetic simulations showing that an unequivocal and unidirectional switching of the vortex core polarization can be achieved by circular field excitation. Switching of the vortex core could also be confirmed by applying a linear in-plane ac field of the same frequency, which excites the vortex gyration independently of the vortex core polarization. The sense of the gyrotopic vortex motion indicates the polarization of the vortex core.
Surprisingly, significant differences have been found in the ac field amplitudes needed for switching the vortex polarization from 'up' to 'down' and from 'down' to 'up'. These differences in the switching thresholds have been observed not only during excitation with circular but also with linear ac fields. Such differences were never observed so far in micromagnetic simulations of 'perfect' samples. Possible explanations for this 'symmetry breaking' will be discussed.

[1] A. Hubert and R. Schäfer, Magnetic Domains - The Analysis of Magnetic Microstructures, Berlin: Springer (1998)

[2] A. Wachowiak et al. Science 298, 577-580 (2002)

[3] D. Huber, Journal of Applied Physics 53, 1899-1900 (1982)

[4] K. Guslienko et al., Journal of Applied Physics 91, 8037-8039 (2002)

[5] T. Okuno et al., J. Magn. Magn. Mater. 240, 1-6 (2002)

[6] A. Thiaville et al., Phys. Rev. B 67, 094410 (2003)

[7] B. Van Waeyenberge et al. Nature 444, 461-464 (2006)

[8] Y. Gaididei et al., Phys. Ref. B 61, 9449-9452 (2000)

[9] V.P. Kravchuk et al., Journal of Applied Physics 102, 043908 (2007)

[10] K.-S. Lee et al., arXiv: 0712.0758 [cond-mat.mtrl-sci]

HC-05

Spin-dynamics and mode structure in lithographically patterned Permalloy nanostructures.

J. M. Shaw[1], M. Schneider[1,2], T. Silva[1], R. McMichael[3], S. Kim[1], W. Johnson[1], P. Kabos[1]
1. National Institute of Standards and Technology, Boulder, CO; 2. University of Montana, Missoula, MT; 3. National Institute of Standards and Technology, Gaithersburg, MD

We use a novel frequency resolved magneto-optic Kerr effect (FR-MOKE) [1] technique to probe the spin-dynamics and mode structure in 50 to 200 nm diameter Permalloy nanodots from 3 to 10 nm in thickness. It is important to understand the high-frequency behavior of such structures for continued development of spintronic technologies. An important question is how scaling and processing in nanostructures affects the magnetic properties such as switching field distributions and switching rates.

In this work, arrays of circular and elliptical nanodots were fabricated from dc magnetron sputter deposited 3 nm Ta/ 10 nm Permalloy/ 4 nm Si3N4 layers on sapphire substrates. Electron beam lithography was then used to create a cross-linked PMMA mask. Ion milling was used to transfer the mask pattern to the deposited magnetic layer. The inset of Fig. 1 shows a secondary electron micrograph of a typical array of 50 nm diameter nanodots.

Uniform precession modes were studied using FR-MOKE, whereby the nanodot arrays is driven by a cw microwave field generated by a coplanar waveguide. The microwave dynamics are detected by focusing a low-noise cw laser beam on the array and analyzing the polarization-modulated reflected light with a polarizer and a 12 GHz broadband photo-diode. The details of this technique and the data analysis used for fitting is given in Ref. 1. Figure 1 shows a typical FR-MOKE spectrum for an array of 50 nm diameter nanodots.

For nanodots greater than 75 nm diameter, two modes are observed with FR-MOKE. The field dependence of the frequency of these two modes is given in Fig. 2(a) and 2(b) for 100 nm and 200 nm nanodots respectively. Micromagnetic simulations [2] for a single ellipsoidal shaped nanomagnet (see insets in Fig. 2) reveal that one mode is concentrated at the edge while the other is concentrated at the center (herein referred to as the “edge” and “center” modes, respectively). The field dependence of the simulated mode-frequency is included in Fig. 2 in fair agreement with the data. We speculate that the small shift in frequency is most likely due to the fact that simulations were done on perfect structures that do not take into account such things as irregular shape, side wall tapering, and dot-to-dot dipole interactions. Figure 3(b) also show an asymmetry in the peaks which is reproduced in the simulations shown in Fig. 3(a). This asymmetry is due to a phase difference between the two modes that occurs when they overlap.

Characterization of the linewidth of these two modes allows us to independently study the homogeneity at the edge and center regions of the nanostructures. Micromagnetic simulations indicate that the linewidths of the two modes should intrinsically be the same as shown in Fig. 3(a) for a perfect structure. However, Figs. 3(b) and 3(c) show that the linewidth for the “edge” mode is approximately a factor of 2 greater. One plausible explanation is that the edge mode frequency is more susceptible to defects at the edges of the nanodots. Such defects would be most likely due to fabrication-induced damage and edge roughness. Such a sensitive dependence of edge mode properties on edge structure has been observed for edge modes in long Permalloy wires. [3] Thus, FR-MOKE could be used to quantitatively measure the edge properties of magnetic nanostructures and ultimately correlate that with processing conditions.

[1] M. L. Schneider, J. M. Shaw, A. B. Kos, Th. Gerrits, T. J. Silva and R. D. McMichael, J. Appl. Phys. 102, 103909 (2007).
[2] M. J. Donahue and D. G. Porter, National Inst. Std. Tech. NISTIR 6376 (1999).
[3] R. D. McMichael and B. B. Maranville, Phys. Rev. B 74, 024424 (2006).

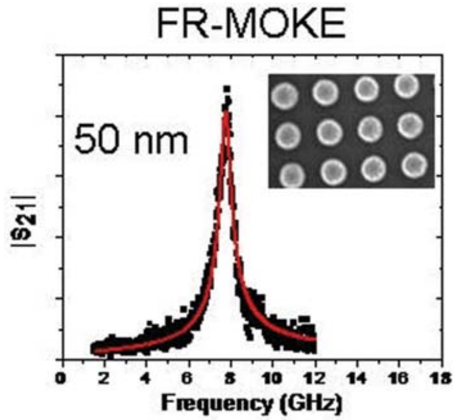

Figure 1. Example of FR-MOKE spectrum for a 50 nm nanodot array. The inset shows an SEM image of the array.

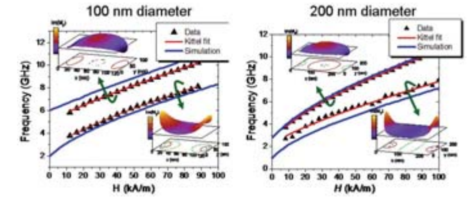

Figure 2. Kittel plots of the experimental and simulated data for (a) 100 nm and (b) 200 nm diameter nanodots. The insets show the spatial map of the corresponding mode amplitude across the nanodot.

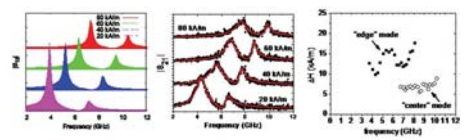

Figure 3. Amplitude as a function of frequency for 100 nm diameter nanodots in the (a) micromagnetic simulations and (b) experiment, along with (c) the extracted linewidths as a function of frequency from the experimental data.

HC-06

Microwave-assisted switching and demagnetizing of NiFe thin films patterned in micro-elements : a domain structure study by Kerr effect.

M. Laval[1], J. Bonnefois[1], J. Bobo[1], F. Issac[2], F. Boust[2]
1. LNMH, CNRS ONERA, Toulouse, France; 2. DEMR, ONERA, Toulouse, France

Many fields of application of magnetic materials require a fundamental study of the switching mechanism of small (micro or nano) magnetic elements. Most studies are oriented to magnetic data storage technologies [1,2], either for solid-state devices (MRAM) or patterned media hard disks. We have another application purpose which is to combine magneto-optics and microwave micro/nano materials for detection of intense electromagnetic pulses (EMP), like the ones emitted by large range radars. For aeronautics applications, the availability of rf magnetic field sensors is crucial for the determination of surface current density in airframes. The technique presently used is based on thermo-emissive foils (e.g. thin conductive layers deposited of polymer films) and infrared detection [3]. This method is only sensitive to the electric field component of the microwaves.
We have developed a combination of time-resolved Kerr magnetometer and stationnary Kerr microscope, coupled with static field electromagnets, microwave generators and strip-lines for the excitation of high permeability micro-elements.
Experimental details :
Permalloy thin films were grown by rf sputtering on oxidized silicon wafers. A 1 kOe static magnetic field was applied in the plane of the substrates in order to induce a magnetic easy axis. Thickness was set in the range 10 to 50 nm in order to keep the magnetization in plane and to have a sufficient response in Kerr effect. Several sets of photolithography masks, containing assemblies of rectangular elements with lateral shapes W(idth) x L(ength) ranging from 10x10 up to 20x160 square microns were used for patterning wafers in sectors of 7x7 square mm. The deposition-induced magnetic easy axis was aligned along the length of the micro-elements. A subsequent 5 nm Si_3N_4 capping layer was rf-sputtered prior to dicing.
Each individual sample was studied by longitudinal Kerr effect (ac field and He :Ne polarized laser). These first measurements reveal low values for the coercive field of our samples (typically from 1 to 10 Oe), as one can expect from large size magnetic elements. Dynamic susceptibility of each sample was analyzed with in a inductive coil in reflexion mode on a vectorial network analyzer. The cutoff frequency of this set up is 2 GHz. Compared to a plain NiFe film which has a gyromagnetic resonance frequency of 0.84 GHz, patterned films exhibit gyromagnetic resonance at larger frequency : 1.28 to 1.31 GHz for 20xL elements (L=20 to 160 microns), more than 2 GHz for 10xL samples. Fitting to LLG equations of the permeability spectrum of the plain film yields an anisotropy film of 8 Oe and a damping coefficient of 0.012. Such model does not apply for patterned elements since it requires uniformly magnetized thin film samples.
We have used a Kerr microscope, equiped with a 300 W UV-filtered Xe:Hg lamp, a standard set of polarizer/analyzer and a wide field objective. Images are collected with a 12 bits CCD camera and are subsequently analyzed for background subtraction and subpixel corrections of spurious sample motion. The optical resolution of our microscope is better than 1 micrometer. The sample holder is equipped with two microwave ports and an adapted strip line with one optical window. Samples are mounted underneath the strip line. The observation window is located in the center of the strip line where the rf field is highly homogeneous. This configuration leads to a more homogeneous magnetic field than with the usual coplanar waveguide used by others. Its drawback is the relative difficulty of accessing to the magnetic elements.

Results :
Magnetization switching field (or coercive field) decreases monotonically from 3.5 Oe for the unexcited elements, down to 2 Oe for 20 W. This decrease, already reported by Nembach et al [1] and Woltersdorf et al [2], is characteristic of the excitation of the transverse magnetization of the elements that favors its reversal. We are presently studying in detail the dependence of coercivity vs. the element dimensions, the microwave power and density. These results will be accompanied with micromagnetic modeling.
Another alternative way we have investigated is the demagnetization of a saturated permalloy element when it is submitted to submicrosecond magnetic field pulses. NiFe square elements (100x100 μm^2) were excited with several series of 25 ns magnetic pulses. The peak magnetic field H_{peak} was adjusted from 0.1 to 10 Oe. Above a threshold value of H_{peak} = 2 Oe, we observe a significant demagnetization of the patterned square with the growth of opposite or transverse domains.
In conclusion, we have demonstrated that it is possible to monitor either the intensity and the frequency of a CW microwave excitation or the intensity, width and number of electromagnetic pulses on magnetic micro elements by Kerr microscopy. The implementation of this technique for microwave metrology is presently in progress.

[1] H. T. Nembach et al., Appl. Phys. Lett. 90, 062503 (2007)

[2] G. Woltersdorf and C. H. Back, Phys. Rev. Lett. 99 (2007) 227207

[3] D. Dalageas and P. Levesque, Rev. Gén. Therm. 37 (1998) 725

[4] D. Spenato et al., J. Phys. D: Appl. Phys. 26 (1993) 1736-1740

HC-07

Modeling of microwave-assisted switching in micron-size magnetic ellipsoids.

R. Yanes[1], *O. Chubykalo-Fesenko*[1], P. Martin Pimentel[2], B. Leven[2], B. Hillebrands[2], V. Tyberkevich[3], A. Slavin[3]
1. POMT, Instituto de Ciencia de Materiales de Madrid, CSIC, Madrid, Spain; 2. Technische Universitaet Kaiserslautern, Kaiserslautern, Germany; 3. Department of Physics, Oakland University, Rochester, MI

The fundamentals of fast magnetisation switching is one of the important problems in magnetism, related to technological applications. Among various possibilities, the microwave-assisted (mw) switching with linearly-polarized excitation could be implimented based, for example, on fast magneto-optic Kerr set-up, synchronized with a microwave field [1]. It has been shown that the mw-assisted switching requires smaller dc external field. The process of understanding the underlying physics is still on-going and several ideas which include fast precessional switching [2], nonlinear phenomena [3], enhanced nucleation or increased domain wall mobility [1,4] could be found in the literature.
In the present work and with the aim to understand the mw-assisted switching in large magnetic elements [1], we use a micromagnetic model to simulate a pemalloy ellipsoid of 4μm x 2 μm by 25 nm dimensions with easy axis parallel to the large ellipsoid dimension (y-axis). Initially the ellipsoid is magnetised along this axis and the dc-applied field is also placed parallel to it. The ac field with large amplitude is directed perpendicular (x-axis). First of all, we notice that the largest effect of the coercivity reduction comes from the deviation of the magnetisation from y-axis, following the ac-field. Thus, the coercivity is reduced simply due to the fact that most of time the resulting field is applied at some angle to the easy axis. Consequently, we compare the mw-assited switching with the situation when we substitute the ac-field with the dc-field of the same amplitude. Our results shows that even in this case the mw-assisted switching requires less dc-field.
Figs.1 show the magnetisation configurations during the static and mw-assisted reversal. We clearly observe that in the second case the ellipsoid is dynamically divided into “domain” structures. The number of “domains” depends strongly on the mw frequency and may be related to the length of the spinwave mode, excited in the system. The division of the ellipsoid into domains during mw-assisted switching is experimentally confirmed by Kerr images in Ref.[5].
Furthermore, during this process the Néel type domain walls appear. The magnetic moments in the center of domain walls are precessing and their mobility may be incremented by mw following the precessional switching effect. Another effect may be related to mw-assisted vortices switching [6], whose multiple appearance is also detected in the system.
We have investigated the switching time for ellipsoid as a function of the mw amplitude and frequency. Since the main features of the nonlinear processes with large-amplitude excitation may resemble that of the parametric resonance ones, we present in Fig.2 our results as a function of the double FMR frequency (evaluated for different applied fields), ω_0 normalized to the ac-frequency υ. Our simulations clearly show the maximum of switching time corresponding to the resonance condition $2\omega_0/\upsilon$ » $2a$. The difference a could be attributed to the nonlinear shift of the precessional frequency due to large-angle motion. Secondly, next-order resonances are also observed. Surprisingly, the switching time appears to be large when the mw frequency coincides with that of the nonlinear FMR one. Having analysed in details the switching process, we observed strong precession of magnetic moments in this case. Consequently, due to the coupling of the mw to the precessional mode, the energy is transfered into this motion and not to the switching process [4]. Finally, we conclude that several of the effects decribed above coincide, making the overall process complicated. However, our simulations clearly confirm the fact that the mw-assisted switching requires less external field and is faster.

[1] H.T.Nembach et al, Appl. Phys.Lett., vol. 90 (2007) p.1.
[2] G.Bertotti et al, IEEE Trans Magn 39 (2003) 2504.
[3] C.Thirion et a, Nature Mater. vol. 2 (2003) p.524.
[4] A.Krasyuk et al Phys. Rev.. Lett. 95, 207201, (2005)
[5] P.Martin Pimental, J Appl. Phys. 102, 063913 (2007)
[6] B. Wayenberge et al Nature 444 (2006) 461

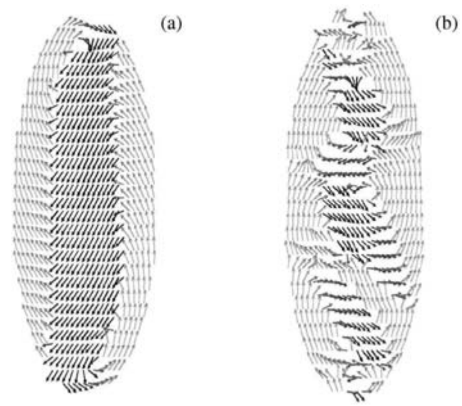

Fig.1 Dynamic magnetisation configuration during static hysteresis (a) and mw-assisted one (b).

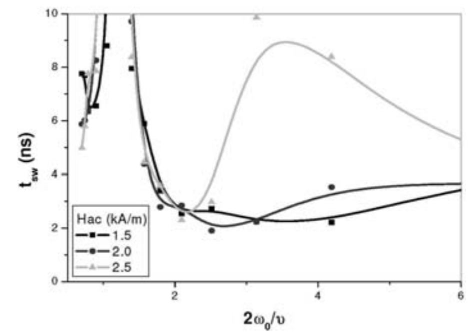

Fig.2 Switching time for the ellipsoid as a function of the inverse mw frequency ν.

HC-08

Nonlinear processes during switching of a thin Permalloy film in different geometries.

K. Livesey[1], H. Nembach[2], M. Kostylev[1], P. Martin-Pimentel[2], S. Hermsdoerfer[2], B. Leven[2], R. Stamps[1], B. Hillebrands[2]
1. School of Physics, University of Western Australia, Crawley, WA, Australia; 2. Fachbereich Physik und Forschungsschwerpunkt MINAS, Technische Universitaet Kaiserslautern, Kaiserslautern, Germany

The study of magnetization switching in thin magnetic films and small magnetic elements is of interest today with the advent of patterned recording media and of MRAM. In this work we present a combined experimental and theoretical study of precessional magnetization switching in thin Py films. We show the evidence for nonlinear processes occurring during large-angle switching [1] that can strongly decrease the coherency of reversal and decrease switching times [2]. We focus on the effect that varying the strength and direction of bias fields may have on the threshold for nonlinearity.
A 10nm Permalloy film was switched by applying a bias field and then a short pulse field at 90 degrees to the bias, which causes the magnetization to precess. The dynamics were measured using a Magneto-Optical Kerr Effect (MOKE) set-up in longitudinal configuration [3]. The magnetization vector can be resolved in all three directions and at all times during its trajectory using this technique. However, recombining the three components of the magnetization vector, it can be seen that the vector length, |M|, is not conserved (see Fig.1.). This is evidence that there are spin waves being parametrically excited in the film that have wavelengths shorter than the laser spot-size used in the experiment.
To compare with experiment we have used a classical, perturbative theory in which we write the magnetic Hamiltonian for the thin film and then solve equations of motion to find analytically the parametric threshold [4]. This is a threshold for four-wave decay of the large-angle precession, induced by the pulse field.
In Fig.2 we plot the minimum value of |M|/M=|m| measured during switching as a function of bias field for both easy and hard axis biasing. A pulsed field of 5.9 Oe (as inferred by macrospin simulations) is used, and there is a uniaxial anisotropy of 7.9 Oe, which is experimentally measured. It can be seen that while for the easy axis biasing the maximum decrease in |M| is 2%, for the hard axis biasing the maximum decrease is a much larger 10%. Also, for both plots there is a smaller decrease in |M| for larger bias fields.
These results can be explained with comparison to our theoretical results. In Fig.3 we have plotted on the left the threshold to see a reduction in |M| (in terms of average angle of precession) for hard (dashed line) and easy (solid line) axis biasing. There is a lower threshold for the hard axis biasing so we would expect the reduction in |M| to be higher in this geometry. This is not the whole story, however, because the "supercriticality" of the system (how far above threshold it is) will also determine the decrease in |M|. On the right of Fig.3 we have plotted the switching angle for hard (dashed line) and easy axis (solid line) biasing, which gives a qualitative description of the precession angles involved during switching. Again, for the hard axis biasing there is a larger switching angle, and so a higher level of supercriticality, and we would expect a much larger decrease in |M|. Also, for larger bias fields, the precession angle goes towards zero.
Although Permalloy has a small uniaxial anisotropy, it has been shown that the direction of biasing is very important in determining the dynamics during switching. There is a much larger nonlinearity for hard-axis biasing at low fields, which means switching will be less coherent but faster in this geometry.

Support by the Hackett Student Fund (UWA), Australian Research Council and the Deutsche Forschungsgemeinschaft within the SPP 1133 is acknowledged.

[1] T.J. Silva, P. Kabos, and M.R. Pufall, Appl. Phys. Lett. **81**, 2205 (2002).

[2] A. Yu. Dobin and R.H. Victora, Phys. Rev. Lett. **90**, 167203 (2003).

[3] H.F. Ding, S. Puetter, H.P. Oeppen and J. Kirschner, Phys. Rev. B **63**, 134425 (2001).

[4] K.L. Livesey, M.P. Kostylev and R.L. Stamps, Phys. Rev. B **75**, 174427 (2007).

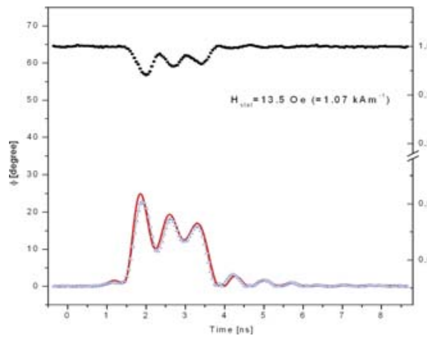

Figure 1. A time-resolved measurement of the excursion angle (bottom) and |m|=|M|/M (top) during precessional switching. Here a bias field of 13.5 Oe, parallel to the easy axis, is applied for 2ns.

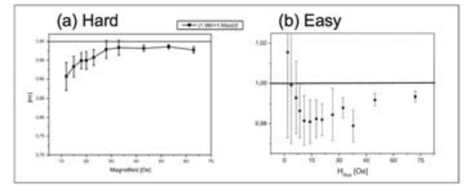

Figure 2. The minimum measured value of |m| = |M|/M during switching as a function of bias field strength for (a) hard and (b) easy axis biasing.

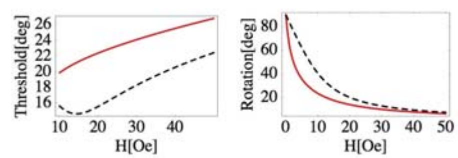

Figure 3. On the left the threshold to measure a decrease in |M| during 2ns is plotted as a function of bias field strength for easy (solid line) and hard (dashed line) axis biasing. On the right, the switching angle is given for the two geometries.

HC-09

Precessional magnetization reversal in composite patterned media: Dependence on applied field parameters.

B. Livshitz[1], H. N. Bertram[2,3], A. Inomata[4], V. Lomakin[1]
1. Department of Electrical and Computer Engineering, UCSD, San Diego, CA; 2. Center for Magnetic Recording Research, UCSD, San Diego, CA; 3. Research Center, Hitachi Global Storage, San Jose, CA; 4. Storage and Intelligent Systems Laboratories, Fujitsu Laboratories Ltd, Atsugi, Japan

Precessional reversal (PR) is a reversal mechanism allowing bypassing an energy barrier thus resulting in a low reversal field [1,2]. Recently, it was shown that compared to PR in homogeneous elements, PR in exchange coupled composite elements is characterized by several unique properties [2,3], including substantial reduction of the reversal field and increase of the critical rise time, viz. rise time required for PR to occur.

Here, we continue the investigation of PR in composite elements. Specifically, we study the dependence of PR parameters on the applied field parameters, including the magnitude, pulse duration, and element coverage. We consider exchange coupled dual-layer elements in Fig. 1. The layers have anisotropies of K_h (hard) and K_s (soft) and identical size of w,$w/2$,w and they are coupled with surface energy J_s. The layers have a damping constant α, saturation magnetization M_s, and exchange length $l_{ex}=A^{1/2}/M_s$(with A the exchange constant). A magnetic field $\mathbf{H}_{\mathrm{ext}}=-H_a(1-2\exp(-2t/\tau))(\mathbf{x}\sin\phi+\mathbf{y}\cos\phi)$ is applied uniformly across the width and through the height of the element but only over a varying percentage of the length direction. Here, ϕ is the field angle, H_a is the field magnitude, and τ is the field rise time. Magnetization reversal occurs when H_a is above a certain reversal field H_r. The analysis is performed by numerically solving the Landau-Lifshitz equation.

Figure 1(a) shows H_r vs. percentage of the applied field coverage for different rise times for the structure parameters shown in the insert. It is found that H_r increases with a decrease of the applied field coverage. The magnetization distribution behavior shows that the increase is associated with non-uniform reversal in horizontal direction. More interestingly, H_r is found to be substantially smaller for a small rise time (τ=20 ps- full curve) than for a large rise time (τ=200 ps- dashed curve). The H_r reduction for small τ is obtained because in this case reversal occurs in the precessional regime [3]. It also should be noted that the PR field reduction for composite elements is much more pronounced than for homogeneous elements [3,4].

A crucial parameter for PR is the critical rise time τ_{crit} [3]. For homogeneous elements $\tau_{crit}=\pi/\gamma H_k$ and it can be extremely small for large values of H_k, which are required for thermal stability in high-density media. The situation is different in the case of composite media. Figure 1(b) depicts τ_{crit} vs. percentage of applied field coverage. The obtained τ_{crit} is significantly (about 8 times) larger than τ_{crit} for homogeneous elements. The values of τ_{crit} can be even larger for other structure parameters. It is also observed that τ_{crit} noticeably decreases with a decrease of the applied field coverage. It follows that by carefully choosing the rise time, one can control the mechanism of reversal for different applied field coverage. This is demonstrated by the dotted curve in Fig. 1(a) that shows H_r for τ=45 ps. It is evident that H_r is very low and almost equals the PR field when the entire element is under the applied field, whereas it is much higher and almost equals the damping reversal field when only a small part of the element is under the applied field. This increased reversal field contrast can have important applications to improve time margin errors in magnetic recording applications.

We also have studied the reversal field behavior for many other parameters of the structure and pulsed applied field, including the applied field magnitude, rise time, pulse duration, and pulse shape. These results will be presented during the conference.

[1] L. He, W. D. Doyle, and H. Fujiwara, *IEEE Trans. Magn.*, **30**, 4086, 1994.

[2] K. Z. Gao and J. Fernandez-de-Castro, *J. Appl. Phys.*, **99**, 08K503, 2006.

[3] B. Livshitz, A. Inomata, N. H. Bertram, and V. Lomakin, *Appl. Phys. Let.*, **91**, 182502, 2007.

[4] B. Livshitz, R. Choi, A. Inomata, N. H. Bertram, and V. Lomakin, *J. Appl. Phys.*, April, 2008, submitted.

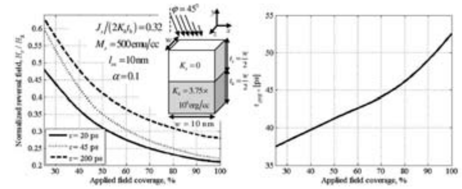

Fig.1 Normalized reversal field (a) and critical rise time (b) as a function of applied field coverage for ϕ=45^0.

HC-10

Dynamics of bubble domains in nanodots with high anisotropy.

C. Moutafis[1], S. Komineas[2], C. F. Vaz[3], J. C. Bland[1], T. Shima[4], T. Seki[5], K. Takanashi[5]
1. Cavendish Laboratory, Cambridge University, Cambridge, United Kingdom; 2. Max-Planck Institute for the Physics of Complex Systems, Dresden, Germany; 3. Applied Physics, Yale University, New Haven, CT; 4. Faculty of Engineering, Tohoku-Gakuin University, Tagajyo, Japan; 5. Institute for Materials Research, Tohoku University, Sendai, Japan

We study the statics and ultra-fast dynamics of magnetic bubbles in finite geometries. We identify transient phenomena that dominate the dynamics and show a way to obtain magnetic bubbles of varying topology in magnetic elements. We also calculate an eigenfrequency, which can provide an easy link with experiment. While the magnetic vortex is well understood as a fundamental state for magnetically soft discs, the question arises as to the corresponding fundamental state in the presence of a strong symmetry breaking anisotropy and its dynamical behavior. Confined single magnetic bubbles have been identified as ground states in nanoscale elements with magnetocrystalline uniaxial perpendicular anisotropy [1-4]. The bubble state presents a magnetic circulation around the centre of the dot and should be viewed as the analogue of the vortex found in soft dots.We have recently shown experimental evidence for the existence of such bubble domains [4], termed the monobubble (Fig.1), and the three-ring state, in suitably designed high-quality circular FePt nanodots. Here, we present Magnetic Force Microscopy imaging of these magnetic states.
A numerical study confirms the range of stability of the observed magnetic states and predicts the phase diagram in parameter space where these states are energetically favourable. The complexity of these multidomain states can be quantified by a topological invariant called the “Skyrmion number”, **N**. While the monobubble is the simplest topologically non-trivial structure (**N** unity) in magnetically hard dots, the three-ring structure has vanishing **N**. The skyrmion number is important for bubble dynamics since it is proportional to the gyrocoupling vector which is directly linked to magnetization dynamics [5]. We perform here a full numerical study of the evolution of bubbles under an external magnetic field gradient in nanodots and describe the unusual dynamics they exhibit. We allow the bubble to evolve under the field and then switch off the field and let it evolve freely until it reaches a remanent state. We use a field which varies by the magnitude of the saturation magnetization along the dot’s diameter. The field used here is particularly strong but the underlying described phenomena should be generic. By calculating the moments of the center of mass and the topological density of the bubble we follow its motion and dynamical behaviour.
Surprisingly, the topological charge moves not across the gradient, but perpendicular to it; in just t=45ps it has moved for 10 l_{ex}. Interestingly, at t=385ps we observe a switch to vanishing topological density. The magnetic configuration is allowed to evolve freely and it relaxes in the center of the dot indicating that this is a metastable state in our system. We thus illustrate a simple sub-nanosecond mechanism to switch from a bubble with skyrmion number unity to a bubble with a vanishing skyrmion number in a finite geometry. This state is not symmetric anymore and it has a slightly larger energy. The circular domain wall now includes a pair of Néel lines. The new configuration’s dynamical behaviour is different to the monobubble’s dynamics. Importantly, this is an ultra-fast mechanism, which should be of interest in devices. We also identify the mechanism to switch back to the original symmetric monobubble state by controlling the applied pulse. We study the monobubble behaviour under various magnetic gradients of different durations and strengths. For low enough fields, we observe a low drive of the bubble without distortion of the domain wall structure. In addition, a displaced bubble with unperturbed domain wall, left to evolve freely, performs a damped periodic motion towards the center of the dot (Fig.2). We thus calculate the corresponding eigenfrequency, which for the specific geometrical characteristics, is approximately 1GHz.

[1] M. Hehn et~al., Science 272, 1782(1996).

[2] G.D. Skidmore,A. Kunz,C.E. Campbell,and E.D. Dahlberg,Phys. Rev. B 70, 012410(2004).

[3] S. Komineas et~al., Phys. Rev. B 71, 060405(R)(2005)

[4] C.Moutafis, S.Komineas, C.A.F. Vaz, J.A.C. Bland, T. Shima, T. Seki, K. Takanashi,Phys.Rev. B 76, 104426(2007)

[5] A.A. Thiele,Phys.Rev.Lett. 30, 230(1973).

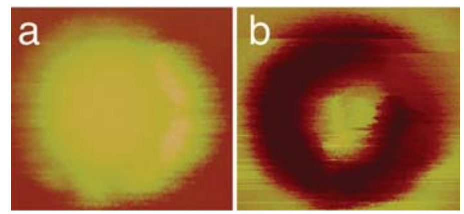

a) The topography of a 500nm diameter FePt nanodot is shown.b) The magnetic image shows a bubble in the center.

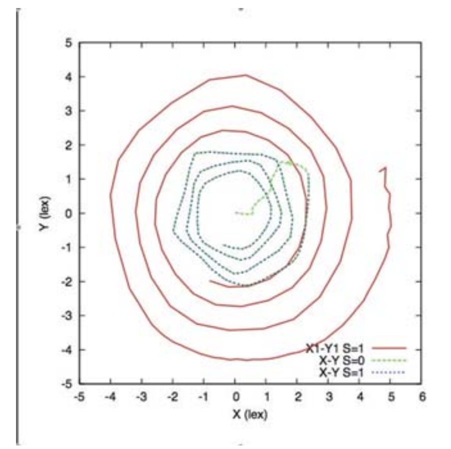

The moments of the center of mass (X,Y) and of the topological density (X1,Y1) are shown. The switching from the bubble with N=0 back to the monobubble with N=1 is shown. After the switch the bubble is off-centered and it enters a periodic motion to the center of the dot.

HD-01

Control of domain wall motion in Permalloy nanowires using magnetostatic interactions.

S. Basu, D. Allwood, T. Schrefl
Department of Engineering Materials, University of Sheffield, Sheffield, United Kingdom

Controlled pinning and depinning of domain walls (DWs) in ferromagnetic nanowires can be used to control the movement of DWs [1, 2]. This may provide additional functionality in DW devices. We have carried out micromagnetic simulations of pinning and depinning of transverse DWs by magnetostatic interactions between two or three Permalloy (Ni80Fe20) nanowires placed side-to-end (T and cross shapes). Figure 1 gives a schematic representation of the wire geometries and shapes used for the study. The wires consist of a 'propagation wire that has an initialised DW on one side, and one or two 'control' wires placed close to the edge of the propagation wire. A linearly increasing applied field is used to move the DW in a nanowire. In order to pass through the junction region, the DW must overcome the magnetostatic interactions with the control wire(s). These may be attractive or repulsive interactions but either case results in an increased 'pass' field compared to propagation elsewhere in the wire. This interaction varies as a function of the wire separations and end shape of the control wire(s). The control wire ends had either flat-ended or of tapered geometries. The wires were 200 nm wide. The separation between the wires was varied from d = 20 – 100 nm.

The pass field is higher when the end shape of the pinning wire is flat compared to when the end shape is tapered. The relative magnetisation direction in the control wires and in the DW was varied. In T shapes, it was either parallel or antiparallel. In cross shapes, the magnetisation configurations in the two control wires with respect to the DW magnetisation was parallel, antiparallel, antiparallel-antiparallel or parallel-parallel as depicted in figure 2a, 2b, 2c and 2d repectively for flat-ended control wires.

The pass field increases with decreasing separation. For example, in T-shaped structures with the tapered end of the control wire close to the propagation wire a 200% increase in pass field is observed when d = 20 nm compared to d = 100 nm (Figure 3). Again, the pass field is nearly doubled to 4.2 mT when the flat end of the control wire is close (20nm separation) to the propagation wire compared to the tapered end of the control wire close (2.2 mT). Figure 4 shows the pass field of the DW as a function of separation between the propagation and the control wire, with the flat end close. The cross shaped geometry was better in pinning the DW for some of the magnetisation configuration for smaller separation. For example, in the configuration where the magnetisation in the control wires is antiparallel to the DW magnetisation, the switching field is double compared to the T-shape with the same separation. When the tapered end is used to pin the DW, the pass field is much lower, compared to when the flat end is used to pin and also comparable to the T-shapes of equal separation. Cross-shapes offer high level of control for DW propagation by changing the magnetisation geometry compared to the T-shapes where little control is possible.

1. M. Kläui, et. al, Physical Review Letters, 94(10) (2005), p. 106601.

2. S. S. P. Parkin, US Patent Application 20040252539 (2004).

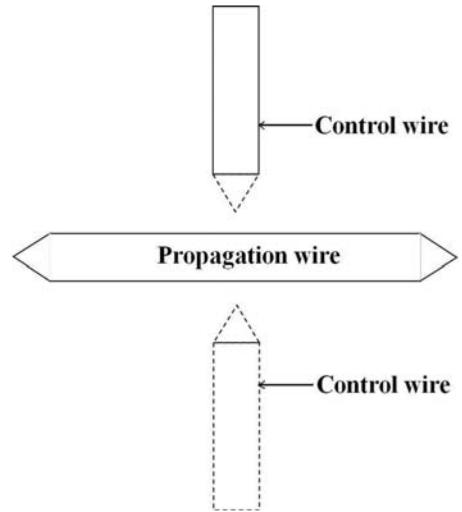

Figure 1: Schematic of the geometries used for the simulations

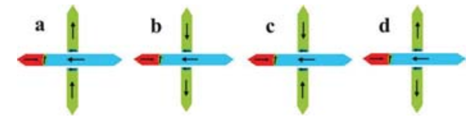

Figure 2: The magnetisation configuration and geometries used for the simulations with cross shapes

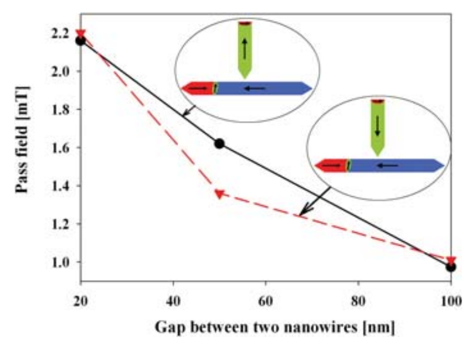

Figure 3: Pass field as a function of separation between nanowires in T-shaped structures

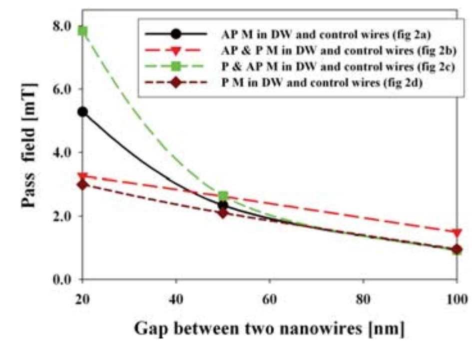

Figure 4: Pass field as a function of separation between nanowires in cross-shaped structures

HD-02

Domain wall depinning from a notch under oscillating currents: the role of non-adiabaticity.

E. Martinez[1], L. Lopez-Diaz[2], O. Alejos[3], L. Torres[2]

1. Ingenieria Electromecanica, University of Burgos, Burgos, Spain; 2. Fisica Aplicada, University of Salamanca, Salamanca, Spain; 3. Electricidad y Electronica, University of Valladolid, Valladolid, Spain

The position of a Domain Wall (DW) in a thin ferromagnetic wire can be manipulated by means of notches, which act as pinning potential wells by locally lowering its magnetostatic energy. The analysis of the current-induced DW depinning from a notch is not only of technological relevance for promising logic and storage devices [1]. It is also interesting from a fundamental point of view, because the comparison between theoretical predictions and experimental observations could be used to ascertain the magnitude of the non-adiabatic spin torque, which is difficult to compute from first principles.

In this talk, the interaction between oscillating spin-polarized electrical currents and a DW initially trapped on a notch in a thin Permalloy nanostrip is investigated by micromagnetic modeling as well as a one-dimensional model which considers the wall as a rigid object [2]. A systematic analysis of the depinning transition is carried out in the frequency domain for several static magnetic fields and AC currents, both at zero and at finite temperature [3].

As an example, we have computed the depinning field as a function of the frequency of the injected current. The results are depicted in Fig. 1 under a constant amplitude current 1A/μm2 at room temperature. Each dot represents the first field at which the DW is depinned with 100% of probability (PD=1) for each frequency of the current. Solid line represents the fitting to the analytical deterministic field in the stationary regime [3]. A dip of the depinning field is observed at the frequency resonance [2].

We have also analyzed a similar pinning potential as experimentally studied by Bedau and coworkers [4]. Their experimental results can be also quantitatively described by the rigid approach if a non-adiabatic parameter in the order of 1 is considered. Such a high value of the non-adiabatic parameter could be related to the large magnetization gradient occurring in a vortex wall, where the magnetization changes by 180 degrees within a few nanometers. This noticeable issue, along with its theoretical implications and details of our model, will be extensively discussed in the presentation.

[1] S. S. Parkin, U.S. Patent No. 6834005 (2004)

[2] E. Martinez et al, Phys. Rev. Lett. 98, 267202 (2007)

[3] E. Martinez et al. Submitted to Phys. Rev. B (2007).

[4] B. Bedau et al. Phys. Rev. Lett. 99, 146601 (2007)

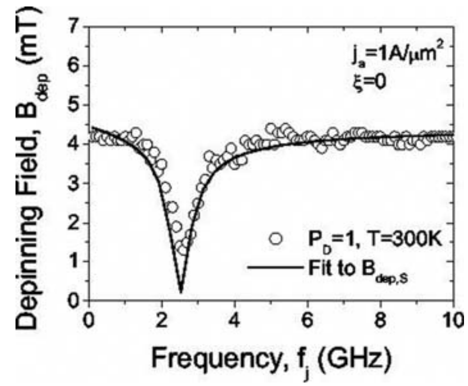

Figure 1. DW Depinning field as a function of the frequency at room temperature. A constant current density of 1A/μm2 is considered.

HD-03

Spin-Polarized Current Induced Switching of Composite Free Layers.

C. Yen, W. Chen, Y. Chen, D. Wang, C. Shen, S. Yang, C. Tsai, Y. Lee, C. Hung, K. Shen, M. Kao
Electronics and Optoelectronics Research Laboratories (EOL), Industrial Technology Research Institute (ITRI), Hsinchu, Taiwan

Spin-poliarized current induced magnetization switching has drawn considerable attentions for the potential applications of high density magnetic random access memory (MRAM). [1] The spin polarized current flows through the magnetic tunnel junctions exerts a spin torque on the magnetic moment of the ferromagnetic layer which is used as the information storage layer (free layer) in MRAM. One of the most challenging targets of the spin torque switching architecture is the reduction of critical current of magnetization reversal while keep the thermal stability at a reasonable level in the mean time. In general, the reduction of critical currents requires a intrinsically softer ferromagnetic material as the free layer or reducing the thickness of free layer. Nevertheless, these approaches contradict the requirement of maintaining thermal stability.

In this work, we propose a composite free layer, which is a sandwiched structure, two ferromagnetic layers separated by a metal layer, and coupled by the RKKY interlayer exchange coupling in parallel. The macrospin models were used to study this structure. The lateral size of model structure is a ellipse with a long axis of 100nm and a short axis of 50nm. The stacks and corresponding parameters are as following: a top soft free layer (layer 1), with a saturation magnetization of 250 emu/c.c., an uniaxial anisotropy of 10 Oe, a thickness of 17.5 angstrom, and a bottom hard layer (layer 2), with a saturation magnetization of 400 emu/c.c., an uniaxial anisotropy of 30 Oe, a thickness of 12.5 angstrom. Assume both layers are experiencing the spin torque simultaneously, and have the same damping constant of 0.02 and polarization of 0.2.

We found that with a 10ns current pulse, a single layer 2 has a switching critical current density of 6.4×10^6 A/cm^2 and a single layer 1 has a switching critical current density of 4.0×10^6 A/cm^2. However, if these two layers are combined together and interlayer exchange coupled with a coupling strength of 0.01 erg/cm^2, the device requires only 4.2×10^6 A/cm^2 of critical current density to switch. These results suggest that the precession of magnetic moment in the soft layer (layer 1) may assist the precession of magnetic moment in the hard layer (layer 2) and make the layer 2 switchable at a much lower current density than the value on its own. In a word, this kind of free layer structure has the potential of existing low switching current density and high thermal stability at the same time. The influences of exchange coupling strength, relative hardness of ferromagnetic layers, spin-torque efficiencies in these two layers, and random thermal perturbations will be addressed by both macrospin and micromagnetism simulations.

[1]Z. Diao, Z. Li, S. Wang, A. Panchula, E. Chen, L.-C. Wang, Y. Huai "Spin-transfer torque switching in magnetic tunnel junctions and spin-transfer torque random access memory" J. Phys. Condens. Matter. vol.19, 165290, 2007.

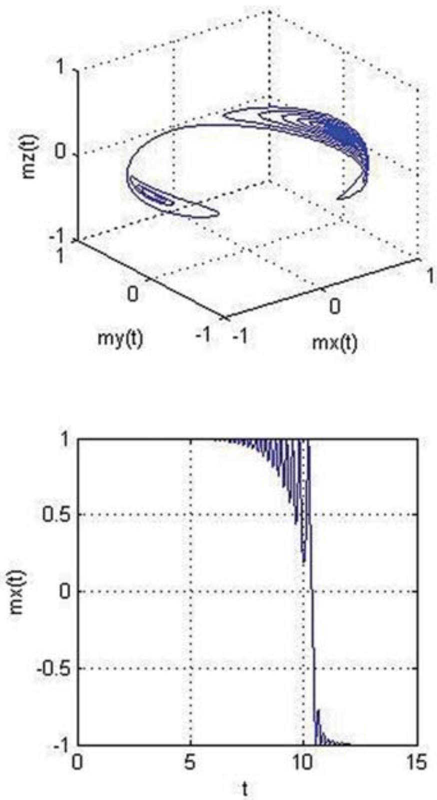

Fig.1 A single free (hard) layer, switched at 6.4×10^6 A/cm^2

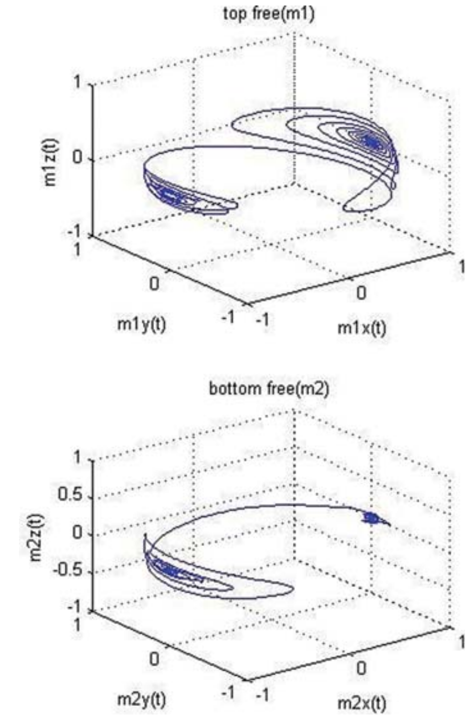

Fig.2 A composite free layer, with a top (soft) layer and a bottom (hard) layer, switched at 4.2×10^6 A/cm^2

HD-04

Switching of vortex chirality in $Ni_{80}Fe_{20}$/Cu/Co nanopillars by a spin-polarized current pulse.

B. C. Choi[1], Y. K. Hong[2], J. Rudge[1], E. Girgis[1], J. Kolthammer[1], A. Lyle[2], G. W. Donohoe[3]
1. Department of Physics & Astronomy, University of Victoria, Victoria, BC, Canada; 2. Department of Electrical and Computer Engineering, University of Alabama, Tuscaloosa, AL; 3. 2Department of Electrical and Computer Engineering, University of Idaho, Moscow, ID

The magnetization dynamics of vortex structures in patterned elements has received considerable attention during the last few years due to its possible applications in high-density magnetic storage devices [1-3]. Recently, it was found that the vortex core magnetization can be switched by applying a short magnetic field pulse with an appropriate strength and duration [3]. For practical applications, however, it is desirable to find a more convenient method, i.e., current-driven switching of the magnetization state of the vortex. Here we report detailed micromagnetic studies of the spin-transfer effect on the vortex magnetization in magnetic multilayer structures. Fig. 1(a) is a schematic of the multilayered structure used in our study. The diameter is 100 nm, and the fixed magnetic layer (Co) is separated from the free magnetic layer (Py) by a 4 nm thick Cu layer. The bottom panel of Fig. 1 shows the initial magnetization configurations in the Py (b) and Co (c) layers, respectively. Each layer contains a single vortex core located at the center of the disk, and M_{Py} and M_{Co} are aligned close to parallel forming a small angle between M_{Py} and M_{Co}. To study the dynamic response of the vortex magnetization to the spin-polarized current pulse, the equilibrium micromagnetic distributions of M_{Py} and M_{Co} are excited by injecting a short current pulse. The current direction is denoted positive when it flows from Py to Co layer. Fig. 2 shows a series of the non-equilibrium configurations of M_{Py} captured at selected times after a negative current pulse of 30 mA ($\approx 1\times10^8$ A/cm^2) with the duration of 200 ps is applied. Following the temporal evolution of the micromagnetic configuration, one finds that individual M_{Py} undergoes the CW rotation, while the whole vortex configuration appears to circulate CCW around the disk center. The image (b), captured at 84 ps after the current pulse is applied, reveals that M_{Py} rotates by $\sim 90^{\circ}$, and with increasing time M_{Py} further rotates by $\sim 180^{\circ}$, as shown in (c) captured at 144 ps. Finally, the vorticity of M_{Py} switches to CW (d). M_{Py} of the switched vortex state, however, is still in a nonequilibrium state, and the dynamics of the energy dissipation after the initial vortex chirality switching involves a series of complex magnetization processes. The magnetization configuration in (d), for instance, reveals a high degree of complexity both due to the nonunifrom distribution of M_{Py} and the creation of an additional vortex-antivortex pair. The pair is found to be a metastable micromagnetic state, and it vanishes without undergoing the annihilation process. As shown in Fig. 2(e), a full relaxation of M_{Py} is reached after about 2 ns after the excitation. By contrast, the micromagnetic distribution of M_{Co} is only slightly perturbed from the initial state through the entire process of the chirality switching of M_{Py}, and no switching of vortex chirality of M_{Co} occurs(f). After the reversal of the vortex chirality of M_{Py} is completed, the curling in-plane magnetizations of M_{Py} and M_{Co} remain aligned nearly antiparallel to each other, implying that the vortex configuration shown in (e) and (f) is an energetically stable micromagnetic state in the nanopillar. Finally, the switched vortex chirality is reversed back to the initial vortex configurations of M_{Py} and M_{Co} by applying a positive current pulse, 25 mA in amplitude and 200 ps in duration. The critical current density required for the back-switching is reduced to about 8×10^7 A/cm^2, which is about 20% lower than the value needed for the negative current pulse discussed in Fig. 2. In conclusion the switching of the vortex chirality of M_{Py} is understood in terms of the spin-transfer torque exerted on M_{Py}. The dynamics of the energy dissipation in the chirality switching involves a series of complex magnetization processes, which includes the magnetization precession and creation of additional vortex and antivortex cores. From an application point of view, the results suggest opportunities to implement the novel switching mechanism to memory device applications, in which vortex states with opposite chiralities in the free layer of a magnetic multlayer may be used as memory bits.

[1] B. Van Waeyenberge et al, Nature 444, 461 (2006).

[2] Q.F. Xiao et al, Appl. Phys. Lett. 89, 262507 (2006),

[3] R. Hertel et al, Phys. Rev. Lett. 98, 117201 (2007).

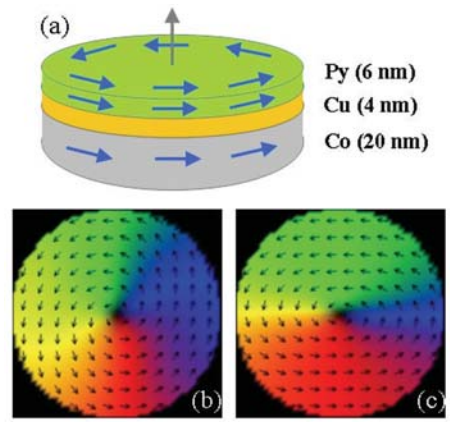

Fig. 1

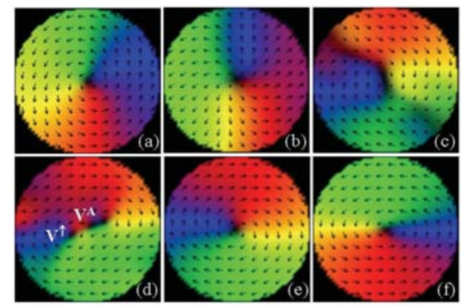

Fig. 2

HD-06

Temperature dependent exchange stiffness in FePt.

D. Hinzke[1], R. F. Evans[1], U. Nowak[1], R. W. Chantrell[1], U. Atxitia[2], O. Chubykalo-Fesenko[2], P. Asselin[3], O. N. Mryasov[3]
1. Physics, University of York, York, United Kingdom; 2. Instituto de Ciencia de Materiales de Madrid, Madrid, Spain; 3. Seagate Research, 1251 Waterfront Place, Pittsburgh, PA

In the present paper we evaluate the temperature dependent properties of the micromagnetic exchange constant in FePt, a material which has been intensively studied due to its potential application as ultra-high density recording media. We introduce different approaches to investigate the scaling of the exchange stiffness A with the magnetization M in a broad temperature range up to the Curie temperature Tc. This scaling behaviour is of interest due to its application for coarser scale micromagnetic simulations, e. g. within the framework of the Landau-Lifshitz-Bloch equation [1,2]. The exchange stiffness is also relevant for pump-probe type and heat assisted magnetic recording (HAMR) simulations [3].
We use a number of approaches to determine the exchange stiffness A within the atomistic resolution. Namely, we model bulk FePt in the chemically ordered phase using an effective classical spin Hamiltonian [4,5]. The layered structure of this phase is responsible for the fact that the interaction within the Fe planes are larger than between different Fe planes. The latter affects the domain wall width as well as its energies [4].
Within this model, we obtain thermodynamic averages, such as the internal energy, by integrating a classical Gilbert equation with Langevin thermal fields at atomic scale until the system reaches equilibrium. The free energy is obtained by integrating the internal energy over the inverse temperature. We force a domain wall in the system by means of boundary conditions. The wall width and the excess free energy yield the micromagnetic anisotropy constant and micromagnetic exchange stiffness [6]. The anisotropy is consistent with independent calculations [4]. The exchange stiffness is shown in the figure for two orientations, perpendicular as well as parallel, of the wall relative to the FePt planes.
Furthermore, for confirmation of this result, we use a generic Hamiltonian using material parameters largely comparable to the effective Hamiltonian described above. Here, we use a constrained Monte Carlo method [7] to force a spin spiral into the system in order to calculate the free energy difference between a system with and without it. This is equivalent to the evaluation of the micromagnetic exchange stiffness. Finally, our third method calculates the spin wave spectrum using Fourier transformation of magnetisation fluctuations [8] in a generic atomistic system. From the spectra we extract the spin wave stiffness, which, on the macroscopic scale, is equivalent to the micromagnetic exchange energy constant.
The comparison of values from the different methods is complicated given that the crossover is difficult to detect from numerical results. However, all these different approaches yield the same magnetisation scaling of the exchange stiffness for temperatures not close to Tc, with exponents close to 1.7. Furthermore, analytical calculation of the domain wall free energy based on mean-field approximation suggests that two different scaling laws exist, one for low temperatures and another one in the high temperature limit, with two different scaling exponents. The reason for the different regimes will be discussed.

[1] D. A. Garanin, Phys. Rev B 55, 3050 (1997)

[2] O. Chubykalo-Fesenko, U. Nowak, R. W. Chantrell, and D. A. Garanin
Phys. Rev. B 74, 094436 (2006)

[3] U. Atxitia, O. Chubykalo-Fesenko, N. Kazantseva, D. Hinzke, U. Nowak, and R. W. Chantrell,
Appl. Phys. Lett 91, 232507 (2007)

[4] O. N. Mryasov, U. Nowak, K. Guslienko, and R. W. Chantrell,
Europhys. Lett. 69, 805 (2005).

[5] U. Nowak, R. Wieser, O. N. Mryasov, K. Guslienko, and R. W. Chantrell,
Phys. Rev. B 72, 172410 (2005)

[6] D. Hinzke, U. Nowak, O. N. Mryasov, and R. W. Chantrell,
Appl. Phys. Lett. 90, 082507 (2007)

[7] P. Asselin, R. F. Evans, D. Hinzke, U. Nowak, and R. W. Chantrell,
to be published

[8] O. Chubykalo, J. D. Hannay, W. Wongsam, R. W. Chantrell, and J. M. Gonzales,
Phys Rev B 65, 184428 (2002)

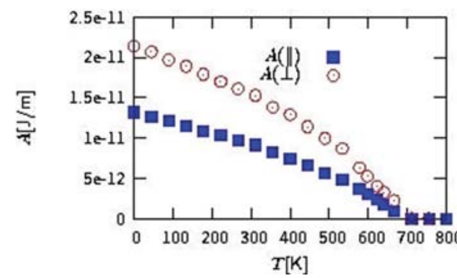

HD-07

An alternative finite element scheme for dynamic micromagnetic computations.

A. Manzin[1], O. Bottauscio[1], M. Chiampi[2]

1. Istituto Nazionale di Ricerca Metrologica, Torino, Italy; 2. Ingegneria Elettrica, Politecnico di Torino, Torino, Italy

Finite difference or finite element techniques are well established numerical methods for the spatial discretization of the Landau-Lifshitz (LL) equation [1]. The finite element method (FEM) enables the use of unstructured meshes, allowing a precise description of complex geometries, and the adaptive mesh refinement. With a 3-D FEM discretization, the unknowns are the three components of the magnetization on each grid node [2], or the projection of the magnetization on each edge of the tetrahedral mesh [3]. In both FEM approaches, the weak formulation reduces the spatial derivative order in the exchange term, but requires the enforcement of the nonconvex constraint. With nodal FEM a possible strategy is the normalization of the magnetization module after every time step [2], but no corrections are imposed on the magnetization direction. The edge FEM makes difficult the introduction of direct corrector schemes; in this case the nonconvex constraint can be approximated by a penalization strategy, which has the drawback of requiring the tune-up of the penalty and mesh parameters [4].

To overcome these difficulties, this paper proposes an alternative solution, which applies the weak formulation in the effective field expression, before solving the LL equation. The three components of the effective field are obtained by a nodal FEM approach, leading to a time-invariant stiffness matrix, which is computed once and for all at the beginning of the dynamic evolution. The instantaneous nodal values of the effective field are then introduced in the LL equation, and the magnetization is locally derived in each FEM node following a time stepping scheme able to preserve the constraint [5]. The magnetostatic field, expressed by the scalar potential, is calculated by solving the Poisson equation either with a hybrid finite element/boundary element method (FEM/BEM) or with an integral Green formulation.

The procedure is applied to the study of magnetization reversal in bulk objects and thin films with a spatially uniform distribution of the initial magnetization and subjected to a uniform and constant applied field. The method validation is obtained by comparison to analytical relationships describing the uniform magnetization state, in the case of spherical particles [6], and to the results performed with the NIST/OOMMF code, in the case of thin films.

Fig. 1 reports the magnetization time evolution in the case of precessional switching in a sphere (diameter of 250 nm) with a unixial anisotropy constant of 150 kJ/m^3 and easy axis along x-direction. The reversal is produced by an external field applied along y-axis. The computations are made with a 3-D coarse mesh having a tetrahedron edge size equal to a tenth of the sphere diameter. Despite the rough discretization, the comparison evidences how the numerical results are in good agreement with the analytical solution when calculating the magnetostatic field through the FEM/BEM approach. The Green formulation introduces numerical errors, which are reduced by refining the mesh of a factor 4.

The precessional switching in a permalloy thin film is shown in Fig. 2. The film is discretized with a 3-D mesh having a tetrahedron edge size Δs comparable to the exchange length; the method converges to the reference solution, calculated with the NIST/OOMM code, provided that the time step Δt is sufficiently small.

[1] J. Fidler and T. Schrefl, "Micromagnetic modelling –the current state of the art," J. Phys. D: Appl. Phys., vol. 33, pp. R135-R156, 2000.

[2] B. Yang and D.R. Fredkin, "Dynamical micromagnetics by the finite element method," IEEE Trans. Magn., vol. 34, pp. 3842-3852, November 1998.

[3] O. Bottauscio, M. Chiampi, and A. Manzin, "An edge element approach for dynamic micromagnetic modelling," To appear on J. Appl. Phys.

[4] A. Prohl, Computational Micromagnetism, Adv. in Numer. Math., vol. XVI, Leipzig: Teubner, 2001.

[5] M. d'Aquino, C. Serpico, and G. Miano, "Geometrical integration of Landau-Lifshitz-Gilbert equation based on the mid-point rule," J. Comp. Phys., vol. 209, pp. 730-753, November 2005.

[6] G. Bertotti and I. Mayergoyz, The Science of Hysteresis. Oxford: Academic Press, 2006.

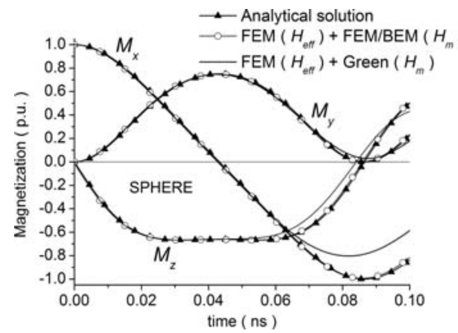

Precessional switching in a sphere with uniaxial anisotropy along x-axis. Time evolution of average magnetization, applying a uniform external field along y-axis (Ha = 0.25 Ms with Ms the saturation magnetization).

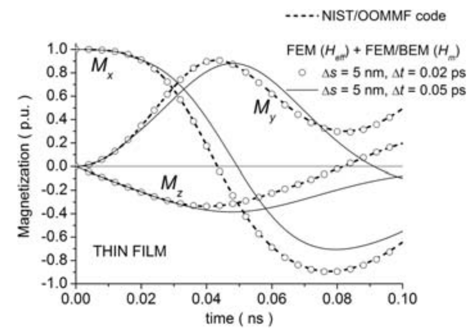

Precessional switching in a permalloy thin film, lying in the x-y plane. Time evolution of average magnetization, applying a uniform external field along y-axis (Ha = 0.063 Ms). The magnetostatic field is computed with the FEM/BEM approach.

HD-08

Innovative weak formulation for the Landau-Lifschitz-Gilbert equation.

H. Szambolics[1,2], J. Toussaint[1,2], L. D. Buda-Prejbeanu[2,3], F. Alouges[4], E. Kritsikis[2,3], O. Fruchart[1]
1. Department of Nanosciences, Institut Neel, CNRS, Grenoble cedex 9, France; 2. Institut National Polytechnique de Grenoble, Grenoble, France; 3. Laboratoire SPINTEC, CEA, Grenoble, France; 4. Laboratoire de Mathématique, Université Paris XI, Orsay, France

An innovative time integration scheme for solving the Landau-Lifschitz-Gilbert (LLG) equations based on the finite element method (FEM) was proposed by Alouges in 2006 [1]. In our paper, we generalize it by taking into account all the energy terms and evidence its robustness and reliability in strongly nonlinear dynamics.
The magnetization distribution corresponding to an equilibrium state of the ferromagnet can be obtained by minimizing the total energy E_{tot} with respect to the orientation of **m(r)** [2]. In the continuous medium approximation, this energy is the sum of several contributions:
$E_{tot}[\mathbf{m}]=\int A_{ex}[\nabla\mathbf{m}]^2dV+\int K_1[1-(\mathbf{u_K}.\mathbf{m})^2]dV-\int\mu_0M_S\mathbf{m}.\mathbf{H_{app}}dV-\int 1/2\mu_0M_S\mathbf{m}.\mathbf{H_m}dV$ (1).
This integral expression depends on the material parameters: A_{ex} the exchange constant, K_1 and $\mathbf{u_K}$ for the uniaxial anisotropy and M_S the spontaneous magnetization. $\mathbf{H_m}$ is the magnetostatic field, solution of Maxwell's equations.
The method adopted here to relax the magnetic configuration to its equilibrium state consists in integrating the dynamic LLG equations:
$\mathbf{v}=-\mu_0\gamma(\mathbf{m}\times\mathbf{H_{eff}})+\alpha(\mathbf{m}\times\mathbf{v})$ (2).
Here $\mathbf{v}$ is $\partial\mathbf{m}/\partial t$ with the constraint $|\mathbf{m}|=1$, γ is the gyromagnetic factor, α is the damping constant and $\mathbf{H_{eff}}$ is the effective field obtained by variational derivation of the total energy E_{tot} with respect to **m(r)**. Following (1) the effective field can be written as the sum of four fields: exchange field $\mathbf{H_{ex}}$, anisotropy field $\mathbf{H_{ani}}$, magnetostatic field $\mathbf{H_m}$ and applied field $\mathbf{H_{app}}$.
Solving Equations (2) using FEM, as explained below, means deriving their weak form and integrating it using the most suitable integration method [3].
Usually, the weak form is obtained by projecting the physical equations onto basis test functions w. These test functions can be piecewise linear or quadratic functions. Our FEM approach is based on an original weak formulation of the LLG equation [1]. Due to the fact that the vector fields **(m,v)** belong to mutually orthogonal subspaces, the projection method is adapted by choosing vector test functions only in the tangent space to **m**. One possibility to do that is by building $\boldsymbol{\phi}=\mathbf{m}\times\mathbf{w}$ such as $\mathbf{m}.\mathbf{w}=0$ without loss of generality. Taking these into account the weak form obtained for the LLG equations reads as:
$\alpha\int\mathbf{w}.\mathbf{v}+\int\mathbf{w}.(\mathbf{m}\times\mathbf{v})+(2A_{ex})/(\mu_0M_S)\int\nabla\mathbf{w}\nabla\mathbf{m}-\int\mathbf{w}.\mathbf{H_{loc}}=0$ (3).
Note that for the exchange term the derivation order of unknowns and test functions has been equilibrated.
The time discretization in our approach looks like a classical θ scheme. It is obtained from the weak form (Eq. 3) by replacing $\mathbf{m}(t)$ by $\mathbf{m_n}+\theta\delta t\mathbf{v_n}$, where $0\leq\theta\leq1$. In particular, $\theta=1/2$ corresponds to a Crank-Nicholson like scheme. Finally Equation 3 can be rewritten as:
$\alpha\int\mathbf{w}.\mathbf{v_n}+\int\mathbf{w}(\mathbf{m_n}\times\mathbf{v_n})+(2A_{ex}\theta\delta t)/(\mu_0M_S)\int\nabla\mathbf{w}\nabla\mathbf{v_n}=-(2A_{ex})/(\mu_0M_S)\int\nabla\mathbf{w}\nabla\mathbf{m_n}+\int\mathbf{w}.\mathbf{H}\{\mathbf{m_n}\}$ (4).
It is important to notice that the system to solve always remains linear, only a normalization of the magnetization is needed at each mesh node and for each iteration, even in the case $\theta=1/2$. This implies that the accuracy of the $\theta=1/2$ scheme is better than the implicit one ($\theta=1$), but is not of order 2 in time.
A key step is to show that the Equation 4 describes a dissipation process. In other terms, one has to check if the energy difference between two consecutive time steps:
$\delta E_n=E\{\mathbf{m_{n+1}}\}-E\{\mathbf{m_n}\}=E\{\mathbf{m_n}+\theta\delta t\mathbf{v_n}\}-E\{\mathbf{m_n}\}$ (5)
is negative. For sake of simplicity, only the exchange term is kept in the following proof. In this context, the system's energy reads as $E\{\mathbf{m_n}\}=\int A_{ex}(\nabla\mathbf{m_n})^2$ at each time step n. Writing down the energy at time step $n+1$ and making use of the weak formulation we manage to obtain the expression of δE_n:
$\delta E_n=-\alpha\delta t\int\mathbf{v_n}^2-(\theta-1/2)\delta t^2(2A_{ex})/(\mu_0M_S)\int(\nabla\mathbf{v_n})^2$ (6).
One remarks that the system's energy decreases in time only if $\theta\in[1/2,1]$.
We present here an application of our finite element approach to magnetic thin films with perpendicular anisotropy of moderate strength. The equilibrium magnetization configuration of such systems consists in a periodic modulation of the perpendicular component of the magnetization leading to parallel stripe domains [4].
To test our approach the relaxation process to equilibrium calculated by FEM is compared with the one obtained by a finite difference (FD) approach implemented in the software GL_FFT (© Institut Néel).
By monitoring the time evolution of the total energy we check that the time integration scheme describes a dissipation process towards equilibrium. A small energy gap below 0.1% is observed at equilibrium between the FD and FEM calculations. This gap can be attributed to the different ways to evaluate the total energy: FD uses local estimations of the magnetization vector and the effective field, whereas in FEM the total energy expression (1) is applied to the magnetization field interpolated on each element. A very good agreement between the results is observed on a large range of time, proving the high accuracy of our original weak form for micromagnetism.

[1] F. Alouges, P. Jaisson, Convergence of a finite elements discretization for Landau-Lifshitz equations, Math. Mod. Meth. Appl. Sci. 16 No. 2 (2006).

[2] W. F. Brown Jr., Micromagnetics, Interscience Publishers, J. Wiley and Sons, New York, 1963.

[3] D. Braess, Finite Elements, second ed., Cambridge University Press, Cambridge, 2001.

[4] J. C. Toussaint, A. Marty, N. Vukadinovic, J. Ben Youssef, M. Labrune, A New Technique For Ferromagnetic Resonance Calculations, Comp. Mat. Sci. 24 (2002).

HD-09

Stochastic dynamics and optimal switching paths in thermally activated magnetization processes of ferromagnetic nanoparticles.

C. Serpico[1], G. Bertotti[2], C. S. Ragusa[3], M. d'Aquino[4], I. D. Mayergoyz[5], P. Ansalone[3]
1. Dipartimento di Ingegneria Elettrica, Università di Napoli "Federico II", Napoli, Italy; 2. Istituto Nazionale di Ricerca Metrologica (INRiM), Torino, Italy; 3. Dipartimento di Ingegneria Elettrica, Politecnico di Torino, Torino, Italy; 4. Dipartimento per le Tecnologie, Università di Napoli "Parthenope", Napoli, Italy; 5. ECE Department and UMIACS, University of Maryland, College Park, MD

Thermal stability in submicron-sized ferromagnetic bodies is one of the crucial issues in magnetic storage technologies and spintronics.
In the last decades, this topic has received considerable attention both from the experimental and the theoretical point of view [1].
Thermally induced magnetization dynamics is usually studied by including appropriate white-noise terms into the classical magnetization dynamics equations,
such as Landau-Lifshitz (LL) or Landau-Lifshitz-Gilbert (LLG) equations [2].
The resulting Langevin-type equation is, from the mathematical point of view, a stochastic and nonlinear differential equation driven by non-additive white noise.
The solutions of this stochastic equation can be found, in principle, by direct stochastic time integration methods. On the other hand, in many situations relevant to applications, ferromagnetic elements are designed to be relatively stable against thermal fluctuations. This means that stable magnetization states are separated by large energy barriers and thermally activated transitions between these states occur on very long time scales. In these conditions, magnetization dynamics has very different time scales of evolution: stochastically perturbed precessional dynamics occurs on the picosecond time scale while thermal activated dynamics may occur on the microsecond second time scale. Since a correct stochastic time integration requires an accurate description also of the fast time scale, direct numerical Langevin simulations may become unfeasible especially when spatially nonuniformities of magnetization have to be taken into account.
The study of thermally activated transitions in these weak noise conditions can be carried out by using appropriate asymptotic techniques, such as nudged elastic band method [3], string method [4] and action functional method [5]. These techniques provide estimates of the probability of certain transitions. The probability is estimated in terms of exponential factors which can by computed by determining the most probable path followed by the state of the system to realize the transition under investigation. In the present work, we use the action functional method which is based on the Freidlin-Wentzell theory [5]. This method is applicable to stochastic systems governed by a generic stochastic differential
equation and it is based on a rigorous mathematical theory. The method is obtained by applying a large deviation principle to the probability that the stochastic trajectories generated by the differential equation are inside a specified set of paths. This probability can be formally written in terms of a Wiener path integral. According to the large deviation principle, one can prove
that the probability associated to this set of paths, in the limit of weak noise, is determined by the path in the set which minimize an appropriate action functional. This path is what is generally called an optimal path. In the case of switching between two stable states `a' and `b', the set of paths of interest is the one given by the paths starting from the point `a' and finishing in an appropriate neighborhood of the point `b'. In this case, the optimal path is also an optimal switching path.

In this work, we study systematically the accuracy, for small but finite noise, of the action functional method. This study is carried out by comparing results of direct stochastic simulations of Langevin LL with those obtained by minimization of the action functional associated to LL equation. To keep the numerical simulations feasible we have limited ourselves to the case of a uniformly magnetized anisotropic nanoparticle. Stochastic time integration is performed by using the mid-point stochastic scheme presented in Ref.[6]. In Fig.1 it is shown typical stochastic evolution of one component of magnetization obtained by stochastic time integration. On the other hand, action functional minimization is performed by a suitable numerical optimization technique.
The detailed analysis of Langevin simulations allows one to carry out an `empirical analysis' of stochastic switching paths and in this way to show how accurate is the estimate obtained by the action functional technique. The complete comparative study of these two techniques will
be presented in details in the full paper.

[1] D. Weller, IEEE Trans. Magn. 39, 3476 (2003)

[2] W. F. Brown, Phys. Rev. 130, 1677 (1963)

[3] R. Dittrich et al., J. Magn. Magn. Mater. 250, 12 (2002)

[4] W. E, W. Ren, E. Vanden-Eijnden, J. Appl. Phys. 93, 2275 (2003)

[5] M.I. Freidlin, A.D. Wentzell, Random Perturbations of Dynamical Systems, Springer, New York, 1998

[6] M. d'Aquino et al., J. Appl. Phys. 99, 08B905 (2006)

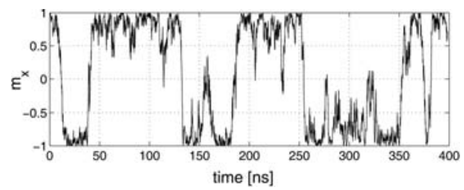

Stochastic dynamics of the component of magnetization along the easy axis of a uniaxial nanoparticle obtained by direct time integration of stochastic LLG.

HD-10

A Study of Pseudoelastic Phenomenon in Ferromagnetic Shape Memory Alloy NiMnGa by Phase-field Simulation.

X. Ma[1], P. Wu[1], J. Zhang[2], L. Chen[2]
1. Department of Physics, University of Science and Technology Beijing, Beijing, China; 2. Department of Materials Science and Engineering, The Pennsylvania State University, University Park, PA

NiMnGa, as an important kind of ferromagnetic shape memory alloy (FSMA), is currently receiving increasing attention due to its large magnetic-field-induced strain (MFIS) since their discovery by Ullakko et al in 1996. However, the effect of external mechanical input on the magnetic behavior in NiMnGa alloy received limited attention. Several authors studied reversible (pseudoelastic) stress-strain behavior of single crystal NiMnGa at a constant magnetic field. It is found that the psedoelastic stress-strain behavior only take place when the applied magnetic field exceeds certain critical value. When the applied field is lower, the quasiplastic behavior appears.

In this work, a phase-field method [1] was used to study the transition from the quasiplastic to pseudoelastic behavior under applied mechanical and magnetic field.In our model, a state of FSMA is described by two fields: a local magnetization field M(r)and a stress-free transformation strain field e. Their evolution may be obtained by solving Landau-Lifshitz-Gilbert(LLG)equation and time–dependent Ginzburg-Landau(TDGL) equation respectively.The parameters of NiMnGa employed in our model are from the references[2].

With no magnetic and stress fields applied, the Domain structure (DS) and Martensitic Microstructure (MS) are generated simultaneously. Two kinds of martensite variants(A and B)were obtained and each martensitic plate contains anti-parallel magnetic domains. The 90 degree magnetic domain walls coincide with twin boundaries.

As shown in Fig 1, a stress was applied along the y axis gradually without an applied magnetic field. In the initial stage of loading process of the quasiplastic behavior, the strain changes a little with the applied stress and both of the DS and MS have no visible deformation. With the increase of the applied stress, the loading curve climbs up rapidly. The martensite variant B grows up continuously and the variant A shrinks simultaneously. In the corresponding magnetic domain structure, the 90 degree domain wall starts to move. When the applied stress is greater than 7Mpa, only a single martensite variant left and a corresponding stripe magnetic domain structure exists. When the stress unloaded, the martensite microstructure remains unchanged, the strain will not reverse, except for the elastic deformation origining from elasticity of the material itself. There is no obvious change in the magnetic domain structure throughout the unloading process. The stress-strain curve under H=150kA/m along x axis is similar to that in Fig. 1.

The pseudoelastic curve under an applied magnetic field of 300kA/m along x is shown in Fig 2. We observed that in each variant, the original anti-parallel domain structure disappeared and were replaced by a single orient magnetic domain structure after applying the magnetic field. As a result, there is only 90 degree domain wall exists. During the loading process,the evolvement of martensite microstructure is exactly the same as the case with no external applied field, except that larger applied stress needed to move the martensite twin boundary. During the unloading stage, firstly, with the decrease of the stress, the strain decrease slowly, the domain structure and the martensite microstructure have no obvious change. But when the applied stress is lower than 0.8Mpa, the strain descends rapidly following the reducing of the stress. As shown in Fig2, the x domain expanded under the external applied magnetic field and the martensite twin boundary also started to move through the magnetoelastic coupling effect, recovering strain to its original state. Also, throughout the loading and unloading process, 90 degree domain wall and the twin boundary are matched. The magnetization-strain curve shows a narrow hysteresis.

From the observed phenomenon above, we can conclude that the 90 degree domain walls coincide with the martinsite twin boundary. Pseudoelastic stress-strain behavior will appear when the external magnetic field is large enough to move the martensite twin boundary through magnetoelastic coupling.

1. J.X.Zhang and L.Q.Chen Acta Mater, 53, 2845 (2005);

2. R.Tickle and R.D.James. J Magn. Magn.Mater 195 627 (1999)

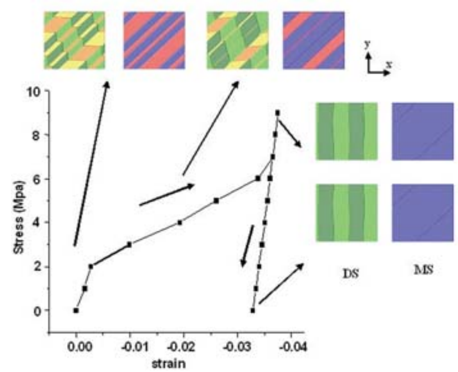

Fig 1: the strain-stress curve of NiMnGa under no applied magnetic field.

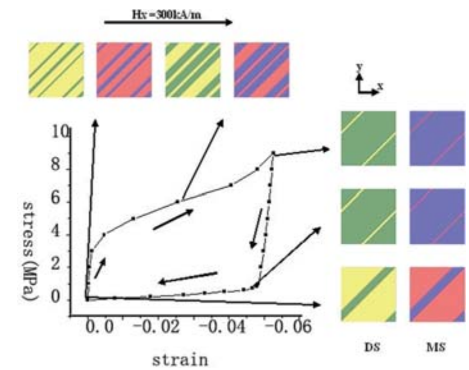

Fig2: the stress-strain curve of NiMnGa under 300kA/m under a stress of 9mpa.

HD-11

Effects of nanowire roughness on spin wave propagation.

S. Bance, T. Schrefl, D. Allwood, G. Hrkac, A. Goncharov
University of Sheffield, Sheffield, United Kingdom

Spin waves are of interest as propagators of information in the field of spin wave logic [1]. Here it is beneficial for their behaviour to be orderly and predictable so that device behaviour is reliable. Reflections from the structural boundaries of the magnetic microstructure may cause interference that would disrupt the useful waves that the devices use. Or in turn, well defined microstructural features may be used to perform certain logic operations. Wire roughness and edge defects can introduce small reflective and diffractive effects that might affect the amplitude and coherence of spin waves propagating through the wire. This work assesses the effect of wire roughness and single notches using finite element micromagnetics.

We first consider the effect of a single, triangular notch on the propagation of spin waves through a nanowire. A permalloy nanowire of width 100 nm and thickness 10nm has a notch of width 50 nm and depth 25 nm on one edge. An external field is applied in a locally confined region at a distance of 200 nm from the notch to generate spin waves that travel outwards along both directions of the wire. Fig. 1 shows the two spin wave packets travelling from the centre to the two ends of the wire. The notch on the right hand side of the wire decreases the spin wave amplitude but does not hinder spin wave propagation. A probe is placed after the notch at a distance of 150 nm from the centre of the notch. The Fourier transform of the transverse magnetization at the probe point shows a decay of the spin wave amplitude and a slight shift of the spin wave frequency if the spin wave packet passes the notch. However, this change is observed only for a notch of width 50 nm and depth 25 nm. For a notch of only half of this size no significant change in the Fourier spectrum is observed due to the presence of the notch (see Fig. 2).

The spin wave propagation across the wire depends on the local initial susceptibility of the transverse magnetization. The wire is split into regions each of length 100 nm in order to calculate the magnetic susceptibility in each region. The local susceptibility at probe points in the vicinity of the notch is similar to the susceptibility at other points along the wire. Whereas the existence of a notch does not perceivably alter the susceptibility in the region around it, the initial susceptibility close to the two wire ends is about two times higher than in the rest of the wire.

Four nanowires with different types of roughness have spin waves generated at their centre, as above, and probes to measure the peak spin wave amplitude at different probe positions along the wire. The results (Fig. 3) show that introducing roughness into the wire can reduce the propagation amplitude of the spin waves.

We conclude that notches in a nanowire can reduce spin wave transmission through the nanowire and may be used to adjust the spin wave frequency. Since wire roughness can be modelled as a series of notches, roughness may also hinder spin wave propagation.

[1] A. Khitun & K. L. Wang, Superlattices and Microstructures 38 pp. 184-200 (2005)

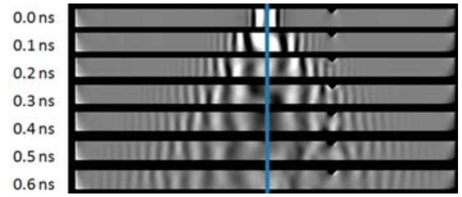

Figure 1. Spin wave propagation from the centre of a 100 nm wide nanowire. The notch does not hinder the propagation of the spin wave packet but reduces the spin wave amplitude. The perpendicular magnetization component is colour coded at different times after perturbing the magnetisation in the wire centre.

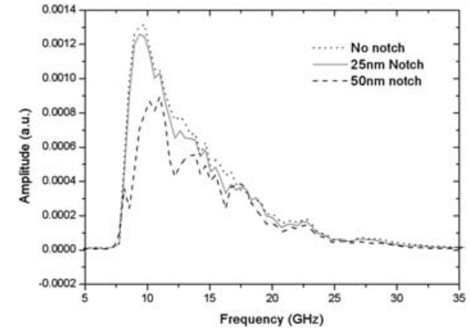

Figure 2. Spin wave frequency plot for a probe positioned after the notch shows reduced transmission of the spin waves for increasing notch size. The Fourier transform of the transverse magnetization is plotted for wires with notch width 50 nm, 25 nm, and no notch.

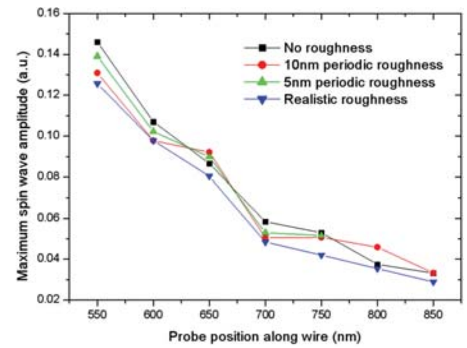

Figure 3. Spin wave maximum amplitudes at positions along a permalloy nanowire. The spin wave amplitude can vary by around 15% depending on the type of roughness used. Shown here are two examples of triangular, periodic roughness of various size as well as realistic roughness taken from a micrograph image. These are compared to a wire with no roughness.

Effect of interface exchange coupling on the reversal of single antiferromagnetic grains in exchange bias systems.

J. Jackson, U. Nowak, R. Chantrell
Physics, University of York, York, United Kingdom

The exchange bias and coercivity increase observed in multilayer systems, consisting of an antiferromagnetic (AFM) layer exchange coupled to a ferromagnetic (FM) layer, are strongly affected by the characteristics of the AFM layer during field reversal. For a single grain in an exchange decoupled AFM film, the size, geometry and interface structure determine whether the AFM sublattice magnetisation reverses and, if reversal does occur, the mechanism of reversal.
Here, zero temperature atomistic simulations using the Landau-Lifshitz-Gilbert equation are presented, modelling the reversal of single antiferromagnetic grain due to the exchange field of an interfacial FM. The transition from collective reversal to incoherent reversal has been studied for systems with perfect interfaces; FM/AFM interfaces with a step like structure having varying proportions of each AFM sublattice coupled to the FM have also been examined.
For the case of perfectly uncompensated interfaces and in the small grain limit, reversal proceeds by coherent rotation analogous to Stoner-Wohlfarth switching. When the grain length is comparable with the material domain wall width, reversal occurs by the introduction and propagation of a domain wall in the AFM grain in accord with the Mauri model [1]. During such domain wall assisted reversal, a distortion of the magnetisation away from the easy axis is introduced into the grain at the interface. This is the minimum energy configuration for small deviations of the ferromagnet orientation from the antiferromagnet easy axis, but becomes metastable as the partial domain wall angle increases. This results in hysteresis in the reversal of the AFM which is considered to be a realistic dynamic effect having an energy barrier corresponding to the domain wall energy of the grain.
When the interface contains a step, AFM ordering is frustrated and a distinct surface domain forms for all orientations of the ferromagnet. This surface domain, which minimises exchange energy at the surface, prohibits coherent AFM magnetisation reversal for all film thicknesses by eliminating the energy barrier of establishing a domain wall within the grain. Because the axial symmetry of the system is broken by the surface step, reversal occurs by collective spin fluctuations out of the interface plane resulting in reversal hysteresis different to that observed for perfect interfaces.
Atomic resolution simulation shows that the dynamics for step-like interfaces cannot be simply described by a varying interface coupling because of the domain structure present at the interface. These simulations provide a framework for advancing micromagnetic simulation studies of the exchange bias effect; realistic reversal energy barriers together with a more accurate description of the import ace of surface inhomogeneity and interface exchange coupling variation can substantially improve Fulcomer-Charap type approaches [2].
It has also been found that the domain wall energy in finite systems depends upon the crystallographic orientation of the major axis of the grain. For systems where the grain axis is aligned along the [111] direction, the energy barrier tends to the energy of a 90 degree domain wall in the limit of infinite film thickness. This effect, which is most pronounced as the aspect ratio of the grain is increased, is important for film thicknesses found in modern sensor devices.

[1]D. Mauri, H.C Siegmann et.al J. Appl. Phys. 62 (1987) 3047

[2]E. Fulcomer and S.H. Charap J. Appl. Phys. 43 (1972) 4190-4200

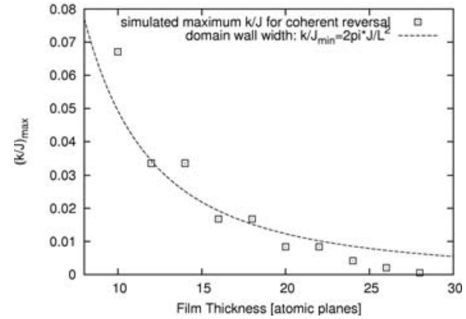

Maximum uniaxial AFM anisotropy for coherent reversal for perfectly uncompensated FM/AFM interfaces. The dotted line shows the prediction of the 1-dimensional Heisenberg model.

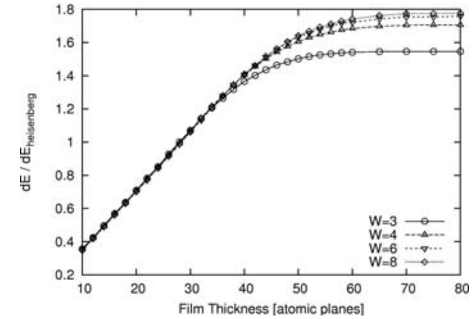

Change in the AFM reversal energy barrier, dE, as a function of Length for different grain widths. For the [111] interface, the energy change is larger than that predicted by the 1-dimensional Heisenberg model. The different lines correspond to varying grain radius (lattice units).

HE-01

Microtexture and Magnetic Microstructure of Sputtered NdFeB Thick Films Destined for Application in Micro-Electro-Mechanical Systems (MEMS).

T. G. Woodcock[1], K. Khlopkov[1], A. Walther[2], N. M. Dempsey[2], D. Givord[2], O. Gutfleisch[1]
1. Institute for Metallic Materials, IFW Dresden, Dresden, Germany; 2. Insitut Néel, CNRS, Grenoble, France

Thick films (5-300 µm) of NdFeB have excellent hard magnetic properties which make them attractive for applications in micro-electro-mechanical systems (MEMS) [1]. Such films have been prepared by a two step process consisting of triode sputtering followed by high temperature annealing of the as-deposited film [2,3,4]. Optimum magnetic properties were achieved for a substrate temperature of 500°C during deposition and an annealing temperature of 750°C for 10 min with a rapid heating rate [3,4]. In this digest, detailed characterisation of the local crystallographic texture and magnetic microstructure of the NdFeB layer are presented.
Triode sputtering was used to deposit {Ta (100 nm) / NdFeB (5 µm) / Ta (100 nm)} multilayers onto 100 mm diameter Si substrates at various temperatures. Details of the deposition procedure are given elsewhere [3,4]. The microtexure of the NdFeB layers was investigated in plan view by electron backscatter diffraction (EBSD) in a FEG-SEM. The magnetic microstructure of the NdFeB layers was investigated using magnetic force microscopy (MFM) using hard magnetic tips.
The misorientation of the NdFeB grains with respect to the ideal orientation [001]//film normal is shown for deposition at 300°C (fig. 1a) and 500°C (fig. 1b). Both films were annealed at 750°C for 10 min after deposition. The grains are coloured according to the misorientation angle given in the colour key. Grain boundaries are shown in black. The grey areas in fig. 1a and b correspond to those electron backscatter diffraction patterns which could not be indexed as the Nd2Fe14B phase. These points are due to imperfections or contamination on the polished surface. Although the proportion of these points is relatively high, significant microtexture information has still been obtained. Blue and dark green grains have a misorientation of < 20° and are therefore considered to be well oriented. Although the sample deposited at 300°C (fig. 1a) has a large fraction of well oriented grains, the sample at 500°C (fig. 1b) is entirely well oriented. This is also shown by the misorientation distribution above the colour key (fig. 1a and b) which is much sharper and has its maximum at a lower angle for the film deposited at 500°C. Sharper texture leads to higher out of plane magnetic anisotropy and therefore to an improved energy product (BHmax) [3].
The magnetic microstructure of the NdFeB films imaged by MFM is shown in fig. 2 for films in the as-deposited state. Bright areas correspond to domains directed out of the plane of the image and dark areas are domains oriented 180° to the bright ones. The films deposited without substrate heating (fig. 2a) and at 400°C (fig. 2b) have magnetic domains typical of amorphous materials. These films were reported to be amorphous in the as-deposited state [3]. The film deposited at 500°C was reported to be crystalline and to display hard magnetic properties [3] and this is reflected in the magnetic microstructure (fig. 2c) which is typical for crystalline materials with high magnetic anisotropy.
A comparison of MFM images of samples in their as-deposited and annealed states will be made. The evolution in the characteristics of the magnetic microstructure, with increasing deposition temperature, will be discussed. The application of EBSD to study microtexture in NdFeB films is a novel approach and is expected to become an important characterisation tool in these systems. A combination of high resolution characterisation techniques is vital for the development of MEMS.

[1] O. Cugat, J. Delamare, and G. Reyne, IEEE Trans. Magn. 2003, 39 (6), 3607-3612

[2] B.A. Kapitanov, N.V. Kornilov, Ya.L. Linetsky, V.Yu. Tsvetkov, J. Magn. Magn. Mater. 1993, 127 (3), 289-297

[3] N.M. Dempsey, A. Walther, F. May, D. Givord, K. Khlopkov and O. Gutfleisch, Appl. Phys. Lett. 2007, 90, 092509, 1-3

[4] A. Walther, K. Khlopkov, O. Gutfleisch, D. Givord and N.M. Dempsey, J. Magn. Magn. Mater. 2007, 316, 174-176

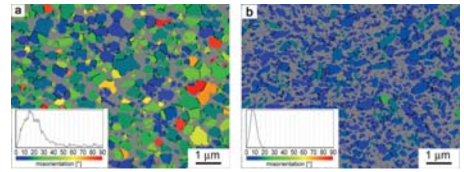

Fig. 1 Plan view EBSD maps showing the misorientation of the NdFeB grains from the ideal orientation [001]//film normal. The corresponding colour key and misorientation distribution are given in both cases. (a) deposited at 300°C. (b) deposited at 500°C. Both films were annealed at 750°C following deposition.

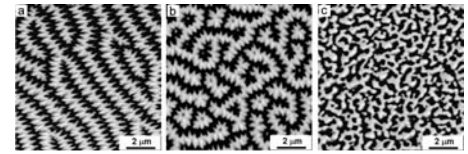

Fig. 2 MFM images of NdFeB films deposited without substrate heating (a), at 400°C (b) and at 500°C (c). The films were in the as-deposited state.

HE-02

Temperature dependent anisotropy in epitaxial Pr-Co films.

A. K. Patra[1], M. Eisterer[2], R. Biele[1,3], S. Fähler[1], L. Schultz[1], V. Neu[1]
1. IFW Dresden, Dresden, Germany; 2. Atomic Institute of the Austrian Universities, Vienna, Austria; 3. University of Technology Dresden, Dresden, Germany

Recently, epitaxial Pr-Co films have been prepared on Cr buffered MgO(110) substrates with a single orientation of the c-axis along the MgO[001] and record values of M_s and energy density ($(BH)_{max}$ = 310 kJ/m^3) [1]. In this work, we focus on the intrinsic properties of such a highly textured, epitaxial $Pr_{15.4}Co_{84.6}$ film, especially on the temperature dependent anisotropy including the spin reorientation transition (SRT).
The magnetic characterization was performed by measuring magnetization curves in a VSM with field applied along different angles with respect to the texture axis of the sample at various temperatures (Fig. 1). To determine the anisotropy constants a full range fitting procedure to the magnetization loops in a field range of 2 to 5 T is performed. The theoretical magnetization loops were calculated based on an energy minimization code including anisotropy energy up to second order (K_1 and K_2) and magnetostatic energy of the magnetization vector in an applied field. A realistic texture spread of 10° was implemented by averaging over a Gauss shaped c-axis distribution around the texture axis of the sample. For a given temperature, measurements at 5 different angles were fitted simultaneously to derive the first and second order anisotropy constant (K_1 and K_2). In Fig. 2 the measured magnetization loops at a temperature of 220 K are shown. For the applied field along the easy axis ($\alpha = 0$), the magnetization curve in the first quadrant reaches a constant value of M_s already at small fields. When the field is applied at an angle to the easy axis ($0 < \alpha \leq 90°$), the field leads to a rotation of the magnetization vector away from the easy axis and consequently the remanent magnetization decreases and the slope of the magnetization loop increases. Fig. 3 shows the first quadrant magnetization curve measured at 100 K (open circle) together with the calculated curve (line) obtained from the minimization routine. It is worth noting, that at this temperature the $Pr_{15.4}Co_{84.6}$ film is below the SRT and the anisotropy energy is minimum in an easy cone configuration around the c-axis. This is apparent from the reduced slope of the magnetization curve at α = 90°, which would intersect the magnetization axis at a non-zero remanence value. The anisotropy constants K_1 and K_2 as a function of temperature are shown in Fig. 4. The measured value of K_1=4.8 MJ/m^3 at room temperature is lower compared to the bulk single crystal value of K_1 = 7.7 MJ/m^3 for $PrCo_5$ [2], whereas the value of K_2 = 1.1 MJ/m^3 is higher. This discrepancy may be due to the high Cobalt content of this $Pr_{15.4}Co_{84.6}$ film, which is optimized for high saturation magnetization or due to the presence of a mixed phase. Nevertheless, the nature of the curves are similar to the bulk with a monotonic increase of K_2 and a decrease of K_1 with decrease in temperature, and a sign reversal of K_1 at about 120 K, which manifests the spin reorientation transition.

[1] A. K. Patra, V. Neu, S. Fähler, R. Groetzschel, S. Bedanta, W. Kleemann and L. Schultz, Phy. Rev. B. 75, 184417 (2007).

[2] E. Tatsumoto, T. Okamoto, H. Fujii, and C. Inoue, J. de Phys. 32, C1-550 (1971).

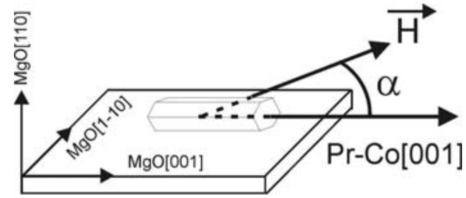

Fig. 1: Field direction with respect to the sample orientation.

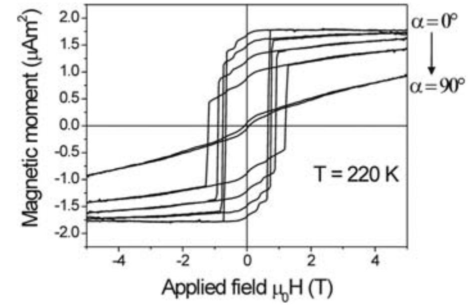

Fig. 2: Magnetization loops of $Pr_{15.4}Co_{74.6}$ measured at 200 K for angle α = 0°, 30°, 45°, 60° and 90° between applied field and the texture axis.

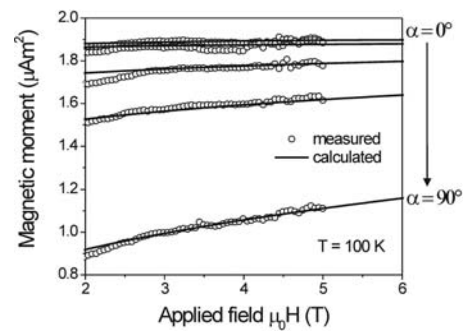

Fig. 3: Measured (open circle) and calculated (line) magnetization curve in the first quadrant for $Pr_{15.4}Co_{74.6}$ at 100 K (angle α as in Fig. 2).

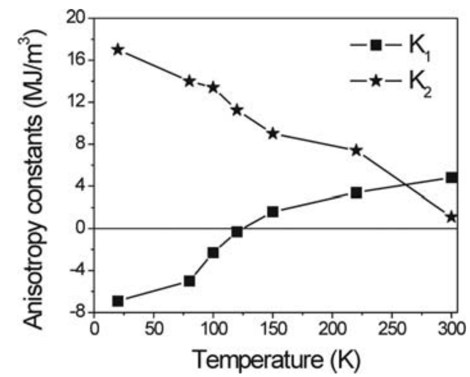

Fig. 4: Temperature dependence of the anisotropy constants K_1 and K_2 of the epitaxial $Pr_{15.4}Co_{74.6}$ film.

HE-03

Sintered Sm_2Co_{17}-based Magnets with Small Additions of Indium.

A. Gabay[1], M. Marinescu[2], J. Liu[2], G. C. Hadjipanayis[1]
1. University of Delaware, Newark, DE; 2. Electron Energy Corporation, Landisville, PA

In the best currently used high-temperature Sm-Co permanent magnets, the coercivity is developed in the bulk state through a multiphase “cellular” nanostructure. To assure this some excess of Sm and 7 - 10 at. % of Cu and Zr must be added to the alloy, which decreases the amount of high-magnetization $Sm_2(Co,Fe)_{17}$ phase. The earlier attempts to obtain “pure” 2:17 magnets were not very successful [1,2], though a maximum energy product of 28 MGOe has been reported for magnets containing Mn [3]. Coercivity of magnets fabricated via sintering of anisotropic micron-size powders critically depends on the state of their grain boundaries. In particular, the high performance of sintered Nd-Fe-B magnets is assured by the low-melting-temperature Nd-rich phase which magnetically insulates the $Nd_2Fe_{14}B$ grains and inhibits nucleation of reversed magnetic domains.
In this work, we analyzed the grain-boundary phases formed in the $Sm_2(Co,Fe)_{17}$ sintered magnets due to small additions of several elements (Ag, C, Ga, In, Sn) and their combinations. Differential thermal analysis (DTA) indicates the appearance of a liquid phase at 1055 - 1070 °C in In-added Sm_2Co_{17} and $Sm_2(Co,Fe)_{17}$ alloys (Fig. 1). According to energy-dispersive spectrometry (EDS), the grain-boundary phase found in the In-added cast alloys and in sintered magnets is enriched in both Sm and In (Fig. 2). Virtually all the added In is concentrated in this phase, where its content reaches 18 - 20 at.%. Due to the lowered solidus temperature, the 2:17 magnets with only 0.5 at.% In exhibit a density of 0.98 times that of the ingot after sintering for 1 h at 1075 °C (Fig. 3a), which is more than 100 degrees lower than the usual sintering temperature of the 2:17 magnets.
The addition of In also led to a significant increase in the coercivity (Fig. 3b), though the reasonable values were obtained only for the $Sm_2(Co,Fe,Mn)_{17}$ matrix phase known to have an enhanced magnetocrystalline anisotropy [3]. The coercivity was found to be very sensitive to the post-sintering heat treatment, as shown in Fig. 4, and it is dramatically reduced if the magnets have been quenched from a temperature lower than 1000 °C after annealing for 1 h at this temperature. This behavior resembles that of the $SmCo_5$ magnets, though the most usual explanation of the latter (the 1:5 phase supposedly decomposes into the 2:17 and 2:7 phases) is hardly applicable to the 2:17 magnets. The coercivity values of optimally annealed magnets with different Sm content are also shown in Fig. 4. In conclusion, the small In additions greatly facilitate sintering of the “pure” 2:17 magnets, but more effort is needed to obtain a high magnetic performance.
This work was supported by Air Force through STTR contract FA9550-07-C-0029.

[1] R.C. Carriker, A.S. Rashidi, AIP Conf. Proc. 10, 608 (1973).

[2] R.S. Perkins, S. Gaiffi, A. Menth, IEEE Trans. Magn. 11, 1431 (1975).

[3] H. Nagel, AIP Conf. Proc. 29, 603 (1976).

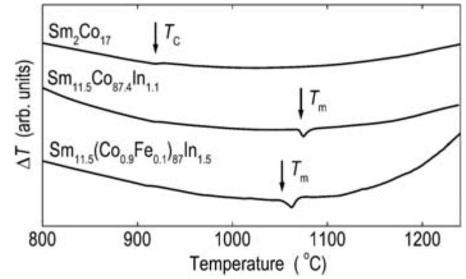

Fig. 1. Heating DTA curves of three Sm-Co -based cast alloys. T_C and T_m indicate the Curie temperature and solidus temperature, respectively.

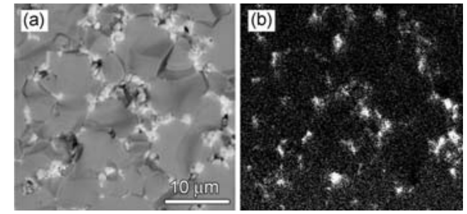

Fig. 2. SEM characterization of $Sm_{12.5}(Co_{0.85}Fe_{0.075}Mn_{0.075})_{86}In_{1.5}$ magnet sintered at 1075 °C: (a) fractured surface and (b) corresponding EDS map for In.

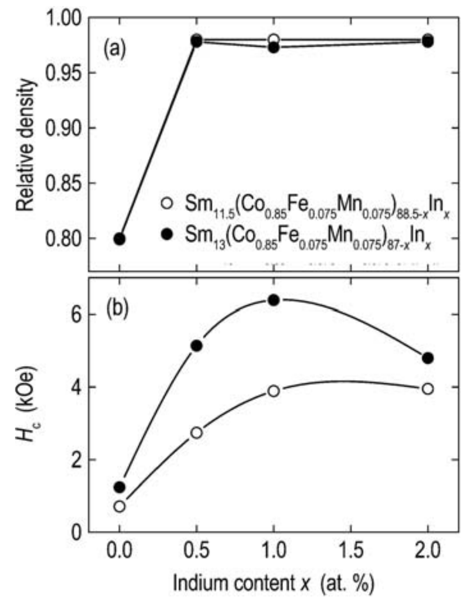

Fig. 3. Effect of In content on relative density and intrinsic coercivity of magnets sintered at 1075 °C and annealed at 1000 - 1050 °C.

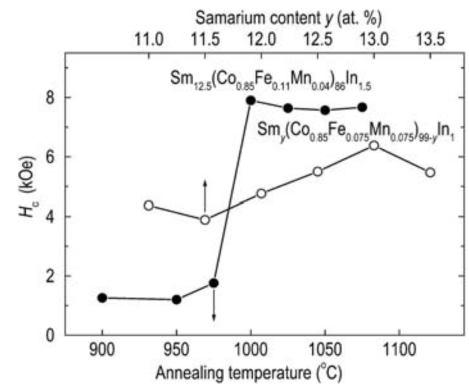

Fig. 4. Effects of post-sintering annealing and Sm content on intrinsic coercivity of magnets sintered at 1075 °C.

HE-04

Prediction of temperature demagnetization of bonded rare earth magnets by finite element analysis.

T. Schliesch, T. Lindner
Max Baermann GmbH, Bergisch Gladbach, Germany

Often permanent magnets suffer irreversible losses of magnetic flux by changes of temperature or by external fields. This especially is of relevance for many sorts of bonded magnets on rare earth basis like NdFeB or SmFeN magnets. Mechanisms for magnetic weakening can be sought in mainly three effects: Passage of magnetization to minor hysteresis curves, change of operating points by magnetic viscosity and flux losses due to oxidation. In our paper we will deal with the analysis of the first two effects. The method we use is applied for homogeneously magnetized magnets as well as for specimen, which have non trivial shape of polarization. Predictions by FEM will be compared with experimental results.
Fig.1a sketches the basic principle of magnetic losses in rare earth magnets due to the movement of operating points to minor hysteresis loops when temperature is changed. Here e.g. a point A changes to B when the magnet is exposed to a high temperature, and finally to C when the sample is cooled down again. In bonded NdFeB magnets such losses due to a movement to recoil curves even start at low magnetic loads, as the most materials show a bent demagnetization curve already at locations close to remanence. On the other hand also magnetic viscosity plays an important role for these sorts of magnets, which can be seen in Fig. 1b. by the flux loss of a bonded NdFeB sample as a function of time. In Fig.1a. this effect can be described by a vertical movement e.g. of point B to point B' at high operating temperatures.
To perform a quantitative description of the irreversible losses of bonded magnets, especially after the exposition to high operating temperatures, we included both effects into the FEM analysis of the related systems. The recoil curve effect was treated by modeling temperature dependent demagnetization curves and by transferring the operating point locations to inner loops when temperature changes and irreversible parts of the demagnetization curve are occupied. The minor curves were modeled as unique curves for simplicity. This process was done for each finite element of the magnet due to the spatial spreading of magnetic loads, which takes place even for homogenously magnetized magnets. The impact of viscosity was modeled by treating it as an additional, time dependent field, which generally is also different at different locations in the magnet. For non homogenous magnets which were magnetized by pulse magnetization, in addition the pulse magnetization process had to be modeled by coupling the coil model with that of the magnetizers circuit and by applying a simple hysteresis model. Fig. 2 shows the degree of saturation for such a non homogenous magnet of rotational shape, which had a two pole bow shaped magnetization in axial direction. In Fig.2 the specimen is only partially saturated. This magnet was analyzed in regard to its losses after temperature exposition in saturated as well as in non saturated state to proof the accuracy of our method under different conditions. All predictions by finite elements were compared to experimental values by comparing computed fields outside the magnet with hall probe measurements.
One of our main results was that a neglect of magnetic viscosity always led to wrong predictions of magnetic losses with an error up to 50%, whereas the inclusion of viscosity resulted in good to adequate correspondences with experimental results. The predicted external fields always were a useful approximation of reality as long as magnetic loads were not to high and as long the upper temperature was within reasonable limits. Fig. 3 shows the change of the axial field maximum on a circular path above the non homogenous magnet of Fig. 2 after different temperature expositions, at different distances to the magnets surface and for different magnetizing voltages.

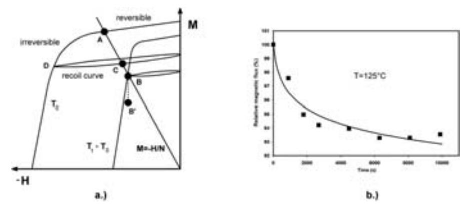

Fig. 1: a): Mechanism of temperature losses in permanent magnets on rare earth basis by movement of operating points to inner branches of hysteresis. b): Magnetic viscosity effect on an isotropic bonded NdFeB sample.

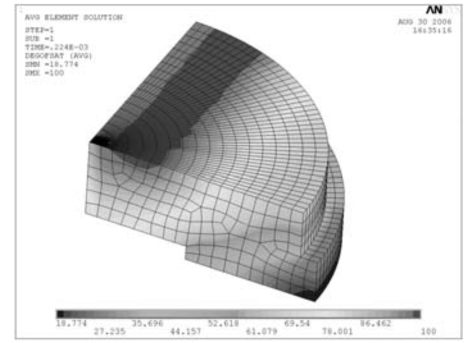

Fig. 2: Degree of saturation (%) of a cylindrical injection molded NdFeB magnet with two pole axial magnetization, U =400V.

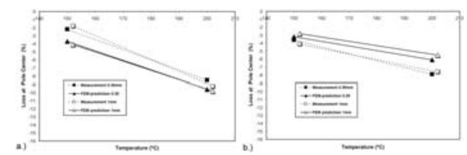

Fig. 3 : Relative change of room temperature flux density at pole center after 2h exposition to high temperatures: a): r=6mm, U=400V; b): r=6mm, U=1500V. Comparison of FEM predictions with Hall probe results.

HE-05

New Dy-substituted Ba hexaferrites with high coercivity.

G. Litsardakis[1], I. Manolakis[1], A. Stergiou[2], C. Serletis[2], K. G. Efthimiadis[2]
1. Dept. of Electrical & Computer Engineering, Aristotle University, Thessaloniki, Greece; 2. Dept. of Physics, Aristotle University, Thessaloniki, Greece

Several rare earth additions have been tried recently in Ba and Sr hexaferrites after the preparation of Sr-La-Co sintered magnets with improved magnetic properties [1]. Addition of Sm, Nd and Pr has resulted in coercivity enhancement which is generally attributed to microstructural effects [2-4]. Single-phase rare-earth substituted hexaferrites have been obtained only with Nd by the chemical coprecipitation method [3] and with Gd by both the classical ceramic [5] and the coprecipitation methods [6]. In this report we present for the first time the synthesis and properties of a new series of Ba-Dy hexaferrites with enhanced coercivity.
Samples with nominal chemical formula $(Ba_{1-x}Dy_x)O\times5.25Fe_2O_3$ (x =0-0.30) were prepared by the chemical coprecipitation method from nitrate salts and then heated at T_h = 900-1200 °C for 2 h. Phase formation and crystal structure have been examined by x-ray powder diffraction with CuKα radiation. The recorded diffraction patterns have been analyzed by the Rietveld method. Magnetization measurements were performed by VSM at room temperature with maximum field 1.8 T.
Diffraction patterns of samples heated at 1000 °C are presented in Fig.1. All samples present the M-type hexaferrite structure (s.g. $P6_3/mmc$, a≈5,88Å και c≈23,2Å) and are single-phase up to x=0.15 for T_h=900 °C and x=0.10 for T_h=1000 °C. Beyond this substitution range, Fe_2O_3 is present as the only secondary phase in small amounts ~ 1-10 %. Formation of α-Fe_2O_3 is also favored by the increase of the heating temperature.
The absence of other phases suggests that Dy is incorporated in the hexaferrite structure in the whole substitution range. This has not been observed in other rare earth substituted hexaferrites, except for Gd [6].
The hysteresis loop of sample x=0.25 για T_h=1000 °C, presenting a coercive field H_c= 441 kA/m (5.6 kOe) is shown in Fig. 2. In Fig. 3 the variation of specific saturation magnetization σ_{sat} and coercivity H_c with substitution x are traced for T_h=1000 °C. Coercivity is high (~365-410 kA/m), and increases significantly up to ~440 kA/m for x=0.15-0.25, at T_h=1000 °C, while it decreases for x=0.30. Magnetization decreases slightly with substitution and ranges between 65-62 Am^2/kg up to x=0.25. The decrease of magnetization is related to the presence of α-Fe_2O_3. The variation of coercivity may be attributed mainly to the influence of Dy on grain growth, according to the studies of the analogous Gd series, $(Ba_{1-x}Gd_x)O\times5.25Fe_2O_3$ [6]. A similar behaviour is observed in Sr-Dy hexaferrites which are currently under study.

[1] Kools, F. et al, J. Magn. Magn. Mater. 242-245 (2002) 1270-1276

[2] Lechevallier, L. et al, J. Magn. Magn. Mater. 269 (2004) 192

[3] Yamamoto H., Isono M. and Kobayashi T., J. Magn. Magn. Mater. 295 (2005) 51-56

[4] Wang J.F, Ponton C.B. and Harris I.R., J. All. Comp. 403 (2005) Issues 1-2, 104-109

[5] G.Litsardakis, I.Manolakis, C.Serletis and K.G.Efthimiadis, J. Magn. Magn. Mater. 310 (2007) e884-886

[6] G.Litsardakis, I.Manolakis, C.Serletis and K.G.Efthimiadis, 52nd MMM Conference (2007), paper CT-07 (to appear in J.Appl.Phys.)

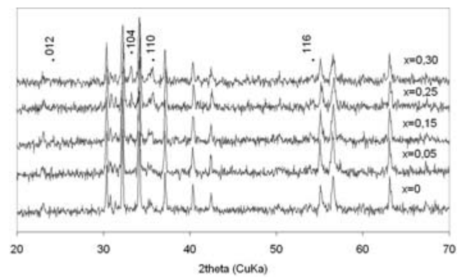

Fig.1 Diffraction patterns of samples $(Ba_{1-x}Dy_x)O\times5.25Fe_2O_3$ (x=0–0.30) heated at 1000 °C. The positions of α-Fe_2O_3 peaks are shown.

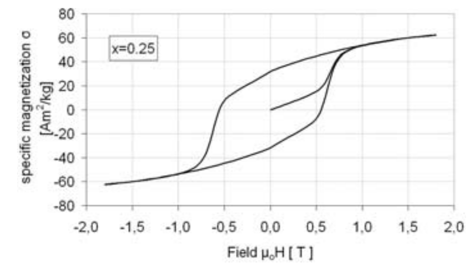

Fig.2 Hysteresis loop for x=0.25 and T=1000 °C

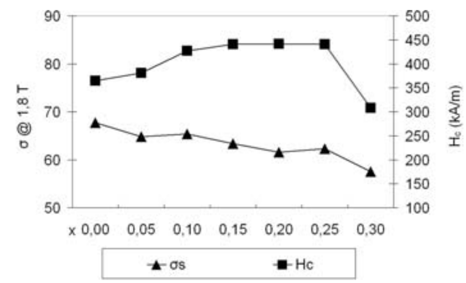

Fig.3 Specific magnetization (△) at 1.8 T and coercivity (■) for x=0-0.3 and T_h=1000 °C

HE-06

Strain-induced exchange bias effects in chemically ordered Pt_3Fe single crystal.

S. Kobayashi, S. Takahashi, Y. Kamada, H. Kikuchi
Faculty of Engineering, Iwate University, Morioka, Japan

The chemically long-range ordered Pt_3Fe alloy has $L1_2$-type superlattice structure and exhibits paramagnetic-antiferromagnetic phase transition at T_1 = 170 K, associated with magnetic structure characterized by propagation vector **q**=(1/2 1/2 0).[1] With decreasing temperature, Pt_3Fe alloy shows another antiferromagnetic phase transition at T_2 = 100 K below which two types of magnetic structures with **q**=(1/2 1/2 0) and (1/2 0 0) coexist.

Plastic deformation on such chemically ordered alloy drastically changes the magnetic property, because it strongly depends on the atomic arrangement and/or the configuration of atom-atom pairs. It was shown that plastic deformation on Pt_3Fe single crystal results in superlattice dislocations with burgers vector of (a/2)<110> and glide plane of {111}, and large spontaneous magnetization shows up even at room temperature after very small plastic deformation by 1.3% strain.[2] The appearance of the large ferromagnetism was explained as due to ferromagnetic domains produced around slip planes where strong ferromagnetic exchange coupling between Fe atoms plays a crucial role. In spite of the understanding of formation mechanism of ferromagnetic domains, however, the coupling between the ferromagnetic domains and antiferromagnetic structure in $L1_2$ matrix has not been studied. In this paper, we report the results of magnetic hysteresis loop measurements on chemically ordered Pt_3Fe single crystals after tensile deformation up to 29.8% strain.

Measurements of magnetic hysteresis loops for lightly deformed Pt_3Fe single crystals were performed using a commercial Quantum Design SQUID magnetometer with magnetic fields up to 50 kOe in the temperature range from 5 to 300 K. We confirmed that ferromagnetism, associated with magnetic hysteresis, appears for all deformed samples in all temperature range below 300 K and found that the loop area and coercive field increase with decreasing temperature. However, when the samples were field-cooled at H = 20 kOe from 300 K, observed magnetic hysteresis loops were found to be shifted toward the negative field, unlike normal hysteresis loops centered at origin obtained after zero-field cooling. Figure 1 shows temperature dependence of field shift toward a negative field i.e. exchange bias H_{eb}, obtained after field cooling at 20 kOe. For all deformed samples, exchange bias effect shows up below T_1 and H_{eb} rapidly increases with decreasing temperature. Increasing the level of deformation first makes H_{eb} increase at each temperature but further deformation rather makes it decrease. Such behavior of H_{eb} was also observed after field cooling at H = 10 kOe, though a decrease of cooling field enhances the exchange bias effect. These observations reflect strong coupling between antiferromagnetic matrix and ferromagnetic domains formed around superlattice dislocations in plastically deformed Pt_3Fe single crystal.

[1] G.E. Bacon and J. Crangle, Proc. Roy. Soc. (London) A272 (1963) 387.

[2] S. Takahashi and Y. Umakoshi, J. Phys.: Condens. Matter 2 (1990) 2133.

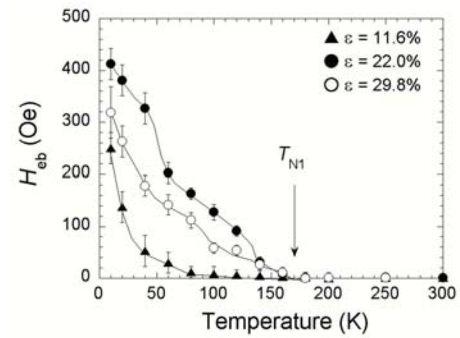

Figure1: Temperatue dependence of H_{eb}, obtained after field cooling at 20 kOe.

HE-07

Fe-Pt thick film magnets prepared by high-speed PLD method.

S. Shibata, *M. Nakano*, T. Yanai, H. Fukunaga
Electronics and Electrical Engineering, Nagasaki University, Nagasaki, Japan

In order to apply Fe-Pt film magnets for dental attachment[1] and medical micro-machines, the films with high energy product and thickness of several tens of microns are needed. A dominant method for obtaining Fe-Pt thick films is a sputtering method. For example, Aoyama et al. reported a 129 micron-thick film with Hc= 580 kA/m and (BH)max = 104 kJ/m3, and a 7 micron-thick Fe-Pt film was reported by Liu et al. to have magnetic properties with Hc= 446 kA/m and (BH)max = 124 kJ/m3 [2][3]. The sputtering method, however, includes the difficulty of deposition speed for a mass-production of the above-mentioned miniaturized devices. This contribution reports PLD(Pulsed Laser Deposition)-fabricated Fe50Pt50 films thicker than 10 microns under the high deposition rate up to approximately 40 microns/h. A Fe-Pt target was ablated with a Nd-YAG pulse laser at the repetition rate of 30 Hz, and the films were deposited on Ta substrates. Before the ablation, the chamber was evacuated down to approximately 0.1 mPa with a molecular turbo pump. The distance between a target and a substrate was fixed at 10 mm. The deposition rate was varied by controlling the laser power between 1 and 9 W at the irradiation exit of a Nd-YAG laser system. The composition of all the obtained films was approximately Fe50Pt50. After an as-deposited sample was magnetized up to 7 T with a pulse magnetizer, magnetic properties were measured with a vibrating sample magnetometer which could apply a magnetic field up to approximately 1800 kA/m reversibly. All films were magnetically isotropic and, therefore, in-plane magnetic properties were shown in this abstract. Figure 1 shows the thickness of Fe-Pt film magnets as a function of the laser power. The deposition rate was proportional to a laser power. The wide deposition rate ranging was realized in our PLD system, and the maximum value of 40 microns/h was approximately 10 times as large as that reported by Aoyama[2]. Although the surface roughness increased with increasing the laser power and the deposition rate, the peeling phenomenon was not observed in all the films. Figure 2 shows the relationship between the laser power and coercivity for the films. The coercivity values of the as-deposited films prepared by the laser power higher than 5.0 W reached approximately 400 kA/m without a post annealing process. An observation of X-ray diffraction patterns for the same samples showed that order and disorder phase transformation occurred with increasing the laser power. We also confirmed that the substrate temperature became higher than 573 K at the laser power of 5 W without a substrate heating system. Figure 3 shows a M-H loop of an as-deposited Fe-Pt film prepared at the laser power of 8 W. The values of coercivity, remanence and (BH)max were 442 kA/m, 0.69 T and 68 kJ/m3, respectively. It was clarified that further improvements in remanence and (BH)max are required for PLD-fabricated Fe-Pt thick film magnets.

[1]Aichi Steel Corporation, H. Aoyama et al., United States Patent, 10/086,454 (2002).

[2]H. Aoyama et al., J. Magn. Soc. Japan 20(1996)237.

[3]W. F. Liu et al., J. Magn. Magn. Mater. 302(2006)201.

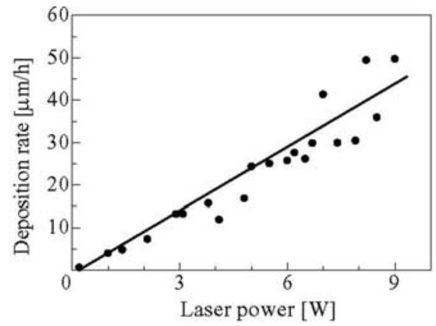

Fig.1 Deposition rate as a function of laser power for PLD-fabricated thick films.

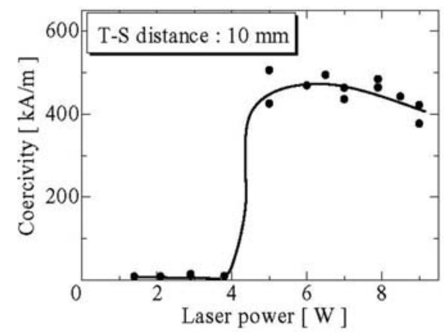

Fig. 2 Coercivity of as-deposited Fe-Pt films as a function of laser power.

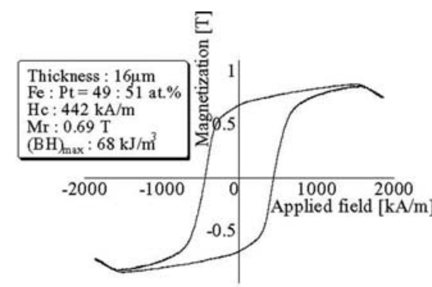

Fig.3 M-H loop of an as-deposited Fe-Pt thick film prepared at laser power of 8 W.

HE-08

Coercivity generation of surface Nd2Fe14B grains and mechanism of fcc-phase formation at Nd/Nd2Fe14B interface in Nd-sputtered Nd-Fe-B sintered magnets.

T. Fukagawa, S. Hirosawa

Magnetic Materials Research Laboratory NEOMAX Company, Hitachi Metals, Ltd., 2-15-17, Egawa, Shimamoto-cho, Mishima-gun, Japan

Introduction

Coercivity of surface grains of an Nd-Fe-B sintered magnet can be measured unequivocally when the magnet is a thin slab with its orientation of the c-axis is parallel to the largest surface. Because of losing a part of a neodymium-rich grain boundary phase, the surface Nd2Fe14B grains have low coercivity after machining. Importantly, the coercivity of the surface grains can be regenerated when the specimen is appropriately annealed after a layer of Nd metal has been sputter deposited on the surface. This observation suggested that HcJ of the surface grains are sensitively dependent on the interface properties near the boundary between the surface of Nd2Fe14B grains and deposited Nd layer. The purpose of the present study is to obtain the microstructure-property relationship describing the regeneration of coercivity of the surface Nd2Fe14B grains.

Experimental method

Thin slices of 4mm-6mm-0.35mm size were prepared from a block of an Nd-Fe-B ternary sintered magnet block. The magnetic field orientation direction was parallel to the 4mm edge. Then the slices were mechanically polished down to a thickness of 0.3mm. Metallic Nd layers of about 2μm thickness were deposited on both 4mm-6mm surfaces (Fig. 1). These samples were annealed in vacuum of about 5×10-3 Pa and quenched in a stream of Ar. The magnetic properties were measured with a vibrating sample magnetometer (VSM) after magnetizing the specimens in a pulsed magnetic field of 3200 kA/m. The microstructures of the Nd film were observed with a transmission electron microscope (TEM) and the selected electron diffraction patterns (SADP) were taken and analyzed.

Experimental result and discussion

When an Nd metallic layer was sputter-deposited on the surface and annealed in the temperature range from 500C° to 675C°, the surface coercivity recovered to its full value identical to the coercivity of the bulk magnet from which the slab was cut out(Fig. 2).

TEM investigations identified phases observed in the Nd films in specimens before (Specimen A) and after (Specimen B) the surface coercivity was recovered. SADPs of these specimens are shown in Fig.3. The whole layer of Nd film was composed of only double hexagonal closed packed (dhcp) phase (metallic Nd) in the specimen A whose surface coercivity wasn't recovered (Fig.3 (a) and (b)). Whereas an fcc phase with the lattice constant of 0.548nm was formed only near the surface Nd2Fe14B grains in the specimen B whose surface coercivity was recovered (Fig.3(c)). The fcc phase is very similar to fcc Nd-O phases that were observed at triple grain boundary junctions in sintered Nd-Fe-B magnets. On the other hand, not only a dhcp but also A-type Nd2O3 (Fig.3 (d)) was observed in the inner layer of the Nd film apart from the interface in the specimen B. A-type Nd2O3 having hexagonal structure of a = 0.382 nm and c = 0.598 nm is the most stable phase among different types of neodymium oxides of the 2:3 stoichiometry. Since the fcc phase is derived from metastable C-type Nd2O3 having cubic structure of a = 1.108 nm, the fcc phase is also a metastable phase. Therefore, it is considered that the formation of the fcc phase results from the interfacial energy with the Nd2Fe14B grains.

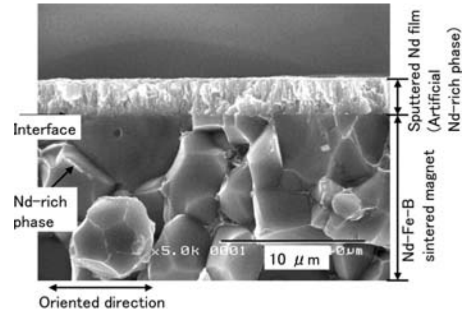

Fig. 1 A SEM micrograph showing the cross section of Nd sputter-deposited Nd-Fe-B sintered magnet.

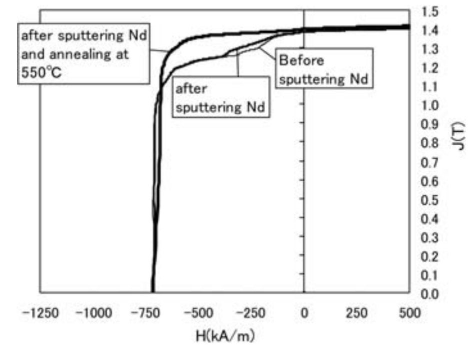

Fig. 2 Effect of Nd sputtering and annealing at 550C° on the degree of the coercive force recovery of the Nd2Fe14B surface grains.

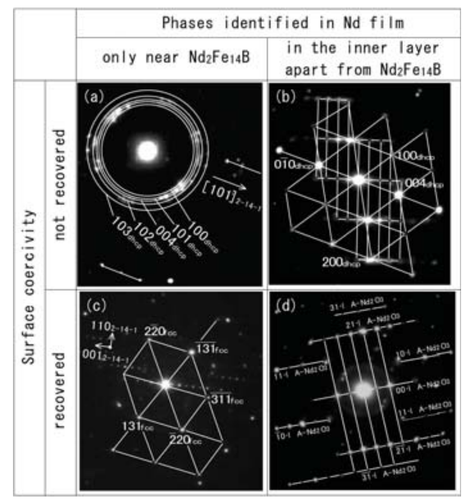

Fig. 3 Selected area diffraction patterns identifying phases near and apart from surface Nd2Fe14B grains in Nd film in the specimens A and B before and after annealing at 550C°, namely before and after the coercivity of the surface grains were recovered, respectively.

HE-09

Wettability and interfacial microstructure between $Nd_2Fe_{14}B$ and Nd-rich phases in Nd-Fe-B alloys.

R. Goto, S. Nishio, M. Matsuura, N. Tezuka, S. Sugimoto
Department of Materials Science, Tohoku University, Sendai, Japan

[Introduction] Nd-Fe-B sintered magnets are well known as permanent magnets with the highest energy products ($(BH)_{max}$) and have been started to use in motors in hybrid electric vehicles (HEV). As high heat resistance and high coercivity are strongly required in HEVs, some amount of Dy is added to Nd-Fe-B magnets. However, the natural abundance of Dy is quite low and the producing country is limited. Therefore, the development of Dy-free or -less Nd-Fe-B sintered magnets with high coercivity is strongly demanded.

The coercivity mechanism is important for increasing coercivity and several candidates of the mechanism have been proposed [1-3]. Although the mechanism has been still discussed, it is generally accepted that Nd-rich phase plays an important role at the interface between $Nd_2Fe_{14}B$ and Nd-rich phases to achieve high coercivity. Consequently, the wettability and interfacial reaction between these two phases are considered to be important. However, there are very few reports related to the wettability besides the report by Knoch *et al*. [4], in which the wettability was measured by the sessile drop method and both Al and Ga addition improve the wettability.

In this study, we investigated the wettability between $Nd_2Fe_{14}B$ and Nd-rich phases to evaluate the reaction process by measuring the change of contact angles under isothermal condition. The wettability was measured by the sessile drop method and a contact angle was adopted as a parameter of the wettability.

[Experimental procedures] Stoichiometric $Nd_2Fe_{14}B$ ingot and two Nd-rich ingots such as $Nd_{72.0}Fe_{26.1}B_{1.9}$ (ternary) and $Nd_{72.0}Fe_{22.4}Cu_{3.7}B_{1.9}$ (Cu-added) were prepared. $Nd_2Fe_{14}B$ ingots were sliced into the plate of 20 x 20 x 1.5 mm^3 and polished by SiC emery papers and oil diamonds. Nd-rich ingots were cut into the block of 2 x 2 x 2 mm^3 and polished in inert gas atmosphere. After polishing, the block of Nd-rich ingot was set on the plate of $Nd_2Fe_{14}B$ ingot on the stage of an infrared image furnace. The samples were heated to 560-720°C at a rate of 50 °C/min, and then kept for 1 h in Ar atmosphere. Time dependence of contact angle between $Nd_2Fe_{14}B$ and Nd-rich ingots was observed by a CCD camera. The angle and time when the contact angle became constant were defined as the saturated angle (θ_s) and completion time (t_{comp}), respectively. Microstructure of the interface between the $Nd_2Fe_{14}B$ and Nd-rich ingots is also observed by a scanning electron microscope (SEM).

[Result] Figure 1 shows the time dependence of contact angles between $Nd_2Fe_{14}B$ and ternary Nd-rich ingots heat-treated at 640-720°C. For the ternary Nd-rich ingots, θ_s and t_{comp} tend to decrease with increasing heat treatment temperature. Although tendency of the change in contact angle is similar for both ternary and Cu-added Nd-rich ingots, the θ_s values for Cu-added Nd-rich ingots are smaller than those for ternary Nd-rich ingots. The activation energies that the wetting achieves equilibrium were estimated from the Arrhenius plot using t_{comp} and temperature. The result is shown in Figure 2. From the figure, the activation energy is estimated to be 196.8 kJ/mol and 162.6 kJ/mol for ternary and Cu-added Nd-rich ingots, respectively.

Therefore, it is concluded that Cu addition improves the wettability of Nd-rich phase to the $Nd_2Fe_{14}B$ phase and the effect is related to the decrease in the activation energy.

[Acknowledgement] A part of this study was financially supported by a Grant-in-Aid for Scientific Research (Scientific Research of Priority Areas "Panoscopic Assembling and High Ordered Functions for Rare Earth Materials (No. 16080202)") from the MEXT in Japan and the Project for Development of Alternative Materials of Rare Metals (Technology Development of Dy Reduction for Rare-earth Permanent Magnets) from the METI in Japan. The authors also thank to Santoku Corporation for providing $Nd_2Fe_{14}B$ and Nd-rich ingots.

[1] M. Sagawa *et al*., IEEE Trans. Magn. **MAG-20** (1984) 1584. [2] S. Hirosawa *et al*., J. Magn. Magn. Mat. **84** (1990) 309. [3] K. Makita *et al*., Appl. Phys. Lett. **74** (1999) 2056. [4] K. G. Knoch, *et al*., IEEE Trans. Magn. **25** (1989) 3426.

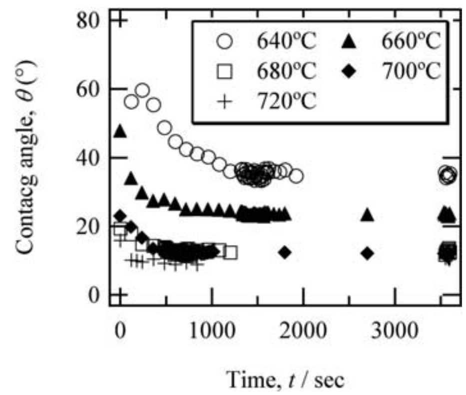

Fig. 1 The time dependence of contact angles between $Nd_2Fe_{14}B$ and ternary Nd-rich ingots heat-treated at 640-720°C.

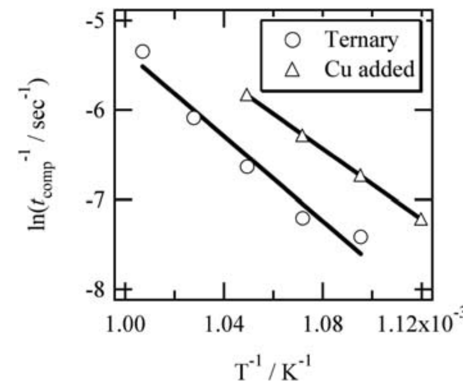

Fig. 2 Arrhenius plot of t_{comp} and heat treatment time for ternary and Cu-added Nd-rich ingots.

HE-10

The role of Cu addition in the coercivity enhancement of sintered Nd-Fe-B magnets.

T. Ohkubo[1,2], W. Li[1], K. Hono[1,2], T. Akiya[3], H. Kato[3]
1. National Institute for Materials Science, Tsukuba, Japan; 2. CREST, JST, Japan; 3. Tohoku University, Sendai, Japan

1. Introduction

It is well known that the coercivities of Nd-Fe-B based sintered magnets are strongly influenced by the aging treatment at around 773K after sintering. This coercivity enhancement by aging can be seen in the sintered magnets that contain approximately 0.5 at.% of Cu [1]. The increase of coercivity should be due to a microstructure effect, since the anisotropy field hardly decreases [2]. Although the previous investigation[3] reported the formation of continuous Nd-rich thin layers surrounding grain boundaries during aging, how Cu is involved in these thin grain boundary phases as well as chemical distribution within Nd-rich grains are not well understood. In this work, we have studied the microstructure differences between the samples with and without Cu addition systematically. Focuses have been put on the distribution of Nd-rich phase and the segregation of Cu, which are thougth to be the dominant factor on the coercivity of sintered Nd-Fe-B magnets.

2. Experimental details

The nominal compositions of the sintered magnets studied in this investigation were Nd14.5Fe79.4B6.1 and Nd14.5Fe79.3B6.1Cu0.1. The sintered magnets were annealed under magnetic field of 140 kOe at 823K. For microstructure investigation, FEG-SEM LEO 1550,1540 EsB cross beam system, TECNAI G2 F30 TEM equipped with GIF and EDX, and Femtosecond laser assisted 3D atom probe (3DAP) were employed.

3. Result and discussion

The coercivities of the Cu-free and Cu-containing samples were 3.6 and 13.6 kOe, respectively, after the magnetic annealing. SEM EsB images of the Cu-containga sample showed thin bright contrast along grain boundaries, while no such contrast was observed from the Cu-free sample (Fig. 1). We have obtained 3D tomography of the brightly imaged Nd-rich phase by sequentially observing BSE images with continous removal of thin volume of samples by FIB as shown in Fig. 2. In the Cu-containing sample, the grain boundary phase continously envelope Nd2Fe14B grains, while in the Cu-free sample, grain boundary phase form only in localized regions near triple junctions. This means that the Nd-rich phase was trapped into the grain boundary junction regions and did not penetrate into the grain boundaries between the Nd2Fe14B phase grains in the Cu-free sample.

Energy filter mapping, and HRTEM images, can further confirmed that the Nd-rich phases in the Cu-containing magnet form a shell around the Nd2Fe14B grains, resulting in decoupling of hard magnetic phases.

Figure 3 shows 3DAP concentration depth profile across a Nd-rich phase/Nd2Fe14B grain interface. The composition within the Nd-rich phase is approximately Nd35Fe30Cu10O25. There is Cu depleted and Cu enriched layers near the interface.

4. Conclusion

With a small amount of Cu addition (0.13 at.%), the coercivity of sintered magnet is significantly increased from 3.6kOe to 13.6kOe after magnetic annealing at 823K. It was found that by Cu addition Nd-rich phases in the magnet form a shell around Nd2Fe14B grains resulting in decoupling of hard magnetic phases, thereby enhancing coercivity. The better wetability of Nd-rich phase around the surface of Nd2Fe14B is originated from the Cu incorporation due to lowered melting point. 3DAP investigation revealed a thin Cu-enriched layer at the interface of Nd-rich phse/Nd2Fe14B phase.

1. W. Fernengel, M. Velicescu, W. Rodewald, P. Schrey, and B. Wall, Proceedings of the Third ISPMM, 1995, p.748.

2. A. Kowalczyk, and A. Wrzeciono, J. Magn. Magn. Mater. 74(1988)260

3. F. Vial, F. Joly, E. Nevalainen, M. Sagawa, K. Hiraga, K.T. Park, J. Magn. Magn. Mater., 242-245(2002)1329

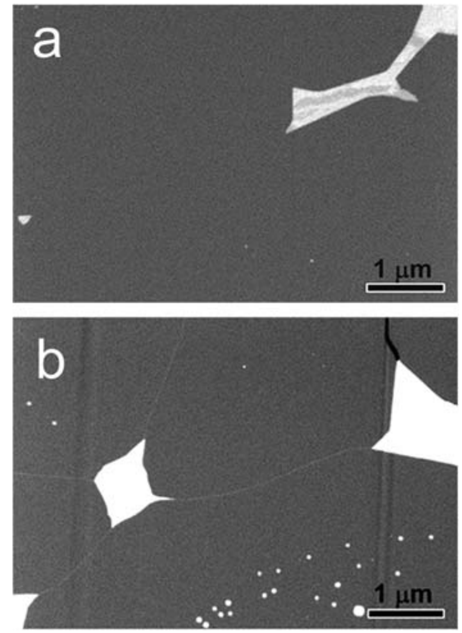

Fig.1 High resolution SEM EsB images of the samples without Cu (a) and with Cu (b).

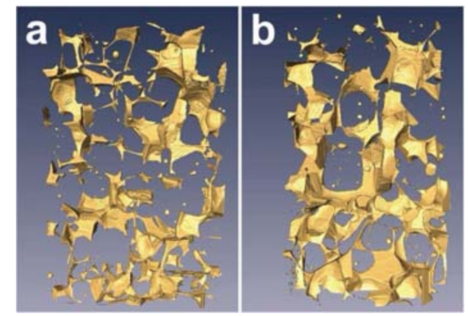

Fig.2 FIB tomography of the samples without Cu (a) and with Cu (b) showing the distribution of Nd rich phase

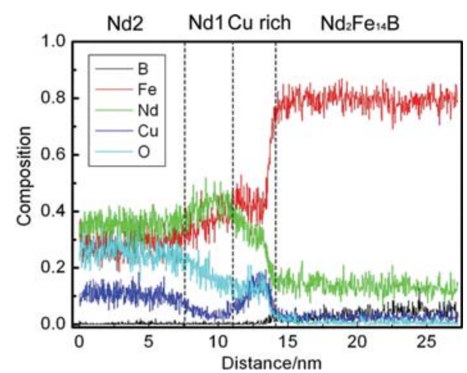

Fig.3 Concentration depth profiles for Nd, Fe, B, Cu, and O determined from the 3DAP analysis.

HE-11

Magnetic Properties of Sm2Co17 & Sm2Co7 Sputtered and Post-annealed Thin Films. Effect of Mo Underlayer.

I. Lucas[1], M. Maicas[2], L. Pérez[3], M. Díaz - Michelena[1]
1. Dto: Space Programs and Space Sciences, I.N.T.A., 28850 Torrejón de Ardoz, Spain; 2. (ISOM) ETSI Telecomunicación, Universidad Politécnica de Madrid (UPM), Madrid, Spain; 3. Dto:Física de Materiales, Universidad Complutense de Madrid (UCM), Madrid, Spain

SmCo hard magnetic films have been extensively studied in the last years due to their applications in microelectromechanical systems (MEMS) [1,2] and recording media [3,4]. Depending on the Sm content of the films, microstructure and magnetic properties change [5]. Sm content is not the only parameter these properties depend on. The Argon pressure and the underlayers used, are also important factors to take into account. Amongst all the possible SmCo phases present in bulk magnets as well as in thin films, $SmCo_5$ has been the most studied. However SmCo present other interesting phases such as $SmCo_7$, Sm_2Co_7 and Sm_2Co_{17}. In this work, we study the dependence of the thin film composition and the crystalline phases on the working pressure and the presence of a Mo underlayer for different annealing processes trying to get a hard magnetic material with an out-of-plane easy axis..

SmCo layers were grown both with and without a 100nm thick Mo underlayer onto Si (100) substrates at different working pressures. Commercial Sm_2Co_{17} sintered targets were used as sputter targets. The base pressure in the chamber was below 5×10^{-7} mbar and the working pressures were 3.5×10^{-3} mbar and 2.5×10^{-2} mbar. The thickness of the SmCo layers was between 550 and 650 nm. All samples were covered with a 30 nm thick Mo layer in order to avoid the sample oxidation. The samples were annealed with three different thermal treatments, two of them without applied magnetic field and the last one with a 2 T magnetic field applied perpendicular to the surface of the sample in order to induce an out-of-plan anisotropy. The two first thermal treatments were carried out in a tubular furnace with a controlled and constant Argon flux at 600°C for an hour. The difference between them is that in the second one, when the temperature is decreasing, there was one step more where the temperature was maintained at 400°C for another hour. The annealing with the applied magnetic field was carried out in a small tubular furnace which is part of a VSM. This annealing had not the 400°C step.

Sputtered SmCo and Mo/SmCo samples are amorphous. Both set of films obtained with the lower working pressure, which have less percentage of Sm [5], present a clearly defined in-plane anisotropy. On the other hand, films obtained using the higher working pressure, whith more Sm content [5], present an anisotropy with an out-of plane contribution. X-ray measurements developed for the samples grown with the different working pressures after the annealing process, demonstrated the presence of Sm_2Co_7 and Sm_2Co_{17} crystalline phases for the samples with Mo underlayer and the presence of $SmCo_5$ and $SmCo_7$ phases for the samples without it. Regarding the desired magnetic properties, we have that coercivity field and remanence increase considerably after annealing in both SmCo and Mo/SmCo samples although the variation is higher in the SmCo thin films. These samples present coercivity values of 0.26 T in-plane and 0.35 T out-of-plane after annealing while Mo/SmCo samples present coercivity values around 0.1T in-plane and 0.15 T out-of-plane. SmCo samples without Mo underlayer become isotropic, with no well defined anisotropy, whereas Mo/SmCo samples anisotropy remain showing just an out-of-plane contribution. Besides, the remanence of the SmCo samples is also higher than in the samples with Mo underlayer (Fig. 1 and Fig. 2). The heat treatment carried out with an applied magnetic field reported no better results because the coercivities and remanence fields are smaller than those obtained by using the first heat treatment.

To summarize we can conclude that we have got thin film SmCo samples that do not present a dominant in-plane crystalline anisotropy with remanences and coercive fields high enough to be used as hard magnetic thin films with out-of-plane magnetization.

[1] V.Neu, U. Hannemann, S. Faehler, B. Holzapfel and L.Schultz, J. Appl. Phys. 91(10) (2002) 8180-8182.

[2] E. Pina, F.J. Palomares, M.A. García, F.Cebollada, A. de Hoyos, J.J. Romero, A. Hernando and J.M.González, J. Magn. Magn. Mater. 290-291 (2005) 1234-1236.

[3] Akimitsu Morisako and Xiaoxi Liu, J. Magn. Magn. Mater. 304 (2006) 46-50.

[4] A. Morisako, I. Kato, S. Takei and X.Liu, J. Magn. Magn. Mater. 303 (2006)

e274-e276.

[5] V. Neu and S.A. Shaheen, J. Appl. Phys. 86(12) 7006-7009(1999).

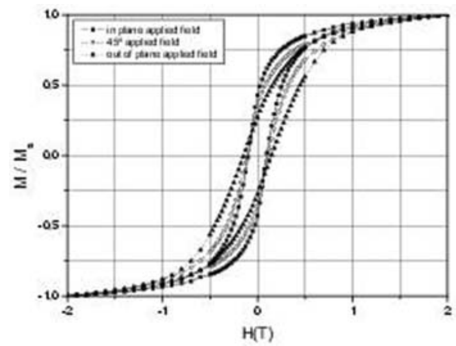

Hysteresis loops of annealed Mo/SmCo films.

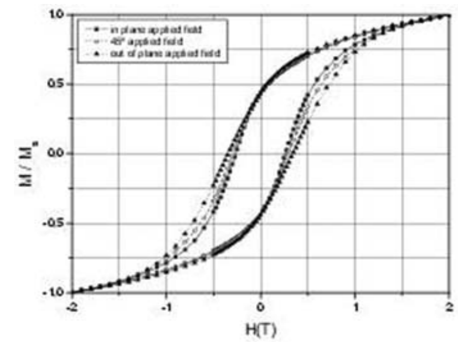

Hysteresis loops of annealed SmCo films.

HE-12

Preparation and magnetic study of the $CoFe_2O_4$-$CoFe_2$ nanocomposite powders.

F. Cabral[1,2], *F. Machado*[1], J. Araújo[2], J. Soares[3], A. Rodrigues[1], A. Araújo[2]
1. Departamento de Física, Universidade Federal de Pernambuco, Recife, Brazil; 2. Departamento de Física Teórica e Experimental, Univesidade Federal do Rio Grande do Norte, Natal, Brazil; 3. Departamento de Física, Univesidade do Estado do Rio Grande do Norte, Mossoró, Brazil

Nowadays, one of the most important goals in material science is to develop new materials at the nanometric scale. Magnetic materials have their physical properties strongly dependent on the size and on local structure of the grains. This has allowed to develop new application in areas such as catalysis, magnetism, optoelectronics and medicine [1]. The cobalt ferrite $CoFe_2O_4$, for instance, was found to be an important magnetic material because of its application in magnetic fluids, in magnetic recording media and also in magnetic resonance imaging. It presents high magneto-crystalline anisotropy, moderate saturation magnetization, remarkable chemical stability and mechanical hardness. $CoFe_2$, in turn, is an important soft-ferromagnetic material with unique properties such as large magnetic permeability and very high saturation magnetization (above 230 emu/g). The nanocomposites $CoFe_2O_4$-$CoFe_2$, on the other hand, have attracted great attention due to their potential use in developing magnetoresistive devices [2]. Besides, they are suitable to investigate the phenomena of the exchange-coupling in soft-hard ferro-ferrimagnetic composite material which is less studied and it is not completely elucidated yet. The ferrimagnetic and the ferromagnetic phases are expected to couple their magnetic moments at the interface between the phases. It is expected that the exchange spring mechanism would allow one to obtain nanocomposite hard magnetic materials combining the hard (high anisotropy) and soft (high magnetization) magnetic properties in such way that the soft phase becomes harder and its high magnetization enhances the energy product $(BH)_{max}$ [3].
In this work we report a detailed studying of the magnetic properties of powders made of nanoparticles composed by a solid-solution of $CoFe_2O_4$-$CoFe_2$. Powders with different relative volume fraction of this two phases were obtained by heat treatments of single phase cobalt ferrite $CoFe_2O_4$ into a flux of high purity hydrogen gas. The composition of the resulting powders presented nano-sized particles with a relative volume fraction of the oxide $CoFe_2O_4$ and of the metallic $CoFe_2$ phases. The amount of $CoFe_2$ in the composite was increased up to 90% vol. by this process. The volume fraction of the two phases were controlled by the hydrogen flux and by the amount of time and temperature which the samples were exposed during the reduction process. The composition, the structure and the morphology of the particles were characterized by using X-ray diffraction and electron microscopy while the magnetic properties were investigated by using a vibrating sample magnetometer. It was found that the saturation magnetization of the nanocomposite powders increase with the volume fraction of the ferromagnetic $CoFe_2$ phase while their coercivity decrease. A maximum at the remanence M_r (= 49,3 emu/g) was observed for the composite containing 90 % vol. of $CoFe_2$ while the maximum energy product $(BH)_{max}$ was found to be 0.62 MGOe. This is 19% higher than the value obtained for single phase $CoFe_2O_4$. The coercive field H_c for this composition was found to be 539 Oe. Moreover, for all the range of volume fractions investigated the powders behaved as magnetic single phase-like showing smooth magnetic field variation at the magnetization hysteresis curves. This result indicate that the ferrimagnetic $CoFe_2O_4$ and ferromagnetic $CoFe_2$ are effectively exchange coupled and that magnetization of both $CoFe_2O_4$ and $CoFe_2$ reverses cooperatively.

Acknowledgments. This work was partially supported by CNPq, FINEP and FACEPE (Brazilian Agencies).

1 - C. T. Campbell, S. C. Parker, and D. E. Starr, Science **298**, 811 (2002); Z. Tang, N. A. Kotov, and M. Giersig, Science **297**, 237 (2002); P. Gould, Nano Today **1**, 34 (2006).

2 - N. Viart, R. Sayed Hassan, C. Mény, P. Panissod, C. Ulhaq-Boullet, J. L. Loison, G. Versini, F. Huber, and G. Pourroy, Appl. Phys. Lett. **86**, 192514 (2005).

3 - H. E. Kneller, and R. Hawig, IEEE Trans. Magn. **MAG-27**, 3588 (1991).

HF-01

Bimodal use of maghemite nanoparticles as contrast agents for magnetic resonance imaging (T1 and T2 CA's) through modulation of their stabilizing coating.

E. Taboada[1], *A. Roig*[1], E. Rodriguez[2], M. Delville[3]
1. Institut de Ciència de Materials de Barcelona, ICMAB-CSIC, Bellaterra, Spain; 2. Center for Molecular Imaging Research, MGH-Harvard Medical Hospital, Boston, MA; 3. Institut de Chimie de la Matière Condensée de Bordeaux, ICMCB-CNRS, Bordeaux, France

In biomedicine, magnetic materials have been used for long time in diagnosis as well as in therapy; some of its applications are found in magnetic resonance imaging (MRI), hyperthermia or magnetic separation. For biomedical use, magnetic nanoparticles are generally preserved as aqueous colloidal dispersions which must fulfill some important requirements: superparamagnetic (SPM) behaviour at room temperature (RT), high saturation magnetization, biocompatibility and stability in physiological media. The SPM behaviour of the particles assures that they will be only magnetized in the presence of an external magnetic field. Lack of toxicity is a fundamental concern as particles are internalized in the patient body or used with cell culture. Finally, stability in physiological media must be guaranteed avoiding the aggregation and precipitation of the particles, since their magnetic properties and biodistribution depend significantly on their size.
Our work has been directed towards the material's aspect of the problem; in particular on the synthesis and characterization of new materials suitable to act as contrast agents for magnetic resonance imaging (CA's for MRI). Based upon on our earlier work (1), dual MRI nanoparticles have been synthesized. On the one hand maghemite nanoparticles (γ-Fe2O3 NPs) of 5 nm of diameter stabilized in water with sodium citrate (γ-Fe2O3-citrate) that act as positive contrast agents (T1-CAs) and on the other hand, maghemite NPs embedded in silica aerogel resulting in negative contrast agents (T2-CA) (γ-Fe2O3-silica aerogel) (see enclosed figure).
The synthesis of maghemite nanoparticles was carried out in organic media by thermal decomposition of iron pentacarbonyl in presence of oleic acid (2). The particles were afterwards dispersed in hexane. The organic colloidal-dispersion, γ-Fe2O3-oleic, is the starting material for our dual system. It is remarkable the narrow particle size distribution achieved by this synthetic route allowing the control over the magnetic properties of the system.
The γ-Fe2O3-citrate aqueous colloidal dispersions were obtained by displacement of the oleic acid adsorbed onto the surface of the particles by the electrolyte sodium citrate. The γ-Fe2O3-citrate NPs are superparamagnetic at RT, with high saturation magnetization (68 emu/g γ-Fe2O3), very close to the maghemite bulk value (76 emu/g γ-Fe2O3) and large considering the small size of the particles.
The γ-Fe2O3-silica aerogel is a composite material formed of sub-micrometric size particles, dispersible in water. The synthesis of the porous silica is done under supercritical conditions of acetone (T > 250°C, P > 200 bar) in the presence of the γ-Fe2O3-oleic particles. The composite particles have a final mean size around 100-200 nm, with big magnetic cores (30-70 nm diameter) built up of non-contacting maghemite NP's and silica aerogel shells. The composite also shows SPM behaviour at RT.
Both γ-Fe2O3-citrate and γ-Fe2O3-silica aerogel, were evaluated as contrast agents for MRI. This is a medical technique able to enhance contrast differences between healthy and pathological tissues. It measures the longitudinal and transversal magnetic relaxation times of the protons. Contrast agents (CA's) are magnetic materials that increase the relaxation rates, enhancing the contrast between tissues. Positive CA's (or T1) increase the longitudinal relaxation rates (r1) and negative CA's (or T2) increase the transversal ones (r2). The r1 value directly depends on the magnetization of the CA and the accessibility of the protons to the CA. On the other side, r2 magnitude is directly dependent on the magnetization of the CA and the ability to produce local magnetic inhomogeneities.
We will show that the relaxation mechanism is hugely dependent on the coating of the maghemite NP's. The values of r1 and r2 values obtained for γ-Fe2O3-citrate give an r2/r1≈1, indicating a positive CA while for γ-Fe2O3-silica aerogel an r2/r1 > 1000 was found indicating a negative CA. Which is the reason for this different relaxometric behavior when both materials contain the same magnetic NP's? The main explanation resides in the clustering of the nanoparticles in the silica matrix. The r2/r1 value for γ-Fe2O3-citrate is near 1 due mainly to the small size of the nanoparticles as well as its very homogeneous dispersion in the medium. In contrast, γ-Fe2O3-silica nanoparticles act as T2-CAs mostly because its big magnetic cores induce large local magnetic inhomogeneities and high increase of the r2 values.
To sum up, we have synthesized and characterized two different magnetic colloidal dispersions with the same magnetic material but with different relaxometric properties. Thus, it has been demonstrated that in view of their final application in life sciences, the coating of magnetic nanoparticles is as relevant as their inherent magnetic properties.

1. Taboada et al. Langmuir, 2007, 23, 4583

2. Sun et al. Science, 2000 287 1989

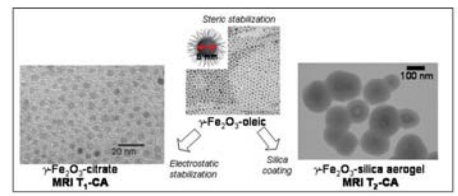

HF-02

Magnetic Hyperthermia with Fe_3O_4 nanoparticles: the Influence of Particle Size and Domain Structure on Energy Absorption.

G. F. Goya[1], E. Lima Jr.[2], A. D. Arelaro[2], T. Torres[1], H. R. Rechenberg[2], L. Rossi[3], C. Marquina[4,1], M. R. Ibarra[1,4]

1. Nanoscience Institute of Aragon, University of Zaragoza, Zaragoza, Spain; 2. Physics Institute, University of Sao Paulo, Sao Paulo, Brazil; 3. Chemistry Institute, University of Sao Paulo, Sao Paulo, Brazil; 4. Instituto de Ciencia de Materiales de Aragón-CSIC, University of Zaragoza, Zaragoza, Spain

Magnetic hyperthermia (MH) is a developing strategy in biomedical research fields, by which the temperature of a target cell or tissue containing ferromagnetic particles can be raised remotely through radio-waves of 100 to 1000 kHz.[1] In this frequency range the heating effects on living tissues, related to electric coupling of dipolar moments and E-component of the waves, are negligible. On the other hand, if magnetic particles are loaded into the target tissue, their magnetic moment interacts with the B-component of these radio waves, releasing the absorbed power as heat. The origin of the energy dissipation when a ferromagnetic nanoparticle is placed on an ac magnetic field is related to magnetic losses through domain wall displacements (in multi-domain particles), and/or Néel relaxation in single domain particles. Energy loss from mechanical rotation of the particles, acting against viscous forces of the liquid medium (Brownian losses) could also contribute al low (< 50 kHz) frequencies. The dominant process will depend on the specific particles used and the applied frequency range. The heating efficiency of a magnetic colloid is measured by the heating power of a given mass m_{NP} of the constituten nanoparticles diluted in a mass m_{ff} of ferrofluid, through the Specific Absorption Rate

$SAR = C_S(m_{ff}/m_{NP})(\Delta T/\Delta t)$ (I)

in W/g, where C_S is the specific heat of the colloid, and $\Delta T/\Delta t$ is obtained from the heating curves of the material. Although SAR values are often given without any further specification,[2,3] it is known that the rate of temperature increase $\Delta T/\Delta t$ is time-dependent. Therefore the values reported in the literature are difficult to compare and evaluate in terms of their actual heating capacity.

In this work we analyze the effect of particle size on SAR values in a series of Fe_3O_4 NPs with increasing mean particle size from 3 to 30 nm, and good control of size dispersion.

Experiments of power absorption as a function of particle size revealed the existence of a sharp increase in SAR values near the single- to multi-domain structure, irrespective of magnetization values, as displayed in figure 1. The largest value obtained was 130 W/g, corresponding to a bimodal particle distribution with average size values of 17 and 25 nm. We discuss the correlation of this behavior with magnetic parameters such as crystalline state of the particles, magnetic anisotropy and coercivity values.

When measured against NP concentration, the SAR values were not constant as expected from eq.(I). We present evidence of other effects such as dipolar interactions among particles, and also the non-adiabaticity effects of experimental protocols used for measurements in ferrofluids, aiming a useful determination of SAR values.

[1]Wilhelm, Claire; Fortin, Jean-Paul; Gazeau, Florence,

J. Nanosci. Nanotech., 7(2007)2933-2937.

[2] Jordan A., Rheinl T.,Waldofner N. and Scholz R.,J. Nanoparticle Res. 2003, 5,597.

[3] Ma M., Wu Y., Zhou J., Sun Y., Zhang Y., Gu N., J. Magn. Magn. Mater. 268 (2004) 33–39.

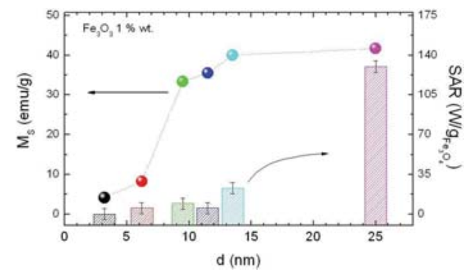

Figure1. Saturation magnetization values, MS, at room temperature (left axis) and the corresponding Specific Absorption Rate values (right axis) for magnetite particles with different mean particle diameters, d. It can be observed a jump in MS values for the larger particles, in a smaller d range than the observed increase of SAR.

HF-03

Synthesis and Cellular Uptake of Foliate-Conjugated Hydrophobic Superparamagnetic Iron Oxide Nanoparticles.

K. Woo[1], J. Moon[1,2], K. Choi[3], K. Yoon[3], T. Seong[2]
1. Nano-Materials Research Center, KIST, Seoul, South Korea; 2. Department of Materials Science and Engineering, Korea University, Seoul, South Korea; 3. Institute for Radiological Imaging Science, Wonkwang University School of Medicine, Iksan, South Korea

Recent advances [1-3] in preparation of monodisperse superparamagnetic iron oxide nanoparticles (SPIONs) in organic medium have accelerated the emergence of surface modification chemistry. However, most of the surface modification chemistry has been focused on the preparation of water-dispersible functional SPIONs. On the other hand, the surface modification study for hydrophobic functional SPIONs has been quite rare and few reports are found. Though not injectable alone, hydrophobic functional SPIONs can have some potential applications as implantable targeting probes [4] or inclusion probe materials in a polymer utilized micelle [5], together with drug delivery. The best advantage of hydrophobic functional SPIONs over hydrophilic ones could be an aggregation-free behavior.
In this investigation, we prepared foliate-conjugated hydrophobic SPIONs and investigated their cellular uptake by KB cell (human epidermoid carcinoma cell), which is one of the representative foliate receptor over-expressed cells, using magnetic resonance (MR) imaging. Foliate-conjugation to imaging probes has been known to target and image breast cancer since some of the breast cancer cells over-express foliate receptors.
Our foliate-conjugated hydrophobic SPIONs were prepared as following. The oleic acid protected SPION (5.5 nm and 11 nm SPION-OA) was prepared according to the published method [1]. To this crude solution at 100°C, 10 mol % iron pentacarbonyl was added with stirring and then heated to reflux. The protecting ligand OA was substituted by decanoic acid (DA) to yield SPION-DA, which was treated with 5 equivalents of mercaptoundecanoic acid (MUA) to produce SPION(-DA)ex(-MUA)5. The carboxylic acid end groups of SPION(-DA)ex(-MUA)5 were conjugated to folic acid (FA) through ethylenediamine bridge, yielding the final product SPION(-DA)ex(-MUA-FA)5.
SPION(-DA)ex(-MUA-FA)5 was hydrophobic and soluble in non-polar solvents such as hexane, toluene, and chloroform. The TEM image analysis implied that each SPION(-DA)ex(-MUA-FA)5 was aggregation-free without its size change in both cases. The cellular tests with/without folic acid and their MR imaging showed efficient uptake of functional hydrophobic SPION(-DA)ex(-MUA-FA)5 to KB cells and about 10% decrease under the inhibition of excess folic acid.

[1] K. Woo et al. Easy synthesis and magnetic properties of iron oxide nanoparticles, Chem. Mater. 16, 2814 (2004).

[2] T. Hyeon et al. Synthesis of highly crystalline and monodisperse maghemite nanocrystallites without a size-selection process, J. Am. Chem. Soc. 123, 12798-12801 (2001).

[3] S. Sun and H. Zeng, Size-controlled synthesis of magnetite nanoparticles, 124. 8204-8205, (2002).

[4] J. Lee et al. Biocompatible polymeric nanoparticles and films containing hydrophobic quantum dots, Mater. Res. Soc. Symp. Proc. 950, 0950-D04-09, (2007).

[5] K. Kim et al. Cell-permeable and biocompatible polymeric nanoparticles for apoptosis imaging, J. Am. Chem. Soc. 128, 3490-3491, (2006).

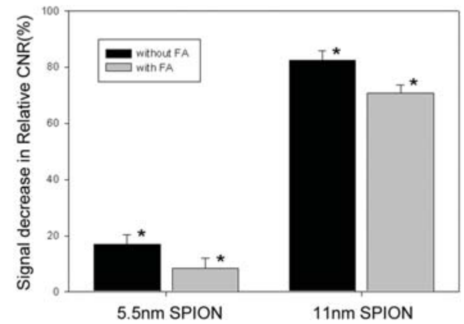

Figure 1. Signal decrease of cellular SPION(-DA)ex(-MUA-FA)5 in relative CNR (%), where CNR (%) = {T2*(cell alone)-T2*(cellular SPION)} x 100/T2*(cell alone).

HF-04

Water based colloids of Fe_3O_4/SiO_2 magnetic nanoparticles with core/shell structure for magnetic hyperthermia.

M. A. Gonzalez-Fernandez[1], T. Torres[2], M. A. Verges[3], G. F. Goya[2], C. J. Serna[1], M. P. Morales[1]
1. Instituto de Ciencia de Materiales de Madrid, CSIC, Madrid, Spain; 2. Institute of Nanoscience of Aragon (INA), University of Zaragoza, Zaragoza, Spain; 3. Department of Organic and Inorganic Chemistry, Universidad de Extremadura, Badajoz, Spain

The interest in using core/shell magnetic nanoparticles (NPs) for biomedical and bioengineering applications has been increasing over the last few years. These magnetic NPs can be widely used for in-vitro as well as in-vivo applications such as magnetic biosensing, cell separation and contrast enhancement in magnetic resonance imaging. Possible future applications are being developed such as tissue repair, magnetic hyperthermia treatment and targeted drug delivery. The size, shape and biochemical coating of these nanoparticles are of critical importance and must be controlled accurately. They must also be thermally and chemically stable and have large magnetic moments. It is therefore very important to optimize these parameters, and to characterize the magnetic properties so that the performance of the final pharmaceutical product can be evaluated. For specific applications such as magnetic inductive hyperthermia (MIH), the rheological properties of the colloids and the efficiency for absorbing RF power on NPs are also major issues that require optimization [1].

In this work core/shell magnetic nanoparticles have been obtained for further use in hyperthermia studies. Magnetite NPs of three different sizes of 30 nm, 50 nm and 110 nm have been prepared, labeled as ASi, BSi and CSi respectively. These magnetic NPs have been furthermore coated with a silica layer of 1 nm (ASi), 4.5 nm (BSi) and 15 nm (CSi). Fig.1 shows TEM images of one of these samples. Colloidal stability has been measured for all samples as a function of pH and surface charge. Silica has several advantages over organic coatings. It is very resistant against biodegradation and avoids unwanted interactions by preventing direct contact of the magnetic cores with other additional agents that might be linked to the silica surface [2]. Furthermore, silica coatings are very stable under aqueous conditions in a very wide range of pH. Through the silica coating it is relatively easy to control the interactions between particles in solution.

Hysteresis loops of magnetite and silica coated magnetite samples at room temperature have been obtained and compared, Fig.2. A slight increase in the coercivity, a clear increase in the squareness and in the area of the hysteresis loop is observed for coated samples compared to pure magnetite samples. Also, zero-field-cooled (ZFC) and field-cooled (FC) magnetisation measurements have been carried out in all samples. The samples were dispersed and stabilized in water and their power absorption efficiency at a frequency of 260 kHz and peak field of 150 Oe was determined in adiabatic experiments from the initial temperature increase of the Temperature vs. time curves. The slope of the curves reached their maximum values within the first five minutes for the 30 nm and 50 nm coated samples. We found that the 30 nm-magnetite NPs have the largest values of specific power absorption (82 W/g of magnetite), whereas for the largest particles (CSi sample) no power absorption was observed within experimental, Fig.3. Since in the largest particles (CSi, size 150 nm) the power absorption is dominated by domain wall displacements, our findings suggest that the optimal nanoparticle for power absorption should be designed to be close to its multi- to single-domain size.

[1] G.F. Goya, R. Fernandez-Pacheco, M. Arruebo, N. Cassinelli, M.R. Ibarra, J. Magn. Magn. Mat., 316,132 (2007)

[2] A. Lu, E.L. Salabas, F. Schüth, Angew. Chem. Int. Ed. 46, 1222, (2007)

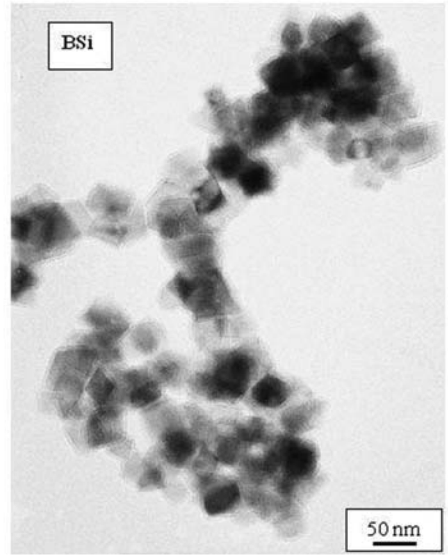

Magnetite NPs coated with a thin silica layer (BSi)

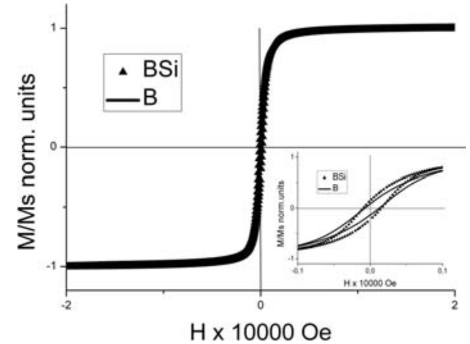

Hysteresis loops of 50 nm magnetite sample pure (B) and coated with silica (BSi). The inset shows a close up of the hysteresis loops at low fields.

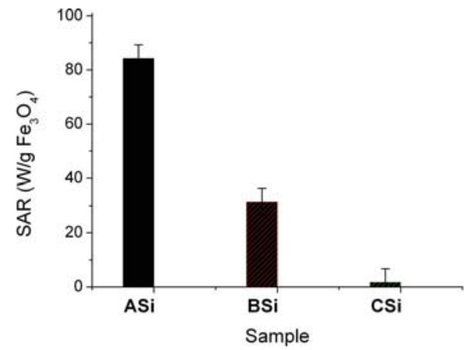

Specific absorption rate of coated samples.

HF-05

Antiferromagnetic susceptibility in ferritin.

N. J. Silva[1], A. Urtizberea[1], A. Millán[1], F. Palacio[1], E. Kampert[2], U. Zeitler[2], H. Rakoto[3], V. S. Amaral[4]

1. Fisica de la Materia Condensada, Instituto de Ciencia de Materiales de Aragón CSIC/Universidad de Zaragoza, Zaragoza, Spain; 2. Radboud Univ. Nijmegen, High Field Magnet Lab, Nijmegen, Netherlands; 3. LNCMP, Toulouse, France; 4. Departamento de Física and CICECO, Universidade de Aveiro, Aveiro, Portugal

The enhancement of χ_{AF} bellow T_N in antiferromagnetic nanoparticles compared to bulk was predicted by Néel and estimated to decrease with temperature [1]. The extra susceptibility (χ_a) is a finite size effect termed superantiferromagnetism arising from the coupling between the external field and the AF easy axis, corresponding to a progressive rotation of the AF axis from surface to surface across the particle, in particles with even number of ferromagnetic spin plans. Finding experimental evidence of superantiferromagnetism is not straightforward as it is necessary to have magnetic particles with small grains with controlled size distribution, and it is necessary to overcome the influence from the uncompensated magnetic moment μ_{un}. In the case of high field measurements, the influence of μ_{un} is related to the non-saturation of the magnetization associated to μ_{un} (M_μ) at the typical applied fields (50 kOe) and temperatures. The absence of a reliable model of the field dependence of M_μ, neither of its approach to saturation, makes the separation between the contribution of χ_{AF} and μ_{un} to the total magnetisation (and the subsequent determination of $\chi_{AF}(T)$) quite difficult.
In previous reports (see, for instance Ref. [2]), $\chi_{AF}(T)$ was found to decrease with temperature based on magnetisation curves measured up to 5×10^4 Oe and analysed without taking into account anisotropy effects. In Ref. [3], it was highlighted that a spurious contribution to $\chi_{AF}(T)$ arise when modelling $M_{mu}(H)$ without considering anisotropy. This spurious contribution decreases with temperature towards zero as anisotropy energy becomes small compared to k_BT and $\mu_{un}H$. Given this scenario, a better insight on $\chi_{AF}(T)$ depends on measurements of the susceptibility at fields higher than those used up to now. With this aim, we present measurements taken up to different maximum fields and different techniques of measuring magnetisation in ferritin, a model system for nanoparticles with AF interactions, where many previous studies were performed.
Ferritin consists of a hollow spherical shell composed of 24 protein subunits surrounding a ferrihydrite-like core. The diameter of the cavity is of the order of 7-8 nm and the average size of the core is 5 nm. Ferritin samples used in the experiments here reported were obtained from Sigma Chemical Company and prepared in powder samples by evaporation of the solvent at room temperature. Magnetisation was determined as a function of field i) up to 9×10^4 Oe at different temperatures using a PPMS system (Quantum Design) with a vibrating sample magnetometer (VSM) option, ii) up to 30×10^4 Oe at different temperatures using an extraction magnetometer in a Bitter magnet (HFML facility, Nijmegen), and iii) up to 50×10^4 Oe at 4.2 K using pick up coils and a pulsed field (LNCMP facility, Toulouse).
From the magnetisation isotherm curves, it is possible to observe the different evolutions of χ_{AF} with temperature when χ_{AF} is estimated at different fields as the derivative of the magnetisation as a function of field dM/dH. To distinguish from the real χ_{AF} obtained for complete μ_{un} saturation, we term the susceptibilities obtained from dM/dH at different (high) fields as high field susceptibility χ_{hf}. In Fig. (1) it is possible to observe that χ_{hf} decreases with temperature when taken at 5×10^4 Oe, in accordance with previous results (see, for instance Ref. [2, 4]). When taken at 9×10^4 Oe, χ_{hf} has a non-monotonic behaviour, increasing and then decreasing with temperature. For $H=30\times10^4$ Oe, χ_{hf} is reduced about 3 times compared to the values at 5×10^4 Oe and increases with temperature from 4.2 to 190 K. This clearly shows that the temperature dependence of the estimated χ_{AF} depends on the field at which is calculated, with the trend to increase with temperature being more evident as the field increases. This effect is associated to the non-saturation of μ_{un} at lower temperatures due to anisotropy.
The value of χ_{hf} found at 50×10^4 Oe and 4.2 K agrees quite well with $\chi_{AF}(0)$ estimated from mean field: 4.68×10^{-5} emu/Oe g_{Fe}, and thus superantiferromagnetism does not play a significant role in ferritin.

[1] L. Néel, C. R. Hebd. Seances Acad. Sci. 253, 1286 (1961).

[2] S. A. Makhlouf, F. T. Parker, and A. E. Berkowitz, Phys. Rev. B. 55, R14717 (1997).

[3] D. E. Madsen, S. Mørup, and M. F. Hansen, J. Mag. Mag. Mat. 305, 95 (2006).

[4] C. Gilles, P. Bonville, K. K. Wong, and S. Mann, Eur. Phys. J. B 17, 417 (2000).

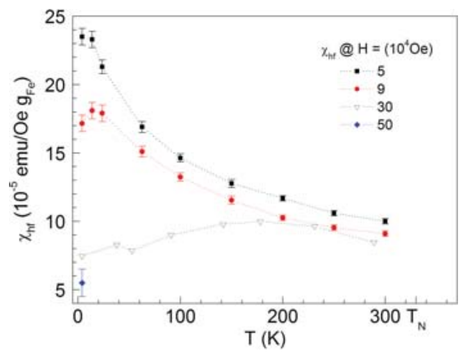

Fig. 1 High field susceptibility χ_{hf}=*dM/dH* obtained at selected fields and temperatures for ferritin.

HF-06

Iron oxide *versus* $Fe_{55}Pt_{45}@Fe_2O_3$ ferromagnetic nanoparticles: improved magnetic properties of core/shell nanostructure for biomedical applications.

L. C. Varanda[1], F. J. Santos[2], I. Momotaro[3], M. Jafelicci Jr.[2]
1. Físico-Química, Instituto de Química de São Carlos - USP, São Carlos, Brazil; 2. Físico-Química, Instituto de Química de Araraquara - UNESP, Araraquara, Brazil; 3. Física, Faculdade de Ciências - UNESP, Bauru, Brazil

Magnetic nanoparticles (NPs) with tailored surface chemistry have been widely studied and mainly due to their strongly potential in vivo biomedical applications such as magnetic resonance imaging, tissue repair, immunoassay, drug delivery, biological fluids detoxification, hyperthermia, and cell separation.[1-3] However, all applications impose requirements on the magnetic nanoparticles properties as chemical composition, biocompatible surface and crystal structures, adsorption, solubility, low own toxicity, high magnetization and small size with narrow particle size distribution. These features improve tissular diffusion, sedimentation times, magnetic response, and allow a targetable delivery in a local specific area of the body.[3] Magnetic iron oxide NPs, such as magnetite (Fe_3O_4), with magnetic moment of 300-400 emu/cc is currently used for thus purpose, and there is significant interest in developing high magnetic moment materials closed to α-Fe (~1000 emu/cc). However, disadvantages of metallic NPs uses reside in their toxicity, highly sensitive to oxidation, and limited biocompatible molecules that could be used to functionalize the metallic surface.[3] In this work, the synthesis and properties of the high magnetic moment Fe_3O_4-coated FePt NPs in a core/shell structure with improved magnetic properties and controlled oxide surface thickness were reported. Recently, we reported a modified polyol process to produce 4 nm-$Fe_{55}Pt_{45}$ ferromagnetic NPs.[4] Combining this process with the seed-mediated growth method, $Fe_{55}Pt_{45}@Fe_3O_4$ nanoparticles were prepared as follows: for coating of 2 nm-Fe_3O_4 shell thickness, oleic acid (1 mmol), oleylamine (1 mmol), $Fe(acac)_3$ (1 mmol), and 1,2-hexadecanediol (5 mmol) in octyl ether were mixed under nitrogen flow in a three-necked round-bottom flask. Then, 4 nm-$Fe_{55}Pt_{45}$ NPs dispersed in hexane (50 mg in 5 mL) were added, the mixture heated at 100 °C for 1 hour, and the temperature raised to reflux (298 °C) under a blanket of nitrogen for 30 min. The suspension was then cooled down to room temperature and the NP separated by ethanol addition and centrifuging. In absence of seeds, 6 nm-Fe_3O_4 NPs were obtained (Fig. 1a), and in presence of FePt seeds the core-shell nanostructure was observed as showed in Fig. 1b for $Fe_{55}Pt_{45}@Fe_3O_4$ with 4 nm core and 2 nm shell. By controlling the ratio of $Fe(acac)_3$ to FePt seeds, the oxide shell thickness can be readily tuned. XRD and EDX analysis show the Fe_3O_4 formation with Fe contents increasing with the increase of the shell thickness. Magnetic measurements show that saturation magnetization (M_S) of the as-synthesized NPs increases from 316 emu/cc to 830 emu/cc, respectively for Fe_3O_4 and core/shell nanostructure(Fig. 1c). Also, core/shell present coercive field (H_C) of only 90 Oe, closed to the superparamagnetic (SPM) behavior with magnetization directions of both core and shell switch coherently. Annealing the core/shell NPs leads to H_C and M_S values of 14.2 kOe and 1045 emu/cc, respectively, for 0.5 nm of shell thickness (Fig. 1d). This magnetization value is close to α-Fe and higher than that annealed pure $Fe_{55}Pt_{45}$ suggesting the presence of a higher moment iron-rich species in a thin layer on NP surface. H_C value increases by transformation of the FePt from fcc to fct phase, which increases the magnetocrystalline anisotropy. Hysteresis loop shape and the remanence ratio (~0.73) indicate effective exchange coupling between hard and soft phases, promoted by existence of a slightly iron oxide thin shell in the annealed composite (HRTEM, Fig. 1b inset). On the other hand, annealing of the 2 nm shell thickness coated-NPs (Fig. 1e) results in a coupled system presenting the exchange bias effect as evidenced by shift of the hysteresys curve and showed in the Fig 1f detail due to a hard and soft magnetic phase formation. This coupling leads a strong decreases in the coercivity value (130 Oe) closed to the SPM behavior, but maintain the high magnetization close to α-Fe. Results infer strong enhancement in the structural and magnetic properties of the core/shell NPs combined with the surface functionalization facility due to presence of the surface oxide layer suggesting potential biomedical applications.

1. Tartaj, P. et al., *J. Magn. Magn. Mater.* **290-291** (2005) pp. 28-34.

2. Klabunde, K. J., Zhang, D. and Sorensen, C., Encapsulated nanometer magnetic particles, US Patent 6.045.925 (2000).

3. Bao, Y. and Krishnan, K. M., *J. Magn. Magn. Mater.* **293** (2005) pp. 15-19.

4. Varanda, L. C. and Jafelicci Jr., M., *J. Am. Chem. Soc.* **128** (2006) pp. 11062-11066.

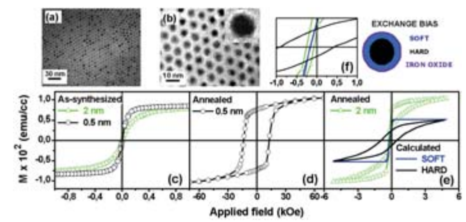

Fig. 1: TEM images of (a) 6 nm- Fe_3O_4 obtained without FePt seeds, (b) core/shell (4 nm/2 nm) $Fe_{55}Pt_{45}@$ Fe_3O_4 nanostructure. Inset shows a single particle of sample (b) after annealing with slightly iron oxide shell. Magnetic hysteresis loops of 4 nm- $Fe_{55}Pt_{45}$ coated with different shell thickness (c) as-synthesized (SPM behavior), and after annealing (d) 0.5 nm (strong ferromagnetic behavior, H_C ~14 kOe), (d) 2 nm showing high magnetization and coercivity close to SPM behavior due to exchange bias effect as showed by curve shift in (f).

HF-07

Surface modified superparamagnetic nanoparticles as a novel magnetic carrier.

M. Lin[1], S. Li[2], J. Gu[1], H. Lee[3], M. Mamoun[2], D. Kim[1]
1. Institute of Science and Technology in Medidicine, Keele University, Stoke-on-Trent, United Kingdom; 2. Materials Chemsitry Divisions, Royal Institute of Technology, Stockholm, Sweden; 3. Department of Materials Science and Engineering, Myongji University, Kyunggi-do, South Korea

Superparamagnetic iron oxide nanoparticles (SPIONs) are good candidates for various biomedical applications, such as magnetic resonance (MR) contrast agents, magnetic targeted drug/gene delivery, and hyperthermia. *In vivo* applications, which require stable colloid under physiological condition and further conjugation with bioactive molecules depending on individual purpose, remain a challenge. Since bare SPIONs tend to form agglomerations and it has barely any functional groups for attachment of bioactive molecules. So dextran and its derivatives have been attractive coating materials due to their biocompatible and hydrophilic characteristics. [1] Dextran stabilized SPIONs are readily commercially available. However, conjugation of bioactive molecules still strongly relies on generation of additional functional groups such as amine and carboxyl groups. Tat peptide conjugation to ammonia soaked dextran coated SPIONs was reported, but the amine activation is very unstable. [2] Carboxymethyl dextran (CMD) is of particular interests as iron oxide coating substances, due to their good biocompatibility and ability to conjugate with bio-molecules. CMD coating has been through physical adsorption and a 19-mer oligonucleotide has been attached to such CMD coated magnetic particles through carboiimide conjugation.[3] However it has shown that long-term storage of CMD nanoparticles eliminates the functioality of such particles, since physically absorbed CMD may dissociate from particles and result in exposure of iron oxide into the environment.

In this work, carboxymethyl activated crosslinked superparamagnetic iron oxide nanoparticles (CM-CL-SPIONs) are developed. CM-CL-SPIONs as backbone nanocarriers have enormous potential in biomedical applications such as MR contrast agent and targeted drug delivery system. The CM-CL-SPIONs have two major advantages as nanocarriers: (1) carboxylic groups of CMD serve as functional groups for attachment of versatile bioactive molecules. (2) CMD coating is continuous and stable. Briefly, dextran coated SPIONs (D-SPIONs) are synthesized by alkaline coprecipitation of Fe3+ and Fe2+ in the presence of dextran, and subsequently crosslinker epichlorohydrin is applied to the colloids. CL-SPIONs were further modified to generate carboxymethyl groups by monochloroacetic acid.

The as-prepared CM-CL-SPIONs were characterized by TEM, FTIR, TGA, DSC and zeta-potential. The particles are spherical in shape, 3-9 nm in diameter, with some degree of agglomeration. (Fig. 1) FTIR spectra confirm the existence of dextran coating; the new peak at 1598 cm-1 on CM-CL-SPIONs is due to carboxylate stretching, indicating the successful carboxymethylation. (Fig. 2) The stability of CM-CL-SPIONs with varied amount of crosslinking degree was investigated. Terminal sterilization (e.g. heat stress, 121 °C, 30 min) is legally required to for pharmaceutical products. However, heat stress cause severe dextran dissociation that is very undesirable and may cause exposures of SPION cores to the environment and subsequent aggregation. Estimation of dextran loss upon heat stress sterilization is very essential, if the product is used *in vivo*. With increased epichlorohydrin amount, the dissociation was suppressed, when reached a certain amount of crosslinking agent (10 %), the dextran lost is at the same level after heat stress (around 4 %), no matter further amount of crosslinker is added.

In conclusion, a versatile and novel magnetic nanocarrier CM-CL-SPIONs for biomedical applications is developed. Attributed to its good stability in water, and ability of conjugation of further biomolecules, CM-CL-SPIONs can be a backbone nanocarrier in biomedical applications.

1. Pankhurst, Q. A. ; Connolly, J. ; Jones, S. K. ; Dobson, J., J. Phy. D: Appl. Phy., 2003. 36: p. R167-R181

2. Lewin, M. ; Carlesso, N. ; Tung, C. ; Tang, X. ; Cory, D. ; Scadden, D. T. ; Weissleder, R.,. Nat. Biotechnol., 2000. 18: p. 410-414.

3. Wagner, K. ; Roder, M. ; Schwalbe, M. ; Pachmann, K. ; Clement, J. H. ; Schnabelrauch, M., Appl. Organo. Chem., 2004. (18): p. 514-519.

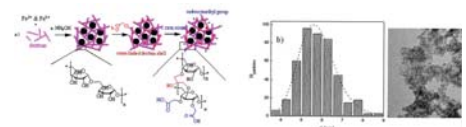

Figure 1. a) illustration of synthetic procedure of CM-CL-SPIONs. b) size distribution and c) TEM image of CM-CL-SPIONs.

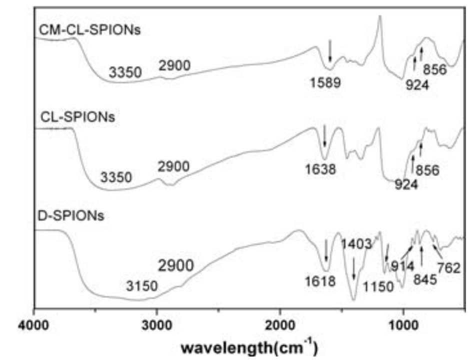

Figure 2. FTIR spectra of D-SPIONs, CL-SPIONs and CM-CL-SPIONs.

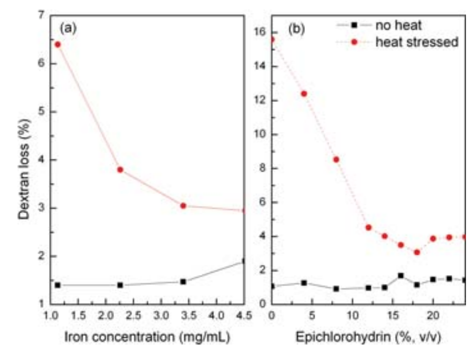

Figure 3. Dextran loss during heat stress. a) with varied particle concentratiojn; b) with varied crosslinker amount.

HF-08

Magnetic porous hollow silica nanospheres for biomedicine application.

H. Ma[1], J. Zhou[1], D. Caruntu[1], M. Yu[1], J. Chen[2], C. O'Connor[1], *W. Zhou*[1]
1. Advanced Materials Research Institute, University of New Orleans, New Orleans, LA; 2. Key Lab for Nanomaterials, Ministry of Education, Beijing University of Chemical Technology, Beijing, China

Introduction

Magnetic nanoparticles (MP) are widely used in biomedical fields such as MRI and targeted drug delivery due to the high saturation magnetization, superparamagnetism, high magnetic susceptibility and low toxicity.[1-4] Among different carrier, silica is a promising material with good biocompatibility. The magnetic hollow silica nanospheres with a character of superparamagnetism are considered to be the proper carriers for magnetically guided targeted delivery and controlled release. In this paper, we report a novel synthetic method for magnetic porous hollow silica nanospheres (MPHSNs), using tetraethoxysilane (TEOS) as precursor, and sacrificed $CaCO_3/Fe_3O_4$ composite nanoparticles and cationic surfactant double templates. The product is potentially capable in bio-medicine applications.

Experiment

At room temperature, 3g $Fe_3O_4/CaCO_3$ composite particles was dispersed ultrasonically into a mixture of 60 ml ethanol and 40 ml H_2O for 30min and then stirred for 30 min. Then add 0.74g CTAB/mixed CTAB&Octane and dispersed ultrasonically for 20 min. [5-7] Add 34 ml ammonia, 3.7 ml TEOS into the reaction mixture to reach 11 of pH. The system was stirred at 500 rpm for 2 h and aged for 6h then filtrated. The cake was dried at 50°C for 6 h and calcined at 550°C for 5 h then immersed in acetic acid solution (HAc: H_2O = 1:15) for 5 h, then washed with H_2O and alcohol, and dried at 75°C for 18 h to yield the MPHSNs. The samples were investigated by Carl Zeiss 1530 VP FESEM, JEOL 2010 TEM, EDS, XRD, ASAP2010 Surface Area Analyzer, Quantum Design MPMS-5S SQUID magnetometer and controlled release test.

Magnetic nanoparticles (MP) are widely used in biomedical fields such as MRI and targeted drug delivery due to the high saturation magnetization, superparamagnetism, high magnetic susceptibility and low toxicity.[1-4] Among different carrier, silica is a promising material with good biocompatibility. The magnetic hollow silica nanospheres with a character of superparamagnetism are considered to be the proper carriers for magnetically guided targeted delivery and controlled release. In this paper, we report a novel synthetic method for magnetic porous hollow silica nanospheres (MPHSNs), using tetraethoxysilane (TEOS) as precursor, and sacrificed $CaCO_3/Fe_3O_4$ composite nanoparticles and cationic surfactant double templates. The product is potentially capable in bio-medicine applications.

Result and discussion

The obtained MPHSNs are shown in Fig.1. MPs are embedded in the cores and EDS analysis implies there is no Ca exists. Fig.2a shows ZFC and FC magnetization data of MPHSN in the temperature range of 10 to 300K. In ZFC, the sample was cooled from 300K to 5K in a zero field, then heated from 5 to 300 K in a field of 100 Oe and the magnetization was measured. In FC, the sample was cooled from 300 K to 5 K in a field of 100 Oe and the magnetization was measured as heated from 5 to 300 K in the field. The MPHSNs exhibit superparamagnetism and ferromagnetism above and below the blocking temperature, as shown in the field-dependent hysteresis loops of MPHSNs in Fig.2b. Fig.3 shows the vitro release behavior of MPHSNs using ibuprofen. MPHSNs using CTAB and Octane as surfactant have the best controlled release effect, indicating the potential capability in bio-medicine.

1. H.H.Yang, S.Q. Zhang, X.L. Chen, Z.X. Zhuang, J.G. Xu and X.R. Wang. Anal. Chem. 76, 1316, 2004.

2.B.I. Haukanes, C. Kvam, BioTechniques 11, 60, 1993.

3.T. Tanaka., T. Matsunaga. Anal. Chem. 72, 3518, 2000.

4.L. Levy, Y. Sahoo, K.S. Kim, E. J. Bergey, and P. N. Prasad, Chem. Mater. 14, 3715, 2002.

5.Y. Lu, Y. Yang, A. Sellinger, M. Lu, J. Huang, H. Fan, R. Haddad, G. Lopez, A.R. Burns, D. Y. Sasaki, J. Shelnutt, C.J. Brinker, Nature 410, 913, 2001.

6.D. Wang, W.L. Zhou, B.F. McCaughy, J.E. Hampsey, X. Ji, Y.B. Jiang, H. Xu, J. Tang, R.H. Schmehl, C.J. O'Connor, C.J. Brinker, Y. Lu, Adv. Mater. 15, 130, 2003.

7.Y. Lu, A. Chemie, International Edition, 45, 7664, 2006.

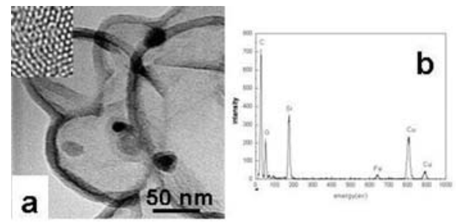

Fig.1 TEM image (a) and EDS spectrum (b) of MPHSNs. The inset is a HREM image, showing pores on the hollow silica shell.

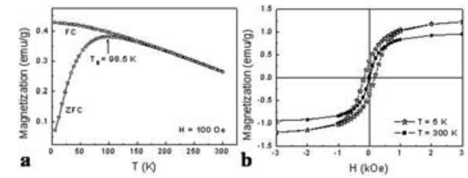

Fig. 2 Magnetic properties of the MHSNs: (a) temperature dependence of magnetization at ZFC and FC conditions; (b) hysteresis loops of the MHSNs at 5 and 300 K.

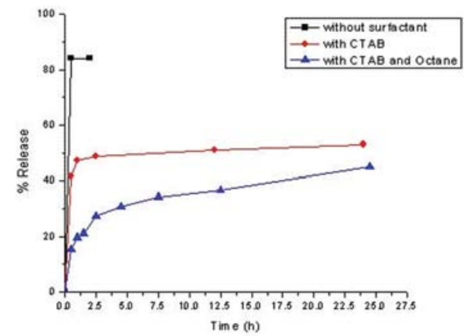

Fig.3 Drug release of ibuprofen from the MPHSNs showing slow release.

HF-09

Hysteresis power loss heating of ferromagnetic nano-particles designed for magnetic thermoablation.

E. Kita[1], H. Yanagihara[1], S. Hashimoto[2], K. Yamada[2], T. Oda[2], M. Kishimoto[3], A. Tasaki[1]
1. Institute of Appield Physics, University of Tsukuba, Tsukuba, Japan; 2. Institute of Clinical Medicine, University of Tsukuba, Tsukuba, Japan; 3. Hitachi Maxell, Ltd.,, Oyamazaki, Japan

Magnetic hyperthermia and thermoablation using small magnetic particles have been a new approach to apply heat power on cancerous cells without surgical operations[1]. Most of researches have been carried out using magnetic fluids which consist of Fe oxides particles basically of superparamagnetic at room temperature. Additionally there are reports using ferromagnetic $MgFe_2O_4$ particles with small coercive force around 20 Oe. In both cases, AC magnetic fields around 100 kHz are widely used. The advantage of superparamagnetic relaxation heating is that particle aggregation due to the magnetic interaction between particles is small. It can be a realistic advantage for the actual medical use, however it has a difficulty in fitting their size properly to the driving frequency. On the other hand, ferromagnetic hysteresis loss heating is free from such condition to the driving frequency and size distribution has less effect on the heating performance. To use this hysteresis loss, it is necessary to apply higher magnetic field than those applied in usual methods with a frequency of 100 kHz. The use of hysteresis loss for heating at lower frequency and high magnetic fields is expected to be another solution to thermoablation. We have tested heating capacity of ferromagnetic nano-particles for thermoablation with rather high coercive force under an AC magnetic field of 10 kHz and 500 Oe.

Co-contained Fe_3O_4 particles were produced by heating the coprecipitants containing Co2+, Fe2+ and Fe3+ ions in alkaline solution at 130 °C for 5 hours using hydrothermal method. The coercivity was controlled from 80 Oe to 320 Oe by changing the content of Co. Sizes of nano-particles were about 20 nm for all samples. Magnetic dc hysteresis loops were measured at room temperature with a vibrating sample magnetometer (VSM). AC magnetic fields were produced in a gap of a ferrite core. AC currents at 10 kHz were provided by a commercial high power audio amplifier. Oxide nano-particles of 50 mg were formed into a cylindrical shape and set at the center of a gap of the ferrite core. Temperature of the sample was recorded by an infrared optical thermometer.

Figure 1 shows an electron micrograph of typical Co-contained Fe_3O_4 particles and well dispersed nano-particles were observed. Magnetic hysteresis loops of Fe oxides particles were recorded under the magnetic field between – 2000 Oe and 2000 Oe where the loop represents its major hysteresis loop and coercive force was about 160 Oe. A minor loop was recorded at the field between -500 and 500 Oe as shown in Fig, 2. Temperature variation of the same sample under the application of 500 Oe (peak) AC field at 10kHz was shown in the Fig. 3.

From the initial slope of the curve, heating power was derived to be 4 W /g. Power loss is expected to be the product of frequency and the area of DC hysteresis. From the 500 Oe minor loop shown in Fig. 2, the loss is estimated to be 6.7 W/g. These results conclude that loss at 10 kHz is fairly well understood by the DC minor loop recorded at the same magnetic field. By choosing magnetic fields strength and elevating the frequency, ferromagnetic hysteresis loss in nano-particles will be another candidate of the heating system.

[1] for example, see R. Hergt and W. Andrä, Magnetic Hyperthermia and Thermoablation in *Magnetism in Medicine* Wiley-VCH, Weinheim 2007, p. 550.

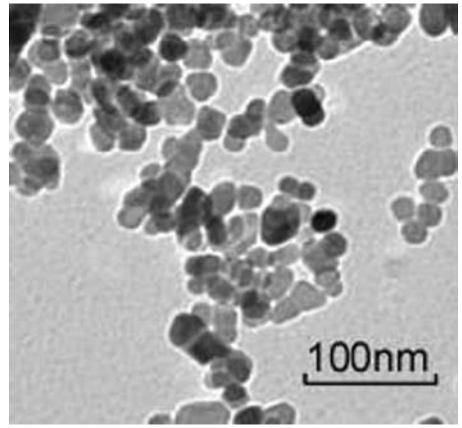

Fig. 1. Electron micrograph of Fe_3O_4 based nano-particles.

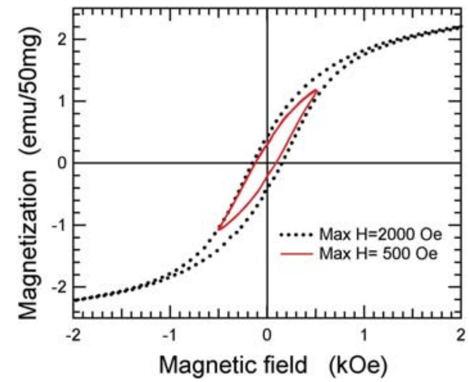

Fig. 2. Hysteresis loops of Fe_3O_4 based nano-particles with a coercive force of 160 Oe.

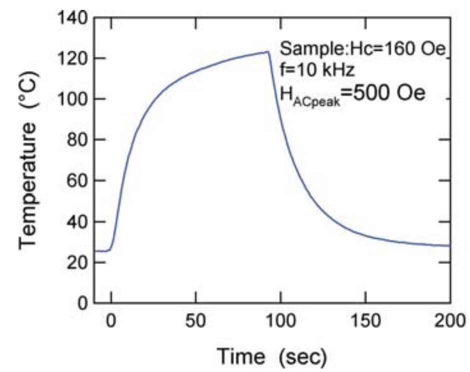

Fig. 3. Heating performance of Fe_3O_4 based nano-particles at 10 kHz.

HG-01

The local atomic Joule magnetostriction of $Fe_{81}Ga_{19}$

M. P. Ruffoni[1], S. Pascarelli[1], R. Grössinger[2], R. Sato-Turtelli[2], R. F. Pettifer[3]
1. European Synchrotron Radiation Facility, Grenoble, France; 2. Technical University of Vienna, Vienna, Austria; 3. Department of Physics, University of Warwick, Coventry, United Kingdom

Using X-ray Absorption Spectroscopy (XAS) in differential mode (DiffXAS), the magnetostriction of a $Fe_{81}Ga_{19}$ splat cooled ribbon has been measured and the strain coefficients quantified. Due to the local atomic nature of XAS, this represents the first microscopic analysis of such a system, and was made possible only by recent advances in synchrotron radiation based techniques, capable of detecting atomic strains on the scale of femtometres [1].
Previously, magnetostriction measurements have relied on macroscopic techniques, commonly via strain gauges. However, such measurements on thin films and ribbons, which tend to be of the greatest importance from a technical perspective, are notoriously difficult. This is in part due to the measured strains being extremely small over a sample thickness of a few tens of microns, but also due to the practicalities of coupling such a sample to a sensor. Consequently, published magnetostriction coefficients vary immensely. In some cases, giant magnetostrictions have been reported for $Fe_{(1-x)}Ga_x$ ribbons [2][3] although doubt has recently been cast upon their validity [4]. This serves to assert a need for a more fundamental approach to measuring magnetostrictive strains. A need which is satisfied by DiffXAS.
Being based upon XAS, DiffXAS probes changes in local atomic structures and is just dependent upon the short-range order of the first one or two atomic shells surrounding an absorbing atom. However, whilst even giant magnetostrictive strains exhibited by a number of rare-earth based Fe alloys are on the very limits of detection by conventional XAS techniques, DiffXAS offers an increase in sensitivity of two orders of magnitude and so makes such strains easily measurable. Direct detection of strains on the scale of tens or hundreds of ppm then becomes possible. Furthermore, in principle, this is true for any type of strain that is reproducible upon the modulation of some external sample property [5].
Additionally, since x-ray absorption is chemically selective, these structural changes may be viewed from different positions within the crystal lattice, and so the underlying significance of different atomic species in the overall process elucidated. Contributions from different types of bonds within the structure may then be decoupled and analysed. Such information has immense value when trying to obtain fundamental knowledge of atomic strains, and particularly when attempting to verify theoretical models. Concerning $Fe_{(1-x)}Ga_x$, a theory for the observed strain enhancement was first put forward by Wu [6] in 2002, which has more recently been developed by Cullen et al. [7] after modelling the behaviour of the material's magnetocrystalline anisotropy. Experimental verification of these proposals has yet to be presented, but is something that DiffXAS has the potential to provide.
Using this technique, we have focused on the problem of enhanced magnetostriction observed in the $Fe_{(1-x)}Ga_x$ system. Such systems have attracted significant interest from a technological and device applications perspective since, although they do not possess truly giant magnetostrictions, they are both absent of expensive rare-earth elements and have desirable mechanical properties. They also show appreciable low-field magnetostriction, saturating at fields of only several hundred Oersteds. Working within these saturation conditions, DiffXAS detects the changes in photoelectron scattering path length induced by structural distortions that occur when the sample's magnetisation vector is modulated between two states – parallel and perpendicular to the x-ray polarisation vector.
Subsequent data analysis uses a framework of Cartesian tensors to model the structural properties of the sample, and *ab initio* XAS theory to model the observed perturbations. From this, the atomic strain tensor may be derived and related to the sample magnetisation vector in order to find the coefficients of the Joule magnetostriction tensor [8]. These coefficients may then be reduced to the more familiar macroscopic λ^{100} and λ^{111} coefficients by exploiting the crystal symmetry elements [8].
Working on a splat cooled foil of $Fe_{81}Ga_{19}$, preliminary analyses performed with this technique have yielded a magnetostriction coefficient of $(3/2)\lambda^{100} = 250\pm20$ppm ($\lambda^{111}$ coefficient is approximately zero for this composition), based upon a disordered A2 structure determined from analysis of the sample's conventional XAS signal. This analysis failed to detect the $D0_3$ structure reported by some authors for this composition. Further experiments are planned to examine the full range of compositions over which magnetostriction enhancement is observed in this system.

[1] R.F. Pettifer, O. Mathon, S. Pascarelli, M.D. Cooke, M.R. J. Gibbs, Nature 435, 79 (2005)

[2] M.C. Zhang, H.L. Jiang, X.X. Gao, J. Zhu, and S.Z. Zhou, J. Appl. Phys. 99, 023903 (2006)

[3] G.D. Liu, L.B. Liu, Z.H. Liu, M. Zhang, J.L. Chen, J.Q. Li, G.H. Wu, Y.X. Li, J.P. Qu, T.S. Chin, J. Appl. Phys. 84, 2124 (2004)

[4] R. Grössinger, R. Sato Turtelli, N. Mehmood, S. Heiss, H. Müller, C. Bormio-Nunes, J. Mag. Mag. Mater., in press

[5] M. P. Ruffoni, R.F. Pettifer, S. Pascarelli, A. Trapananti, O. Mathon in X-Ray Absorption Fine Structure XAFS13, edited by B. Hedman and P. Pianetta, AIP Conf. Proc. No. 882 (AIP, 2007), p. 838.

[6] R. Wu, J. Appl. Phys. 91, 7358 (2002)

[7] J. Cullen, P. Zhao, M. Wuttig, J. Appl. Phys. 101, 123922 (2007)

[8] E du T, de Lacheisserie in Magnetostriction: Theory and Applications of Magnetoelasticity (CRC Press, 1993), p133 and p161-162

HG-02

The Effect of Tempering on the Magnetostriction of Fe-Ga Alloys.

T. A. Lograsso[1,2], M. Huang[1]
1. Institute for Physical Research and Technology, Iowa State University, Ames, IA; 2. Materials and Engineering Physics, Ames Laboratory, Ames, IA

It is well known that the magnetostriction in Fe-Ga alloys depends significantly on thermal history[1,2]. While most studies have investigated properties of Fe-Ga alloys in terms of the cooling rate (quenched vs. slow cooling)[1,2], little attention has been given to the influence of tempering temperature on the magnetostriction. In this paper we report on single crystalline magnetostriction measurements of $Fe_{100-x}Ga_x$ alloys to examine the affect of tempering temperature and time on the tetragonal magnetostrictive constant λ_{100}. These measurements were conducted on the same single crystal to minimize any effect of sample to sample variations in chemistry, misorientation or other sample to sample variations that can have significant influence on the measured strain. We have examined two different compositions; one far from the solubility limit (x=10) where formation of $D0_3$ on cooling is not expected, and the other near the first maximum in magnetostriction (x=18.4) where thermal history is known to have a significant impact on the structure of the alloy[1,2].
All samples were quenched from 1000 °C into water, tempered at various temperatures for 1 hr and then water quenched. Tempering temperatures started at 250 °C because according to Differential Scanning Calorimetry (DSC) analyses of quenched alloys[3], the formation of $D0_3$ phase begins at around this temperature. It can be seen in Fig. 1, for Fe-10 at% Ga alloy, the magnetostriction is invariant with temperature within experimental error, ± 3 ppm. This result is consistent with the Fe-Ga phase equilibria[4] where $D0_3$formation is not expected as this composition is well within the A2 single phase region, from room temperature to 1500 °C. In contrast, as shown in Fig. 2, magnetostriction decreases dramatically with tempering temperature above 300 °C for a composition of Fe-18.4 at% Ga. This decrease in strain occurs unexpectedly at higher temperatures than the observed exothermal peak at around 250 °C in the DSC results[3].
In order to confirm that $D0_3$ formation in the annealed samples leads to the observed decreases in $(3/2)\lambda_{100}$, X-ray diffraction measurements were carried out. Standard θ-2θ X-ray spectra were used to examine the phase evolution with annealing time for the Fe-18.4 at. % Ga crystal, tempered at 350 °C up to 4 hours. A Si internal standard was used to account for any misalignment of the single crystal. It can be seen in Fig. 3a that $D0_3$ was not observed in the water quenched sample and a strong reflection at ~ 64° is from the (200)reflection of the A2 phase[1,3]. After tempering for 1 hour, a small peak at around 30.5° was observed which corresponds to the superlattice $(100)_{A2}$ reflection of the $D0_3$ phase. This peak increases in intensity with longer annealing times as seen in Fig. 3c and Fig. 3d, indicating larger fraction of $D0_3$ phase is formed. These X-ray results are consistent with previous studies[1] in that quenching from high temperature prevents the formation of the $D0_3$ phase resulting in maximum magnetostriction. Further the presents results confirms that $D0_3$ formation result in a decrease in magnetostriction.

1. T. A. Lograsso, A. R. Ross, D. L. Schlagel, A. E. Clark and M. Wun-Fogle, J. Alloys Comp. 350 (2003) p. 95.

2. A. E. Clark, K. B. Hathaway, M. Wun-Fogle, J. B. Restorff, T. A. Lograsso, V. M. Keppens, G. Petculescu and R. A. Taylor, J. Appl. Phys. 93 (2003) p. 8621.

3. S. Datta, M. Huang, J. Raim, T. A. Lograsso and A. B. Flatau, Mat. Sci. &Eng. A., 435-436, 221 (2006).

4. O. Ikeda, R. Kainuma, I. Ohnuma, K. Fukamichi and K. Ishida, J. Alloys and Comp. 347 (2002) p. 198.

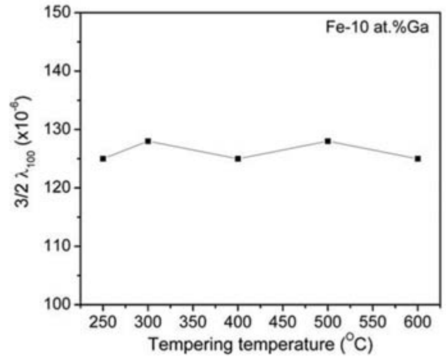

Fig. 1 Magnetostriction vs. tempering temperature for Fe-10 at.%Ga alloy

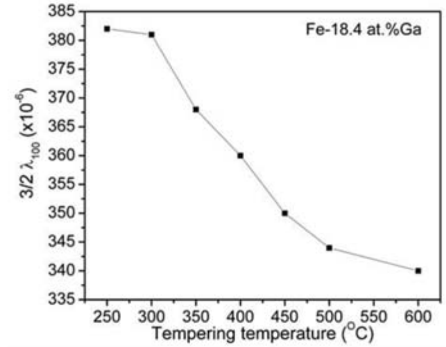

Fig. 2 Magnetostriction vs. tempering temperature for Fe-18.4 at.%Ga alloy

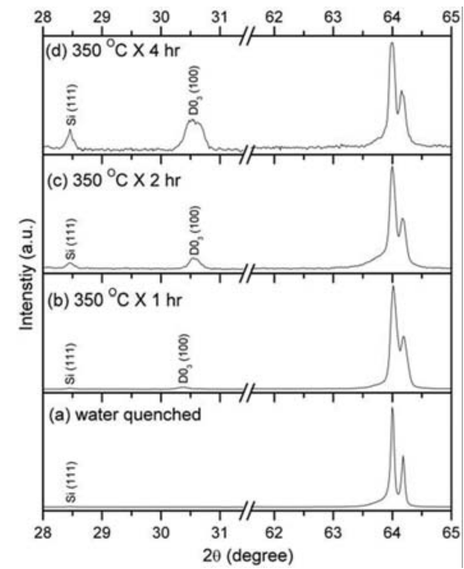

Fig. 3 X-ray results of Fe-18.4 at.%Ga alloy tempered at 350 °C

Magnetic field and stress dependence of FeGa 3-D shaped polycrystalline magnetostrictive materials properties.

N. Lupu, H. Chiriac
Magnetic Materials and Devices, National Institute of Research and Development for Technical Physics, Iasi, Romania

Magnetostrictive materials can be obtained in desirable shapes depending on their final application. The fabrication in variable shapes strongly depends on the method of preparation. Fe–Rare Earth base giant magnetostrictive materials (Terfenol, Sm-Dy-Fe, Fe-Dy, etc.) are generally prepared as rods or bars especially due to the specific conditions to be assured to get the single crystal phase, but also because of their fragility in other shapes (thin films, melt-spun amorphous or polycrystalline ribbons). Despite of their no fragility under mechanical stress conditions, the obtaining of the single phase in Fe-Ga/Fe-Al base alloys which gives the large magnetostriction on preferred direction, impose limitations on preparation, and thus the bulk shapes (rods, bars) are preferred.
In this work, alloy ingots of $Fe_{1-x}Ga_x$ (x = 0.15, 0.175, 0.195, 0.21, 0.225, 0.28) were prepared by arc-melting high purity (> 99.9%) constituent elements multiple times to insure homogeneity. Bulk cast samples as rods of 6 mm in diameter and 40 mm in length, and respectively bars of 3x3x10 mm^3 have been prepared by ejecting the molten alloy in Cu moulds using an ejection pressure of 4 atm. Bulk shaped samples were sealed in quartz tubes with approximately 1 atm. of Ar. Isothermal heat treatments were performed at 1000^0C for 72 hours and then the samples were slow quenched to RT or slow quenched to 800^0C then water quenched.
No texture was evidenced by XRD measurements. In addition to the primary reflections at ~ 44^0 (110) and ~ 64^0 (200), none reflections corresponding to the DO_3 phase were observed. The thermomagnetic measurements confirmed the existence of bcc Fe (A_2 phase), with an additional magnetic transition at around 500^0C for $Fe_{79}Ga_{21}$ melt-spun ribbons. Additionally, the samples are magnetically very soft, which is also confirmed by the λ-H measurements shown below for $Fe_{82.5}Ga_{17.5}$ and $Fe_{80.5}Ga_{19.5}$ cast bars of 3x3x10 mm^3.
The magnetostriction of the 3-D shaped polycrystalline Fe-Ga bulk samples is dependent on the magnitude of the applied stresses during measurements, because of the stored magnetoelastic energy, as shown in Fig. 2. The same behavior is observed for all composition, but the increase of the magnetostriction is smaller for higher Ga contents. Additionally, depending on the composition, applied field direction and the treatment conditions (but mainly on the cooling history) the magnetostriction behaves differently for 21 and 28 at. % Ga, respectively. Such a different behavior is mainly caused by the specific microstructure developed in each polycrystalline Fe-Ga cast sample as a function of composition and annealing conditions (relaxation of internal stresses, presence of microstresses and microstrains, etc.).
All these aspects will be discussed in detail, being extremely important in what concerns the potential applications of such cast 3-D shaped polycrystalline magnetostrictive materials.

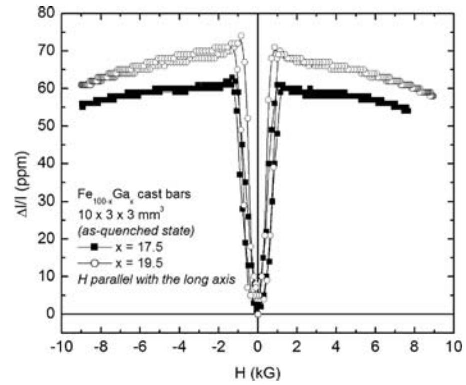

Fig. 1. Room temperature magnetostriction of $Fe_{82.5}Ga_{17.5}$ and $Fe_{80.5}Ga_{19.5}$ polycrystalline cast-bars.

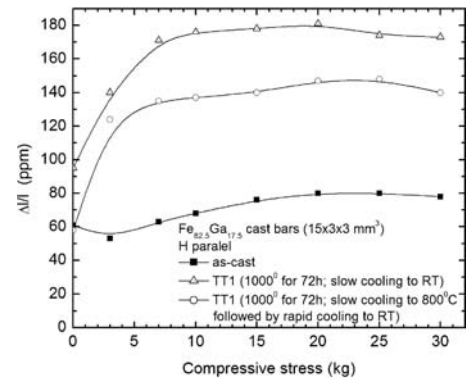

Fig. 2. Applied stress dependence of the magnetostriction for $Fe_{82.5}Ga_{17.5}$ cast bars.

HG-04

Magnetostriction of Fe-X (X = B, Al, Ga,Si, Ge) intermetallic alloys.

G. Roland, S. Reiko, M. Nasir
Inst. of Solid State Physics, Techn. Univ. Vienna, Vienna, Austria

Metallic iron exhibits a rather low magnetostriction of λ(100) = 20 ppm and λ(111) = -21 ppm. However substituting Fe by nonmagnetic elements, such as Ga, Al,… leads very often to a remarkable enhancement of the magnetostriction [1,2].
Table 1 shows the change of the magnetostriction due to substitution in Fe-X systems.
In single crystalline Fe100-xGax a maximum magnetostriction between 17 and at19% Ga was found which can reach values of less than 400 ppm (3/2 λ(100)) at room temperature.
It should be noted that the phase diagram on the Fe-rich side is very similar for substituting Si, Al or Ga. First a statistical substitution of the bcc α-Fe occurs which leads to the A2 structure. For higher amounts of the substituting element the more ordered B2 or even the DO3 structure can occur. Figure 1 shows the structural situation for the Fe-Ga system:
Due to the fact that in polycrystalline materials the relative amount of the different structure types plays a very important role, the production influences the achievable magnetostriction. Comparing Fe-Ga, Fe-Si and Fe-Ge binary systems, all three systems in the Fe-rich region present disordered solid solution in the A2 structure and ordered phases B2 and DO3 for higher concentrations. So recently the magnetostriction was investigated on bulk annealed Fe100-xGex (x = 8, 12, 15, 20). Depending on the composition different crystallographic phases occur. For annealed Fe80Ge20 (T = 600°C) a maximum magnetostriction of -30 x 10-6 was found [7], which is significantly smaller than that of polycrystalline Fe-Ga..
In the last years a large number of papers appeared reporting large and even "giant" magnetostriction values obtained on rapidly quenched Fe-Ga ribbons. The reported "giant" values range from -1100 ppm for a Fe85Ga15 stacked ribbon sample [8], to even larger values such as -2100 ppm in Fe83Ga17 ribbon [9]. However due to careful investigations on the bending problem – depending on the field direction with respect to the ribbon axis - which may occure in such ribbons, doubts exist concerning the reliabilty of these data [10].
In the present paper an overview of actual achieved magnetostriction data on systems Fe-X (X = Al, Ga,Si, Ge) will be given. Of great importance is the applied measuring method. The samples are measured using either a strain gauge method or a capacitance dilatometer. The used geometry (e.g. field direction with respect to ribbon axis) is of large importance. Additionally is the structural situation, which can be influenced by the production method, important with respect to the local degree of disorder. The effect of the local surrounding, the symmetry as well as the microstructure will be discussed.

[1] A.E. Clark, James B. Restorff, M.Wun-Fogle, T.A. Lograsso, D.L. Schlagel; IEEE TRANS. ON MAGN. VOL. 36, NO. 5, (2000) 3238

[2] A.E. Clark, M.Wun-Fogle, J.B. Restorff, T.A. Lograsso, J.R. Cullen; IEEE TRANS. MAGN., VOL. 37, NO. 4, (2001) 2678

[3] R. C. Hall, J. Appl. Phys., vol. 30, (1959) pp. 816–819

[4] R. C. Hall, J. Appl. Phys., vol. 31, (1960) pp. 1037–1038

[5] Landolt-Börnstein Group III Vol.19; Springer Verlag (1994); Chapt. 7.1.2.3

[6] O. Ikeda, R. Kainuma, I. Ohnuma, K. Fukamichi, K. Ishida, J. Alloys Compd. 347 (2002) 198–205

[7] C. Bormio Nunes, R. Sato Turtelli, L. C. Teixeira, P. A. Suzuki, R. Grössinger, C. Barbatti; J. Magn. Magn. Mat. submitted.

[8] G. D. Liu, L. B. Liu, Z. H. Liu, M. Zhang, J. L. Chen, J. Q. Li, and G. H. Wu, Y. X. Li and J. P. Qu, T. S. Chin; Appl. Phys. Let. 84 (2004) 2124

[9] M. C. Zhang,H. L. Jiang, X. X. Gao, J. Zhu, and S. Z. Zhou; J. Appl. Phys. 99 (2006) 23903

[10] R.Grössinger, R.Sato Turtelli, N.Mehmood, S.Heiss; J. Magn. Mat. (2007) accepted

atom % Fe	λ(100) ppm	λ(111) ppm
0**	22	-21
13%Ga	153	-16
17%Ga	207	-
16%Al*	86	-2
5%Si**	27	-7
15.6%Cr*	51	-6
15.6%V*	43	-10

Table1: Magnetostriction constants at room temperature from Fe-X single crystals. *…taken from R.C.Hall [3,4]; **…Landolt Börnstein [5]

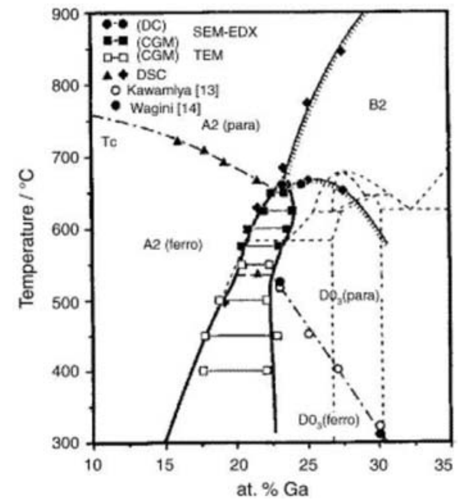

Fig. 1. Metastable Fe–Ga phase diagram [6].

HG-05

Magnetic and magnetoelastic properties of electrodeposited FeGa/CoFeB multilayered films and nanowires arrays.

N. Lupu, P. Pascariu, C. Gherasim, H. Chiriac
Magnetic Materials and Devices, National Institute of Research and Development for Technical Physics, Iasi, Romania

Recently, hybrid structures consisting of a combination of magnetostrictive alloys and soft magnetic materials have been proposed [1]. The multilayered thin films, prepared by conventional sputtering methods, were designed on the basis of "exchange spring" magnets, which consist of two materials with different magnetic properties, exchange coupled in a multilayer system. This behavior is called "exchange magnetostriction" and depends strongly on the thickness of the different layers forming the multilayered structure [2].
This work is focusing on the fabrication and characterization of Fe-Ga/Co-Fe-B multilayered thin films (MTF) and nanowires (MN). Multilayered films 3-4 µm thick have been obtained by electrodepositing 50 consecutive sequences of amorphous Co-Fe-B (20 nm or 60 nm) and Fe-Ga (60 or 20 nm) successive layers. 200 to 300 sequences multilayered nanowires were electrodeposited into commercially available Synkera® nanoporous alumina membranes with pore diameters ranging from 17 to 97 nm, and lengths of 50 µm. CoFeB amorphous alloy has been chosen for its magnetic softness [3], which favors the rotation of the magnetic moments, thus contributing to the appearance and magnitude of the "exchange magnetostriction" effect in the coupled FeGa/CoFeB structures. $[Fe_{1-x}Ga_x/Co_{60}Fe_{20}B_{20}] \times n$ (x = 0.1√0.3) multilayered nanowires were electrochemically deposited into the nanopores from a Watts-type bath, changing the electrochemical potential in the range 0.75 (CoFeB) to 1.7 V (FeGa). The composition of the successive Fe-Ga and Co-Fe-B layers was controlled through optimizing deposition parameters such as ion concentration, buffer acids, and applied voltage. The bath consisted in a single mixed solution of iron(II) sulfate heptahydrate, cobalt(II) sulfate heptahydrate, gallium(III) sulfate hydrate and $C_2H_{10}BN$ combined with boric acid as a pH buffer and small amounts of sodium citrate as complexing agent to keep the ferrous iron and cobalt from oxidizing. Energy dispersive spectroscopy (EDS) was used to check the composition of the electrodeposited nanowires. In order to select only the most suitable conditions for multilayered nanowires preparation, separate thin films of Fe-Ga and Ni-Fe as well as multilayered thin films have been electrodeposited first, using brass substrates.
SEM micrographs of FeGa/CoFeB nanowires show that the multilayered structure is formed. The X-ray diffraction patterns indicates the coexistence of (Fe,Ga) solid-solution phase and amorphous CoFeB in multilayered thin films and nanowires. The coexistence of these phases is evidenced also by the thermomagnetic measurements shown in Fig. 1. The Curie temperature of the amorphous CoFeB is about 430^0C, whereas the second transition at about 700^0C is the ferromagnetic-paramagnetic transition of $Fe_{70}Ga_{30}$ [4].
The combination of $Fe_{1-x}Ga_x$ magnetostrictive material and $Co_{60}Fe_{20}B_{20}$ amorphous soft magnetic material shows good magnetic softness (H_c does not exceed 20 Gs) and gives novel magnetostrictive behavior caused by the formation of twisted spin structures. The coercive field values are smaller than those reported up to now for Fe-Ga single nanowires [5] and Fe-Ga/Py multilayered nanowires [6], and the reason for keeping such reduced coercivities might be again the softness of amorphous Co-Fe-B layer, which allows the rotation of the magnetic moment much faster than if using other interface layers. The intrinsic mechanisms governing the magnetic and magnetoelastic behavior of such "twisted" structures will be discussed in detail considering the magnetic domains structure of the component layers as well as the interlayer phenomena.

[1] E. Quandt, A. Ludwig, J. Betz, K. Mackay, D. Givord, J. Appl. Phys. 81, 5420 (1997).

[2] T. Shima, H. Takahashi, K. Takanashi, H. Fujimori, Sensors and Actuators A 91, 210 (2001).

[3] M. Ciureanu, F. Beron, L. Clime, P. Ciureanu, A. Yelon, T.A. Ovari, R.W. Cochrane, F. Normandin, T. Veres, Electrochimica Acta 50 (2005) 4487.

[4] L. Dai, J. Cullen, M. Wuttig, T. Lograsso, E. Quandt, J. Appl. Phys. 93, 8627 (2003).

[5] P.D. McGary and B.J.H. Stadler, J. Appl. Phys. 97, 10R503 (2005).

[6] N. Lupu, H. Chiriac and P. Pascariu, J. Appl. Phys. (2008) in press.

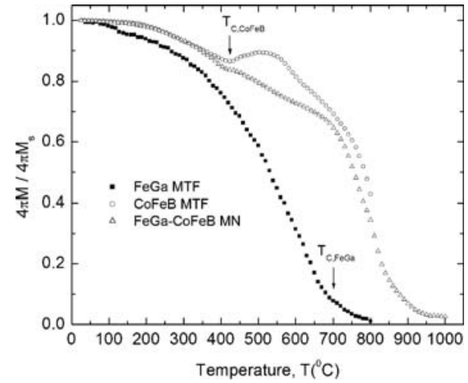

Fig. 1. Thermomagnetic curves of electrodeposited Fe-Ga and Co-Fe-B thin films (MF) and respectively Fe-Ga(60 nm)/Co-Fe-B (20 nm) nanowire arrays (MN) with diameters of 73 nm.

HG-06

Modelling and experimental analysis of magnetostrictive devices: from the material characterisation to their dynamic behaviour.

O. Bottauscio[1], R. Bonin[1], A. Lovisolo[1], P. Roccato[2], C. Sasso[1], M. Zucca[1]
1. Electromagnetics, Istituto Nazionale di Ricerca Metrologica, Torino, Italy; 2. Dip. Ingegneria Elettrica, Politecnico di Torino, Torino, Italy

The prediction of the dynamic behaviour of magnetostrictive (MST) devices is fundamental for their use as active compensators of mechanical vibrations. To this aim, computational tools able to modelling the device response are useful both for the development of fast and reliable control algorithms and in the design of new multipurpose devices [1-2]. These tools have to couple the electromagnetic field equations with the supply circuits, accounting for the magnetoelastic properties of the magnetostrictive rod through the use of physical-based models [3,4].
A first approach coupling electromagnetic field analysis and magnetostrictive models has been proposed in [5], limiting the analysis to the MST rod section. Here the model has been extended to account for the entire device geometry.
The model is based on a finite element (FEM) solution of electromagnetic field equations within a domain describing the MST rod, the enclosure and the supply coil, including eddy currents in the rod. The magnetoelastic properties of the rod are modelled through a Preisach hysteresis model, introducing an effective field, which account for the magnetoelastic interaction [4]. FEM formulation is coupled with the magnetostrictive hysteresis model (MM) using the iterative Fixed Point technique.
MM is identified starting from static magnetoelastic characterisations carried out using a 30 kN dynamometer where an iron yoke was embedded under the moving crossbar to provide magnetic field and stress on a cylindrical Terfenol-D sample. The characterization has been performed under constant stress; the control logic of the dynamometer keeps the mechanical load constant under any change of shape of the sample and therefore compensates the mechanical load yield by the magnetized sample itself and the force due to the poles attraction. Magnetostriction (λ) has been measured by two electric strain gauges, along and transversally to the applied field respectively. Magnetization has been measured by a pick-up coil winded on the sample whereas field was measured by a hall probe placed close to the sample surface such to measure internal field. This set up has allowed the measurement of static hysteresis and magnetostriction loops under the effect of compressive stresses up to 32.5 MPa. The quasi-static measured and reconstructed B-H and λ-H cycles are reported in Fig. 1.
The coupled FEM-MM is applied to the simulation of a device having a bulk Terfenod-D rod. The analysis is extended up to 100 Hz evaluating the device response in terms of magnetic (magnetic flux in the rod) and mechanical properties (rod strain). Both quantities have been compared with measurements performed on the device, equipped with sensors for its complete magneto-mechanical characterisation [6].
Fig. 2 shows the magnetic flux flowing in the rod mid-section as a function of the coil current, comparing computed and measured values. The agreement between experiments and computations is encouraging, and it increases with frequency. The presence of eddy currents inside the magnetostrictive rod determines an enlargement of the hysteresis cycle, even if the same maximum value of the magnetic flux is reached. The corresponding global rod strain at 100 Hz is also shown, in comparison with the curve at 1 Hz.
The numerical implementation and the application to the analysis of the magnetostrictive actuator, comparing the results with experiments, will be shown in the full paper.

[1] S. Mandayam et al., "A fast iterative finite element model for electrodynamic and magnetostrictive vibration adsorbers", IEEE Trans. Magn., Vol. 30, No. 5, 1994, pp. 3300-3303.

[2] S.C. Cao et al., "Modeling dynamic hysteresis for giant magnetostrictive actuator using a hybrid genetic algorithm", IEEE Trans. Magn., Vol. 42, No. 4, 2006, pp. 911-914.

[3] M.J. Dapino et al., "Structural magnetic strain model for magnetostrictive transducer", IEEE Trans. Magn., Vol. 36, No. 3, 2000, pp. 545-556.

[4] M.J. Sablik, D.C. Jiles, "Coupled magnetoelastic theory of magnetic and magnetostrictive hysteresis", IEEE Trans. Magn., Vol. 29, No. 3, 1993, pp. 2113-2123.

[5] O. Bottauscio et al., "Dynamic modelling and experimental analysis of Terfenol-D rods for magnetostrictive actuators", presented at 52nd MMM Conf., Tampa, Florida, Nov. 2007. To appear on J. Appl. Phys.

[6] A. Lovisolo et al., Analysis of magnetostrictive actuator equipped for the electromagnetic and mechanical dynamic characterisation, presented at 18th SMM Conf., Cardiff (UK), Sept. 2007.

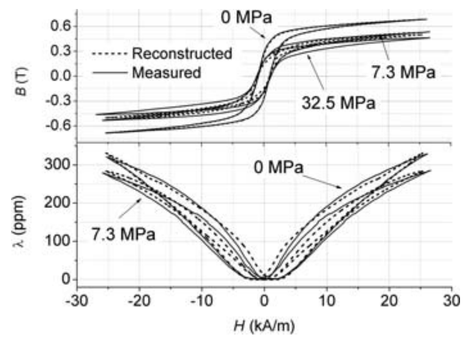

Fig. 1 – Quasistatic B-H and λ-H cycles measured on the rod

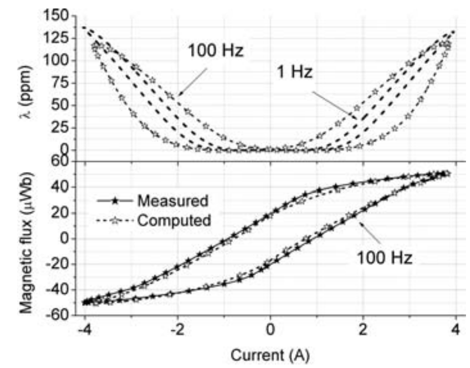

Fig. 2 – Magnetic flux versus coil current at 100 Hz and corresponding rod strain

HG-07

Design of a multipurpose magnetostrictive device.

O. Bottauscio[1], A. Lovisolo[1], P. Roccato[2], *M. Zucca*[1]
1. Electromagnetics, INRIM, Torino, Italy; 2. Dip. Ing. Elettrica, Politecnico di Torino, Torino, Italy

The performances and the use of non-linear actuators, in the micropositioning applications and as active vibration compensators, could be limited by a non proper design of the magnetic circuit and by the approximation, necessarily introduced, in modelling their behaviour for the control environment. Therefore, the use of such devices often requires a specific design, which should take into account two aspects.
First, an effective design implies the availability of modelling tools coupling the electromagnetic field equations with the supply circuits and taking into account the magnetoelastic properties of the magnetostrictive(MST)rod through the use of physical-based models.
Second, an accurate verification of the actual dynamic behaviour of a MST device requires a measurement system able to assess the dynamic magnetic and dynamic electro mechanical characteristics: stress-current (ε-I) and magnetostriction (strain)-current (λ-I), at various frequencies and applied preloads. To this purpose, a measurement device has been proposed in [1].
In this paper, starting from the experience described in [1] and from approach proposed in [2], coupling electromagnetic field analysis and magnetostrictive models, a suitable Finite element – magnetostrictive approach (FEM-MM) has been employed in the design of a MST multipurpose device. This appliance has to be able to assess the magnetic and mechanical characteristics of the magnetoelastic rod housed inside and, thus, to perform the applications in presence of a significant applied load of thousands of Newton.
The work proposes a device configuration shown in Fig.1, where the magnetic circuit has been studied taking into account the presence of different measurement elements (load cell, strain gauges, pick up coils, …) and the need of an higher magnitude and uniformity in magnetic flux density inside the MST rod. The device has been designed with an external case, constituted of magnetic commercial steel C45 which limits the stray field and guarantees a sufficient mechanical strength. Moreover, there is an internal magnetic circuit able to concentrate the magnetic flux inside the rod that, as it is known, has weak magnetic properties. The same C45 material can be used to build the magnetic circuit. The paper discusses, through the FEM-MM results, the effects in using different materials in the frequency range 1 Hz - 100 Hz. As an example, the stray field, the rod magnetization and strain are shown in the following for two different magnetic materials, the already mentioned C45 steel and the Somaloy provided by Hoganas. Fig. 1 evidences how, at the frequency of 10 Hz, Somaloy provides lower stray field whilst Fig. 2 put in evidence how the magnetic configuration guarantees a satisfactory magnetization and uniformity along the rod both at lower and higher frequencies and how the Somaloy circuit suffers a lower demagnetization increasing frequency. Fig. 3 shows how the lower dynamic effects in Somaloy reduce the derating in the time varying strain characteristics. In the full paper a complete analysis also employing other materials, including the effect of permanent magnets, will be provided.

[1] A. Lovisolo, P.E. Roccato, M. Zucca, Analysis of magnetostrictive actuator equipped for the electromagnetic and mechanical dynamic characterisation, presented at 18th SMM Conf., Cardiff (UK), Sept. 2007.

[2] O. Bottauscio, M. Chiampi, A. Lovisolo, P.E. Roccato, M. Zucca, "Dynamic modelling and experimental analysis of Terfenol-D rods for magnetostrictive actuators", presented at 52nd MMM Conf., Tampa, Florida, Nov. 2007. To appear on J. Appl. Phys.

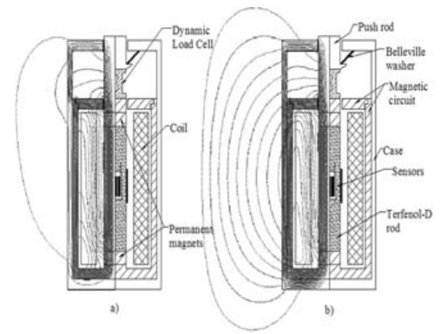

Fig. 1 : multipurpose device. Computed results at 10 Hz. Left hand side: flux lines with a C45 steel case and the Somaloy magnetic circuit. Right hand side: C45 case and C45 magnetic circuit.

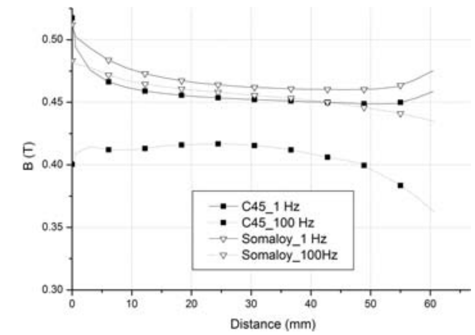

Fig. 2: magnetic flux density along the magnetoelastic rod, computed at two working frequencies for two different magnetic materials. Instant of the current peak.

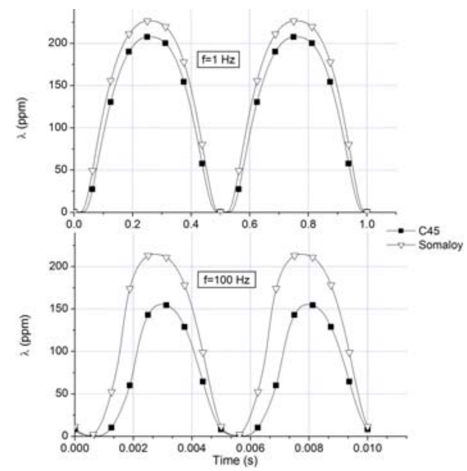

Fig. 3 : time behaviour of the total strain of the rod at two different frequencies for the two considered materials.

HG-08

Temperature dependence of magnetostriction of $Co_{1+x}Ge_xFe_{2-2x}O_4$ for magnetostrictive sensor and actuator applications.

N. Ranvah[1], I. C. Nlebedim[1], S. H. Song[2], Y. Melikhov[1], J. E. Snyder[1], D. C. Jiles[1], A. J. Moses[1], P. I. Williams[1]

1. Wolfson Centre for Magnetics, Cardiff University, Cardiff, United Kingdom; 2. Materials Science and Engineering Department, Iowa State University, Ames, IA

Cobalt ferrite based materials have potential for non-contact magnetostrictive sensor applications due to their low cost, high magnetostriction coefficient λ and high sensitivity to field dλ/dH [1]. In the past, substitution of Cr^{3+}, Mn^{3+} or Ga^{3+} for Fe^{3+} has been used to vary the magnetic and magnetoelastic properties [2]. These properties are greatly affected by the site occupancy of the various ions in the cubic spinel structure. In the current study, the effect of Ge^{4+}/Co^{2+} co-substitution is investigated, which is expected to show different effects than previous trivalent substitutions.

A series of polycrystalline Ge-substituted cobalt ferrite samples, $Co_{1+x}Ge_xFe_{2-2x}O_4$ (x=0, 0.3, 0.6) were prepared by standard powder ceramic techniques [1, 2]. Curie temperatures determined by vibrating sample magnetometry were seen to fall steeply with increasing Ge content (780K, 558K and 407K for x=0, 0.3 and 0.6 respectively). The magnetostriction was measured with a strain gauge setup between temperatures of 250 – 400K at 50K intervals. As an example, Fig. 1 shows magnetostriction curves for all samples at 300 K.

Over the range 250 – 400K, three shapes of magnetostriction curves were observed and classified as shown in Fig. 2. (a). These shapes are due to presence of the two magnetostriction coefficients, λ_{100} and λ_{111}, having opposing signs in cobalt ferrite [5]. Shape-A was obtained when the contribution of λ_{100} to strain, negative in sign, initially increased faster with field than the contribution from λ_{111}. This continued until complete alignment of domains with easy <100> axes. After that the contribution from λ_{111}, opposite in sign, increased faster causing the magnetostriction to decrease in magnitude. This shape was observed for samples with Ge-content x=0 at all temperatures and for x=0.3 at 250 and 300K. Shape-B was observed for samples with x=0.3 at 350 and 400K. With this substitution of Ge/Co the contribution of λ_{100} to field induced strain has become dominant and that of λ_{111} appears negligible. Shape-C was an inverted form of Shape-B, observed for x=0.6 at all temperatures. Apparently either λ_{111} contributions have become dominant or λ_{100} has reversed sign. Field induced strain amplitude for the initial high-sensitivity linear region of each curve, $|\lambda|_{max, linear}$, was determined. For Shape-A, the maxima at the end of linear region were chosen as the $|\lambda|_{max, linear}$. For Shape-B or C, the end of linear region was chosen as the point where |dλ/dH (H)| has decreased to 10% of $|d\lambda/dH|_{max}$ (see Fig. 2. (b)). Fig. 3 shows the temperature dependence of these $|\lambda|_{max, linear}$ and the amplitude of magnetostrictive strain sensitivity $|d\lambda/dH|_{max}$. At 250 K, the magnetostrictive strain amplitude for pure cobalt ferrite is the same as that of $Co_{1.3}Ge_{0.3}Fe_{1.4}O_4$. However, at this temperature, the field at which $Co_{1.3}Ge_{0.3}Fe_{1.4}O_4$ reaches maximum magnetostriction is only 70% of the field at which pure cobalt ferrite attains its maximum. In the design of device applications for this material, this translates to a power saving of 50% over pure cobalt ferrite. Due to its low Curie temperature, $Co_{1.3}Ge_{0.3}Fe_{1.4}O_4$ exhibits less hysteresis at low temperatures, which again is an important consideration for sensor design.

This research was supported by the UK EPSRC under grant number EP/D057094 and by the US NSF under grant number DMR-0402716.

[1] Y.Chen, J.E.Snyder, C.R.Schwichtenberg, K.W.Dennis, R.W.McCallum, and D.C.Jiles, IEEE Trans. Magn. 35, 3652 (1999).

[2] J.A.Paulsen, A.P.Ring, C.C.H.Lo, J.E.Snyder, and D.C.Jiles, J. Appl. Phys. 97, 044502 (2005). S. J. Lee, C. C. H. Lo, P. N. Matlage, S. H. Song, Y. Melikhov, J. E. Snyder, and D. C. Jiles, J. Appl. Phys. 102 073910 (2007). S. H. Song, C. C. H. Lo, S. J. Lee, S. T. Aldini, J. E. Snyder, and D. C. Jiles, J. Appl. Phys. 101, 09C517 (2007).

[3] B.D.Cullity, Introduction to magnetic materials (Addison Wesley, 1972).

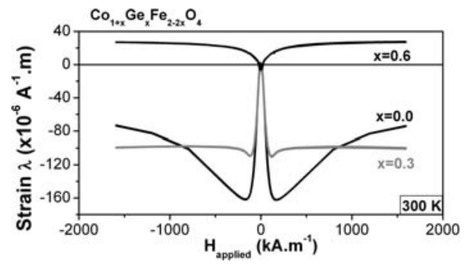

Fig. 1. Magnetostriction curves for $Co_{1+x}Ge_xFe_{2-2x}O_4$ at 300 K.

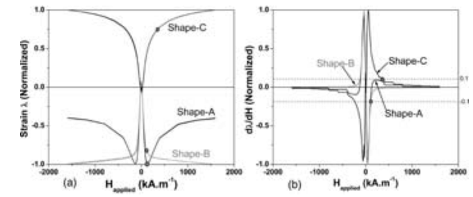

Fig 2. (a) Classification of the different shapes of magnetostriction λ curves. (b) Corresponding dλ/dH curves. Field induced magnetostrictive strain amplitude is marked with filled dots onto the curves.

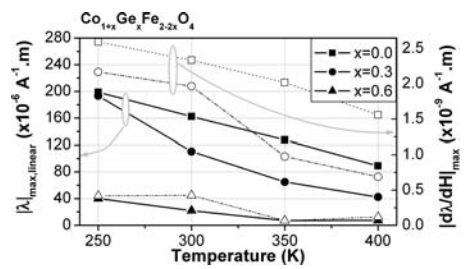

Fig. 3. Solid lines and solid symbols show the field induced magnetostrictive strain amplitude. Dotted lines and hollow symbols show amplitude of field induced strain sensitivity.

HG-09

Magnetostriction studies on antiferromagnetic MnxFe100-x (30≤x≤55) alloys.

M. Yan, T. Ma, J. Zhang, Y. Xu
Department of Materials Science and Engineering, Zhejiang University, Hangzhou, China

Introduction

In the past few decades, giant magnetostriction has been obtained in many magnetic materials, including both ferromagnets and antiferromagnets. Most magnetostrictive materials are ferromagnets, such as TbDyFe and NiMnGa alloys, which have been studied extensively and stepped into practical applications [1-2]. However, researches on magnetostrictive antiferromagnets are still very limited, since they only possess giant magnetostriction at cryogenic temperatures or in relatively strong magnetic fields [3]. Much more recently, at room temperature and in a relatively low magnetic field of 1T, Peng et al found that antiferromagnetic Mn42Fe58 alloy possesses a magnetostriction up to 169 ppm [4], which can be comparable to that of textured ferromagnetic Fe-Ga alloys [5]. This makes it a promising candidate in magnetostrictive applications in addition to its low cost. Meanwhile, the magnetostriction mechanism of antiferromagnetic Mn-Fe alloys remains unclear up to now. This work presents a systemic study on the magnetostriction of antiferromagnetic MnxFe100-x (30≤x≤55) alloys.

Microstructure

MnxFe100-x (x = 30, 35, 40, 50 and 55) alloys were prepared by induction melting method, followed by homogenization for 24h at 1273K, then furnace cooled to room temperature. Fig.1 shows the x-ray diffraction spectra of the MnxFe100-x samples. It can be seen that when x was less than 40, the diffraction peaks can be indexed as two phases. One was the face-centered-cubic (fcc) γ phase, the other was the hexagonal-close-packed (hcp) ε phase. The optical micrograph of Mn30Fe70 alloy also shows the mixed structure of two phases. When x was higher than 40, only γ phase remained in MnxFe100-x alloys.

Magnetostriction

Fig.2 shows the magnetostriction curves of MnxFe100-x (30≤x≤55) alloys up to 1.9 T. It can be seen that the magnetostriction value showed an obvious composition dependence. When Mn content x was less than 40, the magnetostriction at 1.9 T, λ1.9T was below 100×10-6. At x = 40, λ1.9T increased to 209×10-6. When x was further increased to 50 and 55, λ1.9T reached 875×10-6 and 665×10-6, respectively. The 1.9 T field was not high enough to saturate the magnetostriction, thus higher values can be expectable when the magnetic field was further increased. It can be concluded that the MnFe alloys of single γ phase possessed higher magnetostriction than those containing both γ and ε phases.

To understand whether the magnetic-field-induced structural transformation occurred in Mn-Fe alloy, the Mn50Fe50 sample was magnetized by increasing the magnetic field to 1.9 T and then removing the field. The XRD spectrum of the as-magnetized sample is shown in Fig.3. As can be seen, the Mn50Fe50 alloy changed from single γ phase to a mixture of γ+ε phases after magnetizing. That means a magnetic-field-induced phase transformation from γ to ε occurred in Mn50Fe50 alloy. Thus, the large magnetostriction in Mn-Fe alloys of high Mn content should be attributed to the magnetic-field-induced structural transformation.

[1] T. Y. Ma, M. Yan, J. J. Zhang, W. Luo, C. B. Jiang, and H. B. Xu, Appl. Phys. Lett., 90, 102502 (2007)

[2] K. Ullakko, J. K. Huang, C. Kantner, R. C. O'Handley, and V. V. Kokorin, Appl. Phys. Lett., 69, 1966 (1996)

[3] A. N. Lavrov, S. Komiya and Y. Ando, Nature, 418, 385 (2002)

[4] W. Y. Peng and J. H. Zhang, Appl. Phys. Lett., 89, 262501 (2006)

[5] J. L. Weston, A. Butera, T. Lograsso, M. Shamsuzzoha, I. Zana, G. Zangari, and J. Barnard, IEEE Trans. Magn., 38, 2832 (2002)

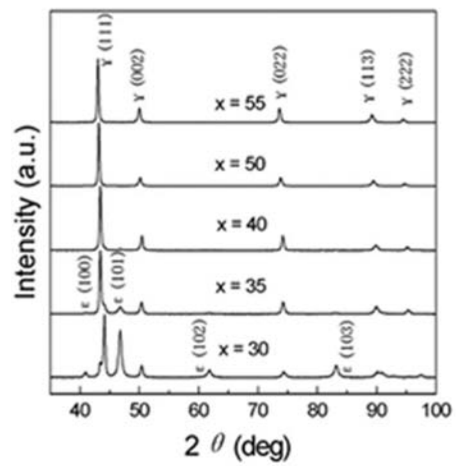

XRD patterns of MnxFe100-x alloys.

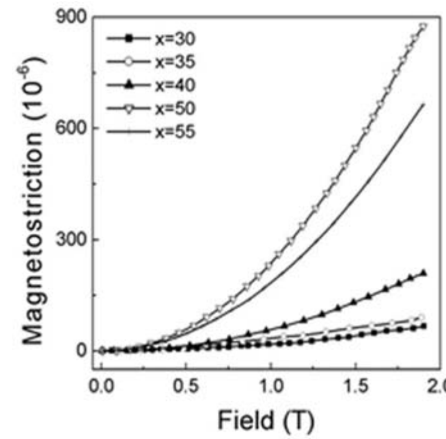

Magnetostriction of MnxFe100-x alloys.

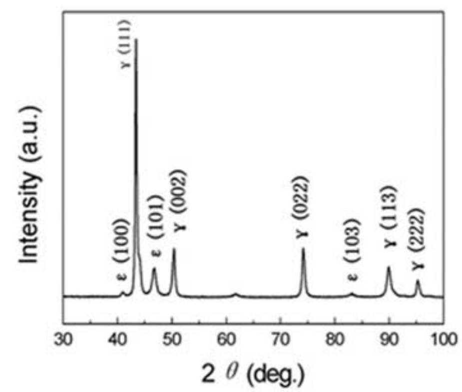

XRD pattern of Mn50Fe50 alloy after magnetizing.

HG-10

Magnetic softening of magnetostrictive $(Fe_{80}Co_{20})_{80}B_{20}$ amorphous thin films with a thickness modulation of the magnetic anisotropy.

J. Prieto[2], M. González-Guerrero[1], D. Ciudad[1], P. Sánchez[1], C. Aroca[1]
1. Física Aplicada, ETSI Telecomunicación UPM, Madrid, Spain; 2. ISOM, Universidad Politécnica de Madrid, Madrid, Spain

In this work we present an innovative method to optimize the magnetic properties of magnetostrictive thin films. For set deposition parameters we are able to reduce the coercivity and to control the magnetic anisotropy, while keeping the total magnetostriction.
The trend for the miniaturization of magnetostrictive sensors and actuators and the promising opportunities of magnetic MEMS produce a constraint in the maximum field that can be applied to activate the magnetostrictive material. These new trends require new materials with high magnetostriction and soft magnetic properties at the same time[1].
Our proposal consists of combining multilayers with crossed magnetic anisotropies. $(Fe_{80}Co_{20})_{80}B_{20}$ magnetostrictive amorphous thin films have been sputtered with 70 W power and 6 mTorr Ar pressure on 2×1.5 mm thermal oxide Si substrates lithographically defined. The magnetic anisotropy in every growing layer is induced by the oblique incidence of the plasma, due to the stress induced during the deposition[2].
In order to vary the magnetic anisotropy direction of the layers during the deposition process, we rotate the sample 90° with respect to the plasma incidence from layer to layer within the multilayers. We have deposited several multilayers, consisting of five identical bilayers composed of two layers with crossed magnetic anisotropies and different thickness (X-9 nm), X ranging from 16 to 30 nm. Note that all the layers have the same composition and therefore they are exchange coupled, being the overall direction of anisotropy the one of the thicker layers[3]. The multilayers are compared with a set of single layer samples with the same total thickness. Figure 1 shows a schematic picture of the samples under study.
The magnetic properties of the samples were measured with a VSM and the magnetostriction of some of them was measured as well through the optical detection of the deflection of cantilevers. All the samples present one well defined anisotropy axis. Figure 2 represents the anisotropy and the coercive field of all the samples of the study along the hard axis of magnetization, as well as the saturation magnetostricion of some of them.
The results show that the multilayers present a much lower magnetic anisotropy than the single layer samples and, though growing with the total thickness of the layer in both kind of samples, the variation of the X/9 thickness ratio in multilayers ensures an almost linear increase of the anisotropy field. Interestingly, the coercive field is observed to decrease in all the multilayer samples respect to their single layer counterparts. Although the coercive plot follows a slightly scattered trend, we have repeated this measurement several times, confirming the reduction of coercivity. In addition, the magnetostriction measurements of some selected multilayers show that multilayering does not affect the magnetostriction of the films.
Furthermore, the magnetic anisotropy is less dispersed in multilayers than in single layer samples, so that the hard axis hysteresis loops of multilayers are much more linear. Figure 3 shows the loops along the easy and the hard axis of magnetization of a multilayer and its single layer counterpart with the same thickness. The loops along the easy axis of magnetization are very similar. However, while the hard axis hysteresis loop of the multilayer sample is very linear in the low field region, it shows a little widening in the single layer, corresponding to domain wall movement.
The origin of these differences seems to lie in the mechanical energy accumulated in each layer. Indeed, Bitter images (not included) show very low mobile Bloch domain walls in multilayers and Neel domain walls in single layers.

[1] E. Quandt et al., J. All. & Comp., **259**, (1997), 126.

[2] M. Kevin Minor et al., J. Appl. Phys., **91**, (2002), 8453.

[3] B. D. Cullity, *Introduction to magnetic materials*, (Addison-Wesley Inc., Massachussets, 1972), p. 244.

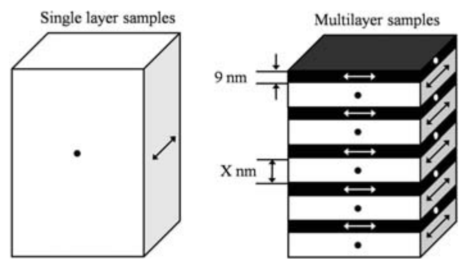

Fig. 1. Schematic picture of the multilayer and the single layer samples with the same overall thickness. The arrows indicate the anisotropy direction of every layer.

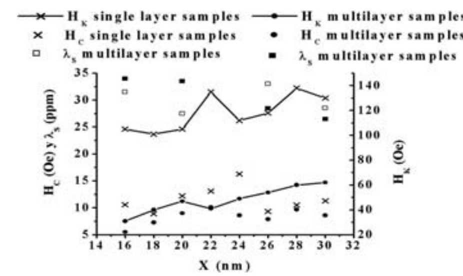

Fig. 2. Anisotropy and coercive (along the hard magnetic axis) fields and absolute magnetostriction of the multilayer 5×(X-9 nm) samples and their single layer counterparts with the same total thickness.

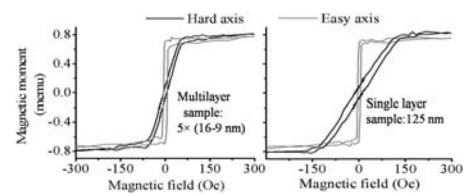

Fig. 3. Hysteresis loops along the hard and easy axis of magnetization of a multilayer sample with X=16 nm and its single layer counterpart with the same total thickness.

HG-11

Fine structure observation near critical temperature in $Gd_5Si_{1.95}Ge_{2.05}$

R. L. Hadimani, Y. Melikhov, J. E. Snyder, D. C. Jiles
Wolfson Centre for Magnetics, Cardiff University, Cardiff, United Kingdom

$Gd_5(Si_xGe_{1-x})_4$ exhibits the largest known room temperature giant magnetocaloric effect near its coupled first order magnetic-structural phase transition. This effect can be utilised for energy efficient refrigeration. The energy conversion efficiency of these refrigerators can reach as high as 60% of Carnot efficiency, which is much larger than the 30% achieved in conventional liquid/vapour cycle refrigeration. This first order magnetic-structural phase transition also involves a colossal magnetostriction of the order of 10,000 ppm [1].

$Gd_5(Si_xGe_{1-x})_4$ has a complex magnetic-structural phase diagram which can be divided into three distinct regions. In the silicon rich region ($0.575 \le x \le 1.0$) there is a second order magnetic phase transition with no associated structural transition. In the germanium rich region ($0 \le x \le 0.3$) there is a first order magnetic-structural transition from Gd_5Si_4-type orthorhombic ferromagnetic phase to Sm_5Ge_4-type orthorhombic antiferromagnetic phase [2]. In the middle region ($0.4 \le x \le 0.503$) there is a first order magnetic-structural phase transition exhibiting the highest magnetocaloric effect [3].

We have carried out a series of measurements on single crystal and polycrystalline $Gd_5Si_{1.95}Ge_{2.05}$ and single crystal $Gd_5Si_2Ge_2$ samples showing magnetostrictive strain as a function of temperature at various magnetic field strengths and magnetostrictive strain as a function of magnetic field at various temperatures with a magnetic field of up to 7 Tesla.

In single crystal $Gd_5Si_{1.95}Ge_{2.05}$, there was fine structure observed in the magnetostriction curve λ (strain) vs. H (field strength) near the critical temperature (Fig 1 and 2). The magnetostriction measurements show that close to the critical temperature, there is a sudden increase in the magnetostrictive strain of about 200-300 ppm (positive) just before the field induced first order phase transition of about 900-1000 ppm (negative). This anomaly was observed for both strain vs. magnetic field at various temperatures and for measurements of strain vs. temperature at various magnetic field strengths. For the polycrystalline $Gd_5Si_{1.95}Ge_{2.05}$ sample the fine structure was not as strong as in the single crystal. The sudden change in the magnetostrictive strain just before the field induced first order phase transition was about 40 ppm (Fig 3).

Measurements of strain as a function of magnetic field strength and temperature were also made on a single crystal $Gd_5Si_2Ge_2$ sample using the same equipment. No sudden change in the strain below the critical temperature was observed (Fig.4).

From these results we conclude that the magnetoelastic behaviour of the $Gd_5(Si_xGe_{1-x})_4$ can shows significant levels of fine structure in the approach to the transition. This fine structure could be indicative of differences in switching field strength for different regions of the material which could be due to the presence of two phases.

This research is supported by the UK Royal Society under a Wolfson Research Merit Award.

[1] M. Han, D. C. Jiles, J. E. Snyder, T. A. Lograsso, and D. L. Schlagel J. Appl. Phys., 95, 6945 (2004).

[2] A. O. Pecharsky, K. A. Gschneidner, V. K. Pecharsky and C. E. Schindler. J. All. Comp., 338, 126 (2002).

[3] V. K. Pecharsky, K. A. Gschneidner Jr., Adv. Mater. 13, 683 (2001).

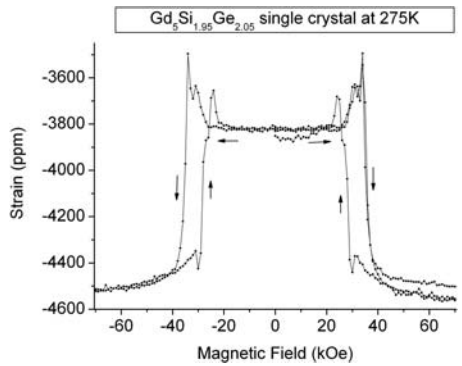

Fig. 1: Magnetostrictive strain vs. field near the critical temperature at 275K.

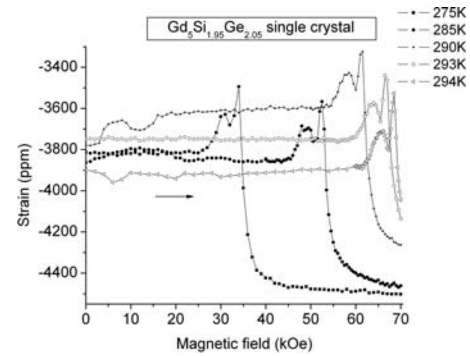

Fig. 2: Magnetostrictive strain vs. field for various temperatures near the critical temperature.

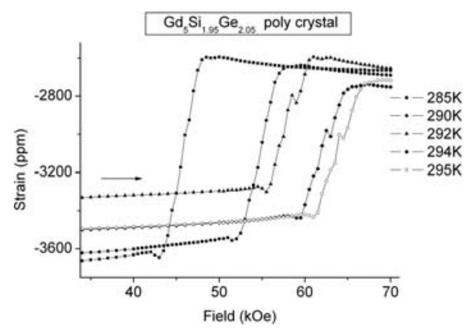

Fig 3: Magnetostrictive strain vs. field for a polycrystalline sample.

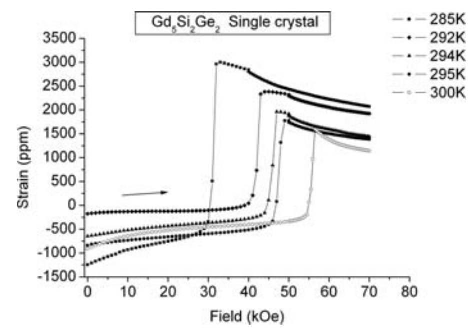

Fig 4: Magnetostrictive strain vs. field for a single crystal Gd5Si2Ge2 sample.

HG-12

On the nature of the Griffiths-like phase behaviour in Gd_5Ge_4 giant magnetocaloric alloy.

N. Pérez[1,2], F. Casanova[2,3], F. Bartolomé[4,5], L. M. García[4,5], S. DeBrion[6], A. Labarta[1,2], X. Batlle[1,2]

1. Fisica Fonamental, Universitat de Barcelona, Barcelona, Spain; 2. Institut de Nanociencia i Nanotecnologia IN2UB, Universitat de Barcelona, Barcelona, Spain; 3. Physics Department, University of California (UCSD), San Diego, CA; 4. Instituto de Ciencia de Materiales de Aragón, CSIC, Zaragoza, Spain; 5. Física de la Materia Condensada, Universidad de Zaragoza, Zaragoza, Spain; 6. Institut Néel, CNRS-UJF, Grenoble, France

The family of compounds $Gd_5(Si_xGe_{1-x})_4$ is well known for showing giant magnetocaloric effect [1,3]. The interplay between the crystallographic and magnetic structures present in these materials configures a rich and complex scenario not yet completely understood, specially in the edge compound Gd_5Ge_4 [4, 5]. In this alloy, a second-order paramagnetic (PM)-to-antiferrromagnetic (AFM) transition occurs at the Néel temperature $T_N \approx 130$ K. The nature of the AFM phase is complex, with competing AFM (between layers) and ferromagnetic (FM) interactions (within layers). The magnetic ordering remains AFM after zero-field-cooling down to 2 K. The application of a certain magnetic field, whose value depends on the temperature, induces a first-order AFM-to-FM magnetostructural transition, which is irreversible at temperatures below ~10 K, partially reversible from ~10 to ~20 K and fully reversible above ~20 K [5]. Here, we study Gd_5Ge_4 alloy with ac magnetic susceptibility and high field magnetization curves. The samples were prepared with high purity (99.99%) Gd and special attention was paid to the temperature stability and ramping rate during the measurements. An anomalous behavior is observed in the real and imaginary parts of the ac susceptibility through a peak around 225 K. This points out to the occurrence of spin clustering due to short-range correlations (SRC) in the PM phase, that is, a Griffiths–like phase behavior [2]. Gradually increasing the applied dc field causes this anomaly at $T_G \approx 225$ K to weaken and finally disappear at 200 Oe. Variation of the ac frequency from 0.1 Hz to 1 kHz shows a shift of T_G to higher temperatures. High magnetic field measurements (isothermal and isofield magnetization curves) were performed in the Grenoble High Magnetic Field Laboratory,with fields up to 23 T within 5 and 300 K. Isothermal magnetization up to 20 K shows gradual reduction of the hysteresis with increasing temperature, associated with the irreversible low-temperature transition [5]. Above 20 K, the transition becomes reversible and shifts to higher fields with increasing temperature. Above 90 K the hysteresis is no longer observable in the investigated field range. At about 80 K, a change in the slope of the magnetization curve is evident. Zero Field Cooled–Field Cooled (ZFC–FC) protocol in isofield curves do not show any difference between the ZFC and FC processes when data are acquired on increasing the temperature. In contrast, in a Field Cooling–Field Heating experiment, a remarkable hysteresis is observed in the first-order transition and, surprisingly enough, in the PM state. All the foregoing sheds some light on the nature of the Griffiths-like phase and evidences that SRC occur both at low and high magnetic fields. Consequently, it is likely that the interplay between the AFM and FM SRC, and the actual nature of the dominant ones, changes with temperature and magnetic field.

[1] V. K. Pecharsky and K. A. Gschneidner, Jr., Giant Magnetocaloric Effect in Gd5(Si2Ge2), *Phys. Rev. Lett.* **78**, 4494 (1997)

[2] C. Magen, P. A. Algarabel, L. Morellon, J. P. Araújo, C. Ritter, M. R. Ibarra, A. M. Pereira, and J. B. Sousa, Observation of a Griffiths-like Phase in the Magnetocaloric Compound $Tb_5Si_2Ge_2$, *Phys. Rev. Lett.* **96**, 167201

[3] F. Casanova, A. Labarta, X. Batlle et al., Direct observation of the magnetic-field-induced entropy change in Gd_5Ge_4 giant magnetocaloric alloys, *Appl. Phys. Lett.* **86**, 262504

[4] F. Casanova, S. de Brion, A. Labarta and X. Batlle, Coexistence of short-range ferromagnetic and antiferromagnetic correlations in Ge-rich Gd_5Ge_4 alloys, *J. Phys. D: Appl. Phys.* **38** 3343–3347

[5] F. Casanova, A. Labarta and X. Batlle, Giant heat dissipation at the low-temperature reversible-irreversible transition in Gd_5Ge_4, *Phys. Rev. B* **72**, 172402 (2005)

HH-01

Spin Dynamics and Gilbert damping of a nanomagnet connected to leads.

A. Núñez[1], R. Duine[2]
1. Departamento de Física, Facultad de Ciencias Físicas y Matemáticas, Universidad de Chile, Santiago, Chile; 2. Institute for Theoretical Physics, Utrecht University, Utrecht, Netherlands

The theoretical description of several spintronics phenomena, is surrounded by several subtle challenging issues. Standing as a major challenge in the description of various phenomena such as current-induced magnetization reversal(2-5) and domain-wall motion(6-12), is their inherent non-equilibrium character. Besides the intrinsic non-equilibrium dynamics of the the magnetization degree of freedom, the nonequilibrium behavior manifests itself in the quasi-particle degrees of freedom that are driven out of equilibrium by the nonzero bias voltage. Due to this, the fluctuation-dissipation theorem cannot be applied to the quasi-particles. This, in part, has led to controversy surrounding the theory of current-induced domain wall motion (7-8). We consider the dynamics of single-domain nanomagnet that is subjected to non-equilibrium conditions. This system is modeled as a quantum spin coupled to two ferromagnetic leads. Starting from this model, and building upon previous work (1), we derive an effective stochastic equation for the dynamics of the magnetization direction using the functional-integral description of the Keldysh-Kadanoff-Baym nonequilibrium theory. We implement a microscopic derivation of the Langevin equation for the magnetization direction degree of freedom. In the limit of adiabatic changes in the magnetization direction it takes on the form of the stochastic Landau-Lifschitz-Gilbert equation. The effect of the ferromagnetic leads is displayed in the form of a spin-transfer-torque term (2-5). We are able to provide microscopic expressions for the Gilbert damping parameter and the strength of the fluctuations, including their bias-voltage dependence. Far from equilibrium it can be expected that the strength of the fluctuations and damping parameter are not related by the fluctuation-dissipation theorem. Our main finding is that in the low-frequency limit it is possible to introduce a voltage-dependent effective temperature that characterizes the fluctuations of the magnetization direction and its transport-steady-state probability distribution function.

In the situation that e V is substantially larger than k_B T, which is usually approached in experiments, we have that:

$k_B T_{eff} = e\, V/4 + k_B\, T/2$.

An effective temperature for magnetization dynamics has been introduced before on phenomenological grounds. Interestingly, the phenomenological expression of Urazhdin et al.(9), found by experimentally studying thermal activation of current-driven magnetization reversal in magnetic trilayers, has the same form as our expression for the effective temperature in the large bias-voltage limit that we derived microscopically. We believe that spin current shot noise may be observable in future experiments and that it may become important for applications as technological progress enables further miniaturization of magnetic materials. Moreover, the formalism presented here is an important step in understanding magnetization noise from a microscopic viewpoint as its generalization to more complicated models is in principle straightforward.

(1) A. S. Núñez and R. A. Duine, to appear in Phys. Rev. B

(2) J.C. Slonczewski, J. Mag. Mag. Mat. 159, L1 (1996).

(3) L. Berger, Phys. Rev. B54, 9353 (1996).

(4) M. Tsoi, A. G. M. Jansen, J. Bass, W.-C. Chiang, M. Seck, V. Tsoi, and P. Wyder, Phys. Rev. Lett. 80, 4281 (1998).

(5) E. B. Myers, D. C. Ralph, J. A. Katine, R. N. Louie, R. A. Buhrman, Science 285, 867 (1999).

(6) G. Tatara and H. Kohno, Phys. Rev. Lett. 92, 086601 (2004); Phys. Rev. Lett. 96, 189702 (2006).

(7) S. E. Barnes and S. Maekawa, Phys. Rev. Lett. 95, 107204 (2005)

(8) S. E. Barnes, Phys. Rev. Lett. 96, 189701 (2006).

(9) S. Urazhdin, N.O. Birge, W.P. Pratt, Jr., and J. Bass, Phys. Rev. Lett. 91, 146803 (2003).

HH-02

Race track memories seen from an ab-initio point of view.

P. Weinberger
1. Center for Computational Nanoscience, Vienna, Austria; 2. Department of Physics, New York University, New York, NY

Magnetic domains and domain walls and their resistivities have become important features of magnetism at the nanoscale (including thin wires or spin valve type arrangements), especially since the discovery of the giant magnetoresistance effect. Here, using the fully relativistic versions of the Screened Korringa-Kohn-Rostoker method and of the Kubo-Greenwood equation equilibrium domain wall widths and corresponding domain wall resistivities are calculated for Co-cFe-(1-c), Co-cNi-(1-c) and Fe-cNi-(1-c) and making use of a multi-scale approach (*). It is found that in Co-cFe-(1-c) the domain wall width becomes rather large at about c=0.4, but does not show an obvious singularity in the vicinity of the bcc to fcc phasetransition. In Co-cNi-(1-c) the domain wall width varies much less in size with respect to the concentration. In particular, it is demonstrated (**) that as compared to the homogeneous infinite systems the anisotropic magnetoresistance is reduced in the presence of a domain wall. This reduction is very small for Co-cFe-(1-c), rather moderate for Co-cNi-(1-c), while for Fe-cNi-(1-c) it is abbout 15%! The results clearly indicate that besides Fe-cNi-(1-c), Co-cNi-(1-c} might be a useful candidate for race track memories.

(*) P. Weinberger, PRL 98, 027205 (2007)

(**) P. Weinberger, PRL, publishing date, probably December 31 issue (2007)

HH-03

DETECTION OF CURRENT-INDUCED OSCILLATIONS OF PINNED DOMAIN WALLS.

M. Kläui[1], D. Bedau[1], S. Krzyk[1], G. Faini[2], L. Vila[2], U. Rüdiger[1]
1. Physics, University of Konstanz, Konstanz, Germany; 2. LPN-CNRS, Marcoussis, France

When combining transport with magnetic materials on the nanoscale, a range of exciting and novel phenomena emerge. Due to the interaction of the current with the magnetization, the spin transfer torque effect leads to current-induced domain wall motion (CIDM) [1-3], which we study in detail. In CIDM, electrons transfer angular momentum and thereby push a domain wall [1-3]. We have comprehensively investigated this effect and observed that this interaction is strongly dependent on the temperature [3] and the wall spin structure [2]. So far, primarily current pulses have been employed to investigate domain wall displacements and strongly stochastic behaviour has been observed.

More reproducible behaviour is found if AC currents are used to excite domain wall oscillations, which are inherently reproducible. To generate a domain wall oscillator a restoring force is necessary, which can be provided by a constriction that generates an attractive potential well for a domain wall, which then acts as a quasiparticle [4]. The depth of the potential well, was found to increase with decreasing constriction width, and the well width was found to extend far beyond the physical size of the constriction [4].

To fully characterize the pinning potential, the curvature has to be determined in addition to the width and the depth. To study the curvature, the resonance frequency of the domain wall has to be ascertained and to this end, we inject AC currents with variable frequency into the structure shown in Fig. 1 (a) [5]. We then measure the depinning field as a function of the injected microwave frequency as shown in Fig. 2 (a) (blue squares) for a transverse wall (Fig. 1 (b)). We observe a dip of the depinning field at a resonance frequency of about 1.3 GHz even for low current densities of 10^{10} A/m^2 and the eigenmode consists of the whole wall moving. Next we consider a pinned vortex wall (Fig. 1 (c)) and a strong dip in the depinning field is observed at around 800 MHz (Fig. 2 (b), blue squares). Here the eigenmode consists of the vortex core oscillation. To obtain the resonance frequencies at variable fields we employ a DC homodyne detection scheme:

As the domain wall oscillates, the resistance of the magnetic structure is modulated due to the anisotropic magnetoresistance in phase with the domain wall position. If the quasiparticle happens to be excited at the resonance frequency, the varying resistance will rectify the injected high frequency current and a DC voltage is developed across the structure. We plot the DC response for the vortex wall pinned at the constriction in Fig. 2 (b) (red line). We see a dispersion-like signal with a change in the sign exactly at the resonance frequency, which allows us to determine the resonance from the DC signal. For the transverse wall the expected signal is much weaker since the oscillation has a smaller amplitude, as visible from the smaller change in the depinning field compared to the vortex wall and this is also reflected in the smaller DC signal (Fig. 2 (a) (red line)).

The domain wall resonance frequency was measured for different external magnetic fields and was found to increase with increasing field so that we can conclude that the potential well curvature can be engineered by varying the external field [5].

To directly determine the potential U(x) we can use the power dependence of the resonance frequency [5]. From the resonance frequency as a function of the power, we obtain the oscillation period and, since the energy of an oscillator is proportional to the square of the driving force, also as a function of the energy in the system. From the energy dependence of the oscillation period we can for the first time directly determine U(x) as shown in Fig. 2 (c) with the absolute width of the potential well determined as described in [4]. The blue dots are calculated from the measured oscillator periods and the red line indicates the parabolic part of the potential well. As expected the domain wall potential flattens far away from the origin, indicating a non-harmonic (non-linear) contribution [5].

[1] C. Marrows, Adv. Phys. 54, 585 (2007).

[2] A. Yamaguchi et al., Phys. Rev. Lett. 92, 077205 (2004); M. Kläui et al., Appl. Phys. Lett. 83, 105 (2004); Phys. Rev. Lett. 94, 106601 (2005); Phys. Rev. Lett. 95, 26601 (2005).

[3] M. Laufenberg et al., Phys. Rev. Lett. 97, 46602 (2006); F. Junginger et al. Appl Phys. Lett. 90, 132506 (2007).

[4] M. Kläui et al., Phys. Rev. Lett. 90, 97202 (2003); Appl. Phys. Lett. 87, 102509 (2005).

[5] D. Bedau et al., Phys. Rev. Lett. 99, 146601 (2007); D. Bedau et al. (unpublished); L. D. Landau and E. M. Lifshitz Theoretical Physics Course – Mechanics, (Butterworth-Heinemann, 1982).

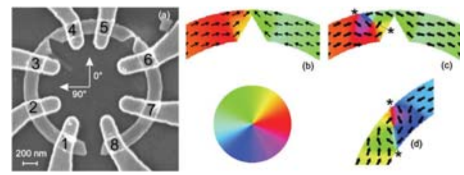

(a) SEM image of the device used with the AC current injected between contacts 3 and 4. Micromagnetic simulations of a pinned transverse wall (b), pinned vortex wall (c) and a free vortex wall (d).

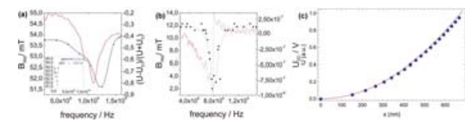

Depinning field (blue squares) and DC signal (red line) for a transverse wall (a) and a vortex wall (b). In (c) the potential U(x) is directly determined and a non-harmonic contribution is found.

HH-04

Current-induced switching of the magnetic vortex core in a ferromagnetic circular dot.

K. Yamada[1], S. Kasai[1], Y. Nakatani[2], K. Kobayashi[1], H. Kohno[3], A. Thiaville[4], T. Ono[1]
1. Institute for Chemical Research, Kyoto University, Uji, Japan; 2. Department of Computer Science, University of Electro-Communications, Chofu, Japan; 3. Graduate School of Engineering Science, Osaka University, Toyonaka, Japan; 4. Laboratoire de Physique des Solides, CNRS and Univ. Paris-Sud, Orsay, France

The magnetic vortex structure [1] observed in ferromagnetic circular dot has been intensively studied recently because of its potential applications to high-density and non-volatile storage media. To realize a magnetic vortex memory, control of the polarity of the vortex core is a key issue. Recently, it has been reported that the polarity can be reversed via the translational motion excited by an ac magnetic field [2]. Here, we demonstrate the reversal of vortex core polarity by an ac excitation current [3,4]. Samples were fabricated by the lift-off method in combination with electron beam lithography onto Si substrates. The diameter and thickness of the Permalloy dot were 1 µm and 50 nm, respectively. The motion was excited by using an ac excitation current generated from arbitrary functional generator (AFG), and the current density was estimated from the reflection signal by using standing wave ratio (SWR) bridge, as shown in Figure 1. The polarity reversal in the vortex core was observed by using magnetic force microscopy (MFM), as shown in Figure 2. The magnetization reversal was observed when the current density (j) exceeds 3×10^{11} A/m^2 and the frequency of the excitation current (f) is 280 MHz $< f <$ 300 MHz. Numerical simulations and theoretical studies revealed the critical role of the dynamical magnetic field induced by the motion of the vortex core [5]. Also, the studies indicate the existence of the threshold velocity. The dynamical magnetic field at the threshold velocity that corresponds to ~2 kOe is sufficient to reverse the vortex polarity.

The above scenario gives a way to control the polarity of the vortex core, not only by an ac current but also by a pulsed current. Recently, we succeeded in reversing the polarity by a pulsed current with a duration of 1 ns.

[1] T. Shinjo *et al*., Science **289**, 930 (2000).

[2] B. Van Waeyenberge *et al*., Nature **444**, 461 (2006).

[3] S. Kasai *et al*., Phys. Rev. Lett. **97**, 107204 (2006).

[4] K. Yamada *et al*., Nature Mater. **6**, 269 (2007).

[5] W. Döring, Z. Naturforchg. a **3**, 378 (1948).

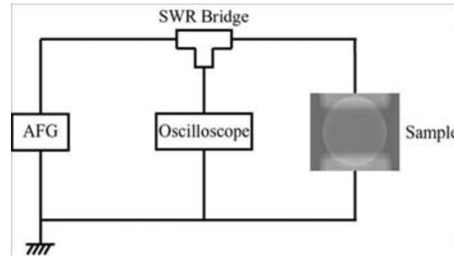

Figure 1. Schematic illustration of the measurement setup used in the experiment. The current is supplied from the AFG to the sample. The current reflected from the sample is measured in the oscilloscope via SWR bridge. The dot shown in the illustration is Scanning Electron Microscopy (SEM) image of the sample. Two wide Au electrodes with 70 nm thickness, through which an ac excitation current is supplied, are also seen.

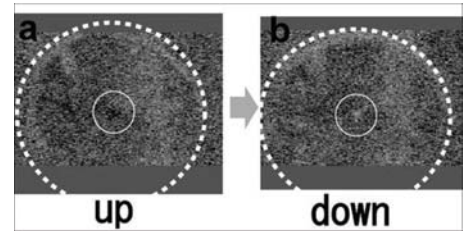

Figure 2. (a) MFM image before the application of the excitation current. A dark spot at the center of the disk (inside the white circle) indicates that the core magnetization points upwards with respect to the paper plane. (b) MFM image after the application of the ac excitation current at frequency f = 290 MHz and current density j = 3.5×10^{11} A/m^2 through the disk with a duration of about 10 s. The dark spot at the center of the disk in (a) changed to a bright spot, indicating the switching of the core magnetization from up to down. The MFM scan area was limited by the experimental time, and the parts of the sample that are necessary to determine the core direction have been omitted from the images. The low MFM contrast for the core is due to the height difference between the disk and the electrodes. The white dotted circle is the perimeter of the Permalloy disk.

HH-05

Magnetization reversal control using a current pulse in Permalloy nanowires.

Y. Togawa[1], T. Kimura[1,2], K. Harada[1,3], T. Akashi[4], T. Matsuda[1,3], A. Tonomura[1,3], Y. Otani[1,2]
1. Frontier Research System, Institute of Physical and Chemical Research (RIKEN), Wako, Japan; 2. Institute for Solid State Physics, University of Tokyo, Kashiwa, Japan; 3. Advanced Research Laboratory, Hitachi, Ltd., Hatoyama, Japan; 4. Hitachi High-Technologies Co., Hitachinaka, Japan

Magnetic memory device records information by magnetic configuration in ferromagnetic elements implemented in the device. Thus, the magnetization switching in the magnetic domain is an important technology in the device operation. While the magnetization reversal using magnetic field is widely utilized to change the magnetic bits of domains in the device, the current-driven magnetization reversal due to the spin transfer torque[1,2] and spin-wave excitation[3] is one of the promising and useful methods to realize the magnetic device of smaller bit size with larger integrated density.

In the present study, we microscopically investigate the magnetization dynamics including the magnetization reversal induced by a current pulse in Permalloy nanowires with in-plane anisotropy by means of Lorentz microscopy and electron holography. We found that the magnetic domain is controllably induced and erased in the uniformly-magnetized wire using a current pulse in small magnetic fields, which enables the magnetization reversal control.

Permalloy wires with a chemical composition of $Ni_{80}Fe_{20}$ are prepared on a Si_3N_4 membrane 30 nm in thickness supported by a Si substrate by electron lithography and lift-off method. Zigzag shaped wire 500 nm in width and 30 nm in thickness is uniformly magnetized along the wire due to strong shape anisotropy when the wire is as-deposited. The magnetization is completely reversed all over the wire in an in-plane magnetic field above 60 Oe applied against the averaged direction of the magnetization. The magnetization is alternately reversed and the magnetic domains are induced in the straight segments of the wire between corners when the in-plane magnetic field as large as 260 Oe is applied perpendicular to the averaged direction of the wire. A variety of the magnetic domain movements occur as a function of applied current density below the Curie temperature T_C[4,5]. In the following, we focus on the magnetization reversal induced by the current pulse in the uniformly-magnetized wire[6].

The probability that the magnetic domain is nucleated by the current pulse changes drastically between 0 % and 100 % depending on whether or not the in-plane magnetic field is applied parallel to the averaged direction of the wire. The magnetization direction in the nucleated magnetic domain is parallel to the applied in-plane magnetic field. These features enable stable and selective manipulation of the magnetic domain state, which will be applicable to the magnetization switching of the magnetic bit. We interpret that observed current-driven magnetization reversal is associated with the spin-wave and thermal excitation in zero magnetic field and its stochastic nature turns into deterministic under small magnetic fields because of Zeeman energy stabilization.

[1] L. Berger, *J. Appl. Phys.* **55**, 1954 (1984). [2] L. Berger, *Phys. Rev. B* **54**, 9353 (1996): J. C. Slonczewski, *J. Magn. Magn. Mater.* **159**, L1 (1996). [3] J. Shibata, G. Tatara, and H. Kohno, *Phys. Rev. Lett.* **94**, 076601 (2005). [4] Y. Togawa *et al., Jpn. J. Appl. Phys.* **45**, L683 (2006). [5] Y. Togawa *et al., Jpn. J. Appl. Phys.* **45**, L1322 (2006). [6] Y. Togawa *et al., Appl. Phys. Lett.* **92**, (2008), in press.

HH-06

Stochastic magnetic field driven domain wall motion in a spin-valve nanowire.

X. Jiang, L. Thomas, R. Moriya, M. Hayashi, B. Bergman, C. Rettner, S. Parkin
IBM Almaden Research Center, San Jose, CA

Field and current driven domain wall (DW) motion in magnetic nanowires has attracted much attention due to its scientific importance and technological potential for logic and storage device applications[1-3]. Here we report single-shot, real-time measurements of the stochastic field-driven motion of domain walls in NiFeCo free layers of spin-valve nanowire devices.

The spin-valve film stacks were deposited onto thermally oxidized silicon wafers by magnetron sputtering. The layer sequence, from bottom to top, is as follows: 3 MgO/ 17.5 $Ir_{24}Mn_{76}$/ 3.5 $Co_{70}Fe_{30}$/ 2.4 Cu/ 1 $Co_{70}Fe_{30}$/ 20 $Ni_{65}Fe_{20}Co_{15}$/ 1 $Co_{70}Fe_{30}$/ 1.5 Ru, where the numbers represent film thicknesses in nanometers. A combination of electron beam lithography, argon ion milling, and optical lithography was used to pattern the films into nanowires with a width of 200 nm and a length of 22 μm.

To measure the field driven DW motion, we inject a DW into the free layer of the spin-valve in the presence of a driving field. The DW propagation along the nanowire leads to a resistance change of the spin-valve due to the giant magnetoresistance effect, which, under a dc bias current, gives rise to a voltage signal that can be sensed by a real time oscilloscope. From single-shot measurements of the signal traces with sub-nanosecond time resolution, we extract the DW's maximum displacement and velocity in real time.

Fig. 1 (a – b) show the histograms of the DW velocity and displacement at fields of 6 Oe, 11 Oe, and 80 Oe. Each histogram of the DW velocity is fit by a Gaussian distribution, as shown by the solid lines in Fig. 1(a). The most probable velocity obtained from the fit is plotted as a function of the driving field in Figs. 1 (c). The DW velocity shows a maximum at ~ 10 Oe, which is the Walker breakdown field H_W[4, 5].

Interestingly, we find that the stochasticity of the DW motion depends strongly on the magnetic field. For fields below (6 Oe) and well above (80 Oe) the Walker breakdown, the DW moves to the end of the nanowire with a well defined velocity. However, for fields just above the Walker breakdown (11 Oe), the DW velocity distribution is very broad. Moreover, the DW tends to stop before reaching the end of the nanowire. This field dependent stochasticity can be understood using a 1-D model of DW dynamics. When the applied magnetic field is below the Walker breakdown, the DW motion is translational, i.e., the DW moves at a constant speed without changing its structure. Such a steady motion of the DW makes it less susceptible to the weak pinning sites in the nanowire since its momentum helps it to overcome these local pinning potentials. When the field exceeds the Walker breakdown, however, such a dynamic equilibrium can no longer be sustained. Instead, the DW motion becomes turbulent and its velocity oscillates with time. In this case, the DW is more likely to be pinned by imperfections in the nanowire whenever its momentum is close to the minimum of the oscillation. Depending on the details of the velocity oscillation and the time when the DW pinning occurs, the average DW velocity may vary considerably. For fields much larger than the Walker breakdown field, the DW still undergoes continuous velocity oscillations as it moves. However, the wall is less likely to be pinned due to the much larger driving force provided by the field. In addition, the oscillation period of the velocity is much shorter compared to the traveling time of the DW in larger fields. As a result, the average velocity shows less variation. Our study suggests that the pinning of a moving DW is a dynamic process, which depends not only on the pinning strength of the imperfections in the wire, but also on the mode of the DW's motion.

[1] L. Berger, J. Appl. Phys. 55, 1954 (1984).

[2] D. A. Allwood, G. Xiong, M. D. Cooke, et al., Science 296, 2003 (2002).

[3] S. S. P. Parkin, U.S. Patent 6 834 005 (2004).

[4] N. L. Schryer and L. R. Walker, J. Appl. Phys. 45, 5406 (1974).

[5] A. P. Malozemoff and J. C. Slonczewski, Magnetic Domain Walls in Bubble Material (Academic Press, New York, 1979).

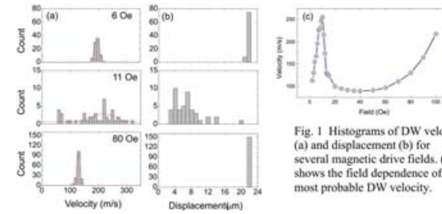

Fig. 1 Histograms of DW velocity (a) and displacement (b) for several magnetic drive fields. (c) shows the field dependence of the most probable DW velocity.

HH-07

Stochastic domain wall motion under a polarized current in wires with perpendicularly magnetized layers.

C. Burrowes[1], D. Ravelosona[1], D. Stanescu[1], N. Vernier[1], C. Chappert[1], B. Terris[2], J. Katine[2], E. Fullerton[3]

1. Institut d'Electronique Fondamentale, Orsay, France; 2. HitachiGST, San Jose, CA; 3. UC San Diego, San Diego, CA

The recently proposed "storage track memories" concept consist in storing information on domain wall (DW) sequences moving in patterned magnetic tracks. Based on recent advances in spin electronics for reading (magnetic tunnel junctions) or writing (spin transfer torque) magnetic information, performances are predicted to be very competitive with potential for high capacity 3D architectures. However in such nanodevices, DWs have to be driven on large distances in narrow wires in presence of lithography induced defects and imperfections from the virgin films. It is then crucial to determine how such defects will affect DW dynamics in presence of a polarized current.

Recently, current induced domain wall depinning on a nanometer scale were reported in nanostructures with high perpendicular magnetic anisotropy (PMA) [1,2]. Such perpendicularly magnetized wires that exhibit very narrow DWs and high pinning fields are model systems to study interaction of DWs with pinning sites. In addition they open new perspectives for more integrated memory devices or logic circuits.

Here, we study current induced steady DW motion on micrometric distances. We use Giant Magnetoresistance (GMR)effect in perpendicularly magnetized spin valves to track DW motion in nanowires. We evidence stochastic behaviour of DWs motion under a polarized current due to the presence of random pinning defects.

We used 40 microns long wires based on [(Co/Pt)/(Co/Ni)]Cu/[(Co/Ni)] spin valves with PMA [2]. A large reservoir allows injecting a single 10nm wide Bloch domain wall into the wires of the free Co/Ni layer. The high GMR ratio of about 1.5% allowed us to detect DW motion in the free layer with high spatial resolution down to 500nm. All experiments are done at room temperature. As seen in Fig. 1(a) for a magnetic field of H=350 Oe, the measurement of GMR as a function of time allows tracking spatially DW motion in the free layer along a 40 microns long and 500nm wide wire and determining its velocity.

We first evidenced that the threshold current value to move DWs at zero field is strongly dependent on the DW position in the wire. Also, it is found that it is not possible to move DWs at zero field on large distances (> 1 micron) by injecting a current through the stripe. These features are consistent with the presence of random pinning sites that interact with the single DW during its propagation in the wire. This is clearly seen in Fig. 1(b) where at H=280 Oe, a DW undergoes many pinning events (plateaus) followed by steady DW motion (abrupt transitions).

The different duration of pinning events indicates a distribution of pinning fields in the wire. These pinning centres are probably due to intrinsic pinning defects from the virgin films since we have managed to reduce the edge roughness arising from patterning down to a few nanometers. In a previous study [2], we have shown that the threshold current is determined by the pinning force. This explains why the threshold current value depends on the DW position in the wire, i.e., a distribution of pinning fields induces a distribution of threshold currents.

As shown in fig. 2, such a distribution of pinning sites in a 1 micron wide wire is responsible for a very stochastic behaviour under either magnetic field solely or the combination of magnetic field and current. Only current above 7mA (5*10^7 A/cm2) under a magnetic field of H=300 Oe are sufficient to get reproducible DW propagation without any pinning in the 40 microns long wire, but then thermal effects may also contribute.

In conclusion, this demonstrates that in films with PMA the control of the random pinning potential is a key factor to get reproducible steady DW motion and increase the DW velocity. We will also show that irradiation with light He+ ions could be an elegant approach to homogenize and control the pinning potential.

This work has been supported by the Région Ile-de-France in the framework of C'nano IdF. C'Nano-IdF is the nanoscience competence center of Paris Region, supported by CNRS, CEA, MESR and Région Ile-de-France.

[1] D.Ravelosona et al, Phys. Rev. Lett 95, 117203 (2005).

[2] D. Ravelosona et al, Appl. Phys. Lett 90, 72508 (2007).

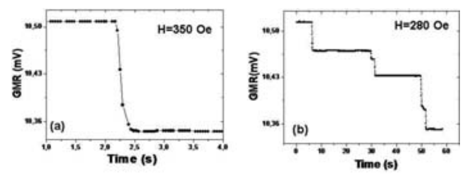

Fig. 1: GMR as function of time at (a) H=350Oe and (b) H=280 Oe for a 500 nm wide and 40 microns long wires.

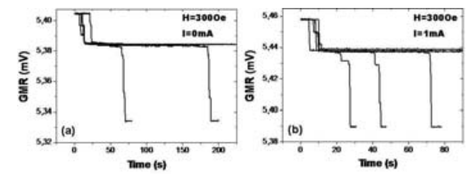

Fig. 2: GMR as function of time at (a) H=300Oe and I=0mA and (b) H=300 Oe and I=1mA. Measurements have been repeated several times, indicating stochastic behaviour.

HH-08

Effect of anisotropy distribution on domain wall motion in nanowires with perpendicular anisotropy.

Y. Nakatani[1], T. Ono[2]
1. Department of Computer Science, University of Electro-Communications, Tokyo, Japan; 2. Kyoto University, Uji, Japan

Spin current-induced domain wall (DW) motion in nano-strips is one of the active subjects, and many works have been reported [1-6]. All of the experimental results with no anisotropy show very large threshold current density for the DW motion (10^{12} A/m^2), but the simulation results show the low threshold current density in the wire with perpendicular anisotropy [7]. Because the distribution of the anisotropy can be considered in the real wire, we investigate the effect of anisotropy distribution on domain wall motion in nanowires with perpendicular anisotropy by micromagnetic simulation.
The cross section size of the wire is 280x6nm, and the cell size used in the simulation is 4x4x6nm. The same calculation method is used in [6] except for the anisotropy distribution. The pinning effect of the anisotropy distribution depends on the magnitude distribution and the space size of the fluctuation [8]. The normal distribution is assumed for the distribution of the magnitude. The m x m (m: block size hereafter) simulation cells are combined and set the same magnitude of the anisotropy to the cells to change the space size.
Figure 1 shows the averaged domain wall velocity <v> as the function of the current velocity u in no anisotropy distribution wire. The threshold current velocity is about 45 m/s with β=0 case, but it can be reduced with 140x6nm wire, because the demagnetizing field acting on the domain wall is small. There are not threshold current with β>0 case same as the no anisotropy wire case [6].
Figure 2 shows the averaged domain wall velocity as the function of the field and the block size of the anisotropy distribution (standard deviation of the anisotropy is 30%). The pinning field becomes maximum with m=10, and very large pinning field (500 Oe), which is the same value obtain by the experiment [9] is realized.
Figure 3 shows the averaged domain wall velocity as the function of the current and the β term. The threshold current is less than half with that of the perfect wire, and the results does not depend on the β term. The domain wall in the strip bends by anisotropy distribution, and the breakdown is occurred from the bend area. The domain wall motion velocity with breakdown only depends on the current velocity [6]. This is the reason why the β term effect is disappeared.
This stidy was supported by New Energy and Industrial Technology Development Organization (NEDO).

[1] L. Berger, Phys. Rev. B, 54, 9353 (1996).

[2] N. Vernier, et. al., Europhys. Lett., 65, 526 (2004).

[3] A. Yamaguchi, et. al., Phys. Rev. Lett. 92, 077204 (2004).

[4] M. Kl\"{aui, et. al., Phys. Rev. Lett., 95, 026601 (2005).

[5] S. Zhang and Z. Li, Phys. Rev. Lett., 93, 127204 (2004).

[6] A. Thiaville, et. al., Europhys. Lett., 69, 990 (2005).

[7] S. Fukami, Digest of MMM conference, FE-06 (2007).

[8] N. Hayashi, et. al., J. Magn. Soc. Jpn., 23, S1, 151 1999).

[9] H. Tanigawa, et. al., Appl. Phys. Express, in press.

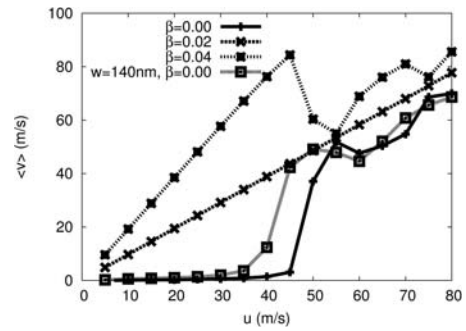

Figure 1. The averaged domain wall velocity <v> as the function of the current velocity u (no anisotropy distribution wire).

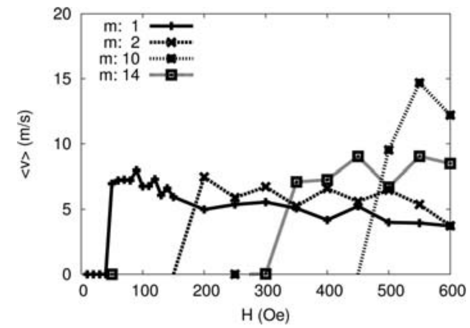

Figure 2. The averaged domain wall velocity <v> as the function of the field H and block size m (standard deviation of the anisotropy is 30%).

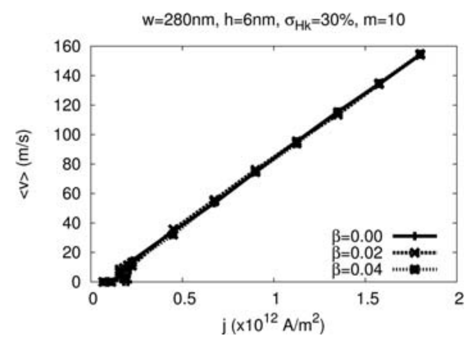

Figure 3. The averaged domain wall velocity <v> as the function of the current velocity u (standard deviation of the anisotropy is 30% and the block size is 10).

HH-09

Current-driven domain wall motion, nucleation, and propagation in a Co/Pt multi-layer strip with a stepped structure.

T. Suzuki, S. Fukami, K. Nagahara, N. Oshima, N. Ishiwata
Device Platforms Res. Labs., NEC, Sagamihara, Japan

Current-driven domain wall (DW) motion in nano-strips with perpendicular magnetic anisotropy is very suitable for spintronics devices such as MARMs because it has the potential to significantly decrease the operation current [1-3]. We have studied current-driven DW motion, nucleation, and propagation in a $[Co(0.7\ nm)/Pt(2\ nm)]_8$ multi-layer strip with a stepped structure by measuring the Hall effect with unique placement of via contacts. The strip is 1.68 µm long and 0.32 µm wide with a 10-nm deep step (Fig. 1), which acts as a pinning site for the DW, and was fabricated by KrF lithography and ion milling. Two via contacts, C_1 and C_2, for a driving current pulse and a via contact C_3 for a sensing current, which is offset in the y-direction, are attached to the strip. Because the sense current has a y-component, which is vertical to the contacts for the voltage, the magnetization direction in a thin region can be detected by measuring the extraordinary Hall effect (EHE) voltage between C_1 and C_2 with a small sense current from C_3 to C_1 or to C_2.
The EHE minor hysteresis loop of the strip after the initialization with -3kOe perpendicular field is shown in Fig. 2. Low and high resistances correspond to negative and positive magnetization in the thin region, respectively. The minor hysteresis loop shows asymmetry of field, and this suggests that the mechanisms for the resistance change are different in the positive and the negative one. The resistance increases at a positive threshold field because of a reverse domain nucleation and propagation in the thin region, but the resistance decreases at the negative threshold field because of a DW depinning from the boundary between the thin and thick regions.
The Hall resistance as a function of current pulse amplitude is shown in Fig. 3 for both of the low and high initial resistance states. Here the positive (negative) current was applied from $C_2(C_1)$ to C_1 (C_2) with a pulse width of 500 ns, and then we measured the Hall resistance. When the positive current is applied for the high resistance state, the resistance decreases to the low state at +5.5 mA, which seems to correspond to the DW motion driven by spin-transfer torque. However, the resistance increase is observed at -5.5 mA for the low resistance state, which should not have the DW. We applied negative current for the low resistance state and then measured the EHE hysteresis loops, which are shown in Fig. 4. The loop for the -4.8 mA one indicates that the threshold field is smaller than that for the zero current although the resistance change at the current is not so large. This suggests the reverse domain nucleates by the smaller current pulse and propagates by field. Moreover, the similar decrease of threshold field is observed after the positive current is applied for the low resistance state although the resistance does not increase to the high state even at +6 mA. Therefore, we deduce that the nucleation by the current occurs regardless of the polarity of the current, while the propagation of the reverse domain depends on the polarity of the current, and this propagation is related to the spin-transfer torque.
A portion of this work is supported by NEDO.

[1] D. Ravelosona *et al.*, Appl. Phys. Lett. **90**, 072508 (2007).

[2] L. S. E. Alvarez *et al.*, J. Appl. Phys. **101**, 09F508 (2007).

[3] S. Fukami *et al.*, 52nd MMM conference, FE-06 (2007).

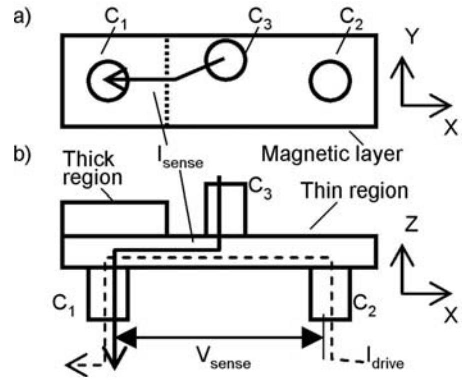

Fig. 1 Schematic depiction of strip with step. a)Layout, b)Cross-section.

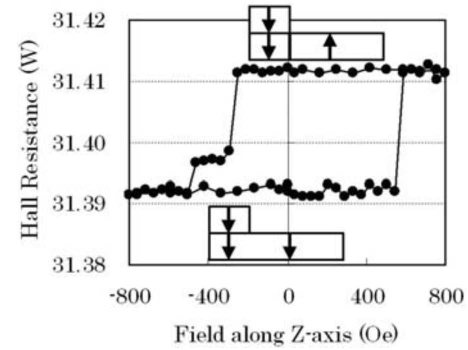

Fig. 2 Hysteresis loop by Hall resistance.

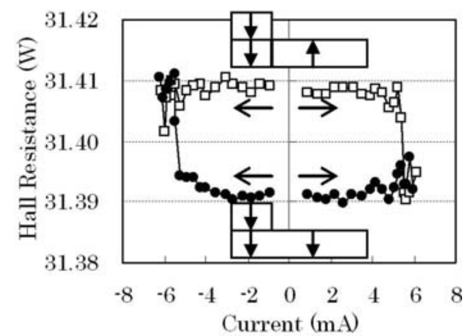

Fig. 3 Hall resistance as a function of current pulse amplitude.

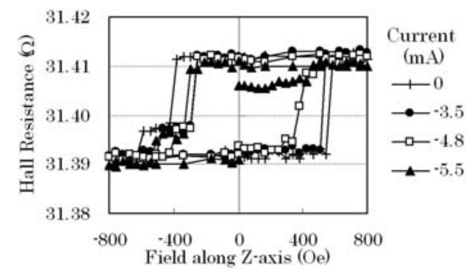

Fig. 4 Hysteresis loops by Hall resistance after applying pulse current.

HH-10

Current-Driven Domain Wall Motion in CoCrPt Wires with Perpendicular Magnetic Anisotropy.

H. Tanigawa[1], K. Kondou[1], T. Koyama[1], K. Nakano[1], S. Kasai[1], N. Ohshima[2], S. Fukami[2], N. Ishiwata[2], *T. Ono*[1]

1. Institute for Chemical Research, Kyoto University, Uji, Japan; 2. Device Platforms Research Laboratories, NEC Corporation, Sagamihara, Japan

Domain wall (DW) motion in magnetic wires by current injection, first predicted by Berger [1], is now investigated extensively [2–7], since in addition to exciting fundamental physics, novel applications based on the current-driven DW motion have been proposed [8-10]. However, we need a high current density of around 1.0×10^12 A/m^2 even in the case of very small DW pinning field of several Oe in the absence of a magnetic field [6]. Thus, it is required to explore a new material system from the viewpoint of practical applications. One of the candidates is the wire with perpendicular anisotropy in which the simulation results show the low threshold current density [11]. In this contribution, we report the current-driven DW motion in a CoCrPt wire with perpendicular magnetic anisotropy by means of the magnetic force microscopy (MFM) [12].

Magnetic nanowires were patterned by electron beam lithography from Pt(2nm)/Co63Cr11Pt26(8nm)/Ru(2nm)/Ta(5nm) films deposited on silicon substrates by dc magnetron sputtering. After the formation of a 280 nm wide current channel, a 2 nm surface layer was etched away from a part of the channel. The etched region has the smaller coercive field than the non-etched region, which allows us to initialize the DW position at the boundary of the two regions by an external magnetic field. A magnetic field of 2 kOe perpendicular to the substrate plane was first applied in order to align the magnetization in one direction (Fig. 1(a)). Then, a DW was introduced by applying a magnetic field of -580 Oe to the counter direction (Fig. 1(b)). After that, the MFM observations were carried out in the absence of a magnetic field.

Figure 1(d) shows an MFM image after the DW introduction. The boundary between the etched and the non-etched regions is shown by the vertical white dashed line. The dark contrast in the left part of the boundary corresponds to a downward magnetization, while the bright contrast in the right part corresponds to the upward magnetization, as shown in Fig. 1(b). Thus, Fig. 1(d) shows that a DW is trapped at the boundary. After the DW introduction, a pulsed-current with the current density of 1.3 × 10^12 A/m^2 and the pulse duration of 8.2 μs was applied through the wire in the absence of a magnetic field, and then the domain structure was observed after each pulsed-current injection. The actual current density in the Co63Cr11Pt26 wire is 1.0 × 10^12 A/m^2 if we take the shunting effect by the Ru/Ta buffer and the Pt capping layers into account.

Figs. 1(e)-1(m) show successive MFM images with one pulse applied between each consecutive image. Current directions are indicated by the horizontal white arrows. DW positions are indicated by the white triangles. The DW always moved opposite to the current direction which is consistent to the DW motion by the spin transfer torque.

We would like to thank Y. Nakatani for valuable discussions. The present work was partly supported by NEDO Spintronics nonvolatile devices project.

[1] L. Berger, J. Appl. Phys. 55, 1954 (1984).

[2] A. Yamaguchi et al., Phys. Rev. Lett., 92, 077205 (2004); Phys. Rev. Lett. 96, 179904(E) (2006).

[3] M. Yamanouchi et al., Nature 428, 539 (2004).

[4] M. Klaui et al., Phys. Rev. Lett. 94, 026601 (2005).

[5] G. S. D. Beach et al.: Phys.Rev. Lett. 97, 057203 (2006).

[6] M. Hayashi et al., Phys. Rev. Lett. 96, 197207 (2006).

[7] D. Ravelosona et al., Appl. Phys. Lett. 072508 (2007).

[8] S. S. P. Parkin, U.S. patent 6,834,005 (2003).

[9] D. A. Allwood et al., Science 296 5575 (2002).

[10] H. Numata et al., 2007 VLSI Tech. Dig. 232 (2007).

[11] S. Fukami et al., 52nd Conference on MMM Abstracts FE-06 (2007).

[12] H. Tanigawa et al., Appl. Phys. Express, in press.

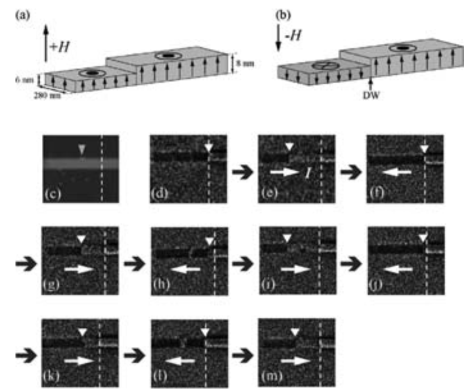

Figure 1 (a) and (b) Schematic illustration of the sample structure with magnetic domain structures. A magnetic field of 2 kOe perpendicular to the substrate plane was first applied in order to align the magnetization in one direction (a). Then, a DW was introduced by applying a magnetic field of -580 Oe to the counter direction (b). (c) Atomic force microscope image of the sample. The boundary between the etched and the non-etched regions is shown by the vertical white dashed line. (d)-(m) Successive MFM images with one pulse applied between each consecutive image. Current direction is indicated by the horizontal white arrows. DW position is indicated by the white triangles.

HH-11

Intrinsic threshold current density of domain wall motion in nano-strips with perpendicular magnetic anisotropy for use in low-write-current MRAMs.

S. Fukami, T. Suzuki, N. Ohshima, K. Nagahara, N. Ishiwata
Device Platforms Research Laboratories, NEC Corporation, Sagamihara, Japan

It has been reported that the threshold current density required to induce domain wall (DW) motion is much smaller for nano-strips with perpendicular magnetic anisotropy (PMA) than for those with in-plane magnetic anisotropy (IMA) [1]. This suggests that current-induced DW motion in PMA strips may have potential for use in low-write-current MRAMs. In this study, we have used micromagnetic simulation to calculate the threshold current density of DW motion in PMA strips as a function of a number of different parameters, and we have considered the results on the basis of a one-dimensional (1D) analysis. Further, on the basis of the obtained results, we have also estimated the writing properties of MRAMs with DW motion.

We first used a Landau-Lifshitz-Gilbert equation containing spin-transfer torque terms [2] to calculate the intrinsic threshold current density, u_w, which here represents the current density required to keep a DW in continuous motion under the assumption of adiabaticity. Figure 1 shows the threshold current density as a function of strip thickness, width, and magnetization. Threshold current density decreases with decreases in the value of each of the parameters. The decrease that accompanies width reduction below 100 nm is particularly significant. We may also note here that the dependence on width and thickness indicates an excellent potential for write-current scaling. Further, we have confirmed our results using a 1D analytical model. In our 1D model, intrinsic threshold current density, u_w, may be expressed as $u_w=\gamma H_k\Delta/2$, where γ is the gyro-magnetic ratio, H_k is the hard-axis anisotropy field of the DW, and Δ is the DW width. Obtained analytical values are plotted in Fig. 1, where H_k has been derived by calculating the Walker field, H_w. The results presented in Fig. 1 show good agreement between 2D simulation values and 1D analytical values. This agreement may be attributed to simple magnetic structural changes that occur in DWs in PMA strips during motion, and it is not seen in IMA strips.

We have found that u_w is a good measure for critical current density even in nano-strips with pinning sites. Figure 2 shows the threshold current density, u_{th}, in nano-strips having various individual notch shapes. This variation results in different threshold field, H_{th}, values. Interestingly, u_{th} values in nano-strips having finite H_{th} values are smaller than u_w values and not strongly dependent on H_{th}. We have found that u_{th} is always smaller than u_w except for excessively large H_{th} values, and this is related to a characteristic depinning mechanism in PMA strips in which pinning potential enhances DW break-down. The fact that u_{th} is relatively independent of H_{th} is an advantage in MRAM devices, for which high energy stability is required.

We also estimated critical current density and corresponding critical current values as a function of strip width for various thicknesses and magnetizations, as shown in Fig. 3. We assumed here that polarization, P, is proportional to magnetization, M_s, and that P=0.7 when M_s=800emu/cc. We also assumed that u_w approximates DW velocity, v_{th}. The results shown in Fig. 3 suggest the potential for MRAMs with DW motion in PMA strips to replace existing memories [3]. For a width of less than roughly 100 nm, for example, we get I_{th}<0.2mA and v_{th}>20m/s.

A portion of this study was supported by NEDO.

[1] S. Fukami et al., 52nd MMM conf., FE-06 (2007), to be published in J. Appl. Phys.

[2] A. Thiaville et al., Europhys. Lett., 69, 990 (2005).

[3] N. Sakimura et al., IEEE J. Solid-State Circuits, 42, 830 (2007).

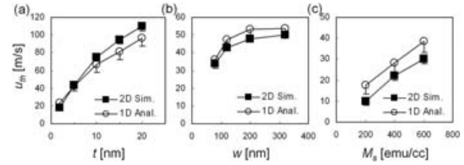

Fig. 1: Intrinsic threshold current density, u_w, as a function of (a) strip thickness, t, (b) width, w, and (c) magnetization, M_s.

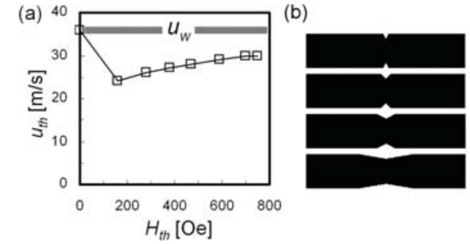

Fig. 2: (a) Threshold current densities, u_{th}, for different threshold field, H_{th}. (b) Strip patterns used for the calculations.

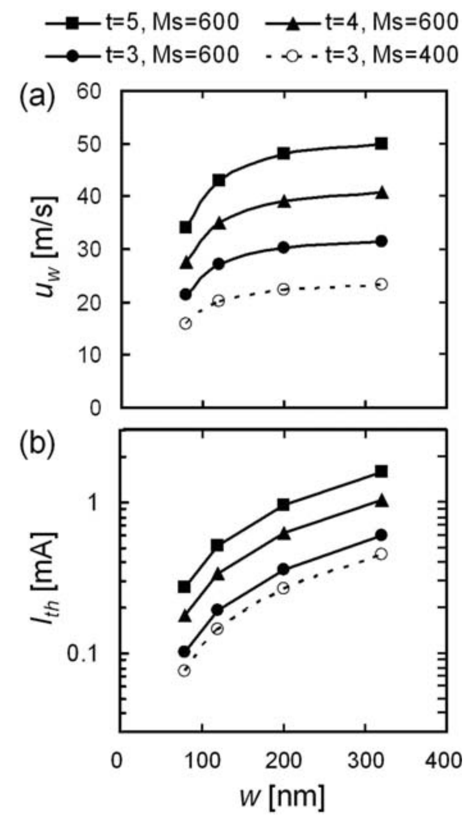

Fig. 3: (a) Intrinsic threshold current density, u_w, and (b) corresponding critical current, I_{th}, as a function of strip width, w, for various thicknesses and magnetizations.

HH-12

Current domain wall dragging in GaMnAs.

N. VERNIER[1,3], L. Thevenard[2], A. Lemaitre[2], A. Miard[2], G. Faini[2], L. Vila[2], J. Ferré[3], J. Adam[3]
1. IEF, Université Paris-Sud, Orsay, France; 2. LPN, CNRS, Marcoussis, France; 3. LPS, Université Paris-sud, Orsay, France

The Diluted Magnetic Semiconductor (DMS) GaMnAs is a promising material. Growing of high quality films is now well controlled, its ferromagnetic nature is quite well understood, and Curie temperature up to 170 K have been reported. As compared to usual ferromagnetic materials, GaMnAs exhibits several interesting features for current domain wall dragging : its magnetization is much lower than usual. What's more, it is possible to work very near the Curie temperature, where domain wall mobility is very high. This is probably why it has been possible to drag domain walls with a much smaller current density than in metals (3 orders of magnitude lower), and GaMnAs appears as a very interesting model system for this kind experiments(1).
Current induced propagation is very different from field induced propagation, one important feature is the fact that the dragging direction doesn't depend on the downstream and upstream magnetization of the domain wall. This has led to propose a new way to store data, called "racetrack"(2) : the tracks don't move, it is the whole domain structure which moves coherently through current domain wall dragging. We report here on experiments carried on perpendicularly magnetized GaMnAs tracks. They show there might be some difficulties to apply the racetracks concept to systems with perpendicular anisotropy.
We have studied propagation of not one single domain wall, but of a whole domain, bounded by a wall upstream and a wall downstream, on a wire of GaMnAs. The wires were made out of a 50 nm thick $Ga_{0.93}Mn_{0.07}As$ film, with T_C= 130K before patterning(3). To get a perpendicular magnetic anisotropy, a buffer layer of GaInAs was inserted between the GaAs substrate and the GaMnAs layer. The patterning was carried out using e-beam lithography to create a protection mask, and Ion Beam Etching to remove GaMnAs everywhere except on the wires. A bigger pad was also kept at the end of the track to enable easy initial nucleation under magnetic field. The track width was 4 μm and its length was 90 μm. The domain structure was checked using polar Kerr imaging. The magnetic state was always checked in zero applied field and current, current was applied during very short pulses.
The result is presented on figure 1 : one can see that the size of the domain fluctuates and tends to increase during propagation. This increase phenomenon is reproducible. After some pulses, a slight decrease of domain length could sometimes be seen (for example figure 1.2 and 1.3) : we have been able to correlate such a decrease to the presence of a defect in the track. Due to it, the front domain wall is slowed down, and the back wall can catch up with him. But once the wall depinned from the defect, the domain size grows again.
This result can be explained by dipolar interactions between domain walls(3,4). Indeed, these interactions are very strong for films with perpendicular anisotropy. For a single domain, each wall is submitted to two forces (figure 2) : the current-induced one, which is the same for both walls, and the repulsive force due to the other wall. When summing these two contributions, the total force applied on the front wall is bigger than the one applied on the back wall (figure 2). So, the front wall moves faster and consequently the domain size increases.
As a conclusion, we have demonstrated that, due to dipolar interaction between domain walls in tracks with perpendicular anisotropy, the domain structure is modified during current-induced propagation.

(1)M. Yamanouchi, D. Chiba, F. Matsukura, T. Dietl, and H. Ohno, Phys. Rev. Lett. 96, 096601 (2006)

(2) S.S. Parkin, US patent 6,834,005 (2004) and 6,898,132 (2005)

(3)L. Thevenard, L. Largeau, O. Mauguin, G. Patriarche, A. Lemaître, N.Vernier, and J. Ferré, Phys. Rev. B 73, 195331 (2006)

(4)M. Bauer, A. Mougin, J. P. Jamet, V. Repain, J. Ferré, R. L. Stamps,H. Bernas, and C. Chappert, Phys. Rev. Lett. 94, 207211 (2005)

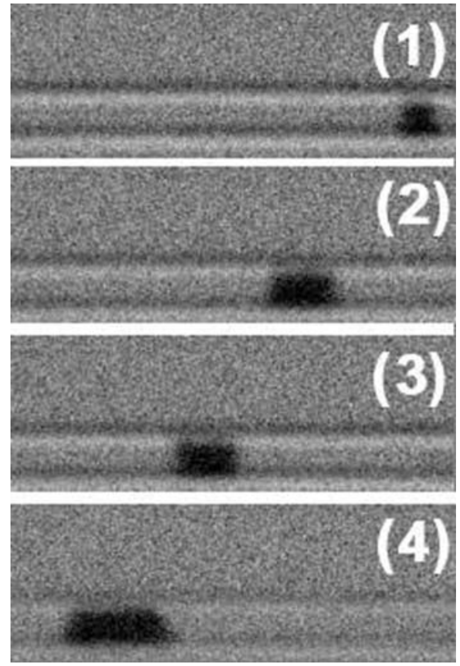

Figure 1 : Polar Kerr snapshots showing the propagation of a magnetic domain in the track at T=100K, after current pulses of density 9x10^{8} A.m^{-2} and duration 6 ms. The size of each snapshot is 44x15μm^{2}

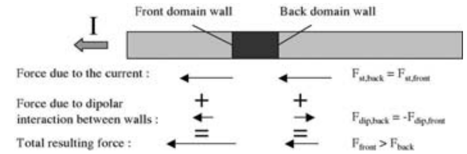

Figure 2 : forces acting on each wall limiting a single domain.

HL-01

Aerodynamic damping on vibration of rotating disks and effects of shroud and top cover.

T. Eguchi
Central Research Laboratory, Hitachi, Ltd., Fujisawa, Japan

This paper experimentally investigated aerodynamic damping for vibration of rotating disks surrounded by a shroud, a top cover, and a base plate.
It was shown that a narrow disk-shroud gap and disk-cover gap causes a large damping effect, and is remarkably effective for suppressing disk flutter vibration of a hard disk drive.
Comparing with squeeze film bearing plate reported by Deeyingyang and Ono, the damping effect caused by the narrow disk-shroud gap is smaller, but it can keep a distance between a disk and an adjacent plate wider and shock tolerance of a HDD better.
This is a great advantage of the narrow disk-shroud gap over the squeeze film bearing plate in terms of applying to commercial hard disk drives.
Experimental setups are shown in Fig. 1.
Frequency response functions (FRFs) measured under vacuum and atmosphere pressures are compared in Fig. 2.
The rotating speed was 9000 rpm (150 Hz), the disk-shroud gap was 0.4 mm, and the top cover was removed in order to place the capacitance probe close to the top disk.
All resonance peaks in the figure are related to normal modes of the rotating disks that appear as disk flutter of a hard disk drive.
These peaks of the disk modes under the atmosphere pressure have more rounded shapes and smaller amplitudes than the vacuum pressure.
Therefore, this figure shows that the air around the disks caused substantial aerodynamic damping effect on the disk vibration.
Hammer tests were performed for various disk-shroud gaps and disk-cover gaps and damping ratios of each the disk modes were computed by using a curve-fit technique.
The results are plotted double logarithmic in Fig. 3-5 by each the disk modes, and can be categorized into four groups.
The first group is the cases that disk-shroud gap was narrower than 0.3 mm, the second group is the cases that disk-shroud gap was wider than 1.0 mm, the third group is an intermediate group between the first and second.
The last group is the cases that disk-cover gap was 0.4 mm.
The results in the last group had very large damping ratios even if the disk-shroud gap was wide.
So, it is likely that the squeeze film damping was working in this group.
In the first and second groups, the results for a certain disk-cover gap were almost on a line respectively.
Solid and dashed lines in the figures represent regression lines for the case that the disk-cover gap was 2.7 mm, and p_1 and p_2 are exponents of the regression expressions.
According to these results, aerodynamic damping was inversely proportional to disk-shroud gap powered by 1.3 to 3 when the disk-shroud gap was narrow, and inversely proportional to disk-shroud gap powered by 0.2 and 0.4 when the disk-shroud gap was wide.
Moreover, another experiments confirmed that the aerodynamic damping effect was independent of the vibration amplitude of the disks.
Therefore, it is thought that the aerodynamic damping effect in the first group came from shear viscosity of the axial flow through the narrow disk-shroud gap rather than dynamic pressure loss.
And, the narrow disk-cover gap improved the effect of the disk-shroud gap.

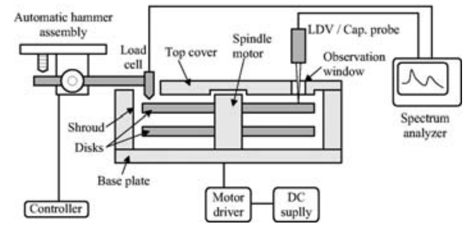

Fig. 1 Experimental setups

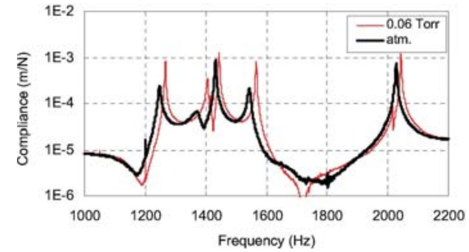

Fig. 2 FRFs under vacuum and atmosphere pressures

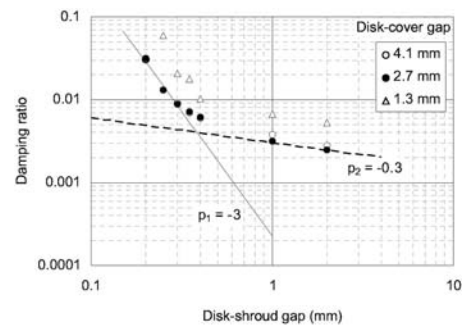

Fig. 3 Damping ratios of (0, 0) mode

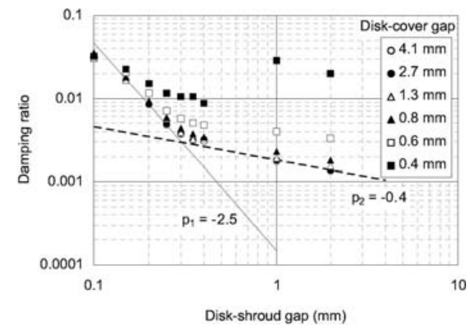

Fig 4. Damping ratios of (0, 1) backward mode

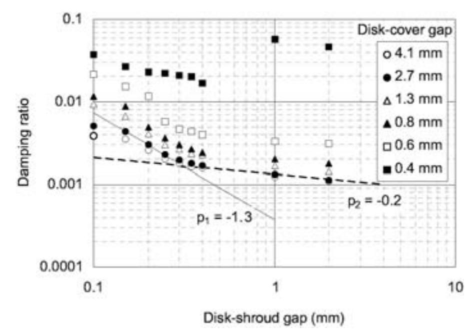

Fig. 5 Damping ratios of (0, 2) backward mode

HL-02

Adaptive frequency identification method for multiple unknown disturbances in HDDs.

Q. Jia[1], Z. Wang[2]
1. Storage Mechanics Lab, Hitachi Asia Ltd, Singapore, Singapore; 2. School of Electrical Engineering and Computer Science, Oregon State University, Corvallis, OR

In hard disk drive (HDD) systems, non-repeatable runout (NRRO) disturbances often contains components with time-varying phases and magnitudes at unknown frequencies. To reject the disturbances, the dominant frequencies of the disturbances usually need to be identified first. As the dominant frequencies of NRRO disturbances often vary with read/write head position (from track to track) and operation environment, for example, temperature, on-line identification is required. On-line adaptation is not easy to be implemented in HDD products due to stability and transient convergence issues. One well-used method to estimate unknown disturbance frequencies is adaptive notch filter [1]. For cases with multiple unknown disturbances, when the dominant frequencies are distinct and roughly known, band-pass filters can be applied to each dominant frequency and thus for each frequency, an adaptive notch filter can be designed independently. However, if the dominant frequencies are totally unknown or very close to each other, it is hard to design the adaptive notch filters independently. In [1], adaptive identification method has been introduced for identification of multiple unknown frequencies. However, the method is very sophisticated and hard to be applied practically. In this paper, a new online adaptive identification method has been proposed. The algorithms of the proposed method are much simplified and thus can be easily implemented in practice.

Suppose the disturbance d(t) with 2 unknown dominant frequencies can be expressed as addition of 2 sinusoidal signals:

$d(t)=A_1 sin(\omega_1+\phi_1)+A_2 sin(\omega_2+\phi_2)$,

where A_i, ω_i *and* ϕ_i, $i=1,2$, are unknown.

Let the adaptive identifier output $d_0(k)$ and identifier error e(k) be

$d_0(k)=4d(k-1)-6d(k-2)+4d(k-3)-d(k-4)-T^4\lambda'_1(k)d(k-4)-T^2\lambda'_2(k)[d(k-2)-2d(k-3)+d(k-4)]$;

$e(k)=d_0(k)-d(k)=-(\lambda'_1(k)-\lambda_1)T^4d(k-4)-(\lambda'_2(k)-\lambda_2)T^2[d(k-2)-2d(k-3)+d(k-4)]$.

T is the sampling time; $\lambda'_i(k)$, $i=1,2$, are the estimates of constant values $\lambda_i(k)$. It can be shown that the adaptive laws based on the gradient algorithm can be designed as:

$\lambda'_1(k+1)= \lambda'_1(k)+\gamma_1 e(k)d(k-4)$;

$\lambda'_2(k+1)= \lambda'_2(k)+\gamma_2 e(k)[d(k-2)-2d(k-3)+d(k-4)]$.

γ_1 and γ_2 are adaptation gains. The unknown frequencies ω_1 and ω_2 can be calculated from the estimation values λ'_1 and λ'_2 easily. Although the discusion has been focused on cases with 2 unknown frequencies, the above adaptive method can be extended to identify n unknown frequencies online. The order of the adaptive identifier will be 2n. The effectiveness of the proposed online adaptive method has been verified by both simulation and experimental studies. Fig.1-2 show the experiment results for applying the proposed method to a 2.5-inch form factor HDD product with 2 dominant unknown disturbances.

From the measured disturbance spectrum shown in Fig. 1, it can be observed that there exit two close dominant frequencies in the HDD system. The adaptive notch filter method can be hardly applied to such kind of HDD systems. The estimated unknown frequencies using proposed online adaptive identification method are shown in Fig. 2. It clearly shows that the adaptive identification process is stable and the transient convergence is fast. The average estimated frequencies are $\omega_1=370Hz$ and $\omega_2=529Hz$, which are exactly the two dominant frequencies shown in Fig.1. Several methods can be applied to attenuate the dominant disturbances based on the identified frequencies. In this paper, adaptive peak filters have been adopted. The position error signals (PES) before and after adaptive attenuation are shown in Fig.3. It is obvious that the dominant disturbances have been significantly attenuated.

[1]C. Kang, C. Kim, "An adaptive notch filter for suppressing mechanical resonance in High track density disk drives,"pp. 638-652, *Microsystem Technologies,* 2005.

[2] X. Xia, "Global frequency estimation using adaptive identifiers," *IEEE Trans. Automatic Control,* Vol. 47, No. 7, pp. 1188-1193, 2002.

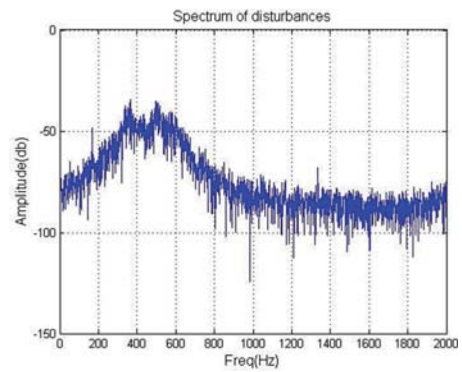

Fig. 1 Spectrum of disturbances

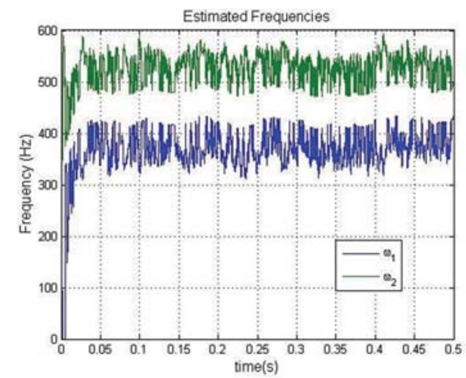

Fig. 2 Estimated dominant frequencies

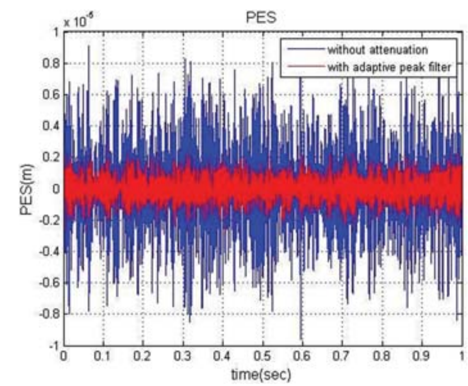

Fig.3 Position error signals: before and after attenuation

HL-03

A disturbance observer design for SPM-based data storage system.

J. Moon[1], C. Chung[1], C. Lee[1], Y. Kim[2]
1. Electrical Engineering, Hanyang University, Seoul, South Korea; 2. Devices & Materials Lab., LG Elite, Seoul, South Korea

Scanning probe microscopy-based data storage (SDS) system is one of the next generation storage devices. Nano scale precision control of SDS stage must be considered to realize the small form factor[1]. SDS stage is fabricated by Micro-Electro-Mechanical System (MEMS), and is the spring-mass-damper system as shown in Fig. 1. The nonlinear effects such as coupling dynamics and parameter uncertainties are the main issues of precision control of SDS stage. In [1], the coupling dynamics are treated as output disturbance and are reduced by the system feedback controller. However, only the feedback controller, it may not be sufficient to reject the output disturbance. Also the parameter uncertainties can arise during the operating time. These problems can be reduced by the enhanced system's sensitivity function.

Disturbance observer (DOB) is known as an effective method to improve the system's sensitivity function. In DOB, the performance and robustness depend on DOB Q-filter. Various methods have been developed to design Q-filter. However, despite all these methods, we still have to determine design parameters of Q-filter for the robustness and performance. Recently, we have proposed robust DOB which is based on robust stabilization and H∞ loop shaping method[2]. The advantage of this method is that the parameters of Q-filter for the robustness and performance can be determined systematically. In this paper, we apply this proposed DOB to SDS system to reduce the stage coupling and parameter uncertainties. The coprime uncertainty DOB model is shown in Fig. 2. In this figure, Fig. 2(a) can be represented to the equivalent model of a single loop controller of Fig. 2(b). Using this equivalent model, we can design DOB with the desired target loop transfer function by H∞ loop shaping method[2].

Fig. 3 shows the singular values of the system feedback controller Kx, and its DOB controller, KDOB. These controllers are designed by H∞ loop shaping method. Fig. 4 shows the experimental results of the sensitivity functions of the closed loop system. The improved sensitivity function is obtained by the proposed DOB. This result indicates that the nonlinear effects of SDS stage can be reduced and the tracking performance can be improved by DOB. Finally the maximum value of the sensitivity function is less than 6dB, the proposed DOB guarantees the robust stability.

[1] A. Pantazi, A. Sebastian, G. Cherubini, M. Lantz, H. Pozidis, H. Routhuizen and E. Eletheriou, "Control of MEMS-based scanning-probe data-storage devices," IEEE Trans. on Control System Technology, Vol. 15, No. 5, pp. 824-841, 2007.

[2] J. Moon, C. W. Lee, C. C. Chung and W. S. Kim, "Design Disturbance Observer via Robust Stabilization and H∞ Loop Shaping Method," to appear in the proceedings of 17th IFAC2008 World Congress.

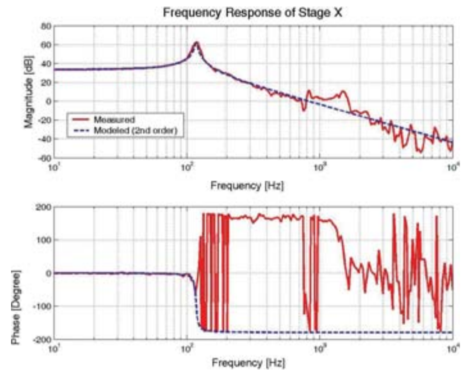

Fig. 1. Frequency response of stage x

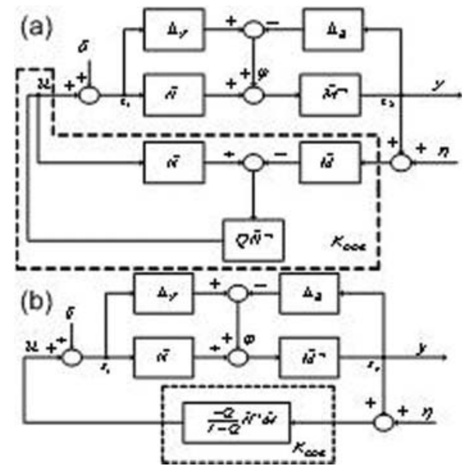

Fig. 2. Coprime uncertainty model of DOB[2]

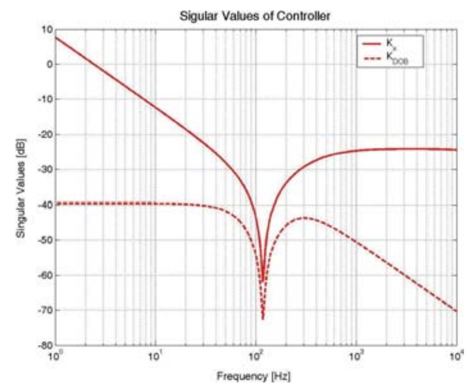

Fig. 3. Singular values of controller

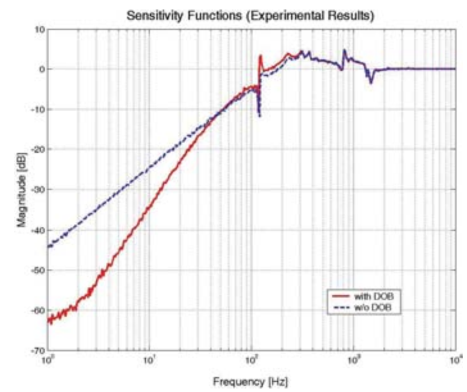

Fig. 4. Sensitivity functions

HL-04

A discrete-time modified sliding mode proximate time optimal servomechanism for SPM-based data storage systems.

J. Jeong[1], C. Lee[1], C. Chung[1], Y. Kim[2]
1. Electrical Engineering, Hanyang University, Seoul, South Korea; 2. Devices & Materials Lab., LG Elite, Seoul, South Korea

The growth rate of data storage density of scanning probe microscope (SPM)-based data Storage (SDS) system has been increased. Thus, access time is one of the key parameters characterizing SDS systems. It is always desirable to minimize the seek time. In Hard Disk Drive, the Proximate Time Optimal Servomechanism (PTOS) was proposed by Workman to reduce chattering problem [1]. The PTOS is robust to model uncertainties, but has slower settling time than time optimal control. To eliminate the common chattering and overshoot problem, variable structure control with sliding mode control, such as Sliding Mode PTOS (SMPTOS) for double integrator system [2] and discrete-time sliding mode control [3], was proposed.

In SDS systems, recently, the Proximate Time Optimal Servomechanism (PTOS) for damped harmonic oscillator model was proposed by IBM [4]. However, this method is difficult to obtain some design parameters satisfying an acceptable overshoot margin both short and long strokes. In this paper, we propose a discrete-time Modified Sliding Mode Proximate Time-Optimal Servomechanism (MSMPTOS). In the proposed method, the convergence rate factor, θ, affects settling time. Fast settling time causes large overshoot, so there is a trade-off between settling time and overshoot in sliding mode control. We applied SMPTOS in SDS systems, but the variable convergence rate factor which is a nonlinear function of position error is used. The convergence rate factor, depending on position error determines the width of unsaturation region. As we use the convergence rate factor varying to position error, the system has the fast settling time with much less overshoot than the previous methods.

Fig. 1 and Fig. 2 illustrate the simulation results of PTOS, SMPTOS and MSMPTOS for the seek operation, where the step input for the X-direction has an amplitude of 35[um]. The seek time of the proposed algorithm obtained from Fig.1 is 3.7[ms] which is smaller than 4.4[ms] in PTOS and 4.1[ms] in SMPTOS. Fig. 2 also shows the input voltage signal of PTOS, SMPTOS and MSMPTOS, which is constrained to ±10V. The control command of MSMPTOS is similar to time optimal control due to use varying θ rather than PTOS and SMPTOS. Phase portrait of PTOS, SMPTOS and MSMPTOS is shown in Fig. 3. This shows velocity profile of MSMPTOS is faster than PTOS and SMPTOS and it results in fast settling time in MSMPTOS.

[1] M. E. Workman, “Adaptive proximate time-optimal servomechanism,” Ph. D. Dissertation, Stanford University, 1987.

[2] D. Q. Zhang and G. X. Guo, “Discrete-time sliding mode proximate time optimal seek control of hard disk drives,” IEE Proc.-Control Theory Appl., Vol. 147, No. 4, pp.440-446, 2000.

[3] Chung Choo Chung, Jae-Wan Jang, and Ho-Seong Lee, “Design of Seek Control of Hard Disk Drive using Discrete-Time Sliding Mode Control,” Proceedings of IEEE International Conference on Control Applications, pp. 533-538, 2004.

[4] A. Sebastian, A. Pantazi, G. Cherubini, M. Lantz, H. Rothuizen, H. Pozidis, and E. Eleftheriou, “Towards faster data access: Seek operations in MEMS-based storage devices,” Proceedings of the IEEE International Conference on Control Applications, pp. 283-288, 2006.

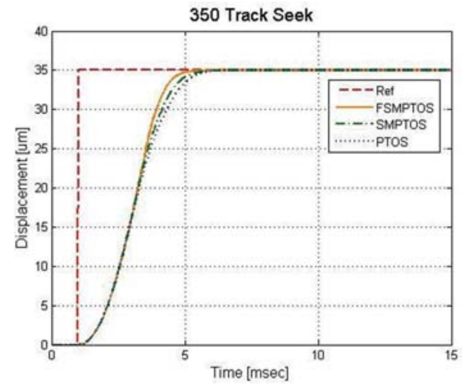

Fig. 1 350 Track seek of PTOS, SMPTOS and MSMPTOS

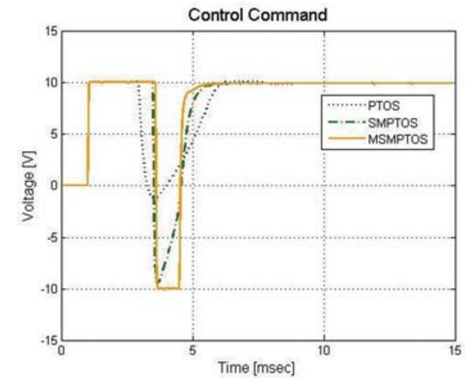

Fig. 2 Control Command of PTOS, SMPTOS and MSMPTOS

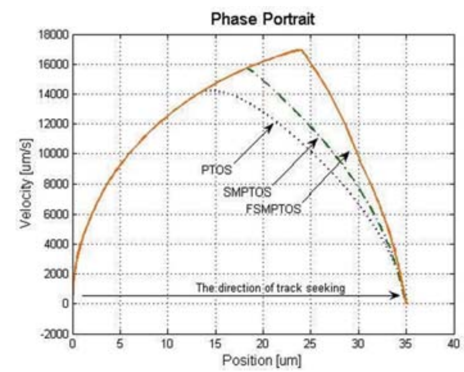

Fig. 3 Phase portrait of PTOS, SMPTOS and MSMPTOS

HL-05

Magnetic recording performance of 'Bit Printing method' on PMR media and its extendability to the higher areal density.

A. Morooka[1], M. Nagao[1], T. Yasunaga[1], K. Nishimaki[2]
1. Recording Media Research Laboratories, FUJI FILM co.,LTD., Odawara, Japan; 2. Production Engineering & Development Center, FUJI FILM co.,LTD., Odawara, Japan

The increase of servo track writing time according to the HDD density and capacity increase is a growing concern of the HDD industry. Servo pattern printing which supports bulk printing of the servo pattern is expected to be the ultimate solution for it(1). There are two printing methods, 'Edge Printing (EP)' and 'Bit printing (BP)' for PMR media. EP method applies horizontal external magnetic field, and its reproduced waveform is not compatible with head writing. On the other hand, BP method applies vertical external magnetic fields, is able to give the waveform like head write. But the experimental result was reported only for micron order bit length pattern(2). This paper describes the BP performance and the extendability to the future high areal density application.
The master with unevenness corresponding to the expected servo pattern is fabricated with lithography, EB-draw and electro plating technique. The magnetic layer of master is made of FeCo sputtered layer. The hard disk is initialized with 10KOe, then master disk is put on the hard disk with uniform contact and the external field is applied toward the opposite direction to the initialization. The reproduced signal was collected using spin stand. The magnetic spacing loss factor was calculated from the experiments with two master disks. One is with 10nm carbon overcoat and the other is without carbon overcoat. It is assumed that the magnitude of the reproduced signal is proportional to bit length and it is inverse proportional to the magnetic spacing. SNR was calculated from S as magnitude of 40MHz and N as integral of magnitude ranging from 0.5MHz to 80MHz.
Fig.1 shows the comparison of head writing signal and BP signal at the bit length of 70nm (λ= 140nm). Even with 70nm bit length, no significant difference between them on the amplitude and the signal shape is observed. This proofs the printed pattern has a good magnetic contrast corresponding to the mater pattern.
Fig.2 shows the spacing loss factors of BP. The spacing loss factor of BP is about 8dB at 80nm bit, it is smaller than that of head write recording (3). This is the merit of BP method. We thought this comes from that magnetic printing is static recording method and is not affected by dynamic recording demagnetization. In addition, the mirror effect of media SUL (Soft Under Layer) works not only for head write recording, but also for BP method.
Fig.3 shows the SNR dependency of 100nm bit length pattern on the applied magnetic field normalized with Hc. In the case of BP, SNR has its peak at the point where Ha is close to Hc. Too large Ha over Hc leads to the initialized magnetization flip of the master depression and too small Ha can't print the pattern which corresponds to the master projections. A simulation result leads that ΔH, which is the magnetic field delta between the vicinity of the master projection and depression, is proportional to the applied external magnetic field Ha(4). From these two facts, the media Hc increase to achieve higher areal density allows BP to apply higher Ha, which leads higher ΔH, and it gives better signal quality. The write element of the head has to control the magnetic flux distribution and amount at the same time and it's difficult to provide enough flux at short bite length, while BP controls the flux amount by hard magnet and controls flux distribution by master pattern separately and it is easy for BP to apply large Ha.
BP performance was demonstrated with 70nm bit length. The head writing compatible waveform signal was obtained with enough signal amplitude. The magnetic spacing loss is enough small and the optimum performance is obtained with the Ha close to media Hc. No significant concern to increase Ha on BP is observed, and BP is suitable for the future short bit length pattern.
The authors would like to thank members of Sugita Lab. of Ibaragi University for their productive discussion.

(1)R.Sugita etc., IEEE Trans.Mag.Vol.36,No.5,pp.2288-2290,2000

(2)A.Saito etc., IEEE Trans.Mag.Vol.38,No.5,pp2195-2197,2002

(3)H.N.Bertram etc., IEEE Trans.Mag.Vol.18,No.6,p1206-1208,1982

(4) R.Sugita etc., To be published in intermag 2008

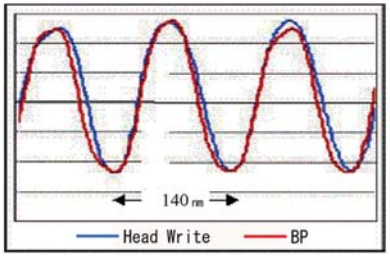

Fig. 1 Waveforms of magnetic head record and Bit Printing

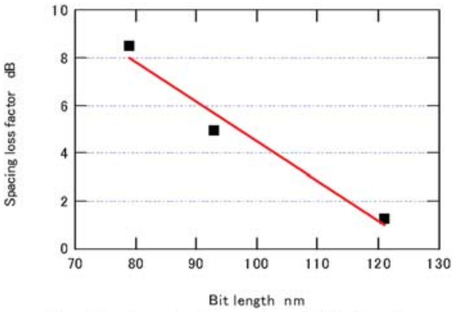

Fig. 2 Spacing loss factor in each bit length

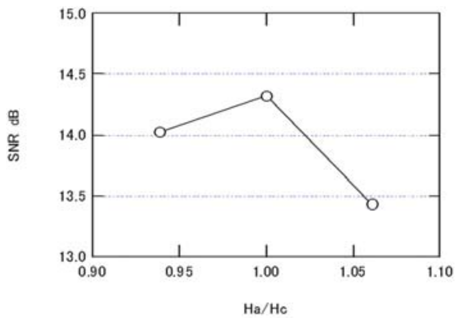

Fig. 3 Reproduction signal SNR in each Ha

HL-06

Using steady solutions of Reynolds-Averaged Navier Stokes (RANS) equations to estimate flow induced vibrations (FIV) of hard disk drive carriage arms.

T. Yip, E. Ong, A. Yudhanto, Z. He, Q. Zhang
Data Storage Institute, Singapore, Singapore

Flow induced vibrations (FIV) caused significant positioning errors to hard disk drives (HDD) particularly the higher rpm types. As a consequence, FIV consitutes a significant portion of NRRO budget during the design stage of higher rpm drives. To compute for FIV, the first step of the most common approach begins from a quantitative description of the HDD flow field. From the velocity and pressure fields, the various forms of time dependent forces from the fluid are quantitified and apply on the solid surfaces of the HDD carriage arms. By assuming a unidirectional coupling from the fluid forces to the solid carriage arms, the dynamic response of the HDD carriage subjected to complexly distributed three dimensional forces from the high speed fluid could be obtained subsequently. The above method was first reported by Kubotera et al (2002) and subsequently extend to the study of FIV on head gimbals assembly by Shimizu et al (2003). The HDD flow fields were obtained from time dependent solutions obtained from Large Eddy Simulation (LES) as described by Shimizu et al (2001). Abrahamson et al (2006) reported a similar LES/FEA approach towards FIV on disk vibrations. Although there is a good agreement between computed and measured results, one of the conclusion from the investigation was the time required to model and compute LES solutions being overly excessive. As a consequence, such LES approach is of limited practical use as a HDD design tool because computational design of experiments are not permitted. It was suggested that the steady solutions of the Reynolds-Averaged Navier Stokes (RANS) equations may be more appropriate for the purpose because of the economy RANS could offer in time. However, it has to be pointed out that RANS equations yield only ensemble averaged descriptions of flow properties. Instantaneous informations of velocities and pressures had been lost during the time–averaging proccess. Therefore, the major challenge of employing RANS equations is to reconstruct time dependent instantaneous fluid forces from the time averaged ones obtained from ensemble averaged HDD flow field. In this investigation, time independent ensemble-averaged turbulent fluid forces to act on hard disk drive carriage arms were first estimated from a statistically averaged Reynolds Averaged Navier Stokes (RANS) description of the flow field inside a 3.5 inch format simpilfied HDD model. Subsequently, by incorporating dominating convective time scales with the turbulent velocity-vorticity interaction terms from the RANS flow field, instantaneous turbulent fluid forces were reconstructed. The corresponding dynamic displacement of hard disk drive carriage arms caused by the estimated instantaneous turbulent fluid forces was computed numerically and validated using a laser Doppler Vibrometer (LDV) experimentally. The proposed FIV code offers tremendous saving in computing time and resources because steady RANS solutions of HDD flow field can be employed instead of time dependent solutions from Large Eddy simulation (LES). Other than computing for weeks and months, estimation of FIV can be expected in just hours or atmost a few days. The new FIV code may potentially be a tool for computational design of experiments of HDD designs. In the present investigation, the RANS description was obtained experimentally with non-intrusive optical measurement using a laser Doppler anemometer (LDA) because experimentally validated RANS solutions from computational fluid dynamics (CFD) of the simlified HDD model were not availabe during the investigation period. Steady solutions of RANS equation obtained by CFD or via LDA measurements are indifferent to the present RANS/FEA approach. However, experimentally validated CFD solutions from RANS equations for the present HDD model were not available yet during the investigation.

1. Kubotera H., Tsuda N., Tetawaki M. and Maruyama, “Aerodynamic Vibration mechanism of Hdd arms predicted by unsteady numerical simulation”, IEEE Transaction on Magnetics, vol. 38, no. 5, September 2002, pages 2201-2203. 2.Shimizu H., Shimizu T., Tokuyama M., Masuda H. and Nakamura S., 2003“Numerical Simulation of Positioning Error Caused by Air-Flow-Induced Vibration of Head Gimbals Assembly in Hard Disk Drive”, IEEE Transaction on Magnetics, vol. 39, no. 2, pp. 806-811.3.Shimizu H., Tokuyama M., Imai, S., Nakamura, S., and Sakai, K., 2001, “Study of aerodynamic characteristics in hard disk drives by numerical simulation,” IEEE Trans. Magn., vol. 37, pp. 831–836.4.Abrahamson, S., Buzek, M., Calihan, T., Isaacson, M. And Ohlsen, D., 2006, “CFD/FEA Simulation to examine airflow induced disk motiom in hard disk drives. ”, ASME/ISPS conference 2006, 21-23 June 2006, Santa Clara C.A., USA.5.Yip T.H., Zhang Q.D., Ong E.H., 2005, “Estimating time-averaged turbulent fluid forces from an ensemble-averaged flow field for engineering applications.” Fluid Structure Interaction III, WIT Press.6. T.H Yip, Q.D Zhang. and B.L. Ibrahim See, 2007, “Flow induced vibrations caused by turbulent jets behind the trailing edges of HDD arms in 15 000 rpm hard disk drives.” ASME ISPS 07, June 18-19, Santa Clara, California, USA.7. Yip T.H., Tan C.K. and Kuan Y.K., 2006, “The behavior of spiral flow structures along the trailing edges of E-block arms under increasing airflow velocities.”, IEEE TRANSACTIONS ON MAGNETICS 42 (10): 2591-2593 OCT 2006.

HL-07

A Novel Settling Controller for Dual-stage Servo Systems.

J. Zhang[1], C. Du[1], S. Ge[2]

1. Data Storage Institute, Singapore, Singapore; 2. Department of Electrical & Computer Engineering, National University of Singapore, Singapore, Singapore

The dual-stage servo system is necessary in the future to support 1 Tb/in2 and beyond. In this paper, we discuss the unique characteristics of settling controller for dual-stage servo system [1, 2]. An initial error shaping (IES) settling controller is designed to shape the position error signal profile before it is fed into the nominal controller. The proposed method is convenient and suitable for real implementation.

Fig. 1 shows a typical master/slave dual stage servo structure for on-track mode. The seeking can very fast respond to the command due to the boosted high servo bandwidth. The whole system has no obvious slow modes, since PZT is used to compensate the slow modes in VCM loop, but it has relatively large overshoot. Therefore, it is important to achieve a smooth and fast settling to deal with the non-zero VCM states when switching from VCM seeking to dual stage on-track mode. The major initial values of VCM states that need to be considered are initial position y0 and velocity v0. Denote VCM plant as Pv: (Av, Bv, Cv), and PZT plant as Pm: (Am, Bm, Cm) with Dv= 0, and Dm= 0. Then the dual-stage plant is described as (1).

IES for initial position y0

For initial position value of VCM, it is equivalent to apply a disturbance at the output as shown in Fig. 2. Our objective is to design a feedforward controller F(z) such that the transient due to y0 is cancelled out. From Fig. 2 we have (2).Obviously, if there is no IES and F(z)=1, the transient of PES while settling is the same as the transient of step response of the closed-loop system. To improve the transient of settling, the mode added inside F(z) should be the inverse of the transient of closed-loop system. In other words, the mode added by F(z) should cancel the undesired on-track modes. F(z) can be designed using ZPETC method [3]. Let Ba(z) and Bu(z) respectively include acceptable and unacceptable zeros of B(z), where acceptable zero means that it is within acceptable circle in the pole/zero maps. Ultimately we can have (3).

Note that Bu*(z^{-1}) is the complex conjugate of Bu(z). Therefore, after (n-m+q) step delay, the second part of the above equation is a moving average of a constant y0, which means PES is zero after (n-m+q) step delay.

IES for initial velocity v0

Let Tv(z) be the transfer function from initial velocity v0 to pes. From Fig.2, we have (4). When x(t) is designed as x(z)=-z^(n-m+q)Tv(z)v0, we have (5). Note that Bu*(z^{-1}) is the complex conjugate of Bu(z), therefore, the first part of the above equation is the moving average of (-Tv(z)v0), which is very close to -Tv(z)v0 due to the fact that it is transient response to slow energy loss stored in VCM. Thus it compensates for the second part.

The simulation results in Fig. 3 and 4 with y0 = 0.5 track show that output settles to on-track very fast (less than 0.2 ms) and with no acoustic problem in control effort. Fig. 5 shows the transient due to v0=2000 track/sec. The curve A is without IES compensation, the curve B is with IES compensation. Fig. 6 and 7 shows the settling performance with IES to compensate y0 and v0. Fig. 8 and 9 are experimental results. With IES, the transient due to the initial position is significantly improved. Although the feedforward controller is of higher order, actually the implementation of this controller is much simple. We only need to create a look up table (LUT) to store the compensator output corresponding to unit initial position and velocity. While online compensating, we only need to multiply the value in LUT with the corresponding initial values and inject into the nominal controller. As we know, the transients for both initial velocity and position are only significant for the first 2 ms. If we use 20 kHz sampling frequency, only 40 points are needed for this compensation. In the future, the simplification and optimal switching condition for this method will be studied.

[1] T. Yamaguchi, et.al, IEEE Trans. On Magnetics, 32(3), pp.1767-1772, May 1996.

[2] M. Kobayashi, et.al, IEEE Trans. on Magnetics, 37(2),

2001, pp. 949-954 Mar. 1999.

[3]M. Tomizuka,ASME J. Dyn. Sys., Meas., and Contr., vol. 109, pp. 65-68, Mar. 1987.

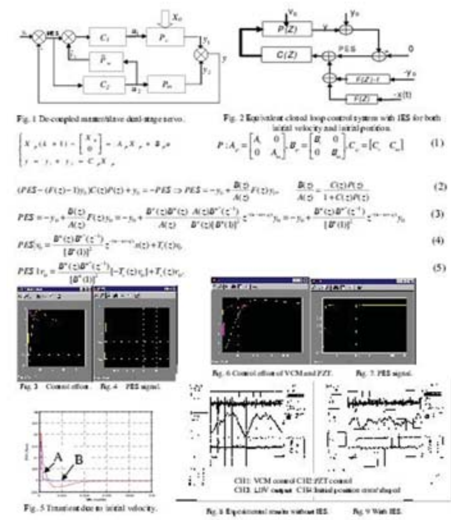

HL-08

PES Generation and Evaluation for Bit Patterned Servo.

S. Zhang, W. Wong
Data Storage Institute, Singapore, Singapore

1. INTRODUCTION
With the proposal of bit-patterned-media (BPM) [1] in next generation magnetic recording system, readback signal profile and media noise profile are expected to be much different from that of previous HDD systems. Evaluating the performance of servo pattern with BPM is therefore necessary to help advanced servo controller design as well as head/media design for future HDD systems. In this work, we developed a simulation platform based on 3D analytical read head modeling and BPM media modeling to generate readback signal from bit-patterned-servo. With this platform, media noise due to manufacturing defects [4] and other head/media parameters can be effectively modeled and their impacts on the performance of the PES generation/demodulation are analyzed.
2. PES GENERATION AND PERFORMANCE EVALUATION
The simulation model is based on the widely used reciprocity principle where the details of the modeling process are addressed in [2]. In this work, we target ultra-high density of 1Tera-bits per square inch (Tbpsi) and above, with a small bit-aspect-ratio (BAR) of 2-4 due to the smallest lithography imprinting feature size.
Amplitude based servo pattern is considered here (full paper will include other servo pattern but omitted here due to size limit of web-submission). Demodulation of PES can be done through either area demodulation or DFT based demodulation [3].
In fig. 1, we illustrate the simulated readback signal from a bit-patterned-servo (BPS) pattern. The readback signal at the track center resembles a waveform commonly seen in amplitude servo pattern. From the 3D readback signal plot it is clear that the signal amplitude drops nonlinearly when the read head moves from the center of the island outwards. This suggests the need of a mapping function that translates the raw PES to the offtrack position of the read head in such system.
In Fig. 2, it shows that the larger the BAR the better the resolution of PES, as well as steeper the curve transitions. Lower density has similar advantage over higher density as shown in Fig. 3. In other words, wider track pitch for the same read head means sharper transition at the servo bursts edge.
In Fig. 4, we compare the PES demodulation noise at different additive white Gaussian noise (AWGN) level. By comparing Fig. 5 with Fig. 4, we can see that 5% island position jitter has roughly the same destructive effect of AWGN in 15dB SNR. This is roughly equivalent with 5% size fluctuation as shown in Fig. 6. These observations and further results maybe used as guidance for manufacturer on the maximum media noise a system can tolerate. But unlike transition jitter noise in conventional continuous media, these media noise are fixed once the media is manufactured and can be dealt as repeatable run out (RRO) instead of non-repeatable run out (NRRO).
3. CONCLUSION
With the help of the 3D analytical signal model for BPM, we can generate readback signal for arbitrary sets of head/media parameters. Servo signal is generated based on this model for bit-patterned-servo. Effects of media noise on PES demodulation noise is analyzed using this platform and useful information on servo design can be obtained from this analysis.
(due to the character limits of web-submission, not all figures are uploaded, but will be available in full paper and presentation)

[1] R. L. White, R. M. H. New, and R. F. W. Pease, “Patterned media: A viable route to 50Gbit/in2?,” IEEE Trans. Magn., vol. 33, pp. 990-995, Jan. 1997

[2] S. Zhang, B. Chen and Z. J. Liu “Effects of Media Imperfection on Readback Signal in Bit Patterned Media Recording”, submitted to IEEE Trans. Mag.

[3] S. Zhang, W. E. Wong, “Evaluation of Servo Patterns for Perpendicular Recording”, Proc. APMRC 2006

[4] B. D. Terris, “Bit patterned media for hard drives,” Proc. TMRC. 2006

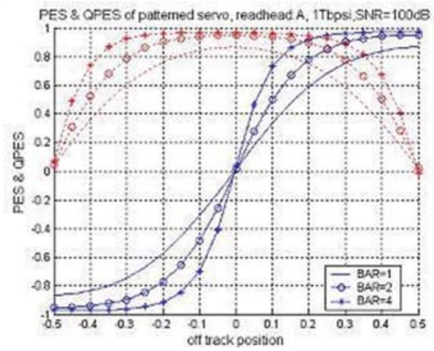

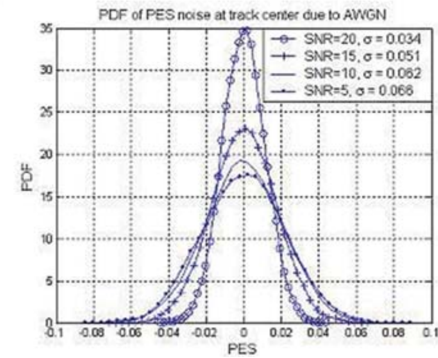

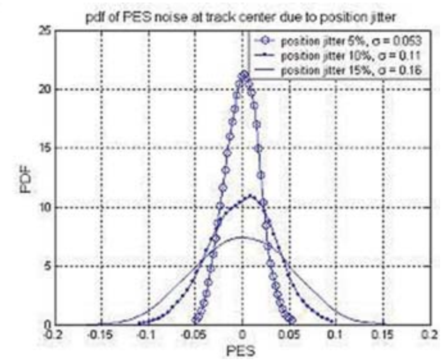

Mean-Adjusted PDNP Detector for Perpendicular Recording Channels With NLTS.

Z. Wu[1], P. H. Siegel[1], J. K. Wolf[1], N. Bertram[1,2]
1. Center for Magnetic Recording Research, University of California, San Diego, La Jolla, CA;
2. Hitachi Global Storage Technologies, San Jose, CA

In high density perpendicular magnetic recording channels, nonlinear transition shift (NLTS) is one of the distortions that can degrade the system performance. Write precompensation is a standard method used to offset the negative effect of NLTS. In this paper, we propose a modified pattern-dependent noise predictive (PDNP) detection algorithm for use on channels with electronics noise, transition jitter noise, and NLTS. We show that this detector can offer significant improvement in bit error rate (BER) compared to conventional Viterbi and PDNP detectors. Moreover, the system performance can be further improved by combining the new detector with a simple write precompensation scheme.

PDNP detectors have been shown to reduce the BER in recording channels with data-dependent media noise and correlated additive Gaussian noise by incorporating pattern-dependent noise prediction into the branch metric computation of the Viterbi algorithm [1][2]. We introduce a "mean-adjusted" PDNP (MA-PDNP) detector that also takes into account the effect of NLTS on the mean and covariance of the channel noise. Equation (1) of Fig. 1 gives the modified branch metric of the proposed detector for a trellis branch e_k at time k. In the equation, r_j denotes the equalized readback sample at time j, while $y_j(e_k)$, $j=k-L_y,\ldots,k$ denote the noiseless channel output samples. The noise variance $\sigma^2(e_k)$, noise prediction coefficients $p_i(e_k)$ and noise means $m_i(e_k)$ corresponding to branch e_k are all data-dependent and may differ from branch to branch.

In our performance simulations, we use the channel model described in equation (2) of Fig. 1. The channel output signal, $z(t)$, incorporates a second-order approximation of the error-function transition response, $s(t)$, whose first and second derivatives are denoted by $s'(t)$ and $s''(t)$, respectively. For the ith transition, d_i, the net transition shift, δ_i, incorporates both NLTS as well as write precompensation (if any), and the random transition jitter, denoted a_i, is assumed to be a Gaussian random variable, independent from transition to transition, with variance σ_J^2. The contribution of AWGN is represented by $n_W(t)$.

As with PDNP detection [2], there are several ways to derive from the MA_PDNP detector a variety of simpler, yet still effective detectors. Strategies for reducing detector complexity include lowering the prediction filter length L_y, limiting the required number of predictors by shortening the data-dependence length L_x, and eliminating trellis states by using feedback of tentative decisions. Our error-rate simulations used PDNP and MA-PDNP detector trellises with the same number of states as the conventional Viterbi detector. The data-dependence range of the noise predictors was set to L_x=6.

Performance results for the MA-PDNP detector are shown in Fig. 2. The simulated system uses a 3-tap equalizer target and an MMSE monic-constraint equalizer design. The channel density and normalized jitter-noise standard deviation are $T_{50}/B = 1$ and $\sigma_J/B = 0.1$, respectively, where B is the channel bit spacing. The signal to noise ratio is defined as $SNR_W=20\log(V_{max}/\sigma_W)$, where σ_W is the standard deviation of the sampled white Gaussian noise. Fig. 2(a) shows that the MA-PDNP detectors with prediction filter lengths $L_y=0,\ldots,3$ are all superior to both the Viterbi detector and the PDNP detector with $L_y=3$. We note that for SNR_W equal to 23dB and 26dB, the BER of the MA-PDNP detector does not depend upon L_y over the range of values considered.

The MA-PDNP detector can be used together with any write precompensation scheme. Fig. 2(b) shows that the system performance can be improved by combining the new detector with simple dibit precompensation. We see that, with large enough L_y, the combined scheme achieves the same performance as a PDNP detector applied to a channel with no NLTS. This is true over a wide range of precompensation values.

[1] A. Kavčić and J. M. Moura, "The Viterbi Algorithm and Markov Noise Memory," IEEE Trans. Inf. Theory, vol. 46, no. 1, pp. 291–301, Jan. 2000.

[2] J. Moon and J. Park, "Pattern-dependent Noise Prediction in Signal-Dependent Noise," IEEE J. Sel. Areas Commun., vol. 19, no. 4, pp. 730–743, Apr. 2001.

$$M(e_k)=\log\left(\sqrt{2\pi\sigma^2(e_k)}\right)+\frac{1}{2\sigma^2(e_k)}\left(\sum_{i=0}^{L_y}p_i(e_k)[r_{k-i}-y_{k-i}(e_k)-m_i(e_k)]\right)^2 \quad (1)$$

$$z(t)=\sum_i d_i\left[s(t-iB)+(a_i+\delta_i)s'(t-iB)+\frac{(a_i+\delta_i)^2}{2}s''(t-iB)\right]+n_W(t) \quad (2)$$

Fig. 1 Equations.

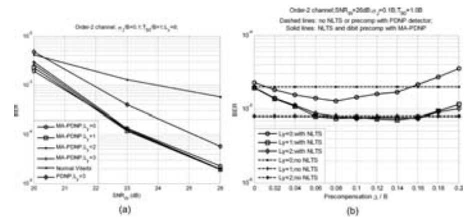

Fig. 2 Simulation results. (a) Comparison between Viterbi, PDNP, and MA-PDNP detectors. (b) MA-PDNP detector with dibit precompensation.

HM-02

Ordered statistics soft decoding of Reed-Solomon codes over intersymbol interference channels.

F. Y. Lim, *A. Kav či ć*, M. Fossorier
University of Hawaii, Manoa, Honolulu, HI

Ordered Statistics Decoding (OSD): The aim of this paper is to implement and test OSD techniques [1,2] over intersymbol interference (ISI) channels. For any [n,k] block code, the principle of OSD is to process low-weight (sparse) error patterns in the k most reliable basis (MRB) positions. However, in ISI channels, the errors in the MRB are observed to consist of sparse error-events (not bit errors). Consequently, an efficient technique needs to process error-events that may occur in the MRB.

Improvements for ISI channels: We define the most-likely path as the (uncoded) signal sequence with the largest likelihood, out of all possible 2^n binary sequences. For any two sequences, the positive difference between their Euclidean distances to the received sequence will be termed the metric difference. The problem of implementing OSD for ISI channels can now be restated as processing error-events with different supports in the MRB in order of increasing metric differences. To reduce the implementation complexity, we do not use the Generalized Viterbi Algorithm [3], which sorts all 2^k possible paths in terms of increasing metric difference, but rather, our proposed solution is a modification of Battail's algorithm [4] which solves a related problem in memoryless AWGN channels.

Battail's Algorithm: We briefly review Battail's algorithm [4], which constructs k lists of low weight error patterns over the k MRB positions. Conceptually, the algorithm orders the error patterns in k FIFO lists. Every error pattern is associated with a unique parent error pattern, and the parent has a lower discrepency [1,2] than any of its children. New error patterns are added for future processing only after the parent has been processed. Using this approach, the lists have been observed to grow quite fast, but Valembois, et al. [4] proposed a solution that involves introducing an additional list to overcome this problem.

Modification for ISI Channels: We create n×S lists, where S is the state size of the ISI channel trellis. Using the Soft-Ouput Viterbi Algorithm [5], we compute and store, for every time instant and every state, the corresponding path difference and error event. We now use Battail's algorithm to process and combine error events (rather than single bit errors). If an error event includes MRB positions, we process it by computing the corresponding codeword and its likelihood. The algorithm is stopped when a pre-determined number of codewords has been processed. Out of all the processed codewords, the most likely is chosen and returned as the decision.

To make the search more efficient, we combine error events only if the errors occur in the MRB positions. We call an error event complete if it diverges from the same state as the most-likely path, and incomplete otherwise. The structure of Battail's algorithm guaranees that all error events of interest are processed if the following rules are followed:

1. Incomplete error events that do not contain MRB positions are discarded.
2. A complete and incomplete error event are combined only if they are not disjoint (e.g. Type I, II).
3. Two complete error events are combined only if both occur in the MRB.

Simulations: We experimented on the perpendicular recording $(1 + D)^2$ ISI channel, for the standard (255,239) Reed-Solomon code binary image. We processed 2 million error patterns, which is approximately $O(n^2)$, thus a similar list size as OSD(2) processing [1]. The performance is compared to that of a "bit" Chase decoder, and the message passing (iterative) decoder proposed by Bellarado-Kavcic [6] for RS codes (which performs similarly to the Jiang-Narayanan iterative decoder [7], but at much lower complexity). We also show the performance of a similar complexity OSD-based decoder (BMA(2, 22) [2]), that was demonstrated to give a 1.5 dB gain on the AWGN channel over HDD. On the ISI channel, our decoder achieves approximately 1 dB gain over HDD, and the BMA only achieves a 0.5 dB gain. The iterative decoder [6,7] performs similarly as the BMA, giving a 0.45 dB gain. The gains of both the new decoder and the BMA come with the cost of $O((1 - R)n^3)$ complexity over GF(2) due to the required Gaussian elimination.

[1] IEEE Trans. on Inform. Theory., vol. 42, no. 3, pp. 738-750, May 1996.

[2] IEEE Trans. on Inform. Theory., vol. 50, no. 5, pp. 796-810, May 2004.

[3] IEEE Trans. on Comm., vol. 43, no. 2/3/4, pp. 277-297, Feb./Mar./Apr. 1995.

[4] IEEE Comm. Letters, vol. 5, no. 11, pp. 456-458,Nov. 2001.

[5] Proc. Global Telecomm. Conf. (GLOBECOM '89), TX, USA, Nov. 1989, pp. 1680-1686.

[6] Proc. IEEE Inform. Theory Workshop (ITW '07), CA, USA, Sept 2007, pp. 138-143.

[7] IEEE Trans. on Inform. Theory., vol. 52, no. 8, pp. 3746-3756, Aug. 2006.

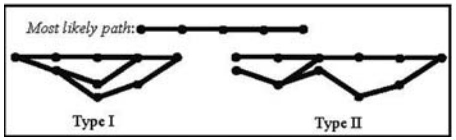

Type I and II error events

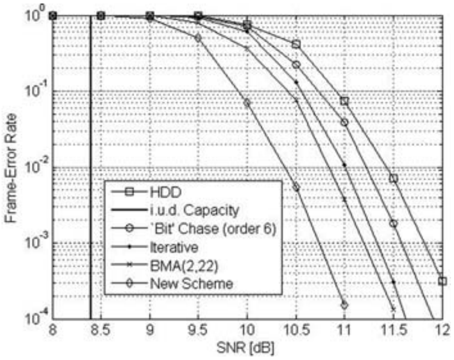

Performances of various algorithms for the (239,255) RS code

HM-03

Enhanced Message Passing in Turbo Product Code.

N. Yeh[1], P. Steiner[1], Y. Li[1,2]
1. Seagate Technology, Fremont, CA; 2. Presently with AMD, Yardley, PA

Introduction:

Iterative code has been shown to provide significant performance advantage but may be slow to converge and even exhibit a residual error floor. It is proposed in this paper to improve the performance of turbo product code with single-bit parity check (TPC/SPC) [1] by adding cyclic redundancy check (CRC) to the sub-blocks. A sub-block can be ensured error free after it passes both the parity check and CRC. At the completion of each iteration, the message from the error free sub-blocks can be modified to greatly increase its confidence level. The artificially high confidence level from those error free sub-block bits results in much more efficient iterations subsequently and greatly lowers the error floor.

Enhanced Message Passing:

Passing the parity check in TPC/SPC does not guarantee the sub-block to be error free since four error bits sitting on a rectangular grid does not cause any parity violation. Additional CRC is required to ensure a sub-block to be free of errors. When all the bits in a sub-block are correctly decoded, the log-likelihood ratio of these bits can be increased to $+\infty$ and $-\infty$, respectively, as shown in Fig. 1. These sub-blocks will have all the bits assigned to the correctly decoded values without going through further local iterations. The artificially high log-likelihood ratios from these bits after interleaving would have good influence on the adjacent bits in soft Viterbi algorithm (SOVA) decoder. It is equivalent to pruning the trellis when there is a definite "0" or a definite "1" as illustrated in Fig. 2. This enhanced message passing enables much more efficient iteration and faster convergence.

Results:

Bathtub curves were measured from high-density head/media on spinstand with on-track first-pass SOVA BER about 10^{-2}. Waveforms were captured and processed through software TPC/SPC channel. A data sector of 512 bytes including CRC is divided into four sub-blocks each with 32x32 bits. The sub-block is encoded to 33x33 bits after adding parity bits. The bits from all the four sub-blocks are interleaved, serialized and recorded onto the disk. It was found that CRC combined with the noise prediction maximum-likelihood (NPML) detection in SOVA [2] gives the best performance. With simultaneous application of NPML and CRC, the burst error profile is greatly improved (Fig. 3) and the residual error floor is brought down well below BER=10^{-9} (Fig. 4). Incremental enhancement of message passing and NPML is plotted in these figures to demonstrate the algorithm capabilities.

Summary:

Enhanced message passing opens opportunities for additional performance gain from traditional TPC/SPC. Application to magnetic recording would allow continuing advancement of areal density in the future.

[1] J. Li, *et al.*, *IEEE Trans. Commun.* **50**, No. 5, pp 723-734 (2002)

[2] E. Eleftheriou. *et al.*, *IEEE Trans. Magn.* **32**, No. 5, pp 3968-3970 (1996)

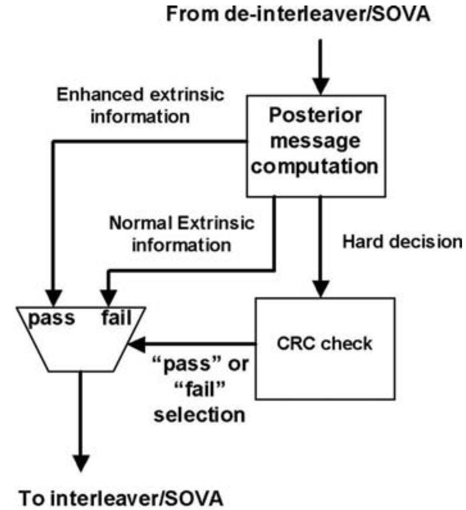

Fig. 1 Enhanced message selection

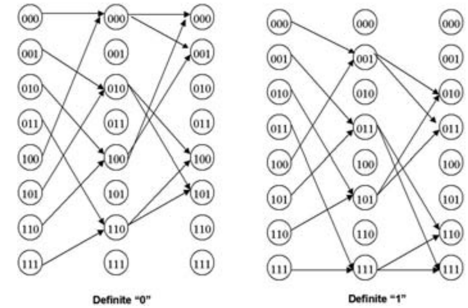

Fig. 2 Branches are pruned when the bit is a sure "0" or a sure "1" in an 8-state Viterbi trellis.

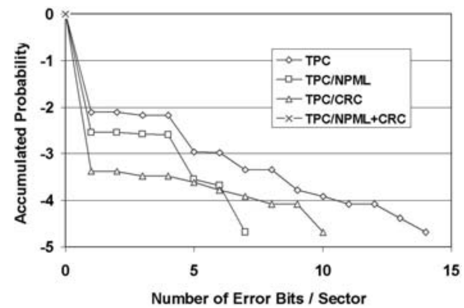

Fig. 3 Burst error profile with application of CRC and NPML

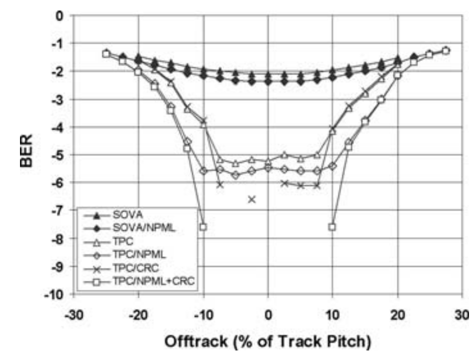

Fig. 4 BER improvement from enhanced message passing

HM-04

A New Burst Detection Method Using Parity Check Matrix of LDPC Code for Bit Flipping Burst-like Signal Degradation.

Y. Nakamura[1], M. Nishimura[1], Y. Okamoto[1], H. Osawa[1], H. Muraoka[2]
1. Graduate School of Science and Engineering, Ehime University, Matsuyama, Japan; 2. RIEC, Tohoku University, Sendai, Japan

I. Introduction

Low-density parity-check (LDPC) coding [1] and iterative decoding system with a burst detector has the resistance to the burst-like signal degradation due to detectable media defects. There is a possibility that the undetectable signal burst called bit flipping gives the fatal influence on the LDPC coding and iterative decoding system with the conventional burst detector using a reproducing waveform, an equalizer output, an a posteriori probability (APP) decoder output and so on [2]. We propose and evaluate a new burst detection method using a check matrix of LDPC code for the bit flipping media defects under the long sector format of 4096 Byte/sector.

II. R/W channel

Fig. 1 shows the block diagram of an R/W system. In this study, we assume that a sector of user data sequence consists of 4096 Bytes. The 128/130(0, 16/8) RLL code and the regular(22, 3) LDPC code are employed. We assume the bit flipping of the length L_{flip} normalized by user bit interval as the undetectable burst-like signal degradation, which is functionally equivalent to flipping the recording sequence as shown in the figure. We also assume a perpendicular magnetic recording (PMR) channel with a hyperbolic tangent isolated waveform [3] at a linear density of K = 1.5 defined as the transition width T_{50} normalized by user bit interval. The noise at the reading point is composed of a jitter-like medium noise and a system noise with power ratio of 8:2. The equalizer is adjusted so as to convert the bit response of R/W channel into a PR1 characteristic [4]. The APP decoder has an autoregressive (AR) channel model as a channel estimator [5]. The iterative decoder consists of an APP decoder and a sum-product (SP) decoder. In this study, we set the iteration limits in the SP and iterative decoders to 5. The burst detector detects the position and length of the bursts by using parity check matrix of the LDPC code. Our proposed burst detector obtains the burst information for iterative decoding from the parity check results of LDPC code. The detector checks whether an error has occurred in each row by parity check, and makes the error flag sequence by the sum of the check results. The error flag sequence consists of "0", "1", "2" and "3" if the column weight is three. The burst information is made by the threshold decision after the moving average of the error flag sequence. The SP decoder decodes the recorded sequence using the constraint of LDPC code from LLR with the burst information by controlling the amplitude of LLR not to cause error propagation due to the burst-like signal degradation. After the given iterations, the output data sequence is recovered by the hard decision and the RLL decoding.

III. Performance comparison

Fig.2 shows the relationship between L_{flip} and the required SNR to achieve the error free detection for about 10M bit sequence. The symbols circle, triangle and square show the performance of LDPC coding and iterative decoding system with the proposed burst detector (LDPC-PCBD), the LDPC coding and iterative decoding system with the conventional burst detector (LDPC-BD) and the erasure correcting system using Reed-Solomon (RS) code (RLL-RS-EC), respectively. As can be seen from the figure, the LDPC-PCBD system shows the better performance and has the resistance to a bit flipping signal burst of about 1500 bits.

IV. Conclusion

We have proposed and evaluated a new burst detection method using a check matrix of LDPC code for the bit flipping signal bursts under a long sector format of 4096 Byte/sector. The results show that the LDPC coding and iterative decoding system with the proposed burst detector shows the better performance and has the resistance to a bit flipping signal burst of about 1500 bits.

Acknowledgment

This work was supported in part by the Grants-in-Aid of the Storage Research Consortium (SRC), Japan.

[1] R. G. Gallager, IRE Trans. Inform. Theory, vol.IT-8, pp.21-28, Jan. 1962.

[2] W. Tan et al., IEEE Trans. Magn., vol.39, no.5, pp.2579-2581, Sept. 2003.

[3] Y. Okamoto et al., J. Magn. Magn. Mater., vol.235, pp.259-264, 2001.

[4] E. R. Kretzmer, IEEE Trans. Commun. Technol., vol.COM-14, no.1, pp.67-68, Feb. 1966.

[5] Y. Nakamura et al., IEEE Trans. Magn., vol.39, no.5, pp.2570-2572, Sept. 2003.

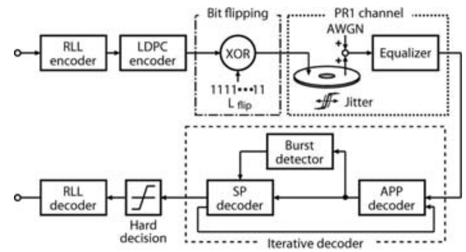

Fig.1 Block diagram of R/W system.

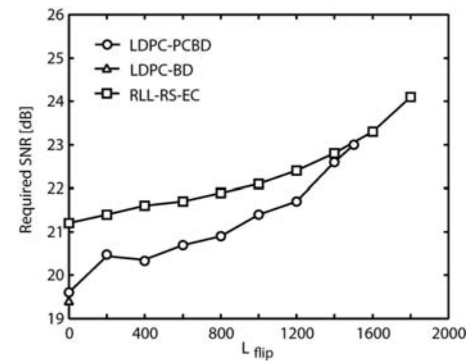

Fig.2 L_{flip} versus required SNR.

Low-Complexity LDPC Decoder Architecture for High-Speed Magnetic Recording.

C. Zhang[1,2], Z. Wang[3], L. Li[1,2], J. Lin[1,2], M. Gao[1,2]
1. Institute of VLSI Design, Physics Department, Nanjing University, Nanjing, China; 2. Key Laboratory of Advanced Photonic and Electronic Materials, Nanjing University, Nanjing, China; 3. School of Electrical Engineering and Computer Science, Oregon State University, Corvallis, OR

Low Density Parity-Check (LDPC) code has been considered in magnetic recording for its outstanding error correcting capability. Recently *shift*-LDPC code structure [1] was proposed for low-complexity high-speed implementation. It was shown in [2] that a 8192-bit LDPC decoder chip in 0.18 μm CMOS technology can achieve over 5Gb/s throughput at 15 iterations with only 11.3 mm^2. In this digest, algorithmic transformations are employed to further reduce the complexity of LDPC decoder
The parity check matrix of a regular (N, M) (c, t) *shift*-LDPC code consists of $c \times t$ submatrixes, where P is a $L \times L$ permutation matrix. In each clock cycle, the column process and the row process are interleaved. One iteration can be finished in t clock cycles. Using Min-Sum algorithm for *shift*-LDPC code has led to significant,memory reduction compared with using Sum-Product algorithm as demonstrated in [1]. In this work, we will introduce 2 algorithmic transformations to further reduce overall hardware. The first one is single minimum scheme, which only requires the single minimum value of all inputs in the check node process [1]. This modified algorithm is provided in Fig. 1. The second one is a non-uniform quantization scheme. Specifically 5-bits are considered per soft message to achieve comparable decoding performance to that using 6-bit per message in the prior design. Table 1 shows how to convert between 6-bit uniformly quantized messages and 5-bit non-uniformly quantized messages. The non-uniformly quantized messages are directly used in Check node Processing Units (CPUs), which find only the minimum values. While in Variable node Processing Units (VPUs), both the expansion and compression blocks are required. Simulation results for a regular (8192, 7168) (4, 32) *shift*-LDPC code is shown in Fig. 2. It can be observed that the proposed Min-Sum algorithm achieves slightly better performances than that with (6:3) uniform quantization scheme.
Based on the non-uniform quantization scheme, the expansion block and the compression block can be easily derived. The overhead of the part of logic is small. Due to the reduced wordlength, the routing complexity and memory usage will be significantly decreased. Fig. 3 shows the structures of CPU and VPU. The proposed *shift*-LDPC decoder has been synthesized in SMIC 0.18μm CMOS technology, using Synopsys Design Compiler. The implementation results in Table 2 show that compared with [2] the proposed design saves 14.2% area with the same throughput. And the new design has big advantages in both throughput, and hardware cost over the one presented in [3] targeting for magnetic recording.

[1] J. Sha, Z.Wang, *et al*, "Efficient Decoder Implementation for QC-LDPC Codes," *IEEE ICCCAS'06*, pp. 2498-2502, June 2006.

[2] J. Sha, Z. Wang, *et al*, "Multi-Gb/s LDPC Code Design and Implementation," *submitted to IEEE Trans. on VLSI Systems* in Oct.2007.

[3] H. Zhong, *et al*, "Area-Efficient Min-Sum Decoder Design for High-Rate Quasi-Cyclic Low-Density Parity-Check Codes in Magnetic Recording," *IEEE Trans. on Magnetics*, vol. 43, no. 12, pp. 4117-4122, Dec. 2007.

Decimal Value	±0.0000	±0.0625	±0.1250	±0.1875	±0.2500	±0.3125	±0.3750	±0.4375	±0.5000~±0.6250	±0.6875	±0.7500	±0.8125	±0.8750	±0.9375	±1.0000~±1.1875	±1.2500~±1.9375
(6:4) Uniform Quan.	x00000	x00001	x00010	x00011	x00100	x00101	x00110	x00111	x01000~x01010	x01011	x01100	x01101	x01110	x01111	x10000~x10011	x10100~x11111
5-bit Non-uniform	x0000	x0001	x0010	x0011	x0100	x0101	x0110	x0111	x1000	x1001	x1010	x1011	x1100	x1101	x1110	x1111

Reference	Code Length	Code Rate	CMOS Technology	Quantization	Decoding Algorithm	Clock Frequency	Throughput	Decoding Iteration	Area	Area Scaled to 65nm
Proposed	8192	7/8	180nm, 1.8V	5-bit	Transformed Min-Sum	317MHz	5.1Gbps	15	9.69mm^2	1.26mm^2
[2]	8192	7/8	180nm, 1.8V	6-bit	Min-Sum	317MHz	5.1Gbps	15	11.3mm^2	1.47mm^2
[3]	9216	8/9	65nm, 0.9V	4-bit	Min-Sum	300MHz	2.1Gbps	16	2.32mm^2	2.32mm^2

The Min-Sum Algorithm with Single Minimum Schemes

. . .

Step. 1 $\beta_{\min} = \min_{i \in V_j} \beta_{ij}$, *N′ defines the mumber of the* min;

if $N' = 1$

then $\beta'_{ij} = \begin{cases} \beta_{\min} + 0.125(if\ \beta_{ij} = \beta_{\min}) \\ 0.68 \times \beta_{\min} \end{cases}$;

else $\beta'_{ij} = 0.68 \times \beta_{\min}$;

end

$L(r_{ij}) = \prod_{i' \in V_j \setminus i} \alpha_{i'j} \cdot \beta'_{ij}$;

Step. 2 . . .

. . .

Output: *decoded bit* $\hat{c}_i$

Fig. 1

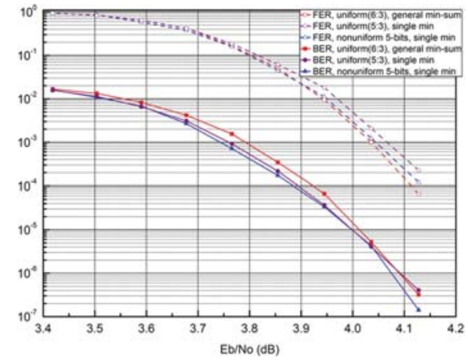

Fig. 2

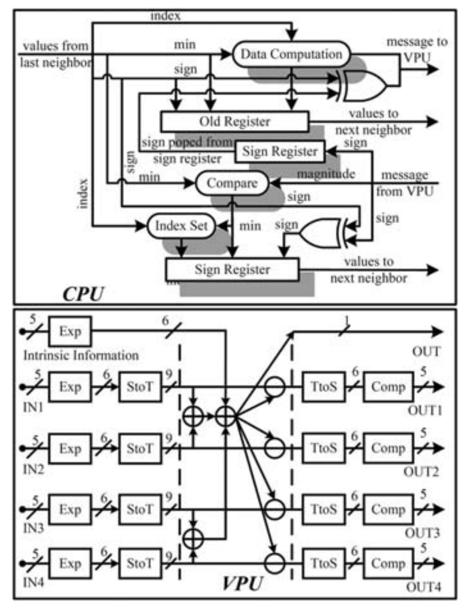

Fig. 3

HM-06

Message-Passing Detector with Serial Concatenated Codes for PMR Channel.

D. Park[1], J. Lee[1], J. Lee[2]
1. School of Electronic Engineering, Soongsil University, Seoul, South Korea; 2. Storage System Division, Samsung Electronics, Suwon, South Korea

Abstract
For higher density perpendicular magnetic recording systems, it is hard to expect improving the performance any more by using only NPML. We exploit serial concatenated system with channel detector and recursive systematic convolutional (RSC) code decoder using message-passing algorithm and evaluate the performance on the perpendicular magnetic recording channel.

1. Introduction

As the density of perpendicular magnetic recording system is getting higher the storage capacity of hard disk drives is increased. However, the higher bit density causes the degradation in signal-to-noise ratio (SNR). Kurkoski and et al. proposed the joint message-passing detector with LDPC code[1]. In this paper, we apply the joint message-passing algorithms between channel detector and recursive systematic convolutional (RSC) code instead of the LDPC code for the simplicity. Furthermore, we even use the max-log method[2] for reducing the complexity. The proposed algorithm is applied to perpendicular magnetic recording (PMR) channel with jitter noise, and we investigate the performance.

2. Perpendicular magnetic recording channel

In PMR channel, the signal-transition step response can be approximated as follows[3].

$g(t)=A\tanh(2t/(0.597\pi T_{50}))$

where A is the maximum amplitude of g(t) and T_{50} is the required time to go from -A/2 to +A/2. The normalized recording density is $K=T_{50}/T_b$, and T_b is the recording bit interval. Then, the read-back signal response can be modeled as follows.

$r(t)=\Sigma^{\infty}_{k=-\infty} a_k[g(t-kT)-g(t-(k+1)T)]+n_w(t)+n_j(t)$

where $n_w(t)$ and $n_j(t)$ are AWGN and jitter noise, respectively.

3. Joint Message-Passing Detector with RSC Decoder

The message-passing algorithm is a state-based parallel algorithm. We propose the joint message-passing detector/decoder for reducing the calculation delay and apply the max-log approximation for low calculation complexity. Fig.1 shows the block diagram of the proposed system using the message-passing detector/decoder and a random interleaver(Π). The channel detector uses the PR(12321) target and $1/(1+D^2+D^3+D^2+D^5)$ precoder. The RSC code has the generator polynomial of $(31,23)_8$.

4. Simulation Result

The user bit density (UBD) for simulation is D=1.7. The normalized recording density is K=UBD/R, where R is the code rate of 0.945(≈4096/4336). Fig. 2 shows the performance with 80% jitter noise and 20% AWGN on the PMR channel when we do the percoding or not. The precoding channel performs 1dB better than non-precoding channel at 10^{-5}BER. Fig. 3 shows the performance that there is 100% AWGN on the PMR channel. We can see that the precoded channel performs 1dB better than non-precoding channel at 10^{-5}BER. As usual, we can notice that the channel iteration improves the decoding performance in both of the precoding and non-precoding cases.

5. Conclusion

We have presented the joint message-passing detector/decoder reducing calculation delay and complexity. The precoding case performs 1dB better than the non-precoding case when there is jitter noise or not. The joint message-passing detector/decoder scheme with one channel iteration performs 1.8dB better than the NPML in PMR channel.

[1] B. M. Kurkoski, P. H. Siegel, J. K. Wolf, "Joint message-passing decoding of LDPC codes and partial-response channels," IEEE Trans. Infor. Theory., vol. 48, no. 6, pp. 1410-1422, June 2002.

[2] A. J. Viterbi, "An intuitive justification and a simplified implementation of the MAP decoder for convolutional codes," IEEE Journal on Seleted Areas in Communications, vol. 16, no. 2, pp. 260-264, Feb. 1998.

[3] M. Madden, M. Öberg, Z. Wu. R. He, "Read channel for perpendicular magnetic recoding," IEEE trans. Magnetics, vol. 40, no. 1, pp. 241-246, Jan. 2004.

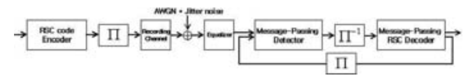

Fig. 1. Block diagram of the system.

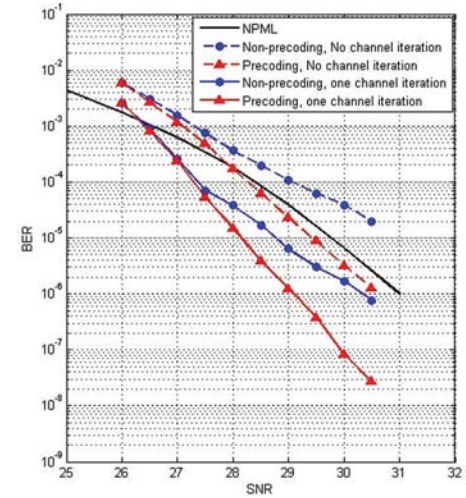

Fig. 2. Bit error rate, Jitter noise : AWGN = 80% : 20%, UBD=1.7.

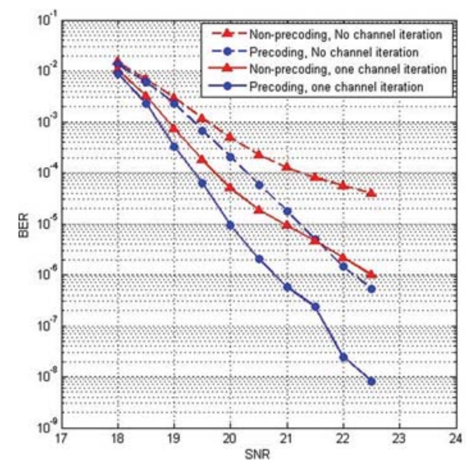

Fig. 3. Bit error rate, 100% AWGN, UBD=1.7.

HM-07

Hardware-Efficient LDPC Decoding for Magnetic Recording.

Z. Cui[1], Z. Wang[1], *X. Zhang*[2], Q. Jia[3]
1. Oregon State University, Corvallis, OR; 2. Case Western Reserve University, Cleveland, OH; 3. Hitachi Asia Ltd, Singapore, Singapore

A. Overview
Quasi-cyclic LDPC (QC-LDPC) codes can achieve very low sector failure rate with very high code rate [1-3] in magnetic recording channel. Conventionally, the switching network of a QC-LDPC decoder is implemented with barrel shifters [3], which generally consume a significant portion of silicon area for high-speed QC-LDPC decoder. Shift matrix structure is much simpler as it can be implemented with one-stage of multiplexer array. However, it is not applicable to general QC-LDPC codes.
In this work, matrix permutation and column grouping schemes are employed to convert the H matrix of a (generic) QC-LDPC code into a shift matrix hence to reduce the implementation complexity for high-speed QC-LDPC decoder. Based on shift matrix structure, we developed an optimized QC-LDPC decoder architecture which employs shuffled message scheduling (proposed by Zhang and Fossorier) to increase decoding converge speed. In this way, only one copy of compressed check-to-variable (C2V) messages is needed and variable-to-check message (V2C) are used on-the-fly. Thus, the VLSI implementation cost of this design is significantly lower over the prior art [3], which used two copies of C2V messages.
B. Matrix Transform
It can be proved that for any no cycle-4 quasi-cyclic LDPC code whose H matrix contains only cyclic shifted identity submatrices and zero submatrices, its H matrix can be converted into a form such that, 1) each submatrix in one block row (denoted as block-row-0) contains only one non-zero row; 2) the block column i+1 is a one-step cyclic shift of the block column i; and 3) each submatrix in any block column (except for the submatrices in the block-row-0) has a row weight of at most one. Fig. 1a shows the permutated H matrix of a QC-LDPC code example. To enable high parallism, the matrix can be arranged as shown in Fig. 1b.
C. Decoder Architecture
We will illustrate the design with the matrix shown in Fig. 1b. The decoder architecture is shown in Fig. 2. Only one copy of compressed C2V messages (i.e., the smallest magnitude, Min1, the second smallest magnitude, Min2, the index of Min1 and all signs) is stored. The R-mem and R-regs are storage components for C2V messages corresponding to the first block row and other block rows of the matrix, respectively. De-comp/pDe-comp units are used to completely/partially recover original C2V messages.. The left and right connection networks are hardware mapping of the edges in tanner graph corresponding to the first block column of the matrix shown in Fig. 1b. A parallel check node unit (CNU), P-CNU, get all input messages in parallel. A recursive CNU, R-CNU, get one or two input messages per clock cycle. Because the proposed matrix transform method minimize the (maximum) row weight (except block-row-0) of a block column, the number of input messages to R-CNUs per cycle is minimized. This helps maximize clock speed and minimize implementation complexity of R-CNUs. P-CNUs are pipelined to match its critical path with that of R-CNUs.
In summary, the shift characteristic in H matrix of generic QC-LDPC has been maximally exploited and the switching network is implemented with very simple one-stage multiplexer array. The matrix permutation method also enables high clock speed and minimizes implementation complexity of CNUs. Shuffled message scheduling is embedded to increase converge speed. Compared to the prior art [3], more than 30% of storage components can be saved and much higher throughput is expected.

[1] K. M. Kurtas, A. V. Kuznetsov, and I. Djurdjevic, "System perspectives for the application of structured LDPC codes to data storage devices," IEEE Transactions on Magnetics, vol. 42, pp. 200–207, Feb. 2006.

[2] X. Hu, B.V.K.V. Kumar, L. Sun, and J. Xie, "Decoding behavior study of LDPC codes under a realistic magnetic recording channel model," IEEE Transactions on Magnetics, vol. 42, pp. 2606–2608, Oct. 2006.

[3] H. Zhong; W. Xu, Ningde Xie, and Tong Zhang, "Area-efficient Min-Sum decoder design for high-rate quasi-cyclic low-density parity-check codes in magnetic recording,"IEEE Transactions on Magnetics, vol. 43, pp. 4117–4122, Dec. 2007.

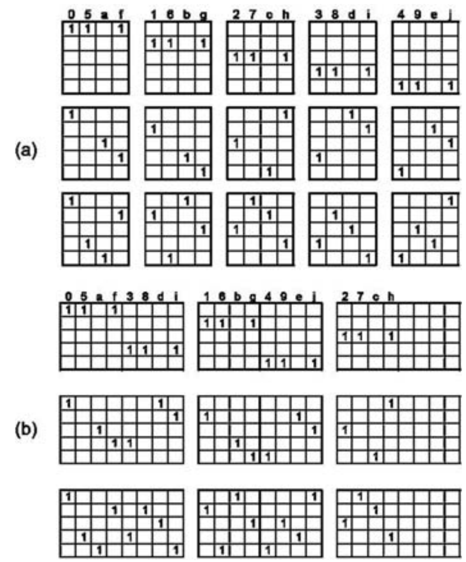

Figure 1. The permutated H matrix of a no cycle-4 quasi-cyclic LDPC code.

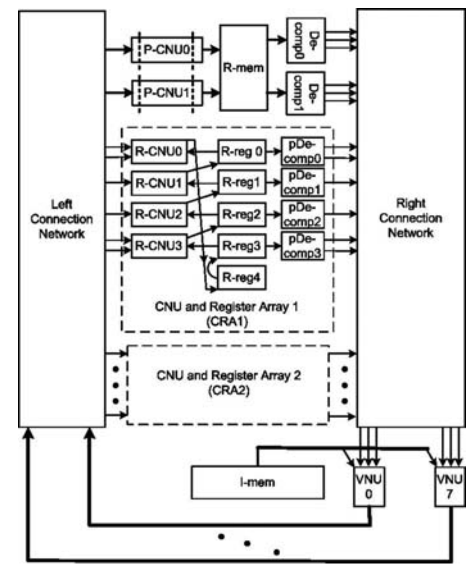

Figure 2. The decoder architecture.

HM-08

Perpendicular Magnetic Recording Channel Equalization Based on Gaussian Sum Approximation.

S. Choi[1], G. Kong[1], H. Cho[1], D. Lee[1], J. Lee[3], J. Lee[2]
1. School of Electrical and Electronic Engineering, Yonsei University, Seoul, South Korea; 2. School of Electronic Engineering, Soongsil University, Seoul, South Korea; 3. Storage System Division, Samsung Electronics, Suwon, South Korea

Perpendicular Magnetic Recording Channel Model : Perpendicular magnetic recording (PMR) scheme is a technology for achieving high magnetic recording density beyond the super-paramagnetic limitation. The PMR system with a single-pole-type (SPT) head provides a practical approach for high-density hard disk drives [1]–[3]. Signal processing techniques play an important role in achieving high-density PMR systems. This paper focuses on equalization techniques of the PMR channels. The mathematical models of the PMR channels in [4], [5] are considered in simulation experiments of this paper.
Equalizer Based on Gaussian Sum Approximations : In this paper, we apply and formulate the Gaussian sum approximation (GSA) in [6], [7] into the PMR channel equalization problem and propose a GSA-ML P equalizer. The proposed GSA-ML P equalizer is a bank of conventional linear filters based on the state and measurement equations for the Kalman filter. In addition, we extend the GSA-ML P equalizer by modifying the state equation for the GSA-ML P equalizer, which is called the GSA-DS-ML equalizer. The GSA-ML P and GSA-DS-ML P have a filter bank with 2^P conventional linear equalizers where P is an integer and combine each output based on the GSA in [6], [7]. The GSA-DS-ML P equalizer uses the information on the previous detected symbol.
Simulation Results : Fig. 1 shows the bit-error-rate (BER) curves for the minimum mean square error (MMSE), Kalman, GSA-ML P and GSA-DS-ML P equalizers and the maximum likelihood sequence estimator (MLSE) bound when the normalized channel density is K=1.6 and the additive white Gaussian noise (AWGN) is considered. The simulation results are omitted when there is the transition jitter noise in the PMR channel model in addition to the AWGN. The proposed equalizers show the better BER performances than the other linear equalizers. The GSA-ML and GSA-DS-ML approaches a BER performance of the MLSE as P increases. Fig. 2 shows the required signal-to-noise ratio (SNR) to obtain the BER of 1.0E-3 for each equalizer when K = 1.6 to 1.9.
Conclusion : In this paper, GSA-ML and GSA-DS-ML equalizers in order to enhance the performance of the conventional linear equalizers are proposed. Through simulation experiments it was found that the proposed equalizers are capable of augmenting the BER performances of the other linear equalizers and approach the BER performances of the MLSE as the number of the filter in the bank increases.

[1] H. Sawaguchi, Y. Nishida, H. Takano, and H. Aoi, "Performance analysis of modified PRML channels for perpendicular recording systems," J. Magn. Magn. Mater., vol. 235, pp. 265–272, 2001.

[2] Y. Okamoto, H. Sumiyoshi, T. Kishigami, M. Akamatsu, H. Osawa, H. Saito, H. Muraoka, and Y. Nakamura, "A study of PRML systems for perpendicular recording using double layered medium," IEEE Trans. Magn., vol. 36, no. 5, pp. 2164–2166, Sep. 2001.

[3] R. Wood, Y. Sonobe, Z. Jin, and B. Wilson, "Perpendicular recording: The promise and the problems," J. Magn. Magn. Mater., vol. 235, pp. 1–9, 2001.

[4] Joohyun Lee and Jaejin Lee, "A Simplified Noise-Predictive Partial Response Maximum Likelihood Detection Using M-Algorithm for Perpendicular Magnetic Recording Channels," IEEE Trans. Magn., vol. 41, no. 2, pp. 1064–1066, Feb. 2005.

[5] Michael Madden, Mats Öberg, Zining Wu, and Runsheng He, "Read Channel for Perpendicular Magnetic Recording," " IEEE Trans. Magn., vol. 40, no. 1, pp. 241–246, Jan. 2004.

[6] D. L. Alspach and H. W. Sorenson, "Nonlinear Bayesian estimation using Gaussian sum approximations", IEEE Trans. Automat. Contr., vol. AC-17, pp.439-447, Sep. 1972.

[7] S. Marcos, "A network of adaptive Kalman filters for data channel equalization", IEEE Trans. Sig. Proc., vol. 48, no. 9, pp. 2620-2627, Sep. 2000.

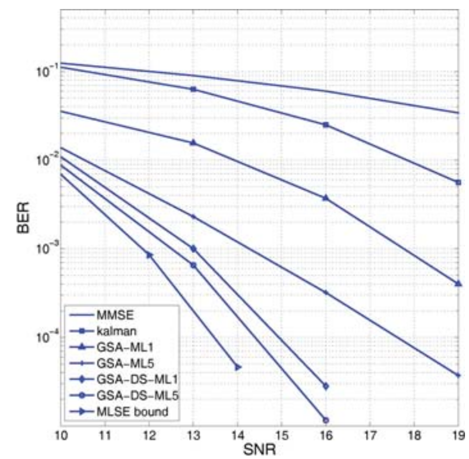

Fig. 1. BER curves of the MMSE, Kalman, GSA-ML P and GSA-DS-ML P equalizers and the MLSE bound when K = 1.6.

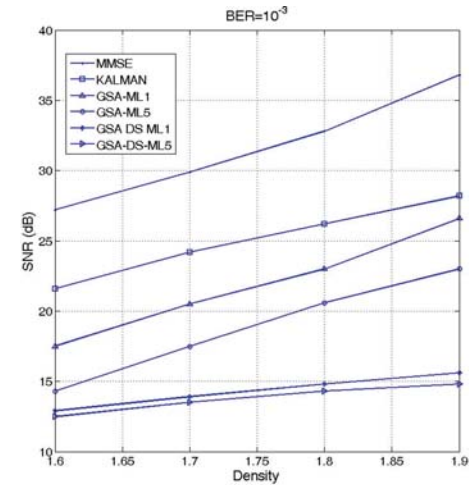

Fig. 2. Required SNR curves to obtain BER = 1.0E-3 for the MMSE, Kalman, GSA-ML P and GSA-DS-ML P equalizers when K = 1.6 to 1.9.

HM-09

Simplified Neural Network Equalizer with Noise Whitening Function for GPRML System.

H. Osawa[1], *M. Hino*[1], N. Shinohara[1], Y. Okamoto[1], Y. Nakamura[1], H. Muraoka[2]

1. Graduate School of Science and Engineering, Ehime University, Matsuyama, Japan; 2. RIEC, Tohoku University, Sendai, Japan

Introduction

The generalized partial response (GPR) channel represented by the transfer polynomial with the noninteger coefficients consists of the PR channel followed by a noise whitening filter which subtracts the noise predicted by the previous noise samples from the output noise of PR channel. In this work, a new constitution method of the simplified neural network equalizer (NNE) with the noise whitening function for the GPR channel is proposed. The long-term bit error rate (BER) performance of GPR class-I maximum likelihood (GPR1ML) system based on the NNE in perpendicular magnetic recording (PMR) with thermal decay is also obtained by computer simulation using our thermal decay model [1].

R/W channel

Fig.1 shows the block diagram of GPR1ML system with NNE. The rate 128/130(0,16/8) code is employed as a run-length-limited (RLL) code. The isolated transition response is assumed to be $h(t)=A\tanh(\ln 3/T_{50})t$ where A is the saturation level and T_{50} is the $-A/2$ to $A/2$ rise time. Here, a normalized linear density is defined as $K=T_{50}/T_b$ where T_b is a user bit interval. The reproducing waveform is generated by using the thermal decay model for a CoPtCr-SiO$_2$ PMR medium with K_uV/kT=60 [1]. It is also assumed that the noise at the reading point consists of an AWGN and a jitter-like medium noise whose power ratio in a bandwidth of $0.6f_b$ is $\sigma^2_W : \sigma^2_J$ where f_b is a user bit rate. The SNR at the reading point is defined as $20\log_{10}A/\sigma$ [dB] where $\sigma^2=\sigma^2_W+\sigma^2_J$ is the total noise power and the percentage of the jitter-like medium noise power to the total noise power as $R_J=\sigma^2_J/\sigma^2\times 100$ [%]. The high-pass filter (HPF) represents the low cut-off characteristic due to AC coupling in a head amplifier which has a normalized low cut-off frequency x_l by f_b. The PR channel response is equalized to a required PR1 target by NNE which consists of a low-pass filter with a normalized high cut-off frequency x_h by f_b and a three-layered neural network [2]. The GPR1 channel output is obtained by subtracting the output of Mth-order noise predictor from PR1 channel output.

Neural Network Equalizer

The neural network having 13-7-1 neurons for the input layer, hidden layer and output layer, respectively, and 98 connections between neurons is assumed. Then, the simplification by thinning out the connections and the noise-whitening are performed by finding the optimal weights of connections based on a hybrid genetic algorithm (HGA) which is the combination algorithm of GA [3] and back-propagation algorithm (BPA) [2]. In HGA, a chromosome of individual is given as a sequence of 98 weights of connections in the neural network. Forty individuals are arranged according to the value of the fitness which is defined as the weighted sum of the negative logarithm of BER of GPR1ML system and the ratio of the initial number of connections to the current number of connections. Here, the prediction coefficients of the noise predictor in GPR1ML system are obtained by using the Levinson-Durbin Algorithm [4] from the autocorrelation function of output noise in the previous-generation NNE. In the current generation, the genetic operations [3] based on the fitness for the GPR1ML system which consists of the previous-generation NNE and noise-whitening filter are performed on the individuals, and then BPA is done where the ideal PR1 response sequence is employed as the desired signal in supervised learning. The next-generation NNE is obtained by rearranging the individuals in descending order of the fitness. These operations are repeated until the fitness of the best individual saturates. The chromosome of this best individual gives the desired weights of the neural network where the connections with a weight of 0 which is brought by the mutation are thinned out.

Results and Discussion

Fig.2 shows the relationship between the BER performance of GPR1ML system and the elapsed time t_E where K=1.5, x_h=0.4, x_l=0.001, SNR=24.5dB, R_J=90% and M=3. The symbols ○, △ and ▽ indicate the performance of GPR1ML system having a simplified NNE with the 11-3-1 neurons and 25 connections, GPR1ML system having a conventional transversal filter (TF) with the number of tap N_t=15 and PR1ML-NNE, respectively. The PR1ML-NNE does not need a noise whitening filter because the NNE based on the proposed method can equip the noise whitening function. The performance of GPR1ML-NNE system is superior to that of GPR1ML-TF system. The PR1ML-NNE system having a two-state Viterbi detector provides the almost equivalent performance to that of GPR1ML-NNE having a 16-state detector.

[1] N. Shinohara et al., IEEE Trans. Magn., vol.43, no.6, pp.2262-2264, June 2007.

[2] R. Rojas, *Neural Networks: A Systematic Introduction*, New York: Springer-Verlag, 1995.

[3] D.E. Goldberg, *Genetic Algorithms*, Boston: Addison-Wesley, 1989.

[4] P. S. Naidu, *Modern Spectrum Analysis of Time Series*, Boca Raton, FL: CRC Press, 1996.

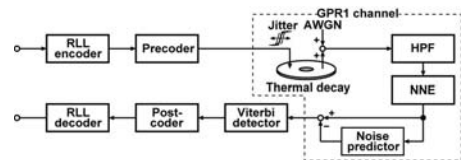

Fig.1 Block diagram of GPR1ML system.

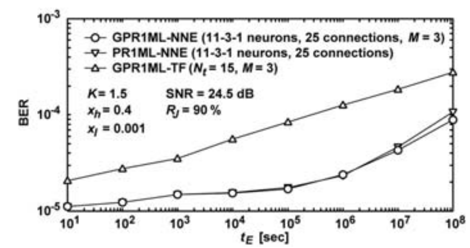

Fig.2 BER vs. elapsed time.

Digital Storage Channel Equalization Using A Bilinear Recursive Polynomial System.

S. Choi[1], H. Cho[1], G. Kong[1], J. Lee[3], J. Lee[2]
1. School of Electrical and Electronic Engineering, Yonsei University, Seoul, South Korea; 2. School of Electronic Engineering, Soognsil University, Seoul, South Korea; 3. Storage System Division, Samsung Electronics, Suwon, South Korea

Motivations : As recording density increases in digital storage systems, distortions are severer. Therefore, more powerful signal processing techniques are essentially demanded. A new nonlinear equalizer based on a bilinear recursive polynomial (BRP) system is introduced and investigated for magnetic channel equalization in this paper.
System Model : To achieve high magnetic recording density beyond the super-paramagnetic limitation the perpendicular magnetic recording (PMR) technique is a promising scheme. For high-density hard disk drives (HDD), the PMR system with a single-pole-type head is considered as a practical approach [1]–[3]. In this paper, we consider the mathematical models of the PMR channels in [4],[5] to conduct simulations for performance comparisons.
Equalizer based on a Bilinear Recursive Polynomial System (BRP) : Fig.1 shows the simplified digital transmission system with the BRP equalizer. The BRP equalizer uses the noisy channel output as well as the 2nd order informations from the noisy channel symbols and the detected symbols as shown FIg. 1. Thererfore the proposed BRP equalizer has a form of a recursive structure.
Simulation Results : The bit error rate(BER, bit error probability) performance of the proposed BRP equalizer is compared with the minimum mean square error (MMSE) and Kalman equalizers and the maximum likelihood sequence estimator (MLSE) bound. The Kalman equalizer also has a recursive structure. Fig. 2 shows the bit-error-rate (BER) curves for the minimum mean square error (MMSE), Kalman, and proposed equalizers and the MLSE bound when the normalized channel density is K=1.6 and the additive white Gaussian noise (AWGN) is considered. The simulation results are omitted when there is the transition jitter noise in the PMR channel model in addition to AWGN. The proposed equalizers show the better BER performances than the other linear equalizers. Fig. 3 shows the required signal-to-noise ratio (SNR) to obtain the BER of 1.0E-3 for each equalizer when K = 1.6 to 1.9. The proposed BRP equalizer provides about 20dB and 10dB of gain over the MMSE and Kalman equalizers at the BER of 1.0E-3 when K = 1.9, respectively.
Conclusion : In this paper, the BRP equalizer in order to enhance the performance of the conventional linear equalizers is proposed. Through simulation experiments it was found that the proposed BRP equalizer with a moderate complexity is capable of augmenting the BER performances of the other linear equalizers.

[1] H. Sawaguchi, Y. Nishida, H. Takano, and H. Aoi, "Performance analysis of modified PRML channels for perpendicular recording systems," J. Magn. Magn. Mater., vol. 235, pp. 265–272, 2001.

[2] Y. Okamoto, H. Sumiyoshi, T. Kishigami, M. Akamatsu, H. Osawa, H. Saito, H. Muraoka, and Y. Nakamura, "A study of PRML systems for perpendicular recording using double layered medium," IEEE Trans. Magn., vol. 36, no. 5, pp. 2164–2166, Sep. 2001.

[3] R. Wood, Y. Sonobe, Z. Jin, and B. Wilson, "Perpendicular recording: The promise and the problems," J. Magn. Magn. Mater., vol. 235, pp. 1–9, 2001.

[4] Joohyun Lee and Jaejin Lee, "A Simplified Noise-Predictive Partial Response Maximum Likelihood Detection Using M-Algorithm for Perpendicular Magnetic Recording Channels," IEEE Trans. Magn., vol. 41, no. 2, pp. 1064–1066, Feb. 2005.

[5] Michael Madden, Mats Öberg, Zining Wu, and Runsheng He, "Read Channel for Perpendicular Magnetic Recording," " IEEE Trans. Magn., vol. 40, no. 1, pp. 241–246, Jan. 2004.

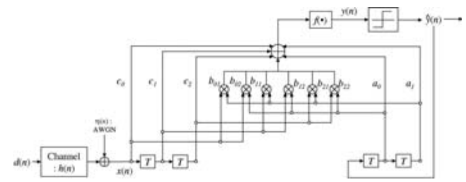

Fig. 1. Simplified digital storage system using the PMR channel and the BRP equalizer.

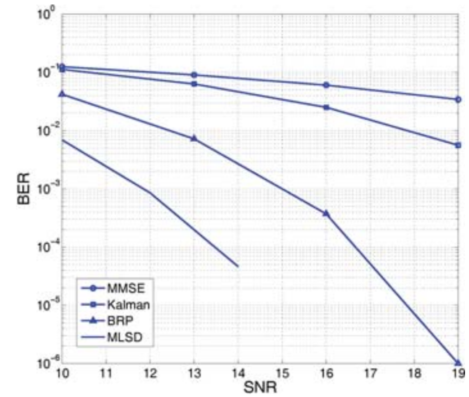

Fig. 2. BER curves of the MMSE, Kalman and BRP equalizers and the MLSE bound when K = 1.6.

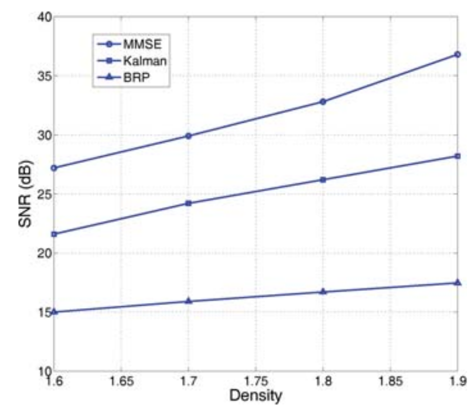

Fig. 3. Required SNR to obtain BER = 1.0E-3 for the MMSE, Kalman and BRP equalizers when K = 1.6 to 1.9.

Interleaved Modified Array Codes (IMAC) Hardware Design and Performance for High-Rate Perpendicular Magnetic Recording Systems.

P. Leekul[1,3], W. Singhaudom[1], P. Supnithi[1,2]
*1. Faculty of Engineering, King Mongkut's Institute of Technology Ladkrabang, Bangkok, Thailand; 2. Data Storage Technology and Applications Research Center (D*STAR), King Mongkut's Institute of Technology Ladkrabang, Bangkok, Thailand; 3. Research Center for Communications and Information Technology (ReCCIT), King Mongkut's Institute of Technology Ladkrabang, Bangkok, Thailand*

Modified Array Codes (MAC) is a structured low-density parity-check (LDPC) code with parity-check matrix described in terms of the parameter (p,j,k), where p is prime and $j \leq k << p$, $\mathbf{0}$ is the pxp null matrix and $\mathbf{I}$ is the pxp identity matrix. The matrix $\mathbf{P}$ is a pxp circulant permutation matrix which shifts the identity matrix $\mathbf{I}$ to the right once. An advantage of modified array code over array code [1] is efficient encoding due to the upper triangular structure of $\mathbf{H}$. Thus, unlike an array code, matrix inversion is unnecessary.

In ISI channel, iterative processing of channel APP decoder and LDPC decoder can cause psue-do cycles even if there is no length-4 cycles in the Tanner graph. A solution is to modify the matrix $\mathbf{H}$ of an array code. In [2], an additional permutation matrix α and a quasi-cyclic matrix ω is used to design an array code. This causes additional interleaving every p columns of the matrix $\mathbf{H}$.

By combining the concepts in [2] and advantages of modified array code, in this paper, we propose an Interleaved Modified Array Codes (IMAC), with a new parity-check matrix H_{IMAC} as shown in Fig. 1.

where is ω a quasi-cyclic matrix. The code rate is $R = 1 - j/k$. An IMAC still has efficient encoding when compared with array codes; there is no need for matrix inversion, and the decoding process is not affected. We design high-rate MAC and IMAC suitable for high-density perpendicular magnetic recording system. The sector size is in the range of 1000 and 4000 bits/sector. We simulate the performance of IMAC and MAC using message-passing algorithm with 30 iterations. For AWGN channel, the results show that the performance of IMAC is superior to MAC for about 0.1-0.2 dB at bit error rate of 10^{-5} as shown in Fig. 2. In addition, the burst error pattern of IMAC is shorter than MAC at both low and high bit error rates. When included in a high-density perpendicular magnetic recording channels with iterative processing and turbo equalization, the SNR gain over MAC is more significant.

We also propose a subblock-based encoder design of QC-LDPC and IMAC for high-rate applications. The parity-check subblock computation is explicitly derived in a recursive manner as shown in Fig. 3, where where $\mathbf{p}_i$, $i = 1,2,\ldots, j$ is a subblock of parity bits of size LxL. Thus, each subsection of parity-check bits can be computed from two parts: the higher-indexed parity-check subsection and all the message subsections. There is a total of j parity subblock equations. We start from the computation of $\mathbf{p}_j$ all the way to $\mathbf{p}_1$. Notice that subblock-type encoding does not require any real multiplication due to the fact that the result of a vector multiplying with permutation matrix is nothing but cyclic-shift the vector to the right by the power of the matrix $\mathbf{P}$. The design is implemented on a Xylinx FPGA platform then the comparison of hardware uasage is then done for serial network, semi-parallel network and fully-parallel network as illustrated in Fig. 4.

[1] J. L. Fan, "Array codes as low-density parity-check codes," in Proc. 2nd Int. Symp. Turbo Codes, Best, France, Sep 2000, pp 543-546.

[2] T. Kanaoka and T. Morita, "Structured LDPC Codes with Reversed MTR/ECC for Magnetic Recording Channels", IEEE Transaction on Magnetics, Vol. 42, No. 10, Oct. 2006, p. 2561-2563.

$$
H_{IMAC}(p,j,k) \triangleq \begin{bmatrix}
\mathbf{I} & \mathbf{I}\omega & \mathbf{I}\omega^2 & \cdots & \mathbf{I}\omega^{(j-1)} & \cdots & \mathbf{I}\omega^{(k-1)} \\
\mathbf{0} & \mathbf{I}\omega & \mathbf{P}\omega^2 & \cdots & \mathbf{P}^{(j-2)}\omega^{(j-1)} & \cdots & \mathbf{P}^{(k-2)}\omega^{(k-1)} \\
\mathbf{0} & \mathbf{0} & \mathbf{I}\omega^2 & \cdots & \mathbf{P}^{2(j-3)}\omega^{(j-1)} & \cdots & \mathbf{P}^{2(k-3)}\omega^{(k-1)} \\
\vdots & \vdots & \vdots & \cdots & \vdots & \cdots & \vdots \\
\mathbf{0} & \mathbf{0} & \cdots & \mathbf{0} & \mathbf{I}\omega^{(j-1)} & \cdots & \mathbf{P}^{(j-1)(k-j)}\omega^{(k-1)}
\end{bmatrix}
$$

Figure 1. The parity-check matrix of Interleaved modifief array code (IMAC).

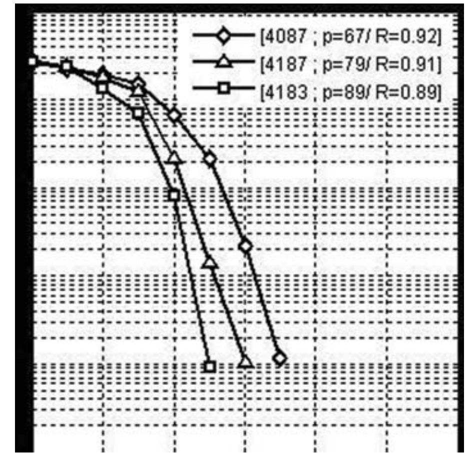

Figure 2. The BER performance of IMAC with sector size ~4000 bits after 30 iterations

$$
\mathbf{p}_j = \sum_{i=1}^{k-j} \mathbf{m}_i P^{(j-1)i}
$$

$$
\mathbf{p}_l = \sum_{i=1}^{j-l} \mathbf{p}_{l+i} P^{(l-1)i} + \sum_{i=1}^{k-j} \mathbf{m}_i P^{(l-1)(j-l+i)}; 1 \leq l \leq j-1
$$

Figure 3. Subblock-based parity-check computation.

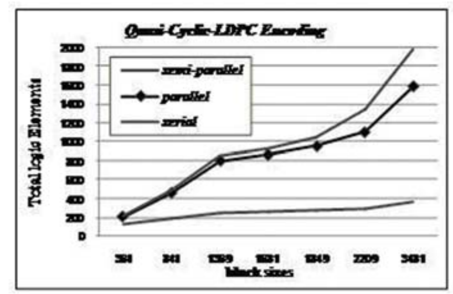

Figure 4. Comparison of hardware usage between Serial, Semi-parallel and Paralell networks.

HM-12

Nonbinary LDPC codes for 4K-byte sectors.

W. Chang, *J. CRUZ*
The University of Oklahoma, Norman, OK

I. INTRODUCTION

Soft iterative decoding of binary low-density parity-check (LDPC) codes provides a considerable coding gain over the Reed-Solomon (RS) codes currently used on perpendicular magnetic recording channels (PMRCs) with the 30-year old sector length standard of 512 bytes. The use of nonbinary LDPC codes further improves performance, especially at high recording densities. With the recent approval of a new and longer sector length standard, it is expected that most hard-disk drives will be formatted using 4K-byte sectors, and is therefore timely to investigate the performance of nonbinary LDPC codes on PMRCs with long sectors. Nonbinary LDPC codes have high complexity on both encoding and decoding. For long sectors, the complexity problem becomes more severe. A way of reducing the encoding complexity is to consider nonbinary quasi-cyclic (QC) LDPC codes. To lower the decoding complexity, we can divide each long sector into short sectors, then encode and decode these short sectors separately.

In this work, we investigate the performance of two encoding schemes for long sectors on PMRCs. In the first scheme, each 4K-byte sector is encoded by a long QC or non-QC nonbinary LDPC code. In the second scheme, each 4K-byte sector is broken into eight 512-byte sectors and then encoded.

II. CODE DESIGN

By shortening and dispersing some RS codes [1], we design a (4, 41)-regular (5207, 4702) long QC-LDPC code over GF (27) and a (3, 30)-regular (930, 839) short QC-LDPC code over GF (25). The long and short non-QC LDPC codes are designed by the progressive edge-growth (PEG) algorithm. We construct a (5202, 4682) PEG-LDPC code over GF (27) and a (911, 820) PEG-LDPC code over GF (25). In addition, we design and simulate long RS and binary LDPC codes to be used as baselines.

III. PERFORMANCE OF NONBINARY LDPC CODES FOR LONG SECTORS

We assume a mix of 90% jitter noise power and 10% electronics noise power in all simulations and consider user densities as low as 0.8741 and as high as 1.2238. Firstly, it is not surprising that nonbinary LDPC codes provide a fairly large coding gain over both binary LDPC and RS codes, and that long nonbinary LDPC codes outperform the short ones, as shown in Fig. 1. Secondly, the coding gains obtained with three turbo iterations are negligible for short nonbinary LDPC codes and barely observable for long nonbinary LDPC codes. Thirdly, as shown in Fig. 2, a maximum of three readings achieves a considerable coding gain for both long and short nonbinary LDPC codes. Although the re-reading scheme makes the short LDPC codes outperform the long ones at low signal-to-noise ratios (SNRs), these coding gains will vanish as the SNR increases.

IV. ERASURE CORRECTION CAPABILITY

We compute the largest correctable erasure length for each code, under iterative decoding and maximum-likelihood (ML) decoding, according to the algorithms proposed in [2] and [3], respectively. The results are listed in Table I. Under ML decoding, PEG-LDPC codes are capable of correcting more erasures than QC-LDPC codes. However, they have similar erasure correction power under iterative decoding. Furthermore, it is intuitive that longer codes can correct longer erasures, which is an advantage of using long LDPC codes. Note that QC-LDPC codes have exactly the same erasure correction capability under ML and iterative decoding, which is an interesting property.

1) L. Zeng, L. Lan, Y. Y. Tai, and S. Lin, "Dispersed Reed-Solomon codes for iterative decoding and construction of q-ary LDPC codes", in Proc. IEEE Global Telecommun. Conf., 2005, pp. 1191-1198.

2) M. Yang and W. E. Ryan, "Performance of efficiently encodable low-density parity-check codes in noise bursts on the EPR4 channel", IEEE Trans. Magn., vol. 40, pp. 507-512, Mar. 2004.

3) C. Di, D. Proietti, I. E. Telatar, T. J. Richardson, and R. L. Urbanke, "Finite-length analysis of low-density parity-check codes on the binary erasure channel", IEEE Trans. Inf. Theory, vol. 48, pp. 1570-1579, June 2002.

Erasure	ML Decoding				Iterative Decoding			
	Short PEG	Short QC	Long PEG	Long QC	Short PEG	Short QC	Long PEG	Long QC
Symbols	89	61	519	253	61	61	259	253
Bits	445	305	3633	1771	305	305	1813	1771

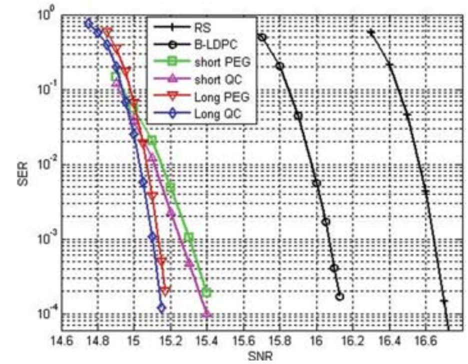

Fig. 1. Performance of nonbinary LDPC coded long sector PMRCs at user density 1.2238.

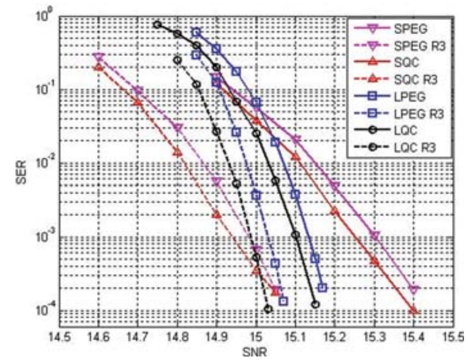

Fig. 2. Performance of nonbinary LDPC coded long sector PMRCs with re-reading at user density 1.2238.

HN-01

Magnetic properties of self-assembled cobalt nanoparticles crystal superlattices.

M. Varon[1], L. Peña[2], L. Balcells[2], V. F. Puntes[1], *B. Martinez*[2]
1. Institut Català de Nanotecnologia, Bellaterra, Spain; 2. Magnetic Materials, ICMAB-CSIC, Bellaterra, Spain

Colloidal dispersed nanoparticles (NP) self assemble into complex structures when segregated from the solvent either by evaporation or precipitation. Thus, different micro and macroscopic structures like opals, fractals, anisotropic structures and others formed by nanoparticles are observed as a result of the balance between electrostatic forces, surface tension, entropy, topography, substrate affinity, among others, and evidently, the size, shape and concentration of the particles. In addition, in ferromagnetic materials, the dipolar magnetic interactions, add a new term in the interactions balance.
The micro and macro self-assembled structures resulting from the evaporation of a solution of cobalt nanoparticles onto a high oriented pyrolytic graphite (HOPG) substrate give a conceptual framework to study the magnetic properties of both the material at the nanometric level and at the macroscopic level on the obtained structures. This is relevant, not only to built up super-structures for specific applications, like compact monolayers for magnetic recording media, but also to elucidate the behavior of nanoparticles in liquid media, often out of equilibrium, aiming to disperse them in biological media.
In this work we report on the static and dynamic magnetic properties of these colloidal and self-assembled structures integrated by Co nanoparticles of about 10 nm in diameter (see Fig. 1). Microstructural characterization of the Co nanoparticles has been performed by using transmission electron microscopy (TEM) (see Fig. 2 left). Self-assembled structures on graphite have been characterized by optical microscopy (see Fig. 2 right) and atomic force microscopy (AFM) (see Fig.3 left). The magnetic force microscopy (MFM) shows the magnetic character of these self-assembled structures (see Fig.3 right).

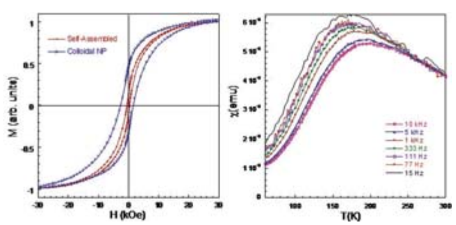

Figure 1. Left) Low temperature (T=10 K) hysteresis loop for colloidal and self-assembled Co naoparticles. Right) Temperature dependence of AC susceptibility for colloidal nanoparticles.

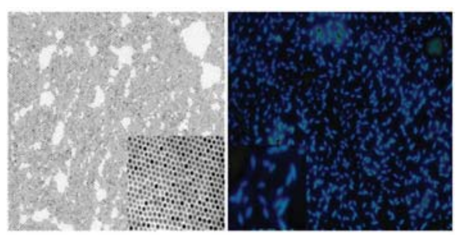

Figure 2. Left) TEM image of 10 nm cobalt nanoparticles. Right) Optical Image of self-assembly structures (5-9μm) of cobalt nanoparticles after its deposition onto HOPG substrate.

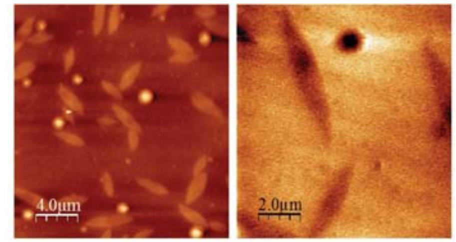

Figure 3. Left) Atomic force microscopy image of self-assemble structures integrated by cobalt nanoparticles. Right) MFM image of some of these structures showing the magnetic character at room temperature.

HN-02

One-Dimensional Hierarchical Nanostructure Generated by Coating SiOX Nanowires with L10 CoPt Nanoparticles.

J. Kim, J. Kim, J. Park, K. Baek, H. Woo, S. Kim, C. Kim, C. Yoon
Materials Science and Engineering, Hanyang University, Seoul, South Korea

Nanosized structures such as nanowires and nanoparticles have recently received considerable interest due to their potential applications in high density storage media [1] and sensors [2]. Especially, L10 CoPt nanoparticle array with the high magnetocrystalline anisotropy and the resulting large coercivity is a candidate for ultra high density magnetic recording media. In the present study, we demonstrate that it is possible to uniformly coat the SiOX nanowires (SiOXNWs) with L10 CoPt nanoparticles by physical deposition to produce one-dimensional hierarchical nanostructure.

In order to grow the SiOXNWs, a monolayer of Au nanoparticles dispersed on a polyimide film was produced by thermally imidizing the polyimide (PI) precursor with thin layer of Au deposited on its top surface. The PI precursor solution was spin coated onto a Si substrate. After depositing 4-nm-thick Au layer on the PI-precursor-coated substrate. the Au/PI/Si sample was cured at 400°C for 1 h in vacuum (~10-3 Pa). The imidized film stack was further treated by thermal annealing at 800°C for 1 hour under vacuum (< 10-3 Pa), followed by another heat-treatment step at 1000°C for 1hour under Ar atmosphere to grow the SiOXNWs. Co-Pt alloy film was produced using dc magnetron sputtering by placing Pt chips on top of a Co target in a mosaic pattern. Initial and post-annealed compositions were verified using energy-dispersive x-ray spectroscopy (EDS).

Figure 1(a) is a scanning electron microscopy image of the dense network of SiOXNWs grown on the Si substrate, based on the vapor-liquid-solid mechanism. The wire diameter ranged from 50 nm to 80 nm. Figure 2 (b) shows a transmission electron microscopy image of the SiOXNWs onto which 6-nm-thick Co-Pt layer was deposited without any pretreatment of the wire surface. Annealing at 650 °C resulted in formation of CoPt nanoparticles on the SiOXNWs surface which acted as a one-dimensional substrate. CoPt particles were uniformly distributed over the nanowire surface. The magnified TEM image in Fig.1 (c) shows that the particle size tended to decrease towards the nanowire edge. In fact, no metal particles were found near the very edge of the nanowire. The average particle size was 2.4 ± 0.9 nm. EDS analysis of the nanoparticles confirms that atomic ratio of Co to Pt was 1:1.5, slightly enriched in Pt due to the preferential loss of Co during annealing [3]. We attempted to control the particle size by multiple depositions of the Co-Pt film on the preexisting particles formed during the initial deposition. When a layer of 1.5-nm-thick Co-Pt was deposited on the preexisting particles, Co-Pt tended to heterogeneously nucleate on the preexisting CoPt particles. The average size of the CoPt particles rose to 5.3 ± 2.1 nm after the third deposition and annealing with somewhat broadened size distribution as a result of impingement of the particles. Figure 2 shows the magnetic hysteresis loop measured at room temperature from the sample which underwent three cycles of Co-Pt deposition and annealing. Although the as-deposited CoPt particles were magnetically soft, the coercivity of the particles annealed at 650°C drastically increased to 550Oe.

We demonstrated that one-dimensional hierarchical nanostructure can be fabricated by simple physical deposition of metal layer on the oxide nanowire surface. The proposed method can be extended to other metal particles for potential use in nano catalyst arrays.

This work was supported by the Korea Ministry of Science and Technology through the Nanoscopia Center of Excellence at Hanyang University.

[1] J. A. Christodoulides, Y. Huang, Y. Zhang, G. C. Hadjipanayis, I. Panagiotopoulos, and D. Niarchos, J. Appl. Phys. 87, 6938 (2000).

[2] Y. Cui, Q. Wei, H. Park, and C. M. Lieber, Science 293, 1289 (2001).

[3] J. H. Kim, J. Kim, N. Oh, Y-H. Kim, C. K. Kim, C. S. Yoon, Sungho Jin, Appl. Phys. Lett. 90, 023117 (2007).

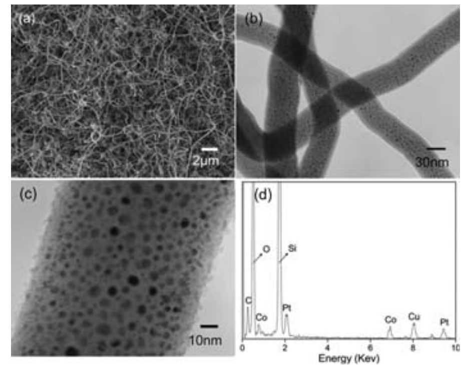

Figure 1. (a) SEM image of the SiOXNWs on the Si substrate. (b) TEM image of the Co40Pt60 nanoparticles on the SiOXNWs after third deposition of Co-Pt alloy annealing at 650°C, (c) Magnified TEM image of the sample in (b), (d) EDS spectrum from the sample in (b) (Cu peak is from the TEM holder).

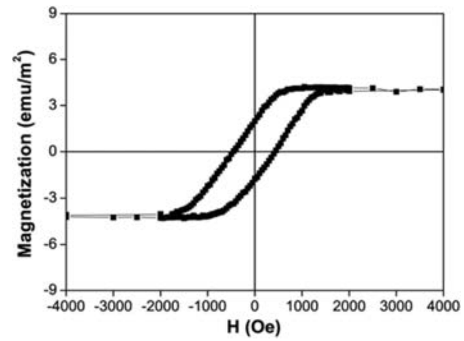

Figure 2. Magnetic hysteresis loops at RT from the CoPt nanoparticles produced by three cycles of deposition and annealing at 650°C.

HN-03

Effects of oxidation and particle size on saturation magnetization of iron nanoparticles.

H. Matsuura[1], K. Seto[2], K. Kawano[1], M. Takahashi[3], T. Ogawa[4]
1. TAIYO YUDEN Co.,Ltd., Takasaki-shi, Japan; 2. Dept. of Elec. Eng., Tohoku Univ., Sendai, Japan; 3. NICHe, Tohoku Univ., Sendai, Japan; 4. CRESS, Tohoku Univ., Sendai, Japan

Superparamagnetic nanoparticles with high saturation magnetization (M_S) have been proposed as a hopeful material for possible application to new nanoparticle/dielectric hybrid material for high frequency devices[1)]. In order to obtain high permeability in the high frequency range, large M_S of nanoparticle is required, and the pure iron is one of attractive candidates. However, the smaller values of M_S than bulk (220 emu/g) were reported in the chemically synthesized iron nanoparticles, and thus, effects of oxidation, particle size and crystalline structure on the M_S of the iron nanoparticle should be clarified. In this study, the effects of oxidation during the synthesis have been precisely investigated by controlling O, O_2 and H_2O impurities in the solvents and the particle size dependence of M_S has been discussed in connection with the oxidation.

Fe nanoparticles has been synthesized by our uniquely developed thermal decomposition method using an iron carbonyl in a glove box under Ar gas atmosphere with 0.1-1ppm of O_2 and H_2O impurities. At first, these impurities dissolved in kerosene and octylether as a solvent, and oleylamine as a surfactant have been removed by a freeze-pump-flaw technique. And then, in order to control the concentration of O, O_2 and H_2O impurities in the reaction solution, addition of H2O, gas bubbling of O_2 or mixing of DOE were performed into the solvent. After injection the $Fe(CO)_5$, the reaction solution was kept at 180 C for 1h. The Fe nanoparticle size was controlled by changing a reaction time from 1 min to 120 min. Particle size and crystalline structure were evaluated by the transmission electron microscopy (TEM). The magnetization curves of the synthesized Fe nanoparticles encapsulated in a quartz tube was measured by a superconducting quantum interference device (SQUID) magnetometer and the M_S was evaluated from the average magnetic moment in the higher field range and the mass of iron obtained from a X-ray Fluorescence Analysis (XRF).

Figure1 shows the dependence of O impurity ratio to iron, O/Fe, in the solvent on M_S of iron nanoparticles at 300K. The average particle size (8.9nm ~9.6nm) and size distribution rarely change by controlling the O impurity ratio in the present range, and rarely change by H_2O/Fe ratio in the range ratio from 0.001 to 0.3. M_S shows independent of the O/Fe ratio in the lower range of O/Fe<10. Assuming that all dissolved O impurity contributes to oxidize the nanoparticle during the synthesis, the decreament in M_S between nanoparticle and bulk should be less than 1%. However, M_S of 152emu/g is obtained at 300K, which is much smaller than the bulk value even at the minimum O/Fe ratio. On the other hand, M_S decreases in the higher range of O/Fe>10, suggesting that the DOE decomposed during the reaction and produced iron-based oxide material because in which the O atom was contained in the DOE molecular structure. Furthermore, the H_2O/Fe ratio rarely contributes the decrease in M_S in the present experimental condition from 10^{-2} to 10^{-5}. These results suggest that the solvent with small amount of O impurities brings about minimal oxidation of iron nanoparticle during the synthesis. Therefore, we concluded that the decrement of M_S could not be explained in terms only of the oxidation in the iron nanoparticles. One possibility to explain the decrement of M_S might be the particle size, namely the increment of the relative surface area might be very crucial for the decrement of M_S. Fig.2 shows the size dependence of M_S of iron nanoparticles at 5K. This result strongly suggests that M_S of the iron nanoparticles depends on the particle size. Nanoparticles with very small size, in addition, has the larger coercitivity than that for the bigger size, indicating the change of the crystalline structure and/or the increment of the surface anisotropy. These features might be due to the increment of the number of surface atoms in each particle, and as a result M_S of the nanoparticles might be decreased.

1) D. Hasegawa, T. Ogawa, M. Yamaguchi, and M. Takahashi, J. Magn. Soc. Jpn., vol. 30,pp528-530, 2006.

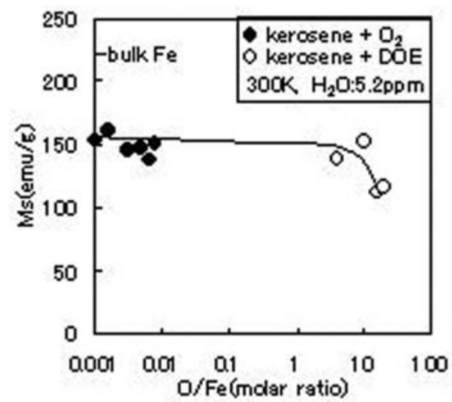

Fig.1 Change of saturation magnetization at 300K by varying the ratio of dissolved O impurity in solvent.

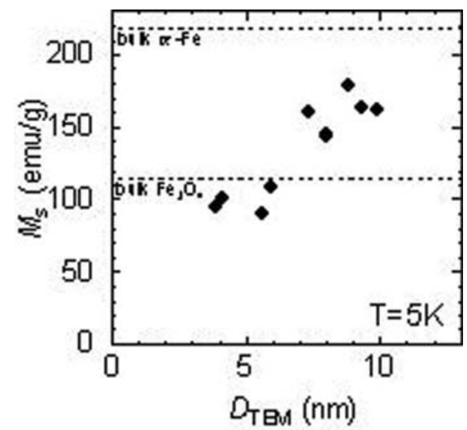

Fig.2 Size dependence of saturation magnetization at 5K for iron nanoparticles.

HN-04

Phase transition of the escape rate for ferromagnetic nanoparticles: A magnetic quantum tunneling study.

J. Florez, P. Vargas
Phys. Dept. USM, Valparaiso, Chile

A study of the phase transition in macroscopic quantum tunneling of a magnetic moment is presented. We show results for different terms in the magneto crystalline anisotropy, these terms can change the behavior of the period of the thermon solution and the quantum to classic transition for the escape rate. Moreover, the transition controlled by the external magnetic field can disappear when higher terms in the anisotropy term are considered.
The phenomena of the macroscopic quantum tunneling and coherent quantum tunneling have been relevant since the intensive studies of Chudnovsky, Caldeira and Leggett and others. Experimental studies have showed the relevance of these phenomena and are now very import in the study of the quantum effects in mesoscopic and nanoscopic magnetic systems. In this work we consider tunneling in a spin model with an applied magnetic field and different contributions to magneto crystalline anisotropy along an easy axes. With the instanton formulation we calculate the period of the thermon solution to escape trajectory, as well as the escape exponent and crossover temperature. In this model, a contribution of the type $H_A(p)=k_p(\mathbf{m.n})^p$ is considered as anisotropy energy (p=2,4,...), m is the magnetic moment and **n** a unitary vector. We also considered an external magnetic field and the total Hamiltonian is $H=-H_xS_x+H_A(p)$. Chudnovsky already showed that in this form with p=2, the external field controls the order of the transition in these spin systems when the field flips the sign of the anharmonic term in the expansion of the equivalent particle potential.
Our results shows the period of the thermon solutions and the escape temperature, which is related to the escape exponent by inverse proportionality, for the configurations with $p=2,k_2=0.8$, and two magnetic fields $H_x=6.1$ and $H_x=11.1$ where the change in the transition has been showed, see Fig.1. Also we calculated the same case adding a new anisotropy term with p=4, $k_4=0.9$, with the same magnetic fields. The results are shown in Figure 2. Other contributions can be also easily considered.
The phase transition between the classic to quantum region is showed in a magnetic system controlled by and external field. The behavior of the period and the escape temperature reproduces previous known calculations. Also, the inclusion of several term in the crystalline anisotropy shows the change from the second to first transition when the magnetic field is below a critical value.

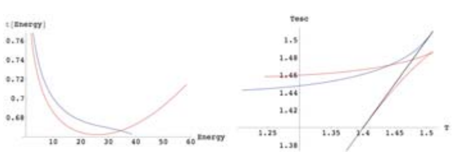

Thermon period as a function of energy (left panel). Escape Temperature as a function of Temperature (right panel). Case with p=2, S=10, and H_x=6.1 (red line) 11.1 (blue line)

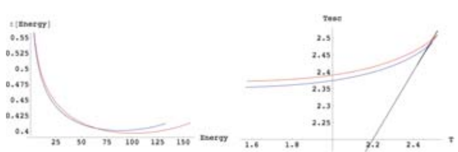

Thermon period as a function of energy (left panel). Escape Temperature as a function of Temperature (right panel). Considering two anisotropy terms p=2 and p=4, S=10, and H_x=6.1 (red line) 11.1 (blue line)

HN-05

Magnetic characterization of nanowire arrays using first order reversal curves.

R. Lavín[1], *J. C. Denardin*[1], J. Escrig[1], D. Altbir[1], A. Cortés[2], H. Gómez[2]
1. Física, USACH, Santiago, Chile; 2. Química, UCV, Valparaíso, Chile

The study of highly ordered arrays of magnetic wires is a topic of growing interest. The high ordering, together with the magnetic nature of the wires, may give rise to outstanding cooperative properties of fundamental and technological interest. In these arrays, inter-element interactions play an important role and have been subject to strong investigation.
In this work, first order reversal curves (FORC) and their respective diagrams have been used to investigate in detail the magnetization reversal process as a function of the interwire interactions in the array. Three hexagonal arrays of Ni nanowires of diameters d=50 nm and different lengths L=1 μm, L=4 μm and L=12 μm have been prepared by electrodeposition into nanopores of alumina membranes with interpore distance D=100 nm [1]. The magnetization measurements were performed with a home-made alternating gradient force magnetometer (AGFM).
In order to understand the role of the length of the nanowires on the interwire interactions, parameters obtained from experimental magnetization measurements and FORC diagrams were compared with micromagnetic simulation [2,3].
The FORC diagrams for the three arrays are shown in Fig1. a to c. A FORC diagram is a contour plot of the probability density function. The FORC diagrams are presented in terms of the coordinates of the switching fields (Hc) and interaction fields (Hi), respectively [4]. In the FORC diagrams of the samples (Fig1. a-c) a very large distribution of the interaction fields (in the direction Hi) is observed, which is expected for highly interacting systems. Another important feature which appears in the diagrams and which is not possible to observe from a simple hysteresis loop is the reversible component of the magnetization. This reversible component vanishes as L increases, as expected, since a system with a significant reversible component of the magnetization has a low coercivity [5].
The coercivity of arrays calculated by means micromagnetic simulations and the normalized magnetostatic interaction energy per wire (Eint) as function of L are shown in Fig1. d. As can be observed in this figure, the interaction per wire, Eint, decreases and the coercivity increases with increasing values of the length L. The experimental data points in the Fig1. d represent the corcivities obtained from hysteresis curves, and are in good agreement with our micromagnetic simulation.
One can also observe from the FORC diagrams (Fig1. a-c) that as L increases the distribution of coercivities increases, as well as the maximum of the distribution of coercivities. This behavior is in agreement with the dependence of measured values of the coercivities (black dots in Fig1. d) and micromagnetic simulations (solid line in Fig1. d). In the FORC diagram of the sample with L=12 μm, a significant increase appears in the distribution of coercivities (which appears as a “tail” in the direction of Hc). It is worth noting that from the FORC diagrams we can also observe a decrease in the distribution of interaction fields as L increases, as expected from the simulations.
In conclusion, FORC diagrams provide a more complete characterization of the system because they provide information of the reversible component of the magnetization and information about the importance of interactions. These factors can not be easily extracted from hysteresis curves.

[1] L. C. da Fontoura, G. Riveros, H. Gómez, A. Cortés, M. Gilles, E. A. Dalchiele and R. E. Marotti, http://arxiv.org/cond-mat/0504573 (2005).

[2] J. Escrig, R. Lavín, J. L. Palma, J. C. Denardin, D. Altbir, A. Cortéz and H. Gomez, Nanotechnology (in press, 2008).

[3] J. Escrig, D. Altbir, M. Jaafar, D. Navas, A. Asenjo, and M. Vázques, Phys. Rev. B 75, 184429 (2007).

[4] C. Pike, A. Roberts and K. Verosub, J. Appl. Phys. 85, 6660 (1999).

[5] L. Spinu, A. Stancu, C. Radu, F. Li, J. B. Wiley, IEEE Trans. Magn. 40, 2116 (2004).

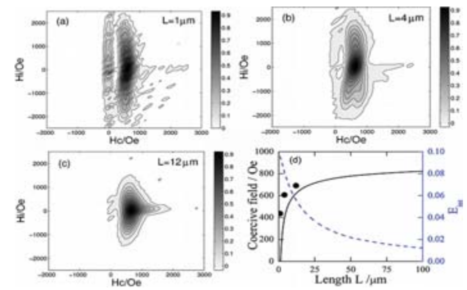

Fig1. (a-c) Normalized FORC diagram for L=1 μm, L=4 μm, and L=12 μm. (d) (solid line) Coercivity of the arrays calculated from micromagnetic model, (black dots) correspond to the measured experimental values, and (dash line) is the normalized magnetostatic interaction energy per wire as a function of the length L.

HN-06

AC susceptibility study of spin dynamics in Fe-doped $La_{0.7}Pb_{0.3}Mn_{0.8}Fe_{0.2}O_3$

L. Fernandez Barquin[1], J. Gutiérrez[2], J. Barandiaran[2], J. Bermejo[2], S. Kaul[3]
1. CITIMAC, Facultad de Ciencias, Universidad de Cantabria, Santander, Spain; 2. Electricidad y Electrónica, UPV / EHU, Fac. Ciencia y Tecnología, Bilbao, Spain; 3. School of Physics, University of Hyderabad, Hyderabad, India

Manganites or mixed manganese oxides of the formula $La_{1-x}M_xMnO_3$ where M is a divalent cation (Pb in our case), are Double Exchange (DE) ferromagnets (FM) that attract great interest in view of their colossal magnetoresistance around the magnetic order temperature. They have a strong tendency to grow in small coherent regions due to the coupling of the magnetic and charge carriers and local distortions like Jahn-Teller or charge ordering. Those ensembles of magnetic atoms at the nanometric scale are known as clusters or grains. Such a tendency is enhanced by doping the Mn with other 3d-metals, like Fe [1], that break up the FM chains by suppressing the DE between Mn ions, and can eventually give rise to spin glass-like structures. The latter magnetic arrangement is consequently maximized with the increase of Fe-content in the compound. Due to the similarities of the relaxation behavior in manganites with the dynamic behavior observed in nanomagnets of strong technological applications, the manganites can be seen as an excellent playground to ascertain the interactions between ensembles of randomly disposed magnetic clusters. In this case, results from dynamic techniques can give insight both into the magnetic coupling and the spatial correlation ranges.
In this work we present recent results obtained by AC magnetic susceptibility experiments in the $La_{0.7}Pb_{0.3}Mn_{1-x}Fe_xO_3$ (x = 0.2) manganite, where the frustration is enhanced respect to the x = 0 compound. All measurements were recorded at several frequencies (100 Hz $\leq f \leq$10 kHz) between 10 K and 220 K in a Quantum Design-PPMS magnetometer, allowing the instantaneous recording of the in-phase (χ') and quadrature (χ") components. The samples were warmed up from helium temperatures at steady heating rates, ranging from 0.1 K/min (where peaks were detected) to 2 K/min, in featureless regions. The amplitudes of the oscillating AC-field were h = 1 and 0.1 Oe.
Among the macroscopic techniques, the AC-susceptibility (ACS) is one of the best suited for a spin dynamic study. This is due to its intrinsic sensitivity to detect very subtle magnetic transitions and/or different magnetic phases and because when there is a need to define a magnetic relaxation process, it is recommendable to cover several decades of measuring time, ideally using a single technique.
In figure 1 (left) we show the measured in-phase and out-of phase responses. Thus, the sample with x=0.2 shows a component with a single broad peak centered around 70 K. This peak looks like as if a single transition should be taking place. By contrast, in it seems that up to three contributions can be present. It is likely that the highest-temperature one (around 100 K) is related to the paramagnetic to ferromagnetic transition which evolves into a blocked or spin-glass peak at around 70 K. Finally the susceptibility displays another shoulder at 50 K more difficult to interpret. Increasing the frequency, the commented features in the curves (marked by arrows) shift to higher temperatures. The detailed analysis of the observed frequency-shift as well as the possible critical behavior of those transitions are the object of the analysis to be presented in this work.
The non-linear susceptibility behavior which can give hints to clarify the critical dynamics, specially for inhomogeneous magnetic systems [2,3]. This kind of analysis has been widely used in other CMR oxides doped with 3-d elements at the Mn^{3+} site [4,5] as well as in quite different families of perovskites [6,7] without such a doping. In our case, the third harmonic component χ'_3 (see figure 1, right) confirms the previously observed two transitions: a sharp one at ≈ 65 K and a well separated broad hump at ≈ 100 K. These results are discussed in terms of the presence of short-range magnetic correlations which can give rise to a ferromagnetic percolated state of a spin-glass-like structure depending on the coupling among those regions.

[1] J. Gutiérrez, F.J. Bermejo, N. Veglio, J.M. Barandiarán, P. Romano, C. Mondelli, M.A. González and A. P. Murani, J. Phys.: Condens. Matter 18 (2006) 9951

[2] D. Chowdury, Spin glasses and other frustrated systems, World Scientific, 1986

[3] H. Ma, H.P. Kunkel and G. Williams, J. Phys.: Cond. Matter 3 (1991) 5563; T. Bitoh, K. Ohba, M. Takamatsu, T. Shirane and S. Chikazawa, J. Mag. Magn. Mat. 222 (2000) 219

[4] D. Verma, A.K. Nigam, T.K. Gundu Rao and D. Bahadur, J- Mag. Mag. Mat. 271 (2004) 172

[5] J. Dho, W.S. Kim and N.H. Hur, Phys. Rev. Lett. 89 (2002) 27202

[6] D.N.H. Nam, R. Mathieu, P. Nordblad, N.V. Khiem and N.X. Phuc, Phys. Rev. B 62 (2000) 1027

[7] V. Markovich, I. Fita, R. Puzniak, M.I. Tsindlekht, A. Wisniewski and G. Gorodetsky, Phys. Rev B 66 (2002) 94409

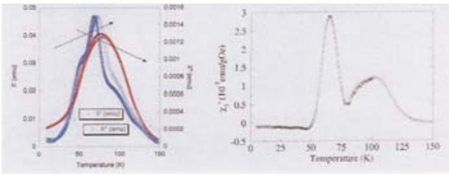

Figure 1. Left: AC-susceptibility behavior of the real and complex components for h = 1 Oe. Frequencies of 500 Hz and 5000 Hz are uniquely shown to clarify the data. The arrows mark the frequency variation found in the transitions. Right: the measured non-linear component, χ'_3 .

HN-07

Exchange coupling in core(ferromagnet)-shell(antiferromagnet) structured nano-particles.

N. N. Phuoc[1], *T. Suzuki*[1], R. W. Chantrell[2], U. Nowak[2]
1. Information Storage Materials Laboratory, Toyota Technological Institute, Nagoya, Japan; 2. Department of Physics, University of York, York, United Kingdom

Exchange coupling in ferromagnetic(FM) and antiferromagnetic(AF) nano-composite particles is an appealing subject among many studies on nano-particles [1] but there is still very little work on this theme. This work hence focuses on the study of the exchange coupling in FePt(core)/FeMn(shell) nano-composite particles by two approaches: atomistic simulation [2] and micromagnetic simulation [3].
The micromagnetic simulation is based on the Landau-Lifshitz-Gilbert equation, where the equilibrium state of the spin configuration is obtained by minimization of the total energy from the random state. The equilibrium state, on the other hand, from the atomistic model is obtained by heating the nano-particles beyond the Curie temperature and cooling down to T = 0K. Another major difference between micromagnetic and atomistic models is that the atomistic approach is based on the calculation at the atomistic level, using a reasonable physical model for the exchange, rather than using the long-wavelength (micromagnetic) approximation [2]. In particular, the Heisenberg form of exchange is used in the atomistic model. In other words, although the cell sizes of both micromagnetic and atomistic models look to be the same, the calculation method is totally different. For micromagnetic cells, a constant value of magnetization is taken while in the atomistic model, the magnetization is averaged over all atoms [2].
Shown in Fig. 1 are some representative spin structures of the core/shell particles obtained from micromagnetic and atomistic simulations with different interlayer exchange coupling constants. It is interesting to see that for the case of weak interlayer coupling, the magnetization arrangement of the core break up into domains even the particle size is very small (4.8 nm) if using micromagnetic simulation. The formation of multiple-domain in this case is unreason-able as it costs a lot of exchange energy in FM system. For stronger interlayer coupling, the core becomes single-domain. Such a behavior cannot be observed if using atomistic simulation. It was reported previously similar failure of the micromagnetic simulation in describing the domain structure and the switching behavior of the hard/soft layers when the interlayer exchange coupling is small [2]. The reason for this failure is possibly due to the under-estimation of the exchange energy for rapid spatial fluctuations of the magnetization by the (continuum) exchange formalism [2]. Another reason for this might be due to the cooling procedure, where the micromagnetic model does not really cool the system and might get trapped in unphysical states while the spin model does really a cooling, i.e. a slow lowering of temperature.
Figure 2 shows the variation of the spin directions of the core and the shell as a function of the anisotropy of the AF shell in the case of strong interlayer coupling. It can be seen that the spins of the core are influenced by the spin of the shell as the K_{AF} increases. In particular, when the K_{AF} is large enough, the FM core spins are canted from the easy axis. As a result, the coecivity of the system is reduced with the increasing of K_{AF}. This behavior and also the discrepancy between atomistic and micromagnetic simulations will be discussed in details in the presentation.

[1] Q.Y. Xu, Y. Kageyama, and T. Suzuki, IEEE Trans. Magn. 41, 3379 (2005).

[2] F. Garcia-Sanchez, O. Chubykalo-Fesenko, O. Mryasov, and R.W. Chantrell, Physica B 372, 328 (2006).

[3] N.N. Phuoc and T. Suzuki, J. Appl. Phys. 101 (2007) 9E501.

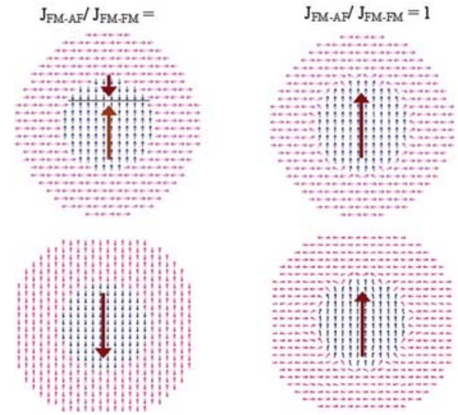

Fig. 1. Spin configurations of the core-shell particles for two cases: weak interlayer coupling (first colum) and strong interlayer coupling (second colum) using micromagnetic (upper row) and atomistic (lower row) simulations.

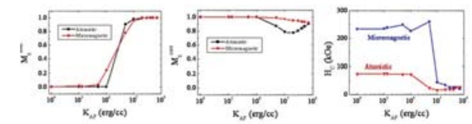

Fig. 2. Magnetization component in z axis of the shell and the core and coercivity as a function of K_{AF}.

HN-08

Single cobalt clusters embedded in isolating matrix.

C. Raufast[1], *A. Tamion*[1], V. Dupuis[1], T. Fournier[2], T. Crozes[2], E. Bernstein[1], E. Bonet[2], W. Wernsdorfer[2]

1. Laboratoire de Physique de la Matière Condensée et Nanostructures, Lyon, France; 2. Institut Néel, CNRS, Grenoble, France

When decreasing the size of the magnet down to the nanometric range, the thermal fluctuation of the magnetization (*superparamagnetic* state) will be seen as an advantage[1] or a poison[2] depending on the expected application. Nevertheless, in both cases, technological improvements require the understanding of dynamical magnetization reversal processes at the nanosecond time scales. Generally, high fields are needed to reverse the magnetization of nanoparticles, which are difficult to achieve in current devices. One way to overcome this limitation is to apply a constant magnetic field, well below the switching field, combined with a radio-frequency (RF) field pulse. The efficiency of this method has been previously demonstrated on a 20 nm cobalt particle by using the micro-SQUID technique[3]. Our aim is to extend this magnetization reversal technique on a cobalt nanoparticle with only 3 nm in diameter, in order to study the dynamics behaviour of only a thousand of spins.

In this paper, we report recent experimental results on the magnetic properties of cobalt clusters prepared by Low Energy Clusters Beam Deposition[2], embedded in insolating matrices. This technique allows us to synthesize highly diluted samples, where clusters are considered as isolated. First of all, from macroscopic measurements on these cluster assemblies we deduce the average structural and magnetic properties (see figure 1).

The final step of this research work consists to use an improved micro-SQUID device coupled with a gold stripe line. With this system, we succeed in the magnetization reversal of a single cobalt cluster at low temperature (T = 35 mK) using a RF pulse (see figure 2).

A qualitative understanding of the magnetization reversal by non-linear resonance can be obtained with the Landau-Lifschitz-Gilbert (LLG) equation.

For each field point inside the Stoner-Wohlfarth astroid, the LLG equation was integrated to calculate the switching times. Assuming that in such Co-nanoparticle, bi-axial surface anisotropy terms dominates all the others terms[4], the anisotropy energy can be written as the sum of second order terms: $E_a = -K_1.m_z^2 + K_2.m_y^2$. The best simulations of the field dependence of the switching field (dynamic Stoner-Wohlfarth astroid) for frequencies of 5-6 GHz and a few nanosecond pulse duration, are obtained for $K_2 = 0.5\ K_1$ and α, the damping term lower than 0.01. Larger studies by varying matrix and clusters size are in progress.

[1]S. Mornet, S. Vasseur, F. Grasset and E. Dugnet, J. Mat.Chem. 14 (2004) 2161

[2]J. Bansmann, S.H. Baker, C. Binns, J.A. Blackman, J.-P. Bucher, J. Dorantes-Dávila, V. Dupuis, L. Favre, D. Kechrakos, A. Kleibert et al. Surface Science Reports 56 (2005) 189

[3]C. Thirion, W. Wernsdorfer and D. Mailly, Nature Materials 2 (2003) 524

[4]M. Jamet, W. Wernsdorfer, C. Thirion, D. Mailly, V. Dupuis, P. Mélinon and A. Perez, Phys. Rev. Letters 86 (2001) 4676

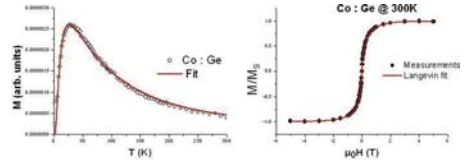

Experimental magnetic susceptibility curve and hysteresis loop of Co nanoparticles embedded in Ge matrix. The fits lead to the clusters magnetic size distribution and the efficient anisotropy constant (K_{eff}).

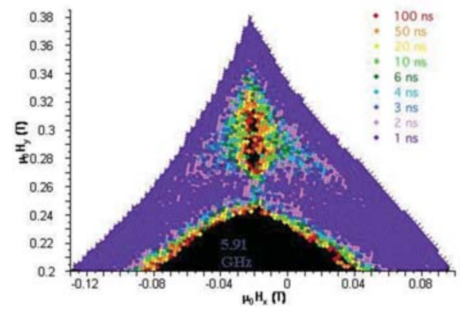

Experimental field dependence of the switching field for a 3 nm single Co particle by applying a RF pulse frequency of 5.91 GHz. For each field point, the shortest pulse length leading to magnetization switching is indicated with a colour. In the black region the magnetization did not reverse whereas the white region is outside the Stoner-Wohlfarth astroid.

HN-09

Thermal relaxation phenomena probed by transverse susceptibility measurements performed at different frequecies.

J. Calleja[1], C. Radu[2], L. Spinu[2], R. Matarranz[1], B. Presa[1], M. Contreras[1]
1. Física, Universidad de Oviedo, Oviedo, Spain; 2. AMRI, University of new Orleans, New Orleans, LA

Thermal relaxation phenomena in particulate media have been extensively studied by several techniques, among them Mössbauer spectroscopy, SQUID magnetometry [1] and Transverse Susceptibility (χ_t) [2]. Superparamagnetic behaviour is observed by using an instrument with a characteristic measuring time τ and at temperatures above the blocking temperature T_B, which depends on the value of the energy barrier KV, K being the magnetic anisotropy constant and V the average volume of a particle. In most experiments, the transition from the superparamagnetic to the ferromagnetic states is investigated using two techniques with very different characteristic measuring times [1]. In this work we present measurements of one physical quantity,χ_t, performed at two different characteristic times below the blocking temperature. As χ_t depends strongly on the value of the observed effective anisotropy energy,$(KV)_{eff}$, it is our aim to show how this value depends on the characteristic time used. Two magnetic media have been chosen, one in which thermal relaxation phenomena are expected to play an important role (Co nanoparticles) and another one in which they are expected to be negligible (continuous polycrystalline CoFe thin films). Co nanoparticles were grown on amorphous Si_3N_4 substrates by triode sputtering at 550°C to favour the formation of nanoparticles. Ex-situ XRD showed that Co crystallizes in the hcp phase without texture. Atomic Force Microscopy results revealed a well-defined nanostructured pattern without coalescence [3]. Polycrystalline CoFe thin films 20 nm thick were deposited on glass substrates. Ex-situ XRD confirmed the bcc structure of the samples with a preferred (110) out-of-plane orientation. TEM measurements showed that the samples were polycristalline. χ_t measurements were performed by two methods. One based on the transverse magnetooptical Kerr effect (MOKE), working at a frequency of 127 Hz [3] and the other one based on a tunnel diode oscillator (TDO) working at 22 MHz [2]. All the samples studied exhibited a magnetic isotropic behaviour. Figure 1a shows the χ_t for a particulate Co thin films with nominal thickness of 3 nm and a mean particle diameter of 15 nm. Although the value of the magnetic field at the peak in the χ_t curves is to be close to the anisotropy field H_k of the particles [4] in this case it is remarkable that: 1) it is too low to be identified as H_k for hcp Co, and 2) it is lower for TS measured at 127 Hz than at 22 MHz. In Figure 1b the χ_t for a CoFe polycrystalline sample is shown. In this case, the measurements performed at 127 Hz and at 22 MHz coincide perfectly. Furthermore, the value of H_k obtained from the χ_t peak is consistent with the magnetocrystalline anisotropy of CoFe: taking $H_k \sim 125$ Oe, and the saturation magnetization Ms = 1700 emu/cm^3 we obtain a magnetic anisotropy constant K ~ 1.1 $\times 10^5$erg / cm^3, a bit lower that the magnetocrystalline value of K for CoFe (1.5×10^5 erg / cm^3) . The slight difference can be attributed to interparticle interaction and anisotropy dispersion [4].
We conclude that in the case of Co nanoparticles the thermal relaxation affects very strongly the value of the effective anisotropy observed. Taking the characteristic measurement time as the inverse of the frequency of the alternating field used, we have τ(MOKE) = 8×10^{-3} s and τ(TDO) = 5×10^{-8} s. The larger the observation time used, the larger the probability for a particle to overcome the energy barrier during the observation. The key parameter governing the transition from one energy minimum to the other is $\alpha = KV / k_BT$. At room temperature, and taking the anisotropy constant of bulk hcp Co ($K = 4.1 \times 10^6$ erg / cm^3) we estimated $\alpha \sim$ 20-50. The medium thermal stability criterion is given by $\alpha \geq 60$ [3]. So the magnetization equilibrium position is not only determined by the value of the applied magnetic field and its orientation with respect to the easy axis but also by the thermal relaxation which favours the switching of the magnetization, yielding an observed effective magnetic anisotropy which is lower than the magnetocrystalline one. These results show that when investigating particulate media thermal relaxation has to be taken into account even when working below the blocking temperature.

[1]G. Xiao, S. H. Liou, A. Levy, J. N. Taylor and C. L. Chien, Phys. Rev. B 34 7573, 1986.

[2]L. Spinu, C. J. O'Connor and H. Srikanth, IEEE Trans. Magn. 37, 2188, 2001.

[3]B. Presa, R. Matarranz, C. Clavero, J. M. García-Martín, J. F. Calleja and M. C. Contreras, J. Appl. Phys. 102, 053901, 2007.

[4]R. Matarranz, M. C. Contreras, G. Pan, B. Presa, J. A. Corrales, J. F. Calleja, J. Appl. Phys. 99, 08Q504, 2006.

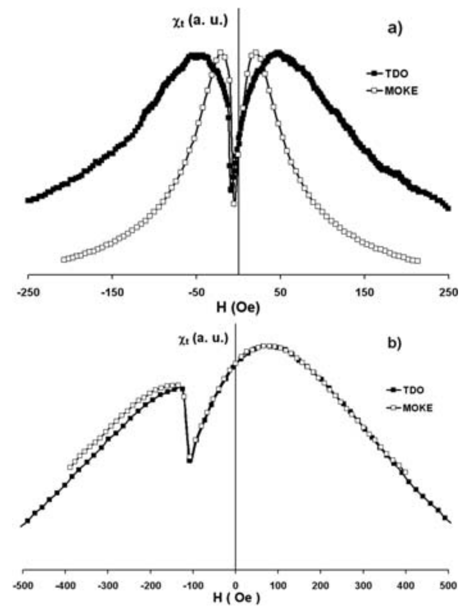

Transverse Susceptibility for Co nanoparticles (a) and polycrystalline CoFe (b) measured at 127 Hz using the magnetooptical Kerr effect (MOKE) and at 22 MHz using a tunnel diode oscilator (TDO).

HN-10

Self-ordered growth of ferrite nanopyramids.

F. Rigato[1], B. B. Nelson-Cheeseman[2], J. Caicedo Roque[1], D. Hrabovsk ý[1], F. Sánchez[1], J. Fontcuberta[1]
1. Magnetic Materials, ICMAB, Bellaterra, Spain; 2. Materials Science and Engineering, University of California, Berkeley, CA

The constant search of increasing the memory density justifies the interest on the production of self-assembled magnetic nano-objects. In studying their magnetic features the first approach consisted, historically, on working with magnetic transition metals (Ni, Fe, Co; see for instance [1]). Recently, nanocolumns of cobalt ferrite, a magnetic oxide, have been grown embedded on a ferroelectric matrix, by a co-deposition process, obtaining composite multiferroic materials of new generation [2]. Magnetoelectric coupling in these nanocomposites is expected to be determined by interface strain, thus detailed control of shape and distribution of the ferromagnetic columns is essential. Deposition temperature is traditionally considered the key parameter [3], however details of the growth, role of the substrate and magnetic structure of the films are not yet fully elucidated. In particular, substrate symmetry and composition can affect the epitaxial character of the nano-objects, determining their magnetic properties.
Aim of this work is to explore and compare the initial growth mechanisms of $CoFe_2O_4$ (CFO) on substrates with different atomic arrangements and thus crystallographic structures. We selected an isostructural spinel ($MgAl_2O_4$, MAO) and a perovskite ($SrTiO_3$, STO) single crystalline substrates, both (001) oriented: we will show that, under the appropriate growth conditions, the formation of pyramidal objects with magnetic behavior is favored *on both* substrates. Lateral size and surface density of the pyramids can be tailored changing the substrate. We emphasize that this, rather than temperature changes, is a preferable way to control the size distribution of the magnetic nanoobjects: in fact, the growth modes generated at different temperatures cannot be easily separated. Moreover, in growing nanocomposites by co-deposition, immiscibility is essential, although limited to a narrow temperature range; otherwise intermixing can occur. For comparison purposes, series of CFO films have also been grown on (111) STO monocrystals: instead of the pyramidal structures observed on (001) substrates, relatively flat CFO surfaces (typically ~10 nm of RMS roughness) constituted by 3D islands are observed.
Samples presented on this work were grown by RF magnetron sputtering, in a mixed atmosphere of argon and oxygen, for a total pressure of 250 mTorr. Deposition duration was 100 minutes and the grow rate was determined by x-ray reflectometry from a thin sample, in which the formation of nano-objects was still in an embryonic phase, and it resulted of the order of 1 Å/min. Morphology was studied by atomic force microscopy (AFM); magnetic characterization was performed by magneto-optical Kerr effect (MOKE). Depositions with substrate temperature of 650 °C, was realized simultaneously on MAO (001) and STO (001): AFM scans of these samples are presented in Fig. 1a and 1b respectively. 3D structures with pyramidal shape are found on the surface: bases are oriented along the substrate crystallographic directions and the lateral size is strongly dependent from the substrate material, resulting double, in average, for the case of STO respect to MAO (~220 nm and ~110 nm respectively). Both images present in an inset graph an analogous deposition, realized with substrate at 700 °C. The higher temperature generates a larger surface density of pyramids, so lateral size is smaller, ~60 nm for both substrates.
When depositing over STO (111), at 650 °C, 3D islands were found, with planar top and triangular bases oriented along the crystal axes of the substrate, reflecting its three-fold symmetry. This growth is promoted by the lower surface energy of CFO (111) face respect to the (001): in fact, for any substrate, the film tends to maximize the (111) surfaces, i.e. the pyramids' faces or the planar tops of the island in the case of STO (111).
Samples deposited over both STO orientations were magnetically characterized by room-temperature MOKE, under an external field up to 1.15 T. MOKE loops with the field applied either perpendicular (polar) or parallel (longitudinal) to the sample surface were collected; longitudinal measurements were collected with the field at two different in-plane angles (0 and 90°). It is found that in both cases the out-of-plane direction is the hard one, whereas the film-plane is an easy plane. For the films grown on (001) substrates, no significant in-plane anisotropy is observed, as expected from the substrates symmetry. However, a similar behavior is observed on (111) substrates. We will discuss on the origin of this unexpected result.
Concluding, we have shown that appropriate substrate selection allows a more efficient growth control of self-assembled ferrimagnetic CoFe2O4 nanostructures. This approach should permit a better understanding of magnetoelectric properties of biferroic nanocomposites.

1. J. Shen and J. Kirschner, Surface Science, 500 (2002) 300

2. H. Zheng, el al., Science, 303 (2004) 661

3. U. Lüders, et al., Phys. Rev. B, 71 (2005) 134419

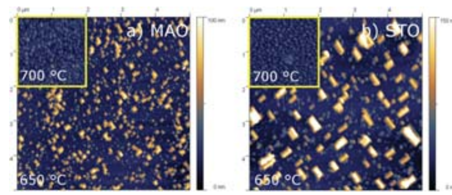

AFM scans of coatings realized at 650 °C over a) MAO (001) and b) STO (001); the respective insets present analogous samples realized at 700 °C, length and color scales are the same as in the principal image.

HN-11

On the low-temperature dependence of the nanoparticle interactions in the $Mn_xZn_{1-x}Fe_2O_4$ system.

A. Mendoza[1], O. Marín[2], D. Reyes[3], A. Ovidio[1], P. Prieto[3]
1. Physics Department, Universidad Nacional de Colombia, Bogotá, Colombia; 2. Magnetic Materials and Nanoestructures, Universidad del Quindío, Armenia, Colombia; 3. Thin Films Group, Universidad del Valle, Cali, Colombia

Magnetic nanoparticles were synthesized by normal micelle micro-emulsion method at room temperature. The ratio between Mn/Zn and Fe cations is adjusted to 1:2 for every sample, the value of x varied in the $0 \leq x \leq 0.75$ range. We estimated nanoparticle size through a chemometric approach introduced by A. Rodinone *et al* [1] as d ~ 33 nm. The ferrite structure was identified by XRD, where peaks can be indexed to planes (220), (311), (400), (422), (511), and (440) of single-phase MnZn ferrite. From the Scherer equation we obtained experimental nanocrystallite size values as d ~ 27-55 nm. These values correspond to the magnitude expected by Rondinone's approach. At 180 K, the ESR spectra were recorded on the nanoparticles with different stoichiometries. A set of dilution samples were prepared by diluting 0.5 mL, 1.0 mL and 1.5 mL in 10 mL water, to obtain variable interparticle distances. ESR shows that the ΔH_{pp} linewidth increases as inter-particle distance L decreases, indicating the existence of magnetic inhomogeneities as the effect of inter-particle interaction on the L scale. This interaction can also be responsible for the resonant field, H_r, shift to higher values. This behavior can be discussed in terms of particle size distribution and inter particle dipole-dipole interaction [2]. If the distance between particles increases, the inter particle dipole-dipole interaction decreases. A set of $Mn_xZn_{1-x}Fe_2O_4$ samples were prepared in the $0 < x < 0.75$ range at the same dilution, e.g., with same inter-particle distance. For $x < 0.5$, the EPR spectra consist of a single resonance signal, strongly symmetrical, with g=2.01. The resonant field is approximately constant for $x \leq 0.5$ $H_r = 3350$G. While the x concentration increases, the Lorentzian character of the signal reduces. The same behavior is observed by feeble dilution of the magnetic particles. These results indicate that x increases the ferrimagnetic character of $Mn_xZn_{1-x}Fe_2O_4$ nanoparticles. For low concentrations, the ΔH_{pp} value remains approximately constant. This was expected, given that at this concentration the single line in the EPR signal at g = 2.01 indicates the presence of Fe3+ of the octahedral sites. For $x \geq 0.5$ close to 1399 G, a second line appears (see Fig. 1) in the EPR signal, corresponding to g = 4.10. This is attributed to a random distribution of the anisotropy in the system, with perpendicular and parallel modes, giving information about the effective anisotropy of the system [3]. As the inset in Fig. 1 shows, the contribution of the second line decreases when x decreases. The latter reinforces the suggestion of a local field created by the Mn in the cell. For high concentrations, the resonant field shifts drastically to 2875G. This phase was verified through hysteresis curves, measured between 10 K to 300 K, by using a Vibrating Spectro-Magnetometer. From the field-cooled (FC) magnetization curves, the behavior of dM/dT (see Fig 2a) as a function of the magnetic field were obtained. This behavior shows a minimum about T_{min} = 145 K, and a soft shift to low temperature as the applied field reduces. Below Tmin a reduction in the rate of ordering moments indicates the existence of strong interactions among particles. A maximum is observed above $T_{max} \approx 25$ K (Fig. 2b) for H > 20 Oe. T_{max} was interpreted as the beginning of a glassy spin-like behavior. The slope of dM/dT can be interpreted as the moments ordering rate. A dependence of this slope as a function of the magnetic field is discussed in the framework of nanoparticle interaction theory.This work was partially supported by COLCIENCIAS under Research Project 1106-05-17612 and CENM, under contract 043-2005.

[1] D.C. Jiles and D.L. Atherton, J. Appl. Phys. vol. 55, pp. 2115-2120, 1984. [2] C. Calle et al., Phys. B., vol. 384, pp. 103-105, 2006. [3] V. H. Calle et al., Phys. Stat. Sol. C, vol. 4, pp. 4197-4220, 2007. [4] M. Fecioru-Morari and A. Stancu, J. Optoelectr. Adv. Mat., vol. 5, pp. 939-944, 2003.

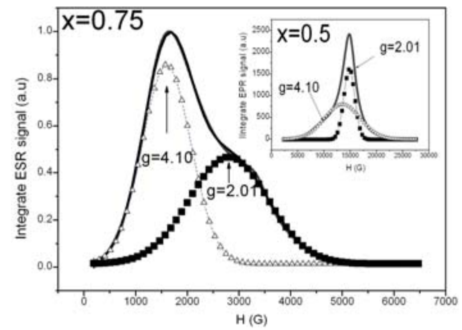

ESR signal for x=0.75 MnxZn1-xFe2O4 sample. Inset for x=0.5

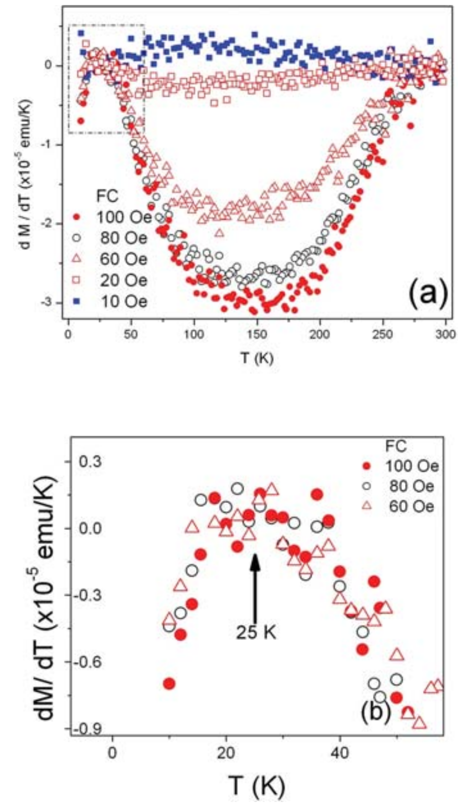

(a) dM/dT for x=0.75 sample obtained from the FC magnetization curve. (b) close up at low temperature.

HN-12

Magnetostatic interactions between magnetic nanotubes.

J. Escrig[1], S. Allende[1], D. Altbir[1], P. Landeros[2], M. Bahiana[3]
1. Departamento de Fisica, Universidad de Santiago de Chile, Santiago, Chile; 2. Departamento de Fisica, Universidad Tecnica Federico Santa Maria, Valparaiso, Chile; 3. Instituto de Fisica, Universidade Federal do Rio de Janeiro, Rio de Janeiro, Brazil

Since the discovery of carbon nanotubes by Iijima in 1991, [1] intense attention has been paid to tubular nanostructures because of their importance for future applications in spintronic devices. [2] In particular, the study of highly ordered arrays of magnetic nanotubes is a topic of growing interest. This is a consequence of the development of experimental techniques that lead to fabricate in a controllable and ordered way such arrays. [3] Magnetic nanotubes may be suitable for applications in biotechnology, where magnetic nanostructures with low density, which can float in solutions, become more useful for in vivo applications. [4] In this way tiny magnetic tubes could provide an unconventional solution for several research problems, and a useful vehicle for imaging and drug delivery applications. In such systems, effects of interparticle interactions are complicated by the fact that the dipolar field depends on the magnetic state of each element, which in turn depends on the field due to adjacent elements. Although the magnetostatic interaction between nanowires has been intensely investigated, [5] tubes have received less attention, in spite of the additional degree of freedom they present; not only can the length and radius be varied, but also the wall thickness.
The purpose of this work is to develop an analytical model for the full long-range magnetostatic interaction between nanotubes that lead us to understand variations of the squareness of the hysteresis of these arrays as a function of the interaction between the elements. Our model goes beyond the dipole-dipole approximation, giving an analytical expression for the interaction in which the shape of the tubes have been taken into account. Using those expressions we developed Monte Carlo simulations to investigate the hysteretic behavior of the array.
Geometrically, tubes are characterized by their external and internal radii, R and a, respectively, and length L. It is convenient to define the ratio β=a/R, so that β=0 represents a solid cylinder (wire) and β close to 1 corresponds to a very narrow tube. We adopt a simplified description of the system, in which the discrete distribution of magnetic moments is replaced by a continuous one characterized by a slowly varying magnetization density $\mathbf{M}(\mathbf{r})$. The full dipolar interaction of an array can be calculated by evaluating the interaction energy between two magnetic bodies and summing up over the array. [5] Thus, the total magnetization can be written as $\mathbf{M}(\mathbf{r})=\mathbf{M_1}(\mathbf{r})+\mathbf{M_2}(\mathbf{r})$, where $\mathbf{M_1}(\mathbf{r})$ and $\mathbf{M_2}(\mathbf{r})$ denote the magnetization of each tube. In this case, the magnetostatic potential $U(\mathbf{r})$ splits up into two components, $U_1(\mathbf{r})$ and $U_2(\mathbf{r})$, associated with the magnetization of each individual tube. Then, the dipolar interaction between both tubes can be written as $E_{int}=\mu\int\mathbf{M_1}(\mathbf{r})\nabla U_2(\mathbf{r})dv$.
In order to evaluate the magnetostatic interaction, it is neccessary to specify the magnetization of each tube. We consider tubes with an axial magnetization defined by $\mathbf{M_i}(\mathbf{r})=M_0\sigma_i\mathbf{z}$, where $\mathbf{z}$ is the unit vector parallel to the axis of the tube and σ_i takes the values ±1, allowing the tube i to point up (σ_i=+1) or down (σ_i=-1) along $\mathbf{z}$. Results are given in units of $\mu_0M^2_0V$, where $V=\pi R^2L(1-\beta^2)$ is the volume and M_0 is the saturation magnetization of each tube.
The interaction between two nanotubes is obtained using the magnetostatic field experienced by one of the tubes due to the other so that the final result reads $Eint=(2\sigma_1\sigma_2/(1-\beta^2))\int(dq/q^2)J_0(qd/L)(J_1(qR/L)-\beta J_1(q\beta R/L))^2(1-e^{-q})$ (1), where J_p is a Bessel function of the first kind and p order and d is the center-to-center distance between the tubes.
Equation (1) has to be solved numerically. However, tubes that motivate this work satisfy L/R>>1, leading us to expand J_1 as $J_1(x)=(x/2)+\Sigma((-1)^k(x/2)^{1+2k}/k!\Gamma(k+2))$. (2) Then we can approximate equation (1) by $E^\lambda_{int}=\sigma_1\sigma_2(R^2(1-\beta^2)/2Ld)\Sigma g_\lambda$, where λ indicates the order of the expansion. An an example, the first term in the sum is $g_1=1-(1/\sqrt{1+(L/d)^2})$.
Figure 1 illustrates the interaction energy between two identical nanotubes (L/R=100) with parallel axial magnetization as a function of 2R/d. When the two tubes are in contact, 2R/d=1; when they are infinitely separated, 2R/d=0. From this figure we can conclude that by increasing the internal radii of the tubes, the magnetostatic interaction between them decreases, changing their magnetic behavior, as evidenced in Monte Carlo simulations. These results lead us to related changes in squareness with β.

[1] S. Iijima, Nature 354, 56 (1991).

[2] S. Sun et al., Science 287, 1989 (2000).

[3] J. Bachmann et al., J. Am. Chem. Soc. 129, 9554 (2007).

[4] M. Eisenstein, Nature Methods 2, 484 (2005).

[5] D. Laroze et al., Nanotechnology 18, 415708 (2007).

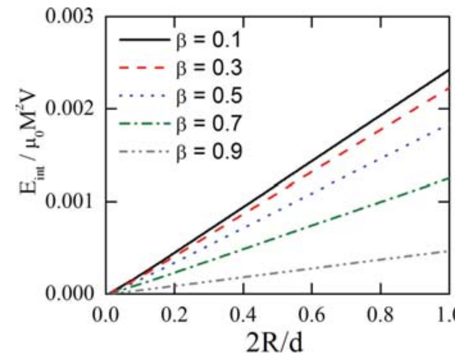

Energy of interaction between two identical nanotubes, L/R=100, with parallel axial magnetization.

HN-13

Magnetic nanowires: from synthesis to permanent magnet applications.

G. Viau[1], Y. Soumare[2], T. Maurer[3], J. Piquemal[2], F. Ott[3], G. Chaboussant[3]
1. LPCNO, INSA Toulouse, TOULOUSE, France; 2. ITODYS, Université Paris7, PARIS, France; 3. LLB, CEA Saclay, ORSAY, France

The key advantage of nanowires is their very large shape anisotropy that can provide a high intrinsic coercivity to the material. A hard magnetic behaviour is expected when the diameter of the wires is small enough to ensure a single domain state. The liquid phase chemical processes are very efficient for the synthesis of monodisperse magnetic particles with a very good control of size and shape. They afford the opportunity to get new insights on the properties of such nano-objects.
By reduction of cobalt and nickel acetate salts in liquid polyols we obtained homogeneous cobalt-nickel metal nanowires with a mean diameter less than 10 nm and a mean length of 200 nm [1,2]. This process was recently extended to the synthesis of pure cobalt wires with the same length by reduction of cobalt carboxylates (*Inset* Fig. 1). The mean diameter is controlled in the range 10-20 nm by varying the cobalt precursor. These wires crystallize in a hcp structure with the crystallographic c-axis laying along the wire axis. HRTEM showed that they are nearly single crystal. The control of the morphology of cobalt and cobalt-nickel particles by reduction in liquid polyol is achieved through a kinetic control of growth of the metal in solution. No template was necessary. We showed that a high growth rate favours the wires whereas platelets and spheres are obtained with lower growth rates. The control the growth step was realized by acting upon three parameters: the basicity of the medium, the metal salts and the polyol that acts both as solvent and as reducing agent.
Magnetic measurements showed a ferromagnetic behaviour at room temperature. Coercivity and remanence strongly depend on the orientation of the wires with respect to the applied field. Square magnetization curves were measured on samples obtained by freezing the wires in toluene under an external field (Fig. 1). For such samples remanence to saturation ratio, M_r/M_s, are close to 1 (Tab. 1). In case of $Co_{80}Ni_{20}$ wires aligned parallel to an external field the magnetization curve was well fitted considering the Stoner Wolfarth model with a dispersion of the nanowires orientation $\sigma = 10°$ (HWHM). The coercivity $H_C = 6.5$ kOe was found to be a sum of two equivalent contributions: a magnetocrystalline anisotropy $H_{MC}= 3$ kOe (which is very close to the value for bulk hexagonal cobalt) and a shape anisotropy which contributes to $H_{shape}= 3.5$ kOe [3]. With pure cobalt wires coercivity values up to 9 kOe at 140K (10 kOe at 5K) were obtained. These higher values are well explained by a higher saturation magnetization of cobalt than alloys. These magnetic properties are very interesting because the coercivity reaches much higher values than magnetic wires obtained by other methods. Arrays of nanowires grown by electrochemical routes are perfectly aligned but never exhibit coercivities higher than 3 kOe even for Fe where the theoretical value could be as high as 10 kOe [4]. These good results are related to the growth process that affords both smaller wire diameter and better crystallinity.
These nanowires may present interesting applications for "high-temperature magnets". The use of 3d transition metals provides high remanence and high Curie temperature (T_C). We showed that the saturation magnetization of cobalt wires is very stable since it is only reduced by 2% at 240°C. In the regime where $T << T_C$ the shape anisotropy is temperature-independent. Thus, we think that these wires could fill a gap between rare earth (RE) magnets like SmCo and AlNiCo magnets. RE magnets have higher coercivities but they show stronger softening upon warming while AlNiCo magnets exhibit much lower coercivities in the whole temperature range of interest.

[1] D. Ung, G. Viau, C. Ricolleau, F. Warmont, P. Gredin, F. Fiévet, *Adv. Mater.*, **17** (2005) 338.

[2] D. Ung, Y. Soumare, N. Chakroune, G. Viau, M.-J. Vaulay, V. Richard, F. Fiévet, *Chem. Mater.*, **19** (2007) 2084.

[3] T. Maurer, F. Ott, G. Chaboussant, Y. Soumare, J.-Y. Piquemal, G. Viau, *Appl. Phys. Lett.*, **91** (2007) 172501.

[4] D.J. Sellmyer, M. Zheng and R. Skomski, *J. Phys.: Condens. Matter* , **13** (2001) R433.

	Pressed powders (300 K)		Aligned wires (140 K)	
Composition	$Co_{80}Ni_{20}$	Co	$Co_{80}Ni_{20}$	Co
H_c (kOe)	3.6	5.0	6.5	9.0
M_r/M_s	0.64	0.62	0.97	0.94

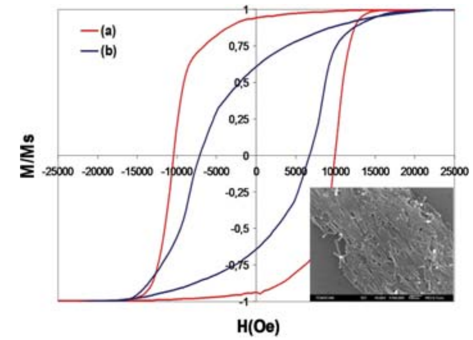

Fig. 1 Magnetization curves of cobalt nanowires at 5K (a) aligned with an external field (b) randomly oriented. *Inset* SEM image of cobalt nanowires.

HN-14

Numerical simulation of magnetic cluster in transition region.

H. Endo[1], Y. Uesaka[1], Y. Nakatani[2], N. Hayashi[3], H. Fukushima[4]
1. Nihon University, Koriyama, Fukushima, Japan; 2. University of Electro-Communications, Chofu, Japan; 3. Individual capacity, Tokyo, Japan; 4. Individual capacity, Chiba, Japan

Introduction

Several authors investigated the effect of magnetic clusters on recording properties [1, 2]. They used models in which the grain sizes and the positions were fixed, a cluster size was formed from several grains and the cluster size did not change through recording processes. On the other hand, we used a perpendicular medium model in which the grain size and its position can be changed. In our previous study, the effects of grain size dispersion and exchange interaction between adjacent grains on magnetic cluster sizes in perpendicular thin films under uniform field were reported [3]. In the present study, the same effects on magnetic cluster size in the transition regions in recorded patterns were estimated. A new method for estimation of magnetic cluster size for magnetic recording was used. Furthermore, the transition shift was investigated in this study.

Calculation conditions

A thin film perpendicular recording medium was represented by a two-dimensional array of hexagonal pillars (grains) for our simulation [4]. The magnetization in each grain was assumed to be uniform and to precess according to the Landau – Lifshits – Gilbert equation. Total number of grains is 4096 (64 × 64), average grain size $< D_{grain}>$ is 6.35 nm, film thickness is 20 nm, packing fraction is 90% and a grain size dispersion, $\sigma/< D_{grain}>$, is changed to 0-30%. In the case of $\sigma/< D_{grain}>$ = 0%, the grains were located in honeycomb structure. In the other cases, the grain sizes were distributed and the center of a grain was moved so that the adjacent grains were not overlapped.

The magnetic properties of the medium are M_s = 800 emu/cm^3, H_k = 12 kOe, exchange stiffness constant $A = (0\text{-}0.15)\times10^{-6}$ erg/cm.

Ten different type media were prepared for each $\sigma/< D_{grain}>$ and A. The effect of thermal switching was calculated according to the Monte – Calro calculation [5]. Ten different patterns were recorded for a medium model with different temperature random numbers; the temperature is 350 K and it is given by a random number for a recording step. On the DC erased state, NLTS 1111 pattern was written. The length of bit was ten times as long as grain size (63.5 nm).

Results and discussion

Two reversed patterns were written on DC erased state. There are four transition regions, T1, T2, T3 and T4. Figure 1(a) shows a typical write pattern. In order to investigate cluster size in the transition regions, we defined that the widths of the transition regions are two grain length.

A scheme of estimation method of magnetic cluster in a transition region is shown in figure 1(b). A rectangular window with width of one-tenth the average grain size and height of the track width was placed on the medium and it was scanned to the down track direction. In the rectangular window, a reversed area which was not separated by a non-reversed area was defined as one cluster (such as cluster 1, cluster 2 in fig. 1(b)). Length of a cluster i^{th} in the cross track direction was defined as CSaxi, and the average of the cluster lengths was named CSax.

Figure 2(a) shows average cluster size as a function of exchange stiffness constant A. The solid lines show average cluster sizes of CSax. The broken line shows cluster sizes which were estimated from M-H loops by using our previous method. These cluster sizes are named CSaa in order to distinguish them from CSax. In the region of the large A, CSaa increases with increasing A and CSax is almost constant. Therefore, CSaa is larger than CSax in the large A region. The CSaa is decreased with increasing $\sigma/< D_{grain}>$, but CSax slightly increases with increasing $\sigma/< D_{grain}>$. Therefore, in magnetic recording, it is inappropriate to use the cluster size estimated from M-H loop for the discussion of medium noise.

Figure 2(b) shows distance between adjacent peaks with various A and $\sigma/< D_{grain}>$ = 0%. The distances between adjacent peaks increase with progressing the recording. In the region of large A ($\geqq 0.03\times10^{-6}$ erg/cm), the distance between peaks became lager than ideal value. In the other grain size dispersion, the same tendency were obtained through $A = (0\text{-}0.15)\times10^{-6}$ erg/cm.

[1] J. J. Miles and B. K. Middleton, IEEE Trans. Magn., 26, 2137(1990).

[2] H. Zhou, H. N. Bertram, M. F. Doerner, and M. Mizamaani, IEEE Trans. Magn., 35, 2712(1999).

[3] H. Endo, Y. Uesaka, Y. Nakatani, N. Hayashi, and H. Fukushima, IEEE Trans. Mag., 42, pp.2969-2971(2006).

[4] H. Endo, Y. Uesaka, Y.Nakatani, N. Hayashi, and H. Fukushima, J. Appl. Phys., 97, p.10E312(2005).

[5] Y. Uesaka, Y. Nakatani, N. Hayashi, and H. Fukushima, J. Magn. Magn. Mater., 174, pp.203-218(1997).

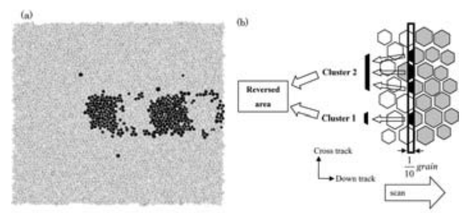

Fig. 1. (a) Typical write pattern, (b) Scheme of estimation method of magnetic cluster in a transition region.

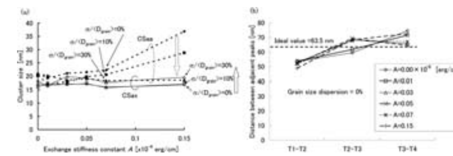

Fig. 2. (a) Average cluster size as a function of exchange stiffness constant *A*, (b) Distance between adjacent peaks with various *A* and $\sigma/< D_{grain}>$ = 0%.

Ligand exchange in gold-coated FePt nanoparticles.

P. de la Presa[1], T. Rueda[1], M. Morales[2], A. Hernando[1]
1. Instituto de Magnetismo Aplicado, UCM, Las Rozas, Spain; 2. ICMM-CSIC, Madrid, Spain

The useful magnetic properties of FePt nanoparticles (NPs) arouse the interest of this material for biological applications.[1] However, the synthetic procedure to obtain high quality NPs involves organic phase processes. The NPs resulting from these procedures are stable in nonpolar solvents (such as hexane) and capped with nonpolar endgroups on their surface. The capping molecules (also called ligands) are typically long-chain alkanes with polar groups that bind to the nanoparticles' surface. To obtain a biocompatible and water dispersible compound the ligands must be exchanged by polar endgroups. Some efforts have been done to found a proper ligand that can bind both Fe and Pt simultaneously. Furthermore, functionalization of the NPs has been recently improved by coating the FePt NPs with gold [2]. The coating procedure requires also an organic phase process resulting in FePt@Au NPs capped by oleic acid and oleylamine and dispersed in hexane.

In this work we present the magnetic properties of gold coated FePt NPs and the study of stable aqueous dispersions of FePt@Au and FePt synthesized after ligand exchange with mercaptoundecanoic acid (MUA). The synthesis of the FePt and FePt@Au Nps is described elsewhere [1,2]. The particle size determined from TEM micrographs goes from 4 nm for the uncoated NPs to a maximum of 10 nm for the gold coated ones indicating that the thickness of the shell ranges from 1 to 3 nm. The magnetic characterization consists in hysteresis cycles at 5K and 300K (see Fig. 1) and zero-field-cooled (ZFC) and field cooled (FC) curves at 100 Oe. The results show that the blocking temperature and coercive field decrease for the gold coating NPs, and it is related to the reduction of the magnetic anisotropy due to the presence of gold atoms at the surface.

The ligand exchange is performed by dispersing the NPs in chloroform containing MUA and stirring during one day; Then NPs are collected by precipitation with ethanol and centrifugation. As can be seen from Fig. 2, the ligand-exchanged NPs are successfully dispersed in water and stable at pH 7. We observe by TEM that, whereas the NPs dispersed in hexane tend to self assembling keeping a certain distance between NPs, in the MUA ligand exchanged NPs there is no sign of pattern, tending to agglomerate instead of self assembling. The hydrodynamic radius of the uncoated, gold coated and the ligand-exchanged NPs is determined by means of dynamic light scattering (DLS). The oleic acid and oleylamine FePt have hydrodynamic diameter (Dh) of about 5 nm, whereas Dh ranges from 7 to 12 nm for gold coated NPs. These values are in agreement with well dispersed NPs which have an organic layer about 1 nm in size surrounding the surface. On the other hand, the ligand-exchanged NPs have a much greater Dh (ranging from 150 to 240 nm) indicating that FePt and the FePt@Au slightly agglomerate during the ligand-exchange process, in agreement with TEM results. The measurement of the isoelectric point shows that the MUA ligand-exchanged NPs have negative charges at the surfaces and are stable in water for pH > 3.

These results make the MUA ligand-exchanges FePt@Au NPs an interesting material for biological applications since the magnetic properties do not vary significantly from the FePt, the size of the agglomerates are around 200 nm and are negatively charged, which can facilitate the cellular uptake of the NPs. Studies of toxicity are underway.

[1] S. Sun, Adv. Mater. 18, 393–403 (2006)

[2] P. de la Presa, M. Multigner, M.P. Morales, T. Rueda, E. Fernández-Pinel, A. Hernando, J. Magn. Magn. Mater. 316, e573 (2007)

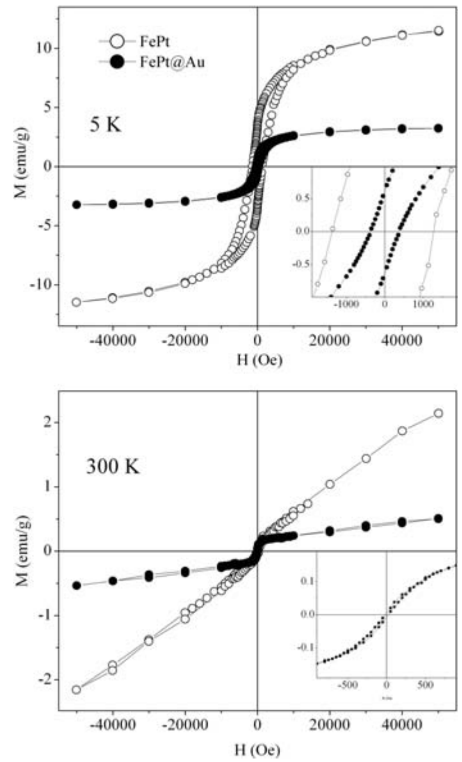

Figure 1: Hysteresis loops at 5 and 300 K of FePt (open circles) and FePt@Au (full circles) NPs

Figure 2:Left: top: FePt@Au dispersed in hexane, bottom: water. Right: top: hexane, bottom: FePt@Au dispersed in water.

HN-16

Magnetic behavior of oleate-capped monodisperse iron oxide nanoparticles prepared in polyol solutions.

G. Caruntu[1,2], D. Caruntu[1,2], C. J. O'Connor[1,2]
1. Advanced Materials Research Institute, New Orleans, LA; 2. Chemistry Department, University of New Orleans, New Orleans, LA

The magnetic characteristics of well-separated monodisperse iron oxide nanoparticles with sizes varying between 6.6 and 17.8 nm prepared in non-aqueous solutions have been investigated. Both morphology and mutual interactions between the nanoparticles have been identified in influencing the magnetic response of the nanopowders. While the smaller nanocrystals exhibit superparamagnetism with blocking temperatures increasing gradually with the particle size, above a critical size the particles are ferromagnetic at room temperature (Fig.1).
Assuming that the particles are non-interacting and possess a uniaxial anisotropy, the corresponding blocking
temperatures (TB) can be used to estimate the values of the anisotropy energy constant (K) of the oleate-capped
Fe_3O_4 nanocrystals. The calculated values of the constant are $K = 4.74 \times 10^5\ Jm^{-3}$ for the particles with an average diameter of 6.6 nm and $K = 1.11 \times 10^5\ Jm^{-3}$ for those with a mean size of 11.6 nm, respectively. These values are about one order of magnitude higher than that of the bulk material($K_{(bulk)} = 0.135\times10^5\ Jm^{-3}$) [1] and were found to increase with decreasing size of the nanoparticles. Additionally, they are slightly larger, but yet in good agreement with the K values estimated by Mossbauer spectroscopy for 6 nm ($K = 1.4 \times 10^5\ Jm^{-3}$) and 12 nm ($K = 0.9\times10^5\ Jm^{-3}$) [2,3] particles or by using the equation $KV = 25\ k_BT$ for 7 nm Fe_3O_4 particles ($K = 2.8\times10^5\ Jm^{-3}$) [4], but much lower than that for to 3–7 nm sized particles obtained by the microemulsion technique ($K = 10^6\ Jm^{-3}$)[5]. The anisotropy constant (K) of the nanocrystalline materials can incorporate different contributions from magnetocrystalline shape and surface anisotropy [4, 6]. Thus, assuming that the magnetocrystalline anisotropy of the Fe_3O_4 nanoparticles prepared in the polyol media is invariant to the reaction conditions (the nature of the solvent, the heating time) and the shape of the nanoparticles does not change significantly with their size, the variation trend in K can be ascribed to the concurrent effect of the interparticle interactions [7] and the surface anisotropy [6]. The saturation magnetization values are slightly smaller than that of the bulk material, suggesting the existence of a disordered spin configuration on their surface. The thickness of the magnetically inert shell estimated from the size variation of the magnetization is 1.9 Å. The dipole–dipole interactions between the particles were tuned by changing the interparticle distances, e.g. by diluting the nanopowders in a non-magnetic matrix at concentrations ranging from 0.25 to 100 wt% (Fig. 2). As the strength of the interactions is decreased with dilution, the energy barrier is substantially lowered; this will induce a drastic decrease of both the blocking temperatures and the coercivity with decreasing concentration of the nanoparticles [8].

[1] Morales M. P. et al. 2005, Chem. Mater. 11 3058.

[2] Ma M. et al. 2004 J. Magn. Magn. Mater. 268 33.

[3] Morup S. et al. 1976 Appl. Phys. 11 63.

[4] Si S. et al. 2004 Chem. Mater. 16 3489.

[5] Lee Y. et al. 2005 Adv. Funct. Mater. 15 503.

[6] Tung L. D. et al. 2002 Physica B 319 116.

[7] Yokoyama M. et al. 1998 J. Magn. Magn. Mater. 183 173.

[8] Vestal C. et al. 2004 J. Phys. Chem. B 108 18222.

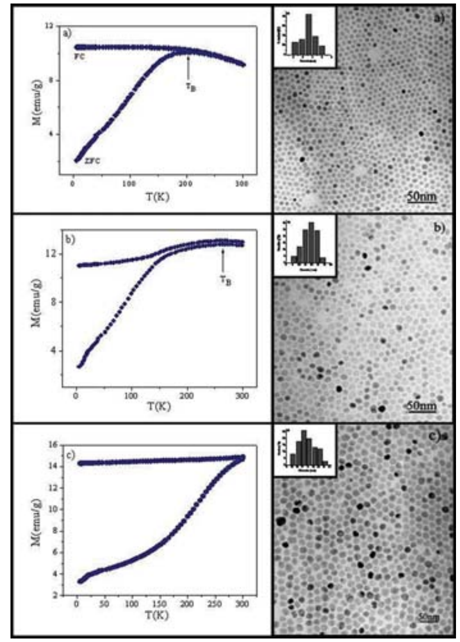

Fig. 1 Zero field (ZFC) and field cooled (FC)curves of the oleate-sized magnetite nanocrystals with differet sizes: 6.6 nm (a); 11.6 nm(b) and 17.8 nm (c). The pictures in the right side show the corresponding TEM micrographs of the nanoparticles.

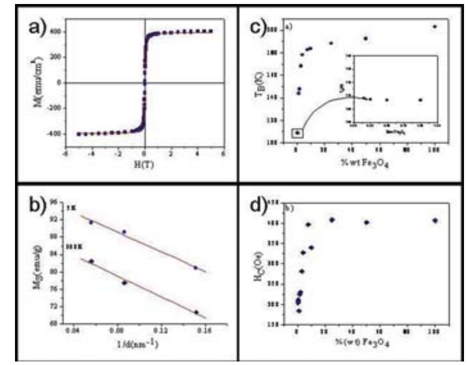

Fig. 2 A typical hysteresis loop for the 17.8 nm magnetite nanoparticles and the coorresponding fit with a Langevin function (a); The variation of the magnetization of differently-sized Fe_3O_4 nanoparticles with the inverse of their diameter (b); Variation of the blocking temperature (c) and the coercivity (d) of 6.6 nm magnetite nanoparticles dispersed in parafin with the dilution

Interplay Between Magnetic Coupling of Magnetic Nanoparticles and Magnetic/Superconducting Proximity Effect.

E. Navarro[1], Y. Huttel[2], A. Cebollada[3], A. Perez-Junquera[4], M. Velez[4], J. I. Martin[4], J. M. Alameda[4], J. L. Vicent[1]

1. Fisica Materiales, Univ. Complutense, Madrid, Spain; 2. Instituto Ciencia de Materiales, CSIC, Madrid, Spain; 3. Instituto Microelectronica de Madrid, CSIC, Madrid, Spain; 4. Fisica, Universidad de Oviedo, Oviedo, Spain

Navarro et al. (1) have reported the magnetic behavior of Fe (100) nanoparticles induced by different capping layers. In that work, they showed that the interplay between the nanoisland sizes and the capping materials is crucial to govern the magnetic coupling among Fe nanoparticles. In this work we are going to address magnetic/superconducting proximity effect between the Fe nanoislands and superconducting films mediated by a capping material. The samples are grown by sputtering technique and following several in-situ steps. First of all, the Fe (100) nanoparticles are grown on sapphire substrates, see Navarro et al (1) for details, after the appropriate capping layer is deposited and finally Nb thin film is grown on top. In situ MOKE hysteresis loops allow us obtaining the magnetic properties of the samples. AFM scans and hysteresis loops are used to extract the nanoparticles morphology, see (1). In this work we will show that the magnetic/superconducting proximity effect is a powerful tool to explore the tuning of magnetic coupling between magnetic nanoparticles mediated by different capping materials. In figures 1,2 we show a typical example. These figures shown an enhancement of the proximity effect due to the strong coupling of the Fe nanoparticles induced by Pt capping, this coupling vanishes in the case of Al capping layer and the Nb film critical temperature increases in comparison with the critical temperature of the Nb/Pt/Fe sample.

(1)E. Navarro, Y. Huttel, C. Clavero, A. Cebollada, G. Armelles, Phys. Rev. B 69, 224419, 2004.

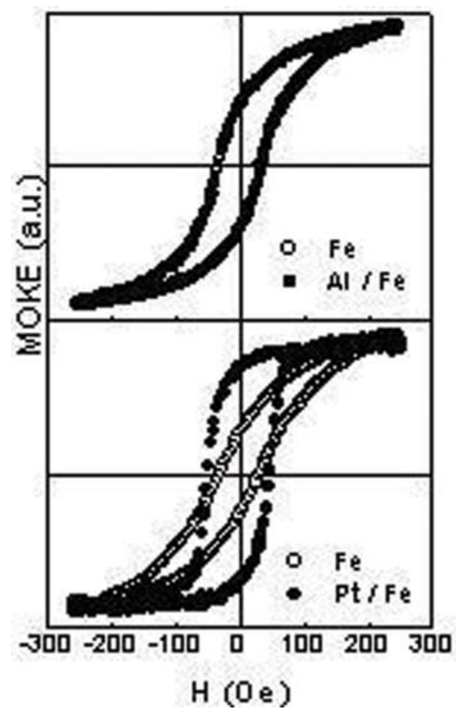

MOKE hysteresis loops of Fe nanoparticles, and Fe nanoparticles with Al or Pt capping layer. Nominal Fe nanoparticle dimensions: Height 1.2 nm and diameter 12 nm. Thickness of the Al or Pt capping layer: 2.5 nm.

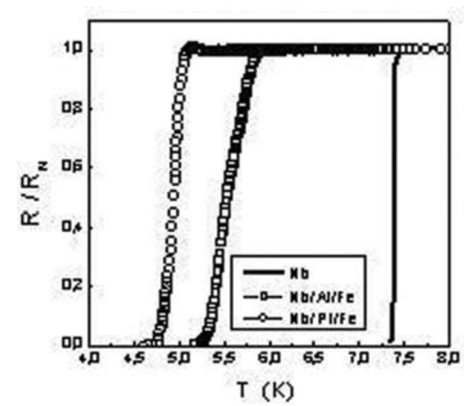

From right to left: Superconducting transition temperatures for: Nb (25 nm thickness)/sapphire sample; Nb (25 nm thickness)/Al (2.5 nm thickness)/Fe (height 1.2 nm and diameter 12 nm)/sapphire sample; Nb (25 nm thickness)/Pt (2.5 nm thickness)/Fe (height 1.2 nm and diameter 12 nm)/sapphire sample.

HO-01

Lube depletion caused by thermal-desorption in heat assisted magnetic recording.

Y. Ma, B. Liu
Data Storage Insitute, Singapore, Singapore

Heat assisted magnetic recording (HAMR) is a promising technique to overcome the superparamagnetic limit. However, it brings about serious problems to the slider-disk interface. One is the lube depletion on disk surface caused by the laser heating. At elevated temperature, lube depletion can be caused by either the desorption of the lube from the disk surface or the decomposition of the lube on the disk surface depending on the relative rate constants for each process [1]. In this article, lube depletion caused by lube desorption from disk surface during laser heating is studied based on adsorption/desorption theory and previous lube transfer studies [2, 3].

A physical model is developed aiming at studying the lube depletion quantitatively. The lube depletion process under laser heating in slider-disk interface and underlying physics are explained. The effects of slider air-bearing pressure and temperature on the saturated vapor pressure of lube, the effect of temperature on lube viscosity, and the difference between the desorption of bonded and unbonded lube molecules on disk surface, etc are also addressed. Then, equations governing the lube depletion are proposed based on the Langmuir and the Brunauer-Emmett-Teller theories.

Lube thinning rate over laser heating area as a function of lube molecular weight is calculated and shown in figure 1. The temperature at laser spot is 450C. The thinning rate decreases dramatically with the increase in the lube molecular weight. To unveil the meaning of the thinning rates, the time for lube in the area from 20 mm to 40 mm in radius on a 3.5” disk surface to thin 1 angstrom is calculated by assuming a 100 nm laser spot size. The results are also shown in figure 1. The time for 6 kDalton Zdol is about 0.42 year, for 7 kDalton Zdol about 19.6 years and for 8 kDalton Zdol about 893 years. It is acceptable if 7 kDalton Zdol is used to deal with the lube depletion problem caused by the lube desorption from disk surface during laser heating.

Lube thinning rate over laser heating area under 180 atm slider air-bearing pressure and the ratio of lube thinning rate under 180 atm over that under 18 atm as a function of lube molecular weight is summarized in figure 2. The temperature at laser spot is 450C. The slider air-bearing pressure shows significant effect on increasing the lube thinning rate and the higher the lube molecular weight the more significant the effect. Therefore, it is very important to avoid designing a slider that produces high air-bearing pressure on the laser heating area in HAMR.

It is also found that lube thinning rate can be reduced significantly by lowering laser heating temperature and lowering lube saturated vapor pressure.

1.Lim, M.S., Gellman, A.J.: Kinetics of laser induced desorption and decomposition of Fomblin Zdol on carbon overcoats. Tribol. Int. 38, 554-561 (2005)

2.Ma, Y.S. Liu, B.: Lube transfer from disk to slider in hard disk drives. Appl. Phys. Lett. 90, 143516 (2007)

3.Ma, Y.S. Liu, B.: Dominant factors in lubricant transfer and accumulation in slider-disk interface. (accepted by Tribol. Lett.)

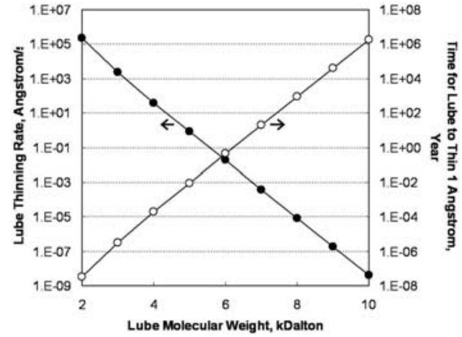

Fig. 1 Lube thinning rate over laser heating area as a function of lube molecular weight and the time for lube in the area from 20 mm to 40 mm in radius on a 3.5” disk surface to thin 1 angstrom at 450C.

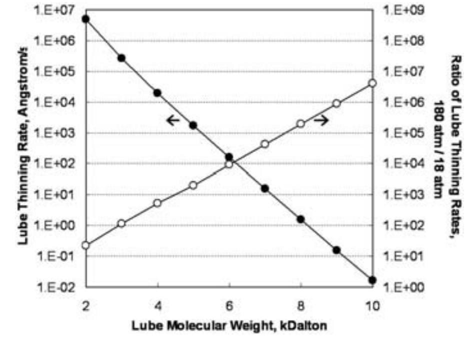

Fig. 2 Lube thinning rate over laser heating area as a function of lube molecular weight under 180 atm slider air-bearing pressure and the ratio of lube thinning rates under 180 atm over that under 18 atm at 450C.

HO-02

Study of slider's flying behavior under by various temperature and humidity conditions.

T. Watanabe, K. Kusakawa
Fuji Electric Device Technology Co.,Ltd, Matsumoto, Japan

[Abstract]
Due to decrease of slider-disk space and usage of Hard Disk Drive under extensive environmental conditions, slider-disk interaction has become more pronounced. Therefore, it is necessary to understand the slider's flying dynamics under extensive environmental conditions.
In this study, we have investigated flyability performances of slider under various temperature and humidity conditions. As the results of touch-down/take-off (TD/TO) tests, it is revealed that water's meniscus formation between slider and disk surface increases slider-disk interaction and degraded slider's flying ability.
[Experiment]
For understanding the temperature and humidity effects on flying slider's behavior, TD/TO tests were performed under various atmosphere conditions. The disk used in this study was coated with a DLC layer and lubricated Fomblin Z-tetraol.
Figure 1 shows the dependence of TD/TO velocities on various temperature and humidity conditions. Under low temperature (22 degree) region, a slight increase in TO velocity is observed as increase of relative humidity. On the other side, remarkable increase was observed under higher temperature region (70 degree) as increase of relative humidity. This result indicates that degradation of slider's flying ability is originated in the water in atmosphere.
[Consideration]
We assumed that high humid air flows between flying slider and disk surface caused the formation of water's meniscus such as Fig.3. According to Kelvin's equation, water's meniscus between two plains is described as follows.
$\mathrm{Ln}(P/P0)=-2\gamma M\cos(\theta)/(RT\rho r)$,where P is vapor pressure at temperature T, P0 is saturated vapor pressure at T, γ is surface energy, M is molecular weight of water, ρ is density of water, θ is contact angle, R is gas constant, T is absolute temperature and r is radius of water's meniscus.
Figure 4 is the correlation between "Diameter of water's meniscus" and "Relative humidity at three temperature conditions (22,55,70 degree)" derived from equation (1).
This figure indicates that the growth of meniscus diameter strongly depends on humidity at high temperature. Moreover, this correlation is similar to that of Fig.1.
Fig5 shows correlation between Diameter of water's meniscus and TD/TO velocity. From this figure, TD/TO velocity strongly depends on the water's meniscus diameter. Therefore, we conclude that the water's meniscus formation degrade slider's flying ability.
[Summary]
We studied the flying slider's behavior under various temperature and humidity atmosphere, and concluded the water's meniscus formation between slider and disk surface increased slider-disk interaction and degraded slider's flying ability under high temperature and high humidity condition. It is expected realizing of hydrophobic surface will be suitable for improving slider's fly-ability.
We will present the method of hydrophobic treatment on the disk surface at meeting.

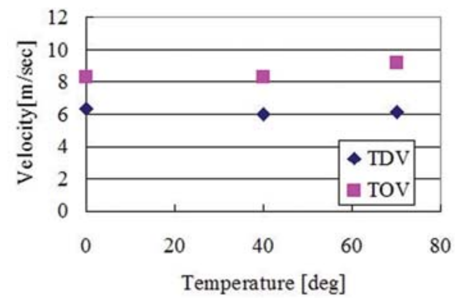

Fig.1 TD/TO Velocity depending on temperature under stable humidity (5%)

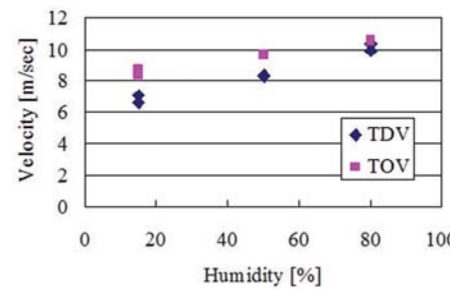

Fig.2 TD/TO Velocity depending on humidity under stable temperature (70 degree)

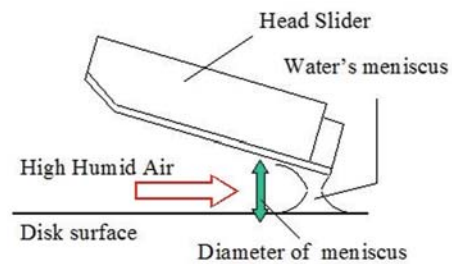

Fig.3 The outline of "meniscus formation" between slider and disk surface

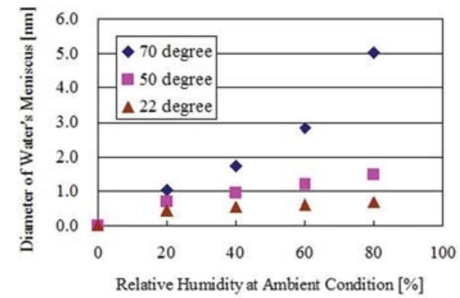

Fig.4 The correlation between diameter of water's meniscus and humidity derived from Kelvin's equation

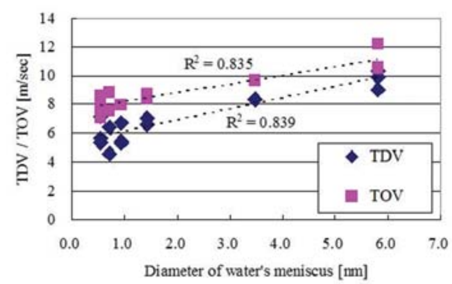

Fig.5 The correlation between TD/TO Velocity and diameter of water's meniscus

HO-03

A novel simulation of air/liquid bearing based on lattice Boltzmann method.

D. Kim, M. S. Jhon, H. Kim
Depart of Chemical Engineering and Data Storage Systems Center, Carnegie Mellon University, Pittsburgh, PA

With the continuous demanding of increasing the areal recording density, head media spacing is expected to be less than 6.5 nm for 1Tbit/in^2 hard disk drive (HDD) implying that the budget for the thickness of lubricant film is 1 nm and with a few nanometer air spacing [1].
Therefore, to accurately model nano-mechanics of head disk interface (HDI), a hybrid approach of air and liquid bearing simultaneously in a non-isothermal environment is required. To achieve this goal we will adopt lattice Boltzmann method (LBM) [2]. LBM has emerged as a promising numerical tool for simulating fluid flows and thermal management with complex physics [2]. The numerous advantages, including clear physical pictures, an inherently transient nature, multi-scale simulation capabilities, and fully parallel algorithms, make LBM to be a strong candidate to model HDI nano-mechanics. Since the application of LBM to air bearing has been reported in other place [3], we will focus on liquid bearing modeling in this paper. Viscoelastic liquid bearing (VLB) [4] can be used as a benchmark problem in studying lubricant rheology in a non-isothermal environment. Due to the high spinning speed of disks and ultra-thin film thickness, the shear rate of this liquid may reach values on the order of 10^{10} sec^{-1}. In this ultra-high shear rate regime, shear thinning effect becomes very subtle. Although the standard modeling for VLB in conjunction with VISqUS technology [5] has been reported in the past [4], we developed a novel three-dimensional mathematical tool based on LBM.
By adopting the Taylor series expansion and least squares based LBM and non-Newtonian fluid models [6], our LBM scheme can predict the flow behavior and stress distribution under an arbitrary shaped slider in three dimensions, which is useful for simulation of VLB. To illustrate the capabilities of our novel LBM methodology, we first simulated the Poiseuille flow in a 3D square duct, which is driven by the pressure difference. Figure 1 shows the nondimensional velocity profiles for Newtonian, truncated power-law, and Bird-Carreau fluids. The power-law exponent was set as 0.9 and the velocity of non-Newtonian fluids (Figs. 1 (b) & (c)) increased in comparison with Newtonian fluid due to shear thinning. LBM described the shear thinning behavior accurately for non-Newtonian fluid models.
After the benchmark study of 3D Poiseuille flow, VLB of a model slider was simulated to illustrate essence of air/liquid bearing simulation. The dummy slider has the dimension of 4 mm × 0.416 mm. The disk is operated at angular velocity of 3,600 rpm and the velocity at pivoting point is 15 m/s. We chose the pitch angle to be 80 μrad and slider flying height h_m=25 nm. Figure 2(a) shows the normalized isothermal pressure profiles for the truncated power-law fluid with n=0.9. The pressure builds up under the slider and reaches maximum near the trailing edge, and then sharply decreases to ambient pressure. In addition to the advantage of transient dynamic calculation, one of the strength of LBM computational tool over the well-known modified Reynolds equation or Boltzmann equation [7] is the direct calculation of stress field, which is critical to determine the friction force or power consumption for HDD. Figure 2(b) shows the isothermal shear stress profiles at the slider bottom surface. As the spacing decreases from leading to trailing edge, the shear rate increases gradually. We are currently developing air/liquid bearing simulation in a non-isothermal environment using LBM to make integrated HDI simulation. This computational tool can be further applied to predict the flow field, temperature and pressure profiles, and shear stress for a slider with complex geometry.

1. J. Gui, *IEEE Trans. Magn.*, **39**, 716 (2003).
2. H. Chen, S. Kandasamy, S. Orszag, R. Shock, S. Succi, and V. Yahkot, *Science*, **301**, 633 (2003).
3. W. T. Kim, M. S. Jhon, Y. Zhou, I. Staroselsky, and H. Chen, *J. Appl. Phys.*, **97**, 10P304 (2005).
4. P. R. Peck, M. S. Jhon, R. F. Simmons, Jr., and T. J. Janstrom, *J. Appl. Phys.*, **75**, 5747 (1994).
5. M. S. Jhon, P. R. Peck, R. F. Simmons, Jr., and T. J. Janstrom, *IEEE Trans. Magn.*, **30**, 410 (1994).
6. W. T. Kim, H. C. Chen, and M. S. Jhon, *J. Appl. Phys.*, **99**, 08N106 (2006).
7. S.-C. Kang, R. M. Crone, and M. S. Jhon, *J. Appl. Phys.*, **85**, 5594 (1999).

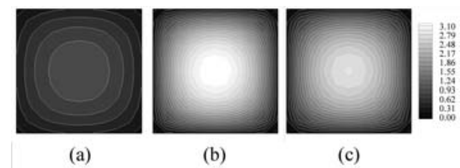

Fig. 1 Nondimensional velocity profiles on the plane perpendicular to the flow direction in the 3D pressure driven square duct for (a) Newtonian, (b) truncated power-law, and (c) Bird-Carreau fluids.

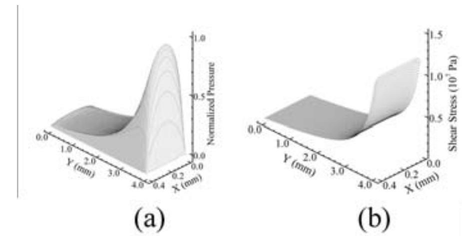

Fig. 2 (a) Normalized pressure profile for a 3D model slider and (b) shear stress profile at the slider bottom surface.

Numerical Simulation of Touchdown/Takeoff of Sphere-Pad Slider.

H. Li[1], J. Li[2], J. Xu[2], Y. Shimizu[2], K. Ono[2], S. Yoshida[1]
1. Storage Mechanics Laboratory, Hitachi Asia Ltd., Singapore, Singapore; 2. Central Research Laboratory, Hitachi Ltd., Kanagawa, Japan

This work numerically simulates of the static TD/TO hysteresis of the sphere-pad slider[1][2] in the terms of meniscus bridge formation and breakage. It proposes a geometry model for the lubricant bridge between the sphere-pad slider and lubricant over the disk surface, and the corresponding meniscus force model. By applying them into the air-bearing simulator, the TD/TO hysteresis of the sphere-pad slider is analyzed.**(1)Mathematical Model of Sphere-pad and Meniscus Bridge** The geometry of the sphere-pad is expressed as a sphere model(Fig.1). The meniscus bridge between the sphere-pad and disk is modeled as Fig. 2. With considering the liquid pressure balances at the meniscus boundary, it can obtain the average contact angle, then the side meniscus radius and ring meniscus radius at given separation[3].**(2)Flying Model of Slider** A three-dimensional (3D) model of sphere-pad slider/disk interface is built(Fig.3). A sphere-pad is designed at the top of slider's trailing pad. There is a smooth air pressure distribution and the achieved mesh size is about 1~2 μm. The air bearing pressure distributions on the slider's ABS with/without the sphere-pad are compared in Fig. 4. **(3)Parametric Study of Mobile Lubricant Thickness on Hysteresis and Meniscus Force** Fig. 5 shows the meniscus forces interaction on the sphere-pad slider under the different mobile lubricant thickness (T). It is found that thinner the mobile lubricant thickness, lower the meniscus force as well as the break height of the meniscus bridge. When T is 0.5, 0.7 and 1.0 nm, the lubricant bridge's break heights are about 1, 3 and 9 nm, respectively. For both two sliders with 5/10 nm height sphere-pads, the break height is kept almost same at the give lubricant thickness, althought the meniscus force is reduced much by the increase of the height of sphere-pad. For example, the meniscus force on the slider with a 5 nm height sphere-pad is about 2 times of that with a 10 nm height sphere-pad. Fig. 6 shows that the FH and RPM hysteresis reduces much with the reduction of T due to the increase of the dispersion pressure. So the reduced mobile lubricant thickness can both reduce the FH and RPM hysteresis as well as the meniscus force.**(4)CONCLUSION** It is found that the reduced mobile lubricant thickness can both reduce the FH and RPM hysteresis as well as the meniscus force. The increase of the Hamaker constant (the absolute value) will reduce the TD/TO hysteresis of FH and RPM of the sphere-pad slider as well as the meniscus force. The increased surface energy will increase the TD/TO hysteresis of FH and RPM of the sphere-pad slider as well as the meniscus force. The large height and small horizontal radius of the sphere-pad can reduce the meniscus force, but do not affect the FH hysteresis much.

[1]K. Ono, "Flying Head Slider," Japan patent: P2005-31007, Filed: January 12, 2005, Published: July 27, 2006.

[2]K. Ono, "Dynamic Instability and Stabilizing Design Concept of Flying Head Slider in Near Contact Region," invited talk, the 8th perpendicular magnetic recording conference, Japan, 2007.

[3]K. Hiromichi, H. Matsuoka, and S. Fukui, "Construction of Interface Model between Two Solid Considering Nano Thin Liquid Layer," Proceedings of JAST Spring Tribology Conference, Tokyo, 2006.

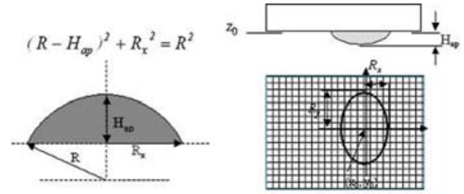

Fig. 1. Geometry model of sphere-pad

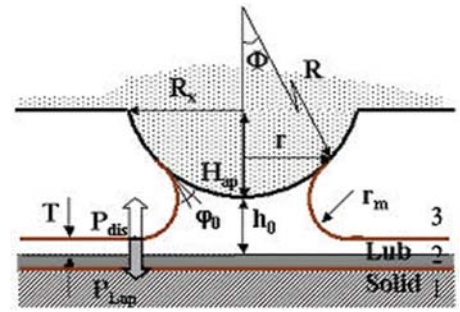

Fig. 2. Model of Meniscus Bridge

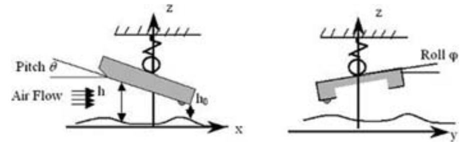

Fig. 3. Three-dimensional model of sphere-pad slider/disk interface

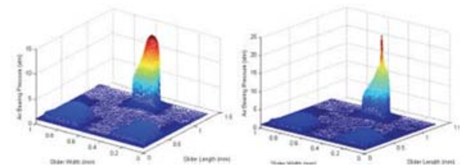

Fig. 4. Air bearing pressure distribution on (a) original slider (b) redistribution on sphere-pad slider of Rx=10 μm and Hap =10 nm

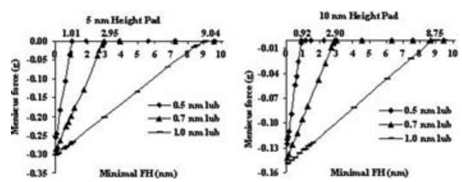

Fig. 5. Meniscus force acting on slider under different mobile lubricant thickness

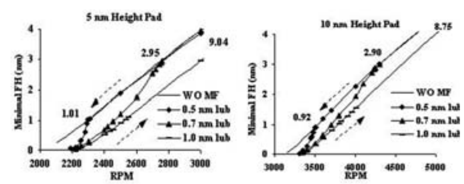

Fig. 6. TD/TO hysteresis under different mobile lubricant thickness

HO-05

Dynamically controlled thermal flying-height control slider.

T. Shiramatsu[1], T. Atsumi[1], M. Kurita[1], Y. Shimizu[1], H. Tanaka[2]
1. Central Research Laboratory, HITACHI, Ltd, Fujisawa-shi, Japan; 2. Hitachi Global Storage Technologies Japan, Ltd., Odawara-shi, Japan

1. Introduction

To achieve ultra-low flying height, magnetic spacing variations due to manufacturing tolerances and temperature-induced thermal protrusion need to be reduced. We have developed a thermal flying-height control (TFC) slider that carries a micro-thermal actuator [1] [2]. Previous TFCs were mainly statically controlled by a constant power supply. Our purpose is to demonstrate dynamic control of a TFC slider to compensate for high-speed magnetic signal modulation using feed-forward control methods.

2. Experimental methods

We used a spin stand and applied the following two feed-forward control methods.
Method 1: Only time domain information was used. The average magnetic signal modulation data without TFC (Fig. 1) was used to adjust TFC power.
Method 2: In addition to time domain information, frequency domain information of a TFC actuator was considered. First, the transfer function of the actuator was calculated from its frequency response. The calculated transfer function P is

$$P = (0.0007072S + 347e6) / (-S-4.356E4) \qquad (1)$$

Next, input data to adjust TFC power was calculated using P and magnetic signal modulation data. In this method, target motion was created by cutting frequency components above 5 kHz using a low-pass filter.

3. Experimental results

The experimental results of methods 1 and 2 are shown in Figs. 2 and 3, respectively. A comparison of modulation by 3-sigma showed that method 1 reduced modulation from 38 mV to 22 mV and method 2 reduced modulation from 38 mV to 18 mV. Method 2 has better compensation than method 1. FFT analysis results are shown in Figs. 4 and 5. Method 2 showed better reduction of modulation in frequencies of 2–5 kHz. A decrease in magnetic signal modulation was confirmed in frequencies up to 5 kHz. The FFT analysis results roughly corresponded to a 5 kHz target frequency.

4. Summary

To dynamically compensate for magnetic signal modulation using TFC, two methods were examined. Method 1 adjusted TFC power using only time domain information. Method 2 adjusted TFC power using frequency domain information in addition to time domain information. Method 2 showed better compensation for magnetic signal modulation due to better compensation at higher frequencies. These results showed that a dynamically controlled TFC is feasible in compensating for kHz order modulation.

[1] M. Kurita et al., Active Flying-height Control Slider Using MEMS Thermal Actuator, Microsystem Technologies, Vol. 12, No. 4, p. 369 (2006).

[2] T. Shiaramatsu et al., Drive Integration of Active Flying-height Control Slider with Micro Thermal Actuator, IEEE Transactions on Magnetics, Vol. 42, No. 10, p. 2513 (2006).

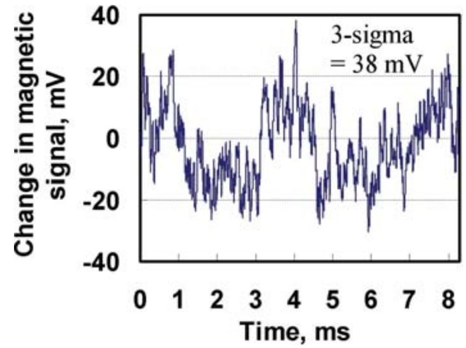

Fig. 1 Magnetic signal modulation

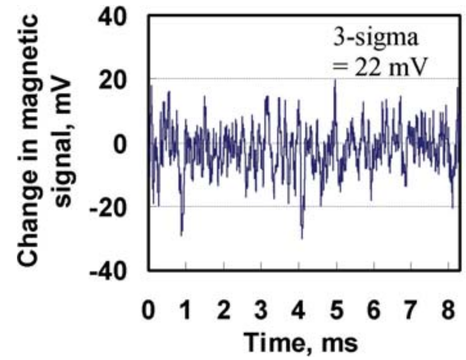

Fig. 2 Magnetic signal modulation during the operation of method 1

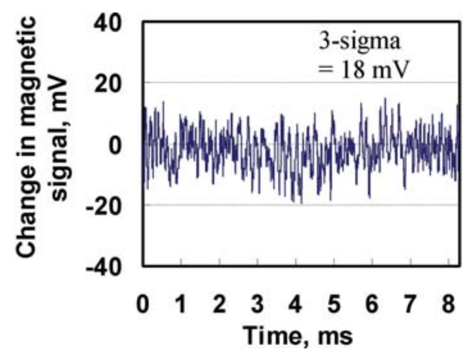

Fig. 3 Magnetic signal modulation during the operation of method 2

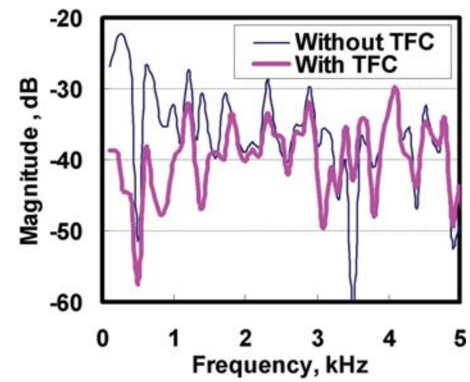

Fig. 4 FFT analysis of method 1

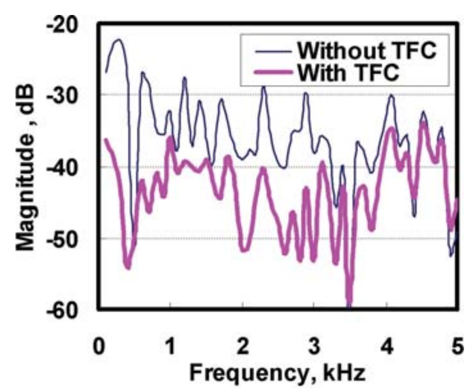

Fig. 5 FFT analysis of method 2

HO-06

Transient analysis of micro thermal actuator for flying height control.

J. Liu[1], J. Li[2], H. Li[1], J. Xu[2], S. Yoshida[1]
1. Storage Mechanics Laboratory, R&D Center, Hitachi Asia Ltd, Singapore, Singapore; 2. Storage Technology Research Center, Hitachi Ltd, Fujisawa, Japan

A spacing of 2.5 nm is required in order to achieve a density of 1 Tbit/in2 in hard disk drives. Static loss of flying height (FH) due to manufacturing tolerance, ambient pressure changes and the temperature variations can cause head disk contact at such a low FH. The dynamic instability should be minimized. All these challenges make a conventional air bearing surface slider an unlikely choice for density of 1 Tbit/in2. Thermal flying height control (TFC) sliders have been recently introduced in commercial products for compensating the static FH loss and reducing the risk of head disk contacts.

Finite element method has been used to model and simulate the static analysis of the temperature distribution and thermal protrusion of the TFC sliders [1]. Experiments were also conducted to verify the nano-protrusion performance and reliability. It was found that the response time of the actuator is about 1ms [2]. Analysis has been conducted to formulate the heat transfer across the head disk interface using velocity slip and temperature jump boundary conditions when a slider flies over a spinning disk [3].

In this paper, a finite element model is created and the cooling effect of the air bearing is included in the model as thermal boundary conditions. Steady-state analysis is firstly performed, the effects of heater input power and distance from ABS to heater were investigated. The results fit well with the previous research results.

Transient simulations are conducted using coupled field finite element analyses to study the bandwidth of the thermal protrusion of the slider, which include the temperature and thermal deformation responses. Firstly we compare the results of two cases, one case we consider the heat transfer on ABS is constant, the other case we consider the heat transfer differs with the pressure differences on ABS. The simulation results show that both the temperature and thermal protrusion of the second case response faster than the constant heat transfer case. It takes about 0.3 ms for the temperature and 0.6 ms for the protrusion to reach static state values. This is because that high pressure or high thermal conduction at the read/write elements location can fasten the temperature and thermal protrusion responses.

In order to compare the responses of power turn on and off, the power is applied from 0 to 0.6 ms and was turned off at 0.6 ms. Time constant(defined as the time for the actuator to reach (1-1/e) times of its full stroke) is used to quantitatively compare the response time of temperature and deformation [1]. Figure 1 (a) and (b) show the time response of temperature and deformation at different locations from the heater. We compare the results of different nodes between actuator and ABS, and at reader position as well. In the figures, D is the distance from ABS. D=15um means the node is inside the slider body,15um away and normal to ABS.D=0 means the node is on the ABS. From figure 1(a), the temperature rise at D=15 um is about 18 degree, but at the reader location is only about 6 degree. And the response time at D=15 um is much faster than at reader location. From Figure 1(b), the deformations only differ about 1 nm from node at ABS plane to node that is 15 um from ABS, and all the response times are similar. Figure 2 listed the response times of the temperature and deformation at D=0 and reader location (T0T and TRT is the temperature response time at D=0 and at reader location respectively, T0D and TRD is the protrusion response time at D=0 and at reader location respectively). It is shown that the response times at these two locations show very small changes and the time constant of power off is slightly longer than power on. The reason for the facts that temperature response strongly depends on distance from the heater is because that the temperature can only transfer from heater to nearby location, and then to further location. But for the deformation response, the expansion around the heater location will push the outer nodes to expand at the same time, thus the response times at different locations are quite similar. When the power is off, no expansion effect exist, the deformations vanish with time and the response time is longer than the expansion time.

The static and other transient results would be included in the full paper.

[1] T. Shiramatsu, M. Kurita, K. Miyake, “Drive Integration of Active Flying-Height Control Slider with Micro Thermal Actuator,” IEEE Trans. Magn., Vol.42, No.10, Oct. 2006, pp: 2513-2515.

[2]M. Kurita, T. Shiramatsu, K. Miyake, “Active Flying-Height Control Slider Using MEMS Thermal Actuator,” Microsyst. Technol., 12 (4) 2006, pp. 369-375.

[3] J. Juang, D. B. Bogy, “Air-Bearing Effects on Actuated Thermal Pole-Tip Protrusion for Hard Disk Drive,” Journal of Trib. Vol. 129, Jul. 2007,

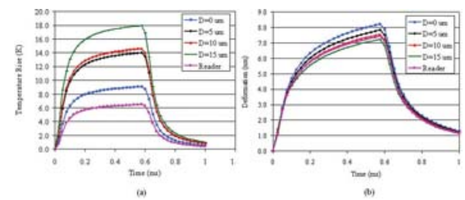

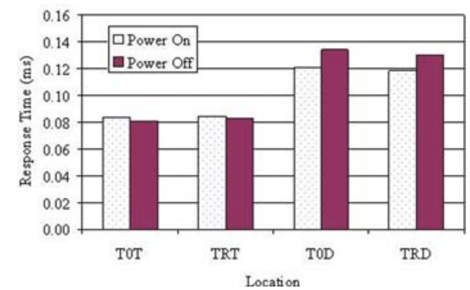

HO-07

Origin of Heater Induced Voltage in Magnetic Recording Heads.

D. Song, M. T. Johnson
Seagate Technologies, Bloomington, MN

Heater induced pole tip protrusion is a popular means of controlling and reducing the head-media spacing (HMS) in a hard disc drive [1]. We found that the heater power can induce a thermoelectric voltage in the transducer. Recall that the thermoelectric effect describes a voltage/current in a circuit where dissimilar metal junctions are placed at different temperatures [2]. In our experiments, recording heads with longitudinal writers were flown on discs. A voltage Vo was applied to the writer leads to obtain a zero net current in the circuit. Thus Vo is the reverse of the thermally induced voltage. Data from three heads showed that the voltage Vo has a parabolic dependence to the heater voltage and is linearly proportional to the heater power (Fig. 1). This suggests that the voltage Vo is thermoelectric in nature and is not due to capacitive coupling.

After studying the writer coil structure, we identified that the dissimilar metal junctions are two Cu/NiFe contacts in the writer coil leads. One contact is positioned next to the heater while the other is substantially further away. Consequently, the two contacts are at different temperatures during heater operation. The measured writer voltage offset is up to 4 mV at 160 mW heater power. Assuming a Seebeck coefficient of 40uV/C [3], this suggests the two interfaces have dT of about 100 C. Our finite-element modeling results using ANSYS indicates that dT is about 64 C for 160 mW heater power. This is within a factor of two compared to the measurement.

The finding implies that one needs to be careful in accounting for voltage offsets during any accurate writer or reader resistance measurements. The effect may be further developed for monitoring temperatures in the transducers if necessary. The effect may also be eliminated by not using dissimilar metals at the contacts, or by placing these contacts such that they are kept at similar temperatures during heater actuation.

[1] D. Meyer, P. Kupinski, US Patent 5991113, 1999

[2] Thermoelectricity, Egli P.H. (Ed.) John Wiley and Sons, New York, 1960

[3] We use the Seebeck coefficient for a Dallas Semiconductor J-type and T-type thermocouples as a guide because the interface contains similar metals. The thermocouples contains Fe-Constantan or Cu-Constantan interfaces and have Seebeck coefficients of 52 uV/C and 42uV/C respectively. Constantan is an alloy of 47wt% Ni in Cu. The specifications can be found at http://www.maxim-ic.com/appnotes.cfm/appnote_number/430.

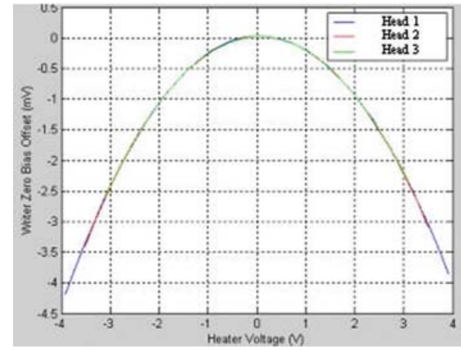

Figure 1: Measured writer offset voltage with zero bias current and various heater voltages on three longitudinal heads.

HO-08

Signal modulation study of TuMR reader near head/disk contact.

N. Kim, Y. Tang, X. Che
Samsung Information Systems America, San jose, CA

Control on head-disk spacing is one of the enabling technologies for continued the higher areal density recording. Flying Height has been significantly reduced over the years and the heating element on heads has been introduced to reduce the spacing even further [1]. The inclusion and proper use of this heater has played a pivotal role in increasing the capacity and the overall performance of magnetic recording.

As this technique allows us the flying height to be in sub nanometer range, proper touch down detection is a necessity for accurate flying height calculation and preventing head-disk interface contact. It is desired to have that detection to be picked up before its catastrophic contact. Such detection could be observed by an acoustic sensor or signal modulation as the head vibration occurs when clearance is minimal [2]. It is also shown that the modulation in an electric signal has the same mechanism vibration with that of acoustic sensor output [3].

Signal modulation has been an excellent indicator for head-disk contact. This resonance signal caused at near contact is generally known as a head vibration. At near contact however, the mechanism of this effect is not well identified. In this paper, we will discuss the origin of this low frequency signal.

The experiment was conducted using a spin stand and a scope to record the read signal from TuMR head. First we checked the head resistance and the signal polarity by injecting a test pulse into the head. We verified the increase of head resistance, resulting in a positive signal on our scope. Heater was used to control on head-disk spacing to create an oscillation when touchdown has occurred. Figure 1a shows the measured signal when head-disk is near contact. From this figure, we can observe clear amplitude change but it is more visible on the positive side. The frequency of the modulation is around 200~300 KHz.

The asymmetrical nature of amplitude modulation can not be explained by Wallace spacing loss. Our study showed that it is caused by a combination of two distinct mechanisms: the magnetic signal amplitude and reader thermal resistance change. To quantify these two effects, the readback signal was passed through a narrow band digital filter centered at recording frequency. The filtered signal was rectified and the envelope was extracted using a low pass digital filter. The Results are plotted in the upper graph of Fig 1b. This envelop represents the magnetic read signal amplitude modulation. To analyze the thermal resistance change effect, the same readback signal was passed through a low pass filter. The result was plotted in the lower part of Fig 1b. The two lines are well synchronized in phase. The well synchronized demodulated magnetic signal and low pass filtered thermal signal suggests that as head-disk spacing is reduced, TuMR resistance increase. This indicates that the temperature has been lowered due to the negative temperature coefficient of the TuMR readers.

This proposition was confirmed with a similar experiment using a GMR reader in which, the magnetic signal amplitude and reader thermal resistance change are synchronized but opposite in phase. Such phase change is expected from the positive temperature coefficient of the GMR readers.

These findings also indicate that the cooling effect increases as the reader approaches the disk surface. Thus, the mechanical vibration of the head results in head-disk spacing change which causes both magnetic signal amplitude modulation (due to Wallace spacing loss) and low frequency reader resistance change (due to thermal cooling effect).

[1] D. Meyer, P. E. Kupinski, and J. C. Liu, “Slider with responsive transducer positioning,” U.S. Patent 5 991 113, Nov. 23, 1999.

[2] W. Shi, L. Zhu, and D. Bogy, “Use of readback signal modulation to measure head/disk spacing variations in magnetic disk files,” IEEE Trans mag. Vol 23, No. 1, pp 233-240, January 1987.

[3] Y.Tang, SY hong, N. Kim and C.Che, “ Overview of Fly height Control applications in Perpendicular Magnetic Recording”,IEEE Trans mag. Vol 43, No. 2, pp 709-714, February 2007.

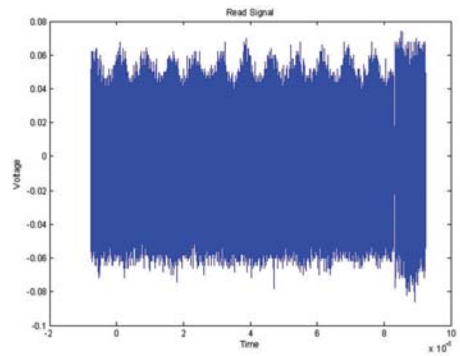

Fig. 1a (Left): The amplitude modulated signal when head –disk is at near contact.

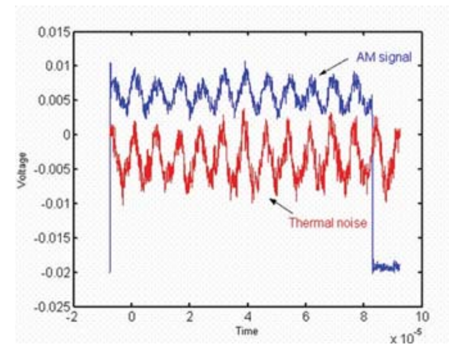

Fig.1b (Right): Demodulated AM signal (upper) and low frequency noise (lower)

HO-09

Nano-mechanics of Perfluoropolyether Films: Compression vs. Tension.

Q. Guo[1,2], P. Chung[1], *M. S. Jhon*[1]
1. Depart of Chemical Engineering and Data Storage Systems Center, Carnegie Mellon University, Pittsburgh, PA; 2. Seagate Technology, Fremont, CA

Molecularly-thin perfluoropolyether (PFPE) lubricant films are commercially used in the magnetic recording media for their long-term reliability. During the hard disk drive operation, the intermittent contact between the slider and lubricant surface inevitably results in the lubricant pick-up, where lubricant molecules could partially transfer to the air bearing surface due to the shear stress and the vertical head-disk interaction and eventually affect the tribological performance of the head-disk-interface (HDI) integration, *i.e.*, lubricant depletion and head vertical displacement. Therefore, compression and tension, the basic vertical modes that PFPE films could undergo, are of technical significance in the HDI integration. Here, using molecular dynamics simulation [1], we examined the nano-mechanics of PFPE films, including compression and tension, along the normal coordinate.
In our "thought experiment," 150 functional PFPE molecules described by the coarse-grained, bead-spring model were simulated onto two solid surfaces facing each other with the horizontal dimension of $15\sigma \times 15\sigma$ and a vertical separation of 25σ (σ is the diameter of the bead). The "compression" mode was achieved by moving the top surface downwards at a constant speed. As the separation becomes less than the Lennard-Jones (LJ) interaction range, interfacial molecules began to interact with each other (Fig. 1b) and eventually formed a nano-confined film (Fig. 1c). During the "tension" process, while the top surface was retracted with the same constant speed, a fluid bridge was formed in between (Fig. 1d), and became thinner and thinner as the wall separation increased (Fig. 1e), and eventually separated into two individual films. Similar nano-mechanics simulation was also performed for nonfunctional PFPE nanofilm, which showed significant difference than functional film. Especially during the "tension" process, with the same time interval, no apparent fluid bridge was observed. Also, its wall separation at the "break" point is much smaller than that of functional PFPEs.
We calculated the normal stress for both nonfunctional and functional PFPEs (Fig. 2). The film normal stress remains constant as the top surface moves downward, but quickly drops when the partial film contact occurs, and eventually reaches the minimum as two separated films completely merge into one confined film. The normal stress may significantly increase with even a minor compressive strain due to the strong intermolecular repulsion force, *i.e.*, the LJ potential. During the tension mechanics, an irreversible normal stress profile was observed, especially for the functional PFPE film, implying the hysteresis phenomenon which may be relevant to the viscoelasticity of PFPE nanofilms and also depend on the retraction rate of the top surface.
The N-mode Maxwell model is employed here to understand the viscoelastic properties of PFPE nanofilms. The simulated "tension" normal stress profile suggests that PFPE molecules may experience two steps of relaxation, especially for functional PFPEs, showing a sharp slope in the beginning of "tension" (backbone-contributed) while the slope gets compromised (endgroup-contributed) once the wall separation is larger than 20σ in Fig. 3.
To satisfy different aspect of disk lubrication requirements, we also explore a multi-component lubricant film system on its fundamentals of nano-mechanics and interfacial properties (*i.e.*, surface tension/disjoining pressure) that have been attempted via both experimental [2] and theoretical tools [3].

1. Q. Guo, Ph.D. Thesis, Carnegie Mellon University, Pittsburgh, PA 2006.
2. C.M. Mate and V.J. Novotny, *J. Chem. Phys.*, **94**, 8420-7 (1991).
3. S. Izumisawa and M.S. Jhon, *IEEE Trans. Magn.*, **42**, 2543-5 (2006).

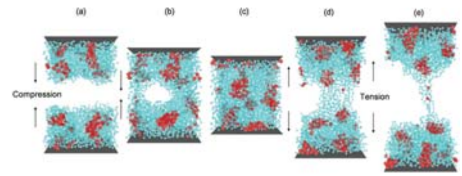

Fig 1. A schematic of the simulated nano-mechanics for functional PFPE films. Note that cyan indicates the backbone beads and red represents the functional endbeads.

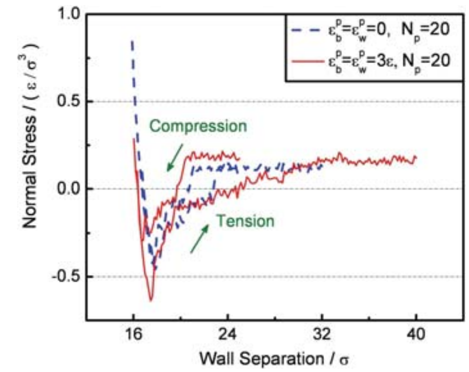

Fig 2. The normal stress of both nonfunctional (dashed lines) and functional (solid) PFPE films.

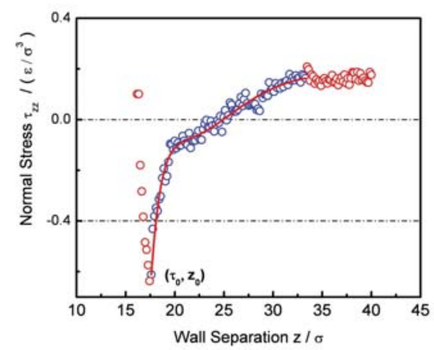

Fig 3. The nonlinear square fit of normal stress data using Maxwell model for functional PFPE films.

HO-10

Ultraviolet Bonding of PFPE with Carbon Overcoat: Surface Energy and Spreading.

H. Chen[2], *P. Chung*[1], M. S. Jhon[1]
1. Depart of Chemical Engineering and Data Storage Systems Center, Carnegie Mellon University, Pittsburgh, PA; 2. Hewlett-Packard Company, San Diego, CA

In this paper, to clarify the bonding mechanism, UV irradiation effects on the molecularly thin PFPE films were investigated by analyzing the surface energy using Lifshit-van der Waals and Lewis acid/base (LW/AB) theory [1]. In the LW/AB theory, the surface energy was decomposed into three components, *i.e.*, LW (γ^{LW}), Lewis acid (γ^{+}), and Lewis base (γ^{-}) surface energy. We have found that the bonding of functional PFPEs with a carbon overcoat is a Lewis acid-base interaction, where the overcoat is an electron donor and functional PFPEs are electron acceptors.
Ztetraol (molecular weight of 2,200 g/mol) were deposited on Seagate disks with ion beam deposited carbon overcoat (COC) via standard dip-coating procedure. These lubricated disks were treated by UV irradiation from a few seconds to 10 min with a low-pressure mercury lamp providing UV light at both 185 nm and 254 nm with the ratio of 1:5. UV irradiations were performed under nitrogen purge to avoid ozone production at room temperature. The contact angles of three test liquids, *i.e.*, DI water, diiodomethane (DIM), and ethylene glycol, were measured on these UV treated disks to determine γ^{LW}, γ^{+}, and γ^{-}. Delubing test was performed to measure the bonded film thickness.
It is found that the total film thickness decreased after 5 mins of UV irradiation. The decease of film thickness indicates the photochemical degradation of PFPE chain and evaporation of short broken chain under UV irradiation. We also found that UV irradiation can enhance the bonding of Ztetraol with ion beam deposited carbon overcoat (< 1 min). However, UV irradiation for longer period (> 1 min) may decrease the bonded film thickness due to the photochemical degradation of PFPE chain.
Figure 1 shows the LW, Lewis acid, and Lewis base surface energies of bare COC and 16Å & 38Å Ztetraol film as a function of UV exposure time. The LW surface energy of Ztetraol film depends weakly on UV exposure time (Fig. 1a). The Lewis acid parameter of Ztetraol film dramatically changed with UV irradiation, which was assigned to the physiochemical changes in the lubricant instead of COC. According to the Lewis acid parameter curve, several stages can be assigned during UV exposure as shown in Fig. 1b. In stage I, the Lewis acid parameter decreased, and the surface became less acidic. In stage II, the Lewis acid parameter increased, which may be due to the dominant photochemical degradation of Ztetraol under UV irradiation. The photochemically degraded PFPE pieces may contain functional groups capable of providing electrons. In stage III, the Lewis acid parameter decreased again then leveled off, which was believed to correlate with the evaporation of broken PFPE.
The Lewis base parameter of bare COC dramatically increased (Fig. 1c), *i.e.*, UV irradiation increased the basicity of the surfaces. It indicates that UV irradiation changes the chemical features of COC. For Ztetraol films, the Lewis base parameter slightly decreased first and reached minimum, then increased (Fig. 1c). The minimum point was related to the maximum bonded film thickness, *i.e.*, 1 min for 16Å Ztetraol and 2 mins for 38Å Ztetraol films.
Short-time UV irradiation can enhance the bonding of functional PFPE, *i.e.*, Ztetraol film with ion bead deposited carbon overcoat, although the energy of UV lights (185 nm and 254 nm) is smaller than the work function of ion beam deposited COC (> 30 eV). It is likely that UV direct photodissociation of PFPE molecules [2] is responsible for the short-time bonding. Long-time UV irradiation degrades the PFPE chain and cause the loss of lubricant by evaporation.

To study the UV effects on the dynamic properties of PFPE film, the spreading profiles of UV irradiated PFPE films were monitored on the partially dip-coated film using optical surface analyzer. Figure 2 shows the spreading profiles of Ztetraol film having the initial thickness of 15 Å without and with 1 min UV irradiation. In comparison to without UV irradiation case, the spreading rate was found to decrease for the films with UV irradiation. We found that the spreading profiles with UV irradiation were much sharper.
L-t plot was adopted to analyze the spreading behaviors. A simple relation $L \propto t^{1/2}$ was found for spreading profiles without UV irradiation indicating diffusion mechanism. With UV irradiation, the spreading of Ztetraol films was retarded, which can be attributed to the enhanced bonding of Ztetraol with overcoat and cross-linking between Ztetraol molecules. In addition, the slope of L-t plot was found to deviate from 0.5. It can be interpreted that UV irradiation produced smaller chain pieces thus led to non-uniform spreading of the film.

1.H.G.Chen,L.Li,P.M.Jones,Y.-T.Hsia,and M.S.Jhon,*IEEE Trans. Magn.*,**43**,2226-8,2006.

2.X.C.Guo and R.J.Waltman,*Langmuir*,**23**,4293-5,2007.

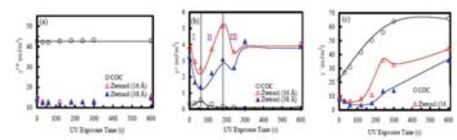

Fig. 1 The (a) LW, (b) Lewis acid, and (c) Lewis base surface energies of bare COC.

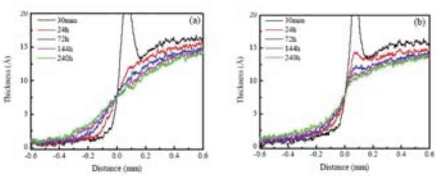

Fig. 2 The spreading profiles of Ztetraol films on carbon overcoat (a) without UV irradiation and (b) with UV irradiation for 1 min.

HO-11

Binary Mixture Lubricant Film of PFPE Lubricants.

P. Chung[1], H. Chen[2], M. S. Jhon[1]
1. Depart of Chemical Engineering and Data Storage Systems Center, Carnegie Mellon University, Pittsburgh, PA; 2. Hewlett-Packard Company, San Diego, CA

New types of disk lubricants, such as Ztetraol Multidentate (ZTMD) and monofunctional (Mono) perfluoropolyether (PFPE), were recently reported to enhance the performance and reliability of hard disk drive with ultra-low head-media spacing (HMS) [1, 2]. However, ZTMD shows good conformation but bad mobility while Mono exhibits better mobility but worse conformation [3]. The mixture of lubricants with different properties may be one solution to meet the harsh requirements of disk lubricants for ultra-low HMS [4]. In this paper, molecular dynamics (MD) simulations with a bead-spring model were employed to examine the detailed structure, conformation, and dynamics of binary mixture lubricant film.
Figure 1 shows the typical snapshots of ZTMD and Z binary mixture monolayer with different volume fraction using MD simulations. The conformation of the binary mixture monolayers was investigated by analyzing the anisotropic radius of gyration (Rgxy/Rgz, where Rgxy and Rgz are parallel and perpendicular components of the radius of gyration, respectively). We found that at the small and large ZTMD volume fraction (ϕ_{ZTMD}) regions, ZTMD as well as Z has flatter conformation than their pure components, which may provide thinner lubricant film thickness. We also calculated the self-diffusion coefficient as a function of volume fraction to quantify the mobility of the binary mixture lubricant. Both self-diffusion coefficients for ZTMD (D_{ZTMD}) and Z as a function of ϕ_{ZTMD} were calculated as shown in Fig. 2. In the region from ϕ_{ZTMD}=0 to 0.45, D_{ZTMD} gradually decreases. The corresponding snapshots (Figs. 1 (a)) illustrate that ZTMD molecules aggregate together due to strong attraction and form isolated islands. With the increase ϕ_{ZTMD}, more ZTMD molecules stick together and the islands become larger and larger, thus the mobility of ZTMD becomes less due to the strong confinement by the surrounding ZTMD molecules. Note that at certain critical volume fraction, ZTMD molecules are all linked together and form connected network structures (Fig. 1 (c)). The transition point from isolated islands to connected network structures is called "percolation threshold," which is approximately 0.45. Beyond the percolation threshold, D_{ZTMD} decreases slightly but at a much smaller rate (Fig. 2). This transition indicates the changes in the diffusion mechanism, *i.e.*, from percolation to reptation process. In the percolation process, the mobile molecules diffuse through the bonded molecules with a random distribution, while, in the reptation process, molecules are laterally constrained and can move only along the path between the gaps of the aggregated molecules (Fig. 3). We also found that the binary mixture of ZTMD and Z with the volume fraction from 0.25 to 0.675 have higher mobility than the pure ZTMD monolayer and keep the desirable conformation, which may be better disk lubricants.
Our simulation results of the static and dynamic properties indicate the advantages of binary mixture monolayer as disk lubricants comparing to their single components. The hysterisis effects on the binary mixture films were further studied. Based on the multi-component lubricants simulations, we systematically constructed the database that described the conformation, morphology, surface coverage, mobility, nano-mechanics, and nano-rheology of PFPE films.

1.Y.Sakane, A.Wakabayashi, L.Li, and P.H.Kasai, *IEEE Trans. Magn.*, **42**, 2501-3, 2006.

2.B.Marchon, X.–C.Guo, H.Deng, T.Karis, H.Deng, Q.Dai, J.Burns, and R.Waltman, *IEEE Trans. Magn.*, **42**, 2504-6, 2006.

3.H.G.Chen, Q.Guo, and M.S.Jhon, *IEEE Trans. Magn.*, **43**, 2247-9, 2007.

4.X.D.Ma, M.Stirniman, H.Tang, and J.Gui, US Patent 6,673,429 B1, 2004.

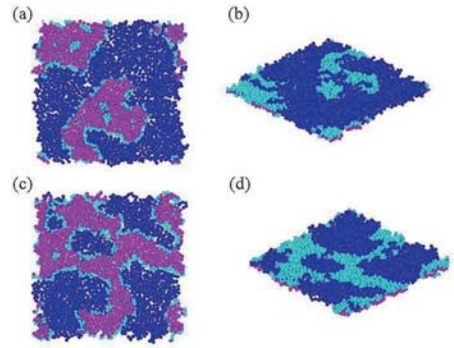

Fig. 1. Snapshots of (a)&(b) ZTMD and Z binary mixture (ϕ_{ZTMD}=0.375); top & side view, (c)&(d) ZTMD and Z binary mixture (ϕ_{ZTMD}=0.5); top & side view.

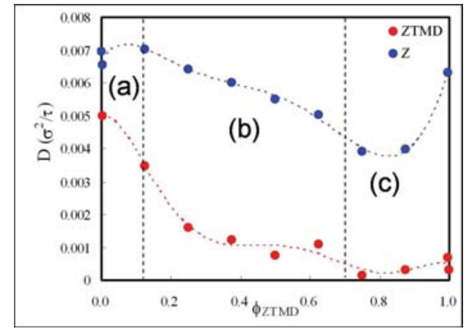

Fig. 2. Self-diffusion coefficient of ZTMD and Z in the binary mixture monolayer as a function of the ZTMD volume fraction for (a) simple diffusion, (b) percolation, and (c) reptation processes.

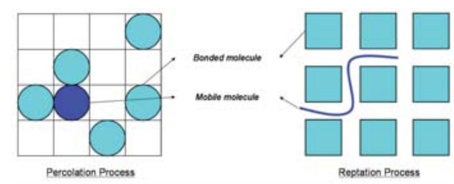

Fig. 3. A schematic of percolation and reptation processes.

HO-12

A Study on Design and Analysis of New Lubricant for Near Contact Recording.

D. Shirakawa, K. Ohnishi
Asahi Glass Co., Ichihara-shi, Japan

As a hard disc drive is required higher recording density and reliability, the technology of the head-disc interface (HDI) is facing more challenging task regarding its tribological performance. In the phase of near contact recording, the conventional lubricants would cause several issues in HDI. For instance, a conventional PFPE that contains weak "-OCF2O-" unit in the main chain due to its manufacturing processes is decomposed in the presence of a Lewis acid catalyst.
In the previous work, we had developed a PFPE "TA-30" that had the improved chemical stability by excluding weak unit[1].
But, TA-30 had lower viscosity than conventional PFPE(Lube-B),so It's thin lubricant layer on disk could't endure the harsh interface condition.
New lubricant"QA-40" improved in these proparties will be discussed at the conference.
They are expected to be suitable for near contact recording lubricant.

[1]D.Shirakawa, IEEE Trans.Magn.,vol.43, pp2253-2255(2007)

HO-13

A new contact model for head disk interface (HDI) with ultrathin liquid film and ultra-small spacing.

H. Matsuoka, H. Kokumai, S. Fukui
Department of Applied Mathematics and Physics, Faculty of Engineering, Tottori University, Tottori, Japan

I. Introduction

An ultrasmall spacing between a flying head slider and a magnetic disk is required for higher recording density in hard disk drives. The head-disk spacing is becoming several nanometers in recent years. The head disk interface (HDI) in such an ultrasmall spacing should be designed considering surface forces [1], instabilities of an ultrathin liquid film spread on the magnetic disk as a lubricant [2], intermittent contact between the head and the disk and so on.

In this study, a new contact model between solids with an ultrathin liquid film on a solid surface has been developed and interaction forces between the elastic sphere and the plane in approach and withdrawal processes have been calculated.

II. Interfacial Regimes

Figure 1 shows schematic geometries of a sphere and a plane coated with an ultrathin liquid film. The spacing between the sphere and the plane, h_0, is assumed to change quasi-statically.

(a) Noncontact regime (see Fig. 1 (a))

Only the van der Waals force, F_{vdW}, is acting on the sphere and the interaction force, F, is given by $F = F_{vdW}$.

(b) Bridged regime (see Fig. 1 (b))

The interaction force, F, consists of the meniscus force, F_m, and the van der Waals force acting through the liquid, F_{vdW_liq}, and is given by $F = F_m + F_{vdW\_liq}$.

(c) Solid contact regime (see Fig. 1 (c))

The interaction force, F, consists of the repulsive contact force, F_{cr}, the adhesion force, F_{ad}, and the meniscus force, F_m, *i.e.*, $F = F_{cr} + F_{ad} + F_m$.

III. Modeling of Liquid Meniscus Bridge

When the spacing becomes small quasi-statically in the noncontact regime (Fig. 1 (a)), the van der Waals attractive force acting on the liquid film surface increases, and consequently, instability of the liquid film surface occurs in the vicinity of the minimum spacing between solids. The liquid meniscus bridge can be formed because of the instability at the spacing of about two times of the liquid film thickness [2].

The Laplace pressure, p_{Lap}, and the disjoining pressure, p_{dis}, are assumed to be balanced in this model, *i.e.*, $p_{Lap} = p_{dis}$. Using the geometrical relationship, we can obtain a meniscus shape equation which gives the filling angle ϕ (see Fig. 1 (b) and (c)). The spacing at the break of the liquid meniscus bridge, h_{0_b}, is also obtained from the meniscus shape equation.

Once the meniscus shape is obtained, the meniscus force, F_m, can be calculated by $F_m = F_{Lap} + F_{cap}$, where F_{Lap} is the Laplace force and F_{cap} is the capillary force.

IV. van der Waals force and Contact Force

The corrected van der Waals pressure equation between multilayers which has been proposed by the authors [3] is used to calculate the van der Waals forces F_{vdW} and F_{vdW_liq}.

The repulsive contact force, F_{cr}, is calculated from well-known Hertz theory, and the adhesion force, F_{ad}, is calculated from the DMT contact model [4].

V. Results

Figure 2 shows the relationship between the minimum spacing, h_0, and the interaction force, F, where the liquid film thickness $T = 1$ nm, surface tension of the liquid $\gamma_L = 24$ mN/m, radius of curvature of the sphere $R = 5$ µm, and contact angle $\theta_0 = 0$ rad. In the approach process, the liquid meniscus bridge is formed at point B because of the instability of the liquid film. The contact between solids occurs at point D. In the withdrawal process, the solid conjunction breaks abruptly at point F. The liquid meniscus bridge is elongated to point H and the meniscus bridge is broken. This result qualitatively agrees with experimental results obtained by the AFM [5]. Moreover, two hysteresis are found; the first comes from the adhesion of the solid and the second comes from the liquid meniscus bridge.

[1] J. N. Israelachvili, *Intermolecular and Surface Forces*, 2nd edition, Academic Press, 1992.

[2] S. Fukui, K. Yorino, K. Yamane, and H. Matsuoka, *Proc. World Tribology Congress III*, WTC2005-63629, 2005.

[3] H. Matsuoka, S. Ohkubo, and S. Fukui, *Microsyst. Technol.*, vol. 11, No. 8 – 10, pp. 824 – 829, Aug. 2005.

[4] B. V. Derjaguin, V. M. Muller, and Yu. P. Toporov, *J. Colloid Interface Sci.*, vol. 53, No. 2, pp. 314 – 326, 1975.

[5] P. M. Jones, M.-L. Wu, C. Platt, L. Li, Y.–T. Hsia, M. Luo, L. R. White, J. Schneider, *Tribology International*, vol. 38, Issues 6 – 7, pp. 528 – 532, June – July 2005.

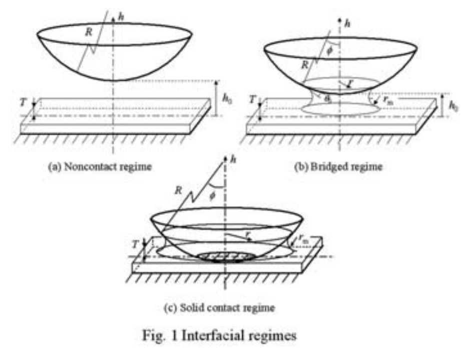

Fig. 1 Interfacial regimes

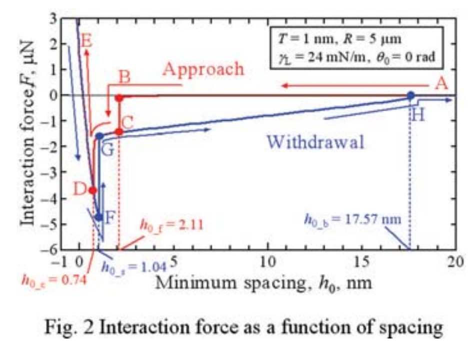

Fig. 2 Interaction force as a function of spacing

HO-14

Density Dependence of Carbon/Magnetic layer for Corrosion/Scratch Resistance on Head-Disk-Interface.

H. Tani, M. Shoda
Head media interface technology, Hitachi Global Storage Technologies Japan, Fujisawa-shi, Japan

1. Introduction

Perpendicular magnetic recording (PMR) disks have increased areal recording density. Generally, PMR disks have the different structure and layer materials including corrosive elements from longitudinal magnetic recording (LMR) disks. Typically, PMR disks have granular magnetic layer with oxide (e.g. SiOx), and soft under layer with soft magnetic metal (e.g. Co, Fe). So, there are some studies about the corrosion behavior of the magnetic disks (1)-(3). On the other hand, scratch resistant of magnetic disks depends on the layered structure of disk (4)-(6).
In this work, we studied about the relationship between the corrosion / scratch resistance and the relative density carbon / magnetic layer derived by TEM-EELS (Electron Energy Loss Spectroscopy). Corrosive metal element extracted on the surface from layers under carbon overcoat generally (3). Scratch damage is affected by the deformation of surface layer and subsurface layer (6). We have suspected the density of carbon overcoat and upper magnetic layer affects both resistance, and we analyzed the relationship between the relative density of both layers and both resistance.

2. Experiment

EELS is the spectroscopic analysis method of electron energy loss through material. Incident electrons generate plasmon by interaction with electrons in material. Transmitted electrons loss energy as same as the energy of the plasmon and we can observe the plasmon energy loss peak. This plasmon energy can be described in the equation (1), where Ne is the valence electron density, ε0 is the vacuum dielectric function, and m* is the electron "effective mass", m being the free-electron mass. The mass density is derived from the valence electron density Ne by assuming the composition of material is same. We can compare the relative density of each layer of disks by plasmon loss energy spectra as shown in Fig. 1.

3. Results and Discussions

The relationship between corrosion count and plasmon peak energy of COC / upper-mag. layer was sturdied. Disks with worse corrosion counts had smaller plasmon peak energy of upper-mag. layer. This result must show the density of COC and upper-mag. layer relates with corrosion property, because higher density COC or upper-mag. layer should reduce corrosive metal extraction to disk surface. Next, we evaluated scratch resistance of several disk samples by the particle injection test. These disks were made by the several process conditions. Figure 2 shows the relationship between the scratch count and the plasmon peak energy of up-mag. layer. We can find the scratch count shows good correlation with the plasmon peak energy of upper-mag. layer, but no correlation with the one of COC. These results suggest that the density of upper-mag. layer is more affective for the scratch resistance than the density of COC. PMR disks have granular magnetic layer with segregated oxide, so the segregated oxide should reduce Young modulus along longitudinal direction, because an oxide has the low modulus, generally. And we suspected PMR disks with granular magnetic layer showed poor scratch resistance, because the magnetic layer deformation was larger.

[1] Rong Ji, Thomas Liew, and T.C.Chong, IEEE Trans. on magn., vol.40, No.4, 2004, p.3192.

[2] E.T.Kuan, D.W.Park, J.Melo, D.Spaulding, J.J.Liu, and K.K.Kim, IEEE Trans. on magn., vol.40, No.4 2004, p.3195.

[3] Qing Dai, Guillermo Prada-Silva, Bing K. Yen, Bruno Marchon, and C.T.Rettner, IEEE Trans. on magn., vol.41, No.10, 2005, p.3055.

[4] R. Tsuchiyama, H. Tani, and Y. Ezawa, JSME, Ibaraki district conference proceedings, Vol.2000 (20000908) p. 103.

[5] M. Shoda,H. Tani, IEEE Trans. on Magn., Volume 39, 2003 p. 893.

[6] L. Thomas, S. Wei Wu, S. Kee Chow, C. Teck Lim, Tribology international, 2000, vol. 33, no 9, p. 611.

$$E_p = \hbar\left(\frac{Ne^2}{\varepsilon_0 m^*}\right)^{\frac{1}{2}} \quad (1)$$

Equation 1, Plasmon loss energy is described in this equation.

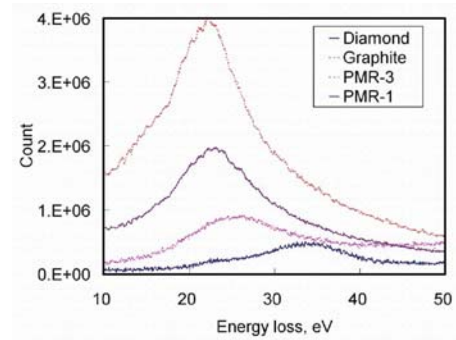

Fig. 1, Plasmon loss energy spectra of carbon layers.

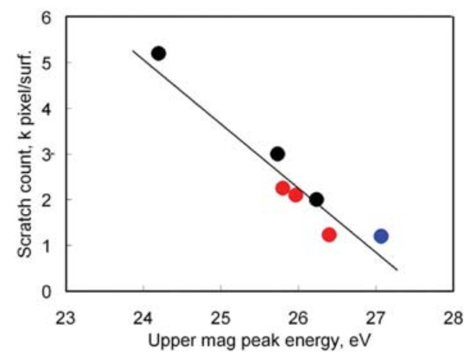

Fig. 2, Relationship between the scratch count and the plasmon peak energy of upper magnetic layer.

HP-01

Crystal structure as an origin of high anisotropy field of FeCoB films with Ru underlayer.

A. Hashimoto[1], K. Hirata[1], T. Matsuu[1], S. Saito[2], *S. Nakagawa*[1]
1. Dept. of Physical Electronics, Tokyo Institute of Technology, Tokyo, Japan; 2. Electronic Engineering, Tohoku University, Sendai, Japan

Introduction
Soft magnetic films with high saturation magnetization M_s are promising candidate for storage and high frequency communication devices. A lot of studies on FeCo-based alloy films with high M_s have been demonstrated and FeCoB was found to be a material with low coercivity H_c and high M_s. Further to these parameter, anisotropy field H_k is also a significant parameter to attain high ferromagnetic resonance frequency $f_r = \gamma(H_k M_s)^{1/2}/2\pi$, where γ is gyro magnetic ratio. It has been reported that FeCoB films fabricated with certain deposition method exhibited remarkably high H_k above 200 Oe [1,2]. While soft magnetic properties are frequently discussed, origins of the remarkable high H_k are not well understood. In this paper, the crystal structure in FeCoB layer possessing very high H_k of 500 Oe was examined by X-Ray diffraction and the origin of high H_k was investigated.
Experimental
FeCoB and Ru layers were deposited on glass substrates by DC facing targets sputtering at room temperature, from pure Ru target and $Fe_{67.2}Co_{28.8}B_4$ alloy targets. The thickness of Ru and FeCoB layers were 5 nm and 200 nm. Ar gas pressure for them in deposition processes were 6 mTorr and 1 mTorr, respectively. Magnetic properties were measured with a vibrating sample magnetometer (VSM) and the crystallographic analysis were performed by X-Ray Diffraction (XRD) with Cu-Kα radiation. XRD patterns were measured in out-of-plane direction to substrate plane and also in-plane direction for various in-plane rotating angle ϕ.
Results and Discussion
M-H curves of a single FeCoB (200 nm) film directly deposited on a substrate are shown in Fig.1(a). Coercivity for easy axis, $H_{c,EA}$ = 130 Oe and that for hard axis, $H_{c,HA}$ = 100 Oe, respectively. The curves indicated little magnetic anisotropy but it was insufficient to assess anistropy field H_k. In contrast, the magnetization curves of substrate/Ru(5 nm)/FeCoB(200 nm) film shown in Fig.1(b) exhibited good soft magnetic properties of $H_{c,EA}$ = 14 Oe and $H_{c,HA}$ = 2.2 Oe and clear uniaxial magnetic anisotropy with H_k of 500 Oe. Easy axis aligns parallel to the facing direction of FeCoB targets, i.e. the direction related with the oblique incidence of dominant sputtering particles. Out-of-plane XRD patterns of both samples indicated only (110) diffraction line of bcc-FeCo crystallite. By contrast, in-plane XRD patterns of them revealed the difference in 2θ diffraction. Fig.2 shows the in-plane XRD patterns of the Ru/FeCoB film for various measurement angle ϕ, defined from the easy axis direction as indicated in the inset. The (110) diffraction line of the high-H_k Ru/FeCoB film gradually expanded as the angle ϕ increased from 0 to 90 deg., whereas low H_k FeCoB film showed no difference in the diffraction patterns for all angles ϕ. The results indicate that the lattice spacing of FeCo(110) $d_{(110),\text{in-plane}}$ of the Ru/FeCoB film along easy axis direction, which corresponded to the facing direction of FeCoB targets, was larger than that along hard axis direction. The expansion ratio was about 0.5 %. It was also observed that the in-plane (200) diffraction was observed in the direction of ϕ of 0 deg., while the (200) diffraction disappeared in the direction of ϕ of 90 deg. These diffraction patterns imply that an alignment of bcc-based crystallites and a distortion of the unit cell by the internal stress can be schematically illustrated as shown in Fig.3. Basically, the high-H_k film consists of Fe based bcc crystallites. The majority of the cubic unit cells aligns with their <100> axis transversely to the easy axis and their (110) plane parallel to the film plane. Furthermore, a compressive stress in the film causes distortion of the unit cell, such as the increase of $d_{(110),\text{in-plane}}$ along the easy axis direction, while the expansion of $d_{(100),\text{in-plane}}$ along the direction transversely to the easy axis is not changed so much. The strain in the distorted cubic model gave the calculated magnetoelastic energy E_{elasic} of 3.8×10^5 erg/cc with measured saturation magnetostriction constant of $\lambda_s=3.2\times10^{-5}$. The E_{elasic} is equivalent to the H_k of 470 Oe which is in good agreement with the measured H_k of 500 Oe.
In conclusion, textured FeCo crystallites as explained above can possibly involve anisotropic magnetoelastic energy which induces the high magnetic anisotropy field H_k in a certain direction.

[1] A.Hashimoto et al., IEEE Transactions on Magnetics, 43, 2007, 2627

[2] M. Munakata et al., IEEE Transactions on Magnetics, 41, 2005, 3262

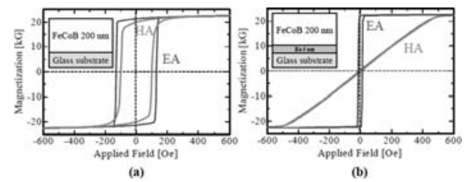

Fig.1 Magnetization curves of (a) FeCoB (200 nm) film and (b) Ru(5nm)/FeCoB(200 nm) film.

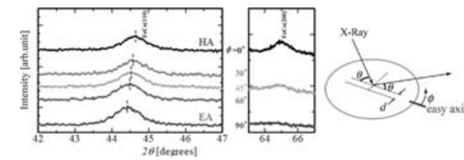

Fig.2 In-plane XRD patterns of Ru(5nm)/FeCoB(200 nm) film.

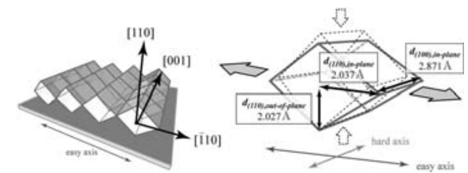

Fig.3 Schematic illustration of the alignment and distortion of crystallites of Ru(5nm)/FeCoB(200 nm) film.

HP-02

Magnetic properties and crystallographic structure of Fe3Pt thin films on glass substrate.

S. Hsiao[1], S. Chen[1], Y. Hsu[1], H. Lee[2], W. Chang[3], F. Yuan[4]
1. Materials science and engineering, Feng Chia University, Taichung, Taiwan; 2. National Synchrotron Radiation Research Center, Hsinchu, Taiwan; 3. Phyics, National Chung Cheng University, Chiayi, Taiwan; 4. Physics, Academia sinica, Taipei, Taiwan

Introduction
Fe3Pt related alloys with L12 superlattice have been studied due to their interesting characteristics, such as martensitic transformation [1] and invar structure [2]. In Fe3Pt thin film system, the excellent soft magnetic properties and magnetic anisotropy were developed recently for application of soft-hard (Fe3Pt-FePt) exchange spring magnets [3] and recording media [4], respectively. However, the magnetic properties and crystallographic structure of isotropic L12 Fe3Pt films were seldom reported. In this paper, the disorder-ordered transformation and resultant properties of sputtered Fe3Pt thin films were investigated by manipulating Fe content, annealing temperature and heating process.
Experimental
Fe100-xPtx (x = 20, 25 and 30) thin films were fabricated by rf magnetron sputtering with background vaccum better than 2.0×10-7 torr. A composite FePt target was made by overlaying a high-purity (99.99%) iron disk with Pt foils (99.99%). Thin films were annealed at 300-700oC by post-annealing or in-situ annealing. Crystallographic structure was identified by x-ray diffraction using Cu Kα radiation. Film thickness was fixed at 51.8 ± 0.5 nm using x-ray reflectivity (XRR) technique. Magnetic properties were measured with a vibrating sample magnetometer (VSM) under a maximum applied field of 12 kOe. Stoicheometric compositions were confirmed by inductively coupled plasma spectroscopy.
Results and Discussion
X-ray diffraction patterns of the Fe75Pt25 samples as a function of annealing temperatures (25~700oC) are shown in Figure 1-(a). Only fundamental (111) reflection can be observed for as-deposited sample, indicating a chemically disordered structure. For films post-annealed above 500oC, the superlattice reflections appear, displaying chemically ordered structure. Moreover, we observed the symmetric profile of (200) reflections in ordered samples, which can be referred to fcc structure. The ordering parameter is close to unity, determined by the integral intensity ratio, indicating a purely ordered fcc Fe3Pt phase for samples post-annealed at 700oC. X-ray diffraction patterns of Fe100-xPtx (x= 20, 25, 30) thin films post annealed at 700oC are shown in Fig. 1-(b). Similar ordered diffraction pattern was found in Fe75Pt25 films. However, for the Fe-rich Fe80Pt20 sample, only disordered reflections were observed.
Hysteresis loops of Fe100-xPtx (x = 20, 25, and 30) thin films post-annealed at 700oC are illustrated in Fig. 2-(a). For Fe75Pt25 and Fe70Pt30 samples, the magnetically soft properties with magnetization of 1270 emu/cm3 and coercivity of about 50 Oe were obtained. However, the Fe80Pt20 samples exhibits a paramagnetic properties. Figure 2-(b). shows the hysteresis loops of Fe75Pt25 samples annealed at 700oC by in-situ annealing and by post-annealing, respectively. Comparing to post-annealing sample, the thin films with in-situ annealing present a hard magnetic properties with coercivity of 2.4 kOe, which can responsible to the formation of L10 FePt phase leading to an asymmetrical (200) reflection confirmed by XRD (not shown). This will be discussed in full paper.
From the above data, we summarize the results: (i) Threshold temperature of fcc L12 ordered Fe3Pt phase should be above 500oC, higher than that of L10 ordered FePt phase. (ii) Samples with highly ordered fcc Fe3Pt phase exhibit magnetically soft properties. (iii) The samples with exceeding Fe content which seems to restrain the formation of ordered Fe3Pt phase, exhibit paramagnetic properties. (iv) Post-annealing appears to be necessary for formation of pure ordered Fe3Pt phase, similar to FePt/Fe3O4 nanoparticle systems [5].

[1] T. Kakeshita et al., Appl. Phys. Lett. 77 1502 (2000)

[2] E. Kisker et al., Phys. Rev. Lett. 58 1784 (1987)

[3] X. Rui et al., Appl. Phys. Lett. 89 122509 (2006)

[4] M. A. I. Nahid and T. Suzuki, Appl. Phys. Lett. 85 4100 (2004)

[5] C. –B. Rong et al., J. Phys. D: Appl. Phys. 40 712 (2007)

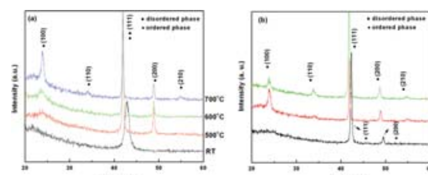

Fig. 1. (a) XRD patterns of Fe75Pt25 samples with differnent post-annealing temperatures. (b) XRD patterns of Fe100-xPtx (x= 20, 25, 30) thin films post-annealed at 700oC.

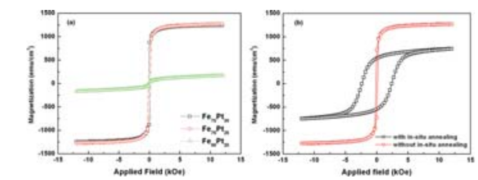

Fig. 2. (a) Hysteresis loops of Fe100-xPtx (x= 20, 25, 30) thin films post-annealed at 700oC. (b) Hysteresis loops of Fe75Pt25 thin films heat treated at 700oC by in-situ annealing and post annealing, respectively.

HP-03

Suppression Of Sm Segregation And Improvement In Thermal Stability By Introducing Ru Underlayer In Co-Sm Amorphous Films.

K. Ikeda[1,2], T. Suzuki[1], T. Sato[2]
1. R&D center, Taiyo Yuden Co., Ltd., Gunma, Japan; 2. Spin device technology center, Shinshu University, Nagano, Japan

Introduction
We have reported that Co-Sm amorphous magnetic films show a large anisotropic magnetic field (Hk) due to the large magnetocrystalline anisotropy of 3d transition metals and rare-earth metal alloys. However, Hk decreases with an increase in the annealing temperature, depending on the crystallization and its closely related phase separation. The deterioration of Hk can be reduced by introducing a Ru underlayer, which effectively improves the various magnetic properties. In order to analyze the effect of the Ru underlayer, we have evaluated the interface structure of Co-Sm films by high-resolution transmission electron microscopy (HR-TEM).
Experimental
Co-Sm magnetic films with a Ru underlayer were deposited on a surface-oxidized silicon substrate by using inductively coupled radio frequency sputtering systems at room temperature. During the deposition, a magnetic field of 100 Oe was applied parallel to the film plane in order to introduce an in-plane uniaxial magnetic anisotropy. The structures of the films were evaluated by HR-TEM. The magnetization curves were measured by using a VSM. The Co-Sm films were annealed from 250 to 600 degrees C. in vacuum without a magnetic field.
Results and discussion
Figure 1 shows the dependence of Hk of the Co-Sm film (with a Sm content of 7 at.%) on the annealing temperature with and without the Ru underlayer. Hk decreases with an increase in the annealing temperature and almost vanishes at 600 degrees C. However, the Hk value of Co-Sm films with the Ru underlayer annealed at temperatures ranging from 250 to 450 degrees C. is larger than that of the films annealed at the corresponding temperatures without the underlayer films, indicating the effect of the underlayer on the suppression of Hk deterioration with annealing. The cross-sectional HR-TEM images of the Co-Sm films (as-deposited and annealed at 350 degrees C.) are shown in Fig. 2 (with the Ru underlayer) and Fig. 3 (without the underlayer). The Co-Sm film with the Ru underlayer exhibits an amorphous-like contrast without the distinct lattice image despite the annealing (Figs. 2a and b). On the other hand, in the as-deposited Co-Sm film without the underlayer, the existence of a very small Sm-related crystalline precipitation is confirmed by a Fourier-transferred image at the Co-Sm film/SiO2 interface (Fig. 3a); further, nanosized crystalline Co and Sm2O3 phases are present at the interface in the film annealed at 350 degrees C. (Fig. 3b). Such thermally induced phase-separations and the following crystallization of the separated phases can be attributed to the instability of the Sm atoms soluble in the Co metal matrix and the resultant Sm segregation due to a significant difference in their atomic radii; this is one of the reasons for the Hk deterioration during annealing. Although the phase-separation and crystallization are enhanced especially at the interface of without underlayer as clearly confirmed by TEM, the gradual undetectable change in nanometer scale with annealing, such as phase separation and atomistic ordering, is expected to occur in the entire film bulk and can also contribute to the Hk deterioration. Actually, independent of the Ru underlayer insertion, the Co-Sm films annealed at 600 degrees C. were observed to be completely crystallized and show almost zero anisotropy magnetic fields. Within the heat-treatment temperature range below 350 degrees C., the Ru underlayer effectively prevents the preferential segregation of Sm at the interface, consequently suppressing the thermally induced degradation of Hk in the Co-Sm films.

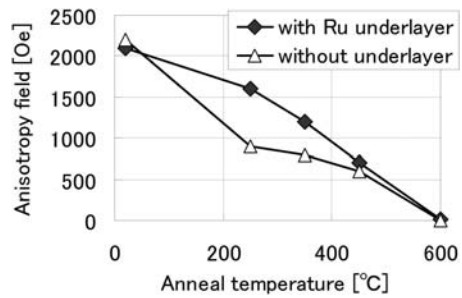

Fig.1 The dependence of Hk of the Co-Sm film on the annealing temperature

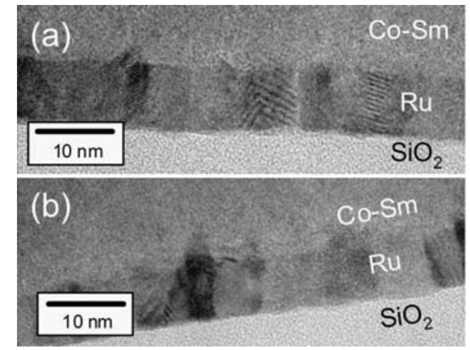

Fig.2 The cross-sectional HR-TEM images of the Co-Sm films with Ru underlayer (a) as deposited (b) 350 degrees C. annealed

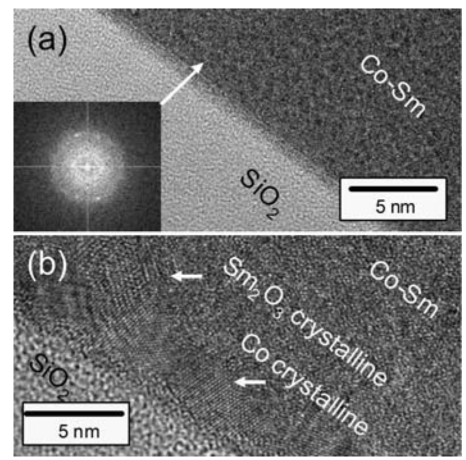

Fig.3 The cross-sectional HR-TEM images of the Co-Sm films without Ru underlayer (a) as deposited (b) 350 degrees C. annealed

HP-04

Magnetic properties of FeCo films prepared by hydrogenous gas reactive sputtering.

X. Liu[1], A. Morisako[2]
1. Department of Information Engineering, Shinshu University, Nagano, Japan; 2. Spin device technology center, Shinshu University, Nagano, Japan

Soft magnetic thin films with high saturation magnetization are required for magnetic head materials in order to saturate the highly coercive media. The $Fe_{1-x}Co_x$, ($0.3 \le x \le 0.4$), alloy has the highest saturation flux density of $4\pi M_s \ge 24$ kG in nature [1]. Much effort has been taken to introduce soft magnetic properties in FeCo thin films [2]-[4]. Additives have been considered to be an effective method because suitable additives can reduce the grain size or control the resistivity [5],. So far, additives that induce soft magnetic properties are AlO, N,etc [5],[6]. However, not all the additives can induce soft magnetic properties in FeCo thin films.
In this experiment, additive of C was introduced into the films by two processes; the first is the convenient process of co-sputtering. The second is introducing hydrogenous gas, such as acetylene into the chamber during sputtering. The magnetic properties of the films prepared by the two processes were compared. It is found that films with $4\pi M_s$ of 23.5 kG and coercivities as small as 1 Oe can be prepared by hydrogenous gas reactive sputtering. While films prepared by co-sputtering have coercivities larger than 40 Oe.
Thin films were prepared by a facing target sputtering system. In the case of co-sputtering, carbon chips were placed onto the FeCo targets. In the case of gas reactive sputtering, acetylene gas was introduced into the chamber. The amount of carbon addition was controlled by the acetylene gas partial pressure for the latter case. For both case, the base pressure of the system is better than 1×10^{-6} Torr.
Transmission electron microscopy results show the grain size of the FeCo films decrease with the increase of carbon addition for both processes. Fig. 1 shows the dependence of magnetization on the acetylene gas partial pressure (a) and the dependence of magnetization on the carbon composition prepared by co-sputtering (b). Of particular interest is that as shown in Fig. 1(a), magnetization of films prepared by gas reactive sputtering first increase slightly then decrease dramatically with the increase of acetylene gas partial pressure. However, magnetization of films prepared by co-sputtering, as shown in Fig. 1(b), almost decrease linearly with the increase of the amount of carbon addition.
All the films show in-plane anisotropic magnetic properties with the magnetic easy axis along the stray field direction. The stray field is due to the magnet behind the target. Fig. 2 shows the dependence of coercivity on the acetylene partial pressure (a) and the dependence of carbon composition for films prepared by co-sputtering (b). It is found that coercivity decrease with the increase of carbon addition for both films. However, films prepared by gas reactive sputtering show coercivity minimum of about 1 Oe in bout easy and hard axis directions. While films prepared by co-sputtering show coercivity larger than 40 Oe in both easy and hard axis directions.
X-ray photoelectron spectroscopy results show films sputtered without hydrogenous gas have impurities of oxygen of about 4 at%. However, oxygen free films can be prepared by introducing hydrogenous gas into the chamber during the sputtering process. This result can explain the results as shown in Fig. 1 (a).
In conclusion, we have compared the magnetic properties of C doped FeCo films prepared by hydrogenous gas reactive sputtering and co-sputtering. Films with $4\pi M_s$ of 23.5 kG and coercivities as small as 1 Oe can be prepared by hydrogenous gas reactive sputtering. XPS results show that oxygen free FeCo films can be prepared by reactive sputtering of hydrogenous gas. While films deposited by co-sputtering have impurities of oxygen as large as 4 at%.

[1] R. M. Bozorth, Ferromagnetism, IEEE, New York, 1993.

[2] S. X. Wang, N. X. Sun, M. Yamaguchi, and S. Yabukami, Nature 407, 150 (2000).

[3] G. Pan and H. Du, J. Appl. Phys. 93, 5498, (2003).

[4] K. Shintaku, K. Yamakawa and K. Ouchi, J. Appl. Phys. 93, 6474 (2003).

[5] S. Ikeda, I. Tagawa, Y. Uehara, T. Kubomiya, J. Kane, M. Kakehi, and A. Chikazawa, IEEE Trans. Magn. 38, 2219 (2002).

[6] N. X. Sun and S. X. Wang, IEEE Teans. Magn. 36, 2506 (2000).

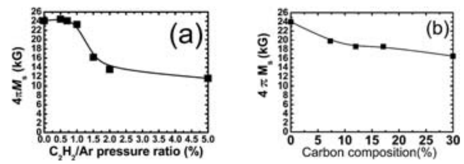

Fig. 1 shows the dependence of magnetization on the acetylene gas partial pressure (a) and the dependence of magnetization on the carbon composition prepared by co-sputtering (b)

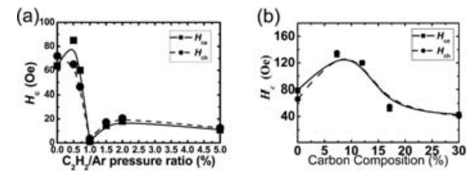

Fig. 2 shows the dependence of coercivity on the acetylene partial pressure (a) and the dependence of carbon composition for films prepared by co-sputtering (b).

HP-05

Nanocrystallyne permalloy thin films obtained by nitrogen IBAD.

P. Prieto[1], J. Camarero[2], J. F. Marco[3], E. Jimenez[2], J. M. Benayas[1], J. M. Sanz[1]
1. Física Aplicada, Universidad Autónoma de Madrid, Madrid, Spain; 2. Física de la Materia Condensada, Universidad Autónoma de Madrid, Madrid, Spain; 3. Instituto de Química Física Rocasolano, CSIC, Madrid, Spain

Permalloy (Fe20Ni80) is well known due to its magnetic properties of high permeability, low coercivity, and small magnetic anisotropy and for its wide use in magnetic recording and sensor industry. Nevertheless, to improve the performance of the permalloy based devices a further optimization of its magnetic properties is required. Several efforts have been performed to optimize the magnetic properties of permalloy thin films by pattering the films or by adding a third element to the FeNi system.
It is also well know that the incorporation of nitrogen by sputtering process on metals induce the formation of fine-grained structures. In the case of Fe, the incorporation of small amount of nitrogen result in a ferromagnetic compound (α'-FexN) with higher magnetic induction and lower coercivity than that of pure α-Fe. In this work we pretend to study the structural changes and the corresponding magnetic effects induced by nitrogen bombardment of Fe20Ni80 during its deposition. With this aim nanocrystalline Fe20Ni80-N films have been deposited on Si (100) substrates at 200oC using a dual ion beam sputtering system. A Fe20Ni80 target has been sputtered with Ar+ ions of 500eV whereas the film is bombarded simultaneously with a controlled mixture of Ar+ and N2+ ions of 55eV energy.
The structure of the films was analyzed using X-Ray diffraction (XRD) at a grazing incidence. The line width at half maximum of the diffraction peaks has been used to estimate the crystallite size using the Scherrer relationship. We have been observed a broadening of the diffraction peaks related to the growth of smaller crystallites when the films are bombarded. The composition of the thin films has been study in terms of resonant RBS. Integral Conversion Electron Mössbauer Spectroscopy (ICEMS) have been used to characterize the deposited films in terms of the grown phases and hyperfine interactions. The magnetic properties were investigated by using vectorial Kerr magnetometry at room temperature.
The ICEM spectra have been recorded in Fig.1 for the non-assisted films as well as for two Fe20Ni80 thin films assisted with 33 and 50% N2+ ions. The spectrum of the non-assisted permalloy film shows a sextet with broad lines that was satisfactory fitted with a hyperfine magnetic field distribution with a maximum located at 27.5 T. The spectrum recorded for the assisted films is very similar to the previous one, although the distribution is slightly narrower and the maximum of the distribution shifted to smaller values (27.1 and 26.0T for 33% and 50 % N2+ assisted films respectively). The spectrum recorded from the 50%N2+ assisted thin film, in addition to the magnetic sextet pattern, shows also a small paramagnetic doublet (13% of the total spectral area) that can be related with the formation of γ'-(Fe0.2Ni0.8)4N. The small decrease in the magnitude of the hyperfine magnetic field might be due to the presence of some interstitial nitrogen atoms within the permalloy lattice in good agreement with the nitrogen content (≈10% at.) estimated by RBS for this last film.
In-plane magnetization components have been measured to determine the magnetic anisotropy and the magnetization reversal process. Fig.2 shows the easy axis M-H loops for the same films as in previous figures but including the results for that assisted with 25% N2+. It is interesting to observe that those films assisted with 25% N2+ and 33% N2+ reduce the coercive field at the easy axis up to values of 0.19mT and 0.36mT respectively with respect to the non-assisted permalloy (i.e. 0.50mT). On the contrary, the incorporation of excess of nitrogen in the film due to the use of a higher concentration of N2+ ions (i.e. 50%) in the assistant beam, causes an increase of the coercive field up to 1.5mT, well above that obtained for the non-assisted film. This is probably related with the small amount of paramagnetic γ'-(Fe0.2Ni0.8)4N found to be present by ICEMS in that film.
In summary we conclude that the soft magnetic properties of permalloy thin films are improve after nanocrystallization by the use of low concentrations of N2+ ions in the assistant beam. However, when the nitrogen is incorporated forming a paramagnetic nitride the soft magnetic properties start to degrade.

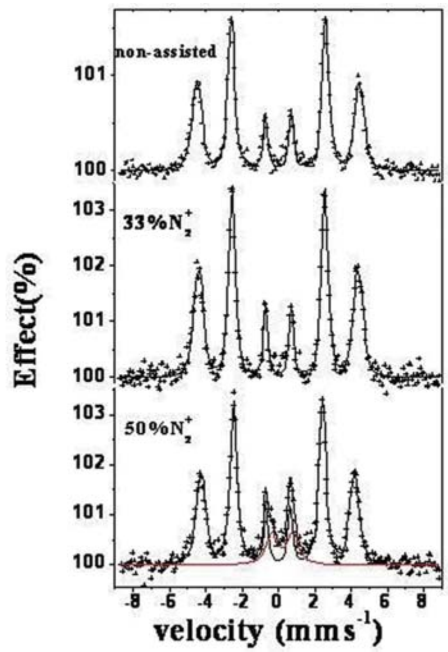

Fig.1 ICEM spectra recorded from the permalloy thin films

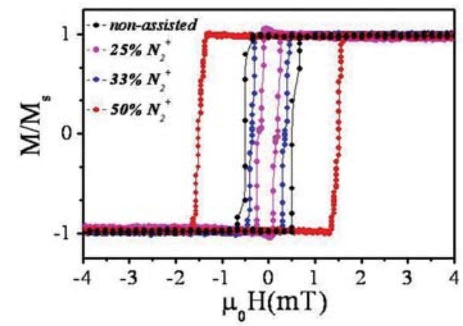

Fig.2 In-plane magnetic hysteresis loops for the longitudinal component of permalloy thin films at the easy axes.

HP-06

Ultra-Soft and High Magnetic Moment CoFe Films Directly Electrodeposited from a B-Reducer Contained Solution.

B. Zong[1], G. Han[1], L. Wang[1], G. Leonard[1], J. Sze[1], L. Shen[2], H. Tan[2], Y. Loh[1], B. Lim[1], B. Liu[1]
1. SMI, Data Storage Institute, A-Star, Singapore, Singapore; 2. Institute of Materials Research & Engineering, A-Star, Singapore, Singapore

The demand of the world market leads to magnetic data storage device advancing towards much smaller dimension and higher capacity.[1] In order to achieve a high capacity in a miniature device, an ultra-soft and high magnetic moment material is required for producing high saturation flux density (Bs), so that the necessary flux densities can be preserved on reducing device dimensions, while simultaneously achieving a low coercivity (Hc) to match the high recording density of magnetic media with high Hc.[2] Although a lot of soft or high Bs magnetic films have been achieved via sputtering, evaporation, and casting, most of them cannot be applied to the fabrication of commercial device.[1,3] Electrodeposition is a simple method to achieve various thickness of soft Fe-based materials.[2] But preventing Fe2+ from oxidization into Fe3+ (which decreases Bs) and minimizing Hc of the metal films are challenges via electrodeposition, hence an ultra-soft (Hc < 5 Oe) magnetic film with high magnetic moment [Bs > 2.4 Tesla (T)] is yet to be achieved.[1] Herein, we report a approach to fabricating ultra-soft magnetic CoFe films from a sulfate salt based solution containing dimethylamine borane (B-reducer) via electrodeposition. In comparison to commonly used strong acidic solutions (pH = 2.4 – 2.8) which contain S-additives (saccharin, Na Lauryl sulfate, etc), the solution containing B-reducer is a semi-neutral medium and has larger process latitude (pH = 3.5 – 4.8). It also does not need a salt-bridge (leading to low efficiency of current)to protect Fe2+ from oxidization. The measurements through AFM show that the thickness of the prepared films ranges from tens of nanometers to micrometers. The magnetic characterizations using VSM and SQUID show that the films possess very soft magnetic property with a Hce and Hch of 6.5 and 2.9 Oe, respectively. The films have a high saturation magnetization of ~2.45 T and good anisotropy.

The CoFe films were electrodeposited on 25 nm CoFe/Si(100) wafers. The FexCo100-x (x = 55 – 68) films were fabricated at the temperature of ~40 cel. deg. from a solution of 0.07 mol/l CoSO4.7H2O, 0.10 mol/l FeSO4.7H2O, 0.5 mol/l NH4Cl, 0.5 mol/l H3BO3, and 2.8 – 3.2 g/l of B-reducer additive. The electroplating system used was a Paddle-Cell with pulse DC power. The atom ratio of Co to Fe in the electrodeposited films was determined by EDS.

Table 1 shows that the addition of B-reducer dramatically decreases the Hc and increases the Bs of Co40Fe60 film (deposited from a current density of 6.0 mA/cm2). The Hce and Hch decreases from 63 and 53 to 6.5 and 2.9 Oe, respectively, while Bs increases from 1.4 to 2.4 T with B-reducer concentration increasing from 0.0 to 3.0 g/l in the electroplating solution. Figure 1 shows that the magnetization curves of the CoFe films from the solutions containing different concentration of B-reducer. It appears that magnetic anisotropy of the films increases with the increase of B-reducer content. Despite no salt-bridge to prevent Fe2+ from oxidization for the solution containing B-reducer, the achieved Bs are still very high and the Hc of the CoFe films are much smaller than these obtained from the solution containing S-additive. It is because B-reducer can reduce Fe3+ (produced during plating) back into Fe2+, which results in a very low content of oxygen in the deposited film. XRD analysis in Figure 2 shows that the added B-reducer leads to a texture structure change of the Co40Fe60 film from CoFe(110) and Fe2O3(209) polycrystalline to CoFe(110) single-crystalline. As a result, the film possesses better anisotropy and its Hc dropped drastically while Bs achieved a high level. Further experiments revealed that too much (> 9 g/l) of B-reducer led to an unstable plating solution. Besides having excellent magnetic properties, our characterizations (in Table 2) indicate that the CoFe films were also good in mechanical and other properties, such as very low surface roughness (Ra) and magnetostriction (λs). Thus, the films have potential applications in future ultra-high density and frequency magnetic recording system, biotechnological, and microelectronic devices.[1,3]

[1] E. I. Cooper et. al. IBM J. Res. and Dev. 49 (1), 103 (2005).

[2] T. Osaka et. al. Electrochem. Solid-Sate Lett. 6, c53 (2003).

[3] Y. Chen et. al. IEEE Trans. Mag. 43, 609 (2006).

Property	No additive	B-reducer (1.5 g/l)	B-reducer (3.0 g/l)	S-additive[1]
Hce (Oe)	63	6.6	6.5	13
Hch (Oe)	53	5.8	2.9	4.8
Bs (T)	1.4	2.1	2.4	2.4

CoFe film	Hce (Oe)	Hch (Oe)	Bs (T)	λs (×10-6)	Surface	Ra (nm)
B.f. anneal	6.5	2.9	2.45	1.6	shining	1.6
A.f. anneal	5.6	1.8	2.42	1.1	shining	1.5

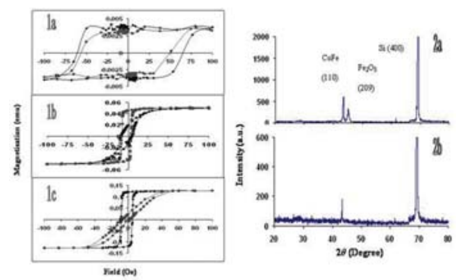

Fig. 1. The *M-H* loops of the Co40Fe60 films electrodeposited from the solutions which contain *B*-reducer of **(a)** 0.0, **(b)** 1.5, and **(c)** 3.0 g/l, respectively at a current density of 6.0 mA/cm2.
Fig. 2. The 2 θ XRD results of 0.6 μm Co40Fe60 films on Si(100) wafer. **(a)** and **(b)** stand for without adding, adding *B*-reducer, respectively.

HP-07

Soft-magnetic CoNiFeP alloy films for high frequency applications.

F. M. Rhen, *S. Roy*
Microsystems Center, Tyndall National Institute, Cork, Ireland

The research in high moment alloy films for high frequency has mostly been driven by applications in magnetic recording heads, microinductors, microtransformers, radars and EMI noise reduction. The basic requirements for materials for high frequency applications are high magnetization saturation, low coercivity, high anisotropy field and high resistivity. High saturation magnetization required for application such as magnetic recording head is to be able to write on magnetic memory elements with high coercivity resulting in higher information density. In case of microfabricated inductors/transformers high saturation magnetization is required to achieve high power density and current handling capability. The most attractive alloy investigated to date is CoNiFe[1], which shows saturation magnetization as high as 2.1 T [2,3]. However, due to low resistivity of CoNiFe (25 μΩ cm) the thickness is limited to submicron when higher operation frequency is required (>100 MHz).
Several approaches have been undertaken to increase resistivity, including the incorporation of sulphur [4,5], and carbon [6] into the deposits. However, these additives also tend to reduce the saturation magnetization. Here, we study the effect of P addition to CoNiFe alloy and its effect on high frequency performance of CoNiFe. We show that films as thick as 10 μm have flat permeability response up to GHz range. The operating frequency is only limited by ferromagnetic resonance of the alloy, which is about 3 GHz (figure 1) depending on the P content.
Acknowledgement: This work has financially been supported by Scientific Foundation of Ireland (SFI) Principal Investigator (PI) grant no 06/IN.1/I98 and Enterprise Ireland (EI) grant no ILRP/05/PEIG/02B
Corresponding author: saibal.roy@tyndall.ie

[1] T.Osaka, M.Takai, K.Hayashi, K.Ohashi, M.Saito, and K.Yamada,Nature 392, 796 (1998)

[2] T. Osaka, M. Takai, K. Hayashi, Y. Sogawa, IEEE Trans, Magn. 34, 1432 (1998)

[3] X. Liu, P. Evan, G. Zangari, IEEE Trans. Magn. 36, 3479 (2000)

[4] I. Tabakovic, S. Riemer, V. Inturi, P. Jallen, A. Thayer, J. Electrochem, Soc. 147, 219 (2000)

[5] M. Takai, K. Hayashi, M. Aoyagi, T. Osaka, J. Electrochem. Soc. 144, L203, (1997)

[6] T. Yokoshima, M. Kaseda, M. Yamada, T. Nakanishi, T. Momma, T. Osaka, IEEE Trans. Magn. 35, 2499 (1999)

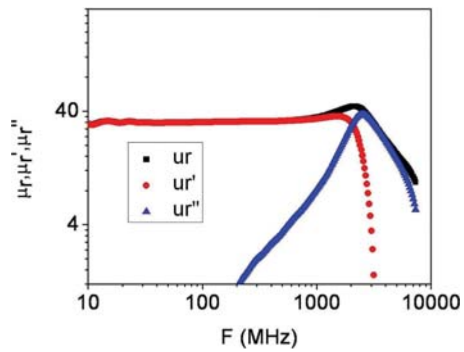

Figure 1. Complex permeability spectra of CoNiFeP alloy film.

HP-08

Spin re-orientation transition in amorphous FeBSi thin-films submitted to thermal treatments.

P. Tiberto, F. Celegato, M. Coisson, F. Vinai
INRIM, Torino, Italy

Ultrathin ferromagnetic films displaying perpendicular anisotropy have been extensively studied in the last decades for practical application in high-density magnetic recording. The magnetic anisotropy governing magnetisation directions is usually strongly dependent on the microstructure and its optimisation turns out to play a key role for thin films application in storage devices [1]. In this frame, magnetic thin films have been obtained by means of RF sputtering technique on Si_3N_4 substrates from a $Fe_{78}B_{13}Si_9$ target. Samples having thickness ranging in the interval 25-300 nm have been produced. X-ray diffraction data indicate that the films have different microstructures varying from fully amorphous to partially nanocrystalline with increasing thickness. In order to relieve the quenched-in stresses during the sputtering, the as-prepared films have been submitted to isothermal furnace annealing in vacuum for temperature varying in the interval 200 – 325 °C. Room-temperature magnetic hysteresis loops have been measured by means of vibrating sample magnetometry on all studied samples. A tailorable spin reorientation transition (SRT) from in-plane single domain-like to out-of-plane multidomain state with increasing film thickness has been observed for samples having thickness higher than 80 nm. These samples are characterised by a two-slope hysteresis loops: a first steep magnetisation jump followed by a linear behavior between remanence and saturation. The lower slope occurring before saturation is related to the development of a perpendicular anisotropy component marking the occurrence of a spin reorientation transition. The magnetic field H_k at which the saturation is reached is connected with the perpendicular anisotropy. Magnetic force microscopy images have been obtained for all studied samples indicating that for films having thickness lower than 80 nm the magnetisation lies in the film plane. Films having higher thickness and diplaying the two-slope hysteresis loops exhibit a stripe domains patterns. The domain width increases on samples with a smaller perpendicular anisotropy value, as expected.

In this work, spin reorientation transition have been studied as a function of sample thickness and perpendicular anisotropy. In particular, the effect of furnace annealing on the transition from in-plane to an out-of-plane configuration will be highlighted. Selected in-plane hysteresis loops of the as–prepared and annealed films having thickness 300 nm are reported as an example in Fig. 1. As it can be clearly observed, the magnetisation behavior indicates an evolution from a out-of-plane configuration towards an in plane magnetisation behavior with increasing annealing temperature. Magnetic domain structures of selected samples, whose hysteresis loops are shown in Fig. 1, are reported in Fig. 2 confirming that the complete relief of quenched-in stresses leads to a in-plane magnetisation behavior.

[1] Ultrathin Magnetic Structures IV: application of nanomagnetism, edited by B. Heinrich and J.A.C. Bland (Springer-Verlag, Berlin 2005).

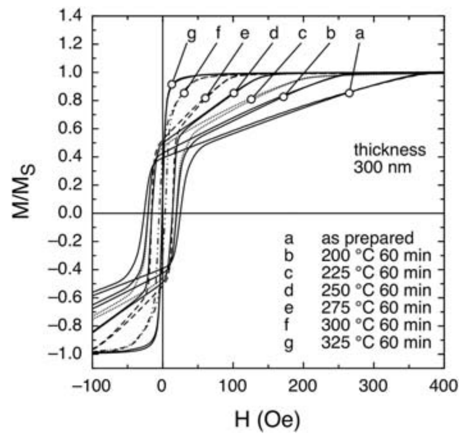

Magnetisation curves with magnetic field H applied along sample length of an as-prepared and selected annealed $Fe_{78}B_{13}Si_9$ thin films having thickness 300 nm.

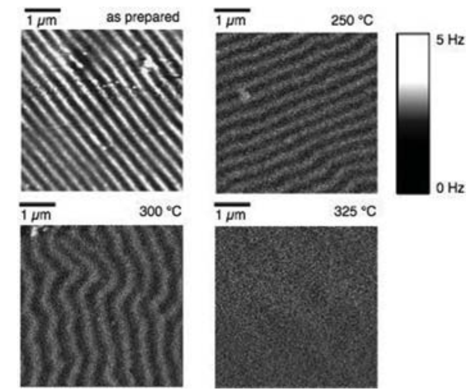

MFM images at magnetic remanence of an as-prepared and selected annealed $Fe_{78}B_{13}Si_9$ thin films having thickness 300 nm.

HP-09

Electroplated Ni_xFe_{100-x}/FeCo Multi-layer Films for Perpendicular Write Heads.

Y. Miyake, M. Matsuoka, M. Kato, H. Kanai, Y. Uehara
fujitsu ltd, Nagano, Japan

Introduction

Perpendicular magnetic recording (PMR) has become the main technology for hard disk drives. For PMR heads in high areal recording density, improvement in overwrite (O/W) and suppression of pole and side-track erasure are required, so high saturation flux density (Bs) and low coercivity (Hc) are demanded in main pole materials. For that purpose, sputtered magnetically soft FeCo multi-layer and electroplated FeCo/non-magnetic NiP laminate films have been studied [1-4]. Main Pole has been fabricated as reverse trapezoid shape or side-shielded heads [1] have been proposed to suppress the side track erasure at skew angle. But it may be difficult to control 3-dimensional shape of the shielded pole having narrow track width. In this paper, we study electroplated Ni_xFe_{100-x}/FeCo multi-layer films for the main pole material having lower Bs with low Hc in the leading edge and higher Bs in the trailing edge. We investigate their magnetic properties and crystal structure and designed the materials for the main pole.

Experiment

The electroplated $[Ni_xFe_{100-x}/FeCo]_2$ films were deposited on a sputtered ruthenium under layer with random crystalline orientation. The electroplated Ni_xFe_{100-x} films were deposited by DC and pulse current in nickel iron electroplating bath. The electroplated FeCo films were deposited by pulse current in iron cobalt electroplating bath. Fig. 1 shows a cross-sectional illustration of $[Ni_xFe_{100-x}/FeCo]_2$ films. Total thickness was fixed in the range from 350 to 500 nm. The composition and thickness of electroplated films were determined by the measurements of X-ray fluorescence (XRF). The in-plane magnetization curves, Hc, and Hk were measured using a B-H loop tracer. Bs was measured at room temperature using the Superconducting-Quantum-Interference-Device (SQUID). The crystal structures of electroplated films were measured using X-ray diffraction (XRD).

Results and discussion

Fig. 2 shows $Ni_xFe_{100-x}/(Ni_xFe_{100-x}+FeCo)$ thickness rate dependences of Hc in electroplated $[Ni_xFe_{100-x}/FeCo]_2$ films with various Ni compositions. Hc decreased dramatically in slight NiFe thickness rate and saturated above the ratio of about 50% in electroplated $[Ni_{35}Fe_{65}$, $Ni_{50}Fe_{50}$, $Ni_{80}Fe_{20}/FeCo]_2$ films, whereas it decreased linearly with increasing the NiFe thickness rate in electroplated $[Ni_{10}Fe_{90}/FeCo]_2$ films. It seems that this drastic decrease in Hc is caused not only by exchange coupling between FeCo and $Ni_{35-80}Fe_{65-20}$, but also by improvement of the crystalline structure and the reduction of the grain size in electroplated FeCo films on electroplated $Ni_{35-80}Fe_{65-20}$ films, because crystal structure contributes to reduction of Hc for easy and hard axis [5].

Conclusions

We have investigated the magnetic properties of electroplated $[Ni_xFe_{100-x}/FeCo]_2$ multi-layer films for perpendicular write heads in high areal recording density, and found that Hc can be dramatically decreased in electroplated $[Ni_{35-80}Fe/FeCo]_2$ films. These multi-layers are expected to suppress the pole and side-track erasure and improve the O/W in narrow track width when used in perpendicular write heads.

[1] Y. Chen, K. Sin, H. Jiang, Y. Tang, K. Sasaki, A. Torabi, L. Wang, M. Park, D. Bai, Y. Shen, P. Luo, F. Lio, K. Stoev, W. Lin and J. Zhu, IEEE Trans. Magn., Vol.43, p.609, Feb. 2007.

[2] M. Kief, V. Inturi, M. Benakli, I. Tabakovic, M. Sun, O. Heinonen, S. Riemer and V. Vas'ko, IEEE Trans. Magn., Vol 44, p113, Jan. 2008.

[3] Y. Okada, H. Hoshiya, T. Okada and M. Fuyama, IEEE Trans. Magn., Vol.40, p.2368, July 2004.

[4] T. Kubomiya, M. Matsuoka, Y. Uehara, S. Ikeda, and Y. Miura, Trans. Mater.Res Soc. Jpn, Vol. 29, p. 1577, 2004.

[5] Y. Miyake, M. Kato, H. Kanai and Y.Uehara, J. Mag.Soc. Jpn, Vol. 29, p. 292,2005.

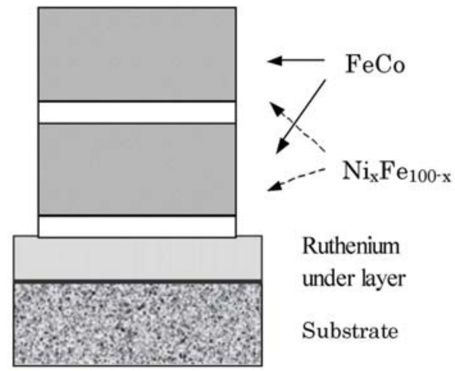

Fig. 1. Cross-sectional illustration of $[Ni_xFe_{100-x}/FeCo]_2$ films.

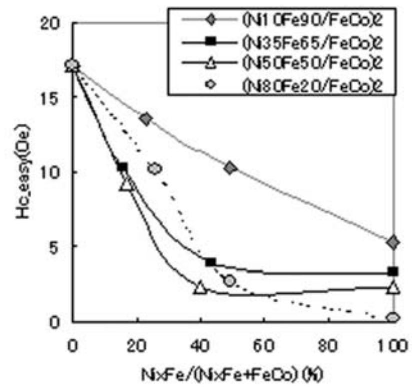

Fig. 2. $Ni_xFe_{100-x}/(Ni_xFe_{100-x}+FeCo)$ thickness rate dependences of H_c in $(Ni_xFe_{100-x}/FeCo)_2$ electroplated films.

HP-10

High temperature electrodeposited multilayer amorphous alloy suitable for integrated inductors.

P. McCloskey[1], B. Jamieson[1], T. O'Donnell[1], D. Gardner[2], M. Morris[3], S. Roy[1]
1. Microsystems Center, Tyndall National Institute, Cork, Ireland; 2. Circuit Research lab, INTEL Corporation, Santa Clara, CA; 3. Chemistry department, University College Cork, Cork, Ireland

INTRODUCTION: The integration of on-chip inductors with magnetic materials into silicon process technology has been a major challenge in the move towards monolithic solutions for wireless communications, RF IC circuits, radar, power delivery, and EMI noise reduction [1]. The use of a magnetic core in such devices has the potential to significantly reduce the footprint required but requires a material that gives very low losses when operating at high frequency. Electrodeposited amorphous Co-P alloys have the advantage of both high resistivity and low coercivity and consequently can show both low eddy current loss and low hysteresis loss. However in order to achieve a low coercivity an approach other than simple direct current (DC) electroplating must be employed since plane DC plated films exhibit perpendicular anisotropy and hence very low permeability and high values of coercivity. In order to have in plane anisotropy and low coercivity a multilayer structure of alternating compositions must be created using either pulse reverse plating [2] or pulse plating at two different current densities [3] [4].
The temperature stability of the magnetic properties is an important consideration because of the processing steps involved in fabricating an inductor consisting of a magnetic core that encloses the windings. Oda et al [5] used small additions of Tungsten to improve crystallisation temperature of amorphous FeCoP alloys. Tungsten has a large atomic weight of 183.8 and it is thought that its large atomic radii plays a role in bringing about an increase in crystallization temperature. However electroplating baths containing Tungsten have a considerable tendency to be unstable. Rhenium has an atomic weight of 186.2 and Brenner [6] describes how it can be readily co-deposited with Iron group metals. The present work is concerned with the characterisation of a novel electrodeposited alloy CoPRe that shows a considerable improvement in temperature stability in comparison with the normal CoP alloy.
EXPERIMENTAL: Plating baths were prepared with the compositions as given in Table 1. The bath composition used in trial 1, was identical to that used in [2] apart from the additions of KReO4. This was added progressively 0.1g/l at a time so that in all 7 samples were produced, the first having no KReO4 addition and the last having an addition of 0.7g/l. In trial 1 the cathode used was 20 µm copper foil. In Trial 2 the effect of changing the Phosphorous content was investigated by varying the quantity of H3PO3 between 30 g/l and 65 g/l, while keeping the KReO4 fixed at 0.7 g/l. In the second trial the material was plated onto Cu foil and onto silicon wafers with a top layer of 500 nm of oxide and a conductive sputtered seed layer consisting of 20 nm Titanium and 200 nm Copper. All the trial 2 samples were plated in the presence of a uniaxial magnetic field of around 200 Oe.
Pulse reverse plating was used in both Trials. In all cases the pulse parameters were kept constant at values found to be optimal for CoP [7]; forward on time, T1=856 ms, forward current density, CD1=151 mA/cm2, reverse on time, T2= 52 ms, reverse current density, CD2=62 mA/cm2 and off time, Toff=80 ms. DC magnetic characterisation was obtained using an ShB Instruments B-H loop tracer. Complex permeability spectra were measured using a Ryowa PMM9G1 permeameter. EDX was used for compositional analysis. DSC analysis was carried out using a Perkin Elmer Pyris 1.

RESULTS: The addition of the Re salt seemed to have no effect on the appearance of the samples. A selection of the samples produced in Trial 1 were subjected to thermal anneals consisting of a 15 minute ramp, a 30 minute dwell at elevated temperature and a 15 minute cooling.
It can be seen that the 300 C anneal dramatically changed the coercivity of the CoP sample but had very little effect on the coercivity of the CoPRe. A similar improvement in thermal stability was obtained for all the CoPRe samples tested.
CONCLUSIONS: A new electrodeposited multilayer amorphous alloy, CoPRe is reported that shows a significant improvement in the thermal stability of its soft magnetic properties in comparison with CoP. The effect of Phosphorous content on the properties of material is investigated.

[1] D. S. Gardner et. al., IEEE International electron device meeting, (IEDM), San Francisco (USA), 11-13 December 2006

[2] J.M. Riveiro, G. Riveiro, IEEE Trans. Mag., 17, No. 6, 3082 (1981).

[3] L.Perez et al, J. Magn. Mag. Mater, 215-216, 337 (2000)

[4] L.Perez et al, Sens. Act. A 109 208 (2004)

[5] Oda et al, US Patent 584494A (1996)

[6] A.Brenner, "Electrodeposition of Alloys", Academic Press, London 1963

[7] P.McCloskey et al, SMM18, Cardiff (UK), 2-5 September 2007

Component(g/l)	Trial 1	Trial 2
H3PO3	65	30-65
CoCO3	39.4	39.4
CoCl2 6H2O	181	181
H3PO4	50	50
KReO4	0-0.7	0.7

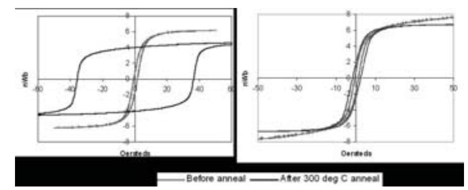

left CoP, right CoPRe

HP-11

Magnetic properties of sputtered permalloy/molibdenum multilayers.

M. Romera[1], M. Maicas[1], R. Ranchal[2], D. Ciudad[1], E. López[2], P. Sánchez[1]
1. ISOM, Universidad Politécnica de Madrid, Madrid, Spain; 2. Física de Materiales, Universidad Complutense de Madrid, Madrid, Spain

Magnetic materials for sensor applications require low internal stress, low coercivity and low magnetostriction while keeping a high permability [1]. Permalloy (Py: Fe20Ni80) fulfil well with these requirements which makes it a good candidate for magnetic sensor applications. Properties like permabillity or linearity of the loops can be controlled by growing Py as a multilayer with alternating perpendicular anisotropies [2]. However for thicknesses over 180 nm sputtered Py films develop perpendicular anisotropy and the magnetic properties degrade notably [3]. Both coercive and saturating fields are nearly 10 times bigger than those measured for thinner films. This anisotropy is induced by the columnar morphology of the sputtered films. Nevertheless, it is possible to obtain low coercivity and high permability if thick Py films are grown as multilayers with a non-magnetic spacer between magnetic layers. In this work we study the properties of Py films grown as multilayers with thin Molibdenum (Mo) spacers.
The multilayers studied were grown by dc magnetron sputtering and the anisotropy induced was controlled by the angle of incidence of the beam. The anisotropy induced by the deposition angle was measured for a single Py layer (125 nm thick) obtaining an anisotropy constant of K=1200 J/m3 which corresponds to an exchange correlation length of 180 nm.
The effect of the sample thickness can be seen in figure 1 which shows the VSM hysteresis loops of Py samples with thicknesses 125, 250 and 375 nm. These loops exhibit quite different behaviour changing from an in-plane anisotropy for the thinner to a clear perpendicular to the plane anisotropy for the others. MFM measurements on the thicker samples show a stripe domain pattern that proves the existence of an anisotropy perpendicular to the sample plane.
A thin Mo spacer of 10 nm results enough to break the magnetic coupling between the Py layers. A Py film with total thickness 250 nm grown as a multilayers with 4 Py layers with Mo (10 nm) spacers was grown. Hysteresis loops show low coercive and saturating fields much lower than those obtained in a Py monolayer with the same thickness (figure 2). The Mo spacer proves to break effectively the magnetic coupling and the columnar morphology maintaining the anisotropy in the plane.
Some authors have found very low coercive field values in Py multilayers for particular thicknesses [3]. In order to study the effect of the thickness in the coercive field of Py/Mo multilayers, 250 nm thick multilayers were grown with a number of Py layers ranging from 2 to 32 with Mo spacers in between. Coercivity was obtained from VSM measurements. Figure 3 shows the coercive field measured as a function of the number of Py layers. A minimum in the coercivity was found for Py layer thicknesses corresponding to 30 nm. This minimum coincides with the transition thickness of a single film where Bloch domain walls change to Néel domain walls. The thickness of Bloch domain walls increases as the Py thickness increases and the thickness of the Néel walls core increases as the Py thickness decreases.
In summary it is observed how the soft magnetic properties of sputtered Py films can be maintained for thicknesses over 180 nm by growing samples as multilayers with thin Mo spacers. The coercivity can be minimized for particular Py thicknesses about 30 nm.

[1] P. Ripka, Magnetic Sensors and Magnetometers, Artech House (2001), p. 88

[2] M. Maicas et al, (sent to European Physical Journal B)

[3] S.F. Cheng, P. Lubitz, Y. Zheng and A. S. Edelstein, J. Magn. Magn. Mat., 282 (2004) 109

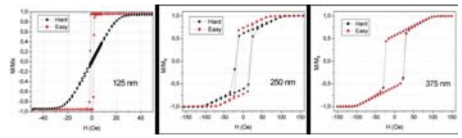

Py hysteresis loops for film thicknesses 125, 250 and 375 nm

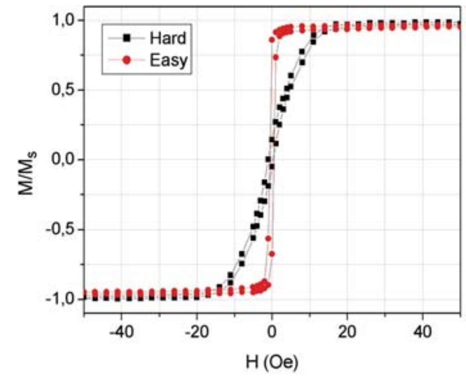

Hysteresis loop of a multilayer consisting in 4 Py layers separated by 10 nm Mo spacers. The total Py thickness is 250 nm.

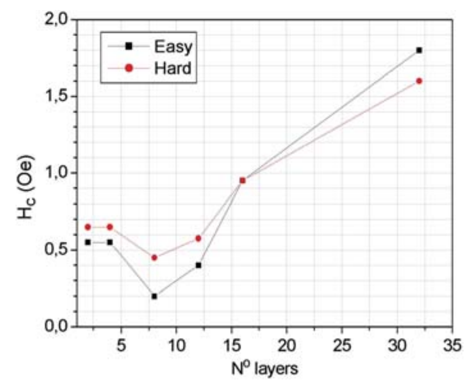

Coercive fields of a Py/Mo multilayer with a total thickness of 250 nm as a function of the number of Py layers

HP-12

Effects of capping layers on damping constants and magnetic properties of CoFeB.

J. Song[1], C. Wang[1], S. Huang[1], C. Lai[1], W. Chen[2], S. Yang[2], K. Shen[2]
1. Department of Materials Science and Engineering, National Tsing Hua University, Hsinchu, Taiwan; 2. ERSO, Industrial Technology Research Institute, Hsinchu, Taiwan

Introduction:
Recently, the amorphous CoFeB is widely used in the MgO-based magnetic tunnel junctions (MTJs) due to its proper magnetic characters. The amorphous CoFeB can also promote the growth of MgO (002), which is very crucial for the high magnetoresistance (MR) ratio. On the other hand, both the magnetic properties and the damping constant (α) of CoFeB are critical factors for spin-transfer or field-switching devices. In this work, we prepared the half-MTJ samples of MgO 1/$Co_{60}Fe_{20}B_{20}$ 2.5/X 5/Ta 5 (unit:nm) to investigate the properties of CoFeB free layer used in MTJs, where X was Cu, MgO or none. Cu was chosen because it can suppress the spin pumping effect and achieve a low damping constant in the NiFe/Cu bilayer [1]. A low switching current of dual-barrier MTJs was reported and the extra MgO barrier was believed to be the major factor [2], but a systematic study of the MgO effect is still lack. In this work, we study the capping layer effects on properties of CoFeB films after different annealing temperatures.
Experiment results & discussion:
All samples were deposited by using a sputtering system with the base pressure better than 1×10^{-8} Torr. Samples were field-annealed in vacuum ($P<1\times10^{-5}$ Torr) for 2 hours at various temperatures up to 360^0C. The α value was obtained from the measurement of the ferromagnetic resonance (FMR) by electron spin resonance (ESR). Magnetic properties were measured by vibrating sample magnetometer (VSM).
A low saturation magnetization M_S of samples of CoFeB/Ta was observed in the as-deposited state, shown in Fig. 1(a), which indicated significant intermixing between Ta and CoFeB layers during deposition. On the other hand, the intermixing seemed to enhance the diffusion of B out of CoFeB for the temperatures up to 300^0C, leading to an increase in M_S and reduction of the damping constant [3]. Since the crystallization of CoFeB typically accompanied the increase in coercivity H_C, the almost unchanged H_C up to 300^0C annealing, shown in Fig. 1(c), implied the crystallization of CoFeB may not occur until the temperature higher than 300^0C. When the annealing temperature reached 360^0C, both improvement of crystallinity of CoFeB and serious intermixing occurred, resulting in the slight decrease of M_S and substantial increase of H_C.
High M_S of the as-deposited samples with the insertion of the Cu layer, shown in Fig. 1(a), revealed that the intermixing was suppressed by the capping of Cu. The slight reduction of M_S and almost unchanged H_C were observed after 360^0C annealing for samples of CoFeB/Cu/Ta. These results indicated that insertion of a Cu layer would prevent B from diffusing out; therefore, the crystallization of CoFeB might start at temperatures higher than 360^0C. In addition, the insertion of a Cu layer led to a low α value even after 360^0C annealing, shown in Fig. 1(b). This low α value confirmed that Cu can also suppress the spin-pumping effect in the CoFeB/Cu system, as reported in NiFe/Cu [1]. The limited intermixing also contributed to the low α value. The decrease in M_S and small α may be beneficial to reduce the switching current for spin-transfer devices.
Insulating capping layer, MgO, exhibited quite different behavior from the previous two samples: significantly high M_S and relatively large H_C and α in the as-deposited CoFeB/MgO/Ta samples. MgO capping seemed to completely restrict the intermixing, resulting in high M_S. We expected to observe a low α value due to insulating characteristics of MgO, which should suppress the spin-pumping effect. Other factors may be taken into account to explain the damping behavior. Dramatic increase of M_S and reduction of α after annealing samples to 300^0C were observed, while the H_C change was quite small. It was reported that the diffusion of boron after annealing may form BO_X at the interface of MgO and CoFeB, which diminish FeO_X and CoO_X [4]; therefore, the extra MgO capping layer might substantially speed the diffusion out of B from CoFeB, leading to increase M_S and decrease α. However, the α and H_C raised again accompanied by the decrease of M_S, which may be attributed to the local oxidization of Co or Fe after annealing at 360^0C,.
In summary, by inserting different capping layers, the α, M_S and H_C of CoFeB can be tuned, which may enable us to adjust the switching current for the spin-transfer devices.

Reference

[1] A. Brataas et al., Phys. Rev. Lett. 88, 117601 (2002)

[2] Y. Huai et al., Appl. Phys. Lett. 90, 132508 (2007)

[3] Y. Ando et al., Jpn. J. Appl. Phys. 45, 3889 (2006)

[4] J. C. Read et al., Appl. Phys. Lett. 90, 132503 (2007)

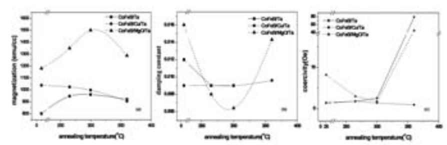

Fig. 1 Variations of (a) M_S, (b) α and (c) H_C with annealing temperature

Direct Observation of Barkhausen Avalanches during Nucleation-Mediated Magnetization Reversal on a nanoscale.

M. Im[1], P. Fischer[1], D. Kim[2], S. Shin[3]
1. CXRO, LBNL, Berkeley, CA; 2. Department of Physics, Chungbuk National University, Cheongju 361-763, South Korea; 3. Department of Physics and Center for Nanospinics of Spintronic Materials, Korea Advanced Institute of Science and Technology, Daejeon 305-701, South Korea

Since the first discovery of Barkhausen avalanches magnetization reversal phenomena are considered as prototype examples of complex dynamical systems exhibiting non-trivial fluctuations which can be described by well defined scaling behavior [1]. Barkhausen avalanches occur in the magnetization reversal process as discrete and sudden magnetization changes under an external magnetic field. Of fundamental interest are fluctuating quantities such as Barkhausen jump size and duration showing a power-law scaling behavior. Most studies reported so far have been mainly performed by theoretical predictions and indirect probes through a classical inductive technique. Recently, substantial progress was enabled by direct observations of the phenomenon using magnetic microscopies [2]. However, they have been carried out on the micrometer scale and concentrated mainly on the Barkhausen avalanches process during the flexible magnetic domain wall motion.
We investigated the Barkhausen avalanches process under nucleation-mediated magnetization reversal at the nanometer scale utilizing high resolution soft X-ray microscopy at beamline 6.1.2 at the Advanced Light Source in Berkeley CA, which provides a spatial resolution down to 15 nm [3]. Nanogranular CoCrPt alloy thin films which are promising candidates for high-density perpendicular magnetic recording media, were prepared by dc magnetron sputtering at ambient temperature. The magnetic domain configurations were recorded at the Co L3 absorption edge (777eV) with varying applied magnetic fields in full hysteresis cycles. Typical domain configurations taken at applied magnetic fields of +400, +200, 0 Oe in the major hysteresis loop are shown in Fig. 1(a). As demonstrated in the figure the magnetization reversal of the CoCrPt sample is governed by the magnetic domain nucleation process. TEM studies indicate that the nucleation-mediated process of magnetization reversal observed in this system is due to switching of individual grains segregated by higher Cr concentration at grain boundaries. Fig. 1 (b) shows the Barkhausen jump distribution in two-dimensional space, where green and red structures represent the Barkhausen avalanches observed at applied magnetic field of +200 and 0 Oe, respectively. One clearly notes that Barkhausen avalanches vividly illustrate the randomness of size, shape, and location. The random behavior in the locations of the Barkahusen avalanches implies that the numerous pinning sites due to the Cr compositional segregation in this system are randomly distributed and strongly localized. The statistical nature of Barkhausen avalanches was studied by repetitive measurement for magnetic domain configurations at each applied magnetic field of +400, +200, 0 Oe. Through a statistical analysis of jump size from several hundreds of domains, the distributions of Barkhausen jump size are obtained (Fig. 2). They exhibit a non-trivial fluctuation and can be described by power-law scaling distributions of $P(T_0) \sim (T_0)^{\tau}$ with a scaling exponent ~1.Scaling exponents taken at applied magnetic field of +200 and 0 Oe are found to be identical within the measurement error. They are consistent with theoretical values derived from a random-field Ising model including the effect of long-range dipolar interaction 4]. Our study experimentally supports a long-standing theoretical prediction, namely that long-range dipolar interactions play a decisive roles in the statistical behavior of Barkahusen avalanches in nucleation-mediated magnetization reversal processes

This work was supported by the DOE, Office of Science, Basic Energy Sciences, Division of Materials Sciences and Engineering.

[1] H.Barkhausen, Z. Phys. 20, 401 (1919).

[2] D.-H. Kim, S.-B. Choe, S.-C. Shin, Phys. Rev. Lett. 90, 87203-1 (2003)

[3] P. Fischer, G. Schütz, G. Schmahl, P. Guttmann, and D. Raasch, Z. f. Physik B 101, 313 (1996).

[4] F. Pazmandi, G. Zarand, and G. T. Zimanyi, Phys. Rev. Lett. 83, 1034 (1999).

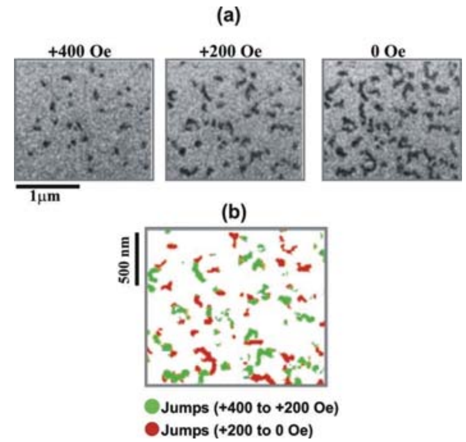

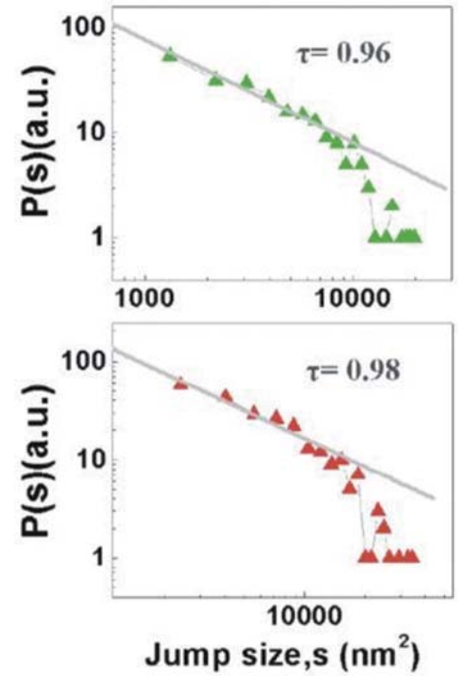

Magnetotransport and exchange-bias in CoCu electrodeposited granular alloys.

M. Plaza[1], L. Perez[1], M. Sánchez[1], A. Fernández-Pacheco[2,3], J. de Teresa[2]
1. Dpt. Fisica de Materiales, Universidad Complutense de Madrid, Madrid, Spain; 2. Instituto de Ciencia de Materiales de Aragón, CSIC-Universidad de Zaragoza, Zaragoza, Spain; 3. Instituto de Nanociencia de Aragón, Universidad de Zaragoza, Zaragoza, Spain

Granular magnetic materials are composed of ferromagnetic nanoparticles inside a non-magnetic conductive matrix. These materials have been deeply studied due to their interesting properties: giant magnetoresistance (GMR) [1], exchange-bias [2] and superparamagnetic behaviour [3]. The study of these properties has led to the use of granular materials in magnetic sensors and devices [4]. We have produced granular electrodeposited CoCu alloys in powder form using a high current density (~10 A/cm2). Electrodeposition was carried out from sulphate-based electrolytes containing 0.5M metal ions and 0.5M boric acid at 20V. The powders were compacted at 120 MPa. A pure Co sample has been also produced following the same procedure.
The figure shows the ω-2θ XRD scans for Co and $Co_{15}Cu_{85}$ samples. Whereas Co sample shows the expected hcp structure, all CoCu samples show fcc structure due to the influence of the Cu matrix. The presence of Cu affects also the grain size of the Co clusters, which is significantly lower in CoCu alloys (~20nm) than in pure Co (~50nm). The figure also shows a detail of the Co-fcc(111) and Cu- fcc (111) peaks. The cobalt peak is shifted to lower angles with respect to the normal position (marked by * in the figure) because the Co structure is 0.7% expanded in the Cu matrix.
The thermal evolution of the GMR ratio for three of the studied samples is shown in the right part of the figure. All samples exhibit the same values of GMR at low temperature (1%), whereas, at high temperature, sample $Co_{12}Cu_{88}$ shows the highest GMR value. At low temperature, scattering at the grain boundaries dominate the GMR effect. Taking into account that all samples present similar structural properties, the same behaviour at low temperature is expected. The thermal dependence of GMR can be fitted with a theoretical calculation based on the model of GMR by Fert et al. [5].
CoCu granular alloys also show exchange bias, most likely due to the antiferromagnetic coupling between the Co clusters and a CoO shell that surrounds them. From these results, comparing with what other authors found in cobalt clusters [2], we suggest that the average particle size may be similar to the grain size (~20nm). Therefore, high-current electrodeposition is a suitable method to produce granular alloys with nanometric ferromagnetic clusters in a non-magnetic metal.

[1] J. Q. Xiao, J. S. Jiang, and C. L. Chien, Phys. Rev. Lett. 68, 3749 (1992).

[2] R. Morel, A. Brenac, and C. Portemont, J. Appl. Phys. 95, 3757 (2004).

[3] R. S. Iskhakov, G. I. Frolov, V. S. Zhigalov, and D. E. Prokof'ev, Tech. Phys. Lett. 30, 51 (2004).

[4] S. Arana, E. Castaño, and F. J. Gracia, IEEE Sensors Journal 4, 221 (2004).

[5] A. Fert and I. A. Campbell, J. Phys. F: Metal Phys. 6, 849 (1976).

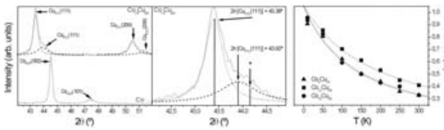

(left) X-ray diffraction ω-2Θ scans for Co and $Co_{15}Cu_{85}$ samples, (center) a detail of the XRD scan showing the fcc-Co and fcc-Cu (111) peaks in the $Co_{15}Cu_{85}$ sample, (right) thermal evolution of the GMR ratio for CoCu samples.

HP-15

High magnetic moment soft thin films for flux concentrators.

I. G. Trindade[1,2], J. Oliveira[1,3], J. Teixeira[1], R. Fermento[1], J. B. Sousa[1,2], S. Cardoso[4], P. P. Freitas[4], J. E. Snyder[5], A. Raghunathan[5]
1. IFIMUP-IN, Porto, Portugal; 2. Physics, Faculdade de Ciências da Universidade do Porto, Porto, Portugal; 3. Faculdade de Ciências da Universidade do Minho, Braga, Portugal; 4. INESC-MN-IN, Lisboa, Portugal; 5. Wolfson Centre for Magnetics, School of Engineering, Cardiff University, Cardiff, United Kingdom

In this paper we describe magnetic thin films prepared by ion beam deposition (Nordiko 3600, INESC-MN) from an alloy target of $(Co_{70}Fe_{30})_{80at\%}B_{20at\%}$. The as-deposited films, with thicknesses up to 40 nm, exhibit an amorphous phase and have a spontaneous magnetic moment, as measured by Hall effect, of 1200 emu/cm^3. An applied field to the substrate, during film growth, induces a uniaxial anisotropy field of 23 Oe, as measured by a B-H looper.

Magnetic flux guides can be used with magnetoresistive sensors to achieve field sensitivities in the picoTesla range and beyond. In those, a non negligible remanent magnetic moment lower the device performance. One way to accomplish null remanent magnetic field in the gap of flux guides consists in integrating a thin, suitable spacer, between two physically identical ferromagnetic layers to provide a long range interlayer antiferromagnetic coupling between the two [1-2] and forming hence a synthetic antiferromagnet [3]. For our purpose, we use thick ferromagnetic layers with a total magnetic thickness in the range of a few hundreds of nanometers, but with high permeability. Ion beam deposition (IBD) is a suitable technique to produce antiferromagnetically coupled films with very smooth interfaces [4], having stabilized single-domain states in the ferromagnetic layers, while maintaining adequate rotational permeability.

The CoFeB has the advantage of having higher spontaneous magnetization than either Permalloy or Co-Zr-Nb (CZN) amorphous alloy, and can have to some degree partial homogeneously distributed crystalline phase by using a suitable buffer layer of Ta 2nm/Ru t_{Ru}. This partial crystalline phase, may have long range interaction through a spacer of Ru and depending upon its thickness, the coupling field between the ferromagnetic layers may be antiferromagnetic. The thickness of Ru of the buffer, on which the multilayer is grown, has considerable effect on the interlayer antiferromagnetic coupling as shown by the M-H curves, presented in Fig. 1, obtained with a vibrating sample magnetometer (VSM). Unlike the CoFeB film deposited directly on a Ta underlayer, films of CoFeB 10nm/(Ru .9nm/CoFeB 10nm)x3 exhibit in the XRD spectra a crystalline peak, around $2\theta= 42\ ^o$, as shown in Fig. 2. The peak is more pronounced if the Ru thickness in the buffer, is 3 nm, than if is 1 nm. These structural results correlate well with the antiferromagnetic coupling field strength, obtained from the M-H curves, with values of 200 Oe and 20 Oe, respectively.

The crystalline phase and texture are discussed. The films, microfabricated into flux guides, consisting of long poles and large yokes, have their magnetization processes characterized by anisotropic magnetoresistance measurements and focused beam magneto-optic Kerr effect. The results are compared with analogous multilayer films that use ferromagnetic layers of Permalloy, also prepared by ion beam deposition in a 4-target Commonwealth Scientific ion beam deposition system (IFIMUP).

[1] S. S. Parkin, Phys. Rev. Lett. 67 (1991), pp. 3598.

[2] M. Maurer, J. C. Ousset, M. Pietcuch, M. F. Ravet and J. P. Sanchez, Mat. Res. Soc. Symp. Proc., 151 (1989) pp. 99.

[3] V. S. Speriosu et al., paper AA-04, presented at Intermag Conference, Seattle 1996.

[4] I. G. Trindade, J. Magn. Mag. Mat., 240 (2002) pp. 232.

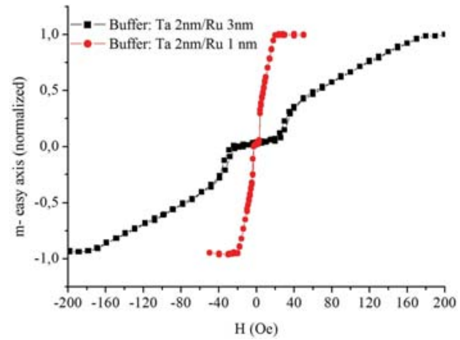

Fig. 1: Easy axis M-H curves as obtained by VSM, corresponding to the films, Glass/Ta 2nm/Ru t<Ru>/(CoFeB 10nm/(Ru .9nm/CoFeB 10nm)x3/Ru 3nm.

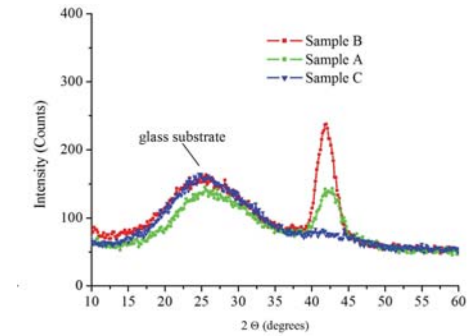

Fig. 2: X-Ray diffraction spectra; Sample A, glass/Ta 2nm/Ru 1nm/CoFeB 10nm/(Ru 0.9nm/CoFeB 10nm)x3/Ru 3nm; Sample B, glass/Ta 2nm/Ru 3nm/CoFeB 10nm/(Ru 0.9nm/CoFeB 10nm)x3/Ru 3nm; Sample C, glass/Ta 2nm/CoFeB 40nm.

HQ-01

Controlling Domain Wall Pinning in Planar Nanowires with Transverse Field and its Application in a Magnetic Memory Cell.

D. Atkinson, D. S. Eastwood, L. K. Bogart
Physics, Durham University, Durham, United Kingdom

Introduction
There has been intensive research interest in the behaviour of individual domain walls in nanowires both in terms of the fundamental physics and for potential applications. For memory applications domain walls trapped at features such as notches or prominences create multiple domains and hence memory states. In contrast to conventional single bit per transistor MRAM this approach presents the opportunity to store multiple data bits for each readout transistor. Here we investigate controlling the interactions of domain walls with asymmetric pinning structures by selecting the magnetization state of the domain wall using a small transverse magnetic field. This provides an additional degree of freedom to the control the pinning and may be exploited in future magnetic memory.
Modelling
Micromagnetic simulations were performed using OOMMF developed by NIST. The modelled structure had a triangular notch of depth 176 nm part way along the length of a 496 nm wide, 8 nm thick nanowire with the nucleation pad at one end. Standar parameters for Permalloy, a cell size of 8 nm and a damping factor, α=0.015 were used in simulations.
Experimental Details
Magnetic nanowires were made by electron beam patterning, thin-film deposition and lift-off. The thickness was 5 nm. Nanowires were 50 μm long and terminated with a wider rectangular 'nucleation pad' to generate domain walls at one end and a triangular point at the other end to prevent nucleation of walls. A triangular notch was located halfway along the length. The magnetization behaviour of individual nanowires was measured using a focused magneto-optic Kerr effect (MOKE) magnetometer.
Results & Discussion
Figure 1 shows some micromagnetic simulations of domain walls interacting with an asymmetric notch (that is only on one side of the nanowire). The direction of the wall moment is controlled by the application of a small (5 Oe) magnetic field transverse to the long axis of the wire. The domain wall is de-pinned from the pad at 45 Oe and propagates along the wire and is pinned at the notch, figure 1b. The wall is pinned up to an axial field of 60 Oe when it propagates along the remainder of the wire. In contrast, when a transverse head-to-head wall is formed with a wall magnetization in the opposite (downward) direction, figure 1c, the wall de-pins from the pad at 45 Oe, but then propagates along the whole length of the wire at 45 Oe and is not pinned at the notch, figure 1d. The MOKE measurements with the laser spot located after the notch showed the switching behavior resulting from de-pinning of domain walls from the notch. For transverse fields below ±5 Oe the de-pinning field showed only some small changes, however, above ±5 Oe the axial switching behaviour changed significantly. For positive transverse fields greater than 5 Oe the negative switching field was reduced while the positive switching field remained the same and for negative transverse fields the opposite behavior was observed with the positive switching field reduced and the negative switching field largely unchanged. Above 5 Oe the transverse field is sufficient to consistently set the magnetization direction of the domain wall that is formed by reversal of the nucleation pad. The transverse field sets the wall magnetization in the same transverse direction for both head-to-head and tail-to-tail domain configurations leading to different domain wall energy states at the notch resulting from the direction of the wall magnetization with respect to the preferred orientation of the domain magnetization around the notch. Therefore, consistent with the micromagnetic simulations, it is suggested that for a head-to-head domain configuration a low pinning field is achieved for wall magnetization that is pointing away from the apex of the notch while for a tail-to-tail configuration a low pinning field is achieved when the wall magnetization is directed towards the apex of the notch.
The pinning behaviour observed is utilized in a concept for multi-bit memory cells applicable as the free-layer in magnetic random access memory where the domain structure is defined by the location of domain walls that either pin or pass-by pinning structures depending upon the domain wall configuration selected. The pinning results and memory concept are described in more detail [1].

[1] D. Atkinson, D.S. Eastwood & L.K. Bogart Appl. Phys. Letts. In press. (2008)

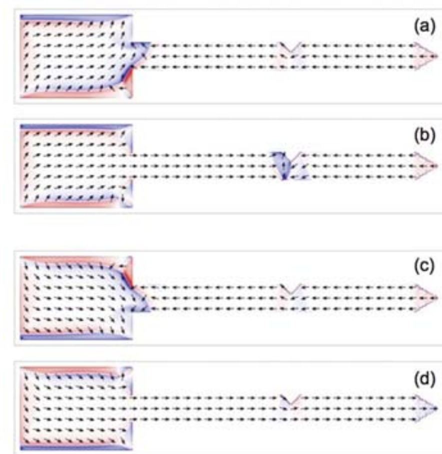

Figure 1. Micromagnetic simulations of the behaviour of walls with different magnetization directions. (a) A head-to-head transverse wall with magnetization pointing upwards and (b) pinning of the wall at the notch after release from the pad at 45 Oe. (c) A head-to-head transverse wall with magnetization pointing downwards and (d) the domain structure at 45 Oe after release of the wall from the pad, the wall has propagated past the notch and swept out of the wire.

HQ-02

Bi-stable memory element based on pinned domain walls in pairs of notches.

E. Martinez[1], L. Lopez-Diaz[2], O. Alejos[3], L. Torres[2]
1. Ingenieria Electromecanica, University of Burgos, Burgos, Spain; 2. Fisica Aplicada, University of Salamanca, Salamanca, Spain; 3. Electricidad y Electronica, University of Valladolid, Valladolid, Spain

Digital information processing relies on the handling of two states, called bits or "0" and "1". A Magnetic Random Access Memory (MRAM) is an array of multilayered elements, each one comprising a soft magnetic layer (free layer) and a hard layer (pinned layer) separated by a non-magnetic layer [1]. Both the free and the pinned layers consist on thin and elongated ferromagnetic dots patterned with lithography, and the shape and dimensions of the free layer are chosen in order to achieve single-domain bi-stable behavior. Bits are stored using the two possible orientations of magnetization in these bi-stable ferromagnetic dots. The information is written on each memory element by passing electrical currents through two orthogonal metallic tracks (work and bit lines), which induce an in-plane magnetic field in the free layer to reverse its magnetization by means of precessional switching. Alternatively, the writing process can be also carried out by means of spin–polarized currents flowing perpendicularly to each multilayer cell [2]. In the reading process, the state of the free layer can be determined by magnetorresistance measurements: if both the free and the pinned layers are magnetized in the same (opposite) direction, the multilayer has low (high) resistance. The two equilibrium states of opposite magnetization are separated by an energy barrier which is related to the dimensions and shape of the free layer. In order to achieve higher density storage, the dimensions of the free layer (and therefore, the energy barrier) must be reduced. However, the superparamagnetic effect, which concerns the loss of magnetic stability as a result of thermal fluctuations when the size of the free becomes small, limits the maximum density of storage information: at finite temperature the magnetization of the free layer can switch from one state to the other just by thermal activation.

It has been recently proposed that bits could be stored in dots displaying a flux-closure magnetic state, coded in the chirality of the structure or in the up-or-down magnetic vortex at the center of the dot [4]. These flux-closure magnetic configurations minimize the magnetostatic coupling between adjacent bits, and they are more stable than single-domain states under thermal fluctuations. However, the vortex configuration in soft samples requires a minimum aspect-ratio under which the single-domain configuration is preferred, so that, the maximum density of storage information is also restricted.
In this work, we explore the possibility of using pinned Domain Walls (DW) on a pair of notches placed in a thin ferromagnetic strip as a simple mechanism to storage information. Here, the bits are stored using the two possible DW positions on each of the two notches of the memory element (see Fig. 1(a)-(b)), and the writing mechanism can be achieved both by means of pulses of in-plane magnetic field and/or electrical current. As an example, Fig. 1(c) shows DW position as a function of time under two magnetic pulses of sinusoidal shape with duration of 20ps and two maximum values. Starting from the initial "0" state, a strength of 55mT (54mT) is (is not) enough to promote the jump of the DW to the "1" state.

Several separations between the two notches are evaluated by means of full micromagnetic modeling as well as a one-dimensional model that considers the DW as a rigid object, both at zero and at room temperature [5]. In the presentation we will show that magnetic field or electrical current pulses can promote transitions between these two well-defined states which are easy, well-controllable, and, faster than previous proposed MRAM devices. Moreover, placing several of these memory elements in the same strip, it will show that the writing mechanism is also highly scalable and selective.

[1] See for example, R. P. Cowburn, J. Appl. Phys. 93, 9310 (2003)

[2] J. Slonczewski. J. Magn. Magn. Mater. 159, L1 (1996)

[3] See for example, E. Martinez et al, Physica B, 372, 286 (2006)

[4] R. Hertel et al. Phys. Rev. Lett. 98, 117202 (2007)

[5] E. Martinez et al, Phys. Rev. Lett. 98, 267202 (2007)

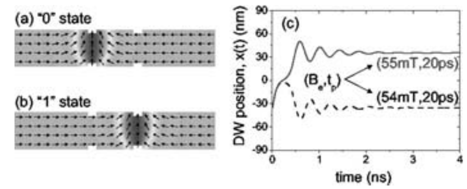

Figure 1. Memory element based on pinned domain walls in a pair of notches. The two states "0" and "1" are depicted in (a) and (b) respectively. (c) DW position as a function of time under two sinusoidal magnetic pulses of 20ps starting from the state "0".

HQ-03

Shingle shot detection of the magnetic domain wall motion by using the TMR effect.

K. Kondou[1], N. Ohshima[2], S. Kasai[1], Y. Nakatani[3], T. Ono[1]
1. Institute for Chemical Research, Kyoto University, Uji, Japan; 2. Device Platforms Reseach Laboratories, NEC Corp., Sagamihara, Japan; 3. Department of Computer Science, University of Electro-communications, Chofu, Japan

The magnetic domain wall (DW) dynamics has been attracting attention these days, because of its underlying potential applications for new spintronics devices, such as the magnetic racetrack memory [1] and magnetic logic device [2]. The operation speed of these devices depends on the DW velocity [3], but it is limited by the precessional motion of the DW known as the Walker breakdown. Until now, several groups have reported about the DW motion by using anisotropic magnetoresistance effect [4] and magneto-optical Kerr effect [5]. These results clearly show the character of the Walker breakdown, but it requires a large number of sampling to obtain a satisfactory averaging. The motion of the DW, however, has a stochastic nature, i.e. each event is not the same. Thus, single shot detection of the domain wall motion with time- and space- resolution is indispensable.

In this presentation, we demonstrate the real-time and real-space detection of the magnetic DW motion by using a tunnel magnetoresistance (TMR) effect. The relative large resistance change due to the TMR effect enables us to perform the single-shot measurement of the magnetic DW motion.

Figure 1 shows the schematic illustration of the sample and circuits for measurement. A Ta(5 nm)/Permalloy(20 nm)/Al-O(0.82 nm)/CoFe(2 nm)/Ru(0.88 nm)/CoFe(2 nm)/PrMn(20 nm) multilayered film was deposited on the thermally oxidized Si substrate. The wire structure was defined by using electron beam lithography and lift-off method. The length and width of the magnetic wire were 55 μm and 0.9 μm, respectively. The region sandwiched by two Au electrodes forms a TMR junction. The resistance of the TMR junction is modulated by the position of the DW in the Permalloy layer. Thus, the TMR junction acts as a detector of the DW motion. The resistance change was converted to voltage by a DC current and monitored by the real-time oscilloscope.

Figure 2 shows the time dependence of the voltage at the TMR junction at H_{ex}= 34.2 Oe. The voltage starts to increase at $t=t_1$, which means the DW arrived at the left side of the Au electrodes. Similarly, the voltage becomes constant after $t=t_2$, which also indicates that the DW went through the Au electrodes. The linear dependence of the voltage on time suggests the DW velocity is constant. The average velocity can be defined as vave=40 μm/(t_2-t_1). Detail studies about the average velocity as a function of the magnetic field shows clear Walker distribution, in spite of the large dispersion due to the stochastic nature of the DW motion. These results suggest the universality of the Walker breakdown phenomena, and the importance of the stochastic nature of the DW motion.

This work was partially supported by NEDO.

[1] S.S. Parkin, US Patent 309, 6, 834, 005 (2004).

[2] D. A. Allwood et al., Science 309, 1688 (2005).

[3] T. Ono et al., Science 284, 468 (1999).

[4] M. Hayashi et al., Phys. Rev. Lett. 98, 037204 (2007)

[5] G. S. D. Beach et al., Nature Mater. 4, 741 (2005).

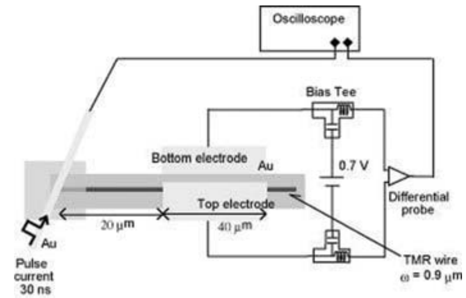

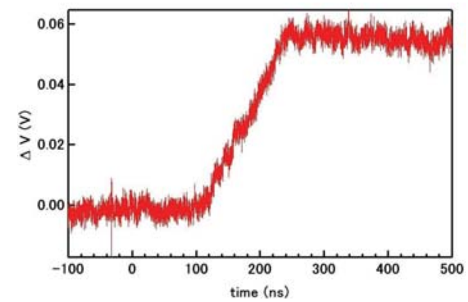

HQ-04

Domain wall injection study in spin valve system with different geometry reservoirs.

K. Cheng[1,2], C. Yu[1], S. Lee[1], Y. Liou[1], Y. Yao[3], J. Wu[3], J. Huang[2]
1. Institute of Physics., Academia Sinica., Taipei, Taiwan; 2. Department of Materials Science and Engineering, National Tsing-Hua University, Hsinchu, Taiwan; 3. Department of Materials Engineering, Tatung University, Taipei, Taiwan

Domain wall injection is a popular topic in Spintronics because it can decrease magnetization switching field (Hs)[1]. In recent studies, it has been demonstrated that the switching field and magnetization reversal process depend strongly on the end shape as well as the width of ferromagnetic wires. The effect of the end shape is attributed to the formation of the end domain or edge domain[2-3]. In this study, we investigate the influence between different shapes of reservoirs and domain magnetization reversal process.

The different geometry patterned wires were fabricated by electron-beam lithography and lift-off process. Five different reservoirs (tip,square,diamond,disk,and ring)on one side of the wires were designed. The other side of the wires was a tip shape. Figure 1 shows a SEM photograph of the wires. The spin valve Co(20nm)/Cu(7nm)/Py(20nm) was used to study the magnetization reversal behavior because the signal of the Giant Magnetoresistance (MR) is much more sensitive in comparison to the Anisotropy MR in a single film. For comparison, a micromagnet simulation software (OOMMF) was used to simulate the spin configurations.

Figure 2 shows typical longitudinal MR curves for all the samples at room temperature. Sample with a tip reservoir is the most difficult one to switch in magnetization reversal process. This indicates that the anisotropic field in the tip shape is the largest, thus it is not easy for domain wall nucleation. On the other hand, domain wall is easy to nucleate in sample with a diamond shape reservoir. For other three kinds of shapes (ring, square,and disk), the value of the switching field Hs is between that of tip and diamond, it is attributed to the domain nucleation process or dipole interaction between the Co and Py films. Diamond and ring shapes have a direct switching, it means the domain wall move quickly through the wires and cause the change easily. The Hs as a function of domain injection angle is plotted in Figure 3. The definition of injection angle is shown in the inset of figure 3. There is a trend that larger injection angle needs bigger switching field. The first group is diamond, square and tip. Diamond has smaller Hs and tip has the biggest value. In diamond shape, magnetic field direction is close to the easy axis, so the domain wall in diamond is easily nucleated than in square. They had similar tendency. The slope of Py is approximately 0.104, and Co is near 0.659. In order to interpret the difference of Hs with the relation to magnetization reversal, the spin configurations were simulated by micromagnet simulation software OOMMF. It is quite consistent with our experimental switching behavior. In tip pattern, the switching behavior is simple and immediate changed. In other structures, it seems like a slowly decrease in the beginning and a suddenly drop off in the next process.

In summary, the diamond shape has the minimum switching field. Results in both Co and Py materials have identical tendency. The spin configurations by OOMMF results also offer good evidence that the different reservoirs have the same magnetic domain, vortex wall, in the sample size we studied. Our experiment provides guidance for taking advantage of different geometry reservoirs.

[1] W. Y. Lee, C. C. Yao, A. Hirohata, Y. B. Xu, H. T. Leung, S. M. Gardiner, S. McPhail, B. C. Choi, D. G. Hasko, and J. A. C. Bland, J. Appl. Phys. 87, 3032 (2000).

[2] K. J. Kirk, J. N. Chapman, and C. D. W. Wilkinson, Appl. Phys. Lett. 71, 539 (1997).

[3] J. Shi, S. Tehrani, T. Zhu, Y. F. Zheng, and J. G. Zhu, Appl. Phys. Lett. 74, 2525 (1999).

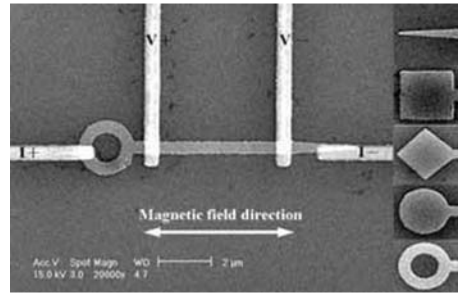

Fig.1 A SEM image of ring shape with I/V contacts. The images on the right show the reservoir parts to the different wires. They are, from top down, tip, square, diamond, disk, and ring structure.

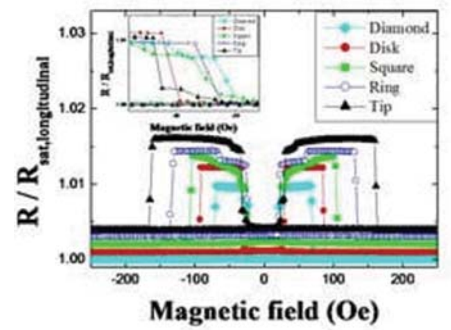

Fig.2 Typical longitudinal MR loops of the wires measured at room temperature. The inset illustrates the small field region.

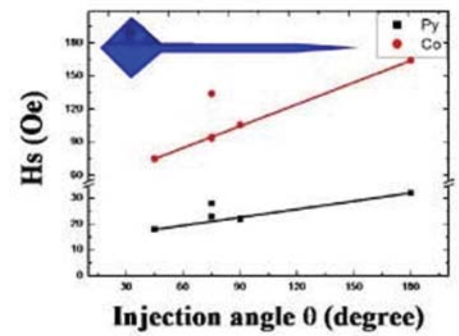

Fig.3 The switching fields of Co and Py versus domain wall injection angle. The inset illustrates the definition of injection angle θ.

HQ-05

Magnetization reversal with domain wall motion in NiFe nanodevices with different pinning sites.

Y. Zhou[1], D. Stickler[2], Y. Du[1], E. Ahmad[1], Z. Lu[1], H. P. Oepen[2], D. Wilton[1], G. Pan[1]
1. Faculty of Technology, University of Plymouth, Plymouth, United Kingdom; 2. Institut für Angewandte Physik, Universität Hamburg, Jungiusstr, Germany

Magnetization reversal process and domain wall (DW) motion in artificial structures such as submicron/nano-scaled or constricted ferromagnetic (FM) wires have been widely researched by magnetoresistance (MR) measurements [1-8]. In this article, different magnetization reversal processes with DW motion in NiFe nanodevices with different pinning sites patterned by ion-milling and FIB milling have been detected and investigated by MR measurements. Two structures have been studied: (a) a 15 nm-thick NiFe micron stripe with a 150 nm-wide nanoconstriction (structure A), and (b) a 15 nm-thick NiFe micron stripe with a submicron triangular element and a 150 nm-wide nanoconstriction (structure B), as shown in the inset of Fig. 1. The ability to control domain wall propagation direction makes them promising for fundamental research and the application of nanowire memory devices.
Structure A: NiFe stripe with a nanoconstriction
For structure A, its longitudinal MR is about -0.17% (Fig. 1-left). When reaching the field of 5.7 Oe, the resistance shows the first jump, indicating that the gradual magnetization reversal in the wide stripe, leading to DWs pinned at the nanoconstriction. When the field reaches the depinning field of the nanoconstriction (20 Oe), the second sharp jump occurs, indicating the depinned DWs annihilate at the nanoconstriction.
The transverse MR magnitude is 0.68% and the MR curve shows a so-called bell-shaped behaviour, that is, an MR enhancement around a zero field [9, 10]. It is argued that this enhancement is due to pining of the DW at the nanoconstriction near a zero field by reversal from saturation, which can be explained by the DW scattering mechanism [10, 11].
Structure B: NiFe stripe with a triangular element and a nanoconstriction
A negative longitudinal MR curve (MR= -0.16%) (Fig. 1-right). Based on micromagnetic simulation results, the three-step switching behaviour can be explained as follows. The right part of the stripe with a lower coercivity first switches the magnetization, and the DW moves towards the nanoconstriction, and then is trapped there, leading to the first resistance jump. Then the resistance keeps increasing gradually, indicating that the left part gradually switches its magnetization until the DW reaches the base of the triangular element. Then the DW experiences pinning there, and the propagation doesn't continue until the field is high enough to overcome the pinning energy induced by the sharp expansion in width. On reaching the field of 13 Oe, the resistance shows the second small jump, which means that the left DW is depinned from the triangular element, and propagates into the apex area, and then gets pinned at the nanoconstriction. On reaching the depinning field of the nanoconstriction (21 Oe), the resistance returns to its original value in the third jump, owing to the annihilation of DWs at the nanoconstriction.
Similarly, for structure B, the so-called bell-shaped behaviour is shown in the transverse MR curve and the magnitude is 0.66%.
We had taken MR measurement of a FIB pre-patterned structure (a NiFe micron stripe with a 500 nm-wide microconstriction). Comparing MR values of these samples, we notice that the transverse MR magnitude of a pre-patterned structure without the bell-shaped behaviour is 0.56%, lower than those of structures A and B, which are 0.68% and 0.66% respectively. Besides, the longitudinal MR value of pre-patterned structure is -0.09%, which is nearly half as large as those of two patterned samples, -0.17% and -0.16%, respectively, which cannot be fully explained by the AMR effect and further confirms some contributions from domain wall MR (DWMR).
For structure A, we fabricated a series of samples with different nanoconstriction widths. The longitudinal MR value decreases from -0.15% to -0.22% when the nanoconstriction width decreases from 200 nm to 80 nm. The DWMR plays a more important role when the nanoconstriction is narrower.

1. T. Ono, H. Miyajima, K. Shigeto, K. Mibu, N. Hosoito, and T. Shinjo, Science 284, 468 (1999).

2. U. Ruediger, J. Yu, S. Zhang, A. D. Kent, and S. S. P. Parkin, Phys. Rev. Let. 80, 5639 (1998).

3. D. A. Allwood, G. Xiong, and R. P. Cowburn, Appl. Phys. Lett. 85, 2848 (2004).

4. A. Himeno, T. Okuno, S. Kasai, T. Ono, S. Nasu, K. Mibu, and T. Shinjo, J. Appl. Phys. 97, 066101 (2005).

5. D. Lacour, J. A. Katine, L. Folks, T. Block, J. R. Childress, M. J. Carey, and B. A. Gurney, Appl. Phys. Lett. 84, 1910 (2004). .

6. M. Tsoi, R. E. Fontana, and S. S. P. Parkin, Appl. Phys. Lett. 83, 2617 (2003).

7. C. K. Lim, T. Devolder, C. Chappert, J. Grollier, V. Cros, A. Vaurès, A. Fert, and G. Faini, Appl. Phys. Lett. 84, 2820 (2004).

8. J. Grollier, P. Boulenc, V. Cros, A. Hamzic, A. Vaure`s, A. Fert. and G. Faini, Appl. Phys. Lett. 83, 509 (2003).

9. A. O. Adeyeye, R. P. Cowburn, and M. E. Welland, J. Appl. Phys. 87, 299 (2000).

10. S. Lepadatu, Y. B. Xu, and E. Ahmad, J. Appl. Phys. 97, 10J708 (2005)

11. P. M. Levy and S. Zhang, Phys. Rev. Lett. 79, 5110 (1997).

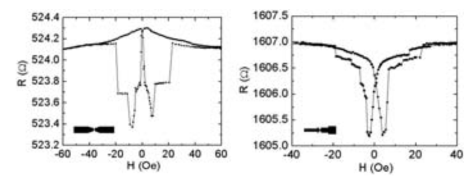

Figure 1: (left) Low field longitudinal MR curve of structure A (inset: schematic diagram of structure A); (right) Low field longitudinal MR curve of structure B (inset: schematic diagram of structure B).

HQ-06

Magnetoresistance of transverse and vortex domain walls in permalloy submicron wires.

C. Yu[1], S. Lee[1], K. Cheng[1], D. Chen[2], E. Haung[3], Y. Liou[1]
1. physics, academica sinica, Taipei, Taiwan; 2. Materials Science & Engineering, Chiao Tung University, Hsinchu, Taiwan; 3. Materials Science & Engineering, University of Tennessee, Knoxville, TN

Lots of efforts have been studied on how the domain wall affects the magneto-transport in magnetic wires. This local spin modulation in the domain wall causes extra contribution to MR that can not be explained by spin-orbit AMR effect, if the quality factor (Q=2K/μOMs, K: anisotropy energy, Ms: saturation magnetization) is Q >1 [1]. Due to the domain wall MR (DWMR or DWR) is still in debate experimentally– positive[2] or negative [3]. Consequently, more experimental evidences are needed to find out the answer of DWMR.
Submicron s-shape and half-ring wires were fabricated by e-beam lithography. The 25 nm thick Ni80Fe20 film was deposited by sputtering on SiO2/Si substrate. There were 7 half-ring units connected in-series in different way, half-ring wire (up-up) and s-shape (up-down) (Fig.1). Outer radius(r) was 2.1 μm of each half-ring and the line width was 0.2 μm. The AMR loops of three different wires (half-ring, s-shape and straight wires)were measured with 4 different angle (θ=0, 30, 60 and 90 degree) at 77K, θ is the angle between H and the long axis of the wire. Compare with the AMR of straight wire, which is about 1.17 %, the AMR effect was suppressed in s-shape wire (AMR ~0.02%) than in half-ring wire (AMR ~0.32%). The reason is attributed to the symmetry of geometry structure. For the half-ring wire, there are overlap regions on the corner of two half-ring units, and AMR (0.32%) is mainly contributed from these corners. To reduce the AMR effect as possible is the key issue to measure the MR contributed by DWMR.
Fig. 2 (half-ring wire) shows the MR loops, and from the MR loops the switching fields Hs at different angles were obtained. The Hs of half-ring wire was -230 Oe at 0 degree and -260 Oe at 30 degree, for the s-shape wire Hs was around -295~ -305 Oe for all the angles. The bell shape of half-ring wire MR loops measured at 60 and 90 degree showed only coherent spin rotation during magnetization reversal process. The different magnetization reversal of half-ring wire resulted from discontinuous domain structure-corner, which was not existed in s-shape wire. In remanent state, the resistivities (ρ) of s-shape wire were almost same value at all angles, the maximum differences of ρ at different angles were below 0.002 μΩ-cm (error of measurement). For the half-ring wire, the ρ of angle 0 and 30 degree were 33.706 μΩ-cm, but the ρ of angle 60 and 90 degree are 33.672 μΩ-cm. The MFM images (Fig.3. (a), (b) half-ring wire and (c) s-shape wire,) shows the domain structures in remanence. There were two domain structures of half-ring wire in remanent state, domain walls (Fig.3.(a)) and magnetic pole (head or tail pole) (Fig.3.(b)) on the corners after magnetized at longitudinal and transverse field. Those different resistivities (0.034 μΩ-cm)in remanent state of half-ring wire were resulted from different domain structures on the corners. There was only one domain configuration of s-shape wire in remanence- magnetic poles on the ends of the wire (Fig. 3 (c)), no matter H was applied in the longitudinal or transverse direction, so no different domain structure to cause different resistivity in remanence. From the MFM images we may interpret the difference of longitudinal and transverse MR in remanence was attributed to two different domain structures on the corners, with domain walls or without domain walls. We calculated the DWMR ratio of half-ring wire was~ +0.02% for every domain wall. The domain structures, on the corners of the half-ring wires, were similar to the two magnetic films in GMR which are antiparallel domains (Fig. 3 (a)) and parallel domains (Fig. 3 (b)). And the current we applied was perpendicular to the walls on the corners. We estimate the DWMR by GMR model [4], and the result is 0.01 ~ +0.05%, which is satisfied with our data.

[1] M. Viret, et al, Phys. Rev. Lett. 85, 3962 (2000).

[2] U. Ebels, et al, Phys. Rev. Lett. 84, 983 (2000).

[3] T. Taniyama, et al,Phys. Rev. Lett. 82, 2780 (1999).

[4] Peter M. Levy, et al, Phys. Rev. Lett. 79, 5110 (1997).

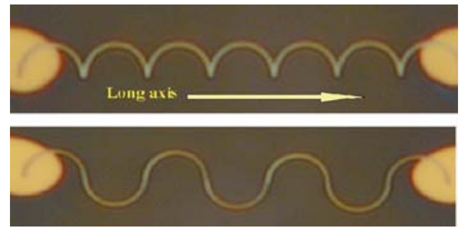

Fig.1. Optical images of half-ring wire, S-hape wire.

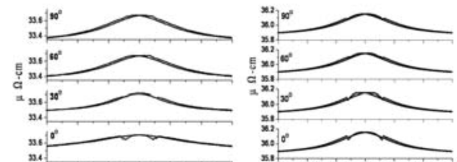

Fig.2. MR loops of half-ring (left) and s-shape wires measured at 4 different angles.

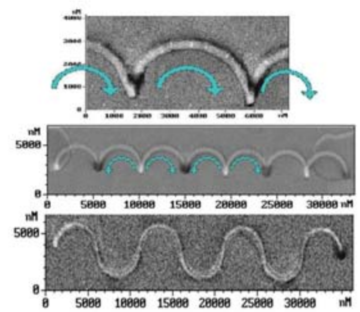

Fig.3 MFM images of the wires at remanence after the wires were magnetized (up) longitudinal, the arrow is guided for eye of the magnetization (middle) transverse for the half-ring wire, (down) both longitudinal and transverse for the s-shape wire.

HQ-07

Domain wall magnetoresistance effect in nanobridges.

Y. Chen[1], *J. Hsu*[1], C. Yu[2], K. Cheng[2], S. Lee[2], Y. Liou[2], Y. Yao[2]
1. Physics, National Taiwan University, Taipei, Taiwan; 2. Physics, Academia Sinica, Taipei, Taiwan

The domain wall magnetoresistance(DWMR) in nano-structured films was extensively studied in the past decade due to rich research topics and great potential application in spin-electronics. However, up to now, DWMR is still under intensive discussions because of conflicts in experimental results. Both positive and negative domain wall magnetoresistance effects have been found. And theoretically it has difficulties in explaining the effect satisfactorily. In this presentation, the extended structure, named as nanobridge(NB), combined by a nanowire of well-defined shape and nanocontact was used and the variation of the magnetoresistance under different external magnetic fields with the sizes (width and length) of nanobridge structures was intensively studied.
Electron-beam lithography and lift-off process were used to prepare Permalloy patterned thin films on Si(100) substrates coated with 100nm SiO2 buffer layers. The Permalloy thin films were deposited by DC magnetron sputtering. The room-temperature magnetoresistance (MR) measurements were made by a four-point technique. The external magnetic field was applied in the in-plane direction. A field of 4k Oe was used to saturate the magnetization and the detailed investigations were carried out from -500 Oe to +500 Oe. The MR results have been compared with the spin configurations obtained by using the micromagnetic simulation software (the Object Oriented Micro Magnetic Framework, OOMMF).
Two sets of NB with bridge lengths 60 nm and 400 nm were used in this study.The width of nanobridge segment of two sets was varied from 40 nm to 100 nm. The samples with long length of 400 nm were denoted as NBL. As examples, three normalized longitudinal MR loops of NBL with widths of 47 nm, 68 nm, and 128 nm were plotted in Fig. 1(a). When the external magnetic field was swept from the saturated magnetic field 4 kOe to zero, the MR value was increased gradually to the maximum value. Further increasing the magnetic filed in the opposite direction, the MR value dropped corresponding to a lower resistance state. The total loop can be visualized as the magnetization reversal process from the variation of anisotropy magnetoresistance (AMR) effect. Because the magnetic state at both sides of NB have already switched via domain wall nucleation and domain wall motion, the magnetic state of NB will maintain its original orientation of magnetization leading to the pinning of two domain walls at the connections between the nanobridge and pad. Therefore, the lower resistance state is a meta-state and arises from the AMR contribution of domain wall's transverse magnetized part. When the magnetic field was continued to increase until it reached certain magnetic field, namely switching field H_{SW}, the depinning of two domain walls caused the complete magnetization reversal of NB. Determined from *R*-*H* loop in Fig. 1(a) it was found that H_{SW} increased as the width of NBL became narrower due to larger shape anisotropy of NB with larger aspect ratio. Another set of samples with short bridge length of 60 nm was denoted as NBS. Following the same procedure, the normalized longitudinal MR loops of NBS samples having widths of 69 nm, 81 nm and 87 nm were plotted in Fig. 1(b). It was noted that the magnetization reversal process of NBS determined from their MR loops differed from those of NBL markedly. The meta-state (or lower resistance state) in the MR loops of Fig. 1(a) possesses a wider field range than that of Fig. 1(b) and the switching field distribution of NBL was larger by 50 Oe than that of NBS. However, a similar trend has been observed for the switching field, which also strongly depends on the width of nanobridge and follows the inverse-width dependence. Stronger shape anisotropy of nanobridge with narrower width will retard the domain walls against depinning into the nanobridge. Furthermore, different domain wall structures, such as transverse domain wall and vortex domain wall,can form in the samples of different sizes. The transverse domain wall does not move so easily as the vortex domain wall causing the difference of the switching fields. Additionally, the shape anisotropy of nanobridge will suppress the domain wall.
In order to explore the MR contribution from the domain wall, some calculations have been carried out. For the nanobridge with 70 nm width, an additional positive domain wall resistance (DWMR) about +0.03% was obtained. Following the same way, a larger additional positive DWR change about +0.07% was obtained for the nanobridge with wider width of about 80 nm, which should be explained by the spin-dependent impurity scattering model, so-called the mistracking model. In this model the condition of tracking between spins of conducting electrons and the orientation of moment within the domain wall in NiFe will determine the magnitude of additional MR contribution. Within the framework of this model, the mistracking contribution to the wider domain wall width is more than to the narrower one. Therefore, a larger positive DWMR is presented in the samples with wider line-width.

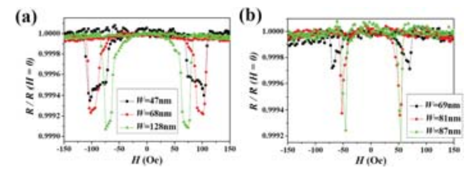

Fig. 1 The normalized magnetoresistance loops for (a) NBs with length 400 nm and width 47 nm, 68 nm and 128 nm, respectively; and (b) for NBs with length 60 nm and width 69 nm, 81 nm and 87 nm, respectively.

HQ-08

Effect of period and linewidth on the magnetization reversal of thin film wire arrays.

S. Moralejo[1], C. Redondo[1], F. J. Castano[2], C. A. Ross[2], F. Castano[1]
1. Depart. Química Física, Univ. País Vasco, Lejona, Spain; 2. Depart. of Material Science and Engineering, MIT, Cambridge, MA

Introduction
The magnetic behaviour and switching field of thin films is significantly modified by patterning them into arrays of one-dimensional wires. Thin film magnetic wires have a variety of possible applications, such as data storage or data processing[1], and it is therefore important to understand the factors that determine their coercivity and magnetization reversal, and the behavior of domain walls. Here, we explore the properties of arrays of ferromagnetic nanowires made by patterning thin films, and analyze how the magnetic behaviour of the array is modified in a controlled way by magnetostatic interactions between the wires.
Experimental
Rectangular 5 x 14 µm2 fields of Ni80Fe20 parallel nanowire arrays were fabricated on top of commercially available oxidized Si substrates by electron-beam lithography and liftoff processing. Fabricated wires had 25 – 150 nm widths and 350 – 600 nm periods, and were patterned from 20nm-thick polycrystalline NiFe films deposited using ion-beam sputtering, as detailed elsewhere[2]. The present work reports on a thorough study of the room temperature hystereis loops of arrays with nominally-identical wires, probed using a focussed MOKE magnetometer (Durham Magneto Optics Ltd. NanoMOKE2TM). Hysteresis loops were obtained using an elliptical laser spot close to 5 x 7 µm2 (FWHM) and averaging ~5000 field cycles at a frequency of 27 Hz, sampling the collective magnetization reversal of 14 wires. The samples were mounted on a rotary stage allowing controlled rotation of the nanowire arrays with respect to the applied field.
Results
Scanning electron micrographs (SEMs) of arrays measured are given in Fig. 1, illustrating the edge quality and pattern geometry.
(Fig.1)
While the coercivity of the unpatterned films are below 1 Oe[2], hysteresis loops of arrays of 500 nm period and upwards are square with coercivities ranging from 225 to 345 Oe and a single Barkhausen jump, suggesting that the collective reversal of all the wires occurs within a narrow switching field distribution. However, for the 400 and 350 nm period arrays, the loops show substantial differences in shape, coercivity and remanence on decreasing the linewidth. Fig. 2 a) illustrates the hysteresis loops of arrays with 350 nm period and 50, 80 and 100 nm wire width. Clear Barkhausen jumps in the 80 nm width array suggest that the reversal of individual wires occurs at different fields. (Note that, because of the shape of the MOKE laser spot, the wires contribute steps of different magnitude to the aggregate hysteresis loop). In contrast, the 50 nm wires do not show distinct jumps, suggesting a more gradual change in magnetization as the field varies, possibly due to domain pinning by the edge roughness. For the array with the widest wires, 100nm, the reversal occurs abruptly and resembles that of arrays with 500nm periods and above. Fig. 2 b) shows the variation of coercivity with array period and wire width. For a width of 125 nm, coercivity decreases with period, but for 80 nm width it increases. At a width of 100 nm the coercivity is nearly independent of period. The insets show that coercivity increases with width for the 350 nm period arrays whereas for the 500 nm period, it decreases. For the 500 nm period the variation of coercivity with wire widths is identical to that of isolated wires.
(Fig.2)

These results suggest an important role for magnetostatic interactions in the reversal of closely-spaced arrays. We expect that in closely spaced wires, the stray fields of the transverse 180deg domain walls can stabilise multidomain structures that are not found in isolated wires, and promotes correlation between domain structures in adjacent wires. This leads to a gradual reversal of the array and consequently a hysteresis loop that does not show Barkhausen jumps. A change in reversal process with array geometry has recently been reported in arrays of long wires and attributed to a change in the energy contributions with geometry[3].

[1] D. A. Allwood et al, Science 309 1688 (2005).

[2] C. Redondo et al, Nanotechnology 17, 2040 (2006).

[3] P. Vavassori et al, J. Magn. Magn. Mater. 316, e31 (2007).

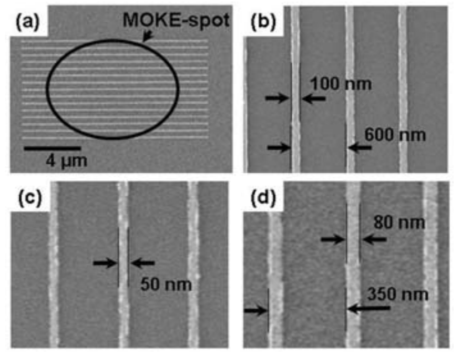

Fig.1. SEMs of 20 nm-thick $Ni_{80}Fe_{20}$ nanowire arrays with a) 100 nm width and 350 nm period , b) 100 nm width and 600 nm period, c) 50 nm width and 350 nm period, and d) 80 nm width and 350 nm period.

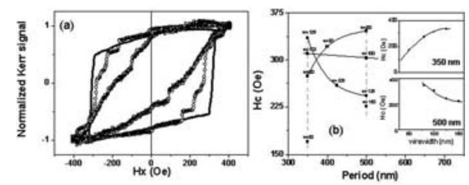

Fig.2. a) Easy axis hysteresis loops for 350 nm period $Ni_{80}Fe_{20}$ patterned wire arrays with widths of 100 nm (solid line), 80nm (open circles) and 50 nm (open squares) respectively, b) Coercivity trends vs period for arrays of different width, indicated above the experimental points. The insets show the dependence of the coercive field for 350 nm (top inset) and 500nm.

Edge Roughness effect on the magnetization reversal process of spin valve submicron wires.

T. Chiang[1,2], C. Yu[1], Y. Chen[1], S. Lee[1], G. Guo[2]
1. Institute of physics, Academia sinica, Taipei, Taiwan; 2. Physics, National Taiwan University, Taipei, Taiwan

Recently, the evolution of nanolithography techniques makes it possible to prepare nano scale pattern with well-defined shapes, which helped us to study the spintronic devices in micromagentic physics. Magnetic domain wall mobility is one of the interesting topics. Whether the switching frequency of a metallic spintronic device can match up with the modern semiconductor electronic device is decided by the mobility of domain wall. Therefore, determination of domain wall mobilities in submicron or nanometer magnetic wires is a crucial topic of interest not only for fundamental research but also for application.
Theoretically, domain wall mobility for bulk magnetic materials can be calculated by $\mu=\gamma\Delta/\alpha$ (γ: gyromagnetic ratio,Δ: domain width, α: spin damping coefficient). There were many experimental results reported. The discrepancies were attributed to roughness effect. How the surface and edge roughness of the wires affect on domain wall motion in different magnetic materials, such as NiFe,Co80Fe10B10 and Co, are the questions we would like to answer in this study.
Our samples had a spin valve structure, X(24nm)\Cu(10nm)\X(12nm) (X=NiFe, Co80Fe10B10 and Co),and theirs widths are 400nm. Different edge 'roughness' was designed by e-beam lithography as periodic spikes along both sides of the samples. The height of the spikes and the pitch (period) could be varied systematically. Figure 1 shows three typical NiFe samples with (a) no designed roughness, (b) 33nm spike height, 116nm pitch, and (c) 51nm spike height, 213nm pitch. The magnetoresistance curve was measured and the domain wall velocity was determined under the same applied magnetic field sweeping rate. Thick and thin layers of NiFe,Co80Fe10B10, and Co had different domain wall velocities during magnetization reversal. The domain wall velocity in the thick layers was faster than the thin ones. The shape of magnetoresistance suggested the same results and indicated that the magnetization reversal of thin layer took place by the pinning and depinning of magnetic domain walls. The roughness of wires made the domain wall to slow down. As the spike height got larger, the domain wall velocity reduced. The pitch effect was not obvious.

In Figure 2, we showed the magnetoresistance curves of the three samples in Figure 1. The number of points on the rising part of the magnetoresistance curve increased as the spike height increased. This result suggested that the domain wall velocity in the thick layer was decreased. The roughness created more pining sites for the domain walls and slowed down the average velocity
As the magnetic materials was varied, our results showed the domain wall velocity in the NiFe was the fastest, the Co was the slowest. In all three different magnetic materials we studied, the spike roughness made the domain wall slowlier.

1.T. Ono et al., Science 284, 468,(1999)

2.Jason Gadbois and Jian-Gang Zhu,IEEE Transactions on magnetics,vol.31,No.6,(1995)

3.M.Hayashi et al., Phys. Rev. Lett. 96, 197207 (2006)

4.M.klaui et al., Phys. Rev. Lett. 95, 026601 (2005)

5.YOSHINOBU NAKATANI et al., Nature Mater. 2, 521–523(2003)

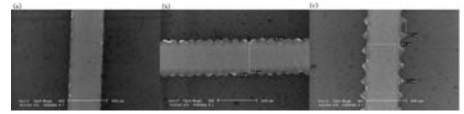

Figure 1. SEM images of NiFe samples (a) no designed roughness, (b) 33nm spike height, 116nm pitch, and (c) 51nm spike height, 213nm pitch.

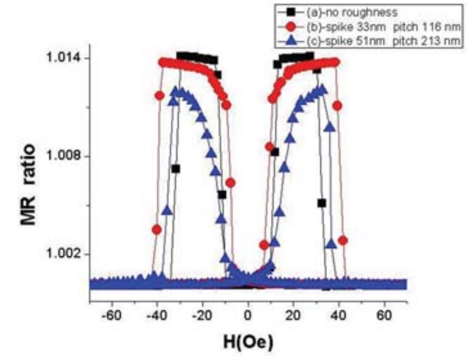

Figure2. Magnetoresistance ratio curves of the three samples in Figure 1.

HQ-10

Study on domain wall moving in a permalloy ring structure.

D. Chen[1], C. Yu[2], Y. Yao[3,1]
1. Department of Material Science and Engineering, National Chiao Tung University, Hsinchu, Taiwan; 2. Institute of Physics, Academia Sinica, Taipei, Taiwan; 3. The Department of Materials Engineering, Tatung University, Taipei, Taiwan

Permalloy (Py) rings were fabricated by electron-beam lithography and the following lift-off technique. The MR measurements were performed at room temperature with applying some constant magnitudes of magnetic field along the direction of the ring plane while rotating the magnetic ring in its plane. Fig.1 shows an SEM image of a Py ring and the configuration in which the contacts of the four-point measurement is arranged. As shown in Fig.2, the rotating MR curves at 4000 Gauss and 100 Gauss reveal obvious difference between the two magnetic configurations. The field at 4000 Gauss hold the most of the local moments parallel to the direction of the field wherever the angle is, hence the resistance is the highest at 0° and the lowest at 90° (or highest at 180° and lowest at 270°). Therefore, the rotating MR signal shows a cosine-like curve. At 100 Gauss, the field is too weak to hold the local moments any more. Instead, the shape anisotropic field forces the local moments aligned to the perimeter of the ring and leave two domain walls at opposite positions in the direction of field. At this magnetization, the field can still drag the two walls in the perimeter of the ring without changing the directions of other moments not present in the walls. Hence, the curve shows more flat region combined with two abrupt sinkages near 90° and 270°. The results of the series of rotating MR measurements by varying magnitude of field reveal a tendency of shift on the angles at which the resistance drops occur with decreasing applied field (Fig.3). The propagation (or moving) of domain wall requires the applied field component tangent to the direction of perimeter at the position where the wall is, thus lower applied field needs larger angle shift to drag domain wall into the region between the two voltage contacts (Fig.4). The tendency of the component changing with varying applied field is shown in Fig.5, in which, the required component to drag domain wall in perimeter, sin(θ), increases with decreasing applied field as explained previously.

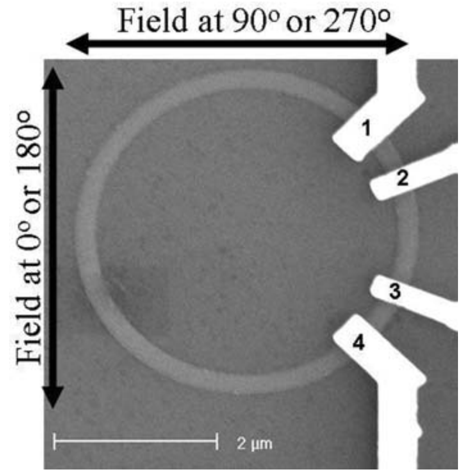

Fig. 1 SEM image. 1 & 4 serve as current contacts, and 2 & 3 as voltage contacts. The bold arrows indicate the definition of the direction at which the field being applied.

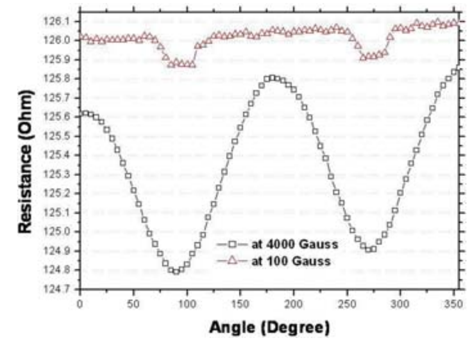

Fig. 2 Rotating MR curves at 100 & 4000 Guass.

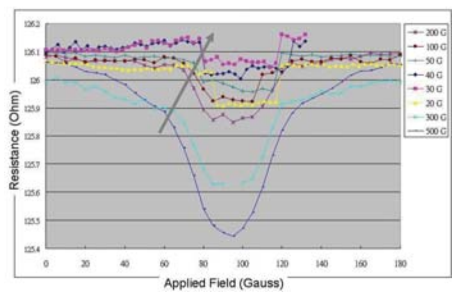

Fig. 3 A series of of rotating MR curves by varying magnitude of field. The angle at which the resistance decrease abruptly shifts toward the direction of angle increasing with decreasing applied field.

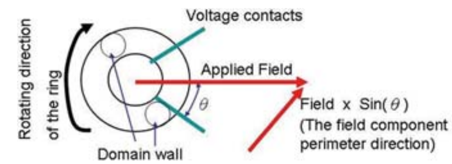

Fig. 4 Schematic diagram of field component.

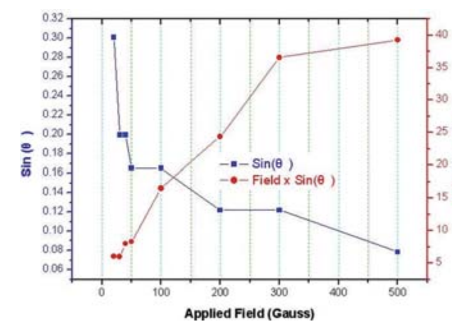

Fig. 5

HQ-11

Magnetic domain wall pinning by the stray field of a ferromagnetic dot array.

P. J. Metaxas[1,3], J. Jamet[1], J. Ferré[1], P. Zermatten[2], G. Gaudin[2], B. Rodmacq[2], A. Schuhl[2], R. L. Stamps[3]
1. Laboratoire de Physique des Solides (UMR CNRS 8502), Université Paris-Sud, Orsay, France; 2. SPINTEC (URA 2512 CNRS/CEA), CEA, Grenoble, France; 3. School of Physics, University of Western Australia, Perth, WA, Australia

In ultrathin weakly disordered Pt/Co/Pt films, structural inhomogeneities create a random pinning potential which impedes domain wall motion, resulting in a type of thermally activated wall motion known as creep [1]. Here we examine how the addition of a spatially periodic pinning potential, produced by the stray field generated by an array of ferromagnetic dots patterned above the film, affects this motion. Introduction of additional pinning via a stray field rather than patterning of the film itself avoids altering the structural properties of the film [2] and hence its intrinsic disorder.
A continuous multilayer Pt/Co sample was first sputter deposited with the following structure: $[Pt(1.8nm)/Co(0.6nm)]_2$ / Pt(5nm) / $[Co(0.6\ nm)/Pt(1.8\ nm)]_4$. The top $[Co/Pt]_4$ multilayer was then patterned into arrays of 200nm wide square dots each separated by 1 μm (Fig 1a). This was done using ion beam etching with a hard Ti mask created by depositing Ti onto a positive resist patterned via electron beam lithography. The strongly ferromagnetically coupled Co layers in the lower $[Pt/Co]_2$ bilayer act effectively as one layer and it is this layer in which we measure the domain wall motion. Both the dots and the continuous layer exhibit perpendicular anisotropy.
Hysteresis loops of the sample were obtained using a conventional polar magneto-optical Kerr effect (PMOKE) magnetometer. The dots display a wide switching field distribution between about 2 kOe and 3 kOe. The domain wall velocity under positive applied fields was then measured in the regions of the continuous film under the dot array using a quasi-static PMOKE microscopy technique [3]. The orientation of the dots' magnetization was set before the velocity measurements by applying a positive or negative saturating field of magnitude 4.2 kOe. The field applied to drive the domain wall was kept below 1 kOe to avoid reversing the dots.
The effect of the dots on wall motion is most pronounced at low applied fields, H, for which the velocity is noticeably lower under the dot arrays than in regions where there are no dots. At high field the dots have only a minimal effect on the propagation of the walls which are rather smooth (Fig 1b). Here, the pinning efficiency of the stray field is reduced due to the large driving force of the applied field and the wall's line tension. This is similar to what is observed in ultrathin Pt/Co/Pt films in the high field viscous regime in which the effect of the film's intrinsic disorder becomes negligible [3]. The low field wall velocity, v, in Pt/Co/Pt films can generally be fitted with the creep law which predicts $\ln(v) \propto -H^{-\mu}$ [1,3]. μ is a universal exponent equal to 1/4 for a 1D interface moving in a 2D weakly disordered medium. In Fig 2 we have plotted ln(v) against $H^{-1/4}$. We observe rather linear behaviour at low field consistent with creep theory despite the addition of the periodic pinning potential.
The creep velocity also depends on the orientation of the dots' magnetization: the velocity is about 2 times larger when the dots are negatively magnetized. In this orientation, the component of the dots' stray field perpendicular to the film plane will be negative directly under the dots and positive around the dots. Although the magnitude of the negative field beneath the dots will be much larger than that of the positive field surrounding the dots, the dots cover only a small portion of the array area. Henceforth, the increased velocity observed when the dots are negatively magnetized is tentatively attributed to the positive stray field in the area located between the dots which reinforces the positive applied field. Indeed, when the dots are negatively magnetized one sees at low field that the domains do in fact propagate most easily between the dots (Fig 1c). This creates a much more dendritic domain pattern than that which is observed when the dots are magnetized positively (Fig 1d).

[1] Lemerle et al, Phys. Rev. Lett., 80, 849, (1998).

[2] Herget et al, IEEE Trans. Mag., 41, 3763 (2005).

[3] Metaxas et al, Phys. Rev. Lett., 99, 217208 (2007).

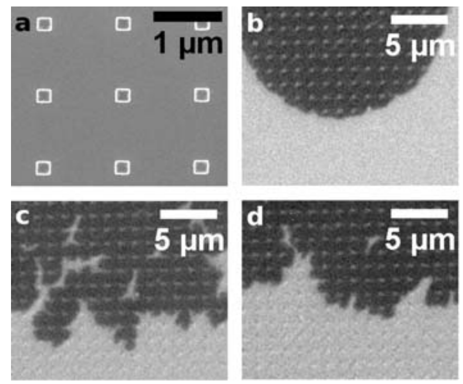

FIG 1: SEM image of a portion of the dot array (a). PMOKE images of domains at high field (H~900 Oe) (b) and at low field (H~100 Oe) with the dots magnetized negatively (c) and positively (d).

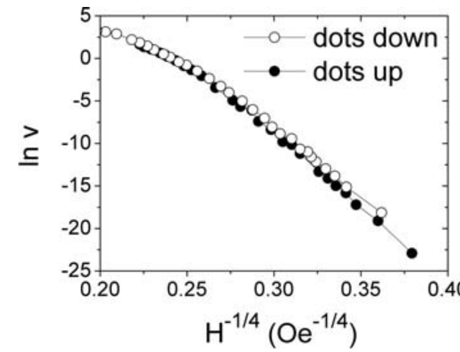

FIG 2: Natural logarithim of the wall velocity underneath the dot arrays plotted against the scaled applied field. The velocity has been measured with the magnetization of the dots oriented in the positive (dots up) and negative (dots down) directions.

HQ-12

Ratchet effects on domain wall motion in 2D magnetic amorphous thin film with arrays of asymmetric holes.

J. I. Martín[1], A. Pérez-Junquera[1], V. I. Marconi[2], A. B. Kolton[2], L. M. Álvarez-Prado[1], Y. Souche[3], A. Alija[1], M. Vélez[1], J. V. Anguita[4], J. M. Alameda[1], J. R. Parrondo[2]

1. Departamento de Física, Universidad de Oviedo - CINN, Oviedo, Spain; 2. Física Atómica, Molecular y Nuclear, and GISC, Universidad Complutense de Madrid, Madrid, Spain; 3. NANO, Institut Néel, CNRS and Universite Joseph Fourier, Grenoble, France; 4. Dispositivos, Sensores y Biosensores, Instituto de Microlectrónica de Madrid (CNM-CSIC), Madrid, Spain

The study of domain wall (DW) propagation in ferromagnetic films has long attracted a great interest since it provides both the basis for a wide number of magnetic devices [1] and a good experimental system to analyze the basic physics of an elastic interface in the presence of either ordered or random pinning defects [2,3]. When the pinning potential is asymmetric it can behave as a ratchet, so that DW propagation is favored in one direction. One of the first ratchet potentials that have been used in the field magnetism are “angelfish” patterns that control the sense of propagation of bubble domains in shift registers [4]. Also, asymmetric motion of domain walls (DWs) in nanowires with triangular [5] or notched [6] shapes has been reported recently. However, up to now, in order to ensure a good control of the DW nucleation/propagation process, in all these cases DW motion has been confined to an essentially 1D path (either by narrow guide rails or by the nanowire geometry), so that its transverse wandering can be neglected. On the other hand, in a thin extended film with a 2D array of asymmetric pinning centers, novel ratchet phenomena can appear since a DW behaves as an elastic line that can distort all along its length in response to the 2D pinning potential.

In this work, the propagation of DWs in extended uniaxial magnetic films patterned with a periodic array of asymmetric holes (see Fig.1) has been studied. For the first time, we have experimentally observed and theoretically simulated the existence of two crossed ratchet effects of opposite sign that change the preferred sense for DW motion depending on whether a flat or a kinked wall is moving [7]. This implies a change in the rectification effect on DW motion as a function of magnetic field that has an interesting consequence from the applied point of view: the system keeps memory of the sign of the last saturating state even in a zero magnetization configuration.

When a magnetic field is applied to push a flat DW across the asymmetric holes, the DW moves more easily (i.e. with lower coercivity) in the direction in which the length of the pinned wall between two antidots increases smoothly as shown in the numerical simulations of a ϕ^4 model presented in Fig.2 [7]. This asymmetric pinning for flat walls has been confirmed experimentally and also with micromagnetic simulations with the OOMMF code [8]. The novel ratchet behavior appears as the pinned wall inside the array develops kinks. This provides an extra mechanism for DW motion only possible in a 2D geometry through upward/downward kink propagation. This novel ratchet mechanism has an opposite sign in comparison to the flat DW ratchet and dominates the low field behavior. The interplay between both ratchets implies that the system keeps memory of the sign of the magnetization before a DW enters the array of asymmetric holes. Thus, it is possible to record several magnetic states introducing DWs in the array and to read them with a low amplitude AC field as can be seen in Fig. 3.

Work supported by Spanish CICYT (grants NAN2004-09087, MOSAICO and FIS2005-07392)

[1] C.D. Mee and E.D. Daniel, Magnetic Storage Handbook(1996) (New York: McGraw-Hill); G. Prinz, J. Magn. Magn. Mater. 200, 57 (1999).

[2] S. Lemerle et al., Phys. Rev. Lett. 80 849 (1998).

[3] E. Martínez et al., Phys. Rev. Lett. 98, 267202 (2007).

[4] N. Hayashi et al., IEEE Trans. on Magn. 8 370 (1972).

[5] D.A. Allwood et al., Appl. Phys. Lett. 85, 2849 (2004).

[6] A. Himeno et al., J. Appl. Phys. 97, 066101 (2005); M. Hayashi et al., Phys. Rev. Lett. 97, 207205 (2006); S. Savel’ev et al., New J. Phys. 7, 82(2005).

[7] A. Pérez-Junquera et al., Phys. Rev. Lett. in press.

[8] OOMMF available at http://math.nist.gov/oommf

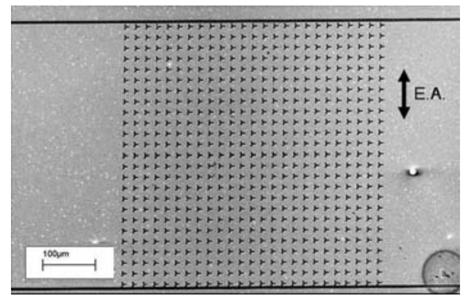

SEM image of an array of asymmetric holes. EA direction is indicated.

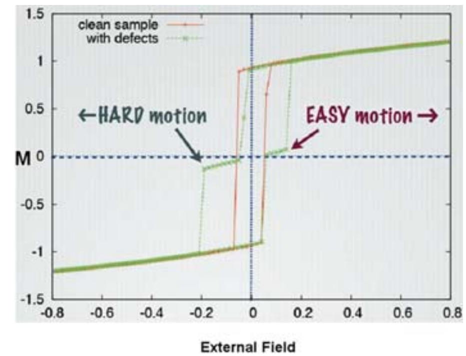

Numerical simulation of the necessary external field in a magnetic reversal process in order to move a wall through a pinning potencial form left to right or viceversa (green line) or through a continous film (red line).

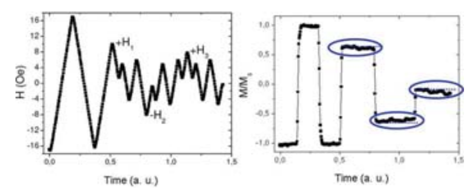

(Left) Field time evolution in order to record three magnetics states in the array. (Right) Corresponding magnetization time evolution, where it can be seen how the reduction of absolute magnetization due to the kinks movement gives the information about the magnetic state.

HR-01

Annealing temperature dependence of tunnel magnetoresistance in MgO-barrier magnetic tunnel junctions with CoFeB electrodes.

S. Ikeda[1], J. Hayakawa[2], Y. Lee[1], K. Miura[2,1], H. Hasegawa[1,2], F. Matsukura[1], H. Ohno[1]
1. Laboratory for Nanoelectronics and Spintronics, RIEC, Tohoku Univ., Sendai, Japan; 2. Advanced Research Laboratory, Hitachi, Ltd., Tokyo, Japan

Introduction

The investigation of magnetic tunnel junction (MTJ) structures (especially MgO barrier system [1]-[5]) that realizes high tunnel magnetoresistance (TMR) is important for development of advanced magnetoresistive random access memories (MRAMs) and hard disk drives (HDDs). TMR ratio of up to 500% at room temperature (RT) has been observed for sputtered CoFeB/MgO/CoFeB MTJs consisting of pseudo-spin valve (P-SV) stacking structure without antiferromagnetic pinning layer such as MnIr [6]. The optimum annealing temperature (T_a=450-525°C) that results in the maximum TMR ratio for P-SV MTJs is higher than that (T_a=360-425°C) of the exchange biased (EB)-SV MTJs with MnIr layer [7], [8]. The absence of diffusion of Mn into the MgO barrier at high T_a above 450°C is a factor for the high TMR ratios in P-SV MTJs. However, the effect of annealing temperature on the high TMR ratio for P-SV MTJs has not yet been fully clarified.

In this study, we investigated the dependence of the TMR ratio on annealing temperature for P-SV MTJs with various CoFeB compositions and thicknesses.

Experiments

The rf-sputtered MTJs studied here have stacking structure of substratre/Ta(5)/Ru(8) /Ta(5) /$(Co_xFe_{100-x})_{80}B_{20}(t_{CoFeB})$/MgO(1.5, 2.1)/$(Co_xFe_{100-x})_{80}B_{20}$(4)/Ta(5)/Ru(5). In CoFeB layer, the B composition was fixed to 20 at% and the composition x of Co was 0 and 75 at%. The bottom CoFeB layer thickness t_{CoFeB} varied from 2.3 to 6.7 nm by using the slide shadow mask technique. All MTJs were fabricated by photolithography and Ar ion milling with a junction size of 0.8×4 μm^2, and then were annealed at T_a=270-525°C for 1h in a vacuum under 4 kOe. The TMR ratio was measured using a dc four-point probe method in the magnetic field range of ±1 kOe.

Results and Discussion

Fig. 1 shows TMR ratios measured at RT as a function of annealing temperature (T_a) for P-SV MTJs with 4.3 nm-thick bottom CoFeB electrodes changed from x = 0% to 75%. In all samples with different CoFeB compositions, TMR ratio increases with increasing T_a and reaches the maximum at 475°C. When all samples annealed at temperature over 500°C, TMR ratios saturate and then gradually decrease. The maximum TMR ratio is 500% at RT (1010% at 5K) for the MTJ with x = 25 and a 2.1nm-thick MgO barrier. The high TMR ratio over 400% was observed for MTJs with x = 25 and 50%.

To understand the reasons for the decreased TMR ratios at high T_a for the P-SV MTJs, high resolution transmission electron microscopy (HRTEM) was employed for structural characterization. Fig. 2 shows the cross-sectional HRTEM images of Ta(5)/Ru(8)/Ta(5)/$(Co_{25}Fe_{75})_{80}B_{20}$(5) /MgO(2.1) /$(Co_{25}Fe_{75})_{80}B_{20}$(4) /Ta(5)/Ru(5) films, which were annealed at (a) 475°C and (b) 600°C. Two features can be pointed out when the samples were annealed at high temperature of 600°C: (i) CoFeB/Ta interfaces become more indistinct and (ii) (001) orientation of CoFeB electrodes deteriorates. Furthermore, energy dispersive x-ray (EDX) analysis (not shown) indicated that Ta diffuses into the CoFeB electrodes and MgO barrier in the sample after annealing at 600°C. Increasing T_a further to 500°C induced the diffusion of Ta into the CoFeB electrodes and MgO barrier, which may be the reason for the drop in TMR ratios in P-SV MTJs. Realization of higher TMR ratio over 500% is expected by suppression of Ta diffusion resulting from high temperature annealing. The application of the thicker CoFeB electrode suppresses Ta diffusion into MgO barrier and results in a high thermal stability, i.e., high TMR ratio through annealing at high T_a.

This work was supported in part by “High-Performance Low-Power Consumption Spin Devices and Storage Systems” program under Research and Development for Next-Generation Information Technology of MEXT.

[1] S. Yuasa *et al*., Nat. Mater. 868, 3 (2004).

[2] S. S. Parkin *et al*., Nat. Mater. 3, 862 (2004).

[3] D. D. Djayaprawira *et al*., Appl. Phys. Lett. 86, 092502 (2005).

[4] J. Hayakawa *et al*., Jpn. J. Appl. Phys, 44, L1267 (2005).

[5]S. Ikeda *et al*., IEEE Trans. Electron Devices, 54, 991 (2007).

[6] Y. M. Lee *et al*., Appl. Phys. Lett., 90, 212507 (2007).

[7] Y. M. Lee *et al*., Appl. Phys. Lett., 89, 042506 (2006).

[8] J. Hayakawa *et al*., Appl. Phys. Lett., 89, 232510 (2006).

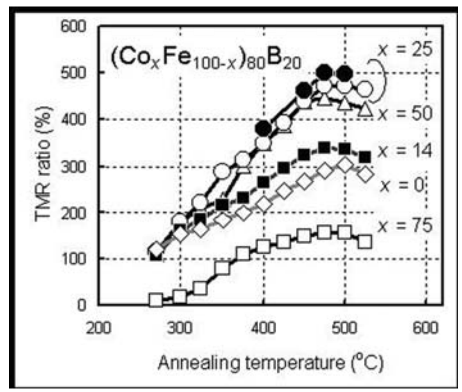

Fig.1. TMR ratio as a function of annealing temperature for P-SV MTJs having CoFeB electrodes with x = 0 %– 75% and t_{CoFeB}=4.3 nm.

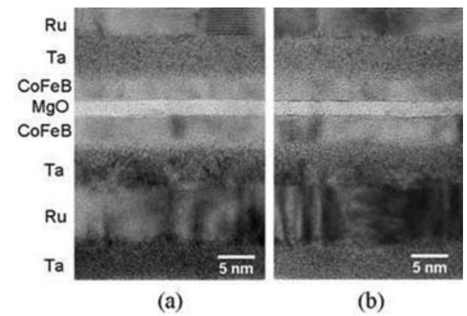

Fig.2. Cross-sectional TEM images for P-SV MTJs (a) after annealing at 475°C, and (b) after annealing at 600°C.

HR-02

Effects of MgO barrier thickness on magnetic anisotropy energy constant in perpendicularly magnetic tunnel junctions of $(Co/Pd)_n/MgO/(Co/Pt)_n$

J. Lee[1,3], C. Lee[1,2], L. Ye[1], S. Wang[1,2], Y. Wang[1], K. Lin[4], Y. Chang[4], T. Wu[1,2]
1. Taiwan SPIN Research Center and Graduate School of Engineering Science and Technology, National Yunlin University of Science and Technology, Douliou, Taiwan; 2. Graduate school of materials science, National Yunlin University of Science and Technology, Douliou, Taiwan; 3. Graduate school of Engineering Science and Technology, National Yunlin University of Science and Technology, Douliou, Taiwan; 4. Laser Application Technology Center, Industrial Technology Research Institute, Tainan, Taiwan

Perpendicularly magnetic tunnel junctions (pMTJ) have been considered as one of the candidates for high density spintronic applications because of their low aspect ratio. The perpendicularly magnetic anisotropy (PMA) energy constant Ku of free and pinned layers in pMTJ, from which the switching field is mainly determined, is a key characteristics for practical application. In the present work, we fabricated a series of multilayered pMTJs and found that Ku oscillates with respect to MgO barrier thickness with a period of about 0.3 nm.

The pMTJs using (Co/Pd) and (Co/Pt) binary multilayers were deposited on a SiNx substrate at room temperature. The stacking of these structures were $SiNx/Pt/(Co/Pd)_{10}$ $/MgO/(Co/Pt)_5$. The magnetic and metallic thin films were deposited by dc magnetron sputtering, while the MgO layer was deposited using the radio-frequency reactive sputtering method. The thickness of the MgO layer varied from 0.6 nm to 2 nm. The Co/Pd multilayer was used as the pinned layer and the Co/Pt multilayer acted as the free layer. The magnetic properties were measured using an alternating gradient magnetometer (AGM). The anisotropy constants Ku were obtained by using the extraordinary Hall Effect (EHE) measurements method [1-3]. Under such configuration, the Hall voltage is proportional to the perpendicular magnetization component which, in turn, depends on the strength of in-plane applied magnetic field and the anisotropy constant. The anisotropy constant Ku can be obtained by assuming that the magnetization direction is determined by minimization of the magnetic energy [3]:

$$E=-H_{app}M\sin\theta-2\pi M^2\sin^2\theta+Ku\sin^2\theta, \qquad (1)$$

where θ is the angle between the magnetization and the film normal.

Fig. 1 shows the normalized extraordinary Hall voltage versus the applied magnetic field for several MgO layer thicknesses. As the in-plane field increases, the perpendicular magnetizations, and thus the Hall voltages, decrease slowly in the beginning; however, as the field larger than 2 kOe, the Hall voltages decrease abruptly. The suddenly drops could be attributed to the magnetization switching change from coherent to incoherent. Hence, only the data before these abrupt drops are taken to estimate the anisotropy constant. The calculated results of anisotropy constant Ku for various MgO barrier thicknesses are shown in Fig. 2. Interestingly enough, the anisotropy constant Ku oscillates with MgO thickness with values between 1.3×10^6 erg/cc and 2.7×10^6 erg/cc, and the oscillation period is about 0.3 nm, which is close to the oscillation period of magnetoresistance observed in epitaxial Fe/MgO/Fe MTJs [4]. An discussion on the effect of oxidation layer thickness from the AGM and CIPT (Current In-Plane tunneling) measurements are also presented in Worledge and Trouilloud [5].

This work was supported by the Department of Industrial Technology, Ministry of Economic Affairs, Republic of China, under Contract No. 95-EC-17-A-01-S1-026, by the National Science Council of Taiwan, Republic of China, under Contract No. NSC 95-2112-M-224-003-MY3., and by the R.O.C. Ministry of Economic Affairs under Grant 6301XSW410.

[1]Wolniansky. P., S. Chase. R. Rosenvold, M. Ruane and M. Mansuripur, "Magneto-optical measurements of hysteresis loop and anisotropy energy constants on amorphous TbxFe1-x alloys", J. Appl. Phys. Vol. 60, 346(1986)

[2] E. C. Stoner and E. P. Wohlfarth :Philos Trans .R. Soc. A 240 (1948) 599.

[3]Te-ho wu, Hong Fu, Hajjar R. A., Mansuripur M.," Measurement of magnetic anisotropy constant for magneto-optical recording media : a comparison of several techniques", J. appl. phys. Vol. 73, pp. 1368-1376(1993).

[4] Rie Matsumoto, Akio Fukushima, Taro Nagahama, Yoshishige Suzuki, Koji Ando, and Shinji Yuasa, Oscillation of giant tunneling magnetoresistance with respect to tunneling barrier thickness in fully epitaxial Fe/MgO/Fe magnetic tunnel junctions, Appl. Phys. Lett. 90, 252506 (2007).

[5] D. C. Worledge and P. L. Trouilloud, "Magnetoresistance measurement of unpatterned magnetic tunnel junction wafers by current-in-plane tunneling", Appl. Phys. Lett. 83, 84 (2003)

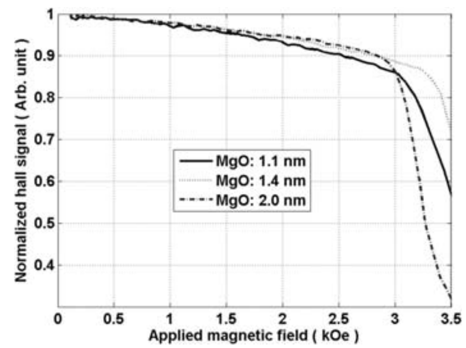

Fig.1 Extraordinary Hall effect measurement of Perpendicular magnetic anisotropy energy constant on pMTJs

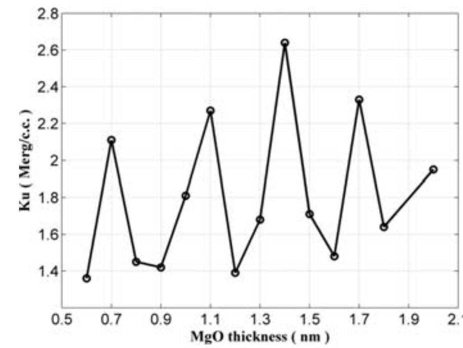

Fig.2 Anisotropy energy constant Ku versus MgO thickness

HR-03

Magnetoresistance Behavior of Bottom Exchange Biased Perpendicular Magnetic Tunnel Junction Based on Pd/Co Multilayers.

D. Lim[1], *K. Kim*[1], S. Lee[1], S. Kim[2], W. Jeung[3]

1. Materials Science and Engineering, Korea University, Seoul, South Korea; 2. Mechanical Design and Automation Engineering, Seoul National University of Technology, Seoul, South Korea; 3. Korea Institute of Science and Technology, P.O.Box 131, Seoul, South Korea

Introduction

Magnetic tunnel junctions (MTJs) with perpendicular anisotropy can increase the memory density of magnetic random access memory (MRAM) by avoiding the magnetization curling phenomena in the low aspect ratio scheme [1]. Co/Pt multilayer with the perpendicular anisotropy was shown to be exchange biased using a conventional FeMn antiferromagnet [2]. In the previous study, we obtained tunneling magneto-resistance (TMR) ratio of 12.6% at R.T. in a pseudo perpendicular magnetic tunnel junction (pMTJ) but a very low TMR ratio in the top exchange biased (TEB)-pMTJ [3]. In this study, we fabricated the bottom exchange biased (BEB)-pMTJ based on Co/Pd multilayers and investigated the effect of multilayer structures, such as underlayer materials and number of bilayers, on the magnetoresistance and perpendicular exchange coupling of the BEB-pMTJs.

Experiments

SiO_2/Pd 9/(Co 0.2/Pd 0.7)$_x$/Co 0.5/Al 1.6 + oxidation/Co 0.5/(Pd 0.7/Co 0.2)$_3$/IrMn 8/Pd 2 stacks and SiO_2/underlayer/IrMn 8/Pd 0~0.7/(Co 0.2/Pd 0.7)$_n$/Co 0.5/Al 1.6 + oxidation/Co 0.5/(Pd 0.7/Co 0.2)$_3$/Pd 2 (numbers in nm) stacks were sputter-deposited on Si substrates for the TEB-pMTJ and the BEB-pMTJ, respectively. The tunnel barrier was formed by oxidizing the Al layers in an RF plasma environment (2.16 W/cm^2 RF power density, 100 mTorr O_2 partial pressure). Junctions were patterned using a set of metal shadow masks with a 200×200 μm^2 opening. The magnetoresistive and magnetic properties of the pMTJ samples were measured using a dc-four point probe and a vibrating sample magnetometer (VSM). The temperature dependence of the TMR was measured using a cryogenic Dewar at temperatures from 10 to 300 K. The surface roughness was measured using atomic force microscopy (AFM) and the scan size was 1×1 μm^2.

Results and Discussion

TMR ratio of the TEB-pMTJ was reduced as compared with the pseudo-pMTJ because in-plane anisotropy of the Co/antiferromagnet (IrMn) interfaces deteriorates the anti-parallel state between the bottom and the top electrodes.[3] When we used the Pd as an underlayer in the BEB-pMTJ stack, the TMR ratio increased a little compared with the TEB-pMTJ. However, the perpendicular exchange coupling and perpendicular anisotropy decreased because the IrMn induced the in-plane anisotropy. To improve the TMR ratio and perpendicular exchange coupling in the BEB-pMTJ, we modified the multilayer structure and the materials, such as underlayer materials, Pd insertion in between the IrMn and the bottom (Co/Pd)$_n$ layer, and the number of bilayers in the bottom (Co/Pd)$_n$. When the Pd layer was inserted, the TMR ratio was improved but the spin polarization and the perpendicular anisotropy were degraded. TMR, R, and ΔR increased as the number of bilayers in the bottom (Pd/Co)$_n$ increased as shown in Fig. 1. Although the perpendicular anisotropy increased as the number of bilayers increased, the perpendicular exchange coupling with the IrMn was not observed in this stack. When we used the NiFe as a buffer layer, the in-plane anisotropy was induced and hence the IrMn coupled with the NiFe in the plane direction. To solve rhis problem, we replaced the Ta/NiFe with the perpendiculary magnetized (Pd/Co)$_n$ as a buffer layer. The perpendiculary exchange coupled pMTJ with the moderate TMR was obtained using the buffer layer of (Pd/Co)$_n$ as shown in Fig. 2 and the exchange coupling field was 147 Oe. In summary, we could improve the TMR ratio in the BEB-pMTJ. A perpendicularly magnetized buffer layers, such as (Pd/Co)$_n$ multilayers should be used to induce the perpendicular exchange coupling with antiferromagnet such as IrMn in the BEB-pMTJ.

[1] N. Nishimura, T. Hirai, A. Koganei, T. Ikeda, K. Okano, Y. Sekiguchi, and Y. Osada, J. Appl. Phys., 91, 5246 (2002).

[2] F. Garcia, G. Casali, S. Auffret, B. Rodmacq, and B. Dieny, J. Appl. Phys., 91, 6905 (2002).

[3] D. Lim, S. Kim, and S.-R. Lee, J. Appl. Phys., 97, 10C902 (2005).

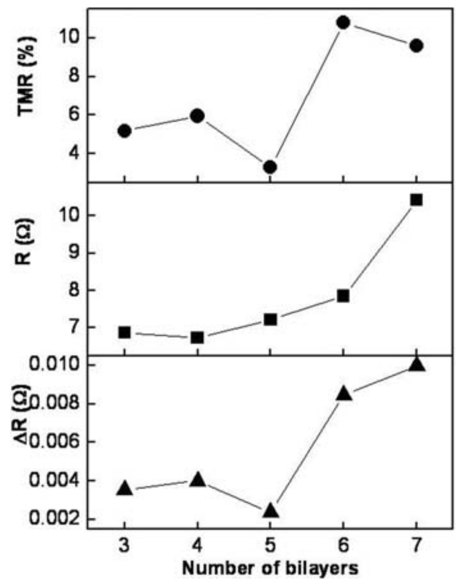

Fig. 1. TMR, R, and ΔR change of BEB-pMTJ as a function of the number of bilayers in the bottom (Co/Pd)$_n$. The pMTJ stack is SiO_2/Ta 5/NiFe 2/IrMn 8/(Co 0.2/Pd 0.7)$_n$/Co 0.5/Al 1.6+Oxidation/Co 0.5/(Pd 0.7/Co 0.2)$_3$/Pd 2 (nm)

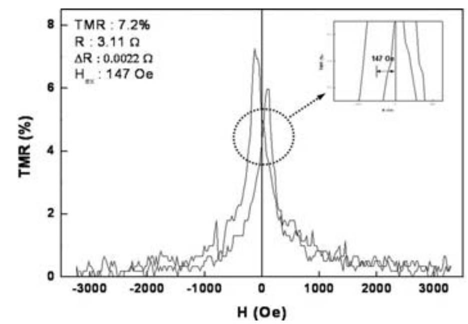

Fig. 2. TMR curve of the BEB-pMTJ with the (Co/Pd)$_n$ underlayer. The pMTJ stack is SiO_2/Pd 9/(Co 0.2/Pd 0.7)$_3$/Co 0.2/IrMn 8/(Co 0.2/Pd 0.7)$_6$/Co 0.5/Al 1.6+Oxidation/Co 0.5/(Pd 0.7/Co 0.2)3/Pd 2 (nm).

HR-04

Improvement of (100) orientation of MgO films deposited at room temperature for perpendicular MTJ.

H. Ohmori, S. Nakagawa
Dept. of Physical Electronics, Tokyo Institute of Technology, Tokyo, Japan

Introduction

MTJs with perpendicular magnetic anisotropy (p-MTJ) are expected to be high density integration and reduce electrical power consumption of MRAM[1],[2]. We fabricated p-MTJ with rare-earth transition metal (RE-TM) amorphous alloy and 3nm-thick MgO(100) tunneling barrier prepared at room temperature and observed 64% TMR ratio[3]. However, large TMR ratio above 100% was not observed despite using Fe(100)/MgO(100)/Fe(100) tunnel junction. We particularly focused the crystallinity and crystallites orientation of MgO(100) textured films and tried to improve MgO crystallinity. Since high temperature treatment such as annealing may cause degradation of perpendicular magnetic anisotropy of RE-TM films, we investigated the appropriate process by changing sputtering condition. MgO crystallinity was improved by the epitaxial growth depended on the crystallographic structure of Fe buffer layer by low MgO deposition rate. Cryatallinity of 3nm-thick MgO tunneling barrier prepared at total gas pressure of 0.5 mTorr and low deposition rate was improved compared to that of the 3nm-thick MgO tunneling barrier prepared in the previous condition.

Experimental

Fe films were deposited by facing targets sputtering system at 0.4 mTorr of Ar gas pressure. Fe films exhibit (100) orientation when these films were deposited directly on glass substrate at low deposition rate below 0.7 nm/min. MgO films were prepared at room temperature by reactive facing targets sputtering system using Ar+O_2 mixture gas and Mg target. MgO deposition conditions were changed by total gas pressure (0.50-1.0 mTorr) and sputtering power (17-130 W). MgO deposition rate were controlled in the range from 0.20 to 1.45 nm/min. Fe(3 nm)/MgO(20 nm) bilayer on glass substrates were prepared at room temperature in order to evaluate MgO crystallinity and crystallites orientation. $Gd_x(Fe_{90}Co_{10})_{1-x}$ and $Tb_x(Fe_{90}Co_{10})_{1-x}$ were prepared by ion beam sputtering method using 0.10 mTorr of Kr gas pressure. MgO crystalline orientation was evaluated by X-ray diffractometer (XRD).

Results and Discussion

Fig.1 (a) shows the variation of MgO crystallinity for various total gas pressure. Integrated intensity, FWHM and $\Delta\theta_{50}$ indicate that total gas pressure of 0.75 mTorr was optimal condition for the crystallinity and crystallites orientation of MgO(100) textured films. Since each input power was almost constant (85-90 W), MgO crystalline were not influenced by input power. However, MgO deposition rate dropped with increase of gas pressure. We think that the improvement of MgO(100) crystalline was caused by increase of collision probability and decay of MgO deposition rate. The distance between the center of targets and the center of substrate was about 15 cm in our sputtering system and mean free path of MgO particle was about 5-8 cm in this gas pressure condition. Therefore, the sputtering particle which can reach substrate decrease with the increase of gas pressure and the deposition rate was dropped. Most particles collide with other particles on the way to the substrate by the increase of gas pressure and the particles which collide once or more lose their momentum. As a result, they depended on the interfacial energy of Fe buffer layer and MgO films exhibited better (100) orientation. Fig.1 (b) shows the change of crystallinity of MgO films for various input power at the same total gas pressure. In the region below 88 W, integrated intensity, FWHM and $\Delta\theta_{50}$ indicate that the crystallinity and crystallites orientation of MgO films improved with the decrease of input power. Interfacial energy was smaller than surface energy with the decrease of input power. In the result, MgO particles depended on the crystallographic structure of Fe surface by the decrease of input power and deposition rate[4]. In conclusion, since the crystallinity and crystallites orientation of MgO films prepared at room temperature were improved by the decay of MgO deposition rate with the change of total gas pressure or input power, the control of deposition rate can be possible to reduce the annealing temperature.

Fig.2 shows the XRD diagrams of 3nm-thick MgO tunneling barrier which was prepared at total gas pressure of 0.5 mTorr and input power of 17 W was improved compared to 3nm-thick MgO in previous condition that revealed 64% of TMR ratio[3]. MgO(200) integrated intensity prepared in this condition was 1.5 times larger than that prepared in previous condition. The further increase of TMR effect can be expected with the improvement of MgO crystalline prepared at room temperature.

[1] N. Nishimura, *et al.*, J. Appl. Phys., 91(8), 5246 (2002).

[2] S. Mangin, *et al.*, Nature mater., 5, 210 (2006).

[3] H. Ohmori, *et al.*, "Perpendiular magnetic tunnel junction with TMR ratio of 64% using MgO(100) barrier layer prepared at room temperature", J. Appl. Phys., in press (2008).

[4] K.-H. Ahn, *et al.*, J. Mater. Res., 17(9), 2334 (2002).

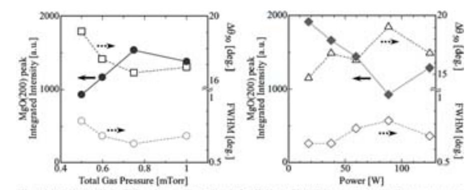

Fig.1 MgO(200) XRD diffraction peak analyses for Fe[3 nm]/MgO[20 nm]; (a) total gas pressure (Ar + O_2 mixture gas) dependence and (b) input power dependence. Film architecture are Fe(3 nm)/MgO(20 nm) on glass substrate. Integrated intensity and full width at half maximum (FWHM) were derived from 2θ-θ diffraction patterns. $\Delta\theta_{50}$ wasderived from rocking curve around each MgO(200) diffraction peaks.

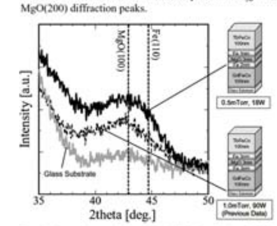

Fig.2 Comparison of the crystallinities of 3nm-thick MgO (100) tunneling barriers by the difference of sputtering condition.

HR-05

Magnetic tunnel junctions formed by oxidation of Mg.

W. Raberg[1], T. Bever[1], M. Hawraneck[1,2], S. Koss[1,3], S. Schmitt[1], J. Zimmer[1]
1. Technology development Sense & Control, Infineon Technologies AG, Neubiberg, Germany; 2. Institut für Materialwissenschaften, Technische Universität Darmstadt, Darmstadt, Germany; 3. Institut für Festkörperphysik, Universität Hannover, Hannover, Germany

When Parkin et. al.[1] and Yuasa et. al. [2] published the first results for MgO-TMR's with values above 200 % in 2004 the resonance was enormous. The high signal amplitude which had been predicted previously by Butler et.al. [3] opened the path to improved performance in magnetic random access memories (MRAMs) as well as magnetic sensor applications and enabled new concepts based on spintronics.
One reason, why it took relatively long to achieve the breakthrough in MgO-barriers was that the approach of oxidizing the metal which is commonly used for the formation of Alox barriers did not seem to be applicable. Achieving a well ordered crystalline layer by first depositing a metallic Mg-layer and then incorporating oxygen atoms is not straightforward. Consequently, the first successful approaches used either reactive deposition of MgO [1] or epitaxy [2].
Results for MgO-barriers formed by oxidation of metallic magnesium have been less encouraging [4], although values of up to 60% have been demonstrated [5]. The gap to the results obtained with the above mentioned methods was attributed to the poor texture present in the MTJ formed by oxidation.
In this work we present results for MgO-based magnetic tunnel junctions formed by radical shower oxidation that show TMR effects of almost 200%. Despite a strong dependence on the Mg-thickness in a single deposition step the process is shown to be scalable to any resistance area product needed in a given application.
MTJ-stacks of the form seed/PtMn/CoFe/Ru/CoFeB/xMg(t_{ox})/CoFeB/cap were deposited using DC-sputtering. The wafers were deposited up to the Mg layer, then oxidized using a radical shower oxidation process. The stack formation was completed by depositing the freelayer and the cap material. The wafers were annealed in a magnetic oven at 350°C for 1 h with a field of 1 T.
Figure 1 shows CIPT results for MR and RA as a function of initial Mg-thickness.
Obviously, a high signal is obtained only for a very thin Mg-layer of 5Å thickness. Even an increase of only 0.5 Å leads to a significant increase in RA and a decrease in MR. A further increase of the Mg-thickness results in an even stronger degradation of the barrier properties. On the other hand, Mg-layers thinner than 5 Å do not result in a functional barrier either, which indicates that the window for obtaining the right texture is indeed very small.
The observed properties of the 5 Å barrier stack are, however, very attractive for spintronic applications: 90% MR at an R*A-product of 13 Ωμm2. Characterization of the magnetic properties confirm the integrity of the barrier. Despite the above described small window significantly larger R*A can be realized. This is achieved by simply repeating the barrier process as often as needed to obtain the desired resistance. Figure 2 shows the results obtained for up to five iterations. The R*A trend follows the exponential law expected for the thickness dependence of a tunnelling process. High MR is obtained throughout the series with maximum values of 180 % and more. The structural homogeneity is astonishing as is observed with HRTEM for fourfold barrier (Fig.3).
This work is supported by the BMBF project 13N9084.

[1] S.S.P. Parkin, C. Kaiser, A. Panchula, P.M. Rice, B. Hughes, M. Samant, S-H. Yang, Nature Materials 3, 862 (2004)

[2] S. Yuasa, T. Nagahama, A. Fukushima, Y. Suzuki, K. Ando, Nature Materials 3, 868 (2004)

[3] W.H. Butler, X.-G. Zhang, T.C. Schulthess, J.M. MacLaren, Phys. Rev. B 63, 054416 (2001)

[4] M. Hehn, C. de Buttet, G. Malinowski, E. Snoeck, C. Tiusan, F. Montaigne, Europ. Phys. J. B, 40(1), 19 (2004)

[5] T. Dimopoulos, G. Gieres, J. Wecker, N. Wiese, Y. Luo, K. Samwer, J. Appl. Phys. 98, 073705 (2005)

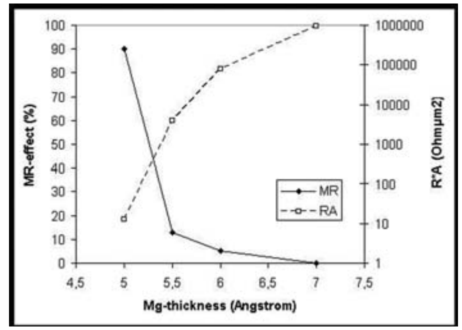

MR and RA as function of initial thickness of single Mg-films.

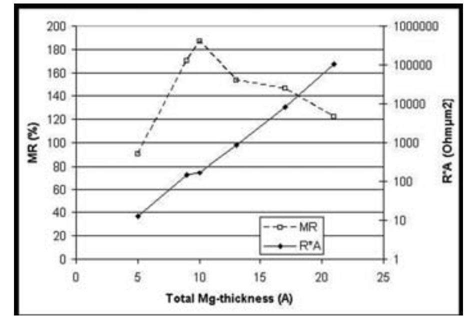

MR * RA vs. cumulated Mg-thickness in the iterative process.

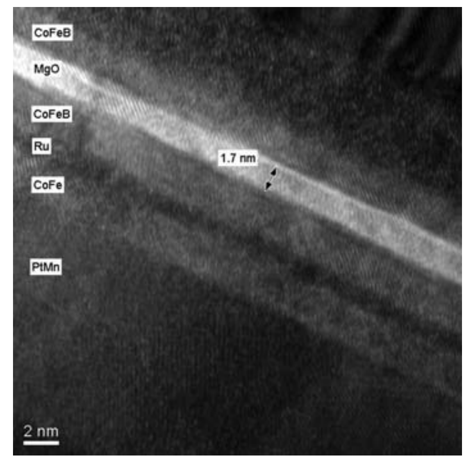

HRTEM image of the MgO barrier formed by four iterations.

HR-06

Influence of boron concentration on tunnel magnetoresistance in CoFeB/MgO/CoFeB magnetic tunnel junctions.

K. Tsunekawa[1], Y. Nagamine[1], Y. Choi[1], F. Ernult[1], D. D. Djayaprawira[1], Y. Kitamoto[2]
1. Electronic Devices Engineering Headquarters, Canon ANELVA Corp., Kawasaki-shi, Japan;
2. Tokyo Institute of Technology, Yokohama-shi, Japan

Introduction:
MgO-based magnetic tunnel junctions (MTJs) using amorphous CoFeB ferromagnetic electrodes have attracted much attention not only due to their huge tunnel magnetoresistance (TMR) effect but also to their suitability for mass production. In this system, the influence of Co/Fe ratio on TMR effect has been investigated, and the Co/Fe ratio of about 25/75 has been found to be an optimum composition to obtain the largest TMR effect [1-2]. In past reports, however, boron concentration had always been constant at about 20 at.%, and thus the influence of boron concentration on TMR effect is still unclear. Therefore, in this study, we prepared CoFeB/MgO/CoFeB MTJs with different boron concentrations under a constant Co/Fe ratio, and investigated the influence of boron concentration on TMR effect.
Experimental:
The MTJs consisting of bottom electrode/Pt49Mn51/Co70Fe30/Ru/(CoFe)100-xBx reference layer (RL) /MgO/(CoFe)100-xBx free layer (FL) /top electrode were prepared on a thermally oxidized silicon wafers using an ultra-high vacuum magnetron sputtering system (Canon ANELVA C-7100). All the metallic layers were deposited by dc sputtering in Ar or Kr atmosphere, and the insulating MgO layer was deposited by rf sputtering directly from a sintered MgO target. The Co/Fe ratio in the (CoFe)100-xBx layers was maintained at around 75/25. When boron concentration of one CoFeB layer was varied, that of another CoFeB layer was fixed at 20 at.%. After deposition, the MTJs were annealed at various temperatures for 2 hours in a magnetic field of 8 kOe.
Results:
Figures 1 and 2 show the dependence of MR ratio on annealing temperature for MTJs with (CoFe)100-xBx RL and (CoFe)100-xBx FL, respectively. It is noted that all MTJs show a local minimum of MR ratio in the annealing temperature dependence experiments. This MR drop is caused by thermal degradation of the synthetic antiferro (SAF) pinned layer and not by degradation of the tunnel juction. The dashed lines in the figures indicate the critical temperature until which the properties of the SAF pinned layer are retained. For the MTJs with (CoFe)100-xBx RL, the critical temperature depends on boron concentration x. Furthermore, when x = 0-5 at.%, the MR ratio is significantly low, only 50-70%, which is equivalent to that of MTJs using an amorphous Al2O3 tunnel barrier. On the other hand, for the MTJs with (CoFe)100-xBx FL, the critical temperature is almost constant between 360°C and 380°C. The MR ratio is always over 100% below the critical temperature and gradually increases with increasing boron concentration x.
The low MR ratio in the MTJs with (CoFe)100-xBx RL when x = 0-5 at.% is caused by the lack of (001)-texture of the MgO layer deposited on top of the RL and by the partial oxidation of the the (CoFe)100-xBx RL after high temperature annealing.

[1] K. Tsunekawa, Y. S. Choi, Y. Nagamine, D. D. Djayaprawira, T. Takeuchi, and Y. Kitamoto, Jpn. J. Appl. Phys. 45 (2006) L1152-L1155.

[2] Y. M. Lee, J. Hayakawa, S. Ikeda, F. Matsukura, and H. Ohno, Appl. Phys. Lett. 90 (2007) 212507.

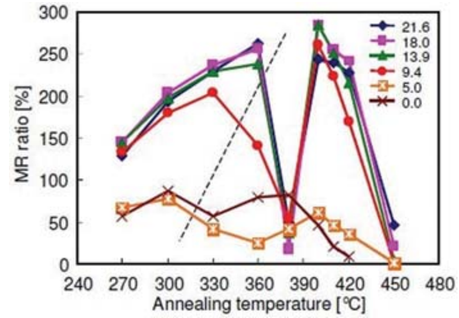

Fig. 1 Dependence of MR ratio on annealing temperature for MTJs with (CoFe)100-xBx RL.

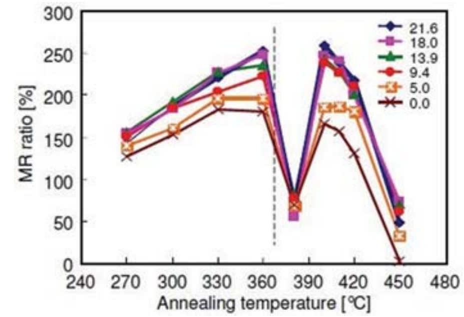

Fig. 2 Dependence of MR ratio on annealing temperature for MTJs with (CoFe)100-xBx FL.

HR-07

Temperature dependence of magnetoresistance in epitaxial Fe/MgO/Fe/IrMn magnetic tunnel junctions.

S. Wang[1,2], *R. Ward*[1], G. Du[2], X. Han[2], C. Wang[3], A. Kohn[3]
1. Department of Physics, University of Oxford, Oxford, United Kingdom; 2. Institute of Physics, Chinese Academy of Sciences, Beijing, China; 3. Department of Materials, University of Oxford, Oxford, United Kingdom

Following theoretical predictions, very high tunnel magnetoresistance (TMR) ratios have been achieved in epitaxial Fe/MgO/Fe MTJ structures [1]. The TMR ratio exhibits both temperature and bias voltage dependences, which play critical roles in device applications. In the present work, we analyse the temperature dependence of TMR of fully epitaxial Fe/MgO/Fe/IrMn MTJs grown by MBE. The temperature dependence of TMR ratio, which rises to over 300% at 10K, is fitted using a model based on the effect of magnetic disorder of the electrodes on the spin polarized tunnelling current.
Structural characterization (RHEED, XRD, HRTEM, see ref [2]) established the epitaxial structures as Fe(001)[100]//MgO(IrMn)(001)[110] with sharp interfaces. Junctions (6x8 μm^2 area, 36 per sample) were patterned by optical lithography combined with Ar ion-beam milling. The magneto-transport properties at different temperatures were measured in a PPMS system using a standard four-probe technique with a magnetic field applied parallel to the [100] Fe easy axis. Figure 1 shows loops of the junction resistance *R* as a function of magnetic field at 300K, 100K, and 10K, measured for an MTJ composition Fe(25)/MgO(3)/Fe(10)/IrMn(10) (thicknesses in nm). A TMR ratio of 170% is found at room temperature which increases to 318% at 10K. Note also in Figure 1 the strong temperature dependence of coercivity and exchange bias field, unlike results of other groups [1], which is attributed to the fully epitaxial nature of the FM/AFM structure in this study. The temperature dependence of the TMR ratio is shown in Figure 2(a) for two different junctions from the same sample as Figure 1. We find a reproducible departure from linearity of the *TMR* vs *T* relationship, and the solid lines in Figure 2(a) are fits based on the model to be described. Figure 2(b) shows the resistances of junction-2 in the P and AP configurations as a function of temperature. R_P is seen to be nearly independent of temperature, which is a characteristic of high quality MgO barriers, while R_{AP} increases monotonically with decreasing temperature.
In order to describe the temperature dependence of *TMR* we have used Slonczewski's [3] expression for the conductance of a tunnel junction: $G = G^0(1 + P_1P_2\cos\theta)$, where P_1, P_2 are the effective polarizations of the FM electrodes and θ is the angle between their magnetisations. This definition is now modified by replacing polarization with magnetization (*M*) and introducing individual angular terms to define the directions of magnetisation in the two electrodes with respect to the direction of the applied field. The close link between polarization and magnetization has been emphasised by previous authors [4]. At temperatures T>0, the direction of the magnetisation in each electrode will deviate from exact alignment with the applied field according to the minimum of the Zeeman plus exchange energies, and the energy terms are different for the P and AP configurations. Taking R_P to be constant, and using the Bloch relation to describe the temperature dependence of magnetisation [4], the TMR ratio can be expressed as :
$TMR = (R_{AP} - R_P)/R_P = R^0_{AP}/R_P[1 - \beta M^0_1 M^0_2(1-\alpha_1 T^{3/2})(1-\alpha_2 T^{3/2})] - 1$ ......(1),
where the fitting parameter β includes the proportionality factor between polarization and magnetization, and α_1, α_2 are the Bloch constants for the two FM layers.
The fits, using Eq. (1), of the experimental TMR data are shown by the solid lines in Figure 2(a). The parameters $\alpha_{1,2}$ were obtained by fitting the magnetization curves of reference Fe and Fe/IrMn layers according to the Bloch equation. The temperature dependence fitting of the TMR ratio has been repeated successfully for MgO barrier thicknesses of 2 and 3 nm. We conclude that the temperature dependence of TMR in epitaxial MgO tunnel junctions is well described by a model based on the magnetic disorder of the two FM electrodes on each side of the barrier.

[1] S. Yuasa, T. Nagahama, A. Fukushima, Y. Suzuki, and K. Ando, Nature Materials 3, 868 (2004)

[2] C. Wang, S. G. Wang, A. Kohn, R. C. C. Ward, and A. K. Petford-Long, IEEE Trans. Magn. 43, 2799 (2007)

[3] J.C. Slonczewski, Phys. Rev. B 39, 6995 (1989)

[4] C. H. Shang, J. Nowak, R. Jansen, and J. S. Moodera, Phys. Rev. B 58, R2917 (1998)

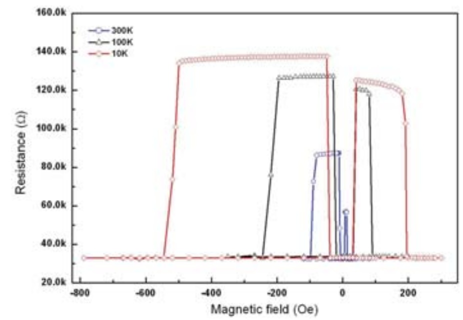

Fig. 1 TMR vs. Field at 300K, 100K, 10K

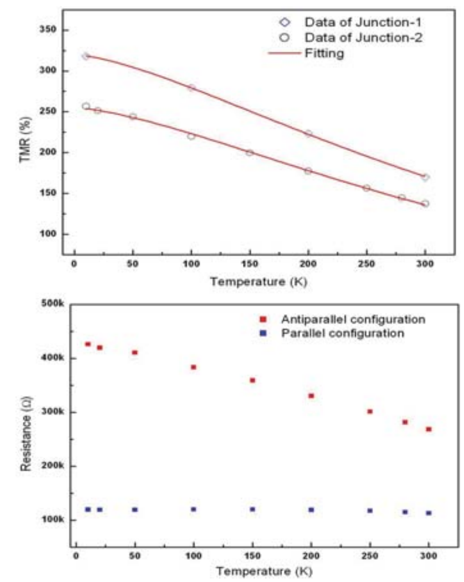

Fig. 2 (a) TMR vs. Temp (b) R_P, R_{AP} vs. Temp

The XRD analysis of pseudo and exchange bias spin valve of MgO based magnetic tunnel junctions.

J. Kanak[1], P. Wisniowski[2], A. Zaleski[1], S. Cardoso[2], P. P. Freitas[2], T. Stobiecki[1]
1. AGH University of Science and Technology, Krakow, Poland; 2. INESC Microsystems and Nanotechnologies, Lisbon, Portugal

Two sets of MTJs: pseudo spin valve (PSV): glass/Ta50/Ru180/Ta30/$(Co_{52}Fe_{48})_{75}B_{25}$150(50)/MgO150(12)/$(Co_{52}Fe_{48})_{75}B_{25}$150(40)/Ru50/Ta50 and exchange biased spin valve (EB-SV): glass/Ta50/Ru180/Ta30/$Pt_{46}Mn_{54}$200/$Co_{82}Fe_{18}$20/Ru9/$(Co_{52}Fe_{48})_{75}B_{25}$150(30)/MgO150(12.5)/$(Co_{52}Fe_{48})_{75}B_{25}$150(30)/Ru50/Ta50 (thicknesses in Å) have been investigated in order to characterize microstructure using XRD methods. Layer thicknesses of MTJs for TMR measurements are given in brackets. The samples were annealed in high vacuum at 340°C, for 1 hour in a magnetic field of 4 kOe applied along the easy axis, and furnace cooled in the field.
Figure 1 shows θ-2θ diffraction profiles in wide 2θ range for PSV (a) and EB-SV (b) measured for as deposited and annealed samples. It was found for both PSV and EB-SV samples that seed layer 50 Å Ta is amorphous. Buffer layer 180 Å Ru is strongly textured in [002] direction. CoFeB ferromagnetic electrodes are amorphous in as-deposited state and crystallize to bcc(200) CoFe phase after annealing. The PtMn antiferromagnet in EB-SV sample transforms after annealing from single fcc(111) to single fct(111) phase. The rocking curves of (002) Ru and (200) MgO show that the texture of these materials essentially increases after annealing.
Figure 2 shows θ-2θ experimental and simulated diffraction profiles in narrow 2θ range for annealed PSV (a) and EB-SV (b), and simulated structure of EB-SV imaged by one dimensional grains (c). The intensities of θ-2θ profiles were calculated from kinematical diffraction theory using the Monte Carlo simulation method. In this approach polycrystalline multilayer structure is generated with the assumption of the Gaussian distribution of crystallite sizes in the perpendicular to the film plane direction. The calculated intensity profiles are in very good agreement with experimental data. The results of simulations are collected in Table 1. Diffraction θ-2θ profiles of the annealed PSV and EB-SV (Fig.3) show that amorphous $(Co_{52}Fe_{48})_{75}B_{25}$ crystallizes to the CoFe bcc (200) phase. Intensity of CoFe (200) peak in PSV sample and texture coefficient is higher than that of EB-SV sample (Table 1). It means that CoFeB layers adjacent to MgO (200) barrier crystallize more effectively when grown on Ta50/Ru180/Ta30 buffer layers in comparison to those which are separated from buffer layers by PtMn200/CoFe20/Ru9. TMR and RA product of MTJs with layer structure equivalent to the samples for XRD investigation are collected in Table 1. Higher TMR for PSV than that of EB-SV sample is probably due to effective crystallization process of amorphous CoFeB layers in the case of PSV stack layers.
In summary, it can be concluded that after annealing CoFeB amorphous layers, which are adjacent to MgO barrier, crystallize coherently with (200) MgO planes.
Acknowledgment: Financial support by the MRTN-CT-2006-035327(SPINSWITCH) and MRTN-CT-2003-504462 (ULTRASMOOTH).

Sample	Ru 180 Å		PtMn 200 Å		CoFeB 150 Å		Ru 50 Å		TMR [%]	RA [kΩμm²]
	D [Å]	texture coef.	D [Å]	texture coef.	D [Å]	texture coef.	D [Å]	texture coef.		
PSV	160	1	-	-	50	0.16	30	0.6	240	25
EB-SV	160	1	55	0.56	50	0.12	30	0.7	180	28

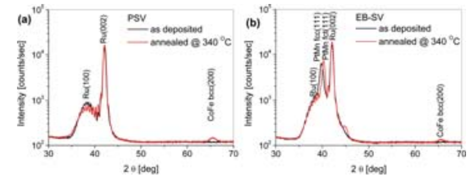

Fig. 1. XRD θ-2θ profiles of PSV (a) and EB-SV (b) MTJs.

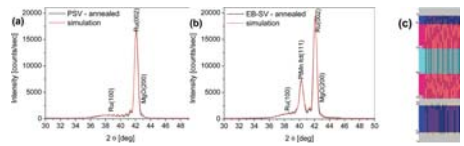

Fig. 2. Measured and simulated XRD θ-2θ profiles of PSV (a) and EB-SV (b) and simulated structure of EB-SV (c).

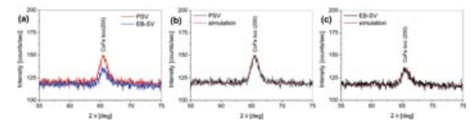

Fig. 3. XRD θ-2θ profiles measured (a) and simulated for annealed PSV (b) and EB-SV (c).

HR-09

The electrical properties of the radically oxidized MgO prepared in different oxidation condition.

C. Shen, S. Yang, C. Yen, W. Chen, Y. Lee, D. Wang, C. Tsai, C. Hung, K. Shen, M. Kao
Electronics and Optoelectronics Research Lab (EOL), Industrial Technology Research Institute (ITRI), Hsinchu, Taiwan

The improvements of the magnetic tunnel junctions (MTJs) with MgO barriers represent the capability of the MRAM device and spin transfer memory because of their high magnetoresistance ratios (MR) and good resistance-area product (RA) control. High MR results above 200% could be realized in the RF sputtered MgO-based MTJs in recent reports[1]; furthermore, reactively sputtered Mg in radical oxidation process also showed good MR behavior about 100% and better resistance-area (RA) and MR uniformity[2]. Although the MR ratio in the post-oxidized MgO MTJ is only half of that in the RF sputtered MgO MTJ, the RA and MR uniformity and distribution are the main points for mass production. Therefore, in this report, the development of uniformity and film properties of the MTJs with post-oxidized MgO barriers has been studied and the MTJ stacks of Ta /PtMn /CoFe /Ru /CoFeB /Barrier Layer /CoFeB /Ta are deposited on the thermally oxidized Si substrate in UHV sputtering system. The barrier layer was prepared by first depositing the Mg metal layer and then radical oxidized it at the atmosphere of oxygen or argon/ oxygen mixed gas. All films were vacuum-annealed ex-situ in a field of 1 Tesla at 360C for 2 hours.

The preparation of the MTJs with radically oxidized MgO is very complicated because there are too many conditions need to be concerned, like deposition power, gas condition, etc.. In this work, we found that the oxidation atmosphere is an important factor for the cell quality. In Figure 1, the MTJs with the MgO barrier made by oxidizing Mg layer under argon/ oxygen mixed gas (type A,B,C) or pure oxygen (type D) showed similar MR ratios about 90% and RA about 300 ohm-um2. However, for the barriers oxidized in mixed argon /oxygen gas, the MTJ device showed the bad performance and large amount of bad dies. Those dies were short and resulted in no MR and RH loops which may be come from the worse oxidization quality by adding the argon gas. In addition, all dies are short when the argon/oxygen ratio was increased to 1 (Type C, 200/200). For type D, oxidizing in the pure oxygen gas, the device showed higher good dies and similar MR ratio.

Furthermore, compared the radically oxidized MgO MTJs with RF sputtered MgO MTJs, we investigated that the MR and RA uniformity in RF MgO MTJs are 8% and 14%. Both of those could be improved to about 3.7% and 8.5% in radically oxidized MgO MTJs. The uniformity is defined as standard deviation per average value.

Consequently, we have demonstrated that the oxidation atmosphere has greatly affected the MTJ device and the radically oxidized MgO MTJs could possess the better uniformity. In the following work, the influence of the oxidation atmosphere on the MgO texture and device performance will be discussed in detail and the uniformity still continued to be improved.

[1] S. S. P. Parkin, Nat. Mater., vol. 3, p. 862, 2004.

[2] S. C. Oh, IEEE TRANS. ON MAG., vol. 42, p. 2642, 2006

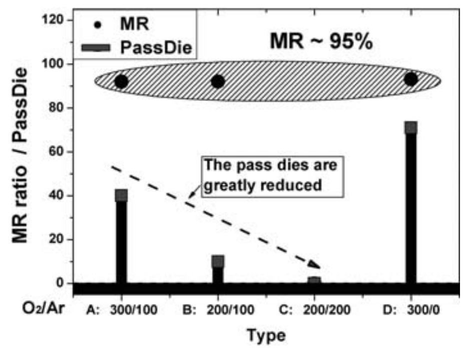

Figure 1 The MR ratios and PassDies of the radically oxidized MgO layer under different oxidation atmosphere

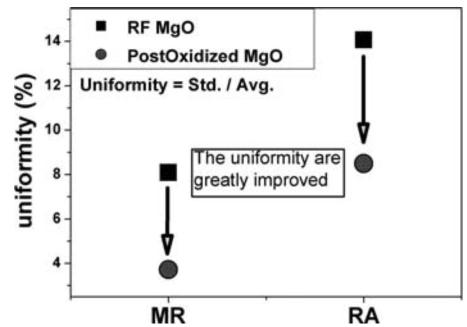

Figure 2 The MR and RA uniformity of the MgO MTJs prepared by the RF sputtered MgO and radically oxidized MgO

HR-10

Effect of Thermal Treatment on Chemical States of CoFeB/MgO/CoFeB Tunnel Junctions.

Y. Han[1], S. Lee[1], J. Hong[1], M. Jung[2], H. Shin[2]
1. Materials Science and Engineering, Yonsei University, Seoul, South Korea; 2. Pohang Accelerator Laboratory, POSTECH, Pohang, South Korea

INTRODUCTION

Magnetic tunnel junctions (MTJs) composed of a crystalline MgO barrier and amorphous CoFeB layers have attracted much attention due to their high TMR values more than 200% at room temperature [1]. Most recently, the pseudo-spin-valve MTJs with rf-sputter-deposited MgO showed that the TMR could reach 500% at room temperature [2]. Magnetic layers of CoFe with B contents over 20 at% followed by high temperature annealing have been required to achieve such high TMR values since they help develop the (001) texture and crystallize the MgO barrier. In our presentation, we discuss changes in the chemical states with different annealing temperatures in the CoFeB free layer and the MgO barrier, and at the interface between CoFeB/MgO/CoFeB.

EXPERIMENTS

We have prepared $Co_{40}Fe_{40}B_{20}$/MgO/$Co_{40}Fe_{40}B_{20}$ MTJs by a UHV sputtering system whose base pressure was lower than 2×10^{-9} Torr and annealed them in vacuum at 275 °C and 380 °C for 2 h each. The MgO was rf-sputter-deposited. We performed the photoemission spectroscopy depth profile on the U7 beamline at the Pohang Light Source, which provides a highly brilliant and monochromatic linear-polarized soft x-ray for high-resolution spectroscopy. We used Ne ions to minimize the ion sputtering damage during the depth profiling, and a beam energy of 635 eV for oxygen and 270 eV for boron and magnesium to improve surface sensitivity. We calibrated the binding energies using the valence-band maximum in valence spectra. The base pressure of the experimental chamber was less than 1×10^{-10} Torr.

RESULTS AND DISCUSSION

As expected, the TMR values of MTJs annealed at 380 °C were much higher than those annealed at 275 °C; 124% vs. 56%, more than double increase. However, changes in the chemical states were not as significant as those in the TMR values. The photoelectron spectra of B, O and Mg did not show great differences in chemical states with the annealing temperatures, except for the relative fraction of oxide phases existed in the CoFeB free (top) and MgO barrier layers, and at the interface between CoFeB (top)/MgO. We found not only the metallic B phase but also two distinguishable boron oxide phases, stoichiometric B_2O_3 and oxygen-deficient BO_x, in the CoFeB layer, which is also confirmed by others [3]. On the other hand, we could not see noticeable evidence of the formation of Co and Fe oxides, irrespective of the annealing temperature. We think that the oxygen sources for B oxides in the free layer were probably originated from our sintered CoFeB target. As we get closer to the interface of CoFeB/MgO, the oxygen-deficient BOx and the metallic B phase started to decrease and finally disappeared in the MgO barrier, as shown in Fig. 1. However, the stoichiometric B_2O_3 phase remained even inside the MgO barrier, confirming the diffusion of B into the MgO barrier during the deposition and the annealing. The relative fraction of B_2O_3 inside the MgO was found to be large when the MTJ was annealed at 380 °C, which indicates that the diffusion of B into MgO was significant at high temperature. In this presentation, we discuss how the chemical states were changed in the CoFeB free layer and the MgO barrier, and at the interface between CoFeB/MgO/CoFeB with different annealing temperatures based on the depth-profile results by high-resolution photoelectron spectroscopy with the synchrotron radiation.

[1] S. S. P. Parkin et al., Nat. Mater. 3, 862; S. Yuasa et al., Nat. Mater. 3, 868 (2004).

[2] Y. M. Lee et al., Appl. Phys. Lett. 90, 212507 (2007)

[3] J. Y. Bae et al., J. Appl. Phys. 99, 08T316 (2006); J. C. Read et al., Appl. Phys. Lett. 90, 132503 (2007); J. Schmalhorst et al., J. Appl. Phys. 102, 053907 (2007)

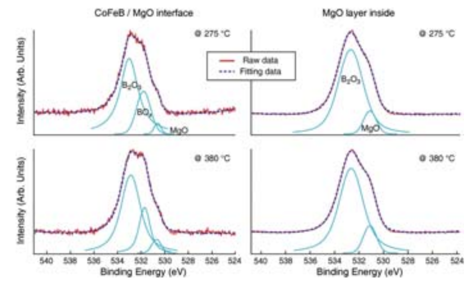

Fig. 1. O 1s photoelectron spectra at the interface between CoFeB/MgO and inside MgO for the two annealing temperatures.

HR-11

Ab intio calculations of the TMR in magnetic tunnel junctions (MTJ): application to Fe/MgO/Fe.

I. Arias, J. I. Cerdá, M. Muñoz
Intercaras y crecimiento, Instituto de Ciencia de Materiales de Madrid, Madrid, Spain

Magnetic Tunnel Junctions (MTJ) consisting of two ferromagnetic (FM) metal layers separated by a thin insulating layer exhibit a large change in the Tunneling Magneto Resistance (TMR) depending on the relative orientation of the magnetization at the FM layers[1]. The origin of the TMR lies in the dependence of the tunneling probability across the MTJ on the spin state. It is now well established that TMR is determined by the electronic structure of the entire junction, and not only by the properties of the FM. Thus, a realistic and reliable description of the TMR must consider the character, symmetry and spin polarization of the electronic states at the FM, but also any interfacial localized states or any evanescent waves inside the insulator which may be expected due to the chemical bonding at the FM/insulator interface. The Fe(001)/MgO(001)/Fe(001) MTJ can be considered as a model system for TMR studies
since it can be fabricated fully epitaxially providing large TMR ratios[2].
The theoretical study of TMR across MTJ is, however, problematic.
Most of current DFT based codes are restricted to the so called "supercell" approach, whereby a 3D periodicity is always assumed for the system to be studied. Low dimensional structures (e.g. clusters or surfaces) are also treated within this framework by simply inserting large vacuum regions along the non-periodic directions. However, the supercell approach is not well suited for electron transport calculations, since semi-infinite leads are required in order to emit or receive electrons into or from the junction. The presence of the leads breaks any periodicity along the transport direction and hence, the "supercell" approach cannot be employed anymore.
To overcome this shortcoming, we have implemented an interface between the DFT-LCAO based SIESTA package[3] and the GREEN code[4], the latter being designed to solve the Green's functions of non-periodic systems such as the MTJ. As depicted in the figure, we first perform two indepedent SIESTA calculations, one for the bulk part of the leads and another one for the MTJ interface, which is defined as a 2D slab comprising the oxide layer sandwiched by several metallic planes (see figure). Full atomic optimizations may be performed at this stage in order to account for any relaxations at the metal-oxide interface. However, in the relaxation process the metal atoms far from the interface are fixed to the bulk positions -this is essential to ensure that selfconsistency is preserved in the matching process described below. From the DFT calculations we extract and save the Hamiltonian matrix elements for both the leads and the MTJ. Our next step consists on constructing the Hamiltonian for an infinite MTJ by attaching the bulk leads to the MTJ interface. To this end we split the system into principal layers (PLs), each PL containing several atomic planes so that only nearest neighbor interactions are taken into account. The Hamiltonian hence becomes block tridigonal and infinite. We may use the Hamiltonian matrix elements obtained from the slab calculation (H_slab) for all the interactions involving the MTJ interface (PL number 0 in the figure), while those obtained from the bulk DFT calculation (H_bulk) may be used for the rest of blocks in the infinite Hamiltonian matrix. The Green's function of such a system is solved exactly via matching techniques[4] and the spin resolved elastic conductance across the junction can then be easily obtained after integration over the 2D Brillouin Zone[4].

We have applied the current approach to the calculation of the TMR across the ideal (epitaxial) Fe/MgO/Fe junction systematically varying the oxide thickness. Although our results are somewhat similar to previous theoretical works on the same system, we also find important issues which differ qualitatively (e.g. the role of atomic relaxations at the interface) and that may provide new insights into the magnetotransport across metal-tunnel junctions.

References:

[1] J.S. Moodera, L.R. Kinder, T.M. Wong and R. Meservey, Phys. Rev. Lett. 74 3273 (1995).

[2] R. Matsumoto, A. Fukushima, T.Nagahama, Y. Suzuki, K. Ando and S. Yuasa, Appl. Phys. Lett. 90, 252506 (2007)

[3] J.M. Soler, E. Artacho, J. Gale, A. García, J. Junquera, P. Ordejón and

D. Sánchez-Portal, J. Phys. Condens. Matter. 14 2745 (2002).

[4] J. Cerdá, M.A. Van Hove, P. Sautet and M. Salmeron,

Physical Review B 56 15885 (1997); see also www.icmm.csic.es/jcerda

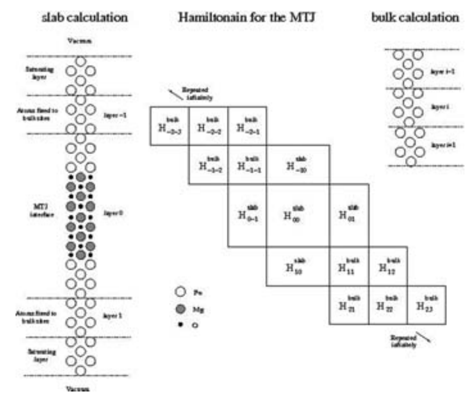

HR-12

Substrate biasing effect on the MgO (001) growth in CoFeB/MgO/CoFeB TMR junctions.

G. Choi, W. Lim, T. Lee
Department of Materials Science and Engineering, KAIST, Daejeon, South Korea

After the theoretical prediction of coherent tunneling in Fe/MgO/Fe MTJ[1,2], high TMR ratio were reported by two groups[3,4]. More recently similar results were reported in CoFeB/MgO/CoFeB MTJ after annealing, which is easier to fabricate. However, good (001) oriented MgO layer on CoFeB layer in thin thickness is not so easy task and reports on high TMR and low RA are limited by several groups. In this work we have studied effect of substrate bias voltage during MgO layer deposition on TMR ratio and RA of CoFeB/MgO/CoFeB MTJ as a function of target-substrate (T-S) distance.

A homemade multi-target UHV sputtering system with back ground pressure of better than 5×10^{-9}Torr was used for the deposition. Si/Ta/NiFe/IrMn/CoFe/Ru/CoFeB/MgO/CoFeB/Ta stacks were deposited and fabricated to $10\times10\mu m^2$ cells by a photolithography and ion beam etching. The patterns were annealed at 400°C in vacuum of 3×10^{-6}Torr with an applied field of 1000 Oe. MgO layer was kept at a constant thickness of 2nm in all experiments. During MgO layer deposition substrate bias was applied.

As sputter power increased from 60W to 200W at 10mTorr with T-S distance of 5cm, TMR was a nearly constant of 250% but RA increased. This suggests some parts of the bottom electrode may be oxidized by O ions or radicals. When the T-S distance was varied from 5 to 10cm. TMR rapidly decreased and RA increased more drastically as shown in Fig. 1. The reason of this behavior can be explained by formation of weaker (001) texture of MgO layer as the T-S distance increases as shown in Fig. 2. Deterioration of the MgO (001) growth must be associated with lower ad-atoms' mobility on the substrate surface as the T-S distance increases. If mobility of ad-atoms is high enough MgO will grow to (001) orientation as (001) surface has the lowest surface energy. It is concluded that in order to get high TMR and low RA high mobility of ad-atoms and reduction of oxidation of the bottom electrode by reducing flux of O ion and radical are needed. As population of ion species decreases faster than that of neutral atom species as T-S distance increases, we increased T-S distance while applying substrate bias voltage to increase ad-atom mobility via Ar ion bombardments. The results are appeared in Fig. 3. In both cases, as bias voltage increases, TMR increases and RA decreases. However, it should be mentioned that when negative bias voltage exceeds -50eV for 20mTorr, TMR was not detected due to strong etching effect on growing MgO surface. High RA must be associated with two major factors; misoriented MgO (001) growth by which broken lattice matching between CoFeB and MgO during post-annealing for coherent tunneling and partial surface oxidation of bottom electrode. In the case of the specimens of TMR beyond 200 or 250% range, the major reason of high RA must be associated with partial surface oxidation of bottom electrode. In this paper, role of H_2O during sputtering process was not studied as we have used a constant back ground pressure condition. The TMR ratio achieved was 352% at RT but RA was $100k\Omega\mu m^2$ range. The RA is much higher value than the previously reported one [5,6].

Applying substrate bias voltage during MgO layer deposition is effective for increasing TMR and lowering RA especially when T-S distance increases. This is due to increased ad-atom mobility by Ar ion bombardment via substrate bias and reduced O ion population as T-S distance increases.

[1] W. H. Butler, X. –G. Zhang, T. C. Schultheiss and J. M. Maclaren, Phys. Rev. B, 63, 054416(2001)

[2] J. Mathon and A. Umerski, Phys. Rev. B, 63, 220403(R)(2001)

[3] S. Yuasa, T. Nagahama, A. Fukushima, Y. Suzuki, and K. Ando, Nature materials, 3, 868(2004)

[4] S. S. P. Parkin, C Kaiser, A. Panchula, P. M. Rice, B. Hughes, M. Samant, and S. H. Yang, Nature materials, 3, 862(2004)

[5] K. Tsunekawa, D. D. Djayaprawira, M. Nagai, H. Maehara, S. Yamagata, N. Watanabe, S. Yuasa, Y. Suzuki, K. Ando, Appl. Phys. Lett., 87, 072503(2005)

[6] J. Hayakawa, S. Ikeda, F. Matsukura, H. Takahashi, and H. Ohno, Jap. J. Appl. Phys., 44, L587(2005)

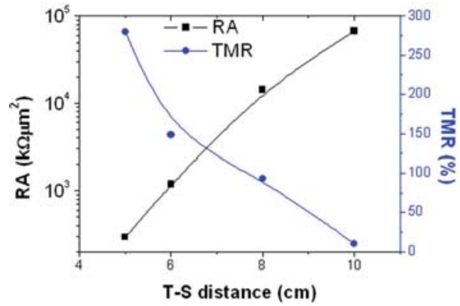

Fig. 1. RA and TMR as a function of T-S distance at pressure 10mTorr and power 100W.

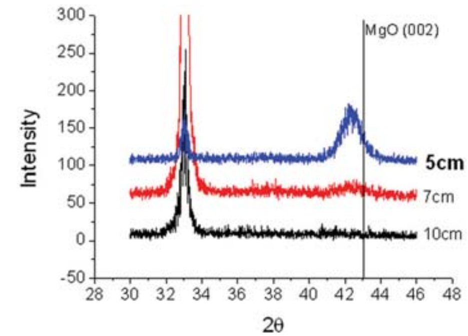

Fig. 2. XRD patterns of SiO_2/Ta(5nm)/ CoFeB(5nm)/MgO(10nm).

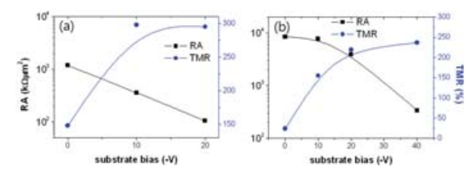

Fig. 3. RA and TMR as a function of substrate bias. (a); T-S distance 6cm, 10mTorr, 100W (b); T-S distance 8cm, 20mTorr, 100W

The bias voltage dependence of inverted magnetoresistance on the annealing temperature in MgO-based magnetic tunnel junctions.

J. Feng, G. Feng, J. Coey
CRANN and school of physics, Trinity College, Dublin, Ireland

MgO-based magnetic tunnel junctions (MTJs) with a main layer sequence Ir22Mn78 (or Fe50Mn50, 10 nm) /Co90Fe10 (2 nm) /Ru (0.85 nm) /CoFeB (0 < t < 3 nm) /MgO (2.5 nm) /CoFeB (3 nm) have been fabricated. The inverted tunneling magnetoresistance (TMR) as high as -55% has been observed at zero bias for these MTJs at t = 1.5 nm. More details can be found in Ref. 1. TMR is defined as (RAP-RP)/RL, RP and RAP are the resistances of MTJs when the magnetizations of the ferromagnetic electrodes in contact with tunnel barrier are parallel and antiparallel, and RL is the lower one. Here we give a detailed description about the bias voltage dependence of the TMR as a function of the annealing temperature (Ta) in these MTJs with a thin CoFeB layer in the pinned synthetic antiferromagnetic CoFe/Ru/CoFeB stack.

Experimental results show that a possible discontinuous CoFeB film may form on Ru when the pinned CoFeB layer in the synthetic antiferromagnetic stack is thin (t < 1.5 nm), and the TMR ratio changes its sign from inverted to normal at a critical bias voltage (VC) without any annealing process. VC is the bias voltage at which TMR = 0, as shown in Fig.1. Figure 1 (a) shows the bias voltage dependence of the TMR ratio for one FeMn- MTJ with t = 0.75 nm, the sign change of the as-grown TMR happens at VC = -0.28 V. The inverted and normal TMR curves at VC = +0.2 and -0.4 V are shown in Figure 1 (b) and (c), respectively. However, no VC can give at as-grown state and Ta = 150 oC for the MTJs with t = 0.5 nm due to no appearance of the obvious TMR. At Ta > 150 oC, the magnetotransport behavior happens, which may be due to certain Ru diffusion in the annealing process.1 It is easy to find that the annealing effect has a key influence for these MgO-based MTJs.

The VC at different CoFeB thicknesses increases largely by increasing the Ta and starts to decrease at a certain Ta (see Fig. 2), which has a similar change compared to that of TMR versus Ta.1 The VC at higher Ta was not attained for the MTJs with t ≥ 0.75 nm because the lager bias voltage was needed to apply and the MTJs were easy to be destroyed. These VC values in Figure 2 are much changed for different CoFeB thicknesses and Tas, which suggests that a strong density-of-states modification at bottom oxide/ferromagnet interface appears.2, 3

Reference

1J. F. Feng, G. Feng, J. M. D. Coey, X. F. Han, and W. S. Zhan, Appl. Phys. Lett. 91, (2007) 102505

2 P. LeClair, B. Hoex, H. Wieldraaijer, J. T. Kohlhepp, H. J. M. Swagten, and W. J. M. de Jonge, Phys. Rev. B 64, (2001) 100406

3C. Tiusan, M. Sicot, M. Hehn, C. Belouard, S. Andrieu, F. Montaigne, and A. Schuhl, Appl. Phys. Lett. 88, (2006) 062512

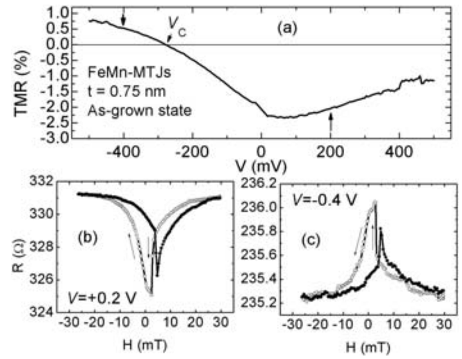

Figure 1 (a) The bias voltage dependence of the TMR ratio in MgO-based FeMn-MTJs with t = 0.75 nm at 300 K. (b) and (c) the inverted and normal TMR curves at V = +0.2 and –0.4 V; the arrow marks in (a) are the detailed bias positions for (b) and (c).

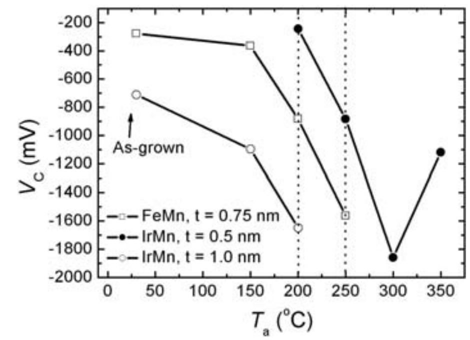

Figure 2 The critical bias voltage as a function of annealing temperature under different pinned CoFeB thicknesses in MgO-based FeMn- & IrMn- MTJs, taken at 300 K.

Detection of an infra red magnetorefractive effect from a layered Fe/MgO/Fe magnetic tunnel junction.

R. T. Mennicke[1], R. Berryman[1], F. Ernult[2], H. Wang[2], Y. Nogi[2], J. A. Matthew[1], *S. M. Thompson*[1], S. Mitani[2], K. Takanashi[2]
1. Physics, University of York, York, United Kingdom; 2. Institute for Materials Research, Tohoku University, Sendai, Japan

In the far infra red (IR), the dielectric response of a metal is directly related to its d.c. electrical conductivity with the result that the refractive index is a function of the electrical resistivity. This is exploited in remote techniques for measuring giant magnetoresistance (GMR) by sensing a change in reflection, transmission or emission in an applied magnetic field [1,2]. In spectral magnetorefractive effect (MRE) measurements, the percentage change in reflected intensity in an applied magnetic field is measured as a function of wavelength. The effective medium approach normally used to model metals breaks down when studying magnetic tunnel junctions (MTJ) due to the presence of the insulating tunnel barrier through which IR transmission is high. Previous work has concentrated on thick film granular tunnelling materials such as Co-Al_2O_3 which contain large volume fractions of insulator, the dielectric properties of which are modified by the magnetic inclusions [3]. Spin dependent effects have been seen in thick granular films in which multiple reflections occur, enhancing the changes which occur in a magnetic field [4,5]. We report the detection of a significant MRE in a patterned tunnel junction, enhanced by the presence of an absorption edge associated with MgO.

The sample (Fig. 1) was prepared by molecular beam epitaxy on an MgO substrate and patterned into 3mm arrays of square pillars of dimensions: 50µm and 5µm. The structure of the MTJ is: MgO(100)/$Mg0_{20nm}$/Fe_{20nm}/$MgO_{1.5nm}$/Fe_{5nm}/Co_{3nm}/Au_{3nm}. The MRE spectra from 2-20µm were measured with randomly polarised IR radiation using a Fourier Transform Infra red Spectrometer in applied fields up to 1.25T, shown in Figs. 2 and 3 for the 5µm pillars. As the film is thin compared to the skin depth of the IR radiation, the raw IR spectrum is dominated by the spectral response of the MgO substrate which contains the longitudinal optic (LO) and transverse optic (TO) phonon modes at 24µm and 13.5µm respectively. This results in a sharp increase in reflectivity as the wavelength is increased at approximately 12.5µm. In 1.25T, the size of the MRE is approximately 0.2% at long wavelengths with a prominent step of magnitude 0.6% at the absorption edge. The MRE scales with the applied field, and has not yet saturated at 1.25T. Control experiments carried out on MgO substrates and the sample holder confirm that the MRE originates from the sample. Fig. 2. is an average of 10 very similar spectra demonstrating the repeatability of the measurement. No significant differences were observed between the 5µm and the 50µm pillars. The origins of the spin-dependent effect are not yet clear; they may result from bulk spin dependent scattering within the magnetic layers, or the more direct effect of spin dependent tunnelling on the dielectric response. The results demonstrate the effectiveness of using a resonant feature in the underlying reflectivity spectrum to enhance an otherwise small MRE, opening the way to using the technique to study a wider range of materials or using the step edge as a magnetic switch.

[1] M. Vopsaroiu et. al. Phys. Rev. B. 70(21): art. no. 214423 (2004)

[2] R.T. Mennicke et. al. J. Magn. Magn. Mater. 303(1) 92 (2005)

[3] H. Kaiju et. al. J. Appl. Phys. 91(10) 7430 (2002)

[4] I. Bykov et. al. Physics of the Solid State 42(3) 498 (2000)

[5] A.S. Granovsky and M. Inoue J. Magn. Magn. Mater. 272-276(1) E1601 (2004)

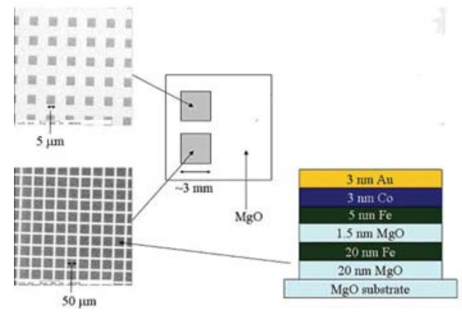

Scanning electron microscope images and schematic diagram showing the structure of the magnetic tunnel junction: MgO(100)/$Mg0_{20nm}$/Fe_{20nm}/$MgO_{1.5nm}$/Fe_{5nm}/Co_{3nm}/Au_{3nm} patterned into 3cm arrays of 5µm and 50µm square pillars.

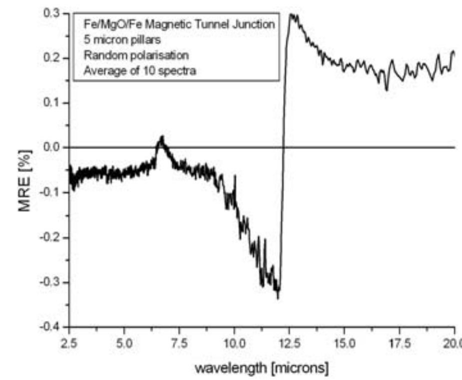

Average of 10 repeats of the MRE spectrum measured at 1.25T from the 5µm pillar region. The sharp feature at 12.5µm occurs at the position of the LO phonon mode of the MgO substrate.

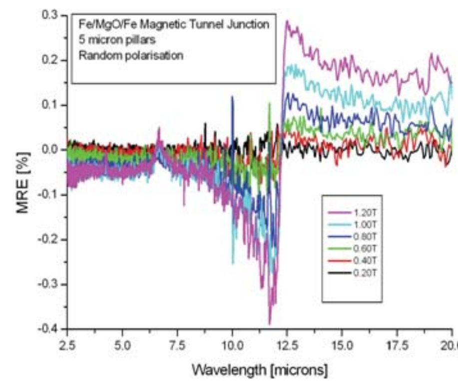

Average MRE spectra measured from the 5µm pillar region of the sample for applied magnetic fields from 0.2 to 1.2T

HR-15

Low Frequency Noise in MgO Magnetic Tunnel Junctions: Hooge's Parameter Dependence on Bias Current Density.

J. M. Almeida[1,2], P. P. Freitas[1,2]
1. INESC - MN, Lisbon, Portugal; 2. Physics, IST, Lisbon, Portugal

Single (SB) and double barrier (DB) magnetic tunnel junctions (MTJs) were deposited with the stacks presented in Figure 1a and 1b. These samples were processed with areas of 200 μm^2 (elliptical junction shape), presented RA products ranging from 20 to 60 kΩ.μm^2 and TMR values up to 110% (Figure 1c).

At low frequencies and for samples showing no Random Telegraph Noise (RTN), 1/f noise dominates: $S_V^{1/f}(V^2/Hz) = \alpha . V_b^2/(A.f)$

where α is the Hooge parameter, A stands for the junction area, S_V the noise power spectrum and V_b the junction bias voltage. Non-magnetic α values depend on barrier properties (RA product), and MTJs low or high resistance states). This work demonstrates that the Hooge parameter, measured on magnetically saturated MTJs, also shows a dependence on the current density flowing through the junctions for both single and double barrier MTJs.

Noise measurements were made for both types of MTJs. Permanent magnets were used to saturate the junction's free layer with an applied field of ± 250 Oe during measurement. Figure 2 shows a set of noise measurements made for a DB MTJ vs. bias current. The Hooge parameters obtained from these curves are plotted in Figure 3. "α" varies from ≈ 9E-9 μm^2 near zero bias to ≈ 1E-9 μm^2 at j = 1.5×10^3 A/cm^2. Similar measurements on SB MTJs show a weaker but still significant decrease of α with bias current (from ≈ 1E-9 μm^2 to ≈ 3E-10 μm^2 in the HR state). The reproducibility of this bias current dependence was verified measuring for both increasing and decreasing current densities.

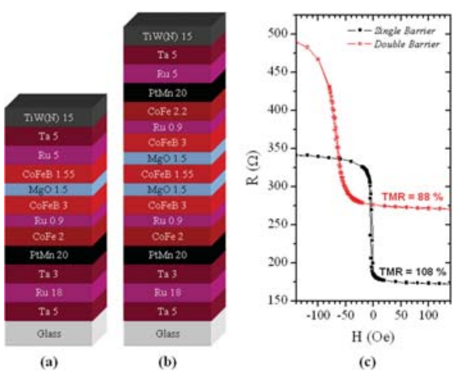

Figure 1 - a) SB stack (thicknesses in nm); b) DB stack; c) Transfer curves for both SB and DB sensors

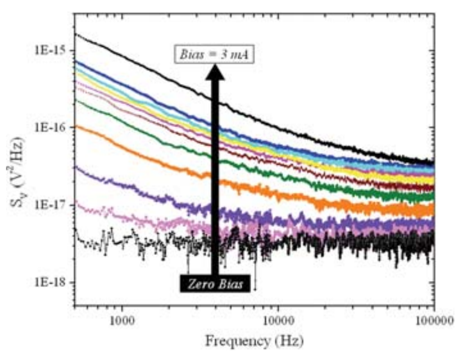

Figure 2 – Noise measurements made in a DB MTJ in the high resistance state for varying bias current

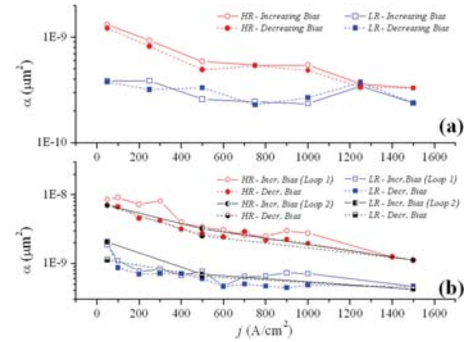

Figure 3 – Hooge parameter obtained for 200 μm^2 junctions in the HR and LR state for: a) SB sensor; and b) DB sensor

HR-16

Magnetization reversal processes of nanostructured magnetic tunnel junction rings.

C. Chen[1], C. Chao[1], C. Kuo[1], J. Ou[1], L. Horng[1], J. Wu[1], T. Wu[2], J. Yang[3], S. Isogami[4], M. Tsunoda[4], M. Takahashi[4]
1. Taiwan SPIN Research Center,National Changhua University of Education, Changhua, Taiwan; 2. Taiwan SPIN Research Center, National Yunlin University of Science & Technology, Yunlin, Taiwan; 3. Institute of Optoelectronic Sciences, National Taiwan Ocean University, Keelung, Taiwan; 4. Graduate school of Electronic Engineering, Tohoku University, Sendai, Japan

Introduction:
Over the last decade, the magnetic tunnel junction (MTJ) devices have been extensively studied due to great potential for spintronic devices. For the aspect of memory application, a good unit cell must possess low field leakage and reversible switching process to enhance storage density and operating mode, respectively. As a result, ring-shaped element was firstly proposed to be the best candidate for magnetic random access memory (MRAM) cell due to its unique shape [1]. The advantage of using the ring-shaped cell is the lack of the energetic core in the center of circular element, giving rise to a simple and reproducible switching behavior [2-3]. In addition, a recent publication has shown nanostructured MTJ rings with current-induced magnetization switching method and thus the storage density is expected to be dramatically increased [4]. However, the mechanism for having many different intermediate states taken place in the free layer switching process in the previous publications is still unclear. Herein, we present a study of a series of nanostructured MTJ rings to investigate the magnetization reversal processes. The concerns are focused on the size dependent free layer switching process and coupling effects.
Experiments:
Stack films consisting of Si/SiO2 50-substrate/ Ta 5/ Ru 40/ Ta 5/ (Co50Fe50)78B22 4/ Mg 0.4/ MgO1.8/ (Co50Fe50)78B22 4/ Ru 0.85/ Co70Fe30 3/ MnIr 7.5/ Ta 5/ Ru 7 -cap (thickness in nm) were first prepared by magnetron sputtering system. Various MTJ rings with outer diameter/linewidth of 0.7µm/100nm and 1µm/100 nm were fabricated using a top-down technique. Firstly, a hard mask of Cr was created by standard electron beam lithography through a lift-off process. Subsequently, a two-step ion-milling was utilized to transfer the ring pattern into the MTJ stack films. A 40 nm SiO2 insulating layer was then sputtered on the whole devices area, followed by an etch-back technique for making the top electrodes. The magnetization reversal processes was investigated using four-terminal magnetoresistance measurements with the external field applied in the film plane.
Results and discussion:
Figure 1 (a) shows the R-H major loop of a MTJ ring with outer diameter/linewidth of 0.7µm/100nm. A significant reduction of biasing field, from 1600 Oe extracted from the AGM data of the sheet film down to 250 Oe measured from the ring device, indicates a strong anisotropy effect in this small ring. Figure 1 (b) presents the minor loop of the abovementioned MTJ ring, in which the magnetoresistance ratio (MR) is about 50 % and the resistant-area product (RA) is about 6400 Ωµm2. Double transition process is examined with fixed magnetization configuration in pinned layer and field-switching process in free layer. A simpler magnetization reversal process in comparison with micronstructured MTJ rings [3] within free layer, i.e. onion to vortex to reversed onion state, was observed. Figure 2 represents the minor loop of the other MTJ ring with diameter/ linewidth of 1µm/ 100nm, in which the MR ratio is about 70 % and the RA is about 3100 Ωµm2. In contrast to the smaller outer diameter MTJ ring, the same transition process is also revealed. The antiparallel coupling, showing the shift of minor loop, are both observed in these patterned MTJ rings, implies that the dipolar coupling of the pinning system of synthetic antiferreomagnet structure is strikingly reduced. Moreover, different transition fields, i.e. Hc1 of onion to vortex and Hc2 of vortex to reversed onion, are also perceived. Notice that the Hc1/Hc2 of 70/120 Oe and 30/125 Oe are observed in diameter/ linewidth of 0.7µm/ 100nm and 1 / 100 nm MTJ rings, respectively. Details of the fabrication and characterization will be discussed.

[1] J. G. Zhu et al., J. Appl. Phys., 87, 6668 (2000).

[2] C. C. Chen et al, IEEE Trans. On Magn., 42, 2766 (2000).

[3] C. C. Chen et al, JMMM, 310, 1900 (2007)

[4] Z. C. Wen et al, APL, 91, 122511 (2007)

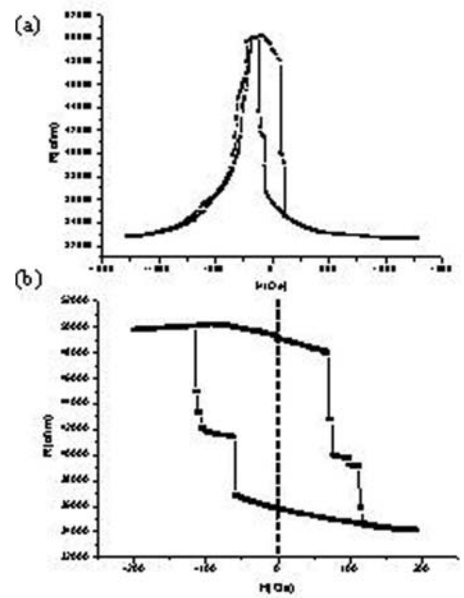

Fig. 1 (a) R-H major loop and (b) minor loop of a ring-shaped MTJ device with outer diameter/ linewidth of 0.7µm/ 100nm. The MR minor loop, with 50% MR ratio and RA~6400 ohm×µm2, reveals a double-transition reversal process.

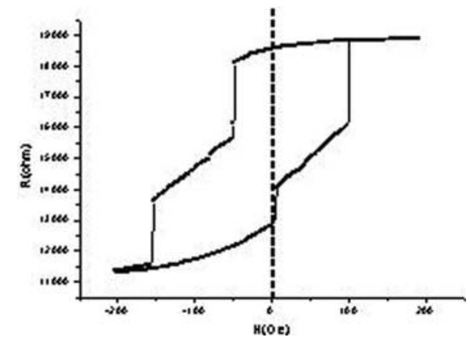

Fig. 2 The MR minor loop of a MTJ ring with outer diameter/ linewidth of 1µm/ 100nm, with 70% MR ratio and RA~3100 ohm×µm2, reveals a double-transition reversal process.

HS-01

First-principles calculations of structural and magnetic properties of Fe/MgO/Fe with interfacial Mg vacancy.

C. Kim, G. Yoon, Y. Chung
Materials Science and Engineering, Hanyang University, Seoul, South Korea

Magnetic tunnel junctions (MTJs) utilizing tunneling magnetoresistance have been strong candidates for the application of spintronic devices. Because the thickness of each thin film is in a few nanometer scale, understanding the influence of the imperfections upon a magnetic properties is becoming increasingly important. We demonstrated theoretically that the electronic structures in Fe(001)/MgO(001)/Fe(001) MTJ are strongly affected by the interfacial Mg vacancy. Using Vienna ab-initio simulation package code, density functional theory calculation was performed. The projector augmented wave-generalized gradient approximation method was employed.
Calculation yielded 1.74 Å of Fe-O distance.(Fig. 1) The Mg-interface atoms positioned 0.19 Å lower than the O atoms while the Fe-interface atoms kept their position. This reconstruction led the consequent fluctuation of the second MgO layer, so that the half of O atoms displaced upwardly whereas another half displaced downward. There were no lateral displacements in the plane parallel to the (001) for both layers regardless of lateral lattice mismatch of 5.5% between the electrode and barrier layers. The layer density of states (DOS) profile for Mg and O atoms in barrier layer showed very large unexpected band in the energy range between the conventional valence band and conduction band.(Fig. 2) Specifically, band gap for interfacial atoms of MgO layer was nearly vanished because of the noise states induced by the hybridization. Most of DOS peaks for Mg- and O-interface atoms consist of s and p. However, there also exist considerable d_{x2-r2} and d_{x2-y2} orbital states. Although the noise of DOS was negligible at Fermi energy of MgO-center, strong enhancement of spin polarization at the energy range from -0.25 eV to -0.1 eV was found. Because of non-symmetric occupancy between spin-up and spin-down states the magnetic moment became 0.20 μ_B.
The absolute amount of both majority and minority DOS was approximately zero as shown in Fig. 3. However, it was clearly seen that the distribution of spin polarization values of MgO was spread in almost same range of the polarization of Fe layers. It can be reasonably inferred that the induced DOS and unexpected polarization for atoms in the barrier layer resulted from the hybridization of 2p states of Mg and O ions with 3d band of Fe atoms, which involved in the junction formation. Furthermore the third and fourth slabs of Fe layer exhibit the negative polarization. Consequently, relatively small magnetic moment for those two atomic slabs was predicted.(Fig. 3)
The energy gap between the valence and conduction bands yielded 7.5 eV commonly to both spin channels.(Fig. 4) At approximately -2.5 eV, single impurity state was induced for majority channel, and additional sub band at -3.0 eV was found for minority channel. Contrary to existence of 1.3 eV of energy mismatch between both spin channels of the Mg-interface atom, the bands of Mg-center atom positioned at same energy level. The small gap opened in majority channel of interfacial O atom, but the unexpected noise exists, which remained in O-center layer as well. Among the noise states there were only negligible d states whereas the other band region contains significant d_{yz} and d<sib>xz states for valence, and d^{xy}, d^{yz}, and d^{x2-r2} for conduction band. It was obvious that the electronic structure of Fe layer propagated into the barrier layer, and the influence on the O atoms was much stronger than the Mg atoms.

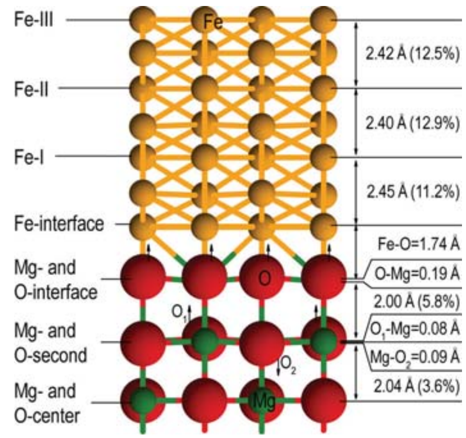

Fig. 1. Optimized structure of Fe/MgO/Fe with interfacial Mg vacancy.

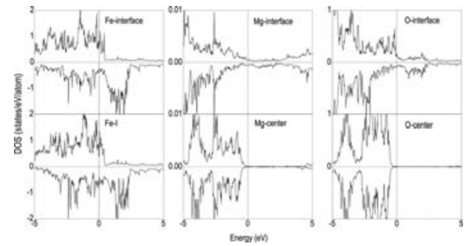

Fig. 2. LDOS for Fe/MgO/Fe with interfacial Mg vacancy.

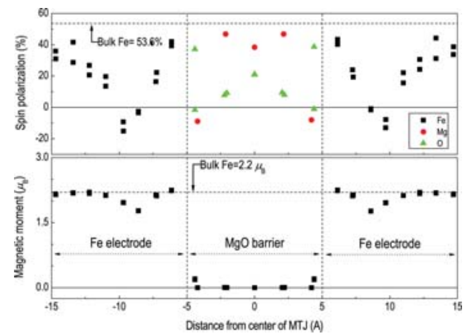

Fig. 3. Spin polarization and magnetic moment for Fe/MgO/Fe with interfacial Mg vacancy.

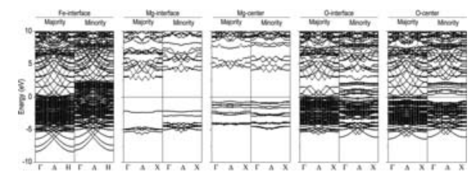

Fig. 4. Band structure for Fe Mg, and O atoms in the MTJ with interfacial Mg vacancy.

HS-02

Ab-initio spin-dependent electronic transport calculations of MTJ with low band-gap insulating oxides with rock salt structure.

A. Furuya[1], A. Fujisaki[1], H. Kanai[2], K. Noma[2], K. Kobayashi[2], Y. Uehara[2]
1. Simulation Technology Development Division, FUJITSU Advanced Technologies Ltd, Kawasaki, Japan; 2. Head Division, Storage Products Group, Fujitsu Ltd, Nagano, Japan

The tunneling magneto resistive (TMR) head [1,2] is widely used as HDD read sensor. Although several barrier materials were studied for its application, MgO-TMR leads to great success to achieve large MR ratio over 200% [3-7]. On the other hand, in terms of sensor resistive, the MR head whose resistance-area product (RA) is around 0.1Ohm micron2, is needed for 1 Tbit/in2 recording [8]. Thin barrier layer under 1nm in thickness has low-RA under 1 Ohm micron2 [8], however, it is difficult to sustain high-MR ratio and high-breakdown voltage. Therefore, insulators of high MR ratio and low barrier height are needed for next breakthrough beyond MgO-TMR. In this study, we report ab-initio electronic transport calculations for new magnetic tunneling junction (MTJ) structures with low band-gap insulator.
We performed transmission calculations based on NEGF method [8] formulated by linear combination of pseudo atomic orbitals(LCAO) [9]. All results are calculated by OpenMX which is electronic structure calculation code based on DFT [10]. As insulating materials for a barrier layer sandwiched between ferromagnetic layers, we examined MgO, ZnO and CaO, which are insulating oxides with rock salt structure. These materials are suitable to replace the MgO layer and to make a good interface with (001) aligned bcc Fe layer.

Table 1 shows calculated electronic transport properties of MTJ in the cases of six atomic layers of MgO, ZnO and CaO sandwiched between bcc Fe ferromagnetic layers. The MTJ with the MgO layer has the large MR ratio over 1000% [3,4], because the MgO layer can transmit mainly delta 1 electrons which construct the eigen-state of majority spin near the Fermi level. On the other hand, MTJs with ZnO and CaO layer have low RA and low MR ratio. This reason is investigated by transmission and spectral function [8]. Fig. 1 shows the transmission in k-space of MTJ with ZnO layer (a) and CaO layer (b). In the case of ZnO, the delta 1 electron near gamma point in k-space tunnels through the insulator layer similar to MgO's result, however, this result indicates that MTJ has lower RA than that of MgO, because ZnO has delta 1 eigen-state as LUMO state with low excitation energy. On the other hand, MTJ with CaO layer has different transmission whose peak are located near k=(0.5,0.5). Because CaO has delta 5 eigen-state as LUMO at k=(0.5,0.5), MTJ with CaO can transmit only delta 5 electrons. These results show that ZnO has same symmetry filtering effect similar to MgO, and ZnO is a candidate to be compounded or formed multi-layer with MgO for low RA and high MR ratio. Next, we examined the MTJ with ideal tri-layer structure MgO(1L)/ZnO(4L)/MgO(1L). Fig. 2 shows transmission of majority spin at parallel configuration and spectral function at anti-parallel configuration which is compared with that of ZnO mono-layer. In ZnO mono-layer case, interfacial resonant state is observed and decreases the MR ratio. The tri-layer suppresses this resonant state by inserting MgO at the interface, has a large MR ratio, calculated value is 1300%.

[1] T. Miyazaki and N. Tezuka: J. Magn. Magn. Mater. 139, 231 (1995).

[2] J. S. Moodera, L. R. Kinder, T. M. Wong and R. Meservey : Phys. Rev. Lett. 74, 3273 (1995).

[3] W. H. Butler, X.-G. Zhang, T. C. Schulthess and J. M. MacLaren : Phys. Rev. B, 63, 054416(2001)

[4] J. Mathon, and A. Umerski : Phys. Rev. B 63, 220403R (2001).

[5] S. Yuasa, T. Nagahama, A. Fukushima, Y. Suzuki, and K. Ando : Nat. Mater. 3, 868 (2004)

[6] S. P. Parkin, C. Kaiser, A. Panchula, P. M. Rice, B. Hughes, M. Samant and S.-H. Yang, : Nat. Mater. 3, 862(2004)

[7] D. Djayaprawira, K. Tsunekawa, et al : Appl. Phys. Lett. 86, 092502 (2005)

[8] S. Datta : Electronic Transport in Mesoscopic Systems, Cambridge University Press(1995)

[9] These calculations are performed on NEGF implemented OpenMX coded by T. Ozaki, H. Kondo and H. Kino.

[10] T. Ozaki, Phys. Rev. B 67, 155108 (2003)

Insulator layer	Band gap (calc.)[eV]	RApc(Parallel)	RAapc(Anti-parallel)	MR ratio
Fe/MgO(6L)/Fe	4.2	4.5	93	2000%
Fe/ZnO(6L)/Fe	1.0	0.087	0.178	110%
Fe/CaO(6L)/Fe	3.5	0.36	1.04	200%

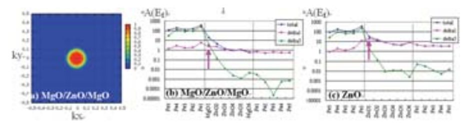

(a)transmission profile of majority spin in k-space at parallel configuration in the case of MgO/ZnO/MgO tri-layer Spectral function profiles at anti-parallel configuration in the case of tri-layer(b) and ZnO mon-layer(c).

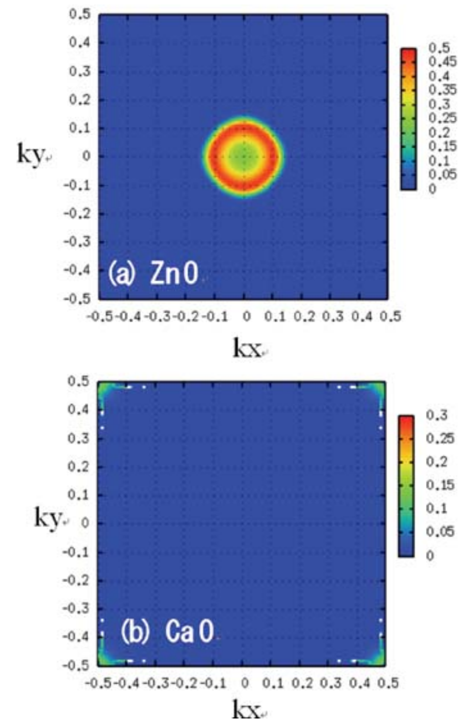

Transmission profile of majority spin in k-space at parallel configuration, (a)in the case of MTJ with ZnO layer, (b) in the case of MTJ with CaO layer

HS-03

Inhomogeneity and magnetism in diluted magnetic semiconductors.

B. Sanyal, R. Knut, O. Granas, D. M. Iusan, O. Karis, O. Eriksson
Department of Physics, Uppsala University, Uppsala, Sweden

In semiconductor spintronics [1], the spin of the electron is manipulated by the control of charge carriers. Two major tasks are involved in the realization of a successful diluted magnetic semiconductor (DMS) to be used in future spintronic devices: a well characterized sample without inhomogeneities and the occurrence of ferromagnetic order at room temperature and above. However, a wide variation of experimental results [2] showing strong or weak ferromagnetism or paramagnetism, exists for Co doped ZnO diluted magnetic semiconductor indicating the absence of homogeneity in the samples.Recently, it was shown from experiments [3] that the high temperature ferromagnetism in DMS materials without charge carriers can originate from the nanocrystals of magnetic ions. The increased density of magnetic ions in certain regions of the samples reflects inhomogeneities.
Here, we have studied the chemical and magnetic interactions in Co doped ZnO diluted magnetic semiconductor by {\it ab-initio} density functional calculations. We have performed electronic structure calculations using a Green's function Korringa-Kohn-Rostoker (KKR) method [4]. The chemical and magnetic disorder were simulated by the use of coherent potential approximation (CPA). The Heisenberg pair-exchange parameters were determined using the theory of Liechtenstein {\it et al.} [5]. The chemical pair interactions were calculated using the generalized perturbation method. To generate the atomic configurations, we performed Monte-Carlo simulations (MCS) on an Ising model Hamiltonian. To allow for different stages of growth, we terminated our simulations after different number of Monte-Carlo steps. The corresponding atomic configurations were used for the calculation of magnetization using the calculated magnetic exchange interaction parameters. These simulations were done by a single spin flip Metropolis algorithm. Curie temperatures were estimated from the magnetization vs. temperature plots.
The calculated first neighbor chemical interaction is very strong indicating a strong tendency of clustering between the Co atoms hence paving the way towards a phase separation commonly known as spinodal decomposition. Both chemical and magnetic pair interaction parameters are short-ranged with a large first neighbor interaction.
Magnetization is strongly dependent on the configurations of magnetic atoms. For 10 $\%$ of Co, at an early stage in the annealing process, the spins can interact with each other and a long-range ferromagnetic order is established. So, a well defined magnetization vs. temperature curve is obtained showing a finite T$_C$ (Fig.1). However, after 2000 MC steps, the Co clusters have become so large so as to effectively absorb all Co atoms in the simulation cell. We are left with a system with clusters of Co atoms which are separated far from each other, which has the consequence that they cannot interact with each other to establish a magnetic percolation path. As a result, we do not observe ferromagnetism in the system. Any magnetic response from such materials should rather be referred to as super paramagnetic.
The situation is different for 30 $\%$ Co. Here a consistent increase in T$_{C}$ with an increase in MCS step is clearly observed in Fig.1. For a homogeneous distribution of Co atoms in the beginning of the annealing process, the estimated T$_{C}$ is around 200K. At a very large number of MCS step 20000, one observes an extremely high T$_{C}$ indicating the formation of a metallic Co in a big spanning cluster throughout the system. As the Co atoms are close to each other in a spanning cluster, it is very easy to interact with each other with this strong ferromagnetic interaction. This phenomenon explains qualitatively the wide variation of results on the ordering temperatures obtained in experiments.

[1] {\it Semiconductor spintronics and quantum computation}, edited by D. D. Awschalom, D. Loss and N. Samarth, Springer, Berlin (2002).

[2] H-J Lee, S-Y. Jeong, C. R. Cho and C. H. Park, Appl. Phys. Lett. {\bf 81}, 4020 (2002); M. Venkatesan, C. B. Fitzgerald, J. G. Lunney and J. M. D. Coey, Phys. Rev. Lett. {\bf 93}, 177206 (2004); K. R. Kittilstved, N. S. Norberg and D. R. Gamelin, Phys. Rev. Lett. {\bf 94}, 147209 (2005).

[3] S. Kuroda, N. Nishizawa, K. Takita, M. Mitome, Y. Bando, K. Osuch and T. Dietl, Nat. Mat. {\bf 6}, 440 (2007).

[4] I. A. Abrikosov and H. L. Skriver, Phys. Rev. B {\bf 47}, 16532 (1993); A. V. Ruban and H. L. Skriver, Comput. Mater Sci. {\bf 15}, 119 (1999).

[5] A. I. Liechtenstein, M. I. Katsnelson, V. P. Antropov and V. A. Gubanov, J. Magn. Magn. Mater. {\bf 67}, 65 (1987).

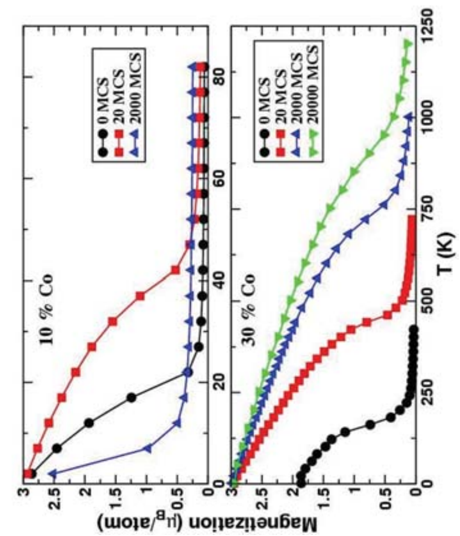

Magnetization versus temperature for 10 $\%$ (upper panel) and 30 $\%$ (lower panel) Co. Magnetization data for different Monte-Carlo simulation (MCS) steps are shown.

HS-04

Interface magnetism in Fe_2O_3-$FeTiO_3$ heterostructures.

S. Sadat Nabi, R. Pentcheva
department of earth and environmental sciences, section crystallography, Ludwig Maximilain University of Munich, Munich, Germany

Charge mismatch at complex oxide interfaces can give rise to properties and functionality distinct from the bulk [1,2,3,4]. The unique magnetic behavior of the hematite-ilmenite system [5] has received revived interest as a possible cause for magnetic anomalies in the Earth's crust and on other planets [6]. In addition, Ti doped hematite is a potential material in the search of a room temperature(RT) ferromagnetic semiconductor for spintronic devices [3,7,8]. To explain the strong and stable remanent magnetization in nanoscale exsolutions of the canted antiferromagnet (AFM) hematite and the RT paramagnet ilmenite, Robinson et al.[9] proposed a mixed Fe^{2+} and Fe^{3+} contact layer. This so called lamellar magnetism (LM) hypothesis is based on bond valence arguments and kinetic Monte Carlo simulation with empirical parameters, but a microscopic understanding from first principles was lacking so far.
To this end we have performed DFT calculations on solid solutions and heterostructures of hematite and ilmenite using the FP-APW method in the WIEN2k-code [10].
As a starting point we have modelled the end members α-Fe_2O_3 and $FeTiO_3$ in a hexagonal primitive unit cell containing 30 and 60 atoms, respectively (Fig.1). We find that the inclusion of electronic correlations within the LDA+U method [11,12] is decisive to obtain the correct ground state and band gap of the bulk materials i.e. AFM coupling of Fe layers in α-Fe_2O_3 with Fe in the Fe^{3+} oxidation state and a Fe^{2+} and Ti^{4+} ground state configuration in $FeTiO_3$.
varying systematically the concentration, distribution and charge state of Ti (Fe) incorporated in a α-Fe_2O_3 ($FeTiO_3$) host we explore different scenarios for the charge compensation mechanism in this system and its consequences for the magnetic and electronic behavior. A phase diagram of the different configurations showing the stability with respect to the end members as a function of Ti-doping is shown in Fig.2. Each Ti ion, irrespective of the charge state (3+ or 4+) adds a defect magnetic moment of 4μB to the system. Ti incorporation in the same spin-sublattice which maximizes the net magnetic moment is slightly preferred to substitution in different spin-sublattices in agreement with previous LDA+U results [13]. However, we find a clear preference to form layered arrangements as opposed to solid solutions. When Ti substitutes for Fe^{3+} in the hematite host, it is not inert as commonly assumed but plays an active role in charge compensation and the emergence of magnetism: in a single Ti layer in hematite the preferred charge state is Ti^{3+}, Fe^{3+}. The spatial distribution of the majority spin density with an occupied d_{z^2} orbital at the Ti^{3+}-sites across the interface is shown in Fig. 1a. As soon as a thicker ilmenite-like block forms, the most favorable compensation mechanism is through Ti^{4+} and a disproportionation in the Fe contact layer in Fe^{2+}, Fe^{3+} (Fig.1b) giving first theoretical evidence from correlated band theory for the lamellar magnetism hypothesis [14].
The band gap reduces to 0.7-1.0 eV and in some cases (at 66% Ti-doping) to half-metallic behavior, making this system a promising candidate for spintronics applications.

[1]A.Ohtomo, et al., Nature 419, 378 (2002)

[2]A.Brinkman, et al., Nat. Mat. 6, 493 (2007)

[3]N.Reyren, et al., Science, 317, 1196 (2007)

[4]R.Pentcheva and W.E.Pickett, PRL, 99, 016802 (2007)

[5]Y.Ishikawa, JPSJ, 13, 37 (1958)

[6]S.A.McEnroe, et al., Earth Planet. Sci. Lett. 224,461 (2004)

[7]Y.Takada, et al., J. Magn. Magn. Mat. 310, 2108(2007)

[8]H.Hojo, et al., APL, 89, 142503 (2006)

[9]P.Robinson, et al., Nature 418, 517 (2002)

[10]P.Blaha, et al., ISBN 3-9501031-1-2(2001)

[11]J.P.Perdew, et al., PRL, 77, 3865,(1996)

[12]V.I.Anisimov, et al., PRB,48, 16929 (1993)

[13]J.Velev, et al., PRB, 71, 205208 (2005)

[14]R.Pentcheva and H.Sadat Nabi, submitted to PRL

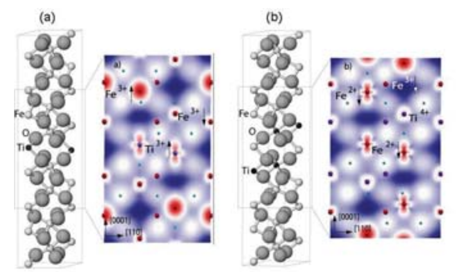

Fig. 1 Side view of the 60 atom simulation cell of a single (a) and double (b) Ti layer incorporated in hematite. Iron, oxygen and titanium are marked by grey, dark grey and black circles, respectively. Fig. a) and b) are showing also the majority and minority spin density for the most favourable charge configurations through the interface for the single (Ti^{3+}, Fe^{3+}) and the double Ti layer in hematite host (Fe^{2+}, Fe^{3+} in the contact layer).

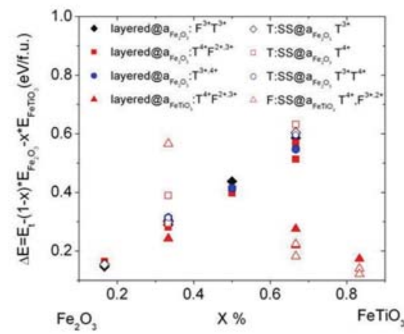

Fig. 2) Formation energy with respect to the end embers as a function of ilmenite concentration x. Layered arrangements are denoted with full symbols, solid solutions with open ones.

Charge, magnetic and orbital order at perovskite interfaces.

R. Pentcheva[1], W. E. Pickett[2]
1. Department of Earth and Environmental Sciences,Section Crystallography, University of Munich, Munich, Germany; 2. Department of Physics, University of California, Davis, CA

Transition metal oxides exhibit a rich spectrum of properties such as ferroelectricity, magnetism, superconductivity, Mott insulator-metal transition and colossal magnetoresistance, to name only a few. Oxide heterostructures offer not only the possibility to combine these properties in one material, but also to generate novel functionalities that do not exist in the parent compounds. The conductivity measured at the interfaces between the Mott insulator LaTiO3 and the band insulator SrTiO3 [1] but also between the two simple band insulators LaAlO3 (LAO) and SrTiO3 [2] has triggered intensive research and excitement both on the theoretical and experimental side. Recently LaAlO3/SrTiO3 interfaces were reported to be magnetic [3] and even superconducting [4].
To explain these results we have performed density-functional theory (DFT) calculations including a Hubbard U on a variety of LaTiO3/SrTiO3 and LaAlO3/SrTiO3 superlattices where we have varied the number of layers of each material. We find that the charge mismatch at the LaTiO3/SrTiO3 as well as the n-type LaAlO3/SrTiO3 interface (a LaO layer next to a TiO2-layer analogous to the Mott insulator LaTiO3) is accommodated by charge disproportionation on the Ti-sublattice in the interface layer in Ti3+ and Ti4+. The charge density distribution of the occupied d-states in Fig 1a) shows that this state is not only charge ordered (CO) with Ti3+ and Ti4+ arranged in a checkerboard manner, but also orbitally ordered with an occupied dxy-orbital at the Ti3+-sites. These results point at additional compensation mechanisms in complex oxides with multivalent cations that are not available in conventional semiconductor heterostructures. We find a slight preference for an antiferromagnetic (AFM) alignment of the Ti3+ spins [5,6], but with a periodicity that is different than in bulk AFM-G type LaTiO3. This result is particularly interesting for the n-type LaAlO3/SrTiO3 interface, because here the corresponding bulk materials are not magnetic. First experimental evidence for localized magnetic moments in this system is given by Brinkmann et al. [3].
While for the ideal positions of the atoms a 1LTO/5STO superlattice is insulating in the strong interactions regime (U=8eV, J=1 eV), lattice relaxations lead to a metallic behavior (cf. Fig 1b) and c)). We also discuss the influence of lattice relaxation on the electronic and magnetic properties of more isolated interfaces in a 5LAO/5STO-heterostructure.
An enhanced complexity with respect to orbital occupation is observed at the LaVO3/SrTiO3 interface. The charge mismatch at this d2-d0 interface can be accommodated either by Ti3+ or promote V4+. Both compensation mechanisms and the resulting magnetic and orbital order will be discussed in the context of recent experimental findings [7].

[1] A. Ohtomo, D.A. Muller, J.L. Grazul, and H.Y. Hwang, Nature 419, 378 (2002).

[2] A. Ohtomo and H. Y. Hwang, Nature 427, 423 (2004).

[3] A. Brinkman, et al., Nature Materials, 6, 493 (2006).

[4] N. Reyren, et al., Science 317, 1196 (2007).

[5] R. Pentcheva and W.E. Pickett, Phys. Rev. Lett. 99, 016802 (2007).

[6] R. Pentcheva and W.E. Pickett, Phys. Rev. B 74, 035112 (2006).

[7] Y. Hotta, T. Suzaki, and H.Y. Hwang, Phys. Rev. Lett. 99, 236805 (2007).

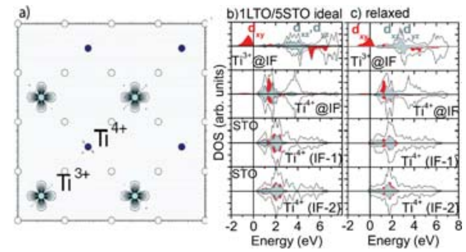

Fig. 1: a) Charge distribution of the occupied 3d-states in the TiO2 interface layer in a LaTiO3/SrTiO3 superlattice. Ti3+ and Ti4+ are ordered in a checkerboard arrangement with a dxy-orbital occupied at the Ti3+-sites; b) and c) layer-resolved density of states for the Ti 3d-states for an ideal and relaxed 1ML LTO/5ML STO-heterostructure. The relaxed structure is metallic [5].

HS-06

Magnetism of conduction band, exchange interactions and magneto-caloric effects in pure hcp Gd: a first-principles calculations.

S. Khmelevskyi[1], A. V. Ruban[2], I. Turek[3], P. Mohn[1]
1. Center for Computational Materials Science, Vienna Technical University, Vienna, Austria; 2. Royal Unicersity of Technology, Stockholm, Sweden; 3. Charles University, Prague, Czech Republic

The pure Gd metal exhibits an example of model system where a strongly correlated and well-localized magnetic 4f-electronic subsystem interacts with broad spd-conduction band. The intensive spectroscopic studies of the last decade have revealed a highly non-trivial behavior of the conduction band at finite temperatures due to increasing thermal disorder of the localized 4f-moments. We present a first-principles theoretical framework, which gives a description and physical explanation of microscopical photoemission probes as well as macroscopical behavior such as the anomalous thermal expansion and a value of the Curie temperature. In order to describe an electronic structure of the conduction band we model thermal disorder of 4f-moments using Disordered Local Moment approach. The calulations are püerformed within the Korringa-Kohn-Rostokker band structure formalism in the framework of the Local Spin Density Approximation. The local moments associated with 4f-states are treated by an open core model. We find that the local splitting of the conduction band remain finite in paramagnetic state, but order of magnitude smaller than in FM ground state. We also show that changes in the electronic structure of conduction band lead to the strong temperature dependent renormalization of magnetic interactions between localized 4f-moments. The magnetic interactions have been calculated using first-principles magnetic force theorem and then used to derive the Curie temperature of hcp Gd from statistical Monte-Carlo simulations. Having estimations of the exchange constants in paramagnetic state and their dependence on the total magnetization, we calculate also a magnetic specific heat dependencies on the external magnetic field and thus a give a first principles description of the magnetocaloric effect in pure Gd.

HS-07

Ab-initio magneto-optical properties of bcc Ni/Ni(100).

C. Etz[1], A. Vernes[1], L. Szunyogh[1,2], P. Weinberger[1]
1. Center for Computational Materials Science, Vienna University of Technology, Vienna, Austria; 2. Department of Theoretical Physics, Budapest University of Technology and Economics, Budapest, Hungary

By using the Luttinger formula and the spin-polarized relativistic screened Korringa-Kohn-Rostoker method, the inter- and intra-layer contributions $\boldsymbol{\sigma}^{pq}(\omega)$ to the complex optical conductivity have been computed for a photon wave length $\lambda = 633$ nm and both bcc $Vac_N vac/Ni_N lay/Ni(100)$ and $Ni(100)/Ni_N lay/Ni(100)$ respectively, layered systems showing an in-plane magnetization. By comparing the layer-resolved permittivities with that of the semi-infinite bulk substrate, it is shown that with the exception of the xy components all other permittivity tensor elements are dominated by contributions arising from the surface.

Ab-initio Kerr angles obtained via the 2×2 matrix technique for an arbitrary linearly polarized light at oblique incidence within the 0yz plane prove that the appropriate formulas for Kerr angles, widely used in the literature, are valid for a relatively large range of incidence angles.

The calculated Fresnel coefficients show that besides the magnitude of the average magnetization, they only depend on the angle of incidence θ. Within the range of validity of the appropriate formulas

$\theta_K = \theta^l{}_K m_l + \theta^q{}_K m_l m_t$ (1a)

$\varepsilon_K = \varepsilon^l{}_K m_l + \varepsilon^q{}_K m_l m_t$ (1b)

the θ-dependence of the linear Fresnel coefficients was found to scale as sinθ confirming the experimental expectation, whereas the quadratic Fresnel coefficients are almost independent of θ. (see Fig.1)

With these highly accurate Fresnel coefficients, the appropriate formulas in Eqs.(1) can be applied to determine Kerr angles for any arbitrary direction of a uniform in-plane magnetization. A comparison of the calculated Kerr angles obtained via the 2×2 matrix technique with those determined by using the two-media approach (see Fig.2) evidences that the latter only applies for a normal incidence, whereas for arbitrary oblique incidences about 75% of the magnitude of Kerr rotation angles comes from surface contributions.

1. J. Zabloudil, R. Hammerling, L. Szunyogh, and P. Weinberger, Electron Scattering in Solid Matter: A Theoretical and Computational Treatise, Solid-State Sciences (Springer Verlag, Berlin, 2005)

2. R. Kubo, J. Phys. Soc. Japan **12**, 570 (1957)

3. A. Vernes, L. Szunyogh, and P. Weinberger, Phase Transitions **75**, 167 (2002).

4. A. Vernes, Philos. Mag. **86**, 1973 (2006)

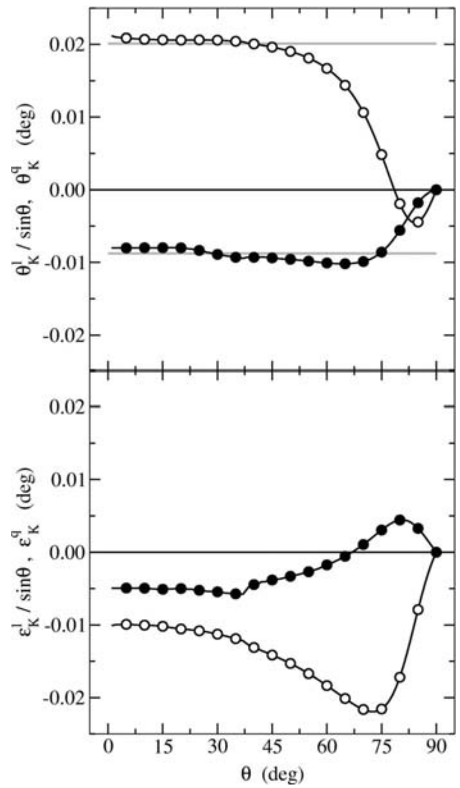

FIG. 1: Fresnel coefficients for *p*-polarized light incident within the 0yz plane (λ = 633 nm) in bcc Ni/Ni(100) as a function of the angle of incidence θ, see Eqs.(1). sinθ-scaled linear and plain quadratic Fresnel coefficients are shown by open and full circles, respectively.

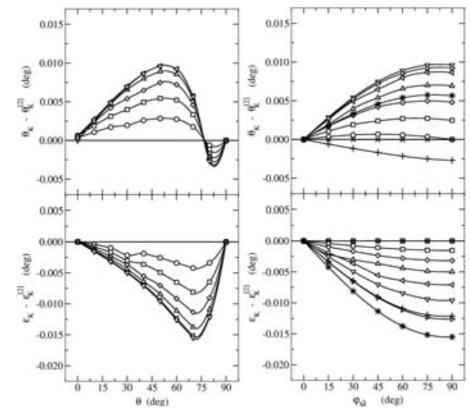

FIG. 2: Differences in the Kerr angles for oblique incidence of *p*-polarized light in 0yz plane (λ = 633 nm) and bcc Ni/Ni(100), when using the 2×2 matrix technique and the two-media approach as a function of the incidence angle θ (left) or the polar angle ϕ_M (right). In the left panel circles, squares, diamonds and triangles (up, left and down) refer to Kerr angles obtained for a polar angle ϕ_M= 15°, 30°, 45°, 60°, 75°, 90° (open symbols), in the right panel circles, squares, diamonds and triangles (up, left, down and right) represent Kerr angles obtained for an angle of incidence θ = 0°, 10°, ..., 60°(open symbols), stars, pluses and crosses stand for θ = 70°, 80°, 90°.

HS-08

Influence of external magnetic field on the resistivity of a one-dimensional Neel type magnetic domain wall in presence of Rashba spin-orbit coupling.

M. Ghanaatshoar[1], V. Fallahi[1], M. M. Tehranchi[1], A. Phirouznia[2]
1. Laser and Plasma research institute, Shahid Beheshti University, Tehran, Iran; 2. Department of physics, Azarbaijan University of Tarbiat Moallem, Tabriz, Iran

Magnetic nanowires offer new prospect for spintronic devices such as sensor, switch and data storage memory. In these systems spin-dependent scattering makes accountable role in the electrical resistance. In addition, the long dephasing time of electron's spin and easy manipulation of the spin polarization by an external magnetic field, have made these kinds of materials to be one of the suitable candidates for information transmission devices. Spin relaxation time can be affected by various interaction mechanisms. It is well known that the domain walls (DWs) in the nanowires cause spin-flip scattering via coupling of two spin states [1]. Furthermore, presence of Rashba spin-orbit interaction which arises due to asymmetry of confining potential in the low dimensional systems can decrease the relaxation rates of electrons and consequently change the DW resistance [2]. However, by applying external magnetic field, one can eliminate the spin-flip scattering via Rashba spin-orbit interaction.
In this paper, we systematically investigate how the interplay between the Rashba spin-orbit interaction and Zeeman coupling affects the electron transport through the 1-dimensional (1-D) DWs. Confinement of the electrons in one dimension eliminates the magnetic part of the Lorentz force which is exerted on electrons, but the magnetic field still contributes in collision term through the Zeeman interaction. The studies have been carried out on the ideal 1-D linear Neel type DWs which are shown in Figure (1). For a smooth linear DW, the local direction of magnetization can be described by $\theta(z)=\pi z/d$ in which d is the DW width and θ is the angle between the local direction of magnetization and wire axis (z axis). We suppose that the magnetic field do not affect the DW configuration.
The Hamiltonian of the system can be written as
$H=H_0+H_{sf}+H_Z+H_R$
where H_0 contains periodic potential and kinetic energy, H_{sf} is the s-f exchange between the conduction electrons and the localized magnetic moments, H_Z is the Zeeman interaction and H_R represents the Rashba coupling Hamiltonian. The appropriate spin-orbit coupling Hamiltonian operator for electrons moving with a well-defined k along the DW can be written as
$H_R=2\pi\gamma_R/h\ \sigma.(n\times p)$
where h is planck's constant, p is the momentum of the electron, n is the induced electric field direction due to structure inversion asymmetry and σ is the spin operator. We have considered that the asymmetry of electrical potential in the z direction is negligible in compare to the transverse direction. In the limit of $\varepsilon_F>>\Delta$ in which ε_F is Fermi energy and Δ is the exchange interaction constant, it is straightforward to show that only the terms of H_R which are proportional to σ_y, can contribute to elastic scattering. By introducing transverse external magnetic field along the ±y direction, one can control the strength of Rashba spin-orbit interaction.
To determine the eigenstates of H_0+H_{sf}, we apply an approach based on the perturbation method [3]. In this approach, for a linear DW and up to any order of approximation, the s-f interaction can not produce any mixing between different k-states. Treating of the Rashba and Zeeman scattering mechanisms has been based on Boltzmann transport equation, within the relaxation time approximation. Through this formalism, we can determine the relaxation times and the resistivity of the DW. Figure (2) indicates the DW resistivity versus applied magnetic field. As can be seen, when the scattering amplitude associated with the Zeeman interaction is comparable to that of the Rashba interaction at the Fermi level, the contribution of the external magnetic field to the DW resistivity can be canceled out.

[1] V.K. Dugaev, J. Berakdar, J. Barnas, W. Dobrowolski, V.F. Mitin, M. Vieira, Materials Science and Engineering C, 25 (2005) 705.

[2] A. Phirouznia, M. M. Tehranchi and M. Ghanaatshoar, Phys. Rev. B, 75 (2007) 224403.

[3] P. M. Levy and S. Zhang, Phys. Rev. Lett., 79 (1997) 5110.

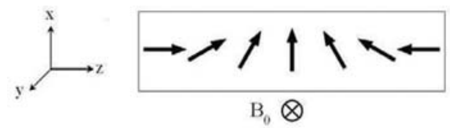

Figure (1): A 180° Neel type domain wall. The external magnetic field is applied along the y axis.

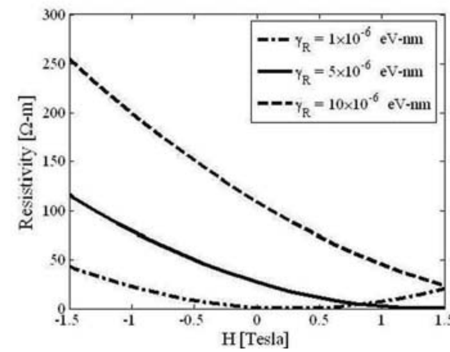

Figure (2): Resistivity of the DW (20 nm width) versus external transverse magnetic field for different values of Rashba interaction strength.

HS-09

Ab-initio study on the magnetic structures in the ordered Mn_3Pt alloy.

Y. Kota, H. Tsuchiura, A. Sakuma
Applied Physics, Tohoku University, Sendai, Japan

1) Introduction

Geometrically frustrated antiferromagnetic (AF) systems have been extensively studied because they show many unusual behaviors in magnetic and thermal properties. Their classical ground state has a thermodynamic degeneracy with a potential instability to various magnetic phases. In general, thermal fluctuations may drive symmetry breaking to the phase with the largest entropy, and leads to the possibility of phase transitions between different magnetic phases. The magnetically ordered Mn_3Pt alloy has long been studied [1-4], and considered to be such a system, which shows an order-order phase transition between two AF phases. The magnetic structures of these two phases are determined by neutron scattering measurements. In the low temperature phase (D-phase) realized below T_t = 400K [2], the spin moments of the three Mn atoms in the unit cell order in a triangular arrangement in the (111) plane, each spin pointing to the center of the triangle, shown Fig. 1 (a). In the high temperature phase (F-phase) in the temperature range of $T_t < T < T_N$ = 475K, in contrast, a collinear magnetic structure shown in Fig. 1 (a) is realized. A peculiar feature of the F-phase is that one third of Mn atoms on the sites where the magnetic mean-field is cancelled have no magnetic moments. Recently, it has been suggested experimentally that the spins of these one third Mn atoms are not paramagnetic but strongly fluctuating [4]. Motivated by these backgrounds, we study the stabilities of various magnetic structures in the ordered Mn_3Pt alloy by using *ab-initio* calculation techniques based on the density functional theory (DFT).

2) Calculation method and model

In this work, DFT calculations have been carried out in conjunction with the generalized gradient approximation (GGA) projector augmented-wave (PAW) potentials, by using the Vienna *ab initio* simulation package (VASP) [5,6]. The lattice constants are set to experimental values of a=b=c=3.833Å for the D-phase [1], while a=b=3.882Å and c=3.876Å for the F-phase [4].

3) Results and Discussion

First, let us look at the ground state of the Mn_3Pt. Taking account of the spin-orbit interaction, we actually obtain the D-phase magnetic structure as the lowest energy state of the system. The magnetic moment obtained here is $3.09\mu_B$ per Mn atom, which is in fairly good agreement with the experimental value $3.0\pm0.3\mu_B$ [2]. This non-collinear magnetic structure has been theoretically proposed for Mn_3Pt within a spin-wave theory for the classical Heisenberg model [3]. We note here that, the spin structure of the D-phase is now unambiguously determined from the theoretical point of view.

Next we study the magnetic structures with higher energies, which may be relevant to the F-phase. We find that the structure with one third of Mn atoms having no magnetic moment is energetically so much unfavorable that it may be irrelevant to the F-phase. Instead, we introduce noncollinear magnetic structures with additional spins on the one third Mn atoms shown in Fig. 1 (b). Although this structure appears different from the collinear structure experimentally proposed for the F-phase (Fig. 1 (a)), we confirm that it is energetically much lower (about 1.7eV per unit cell) than the collinear structure. It should be noted that this magnetic structure has four-hold symmetry around the *c*-axis and can easily rotate within the *c*-plane, which leads us to suggest that the spatially or thermally averaged magnetic structure can be equivalent to the structure of Fig. 1 (a). Moreover, we also confirm that if the relative angle between the additional spins and the *c*-axis change from 0 to 90 degrees, the energy of the system per unit cell varies only in order of 0.001eV. This implies the possibility that the additional spin moments can thermally fluctuate in the temperature range 400 < T < 475K, where the F-phase is realized. This result may support the experimentally proposed model [4]. We will also discuss the thermal fluctuation effects in more detail by estimating the exchange interaction constants for Mn_3Pt within the *ab-initio* calculations.

1) E. Krén, G. Kádár, L. Pál, J. Sólyom, P. Szabó and T. Tarnóczi, Phys. Rev. **171**, 574 (1968).

2) H. Yasui, T. Kaneko, H. Yoshida, S. Abe, K. Kamigaki and N. Mori, J. Phys. Soc. Jpn. **56**, 4532 (1987).

3) M. W. Long and A. Bayri, J. Phys.: Condensed Matter **5**, 7719 (1993).

4) T. Ikeda and Y. Tsunoda, J. Phys. Soc. Jpn. **72**, 2614 (2003).

5) G. Kresse and J. Furthmüller, Phys. Rev. B **54**, 11169 (1996); Comput. Mater. Sci. **6**, 15 (1996).

6) G. Kresse and J. Hafner, Phys. Rev. B **47**, 558 (1993).

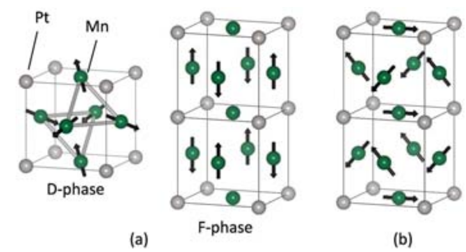

Figure. 1. (a) The magnetic structures for the ordered Mn_3Pt in the D-phase and F-phase, proposed by the experiments. (b) A magnetic structure proposed as a relevant state of the F-phase.

HS-10

Half-metallicity of the bulk and the (001) surface for full Heusler alloy Co_2HfSi: a first-principles study.

Y. Jin, *J. Lee*
Physics, Inha University, Incheon, South Korea

Introduction

One of the crucial issues in recent rapidly developing field of spintronics is to obtain efficient spin-injections from ferromagnets into semiconductors. Half-metallic ferromagnets are regarded as promising sources for spin-injection due to the complete spin-polarization at the Fermi level. Many of the Co2-based full Heusler alloys Co_2YSi (Y=3d and 4d transition metals) were predicted to be half-metallic by band structure calculations [1,2,3]. On the other hand, the measured spin-polarizations for several half-metallic ferromagnets from the surface sensitive techniques such as point contact Andreev reflection spectroscopy are lower than 100% [4] and it was suggested that the atomic disorder or surface effects were responsible for the discrepancies between the theoretical predictions and the experimental observations [5]..

In this work, we predicted that the Co_2HfSi compound, the Co_2-based full Heusler alloy containing 5d transition metal, is half-metallic by the first-principles band structure calculation. We also calculated the surface electronic structure of Co_2HfSi (001) and discussed the half-metalliciy at the surface.

Model and calculational method

We first found that the bulk Co_2HfSi is half-metallic at the equilibrium lattice constant of a = 11.317 a.u. In order to investigate the surface electronic structure, we have considered two types of surface terminations along the (001) plane: the Co atoms terminated (Co-term) and the Hf and Si atoms terminated (HfSi-term) surfaces. The Co-term and HfSi-term were modeled by two single slabs with 11 and 13 atomic layers, respectively. The two-dimensional (2D) lattice constant was taken to be 8.002 a.u. and the interlayer distant was taken to be 2.829 a.u. which is a quarter of the calculated equilibrium lattice constant. The Kohn-Sham equation was solved by means of the all-electron full-potential linearized augmented plane wave method within the GGA [8]. Lattice harmonics with $l\leq 8$ were employed for describing the wave functions, charge, and potential inside the muffin-tin (MT) spheres. Core states were treated fully relativistically and valence states were treated scalar relativistically.

Results and discussions

The calculated atom-resolved density of states (DOS) for the Co-term and HfSi-term (001) slabs are presented in Fig. 1. The results for bulk Co2HfSi are also given for comparison. The minority spins are factored by -1 and the Fermi levels are set to zero. As we can see in Fig. 1, there is a band gap of 0.69 eV in the minority states for bulk Co_2HfSi which indicates that the bulk Co2HfSi is a half-metallic ferromagnet. The calculated magnetic moment of Co_2HfSi is an integer value of 2.00 μ_B/f.u. which follows the Slater-Pauling rule [9]. For the HfSi-term of the Co_2HfSi(001), the surface retains the half-metallic character as in the bulk, while the minority spin band gap was much reduced compared to that of the bulk. On the other hand, the surface of the Co-term loses the half-metallicity because the occupied minority states shift to higher energy region. The magnetic moments of the Hf(S) in the HfSi-term and the Co(S) in the Co-term, calculated to be -0.05 and 0.98 μ_B, respectively, were slightly smaller than those of the bulk (-0.07 and 1.05 μ_B for the Hf and Co atoms, respectively).

[1] H. C. Kandpal, G. H. Fecher, and C. Felser, *J. Phys. D: Appl. Phys.* vol. 40, p1507 (2007).

[2] X. Q. Chen, R. Podloucky, and P. Rogl, . *J. Appl. Phys.* vol. 100, p113901 (2006)

[3] Y. J. Jin and J. I. Lee, *J. Korean Phys. Soc.* vol. 51, p155 (2007)

[4] L. J. Singh, Z. H. Barder, Y. Miyoshi, Y. Bugoslavsky, W. R. Branford, and L. F. Cohen, *Appl. Phys. Lett.* vol. 84, p2367 (2004)

[5] D. Ristoiu, J.P. Nozières, C.N. Borca, B. Borca, and P.A. Dowben, *Appl. Phys. Lett.* vol. 76, p2349 (2000)

[6] Galanakis, *J. Phys.: Condens. Matter* vol. 14, p6329 (2002).

[7] E. Wimmer, H. Krakauer, M. Weinert, and A. J. Freeman, *Phys. Rev. B*vol. 24, p864 (1981), and references therein. M. Weinert, E. Wimmer, and A. J. Freeman, *Phys. Rev. B*vol. 26, p4571 (1982).

[8] J.P. Perdew and Y. Wang, *Phys. Rev. B* vol. 45, p13244 (1992).

[9] I. Galanakis, P. Mavropoulos, P. H. Dederichs, *J. Phys. D: Appl. Phys.* vol.39, p765 (2006).

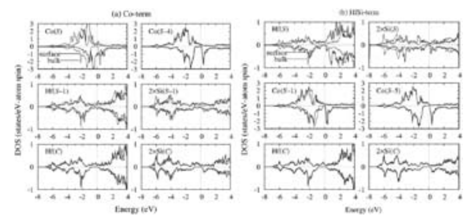

Fig. 1. Calculated spin-polarized DOS for the (a) Co-term and (b) HfSi-term $Co_2HfSi(001)$ surfaces. Those for bulk Co_2HfSi were also presented for comparison. The solid- and the dotted lines denote the surfaces and bulk results, respectively . The DOS values for spin down states are multiplied by -1, and the Fermi levels are set to zero.

HS-11

Magnetic properties of the antiperovskite Co_4N(001) surfaces: a first-principles study.

I. Kim[1], B. Bialek[2], J. Lee[2]
1. Grad. Inst. Ferrous Tech. (GIFT), POSTECH, Pohang, South Korea; 2. Physics, Inha University, Incheon, South Korea

Ferromagnetic transition metal nitrides are technologically interesting materials which are more and more applied in the areas such as a high density magnetic recording. Especially cobalt nitride films are considered to be promising materials for the application because of their high chemical stability and a large saturation magnetization. It is known that the cobalt-nitrogen system may contain many phases, among them is the richest in cobalt Co_4N [1]. The structure of Co_4N may be thought as face-centered-cubic (*fcc*) cobalt with N atom inserted in the center of the cube. In such structure two types of Co atoms may be distinguished: one positioned at the corner of the cube (denoted as Co^I) and the other placed in the center of the cube face (Co^{II}). Recently, an *ab initio* study has been undertaken in order to understand the electronic and magnetic properties of such structured bulk Co_4N [2]. It was shown that the magnetic properties of cobalt atoms in the structure are strongly correlated with the atoms chemical surrounding, i.e. Co^{II}, which are involved in creation of a bond with N atom, have smaller magnetic moments, while Co^I at the corner sites retain their isolated character, similarly to the atoms of *fcc* Co.
For further applications of Co_4N, a comprehensive study of the electronic and magnetic properties of its surfaces is equally essential as the understanding of the bulk properties. In this paper we discuss the electronic and magnetic properties of the antiperovskite Co_4N(001) surfaces based on a first–principles method.
The calculations were carried out for a single slab representing the (001) surface of Co_4N. We considered two possible surface terminations, that is Co- and CoN-terminated surfaces (denoted as Co-Term and CoN-Term, respectively). In the first system, the slab consisted of 13 layers cut from the bulk structure, which lattice constant equal to 6.7788 a.u. was taken from experimental data [3]. In the CoN-Term slab there were 11 layers. We employed the all-electron full-potential linearized augmented plane wave (FLAPW) method [4,5] with the generalized gradient approximation (GGA) [6].
The calculated atom-resolved local density of states (DOS) for the Co-Term and CoN-Term (001) (001) surface of Co4N are shown in Fig. 1. Four layers ae concerned in each of the two sysytems: the surface (S), the first sub-surface (S-1), the center (C), and next to the center (S-4 in Co-Term and S-3 in CoN-Term) layer. We found that the DOS for CoI(S) in the Co-Term surface is narrower than the DOS for CoI in the bulk. The exchange splitting in the Co^I(S) is larger compared to the center layer due to the surface effect, which suggests an enhancement of the magnetic moment. The calculated DOS for CoII (S) of the CoN-Term shows no increase of exchange splitting, which is due to the hybridization with the surface N atom. The surface states are found around -1 eV of the spin-down states in both Co^I(S) atom of Co-Term and Co^{II}(S) atom of CoN-Term. The surface states of CoII(S) atom of CoN-Term split into two peaks, which are thought as the effect of the surface nitrogen bands.
The calculated magetic moment (MM) on Co atoms in the most inner layers of the two investigated slabs are 1.91 and 1.37 μ_B on Co^I and Co^{II}, respectively, which is consistent with the results reported for bulk Co_4N [2]. The magnetic properties of the surface Co atoms depend strongly on the atoms surrounding. In the Co-Term slab the value of MM on Co^I(S) is 2.03 μ_B, considerably larger than that on Co^I(S-4). In contrary, the calculated MM on the Co^{II}(S) atom in CoN-Term slab is reduced to 1.27 μB, which is even lower than the MM on CoII atoms in inner layers. This behaviour may be explained by an enhancement of the surface N *p* and Co *d* states hybridization, which is confirmed by the split surface states for Co^{II} atom in the CoN-Term slab. A similar reduction of Co^{II} magnetization is seen also in the (S-1) layer of the Co-Term structure, which confirms the importance of the presence of nitrogen for tailoring the magnetic properties of CoII atom in the nitride.

[1] K. Suzuki, T. Kaneko, H. Yoshida, H. Morita, H. Fujimoi, *J. Alloys Comp.*, vol. 224, p. 232, 1995.

[2] S. F. Matar, A. Houari, M. A. Belkhir, *Phys. Rev. B*, vol. 75, p. 245109, 2007.

[3] K. Oda, T. Yoshio, and K. Oda, *J. Mater. Sci.*, vol. 22, p. 2729, 1987

[4] E. Wimmer, H. Krakauer, M. Weinert, and A. J. Freeman, *Phys. Rev. B*, vol. 24, p. 864, 1981, and references therein.

[5] M. Weinert, E. Wimmer, and A. J. Freeman, *Phys. Rev. B*, vol. 26, p. 4571, 1982.

[6] J. P. Perdew, K. Burke, and M. Ernzernhof, *Phys. Rev. Lett.*, vol. 77 p. 3865, 1996; ibid. vol. 78, p. 1396(E), 1997.

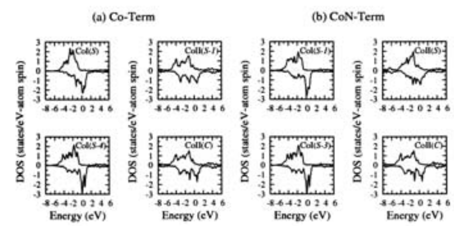

Fig. 1. Spin-polarized atom-resloved DOS for the (a) Co-Term and (b) CoN-Term Co_4N (001) surface. The DOS values for spin down states are multiplied by -1, and the Fermi levels are set to zero.

HS-12

A first principles study of Thiol-Capped Au Nanoparticles.

R. Cuadrado, J. Cerdá
Intercaras y Crecimiento, Instituto de Ciencia de Materiales de Madrid, Madrid, Spain

I. Introduction
During the last years, nanoparticles (NPs) have become a subject of major research due to their new optical, electronic and/or magnetic properties which may be controlled by varying the NP size or shape. Functionalizing these NPs with adequate organic capping layers further provides chemical specificity to the clusters, thus becoming highly interesting for biological applications. Gold NPs have received great attention because bulk gold is inert and, most surprisingly, several experiments recently reported on the ferromagnetic nature of these Au Nps [1]. There exist, however, conflicting results regarding the conditions required for achieving such magnetic clusters; whereas the first experiments required sulfur based capping ligands (alkane-thiols), subsequent theoretical and experimental works point to the existence of a a permanent magnetism in bare gold clusters [2]. In this work, we address precisely the role that an alkane-thiol capping layer plays on the properties of Au NPs by means of ab initio Density Functional Theory (DFT) based calculations.
II.Theoretical
We have modeled Au clusters of different sizes ranging from just 1 up to 38 gold atoms. The two largest clusters considered, Au38 and Au14, where chosen with octahedral shapes preserving the bulk fcc arrangement. In order to reduce the computational load, we considered short alkane-thiols of just two C atoms (S-C2H5) and systematically varied the thiol coverage for each of the Au clusters. In order to generate initial configurations for the thiol-capped clusters, we first performed Molecular Dynamics (MD) calculations at a fixed temperature of 300 K (Nosé thermostat) employing simple two-body Lennard-Jones potentials. Following a recent XRD structural study of thiol films on an Au surface [3], a different set of initial configurations was additionally created by attaching an extra gold atom to the thiol (Au-S-C2H5) and performing further MD runs. The structure of these clusters was then studied with the DFT based SIESTA code under the Local Density Approximation (LDA) employing scalar relativistic pseudopotentials [4]. All the clusters were fully relaxed and their electronic and magnetic structure were determined by inspecting the resulting atom projected Density of States (PDOS) together with any net magnetic moments.
III. Results
Figure 1 shows several relaxed clusters for the Au38 cluster and for different thiol coverages. The optimized structures show that the S atoms are predominantly 2 fold coordinated to the surface gold atoms. although structures having 1 and 3 coordination numbers were also found. The highest coverage considered here were 24 thiols, which amounts to a 3:4 ratio between the number of gold surface atoms and the number of thiols. As the coverage is increased, the reconstruction at the NP surface becomes more prominent. Figure 2 shows the distribution of Au-Au distances as a function of coverage. A shift in the first peak from 2.75 A to 2.85 A can be clearly followed as the coverage increases, in good accordance with the experimental findings[1].
As our main result, we have not found any evidence for magnetism in any of the large clusters studied; the spin polarization vanished in all cases.
Figure 3 shows the evolution of the DOS for the Au38 cluster and for different thiol coverages. We include the projections on the gold and sulfur atoms as well as on the organic ligands (C3H5). As the coverage increases, the peaks are smeared and bands are formed implying that electrons become delocalized. Most interestingly, any peaks related to the gold atoms and close to the Fermi level disappear thus reducing the number of d-holes. We thus conclude that thiol capping does not help the development of any spin polarization in the Au NPs.

[1] P. Crespo et al, Phys. Rev. Lett. 93, 087204(2004).

[2] Y. Yamamoto et al., Phys. Rev. Lett. 93-11, 116801(2004)

[3] Miao Yu et al. Phys. Rev. Lett. 97, 166102(2006)

[4] José M. Soler et al, J. Phys.: Condens. Matter 14, 2745-2779 (2002).

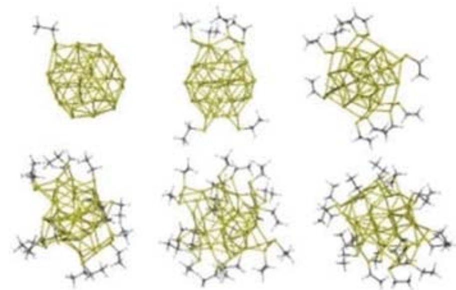

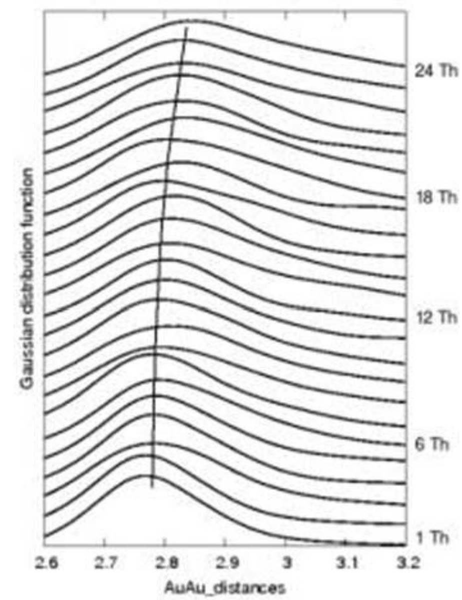

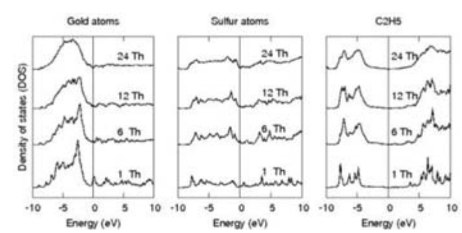

HS-13

The Study of Magnetic Properties of Fe2Sm Using Ab- Initio Calculation.

M. Imaizumi[1], *L. C. Varanda*[2], M. Jafelicci Jr[3]
1. Fisica, Universidade Estadual Julio de Mesquita Filho, Bauru, Brazil; 2. Química, Universidade de São Paulo, São Carlos, Brazil; 3. Qúimica, Universidade Estadual Paulista Júlio de Mesquita Filho, Araraquara, Brazil

Rare-earth metals as Sm combines with iron metal to form intermetallic Fe2Sm compound and its crystallizes in the MgCu2 (Fd3m) Laves phase. In this structure the Sm atoms are equivalent to Mg atoms, occupying equivalent sites with cubic point symmetry and this intermetallic compound behaves ferromagnetically. Then, in this context, motivates us to investigate theoretically the magnetic behavior of the Fe2Sm compound. We used the self-consistent spin-polarized energy band calculation, using full potential linearized augmented plane waves method (FP-LAPW) with APW + lo [1]. These calculations are based on the first-principles functional-density theory (DFT) with the general gradient approximation (GGA) for exchange and correlation potential [2] and provide total density of states, total energy as function of volume and band energy dispersion. The calculated magnetic spins moments are 5.41μB for samarium atoms and 2.90 μB for iron atoms, respectively. Figure 1 shows the ferromagnetic behavior of the material by the the difference observed between the total density of states of spins up and spins down [3] and figure 2 shows the behavior of the total energy as function of volume with an equilibrium volume of 643.2910 (bohr**3) and a bulk modulus of 33.988 GPa [4].

[1] P. Blaha, K. Schwarz,G.K.H.Madsen, D.Kvasnicka and J. Luitz, Wien2k, An Augmented +Local Orbitals Program For Calculating Crystal Properties. (Karlheinz Schwarz, Tech.University of Vienna, Austria), 2001.

[2] J. J. Perdew, K. Burke, and M. Ernzerhof, Phys. Rev. Lett. 77, 3865, 1996.

[3] K. Schwarz and P. Mohn, J. Phys. F: Met. Phys., 14, L129, 1984.

[4] F.D. Murnaghan, Proc. Natl. Acad. Sci., USA 30, 244, 1944.

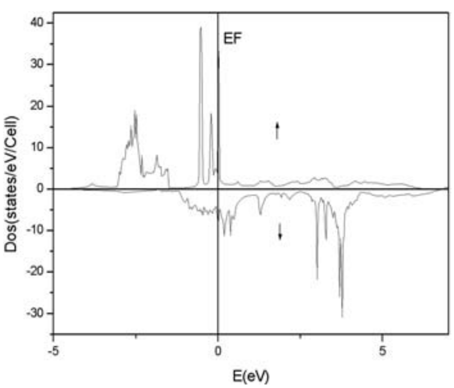

Figure 1- Total density of states of electrons with spins up and spins down.

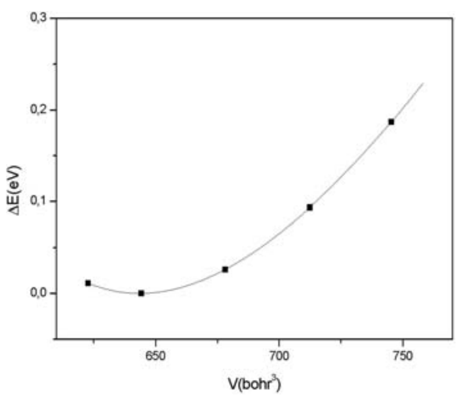

Figure 2 - Total energy as function of volume for ferromagnetic phase.

HS-14

Energy spectrum of S=1/2 Heisenberg systems via a recursive diagonalization method.

F. C. Souza, V. L. Líbero
Departamento de Física e Informática, Instituto de Física de São Carlos, Universidade de São Paulo, São Carlos, Brazil

Introduction. Quantum spin systems are among the most important subjects in condensed-matter physics and recently have motivated many applications, for instance in the new area of spintronics [1]. An example is the work at IBM, using low-temperature scanning tunneling microscopy were able to measure the exchange interactions between individual spins in small manganese chains [2]. A Heisenberg like Hamiltonian was used to analyze the experimental results. They also measured the spin excitation spectrum of these structures, constituting of linear chains of one to ten atoms. The most striking features of these systems are found in the antiferromagnetic compounds, generally the hardest to diagonalize. The difficulties arise especially when the system presents broken symmetry. In this case even well-established methods like Lanczos [3], or Monte Carlo [4], encounter serious limitations. In this work we propose a new numerical diagonalization method which works even in the absence of translational invariance. **The recursive method.** We applied this method to the isotropic spin-1/2 Heisenberg model. Besides conservation of the z-component of the total spin, S^z, we also exploit conservation of the square of the total spin, S^2, a much more complicated procedure that renders an additional block diagonalization. Moreover, we diagonalize a chain with N spins using the eigenvectors obtained from previous diagonalization of a chain with N-1 spins. The N-site Hamiltonian, H_N is built using basis-vectors generated from the direct product of the eigenvectors of the H_{N-1} and the states up and down of the added N-th spin, by means of suitable Clebsch-Gordan coefficients. The matrix elements of the H_N are then expressed in terms of invariant matrix elements through the Wigner-Eckart theorem. The procedure is easily adapted for the two-leg ladder, an experimentally relevant system with a chain as a particular case. **Results.** Using a desktop microcomputer we were able to obtain the entire energy spectrum for chains with up to 20 spins 1/2 (10 rungs for ladders) with fourteen figures of precision. For larger chains, the recursive diagonalization allows a simple truncation scheme that reduces the size of the basis with some controllable reduction of accuracy. The key idea is, to build at each iteration the basis-vector not using all eigenstates from the previous iteration, but a fraction of them. The more eigenstates kept at each iteration, the higher accuracy the spectrum will have. For instance, for an open chain with 128 spins 1/2 the exact ground-state energy is known as e_0/J=-0.441683. Using our recursive procedure, we obtain e_0/J=-0.44166(3), with a maximum of 10000 states kept at each iteration. The number in parenthesis means the deviation from a simulation keeping 5000 states. The deviation from the exact result is just 0.005%. The iterative procedure is also easily implemented for spin-1/2 chains with few spin impurities S located at any position along the chain. It is also straightforward to code the procedure for spin ladders for any ratio of the rung and leg exchange couplings. Having the entire spectrum evaluated with controlled accuracy, we are now investigating thermodynamical quantities for the same systems. **Summary**. We have proposed an iterative diagonalization method exploiting the conservation of S^2 and S^z, and implemented it for the Heisenberg model. The method is also adaptable to other strong correlated systems like the Hubbard model. It is time and memory intensive, but still more economic than Lanczos exact diagonalization or Monte Carlo methods. For large chains, the low-lying energy levels are obtained with high accuracy after an energy cuttoff. The presence of spin impurities, bond defects or borders does not pose any additional problem.

[1] H. Brune, Science **312**, 1005 (2006).

[2] C. F. Hirjibehedin, C. P. Lutz, A. J. Heinrich, Science **312**, 1021 (2006).

[3] G. Grosso, L. Martinelli, G. P. Parravicini, Phys. Rev. B **51**, 13033 (1995).

[4] M. J. de Oliveira, Phys. Rev. B **48**, 6141 (1993).

[5] T. Barnes, E. Dagotto, J. Riera, E. S. Swanson, Phys. Rev. B **47**, 3196 (1993).

L	α=0	α=0.2	α=0.4	α=0.6	α=0.8	α=1.0
12	0.428508	0.435168	0.454459	0.483438	0.520386	0.564158
16	0.431983(1)	0.439115(1)	0.458664(1)	0.487490	0.524167	0.567629
20	0.434121(9)	0.441577(5)	0.461205(3)	0.489924(1)	0.526436(1)	0.569712(1)
24	0.435564(20)	0.443247(13)	0.462901(7)	0.491545(3)	0.527948(2)	0.571100(1)
28	0.436594(32)	0.444446(24)	0.464110(14)	0.492703(6)	0.529027(4)	0.572091(2)
32	0.437363(49)	0.445344(44)	0.465014(24)	0.493569(10)	0.529836(7)	0.572834(4)

Ground-state energy per spin ($-E_o/(2LJ)$) of the 2xL Heisenberg ladder with open boundary conditions (6000 states kept).

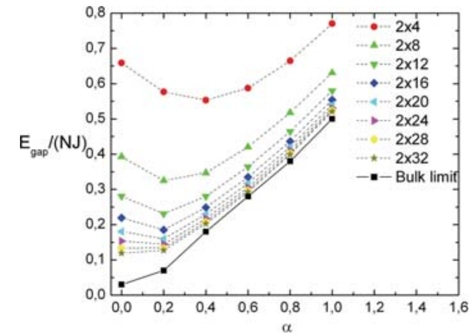

Singlet-triplet energy gap of the 2xL Heisenberg ladder (open boundary condition). Bulk limit data were obtained from Ref.[5] .

HS-15

Density Functional Theory for Heisenberg Spin-1/2 Chains With Bond Defects.

V. L. Líbero, P. H. Penteado
Departamento de Física e Informática, Instituto de Física de São Carlos, Universidade de São Paulo, São Carlos, Brazil

Introduction. The development of new magnetic materials is close related to our comprehension of the fundamental models of magnetism. As could be expected, the pioneering theoretical studies were in magnetic chains or lattices with complete translational invariance, i.e., systems without impurities, bond defects or border effects. The Bethe ansatz solution for the infinite Heisenberg chain of spin 1/2 is the best example of such a system. We learned a lot from those clean chains, but even a superficial inspection reveals that real materials unavoidably have impurities or defects. Frequently, to obtain special properties impurities or defects are insert even in clean materials. Thus, in material science, models and techniques developed for systems with broken symmetry are crucial.

The model. The most important spin model is the Heisenberg model, defined to describe a collection of localized spins coupled by exchange interactions, usually restrict to nearest neighbour spins [1]. Its aplicability goes beyond Physics and extends to Chemistry and Biology as well. In particular for antiferromagnetic ordering, its comprehension is far from complete and becomes even more challenging for inhomogeneous systems.

The procedure. Density Functional Theory (DFT) in the local-density approximation allows to obtain estimates for ground-state properties of inhomogeneous systems by exploiting many body calculations for homogeneous systems [2]. Although created for electronic systems, recently, DFT was formulated for the Heisenberg Model, and a local-spin approximation (LSA) to the ground-state spin functional was proposed [3,4]. This approximation permits the study of inhomogeneous systems with impurity spins in chains or lattices of arbitrary size with uniform exchange interaction. Ref.[5] presented a local functional applicable to nonuniform bond interactions, that improved on the mean-field approximation. Here we present a non-local functional of the bond interactions that further improves the results. This is relevant for instance in the study of the S=1/2 alternating-bond Heisenberg chain, in which the exchange coupling alternates (values or even sign) from site-to-site [6].

Consider a chain of spin 1/2 with alternating bonds J and αJ. A precise estimate for the ground state Eo(α) is known from Ref.[6] for $\alpha<1$. For $\alpha>1$ we may use the relation $Eo(\alpha)=\alpha Eo(1/\alpha)$. The DFT-LSA approach first looks for a homogeneous system as a starting point. Our alternating chain is homogeneous if seen as made of pair of bonds J and αJ. After that, we define the correlation energy $Ec(\alpha)=Eo(\alpha)-E^{MF}(\alpha)$, where E^{MF} is the well known mean-field energy term. Now, for a chain with arbitrary exchange interactions J_i, i.e., an arbitrary set of $\alpha_i=J_{i+1}/J_i$, a local approximation for the correlation is obtained by replacing Ec(α) by Ec[α_i]. Therefore, $Eo[\alpha_i] = E^{MF}[\alpha_i]+Ec[\alpha_i]$. Note that the only approximation is in Ec, since E^{MF} is known exactly. This local functional of α_i is in fact non-local in the exchange coupling J_i; this is the first non-local functional of bond coupling for Heisenberg models and provides much better estimates than the previous local approximation presented in Ref.[5].

Results. We compare results from our DFT procedure to exact numerical diagonalization of the model Hamiltonians for chains with 24 spins and periodic boundary condition. We illustrate the method in the case in which all bonds have the same exchange iteraction J (α_i=1) except one bond with J'= βJ. Note that this case represents a very inhomogeneous situation relative to the alternating chain. The following table contains representative results:

β	-Eo/J	Exact
0.2	0.43596	0.43598
0.5	0.43692	0.43775
0.9	0.44005	0.44282
1.5	0.45459	0.45560

For β close to unity, the agreement is not expect to be as good as for β much less than one or β much bigger than one, since the expression for the ground-state energy for the homogeneous system, Eo(α), is an approximation valid for α nonequal to one.

Summary We developed a non-local functional of the bond exchange interactions for the ground-state energy of quantum spin chains. We obtain good estimates for large chains with arbitrary distribution of bond interactions, at no extra computational costs as compared to a simple mean-field calculation. The agreement with exact numerical diagonalization is very good even for many bond defects.

[1] W. Heisenberg, Z. Phys. **38**, 441 (1926), Z. Phys. **49**, 619 (1928).

[2] P. Hohenberg and W. Kohn, Phys. Rev. **136**, B864 (1964); W. Kohn, Rev. Mod. Phys. **71**, 1253 (1999).

[3] Valter L. Líbero and K. Capelle, Phys. Rev. B **68**, 024423 (2003); Int. J. Quantum Chem., **105**, 679 (2005); Physica B **384**, 179 (2006).

[4] P. E. G. Assis, Valter. L. Líbero and K. Capelle, Phys. Rev. B **71**, 052402 (2005).

[5] Valter L. Líbero, K. Capelle, F. C. Souza and A. P. Fávaro, JMMM (2007), accepted for publication, code libero044.

[6] T. Barnes, J. Riera and D. A. Tennant, Phys. Rev. B **59**, 11384 (1999).

HS-16

Ab initio DFT study of half-metallic character in Sr_2CoReO_6 complex perovskite.

J. Roa-Rojas, M. Bonilla, J. A. Rodriguez, F. Fajardo, D. A. Landinez-Tellez
Dept. of Physics, Universidad Nacional de Colombia, Bogotá, Colombia

The extensive half-metallicity studies in double perovskite materials are related with the technological applications in *spintronic* devices, such as spin valves, sources for spin polarized electrons and magnetic information storage systems. The aim of this work is to carry out a *ab-initio* study of the complex perovskite Sr_2CoReO_6, which was reported as antiferromagnetic with low Néel temperature T_N = 65 K[1].
Calculations of electronic structure for Sr_2CoReO_6 were performed with the FP-LAPW method, in the framework of the Density Funcional Theory [2,3] as implemented in the wien2k code[4]. We have used the following parameters for the program: RMT×Kmax=8, the muffin-tin radii (in u.a.) of 2.5, 1.96, 1.96 and 1.69 for Sr, Co, Re, and O respectively. 196 k-points were used in the irreducible Brillouin zone. Calculations were performed with the structure I4/m (space group #87). The total energy versus volume of unit cell was fit to the Murnaghan state equation. From this fitting, we obtain the lattice parameters a=5.533 Å and c=7.859 Å, which correspond to c/a=1.42, which are in a good agreement with experimental results [1].
As it is shown in figure 1, the Density of States (DOS) shows a clear half-metallic nature for the material: the spin up channel has a semiconducting behavior, with a gap of 0.27 eV, and the spin down evidences a conductor behavior.
In the $A_2BB'O_6$ complex perovskite, the effect of oxygen on the B and B'(transition metal cations) produces a splitting in the bands due to the crystalline field. It is known that for no cubic structures, d_{xz} and d_{yz} behave as a single level d_{xz+yz}. It is because of the lost of symmetry in the structure, due the deformation of a cubic cell to create a tetragonal structure. Another explanation is related to the possibility that usual states are not divided in d_{eg} (high energy) and d_{t2g} (low energy) but in d_{z^2}(high energy) and $d_{x^2-y^2}$ and d_{xz+yz} (low energy) levels. Due to the magnetic characteristic of B and B' cations, an exchange splitting has place. It is observed as a difference between up-d_{eg} and down states, and a difference between up-d_{t2g} and down states. In order to study these effects, calculations of projected DOS on the like atomic-orbitals have been performed for Co and Re. In figure 2, it is observed that spin-down-low-energy states (which is extended from ~-1.88 eV to ~0.84 eV) contribute to the conduction band, while high energy levels contribute to the unoccupied states above the Fermi level (from ~0.9 to ~2.5 eV). On the other hand, spin-up-high-energy states contribute below the Fermi level from ~-1.69 eV to ~-0.16 eV.
Low energy states are observed below -3.00 eV. We have determined that up and down high energy states do not contribute significantly to the density of states and appear above ~3.5 eV. Up-spin-low energy states are located close and above the Fermi level at E > 0.15 eV. Down-spin-low energy states belong to the conduction band. It is expected from the possible valences of Re, +5 or +6, which represent an effective magnetic moment due to the $5d^1$ or $5d^2$ electronic configurations.
In summary, structural and electronic properties of the Sr_2CoReO_6 material were investigated. Our study reveals that this material is half-metallic. As expected for such systems, effective magnetic moment of cell, predominantly due to Co, is an integer number of Bohr magneton. Additionally, we use the partial densities of states of electronic orbital to discuss some aspects of the underlying physics in these systems and to correlate our results with reported methodologies, which consider a new mechanism as responsible of the magnetic interactions in perovskite compounds.

[1] H. Kato et al, Phys. Rev. B 69, 184412 (2004)

[2] P. Hohenberg, W. Khon, Phys. Rev. 136 (1964) B864.

[3] W. Khon, L. S. Sham, Phys. Rev. 140 (1965) A1133.

[4] P. Blaha, K. Schwarz, G. K. H. Madsen, D. Kvasnicka, J. Luitz, WIEN2k, An Aug-mented Plane Wave + Local Orbitals Program for Calculating Crystal Properties (Karlheinz Schwarz, Techn. Universität Wien, Austria, 2001), ISBN 3-9501031-1-2.

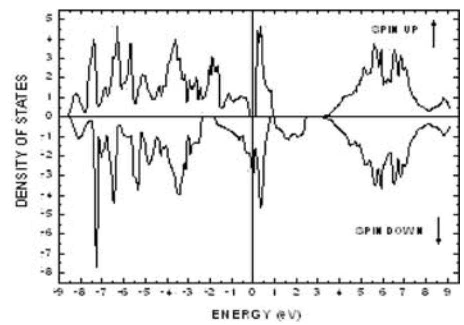

Fig. 1. Total density of states for Sr_2CoReO_6 complex perovskite.

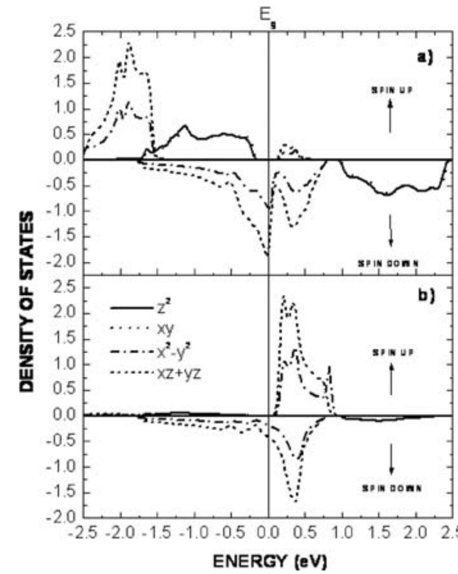

Fig. 2. Projected DOS for *d*-like atomic orbitals of Sr_2CoReO_6 material: a) *d*-DOS of Co and b) *d*-DOS of Re for the spin-up and spin-down polarizations. High energies of up and down levels are superposed.

HT-01

Combinations of decoding algorithm for LDPC codes by tensor product decoding.

H. Kamabe
Information Science, Gifu University, Gifu, Japan

1. Introduction

A power constraint of electronic circuits for encoding and decoding is rather severe in storage devices in mobile systems. We combine bit flipping decoding algorithms (simple, fast but not good enough), denoted by D_{1} below, and the sum-product decoding algorithm (complex, power consuming but very good), denoted by D_{2} below, by using the concept of Tensor Product Codes[1] in order to save the power for decoding retrieved signals without much code rate loss.

2. Method

We use 3 error correcting codes as constituent codes of our coding scheme, say, C_{1}, C_{2} and C_{3}. Here, C_{2} is a repetition code of length 3 and C_{3} an LDPC code. We explain our coding scheme using a single parity check code as C_{1} for simplicity. A code word generated by our coding scheme is schematically given as follows

$c_{11} c_{21} .... c_{k1} c_{(k+1)1} .... c_{n1}$,
$c_{12} c_{22} .... c_{k2} c_{(k+1)2} .... c_{n2}$,
$c_{13} c_{23} .... c_{k3} c_{(k+1)3} .... c_{n3}$.

2.1 Encoding

We assume that C_{3} is a systematic code.

(1) We encode $c_{11} c_{21} ... c_{k1}$ by C_{3} and obtain parity bits $c_{(k+1)1} ... c_{n1}$.
(2) We calculate a syndrome s_{1} of $c_{11} ... c_{k1}$ for the single parity check code C_{1}.
(3) We determine c_{1j} so that a syndrome bit of $c_{1j}... c_{kj}$ for C_{1} is equal to s_{1} for $j=2,3$.
(4) We encode $c_{1j} ... c_{kj}$ by C_{3} and obtain parity bits $c_{(k+1)j}...c_{nj}$ for $j=2,3$.
(5) We record or transmit c_{ij} but do not record s_{1}. We call $c_{1i} c_{2i} ... c_{ni}$ the i-th block.

2.3 Decoding

Let $\{y_{ij}\}$ be retrieved signals.

(1) We apply the decoding method D_{1} to each block $y_{1i}...y_{ni}$ and obtain $z_{1i}...z_{ni}$.
(2) We calculate a syndrome bit t_{i} of $z_{1i}...z_{ki}$ for C_{1}.
(3) We decode $t_{1}t_{2} t_{3}$ as a code word of C_{2}.
(4) If we find an erroneous bit in the previous step, say t_{i}, we try to decode the i-th block again by the decoding method D_{2}.

Note that the error correcting performance of D_{2} is better than that of D_{1}.

3. Results

We show simulation results of the above decoding scheme where we use a Hamming code as C_{1}. In Fig.1 we show error correcting performance of our coding scheme. `mQBF’ is a decoding algorithm based on the bit flipping. It uses only integer values in each iteration process but has a relatively better error correcting performance. $C_{3}$ is an `s2.94.594’ code available from the Mackay’s database for LDPC codes. When we use the Hamming code as C_{2}, we can have some variants of our coding scheme because a syndrome of the code is a vector of length greater than 1. `TP-Hamming-1Correct’ and `TP-Hamming-AllCorrect’ mean two of these variants. Our coding scheme is far better than mQBF and the probability for invoking the Sum-product decoding is low when the SNR is large enough. This may imply that the power consumption of our coding scheme may be low. Our coding scheme can be modified so that the information about erroneous block is used in the first decoding process by D_{1}. We must investigate better combinations of C_{1}, C_{2} and C_{3}.

4. Properties

(1) Code rate
We use C_{2} to find errors in outputs of D_{1}. A similar mechanism can be implemented by a serial concatenation coding scheme of C_{2} and C_{3}. But we can reduce the rate loss by our coding scheme.
(2) Error detecting capability
Our coding scheme can find an erroneous block correctly when the number of erroneous blocks is at most one.
(3) Error Propagation
Our decoding method is analogous to the decoding procedure for a Tensor Product code[1] which we use to reduce the code rate. An integrated interleaving error correcting(IIEC) is another technique to reduce the code rate[2]. Although a lot of errors in integrated parity bits in the IIEC propagate through a block, there is no error propagation in our decoding scheme because integrated parity bits are used only to find erroneous blocks.
(4) Power consumption
From Fig. 2 we note that our coding scheme reduces the power consumption while keeping the better error correcting performance of D_{2}.

[1] J. K. Wolf, An Introduction to Tensor Product Codes and Applications to Digital Storage Systems, Proceedings of ITW2006, pp. 6–10, 2006.

[2] M.Hassner, K.Abdel-Ghaffer, A.Patel, R.Koetter and B.Trager, Integrated Interleaving — A Novel ECC Architecture, IEEE Trans. Magn., vol. 37, pp. 773—775, 2001.

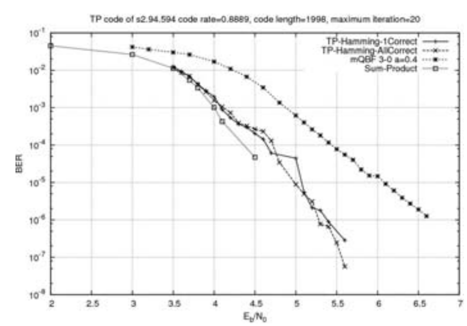

Fig. 1

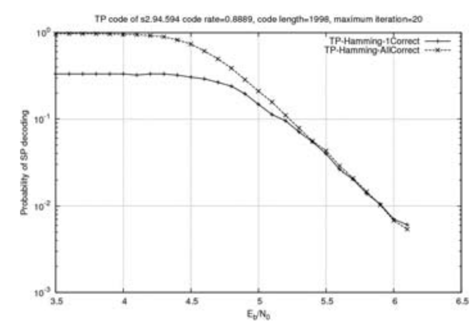

Fig. 2

HT-02

Performance Evaluation of Combined Post-processor Based on Likely Error Pattern and Parity Check Targeting under Write Pre-compensation in PMR Channel with NLTS.

Y. Okamoto[1], *T. Bushisue*[1], Y. Nakanura[1], H. Osawa[1], H. Muraoka[2]
1. Graduate School of Science and Engineering, Ehime University, Matsuyama, Japan; 2. RIEC, Tohoku University, Sendai, Japan

Introduction

We proposed a post-processor without parity check code for PRML channel[1]. The post-processor targets the likely error patterns due to jitter-like medium noise which depends on the recording sequence, and corrects without support provided by parity check. It requires a write pre-compensator (WPC) to offer good performance in perpendicular magnetic recording (PMR) channel with nonlinear transition shift (NLTS) [2]. Furthermore, it introduces parity check (PC) code to decrease the mis-correction in error pattern targeting and to correct the uncovered error patterns. In this study, the PRML channel with the combined post-processor (CPP) is evaluated under WPC in PMR channel with NLTS and is compared to PRML-AR channel with a complex autoregressive (AR) model [3] as channel estimator.

PRML channel with write pre-compensator and post-processor

Fig.1 shows the block diagram of PRML channel with CPP. The system employs the 4-interleaved PC code with coding rate of 128/132. The data sequence is recorded after the WPC in the PMR channel with NLTS. The amount of NLTS is measured by using 5th harmonic method [4] for R/W experimental data obtained by a sprinstand. We use a hyperbolic tangent like function defined by the saturation level A and the rising time T_{50} as the isolated reproducing waveform for the step-like recording waveform [5] in computer simulation. We adopt a generalized partial response (GPR) channel [6] based on PR1 channel which requires a Viterbi detector (VD) with 16 states. The VD estimates the detector input sequence using a simple signal estimator, or it does not use a complex noise estimator like AR model. The CPP consists of two classes of error correction units. The first unit called PPE corrects the particular decision errors of GPRML channel due to jitter-like medium noise [1]. The second unit called PPP corrects the remaining errors composed of the other uncovered error patterns and the mis-corrected errors by PPE. The PPE and PPP units use the squared distance increase [7] as the reliable information. It is calculated by a simple signal estimator which is the same as the VD.

BER performance comparison

Fig.2 shows the bit error rate (BER) performance of proposed GPRML-CPP, GPRML-PPE, simple GPRML and GPRML-AR channels with symbols ○, △, ●, and ■, respectively. The parameters are set to the normalized linear density $K=T_{50}/T_b=1.2$ by a bit interval T_b, SNR=19.5dB defined by the saturation level A and the rms value of total noise at the reading point, the percentage of jitter-like noise R_j=80%, the normalized cut-off frequency of low-pass filter x_h=0.4 by a bit-rate f_b, and the tap number of transversal filter N_t=15. The amounts of NLTS normalized by a bit interval T_b are 0.031, 0.133, 0.139, and 0.142 for the respective transition intervals of T_b, $2T_b$, $3T_b$, over $4T_b$. The WPC shifts the transition with longer interval than Tb from the previous transition to the post direction by L_{comp} [%] of T_b. From the figure, the optimum amounts L_{comp} of pre-compensation which provide the lowest BERs are different for respective GPRML channels. Though the performance of GPRML-PPE is inferior to that of GPRML-AR, GPRML-CPP shows the slightly better performance than GPRML-AR in spite of rate loss due to PC code.

Conclusion

The PRML channel with CPP has been evaluated under WPC in PMR channel with NLTS and compared to PRML-AR channel with an AR model as a channel estimator. The results show that GPRML-CPP shows the slightly better performance than the complex GPRML-AR in spite of rate loss due to PC code.

[1] Y. Okamoto et al., The digests of MMM-INTERMAG 2007, AQ-05, Jan. 2007.

[2] K. Senanan et al., IEEE Trans. Magn., vol.38, no.4, pp.1664-1669, July 2002.

[3] A. Kav či ć et al., IEEE Trans. Magn., vol.34, no.3, pp.763-771, May 1998.

[4] Y. Tang et al., IEEE Trans. Magn., vol.27, no.6, pp.5316-5318, Nov. 1991.

[5] Y. Okamoto et al., J. M. M. M., vol.235, pp.259-264, 2001.

[6] J. D. Coker et al., IEEE Trans. Magn., vol.34, no.1, pp.110-117, Jan. 1998.

[7] Z. Wu, *Coding and iterative detection for magnetic recording channels*, Kluwer Academic Publishers, 2000.

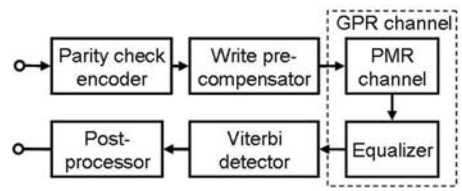

Fig. 1 Block diagram of PRML system with combined post-processor

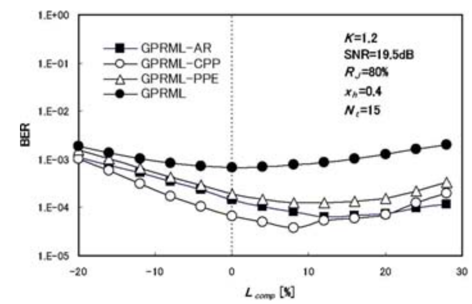

Fig. 2 BER perormance of PRML channels for L_{comp}

HT-03

Performance comparison of various error correcting strategies using perpendicular magnetic recording data series.

S. Mita, H. Matsui
Toyota Technological Institute, Nagoya, Japan

Introduction
The choice of error correcting strategy is a key point in implementing HDD with high data reliability. We have evaluated the performance of the following typical three error correcting methods that have nearly the same code rate of 0.93 at a bit error rate of around 10-3 and higher using real perpendicular magnetic recording channel data series. This bit error rate may be expected as the worst case for practical use.
(a) Finite geometry LDPC codes [1]
(b) Parity product codes
(c) Reed-Solomon codes with hard decision decoding
Measurement
Figure 1 represents a performance evaluation process. 6 bit quantized data series sampled at adequate timing instants are fed into a simple DC restoration process using signal envelope detection and equalized to partial response class 1 waveform by using
9 –tap transversal filter. Then, LLRs are calculated by applying BCJR algorithm to PR1 trellis structure (PR1 detector). We have adopted two types of PR1 detector such as a conventional 2-state PR1 detector and our proposed 4-state PR1 detector [2] using multi-chip structure. These LLRs are provided to various error correcting decoders above mentioned. Hard decision bits generated from LLRs are provided for the Reed-Solomon decoder. The number of error included in retrieved data series are counted in correspondence with original data series.
Structure of error correcting codes
(a) Finite geometry LDPC code
We have used a Type-2 Projective Geometry-LDPC code (PG-LDPC) whose code length is 5797 and code rate is 0.949. Moreover, we have estimated another code length, the shortened PG-LDPC code whose code length is 4296. The code rate of the shortened PG-LDPC codes is set to 0.931. As well known, these LDPC codes do not include 4-cycle. These encoders have the form of quasi-cyclic structure adequate for easy implementation. We have used sum-product algorithm as a decoding algorithm.
(b) Parity product code
We have attempted to evaluate the parity product codesof 83×51 matrix including 4100 data bits, 82 horizontal parity bits and 51 vertical parity bits. This code rate is approximately 0.968. Moreover, we have adopted a random inter-leaver of 4100 bits that can cover an entire sector data.
(c) Reed-Solomon code
RS code over a field GF (2^10) are selected, which can cover one sector of 512 bytes with redundant part for 15 correctable errors. Thus, the total code length must be 440 symbols. Its redundant part is 30 symbols, which is equal to 300 bits. Its code rate is approximately 0.931.
Comparison of error correcting capability
(a)Figure 2 shows one example of the decoding performance of both PG-LDPC code and the shortened code. LDPC decoding of small noise data (bit error rate of approximately 10-3 with 2-state PR1 detector) is completed after 3 iterations. Furthermore, the error rate of PG-LDPC code with a code rate of 0.949 is 10 times greater than that of shortened PG-LDPC code. On the other hand, LDPC decoding of large noise data (bit error rate of approximately 5x10-3) can not correct errors even after 9 iterations. Proposed 4-state PR1 detector halves number of errors of 2-state PR1 at a bit error rate of 10-3. Table1 shows the number of residual errors included in 4296 bits after iteration. This small improvement is useful in high error rate area.
(b)A combination of parity product codes with code rate 0.97 and 4-state PR1 detector can improve bit error rate by two orders at a bit error rate of 10-3 . Residual errors can be corrected by using RS codes with a code rate of 0.96. Total code rate of the combination is approximately 0.93.
(c) The maximum number of symbol errors included in one sector was 6 for the 4-state PR1 detector and 12 for the 2-state PR1 during total 2000 sectors. Therefore, surprisingly, Reed-Solomon codes with hard decision decoding can correct these errors completely.
Concluding remarks
Consequently, increasing RS codes redundancy and adding soft decision capability for a part of redundancy as well as hard decision capability could be one of the best choices for the worst error rate of around 10-3 in future HDD.

[1]Y. Kou et al., “Low-Density Parity-Check Codes Based on Finite Geometries: A Rediscovery and New Results,” IEEE Trans. Information Theory, Vol-42, No.7, November 2001.

[2] S. Mita, “A Robust Detector Based on a Combination of PR1 and EEPR4 for Perpendicular Magnetic Recording,” IEEE Trans. Magn., Vol-42, No.10, October, 2006.

Iteration	1	2	3
2-state PR1	3292	609	11
4-state PR1	3119	371	3

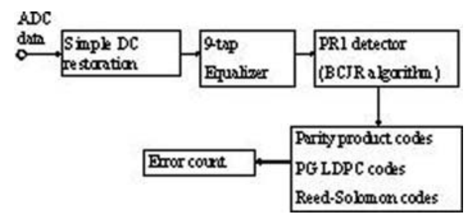

Fig.1 Measurement process

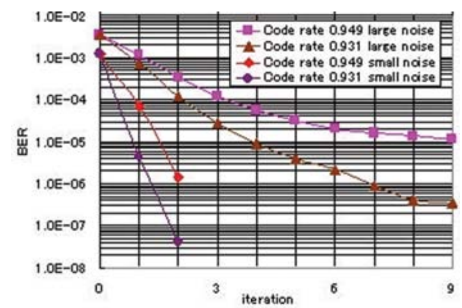

Fig.2 Error rate of PG-LDPC code

HT-04

EPCC-based Channel-Optimized LDPC coding.

H. S. Alhussien, *J. Moon*
CDSLAB, Electrical and Computer Engineering, University of Minnesota Twin Cities, Minneapolis, MN

Low density parity check (LDPC) codes are gaining wide interest in the implementation of the perpendicular magnetic recording (PMR) read channel. The PMR read signal is corrupted by intersymbol interference (ISI) and a mix of Gaussian electronic and media noises. For this kind of environment, even state of the art soft decoding of the currently implemented Reed-Solomon (RS) codes shows a significant gap to the binary constrained channel capacity. On the other hand, turbo equalization (TE) based on the iterative exchange of soft information between the channel detector and the message passing decoder (MPD) of LDPC can potentially close the gap to channel capacity. Moreover, the gap to capacity can be reduced by optimizing the LDPC matched to the channel using density evolution techniques. However, the resulting random irregular parity check matrix requires high encoding complexity.

To design a channel optimized high-rate TE system with low encoding complexity, we propose to concatenate a very high-rate specialized inner error pattern correction code (EPCC) to an outer structured LDPC code. This is motivated by the sector error rate (SER) gains observed when EPCC serves as an inner code for RS at a manageable added complexity [2]. Furthermore, EPCC enhances the overall bit error rate (BER) of TE systems for a wide range of operating rates [3].

We compare the BER and SER performance of TE based on a standalone quasi-cyclic (QC) LDPC [3] iteratively decoded with the channel, to the performance of the same TE with an EPCC soft-in soft-out (SISO) decoder standing at the output of the channel detector and LDPC MPD input. In this presentation, we show results for a 1+D ISI channel corrupted by additive-white-Gaussian-noise (AWGN) experiencing a noise penalty proportional to $10\times\log_{10}(1/R)$, where R is the coding rate. In the final version of this work, we will study the performance in a jitter dominant environment with $10\times\log_{10}(1/R^2)$ noise penalty.

The EPCC proposed in [1] and [2] is designed such that for a given set of dominant error patterns, inherent in an ISI channel, any single dominant error pattern occurrence as well as a significant portion of their multiple occurrences can be corrected. Here, We design a 0.98 rate (630, 616) EPCC targeting the 10 most dominant error events of the 1+D channel, those are of length 1 to 10 and are of the form ±[2,-2,2,-2,…]. Details on the design of the EPCC algebraic single pattern correcting code can be found in [2], the correction capability of the algebraic decoder is extended through list decoding [2][3] by using a parallel bank of such decoders. The list decoder uses channel observation in addition to *a priori* soft information generated by the maximum *a posteriori* (MAP) channel detector to build a list of candidate codewords through algebraic decoding of 25 most probable test patterns, where a test word is constructed by corrupting the maximum likelihood word at the output of the MAP detector by a predetermined combination of the most probable error events. Then, by the utility of error-event-matched *local* correlators to evaluate candidate codeword probabilities, bit-level soft output information is calculated and passed to the LDPC MPD, which in turn, generates extrinsic information to be fed back to the MAP channel detector [3]. The system block diagram is shown in Fig.1.

The outer QCLDPC is designed using the algebraic structured technique in [4] to have performance that rivals the best comparable random codes. We construct a regular (4251, 3926) QCLDPC of rate 0.92, and column and row weights of 3, and 39 respectively. Each sector-wide LDPC codeword is encoded into 7 EPCC codewords and 10 LDPC iterations are implemented per turbo iteration where the overall EPC-QLDPC coding rate is 0.9.

As can be seen is Fig.2, simulation results show that with only 5 turbo iterations of EPC-QCLDPC, a SER of 10^{-4} is achievable at an SNR that is more than 1 dB less than that of standalone QCLDPC.

[1] J. Park, and J. Moon, "High-Rate Error Correction Codes Targeting Dominant Error Patterns," in IEEE Trans. Magn., vol. 42, no. 10, pp. 2573-2575, Oct. 2006.

[2] J. Park, and J. Moon, "Error-Pattern-Correcting Cyclic Codes Tailored to A Prescribed Set of Error Cluster Patterns," in IEEE Trans. Inform. Theory, submitted for publication.

[3] H. Alhussien, J. Park, and J. Moon, "Iterative Decoding Based on Error Pattern Correction," in IEEE Trans. Magn., vol.44, no.1, pp.181-186, Jan. 2008.

[4] R. M. Tanner, D. Sridhara, A. Sridharan, T. E. Fuja, and D. J. Costello, JR. "LDPC block and convolutional codes based on circulant matrices," in IEEE Trans. Inform. Theory, vol. IT-50, pp. 2966-2984, Dec. 2004.

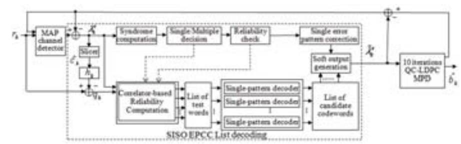

Fig.1: Iterative decoding of ISI channel, EPCC, and QCLDPC.

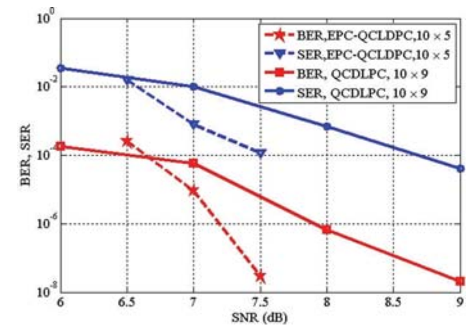

Fig.2: BER and SER comparison of standalone QCLDPC and EPCC-enhanced QCLDPC for a 1+D ISI channel and AWGN.

HT-05

On Imposing an RLL Constraint without Explicit RLL Coding.

J. Park, J. Moon
Electrical and Computer Engineering, University of Minnesota, Minneapolis, MN

In most recording systems, the maximum runs of consecutive like bits and alternating bits are respectively limited to (k+1) and (g+1), based on the non-return-to-zero (NRZ) convention. The k constraint provides adequate timing information to the clock recovery circuit while the g constraint limits the path memory length in the implementation of the Viterbi algorithm. While run-length limited (RLL) coding is typically employed to impose this $\{k,g\}$-constraint, the rate loss associated with the RLL code results in a significant loss of effective signal-to-noise ratio (SNR). A large codeword length can be utilized to mitigate the rate loss effect but this would require reverse concatenation between the error correction code and the RLL code. In this work, we propose a different approach to imposing the $\{k,g\}$-constraint. Our approach does not utilize an explicit RLL coding. The idea is to make use of an error-pattern-correcting code (EPCC) that is highly tailored to a set of dominant error patterns [1]. This code has been shown to provide a significant coding gain [1][2], but here we show that it can also be used to completely eliminate the need for explicit RLL coding. The specific approach is to force a short error pattern in the middle of a prolonged absence of bit transitions as well as a long string of consecutive transitions, after EPCC encoding is done. In the read side, the combined action of EPCC decoding and typical error correction code decoding eliminates the forced error patterns with high probability. This scheme is reminiscent of the method based on the insertion of a detectable pattern with a cyclic redundancy check (CRC) code [3]. The difference is that the present method utilizes a more aggressive error-pattern *correcting* code that can handle multiple occurrences of error patterns including the inserted pattern. Obviously, the inserted pattern must be detected/corrected by the EPCC, and any pattern that contains relatively short transitions can be chosen for this purpose. The inserted pattern is removed whenever it appears at the channel detector output, by using a pattern removal block, as seen in Fig. 1. Afterwards, the error between the detector input and the pattern-removed detector output convolved with the known intersymbol interference (ISI) channel drives the local pattern correlator bank. In this way, when the error flag is raised, the forced pattern and its possible positions can be identified based on the captured syndrome, and the local correlator matched to that pattern will successfully produce a high output at the inserted position. With both the algebraic information and the pattern-level reliability measures provided by local error-pattern correlators matched to the targeted error patterns, including the inserted pattern, the EPCC list decoder based on a set of test word-error events [2] can correct multiple occurrences of error patterns. For the ISI channel response $5+6D-D^3$, a (630,616) EPCC based on the generator polynomial $g(x) = (1+x^3+x^5+x^8)(1+x+x^6)$ has been constructed in [1][2] to identify ten dominant error patterns. Assuming a 20-symbol-correcting outer (450,410) Reed-Solomon (RS) code, the sector error rates (SERs) of the proposed scheme are compared for various $\{k,g\}$ values (Fig. 2). In order to attain the given $\{k,g\}$ constraints, a single-bit error pattern, which is one of the targeted dominant error patterns, is chosen as the insertion pattern. Here, the SERs above 10^{-5} represent actual counts, whereas the lower SERs were computed based on the block multinomial distribution. The employed EPCC list decoder attempts to correct up to triple error patterns within the codeword using 26 test words. It is seen that there is virtually no performance penalty in inserting patterns to impose the $\{k,g\}=\{20,20\}$ compared to the no-insertion case, i.e., $\{k,g\}=\{\infty,\infty\}$. Compared to the case of the Viterbi detector plus RS code only (no EPCC), the $\{20,20\}$-imposed EPCC system yields about 0.5 dB coding gain at SER=10^{-7} while completely eliminating the need for explicit RLL coding.

[1] J. Park and J. Moon, “A New Class of Error-Pattern-Correcting Codes Capable of Handling Multiple Error Occurrences,” *IEEE Trans. Magn.*, vol. 43, no. 6, pp. 2268-2270, Jun. 2007.

[2] J. Park and J. Moon, “Error-Pattern-Correcting Cyclic Codes Tailored to A Prescribed Set of Error Cluster Patterns,” under review for *IEEE Trans. Inform. Theory*.

[3] J. Park and J. Moon, “Imposing a k-constraint in Recording Systems Employing Post-Viterbi Error Correction,” *IEEE Trans. Magn.*, vol. 41, no. 10, pp. 2995-2997, Oct. 2005.

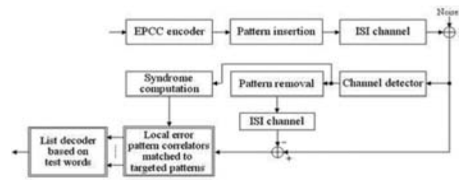

Fig. 1: The $\{k,g\}$-constraint strategy based on error-pattern-correcting code

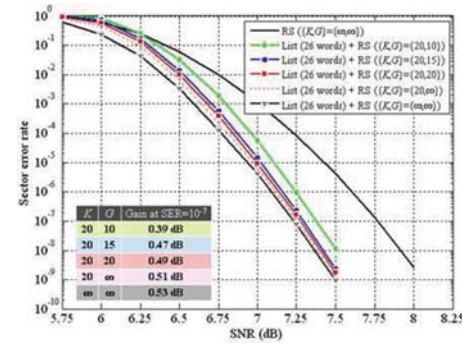

Fig. 2: Sector error rates for various $\{k,g\}$-constraints

HT-06

On the use of averaging to estimate the dibit response.

M. Ting
Seagate Technology, Pittsburgh, PA

I. INTRODUCTION

<p>The dibit response of a magnetic recording system is useful in various ways: for example, its width is an indication of the amount of inter-symbol interference (ISI) in the magnetic recording channel. In the magnetics literature, the dibit response is typically estimated assuming knowledge of the written bit sequence and the noiseless readback signal [1], [2]. Magnetic recording systems, however, have various sources of noise. These include transition and additive noise [3]. In [2], a method to obtain the noiseless readback signal was proposed in which one used spatial and temporal averaging to reduce the transition and additive noise respectively.

<p>This work considers the effect of independent and identically distributed (i.i.d.) transition position jitter and additive noise in the readback signal. We assume that a second-order Taylor series expansion can be applied to the transition response terms with position jitter. We then show that the averaging method of [2] results in a biased estimate of the noiseless readback signal. Assuming that the position jitter has zero mean, the bias in the estimate is proportional to the position jitter variance. Suppose that a transition sequence is written I times around a track, and J rereads of the I sequences are obtained. Application of the Central Limit Theorem shows that the variance of the estimate due to the additive noise decreases by a factor of $(IJ)^{-1}$. The variance of the estimate due to the transition position jitter decreases by a factor of I^{-1}. Explicit forms for the distributions of the transition jitter and additive noise are not used: the result therefore has the appeal of being broadly applicable to various noise distributions.

II. READBACK SIGNAL MODEL AND NOISELESS ESTIMATOR

<p>Denote the transition bits $b_n \in \{0,\pm1\}$. The readback signal y(t) is oversampled at $R \in N$ times the data rate. Let T be the bit period and T_s the sampling time period: note that $RT_s = T$. We consider transition position jitter and additive noise, so that the sampled readback is $y_n = \Sigma_k b_k h(nT_s - kT + e_p(k)) + e_a(n)$ … (**1**), where h(●) is the transition response; $e_p(n)$ is the transition position jitter; and $e_a(n)$ is additive noise [3, (1)]. Assume that

$e_p(n)$ is an i.i.d. sequence with $E[e_p(n)] = 0$ and finite second and fourth order moments.

$e_a(n)$ is an i.i.d. sequence with $E[e_a(n)] = 0$ and $E|e_a(n)|^2 < \infty$.

~~<\>>~~

~~For a continuous time signal x(t), let $x_d(n) := x(nT_s)$ denote the sampled discrete time signal, e.g., $h_d(n) = h(nT_s)$, etc. For a sequence x(n), $x_{(R)}(n)$ is x(n) upsampled by R. Define $x(n) * y(n) := \Sigma_k x(k)y(n-k)$ and $s_n := b_{(R)}(n)*h_d(n)$. Note that s_n is the *noiseless* readback signal.~~

~~<p>Let $s°_n$ be the estimator of s(n) proposed in [2]. It is formed as follows: denote by $y_{ij}(n)$ the *j*th readback of the *i*th track location, for $1 \le i \le I$ and $1 \le j \le J$. Then, $s°_n = (IJ)^{-1} \Sigma_{i,j}\, y_{ij}(n)$ … (**2**).~~

~~III. ASYMPTOTIC RESULTS~~

~~Define σ^2_{ep} to be the variance of $e_p(n)$. One can show that $s°_n \to s_n + ½\sigma^2_{ep}[b_{(R)}(n)*h''_d(n)]$ (a.s.) as $I,J \to \infty$ … (**3**), where "a.s." denotes almost sure convergence. The variance results are omitted for lack of space.~~

~~IV. SIMULATION~~

~~<p>The readback signal model (1) is simulated with: the perpendicular recording channel at normalized density $D_s = 2$ and $R = 10$; $e_p(n)$ being i.i.d. Gaussian $N(0, \sigma^2_{ep})$ truncated to $[-T/2, T/2]$; and $e_a(n)$ i.i.d. $N(0,\sigma^2_{ea})$. T denotes the bit period. The data bits $a_n \in \{\pm1\}$ are taken to be three periods of a pseudorandom (PRB) sequence generated by the primitive polynomial x^7+x^4+1, and $b_n=(a_n-a_{n-1})/2$. The signal to noise ratio (SNR) is 15 dB in the oversampled domain with a noise mix of 50% jitter and 50% additive noise: see [4].~~

~~The empirical and theoretical asymptotic bias of $s°_n$ are illustrated in Fig. 1 for one PRB period. The transitions in the signals match well; however, the amplitudes of the peaks and valleys do not. There are two possible reasons. The first is that the theoretical bias term is derived in the asymptotic regime: a larger value of I may be required. The second is that a second-order Taylor series expansion may be insufficient, and higher-order terms need to be considered.~~

D. Palmer, P. Ziperovich, R. Wood, and T. D. Howell, "Identification of nonlinear effects using pseudorandom sequences," IEEE Trans. Magn., vol. MAG-23, no. 5, pp. 2377–2379, 1987.

I. Ozgunes and W. R. Eppler, "Synchronization-Free Dibit Response Extraction From PRBS Waveforms," IEEE Trans. Magn., vol. 39, no. 5, pp. 2225–2227, 2003.

J. Moon, "Discrete-Time Modeling of Transition-Noise-Dominant Channels and Study of Detection Performance," IEEE Trans. Magn., vol. 27, no. 6, pp. 4573–4578, 1991.

J. Moon, "Signal-to-Noise Ratio Definition for Magnetic Recording Channels with Transition Noise," IEEE Trans. Magn., vol. 36, no. 5, pp. 3881–3883, 2000.

~~<\>>~~

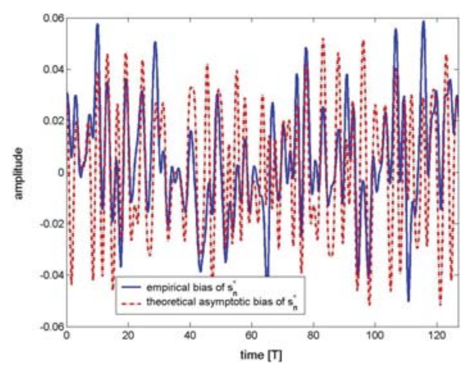

Fig. 1. Comparison of the empirical and theoretical asymptotic bias of the estimator $s°_n$ for a PRB sequence of length 127. The horizontal axis is given in units of T, the bit period.

HT-07

Two-Dimensional Pulse Response and Media Noise Modeling for Bit-Patterned Media Channels.

S. Nabavi[1,2], *V. Bhagavatula*[1,2], J. A. Bain[1,2]
1. Data Storage Systems Center (DSSC),, Pittsburgh, PA; 2. ECE, Carnegie Mellon University, Pittsburgh, PA

I. Introduction
Bit-patterned media (BPM) is one of the promising technologies that is being considered for storage densities of 1 Tbit/in^2 and higher. In BPM, in order to achieve high densities, the bits or magnetic islands should be very close to each other, i.e., both the track pitch and the bit period must be very small. As a result, there will be inter-track interference (ITI) in addition to inter-symbol interference (ISI) [1], [2]. In other words, in BPM, the interference is in 2D. Also in BPM, the media noise is different from that in conventional magnetic recording systems [3]. In BPM a major part of the media noise is due to the fabrication imperfections, therefore the media noise is correlated and affects both the along-track pulse response and the track profile. In this work, to obtain a more realistic channel model, we develop a 2D pulse response to model the 2D interference and the media noise. We also fit an analytical model to the 2D pulse response of BPM to simplify the channel model.
II. Channel modeling
We obtain the 2D pulse response using the three-dimensional (3D) reciprocity integral based on the magnetic potential of the magneto-resistive (MR) read head. We apply the MR read head surface magnetic potential approximated by Weisen et al. [4], to obtain the head magnetic potential [4], [5]. In this work, we use the numerical approach to calculate the 3D reciprocity integral and the head magnetic potential. From the 2D pulse response, we obtain the readback signal by applying 2D linear superposition to model both the ITI and the ISI. We consider fluctuations in island locations and sizes as the sources of media noise [3]. Fluctuations in the location are modeled by using suitably random sampling points of the 2D pulse response. Because the size fluctuations change the shape of the 2D pulse response, we use the first-order Taylor series expansion to approximate this media noise. The correlated noise is obtained by applying a digital filter to white Gaussian noise. To find an analytical or closed-form expression for the 2D pulse response, we fit a surface to the numerical 2D pulse response. A 2D Gaussian pulse appears to be a good candidate for an analytical model of BPM pulse response.
III. Simulation results
An example of a numerical 2D pulse response for a square magnetic island with length 11 nm, height 10 nm, and fly height 10 nm and with soft under layer (SUL) is shown in Fig .1. For this pulse, the MR element has a thickness of 4 nm and width of 20 nm and the shield-to-shield gap is 20 nm. In this work, we focus on the density of 1.5 Tbit/in^2, corresponding to a bit period and the track pitch of 21 nm. A generalized partial response (GPR) equalizer and corresponding Viterbi detector are employed in the channel simulator. The results of modeling the media noise for different values of noise are shown in Fig. 2, where SNR_e is the inverse of electronic noise power in db when using normalized 2D pulse response. It seems that to achieve reasonable bit error rates (BERs), the size fluctuations and the location fluctuations should be smaller than 8% of the bit period. The simulation results also show that correlated noise degrades the performance of the channel even more. The mean square error between the numerical pulse response and the 2D Gaussian pulse response with the same along-track and cross-track PW50s is of the order of 10^{-4}. Also the BER performance of the channel modeled by the 2D Gaussian pulse is very close to that based on the numerical pulse.

[1] P. W. Nutter, I. T. Ntokas, B. K. Middleton, and D.T. Wilton, “Effect of Island Distribution on Error Rate Performance in Patterned Media,” IEEE Trans. Magn., vol. 41, no. 10, pp. 3214-3216, 2005.

[2] S. Nabavi, B. V. K. Vijaya Kumar, and J. Zhu, “Modifying Viterbi Algorithm to Mitigate Inter-track Interference in Bit-Patterned Media,” IEEE Trans. Magn., vol. 43, no. 6, pp. 2274-2276, 2007.

[3] H. J. Richter, A. Y. Dobin, O. Heinonen, K. Z. Gao, R. J. M. V. D. Veerdonk, R. T. Lynch, J.Xue, D. Weller, P. Asselin, M. F. Erden, and R. M. Brockie, “Recording on Bit-patterned Media at Dnsities of 1 Tb/in2 and beyond,” IEEE Trans. Magn., vol. 42, no. 10, pp. 2255-2260, 2006.

[4] K. Wiesen, and B. Cross, “GMR Head Side-Reading and Bit Aspect Ratio,” IEEE Trans. Magn., vol. 39, no. 5,pp 2609-2611, 2003.

[5] S. W. Yuan, and H. N. Bertram, “Off-track Spacing Loss of Shielded MR Heads,” IEEE Trans. Magn., vol. 30, no.3,pp 1267-1273,1994.

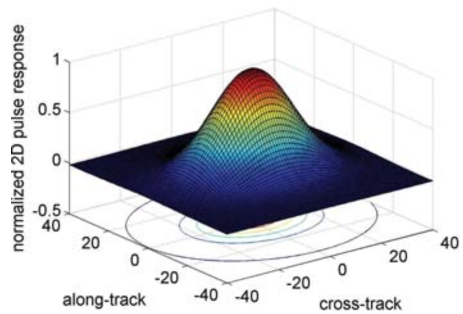

Fig. 1. A 2D pulse response for BPM

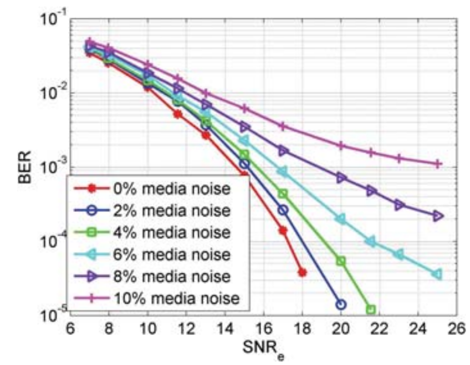

Fig. 2. BER vs SNR_e for white media noise

HT-08

Soft Feedback Equalization for Patterned Media Storage.

M. Keskinoz
Electronics Engineering, Sabanci University, Istanbul, Turkey

Patterned Media Storage (PMS) has recently got a lot of attention since it has a potential to provide ultra-high recording densities of 1 Tb/in2 and beyond [1]. In PMS, the information is stored in the isolated single domain magnetic islands and islands are distributed both along the track and across the track directions. The 2D discrete noisy readback signal of PMS can be expressed as $r_{ij}=a_{ij}\odot h_{ij}+n_{ij}$ where a_{ij} represents the i th binary information bit of the j th track, h_{ij} is the 2D island response sampled at island period along track direction, T_x, and island period across-track direction, T_y, and n_{ij} is the receiver electronics noise which is modeled additive-white Gaussian noise (AWGN) with zero mean variance σ^2.

In this work, we consider only PMS with a SUL and generate the 2D island response to produce similar characteristics as in reference [1] using a square island of length of 12.5 nm.For a high areal density PMS, both inter-track interference (ITI) and inter-symbol interference (ISI), and noise severely degrade the bit error rate (BER) performance of the system. To mitigate the effects of these adverse effects and obtain a capacity increase, in literature, the linear minimum mean squared error (LMMSE) equalization following by threshold (TD) detection, pseudo-decision feedback equalization (PDFE) has been proposed [2]. Under severe 2D-ISI, the performance of PDFE has been shown to be quite better as compared to LMMSE in the numerical experiments since PDFE uses self-iterations to improve hard decisions obtained after the LMMSE equalization followed by threshold detection. To further improve the performance of the PDFE, we develop a method called soft feedback equalization (SFE) that produces soft information rather than hard decisions after the LMMSE equalization and exchanges that between its self-iterations. In SFE,the LMMSE equalizer output is used to calculate the soft information called "extrinsic information" about a particular symbol a_{ij} as shown in Fig.1 Therefore, we first design a simple extrinsic information calculator which outputs the extrinsic log likelihood ratio(LLR) of each information symbol. The calculated extrinsic LLRs are then used to determine the mean of the channel outputs which is later subtracted from the channel outputs to perform LMMSE estimation. To initialize the SFE equalization, we set a priori information of all information bits to zero. After the first iteration, we obtain the extrinsic LLR at the output of the equalizer and it can be used as a priori information for the next iteration of the equalization process.

We also compare the performance of SFE with LMMSE and, PDFE and SFE for different recording densities that equal to $1/(T_x T_y)$*bits/unit area* . In our numerical experiments, for this aim, we consider only T_x= 14.13 nm and vary the island period along the track direction, T_y, as 31.2 nm, and 17.83 nm to obtain areal density D of 1.45 and 2.53 (Tera-bits/inch2) respectively. For these values of island periods and corresponding recording densities, the channel has a support of Lx =5 and Ly =5 at most. In PDFE and SFE, we use 2 iterations and we observed that using more iteration does not help to improve the performance. To keep the complexity of PDFE and SFE small, we only employ a 3x3 LMMSE equalizer.

During our simulations,we observe that PDFE and SFE converge using one iteration and two iterations for D= 1.45 and D=2.53 Tbits/ inch2 respectively. For the target BER of 10^{-4} and D=1.45 both PDFE and SFE provide SNR gain of 1.25 dB over LMMSE. For this track density since the amount of 2D-ISI is relatively small and hence SFE didn't provide any SNR improvement over PDFE. For the same target BER and D=2.53, PDFE and SFE and provide SNR gain of 4.5 dB and 8 dB over LMMSE respectively. For this density, the performance of SFE is superior and it provides SNR gain of 3.5 dB compared to PDFE with two iterations. Hence, we conclude that under very high areal density and severe 2D-ISI, employing more iterations in SFE can result in higher SNR gains over both LMMSE and PDFE and therefore SFE has a high potential to be used in a ultra-high capacity PMS.

[1] P. W. Nutter, I. T. Ntokas, and B. K. Middleton, "An Investigation of the Effects of Media Characteristics on Read Channel Performance for Patterned Media Storage," IEEE Trans. Magn., vol. 41, no. 11, pp. 4327-4334, 2005.

[2] B. M. King and M. A. Neifeld, "Parallel detection algorithms for page-oriented optical memories," Appl. Opt. 37, 6275-6298 (1998).

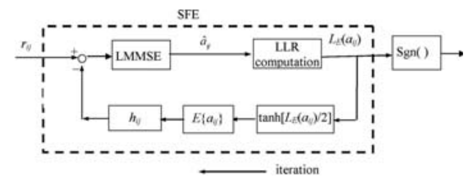

Fig. 1. Schematic of soft feedback equalizer (SFE).

HT-09

Signal Modeling for Ultra-high Density Bit Patterned Media and Performance Evaluation.

S. Zhang, Z. Qin, X. Zou
Data Storage Institute, Singapore, Singapore

1. INTRODUCTION

Bit-patterned-media (BPM) has been proposed as a candidate for next generation hard disk drives (HDD) [1]. However, manufacturing imperfections can cause these islands to vary in shape/size as well as their geometric locations. In this work, we look into the effects of such manufacturing defects on the signal characteristics and performance with a modeling technique based on our newly developed analytical 3D GMR sensor profile and the reciprocity principle [2].

2. SIGNAL AND CHANNEL MODELING

We simulated 2 heads of different geometric parameters listed in Table 1. On the media side, we target ultra-high density recording of 1 tera-bit per square inch (Tbpsi) and above, with a small bit-aspect-ratio (BAR) of 2 or 4 as the minimum lithographic imprinting feature size sets a lower limit on the island diameter. Based on the read head geometry, the ISI and ITI profile are summarized in Table 2.

Signal generation for BPM is based on the 3D read head profile derived in [2]. We compare the readback signal due to a single transition with those generated using mathematical models, such as error function, hyperbolic tangent function and other physics based model such as the Roger-Potter model [3]. From Fig. 1, we can see that error function and hyperbolic tangent function as well as R-P model matches well to our analytical model, but still not as accurate in modeling the tailing (under-shoot) part of the transition. Therefore we further improve these models by calculating two transitions matched to the media top readback and media bottom readback and combine them accordingly. These improved mathematical models match better to our analytical readback. Another example of this technique is given in Fig. 2 for readback pulse due to a single island in BPM. Also shown in this figure is the interference caused to the neighboring track after being normalized to the same amplitude of the on-track pulse to better illustrate the shape change.

3. PERFORMANCE OF A HIGH RATE LDPC CODES WITH BPM

With the accurate signal generation model for BPM developed, we then conduct channel performance with a 4096/4544 LDPC encoder, a minimum-mean-square-error (MMSE) equalizer, followed by an iterative detector/decoder which consists of a soft-input soft-output BCJR detector and an LDPC decoder. The SNR definition in our result plot is the ratio between the summation of channel coefficient (ISI coefficients) square and the noise power. Therefore longer ISI span means lower effective SNR for each bit.

Bit-error-rate (BER) curves and frame-error-rate (FER) curves are obtained for different head/ density/ BAR combinations in Fig. 3 and Fig. 4. From Table 2 we can see that ITI for smaller BAR can be quite severe at high recording density, resulting very poor performance.

In Fig. 5-6, we explore the effects of island position jitter levels as they could be quite severe in real product [4]. For example, 15% island position jitter roughly translates into 1.5dB SNR loss when comparing the error rate performance, for both read heads. However, the effect of island size fluctuation at different head/density can be quite different. In Fig. 7, 10% island size variation roughly translates into 0.5dB SNR loss for small head and low density, while it translates into about 2dB for larger head and double the density in Fig. 8. With read head B and density 2Tb/in2, 15% island size variation equals nearly 7dB in SNR loss.

4.SUMMARY

In this work we developed a signal generation model for BPM recording system based on analytical 3D read head profile and reciprocity principle. We also proposed method to tune simple mathematical model with parameters extracted from analytical model for faster signal generation. Simulation of BPM recording system with advanced channel algorithm is conducted and effects of media noise on performance are discussed.

(full table/figures/references can only be provided in full paper due to charater limits in web-submission)

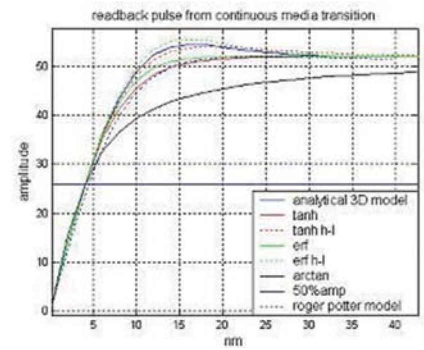

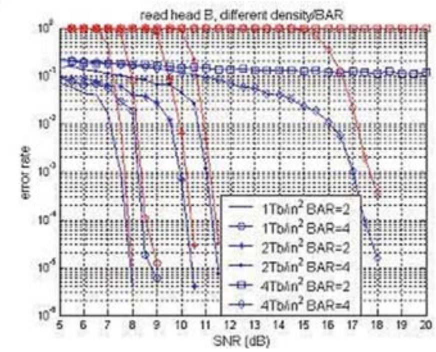

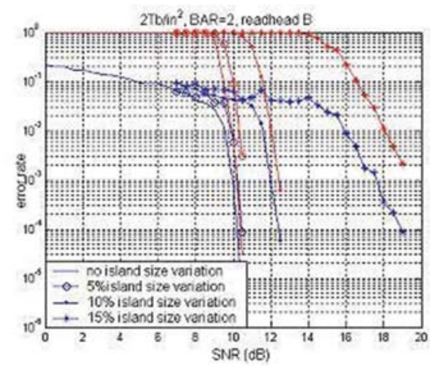

Equalization and detection for patterned media recording.

S. Karakulak[1], P. H. Siegel[1], J. K. Wolf[1], H. Bertram[1,2]
1. Electrical and Computer Engineering Dept., Center for Magnetic Recording Research, UCSD, La Jolla, CA; 2. Hitachi Global Storage Technologies, San Jose, CA

Patterned media recording, where bits are stored on predefined, signal domain magnetic islands, may provide an alternative to conventional recording on continuous media. In this paper, we present a very simple equalization procedure and compare several different detection methods for patterned media recording channels [1].<p>
In the read channel model considered here, a track consists of three parallel sub-tracks, and the read head, when centered over the middle sub-track, spans a specified fraction of the outer sub-tracks. Electronics noise, modeled as AWGN with mean zero and variance σ^2, is assumed to corrupt the output of the read head. For certain recording densities, the noiseless discrete-time readback model can be represented by a 3x3 channel response matrix H, shown in (1) of Fig. 1. Each cross-track triplet of islands represents one of 8 possible recorded symbols. The channel represented by H has memory equal to 2 symbols, so the trellis representing the noiseless channel output sequences has 8^2 =64 states, and from each state there are 8 outgoing branches. When the channel response matrix has cross-track symmetry, the number of states can be reduced to 6^2=36 with 6 outgoing branches from each state. If, in addition, the corner entries are equal to zero, the number of states can be reduced to 2^2=4 with 3 parallel branches between each pair of connected states [2]. In the reduced-state trellis structures, some output sequences may be generated by more than one input sequence. Therefore, when using these trellises as the basis for symbol detection, we may have to use a restricted input symbol alphabet [1]. Alternatively, we may use them for detection of the middle sub-track only. <p>
We consider maximum-likelihood (ML) detection of symbol sequences or bit sequences, as well as maximum a-posteriori (MAP) detection of symbols or bits. The ML detector uses the Viterbi algorithm to find the ML symbol sequence, with a simple modification for ML bit sequence detection. The MAP symbol detector uses the Bahl-Cocke-Jelinek-Raviv (BCJR) algorithm, which we can modify slightly to obtain the a posteriori probability ratio (APPR) of the coded bits for MAP bit detection. Specifically, if $u_{i,0}$ represents a recorded bit on the middle sub-track at time index i and $\underline{y}$ represents the channel output samples, the modified BCJR algorithm outputs the APPR in (2) of Fig. 1, where S_i^{-1} and S_i^{1} are, respectively, the set of trellis branches (s_{i-1},s_i) corresponding to input bit -1 and 1.<p>
We compare the performance of four different schemes using the channel response introduced by Nabavi et al [2], H_1, shown in Fig. 2. The first scheme uses an ML bit sequence detector whereas the second scheme uses an MAP bit detector. Both detectors use a trellis with 36 states and 6 outgoing branches per state. In the third scheme, we use a one-dimensional MMSE equalizer with finite impulse response (FIR) designed using an adaptation of the method in [3] but with a 3x3 target response G having corner entries equal to zero and $g_{-1,0}$=1 [2]. The detector trellis has 4 states with 3 parallel branches between each connected pair of states. We use the Viterbi algorithm with squared-Euclidean metric to detect the middle sub-track bit sequence. (Since the equalizer colors the electronics noise, this detector is no longer ML.) The fourth scheme was introduced by Nabavi et al. [2] for the same channel model. Their detector also uses the Viterbi algorithm on a trellis with 4 states and with 3 parallel branches between each connected pair of states. The detector complexity of the first and second schemes is considerably greater than that of the third and the fourth schemes. For channel response matrix H_2 shown in Fig. 2, we simulate the first three schemes.<p>

The simulation results are shown in Fig. 3 for H_1 and H_2. The signal to noise ratio (SNR) is defined as $20\log10(V_p/\sigma)$ where V_p=1. In all equalized systems, the FIR filters were limited to 11 taps. For channel H_1, the first three schemes substantially outperform the fourth scheme where the results are taken from [2]. At a target bit error rate of 10^{-4}, the proposed schemes provide a gain of 1.5dB for channel H_1. For channel H_2, the first three schemes have approximately the same performance.

1. S. Karakulak, P. H. Siegel, J. K. Wolf and H. N. Bertram, “A New Read Channel Model for Patterned Media Storage,” *IEEE Trans. Magn.*, vol. 44, no. 1, pp. 193-197, Jan. 2008.<p>

2. S. Nabavi, B. V. K. V. Kumar and J-G. Zhu, “Modifying Viterbi Algorithm to Mitigate Intertrack Interference in Bit-Patterned Media,” *IEEE Trans. Magn.*, vol. 43, no. 6, pp. 2274-2276, June 2007.<p>

3. J. Moon and W. Zeng, “Equalization for Maximum Likelihood Detector,” *IEEE Trans. Magn.*, vol. 31, no. 2, pp. 1083-1088, March 1995.

$$H = \begin{pmatrix} h_{-2,-1} & h_{-1,-1} & h_{0,-1} \\ h_{-2,0} & h_{-1,0} & h_{0,0} \\ h_{-2,1} & h_{-1,1} & h_{0,1} \end{pmatrix} \quad (1) \qquad \frac{P[u_{i,0}=-1|\underline{y}]}{P[u_{i,0}=1|\underline{y}]} = \frac{\sum_{S_i^{-1}} P[s_{i-1},s_i,\underline{y}]}{\sum_{S_i^{1}} P[s_{i-1},s_i,\underline{y}]} \quad (2)$$

Fig. 1 The channel response matrix *H* and the APPR for the coded bit $u_{i,0}$.

$$H_1 = \begin{pmatrix} -0.023 & 0.264 & -0.023 \\ -0.087 & 1 & -0.087 \\ -0.023 & 0.264 & -0.023 \end{pmatrix} \qquad H_2 = \begin{pmatrix} 0.0347 & 0.2297 & 0.0347 \\ 0.1277 & 1 & 0.1277 \\ 0.0347 & 0.2297 & 0.0347 \end{pmatrix}$$

Fig. 2 The channel response matrices H_1 and H_2.

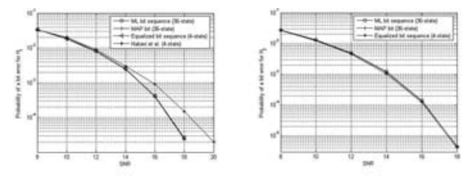

Fig. 3 (a) Simulation results for H_1. Fig. 3 (b) Simulation results for H_2.

Understanding sources of errors in bit patterned media to improve read channel performance.

Y. Shi, P. W. Nutter, J. J. Miles
School of Computer Science, The University of Manchester, Manchester, United Kingdom

It is believed that the superparamagnetic limit will restrict the storage density of continuous magnetic media to approximately 1Tb/in^2. Consequently, research has been directed into the development of new storage paradigms to overcome this limit, such as the use of bit patterned media [1]. However, there are considerable problems that need to be overcome in order to fabricate a patterned magnetic storage medium with densities in excess of 1Tbit/in^2. The limitations of practical fabrication techniques result in a variation in the size and position of the fabricated islands that manifests itself as jitter in the replay signal; this inevitably has a detrimental effect on the bit-error-rate (BER) performance of the read channel [2]. Recent work investigating read channel designs for bit patterned media has shown that the application of low density parity-check (LDPC) codes offers improved BER performance in the presence of lithography jitter [2]. However the differing effects of size and position variation upon read errors has not been studied. In this paper, we separate island position and size variations and investigate their effects on the read channel performance. We then propose an extended trellis structure that can be shown to improve the BER performance with position jitter present, without the complexity of LDPC codes.

To predict the performance of the read channel in terms of BER performance against replay signal-to-noise ratio (SNR), a simulation of the data recovery process has been developed [2,3]. The simulation consists of a read channel model and a 3-D replay model which takes into account the geometrical aspects of both the patterned storage medium and the GMR sensor. The read channel model consists of an FIR to equalise recovered samples to a [0.1, 1, 0.1] PR target, followed by a Viterbi decoder. In the following analysis a patterned medium comprising of a track of square islands with island length and period of 12.5nm and 25nm respectively has been adopted, corresponding to 1Tbit/in^2; the read sensor dimensions are given in [3]. The variation in island position and size are assumed to have a Gaussian distribution [2,3], with standard deviation, σ, specified in terms of a percentage of the island period. Figure 1*a*) illustrates BER v. SNR curves for four cases using a conventional trellis: no jitter (solid); 10% island position jitter (dashed); 10% island size jitter (dotted); and 10% island position and size jitter (dash-dot). The introduction of jitter, whatever its source, has a detrimental effect on the performance of the read channel, and the degradation in performance is dominated by variations in island size. In order to combat the effects of position jitter, an extended trellis has been introduced, to replace the standard trellis. In the extended trellis, the states are defined by both the state of the magnetised islands and the discrete values representing a position shift of each island due to jitter. The pulse amplitude with fixed jitter is determined to characterise the amplitude due to each magnetised island, and the ideal output value of the branches from one state to the next is calculated accordingly. In the extended trellis the state bits and the contributions of position jitter are considered when selecting the most likely input sequence. A similar approach has been used for transition jitter estimation in perpendicular storage media [4]. However, unlike transition jitter in perpendicular media, position jitter is signal-independent and uncorrelated and thus causes the state definitions and the transitions between states to differ from the solution described in [4]. Here we use a PR target of tap length 3 and choose 3 discrete jitter levels, {-2.5nm,0,+2.5nm} for σ=10%, which results in 36 states in the extended trellis. The configuration of the extended trellis depends upon the known amount of jitter present. Figure 1*b*) demonstrates the improvement in BER performance that is observed when adopting the proposed extended trellis in the presence of 10% position jitter (dotted line), compared with the use of the standard trellis (dashed line).

We have shown that read channel performance in bit patterned media is degraded by the presence of variations in island position and size and that variations in island size are a more significant source of error. We have investigated new trellis designs that can be shown to offer improved read channel performance, initially in the presence of island position variations in the media. This work will be extended by investigating optimal trellis designs and alternative extended trellis designs that offer improved performance in the presence of island size jitter and both island position and size jitter, as well investigating reduced complexity designs.

[1] R. J. White et al., IEEE Trans. Mag., vol. 33, pp. 990-995, 1997.

[2] I. T. Ntokas et al., IEEE Trans. Mag., vol. 43, pp. 3923-3929, 2007.

[3] P. W. Nutter et al., IEEE Trans. Mag., vol. 41, pp. 4327-4334, 2005.

[4] X. Zhang and R. Negi, J. Appl. Phys., vol. 99, pp. 08K505-1-3, 2006.

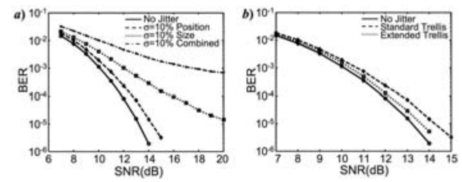

Figure 1 BER v. SNR curves: *a*) with different origins of jitter using the standard trellis, *b*) with 10% position jitter and the extended trellis

Global timing control for tape storage channels.

S. Ölçer[1], J. Jelitto[1], R. A. Hutchins[2]
1. IBM Zurich Research Laboratory, Rüschlikon, Switzerland; 2. IBM STG, Tucson, AZ

Efficient symbol timing recovery is a key issue in read channels for data storage systems. In particular, approaching the Shannon-limit performance requires highly robust solutions, capable of reliable operation under low signal-to-noise ratio (SNR) conditions. In tape-based data storage, timing recovery problems are exacerbated by disturbances such as dropout events, instantaneous speed variations, or nonlinear signal distortion, which erode the available SNR margins further. Degraded channel conditions typically lead to "cycle slip" or temporary "loss-of-lock" events. Although techniques for symbol synchronization in low SNR have been proposed, e.g., [1]-[5], complexity usually is an obstacle for practical applications.

Here, a new approach is introduced for robust timing recovery called global timing control (GTC). The proposed technique exploits the multi-channel nature of tape storage systems. The idea of GTC is to combine the timing information provided by a plurality of channels and generate "global" control signals that are used by all channels for their timing recovery functions. Channels subject to disturbance are aided with the timing information from channels operating under more reliable conditions.

The GTC scheme is derived by applying results from optimum filtering theory to the state-space model of the timing process in an N-channel system. The optimal solution obtained can be regarded as N second-order phase-locked loops (PLLs) coupled by a multi-input multi-output (MIMO) loop filter with time-varying coefficients. The paper describes how practical GTC schemes are obtained from the optimal solution. A particularly simple solution is shown in Fig. 1 for a 2-channel system. Here, $\gamma^{(1)}$ and $\gamma^{(2)}$ denote the loop coefficients for the proportional terms. The factors $w_k^{(1)}$ and $w_k^{(2)}$ weight, at time k, the contribution of each phase-error signal to the global frequency estimation; together with $\sqrt{\zeta}$ they form the loop coefficients for the integral terms. The coefficient values are derived from Kalman filtering theory. To simplify computations, the weights $w_k^{(i)}$, i=1,...,N, can be approximated, e.g., by using the SNRs at the read-channel detection points (SNRDs). The simplest implementation uses equal-weight combining with weights 1/N for all N channels.

The performance of the GTC scheme was analyzed using readback waveforms captured in a commercial tape drive. Three cases were considered, corresponding to waveforms with increasingly higher linear recording densities. Data were written onto 16 tracks in "sectors" of 8 Kbits separated by synchronization (Sync) patterns. The waveforms were captured from 16 parallel channels, with each waveform extending over 32 sectors. A 16-channel software read channel was used to process the waveforms. Timing recovery was performed either independently on each channel (local mode) or in GTC mode. Performance results showed that adaptive weighting usually achieves some improvement over equal gain weighting. The implementation loss introduced by the simplifications is very small. The results in Table I demonstrate the robustness of GTC and its resilience against loss-of-lock phenomena ("missed sectors" are due to missed Sync patterns and indicate loss-of-lock). Hence, a significant improvement is achieved over local timing control. The simplified GTC scheme using SNRD-based weighting incurs a fairly low implementation complexity. GTC can be applied to other storage technologies that use multi-track recording.

[1] J. Moon, J. Lee, and D. Yoon, "Joint gain and timing recovery with applications to magnetic tape storage," IEEE Trans. Magn., Vol. 43, No. 6, pp. 2328-2330, June 2007.

[2] P. Kovintavewat, J. R. Barry, M. F. Erden, and E. Kurtas, "Per-survivor timing recovery for uncoded partial response channels," Proc. Globecom 2004, pp. 2715-2719.

[3] J. Liu, H. Song, and B. V. K. Vijaya Kumar, "Dual segmented Kalman filters based symbol timing recovery for low-SNR partial response data storage channels," Proc. Globecom 2003, pp. 4084-4090.

[4] A. R. Nayak, J. R. Barry, and S. W. McLaughlin, "Joint timing recovery and turbo equalization for coded partial response channels," IEEE Trans. Magn., Vol. 38, No. 5, pp. 2295-2297, Sep. 2002.

[5] J. R. Barry, A. Kavcic, S. W. McLaughlin, A. Nayak, and W. Zeng, "Iterative timing recovery," IEEE Signal Processing Mag., Vol. 21, No. 1, pp. 89-102, Jan. 2004.

	Nominal linear density		Higher linear density		Highest linear density	
Weighting Scheme	No GTC	GTC (SNRD)	No GTC	GTC (SNRD)	No GTC	GTC (SNRD)
Number of Bit Errors	61,639	1,354	104,749	6,928	242,927	10,368
Bit Error Rate	1.5×10^{-2}	3.3×10^{-4}	2.6×10^{-2}	1.7×10^{-3}	5.9×10^{-2}	2.5×10^{-3}
Missed Sectors	4	0	4	1	4	2

Table I: Detection performance w/ and w/o GTC

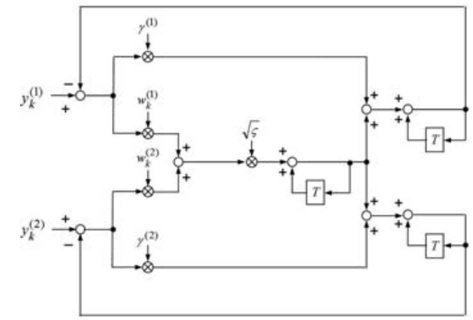

Fig. 1. GTC for a 2-channel system: $\gamma^{(1)}$ and $\gamma^{(2)}$ denote input phases for channels 1 and 2, respectively, and T represents the bit duration.

HU-01

Multilayered thin film structure for negative permeability.

S. Cho[1], J. Kim[1], K. Kim[2]
1. Metallurgy and materials engineering, Hanyang University, Ansan, South Korea; 2. Physics, Yeungnam University, Gyeongsan, South Korea

Introduction

In recent, electromagnetic and communication devices are faced with the physical limitation of electromagnetic materials. This physical limitation is suggested to be overcome by the development of new artificial meta-materials, which have negative permittivity and permeability. Thus these meta-materials are generally known as LHM (Left-Handed Material) and NRIM (Negative Refractive Index Material) suggested by Veselago in 1968 [1]. This negative value of permittivity and permeability of LHM is expected to show different electromagnetic response, which is not found in nature, such as negative refractive constant. Therefore, LHM can apply to various new electromagnetic and communication devices in frequency ranges from MHz to THz without less design space constraint.

Up to now, LHM are realized as a circuitry type by using a SRR (Split Ring Resonator) and thin wire structure [2, 3]. Because this circuitry type LHM requires large volume and complicate fabrication process, it is of prime interest to develop a non-circuitry type LHM with simple fabrication process and small volume. In this study, we suggest a new non-circuitry type LHM with a multilayered thin film structure. This new LHM is expected to bring a new design concept and paradigm of LHM.

Experimental Procedures

In this experiment, two kinds of multilayered thin film structures were designed and fabricated on corning glass: the one is a non-insulating type structure with Cu (20nm) / Ni80Fe20 (100nm) / Cu (20nm) and the other an insulating type structure with Cu (20nm) / SiO2 (10nm) / Ni80Fe20 (100nm) / SiO2 (10nm) / Cu (20nm). The metal thin film layers were grown by a RF magnetron sputtering method in Ar plasma atmosphere (working pressure: 2 mTorr, working power: 300 W) and the insulating layer (SiO2), deposited by a chemical vapor deposition method (deposition temperature: 300°C, working pressure: 1000 mTorr, carrier gas: SiH4, working power: 20 W). The permeability of the thin film structures was measured by a broadband CPW (Coplanar Waveguide, a dimension of $0.1 \times 5.2 \times 0.003$mm) method which was discussed in other literature [4].

Results and Discussions

Fig. 1 shows the S-Parameter variations of CPW loaded with multilayered thin films versus the operation frequency. As shown in the figure, the values of S11 and S21 were changed by the loading of the thin films. In particular, the value of S21 is larger than that of S11 when a non-insulating type sample is loaded on the CPW. In order to extract the permeability of these multilayered samples, a broadband CPW method was used and the results are shown in Fig. 2. As shown in the Fig. 2 (a), the magnetic resonance of the non-insulating type sample is observed to occur at ~ 1.5 GHz. This magnetic resonance should be related to the resonance of the Ni80Fe20 layer. However, the real value of the permeability is shown to be decreased although the operation frequency is increased over the resonance frequency. This should indicate that this material have negative permeability over resonance frequency. Contrary to the non-insulating sample, there is no indication of magnetic resonance in the insulating sample. Moreover, the real part of permeability in the insulating type material shows a constant negative value of -40 up to ~15 GHz.

These experimental results show that meta-materials with negative permeability can be fabricated by a multi-layer structure. This finding suggested that LHM could be very innovative materials for EM and communication devices.

[1] V.G. Veselago, Sov. Phys. USPEKHI 10, 509 (1968)

[2] J.B. Pendry, A.J. Holden, D.J. Robbins, and W.J. Stewart, IEEE Trans. Microwave Theory Tech. 47, 2075 (1999)

[3] D.R. Smith, Willie J. Padilla, D.C. Vier, S.C. Nemat-Nasser, and S. Schultz, Phys. Rev. Lett. 84, 4184 (2000)

[4] S.G. Cho, J. Kim, I. Kim, K.H. Kim, and M. Yamaguchi, Phys. Stat. Sol. (a) 204, 4133 (2007)

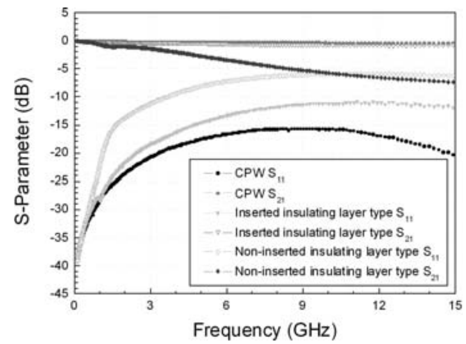

S-Parameter of CPW and multilayered thin film

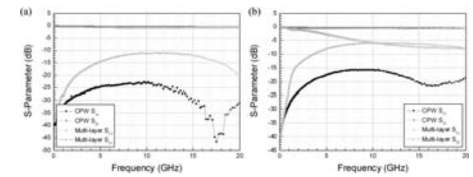

Negative permeability of multilayered thin film by broadband CPW method, (a) inserted non-insulating type, (b) inserted insulating type

HU-02

Interlayer exchange coupling in $Co_2FeAl_{0.5}Si_{0.5}/Cr/Co_2FeAl_{0.5}Si_{0.5}$ trilayers.

T. Furubayashi[1], K. Kodama[2], K. Inomata[1], K. Hono[1]
1. Magnetic Materials Center, National Institute for Materials Science, Tsukuba, Japan; 2. Graduate School of Pure and Applied Sciences, University of Tsukuba, Tsukuba, Japan

Much attention has been paid to the problem of interlayer exchange coupling in multilayered films consisting of half metallic full-Heusler alloys. Ambrose et al. [1] reported that, in Co_2MnGe(CMG)/V/CMG and CMG/Mn/CMG trilayers, the magnetizations of two CMG layers couples with 90 degrees to each other, while the CMG/Cr/CMG films exhibited no significant coupling. Recently, Wang el al. [2] showed that (001) epitaxial Co_2MnSi(CMS)/Cr/CMS films show very strong 90-degree interlayer exchange coupling. In this system, the biquadratic coupling is dominant while the bilinear component, which gives parallel or antiparallel couplings, is negligibly small. The mechanism of such strong 90 degree coupling is still unclear. It is of much interest to see if such a property is observed commonly in Heusler alloys or half metals. For obtaining further insights in this problem, we have examined trilayers consisting of a Heusler alloy $Co_2FeAl_{0.5}Si_{0.5}$ (CFAS). Tezuka et al. [3] reported that magnetic tunnel junctions with the structure CFAS/MgO/CFAS show high MR ratio reaching 220 % at room temperature. CFAS is expected to have a high spin polarization, so is promising for various spintronic applications. In this work, magnetic properties were examined for both (001) epitaxial and polycrystalline films with the trilayer structure of CFAS/Cr/CFAS. Such trilayers are of much interest in view of potential applications to GMR devices not only from physical viewpoints.

Layered structures with CFAS Heusler ally were grown by dc magnetron sputtering in an ultrahigh vacuum system with the base pressure lower than 5×10^{-7} Pa. The films were deposited upon MgO (001) single crystalline substrates and thermally oxidized Si substrates at room temperature (RT) with the layer structure of Cr(30)/CFAS(20)/Cr(t)/CFAS(5)/Ta(5) in nm from the bottom. After depositing the bottom CFAS(20) layer, the films were annealed at 400 °C in situ for improving the structure order and then cooled to RT. Layers of Cr and CFAS deposited on MgO (001) single crystals were found to show epitaxial (001) growth. The CFAS was in the B2 structure. In contrast, the films deposited on SiO_2 were polycrystalline with no significant texture, in which the CFAS was in the A2 disordered structure.

Magnetization curves were recorded at RT using VSM with a magnetic field applied in the film plane. For epitaxial films prepared on MgO (001), a magnetic field was in the direction parallel to the [110] axis of CFAS, the easy direction.

The magnetization curves, as shown in Fig. 1, exhibit different behaviors for two samples with different Cr interlayer thicknesses of (a) 2.5 nm and (b) 1.5 nm. The results obviously indicate nonferromagnetic coupling between two CFAS layers through the 1.5 nm thick Cr layer. In the sample deposited on MgO (001), we obtain $M_R/M_S = 0.82$, where M_R is the remanent magnetization and M_S is the saturation magnetization. This value is near 0.8 expected for the case that the two CFAS layers with the different layer thicknesses have 90 degree coupling. Thus, in the CFAS/Cr/CFAS film grown epitaxially on MgO (001), biqadratic coupling is dominant, as observed in the CMS/Cr/CMS (001) system [2]. Note that the polycrystalline film deposited on SiO_2 shows smaller M_R/M_S of 0.65, which is near the value 0.6 expected for an antiferromagnetic coupling. This result indicates that, in the polycrystalline CFAS/Cr/CFAS film, the bilinear coupling exists in addition to the biquadratic coupling. In other words, the amplitude of the bilinear coupling strongly depends on the crystal orientation. It is negligibly small compared with the biquadratic one when stacked in the (001) direction. Thus the interlayer couplings would depend on the band structure of Cr and CFAS for different direction of the electron propagation.

In summary, interlayer couplings were examined for both (001) epitaxial and polycrystalline CFAS/Cr/CFAS layered films. Strong couplings were observed for the films with the 1.5 nm thick Cr interlayer. A 90-degree coupling is dominant in the (001) epitaxial film, similarly with the CMS/Cr/CMS system. In contrast, an antiparallel coupling also exists in the polycrystalline one. Thus, the interlayer couplings in this system strongly depends on the crystal orientation of the layers. The mechanism of the interlayer couplings is expected to be clarified theoretically by accounting for the electronic structure of both Cr and CFAS.

[1] T. Ambrose, J. J. Krebs, and G. A. Prinz, J. Appl. Phys., 89, 7522 (2001).

[2] H. Wang, A. Sato, K. Saito, S. Mitani, K. Takanashi and K. Yakushiji, Appl. Phys. Lett., 90, 142510(2007).

[3] N. Tezuka, N. Ikeda, S. Sugimoto and K. Inomata, Japan. J. Appl. Phys., 46, L454 (2007).

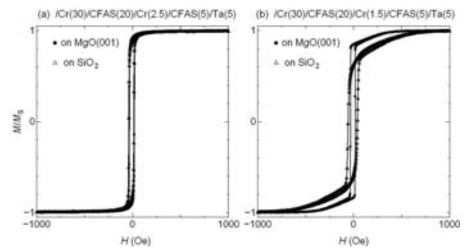

Fig. 1: Magnetization curves recorded at room temperature for the films with indicated thicknesses in nm.

HU-03

Thickness and Temperature Dependence of Extraordinary Hall Effect in Interlayer Coupled [Pt/Co]$_5$/Ru/[Co/Pt]$_5$ Multilayers with Perpendicular Anisotropy.

J. Zhao[1], Y. Wang[1], S. Zhang[2], X. Han[1]
1. State Key Laboratory of Magnetism, Institute of Physics, Chinese Academy of Science, Beijing, China; 2. Department of Physics and Astronomy, University of Missouri–Columbia, Columbia, MO

Due to spin-orbit interaction and the strong hybridization between Pt-5d and Co-3d at the Pt/Co interface in Co/Pt multilayers (MLs), its extraordinary Hall effect (EHE) is substantially larger. It may serve as a good electric transporter for the measurement of hysteresis loop because the Hall resistivity is proportional to the perpendicular component of magnetization[1].
Because the dependence of the interlayer coupling oscillatory behavior and extraordinary Hall effect on the thickness of the nomagnetic (NM) Pt and the ferromagnetic (FM) Co have been reported previously [2,3], our this work is focused on the temperature dependence of EHE in the interlayer coupled Co/Pt MLs, in which the spacer layer is Ru between (Pt/Co)n and (Co/Pt)n.
The Hall effect was measured for some selected interlayer antiferromagnetic(AF) coupling samples by four probe method from 300K to 4.2K, as shown in Fig. 3. Only the extraordinary term contributes to the Hall resistivity, i.e. it is only proportional to the magnetization. The saturation field Hs and interlayer AF coupling field Hex decay linearly with the increase of T, while EHE enhances with the increase of T. An inflexion point appears at the temperature of about 125K, where the alignment of the magnetization vectors of the top and bottom Co/Pt MLs begins to deviate from the previous complete antiparallel state. Such behavior can be explained by the competition between magnetic anisotropy energy and interlayer AF coupling energy. As the perpendicular anisotropy field is stronger increased than that of the interlayer coupling field Hex during decreasing temperature, it become difficult to turn the magnetic vector in one layer to the opposite direction on the reversal process. It is known that skew scattering and side jump contribute to Hall resistivity near RT[4], however, the skew scattering dominates at low temperature according to our results.

[1] L. Berger and G. Bergmann, in The Hall effect and Its Applications, edited by C. L. Chien and . R. Westgate (Plenum Press, New York, 1980).

[2] J. Zhao, Y. J. Wang, X. F. Han, "Thickness Dependence of Oscillatory Interlayer coupling and Extraordinary Hall Effect in [Pt/Co]5/Ru(Cu)/[Co/Pt]5 Multilayers", The 6th IEEE International Symposium on Metallic Multilayers, poster presentation (Wed-P16), Perth, Australia.

[3] J.Zhao, Y. J. Wang, Y.Z. Liu, Z. Zhang, X .F. Han, "Perpendicular Anisotropy dependence of Oscillatory Interlayer Coupling Behavior in [Pt/Co]$_5$/Ru/[Co/Pt]$_5$ Multilayers", submitted to Journal of Applied Physics, in review

[4] S. Zhang, Phys. Rev. B 51, 3632(1995)

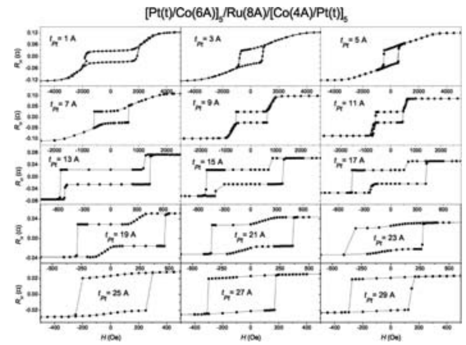

Fig.1 Pt layer thickness dependence of Hall hysteresis loop.

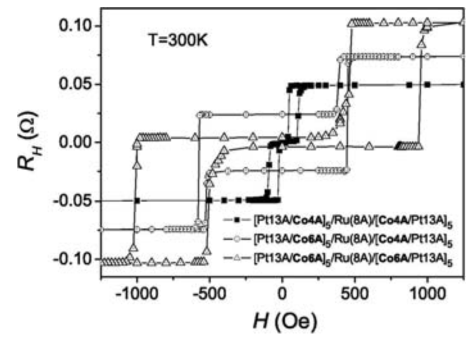

Fig.2 Co layer thickness dependence of Hall hysteresis loop.

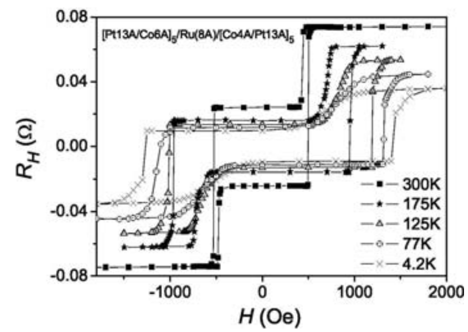

Fig.3 Temperature dependence of Hall hysteresis loop.

HU-04

Effect of antiferromagnetic interlayer coupling on domain wall creep in a system with perpendicular anisotropy.

P. J. Metaxas[1,2], J. Jamet[1], J. Ferré[1], B. Rodmacq[3], B. Dieny[3], R. L. Stamps[2]
1. Laboratoire de Physique des Solides (UMR CNRS 8502), Université Paris-Sud, Orsay, France; 2. School of Physics, University of Western Australia, Crawley, WA, Australia; 3. SPINTEC (URA 2512 CNRS/CEA), CEA, Grenoble, France

We have measured low field domain wall motion in a weakly disordered ultrathin Co film coupled (through a Pt spacer) to a second, magnetically harder Co layer. We examine how the effective coupling field created by the antiferromagnetic coupling to the harder layer results in asymmetric domain wall creep motion. The coupling field is determined from the wall velocity measurements by way of a modified creep expression which takes the effective coupling field into account.

The sample was sputter deposited at ambient temperature onto an etched Si substrate and has the following structure: Pt(4.5 nm) / Co(0.5 nm) / Pt(4 nm) / Co(0.8 nm) / Pt(3.5 nm). Both Co layers exhibit perpendicular anisotropy with the thinner Co layer being the magnetically softer one (Fig 1). Interlayer coupling in such films is thought to result from a combination of RKKY and orange-peel coupling [1]. The antiferromagnetic interlayer coupling in this particular film can be first evidenced from the leftward shift of the minor hysteresis loop of the soft layer (inset of Fig 1), obtained while keeping the harder Co layer negatively staurated. The observed shift can be interpreted in terms of an effective coupling field, H_J=5.2±2.0 Oe, which acts on the soft layer during reversal [2]. While this is a common method of determining H_J, ambiguities can exist due to the multiple reversal processes (domain nucleation and wall propagation) occuring during reversal [3]. A more relevant and easily interpreted measurement is to determine the effect of the coupling field on individual reversal processes [4].

We have measured the velocity of domain walls in the soft layer under both positive and negative applied fields, H, while keeping the hard layer (to which the soft layer is coupled) negatively saturated. This was done using a quasi-static PMOKE microscopy technique [5]. An asymmetry was found for velocities measured for H>0 and H<0 (Fig 2) which resulted from the different relative directions of the applied field and coupling field (which was always positive) in the two cases. For H>0, H_J reinforced the applied field whereas for H<0, H_J worked against the applied field, resulting in a lower wall velocity.

In single layer ultrathin Pt/Co/Pt films, low field domain wall motion can be understood [5,6] in terms of interface creep theory [7] for which we expect $v \propto \exp[-(E_B/k_bT)H^{-\mu}]$. E_B characterizes the pinning potential induced by the structural disorder in the film and μ is a universal exponent equal to 1/4 for a 1D interface (domain wall) in a 2D weakly disordered medium. This expression however cannot be used to describe our data since it does not take the effective coupling field into account. We therefore modified the standard expression, including the effective coupling field resulting from the interlayer coupling as a component of the total effective field acting on the wall (as done for viscous wall motion [4]). This yields $|v| \propto \exp[-(E_B/kbT)|H+H_J|^{-\mu}]$. We then tested if this approach could reconcile the H>0 and H<0 data sets, treating H_J as a fitting parameter and searching for the value which overlapped the two data sets. The two data sets could indeed be reconciled with H_J=4.9±0.2 Oe, consistent with the value determined from the loop shift. The ln(v) data (inset of Fig 2) is linear in the corrected total scaled field $|H+H_J|^{-1/4}$ up to about 300 Oe confirming the validity of the universal creep exponent μ=1/4 for describing the low field wall motion once H_J is taken into account. As expected, E_B (which describes the film's intrinsic disorder) does not show any appreciable dependence upon the relative directions of H and H_J.

[1] Moritz et al, Europhys. Lett., 65, 123 (2004).

[2] Grolier et al, Phys. Rev. Lett., 71, 3023 (1993).

[3] Pennec et al, Phys. Rev. B., 69, 180402(R) (2004).

[4] Fukumoto et al, J. Magn. Magn. Mater., 293, 863 (2005).

[5] Metaxas et al, Phys. Rev. Lett., 99, 217208 (2007).

[6] Lemerle et al, Phys. Rev. Lett., 80, 849 (1998).

[7] Chauve et al, Phys. Rev. B, 62, 6241 (2000).

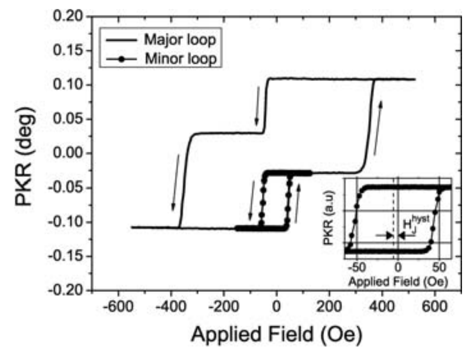

FIG 1: Major and minor polar Kerr rotation (PKR) hysteresis loops (field sweep rate: 0.4 kOe/s) with field applied perpendicular to the film plane. Arrows indicate field cycling direction. Inset shows shifted minor loop of soft layer.

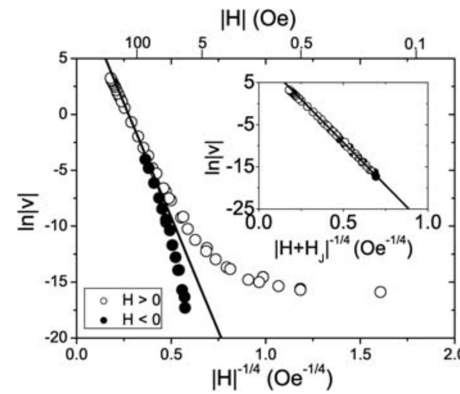

FIG 2: Asymmetric domain dynamics in the soft layer under positive and negative applied fields. Inset shows the same data corrected by including the coupling field (4.9 Oe) in the creep law. Solid line is a linear fit to the corrected data.

HU-05

Spin-glass-like magnetic behaviour of Tb/Si and Tb/Ti nanoscale multilayers.

A. V. Svalov[1,2], V. O. Vas'kovskiy[1], J. M. Barandiarán[2], I. Orue[3], R. Lopez Anton[4,5], G. V. Kurlyandskaya[2]
1. Ural State University, Ekaterinburg, Russian Federation; 2. Electricidad y Electrónica, Universidad del País Vasco (UPV/EHU), Bilbao, Spain; 3. SGiker, Universidad del País Vasco (UPV/EHU), Bilbao, Spain; 4. Instituto de Ciencia de Materiales de Aragón, CSIC-Universidad de Zaragoza, Zaragoza, Spain; 5. ISIS Facility, Science and Technology Facilities Council, Rutherford Appleton Laboratory, Harwell Science and Innovation Campus, Didcot, United Kingdom

Magnetic properties of low dimensional objects (layers and particles) depend on their size. In some cases the size dependence of magnetic ordering temperature T_{ord} for rare-earths (RE) layers, e.g. for $[Gd/X]_n$ and $[Tb/X]_n$ multilayers, where X is a nonmagnetic spacer, can be described satisfactorily by a finite size scaling theory [1-4]. However, when the thickness of the RE layers decreases down to a few nanometers, deviations from this law appear [2,4]. The objective of this work is the study of the structure and magnetic properties of Tb/Si and Tb/Ti nanoscale multilayers aiming to understand the cause of the observed size dependence.

The multilayers were prepared by alternative deposition of Tb layers and nonmagnetic spacers onto glass substrates by rf-sputtering. The thickness of Tb layers (L_{Tb}) varied from 1.5 nm to 12 nm and total thickness of magnetic component in the multilayers was 90 or 120 nm. The spacer thickness was 2 nm. Magnetic properties were measured using a SQUID magnetometer. The microstructure was examined by X-ray diffraction and transmission electron microscopy. Small angle X-ray diffraction was used to determine the quality of the layers in multilayered structures.

Zero Field Cooling (ZFC) and Field Cooling (FC) dc susceptibility χ_{dc} was measured in 120 Oe. For all samples ZFC curves had a maximum at certain temperature T_m. Below T_m a clear difference between the FC and ZFC curves was observed. Such a behavior of the magnetization is typical both for spin glass [6], and for superparamagnetic objects [5]. However this feature may also be a consequence of the high crystalline magnetic anisotropy of terbium at low temperatures. It was observed that T_{ord} and T_m depend on the type of the material of the nonmagnetic spacer at $L_{Tb} < 10$ nm, e.g. for $[Tb(1.5nm)/Ti]_{60}$ and $[Tb(1.5nm)/Si]_{60}$ multilayers T_m is 80 K and 9 K, respectively (Fig. 1). For $[Tb(1.5nm)/Si]_{60}$ multilayers ac susceptibility χ_{ac} was measured also for different frequencies (10-700 Hz) and 4 Oe ac magnetic field. The susceptibility peak shows an increase in intensity and a shift to lower temperatures with decreasing frequency, consistent with the classic spin glass behavior. The value of the effective moment μ calculated according to Curie-Weiss law for $[Tb(1.5nm)/Si]_{60}$ multilayers is within 10% of the expected value for trivalent Tb (9.72 μ_B).

Fig. 2 shows the hysteresis loops of the $[Tb(1.5nm)/Si]_{60}$ multilayer measured below and above T_m. The shape of the $M(H)$ curves is reminiscent of that of the superparamagnetic particles with blocking temperature $T_b = T_m$. The superparamagnetic behavior can be also confirmed by the usual superposition of the magnetization vs H/T curves above 10 K (Fig.2, inset). If one consider the value of the anisotropy constant of the bulk Tb (5.5×10^8 erg/cm^3) in case of $[Tb(1.5nm)/Si]_{60}$ multilayer, the size of the superparamagnetic particles can be estimated as 1.5 nm. The hysteresis loops of the $[Tb(1.5nm)/Ti]_{60}$ multilayer measured at the same temperatures have different shapes (Fig. 3). It was found that the coercivity H_c at 80 K (Fig. 3, inset) is comparable to the applied field of 120 Oe for which the ZFC curve has a maximum at $T_m = 80$ K.

In summary, the size dependence of T_{ord} for Tb/Ti multilayers can be satisfactorily described by a finite size theory up to $L_{Tb} = 1.5$ nm and the observed spin-glass like behaviour is caused by the high crystalline magnetic anisotropy of terbium. For Tb/Si multilayers with $L_{Tb} \leq 3$ nm the spin-glass like behaviour can be due to the formation of superparamagnetic particles of Tb and/or Tb-Si spin-glass alloys.

One of the authors (GVK) acknowledges the Ramon y Cajal Fellowship of the Spanish MEC. This work was supported by the RF project RNP.2.1.1.6945, Ural and Siberian Divisions of RAS under Grant no. 32-2007, and Spanish MEC (project MAT_2005-06806-C04-03). The magnetization measurements were performed at the Cryomagnetic Center, Institute of Metal Physics UD RAS and general research Services (SGiker) of the University of the Basque Country UPV-EHU.

[1] J. Samuel Jiang, C.L. Chien, J. Appl. Phys. 79 (1996) 5615.

[2] Y. Li, C. Polyaczyk, D. Riegel, Surf. Sci. 402-404 (1998) 386.

[3] M.J. O'Shea, P. Perera, J. Appl. Phys. 85 (1999) 4322.

[4] A.V. Svalov, V.O. Vas'kovskiy, G.V. Kurlyandskaya, J.M. Barandiaran, I. Orue, N.N. Schegoleva, A.N. Sorokin, Chin. Phys. Lett. 23 (2006) 196.

[5] N.B. Shevchenko, J.A. Christodoulides, G.C. Hadjipanayis, Appl. Phys. Lett. 74 (1999) 1478.

[6] J.J. Hauser, Solid State Comm. 55 (1985) 163.

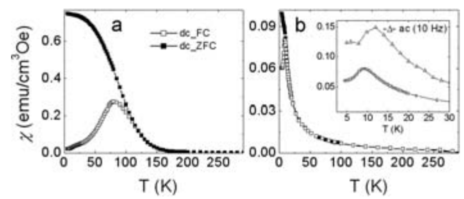

Fig. 1. χ_{dc} **and** χ_{ac} **for** $[Tb(1.5nm)/Ti]_{60}$ **(a) and** $[Tb(1.5nm)/Si]_{60}$ **(b) multilayers.**

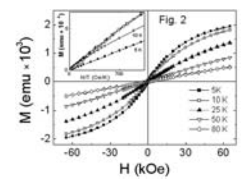

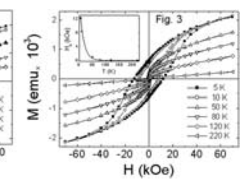

Fig. 2. $M(H)$ **for** $[Tb(1.5nm)/Si]_{60}$ **multilayers for various temperatures. Inset:** M **as a function of** H/T**. Fig. 3.** $M(H)$ **for** $[Tb(1.5nm)/Ti]_{60}$ **multilayers for various temperatures. Inset:** H_c **vs** T**.**

HU-06

Magnetoimpedance in permalloy-based multilayers: effect of Ag and Cu spacers.

A. de Andrade[1], A. Viegas[2], R. da Silva[3], M. Corrêa[4], R. Sommer[5]
1. Universidade Federal de Santa Maria, Frederico Westphalen, Brazil; 2. Universidade Federal de Santa Catarina, Florianópolis, Brazil; 3. Universidade Federal do Rio Grande do Sul, Porto Alegre, Brazil; 4. Universidade Federal do Pampa, Caçapava do Sul, Brazil; 5. Centro Brasileiro de Pesquisas Físicas, Rio de Janeiro, Brazil

Multilayered films appear to be a good solution to relief the stress stored during the sputtering deposition of thick the ferromagnetic layers for magnetoimpedance sensors, as well as to tailor the DC impedance of a given device. The accumulated stresses contribute to an increase in the dispersion and strength of the effective anisotropy which, in turn, decreases the permeability and magnetoimpedance (MI) in these materials.
In particular, permalloy-based multilayered films are used in much read/write magnetic devices due to the excellent soft magnetic properties and signal/noise ratios obtained is such devices. MI sensors based in permalloy and permalloy-based multilayers become attractive as the can be integrated with the electronics or pre-existing read/write devices without extra processing steps.
In this work, we report a comparative study of the MI is investigated in both, Py/Ag and Py/Cu multilayers, produced by magnetron sputtering over glass substrates. The samples were produced with the number of bilayers 15, 30, 50, 70 and 100. The MI measurements were performed in the samples with t_{Py}/t_{Ag} and t_{Py}/t_{Cu} ratio thickness of 10/0.7, 10/2.5 and 10/10. The thickness of the permalloy layer was fixed as 10nm. The impedance spectra $Z(f,H)=R(f,H)+jX(f,H)$ was measured with an impedance analyzer HP4396B at frequencies in the range 100kHz - 1.8GHz with an strip line microwave sample holder under a slowly varying magnetic field. The samples were cut in two different directions: longitudinal and transverse (relative to motion of the substrates during the deposition process) as a transverse anisotropy appeared in some of the samples. The magnetoimpedance measurements were performed with the probe current flowing in these two directions.
For the Py/Cu multilayers, we observed single peak structures in both directions up to the highest frequency, which is consistent with in-plane isotropic magnetic properties. Some magnetoimpedance *vs.* field curves for the [Py(100Å)/Cu(25Å)] x n sample with n = 15 and 100, are shown in figure 1 below.
For the Py/Ag samples, however, a characteristic single peak at longitudinal direction and double peak at transverse one were observed, as shown in figure 2.a. This behavior is in accordance with the predominantly uniaxial properties observed in these samples. The highest MI ratios were observed for samples with 100 bilayers. Interestingly, both materials (Py/Ag and Py/Cu) present almost the same maximum MI ratio: 250% for 2.5nm of Cu or Ag and 10nm of Permalloy, both with 100 bilayers.
Moreover, for some Py/Ag samples with small number of bilayers, the frequency and field dependent impedance curves show multiple-peak structures (see figure 2.a), characteristic of multiple FMR lines. This effect was stronger for samples with thickness ratio t_{Py}/t_{Ag}=4. These features are the fingerprint of a complex dynamics, possibly associated with the magnetic coupling between individual layers.

[1] P. Delooze, L. V. Panina, D. J. Mapps, K. Ueno and H. Sano, J. Magn. Magn. Mater., 272 (2004) 2266;

[2] A.M.H. de Andrade, R.B. da Silva, M.A. Corrêa, A.D.C. Viegas, A.M. Severino and R.L. Sommer, J. Magn. Magn. Mater., 272 (2004) 1846.

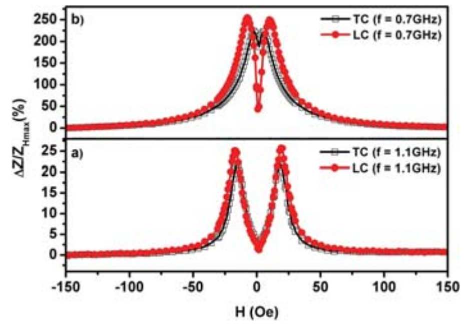

Figure 1. MI(%) curves in multilayers [Py(100Å)/Cu(25Å)] a) 15 bilayers and b) 100 bilayers.

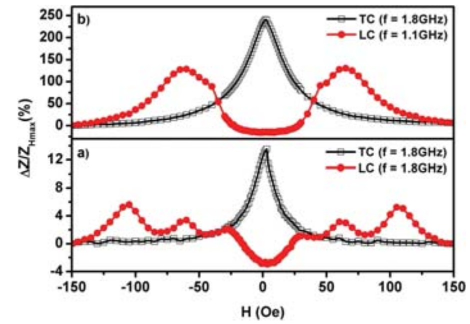

Figure 2. MI(%) curves in multilayers [Py(100Å)/Ag(25Å)] a) 15 bilayers and b) 100 bilayers.

HU-07

Structural Characterization of Ferromagnetic Mn/ZnO Multilayers.

E. Céspedes, A. Espinosa, M. García-Hernández, A. de Andrés, C. Prieto
Instituto de Ciencia de Materiales de Madrid, Consejo Superior de Investigaciones Científicas (CSIC), Madrid, Spain

Mn-Zn-O system has attracted great theoretical and experimental attention in the last years due to its potential functionalities in spintronics as a wide band gap diluted magnetic semiconductor (DMS). Since Dietl et al.[1] predicted the possibility of room-temperature ferromagnetism (RTFM) in p-type $Zn_{1-x}Mn_xO$, ferromagnetism with transition temperatures above RT has been experimentally obtained in Zn-Mn-O films prepared by different methods. However, experimental results obtained up to date have been very controversial and the origin of RTFM has been attributed either to an intrinsic or extrinsic property.[2] The role of Mn-ZnO interfaces, a quite unexplored field, has been claimed to be of great importance in the FM behaviour of these materials.[3,4]
In this work, in order to study interfaces in the Mn-Zn-O system, a series of $(ZnO_{3nm}/Mn_t)_n$ multilayers was prepared by magnetron sputtering on Si(100) substrates at room temperature (RT). The nominal Mn layer thickness, t, was varied from 6 to 0.1 nm while the number of bilayers, n, was increased from 5 to 75 to keep the total amount of Mn constant.
Structural information, as bilayer thickness and roughness, was obtained from X-ray reflectivity (XRR) measurements, carried out on a Bruker D8 X-ray diffractometer.
Magnetic properties were measured with a "Quantum Design" Superconducting Quantum Interference Device system up to 5 T. The magnetic behaviour of these samples varies within the series and ferromagnetic order gets favoured by increasing the Mn layer thickness (t). The transition temperature, T_C, is always above 400 K for these ferromagnetic samples.
X-ray absorption spectroscopy (XAS) measurements at the Mn K-edge were made at SpLine and Dubble beamlines (ESRF) in fluorescence detection mode. X-ray absorption near-edge structure (XANES) results indicate a variation of the Mn oxidation state with t. Mn valence states close to +2 are found for samples that exhibit ferromagnetic order while higher Mn oxidation states are obtained as t is reduced. The presence of pure metallic Mn is discarded in every sample. Further XANES analysis points towards the existence of two different Mn environments in samples with high t values. By comparison with reference XANES spectra, not only the existence of Mn in ZnO wurtzite structure, but also Mn in rocksalt lattice is revealed.
X-ray diffraction experiments were performed at SpLine (ESRF) at 14 KeV (λ = 0.8857 Å). Θ-2Θ and grazing incidence high-angle X-ray diffraction spectra revealed that all multilayers contain ZnO wurtzite nanocrystals. Samples show texture in the (002) crystallographic direction. The size of these nanocrystals is of the ZnO layer thickness order (3 nm) in samples with t sufficiently high. In the case of samples with very thin Mn layers, though, crystalline grains above 7 nm are found, evidencing no restriction to the ZnO grain size in the out-of-plane direction; showing that for these small t, Mn deposition does not hamper ZnO growth. MnO nanocrystals are also identified, but just in samples with high values of t, in agreement with XAS results, where coexistence of wurtzite and rocksalt is identified. No traces of metallic Mn or other Mn-Zn-O phases are found from diffraction measurements.
According to the growth conditions, a model is proposed to explain all the obtained results. For all the samples, the oxygen excess at the surface of the lately deposited ZnO layer can provide a highly oxidized state to the very close Mn atoms and therefore, a small Mn^{4+} fraction should be expected at the first growth stage of the Mn layers. For samples with very thin Mn layers, no appreciable differences are expected between top or bottom of the Mn layer, leading to the formation of MnO_2 in the entire Mn layer. Due to big differences in the ionic radii, neither Mn^{4+} diffusion into ZnO nor Zn^{2+} diffusion in MnO_2 are expected. For samples with high t values, though, high reactivity of freshly deposited Mn along with competition between Mn and Zn to share oxygen explains interdiffusion and the formation of mixed $Zn_{1-x}Mn_xO$, with rocksalt and wurtzite phases coexisting. Further analysis of magnetic and XAS results indicates a relation between the Mn amount into ZnO lattice and the obtained saturation magnetization values, what points towards Mn diluted into ZnO as the origin of the obtained ferromagnetism.

[1] T. Dietl, H. Ohno, F. Matsukura, J. Cibert, D. Ferrand, Science 287, 1019 (2000).

[2] S. A. Chambers, Surface Science Reports 61, 345 (2006).

[3] C. Kundaliya, S.B. Ogale, S.E. Lofland, S. Dhar, C.J. Metting, S.R. Shinde, Z. Ma, B. Varughese, K.V. Ramanujachary, L. Salamanca-Riba, and T. Venkatesan, Nat. Mater. 3, 709 (2004).

[4] M. A. García, M. L. Ruiz-González, A. Quesada, J. L. Costa-Krämer, J. F. Fernández, S. J. Khatib, A. Wennberg, A. C. Caballero, M. S. Martín-González, M. Villegas, F. Briones, J.M. González-Calbet, and A. Hernando, Phys. Rev. Lett. 94, 217206 (2005).

Structural control of magnetic properties in Co/Pd multilayer for heat assisted perpendicular MRAM application.

B. Purnama, K. Waseda, S. Yoshimura, Y. Nozaki, *K. Matsuyama*
Electronics, Kyushu University, Fukuoka, Japan

Thermally assisted magnetization reversal is a promising scheme to utilize a superior data storage performance of recently developed ultra-high perpendicular anisotropy materials in MRAM technology[1]. A moderate value of magnetization switching field and sensitive temperature dependence are required for MRAM memory cell, where a fast memory operation should be performed with a tolerable amplitude of conductor current at an elevated temperature. In order to satisfy the above technological demands, structural control of coercive field H_c and whose temperature dependence have been systematically studied for Co/Pd multilayer. Samples were deposited on glass substrates by a tandem type DC magnetron sputtering with a muti-cathode system (Anelva SPC-350). Magnetic and structural properties in as-grown films were characterized with VSM and XRD measurements, respectively. The extraordinary Hall resistance R_H was measured for the microstructured samples with overlaid 4-terminal Ti/Au electrodes, fabricated with photolithography and following lift-off process.

Fig. 1(a) shows R_H hysteresis curves measured at various temperatures, ranged from 23°C to 150°C. The square hysteresis is observed up to 100°C, suggesting a nucleation type magnetization reversal at high temperatures. The value of H_c linearly decreases with the increase of temperature and is extrapolate to zero value at 150°C, defined as a threshold temperature T_{th}, as shown in Fig. 1(b). The sensitive temperature dependence of the coercivity can be associated with a thermally activated magnetization process, since the perpendicular anisotropy is still remained at T_{th}, as shown in Fig. 1(a). The H_c decreases with the increase of Co layer thickness t_{Co}, except a very thin thickness of 1 Å, suggesting an aspect of interface anisotropy[2]. While, the T_{th} linearly increases with the increase of t_{Co}. Resultantly, complementary properties for H_c and T_{th} are realized by adjusting the t_{Co}, which can be utilized for an exchange coupled bi-layer in a heat assisted MRAM architecture[3]. Practical data stability was confirmed by a sufficient value of the activation energy E_a for magnetization reversal, estimated from a field sweep rate dependence of coercive fields. A typical value of E_a obtained by fitting the experimental results to the Sharrock formula[4] was 100 for a sample of [Co(1.7 Å)/Pd(8.0 Å)]$_{20}$. The magnetic properties can be also controlled with the repetition number N of Co/Pd bi-layer, as shown in Fig. 2(b). The monotonous increase of H_c and T_{th} can be associated with the crystalline structural change due to the increase of film thickness. Drastic enhancement of coercivity was also attained by adding a Pd under layer of 10 nm, while keeping a low T_{th}, that is H_c = 2.1 kOe (@ 23°C) and T_{th} = 200°C.

[1] R. S. Beech et al., J. Appl. Phys. 87, 6403 (2000).

[2] F. J. A. Broeder et al., J. Appl. Phys. 61, 4317 (1987).

[3] Y. Nozaki et al., J. Magn. Soc. Jpn., 30, 574 (2006).

[4] M. P. Sharrock et al., IEEE. Trans. Magn., 17, 3020 (1981).

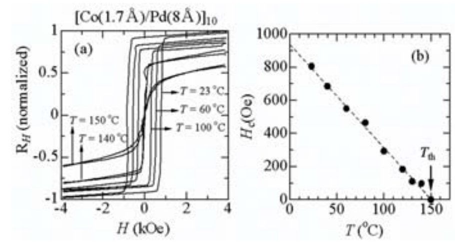

Fig. 1 (a) Extraordinary Hall resistance hysteresis of [Co(1.7 Å)/Pd(8 Å)]$_{10}$ measured at various temperatures. (b) Temperature dependence of coercive field H_c.

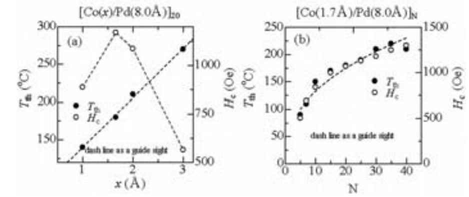

Fig. 2 Coercive fields H_c and threshold temperature T_{th} as a functions vs. (a) Co thickness layer t_{Co} and (b) repetition number N of Co/Pd bi-layer

HU-09

Antiferromagnetic Exchange Coupling at Interface between Fe_3O_4(001) and Fe(001) Epitaxial Films.

H. Yanagihara, A. Ohnishi, J. Hagiwara, Y. Toyada, E. Kita
Applied Physics, Univ. Tsukuba, Tsukuba, Japan

Interlayer exchange coupling (IEC) between two ferromagnetic layers is important phenomenon for magnetic recording technologies. Most of the reported IEC systems consist of two ferromagnetic metal (FMM) layers separated by a non-magnetic metal (NMM) spacer. Depending on the NMM layer thickness and the material, the IEC changes its sign as well as the coupling energy, explained by the picture of RKKY interaction or spin-dependent quantum well state. In contrast, the hybrid structure of two ferromagnetic layers without the spacer mostly gives ferromagnetic coupling or no magnetic coupling, and the direct exchange type of antiferromagnetic coupling is hardly observed at the interface between two ferromagnetic layers. In this presentation we report the strong antiferromagnetic exchange coupling in Fe_3O_4/Fe(001) epitaxial layers.
All samples were grown by using a molecular beam epitaxy (MBE)[1]. Base pressure was better than $1x10^{-8}$ Torr. We used cleaved MgO(001) as substrates. Prior to the film growth, the substrates were annealed at 700 ^oC to remove surface contaminations. After decreasing the temperature to 280 ^oC, Fe_3O_4 layers were grown by reactive MBE technique with oxygen gas. During the Fe_3O_4 growth, the chamber pressure was kept as 4 $x10^{-6}$ Torr. The Fe layers were grown at room temperature and at the pressure of ~ $x10^{-8}$ Torr. We finally deposited 2 nm of Au thin films as a protection layer. The typical sample structure was MgO(001) substrate/ Fe_3O_4(13 nm)/ Fe (3 nm)/ Au(2 nm). In some samples we also inserted thin MgO(001) spacers to investigate a role of the interface on the coupling between Fe_3O_4 and Fe(001). We monitored the growth process with a reflection high energy electron diffraction (RHEED) technique. In order to estimate the interface exchange constant for the antiferromagnetically coupled layers, the magnetic moments of both Fe_3O_4 and Fe layers were designed to be the same. Magnetization measurements were carried out by using a commercial SQUID magnetometer and a magneto-optical Kerr effect (MOKE) at room temperature.
A RHEED image during the Fe_3O_4 growth is shown in Fig.1. Up to the 13 nm thick of Fe_3O_4, the intensity of the specular reflection spot oscillates as a function of the growth time. The oscillation period corresponds to the thickness of 0.21 nm which is equal to a quarter of the unit cell of Fe_3O_4 (a = 0.84 nm). Therefore the interface of Fe_3O_4/Fe is expected to be quite sharp. The RHEED pattern of the Fe (001) is a little spotty but still suggesting a high crystalline quality.
Magnetization curve measured at room temperature is shown in Fig. 2. At the remanence state, the magnetic moment is nearly canceled out and the saturation field is larger than H = 10 kOe which is much higher than both of the Fe and Fe_3O_4 films. In addition, the saturated value of the magnetic moment corresponds to the sum of the two layers, indicating the existence of strong antiferromagnetic coupling between Fe_3O_4 and Fe at the interface. The estimated value of the coupling constant from the *MH* curve is J ~ -2 erg/cm^2. A thin MgO(001) spacer inserted between two ferromagnetic layers, reduced the coupling constants, in contrast to the case of γ-Fe_2O_3 / MgO/Fe(001) in which the strong antiferromagnetic coupling appeared with 0.6 nm of MgO and the direct exchange is ferromagnetic between γ-Fe_2O_3 and Fe(001) layers[2].
Although the mechanism of this direct-exchange type strong antiferromagnetic coupling is unknown at this point, the unique electronic structure of the Fe_3O_4 is crucial to reveal such a strong exchange coupling with a negative constant. According to a band calculation for Fe_3O_4, the DOS of conductive (or high temperature) state is half-metallic [3]. The minority state of the Fe_3O_4 has a Fermi surface and the majority one has a band-gap, suggesting that only the minority spin-state can be mixed with the electronic state in Fe. The observed strong antiferromagnetic coupling might be understood along with this framework.

[1] H. Yanagihara, M. Hsegawa, E. Kita, Y. Wakabayashi, H. Sawa, and K. Siratori, J. Phys. Soc. Jpn. 75, 054708 (2006).

[2] H. Yanagihara, Y. Toyoda, and Eiji Kita. J. Appl. Phys. 101, 09D101 (2007).

[3] A. Yanase and K. Siratoi, J. Phys. Soc. Jpn. 53, 312 (1984).

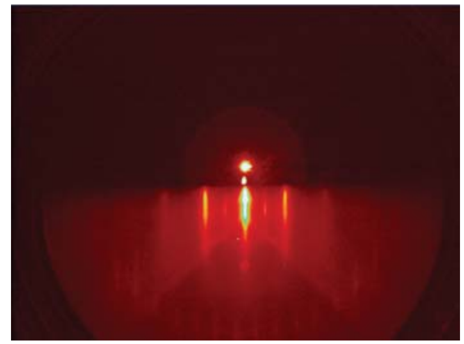

FIG. 1. RHEED image of Fe_3O_4(001).

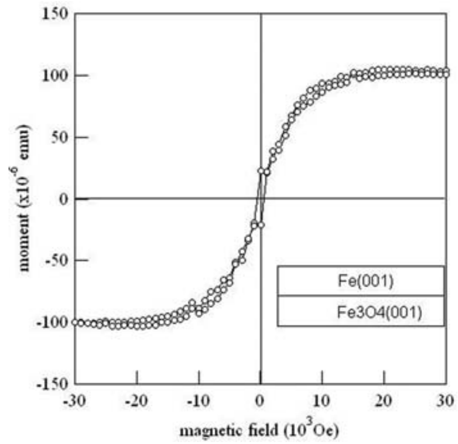

FIG. 2. *MH* curve of Fe_3O_4 bilayer.

HU-10

Preparation of Longitudinally Oriented CoCrPt Thin Film in GMR Head at Room Temperature.

X. Liu[1], Z. Li[1], S. Li[1], W. Shi[1], *F. Wei*[1], D. Wei[2], J. Cao[3]

1. Lanzhou University, Research Institute of Magnetic Materials, Lanzhou, China; 2. Tsinghua University, Key Laboratory of Advanced Materials Department and Engineering, Beijing, China; 3. Lanzhou University, Research Institute of Magnetic Materials(Now woking in INESC-Microsystems and Nanotechnologies (INESC-MN), R.Alves Redol 9-1, 1000-29 Lisbon, Portugal), Lanzhou, China

The CoCrPt thin films can be used as longitudinal magnetic recording media or bias layers which provides longitudinal field in spin valve GMR read heads. For its application in GMR heads, not only the crystallographic c-axis should lie in the film plane[1], but also the room-temperature preparation of the thin film is required to match with the micro-electronic device processing procedure. In this work, the CoCrPt film, CoCr interlayer and CrW underlayer were prepared by DC and RF co-sputtering method using the CM-18 magnetron sputtering system. It is difficult to obtain Cr (200) texture on amorphous SiO_2 substrate.

We find that the doping of W element is helpful to improve the film texture, and the CrW alloy film has (200) preferential orientation with tungsten's atomic percentage from 5 to 22%[2]. The CoCrPt films deposited on the CrW underlayer with (200) texture show a (10-11) orientation texture, but not the expected (11-20)texture; and the angle between the [10-11] and [0001] crystal orientation is about 28°. A 5nm CoCr intermediate layer is helpful to achieve a good (11-20) orientation of CoCrPt films, just shown in Fig1. This may be interpreted that the additions of W enhance an expansion of Cr lattice, and it is not favorable for formation of CoCrPt (11-20)texture. The CoCr intermediate layer plays a role to modulate the misfits between both.

The relationships between with Pt atomic contents and magnetic properties are also studied, as shown in Fig 2. When the Pt content rises from 8.5% to 25%, the lattice constant *a* increases from 2.537À to 2.617À, and the in-plane coercivity Hc is enhanced from 950 Oe to 3200 Oe, which suggests that the in-plane magnetostriction with a residual compressive stress would enlarge the longitudinal coercivity.

It is well known that the coercivity is controlled by the magnetic anisotropy of materials, mostly the magnetocrystalline anisotropy, but sometimes the magnetostriction or magneto-elastic anisotropy is also important. The magneto-elastic anisotropy is a result of the residual stress in the material. For the CoCrPt multilayer, the stress may arise from internal and external mechanical stress: a thermal component owing to the difference in the thermal expansion coefficients of the CoCrPt thin film and CrW underlayer, and an intrinsic one resulting from the structure of the film, such as the lattice deformation.

In the simulation part of M-H loops, the magnetocrystalline anisotropy is determined by the law of approach to saturation; and the magneto-elastic anisotropy is analyzed by using micromagnetic model[3]. For the film with 0.85 at% Pt,the simulated results are shown in Fig 3. It is found that the in-plane magneto-elastic effect with a residual compressive stress on the order of 1.14Gpa tends to enlarge the longitudinal coercivity, squareness, and enduce the open-up between the tails of the longitudinal and perpendicular loops. The simulated in-plane M-H loop agrees well with the experimental results, the deviation of the perpendicular loop maybe due to other anisotropy contributions, such as shape and interface anisotropies[4], which will be discussed in this work.

[1] M.E. Mehery and D.E laughlzn Acta Mater 48. 223-238 (2000)

[2] Jiangwei Cao, Jun Cai, Yan liu, Zheng Yang and Fulin Wei J. Appl. Phys.99,08F901 (2006)

[3] Zhenghua Li, Jiangwei Cao, Fulin Wei, Kun Piao, Shenxian She and Dan Wei, JOURNAL OF APPLIED PHYSICS 102, 113918 (2007)

[4] R. Jungblut, M. T. Johnson, J. aan de Stegge, A. Reinders, and F. J. A. den Broeder, J. Appl. Phys. 75 (lo), 15 May 1994

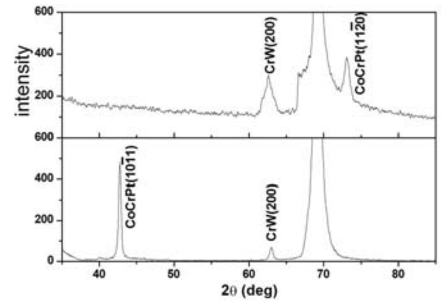

Fig 1 XRD pattern of (a) CoCrPt(50nm)/CoCr(5nm)/CrW(50nm)/SiO_2 (b) CoCrPt(50nm) /CrW(50nm)/SiO_2

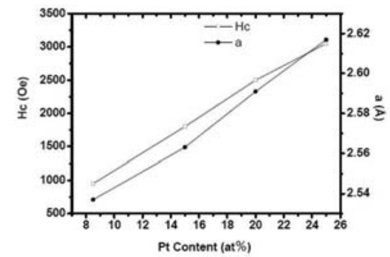

Fig 2. Relationship between the magnetic proterity Hc in-plane and crystal parameter a with Pt content(at%).

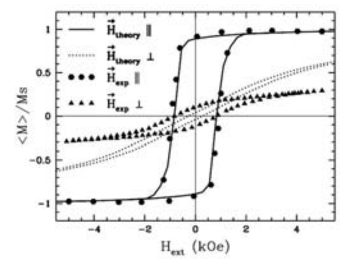

Fig.3: Simulated longitudinal (solid lines) and perpendicular (dotted lines) loops compared with the experiment results (hexangular and triangular dots) .

HU-11

Molecular dynamics investigation on interfacial mixing behavior in transition metals (Fe, Co, Ni)- Al multilayer system.

S. Lee, H. Park, Y. Chung
Department of Materials Science & Engineering, Hanyang University, Seoul, South Korea

1. Introduction

It has been generally known that the interface between metals or metal and insulator had a critical role in the spin polarization of the junction, and the spin polarization for the tunneling characteristics is strongly dependent on the structural quality of the tunnel junction [1]. For MRAM application, ordered and uniform thin films less than 1-2 nm are essentially required for the coherency of the device. Accordingly, a considerable amount of interest has been focused on the chemically affinitive interface between transition metal and Al. In this work, the intermixing characteristic of the Co, Fe, and Ni on Al(001) substrate surface was quantitatively investigated by molecular dynamics simulation.

2. Calculation Methods

The position of the bottommost two layers for Al(001) substrate were fixed at 0 K. The temperature of other layers was set to 300 K. The incident energy of adatoms was set to 0.1 eV. The adatom was added at a distance of 20 Å from the substrate surface. The positions of the adatoms were randomly selected in the x, y-plane and the incident angles were set to be normal to the substrate. The MD time step was set to 1 femto-second(fs) and the system was fully relaxed for each additional adatom in the limit of 5 pico-second(ps).

3. Results and Discussion

The arriving Co, Fe, and Ni adatom was initially absorbed into a hollow site of the substrate surface layer (Fig. 1(a)). The Co, Fe, and Ni adatom then interchanged with the substrate Al atom below the surface, and the exchanged Al atom finally comes to reside in the hollow site on the Al surface (Fig. 1(b)). A time of only 1 ps was sufficient for the adatom to mix with the Al(001) surface at room temperature. Active surface alloying can be explained by the corresponding surface energy. Because the surface energy of Al(001) is much lower than that of Co, Fe, and Ni(001), the adsorbate films could be incorporated into the Al substrate. Moreover, the maximum local acceleration coming from the strong affinity between Al adatom and surface Co, Fe, and Ni atom was in the range of 2~4 eV. It can be reasonably expected that the adatoms could be considered as being mixed with the Al substrate in spite of the low adatom incident energy of 0.1 eV at room temperature. The mixing length and ratio for Fe was found to be the lowest value among these systems and the degree of mixing at the interface could be dependent on locally accelerated energy of each adatom near the Al substrate surface (Table 1). These results showed a similar tendency with that of an experimental report [2]. When Co, Fe, and Ni atoms are deposited on Al substrate up to 10 monolayers (Fig. 2), Fe atoms were incorporated into the substrate less than Co and Ni atoms. The origin of these phenomena can be found be in the difference in cohesive energy. Moreover, it can be inferred that interfacial structure for Co/Al(001) was apparently revealed to be the most forming B2 structure (Fig. 2(a)), since perfect B2 structure indicates the structure in which the first atomic layer has 100 at% substrate atom - 0 at% adsorbate atom and the second atomic layer has 0 at% substrate atom- 100 at% adsorbate atom (mixing layers) repeatedly. Additionally, the interfacial structure for Co, Fe, Ni on Al substrate surface was quantitatively analyzed by pair correlation function (PCF).

[1] J. M. De Tersa, A Barthelemy, A. Fert, J. P. Contour, F. Montaigne, and P. Seneor, Science 286, 507 (1999).

[2] J. D. R. Buchanan, T. P. A. Hase, B. K. Tanner, P. J. Chen, L. Gan, C. J. Powell, and W. F. Egelhoff Jr., Phys. Rev. B 66, 104427 (2002).

System	Mixing length 1)	Mixing ratio 2)	Maximum local acceleration
Co/Al	1.50 Å	90.0 %	3.50 eV
Fe/Al	0.86 Å	88.0 %	2.00 eV
Ni/Al	1.69 Å	94.0 %	3.70 eV

Table 1. Calculated mixing length and ratio, and locally accelerated energy 1)Average penetration distance of incorporated adatoms measured from the original surface of the substrate. 2)Proportion of the number of penetrated adatoms to the total number of adatoms during 1000 random depositions of individual adatoms on the clean Al(001) substrate surface

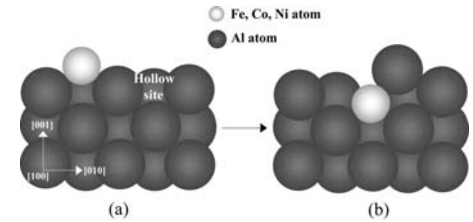

Fig.1.Schematic diagram (side view) of exchange diffusion mechanism of Co, Fe, and Ni adatom on Al(001) substrate. The incorporation path of each adatoms are from (a) a hollow site to (b) a substitutional site of the Al(001) surface. .

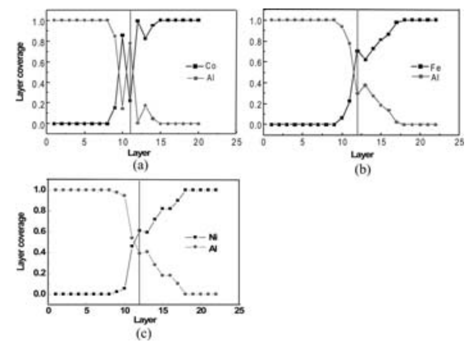

Fig.2. Layer coverage fraction of Co, Fe, Ni atoms with 0.1 eV on Al(001) surface at 300 K along the z-axis direction. The centeral solid line corresponds to the surface of Al substrate before deposition.

HU-12

Intermedium zero-magnetization state in Co/TiO2/Co trilayer.

Y. Wu[1,2], *J. G. Lin*[1,3], C. Chang[2,3]
1. Center for Condensed Matter Sciences, National Taiwan University, Taipei, Taiwan; 2. Department of Physics, National Taiwan University, Taipei, Taiwan; 3. Center for Nanostorage research, National Taiwan University, Taipei, Taiwan

I. INTRODUCTION

The antiferromagnetic interlayer coupling in layered magnetic system was observed in 1986 and suggested to be Heisenberg type. However, the observation of one-half of the saturation magnetization in Fe/Cr/Fe prevailed that another type of magnetic interlayer coupling might occur, which was named as biquadratic interlayer coupling. Generally speaking, the understanding of the nature of magnetic interlayer coupling between magnetic layers is important from both scientific and industrial application points of view. In this work, the coupling between two Co thin layers separated by a TiO2 (X nm) layer with various thickness X is investigated. We observe an intermediate zero-magnetization state at some finite interval of applied field for the sample of X = 8. The nature of this intermedium state is proposed to be the either the meta-stable state at which the direction of total moment is perpendicular to the applied field or an antiferromagnetic state with a pinned Co-layer by interface roughness.

II. EXPERIMENT

A series of Co/TiO2(X nm)/Co trilayers with the thickness of amorphous TiO2 spacer X varying from 2 to 10 nm are synthesized on TiO2/Si(100) at room temperature. The thickness of the Co ferromagnetic layers was fixed to be 20 nm in all samples. For comparison, a sample with pure Co layer of 40 nm (X = 0) is also prepared. The field dependent in-plane magnetization (M-H) was measured at 300, 80 and 10 K with a physical-property-measurement system (PPMS, Quantum Design model 6000). Scanning electron microscopy (SEM, JEOL 6700) was used to determine the thickness of each layer. Atomic force microscopy (AFM) was utilized for the morphology of TiO2(X)/Co(20nm)/TiO2(10nm) layers. X-ray diffraction patterns of the samples were taken with PANalytical X'Pert PRO system.

III. RESULTS AND DISCUSSION

Figure 1 is the plot of M-H at 10 K for the samples with X = 0 to 10. It indicates that the value of the Hc for all samples get much larger than those measured at room temperature. Moreover, the sample of X= 8 show a very unusual behavior with two steps of zero magnetization at -10 Oe < H < -50 Oe and 30 Oe < H < 80 Oe. This two-step feature of X = 8 also occurs at 80 K within two narrower intervals of (-10 Oe, -40 Oe) and (30 Oe, 60 Oe). Figure 2 shows the plot of M-H for X = 8 at 80 K and 10 K with respect to the symbols of open and close squares. The occurrence of zero magnetization at a finite interval of field implies a meta-stable state between two field-parallel ferromagnetic states. Comparing our M-H results with that in NiFe/SiO2/CoFe [8], the observed zero magnetization in our sample of X = 8 seems resemble to the AFM state under a single domain model. However, the major difference between our sample and NiFe/SiO2/CoFe is that our two Co-layers are identical, meaning the same switching field for these two Co-layers; while NiFe and CoFe have very different coercivities of 25 Oe and 130 Oe respectively. Therefore, it is hard to explain why two Co-layers can form an AFM state without an additional pinned layer, unless the interface roughness provides a directional pinning mechanism. The other possibility is that when two coupled Co-layers rotate together, they are temporarily pinned at the direction perpendicular to the filed, under the circumstance that the domain structure prefers a directional pinning force.

IV. CONCLUSION

A series of Co/TiO2(X)/Co trilayers with X = 0 to 10 nm are synthesized. In the M-H curves at 10 and 80 K, the samples with X = 2 and 4 nm exhibit weakly coupled FM behaviors. As increasing the spacer layer thickness up to 6 nm, the percolation/pinhole effect disappears, and the interlayer coupling becomes dominating. Our salient finding is the observation of an intermedium zero-magnetization state for X = 8, which maybe associated with a meta-stable FM state with the direction of magnetic moment perpendicular to the applied field or an AFM state with one of Co-layers pinned by surface roughness.

ACKNOWLEDGMENT
This work is supported by the Ministry of Economics Affair (95-EC-17-A-08-S1-0006) and the National Science Counsel of R. O. C. (NSC-95-2120-M-002-002 and NSC 95-2752-M-002-006-PAE).

[1] C. L. Platt, M.R. McCartney, F.T. Parker, A. E. Berkowitz, Phys. Rev. B 61, 9633 (2000).

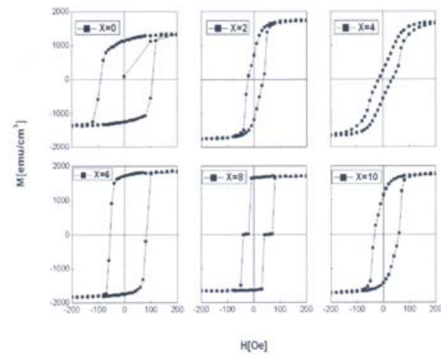

Fig. 1 M-H curve measured at 10 K, for various Co/TiO2(X nm)/Co trilayer with X = 0 to 10.

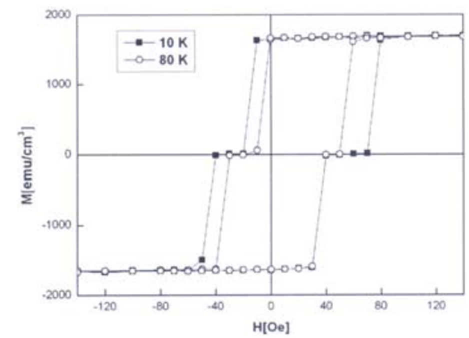

Fig. 2 M-H curve for Co/TiO2(8 nm)/Co at 10 and 80 K with respect to the close squares and open circles.

Fe_3O_4/MgO/Fe heteroepitaxial structures for magnetic tunnel junctions.

J. Orna[1,2], L. Morellon[1,2], P. A. Algarabel[2], J. A. Pardo[1,3], S. Sangiao[1], C. Magen[4], J. M. De Teresa[2], M. R. Ibarra[1,2]
1. Instituto de Nanociencia de Aragón (INA), Universidad de Zaragoza, Zaragoza, Spain; 2. Instituto de Ciencia de Materiales de Aragon (ICMA), Universidad de Zaragoza-CSIC, Zaragoza, Spain; 3. Departamento de Ciencia y Tecnología de Materiales y Fluidos, Universidad de Zaragoza, Zaragoza, Spain; 4. Materials Science and Technology Division, Oak Ridge National Laboratory, Oak Ridge, TN

Magnetite (Fe_3O_4) is a half-metallic ferromagnet with a high Curie temperature (860 K) that is expected to exhibit suitable properties for its implementation in spintronic devices [1-3]. In addition, the interest in spintronic structures based on magnetic oxides has increased recently [4]. MgO is a serious candidate as tunnel barrier because of the small lattice mismatch with the Fe_3O_4 (0.3%) electrode [5-7]. Nevertheless, the performance of Fe_3O_4-based magnetic tunnel junctions (MTJs) has been limited with scattered values and a maximum of -14% at room temperature [8, 9]. Other tunnel barriers were not significantly better [10-12]. We believe that prior to application in real devices, the epitaxial growth of heterostructures with Fe_3O_4 and MgO should be further optimized. In this work we report the growth of epitaxial Fe_3O_4/MgO/Fe heterostructures on MgO (001) substrates by means of pulsed laser deposition (PLD) and their structural and magnetic properties.
We have grown epitaxial Fe_3O_4 and Fe thin films on single-crystal MgO (001) substrates by PLD using a KrF laser (248 nm). Stoichiometric polycrystalline Fe_3O_4 and MgO, and pure (99.99%) Fe targets have been used. All layers have been deposited in ultra-high vacuum (base pressure $< 5\times10^{-9}$ Torr) at substrate temperatures of 400 °C for Fe_3O_4 and between room-temperature (RT) and 400 °C for Fe and MgO layers. Individual thin films and Fe_3O_4/MgO/Fe heterostructures on MgO (001) have been characterized by X-ray diffraction (θ-2θ, ω scans, Φ scans, and reciprocal space maps) and X-ray reflectivity (XRR), high-resolution transmission electron microscopy (HRTEM) and VSM and SQUID magnetometry. Previous magnetoresistance and anomalous Hall effect measurements in our epitaxial Fe_3O_4 thin films have been published elsewhere [13, 14].
After optimizing the growth conditions and fully characterizing the single Fe_3O_4 and Fe layers onto MgO (001), we undertook the growth of the full Fe_3O_4/MgO/Fe heterostructures by PLD. HRTEM data (not shown here) demonstrate a high crystallinity of the MgO (001) tunnel barrier and sharp interfaces. XRR in a selected heterostructure where both MgO barrier and Fe counterelectrode have been deposited at RT are shown in Fig. 1. As can be seen from the fit the rms roughnesses are relatively low, ~0.2 nm, this being indispensable for future MTJs. The RT hysteresis loop in a sample grown in similar conditions, Fig. 2a, reveals an independent switching of both Fe_3O_4 and Fe electrodes, this also being required for tunnel magnetoresistance. The low field (500 Oe) temperature dependence of the magnetization of the same sample as seen in Fig. 2b displays a clear and sharp drop at the Verwey transition, T_V=115 K, demonstrating the high quality of the Fe_3O_4 layer.
We have produced high quality epitaxial Fe_3O_4/MgO/Fe heterostructures by PLD. To our knowledge, this type of heterostructure has not been grown before by PLD. Microfabrication of MTJs from these is in progress.

[1] K. Gosh et al., Appl. Phys. Lett. **73**, 689 (1998)

[2] X. W. Li et al., Appl. Phys. Lett. **73**, 3282 (1998)

[3] P. Seneor et al., Appl. Phys. Lett. **74**, 4017 (1999)

[4] M. Bibes and A. Barthélémy, IEEE Trans. on Electron Devices **54**, 1003 (2007)

[5] T. Kiyomura et al., J. Appl. Phys. **88**, 4768 (2000)

[6] W. Kim et al., J. Appl. Phys. **93**, 8032 (2003)

[7] X. Jin et al., J. Magn. Magn. Mater. **286**, 128 (2005)

[8] P. J. van der Zaag et al., J. Magn. Magn. Mater. **211**, 301 (2000)

[9] T. Kado et al., J. Appl. Phys. **101**, 09J511 (2007)

[10] K. S. Yoon et al., J. Magn. Magn. Mater. **285**, 125 (2005)

[11] D. Reisinger et al., cond-mat/0407725

[12] S. Parkin et al., Proc. IEEE **91**, 661 (2003)

[13] J.M. De Teresa et al., Microelectr. Eng. **84**, 1660 (2007)

[14] A. Fernandez-Pacheco et al., submitted to Phys. Rev. B (2008)

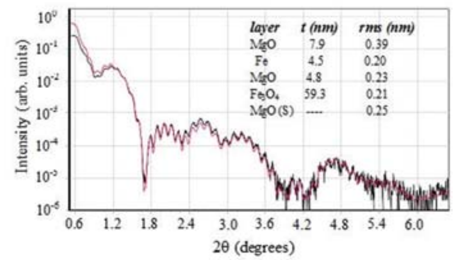

FIGURE1. X-ray Reflectivity (XRR) of a selected Fe_3O_4/MgO/Fe heterostructure. The red line is the fit by using the software package LEPTOS from Bruker AXS. The derived thickness and rms roughness of all layers and interphases have been listed as an inset.

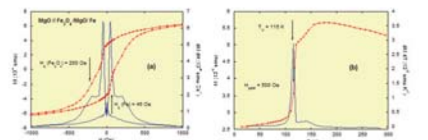

FIGURE 2. (a) Room-temperature hysteresis loop of a Fe_3O_4 (70.9 nm)/MgO (3.7 nm)/Fe (5.6 nm)/Au (5.3 nm) heterostructure. The switching fields of both electrodes have been marked. (b) Temperature dependence of the magnetization in a field of 500 Oe of the same sample. The onset of the Verwey transition is indicated.

HU-14

Thermal stability of top-type synthetic antiferromangetic spin-valve structure in (001) orientated MgO-based MTJs.

C. Chen[1], C. Lai[1], W. Chen[2], K. Shen[2], H. Bor[3]
1. Department of Materials Science and Engineering, National Tsing Hua University, Hsinchu, Taiwan; 2. Electronics Research and Service Organization, Industrial Technology Research Institute, Hsinchu, Taiwan; 3. Materials and Electro-Optics Research Division, Chuang-Shan institute of Science and Technology, Tauyoun, Taiwan

Introduction:

Recently, MgO-based MTJs have attracted much attention due to ultra high MR ratio and low RA products [1], which may make MRAM compatible in commercial applications. The synthetic antiferromagnetic (SAF) structure is extensively used in the fabrication of MTJs not only to get better thermal stability but also to avoid biasing effect on the free layer due to the stray field, especially when the pattern size is small [2],[3]. In this work, we investigated the thermal stability of the SAF structure, FM/Ru/$Co_{50}Fe_{50}$ in the top-type MgO-based MTJs, where $Co_{50}Fe_{50}$, $Co_{40}Fe_{40}B_{20}$, $Co_{40}Fe_{40}B_{20}$/$Co_{50}Fe_{50}$, and $Co_{50}Fe_{50}$/$Co_{40}Fe_{40}B_{20}$ were used as the FM layer. We found that orientations of FM and Ru influenced the thermal stability of the SAF structure.

Experiment results & discussion:

We prepared the full stack structure, consisting of substrate/Ta(20)/$Co_{40}Fe_{40}B_{20}$(3)/MgO(2)/FM(3)/Ru(0.9)/$Co_{50}Fe_{50}$(3)/IrMn(10)/Ta(40) (unit: nm), where (002) $Co_{50}Fe_{50}$(3 nm), amorphous $Co_{40}Fe_{40}B_{20}$(3 nm), amorphous $Co_{40}Fe_{40}B_{20}$(1.5 nm)/(110) $Co_{50}Fe_{50}$(1.5 nm), and (002) $Co_{50}Fe_{50}$(1.5 nm)/ amorphous $Co_{40}Fe_{40}B_{20}$(1.5 nm) were used as the FM layer. All films were deposited by using a magnetron sputtering system with a base pressure less than $5x10^{-8}$ Torr and an in-plane magnetic field of 80 Oe was applied during deposition to define the anisotropic direction. In our layer structure, the orientation of the FM layer can be tuned to amorphous, (002), or (110) direction while the MgO barrier remains (001)-orientated. The MTJ films were annealed for 1hr at various temperatures in a vacuum of 2×10^{-5} Torr under a magnetic field of 7 kOe. The magnetic and structural properties were measured by a vibrating sample magnetometer (VSM) and an X-ray diffractometer (XRD) using Cu Kα radiation, respectively.

The strength of the RKKY coupling was correlated to FM/Ru interface, shown in Fig. 1, where CoFe/Ru showed larger coupling strength than CoFeB/Ru in the as-deposited state no matter which orientation CoFe was. However, after annealing at high temperatures, a remarkable drop of RKKY coupling was observed in (002) CoFe/Ru/CoFe interface with an antiferromagnetic layer, IrMn. The RKKY antiparallel coupling between adjacent CoFe layers was completely destroyed after 275 ^{o}C annealing, leading to a single biased pinned loop. For comparison, we prepared the similar structure without the IrMn layer, Ta(20)/CoFeB(3)/MgO(2)/CoFe(3)/Ru(0.9)/CoFe(3)/Ta(2) to examine how the annealing process affected the RKKY coupling. The strength of RKKY coupling with (002) CoFe as the FM layer is about the same even after thermal treatment, which strongly indicated that Mn diffusion was the main reason to deteriorate the antiferromagnetic coupling of CoFe/Ru/CoFe. The Ru spacer has been known as an effective diffusion barrier for Mn in the bottom-type SAF, in which CoFe is (110). To clarify if the orientations of FM and Ru affected the roles of the diffusion barrier, Ru, we prepared samples consisting of substrate/MgO(2)/FM(3)/Ru(15)/Ta(2). XRD results revealed that all samples showed strong (002) Ru intensity except for (002) CoFe as the FM layer in the as-deposited and annealed states. From TEM cross-sectional images, (002) CoFe/Ru/CoFe showed serious diffusion while other samples still kept sharp interfaces after 275 ^{o}C annealing. These results implied that Ru is no longer an effective diffusion barrier for Mn with (002) CoFe and the thermal stability of SAF is strongly correlated to the orientations of FM and Ru.

[1] K. Tsunekawa, D. D. Djayaprawira, M. Nagai, H. Maehara, S. Yamagata, N. Watanabe, S. Yuasa, Y. Suzuki, and K. Ando, Appl. Phys. Lett. 87. 072503 (2005)

[2] X.Liu, D. Mazumdar, W. Shen, B. D. Schrag, and G. Xiao, Appl. Phys. Lett. 89. 023504 (2006)

[3] Y. M. Lee, J. Hayakawa, S. Ikeda, F. Matsukura, and H. Ohno, Appl. Phys. Lett. 89. 042506 (2006)

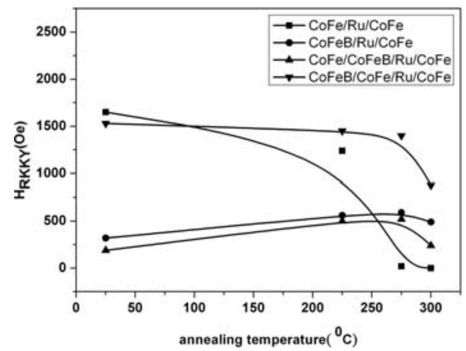

Fig. 1 H_{RKKY} V.S. annealing temperature in FM/Ru/CoFe with different FM materials

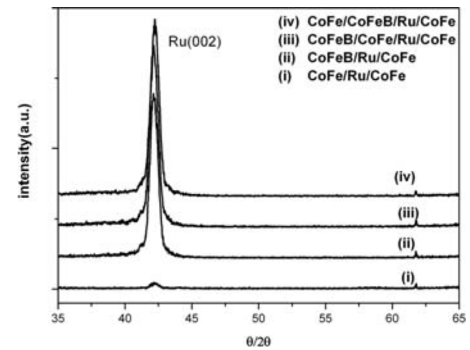

Fig. 2 XRD results of substrate/MgO(2 nm)/FM(2 nm)/Ru(15 nm)/Ta(2 nm). FMs are $Co_{50}Fe_{50}$, $Co_{40}Fe_{40}B_{20}$, $Co_{40}Fe_{40}B_{20}$/ $Co_{50}Fe_{50}$, and $Co_{50}Fe_{50}$/ $Co_{40}Fe_{40}B_{20}$

HV-01

Numerical Analysis of Heat Transfer Mechanisms Induced by Laser Heating in Far- and Near- Field HAMR Systems.

R. Ikkawi[1], N. Amos[1], A. Balandin[1], D. Litvinov[2], S. Khizroev[1]
1. Electrical Engineering, University of California, Riverside, Riverside, CA; 2. Center for Nanomagnetic Systems, University of Houston, Houston, TX

Heat-assisted magnetic recording (HAMR) systems utilize the phenomenon during which the magnetic properties of the recording media could be locally modified via heating (optionally, by an optical source in the near field) to temperature in the vicinity of the Curie value of the media material [1]. As a result, heat induced by the optical source can temporarily reduce the magnetic coercivity of high anisotropy material to a level attainable by the magnetic writing head, thus making it feasible to record on relatively small ultra-high anisotropy (and thermally stable) grains, consequently dramatically enhancing the areal density. In other words, in a HAMR system, certain transfer of heat at nanoscale is initiated by a source. This energy transport affects the physical properties of the recording media as well as the stability of the system. This paper will present of a numerical analysis of heat transfer mechanisms induced by laser heating in far- and near-field HAMR systems.
The absorption of electromagnetic waves by the recording media will induce heat due to the electron-phonon interplay. Thus, the thermal behavior of energy carriers, particularly, electrons and phonons should be considered during the numerical analysis for predicting the transient thermal transport in the magnetic media. The absorption process can be considered as a secondary source of energy inside the material. It is the secondary source, rather than the beam generated by the laser device, that will determine the dynamics of the irradiated material. A laser beam will be used to locally heat a magnetic thin film deposited on glass substrates spinning at 5400-7200 rpm with respect to the stationary light source. The beam penetration depth, which can be described with an absorption coefficient, depends on the ambient temperature. Therefore, the model will examine the penetration depth and the influence of the disk rotation on the transient temperature distribution and cooling effects. Figure 1 shows calculated temperature rise induced by different power levels. Figure 2 shows the effect of spinning frequency on convective cooling as compared to no cooling effects. The simulation model considers the laser beam to have an infinitesimal width that will vary from diffraction limited spot sizes (~λ/2) to 50-nm spot sizes in the near-field regime of the emitting source to address the heating issues associated with both HAMR setups: far- and near-field. The transient energy-balance equation solved is given by Expression 1, where the boundary condition on the heated boundary of the disk was assigned to assess cooling effects resulted by air-convective cooling and surface radiation, as given by Expression 2.

T. McDaniel, W. Challener, “Issues in heat-assisted perpendicular recording,” IEEE Trans. Magn. 39 (4), 1972-9 (2003)

$$\rho . C_p . \frac{\partial T}{\partial t} + \nabla .(-K \nabla T) = Q \tag{1}$$

$$-n.(-k \nabla T) = q_0 + h(T_{inf} - T) + \varepsilon\sigma (T_{amb}^4 - T^4) \tag{2}$$

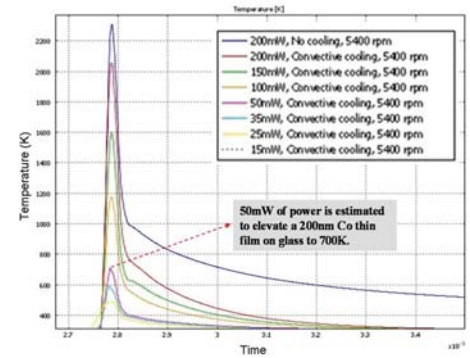

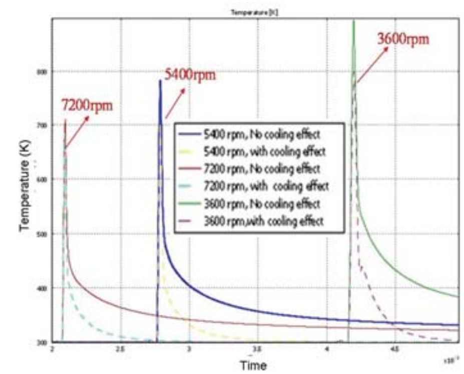

Micromagnetic studies of probe recording on magnetic nanocaps.

A. Goncharov[1], T. Schrefl[1], P. Kappenberger[2], G. Hrkac[1], J. Dean[1], S. Bance[1], M. Albrecht[3]
1. Engineering Materials, The University of Sheffield, Sheffield, United Kingdom; 2. Nano-scale Materials Science, Empa-Materials Science & Technology, Dübendorf, Switzerland; 3. Surface and Interface Physics, Chemnitz University of Technology, Chemnitz, Germany

Recently fabricated Co/Pd nanocap arrays have been shown to be a promising candidate for the magnetic recording with densities above 1 Tbit/inch^2 [1]. We present results on micromagnetic studies of possibilities of the MFM tip recording on these nanostructures. For these studies a nanocap with 20 nm diameter and Co coated tips were used. First, we investigated the impact of different tip geometries and coatings onto the tip apex field. Further, the results of integrated recording simulations and the impact of the bias field on the stability of the magnetization direction in the nanocaps is discussed.

In order to estimate an impact of the material properties and a geometry of the magnetic coating on the stray field, produced by an MFM tip, full micromagnetic studies have been performed. Three ferromagnetic parameters (M_s, K, and A) of the layer and its shape were varied. The three different MFM tip coatings, corresponding to conical and pyramidal shaped tips were modelled. The results are grouped into parts describing the dependence of the stray field on the following parameters: film thickness, saturation magnetization, magnetocrystalline anisotropy, exchange constant. As a starting point, values from bulk hcp cobalt for the anisotropy (K_1 = 4.5e10^5 J/m^3, K_2 =1.5e10^5 J/m^3), exchange (A = 1.3e10^{-11} J/m) and saturation magnetization (M_s = 1.76T / μ_0) were taken. Our results show, that significant decrease in the anisotropy of the magnetic material does not influence the stray field of the tip, as the magnetization configuration is governed by the shape anisotropy of the high aspect ratio tips. In addition, Our data suggests that the exchange constant does not affect the stray field significantly within a realistic range of values. High values of the magnetization polarization can help to increase the stray field, but also introduce higher demagnetizing field, which degrades the performance of the tip. The impact of the film thickness on the stray field is an important parameter as it is the only feasible parameter that can be varied in the coating of the MFM tips if the magnetic material is not changed. It has a significant influence on the stray field generation. The strength of the field can be increased by the factor of two by changing the coating thickness from 4 nm to 7 nm. This dependence has been simulated for two tip shapes, the conical and the pyramidal shape with one covered facet.

Recording simulations for writing bits using an MFM tip were performed at 0 K using tip with a conical shape, with a bottom diameter of 10 nm and the coating thickness of 5 nm. A sphere size of 20 nm was chosen for these simulations, covered with a magnetic nanocap of 3.5 nm film thickness on top. For the cap to be thermally stable a magnetocrystalline anisotropy constant of 4.77e10^5 J/m^3 was taken. This value corresponds to an effective energy barrier of 50 k_BT, which is required for magnetic storage application. The exchange constant and M_s were set to 1.0e10^{-11} J/m and 0.6 T, respectively. It was shown that a successful writing is only possible if unrealistically low anisotropy values for the cap material are assumed (K < 10^4 J/m^3). This leads to thermally unstable media and thus is not suited for a practical storage application. Further simulations were made at 300 K that included thermal activation during the recording process. Thermal fluctuations assist in the recording process, but their effect was found to be to small to sufficiently lower the switching field of the nanocaps in order to be writable with a MFM tip. When writing on nanocaps using a locally applied magnetic bias field, it is possible to achieve selective switching of single nanocaps. The sum of the bias field and the field from the MFM tip exceeds the coercive field of the cap and switching is possible. The optimal bias field for 20 nm caps at 300 K was found to have a magnitude of at least 0.22 T at an angle of 20 degrees with the film normal. The bias field has to reduce the energy barrier to 16 k_BT. Together with the reduction of the 10 k_BT by the field of the tip this will lead to 6 k_BT. The target cap can be switched with the field from the tip within 1 ns by the help of thermal fluctuations. However, all caps in the array that are subject to the bias field have a relaxation time of about 10 microseconds. For 10^4 write cycles, the accumulated field exposure time, will be 10 microseconds which can give rise to adjacent track erasure.The way to overcome this problem is to increase the stray field strength of the tips by using thicker coatings or harder magnetic materials or employ local anisotropy reduction in the caps such as heat assisted magnetic recording.

[1] T Ulbrich et al., Phys. Rev. Lett. 96, 077202 (2006)

HV-03

Compositional dependence of g-factor and damping constant of GdFeCo amorphous alloy films.

T. Kato[1], K. Nakazawa[2], R. Komiya[2], N. Nishizawa[3], S. Tsunashima[2], S. Iwata[1]

1. Department of Quantum Engineering, Nagoya University, Nagoya, Japan; 2. Department of Electrical Engineering and Computer Science, Nagoya University, Nagoya, Japan; 3. Osaka University, Suita, Japan

Understanding of the magnetization dynamics in magnetic thin films is one of the recent critical issues to develop ultra-high speed magnetic sensors and memories. Ferrimagnetic rare-earth (RE) transition metal (TM) systems are known to be possible to compensate their angular momentums even at the RE-TM composition having a small saturation magnetization due to the difference of the g-factors between RE and TM sublattice magnetic moments. Thus, in such systems, divergence of the effective g factor at the angular momentum compensation point is expected, which is considered to contribute to the fast magnetization reversal. Recently, spin dynamics of GdFeCo [1] and GdCo [2] alloys were measured by pump-probe setup using a Ti sapphire fs laser, and the temperature dependence of the precessional frequency and effective damping factor has been reported. Here we report the magnetization dynamics of GdFeCo with various compositions measured by pump-probe method using an ultra short pulse fiber laser, which has characteristics of high power and excellent stability and is available recently. The compositional dependence of g-factor and damping constant of GdFeCo films has been evaluated and discusses together with the data taken by ferromagnetic resonance (FMR).

SiN (140 nm) / GdFeCo (30 nm) / AlCu (100 nm) / SiN (10 nm) / oxidized Si substrate was prepared by a magnetron sputtering method. Hysteresis loops were measured by an alternating gradient field magnetometer (AGM), and Kerr loops were checked by a polarized angle modulation method. Time-domain magnetization dynamics of GdFeCo was measured by pump-probe method using high-power fiber laser with a wavelength of 1560 nm, a pulse width of 1 psec, a maximum energy of 2 μJ/pulse, and a repetition frequency of 200 kHz. The pump and probe beams were focused onto GdFeCo films with a diameter of 60 μmϕ and 15 μmϕ, respectively. The probe beam was incident normal to the film surface and the polarization of the reflected probe beam was analyzed to monitor the perpendicular component of the magnetization, M_z, after the illumination of the pump beam. During the measurements, an external field of 2 kOe was applied 45 deg from the film normal direction. Ferromagnetic resonance (FMR) spectra at room temperature were obtained by an X-band spectrometer ($f \sim 9.15$ GHz) applying an external field parallel or perpendicular to the film plane.

Just as in the reported papers [1, 2], the time-domain magnetization dynamics of the GdFeCo film showed a sudden drop of the M_z component at delay time of $\Delta t \approx 0$, due to the laser induced demagnetization and a clear oscillation during the recovery of M_z, which allow to estimate effective g-factor g_{eff} and effective damping constant α_{eff} using a numerical calculation of Landau-Lifshitz-Gilbert equation [3]. Figure 1 shows the compositional dependences of precessional frequency f, g_{eff} and α_{eff} of the GdFeCo films obtained from the pump-probe data (closed circles). The precessional frequency took a maximum near the magnetization compensation point C_{M}, while the g_{eff} increases around the angular momentum compensation point C_{A}. This means that the increase of the precessional frequency f near C_{M} is due to the increase of the anisotropy field near C_{M} as well as the increase of g_{eff} near C_{A}. The compositional dependences of g_{eff} and α_{eff} are roughly described by a mean-field model [4]. The g_{eff} calculated by the mean-field model assuming the g-factors of Gd and FeCo to be 2.0 and 2.2, respectively, are drawn as a solid line in the figure. The calculated g_{eff} shows a divergence at C_{A}, which is qualitatively consistent with the experiment. The g_{eff} and α_{eff} are also estimated from the FMR spectra, which are plotted in Fig. 1 as a comparison (open circles). The data from the FMR spectra agree well with those from the pump-probe measurement except for near C_{M} and C_{A}. The FMR method cannot excite the magnetization near the magnetization compensation point C_{M} because of the small magnetization. However the pump-probe measurement utilize the laser pulse to excite the spin system, so that it is possible to observe the oscillation of the magnetization and possible to estimate g_{eff} and α_{eff}.

[1] C. D. Stanciu, A. V. Kimel, F. Hansteen, A. Tsukamoto, A. Itoh, A. Kirilyuk, and Th. Rasing: Phys. Rev. B **73** (2006) 220402.

[2] M. Binder, A. Weber, O. Mosendz, G. Woltersdorf, M. Izquierdo, I. Neudecker, J. R. Dahn, T. D. Hatchard, J.-U. Thiele, C. H. Back, and M. R. Scheinfein: Phys. Rev. B **74** (2006) 134404.

[3] Y. Nakatani, Y. Uesaka, N. Hayashi: Jpn. J. Appl. Phys., **28** (1989) 2485.

[4] R. K. Wangsness: Phys. Rev. **91** (1953) 1085.

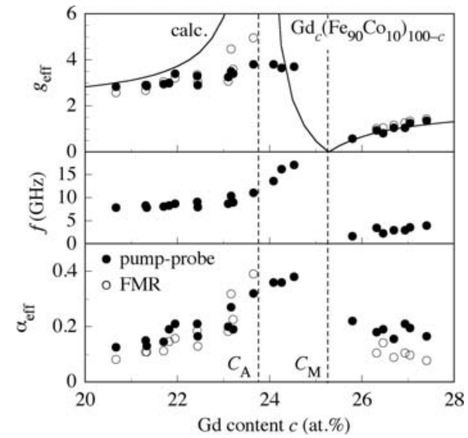

Fig. 1 Compositional dependences of effective g-factor g_{eff}, precession frequency f, and Gilbert damping parameter α_{eff}, of GdFeCo films. The solid line indicates the g_{eff} calculated by the mean-field model [4].

HV-04

Magneto-optical properties of nanometer crystal giant magneto-optical BiAlDyIG thin film materials post-treated by rapid recurrent thermal annealing (RRTA) method.

Q. Yang, H. Zhang, Q. Wen, Y. Liu
University of Electronic Science and Technology of China, Chengdu, China

BiAlDyIG film is an outstanding candidate for next generation magneto-optical (M-O) recording for its intense magneto-optical effect in shortwave length and proper uniaxial anisotropy property. However, the BiAlDyIG films prepared by sputtering or sol-gel method, after treating by common thermal annealing (CTA), have big crystal grains which are much larger than the size of magnetic domain, leading to a deformation of domains and decrease of signal-noise-ratio. Different methods have been applied to solve this problem, such as ions doping, annealing process optimizing, but the effect is very limited. Suzuki developed a rapid thermal annealing (RTA) method to treat the Bi-YIG films [1]. On this basis, a recurrent rapid thermal annealing (RRTA) method was developed by Dr. Zhang [2, 3]; it provides more conditions to optimize annealing technology comparing to RTA method; so the RRTA technology is a better choose based on the magnetic properties of the film, and ultra-fine crystal grains and small surface roughness can be obtained. Since the sol-gel method was successfully applied to prepare the bismuth substituted YIG film [4], the main difficulty now is how to fine the crystal grains and increase the signal-noise-ratio of the magneto-optical disk.

In this paper, the formula of BiAlDyIG film with giant magneto-optical effect within blue and violet light ranges is obtained. Based on the electric dipole transition model of four energy levels, the frequency spectrum of Faraday angle in blue and violet light ranges has been analyzed. According to theoretical results, the optimized stoichiometric compositions is BiyDy3-yFe5-xAlxO12 with x=0.8 ~ 1.2 and y=1.0 ~ 1.96., and then high quality BiAlDyIG thin films have been prepared by a sol-gel method and post-treated by RRTA method. The effects of RRTA on Faraday angle of the films have been studied in detailed, a maximum Faraday angle of 4.9degree in the 450nm thickness film (Bi1.96Dy1.04Fe4AlO12) was obtained, which is about 2.0degree larger than that of the common thermal annealed (CTA) samples. These results are potentially helpful to improve the recording density and signal-noise-ratio of magneto-optical disk.

1. T. Suzuki, G..Zharchuk, G.Gorman, Magnetic and MO properties and kinetics of rapid-thermally crystallized Bi substituted garnet films, IEEE Trans. Magn. 1990,216(5):1927

2. S.J.Zhang, X.Y.Guo, F.P.Zhang et al., Effect of rapid recurrent annealing on structure and magneto-optical properties of garnet films, J.Appl.Phys., 1993,73(10 Part 2B):6832

3. H.W.Zhang, The magnetic and structure of fine grain garnet films, J.Magnetisim Magnetic Materials,1995,149(10):288

4. T.Mizuno, M.Gomi, Magneto-optical properties of Bi substituted garnet films prepared by pyrolysis, IEEE Trans. Magn., 1986,22(5):1236

HV-05

Prospect for Optically Assisted Magnetic Recording using Amorphous Film of Rare Earth-Transition Metal Alloy.

M. Murakami
Electro-mechanical Components Business Unit, Panasonic Electronic Devices Co., Ltd., Kadoma, Japan

A magneto-optical (MO) recording material is candidate for high-density optically recording. Controlling the microstructure of the sputtering process and layer structure was found to be an effective way of managing the magnetic properties of the amorphous Rare earth-Transition metal film for memory devices. [1] The relationship between MsHc and microstructure in recording layer is discussed, and it is found that the columnar structure is effective for tiny mark recording.
Coecivity of conventional magnetic recording material necessarily enhanced to solve the thermal stability for tiny mark recording. There are some solutions in recording materials but it is quite difficult to apply a huge magnetic field. Under these backgrounds, optically assisted magnetic recording, which is similar approach to MO high-density magnetic recording. This paper describes the prospect for a tiny domain stability using MO recording materials. Our approaches and results for ultra-high density recording are also discussed.

[1] M. Murakami and M. Birukawa, IEEE Trans. Magn., Vol. 2, No.5, p.3178 (2003).

Feasibility of Perpendicular Magnetic Printing at 1 $\mathrm{Tbit/inch^2}$

T. Komine, T. Murata, Y. Sakaguchi, Y. Hosoya, N. Suhaimi, R. Sugita
Department of Media and Telecommunications Engineering, Ibaraki University, Hitachi, Japan

1. Introduction

As the high density hard disks (HDs) are in high demand, a method to realize the 1 $\mathrm{Tbit/inch^2}$ HD with perpendicular magnetic recording has been investigated. A perpendicular magnetic printing, which can write servo signals with high speed, high accuracy and low cost, has been studied [1]. However, feasibility of the perpendicular magnetic printing for ultra-high density HDs has not been discussed yet. In this study, the feasibility is investigated by using the micromagnetic simulation.

2. Simulation method

Fig. 1 shows the simulation model used in this study. Table 1 shows the parameters of master and slave media for recording density of 0.25, 0.5 and 1 $\mathrm{Tbit/inch^2}$. First, magnetic field distribution near the master media was calculated by using the three-dimensional finite element method (3D-FEM) when the printing field was applied in the perpendicular direction to the recording layer. Next, the magnetization distribution of the recording layer of the slave media was computed by the LLG equation with the magnetic field distribution calculated by the 3D-FEM [1]. It was assumed that the averaged anisotropy field H_k increased and the spacing between master and slave media became smaller as the recording density increased. The recording layer was composed of rectangular parallelepiped single domain particles whose size was $5\times5\times20$ $\mathrm{nm^3}$. The z-component calculated magnetization was compared with the z-component of ideal printed magnetization, and printing performance was estimated for each recording density. The printing performance is 100 % when printed pattern equals master pattern.

3. Results and discussion

Fig. 2 shows the magnetization distribution of the recording layer printed at the recording density of 0.25 and 1 $\mathrm{Tbit/inch^2}$. The exchange constant was set to 1.5×10^{-7} erg/cm. The printing field was the same value as the coercivity H_c of the recording layer. It was reported in the previous study that in order to obtain the best printing characteristics, the printing field should be applied at much the same value as H_c. In Fig. 2, white and black areas represent $M_z/M_s = -1$ and 1, respectively. For 0.25 $\mathrm{Tbit/inch^2}$, the magnetization was reversed at the contact area of slave and master media, and the initial magnetization was preserved at the non-contact area. The magnetization was not reversed at the center of the contact area, because the magnetic field at the center of the magnetic pattern of master has no in-plane component. For 1 $\mathrm{Tbit/inch^2}$, the magnetization at the contact area was reversed all over, but the reverse region was enlarged owing to increase of the reversed particle by the exchange interaction. Fig. 3 shows the recording density dependence of maximum value of printing performance in each recording density. Although the printing performance slightly deteriorated at 1 $\mathrm{Tbit/inch^2}$, the printing performance maintained 70%. This result shows that perpendicular magnetic printing at 1 $\mathrm{Tbit/inch^2}$ is feasible.

4. Conclusion

The feasibility of perpendicular magnetic printing for ultra-high density HDs was investigated. As results, it was clarified that the printing performance does not deteriorate much and the perpendicular magnetic printing is feasible even at ultra-high density.

Acknowledgment

This research was supported in part by the '07 Industrial Technology Research Grant Program of the New Energy and Industrial Technology Development Organization (NEDO) of Japan. The authors would like to thank members of Fuji Film Co., Ltd. for their fruitful discussion.

[1] T. Komine, A. Izumi, T. Murata and R. Sugita: J. Magn. Soc. Jpn., 31, 173 (2007).

Recording density [T bit /inch^2]	Master media	Recording layer of slave media						Spacing between master and slave media [nm]
	Size of magnetic pattern [nm^3]	Saturation magnetization M_s [emu/cm^3]	Coercivity Hc [kOe]	Anisotropy field Hk [kOe]	C-axis distribution Δθ50 [°]	Exchange constant A [10-7erg/cm]		
0.25	50×50×50	550	6	11	5	0.5 - 2.5		10
0.5	35×35×35	550	9	14	5	0.5 - 2.5		5
1	25×25×25	550	12	17	5	0.5 - 2.5		2.5

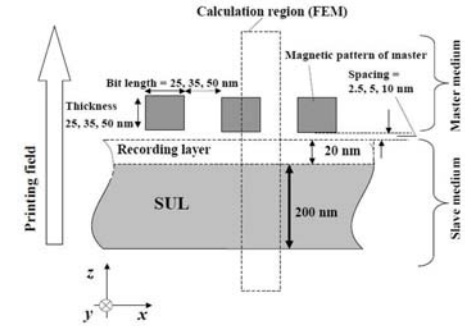

Fig. 1 Calculation model.

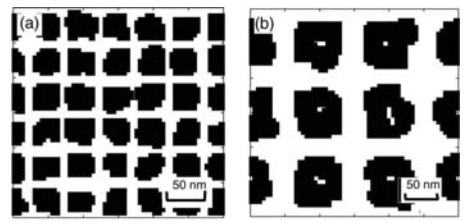

Fig. 2 Magnetziation distributions of (a) 0.25 $\mathrm{Tbit/inch^2}$ and (b) 1 $\mathrm{Tbit/inch^2}$.

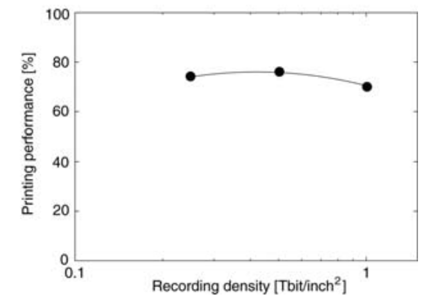

Fig. 3 Recording density dependence of printing performance.

HW-02

Off-Track Performance and Track-Edge Structure in Narrow Track Perpendicular Magnetic Recording.

K. Miura, T. Ogawa, H. Muraoka, H. Aoi, Y. Nakamura
RIEC, Tohoku University, Sendai, Japan

For the steady growth of track density, writing field fringing and fluctuated track edge structure have to be urgently improved. Particulary erase-band (EB) and/or track edge noise is becoming the most significant issue to narrower the track pitch. For this aim, recorded magnetization distribution at track-edges should be clarify and recording parameter must be optimized. We proposed accurate estimation of erase band width (EBW) [1]. From this measurement, accurate track edge position and EBW in off-track noise profile can be known. In this study, the location of track-edge noise was specified using the accurate EBW and magnetic write width (MWW). Influence of the EB on the off-track capability (OTC) versus track pitch, or the '747' performance, that governs attainable track density is also investigated.

A spinstand was used for the measurements of read write properties with a hardware error rate tester (BES #M6) for the measurement of the 747 curves. A trailing-shield single-pole writer with a GMR reader was employed. The write and read width T_{ww} and T_{wr} were 160 nm and 100 nm, respectively. Coupled granular and continuous (CGC) perpendicular media [2] were tested, in which the contnous layer thickness was varied to control in-plane exchange coupling of the recording layer. Our precise measurement for track width and EB [4] was employed.

Measured off-track profile of media noise is shown in Fig. 1, in which the noise power was reduced to that for track width of 10 nm. First wide area was dc-erased, then one track erasure with opposite polarity dc current was carried out. In the figure written track position and EB measured for 300 kfci track is also depicted. The noise power from the EB was relatively large as the peak around the EB was observed. Since large medium noise emanated from the EB, the error rate performance at track-edge EB will be influenced by this EB noise.

Past analyses for the 747 curve presumed that the EB exhibited noise minimal [5], however above experiment rather large medium noise was observed. The 747 curves modeled according to the noise amplitude at EB using the calculation in which signal and noise are proportional to corresponding on-track width [5]. Fig. 2 schematically shows three assumptions. In the case of model #1 old data is noisy but EB shows no noise or quiet, in model #2 both EB and old data are noisy, and in model #3 the EB is noisy but no old data. The signal in the adjacent track always acts as cross-talk noise. Fig. 3 shows the 747 curves of the three models with experimental data. Because the measurement of 747 curve carried out under the condition of DC erase background, model #3 seemed to be the most suitable for the condition. The bump of 747 curve was notably seen only in the model #1, which indicates that the bump is observed in the case of the quiet EB. No bump appeared when EB generates noise.

Normalized 747 curves for three CGC media samples with various in-plane exchange couplings are shown in Fig. 4. The sample #1 had the thickest continuous layer, which has larger strong in-plane coupling, and its EB noise was large. While, in the case of medium #4 an obvious bump appeared, in which the contineous layer thickness is the thinest among these samples. The noise of the EB suppresses the bump that improve OTC. Therefore, a large medium noise from the EB deteriorates attainable track density in the 747 performance. In this experiments it is revealed that the reduction of EB noise due to the optimization of in-plain exchange coupling in perpendicular magnetic recording is crucial for high track density recording.

This work was supported in part by the RR2002 program of MEXT, and Research and Development for Next-Generation Information Technology of MEXT.

[1] K. Miura et al.,: Digest of Intermag 2007, EG-05.

[2] Y. Sonobe et al.,: IEEE Trans. Magn., 38, 2006(2002).

[3] Zhong-Heng Lin et al.,: IEEE Trans. Magn., 41, pp. 3067-3069 (2005).

[4] H. Yamada et al.,: IEEE Trans. Magn., 34, pp. 1468-1470 (1998).

[5] J. K. Lee et al.,: IEEE Trans. Magn., 26, 2475-2477(1990) .

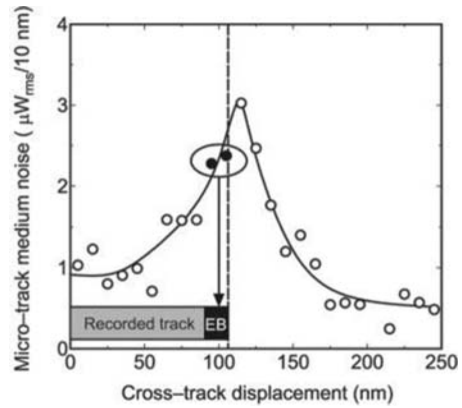

Measured cross-track noise profile. The plots were reduced to the noise power for track width of 10 nm.

Schematics of the 747 curve models. Media noise was assumed to emanate from the gray areas.

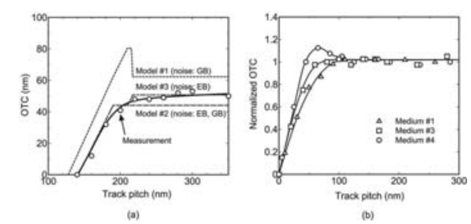

(a)Dependence of off-track capability (OTC) on the squeezed track pitch. Calculated results obtained by the three analytical models were shown in three dashed lines. (b) Normalized OTC versus track pitch for CGC media samples with various in-plain exchange coupling.

HW-03

Microwave assisted magnetization reversal and its thermal activation.

S. Okamoto, N. Kikuchi, O. Kitakami
IMRAM, Tohoku University, Sendai, Japan

Magnetic recording has been a fundamental technology in the present high density storage system. However, further increase of the recording density strongly requires a new advanced recording technique. Very recently, the microwave assisted magnetic recording (MAMR) has been explored both experimentally and theoretically [1-3]. In this study, we discuss the effectiveness of MAMR on the perpendicular magnetic recording and its thermal activation.

Dynamical magnetization motion and the switching field H_{sw} are calculated by using the Landau-Lifshitz-Gilbert (LLG) equation of motion without thermal fluctuation. The external reverse dc field H_{dc} is applied along the easy magnetization axis, and the sinusoidal ac field h_{ac} is applied perpendicular to H_{dc}. Taking into account the recording conditions of the present perpendicular recording, H_{dc} is applied in the form of a rectangular pulse with the rise time of 0.1 nsec and width of 1 nsec. A single spin nanoparticle with the anisotropy field H_k of 20 kOe is treated in this calculation. Fig. 1 shows the 2D mapping of magnetization switching under the conditions of h_{ac} = 1 kOe and the Gilbert damping α = 0.06 as functions of $H_{dc}/H_{sw}(0)$ and the ac frequency f_{ac}, where $H_{sw}(0)$ is the static switching field for h_{ac} = 0. Note that the switching field H_{sw} significantly reduces along the condition of ferromagnetic resonance (FMR) indicated by the thick line in Fig. 1, suggesting that the magnetization switching is brought about by the absorption of microwave energy. The effective absorption of microwave energy excites precessional motion of magnetization, resulting in the magnetization switching when the precessing spin crosses over the energy barrier into the energy minimum. This mechanism is very similar to that for spin transfer switching (STS). It is easily understood that the MAMR strongly depends on α and h_{ac}. Figs. 2(a) and (c) show the minimum H_{sw} obtained at each condition as functions of α and h_{ac}, respectively, and Figs. 2(b) and (d) show the f_{ac} which gives the minimum H_{sw} shown in Figs. 2(a) and (c). It is clearly noticed that the smaller α effectively reduces the H_{sw}, and H_{sw} is almost saturated when the α is smaller than 0.02. On the other hand, the H_{sw} linearly decreases with increasing h_{ac}. Thus, it is concluded that MAMR is very effective to reduce the magnetic field necessary for saturation recording.

Since magnetic recording systems operate at the ambient temperature, thermal activation in the MAMR process should be taken into account as well as the conventional magnetic recording. For this purpose, we adopt almost the same idea developed for STS [4]. The effective Gilbert damping α_{eff} can be derived from the LLG equation under the FMR condition, and it can be described as $\alpha_{eff} = \alpha - (h_{ac}/H_{eff}) \times (1/\sin\theta_0)$, where $H_{eff} = H_{dc} + H_k$, θ_0 is the angle of the precessional motion of magnetization with respect to the easy axis under the assumption of the steady state. Finally, by using the relation of $\alpha T = \alpha_{eff} T_{eff}$ based on the fluctuation-dissipation theorem, the fictious temperature T_{eff} is obtained. Thus, the widely used analytical expressions for thermal activation events, such as Sharrock formula, with T_{eff} instead of the actual temperature T can be applied to MAMR.

This work is partially supported by the "Research and Development for Next-Generation Information Technology of MEXT" and Grant-in-Aid for Scientific Research from MEXT and the Storage Research Consortium in Japan.

[1] C. Thirion, W. Wernsdorfer, and D. Mailly, Nat. Mater. 2, 524 (2003).

[2] J.-G. Zhu, X. Zhu, and Y. Tang, IEEE Trans. Magn. 44, 125 (2008).

[3] Y. Nozaki, M. Ohta, S. Taharazaka, K. Tateishi, S. Yoshimura, K. Matsuyama, Appl. Phys. Lett. 91, 082510 (2007).

[4] R. H. Koch, J. A. Katine, and J. Z. Sun, Phys. Rev. Lett. 92, 088302 (2004).

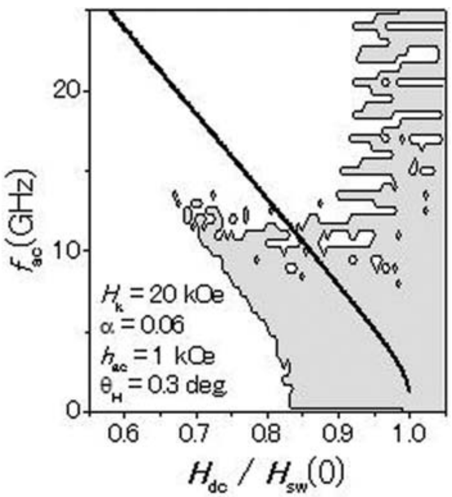

Fig. 1 2D mapping of switched area (gray zone) of a single spin nanomagnet as functions of $H_{dc}/H_{sw}(0)$ and f_{ac}.

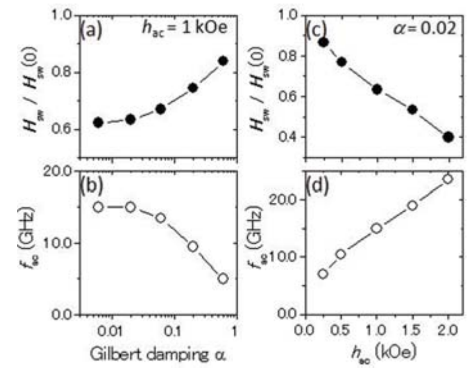

Fig. 2 Minimum H_{sw} ((a) and (c)) and corresponding f_{ac} ((b) and (d)) as functions of α and h_{ac}, respectively.

HW-04

Prediction on the recording performance of exchange coupled composite media and discrete track media.

Y. Tahk, J. Lee, S. Lee
Storage System Division, Samsung Electronics, Suwon, South Korea

Recently, PMR media with dual or triple magnetic layer show feasibility of high areal density more than 250 Gbpsi. However, the conventional PMR head media system will be under lack of head field and difficulty in the control of grain size and coercivity of media. To satisfy these needs of head/media industry, ECC (Exchange Coupled Composite) media [1] and DTR (Discrete Track Recording) media have been proposed and studied. The basic idea of the exchange coupled composite media(ECC media or semi-ECC media) is to overcome the write head field deficiency by utilizing magnetostatic and exchange coupling field from semi-hard layer(semi-ECC case) or soft layer(ECC case) which switches at lower field. Discrete track media has grooves which separate tracks physically and magnetically. In this paper, comparison results of magnetic recording performance of both types of media through micromagnetic modeling will be shown and the synergy of two kinds of media concept.

In the present work, full 3D-micromagnetic simulations of the exchange-coupled composite media were performed to understand the read/write properties by changing interlayer exchange coupling strengths (Jex) between top magnetic layer and bottom magnetic layer, each layer's thickness, crystalline magneto anisotropy constant (Ku), and intergranular exchange coupling constant (A*) within each magnetic layer.

SNR result shows the semi-ECC media with weak exchange coupling is not desirable. To understand why the media with insufficient Jex do not have good read/write performance, dynamic M-H loop of each layer in the ECC media was compared. To configure out the switching mode of top and bottom layer, the magnetization of each layer was obtained separately. Obviously, top magnetic layer which has lower Hc is switched first and it makes magneto static field to help switch the higher coercive bottom layer. It should be noted that not sufficient exchange coupling gives kink in the hysteresis loop. Intuitionally, these characteristics seem to be unique in ECC media.

However, in view of dynamic writing, this kind of big difference in Hc will result the transition time shift between top and bottom layer. For better understanding writing process of ECC type media, it will be helpful to check magnetic dynamics of each magnetic layer when writing current is changed from positive to negative. As shown in Fig. 1, ECC media with insufficient Jex have unclear transition shape and blurred write bubble. This kind of irregular transition shape is from the mismatch in transition timing. When the difference in the dynamic coercivity (Hc) of top and bottom magnetic layers is big, ECC media with weak interlayer exchange coupling strength do not give desirable SNR and need more exchange coupling strength.

ECC media and Semi-ECC media show maximum on-track SNR (single track). However, more likely ECC media is a little bit easier to squeeze compared with Semi-ECC media with higher Hc of top mag-layers. DTR was implanted to ECC media to get higher TPI performance. DTR (75 % Land : 25% Groove) with ECC media gives extra 2dB SNR gain at squeezed condition with side writing. When the groove portion is increased to 33 % or higher, SNR gain is less than 1 dB.

As shown in Fig.2, optimized triple magnetic layered semi-ECC media with Jex of about 0.6 erg/cm2 shows higher SNR than the very strongly exchange coupled composite media like conventional media. Expected SNR gain from optimized ECC design compared with conventional dual-magnetic layer media can be higher than about 3 dB. However, the magnetic distribution such as Hk distribution and Jex distribution should be well evenly controlled. More enhanced semi-ECC media will be possible breakthrough for the near future and the ultra high density recording above 600 Gbpsi can be realized by DTR combined with ECC media.

R.H. Victora, X. Shen, IEEE Trans. Magn. 41 (2005)

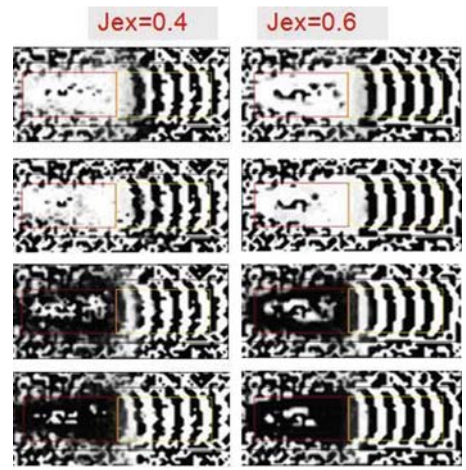

Fig.1. Magnetic dynamics of top semi-hard layer in semi-ECC media with different Jex during writing process.

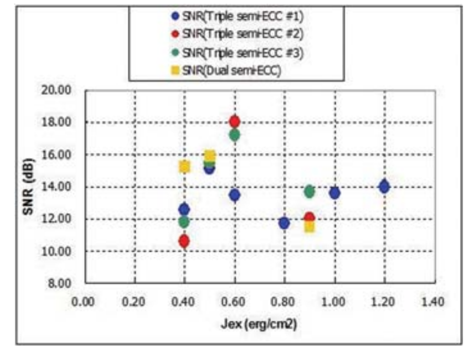

Fig.2. SNR of various semi-ECC media with variation of exchange coupling. Semi-ECC #1 has a Hc distribution of 1 sigma = 7 % and the other cases have Hc distribution of 1 sigma = 3.5 %.

HW-05

Attempt Frequency with Respect to Field Dependence and Modified Sharrck'S Formula for Perpendicular Recording Media.

M. Igarashi[1], Y. Sugita[2]
1. Hitachi, Ltd., Kokubunji, Japan; 2. Tohoku Institute of Technology, Sendai, Japan

In the previous work using micromagnetic simulation, we have found that time-dependent remanent coercivities $H_{cr}(t)$ for perpendicular recording media (PRM) are well expressed by Sharrock's formula[1, 2] with assuming a constant value of the attempt frequency f_o as written by Eq. (1).
Here H_{cro} and t are the switching field of recording medium and the elapse time, respectively. The thermal stability factor K_β is defined by K_uV/kT, where K_u, V, and kT are the uniaxial anisotropy energy, the switching volume, and the thermal energy, respectively. However, f_o is theoretically written by Brown for a single magnetic particle as a function of the external field H as written by Eqs. (2, 3)[3].
Here $h(=H/H_{cro})$, γ, H_k, and α are the normalized field, the gyro-magnetic ratio, the magnetic anisotropy field, and the Gilbert damping constant, respectively.
In this study, f_o as a function of the external field and a modified Sharrock's formula for PRM are discussed.
A 64x64 array of uniform hexagonal prism grains with a diameter D of 8.5 nm and a height t_{mag} of 12.0 nm was used to simulate a medium. The separation between grains d was 0.5-10 nm. In each grain, the magnetization rotates coherently and interacts with the neighbors by a weak exchange coupling. The easy axis of each grain was perpendicular to the film plane with a distribution of 3 degrees. The value of the uniaxial perpendicular anisotropy energy K_u was 4.0Merg/cm^3 with a normal dispersion of ±10%. A constant value of the attempt frequency f_o*, K_β, and H_{cro} were determined in order that 12 points of calculated H_{cr} vs. t satisfy Eq.(1) simultaneously[2]. Also f_{oo} was determined from the 12 points of calculated H_{cr} vs. t using modified Sharrock's formula in which f_o is replaced by $f_o(h)$ in Eq.(1).
Figure 1 shows f_{oo} along with f_o* as a function of the inter-grain exchange surface energy density w. Both f_{oo} and f_o* decrease with increasing w initially below a critical value w_c, and increases above w_c. The reason for the initial decrease of f_o with w below w_c is that the increment of f_o by the magnetostatic coupling is being lowered by the exchange coupling with increasing w[4]. It should be noted that f_{oo} is clearly larger than f_o* for each w. Table 1 shows the ratio of f_o* to f_{o-c}^*. Here f_{o-c}^* is obtained from Eq.(2) using f_{oo} and the average field of 12 points of H_{cr} calculated. The ratios are roughly equal to 1.0. This means that the field dependence of the Brown's attempt frequency is valid for PRM and the modified Sharrock's formula should be used in strict discussions.
You should note that the values of f_{oo} discussed here for PMR are much larger than that for a single particle in Eq.(3). Inter grain exchange and magneto static couplings increase f_{oo}. This large f_{oo} is also consistent with the results of f_o in exchange coupled nano-chains [5] and graded media [6].

[1] M. P. Sharrock and J. T. McKinny, "Kinetic Effects in Coercivity Measurements," IEEE Trans. Magn., 17, pp3020-3022 (1981).

[2] M. Igarashi, F. Akagi, and Y. Sugita, "Validity of Values of Thermal Stability and Switching Field in Recording Medium Obtained by Using Sharrock's Formula," IEEE Tran. Magn. 42, pp2399-2401 (2006).

[3] W. F. Brown, Jr., "Thermal fluctuation of a Single-Domain Particle," Phys. Rev., vol.130, No.5, pp1677-1686(1963).

[4] M. Igarashi and Y. Sugita, "Study of Attempt Frequency in Sharrock's Formula for Perpendicular Recording Hard Disk Media," 15pD-02, PMRC2007 and FQ-08, MMM2007.

[5] A.Y. Dobin, "Attempt frequency of thermally activated non-coherent switching in nanomagnets," ER-02, MMM2007.

[6] G.T. Zimanyi, "Graded media: optimization and energy barriers," FC-07, MMM2007.

w (erg/cm^2)	f_{oo} (GHz)	h_{av}	f_{o-c}^* (GHz)	f_o^* (GHz)	f_o^*/f_{o-c}^*
0	4.3E+02	0.595	1.1E+02	1.5E+02	1.3
0.1	1.2E+02	0.564	3.6E+01	4.0E+01	1.1
0.25	4.9E+01	0.545	1.6E+01	1.5E+01	0.9
0.5	7.3E+02	0.578	2.1E+02	2.7E+02	1.3
0.75	2.5E+04	0.705	3.6E+03	8.6E+03	2.4
1.0	2.7E+07	0.772	2.4E+06	1.4E+06	0.6

Table 1. h_{av}:the normalized average field of 12 points of H_{cr} by H_{cro} $f_{o-c}^*=f_{oo}\times(1-h_{av}^2)(1-h_{av})$

Equations

$$H_{cr}(t) = H_{cro}\left(1-\left(\frac{\ln(t)+\ln(f_o/\ln 2)}{K_\beta}\right)^c\right). \quad (1)$$

$$f_o(h) = f_{oo}(1-h^2)(1\pm h), \quad (2)$$

$$f_{oo} \equiv \frac{\gamma H_k \alpha}{\sqrt{\pi}(1+\alpha^2)}\sqrt{K_\beta}. \quad (3)$$

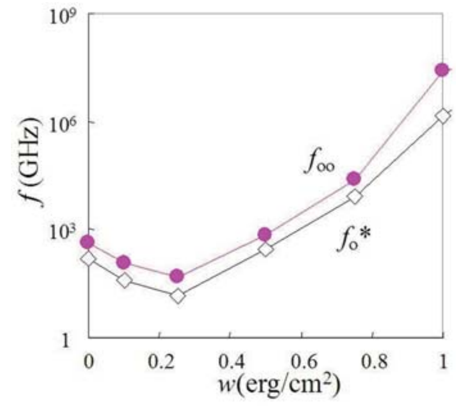

Fig. 1. f_{oo} and f_o* as a function of the exchange surface energy density w (K_u=4.0 Merg/cm^3).

HW-06

Effect of demagnetizing field distribution in discrete track media recording.

Y. Kawato[1], A. Nakamura[1], A. Yatagai[2], Y. Nishida[2], K. Ito[1], S. Nosaki[1], Y. Hirayama[1], Y. Hosoe[1]
1. Central Research Laboratory, Hitachi, Ltd., Kokubunji, Japan; 2. Advanced HDD Technology Laboratory, Hitachi Global Storage Technologies, Fujisawa, Japan

Introduction

After the technology transition from longitudinal to perpendicular magnetic recording (PMR) in hard disk drives, some classic recording methods attract lots of attention as a way to realize areal density of tera-bits per square inch. Patterned media, including discrete track media (DTM) [1], [2] and bit patterned media, is one of those methods. DTM, shown in Figure 1, consists of pre-patterned data tracks, or lands, separated by non-magnetic bands. DTM recording is considered the first comer among the novel recording schemes because it has higher affinity for conventional PMR than others. It has been recently reported that DTM realizes higher tracks-per-inch (TPI) than PMR [3].

Demagnetizing field distribution in recording layer

Figure 2 shows calculated demagnetization (demag)-field distribution along the cross-track direction. A 2-dimensional surface charge model was used, so the bit length was assumed to be infinite. The effect of the soft under-layer was taken into account as a perfect mirror image. The field strength was calculated at the through-thickness center and normalized by $4\pi M_s$ of the recording layer. The thickness of the recording and seed layers were assumed to be 16 and 10 nm respectively. For the sake of comparison between PMR and DTM recordings, we also assumed that the magnetic write width was 68 nm for PMR and the land width was 48 nm for DTM. It means that the PMR write width was 90% of the track-pitch (Tp) and the DTM land-width was 60% of Tp when Tp was 76 nm. The land-width/Tp ratio of 60% was based on a demonstration by TDK in 2006 [4]. It is clear that the demag-field of DTM is smaller than that of PMR recording layer. For example, the reduction rate was 7% at the track center and 60% at the off-track position of 30 nm. We have studied the effect of the reduction in the demag-field on some recording performances.

Influence on thermal Decay

The demag-field directly affects magnetization stability as well as the recording process. So we have computed a thermal decay process using micro-magnetic simulation. Figure 3 is the calculated signal deterioration depending on elapsed time after writing. Note that the temperature was set extremely high to accelerate thermal switching. It shows that the decay rate for DTM was much smaller than that for PMR in this condition. So DTM recording can be a thermally stable storage system.

Improvement in robustness against adjacent track erasure

Figure 4 indicates the so-called '747-curve' measured for PMR and DTM using spin-stand . Same media material and recording head were used for this measurement. The point at which off-track capability goes to zero can be interpreted as the adjacent write position where the target track vanishes. So the difference of the points between PMR and DTM means that DTM recording is more stable against track squeezing. Reduction in the demag-field at the land edge would be one of the major factors of this characteristic.

[1] L. F. Shew, IEEE Trans. Broadcast Television Receivers, vol. BTR-9, pp. 56-62, 1963.

[2] S. E. Lambert, I. L. Sanders, A. M. Patlach, and M. T. Krounbi, IEEE Trans. Magn., vol. MAG-23, no. 5, pp. 3690-3692, Sep. 1987.

[3] X. Che, K. S. Moon, Y. Tang, N. Y. Kim, S. Y. Kim, H. J. Lee, M. Moneck, J. G. Zhu, and N. Takahashi, IEEE Trans. Magn., vol. MAG-43, no. 12, pp. 4106-4112, Dec. 2007.

[4] CEATEC JAPAN 2006.

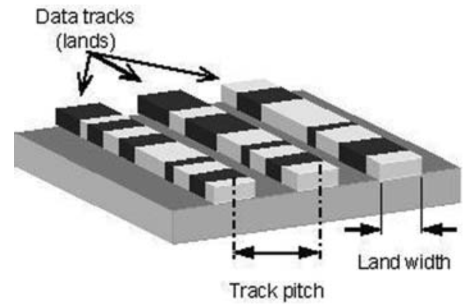

Fig.1 Schematic of discrete track media

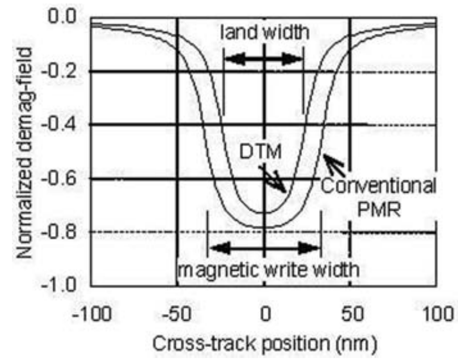

Fig.2 Cross-track profile of demag-field (calculated)

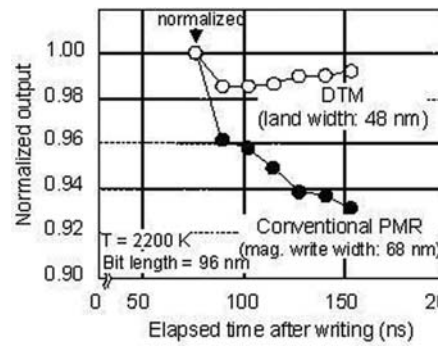

Fig.3 Thermal decay of output signal (calculated)

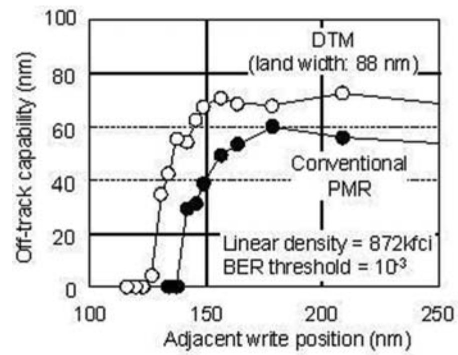

Fig.4 747 curve (measured)

HW-07

The effect of write head current on adjacent track erasure.

J. S. Dean[1], M. A. Bashir[1], A. Goncharov[1], G. Hrkac[1], S. Bance[1], T. Schrefl[1], A. Cazacu[2], M. Gubbins[2], R. R. Lamberton[2], D. Suess[3]
1. Engineering materials, Univerisity of Sheffield, Sheffield, United Kingdom; 2. Seagate Technology, Derry, United Kingdom; 3. Solid State Physics, Vienna University of Technology, Vienna, Austria

One significant limitation of magnetic recording is the super paramagnetic effect. This is the effect where ambient thermal energy can overcome the energy barrier within the media leading to possible read errors. Thermally induced magnetization reversal is also thought to be one of the major sources of adjacent track erasure [1]. As the write head passes close to the pre-written bits, the stray field of the writer lowers the energy barrier of the grains in the neighboring track grains. Any given track must sustain a large number of adjacent write operations. Therefore a weak cross-track stray field may destabilize the magnetization in adjacent grains over the life time of the disk.
Presented here are results of a study on the effect of the write head current on cross track erasure. This work also addresses some basic specifications for media design for maintaining grain stability whilst still providing the highest areal density possible. Focusing on exchange spring media (15nm thick, Js = 0.6 T), where hard (7.5 nm, Kh=0.8×106 Jm-3) and soft (7.5 nm, Ks=0.2×106 Jm-3) phases are perfectly coupled, we calculate the energy barrier under the influence of the cross-track stray field using the nudged-elastic band method [2] coupled with a finite element micro magnetic approach [3-4]. The energy barrier is computed for a series of grains, as a function of the distance between the centre of one single grain (6 nm diameter) and the centre of the current track. For comparison the energy barrier of a single grain in zero magnetic field is found be 45.3kBT300.
The stray field of the writer is non-uniform over the cross section of a grain in the adjacent track. In order to allow for the non-uniformity of the cross-track stray field a novel approach is applied. First the field of a 100 nm wide single pole writer with trailing shield is computed using the Flux3D FEM solver from CEDRAT. Then the energy barrier is calculated using a subdiscretized grain exposed to the non-uniform cross-track stray field. From the energy barrier we estimated the maximum accumulated field exposure time that is allowed before adjacent track erasure occurs due to thermal activation by computing the grain's lifetime with the Arhenius Neel formula assuming an attempt frequency of 1 GHz. The maximum accumulated field exposure time can be converted into the number of passes the write head can achieve before cross track erasure.
In order to give an estimate of the track density, we assumed a maximum accumulated field exposure time of 1 second that corresponds to 109 passlines. Using this method the track density was calculated for different write currents. It is found that for a current of 45 mA erasure begins to occur at 88 nm from the center of the write head, leading to a track width of 176 nm. This is considerably wider than the write width that was calculated micro-magnetically to be 105 nm for a write current of 45 mA. The comparison with a single phase media shows that adjacent track erasure problem observed experimentally in composite media might be induced by high inter-grain exchange interactions in composite media. Neglecting inter-grain exchange interactions, a single phase shows an erasure distance (distance of the track center to first stable grain for a total field exposure time of one second) of 113 nm as compared to 88 nm for the composite media. For this comparison the anisotropy of the single phase media was carefully chosen so that both single phase and composite media showed the same write width.
For the exchange spring media, the erase distance decreases to 83 nm and 75 nm for write currents of 35 mA and 25 mA, respectively. The reduction of the write current to 35 mA decreases the write width to approximately 88 nm, however no bit is generated at 25 mA.
In summary, we present a method to estimate the track density taking into account thermally induced magnetization reversal und the influence of the cross-track write field. It is also shown that cross track erasure can be reduced allowing a much higher track density for a given writer by careful controlling the write current.

[1] H. J. Richter, J. Phys. D: Appl. Phys. 40 R149 (2007).

[2] G. Henkelman and H. Jonsson, J. Chem. Phys. 113, 9978 (2000).

[3] R. Dittrich, T. Schrefl, D. Suess et al., J. Magn. Magn. Mater. 250, 12 (2002)

[4] D. Suess, S. Eder, J. Lee et al., Physical Review B 75 (17), 174430 (2007).

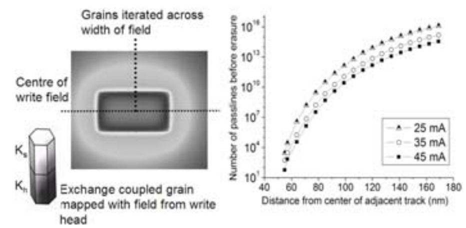

Fig. 1. Left: The magnetic field of the writer (45 mA) is fully mapped onto a grain of two phase media (show bottom right for a mapped position of 72 nm from center). The energy barrier under the influence of the field is computed to give the lifetime as a function of distance. A cross track erasure profile can then be generated. Right: The number of passlines which can be achieved before cross track erasure occurs for differing write currents.

HW-08

Study of Overwrite Generated Twisted Transition Written by Trapezoid Shape Single Pole.

S. Hu, Z. Yuan, B. Liu
Data Storage Institute, Singapore, Singapore

A combination of single pole writer and soft underlayer was proposed to be a configuration for perpendicular recording system[1]. It was found later that there is a track edge erasure issue with the single pole writer when the single pole writer is driven by a rotary actuator. A trapezoid single pole writer was then proposed to solve such problem and maintain the track width at large skew angle. The trapezoid shape pole generates a same type of write bubble. The overall superposition of magnetostatic field of trailing edge transition at different off track positions could be different when the write field is in opposite polarity to the media previous magnetization. It can cause the transition to be twisted [2].
This work uses even harmonic ripple effect[3] to modulate the demagnetic field in the perpendicular medium and reveals the phenomenon of overwrite generated twisted transitions at different skew angles.
Experimental investigations were conducted on the Guzik spin stand v2202. Commercial perpendicular disks and trapezoid single pole writer-TMR reader were used in the test.
In this work, the bit length is selected to be equal to the write pole thickness. When the trapezoid single pole writer is at different skew angles, two regions (which are lined by the trapezoid single pole, track edges and the pre-recorded bit boundary) are varied. This is to enable the pre-magnetization of the two regions in the perpendicular medium to make different contribution to the transition shift.
Fig. 1 shows the ripple waveform maps at different skew angles (0°, ±10°). It is noticed that there are two peak regions in the ripple waveform, the left peak region and the right peak region in the ripple waveform map at skew angle 0° (Fig.1b). As the skew angle increases from 0° to 10°, the two even harmonic peak regions are inclined to one direction. And the left peak region becomes more obvious (Fig. 1a). It shows there is a big even harmonic peak in the left side along the cross track direction. When the skew angle changes from 0° to -10° (Fig. 1c), the ripple waveforms maps are inclined to the opposite directions and the shapes of the two ripple waveform peak regions are changed also. For the given test trapezoid single pole, taking skew angle +10° for example, the right slope side of the trapezoid type pole is aligned to the track right edge. So the pre-magnetization of the left region in the recording medium uncovered by the trapezoid pole will affect the total magnetic field obviously. It can cause transition twisted.
The averaged twisted read-back signal maps at skew angle -10° and +10° are plotted in Fig 2 and Fig 3 respectively. It is noticed that the twisted transitions shown in Fig 2 and Fig 3 are different as skew angle changes. Fig 4 and Fig 5 show the pulse period variations at different positions along the cross track direction at skew angle α=-10°. The pulse period time variations increase from track center (label "8uin") to the track side (label "12uin").

1) Roger Wood, et al, JMMM, 235,1-9(2001)

2) Sheng-Bin Hu, et al, PMRC2007, 16aA-04

3) Rui.Xian, et al, IEEE trans. Magn.,40, 2601-2603(2004)

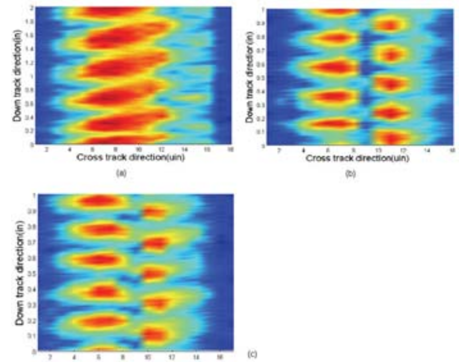

Fig 1 Even harmonic ripple maps (a)+10°, (b) 0°, (c)-10°.

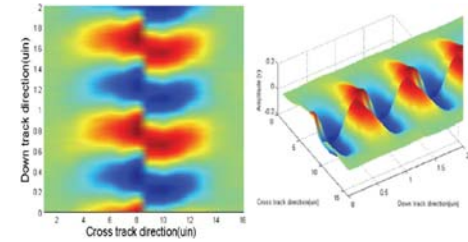

Fig 2 Twisted transitions at -10°

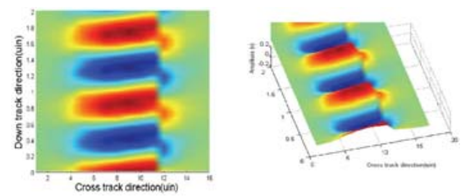

Fig 3 Twisted transitions at +10°

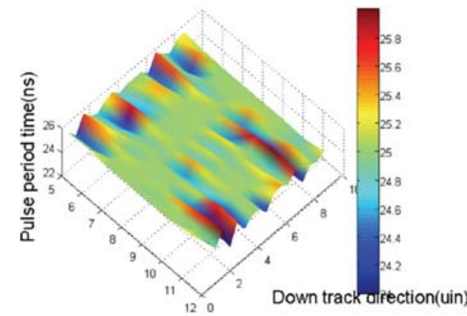

Fig 4 3D view of pulse period time variations at -10°

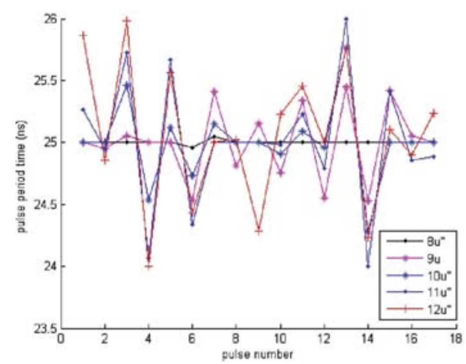

Fig 5 Pulse period time variations at -10°

Reverse DC erase noise analysis on exchange coupled composite PMR media.

S. Hong, Y. Tang, X. Che
SISA, San Jose, CA

PMR Media	Magnetic Properties				
	Hc (Oe)	Hn (Oe)	tMag (nm)	tSUL (nm)	Bs-SUL (T)
ECC	4640	- 1360	16	50	1.5
Con.	4800	- 2065	16	50	1.5

Recently, the exchange coupled composite (ECC) media has been proposed to decrease the switching field without degrading the media thermal stability [1]. Furthermore, micromagnetic modeling for the systematic study on the recording performance of ECC media showed that the soft magnetic layer with high saturation magnetization and low anisotropy field cause unfavorable adjacent track encroachment (ATE) performance in recording [2]. It is desirable to experimentally confirm this phenomenon in ECC PMR media. In this work, we applied the reverse DC erase medium noise measurement method to estimate DC noise in ECC media. We also discussed the role of negative nucleation field and writer's return pole field in the ATE performance of an ECC media structure. ECC and conventional PMR media with similar intermediate layer (IL), soft magnetic underlayer (SUL) structure, and different magnetic properties as shown in Table 1 were used in this study. Reverse DC erase medium noise and recording performances were characterized using tapered writer pole with Bs = 2.3 T and tunneling magnetoresistance (TMR) read head with a shield gap of about 35 nm.

Normalized rms noise for both ECC and conventional PMR media was shown in Fig. 1. Starting from AC erased background, we first DC erase in one direction then erase with opposite current in different magnitude. The noise after reverse current erasure was recorded. As the opposite erasure current increases, the conventional media showed that the noise power increased, peaked at about 9mA and decrease back to the low noise state. For ECC media, the noise also peaked at about the same current but the increase started earlier than for the conventional media. The earlier start of noise increase is consistent with the relatively low negative nucleation field (Hn) value of the ECC media. Another qualitative noise property difference between conventional and ECC media is at erase current above 30mA. Here ECC media noise increases with write current while conventional media noise does not. This may come from the return field of the write head. Since ECC media has lower Hn, partial erasure can occur at high write current.

Fig. 2 showed ATE quantified by averaging the percentage loss of the track average amplitude (TAA) over the 23 tracks with increased write current. The ECC media with lower negative nucleation field showed much higher ATE compared to conventional PMR media having higher negative nucleation field. Especially, ATE of ECC media is getting worse with increased writing current. One possible interpretation of this poor ATE on ECC media is that, comparing to conventional PMR media, partial erasure occurs at smaller write current as shown in the reverse DC erase noise experiment.

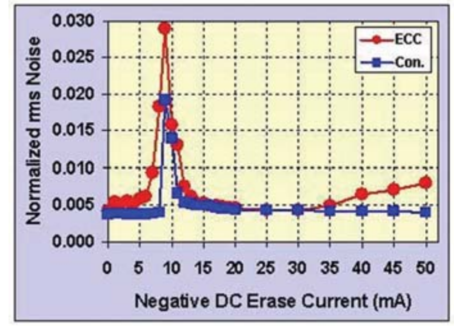

Fig. 1. Measured medium noise of ECC and conventional PMR media as function of the reverse DC erase write current.

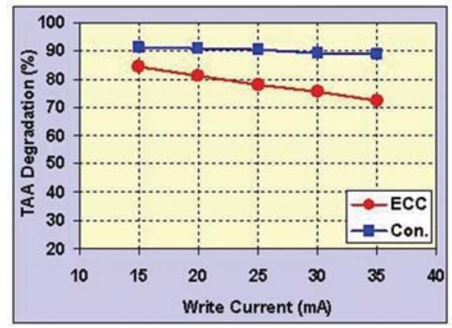

Fig. 2. Comparison of ATE performance between ECC and conventional PMR media with increased write current.

[1] R. H. Victora and X. Shen, "Composite media for perpendicular magnetic recording," IEEE Trans. Magn., vol. 41, pp. 537–542, 2005.

[2] Yuhui Tang, Sooyoul Hong, Xiaodong Che and Jian-Gang Zhu, "Optimization of perpendicular recording on exchange coupled composite media" abstract to MMM 2007.

HW-10

Influence of the media magnetization patterns on the domain structure in the reader stack with the asymmetric stabilization.

E. Haftek[1], *V. Nandakumar*[2], M. Benakli[3]
1. Electrical Integration, Seagate Technology, Bloomington, MN; 2. Servo Format Engineering, Seagate Technology, Shakopee, MN; 3. Recording Sub-systems Organization, Seagate Technology, Bloomington, MN

Introduction:
Reader instabilities are known to be a critical factor in the reader design, and are expected to increase in importance as we scale down the read sensor dimensions. Many techniques, such as transverse curves, have been developed to screen sensors with read instability. These techniques, however, offer limited insight on the origin of the instability. In this work the cross track profile of the sensor is used to characterize bad sensors. The advantage of this technique is higher spatial resolution in locating of the source of the instability. The spatial resolution is obtained by subjecting the sensor to the media non-uniform stress field, as described in the procedure below.
Experiment:
First a typical perpendicular media is prepared by recording low frequency pattern on a DC background. The sensor under investigation is then used to generate a readback map as shown in figure 1. A digital oscilloscope was used to collect very high resolution down track samples of the written pattern. The voltage color map is generated by consecutive readback at different off-track positions moving from OD to ID (the offtrack position shown in the x-axis of figure 1) at small, accurate crosstrack steps. The samples were aligned to remove trigger and sampling jitter. This non-destructible method allows for repeated captures with the same components. All the experiments were conducted on a spinstand tester at 15000 rpm, and the tracks were written with a fast-rise time written current waveform a square wave pattern. The tester was also equipped with a servo system that helped limit the thermal drift through active piezo-compensation. Heads with known bias asymmetry were selected for the experiments.
Observation:
An asymmetry is observed in the captured read back voltage, and summarized in the cross track profile shown in figure 2. By changing the direction of the scan (moving from ID to OD), the crosstrack profile shows a noisy signature on the ID side of the profile (see figure 3).
The observed hysteretic (ID to OD in fig 2 versus OD to ID in fig 3) and noisy behavior (on the OD side) of the crosstrack profile (fig 2 and 3) is an indication of the existence of metastable state in the reader stack. As the weak region of the reader stack goes over edge of the DC region it is subjected to an additional bias field. This bias field changes the energy barrier for the metastable state leading to a stochastic response of the reader. Depending on the direction of the scan the metastable region of the sensor is subjected to a different history of media contribution to the bias field, which explains the hysteretic behavior of the track profile. Also a noise free crosstrack profile is expected if both the DC field and scan direction are combined to provide a stabilizing field (parallel to permanent magnet field) prior to the free layer approach to the center track. This allows to position the metastable region of the reader stack on the bottom side of stack. This conclusion is to be confirmed by micromagnetic modeling, and further experimental data with different preconditioning of the adjacent tracks, and will be included in the final publication of these results.
Acknowledgements: The authors thank Al van der schans and Debra Wozniak for their contributions in obtaining the empirical results.

1) Thermally Excited Low Frequency Magnetic Noise in CPP Structure MR Heads, IEEE TRANSACTIONS ON MAGNETICS, VOL. 43, NO. 6, JUNE 2007 page 2187

2) Is Electrical 1/f Noise in Tunneling Magnetoresistive Heads a Form of Equilibrium Noise?, IEEE TRANSACTIONS ON MAGNETICS, VOL. 43, NO. 6, JUNE

2007 page 2193

3) Electrical Low-Frequency Noise in Tunneling Magnetoresitive Heads: Phenomena and Origins, IEEE TRANSACTIONS ON MAGNETICS, VOL. 43, NO. 2,

FEBRUARY 2007 page 663

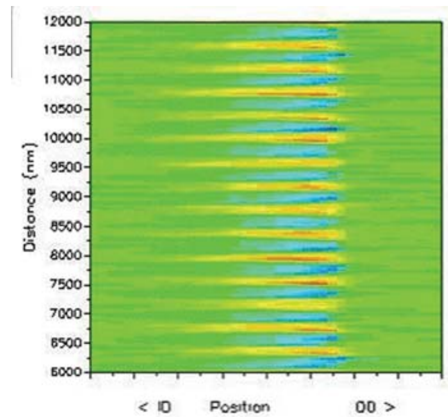

Fig1: Readback amplitude map for a 170kFCI center track pattern on a positive DC background

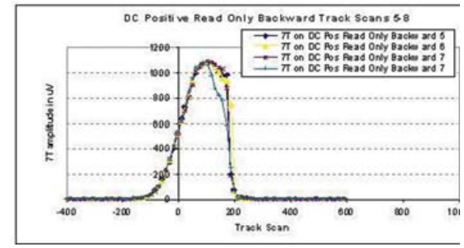

Fig. 2: Repeated cross track profile as read sensor scan the tracks moving from OD to ID

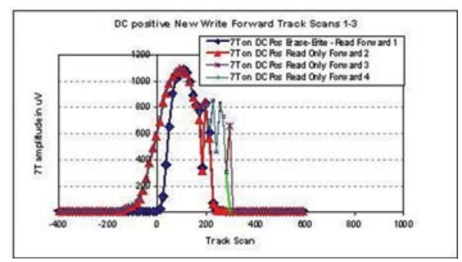

Fig. 3: Repeated cross track profile as read sensor scan the tracks moving from OD to ID

HW-11

A Novel Algorithm for Unknown Periodic Disturbance Cancellation in HDD.

L. Hui[2,1], D. Chunling[1], W. Youyi[2]
1. MRC, DSI, Singapore, Singapore; 2. NTU, Singapore, Singapore

Identification of disturbance frequency in HDDs is usually done in so-called track -following control where the read/writhe head is positioned at the center of a particular data track. Many methods such as AIM [1] and AFC have been used for this case. In this paper, we propose a new method to cancel periodic disturbances.

In order to cancel the periodic disturbances, we suppose to build a new signal which is approximate to the disturbance and add its opposite value to the command signal.

Fig.1 shows the system structure of proposed algorithm, where u, y and w are the system command, output and disturbance respectively. The internal model principle can effectively estimate the dominate frequency of PES, which is also the fundamental frequency of disturbance; while a disturbance rebuilder use the frequency estimation and a signal generated by the difference of output pass through the inverse of plant and input signal to rebuild a signal which approximates the periodic disturbance. Then the disturbance will be cancelled by adding the opposite value of this signal to the command signal.

The frequency estimator derived from the discrete time representation of AIM has a form of $X1(k)=2\cos(\omega T)X1(k-1)-X1(k-2)+Kf(1-\cos(\omega T))(e(k-1)-e(k))$, $X2=2\cos(\omega T)X2(k-1)-X2(k-2)+Kf/\omega\sin(\omega T)(e(k-1)-e(k))$, $\omega(k-1)=\omega(k)-Ke*(e(k)*X1(k))/(X1(k)^2+X2(k)^2)$.

When using AIM method, the frequency estimation will not converge in the first stage if we choose a larger estimation gain Ke in order to achieve high converge speed. While this problem will be solved if we know the range of the disturbance frequency and add an estimator band constrain. Fig.2 shows estimation of disturbance with frequency of 700 Hz and 2000 Hz. When adding 200 Hz and 500 Hz lower band constrains respectively, the frequency estimation speeds have significant advanced.

For disturbance which has single frequency component, magnitude and phase estimation can be achieved by two parameters estimation [2].

Suppose $\Theta(k)=[\alpha(k),\beta(k)]$, which are the coefficients of $\cos(\omega T)$ and $\sin(\omega T)$, then $\Theta(k)$ can be estimated by the recursive least squares parameter adaptation algorithm:

$\Theta(k)=\Theta(k-1)+F(k)*\Phi'(k)*\varepsilon(k)/(1+\Phi'(k)*F(k)*\Phi(k))$, $F(k+1)=1/\lambda*[F(k)-F(k)*\Phi(k)*\Phi'(k)*F(k)]/(\lambda+\Phi'(k)*F(k)*\Phi(k))]$

where $\Phi(k)=[\cos(\omega kT),\sin(\omega kT)]'$ and $\varepsilon(k)=P^{(-1)}y(k-1)-u(k-1)-\Theta(k)\Phi(k-1)$, the signals have one sample time delay to achieve plant inverse causal.

For the disturbance which has harmonic components, the frequency estimation in [1] can also get the fundamental frequency. And the similar method can be used to estimate the parameters corresponding to the several main harmonic components. For disturbance which has not harmonic components, there should be several frequency estimators to get the different frequencies, and estimate the corresponding parameters similarly.

Another idea for dealing with multi-frequency case is that each signal can be represented by a nonlinear function. Then a 3rd order polynomial function which has coefficients of each power time-varying can approximately represent the signal according to Taylor's series. In this case, following the above method, we just replace the parameter by $\Theta(k)=[a0(k),a1(k),a2(k),a3(k)]$ and $\Phi(k)=[1,kT,(kT)^2,(kT)^3]$, and there is no need to estimate the disturbance frequency.

To support the algorithm, several simulations have been done. Fig.3 reflects the effect of the proposed algorithm dealing with the single frequency disturbance which has phase change and magnitude change. Fig. 3 shows that this method can efficiently cancel the disturbance with single frequency. Fig 4 shows results to deal with multi-frequencies disturbance cases. In Fig 4 (a), a harmonics disturbance was added in the simulation, while Fig 4 (b) presents a disturbance which has several different harmonics and non-harmonic frequency cases. Result presents that the 3rd order polynomial fitting method has better performance and robustness to observer noise. The reason for those phenomena is that for multi-frequencies cases, one frequency estimator can not bring out all the frequencies in disturbance. Even the estimator number is sufficient, it can not be sure that estimator can converge to a different frequency. So the signal fitting will not perform well.

The future work will be conducted to improve and verify the multi-frequency estimation method and investigate how the time delays affect on the performance.

[1] L. J. Brown and Q. Zhang, IEEE Trans on Signal Processing,Jun 2003.1538-1545.

[2] Q. Zheng and M. Tomizuka, IEEE Trans.on Magnitics, Sep 2007.3756-3762

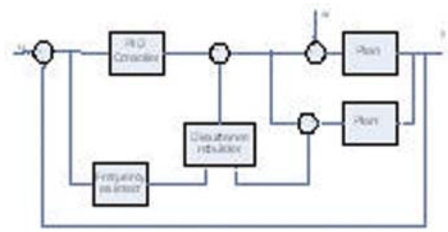

Fig.1 The structure of the system

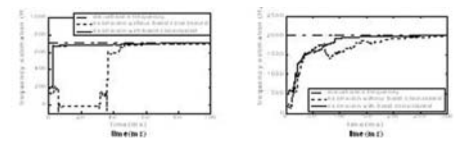

Fig.2 frequency estimation improvement by adding band constrained

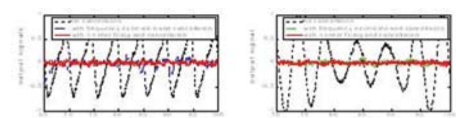

A

B

C

D

E

F

G

H

I

J

L

M

N

O

P

Q

R

S

T

U

V

W

X

Y

Z